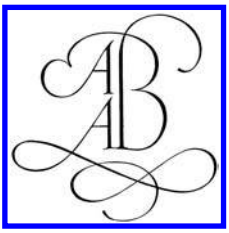
RIVER FLOW 2006

Copyright © 2006 Taylor & Francis Group plc, London, UK



BALKEMA – Proceedings and Monographs
in Engineering, Water and Earth Sciences

Copyright © 2006 Taylor & Francis Group plc, London, UK

PROCEEDINGS OF THE INTERNATIONAL CONFERENCE ON FLUVIAL HYDRAULICS, LISBON, PORTUGAL, 6–8 SEPTEMBER 2006

River Flow 2006

Editors

Rui M.L. Ferreira
Instituto Superior Técnico, Technical University of Lisbon, Lisboa, Portugal

Elsa C.T.L. Alves
Laboratório Nacional de Engenharia Civil, Lisboa, Portugal

João G.A.B. Leal
Universidade da Beira Interior, Covilhã, Portugal

António H. Cardoso
Instituto Superior Técnico, Technical University of Lisbon, Lisboa, Portugal

VOLUME 1-2



Taylor & Francis
Taylor & Francis Group
LONDON / LEIDEN / NEW YORK / PHILADELPHIA / SINGAPORE

Copyright © 2006 Taylor & Francis Group plc, London, UK

Copyright © 2006 Taylor & Francis Group plc, London, UK

All rights reserved. No part of this publication or the information contained herein may be reproduced, stored in a retrieval system, or transmitted in any form or by any means, electronic, mechanical, by photocopying, recording or otherwise, without written prior permission from the publisher.

Although all care is taken to ensure the integrity and quality of this publication and the information herein, no responsibility is assumed by the publishers nor the author for any damage to property or persons as a result of operation or use of this publication and/or the information contained herein.

Published by: Taylor & Francis/Balkema
P.O. Box 447, 2300 AK Leiden, The Netherlands
e-mail: Pub.NL@tandf.co.uk
www.taylorandfrancis.co.uk/engineering, www.crcpress.com

ISBN10 set: 0-415-40815-6
ISBN10 Volume 1: 0-415-40810-5
ISBN10 Volume 2: 0-415-40814-8

ISBN13 set: 978-0-415-40815-8
ISBN13 Volume 1: 978-0-415-40810-3
ISBN13 Volume 2: 978-0-415-40814-1

Printed in Great Britain

Copyright © 2006 Taylor & Francis Group plc, London, UK

Table of Contents

Preface XIX
Organisation XXIII
Organising institutions and sponsors XXV
Acknowledgements XXVII

VOLUME 1

Keynote lectures

Large scale river morphodynamics: Application to the Mississippi Delta 3
G. Parker, O. Sequeiros & River Morphodyamics Class of Spring, 2006

Rivers and floods: A concern for people, a problem for engineers, a challenge for research 13
Y. Zech, S. Soares-Frazão, D. Bousmar, B. Spinewine, C. Dal Cin & C. Savary

Engineering case studies

Recent training of the lower Rhine River to increase Inland Water Transport potentials: A mix of permanent and recurrent measures 31
H. Havinga, M. Taal, R. Smedes, G.J. Klaassen, N. Douben & C.J. Sloff

Case study: River restoration projects along the Isar (Germany) 51
W. Binder

Sediment transportation in the Yangtze River and impacts of the three gorges project 61
Z.Y. Wang & Y.T. Li

A. River hydrodynamics

A.1. Turbulent open-channel flow and transport phenomena

Unsteady turbulence characteristics in an undular bore 79
C. Koch & H. Chanson

On the definition of the shear velocity in rough bed open channel flows 89
D. Pokrajac, J.J. Finnigan, C. Manes, I. McEwan & V. Nikora

Large eddy simulation of the two phase flow 99
F. Gallerano, L. Melilla & G. Cannata

Turbulent processes at the entrance of a pool using flow visualization 109
G.A. Marquis & A.G. Roy

A laboratory investigation on the advection of free surface fluctuations in turbulent open-channel flows 119
H. Miyamoto

Turbulent wake region of large roughness elements: Combining flow visualization and high frequency velocity measurements 125
R.W.J. Lacey & A.G. Roy

A new perspective on sidewall correction procedures, based on SKM modelling 135
J. Chlebek & D.W. Knight

Copyright © 2006 Taylor & Francis Group plc, London, UK

Open-channel side-cavities: A comparison of field and flume experiments 145
J. Le Coz, W. Brevis, Y. Niño, A. Paquier & N. Rivière

Spatially averaged near-bed flow field over rough armor layers 153
J. Aberle

Parameterisation of the vertical velocity profile in the wall region over rough surfaces 163
K. Koll

Secondary flow and velocity redistribution by bubble screens in open channel bends 173
J.H.A. Wijbenga, R. Schielen, K. Blanckaert & F. Buschman

Detection and reconstruction of coherent structures based on wavelet multiresolution analysis 181
M.J. Franca & U. Lemmin

Equivalent velocity profile for turbulent flows over gravel riverbeds 189
M.J. Franca & W. Czernuszenko

Admissible and inadmissible simplifications of pollution transport equations 199
P.M. Rowiński & M.B. Kalinowska

Fundamental characteristics of high velocity flows in a sinuous meandering channel in the vicinity of resonance 209
T. Hosoda & M. Nishihama

Smoothly limited finite-volume modelling of rapidly varying river flows 219
T. Krámer & J. Józsa

Large eddy simulation of fully-developed turbulent flow through submerged vegetation 227
T. Stoesser, C. Liang, W. Rodi & G.H. Jirka

Experimental characterization and visualization of mass exchange process in dead zones in rivers 235
W. Brevis, Y. Niño & J. Vargas

Coherent structure of horizontal eddies in meandering compound open-channel flow by using multi-layer scanning PIV 243
M. Sanjou, I. Nezu, T. Doi & H. Quang

Large eddy simulation of turbulent structure in meandering compound open-channel flow 253
M. Sanjou & I. Nezu

Emergence of large-scale coherent structures in a shallow separating flow 261
H. Talstra, W.S.J. Uijttewaal & G.S. Stelling

A.2. Flood propagation and channel/floodplain interactions

Finite element hydrodynamic modeling in a river 273
K.-Y. Han, C.-H. Baek & J.-W. Noh

Fourth order balanced WENO schemes for shallow water equations 281
V. Caleffi & A. Valiani

Two-dimensional numerical simulation of flood propagation in presence of buildings 291
C. Costanzo & F. Macchione

A practical approach to estimating the flow capacity of rivers – Application and analysis 303
C. McGahey, P.G. Samuels & D.W. Knight

Diffusion wave based modeling of flood inundation based on sub-grid connectivity 313
D. Yu & S.N. Lane

Experiments on the flow in a enlarging compound channel 323
D. Bousmar, S. Proust & Y. Zech

Copyright © 2006 Taylor & Francis Group plc, London, UK

Stage-discharge modelling in mobile bed compound channel 333
D. Bousmar, S. Atabay, D.W. Knight & Y. Zech

Performance of several hybrid numerical schemes to determine flooding extent 343
I. Villanueva & N.G. Wright

Roughness coefficient for flood plains with macro roughness elements 351
I. Aydin, M.A. Kokpinar & M. Ustaomer

Discretization of the friction term in the shallow water equations 359
J. Murillo, J. Burguete, P. Brufau & P. Garcia-Navarro

Numerical simulations on the Paraná de las Palmas River 367
J.M. Viscardi, A. Pujol, V. Weitbrecht, G.H. Jirka & N.R. Olsen

Selection of interface plane in the assessment of discharge in two stage meandering and straight compound channels 379
K.C. Patra & K.K. Khatua

Mathematical modelling and analysis of river flows in transitional waters 389
M. Santos & J. Hipólito

Modelling the distribution of boundary shear stress in open channel flows 397
M. Omran & D.W. Knight

A methodology for computing non-uniform flows in compound channels 405
S. Proust, D. Bousmar, N. Rivière, A. Paquier & Y. Zech

A coupled 1D to 2D model for flood plain simulation 415
V. Roubtsova, G. Tchamen, J. Abdo & R. Kahawita

1D complex modelling with lateral exchanges coupling two reaches 421
N. Goutal, C. Cheviet & G. Duvivier

A.3. Dam-break and highly unsteady open-channel flow

A marching in space and time solver for the complete 2D shallow water equations: Application to real test cases 429
C. Aricò, C. Nasello & T. Tucciarelli

An application of BGK numerical method to tidal flow 439
D. Jiaquan

A robust implementation of Riemann solvers for one-dimensional free surface flow simulation in natural rivers 445
G.W. Tchamen, T.T. Quach & R. Kahawita

1-Dimensional numerical analysis of tsunami in river 455
H. Yasuda

Analytical solutions of laminar and turbulent dam break wave 465
H. Chanson

Efficient implicit upwind schemes for river flow simulation with or without shocks 475
J. Burguete, P. Garcia-Navarro, P. Brufau & J. Murillo

Numerical and experimental modelling of the generation and propagation of waves caused by landslides into reservoirs and their effects on dams 483
R.F. de Carvalho & J.S.A. do Carmo

High-order finite volume modelling of one-dimensional flows 493
L. Cozzolino & D. Pianese

Copyright © 2006 Taylor & Francis Group plc, London, UK

Nonparallel spatial stability of shallow water flow down an inclined plane of arbitrary slope 503
P. Bohorquez & R. Fernandez-Feria

Dam-break flow experiments in simplified city layouts 513
S. Soares-Frazão, B. Spinewine, A. Duthoit, J.F. Deswijsen & Y. Zech

A.4. Vegetated beds and flow resistance

Evolution of mixing layers in turbulent flow over submersed vegetation: Field experiments and measurement study 525
A. Sukhodolov & T. Sukhodolova

A new 1D-numerical model for flexible vegetated channels 535
D. Velasco, A. Bateman & V. Medina

Steady 1D water surface model of natural rivers with vegetated floodplain: An application to the Lower Biebrza 545
D. Świątek, J. Kubrak & J. Chormański

Experimental investigation of flow characteristics in vegetated channels 555
F.G. Carollo, V. Ferro & D. Termini

A two-dimensional lattice model for describing the open channel flow with vegetation 565
F.J. Jiménez-Hornero, J.V. Giráldez, A.M. Laguna, S.J. Bennett & C.V. Alonso

Depth-averaged flow in presence of submerged cylindrical elements 575
F. Huthoff, D.C.M. Augustijn & S.J.M.H. Hulscher

Turbulent structure and dispersive properties in vegetated canopy open-channel flows 583
I. Nezu, M. Sanjou & T. Okamoto

Influence of aquatic plants on the flow resistance and the hydraulic capacity of vegetated rivers 593
L. De Doncker, P. Troch, R. Verhoeven, K. Bal & P. Meire

Experimental study of flexible and rigid vegetation in an open channel 603
M. Ben Meftah, F. De Serio, D. Malcangio, A.F. Petrillo & M. Mossa

Longitudinal dispersion in vegetated channels 613
E. Murphy, M. Ghisalberti & H.M. Nepf

Turbulent characteristics of flows through emergent vegetation 623
P.M. Rowiński & A. Mazurczyk

Longitudinal dispersion in a lowland river with submersed vegetation 631
T. Sukhodolova, A. Sukhodolov, H-P. Kozerski & J. Köhler

Effects of aquatic and bank-side vegetation on hydraulic performance of small streams 639
V. Nikora, S. Larned, K. Debnath, G. Copper, M. Reid & N. Nikora

Interaction of vegetation, current and sedimentation 647
S. Schneider, F. Nestmann & B. Lehmann

A.5. Interaction with structures

Large-scale motion induced by turbulent plunging jets in pools created by scouring of the riverbed 657
P. Manso, A. Schleiss, J.-L. Boillat & E. Bollaert

Numerical investigation of the turbulent flow around a bridge abutment 667
A. Teruzzi, F. Ballio, S. Salon & V. Armenio

The shallow flow around a single groyne under submerged and emerged conditions 673
A. Kadota, K. Suzuki & W.S.J. Uijttewaal

Copyright © 2006 Taylor & Francis Group plc, London, UK

Diverse riverbed figuration by using skew spur-dike groups 683
A. Tominaga & D. Matsumoto

Turbulence analysis of vertical slot fish pass by in situ measurements and CFD modelling 693
B. Sokoray-Varga, S. Baranya & J. Józsa

Stability analysis of turbulent water jets onto both rigid and mobile beds 701
C. Adduce, M. la Rocca & P. Mele

Investigation of the velocity and pressure fluctuations distributions inside the turbulent horseshoe vortex system around a circular bridge pier 709
G. Kirkil, G. Constantinescu & R. Ettema

The scour-hole problem due to sluice gates: Quadrant analysis of the turbulence characteristics in the presence of Görtler vortices 719
I. Albayrak & U. Lemmin

Temporal flow evolution of sediment embedded circular bridge piers 729
J. Unger & W.H. Hager

A numerical model for local scour at piers according to the unit stream power approach 741
M.E. Cunninghame & N.P. Armitage

Conservative scheme for flow numerical modeling of submerged bridges 747
M. Catella & G. Bechi

Turbulent flow field modeling as an aid to the analysis of scour and for a protection scheme 757
R. Aragão, V.S. Srinivasan, K. Suzuki & A. Kadota

Predictions of turbulent flows around a bridge pier using various numerical models 767
I. Kimura, T. Hosoda & S. Onada

B. River Morphodynamics and sediment transport

B.1. Mechanics of sediment transport

Validation of a new model to account for bed slope effect for prediction of equilibrium condition in loose bed channels with significant suspended sediment transport 779
J. Zeng, G. Constantinescu & L. Weber

A PIV/PTV experiment on sediment transport in a horizontal open channel flow 789
W.A. Breugem & W.S.J. Uijttewaal

Towards a Direct Numerical Simulation (DNS) of particle motion close to river beds 799
A.E. González, F.A. Bombardelli & Y. Niño

Modelling sorting over the lee face of individual bed forms 807
A. Blom & M.G. Kleinhans

Entrapment of fines in coarse sediment beds 817
B.G. Krishnappan & P. Engel

Can a two-layer morphological model compete with common sediment transport formulae? 825
C. Savary & Y. Zech

Wide solid-discharge fluctuations and collective effects in bed-load transport 833
C. Ancey, T. Böhm, P. Frey & M. Jodeau

SETRAC – A sediment routing model for steep torrent channels 843
D. Rickenmann, M. Chiari & K. Friedl

Influence of sand shape to vertical sorting under uniform flow condition 853
E. Harada & H. Gotoh

Copyright © 2006 Taylor & Francis Group plc, London, UK

Investigation of flow hydrodynamics under equilibrium bedload transport conditions using PIV 859
F. Bigillon, G. Couronné, J.Y. Champagne, A. Recking & P. Frey

The resistance of transported sediment 867
G. Smart

Development of a hybrid adaptive neuro-fuzzy system for the prediction of sediment transport 877
M. Valyrakis, P. Diplas, C.L. Dancey, T. Akar & A.O. Celik

Experimental study of bed load on steep slopes 887
P. Frey, M. Dufresne, T. Böhm, M. Jodeau & C. Ancey

Downstream fining of sediments in the Meuse River 895
R. Murillo-Muñoz & G.J. Klaassen

Cohesive sediment removal from a fixed bed 907
R. Della Morte, C. Mucherino, D. Pianese & F. Pirozzi

Modeling granular sediment transport over water worked gravels within a CFD framework 913
R.J. Hardy

The beginning of sediment transport – A different approach 919
R. Aleixo & R. Maia

Marbles in oil, just like a river? 927
S.M. Cameron, S.E. Coleman, B.W. Melville & V.I. Nikora

Bed load fluctuations and channel processes in a braided network laboratory model 937
W. Bertoldi, T. Amplatz, S. Miori, L. Zanoni & M. Tubino

Conceptual model for the bedload layer of gravel bed streams based on laboratory observations 947
R.M.L. Ferreira, J.G.A.B. Leal & A.H. Cardoso

Energy dissipation downstream of dams established in alluvial beds 957
A. Sá Lopes, M.F. Proença & R. Maia

B.2. Bed forms and flow resistance

Modelling morphodynamic evolution of river dunes 969
A.J. Paarlberg, C.M. Dohmen-Janssen, S.J.M.H. Hulscher, J. van der Berg & A.P.P. Termes

Field investigations of sand-gravel bed forms within the Raba River, Poland 979
A. Radecki-Pawlik, P.A. Carling, E. Slowik-Opoka, L. Książek & R. Breakspeare

Semi-empirical model to predict mobile bed evolution in presence of a side overflow 985
B. Rosier, J.-L. Boillat & A.J. Schleiss

Morphology, flow and sediment transport over a natural 3D dune field: Rio Paraná, Argentina 997
D.R. Parsons, J.L. Best, S.N. Lane, R.J. Hardy, R. Kostaschuk, D. Shugar & O. Orfeo

Flow resistance associated to a schematic step-pool pattern 1005
F. Canovaro & L. Solari

Three-dimensional properties of laboratory sand waves obtained from two-dimensional autocorrelation analysis 1013
H. Friedrich, B.W. Melville, S.E. Coleman, T.M. Clunie, V.I. Nikora & D.G. Goring

Spatial development of turbulent open channel flow over bottom with multiple dunes 1023
N.Th. Fourniotis, A.A. Dimas & A.C. Demetracopoulos

Bed forms and transport characteristics of a partly cohesive sediment 1033
R. Banasiak & R. Verhoeven

Bed morphology and flow resistance in steep open channels with varying widths 1039
R.B. Weichert, G.R. Bezzola & H.E. Minor

Copyright © 2006 Taylor & Francis Group plc, London, UK

A vertical two-dimensional morphodynamic model for bedform simulation 1049
S. Giri & Y. Shimizu

Experimental study on steady flow in a channel with macro-roughness at the side walls 1059
T. Meile, J.-L. Boillat, J. Dubois & A.J. Schleiss

Weakly nonlinear analysis on interaction of alternate bars and double-row bars 1069
Y. Watanabe & K. Hasegawa

Three-dimensional numerical modeling of flows over a natural dune field 1077
R.J. Hardy, D.R. Parsons, J.L. Best, S.N. Lane, R. Kostaschuk & O. Orfeo

B.3. Large scale river morphology and morphodynamics

Effect of vegetation growth and unsteady characteristics of water supply on formative condition of mesoscale channel configuration 1087
H. Takebayashi, M. Teraoka, T. Okabe & S. Egashira

Location of hills and deeps in meandering streams: An experimental study 1097
A.M.F. da Silva & T. El-Tahawy

VOLUME 2

B.3. Large scale river morphology and morphodynamics (continued)

On the bed deformation in meandering streams 1119
A.M.F. da Silva & M.S. Yalin

Gravitational effects on river morphodynamics 1129
S. Francalanci, L. Solari & G. Vignoli

Entropy and river meander planform 1137
A.J. Teuling, S.J. van Andel, P.A. Troch & A.J.F. Hoitink

Downstream stable channel configuration: Preliminary analysis 1147
B. Mengoni & E. Paris

Two-layer approach for transcritical flow on mobile bed: Nickpoint migration 1155
C. Savary, M. Bellal & Y. Zech

On the effect of the bed morphology on the river confluence hydrodynamics 1165
D. Đorđević & M. Jovanović

The overdeepening theory in river morphodynamics: Two decades of shifting interpretations 1175
E. Mosselman, M. Tubino & G. Zolezzi

Prevalent morphodynamic regime and short-term dynamics of meandering rivers 1183
G. Zolezzi, R. Luchi & D. Marchiori

Migration of a dredging pit in the Rhone River 1193
J.-L. Boillat, J. Dubois & N. Nilipour

Bed levelling investigations on transverse sloped beds 1203
J.U. Wiesemann, P. Mewis & U. Zanke

Effective use of non-erodible layers for improving navigability 1211
C.J. Sloff, E. Mosselman & J. Sieben

Copyright © 2006 Taylor & Francis Group plc, London, UK

Morphodynamic modeling of sand bar evolution under unsteady flow 1221
K. Kobayashi, Y. Shimizu, S. Giri & Y. Watanabe

Experimental investigation on flow expansions over fans 1231
L. Sittoni, C. Paola, J. Fedele & M. Tubino

Investigation on the dominant discharge in DEZ River and the effect of DEZ Dam on it 1237
M.A. Pourhasan, H.R. Sadeghi, P.S. Mirja'fari & S. Fartoos

Large-scale turbulence and river morphology 1243
M.S. Yalin

Analysis of water and sediment flows over an alternate bar in a gravel bed river 1251
M. Jodeau & A. Paquier

ECOMSED – Three dimensional modeling in rivers 1259
M.A. Mekonnen & B. Dargahi

3D modeling of transient bed deformation in sine-generated laboratory channel with two different width to depth ratios 1269
N. Rüther & N.R.B. Olsen

Morphology and flow structures in a large confluence-diffluence: Rio Paraná, Argentina 1277
O. Orfeo, D.R. Parsons, J.L. Best, S.N. Lane, R.J. Hardy, R. Kostaschuk, R.N. Szupiany & M.L. Amsler

Unsteadiness effects on the morphological behaviour of gravel-bed river bifurcations 1283
S. Miori, R. Repetto & M. Tubino

Sediment dynamics in anabranched channels of the Loire River: The study case of Ingrandes (France) 1293
S. Rodrigues, J.N. Gautier & J.J. Peters

Man-induced morphological processes in Warta river (Poland), and their impact on the evolution of hydrological conditions 1301
T. Dysarz, J. Wicher-Dysarz & B. Przedwojski

Morphological description of river bifurcations in gravel-bed braided networks 1311
W. Bertoldi, S. Miori, M. Salvaro, L. Zanoni & M. Tubino

Study on river change and sediment transportation of Tan Chau reach in lower Mekong river 1319
X.L. Luu, S. Egashira & H. Takebayashi

Morphodynamics of mountain rivers following repeated sediment release from reservoirs 1329
G. Fasolato, P. Ronco & M. Tregnaghi

Analysis of sediment transport during floods in a large river 1337
J.S. Rocha & J.N. Fernandes

The case of the Zambezi River in Mozambique: Some investigations on solid transport phenomena downstream Cahora Bassa Dam 1345
P. Ronco, G. Fasolato & G. Di Silvio

Effect of upstream meanders on bifurcation stability and sediment division in 1D, 2D and 3D models 1355
M. Kleinhans, B. Jagers, E. Mosselman & K. Sloff

Bed Load Management at the River Lech – A physical model 1363
U. Stephan & K. Wibmer

B.4. Debris and hyperconcentrated flows

Intermittency of rheological regimes in uniform liquid-granular flows 1375
A. Armanini, M. Larcher & L. Fraccarollo

Copyright © 2006 Taylor & Francis Group plc, London, UK

Morphological modelling of hyperconcentrated floods in the Yellow River 1383
D.S. van Maren, J.C. Winterwerp, B.S. Wu & J.J. Zhou

Fluctuations in surface granular flow via a PIV-edge detection technique 1393
D. Berzi, L. La Rosa, S. Malavasi & A. Radice

Numerical simulations of the covering a house by a debris flow 1401
E. Harada, T. Hosoda & H. Gotoh

Frictional surface flow of a dry granular medium 1407
D. Berzi & E. Larcan

Experiments on the impact process of dry and saturated mixtures against obstacles of various shapes 1413
P. Ghilardi, M. Pagliardi & B. Zanuttigh

Limiting conditions for the existence of permanent periodic roll waves in stony debris flows 1421
S. Longo

Instability and kinematic for sand-water mixture or dry sand flowing past a circular cylinder 1433
S. Longo, A. Valiani & L. Lanza

B.5. Geomorphic dam-break flows and breach formation

A new approach to solving boundary conditions in shallow water equations using a Riemann solver 1443
V.C. Medina Iglesias, A. Bateman Pinzon & D. Velasco Montes

The role of quasi-conservative form for morphodynamic modelling in river flow computations 1453
A. Siviglia, G. Nobile & M. Colombini

Front dynamics of a water surge at high Reynolds number: Similarity solutions to the Saint-Venant equations 1463
C. Ancey, S. Cochard, M. Rentschler & S. Wiederseiner

Fully-2D and *quasi*-2D modeling of flooding scenarios due to embankment failure 1473
F. Aureli, P. Mignosa, C. Ziveri & A. Maranzoni

Two-dimensional dam-break simulation over movable beds with an unstructured mesh 1483
J.A. Vásquez & J.G.A.B. Leal

Numerical simulation of 2D dam break on mobile bed 1493
M. Greco, M. Iervolino & A. Leopardi

One dimensional modeling of dam break flow over erodible sediment bed 1501
P. Costabile & F. Macchione

Dike erosion – A preliminary outlook 1511
W.H. Hager & J. Unger

Discontinuities in geomorphic dam-break flows 1521
R.M.L. Ferreira, S. Amaral, J.G.B. Leal & B. Spinewine

Experimental study of landslide-induced flooding in open channels 1531
J. Yan, Z. Cao & L. Chen

Dam-break propagation over a movable bed in a non-prismatic channel 1541
J.G.A.B. Leal, P. Silva & R.M.L. Ferreira

Levee breach process of a river by overflow erosion 1547
T. Tsujimoto, A. Mizoguchi & A. Maeda

Copyright © 2006 Taylor & Francis Group plc, London, UK

B.6. Sedimentation in reservoirs

A 3-D numerical investigation of the development of density driven finite-channel lock-release currents at high Grashof numbers 1559
S.K. Ooi, G. Constantinescu & L. Weber

Bedload transport in the case of seepage flow 1569
S. Francalanci, G. Parker & L. Solari

Long-term morphological behavior of Verbois reservoir (Geneva) 1577
E. Bollaert, S. André, S. Diouf, D. Sidler & S. Ferretti

1D Process-based modelling of reservoir sedimentation: A case study for the Barasona reservoir in Spain 1585
G.L. Mamede, A. Bronstert, T. Francke, E.N. Müller, J.C. de Araujo, R.J. Batalla & A. Güntner

Deposition of fine particles varying with their cohesiveness 1595
G. Hillebrand & F. Nestmann

Measurement of flow patterns within an Alpine reservoir 1601
H. Knoblauch, H. Badura & J. Schneider

Reservoir sedimentation: 1D model of turbidity currents and delta deposits 1607
J. González, A. Tamburrino & Y. Niño

Jets opposing flow on inclines 1617
J. Bühler, Ch. Oehy & A.J. Schleiss

Experimental study of suspended sediment transport and deposition in a rectangular shallow reservoir 1623
S.A. Kantoush, E.F.R. Bollaert, J.-L. Boillat, A.J. Schleiss & W.S.J. Uijttewaal

Effects of flushing of two reservoirs in Spain 1633
R. Cobo Rayán & C. Mateos Iguacel

B.7. Local scour and protection

Time evolution of erosion depth and sediment motion for abutment scour in a pressure duct 1639
A. Radice, S. Malavasi & F. Ballio

Local scour at elliptical guide banks in plain rivers 1649
B. Gjunsburgs, R.R. Neilands & E. Govsha

Local scouring at bridge piers and abutments: Time evolution and equilibrium 1657
C. Grimaldi, R. Gaudio, A.H. Cardoso & F. Calomino

Diversity of streambed features caused by open-slot groundsills 1665
C.C. Wu & Y.-C. Lin

Riprap design for spur protection 1673
C. Gisonni & W.H. Hager

Numerical simulation of flow and local scour around hydraulic structures 1683
H. Zhang, H. Nakagawa, Y. Muto, Y. Baba & T. Ishigaki

Dimensional analysis of bridge pier scour and the role of flow intensity 1695
L. Teixeira, G. López, G. Simarro, E. Fernandez & M. Ortega-Sánchez

Maximum scour depth around spur dikes 1701
M. Azarderakhsh, H. Norouzi & M. Ghodsian

Modelling the flow and morphology in groyne fieds 1707
M.F.M. Yossef & R. Rupprecht

Copyright © 2006 Taylor & Francis Group plc, London, UK

Experimental study of the scour regimes downstream of an apron for intermediate tailwater depths 1715
P. Espa & S. Sibilla

Scour protection downstream of block ramps 1725
S. Pagliara & M. Palermo

Temporal patterns of the maximum scour depth around a pier 1731
G. Oliveto & A. Di Domenico

Riverbed scour induced by a long constriction 1737
G. Oliveto, B. Onorati & V. Comuniello

Clear-water scour at bridge piers and abutments 1743
U.C. Kothyari, W.H. Hager & G. Oliveto

Clear water scour analysis around groynes and bridge abutments 1749
C. Marson, V. Fiorotto, E. Caroni & L. Da Deppo

Sediment supply effect on local scouring at bed sills in high gradient streams 1759
M. Tregnaghi, A. Marion & F. Comiti

Riprap protection of vertical-wall bridge abutments 1765
C.M.S. Fael, C.A.M. Ramos & A.H. Cardoso

Geometrical effects in non-continuous riprap stability 1775
G.A. Mazza de Almeida & J.P. Martín-Vide

B.8. Bank erosion and protection

An integrated model for the evolution of channel morphology, including cohesive bank erosion 1785
A.N. Menéndez, P.E. García, J.R. Ardila, C.E. Laciana & A. Sfriso

Bend scour reduction and flow pattern modification by an outer bank footing 1793
M. Roca, J.P. Martín-Vide & K. Blanckaert

Self widening by lateral erosion in gravel bed rivers 1801
P. Requena, R.B. Weichert & H.-E. Minor

C. Interdisciplinary approaches for river management

C.1. Innovative field and laboratory instrumentation

DPIV study of the turbulent boundary layer over V-shaped cavities 1813
A. Amador, M. Sánchez-Juny & J. Dolz

Time variation of three-dimensional scour geometry 1823
O. Link & U. Zanke

Discharge measurement using Large Scale PIV under varied flow conditions – Recent results, accuracy and perspectives 1829
A. Hauet, J.D. Creutin, P. Belleudy, M. Muste & W. Krajewski

Discharge measurements in a small ungauged river: Comparison between conventional current-meter and tracer dilution methods 1835
A. Bolognesi, G. Gottardi & M. Maglionico

Recirculating flow assessment from aDcp, LS-PIV and 2Dh modelling 1843
J. Le Coz, A. Hauet, F. Védie, G. Dramais, B. Chastan & A. Paquier

Filtering ADV data on highly turbulent free surface flow 1853
L. Cea, L. Pena & J. Puertas

Copyright © 2006 Taylor & Francis Group plc, London, UK

Accurate measurements of free-surface in the dam-break problem 1863
S. Cochard & C. Ancey

Study on river-discharge measurements with a bottom-mounted ADCP 1873
Y. Nihei & T. Sakai

Experimental procedure to obtain 2D time-space high-speed water surfaces 1879
A. Bateman, A. Granados, V. Medina, D. Velasco & M. Nalesso

A three-dimensional model of flow dynamics around paired deflectors for fish habitat enhancement 1889
D.M. Carré, S.J. Gaskin & P.M. Biron

C.2. Information technologies and modelling tools for river management

How advances in hydraulic modelling can contribute to solve real problems of flooding: Three examples 1899
A. Paquier

Solute transfer from soil surface to runoff as a boundary condition in open channel flow modeling 1907
M. Nofuentes, M.J. Polo, J.V. Giráldez & L. Mateos

Loose-bed models for river structure design: Two example studies on river Po 1915
M. Guerrero & A. Lamberti

River Energy Auditing Scheme (REAS) for catchment flood management planning 1923
N.P. Wallerstein, P.J. Soar & C.R. Thorne

Fluid–structure interaction modeling with a coupled 1D–2D free surface flow solver 1933
S. Erpicum, P. Archambeau, B. Dewals, S. Detrembleur & M. Pirotton

Roughness parameterization for 2D hydrodynamic models from QuickBird spaceborne imagery 1941
S. Rath, B. Gunawan, E. Pasche, A. Frick & U. Teschke

Multi-attribute decision making and cost-sharing tool for planning urban river rehabilitation schemes 1947
M. Brilly & S. Rusjan

The influence of errors in Digital Terrain Models on flood flow routes 1955
S. Néelz & G. Pender

One-dimensional flow modelling and a case study of the River Rhine 1963
T. Bleninger, J.D. Fenton & R. Zentgraf

River Po low water training: The importance of mathematical modeling to support designing activities 1973
L. Schippa, S. Pavan & S. Colonna

Sustainable navigation Rhine Delta branches, a reconnaissance of strategies 1985
G.J. Akkerman, M.A. van Heereveld, H.J. Barneveld & R.J. Smedes

C.3. River habitat management and restoration

Mathematical modeling of the biogeochemistry of dissolved and sediment associated trace metal contaminants in riverine systems 1993
A. Massoudieh, F.A. Bombardelli, T.R. Ginn & P.G. Green

The application of hydrodynamic models as integrative tool between flood protection and ecological demands using a morphologically based evaluation method 2001
C. Hauer, M. Liedermann & H. Habersack

Copyright © 2006 Taylor & Francis Group plc, London, UK

River habitat model using energy budget characteristics and experiment on improvement of river physical environment 2007
H. Yabe

Flow-vegetation-sediment interaction: Research challenges 2017
J. Järvelä, J. Aberle, A. Dittrich, H.P. Rauch & I. Schnauder

Multi-purpose shallow reservoir: Synergies between ecology and energy production 2027
P. Heller, E. Bollaert, A.J. Schleiss, M. Pellaud & R. Schlaepfer

Optimizing the flow pattern in culverts for small upstream migrating fish using a numerical 3D Code 2037
R. Feurich & J. Boubée

Fuzzy modelling of habitat suitability using 2D and 3D hydrodynamic models: Biological challenges 2043
S.N. Lane, D.C. Mould, P.E. Carbonneau, R.J. Hardy & N. Bergeron

Modeling approach to simulate habitat dynamics 2055
S. Wieprecht, A. Eisner & M. Noack

Comparison of suitability for living of ayu, *Plecoglossus Altivelis*, between pools and rapids 2065
T. Nagaya, Y. Shiraishi, K. Onitsuka, M. Higashino, T. Takami, N. Otsuka, J. Akiyama, H. Ozeki, Y. Nakagawa & H. Hatanaka

Interaction between flow and growth of Periphyton in sand river 2073
Y. Toda, T. Tsujimoto, T. Ikeda & Y. Tadakuma

Evaluation of environmental impacts resulting from river regulation works: A case study from Portugal 2081
A.E. Barbosa, E. Alves, R.M.V. Cortes, P.M. Silva-Santos, F. Aguiar & T. Ferreira

Methodology and techniques for urban river rehabilitation 2093
J.S. Rocha

C.4. Management of risk associated to floods and man-induced river hazards

Flood management system – A newly developed instrument based on WebGIS and CMS and the improvement of basis data 2105
A. Koch, M. Tzschirner & R. Jüpner

Palaeoflood records applied to assess dam safety in SE Spain 2113
G. Benito, M. Rico, V.R. Thorndycraft, Y. Sánchez-Moya, A. Sopeña, A. Díez Herrero & A. Jiménez

Development of a flood inundation model for extreme flood analysis 2121
K.-Y. Han, G. Kim, K.-H. Choi & J.-T. Lee

A management system to optimize reservoir control in the case of floods 2127
R. Pohl & A. Bornschein

Using results of mathematical modeling of debris flows for optimization of a river channel form to convey debris flows and floods 2137
R. Fazarinc, B. Majes & M. Mikoš

Climate change, sediment delivery and flood risk explored using two-dimensional inundation modelling 2147
S.N. Lane, R.J. Hardy, D. Yu, V. Tayefi & S.C. Reid

Consideration of protection works in hazard assessment – A case study 2157
W. Gostner & B. Mazzorana

Copyright © 2006 Taylor & Francis Group plc, London, UK

Innovative aspects of design concept for comprehensive flood scheme for Water of Leith, Dunedin, South Island, New Zealand 2167
M.G. Webby, T.G. Parsons, S.E. Coleman, B.W. Melville, G. Palmer & G. Collings

YTSS. Yangtze Special Session

Changes of sediment deposition and erosion at Chongqing reach in backwater area of Three Gorges Project 2179
A.Y.J. Lu, C.W. Xu, L.Q. Zuo & B.Z.Y. Wang

A preliminary study on the local abrupt descent of downstream water level near the Three Georges Dam 2189
Z. Sun, Y. Li, M. Li & Y. Huang

Habitat suitability index model of four major Chinese carp species in the Yangtze River 2195
A.Y.J. Yi, Z.Y. Wang & B.Y.J. Lu

Influence of flow and sediment inputs on channel sediment delivery ratio: An example of the Yichang – Hankou Reach, Yangtze River, China 2203
J.X. Xu

Restore water levels in the river channel downstream of the Three Gorges Reservoir: A numerical simulation 2211
G. Zhou, H. Wang, D.D. Jia & X.J. Shao

The evolution analysis of Fengcheng reach under the changing conditions 2221
L. Chen, J. He, Z.G. Wang & W.S. Xu

Impacts of the Three Gorges Project on flood in the middle reach of Yangtze River 2229
Y. Li, Y. Liu, Z. Sun & J. Deng

Copyright © 2006 Taylor & Francis Group plc, London, UK

Preface

E a cidade,
chamam-lhe Lisboa,
mas é só o rio
que é verdade
só o rio,
é a casa de água,
casa da cidade em que vim nascer.

from "O Tejo", performed by Madredeus,
lyrics by Pedro Ayres de Magalhães

Rivers are embedded into the very fabric of civilization. The knowledge of river hydraulics was passed over different civilizations, being remarkable the Babylonians, Egyptians, Greeks and Romans. Sophisticated irrigation works are reported in China, in the 3rd century BC, and drainage systems were found in cities belonging to the Indus civilization.

In what concerns societies' superstructure, rivers operate as complex and diverse symbols within religious, political or otherwise cultural contexts. Their meaning and usage are often conflicting: in the Hindu, Muslim and Jewish-Christian traditions rivers are endowed with the benign characteristics of pure water, those of cleaning, purifying and regenerating; yet, river waters can be the vehicle of corruption and can even be poisonous, as was the case of the spring waters of River Styx, described by Pausanias the geographer.

Rivers are tokens of fertility; their allegoric use often endorses the world of the Mother, of *natura*. Anqet, the goddess of the Nile in the Old Kingdom, was simultaneously "the embracer" and "the nourisher" of the fields, qualities that evoke the sedimentation of fertile soil during the Nile floods. Sedimentation can be also associated to the death of water streams and used as a metaphor of death and suffering: in Dante's Divine Comedy, the souls of those possessed by wrath and insolence are punished in the muddy marshes along the Styx.

Thoreau, travelling up the Merrimack River, wrote that "rivers must have been the guides which conducted the footsteps of the first travellers". The displacement may be literal but may also be a metaphor of an inner journey or a path to enlightenment. In the pilgrimage of River Narmada, both senses are at use; pilgrims would walk up the river to its spring and, on the other margin, would walk down to its mouth. In the process, the pilgrims could achieve enlightenment and purification. The river is ever present in the journey undertaken by Siddharta, in Herman Hesse's novel. His ultimate synthesis of the world of the senses and the world of pure contemplation is made possible by understanding the message contained in the river, literally by listening to the sound of its waters.

Rivers can also be obstacles in the path. Their crossing may stand for a rite of passage or an act of reconnaissance of owns free will, for instance Siddhartha's crossing of the river into the world of senses. However, crossing the river may also stand for the initiation of an inevitable chain of events; they can represent a mark beyond which free-will matters little, best exemplified by current allegoric use of Caesar's crossing of the Rubicon.

Rivers are political boundaries. However, they can also be attractors that convey identity to the communities that live along their margins. Numerous examples can be drawn, from the community of avieiros of Escaroupim, River Tagus, to the Isis and Oxford canal boat community.

The myth of a great flood, simultaneously destroying all but a small number of chosen living creatures and cleaning the land of all sin, is inscribed in many cultures and religious traditions. Virtually all the civilizations that we acknowledge as ancestors of ours came into being in the fertile valleys of large rivers. It is thus reasonable to believe that they should have experienced, at some point of their development, the devastating effects of river floods.

Generalising, the key concept of experimentation must have certainly guided communities' interaction with rivers. It can be traced in the process by which the heterogeneous and often contradicting allegoric usages of the

Copyright © 2006 Taylor & Francis Group plc, London, UK

river were inscribed in the languages. Conflicting meanings simply reflect the tensions arisen as societies evolve in articulation with their economical base. For instance, rivers have always supported human life by providing water for household consumption, for irrigation and for industry and their flood plains provided nutrients for agriculture. However, misuse of the sources of fresh water and bad agricultural techniques leads to water quality degradation. If the demographic pressure is too intense, river waters may even become the carriers of epidemic vectors.

Hydropower plants were essential to the development of industrial modes of production. Yet, the impacts of large dams are difficult to dissipate and may dramatically reduce rivers' potential to support wildlife and traditional economic activities. Riverbed sand, mud and pebbles have been used in building industry since the dawn of times. Again, overexploitation of these resources leads to oversimplification of their life. Furthermore, river's landscape value, often crucial for the collective identity of riverine communities, is built in permanent tension with its economic value. In particular, navigability requirements and flood defence structures are often seen as aggressions to the river's landscape and to its role as support of diverse biotopes.

In recent years, due to exponential population growth, these conflicting pressures have become more intense. As a result, river management has increasingly been carried out with close attention to the long term impact of river works. There is greater recognition that enforcing quality environments and promoting human development in the river space can be met at one and the same time, by working *with* rather than against nature. In other words, it is necessary to work with a deep knowledge of river phenomena. Such an approach is a clear application of the principles of sustainable development.

In what concerns the knowledge of the river processes, a change from the philosophical science of the Scholastics toward the observational science of the present day came perceptible during the Renaissance. Such change is best exemplified by Leonardo da Vinci's prolific production of drawings depicting flow phenomena. Fluvial Hydraulics is nowadays rooted in engineering practice and scientific research. Recent developments in fluid and sediment mechanics, namely in what concerns turbulent flows and flows of granular material, have provided Fluvial Hydraulics with the formal apparatus to sustain within itself research programs envisaging the integration of basic phenomenological knowledge into practical engineering works. Hence, defined as the discipline, or set of disciplines, geared toward the joint study of the processes of entrainment, erosion, deposition and transport of sediment and the mechanics of open-channel flows with mobile boundaries, Fluvial Hydraulics is more than ever solicited to guide engineering works, evaluate environmental impacts and mitigate hazards. New engineering tools emerge from advances in physical understanding, computation methods and measuring techniques.

River Flow 2006 was organized under the auspices of the Fluvial Hydraulics Section of the International Association of Hydraulic Engineering and Research (IAHR). River Flow conferences are intended to be exceptional forums for scientists and engineers working on Fluvial Hydraulics and river-related disciplines. The hearty spirit of the first edition, in Louvain-la-Neuve in 2002, encouraged the prosecution of the conference series. The ensuing conferences have registered an increasing participation of members of our community of river engineers and researchers, a clear indication of the relevance of such a forum.

The Local Organizing Committee of River Flow 2006 has received 546 abstracts, of which 486 were considered to be aligned with the conference topics. Subsequently, 358 papers were submitted by engineers and researchers of 49 countries from all 5 inhabited continents. The International Scientific Committee has, finally, selected 239 to be included in this proceedings book. Of these, 67% were considered for oral presentation and 33% were selected for the poster sessions. The accepted contributions cover essentially River hydrodynamics, River morphodynamics and sediment transport, and Interdisciplinary approaches for river management.

A distinctive feature of River Flow conferences has been the existence of Master Classes the day preceding the formal opening of the Conference. They are intended for PhD or MSc students or young researchers working on Fluvial Hydraulics or related disciplines. They represent a unique opportunity for students to address senior scientists, meet peers working on similar topics and identify possible collaborations for the continuation of their work. The response to this initiative exceeded the best initial expectations: 7 Master Classes were run, enrolling 41 students from 14 countries and 14 masters. This is an indication of the vitality of Fluvial Hydraulics and a contribution for the continuity of the IAHR.

In 1999, the IAHR added "Engineering" to its official designation. This symbolic gesture signalled IAHR's ever present will to enrol engineering practitioners in the prosecution of its main objective, the promotion of the advancement and the exchange of knowledge in water related subjects. The Local Organizing Committee has decided to implement the new concept of "engineering case studies" in the attempt to encourage practitioners with different approaches and backgrounds to participate in the technical and scientific debate of the conference. Engineering case studies were given the visibility and relative importance of keynote lectures. The initiative was successful and its continuation is recommended: 13 candidate case studies were received for 3 to be presented.

Copyright © 2006 Taylor & Francis Group plc, London, UK

River Flow 2006 introduced a special session dedicated to the Yangtze River, a suggestion made by Professor Zhaoyin Wang. The organizing committee of River Flow 2006 acknowledged the idea enthusiastically and sought to transform it into a perennial trait of River Flow conferences: it was proposed to IAHR that all future editions should have a session dedicated to a particular river. Such river should be chosen on the basis of its symbolic importance for human communities, for the social relevance and impact of engineering works performed upon it or for the innovative aspects shown by the engineering practices led by their managing authorities.

The Local Organising Committee of River Flow 2006

Copyright © 2006 Taylor & Francis Group plc, London, UK

Organisation

Members of the International Scientific Committee

A.B. Almeida	Instituto Superior Técnico, Portugal
M. Altinakar	The University of Mississippi, USA
A. Armanini	Università di Trento, Italy
N.P. Armitage	University of Cape Town, South Africa
Ph. Belleudy	Université Joseph Fourier, France
R. Bettess	HR Wallingford, UK
J.-P. Bouchard	Electricitè de France, France
D. Bousmar	Ministère Wallon de l'Equipement et des Transports, Belgium
J.A. Carmo	Universidade de Coimbra, Portugal
L. Fraccarollo	Università di Trento, Italy
M. Garcia	The University of Illinois, USA
P. Garcia Navarro	Universidad de Zaragoza, Spain
W. Graf	EPF Lausanne, Switzerland
M. Greco	Università di Napoli Federico II, Italy
W. H. Hager	ETH Zürich, Switzerland
F. Holly	Forrest Holly & Associates, USA
J.T. Jenkins	Cornell University, USA
G.H. Jirka	Universität Karlsruhe, Germany
J. Józsa	Budapesti Müszaki és Gazdaságtudományi Egyetem, Hungary
P. Julien	Colorado State University, USA
G. Klaassen	UNESCO-IHE Institute for Water Education, The Netherlands
U.C. Kothyari	Indian Institute of Technology, India
A. Lara Dominguez	Centro de Estudios y Experimentación de Obras Públicas, Spain
M. Leclerc	INRS- Centre Eau, Terre & Environnement, Canada
J.P. Martín-Vide	Universitat Politècnica de Catalunya, Spain
B.W. Melville	The University of Auckland, New Zealand
I. Nezu	Kyoto University, Japan
V. Nikora	University of Aberdeen, UK
Y. Niño	University of Chile, Chile
T. Papanicolaou	The University of Iowa, USA
G. Parker	The University of Illinois, USA
C.M. Ramos	Laboratório Nacional de Engenharia Civil, Portugal
K.G. Ranga Raju	Indian Institute of Technology Roorkee, India
P. Samuels	HR Wallingford, UK
F. Schöberl	Innsbruck University, Austria
G. Seminara	Università di Genova, Italy
H. Shaheen	An-Najah National University, Palestine
A.M. da Silva	Queen's University, Canada
T. Tsujimoto	Nagoya University, Japan
W. Uijttewaal	Technical University Delft, The Netherlands
O. Vasiliev	Institute for Water and Environmental Problems, Russia
H.J. de Vriend	Technical University Delft, The Netherlands
Z.Y. Wang	Tsinghua University, P. R. of China
S. Wieprecht	Universität Stuttgart, Germany
M.S. Yalin	Queen's University, Canada
F. Yazdandoost	K.N.Toosi University of Technology, Iran
Y. Zech	Université catholique de Louvain, Belgium

Copyright © 2006 Taylor & Francis Group plc, London, UK

E. Ben Slama	Electricitè de France, France
M. Roca-Collell	Universitat Politècnica de Catalunya, Spain
A. Tominaga	Nagoya Institute of Technology, Japan
K. Onitsuka	Kyushu Institute of Technology, Japan

Members of the Local Organising Committee

A.H. Cardoso	Instituto Superior Técnico, Portugal, Chairman
J.S. Rocha	Laboratório Nacional de Engenharia Civil, Portugal, Co-chairman
R. Ferreira	Instituto Superior Técnico, Portugal, Secretary
E. Alves	Laboratório Nacional de Engenharia Civil, Portugal
R. Maia	Universidade do Porto, Portugal
J. Leal	Universidade da Beira Interior, Portugal
M. Franca	Instituto Superior Técnico, Portugal
T. Fonseca	Laboratório Nacional de Engenharia Civil, Portugal
C. George	IAHR Executive Director, UK

Copyright © 2006 Taylor & Francis Group plc, London, UK

Organising institutions and sponsors

River Flow 2006 was organised by the following institutions.







The following organisations sponsored the conference.









Copyright © 2006 Taylor & Francis Group plc, London, UK

Acknowledgements

River Flow 2006 was jointly organised by the Instituto Superior Técnico (IST) and the Laboratório Nacional de Engenharia Civil (LNEC), both in Lisbon. It took place in LNEC between the 5th and the 8th of September 2006. Its preparation begun much earlier, sometime in March 2004. Over the course of these two and a half years, many people and organisations were directly and indirectly involved in the many tasks that constituted the work program of the conference.

We are first and foremost grateful to all researchers and practitioners working in river-related disciplines that chose to participate in River Flow 2006 by sending their abstracts, papers and case-studies. Their collaboration reiterated the vitality of our rivers community, surely one of the most active groups within IAHR. Special thanks to the students that applied to the Master Classes and whose enthusiasm guarantees a bright future to our community.

The success of the conference was materialized in a record number of contributions accepted for reviewing. The role of the International Scientific Committee was therefore paramount. We are indebted to its members for the in-depth reviewing of the manuscripts, a task carried out with overall excellence, rare in conferences, despite the limited time available.

Such a selective conference, involving so many students at reduced fees, is only financially sustainable with some level of sponsorship. We acknowledge the support of Câmara Municipal de Lisboa (CML), AdP – Águas de Portugal, EDP – Energias de Portugal and FLAD – Fundação Luso-Americana. The support of these institutions has made it possible to attribute five scholarships to participants from developing countries and partly cover the expenses of a large number of Masters.

Complementing the work of the Local Organising Committee (LOC) in IST, there was the dedicated and competent contribution of Mrs. Dulce Fernandes. She was present in all crucial moments of receiving, printing and organizing the manuscripts of all authors and, for that matter, she deserves our deepest recognition.

The preparation of River Flow 2006 benefited, at several stages, from the experience of the organisers of previous editions. For that matter, we are indebted to Didier Bousmar, Yves Zech and Massimo Greco for their ever present willingness to collaborate with us.

The image of the conference was essentially a product of collective work within the LOC. In what concerns the design and the maintenance of the webpage, we acknowledge the valuable contribution of Americo Louro at LNEC. A word of appreciation to Helena Elias for her contribution in the redesign of the logo and for the preparation of the presentation that, in June 2004, in Naples, introduced River Flow 2006.

The involvement of IAHR was fundamental for the divulgation of the conference. For their efforts, we endorse our gratitude to Estíbaliz Serrano and Cristina Moreno. At last, the preparation of the manuscripts often required the intervention of the publisher, Taylor & Francis/A. A. Balkema. Our recognition goes to Léon Bijnsdorp, Lukas Goosen, Maartje Kuipers and remaining staff involved.

The Local Organising Committee of River Flow 2006

Copyright © 2006 Taylor & Francis Group plc, London, UK

Keynote lectures

Copyright © 2006 Taylor & Francis Group plc, London, UK

Large scale river morphodynamics: Application to the Mississippi Delta

G. Parker
University of Illinois, Dept. of Civil & Environmental Engineering & Dept. of Geology, Urbana, Illinois, USA

O. Sequeiros
University of Illinois, Dept. of Civil & Environmental Engineering, Urbana, Illinois, USA

River Morphodynamics Class of Spring, 2006
University of Illinois: see Acknowledgements

ABSTRACT: The delta of the Mississippi River is in jeopardy. It is rapidly subsiding into the Gulf of Mexico. Delta marshland is being drowned and the shoreline is moving northward toward New Orleans. The cause of these problems is the levee system along the Mississippi River, which prevents the replenishment of sediment to the delta. One way to restore the delta is through the use of one or more controlled partial avulsions of the Mississippi River. The design of such diversions represents a monumental task. A natural example of an avulsion in the Mississippi Delta, however, offers an excellent opportunity to test the concept of land building via river diversions. The Atchafalaya River is a distributary of the Mississippi River. During the flood of 1973, part of the Atchafalaya River avulsed into a man-made channel. The Wax Lake Delta at the mouth of the channel has been building seaward since then. Here a morphodynamic model of the Wax Lake Delta is presented and tested against field data. While the model is preliminary, the fact that it captures the process of land building at the Wax Lake Delta suggests that it can be adapted to the design of a major controlled partial avulsion of the Mississippi River into, for example, Barataria Bay.

1 INTRODUCTION

The extensive levees on lower Mississippi River serve an essential role in a) protecting human lives and infrastructure in New Orleans and the Mississippi Delta and b) preventing an avulsion of the river that would render New Orleans useless as a port. These same levees, however, prevent sediment delivery to the Mississippi Delta itself.

Under natural conditions, the delta was maintained by two counteracting processes; sediment deposition and avulsion which cause the delta to build up and prograde seaward, and compaction of fine-grained delta sediment under its own weight, which causes the delta to subside into the Gulf of Mexico. Under present conditions the delta is subsiding without any sediment replenishment. As a result delta marshland is sinking into the sea and the shoreline is rapidly advancing northward (Hallowell, 2001).

Land loss in the Mississippi Delta has resulted in the disappearance of or damage to large tracts of marshland habitat of unique ecological value. It has forced many Delta inhabitants to move elsewhere, and has damaged the livelihood of many more. In addition the northward movement of the shoreline has reduced the land buffer needed to damp hurricane storm surge, and thus placed New Orleans at risk to powerful hurricanes.

This vulnerability is highlighted by the Hurricane Katrina disaster of August, 2005, which caused a public emergency of major proportions, and rendered the city uninhabitable for months. Figure 1 shows satellite images of the Mississippi Delta just before and after the disaster. The damage to the Delta and the increased risk to New Orleans is clear from the images.

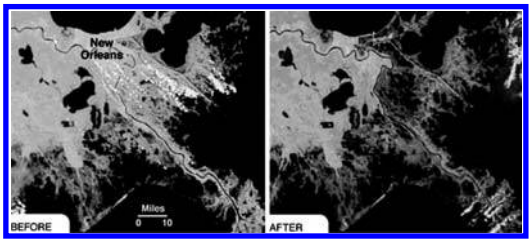


Figure 1. Satellite images of the Mississippi Delta near New Orleans before and after Hurricane Katrina. The image is from the New York Times.

Copyright © 2006 Taylor & Francis Group plc, London, UK

Various proposals have been offered in order to restore the Delta. Among the most attractive of these consists of one or more partial, controlled avulsions of the river either upstream or downstream of New Orleans. These avulsions would be accomplished by means of massive diversion structures of the general type that are already in place at the junction of the Mississippi River and the Old River in northern Louisiana, shown in Figure 2 and located in Figure 3. The Old River Control Structures allow a controlled amount of Mississippi River floodwater to flow into the Old River, and thence into the Atchafalaya River, while preventing a complete capture of the Mississippi River by the Atchafalaya River. Part of the structure nearly failed in the historic flood of 1973; the severe consequences of such a failure are outlined in Kazmann and Johnson (1980). This near failure highlights the importance of careful design of any diversion structures designed to restore sediment to the Delta.



Figure 2. Aerial view of the Old River Control Structures on the Mississippi River, Louisiana. The Mississippi River is to the right; flow in it is from top to bottom.

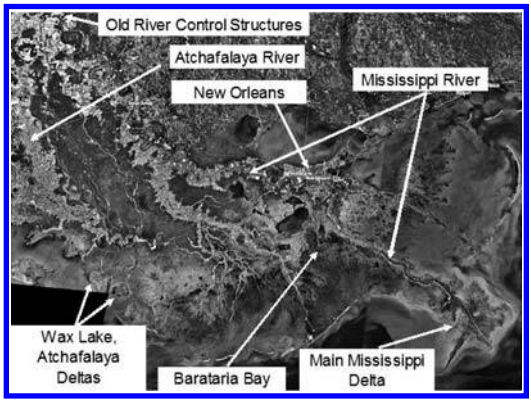


Figure 3. The NASA WorldWind satellite image serves as a locator map for New Orleans, the Mississippi and Atchafalaya Rivers, the Old River Control Structures, the Main Mississippi Delta, the Wax Lake and Atchafalaya Deltas and Barataria Bay circa 2006.

The flood of 1973 also had a consequence that has provided an invaluable case history for restoring the Delta. During that flood, part of the Atchafalaya River near its own delta partially avulsed into a man-made channel known as the Wax Lake Outlet. Ever since that avulsion a new delta at its outlet, the Wax Lake Delta has been building into the Gulf of Mexico. The subsequent growth of the Wax Lake Delta has been monitored by Louisiana researchers (Roberts and Coleman, 1996; Roberts et al, 1997). The locations of New Orleans, the Mississippi and Atchafalaya Rivers, the main mouth of the Mississippi River and the Wax Lake and Atchafalaya Deltas are shown in Figure 3. The Wax Lake Delta itself is shown in Figure 4.

The well-documented growth of the Wax Lake Delta allows an opportunity for "proof of concept" of land building by river diversions. If a morphodynamic model of river-delta evolution can predict the observed evolution of the Wax Lake Delta with a) reasonable accuracy and b) a minimum of "tuning", such a model can be adapted into a powerful tool to aid delta restoration. The tool could be used to study a variety of options for one or more much larger controlled avulsions upstream or downstream of New Orleans, so serving as part of the design of an optimal scheme for land building and delta reconstruction, with minimum negative influence on the economy and habitability of the Delta as a whole and New Orleans in particular.

Here a morphodynamic model of the Wax Lake Delta and the fluvial reach immediately upstream is outlined and compared against available data. The

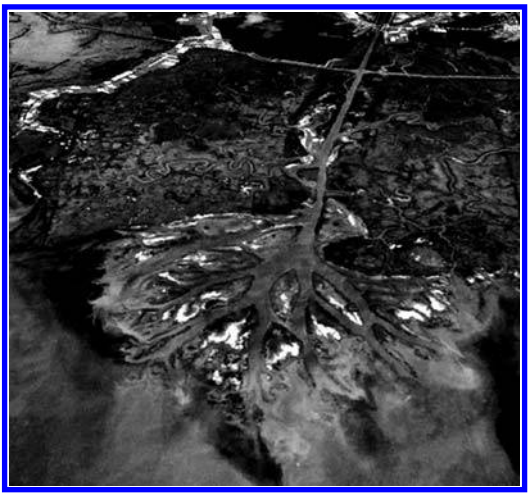


Figure 4. NASA WorldWind satellite image of the Wax Lake Delta, Louisiana as of 2006.

Copyright © 2006 Taylor & Francis Group plc, London, UK

results, while preliminary, are encouraging in terms of the use of controlled diversions to build land.

2 THE WAX LAKE DELTA

The Wax Lake Delta is a fan-delta located at the mouth of the Wax Lake Outlet (Figure 5). The Wax Lake Outlet is a man-made channel that was excavated in 1941. It connects the southeastern corner of Six Mile Lake with Atchafalaya Bay of the Gulf of Mexico. Six Mile Lake is in turn connected to the lower Atchafalaya River (Figure 5; DuMars, 2002).

The Wax Lake Outlet was designed to divert part of the flood flow of the Atchafalaya River. As recently as 1972 the shoreline along Atchafalaya Bay was eroding. The epic flood of the Mississipppi River of 1973 reversed this process (Roberts *et al.*, 1997). A partial avulsion of the Atchafalaya River to the Wax Lake Outlet significantly increased the flow to the Wax Lake Delta.

Subsequent to the flood of 1973 the Old River Control Structures have been used to divert both water and sediment from the Mississippi River to the Atchafalaya River in a prescribed manner. While the design diversion is 30% of the flow of the Mississippi River, as much as 50% of the Mississippi's discharge and over 60% of its suspended load has been flowing into the Atchafalaya River (Roberts *et al.*, 2003a). This delivery of sediment has caused both the Atchafalaya Delta itself and the subsidiary Wax Lake Delta to prograde significantly since 1973. As progressively more flow was captured by the Wax Lake Outlet, a control structure was placed on it in 1988. The structure limited the flow down the Wax Lake Outlet during normal flow, but was less effective at high flows. The structure was finally removed in 1994 (Roberts *et al.*, 2003a).

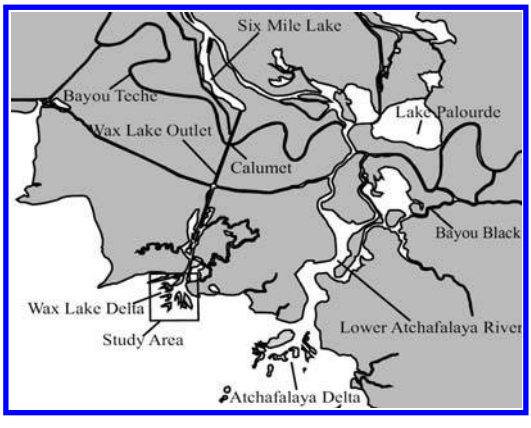


Figure 5. Map showing the Atchafalaya River, Six Mile Lake, the Wax Lake Outlet and the Wax Lake Delta. From DuMars (2002).

As of 2006 the Wax Lake Delta continues to prograde into Atchafalaya Bay (Figure 4). While not specifically intended to do so, it serves to illustrate how the sediment-laden water of the Mississippi River can be used to build land.

3 ELEMENTS THAT MUST BE CAPTURED BY THE MORPHODYNAMIC MODEL

A predictive morphodynamic model of the evolution of the Wax Lake Delta must include at least the following elements:

- account for the flood hydrology of the Atchafalaya River and the Wax Lake Outlet (WLO);
- partition water and sediment in the Atchafalaya River between the WLO and the Atchafalaya River below the outlet;
- discriminate between sand and mud delivered to the WLO;
- account for the Wax Lake Delta as well as a reach of the WLO upstream;
- specify the efficiency of deposition of sand and mud in the WLO, its adjacent "floodplain" and the delta itself; and
- account for the effects of both delta subsidence and sea level rise.

4 MODEL GEOMETRY

The model geometry is illustrated in Figures 6 and 7. A fluvial reach of specified down-valley length L_f and "floodplain" width B_f corresponding to part of the WLO is connected to a fan-delta reach corresponding to the Wax Lake Delta. The downvalley coordinate on the fluvial reach is denoted as x; channel width on the fluvial reach is a variable denoted as B_{fc}.

The fan-delta has specified fan angle θ. The radial coordinate from the fan-delta apex is denoted as r, such that r_u denotes a specified distance to the upstream end of the fan-delta and r_d denotes the distance from the vertex to the topset-foreset break (shoreline). In so far as the delta is prograding, r_d must be allowed to be a function of time t. Under conditions of any given flood flow there may be more than one active channel on the fan-delta; their amalgamated width is a variable denoted as B_{dc}. That part of the fan-delta that is not channelized at any given time is referred to as "floodplain" below. The width of the fan-delta is given as

$$B_d = \theta r \tag{1}$$

River bed elevation on the fluvial reach is denoted as η_f; the corresponding elevation on the fan-delta reach is denotes as η_d (Figure 7). The distance from the fan vertex to the junction between the base of the

Copyright © 2006 Taylor & Francis Group plc, London, UK

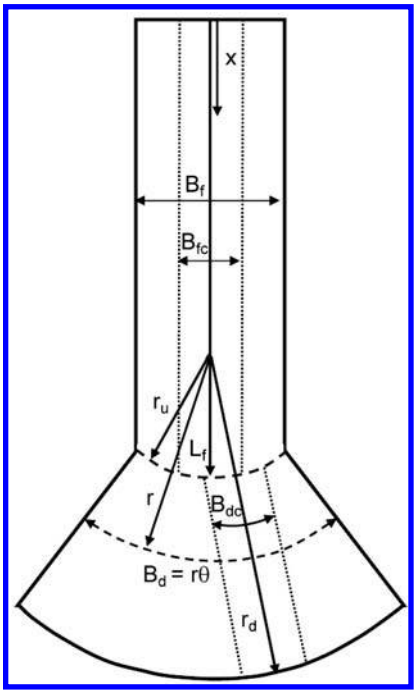


Figure 6. Definition diagram for planform of the fluvial and fan-delta reaches.

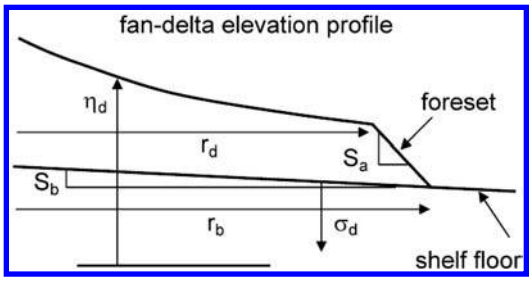


Figure 7. Definition diagram cross-section of the fan-delta reach.

foreset and the shelf floor is denoted as r_b. The shelf floor below the fan-delta reach is taken to have constant slope S_b and to be subsiding at rate σ_d, and the basement below the fluvial reach is subsiding at rate σ_f. Both subsidence rates are taken to be specified parameters. The fan-delta is assumed to prograde with a specified foreset angle S_a (Figure 7).

5 EXNER EQUATION OF SEDIMENT CONTINUITY

Rivers are morphologically active during floods. To capture this in a simple way, the river is assumed to be at bankfull flow Q_{bf} for fraction of time I_f, when it is morphologically active; otherwise the river is assumed to be morphologically inactive. The value of I_f is determined by the constraint that the river transports its mean annual bed material load at bankfull flow sustained for fraction I_f of a year (Wright and Parker, 2005).

Sand-bed rivers such as the Mississippi River and its distributaries carry far more mud than sand. For example, Allison *et al.* (2005) estimate that the Lower Mississippi carries annual loads of 124 Mt/year of mud but only about 6 Mt/year of sand. Here the sand is allowed to exchange with the bed, so constituting bed material load, but the mud is allowed to exchange only with the floodplain.

As the channel progrades, the deposit is spread across the entire floodplain (fluvial reach). Here the following parameters are defined for the fluvial and fan-delta reaches, denoted respectively by the final subscripts "*f*" and "*d*"; total bed material (sand) volume transport rates at bankfull flow Q_{tbff} and Q_{tbfd}, channel sinuosity Ω_f and Ω_d and deposit porosity λ_{pf} and λ_{pd}. It is assumed that for each volume unit of sand deposited in the channel-floodplain complex Λ_f units of mud are deposited in the channel-floodplain complex of the fluvial reach and Λ_d units are deposited in the corresponding complex of the fan-delta reach.

The time-averaged Exner equation of sediment continuity thus takes the following respective forms on the fluvial and fan-delta reaches;

$$(1-\lambda_{pf})\left(\frac{\partial \eta_f}{\partial t}+\sigma_f\right)=-\Omega_f\frac{I_f(1+\Lambda_f)}{B_f}\frac{\partial Q_{tbff}}{\partial x} \tag{2a}$$

$$(1-\lambda_{pd})\left(\frac{\partial \eta_d}{\partial t}+\sigma_d\right)=-\Omega_d\frac{I_f(1+\Lambda_d)}{B_d}\frac{\partial Q_{tbfd}}{\partial r} \tag{2b}$$

6 FLOW AND SEDIMENT TRANSPORT

Channel hydraulics at bankfull flow is described in terms of a quasi-steady backwater formulation. Thus where U = bankfull flow velocity, H = bankfull flow depth, S = bed slope, C_f = a dimensionless bed friction coefficient and g denotes the acceleration of gravity, the shallow-water equation of momentum balance takes the following respective forms on the fluvial and fan-delta reaches;

$$U_f\frac{dU_f}{dx}=-g\frac{dH_f}{dx}+gS_f-C_{ff}\frac{U_f^2}{H_f} \tag{3a}$$

$$U_d\frac{dU_d}{dr}=-g\frac{dH_d}{dr}+gS_d-C_{fd}\frac{U_d^2}{H_d} \tag{3b}$$

where the final subscript "*f*" denotes the fluvial reach and the final subscript "*d*" denotes the fan-delta reach.

Copyright © 2006 Taylor & Francis Group plc, London, UK

Here the bed slopes S are given by the respective forms

$$S_f = -\frac{\partial \eta_f}{\partial x} \quad , \quad S_d = -\frac{\partial \eta_d}{\partial r} \tag{3c,d}$$

In (3a) and (3b) the friction coefficients are treated as constants specified in terms of the corresponding dimensionless Chezy resistance coefficient Cz, such that

$$C_{ff} = Cz_f^{-1/2} \quad , \quad C_{fd} = Cz_d^{-1/2} \tag{4a,b}$$

The boundary condition on (3b) is one of specified elevation of standing water (base level) $\xi_d(t)$ in Atchafalaya Bay. Thus at the delta shoreline $r = r_d(t)$ is the position of the topset-foreset break (shoreline),

$$(\eta_d + H_d)_{r=r_d} = \xi_d(t) \tag{5a}$$

Here tides, which are in any case rather low in the Gulf of Mexico, are neglected for simplicity. The corresponding boundary condition on (3a) is continuity in water surface elevation;

$$(\eta_f + H_f)_{x=L_f} = (\eta_d + H_d)_{r=r_s} \tag{5b}$$

The mobility of bed material load (sand) can be quantified in terms of the Shields number τ_{bf}^* at bankfull flow, here defined as

$$\tau_{bf}^* = \frac{C_f U^2}{RgD} \tag{6}$$

where R denotes the submerged specific gravity of the sand (taken here to equal 1.65 for quartz) and D denotes the characteristic size of the sand in the river bed, here assumed to be a specified constant that is identical in the fluvial and fan-delta reaches. Sand transport is described in terms of the total bed material relation of Engelund and Hansen (1967); where B_c denotes the bankfull width of the channel (taking the values B_{fc} on the fluvial reach and B_{dc} on the fan-delta reach),

$$Q_{tbf} = B_c \sqrt{RgD}\, D \frac{0.05}{C_f} (\tau_{bf}^*)^{5/2} \tag{7}$$

7 DOWNSTREAM VARYING BANKFULL CHANNEL GEOMETRY

A simple way to describe the bankfull characteristics of a channel is in terms of a specified channel-forming bankfull Shields number τ_{bf}^*. Parker *et al.* (1998) and Parker (2004) have found that the following approximate closure is appropriate for sand-bed streams:

$$\tau_{bf}^* = 1.86 \tag{8}$$

Equation (6) can then be rearranged to yield the following relation for bankfull flow velocity U;

$$\frac{U}{\sqrt{RgD}} = \left(\frac{\tau_{bf}^*}{C_f}\right)^{1/2} \tag{9}$$

Thus for constant values of τ_{bf}^*, C_f, grain size D and sediment submerged specific gravity R, (9) specifies a bankfull flow velocity U that remains constant in the downstream direction. Substituting (9) into (3a) and (3b) and reducing, the following forms are found for the fluvial and fan-delta reaches;

$$\frac{dH_f}{dx} = S_f - R\tau_{bf}^* \frac{D}{H_f} \tag{10a}$$

$$\frac{dH_d}{dr} = S_d - R\tau_{bf}^* \frac{D}{H_d} \tag{10b}$$

For a given river profile on the fan-delta $\eta_d(r,t)$ at any time t, (10b) can be solved subject to (5a) to determine the streamwise variation in bankfull depth H_d on the fan-delta. Then (10a) can be solved subject to (5b) to determine the streamwise variation in bankfull depth on the fluvial reach. It is here assumed that the river has no tributaries over the reach of interest, so that bankfull water discharge Q_{bf} is constant in the streamwise direction, taking the same values on the fluvial and fan-delta reaches. Water continuity requires that

$$Q_{bf} = B_c U H \tag{11}$$

in which case the streamwise varying bankfull width is given from (7) and (11) as

$$B_c = \left(\frac{C_f}{\tau_{bf}^*}\right)^{1/2} \frac{Q_{bf}}{\sqrt{RgD}\, H} \tag{12}$$

Once the streamwise variation of H_d and B_{dc} (fan-delta reach) and H_f and B_{fc} (fluvial reach) are computed for a given bed profile, the streamwise variation in total bed material loads Q_{tbfd} (fan-delta reach) and Q_{tbff} (fluvial reach) are computed from (7).

8 SHOCK AND CONTINUITY CONDITIONS

The morphodynamic model has two moving boundaries: the position $r = r_d(t)$ denoting the distance from the fan vertex to the topset-foreset break (shoreline) and the position $r = r_b(t)$ denoting the distance form the fan vertex to the foreset-bottomset break (Figures 6 and 7).

Shoreline migration can be specified in terms of a shock condition (Swenson *et al.*, 2000; Kostic and Parker, 2003). The shoreline is located at $r = r_d(t)$, and

Copyright © 2006 Taylor & Francis Group plc, London, UK

bed elevation there is $\eta_d[r_d(t),t]$. It is assumed that the delta progrades with constant foreset slope S_a. The foreset elevation profile is thus given as

$$\eta(r,t)=\eta_d[r_d(t),t]-S_a[r-r_d(t)] \tag{13}$$

The shock condition is obtained by integrating (2b) from $r=r_d$ to $r=r_b$ subject to (1) and (13). This results in the relation

$$\frac{1}{2}(r_b^2-r_d^2)\theta_f\left[\left.\frac{\partial\eta_d}{\partial t}\right|_{r_d}+\sigma_d+(S_a-S_{dd})\dot{r}_d\right]= \Omega_d\frac{(1+\Lambda_d)}{(1-\lambda_{pd})}Q_{tbfdd} \tag{14}$$

where

$$\dot{r}_d=\frac{dr_d}{dt} \tag{15}$$

denotes the speed of progradation of the shoreline and

$$S_{dd}=-\left.\frac{\partial\eta_d}{\partial x}\right|_{r_d}\quad,\quad Q_{tbfdd}=Q_{tbfd}\big|_{r_d} \tag{16a,b}$$

A relation for the migration speed of the position of the foreset-shelf floor break can be obtained by imposing elevation continuity there. This condition is seen from (13) and Figure 7 to take the form

$$\eta_b(x,t)=\eta_d[r_d(t),t]-S_a[r_b(t)-r_d(t)] \tag{17}$$

Noting that by definition

$$\sigma_d=-\frac{\partial\eta_b}{\partial t}\quad,\quad S_b=-\frac{\partial\eta_b}{\partial x} \tag{18a,b}$$

and taking the derivative of (17) with respect to time, it is found that

$$(S_a-S_b)\dot{r}_b=(S_a-S_{dd})\dot{r}_d+\left.\frac{\partial\eta_d}{\partial t}\right|_{r_d}+\sigma_d \tag{19}$$

where

$$\dot{r}_b=\frac{dr_b}{dt} \tag{20}$$

9 SOLUTION AND TRANSFORMATION TO MOVING BOUNDARY COORDINATES

The specification of the problem is completed by one upstream boundary condition and one more continuity condition. The input volume bed material transport rate Q_{tbfu} must be specified at the upstream end of the fluvial reach;

$$Q_{tbff}\big|_{x=0}=Q_{tbfu} \tag{21}$$

In addition, the bed material transport rate should be continuous at the junction between the fluvial and fan-delta reaches;

$$Q_{btff}\big|_{x=L_d}=Q_{tbfd}\big|_{r=r_a} \tag{22}$$

The solution method can now be described as follows. Time and space must be appropriately discretized to allow a numerical solution, using spatial nodes separated by appropriate spatial steps Δx and Δr and an appropriate time step Δt. At any given time it is assumed that the bed profiles $\eta_d(x,t)$ and $\eta_f(x,t)$ are known. First (11b) is solved numerically by stepping upstream subject to (5a) to determine the bankfull depth profile H_d over the fan-delta reach. Then (11a) is solved by stepping upstream subject to (5b) to determine the bank depth profile H_f over the fluvial reach. Bankfull channel widths B_{fc} and B_{dc} are then solved algebraically from (12). The volume transport rates of bed material load at bankfull flow are computed algebraically from (7).

Equations (2a) and (2b) are then solved numerically to determine the bed elevation profiles η_d and η_f at one time step later. In the fan-delta reach, the volume bed material transport rates are given from (7) at all internal nodes. At the upstream node of this reach the continuity condition (22) is applied. At the downstream node of this reach the shock condition (14) is applied to determine the new position of the delta shoreline. Equation (17) is applied to determine the new position of the foreset-shelf floor break.

The initial conditions for the problem are specified initial bed profiles and shoreline position;

$$\eta_f\big|_{t=0}=\eta_{fI}(x) \tag{23}$$

$$\eta_d\big|_{t=0}=\eta_{dI}(x) \tag{24}$$

$$r_d\big|_{t=o}=r_{dI} \tag{25}$$

Here (23) and (24) are implemented in terms a) specified constant initial bed slopes S_{dI} and S_{fI} on the fan-delta and fluvial reaches, respectively, b) a specified initial delta height $\Delta\eta_I$, where

$$\Delta\eta_I=\{\eta_d[r_d(t),t]-\eta_b[r_b(t),t]\}_{t=0} \tag{26}$$

and c) an initial depth of submergence of the topset-foreset break below sea level;

$$H_d[r_d(t),t]\big|_{t=0}=\xi_d(0)-\eta_d[r_d(t),t]\big|_{t=0}=H_{ddI} \tag{27}$$

The initial elevation of standing water must be specified as well;

$$\xi_d(0)=\xi_{dI} \tag{28}$$

In the present analysis base level is assumed to rise at a specified constant rate $\dot{\xi}_d$.

The fact that the fan-delta reach includes two moving boundaries suggests the utility of solving

Copyright © 2006 Taylor & Francis Group plc, London, UK

the problem within this domain in moving-boundary coordinates. These are introduced as follows;

$$\bar{r} = \frac{r - r_u}{r_d(t) - r_u} \quad , \quad \bar{t} = t \tag{29}$$

Equation (2b), (10b), (14) and (19) thus transform to the respective forms

$$(1-\lambda_{pd})\theta \bar{r} r_d \left[\frac{\partial \eta_d}{\partial \bar{t}} + \sigma_d - \left(\frac{\bar{r}\dot{r}_d}{r_d - r_u} \right) \frac{\partial \eta_d}{\partial \bar{r}} \right] = - \Omega_d \frac{I_f (1+\Lambda_d)}{(r_d - r_u)} \frac{\partial Q_{tbff}}{\partial \bar{r}} \tag{30}$$

$$\frac{1}{r_d - r_u} \frac{dH_d}{d\bar{r}} = -\frac{1}{r_d - r_u} \frac{\partial \eta_d}{\partial \bar{r}} - R\dot{\tau}_{bf}^* \frac{D}{H_d} \tag{31}$$

$$\frac{1}{2}(r_b^2 - r_d^2)\theta_f \left[\left. \frac{\partial \eta_d}{\partial \bar{t}} \right|_{\bar{r}=1} + \sigma_d + S_a \dot{r}_d \right] = \Omega_d \frac{(1+\Lambda_d)}{(1-\lambda_{pd})} Q_{tbfdd} \tag{32}$$

$$(S_a - S_b)\dot{r}_b = S_a \dot{r}_d + \left. \frac{\partial \eta_d}{\partial \bar{t}} \right|_{\bar{r}=1} + \sigma_d \tag{33}$$

10 MODEL INPUT

Input data were gleaned from a) sediment data on the web site of the US Geological Survey, b) information provided by the US Army Corps of Engineers and c) published papers and reports including Roberts and Coleman (1996), Roberts *et al.* (1997), Majersky *et al.* (1997), DuMars (2002), Roberts *et al.* (2003a,b) and Wellner *et al.* (2006). Some poorly-constrained parameters were refined in the course of performing numerical runs, but arbitrary adjustments of the input parameters were kept to a minimum.

The following parameters were used for the results reported here: $D = 0.10$ mm, $R = 1.65$, $Q_{bf} = 4100\ \mathrm{m^3/s}$. $I_f = 0.27$, $Q_{tbfu} = 0.292\ \mathrm{m^3/s}$ (corresponding to 6.58 Mt/year of sand), $\tau_{bf}^* = 1.86$, $L_f = 25{,}000$ m, $B_f = 800$ m, $\theta = 120°$, $S_a = 0.002$, $S_b = 0.00018$, $Cz_f = Cz_d = 20$, $\lambda_{pf} = \lambda_{pd} = 0.6$, $\Omega_f = \Omega_d = 1$, $\Lambda_f = \Lambda_d = 0.49$, $\sigma_f = 0$, $\sigma_d = 5.8$ mm/year, $\dot{\xi}_d = 1.2$ mm/year, $\Delta\eta_I = 2.0$ m, $H_{ddI} = 5.1$ m, $(r_{dI} - r_u) = 4{,}300$ m, $r_u = B_f/\theta = 382$ m, $S_{fI} = 0.000062$ and $S_{dI} = 0.00014$. The modelling was commenced starting in year 1981 rather than 1973, because Majersky *et al.* (1997) suggest that it was in this year that upstream deposition became sufficient to allow the Wax Lake Delta to start prograding in its present rapid mode.

11 PRELIMINARY MODEL RESULTS

Figure 8 shows a plot of the position of the delta front r_d as a function of years since 1980. Both the model predictions and four data points extracted from three sources are shown. Figure 9 shows a plot of delta surface area of time as a function of years since 1980. Both the model predictions and five data points from two sources are shown.

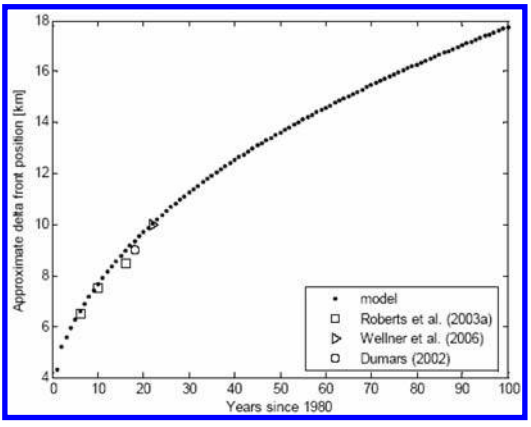


Figure 8. Plot of delta front (shoreline) position as a function of time since 1980.

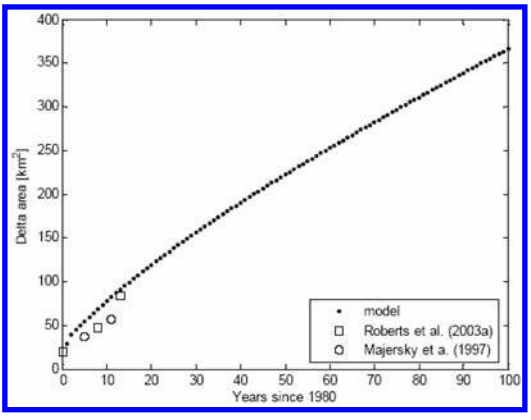


Figure 9. Plot of delta surface area as a function of time since 1980.

The results of these figures are highly preliminary, but they indicate that morphodynamic modeling of land building in the Mississippi Delta is feasible, and can yield reasonable predictions. Figure 10 shows a satellite photograph in which the projected delta front of Wax Lake is estimated out to year 2081. The Wax Lake Delta cannot in fact grow as large as indicated by year 2081, because before then it would partially merge with the Atchafalaya Delta.

12 NOTES OF CAUTION

The morphodynamic model of Wax Lake presented here is preliminary and incomplete in many ways. The

Copyright © 2006 Taylor & Francis Group plc, London, UK

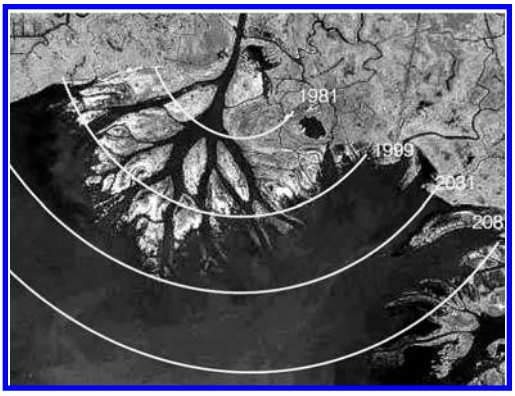


Figure 10. Predictions of the model for the shoreline of Wax Lake Delta overlain onto a satellite image from January 1999.

following revisions and additions need to be made to the model before practical application:

- modification from a single sand grain size to a sand grain size distribution;
- quantitative description of the role of vegetation in increasing the trapping rate of mud in the delta;
- incorporation of removal of delta sediment offshore due to the effect of e.g. cold fronts and hurricanes (Roberts *et al.*, 2003);
- a more detailed description of subsidence, if possible with a link to sediment loading; and
- clarification of the role, if any, of tides on delta dynamics.

It hardly needs pointing out that the morphodynamic model could not have been developed to the present point without the years of patient field campaigns carried out by H. Roberts and colleagues in Louisiana. There are nevertheless important gaps in the data base which need filling by means of further field campaigns.

13 IMPLICATIONS FOR RESTORATION OF THE MISSISSIPPI DELTA

The results of this study, though preliminary, lend support to the concept of building land in the Mississippi Delta by means of one of more controlled partial avulsions. Each such avulsion would involve a) a rigorously-designed diversion structure that would play a role similar to the Old River Control Structures, b) less rigorously designed levees that confine the flow within the diversion channel until the intended depositional zone is reached, and c) the absence of any and all levees and control structures within this depositional zone, to allow the river to do what it does best, in a delta, i.e. build new land.



Figure 11. Possible locations for controlled partial avulsions of the Mississippi River into Barataria Bay.

A primary candidate for such a depositional zone is Barataria Bay (Figure 3). Barataria Bay has been a zone of significant marshland loss in recent years. It is strategically located just south of New Orleans. In addition, it constitutes an area that is relatively sheltered, and thus less subject to the offshore removal of sediment by cold fronts and hurricanes (Roberts *et al.*,2003b).

Two possible sites for diversions are shown in Figure 11. One would divert part of the river into Barataria Bay upstream of New Orleans, and the other would divert part of the river downstream of New Orleans. An extended and refined version of the morphodynamic model presented here combined with extensive field data could be used as part of the design process in selecting a diversion.

There are many issues in regard to such controlled avulsions which need to be considered carefully, but which are beyond the scope of the present model. For example, a partial diversion downstream of New Orleans could cause a wave of degradation to sweep upstream, with potential damage to bridges, pipeline crossings etc. A partial diversion upstream of New Orleans could cause excessive siltation in the Port of New Orleans. If the diversion were sustained during low flow it could allow a salt wedge to move so far upstream as to contaminate the drinking water of New Orleans. In order to address these issues, the morphodynamic model presented here must be linked to purely channel-based models that can predict channel degradation and aggradation such as that of Meselhe *et al.* (2005).

Issues which need to be considered go beyond those involving the channel of the Mississippi River

Copyright © 2006 Taylor & Francis Group plc, London, UK

itself. Any scheme for controlled partial avulsions will require large expenditures of funds. The beneficial results may take decades to realize. In addition, any controlled partial avulsion is likely to have at least some negative consequences. These could, for example include siltation in the Intracoastal Waterway.

In point of fact, Hurricane Katrina was not needed to convince river and delta specialists that the negative consequences of doing nothing in the Mississippi Delta are likely to be far greater, in financial, social and ecological terms (Fischetti, 2001). The time has come to move forward with plans to use the sediment of the Mississippi River to restore the delta. Morphodynamic models of land building have an important role to play in this planning.

ACKNOWLEDGEMENTS

This paper is a contribution to the research effort of the National Center for Earth-surface Dynamics (NCED), a National Science Foundation (NSF) Science and Technology Center. The authors express their sincere thanks to Harry Roberts of Louisiana State University for his generous sharing of data and insight. Robert Twilley, also of Louisiana State University, Chris Paola and Efi Foufoula-Georgiou of NCED and H. Rich Lane of NSF strongly encouraged the pursuit of this research at a time when it appeared as though crucial support was lacking from NSF's Office of Integrative Activities. The cooperation of Mead Allison of Tulane University, John McCorquodale of the University of New Orleans and Ehab Meselhe of the University of Louisiana Lafayatte is gratefully acknowledged. The data collection exercise for the Wax Lake Delta was diligently carried out by the students in the first author's graduate course on river morphodynamics in the first term of 2006. The second author was one of these students: the others are Javier Ancalle, Corrie Bondar, Shane Csiki, Hsi-Heng Dai, Daniel Gambill, Christopher Hamblen, Ciaran Harman, Robert Haydel, Juan Martin-Vide, Stephen McKay, Diego Oviedo-Salcedo, Francisco Pedocchi, James Powell Joy Rexshell and Enrica Viparelli.

REFERENCES

Allison, M.A., Nittrouer, J.A. & Galler, J.J. 2005. The supply side of Mississippi river delta restoration: can the river provide the sediment we need? *Eos Trans*, AGU, 86(52), Fall Meet. Suppl., Abstract H42C-03.

DuMars, A.J. 2002. *Distributary mouth bar formation and channel bifurcation in the Wax Lake Delta, Atchafalaya Bay, Louisiana*. M.S. thesis, Louisiana State University, 88 p.

Engelund, F. & Hansen, E. 1967. *A Monograph on Sediment Transport in Alluvial Streams*. Technisk Vorlag, Copenhagen, Denmark.

Fischetti, M. 2001. Drowning New Orleans. *Scientific American*, October, 10 p.

Hallowell, C. 2001. *Holding Back the Sea*. HarperCollins, New York, USA.

Kazmann, R.G. & Johnson, D.B. 1980. If the Old River Control Structure fails? *Bulletin* 12, Louisiana Water Resources Research Institute, Louisiana State University, USA.

Kostic, S. & Parker, G. 2003. Progradational sand-mud deltas in lakes and reservoirs Part 1. Theory and numerical modeling. *Journal of Hydraulic Research*, 41(2), 127–140.

Majersky S., Roberts, H.H., Cunningham, R., Kemp, G.P. & Chacko, J.J. 1997. Facies Development in the Wax Lake Outlet Delta: Present and Future Trends. *Basin Research Institute Bulletin*, 50–56.

Meselhe E.A., Habib E.H., Griborio A.G., Chen C., Gautam S., McCorquodale A., Georgiou I., & Stronach J.A. 2005. Multidimensional modeling of the Lower Mississippi River. *Proceedings,* 9th International Conference on Estuarine and Coastal Modeling in Charleston, South Carolina October 31 to November 2.

Parker, G., Paola, C., Whipple, K.X. and Mohrig, D. 1998. Alluvial fans formed by channelized fluvial and sheet flow: theory. *Journal of Hydraulic Engineering*, 124(10), 1–11, 1998.

Parker, G. 2004. Chapter 24: Approximate formulation for slope and bankfull geometry of rivers. *1D Sediment Transport Morphodynamics with Applications to Rivers and Turbidity Currents*, downloadable at: http://cee.uiuc.edu/people/parkerg/morphodynamics e-book.htm.

Roberts, H.H. & Coleman, J.M. 1996. Holocene evolution of the deltaic plain; a perspective, from Fisk to present. *Engineering Geology*, 45(1-4), 113–138.

Roberts, H.H., Cunningham, R. Walker, N. & Majersky, S. 1997. Evolution of sedimentary architecture and surface morphology; Atchafalaya and Wax Lake deltas (1973–1994). *Am Assoc Petrol. Geol. Bulletin*, 81(9).

Roberts, H.H., J. M. Coleman, S.J. Bentley, N. Walker, 2003a. An embryonic major delta lobe: A new generation of delta studies in the Atchafalaya-Wax Lake delta system. *Transactions*, Gulf Coast Association of Geological Societies 53, 690–703.

Roberts, H.H., Beaubouef, R.T. Walker, N. Stone, G.W., Bentley, S., Sheremet, A. & Van Heerden, I. 2003b. Sand-rich bay head deltas in Atchafalaya Bay (Louisiana): Winnowing by cold front forcing. *Proceedings* Coastal Sediment '03, Clearwater, FL, 1–15.

Swenson, J.B., Voller, V.R., Paola, C., Parker, G. & Marr, J. 2000. Fluvio-deltaic sedimentation: A generalized Stefan problem. European Journal of Applied Math., 11, 433–452.

Wright, S. & Parker, G. 2005. Modeling downstream fining in sand-bed rivers. II: Application. S. Wright and G. Parker. *Journal of Hydraulic Research*, 43(6), 620–630, 2005.

Wellner, R.W., Beaubouef, R.T., Van Wagoner, J.C., Roberts, H.H. & Sun, T. 2006. Jet-plume depositional bodies –the primary building blocks of Wax Lake Delta. *Unpublished Report* to ExxonMobil, personally communicated by H.H. Roberts.

Copyright © 2006 Taylor & Francis Group plc, London, UK

Rivers and floods: A concern for people, a problem for engineers, a challenge for research

Y. Zech
Université catholique de Louvain UCL, Dept Civil & Environmental Engineering, Louvain-la-Neuve, Belgium

S. Soares-Frazão
UCL, Dept Civil & Environmental Engineering and Fonds National de la Recherche Scientifique, Belgium

D. Bousmar
Laboratoire de recherches hydrauliques, Walloon Ministry of Equipment and Transport, Châtelet, Belgium

B. Spinewine, C. Dal Cin & C. Savary
UCL, Dept Civil & Environmental Engineering, Louvain-la-Neuve, Belgium

ABSTRACT: Practitioners did not wait for a complete achievement of knowledge to design and build flood defence structures, and to prepare emergency plans. As a consequence, research and practice often evolve in parallel worlds, without many interactions. To address end-user needs, research should thus develop adapted models, close to the physics, simple to implement, easy to calibrate, validated against idealised experiments and not too demanding in data. Three examples inspired by this philosophy are proposed: a model accounting for interactions between subsections in compound channels, an analogue 1-D model for a dam-break wave in a sharp bend, and a two-layer model for sediment movement induced by a dam-break wave.

1 INTRODUCTION

Rivers are among the most fascinating creations in nature, closely related to human development and well being. Rivers are involved in essential human activities: irrigation for agriculture, drinking water, energy and transportation.

But rivers also raise a lot of problems: floods and inundation often threaten human activities, rivers may convey chemical or biological pollution, or they may constitute an obstacle to mobility.

Among those problems, floods represent something special. They are a part of the river life and participate to its general equilibrium and evolution. River themselves have organised a natural system to mitigate their excesses. Floodplains may be considered as the most ingenious arrangement of flood regulation. The problem is that riverside areas are so attractive that more than 1.5 billions persons live in a floodplain, often unconsciously.

Modelling floods is thus of primary importance to take the best measures in order to manage their occurrence and mitigate their consequences.

1.1 *Short history of flood modelling*

Mitigation and management of floods and inundation is a very old problem for engineers, well before scientists could propose usable models. Designers could not wait for a complete knowledge and understanding of river behaviour before undertaking protective works. Often, those works were really successful, thanks to the good feeling of the river engineers of the past. But those empirical efforts did not always succeed, and sometimes ill-designed structures may have aggravated the risks of overflow consequences, compared to the natural situation.

In the history of flood defence, action has thus sometimes preceded reflection, at least accurate reflection.

During the 19th century, many works were carried out in rivers (e.g. Rhine, Rhône and Garonne, for Western Europe). These works were not all conducted in a blind way. Sometimes, the main characteristics of the natural river were defined from observation and one of the merits of those practitioners, like Fargue for the Garonne River, was to presume that the natural

Copyright © 2006 Taylor & Francis Group plc, London, UK

behaviour of a river was the best guideline for river works. The first source of knowledge about rivers was thus field observation, but the part of interpretation and empiricism was too large to avoid spectacular failures.

A part of the 20th-century progresses in modelling river floods was thus motivated by the urgency to face the failures in design of the former century. This is an uncommon situation in engineering where fundamental and applied researches generally precede application.

The first theoretical approaches of open-surface hydraulics were developed in a simplified context of straight prismatic channels with very simple geometry. The gap between those assumptions and the complexity of the reality was so large, that mathematical models issued from those pioneering approaches were not, or very approximately applied in real-life rivers.

In the same time, for complex river features or structures, laboratory scale models developed extensively, maybe more than in any other branch of learning. Some major laboratories were built mainly around such models devoted to main river reaches or estuaries.

An unexpected consequence of that was a resistance to mathematical model development and use, compared, for example, to fluid dynamics models in aeronautics. Indeed, during years, in consulting companies, numerical schemes developed by some pioneers (see for instance Miller & Yevjevich, 1975; Abbott, 1979; Cunge et al., 1980) were considered as limited to simplest cases and their feasibility was to be controlled by scale models.

The golden age of large-scale models ended mainly due to the increase of manpower costs, making impossible the construction and the maintenance of those models.

The too expensive physical models were thus rapidly replaced by software suites, generally based on the pioneers' work, developed above all for engineering purposes, with rather simplified reality description, but sophisticated interfaces for friendly use in data introduction and result interpretation.

1.2 *Which future for research in flood modelling?*

The progresses of theoretical and numerical modelling have been slowed down in a first time by the supremacy of physical models, which were the only ones able to account for complex situations. Similarly, the advantages offered by user-friendly packages generated some resistance to new theoretical developments.

This would not be a problem if all the practical issues were addressed by the existing packages. But in river engineering and management, major catastrophic events frequently recall that neither knowledge, nor techniques nor management are yet perfect.

Researchers propose more accurate physical description of the phenomena and more sophisticated numerical formulations. Practitioners are not only interested in accuracy but also in data treatment, user-friendly aspects, aided-interpretation of results, practical design of fluvial structures.

Each one develops as far as possible his own logic, sometimes leading to impossible synthesis. Indeed, why to elaborate a description so complicated that the numerical approach becomes unfeasible? Why to develop a model with so many parameters to calibrate that the usability is compromised? Why to construct a huge data set if this information is too large to be used in practice? Why to build a refined model if the required data are not available? Why to design complex scale models when simple experiments could produce simple results easier to use for calibration?

All the actors of fluvial hydraulics developments should size their own efforts according to the other approaches.

For the last ten years, the hydraulic research team of the *Université catholique de Louvain* (Belgium) had the opportunity to enter most of those aspects of research in river hydraulics and engineering applied to flood modelling. This context of diversified approaches has progressively led to a change in research methodology, privileging simple models, close to the physics, validated against idealised experiments and not too demanding in data for practical use. The present paper aims at sharing some experience gained from this philosophy, without pretending at all that this is the unique efficient approach, or that the presented models are the best ones.

This point of view will be illustrated through three topics of flood hydraulics: flow in compound channels (overbank floods), severe transient flows due to dam- or dike break and interaction between severe transient flows and sediments.

For each of those topics, the paper will organise in the following way: some key problems to be solved, the development of new ideas and models along with simple idealised experiments, and the critique of their applicability in terms of data requirements as well for calibration as for use.

2 OVERBANK FLOODS

The determination of water profile in compound channels is one of the major issues of flood modelling. Indeed, most of the human housing and activity, attracted by the proximity of the river, take place in the floodplains.

2.1 *A key problem to be solved: interactions between subsections*

The determination of the water profile in compound channels is not simple, as the flow behaviour in the

Copyright © 2006 Taylor & Francis Group plc, London, UK

main channel and in the floodplains are distinct. The main channel is deeper, smoother and more uniform, while the floodplain is shallower, rougher and irregular. The typical velocity of various subsections may be very different leading to complex interactions between flows in each subsection.

The simplest assumption is to consider the whole cross section. This could be seen as an interaction between subsections strong enough to force the velocity to be uniform in the whole cross section. In this so-called Single Channel Method (SCM), uniform-flow equations like Manning relation may be used:

$$Q = \frac{AR^{2/3}}{n} S_0^{1/2} = K S_0^{1/2} = K S_f^{1/2} \quad (1)$$

where Q is the discharge, A and R are the cross-section area and hydraulic radius, respectively, both depending on the water level, n the averaged roughness, S_0 and S_f the bottom and the friction slopes (assumed to be equal in uniform flow). The parameter K is defined as the cross-section conveyance, depending on the water depth and on the cross-section geometry and roughness.

The water profile may be computed using the Bernoulli equation (solved for example by the standard step method), assuming that the head loss for a specific reach is equal to the head loss in the reach for a uniform flow having the same hydraulic radius and average velocity (French 1985): the energy slope S_f can thus be expressed from (1):

$$S_f = \left(\frac{Q}{A R^{2/3}/n} \right)^2 = \left(\frac{Q}{K} \right)^2 \quad (2)$$

At the opposite of the SCM, the popular Divided Channel Method (DCM) considers separate subsections, neglecting their mutual interactions. The channel cross section is decomposed into three reasonably homogeneous subsections (Fig. 1) in such a way that the velocity field in each subsection can be assumed to be uniform and the subsection discharge Q_i can be estimated by the Manning formula (Lotter, 1933):

$$Q = \sum_i Q_i = \sum_i \frac{A_i R_i^{2/3}}{n_i} S_0^{1/2} = \sum_i K_i S_0^{1/2} \quad (3)$$

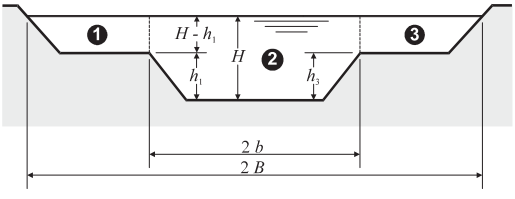


Figure 1. Subsections of compound channels.

where subscript i stands for subsection i. For computing the subsection characteristics A_i and R_i, the limits between the subsections can be vertical, diagonal or horizontal, the most common and practical choice being the vertical ones.

The Divided Channel Method gives better results than the Single Channel one and provides an energy slope value that can easily be included in computational schemes. It is therefore widely used in compound channel packages such as HEC-2 or HEC-RAS (*HEC-2*, 1990). Nevertheless it does not take the momentum transfer into account and thus tends to overestimate the total channel discharge.

A first way to correct the subsection discharges is to consider an apparent shear stress acting at the shear layer between main channel and floodplain. Several empirical shear stress formulae were experimentally established but they generally refer to one particular tested geometry and are difficult to apply to other data (Knight & Shiono, 1996). Moreover, there is no straightforward way to deduce an energy slope value from this kind of models, hindering their exploitation to water-profile computations.

The main progresses have been achieved during the last 20 years in the UK, especially based on large-scale experiments carried out in the Flood Channel Facility (FCF) at Wallingford. Empirical formulae (Ackers, 1993) or analytical methods (Shiono & Knight, 1991) have been developed for prismatic channels.

Those developments significantly improve the prediction of the stage-discharge relationship, but they do not always explicitly represent the physics of the phenomena and require tedious calibrations.

2.2 *A tentative new model: the Exchange Discharge Model (EDM)*

The development of a new model (Bousmar & Zech, 1999) was conducted by some simple guidelines:

(1) to use one-dimensional scheme to reduce the amount of required data and to limit the computation time;
(2) to keep close to the physics by explicitly expressing the momentum exchanges between subsections;
(3) to use a limited number of parameters to be calibrated and to define these physically;
(4) to provide an energy slope value, which can easily be included in computational schemes.

Those principles were dictated by the need to use the new method immediately in real-life applications.

2.2.1 *Physical principles*

In straight compound channels, due to the shear layer at the main channel-floodplain interface, large-scale vortices appear. These vortices can be seen as a turbulent exchange discharge through the interface (Fig. 2).

Copyright © 2006 Taylor & Francis Group plc, London, UK

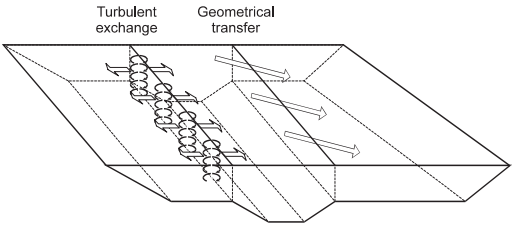


Figure 2. Flow exchange at the interfaces between main channel and floodplains.

Rather than giving an estimate of an apparent shear stress, Bertrand (1994) proposed to model the momentum transfer between subsections by the product of the mass of water flowing through the interface by the velocity gradient at this interface.

This model is easy to extend to non-uniform and/or non-prismatic flows where a lateral discharge occurs through the interface due to a modification of flow distribution in the subsections (Yen et al. 1985). This geometrical transfer discharge (Fig. 2) can be added to the turbulent exchange to get a global estimation of the momentum transfer.

2.2.2 *Governing equations*

Each subsection of a compound channel acts as a channel submitted to a lateral flow per unit length q_l, which consists in an inflow component q_{in} and/or an outflow component q_{out}. Inflow and outflow are normally mutually exclusive, except for turbulent exchanges due to fluctuations, where mass transfer is equal to zero but not momentum transfer. Conservation of *mass* may be written:

$$\frac{\partial A}{\partial t}+\frac{\partial Q}{\partial x}=q_l=q_{in}-q_{out} \tag{4}$$

where A is the cross-section area, and Q the discharge.

On the other hand, the net rate of *momentum* flux into a control volume plus the sum of the forces (gravity, friction, pressure) acting on the control volume is equal to the rate of accumulation of momentum within the control volume (Fig. 3):

$$\frac{\partial}{\partial t}(\rho AU)=-\frac{\partial}{\partial x}(\rho AU^2)+\rho q_{in}u_l-\rho q_{out}U -\rho gA\frac{\partial z}{\partial x}-\rho gAS_f \tag{5}$$

where ρ is the density of water, g is the gravity constant, S_f is the friction slope, estimated for example by (2), $U=Q/A$ is the mean velocity, z the water level; and u_l the lateral-inflow velocity component in the direction of the main flow.

Of course, lateral inflow q_{in} and outflow q_{out} in (4) and (5) may be composed of several parts, which is the case for a main channel flanked by two floodplains.

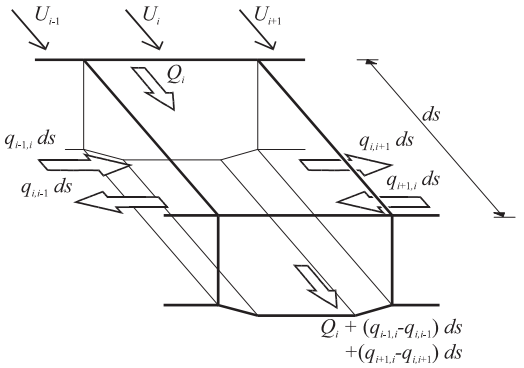


Figure 3. Momentum balance for a sub-section i Developing (5) yields.

$$A\frac{\partial U}{\partial t}+U\frac{\partial A}{\partial t}+AU\frac{\partial U}{\partial x}+U\frac{\partial AU}{\partial x}+gA\frac{\partial z}{\partial x} =q_{in}u_l-q_{out}U-gAS_f \tag{6}$$

which may be simplified, subtracting to (6) the continuity equation (4) multiplied by U:

$$A\frac{\partial U}{\partial t}+gA\frac{\partial}{\partial x}\left(z+\frac{U^2}{2g}\right)=q_{in}(u_l-U)-gAS_f \tag{7}$$

showing that only the lateral inflow influences the momentum, while the outflow effect is implicitly included in the kinetic head variation. An important consequence of this asymmetry between in- and outflow effect is that there exists a momentum transfer due to turbulence even if the average mass transfer is equal to zero.

2.2.3 *Head losses relations*

In case of steady flow, the first term of (7) disappears, and the opposite of the partial derivative of the second term may be defined as a head loss per unit length S_e,

$$S_e=-\frac{\partial}{\partial x}\left(z+\frac{U^2}{2g}\right)=S_f+S_a=S_f(1+\chi) \tag{8}$$

where S_a is an additional head loss due to the exchange of momentum induced by q_{in}. Using (7) generalised to the case of multiple inflows, (8) can be written for a subsection i between a right subsection $i-1$ and a left subsection $i+1$ (Fig. 3)

$$S_{a,i}=S_{f,i}\chi_i=\frac{q_{i-1,i}(U_i-u_{i-1})+q_{i+1,i}(U_i-u_{i+1})}{gA_i} \tag{9}$$

in which $q_{i-1,i}$ is the unit lateral inflow from subsection $i-1$ to subsection i, and u_{i-1} the lateral inflow longitudinal velocity.

Copyright © 2006 Taylor & Francis Group plc, London, UK

2.2.4 *Exchange discharges*

The exchange discharges q is divided in two parts: q^t, due to turbulent exchanges, and q^g, associated to mass transfer due to change in cross-section geometry.

According to Bertrand's proposal (1994), we assume that both lateral discharges q^t_{cf} and q^t_{fc}, respectively from the main channel to a floodplain and from this floodplain to the main channel, are equal to the product of the depth-averaged turbulent part of the transversal velocity by the interface area per unit length,

$$q^t_{cf} = q^t_{fc} = \left|\overline{v'}\right|(H - h_1) = \psi' \left|U_c - U_f\right|(H - h_1) \qquad (10)$$

where H and h_1 are the water and the bank levels above the main-channel bottom (Fig. 1). According to the Boussinesq assumption, the average turbulent transversal velocity is assumed to be proportional to the absolute value of the longitudinal velocity difference between subsections.

If there is a change in geometry (widening or narrowing of floodplain cross-section area) or in water depth (gradually varied flow), the conveyance in the floodplain increases or decreases, forcing through the interface a geometrical transfer discharge q^g_{cf} or q^g_{fc}. For example, if the change in geometry is such that the floodplain conveyance K_f increases,

$$q^g_{fc} = 0 \quad \text{and} \quad q^g_{cf} = \frac{dQ_f}{dx} = \frac{dK_f}{dx} S^{1/2}_{f,f} \qquad (11)$$

neglecting the variation of the friction slope on the floodplain $S_{f,f}$ on the considered interval. This result may be generalised as:

$$q^g_{fc} = \psi^g \kappa_{fc} \frac{dK_f}{dx} S^{1/2}_{f,f} \qquad (12a)$$

$$q^g_{cf} = \psi^g \kappa_{cf} \frac{dK_f}{dx} S^{1/2}_{f,f} \qquad (12b)$$

where κ_{fc} and κ_{cf} take the appropriate values, respectively (0, 1) for $dK_f/dx > 0$ and $(-1, 0)$ for $dK_f/dx < 0$. A proportionality factor ψ^g has also been included to take into account the fact that a change in conveyance does not induce an immediate mass transfer.

2.2.5 *Practical evaluation of flow*

The key assumption is to consider in each subsection i, a distinct friction slope S_{fi}, a distinct additional loss S_{ai}, and thus a distinct ratio χ_i, but a unique total energy slope S_e in all subsections, according to the one-dimensional modelling. This assumption means that the river adjusts its energy budget in such a way that the differences in head are constant between adjacent subsections.

Thus we can write the Manning equation for each subsection:

$$Q_i = A_i U_i = \frac{A_i R_i^{2/3}}{n_i} S^{1/2}_{fi} = K_i S^{1/2}_{fi} = K_i \left(\frac{S_e}{1+\chi_i}\right)^{1/2} \qquad (13)$$

from which the subsection velocity U_i can be evaluated.

Applying (9), for example to the subsection 1 of Fig. 1 (the only connection is with the subsection 2), yields,

$$\chi_1 = q_{2,1} \frac{(U_1 - u_2)}{g A_1 S_{f,1}} = \left(q^t_{2,1} + q^g_{2,1}\right) \frac{(U_1 - u_2)}{g A_1 S_{f,1}} \qquad (14)$$

recalling that $q = q^t + q^g$.

Computing $q^t_{2,1}$ from (10), $q^g_{2,1}$ from (12), and the velocities U_i from (13), (14) reads after some simplifications:

$$\chi_1 = \left[\psi'(H - h_1)\left(\frac{R_2^{2/3}}{n_2}\left(\frac{1+\chi_1}{1+\chi_2}\right)^{1/2} - \frac{R_1^{2/3}}{n_1}\right) + \psi^g \kappa_{21} \frac{dK_1}{dx}\right] \left[\frac{R_1^{2/3}}{n_1} - \frac{R_2^{2/3}}{n_2}\left(\frac{1+\chi_1}{1+\chi_2}\right)^{1/2}\right] \frac{1}{g A_1} \qquad (15)$$

Similar equations may be derived for χ_2 (with interactions between subsections 1 and 3) and for χ_3 (with interactions with subsection 2). For a given depth H, the partial section A_i and hydraulic radius R_i may be computed geometrically for each subsections, and a set of non-linear equations in χ_i results:

$$\chi_1 = f(\chi_1, \chi_2) \qquad (16a)$$

$$\chi_2 = f(\chi_1, \chi_2, \chi_3) \qquad (16b)$$

$$\chi_3 = f(\chi_2, \chi_3) \qquad (16c)$$

which can be solved for example by a Newton-Raphson algorithm.

2.2.5.1 Stage-discharge in uniform flow

Given the values of χ_i, it is possible to compute the subsection discharges Q_i by the adapted Manning equation (13) for an uniform flow at a given depth H with an head slope S_e postulated equal to the channel bottom slope S_0 if the latter may be defined. The total discharge Q in the cross-section is the sum of the corrected subsection discharges,

$$Q = \sum_i Q_i = \sum_i \left(\frac{K_i}{(1+\chi_i)^{1/2}}\right) S_e^{1/2} \qquad (17)$$

The discharge is thus computed in a similar way as the Divided Channel Method, but with corrected conveyance in each subsection.

Copyright © 2006 Taylor & Francis Group plc, London, UK

2.2.5.2 Energy slope for varied-flow computation

Equation (17) also leads to a direct computation of the energy slope for a given discharge, a given water level and the associate cross-section geometry. A coefficient χ may be defined for the whole cross-section as a global correction applied to the friction slope S_f computed from the Divided Channel Method (see Eq. 3 with $S_f = S_0$):

$$S_e = S_f(1+\chi) = \left(\frac{Q}{\sum_i K_i}\right)^2 (1+\chi) \qquad (18)$$

Introducing the discharge (17) into (18) yields,

$$\chi = \left(\frac{\sum_i K_i}{\sum_i \left(K_i/(1+\chi_i)^{1/2}\right)}\right)^2 - 1 \qquad (19)$$

making possible the use of any method to solve (5) or the Bernoulli equation, just substituting the total head loss S_e to the friction loss S_f, in order to compute the water profile in non-uniform flow.

2.3 *Applicability*

Most of the initial objectives are reached: the model is simple and may be easily implemented in common computation procedures as the standard-step method. The method was successfully tested against laboratory data (Bousmar & Zech, 1999).

Only two parameters are to be calibrated: the turbulent exchange coefficient ψ^t, which revealed from comparisons with experimental data to be rather constant ($\psi^t = 0.16$), and the geometrical exchange correction factor ψ^g, whose the value of 0.5 initially adopted (Bousmar & Zech, 1999) has to be refined.

2.3.1 *Validation*

A challenging example is a 4-km meandering reach of River Sambre, Belgium (Fig. 4). Grassland floodplains, on both sides of the main channel were flooded several times during the last years. Accurate topographic data (with cross-section profiles known at intervals of about 100 m, including floodplains) are available. For 18 flood events, discharge was measured together with upstream and downstream water levels, making possible a roughness evaluation in main channel and floodplains.

For each gauged discharge, a water profile was computed from the corresponding measured downstream depth. Three different methods were used: the Single Channel Method, the Divided Channel Method (using HEC-2) and the Exchange Discharge Model. They are synthesised in Fig. 5: each gauged discharge presents

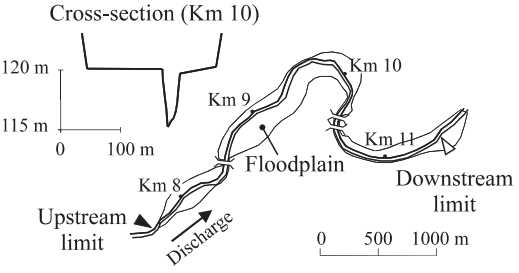


Figure 4. Scheme of River Sambre modelled reach.

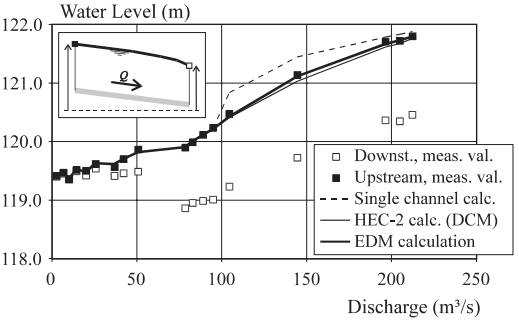


Figure 5. Water-profile computation in River Sambre, Belgium. Measured downstream water levels, measured and computed upstream water levels (lines between points are only drawn for figure legibility). Manning roughness coefficients are, for SCM: $n = 0.026$; for DCM: $n_c = 0.026$, $n_f = 0.100$; and for EDM: $n_c = 0.026$, $n_f = 0.031$.

its specific downstream water level, the upstream calculated levels are shown compared to the measured values.

The results show that the SCM clearly over-estimate the energy slope (difference between up- and downstream levels) for low overflow. HEC-2 (DCM) gives better results, as the energy slope evolution is better estimated. Nevertheless, computations with various floodplain roughness coefficients show that its value can vary in the range $n_f = 0.100 \ldots 1.000$ which are unrealistic.

The Exchange Discharge Model gives better results, with a floodplain roughness coefficient $n_f = 0.031$, which is coherent with field observations on grasslands. For the largest discharge ($Q = 205\ \mathrm{m^3/s}$), the additional loss S_a due to interaction can represent up to 25% of the total losses S_e.

2.3.2 *Application to Meuse River (Belgium)*

The Meuse River, whose the watershed covers 12220 km^2 (73.3% of the Walloon territory in Belgium), has suffered two big floods in 1993 and 1995, with damages partly due to poor information available to decision makers and to population in general.

Copyright © 2006 Taylor & Francis Group plc, London, UK

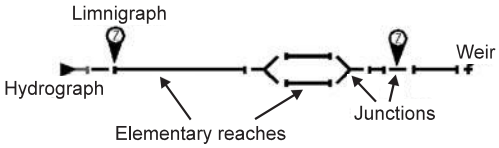


Figure 6. Network scheme of a River Meuse reach.

The Service of Hydrologic Studies (SETHY) of the Walloon Ministry of Equipment and Transport has piloted an ambitious project aiming at giving a real-time forecasting of the water levels and flooded area, with a prediction of 18 hours (Dal Cin et al., 2005). The project is an integration of various techniques:

(1) construction of accurate geometry data base: bed profiles by swath bathymetry, which records depth profiles across tracks from a boat whose motion sensors measure the roll, pitch and heave and DGPS gives position; survey of the floodplains by an airborne laser, yielding a DTM with one measured point per m^2;
(2) prediction of the inflow discharges from the upper valley and from the tributaries: rainfall, non-linear production function, linear transfer function (Moens & Bastin, 1995);
(3) flood propagation in the river, including the effects of control structures (dams and gates);
(4) delineation of flooded areas using GIS tools.

The authors were involved in most of those types of task, except the prediction of the inflows. This multiple involvement naturally imposed an integrated approach. As the river reach was long (one thousand cross-sections for 90 km) and the computation time allowed to obtain real-time prediction was rather short, a one-dimensional model was preferred with a four-point Preissmann implicit scheme.

As the river features some islands and is controlled by several dams (12 in the studied reach), an organisation in sub-reaches was adopted, with "elements" interacting mutually (Fig. 6).

For the determination of cross sections, a simplification of the polylines issued from the DTM and the bathymetry was required to minimise the data size without altering the computation of the characteristics (area A, wetted perimeter P, hydraulic radius R). It was observed that one of the most delicate points was the merging of submerged and emerged data, issued from various sources, not always compatible. In particular the definition of the overbank level is important for the EDM.

The Exchange Discharge Model revealed to improve considerably the results without slowing down too much the computation process (Fig. 7).

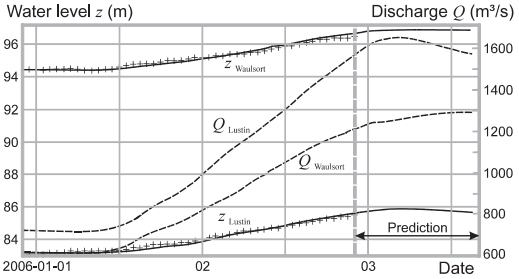


Figure 7. Meuse River: measured (+) and simulated (lines) water levels and discharge (18-hour forecasting).

3 SUDDEN FLOODS

Another challenging problem is the modelling of sudden floods following a structure failure (a dam break or a dike breach) or from an extreme rain-peak.

This kind of flood is fortunately less frequent than overbank floods. However this low probability of occurrence is to be confronted to the magnitude of the associated risk, in terms of casualties and damages to the properties and to the social organisation.

Dam or dike failures are rare but they constitute one of the heaviest threats for the downstream population. People, and thus also decision-makers, less and less accept to consider this event as an uncontrolled fatality. Legal obligations were progressively imposed to the dam owners to investigate the consequences of a potential failure, and to prepare adapted warning systems and rescue plans.

This explains why so many efforts were carried out during the last 20 years, to improve the modelling of such an event. Generally companies in charge of dams developed their own expertise with or without the support of research organisations. Models issued from these developments are often efficient enough to address the legal requirements. In some cases, such models or methods have even become the rule with a trend to fix the procedures.

In parallel, researchers, fascinated by such an interesting problem, have continued to improve their methods. These are more and more accurate but generally heavier to apply. As a consequence, application of such developments in the practice remains limited. A kind of gap has resulted between the practitioners a little reluctant to rerun their computations, and the researchers.

Another difficulty is that the accuracy of new developments has to be confronted to real-life data. Such data are (fortunately) rare and inaccurate, as, in case of catastrophic events, measurements are not the first people's concern. Of course it is sometimes possible to replay the event at a laboratory scale with accurate measurement, but scale models are generally too expensive and also too complex for giving a clear guidance in numerical model calibration.

Copyright © 2006 Taylor & Francis Group plc, London, UK

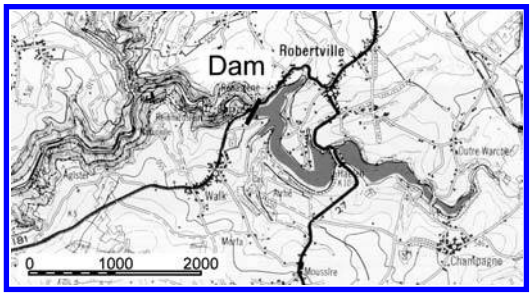


Figure 8. Robertville dam, in the Warche valley (Belgium).

3.1 *An example of key problem to be solved: effect of bends on dam-break waves*

A recent dam-break study on a Belgian valley highlighted important differences in the computed wave arrival time between one- and two-dimensional models: the one-dimensional model, generally preferred for large-scale simulations, predicted a much faster wave than the two-dimensional model (6 minutes instead of 50 minutes to reach the first town downstream).

How to explain such a difference? The valley slope is steep, with multiple sharp bends (Fig. 8), and it was suspected that the important head and momentum losses occurring in the bends, which are not taken into account by the one-dimensional model, were at the origin of the observed difference.

3.2 *A tentative approach: basic experiments and simplified models*

3.2.1 *The basic one-dimensional model*

To represent the dam-break wave in a natural valley, a one-dimensional approach is possible as far as changes in cross-section geometry are accounted for.

The computation is thus founded on an appropriate form of shallow-water equations (Capart et al., 1997; Soares-Frazão, 2002):

$$\frac{\partial \mathbf{U}}{\partial t} + \frac{\partial \mathbf{F}}{\partial x} = \mathbf{S} \tag{20a}$$

with

$$\mathbf{U} = \begin{pmatrix} A \\ Q \end{pmatrix}, \ \mathbf{F} = \begin{pmatrix} Q \\ VQ + gI_1 \end{pmatrix}, \ \mathbf{S} = \begin{pmatrix} 0 \\ \frac{\partial}{\partial x}\left(gI_1|_{\bar{z}}\right) - gAS_f \end{pmatrix} \tag{20b}$$

where A is the cross-section area, Q the discharge and I_1 the cross-section static momentum accounting for the hydrostatic pressure (Fig. 9)

$$I_1 = \int_0^h (h-\eta)\, b(\eta)\, d\eta \tag{21}$$

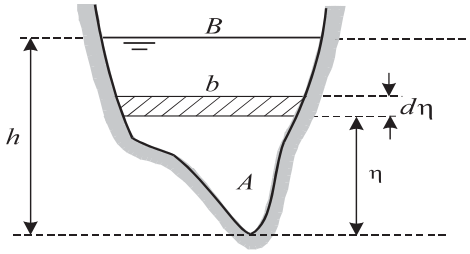


Figure 9. Static moment definition.

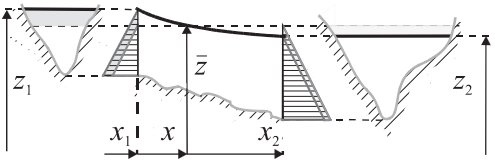


Figure 10. Hydrostatic pressure in non-prismatic channel.

In the source terms, the difference in gI_1 for a given mean water level accounts for the effect on the hydrostatic pressure, as well the effect of the changes in cross-section width as the effect of the bottom slope (Fig. 10).

This formulation, applied to a finite-volume scheme, appeared to be very efficient even for irregular valleys, except if these feature significant changes in direction. Further investigations about this particular point were thus carried out (Soares-Frazão, 2002; Soares-Frazão & Zech, 2002).

3.2.2 *A basic experiment: a 90° sharp bend*

To investigate more deeply the problem posed by sharp bends, and compare the performances of two- and one-dimensional modelling, a simplified case was investigated: a dam-break flow in a channel with a 90° sharp bend. Therefore, an experimental channel with such a 90° bend was built in the laboratory of the Civil Engineering Department of the Université catholique de Louvain, Belgium, and some computations were performed with various levels of sophistication (Fig. 11).

Experiments in the 90°-bend channel showed that the change in flow direction occurs abruptly as depicted on Fig. 12 at various times from a 2-D computation.

The supercritical flow induced by the dam break reflects against the bend, its velocity becomes zero and the water level rises (Fig. 12a). Then, this water column falls down (Fig. 12b) and a new water front propagates both in the downstream and upstream reaches (Fig. 12c). In the upstream direction, this results in a bore receding to the reservoir, with the consequence

Copyright © 2006 Taylor & Francis Group plc, London, UK

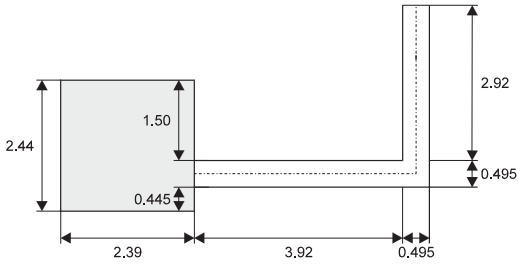


Figure 11. Sharp bend: experimental set-up.

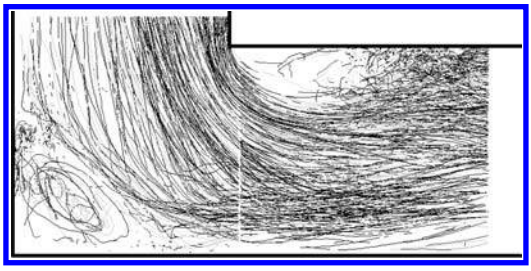


Figure 13. Trajectories in the bend.

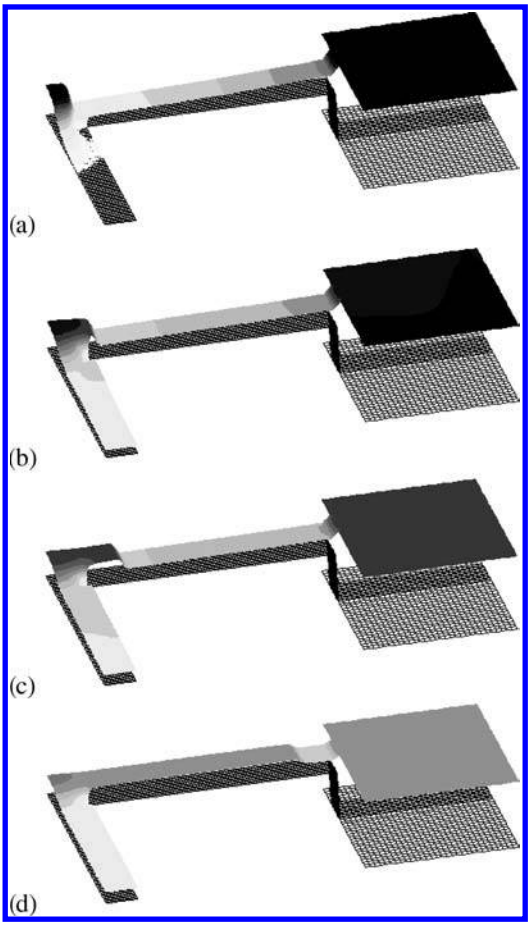


Figure 12. Dam-break flow in a 90˚ bend at times (a) 3 s, (b) 5 s, (c) 7 s, and (d) 14 s.

that the flow at the head of the bore is now subcritical, and thus much slower than the initial supercritical flow (Fig. 12d).

The abrupt change in direction can be explained as follows. In the initial supercritical stage, the kinetic energy is dominant. Then, when the water is suddenly stopped in the bend, its kinetic energy is transformed into potential energy (rise of the water surface) while important head losses occur. Contrarily to kinetic energy, which is associated with velocity vectors with a given direction, the potential energy is purely scalar without any preferential direction. This potential energy then transforms back into kinetic energy, with velocities oriented in the downstream-reach direction.

3.2.3 *An equivalent one-dimensional model for the bend*

Developing the bend channel as a straight one, the water profile along the developed channel shows interesting similarities with the water profile obtained in a case of channel locally constricted. A bore forms just upstream the channel narrowing, similarly to what happens upstream the bend.

Using a digital imaging technique to measure the surface-velocity field in the bend (Capart et al., 2002; Spinewine et al., 2003), it was possible to reconstruct the flow trajectories. Such trajectories measured over the time interval [6 s–7 s] are shown on Fig. 13.

It appears that the active flow region does not extend over the whole channel cross section in the bend: there is a dead zone in the outer corner, and a shadow zone just downstream from the inner corner. The flow thus seems to reproduce a kind of local constriction, supporting the idea of a similarity in the consequences of those two topographical singularities.

Combining the flow trajectories in the bend over different time intervals, it was possible to define an average local constriction in a straight channel corresponding to effect of the bend (Fig. 14).

This fictitious channel was thus used to simulate a dam-break flow under the same initial conditions as for the bend test case. Results show a good agreement between 1-D analogue, 2-D computations and measurements, except regarding the time of the reflected front (Fig. 15a, gauge C2). The water level is exaggerated in gauge C3, but the water release at gauge C4 (Fig. 15b) is even better captured by the analogue 1-D than by the full 2-D model.

Copyright © 2006 Taylor & Francis Group plc, London, UK

3.3 *Applicability*

Of course, equivalent one-dimensional models do not pretend to reach the performance of a complete two- or three-dimensional model, but they may offer to the practitioners an interesting substitute for these, in the frequent case where no complete information is available on the valley topography.

It is clear also that such analogues have to be further investigated to form a usable catalogue, and the only way to do that is a mix of some basic experiments for idealised geometry, and methodical accurate computations with full models in order to scan the whole range of possible situations.

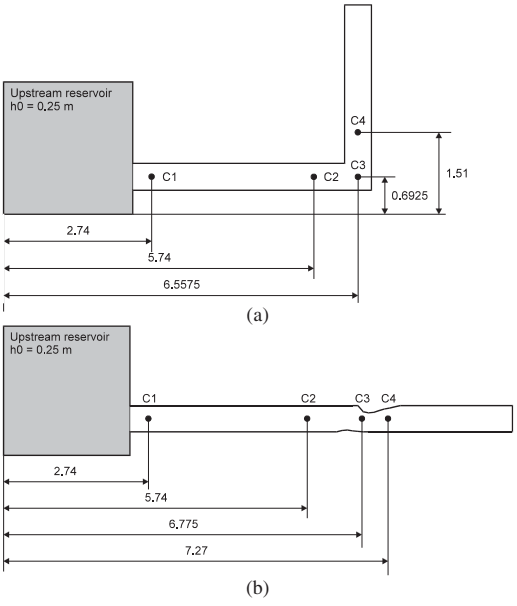


Figure 14. Constriction as an analogue to the bend.

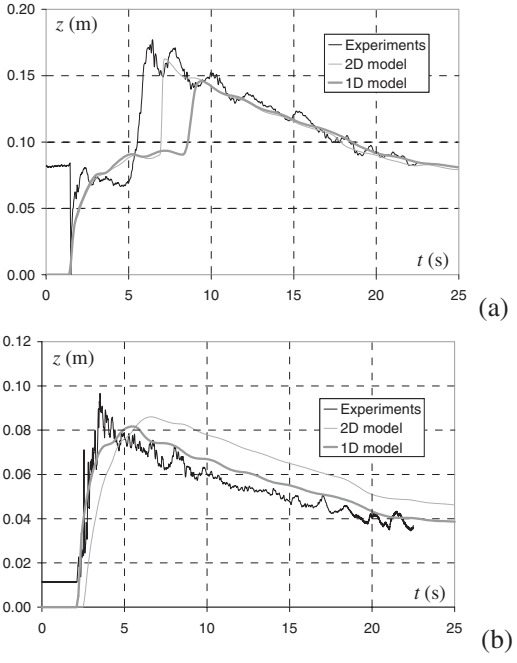


Figure 15. Comparisons between experiments, analogue 1-D model and full 2-D model at gauges C2 (a) and C4 (b).

4 SUDDEN FLOODS AND SEDIMENTS

In a number of ancient and recent catastrophes, floods from dam or dike failures have induced severe soil movements in various forms: debris flows, mud flows, floating debris and sediment-laden currents (Costa and Schuster, 1988). Fig. 16 presents some estimates of the volume of sediment material moved by such flows, gathered from published cases studies (Capart, 2000; Capart et al., 2001). In some cases, the volume of entrained material can reach the same order of magnitude (up to millions of cubic meters) as the initial volume of water released from the failed dam.

Also, this solid transport often causes more damages and casualties than the liquid flood and the means required to restore the devastated area are considerably heavier.

Moreover, presence of solid transport seriously affects the evaluation as well of the maximal water level as of the arrival time of a dam-break wave.

However, at the current stage of development of numerical simulation tools, it is impossible for practitioners to accurately account for such a sediment mobilisation and movement.

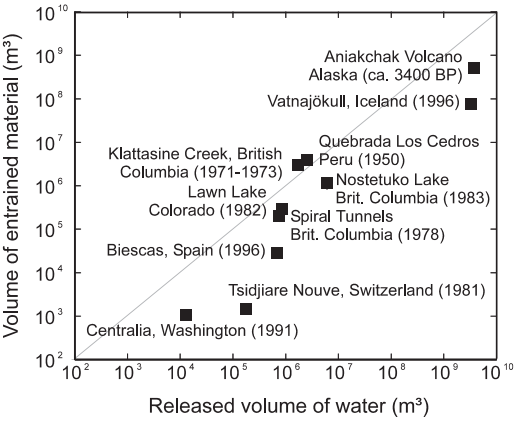


Figure 16. Entrained material from dam or dike failures (Capart, 2000).

Copyright © 2006 Taylor & Francis Group plc, London, UK

4.1 *A key problem: sediment mobilisation and expansion*

Dam-break induced geomorphic flows generate intense erosion and solid transport, resulting in dramatic and rapid evolution of the valley geometry.

Close to the broken dam, rapid and strong erosion accompanies the development of the dam-break wave. The flow exhibits noticeable free surface features: wave breaking occurs at the centre (near the initial location of the dam), and a nearly vertical wall of water and debris overruns the sediment bed at the wave forefront (Capart, 2000), resulting in an intense transient debris flow (Fig. 17).

Behind the debris-flow front, the behaviour appears to be completely different: inertial effects and bulking of sediments may play a significant role.

Common geomorphic models are based on the Saint-Venant – Exner equations, adding to the common continuity and momentum conservation of the liquid phase (see Eqs. 20, for example) an equation for the continuity of the sediment phase. In this approach, the solid transport is not a main unknown and is evaluated externally by a closure equation (for instance a Meyer-Peter – Müller formula).

The main drawback of such a method is that the common solid-transport formulae have been developed in uniform regime, yielding an equilibrium transport capacity, which has no chance to occur under dam-break conditions.

The key point is thus to take into account the complete mechanism of sediment mobilisation, including the inertia of the grains, the momentum required for their acceleration and the expansion needed for their movement.

4.2 *A tentative new description: the two-layer model*

To fulfil the above requirements, the key idea is to consider separately the layer of moving sediments from moving water to make exchanges possible between the two layers.

4.2.1 *Physical description*

The two-layer model presented here is due to Spinewine (2005) and is based on the pioneering work by Capart (2000), progressively improved by Capart & Young (2002), Spinewine (2003).

The sediments are moving in a dense layer, with negligible suspension in the upper layer. The flow is thus represented by the following layers: (a) the upper layer consisting in clear water of depth h_w, (b) the moving sediment layer h_s and (c) the fixed-bed layer, having the bed level z_b as upper limit (Fig. 18).

To give the model the required degrees of freedom the velocities of the two moving layers are distinct: ($u_s \neq u_w$) and the concentrations of the bottom and of the moving layer are not the same ($C_s \neq C_b$) to account for the expansion required by the grain mobilisation.

4.2.2 *Governing equations*

Defining the erosion rate (negative in the case of deposition) as

$$\frac{\partial z_b}{\partial t} = -e_b \tag{22a}$$

it is possible to express the continuity of both the water and the water/sediment mixture layers:

$$\frac{\partial h_w}{\partial t} + \frac{\partial}{\partial x}\left(h_w u_w\right) = -e_b \frac{C_b - C_s}{C_s} \tag{22b}$$

$$\frac{\partial h_s}{\partial t} + \frac{\partial}{\partial x}\left(h_s u_s\right) = e_b \frac{C_b}{C_s} \tag{22c}$$

Those equations can be compared to (4). The right-hand side of (22c) indeed represents the in- or outflow, taking into account the change in concentration of an amount of material passing from the fixed bed to the moving-sediment layer (due to the expansion, the volume is greater in case of erosion), and the call of water from the upper layer to fill the void so-generated, which induces a loss for this upper layer as represented in the right-hand side of (22b).

Using a shallow-water approach, with the assumption of a hydrostatic pressure distribution, the momentum conservation of those moving layers reads:

$$\frac{\partial (h_w u_w)}{\partial t} + \frac{\partial}{\partial x}\left(h_w u_w^2 + \frac{g h_w^2}{2}\right) + g h_w \frac{\partial}{\partial x}\left(z_b + h_s\right) = -e_b \frac{C_b - C_s}{C_s} u_1 - \frac{\tau_w}{\rho_w} \tag{22d}$$

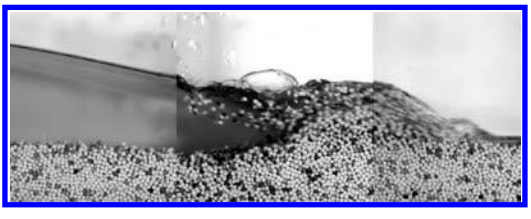


Figure 17. Near-field water/sediment flow (Université catholique de Louvain).

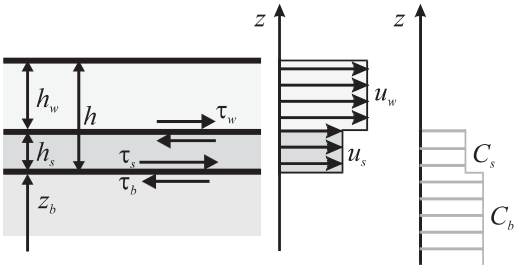


Figure 18. Two-layer model scheme.

Copyright © 2006 Taylor & Francis Group plc, London, UK

$$\frac{\partial(h_s u_s)}{\partial t}+\frac{\partial}{\partial x}\left(h_s u_s^2+\frac{g h_s^2}{2}\right)+g h_s\left(\frac{\partial z_b}{\partial x}+\frac{\rho_w}{\rho'_s}\frac{\partial h_w}{\partial x}\right) = \frac{\rho_w}{\rho'_s}\frac{C_b-C_s}{C_s}e_b\,u_1+\frac{\tau_w}{\rho'_s}-\frac{\tau_b}{\rho'_s} \quad (22e)$$

where $\rho'_s=\rho_w(1-C_s)+\rho_s C_s$ is the volumetric mass of the moving mixture layer h_s. Those equations may be compared to (6).

The asymmetrical exchange of momentum in case of erosion or deposition is taken into consideration in the following way: $u_1=u_w$ if $e_b>0$ while $u_1=u_s$ if $e_b<0$. For details about the above equations see Spinewine (2005)

In this model the five dependent variables are h_w, h_s, z_b, $(h_w u_w)$ and $(h_s u_s)$. The erosion rate e_b (negative in the case of deposition) results from the inequality between the shear stresses τ_s and τ_b on both faces of the bed interface:

$$e_b=\frac{1}{\rho'_b\,|u_s|}\left(\tau_s-\tau_b\right) \quad (23)$$

where $\rho'_b=\rho_w(1-C_b)+\rho_s C_b$ is the volumetric mass of the bottom layer at rest. Closure equations are required for τ_w, τ_s and τ_b. The shear stresses τ_w and τ_s are evaluated from the turbulent friction:

$$\tau_w=\rho_w C_{fw}\left(u_w-u_s\right)^2 \quad (24)$$

$$\tau_s=\rho'_s C_{fs}\,u_s^2 \quad (25)$$

while τ_b depends on the critical shear stress c, and on the internal friction angle ϕ:

$$\tau_b=c+\sigma'\tan\phi=c+\left(\rho'_s-\rho_w\right)g\,h_s\,\tan\phi \quad (26)$$

where σ' is the effective pressure.

4.2.3 *Model calibration*

Some variables in (22–26) are physically determined: ρ_w, ρ_s, C_b, C_s, c and ϕ. The only coefficients impossible to measure directly are the friction coefficients C_{fw} and C_{fs}.

These parameters are not easy to calibrate by means of experiments, as the above model relies on some simplifications: the velocity is considered as uniform in both layers leading to a discontinuity at the interface. This fictitious discontinuity, useful to derive the erosion rate is not really present in the reality, where the interfaces are not so sharp. It is thus difficult to define exactly what and how to measure in order to calibrate (24) and (25).

Fortunately, using the uniform-flow condition as a reference (Zech et al., 2005) it is possible to find a good approximation of the two friction coefficients only by comparison, for one given situation, between results from the model with results from any uniform-flow formula (Manning for example), and any solid-transport formula (for instance Meyer-Peter–Müller).

In uniform-flow conditions, (22d) and (22e) simplify since the partial derivatives $\partial/\partial t=0$ and $\partial/\partial x=0$, except $\partial z_b/\partial x=-S_0$, S_0 being the bottom slope:

$$-g h_w\frac{\partial z_b}{\partial x}=g h_w S_0=\frac{\tau_w}{\rho_w} \quad (27)$$

$$-g h_s\frac{\partial z_b}{\partial x}=g h_s S_0=\frac{\tau_b}{\rho'_s}-\frac{\tau_w}{\rho'_s} \quad (28)$$

In uniform-flow conditions, the solid transport is in equilibrium, which means that neither erosion nor deposition occurs; thus (23) reduces to the condition,

$$\tau_b=\tau_s \quad (29)$$

If we now define the unit liquid and solid discharges,

$$q_w=u_w h_w \quad (30)$$

$$q_s=u_s h_s \quad (31)$$

Equations (24–31) form a set of 8 uniform-flow equations linking 12 parameters: S_0, q_w, q_s, h_w, h_s, u_w, u_s, τ_w, τ_s, τ_b, C_{fw} and C_{fs}. If 4 of them are known, the others may be deduced.

It is thus possible to calibrate the two friction coefficients, C_{fw} and C_{fs}.

For example, for a given discharge q_w in a channel of slope S_0 with mobile bed with a characteristic diameter d, the Manning roughness coefficient n may be evaluated from the Strickler formula,

$$K=\frac{1}{n}=\frac{26}{d^{1/6}} \quad (32)$$

and the water depth h_w may thus be deduced from the Manning uniform-flow relation:

$$q_w=\frac{1}{n}h_w^{5/3}S_0^{1/2} \quad (33)$$

If we now compute the solid discharge q_s from any empirical formula, we obtain the 4 parameters (two imposed: the discharge q_w and the slope S_0; two calculated: the water depth h_w, and the solid discharge q_s) required to compute the 8 others from (24–31) and among them the two coefficients to calibrate: C_{fw} and C_{fs}.

4.2.4 *Some typical results*

Once those coefficients are calibrated, one may investigate the behaviour of the two-layer model in other uniform-flow conditions by considering various combinations of q_w and S_0. For each combination, it is possible to compute q_s, h_w, h_s,u_w,u_s, τ_w, τ_s and τ_b.

Copyright © 2006 Taylor & Francis Group plc, London, UK

To analyse the two-layer model behaviour, an example was computed with the following data: a unit water discharge $q_w = 10\,\mathrm{m}^3/\mathrm{s/m}$ in a channel, whose bed is constituted of uniform grains of diameter d varying from 1 to 10 mm; the density $\rho_s/\rho_w = 2.65$, and the internal friction angle $\phi = 30°$.

For each diameter, the calibration of C_{fw} and C_{fs} was done for a bottom slope S_0 corresponding to the value of the Froude number $\mathbf{Fr} = 1$. The corresponding transport q_s and critical shear stress c are evaluated from Meyer-Peter-Müller formula.

Then, for each diameter a range of bottom slopes is explored. Using the set of equations (24–31), it is possible to compute the various parameters as a function of the Froude number defined as,

$$\mathbf{Fr} = \frac{u_w}{\sqrt{g\,h_w}} \tag{34}$$

Some results about the sediment layer depth h_s and velocity u_s are given in Figures 19 and 20. By increasing bottom slope S_0 (thus by increasing Froude numbers), the solid discharge q_s also increases, due for a part to the increase of sediment velocity u_s but mainly to the development in depth of the sediment layer.

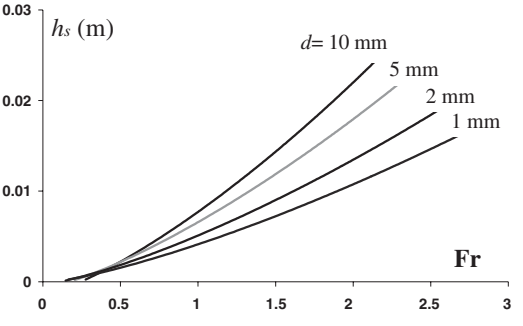


Figure 19. Uniform flow ($q_w = 10\,\mathrm{m}^3/\mathrm{s/m}$): relationship between sediment-layer depth and Froude number (two-layer model).

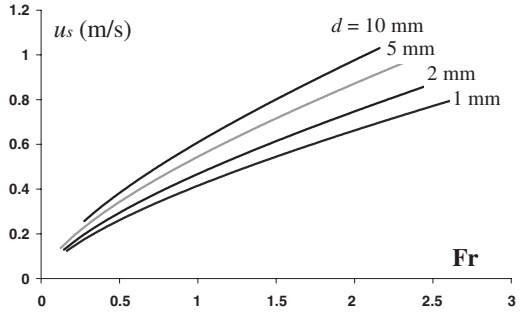


Figure 20. Uniform flow ($q_w = 10\,\mathrm{m}^3/\mathrm{s/m}$): relationship between sediment-layer velocity and Froude number (two-layer model).

4.3 *Applicability*

The two-layer model was tested against experimental data of dam-break induced wave.

Experiments were carried out at the *Université catholique de Louvain* (Spinewine, 2005, Spinewine and Zech, submitted). The set-up is sketched in Figure 21 with the following characteristic dimensions: an initial water layer of depth $h_{w,0} = 0.35$ m in the reservoir, and a fully saturated bed of thickness $h_{b,0} = 0.05$ m. The bed material consisted of cylindrical PVC pellets, with the following measured characteristics: $d = 3.92$ mm, $\rho_s = 1580\,\mathrm{kg/m}^3$, $\phi = 38°$, $C_b = 0.58$. The concentration of the moving layer was estimated from digital imaging measurements: $C_s = 0.22$.

Figure 22 shows a comparison between measurements (obtained from digital imaging techniques, indicated in the background of the figure) and computations by the two-layer model (thick black lines). Regarding the wave front, the agreement is excellent, as well for the arrival time as for the layer thickness. Near the initial position of the gate (abscissa 0), the early stage (Fig. 22a: $t = 0.25$ s) features a zone of fluidisation of the sediments, which corresponds to the sediments mobilised to fill the void created by the gate drop (the gate moves downwards). Of course, this particular phenomenon is not represented in the computation. In the next times (Fig. 22b: $t = 0.50$ s; Fig. 22c: $t = 0.75$ s), bed forms (antidunes-like) appear, probably initiated by the initial fall of the water mass. This phenomenon, involving significant vertical velocity components has no chance to be reproduced by a shallow-water model, where only horizontal velocities are taken into account.

The same experiments (initial water layer of depth $h_{w,0} = 0.35$ m in the reservoir, and fully saturated bed of thickness $h_{b,0} = 0.05$ m) were carried out, with a bed of sand with the following characteristics: $d = 1.82$ mm, $\rho_s = 2680\,\mathrm{kg/m}^3$, $\phi = 30°$, $C_b = 0.53$. The concentration of the moving layer was estimated from digital imaging: $C_s = 0.22$, the same as in the PVC-pellet case.

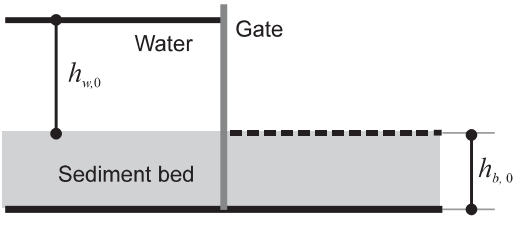


Figure 21. Scheme of the dam-break experiment (UCL).

Copyright © 2006 Taylor & Francis Group plc, London, UK

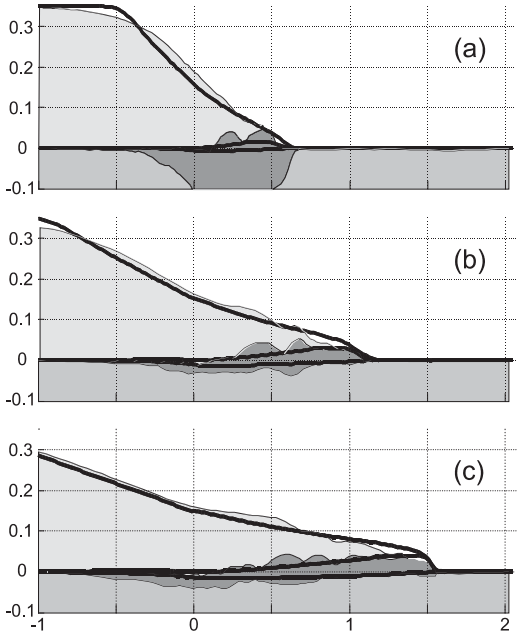


Figure 22. Dam break with PVC pellets: comparison between experiments and numerical results at times (a) $t = 0.25$ s, (b) $t = 0.50$ s and (c) $t = 0.75$ s. Grey-scale zones feature the measurements while the thick lines represent the model result. The dimensions are in metres.

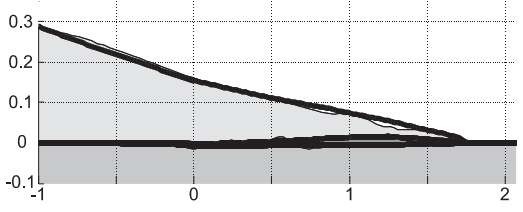


Figure 23. Dam break with sand: comparison between experiments and numerical results at time $t = 0.75$ s. Grey-scale zones feature the measurements while the thick lines represent the model result.

A comparison is presented in Figure 23, for the time $t = 0.75$ s. Due to the higher density, it appears that the erosion is less effective than in the former example. Thus, the thickness of mobilised material is significantly affected.

It is interesting to notice that the two calibrated parameters keep the same value for both experiments ($C_{fw} = 0.005$ and $C_{fs} = 0.04$).

Other experiments were carried out for testing the capacity of the two-layer model in representing the water and sediment movement following a dam-break event (Spinewine, 2005; Zech et al., submitted).

It is clear that all the problems are not solved with this kind of approach. It is clear also that this type of model is far from application in real-life situations, above all if the scale of the problem is large. But, featuring an excellent agreement with basic experiments, the model is really closer to the physics than the common ones and also less demanding in calibration efforts. In that sense, it is promising in terms of generalisation and interpretation.

5 CONCLUSIONS

Fluvial hydraulics, above all in modelling extreme events, is still in progress. Many important phenomena are commonly described in a too rough way. The model based on such rough descriptions may hide some aspects of the reality leading to a false perception of the risks.

All sciences present such a stage of rough description in their history. The danger for fluvial engineering is that so much has yet been designed and realised that inclusion of new knowledge could open an endless and discouraging review of past decisions.

As a consequence, the threat for fluvial science is to progress just for itself, progressively loosing the contact with the practice and the care for applicability.

The few examples developed here show that a median way is possible. Simple models, based on accurate physical description and on basic scale experiments, may seduce the practitioner, as far as those models take care of their concerns.

With such a spirit, fluvial hydraulics remains one of the most exciting fields of research, at the crossing between new knowledge to discover and high responsibility to exert in well being and safety of people.

REFERENCES

Abbott, M.B. 1979. *Computational hydraulics*, Pitman, London, UK

Ackers, P. 1993. "Flow formulae for straight two-stage channels", *Journal of Hydraulic Research, IAHR*, 31(4), 509–531

Bertrand, G. 1994. *Le calcul d'axes hydrauliques dans les rivières à plaines inondables.* Mémoire de Stage, Ministère Wallon de l'Equipement et des Transports, D. 213, Châtelet, Belgium (in French)

Bousmar, D. 2002. *Flow modelling in compound channels. Momentum transfer between main channel and prismatic or non-prismatic floodplains*, Ph.D. thesis, Université catholique de Louvain, Louvain-la-Neuve, Belgium

Bousmar, D. & Zech, Y. 1999. Momentum transfer for practical flow computation in compound channels, *Journal of Hydraulic Engineering*, American Society of Civil Engineers (ASCE), vol. 125, n 7. 696–706

Copyright © 2006 Taylor & Francis Group plc, London, UK

Capart, H. 2000. *Dam-break induced geomorphic flows.* Ph.D. thesis, Université catholique de Louvain, Louvain-la-Neuve, Belgium

Capart, H., Huang, S.Y., Young, D.L. & Zech, Y. 1997. Upwind routing of typhoon floods through a mountainous island river network : the Tanshui in Northern Taiwan, *Proc. 3rd Int. Conference on River Flood Hydraulics*, Stellenbosch, South Africa, 91–100

Capart, H., Bellal, M., Boxus, L., De Roover, C. & Zech, Y. 1998. Approach to morphological equilibrium for steep-sloped river beds. *Proceedings of the seventh International Symposium on River Sedimentation, Hong Kong*: 231–237

Capart, H., Young, D.L. & Zech, Y. 2001. Dam-break induced debris flow, *Special publication of the International Association of Sedimentologists*, vol. 31, 149–156

Capart, H. & Young, D.L. 2002. Two-layer shallow water computations of torrential geomorphic flows. *Proceedings River Flow 2002*, Louvain-la-Neuve, Belgium: 1003–1012

Capart, H., Young, D.L. & Zech, Y. 2002. Voronoï imaging methods for the measurements of granular flows, *Experiments in Fluids*, vol. 32(1), 121–135

Costa, J.E. & Schuster, R.L. 1988. The formation and failure of natural dams. *Bull. Geol. Soc. Am.*, 100: 1054–1068

Cunge, J.A., Holly, F.M. Jr. & Verwey, A. 1980. *Practical aspects of computational river hydraulics*, Pitman, London, UK

Chang, H.H. 1992. *Fluvial Processes in River Engineering.* Malabar, Florida: Krieger Publishing Company

Dal Cin, C., Moens, L., Dierickx, Ph., Bastin, G. & Zech, Y. 2005. An integrated approach for real-time flood-map forecasting on the Belgian Meuse River, *Natural Hazards*, Volume 36, Issue 1–2, 237–256

Fraccarollo, L. & Capart, H. 2002. Riemann wave description of erosional dam-break flows. *Journal of Fluid Mechanics* 461: 183–228.

French, R.H. 1985. *Open-channel hydraulics*, McGraw-Hill, New-York, N.Y.

HEC-2 water surface profiles, users manual. 1990. USACE, Hydrologic Engineering Center, Davis, California, USA

Jansen, P.Ph., Van Bendegom, L., Van Den Berg, J., de Vries, M. & Zanen, A. 1979. *Principles of River Engineering. The non-tidal alluvial river*. London, UK: Pitman,

Knight, D.W. & Shiono, K. 1996. River Channel and flood plain hydraulics. *Flood plain processes*, M. Anderson, D. Walling and P. Bates, eds., J. Wiley & Sons, U.K., 139–181

Lotter, G.K. 1933. Considerations on hydraulic design of channels with different roughness of walls. *Trans. All Union Scientific Research*, Institute of Hydraulic Engineering, Leningrad, 238–241.

Miller, W.A., Jr. & Yevjevich, V. 1975. *Unsteady flow in open channels.* Water resources Publications, Fort Collins, Colorado, USA

Shiono, K. & Knight, D.W. 1991. Turbulent open channel flows with variable depth across the channel. *J. Fluid Mech.*, 222, 617–646. (Errata in 231, 693)

Soares-Frazão, S. 2002. *Dam-break induced flows in complex topographies. Theoretical, numerical and experimental approaches*, Ph.D. thesis, Université catholique de Louvain, Louvain-la-Neuve, Belgium

Soares-Frazão, S. & Zech, Y. 2002. Dam-break in channels with 90° bend, *Journal of Hydraulic Engineering*, American Society of Civil Engineers (ASCE), vol. 128, n 11, 956–968

Spinewine, B. 2003 *Ecoulements transitoires sévères d'un milieu diphasique liquide/granulaire (eau/sédiments), en tenant compte du couplage rhéologique entre les deux phases et des composantes verticales du mouvement* (in French). M.Sc. thesis. Université catholique de Louvain, Louvain-la-Neuve, Belgium

Spinewine, B. 2005. *Two-layer flow behaviour and the effects of granular dilatancy in dam-break induced sheet-flow*, Ph.D. thesis. Université catholique de Louvain, Louvain-la-Neuve, Belgium

Spinewine, B., Capart H., Larcher M. & Zech Y. 2003. Three-dimensional Voronoï imaging methods for the measurement of near-wall particulate flows, *Experiments in Fluids*, vol. 34(2), 2003, pp. 227–241

Spinewine, B. & Zech, Y., submitted. Experimental dam-break waves on movable beds. I: A flat bed test-case

Yen, B.C. 1973. Open-channel flow equation revisited. *J. Engrg Mech. Div.*, ASCE, 99(5), 979–1003

Zech, Y., Soares-Frazão, S., Spinewine, B., Bellal, M., Savary, C. 2005. The morphodynamics of super- and transcritical flow, *Proceedings Conference on River, Coastal and Estuarine Morphodynamics, RCEM 2005*, Urbana, Illinois, USA, Vol. 1, pp. 239–251

Zech, Y., Soares-Frazão, S., Spinewine, B., le Grelle, N., submitted. Dam-break induced sediment movement. Findings and conclusions of the European IMPACT research.

Copyright © 2006 Taylor & Francis Group plc, London, UK

Engineering case studies

Copyright © 2006 Taylor & Francis Group plc, London, UK

Recent training of the lower Rhine River to increase Inland Water Transport potentials: A mix of permanent and recurrent measures

H. Havinga*, M. Taal & R. Smedes
Ministry of Transport, Public Works and Water Management, Directorate General Rijkswaterstaat, Arnhem, The Netherlands

G.J. Klaassen & N. Douben
UNESCO-IHE, Delft, The Netherlands

C.J. Sloff*
WL | Delft Hydraulics, Delft, The Netherlands
** Delft University of Technology*

ABSTRACT: Inland navigation is very important for national and international transport to and from the Netherlands. River management of the main Dutch Rhine branch, the Waal River, aims at improving navigation conditions, at the same time taking into account other, sometimes conflicting interests. Therefore integrated approaches are demanded to implement improvement measures. This paper focuses on the river improvement measures, executed in the Waal River for the benefit of navigation since 1995. The impact of executed and planned measures for navigation on the morphology of the river is discussed. New in the approach since 1995 is that in addition to (essentially traditional) permanent bend improvement measures, recurrent measures like (systematic) dredging and sediment feeding schemes are becoming increasingly important. This signals a change in policy of the Dutch Public Works Department, which traditionally preferred permanent fixed solutions. Special emphasis is given to the specific in-depth field and mathematical modelling studies, which were carried out to understand the morphological processes in this engineered river, the interaction between structures and the river and the relevant time and spatial scales of effects and impacts of the recurrent methods. The need for a master plan taking into account the autonomic trends to facilitate a sustainable development of the river system is underlined.

1 INTRODUCTION

In the past two centuries the Rhine River has been heavily regulated for the benefit of flood protection and navigation. The Rhine basin has profited enormously from these efforts: the area is one of the world's most prosperous regions. For the Netherlands and Germany Inland Water Transport (IWT) is a very important mode of transport. More than 50% of goods arriving from overseas in Rotterdam seaport are transported to Germany by ship over the Rhine River. The implemented regulation measures, however, caused severe riverbed degradation by the normalization and narrowing of the river channel and the large reduction of natural flooding area (Havinga and Smits 2000). Moreover, bank protection works and the cultivation of the floodplains for cattle breeding and agriculture reduced the bio-diversity in the river (Smits et al 2000). In the last decades, the Rhine bordering governments wish to improve the situation, i.e. to increase bio-diversity, to return some of the river's original resilience and to maintain or even increase the level of flood protection. At the same time the conditions for inland navigation must improve, taking into account an integrated approach to river management. To this end the Dutch Ministry of Transport, Public Works and Water Management, Directorate General Rijkswaterstaat (RWS) presented the Waal project in the mid 1990-ies (Rijkswaterstaat, 1995). New in the approach since 1995 is that in addition to (essentially traditional) permanent bend improvement measures, recurrent measures like (systematic) dredging and sediment feeding schemes are increasingly playing a role. In this paper recently executed measures within the framework of the Waal project are described and results are evaluated.

Nowadays proper river management also takes into account sustainability of measures, beside their effectiveness. In the Netherlands large river improvement schemes are prepared to maintain the level of flood protection (project Room for the River) and to increase the fairway width and depth (project Sustainable

Copyright © 2006 Taylor & Francis Group plc, London, UK

Fairway Rhine delta). To this end reliable predictions of the (morphologic) behaviour of the river system are required to facilitate the necessary decision-making. In view of the character of this paper (an "engineering case study") an overview is presented of the Waal project. Many detailed studies were carried out as part of this Waal project. In a number of boxes the studies, which are of specific interest for fluvial hydraulics, are presented.

2 WAAL RIVER CHARACTERISTICS

2.1 *General lay-out*

The general layout of the Rhine River in The Netherlands is presented in Figure 1. The river enters The Netherlands from Germany. Slightly downstream it bifurcates into two channels, the Waal River and the Pannerdens Kanaal. The latter channel bifurcates again into the IJssel River and the Lower Rhine-Lek River at the city of Arnhem (not named in Figure 1) near Driel. The Waal River is the most important Rhine branch, carrying about 2/3 of the Rhine discharge entering from Germany. This distributary is also the main fairway between Rotterdam (one of the largest sea ports of the world) and the German hinterland. The IJssel is the smallest of the three distributaries (carries about 1/9 of the Rhine flows), but it is important as fairway to the eastern and northern part of The Netherlands.

The two bifurcations in the Netherlands are called Pannerdense Kop and IJsselkop. They are important river features as they determine the flow to the different distributaries. Much effort has been spent to stabilize these bifurcations with their specific flow and sediment distributions. More information on in particular the Pannerdense Kop is presented later in this paper.

The Waal River (see Figure 1) is characterised by some sharp bends between the Pannerdense Kop and Nijmegen and another one downstream of Tiel (here referred to as the bend St. Andries). The reach between Nijmegen and St. Andries is referred to in this paper as the Middle Waal.

2.2 *Waal river data*

The main characteristics of the Waal River are:

- slope about 10^{-4} (0.1 m/km)
- mean depth: 5 m
- width low water bed: 260 m
- discharges: low discharge $Q_{5\%} = 800\,m^3/s$; mean discharge $Q_{50\%} = 1{,}600\,m^3/s$; design flood discharge $Q_{0.08\%} = 10{,}000\,m^3/s$
- bed material composition: $D_{10} = 0.4$ mm; $D_{50} = 1.5$ mm; $D_{90} = 6$ mm
- yearly sediment load $S_{year} = 500{,}000\,m^3$.

Figure 2 shows a schematised cross-section of the Waal River with the following elements: a low-flow channel which is used as fairway, groynes extending into the flow reducing the width of the river and stabilizing the main channel, a floodplain on both sides of the river and in total several kilometres wide, summer dikes to prevent flooding during low summer floods and a main levee designed to withstand the design flood (with a probability of 8% in 100 years).

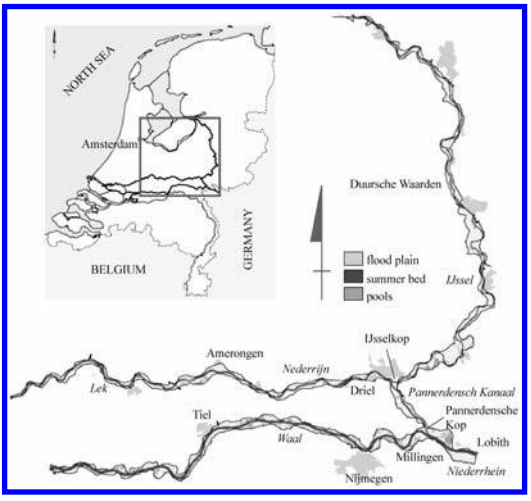


Figure 1. The Rhine River in The Netherlands: two bifurcations, three distributaries of which the Waal River is the most important for inland navigation.

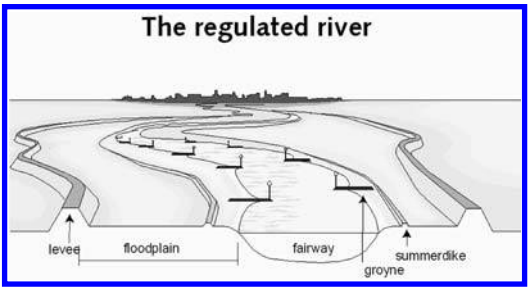


Figure 2. Schematised cross-section of the Waal River.

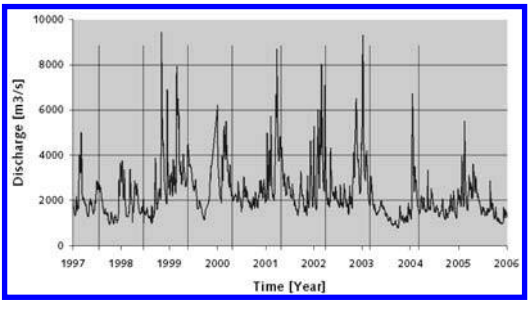


Figure 3. Hydrograph of Waal River over the years 1997–2005.

Figure 3 presents the hydrograph of the Waal River for some recent years. Fairly irregular floods

Copyright © 2006 Taylor & Francis Group plc, London, UK

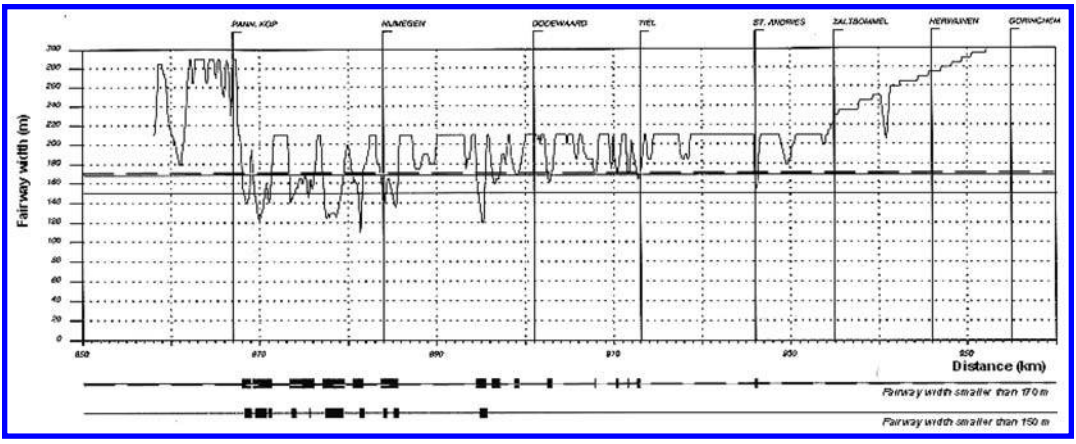


Figure 4. Nautical bottlenecks in the Waal River for 150 and 170 m wide channel, 2.5 m below OLR (1995, flow from left to right).

Table 1. Conflicting interests and different conditions they are posing to the Waal River.

Interest	Preferred geometry	Defences	Preferred hydrological conditions
Safety against flooding	Summer dikes Winter dikes Groynes (to prevent ice jams)	"Fixed" constructions Rock	Guarding maximum design water levels and discharge distributions
Navigation	Summer dikes Deep minor bed (groynes)	"Fixed" constructions Rock	Minimum of 2.8 m water depth: total discharge through minor bed
Agriculture (cattle breeding)	Summer dikes Polder dikes Grass No natural vegetation	"Fixed" constructions	No inundation (at least not in periods that the cattle is in the floodplains)
Ecology	No summer dikes Secondary channels Natural vegetation Islands	No constructions	Frequent inundation

characterize the yearly hydrograph during spring and fall and low-flow periods during the summer with occasional small floods. The summer dikes prevent flooding during summer.

2.3 *Sailing conditions in 1995*

Figure 4 shows the in 1995 present bottle-necks in the Waal River applying the existing fairway dimensions of a navigation channel, which is 150 m wide and 2.5 m deep, referring to the reference of the Agreed Low Water level (OLR in Dutch), which is related to the $Q_{5\%}$ discharge that is exceeded by 95% of the daily discharges. The figure also shows the increase of the number of bottle-necks when the width is increased to 170 m.

2.4 *Conflict of interests*

Several functions of the Rhine branches can be recognized. The primary function of the river is the safe discharge of water, sediment and ice. It is assured by the Dutch system of minor beds and floodplains with elements like summer dikes, winter dikes and groynes. Added secondary functions are navigation, agriculture, sand and gravel mining, recreation and ecology, the latter elements becoming increasingly important in recent years. However, these different functions pose different and often conflicting demands upon the river system (see Table 1). The "traditional" functions, namely safety against flooding, navigation and agriculture go together quite well, considering the nature of required river works. These functions do not pose large policy problems to river administration, apart from optimisation questions (e.g. the Lower Rhine canalisation). However, the ecology function is quite a different matter, which appears to be difficult to integrate into river administration.

Together with the concern to increase ecological values, also emphasis is laid upon using river measures that ensure the resilience of the Rhine river system

Copyright © 2006 Taylor & Francis Group plc, London, UK

(Havinga and Smits 2000). River measures should be designed in such a way that they cause only local effects and do not affect the entire system. This condition turns out to be very decisive in the development of river improvement schemes.

3 RHINE AND WAAL FAIRWAY IMPROVEMENT IN HISTORICAL PERSPECTIVE

3.1 *Introduction*

Since many centuries mankind has been working in and along the Rhine River to improve living conditions. This was done in The Netherlands as well, where the first river regulation works consisted of local dikes for flood protection. Groynes and longitudinal dikes along the riverbed were built, to prevent erosion of the banks and to catch sediment to create farmland in the floodplain. Later also secondary channels were closed and river bends were cut off. These measures were intended to increase and maintain flow velocities in the main channel, thus preventing the formation of sandbanks. In winter periods, these shallows were prone to the development of ice jams at locations where converging flow occurred. These ice jams caused backwaters, which created a serious threat to the dikes sometimes leading, to overflow and breaches (Figure 5).

The river regulation triggered higher velocities in the low water bed, which induced larger water depths and lower slopes, resulting in lower bed levels. Because of this it turned out that these measures had also been beneficial for navigation, because they had deepened the main channel. In order to optimise the navigation channel so-called "width normalisations" were carried out. Width normalisation means that the low water bed is limited to one main channel with a constant (normal) width. Groynes were constructed at regular intervals, which confined the low water bed into a narrower channel and kept the water flow away from the erodible bank. In the 19th and 20th centuries, after many uncoordinated regulations, two large-scale width normalisations were carried out in the Waal River (Figure 6). Until recently the agreed fairway dimensions of the Waal River are 150 m wide and 2.5 m during OLR. If this water depth was not met under these conditions, Public Works Department would carry out local dredging.

3.2 *Rhine bifurcations*

In addition to the regulation works carried out in the different distributaries of the Rhine River, in the past there was also a lot of interest and works carried out in relation to the flow distribution over the three branches. Box 1 provides some details on the bifurcations, the works carried out in the past, and the studies carried



Figure 5. Dike breach by ice dam.

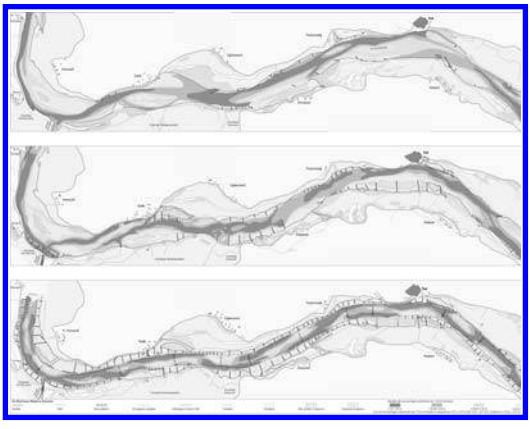


Figure 6. Normalisation of Waal River near Tiel in the 19th century (river planforms from 1831–1835, 1872–1873 and 1888–1989). Note the increasing number of groynes and the decrease of the width of the Waal River.

out recently to better understand the functioning of these bifucations. In principle the distribution could be changed as well, to better serve the different interests, but this can only be done when there is a sufficient undertanding of the consequences. Hence at present many studies are carried out to obtain such a better insight. These include field studies and numerical models with different levels of complexity regarding graded sediment, sorting, and roughness and bed forms. For more details see Sloff et al.(2003).

3.3 *20th century proposals for Waal bend cut-offs*

Between 1960 and 1980, many plans have been devised to cut off the last remaining major bends in the Waal River near Nijmegen and near St. Andries (see Figure 1 and Figure B2 below). Many studies were carried out, both to optimise the layout of the cut-offs, but also the impact of the cut-offs on the flow distribution at Pannerdense Kop bifurcation. Cutting off a bend will lower the upstream stages and this will cause

Copyright © 2006 Taylor & Francis Group plc, London, UK

Box 1. History of the two Rhine bifurcations in The Netherlands

The two bifurcations of the Rhine in the Netherlands are Pannerdense Kop and IJsselkop (see Figure 1). These bifurcations are important river features as they determine the flow to the different distributaries. In the past much effort has been spent to stabilize these bifurcations and the flow and sediment distributions, and many studies have been carried out to better understand their functioning, in the field, in scale models and with mathematical models.

The distribution of Rhine water over the different Dutch Rhine branches (today at the village of Pannerden and the city of Arnhem) caused many problems in the past. Especially the IJssel River showed a strong tendency to aggrade, causing flooding along this river and along the Waal River. The shape of the bifurcations contributed a lot to the unfavourable discharge distributions (see Figure B1a).

Also the waterborne transport to the north suffered greatly from the poor water conveyance of the Nederrijn and IJssel Rivers. In the 17th century there was a lot of (commercial) competition between cities and provinces situated along the Waal en IJssel River. So, when for the military defense of the provinces of Holland (the Spanish armies could cross the northern rivers by foot) a channel was dug between the Nederrijn River and the upstream part of the Waal River, the cities along the Waal River for a number of years obstructed the connection with the Nederrijn River. Finally, after many meetings it was agreed to make an open waterway between the two rivers (Pannerdensch Kanaal), see also Van der Ven, 1976. The shortcut moved the bifurcation further downstream (Figure B1b).

Though this considerably improved the conveyance of the Nederrijn, problems of aggradation and floodings persisted. It took another 75 years before plans were adopted to improve the mouth of the Pannerdens Kanaal. To enable the building of a new bifurcation dam, use was made of a shoal that appeared in front of the bifurcation after a winter with a lot of ice. Also, a new river mouth of the IJssel River had been built (by digging a new canal through the Pley foreland). From the end of the 18th century the discharge distribution had been stabilized, which gave start to the extensive general river training of the Dutch Rhine branches. Leading for the design of river works became the politically agreed waterdivision (1745), according to which the Waal River would convey 2/3^{d} of the total Rhine discharge, and the IJssel River 1/9th. Since then these ratio's have not been changed, so measures for flood defense and navigation have been designed accordingly.

Presently there is a renewed interest in the functioning of the bifurcations. The construction of three barrages in the Nederrijn-Lek and other developments might have had an impact on flow and discharge distribution. Two scale models of the bifurcations were operated in the 1960-ies and 1970-ies. The model study of the IJsselkop was carried out with uniform sediment, but the later model for the Pannerdense Kop was done with graded sediment. Some information on the Pannerdense Kop model is provided in Sloff et al (2003). Recently also attempts have been made to model the Pannerdense Kop with numerical models as well. In the 1980-ies it was found that a 2D

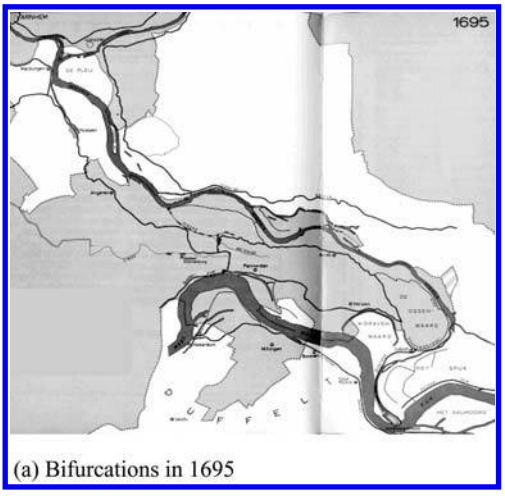


Figure B1. Changes in the two main bifurcations of the Rhine River in The Netherlands.

(depth averaged) model with uniform sediment and a spatially constant Chezy roughness (for a dominant Rhine discharge of 2,400 m^3/s) resulted in a fair reproduction of bed topography and the flow and sediment distribution at the bifurcation.

More recent simulations with Delft3D graded in its depth-averaged mode, but applying recent field data on the bed composition of the bifurcation resulted in poorer results. This model allows for longitudinal and lateral sorting and was expected to yield even better results. Only by including a spatially varying Chezy roughness coefficient, better simulations could be found (Sloff et al, 2003). This suggests that there is a strong interaction between bed-composition patterns, roughness and bed topography. A topic urgently needing more study.

Copyright © 2006 Taylor & Francis Group plc, London, UK

Box 2. Scale model M1278 Waal bend Nijmegen – in retrospect a turning point

In the 1980s it was planned to cut off the two bends upstream of Nijmegen (see Figure B2). The purpose of this measure was to eliminate a number of sharp bends downstream of the Pannerdense Kop bifurcation, and in particular to increase the bend radius of the bend near Nijmegen. This would have had a very beneficial effect on the available draught (=depth available for ships). Although finally these cut-offs were not carried out, in retrospect this model study can be considered to be a turning point in the understanding of 2D river morphology and the use of models in The Netherlands.

To study this possible measure a physical model was constructed which was characterized by:

- distortion 2.5 (horizontal scale 100, vertical scale 40) in line with the roughness condition;
- sand as bed material (particle size scale 4);
- slope about 5 times larger than required when considering only the distortion;
- deviation from the Froude condition (Froude scale 0.4, Froude number model 0.4);
- ideal velocity scale (implying that the Shields number was the same in model and prototype);
- bed load dominant.

For more details on the scaling procedure used see Struiksma (1987). Because the client (RWS = Public Works Department, The Netherlands) was not satisfied with the results of the calibration, WL/Delft Hydraulics was requested to do an investigation into scale effects in mobile bed river models. In the resulting report it is concluded for the first time that in a distorted model (common for mobile bed models) the beginning of a bend is always subject to serious scale effects.

In the same period and by the same researcher and others (as part of a larger group united in the so-called TOW Rivers – long lasting research funded by RWS) extensive research was carried out on

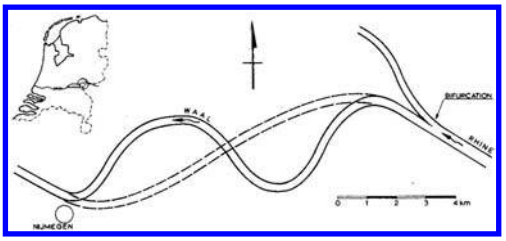


Figure B2. Proposed cut-offs Waal bends near Nijmegen.

morphological phenomena in bends, which culminated in the prize-winning paper by Struiksma et al (1985), in which for the first time the importance of redistribution processes in the beginning of bends was explained and quantified. Using these results Struiksma (1987) managed to fully understand and explain the substantial scale effects in the simulation of bends in mobile bed models with dominant bed load. Based on the understanding on phenomena in bends WL/Delft Hydraulics developed 2D depth averaged morphological models with spiral flow added to arrive at a quasi 3D flow pattern (Struiksma, 1985), which nowadays is included in the Delft3D modelling suite.

In retrospect the study in scale effects in the mobile models turned out to be the transition from the exclusive use of the scale models for 2D morphological problems to the present conditions where most of these studies are done with mathematical models. In these models it is nowadays also possible to consider suspended sediment and the effect of gradation and sorting. Interestingly a similar model was used recently to study scale effects in a scale model with dominant suspended load (Haque et al, 2006), which is a good indication of the changing role of scale and mathematical models in investigations for river engineering projects.

that more flow will enter the Waal River. Eventually none of these plans have been executed, because of an increased awareness of ecological interests and the bad economic situation in the late nineteen-seventies. Box 2 provides more information on this issue.

3.4 *Necessary increased use of IWT potentials*

When it became clear that the anticipated bend cut-off could no longer play part in regulation schemes, bend improvement measures were designed. In 1982 the removal of a bridge pier centred in the fairway of the river bend at Nijmegen gave a start to a general improvement of the Waal River. The admission in 1986 (Anonymous, 1988) of 6-barge push-tows underlined the necessity to increase the fairway dimensions. This triggered a study which was started in the late 1980-ies and which resulted in the so-called Waal project, which is the topic of the remaining part of this paper.

4 OVERVIEW OF RECENT IMPROVEMENTS: THE WAAL PROJECT

In 1994 RWS proposed up the so-called Waal programme, a master plan that combined several different projects to improve navigation conditions on the Waal River (bend improvement, increased fairway

Copyright © 2006 Taylor & Francis Group plc, London, UK

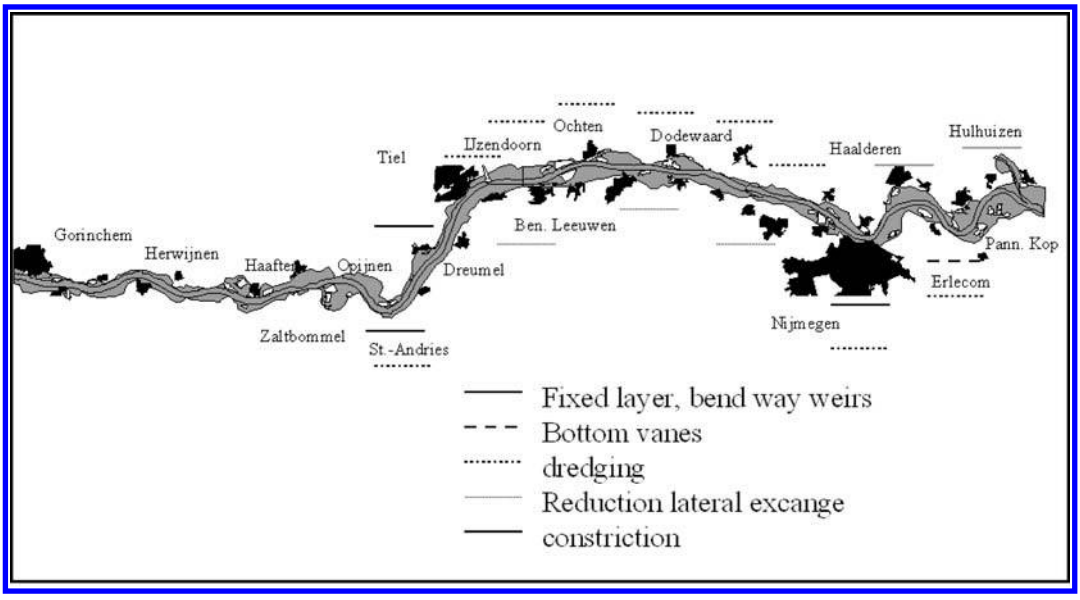


Figure 7. Overview of measures proposed as part of the Waal Project (refugee harbours not indicated).

dimensions, refugee harbours and extended radar coverage). In a visionary report the possibilities to improve the conditions for IWT on the Dutch Waal River were evaluated (Rijkswaterstaat, 1993). Now it was decided to upgrade the fairway substantially. It was also decided to try to stop the ongoing degradation of the bed level, caused by river regulation measures (dikes, groynes, bend cutoffs) that inflicted smaller slopes and larger depth's. This scouring of the bed will 'autonomously' go on for at least another 100 years (Baur, 2003).

The objectives of the Waal programme can be summarized as follows:

- Fairway dimensions of 170 m × 2,80 m available at OLR starting in the year 2004.
- Only apply measures, which do not accelerate the autonomous degradation of the river bed, which in the 1990-ies and also currently amounts to about one cm/year.
- Obtain surplus values for the river's ecosystem by integrating floodplain rehabilitation plans.

Furthermore the different technical solutions had to respect a number of boundary conditions regarding the discharge distributions at bifurcations, besides low water levels and peak flow levels in order to safeguard levels of flood protection and navigation.

Evaluation factors comprised effectiveness (width and depth increase), costs, backwater effects and ecological impact. Any distant response (large scale system effects in place and time) should be prevented.

Evaluation of the solutions led to the application of local river measures (Havinga 1996). The time horizon of the Waal programme was 2010; a study of the conditions beyond 2010 was only recently started (see Chapter 7).

Quite essential in the approach taken is that the engineering measures proposed are *a combination of permanent structures and recurrent measures*. Moreover, nautical bottlenecks that cannot be mitigated by engineering measures are tackled with traffic measures: regulation and traffic control. Also a number of so-called refugee harbours (mutual sailing distance 20 km) have been constructed.

In the original Waal project plan the following technical measures were envisaged (see also Figure 7):

(a) *Permanent measures* (from upstream to downstream)
- Bottom vanes or bendway weirs in the bends upstream of Nijmegen.
- For the reach between Nijmegen and St Andries stabilization of discharge ratio between low water bed and floodplain during peak flows plus width constriction.
- Bottom vanes or bendway weirs in the bend of St. Andries.

(b) *Recurrent measures*
- Dredging in the bend of Nijmegen (fixed layer already constructed in 1986).
- Large-scale dredging in the Middle Waal.
- Dredging in the bend of Opijnen.

Copyright © 2006 Taylor & Francis Group plc, London, UK

In the end certain measures have not (yet) been carried out for different reasons: expected low effectiveness and reduced confidence in a proposed solution (bottom vanes), postponement (stabilizing discharge distribution between low water bed and floodplain plus local width constriction) and awaiting possible integration with measures within the so-called Room for the River project. Upstream of Nijmegen only in the bend Erlecom bendway weirs were placed; the improvement method for the other bends upstream of Nijmegen has still to be decided upon. At present additional dredging is required in all remaining bottlenecks.

5 PERMANENT BEND IMPROVEMENTS

5.1 *General*

In 1990 new research on improvement of river bends was initiated, leaving aside the cut-off option for ecological and landscape reasons and for the possible impact of bend cut-offs on the discharge distribution. This implied that apart from dredging the fairway width in bends could only be increased by measures limited to the low water bed, like fixed layers, bendway weirs (submerged groynes) and bottom vanes (Rijkswaterstaat, 1991).

By now much experience has been gained on measures in bends: fixed layers (Figure 8) were applied in the bends Nijmegen (1985) and St.-Andries (1998), and bendway weirs (Figure 9) were applied in the bend Erlecom (1996).

A fixed layer in the outer bend consists of a partly filled up outer bend with sand and gravel, protected by a layer of riprap. This measure raises the bed level, which initially decreases the overall flow area. The rough surface of the stones increases the hydraulic roughness in the outer bend. Both effects cause water velocities and sediment transport in the inner bend to increase, degrading the riverbed and subsequently increasing the overall flow area again.

Bendway weirs in the outer bend are in fact submerged groynes, constructed with sand, geo-textile and riprap, reducing the spiral flow near the riverbed. They show a slight inclination upstream in order to decrease the spiral flow even further and to direct the sediment transport near the bed to the outer bend. In this way the bed in the outer bend is aggraded and the bed in the inner bend is degraded, yielding a larger fairway width. The resistance to flow of the bendway weirs also redirects the flow to the inner bend, which adds to the eroding effect.

5.2 *Investigations carried out during design phase*

In the design phase the hydraulic and morphological effects of the bend measures were investigated

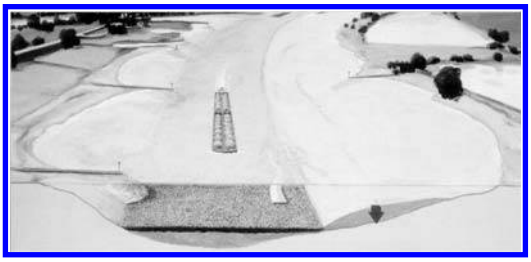


Figure 8. Fixed layer (C. Nuyten).



Figure 9. Bendway weirs (C. Nuyten).

in various ways by WL|Delft Hydraulics. The fixed layer at Nijmegen was designed between 1980 and 1985 using a physical scale model and a numerical 2-D morphological model (SEDIBO, a predecessor of Delft3D). The second fixed layer at St.-Andries was designed using only a numerical morphological 2-D model (RIVCOM, another predecessor of Delft3D), flagging the experience obtained and the increased confidence in numerical models. The bendway weirs have been investigated using a physical scale model and a 2-D morphological model (RIVCOM).

The models have always been used in a comparative way. First a reference situation was calibrated, using prototype data and (if available) scale model data. Cross-sectional velocities and depth contours are the main calibration parameters. Next the new bend configuration is implemented in the model and the relative improvement is measured or simulated. This is interpreted towards improved sailing conditions. The simulated results were so promising that the proposed measures were implemented.

5.3 *Construction*

The fixed layer of St. Andries was built using a rock coverage, consisting of stones with specific specifications, to avoid the use of a separate filter layer. During construction a sandpit was maintained upstream, to avoid immediate coverage of the fixed layer, which would endanger a correct measurement (by multibeam soundings) of the top level of this layer. To obtain

Copyright © 2006 Taylor & Francis Group plc, London, UK

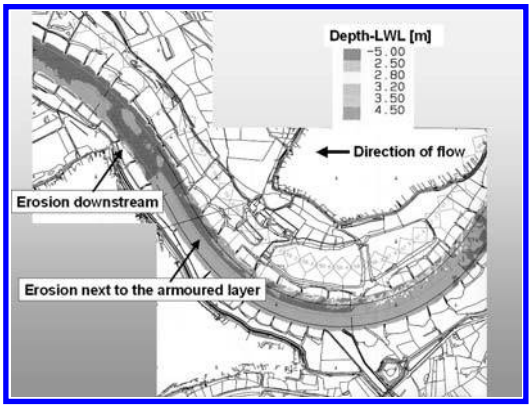


Figure 10. Bed topography in bend St.-Andries after construction of fixed layer (note deep scour hole downstream of the fixed layer and the shoal in the inner bend).

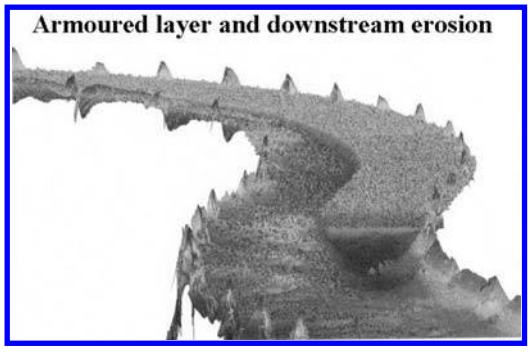


Figure 11. 3D image of fixed layer in bend St.-Andries on the basis of multi-beam soundings (looking upstream).

reliable sounding data, for the first time a multi-beam sounding system was used extensively. This instrument together with GIS techniques offered the possibility to monitor closely the dumping process of sand, gravel and stone. Also the morphologic changes could be followed in detail. Figure 10 shows the final bed topography and Figure 11 shows a 3-D view of the lower end of the construction in the bend St.-Andries.

5.4 *Effect of measures*

In the bend of Nijmegen the increase of the fairway width amounts to about 50 m (with an available depth of 2,50 m at $Q_{5\%}$), while the applied 2-D morphological model had predicted 35 m. The width increase in the bend of St. Andries is about 45 m, while 35 m had been predicted. The fairway width increase in the bend near Erlecom (bendway weirs) appears to be 25 m, which corresponds to what had been predicted. Furthermore it can be noted that the width

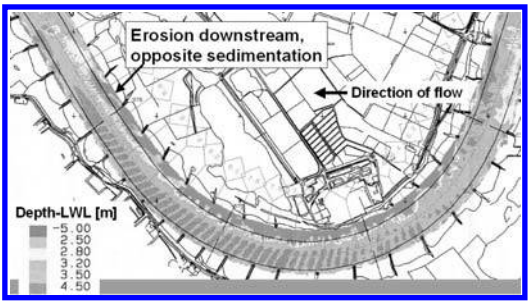


Figure 12. Bendway weirs in bend Erlecom.

changes occurred rather quickly: about 80% of the cross-sectional changes took place within 2 years.

Compared to the impact of a fixed layer in the outer bend the impact of the bendway weirs (in bend near Erlecom) on the navigation width is less, as a consequence the downstream effects are also less (see Figure 12 showing an erosion hole of approximately 2 m downstream of the bendway weirs, and no severe shoaling along the inner bend).

All computations used for the design of fixed layers show severe erosion immediately downstream of the fixed layer and shoaling in the inner bend on the opposite side. However, the prototype data show only about half of the predicted erosion and shoaling (see the Figures 10 and 11). Still this creates a problem and a special study was carried out to understand the cause of the shoaling and to investigate possible mitigating measures (see Box 3).

5.5 *Far field impact of bend measures*

The construction of fixed layers or bendway weirs also has an impact on the bed degradation on a larger spatial and time scale. Figure 13 shows the (moving averaged) bed level development (longitudinal profile) of the Waal River using yearly soundings (cross-sections every 125 m) for the past 20-year period. The three lines refer to the years 1979, 1989 and 1999. The autonomous bed level degradation of about 0.5 m in 20 years clearly can be observed. The armoured layer of Nijmegen, constructed in 1985 locally fixes the bed level, and it causes degradation, which travels downstream. No upstream effect can be deducted. Ignoring the autonomous degradation the conclusion can be drawn that the erosion pit travels downstream with an average rate of 1,5 km/year, which equals the theoretical celerity of a disturbance in the bed (c_b).

Compared to the impact of a fixed layer in the outer bend the impact of bendway weirs on navigation width is less. As a consequence, the downstream impacts are also less. The main concern with fixed layers and bendway weirs is the fact that they create hard points in the river, which with continuing degradation will become a bottleneck themselves in due time.

Copyright © 2006 Taylor & Francis Group plc, London, UK

Box 3. Fixed layer in outer bend near St. Andries and its near-field morphological effect

In the bend near St. Andries a fixed layer in the outer bend was implemented in the year 1998. The purpose of this fixed layer was to fill up the outer bend, which subsequently would lead to erosion of the pronounced point bar in the inner bend. This indeed did occur, resulting in improved sailing conditions in this bend. However, after a few years also some negative morphological impacts were observed. Firstly the unprotected inner bend eroded seriously, endangering the stability of the fixed layer in lateral direction. Secondly downstream of the fixed layer an erosion pit (depth approx. 2,5 m) occurred, threatening the stability of the downstream end of the fixed layer. Finally a shoal developed at the same location but along the inner bend (with a height approx. 1 m). This shoal at St.-Andries has regularly to be removed by dredging. Figure 10 shows an image of the riverbed in the bends at St. Andries, made by multi-beam soundings. This map shows the downstream effects clearly. A study was carried out (van Reen, 2000) to understand the cause of these morphological changes and to propose remedial measures.

The key for understanding these morphological changes is given in Figure B3.1. The dense coverage of sounding data also enabled a good view of the sediment transport over the fixed layer. Figure B3.1 gives an impression of the sediment coverage of this fixed layer, using standard deviations of measured depths. The larger values of the standard deviation indicate uncovered rock, while the smaller values correspond to a fixed layer where the area between the stones is filled in by sediment, which is transported over the fixed layer. From the figure it can be deduced that the sediment on the fixed layer is swept towards the inner bend. This is explained by the effect of the spiral flow, which – because of the fixed layer being horizontal – is not compensated by the lateral slope of the bed, as is the case in alluvial bends. The direction of the near bed flow clearly can be deducted from the pattern. The locations with sediment transport were qualitatively checked using a bed load transport sampler (Wilbers, 2000).

The consequence of the sediment transport pattern, as shown in Figure B3.1, was studied by van Reen (2000) and later by Sloff et al (2006). For axi-symmetric conditions all sediment, which in the reach upstream of the bend is transported over the full width, now is transported in the narrow alluvial strip next to the fixed layer. Applying the improved Lane's balance (Klaassen, 1995) it could be shown that for the conditions in the Waal River near St. Andries the narrow alluvial reach will respond with an increased depth. This explains the deep trough next to the fixed layer, which can be observed in the Figures 10 and 11. Van Reen (2000) developed an analytical model to determine the depth next to such fixed layers as a function of the lateral extent and relative level of the fixed layer. A similar model was later verified by Sloff et al (2006) using field and flume data.

Also the erosion downstream of the fixed layer and the shoaling at the same location but in the inner bend could be explained by the shift of the sediment transport towards the inner bend. Where the fixed layer ends, the reach along the outer bend has a large sediment transport capacity but no sediment is supplied from upstream. Hence this sediment is picked up from the riverbed and causes the serious erosion. The flow in the inner bend is attracted by this deeper part and this causes re-distribution of the flow

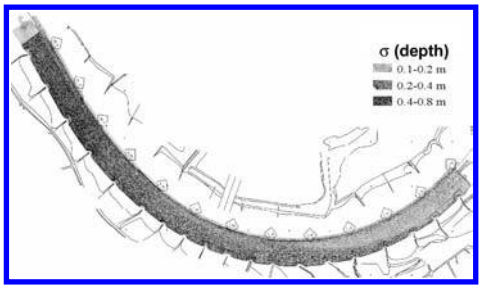


Figure B3.1 Standard deviation (σ) of bed levels of the fixed layer, showing the sediment coverage (large standard deviation = no sediment).

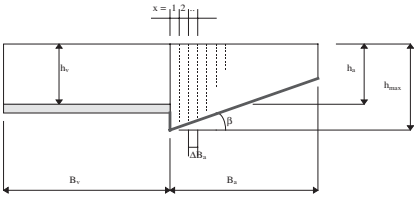


Figure B3.2 Schematised cross-section for axisymmetric conditions with fixed layer in outer bend (van Reen, 2000).

downstream of the termination of the fixed layer. As a consequence the transport capacity along the inner bend reduces and sand is deposited forming a shoal. The re-distribution of flow and sediment is governed by the same process as is dominant in the beginning of a bend. Also the same longitudinal scales (λ_w, λ_s, L_p and L_D), which were introduced by Struiksma et al (1985) are relevant here. Van Reen (2000) applied Delft3D in the depth averaged and quasi-3D mode (with spiral flow added after the flow pattern has been simulated) to show that indeed the re-distribution of flow and sediment is causing the morphological phenomena observed.

In a further step in his study Van Reen (2000) explored possibilities to prevent in particular the shoaling in the inner bend downstream of where the fixed layer terminates. It was shown that one possibility is to extend the fixed layer to the point bar in the next opposite bend downstream. Here the sediment distribution downstream of the fixed layer is in correspondence with the sediment distribution in an alluvial bend. By selecting the termination point of the fixed layer in an intelligent way it is even possible to improve the sailing conditions in this downstream bend as well. It should be mentioned here that initially it was indeed planned to extend the fixed layer in downstream direction, but budgetary problems forced the fixed layer to terminate earlier.

Another option is to try to force the sediment transported in the inner bend to the outer bend. This could be done by bottom vanes, but these may affect the navigability, as they extend into the flow. It could be considered to make the upper part of the bottom vanes flexible, but until now no acceptable solutions have been found. As an alternative the possibility of applying vortex excluders is presently being studied.

Copyright © 2006 Taylor & Francis Group plc, London, UK

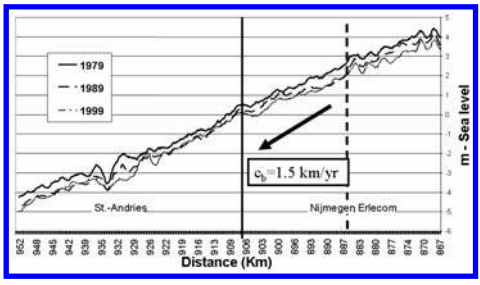


Figure 13. Bed degradation of the Waal River in the period 1979–1999 with an erosion of approximately 0.5 m.

6 DREDGING IN THE MIDDLE WAAL RIVER

6.1 *Introduction*

As indicated in Chapter 4 on the Waal programme dredging has been considered, but as a tool that should be used in addition to other constructive measures. Only in the straightened Middle Waal Nijmegen – Tiel – St.-Andries (see Figure 7) systematic dredging has been developed as an alternative for additional normalisation works.

To maintain a fairway for navigation in alluvial rivers dredging might be needed. In principle dredging operations should be planned and executed considering maximal flexibility, because the moment of dredging is not known far in advance. Actual and historical discharges determine bed levels and bedforms, which may hamper navigation. Some forecasting can be done, using the trend of the actual discharges, mean hydrographs and forecasting techniques for water discharge and morphology (see also Section 6.5). As the limitations of the fairway dimensions are of a dynamic nature, also dredging must be dynamic. Dynamic bed level variations will always be present in a river, even in the case that the low water bed width is restricted to the required fairway width. Moreover, every geometrical discontinuity – both in the channel as well as in the floodplain – in principle will generate erosion or sedimentation waves, which will propagate through the river system (Van Vuren 2005). To complicate things even more, also the relation between hydraulic conditions and bedforms is not unique, leading to surprises concerning the Least Available Depth (LAD's) in a reach.

For river management dredging is a measure, which by its nature is recurrent, and that has to be weighed against more structural measures, like normalisation (building groynes, longitudinal dams) and bend regulation measures. Modifying the dimensions of existing groynes and local summer dikes influences the riverbed morphology and consequently the required amounts to be dredged. Dredging can be a good option in situations where the execution of several river training measures is not certain, where the impact of (e.g. Room for the River) measures are not well known, or where funding is too limited to allow for expensive structural measures. However, once the choice for dredging as a systematic recurrent measure has been made, long term future funding is required which may be a problem. A year with reduced budget means a year with hampered navigation. This may have large consequences if transport companies turn to other modes of transport (truck, rail) and do not return to IWT as their preferred mode of transport.

6.2 *Pilot projects*

To gain more experience on dredging on the Middle Waal, several dredging projects have been executed in the reach between Nijmegen and Zaltbommel (see Figure 7) in the period 1998–2002. The aim of these projects was twofold (Groen, 2002 and 2004): (i) maintaining a fairway with dimensions of (at least) 2,5 m depth and 150 m wide at OLR and (ii) gathering experience with systematic dredging as a means to enlarge the fairway. With this in mind between 1998 and 2000 in total four reaches of 2 km were dredged to the standard of 150 m by 2.5 m, and some small reaches slightly deeper (see also Box 4). The development of the bed topography of the river was monitored to identify the response of the river to dredging, both during medium and low flows and during a peak flow. To determine changes in time frequent multi-beam soundings were carried out. The data were analysed in different ways.

Firstly the data were entered into a GIS package (ArcView) and subsequently analysed. This was done at two levels of detail (see the study by Schepman (2000) and Box 4). Locally the re-emergence of shoals was studied and the possible cause identified. Secondly the reduction of the total dredged quantities was studied and also this was tested versus the assumed relaxation behaviour (see also Box 5). These analyses, in combination with additional studies allowed deriving expressions, which predict the development of a dredged reach over time. After a major flood the effect of dredging in the previous period is almost lost and the river is back to its "natural" state before dredging. This implies that dredging is required after every major flood.

The second way of analysing the monitoring results was to study the Least Available Depth (LAD) on the Waal River, which is daily established by measuring the available depth at a number of locations. This is a very relevant parameter as the LAD's are used as a basis for the decision how deep ships will be loaded and it is moreover the basis for compensating the shipping companies when not sufficient draught would be available. For the results of this study see Section 6.7.

It should be noted that in addition to the pilot projects described above also some other pilotprojects

Copyright © 2006 Taylor & Francis Group plc, London, UK

Box 4. Pilot Project Morphology

One of the pilot projects carried out in the preparatory phase of the large-scale dredging of the Middle Waal River (see §6.2) was the Pilot Project Morphology. The aim of the project was to better understand the morphology of the Waal River without and with dredging. Regarding the morphology without dredging, the pilot project was in particular meant to identify the cause of shoals in the Middle Waal and their occurrence and behaviour under variable flow conditions. For the conditions with dredging the interest was how quickly shoals would appear again and which morphological features would be dominant in this respect. This is relevant for the development of a prediction method for how the river responds to dredging. Such a prediction method can help in the decision on where and how much has to be dredged. Over-deepening by dredging can be considered as well.

The Pilot Project covered a period of about two years, from March 1998 to May 2000. During this period two times capital dredging was carried out at in four locations of 2 km in the Middle Waal River (see figure B4.1).

The dredging aimed at lowering the bed level in the whole reach down to OLR – 2.8 m at most places, and at one location down to OLR – 3.2 m. The reaches in which dredging was carried out were monitored by means of multi-beams soundings, resulting in a very dense measuring grid. During the period of slightly more than 2 years, two floods occurred (see Figure B4.2) and in total 23 soundings were carried out (about one sounding every month). These measurements were subsequently entered into ArcView and a number of calculations were carried out in the ArcView environment. To get a better insight into the bed topography of the Middle Waal River without dredging also a number of JDP's (yearly cross-sectional soundings) of 12 previous years were used. The JDP's are single beam soundings at a mutual distance of 125 m, giving only a limited coverage of the riverbed. The effect of dunes, which can be reduced in ArcView by taking a centred average, cannot be eliminated from JDP's. The data collected during the Pilot Project Morphology were elaborated by Schepman (2000). Some results of this study are presented in this box.

Some basic assumptions made during the analysis of the soundings are:

- the bed topography of the Middle Waal River can be divided in a forced bed topography and free moving features,
- the forced bed topography which is hardly varying in time and is determined by the planform of the river,
- the morphological features which can move freely are superimposed on the forced bed topography,
- after dredging the bed topography of the river will return to its natural shape with some delay in time,
- the recovery process is a combination of a pure relaxation and translation.

The major conclusions from the study of Schepman (2000), apart from the observation that this approach using a combination of multi-beam soundings with ArcView is very fruitful, are:

- the forced bed topography is determined by the planform of the river and consists of point bars in combination with the so-called "groyne flames", features linked to the position of the groynes along the low-flow channel,
- the free features are a combination of bedforms and of deposits in the low-water channel, which are generated during periods when the floodplain is flooded and non-uniformity of the floodplains causes deposits (so "forced" by the floodplain geometry), which start to behave as free features once the flow is below bankfull,
- there is a clear difference between the height of the free features in the Northern half of the river (larger) and in the Southern half (smaller), which is most probably caused by navigation (having more draught when sailing upstream),
- the recovery of dredged reaches is faster where much dredging has been carried out: the deeper the dredged reach, the quicker the recovery,
- recovery is fastest in the beginning of point bars (Box 5),
- during low flow conditions the recovery is limited, whereas major recovery takes place during floods,
- the effect of dredging after the previous flood is still noticeable after the next flood,
- in addition to relaxation also translation plays a significant role and has to be taken into account when predicting the response of the river to dredging operations.

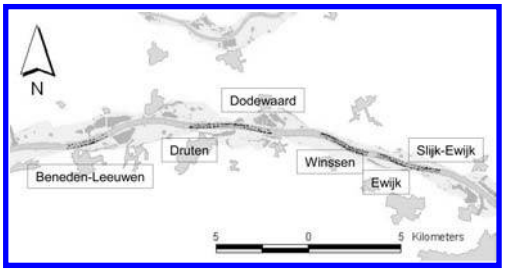


Figure B4.1 Dredging locations Pilot Project Morphology.

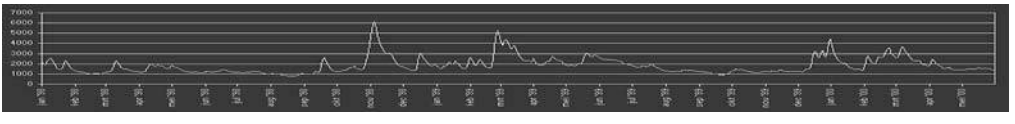


Figure B4.2 Discharge variation during Pilot Project Morphology.

Copyright © 2006 Taylor & Francis Group plc, London, UK

Box 5. Prediction of the recovery rate of dredging operations using numerical models

A dredging (and dumping) operation can be considered as a temporary disturbance of the regular cross-section, after which in time the cross-section gradually restores to the undisturbed situation. This process is governed by a one-dimensional propagation process, causing a gradual filling of dredged holes from upstream, and by a two-dimensional process related to transverse flow and transport effects in a (bend) cross-section. If morphological development on the scale of hundred of meters to kilometres is considered the filling process can be approached by an elliptic function:

$$z(t) = z^{+}(0)e^{-t/T_s} + z(t=\infty)\left[1 - e^{-t/T_s}\right]$$

in which t = time, T_s = time-scale of adaptation, z = spatially averaged bed level of a section, z(t = ∞) = long term bed level at low-flow conditions, and z + (0) = average bed level after dredging. Note that to compute the representative bed level additional terms have to be added to include the spatial variations (standard deviation), e.g. by dunes in a section.

To assess the time evolution of dredged holes and fills in the Waal River, a 2-D, depth-averaged morphological model was applied that is capable of reproducing these processes. The aim of these calculations has been to find approximate time-scales for filling of the dredged holes at subsequent sections along the river. As the filling process is highly dependent on the sediment-transport rate, and hence on the expected discharge, these calculations have been carried out for a range of discharges and dredging operations (primarily dredging of point bars).

The 2D model has been calibrated to reproduce the time-average alternately pool and point-bar pattern that is characteristic for the meandering Waal River, and to reproduce the time-scale of propagation of large bed forms which is about 1 km/year. The model has a length of about 84 km, a grid size of about 50 m (length) times 20 m (width), i.e.14 cells in transverse direction, covering only the main channel between the groynes. In the model D_{50} = ca. 1 mm has been used which slightly differs from the average river sediment. Transport rates can be approximated well using the Engelund and Hansen transport

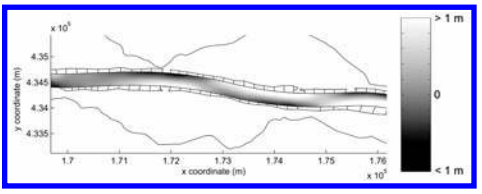


Figure B5.1 2D bed topography of the straightened Middle Waal River.

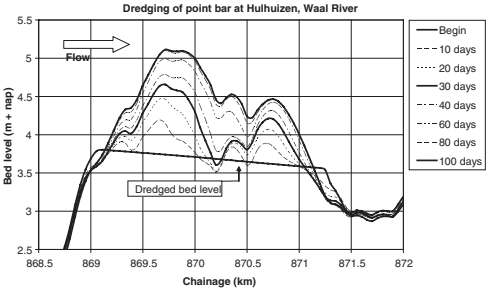


Figure B5.2 Simulated bed levels changes of a point bar after dredging.

formula (1967) for total load. Spiral flow and transverse-slope effects, that essentially determine 2-D effects in the river bends, are computed using the approach of Talmon et al. (1995).

Above figures show some results of the model.

By subtracting the simulated bed levels for the reference situation (without dredging) from the simulated results with dredging, it is possible to construct the elliptic filling process, and derive the time scale T_s. The value of T_s is in the order of 100 days (depending on discharge, dredging depth, section length, etc.).

In many dredging operations the depth-gain is reached by removal of dunes, which gradually grow up again in time. The growth of dunes does not follow from the 2-D simulation, but is derived from relations from observed dune development. The empirically derived development (growth) of dunes is discharge dependent. Its effect on available depths should be superimposed on the effect from the 2D model simulations.

were carried out e.g. to study different dredging methods.

6.3 *Dredging strategy*

In view of the experience gained during the pilot dredging it was decided to differentiate between two main types of dredging: (i) profile dredging and (ii) local spot dredging. When *profile dredging* is applied the exact fairway dimensions are dredged, taking into account 0.4 m extra dredging when OLR–2.8 m is used as reference. Profile dredging in terms of the volume to be dredged can easily be in the order of the yearly sediment transport in the Waal (see Section 2.2).

Copyright © 2006 Taylor & Francis Group plc, London, UK

Profile dredging is done at the beginning of a dredging programme and usually is required after a major flood (in principle every year, although sometimes it is not needed when the flood was low). After having established the fairway, its dimensions are maintained by *local spot dredging*, i.e. the removal of local shoals and dunes. Local spot dredging can be several thousands of cubic meters per year per spot.

6.4 *Dredging and dumping spoils*

In the past ten years various methods of dredging and dumping of the dredged material were tested on the Waal River. In advance it should be noted that in order to slow down the autonomous bed degradation, all the dredged material is dumped in the river again.

Where to dredge is usually easily determined on the basis of soundings and extrapolations of water level and bed level trends. In the dredging/dumping procedure finding a suitable place to dump the dredged material is a much larger problem. At first glance the deeper spots in the river seem logic dumping sites. However, these spots are maintained deep by the river (hydraulics) itself, and as a consequence the dumped sediment eventually will be transported further downstream and settled in locations with low flow velocities, and may increase existing shoals. Spoil dumped in outer bends appeared to stay there for more than 50% until the peak flow occurred, so depending on the hydrograph, dumping in outer bends can be considered an option for temporary storage of dredged material (Groen, 2002). The same holds for dumping in the erosion pit immediately downstream of a fixed layer. If bendway weirs have been applied, dumping in the space between them can be considered as well, as they also temporarily store the sediment.

Dumping in groyne fields is a very attractive method. Here the location of dumping (close to the low water bed or higher on the banks) defines the rate at which sediment will be supplied back to the main channel. In practice application of this method may be hampered by legislation regarding conditions to the possible contamination of the sediments (in particular regarding the receiving sediment in the groyne fields as the dredged material is of good quality). It also requires study of the local flow patterns during peak flows to estimate the supply rate. Nevertheless dumping in groyne fields is considered a sustainable sediment management solution.

To slow down the ongoing bed degradation the dredged material actually is dumped upstream of the dredging location. In this way the extra sediment supply increases the bed slope. Logically this might mean that the volumes to be dredged are increasing. This upstream dumping is subject to criticism and after investigations this procedure may be changed into dumping downstream.

6.5 *Decision support system*

For the determination of when and where to dredge a Decision Support System was developed. More details on the DSS Dredging on the Waal are given in Box 6 and in Douben & Werners (2000). At present the DSS is mainly used for data storage and presentation. This is due to the fact that until now the fairway is still maintained at the dimensions of 150 m by 2.50 m. Available experience is in this case a good alternative for the use of the DSS. It is expected that when the Middle Waal will have to be maintained by dredging to fulfil the required fairway dimensions of 170 m $\times$ 2.80, the DSS will be used again extensively.

6.6 *Effect of dredging on LAD's*

As mentioned before also the impact of dredging on the Least Available Depths (LAD's) was studied. Amazingly it turned out that dredging of the Waal did not increase the available draught for the ships. A number of reasons appear to be responsible for this disappointing result:

- The downstream shoal of the fixed layer in the bend near St Andries presented a fairly constant bottleneck, which constricts the width (and the LAD). This bottleneck is new (and linked to the construction of the fixed layer; studies are carried out to eliminate this new bottleneck. The shoals downstream of the other bend improvement structures in the bends Erlecom and Nijmegen were not critical.
- According to the dredging contract RWS prescribed the dredging locations, which contributed to the fact that the contractor could not respond in time to rapid changes in bed levels.
- Insufficient dredging downstream of the area. prescribed in the contract.

These observations resulted in the decision (i) to find a more permanent solution for the shoaling downstream of the fixed layer at St Andries and (ii) to develop a different form of contract between RWS and the dredging contractor to make the latter responsible for the maintenance of the fairway dimensions (see Section 6.7).

6.7 *Flexible contract*

With help of the experiences described in Section 6.6 it was decided to develop a new form of contract for dredging the Waal River, whereby the contractor is held responsible for every flaw in the required fairway dimensions, i.e. a smaller LAD than 2,5 m at OLR, with accompanying prescribed widths in the contracted river reaches. Early experiences with this new form of contract demonstrate that the cost of dredging decreased in the order of 50% and that the required fairway dimension can be maintained, apart from the known local shoals downstream of the permanent bend regulation measures.

Copyright © 2006 Taylor & Francis Group plc, London, UK

Box 6. Decision support system for dredging

Operational decision-making about maintenance dredging in an engineered river like the Waal is complex; future discharges, water levels and morphological changes remain uncertain. A Decision Support System (DSS) to optimise maintenance dredging has been developed, which is based on the combination of bathymetric monitoring-data and simplified water level and morphological predictions. The DSS facilitates decision-making on dredging activities during critical low-water periods and after the recession of peak flows. In addition, the DSS analyses dredging and dumping strategies, maintains a database with dredging information, determines relative economic benefits and visualises the effects of different strategies.

The DSS contains five main components (modules): (i) data input, (ii) data management, (iii) calculation & analyses, (iv) presentation & interface and (v) assessment & evaluation.

By defining several boundary conditions, the user can compose dredging strategies, focussing on dredging and dumping volumes in time and space, including short and/or long term water level and morphological predictions and estimations of relative benefits. Readjustment of boundary conditions provides the opportunity to set time related priorities and to compare and optimise dredging strategies. Strategies and their consequences can be visualised in the presentation module.

The DSS contains three different prediction methods: (i) water level predictions, (ii) morphological predictions and (iii) estimation of relative benefits. Long-term water level predictions (up to 6 months) are based on the base flow concept (Lyne-Hollick algorithm) in combination with regression equations for the Rhine River. Short-term water level predictions (up to a fortnight) are calculated with an extended version of a Multi Linear Regression (MLR) model, based on statistical relations between several upstream water level gauges and rainfall stations.

Morphological predictions are based on 'conceptualised' empirical knowledge in combination with (weekly) bathymetric measurements, providing the user guidelines for future bed level developments and morphological recovery after dredging. A distinction is made between forced morphological phenomena (as a result of the river geometry) and free moving bed forms such as dunes.

In the DSS also a methodology to estimate relative benefits (comparative transportation costs) of inland shipping is included. It is based on an increasing normative depth as a result of dredging activities, which (theoretically) results in an increasing loading capacity. For more details on this module see Douben and Werners (2000).

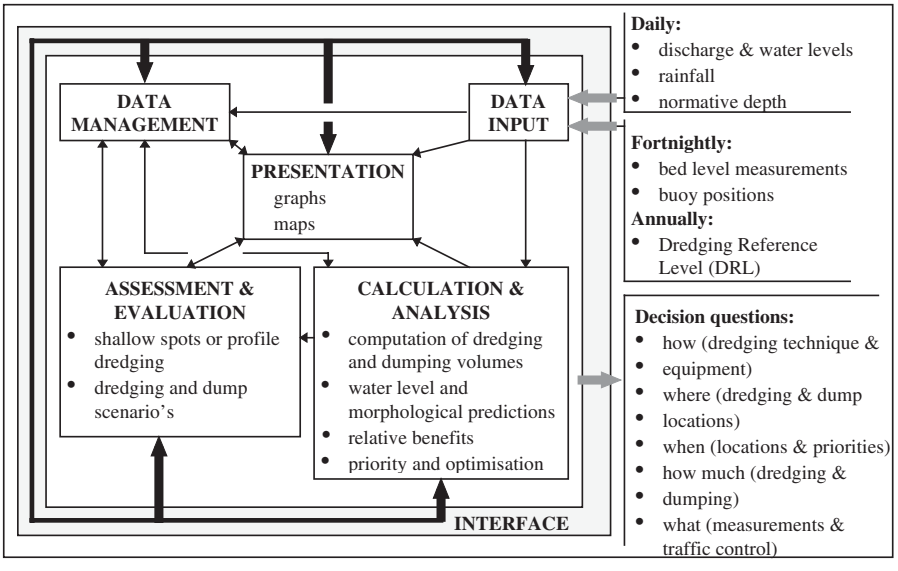


Figure B6. Schematic set-up of Decision Support System for dredging on the River Waal.

Copyright © 2006 Taylor & Francis Group plc, London, UK

7 TOWARDS A MORE SUSTAINABLE APPROACH FOR IWT

7.1 *Long term trends*

The Rhine delta has always been very important for the safety of Holland. For each of the downstream branches the level of flood protection, navigation potential and fresh water supply is determined by the (in principle) unregulated discharge distributions at two bifurcations. Though the discharge distributions appear to be remarkably stable, this is not certain during extreme peak flows. Recent observations of developments of bed levels, water levels and discharge distributions show tendencies that are worrying. The ongoing bed degradation of the upstream reaches of the Dutch Rhine branches leads to less discharge flowing into the Waal River, which is part of the main transport route to the German Ruhr area. Germany tries to stop this degradation by armouring the bed and by sediment feeding. Continued lowering of the water level in the Dutch waters would lead to a gradual reduction of draught near the border and increased upstream bed degradation.

Flood management measures, such as flood channels and lowering of summer embankments, may influence the flow pattern in the main channel during low flow conditions. Lowered water levels or sedimentation in the fairway might hamper navigation or require costly measures like dredging. The reintroduction in the (regulated) river system of unprotected banks, secondary channels and patches of naturally evolving vegetation – all aimed at increasing the ecological potential and biodiversity – will also have an impact on flood levels and navigation.

A large number of flood management projects are in preparation along the Rhine branches. Because these rivers are also important IWT routes, it appears necessary to deal with negative effects of flood management works on navigation and vice versa.

7.2 *Towards a Sustainable Fairway Rhine delta*

The combination of the requirements for navigation with the targets set by the "Room for the River" project has given rise to the Sustainable Fairway Rhine delta (SFR) project which should lead to an integrated solution that allows for a maintainable fairway on the main transport routes. It is expected that measures like local bed armouring, sediment supply schemes, adaptation of normal widths and modifying groyne dimensions will be part of the solution.

Besides the fact that the (autonomous) bed degradation has to be stopped, the main goals of SFR are the following:

- Assure a fairway (170 m wide and 2.8 m deep during low stages) that can also be maintained in the long run (both technically and financially).
- Use of sustainable measures that also in the long run can cope with system developments, so that possible future bottlenecks can be avoided. In this respect sustainability also is related to (financially) maintainability.
- Development of an optimal maintenance program.

It can be stated that the SFR project is a new master plan, which adds sustainability to the original Waal project.

For the choice of a set of measures the impact of the measures on the different user functions should be known. Therefore a prediction tool is being developed, that must be able to simulate the relevant processes with sufficient accuracy. This includes the following aspects:

- Simulation of the supply of sediment consisting of sediment with a different composition than the local alluvial material.
- Simulation of the effect of non-erodible layers in combination with non-uniform sediments.
- Simulation of the morphological development of the river system including the two bifurcations in combination with the flood plain areas on both sides of the river branches (including all above-mentioned aspects of groynes, vegetation and summer embankments).

7.3 *Sediment management*

Measures have to be investigated that contribute to sustainable river management to stop the degradation of both the bed and water levels. An extensive study on possible measures already has been carried out for the reach Emmerich-Lobith at the Dutch-German border (Baur, 2003), which shows the most severe degradation between Duisburg and Werkendam. In this study a 2-D morphologic model has been used to define solutions to stop the autonomous bed degradation and to increase the fairway depth. It appeared from this study that solutions can be found using combinations of engineering measures with bed-load supply, the construction of armoured layers and local groyne adaptation. From a multi-criteria analysis, a combination of measures with the following elements turned out to be the best solution:

- Non-erodible layers in the deep outer bends (see Figure 14).
- Bed-load supply upstream (4000 tons/week, every second year) and a total of 4000 tons/week in the project area, which results in a total supply of approximately 200,000 m^3/year.
- Local dredging.

It was assumed that no sediment is taken out of the river: the material dredged in the fairway is dumped in deep areas. The locations for bed-load supply and dumping of the dredged material only slightly affects

Copyright © 2006 Taylor & Francis Group plc, London, UK

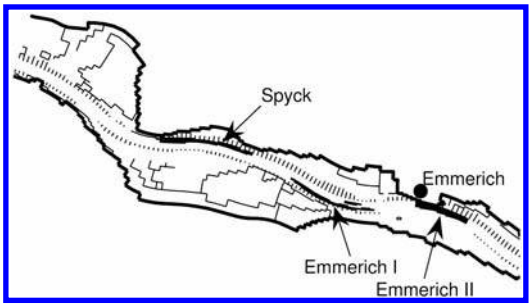


Figure 14. Identified non-erodible layers in border reach.

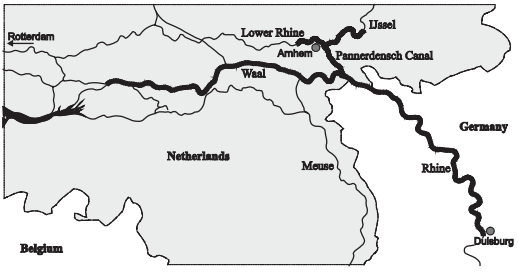


Figure 15. Study reach of the common German-Dutch Rhine.

the scoring of the combinations of measures. The erosion averaged over the whole project area will be reduced by these engineering measures from 50 cm to about 5 cm between 2000 and 2025.

In a recent study on sediment feeding of the Rhine River near the Dutch-German border (Schwerdtfeger, 2004; see Box 7) different feeding strategies related to the grain size distribution and feeding locations were investigated, all of them intended to stop the on-going degradation in this area (no attention was given to maintaining the fairway). A 1-D graded morphologic model was used. It was concluded that the amount of sediment to be fed (around 200.000 m^3/year) was rather independent of the grain size distribution, but that the number of feeding inputs increases as the maximum diameter or the D_{50} of the suppletion also increases. For the effect on downstream areas it is important to note that more sediment is transported downstream when the supplied mixture is richer in fractions near the D_{50}. The addition of finer material may be appropriate if the aim is to quickly stabilize river reaches downstream. A complicating factor can be bedforms, which may develop using finer sediments and the accompanying reduction of the draught.

Though sediment feeding can be applied without great risk a number of aspects need attention. Changing grain size distributions of sediment mixtures cost a lot of money. If feeding material is used which differs from the original bed composition phenomena may be observed that relates to the following aspects:

- Different bedforms.
- Different lateral slopes in bends including point bars.
- Effect on navigability, because of shoals and propagating sand waves.
- Different effect of ship induced currents on bed levels.

These aspects need to be studied carefully.

7.4 *Structural measures*

Though a lot of experience has been collected with dredging as a maintenance tool, experience shows that dredging cannot be used as a means to create and sustainably maintain the targeted fairway with larger dimensions. Taking into account lessons learnt from past training schemes, it is clear that a new round of (traditional) river regulation measures should only be considered with great care. Therefore a large 2-dimensional morphologic model should be used that can show the river system changes also in the long run (Havinga et al, 2005). Figure 15 shows the study reach. Though many measures can be contemplated, with the experience from river measures already carried out in the past or recently investigated, only a few types of measures are convenient to use in a sustainable river training scheme. They are:

- Modification of normal width's to neutralize the increase or decrease in sediment transport capacities.
- Fixed layers: to fix the bed levels.
- Groyne adaptations: to decrease water level set-up and create a better alignment of the fairway.
- Sediment management: to meet the river's sediment demand.

7.5 *Discussion: investigation and the sequence of application of measures and the order of application*

As indicated before each combination of above-mentioned measures should be carefully investigated with morphological models. However, the reliability of such models is limited. Aspects like graded bed material, simulation of flow in groyne fields and correct simulation of cross-sectional slopes, local shoals and bedforms are not yet well represented in these models. Nevertheless they provide interesting information on the effects of measures. Especially a complete 2D morphologic model of the Rhine branches, from Duisburg (Germany) to the tidal area of the Waal River, including the two bifurcations can be very useful, in particular when this model is calibrated with results of measures already carried out. In future more detailed physics can be included to increase the forecasting capability of the model.

Copyright © 2006 Taylor & Francis Group plc, London, UK

Box 7. Simulation of effect of artificial sediment feeding

To reduce or even stop the ongoing degradation of the river bed of the Rhine River different possibilities are available. One possibility is to start feeding sediment to the river. This method has been applied successfully in Germany downstream of the Iffezheim barrage. Presently also more downstream in Germany sediment is supplied to the river. So also in The Netherlands this method is being considered.

When applying sediment feeding as a measure a number of questions have to be answered, notably:

- how much sediment will be supplied?
- where will the sediment be supplied (in one location or over a long reach and in outer bends, in the groyne fields or at other locations?
- when will the sediment be supplied (e.g. only during the flood season?)?
- what should be the size and gradation of the supply material?

The quantities to be supplied each year were determined in a recent study (WL/Delft Hydraulics, 2002/2003) and are about 200,000 m3/year. The experience from Iffezheim will surely be useful, but in Iffezheim great efforts are being made to supply to the river a very accurately composed mixture exactly corresponding to the bed material transported by the river (Droege, 1992a & 1992b; Nestmann, 1992). The preparation of this mixture is very expensive. It would be preferable if a commercially available mixture could be used. Moreover it might be considered to use the artificial sediment feeding to slowly change the bed composition of the river, if this would have advantages.

To study the effect of supplying different types of sediment to the river a study was carried out by Schwerdtfeger (2004), applying the SOBEK package, 1-D software developed by WL/Delft Hydraulics together with RIZA, which is a one-dimensional open-channel dynamic numerical modelling system, including in this application the morphology mode for graded sediments. Morphological changes are simulated by means of bed-material conservation (sediment continuity equation for bed-load material). The changes of composition are computed from the continuity equations per fraction for the separate layers, and by the bed-load transport simulation per fraction. Changes in composition of the active layer are caused by differential transport of the different fractions. The model uses the Hirano active layer approach (see Ribberink, 1987), and the active layer thickness can be selected as a fixed value or can be linked to e.g. the bedform height. The different parameters in the model (roughness, sediment transport formula, etc.) were selected to represent the Rhine River. For more details see Schwerdtfeger (2004).

There was one serious problem with the modelling approach. In the reach modelled the size of the bed material changes rapidly (Figure B7.1). This might be caused by abrasion, but abrasion rates would have to be excessive in this particular reach. Often the modelling approach is that the basis for the model is a base case in which no changes occur. In the case of a graded model with a reduction of grain size in downstream direction, it is not possible to define a base case where no net bed level and bed composition changes are taking place if no feeding is applied. Hence the modelling used the approach of simulating the conditions over a period of 20 years ahead without and with artificial feeding. The differences were used as assessment criterion.

A typical result of the study of Schwerdtfeger (2004) is shown in Figure B7.2. It is proposed to supply the sediment to the river divided over a number of feeding points to reduce

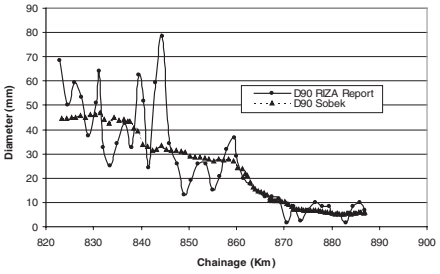


Figure B7.1 Reduction in grain size in the Rhine River in the German-The Netherlands border reach.

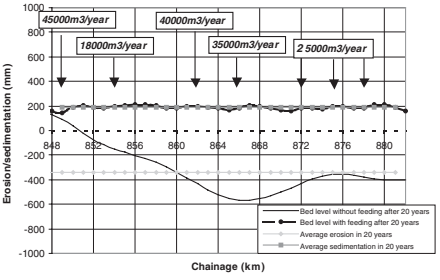


Figure B7.2 Possible feeding strategy and effect on bed degradation.

possible irregularities in the riverbed. Schwerdtfeger (2004), who studied only morphological issues and e.g. not practical aspects as mentioned above, concluded the following:

- Sediment feeding is an attractive and sustainable measure, giving a lot of flexibility (quantities and composition can be changed over the years on the basis of experience).
- It is possible to change the bed material characteristics of the Rhine River by artificial bed material different from the bed material present in the river.
- How quickly these changes in bed material proceed is dominated by the thickness of the active layer (however there is much uncertainty on the thickness of this active layer in a river reach with a very graded bed material consisting of gravel and sand).

More detailed studies are needed to develop appropriate feeding strategies (where, how much, when). Moreover it is proposed to do a number of additional studies related to the impact of possible changes in the composition of the bed material on other aspects of the river. Some aspects to be studied are (i) the effect of sorting on the lateral slope of bands, (ii) the effect of navigation, (iii) the morphological interaction with the groyne fields, etc.

Based on these results it was proposed to develop a pilot project for artificial feeding of sediment to the Rhine River. This project should be accompanied by a properly designed monitoring study including frequent and comprehensive sampling with the objective to monitor the impact of the feeding on bed degradation and bed composition and other aspects and when needed to adjust the feeding strategy. Simultaneously the current existing graded-sediment models could be improved.

Copyright © 2006 Taylor & Francis Group plc, London, UK

Accepting the limited reliability of morphologic models, measures should be applied with care and the sequence of their application must follow a certain order. Modifying the normal widths is done by adapting groyne lengths, which is a very costly procedure (round € 300.000/groyne, in total 400 groynes), so this should be combined with other groyne modifications. As the required normal width to neutralize changes in sediment transport capacity is computed with morphologic models and the measure is far from flexible, this measure should be investigated thoroughly. From experience we know that with the available models the location and dimensions of armoured layers can be defined fairly well, so though these measures are also very costly and non flexible, they could be applied in short notice. Sediment management can be applied immediately as this is a flexible measure, which can be stopped and altered very easily.

7.6 *Long-term developments in navigation*

The transport capacity of the Waal River is already very large. It has been estimated that the actual used capacity can easily be tripled without having to invest large amounts of money in this waterway, maintaining the actual fairway. To further increase the economical use of the river, tools are being developed that can present the actual bed geometry in the wheel house (electronic chart display information system or ECDIS). In this way the skipper can judge better the ship's course. This may result in a more chaotic navigation pattern, when different types of ships choose different sailing routes. So, with the intention not to decrease the safety level of inland navigation, a system of individual guidance of ships (water traffic control) may be necessary. With ECDIS and a water traffic control system the use of the available fairway can be optimised.

However, there is still another way to increase the transport capacity of the river, i.e. to make use of larger water depths. Apparently in case of the Rhine navigation the choice was made to make use of limited draft and several shipping lanes. In this way many types of ships can sail the Rhine River, its tributaries and the smaller feeder canals. Another strategy can be to limit the width of the fairway for the benefit of larger drafts. This can be demanded when a strong increase of transported volumes of goods has to be faced. The actual fairway of the Waal River enables up to 5 shipping lanes. When the number of shipping lanes is reduced to 3 or even less, the draft of the ships can increase substantially. However, the fairway width might decrease to around 100 m. A consequence of such a fairway is the creation of in-line navigation, which is considered a major drawback of this system. Probably additional measures at crossings will be needed.

8 DISCUSSION

In this paper an overview is presented of river measures carried out in the Waal River during the past 10 years to increase navigation potentials. Though a well motivated master plan was available, a number of works have not been executed and/or have been replaced by alternative measures, due to budget problems and growing insecurity about the effectiveness of certain measures (e.g. bottom vanes). This is not a unique situation, neither for the Netherlands, nor for this era; also in the past this situation frequently happened. Nevertheless it can be concluded that for sustainable development of navigation and other river functions, it is essential to have a master plan in which the long-term autonomous development of the river system is leading. Any planned river measures that deviate from measures envisaged in the master plan, should be of a reversible nature. In view of this the relatively extensive dredging operations in the Waal River, which temporarily (or permanently?) replace more structural measures, are a logical step in the implementation of the original Waal project.

The demands on the layout of the Waal River are large: the combination of user functions with ecology and the desire to obtain sustainable (and maintainable) solutions to optimise the user functions, poses complex questions. Answers have to be sought using 2-D simulation models (also with movable bed), utilizing the best understanding available.

River management has to deal with the natural dynamics of the river. The related uncertainties limit flood safety and navigation opportunities. In the past centuries coping with these uncertainties was also translated in a river lay-out in which (most) people could survive flooding and accepted the nuisances, e.g. small draughts or no sailing at all. Today, the situation is quite different: the regulation of the discharge distributions in the 18th century led to a high flood protection standard and to reliable navigation conditions. Further improvements for navigation can be found in reducing the uncertainties in forecasting of navigation depths. This touches upon a whole range of "river flow" subjects related to forecasting of discharges, water levels, bed levels and bedforms, in which uncertainty plays a major role and where probabilistic approaches are appropriate.

REFERENCES

Anonymous (1988), Six-barge push-tow trials. PIANC Special Bulletin

Baur, T. (2003), Border project Rhine River, Report 4 Investigation of combination of engineering measures with 2-D morphological model, WL/Delft Hydraulics, Report Q2496 (in Dutch and German)

Copyright © 2006 Taylor & Francis Group plc, London, UK

Droege, B. (1992a), Change of River Morphology by controlled erosion and deposition – Bed Load Budget of the Rhine River, 5th Intern. Symp. on River Sedim., Karlsruhe
Droege, B. (1992b), Recent Morphologic Development of the Rhine River, 5th Intern. Symp. on River Sedim., Karlsruhe
Douben. N. & S.E. Werners (2001), Decision Support System for Maintenance Dredging in the River Rhine, Proc. XXIX IAHR Congress, Beijing, China, Vol. II, pp. 812–820.
Engelund, F. en E. Hansen (1967), A monograph on sediment transport in alluvial streams. Teknisk Forlag, Kopenhagen
Groen, M. (2002), Analysis of dredging in outer bend of the Waal River near Hulhuizen, Ministry of Public Works and Transport, Rijkswaterstaat Oost-Nederland, (in Dutch)
Groen, M. (2004), Effects of dredging on Least Available Depth in the Waal River. Ministry of Public Works and Transport, Rijkswaterstaat Oost-Nederland (in Dutch)
Haque, M.M., Klaassen, G.J. and Enggrob, H.G. (2006), Scale effects in movable bed models of rivers with dominant suspended load, Proc. EWRI (ASCE) Symposium Nebraska
Havinga, H., Jagers, H.R.A. and Sloff, C.J. (2005), Knowledge requirements for sustainable fairway management, Proc. 3rd Symp. On River, Coastal and Estuarine Morphodynamics, Minnesota, USA
Havinga, H., Waal project: Design report (in Dutch). Ministry of Public Works and Transport, Rijkswaterstaat, Directie Oost-Nederland, 1996
Havinga, H. and Smits, A.J.M. (2000), River management along the Rhine: a retrospective view. In: Smits, A.J.M., Nienhuis, P.H. & Leuven, R.S.E.W. (Eds.) New Approaches to River Management, Backhuys Publishers, Leiden, 15–32
Huisman, P., Cramer, W., Van Ee, G., Hooghart, J.C., Salz, H. & Zuidema, F.C. (1999), Water in the Netherlands, Netherlands Hydrological Society, Delft
Jansen, P.Ph., Van Bendegom, L., Van den Berg, J., De Vries, M. & Zanen, A. (1979), Principles of river engineering, Pitman Publishing Ltd. London.
Klaassen, G.J. (1995), Lane's balance revisited, Proc. 6th Intern. Symposium on River Sedimentation, New Delhi (India), pp. 671–686
Klaassen, G.J. and Sloff, C.J. (2000), Prediction bed topography and recovery after dredging in the Waal, WL/Delft Hydraulics, Report Q2669 (in Dutch)
Nestmann, F. (1992), Improvement of the Upper Rhine, Tail Water (TW) Iffezheim, 5th Intern. Symp. on River Sedimentation, Karlsruhe
Ribberink, J.S. (1987), Mathematical modelling of one-dimensional morphological changes in rivers with non-uniform sediment, TU Delft, Ph.D. thesis.
Rijkswaterstaat (1991), Research Bend improvement Measures Waal River Ministry of Public Works and Transport, Rijkswaterstaat, Directie Gelderland, Resource Analysis, WL|Delft Hydraulics, Stichting voor Toegepaste landschapsecologie (in Dutch)
Rijkswaterstaat (1993), Waal: Future Main Transport Axis (in Dutch). Ministry of Public Works and Transport, Rijkswaterstaat, Directie Gelderland (in Dutch)
Schepman, F. (2000), Morphology of the Middle Waal without and with dredging, Delft University of Technology, The Netherlands, M.Sc. report (in Dutch)
Schwerdtfeger, C.M. (2004), Sediment feeding to reduce bed degradation of the Rhine River near the German/Dutch border, UNESCO-IHE, MSc Thesis HE 177
Sloff. C.J. (2001), Morphological study DSS Dredging with Delft2D-Rivers, WL/Delft Hydraulics, Report Q2844 (in Dutch)
Sloff, C.J., Bernabe, M. and Baur, T. (2003), On the stability of the Pannerdense Kop river bifurcation, Proc. 3rd Symp. On River, Coastal and Estuarine Morphodynamics, Barcelona, pp. 1001–1011
Sloff, C.J., Mosselman, E. and Sieben, J. (2006), Effective use of non-erodible layers for improving navigability, Proc. River Flow 2006, Lisbon, Portugal
Smits, A.J.M., Havinga, H. and Marteijn, E.C.L. (2000), New concepts in river and water management in the Rhine River basin: how to live with the unexpected? In: Smits, A.J.M., Nienhuis, P.H. & Leuven, R.S.E.W. (Eds.). New Approaches to River Management, Backhuys Publishers, Leiden, pp. 267–286
Struiksma, N. (1978), Scale effects in river models with movable bed, WL/Delft Hydraulics, Report R1119 (in Dutch)
Struiksma, N. (1985), Prediction of 2-D bed topography in rivers, J. Hydr. Engrg., ASCE, Vol.111, No.8, pp.1169–1182
Struiksma, N. (1990), Scale effects in the reproduction of overall bed topography in river models, In Shen, H.W. (1990), IAHR symposium on scale effects in modelling sediment transport, Toronto, Canada, 1986
Struiksma, N., Olesen, K.W., Flokstra, C. and de Vriend, H.J. (1985), Bed deformation in curved alluvial channels, Journ. Hydr. Res., IAHR, Vol.23, No.1, pp.57–79
Talmon, A.M., N. Struiksma, and M.C.L.M. van Mierlo (1995), Laboratory measurements of the direction of sediment transport on transverse alluvial bed slopes, J. of Hydraulic Research, IAHR, Vol. 33, No. 4, p.495–517.
Ten Brinke, W. (2004), The Dutch Rhine, A restrained river, Publ. Veen Magazines BV, Diemen, 228 pp.
Van der Ven, G.P. (1976), At the cradle of Rijkswaterstaat. History of the development of the Pannerdens Kanaal, De Wilbur Peers, Zutphen
Van Reen, M.J. (2000), Morphological problems near the fixed layer at St. Andries, Delft University of Technology, The Netherlands, M.Sc. thesis report (in Dutch)
Van Vuren, S. (2005), Stochastic modelling of river morphology. PhD thesis: Delft University of Technology, Delft
Wilbers, A.W.E. (2000), Bed load transport in the bend St.-Andries, University of Utrecht (in Dutch)
WL/Delft Hydraulics (2002/2003), Grensproject Bovenrijn, WL/Delft Hydraulics, Reports Q2496, Fases 1, 2, 3 and 4
Wolters, A. (1998), Case-study fixed layer Nijmegen, Ministry of Public Works and Transport, Rijkswaterstaat, RIZA (in Dutch).

Copyright © 2006 Taylor & Francis Group plc, London, UK

Case study: River restoration projects along the Isar (Germany)

W. Binder
Bayerisches Landesamt für Umwelt, Munich, Germany

ABSTRACT: Like most of the larger rivers in middle Europe sections of the Isar, flowing from the Alps down to the Danube, were canalised more than hundred years ago, to improve flood control and the use of hydropower. The floods in the last two decades showed the needs to improve flood protection and accelerated the discussions about more nature and outdoor recreation along the canalised rivers. The basic for restoration projects are regional river concepts. They contain the guidelines for local projects. Such concepts as well each single local restoration project requires teamwork, needs ecological understanding, technical knowledge in hydraulics/ construction and social acceptance. They have to be supported by the public e.g. engaged Non Governmental Organisations (NGO). Engineers, architects and experts of different fields e.g. nature conservation, wildlife, agriculture, forestry and fishery are working together to find win-win-solutions. The case study Isar, includes projects in the city of Munich and outside in the rural floodplains, describing planning steps, river restoration objectives and measurements and also the importance of public participation.

1 INTRODUCTION

More than 150 years of river and drainage works in many parts within Europe and also other places in the world couldn't ban the danger of floods, but brought a loss of nature to rivers, streams and wetlands.

Within the last three decades restoration projects were started and river restoration is finding growing interests in many states in Europe, but also in the USA, in Australia and Japan. Especially the floods in 1995, 1999, 2002 and 2005 in Central Europe pushed programs for flood protection and restoration. Today the objectives are to preserve natural retention areas and to restore rivers beside technical flood control works. River assessment methods where developed, to show how much of the hydromorphological components in our rivers have been altered by river works and where river restoration should be concentrated to improve the ecology.

Many projects were completed in the last two decades dealing with river restoration. Not all of them were perfect, some are already redesigned by floods. But there are many successful projects along streams and rivers, where we can learn by studying the technical solutions and the experiences which were made. Not all restoration projects needs a lot of construction work, also maintenance work, wisely done, can improve the ecological quality of fluvial systems and can meet the demands of the Water Framework Directive and of Natura 2000.

2 SITUATION OF RIVERS AND STREAMS IN MIDDLE EUROPE

Channelled, incised, dammed, most of the rivers and streams in middle Europe have been altered in the last 150 years to improve shipping, the use of hydropower, land drainage and flood control of rural and urban areas. Close connected with these alternations of rivers and streams were the loss of biotops for animals and plants. The floods of the last decade brought heavily damages and losses for urban areas, since there is not enough open space anymore for the water.

The assessment of the hydromorphological feature of rivers and streams in Germany shows that 2/3 of all assessed rivers have strong deficits or are completely unnatural. The surveys for the European Water Framework Directive (WFD) confirm that most of the rivers in Germany are endangered to reach the good ecological status for the biological quality components due to hydromorphological deficits. Bayerisches Landesamt für Wasserwirtschaft et al. (2001).

3 GUIDELINE FOR RESTORATION PROJECTS: THE ECOLOGICAL FUNCTIONS OF RIVERS AND STREAMS

3.1 *Principles*

Rivers and streams are dynamic systems. They are formed by the natural characteristics of the drainage

Copyright © 2006 Taylor & Francis Group plc, London, UK

basin, climate, geology, tectonic, vegetation and land-use. Depending on the precipitation rainfall and storage capacity the discharge is fluctuating. The power of running water and the amount of transported solids influence the morphological process and the geometry of the river channel.

This includes bank erosion and sedimentation, the rebuilding of riffles and pools and the migration of the riverbed within the alluvial plain. The geometric features of the river channel e.g. planform, longitudinal and cross sections as well the substrate in the river channel are depending from the conditions in the watershed area. River and floodplain are an unit. Mangelsdorf et al. (1980).

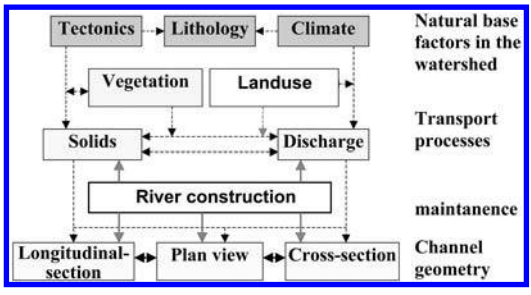


Figure 1. Modification of hydromorphological processes caused by river construction.

The ecological functions are impounded by river construction and regularly maintenance, controlling the morphodynamic processes. They change such dynamic rivers into static systems, causing ecological deficits.

The model for restoration describes the naturally ecological function of a river system. Rivers are called natural, if they are not polluted and can migrate freely in the flood-plain. This is a continuos process in time and space. The transport of water and solids is not interrupted by weirs or bank fixation. The vegetation along the river and in the flood plain is in natural succession, its zonation spans from pioneer vegetation to alluvial woodland. The migration of the river bed, pushed during floods, lead to a continuos replacement of typical structures. Natural river systems flood several times the year. They are housing a mosaic of biotops for animals and plants. This explains why natural river systems offer such a wide range of habitats, if their ecological functions are not affected. Their reference status is equal to the high ecological status of the WFD.



Figure 2. Natural section of the Isar near the alps, showing the alpine character.

Copyright © 2006 Taylor & Francis Group plc, London, UK

3.2 *Planning process*

The basic for river restoration projects are planning concepts for contiguous river sections, mostly done in the scale 1:25.000. Following these concepts restoration projects are done in the scale 1:5.000 to 1:1000. Regional river restoration concepts are helpful for the planning and communication processes with experts, members of the administration, Non Governmental Organisations (NGO) and the public. Such concepts assist the transparency of the planning processes and accelerate the decisions for local restoration projects. There are several planning steps for restoration projects.

Step 1: to develop the reference status for the river landscape.
Step 2: to asses the status quo.
Step 3: to find the deficits by comparison of reference status and status quo.
Step 4: to shows the restrictions for the restoration project.
Step 5: to develop the objectives for the restoration project.
Step 6: to improve the ecological functions of the river system; the measurements have to be placed and the costs estimated.

The objectives for river restoration projects are:

- to improve flood control e.g. in urban areas and outside urban areas strengthen the natural retention capacities
- to enforce the ecological function of the river system and to give more space to the river within the flood plain
- to allow the natural morphodynamics processes
- to find new techniques for mitigation to support or to limit morphodynamic processes
- to win stakeholders, residents and others for river restoration projects by information and participation
- to improve the recreational value of the riverside.

The planning process should be interdisciplinary and should integrate other plans and programs within a county or community related to the restoration project. These can be e.g. programs for city development, for clean water, reducing the pollution from point and non point sources. Interests of stakeholders e.g. fishery, nature conservation and of land owners, especially farmers along rivers and streams have also to be reviewed. Binder (2000).

Public Participation has to be integrated in the planning process to support the restoration projects. Agenda groups on regional and local level are formed to exchange ideas and practical experiences with experts and to accompany restoration projects. This includes to realize the needs for flood control, for natural retention of waters, for the ecological improvement of the system, for nature conservation and the possibilities and limitations for recreation.

4 RESTORATION PROJECTS ALONG THE ISAR, GENERAL INFORMATIONS

There are several restoration projects along the Isar, they include projects in urban areas like the Isarplan Munich and restoration projects north and south of Munich in rural zones.

Before these projects will be described, some general information about the river Isar are given: Bayerisches Landesamt für Wasserwirtschaft et al. (2001).

4.1 *The Isar*

The Isar runs from the Karwendel Alps to the Danube. It watershed covers about 9 000 km with about 2,5 million of habitats, more than 1,5 million in the city of Munich. The length of the river is more than 260 km. The annual precipitation in the mountain areas are more than 2000 mm/a, close to the Danube less than 700 mm/a. Floods occur mainly from spring to fall. The discharges in Munich are:

NMQ	(low flow)	ca. 40 m^3/s
MQ	(medium flow)	ca. 90 m^3/s
HQ	(high flow)	ca. 350 m^3/s
HQ	(Spring 1999)	ca. 870 m^3/s
HHQ	(maximum flow)	1440 m^3/s

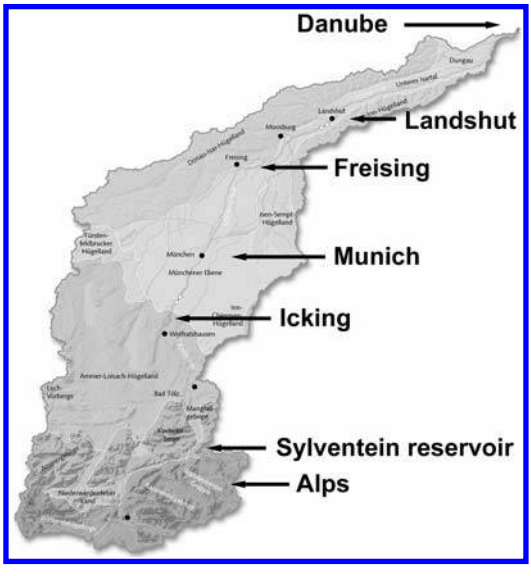


Figure 3. Watershed of the Isar.

Copyright © 2006 Taylor & Francis Group plc, London, UK

4.2 *Isar before canalisation*

Up to the beginning of the 19th century the Isar was a free flowing braided river system from the Alps down to the Danube. During low flow the water gets nearly lost between a corridor of gravel banks within a belt of alluvial woodland. Wetland with oxbows and groundwater streams accompanied the river system. The dynamics processes of erosion and sedimentation provided biotops for alpine plants and special animals. The zonation and the succession of the vegetation were controlled by floods and transport of gravel and sediments.

4.3 *River canalisation*

On the beginning of the 19th century river construction started. The objective was to get the river in a fixed bed, to improve rafting and to reduce flooding. The first construction work was done in the cities of Munich and Landshut. About 100 years later, at the beginning of the 20th century the canalisation of the Isar from Munich down to the Danube was completed, dikes were been built to protect urban and rural land from flooding. Between 1954 and 1959 the Sylvenstein Dam was built as a flood reservoir to improve the flood control in the Isar valley down to Landshut.

4.4 *Hydropower*

Already in the middle age water was used to run mills. Along the Isar only large communities like the cities of Munich and Landshut were able to build and to maintain weirs, which were endangered by each large flood. Water was taken at these weirs in channels to run mills. The streams in the "English Garden" in Munich remember for such systems.

The technical development at the beginning of the 20th century allowed using hydropower to get electricity. This was the start to built weirs and channels at the upper part of the Isar to withdraw the water from the river bed into channels to transport it to Hydropower plants. The riverbed itself remains for the most time of the year mostly dry, only to carry the water during floods. With the renewing of the concessions for this river sections in the last years (1995), minimum discharge in the river bed are guaranteed and restoration projects were started, financed by the hydropower companies.

Between 1948 and 1984 the Isar between Landshut and the Danube were dammed with a chain of hydropower plants, creating an artificial river landscape. Some of these lakes are built with Islands and natural zones. They will reach the good ecological satuts, which is asked for Heavily Modified Water Bodies (HMWB) by the WFD.



Figure 4. The dammed Isar north of Landshut built with islands and natural zones. This HMWB will reach the good ecological status.

4.5 *Natura 2000*

Besides the alternation of the Isar from a free flowing river and the loss of habitats, there are today many protected natural areas, especially from the Alps down to Landshut. In this section a wide corridor of woodland follows the river, only disrupted by the cities of Bad Tölz and Munich. The Isar, as an alpine river, offers a corridor of habitats for alpine animals and plants migrating from the Alps down to the Danube. For this reason more than 100 km of the Isar, flowing in Bavaria are reported for Natura 2000, covering biotops with rare specious of animal and plants, protected at an European level.

4.6 *Program for flood control 2020 in Bavaria*

Restoration projects along the Isar are on the way, to improve the ecological quality of the river and the flood plain. They include taking out bank fixation, where enough land is available, to start again the hydromorphological processes. This includes projects for gravel transport and the construction of By-passes at weirs for the migration of fishes. These restoration projects are parts of the Program "Hochwasserschutz in Bayern" which improves flood control by technical measurements and also by restoring the natural retention capacity of the flood plain, up to the year 2020, spending 2 bn of Euros.

4.7 *Public participation*

For the habitants of Munich and upper Bavaria the Isar is their river. Numerous books and magazines are published describing land and people of the Isar Valley. Isar is synonym for easy life, enjoying outdoor recreation and nature adventures. Already more than 100 years ago, the Isar valley was in the focus of painters and nature oriented people. To protect the beauty of the landscape, organisations were founded like: Isartalverein, Verein zum Schutz der

Copyright © 2006 Taylor & Francis Group plc, London, UK

Bergwelt, Bund Naturschutz in Bayern, Landesbund für Vogelschutz and others. Also the hunters and fisherman were well organised. All these NGO are fighting since decades for the river Isar. Thanks the engagement of these groups the Isar shows especially between Munich and the Alps still its alpine character. Today the NGO are organised in the Isarallianz, a federation of nature, environmental and sports organisations to escort the implementation of the restoration projects along the Isar step by step.

5 CASE STUDY ISAR IN MUNICH, THE ISAR-PLAN

In Munich the Isar get restored for a length of 8 km. The City of Munich and the State Office for Watermanagement put up the ISARPLAN to improve flood control, ecological functions and recreation. For this a planning group was installed with water engineers, landscape architects, city planners and biologist working together. The planning steps included meeting with citizen groups and members of all kind of NGO, like nature conservation-, fisher- and kayak-groups, they all were represented by the Isarallianz. The planning stage of the restoration project was implemented 1995, in fall 2000 the work started. Today 6 km of the project are restored, the last sector of about two km was approved by the city council in spring 2005 and will be finished 2007. The project will cost about 28 Mio Euro; 55% is paid by the State of Bavaria, a part of it is sponsored by the European Commission and 45% covers the city of Munich. Hafner (2001).



Figure 5. Canalised Isar (since 1900) in the city of Munich.

5.1 *Starting position*

The Isar in Munich got canalised about 1900 in a double trapeze profile, with the river bed and a flood plain. The floodplain is limited by walls and dikes. There were no gravel banks. The steep banks got protected with heavy stonework and concrete. To step down to the water was quite dangerous and needed to be sporty, for kids and olds. Small weirs had to prevent the incising in the river bed, they interrupted the longitudinal connectivity for boats and fishes. The flood corridor was grassland, regularly mowed and maintained as green grounds for soccer and other sports. Due to the discharge for floods, there were only a limited amount of trees and shrubs.

The water is taken into a channel to produce electricity, so more than 6 km of the 8 km restoration section has only a minimum flow of 5 m^3/s, but has to take the floods. At the moment there are discussions with the hydropower company to raise the minimum flow up to 15 m^3/s.

5.2 *Reference site*

The reference for the planning group was the "Flaucher" a natural section of the river in the city, where a historic weir widens the river bed with banks of gravel. The idea of the plans is to enlarge the cross sections of the river bed for the 100 year flood, to give the gravel banks back to the Isar by widen the river bed and to improve the longitudinal connectivity by replacing the weirs through ramps. With these principle measurements the objectives of the Isarlpan flood control, ecology and recreation can be covered.

5.3 *Planing approach and public participation*

In urban areas, where available space is limited, river restoration projects are mostly restricted to restore and to maintain the typical structures of the river channel. In Munich the flood corridor offering some space is integrated in the restoration project. From the start of the Isarplan 1995 the public was asked to accompany the planing process. People has been interviewed about the new river and what they would prefer. Their answers were different: The younger people were asking for more gravel banks and an open, easy access to the waterline, the older to keep the grassland. The compromise was to widen the river for 30% to bring back the gravel bank, but keep about 60% of the grassland for playground (soccer) and for the dogs. The main results of these interviews are:

- Bring the alpine character of the Isar back into the city.
- Enlarge the gravel banks along the river, especially wanted by the youngsters.
- Keep the flood meadows wanted by the oldies, (the dogs like grassland).

Copyright © 2006 Taylor & Francis Group plc, London, UK

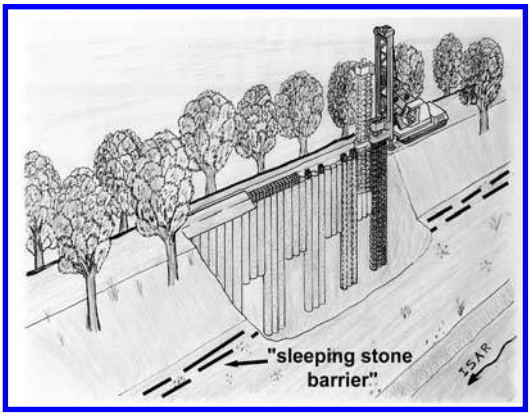


Figure 6. Lack of space to rebuilt the dikes, they got improved by steel pillars and a suspension of bentonit drilled in the dike. The bank fixation was taken out and replaced by a buried stone barrier in front of the dike.

- Keep the tress and the nature vegetation.
- Improve sun bathing along and and bathing in the river.
- Improve the function of the Isar corridor for pedestrian and cyclists, longitudinal north south connectivity within the city along the Isar.
- Improve the lateral connectivity with the quarters east and west the Isar.
- Avoid spectacular attraction along the river, because the area is already under strong pressure of recreation and should not attract additional visitors.

5.4 *Planning competition*

For the last restoration section in the city, south of Deutsches Museum, architects and engineers were invited into a competition to find a acceptable solution. The winner recommended a more formal solution, but this was resisted by the Citizens of the surrounding quarters. After a mediation process a solution now is found, which follows the restoration principles, which were chosen for the sections, already finished.

5.5 *Flood protection measurement*

The main objective of the Isarplan is to improve flood protection for a hundred year flood. To achieve this, the river canal has to be widening, the bank and the adjacent flood corridor were lowered to enlarge the hydraulic section for the discharge of water. The existing dikes have to be improved. For this the bank fixation was taken out and placed by gravel banks. To restrain the river within flood corridor, the fixation of the bank is replaced by and hidden stone barrier, buried in front of dikes, to limit the migration of the river canal and prevent damages of the dike. The dikes have to be improved for the 100year flood. The sections, covered with trees, got enforced by drilling in a mixture of concrete and bentonit, armed with steel pylons into the dikes.

5.6 *Hydraulic modelling*

The widening of the river bed improved the deposits for gravel, so, the gravel banks, a natural part of alpine river systems are back again even in the city, changing their position with each flood. The remodelling of the river canal and the floodplain opens the access for people to the water edge. To make sure that these measurements will resist flood a hydraulic model in the scale 1:30 was built.

5.7 *Ecological and recreational improvements*

Widening the river bed improves the structural variability and with this habitats for plants and animals. The existing vegetation was carefully documented, especially the trees, to avoid losses of natural vegetation and trees. Grassland vegetation with rare species was transplanted to places already restored. Reseeding of grassland was done with a mixture of grass and flowers, harvested on natural grassland along the Isar. Removing weirs and to replace them by ramps brought back the longitudinal connectivity in the river. The bed sediments with the hyporeic interstitial, before stabilised by this weirs, now can be transported during floods; the substrate of gravel and sand, now revived can serve again as spooning places for fishes and other habitants of the riverbed.

5.8 *Recreation*

The opening of the river by widening and lowering the bank, getting islands and gravel banks, improves the recreation facilities along the river in the centre of a city with more than one million of habitants. The new Isar attracts during warm and sunny days ten thousands of visitors, bathing in the sun or in the water, celebrating parties day and night. The restored Isar serves a giant public swimming pool, that also means more public toilets and more maintenance of the river corridor, which is used as a public park during the summer season.

The crowds of people, tied to the river in Munich, will not spoil the more natural sections north and south of Munich with their high value for nature conservation, especially with their habitats for rare and protected species of plants and animals.

5.9 *Hygienic situation*

Since 2005 the Isar in Munich offers in normal days bathing water quality, as this is ask by the Europeandirective for water bathing quality. To achieve

Copyright © 2006 Taylor & Francis Group plc, London, UK



Figure 7. The proposal of the planing competition for the new Isar. Left: a more formal solution. Right: a more nature oriented solution.



Figure 8. The new Isar with an enlarged flood corridor.

this, the sewage treatment plants between the Alps and Munich are running from April to October UV radiation, which treat the outflow. This radiation reduces the bacteria loads during normal flows for about 50%. This is possible, because in the watershed of the upper Isar industrial zones and population is relatively low, compared to some other watershed in Germany. It is covered to more than 50% with woodland and the sewage treatment plants have a very high standard. To keep this high water quality also in Munich, the City of Munich put up a program more than 20 years ago, to enlarge the storage capacity of the sewage system and to reduce the direct discharge of polluted water into the Issuer e.g. stormwater. This high water quality can not be guaranteed during floods, in such times the water is polluted by many non point sources. But since the Isar is a flowing river, it takes only some few days after the flood, that the water quality reaches again a quality, which allows bathing. Bayerisches Landesamt für Wasserwirtschaft (2003).

5.10 *Construction processes*

The planning and construction processes were closely watched by the public. Information was given to the local districts, neighbouring the Isar, the Isar Allianz and to the general public.

The construction time is during October and April, starting 1999. This is the time were the discharge of the Isar, due to snow and ice in the alpine mountains, is low, also the pressure of recreation is during the winter season less.

Copyright © 2006 Taylor & Francis Group plc, London, UK

The first section of the restoration work was done in a pilot project to get experiences with these new steps in river restoration. Especially the design of the new bank and floodplain needs a sensitive understanding. To protect bed erosion the old weirs are replaced by ramps, using a technique, developed for alpine river systems. Workshops and excursions were organised to change experiences and find solutions.

During the construction time are some specialties to mention:

- The problem of removing ammunition and bombs from World War II.
- The removal of contaminated soil, which has to be transported to deposit places outside the city, causing high costs.

5.11 *Flood 9/2005*

For the planners the task was to find a solution, which compromises between the technical standards, the ecological needs and the demands for recreation, and finally which also will resist a one hundred years flood.

This flood took place about 9/2005. The new Isar passed successful this test, with a discharge more than 1100 m^3/s. Damages were especially along one relatively sharp outside curve. Because the trees and the natural grassland vegetation in this sector had to be conserved, it was not allowed to straighten this curve. So the flood did it. The bank, even fixed with heavy stonework, exposed to the high velocity of the water flow, got washed away. The trees along the bank, which were carefully protected during the construction time, were taken by the flood. The river widened the bed. With this additional space, taken by the river, a new bank line could be chosen, which correspondents better with the hydraulic needs.

With this flood gravel was transported without problem through the redesigned sections. But a huge amount of trees, shrubs an wooden debris were deposited at the gravel bank and has to be taken away. But this is has also been always occurred after floods, even before the Isar was restored.

The city of Munich is responsible for the maintenance for the Isar. The cost to maintain the corridor, which is comparable to a public park or a public swimming pool, are slightly higher than before, because the new Isar attracts more guests than before. Binder (2004).

6 RESTORATION PROJECTS OUTSIDE URBAN AREAS

Outside urban areas the objective for restoration projects is to restore the ecological functions with a minimum of intervention. That means: bring back the dynamic processes. An important precondition for this is that enough land is available. In such areas the hydromorphological processes can be started again by taking out the bank fixation. Such restoration projects need space and time and can be done in rural areas. Binder, Hoelscher-Obermaier (2003).

6.1 *Isar near Icking, south of Munich*

South of Munich the Isar flows in the floodplain within a corridor of alluvial woodland. The water of the Isar is taken in cannels to generate electricity. The concession experiences 1997. To get a new concession the power company was asked to raise the minimum flow from and contribute to the cost of river restoration about 50%, based on a river restoration concept. The objectives for river restoration in rural areas are mentioned in chapter 3.

The restoration costs:

- Removing the bank fixations (the concrete stone protection was shredded and given back to the river): approx. 2,5 Mio Euros.
- Building a bypass at the weir in Icking: approx. 200.000 Euros.

Not included in these costs is the land, given back to the river. The land is owned by the state of Bavaria.

Also not included are costs for the loss of energy, since with the new permission since 1997 the minimum discharge in the river is raised from 5 m^3/s to 15 m^3/s.

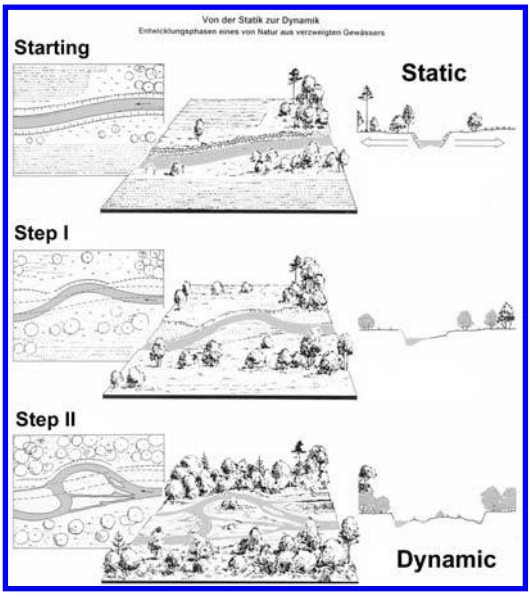


Figure 9. From static back to dynamic system, restoration steps of a cannalised river.

Copyright © 2006 Taylor & Francis Group plc, London, UK

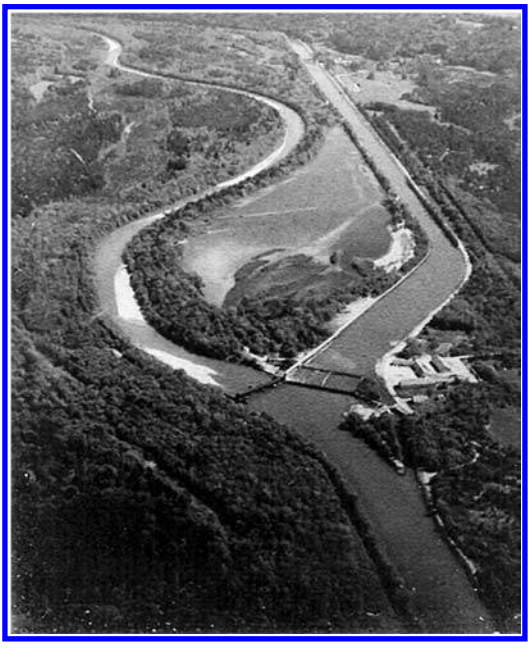


Figure 10. The Isar with the canal and the weir Icking, built 1925–1928.



Figure 11. The Isar and the weir Icking, 2001, after removing the bank pavement. The dynamic of the river is restoring a natural bed, migrating into the alluvial woodland.

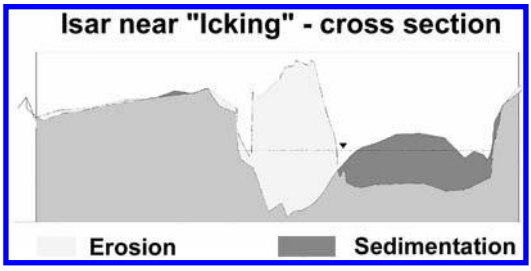


Figure 12. The widening of the river bed between 1997 and 2001, after the removal of the bank protection.

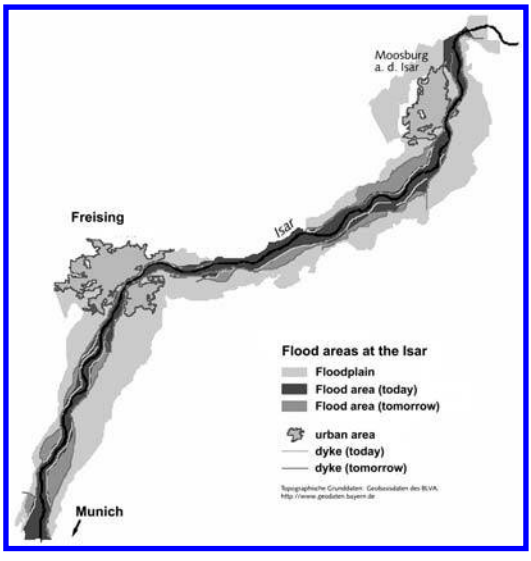


Figure 13. The Isar north of Munich.

6.2 *Isar, north of Munich*

70 km length and about 5000 ha alluvial plan, 3 500 ha woodlands. Most of the area is reported for Natura 2000. The water of the Isar between Munich and Landshut is taken into a channel, for the use of hydropower. The concession expired 2001 and got reviewed. The power company has to keep the minimum discharge in the river between 13 m^3/s and 17 m^3/s and has to pay 20 Million Euros within 10 years for restoration works, which will be done by the state and subsidies by the EU. The basic for this agreement was a river restoration concept. It shows:

- To improve flood control. For this the dikes has to be rebuilt. The old dikes are taken out from and are built at the edge of the woodland with the standards of today. Removing the old dikes, the retention area in causes of floods is enlarged by 1000 ha, from 1600 ha to 2600 ha.
- To replace weirs by ramps to improve the longitudinal connectivity.

Copyright © 2006 Taylor & Francis Group plc, London, UK



Figure 14. Weirs, brought in to stop bed erosion, are replaced by ramps to restore the lateral connectivity.



Figure 15. With widening the flood plain bank protection is withdrawn, the morphodynamic processes can start again, widening the once canalised river bed. The eroded tree improve the structures e.g. for fishes.

- Bank fixations are taken out, so the hydromorphodynamic processes of erosion and sedimentation of the once braided river system can start again. The land is own by the states, who is also in charge for the river.

7 OUTLOOK

There are not many cities in the world with more than a million of habitants, with a river in its middle, were people can bath. And there are also not many rivers in the vicinity of an urban agglomeration like the rural zones north and south of Munich, were the wilderness of a river is coming back by restoration projects. Here flood protection, ecology, recreation and nature conservation (Natura 2000 areas) are combined in win-win projects, done by an engaged team of engineers, landscape architects, supported by stakeholders and public participation through all decision making levels from the beginning. The people in the urban agglomeration of Munich gets back a river, showing again its alpine character, offering recreation facilities and also the beauties and secrets of nature.



Figure 16. River and floodplain as an unit, at least during floods. The Isar-flood 2002 near Freising.

REFERENCES

Bayerisches Landesamt für Wasserwirtschaft and Bayerisches Landesamt für Umweltschutz (eds) 2001. *Flusslandschaft Isar von der Landesgrenze bis Landshut – Leitbilder, Entwicklungsziele, Maßnahmenhinweise.* München-Augsburg.

Bayerisches Landesamt für Wasserwirtschaft (ed.) 2003. *Verbesserung der hygienischen Situation an der Oberen Isar*, München, p. 4.

Binder, W. 2004. *Die Isar.* in: Jürging, P. and Patt H. (eds), Fließgewässer- und Auenentwicklung, p. 416–428, Berlin-Heidelberg: Springer.

Binder, W. and Hoelscher-Obermaier, R., 2003: *Die Wildflusslandschaft Isar*, in: Garten und Landschaft 12/2003, München: Callwey.

Binder, W. 2000. *A experenencia da recabililitacao fluvial no Estadoda Baviera, Alemanha*. In: Moreira, I., da Graca Saraiva, M. & Correia, F. N. (eds): Gestai ambiental des sitemas fluvials, p. 485–496, Lisboa: Isapress.

Hafner; K. 2001. *Neues Leben für die Isar – 2,5 km bereits renaturiert.* Jahresbericht 2000/2001 des Isartalvereins. V., p. 30–34. München.

Mangelsdorf, J., Scheurmann, K., Weiß, F.-H. 1980. *River morphology.* Berlin-Heidelberg: Springer.

Copyright © 2006 Taylor & Francis Group plc, London, UK

Sediment transportation in the Yangtze River and impacts of the three gorges project

Z.Y. Wang
Professor, Dept. of Hydraulic Engineering, Tsinghua University, Beijing, China

Y.T. Li
Professor, Wuhan University, Luojia Hill, Wuhan, Hubei Province, China

ABSTRACT: The 6300-km long Yangtze River is the largest and longest river in China with a drainage area of 1.80 million km^2. The sediment transportation in the river is complex. Debris flow frequently occurs in the dry and hot valleys in the upstream reaches and has become the main form of sediment transportation from numerous gullies to the tributaries of the Yangtze River. The sediment carrying capacity of the debris flows is 40 times higher than normal sediment laden flows. The total sediment yield from the drainage area of the upper reaches is 2.17 billion tons per year. The sediment carrying capacity of the currents in the tributaries is much lower than load from debris flows and only a small part of the total sediment load from gullies is transported into the Yangtze River. The annual runoff increases from upstream to downstream along the course but the annual sediment load increases from the source to Yichang (the Three Gorges Dam site) reaching its highest amount of about 500 million tons/year. Downstream of Yichang the river flows out of the mountains and enters its alluvial reaches in the middle and lower reaches. Sediment load in the upper reaches is proportional to the flow discharge in flood and low flow seasons. The sediment load in the middle and lower reaches is proportional to the flow discharge in the low flow season but is not related to the discharge in the flood season because a lot of sediment is wash load in the flood season. The sediment load reduced along the course in the middle reaches due to deposition. The riverbed profile in the middle and lower reaches was developing toward the equilibrium profile defined by the minimum stream power but the impoundment of the Three Gorges Reservoir interrupts and modifiers this fluvial process. The Three Gorges Project on the Yangtze River is the largest hydro-project in China, which is regulating the flow for power generation. To mitigate reservoir sedimentation and channel erosion in the downstream reaches, the reservoir is operate in the mode of "storing the clear and releasing the turbid", which is the main strategy for sedimentation control. The sediment transportation in the middle and lower reaches is affected and the middle reaches have changed from siltation to erosion since the impoundment of the reservoir in 2002.

1 INTRODUCTION

The 6300-km long Yangtze River is the largest and longest river in China with a drainage area of 1.80 million km^2, as shown in Figure 1. The figure also shows the locations of hydrological stations, meteorological stations, tributaries, riparian lakes, and debris flow areas. Below the map is the diagram of a cross section through Batang-Chongqing-Poyang lake, showing the elevation of the basin from the origin in the west to the river mouth in the east. The Yangtze Basin has elevation varying from 5,000 m to the 0 m with latitude from N25° to N35°. The river flows through the Qinghai-Tibet Plateau, Yunnan-Guizhou Plateau, Sichuan Basin, Three Gorges, Jiang-Han Plain, Lower Yangtze Plain, and pours into the East China Sea at Shanghai. From the source to Yichang (Three Gorges Dam site) is the upper reach, from Yichang to Hukou (Poyang Lake mouth) is the middle reach, from Hukou to Datong is the lower reach, and below Datong is the estuary. In China, the river is called Changjang (long river), with special names for different stretches: the lower reaches is called Yangtze River; the middle reaches are called Jingjiang River; the reach from Yichang to Yibin is called Chuanjiang River, from Yibin to Batang is called Jinsha River, and from Batang to the origin is called Tongian River (heaven river).

The sediment transportation in the river is complex. Debris flow frequently occurs in many gullies in the dry and hot valleys and has become the main form of sediment transportation from numerous gullies to the tributaries of the Yangtze River. The sediment carrying capacity of the debris flows is more than 40 times higher than normal sediment laden flows. The total

Copyright © 2006 Taylor & Francis Group plc, London, UK

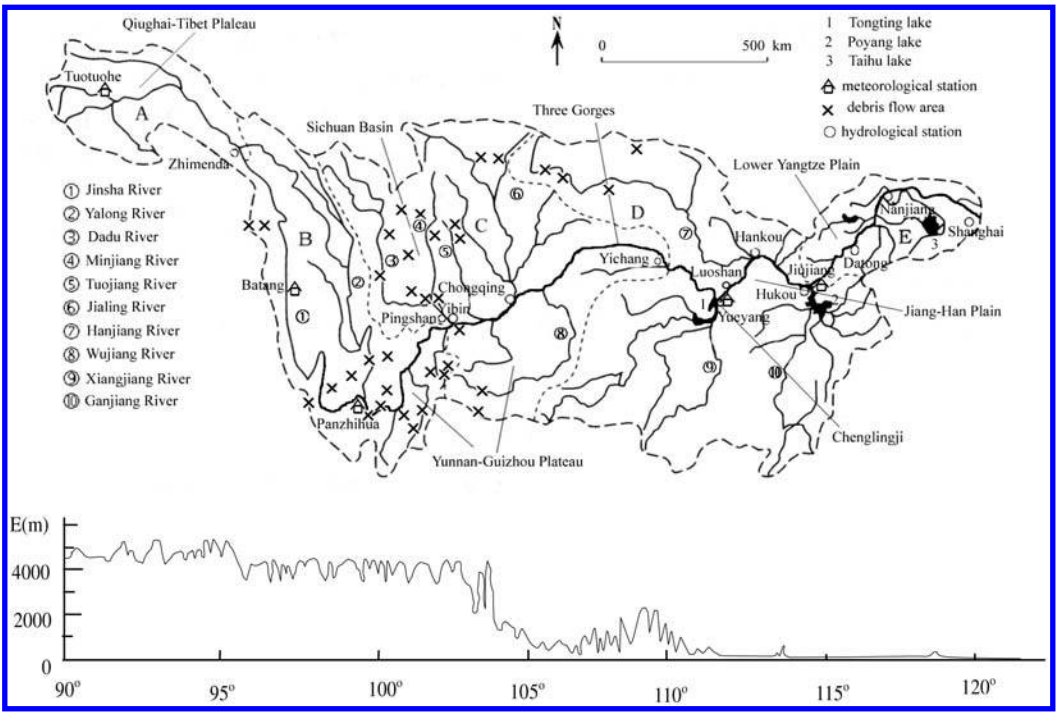


Figure 1. The Yangtze River Basin, showing the locations of the hydrological stations, meteorological stations, tributaries, riparian lakes, and the debris flow areas; and the watershed topography on an east-west line from Batang through Chongqing and Poyang Lake to the East China Sea.

sediment yield from the drainage area of the upper reaches is 2.17 billion tons per year. The sediment carrying capacity of the currents in the tributaries is much lower than load from debris flows and only a small part of the total sediment load from gullies is transported into the Yangtze River. The annual runoff and sediment load varies along its course. The annual runoff increases from upstream to downstream but the annual sediment load increases from the source to Yichang (the Three Gorges Dam site) reaching its highest amount of about 500 million tons/year. Downstream of Yichang the river flows out of the mountains and enters its alluvial reaches. The sediment load reduces from Yichang to Hankou due to deposition.

There have been quite a few studies on the sediment in the Yangtze River. Lu and Higgitt (1998) studied the sediment yield from the tributaries of the upper Yangtze River basin in the period 1956–1987 and indicated that ten stations, mainly located on the Dadu River and Wujiang River have shown increasing sediment yield, and six stations, located on the upper Jialing River and Tuojiang River have experienced decreasing sediment yield. Most of the observed decreases in sediment yield are associated with large reservoirs on these rivers. Zhang and Wen (2004) also studied sediment yield of the upper Yangtze River and illustrated a decrease in sediment yield in the Jialing River and an increase in the Jinsha River during the period from the 1950s to the 1990s. It was apparent that the decreasing sediment yield in the Jialing River was due to construction of reservoirs, reforestation, and soil and water conservation efforts. Land degradation, engineering, and channel activities were responsible for the increase in sediment yield of the Jinsha River. Higgitt and Lu (2001) examined sediment yield and its response to catchment disturbance and environmental variables in the upper Yangtze River basin and illustrated that a significant increase in sediment yield has occurred over about 8% of the catchment area while about 3% of the catchment has experienced decreasing sediment yields.

Investigation of the temporal and spatial variability of sediment transport within the upper Yangtze River catchment leads to the following paradox. There is evidence that the extent and magnitude of soil erosion across southern China has increased dramatically during the last 30–40 years (Smil, 1993; Wen, 1993; Lu and Higgitt, 1999; Edmonds, 1994). But there is no evidence of sediment load increasing at the Yichang Hydrological Station delivered from the upper Yangtze River catchment. Moreover, many studies have indicated that the total soil erosion from the upper reaches

Copyright © 2006 Taylor & Francis Group plc, London, UK

of the Yangtze River is around 2.2 billion tons per year (Tang et al., 2004). But the sediment load measured at Yichang is only about 500 million tons per year. A large volume of sediment is stored somewhere in the upper reaches.

The Three Gorges Dam, which is still under construction, is at Sandouping, 38 km upstream from Yichang (Fig. 1). The main purposes of the project are flood control, power generation and navigation. The dam is 185 m high and the storage capacity of the reservoir is 39.3 billion m^3, in which 17.2 billion m^3 are for sedimentation and 22.1 billion m^3 for flood control. The dam controls 1 million km^2 of drainage area. The hydroelectric station of the TGP will be the biggest in the world, with an installed capacity of 17,680 MW and an annual generation of 84 billion kWH. The project may replace several thermal power stations, thus reduce the consumption of coal by 50 million tons every year and cut carbon dioxide, sulphur-dioxide, carbon monoxide and nitrogen-oxide emissions by 100 million tons, 2 million tons and 10,000 tons and 370,000 tons, respectively. The project will improve navigation conditions from Yichang to Chongqing, by eliminating shoals, deepening and widening the shipping lanes and reducing river currents, and thus enable 10,000-ton tow-boats to sail right up to Chongqing. The annual shipping capacity will increase to 50 million tons from the present 10 million tons and transport costs will be cut by 35–37%.

The Three Gorges Reservoir began to fill in 2002 and the pool level is around 140 m. The water level will rise to the planned normal pool level 175 m in 2009 when the project will be completed. Sedimentation in the Three Gorges Reservoir and erosion of the downstream reaches by the released relatively clearer water from the reservoir has changed the sediment transportation in the river. Operation schemes and management strategies of the reservoir are important to control sedimentation in the reservoir and erosion in the downstream reaches. This paper studies the sediment load in different reaches and the impacts of the Three Gorges Dam on the sediment transportation in the river.

2 SOIL EROSION AND SEDIMENT STORAGE IN THE UPPER YANGTZE RIVER BASIN

There are three different climate patterns in the basin. Figure 2 shows typical climate diagrams for the three zones. It is cold in the source area on the Qinghai-Tibet Plateau and the Tuotuohe Meteorological Station has a typical cold climate pattern (Fig. 2). It is hot and dry in the Jinsha River reach from Batang to Yibin, as shown in the middle of Figure 2 for the Panzhihua Meteorological Station. The area experiences high erosion and is the main source of sediment for the Yangtze River. In the middle and lower reaches it is wet and warm, with the Jiujiang Station shown as an example in Figure 2. The tributaries in the middle and lower reaches contribute little sediment but input 50% of discharge to the Yangtze River.

A parameter is defined to represent the wetness, W, as follows:

$$W = \frac{R}{300mm} - \frac{T}{100^\circ C} \quad (1)$$

in which R is monthly average precipitation in millimeters and T is the monthly average temperature in degree Celcious. A positive W value means a wet climate and well-developing vegetation, but a negative W value implies a dry climate and poor vegetation. At Tuotuohe and Yushu (Zhimenda) the average temperature is low but the wetness is positive, because the evaporation is low. Because of the low temperature and cold climate, vegetation may slowly develop but mainly is herbaceous. The Jinsha River basin (from Batang to Yibin) is called dry and hot valleys, with annual average temperature about 20°C, but monthly average rainfall from December to April is less than 10 mm and the wetness number is negative resulting in poor vegetation. In summer from June to September, the monthly rainfall is more than 120 mm, which causes high soil erosion. The area has experienced extremely high tectonic motions and the rocks have been cut into small pieces. The topsoil layer is thin. Splash erosion, sheet erosion, and rill erosion are moderate but gully erosion is extremely intensive. The rate of erosion per area is very high and the sediment eroded from the area is composed of silt, sand, gravel, cobbles, boulders, and a small amount of clay. More than 50% of the sediment load to the middle and lower Yangtze River are from the Jinsha River basin.

Soil erosion, sediment load, and sediment storage have been measured and the data have been analyzed. There are many hydrological stations and numerous monitored cross sections and gauging stations on the river and its tributaries. Regular measurements are performed daily at the hydrological stations, including stage, velocity, discharge, suspended sediment concentration, and rate of bed load transportation. The later is measured by using bed load samplers. Channel bed deformation is measured occasionally at all stations and at the monitored cross sections on the rivers, ravines, and gullies. The error in bed elevation measurement is less than 5 mm and the error in horizontal positioning is less than 50 mm. The sediment load of the river is calculated with the flow discharge, suspended sediment concentration, and rate of bed load transportation. Because the bed load is less than 1% of the total load, the relatively large error in bed load measurement does not affect the accuracy of the total sediment load measurement. The volume of sediment deposition on the riverbed and reservoirs is calculated with the measured cross sections.

Copyright © 2006 Taylor & Francis Group plc, London, UK

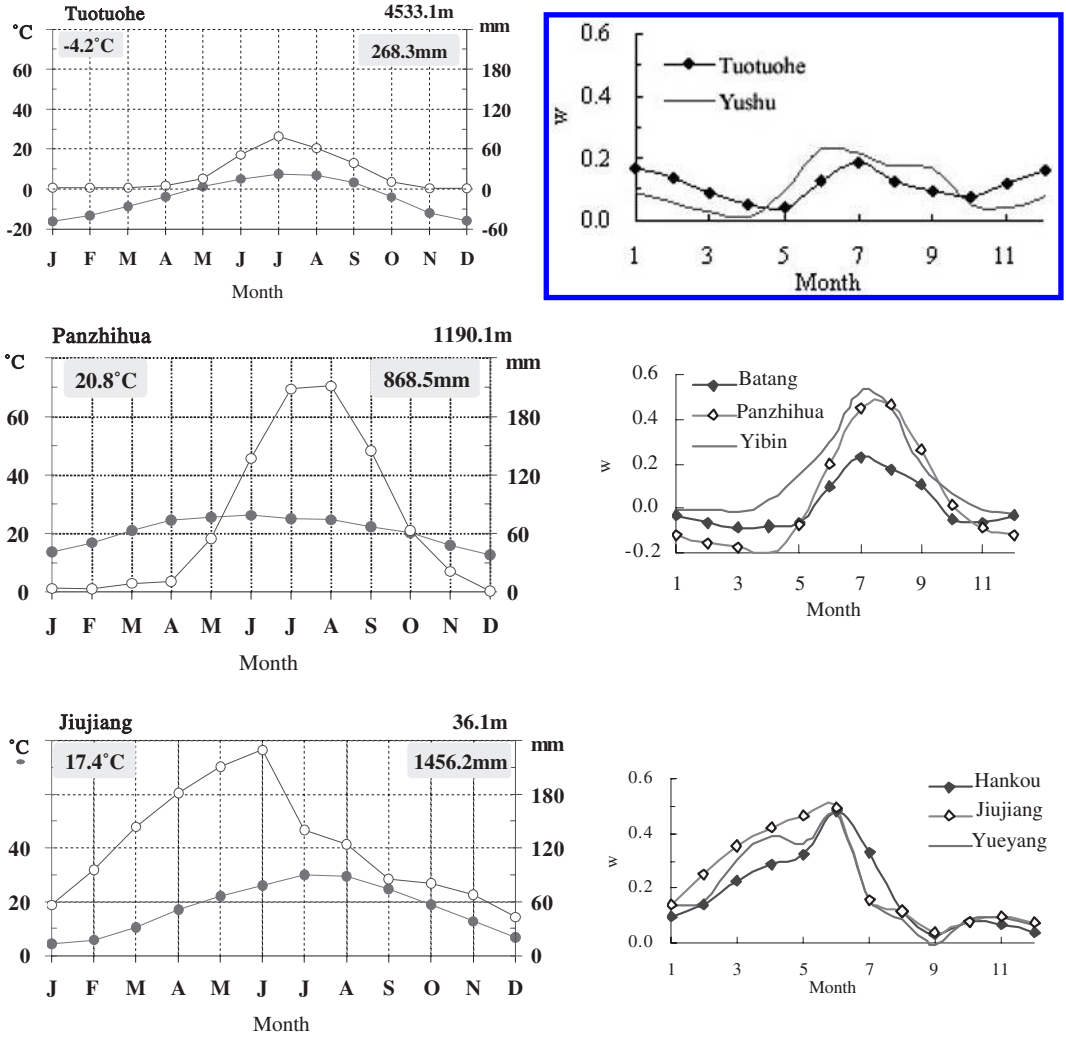


Figure 2. Climate diagrams showing monthly average temperature and precipitation and distributions of wetness number (W) of three typical climate patterns in the Yangtze River basin (note: the climate diagrams also list the elevation, the mean annual temperature and total annual precipitation. Data Source: Climatic Data Center, National Meteorological Information Center, CMA).

Soil erosion is measured in the following ways: (1) the soil erosion areas are determined by field investigations; (2) for each soil erosion area, the rate of sediment load transportation is measured at the downstream end of the small wartershed (generally several tens to a hundred square kilometers); (3) the rate of sediment erosion is calculated with the total load per year over the area of the watershed; or (4) the rate of soil erosion is directly measured by collecting the sediment eroded from a 100 m^2 sample plot, which is isolated by using low steel plate walls during rain falls; (5) the amount of soil erosion from all small watersheds is summed to obtain the total amount of soil erosion from the basin.

The total amount of soil erosion from the upper Yangtze River Basin is reported at 1.6–2.24 billion tons per year, depending on the statistics. Yu et al. (1991) evaluated statistics and reported the total soil erosion from the upper Yangtze River basin as 1.6 billion tons per year. Tang et al. (2004) presented the value of 2.24 billion tons per year. Yu (2003) adopted the value at 2.179 billion tons per year. The ministry of water resources reported the total soil erosion determined by remote sensing performed in 1990, which agrees with

Copyright © 2006 Taylor & Francis Group plc, London, UK

Table 1. Sediment yield per area from debris flow gullies in the upper Yangtze River basin.

Debris flow Gully	Area (km^2)	Sediment yield per area ($t/km^2.yr$)	Period of measurement	References
Guxiang gully	26.00	470,020	1964–1965	Wang & Zhang, 1985
Liuwan gully	1.97	124,970	1963	Yang, 1985
Huoshao gully	2.03	126,100	1973	Yang, 1985
Niwan gully	10.30	65,500	1965	Yang, 1985
Hunshui gully	4.50	374,240	1976–1978	Zhang & Liu, 1989
Jiangjia Ravine	48.60	142,200	1965–2002	MWRC, 2000

the value around 2.2 billion tons (ACRS, 1990). Yu (2003) indicated that the Jinsha, Jialing and Minjiang River basins are the main sediment sources for the Yangtze River, with average annual soil erosion 829 million tons, 559 million tons and 253 million tons.

The total soil erosion from the upstream reaches of the Yangtze River is 2.179 billion tons per year. But the long-term average suspended load at Yichang before the impoundment of the Gezhouba Dam – the first dam on the river – in 1980 was 514 million tons, with an additional sum of bed load of 9.54 million tons (sand bed load 8.78 million tons plus gravel bed load 0.758 million tons) (TGP Water Survey, 2005). The difference between the volumes of the total soil erosion from upper Yangtze River basin and sediment load at Yichang is 1.655 billion tons. Where does the huge amount of sediment go?

The Jinsha River basin (upstream Yangtze River basin from the source to Yibin) is the most sediment source of the Yangtze River, with total soil erosion of 829 million tons per year. As shown in Figure 1. there are many debris flow areas in the basin and the slope in the basin is quite high. Table 1 shows the sediment yield from several debris flow gullies measured at the downstream end of the gullies. The sediment yield per area from the debris flow gullies is generally more than 40 times higher than the basin average. For example, the Xiaojiang River is a tributary of the Jinsha River as shown in Figure 3. which is 138 km long and has a drainage area of 3043 km^2. There are 107 debris flow gullies in the small river basin, among which the Jiangjia Ravine is the most well-known because of its high frequency of debris flow events, and they transport huge amounts of sediment into the Xiaojiang River every year. The sediment yield from the Jiangjia Ravine is 142,200 $t/km^2.yr$, of which only 2% can be transported downstream by the Xiaojiang River.

Figure 4 shows the aggradation and degradation of the Jiangjia Ravine in the periods 1957–1985 and 1957–2002 (He et al., 2003). Gully erosion is the main type of erosion, which produces 75–83% of the total sediment yield from the ravine. The eroded sediment from the upstream reaches was transported in debris flows and deposited in the downstream reaches of the ravine. The gully bed aggraded by more than 40 m in the period of 1957–2002. A huge amount of sediment is stored in the downstream reaches and the mouth of the ravine. The same story occurred in numerous debris flow gullies. All the mouths of the debris flow gullies along the Xiaojiang River have been silted up by several tens of meters in the past 50 years.

Figure 5 shows the size distributions of debris flows in the upper reaches of the Yangtze River in comparison with the size distributions of suspended load at Yichang and Datong Hydrological Stations (Kang et al. 2004, Xu 2005, Wang et al. 2001, Xie et al. 2004, & Wan et al. 2003). Only the fine part of sediment eroded from the basin is transported into the Yangtze River. Dividing the sediment into n-fractions with diameter in the ranges $D_1 \sim D_2$, $D_2 \sim D_3$, $D_3 \sim D_4$, … in which the subscript 1,2,3, are the order numbers. If the cumulative percentage corresponding to D_i and D_{i+1} on a sediment size distribution curve in the figure is P_i and P_{i+1}, $\Delta P_i = P_{i+1} - P_i$ is the percentage of the i-th fraction. The amount of sediment of diameter in the range $D_i \sim D_{i+1}$ depositing in a river reach between an upstream section and a downstream section, S_{di}, is given by:

$$S_{di} = S_{up}(\Delta P_i)_{up} - S_{down}(\Delta P_i)_{down} \quad (2)$$

in which the subscripts up and down represent upstream section and downstream section of the river, S_{up} and S_{down} are sediment loads in the upstream section and downstream section.

The sediment eroded from the upper reaches of the Yangtze River is complex and it is difficult to calculate the average size distribution. However, mass sediment transportation in the most upstream tributaries and gullies is in the forms of landslides and debris flows. If the curve of S7 (the Little Haihe River, a tributary of the Xiaojiang River), which is average sediment size distribution of debris flows and hyperconcentrated flows, is used to represent the size distribution of sediment eroded from the upper reaches, the amount of sediment storage of different fractions can be estimated with Equation (2). At the Yichang station, gravel bed load composes only 0.15% and sand bed load 1.7% of the total load, the size distribution curve of suspended load can be approximately regarded as the size distribution of total load. The amount of sediment deposition in the gullies and tributaries can be calculated by using

Copyright © 2006 Taylor & Francis Group plc, London, UK

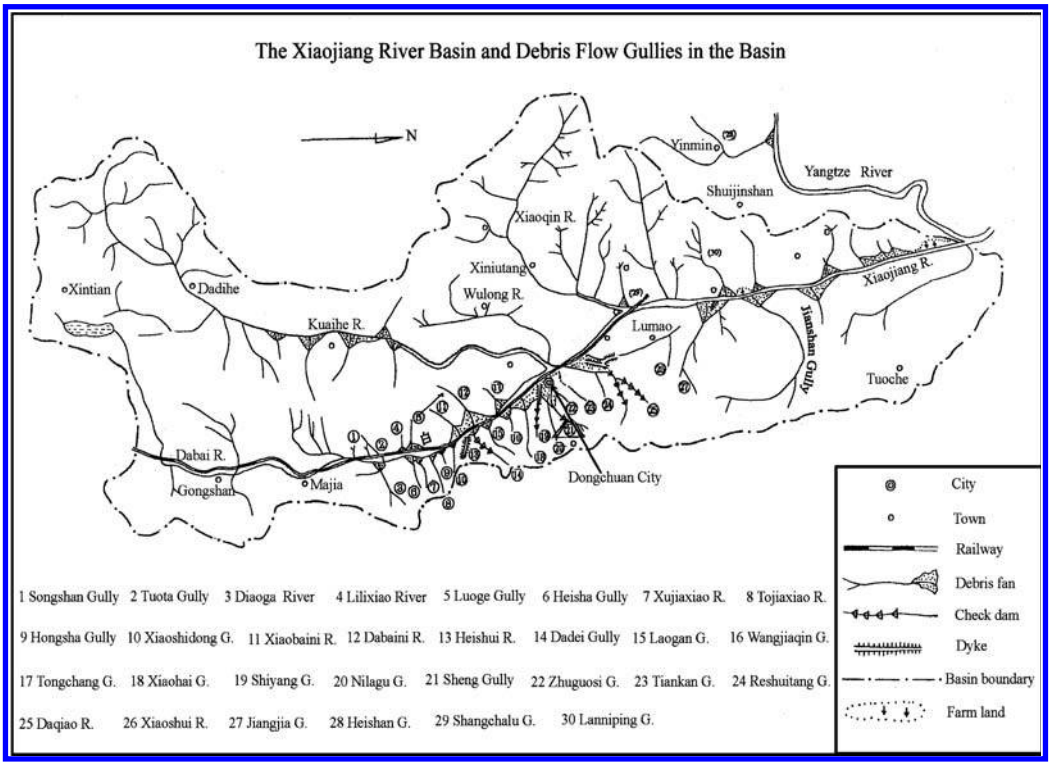


Figure 3. The Xiaojiang River Basin and debris flow gullies in the basin (provided by Zhicheng Kang, Institute of Mountain Hazard and Environment, Chinese Academy of Sciences).

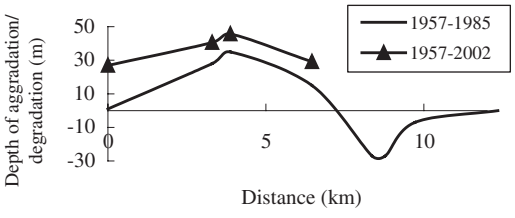


Figure 4. Aggradation and degradation of the Jiangjia Ravine in the periods 1957–1985 and 1957–2002 as a function of distance from the ravine mouth.

Equation (2) and taking figures for the upstream section from S7 and for the downstream section from the size distribution curve of Yichang as follows:

For the fraction coarser than 0.5 mm, $S_d = 2179^* 0.55 = 1198$ million tons

For the fraction in the range $0.05 \sim 0.5$ mm, $S_d = 2179^* 0.22 - 514^* 0.35 = 300$ million tons

For the fraction finer than 0.05 mm, $S_d = 2179^* 0.23 - 514^* 0.65 = 167$ million tons.

In other words, almost all the sediment coarser than 0.5 mm eroded from the watershed deposits in the gullies and tributaries of the upper Yangtze River basin; 300 of the 480 million tons of sediment of diameter in the range of $0.05 \sim 0.5$ mm and 167 of the 501 million tons of sediment finer than 0.05 mm deposit in the gullies and the tributaries of the upper Yangtze River basin.

3 SEDIMENT TRANSPORTATION

The sediment transportation in the river is complex. The sediment carrying capacity of the currents in the tributaries is much lower than the load from debris flows and only a small part of the total sediment load from gullies is transported into the Yangtze River. The sediment load in the river varies along its course because the runoff increases but the energy slope decreases along the course. Figure 6 shows the annual runoff and sediment load in the Yangtze River along its course. The annual runoff increases from upstream to downstream with the annual water at Yichang about 450 billion m^3. The annual sediment load increases from the source to Yichang (the Three Gorges dam site is at 4400 km in Fig. 1) reaching its highest amount

Copyright © 2006 Taylor & Francis Group plc, London, UK

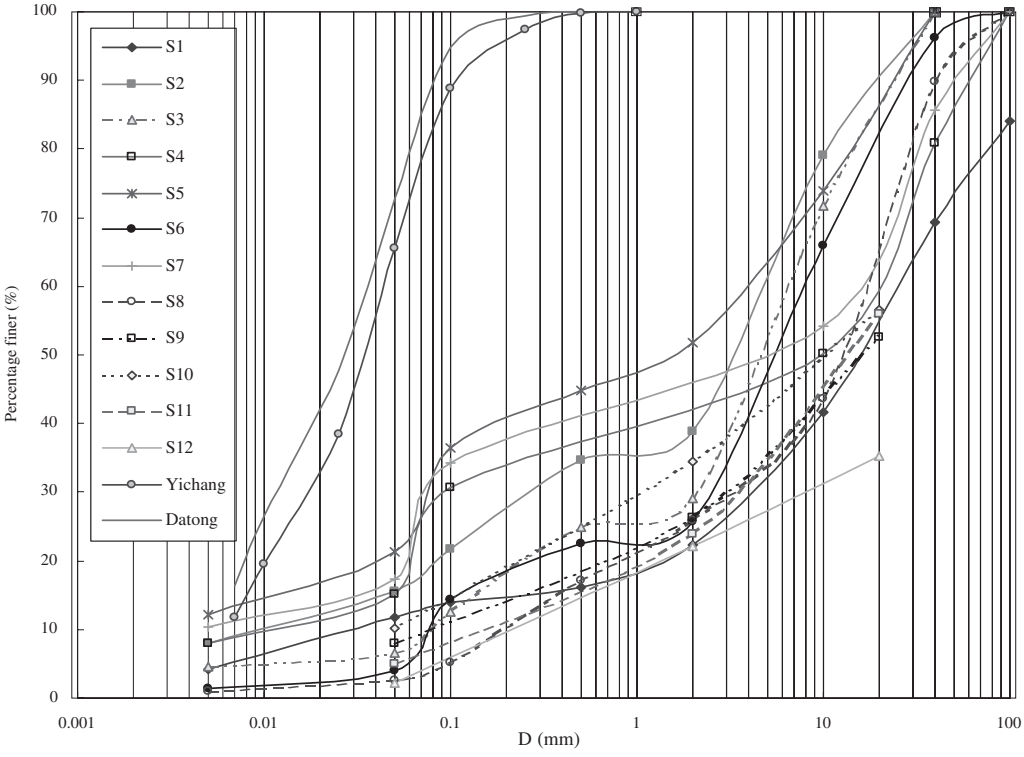


Figure 5. Comparison of the size distributions of sediment transported by debris flow from gullies to the tributaries of the Yangtze River with and those of suspended load at Yichang and Datong stations in the Yangtze River.
Note: S1–S12 are size distributions of debris flows in the upper Yangtze River basin: S1 = Little Xujia River; S2 = Big Baini Ravine; S3 = Tongchangqing Gully; S4 = Dade Gully; S5 = Little Haihe River; S6 = Jiangjia Ravine; S7 = Daduo Ravine; S8 = Xiaojiang River; S9 = Sunshuihe Gully; S10 = Niurihe Gully; S11 = An-Ning River; S12 = Yalong River.

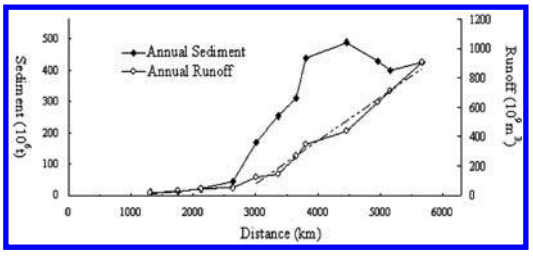


Figure 6. Distribution of annual runoff and sediment load along the course of the Yangtze River (The points are the average value for the period of 1950–2000 with data measured at the stations from left to right: Zhimenda, Batang, Panzhihua, Shigu, Qiaojia, Pingshan, Zhutuo, Cuntan, Yichang, Luoshan,Hankou,and Da-tong).
Note: The source of the data and period of statistics are: Zhimenda 1957–1999 (Wu & Yu 2002), Batang and Shigu, 1954∼1987 (Pan 1999), Panzhihua,1964∼1996 (Zhang & Wen 2002); Qiaojia, 1958∼1992 (Deng 1997); Datong, Hankou, Yichang, Pingshan, 1950∼2002 & Zhutuo, 1950∼2000 (MWRC 2000, 2001 & 2002); Cuntan, 1950∼2000 (Wang & Yi 2003); Luoshan, 1956∼1995(Pan & Lu 1999).

of about 500 million tons/year. The median diameter of suspended load at Yichang is 0.033 mm and the median diameter of bed load is 24 mm. Downstream of Yichang the river flows out of the mountains and enters its alluvial reaches. The sediment load reduces from Yichang to Hankou due to deposition.

Figure 7 shows the water-sediment diagrams at four hydrological stations on the Yangtze River, in which the horizontal axis is the year of the statistics, the left vertical axis is the annual runoff volume and the right vertical axis is the annual sediment load at the given hydrological station. The scales of the two vertical axes are set such that the long term average runoff and the long term average sediment load have the same position for the Datong Station, which is the most downstream station between the lower reaches and the estuary of the river. In the diagram the load and runoff are comparable and mutually convertible. A given runoff also represents the amount of sediment load the runoff can transport into the ocean. For the Pinshan (Yibin) and Yichang Stations, the curve of sediment load is much higher than the curve of runoff,

Copyright © 2006 Taylor & Francis Group plc, London, UK

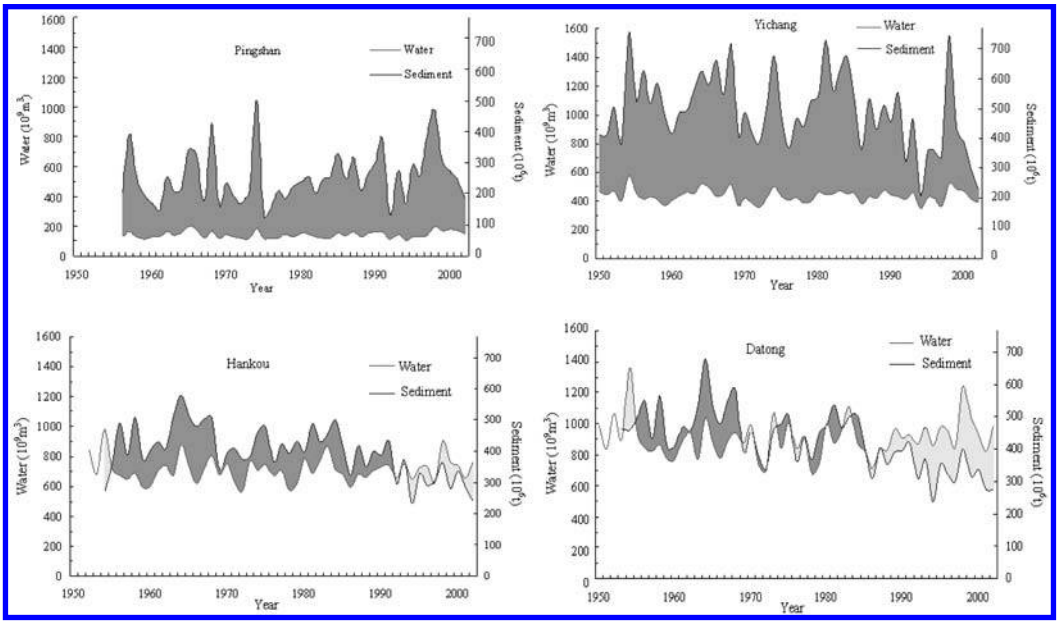


Figure 7. Water-sediment diagrams of the Pingshan (Yibin), Yichang, Hankou (Wuhan), and Datong hydrological stations on the Yangtze River; Beibei station on the Jialing River; Huangzhuan station on the Hanjiang River; Chenglingji Station on Tongting Lake; and Hukou station on Poyang lake.

which implies that the load is more than the capacity of the flow and the difference between the two curves (black area) implies aggradation downstream. Both the runoff and load curves increase from Pinshan to Yichang but the load curve increases more and the black area becomes larger. From Yichang to Hankou (Wuhan), however, the runoff curve increases but the load curve reduces and the black area is much smaller, which implies a huge amount of sediment deposits in the reach between the two stations. At Datong Station the period from the mid of the 1950s to the end of the 1960s is a "black" period, during which more sediment load than the average came to the estuary. Since then the sediment load has been continuously reducing and the load curve is much lower than the runoff curve.

The middle and lower reaches of the Yangtze River are alluvial and the sediment load varies in accordance with the sediment carrying capacity of the flow. Thus, sediment load is related to the flow discharge. Figure 8 shows the relations between the total sediment load and water discharge at the Yichang, Hankou, and Datong stations in different seasons. At Yichang (upper reaches), the sediment load is always proportional to the flow discharge because both sediment and water are from the upper reaches. At Hankou and Datong Stations (middle and lower reaches), however, the sediment load is proportional to the flow discharge in the low flow season from January to June and from October to December, but the load is not related to the discharge in the flood season from July to September. In the middle and lower reaches, sediment consists mainly of bed material load in the low flow season. The higher the flow discharge, the more sediment is eroded from the channel bed, and, therefore, the higher the sediment load. In the flood season, however, a lot of sediment is transported from upstream reaches but half of the water is from the middle and lower reaches. Sediment and water are from different reaches and a huge amount of sediment load is wash load, therefore, the sediment load is not strongly related to flow discharge.

Wang & Dittrich (1992) used the Rouse number Z to differentiate wash load and bed material load, in which the Rouse number is defined as:

$$Z = \frac{\omega}{\kappa U_*} \tag{3}$$

in which ω is the fall velocity of the sediment particles; $\kappa = 0.41$ is the von Karman constant, and $U_* = \sqrt{gsR}$ is the shear velocity, s is bed slope, R is the hydraulic radius of the flow and is equal to the average depth in a wide river channel. Wang and Dittrich analyzed the rate of sediment transportation at high concentrations under different flow conditions and found that some coarse sediment may wash downstream for several hundred kilometers without exchange with the bed sediment at high flow intensities. Thence they

Copyright © 2006 Taylor & Francis Group plc, London, UK

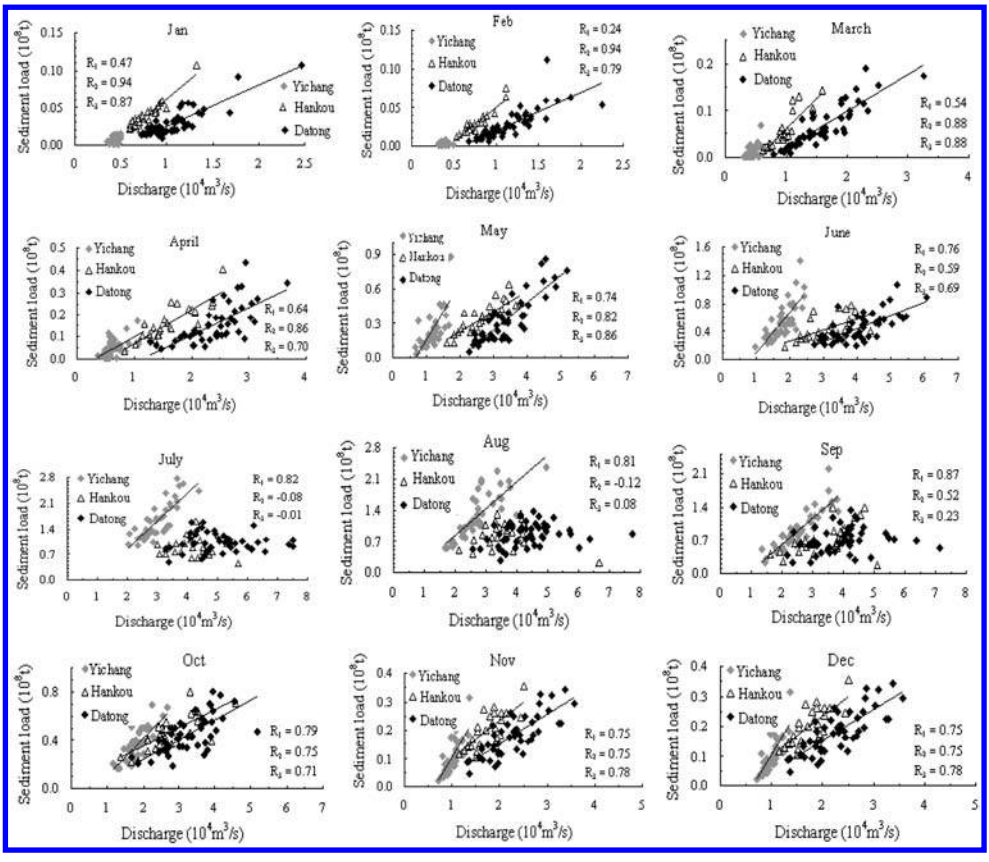


Figure 8. Relations between the sediment load and flow discharge at the Yichang (1, upper reaches), Hankou (2, middle reaches) and Datong (3, lower reaches) stations in different seasons, where Rn is the correlation coefficient of these relations.

proposed the following for identification of bed load, suspended bed material load, and wash load:

$$Bed\ Load > Z = 3 > Suspended\ Bed\ Material\ load > Z = 0.06 > Wash\ Load \quad (4)$$

Figure 9 shows the calculated Rouse number at the Datong station in flood and low flow seasons as a function of the flow depth. In the calculation the fall velocity is determined for the median diameter of the suspended sediment load. In the low flow season, the Rouse number is in the range of 0.1–0.25 and the suspended sediment is bed material load; and in the flood season, however, the Rouse number is mostly smaller than 0.06 and thence the suspended sediment is wash load.

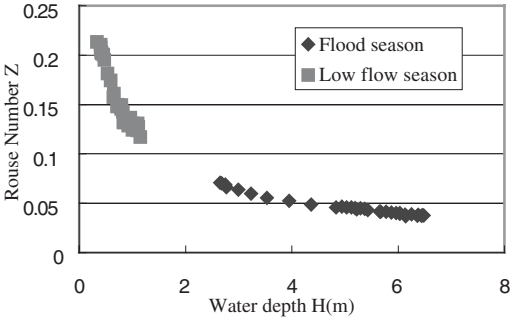


Figure 9. The calculated Rouse number at the Datong station in flood and low flow seasons as a function of the flow depth.

4 FLUVIAL PROCESS IN THE MIDDLE AND LOWER REACHES

The fluvial process and lateral movement of the channel is now constrained by the grand levees in the middle and lower reaches of the river. Sediment deposition and erosion mainly affect the longitudinal profile of the river. According to the minimum stream power theory, the morphology of fluvial rivers develops to reach

Copyright © 2006 Taylor & Francis Group plc, London, UK

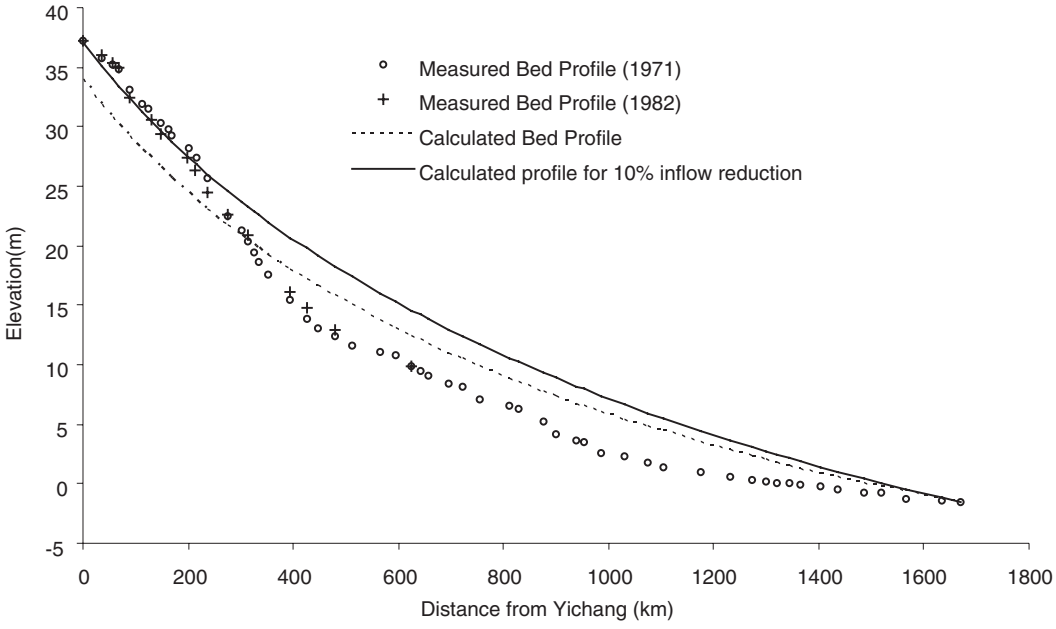


Figure 10. Longitudinal bed profiles of the middle and lower Yangtze River in comparison with the equilibrium bed profile required to reach the minimum stream power.

the minimum stream power (Yang 1996). This can be described by the following equation:

$$\frac{dP}{dx} = \frac{d}{dx}(\gamma s Q) = \gamma(Q\frac{ds}{dx} + s\frac{dQ}{dx}) = 0 \qquad (5)$$

in which Q is the annual discharge, γ is the specific weight of water, s is the bed slope and x is the distance down the river. The equilibrium bed slope can then be calculated with the following formula:

$$s_{n+1} = \frac{s_n}{Q_n}[Q_n - \frac{\Delta Q_n}{\Delta x_n}(x_{n+1} - x_{n-1})] \qquad (6)$$

For the fluvial reaches of the Yangtze River (downstream from Yichang), the discharge increases along the course due to the inflow from tributaries; thus, the equilibrium slope decreases along the course. The river exhibits a concave downward riverbed profile, as shown in the measured profiles in 1971 and 1981 in Figure 10. The fluvial process is developing toward the calculated profile (dashed curve). The inflow of water from the tributaries in the middle and lower reaches is reducing due to water diversion for economic development and agriculture. Assuming a reduction in the reach of about 10%, the equilibrium river bed profile will be different as shown in Figure 10 (solid curve). It is clear that the measured bed profile develops toward the equilibrium profile.

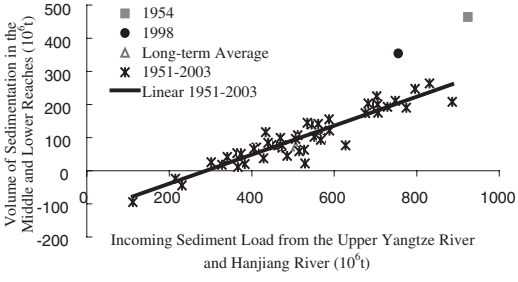


Figure 11. Relation of the net sedimentation in the middle and lower Yangtze River with the incoming sediment load from the upper Yangtze River (measured at Yichang) and the Hanjiang River (sedimentation in Tongting Lake is not included in the net sedimentation).

The equilibrium bed profile is higher than the present profile and sedimentation dominates the fluvial process of the middle and lower reaches. Still a huge amount of sediment is needed for the riverbed to reach the equilibrium profile. Nevertheless, the volume of annual sedimentation in the middle and lower reaches depends on the incoming load. Generally speaking, the higher the incoming sediment load from the upper reaches, the more sediment deposits in the middle and lower reaches. Figure 11 shows the relation between the net sedimentation (the volume of sedimentation minus erosion) and incoming sediment load

Copyright © 2006 Taylor & Francis Group plc, London, UK

from the upper reaches (measured at Yichang) and the Hanjiang River, in which the sedimentation in Tongting Lake is not included in the net sedimentation. The sediment load from Yichang and the Hanjiang River is more than 95% of the total sediment transported into the middle and lower reaches of the Yangtze River, to which the total incoming load refers in the following text. The net sedimentation in the middle and lower reaches increases linearly with the total incoming load. If the total incoming load is more than 280 million tons, sedimentation occurs in the river; if the total incoming load is around 500 million tons, 100 million tons of the sediment will deposit in the river. In the period of 1955–2000, the annual siltation rate of the average riverbed elevation for several reaches is as follows:

Yichang – Chenglingji −2.7 cm/yr;
Chenglingji – Luoshan +1.0 cm/yr;
Luoshan – Hankou +2.0 cm/yr;
Hankou – Jiujiang +3.0 cm/yr;
Jiujiang – Datong +1.8 cm/yr.

If there were no interruption by human activities, the fluvial process to reach the minimum stream power would continue for a long period of time because the present bed profile is still far from the equilibrium profile.

5 SEDIMENTATION IN THE THREE GORGES RESERVOIR

The Three Gorges Reservoir, which is still under construction and will have a storage capacity of 39 billion m^3. The reservoir, located 37 km upstream of the Yichang Station, began to fill in June 2002. The pool level is now around 140 m and will rise to the normal pool level of 175 m in 2009. The filling of the reservoir has caused further reduction in the sediment load to the middle and lower reaches. The reservoir is trapping sediment and releasing flow starving of sediment. The rate of sedimentation in the reservoir depends mainly on the pool levels and operation scheme. The normal pool level (NPL) is set at 175 m, and the flood control level (FCL), to which the pool will be drawn down at the beginning of the flood season generally in June, is set at 145 m. The reservoir is impounded to 175 m after the flood season, usually from the beginning of Oct. and drawn down to 145 m before and during flood. FCL is the major factor affecting the sediment deposition amount in the reservoir.

The main strategy for sedimentation control is "storing the clear and releasing the turbid" (Sedimentation Panel 1988). Sediment transportation in the Yangtze River occurs, of 80–90% of annual sediment load with 50–60% of annual runoff water, in 2–4 months of the flood season. The pool level is drawn down from 175 m to 145 m from June to September when

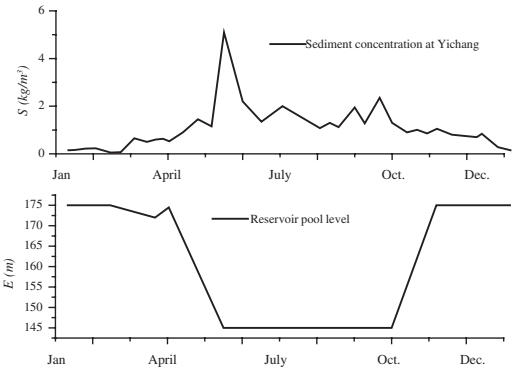


Figure 12. Typical processes of sediment concentration at Yichang and the operational pool level of the reservoir for sedimentation control.

the sediment concentration is high, allowing the turbid water wash through the dam. The reservoir stores water from October when the income water becomes clear. Figure 12 shows the typical seasonal variations of sediment concentration at Yichang and the operational pool level for sedimentation control, in which the distribution of sediment concentration is the average in the 1960s.

By employing the strategy of "storing the clear and releasing the turbid", much less sediment will deposit in the reservoir while the reservoir will be still able to store enough water for power generation in the low flow seasons. Although the pool level is drawn down to FCL, the stage in a 400 km long reach within the reservoir is 10–70 m higher than those without the dam and the average velocity is much slower. For a discharge of 30,000 m^3/s, the average velocity would be 1.5–3.5 m/s if there were no dam, and it is only 0.3–1.3 m/s with the dam. Therefore, sedimentation occurs and the riverbed is silted up.

The sedimentation in the TGP reservoir is calculated with numerical models. Han developed a one-dimensional mathematical model of sedimentation based on the equation of on-equilibrium transport of sediment. In the model Han employed the Manning's formula, the continuity equation and the following sediment equation (Han 1979, Lin et al. 1983):

$$\frac{\partial(hS)}{\partial t}+\frac{\partial(qS)}{\partial x}+\alpha\omega(S-\Phi)=0 \qquad (7)$$

where h is the depth of flow, S the mean concentration of sediment in a cross section, q the water discharge per unit width, ω the fall velocity of sediment, α a variable coefficient. The subscripts x and t denote the independent variables in partial differentiation. Φ is the mean concentration of sediment corresponding to the capacity of sediment transport and represents

Copyright © 2006 Taylor & Francis Group plc, London, UK

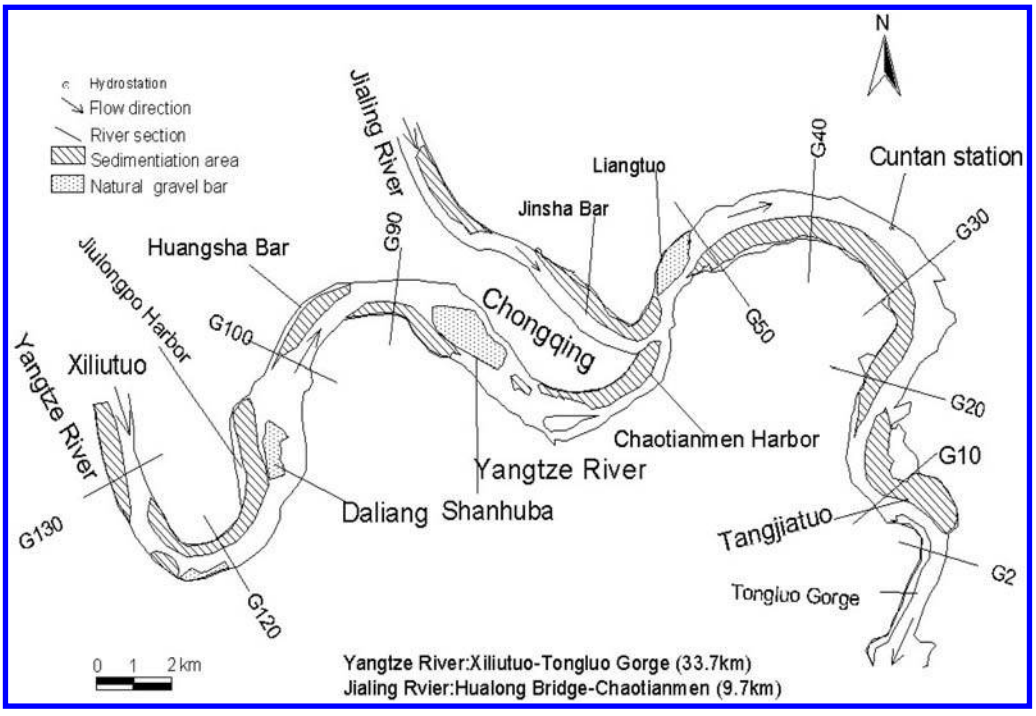


Figure 13. Sedimentation in the Chongqing reach after 80 years operation of the TGP reservoir (Physical model experimental results). The shadowed areas indicate the places where cumulative sedimentation would occur. G2 – G130 represent the measurement cross sections (Wang et al. 1990).

the suspended sediment-carrying capacity of the flow, which is given by:

$$\Phi = 0.03 \frac{Q^{2.76} B^{0.92}}{A^{3.68} \omega^{0.92}} \quad (8)$$

in which Q is the discharge, A is the wet area and B the width of the channel. In this model, Han specifies the values of α to be 0.25 for the case of deposition and 1.0 for the case of erosion on the basis of considerable amount of field data.

Calculation with the numerical model shows that the sedimentation volume in the reservoir will be 8 billion m^3 in 30 years, 14 billion m^3 in 60 years, and 16 billion m^3 in 90 years. Then the accumulative sedimentation amount will approach equilibrium and will increase very slowly thenceforth. The total sedimentation in 120 years will be about 17 billion m^3 (Sedimentation Panel of TGP 2002).

The impoundment of the reservoir also caused sedimentation in the fluctuating backwater region, in which the water level in the low flow season will be higher than before the impoundment but will be the same as before in flood season as the pool level reduces to 145 m. Sediment deposits during the low flow season and can not be scoured down before the flood season, which causes thence problems for navigation and harbor operation. The industrial hub – Chongqing City – is located at about 600 km upstream of the dam and is in the fluctuating backwater region. The Jialing River flows into the Yangtze River at Chongqing. In Chongqing, Chaotianmen harbor is a passenger ship terminal and Jiulongpo Harbor is the most important freight ship terminal in southwest China.

Scale model experiments have been performed to study the sedimentation problems in a 33 km-long section around Chongqing. The experiments showed that impoundment of the reservoir will cause sediment deposition at the apron of the harbors, as shown in Figure 13. The shadowed areas in the figure indicate the places where cumulative sedimentation would occur. There are two channels separated by the Daliang Bar. Water flows in the west channel during low flow season and the main stream flow shifted to the east channel during flood, but the west channel maintains around-the-year a depth over 3 meters, which is necessary for the harbor. After 80 years impoundment of TGP, however, cumulative sedimentation would occur in the west channel, which could result in blockage of the channel eventually. The harbor facilities would not be usable if dredging or other technical measures were not taken. The experiments demonstrated that

Copyright © 2006 Taylor & Francis Group plc, London, UK

the problem can be solved by building spur dykes and groins to regulate the flow. The dykes and groins will narrow the channel and concentrate the flow, so that flow velocity in the west channel can be enhanced, which can prevent sediment from depositing (Wang et al., 1990). With a budget of about $ 100 million, the regulation works will be able to control sedimentation and preserve and improve the navigation and harbor conditions within the Chongqing reach.

6 DEGRADATION OF THE MIDDLE AND LOWER YANGTZE RIVER DUE TO THE THREE GORGES RESERVOIR

Because the TGP reservoir will release clear water to the downstream reaches during non-flood season, the riverbed will be scoured down. The discharge will be higher from January to May but lower from October to November than those without the dam (Fig. 14a). It will remain unchanged during flood season from July to September. Sediment load to the downstream reaches will be less due to trapping in the reservoir. Figure14b shows the calculated annual sediment load released to the downstream reaches, compared with the annual sediment load at Yichang under natural conditions (recycle of the data in the period 1961–1970). The sediment load will be greatly reduced by the trapping of the reservoir in the first 50 years. The load reduction must cause degradation of the downstream reaches (Tsinghua 2002).

The 1-D model by Han calculated the amount of sediment that will be scoured from the riverbed from Yichang to Wuhan. The clear water released from the TGP reservoir will scour 1.7 billion m^3 in the first 20 years, about 2.9 billion m^3 in 40 years, 3.7 billion m^3 in 60 years and 3.9 billion m^3 in 80 years. Thence, resiltation will occur. The scour and reduction of riverbed will cause flood stage reduction, which will be 3 m at Shashi and 0.75 m at Wuhan for a flood of discharge 30,000 m^3/s. The riverbed scour and stage reduction will be more obvious in a reach near the dam. The riverbed of a 150 km long reach from Yichang to Shashi will be scoured down by more than 0.5 m in first 20 years with a total scoured sediment volume of 252 million m^3. Gravel bed section will be scoured down by about 0.5 m and some sand bed sections may be scoured by about 10 m. The flood stage then will be reduced by more than 1.5 m in the reach (Sedimentation Panel 2002).

In the numerical model the data of water and sediment load measured in 1961–1970 were used. In the past 20 years the sediment load to Yichang has remarkably reduced, as shown in Figure 7. This trend is continuing because more and more reservoirs with different scales have been built in the river basin and more and more sediment load is trapped by the reservoirs. There were 45,647 reservoirs of different sizes in the Yangtze

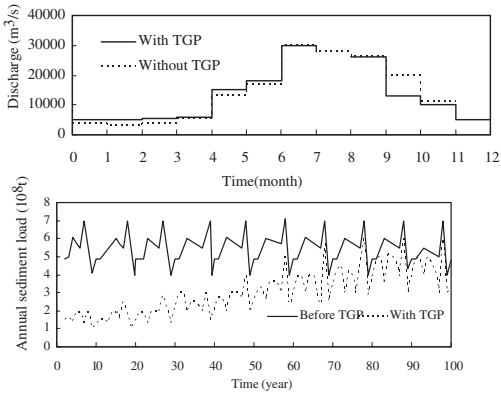


Figure 14. (a) Month-mean discharges under the natural conditions and with the regulation of the TGP reservoir. (b) Variation process of annual sediment load released to the downstream reaches from the reservoir compared with the annual sediment load at Yichang under natural conditions (recycle of the data in the period 1961–1970) (Sedimentation Panel, 2002).

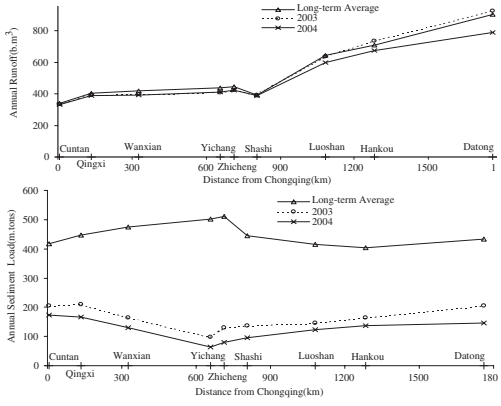


Figure 15. The annual runoff and sediment load after the impoundment of the Three Gorges Reservoir in comparison with the long-term (1951–2001) average values at the hydrological stations along the Yangtze River (after Sediment Panel 2005).

River basin with a total storage capacity of 170.5 billion m^3 up to 2003, among which 143 reservoirs are large with storage capacities over 100 million m^3. The real sediment load entered into the reservoir and released to the middle and lower reaches are less than the calculated values. Figure 15 shows the distributions of runoff and sediment load along the course in 2003 and 2004, in which the long-term average distributions of runoff and sediment load in the period of 1950–2002 are shown for comparison. The distributions of runoff in 2003 and 2004 are almost the same as the long-term average but the distribution of sediment load

Copyright © 2006 Taylor & Francis Group plc, London, UK

changed greatly. The long-term average sediment load reduced from Yichang to Hankou due to sedimentation in the reach; but the sediment load in 2003 and 2004 increases from Yichang to Hankou because the sediment concentration is too low and erosion occurred in the reach. It is predicted that riverbed erosion will dominate the fluvial process for 40 years (Wang et al. 2005). The figure also shows that the released sediment load at Yichang is more than half of the sediment load entered into the reservoir at Cuntan because the pool level was maintained around 140 m. In other words, the strategy "storing the clear and releasing the turbid" may control reservoir sedimentation.

7 CONCLUSIONS

Sediment transportation in the Yangtze River is complex. The total soil erosion from upper Yangtze River basin is about 2.2 billion tons per year, of which 1.7 billion tons deposit in the gullies and tributaries and about 0.5 billion tons are transported into the upper Yangtze River. Debris flow is the main form of sediment transportation from numerous gullies to the tributaries of the upper Yangtze River. The annual runoff increases from upstream to downstream along the course but the annual sediment load increases from the source to Yichang (the Three Gorges Dam site) reaching its highest amount of about 500 million tons/year, and then reduces along the course in the middle reaches. In the upper reaches of the Yangtze River, the sediment load is proportional to the flow discharge because both sediment and water are from upper reaches. In the lower reaches, however, sediment comes from upstream reaches in flood season, but half of the water is from the middle and lower reaches. A huge amount of sediment load is wash load, thence sediment load exhibits a very poor relation with flow discharge. In low flow season, not enough sediment is transported from the upper reaches, and much sediment load is from the riverbed. Therefore, the sediment load in low flow season consists mainly of bed material load and is proportional to the flow discharge. The riverbed profile in the middle and lower reaches is developing toward the equilibrium profile of minimum stream power but the impoundment of the Three Gorges Reservoir interrupts the fluvial process. The annual sediment load in the Yangtze River has reduced due to sediment trapping in numerous reservoirs. And the reduction is even higher after the impoundment of the Three Gorges Reservoir. The middle reaches of the river have changed from siltation to erosion because the sediment concentration released from the Three Gorges Reservoir is too low. It is predicted that riverbed erosion will dominate the fluvial process for 40 years. The first two years operation of the reservoir shows that more than half of the sediment load entered into the reservoir can be released to the downstream reaches.

ACKNOWLEDGEMENT

The study is supported by the 973 program 2003CB415206 and Science Fund for creative research group 50221903-3.

REFERENCES

ACRS. 1990. *Statistics of soil erosion by using remote sensing, Application Center of Remote Sensing Technology, Ministry of Water Resources of China* (in Chinese).

Chen, Z.Y. Li, J.F. Shen, H.T. & Wang, Z.H. 2001. Yangtze River of China: historical analysis of discharge variability and sediment flux, *Geomorphology*. 41: 77–91.

Deng, X.G. 1997. Analyses on the areas of sediment yield and sediment transportation in the Jinsha River basin, *Sichuan Hydropower*. 16(1): 23–25 (in Chinese).

Edmonds, R.L. 1994. *Patterns of China's Lost Harmony: A Survey of the Country's Environmental Degradation and Protection*. Routledge, London.

Han, Q.W. 1979. On non-equilibrium transport of non-uniform suspended sediment, *Science Bulletin.* 24(17) (in Chinese).

He, Y.P. Sun, E.Z. & You, Y. 2003. Monitoring of sedimentation and erosion of the Jiangjia Ravine, *Study report for the key NSFC research project* No.49831010. (in Chinese).

Higgitt D.L. & Lu X.X. 2001. Sediment delivery to the three gorges: 1. Catchment controls, *Geomorphology.* 41: 143–156.

Kang Z. Li, Z. Ma, A. & Luo, J. 2004. *Debris Flow Studies in China*. Science Press, Beijing (in Chinese).

Lin, B.(P.) N. Huan, J. & Li, X. 1983. Unsteady transport of suspended load at small concentrations, *J. of Hydraulic Engineering.* ASCE Proceedings, 109(1).

Lu X.X. & Higgitt D. L. 1998. Recent Changes of Sediment Yield in the Upper Yangtze, China, *Environmental Management* 22(5): 697–709.

Lu, X.X. & Higgitt, D.L. 1999. Sediment yield variability in the Upper Yangtze, China, *Earth Surface Processes and Landforms*. 24: 1077–1093.

MWRC (Ministry of Water Resources of China). 2000. China Sediment Gazette-2000, *Ministry of Water Resources of China* (in Chinese).

MWRC. 2001. China Sediment Gazette-2001, *Ministry of Water Resources of China* (in Chinese).

MWRC. 2001. China Sediment Gazette-2002, *Ministry of Water Resources of China* (in Chinese).

Pan, J.G. 1999. Characteristics of sediment transportation in the Jinsha River, *Sediment Research.* (2): 46–49 (in Chinese).

Pan, Q.X. and Lu, J.Y. 1999. Analysis of fluvial process of the middle reaches of the Yangtze River, *People's Yangtze River.* 30(2): 32–34 (in Chinese).

Sedimentation Panel for TGP Project. 1988. *Suggestion for the pool level schemes for the Yangtze River Three Gorges Project, Proceedings of the Sedimentation Studies for the Yangtze River Three Gorges Project (160 m–180 m Schemes)*, Department of Science and Technology, the Ministry of Water Resources of China (in Chinese).

Sedimentation Panel for TGP. 2002. *Comprehensive analysis on "9.5" sedimentation study results for the Three gorges Project on the Yangtze River,* Intellectual Copyright Press (in Chinese).

Copyright © 2006 Taylor & Francis Group plc, London, UK

Sediment Panel for TGP Project. 2005. Field investigation of the channel bed of the Yichang-Jiujiang section of the Ynagtze River, *Sediment Panel for the Three Gorges Project, June 2005.* (in Chinese).

Smil, V. 1993. *China's Environmental Crisis: An Inquiry Into the Limits of National Development*, M.E. Sharpe, New York.

Tang, K.L. (Editor) 2004. China *Soil Conservation*, Chinese Science Press.: 264 (in Chinese).

TGP Water Survey. 2005. Introduction about the Yichang Hydrological Station, *The Three Gorges Hydrology and Water Resource Survey Bureau*. (in Chinese).

Tsinghua University. 2002. Comparison and assessment of the calculation results of erosion and sedimentation of the Yangtze River from the TGP dam down to Datong with a 1D models, *Sedimentation Studies for the Yangtze River Three Gorges Project.* Vol.7. China Patent Press (in Chinese).

Wan, X. Li, J. He, Q. Xiang, W. & Wu, H. 2003. Variation of the sediment flux in the middle and lower Yangtze River, *Sediment Research.* (4): 29–35 (in Chinese).

Wang, L. & Yi, Y. 2003. Analysis of water and sediment load at Cuntan Station on the Yangtze River, *Water Resources and Hydro-Power analysis* (in Chinese).

Wang, W.R. & Zhang, S.C. 1985. *Characteristics of debris flow in the Guxiang Gully in Tibet, Research Paper Corpus,* No.4, Research Institute of Glaciology and Cryology (in Chinese).

Wang, Y. Zhan, Q. & Yan, B. 2001. *Structure and Rheological Properties of Debris Flows,* Hunan Science Press, Changsha (in Chinese).

Wang, Z.Y. Lu, X.Z. Zeng, Q.H. 1990. *Physical model experimental study on sedimentation in the Chongqing reach of the Yantze River for the Three Gorges Project – a report for the 175 m scheme, in the Collection of Research Results on the Sedimentation in the Chongqing reach of the Yangtze River*, Report, China Institute of Water Resources and Hydro-Power Research (in Chinese).

Wang, Z.Y. & Dittrich, A. 1992. A study on problems in suspended sediment transportation, Proceedings, *2-nd International Conference on Hydraulics and Environmental Modelling of Coastal, Estuarine and River Waters,* Ashgate, England.: 467–478.

Wang, Z.Y. Lee, J. H.W. & Cheng, D.S. 2005. Impacts of the TGP project on the Yangtze River ecology and management strategies, *International Journal of River Basin Management*. 3(4): 237–246.

Wen, D.Z. 1993. Soil erosion and conservation in China. In: Pimental, D. ed., *World Soil Erosion and Conservation.* Cambridge Univ. Press, Cambridge.: 63–85.

Wu, H. & Yu, X.G. 2002. Variation of water and sediment load in the origin area of the Yangtze River in the past 40 years, *Resources and Environment of the Yangtze River Basin.* 11 (2): 175–178. (in Chinese).

Xie, H. Zhong, D. Li, Y. & Wei, F. 2004, Characteristics of debris flow disasters in the upper Yangtze River Basin, *Resources and Environment of the Yangtze River Basin.* 13 (1): 94–99 (in Chinese).

Xu, J.X. 2005. Variation of the suspended sediment size in the upper Yangtze River in the past 40 years and its relationship with human activities, *Sediment Research*. 3: 8–16 (in Chinese).

Yang, C. Ted 1996. *Sediment Transport-Theory and Practice,* The McGraw-Hill Companies, Inc., New York, St. Louis, San Francisco.

Yang, Z.N. 1985. *A discussion on the velocity formulae of rainfall debris flows,* Research Paper Corpus, Research Institute of Glaciology and Cryology (4) (in Chinese).

Yu, J.R. Shi, L.R. & Feng, M.H. 1991 Soil erosion and river sediment in the upper stream reaches of the Yangtze River, *Bulletin of Water Resources.* 11(1): 9–17 (in Chinese).

Yu, X.G. 2003. *Research on the sustainable development of the Yangtze River Basin*, Chinese Science Press.: 280 (in Chinese).

Zhang, X.B. & Wen, A.B. 2002 Causes of variation in sediment load in the upper Yangtze River and its tributaries in the recent period, *Shuilixuebao*. (4): 56–59 (in Chinese).

Zhang, X.B. & Liu J. 1989. *Debris flows in the Dayingjiang Basin in Yunnan,* Chengdu Atlas Press (in Chinese).

Zhang, X.B. & Wen, A.B. 2004. Current changes of sediment yields in the upper Yangtze River and its two biggest tributaries, China, *Global and Planetary Change*. 41: 221–227.

Copyright © 2006 Taylor & Francis Group plc, London, UK

A. River hydrodynamics

A.1. Turbulent open-channel flow and transport phenomena

Copyright © 2006 Taylor & Francis Group plc, London, UK

Unsteady turbulence characteristics in an undular bore

C. Koch
Formerly: Civil Engineering, The University of Queensland, Brisbane, Australia

H. Chanson
Civil Engineering, The University of Queensland, Brisbane, Australia

ABSTRACT: When a river mouth has a flat converging shape with a tidal range exceeding 6 to 9 m, the river may experience a tidal bore. A tidal bore is a positive surge, and the aim of the study is to detail the turbulent field beneath an undular bore. New unsteady experiments were conducted in a large channel. Turbulence measurements were performed with high-temporal resolution using side-looking acoustic Doppler velocimetry. Detailed turbulent measurements were conducted along a vertical profile for a Froude number of 1.4. Instantaneous velocity measurements showed a marked flow deceleration at all vertical elevations. Turbulent stresses were deduced from high-pass filtered data. Maximum Reynolds stresses were observed beneath the whelps, under and just before each crest. The findings suggest that preferential bed erosion takes place beneath each wave crest, and the eroded material is advected in the undular wave motion behind the bore front.

1 INTRODUCTION

In macro-tidal estuaries, a tidal bore may form during spring tide conditions when the flood tide is confined to a narrow channel. The bore is a series of waves propagating upstream as the tidal flow turns to rising (Fig. 1). The occurrence of tidal bores has a significant impact on river mouths and estuarine systems. Bed erosion and scour take place beneath the bore front while suspended matters are carried upwards in the ensuing wave motion. The process contributes to significant sediment transport with deposition in upstream intertidal areas. Tidal bores induce also strong mixing and dispersion in the river mouth, but classical mixing theories do not account for such type of discontinuities. The existence of tidal bores is based upon a fragile hydrodynamic balance which may be easily disturbed by changes in boundary conditions and freshwater inflow (e.g. Chanson 2004a, 2005a).

There are numerous visual accounts of tidal bores. Most occurrences showed well-defined undulations behind the leading wave, that is an undular bore process. The other type of bore is the breaking bore that is rarely seen, but for a few exceptions. Field measurements in tidal bores are very limited and most studies recorded a limited number of parameters with relatively coarse resolutions in terms of time scales, spatial resolutions and velocity magnitudes. All field studies were fixed-point measurements, but a tidal bore is a very dynamic process which extends over several kilometres, sometimes tens of kilometres, and the bore shape and characteristics evolve rapidly with time in response to change in bathymetry. Figure 1B illustrates a tidal bore event in the Baie du Mont Saint Michel, France. The bore front travelled with an average celerity of about 2.7 m/s, but its shape changed constantly with time, sometime disappearing in the deep water channel, while a breaking front was observed in the shallower waters near the banks (Chanson 2005b).

The aim of the study is to detail the turbulence field in an undular tidal bore under controlled flow conditions. New experiments were conducted in a large channel ($L = 12$ m, $W = 0.5$ m). Detailed free-surface and turbulence measurements were performed with high-temporal resolution (50 Hz) using side-looking acoustic Doppler velocimetry and non-intrusive free-surface measurement devices. It is the purpose of this paper to present new compelling evidences on the hydrodynamics of undular bore front.

1.1 *Bibliographic review*

Positive surges and bores were studied by hydraulicians and applied mathematicians. Major contributions included Barré de Saint Venant (1871), Boussinesq (1877), Lemoine (1948), Serre (1953) and Benjamin and Lighthill (1954). Classical experimental investigations of undular bores included Bazin (1865), Favre (1935), Sandover and Holmes (1962), Benet and Cunge (1971) and Treske (1994). Ponsy and

Copyright © 2006 Taylor & Francis Group plc, London, UK



(A) Undular tidal bore of the Dordogne river (France) at St Pardon on 6 Aug. 2004 (Courtesy of Pierre-Yves Lagrée) - View from left bank with bore propagating from left to right



(B) Tidal bore of the Selune river (France) on 7 April 2004 at Roche-Torin (Photograph by Hubert Chanson) - The bore front disappeared briefly in the deep channel section while an undular bore was seen besides, with breaking bores in shallower waters and the bore front advancing over dry bed in foreground

Figure 1. Photographs of undular tidal bores.

Carbonnell (1966) presented superb, detailed three-dimensional free-surface profile measurements in prototype trapezoidal channels. However most experimental studies were limited to visual observations and sometimes free-surface measurements. These rarely encompassed turbulence but a few limited studies (e.g. Hornung et al. 1995).

Field measurements in tidal bores are few: e.g., Lewis (1972) and Huntley (2003) in the Dee river (UK), Wolanski et al. (2004) in the Daly river (Australia), Kjerfve and Ferreira (1993) in Rio Mearim (Brazil). All these studies were limited to a very small number of occurrences.

2 EXPERIMENTAL FACILITIES

2.1 *Channel and instrumentation*

Experiments were performed in a 0.5 m wide 12 m long horizontal flume (Fig. 2). Waters were supplied by a constant head tank. A tainter gate was located next to

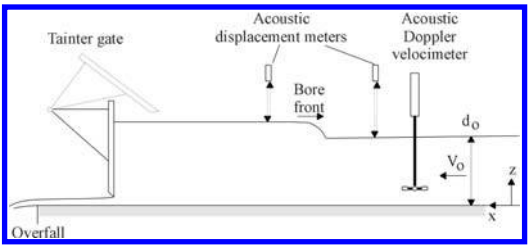


Figure 2. Sketch of experimental channel.

the downstream end of the channel ($x = 11.15$ m). Its controlled and rapid closure induced a positive surge propagating upstream. Steady flow rates were measured with bend meters which were calibrated in-situ with a large V-notch weir. The percentage of error was expected to be less than 2%. In steady flows, the water depths were measured using rail mounted pointer gauges and acoustic displacement meters. Unsteady water depths are measured with acoustic displacement meters Microsonic™ Mic + 25/IU/TC with an accuracy of 0.18 mm and a response time of 50 ms. The acoustic displacement readings were compared with instantaneous free-surface profiles captured with a high-speed camera. The results were found to be within the accuracy of the systems, although a few spurious points were sometimes observed. The displacement meter output was a function of the strength of the acoustic signal reflected by the free-surface. When the free-surface was not horizontal, some erroneous points were recorded. These were relatively isolated and easily ignored.

In steady flows, velocity measurements were conducted with a Prandtl-Pitot tube (3.3 mm Ø) previously calibrated as a Preston tube based upon in-situ experiments (Chanson 2000). Turbulent velocity measurements were conducted with an acoustic Doppler velocimeter Sontek™ 16 MHz micro-ADV at $x = 5$ m. The probe sensor had a two-dimensional side-looking head with a distance to sampling volume of 5 cm. With this arrangement, the closest measurement distance from the bed was 7.2 mm. The V_x velocity component was aligned with the longitudinal flow direction and positive downstream, while the transverse velocity component V_y was oriented normal to the channel sidewall and positive towards the left sidewall. The velocity range was 1.0 m/s, most unsteady flow experiments were conducted with 50 Hz sampling rate and the data accuracy was 1%. The translation of Pitot tube and ADV probe in the vertical direction was controlled by a fine adjustment travelling mechanism connected to a Mitutoyo™ digimatic scale unit. The error on the vertical position of the probe was $\Delta z < 0.025$ mm. The accuracy on the longitudinal position was estimated as $\Delta x < \pm 2$ mm. The accuracy on the transverse position of the probe was less than 1 mm.

Copyright © 2006 Taylor & Francis Group plc, London, UK

Table 1. Experimental flow conditions.

Q m^3/s	d_o m	U m/s	d_{conj} m	Fr	Remarks
0.0403	0.0795	0.140	0.0957	1.31	Undular bores
0.0403	0.0795	0.235	0.103	1.41	ADV measurements.
0.0403	0.0785	0.238	0.109	1.44	
0.0406	0.0790	0.286	0.117	1.49	
0.0403	0.0785	0.315	0.120	1.53	
0.04015	0.0790	0.456	0.135	1.67	Some breaking at 1st wave crest
0.0406	0.0795	0.549	0.145	1.77	Breaking bore.

* d_o: initial flow depth d_{conj}: measured conjugate flow depth; Q: steady discharge; U: bore celerity.

Additional informations were obtained with digital cameras Panasonic™ Limux DMC-FZ20GN and Canon™ A85, and a digital video-camera Sony™ DV-CCD DCR-TRV900. Further details on the experimental facility were reported by Koch and Chanson (2005).

2.2 *Tidal bore generation*

For each experiment, the initial steady flow was uncontrolled and gradually-varied. It was established for at least 10 minutes prior to measurements. A bore was generated by the rapid partial closure of the downstream gate. The gate closure occurred in less than 0.1 sec. Flow measurements and data acquisition were started for 2 minutes prior to gate closure. After gate closure, the travelling bore propagated upstream against the gradually-varied flow over the full channel length. Each experiment was stopped when the bore front reached the intake structure. Tests were repeated systematically for different gate closures (Table 1).

Detailed velocity and free-surface elevation measurements were performed with the acoustic Doppler velocimeter (ADV) located at $x = 5$ m from the channel intake and at several transverse positions $y/W = 0.5$, 0.75, 0.90 and 0.95, where x is the distance from the upstream channel end, y is the transverse distance measured from the right sidewall and W is the channel width ($W = 0.5$ m). The acoustic displacement meters were located at $x = 10.95$ m, 7.25 m, 6 m, 5.1 m and 5 m. The latter displacement meter sampled the free-surface elevation immediately above the ADV sampling volume, while the other sensors were placed on the channel centreline.

2.3 *Initial steady flow conditions*

The initial steady flow was partially-developed with $\delta/d_o = 0.6$ to 0.8 at the sampling location ($x = 5$ m). Both ADV and Prandtl-Pitot tube data compared favourably with a 1/7th power law in the boundary layer. The shear velocity was estimated using the Preston-Prandtl-Pitot tube and a match between velocity data and logarithmic velocity law in the inner flow layer. The results were close and yielded: $V_* = 0.044$ m/s. Importantly, the data, including the vertical distributions of Reynolds stresses, showed good qualitative and quantitative agreement with the detailed experiments of Xie (1988) and Tachie (2001) in smooth open channel flows. Further details on the initial flow properties were described in Koch and Chanson (2005, pp. 21–37).

2.4 *Acoustic Doppler velocity metrology*

Acoustic Doppler velocimetry (ADV) is designed to record instantaneous velocity components at a single-point with relatively high frequency. Past and present experiences demonstrated many problems. In steady turbulent flows, the ADV velocity fluctuations characterise the combined effects of the Doppler noise, signal aliasing, velocity fluctuations, turbulent shear and other disturbances (Lemmin and Lhermitte 1999, McLelland and Nicholas 2000, Chanson et al. 2005). For all experiments, present experience demonstrated recurrent problems with the velocity data, including low correlations and low signal to noise ratios. The situation improved by mixing some vegetable dye (Dytex Dye™ Ocean Blue) in the entire water recirculation system. Other problems were experienced with boundary proximity.

In steady flows, detailed comparisons between ADV and Prandtl-Pitot tube data were conducted at $y = 0.473$, 0.450, and 0.375 m (or 27, 50 and 125 mm from the left sidewall) with the micro ADV sensors facing the left sidewall, where y is the transverse distance from the right wall. Experimental data indicated that the streamwise velocity data were not affected by the presence of the channel bed at $y = 0.450$ and 0.375 m as observed at $y = 0.250$ m. But the ADV data underestimated the velocity in the vicinity of a sidewall ($y > 0.455$ mm). This was associated with a drastic decrease in average signal correlations, average signal-to-noise ratios and amplitudes next to the wall (Koch and Chanson 2005).

While several ADV post-processing techniques were devised for steady flows (e.g. Goring and Nikora 2002, Wahl 2003), these post-processing techniques are not applicable to unsteady flows (e.g. Nikora 2004, *Person. Comm.*, Chanson et al. 2005). In the present study, unsteady flow post-processing was limited to a removal of communication errors and a replacement by interpolation. Beneath the undular surge, the ADV probe outputs showed systematically a lower proportion of errors and "spikes" while the bore front passage was associated with some increase in average

Copyright © 2006 Taylor & Francis Group plc, London, UK

signal-to-noise ratios, average signal correlations and to a lesser extent signal amplitudes. Although these observations were not "true" validation, they tended to support the use of Acoustic Doppler devices in such a highly unsteady flow situation.

2.5 *Reynolds stress calculation in rapidly-varied flow motion*

In turbulence studies, the measured statistics are based upon the analysis of instantaneous turbulent velocity data : $v = V - \bar{V}$, where $\bar{V}$ is a time-average velocity. If the flow is "gradually time-variable", $\bar{V}$ must be a low-pass filtered velocity component, or variable-interval time average VITA (Piquet 1999). The cutoff frequency must be selected such that the averaging time is greater than the characteristic period of fluctuations, and small with respect to the characteristic period for the time-evolution of the mean properties.

In undular surge flow, the Eulerian flow properties showed an oscillating pattern with a period of about 2.4 s that corresponded to the period of the free-surface undulations. The unsteady data were therefore filtered with a low/high-pass filter threshold greater than 0.4 Hz (i.e. 1/2.4 s) and smaller than the Nyquist frequency (herein 25 Hz). The cutoff frequency was selected as 1 Hz based upon a sensitivity analysis (Koch and Chanson 2005, pp. A51-A55). The same filtering technique was applied to both streamwise and transverse velocity components, and Reynolds stresses were calculated from the high-pass filtered signals.

3 UNDULAR BORE FREE-SURFACE PROFILES

3.1 *Presentation*

Undular bores were observed for surges Froude numbers less than 1.7, where the surge Froude number is defined as:

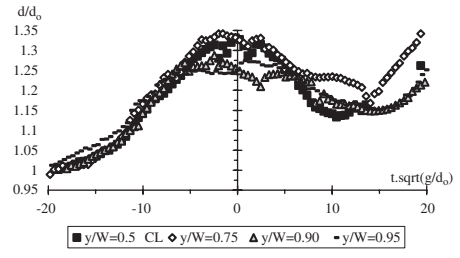
$$Fr = \frac{U + V_o}{\sqrt{g\, d_o}} \quad (1)$$

with V_o is the initial flow velocity, U is the bore front celerity for an observer fixed on the bank, g is the gravity acceleration and d_o is the initial water depth (Henderson 1966, Chanson 2004a,b). Measured initial depths and surge celerities are listed in Table 1.

The undular bores propagated upstream relatively slowly and the bore front was followed by a train of well-formed undulations. For low surge Froude numbers ($1 \leq Fr < 1.4$ to 1.5), the free-surface undulations had a "smooth" appearance and no wave breaking wave observed. Some cross-waves were seen developing upstream of the first wave crest and intersecting next to the first crest (Fig. 3A). For intermediate surge



(A) Photograph of advancing undular bore, looking downstream with cross-waves intersecting on the first wave crest



(B) First wave crest free-surface profiles at x = 5 m and 4 transverse locations

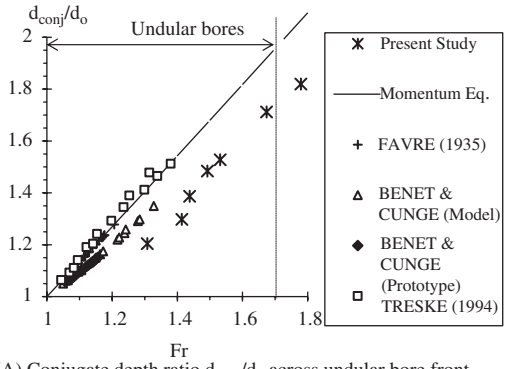
Figure 3. Undular bore free-surface profile ($Fr = 1.4$, $d_o = 0.079$ m).

Froude numbers (i.e. 1.4 to 1.5 < Fr < 1.7), some slight wave breaking was observed at the first crest, and the ensuing free-surface undulations were flatter. For larger Froude numbers (i.e. $Fr \geq 1.7$), a breaking surge was seen.

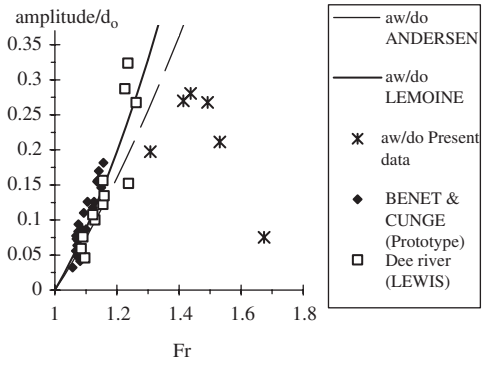
Typical instantaneous free-surface profiles are presented in Figure 3B. Each curve shows the instantaneous dimensionless flow depth d/d_o as a function of a dimensionless time $t\sqrt{g/d_o}$ for the first wave crest. Figure 3B shows data collected at $x = 5$ m for four transverse locations, illustrating the three-dimensional nature of the flow. At the first wave crest, the water levels were higher next to the centreline ($y/W = 0.5$ & 0.75) than next to the sidewall ($y/W = 0.95$ & 0.90) (Fig. 3B).

The data showed a gradual evolution of the undular bore shape as it propagated upstream. It is conceivable that the bore was not fully-developed. However the data tended to suggest a gradual reduction of the bore height with increasing distance from the downstream gate. Such a trend was consistent with a fully-developed bore propagating against a gradually-varied flow with a S2 backwater profiles. In the present study, longitudinal free-surface measurements in steady flows suggested indeed a S2 profile between $x = 5$ and 7 m.

Copyright © 2006 Taylor & Francis Group plc, London, UK



(A) Conjugate depth ratio d_{conj}/d_o across undular bore front – Comparison between momentum principle and experiments



(B) Dimensionless free-surface undulation amplitude (first wavelength) – Comparison between Lemoine's (1948) theory, Andersen's (1978) theory, laboratory data (Present study), prototype data (Benet and Cunge 1971) and tidal bore field observations (Lewis 1972)

Figure 4. Dimensionless properties of undular bores.

3.2 *Undular bore properties*

In a fully-developed bore, the ratio of conjugate depths (d_{conj}/d_o) must satisfy the continuity and momentum equations :

$$\frac{d_{conj}}{d_o} = \frac{1}{2} * \left(\sqrt{1 + 8\,Fr^2} - 1 \right) \quad (2)$$

where d_{conj} is the depth immediately behind the bore. Experimental results are presented in Figure 4A, where the ratio d_{conj}/d_o is plotted as a function of the Froude number. Present data are compared with Equation (2) and with past experiments. The data showed slightly lower conjugate depth ratios for $1.1 < Fr < 1.7$. In undular bores, the estimate of the conjugate depth d_{conj} is somewhat arbitrary. For all data the conjugate depth d_{conj} was estimated as the average of wave crest and trough depths. The averaging process assumed a symmetrical wave pattern that was not supported by experimental data.

Undulation amplitude and wave length data were also compared with previous studies and with the theories of Lemoine (1948) and Andersen (1978). Lemoine (1948) assumed that the energy dissipation takes place by radiation of sinusoidal wave train, while Andersen (1978) developed a solution of the Boussinesq equation. Present data showed a good agreement with earlier studies. Interestingly, the data agreed reasonably well with Lemoine's theory although the latter was based upon a sinusoidal wave assumption. Present results do not support claims that cnoidal wave theory yields better agreement with experimental data (e.g. Benjamin and Lighthill 1954).

Figure 4B compares undular wave amplitudes with undular tidal bore observations in the Dee river (Lewis 1972). Note that the wave amplitude (Fig. 4B) decreased sharply immediately before the disappearance of free-surface undulations. Treske (1994) reported a similar trend. It is believed that the flow conditions associated with maximum wave amplitude occurred immediately before the appearance of some wave breaking at the first wave crest: i.e. for Fr ~1.4 to 1.5 in the present study.

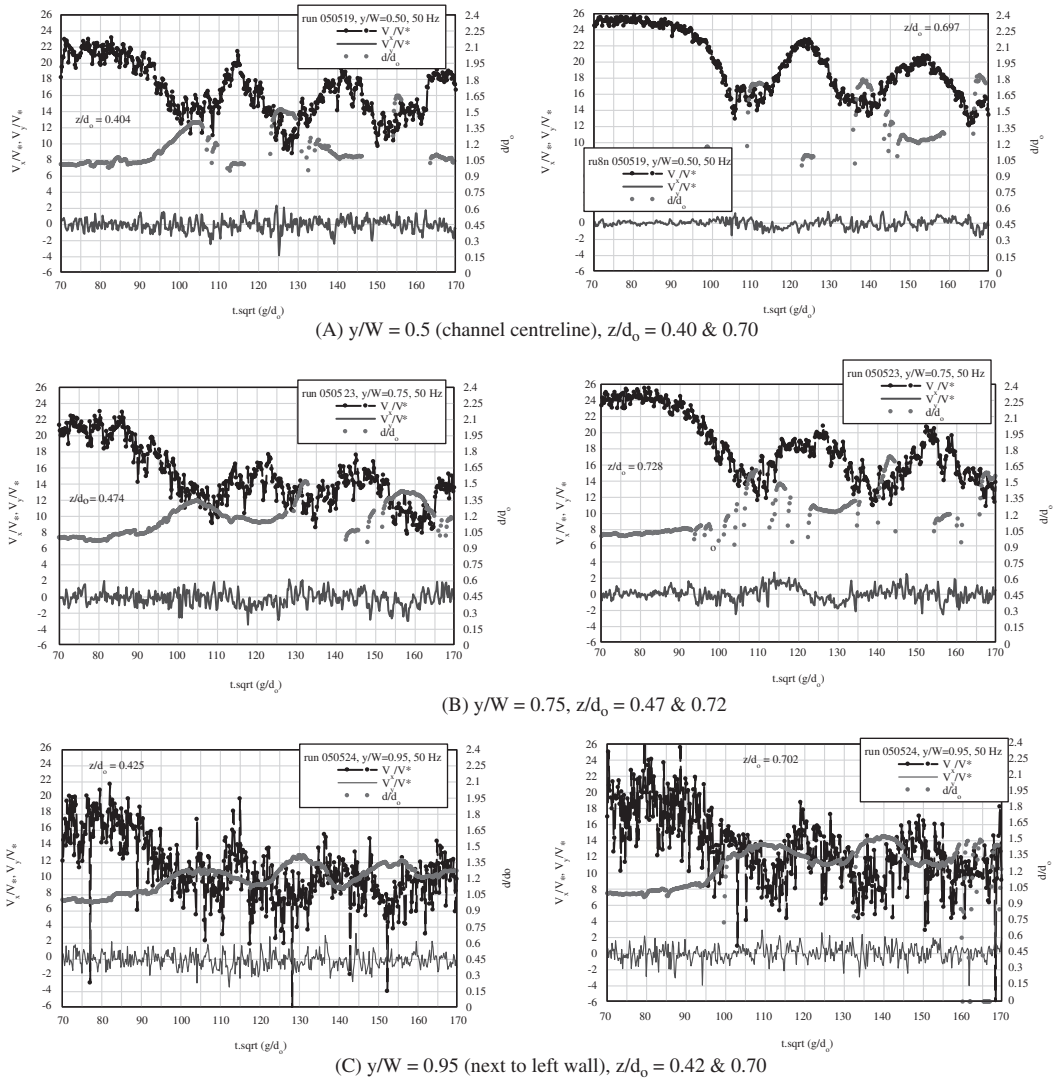
4 TURBULENT VELOCITIES BENEATH UNDULAR BORE

4.1 *Instantaneous velocity measurements*

Unsteady velocity measurements were performed beneath an undular bore for a surge Froude number of Fr = 1.4 (Table 1). The acoustic Doppler velocimetry (ADV) system was positioned at x = 5 m and each experiment was conducted at several vertical elevations z and transverse locations y. Figure 5 illustrate the effects of undular bore passage on the turbulent velocity field at a fixed point. Each graph presents the dimensionless velocities V_x/V_* and V_y/V_*, and water depth d/d_o, where d_o is the initial water depth and V_* is the shear velocity measured on the channel centreline in steady flows ($V_* = 0.044$ m/s). The time t is zero at 10 s prior to the first wave crest passage. Figure 5A shows centreline data while Figures 5B and 5C present data at other transverse locations (y/W = 0.75 & 0.95). Figure 6 presents details of the flow field next to the first wave crest.

Experimental results indicated some basic features. The streamwise velocity component decreased rapidly with the passage of the first wave crest and oscillated with time with the same period as and out of phase with the surface undulations (Fig. 5). Maximum velocities were observed beneath the wave troughs and minimum velocities below the wave crests. The trend was seen at all vertical and transverse locations, and it was consistent with irrotational flow theory. Note that the

Copyright © 2006 Taylor & Francis Group plc, London, UK



(A) y/W = 0.5 (channel centreline), z/d_o = 0.40 & 0.70

(B) y/W = 0.75, z/d_o = 0.47 & 0.72

(C) y/W = 0.95 (next to left wall), z/d_o = 0.42 & 0.70

Figure 5. Instantaneous dimensionless velocities V_x/V_* and V_y/V_* beneath an undular bore (Fr = 1.4).

streamwise velocities were always positive, although a few negative instantaneous V_x velocities were seldom detected next to the side wall (Fig. 5C).

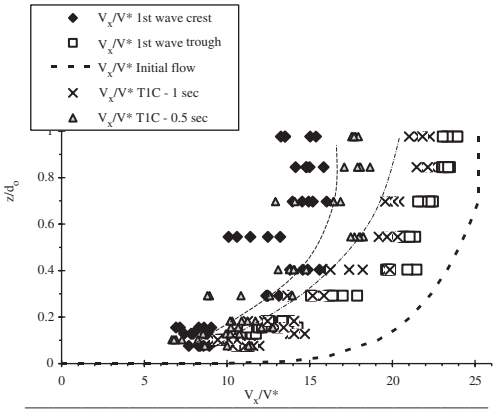
In the upper flow region ($z/d_o > 0.5$), large fluctuations of velocities were observed beneath the undulations. At a given height, the deviations of instantaneous velocities from an overall data trend were larger than the initial turbulent velocity fluctuations prior to the bore passage. For example, in Figure 5A for $t\sqrt{g/d_o} > 90$ to 100. Since the measurements were Eulerian, the measured fluctuations included the contributions of the velocity deviation from an ensemble average and the time-variation of the ensemble average.

At the highest sampling points (e.g. $z/d_o = 0.7$, Fig. 5A & 5B), the transverse velocity V_y data tended to oscillate with the same period as and in phase with the free-surface.

4.2 *Remarks*

In an undular bore, theoretical considerations and flow net analysis predict significant velocity redistributions between wave crests and troughs associated with

Copyright © 2006 Taylor & Francis Group plc, London, UK



	Initial flow	T1C -1 sec.	T1C -0.5 sec.	1st wave crest	1st wave trough
t(s) =	0	9.0	9.5	10.0	11.05
d/d_o =	1	1.14	1.24	1.80	1.05

Figure 6. Redistributions of dimensionless vertical velocity profiles (V_x/V_*) beneath the first wave crest of an undular surge (Fr = 1.4, centreline data) – At each vertical elevation, 5 instantaneous, consecutive data samples are shown.

pressure gradients greater than hydrostatic beneath wave trough and less than hydrostatic beneath crest (e.g. Rouse 1938, Montes and Chanson 1998). Figure 6 illustrates the redistribution of vertical velocity profiles with time during the propagation of the first free-surface undulation. At each vertical elevation, five instantaneous, consecutive velocity samples are plotted as functions of the vertical elevation. Similarly, five consecutive data samples at each elevation are shown for 1 s before the passage of the first wave crest (T1C–1 sec.), 0.5 s prior to the first crest (T1C – 0.5 sec.), and at the following wave trough. The initial velocity profile is shown in thick dashed line for comparison. Trend lines are shown for (T1C-1 s) and (T1C-0.5 s) also (thin dashed lines).

Present data showed experimental trends that were in agreement with irrotational flow motion theory. But the ideal fluid flow theory is based upon the assumption of frictionless fluid. It does not account for bed and sidewall friction, nor for the initial turbulence flow conditions and turbulence structure. The presence of boundary shear contributes to some energy dissipation as well as the generation of vorticity. When a bore propagates upstream against a current, the average vorticity is positive.

Note also that the velocity redistributions presented a different pattern to that observed beneath undular hydraulic jumps (e.g. Chanson 1995). Several researchers argued that there are indeed fundamental differences between the two types of flows (Montes 1979, Montes and Chanson 1998).

5 TURBULENT REYNOLDS STRESSES BENEATH UNDULAR BORE

5.1 *Instantaneous Reynolds stresses*

Reynolds stress data showed large turbulent stresses below the surge front and ensuing undulations (Fig. 7). This is seen in Figure 7 for $t\sqrt{g/d_o} > 90$. Figure 7 presents both normal and tangential instantaneous turbulent stresses. Reynolds stresses were significantly larger than in the initial steady flow. In particular, intense normal and tangential stresses were consistently seen beneath wave crests and just before each crest. These turbulent stresses were larger than beneath the adjacent wave troughs (Fig. 7). The data showed also larger Reynolds stresses at the lower sampling locations including next to the bed. Comparatively smaller Reynolds stresses were measured at higher sampling locations, although the Reynolds stress levels were always larger beneath the undulations than in the initial steady flow.

5.2 *Turbulent dissipation and mixing*

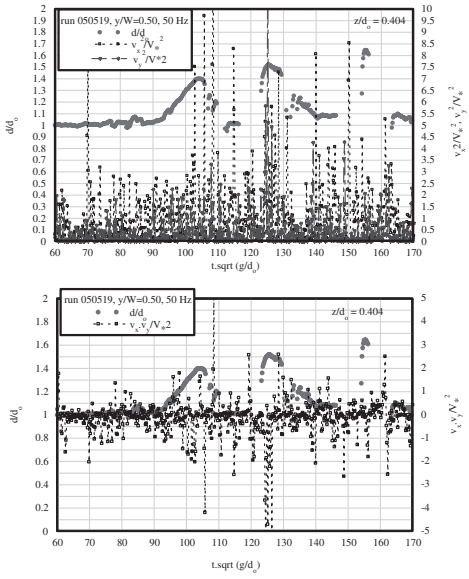
In a river, the passage of an undular bore is always associated with very significant turbulence and mixing as demonstrated by field observations. Evidences included repeated impact and damage to field measurement equipments: e.g., in Rio Mearim (Kjerfve and Ferreira 1993), in the Daly river (Wolanski et al. 2004), in the Dee river (Lewis 1972). Further demonstrations covered major damage to river banks, shipping and navigation. Other tragic evidences included numerous drownings in tidal bores and "whelps" (Malandain 1988).

At a point fixed in space, the passage of the bore front and ensuing undulations is associated with rapid fluctuations of vertical pressure and velocity distributions between adjacent wave crests and troughs (e.g. Figs. 5 & 6). This type of mixing is supported by strong turbulence measured in undular bores and sediment advection observations behind bore front.

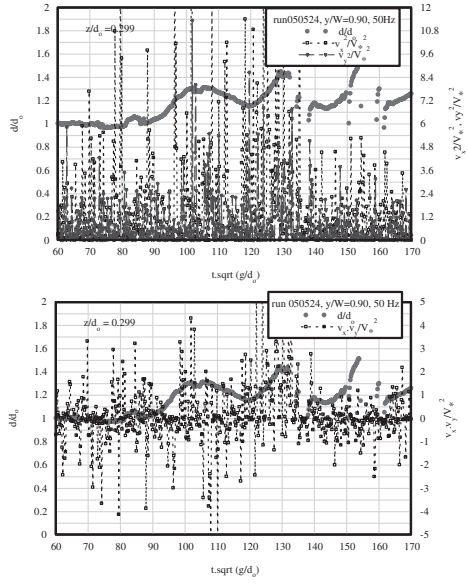
Second, large volumes of sediments are advected upstream behind tidal bores as observed by numerous researchers (Chen et al. 1990, Tessier and Terwindt 1994). In the Rio Mearim, Kjerfve and Ferreira (1993) reported: "*in shallow areas, the water boiled violently after the passage of the bore and became brownish-black*". All studies showed that the arrival of an undular bore was associated with intense bed material mixing. Chanson (2001, 2005a,b) argued that sediment suspension beneath the "whelps" is sustained by strong wave motion for relatively long periods. In the Dordogne river, he observed some intense wave motion lasting more than 20 minutes after the bore passage.

Third some turbulent energy is dissipated in vortical structures advected behind the surge front. The role of

Copyright © 2006 Taylor & Francis Group plc, London, UK



(A) y/W = 0.50 (Centreline), $z/d_o = 0.40$: (A1) Normal Reynolds stresses (v_x^2/V^{*2}, v_y^2/V^{*2}) (A2) Tangential Reynolds stress ($v_x * v_y/V^{*2}$)



(B) y/W = 0.90, $z/d_o = 0.30$: (B1) Normal Reynolds stresses (v_x^2/V^{*2}, v_y^2/V^{*2}) (B2) Tangential Reynolds stress ($v_x * v_y/V^{*2}$)

Figure 7. Dimensionless normal and tangential Reynolds stresses beneath undular bore (Fr = 1.4).

these large-scale turbulent structures was highlighted by Hornung et al. (1995). It is thought however that these may be highly dependant upon the initial flow conditions. For example, Hornung et al. (1995) studied positive surges propagating in initially still waters,



Figure 8. Surface on the first wave crest of the Amazon river bore (pororoca) (P. Lespinasse 2005, courtesy of FR3 & TV5 Asie).

while the present study investigated a bore propagating against a steady current.

Present experimental evidences showed that the arrival of an undular bore was characterised by very rapid changes in streamwise velocities and by large fluctuations in transverse velocities at all transverse locations. This was associated with relatively large instantaneous turbulent Reynolds stresses beneath the undulations at most vertical elevations (for Fr = 1.4 and $y/d_o < 1$). In Nature, the initial steady flow conditions are often quiescent. The arrival and passage of an undular bore must be associated with significant bed material scour and pickup. Such a sediment erosion process is an Eulerian problem, and present experimental results are directly applicable. The ensuing sediment suspension and advection behind the bore front is a Lagrangian problem however.

In an undular bore, maximum Reynolds stresses were observed beneath the wave crests (Fig. 7), and the results suggested repeated high shear and scour just before and below each wave crest. Eroded bed material is then placed into suspension and advected in the "whelps" and wave motion behind the leading wave. Such a mechanism was proposed by Donnelly and Chanson (2002,2005) based upon a quasi-steady flow analogy.

Note that the present study was conducted in tidal bores resulting from partial gate closure. The experimental setup was selected to generate under controlled flow conditions a range of undular bores with the same initial conditions. It is acknowledged that these initial conditions might not be typical of tidal bores in natural estuaries (Fig. 8) because there was no complete flow reversal after bore front passage. Further present

Copyright © 2006 Taylor & Francis Group plc, London, UK

results focused on the bore front and the short period immediately after bore passage.

6 CONCLUSION

Limited quantitative information is available to date on the turbulence induced by undular tidal bores because the hydrodynamics and turbulence field were not studied with fine instrumentation under well-defined conditions. In the present study, new experiments were conducted under controlled flow conditions in a large channel. Detailed turbulence measurements were performed with a high-temporal resolution (50 Hz) using side-looking acoustic Doppler velocimetry and non-intrusive free-surface measurement devices. The experiments were designed to study a range of undular bores with a minimum number of dependant variables. Using one set of initial flow conditions, experiments were performed in undular surges resulting from a rapid gate closure at the downstream end of the flume and propagating upstream against the initial flow. The only dependant variable was the downstream gate opening after closure.

Undular bores were observed for surges Froude numbers less than 1.7 although some breaking was observed at the first crest for 1.4 to $1.5 < Fr < 1.7$. Free-surface profiles compared favourably with past measurements in positive surge and tidal bores. The present study demonstrated unique features of tidal bore fronts. Velocity measurements with high-temporal resolution showed a marked effect of the bore passage. Longitudinal velocities were characterised by rapid flow deceleration at all vertical elevations, while large fluctuations of transverse velocities were recorded beneath the front. Turbulent Reynolds stress data highlighted high levels in the lower flow region including next to the bed, and maximum normal and tangential stresses were observed immediately upstream of and at wave crests. Hence bed erosion may take place beneath each wave crest, and the eroded material and other scalars are advected in the "whelps" and wave motion behind the first wave crest. These would be consistent with very-strong turbulence levels observed behind tidal bores in the field (Fig. 8).

While the present study allowed a detailed comparison of the effects of undular bores, it was limited to one set of initial flow conditions. Further works should encompass a wider range of inflow conditions and surge generation, including positive surges propagating downstream and tidal bore flows with complete flow reversal.

ACKNOWLEDGEMENTS

The writers thank Professor Michele Mossa (Politecnico di Bari, Italy) for his valuable input. They thank also Graham Illidge (The University of Queensland) for his technical assistance. Hubert Chanson thanks all the people who provided him with relevant information, in particular Dr Eric Jones (Proudman Oceanographic Laboratory) and Professor David Huntley (University of Plymouth, UK).

REFERENCES

Barré de Saint Venant, A.J.C. (1871). "Théorie et Equations Générales du Mouvement Non Permanent des Eaux Courantes." *Comptes Rendus des séances de l'Académie des Sciences*, Paris, France, Séance 17 July 1871, Vol. 73, pp. 147–154 (in French).

Bazin, H. (1865b). "Recherches Expérimentales sur la Propagation des Ondes." *Mémoires présentés par divers savants à l'Académie des Sciences*, Paris, France, Vol. 19, pp. 495–644 (in French).

Benet, F., and Cunge, J.A. (1971). "Analysis of Experiments on Secondary Undulations caused by Surge Waves in Trapezoidal Channels." *Jl of Hyd. Res.*, IAHR, Vol. 9, No. 1, pp. 11–33.

Benjamin, T.B., and Lighthill, M.J. (1954). "On Cnoidal Waves and Bores." *Proc. Royal Soc. of London, Series A, Math. & Phys. Sc.*, Vol. 224, No. 1159, pp. 448–460.

Boussinesq, J.V. (1877). "Essai sur la Théorie des Eaux Courantes." *Mémoires présentés par divers savants à l'Académie des Sciences*, Paris, France, Vol. 23, Série 3, No. 1, supplément 24, pp. 1–680 (in French).

Chanson, H. (1995). "Flow Characteristics of Undular Hydraulic Jumps. Comparison with Near-Critical Flows." *Report CH45/95*, Dept. of Civil Engineering, University of Queensland, Australia, June, 202 pages.

Chanson, H. (2000). "Boundary Shear Stress Measurements in Undular Flows: Application to Standing Wave Bed Forms." *Water Res. Res.*, Vol. 36, No. 10, pp. 3063–3076.

Chanson, H. (2001). "Flow Field in a Tidal Bore : a Physical Model." *Proc. 29th IAHR Congress*, Beijing, China, Theme E, Tsinghua University Press, Beijing, G. LI Ed., pp. 365–373.

Chanson, H. (2004a). "The Hydraulics of Open Channel Flows : An Introduction." *Butterworth-Heinemann*, Oxford, UK, 2nd edition, 630 pages.

Chanson, H. (2004b). "Environmental Hydraulics of Open Channel Flows." *Elsevier Butterworth-Heinemann*, Oxford, UK, 483 pages.

Chanson, H. (2005a). "Physical Modelling of the Flow Field in an Undular Tidal Bore." *Jl of Hyd. Res.*, IAHR, Vol. 43, No. 3, pp. 234–244.

Chanson, H. (2005b). "Tidal Bore Processes in the Baie du Mont Saint Michel (France): Field Observations and Discussion." *Proc. 31th Biennial IAHR Congress*, Seoul, Korea, B.H. JUN, S.I. LEE, I.W. SEO and G.W. CHOI Editors, Theme E.4, Paper 0062, pp. 4037–4046.

Chanson, H., Trevethan, M., and Aoki, S. (2005). "Acoustic Doppler Velocimetry (ADV) in a Small Estuarine System. Field Experience and "Despiking"." *Proc. 31th Biennial IAHR Congress*, Seoul, Korea, B.H. JUN, S.I. LEE, I.W. SEO and G.W. CHOI Editors, Theme E2, Paper 0161, pp. 3954–3966.

Chen, Jiyu, LIU, Cangzi, Zhang, Chongle, and Walker, H.J. (1990). "Geomorphological Development and

Copyright © 2006 Taylor & Francis Group plc, London, UK

Sedimentation in Qiantang Estuary and Hangzhou Bay." *Jl of Coastal Res.*, Vol. 6, No. 3, pp. 559–572.
Donnelly, C., and Chanson, H. (2002). "Environmental impact of a Tidal Bore on Tropical Rivers." *Proc. 5th Intl River Management Symp.*, Brisbane, Australia, Sept., 3–6, 9 pages (PDF: www.uq.edu.au/∼e2hchans/reprints/riv02_1.pdf).
Donnelly, C., and Chanson, H. (2005). "Environmental Impact of Undular Tidal Bores in Tropical Rivers." *Environmental Fluid Mechanics*, Vol. 5, No. 5, pp. 481–494.
Favre, H. (1935). "Etude Théorique et Expérimentale des Ondes de Translation dans les Canaux Découverts." *Dunod*, Paris, France (in French).
Goring, D.G., and Nikora, V.I. (2002). "Despiking Acoustic Doppler Velocimeter Data." *Jl of Hyd. Engrg.*, ASCE, Vol. 128, No. 1, pp. 117–126. Discussion: Vol. 129, No. 6, pp. 484–489.
Henderson, F.M. (1966). "Open Channel Flow." *MacMillan Company*, New York, USA.
Hornung, H.G., Willert, C., and Turner, S. (1995). "The Flow Field Downsteam of a Hydraulic Jump." *Jl of Fluid Mech.*, Vol. 287, pp. 299–316.
Huntley, D.A. (2003), *Person. Comm.*.
Kjerfve, B., and Ferreira, H.O. (1993). "Tidal Bores: First Ever Measurements." *Ciência e Cultura (Jl of the Brazilian Assoc. for the Advancement of Science)*, Vol. 45, No. 2, March/April, pp. 135–138.
Koch, C., and Chanson, H. (2005). "An Experimental Study of Tidal Bores and Positive Surges: Hydrodynamics and Turbulence of the Bore Front." *Report No. CH56/05*, Dept. of Civil Engineering, The University of Queensland, Brisbane, Australia, July, 170 pages.
Lemmin, U., and Lhermitte, R. (1999). "ADV Measurements of Turbulence: can we Improve their Interpretation ? Discussion" *Jl of Hyd. Engrg.*, ASCE, Vol. 125, No. 6, pp. 987–988.
Lemoine, R. (1948). "Sur les Ondes Positives de Translation dans les Canaux et sur le Ressaut Ondulé de Faible Amplitude." *Jl La Houille Blanche*, Mar-Apr., pp. 183–185 (in French).
Lespinasse, P. (2005). "Sons of the Moon / Les Fils de la Lune." *Grand Angle Production*, France, 50 min..
Lewis, A.W. (1972). "Field Studies of a Tidal Bore in the River Dee." *M.Sc. thesis*, Marine Science Laboratories, University College of North Wales, Bangor, UK.
McLelland, S.J., and Nicholas, A.P. (2000). "A New Method for Evaluating Errors in High-Frequency ADV Measurements." *Hydrological Processes*, Vol. 14, pp. 351–366.
Malandain, J.J. (1988). "La Seine au Temps du Mascaret." *Le Chasse-Marée*, No. 34, pp. 30–45 (in French).
Montes, J.S. (1979). "Undular Hydraulic Jump - Discussion." *Jl of Hyd. Div.*, ASCE, Vol. 105, No. HY9, pp. 1208–1211.
Montes, J.S., and Chanson, H. (1998). "Characteristics of Undular Hydraulic Jumps. Results and Calculations." *Jl of Hyd. Engrg.*, ASCE, Vol. 124, No. 2, pp. 192–205.
Piquet, J. (1999). "Turbulent Flows. Models and Physics." *Springer*, Berlin, Germany, 761 pages.
Ponsy, J., and Carbonnell, M. (1966). "Etude Photogrammétrique d'Intumescences dans le Canal de l'Usine d'Oraison (Basses-Alpes)." *Jl Soc. Française de Photogram.*, Vol. 22, pp. 18–28.
Rouse, H. (1938). "Fluid Mechanics for Hydraulic Engineers." *McGraw-Hill Publ.*, New York, USA (also Dover Publ., New York, USA, 1961, 422 pages)
Sandover, J.A., and Holmes, P. (1962). "The Hydraulic Jump in Trapezoidal Channels." *Water Power*, Vol. 14, Nov., pp. 445–449.
Serre, F. (1953). "Contribution à l'Etude des Ecoulements Permanents et Variables dans les Canaux." *Jl La Houille Blanche*, Dec., pp. 830–872 (in French).
Tachie, M.F. (2001). "Open Channel Turbulent Boundary Layers and Wall Jets on Rough Surfaces." *Ph.D. thesis*, Dept. of Mech. Eng., Univers. of Saskatchewan, Canada, 238 pages.
Tessier, B., and Terwindt, J.H.J. (1994). "An Example of Soft-Sediment Deformations in an Intertidal Environment - The Effect of a Tidal Bore". *Comptes-Rendus de l'Académie des Sciences*, Série II, Vol. 319, No. 2, Part 2, pp. 217–233.
Treske, A. (1994). "Undular Bores (Favre-Waves) in Open Channels - Experimental Studies." *Jl of Hyd. Res.*, IAHR, Vol. 32, No. 3, pp. 355-370. Discussion : Vol. 33, No. 3, pp. 274–278.
Wahl, T.L. (2003). "Despiking Acoustic Doppler Velocimeter Data. Discussion." *Jl of Hyd. Engrg.*, ASCE, Vol. 129, No. 6, pp. 484–487.
Wolanski, E., Williams, D., Spagnol, S., and Chanson, H. (2004). "Undular Tidal Bore Dynamics in the Daly Estuary, Northern Australia." *Estuarine, Coastal and Shelf Science*, Vol. 60, No. 4, pp. 629–636.
Xie, Q. (1998). "Turbulent flows in non-uniform open channels: experimental measurements and numerical modelling." *Ph.D. thesis*, Dept. of Civil Eng., University of Queensland, Australia, 339 pages.

Copyright © 2006 Taylor & Francis Group plc, London, UK

On the definition of the shear velocity in rough bed open channel flows

D. Pokrajac
Department of Engineering, University of Aberdeen, Aberdeen, UK

J.J. Finnigan
CSIRO, Marine and Atmospheric Research, Canberra, Australia

C. Manes, I. McEwan & V. Nikora
Department of Engineering, University of Aberdeen, Aberdeen, UK

ABSTRACT: Shear velocity u_* is a well-known fundamental velocity scale of the wall turbulence, widely used for scaling various flow quantities such as mean velocity and turbulent intensities. The definition of shear velocity is closely related to the universal Logarithmic law of the wall, which was originally derived for constant shear stress boundary layers. Because the shear stress is constant, the momentum flux ρu_*^2 is equal to the wall shear stress, so u_* is often understood as some kind of synonym for the wall shear stress. The universal Log-law is also used for the flows with linear shear stress such as pipe flows and uniform open channel flows. In such flows the turbulent momentum flux delivered to the roughness differs from the wall shear stress, but the difference is negligible for the rough walls where boundary layer thickness (flow depth in case of uniform open channel flow), is much larger than roughness height. In rough wall flows where the flow depth and the roughness height are of the similar order, the difference between the turbulent momentum flux representative of the free outer flow and the wall shear stress may become significant. For such flows it is important to distinguish between the wall shear stress and the shear stress used for evaluation of the shear velocity. This paper highlights the problems associated with the definition of the shear velocity in shallow open channel flows and its use for evaluation of the bed shear stress. The influence of the definition of u_* on the data analysis is illustrated using experimental results.

1 INTRODUCTION

Open channel flows over rough beds are of considerable engineering interest, but there are still some uncertainties about them. One of the difficulties in investigating such flows is that flow properties near the bed are spatially inhomogeneous. Instead of studying time-averaged flow properties which vary in space, it is more convenient to investigate double-averaged flow properties, using the double-averaged (in time/ensemble and spatial domains) Navier-Stokes equations. The idea of spatial flow averaging was first introduced in hydraulics by Smith and McLean (1977). The development of a new methodology based on spatially averaged equations was initiated by Wilson and Shaw (1977) for describing atmospheric flows within vegetation canopies. The atmospheric physicists Raupach and Shaw (1982), Finnigan (1985), Raupach et al. (1991), provided the mathematical basis for a new set of equations.

Double-averaging methodology provides clear definitions of some basic concepts in rough bed open channel flow. For instance, although local flow properties near rough bed always vary in space, globally uniform flow is defined by the requirement that the double-average flow properties do not change in the streamwise direction (Nikora et al., submitted). Furthermore DAM provides strict definitions of the spatially-averaged or macroscopic momentum balance, fluid shear stress and bed shear stress.

However, there is one more question about the rough bed flows that has so far been neglected. Rough beds have complex geometry such that the bed level (height above an arbitrary bed-parallel datum) varies in space. In DAM this variation is expressed by a single parameter – the roughness porosity function, equal to volume of water/total volume within the spatial averaging domain (thin bed-parallel slices). The porosity function varies between one, above the roughness crests, and zero (for impermeable bed), below the lowest roughness troughs. At the level of the roughness crest this variation can be abrupt or gradual, depending on the roughness geometry. In either case it is not clear *a priori* where exactly, between roughness crests

Copyright © 2006 Taylor & Francis Group plc, London, UK

and troughs, is the appropriate position of an equivalent imaginary bed i.e. the idealised sharp interface between turbulent flow and the rough wall. This affects the definition of basic concepts such as flow depth and the shear velocity, especially for flows with small relative submergence (flow depth/roughness height ratio).

The shear or friction velocity is usually defined as the velocity scale of the momentum absorbed by the bed. It can be evaluated either at the roughness crests, where the bed starts extracting momentum from the flow, or at the troughs, where the total momentum is absorbed, or somewhere between them. Various versions are present in the literature and yet called the same name. It introduces confusion and makes it difficult to compare published data.

In this paper we present a case for defining the universal velocity scale u_* in rough bed flows from the shear stress at the roughness crests, rather than from the total momentum extracted from the flow i.e. from the bed shear stress. In order to clearly define the bed shear stress we first use DAM to summarise the momentum balance in uniform flows over rough beds. We then revisit the original derivations of the universal Log-law where u_* was first introduced, and point out that the Log-law was first developed for constant shear stress boundary layers, so it does not answer the question about the appropriate definition of the shear velocity. In case of rough bed open channel flows with linear shear stress only the shear velocity associated with the roughness crest has a potential to be universal, so it is adopted as the appropriate velocity scale for scaling flow properties. The consequences of using the velocity scale based on the bed shear stress instead are illustrated using a case from the literature and our own experiments.

2 DOUBLE-AVERAGED OPEN CHANNEL FLOW

We consider steady uniform two-dimensional open channel flow over a rough bed. A right-hand co-ordinate system is used with $x =$ streamwise, $y =$ lateral and $z =$ bed-normal coordinates, and the velocity components in x, y, z direction are denoted by u, v, w respectively (Fig. 1). Roughness height is denoted by k. and the origin of z is placed at the roughness crest. For simplicity, roughness elements have identical height. In natural sediments, where this is clearly not the case, some statistical property of the bed level e.g. $z_{99\%}$can be used as a global level of roughness crest.

The double-averaged momentum equations are obtained by averaging Reynolds equations over thin bed-parallel volumes dV (Fig. 1). These volumes may intersect with the bed so in general they contain both

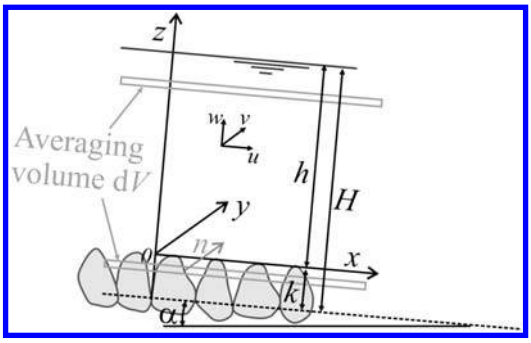


Figure 1. Definition sketch.

water and the grains. The double-averaged momentum equation in x direction is (Nikora et al. 2004)

$$\phi\rho g \sin\alpha = f_x - \frac{\partial \phi \tau_{xz}}{\partial z}, \tag{1}$$

where g = gravitational acceleration, $\rho =$ density, $\alpha =$ angle between the bed and the horizontal datum, $\phi =$ porosity of the rough bed=volume of water/total volume dV, τ_{xz} is the fluid shear stress and f_x is the total drag force exerted by the fluid on the roughness per unit plan area and unit height dz. For an averaging volume above the roughness crests dV contains only water, so $\phi = 1$ and f_x vanishes from the equation. The fluid shear stress is

$$\tau_{xz} = \rho\left\langle \nu \frac{\partial \overline{u}}{\partial z} \right\rangle - \rho\langle \overline{u'w'} \rangle - \rho\langle \tilde{u}\tilde{w} \rangle, \tag{2}$$

where the three terms are the spatially averaged viscous stress, the spatially averaged turbulent stress and the form-induced stress, respectively. The over-bar denotes time average, $' =$ fluctuation, $\langle\ \rangle =$ spatial average and tilde = the deviation of a time-averaged quantity from its spatial average. The drag term is obtained by integrating local pressure and viscous stress over the interface between water and grains, S, within the averaging volume dV:

$$f_x = -\frac{1}{dV}\iint_S \overline{p} n_x dS + \frac{1}{dV}\iint_S \mu\left[\frac{\partial \overline{u}}{\partial x}n_x + \frac{\partial \overline{u}}{\partial y}n_y + \frac{\partial \overline{u}}{\partial z}n_z\right] dS \tag{3}$$

where n_x, n_y, n_z are the components of the unit vector $\boldsymbol{n}$, normal to the surface dS, pointing into the fluid (Fig. 1).

Spatial averaging smoothes spatial heterogeneity of the flow near the rough bed in (x, y) planes, so that all flow variables are represented as profiles in z. The lowest point in such profiles is the lowest point of the bed roughness. Time-averaged flow depth measured from that point is denoted by H, and time-averaged flow depth measured from the roughness crests is h.

Copyright © 2006 Taylor & Francis Group plc, London, UK

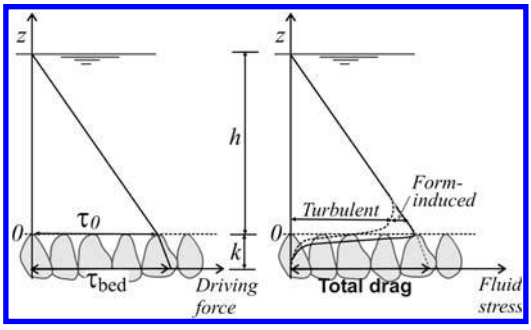


Figure 2. Momentum balance in 2d rough bed flow.

2.1 *Momentum balance*

In boundary layer terminology open channel flow belongs to 'constant pressure gradient' boundary layer flow, because its driving force, gravity, plays a role in the momentum balance analogous to the pressure gradient. In steady uniform flow over a rough bed the terms of momentum balance can be obtained by integrating the momentum equation (1) over z. (Nikora et al. 2001, Nikora et al., submitted). For any bed-parallel plane above the roughness top (Fig. 2) the total driving force or momentum supply (per unit plan area) between the plane and the free water surface is

$$\int_z^h \rho g \sin\alpha \, dz \cong \rho g S (h - z), \tag{4}$$

where $z =$ height of the plane above the roughness top and $S =$ bed slope (Fig. 2 left). It is in balance with the momentum flux through the plane at the height z, $\tau_{xz}(z)$, so τ_{xz} increases linearly, starting from the zero at the free surface. Far away from the roughness both viscous stress and form-induced stress are negligible so τ_{xz} is turbulent shear stress. Near the roughness crest persistent vortices behind roughness elements cause form-induced momentum flux so momentum is transferred from the flow above by both turbulent and form-induced shear stress (Fig. 2 right). At the roughness crest, $z = 0$, the momentum flux from the flow above the roughness is just sufficient to balance ρghS, so the fluid shear stress is

$$\tau_0 = \rho ghS. \tag{5}$$

Below the roughness crest, between the plane $z = 0$ and a bed-parallel plane at level z there is an additional momentum supply of $\phi\rho g(0 - z)S$. The corresponding total momentum supply of $\rho gS[h + \phi(0 - z)]$ is partly transferred further down via fluid shear stress and partly transferred to the roughness via form drag and viscous drag , which act as momentum sinks. At the level of the roughness troughs fluid shear stress diminishes and the total momentum from the flow above is transferred to the roughness:

$$\rho gS(h + \phi k) = \int_{-k}^{0} f_x dz \tag{6}$$

The total momentum flux from the fluid flow is therefore in balance with the total drag. The total drag exerted by the fluid on all roughness elements, per unit plan area of the bed, is the spatially averaged or macroscopic bed shear stress,

$$\tau_{bed} = \rho gh(S + \phi k). \tag{7}$$

Due to the additional momentum supply below the roughness top, the bed shear stress τ_{bed} differs from the fluid shear stress at the roughness top τ_0

2.2 *Flow layers*

In 'deep' rough bed flows, where the influence of the bed roughness is significant only over a small part of the flow depth (less than around 0.15–0.2 h), the following layers can be distinguished:

(i) The *Outer Layer,* similar to the outer layer for flows over hydraulically smooth beds, with the characteristic scales: the shear velocity, u_*, the maximum velocity, U_∞ (assumed to occur at the free surface), flow depth, h, and the distance above the zero-plane. (zero-plane= origin of the Log-law).

(ii) The *Logarithmic layer,* with the scales u_*, and the distance above the zero-plane. A single length scale exists only over a region far away from both the water surface and the rough bed so that it is not influenced by their respective length scales.

(iii) The *Roughness layer,* also called the *Roughness sub-layer,* is strongly influenced by the set of surface length scales L_i that describe bed geometry, including characteristic roughness height, k, so its characteristic scales are u_*, and L_i. This layer may extend up to $4k$ above the roughness crest (Raupach et al. 1991). Flow within the Roughness sub-layer is strongly affected by coherent eddies generated at the top of the roughness. In plant canopy flows the relevant length scale of the Roughness sub-layer is determined by the vorticity thickness $\delta_w = u(0)/(du/dz)(0)$ (Raupach et al. 1996). This was also observed in flows over relatively dense aquatic vegetation canopy (Nepf & Vivoni, 2000, Poggi et al. 2004).

For relatively shallow open channel flows some of the layers may be absent, because the Roughness sub-layer covers the part of the flow profile 'reserved' for the Log-layer, or even extends to the free surface, obliterating the Outer layer as well.

When all three flow layers are present they have a single velocity scale u_*. The Logarithmic layer has only

Copyright © 2006 Taylor & Francis Group plc, London, UK

one spatial scale, so it offers the simplest framework for studying u_*. For that reason the definition of the shear velocity and its application in boundary layer theory are closely related to the universal Logarithmic law of the wall.

3 THE UNIVERSAL LOG-LAW

The universal Log-law was originally derived for constant shear stress (zero pressure gradient) boundary layers over smooth walls. It can be derived in several ways. The two well-known approaches are:

(i) The overlap approach where the dimensional analysis is combined with asymptotic matching (Millikan, 1939, Yaglom, 1979). Asymptotic matching requires a clear scale separation between the boundary layer thickness and the thickness of the Roughness sub-layer. This derivation does not rely on the constant shear stress: the only assumption is that a single velocity scale u_* is responsible for momentum transfer from the outer flow to the wall. This velocity scale is usually called the friction velocity and calculated from the wall shear stress. Due to the scale separation, the difference between the momentum absorbed at the level of roughness crests and troughs, i.e. between τ_0 and τ_{bed}, is negligible.

(ii) The momentum flux approach where the momentum balance equation ($\tau_{xz} = -\rho\overline{u'w'} = \tau_{wall}$) is combined with an assumption about the relationship between turbulent momentum flux (turbulent shear stress) and velocity gradient either directly (Landau, 1944, Monin and Yaglom 1971) or through an assumption on the mixing length or turbulent viscosity. This approach requires that the fluid shear stress and the related velocity scale u_* are constant along z. In such case it clearly makes no difference whether u_* is evaluated at the roughness crests or troughs.

In either of the two approaches the condition for the existence and use of the Logarithmic layer is that it occurs far enough from both boundaries (at sufficient distance from the wall, in terms of wall units z^+, and at the same time at height much smaller than the boundary layer thickness), so that the only remaining relevant length scale is the distance from the wall z. In the 'overlap' approach this assumption is explicit. In the 'momentum flux' approach the assumed relationship between shear stress and velocity gradient is valid only in the vicinity of the wall where the turbulent momentum flux is not affected by the outer flow scales.

The Log-law for boundary layers over rough walls can be stated as

$$\frac{\overline{u}}{u_*} = \frac{1}{\kappa}\log\left(\frac{z+d}{z_0}\right) \tag{8}$$

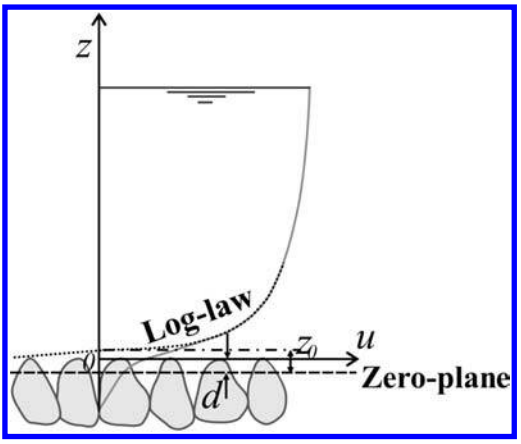


Figure 3. Logarithmic velocity profile above rough bed.

where κ is the universal von Karman constant and d defines the origin of the logarithmic velocity profile (Fig. 3). Due to the complex wall geometry and flow interactions, the position of this origin is not *a priory* known, so it has to be found by fitting. Experimental evidence shows that the origin of the Log-law, called zero-plane, is typically located between roughness crests and troughs and that it moves towards the troughs for more energetic flow and sparse roughness elements (Nikora et al. 2002). The zero-plane position at $z = -d$ implies that the length scale relevant within the Log-layer is $z + d$. If the Log-law is derived for a constant shear stress boundary layer, with the mixing length assumed proportional to the distance from the origin, $\ell = \kappa(z + d)$, the zero plane defines the position where the mixing length is zero.

The roughness length z_0 is formally an integration constant of the Log-law (height above the zero-plane where the velocity obtained from the Log-law is zero, Fig. 3). It depends on the roughness characteristics and is a measure of the efficiency of the surface in absorbing momentum.

The Log layer has to be outside the direct influence of the surface roughness, so it must be located above the Roughness sub-layer. On the other hand, to ensure that the Log-layer is sufficiently far away from the outer boundary of the boundary layer, it is assumed to be limited to some small portion, usually 0.15–0.2 of the boundary layer thickness. In cases where roughness generates a significant Roughness sub-layer which spreads higher than 0.15–0.2 of the boundary layer the Log-layer does not have enough space to develop.

The Log-law is also widely used for boundary layers with linear shear stress such as pipe flows and open channel flows with $h, H \gg k$. The 'overlap' derivation of Log-law explains why it works well with variable shear stress (provided that $h, H \gg k$). It can also be

Copyright © 2006 Taylor & Francis Group plc, London, UK

argued that the shear stress is still approximately constant between the wall and the Log-layer because the Log-layer has to be close to the wall (Monin & Yaglom, 1971),

In shallow open channel flows over rough bed the roughness height is comparable to water depth. Neither the 'overlap' approach nor the 'momentum balance' approach is applicable, since there is no scale separation and the shear stress is not constant. There is no theoretical basis for the universal Log-law and the velocity scale responsible for momentum transfer between the Outer layer and the bed becomes less obvious and Despite that, many investigators present experimental data fitted to the logarithmic equation (8) and scaled with the shear velocity u_*. The choice of u_* in shallow open channel flows is discussed in the remaining part of the paper.

4 DEFINITION OF THE SHEAR VELOCITY

The shear velocity u_* discussed here is a velocity scale expected to universally collapse data for rough bed open channel flows including flows with low relative submergence (with and without the-log layer). In other contexts e.g. sediment entrainment and sediment transport different definitions of u_* are required.

Although the u_* was first introduced in the context of the Log-law, the original derivations of the Log-law do not provide a general definition of the u_* which would be applicable to the boundary layers with variable shear stress where the roughness height is comparable with the boundary layer thickness. They associate u_* with the momentum absorbed by the wall. However this definition does not specify where exactly (along the roughness height k) is this momentum to be evaluated. This is the reason why there is no general consensus in the literature on the appropriate choice of the u_*. The following options exist:

- $u_*^{\text{bed}} = \sqrt{\tau_{\text{bed}}}$, where τ_{bed} is the bed shear stress. This classical approach, which assumes that u_* is an equivalent way of expressing the bed shear stress, is widely used in the open channel flow literature (e.g. Bayazit 1976, Ditrich & Koll, 1997, Katul et al. 2002, Rowinski et al.).
- $u_*^0 = \sqrt{\tau_0}$, where τ_0 is the total fluid shear stress at the roughness crest (at $z = 0$ in Figure 2). This approach is consistently used in the canopy flow literature (e.g. Finnigan 2000, Poggi et al. 2004, Jarvela, 2005), but may be found in open channel flow papers (e.g. Nakagawa 1991).
- $u_*^d = \sqrt{\tau_d}$, where τ_d is the total fluid shear stress extrapolated to the level of zero plane, $z = -d$ (Nepf & Vivoni, 2000, Ditrich & Koll, 1997).
- $u_*^{\log} = \sqrt{\tau_{\log}}$, where $\tau_{\log}$ is the shear stress that corresponds to u_* obtained by fitting experimental data (with the assumed $\kappa = 0.4$) to the logarithmic formula (8). (Wang et al. 1993, Wang & Dong 1996). It is not clear where exactly is $\tau_{\log}$ in the shear stress profile.

The first option clearly cannot yield the universal velocity scale because the bed shear stress depends on the roughness porosity function ϕ, which is not universal. To illustrate this let us assume flow over a bed composed of closely packed rods forming a porous medium with very low permeability, so that only a thin uppermost layer of the porous bed interacts with the mean velocity profile above, while below this layer flow is driven solely by the momentum supplied by gravity within the bed. Increasing height of the rods would not affect the mean velocity profile of the free surface flow above them, they would remain identical. However if we choose to scale them with the shear velocity calculated from the bed shear stress the scaled velocity profiles would differ by a factor proportional to the increase in the height of the rods. Thus we would detect a non-physical suppression of velocities, which is an artefact of the selection of the shear velocity.

Two other options, zero-plane and the Log-layer, rely on the existence of the Log-layer and the universal Log-law. This makes it impossible to use them for shallow flows where the existence of the universal Log-layer is questionable.

The remaining option of defining the u_* from the fluid shear stress at the roughness crest is the simplest and the least ambiguous one. In order to achieve uniform flow, flow depth, the velocity profile and the turbulence structure must adjust to deliver a momentum flux to the roughness that just balances the gravity forcing of the free fluid. This momentum flux is τ_0 and the corresponding velocity scale is u_*^0. At the roughness crest form drag and viscous drag start affecting the flow introducing a major change in flow physics. Below the roughness crest flow adjusts to the microphysics of drag and porosity in the roughness, so that the bed shear stress and the corresponding velocity scale reflect them, rather than solely the characteristics of free fluid. For these reasons we have adopted the shear velocity associated with the shear stress at the roughness crest as the appropriate velocity scale for scaling turbulent flow quantities across the whole flow profile.

5 SHEAR VELOCITY AND THE DATA INTERPRETATION

Shear velocity is widely used as a universal velocity scale, often in the context of the Log-law, but also for scaling the data on shallow rough bed open channel flows where the Log-layer is not present (e.g Katul et al. 2002). In this section we first analyse how the

Copyright © 2006 Taylor & Francis Group plc, London, UK

choice of the shear velocity affects the parameters of the Log-law in its original form (8) and present an example from the literature. We then demonstrate, using our own measurements of turbulent intensities, the general effect of the shear velocity definition on interpretation of data on shallow flows over rough bed.

Only the conventional 'bed shear stress' shear velocity is compared with the adopted 'roughness crest' shear velocity. The effect of other versions of the shear velocity definition, listed in the previous section, can be easily evaluated using an analogous procedure. From the momentum balance explained in the section 2.1 (Fig 2) it follows that the bed shear stress and the fluid shear stress at the roughness crests are related as

$$\frac{\tau_{\text{bed}}}{\tau_0} = \frac{h+\phi k}{h} \tag{9}$$

so that

$$\frac{u_*^{\text{bed}}}{u_*^0} = \sqrt{\frac{\tau_{\text{bed}}}{\tau_0}} \tag{10}$$

Obviously using u_*^{bed} as approximation of u_*^0 always overestimates it. The ratios $\tau_*^{\text{bed}}/\tau_*^0$ and u_*^{bed}/u_*^0 are plotted in Figure 4 as functions of the relative submergence H/k for three typical values of porosity ϕ Porosity 0.3–0.5 is approximately the range that can be expected in natural gravel beds, while 0.9 or higher may occur in aquatic vegetation. In the former case the difference between u_*^{bed} and u_*^0 becomes significant (larger than 10%) for the relative submergences less than 2.5-3.5 while in the latter case it happens for those less than 5. The graphs evaluate the effect of using u_*^{bed} instead of u_*^0 on the quantities scaled with the shear velocity. Two examples are presented in the following text to illustrate the consequences of this effect.

5.1 *Mean velocity and Log-law parameters*

Applicability of the universal Log-law to shallow open channel flows and the alternative formulations of the log-law (adjusted to linear shear stress and flows without clear scale separation) are beyond the scope of this paper. Here we analyse solely a case, often found in the literature, of fitting the conventional logarithmic velocity profile given by (8) to the experimental velocity data for shallow flows with low relative submergence H/k.

For a given set of experimental data, fitting to the log-law produces a single ratio κ/u_*, provided that κ/u_* and d wee both determined by fitting, The most obvious way to demonstrate this is by differentiating the log formula for u with respect to z, which yields (Nikora et al. 2002)

$$\left(\frac{du}{dz}\right)^{-1} = \frac{\kappa}{u_*}(z+d) \tag{11}$$

A given data set has a given set of velocity gradients. The slope of the best-fit line through their reciprocal values gives the ratio κ/u_* and the intercept gives the position of the zero-plane d.

The shear velocity evaluated from the bed shear stress is over-estimated by the factor shown in Figure 4, so that κ is over-estimated by the same factor. This means that for flows with very small relative submergence using the 'bed shear stress' shear velocity instead of the 'roughness crest' velocity can have significant influence on the reported values of the von Karman constant.

Figure 5 shows the results of Bayazit, 1976, who reported gradually increasing von Karman constant as the relative submergence decreased. The values of κ were evaluated by fitting the velocity data to the Log-law, with the position of the zero-plane $d = 0.33\,k$ below the roughness crest for all experiments. In the same paper Bayazit made a comment that these large values of κ for small relative submergences may be due to the wrong choice of the velocity scale u_*, but did

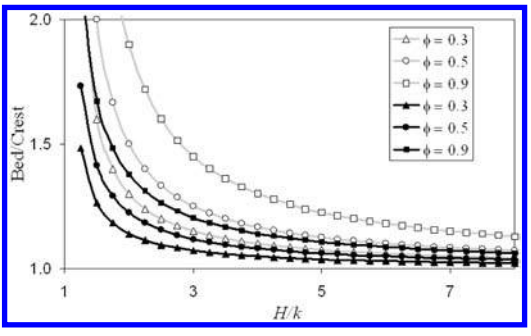


Figure 4. Ratio between the bed shear stress and the shear stress at the roughness crest (white symbols) and between the corresponding shear velocities (black symbols), for a range of relative submergences H/k and 3 different porosities ϕ.

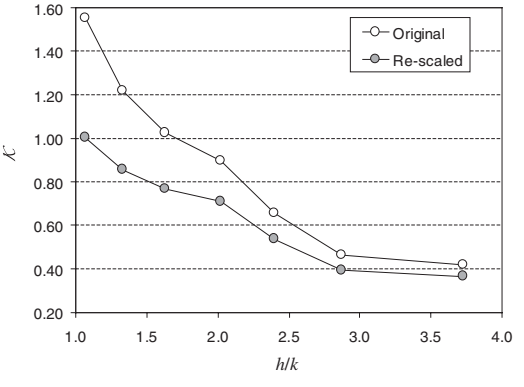


Figure 5. Von Karman constant reported in Bayazit, 1976 and re-calculated with the 'roughness crest' shear velocity.

Copyright © 2006 Taylor & Francis Group plc, London, UK

not attempt to correct it. These values of κ are here re-calculated with the 'roughness crest' shear velocity u_*^0 instead of the 'bed shear stress' u_*^{bed} from the original paper. Figure 5 shows that the correction significantly changes κ values.

This discussion is not aimed at listing all potential problems with fitting the velocity data to the logarithmic law. The aim is to point out just one particular source of error. The literature on shallow rough bed flows contains a range of values of von Karman constant. In cases where the reported values of κ are less than 0.4 the correction for u_*^{bed}/u_*^0 would further reduce them. In flows with small to intermediate relative submergence the universal Log-layer is often not present, so there is no reason for κ obtained by fitting the velocity data to have the universal value. However it is important to realise that without a physically based and consistent velocity scale u_* it is very difficult or impossible to compare different experimental data. Correcting the data for bias introduced by using u_*^{bed} would clarify the genuine influence of the relative submergence and other parameters that affect velocity profiles.

An inverse situation happens when the u_*, determined by fitting the log-law to the measured velocity profile (assuming $\kappa = 0.4$), is used for evaluation of the bed shear stress or the friction factor. This is frequent in field measurements, where using u_* is a simpler and more robust alternative to the direct measurement of the shear stress. In such cases the result of fitting is the 'roughness crest' shear velocity u_*^0, but it is used as if it were 'bed shear stress' velocity u_*^{bed}. Since u_*^0 is always less than u_*^{bed}, this means that, even if the assumed $\kappa = 0.4$ is correct, the bed shear stress and the friction factor are underestimated by factors shown in Figure 4.

The above analysis applies to the cases where κ/u_* and d were both found by fitting. However the position of the zero-plane is sometimes found using the centre-of-pressure method (Jackson, 1981). This method is not applicable to 'constant pressure gradient' boundary layers because the momentum supply below the roughness crest affects the position of the centre of drag. If d was evaluated using this method the error would combine with the error in u_* and further affect the value of κ.

For rough bed open channel flows with small to intermediate relative submergence the use of the Log-law in its original form is questionable and alternative options should be explored. In any case, in future efforts to compile available experimental data it is very important to make a clear distinction between the non-universal 'bed shear stress' velocity scale u_*^{bed}, which depends on the particular roughness geometry and the 'roughness crest' velocity scale u_*^0, which has a potential to universally collapse the experimental data.

5.2 *Turbulent intensities*

The difference between the 'bed shear stress' and 'roughness crest' shear velocity has an important influence on the turbulence characteristics reported for the rough bed shallow open channel flows. For instance turbulent intensities are usually scaled with the u_*, and compared with the corresponding dimensionless turbulent intensities measured in deep rough bed flows or smooth bed flows. Scaling the turbulent intensities for deep flows is not sensitive to the difference between u_*^0 and u_*^{bed}, but for shallow flows the difference becomes significant. Using u_*^{bed} instead of u_*^0 for scaling introduces an artificial suppression of turbulent intensities, caused by the choice of the velocity scale rather than the real physics. The 'suppression factor' progressively increases with decreasing relative submergence. The maximum turbulent intensity (scaled with u_*) is known to decrease when the relative submergence decreases (Wang et al. 1993, Ditrich & Koll 1997). Part of this finding may be the artefact of the choice of the velocity scale.

To explore this possibility we first re-calculated the results from Bayazit (1976), where turbulent intensities were fitted to the formula

$$\frac{\sigma_u}{u_*} = A + B \ln \frac{u_* z}{\nu}. \tag{12}$$

In Bayazit (1976), turbulent intensities scaled with u_* and plotted against $\ln u_* z/\nu$ do not collapse for different relative submergences. Instead, they follow a set of parallel lines, indicating that only the coefficient A from (12) is responsible for the reduction of turbulent intensities as the relative submergence (h/k) decreases. Figure 6 shows the values of A from the original paper and those corresponding to 'roughness crest' u_* as a velocity scale. The re-calculated A values vary much less, indicating very small variation of turbulent intensities with relative submergence. It is

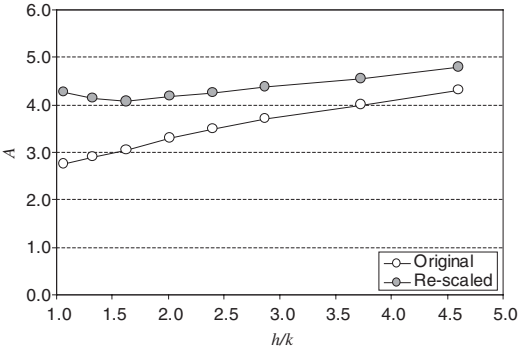


Figure 6. The constant A (eq. 5) defining maximum turbulent intensities σ_u reported in Bayazit, 1976 and re-scaled with the 'roughness crest' shear velocity.

Copyright © 2006 Taylor & Francis Group plc, London, UK

clear that turbulent intensities profiles would collapse much better when scaled with the 'roughness crest' shear velocity.

Further analysis was performed with our own measurements of flow over a single layer of spheres packed in the cubic pattern. All the experiments were carried out under uniform, fully turbulent rough flow conditions. The aspect ratio varied from 18-5.4 for which we can assume that the flow was two-dimensional (Kironoto and Graf 1994). The main hydraulic parameters for the experiments are shown in Table 1. Measurements were carried out using Particle Image Velocimetry along two vertical planes along the flume axis, one plane through the centres of the spheres and another through their connections. The results presented below were obtained by averaging the results for these two planes. More detailed description of the experimental procedures can be found in (Manes et al. submitted). Figure 7 shows turbulent intensities $\sigma_u = \sqrt{\overline{u'^2}}$ and $\sigma_w = \sqrt{\overline{w'^2}}$ measured in the experiments **E1, E2, E3**, once scaled with the 'roughness crest' shear velocity u_*^0 and once with the 'bed shear stress shear velocity u_*^{bed}. The values of the shear stress at the roughness crest and the bed shear stress were determined by the extrapolation of the Reynolds stress

Table 1. Experimental conditions.

Experiment	E1	E2	E3
Bed slope	1:400	1:400	1:200
Sphere diameter, k(mm)	12	12	12
Depth h(m)1.3	22	42	21
Maximum depth H(mm)	34	54	33
Relative submergence (H/k)	2.83	4.5	2.75
Shear velocity u_* (m/s)	0.0235	0.0300	0.0301
Roughness Reynolds number	141	180	181
Average profile velocity (m/s)	0.210	0.340	0.286
u_{bed}/u_*	1.13	1.07	1.14

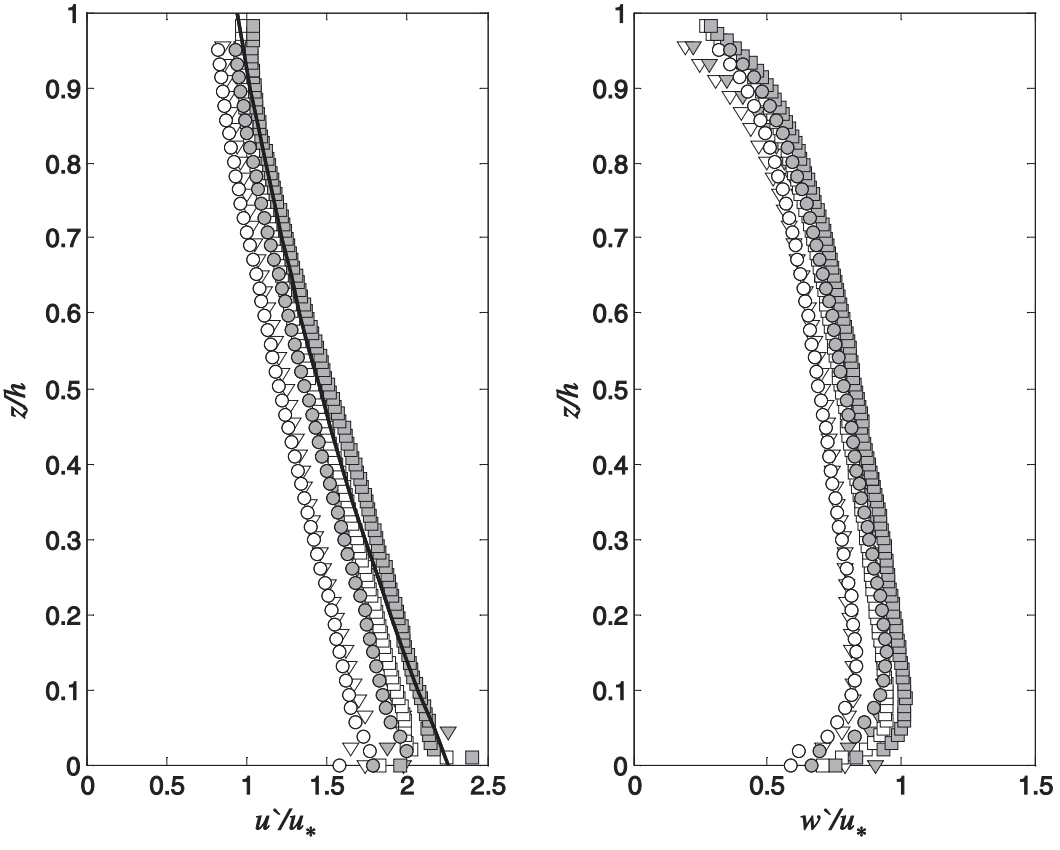


Figure 7. Turbulent intensities σ_u and σ_w scaled with the 'roughness crest' shear velocity (grey symbols) and the 'bed shear stress' shear velocity (white symbols) in experiments E1 (circles), E2 (squares) and E3 (triangles); σ_u is compared with turbulent intensities in flow over smooth bed (Nezu & Rodi 1986, line).

Copyright © 2006 Taylor & Francis Group plc, London, UK

profiles to the appropriate level (the roughness crest and the mean bed level $z = -\phi k$ consequently). The dimensionless profiles of turbulent intensity collapse reasonably well between the experiments when scaled with the 'roughness crest' shear velocity. When scaled with the 'bed shear stress' shear velocity, the turbulent intensities for the two shallower experiments (circles and triangles in Fig. 7) clearly stand out, showing the suppression of the turbulent intensities which is solely the artefact of the choice of the velocity scale u_*. It is interesting to compare the scaled turbulent intensities σ_u with those for the smooth bed flow (Nezu & Rodi, 1986), shown in the same figure. Judging by the data scaled with the 'bed shear stress' velocity scale, the turbulent intensities are suppressed in shallow flow over rough bed compared to smooth bed, while the data scaled with the 'roughness crest' velocity scale indicate that they are similar. As expected, in the experiment **E2** with deeper flow than in other two experiments, this difference vanishes.

These results illustrate how we can reach a different conclusion about turbulent intensities in rough bed shallow flows, solely because of the choice of the shear velocity with which to scale experimental data. For flow over spheres with uniform diameter using the correct velocity scale reveals the similarity of turbulent intensities between smooth-bed and rough-bed flows, while the inappropriate scale causes the non-existent, artificial, suppression of turbulent intensities.

6 CONCLUSIONS

The paper is focussed on the definition of the shear velocity which is to be used, as universal velocity scale, for scaling properties of free-surface turbulent flows over rough bed. In the literature there are several different definitions of the shear velocity, each with the different associated shear stress. The two most common definitions are based on the shear stress at the level of the roughness crest and the bed shear stress. In deep flows, where the water depth is much larger than the roughness height, the different definitions give approximately equal values of the shear velocity. In shallow flows, however, the differences between these values can be significant.

This is the reason why for shallow rough bed flows the definition of the shear velocity requires closer inspection. In this paper we present a case for adopting the shear velocity evaluated from the shear stress at the roughness crest as the universal velocity scale. There are clear reasons against using the bed shear stress, inasmuch as the shear velocity must be interpreted as the universal velocity scale of the free fluid flow in the outer layer. (The velocity scale calculated from the bed shear stress is the appropriate choice in some other context e.g. sediment transport). It was shown that scaling with the velocity scale based on the bed shear stress produces artificially increased von Karman constant and artificially suppressed turbulent intensities. For shallow flows this can significantly affect data interpretation.

ACKNOWLEDGEMENTS

This investigation was carried out as part of an experimental programme funded by the United Kingdom Engineering and Physical Sciences Research Council (Grant GR/R51865/01).

REFERENCES

Bayazit, M. 1976. Free surface flow in a channel of large relative roughness, *J. Hydraul. Res.*, 14(2): 115–126.

Dittrich, A., & Koll, K. 1997. Velocity field and resistance of flow over rough surface with large and small relative submergence. *Int. J. Sediment Res*., 12(3): 21–33.

Finnigan, J.J. 1985. Turbulent transport in flexible plant canopies. *The forest-atmosphere interactions*, B.A. Hutchinson and B.B. Hicks, eds., Reidel, Dodrecht, The Netherlands, pp. 443–480.

Finnigan, J.J. 2000. Turbulence in plant canopies. *Annu. Rev. Fluid. Mech*., 32: 519–571.

Jackson, P.S. 1981. On the displacement height in the logarithmic velocity profile, *J. Fluid Mech.*, 111:15–26.

Jarvela, J. 2005. Effect of submerged flexible vegetation on flow structure and resistance. *Jour. Hyd.*, 307: 233–241.

Katul, G., Wiberg, P., Albertson, J., & Hornberger, G. 2002. A mixing layer theory for flow resistance in shallow streams. *Water Resour. Res.,* 38(11):1250–1257.

Kironoto, B.A., & Graf, W.H. 1994. Turbulence characteristics in rough uniform open-channel flow. *Proc., Instn. Civ. Enrg. Water, Maritime, and Energy,* 106: 333–344.

Manes, C., Pokrajac, D., & McEwan, I. Double averaged open channel flows with small relative submergence. Submitted to *J. Hydraul. Eng.,* ASCE.

Millikan, C.D. 1939. A critical discussion of turbulent flows in channels and circular tubes. in *Proc. Fifth. Int. Conngr. Appl. Mech*.: 386–392.

Monin, A.S. & Yaglom, A.M. 1971. *Statistical fluid mechanics: Mechanics of turbulence*, Vol. 1. MIT Press, Boston, Mass.

Nakagawa, H., Tsujimoto, T., & Shimizu, Y. 1991. Turbulent flow with small relative submergence, in *Lecture Notes in Earth Sciences*, pp. 33–44.

Nepf, H.M., & Vivoni, E.R. 2000. Flow structure in depth-limited, vegetated flow. *J. Geophys. Res.*, 105(C12): 28547–28557

Nezu, I., & Rodi, W. 1986. Open-channel flow measurements with a laser Doppler anemometer, *J. Hydraul. Eng.,* 112(5): 335–355.

Nikora, V.I., Goring, D.G., McEwan, I.K., & Griffiths, G. 2001. Spatially averaged open-channel flow over rough bed. *J. Hydraul. Eng.,* ASCE 127(2): 123–133.

Nikora, V., Koll, K., McLean S., Dittrich, A., & Aberle, J. 2002. Zero-plane displacement for rough-bed open-channel flows. in *Proceedings of the International*

Copyright © 2006 Taylor & Francis Group plc, London, UK

Conference on Fluvial Hydraulics River Flow 2002, September 4–6, 2002, Louvain-la-Neuve, Belgium, pp. 83–92.

Nikora, V., Koll, K., McEwan, I., McLean, S., & Dittrich, A. 2004. Velocity distribution in the roughness layer of rough-bed flows, *J. Hydraul. Eng*., ASCE, 130(7), 1036–1042.

Nikora, V., McEwan, I., McLean, S., Coleman, S., Pokrajac, D., & Walters, R. Double averaging concept for rough-bed open-channel and overland flows. Theoretical background, submitted to *J. Hydraul. Eng.,* ASCE.

Poggi, D., Porporato, A., Ridolfi, L., Albertson, J.D., & Katul, G.G. 2004. The effect of vegetation density on canopy sub-layer turbulence, *Boundary-Layer Meteorology*, 111: 565–587.

Raupach, M.R. & Shaw, R.H. 1982. Averaging procedures for flow within vegetation canopies. *Boundary-Layer Meteorology*, 22: 79–90.

Raupach, M.R., Antonia, R. A., & Rajagopalan, S. 1991 Rough-wall turbulent boundary layers. *Applied Mech. Rev.* 44: 1–24.

Rowinski, P., Aberle, J., & Mazurczyk, A. 2005. Shear velocity estimation in hydraulic research. *Acta Geophysica Polonica* 53(4): 567–583.

Smith, J.D. & McLean, S.R. 1977. Spatially averaged flow over a wavy surface. *J. Geophys. Res.*, 83(12): 1735–1746.

Wilson, N.R. & Shaw, R.H. 1977. A higher order closure model for canopy flow. *J. Appl. Meteorology*, 16: 1197–1205.

Wang, J., Dong, Z., Chen, C., & Xia, Z. 1993. The effects of bed roughness on the distribution of turbulent intensities in open channel flow, Jour. Hyd. Res. 31(1): 89–98.

Wang, J., & Dong, Z. 1996. Open-channel turbulent flow over non-uniform gravel beds, *Appl. Sci. Res* 56: 243–254.

Yaglom, A.M. 1979. Similarity laws for constant-pressure and pressure-gradient turbulent wall flows, *Ann. Rev. Fluid Mech*., 11:505–540.

Copyright © 2006 Taylor & Francis Group plc, London, UK

Large eddy simulation of the two phase flow

F. Gallerano, L. Melilla & G. Cannata
Dipartimento di Idraulica, Trasporti e Strade, Università "La Sapienza", Roma, Italia

ABSTRACT: A new LES model is proposed together with a new methodology for the simulation of concentration fields of suspended solids coherent with the LES methodology. The proposed closure relation for the generalized SGS turbulent stress tensor: complies with the principle of turbulent frame indifference; takes into account both the anisotropy of the turbulence velocity scales and turbulence length scales; removes any balance assumption between the production and dissipation of SGS turbulent kinetic energy. In the proposed model the generalized SGS turbulent stress tensor is related exclusively to the generalized SGS turbulent kinetic energy (which is calculated by means of its balance equation) and the modified Leonard tensor. The concentration field is simulated by the spatially filtered equation of the concentration. In this equation the first-order tensor (produced by the correlation between the velocity and the concentration) is related to the gradient of the resolved concentrations according to an original dynamic Germano procedure.

1 INTRODUCTION

The numerical integration of the equations for Large Eddy Simulation (LES) of turbulent flows requires the formulation of closure relations for the generalized sub grid scale (SGS) turbulent stress tensor

$$\tau_{ij} = \tau(u_i, u_j) = \overline{u_i u_j} - \bar{u}_i \bar{u}_j \tag{1}$$

where u_i is the ith component of the instantaneous velocity and the overbar represents the application of the spatial filter.

Breaking down the instantaneous velocity which appears on the right hand side of Equation 1 into filtered (resolved) and fluctuating components,

$$\bar{u}_i \quad , \quad u_i' = u_i - \bar{u}_i ,$$

the SGS turbulent stress tensor can be split into three tensors:

$$\tau_{ij} = L_{ij}^m + C_{ij}^m + R_{ij}^m$$

called, respectively, modified Leonard tensor, modified cross tensor and modified Reynolds tensor and defined as follows (Germano 1992):

$$L_{ij}^m = \tau(\bar{u}_i, \bar{u}_j) = \overline{\bar{u}_i \bar{u}_j} - \bar{\bar{u}}_i \bar{\bar{u}}_j \tag{2}$$

$$C_{ij}^m = \tau(\bar{u}_i, u_j') + \tau(u_i', \bar{u}_j) = \overline{\bar{u}_i u_j'} - \bar{\bar{u}}_i \bar{u}_j' + \overline{u_i' \bar{u}_j} - \bar{u}_i' \bar{\bar{u}}_j \tag{3}$$

$$R_{ij}^m = \tau(u_i', u_j') = \overline{u_i' u_j'} - \bar{u}_i' \bar{u}_j' \tag{4}$$

In this paper a Large-Eddy-Simulation model (which overcomes the drawbacks of the models currently present in the literature) is presented. These include all dynamic Smagorinskv-type SGS models (e.g., Dynamic Smagorinsky Mode DSM (Germano et al. 1991), Dynamic Mixed Model DMM1 (Zang et al. 1993), DMM2 (Vreman et al. 1994), Lagrangian Dynamic Model LDM (Meneveau 1996), Dynamic Two-parameter Model DTM (Salvetti & Banerjee 1995)), in which the generalized SGS turbulent stress tensor is related to the resolved strain-rate tensor by means of a scalar eddy viscosity. It is assumed in these models that the eddy viscosity is a scalar proportional to the cubic root of the generalized SGS turbulent kinetic energy dissipation and that such dissipation is locally and instantaneously balanced by the production of the generalized SGS turbulent kinetic energy (i.e., by the rate of kinetic energy per unit of mass transferred from the large scales, larger than the filter size, to the unresolved ones). Consequently, it is evident that the dynamic Smagorinsky-type SGS models are fraught with three relevant drawbacks. The first drawback is represented by the scalar definition of the eddy viscosity; the second one concerns the local balance assumption of the generalized SGS turbulent kinetic energy production and dissipation, whilst the third drawback is related to the dynamic calculation of the coefficient used to model the eddy viscosity (Smagorinsky coefficient).

The scalar definition (first inconsistency) of the eddy viscosity is equivalent to assuming that the principal axes of the generalized SGS turbulent stress tensor, or the unresolved part of it (represented by the cross and Reynolds terms), are aligned with the principal axes of the resolved strain-rate tensor. This

Copyright © 2006 Taylor & Francis Group plc, London, UK

assumption has been disproved by many experimental tests and by DNS, which demonstrate that there is no alignment between the generalized SGS turbulent stress tensor, or the unresolved part of it, and the resolved strain-rate tensor (Tao et al. 2000, Meneveau & Katz 2000). Moreover, the eddy viscosity is proportional to the product of two terms, of which the dimensions are, respectively, those of a length and a velocity (Tennekes & Lumley 1972). These terms, which represent, respectively, the turbulence length scales and turbulence velocity scales, are, more generally, second-order tensors of which the product is a fourth-order tensor which represents the eddy viscosity (Monin & Yaglom 1972).

The scalar definition of the eddy viscosity, used in the above-mentioned dynamic Smagorinsky-type SGS models, presupposes the existence of a single turbulence velocity scale and a single turbulence length scale. This is equivalent to assuming that the second-order tensors which represent the turbulence length scales and the turbulence velocity scales are isotropic and that, therefore, the turbulence is isotropic. In this manner, the turbulence anisotropy induced by the continuous transfer of energy from the mean flow towards the turbulent fluctuations, which is generally extremely anisotropic, is not considered. Even though the energy cascade process causes a reduction of the turbulence anisotropy, many authors (Speziale & Gatski 1997, Sreenivasan 1991) demonstrated that even in the dissipation range of the smallest turbulent scales, where viscous dissipation occurs, there is a high anisotropy level even at high Reynolds numbers.

The second inconsistency of the Smagorinsky dynamic models is related to the assumption of a local and instantaneous balance between production and dissipation of the generalized SGS turbulent kinetic energy, formulated in the above-mentioned models to obtain the turbulent viscosity expression. This assumption is confirmed statistically and never instantaneously, and only locally at the scales associated with wavenumbers within the inertial subrange, and the latter exists only for isotropic turbulence and at high Reynolds numbers. Moreover, since the dissipation of the generalized SGS turbulent kinetic energy is, by definition, positive, the assumption of local balance implies that also the production of generalized SGS turbulent kinetic energy is positive. However, the assumption that the production is always positive implies that the energy transfer always occurs from the largest to the smallest scales and prevents positive transfers of kinetic energy from the subgrid scales to the resolved ones (backscatter). Since the energy exchange processes between the resolved and unresolved scales generally occur in both directions (forward scatter and back scatter), as has been observed by various authors (Piomelli et al. 1991, Horiuti 1989), the assumption that the production of generalized SGS turbulent kinetic energy is always positive does not enable the complexity of the energy exchange processes which characterize the turbulence to be adequately taken into account.

The third inconsistency of the dynamic models concerns the calculation of the above mentioned Smagorinsky coefficient C_s. It is calculated with variational methods, (e.g. with a least squares minimization method (Lilly 1992) or Lagrangian method (Meneveau et al. 1996)). These methods identify a single value of the scalar coefficient C_s from a system of five independent scalar equations relating the components of the anisotropic part of the generalized SGS turbulent stress tensor to the components of the resolved strain-rate tensor. This procedure does not provide completely acceptable results. Moreover, when simulating confined flows at high Reynolds number, the results of the dynamic procedure are of doubtful reliability in the region close to the wall including both the viscous sublayer and the buffer layer (Sarghini et al. 1999). In this region, the filter width used in the dynamic procedure is larger than most eddies that govern the momentum and energy transfer. Consequently, the dynamic procedure used under these conditions for the calculation of the coefficient C_s is not able to fully account for the local subgrid dissipative processes that affect the entire domain.

Another group of SGS models is made up of models that are based on the assumption of scale similarity, according to which there is a strict analogy between the hydrodynamic characteristics of the scales of motion which are contiguous in wavenumber space. This assumption is evidently justified by the characteristics of the energy cascade process that transfers the turbulent kinetic energy from the mean velocity field towards the largest turbulent scales and then towards the smallest by vortex stretching. The scale similarity models of Bardina et al. (1983) and of Liu et al. (1994) unlike the Smagorinsky dynamic models, assume neither local isotropy of the turbulence scales, nor alignment of the generalized SGS turbulent stress tensor with the resolved strain-rate sensor, nor local balance between production and dissipation of generalized SGS turbulent kinetic energy. In particular, Bardina et al. (1983) use scale similarity and assume that

$$\tau_{ij} = L_{ij} + rL_{ij} \tag{5}$$

in which

$$L_{ij} = \overline{\bar{u}_i \bar{u}_j} - \bar{u}_i \bar{u}_j \tag{6}$$

is the Leonard term and C_b is a dimensionless coefficient.

The scale similarity model of Bardina et al. (1983) and those derived from it, even though they eliminate the main inconsistencies of the Smagorinsky dynamic

Copyright © 2006 Taylor & Francis Group plc, London, UK

models, have the drawback of being insufficiently dissipative, i.e. they are not able to guarantee an adequate energy drain from the grid scales to the subgrid scales.

In this paper a new scale similarity model is proposed in which the SGS stress tensor is related to the modified Leonard stress tensor and the generalized SGS turbulent kinetic energy, which is calculated by its balance equation.

In such a way it is possible to guarantee an adequate energy drain from the grid scales to the subgrid scales without adding an eddy viscosity type term.

In this paper the main drawbacks of the large eddy simulation models present in literature are overcome and a new LES model is proposed, along with a new methodology for the simulation of concentration fields of the solids in suspension, coherent with the LES methodology.

In the proposed model: (a) there is no coefficient which appears in the closure relation for the generalized SGS turbulent stress tensor; (b) the generalized SGS turbulent stress tensor is related exclusively to the generalized SGS turbulent kinetic energy and the modified Leonard tensor; (c) the viscous dissipation ε of the generalized SGS turbulent kinetic energy is calculated directly by its balance equation, thereby overcoming the inconsistencies concerning the modelling of ε. The closure relation at the basis of the proposed Two-Equation Model (TEM): (a) complies with the principle of turbulent frame indifference; (b) takes into account both the anisotropy of the turbulence velocity scales and of the turbulence length scales; (c) removes any assumption of balance between the production and dissipation of the turbulent kinetic energy; (d) allows the use of a filter of which the width is not necessarily associated with the wavenumbers lying within the inertial subrange; (e) assumes scale similarity; (f) guarantees an adequate energy drain from the grid scales to the subgrid scales and guarantees backscatter; (g) overcomes the inconsistencies linked to the dynamic calculation of the closure coefficient used in the modelling of the generalized SGS turbulent stress tensor.

The concentration field is simulated by the spatially filtered concentration equation. In this equation the first-order tensor (produced by the correlation between the velocity and the concentration) is related to the gradient of the resolved concentrations according to an original dynamic Germano procedure.

2 A NEW LES MODEL

2.1 *The turbulence model*

According to Bardina's scale similarity assumption, the generalized SGS turbulent stress tensor can be expressed by

$$\tau_{ij} = (1+r)L_{ij}^m \tag{7}$$

where r is an unknown scalar coefficient and L_{ij}^m is the modified Leonard tensor.

In this paper it is demonstrated that, starting from the scale similarity assumption in 7, (by simple mathematical calculations) a closure relation is reached for the generalized SGS turbulent stress tensor, in which there appears no coefficient to be calibrate or to calculate dynamically and which is given by the following relation:

$$\tau_{ij} = \left(\frac{2E}{L_{kk}^m}\right) L_{ij}^m \tag{8}$$

Such a relation is not present in literature and has never been presented by other authors.

It is easy to verify that as, by definition, the generalized SGS turbulent kinetic energy equal to half the trace of the generalized SGS turbulent stress tensor (Germano 1992),

$$E = \frac{\tau_{kk}}{2} \tag{9}$$

from Equation 7 is obtained

$$\tau_{kk} = (1+r)L_{kk}^m \quad \text{where} \quad r = \frac{2E - L_{kk}^m}{L_{kk}^m} \tag{10}$$

Introducing 10 into 7 gives:

$$\tau_{ij} = \left(1 + \frac{2E - L_{kk}^m}{L_{kk}^m}\right) L_{ij}^m = \left(\frac{2E}{L_{kk}^m}\right) L_{ij}^m \tag{11}$$

The closure relation 11 is obtained without any assumption of local balance between the production and dissipation of generalized SGS turbulent kinetic energy and may thus be considered applicable to LES with the filter width falling into the range of wave numbers greater than the wave number corresponding to the maximum turbulent kinetic energy.

The closure relation 11 for the generalized SGS turbulent stress tensor: (a) complies with the principle of turbulent frame indifference given that it relates only objective tensors; (b) takes into account both the anisotropy of the turbulence velocity scales and turbulence length scales; (c) assumes scale similarity; (d) guarantees an adequate energy drain from the grid scales to the subgrid scales and guarantees backscatter; (e) overcomes the inconsistencies linked to the dynamic calculation of the closure coefficient used in the modelling of the generalized SGS turbulent stress tensor.

The generalized SGS turbulent kinetic energy, E, is calculated by solving its balance equation, defined by the following equation:

$$\frac{DE}{Dt} = -\frac{1}{2}\frac{\partial \tau(u_k,u_k,u_m)}{\partial x_m} - \tau_{mk}\frac{\partial \bar{u}_k}{\partial x_m} - \frac{\partial \tau(p,u_m)}{\partial x_m} + \nu\frac{\partial^2 E}{\partial x_m \partial x_m} + \tau(F_{ok},u_k) - \nu\tau\left(\frac{\partial u_k}{\partial x_m},\frac{\partial u_k}{\partial x_m}\right) \tag{12}$$

Copyright © 2006 Taylor & Francis Group plc, London, UK

The 1st and 3rd terms of the right-hand side of Equation 12 express the turbulent diffusion of the generalized SGS turbulent kinetic energy:

$$\frac{1}{2}\frac{\partial \tau(u_i,u_i,u_k)}{\partial x_k}+\frac{\partial \tau(p,u_k)}{\partial x_k}=\frac{\partial (F_E)_k}{\partial x_k} \tag{13}$$

The following equation is used for the calculation of $(F_E)_k$

$$(F_E)_k = D\sqrt{E}\,\overline{\Delta}\frac{\partial E}{\partial x_k} \tag{14}$$

Scalar coefficient D is dynamically calculated by means of a Germano identity applied to the 1st and 3rd terms on the right-hand side of Equation 12

$$\left(F_E^T\right)_k-\widetilde{(F_E)}_k=\frac{1}{2}T(u_i,u_i,u_k)-\frac{1}{2}\widetilde{\tau(u_i,u_i,u_k)} +T(p,u_k)-\widetilde{\tau(p,u_k)} \tag{15}$$

where the first term on the left-hand side of Equation 15 is the turbulent diffusion of the generalized SGS turbulent kinetic energy at the test level, the symbol $\widetilde{(.)}$ indicates the filter operation at the test level and

$$T(f,g)=\widetilde{\overline{f}\,\overline{g}}-\widetilde{\overline{f}}\,\widetilde{\overline{g}} \tag{16}$$

$$T(f,g,h)=\widetilde{\overline{f}\,\overline{g}\,\overline{h}}-\widetilde{\overline{f}}\,\widetilde{\overline{g}}\,\widetilde{\overline{h}} -\widetilde{\overline{f}}\,T(g,h)-\widetilde{\overline{g}}\,T(f,h)-\widetilde{\overline{h}}\,T(f,g) \tag{17}$$

are, respectively, the generalized second and third order central moment at the test level (Germano 1992). According to 16 and 17, Equation 15 reads.

$$\left(F_E^T\right)_k-\widetilde{(F_E)}_k=\frac{1}{2}\widetilde{\overline{u_i}\,\overline{u_i}\,\overline{u_k}}-\frac{1}{2}\widetilde{\overline{u}}_i\widetilde{\overline{u}}_i\widetilde{\overline{u}}_k -\frac{1}{2}\widetilde{\overline{u}}_k T(u_i,u_i)+\frac{1}{2}\widetilde{\overline{u}_k\tau(u_i,u_i)}-\widetilde{\overline{u}}_i T(u_i,u_k) +\widetilde{\overline{u}_i\,\tau(u_i,u_k)}+T(p,u_k)-\widetilde{\tau(p,u_k)} \tag{18}$$

Using Equation 14, the left-hand side term of Equation 15 takes the form

$$\left(F_E^T\right)_k-\widetilde{(F_E)}_k=D\sqrt{E^T}\,\overline{\Delta}^T\frac{\partial E^T}{\partial x_k}-\widetilde{D\sqrt{E}\Delta}\frac{\partial \overline{E}}{\partial x_k} \tag{19}$$

where E^T is the generalized SGS turbulent kinetic energy at the test level. The coefficient D is calculated by introducing 19 into 18.

The last term on the right-hand side of Equation 12 is defined as viscous dissipation:

$$\varepsilon=\nu\tau\left(\frac{\partial u_i}{\partial x_j},\frac{\partial u_i}{\partial x_j}\right) \tag{20}$$

In the proposed LES model a further balance equation is introduced for the subgrid viscous dissipation ε. This equation, expressed in terms of the generalized central moments, takes the form (Gallerano et al. 2005):

$$\frac{\partial \varepsilon}{\partial t}+\frac{\partial \overline{u}_k\varepsilon}{\partial x_k}-\nu\frac{\partial^2\varepsilon}{\partial x_k\partial x_k}+\nu\frac{\partial}{\partial x_k}\tau\left(u_k,\frac{\partial u_i}{\partial x_j},\frac{\partial u_i}{\partial x_j}\right)+ 2\nu\frac{\partial}{\partial x_k}\left(\frac{\partial \overline{u}_i}{\partial x_j}\tau\left(u_k,\frac{\partial u_i}{\partial x_j}\right)\right)+2\nu\frac{\partial}{\partial x_k}\tau\left(\frac{\partial u_k}{\partial x_i},\frac{\partial p}{\partial x_i}\right)+ -2\nu\frac{\partial}{\partial x_k}\left(\frac{\partial \overline{u}_i}{\partial x_j}\frac{\partial \tau_{ik}}{\partial x_j}\right)+2\nu\tau\left(\frac{\partial u_i}{\partial x_k},\frac{\partial u_k}{\partial x_j},\frac{\partial u_i}{\partial x_j}\right) +2\nu\frac{\partial \overline{u}_k}{\partial x_j}\tau\left(\frac{\partial u_i}{\partial x_k},\frac{\partial u_i}{\partial x_j}\right)+2\nu\frac{\partial \overline{u}_i}{\partial x_k}\tau\left(\frac{\partial u_k}{\partial x_j},\frac{\partial u_i}{\partial x_j}\right)+ 2\nu\frac{\partial \overline{u}_i}{\partial x_j}\tau\left(\frac{\partial u_i}{\partial x_k},\frac{\partial u_k}{\partial x_j}\right)+2\nu\frac{\partial \tau_{ik}}{\partial x_j}\frac{\partial^2\overline{u}_i}{\partial x_j\partial x_k}+ 2\nu^2\tau\left(\frac{\partial^2 u_i}{\partial x_j\partial x_k},\frac{\partial^2 u_i}{\partial x_j\partial x_k}\right)-2\nu\tau\left(\frac{\partial u_i}{\partial x_j},\frac{\partial F_{0i}}{\partial x_j}\right)=0 \tag{21}$$

In this paper an original expression is proposed for the "modeled" form of the balance equation for the generalized SGS turbulent kinetic energy dissipation, in which the unknown tensors are modeled by adopting the hypothesis of scale similarity and Equation 21 takes the form:

$$\frac{\partial \varepsilon}{\partial t}+\frac{\partial \overline{u}_k\varepsilon}{\partial x_k}-\nu\frac{\partial^2\varepsilon}{\partial x_k\partial x_k}+\frac{\partial}{\partial x_k}C_{F_\varepsilon}\frac{E^2}{\varepsilon}\frac{L_{kl}^m}{L_{jj}^m}\frac{\partial \varepsilon}{\partial x_l} +2\nu\frac{\partial}{\partial x_k}\left(\frac{\partial \overline{u}_i}{\partial x_j}\left(\frac{C_{F^1_\varepsilon}\dfrac{E}{\varepsilon}\dfrac{\partial \varepsilon}{\partial x_q}\delta_q}{\tau\left(\overline{u}_n,\dfrac{\partial \overline{u}_n}{\partial x_n}\right)}\tau\left(\overline{u}_k,\frac{\partial \overline{u}_i}{\partial x_j}\right)\right)\right) -2\nu\frac{\partial}{\partial x_k}\left(\frac{\partial \overline{u}_i}{\partial x_j}\frac{\partial}{\partial x_j}\left(\frac{2E}{L_{qq}{}^m}L_{ik}{}^m\right)\right)-C_{P_\varepsilon}\frac{\varepsilon(-L^m{}_{ij}\overline{S}_{ij})}{L^m{}_{kk}} +2\nu\frac{\partial \overline{u}_k}{\partial x_j}\frac{\dfrac{\varepsilon}{\nu}\tau\left(\dfrac{\partial \overline{u}_i}{\partial x_k},\dfrac{\partial \overline{u}_i}{\partial x_j}\right)}{\tau\left(\dfrac{\partial \overline{u}_q}{\partial x_n},\dfrac{\partial \overline{u}_q}{\partial x_n}\right)}+2\nu\frac{\partial \overline{u}_i}{\partial x_k}\frac{\dfrac{\varepsilon}{\nu}\tau\left(\dfrac{\partial \overline{u}_k}{\partial x_j},\dfrac{\partial \overline{u}_i}{\partial x_j}\right)}{\tau\left(\dfrac{\partial \overline{u}_q}{\partial x_n},\dfrac{\partial \overline{u}_q}{\partial x_n}\right)} +2\nu\frac{\partial \overline{u}_i}{\partial x_j}\frac{\dfrac{\varepsilon}{\nu}\tau\left(\dfrac{\partial \overline{u}_i}{\partial x_k},\dfrac{\partial \overline{u}_k}{\partial x_j}\right)}{\tau\left(\dfrac{\partial \overline{u}_q}{\partial x_s},\dfrac{\partial \overline{u}_s}{\partial x_q}\right)}+2\nu\frac{\partial}{\partial x_j}\left(\frac{2E}{L_{nn}^m}L_{ik}^m\right)\frac{\partial^2\overline{u}_i}{\partial x_j\partial x_k} +C_{D_\varepsilon}\frac{\varepsilon^2}{E}=0 \tag{22}$$

Copyright © 2006 Taylor & Francis Group plc, London, UK

where $\delta_i = (1,1,1)$ and in which the closure coefficients are calculated dynamically by means of the Germano identities.

2.2 *The spatially filtered concentration equation*

The filtered equation of the concentration of suspended solids is:

$$\frac{\partial \overline{C}}{\partial t} + \frac{\partial \overline{u}_i \overline{C}}{\partial x_i} + \frac{\partial}{\partial x_i}\left(\overline{u_i C} - \overline{u}_i \overline{C}\right) = 0 \tag{23}$$

where $\bar{C}$ represents the spatially filtered concentration field.

The last term of Equation 23 is a first-order tensor given by the generalized central moment relative to the velocity vector and the concentration and is defined as follows:

$$a_i = \tau\left(u_i, C\right) = \left(\overline{u_i C} - \overline{u}_i \overline{C}\right) \tag{24}$$

The above tensor can be split in terms of generalized central moments:

$$a_i = L_i^C + C_i^C + R_i^C \tag{25}$$

where:

$$L_i^C = \tau\left(\overline{u}_i, \overline{C}\right) = \overline{\overline{u}_i \overline{C}} - \overline{\overline{u}_i}\,\overline{\overline{C}}$$

$$C_i^C = \tau\left(\overline{u}_i, C'\right) + \tau\left(u_i', \overline{C}\right) = \left(\overline{\overline{u}_i C'} - \overline{\overline{u}_i}\,\overline{C'} + \overline{u_i' \overline{C}} - \overline{u'}\,\overline{\overline{C}}\right)$$

$$R_i^C = \tau\left(u_i', C'\right) = \overline{u_i' C'} - \overline{u_i'}\,\overline{C'}$$

The sum of the second and third term on the right hand side of Equation 25 represents an unknown first-order tensor. In this paper a new closure relation for this unknown tensor is proposed.

The closure relation between this unresolved tensor and the gradient of the filtered concentration is defined by a second-order tensor which is assumed proportional to the subgrid turbulent velocity scale and the turbulence length scale:

$$v_{ij}^C = c_c \sqrt{E} d_{ij} \tag{26}$$

the above closure relation is:

$$C_i^C + R_i^C = c_c \sqrt{E} d_{in} \frac{\partial \overline{C}}{\partial x_n} \tag{27}$$

Let $T(u_i, C)$ be the generalized central moment at the test level related to the velocity vector and the concentration, the following first-order tensor is defined

$$A_i = T\left(u_i, C\right) = \widetilde{\overline{u_i C}} - \tilde{\overline{u}}_i \tilde{\overline{C}} \tag{28}$$

which in terms of generalized central moments can be split as:

$$A_i = L_i^T + C_i^T + R_i^T \tag{29}$$

where:

$$L_i^T = T\left(\tilde{\overline{u}}_i, \tilde{\overline{C}}\right) = \widetilde{\tilde{\overline{u}}_i \tilde{\overline{C}}} - \tilde{\tilde{\overline{u}}}_i \tilde{\tilde{\overline{C}}}$$

$$C_i^T = T\left(\tilde{\overline{u}}_i, C'\right) + T\left(u_i', \tilde{\overline{C}}\right) = \left(\widetilde{\tilde{\overline{u}}_i C'} - \tilde{\tilde{\overline{u}}}_i \tilde{\overline{C'}} + \widetilde{u_i' \tilde{\overline{C}}} - \tilde{\overline{u'}}\,\tilde{\tilde{\overline{C}}}\right)$$

$$R_i^T = T\left(u_i', C'\right) = \widetilde{\overline{u_i' C'}} - \tilde{\overline{u_i'}}\,\tilde{\overline{C'}}$$

The sum of the last two terms on the right hand side of Equation 29 is an unknown quantity that is modeled with an expression analogous to Equation 27:

$$C_i^T + R_i^T = c_c \sqrt{E^T} d_{in}^T \frac{\partial \tilde{\overline{C}}}{\partial x_n} \tag{30}$$

The calculation of the coefficient c_c is carried out by using the following identity

$$A_i - \tilde{a}_i = \widetilde{\overline{u_i C}} - \tilde{\overline{u}}_i \tilde{\overline{C}} \tag{31}$$

Equation 31, with the use of the closure relations expressed by Equations 27 and 30, becomes

$$c_c \sqrt{E^T} d_{in}^T \frac{\partial \tilde{\overline{C}}}{\partial x_n} - \widetilde{c_c \sqrt{E} d_{in} \frac{\partial \overline{C}}{\partial x_n}} = \widetilde{u_i \overline{C}} - \tilde{u}_i \tilde{\overline{C}} - \widetilde{\tilde{u}_i \tilde{\overline{C}}} + \tilde{u}_i \tilde{\tilde{\overline{C}}} + \widetilde{u_i \tilde{\overline{C}}} - \tilde{u}_i \tilde{\tilde{\overline{C}}} \tag{32}$$

where E^T indicates the SGS kinetic energy relative to the test-filter and d_{in}^T indicates the second-order tensor associated with the turbulence length scales relative to the test-filter.

Equation 32 allows the dynamic calculation of the coefficient c_c.

The numerical integration of Equation 23 for the simulation of the filtered concentration field of suspended solids may be carried out once the boundary conditions have been defined.

The plane, in proximity to the bottom, which defines the boundary for the concentration field is placed immediately above the viscous sublayer, inside the buffer layer: the "Reference Concentration", C_r, is imposed on the plane as a boundary condition.

Copyright © 2006 Taylor & Francis Group plc, London, UK

This reference concentration is calculated as a function of the resolved tangential stress at the bottom and the critical stress representing the threshold beyond which the movement of solid particles from the bottom is produced.

In particular, in the proposed model the value of the local and instantaneous reference concentration, C_r, is related to the resolved velocity field at the bottom by means of the formula proposed by Van Rijn (1985). The aforesaid Van Rijn formula reads:

$$C_r = 0{,}015\left(\frac{D_p}{a}\right)\left(\frac{T^{1,5}}{D_*^{0,3}}\right) \tag{33}$$

in which
a: distance from the bottom at which C_r is calculated
D_p: diameter of the solid particles

$$D_* = D_p\left[\frac{(\delta-1)g}{\nu}\right]^{1/3} \quad \begin{cases} \delta: \text{relative density of the particle} \\ \nu: \text{kinetic viscosity} \end{cases} \tag{34}$$

$$T = \frac{\overline{u}_*^2 - u_{*crit}^2}{u_{*crit}^2} \tag{35}$$

and the quantity $\overline{u}*^2$ which appears in Equation 35 is linked to the tangential stress at the bottom, τ_f, produced at each time step by the tangential resolved velocity component at the bottom, $\overline{u}$, by means of the following relation:

$$\overline{u}_*^2 = \frac{\tau_f}{\rho} = \nu\frac{\partial \overline{u}}{\partial y} \tag{36}$$

3 RESULTS AND DISCUSSION

The symbol $\langle . \rangle$ represents the Reynolds average and the friction velocity based Reynolds number is given by:

$$Re_\tau = \langle u_* \rangle L/\nu.$$

Turbulent channel flows (between two flat parallel plates placed at a distance of $2L$) are simulated with the proposed Large Eddy Simulation model at different friction-velocity-based Reynolds numbers, ranging from 395 to 2,340.

In order to validate the proposed closure relation for the generalized SGS turbulent stress tensor, the numerical results obtained with the proposed model are compared with DNS results and with experimental data.

The proposed model is used to simulate the phenomenon of the re-suspension (from the bottom) of solid particles in a channel flow.

The values of the diameter and the relative density of the solid particles are, respectively, equal to 100 μm and 1.65.

The simulation of the velocity and concentration fields in a channel flow is performed at Reynolds number $Re_\tau = 600$.

In Figure 1 is plotted the profile of the time-averaged streamwise velocity component obtained with the proposed model compared with the profile obtained with DNS (Mansour et al.) and the Dynamic Mixed Model, DMM (Zang et al. 1993), for flows at $Re_\tau = 395$. The figure shows that the profile obtained with the proposed model agrees more the DNS velocity profile than with the profile obtained with the DMM, both in the boundary layer and in the region inside the channel.

Figure 2 shows the profiles of the component $<u_1' u_3'>$ of the Reynolds stress tensor, (where indexes

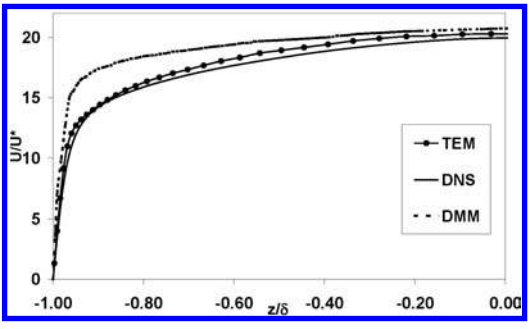


Figure 1. Time-averaged streamwise velocities. Comparison between DNS and LES results obtained with DMM and the proposed model (TEM). Channel flow, $Re_\tau = 395$.

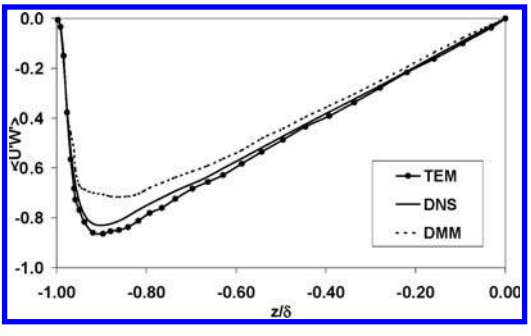


Figure 2. Reynolds stress $<u_1' u_3'>$. (indexes (1) and (3) denote, respectively the streamwise and wall-normal directions) Comparison between DNS and LES results obtained with the dynamic mixed model (DMM) and the proposed model (TEM). Channel flow, $Re_\tau = 395$.

Copyright © 2006 Taylor & Francis Group plc, London, UK

1 and 3 denote, respectively, the streamwise and wall-normal directions), obtained from the simulations carried out with the proposed model compared with the profiles of the analogous component obtained from DNS and from simulations carried out with the DMM at $Re_\tau = 395$. As can be seen from figure 2, the profile of the component $<u_1' u_3'>$ calculated with the proposed model yields a similar profile to that of the corresponding component of the Reynolds stress tensor obtained by the DNS, whilst the DMM provides values which are greatly underestimated.

Figure 3 shows the profile averaged streamwise velocity component for a channel flow at $Re_\tau = 2340$ obtained with the proposed model compared with the profile of the analogous velocity component measured experimentally (Comte-Bellott). The agreement between the two velocity profiles is very good.

Figure 4 compares the profile of the component $<u_1' u_3'>$ of the Reynolds stress tensor calculated with the proposed model with the profile of the similar component of the Reynolds tensor obtained from experimental measurements, for a channel flow at $Re_\tau = 2340$. Figure 4 shows that at $Re_\tau = 2340$ the proposed model provides a profile of the component $<u_1' u_3'>$ in agreement with that of the corresponding component of the Reynolds stress tensor obtained from the experimental measurements.

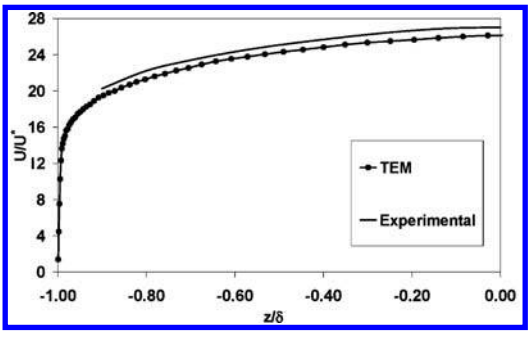


Figure 3. Time-averaged streamwise velocities. Comparison between experimental measurements and LES results obtained with the proposed model (TEM). Channel flow, $Re_\tau = 2340$.

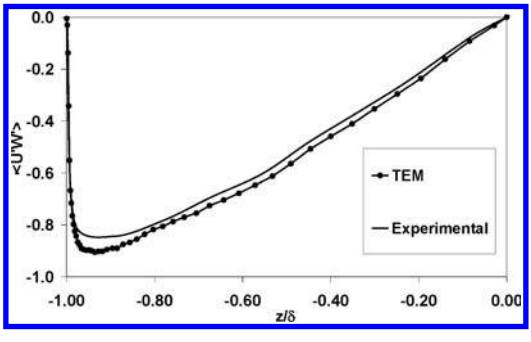


Figure 4. Reynolds stress $<U'W'>$. Comparison between experimental measurements and LES results obtained with the proposed model (TEM). Channel flow, $Re_\tau = 2340$.

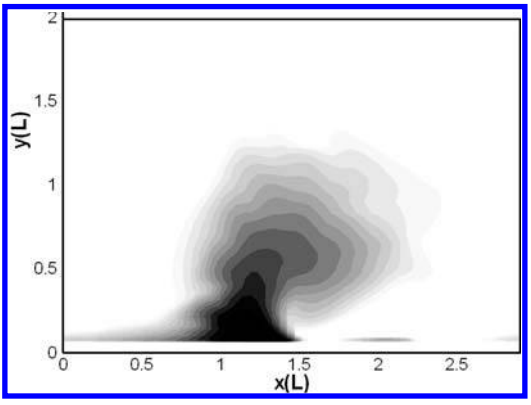


Figure 5. Channel flow: filtered concentration field.

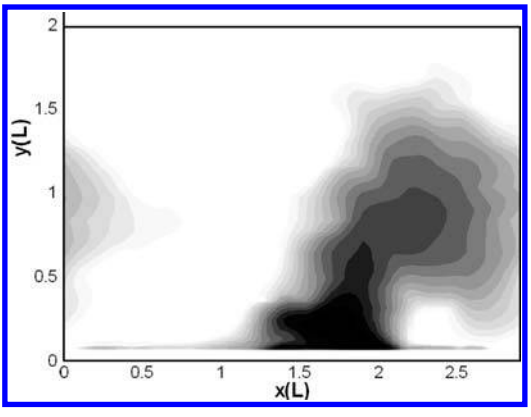


Figure 6. Channel flow: filtered concentration field.

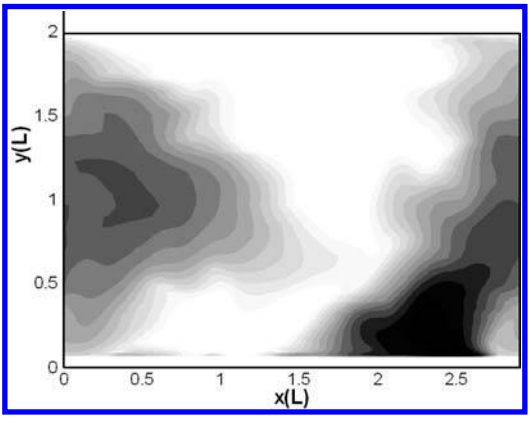


Figure 7. Channel flow: filtered concentration field.

Copyright © 2006 Taylor & Francis Group plc, London, UK

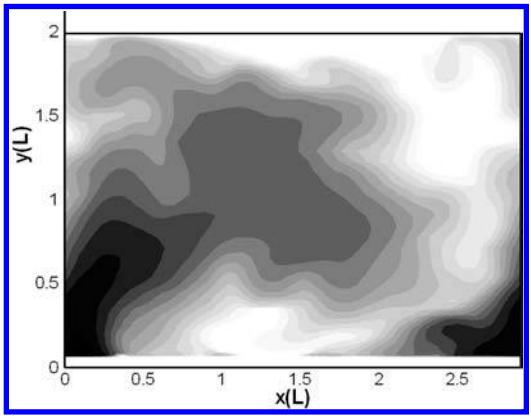


Figure 8. Channel flow: filtered concentration field.

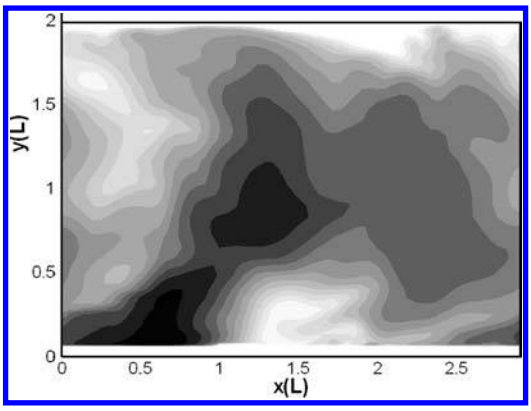


Figure 9. Channel flow: filtered concentration field.

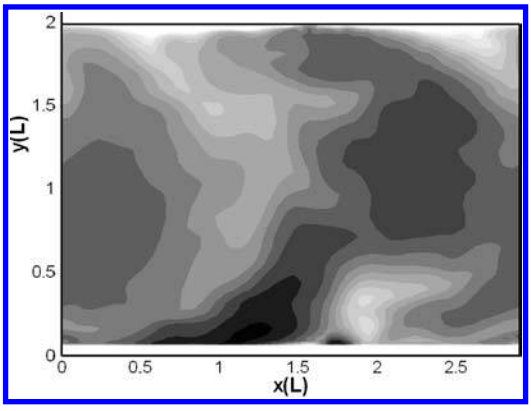


Figure 10. Channel flow: filtered concentration field.

In Figures 5–10 is shown a sequence of longitudinal sections of instantaneous solid particles concentration fields relative to the transitory interval during which the phenomenon of the re-suspension begins and develops from the bottom and the transport of solid particles inside the channel.

Periodic boundary conditions on the velocity and concentration fields in the streamwise direction allow the numerical simulation of the concentration field which occurs in a channel of infinite length having an erodible particle bed.

Figure 5 shows the filtered concentration field (at an instant of the numerical simulation): from the figure it is possible to see how some vortices (characterized by a high content of the turbulent kinetic energy and located between the abscissa $x > 1$ and $x < 1.5$) are able to produce instant values of friction velocity that may generate the re-suspension of the solid particles.

In Figures 6–10 it is shown how the concentration field values change over time: these variations are the result of the streamwise movement of the aforesaid vortices: the increases of the instantaneous friction velocity (associated to the vortices) and the streamwise movement of the vortices with high value of kinetic energy produce an increase of the value of the reference concentration and a streamwise movement of the bottom regions characterized by the re-suspension of the solid particles.

After a high number of iterations a statistically steady condition for both the solid and the liquid phase is verified.

By applying a Reynolds average to the spatially filtered concentration values (for a time higher than the integral time scale of turbulence) a statistically steady vertical concentration profile of the solids in suspension is obtained:

$$\left\langle \overline{C}(y) \right\rangle = \int_0^{T_0} \overline{C}(y,t)\,dt \qquad (37)$$

where y is the vertical coordinate and T_0 the time over which the average is calculated.

The numerical results of the concentration vertical profile, obtained by Equation 37, are compared with the experimental measures concentration of Gallerano & Cioffi (1991) in a channel of rectangular area with an erodible particle bed, in steady conditions.

The theoretical profile of the Reynolds averaged concentration values is also calculated by adopting the following Van Rijn's formula in the same average hydrodynamic conditions and for the same particle characteristics of the LES simulations:

$$\frac{\langle C \rangle}{\langle C_r \rangle} = \left[\frac{a(H-y)}{y(H-a)} \right]^{Z} \qquad (38)$$

where

$$Z' = Z + \tau; \qquad \tau = 2.5 \left[\frac{\omega_0}{\langle u_* \rangle} \right]^{0.8} \left[\frac{\langle C_r \rangle}{0.65} \right]^{0.4} \qquad (39)$$

Copyright © 2006 Taylor & Francis Group plc, London, UK

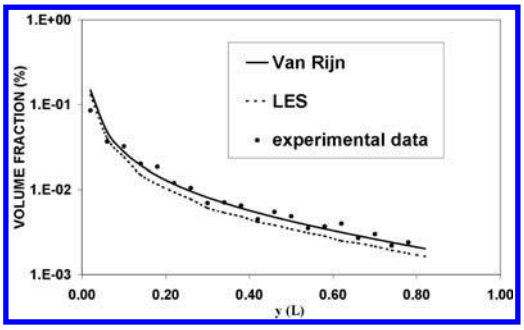


Figure 11. Comparison between experimental data (Cioffi & Gallerano, 1991), Van Rijn's formula values and Reynolds averaged LES values.

$$Z = \frac{\omega_0}{K_\beta k u_*} \; ; \qquad K_\beta = 1 + 2\left[\frac{\omega_0}{\langle u_* \rangle}\right]^2 \tag{40}$$

ω_0 : terminal velocity; k: Von Karman constant
$\langle C_r \rangle$: Reference Concentration calculated by means of Equation 33 in which

$$T = \frac{\langle u_* \rangle^2 - u_{*crit}^2}{u_{*crit}^2} \tag{41}$$

and the parameter a, that appears in the Equation 33 and 38, is assumed equal to the distance from the bottom where the plane on which the Reference Concentration is assigned is placed. In this case a is assumed equal to 12 wall units, where the wall unit

$$y^+ = \frac{y\langle u_* \rangle}{\nu} \tag{42}$$

is calculated using the friction velocity obtained with the Reynolds number of the numerical simulation of the channel flow:

$$\langle u_* \rangle = \frac{Re_\tau \nu}{D} \tag{43}$$

In Figure 11 the vertical concentration profile, obtained by averaging (over time) the spatially filtered concentration values (calculated by means of the proposed numerical model), is compared with the vertical concentration profile measured experimentally by Cioffi & Gallerano (1991) in stationary conditions and with the vertical concentration profile calculated theoretically by means of Van Rijn's formula.

4 CONCLUSIONS

In this paper a new LES model is presented together with a new methodology for the simulation of concentration fields of solids in suspension which is coherent with the LES methodology.

A new constitutive equation, relating the generalized SGS turbulent stress tensor to the resolved kinematic quantities, is proposed. The closure relation on the basis of the proposed model (a) respects the principle of turbulence frame indifference (Hutter & Johnk 2004); (b) takes into account both the anisotropy of the turbulence velocity scales and of the turbulence length scales; (c) removes any balance assumption between the production and dissipation of turbulent kinetic energy; (d) assumes scale similarity.

In the proposed model: (a) the generalized SGS turbulent stress tensor is related exclusively to the generalized SGS turbulent kinetic energy (which is calculated by means of its balance equation) and the modified Leonard tensor; (b) the viscous dissipation ε of the generalized SGS turbulent kinetic energy is calculated by solving the ε balance equation.

Turbulent flows have been simulated with the proposed model between two flat and parallel plates (turbulent channel flow) at friction-velocity-based Reynolds numbers ranging from 395 to 2340. The closure relation between the generalized SGS turbulent stress tensor and the resolved kinematic quantities, used in the proposed model, improves the agreement between the results obtained with LES and those obtained with DNS and with experimental measurements and it allows the simulation of high Reynolds number flows.

The concentration field is simulated by the spatially filtered equation of the concentration. In this equation the first order tensor (produced by the correlation between velocity and concentration) is related to the gradient of the resolved concentrations according to an original dynamic Germano procedure.

The vertical concentration profile, obtained by averaging (over time) the spatially filtered concentration values (calculated by means of the proposed numerical model), are in agreement with the experimental data.

REFERENCES

Bardina, J, Ferziger, J.H. & Reynolds, W.C. 1983. Inproved turbulence models based on large eddy simulation of homogeneous, incompressible, turbulent, flows. *Ph.D. dissertation*. Department of Mechanical Engineering, Stanford University.

Comte-Bellott, G. High Reynolds number vhannel flow experiment. *AGARD Advisory Report*, 343.

Gallerano, F. & Cioffi, F.1991. Velocity and concentration profiles of solid particles in a channel with moveable and erodible bed. *Journal of Hydraulic Research* 29 (3): 387–400.

Gallerano, F., Pasero, E. & Cannata, G. 2005. A dynamic two-equation Sub Grid Scale model. *Continuum Mech. Thermodyn.* 17: 101–123.

Gallerano, F. & Napoli, E. 1999. A dynamic tensorial sub-grid scale model. *Continuum Mech. Thermodyn*, 11: 1–14.

Gallerano, F. & Napoli, E. 2000. Balance equation of the generalized sub-grid scale (SGS) turbulent kinetic energy in

Copyright © 2006 Taylor & Francis Group plc, London, UK

a new tensorial dynamic mixed model. *Continuum Mech. Thermodyn*. 19: 1–16.
Germano, M., Piomelli, U., Moin, P. & Cabot, W.H. 1991. A dynamic subgrid scale eddy viscosity model. *Phys. Fluids* A3: 1760–1765.
Germano, M. 1992. Turbulence: the filtering approach. *J. Fluid Mech.* 238: 323–336.
Ghosal, S., Lund, T.S., Moin, P. & Aksevoll, K. 1995. A dynamic localisation model for large-eddy simulation of turbulent flows. *J. Fluid Mech.* 286: 229–255.
Joeng, J. & Hussain, F. 1995. On the identification of a vortex. *J.Fluid Mech.* 285: 69–94.
Horiuti, K. 1989. The role of the Bardina model in large eddy simulation of turbulent channel flow. *Phys. Fluids* A1: 426–428.
Hutter, K. & Jonk, K. 2004. *Continum Methods of Physical of Modeling*. Springer.
Lilly, D.K. 1992. A proposed modification of the Germano subgrid scale closure method. *Phys. Fluids* A4: 633–635.
Liu, S., Meneveau, C. & Katz, J. 1994. On the properties of similarity subgrid-scale models as deduced from measurements in a turbulent jet. *J Fluid Mech*. 275: 83–119.
Mansour, N.N., Moser, R.D. & Kim, J. Fully developed turbulent channel flow simulation. *AGARD Advisory Report*, 343.
Meneveau, C., Lund, T.S. & Cabot, W.H. 1996. A Lagrangian dynamic subgrid-scale model of turbulence. *J. Fluid Mech.* 319: 353–385.
Meneveau, C. & Katz, J. 2000. Scale-invariance and turbulence models for large-eddy simulation. *Ann. Rev. Fluid Mech*. 32: 1–32.
Monin, A.S. & Yaglom, A.M. 1972. Statistical Fluid Mechanics: Mechanics of Turbulence. *MIT Press*, Cambridge, England.
Piomelli, U., Cabot, W.H., Moin, P. & Lee, S. 1991. Subgrid-scale backscatter in turbulent and transitional flows. *Phys. Fluids* A3: 1766–1771.
Salvetti, V.M. & Banerjee, S. 1995. A priori tests of a new dynamic subgrid-scale model for finite difference large-eddy simulations. *Phys. Fluids* 7: 2831–2847.
Speziale, C.G. & Gatski, T.B. 1997. Analysis and modelling of anisotropies in the dissipation rate of turbulence. *J Fluid Mech*. 344: 155–180.
Sreenivasan, K.R. 1991. On local isotropy of passive scalars in turbulent shear flows. *Proc. R. Soc. London* A 434: 165–182.
Tao, B., Katz, J. & Meneveau, C. 2000. Geometry and scale relationships in high Reynolds number turbulence determined from three-dimensional holographic velocimetry. *Phys. Fluids* 12: 941–944.
Tennekes, K. & Lumley, J.L. (1972) A first course in turbulence. *MIT Press*, Cambridge, Mass.
Van Rijn, L.C., Sediment transport. 1985. *Delft Hydraulic Laborator.* 334.
Zang, Y., Street, R.L. & Koseff, J.R. 1993. A dynamic mixed subgrid-scale model and its application to turbulent recirculating flows. *Phys. Fluids.* A 5: 3186–3196.

Copyright © 2006 Taylor & Francis Group plc, London, UK

Turbulent processes at the entrance of a pool using flow visualization

G.A. Marquis & A.G. Roy
Chaire de recherche du Canada en dynamique fluviale
Département de géographie, Université de Montréal, Montréal, Québec, Canada

ABSTRACT: We examine the response of the turbulent flow processes to changes in bed morphology at the entrance of a pool. Flow visualization and high frequency velocity measurements are combined along a transect where depth increases over a short distance. Velocity data revealed an increased spatial coherence of the turbulent flow structures along the transect. Results from the visualization showed a clear transition in the spatial and temporal scales of the turbulent events. As depth increases, there is a transition in the scale of roughness from a clast dominated boundary layer to a large bedform dominance and turbulent events adjust to this change. Turbulent events that develop in the lee of the slope at the entrance of the pool are more regular and they advect less frequently but more powerfully towards the surface. This bedform-turbulent flow structure interaction may be significant for sediment transport and flow mixing within pools.

1 INTRODUCTION

The turbulent structure of the flow in a river is often described by mean parameters such as turbulence intensity and turbulent kinetic energy. However, individual turbulent events may be significant for river processes like sediment transport and water column mixing (Nelson et al. 1995). Turbulent events in a gravel-bed river mainly occur as large-scale turbulent flow structures, which are ubiquitous and dominant features of the fluvial turbulent boundary layer (Roy et al. 2004). Large-scale turbulent structures are composed of alternating high- and low-speed wedges that scale with outer flow variables such as flow depth (Y). Wedges are narrow (0.5 to $1Y$), elongated (2 to $6Y$) and generally occupy the entire flow depth. Low-speed wedges are ejection-like structures with vertical velocity being positive most of the time. In contrast, high-speed wedges are sweep-like structures with a mostly negative vertical velocity. Those two counterparts, the ejection and the sweep, form the well known bursting process.

Evidence to substantiate the presence and role of these large-scale turbulent flow structures has come from high frequency velocity measurements as well as from flow visualization. While high frequency velocity measurements have been extensively used in river flows, visualization has mostly been limited to flume experiments where it is possible to control the conditions. For instance, flow visualization provides very rich spatio-temporal information on the turbulent flow field. In a river, flow visualization measurements are laborious and only a few researchers have chosen this method to investigate flow turbulence. However, the information provided by visualization is complementary to point velocity measurements, mostly used is shallow flows (Roy et al. 1999). Automated quantification of images recorded in the field has not been fully exploited until now, because the complex images require many transformations before being usable. Also, the quantification of turbulence based on the visual analysis is subject to operator errors and is time consuming. Nevertheless, this type of analysis reveals an excellent correspondence with results derived from the velocity measurements. For example, Paiement-Paradis et al. (2003) showed that the two methods result in similar power law scalings of the frequency distributions for individual turbulent event duration. Generally, the qualitative and the quantitative information manually extracted from the images have allowed to confirm and extrapolate the results from velocity measurement (e.g. Roy et al. 1999, 2004). Until now, *in situ* flow visualization has been only used to study small scale turbulent processes in uniform flows above rough beds and not to examine larger scale bedform-flow interactions.

Several researchers have emphasized the necessity of investigating turbulent flow processes to better understand the complex relationships between bedforms, sediment transport and flow in rivers with pool-riffle morphology (e.g. Clifford 1993). These bedforms impose repeated constraints on the flow by

Copyright © 2006 Taylor & Francis Group plc, London, UK

inducing depth changes in the channel, thus affecting flow turbulent parameters as well as individual turbulent events. In a flume experiment, Thompson (2004) found that the acceleration of the flow at the exit of a pool where flow depth is decreasing produced a non-linear increase of the velocity standard-deviation in the downstream direction. He hypothesized that turbulence intensity increases at the exit of the pool thus leading to an increased dissipation of energy, a mechanism that may be critical for sediment transport. Consequently, the length of the pool is optimized to the mean hydraulic conditions. To our knowledge, no study has investigated the effects of a large bedform on individual turbulent events in a pool-riffle river.

In this paper, our aim is to characterize the effects of increasing flow depth on the turbulent processes at the entrance of a pool in a gravel-bed river. Individual turbulent events that correspond to wedges are the focus of this study. We have used a combination of high frequency velocity measurements and flow visualization. We have also developed a new protocol to automate the quantification of the information extracted from the images. This paper will focus on the visualization results. Velocity measurements will mainly be used to confirm visualization analysis and describe the global characteristics of the flow at the entrance of a pool.

2 METHODS

2.1 *Sampling design*

Field work was conducted in the Eaton-Nord River, Estrie, Québec, Canada. This gravel-bed river is characterized by well defined pool-riffle sequences. The study site is a deep forced-pool induced by a bedrock outcrop on one of the river banks (Figs. 1a, 2). The consequence of this morphology is a flow field where depth increases over a short distance from the riffle to the pool. The study section is 10 m wide and depth (Y) varies from 0.3 to 1.0 m. At the study site, the bed is composed of loose gravel and D_{50} of the substrate is 19 mm with a sorting coefficient of 0.89. During field sampling, particles on the bed were at the threshold of mobility. Mean velocity (U) was around 0.90 ms^{-1} along the transect. No flow deceleration trend was observed because the depth increase occurred at the same time as the flow constriction (Tab. 1). However, the standard deviation of longitudinal velocity (s_u) shows a decreasing trend (Tab. 1). As a consequence of the flow high velocity and complex morphology, the Reynolds number is high (Re = 250 000 to 500 000).

Measurements were taken along a transect in the center of the reach at the entrance of the pool, where most of the depth transition between the riffle and the pool is observed (Fig. 2). All the measurements were taken upstream from the entrance of a secondary channel into the pool (Fig. 2). The study site was divided into four zones where similar measurements were taken (Fig. 1b). Bed topography is irregular along the measurement section and depth increases in two steps. Bed roughness also changes along the section and the central zones (B and C) present larger particles than those in zones A and D (Tab. 1). Visualization and

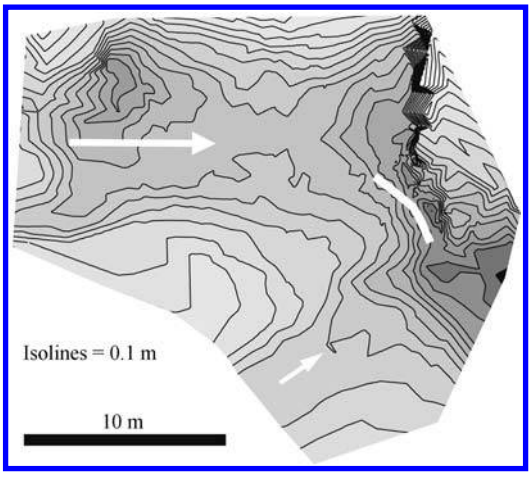


Figure 2. Topographic map of the study reach. Arrows represent flow direction, the longer arrow represent the flow of the main channel. The line indicates the location of the transect of measurements.

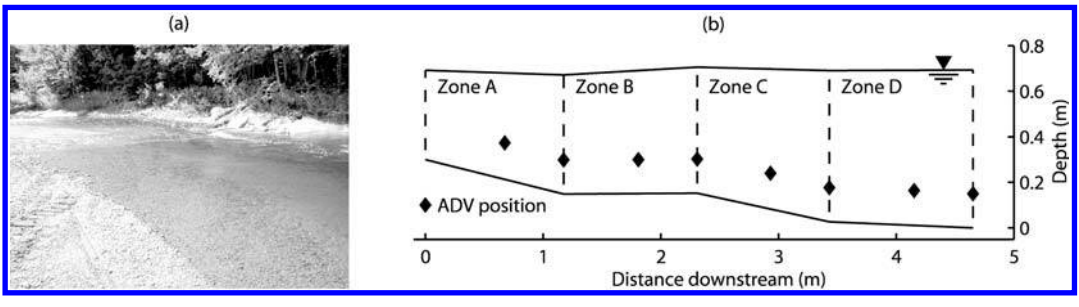


Figure 1. (a) Study reach, upstream view. (b) Sampling design.

Copyright © 2006 Taylor & Francis Group plc, London, UK

velocity measurements were carried out successively within each zone.

Velocity measurements were recorded with two acoustic Doppler velocimeters (SonTek, 10 MHz ADV). Flow velocities are measured in three dimensions at a frequency of 25 Hz in a sampling volume of 250 mm^3. In each zone of the study site, one ADV was positioned at the downstream end of the zone and one ADV was placed 0.50 m upstream (Fig. 1b). This design was chosen in order to characterize the flow field in the downstream half of each zone where the visualization patterns are well developed. The velocimeters were fixed on wading rods and held by operators. The sampling volume was located at 0.15 m above the bed, an adequate distance to capture the large-scale turbulent flow structures without the local perturbations in the vicinity of the bed (Roy et al. 2004). This strategy allows the comparison of the velocity measurements with the visualization data. In further analysis, only the longitudinal (u) and vertical (v) velocity components were used, as the data obtained from the visualization only concern these two dimensions.

To observe turbulent events, dye (powder milk) was injected at the bed surface and filmed with a video camera (Sony, model DCR-TV18) protected by a waterproof casing (Amphibico). The high flow velocity challenges the quality of the flow visualization measurements as the dye is advected very quickly. The injection of the dye at the bed surface ensures that it will be picked up by the ejection-like events that are characterized by an upward vertical velocity (Roy et al. 1999). These events overlap with the low-speed wedges. The dye was injected at a single point at the upstream limit of each zone. The camera was orientated perpendicularly to the flow direction. The camera captured images of 1.10 to 1.22 m wide at the center of the plane delineated by the dye (Fig. 1b, Tab. 1). The frequency of image acquisition (30 Hz) is similar to the sampling frequency of velocity (25 Hz) thus the measurements can be easily compared.

Three minutes were kept of each film and velocity records for further analysis. Buffin-Bélanger & Roy (2005) suggested that records of 60–90 s were sufficient to estimate the mean and turbulent flow properties in a gravel-bed river. From the films, the frequency of occurrence of turbulent events that reach a height of $0.5Y$ was between 0.4 and 1.0 s^{-1}. Therefore, a three minute record should be representative of the turbulent flow structure in conditions of high flow velocity where turbulent events occur at a high frequency.

Table 1. Characteristics of the sampling sites.

	Zone A		Zone B		Zone C		Zone D	
Width (m)	1.17		1.14		1.12		1.22	
D_{50} (m)	0.017		0.020		0.023		0.016	
ADV	A1	A2	B1	B2	C1	C2	D1	D2
Y (m)	0.35	0.45	0.50	0.52	0.58	0.63	0.64	0.65
y/Y	0.43	0.33	0.30	0.29	0.26	0.24	0.23	0.23
U (ms^{-1})	0.93	0.82	0.77	0.96	0.87	0.91	0.96	0.93
s_u (ms^{-1})	0.19	0.20	0.17	0.15	0.15	0.14	0.16	0.16
s_v (ms^{-1})	0.10	0.11	0.09	0.11	0.09	0.09	0.10	0.10

2.2 *Velocity data validation and analysis*

ADVs are instruments sensible to multiple sources of environmental noise (Voulgaris & Throwbridge 1998, MacLelland & Nicholas 2000, Goring & Nikora 2002). It is therefore necessary to evaluate the velocity data quality and to apply the appropriate corrections. In the present study, mean signal correlations are between 78% and 82% and mean signal to noise ratios are between 35 and 40dB. According to the recommendations of the manufacturer, these values should ensure good data quality (SonTek documentation 2002). Spikes in the series were detected using the method presented by Goring & Nikora (2002) and were removed and replaced by linear interpolation using the nearest neighbors of the deleted points. Noise associated with the Doppler effect in high frequencies was removed with a third order low-pass Butterworth filter as recommended by Roy et al. (1997). This filter affects the slope of the power spectrum in the high frequency region and brings the value closer to $-5/3$, a characteristic value of velocity in the inertial subrange of the turbulent boundary layer (Panofsky & Dutton 1984). For means of comparisons between the different velocity measurements, the averages of the vertical (V) and lateral (W) velocity components should be equal to zero over three minute records. The average angles in the longitudinal/vertical plane were between $-5°$ and $2°$. Such angles are believed to be more attributed to the misalignment of the instruments rather than by secondary currents (Roy et al. 1996a). All velocity signals were therefore rotated to bring the angles to $0°$. Finally, the velocity time series were detrended. For some analysis, the longitudinal (u') and vertical (v') velocity fluctuations were used, where

$$u' = u - U \quad \& \quad v' = v - V \tag{1}$$

The analyses of the velocity measurements are conducted in two parts. Firstly, the coherence of the turbulent flow structure is assessed by a space-time correlation analysis. The spatial coherence is estimated from the maximum value of the cross-correlation function (CCF) between simultaneous pairs of ADV time series in each of the four zones. The CCF is estimated for longitudinal and vertical velocity. The maximum correlation coefficient is indicative of the coherence of the turbulent flow structures maintained between two separated points of measurements (Nakagawa & Nezu, 1981).

Copyright © 2006 Taylor & Francis Group plc, London, UK

Secondly, we analyzed the dynamics of individual turbulent events using the modified U-Level technique developed by Luchik & Tiederman (1987). It detects low- and high-speed wedges solely from the longitudinal velocity component. The detection of a turbulent event begins when

$$|u'| > ks_U \quad \text{and ends when} \quad |u'| < pks_U \tag{2}$$

where k is a threshold value, s_u is the standard deviation and p takes a value between 0 and 1. In this paper, a threshold of $k = 0$ is used so that every portion of the signal is categorized as a low or a high-speed wedge. The U-level with $k = 0$ was chosen for its reliability to be compared with the visualization analysis (Paiement-Paradis et al. 2003, Roy et al. 2004).

2.3 *Visualization data validation and analysis*

Before extracting quantitative data from the films it is necessary to reclassify the images. Most of the information on turbulent dynamics is derived from the spatio-temporal evolution of the cloud formed by the dye. Because the injection point is in the clasts at the bed, the dye elevates within the water column with ejections of fluid from the near-bed region. When the dye remains close to the bed, we assume that it corresponds to the passage of sweeps. Therefore, we have chosen to isolate the dye in order to obtain a film of binary type images as shown in Figure 3. The raw images of the films (Fig. 3a) are composed of three color layers (red green blue, RGB mode). Hence, the first step is to reduce each frame in a single layer to facilitate further handling by saving computer memory space. The addition of the red and blue layers has the advantage of enhancing the brightness of the dye in comparison with the ambient environment (Fig. 3b). Once this is done, only the portion of the images where the dye is visible in the flow field is kept (Figs. 3b, c, d).

The next step is the application of a threshold to all the frames to obtain a film of binary fluctuations of the dye (presence/absence) (Fig. 3c). The value of the threshold is determined from the pixel intensity distribution in the flow field of the whole film. In the absence of dye in the flow, pixel intensity varies little over time. In the presence of dye, the distribution of pixel intensity values for a single pixel time series is skewed to the right. From experience, pixel intensity values higher than the mean of the distribution correspond to the presence of the dye. Thus, the threshold is determined by trial-and-error around the mean value of pixel intensity. The effects of a given threshold is checked by a visual assessment of the goodness-of-fit between the original contour of the dye on the raw image and the contour of the dye cloud delineated at that threshold on the binary image. The value of the threshold for each film varies with the saturation of the images, which is essentially a function of depth, water turbidity and the intensity and orientation of the sun.

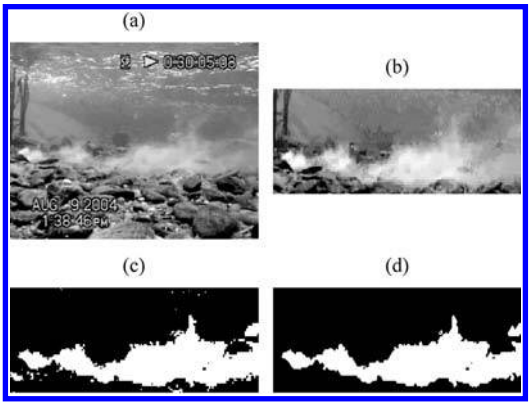


Figure 3. Steps in the reclassification of the images of the flow visualization analysis. Width of the frame is 1.17 m. (a) Raw image. (b) Red and blue layers added. (c) Raw binary image. (d) Filtered binary image.

The last step before the films are ready for quantitative analysis is the filtering of each frame to remove the noise (Fig. 3d). The noise is mainly due to objects that have the same saturation signature than the cloud of milk. This step requires being cautious because the noise has to be removed without affecting the shape of the cloud of dye. Therefore, classical median or mode filters cannot be used. The noise may also be unstable due to the variation of the sun reflection on the bed particles. As the noise is not always located at the same position in the image, the filtering operation cannot be facilitated by applying a mask. The best differentiation criterion is the size of the objects. The noise is always due to objects smaller than the cloud of dye. In order to leave untouched the cloud of dye and to remove the noise at a satisfying level, an algorithm was designed to detect isolated groups of pixels by scanning each frame with a moving window. Finally, all the films are rescaled to allow comparison between each zone.

The first type of visualization analysis consists of extracting time series from strategic and meaningful positions in the flow field. The reclassified images show the occurrence of low-speed wedges when the dye is present and it advects downstream and high-speed wedges when the dye is absent. Time series were built from the variation of a single pixel, which represents roughly 10–15 mm^2. All series were extracted from the downstream half of the images where the dye can reach $0.5Y$ above bed. At a distance of $1Y$ from the dye injection point, the turbulent structures are well developed, enough to characterize their dynamics (Paiement-Paradis et al. 2003). A first set of visualization time series are taken at the location of the ADVs (Fig. 1b). A second set of visualization time series

Copyright © 2006 Taylor & Francis Group plc, London, UK

are extracted from each pixel along a vertical profile between $0.25Y$ and $0.5Y$ located at $1.5Y$ downstream of the injection point. These heights were chosen because below $0.25Y$ the dye is too homogenous and above $0.5Y$ it becomes too sparse and diluted.

In order to describe the spatio-temporal dynamics of the largest individual turbulent events, fifteen wedges were selected visually in each film over the three minute duration. A large turbulent event is defined as a structure that extends vertically above $0.5Y$ and that occupies a large surface in the image. For each turbulent event, three time steps were kept to represent its evolution. One frame is extracted when the turbulent event is the most developed. From that frame, one is extracted 10 frames before (1/3 s) and another one 20 frames before (2/3 s). We chose to analyze 15 major events per film because it is approximately the number of very large turbulent events that occur during three minutes. These few structures may contribute a large part of the Reynolds shear stress because of the important fluctuations in vertical velocity (Lu & Willmarth 1973).

3 RESULTS

3.1 *Reliability of the automated analysis of the turbulent flow structures*

To confirm the reliability of the automated procedure, we compared the results of the image analysis with those obtained from the modified U-level technique applied to the streamwise velocity component as shown in Figure 4a, b, c. The visualization results for the points located where ADV measurements were taken (Fig. 1b) have similar characteristics than the U-level analysis. Along the transect, the mean durations of turbulent events show approximately the same trend for the visualization and velocimetry (Fig. 4a). The main difference between the two methods is in the frequency of occurrence of turbulent events (Fig. 4b). The frequency of occurrence is obtained by dividing the number of events detected by the length of the time series. The visualization analysis underestimates the number of turbulent events. This underestimation is more pronounced for short turbulent events because of the rapid dilution of the dye within the high velocity flow. This phenomenon explains the slight overestimation of the mean duration of events (Fig. 4a).

The frequency distribution of the duration of turbulent events should display a power law scaling as reported by Paiement-Paradis et al. (2003). For example, at the downstream end in zone D, the low-speed wedges detected from the images and from the velocity time series have similar frequency distribution shapes (Fig. 5). The number of events in each class is less for visualization results than for the velocity time series (Fig. 5). The power law slopes of the frequency

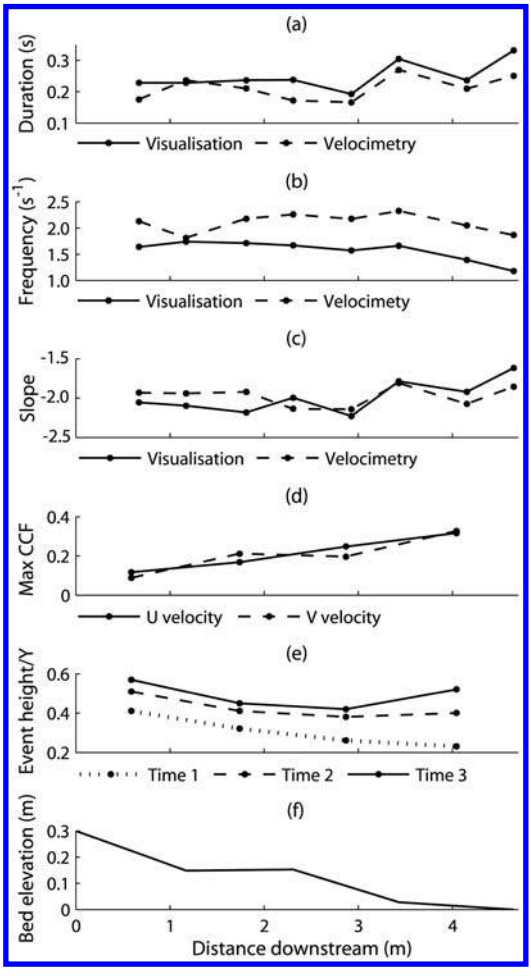


Figure 4. Characteristics of low-speed wedges in each zone as estimated through visualization and ADV measurements (U-level detection), (a) Mean duration; (b) Frequency of occurrence (or number of events per second); (c) Power law slope of the frequency distribution of events duration; (d) Maximum cross-correlation function; (e) Event height normalized on depth (Y) of the 15 largest events in the three minute films at three time steps; (f) Bed topography.

distribution of low-speed turbulent events duration along the transect are shown in Figure 4c. The range and trend of the values are similar for both methods. This means that the ratio between short and long turbulent events is the same even though there is an offset in the number of events detected by the methods. These results tend to show that the data obtained from the protocol to analyze the images yields reliable information even tough flow conditions were challenging for such a visualization experiment. There is a need, however, to be cautious with the absolute values of the

Copyright © 2006 Taylor & Francis Group plc, London, UK

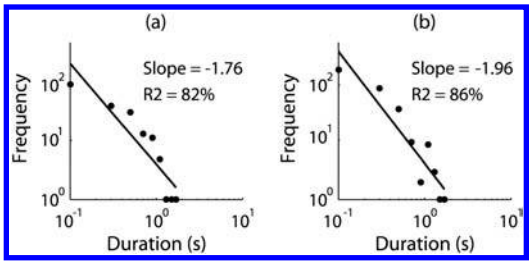


Figure 5. Frequency distribution of the duration of the low-speed wedges for location D2, at the downstream end in zone D, (a) Flow visualization; (b) ADV velocity measurements.

results obtained from the visualization analysis as the procedure is still in development.

3.2 *Flow spatial coherence*

The spatial coherence of turbulent flow is assessed from the correlation analysis in the velocity time series. The maximum correlation coefficients of the CCF between two simultaneous ADV represent the coherence of the turbulent flow structures between two points in the flow. Figure 4d shows that for both the longitudinal and vertical velocity components, the maximum of the CCFs per pair of ADVs increases in the downstream direction. Surprisingly is the value of the maximum of the CCFs of the vertical velocity component is in the same range as the value for longitudinal velocity component (Fig. 4c). Usually, the vertical component of the velocity is less coherent than the longitudinal component (Roy et al. 1996b). Here, there is an enhanced coherence of the vertical velocity component.

3.3 *Events duration, time interval and frequency*

In Figure 4a, b and c, the mean duration of turbulent events, the frequency of occurrence of turbulent events, and the power law slopes of the frequency distribution of the turbulent events duration are similar in zones A and B. A break in these values occurs at the downstream end in zone C showing that the characteristics of the turbulent events are changing with an increasing depth. This effect is still present in zone D where the turbulent events are still adjusting to the increase in flow depth.

The results of the image analysis of the vertical profiles between $0.25Y$ and $0.5Y$ located at $1.5Y$ downstream of the injection point for each zone are shown in Figure 6. The mean duration of events is decreasing from the bed to the surface (Fig. 6a). This result was expected as the dye is injected at the bed and progressively advected towards the surface. The four zones have approximately the same vertical profile of mean turbulent event durations (Fig. 6a). However, the durations of events in zone D have a larger standard deviation than those in the three upstream zones (Fig. 6b). Turbulent events in zone D also display a lower frequency of occurrence in time (Fig. 6c) and consequently, a larger mean time interval between turbulent events (Fig. 6d). The mean time interval between turbulent events is the mean duration between two successive low-speed wedges events. It is shown in Figure 6e that the relationships between the frequency of occurrence of turbulent events and the mean time interval between events have the same trend in the four zones. When relative height above bed is plotted against the ratio between mean events duration and the mean time interval between events, the four zones become distinct from one another (Fig. 6f). The profile in zone A has the highest ratio values, followed by zones C, B and D where the smallest ratio values are observed.

3.4 *Spatio-temporal evolution of turbulent events*

The characteristics of low-speed wedges presented in Figure 6 indicate that turbulent processes at the downstream end of the entrance of the pool, where the flow is deeper, are different than those seen at the beginning of the flow expansion. To investigate further these processes, we examined the spatio-temporal evolution of the shape and size of 15 large turbulent events in each zone. The results are shown in Figure 7. The three first rows in the figure present the superimposition of the 15 frames for each time step in each zone. The darker portions of the images represent the areas where most of the events have passed. Visually, we see that turbulent events in zones A and D are larger and that their shapes are more regular than those in zones B and C. This holds true for the three time steps. The saturated black area is smaller for zones B and C while the gray cloud occupies a larger portion of the image. In other words, the large turbulent events in zones B and C tend to be smaller and their evolution in space is more irregular. The structures do not tend to follow a similar path. Turbulent events in zone D are the most regular and the largest. They are very well defined in space through time for the three time steps displaying a greater consistency in their trajectories as they advect downstream. Visual observation of their evolution on the film showed that the vortices were not only larger than in the other zones but also that they rotated more slowly.

The fourth row of Figure 7 displays all the turbulent structures for the 15 events at the three time steps for each zone, for a total of 45 images superimposed. This superimposition of the temporal evolution reveals a net transition in the turbulent processes. For large turbulent events in zones A to C, the head of the cloud of each time step where the dye has passed quite consistently is visible (Fig. 7). When an ejection-like event forms, it rapidly grows vertically before

Copyright © 2006 Taylor & Francis Group plc, London, UK

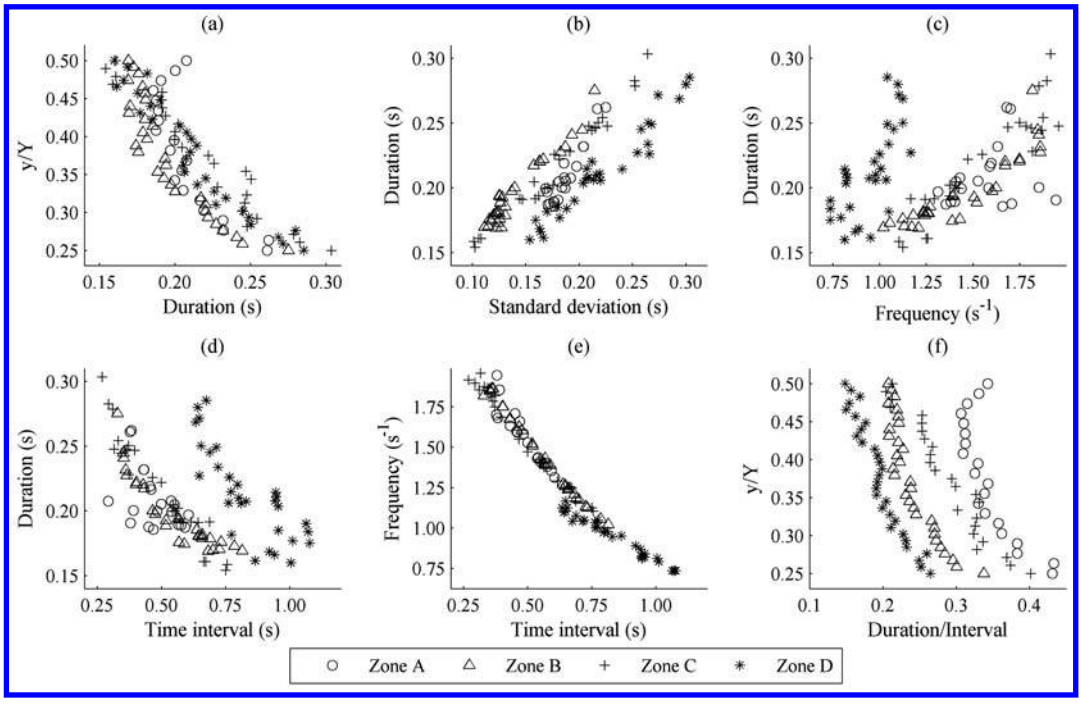


Figure 6. Characteristics of the low-speed wedges detected from images analysis of the vertical profiles between 0.25Y and 0.5Y located at 1.5Y downstream of the injection point. (a) Mean duration in function of relative depth. (b) Relation between mean duration and the standard-deviation of duration. (c) Relation between mean duration and frequency of occurrence. (d) Relation between mean duration and mean time interval between events. (e) Relation between frequency of occurrence and mean time interval between events. (f) Ratio between mean duration and mean time interval between events in function of relative depth.

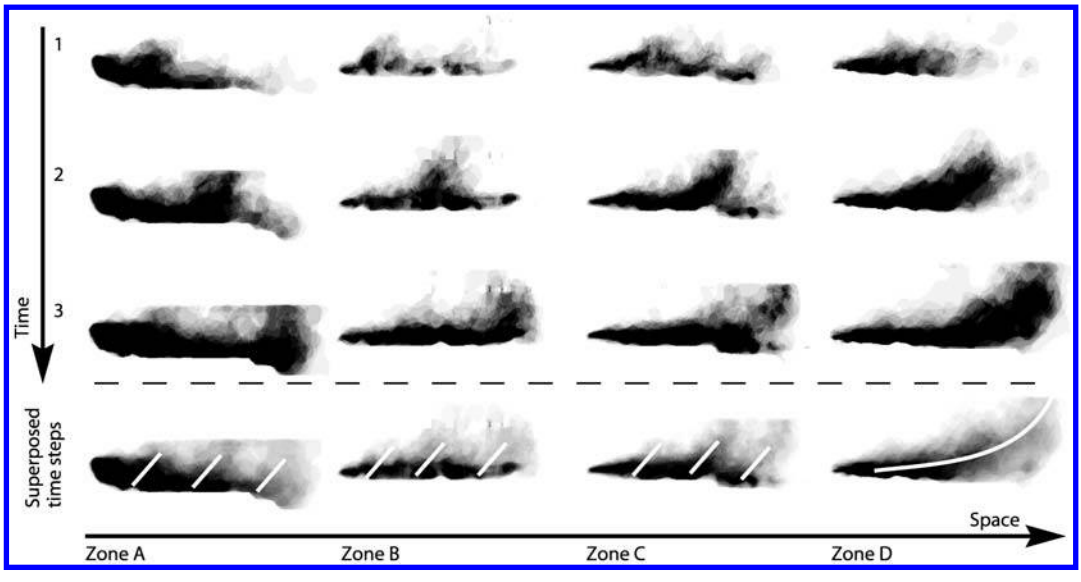


Figure 7. Spatio-temporal evolution of the 15 largest turbulent events. Each image is the superposition of the 15 images of one zone for each time step. The last row is the superposition of all the images for each zone where white lines outlined the turbulent events heads of each time step. Total length of the space arrow represents 4.65 m.

Copyright © 2006 Taylor & Francis Group plc, London, UK

being advected downstream. The structures maintain a constant angle of approximately 40° relative to the bed. The structure heads for time steps 1 and 2 of the turbulent events in zone D are not visible in the time superimposed images (Fig. 7). When an event in zone D is initiated, it always grows in the same direction. Even though this speculation remains to be fully demonstrated, the evidence presented here clearly shows a different mode of development for the large turbulent structures. Figure 4e presents the mean maximum height of turbulent events normalized by depth for each time step at each zone. The vertical extent of the large turbulent events is smaller in zone B and C. As we progress into the pool, the vertical development of the structures occurs later but faster. This indicates a dominance of the vertical velocity component which has an enhanced coherence as indicated by the maximum correlation of the CCFs (Fig. 4d).

4 DISCUSSION

The results presented in this paper link the study of individual turbulent events processes to a large bedform such as a pool where a rapid vertical flow expansion is observed in a gravel-bed river. The use of flow visualization has been shown to provide a complementary approach to the analysis of velocity measurements to describe and understand the spatio-temporal characteristics of the turbulent processes. The data show a transition in turbulent processes occurring at the entrance of a pool. In general, the agreement between the two methods is good even tough the number and duration of the detected turbulent events may differ. It is necessary, at this point, to use the results of the new visualization automation procedure with care. The procedure that we have used shows promising results but still needs further refinement.

The measurements where intentionally done in the transition zone between a riffle and a pool because we consider that key processes occur in this zone between these two large bedform features. Most of previous flow measurements in pool-riffle units have been done over representative cross-sections of pools or riffles without covering the transition zones (e.g. Clifford 1993, Clifford & French 1993, Robert 1997). It is well accepted that the turbulent flow structure is different between riffles and pools (e.g. Cliffford 1993, Robert 1997). Thompson (2004) has focused his study on the exit of a pool which is the transition zone between a pool and a riffle. However, he did not explore individual turbulent events characteristics.

The turbulent structures present a range of characteristics at the entrance of the pool because the morphology of the study reach is complex. From the results presented here, three main characteristics of the flow field seems significant to the change of scale of the turbulent processes identified: (1) The spatial flow coherence increases as flow depth expands which favors the maintenance of the structure of the flow. (2) The vertical velocity spatial coherence is as important as that of the longitudinal velocity. This enhanced coherence in the vertical velocity component is induced by the flow expansion. This is visible in Figure 7 where large turbulent events tend to develop very early, mostly in zones A, B and C. The vertical development of large turbulent events in zone D is important also but it occurs much later in the evolution of the structures (Fig. 4e). (3) Even tough there is no apparent deceleration of the flow as depth increases because of the flow constriction induced by the bedrock outcrop, there is a decreasing trend of the standard deviations of the longitudinal velocity (Tab. 1). This is in agreement with the results of Thompson (2004) who found an increase of the standard deviation of the longitudinal velocity component at the exit of a pool. Although the downstream trend of velocity standard deviations may not be statistically significant, it is consistent with the results shown in Figure 7. Lower turbulence intensity at the downstream end of the entrance of the pool may explain that large turbulent events in zone D are larger and more regular than those in the upstream zones.

By a combination of approaches, we have identified changes in the scale of the turbulent processes. There is an apparent shift between particle-influenced turbulent processes to bedform-influenced turbulent processes as flow depth increases. Ejection-like structures occur in zones A, B and C as shown by the intense vertical development of the turbulent events. This vertical motion occurs early and it propagates in the flow field at a constant angle relative to the bed. The mean angle of 40° is similar to that found by Buffin-Bélanger et al. (2000) for low-speed wedges. These events should reflect the development of a turbulent boundary layer over a rough and irregular bed composed of heterometric clasts (Grass et al. 1991). At the downstream end of the transect, in zone D, large turbulent events propagate while maintaining a constant direction in such a way that the angle relative to the bed varies along the turbulent structure. This would be more typical of eddy shedding structures where flow separation induced by the rapid flow depth expansion over a short distance may play a role. This type of turbulent environment has already been identified for obstacles bed features like dunes and pebble clusters (e.g. Bennett & Best 1995, Buffin-Bélanger & Roy 1998). Brayshaw et al. (1983) have speculated that riffles may act as an obstacle in the flow and be considered as giant pebble clusters. As the velocity data were not dense enough along the transect, no shear zone indicating a flow separation could be identified at our site. Furthermore, the ratio between the flow

Copyright © 2006 Taylor & Francis Group plc, London, UK

depth and the bedform radius influencing turbulent processes is lower for riffles than for pebble clusters or dunes. Thus, the role of eddy shedding structures on the turbulent flow is still speculative. On the other hand, all zones show a very consistent pattern in the relationships between the frequency of occurrence of turbulent events and the time interval between successive events. The relationships have similar slope perhaps because they all pertain to low-speed wedges independent of their scale. Thus, the signature of turbulent events in zone D may be more closely associated with the flow environment that develops in the lee of large scale bedforms.

The transition in the scale of boundary roughness influence is detectable by the spatio-temporal evolution of the shape of the large turbulent events in zones B and C. In Figure 4e, their vertical development is less important than in zone A and D. The consequence of the flow expansion seems to create temporarily a zone where turbulent structures are not fully adjusted to the morphologic constraints and their development in the vertical direction is broken in many small vortices (Fig. 7). The ratios between the mean duration of turbulent events and the mean time interval between events for each zone show that there is a slight transition in turbulent characteristics along the transect (Fig. 6f). The shift in the scale of turbulent processes in zone D is confirmed by the results of all analysis. Turbulent events in zone D have a larger standard deviation of durations (Fig. 6b), a lower frequency of occurrence in time (Fig. 6c) and a longer mean time intervals between turbulent events (Fig. 6d). All these characteristics scale more closely to the bedform conditions than with only the local bed roughness. Events of zone D are larger, better organized and they eject powerfully as shown in Figures 4e, 7. This is consistent with a shift from the dominance of the boundary roughness type seen at the entrance of the pool.

5 CONCLUSION

When depth increases in a river channel, as it is the case at the entrance of a pool, the constraint on the average and turbulent flow properties is important and dynamic. Using flow visualization data obtained from an automated protocol for the analysis of the images, we have found a clear transition in the scale of the turbulent processes of individual ejection turbulent events. The flow is characterized by an increasing spatial coherence from the riffle to the pool head and the strong dominance of the vertical velocity component in the evolution of the turbulent structures. As we progress into the pool, the scale of the boundary roughness changes from local bed conditions dominated by heterometric grains to a large bedform condition. This change in boundary roughness conditions seems to lead to a shift in the scale of turbulent processes. As depth increases, there is a shift between more frequent ejections to less frequent but more regular and more powerful ejections. This transition in the scale of turbulent events is forced by the rapid flow expansion at the entrance of the pool. It is difficult to describe the exact nature of this transition and further work is required to understand the interactions between large bedforms and the turbulent flow structure. These interactions may be significant for sediment transport, bedform formation and maintenance and for vertical flow mixing within the pool.

ACKNOWLEDGEMENTS

This research is part of program of the Chaire de recherche du Canada en dynamique fluvial. The authors would like to thank the National Sciences and Engineering Research Council of Canada for the financial support. Comments on an earlier version of this paper of Pascale Biron were helpful. Discussions with Jay Lacey have been incentives. We are grateful to Annie Cassista, Isabelle Gagnon and Julie Thérien for their assistance in the field.

REFERENCES

Bennett, S.J. & Best, J.L. 1996. Mean flow and turbulence over fixed ripples. In P. Ashworth, J.L. Best, S.J. Bennett & S.J. McLelland (eds), *Coherent flow Structures in Open Channels*: 281–304. Chichester: John Wiley & Sons.

Brayshaw, A.C., Frostick, L.E. & Reid, I. 1983. The hydrodynamics of particle clusters and sediment entrainment in coarse alluvial channels. Sedimentology 30(1): 137–143.

Buffin-Bélanger, T. & Roy, A.G. 1998. Effects of a pebble cluster on the turbulent structure of a depth-limited flow in a gravel-bed River. *Geomorphology* 25(3–4): 249–267.

Buffin-Bélanger, T. & Roy, A.G. 2005. 1 min in the life of a river: selecting the optimal length for the measurement of turbulence in fluvial boundary layers. *Geomorphology* 68(1–2): 77–94.

Buffin-Bélanger, T., Roy, A.G. & Kirkbride, A.D. 2000. On large-scale flow structures in a gravel-bed river. *Geomorphology* 32(3-4): 417–435.

Clifford, N.J. 1993. Formation of riffle pool sequences – Field evidence for an autogenetic process. *Sedimentary Geology* 85(1–4): 39–51.

Clifford, N.J & French, J.R. 1993. Monitoring and analysis of turbulence in geophysicals boundaries: some analytical and conceptual issues. In N.J. Clifford, J.R. French & J. Hardisty (eds), *Turbulence: Perspectives on flow and sediment transport*: 93–120. Chichester: John Wiley & Sons.

Goring, D.G. & Nikora, V.I. 2002. Despiking Acoustic Doppler Velocimeter data. *Journal of hydraulic engineering* 128(1): 117–126.

Copyright © 2006 Taylor & Francis Group plc, London, UK

Grass, A.J., Stuart, R.J. & Mansour-Tehrani, M. 1991. Vortical structures and coherent motion in turbulent-flow over smooth and rough boundaries. *Philosophical Transactions of the Royal Society of London* (Series A-Mathematical Physical and Engineering Sciences) 336(1640): 35–65.

Lu, S.S. & Willmarth, W.W. 1973. Measurements of the structure of the Reynolds stress in a turbulent boundary layer. *Journal of Fluid Mechanics* 60: 481–511.

Luchik, T.S. & Tiederman, W.G. 1987. Timescale and structure of ejections and bursts in turbulent channel flows. *Journal of Fluid Mechanics* 174: 529–552.

Mclelland, S.J. & Nicholas, A.P. 2000. A new method for evaluating errors in high-frequency ADV measurements. *Hydrological Processes* 14(2): 351–366.

Nakagawa H. & Nezu I. 1981. Structure of space-time correlations of bursting phenomena in an open-channel flow. *Journal of Fluid Mechanics* 104:1–43.

Nelson, J.M., Shreve, R.L., Mclean, S.R. & Drake, T.G. 1995. Role of near-bed turbulence structure in bed-load transport and bed form mechanics. *Water Resources Research* 31(8): 2071–2086.

Paiement-Paradis, G., Buffin-Bélanger, T. & Roy, A.G. 2003. Scalings for large turbulent flow structures in gravel-bed rivers. *Geophysical Research Letters* 30 (14): 1773, doi:10.1029/2003GL017553.

Panofsky, H.A. & Dutton, J.A. 1984. Atmospheric turbulence: models and methods for engineering applications. New York: John Wiley & Sons.

Robert, A. 1997. Characteristics of velocity profiles along riffle-pool sequences and estimates of bed shear stress. *Geomorphology* 19(1–2): 89–98.

Roy, A.G., Biron, P. & Deserres, B. 1996a. On the necessity of applying a rotation to instantaneous velocity measurements in river flows. *Earth Surface Processes and Landforms* 21(9): 817–827.

Roy, A.G., Biron, P.M., Buffin-Bélanger, T. & Levasseur, M. 1999. Combined visual and quantitative techniques in the study of natural turbulent flows. *Water Resources Research* 35(3): 871–877.

Roy, A.G., Biron, P.M. & Lapointe, M.F. 1997. Implications of low-pass filtering on power spectra and autocorrelation functions of turbulent velocity signals. *Mathematical Geology* 29(5): 653–668.

Roy, A.G., Buffin-Bélanger, T. & Deland S. 1996b. Scales of turbulent coherent flow structures in a gravel-bed river. In P. Ashworth, J.L. Best, S.J. Bennett & S.J. McLelland (eds), *Coherent flow Structures in Open Channels*: 147–164. Chichester: John Wiley & Sons.

Roy, A.G., Buffin-Bélanger, T., Lamarre, H. & Kirkbride, A.D. 2004. Size, shape and dynamics of large-scale turbulent flow structures in a gravel-bed river. *Journal of Fluid Mechanics* 500: 1–27.

SonTek/YSI Inc. 2002. SonTek ADVField Acoustic Doppler Velocimeter, technical documentation. San Diego: SonTek/YSI Inc.

Thompson, D.M. 2004. The influence of pool length on local turbulence production and energy slope: a flume experiment. *Earth Surface Processes and Landforms* 29(11): 1341–1358.

Voulgaris, G. & Trowbridge, J.H. 1998. Evaluation of the Acoustic Doppler Velocimeter (ADV) for turbulence measurements. *Journal of Atmospheric and Oceanic Technology* 15(1): 272–289.

Copyright © 2006 Taylor & Francis Group plc, London, UK

A laboratory investigation on the advection of free surface fluctuations in turbulent open-channel flows

H. Miyamoto
Department of Civil Engineering, Kobe University, Kobe, Japan

ABSTRACT: The advection characteristics of both water surface fluctuations and turbulence in turbulent open-channel flows were experimentally examined in this paper. We used a simultaneous image measurement method to obtain instantaneous velocity vectors and the corresponding water surface profiles in a vertical cross section of the open-channel. Time series of the water surface profiles indicated that the water surface fluctuations were propagated with a constant advection velocity in each experimental case. The space-time correlation analysis of the water surface fluctuations and turbulence disclosed that the advection velocity of the water surface fluctuations was always smaller than the mean bulk velocity, while that of the turbulence above the near-bed region was the same as the mean velocity, well-known as Taylor's hypothesis of the frozen-turbulence approximation. It was also found that the ratio of the advection velocity of the water surface fluctuations to the mean bulk velocity became smaller as the Froude number decreased.

1 INTRODUCTION

Understanding behavior of the water surface in turbulent open-channel flows has become important from the viewpoint of the aquatic environment of rivers because it could affect the turbulence structures that regulate the gas transfer and the momentum exchange across the water surface. In addition, the spatial distributions of the water surface fluctuations in rivers could be used effectively to measure the surface velocity and flow discharge by using their video images and appropriate image processing methods (Fujita & Komura 1994, Fujita et al. 1998). However, we have had little knowledge about physical relationships between the water surface fluctuations and the turbulent flows immediately under the free surface when a Froude number becomes large and the surface fluctuations are considerably pronounced. This lack of knowledge makes us difficult to understand the transport phenomena around the turbulent water surface as well as to evaluate the validity of the river surface images for the velocity measurements. Therefore, fundamental laboratory experiments with a special focus on the free surface turbulence are indispensable for better understanding of the phenomena.

As for the recent experimental approaches on turbulent open-channel flows emphasizing water surface effects, many research works have been carried out. Among them, the authors measured velocity vectors and the corresponding water surface profiles by using a simultaneous image measurement method (Miyamoto et al. 2003a) with a high resolution CCD camera and a YAG laser. Then, by using POD (proper orthogonal decomposition) and space correlation analysis to the measurement data, they revealed that there were the specific correlation structures between the water surface fluctuations and turbulence structures having the same spatial scale (Miyamoto & Shimoyama 2003b, 2004a). Moreover, they found that a surface-influenced-layer existed immediately under the free surface of turbulent open-channel flows and its depth changed with the Froude number (Miyamoto & Shimoyama 2004b). Nezu & Nakayama (1998a, 1998b) measured the water surface fluctuations and turbulence by using a LDA (laser Doppler anemometer) and an ultra-sonic displacement sensor. They reported that the turbulence structures of open-channel flows near the surface region differed much from those of pipe flows through the examination of turbulence statistics and its energy budget (Nezu & Nakayama 1998a) and that there was a relationship between the organized vortices near the channel bed and those near the water surface by applying the space-time correlation analysis (Nezu & Nakayama 1998b). However, the advection characteristics of the water surface fluctuations have not yet been understood in detail because of the lack of the spatial and temporal resolutions of the measurements installed in the previous experimental works.

In this paper, a laboratory experiment was carried out to examine advection characteristics of both the water surface fluctuations and turbulence in open-channel flows by using a space-time correlation analysis in order to evaluate their relations to the mean velocity field. Instantaneous velocity vectors and the

Copyright © 2006 Taylor & Francis Group plc, London, UK

corresponding water surface profiles analyzed here were experimentally obtained by the simultaneous image measurement method (Miyamoto et al. 2003a). Moreover, we investigated the Froude number dependence of the advection characteristics of the water surface fluctuations as well.

2 LABORATORY EXPERIMENTS AND SIMULTANEOUS IMAGE MEASUREMENTS

2.1 *Hydraulic conditions*

The laboratory experiments reported here were conducted in a clear acrylic flume with the length of 10 m and the width $B = 0.25$ m. The measurement cross section was a vertical cross section along with the longitudinal direction of the flow and it was located at 7.5 m downstream from the inlet tank. It was expected that the turbulent boundary layer generated from the channel bed was fully developed at the measurement cross section. The hydraulic conditions are listed in Table 1. In the experiments, we kept the Reynolds number based on the mean bulk velocity $\overline{U}$ and the mean water depth H with the kinematic viscosity ν, $Re = \overline{U}H/\nu$, a constant ($=2.0 \times 10^4$), while we changed the Froude number based on $\overline{U}$ and H with the gravitational acceleration g, $Fr = \overline{U}/\sqrt{gH}$, from 0.81 (subcritical flow conditions) to 2.33 (supercritical flow conditions). In the hydraulic conditions, we choose relatively high Froude number in which the water surface fluctuations were expected to be pronounced. The range of the Froude number examined here was overlapped in half of the Cases with that examined in Nezu & Nakayama (1998a, 1998b). Relatively lower Froude numbers, which correspond to the condition of real river floods, will be examined in the next research step. In addition, we kept an aspect ratio of channel B/H greater than 6.0 throughout the experiments so that we could obtain the two-dimensional flow characteristics in long-term turbulence structures in the central zone of the channel, where effects of the side-wall friction almost disappears (Nezu & Nakagawa 1993).

2.2 *Simultaneous image measurements of water surface profiles and velocity vectors*

A schematic view of the image measurement system used in the laboratory experiments is shown in Figure 1. The image measurement system was composed of several pieces of equipment, i.e., an argon-ion laser with a laser beam expander, a high speed CCD camera, a monitor and a digital video deck, a PC with an image memory board and so forth. We used particles with diameters of 0.075–0.150 mm and with a specific gravity of 1.02 as a tracer for visualization. A flow field, where the tracer particles were seeded, was visualized by a laser light sheet, as shown in Figure 1. On one hand, the visualized images of the flow fields were captured by the high-speed CCD camera and were recorded in the PC. Images of the water surface profiles, on the other hand, were taken through the mirror so that the water surface would not be hidden by a meniscus of a water surface on the front channel wall. As a result, the images of both the flow field and the water surface profile on the vertical laser light plane were simultaneously captured in the same image flame. In the image processing technique, an edge extraction algorism was used to detect the location of the water surface, while a particle image velocimetry (PIV) was applied to measure the velocity vectors (Miyamoto et al. 2003a). In the image measurements, the sampling intervals of the velocity vectors (temporal resolution) were 1/400 seconds (Case 1 in Table 1) and 1/240 seconds (the other Cases in Table 1), and the pixel sizes of the image (spatial resolution) were ranged from 0.18 to 0.36 mm. Calculating statistics of the turbulent open-channel flows, we used measurement data of 6500–10900 images, of which the difference depended on the experimental Cases in Table 1, to converge the statistical values.

With regard to the reference flame introduced in this study, x, y in the Cartesian coordinate denote the streamwise direction (positive downward) and vertical

Table 1. Hydraulic conditions.

Case #	Q^* cm^3/s	H^* cm	$\overline{U}^*$ cm/s	$U_*{}^*$ cm/s	$1/I^*$	Fr^*	Re^*
1	5.0×10^3	2.0	102.1	5.17	1/65	2.33	2.0×10^4
2	5.0×10^3	2.5	79.3	4.20	1/134	1.60	2.0×10^4
3	5.0×10^3	3.0	67.1	3.51	1/215	1.24	2.0×10^4
4	5.0×10^3	3.5	56.5	3.01	1/347	0.96	2.0×10^4
5	5.0×10^3	4.0	50.4	2.75	1/476	0.81	2.0×10^4

*Q: flow discharge, H: mean water depth, $\overline{U}$: mean bulk velocity, U_*: friction velocity, I: bed slope, Fr: ($\overline{U}/\sqrt{gH}$) Froude number, Re: ($\overline{U}\,H/\nu$) Reynolds number, g: gravitational acceleration, and ν: kinematic viscosity of water.

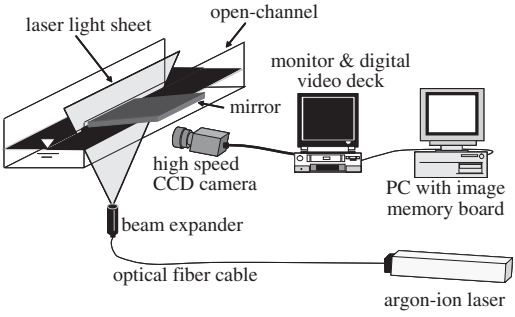


Figure 1. Schematic of the image measurement system for turbulent open-channel flows with the water surface profiles.

Copyright © 2006 Taylor & Francis Group plc, London, UK

direction (positive upward), respectively, with the origin at a point on the channel bed. u, v denote the components of the instantaneous velocities in the x-, y-directions, respectively; U, V, the time-averaged (or the ensemble-averaged) mean velocities; and u', v', the velocity fluctuations. The $\overline{U}$ represents the mean bulk velocity ($=Q/BH$). As regards the water surface, the h denotes the profile of the instantaneous water depth, while H and h' are the mean and fluctuation components of the water depth h, respectively.

3 METHOD OF SPACE–TIME CORRELATION ANALYSIS

In this study, we examined the advection characteristics of both the water surface fluctuations and turbulence in open-channel flows by using the space-time correlation analysis. Analyzed here were the water surface fluctuation h' and the x-directional component of the velocity fluctuations u', as will be mentioned later.

The space-time correlation coefficient of a fluctuation $f(x_{\mathrm{ref}}, t_{\mathrm{p}})$ with $g(x, t_{\mathrm{p}}+\tau)$ is given as the following equation.

$$COR_{fg}(x;\tau)=\frac{\sum_{\mathrm{p=1}}^{\mathrm{M}} f(x_{\mathrm{ref}},t_{\mathrm{p}})\,g(x,t_{\mathrm{p}}+\tau)}{(\sum_{\mathrm{p=1}}^{\mathrm{M}} f(x_{\mathrm{ref}},t_{\mathrm{p}})^2)^{1/2}\cdot(\sum_{\mathrm{p=1}}^{\mathrm{M}} g(x,t_{\mathrm{p}}+\tau)^2)^{1/2}}, \quad (1)$$

where x_{ref} and x denote position vectors of the fluctuations f and g, respectively, and the word '*ref*' of the x_{ref} represents the fixed reference position of the correlation calculation. The t_{p} denotes the discrete time; M, the number of the whole discrete time; and τ, the time lag between the fluctuations f and g.

4 RESULTS AND DISCUSSION

4.1 *Instantaneous velocity fields*

Instantaneous velocity vectors and the corresponding water depth obtained by the simultaneous image measurement are shown in Figure 2 (Case 2; $Fr=1.60$). The velocity vectors near the channel bed are fluctuated vertically with certain spatial extent mainly due to the bed shear. Although the water surface is almost horizontal, there exist small ripples with the spatial scales of 3–4 cm. We used these fluctuation data of the measurements with the sampling intervals 1/400 or 1/240 sec to examine their advection characteristics.

4.2 *Instantaneous water surface profiles and their time sequence*

Four successive water surface profiles with the time difference of 1/80 sec are shown in Figure 3 (Case 2;

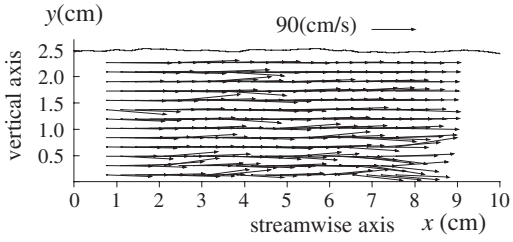


Figure 2. Instantaneous velocity vectors with the corresponding water surface profile. Case 2, $Fr=1.60$.

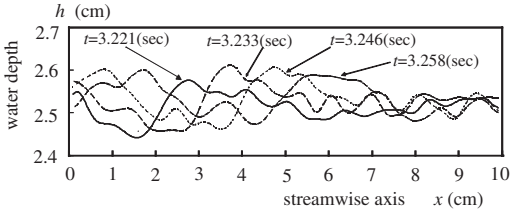


Figure 3. Temporal change of the water surface profiles. Case 2, $Fr=1.60$.

$Fr=1.60$). The instantaneous water depth of the Case 2 is spatially fluctuated with ± 0.1 cm around the mean depth H. The water surface fluctuations are moving downstream with a constant phase speed, although the shape of water surface is slightly changed with time. Moreover, the water surface fluctuations seem to be wave-like motions since a new crest appears at the upstream side of the channel at $t=3.246$ and 3.258 sec.

To examine the advection velocity of the water surface fluctuation as shown in Figure 3, as well as to investigate its relations to the mean bulk velocity and the advection velocity of turbulence, we applied the space-time correlation analysis to the experimental data. Before the correlation analysis, we examined the statistics of both the flow and water surface components in the following subsection.

4.3 *Turbulence statistics of the velocity and water surface*

The distributions of mean velocity U^+ and x-directional turbulent intensity $\sqrt{\overline{u'^2}}/U_*$ are shown in Figures 4 and 5, respectively. Here, $U^+=U/U_*$ and $y^+=yU_*/\nu$ in Figure 4. The vertical axis of Figure 4 is shifted in each Case for the comparison between Cases; the curve of Case 3 represents the original log-law curve for a smooth bed, while the other curves are vertically shifted form it with ± 4 and ± 8, respectively. The experimental values of U^+ are in very good agreement with the calculated log-law curves. In Case 4 of Figure 4, whose Froude number has a near critical value ($Fr=0.96$), there is a specific wake region

Copyright © 2006 Taylor & Francis Group plc, London, UK

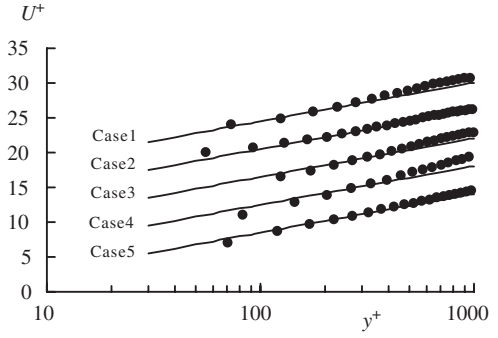


Figure 4. Mean velocity distributions. The experimental values are plotted with the log-law curve. The vertical axis of the figure is shifted for the comparison among the cases; the curve of Case 3 represents the original log-law curve for a smooth bed, while the other curves are vertically shifted form it with ±4 and ±8, respectively.

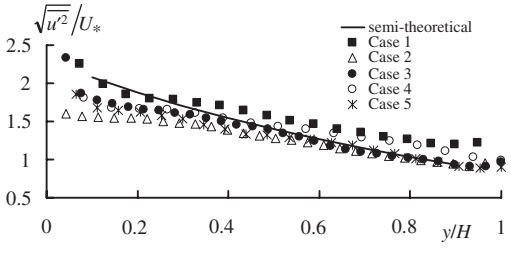


Figure 5. Distributions of x-directional turbulent intensity. The experimental data are plotted with the semi-theoretical curve (Nezu & Nakagawa 1993).

near the water surface. With respect to the turbulence intensity $\sqrt{\overline{u'^2}}/U_*$ shown in Figure 5, the experimental values agree well with the semi-theoretical curves by Nezu & Nakagawa (1993). The values of the intensity decrease toward the water surface region.

The relationship between the intensity of water surface fluctuations $\sqrt{\overline{h'^2}}/H$ and the Froude number Fr is shown in Figure 6. The values of $\sqrt{\overline{h'^2}}/H$ in this study become large as Fr increases. This feature with Fr is almost the same as the results of Nakase et al. (2000). However, a sharp increase around the critical flow condition ($Fr = 1$) reported by Nezu & Nakayama (1998b) is not observed in this study. Since the data of Nakase et al. (2000) also do not have the sharp increase in some cases, it should be necessary to take different approaches that are taken into account interactions of the water surface fluctuations with the turbulence structures under the water surface.

Consequently, from these results of the statistics, the high accuracy of the velocity components and the water surface fluctuations measured by using the simultaneous image measurements is verified.

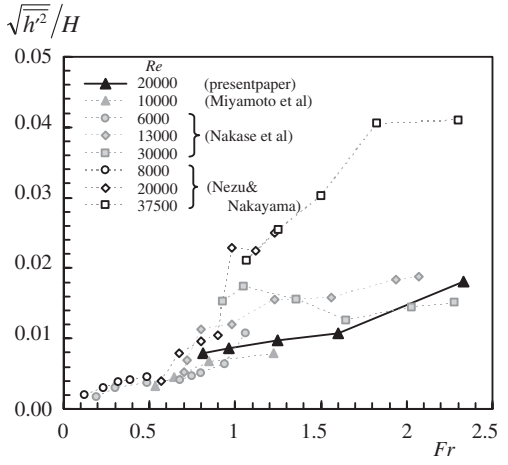


Figure 6. Relationship between the intensity of the water surface fluctuation and the Froude number.

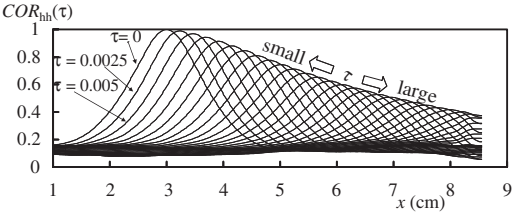


Figure 7. Profiles of the space–time correlation coefficients of the water surface fluctuations in each time lag. Case 1, $Fr = 2.33$. The reference point of the correlation: $x_{ref} = 3.0$ cm.

4.4 *Space–time correlation of the water surface fluctuations and turbulence*

In this subsection, the space-time correlation analysis (Equation (1)) was applied to the experimental data to examine the advection characteristics of both the turbulence and water surface fluctuations.

Figure 7 shows the profiles of the space-time auto-correlation coefficients of the water surface fluctuations $COR_{hh}(x; \tau)$ with the time lag τ in Case 1 ($Fr = 2.33$). These profiles with the time lag $\tau = 0$ to 0.075 sec with the interval of 0.0025 sec are superposed on the figure and the time τ lag becomes large from the left to the right of the figure. The profile of the space correlation coefficients with time lag $\tau = 0$ has a bell-like shape with the maximal value of unity at the reference point $x_{ref} = 3.0$ cm. The maximal values of the profile $COR_{hh}(x; \tau)$ become small and their locations move downstream as the time lag τ increases. The moving rate of the locations of the maximal $COR_{hh}(x; \tau)$ represents the averaged advection velocity of the water surface fluctuations.

Copyright © 2006 Taylor & Francis Group plc, London, UK

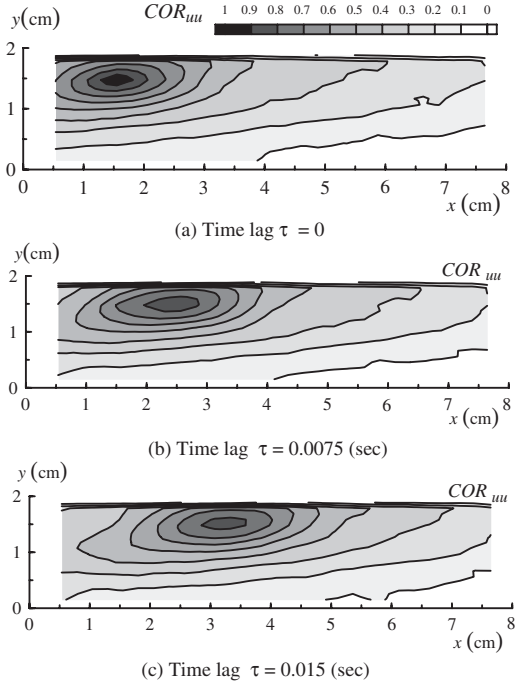


Figure 8. Contour maps of the space-time correlation coefficients of the x-directional velocity fluctuation. Case 1, $Fr = 2.33$. The reference point of the correlation: $(x_{ref}, y_{ref}) = (1.56, 1.47)$ cm.

Figure 8 shows the contour maps of the space-time auto-correlation coefficients of the x-directional velocity fluctuation COR_{uu} in Case 1 ($Fr = 2.33$). The reference point are at $(x_{ref}, y_{ref}) = (1.56, 1.47)$ cm, which is located at $0.75 \times H$ near the water surface. In Figure 8, the maximal values of the correlation coefficients COR_{uu} decrease with time lag τ and their locations move downstream with a constant speed, as same behavior as the cases of the water surface fluctuations.

These characteristics of the correlation coefficients with the time lag τ are qualitatively the same throughout the whole experimental cases both in the water surface fluctuations and the turbulence. Therefore, the advection velocities can be calculated from the movement of the locations of the maximal correlation coefficients.

4.5 *Advection characteristics of the water surface fluctuations and turbulence*

Figure 9 shows the relationship between the advection velocities of the x-directional velocity fluctuation $C_{u'}$ and the time averaged mean velocity $U(y)$. The advection velocity $C_{u'}$ is calculated from the space-time auto-correlation coefficients of the turbulence,

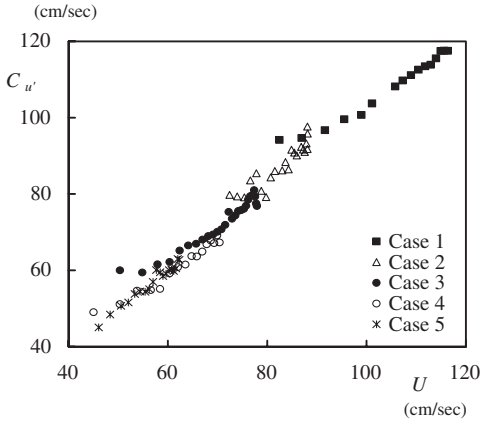


Figure 9. Relationship between the advection velocity of the x-directional velocity fluctuation and the time averaged velocity.

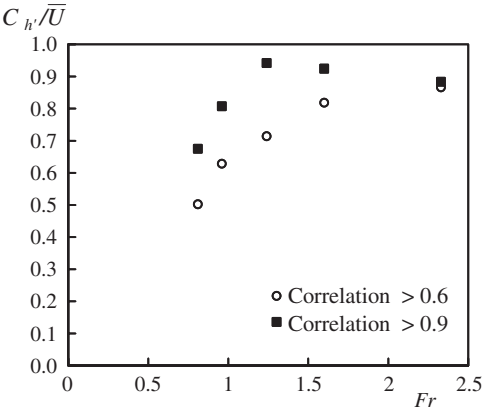


Figure 10. Relationship between the advection velocity of the water surface fluctuation and the Froude number.

as mentioned in the previous subsection. We chose the reference points from near the water surface to near the channel bed and calculate the corresponding advection velocities. It is evident from the Figure 9 that the magnitude of the advection velocity $C_{u'}$ is almost the same as that of the time averaged mean velocity $U(y)$ in whole experiments except near the channel bed region. It indicates that turbulence in the open-channel flows above the near bed region is transported with the time averaged local mean velocity. Therefore, Taylor's hypothesis of the frozen-turbulence approximation (Tennekes & Lumley 1972) is verified above the near bed region. In the near bed region for the Cases 1 to 4, however, the advection velocity $C_{u'}$ is larger than the time averaged mean velocity $U(y)$. Similar result for rough-bed open channel flows was earlier reported in Nikora and Goring (2000). Although our results are for the smooth-bed flows, Nikora and Goring's data and

Copyright © 2006 Taylor & Francis Group plc, London, UK

our data show similar effect in the near bed region. This fact could asserts that the frozen-turbulence approximation is valid only if the turbulence intensity is much smaller than the local mean velocity $U(y)$ not only in grid-generated turbulence (Tennekes & Lumley 1972) but also in both smooth- and rough-bed open channel flows (Nikora and Goring, 2000, present study).

Figure 10 shows the relationship between the non-dimensional advection velocity of the water surface fluctuations $C_{h'}/\overline{U}$ and the Froude number Fr in each Case. The symbols ■ and ○ represent the values calculating from the correlation coefficients larger than 0.9 and 0.6, respectively, implying that the values of ■ represent longer time averaged advection velocity than that of ○. It is found from Figure 10 that the advection velocity $C_{h'}$ has smaller value than the mean bulk velocity $\overline{U}$ in the whole experiments. Since the time averaged local mean velocity $U(y)$ near the water surface has larger value than the mean bulk velocity $\overline{U}$ in general, the advection velocity of the water surface fluctuations $C_{h'}$ has smaller value than the time averaged velocity $U(y)$ near the water surface as well. This evidence with regard to the advection characteristics of the water surface fluctuations is much difference from that of the velocity fluctuations of open-channel flows as mentioned above. Moreover, the value of $C_{h'}/\overline{U}$ decreases as the Froude number Fr becomes small. In the subcritical flow conditions ($Fr < 1.0$), in particular, the advection velocity $C_{h'}$ has considerably smaller value than the mean bulk velocity $\overline{U}$.

5 CONCLUDING REMARKS

The laboratory experiments on turbulent open-channel flows with $Re = 2.0 \times 10^4$ and $Fr = 0.81-2.33$ were conducted to investigate the advection characteristics of both the water surface fluctuations and the turbulence beneath the free surface. The space–time correlation analysis disclosed that the advection velocity of the water surface fluctuations was always smaller than the mean bulk velocity, while that of the turbulence above the near bed region was the same as the mean velocity, which was well-known as Taylor's hypothesis of the frozen-turbulence approximation. Moreover, it was found that the ratio of the advection velocity of the water surface fluctuation to the mean bulk velocity became smaller as the Froude number decreased. It implies from these results and discussion that the simple correlation approaches for the surface velocity measurements of real rivers (e.g. Fujita et al. 1994, 1998) may calculate the velocity relatively smaller than the true value. However, as the examination in this study is limited in the laboratory experiments with the specific hydraulic conditions, further research works should be carried out to evaluate scale effects of the laboratory experiments for the better understanding of the free surface phenomena of real river flows.

ACKNOWLEDGEMENTS

Partial Support from the Ministry of Education, Culture, Sports, Science and Technology, Grant-in-Aid for Young Scientists (B) (No. 18760374, Head Investigator: Dr. Hitoshi Miyamoto of Kobe University) is gratefully acknowledged. I wish to thank to K. Shimoyama and K. Inaoka, my former students of Kobe University, for their assistance on the laboratory experiments.

REFERENCES

Fujita, I. and Komura S. 1994. Application of video image analysis for measurements of river-surface flows, *Proceedings of Hydraulic Engineering*, JSCE, Vol.38, pp.733–738 (in Japanese)

Fujita, I., Muste, M., and Kruger, A. 1998. Large-scale particle image velocimetry for flow analysis in hydraulic applications, *J. Hydr. Res*., Vol.36, No.3, pp.397–414.

Miyamoto, H., Kanda, T., Ooe, K., and Shimoyama, K. 2003a. Simultaneous measurements of water-surface and velocity using image processing technique and analysis of open-channel flow over concave bed with water-surface fluctuation, *Journal of Hydraulic, Coastal and Environmental Engineering*, JSCE, No.726/II-62, pp.41–53 (in Japanese)

Miyamoto, H. and Shimoyama, K. 2003b. Spatial correlation structures of water surface fluctuation and turbulence in open-channel flows, *Annual Journal of Hydraulic Engineering*, JSCE, Vol.47, pp.439–444 (in Japanese)

Miyamoto, H. and Shimoyama, K. 2004a. Spatial correlation structures of water surface fluctuation with turbulence in open-channel flows, *Journal of Hydroscience and Hydraulic Engineering*, JSCE, Vol.22, No.1, pp.37–50.

Miyamoto, H. and Shimoyama, K. 2004b. Experimental study on influence range of water surface fluctuations in turbulent open-channel flows, *The 6th International Conference on Hydroscience and Engineering(ICHE-2004)*, Brisbane, Australia, on Proc.CD-ROM.

Nakase, Y., Yokojima, S., Nakayama, A., and Fujita, I. 2000. Measurements of surface fluctuations in open-channel turbulent flow using ultra-sonic and laser displacement sensors, *Proceedings of 2000 Meeting of Japan Society of Fluid Mechanics*, pp.243–244, Kyoto, Japan (in Japanese)

Nezu, I. and Nakayama, T. 1998a. Space-time correlation structures of coherent vortices near the free surface, *Journal of Hydraulic, Coastal and Environmental Engineering*, JSCE, No.586/II-42, pp.51–60 (in Japanese)

Nezu, I. and Nakayama, T. 1998b. Relationship between turbulent structures near the free-surface and surface-wave fluctuations, *Journal of Hydraulic, Coastal and Environmental Engineering*, JSCE, No.593/II-43, pp.69–78 (in Japanese)

Nezu, I. and Nakagawa, H. 1993. *Turbulence in open-channel flows*, IAHR-Monograph, A.A.Balkema, Rotterdam.

Nikora, V. and Goring, D. 2000. Eddy convection velocity and Taylor's hypothesis of 'frozen' turbulence in a rough-bed open-channel flow, *Journal of Hydroscience and Hydraulic Engineering*, JSCE, Vol.18, No.2, pp.75–91.

Tennekes, H. and Lumley, J.L. 1972. *A first course in turbulence*, pp.248–256, The MIT Press, Massachusetts.

Copyright © 2006 Taylor & Francis Group plc, London, UK

Turbulent wake region of large roughness elements: Combining flow visualization and high frequency velocity measurements

R.W.J. Lacey & A.G. Roy
Département de géographie, Université de Montréal, Succursale Centre-Ville, Montréal

ABSTRACT: This study characterizes the shear layer and associated shedding properties of an isolated in situ submerged pebble clusters using combined flow visualization and high frequency three-dimensional velocity (acoustic Doppler velocimeter, ADV) measurements. We outline a new method for synchronizing digital video recordings and instantaneous velocity measurements and obtained a precision to within one time step which is a vast improvement over previous in situ methods. The synchronized measurements were used to investigate the behavior of the shear layer and shedding vortices under the influence of large-scale (LS) coherent flow structures. Two scales of shedding structures were observed: small-scale initial shear layer instability vortices and larger-scale coherent structures resulting from the rollup and expansion of the initial small-scale vortices. Dominant frequencies estimated through spectral analysis, visual estimation and the Strouhal relationship were in generally good agreement.

1 INTRODUCTION

Large-scale (LS) flow structures appear to be common features of gravel-bed rivers (Roy et al. 2004) and consist of depth scaled intermittent fronts of high-speed fluid which are mainly directed towards the bed (sweeps) and of low-speed fluid that predominantly move towards the free surface (ejections). Sweeps and ejections have been found to contribute to the bulk of positive Reynolds shear stress and as such exert a considerable influence on local sediment dynamics (Williams et al. 1989). The origin of LS structures is still unclear, and it has been suggested that they are produced by topographic features such as changes in channel geometry and separation of flow over bed forms (Dinehart 1999). LS structures appear to have a strong persistence and have been found to influence the shedding motions of isolated pebble clusters (Buffin-Bélanger & Roy 1998, Roy et al. 1999, Buffin-Bélanger et al. 2001). Large roughness elements such as isolated boulders and pebble clusters are frequent features in gravel-bed rivers (Brayshaw 1984). The wake induced by a roughness element provides an effective means of flow resistance through turbulent momentum exchange. Given previous constraints on the synchronization of field velocity measurements and visualization techniques there is still a lack of understanding of the small-scale shedding processes and behavior of in situ shear layers under the influence of LS structures.

Shear layer behavior has been investigated in laboratory studies of mixing layers (Winant & Browand 1974) and around bluff bodies (Nakamura 1993, Roshko 1993), as well as in situ at stream confluences (Biron et al. 1993, Rhoads & Sukhodolov 2004). Relatively few studies have focused on in situ shear layers around pebble clusters (Buffin-Bélanger et al. 2001). The results from bluff body studies are particularly applicable to the characteristics of pebble cluster shear layers, as all shear layers have identifiable characteristic structures (Fuchs et al. 1980). Bluff bodies like pebble clusters are characterized by a flow separation zone, shear layer instability and the associated shedding vortices (Roshko 1993). The flow around a bluff body is described by two basic length scales, the thickness of the separated shear layer, h_l, and the body size, h_s (Nakamura 1993). The rolling up of the initial shear layer causes a train of small-scale vortices (referred to as a Karman vortex street for low Reynolds numbers). Small-scale instability vortices are a common characteristic of shear layers and have been observed in laboratory experiments on spheres (Taneda 1978). The steady broadening of the initial shear layer gives rise to a new set of larger structures downstream where at some fixed point the dominant frequency scales with roughness element diameter (Fuchs et al. 1980). The shift from small to larger scale vortex structures can under certain conditions be the result of vortex pairing and coalescence (Winant & Browand 1974) which enables the adjustment of the

Copyright © 2006 Taylor & Francis Group plc, London, UK

smaller initial scales to the larger scales at a distance equivalent to several h_s downstream and eventually leads to fully developed turbulent flow (Fuchs et al. 1980).

Using insights from bluff body studies, the current research characterizes shear layer behavior (under the influence of LS turbulent flow structures) and the associated shedding properties of an isolated in situ submerged pebble cluster using combined flow visualization and high frequency three-dimensional velocity measurements. As well, we investigate the use of a promising new technique for synchronizing digital video recordings and instantaneous velocity measurements. Synchronizing field equipment is very challenging at high measurement frequencies. In turbulent studies, the instantaneous velocity can change dramatically over one time step making it very difficult to synchronize video images with specific velocity fluctuations. Past studies, have managed to synchronize video recordings (measured at 30 Hz) and instantaneous velocity measurements (measured at 20 Hz) to within 0.5 s using a sound marker emitted by the laptop computer as the measurements were started (Roy et al. 1999, Buffin-Bélanger et al. 2001). Yet due to the lack of high frequency precision, only large coherent structures could be properly compared and characterized with certainty. The method outlined in the current study allows us to synchronize concurrent measurements at a much higher precision.

2 FIELD SITE AND EXPERIMENTAL PROCEDURES

The study site is located on the Eaton North River in the Eastern Townships, Quebec, Canada. The Eaton North is a gravel-bed river with a $D_{50} = 0.035$ m and a bank full width of 30 m. Several large clast sediments (>0.20 m) are scattered sporadically throughout the reach some of which form the keystones of pebble clusters (Lamarre & Roy 2001). An aluminum 1.5 m square frame was positioned overtop of a naturally occurring pebble cluster. The frame (Fig. 1a) was used to support four SonTek acoustic Doppler velocimeters (ADVs) and an underwater Sony digital video camera (Fig. 1b). The ADVs were arranged along a longitudinal (streamwise, x) transect that crossed overtop of the pebble cluster. The mean water depth (Z) within the sampling area was 0.43 m. The A and B axes of the keystone anchoring the pebble cluster were 0.44 m and 0.30 m respectively. The maximum protrusion, h_s, of the cluster was 0.17 m. The bed topography was measured in detail using a Trimble series 5000 total station and is presented in Figure 2a.

An array of four ADVs was used in this study. The ADVs were deployed along the streamwise transect. During the experiment three ADVs were kept at



Figure 1. (a) ADV and digital video camera support frame on the Eaton North River. Flow is from left to right; (b) digital video camera within underwater case.

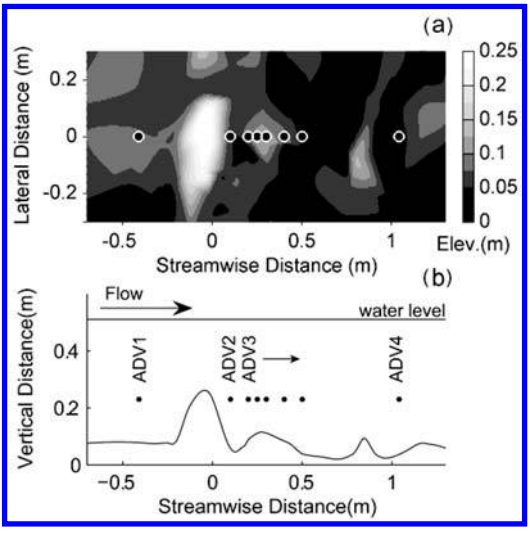


Figure 2. (a) Digital elevation model with ADV sampling locations; (b) Bed profile with ADV sampling volume locations.

stationary positions while one was shifted downstream along the frame to specific measurement locations. The stationary probes were positioned as follows (relative to the lee edge of the pebble cluster): ADV1 at $x = -0.4$ m, ADV2 at $x = 0.1$ m and ADV4 at $x = 1.05$ m. The roving probe ADV3 was located at $x = 0.2$ m for the first set of measurements and was shifted downstream to the positions $x = 0.25$ m, $x = 0.3$ m, $x = 0.4$ m, $x = 0.5$ m for the four subsequent sets of velocity measurements. The centre line bed profile and ADV sampling volume locations are presented in Figure 2b. The array of ADVs was adjusted to a height above the bed to ensure that the sampling volumes of ADV2 and ADV3 were located within the

Copyright © 2006 Taylor & Francis Group plc, London, UK

shear layer in the lee of the pebble cluster. This was accomplished by measuring and analyzing instantaneous velocities in the field at several heights in order to delineate where the shear layer was present. From the velocity time series and spectral density functions it was determined that locating the sampling volumes at a height of 0.02 m below the top of the pebble cluster adequately represented the velocity variations induced by the shear layer.

The digital video camera was housed in a waterproof case and was positioned underwater at a lateral distance of 0.6 m from the ADVs sampling array to give a profile view (x–z plane) which included the lee side of the pebble cluster and the two middle probes (ADV2 and ADV3) directly downstream of the cluster. A neutrally buoyant tracer was prepared by mixing small amounts of non-toxic white latex paint with river water. The tracer was injected continuously into the recirculation zone directly behind the cluster at $x = 0$ m where it could be passively entrained into the overlying shear layer.

Five sets of digital videos were recorded while measuring simultaneously the 3D instantaneous streamwise, u, lateral, v, and vertical, w, velocities. For each subsequent set of measurements the roving probe was shifted downstream along the frame. The video and velocity measurements were initially synchronized by touching the ADVs acoustic transmitter while recording. The ADV responds with large spikes in the signal to noise ratio output and the film captures the hand movement. The sampling frequencies for the ADVs and the digital video camera are 25 Hz and 30 Hz, respectively. Velocity time series were recorded for longer than 6 min, with the exception of the first series which was 4 min in length. Video record lengths were longer than 4 min with the exception of the first film which had a length of 2 min.

3 DATA TREATMENT AND ANALYSIS

The instantaneous velocity time series were visually inspected for irregularities and low signal correlations. With the exception of the velocities measured near the cluster on the downstream side, the majority of the velocity signal correlations were above the 70% rejection limit suggested as a quality control measure by the ADV manufacturer. Failure to remove velocity values with low correlation has been found to introduce bias into both mean velocity values and turbulent statistics (Lane et al. 1998). The velocities measured in the near-shear layer had signal correlations of between 65% and 70%, most likely induced by the high shearing of the flow occurring in the ADV sampling volume. These time series were kept in the analysis in spite of having signal correlations lower than 70% as their velocity spectra indicated an adequate fit with the Kolmogorov $-5/3$ power scale in the inertial subrange. These measurements were also taken at points that were crucial to characterize the dynamics of the shear layer.

The u, v, and w velocity series, u_{i} where i represents the velocity component, were back transformed to beam velocities and obvious spikes from the time series were removed using the Goring & Nikora (2002) phase-space thresholding method replacing them with interpolated values based on adjacent time-step velocities. In order to keep the correlations between velocity signals free of the auto-correlation implicitly added by filters, a low-pass filter was not applied to the time series as is commonly done to remove possible aliasing effects induced by high frequency Doppler noise. Mean lateral velocities were expected to be close to zero given attempts in the field to align the support frame in the streamwise direction. It was found that time averaged lateral velocities, V, were systematically offset. All velocity time series were rotated in the lateral plane, using polar coordinates, by an angle of 8.5° obtained as the mean offset angle of ADV1 and ADV4. These two probes were considered to represent the average flow direction as they are less influenced by the pebble cluster. The rotation angle was selective to give a general downstream orientation to all probes and as such does not bring the V of a single probe to a zero value.

Blue and red hue saturation values, HSVs, were extracted from each digital image of the films to give a time series of the image intensity, I_n, at the estimated sampling volume locations of ADV2 and ADV3 (see Marquis & Roy (2006) for more information on this technique). As the films are recorded at 30 Hz, the I_n, time series were resampled at 25 Hz in order to cross-correlate and compare them with the 25 Hz velocity time series. Using cross-correlation and varying the time lags we were able to precisely synchronize I_n and u_{i}. The correlations between I_n and u_{i} were further improved by adjusting slightly the initial estimate of the ADV sampling volume location on the digital film frames. A roving nine point 15 by 15 pixels window was used to isolate the pixel with maximum correlation with the ADV measurements. Given these cross-correlation methods and the initial field synchronization the ADV time series and the digital films could be matched to within one time step.

To enhance the visualization of the injected tracer, the RGB color levels of the digital films were adjusted and extracted to produce contrasting greyscale films which much facilitate the manual identification and quantification of the coherent turbulent flow structures. The behavior of the shedding structures and the shear layer was compared with the synchronized u_{i} data. The response of the shear layer to the passage of large-scale events was assessed. The frequency, f, of small-scale instability vortices and large-scale

Copyright © 2006 Taylor & Francis Group plc, London, UK

shedding structures was quantified utilizing tracer presence and absence. Identification was based on the characteristic form of a vortex street where vortices contain a much higher level of tracer than the surrounding fluid. While the small-scale instability vortices were easily discerned the detection of LS shedding structures was found to be more difficult due to the complex flow paths and quick dissipation of the tracer. A detection scheme was used, where at a distance of c. $1.5Z$ downstream and at a height of h_s, a structure was detected when an absence of tracer was followed by a large-scale front of rotating fluid with a high tracer concentration. The frequencies of the small and LS shedding structures were compared with the velocity and I_n power spectra and with the shedding frequency predicted by the Strouhal relationship:

$$f = S_r U / h_s \tag{1}$$

where S_r is the Strouhal number. Laboratory and field studies on shear layers have found S_r values ranging from 0.1 to 0.25 (Venditti and Bauer 2005).

Mean turbulent statistics were calculated at each ADV measurement location. These statistics included the root mean squared (RMS), u', v', w'; turbulent kinetic energy $k_e = 0.5(u'^2 + v'^2 + w'^2)$; Reynolds shear stress $\tau_{uw} = -\rho u'w'$, where ρ is the water density.

Space-time correlations (STC) between velocity time series measured simultaneously with each ADV were estimated as follows:

$$r_{u_i u_j}(\Delta x, \Delta t) = \frac{\sum_{k=1}^{n} u_i(x_k, t_k) \cdot u_j(x_k + \Delta x, t_k + \Delta t)}{u_i' u_j'} \tag{2}$$

where r is the space-time correlation between u_i and u_j, Δx is the separation distance between the points where velocity time series i and j were measured, and Δt is the temporal lag between velocity measurements in a series. Equation 2 was also used to estimate the autocorrelation function (ACF) for each velocity component (by setting $\Delta x = 0$). The integral time scale (ITS) of each velocity component was obtained by integrating the ACF up to the time lag at which the correlation is not significantly different from zero ($\alpha = 0.05$).

The digital film I_n time series were cross-correlated with velocity time series by:

$$r_{u_i I_n}(\Delta t) = \frac{\sum_{k=1}^{n} u_i(t_k) \cdot I_n(t_k + \Delta t)}{u_i' I_n'} \tag{3}$$

where I_n' is the standard deviation of I_n.

U-Level event analysis was used to determine the occurrence of high- or low-speed events (Luchick & Tiederman 1987). This is a conditional sampling method that estimates the frequency and duration of the streamwise velocity excursions higher and lower than the mean. As we were interested in determining the occurrence of LS events, we used a threshold (H) of $H = 0$ and a minimum duration of 5 time steps as suggested by Paiement-Paradis et al. (2003).

Velocity spectra were estimated using discrete fast Fourier transforms (fft) of each data series given by:

$$S_{uu}(\omega) = \frac{1}{Tn}\left|\sum_{i=1}^{n} x_i e^{-j\omega i}\right|^2 \tag{4}$$

where T is the sampling interval, n is the number of measurements in the series, x_i is the time domain signal and ω angular frequency. Velocity and I_n spectra were investigated to determine the occurrence of a shedding motion which would appear in a particular range of frequencies.

4 RESULTS AND DISCUSSION

The mean velocities, U, V, W, and turbulent statistics at each sampling location are presented in Table 1. U is reduced in the pebble cluster wake zone and regains its upstream velocities at $x = 1.05$ m ($x = 6.2h_s$) downstream from the cluster. Mean w values show that the flow is directed towards the surface as the flow approaches the pebble cluster and that it is then strongly directed towards the bed in the lee of the cluster. RMS values for all velocity components increase in the wake of the pebble cluster indicating high turbulent energy. The fluctuations in the lateral velocity component, v', are almost equal to those for the streamwise velocity component u', directly behind the cluster. The k_e increases by a factor of 2.5 in the near-wake of the cluster. The increased RMS and k_e values recorded in the wake of the pebble cluster are consistent with other studies investigating the spatial distribution of turbulence around pebble clusters (Buffin-Bélanger & Roy 1998, Lawless & Robert 2001). The integral time scale of all velocity components decreases by a factor of 2 with the exception of the high ITSu at $x = 0.25$ m where the value is larger than what is observed for the upstream measurements ($x = -0.4$ m). The integral time scale gives an indication of the average size of the correlated structures within the flow or the mean life-time of individual eddies (Townsend 1976). Given previous studies where ITSu decreased in the wake of a pebble cluster due to the shedding of smaller scale structures (Buffin-Bélanger & Roy, 1998), the increase of ITSu at $x = 0.25$ is unexpected. This high ITSu value occurs at the same location as the highest Reynolds shear stress recorded. The value of the Reynolds shear stress ($-\rho u'v'$) at $x = 0.25$ m is a factor of 3 greater than the shear stress estimated upstream

Copyright © 2006 Taylor & Francis Group plc, London, UK

Table 1. Mean velocities, turbulent statistics and integral time scales.

Probe	x m	U cm s^{-1}	V cm s^{-1}	W cm s^{-1}	u' cm^2 s^{-2}	v' cm^2 s^{-2}	w' cm^2 s^{-2}	k_e cm^2 s^{-2}	ITSu s	ITSv s	ITSw s	$-\rho u'v'$ N m^{-2}
ADV1	−0.40	80	1	2	18	14	11	316	0.25	0.08	0.09	8.2
ADV2	0.10	46	−7	−5	27	25	16	805	0.10	0.04	0.05	22.2
ADV3-1	0.20	56	−2	−8	27	23	16	744	0.10	0.05	0.07	23.6
ADV3-2	0.25	61	−6	−13	28	22	16	772	0.26	0.05	0.07	25.1
ADV3-3	0.30	64	−6	−12	27	21	16	687	0.14	0.06	0.08	23.2
ADV3-4	0.40	67	−5	−9	25	19	14	611	0.14	0.06	0.08	20.3
ADV3-5	0.50	67	−4	−7	23	18	14	531	0.16	0.06	0.09	17.6
ADV4	1.05	79	−2	0	16	14	10	278	0.21	0.07	0.12	6.9

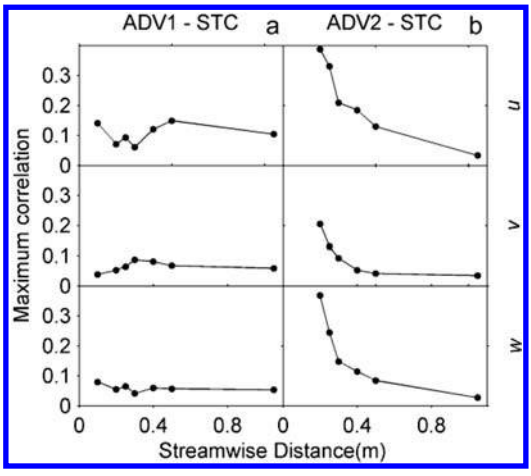


Figure 3. Maximum space-time correlations (a) between ADV1 located at $x = -0.4$ m and all downstream probe locations; (b) between ADV2 located at $x = 0.1$ m and all downstream probe locations.

of the cluster. Inspection of the film, recorded during the velocity measurements at $x = 0.25$ m did not reveal any insight on the unexpectedly high ITSu estimated by ADV3. The high ITSu value is an indication that through the shedding process the size of the mean vortices measured at $x = 0.25$ m is generally larger than elsewhere in the cluster wake.

The persistence and behavior of coherent turbulent flow structures were investigated through space-time correlation analysis (STC). The maximum correlation coefficients obtained in the STC analysis between pairs of probes for each velocity component are presented in Figure 3. Figure 3a presents the maximum STC of ADV1 velocity time series with the time series measured at the downstream sampling locations.

The u series measured by ADV1 at $x = -0.4$ m show a significant correlation with time series measured at $x = 0.1$ m (located in the wake of the pebble cluster). The correlation decreases at $x = 0.2$ m, yet increases further downstream at $x = 0.4$ m. The robustness of

Table 2. Cross-correlation coefficients between velocity time series and and I_n measurements from the images.

Probe	x m	u	v	w
ADV2	0.1	−0.43	0.10	0.39
ADV3-1	0.2	−0.37	0.06	0.37
ADV3-2	0.25	−0.37	0.18	0.34
ADV3-3	0.3	−0.30	0.15	0.29
ADV3-4	0.4	−0.38	0.17	0.38
ADV3-5	0.5	−0.30	0.15	0.31

the u component correlations is an indication of the very local effect of the cluster on the coherent flow structures advecting from upstream and indicates that some structures persist downstream in spite of having passed the cluster. The maximum correlation coefficients between measurements of ADV2 and the downstream sampling locations (Fig. 3b) indicate an expected trend of decreasing correlations with distance. The correlations for the u and w velocity components are seen to be much higher and the structures more persistent than for v component correlations. This is perhaps due to the formation of vortices that have a weak lateral component that shed from the cluster. Unlike the upstream velocities measured at ADV1, the structures generated in the clusters near wake are less persistent as determined by the near zero correlation between $x = 0.1$ m and $x = 1.05$ m.

Table 2 presents the cross-correlations between the simultaneous velocity and image intensity time series. The values are very well correlated. A strong negative correlation is observed between u and I_n which occurs at a time lag of 0, while a strong positive correlation is seen between the w and I_n occurring at time lag of -1 steps (0.04 s). The strength of the correlations is surprisingly good and the correlations are generally higher than the maximum values of the STC obtained between the measurements of adjacent ADVs. The correlations for the v component are much less than for the other two components and occur at a time lag

Copyright © 2006 Taylor & Francis Group plc, London, UK

of between −3 and −4 steps. The smaller correlation values for v is not surprising as I_n is estimated from two dimensional images of the x–z plane and is therefore much less sensitive to the variations in the lateral direction. A slight decreasing correlation trend is observed with distance from the point of tracer injection ($x = 0$ m), with the exception of the ADV3 at $x = 0.4$ m. The higher correlations values during this set of measurements are perhaps explained by an increased concentration of white paint when preparing the tracer or changing ambient light conditions during the recordings.

The correlation values in Table 2 are fundamental for observing and characterizing the behavior of coherent turbulent flow structures seen in the enhanced film images. The negative correlation of I_n with u indicates that for the same time step an increased image intensity can be directly associated with a slower u. From the positive correlation between I_n and w (at a time lag of −1) we understand that an increased image intensity is followed after one time step by a fluid motion towards the surface.

Preliminary analysis of the shear layer behavior observed in the films has identified two scales of coherent flow structures. Within the shear layer, initial small-scale instability vortices are perceived which are seen to form while still in contact with the lee side of the cluster. As these small-scale structures elongate away from the cluster their behavior differs greatly depending on the surrounding fluid conditions. Under neutral conditions the small-scale vortices seem to shed off from the cluster at regular intervals with or without strong vorticity (clockwise rotation). The passage of a sweep intermittently enhances the rollup and pairing of the instability vortices compressing the vortices against or into the recirculation zone. The rollup and expansion of the initial instability vortices produces the second larger-scale coherent flow structures observed which are much more difficult to discern due to flow complexity and tracer dissipation.

An example of these coherent structure characteristics are presented in Figure 4 along with the simultaneous fluctuating u, w and I_n time series. A sequence of 15 enhanced images is presented, starting at $t = 31.7$ s and ending with $t = 32.3$ s. The images and velocities were measured under the condition where ADV2 and ADV3 were 0.15 m apart, at $x = 0.1$ m and $x = 0.25$ m, respectively. ADV2 is the upstream (left) probe in the image. In the initial frame ($t = 31.7$ s), we see two coherent flow structures advecting downstream with an inclination towards the surface and a positive vertical velocity. The positive vertical velocity is recorded in the ADV2 and ADV3 time series plots at $t < 31.75$ s. Adjacent to the cluster a third coherent structure is forming. Subsequent images show how the forming structure is fed by smaller scale initial shear layer instabilities as observed by Taneda (1978). Three separate small-scale vortices can be observed to shed from the cluster at $t = 31.73$ s, $t = 31.83$ s and $t = 31.93$ s. Detailed comparison of the film images with the I_n plots shows that high I_n is often related to the center the coherent vortices. Visual comparisons with the velocity signals indicates an increased u velocity directed towards the bed as the clockwise rotating vortex approaches and induces slower u directed towards the surface as it exits the sampling volume. In Figure 4, the coalesced vortex structure is shed downstream at $t = 32.10$ s and is recorded with positive u and negative w as the front of the clockwise rotating vortex passes through the sampling volume of ADV3. A spike in the intensity is observed in the I_n ADV3 sampling volume plot at $t = 32.23$ s. These relationships are more difficult to see closer to the cluster as the structures are smaller and pass very quickly through the ADV sampling volume, yet the small scale vortices are represented as fluctuating peaks in the u and w velocity signals of ADV2 and in the I_n values.

The behavior of the shear layer and shedding vortices under the influence of a LS ejection event which is defined as a low-speed wedge, detected using U-level analysis, is depicted in the series of enhanced images presented in Figure 5. The sequence of images from $t = 14.33$ s to $t = 15.27$ s was obtained from the set of measurements where ADV2 and ADV3 were separated by 0.10 m, at $x = 0.1$ m and $x = 0.20$ m, respectively. The synchronous time series of u, w, and I_n are presented below the images from $t = 13.5$ s to $t = 15.5$ s. The average coherent structure advection time between ADV1 at $x = -0.4$ m and ADV2 at $x = -0.1$ m determined through STC analysis is 0.76 s. The LS burst event detected for ADV1 at $t = 13.8$ s reaches ADV2 at $t = 14.56$ s which is consistent with the ADV2 velocity plot. The event is also clearly observed in the ADV3 velocity plot where it occurs at $t = 14.75$ s. The shear layer reacts to the arrival of the burst event by expanding upwards towards the surface as seen in the image at t = 14.60 s. The small-scale instability vortices loose most of their rotation as they are ejected towards the surface. This behavior is demonstrated by the downstream coherent structure seen in the image at $t = 14.87$ s which expands yet retains much of its original orientation as it advects downstream. For the time sequence given here, the peaks in the I_n plots fit well with the peaks in the w plots. A small duration LS sweep event precedes the LS burst event and the shear layer is seen to be compressed towards the bed in the image at $t = 14.47$ s. The results presented here show similar dynamics in the lee of the cluster as what has been reported by Buffin-Bélanger et al. (2001). The shedding motion seemed to expand vertically as a low-speed wedge flowed overtop of the cluster and was suppressed during the passage of a high-speed wedge.

Copyright © 2006 Taylor & Francis Group plc, London, UK

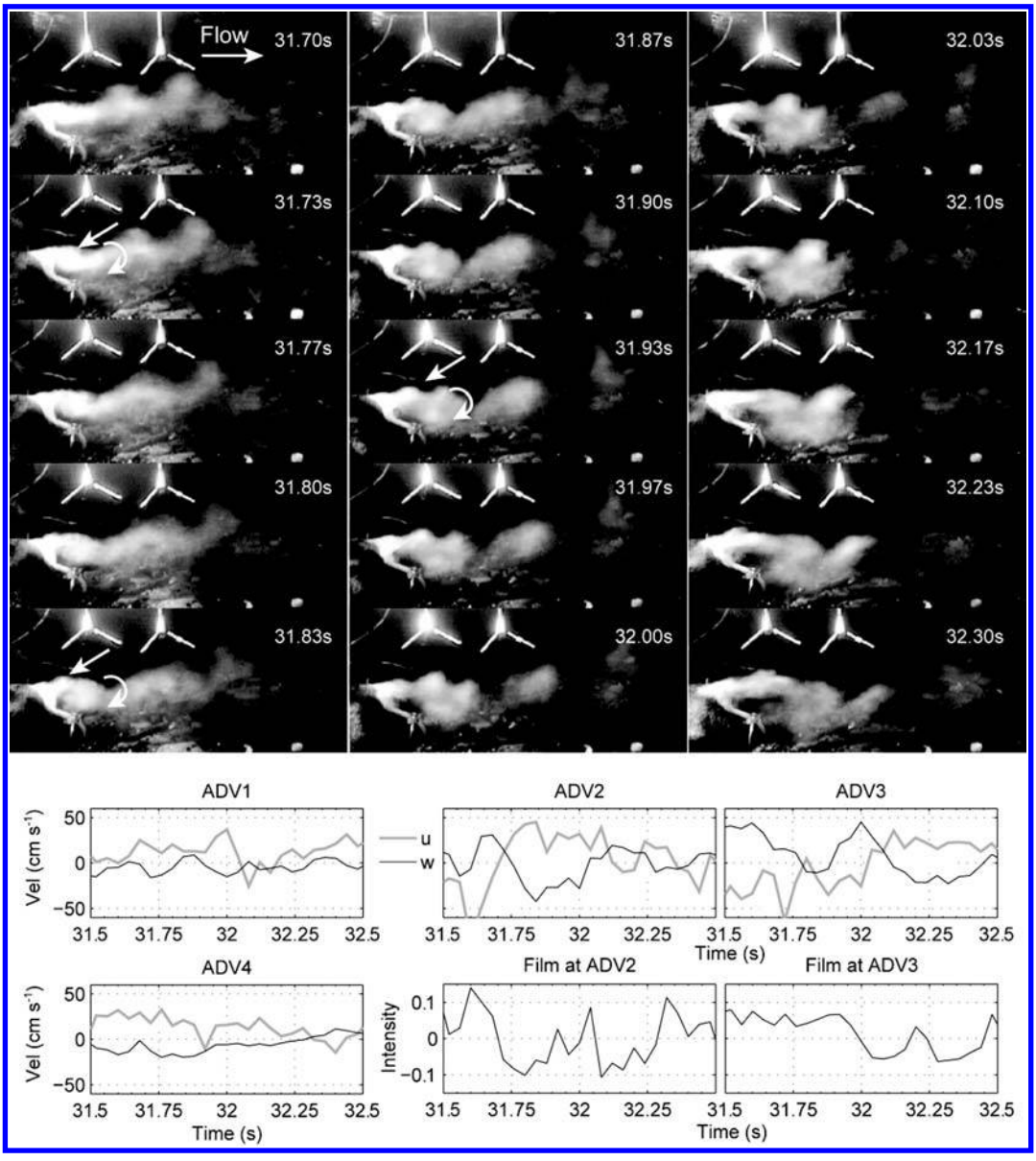


Figure 4. Sequence of 15 enhanced images, starting at $t = 31.7$ s and ending with $t = 32.3$ s. Plots of the simultaneous fluctuating u, w and I_n time series starting at $t = 31.5$ s and ending with $t = 32.5$ are presented below the images. The images present ADV2 and ADV3 (downstream), at $x = 0.10$ m and $x = 0.25$ m, respectively. Arrows highlight shedding of initial instability vortices as well as indicating preferential flow direction.

The peaks in the velocity power spectra for the time series measured by ADV2 at $x = 0.1$ m and ADV3 at $x = 0.25$ (Fig. 6a) compare well with their respective image intensity power spectra (Fig. 6b) and indicate two scales of shedding frequencies. At the $x = 0.1$ m measurement location, a high frequency peak at c. 5.5 Hz is evident in the I_n power spectra. This peak is also seen in the velocity spectra (Fig. 6a) where it occurs over a broader range of frequencies. A second lower frequency peak at c. 1.8 Hz corresponding to the structures that have coalesced into larger scale features is observed in both I_n and the w power spectra although

Copyright © 2006 Taylor & Francis Group plc, London, UK

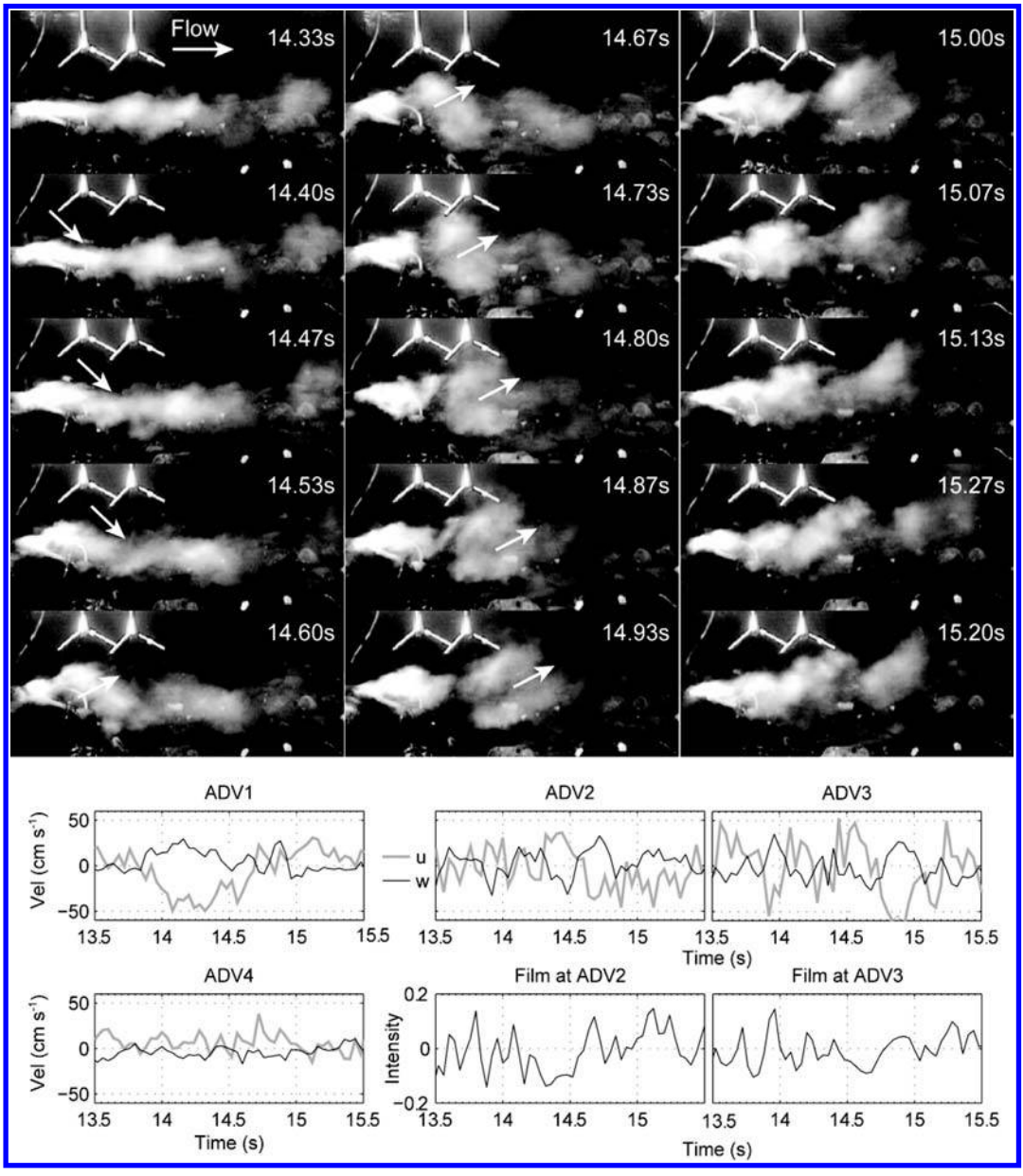


Figure 5. Sequence of 15 enhanced images, starting at $t = 14.33$ s and ending with $t = 15.20$ s. Plots of the simultaneous fluctuating u, w and In time series starting at $t = 13.5$ s and ending with $t = 15.5$ are presented below the images. The images present ADV2 and ADV3 (downstream), at $x = 0.10$ m and $x = 0.2$ m, respectively. Arrows indicate presence and direction of LS flow structures.

it is much less evident in the w spectra. Similar peaks are observed at $x = 0.25$ m, yet they are shifted slightly towards the lower frequency end. The lower frequency w spectral peak is much more evident than at $x = 0.1$ m and occurs at c. 1.2 Hz. The shift in frequency with distance downstream from the cluster may be explained by the intermittent coalescence or dissipation of the smaller-scale vortices. This type of frequency shift has been observed in shallow mixing layer studies and

Copyright © 2006 Taylor & Francis Group plc, London, UK

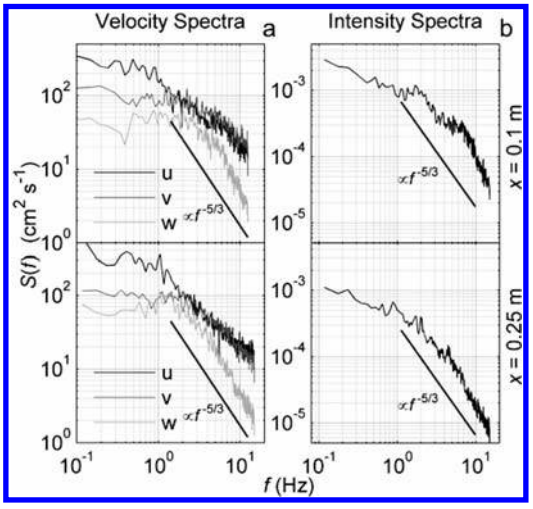


Figure 6. Spectral density functions at $x = 0.1$ m and $x = 0.25$ m for (a) Fluctuating velocity time series (cm^2 s^{-1}); (b) Image intensity time series.

was associated the coalescence and growth of shedding vortices (Uijttewaal & Tukker 1998).

Visual inspection and analysis of the films identified the high frequency observed in the velocity and I_n spectra (5.5 Hz) and could associated it with the formation the small-scale initial shear layer instability vortices. The lower frequency shedding is much more difficult to perceive in the film due to the complexity of the flow paths and the rapid dissipation of the tracer. Using the outlined detection scheme a frequency of *c*. 1.0 Hz was estimated. This frequency is in good agreement with the value predicted by the Strouhal relationship (Equation 1) of *c*. 0.85 Hz.

5 CONCLUSIONS

In order to fully understand the in situ characteristics and processes involved with the shear layer and associated shedding vortices of a pebble cluster at high *Re*, it is important to gain a visual picture of the phenomena. A large benefit is obtained by synchronizing the instantaneous velocity time series with the visualization at the frequency over which the processes are varying. Using the synchronization method presented here, we were able to match the instantaneous velocity fluctuations to within one time step of the concurrent video records and gain a better understanding of the in situ shedding behavior. It was then possible to relate short duration velocity trajectories to the behavior of the small-scale instability vortices. These small-scale vortices were seen to shed from the cluster and intermittently coalesce into larger scale vortical structures. Their intermittent behavior was in part influenced by the passage of LS events. The LS sweep event was seen to compress the shear layer towards the bed and enhance the coalescence of the initial shear layer instability vortices into larger-scale vortices. With the passage of the LS ejection event the small-scale shear layer vortices expanded towards the surface losing some of their clockwise rotating velocities. The LS structures were found to be robust: retaining significant levels of structure coherence after passing overtop of the pebble cluster and the shear layer.

The image intensity showed a strong correlation with the *u* and *w* component velocity time series. Their respective spectral density functions had similar shapes and power law scalings suggesting that I_n could be used as a proxy for detecting the frequency of shedding structures when the peak shedding frequencies in the velocity spectra are less evident.

Due to the intermittent behavior of the shear layer it is difficult to attribute the frequency shift in the velocity and I_n spectra solely to coalescence. The shear layer inherently expands with downstream distance and the shift to lower frequency modes may be more of a measurement of the vortex growth and expansion than to coalescence. Shear layer expansion is a function of *Re* and an area of future work would be to examine if the in situ shear layer behavior characterized in this study occurs in gravel-bed rivers over a range of *Re*.

ACKNOWLEDGEMENTS

This research was conducted as part of the program of The Canada Research Chair in Fluvial Dynamics. Funding was provided by the National Sciences and Engineering Research Council and by the Canadian Foundation for Innovation. The authors wish to thank Genevieve Marquis for her invaluable help in the field and her video processing know-how. We furthermore wish to thank the anonymous reviewer for his constructive criticism.

REFERENCES

Biron, P., De Serres, B., Roy, A.G., & Best, J.L. 1993. Shear layer turbulence at an unequal depth channel confluence. In: Clifford, N.J., French, J.R., and Hardisty, J. (eds), *Turbulence: perspectives on flow and sediment transport*: 197–213. John Wiley & Sons Ltd.

Brayshaw, A.C. 1984. Characteristics and origin of cluster bedforms in coarse-grained alluvial channels. In: Koster, E.H. and Steel, R.J. (eds), *Sedimentology of gravels and conglomerates*: 77–85. Canadian Society of Petroleum Geologists.

Buffin-Belanger, T. & Roy, A.G. 1998. Effects of a pebble cluster on the turbulent structure of a depth-limited flow in a gravel-bed river. *Geomorphology* 25 (3–4): 249–267.

Buffin-Bélanger, T., Roy, A., & Levasseur, M. 2001. Interactions entre les structures d'échappement et les structures

Copyright © 2006 Taylor & Francis Group plc, London, UK

a grande échelle dans l'écoulement turbulent des rivieres a lit de graviers. *Revue des Sciences de l'Eau* 14 (3): 381–407.

Dinehart, R.L. 1999. Correlative velocity fluctuations over a gravel river bed. *Water Resources Research* 35 (2): 569–582.

Fuchs, H. V, Mercker, E. & Michel, U. 1980. Mode expansion of coherent structures in the wake of a circular disk. In L.J.S. Bradbury, F. Durst, B.E. Launder, F.W. Schmidt & J.H. Whitelaw (eds), *Turbulent Shear Flows 2*: 282–296. New York: Springer-Verlag.

Goring, D.G. & Nikora, V.I. 2002. Despiking acoustic Doppler velocimeter data. *Journal of Hydraulic Engineering-ASCE* 128 (1): 117–126.

Lamarre, H. & Roy, A.G. 2001. Organisation morphologique des blocs et des amas de galets dans les cours d'eau a lit de graviers. *Géographie physique et Quaternaire* 55 (3): 275–287.

Lane, S.N., Biron, P.M., Bradbrook, K.F., Butler, J.B., Chandler, J.H., Crowell, M.D., Mclelland, S.J., Richards, K.S., & Roy, A.G. 1998. Three-dimensional measurement of river channel flow processes using acoustic Doppler velocimetry. *Earth Surface Processes and Landforms* 23 (13): 1247–1267.

Lawless, M. & Robert, A. 2001. Three-dimensional flow structure around small-scale bedforms in a simulated gravel-bed environment. *Earth Surface Processes and Landforms* 26 (5): 507–522.

Luchick, T.S. & Tiederman, W.G. 1987. Timescale and structure of ejections and bursts in turbulent channel flows. *Journal of Fluid Mechanics* 174: 529–552.

Marquis, G. & Roy, A.G. 2006. Turbulent processes at the entrance of a pool using flow visualization. Proceedings in: *River Flow 2006, International Conference on Fluvial Hydraulics, September 6–8, Lisboa, Portugal.* Balkema.

Nakamura, Y. 1993. Bluff-body aerodynamics and turbulence. *Journal of Wind Engineering and Industrial Aerodynamics* 49 (1–3): 65–78.

Paiement-Paradis, G., Buffin-Belanger, T., & Roy, A.G. 2003. Scalings for large turbulent flow structures in gravel-bed rivers. *Geophysical Research Letters* 30 (14).

Rhoads, B.L. & Sukhodolov, A.N. 2004. Spatial and temporal structure of shear layer turbulence at a stream confluence. *Water Resources Research* 40 (6).

Roshko, A. 1993. Perspectives on bluff-body aerodynamics. *Journal of Wind Engineering and Industrial Aerodynamics* 49 (1–3): 79–100.

Roy, A.G., Biron, P.M., Buffin-Belanger, T., & Levasseur, M. 1999. Combined visual and quantitative techniques in the study of natural turbulent flows. *Water Resources Research* 35 (3): 871–877.

Roy, A.G., Buffin-Belanger, T., Lamarre, H., & Kirkbride, A.D. 2004. Size, shape and dynamics of large-scale turbulent flow structures in a gravel-bed river. *Journal of Fluid Mechanics* 500: 1–27.

Taneda, S. 1978. Visual observations of the flow past a sphere at Reynolds numbers between 10^4 and 10^6. *Journal of Fluid Mechanics* 85: 187–192.

Townsend, A. A. 1976. *The Structure of Turbulent Shear Flow*. Cambridge, Cambridge University Press.

Uijttewaal, W.S.J. & Tukker, J. 1998. Development of quasi two-dimensional structures in a shallow free-surface mixing layer. *Experiments in Fluids* 24 (3): 192–200.

Venditti, J.G. & Bauer, B.O. 2005. Turbulent flow over a dune: green river, Colorado. *Earth Surface Processes and Landforms* 30 (3): 289–304.

Williams, J.J., Thorne, P.D., & Heathershaw, A.D. 1989. Measurements of turbulence in the benthic boundary-layer over a gravel bed. *Sedimentology* 36 (6): 959–971.

Winant, C.D. & Browand, F.K. 1974. Vortex pairing: the mechanism of turbulent mixing-layer growth at moderate Reynolds number. *Journal of Fluid Mechanics* 63 (2): 237–255.

Copyright © 2006 Taylor & Francis Group plc, London, UK

A new perspective on sidewall correction procedures, based on SKM modelling

J. Chlebek & D.W. Knight
The University of Birmingham, Department of Civil Engineering, Birmingham, UK

ABSTRACT: This paper explores whether a simple depth-averaged flow model, based on the RANS equations, can provide the engineer with a relatively simple tool that can be used to estimate the shear force taken by the sidewalls of rectangular channels for a given aspect ratio. The Shiono & Knight Method (SKM) is used in conjunction with an extensive experimental data set of boundary shear stress measurements to investigate the issue over a wide range of aspect ratios ($0.3 < Asp < 20$). Particular consideration is given to the calibration of the three governing parameters, f, λ and Γ within SKM, bearing in mind the two requirements of simulating both the correct channel discharge and the percentage of the total shear force that is taken by the channel sidewalls. This exploratory attempt, using only one panel to simulate the flow in one half of the rectangular channel, appears to be promising and some equations are presented for the three calibration parameters based on this preliminary analysis. Further work is required to elucidate the physical basis of these equations, to undertake more detailed modelling using multi-panels and to study heterogeneous roughness effects.

1 INTRODUCTION

Sidewall correction procedures are commonly used to process experimental flume or channel data where the influence of the sidewalls is to be excluded from the analysis of bed related phenomena. Typically they reduce an otherwise essentially 3-D flow problem down to a quasi 2-D flow problem.

Although sidewall procedures are well known and have been fully documented by various authors, such as Vanoni & Brooks (1957), Brownlie (1981) and Chang (1992), their application still raises concerns about the underlying physics and level of approximation. Indeed the very number of 'simple' equations for dealing with composite roughness, as illustrated by Table 7 in Yen (1991), or the use of 'shape' effects by Kazemipour & Apelt (1979), indicate the complexity of the physical problem.

The modelling of flow in straight prismatic channels is surprisingly difficult, as shown by Nezu & Nakagawa (1993) and Chiu & Chiou (1986). This is due in part to the nature of the anisotropic turbulence, governed by the channel geometry and roughness distribution, the consequent formation of secondary flow cells and the level of turbulence closure.

This paper explores whether a depth-averaged flow model can provide the engineer with a relatively simple tool that can predict the shear force taken by the sidewalls of a rectangular channel with a given aspect ratio. The flow modelling is based on the Shiono & Knight Method (SKM), described elsewhere by Shiono & Knight (1988 & 1991) and the results are benchmarked against an extensive set of experimental data by Knight et al. (1984), Knight & Patel (1985a & b) and Rhodes & Knight (1994).

2 THEORETICAL BACKGROUND

2.1 *Introduction*

For steady flow in a prismatic open channel, the equation for the streamwise momentum may be combined with the continuity equation to give:

$$\rho\left[\frac{\partial UV}{\partial y}+\frac{\partial UW}{\partial z}\right]=\rho gS+\frac{\partial}{\partial y}(-\rho\overline{uv})+\frac{\partial}{\partial z}(-\rho\overline{uw}) \quad (1)$$

where U, V, W are the mean velocity components in the x (streamwise), y (lateral) and z (normal to bed) directions respectively, u, v, w are turbulent fluctuations of velocity with respect to the mean, ρ is the density of water, and S is the bed slope gradient ($S = \sin\theta$). See Figure 1(a) for notation.

The depth-mean-averaged momentum equation can be obtained by integrating (1) over the water depth, H, provided $W(H) = W(0) = 0$, and is given by Shiono & Knight (1988) in the form:

$$\frac{\partial\left[H(\rho UV)_d\right]}{\partial y}=\rho gHS+\frac{\partial H\overline{\tau}_{yz}}{\partial y}-\tau_b\sqrt{1+\frac{1}{s^2}} \quad (2)$$

Copyright © 2006 Taylor & Francis Group plc, London, UK

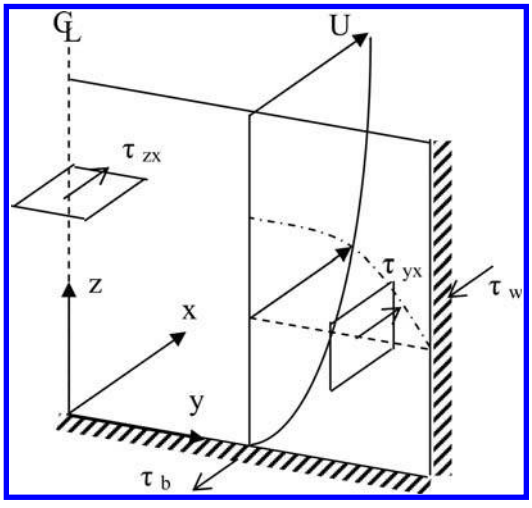


Figure 1(a). Bed and wall shear.

in which τ_b is the bed shear stress, s is the side slope (1:s = vertical: horizontal), and

$$(\rho UV)_d = \frac{1}{H}\int_0^H (\rho UV)dz\,;\ \bar{\tau}_{yx} = \frac{1}{H}\int_0^H (-\rho uv)dz \qquad (3)$$

Using an eddy viscosity approach for dealing with the Reynolds stress term, $\bar{\tau}_{yx}$, then

$$\bar{\tau}_{yx} = \rho\bar{\varepsilon}_{yx}\frac{\partial U_d}{\partial y} \qquad (4a)$$

$$\bar{\varepsilon}_{yx} = \lambda U_* H \qquad (4b)$$

where λ is the dimensionless eddy viscosity coefficient and U_* ($=\tau_b/\rho^{1/2}$) is the local shear velocity. The local boundary shear stress, τ_b, may be related to the depth-mean velocity, U_d, by use of the Darcy-Weisbach friction coefficient, f, giving

$$\tau_b = \rho\frac{f}{8}U_d^{\,2} \qquad (5a)$$

$$U_* = \sqrt{\frac{f}{8}}U_d \qquad (5b)$$

Then, substituting (4) and (5) into (2) yields:

$$\rho gHS - \rho\frac{f}{8}U_b^{\,2}\sqrt{1+\frac{1}{s^2}} + \frac{\partial}{\partial y}\left[\rho\lambda H^2\sqrt{\frac{f}{8}}U_d\frac{\partial U_d}{\partial y}\right] = \frac{\partial}{\partial y}\left[H(\rho UV)_d\right] \qquad (6)$$

Experimental results by Shiono & Knight (1991) show that in overbank flow the shear stress due to secondary flow, $(\rho UV)_d$, varies approximately linearly in certain regions of a channel. Using this concept, the lateral gradient of the secondary flow force per unit length of the channel may then be written as

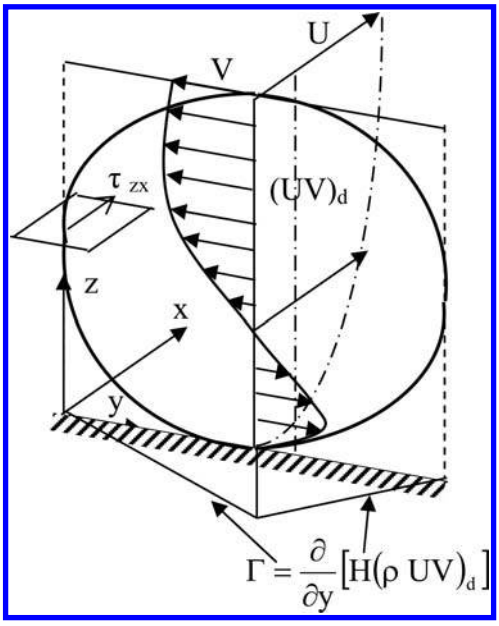


Figure 1(b). Depth-averaged secondary flow term.

$$\frac{\partial}{\partial y}\left[H(\rho UV)_d\right] = \Gamma \qquad (7)$$

where Γ is a dimensionless secondary flow parameter, which is different for different flow regions, as illustrated in Figure 1(b) for a rectangular channel. Thus Eq. (2) may be expressed in a simpler form as

$$\tau_b\sqrt{1+\frac{1}{s^2}} = \rho gHS + \frac{\partial H\bar{\tau}_{yz}}{\partial y} - \Gamma \qquad (8)$$

2.2 *Analytical solution for U_d*

An analytical solution to (6) has been obtained by Shiono & Knight (1988) for two cases, depending on whether the depth is constant or varying across the section. See Knight & Shiono (1996) and Abril & Knight (2004) for further details.

For a sub-area with a constant water depth, H, the analytic U_d distribution has the form:

$$U_d = \left[A_1 e^{my} + A_2 e^{-my} + k\right]^{1/2} \qquad (9)$$

$$\text{where } k = \frac{8gSH}{f}(1-\beta) \qquad (10)$$

Copyright © 2006 Taylor & Francis Group plc, London, UK

$$\gamma = \sqrt{\frac{2}{\lambda}}\left(\frac{f}{8}\right)^{\frac{1}{4}}\frac{1}{H} \tag{11}$$

$$\beta = \frac{\Gamma}{\rho g H S} \tag{12}$$

A_1 & A_2 can be determined by considering the relevant boundary conditions of flow continuity and the no-slip condition at the wall, as shown by Knight et al. (2004). For a simple rectangular channel of semi-width, b, with symmetric flow parameters, using just a single panel to represent half the cross-section, the two A coefficients are

$$A_1 = A_2 = -\frac{k\sinh(\gamma b)}{\sinh(2\gamma b)} = -\frac{k}{2\cosh(\gamma b)} \tag{13}$$

Thus for a rectangular channel, Eq. (9) becomes

$$U_d = \left[C_1\cosh(\gamma y) + C_2\right]^{1/2} \tag{14}$$

$$\text{where } C_1 = -\frac{k}{\cosh(\gamma b)};\ C_2 = \frac{8gSH}{f}(1-\beta) \tag{15}$$

2.3 *Analytical solution for* τ_b

The bed shear stress distribution is given via (5a) as

$$\tau_b = \rho\frac{f}{8}\left[C_1\cosh(\gamma y) + C_2\right] \tag{16}$$

The mean bed shear stress, $\bar{\tau}_b$, is then obtained by integration of (16), to give

$$\bar{\tau}_b = \frac{\rho f}{8}\left[\frac{C_1}{\gamma b}\sinh(\gamma b) + C_2\right] \tag{17}$$

and the shear force on the bed, SF_b ($= \bar{\tau}_b \times 2b$) is

$$SF_b = 2b\rho g H S(1-\beta)\left[1 - \frac{\sinh(\gamma b)}{\gamma b\cosh(\gamma b)}\right] \tag{18}$$

The mean wall shear force, SF_w, (both walls) may then be calculated from a force balance:

$$\tau_o P = SF_b + SF_w \tag{19}$$

where P is the total wetted perimeter and τ_o is the mean boundary shear stress ($= \rho g R S_o$). Thus

$$SF_w = \rho g A S - SF_b \tag{20}$$

The percentage of the total shear force that acts on the walls is then given by

$$\%SF_w = 100 \text{ x } SF_w/\rho gAS \tag{21}$$

Eqs (18) to (21) may then be used to produce a theoretical $\%SF_w$ v 2b/H (aspect ratio) relationship for a rectangular channel. This approach is thus different from those given by other researchers such as Guo & Julien (2005) and Yang & Lim (1997).

3 EXPERIMENTAL WORK

3.1 *Open channel flow data*

The open channel flow data used herein were obtained from earlier experimental work by Knight et al. (1984). The experiments were performed in a non-tilting 15 m long flume with a bed slope $S_o = 9.66 \times 10^{-4}$. The flume was 610 mm wide, and 3 smaller flumes were built inside it with widths of 70, 152 & 381 mm, making it possible to conduct 4 series of experiments in 4 flumes at various depths, giving aspect ratios varying from approximately 0.3 to 20. Ancillary experiments were conducted in rectangular ducts, using air as a medium, to investigate a larger range of aspect ratios than were possible with open channels, in some cases up to 50 (Rhodes & Knight, 1994). However, only the flume data are analysed here. It should be noted also that in this paper the aspect ratio, *Asp*, of the rectangular channel (i.e. channel width/depth ratio = 2b/h) is used throughout, although when combining rectangular and trapezoidal channel data together it is more convenient to use the wetted perimeter ratio, $P_b/P_w (= Asp/2)$, as shown by Knight et al. (1994).

3.2 *Experimental procedure*

Prior to every test in a particular flume, ancillary experiments was carried out with M1 and M2 profiles in order to ascertain the precise tailgate setting that gave the normal depth for a given discharge. Once normal depth conditions were established for a given discharge, individual velocity measurements were made within the cross section using a small propeller meter and boundary shear stress measurements made around the wetted perimeter using a Preston tube. The individual readings were subsequently numerically integrated and compared with the overall values, obtained respectively from a Venturi meter or the energy slope ($\tau_o = \rho g R S_o$). Typically, errors of ±3% and ±6% were tolerated in either integrated discharge or boundary shear. These data, along with other data, are available on the website www.flowdata.bham.ac.uk.

4 MODELLING WORK

4.1 *Influence of calibration parameters*

Some initial results are presented in Tables 1 & 2 that illustrate the influence of the 3 calibration parameters, f, λ and Γ used within the SKM. These were undertaken for one particular channel (152 mm wide) at one particular depth (200 mm). The effect of varying λ on the velocity distribution, while holding f and Γ constant, is shown in Figure 2 and the general effect on $\%SF_w$ and Q of varying all 3 parameters is shown in Table 1.

Copyright © 2006 Taylor & Francis Group plc, London, UK

Table 1. Effect of varying calibration parameters.

Vary	Fixed	+/−	$\%SF_w$	Q
f	λ & Γ	increase f	down	down
		decrease f	up	up
λ	f & Γ	increase λ	up	down
		decrease λ	down	up
Γ	f & λ	increase Γ	up	down
		decrease Γ	down	up

Table 2. Effect of varying parameters on values of $\%SF_w$ & Q for 152 mm wide channel at H = 200 mm.

f	λ	Γ	$\%SF_w$ (%)	Q (l/s)
0.018	0.011	0.047	73.08	13.78
0.040	0.011	0.047	65.23	10.46
0.005	0.011	0.047	83.08	20.52
0.018	0.030	0.047	87.54	9.36
0.018	0.005	0.047	57.44	17.35
0.018	0.011	0.500	79.68	11.97
0.018	0.011	0.000	72.93	13.95

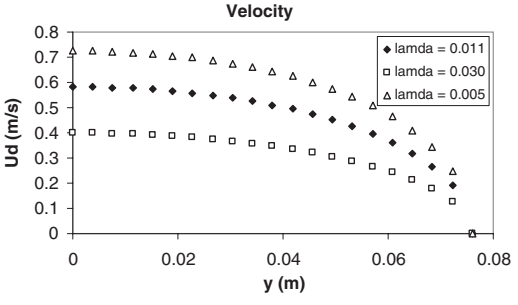


Figure 2. Effect of λ on lateral distribution of velocity in a rectangular channel.

In general, it is found that for a given depth, H, when λ was increased, with fixed f & Γ, it caused $\%SF_w$ to increase and Q to decrease. This is consistent with the results in Figure 2 and physical reasoning. The reverse occurred when λ was decreased. Table 2 illustrates these changes quantitatively, based on this one depth (H = 200 mm) with reference values of $\%SF_w$ and Q of 73.08% and 13.78 l/s respectively.

Table 2 indicates that the effect of varying the 3 parameters is large, as would be expected from physical arguments. Some analysis was therefore undertaken on the sensitivity of each parameter prior to optimising the parameters simultaneously for all flumes over the entire range of discharges and aspect ratios. The 152 mm (= 2b) flume data were selected for this preliminary analysis.

4.2 *Preliminary optimisation and error analysis*

Errors in the modelled values of channel discharge, Q, and the percentage of the total shear force carried by the walls, $\%SF_w$ were determined for each of the 7 depths used in this particular series of experiments, for specific values of the parameters f, λ and Γ. The experiments covered a fairly narrow bandwidth of aspect ratios ($0.99 < Asp < 2.00$) and were undertaken with depths of 153.0, 125.9, 113.6, 102.6, 97.0, 85.8 & 76.0 mm (or $0.50 < P_b/P_w < 1.00$). The discharges ranged from 9.85 l/s to 3.90 l/s and the velocities from 0.424 m/s to 0.338 m/s.

A different procedure was adopted later when optimising the parameters for all data, as in that case 7 pre-selected depths were chosen and the experimental $\%SF_w$ & Q data carefully interpolated in order to make direct comparisons between the data and modelled results at specific aspect ratios.

As the channels being modelled were symmetric, with an assumed constant local friction factor across the channel, it was only necessary to model one half of the cross section. In order to simplify the analysis further in these preliminary tests, only one panel was used to represent this half of the channel. This is known to be inaccurate, especially when modelling the boundary shear stresses, but is not an unreasonable approach when obtaining mean calibration parameters. These mean values may then be used later to undertake more detailed modelling, using 2, 4 and 'n' panels to represent the cross section.

The general approach was to assume values for 2 variables and then vary the other until the modelled values of discharge and $\%SF_W$ were comparable to those measured. The first variable that was calibrated was f, as this has been found to be the most influential. Next, the 'best' value of f was used in conjunction with an initial guess for Γ and λ was varied. Subsequently, the 'best' values of f and λ were used and Γ altered until the optimum solution was found. It should be noted that this order of calibration might not be applicable in all cases, as for example in meandering channels where Γ becomes more significant due to the enhanced secondary flows, as also may occur in overbank flow.

Even though only half the channel was modelled using 1 panel with a given set of f, λ and Γ variables, the panel was sub-divided further into 20 slices and the equations applied to each slice. The velocities from all slices were then laterally integrated to give the discharge for the whole channel.

Initial values of λ and Γ were assumed to be 0.02 and 0.05 respectively, and f values were then varied from 0.010 to 0.046 in increments of 0.002. In some cases the most suitable value for a parameter, f for example, will differ depending on which target variable is being compared, i.e. discharge, Q, or percentage shear force on the walls, $\%SF_w$. This is illustrated in

Copyright © 2006 Taylor & Francis Group plc, London, UK

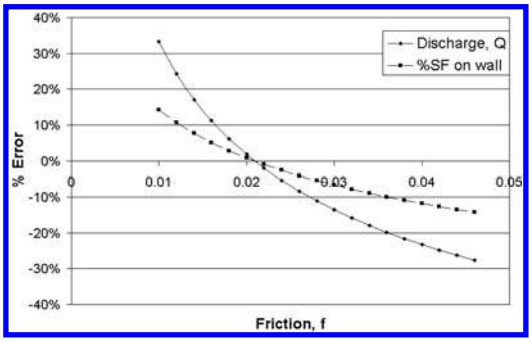


Figure 3. Errors in modelled Q and $\%SF_w$ associated with calibrating f (Experiment 2: h = 85.8 mm & Q = 4.80 l/s).

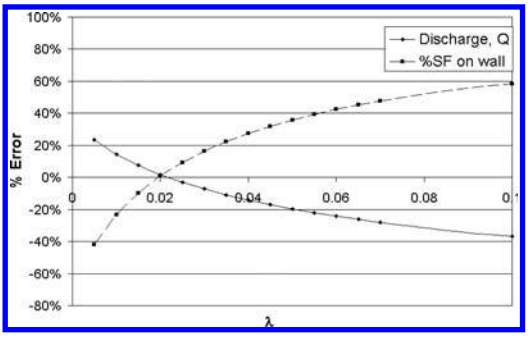


Figure 5. Errors in modelled Q and $\%SF_w$ associated with calibrating λ (Experiment 2: h = 85.8 mm, Q = 4.80 l/s).

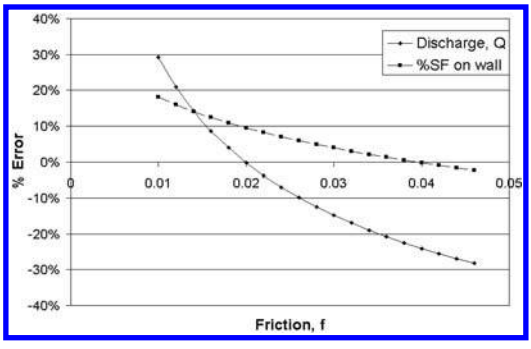


Figure 4. Errors in modelled Q and $\%SF_w$ associated with calibrating f (Experiment 7: h = 153.0 mm, Q = 9.85 l/s).

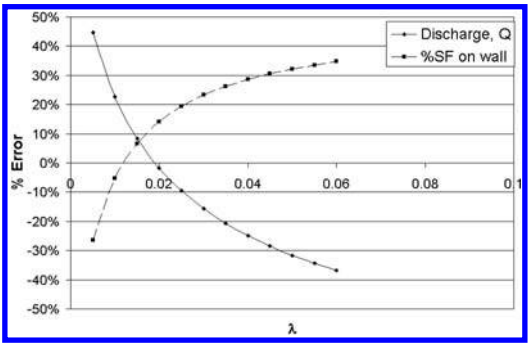


Figure 6. Errors in modelled Q and $\%SF_w$ associated with calibrating λ (Experiment 7: h = 153.0 mm, Q = 9.85 l/s).

Figures 3 & 4 for two particular tests. Experiment 2 had a low depth, with an aspect ratio, *Asp*, equal to 1.77, whereas Experiment 7 had a higher depth and an aspect ratio of 0.99. In Figure 3 it is seen that an f value of 0.021 gives the best result for both Q and $\%SF_w$, whereas in Figure 4 it is seen that the optimum f values are different for each variable ($f \approx 0.020$ for Q and ≈ 0.040 for $\%SF_w$). The errors follow the trends already indicated in Table 1.

Similar problems existed with the calibration of λ but since this parameter had a lower impact on the overall results it was less evident. In cases such as Experiment 7, a decision was made to calibrate λ using all possible values of f. Although this was perhaps tedious, it confirmed that the value of λ changed little. In such cases therefore, a judgement call was required and the combination of f and λ that gave the lowest and somewhat similar errors for discharge and shear force, was selected. In Figure 5 for example, the zero error point associated with discharge coincides with the zero error point for $\%SF_W$, at around $\lambda = 0.020$. However, the same cannot be said of Figure 6, where the zero error points for Q and $\%SF_w$ are again quite distinct, as already seen in Figure 4. In this case (Experiment 7), a λ value of 0.014 was taken as the optimum solution, i.e. in between the two zero error intersection points. This results in errors of approximately 8% in both cases.

A similar procedure was adopted for Γ. The optimum value was again chosen as being the mean value between two zero error intersection points, even though in some cases, the errors were quite large (i.e. ~10%).

Having obtained the optimum values for the 3 calibration parameters that give the best overall discharge and shear force results, the modelled lateral distributions of velocity and boundary shear stress were then compared with the measured ones. It was anticipated that the calculated distributions would not bear much resemblance to the measured ones, on account of using just a single panel in the modelling work, since it is known that then the perturbations that occur in the boundary shear stress due to secondary flow cells cannot be reproduced. An example of these perturbations is shown in Figure 7, taken from the rectangular duct flow experiments of Knight & Patel (1985). In order to model such perturbations accurately, the channel needs to be divided into several panels, each further sub-divided into slices, and the SKM applied to each panel. See Omran & Knight (2006) for further details.

Copyright © 2006 Taylor & Francis Group plc, London, UK

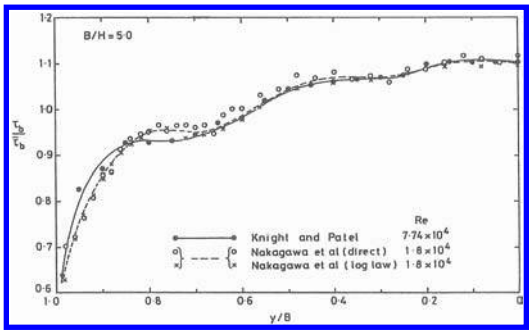


Figure 7. Lateral distributions of boundary shear stress in a rectangular duct (Knight & Patel, 1985).

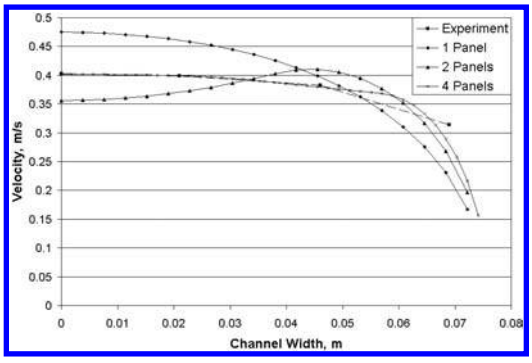


Figure 8. Comparison between modelled and actual lateral distribution of U_d (Experiment 2: h = 85.8 mm, Q = 4.80 l/s).

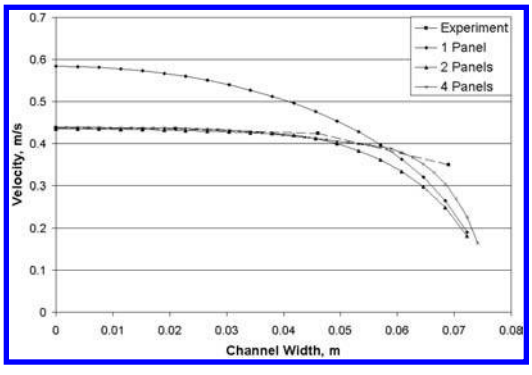


Figure 9. Comparison between modelled and actual lateral distribution of U_d (Experiment 7: h = 153.0 mm, Q = 9.85 l/s).

Two examples of the modelled distributions of depth-averaged velocity, U_d, using just one panel, are shown in Figures 8 & 9. The modelled and actual distributions clearly differ although the general shape of the curves are similar. The model fails to accurately predict the velocity distributions, which then has a knock-on effect on the prediction of the corresponding boundary

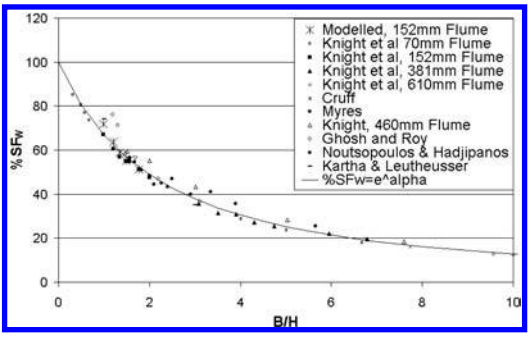


Figure 10. Comparison of modelled results (2b = 152 mm set) with Knight et al's original (1982) equation for $\%SF_W$ (Eq. 23).

shear stress distributions. Despite these obvious shortcomings, these preliminary results compare quite well with the mean shear force results obtained by Knight *et al* (1982), as shown in Figure 10. Also shown in Figure 10 is the original exponential form of equation for $\%SF_w$ v *Asp*, as given by Equations (22) & (23):

$$\%SF_W = e^{\alpha} \tag{22}$$

where, for open channel flow

$$\alpha = -3.230 \log_{10}\left(\frac{2b}{H} + 3\right) + 6.146 \tag{23}$$

In Figures 8 & 9 the one panel solution is shown alongside the 2 and 4 panel solutions. The 2 and 4 panel solutions have a constant λ of 0.07 but the values of f and Γ have been varied between panels. It can clearly be seen though that by increasing the number of panels the user gains more control over the model as each section of the channel can be modelled somewhat independently.

It should be noted that the modelled data in Figure 10 are only those for the 152 mm flume experiments. Although this preliminary analysis serves to show the good agreement between the modelled $\%SF_w$ and experimental results for $1.0 < Asp < 2.0$, data from all 4 rectangular flumes are shown next.

4.3 *Optimisation of parameters using all data*

Having established an understanding of the influence of each calibration parameter, and a procedure for calibration using data from one flume, the data sets from all 4 flumes were then used together. The aim was to obtain an optimized set of calibration coefficients for flow in rectangular open channels for as wide a range of aspect ratios as possible, albeit still modelling them with a single panel.

In order to standardise the modelling results, it was decided to set a maximum allowable error for every

Copyright © 2006 Taylor & Francis Group plc, London, UK

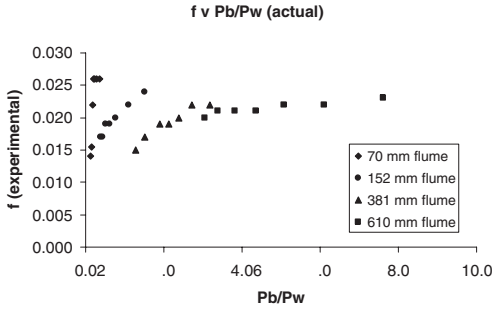


Figure 11. Best-fit f values used in modelling all data from the 4 flumes.

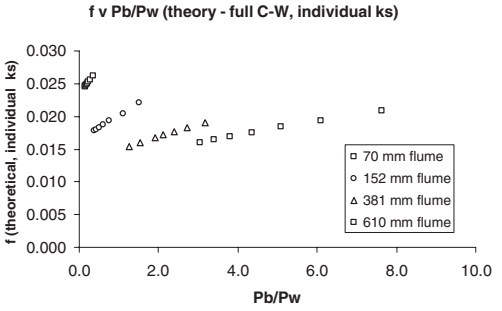


Figure 12. Theoretical f values based on Eq. (25), assuming a rough channel (single optimised k_s value for each flume).

experiment of ±5% for both the discharge, Q, and the percentage of the total shear force acting on the walls, $\%SF_w$. Furthermore, in order to make direct comparisons between different data sets and modelled results at specific aspect ratios, 7 pre-selected depths were chosen for each flume and the experimental $\%SF_w$ & Q data carefully interpolated from the series data for that particular flume. This had the added advantage of smoothing what was already good experimental data, with known errors, into 56 reliable paired $\%SF_w$ & Q target values. For each of these 28 target simulations, each of the f, λ and Γ parameter was varied 10 times over a small optimised bandwidth, making a total of 840 numerical experiments. Conclusions were then made about the choice of parameters.

As an example, the optimized f values are shown in Figure 11, using the wetted perimeter ratio, P_b/P_w as a surrogate for the aspect ratio, Asp ($=2b/H = 2P_b/P_w$), since trapezoidal channel data may then be easily added. It may be seen that each flume, covering a specific range of aspect ratios, produced a discrete curve.

Using the Colebrook-White equation, it is possible to account for the pattern of best-fit f values shown in Figure 11 in the following manner. Since for a rectangular channel $R = A/P = 2bh/(2b + 2h)$ it follows that $R = h/(1 + 2/Asp)$, where Asp = aspect ratio (total width/depth). Inserting these into the standard Colebrook-White equation

$$\frac{1}{\sqrt{f}} = -2.0\log\left[\frac{k_s}{3.71d} + \frac{2.51}{(ud/\nu)\sqrt{f}}\right] \quad (24)$$

and replacing d = pipe diameter by 4R, gives

$$\frac{1}{\sqrt{f}} = -2.0\log\left[\frac{k_s}{14.84\{1+2/Asp\}} + \frac{2.51\nu}{4\sqrt{8gS_f}\{h/(1+2/Asp)\}^{3/2}}\right] \quad (25)$$

where $Asp = 2b/h$ for a rectangular channel of semi-breadth b. Equation (25) thus indicates that the f value

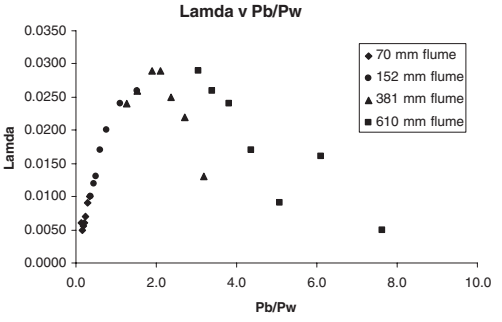


Figure 13. Best-fit λ values used in modelling all data from the 4 flumes.

depends solely on the k_s and Asp values. Equation (25) is illustrated in Figure 12 for a rough channel with the k_s values selected to fit the entire data set from each individual flume. The similarity between the predicted and observed data in Figures 11 & 12 respectively is good. Thus Equation (25) affords a theoretical basis for estimating the friction factors in rectangular channels for all aspect ratios, Asp, once k_s is either specified or known.

A similar procedure was adopted for both the λ and Γ parameters and the optimised results plotted out to observe any underlying trend or relationship. The best-fit results are shown in Figures 13 & 14 respectively. The best–fit equations through the data from all 4 flumes were:

$$\lambda = 6.25x10^{-5}Asp^3 - 0.001625Asp^2 + 0.01145Asp + 0.0032 \quad (26)$$

$$\Gamma = -0.0002Asp^2 + 0.00105Asp + 0.0464 \quad (27)$$

Equations (25)–(26) thus provide the basis for the selection of the 3 calibration parameters, f, λ and Γ for flow in rectangular open channels.

Copyright © 2006 Taylor & Francis Group plc, London, UK

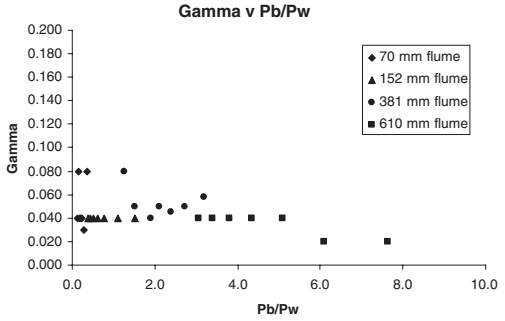


Figure 14. Best-fit Γ values used in modelling all data from the 4 flumes.

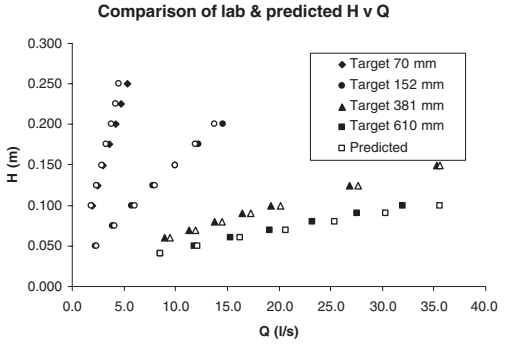


Figure 15. Comparison of laboratory and predicted H v Q values for all flumes.

5 APPLICATION OF MODELLING TOOL

5.1 *Prediction of stage-discharge relationships*

As a check on the optimised calibration coefficients, which were based on interpolated data, Equations (25)–(27) were applied to all the actual flume data. This also illustrates how an engineer might use this novel approach in practice. Figure 15 shows a comparison between the modelled and experimental stage-discharge relationships for the 4 flumes. The agreement is good, despite using a single k_s value for each flume ($k_s = 0.1$, 0.0001, 0.001 & 0.001 mm for the 70, 152, 381 & 610 mm flumes respectively). The predicted curves come from applying the Darcy-Weisbach equations with Eq. (25) supplying the f value, based on the relevant Asp and mean k_s value for each flume. It is apparent that the predicted stage-discharge relationships, using the SKM are in reasonably close agreement with theexperimental ones, indicating that the method is valid over a wide range of aspect ratios ($0.3 < Asp < 20$), as 4 different data sets were used from 4 separate flumes.

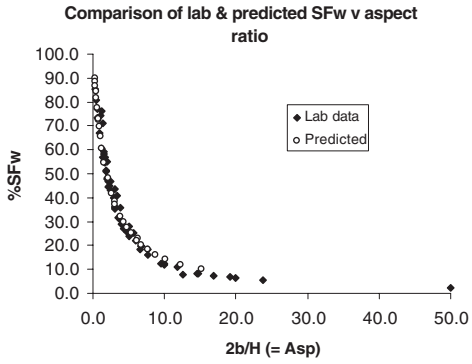


Figure 16. Comparison of modelled results (all data) with Knight et al's (1994) equation for $\%SF_W$ (Eqs. 28–30).

5.2 *Prediction of stage-sidewall shear force relationship*

The sidewall correction procedure outlined in the preceding sections was then tested by applying it to all 4 flumes, using Equations (25)–27) to supply values of the calibration coefficients required in the SKM. Figure 16 shows that the predicted values for the percentage of the total shear force acting on the walls, $\%SF_w$, are in good agreement with the actual experimental data. They are also in agreement with the more general equations for flow in rectangular and trapezoidal channels, provided Knight et al. (1994) for subcritical flow, in the form:

$$\%SF_W = C_{sf} e^{\alpha} \tag{28}$$

$$\alpha = -3.230 \log_{10}\left(\frac{P_b}{P_w C_2} + 1.0\right) + 4.6052 \tag{29}$$

where $C_2 = 1.50$, and $C_{sf} = 1.0$ for $P_b/P_w < 6.546$

$$C_{sf} = 0.5857(P_b/P_w)^{0.28471} \tag{30}$$

It may be noticed in Figure 16 that there is a slight divergence at high aspect ratios ($Asp > 20$), and this is under investigation, using a wider set of data as given in Knight et al. (1994). Figure 17 shows these data, drawn from many open channel flow and duct experiments.

5.3 *Prediction of mean bed shear stress*

Having established the $\%SF_w$ v Asp relationship, it is possible to obtain the mean wall and bed shear stresses via Eqs (20) & (21). The mean bed shear stress may be expressed as

$$\frac{\bar{\tau}_b}{\rho g H S_o} = \left[1 - \frac{\%SF_w}{100}\right] \tag{31}$$

Copyright © 2006 Taylor & Francis Group plc, London, UK

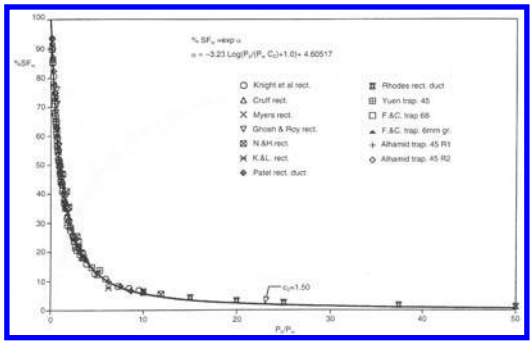


Figure 17. Comparison of channel and duct $\%SF_w$ values in rectangular and trapezoidal channels (Knight et al, 1994).

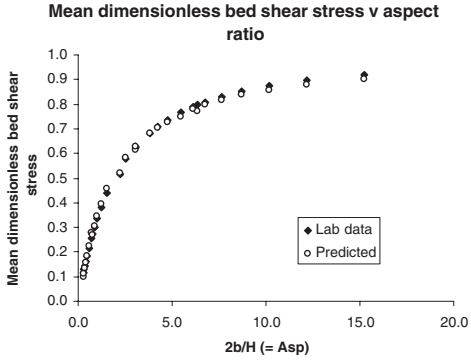


Figure 18. Predicted mean bed shear stress for rectangular channels.

The predicted relationship is shown in Figure 18, together with the experimental data. The agreement is inevitably good on account of the good agreement already shown in Figure 16. Eq. (31) may then be used to estimate how wide a channel will need to be before two-dimensional flow can be assumed. As can be seen, the mean bed shear stress is significantly different from its 2-D value even at large aspect ratios (e.g. $0.95 < \overline{\tau}_b / \rho g H S_o < 1.0$ only when $Asp > 25$.

5.4 *Extension of method to deal with heterogeneous roughness*

The application of this method to channels where there is differential roughness between the bed and the walls, as often occurs in practice in culverts or in flume studies, is not presented herein. However, it should be possible to adjust the λ coefficients and to link them to values of relative roughness, k_{sb}/k_{sw}, where the subscripts *b* & *w* stand for the bed and walls respectively. Some experimental data exist for these conditions, as described by Knight & Alhamid (1992) and shown in www.flowdata.bham.ac.uk.

6 DISCUSSION OF RESULTS

It has been shown elsewhere (e.g. Knight & Shiono (1996) and Abril & Knight (2004)) that the SKM is capable of modelling channels of various cross-sections both accurately and with a minimum of computational effort. This paper has now shown that the SKM is capable of being applied to rectangular channels to give the mean shear force acting on either the bed or the walls. A range of flume data has validated the results over a wide range of aspect ratios ($0.3 < Asp < 20$). Guidance has been given via Eqs (25–27) to the selection of the three calibration coefficients f, λ and Γ. The significance of the calibration values for the 3 parameters lies not so much in the equations, which are based on a preliminary analysis, but in their numerical values.

With regard to the friction factor, f, it is clear from Eq. (25) that the geometric properties of each channel are implicit in the aspect ratio, and therefore the calibrated results show what one might expect, that as Asp increases, f will increase for shallower depths if it is assumed that k_s remains constant for a given surface material. The average k_s values used for each flume were in fact in reasonable accord with experimentally back-calculated values. The 152 mm flume was the first to be tested and built to a high specification, thus having the lowest k_s value. The narrowest flume (70 mm) had the highest k_s value due to the difficulty in assembly. The accuracy obtained for mean values (i.e. <5% error in both Q and SF_w) were not difficult to obtain, and could be improved by simply choosing individual k_s values for each experiment.

The lamda values indicate the lateral shear from the sidewalls and it is instructive to observe that they increase from a low value to a peak at around $Asp = 4$. The discharges are more sensitive to λ than $\%SF_w$ as the velocity distributions show in Figure 2. Since the gradient of velocity is only large near the wall, the influence of λ diminishes as the channel widens. This is also true for large river channels with overbank flow, where the intense shear zone is confined to a relatively small region. However the range of λ values is large, albeit the absolute values used herein are relatively low (typically $\lambda = 0.07$–0.13).

The Γ values are clearly not very significant as using a single panel is not necessarily the best approach, and only used herein as a preliminary modelling experiment. Rectangular channels are actually more difficult to model with a depth-averaged model, by virtue of the fact that in the corner region there are generally two cells present on top of each other, and depth averaging as envisaged in Figure 1 breaks down. Figure 1(b) only shows a single cell operating over the entire depth, as is often conceptualised for wide systems where the cell size scales with the depth and a

Copyright © 2006 Taylor & Francis Group plc, London, UK

pair of contra-rotating cells have a spacing of twice the depth.

Although there are clearly more issues requiring investigation, the modelling approach outlined in this paper does offer an alternative method to obtaining reasonably accurate estimates of mean wall or bed shear, commensurate with the accurate values for the overall discharge. Since many methods give one and not the other, this is offered as a first step in a novel line of attack. The accuracy of the lateral distributions of velocity and boundary shear stress could easily be improved by the incorporation of more panels within the channel.

7 CONCLUSIONS

The SKM has been shown to be applicable to simulating the main physical features of flow in rectangular channels, giving the lateral distributions of both depth-averaged velocity and boundary shear stress.

The method provides a way of determining the proportion of the total shear force that acts on the sidewalls, thus enabling the mean bed shear stress to be determined with the minimum of computational effort. Equations have been given for the general trend in the three calibration coefficients, f, λ and Γ.

Further work is required to elucidate the equations and to undertake more detailed modelling using multi-panels with heterogeneous roughness.

ACKNOWLEDGMENTS

The first author would like to thank the Engineering and Physical Sciences Research Council (EPSRC) for their financial support towards her research studentship at the University of Birmingham.

REFERENCES

Abril, J.B. and Knight, D.W., 2004, Stage-discharge prediction for rivers in flood applying a depth-averaged model, *Journal of Hydraulic Research*, IAHR, 42, No. 6, 616–629.

Brownlie, W.R. 1981, Re-examination of Nikuradse roughness data, *Journal of the Hydraulics Division*, ASCE, Vol. 107, HY1, Jan., 115–119.

Chang, H.H., 1988, Fluvial processes in river engineering, J. Wiley & Sons.

Chiu, C.L. and Chiou, J.D., 1986, Structure of 3-D flow in rectangular open channels, *Journal of Hydraulic Engineering*, ASCE, Vol. 112, No. 11, Nov., 1050–1068.

Guo, J. and Julien, P.Y., 2005, Shear stress in smooth rectangular open-channel flows, *Journal of Hydraulic Engineering*, ASCE, Vol.131, No.1, January, 30–37.

Kazemipour, A.K. and Apelt, C.J., 1979, Shape effects on resistance to uniform flow in open channels, *Journal of Hydraulic Research*, IAHR, Vol. 17, No. 2, 129–147.

Knight, D.W. et al, 1982, Boundary shear stress distribution in open channel and closed conduit flows, *Euromech 156*, Mechanics of Sediment Transport, Istanbul, 33–40.

Knight, D.W., Demetriou, J.D. and Hamed, M.E., 1984, Boundary shear in smooth rectangular channels, *Journal of Hydraulic Engineering,* ASCE, Vol. 110, No. 4, April, 405–422.

Knight, D.W. and Patel, H.S., 1985a, Boundary shear in smooth rectangular ducts, *Journal of Hydraulic Engineering*, ASCE, Vol.111, No.1, Paper 19408, 29–47.

Knight, D.W. and Patel, H.S., 1985b, Boundary shear stress distributions in rectangular duct flow, *Proc. 2nd Int. Symposium on Refined Flow Modelling and Turbulence Measurements*, Iowa, USA, Sept., Hemisphere Publishing Co., I22-1 to I22-10.

Knight, D.W., Yuen, K.W.H. and Alhamid, A.A.I., 1994, Boundary shear stress distributions in open channel flow, in *Physical Mechanisms of Mixing and Transport in the Environment,* (Eds K. Beven, P. Chatwin & J. Millbank), J. Wiley, Chapter 4, 51–87.

Knight, D.W. and Shiono, K., 1996, River channel and floodplain hydraulics, in *Floodplain Processes*, (Eds Anderson, Walling & Bates), Chapter 5, J Wiley, 139–181.

Knight, D.W., Omran, M. & Abril, J.B., 2004, Boundary conditions between panels in depth-averaged flow models revisited, *River Flow 2004, Proc. 2nd Int. Conf. on Fluvial Hydraulics, 23-25 June, Napoli, Italy* [Eds M. Greco, A. Carravetta & R.D. Morte], Vol. 1, 371–380.

Nezu, I. and Nakagawa, H., 1993, Turbulence in open-channel flow, IAHR Monograph, Balkema.

Omran, M. & Knight, D.W., 2006, Modelling the distribution of boundary shear stress in open channel flows, *RiverFlow 2006*, Lisbon, Portugal (in print).

Rhodes, D.G. and Knight, D.W., 1994, Distribution of shear force on boundary of smooth rectangular ducts, *Journal of Hydraulic Engineering*, ASCE, Vol.120, No.7, 787–807.

Shiono, K. and Knight, D.W., 1988, Two-dimensional analytical solution for a compound channel, *Proc. 3rd Int. Symposium on Refined Flow Modelling and Turbulence Measurements,* Tokyo, Japan, July, 503–510.

Shiono, K. and Knight, D.W., 1991, Turbulent open channel flows with variable depth across the channel, *Journal of Fluid Mechanics*, Vol. 222, 617–646 (and Vol. 231, October, p 693).

Vanoni, V.A. and Brooks, N.H., 1957, Laboratory studies of the roughness and suspended load of alluvial streams, *Sedimentation Laboratory Report No. E68*, California Institute of Technology, Pasadena, USA.

Yang, S.Q. and Lim, S.Y., 1997, Mechanism of energy transportation and turbulent flow in a 3D channel, *Journal of Hydraulic Engineering*, ASCE, Vol. 123, No. 8, August, 684–692.

Yen, B.C., 1991, Channel flow resistance: centennial of Manning's formula, Water Resources Publications, Colorado, USA.

Copyright © 2006 Taylor & Francis Group plc, London, UK

Open-channel side-cavities: A comparison of field and flume experiments

J. Le Coz[1], W. Brevis[2], Y. Niño[2], A. Paquier[1] & N. Rivière[3]
[1]*Cemagref, Unité de Recherche Hydrologie-Hydraulique, 3 bis quai Chauveau, CP 220 F-69336, Lyon Cedex 09, FRANCE*
[2]*Universidad de Chile, Departamento de Ingeniería Civil, Av. Blanco Encalada 2002 3er Piso, Santiago, CHILE*
[3]*LMFA (CNRS UMR 5509), INSA Lyon, Bât. Jacquard, 20 av. Einstein, 69621 Villeurbanne Cedex, FRANCE*

ABSTRACT: Side-cavities are common along natural and channelized rivers. In this paper, results of flume experiments in a rectangular side-cavity (length to width ratio L/W = 2) are compared with field observations of a similar, though topographically more complex, dead zone. The main flow in the flume was kept steady, sub-critical (Fr = 0.36) and turbulent ($Re = 3.9 \times 10^4$). Field measurements were performed during small floods with contrasted discharges. In the river main flow, the Froude number was about 0.5 and the Reynolds number about 2×10^6. In the laboratory, flow structure was investigated at three different depth levels within the side-cavity, by means of PTV (Particle Tracking Velocimetry). In situ, flow dynamics features were explored by acoustic Doppler current profiler (aDcp) and video analysis (LS-PIV). Both experimental and field cases show similar mean flow patterns. Flume experiments offer a detailed view of a two-gyre system: a primary gyre takes up three quarters of the cavity area while a secondary contra-rotating gyre occupies the upstream inner corner of the side-cavity. In the field case, the primary gyre also develops, in close connection with morphological patterns. The secondary gyre, atrophied and non-persistent, is replaced by non-eroded materials that fill in the upper corner of the cavity.

1 SIDE-CAVITIES ALONG RIVERS

Side-cavities or embayments are common along natural and channelized rivers. The physical knowledge of the flow structure developing in these so-called dead zones is important from an environmental point of view. It can also help engineers design hydraulic structures such as groin fields and spur dykes.

Very few detailed field investigations of open-channel flow in side-cavities have been reported (cf. e.g. Sukhodolov et al. (2002), Sukhodolov et al. (2004)). Various flume studies (Kimura and Hosoda 1997; Uijttewaal et al. 2001; Muto et al. 2000b; Langendoen et al. 1994; Nezu and Onitsuka 2002) have stressed the determination of flow patterns by the length to width ratio L/W of the side-cavity: a stable one-gyre system for $L/W \approx 1$, an unstable two-gyre system else. Mass exchange appears to be mainly caused by intermittent inflows driven by shear instabilities at the interface (Kimura and Hosoda 1997; Uijttewaal et al. 2001; Muto et al. 2000b).

In this paper, results of flume experiments in a rectangular side-cavity (L/W = 2) are compared with field observations of a similar, though topographically more complex, dead zone. The natural side-cavity corresponds to the junction between a river and the downstream part of a cut-off meander.

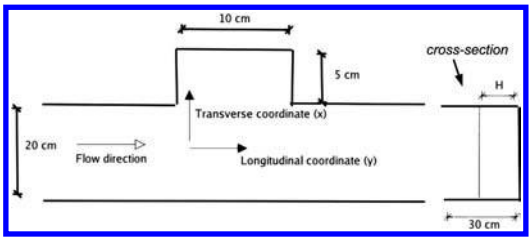


Figure 1. Experimental set-up schematic representation.

2 FLOW PATTERNS IN AN EXPERIMENTAL SIDE-CAVITY

2.1 *Experimental set-up*

Experiments were conducted at the University of Chile, in a 1,200 cm long, 20 cm wide, 30 cm deep flume with a longitudinal slope of 0.001. The side-cavity was located 300 cm upstream from the end of the flume. A schematic representation of the experimental set-up can be seen in Fig. 1. Hydraulic conditions for the experiments, depth (H), flow (Q), mean velocity (U), hydraulic radius (R_h), Reynolds number ($Re = UH/\nu$), and Froude number ($Fr = U/\sqrt{gH}$) are summarized in Table 1.

Copyright © 2006 Taylor & Francis Group plc, London, UK

Table 1. Experimental hydraulic conditions.

H [cm]	Q [cm^3/s]	U [cm/s]	R_h [cm]	Re	Fr
10.7	7,800	36.4	5.17	3.9×10^4	0.36

The cavity was 10 cm long (L) and 5 cm wide (W) and consequently the aspect ratio was L/W = 2. This configuration was chosen because it is more similar to dead zones in rivers than deep cavities. For instance, it shows some aspects of the flow between river groins, which is interesting from a river engineering point of view (Weitbrecht et al. 2002; Uijttewaal et al. 2001). This kind of cavities (aspect ratio 2) presents a higher mass exchange than cavities with aspect ratios close to 1. The exchange process is dominated by several instabilities in comparison with deep cavities where mass exchange is governed by the main gyre (Shankar and Deshpande 2000).

The implemented PTV-System was composed by a 400 MW two-colour laser beam and by a 30 Hz digital camera. Acrylic particles were used. PTV was employed due to the sensitivity of the cavity flow structure to external perturbations. This phenomenon was observed by Nezu et al. (2005) in a rectangular cavity with the same aspect ratio of 2. This made the use of an acoustic Doppler velocimeter (aDv) inside the cavity unsuitable, so this sensor was employed only for measurements in the channel and at the interface between the main flow and the cavity.

2.2 *Particle Tracking Velocimetry (PTV)*

This method was implemented in Matlab for flow structure determination. The main characteristics of PTV is that information can be obtained from each particle in the flow, which constitutes a clear difference with Particle Image Velocimetry (PIV) where information is averaged over a group of particles. PTV provides velocity samples along particle trajectories, i.e. in a Lagrangian frame of reference. Thus it differs from PIV by the fact velocity is measured at random locations instead of over a regular grid (Cenedese and Querzoli 1997). Flow field determination was obtained by application of a dynamic, binary, spatial cross-correlation analysis between two sequential images, according to an algorithm proposed by Hassan et al. (1992). From the random distribution of samples the velocity field over a regular grid can be obtained by interpolation. Following the results obtained by David et al. (2002), the *Inverse Distance Weighting Method* with a Gaussian adaptive window was used for velocity interpolation. As a conclusion the authors point out that this method gives reliable results for strong velocity gradients. The implemented algorithm was tested on synthetic data obtained by a computational implementation of inviscid flow around a cylinder (Hassan et al. 1992) using standard images provided by the Visualization Society of Japan. Spurious vectors (less than 10%) were eliminated thanks to correlation and direction-magnitude filters.

Musalem (1999) from dimensional analysis and Valdes (1995) from error propagation in the PTV method concluded that errors in velocity and vorticity measurements are about 15% and 20% respectively. To reduce errors the threshold level for light intensity in video images must be chosen carefully and particle density must be high. The three measurements reported here were performed for the same hydraulic conditions by recording 1,000 pairs of frames for planes at 20, 60 and 100 mm over channel bottom.

2.3 *Flow structure*

2.3.1 *Velocity field*

Velocity fields averaged over each image time-series are presented in Figs 2, 3 and 4, for three different cavity depth levels. The origin of coordinates is the upstream cavity corner. As in previous results obtained by Weitbrecht and Jirka (2001) and Uijttewaal et al. (2001) for river groins and Muto et al. (2000a) for river embayment, it is possible to identify a two-gyre system. The main gyre (anticlockwise rotation), which occupies three fourths of the cavity area, is driven by the main channel flow and the secondary gyre (clockwise rotation) is driven by the primary gyre. The primary gyre core (velocity nearly zero) does not change its position at the three levels and it is also possible to recognize a high velocity zone at the interface between both gyres. The low velocity region is maximum at elevation 20 mm. In general, velocity magnitude does not suffer important changes with depth and the maximum magnitude is at most 6 times lower than the main channel mean velocity. From vector fields, the main inflow zone in the cavity can be identified and is located at the downstream corner for all three elevations.

2.3.2 *Vorticity*

Vorticity fields are shown in Figs 5, 6, and 7. A comparison between the three levels suggests that the main change in vorticity occurs in the low velocity region (upstream zone). A displacement of the maximum vorticity area towards the interface is observed as the bottom of the cavity is approached. Besides, there is a zone of high vorticity produced by shear between the cavity and the main channel flow, and another one between the primary gyre and the wall. This is mainly due to the high velocity gradient produced by the high velocity zone, described above.

2.3.3 *Streamlines*

The streamlines (Figs 8, 9, 10) show that there is an evolution of the secondary gyre with depth. The secondary gyre even disappears at elevation 20 mm.

Copyright © 2006 Taylor & Francis Group plc, London, UK

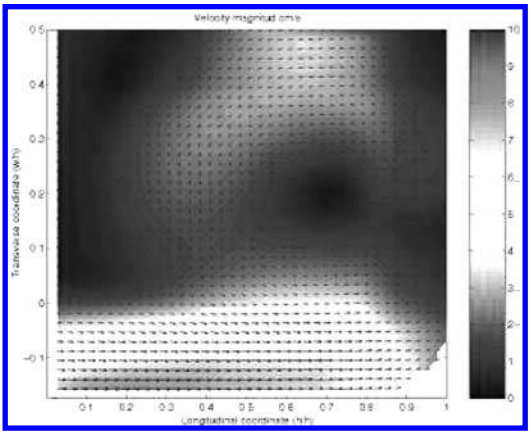


Figure 2. Time-averaged velocity field (100 mm).

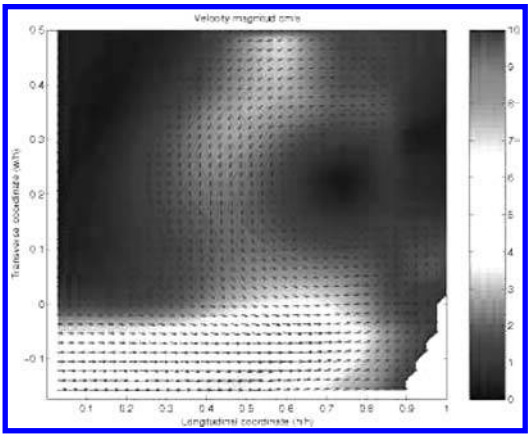


Figure 3. Time-averaged velocity field (60 mm).

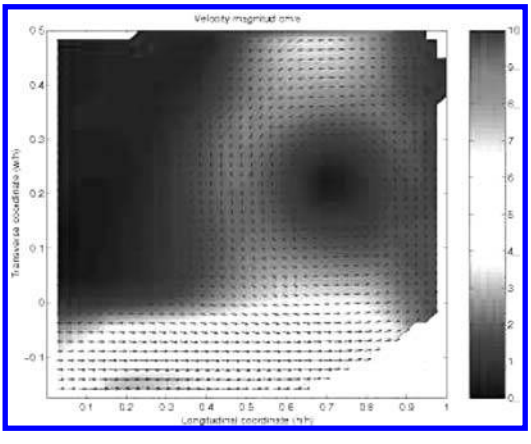


Figure 4. Time-averaged velocity field (20 mm).

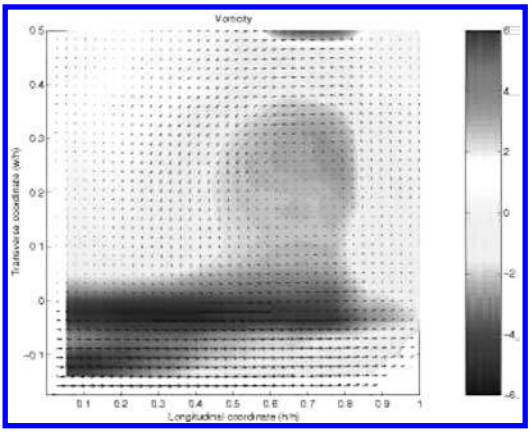


Figure 5. Time-averaged velocity contours (100 mm).

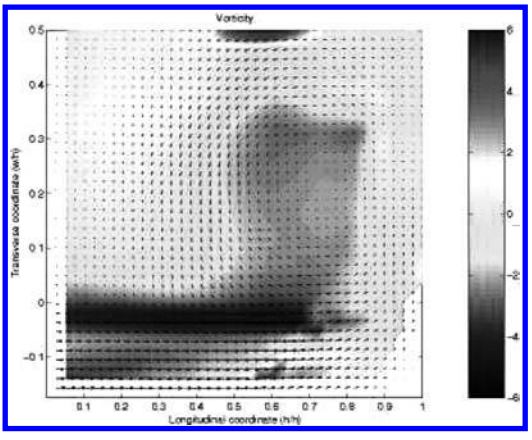


Figure 6. Time-averaged velocity contours (60 mm).

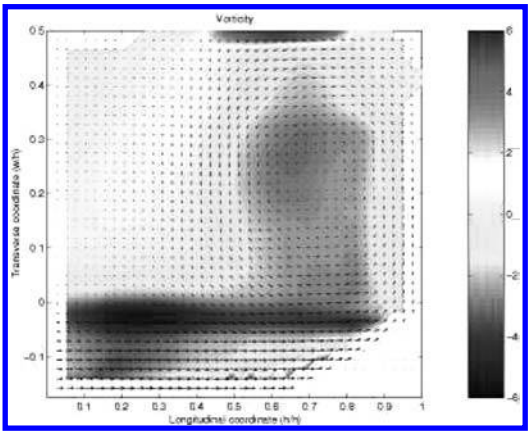


Figure 7. Time-averaged velocity contours (20 mm).

Copyright © 2006 Taylor & Francis Group plc, London, UK

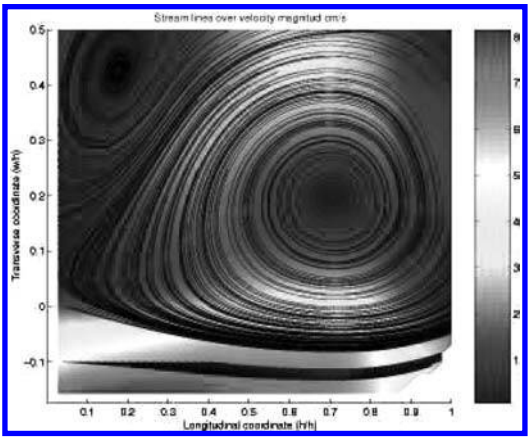


Figure 8. Streamlines over mean velocity (100 mm).

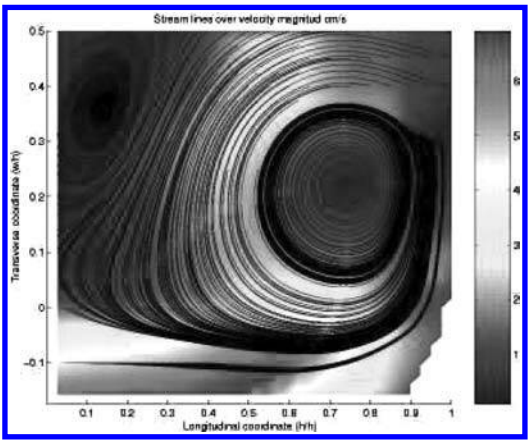


Figure 9. Streamlines over mean velocity (60 mm).

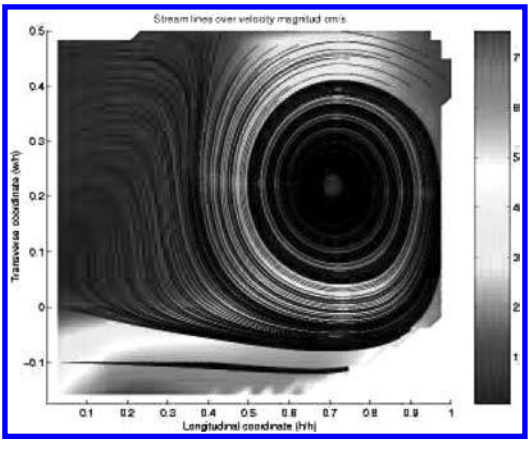


Figure 10. Streamlines over mean velocity (20 mm).

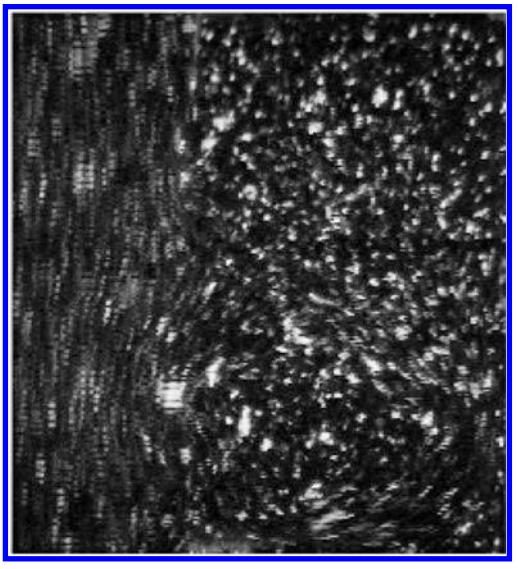


Figure 11. Instantaneous particle position at 100 mm (t = 0 s).

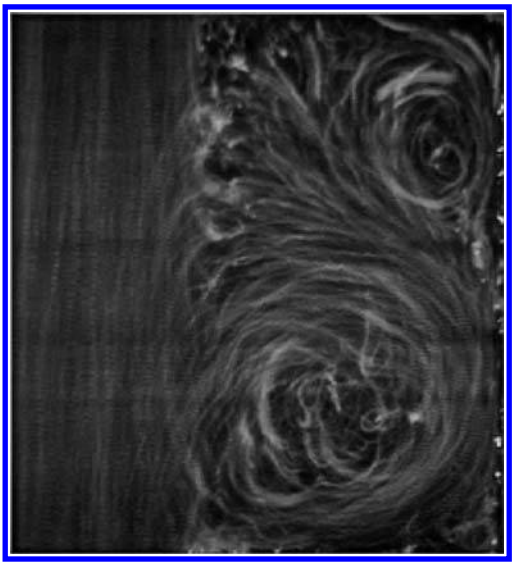


Figure 12. Streaklines at 100 mm (t = 0.33 s).

The primary gyre slightly changes its size with depth and allows structure changes in the low velocity region. It can be noticed that one part of the main gyre is located outside the cavity.

2.3.4 *Streaklines*

Figs 11, 12, 13 show a long time exposure sequence of video images that was obtained by superposition of frames taken from PTV measurements at the same

Copyright © 2006 Taylor & Francis Group plc, London, UK

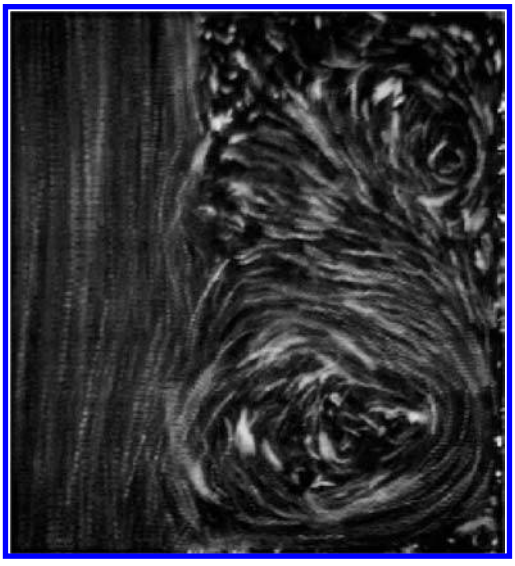


Figure 13. Streaklines at 100 mm (t = 1.33 s).

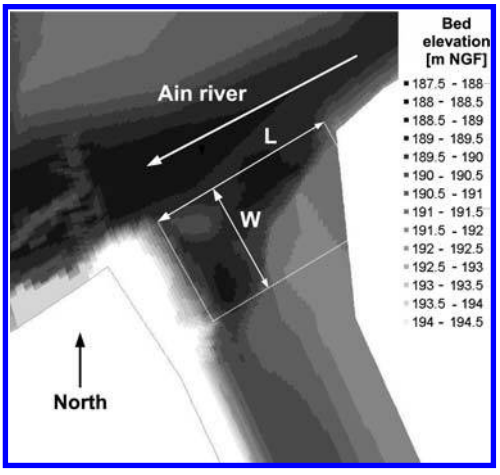


Figure 14. Topographic view of the natural side-cavity.



Figure 15. Low-water view of the natural side-cavity *Recirculating flow from the Ain river (A); central gravel-bar (B); end of the rip-rap embankment (C); dead tree transported by the last flood (D); sand deposit (E); non-eroded right-bank materials (F); bank erosion (G); trees growing on the abandoned point-bar (H).*

cavity depth level, near the free surface. These pictures show that results obtained by PTV are in agreement with the movement of seeded particles in the cavity. The primary gyre and the secondary gyre as well as the internal shear region between both gyres can be clearly observed.

From image analysis it was possible to detect a displacement of both gyres over time. An important effect of this is the perturbation of the shear layer by the main gyre and a consequent increase of the shear layer instability. This process affects the size of billows allowing a more intense mass exchange from channel to cavity. In Fig. 12 some particles are leaving the cavity in the middle part of the cavity-channel interface, in the outflow region.

Another important observation is the direction of particles coming from the interface between gyres: one part of the particles goes to the secondary gyre, one part to the region close to the upstream corner and the rest remains inside the main gyre or leaves the cavity.

3 FLOW PATTERNS IN A NATURAL SIDE-CAVITY

3.1 *Real case geometry*

The field study area is located at the junction of the Ain river, South Eastern France, and one of its former channels. The "Port-Galand" abandoned channel was a slightly sinuous meander that was artificially cut off in 1964 to protect a bridge. In the vicinity of the abandoned channel's mouth, the river reach between two natural sills is quite straight, with one riffle upstream and the other just downstream the study area. The local gradient is estimated to be 0.4% and the median grain size to $d_{50} = 0.021$ m with low dispersion: $S = \sqrt{\frac{d_{84}}{d_{16}}} = 1.7$ (Rollet 2002).

The left bank of the abandoned channel is made of a rip-rap embankment, while the right bank is made of erodible though vegetalized alluvial deposits. The junction angle is close to 90° (Fig. 14), so that the flow area of interest can be likened to a roughly rectangular side-cavity of length $L \approx 55$ m and width $W \approx 30$ m (aspect ratio $L/W \approx 1.8$, close to that of the flume case).

Copyright © 2006 Taylor & Francis Group plc, London, UK

The particular shape of this natural side-cavity (Fig. 15) stems from:

- the primary morphology of the former river channel;
- the left-side straight unerodible embankment (with a small apex visible on Fig. 14);
- the erosion of the right bank like an upstream pointing triangle;
- the remaining part of the right bank materials, occupying the upper outer corner of the equivalent rectangle.

Furthermore the bottom of the cavity is not flat, mainly because of a central gravel-bar deposit. In spite of a sand deposit partly closing its outer side, the cavity is directly connected to a series of elongated oxbow-lakes, where waters are quite still and suspended sediments can settle down.

3.2 *Flow conditions*

In early 2005, four campaigns of in situ hydrodynamical measurements were carried out: acoustic Doppler current profiler (aDcp) and Large-Scale PIV (LS-PIV) data were acquired and post-processed. The observed velocity fields in the natural side-cavity were compared with 2Dh hydrodynamical modelling outputs (*Cemagref* RUBAR20 code). Further details can be found in Le Coz et al. (2006).

River discharge estimates were provided by the local gauging station by courtesy of the Compagnie Nationale du Rhône (CNR). The pressure gauge is located at the very end of the rip-rap embankment.

As no measurement was performed in the river main flow itself, a 1D hydrodynamic model (*Cemagref* MAGE6 code) was calibrated and used to estimate hydraulic parameters for the four campaigns (cf. Table 2). Upstream boundary condition consisted of discharge time series from the "Pont-de-Chazey" gauging station (DIREN Rhône-Alpes) located 15 km upstream the study site. The experimental rating curve of "Port-Galand" gauging station (CNR) was used as a downstream boundary condition. The model was calibrated against water level series from two *Cemagref* pressure gauges located between "Pont-de-Chazey" and "Port-Galand" gauging stations.

From these simulated results (cf. Table 2), it can be confirmed that close to the study area, the river flow was sub-critical ($Fr \approx 0.5$) and highly turbulent ($Re \approx 2 \times 10^6$).

The reliability of these estimates was checked by analysing an aDcp transect acquired by the CNR on 1998, September 14th, about 100 metres upstream from the study site. Hydraulic condition parameters were: $Q = 290\,m^3/s$, $U = 1.32\,m/s$, $R_h = 1.49\,m$, $Fr = 0.34$ and $Re = 1.97 \times 10^6$. These estimates from experimental aDcp data have the same order of magnitude as 1D-modelling outputs (Table 2). Discrepancies may be explained by differences between the aDcp transect section in 1998 and the interpolated computational geometry from a 2004 topographic survey.

Table 2. Hydraulic conditions during measurement campaigns from 1D simulation (Q river discharge, U mean velocity, R_h: hydraulic radius, Fr: Froude number, Re: Reynolds number).

Campaigns dates	aDcp1 050304	LS-PIV1 050214	LS-PIV2 050408	aDcp2 050425
$Q\ [m^3/s]$	200	325	365	650
$U\ [m/s]$	1.42	1.60	1.63	1.79
$R_h\ [m]$	1.06	1.06	1.11	1.68
Fr	0.44	0.50	0.49	0.44
$Re\ (\times 10^6)$	1.51	1.69	1.81	3.00

As reported in Le Coz et al. (2006), river discharge time series recorded during each measurement campaign show various trends. In particular, the aDcp1 campaign was performed during fairly steady conditions (mean discharge $Q = 200\,m^3/s$, $+0.5\%$ of Q per hour), whereas the aDcp2 campaign was performed during the end of the rising limb of a $700\,m^3/s$ flood (mean discharge $Q = 650\,m^3/s$, $+3.5\%$ of Q per hour).

3.3 *Horizontal flow patterns*

All over the investigated range of discharge values – from $200\,m^3/s$ to $650\,m^3/s$ – the observed mean velocity field organizes according to a clear persistent one-gyre system (cf. Fig. 16 and Le Coz et al. (2006)). A large recirculating flow occupies almost the whole side-cavity, rotating around a central gravel-bar deposit corresponding to low velocities. This primary gyre is distorted as it skirts round the gravel-bar's long apex that points towards the entrance of the oxbow-lake. Velocity intensities in the gyre are close to 0.5–0.8 m/s i.e. about 3 times lower than typical velocities in the main channel.

Averaged velocity fields from March, 4th (aDcp1) and April, 25th (aDcp2) campaigns show quite different patterns (Fig. 16). For aDcp2, the primary gyre is more distorted towards the first oxbow-lake of the abandoned channel. "Input" velocities seem much stronger than "output" ones. Computed discharges from aDcp data are clearly negative, with several m^3/s entering the former channel. This can be explained by severely unsteady conditions due to the several hour rising limb of the flood preceding and including the campaign time span. For aDcp1, input and output velocity intensities are quite balanced and the mean recirculating flow does not seem to enter the oxbow-lake. The computed mean discharges through the 5 aDcp1 transects are quite close to 0 ($|Q| < 1\,m^3/s$) as expected for stationary river discharge conditions. Therefore aDcp1 mean velocity patterns should be

Copyright © 2006 Taylor & Francis Group plc, London, UK

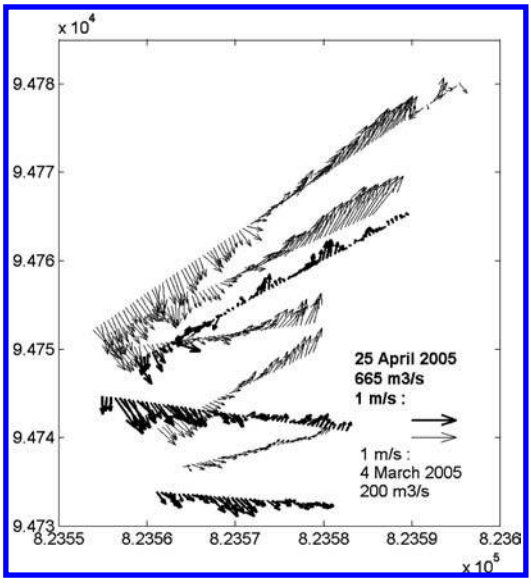


Figure 16. Depth-averaged velocities from interpolated aDcp data. *Equal East and North coordinates in metres*.

considered a reference to be compared with patterns observed in the flume case.

However aDcp instantaneous velocity fields can be quite different from averaged ones (cf. Le Coz et al. (2006)). Non-interpolated data clearly show instabilities that can be compared with fluctuating flow patterns also reported in the experimental side-cavity. Unstable structures connected with intermittent engulfing inflows and water level oscillation were indeed observed in situ (Védie 2005). As a consequence, a secondary contra-rotating gyre intermittently forms in the upstream corner of the cavity (Le Coz et al. 2006). In comparison with the flume secondary gyre, this gyre is very small and degenerated but it causes a local bank erosion (G on Fig. 15).

4 CONCLUSIONS AND PERSPECTIVES

Mean horizontal flow patterns in open-channel side-cavities from flume and field experiments have been depicted and compared. In spite of differences in geometry and hydraulic conditions, the field case may be assimilated to the two-gyre flume case through a so-called "equivalent rectangle" postulate: by means of bank erosion processes, the geometry of the natural side-cavity tends towards a rectangular shape with $L/W \approx 2$ as a morphodynamical equilibrium.

Flume observations show that momentum is transferred from the main flow to the primary gyre through a first unstable mixing-layer, then from the primary gyre to the secondary gyre through a second unstable mixing-layer. What may occur in the field study case is that enough energy is given to the primary gyre to erode the right former-channel bank, but the secondary gyre is too weak to do so. Thus the resulting side-cavity shape would mainly stem from the shape of the primary gyre in the flume case.

From both scientific and engineering points of view, it would be interesting to check this postulate, especially in order to ensure the morphological stability of restored side-cavities. The investigation of different field cases – for instance with both banks erodible – and further flume observations – for instance with variable or erodible walls – would help.

ACKNOWLEDGEMENTS

This work was supported by the *Cemagref* and the University of Chile. Funding was provided by Région Rhône-Alpes, by the National (French) Hydrological Research Programme (ACI ECCO PNRH), by the FONDECYT Project N. 1040494 and the Scholarship Programme of the National (Chilean) Commission of Science and Technology Research, CONICYT. We are grateful to G. Dramais, A. Hauet, F. Védie, T. Pantel (CNR), G. Pierrefeu (CNR) and to the technical staff of the University of Chile for their precious support.

REFERENCES

Cenedese, A. and G. Querzoli (1997). Lagrangian statistics and transilient matrix measurements by PTV in a convective boundary layer. *Measurement Science and Technology 8*(12), 1553–1561.

David, L., A. Esnault, and D. Calluaud (2002). Comparison of interpolation techniques for 2D and 3D velocimetry. *11th International Symposia on Application of Laser techniques to Fluid Mechanics, Lisboa, Portugal*.

Hassan, Y., T. Blanchat, and C. Seeley Jr. (1992). PIV flow visualization using particle tracking techniques. *Measurement Science and Technology 3*(7), 633–642.

Kimura, I. and T. Hosoda (1997). Fundamental properties of flows in open channel with dead zone. *Journal of Hydraulic Engineering 123*(2), 98–107.

Langendoen, E. J., C. Kranenburg, and R. Booij (1994). Flow patterns and exchange of matter in tidal harbours. *Journal of Hydraulic Research 32*(2), 259–270.

Le Coz, J., A. Hauet, F. Védie, G. Dramais, B. Chastan, and A. Paquier (2006). Recirculating flow assessment from aDcp, LS-PIV and 2Dh modelling. In *RiverFlow2006*, Lisbon, Portugal.

Musalem, R. (1999). Medición de campos de velocidades instantáneas en canales mediante procesamiento de imagenes. *Memoria de título, Depto. Ingeniería Civil. Universidad de Chile*.

Muto, Y., H. Imamoto, and T. Ishigaki (2000a). Turbulence characteristics of a shear flow in an embayment attached to a straight open channel. *Advances in Hydro-science and Engineering Seoul Korea 4*.

Copyright © 2006 Taylor & Francis Group plc, London, UK

Muto, Y., H. Imamoto, and T. Ishigaki (2000b). Velocity measurements in a straight open channel with a rectangular embayment. In *12th congress of APD-IAHR*, Bangkok, Thailand, pp. 353.

Nezu, I. and K. Onitsuka (2002). PIV measurements of side-cavity open-channel flows – Wando models in rivers. *Journal of Visualization 5*(1), 77–84.

Nezu, I., M. Yano, and Y. Mitsunari (2005). Hydrodynamic and concentration properties in permeable side-cavity open-channel flow by digital visualization technique. *Environmental Hydraulics and sustainable Water Management II*, 1617–1623.

Rollet, A.-J. (2002). Les effets du barrage d'Allement sur la granulométrie du lit de la basse rivière d'Ain : essai méthodologique par analyse d'image. Technical report, Université Lyon 3.

Shankar, P. and M. Deshpande (2000). Fluid mechanics in the driven cavity. *Annual Review of Fluid Mechanics 32*, 93–136.

Sukhodolov, A., C. Engelhardt, A. Kruger, and H. Bungartz (2004). Case study: turbulent flow and sediment distributions in a groyne field. *Journal of Hydraulic Engineering 130*(1), 1–9.

Sukhodolov, A., W. Uijttewaal, and C. Engelhardt (2002). On the correspondence between morphological and hydrodynamical patterns of groyne fields. *Earth Surface Processes and Landforms 27*(3), 289–305.

Uijttewaal, W. S. J., D. Lehmann, and A. Van Mazijk (2001). Exchange processes between a river and its groyne fields: model experiments. *Journal of Hydraulic Engineering 127*(11), 928–936.

Valdes, I. (1995). Habilitación de una instalación experimental y del sistema de adquisición y procesamiento de datos para el estudio de estructuras turbulentas en canales. *Memoria de título, Depto. Ingeniería Civil. Universidad de Chile*.

Védie, F. (2005). Régimes d'écoulements aux embouchures de bras morts. Etude hydraulique de la lône de Port-Galland. Technical report, Cemagref.

Weitbrecht, V. and G. Jirka (2001). Flow patterns in dead zones of rivers and their effect on exchange processes. *Proceedings of the 2001 International Symposium on Environmental Hydraulics*.

Weitbrecht, V., G. Kuhn, and G. Jirka (2002). Large scale PIV-measurements at the surface of shallow water flows. *Flow Measurement and Instrumentation 13*(5–6), 237–245.

Copyright © 2006 Taylor & Francis Group plc, London, UK

Spatially averaged near-bed flow field over rough armor layers

J. Aberle
Leichtweiss-Institute for Hydraulic Engineering, Technical University of Braunschweig, Germany

ABSTRACT: Results of a laboratory study carried out to investigate the interaction between water worked gravel-bed roughness and the near-bed flow field are presented. Vertical velocity profiles were measured with a 3D-Laser Doppler Anemometer at 24 randomly distributed locations within a defined test section. Bed topography was scanned with a laser displacement meter. The spatial heterogeneity of flow velocities and turbulence parameters in the near-bed region is shown by means of form-induced stresses which follow from the double-averaged Navier-Stokes equations. Form induced stresses are also used to investigate the subdivision of the near-bed flow field into roughness and logarithmic layer dependent on roughness geometry. The influence of the definition of geometrical roughness parameters on hydraulic parameters such as water depth and bed shear stress is discussed.

1 INTRODUCTION

The understanding of the near-bed flow structure over rough natural beds is important for many hydraulic engineering and ecological applications. An abundance of studies have been carried out to explore the theoretical aspects of turbulent structures over rough beds (e.g., Nezu & Nakagawa 1993, Kironoto & Graf 1994, Song & Graf 1994, Nezu 2005). Most of these studies focused on the investigation of the flow field at distances from the bed greater than the roughness height and for flows with large relative submergence. Recent investigations on the near-bed flow structure of flows over irregular rough beds for both, large and shallow water depths resulted in improved approaches for the description of turbulence and the near-bed velocity distribution (e.g., Dittrich & Koll 1997, Dancey et al. 2000, Shvidchenko & Pender 2001, Nikora et al. 2001, 2004, Koll 2002, Tachie et al. 2004, Carollo et al. 2005). However, these approaches still require parameterization and validation.

Most investigations of the flow structure in the near-bed region have been based on the Reynolds equations which were used for both modelling and interpretation of experimental data. However, the near-bed turbulent flow field over rough surfaces is spatially heterogeneous and depends on roughness characteristics. Thus, theoretical considerations based on measurements at a single location cannot be generalized, indicating that the application of the time-averaged momentum equations is inconvenient and impracticable. Giménez-Curto & Corniero Lera (1996) and Nikora et al. (2001, 2005a) concluded that 2D approximations based on the Reynolds equations as well as similarity considerations for time-averaged variables are not possible for the near-bed region. Instead, a detailed analysis of near-bed hydrodynamics requires the consideration of the flow field over a certain spatial scale. Such an approach has been used by researchers to compare flow characteristics at different locations at a small spatial scale (e.g., Lamarre & Roy 2005) or by considering mean velocities and turbulence characteristics to some extent averaged in the space domain, though the averaging operation was not defined explicitly (e.g., Dancey et al. 2000, Lawless and Robert 2001, Carollo et al. 2005).

A methodological approach to investigate rough bed flows is to volume average (within a thin slab) or area average (in planes parallel to the bed) the Reynolds equations. The spatially and temporally averaged Navier-Stokes equations relate to the time-averaged equations as the time-averaged equations relate to the equations for instantaneous hydrodynamic variables. The double averaged Navier-Stokes equations were first introduced by Wilson & Shaw (1977) and further developed by Raupach & Shaw (1982), Finnigan (1985), Raupach et al. (1991), and Giménez-Curto & Corniera Lera (1996). In hydraulics, the idea of spatial flow averaging was first introduced by Smith & McLean (1977) and was recently adopted by various researchers (e.g., Nikora et al. 2001, 2002, 2004, Lopez & Garcia 2001, Righetti & Armanini 2002, Aberle & Koll 2004, Aberle et al. 2004, Campbell et al. 2005, Armanini & Gregoretti 2006). The theoretical background of this methodology and examples of applications for studying rough-bed flows have been described recently in detail in Nikora et al. (2005a, b).

Copyright © 2006 Taylor & Francis Group plc, London, UK

This paper investigates the applicability of the double-averaged momentum equations in order to identify the roughness and the logarithmic layer for flows over gravel beds. The theoretical background of the double averaged velocity distribution in the roughness and the logarithmic layer are briefly discussed. Specifically designed laboratory experiments are described and the data from these experiments are analysed using the double-averaging methodology. The data analysis procedure and the influence of the roughness geometry on flow velocity distribution, form-induced stresses, and layer separation is discussed.

2 BACKGROUND

The double-averaged (in time and space) momentum equations can be written as (Nikora et al. 2005a):

$$\frac{\partial\langle\overline{u}_i\rangle}{\partial t}+\langle\overline{u}_j\rangle\frac{\partial\langle\overline{u}_i\rangle}{\partial x_j}=g_i-\frac{1}{\rho\phi}\frac{\partial\phi\langle\overline{p}\rangle}{\partial x_i}-\frac{1}{\phi}\frac{\partial\phi\langle\overline{u_i'u_j'}\rangle}{\partial x_j}-\frac{1}{\phi}\frac{\partial\phi\langle\tilde{u}_i\tilde{u}_j\rangle}{\partial x_j}+\frac{1}{\phi}\frac{\partial}{\partial x_j}\phi\left\langle\overline{\nu\frac{\partial u_i}{\partial x_j}}\right\rangle+\frac{1}{\rho}\frac{1}{\phi}\frac{1}{V_0}\overline{\iint_{S_{int}}pn_i dS}-\frac{1}{\phi}\frac{1}{V_0}\overline{\iint_{S_{int}}\nu\frac{\partial u_i}{\partial x_j}n_i dS} \quad (1)$$

where $u_i = i$ th component of the velocity vector; $p =$ pressure; $g_i = i$ th component of the gravity acceleration; $t =$ time; $x_i =$ coordinate; $\rho =$ fluid density; $\nu =$ kinematic viscosity; $\phi =$ roughness density function which is defined as V_f/V_0 with $V_f =$ volume of water in the averaging domain and $V_0 =$ total volume of the averaging domain (thin slab parallel to the mean bed); $n =$ inwardly-directed unit vector normal to the bed surface (into the fluid); and $S_{int} =$ extent of water-bed interface. The overbars in Equation 1 denote time averaged variables and angle brackets spatial (volume) averaged variables, respectively. Instantaneous variables are decomposed into time averaged and fluctuating parts according to $\theta_i = \overline{\theta}_i + \theta_i'$ and time averaged variables are decomposed into spatially averaged and spatial fluctuation parts according to $\overline{\theta}_i = \langle\overline{\theta}_i\rangle + \tilde{\theta}_i$. Theoretical considerations related to the averaging procedure are discussed in Nikora et al. (2005a).

The two integrals in Equation 1 characterize form drag f_{pi} and viscous drag f_{vi} per unit fluid volume and are defined only below the roughness crest. Both terms, together with the form-induced stresses $\langle\tilde{u}_i\tilde{u}_j\rangle$ are additional terms when Equation 1 is compared with the conventional time averaged equations. For two-dimensional, steady, uniform flow conditions over a fixed rough bed and a flat water surface, the longitudinal component of Equation 1 reduces to:

$$\rho g S_b+\frac{1}{\phi}\frac{\partial\phi\tau}{\partial z}+f_p+f_v=0 \quad (2)$$

where $S_b =$ bed slope and $\tau =$ total fluid stress. The total fluid stress contains three components, turbulent, form induced, and viscous stresses:

$$\tau=\rho\left[-\left\langle\overline{u'w'}\right\rangle-\langle\tilde{u}\tilde{w}\rangle+\frac{\nu}{\phi}\frac{d\phi\langle\overline{u}\rangle}{dz}\right] \quad (3)$$

For turbulent flows where $-\langle\tilde{u}\tilde{w}\rangle$, f_{pi}, and $f_{vi}=0$ Equation 2 is equivalent to the expression which can be derived from the Reynolds equations. Thus, integration of Equation 2 yields:

$$\rho g S_b\left(z_{ws}-z\right)=-\left\langle\overline{u'w'}\right\rangle(z) \quad (4)$$

In the flow region closer to, but still above the roughness elements, the form induced stresses may contribute significantly to the momentum equation while f_{pi} and $f_{vi}=0$. Thus, integration of Equation 2 yields:

$$\rho g S_b\left(z_{ws}-z\right)=-\left\langle\overline{u'w'}\right\rangle(z)-\langle\tilde{u}\tilde{w}\rangle(z) \quad (5)$$

Below the roughness crest z_c, the drag terms f_{pi}, and f_{vi} must be taken into account and integration of Equation 2 yields:

$$\rho g S_b\left(z_{ws}-z_c+\int_z^{z_c}\phi dz\right)-\phi\left\langle\overline{u'w'}\right\rangle(z)-\phi\langle\tilde{u}\tilde{w}\rangle(z)+\int_z^{z_c}\left(f_p+f_v\right)dz=0 \quad (6)$$

Based on Equations 4–6 it becomes possible to derive relationships for the velocity distribution in the logarithmic layer (above roughness crest) and in the roughness layer. The logarithmic velocity distribution can be derived by Equation 4 and the mixing length approach. Defining mixing length as $l=\kappa(z-d)$ results in:

$$\frac{d\langle\overline{u}\rangle}{dz}=\frac{\kappa}{u_*(z-d)} \quad (7)$$

where $d =$ zero-plane displacement and $\kappa =$ von Kármán constant. The physical background of zero-plane displacement is described in detail in Nikora et al.

Copyright © 2006 Taylor & Francis Group plc, London, UK

(2002) and Koll (2002). Integration of Equation 7 yields the velocity distribution:

$$\frac{\langle \overline{u} \rangle}{u_*} = \frac{1}{\kappa} \ln \frac{(z-d)}{(z_R-d)} + \frac{\langle \overline{u} \rangle_R}{u_*} \quad (8)$$

where z_R = geodetic height of the roughness layer and $\langle \overline{u} \rangle_R$ = double averaged velocity at z_R. Equation 8 shows that the lower boundary of the logarithmic velocity distribution is identical to the upper boundary of the roughness layer. Recent approaches for parameterization of Equation 8 are found, e.g., in Koll (2006).

Conceptual models for an exponential, linear, and constant velocity distribution in the roughness layer have been derived by Nikora et al. (2004). For gravel beds, Nikora et al. (2004) suggested a linear velocity distribution. The prerequisite for a linear velocity distribution is a monotonically decaying roughness density function ϕ towards the lower boundary. Assuming that the total drag term $(f_p + f_v)$ monotonically increases towards the lower boundary, it can be postulated that $\phi(f_{pi} + f_{vi} - \rho g S_b)$ is approximately constant. Shear stress in the roughness layer can be parameterized as $\phi\tau/\rho = k\langle \overline{u} \rangle / u_*$, where k = constant factor. Hence, the following model for a linear velocity distribution is obtained from Equation 6:

$$\frac{\langle \overline{u} \rangle(z) - \langle \overline{u} \rangle(z_R)}{u_*} = \frac{z - z_R}{l_R} \quad (9)$$

where $l_R = \rho k u_*^2 / \phi(f_v + f_p - \rho g S_b)$ corresponds to a shear length scale which characterizes flow dynamics in the roughness layer and does not depend on the vertical coordinate z. Linear velocity distributions in the roughness layer of gravel beds have been identified by, e.g., Dittrich et al. (1996), Nikora et al. (2001), Koll (2002), and Nikora et al. (2004).

3 EXPERIMENTS

Experiments were carried out in a 20 m long, 0.90 m wide and 0.60 m high tilting flume in the laboratory of the Leichtweiss-Institute for Hydraulic Engineering, Technical University of Braunschweig. The experiments were carried out with a constant flume slope of $S = 0.0027$. The discharge Q was adjusted by a valve and measured by an inductive flow meter. Eight piezometers were installed in the flume ($\Delta x = 1.00$ m) and the water surface slope was calculated from linear regression.

A coarse sediment mixture (0.63 mm < d < 64 mm, $d_{50} = 5$ mm) was used as movable bed material for the development of water worked roughness structures. The well-mixed sediment was placed in the flume at the start of the experiments and an armoring discharge $Q_1 = 120$ l/s was then run until the bed-material transport rate became negligible, indicating a stable armored bed surface. The grain-size distribution of the armor layer was determined by using a photographic technique (see Aberle & Koll 2004 and Aberle et al. 2004 for details). Armor layer topography was measured along the 2.40 m long and 0.36 m wide test section with a laser displacement meter. The test section was located 9 m downstream of the flume inlet and its width was smaller than the total flume width to reduce side wall effects. Longitudinal bed profiles were recorded with a sampling interval of $\Delta x = 1.0$ mm and a lateral spacing of $\Delta y = 4$ mm. These data were used to determine the roughness geometry function ϕ. Detailed analysis of the roughness geometry of the different armor layers can be found in Aberle & Nikora (2006).

In a next experimental step, 24 randomly-distributed vertical profiles of 3D velocities were measured for a range of water discharges, less than or equal to Q_1, using a Dantec 3D Laser Doppler Anemometer (LDA). The LDA-system consists of a fully automated traverse system, a 4W Argon-Ion laser, a F80 flow processor and two watertight 27 mm probes with a focal length of 198 mm in water. A 2D probe transmits two orthogonal pairs of beams (514.5 and 488 nm) while the 1D probe, positioned at a 30° angle to the 2D probe, transmits the third pair of beams (476.5 nm) (see Figure 1). Flow velocities (u, v, w) are calculated using coincident LDA-velocity measurements via a transformation matrix (Dantec 2003).

The measurements were carried out with submerged probes to enable flow velocity measurements within the roughness layer. For water depths smaller than the focal length of the LDA probes, the probes were placed in a specifically designed tank with a glass bottom. The tank was filled with water and immersed 1–2 cm in the water body (Figure 1). Flow velocities were measured from 5 cm below the tank bottom

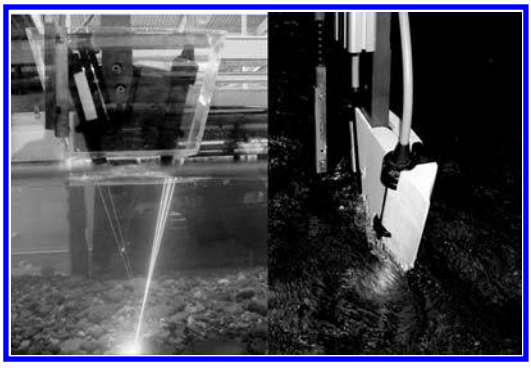


Figure 1. Tank setup for LDA-measurements (left) and measurement situation using submerged probes with aerodynamic housing (right).

Copyright © 2006 Taylor & Francis Group plc, London, UK

Table 1. Discharge, characteristic grain-size d_{50}, standard deviation of bed elevations s, and water surface slope for the analyzed experiments.

Q_{armor} l/s	Q l/s	d_{50} mm	s mm	S –
120	92	11.1	4.8	0.0027
180	91	13.6	6.3	0.0026
220	90	18.4	8.2	0.0026
250a	91	19.5	10.9	0.0028
250b	90	19.6	10.8	0.0028

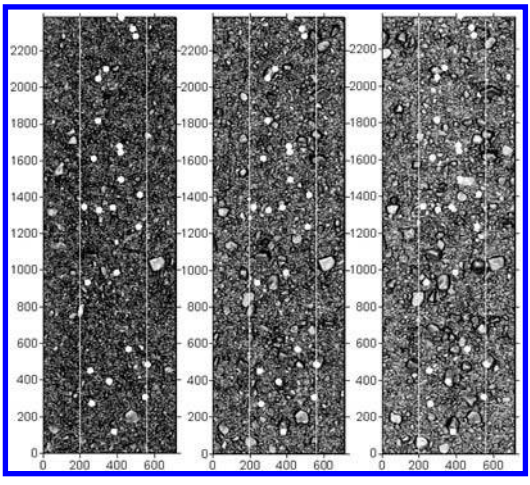


Figure 2. Armor layer topography after armoring discharges of 120, 220, and 250 l/s (from left to right). The lines indicate the test section and the points indicate the location of the velocity profiles in the xy-plane.

to the bed. For flows with water depths significantly larger than the focal length of the probes, the probes were directly immersed. For this setup, a special aerodynamic housing was constructed to minimize flow resistance (Figure 1). Flow velocities were measured until the level of the probes was equal to the water level. Then the LDA-system was changed to the tank setup to measure flow velocities at the upper levels (from 5 cm underneath the tank). Investigations of Beyer (2004) showed that the aerodynamic housing had no influence on the flow field at the level of the sampling volume. For the tank it was found that the flow field was not influenced by the setup for distances to the tank bottom larger than 5 cm.

The vertical sampling resolution of the velocity measurements was $\Delta_z = 2$ mm below roughness crest, $\Delta_z = 4$ mm above roughness crest, and $\Delta_z = 10$ mm in the outer flow field. The sampling time at each point was 1 min (for considerations of sampling time see, e.g., Buffin-Bélanger & Roy 2005) and the sampling frequencies ranged from approximately 20–100 Hz. LDA measurements were performed in planes parallel to the bed slope to simplify the spatial averaging procedure. The spatial averaging procedure was only carried out for planes where 12 or more measurement points were available. All profiles and water levels are referenced to the topography data.

After the LDA-measurements were finished the bed forming discharge Q_1 was increased for the next step to a value $Q_2 = 180$ l/s, so that the existing armor layer was destroyed and a new one developed. The above measurements were repeated and velocity profiles were recorded at the same locations in the $x-y$ plane as for the first run. The procedure was continued for discharges $Q_3 = 220$ l/s, $Q_4 = 250$a l/s, and $Q_5 = 250$b l/s. The bed was armored twice for a discharge of 250 l/s because it was accidentally destroyed in an upstream section during the LDA measurements over the armor layer formed by $Q_4 = 250$a l/s. Therefore, the armoring procedure and measurements were repeated ($Q_5 = 250$b l/s).

In this paper, data from experiments carried out with a measuring discharge of $Q = 90$ l/s are analyzed. Table 1 summarizes the armoring discharges of the successive developed armor layer, the discharge during the LDA-measurements, characteristic grain-size d_{50}, standard deviation of bed elevations s, and water surface slope S. Armor layer topography for the beds formed by $Q_a = 120$, 220, and 250 l/s and the location of the velocity profiles are shown in Figure 2.

4 DEFINITION OF BED LEVELS

Before the velocity data are presented it is necessary to highlight the problem of the accurate definition of geometrical roughness height. In the case of geometrically well defined and identical roughness elements such as cubes or spheres placed on a steel bottom, the definition of roughness height is straightforward. However, in the case of random roughness beds, local effects due to the nature of the bed may significantly influence estimates of roughness height, water depth, bed shear stress, and shear velocity (Rowinski et al. 2005). For example, it is not clear how to unambiguously define roughness trough and crest. One local deep depression in the surface may bias the estimate of the lowermost point of the surface, z_t. Similarly, one single particle protruding significantly through the surface may bias the estimate of the uppermost point of the surface, z_c. Therefore, the effective roughness height does not necessarily equal $(z_c - z_t)$.

A similar problem is encountered when the water depth is defined. Arbitrary definitions comprise the distance from the water surface to roughness crest $(z_{ws} - z_c)$, to mean bed level $(z_{ws} - z_m)$ or to roughness trough $(z_{ws} - z_t)$. Table 2 highlights the influence

Copyright © 2006 Taylor & Francis Group plc, London, UK

Table 2. Relative submergences and bed shear stress for the experiments carried out with $Q = 90$ l/s over surfaces armored with different discharges Q_a.

Q_a	l/s	120	180	220	250a	250b
h_{100}/Δ_{100}	–	3.4	2.5	2.1	1.8	1.7
h_{99}/Δ_{99}	–	6.3	5.0	3.5	2.6	2.5
h_{95}/Δ_{95}	–	8.9	7.2	5.5	4.0	3.8
h_{m}/Δ_{95}	–	9.4	7.8	6.1	4.6	4.4
h_{05}/Δ_{95}	–	9.9	8.2	6.5	5.0	4.8
h_{01}/Δ_{99}	–	7.3	6.0	4.5	3.6	3.5
h_{0}/Δ_{100}	–	4.4	3.5	3.1	2.8	2.7
τ_{100}	N/m^2	3.4	3.2	3.3	3.7	3.5
τ_{99}	N/m^2	3.7	3.7	3.7	3.9	3.9
τ_{95}	N/m^2	3.8	3.8	3.9	4.2	4.1
τ_{m}	N/m^2	4.0	4.1	4.2	4.7	4.6
τ_{05}	N/m^2	4.0	4.1	4.3	4.8	4.8
τ_{01}	N/m^2	4.0	4.1	4.3	4.8	4.8
τ_{0}	N/m^2	4.0	4.1	4.3	4.8	4.8

$h_{xx} = z_{ws} - z_{xx}$; $\Delta_{xx} = z_{xx} - z_{(100-xx)}$

$$\tau_{xx} = \rho g S(z_{ws} - z_{100}) + \rho g S \int_{z_{xx}}^{z_{100}} \phi dz$$

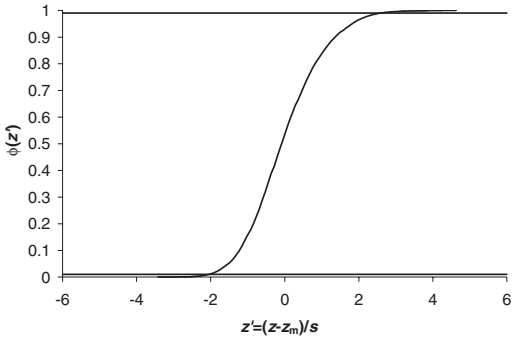


Figure 3. Averaged roughness density function $\phi(z')$ for the bed armored with $Q = 120$ l/s. z is bed elevation, z_m is mean bed elevation and s is standard deviation of bed elevations.

of different definitions of roughness height and water depth on values of relative submergence and bed shear stress. In Table 2, water depth h_{xx} is defined as the distance from the water surface to the level of xx-th percentile of the cumulative frequency distribution of bed elevations, z_{xx}. The frequency distribution can easily be obtained from the bed scans (see Figure 3) and the index xx denotes the upper percentile for which xx % of observed bed elevations are larger than z_t (e.g., z_{100} denotes roughness crest and hence $h_{100} = z_{ws} - z_{100}$). Roughness height Δ_{xx} is defined as the distance between the geodetic height of the upper percentile to its lower counterpart, e.g., $\Delta_{99} = z_{99} - z_{01}$. Bed shear stress τ_{xx} is estimated from depth slope product by taking into account the roughness density function ϕ.

Table 2 shows the influence of the various definitions on relative submergence and bed shear stress. Considering the same flow situation, relative submergence may vary up to 300% and differences in bed shear stress range from 0.6–1.3 N/m^2. Bearing in mind that relative submergence h/Δ is used to classify flows (e.g., large, medium, and small relative submergence) the significance of an appropriate definition of water depth and roughness height becomes apparent.

In the following analysis, roughness crest and roughness trough are defined as z_{99} and z_{01}, respectively. This definition was chosen to minimize local effects due to random nature of the bed and measurement errors. Figure 3 shows the filter defined by z_{99} and z_{01} exemplarily for the roughness density function (which is equivalent to the cumulative frequency distribution) of the bed armored with $Q_a = 120$ l/s. The two horizontal lines indicate the 1st and the 99th percentile. Below the 99th percentile (and above the 1st percentile), the ϕ function is characterized by curvature. Above the 99th percentile (and below the 1st percentile), ϕ does not change significantly. Similar results have been obtained for the ϕ functions of the other armor layers. Therefore it can be concluded that these percentiles are suitable for filtering outliers from the data.

In general, the shape of the ϕ-function reflects a near-Gaussian distribution of bed elevations. In reality, however, ϕ tends to a non-zero value of the bed porosity (0.28 in this case), not to zero. This discrepancy shows a limitation of the laser displacement technique. Additional measurements have been carried out to derive a correction function for ϕ in the lower part of the roughness layer (Aberle, in prep).

5 ANALYSIS OF MEAN VELOCITY PROFILES

Figure 4 shows the double averaged velocity component in flow direction $\langle \overline{u} \rangle$ over the normalized depth $(z - z_{99})/\Delta_{99}$. Above the roughness crest the velocity profiles are characterized by a logarithmic shape. Closer to and below the roughness crest, the curvature of the profiles diminishes and the velocity profiles can be approximated by straight lines. Furthermore, Figure 4 shows that flow velocities above the roughness crest are, at the same dimensionless height, larger for rougher armor layers than for smoother ones. This effect is associated with roughness geometry and (arbitrary) definition of roughness crest.

The parameterization of the velocity distribution according to Equations 8 and 9 requires the subdivision of the flow field in a roughness and logarithmic layer, respectively. Various investigations showed that the geodetic height of the upper boundary of the roughness layer z_R is closely related to the roughness crest

Copyright © 2006 Taylor & Francis Group plc, London, UK

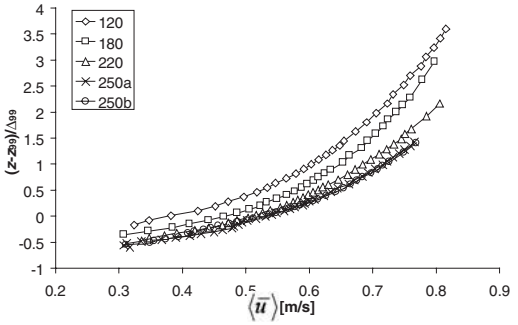


Figure 4. Double Averaged velocity distributions for $Q = 90$ l/s over different armor layers. The legend indicates the armoring discharge of the corresponding armor layer.

(e.g., Dittrich & Koll 1997, Campbell 2005, Carollo et al. 2005, Koll 2006). Therefore, the velocity data were in a first step analyzed in the region close-by z_{99}. Assuming a linear velocity distribution in the roughness layer (Equation 9), the data were fitted by linear regression so that a maximum squared regression coefficient R^2 was obtained. The geodetic height of the uppermost data point from this fit was assigned z_R.

Table 3 summarizes the identified linear ranges with respect to z_{99}, the corresponding ϕ values and R^2 estimates. Table 3 shows that the geodetic height of the roughness layer is located between z_{99} and z_{100} and hence, indeed, closely related to the roughness crest. Only for the experiment over the bed armored with $Q_a = 250$a l/s, z_R was found to be 3 mm above z_{100}. A second linear range within the roughness layer could be found for the flows over the beds armored with 180, 220 and 250 l/s. A second linear range has been suggested also by Dittrich et al. (1996) and Koll (2002). A closer investigation of the slope of the linear velocity profiles revealed a relationship between the shear length scale l_R and the standard deviation of bed elevations s. Such a behavior is expected, since l_R characterizes flow dynamics within the roughness layer and s has been identified as a suitable roughness parameter for gravel-bed rivers (Aberle & Smart 2003, Smart et al. 2004).

The parameterization of the log-range (Equation 8) requires the adequate estimation of the displacement length d. In order to estimate d, the approach of Nikora et al. (2002) is used. Equation 7 can be written as:

$$\left(\frac{d\langle\overline{u}\rangle}{dz}\right)^{-1} = \frac{u_*}{\kappa}(z-d) \qquad (10)$$

Thus, plotting the reciprocal value of the velocity gradient over the vertical coordinate z, it becomes possible to estimate d. The prerequisite for an adequate estimation of d is the knowledge of the lower

Table 3. Ranges of linear flow velocity distribution, corresponding ϕ values, and squared regression coefficient.

Q_a l/s	$z_{R2} - z_{99}$ m	ϕ_{R2} –	$z_R - z_{99}$ m	ϕ_R –	R^2 –
120	−0.002	0.976	0.002	0.996	0.997
180	−0.008	0.996	0.014	1.000	0.996
220	−0.007	0.962	0.011	0.999	0.997
250a	−0.009	0.965	0.011	1.000	0.995
250b	−0.018	0.902	0.002	0.993	0.998

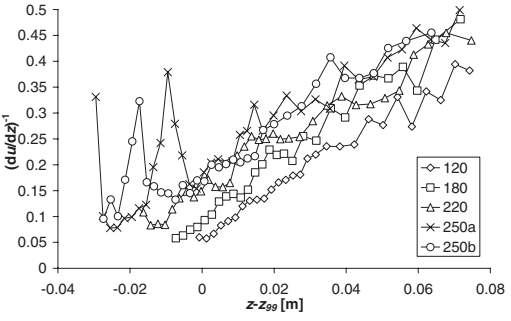


Figure 5. Reciprocal smoothed velocity gradients for the velocity distributions shown in Figure 4. The legend indicates the armoring discharge of the corresponding armor layer.

(z_R) and the upper boundary (z_L) of the logarithmic region. The numerical value for d follows then from linear regression coefficients of the relationship in Equation 10. Figure 5 shows the reciprocal values of smoothed velocity gradients as a function of the vertical distance to z_{99}. The gradients were smoothed by applying a moving average procedure over three adjacent points for both, vertical coordinate z and $\langle\overline{u}\rangle$. The smoothing procedure for the gradients became necessary, since estimating velocity derivatives from point velocity measurements belongs to the class of the so-called ill-posed problems (e.g., Bertero et al. 1988).

Figure 5 shows that the gradients, although smoothed, are still characterized by some scatter. The scatter is, especially for larger values of $z - z_{99}$, associated with the distance between measurement points (ill-posed problem), measurement noise, secondary currents and a wavy water surface. Nonetheless, Figure 5 provides the possibility to verify the estimates of z_R. A linear flow velocity distribution requires a constant velocity gradient. Such constant regions may be identified for the z_R boundaries given in Table 3.

Furthermore, Figure 5 shows that the slope of the reciprocal gradients is not constant over water depth. Thus, to be able to compare the velocity data close to the roughness crest, the data range from z_R to the

Copyright © 2006 Taylor & Francis Group plc, London, UK

Table 4. Parameters of logarithmic range.

Q_a l/s	$z_R - z_{99}$ m	$z_L - z_{99}$ m	R^2 –	ϕ_d –
120	0.002	0.026	0.999	0.584
180	0.014	0.024	0.999	0.108
220	0.011	0.023	0.999	0.010
250a	0.011	0.029	0.995	0.010
250b	0.002	0.026	0.999	0.618

geodetic height $0.2(z_{ws} - z_{99}) + z_{99}$ has been arbitrarily chosen as the upper boundary for the log-range. The lower boundary z_R is known from roughness layer analysis. The upper limit corresponds to approximately 20% of the water depth and was chosen with regard to the limitation of the log-law (see Nezu & Nakagawa 1993).

However, the fit of the data in this region resulted in unrealistically small values for the displacement length d for some of the data sets, i.e., d was located below the roughness trough. The reason for this inconsistency was associated with the scatter of the gradients, and thus the fitting procedure was refined by using the original velocity data. The data were fitted by the function $\langle \overline{u} \rangle = a \ln(z - d) + b$ (with a, b = constants). For the procedure, d was initially set to z_{01} (roughness trough) and then raised by increments of 1 mm. The value of d that provided the highest correlation coefficient was selected as the zero-plane displacement d. The fit region, the corresponding R^2 value, and the value of the roughness density function at the geodetic height of d are presented in Table 4.

All logarithmic fits are characterized by correlation coefficients $R^2 \approx 1$. However, a wide range of d-values may be found which yield $R^2 \approx 1$. This shows that the used procedure with small increments for d is important to avoid subjectively biased choice of d. The identified levels of d vary from the defined lower boundary at z_{01} to z_{60}. Low estimates of d are assumed to be associated with the chosen fit range. This issue will be investigated in more detail in the future.

6 ANALYSIS OF SPATIAL STRESSES

The double averaging approach makes it possible to investigate the spatial heterogeneity of the flow field by examining form induced stresses. In the following, the distribution of form induced and Reynolds stresses are examined in more detail to investigate the relationship between characteristic coordinates derived from the stress-profiles with boundaries for layer separation.

The form induced stresses $\langle \tilde{u}^2 \rangle$ correspond to the variance of the mean velocities in the measurement plane and seem, therefore, to be a suitable parameter to investigate layer separation. The investigations of Koll (2002) and Campbell (2005) showed that, for flows over geometrically well defined roughness elements, layer separation is possible by investigating $\langle \tilde{u}^2 \rangle$. In these studies, $\langle \tilde{u}^2 \rangle$ was approximately zero down to the roughness crest and then rapidly increasing below roughness tops.

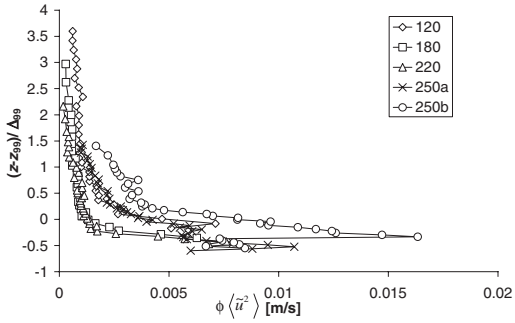


Figure 6. Distribution of form induced stresses $\langle \tilde{u}^2 \rangle$. Note that $\phi = 1$ above the absolute roughness crest. The legend indicates the armoring discharge of the corresponding armor layer.

Table 5. Characteristic vertical coordinates of form induced and Reynolds stresses.

Q_{armor} l/s	$\langle \tilde{u}^2 \rangle_{inc}$ $z - z_{99}$ m	$\langle \tilde{u}^2 \rangle_{con}$ $z - z_{99}$ m	$-\langle \overline{u'w'} \rangle_{lin}$ $z - z_{99}$ m	$-\langle \overline{u'w'} \rangle - \langle \tilde{u}\tilde{w} \rangle_{lin}$ $z - z_{99}$ m
120	0.022	0.056	0.028	0.018
180	0.002	0.026	0.034	0.012
220	0.003	0.029	0.029	0.015
250a	0.015	0.029	0.025	−0.001
250b	0.014	0.042	0.014	0.010

Figure 6 shows the distribution of the form induced stresses $\langle \tilde{u}^2 \rangle$ obtained within this study. The influence of the roughness is taken into account by multiplying the $\langle \tilde{u}^2 \rangle$ values with the roughness density function ϕ (note that $\phi = 1$ above the absolute roughness crest). A closer examination of the $\langle \tilde{u}^2 \rangle$ profiles in Figure 6 reveals that the profiles are characterized by a small but monotonically increase from the outer layer towards the bed. At a certain height $\langle \tilde{u}^2 \rangle$ remains then approximately constant for a certain region before it significantly increases. The corresponding distances of these boundaries ($\langle \tilde{u}^2 \rangle_{const}$ and $\langle \tilde{u}^2 \rangle_{inc}$) to z_{99} are summarized in Table 5. Maximum values occur throughout below z_{99}, i.e. below the roughness crest.

The upper boundary of the constant $\langle \tilde{u}^2 \rangle$-range (column $\langle \tilde{u}^2 \rangle_{con}$ in Table 5) indicates an overlap of this region with the (defined) logarithmic layer for the experiments over the beds armored with 180–250b l/s

Copyright © 2006 Taylor & Francis Group plc, London, UK

(see Table 4). Besides, for the flows over beds armored with 180, 220, and 250a l/s, the upper boundary of the constant $\langle\tilde{u}^2\rangle$-range corresponds approximately to the upper level of the (defined) log-range, i.e. to approximately 20% of water depth. For the flow over the bed armored with 120 l/s, only two data points of the constant $\langle\tilde{u}^2\rangle$-layer overlap with the log-range. The log-range itself falls into the region where $\langle\tilde{u}^2\rangle$ gradually increases (although the values are small, Figure 6). On the other hand, from Figure 6 it would be possible to estimate two more constant $\langle\tilde{u}^2\rangle$-ranges, which would overlap with the log-layer for this particular experiment. However, within this analysis, these "two subjective constant" ranges were interpreted to be part of the rapidly increasing range of $\langle\tilde{u}^2\rangle$.

The rapid increase of $\langle\tilde{u}^2\rangle$ (column $\langle\tilde{u}^2\rangle_{\text{inc}}$ in Table 5) occurs for two beds (armored with 180 and 220 l/s) between z_{99} and z_{100} and for three beds (armored with 120, 250a, and 250b l/s) above z_{100}. The distances to z_{100} range between 0.001 and 0.012 m. Thus, it is not possible to directly relate z_R, estimated from the regression analysis, with the shape of $\langle\tilde{u}^2\rangle$ for the five data sets under investigation. For natural shaped particles glued to a flume steel bottom, the investigations of Koll (2002) showed that the $\langle\tilde{u}^2\rangle$-profiles were characterized by a similar shape as shown in Figure 6. However, in contrast to the results obtained within this study, Koll (2002) concluded that z_R is related to the point of rapid increase. The different results may be associated with roughness density and porosity of the subsurface material. In fact, gluing natural shaped particles onto a steel bottom results, compared to a bed with a porous sublayer, in a different roughness density function and roughness structure. Further data is available to explore this point in more detail in the near future.

Reynolds stresses $-\langle\overline{u'w'}\rangle$ and form induced stresses $-\langle\tilde{u}\tilde{w}\rangle$ are presented in Figure 7. At larger distances to the roughness crest, Reynolds stresses $-\langle\overline{u'w'}\rangle$ are linearly distributed. Below this linear distribution, $-\langle\overline{u'w'}\rangle$ may be approximated by a constant value for a certain range before a decrease becomes apparent. The measurements in the roughness layer covered, as a maximum, the region from the roughness crest to the mean bed level. Therefore it is not possible to discuss the shape of the profiles in the lower portion of the roughness layer in more detail. Table 5 shows the levels to which a linear Reynolds stress distribution $-\langle\overline{u'w'}\rangle$ is apparent from Figure 7. The level was determined by maximizing R^2 values when fitting a straight line to the $-\langle\overline{u'w'}\rangle$-data. The values given in Table 5 indicate that the (defined) log-layer is, in general, part of the constant region of the $-\langle\overline{u'w'}\rangle$-range.

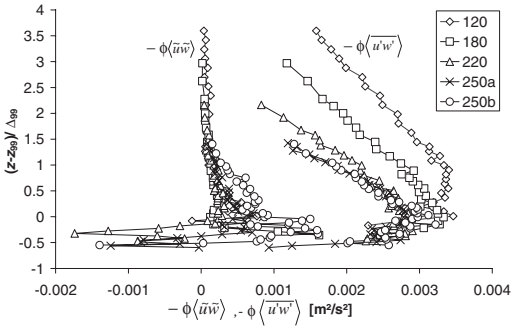


Figure 7. Reynolds stresses and form induced stresses. Note that $\phi = 1$ above the absolute roughness crest. The legend indicates the armoring discharge of the corresponding armor layer.

Figure 7 demonstrates that the form-induced stresses $-\langle\tilde{u}\tilde{w}\rangle$ are not negligible within the roughness layer and, thus, are a significant component in the momentum balance over water-worked gravel beds (see Equation 5). On the other hand, at greater distances from the bed, $-\langle\tilde{u}\tilde{w}\rangle \approx 0$ and the influence of the form induced stresses are negligible. It is interesting to note that closer to the bed, $-\langle\tilde{u}\tilde{w}\rangle$ gradually increases. This increase results in a prolongation of the linearity of the sum $-\langle\overline{u'w'}\rangle - \langle\tilde{u}\tilde{w}\rangle$ compared to the linear portion of $-\langle\overline{u'w'}\rangle$ (see Table 5). The boundaries of the linear portion of $-\langle\overline{u'w'}\rangle - \langle\tilde{u}\tilde{w}\rangle$ (taking into account the roughness density function ϕ) have been estimated using the same procedure as for $-\langle\overline{u'w'}\rangle$. The linear range extends below 20% of the water depth.

Below the linear range, $-\langle\overline{u'w'}\rangle - \langle\tilde{u}\tilde{w}\rangle$ can be approximated by a constant value. Such constant ranges are apparent within or in the vicinity of the range defined by the linear velocity distribution (i.e., close-by z_{100}). The existence of a constant range of $-\langle\overline{u'w'}\rangle - \langle\tilde{u}\tilde{w}\rangle$ below the roughness crest is important, since it justifies the assumption that $\phi(f_{pi} + f_{vi} - \rho g S_b)$ is approximately constant in the roughness layer (follows from Equation 6), and hence the existence of a linear flow velocity profile.

7 SUMMARY AND CONCLUSION

In this paper, the double averaging approach was used to investigate the near-bed flow field of flows over natural gravel bed surfaces. Difficulties concerning the definition of roughness height, water levels, and bed shear stress were discussed with respect to experimental data for flows over different armor layers. This analysis showed that it is important to unambiguously define the datum for roughness crest and trough to make different studies comparable. For gravel beds, the 99th and 1st percentile of the cumulative frequency distribution of bed elevations were suggested as roughness crest and trough, respectively. However, the analysis of the flow velocity data revealed that

Copyright © 2006 Taylor & Francis Group plc, London, UK

by normalizing the vertical coordinate with this definition, the data curves did not collapse. Therefore, the definition of roughness height will be investigated further.

The data were used to investigate the near-bed mean velocity distribution with regard to layer separation. Within the roughness layer, a linear flow velocity distribution could be identified. The shear length scale within the roughness layer was found to be correlated with the standard deviation of bed elevations. The analysis of the form induced stresses indicated that the basic assumption for the linear flow velocity distribution in the roughness layer $[\phi(f_{pi} + f_{vi} - \rho g S_b) = \text{const.}]$ was valid. The upper boundary of the roughness layer, z_R, was estimated from a linear regression of the velocity data and was found to be located between z_{99} and z_{100}.

The zero-plane displacement d was found to be located within the roughness layer. However, the data fitting procedure revealed a strong dependency of d on the data analysis method and underlying assumptions (e.g., roughness trough). Within this study it was assumed that the logarithmic layer commences at z_R and its upper limit was defined to be at the geodetic height $0.2(z_{ws} - z_{99}) + z_{99}$.

The investigation of the spatial terms revealed their importance for the description of rough bed flows and their significant contribution to the momentum equation in the roughness layer. The profiles of the form induced stresses showed a distinct behavior. However, it was not possible to unambiguously relate characteristic levels of the stress profiles (such as sudden increase of $\phi\langle\tilde{u}^2\rangle$) to z_R as estimated from the regression analysis. Therefore, the turbulent intensity $\langle\overline{u'^2}\rangle$ will be included into the analysis of the location of z_R in the future. The next steps will include also the comparison of the parameters of the equations describing the velocity distribution in the linear and logarithmic range. The parameters will be estimated using (i) regression analysis; and (ii) the data identified from characteristic ranges from spatial and turbulent stresses. Further approaches for parameterization of the equations for the velocity distribution will be included into this comparison (e.g., Katul et al. 2002, Koll 2006). For this purpose, further data are available, covering a wide range of discharges, bed slopes, and roughness. Such a consideration will provide deeper insight into the relationship between roughness geometry, form induced stresses and flow velocities.

ACKNOWLEDGEMENTS

The research was conducted under contract DI-651/4-3 from DFG (Deutsche Forschungsgemeinschaft). A. Dittrich and K. Koll provided helpful advice and generous support to this project. U. Ecklebe, G. Beyer, T. Schoneboom, and M. Oppermann provided technical support. The author is grateful for useful discussions and suggestions to V. Nikora, R. Walters, S. McLean, J. Järvelä and to all participants of the 'double-averaging' workshops.

REFERENCES

Aberle, J. & Smart, G.M. 2003. The influence of roughness structure on flow resistance on steep slopes. *J. Hydraul. Res*. 41(3): 259–269.

Aberle, J., & Koll, K. 2004. Double-averaged flow field over static armor layers. *Proc. of the Int. Conf. on Fluvial Hydraulics* "*RiverFlow 2004*", Naples, Italy, Vol. 1: pp. 225–233.

Aberle, J., & Nikora, V. 2006. Statistical properties of armored gravel-bed surfaces. *Water Resour. Res.,* submitted.

Aberle, J., Dittrich, A., Koll, K., Schoneboom, T. 2004. Sohlnahes turbulentes Strömungsfeld. In *Proc. of the BAW-Workshop: Boden- und Sohl-Stabilität – Betrachtungen an der Schnittstelle zwischen Geotechnik und Wasserbau,* 17.09.2004, Bundesanstalt für Wasserbau, Karlsruhe (in German).

Armanini, A. & Gregoretti, C. 2006. Incipient sediment motion at high slopes in uniform flow condition. *Water Resour. Res.* 41: W12431, doi:10.1029/2005WR004001.

Bertero, M., Poggio, T.A. and Torre, V. 1988. Ill-posed problems in early vision. *Proceedings of the IEEE* 76(8): 869–889.

Beyer, G. 2004. Strömungsoptimierung einer 3D-Laser Doppler Anemometer Anlage. *Diplomarbeit*, Leichtweiß-Institut für Wasserbau, TU Braunschweig (in German).

Buffin-Bélanger, T., & Roy, A. G. 2005. 1 min in the life of a river: selecting the optimal record length for the measurement of turbulence in fluvial boundary layers. *Geomorphology* 68: 77–94.

Campbell, L.J. 2005. Double-Averaged Open-Channel Flow over Regular Rough Beds, PhD thesis, University of Aberdeen, pp. 225.

Campbell, L., McEwan, I., Nikora, V., Pokrajac, D., Gallagher, M. Manes, C. 2005. Bed-load effects on hydrodynamics of rough-bed open-channel flows. *J. Hydraul. Eng.* 131(7): 576–585.

Carollo, F.G., Ferro, V., Termini, D. 2005. Analyzing turbulence intensity in gravel bed channels. *J. Hydraul. Eng.*, 131(12): 1050–1061.

Dancey, C.L., Balakrishnan, M., Diplas, P., Papanicolaou, A.N. 2000. The spatial inhomogeneity of turbulence above a fully rough, packed bed in open channel flow. *Experiments in Fluids* 29: 402–410.

Dantec 2003. BSA Flow Software V. 2.1 Installation & User's guide. Dantec Dynamics A/S, Denmark.

Dittrich, A. & Koll, K. 1997. Velocity field and resistance of flow over rough surface with large and small relative submergence. *Int. J. Sediment Res.* 12(3), 21–33.

Dittrich, A., Nestmann, F., Ergenzinger, P. 1996. Ratio of lift and shear forces over rough surfaces. In P.J. Ashworth, S. Bennett, J.L. Best, S.J. McLelland (eds), *Coherent Flow Structures in Open Channels*: 125-146. Chichester: John Wiley & Sons Ltd.

Finnigan, J.J. 1985. Turbulent transport in flexible plant canopies. In B.A. Hutchinson & B.B. Hicks (eds),

Copyright © 2006 Taylor & Francis Group plc, London, UK

The Forest-Atmosphere Interaction: 443–480. Dordrecht: D. Reidel Publishing Co.

Giménez-Curto, L.A. & Corniero Lera, M.A. 1996. Oscillating turbulent flow over very rough surfaces. *J. Geoph. Res.* 101(C9): 20,745–20,758.

Katul, G., Wiberg, P., Albertson, J., Hornberger, G. 2002. A mixing layer theory for flow resistance in shallow streams. *Water Resour. Res.* 38(11): 32-1–32-8.

Kironoto, B.A. & Graf, W.H. 1994. Turbulence characteristics in rough uniform open-channel flow. *Proc. Instn. Civ. Engrg. Water, Maritime, and Energy* 106: 333–344.

Koll, K. 2002. Feststofftransport und Geschwindigkeitsverteilung in Raugerinnen. *[online], Karlsruhe, Univ., Fak. f. Bauingenieur- und Vermessungswesen, Diss. v. 12.07.2002*: http://www. ubka.uni-karlsruhe.de/cgibin/psview?document=2002/bau-verm/12 (in German).

Koll, K. 2006. Parameterisation of the vertical velocity profile in the wall region over rough surfaces. *Proc. River Flow 2006* (this issue).

Lamarre, H. & Roy, A.G. 2005. Reach scale variability of turbulent flow characteristics in a gravel-bed river. *Geomorphology* 68: 95–113.

Lawless, M. & Robert, A. 2001. Scales of boundary resistance in coarse-grained channels: turbulent velocity profiles and implications. *Geomorphology* 39: 221–238.

Lopez, F. & Garcia, M.H. 2001. Mean flow and turbulence structure of open-channel flow through emergent vegetation. *J. Hydraul. Eng.* 127(5): 392–402.

Nezu, I. 2005. Open-channel flow turbulence and its research prospect in the 21st century. *J. Hydraul. Eng.,* 131(4): 229–246.

Nezu, I. & Nakagawa, H. 1993. Turbulence in open-channel flows, Rotterdam: Balkema.

Nikora, V., Goring, D., McEwan, I., Griffiths, G. 2001. Spatially averaged open-channel flow over rough bed. *J. Hydraul. Eng.* 127(2): 123–133.

Nikora, V., Koll, K., McLean, S., Dittrich, A., Aberle, J. 2002. Zero-plane displacement for rough-bed open-channel flows. *Proc. of the Int. Symp. on Fluvial Hydraulics "RiverFlow2002"*, Louvain-la-Neuve, Belgium: pp. 83–92.

Nikora, V., Koll, K., McEwan, I., McLean, S., Dittrich, A. 2004. Velocity distribution in the roughness layer of rough-bed flows. *J. Hydraul. Eng.*, 130(10): 1036–1042.

Nikora; V., McEwan, I., McLean, S., Coleman, S., Pokrajac, D., Walters, R. 2005a. Double averaging concept for rough-bed open-channel and overland flows: Theoretical background. *J. Hydraul. Eng.*, submitted.

Nikora; V., McLean, S., Coleman, S., Pokrajac, D., McEwan, I., Campbell, L., Aberle, J., Clunie, D., Koll, K. 2005b. Double averaging concept for rough-bed open-channel and overland flows: Applications. *J. Hydraul. Eng.*, submitted.

Raupach, M.R. & Shaw, R.H. 1982. Averaging procedures for flow within vegetation canopies. *Bound.-Layer Meteorol.* 22: 79–90.

Raupach, M.R., Antonia, R.A., Rajagopalan, S. 1991. Rough-wall turbulent boundary layers. *Appl. Mech. Rev.* 44(1): 1–25.

Rowinski, P.M., Aberle, J. and Mazurczyk, A. 2005. Shear velocity estimation in hydraulic research. *Acta Geophysica Polonica* 53(4): 567–583.

Righetti, M. & Armanini, A. 2002. Flow resistance in open channel flows with sparsely distributed bushes. *J. Hydrol.* 269: 55–64.

Shvidchenko, A.B. & Pender, G. 2001. Macroturbulent structure of open-channel flow over gravel beds. *Water Resources Research* 37(3): 709–719.

Smart, G.M., Aberle, J., Duncan, M. and Walsh, J. 2004. Measurement and analysis of alluvial bed roughness. *J.Hydraul. Res.* 42(3): 227–237.

Smith, J.D. & McLean, S.R. 1977. Spatially averaged flow field over a wavy surface. *J. Geophys. Res.* 83(12): 1735–1746.

Song, T. & Graf, W.H. 1994. Non-uniform open-channel flow over a rough bed. *Journal of Hydroscience and Hydraulic Engineering* 12(1): 1–25.

Tachie, M.F., Bergstrom, D.J., Balachandar, R. 2004. Roughness effects on the mixing properties in open channel turbulent boundary layers. *Journal of Fluids Engineering* 126: 1025–1032.

Wilson, N.R. & Shaw, R.H. 1977. A higher order closure model for canopy flow. *J. Appl. Meteorol.* 16: 1197–1205.

Copyright © 2006 Taylor & Francis Group plc, London, UK

Parameterisation of the vertical velocity profile in the wall region over rough surfaces

K. Koll
Leichtweiss – Institute for Hydraulic Engineering, Braunschweig Technical University, Germany

ABSTRACT: Analyses of vertical velocity profiles over rough surfaces result in parameters which often have no physical meaning, especially if the relative submergence decreases. Assumptions are required which complicate comparative analysis of data sets. A recently published definition of the zero-plane displacement height d allows for the determination of d solely from velocity measurements, instead of fitting it to a fixed value of the von Kármán constant. Based on this definition, a parameterisation of the vertical velocity profile within the wall region was developed as well as a methodology to determine the parameters. The parameterisation and the methodology were tested with a dataset of vertical velocity profiles measured over artificial and natural roughnesses. Dependencies of the parameters on roughness and flow characteristics were investigated. The results support the suggested parameterisation. The methodology is validated for flow over artificial surfaces whereas improvement is required for analyses of flow over natural beds.

1 INTRODUCTION

Since the development of the logarithmic law of the wall for rough beds the meaning and determination of its parameters κ, d, k_S, and B has been discussed. The parameters are related to each other as $\kappa = 0.4$ should be constant, d is used to keep it constant, and k_S results in combination with the assumption that also $B = 8.5$ is constant.

Problems in determining meaningful values of k_S and d as well as κ-values different from 0.4 are reported throughout the literature of the last decades (e.g. Vanoni & Nomicos 1959, O'Loughlin & Annambhotla 1969, Nowell & Church, 1979, Gust & Southard 1983, Nakagawa et al. 1991, Dittrich & Koll 1997, Nikora & Goring 2000). The problems are grounded in the assumed constancy of κ and, thus, in the definition of d.

The re-definition of the zero-plane displacement height (Nikora et al. 2002) allowed for the development of a new procedure to determine the parameters of the vertical velocity profile within the wall region. Assumptions of fixed values are not required, and thus dependencies of the velocity parameters on flow and roughness parameters can be studied.

In the following based on a brief summary of the derivation of the log-law of the wall the new parameters to describe the velocity profile are introduced and the modified formulas are derived. The procedure to determine the velocity parameters is presented and tested with flume data measured over artificial and water-worked surfaces with low and medium relative submergence. Correlations between velocity, and roughness and flow parameters are discussed.

2 VERTICAL VELOCITY PROFILE

Parameterisation of the velocity profile and mathematical description of the velocity distribution require a subdivision of the turbulent flow field into several layers. The layer separation and geometric parameters are shown in Figure 1.

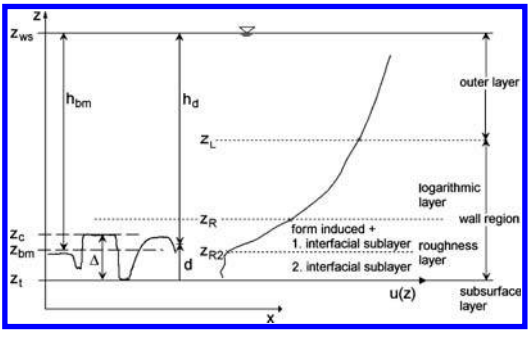


Figure 1. Sketch of layer separation and geometric parameters.

Copyright © 2006 Taylor & Francis Group plc, London, UK

2.1 *Layers of the vertical velocity profile*

The flow field over rough permeable beds can be subdivided into three main layers: the outer layer, the wall region, and the subsurface layer. The wall region includes the logarithmic layer and the roughness layer. The latter contains the form induced sublayer, located just above the roughness crests, and the interfacial sublayer, between the roughness crests and troughs. Velocity measurements over beds with artificial roughnesses indicate that the interfacial sublayer also consists of two parts (Dittrich et al. 1996, Koll 2002).

Following Nikora et al. (2006) the roughness crests z_c and the roughness troughs z_t are defined as the elevations for which 99% of observed bed elevations are smaller than z_c and larger than z_t, respectively. A detailed discussion of roughness geometries can be found in Aberle & Nikora (2006). The height of the interfacial sublayer $\Delta = z_c - z_t$ corresponds to the geometric height of the roughness elements in case of single element roughnesses.

The flow in the form induced sublayer may be influenced by wakes of roughness elements. Thus, the top of the roughness layer z_R -determined from velocity data- is expected to be located above the roughness crests. The height z_{R2}, where the interfacial sublayer is subdivided, results also from velocity data.

The possible minimum height of z_R and, therefore of the lower boundary of the logarithmic layer is z_c. An extension of the logarithmic profile into the layer dominated by characteristics of the roughness is not meaningful, because the derivation of the logarithmic law is based on the assumptions that the shear stress is constant, and that the mixing length increases linearly with the distance from the wall (e.g. von Kármán 1930, Prandtl 1933). The upper boundary of the logarithmic layer z_L is also limited due to these assumptions. According to the conservative limitation of the logarithmic layer the top z_L is set to 20% of the flow depth above the roughness layer. However, discussions about the upper boundary of the logarithmic layer are as yet not conclusive.

2.2 *Equations for the vertical velocity profile in the wall region*

Simplification of the Reynolds equations for two-dimensional, steady, uniform, fully developed open-channel flow results in the basic equation for the derivation of the vertical distribution of the streamwise velocity component (e.g. Nezu & Nakagawa 1993)

$$\frac{\tau_0}{\rho} = u_*^2 = \nu \frac{\mathrm{d}\overline{u}}{\mathrm{d}z} - \overline{u'w'} \tag{1}$$

where $\tau_0 =$ bed shear stress, $\rho =$ fluid density, $u_* =$ shear velocity, $\nu =$ fluid viscosity, $\overline{u} =$ time averaged velocity in streamwise direction, $z =$ vertical coordinate, and $-\overline{u'w'} =$ Reynolds (turbulent) stress with u' and $w' =$ fluctuating part of the velocity components in streamwise and vertical direction, respectively.

By analogy with the viscous stress Boussinesq introduced the turbulent viscosity ν_T to calculate the turbulent stress

$$-\overline{u'w'} = \nu_T \frac{\mathrm{d}\overline{u}}{\mathrm{d}z} \tag{2}$$

Moreover, in rough bed flows the viscous stress is negligible and Equation 1 becomes

$$u_*^2 = \nu_T \frac{\mathrm{d}\overline{u}}{\mathrm{d}z} \tag{3}$$

which is the basic equation to derive the formulas of the vertical velocity profile within the wall region. The problem then to be solved is the determination of ν_T.

2.2.1 *Logarithmic layer*

Prandtl (1933) developed the well known mixing length approach to calculate ν_T within the logarithmic layer

$$\nu_L = l_L^2 \frac{\mathrm{d}\overline{u}}{\mathrm{d}z} \tag{4}$$

where $\nu_L =$ turbulent viscosity of the logarithmic layer considering only time dependent turbulence and $l_L =$ mixing length of the logarithmic layer. Close to the wall it can be reasonably assumed that l_L increases linearily with the vertical coordinate z (von Kármán 1930). Prandtl (1933) used the von Kármán constant κ as constant of proportionality which leads to

$$l_L = \kappa z \tag{5}$$

Substitution of Equations 4 and 5 into Equation 3 and integration results in the formula for the logarithmic profile

$$\frac{\overline{u}(z)}{u_*} = \frac{1}{\kappa} \ln z + const. \tag{6}$$

where *const.* = constant of integration, which depends on the hydraulic roughness of the surface. For hydraulically smooth surfaces it is determined with the boundary condition in the height of the viscous layer. The existence of the buffer layer is neglected.

For hydraulically rough surfaces the viscous layer vanishes in the interfacial sublayer, and thus cannot be used as a boundary condition. Nikuradse (1933a,b), who investigated flow over a surface roughened with a single layer of sand with diameter k_S, chose the top of the roughness elements as lower boundary of

Copyright © 2006 Taylor & Francis Group plc, London, UK

the logarithmic layer, i.e. he determined the boundary condition in the height $z = k_S$. He found the ratio of $\bar{u}(z = k_S)/u_*$ as well as the parameter κ to be constant for hydraulically rough surfaces and formulated the logarithmic law for flow over rough surfaces

$$\frac{\bar{u}(z)}{u_*} = \frac{1}{\kappa} \ln \frac{z}{k_S} + B \tag{7}$$

with $\kappa = 0.4$ and $B = 8.48$.

With increasing geometric roughness height, measured velocities and velocities calculated with Equation 7 correspond less and less. Clauser (1956) attributed this problem to the origin of the vertical coordinate z. He introduced the zero-plane displacement height d and explained it as the height where the logarithmic profile calculated with Equation 7 theoretically becomes zero. Thus, Equation 5 becomes

$$l_L = \kappa(z - d) \tag{8}$$

and Equation 7 becomes

$$\frac{\bar{u}(z)}{u_*} = \frac{1}{\kappa} \ln \frac{(z - d)}{k_S} + B \tag{9}$$

if z starts from below the roughness crests, e.g. from z_t. The parameter d is used to keep κ constant. Nowadays, Equation 9 with $\kappa = 0.4$ and $B = 8.5$ is known as the "log-law of the wall". As aforementioned, the applicability of Equation 9 is limited to a height of 15 to 20% of the water depth due to the assumptions of a linear relation between l_L and z and a constant shear stress.

The equivalent sand roughness k_S became a measure for the hydraulic effect of the bed roughness. Experiments with a further increasing roughness height and, especially, with decreasing relative submergence resulted in k_S-values difficult to explain. For instance, Figure 2 shows the ratio of k_S/Δ as a function of the relative submergence.

Values $k_S/\Delta < 1$ mean that the hydraulic roughness height is smaller than the geometric roughness height, which is not meaningful. Moreover, it implies that the logarithmic velocity profile is valid within the roughness layer. Nakagawa et al. (1991) among others denied this possibility because Reynolds stress decreases below the roughness crests, which contradicts the assumption of a constant shear stress.

Often researchers tried to overcome the problem by using Δ instead of k_S (e.g. Nowell & Church 1979). In that case, k_S is no longer related to the flow, and thus looses its meaning as the hydraulic roughness. Similar problems arise with the zero-plane displacement height d. Consequently, the existence of a logarithmic layer for flow over very rough beds and with low relative submergence often cast in doubt (e.g. Bayazit

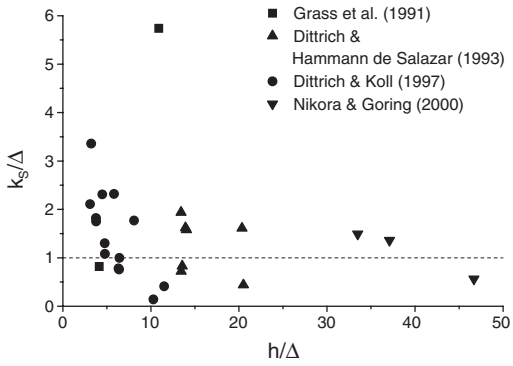


Figure 2. Relation between k_S/Δ and relative submergence h/Δ.

1982). On the other hand, published data (e.g. Bayazit 1982, Dittrich & Koll 1997) show that a region with a logarithmic shape of the velocity profile exists even at low relative submergence.

The problems can be reduced to the requirement that $\kappa = 0.4$ has to be universal – at least in the context considered. It can be shown that κ is not necessarily universal (Koll 2002) but this discussion is however beyond the scope of this paper.

The investigation of the parameters of the vertical velocity profile as a function of roughness and flow requires the variability of all parameters, and thus a re-definition of the zero-plane displacement height d. The new definition introduced by Nikora et al. (2002) explains the physical meaning of d as the level that large-scale turbulent eddies feel as the "bed". It follows that at the height d the mixing length l_L is zero (for more details see Nikora et al. 2002, Koll 2002), i.e.

$$d = z(l_L = 0) \tag{10}$$

Starting again from Equation 6, the constant of integration is determined with the boundary condition $\bar{u}(z = z_R) = u_R$ in the height of the roughness layer z_R. Thus, Equation 6 together with Equation 8 becomes

$$\frac{\bar{u}(z)}{u_*} = \frac{1}{\kappa} \ln \frac{z - d}{z_R - d} + \frac{u_R}{u_*} \tag{11}$$

The parameters κ, d, z_R, and u_R/u_* can be determined from measured velocity profiles without any further assumptions (see Section 3).

2.2.2 *Roughness layer*

The shape of the vertical velocity profile in the roughness layer depends on the geometry of the roughness (Nikora et al. 2004). In case of gravel and comparable artificial roughness elements, the velocity profile follows most probably a linear relation. Using the mixing length concept of Prandtl (1933), linearity implies

Copyright © 2006 Taylor & Francis Group plc, London, UK

that the mixing length in the roughness layer l_R is independent of the vertical coordinate. Assuming that the velocity fluctuation u' scales with $\bar{u}$, and that w' scales with u_* the turbulent viscosity within the roughness layer becomes

$$\nu_R = l_R\, u_* \tag{12}$$

where ν_R = turbulent viscosity within the roughness layer considering turbulence due to roughness.

Substitution of Equation 12 into Equation 3 gives

$$u_* = l_R \frac{\mathrm{d}\bar{u}}{\mathrm{d}z} \tag{13}$$

With the boundary condition $\bar{u}(z = z_R) = u_R$ at the upper boundary of the roughness layer integration leads to the formula for the velocity profile within the roughness layer

$$\frac{\bar{u}(z)}{u_*} = \frac{z - z_R}{l_R} + \frac{u_R}{u_*} \tag{14}$$

Note that it is not distinguished between the form induced sublayer and the interfacial sublayer.

As mentioned previously, the interfacial sublayer can be subdivided into two parts. Although only very little data is available for the lower part, in a first approach it is assumed that the velocity profile follows a linear distribution, too. The formula is derived in analogy to Equation 14 using the boundary condition at the upper boundary of the lower part, i.e. $\bar{u}(z = z_{R2}) = u_{R2}$,

$$\frac{\bar{u}(z)}{u_*} = \frac{z - z_{R2}}{l_{R2}} + \frac{u_{R2}}{u_*} \tag{15}$$

where l_{R2} = mixing length of the lower part of the roughness layer.

The parameters l_R, l_{R2} and u_{R2} can be determined directly from velocity measurements.

3 DETERMINATION OF THE PARAMETERS OF THE VELOCITY PROFILE

The parameters to be determined from measurements of the vertical profile of the streamwise velocity component are summarised in Table 1.

First, the boundaries of the layers have to be determined. Here, linear and logarithmic regression analyses for the roughness and the logarithmic layer, respectively, are used to obtain z_{R2} and z_R. z_L depends on z_R and is calculated with Equation 16.

$$z_L = 0.2(z_{WS} - z_R) + z_R \tag{16}$$

where z_{WS} = water surface level.

Table 1. Parameters of the velocity profile.

Layer	Parameter	
Logarithmic layer	upper boundary	z_L
	constant of proportionality	κ
	zero-plane displacement height	d
Roughness layer (upper part)	upper boundary	z_R
	velocity at height z_R	u_R
	mixing length	l_R
Roughness layer (lower part)	upper boundary	z_{R2}
	velocity at height z_{R2}	u_{R2}
	mixing length	l_{R2}

The velocities u_{R2} and u_R are the velocities at z_{R2} and z_R, respectively, and consequently result directly from the measurements.

The procedure to determine l_{R2} and l_R is identical and, therefore, is exemplarily shown for l_R. Plotting velocities $\bar{u}$ over the vertical coordinate z and employing linear regression results in a straight line with a gradient $m_R = d\bar{u}/dz$. Comparison with Equation 13 gives the formula to calculate l_R

$$l_R = \frac{u_*}{\mathrm{d}\bar{u}/\mathrm{d}z} = \frac{u_*}{m_R} \tag{17}$$

The shear velocity u_* is calculated with the gravity method

$$u_* = \sqrt{g h_d S} = \sqrt{g(z_{WS} - d)S} \tag{18}$$

where g = acceleration of gravity, $h_d = z_{WS} - d$ = water depth, and S = bed slope. Water depth is used here instead of hydraulic radius because the surfaces under consideration are very rough compared to the walls.

However, the zero-plane displacement height d is required to calculate u_* and, thus, l_R. With Equations 3, 4, and 8 it follows

$$u_* = l_L \frac{\mathrm{d}\bar{u}}{\mathrm{d}z} = \kappa(z - d)\frac{\mathrm{d}\bar{u}}{\mathrm{d}z} \tag{19}$$

and thus

$$\frac{l_L}{u_*} = \frac{1}{\mathrm{d}\bar{u}/\mathrm{d}z} \tag{20}$$

Plotting Equation 20 as a function of z and employing linear regression within the logarithmic layer gives the formula of the straight line

$$\frac{l_L}{u_*} = m_L\, z + b_L \tag{21}$$

where m_L = gradient and b_L = intercept of the ordinate.

Copyright © 2006 Taylor & Francis Group plc, London, UK

With the definition of d (Equation 10) the zero-plane displacement height can be calculated with the parameters of the linear regression

$$d = -\frac{b_L}{m_L} \tag{22}$$

and, thus, u_* can be calculated. Finally, comparison of the coefficients of Equations 8 and 21 gives

$$\kappa = m_L\, u_* \tag{23}$$

4 EXPERIMENTAL DATA

Equations 11, 14, and 15 and the method to determine the parameters of the velocity profile (Tab. 1) are tested with data measured with Laser Doppler Anemometry (LDA) over different kinds of roughnesses.

Artificial surfaces were designed using glass beads and PVC cubes as well as uniformly-sized gravel. A single layer of elements was glued to the steel bottom of the flume (flume width $W = 30$ cm). For more details on the experiments see Koll (2002). In addition to the geometric height of the roughness elements, the spacing between the elements was varied. The roughness density is calculated with Equation 24.

$$c_k = \frac{z_{bm}}{\Delta} \tag{24}$$

where c_k = roughness density, and z_{bm} = volumetrically averaged height of the roughness.

The irregularity of the surface of the bed roughness is described by the parameter σ_k/Δ where σ_k is the standard deviation of the bed elevations obtained by scanning the surface with a laser displacement meter.

Moreover, velocity data measured in flow over a natural surface are used. A coarse sediment mixture (grain diameters between 0.63 mm and 64 mm) was placed in the flume (flume width $W = 90$ cm) and leveled to give a thickness of 20 cm. A static armour layer ($d_{50} = 19.6$ mm) was subsequently allowed to develop by adjusting the discharge to 250 l/s and keeping it constant until the sediment transport rate was negligible. For more details on the flume and the methodology see Aberle & Koll (2004) and Aberle (2006).

The characteristics of the roughnesses are summarized in Table 2.

For each roughness, several discharges were adjusted resulting in a range of relative submergence between 2.9 and 20.3. The Froude number was always well below unity and the Reynolds number with a minimum of 41,333 indicated turbulent flow throughout. The lowest grain Reynolds number Re_* was 450 and the surfaces could therefore be considered as hydraulically rough. The width to depth ratio varied between 1.2 and 5.6. Although this ratio is quite small, it has

Table 2. Characteristics of the bed roughnesses.

Roughness	Name	Δ cm	c_k –	σ_k/Δ –	Symbol
Beads	RK-b[a)]	0.83	0.51/0.54	0.42/0.41	○
Cubes	RK-c[a)]	0.80	0.25/0.53	0.46/0.49	□
Gravel	R0[b)]	2.80	0.48	0.56	△
	RI[c)]	2.00	0.59	–*)	▲
	RII[c)]	2.50	0.31	–*)	▽
	RIII[c)]	3.50	0.25	–*)	▼
Armour layer	RA250	5.53	0.38	0.20	∗

a) Dittrich & Hammann de Salazar (1993)
b) Dittrich & Koll (1997)
c) Koll (2002)
*) not available

to be taken into account that the bed surfaces were very rough compared to the walls. Note that the aforementioned values are calculated using $h_{bm} = z_{WS} - z_{bm}$ instead of $h_d = z_{WS} - d$ in order to make them comparable with the ranges of published data. However, the relative submergence h_d/Δ *is* used to characterise the flow when discussing dependencies of the velocity parameters.

The measurements were made at three to five locations in case of the artificial beds. This number appears to be too low to analyse spatial variations. Double averaged velocities (in time and in space) can however be used for analyses, as spatial averaging does not change the formulas derived in Section 2 (e.g. Nikora et al. 2001). Thus, the time averaged velocities $\bar{u}$ are replaced by the double averaged velocities $\langle\bar{u}\rangle$. In case of the static armour layer, measurements were made at 24 locations. Preliminary results of analysis of spatial terms are given in Aberle (2006).

5 RESULTS

The applicability of Equations 11, 14 and 15 as well as of the methodology to determine the accordant parameters can be proofed by plotting the standardised velocity profiles. The plots are shown in Figures 3 and 4 for the logarithmic layer and the upper part of the roughness layer, respectively. Both plots show good matches of the standardised velocity profiles measured over very different bed roughnesses.

However, no good results were obtained for the lower part of the roughness layer, and therefore only the parameters of the logarithmic and the upper part of the roughness layer are discussed in the following.

5.1 *Parameters of the logarithmic layer*

The parameters of the logarithmic layer (Table 1) are expected to depend on flow parameters as well as on

Copyright © 2006 Taylor & Francis Group plc, London, UK

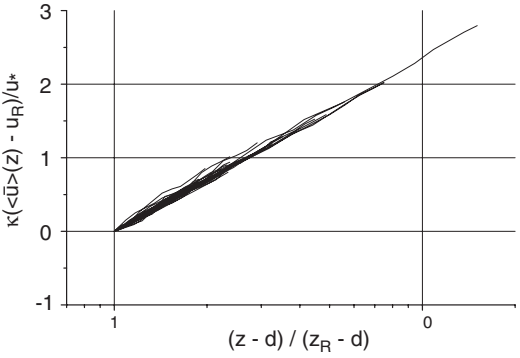


Figure 3. Standardised velocity profile in the logarithmic layer.

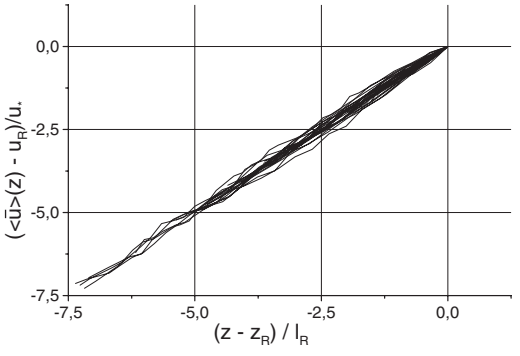


Figure 4. Standardised velocity profile in the upper part of the roughness layer.

roughness parameters. The relative submergence is used to characterise the flow. Geometric roughness height and irregularity of the bed surface are used to describe the roughness.

The zero-plane displacement height d as a function of the geometric roughness height Δ is shown in Figure 5. Considering only the artificial surfaces (beads, cubes, and gravel) d increases with Δ, and a functional relation seems to be inherent. Taking additionally into account the data of the water-worked bed the implication is not supported.

Several reasons for the different behaviour of the armour layer can be suggested. The main differences are that the bed is permeable instead of single layered and that it is water-worked instead of man-made. The roughness elements of the artificial surfaces were glued to the flume bed to avoid erosion. Thus, it was possible to design flow situations which do not exist for water-worked beds. Especially, the determination of the geometric roughness height in case of the water-worked topography contains distinct uncertainties (see Aberle 2006). Moreover, the determination of the boundary between logarithmic and roughness

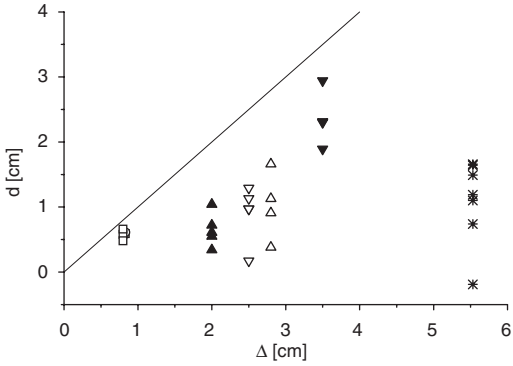


Figure 5. Relation between displacement height d and geometric roughness height Δ (for symbols see Table 2).

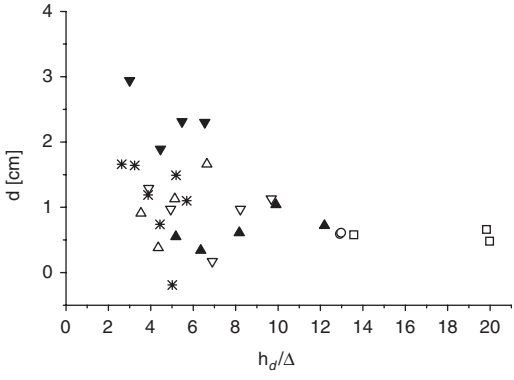


Figure 6. Relation between displacement height d and relative submergence h_d/Δ (for symbols see Table 2).

layer z_R by regression analysis seems to be inappropriate for natural surfaces. Small changes in z_R can change d significantly.

However, d cannot be solely dependent on Δ as the values determined for different flows over the same bed scatter remarkably. Analyses of dependencies on flow parameters show a decrease of d with increasing relative submergence h_d/Δ when looking at the overall shape of the plot (Fig. 6). However, closer examination of the values for single roughness configurations do not support the trend. It has to be considered that the range of relative submergence for each roughness was quite small.

Analyses of κ reveal that it is not a universal constant but depends on the irregularity of the surface σ_k/Δ as well as on the relative submergence. These parameters influence the formation and the expansion, respectively, of coherent turbulent flow structures, and thus the gradient of the velocity profile (e.g. Kirkbride 1993, Sirovich & Karlsson 1997). The relations are shown in Figures 7 and 8.

Copyright © 2006 Taylor & Francis Group plc, London, UK

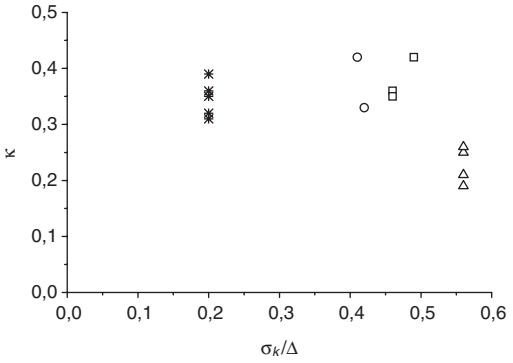


Figure 7. Relation between constant of proportionality κ and irregularity of the bed surface σ_k/Δ (for symbols see Table 2).

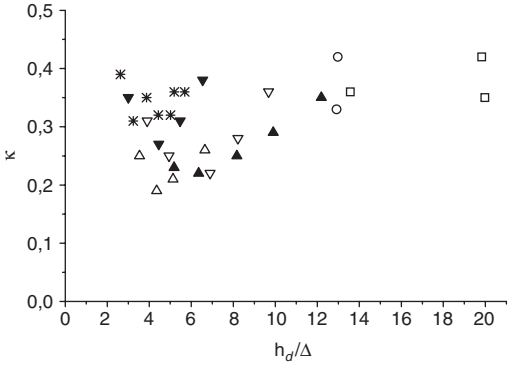


Figure 8. Relation between the constant of proportionality κ and relative submergence h_d/Δ (for symbols see Table 2).

For both, regular surfaces and large relative submergences, κ approaches a value of 0.4. It decreases significantly if the bed surface becomes more irregular and if the water depth related to the roughness height decreases.

Moreover, κ seems to reach a minimum at h_d/Δ between 7 and 4 and increases again for further decreasing relative submergence. This behaviour needs further investigation as an explanation cannot be given at the moment.

5.2 *Parameters of the roughness layer*

In Figure 9 the mixing length of the roughness layer l_R is shown as a function of Δ (note that in the following only the upper part of the roughness layer, i.e. form induced and first interfacial sublayer, is discussed).

For the artificial surfaces the linear increase of l_R with Δ is evident. The values of l_R determined for one roughness and several discharges show only small scatter. This result suggests that l_R is not influenced by flow characteristics.

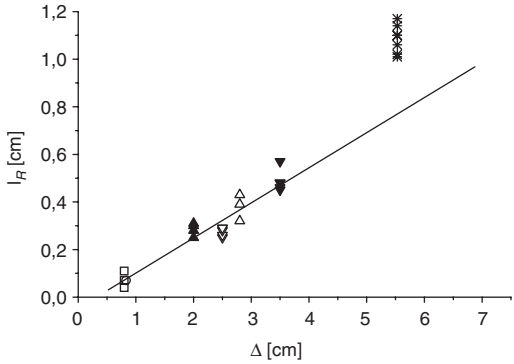


Figure 9. Relation between the mixing length of the roughness layer l_R and the geometric roughness height Δ (for symbols see Table 2).

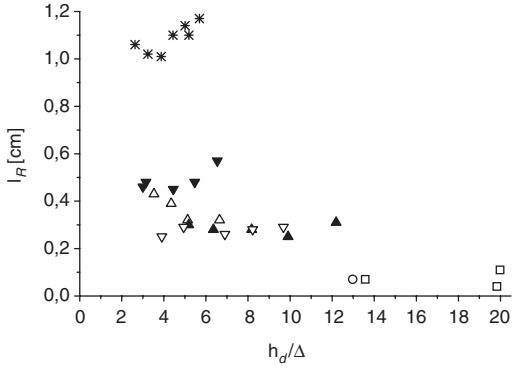


Figure 10. Relation between the mixing length of the roughness layer l_R and relative submergence h_d/Δ (for symbols see Table 2).

The values obtained from the water-worked bed do not follow the linear relation given by the artificial roughnesses but are clearly above the straight line. Moreover, the scatter of l_R is much larger. The most probable explanation for the scatter are the different flow conditions. The mixing length is plotted as a function of h_d/Δ in Figure 10.

The data are grouped according to the preparation of the surface, i.e. man-made and water-worked beds, as well as to the shape of the roughness elements for the flows over artificial surfaces, i.e. gravel, and beads and cubes. The classification cannot be compensated by scaling l_R with another geometric parameter, which indicates the influence of the shape of the roughness elements on the flow field.

The overall shape of the plot shows a decrease of l_R with increasing relative submergence, whereas the trends for single roughnesses are not consistent. Only for the natural bed a dependence on the relative submergence can be observed, but in the opposite

Copyright © 2006 Taylor & Francis Group plc, London, UK

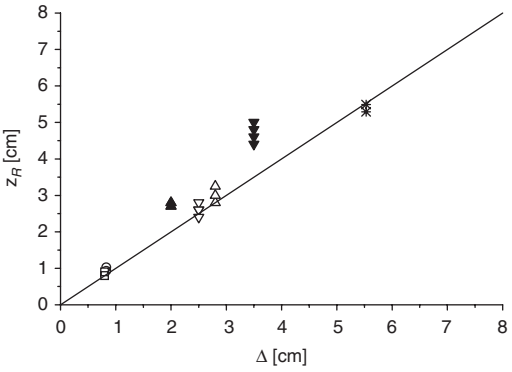


Figure 11. Relation between the upper boundary of the roughness layer z_R and the geometric roughness height Δ (for symbols see Table 2).

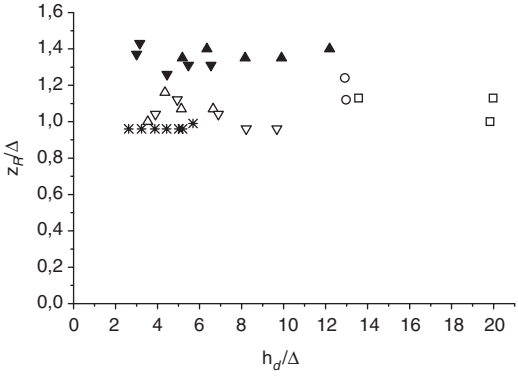


Figure 12. Relation between the upper boundary of the roughness layer normalized with the geometric roughness height and relative submergence h_d/Δ (for symbols see Table 2).

way: l_R increases with increasing h_d/Δ. As mentioned in context with the zero-plane displacement height the findings for the permeable water-worked bed are not consistent with the ones for artificial surfaces.

As the mixing length of the roughness layer also the upper boundary of the layer z_R linearly increases with Δ as can be seen in Figure 11. Again a different behaviour of impermeable man-made and permeable water-worked beds can be observed. As expected, the roughness layer is located at least at the height of the roughness crests in case of the artificial surfaces. z_R is below the roughness crests in case of the armour layer. This finding is not meaningful, as it implements that the logarithmic law would be valid within the roughness layer. Two reasons can be given for the contradiction. First, the definition of the roughness crests z_c as the elevation for which 99% of observed bed elevations are smaller than z_c can be inappropriate. Choosing, for instance, 95% instead of 99% would eliminate the contradiction. And second, as stated above, the determination of the boundary between logarithmic and roughness layer by regression analysis seems to be not sufficiently accurate for natural surfaces.

Plotting z_R as a function of h_d/Δ a plot similar to Figure 10 results. Scaling z_R with Δ and plotting it as a function of the relative submergence (Fig. 12) the classification of the different surfaces almost vanishes.

However, compared to the parameters of the logarithmic layer, the parameters of the roughness layer show only a weak dependence on flow characteristics, if at all. This suggests that it could be possible to parameterise the velocity profile with characteristics of the bed roughness.

The parameter z_R could be treated as the length scale of the bed roughness. It influences the parameters of the logarithmic layer in that way that it defines the lower boundary for analysis of the logarithmic layer. Therefore, thorough determination of z_R is required.

A promising approach to refine the technique of determining the boundary between roughness and logarithmic layer is the adaptation of the double-averaged Navier-Stokes equations (DANS). Due to the spatial averaging the spatial heterogeneity of the flow can be investigated, which then will be related to geometric characteristics of the bed roughness. First results are presented in Aberle (2006).

6 CONCLUSION

Based on the re-definition of the zero-plane displacement height a new parameterisation of the vertical velocity profile within the wall region was developed and a methodology for determination of the parameters was suggested. The parameterisation was tested with velocity data measured over man-made and water-worked surfaces. Dependencies of the velocity parameters on roughness and flow characteristics were investigated.

Scaling of the velocity and the length scale with the appropriate parameters confirmed the parameterisation. Moreover, the study of parameters revealed dependencies for the velocity profiles measured over artificial surfaces. However, the data obtained from the measurements of the flow over a water-worked armour layer show some deviations compared to the data of the artificial surfaces. The inconsistency can be mainly related to the definition of the geometric roughness height and to the determination of the upper boundary of the roughness layer.

The results of the study emphasise the importance of the analysis of the spatial characteristics of the flow field as well as of the roughness density function of water-worked beds, which are under investigation at the moment.

Copyright © 2006 Taylor & Francis Group plc, London, UK

ACKNOWLEDGEMENTS

The research was supported by the European Commission, contracts EV5V-CT92-0179 and ENV4-CT96-0247, grant 447 NSL-111/01/1 from DFG (Deutsche Forschungsgemeinschaft, Germany), and contract DI-651/4-3 from DFG. A. Dittrich and J. Aberle provided helpful advice and generous support to this project. The author is grateful for useful discussions and suggestions to V. Nikora and to all participants of the 'double-averaging' workshops.

REFERENCES

Aberle, J. 2006. Spatially averaged near-bed flow field over rough armor layers. *Proc. of the Int. Conf. on Fluvial Hydraulics* "*RiverFlow 2006*" (this issue).

Aberle, J. & Koll, K. 2004. Double-averaged flow field over static armor layers. *Proc. of the Int. Conf. on Fluvial Hydraulics* "*RiverFlow 2004*", Naples, Italy, Vol. 1: 225–233.

Aberle, J. & Nikora, V. 2006. Statistical properties of armored gravel-bed surfaces. *Water Resour. Res.*, submitted.

Bayazit, M. 1982. Flow structure and sediment transport mechanics in steep channels. *Euromech 156: Mechanics of Sediment Transport*, Istanbul: 197–206.

Clauser, F.H. 1956. The turbulent boundary layer. *Adv. App. Mech.*, Vol. 4: 1–51.

Dittrich, A. & Hammann de Salazar, K. 1993. Bed instability caused by clear water flow. *Final Report of the Project Eroslope (EV5V-CT92-0179).*

Dittrich, A. & Koll, K., 1997. Velocity field and resistance of flow over rough surface with large and small relative submergence. *Int. J. Sediment Res.* 12(3): 21–33.

Dittrich, A., Nestmann, F. & Ergenzinger, P. 1996. Ratio of lift and shear forces over rough surfaces. In: *Coherent Flow Structures in Open Channels.* Eds. P.J. Ashworth, S. Bennett, J.L. Best, S.J. McLelland, John Wiley & Sons Ltd., Chichester, U.K.: 125–146.

Gust, G. & Southard, J.B. 1983. Effects of weak bed load on the universal law of the wall. *J. Geophys. Res.*, 88(C10): 5939–5952.

von Kármán, Th. 1930. Mechanische Ähnlichkeit und Turbulenz. *Nachr. Ges. Wiss.*, Math.-Phys. Kl.: 58–76.

Kirkbride, A. 1993. Observations of the influence of bed roughness on turbulence structure in depth limited flows over gravel beds. In: *Turbulence: Perspectives on flow and sediment transport.* Eds. N.J. Clifford, J.R. French, J. Hardisty, John Wiley & Sons Ltd., Chichester, U.K.: 185–196.

Koll, K. 2002. Feststofftransport und Geschwindigkeitsverteilung in Raugerinnen. [online], Karlsruhe, Univ., Fak. f. Bauingenieur- und Vermessungswesen, Diss. v. 12.07.2002, http://www.ubka.uni-karlsruhe.de/cgibin/psview?document=2002/bau-verm/12.

Nakagawa, H., Tsujimoto, T. & Shimizu, Y. 1991. Turbulent flow with small relative submergence. *Lecture Notes in Earth Sciences "Fluvial Hydraulics of Mountain Regions"*, 37, Eds. A. Armanini & G. Di Silvio, Springer Verlag: 33–44.

Nezu, I. & Nakagawa, H. 1993. *Turbulence in open-channel flows*. IAHR Monograph, A.A. Balkema, Rotterdam, Brookfield, ISBN 90 5410 118 0

Nikora, V.I. & Goring, D.G. 2000. Flow turbulence over fixed and weakly mobile gravel beds. *J. Hydr. Eng.*, 126(9): 679–690.

Nikora, V., Goring, D., McEwan, I. & Griffiths, G. 2001. Spatially averaged open-channel flow over rough bed. *J. Hydraul. Eng.* 127(2): 123–133.

Nikora, V., Koll, K., McEwan, I., McLean, S. & Dittrich, A. 2004. Velocity distribution in the roughnes layer of rough-bed flows. *J. Hydraul. Eng.* 130(10): 1036–1042.

Nikora, V., Koll, K., McLean, S., Dittrich, A. & Aberle, J. 2002. Zero-plane displacement for rough-bed open-channel flows. *Proc. Int. Symp. on Fluvial Hydraulics "RiverFlow2002"*, Louvain-la-Neuve, Belgium: 83–92.

Nikora, V., McLean, S., Coleman, S., Pokrajac, D., McEwan, I., Campbell, L., Aberle, J., Clunie, D. & Koll, K. 2006. Double-averaging concept for rough-bed open-channel and overland flows: Applications. *J. Hydr. Eng.*, submitted.

Nikuradse, J. 1933a. Gesetzmäßigkeiten der turbulenten Strömung in glatten Rohren. *Zeitschrift des Vereins deutscher Ingenieure*, 77(2): 48.

Nikuradse, J. 1933b. Strömungsgesetze in rauhen Rohren. *Zeitschrift des Vereins deutscher Ingenieure*, 77(39): 1075–1076.

Nowell, A.R.M. & Church, M. 1979. Turbulent flow in a depth-limited boundary layer. *J. Geophysical Res.*, 84(C8): 4816–4824.

O'Loughlin, E.M. & Annambhotla, V.S.S. 1969. Flow phenomena near rough boundaries. *J. Hydr. Res.*, 7(2): 231–250.

Prandtl, L. 1933. Neuere Ergebnisse der Turbulenzforschung. *Zeitschrift des Vereins deutscher Ingenieure*, 77(5): 105–113.

Sirovich, L. & Karlsson, S. 1997. Turbulent drag reduction by passive mechanisms. *Nature.* Vol. 388: 753–755.

Vanoni, V.A. & Nomicos, G.N. 1959. Resistance properties of sediment-laden streams. *J. Hydr. Div.*, 85(HY5): 77–107.

Copyright © 2006 Taylor & Francis Group plc, London, UK

Secondary flow and velocity redistribution by bubble screens in open channel bends

J.H.A. Wijbenga
$HKV_{consultants}$, Lelystad, The Netherlands

R. Schielen
Ministry of Transport, Public Works and Water Management, Institute for Inland Water Management and Waste Water Treatment, Arnhem, The Netherlands, and Twente University, Water Engineering and Management, Enschede, The Netherlands

K. Blanckaert
ICARE-ENAC Ecole Polytechnique Fédérale (EPFL), Lausanne, Switzerland

F. Buschman
Hydrology and Quantitative Water Management Group, Wageningen University, Wageningen, The Netherlands

ABSTRACT: In rivers flowing in their own alluvial deposits, the curvature induced circulation results in a cross section with deep outer bends and shallow inner bends, which reduces the depth and width of navigation. In the past various solutions have been proposed to increase the width of navigation through temporary dredging and/or costly non reversible river engineering works. The present paper presents results of preliminary experiments to reduce the influence of the curvature induced circulation by means of a counteracting circulation, generated by a bubble screen along the outer bend. With a bubble screen in operation, two counter rotating circulation cells exist, with a downward flow at the junction of both cells. Due to the presence of the bubble induced circulation, the core of maximum bed shear stress shifts in the direction of the inner bend, while the curvature induced circulation is crushed in inward direction. Increasing the width of navigation seems feasible although many questions still have to be resolved.

1 INTRODUCTION

It is well known that in natural rivers, the bottom configuration is seldom flat. On all spatial scales, bed forms develop, varying from very small ripples to very large alternating bars. For an elaboration of the scale-issue, we refer to Seminara (1995), De Vriend (1999) and Baptist (2005). This paper concentrates on the mega-scale, which is the scale of bars rather than dunes of ripples.

In straight rivers, a pattern of alternating bars is often found, depending on the width-to-depth ratio of the channel. This is a *free* instability, which arises spontaneously due to the fact that there are always small perturbations present on the river bed which grow to finite amplitudes if the conditions are right (for a theoretical analysis of free bars, see for instance Schielen et al 1993).

In open-channel bends, the curvature of the channel gives rise to a *forced* instability which forms the so bar pool bed topography with a point bar in the inner bend and a scour hole in the outer bend (Fargue 1868, Odgaard 1981, etc).

This paper will focus on open-channel bends, although the technique presented can also be applied in straight rivers.

For this paper, it suffices to mention that the bend topography is mainly shaped by the interaction between the velocity distribution, the secondary circulation and the bed topography itself.

This secondary circulation, also called spiral flow or helical flow, is a typical feature of flow in open-channel bends (see Fig. 1, Van Bendegom 1947, Rozovskii 1957, de Vriend 1981, Blanckaert and de Vriend 2003, 2004).

Point bars in the inner bend often cause hinder for shipping because the width of the navigation channel is decreased. This problem is of special importance for the Dutch river Waal (one of the Rhine-branches), which is one of the main shipping routes in Europe. For

Copyright © 2006 Taylor & Francis Group plc, London, UK

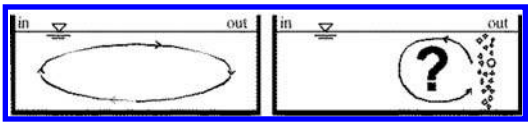


Figure 1. Conceptual sketch of (left) secondary circulation in open-channel bends; (right) the bubble-screen technique.

the Waal, the problems are even more pregnant because in the upper reach, there are several sharp bends which induce large point bars. There are in principal two ways to avoid the existence of point bars: influence the flow, or protect the bed.

The flow can be influenced by the construction of bottom vanes, which actually prevent the secondary circulation to develop. A disadvantage of this method is that it is a fixed construction on the bed, and hence it is a possible threat for the ships. Bottom vanes are applied in for instance Bangladesh, see Hossain et al (2005) and Jongeling and Flokstra (2001), and, in the past, have been considered in the Dutch river IJssel. However, due to the aforementioned threat to the ships, they have never been constructed.

A method which acts on the bed is the construction of a fixed layer in the outer bend. The mechanism is that due to the fixed layer, the outer bend can no longer erode, and hence no material can be transported to the inner bend. Thus, point bars can not develop. Disadvantage of this method is again that it is a fixed construction. As the bed-level in the eastern part of the Netherlands is decreasing, the river Rhine cuts itself deeper in the land and hence, a construction like a fixed layer may also become an obstacle for shipping.

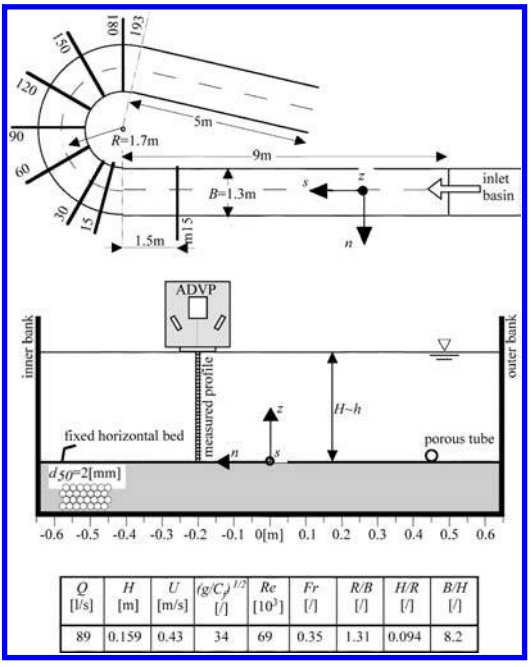
A third method to prevent point bars is the construction of groynes with a limited height ('bed-groynes' or submerged groynes). The maintenance of these underwater groynes however, is far from easy and they are often destroyed under high-water conditions.

In this paper, we describe the method and results of a new, and non-permanent way to perturb the secondary circulation. The central idea is to counteract the downward movement of the secondary circulation by releasing rising air bubbles. The bubble screen drags the flow upwards, and hence, the secondary circulation is perturbed. Figure 1 schematically illustrates this technique.

At forehand, it is not clear how the bubble screen will influence the flow pattern. The main research questions of this paper therefore are:

1. Can a bubble-screen counteract the development of the curvature induced secondary circulation ?
2. What are the characteristics of the remaining flow pattern?

This paper briefly describes the laboratory flume and the experimental conditions, presents the results and discusses them with respect to the navigable width.



Q [l/s]	H [m]	U [m/s]	$(g/C_f)^{1/2}$ [/]	Re [10^3]	Fr [/]	R/B [/]	H/R [/]	B/H [/]
89	0.159	0.43	34	69	0.35	1.31	0.094	8.2

Figure 2. Experimental set-up, reference system, ADVP and hydraulic conditions. B = flume width, H = water depth, R = radius of curvature, U = flow velocity, Q = discharge, Re = Reynolds number, Fr = Froude number.

2 EXPERIMENTS

To investigate the influence of a bubble-screen on the secondary circulation in a bend, experiments were carried out in the strongly curved laboratory flume at the École Polytechnique Fédérale de Lausanne (EPFL) in Switzerland. The curved flume, see Figure 2, consists of a straight inflow reach of 9 m, a 193° curved reach with a 1.7 m radius of curvature for the centreline and a straight outflow reach of 5 m. The width of the flume is 1.3 m, with a rectangular cross section. The bed slope of the inflow reach is 0.22%, while the bend and the outflow reaches are horizontal. The flume bed and the outer bank were artificially roughened with sand, having an average grain size of 2 mm, glued to the surface, whereas the inner bank was made of Plexiglass.

From earlier experiments in the flume (see Blanckaert 2002a) extensive reference data with respect to the unperturbed secondary circulation, is available for a water depth of 0,159 m. To be able to compare results of the experiments at hand with the earlier experiments similar flow conditions were installed, see Figure 2.

For the bubble-screen, use was made of a porous tube, which was placed from the bend entry till the bend exit at a distance of 0,20 m from the outer wall at the location where the downward velocities were largest in the reference experiments without

Copyright © 2006 Taylor & Francis Group plc, London, UK

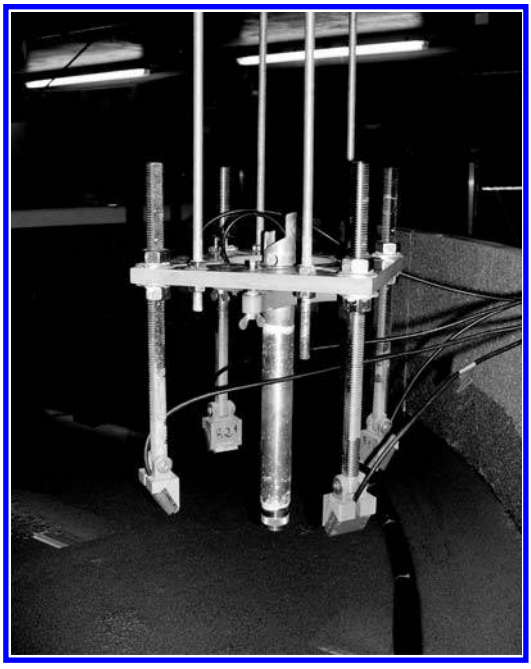


Figure 3. Acoustic Doppler Velocity Profiler (ADVP).

bubble-screen. The holes in the tube are very fine and located on both sides of the diameter, approximately 3 mm apart in longitudinal direction, resulting in bubbles with a diameter of 0.002 m till 0.015 m. The tube was on both sides connected to the same compressor enabling a more or less constant air pressure along the whole length of the tube. The pressure in the tube was measured and could be regulated with a valve. Preliminary tests indicated an optimal pressure of 3 bar, which fortunately coincided with the recommended pressure for the tube.

For the flume a curvilinear coordinate system is defined with s-direction along the centreline of the flume, a transversal axis n, perpendicular to the centreline, positive in outward direction and a vertical z-axis perpendicular to the plane through s and n and positive in upward direction, see Figure 2.

Water levels, bed levels and flow velocities were measured in the cross-sections at an angle of 15°, 30°, 60° 90°, 120°, 150° and 180° in the bend and included the transversal locations, $n = [-0.5, -0.4, -0.3, -0.2, -0.1, 0, 0.1, 0.2, 0.3, 0.4, 0.5]$ m.

The flow velocities, either with or without bubble-screen, were measured with an Acoustic Doppler Velocity Profiler (ADVP), designed at EPFL. Sample time was 180s. The system is based on a central emitter (see Figure 3) which periodically sends an acoustic signal with a frequency of 1 Mhz in the vertical downward direction. From the returning signal of four receivers surrounding the emitter, the time-averaged velocities and velocity fluctuations in the three directions (v_s, v_n and v_z) are derived. The ADVP has the major advantage of measuring entire profiles at one go. Because the flow in the upper 0,02 m of the water column is perturbed by the ADVP, the velocities in this layer were extrapolated by means of procedures outlined by Blanckaert and Graf (2001). For a more detailed description of the ADVP, see Lemmin and Rolland (1997) or Blanckaert and Lemmin (2006).

3 EXPERIMENTAL RESULTS

In general, the flow in river bends is decomposed along the reference axes. The decomposition results in a cross-flow, $U_n = \langle v_n \rangle$ that represents the translatory motion, and the two components (v_n^*, v_z) which represents the circulatory motion, see Bradshaw (1987):

$$\begin{cases} v_s = U_s + v_s^* \\ v_n = U_n + v_n^* \\ v_z \end{cases} \quad (1)$$

To illustrate the effect of the bubble screen on the flow, Figures 4 to 7 compare features of the flow field with and without bubble screen. Figures 4 and 5 show the normalized quantities $(v_n^*, v_z)/U$ and v_s/U in the cross-section at 90° in the bend, whereas Figures 6 and 7 show the evolution around the bend of some depth-averaged flow quantities.

In Figure 4, where the flow velocities for the reference situation without bubbles are given, a curvature induced cell of secondary circulation is clearly visible. It extents over the entire width of the cross-section and reaches maximum transversal and vertical velocities of about $v_n = \pm\ 0.2\ \mathrm{ms}^{-1}$ and $v_z = \pm 0.025\ \mathrm{ms}^{-1}$, respectively. The inclination of the isolines of v_s are illustrative of advective momentum transport by this secondary circulation.

In Figure 5 the flow velocities are given for the same hydraulic conditions and in the same cross section but now with the bubble screen in operation. In the cross section between $n = -0.5$ and $n = 0.4$ two circulation cells can be observed, the curvature induced circulation, smaller in size, more or less equal in strength and direction of rotation and the bubble induced circulation, covering roughly half of the flume width and with a rotation opposite of the curvature induced circulation. The bubble induced circulation is only slightly weaker than the curvature induced one. The vertical downstream velocity at the junction of both cells is amplified and reaches maximum values of about $v_z = -0.055\ \mathrm{ms}^{-1}$. Maximum transversal and vertical velocities are about $v_n = \pm 0.2\ \mathrm{ms}^{-1}$ and $v_z = \pm 0.025\ \mathrm{ms}^{-1}$, respectively.

Copyright © 2006 Taylor & Francis Group plc, London, UK

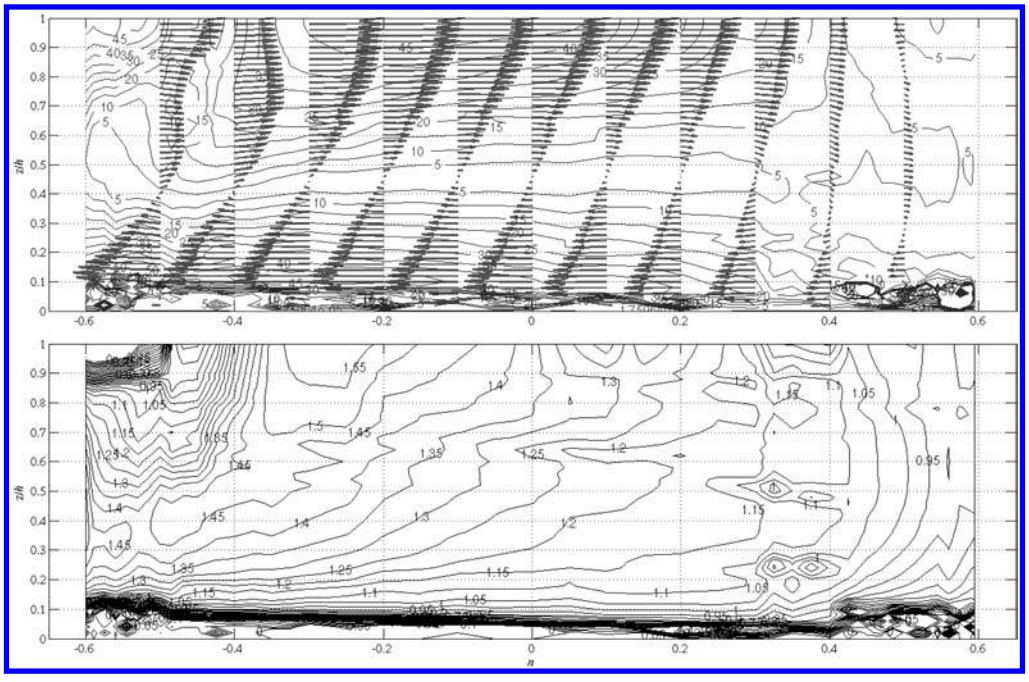


Figure 4. Patterns of normalized secondary circulation, $(v_n^*, v_z)/U$ (isolines show vector magnitude in [%]), and downstream velocity, v_s/U, measured in the cross-sections at 90° without bubble screen. Horizontal axis n, vertical axis z/h.

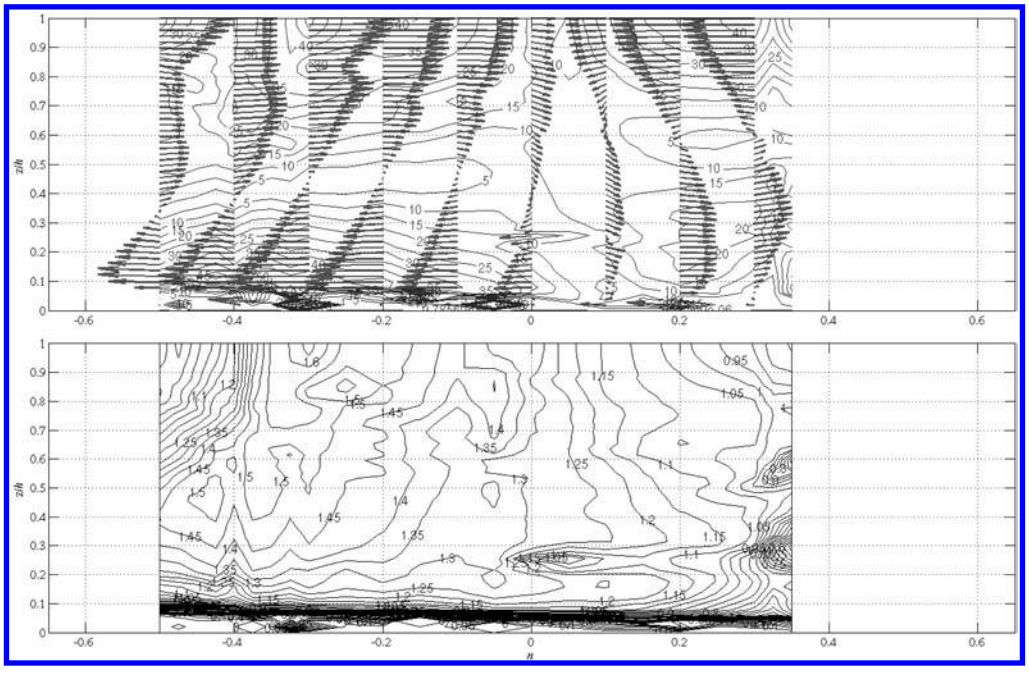


Figure 5. Patterns of normalized secondary circulation, $(v_n^*, v_z)/U$ (isolines show vector magnitude in [%]), and downstream velocity, v_s/U, measured in the cross-sections at 90° without bubble screen. Horizontal axis n, vertical axis z/h.

Copyright © 2006 Taylor & Francis Group plc, London, UK

The secondary circulation pattern is well visualized by means of the functional ψ, defined as:

$$\psi = \frac{1}{2}(\psi_n + \psi_z)$$

$$\psi_n = -(1+n/R)\int_{z_b}^{z} v_n^* dz$$

$$\psi_z = \int_{-B/2}^{B/2}(1+n/R)v_z dn - \langle\langle\psi_z\rangle\rangle + \langle\langle\psi_n\rangle\rangle \qquad (2)$$

The factor $(1+n/R)$ accounts for the divergence of the transversal coordinate axis. $\langle\langle\psi_n\rangle\rangle$ and $\langle\langle\psi_z\rangle\rangle$ represent the grid-averaged value of ψ_n and ψ_z, respectively.

In fully-developed curved flow ($\partial/\partial s = 0$, infinite bend), $\psi_n = \psi_z$ and ψ represents the classical definition of the streamfunction (Batchelor 1967), whence the functional ψ will be called pseudo-streamfunction hereafter.

This pseudo-streamfunction has the advantage of being a scalar quantity, contrary to the secondary circulation vector (v_n^*, v_z). Patterns of secondary circulation measured in the same experimental set-up have been presented by Blanckaert (2002b) by means of a similar pseudo-streamfunction.

Figure 6 shows the strength of the secondary circulation parameterized by the normalized depth-averaged pseudo-streamfunction, $100\langle\psi\rangle/(UH)$. In the experiment without bubble screen, only a curvature induced secondary circulation cell exists, whereas an additional bubble generated circulation cell exists in the presence of the bubble screen. The bubble induced circulation pushes the curvature induced circulation towards the inner bend and reduces its transversal extent, but has hardly any influence on its strength.

In both experiments the secondary circulation develops at the bend entry, reaches its maximum at approximately 90^o in the bend and weakens further downstream.

Figure 7 shows the distribution of the downstream bed shear stress component, τ_{bs}, estimated with the Chézy type relation

$$\tau_b = C_f U_s^2 \qquad (3)$$

and normalized by means of the flume averaged bed shear stress,

$$\langle\langle\tau_b\rangle\rangle = \rho C_f U^2 \qquad (4)$$

where $U = Q/(BH)$ is the flume averaged velocity.

Without a bubble induced circulation cell the core of the high bed shear stress starts at the upstream side at the inner bend and gradually shifts to the outer bend, which is reached at the bend exit. With a bubble induced circulation cell the core of the highest bed shear stress does not migrate further than the junction of both circulation cells, which is found near the centreline of the flume. The bed shear stress decreases towards both banks.

The maximum value of the bed shear stress is higher in the presence of the bubble screen. This maximum value in the bend is about twice as high as the flume averaged value $\langle\langle\tau_b\rangle\rangle$ that would occur in a straight flow.

4 DISCUSSION

The experiments in the strongly curved flume with fixed flat bed show that a bubble induced circulation cell is able to reduce the size of the curvature induced circulation cell.

In case of an alluvial erodible bed, the curvature induced circulation cell would transport the sediment from the outer bend to the inner bend due to the direction of the flow at the river bed. For equilibrium conditions the drag force of the flow in n-direction balances the gravitational force in the same direction. It is expected that, in case of a combination of curvature induced and bubble induced circulation cells, the thalweg would follow the line through the downward junction of both cells and that the cross sectional bed level gradient will be roughly zero along this line. Because of the decrease in size of the curvature induced circulation cell the position of the thalweg would be closer to the centreline. The circulation strength of the curvature induced cell is hardly reduced, so the cross sectional bed slope at the inner bend would be approximately equal to the slope without bubble induced circulation. Due to the shift in thalweg one may nevertheless expect an increase in navigational width, see Figure 8. However, as the experiments so far have only been carried out with a fixed bed, the situation that is indicated in figure 8 remains somewhat speculative. Especially the velocity distribution and shear stress consequences in case of an erodible bed need to be examined.

The main advantage of a bubble screen compared to other techniques, which try to avoid the existence of point bars, is its reversibility. Whenever the compression stops, the bubbles are no longer present, and the flow pattern goes back to normal. In periods of low discharge (and little morphological activity), there is no need for the bubble screen to be present. Only when sediment redistribution is likely to cause problems (this is typically during high discharges) the bubble screen needs to be activated. As a nice side-effect, it may also have an additional positive effect on the ecology in the river. Existing techniques like bottom vanes or fixed layers are always present, and hence do also have an effect at low discharges. This effect is not always appreciated.

Copyright © 2006 Taylor & Francis Group plc, London, UK

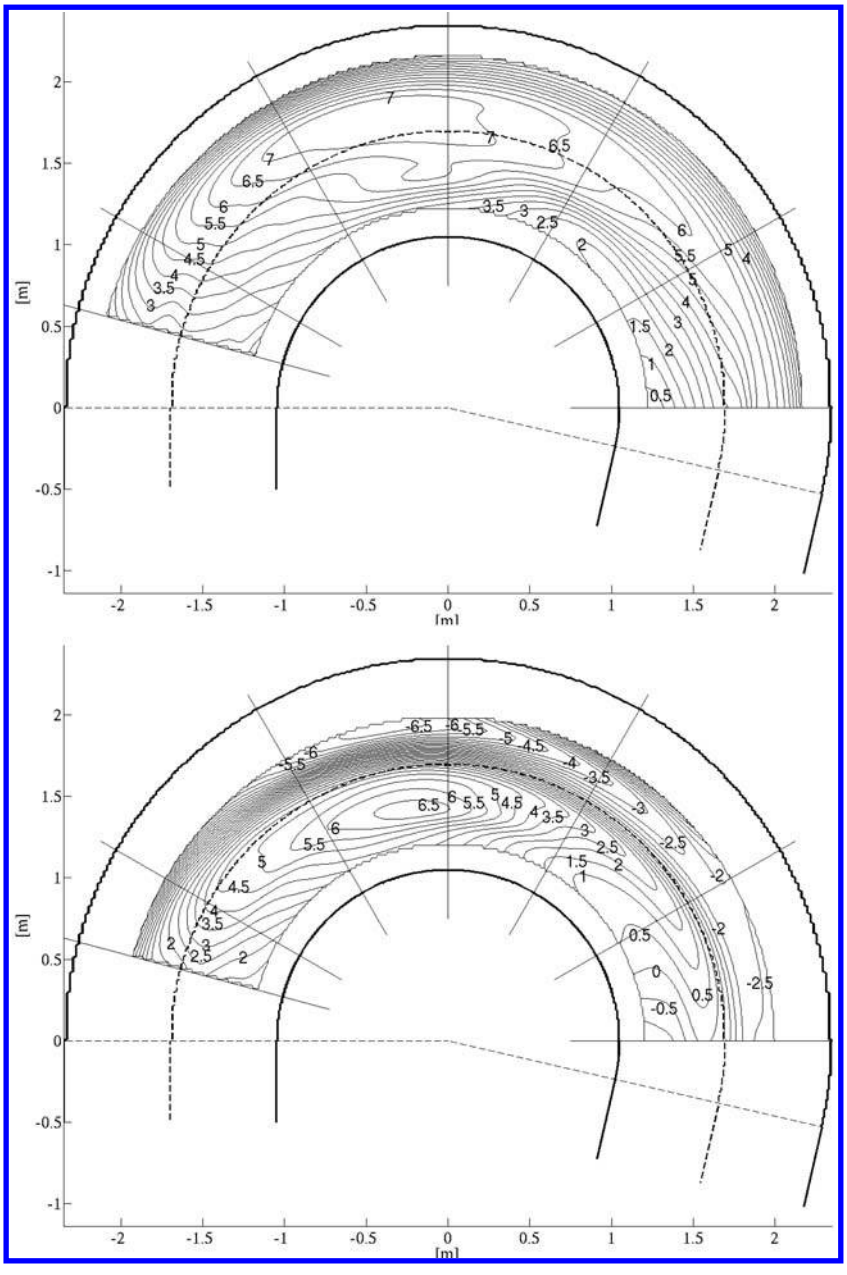


Figure 6. Distribution of the normalized depth-averaged secondary circulation strength $100\langle\psi\rangle/(UH)$ in the bend, (top) Reference situation without bubble screen. (bottom) With bubble screen. Bend entry/exit at the left/right. Measured cross-sections at 15°, 30°, 60°, 90°, 120°, 150° and 180° indicated.

Before applying this technique in practice, further research is needed with respect to technical and economical aspects. The principal seems to work in a flume, but is it also applicable in a real river? The width-to-depth ratio of the flume was about 8.3, while a real river like the Waal has typically width-to-depth ratios over 50. Not only is there a question with respect to the mechanism (will there also appear two cells) but there is also the technical question with respect to the generation of bubbles (which obviously must be an order of magnitude larger than in the experiment) and the energy needed for that.

Copyright © 2006 Taylor & Francis Group plc, London, UK

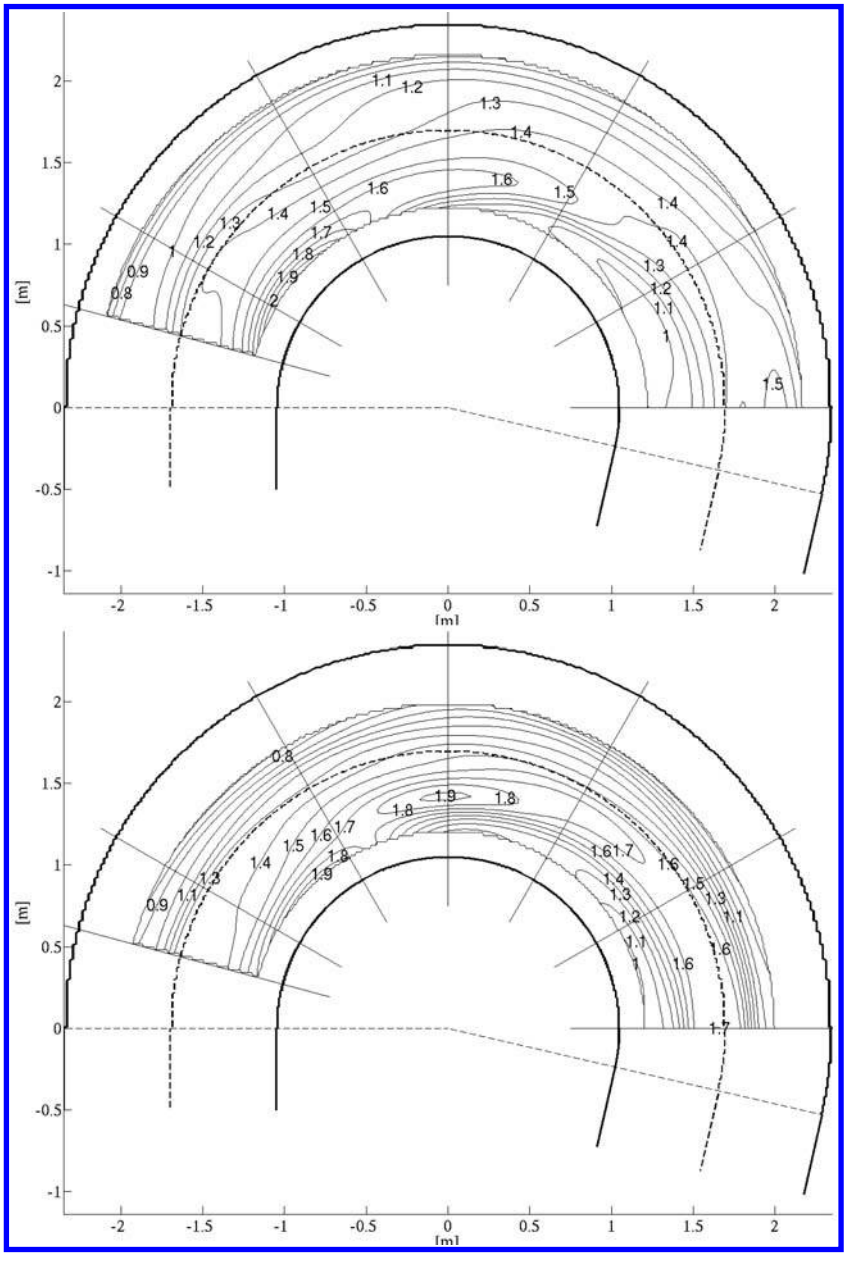


Figure 7. Distribution of the normalized downstream bed shear stress, $\tau_{bs}/\langle\langle\tau_b\rangle\rangle$ in the bend, (top) Reference situation without bubble screen. (bottom) With bubble screen. Bend entry/exit at the left/right. Measured cross-sections at 15°, 30°, 60°, 90°, 120°, 150° and 180° indicated.

5 CONCLUSION

Preliminary experiments in a strongly curved flume convincingly show that a bubble screen reduces the width extent of the curvature induced circulation cell.

A bubble induced circulation cell develops that is roughly similar in strength, but smaller in spanwise extent. It exists next to the counter rotating curvature induced circulation cell, which is shifted in inward direction but hardly reduced in strength. The core of

Copyright © 2006 Taylor & Francis Group plc, London, UK

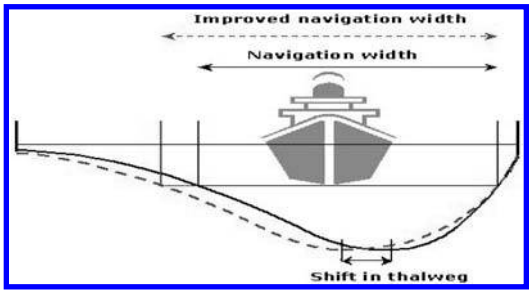


Figure 8. Possible improvement in width of navigation in case of curvature induced and bubble induced circulation cells.

maximum downstream velocities is shifted from near the outer bank in inward direction to the junction of both circulation cells. Over a mobile bed, this would result in a more uniform depth distribution with a maximum depth at the junction of both circulation cells.

Before applying this technique in real life situations however, further technical questions need to be resolved, such as:

- Do the conclusions still hold in the case of an erodible bed?
- During which period of time or during which flow conditions is a bubble screen most effective to increase the width for navigation?
- How much energy is required for such a period?
- Would the navigation be hampered by a bubble screen?
- Will there be an increase in bank erosion at the outer bank?

Besides demonstrating the potential of the bubble screen technique, the measurements provide detailed data on the 3D flow field in open-channel bends, which can be useful for validation of numerical models.

REFERENCES

Baptist, M. (2005): "Modelling floodplain bio geomorphology." Thesis Delft University.

Batchelor, G.K. (1967). "An introduction to fluid dynamics". Cambridge University Press.

Blanckaert, K. (2002a): "Flow and turbulence in sharp open-channel bends." PhD-thesis Nr 2545, Ecole Polytechnique Fédérale de Lausanne, Switzerland. (see "ftp: //lrhmac15.,epfl.ch/Pub/ Thesis/Blanckaert/PhD").

Blanckaert K. (2002b). "Secondary currents measured in sharp open-channel bends." Proc. River Flow 2002, Louvain, Belgium.

Blanckaert, K. & de Vriend, H.J. (2003). "Non-linear modeling of mean flow redistribution in curved open channels." Water Resources Res., AGU, 39(12), 1375. (doi:10.1029/2003WR002068)

Blanckaert, K., and de Vriend, H. J. (2004). "Secondary flow in sharp open-channel bends." J. Fluid Mech, Vol. 498, 353-380. (doi:10.1017/S0022112003006979).

Blanckaert, K. & Graf, W. H. (2001). "Experiments on flow in an open-channel bend. Mean flow and turbulence." J. Hydr. Engng, ASCE, 127(10), 835-847.

Blanckaert, K. & Lemmin, U. (2006). "Means of noise reduction in acoustic turbulence measurements." J. Hydr. Res., IAHR., 44(1), 3-17.

Bradshaw, P. (1987). "Turbulent secondary flows." Annual Review Fluid Mechanics, 53-74.

de Vriend, H.J. (1981): "Velocity redistribution in curved rectangular channels". J. Fluid Mech., Cambridge Univ. Press, 107, 423-439.

de Vriend, H.J. (1999): "Long-term morpho dynamics of alluvial rivers and coasts." In. G. Bianchi (Ed.), Environmental applications of mechanics and computer science (p. 1-19). CISM Courses and Lectures. No. 409, Springer Wine New York.

Fargue L (1868). "Etude sur la corrélation entre la configuration du lit et la profondeur d'eau dans les rivières à fond mobile". Annales des Ponts et Chaussées.

Hossain, M.M., Rahman, K.M., Ferdousi, S., Islam, M.Z. & Mosselman, E. ,2005, "Bottom vanes to mitigate erosion hazard in medium sized rivers of Bangladesh", Proceedings of International Conference on Disaster Management Achievements and Challenges, 18-20 November 2005, Nepal.

Jongeling, T.H.G., and Flokstra, C, "Bodemschermen. Stromingskrachten en snelheidsveld bij variatie van de schermhoogte." (In Dutch). Delft Cluster Report, the Netherlands, 2001.

Lemmin, U. & Rolland, T. (1997). "Acoustic velocity profiler for laboratory and field studies." J. Hydr. Engng, ASCE, 123(12), 1089-1098.

Odgaard, A.J. (1981). "Transverse bed slope in alluvial channel bends." J. hydr. Div., ASCE, 107(HY12), 1677-1693.

Rozovskii, I.L. (1957): "Flow of Water in Bends of Open channels." Acad. Of Sciences of the Ukrainian S.S.R., Inst. Of Hydrology and Hydraulic Eng. Kiev.

Schielen, R.M.J., Doelman, A & De Swart, H.E. (1993): "On the non-linear dynamics of free bars in straight channels." J. of Fluid Mech. 252: 325–356.

Seminara, G. (1995): "Invitation to river morpho dynamics." In A. Doelman and A. van Harten (eds.) Non-linear dynamics and pattern formation in the natural environment (p. 269-294), Pitman Research Notes in Mathematics (335), Longman, Essex.

van Bendegom, L. (1947): "Enige beschouwingen over rivierverbeteringen." (in Dutch). De Ingenieur, 59, 4, B&W. pp. B1-B12. ("Some considerations on river morphology and river training.")

Copyright © 2006 Taylor & Francis Group plc, London, UK

Detection and reconstruction of coherent structures based on wavelet multiresolution analysis

M.J. Franca
Laboratoire d'Hydraulique Environnementale – École Polytechnique Fédérale de Lausanne, Switzerland
Present address: Instituto Superior Técnico – Technical University of Lisbon, Portugal

U. Lemmin
Laboratoire d'Hydraulique Environnementale – École Polytechnique Fédérale de Lausanne, Switzerland

ABSTRACT: In turbulent river flows, coherent structures play a major role in transport and mixing processes. Coherent structures appear as non-stationary randomly distributed singularities in turbulent velocity signals. Wavelet analysis which characterizes signal variability both in time and space is well suited for the analysis of isolated phenomena such as coherent structures. With wavelet decomposition we may represent individual features of the instantaneous signal within a pre-determined scale. We developed a coherent structure detection technique based on wavelet multiresolution analysis, conditioned by event scale and amplitude. The samples are chosen using a correlation threshold condition. 3D reconstruction is made by composite averaging. We assess the relationship between coherent structures and other large- or small-scale flow features and the contribution of individual events to the turbulent flow structure such as velocity profile, Reynolds stress tensor and TKE budget. We apply our method to Acoustic Doppler Velocity Profiler measurements in a gravel-bed river.

1 INTRODUCTION

In geophysical flows, momentary variations of the velocity are related to such processes as the suspension of sediments and the dispersion of pollutants in the water. Coherent structures consist of macroscale "organized" phenomena, belonging to the productive range of the spectral space. In the inertial and the dissipative ranges, turbulence is essentially random and isotropic, composed of fine scale features such as small scale eddies. Coherent structures have a short life cycle. They cannot be identified with a time averaged analysis and require an investigation based on time and space correlation measurements or flow visualization techniques. In laminar and transitional flows, coherent structures occur periodically, whereas in turbulent flows they occur randomly in space and time. Hence, in addition to flow visualization techniques, conditional sampling and statistics techniques have to be used in the detection and characterization of coherent structures. Several authors applied conditional statistics to turbulence studies (Antonia & Atkinson 1973, Nakagawa & Nezu 1977 and Hurther & Lemmin 2000). Adrian et al. (2000) compared Reynolds decomposition, Galilean and LES techniques. In this study we will use Reynolds time-averaged decomposition.

Here we make use of conditional sampling techniques and the wavelet multilevel decomposition of single point instantaneous velocity measurements. Wavelet analysis is a suitable tool for the study of turbulence in geophysical flows. Foufoula-Georgiou & Kumar (1994) presented a compilation of papers dealing with the application of wavelet analysis in geophysics. Turner et al. (1994) examined scales and the location of flow structures related to temperature and flux data of atmospheric flow above a forest canopy. Yoshida & Nezu (2004) used wavelet analysis to study the importance of the bursting process near the free surface for gas transfer in open-channel flows.

We use velocity data obtained with the ADVP instrument in a river in order to develop a detection algorithm for coherent structures. This is based on wavelet multilevel decomposition of 3D instantaneous velocity profiles measured at one location over the whole water depth. A conditioned sample is created with scale, amplitude and cross-correlation threshold methods. Thereafter, the single-point detected structure is reconstructed three-dimensionally by a normalized composite average. We subsequently reconstruct the 3D flow structure over the whole water depth. The reconstructed structure and its time distribution in the instantaneous velocity signal are discussed.

Copyright © 2006 Taylor & Francis Group plc, London, UK

The method is demonstrated for Quadrant II (QII) structures (ejections) but may be generalized to other quadrants. With the detection technique we were able to identify and analyze several sequential bursting packets of coherent structures. The influence of packet dynamics on the velocity profile, Reynolds stress tensor (RST) and TKE production are investigated.

The notation adopted for the Reynolds velocity decomposition is streamwise, $u = \overline{u} + u'$; spanwise, $v = \overline{v} + v'$; vertical, $w = \overline{w} + w'$ (time mean and $'$ instantaneous value). When referring to $v = \overline{v}_i + v'_i$, v is velocity and the subscript i $\{1, 2, 3\} \equiv$ is one of the 3D Cartesian coordinates $\{x, y, z\}$.

2 COHERENT STRUCTURE SAMPLING

2.1 *Wavelet discrete transform and multiresolution analysis*

Wavelet analysis is capable of localizing signal variability simultaneously both in time and scale (scale here refers to time duration) (Kantha & Clayson 2000). Contrary to Fourier based analysis, wavelet analysis can deal with non-stationary signals with randomly distributed singularities, such as the occurrence of coherent structures in turbulent velocity time series. In wavelet decomposition, the wavelet functions are scaled locally (dilation or contraction) in order to represent singularities. Thus, boundaries do not influence the local description of the signal. Fargé (1992) presented an introductory text on the use of wavelet transform in the study of turbulent signals. This paper is based on Fargé (1992), Foufoula-Georgiou & Kumar (1994), Kumar & Foufoula-Georgiou (1997) and Mallat (1999). Only 1D wavelet analysis is used.

In the continuous wavelet transform, the wavelet function $\psi_{\lambda,t}(t)$ is parameterized by the real values of scale λ and time location t, whereas in the discrete wavelet transform $\psi_{m,n}(t)$ it is parameterized by the integers m and n. As in Fourier analysis, we can apply a wavelet transform using appropriate wavelet functions and discrete scale and location parameters (m and n). The process consists of evaluating the signal locally (the wavelet covers all the time locations) in several modes, each corresponding to a defined scale. The scale is defined by the expansion of $\lambda = \lambda_0^m$, where λ_0 is a fixed dilation step and m an integer. The time step to analyze the signal is a function of the chosen scale, $t = nt_0\lambda_0^m$. In this way, the time domain is covered by the discrete analysis.

A wavelet frame, which is characterized by the scale λ corresponds to each of the wavelets $\psi_{m,n}(t)$. The partial reconstruction of the signal conditioned by the wavelet frame defined by m corresponds to one decomposition mode. Wavelet multiresolution consists of the decomposition of the original turbulence signal into one coarse set (the approximation) and several others with progressively smaller scale resolution (the details). Once the multilevel wavelet discretization of the signal is made, each level of the signal is reconstructed resulting in several low-resolution data series corresponding to each wavelet frame scale. A scale resolution higher than the scale of the last lower level of decomposition corresponds to the approximation. The signal may be successively reconstructed by adding the approximation (S) to the consecutive level details (D_λ). Multiresolution analysis allows estimating the energy partition throughout the different scale frames associated with the decomposition modes. We may estimate the contribution of each wavelet frame to the streamwise flow energy by calculating the detail variance:

$$\overline{D_{\lambda,u'}{}^2} = \frac{\sum_{n=1}^{N_{time}} D_{\lambda,u'}(n)}{N_{time}} \qquad (1)$$

where $D_{\lambda,u'}$ = instantaneous detail of the instantaneous streamwise velocity associated with scale λ; n = the integer defining the time step; and N_{time} = total number of time steps (the addition is made for the entire time domain).

We will now introduce a coherent structure detection technique and apply it to a single decomposition mode of the instantaneous 3D velocities measured at one level of the velocity profile. Subsequently the reconstruction of the velocity profile is made taking into account the detected events.

2.2 *Wavelet-frame conditional quadrant analysis*

The statistical distribution of coherent structures in the $\{x\text{-}z\}$ plane may be analyzed by means of the threshold-based conditional sampling of instantaneous shear events $\varepsilon' = u'w'$, combined with their quadrant location (Nakagawa and Nezu, 1977). The quadrant technique consists of analyzing the distribution of the instantaneous shear events ε' in the four quadrants of the $\{x\text{-}z\}$ plane in order to detect coherent motions. For the positive detection of an event, a comparison of the relative amplitude of the instantaneous shear stress with a threshold value H is also required. Events for which the relative shear stress values ($\varepsilon'/\overline{u'w'}$) are lower than a threshold value H are called hole events. Using wavelet multilevel decomposition of the instantaneous signals, we may condition the analysis of the coherent structures to a wavelet frame, by restricting the quadrant analysis to a chosen structure scale:

$$H_{\varepsilon\uparrow\lambda} = \frac{D_{\lambda,\varepsilon'}}{D_{\lambda,u'}D_{\lambda,w'}} \qquad (2)$$

where $D_{\lambda,\varepsilon'}$ = time series of the instantaneous shear stress detail associated with scale λ, defined as

Copyright © 2006 Taylor & Francis Group plc, London, UK

$D_{\lambda,\varepsilon'} = D_{\lambda,u'} D_{\lambda,w'}$. $D_{\lambda,w'}$ is the instantaneous detail of the instantaneous vertical velocity associated with scale λ.

2.3 *Wavelet-frame threshold and cross-correlation conditional sampling*

We discussed how to sample coherent structures according to their scale, quadrant location and shear amplitude. Now we define a time window around the detected structures in a determined wavelet frame centred at the location of the instantaneous shear event detected as relevant (t_ε). Its range ($t_\varepsilon \pm \Delta t_\varepsilon$) is defined by the following window parameter ξ:

$$\Delta t_\varepsilon = \frac{\xi}{2}\lambda \tag{3}$$

The choice for the event reconstruction may be refined with an analysis based on the cross-correlation between individual data windows. A correlation coefficient threshold H_ρ below which the windowed instantaneous velocity data are rejected is defined as:

$$\begin{cases} \rho_{\tilde{v}_i'|\xi, v_i'|\xi} = \dfrac{C_{\tilde{v}_i'|\xi, v_i'|\xi}}{\sigma_{\tilde{v}_i'|\xi}\ \sigma_{v_i'|\xi}} \\ \text{if } \rho_{\tilde{v}_i'|\xi, v_i'|\xi} < H_\rho,\ v_i'|_\xi \text{ is rejected} \end{cases} \tag{4}$$

where $\rho_{\tilde{v}_i'|\xi, v_i'|\xi}$ = correlation coefficient between a windowed instantaneous velocity ($v_i'|_\xi$) and the composite average within the window ($\tilde{v}_i'|_\xi$); $C_{\tilde{v}_i'|\xi, v_i'|\xi}$ = covariance between $\tilde{v}_i'|_\xi$ and $v_i'|_\xi$; and $\sigma_{\tilde{v}_i'|\xi}$ and $\sigma_{v_i'|\xi}$ = standard deviations of $\tilde{v}_i'|_\xi$ and $v_i'|_\xi$, respectively. Appropriate normalization is made for the representation of the identified shear events. The time variable is normalized by the scale corresponding to the wavelet frame used as a basis to identify the structures (t^+). The velocities are normalized by the event amplitude within the time window:

$$v_i'^{+} = \frac{v_i'|_\xi}{\max(v_i'|_\xi) - \min(v_i'|_\xi)} \tag{5}$$

2.4 *Method*

Using the wavelet multilevel decomposition of the signal, a conditional sampling technique is presented that allows detecting and windowing similar coherent motion in a given velocity signal. The main steps of the procedure are:

1) Wavelet discrete transform of the turbulent velocity signal: multilevel decomposition of the signal into several wavelet-frames.
2) Multiresolution decomposition: reconstruction of each wavelet-frame resulting in several low-resolution data series corresponding to different time scales.
3) Scale conditional sampling of the decomposed signal with a chosen reference scale (λ).
4) Quadrant analysis and threshold-based ($H_{\varepsilon'|\lambda}$) sampling of instantaneous shear events conditioned by the chosen scale (λ).
5) Windowing and composite averaging of the detected structures with a defined window parameter (ξ).
6) Correlation coefficient threshold (H_ρ) re-sampling: refinement of the windowed events based on the coherence of different instantaneous events detected within the defined window.
7) Normalization and composite averaging of the windowed events: time normalized by the scale λ, and velocities normalized by the event amplitude (Eq. 5: u^+, v^+ and w^+ respectively for streamwise, spanwise and vertical components).

3 RIVER MEASUREMENTS

This research is based on a timeseries of instantaneous velocity profiles measured in the Swiss river Venoge (canton of Vaud) during the summer of 2004, under stationary shallow water flow conditions. The measuring position was located about 90 m upstream of the Moulin de Lussery. The hydraulic characteristics of the river and of the measured profile are shown in Table 1. where Q = river discharge; S = river slope; h = water depth; $\overline{U}$ = depth-averaged streamwise mean velocity; Re = Reynolds number; Fr = Froude number; u^* = shear velocity estimated using the eddy-correlation method (Monin and Yaglom 1971); D_{50} = bottom grain size diameter for which 50% of the grain diameters are smaller. The riverbed material grain distribution was sampled according to the Wolman (1954) method. The riverbed is hydraulically rough, with coarse gravel and randomly spaced macro-roughness elements scaling with as much as half the water depth (0.5 h). We used the deployable ADVP developed at the LHE-EPFL, which allows measuring 3D quasi-instantaneous velocity profiles over the entire depth of the flow in rivers (Rolland & Lemmin 1997). Data were sampled for 211 s at a frequency of 26 Hz. We implemented a dealiasing method which

Table 1. Summary of the river flow characteristics.

Q (m^3/s)	S (%)	h (m)	$\overline{U}$ (m/s)	Re ($\times 10^4$)	Fr (−)	u^* (m/s)	D_{50} (mm)
0.76	0.33	0.17	0.60	6.4	0.29	0.040	68

Copyright © 2006 Taylor & Francis Group plc, London, UK

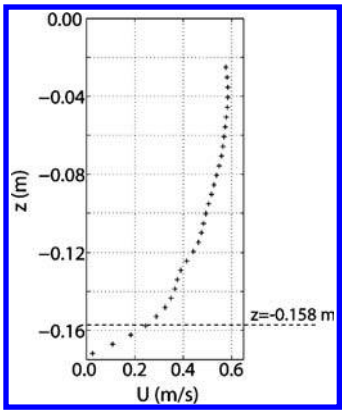


Figure 1. Mean velocity profile U. Horizontal dashed line: location of the analyzed gate.

corrects the instantaneous Doppler frequencies measured by the four receivers (Franca & Lemmin 2006). The vertical resolution of the measurements is around 0.5 cm. Figure 1 shows the mean velocity (U) profile. The coherent structure analysis was applied to a point which is located in the boundary layer of the logarithmic velocity profile, 1.4 cm above the riverbed (Fig. 1).

4 RESULTS

4.1 *Detection and single point 3D reconstruction*

Coherent structures were sampled according to the method described in Section 2. In Table 2 we indicate the parameters used for the application of the analysis. where N is the number of decomposition levels. The chosen scale ($\lambda = 0.43$ s) corresponds to the most energetic scale in the timeseries. The length of the most energetic coherent structures corresponds to a macro scale with an order of magnitude situated between a characteristic bed grain dimension ($\approx D_{50}$) and the water depth (h). Its value is around $\lambda = 0.43$–0.86 s (in length scale, $\Lambda \approx 0.10$ to 0.20 m). An $N = 8$ level wavelet decomposition with the Daubechies type D4 function (Daubechies 1988) is sufficient to describe the energy partition throughout the different structure scales present in the flow. At this scale, negative shear events situated in QII and QIV are predominant. Restricting our analysis to coherent structures belonging to QII and to a threshold level of $H_{\varepsilon'|\lambda=0.43} = 5,46$ shear events are detected. A high degree of scattering around the mean value is found in the individual windowed data series. By windowing the detected events with a window-parameter $\xi = 2.2$, and a refinement using a correlation coefficient threshold of $H_\rho = 0.5$, this number is reduced to 20 events. Under these conditions we reconstructed a composite 3D normalized

Table 2. Parameters used for detecting and sampling coherent structures.

N (–)	*Wavelet type* (–)	λ (s)	*Shear event* (–)	$H_{\varepsilon'\|\lambda}$ (–)	ξ (–)	H_ρ (–)
8	Daubechies D4	0.43	Ejection	5	2.2	0.5

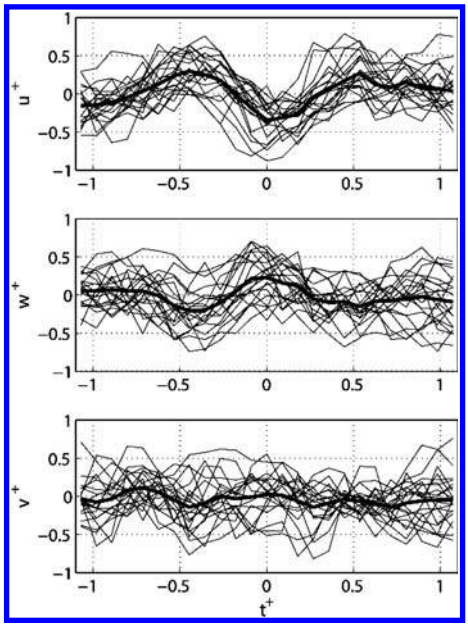


Figure 2. Normalized instantaneous velocity data and composite average (thick line), corresponding to 20 sampled coherent events.

coherent structure at a single-point using the three components of the instantaneous signal.

The windowed composite average ($\tilde{v}_i'|_{\xi=2.2}$) are presented (Figure 2) in the data time series of the corresponding instantaneous streamwise, vertical and spanwise velocity components ($v_i'|_{\xi=2.2}$). In Figure 3 the reconstructed coherent structures from the composite-averaged three velocity components are shown within the selected window.

Coherence exists between the sampled events in the three Cartesian components. Before and after the occurrence of the detected ejection ($t_\varepsilon = 0$ s), lower amplitude sweeps occur (u^+ and w^+ fields). This is a characteristic of the bursting phenomenon. Some in-phase movement is seen in the spanwise velocity data.

The existence of sweeps before and after the detected ejection is a coherent event in all selected structures. Thus, the detection process allows isolating a combined sweep-ejection cycle. In the 3D reconstructed coherent structure, the three velocity components present a statistical coherent structure, mainly in

Copyright © 2006 Taylor & Francis Group plc, London, UK

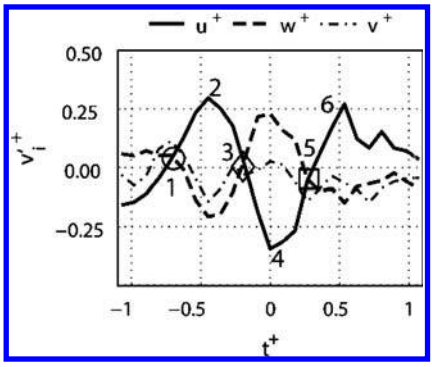


Figure 3. Reconstruction of the detected coherent structure normalized by the local variables. The three velocity components are plotted as a function of time. Symbols ◯ and □ represent the beginning and the end of the sweep-ejection cycle (point 1 and 5 in the figure), and ◇ the beginning of the detected ejection (point 3). Labels are explained in the text.

the $\{x\text{-}z\}$ direction. Six key moments are identified in the process. In chronological order, they are:

1) When all three instantaneous velocity components have low amplitudes;
2) Local maximum amplitude of the u' signal in the first sweep (S1);
3) Before the beginning of the detected ejection when all three instantaneous velocity components again have low amplitudes;
4) High amplitude ejection located in the center of the frame (E1);
5) End of the detected ejection, the three instantaneous velocity components once again have low amplitudes;
6) Local maximum of the u' signal amplitude in the second sweep (S2).

Moments 1, 3 and 5 may be called "stop" points, since all three velocity components simultaneously have low amplitudes and roughly the same value. The spanwise component evolution is in-phase with the vertical component and out-of-phase with the streamwise component, suggesting an interaction between the three components.

4.2 *Reconstruction of the velocity profile*

Having reconstructed one sweep-ejection cycle three-dimensionally in a single point, it is now possible to analyze the remaining water column. The same framing and composite averaging method is applied to the profile, using the time position detected from the single point analysis (the single point analyzed is considered as the detection point for the velocity profile). In Figure 4 the composite averages of the velocity components are represented for the six key moments of the detected cycle indicated in Figure 3.

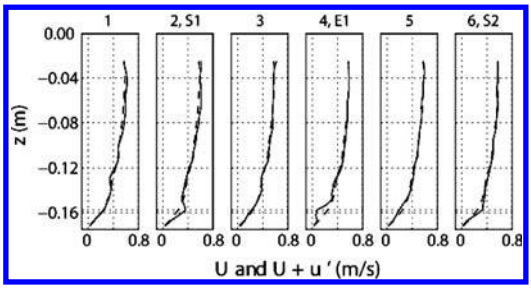


Figure 4. Mean (dashed line) and composite averages (continuous lines) of the streamwise velocity profiles, corresponding to six "key moments" indicated in Figure 3.

The momentary deformation of the velocity profile due to the sweeps and ejections is evident. The streamwise velocity profile acquires its time mean value immediately before and after the events at the so-called "stop" points. The plots of the instantaneous streamwise velocity profiles clearly show the position of the sweep-ejection-sweep cycle detected. The existence of complementary shear events suggest a certain packet behaviour. We are thus in the presence of a bursting packet composed of a sequence of sweeps, S1 and S2 and an ejection, E1.

4.3 *Effect of the passage of the bursting packet on the turbulence intensities*

In this section we analyse the effect of the passage of the bursting packet on the distribution of turbulent intensities (TIs), composite-averaged within the predefined frame. The TIs or normal components of the Reynolds stress tensor (RST) correspond to the variance of the three velocity components ($\overline{v_i'^2}$). The composite-variance calculated within the predefined frame is denoted by $\widetilde{v_i^2}$. The normal stresses define the turbulent energy content of the flow. Since they are production features of the flow, coherent structures are expected to enhance the turbulent energy during their passage. The total mean and composite-averaged (within the frame) TI profiles is presented in Figure 5. The composite-averaged values are denoted by the symbol $\sim$. Both are normalized by the peak values of the mean distribution.

The peak values of the TIs are $\overline{u_{\max}'^2} = 0.0061\ \mathrm{m^2 s^{-2}}$, $\overline{v_{\max}'^2} = 0.0015\ \mathrm{m^2 s^{-2}}$ and $\overline{w_{\max}'^2} = 0.0010\ \mathrm{m^2 s^{-2}}$. As expected, the TIs are enhanced by the bursting packet sequence. Compared with the total time mean, the spanwise TI (Fig. 5b) presents a peak enhancement of about 25 times. This suggests that compared to the background fluctuating field, the component in this direction is particularly strong during these events. The ratio of the peak enhancements for the streamwise (Fig. 5a) and spanwise composite (Fig. 5b) TI is

Copyright © 2006 Taylor & Francis Group plc, London, UK

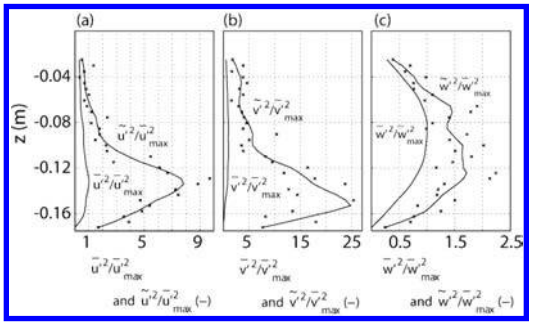


Figure 5. TI profiles, total mean and composite-averaged within the frame defined by $\xi = 2.9$, normalized by the local peaks of the total mean distributions. (a) streamwise, (b) spanwise, (c) vertical TI.

$\frac{\tilde{v}'^2_{max}}{\tilde{u}'^2_{max}} \approx 0.77$. On the average the turbulence structure of the flow is determined by the streamwise velocity component. However, strong short-term processes, such as the sequential bursting packet discussed here, are 3D with an important spanwise component. The determination of streamwise friction velocities by a 2D analysis will thus distort the estimate of the instantaneous bottom drag and provide erroneous information on sediment/mass suspension and transport across the boundary layer.

These results support the observations by Franca (2005) which indicated that 2D friction velocity concepts may not be siutable to determine bottom stress for sediment transport calculations in shallow rough bed rivers. The vertical TI profile (Fig. 5c) is 1 to 2 times greater than the total time average value. The increase is due to the additional vertical momentum introduced into the flow by the packet process. Reynolds shear stress distributions (not shown here) confirm that the strongest transport/suspension processes may occur along both the streamwise and spanwise direction, in agreement with the above observed effect on the friction velocity.

4.4 *Effect of the passage of the bursting packet on the instantaneous TKE budget*

The turbulent kinetic energy (TKE) transport equation, also known as the TKE budget, represents the dynamic equilibrium of the energy terms due to the turbulent motion of the flow. For an incompressible flow of an isothermal fluid, the TKE equation is (Schlichting 1968):

$$\frac{D\overline{k'}}{Dt} = P + D - \varepsilon \tag{6}$$

where $\overline{k'}$ is the temporal mean of the turbulent kinetic energy (TKE: $k' = u'^2 + v'^2 + w'^2$); P is the production rate or generation of TKE by the interaction of Reynolds stress and mean shear; D is the diffusive term; and ε is the dissipation rate. The diffusive term D is negligible for high Reynolds number flows.

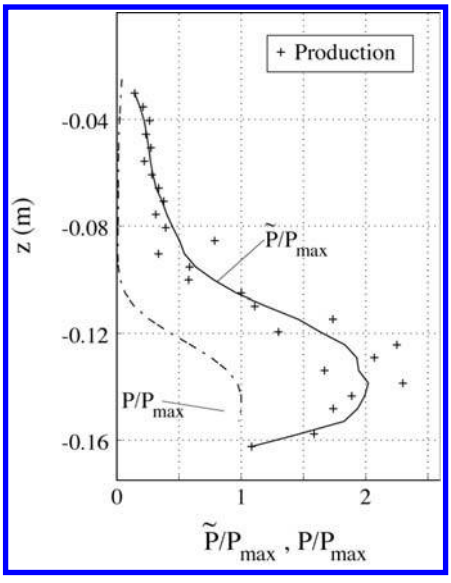


Figure 6. Composite-averaged production $\tilde{P}$, within the frame defined by $\xi = 2.9$, normalized by the peak of the mean distribution.

Background small-scale turbulence present throughout the flow produces dissipation, but production results from individual large-scale events such as the coherent structures described here. The instantaneous production term of TKE, P', is defined by

$$P' = -\overline{v'_i v'_j} \frac{\partial v_i}{\partial x_j} \tag{7}$$

ADVP measurements do not allow direct access to the instantaneous spanwise gradients ($\partial/\partial y$). In order to estimate instantaneous production, we assume that $\frac{\partial u}{\partial y} \approx \frac{\partial v}{\partial x}$, $\frac{\partial w}{\partial y} \approx \frac{\partial v}{\partial z}$, and $\frac{\partial v}{\partial y} \approx \frac{\partial w}{\partial z}$. The streamwise gradients are determined using Taylor's frozen hypothesis. Figure 6 shows the composite-averaged production $\tilde{P}$ profile normalized by the peak of the mean distribution. The maximum increase in the production rate due to the bursting packet is about two times the mean production peak. Despite their short duration, coherent structure packets are highly productive.

5 CONCLUSIONS

Using ADVP measurements in a shallow river, we developed a method for identifying and reconstructing

Copyright © 2006 Taylor & Francis Group plc, London, UK

coherent structures based on a wavelet multiresolution analysis. Coherent structures were detected by analyzing the turbulent velocity signal at one level located in the boundary layer. The reconstruction in time and 3D space was carried out using instantaneous velocity profile measurements. The reconstructed signal provided a visualization of a sequential bursting packet of coherent motion.

The time reconstruction and the phase plots between the three Cartesian components of the reconstruction allowed the following observations:

- The three velocity components present statistical coherent motion.
- A sweep (QIV) was detected before an ejection, with equivalent amplitude and time duration; the compositely reconstructed coherent motion may be a signature of a bursting process.
- A second but weaker sweep (QIV) is observed after the detected ejection.
- Between the sweeps and ejections we observed what may be called "stop" points where all the three components of the instantaneous velocity have low-activity periods simultaneously.
- In summary, the sequence of the movement inside the frame may be characterized by six consecutive key moments: 1) "stop" point; 2) first sweep (S1); 3) "stop" point; 4) ejection, located in the center of the frame (E1); 5) "stop" point; 6) second sweep (S2) (see Figure 3).

We reconstructed the detected coherent motion in the profile, compositely time-averaging the 3D velocity in the water depth. The momentary deformation of the velocity profiles is obvious in the vertical and the streamwise component. The ejection E1 covers a certain scale domain in the water column. An enhancement of the streamwise velocity is limited to the lower layer, whereas the vertical component is affected until $z/h \approx 0.50$. The spanwise velocity profiles are not conclusive. Nevertheless, strong variations of this component occur before the onset of sweeps, suggesting a certain relationship with the shear events in the $\{x\text{-}z\}$ plane. Lateral momentum transfer seems to exist between adjacent ejections and sweeps.

We also analyzed the impact of the passage of the coherent structures packet on the turbulence distribution in the flow, mainly on the RST and on the TKE production. We compared the total time-averaged quantities with frame averages.

The spanwise turbulence intensities are enhanced during the passage of a packet, momentarily equaling the streamwise intensities. Transport and suspension processes, characterized by single or short events, may thus occur in both horizontal directions. The observed packet is highly energetic, and it produces twice the mean peak production during a relatively short period of time.

Based on the present measurements, further systematic research will be conducted in the 3D measuring grid, in order to develop an overall concept of the influence of bursting events on transport and mixing processes in rivers. These extremely energetic events are rare but of great importance in the processes described here. Therefore new approaches are needed in geophysical modeling in order to take their contribution into account.

ACKNOWLEDGEMENTS

The authors wish to acknowledge the financial support by the Swiss National Science Foundation (2000-063818) and the Portuguese Science and Technology Foundation (BD 6727/2001). We are most grateful to Gene Terray for introducing us to wavelet analysis.

REFERENCES

Adrian, R.J., Christensen, K.T. & Liu, Z.C. 2000. Analysis and interpretation of instantaneous turbulent velocity fields. *Exp. Fluids* 29: 275–290.

Antonia, R.A. & Atkinson, J.D. 1973. High-order moments of Reynolds shear stress fluctuations in a turbulent boundary layer. *J. Fluid Mech.* 58(3): 581–593.

Daubechies, I. 1988. Orthonormal bases of compactly supported wavelets. *Comm. Pure Appl. Math.* XLI: 909–996.

Fargé, M. 1992. Wavelet transforms and their applications to turbulence. *Ann. Rev. Fluid Mech.* 24: 395–457.

Foufoula-Georgiou, E. & Kumar, P. (ed.) 1994. *Wavelets in geophysics*. San Diego: Academic Press.

Franca, M.J. & Lemmin, U. 2006. Eliminating velocity aliasing in acoustic Doppler velocity profiler data. *Meas. Sci. Technol.* 17: 313–322.

Franca, M.J. 2005. *A field study of turbulent flows in shallow gravel-bed rivers*. PhD dissertation No. 3393, Lausanne: École Polytechnique Fédérale de Lausanne.

Hurther, D. & Lemmin, U. 2000. Shear stress statistics and wall similarity analysis in turbulent boundary layers using a high-resolution 3-D ADVP. *IEEE J. Oc. Eng.* 25(4): 446–457.

Kantha, L.H. & Clayson, C.A. 2000. *Small scale processes in geophysical fluid flows*. San Diego: Academic Press.

Kumar, P. & Foufoula-Georgiou, E. 1997. Wavelet analysis for geophysical applications. *Rev. Geoph.* 35(4): 385–412.

Mallat, S. 1999. *A wavelet tour of signal processing*. San Diego: Academic Press.

Monin, A.S. & Yaglom, A.M. 1971. *Statistical Fluid Mechanics: Mechanics of Turbulence – Vol. 1*. Cambridge: The MIT Press.

Nakagawa, H. & Nezu, I. 1977. Prediction of the contributions to the Reynolds stress from bursting events in open-channel flows. *J. Fluid Mech.* 80(1): 99–128.

Rolland, T. & Lemmin, U. 1997. A two-component acoustic velocity profiler for use in turbulent open-channel flow. *J. Hydr. Res.* 35(4): 545.

Copyright © 2006 Taylor & Francis Group plc, London, UK

Schlichting, H. 1968. *Boundary-layer theory*. New York: McGraw-Hill.

Turner, B.J., Leclerc, M.Y., Gauthier, M., Moore, K.E. & Fitzjarrald, D.R. 1994. Identification of turbulence structures above a forest canopy using a wavelet transform. *J. Geoph. Res.* 99(D1): 1919–1926.

Wolman, M.G. 1954. A method of sampling coarse river-bed material. *Trans. Amer. Geoph. Un.* 35(6): 951.

Yoshida, K. & Nezu, I. 2005. Experimental study on air-water interfacial turbulent hydrodynamics and gas transfer in wind-induced open channel-flows. In Lee & Lam (eds.), *Environmental Hydraulics and Sustainable Water Management; Proc. 4th Intern. Symp. Environmental Hydraulics – IAHR, Hong Kong, 15–18 December 2004.* London: Taylor & Francis Group.

Copyright © 2006 Taylor & Francis Group plc, London, UK

Equivalent velocity profile for turbulent flows over gravel riverbeds

M.J. Franca
Instituto Superior Técnico – Technical University of Lisbon, Portugal

W. Czernuszenko
Institute of Geophysics, Polish Academy of Sciences, Warsaw, Poland

ABSTRACT: Practitioners need simple estimates of the mean velocity distribution dependent on easy-measurable river characteristics. A simple formulation of the 2D mean velocity profile is thus essential. Recent field measurements obtained with the Acoustic Doppler Velocity Profiler (ADVP) in gravel-bed rivers showed that above the roughness layer the logarithmic law describes the mean velocity distribution fairly well. However, roughness parameters representing local flow conditions differ. It is assumed that the turbulence structure above the roughness layer may be described by the log-law, scaled with height, friction velocity, absolute size of the elements forming the equivalent bed roughness (k) and a coefficient designated by the letter "B". The authors present here a parameterization of the log-law, for turbulent rough flows over gravel riverbeds, where the equivalent roughness is physically based on the bottom roughness protuberances and the coefficient B should represent the bottom geometry.

1 INTRODUCTION

For practical purposes in river engineering it is essential to estimate the flow resistance based in simple measurable quantities. The widely applied logarithmic law to the description of the velocity distribution was object of numerous laboratory studies conducted under idealized conditions of uniform flow and flat beds with fairly homogeneous bed roughness distribution. Conditions like these are rarely found in actual rivers. Field measurements under diverse conditions are desirable for the validation of the existent concepts on river processes with respect to sediment transport, morphology evolution, secondary flows and mixing and transport of matter.

For low values of blockage ratio (h/D, where h is the water depth and D a representative grain diameter), due to the three-dimensionality of the flow, self-similarity of the turbulent flow does not exist inside the roughness layer (Nikora & Smart 1997, Smart 1999, Franca 2005a). Field results show nevertheless that the logarithmic layer is still found on gravel-bed rivers. Franca (2005a) identified three types of velocity profiles for the present measurements: logarithmic, s-shaped and double-logarithmic. The velocity inflection resulting in a s-shaped profile is due to the presence of large scale bed obstacles, whereas the double-logarithmic profiles happen downstream corresponding to the transition to "purely" logarithmic profiles. The extent of the velocity inflection depends on the size of the bed obstacle. Nevertheless, above the roughness layer the flow becomes nearly 2D again and the effects of the bed roughness blend in one single effect causing a linear shear stress with the slope uniformly distributed throughout the river (Franca 2005b). The actual shear in the roughness layer will determine the shear stress distribution throughout the remaining water depth.

If the roughness layer is not too large when compared with the flow depth, it may be possible to parameterize the overall velocity distribution and the flow resistance of gravel river flows over irregular beds (macro-scale roughness), using an equivalent logarithmic 2D velocity profile. Bottom shear would be replaced by the shear at the roughness height.

To both log-law parameters, equivalent roughness and coefficient B, a geometry significance should be attributed, as was the intention since the first studies on the subject (Schlitling 1968). Pitlick (1992) and Baiamonte & Ferro (1997) refer to the equivalent roughness as being 3.0 to 3.5 times the D_{84} (which reflects the deposition of the coarse elements), and Franca & Lemmin (2004) affirm that the mean roughness value is equivalent to D_{84}. The attribution of a physically based value for the equivalent roughness and the definition of the shear or friction velocity resulting from the consideration of uniform flow over a river stretch leaves open the determination of the geometry parameter B. In open-channel rough

Copyright © 2006 Taylor & Francis Group plc, London, UK

turbulent flows, parameter B is commonly attributed the value $8.5 \pm 15\%$ (Monin & Yanglom 1971). Recent developments were made on the attempt to clarify the parameterization of B (Czernusnzenko & Rylov 2004); while the equivalent roughness shall represent the actual confinement introduced by the bed grains in the flow, the parameter B shall be related to the geometry of the bed forms. In gravel-bed rivers, bed forms are typically shaped by the large-scale grains that may under certain circumstances accumulate in coherent regions of the bottom, exerting consequently influence in the flow structure (see Franca & Lemmin 2005). The authors here want to meet up with the idea of physical definition of the equivalent roughness, discussing consequently the geometry signification of the value B.

We will discuss the parameterization of a logarithmic profile for double averaged velocities profiles, in time and space as suggested by Nikora et al. (2001), applied to river velocity measurements. This study is based on field measurements made with the deployable 3D Acoustic Doppler Velocity Profiler (ADVP) in the Swiss rivers Venoge and Chamberonne.

2 THEORETICAL FRAMEWORK

2.1 *Basic hydrodynamic equations*

Three-dimensional, steady and uniform turbulent flow in open channels is governed by the Reynolds – (ensemble) averaged Navier-Stokes (RANS) equations. Continuity and momentum equations for incompressible turbulent flows may be written using the Cartesian tensor notation, respectively:

$$\frac{\partial U_i}{\partial x_i} = 0 \tag{1}$$

$$U_j \frac{\partial U_i}{\partial x_j} = -\frac{1}{\rho}\frac{\partial p}{\partial x_i} + F_i - \frac{\partial}{\partial x_j}\left(\overline{u_i u_j} - \nu \frac{\partial U_i}{\partial x_j}\right) \tag{2}$$

where U_i = i-th component of the time average velocity (i = 1,2,3); p = pressure; ρ = density; F = driving force (F = (g cos α, g sin α, 0), α is the angle corresponding to the river slope) and u_i = i-th component of the instantaneous velocity. A notation of x for horizontal (longitudinal), y for lateral coordinates and z for vertical as well as U, V, W for corresponding velocity components will be used throughout the paper.

However, in open channel flows with irregular beds, these equations are not suitable due to the highly 3D structure of the mean flow. In this case the ensemble averaged flows, at least in the very neighborhood of irregular rough boundary, is strongly spatially heterogeneous. Thus, for any vertical located at (x, y), there is a different local vertical velocity distribution $U(z)$

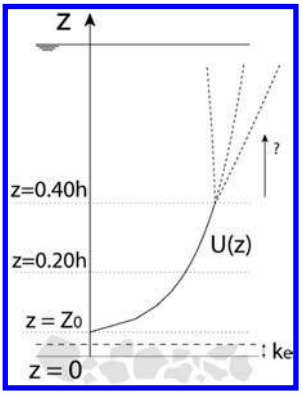


Figure 1. Equivalent logarithmic profile: definition of the roughness length and equivalent roughness.

consequence of the strong spatial variation of the 3D hydraulic conditions. It will be assumed that at some distances from the bed the local profile is defined by the logarithmic law with different parameters (Fig. 1). This assumption is supported by field measurements (Franca 2005b).

Civil and environmental engineers do not need very precise 3D details of the velocity distribution but very often 1D vertical velocity profile description is just enough for their practical applications. This 1D vertical velocity profile should be equivalent to the real 3D in terms of local averaged momentum, i.e., discharges calculated based on these profiles must be the same

$$\int_0^h \int_{y-b/2}^{y+b/2} U(x = const, y, z)\,dy\,dz = b\int_0^h \langle U\rangle(z)\,dz \tag{3}$$

for any x. <> represents spatial averaging. The theoretical level of bed ($z = 0$) is defined as the lowest level of the roughness elements, $U(x, y, 0)$ is not defined to all points belonging to the area of integration. b and h are channel width and depth, respectively.

Double-average velocity (in time and space) is defined as (Nikora et al. 2001)

$$\langle U\rangle(z) = \frac{1}{A}\iint_{D(x,y,z)} \overline{U(x', y', z' = const)}\,dx'\,dy' \tag{4}$$

where the domain $D(x, y, z)$ is a control area located parallel to the plane z = const (assumed parallel to mean bed) centered at the point (x, y). The area of the domain is equal to A, and it is wide and long enough when compared to the characteristic wavelengths of the lateral and longitudinal differences in the velocity distribution.

Longitudinal RANS equations (Eq. 2 to i = 1) may thus be subjected to spatial averaging. First the ensemble average variables (velocity and pressure) are split up into two terms, one double-averaged and

Copyright © 2006 Taylor & Francis Group plc, London, UK

one representing the deviation from this average as follows:

$$\begin{aligned} &U(x,y,z) = \langle U \rangle(z) + \tilde{u}\,(x,y,z) \quad for\ all\ (x,y) \in A, \\ &\langle \tilde{u} \rangle = 0 \\ &p(x,y,z) = \langle p \rangle(z) + \tilde{p}(x,y,z) \\ &\langle \tilde{p} \rangle = 0 \end{aligned} \tag{5}$$

where the tilde denotes the disturbance in the flow variables, i.e., the difference between the double-averaged and time averaged values. One notes that the double-averaged variables are the same in all points belonging to the area of averaging. It is convenient to relate these variables with the location of center of gravity of the area of averaging – A. Choosing appropriate sizes of averaging area, the averaging variables would be only function of the vertical coordinate inside this.

2.2 *Flow above the crest of roughness elements*

Applying Equation 5 to average the momentum and continuity equations over the roughness crests, one can obtain the so called double-averaged (in time and space) (Nikora et al. 2001) equations for conservation of momentum,

$$\langle U_j \rangle \frac{\partial \langle U_i \rangle}{\partial x_j} = g_i - \frac{1}{\rho}\frac{\partial \langle p \rangle}{\partial x_i} - \frac{\partial \langle \overline{u_i u_j} \rangle}{\partial x_j} - \frac{\partial \langle \tilde{u}_i \tilde{u}_j \rangle}{\partial x_j} + \frac{\partial}{\partial x_j}\left\langle \nu \frac{\partial U_i}{\partial x_j} \right\rangle \tag{6}$$

and double-averaged continuity equation

$$\frac{\partial \phi \langle U_i \rangle}{\partial x_i} = 0 \tag{7}$$

It is easy to show that in the z-momentum equation the vertical pressure distribution is close to hydrostatic. The x-momentum equation is simplified to,

$$\frac{\partial}{\partial y}\left(-\langle \overline{u'w'} \rangle - \langle \tilde{u}\,\tilde{w} \rangle + \nu \frac{\partial \langle U \rangle}{\partial z} \right) = g \sin\alpha + \langle W \rangle \frac{\partial}{\partial z} \langle U \rangle \tag{8}$$

After integration of Equation 8 across the boundary layer, one can obtain the formula for distribution of the total shear stresses in the form

$$\begin{aligned} &\frac{\tau_{total}(z)}{\rho} = \left(-\langle \overline{u'w'} \rangle - \langle \tilde{u}\,\tilde{w} \rangle + \nu \frac{\partial \langle U \rangle}{\partial z} \right) = \\ &ghS_f \left(1 - \frac{z}{h} \right) + \int_0^z \langle W \rangle \frac{\partial}{\partial z} \langle U \rangle dz \end{aligned} \tag{9}$$

One can realize that the shear stress in open channel flows includes the contributions of the wall shear stress (caused by pressure and gravity force) and convective inertia. The inertia force disturbs the linear distribution of shear stresses.

The total shear stress in double-averaged formulation comprises three components,: mean Reynolds (τ_t) stresses, a new stress (τ_f) (Eq. 9) called "form-induced stress" or simply "form stress" (Gimenez-Curto & Lera 1996) and mean viscous or laminar stresses (τ_v). The maximum bed shear stress has therefore three components τ_{ov}, τ_{ot}, and τ_{of} and it appears at the roughness height. At this level, the laminar shear stresses are negligible compared with two other stresses. Laminar stresses are essential only in laminar sublayer, which is rather thin in rough turbulent flows. The thickness of laminar sublayer is very difficult to estimate. Omitting the laminar stresses in Equation 9 and considering the convective inertia negligible when compared to the others, the equation of the total shear stresses can be written in the form

$$-\langle \overline{u'w'} \rangle - \langle \tilde{u}\,\tilde{w} \rangle = U^{*}{}_{e}^{\,2} \left(1 - \frac{z}{h} \right) \tag{10}$$

where $U^{*}{}_{e} = (\tau_0/\rho)^{0.5}$ is the friction velocity and $\tau_0 = \rho g h \sin\alpha$ is the bottom shear stresses. Equation 10 says that the total shear stress still varies linearly with the distance from the bed. To solve Equation 10 one has to define the first two terms of the equation. It is assumed that the sum of both terms can be modeled similarly to the Prandtl mixing length theory as follows:

$$\tau_{total} \equiv \tau_t + \tau_f = \rho l_e^2 \left(\frac{\partial \langle U \rangle}{\partial z} \right)^2 \tag{11}$$

where $l_e =$ is defined by analogy with the Prandtl's mixing length.

It is reasonable to assume that the double-averaged velocity profile can be obtained from Equation 10 with the total stresses expressed by Equation 11. Through this equation in similar way as it was done in classical hydraulics, one may get the velocity profile in the logarithmic layer in the form

$$\frac{\langle U \rangle}{U^{*}{}_{e}} = \frac{1}{\kappa_e} \ln \frac{z}{k_e} + B_e \tag{12}$$

where $U_e^* =$ friction velocity for the total shear stresses, i.e., turbulent and form stresses; $k_e =$ equivalent roughness; $\kappa_e =$ equivalent von Karman parameter; and subscript "e" represent equivalent coefficients. The relationship is only valid to flows in rough turbulent regime, i.e. for Reynolds numbers $(U^*k/\nu) > Re^*_{cr} = 70$ (Nezu and Nakagawa 1993).

Copyright © 2006 Taylor & Francis Group plc, London, UK

Table 1. Summary of the flow characteristics.

River	Q (m^3/s)	S (%)	h (m)	b (m/s)	Re ($\times 10^4$)	Fr (−)	D_{84} (mm)
Ven.	0.80	0.33	0.20	6.30	3–14	0.2–0.9	74
Chamb.	0.55	0.26	0.29	5.75	4–12	0.2–0.4	81

3 FIELD MEASUREMENTS

The 3D ADVP field measurements were made at two different gravel-bed Swiss rivers, the Venoge and the Chamberonne, in the summer of 2003. The measurements were made on low water periods, during a single day and under stationary flow conditions (confirmed by the data from the Swiss Hydrological and Geological Services). The cross-section locations were: 120 m upstream from the Moulin de Lussery, for the Venoge; 385 m upstream from the last bridge before the lake Geneva, for the river Chamberonne. Table 1 shows the river main characteristics at the time of the measurements: where S = mean river slope; Q = discharge; h = the water depth; b = river width; Re = Reynolds number; Fr = local Froude number; D_{84} = bottom grain size for which 50% and 84% of the grain diameters are smaller. The riverbed material was sampled according to the Wolman (1954) technique.

The aspect ratio of the river (b/h) is 31.5 and 20.5 for the Venoge and Chamberonne rivers, corresponding both to shallow water or wide open-channel flows. The river slopes were determined with topographic data provided by IATE/HYDRAM (1996), for the Venoge, and by "Gesrau system" (SESA – Canton of Vaud), for the Chamberonne. The river slope and the Froude number are within the range specified by Bathurst et al. (1981) to boulder-bed rivers. The riverbed is hydraulically rough, composed of coarse gravel and randomly spaced macro-roughness elements (some of these scale with half of the water depth, $D \approx 0.5\,h$). There was no sediment transport during the measurements.

The profiles were measured across the section starting from the right riverbank ($y/W = 0$). We assumed symmetrical conditions in the river flow, and only measured across half of the river width (Fig. 2).

The 25 velocity profiles were measured in the river Venoge with a horizontal spacing of 10 to 12.5 cm, and 24 velocity profiles in the Chamberonne with a horizontal spacing of 5 to 12.5 cm. For both cases data acquisition was made during 5 minutes, which is sufficient according to Bergeron & Abrahams (1992). The profiles depth varies between 0.12 m and 0.20 m for the river Venoge and between 0.15 and 0.29 for the river Chamberonne. The actual river water depth considered for the present analysis is the correspondent to the deepest profile.

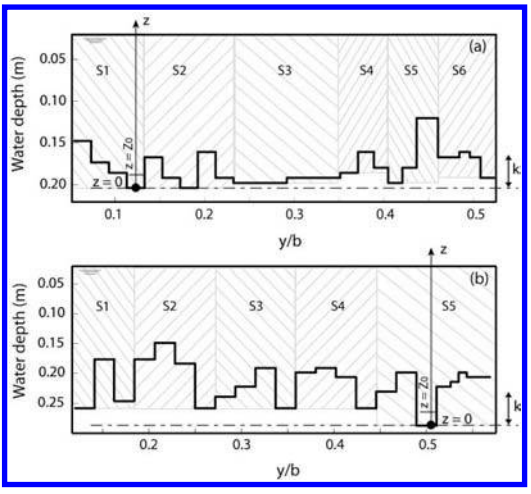


Figure 2. River bottom and length scales for parameterization of the logarithmic law. Definition of the origin of the vertical Cartesian axis. (a) River Venoge, (b) River Chamberonne.

4 INSTRUMENTATION

The deployable 3D ADVP developed at the Laboratoire d'Hydraulique Environnementale (LHE) was used for the present measurements. It allows quasi-instantaneous velocity profiling throughout the water depth, in laboratory flumes and natural rivers. ADVP time and space resolution is enough to quantitatively estimate the main turbulent quantities, within the production and inertial spectral space. A thorough description of the ADVP working principle is given in the literature (Rolland & Lemmin 1997). We used the multistatic configuration of the ADVP, where four different receivers exist to one ultra-sound emitter, providing one redundancy in the conversion of the measured Doppler shift to the 3D Cartesian space velocity components. This redundancy is used to eliminate signal noise and to control the data quality (Hurther & Lemmin 2000). A Pulse Repetition Frequency (PRF) of 2000 Hz and a Number of Pulse Pairs (NPP) equal to 32 was used for the estimation of the Doppler shift and subsequently the flow velocity. This results in an unfiltered sample frequency of 62.5 Hz. Though a low degree of dealiasing was expected on the river data given the PRF used and the flow velocity, a rectifying algorithm based no the signal time history was applied (Franca & Lemmin 2005). A metallic structure was especially conceived to the ADVP displacement in the field (Fig. 3), allowing covering a whole cross-section and the streamwise movement with a relative rapidity.

The instrumentation is kept always at the same vertical distance from the water surface, and the structure

Copyright © 2006 Taylor & Francis Group plc, London, UK



Figure 3. Study reach and deployable ADVP apparatus installed at the river Venoge.

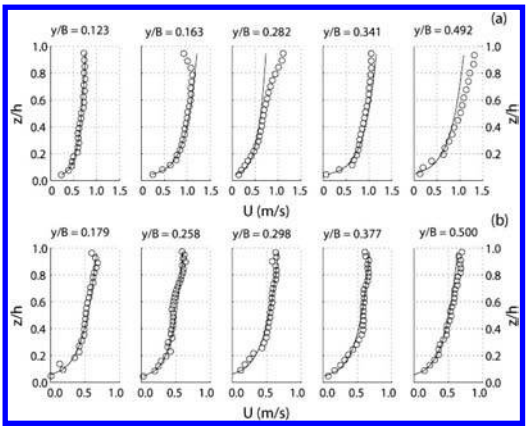


Figure 4. Mean measured velocity profiles with local logarithmic fit curves (continuous lines), for several positions from both rivers. (a) River Venoge, (b) River Chamberonne.

was built to minimize the disturbance of the flow and the vibration of the ADVP.

5 FIELD RESULTS

5.1 *Mean velocity distribution*

Franca & Lemmin (2004) analyzed partially the present data and concluded that the logarithmic layer is found in the lower layers of the majority of the measured profiles. In more than 65% of the profiles, the log law can be applied without apparent deviations up to $z/\delta = 0.4$ (Fig. 4).

Using the distribution of the local Nikuradse equivalent roughness values determined from the log-law, for $B = 8.5$, Franca and Lemmin (2004) concluded that $k_{e,50}$ (defined as the equivalent roughness for which 50% of the values are higher) could be taken equal to the value D_{84} of the gravel diameter distribution (this calculation was made only for the profiles where the logarithmic law could be adjusted). The cross-section averaged values of friction velocity are 0.076 and 0.059 m/s, respectively for the Venoge and Chamberonne rivers.

Above $z/\delta = 0.40$ the mean velocity profiles show deviations from the logarithmic profile in the positive and in the negative direction of the flow. In some profiles a wake effect is detected in the lower layers of the flow, inside the roughness sublayer (Nikora & Smart 1997). This effect corresponds to the s-type velocity profiles observed in gravel-bed streams in the presence of large obstacles (Marchand et al. 1984, Bathurst 1988, Katul et al. 2002, Carravetta & Della Morte 2004, Franca 2005a). The s-profile is a direct result from the riverbed perturbation. Downstream this, a double boundary layer is formed: an inner bottom sheared log-layer exists due to the momentum redistribution throughout the water depth and lateral momentum convection around the bed obstacle. In both flows, there is a large dependency of the flow resistance on the bed forms, thus the local roughness parameterization has a strong cross-section variation. Smart (1999) refers to the dependence of roughness parameters other than grain diameter, namely on the bed forms, bed load, lateral velocity gradients and upstream conditions. Nevertheless, given the field results, the logarithmic law, properly parameterized, is still able to describe the actual velocity distribution to these flows. Franca (2005b) verified that above the roughness layer, the Reynolds shear stress distribution ($\overline{u'w'}$) is nevertheless linear with z.

5.2 *Estimation of the friction velocity from the shear stress measurements to each measured profile*

The ADVP provide us with the 3D instantaneous velocity profiles. The determination of the six Reynolds stress tensor components throughout each measured profile is thus trivial from the measured data. The measurements allow us to compute the local bottom friction velocity from the Reynolds x-z plane shear stress. Turbulent or Reynolds shear stress distribution $\tau_t(z)$ is given by:

$$\frac{\tau_t}{\rho} = -\overline{u'w'} \tag{13}$$

The vertical shear distribution follows a linear trend with slope equal to the bottom shear stress. From the friction velocity definition, the calculation of U^* comes:

$$U^{*2} = \frac{-\overline{u'w'}}{1 - z/h} \tag{14}$$

Copyright © 2006 Taylor & Francis Group plc, London, UK

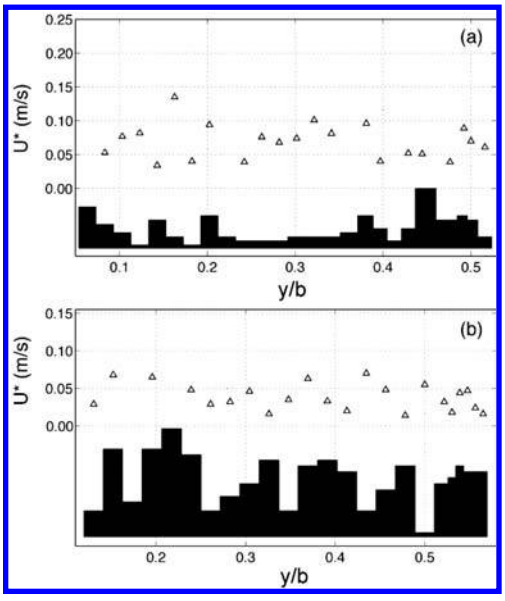


Figure 5. Bottom friction velocity U^* across the sections of the rivers Venoge (a) and Chamberonne (b), estimated from the shear stress distributions.

For both river measurements the shear stress distribution is not always linear due to the three-dimensionality and the presence of large obstacles within the flow. For the bottom friction velocity estimations, we considered only the linear layer closer to the bottom (methodology followed by Wang et al. 2003, for instance), being some of the profiles omitted. In Figure 5 we show the bottom friction velocities results for each profile. The cross-section averaged values of the friction velocity are 0.069 m/s and 0.041 m/s, respectively for the river Venoge and Chamberonne (standard deviations of 0.026 and 0.018 m/s).

In the Venoge case, the averaged friction velocity values, estimated from both the log-law with $B = 8.5$ and from the shear stress measurements, match reasonably well (within an interval error of 10%). In the Chamberonne river, however, the friction velocity estimated from the shear measurements is about 70% of the value determined by the log-law. The discrepancies show the importance of spatial-averaging in the parameterization of turbulent flows over large-scale roughness, as a means to obtain practical information on the flow.

6 PARAMETERIZATION OF THE THEORETICAL LOGARITHMIC PROFILES FOR EACH STRIPE: k_e AND B_e

The spatial averaging of shear stress measurements was made dividing both cross-sections in six and five

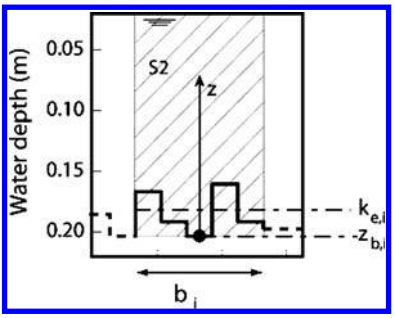


Figure 6. Example of equivalent roughness geometric definition for each cross-section stripe.

Table 2. Parameterization of the logarithmic profiles for each stripe – river Venoge.

Stripe	Profiles	h (m)	k_e (m)	U^* (m/s)	B_e (−)
1	1–4	0.147	0.030	0.071	5.5
2	5–9	0.160	0.022	0.076	5.6
3	10–15	0.191	0.030	0.073	7.0
4	16–18	0.160	0.015	0.068	9.2
5	19–21	0.120	0.046	0.052	13.5
6	22–25	0.160	0.011	0.065	4.1
Averaged values			0.026	0.069	7.5

lateral stripes, for Venoge and Chamberonne respectively (see Fig. 2). We defined equivalent stripes taking into account the wavelength of lateral changes in the velocity distribution (Fig. 6).

This way we attributed to the roughness parameter k local meaning in terms of flow disturbance. The logarithmic law (Eq. 12) was thus parameterized to each stripe, accounting for the individual parameterization of each individual profile inside the stripe. The equivalent roughness ($k_{i,e}$) was determined as the mean bed level variation inside each stripe. The friction velocity for each stripe ($U^*_{i,e}$) is the average of the several profiles, determined from Reynolds shear stress distributions (in the average process we take into account the spacing between the profiles). The equivalent geometry parameter for each stripe $B_{i,e}$ is determined from regression of Equation 12 against the measured field data (Tables 2 and 3).

The cross-section results were obtained from a weighted average using the stripe width. In Figure 7 we present the results of the logarithmic law parameterization for each stripe across the rivers.

The first noticeable remark is the difference between the B values determined for both rivers. For the river Venoge the parameter B is within the expected interval for hydraulically turbulent rough flows though near the lower limit of the interval defined by $8.5 \pm 15\%$ (Monin & Yanglom 1971). For

Copyright © 2006 Taylor & Francis Group plc, London, UK

Table 3. Parameterization of the logarithmic profiles for each stripe – river Chamberonne.

Stripe	Profiles	h (m)	k_e (m)	U^* (m/s)	B_e (−)
1	1–3	0.174	0.055	0.049	8.1
2	4–7	0.147	0.043	0.047	8.2
3	8–11	0.189	0.037	0.032	11.9
4	12–15	0.189	0.023	0.047	8.3
5	16–24	0.196	0.020	0.033	9.5
Averaged values			0.033	0.041	9.3

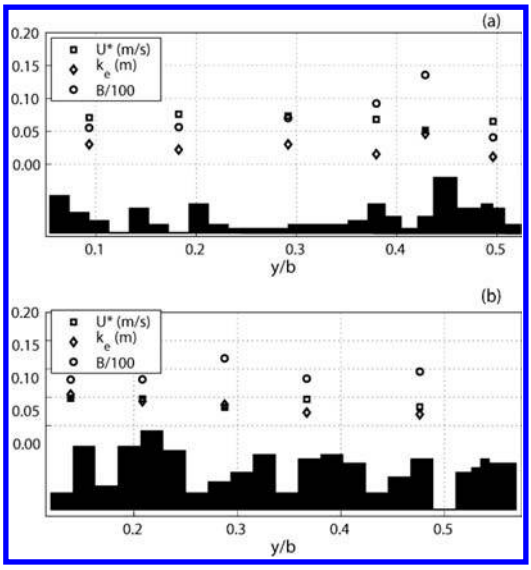


Figure 7. Results from the parameterization of each individual stripe. (a) river Venoge, (b) river Chamberonne.

the Chamberonne, the value B is within the referred interval, this time near its upper limit. From Figures 5 and 7, we see that the density of the bed protuberances is different in both cases. In our opinion the protuberances density is a factor that should be taken into account in the roughness parameterization of the flow. Further studies shall be carried out where a concept of roughness density is included as a determinant variable.

7 PARAMETERIZATION OF THE CROSS-SECTION EQUIVALENT VELOCITY PROFILE

We intend to discuss the parameterization of the logarithmic law for the description of the velocity profiles, as a function of easy measurable variables to be used by practical engineers. The definition of the water depth

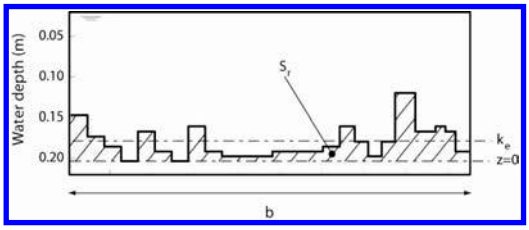


Figure 8. Example of geometric definition of the equivalent roughness using the area occupied by the bed forms – k_{e-4}.

was already referred as corresponding to the deepest measured profile. We parameterized a cross-section equivalent logarithmic profile using the discharge equality as comparison criteria between the theoretical results and the field data. The local discharge values obtained from the measured velocity profiles was compared to the averaged results obtained from the individual stripes parameterization (Tables 2 and 3). Estimates of U^* based in the shear stress measurements (Tables 2 and 3) will be used to our global cross-section parameterization.

To determine the equivalent roughness for the whole river cross-section (k_e) several empirical methods were tested and compared with our data:

$$k_{e,1} = D_{84} \quad (15a)$$

$$k_{e,2} = D_{50} \quad (15b)$$

$$k_{e,3} = S_r / W \quad (15c)$$

$$k_{e,4} = \sigma_{(h_i - h)} \quad (15d)$$

$$k_{e,5} = \sigma_D \quad (15e)$$

where S_r = area occupied by the bed forms (macro-scale gravel) above the reference level (Fig. 8); σ = standard deviation; h_i = depth of each measured profile; and D = bed grain diameter distribution. Several authors refer the value D_{84} being representative for the bottom roughness in gravel-bed rivers (Franca & Lemmin 2004, Smart 1999). Gravel riverbed forms are the result of the individual elements that constitutes the bottom (Fig. 2), hence it is believed that a higher representative diameter as the D_{84} reflect their particular interference on the flow.

The determination of the equivalent velocity profile parameters is made considering the unitary discharge in the river. The real unitary discharge ($q_r = Q/W$, discharge/river width) was calculated directly from the velocity data. The theoretical unitary discharge (q_t) was calculated from the logarithmic model for the velocity distribution, which uses the roughness length as parameter.

$$q_t(Z_0 < z < z_u) = \int_{Z_0}^{z_u} u_t(z)dz = \int_{Z_0}^{z_u} \frac{U^*}{\kappa} \ln\left(\frac{z}{Z_0}\right) dz \quad (16)$$

Copyright © 2006 Taylor & Francis Group plc, London, UK

Table 4. Parameterization of the logarithmic equivalent profiles for each river.

River	q_r (m^2/s)	U^* (m/s)	h (m)	Z_0 (mm)	K_e (mm)	B_e (−)
Venoge	0.016	0.069	0.20	1.4	$K_{e,1} = 74$	9.7
					$K_{e,2} = 40$	8.2
					$K_{e,3} = 24$	6.9
					$K_{e,4} = 20$	6.5
					$K_{e,5} = 23$	6.8
Chamberonne	0.018	0.041	0.29	1.0	$K_{e,1} = 81$	10.8
					$K_{e,2} = 49$	9.6
					$K_{e,3} = 70$	10.5
					$K_{e,4} = 34$	8.7
					$K_{e,5} = 22$	7.7

The roughness length represents the origin of the logarithmic fit to the actual flow velocity and z_u a position near the water level. The integration is made in a layer where the velocity profile is closer to logarithmic ($z_u/h \approx 0.20$). The roughness length can easily be related with other log-law parameters by

$$Z_0 = e^{-B\kappa} k_e \tag{17}$$

Making $q_t = q_r$, we have the non-linear equation which allows the determination of the cross-section equivalent roughness length as a function of the real local unitary discharge:

$$q_r(Z_0 < z < z_u) = \frac{U^*}{\kappa}\left[Z_0 + 0.2h\left(\ln\left(\frac{z_u}{Z_0}\right) - 1 \right)\right] \tag{18}$$

In Table 4 we present the summary of the parameterization of the logarithmic velocity for both rivers.

Considering the parameter B equal to the referenced value of 8.5, the adequate equivalent roughness to be considered would correspond to Equations (15b) and (15d), respectively to the Venoge and Chamberonne rivers. Both correspond to mean values of the variations of the bottom levels. In this case the individual gravel grains are the responsible for the bottom forms. Again we have different conclusions to the different rivers, indicating that an extra parameter representing the bed level variability could be important in the roughness parameterization.

8 SUMMARY

RANS equations are not suitable for irregular rough boundary flows especially in near-bed region where flows are highly 3D and heterogeneous. Boundary irregularities generate perturbations in ensemble-averaged flows, which have been already detected experimentally in steady flows. The velocity profiles are determined by the effects of these disturbances. In order to smooth out the flow irregularities, a special, spatial averaging operation has to be applied to RANS equations. It results in the double-averaged (in both time and space) Navier-Stokes (DANS) equations, which are used to describe the uniform vertical velocity profile. To solve the double-averaged equations we define the so called "form-induced stress" (τ_f). In this text we presented the DANS equations and derived subsequently on equivalent logarithmic law to describe the vertical distribution of the double-averaged streamwise velocity. With field results we discuss the parameterization and definition the equivalent velocity profile.

We estimated cross-section averaged values of friction velocity using both the adaptation of a log-law to the measured velocity profiles, and the shear stress measurements. The results showed discrepancies, especially in the Chamberonne case, emphasizing the practical importance of applying the spatial-averaging techniques to extreme rough cases as the present ones.

The cross-sections were divided in several stripes and to each an equivalent logarithmic velocity profile was derived. From the overall analysis of the results we concluded that the roughness density (or protuberances density) seems to be a determinant factor in the roughness parameterization of the flow.

The use of a variable representing the mean variation of the river bottom constitutes the more indicated estimation for the equivalent roughness. Given the nature of the river, the individual gravel grains are the responsible for the bottom forms.

The original derivation of the time-averaged velocity logarithmic profile was carried out under idealized conditions of open-channel uniform flow and flat beds with fairly homogeneous bed roughness distribution. The analysis of flows with irregular bed as in Venoge and Chamberonne rivers is only possible using space averaged techniques to smooth out the large gradients in the turbulent flow structure.

9 CONCLUSIONS

The presented theoretical background of the equivalent velocity profile allows for adopting the classical log-law to describe the vertical velocity distribution in open-channel flows over irregular bed roughness.

The idea of equivalent velocity profile is supported by river velocity measurements, where beyond a certain distance from the bed the velocity distribution is fairly logarithmic. The velocity distribution is in this case totally defined by the friction velocity and two other parameters characterizing the river bottom, the equivalent roughness k_e, and the dimensionless geometric coefficient B_e.

Equivalent parameters of the logarithmic distribution of the velocities constitute a type of averaged

Copyright © 2006 Taylor & Francis Group plc, London, UK

values of local velocity parameters such as the height of roughness elements disturbing the momentum flux, bed shear stresses and the grain geometry.

ACKNOWLEDGEMENTS

M. J. Franca acknowledges the financial support of the Portuguese Science and Technology Foundation (BPD 21712/2005) and the Swiss National Science Foundation (2000-063818). W. Czernuszenko acknowledges the grant 2 P04D 026 29 from the Ministry of Education and Science, Poland. This contribution was the result of a collaboration sponsored by the program GEODEV. M.J. Franca acknowledges Ulrich Lemmin supervision during the present measurements.

REFERENCES

Baiamonte, G. & Ferro, V. 1997. The influence of roughness geometry and Shields parameter on flow resistance in gravel-bed channels. *Earth Surface Processes and Landforms* 22: 759–772.

Bathurst, J.C. 1988. Velocity profile in high-gradient, boulder-bed channels. *Proc. Int. Conf. Fluvial Hydraulics*, Budapest.

Bathurst, J.C., Li R.M. & Simons, D.B. 1981. Resistance equation for large-scale roughness. *J. Hydr. Eng.* 107(12): 1593–1613.

Bergeron, N.E. & Abrahams, A.D. 1992. Estimating shear velocity and roughness length from velocity profiles. *Water Resour. Res.* 28(8): 2155–2158.

Carravetta, A. & Della Morte R. 2004. Response of velocity to a sudden change of the bed roughness in sub critical open channel flow. *Proc. Riverflow 2004, Naples, 23–25 June 2004.* Balkema.

Czernuszenko, W. & Rylov, A. 2004. 3D turbulent flow over irregular bed surfaces. *Proc. Riverflow 2004, Naples, 23–25 June 2004.* Balkema.

Franca, M.J. & Lemmin, U. 2004. A field study of extremely rough, three-dimensional river flow. *Proc. 4th IAHR International Symposium on Environmental Hydraulics, Hong Kong, 15–18 December 2004.* Balkema.

Franca, M.J. & Lemmin, U. 2005. Cross-section periodicity of turbulent gravel-bed river flows. *Proc. 4th RCEM, Urbana (Il), 3–7 October 2005.* Taylor & Francis.

Franca, M.J. 2005a. Flow dynamics over gravel riverbed. *Proc. XXXI IAHR Congress, Seoul,* 11–16 September 2005.

Franca, M.J. 2005b. *A field study of turbulent flows in shallow gravel-bed rivers*. PhD dissertation No. 3393, Lausanne: École Polytechnique Fédérale de Lausanne.

Franca, M.J. & Lemmin, U. 2006. Eliminating velocity aliasing in acoustic Doppler velocity profiler data. *Meas. Sci. Technol.* 17: 313–322.

Gimenez-Curto, L.A. & Lera, M.A.C. 1996. Oscillating turbulent flow over rough surfaces. *J. Geoph. Res.* 101(C9): 20745–20758.

Hurther, D. & Lemmin, U. 2000. A correction method for turbulence measurements with a 3D acoustic Doppler velocity profiler. *J. Atmosph. Ocean. Technol.* 18: 446–458.

IATE/HYDRAM 1996. Profil en long, profils en travers, et courbes de tarage des sections relevées. *Rapport d'étude du Bassin Versant de la Venoge (EPFL)*, Lausanne.

Katul, G., Wiberg, P., Albertson, J. & Hornberger G. 2002. A mixing layer theory for flow resistance in shallow streams. *Water Resour. Res.* 38(11): 1250.

Marchand, J.P., Jarret, R.D. & Jones, L.L. 1984. Velocity profile, surface slope, and bed material size for selected streams in Colorado. *U.S. Geol. Surv. Open File Rep.* 84–733.

Monin, A.S. & Yaglom, A.M. 1971. *Statistical Fluid Mechanics: Mechanics of Turbulence – Vol. 1*. Cambridge (MA): MIT Press.

Nezu, I. & Nakagawa, H. 1993. *Turbulence in open-channel flows*. Rotterdam: A.A. Balkema.

Nikora, V. & Smart, G.M. 1997. Turbulence characteristics of New Zealand gravel-bed rivers. *J. Hydr. Eng.* 123(9): 764–773.

Nikora, V., Goring, D., McEwan, I. & Griffiths G. 2001. Spatially averaged open-channel flow over rough bed. *J. Hydr. Eng.* 127(2): 123–133.

Pitlick, J. 1992. Flow resistance under conditions of intense gravel transport. *Water Resour. Res.* 28(3): 891–903.

Rolland, T. & Lemmin, U. 1997. A two-component acoustic velocity profiler for use in turbulent open-channel flow. *J. Hydr. Res.* 35(4): 545–561.

Schlichting, H. 1968. *Boundary-layer theory*. New York: McGraw-Hill.

Smart, G.M. 1999. Turbulent velocity profiles and boundary shear in gravel bed rivers. *J. Hydr. Eng.* 125(2): 106–116.

Wang, Z.Q., Cheng, N.S., Chiew , Y.M. & Chen, X.W. 2003. Secondary flows in open channel with smooth and rough bed strips. *Proc. XXX IAHR Congress*, *Thessaloniki, 24–29 August 2003.* IAHR.

Wolman, M.G. 1954. A method of sampling coarse riverbed material. *Transactions American Geophysical Union* 35(6): 951–956.

Copyright © 2006 Taylor & Francis Group plc, London, UK

Admissible and inadmissible simplifications of pollution transport equations

P.M. Rowiński & M.B. Kalinowska
Institute of Geophysics, Polish Academy of Sciences, Warsaw, Poland

ABSTRACT: In general, pollution transport should be represented by 3D advection-diffusion equations but solution of such equations requires a lot of information which in most cases is not available and is computationally very expensive. Therefore different simplifications have been proposed, they mostly pertain to the reduction of the dimensionality of the problem and omitting of the terms considered as small in comparison to others. In practice very often the assumptions that allow for such simplifications are forgotten and therefore the obtained results may appear to be of disputable validity. An example can be the use of a diagonal dispersion tensor in the governing equations even in geometrically complex (and hence anisotropic) situations. Such treatment introduces unacceptable errors which very often are reduced by artificial manipulation of various coefficients. In this paper different model simplifications are discussed and the emphasis is put on their justification or disapproving, depending on the particular context of problem under consideration.

1 INTRODUCTION

Water quality predictions in rivers require development of a model that is able to capture the basic physical features of the process and depends only on the variables that are available in case under consideration. A very crucial and often made assumption is the limitation to the neutrally buoyant substances. The analysis of such micropollutants like heavy metals (e.g. mercury, cadmium, lead) would go along different line. The reason is that these substances may be present in three states in the system considered: in dissolved form as well as in solid phase mostly present in the suspended solids and in the sediment below. In case when these pollutants are in the solid form the relevant description of their transport should appeal to the dynamics of two-phase flows. The solid grains may move in the form of rolling, saltation and suspension. The manner of their motion depends on many factors, like the position at which the particle initiates to move, its size, shape, density relative to the carrier fluid, as well as turbulent properties of the flow. In general the way in which a particle moves is a direct effect of the role and significance of particular forces acting on a grain and also the variability of other solid particles concentration in its neighborhood. When considering the motion of such particle in a Lagrangian frame all the mentioned forces would have to be considered, namely the drag force, the drifting force due to turbulence, lift force and the combination of the weight and buoyancy of the particle. Additionally some supplementary model of a stochastic nature, responsible for the collision of the considered particle with solid boundaries would have to be built.

Let us assume that the considered mixture is passive that is one, in which the fluid-particle interaction does not affect the dynamics of the flow. Otherwise one would have to include momentum considerations in order to properly represent certain two-phase flows.

Further limitation is the consideration of the fate of solutes only, i.e. the substances that are dissolved in the water. Throughout the paper, we use the macroscopic treatment, i.e. the theory of continuum. Because of practical importance, we do not care about the motion of individual particles of the matter and are interested only in the resultant effects due to the motion of a large number of particles. It is possible because in practical problems the smallest length scales of interest are much larger than the distance between molecules.

In principle the physical processes during the transport of any constituent are three dimensional and should be described by three dimensional (3D) advection-diffusion equation together with the description of 3D velocity field. Advection-diffusion equation (ADE) already imposes so-called one-way coupling, i.e. the particles dispersed in a carrier flow have negligible effect on turbulence. It means that particle spread in this regime depends on the state of turbulence but due to the negligible concentration of the particles the momentum transfer from the particles to the turbulence has an insignificant effect on the flow (Elghobashi 1994). In most cases it is an acceptable assumption. Three dimensional ADE is, however, still too demanding in respect to data and the data for such

Copyright © 2006 Taylor & Francis Group plc, London, UK

models are mainly available for academic purposes. Therefore usually further simplifications are sought in practice.

2 TRANSPORT EQUATIONS

In general three-dimensional case, construction of the mass transport equation for a dissolved quantity requires the application of the Reynolds hypothesis allowing for the decomposition of the velocities and concentrations into mean and fluctuating values, and further additional information about the turbulent mass flux, for example based on a linear relationship between the turbulent flux and the gradient of the mean concentration. The main obstacles to progress in that approach is the lack of reliable theory which relates the spatial variation of turbulent diffusion coefficients to flow and boundary conditions, mathematical difficulties in solving the transport equation for variable diffusion coefficients and realistic spatial domains. Another important problem is the lack of knowledge of the realistic detailed 3D velocity field. 3D approach is probably suitable in the vicinity of the injection point in the river when one is interested in studying the heterogeneity in vertical and lateral directions. Such strong heterogeneity may occur due to the variability of river geometry like meanders, or the ones caused by fairways and weirs.

Various simplifications of the model are necessary to tackle real life problems. One option is to eliminate one or two dimensions in cases where such operation is justified by the conditions in the considered river reach. This elimination may be realized by relevant averaging of the governing equations (both hydrodynamics and mass transfer equation at the same time). It is usually the case that in the mid-field region the governing equations may be averaged over the depth giving two-dimensional models. In the far field, in case when the river geometry allows doing this, one is mostly interested in the cross-sectionally averaged concentrations. The governing equations may be then averaged over the cross-section, which results in a one-dimensional model of the spread of the constituent under consideration. Two-dimensional case will be considered in more detail in the next section. Let us therefore briefly discuss the problem of 1D modeling. A long tradition in the application of the longitudinal dispersion model exists. Such model is very useful for designing outfalls or water intakes and first of all for evaluating risks from, for example accidental releases of hazardous contaminants. 1D models are the easiest in application and not such detailed knowledge about the hydraulic characteristics of the considered reach is required as in case of 2D and 3D approaches. One has to realize, however, about the restrictions that 1D models are burdened (Rutherford, 1994; Sukhodolov et al. 1998, Jirka & Volker 2005). 1D model in the traditional Fickian form applies only in relatively simple river reaches (in terms of the geometry) and only after some initial mixing period (the solute concentration should be well distributed over the channel width). A widely applied criterion for the validity of the equation is that the time from the instant of release t should be greater than $0.4\,B^2/E_L$ where B is the channel width and E_L is the longitudinal dispersion coefficient. The advection-dispersion equation has been successfully applied for many real cases; nevertheless very often the questions about its applicability arise. The tail of a solute tracer pulse is often more pronounced than can be accounted for by the traditional advection-dispersion model. A common method for simulating these long tails has been to allow for storage zones along the stream channel (Czernuszenko et al. 1998, van Mazijk & Veling 2005). These storage zones are assumed to be stagnant relative to the longitudinal flow of the stream and to obey a first-order mass transfer type of exchange relationship. Very often a quicker decrease of the concentration maximum than follows from Fickian equation is observed. Also a nonlinear growth of the concentration distribution variance and dependence of the dispersion coefficient on time has been often manifested in experimental studies.

3 TWO-DIMENSIONAL TRANSPORT EQUATION

As mentioned before, in situations where the concentration is rather uniform along each individual vertical line, the depth averaging of every quantity is made to reduce the dimensionality of the problem. As a result the depth-averaged, two-dimensional advection-diffusion transport equation is readily obtained in the form:

$$h\left(\frac{\partial c}{\partial t}+v_x\frac{\partial c}{\partial x}+v_y\frac{\partial c}{\partial y}\right)= \frac{\partial}{\partial x}\left(hD_{xx}\frac{\partial c}{\partial x}+hD_{xy}\frac{\partial c}{\partial y}\right)+\frac{\partial}{\partial y}\left(hD_{yy}\frac{\partial c}{\partial y}+hD_{yx}\frac{\partial c}{\partial y}\right); \quad (1)$$

where t = time; (x, y) = longitudinal and transverse coordinates; (v_x, v_y) = depth-averaged velocities in x and y directions; $c(x, y, t)$ = depth-averaged solute concentration; h = local depth; D_{xx}, D_{xy}, D_{yx}, D_{yy} = dispersion coefficients. One needs to remember that new dispersion fluxes account for both the non-uniformity of velocities over the depth of flow as well as turbulent diffusion. In general the dispersion coefficients in Cartesian coordinates form a non-diagonal dispersion tensor:

$$\mathbf{D}=\begin{bmatrix} D_{xx} & D_{xy} \\ D_{yx} & D_{yy} \end{bmatrix}. \quad (2)$$

Copyright © 2006 Taylor & Francis Group plc, London, UK

In case when the flow direction is parallel to the x-axis, the off-diagonal elements of the dispersion tensor vanish. In such case the transport equation (Eq. 1) can be simplified to the form:

$$h\left(\frac{\partial c}{\partial t}+v_x\frac{\partial c}{\partial x}+v_y\frac{\partial c}{\partial y}\right)= \frac{\partial}{\partial x}\left(hD_{xx}\frac{\partial c}{\partial x}\right)+\frac{\partial}{\partial y}\left(hD_{yy}\frac{\partial c}{\partial y}\right). \quad (3)$$

However, in the realistic cases when an actual river is described, it is impossible to choose a coordinate system with the x-axis parallel to the flow direction for all points of the flow, and hence the full version of the transport equation (Eq. 1) should be used. Literature survey shows that the simplified form of the model is often used, even in very complex situations without any special justification. In the frame where the dispersion tensor is diagonal, D_{xx} element is marked D_L and refers to longitudinal dispersion coefficient, and D_{yy} is marked D_T and refers to transverse dispersion coefficient. D_L and D_T can be measured experimentally. There are numerous phenomenological formulae for calculating dispersion coefficients in literature (e.g. Rutherford 1994). In principle dispersion coefficients depend on channel geometry and turbulent flow structure and their estimation may become a very difficult task.

The use of the same coordinate system for the whole channel may lead to misleading results. To avoid this problem very often transport equations are formulated in a curvilinear coordinate system but it creates other sorts of problems. This matter is discussed e.g. in (Holley & Jirka 1986). In case of Cartesian coordinate systems for some parts of the channel it maybe necessary to use all the dispersion tensor components:

$$\mathbf{D}_D=\begin{bmatrix}D_L & 0\\ 0 & D_T\end{bmatrix}\rightarrow \mathbf{D}=\begin{bmatrix}D_{xx} & D_{xy}\\ D_{yx} & D_{yy}\end{bmatrix}. \quad (4)$$

Mathematically correct way of getting the full tensor $\mathbf{D}$ from the diagonal form $\mathbf{D}_D$ is tensor rotation with the rotation matrix $\mathbf{R}$:

$$\mathbf{D}=\mathbf{R}(\alpha)\cdot\mathbf{D}_\mathbf{D}\cdot\mathbf{R}^{-1}(\alpha); \quad (5)$$

where: $\alpha =$ angle between flow direction and x-axis;

$$\mathbf{R}=\begin{bmatrix}\cos\alpha & -\sin\alpha\\ \sin\alpha & \cos\alpha\end{bmatrix}.$$

It yields:

$$D_{xx}=D_T+D\frac{v_x^2}{v^2};$$
$$D_{xy}=D_{yx}=D\frac{v_x v_y}{v^2}; \quad (6)$$
$$D_{yy}=D_T+D\frac{v_y^2}{v^2};$$

where: $D=D_L-D_T$, $v=\sqrt{v_x^2+v_y^2}$.

For brevity this full method will further be called *rotation*.

Due to the fact that the simplified form of the transport equation is commonly used, a number of approximated methods of the tensor transformation (without off-diagonal components) are reviewed below to reveal under what conditions such simplifications are admissible. The common feature of all these methods is that the tensor stays diagonal after the transformation. A short description of various simplifications used *correctly* or *incorrectly* is given below.

3.1 *Quasi rotation*

As mentioned above a correct way of the rotation of the dispersion tensor is given by Equation 5. To get the diagonal tensor the off-diagonal elements D_{xy}, D_{yx} are often arbitrarily set to 0. Then tensor elements become:

$$D_{xx}=D_T+D\frac{v_x^2}{v^2};$$
$$D_{xy}=D_{yx}=0; \quad (7)$$
$$D_{yy}=D_T+D\frac{v_y^2}{v^2}.$$

3.2 *Vector-like rotation*

D_L and D_T elements are considered to form a vector.

$$\mathbf{D}_V=\begin{bmatrix}D_L\\ D_T\end{bmatrix}\rightarrow \mathbf{D}=\begin{bmatrix}D_{xx}\\ D_{yy}\end{bmatrix}. \quad (8)$$

Such vector is based on longitudinal and transversal dispersion coefficients, D_L and D_T. The resulting vector is rotated according to the vector rotation rule:

$$\mathbf{D}=\mathbf{R}(\alpha)\cdot\mathbf{D}_V. \quad (9)$$

Copyright © 2006 Taylor & Francis Group plc, London, UK

If any element of the vector turns out to be negative an absolute value is taken instead. Finally transformed dispersion components are:

$$\begin{aligned} D_{xx} &= \left| D_L \frac{v_x}{v} - D_T \frac{v_y}{v} \right|; \\ D_{xy} &= D_{yx} = 0; \\ D_{yy} &= \left| D_L \frac{v_y}{v} + D_T \frac{v_x}{v} \right|. \end{aligned} \tag{10}$$

3.3 *Identity transformation*

In this case the considered dispersion tensor is not transformed at all. Independently from the orientation of the coordinate system the tensor elements are always the same:

$$\begin{aligned} D_{xx} &= D_L; \\ D_{xy} &= D_{yx} = 0; \\ D_{yy} &= D_T. \end{aligned} \tag{11}$$

This is actually an approach very often applied in practice, usually without consciousness of the committed error. Authors just omit inconvenient terms in transport equations, even if the considered geometry does not allow for that.

Each simplified approach introduces some errors. Further in the paper the differences between the solutions of the simplified equation and the analytical solution for the simple case where the full equation can be solved, will be shown. It allows to judge under what conditions the assumed simplifications are admissible.

4 COMPUTATIONAL TESTS

Computations were performed away from the boundaries for a straight, rectangular channel (Fig. 1) forming different angles α with the axis of abscissa. Respective computer program was created in C++ computing language and compiled under Linux Red Hat operating system. Visualization of results was done with use of an Object-Oriented Data Analysis Framework ROOT – the program created in CERN – European Organization for Nuclear Research (Brun & Rademakers 1996). For numerical solutions of the transport equation various finite differences methods have been applied. Two of them (Crank Nicolson and Upwind schemes) have been compared in (Kalinowska & Rowiński 2004). The results presented herein were obtained by means of Alternating Direction Implicit style scheme (Douglas 1955, Peaceman & Rachford 1955). This scheme is stable, accurate and relatively fast.

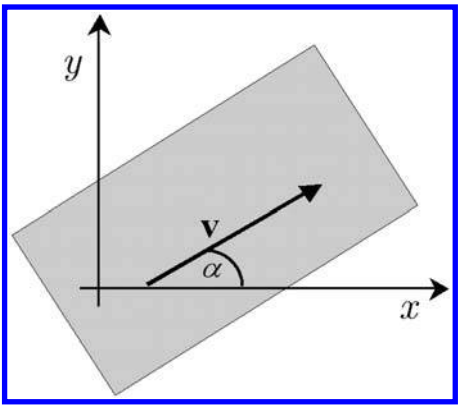


Figure 1. Scheme of straight, rectangular channel, used for computations.

For simplicity in the following tests it was assumed that velocity was uniformly distributed across the channel and equal to $v = 0.15$ m/s, transversal velocity was zero and the depth was constant in the whole channel. The computational time step was assumed as $\Delta t = 1$ s, whereas the grid spacing was $\Delta x = \Delta y = 1$ m. Dispersion coefficients were set as: $D_L = 0.75$ m^2/s, $D_T = 0.1$ m^2/s.

Table 1 provides the values of dispersion coefficients evaluated in the framework of all discussed methods. The differences between those coefficients are small only for angles close to 0° and 90° (with exception of identity transformation). It is worth mentioning the significant values of the "off-diagonal" values of dispersion elements in case of non-trivial angles α.

It is not meaningless how the solute is introduced into the flow and therefore instantaneous and continuous releases will be treated separately in the following numerical tests.

4.1 *Pulse release*

With the initial condition set as a Dirac delta function and with constant velocity and dispersion coefficients, the solution of 2D advection-diffusion equation (Eq. 1), away from the boundaries, is in the form of 2D Gaussian distribution (Smith & Yongming, 2001):

$$c(\mathbf{x},t) = \frac{M}{2\pi\sqrt{4t^2 D}} \exp\left\{ -\frac{(x-\mu_x)^2}{4tD/D_{yy}} \right\} \exp\left\{ -\frac{(y-\mu_y)^2}{4tD/D_{xx}} \right\} \exp\left\{ \frac{(x-\mu_x)(y-\mu_y)}{2tD/D_{xy}} \right\} \tag{12}$$

where: M is the mass released at a point (x_0, y_0) and time $t = 0$; $\mu_x = x_0 + v_x t$; $\mu_y = y_0 + v_y t$; $D = D_{xx} D_{yy} - D_{xy}^2$.

Copyright © 2006 Taylor & Francis Group plc, London, UK

Table 1. Dispersion coefficients for different angles, calculated using different methods.

Angle α	Method of calculation											
	Rotation			Quasi rotation			Vector-like rotation			Identity transformation		
	D_{xx}	D_{xy}	D_{yy}	D_{xx}	D_{xy}	D_{yy}	D_{xx}	D_{xy}	D_{yy}	D_{xx}	D_{xy}	D_{yy}
0°	0.75	0	0.1	0.75	0	0.1	0.75	0	0.1	0.75	0	0.1
5°	0.745	0.056	0.105	0.745	0	0.105	0.738	0	0.165	0.75	0	0.1
10°	0.730	0.111	0.119	0.730	0	0.119	0.721	0	0.229	0.75	0	0.1
15°	0.706	0.162	0.143	0.706	0	0.143	0.698	0	0.290	0.75	0	0.1
30°	0.587	0.281	0.262	0.587	0	0.262	0.599	0	0.461	0.75	0	0.1
45°	0.425	0.325	0.425	0.425	0	0.425	0.460	0	0.601	0.75	0	0.1
60°	0.262	0.281	0.587	0.262	0	0.587	0.288	0	0.699	0.75	0	0.1
90°	0.1	0	0.75	0.1	0	0.75	0.1	0	0.75	0.75	0	0.1

All calculation made for $D_L = 0.75$ and $D_T = 0.1$;
Values are round off to the nearest thousandth.

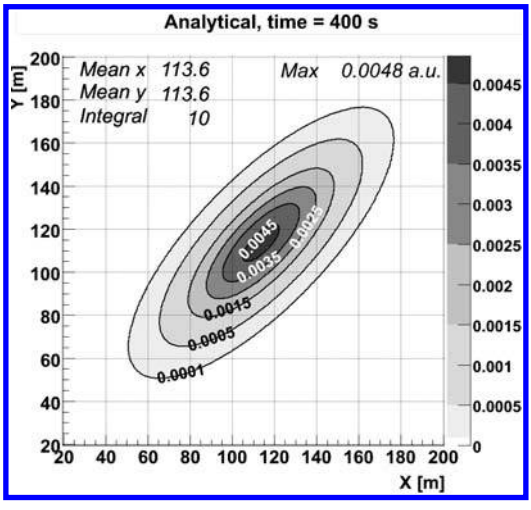


Figure 2. Analytical solution for the pulse release of the substance after 400 s from the release, $\alpha = 45°$.

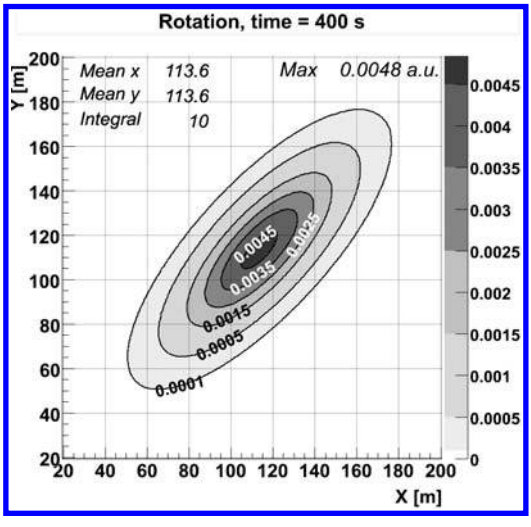


Figure 3. Numerical solution by means of full tensor rotation for the pulse release after 400 s, $\alpha = 45°$.

In our case the mass ($M = 10$ *arbitrary units*) has been injected instantaneously at a point $x_0 = 50$ m, $y_0 = 50$ m. For numerical simulations as an initial concentration (pulse release), the analytical solution after 200 seconds has been taken. In Figures 3 to 10 the results after 400 time steps (after elapsing 400 seconds from the initial time instant) of numerical simulation have been presented. One can compare these results with the analytical solution shown in Figure 2.

All the methods provide identical results as the analytical solution in cases when the angle formed between the channel and the x-axis is equal to 0 or 90° (the only exception is the identity transformation method under 90°). In other cases ($0° < \alpha < 90°$) only the method with the applied full dispersion tensor gives the same result as the analytical method. Figures 3 to 10 reveal most extreme situation when $\alpha = 45°$ – then the differences with the analytical solution are most pronounced. It is worth to note that the difference between the analytical solution and the simplified solutions depend on both the selected method of the transformation of the dispersion tensor and on the angle α. Identity transformation causes that the maximum difference between the analytical solution and the simplified one increases together with the increase of α (Fig. 11) whereas quasi rotation makes that difference symmetrical in relation to $\alpha = 45°$ and that difference diminishes close to $\alpha = 0°$ and $\alpha = 90°$. Vector-like rotation method produces still larger differences (there are small only for angels close to 0° and 90°). That difference for the full tensor rotation method is of the order of 10^{-5} to 10^{-6} and is not visible on the plot.

Copyright © 2006 Taylor & Francis Group plc, London, UK

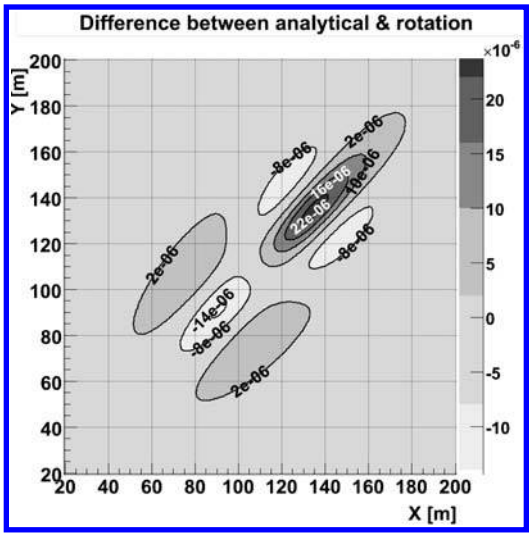


Figure 4. Difference between numerical (rotation) and analytical solutions for the pulse release after 400 s.

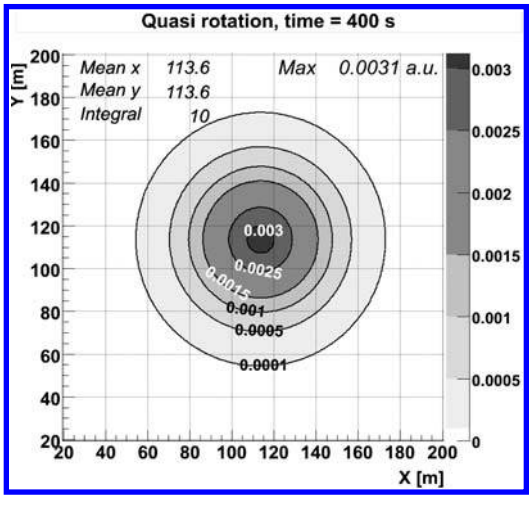


Figure 5. Numerical solution by means of quasi tensor rotation for the pulse release after 400 s, $\alpha = 45°$.

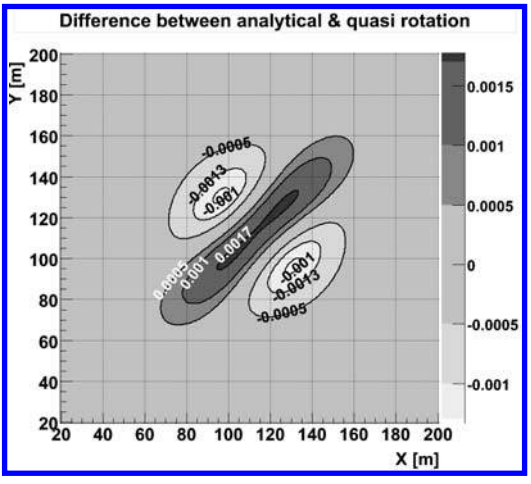


Figure 6. Difference between numerical (quasi rotation) and analytical solutions for the pulse release after 400 s.

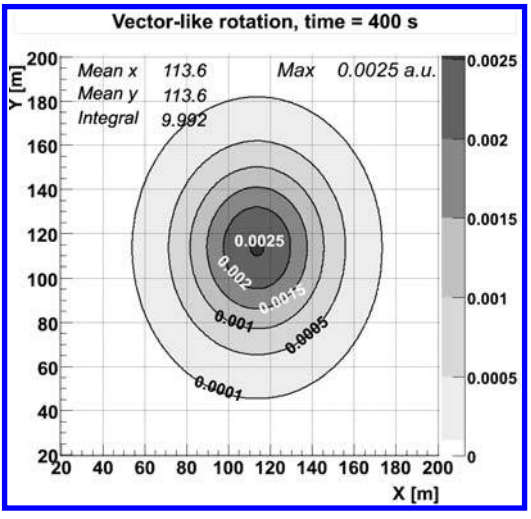


Figure 7. Numerical solution by means of vector-like rotation for the pulse release after 400 s, $\alpha = 45°$.

Environmental criteria cause that information about the maximum concentration of the solute is of special importance. Figure 12 shows the relation between the maxima of concentration obtained with the use of the described methods and the angle α. It is crucial that the maxima of the solute concentration are transformed in a correct way (in respect to their location, not value) independently of the method, which is readily seen in Figures 3 to 10 (note Mean x and Mean y). But the values of those maximum concentrations are very much determined by the method, especially for the angles remote from 0 and 90 degrees. The method with full dispersion tensor as well as the one with identity transformation also provide good estimates of the values of maximum concentration (which in case of the analytical solution for the assumed input data was equal to 0.0048 a.u.). Those observations show that when the investigated problem relates mostly to the maximum values of concentrations, the freedom in the choice of the method is much larger, which may save computational cost. The modeler, however, has to remember that the simplified methods will not provide a reliable pattern of the solute spread in the channel.

Copyright © 2006 Taylor & Francis Group plc, London, UK

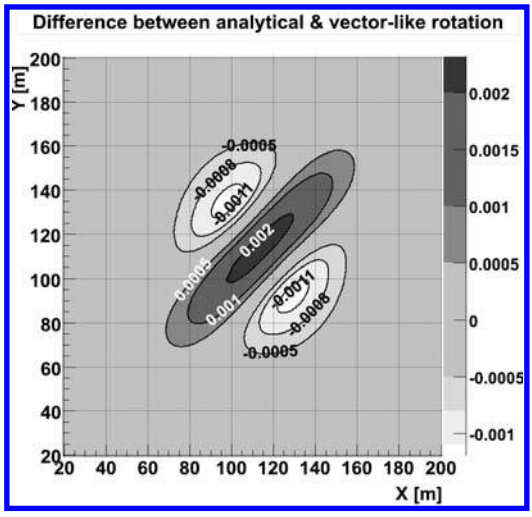


Figure 8. Difference between numerical (vector-like rotation) and analytical solutions for the pulse release after 400 s.

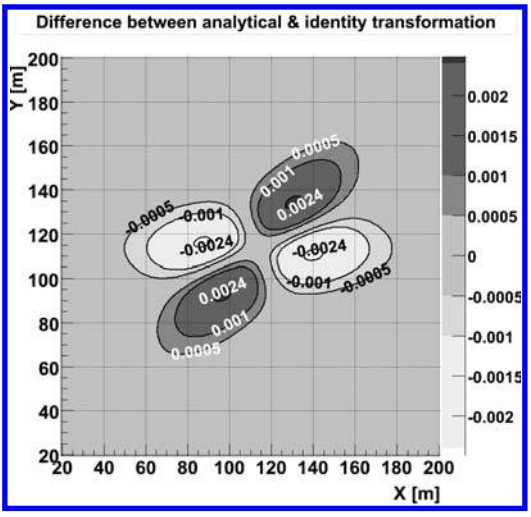


Figure 10. Difference between numerical (identity transformation) and analytical solutions for the pulse release after 400 s.

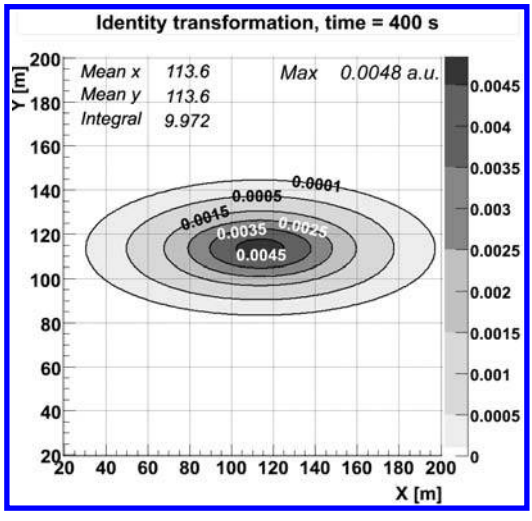


Figure 9. Numerical solution by means of identity transformation for the pulse release after 400 s, $\alpha = 45°$.

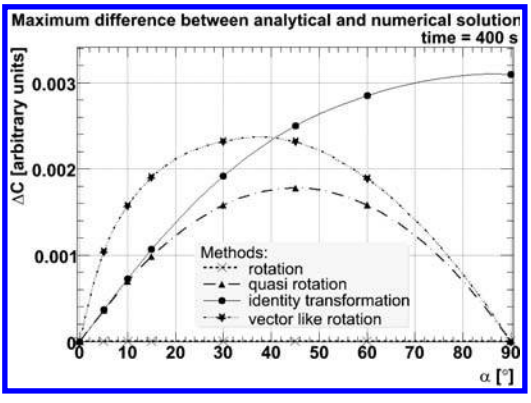


Figure 11. Maximum difference between numerical and analytical solutions for different methods of the dispersion tensor transformations for the pulse release. The difference is plotted as a function of the angle α.

4.2 *Continuous release*

In this case the boundary condition is given in the form of a continuous release at the rate 1[a.u.] per second. The source is located at the point $x_0 = 100$ m, $y_0 = 100$ m. An analytical solution is not achievable in such case so the results of the numerical simulations by means of the simplified methods will be compared with the method in which a complete dispersion tensor rotation is performed. Again the results for the worst case, when the channel forms the angle of 45° with the x-axis, are presented. Figures 13–16 present a snapshot of the numerical results at time instant 1000 s after the discharge of the solute. It is easily seen that all the simplified methods produce much more widespread plume and in case of the so-called identity transformation of dispersion tensor, the plume tends to bend towards one edge. It is again very interesting to judge what information can be gained on the maxima of the solute concentration with use of different methods and for different angles α. As expected, all methods (but identity transformation method) give exact values of the maximum concentration for $\alpha = 0°$ and $\alpha = 90°$ (identity transformation produces true results only

Copyright © 2006 Taylor & Francis Group plc, London, UK

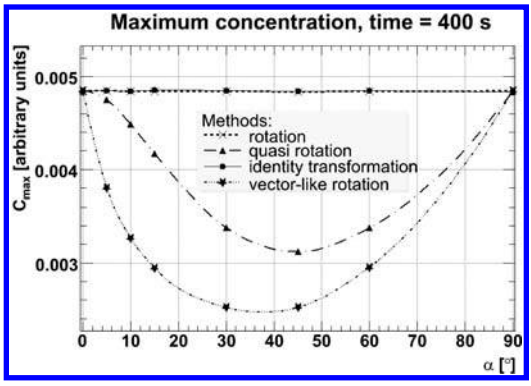


Figure 12. Maximum concentration for different methods of the dispersion tensor transformations for the pulse release. The maximum concentration is plotted as a function of the angle α.

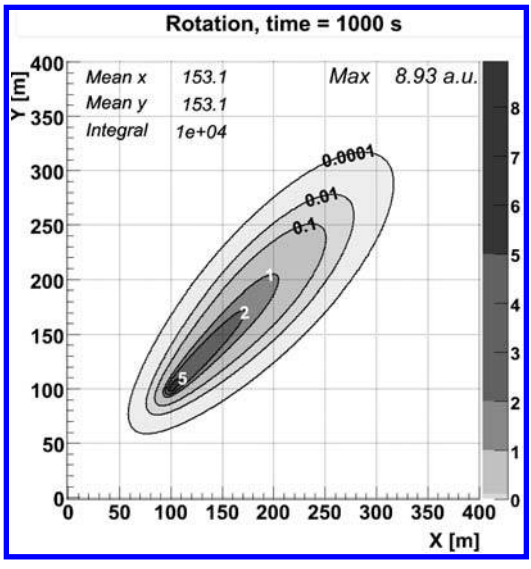


Figure 13. Numerical solution by means of full tensor rotation for the continuous release after 1000 s, $\alpha = 45°$.

when $\alpha = 0°$). Maximum concentration versus angle α in this case for all discussed methods are presented in Figure 17. Note that the error in case of the identity transformation increases with the increase of the angle α and achieves the largest value when $\alpha = 90°$. The noticeable slight oscillations in the solutions with the full dispersion tensor are associated with the method of discretization of the concentration values in a rectangular mesh. Each method causes that the maximum concentration stabilizes at a different level (Figs. 18a–18c) and the differences with the general method are largest at the angle equal to 45°. It shows that in case of continuous release the information about maximum

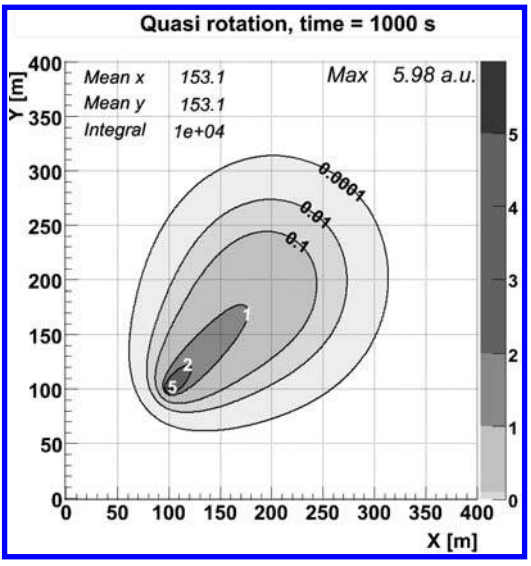


Figure 14. Numerical solution by means of quasi tensor rotation for the pulse release after 1000 s, $\alpha = 45°$.

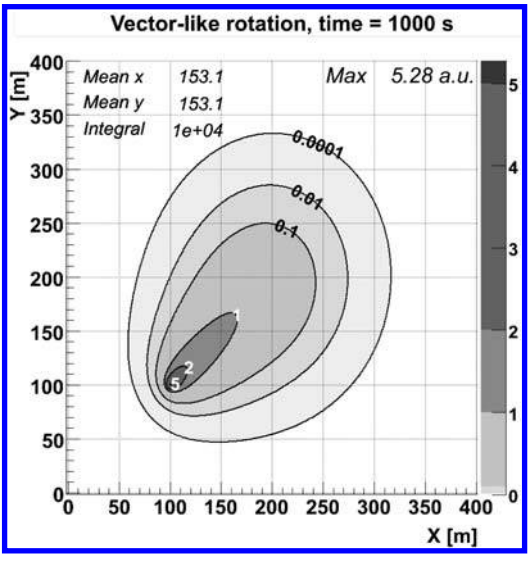


Figure 15. Numerical solution by means of vector-like rotation for the pulse release after 400 s, $\alpha = 45°$.

concentrations can be misleading when the simplified methods are applied.

5 CONCLUSIONS

A common practice in water quality modeling is the simplification of the original equations in order to

Copyright © 2006 Taylor & Francis Group plc, London, UK

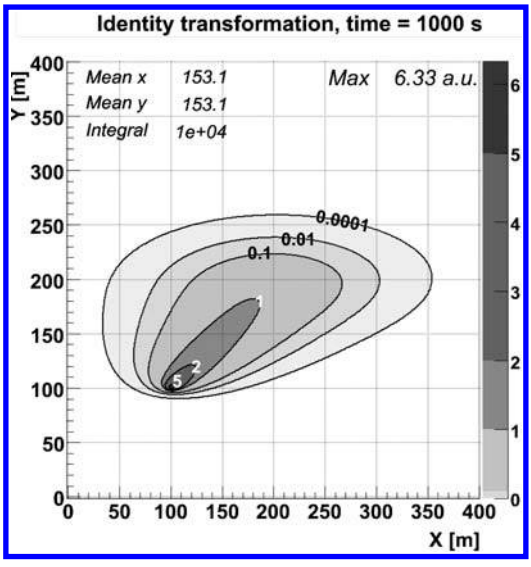


Figure 16. Numerical solution by means of identity transformation for the pulse release after 400 s, $\alpha = 45°$.

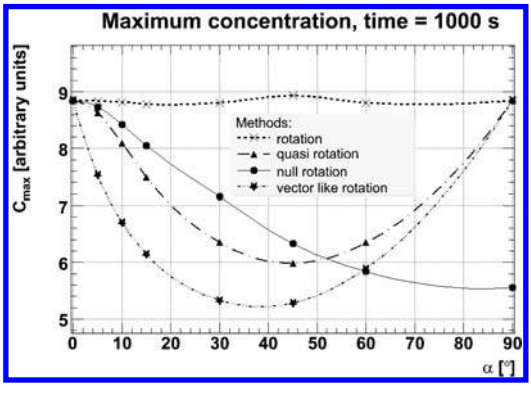


Figure 17. Maximum concentration for different methods of the dispersion tensor transformations for the continues release. The maximum concentration is plotted as a function of the angle α.

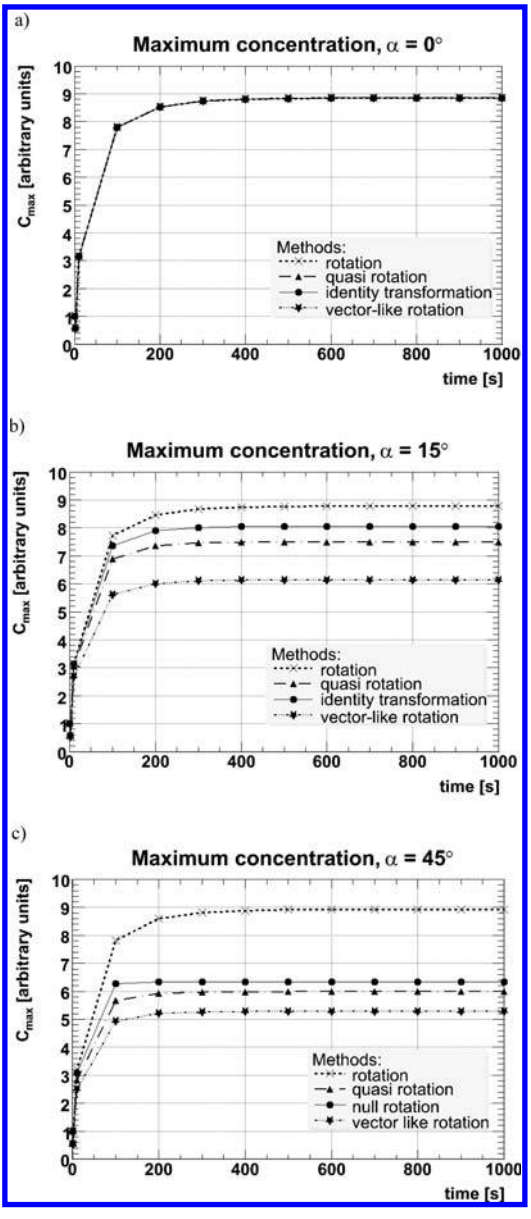


Figure 18. Maximum concentration for different methods of the dispersion tensor transformations for the continues release. The maximum concentration is plotted as a function of the simulation time. a) $\alpha = 0°$; b) $\alpha = 15°$; c) $\alpha = 45°$.

be able to tackle a real-life problem with the achievable data. Simplifications are usually justified under a set of additional assumptions, which very often are ignored in considerations. It very often leads to misleading, loaded with important errors or even totally wrong results. This study clearly shows that care has to be taken when a particular version of a transport equation is applied to a specified problem. Special attention has been paid to the often-encountered practice of neglecting the mixed derivatives in the transport equations independently of the complexity of the domain of computations. In principle such simplified methods are applicable for pulse releases when one is interested in maximum concentrations only or when α is small and varies insignificantly along the channel.

Copyright © 2006 Taylor & Francis Group plc, London, UK

ACKNOWLEDGEMENT

This work was supported by grant 2 P04D 026 29 from Ministry of Education and Science, Poland.

REFERENCES

Brun R. & Rademakers F. 1997. ROOT – An Object Oriented Data Analysis Framework. *Nucl. Inst. & Meth. in Phys. Res. A*, 389:81–86; http://root.cern.ch/.

Czernuszenko W. 1990. Dispersion of pollutants in flowing surface water. In *Encyclopedia of Fluid Mechanics*, 10, Surface and Groundwater Flow Phenomena, Gulf Publishing Company, Houston, London, Paris.

Czernuszenko W., Rowiński P.M. & Sukhodolov A. 1998. Experimental and numerical validation of dead-zone model for longitudinal dispersion in rivers. *Journal of Hydraulic Research*, 36(2):269–280.

Douglas J. 1955. On the numerical integration of $\partial^2 u/\partial x^2 + \partial^2 u/\ \partial y^2 = \partial u/\partial tt$ by implicit methods. *J. Soc. Indust. Appl. Math.*, 3(1):42–65, USA.

Elgobashi S. 1994. On predicting particle-laden turbulent flows, *Applied Scientific Research*, 52:309–329.

Holley E.R. & Jirka G.H. 1986. Mixing in Rivers. In *Technical Report E-86-11*, US Army Engineer Waterways Experiment Station, Vicksburg, Miss.

Jirka G.H. & Volker W. 2005. Mixing models for water quality management in rivers: continuous and instantaneous pollutant release. In Czernuszenko W. & Rowiński P.M. (eds), *Water Quality Hazards and Dispersion of Pollutants*: 1–34, Springer, USA.

Kalinowska M.B. & Rowiński P.M. 2004. Comparison of numerical schemes for two-dimensional mixing models for rivers. In Majewski W. (ed.), *Hydraulic Problems in Environmental Engineering*, *XXIV International School of Hydraulics, Jastrzębia Góra:* 97–104.

Peaceman D.W. & Rachford H.H. 1955. The numerical solution of parabolic and elliptic differential equations. *J. Soc. Indust. Appl. Math.* 3(1):28–42, USA.

Rutherford, J.C. 1994. *River Mixing*, Wiley, Chichester, England.

Smith R. & Yongming T. 2001. Optimal and near-optimal advection-diffusion finite difference schemes VI. In *Proc. R. Soc. Lond. A*, 457: 2379–2396.

Sukhodolov A., Nikora V.I., Rowiński P.M., Czernuszenko W. 1998. A case study of longitudinal dispersion in small lowland rivers. *Water Environment Research* 69(7):1246–1253.

Van Mazijk A. & Veling E.J.M. 2005. Mixing models for water quality management in rivers: continuous and instantaneous pollutant release. In Czernuszenko W. & Rowiński P.M. (eds), *Water Quality Hazards and Dispersion of Pollutants*: 143–168, Springer, USA.

Copyright © 2006 Taylor & Francis Group plc, London, UK

Fundamental characteristics of high velocity flows in a sinuous meandering channel in the vicinity of resonance

T. Hosoda & M. Nishihama
Dept. of Urban Management, Faculty of Engineering, Kyoto University, Kyoto, Japan

ABSTRACT: Fundamental characteristics of high velocity flows in a sinuous meandering channel were investigated theoretically and experimentally. It was shown that the flow characteristics can be classified into two patterns, i.e., out-of-phase and in-phase, by the resonance relation between water surface and channel meandering based on the solutions of the linearized shallow water equations. The experimental results agree well with the theoretical findings within the limited range of flow conditions. We also carried out the numerical simulations by using a shallow water flow model to clarify the non-linear features of water surface profile patterns in the vicinity of the resonance relation. The calculated results of water surface profile were visualized, and compared with the experimental results to verify the numerical model. The calculated results showed some fundamental characteristics such that the phase lag between water surface variations along the side wall and the sinuous channel becomes around 90 degree in the neighborhood of the resonance relation.

1 INTRODUCTION

Fundamental characteristics of high velocity flows in a sinuous open channel (refer to Figure 1) have been investigated by many researchers of hydraulics and river engineering as a typical model for meandering rivers with point bars. Engelund (1974) derived the linear solution of shallow flow equations in a sinuous channel to calculate the erodible bed topography around channel bends. Ikeda, Parker & Sawai (1981) also utilized the solution of the shallow flow equations to investigate the initiation of river meandering. It can be noted that the resonance relation between water surface and channel meandering is not included in the solution that Engelund and Ikeda et al. used, because the inertia terms of the momentum equation in the transverse direction are neglected. Note that resonance in this paper doesn't mean the response between channel meandering and bed topography.

Hasegawa (1980) derived the approximate solution of the linearized shallow flow equations with the inertia terms in the momentum equation along the transverse direction using the Galerkin method to investigate the response of bottom bed to channel meandering. Blondeaux & Seminara (1985) derived the complete linear solution using the same basic equations for the same purpose as Hasegawa (1980). They also derived the solution for the bottom topography combining the sediment transport equation with the shallow flow equations. They claimed that the resonance between channel meandering and bed topography can be explained by the solution and the resonance relation between water surface and channel meandering is also included in the solution. However, since the flow regime near the resonance relation of water surface is super-critical, the flow behaviors near the resonance were not necessary taken into account in the studies of bed topography in meandering channels.

Hosoda (1999) studied the fundamental characteristics of high velocity flows in a sinuous channel using hydraulic experiments. Based on the solutions of the linearized shallow water equations, it was shown that the flow patterns can be basically classified by the resonance relation between water surface and channel meandering. It was shown that the experimental results agreed well with the theoretical findings within the limited range of flow conditions.

In this study, we carried out numerical simulations by using shallow flow equations to clarify the non-linear response of water surface profile near the resonance relation. The calculated results of water surface profile were visualized, and compared with the experimental results to verify the numerical model. It was pointed out that a typical water surface pattern with hydraulic jump appears near the resonance when the inclination of the flume increases.

2 CLASSIFICATION OF FLOW PATTERNS BASED ON THE LINEAR THEORY

2.1 *Summary of linear theory*

For the sake of easy understanding, a summary of derivation process for the simplified linear theory on

Copyright © 2006 Taylor & Francis Group plc, London, UK

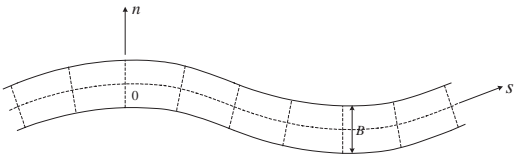


Figure 1. Plan form of a sinuous open channel.

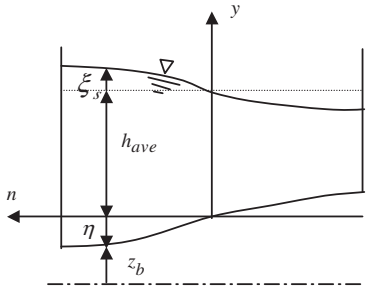


Figure 2. Cross-sectional view of a sinuous open channel.

the response of water surface to channel meandering is presented below.

2.1.1 *Basic equations*

Referring to Figures 1 and 2, the common shallow flow equations, which consist of the continuity equation and the momentum equations, based on the curvilinear orthogonal coordinates are described as follows.

$$\frac{r_0}{r_0+n}\frac{\partial hu_s}{\partial s}+\frac{\partial hu_n}{\partial n}+\frac{hu_n}{r_0+n}=0 \tag{1}$$

$$\frac{r_0}{r_0+n}u_s\frac{\partial u_s}{\partial s}+u_n\frac{\partial u_s}{\partial n}+\frac{u_su_n}{r_0+n}= \frac{r_0}{r_0+n}\left(-g\frac{\partial \xi_s}{\partial s}+g\frac{\partial z_b}{\partial s}\right)-\frac{\tau_{bs}}{\rho h} \tag{2}$$

$$\frac{r_0}{r_0+n}u_s\frac{\partial u_n}{\partial s}+u_n\frac{\partial u_n}{\partial n}-\frac{u_s^{\,2}}{r_0+n}= -g\frac{\partial \xi_s}{\partial n}-\frac{\tau_{bn}}{\rho h} \tag{3}$$

where (s,n): orthogonal curvilinear coordinates, (u_s,u_n): depth averaged velocity vectors in the (s,n) directions, h: depth, ξ_s: water surface elevation, z_b: bottom elevation, (τ_{bs},τ_{bn}): bottom shear stress vectors, r_0: curvature radius along the channel center line.

The sine-generated curve defined by Eq. (4) is assumed as the line of the channel centerline.

$$\frac{1}{r_0}=\frac{1}{R}\cos\left(\frac{2\pi s}{L}\right) \tag{4}$$

where R: minimum curvature radius at the apex of the center line, L: wave length of sinuous channel.

In the previous theoretical studies, the bottom shear stresses are evaluated by the following formulas with friction coefficient.

$$\frac{\tau_{bs}}{\rho}=c_f u_s\sqrt{u_s^{\,2}+u_n^{\,2}},\ \frac{\tau_{bn}}{\rho}=c_f u_n\sqrt{u_s^{\,2}+u_n^{\,2}} \tag{5}$$

where c_f: friction coefficient.

2.1.2 *Linearized equations*

Using the bottom slope along the channel center line as $I_0\approx-\frac{\partial z_b}{\partial s}$, the normal depth, h_0, and the averaged velocity, U, are defined by the following equations.

$$gI_0=c_f\frac{U^2}{h_0},h_0=\frac{q}{U} \tag{6}$$

where q: unit width discharge (discharge divided by channel width).

Firstly, the basic equations are transformed into a non-dimensional form using the following non-dimensional variables.

[definition of non-dimensional variables]

$$u_s'=\frac{u_s}{U},u_n'=\frac{u_n}{U},h'=\frac{h}{h_0},\xi_s'=\frac{\xi}{h_0},\eta'=\frac{z_b}{h_0},$$
$$s'=\frac{s}{h_0},n'=\frac{n}{h_0},\nu=\frac{h_0}{R},\lambda=\frac{2\pi h_0}{L},Fr_0=\frac{U}{\sqrt{gh_0}}$$

Then, the linearized equations, Eqs. (8)–(10), are derived by substituting the expressions in Eq. (7) into Eqs. (1), (2) and (3).

$$u_s'=1+\nu u_1,\ u_n'=\nu v_1,\ h'=1+\nu\left(\xi_{s1}+\eta_1\right) \tag{7}$$

$$\frac{\partial u_1}{\partial s'}+\frac{\partial\left(\xi_{s1}+\eta_1\right)}{\partial s'}+\frac{\partial v_1}{\partial n'}=0 \tag{8}$$

$$\frac{\partial u_1}{\partial s'}+\frac{1}{Fr_0^{\,2}}\frac{\partial \xi_{s1}}{\partial s'}+c_f\left\{2u_1-\left(\xi_{s1}+\eta_1\right)\right\}= -c_f n'\cos\lambda s' \tag{9}$$

$$\frac{\partial v_1}{\partial s'}+\frac{1}{Fr_0^{\,2}}\frac{\partial \xi_{s1}}{\partial n'}+c_f v_1=\cos\lambda s' \tag{10}$$

For simplicity, the prime sign ′ indicating the non-dimensional variables henceforth omitted.

2.1.3 *Approximate linear solutions*

Hasegawa (1980) derived the approximate solutions by using the Galerkin method. Blondeaux & Seminara (1985) derived complete solutions combining the

Copyright © 2006 Taylor & Francis Group plc, London, UK

sediment transport equation with the shallow flow equations. Simpler solutions are shown below to understand the fundamental features of the response of water surface to channel meandering (Hosoda(1999)).

It should be noted that in the bend theory by Ikeda et al. (1981) the first and third terms in the left side of Eq. (10) are neglected and the resonance between water surface and channel meandering is not included in the theory.

Substituting the relations, Eqs.(11a)–(11d), into Eqs. (8)–(10) and setting the coefficients of $\sin(\lambda s)$ and $\cos(\lambda s)$ to be zero, the linear solutions are obtained with the coefficients, $\hat{a} - \hat{l}$, defined below.

$$\xi_{s1} = Fr_0^{\,2} n \cos \lambda s + \xi_{s11} n \cos\left(\lambda s + \phi_{\xi_{s11}}\right) \tag{11a}$$

$$\eta_1 = \eta_{11} n \cos\left(\lambda s + \phi_{\eta_{11}}\right) \tag{11b}$$

$$u_1 = u_{11} n \cos\left(\lambda s + \phi_{u_{11}}\right) \tag{11c}$$

$$v_1 = v_{10}\left(1 - \frac{n^2}{\varepsilon^2}\right) n \cos\left(\lambda s + \phi_{v_{10}}\right) \tag{11d}$$

where ε is defined as $\varepsilon \equiv B/(2h_0)$.

$$\hat{a} = \xi_{s11}\cos\phi_{\xi_{s11}},\ \hat{b} = \xi_{s11}\sin\phi_{\xi_{s11}},$$
$$\hat{e} = u_{11}\cos\phi_{u_{11}},\ \hat{f} = u_{11}\sin\phi_{u_{11}},$$
$$\hat{i} = v_{10}\cos\phi_{v_{10}},\ \hat{j} = v_{10}\sin\phi_{v_{10}},$$
$$\hat{k} = \eta_{11}\cos\phi_{\eta_{11}},\ \hat{l} = \eta_{11}\sin\phi_{\eta_{11}}$$

The coefficients $\hat{a}$ and $\hat{b}$ are calculated by the following relations.

$$\hat{a} = \frac{QS - PR}{P^2 + Q^2},\ \hat{b} = \frac{QR + PS}{P^2 + Q^2} \tag{12}$$

where P, Q, R and S are related to the hydraulic variables defined by the following equations.

$$P = \lambda c_f A_1 + \frac{2}{\varepsilon^2 \lambda}\frac{A_3}{c_f^{\,2} + \lambda^2}\frac{c_f}{Fr_0^{\,2}},$$
$$Q = A_2 + A_3 - \frac{2}{\varepsilon^2}\frac{A_3}{c_f^{\,2} + \lambda^2}\frac{1}{Fr_0^{\,2}},$$
$$R = -\left(A_3 + 2c_f^{\,2}\right)\hat{l} + \lambda c_f\left(1 - \hat{k} - Fr_0^{\,2}\right)$$
$$S = -A_3\left(\hat{k} + Fr_0^{\,2}\right) - \lambda c_f \hat{l} + \lambda^2 + c_f^{\,2}\left(1 + \hat{k} - Fr_0^{\,2}\right),$$
$$A_1 = \frac{2}{Fr_0^{\,2}} + 1,\ A_2 = 2c_f^{\,2} - \frac{\lambda^2}{Fr_0^{\,2}},\ A_3 = 4c_f^{\,2} + \lambda^2$$

The bottom variations, $\hat{k}$ and $\hat{l}$, are given as the boundary conditions. Since the bottom surface of the flume used for the hydraulic experiments is flat, $\hat{k}$ and $\hat{l}$ are set to be zero in this study.

$\hat{i}, \hat{j}, \hat{e}$ and $\hat{f}$ are given by the following equations.

$$\hat{i} = \frac{-c_f\hat{a} - \lambda\hat{b}}{Fr_0^{\,2}\left(c_f^{\,2} + \lambda^2\right)},\ \hat{j} = \frac{+\lambda\hat{a} - c_f\hat{b}}{Fr_0^{\,2}\left(c_f^{\,2} + \lambda^2\right)}$$
$$\hat{e} = -\hat{a} - \left(\hat{k} + Fr_0^{\,2}\right) + \frac{2}{\varepsilon^2\lambda}\hat{j},\ \hat{f} = -\hat{b} - \hat{l} - \frac{2}{\varepsilon^2\lambda}\hat{i}$$

2.1.4 *Resonance relation*

According to the linear theory described above, the flow characteristics are categorized by the following four non-dimensional parameters.

$$\nu = \frac{h_0}{R}, \varepsilon = \frac{B}{2h_0},\ \lambda = 2\pi\frac{h_0}{L},\ Fr_0 = \frac{U}{\sqrt{gh_0}}$$

In this study, since the experiments were carried out using the sinuous channel with constant value of L/B, it is convenient to use L/B instead of λ using the relation $\lambda = \frac{\pi}{\varepsilon}\frac{1}{L/B}$.

Using Eq. (11), ξ_{s1} is described by Eq. (13a) and the variations of water surface along the right side wall, ξ_{sw}, are also given by Eq. (13b).

$$\xi_{s1} = n\left(Fr_0^{\,2} + \hat{a}\right)\cos(\lambda s) - n\hat{b}\sin(\lambda s) \tag{13a}$$

$$\xi_{sw} = Amp \bullet \cos\left(\lambda s + \Phi_{\xi_s}\right) \tag{13b}$$

where Amp and Φ_ξ are defined by

$$Amp = \varepsilon\sqrt{\left(Fr_0^{\,2} + \hat{a}\right)^2 + \hat{b}^2} \tag{14a}$$

and

$$\cos(\Phi_{\xi_s}) = \frac{\varepsilon\left(Fr_0^{\,2} + \hat{a}\right)}{Amp},\ \sin(\Phi_{\xi_s}) = \frac{\varepsilon\hat{b}}{Amp} \tag{14b}$$

If the terms with c_f are neglected from Eq. (12), Amp is reduced to the following equation.

$$Amp = \varepsilon\frac{\frac{2}{\varepsilon^2}}{\left|\lambda^2 - \frac{1}{Fr_0^{\,2}}\left(\lambda^2 + \frac{2}{\varepsilon^2}\right)\right|}$$
$$= \varepsilon\frac{2}{\left|\frac{\pi^2}{(L/B)} - \frac{1}{Fr_0^{\,2}}\left(\frac{\pi^2}{(L/B)} + 2\right)\right|} \tag{15}$$

Copyright © 2006 Taylor & Francis Group plc, London, UK

The resonance relation is defined as the relation where the amplitude of water surface variations becomes to infinity, and given by Eq. (16).

$$\lambda^2 - \frac{1}{Fr_0{}^2}\left(\lambda^2 + \frac{2}{\varepsilon^2}\right) = 0 \quad \text{or} \quad Fr_0 = \sqrt{1 + \frac{2}{\pi^2}\left(\frac{L}{B}\right)^2} \tag{16}$$

Figure 3 shows the relation between the amplitude of depth variations along the side wall and the averaged Froude number described by Eq. (15).

The phase lag between the water surface variations along the right side wall and sinuous channel is also determined using Eq. (16). As shown in Figure 4, the variations show in-phase pattern with $\Phi_\xi = 0$ in the region below Eq. (16) and out-of-phase pattern with $\Phi_\xi = \pi$ above Eq. (16). In-phase pattern indicates that maximum depth occurs near an apex of the outer side wall due to the effect of centrifugal force and the minimum depth near an apex of the inner side-wall.

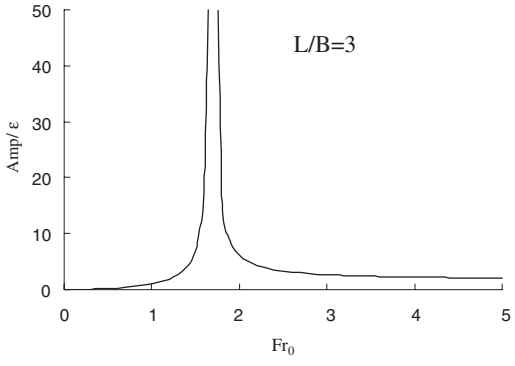


Figure 3. Relation between Amp/ε and Fr_0.

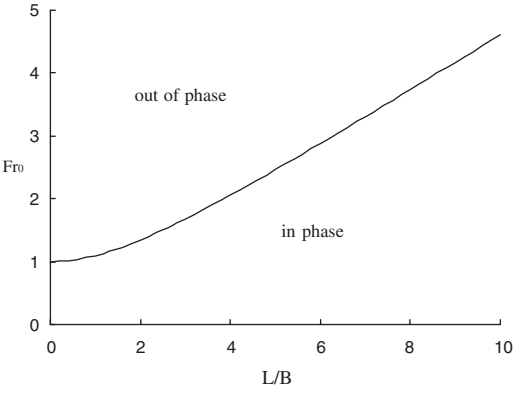


Figure 4. Classification of flow pattern.

3 NUMERICAL MODEL

3.1 *Fundamental equations*

Using the depth averaged shallow flow equations in a generalized curvilinear coordinate, we carried out the numerical simulations of high velocity flows in a sinuous open channel under various hydraulic conditions such as discharge, channel slope, etc.

Common fundamental equations in a Cartesian coordinate, which consists of depth averaged continuity equation and momentum equations, are denoted as follows (refer to Nagata & Hosoda (2000)):

[Depth averaged continuity equation]

$$\frac{\partial h}{\partial t} + \frac{\partial M}{\partial x} + \frac{\partial N}{\partial y} = 0 \tag{17}$$

[Depth averaged momentum equations]

$$\frac{\partial M}{\partial t} + \frac{\partial uM}{\partial x} + \frac{\partial vM}{\partial y} = -gh\frac{\partial z_s}{\partial x} - \frac{\tau_{bx}}{\rho} + \frac{\partial}{\partial x}\left(-\overline{u'^2}h\right) + \frac{\partial}{\partial y}\left(-\overline{u'v'}h\right) \tag{18a}$$

$$\frac{\partial N}{\partial t} + \frac{\partial uN}{\partial x} + \frac{\partial vN}{\partial y} = -gh\frac{\partial z_s}{\partial y} - \frac{\tau_{by}}{\rho} + \frac{\partial}{\partial x}\left(-\overline{u'v'}h\right) + \frac{\partial}{\partial y}\left(-\overline{v'^2}h\right) \tag{18b}$$

where t: time, (x,y): spatial coordinates, (u,v): components of depth averaged velocity vectors in x,y directions, (M,N): components of depth averaged discharge flux vectors in x,y directions, g: gravity acceleration, h: depth, ρ: density of water, z_s: water surface elevation from a datum plane, (τ_{bx},τ_{by}): components of bottom stress vectors, $-\overline{u'^2}$, $-\overline{u'v'}$, $-\overline{v'^2}$: components of depth averaged Reynolds stress tensors.

The bottom shear stresses are evaluated by Manning's formula, Eq. (19).

$$\tau_{bx} = \frac{\rho g n^2 u\sqrt{u^2+v^2}}{h^{1/3}}, \quad \tau_{by} = \frac{\rho g n^2 v\sqrt{u^2+v^2}}{h^{1/3}} \tag{19}$$

The depth averaged Reynolds stresses are evaluated by the following equations.

$$-\overline{u'^2} = 2D_h\left(\frac{\partial u}{\partial x}\right) - \frac{2}{3}k, \quad -\overline{u'v'} = D_h\left(\frac{\partial u}{\partial y} + \frac{\partial v}{\partial x}\right),$$
$$-\overline{v'^2} = 2D_h\left(\frac{\partial v}{\partial y}\right) - \frac{2}{3}k \tag{20a}$$

$$D_h = \alpha h u_* \tag{20b}$$

Copyright © 2006 Taylor & Francis Group plc, London, UK

where D_h: eddy viscosity, k: depth averaged turbulent kinetic energy evaluated by Eq. (21), α: constant (=0.3), u_*: friction velocity defined by

$$\sqrt{\sqrt{(\tau_{bx}{}^2+\tau_{by}{}^2)}/\rho}\,.$$

$$k=2.07u_*^2 \tag{21}$$

Fundamental equations (17)–(18a,b) in a Cartesian coordinate are transformed into the equations in a generalized curvilinear coordinate system.

[Depth averaged continuity equation]

$$\frac{\partial}{\partial t}\left(\frac{h}{J}\right)+\frac{\partial}{\partial \xi}\left(\frac{Uh}{J}\right)+\frac{\partial}{\partial \eta}\left(\frac{Vh}{J}\right)=0 \tag{22}$$

[Depth averaged momentum equations]

$$\begin{aligned}
&\frac{\partial}{\partial t}\left(\frac{Q^\xi}{J}\right)+\frac{\partial}{\partial \xi}\left(\frac{UQ^\xi}{J}\right)+\frac{\partial}{\partial \eta}\left(\frac{VQ^\xi}{J}\right)\\
&-\frac{M}{J}\left(U\frac{\partial \xi_x}{\partial \xi}+V\frac{\partial \xi_x}{\partial \eta}\right)-\frac{N}{J}\left(U\frac{\partial \xi_y}{\partial \xi}+V\frac{\partial \xi_y}{\partial \eta}\right)\\
&=-gh\left(\frac{\xi_x^2+\xi_y^2}{J}\frac{\partial z_s}{\partial \xi}+\frac{\xi_x\eta_x+\xi_y\eta_y}{J}\frac{\partial z_s}{\partial \eta}\right)\\
&-\frac{\tau_b^\xi}{\rho J}+\frac{\xi_x^2}{J}\frac{\partial}{\partial \xi}\left(-\overline{u'^2}h\right)+\frac{\xi_x\eta_x}{J}\frac{\partial}{\partial \eta}\left(-\overline{u'^2}h\right)
\end{aligned} \tag{23}$$

$$\begin{aligned}
&+\frac{\xi_y^2}{J}\frac{\partial}{\partial \xi}\left(-\overline{v'^2}h\right)+\frac{\xi_y\eta_y}{J}\frac{\partial}{\partial \eta}\left(-\overline{v'^2}h\right)\\
&+\frac{\xi_x\eta_y+\xi_y\eta_x}{J}\frac{\partial}{\partial \eta}\left(-\overline{u'v'}h\right)+\frac{2\xi_x\xi_y}{J}\frac{\partial}{\partial \xi}\left(-\overline{u'v'}h\right)\\
&\frac{\partial}{\partial t}\left(\frac{Q^\eta}{J}\right)+\frac{\partial}{\partial \xi}\left(\frac{UQ^\eta}{J}\right)+\frac{\partial}{\partial \eta}\left(\frac{VQ^\eta}{J}\right)\\
&-\frac{M}{J}\left(U\frac{\partial \eta_x}{\partial \xi}+V\frac{\partial \eta_x}{\partial \eta}\right)-\frac{N}{J}\left(U\frac{\partial \eta_y}{\partial \xi}+V\frac{\partial \eta_y}{\partial \eta}\right)\\
&=-gh\left(\frac{\xi_x\eta_x+\xi_y\eta_y}{J}\frac{\partial z_s}{\partial \xi}+\frac{\eta_x^2+\eta_y^2}{J}\frac{\partial z_s}{\partial \eta}\right)\\
&-\frac{\tau_b^\eta}{\rho J}+\frac{\xi_x\eta_x}{J}\frac{\partial}{\partial \xi}\left(-\overline{u'^2}h\right)+\frac{\eta_x^2}{J}\frac{\partial}{\partial \eta}\left(-\overline{u'^2}h\right)\\
&+\frac{\xi_y\eta_y}{J}\frac{\partial}{\partial \xi}\left(-\overline{v'^2}h\right)+\frac{\eta_y^2}{J}\frac{\partial}{\partial \eta}\left(-\overline{v'^2}h\right)\\
&+\frac{\xi_x\eta_y+\xi_y\eta_x}{J}\frac{\partial}{\partial \xi}\left(-\overline{u'v'}h\right)+\frac{2\eta_x\eta_y}{J}\frac{\partial}{\partial \xi}\left(-\overline{u'v'}h\right)
\end{aligned} \tag{24}$$

where (ξ,η): generalized curvilinear coordinates, J: Jacobian of coordinate transformation defined by $J=1/(x_\xi y_\eta - x_\eta y_\xi)$, (U,V): contravariant components of velocity vectors defined by Eq. (25).

$$U=\xi_x u+\xi_y v, V=\eta_x u+\eta_y v \tag{25}$$

where(Q^ξ,Q^η): contravariant components of discharge flux vectors defined by Eq. (26), and (τ_b^ξ,τ_b^η): contravariant components of bottom shear stress vectors defined by Eq. (27).

$$Q^\xi=\xi_x M+\xi_y N, Q^\eta=\eta_x M+\eta_y N \tag{26}$$

$$\tau_b^\xi=\xi_x\tau_{bx}+\xi_y\tau_{by}, \tau_b^\eta=\eta_x\tau_{bx}+\eta_y\tau_{by} \tag{27}$$

3.2 *Numerical method*

We used the Finite Volume Method with staggered allocation of hydraulic variables as a numerical method for the numerical simulations. The details and the other basic items on numerical simulations are described in Kimura & Hosoda (1997) and Nagata & Hosoda (2000).

4 RESULTS OF HYDRAULIC EXPERIMENTS

We conducted the hydraulic experiments to investigate the response of water surface profiles with channel slope, discharge, etc. The three types of sinuous side walls, whose curvature radius is given by Eq. (4) (refer to Figure 5), were set on the straight tilting flume with flat bed.

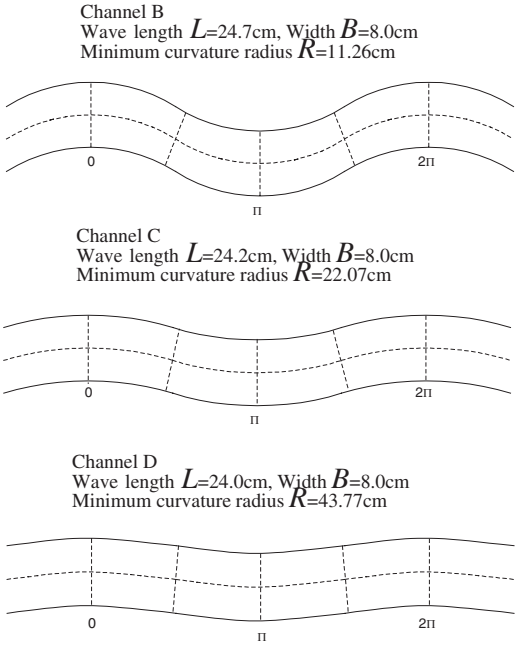


Figure 5. Flumes B, C, D used for experiments.

Copyright © 2006 Taylor & Francis Group plc, London, UK

Table 1. Hydraulic variables of experiments.

	Averaged depth (cm)	Averaged velocity(cm/s)	Minimum curvature radius R (cm)	slope	Froude number	λ	e	ν
RunB1-1	2.29	20.02	11.26	1/150	0.42	0.583	1.747	0.203
RunB2-2	1.42	32.23	11.26	1/64	0.86	0.361	2.817	0.126
RunB3-1	1.73	45.05	11.26	1/26	1.33	0.44	2.312	0.154
RunB3-2	0.61	38.58	11.26	1/26	1.58	0.155	6.557	0.054
RunC1-1	1.48	46.83	22.07	1/64	1.23	0.384	2.703	0.067
RunC2-1	1.09	61.82	22.07	1/26	1.89	0.283	3.67	0.049
RunC2-2	0.59	53.51	22.07	1/26	2.2	0.153	6.78	0.027
RunC3-1	0.49	68.04	22.07	1/20	3.12	0.127	8.163	0.022
RunD1-1	1.09	42.54	43.77	1/64	1.3	0.285	3.67	0.025
RunD1-2	0.68	29.31	43.77	1/64	1.13	0.178	5.882	0.016
RunD2-1	0.59	63.69	43.77	1/26	2.64	0.154	6.78	0.013
RunD2-2	1.01	73.44	43.77	1/26	2.33	0.264	3.96	0.023
RunD3-1	0.61	77.5	43.77	1/20	3.16	0.16	6.557	0.014
RunD3-2	0.81	80.42	43.77	1/20	2.86	0.212	4.938	0.019

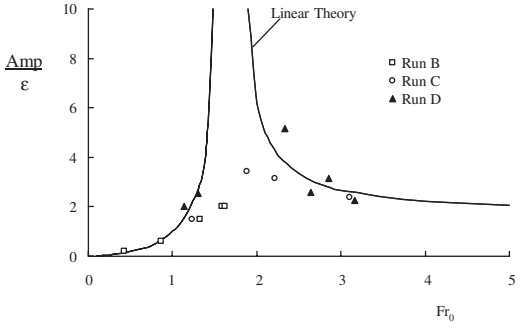


Figure 6. Relation between Amp/ε and Fr_0.

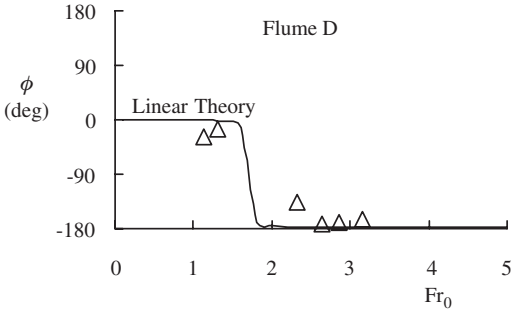


Figure 7. Relation between Φ_ξ and Fr_0 (Flume D).

The hydraulic conditions used in the experiments are listed in Table 1. Plane two-dimensional variations of water surface were measured using a point gage.

Figure 6 shows the relation between Amp/ε and Fr_0 from both the linear solution, Eq. (15), and the experiments. The experimental results are in good agreement with the linear solution in the region a little apart from the resonance relation.

Figures 7 and 8 show the relation of the phase lag, Φ_ξ, and Fr_0 with the linear solution. The results of flume D having the side wall of large curvature radius are in good agreement with the linear solution. But the results of flume B with the side wall of small curvature radius are not compatible with the linear solution due to the non-linear effects.

Some results of the water surface variations along the right side wall are shown in Figures 9, 10 and 11. Figure 9 (Run D1-1) shows in-phase pattern with low Froude number, and Figure 10 out-of-phase pattern with high Froude number. Figure 11 (Run B3-2) shows the pattern with $\Phi_\xi = \pi/2$ under the resonance condition.

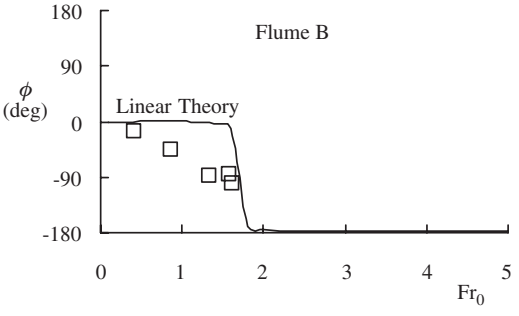


Figure 8. Relation between Φ_ξ and Fr_0 (Flume B).

In the following section, the three dimensional water surface patterns are shown using the numerical results with aid of computer graphics, and the characteristics of the transition of profiles around the resonance relation are discussed.

Copyright © 2006 Taylor & Francis Group plc, London, UK

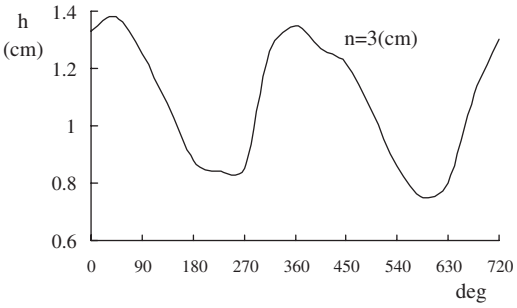


Figure 9. Water surface variations of out-of-phase pattern along the right side wall (Run D1-1).

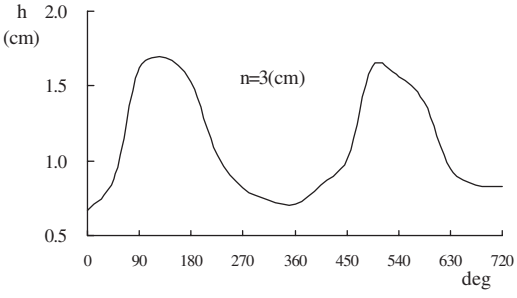


Figure 10. Water surface variations of in-phase pattern along the right side wall (Run D2-2).

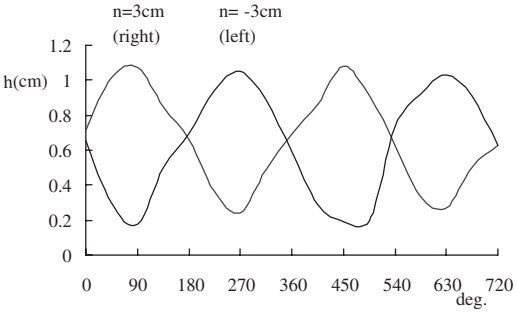


Figure 11. Water surface variations of in-phase pattern along the right side wall (Run B3-2).

5 DISCUSSIONS OF CALCULATED RESULTS

5.1 *Verification of numerical model*

In order to verify the numerical model, the numerical simulations were carried out under the same conditions of hydraulic experiments.

Figure 12 shows the comparison of the calculated to the experimental results on the longitudinal variations of water surface profile of Run D2-2, and Figure 13

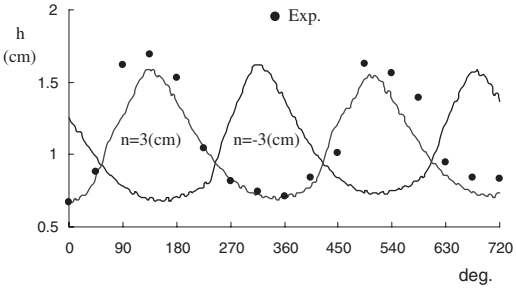


Figure 12. Comparison of longitudinal water surface distributions (Run D2-2).

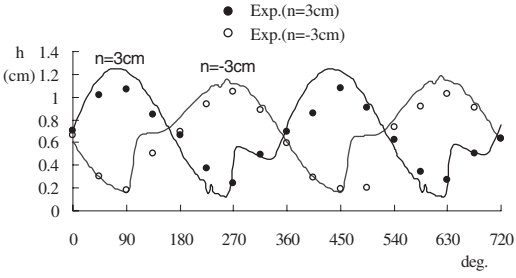


Figure 13. Comparison of longitudinal water surface distributions (Run B3-2).

shows the results of Run B3-2. These two figures indicate that the calculated results are in good agreement with the experimental results.

Figures 14 and 15 show the photographs of the experimental results and the computer graphics created using the calculated results under the same hydraulic conditions. Since the typical features of flow patterns observed in the experimental results are well reproduced in the computational results, the numerical model seems to be applicable to investigate the characteristics of flow response near a resonance relation.

5.2 *Change of flow patterns*

The change of flow patterns from in-phase to out-of-phase are shown in Figures 16 and 17 for flume B and D, respectively. We can observe in these figures that when the Froude number (channel slope) exceeds the value of resonance, the flow patterns are changed from in-phase to out-of-phase. A typical water surface profile with hydraulic jump in the central part of flume is observed at the resonance condition as shown in the middle of Figure 17, which can also be seen in Figures 14 and 15.

Figures 18 and 19 show the water surface variations along the right side wall. Both figures show that the

Copyright © 2006 Taylor & Francis Group plc, London, UK

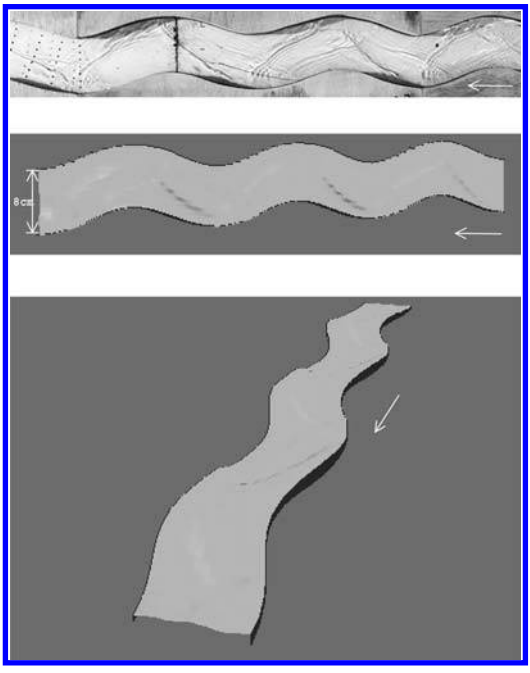


Figure 14. Comparisons of water surface profiles observed in hydraulic experiments with calculated results (Run B3-2, near the resonance condition).

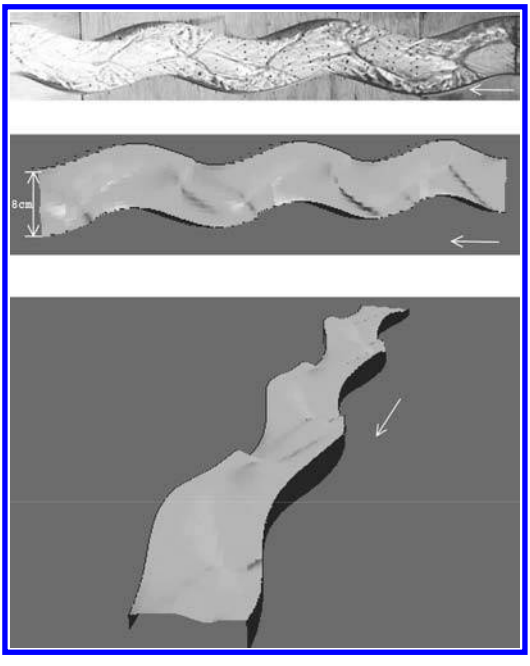


Figure 15. Comparisons of water surface profiles observed in hydraulic experiments with calculated results (Run B3-1, near the resonance condition).

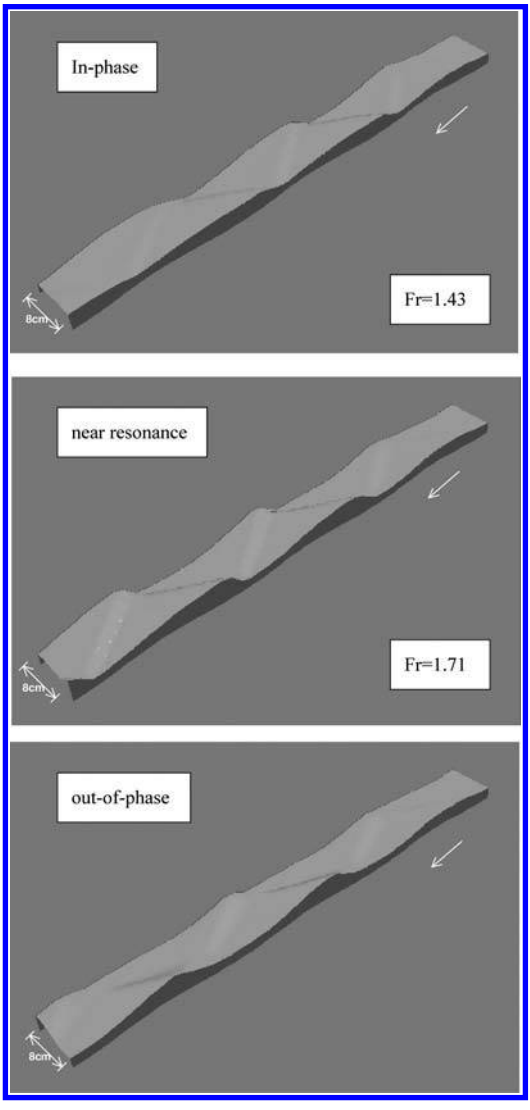


Figure 16. Change of flow pattern with the increase of channel slope (Flume D).

phase lag between water surface variations and sinuous side wall is in-phase for the flows whose Froude number is smaller than the resonance Froude number, and is likely to out-of phase for the flows whose Froude number is larger then the resonance one. The phase lag around the resonance condition is about 90 degrees.

5.3 *Increase of flow resistance*

Figure 20 shows the relation between the calculated averaged flow depth and the bottom slope of the

Copyright © 2006 Taylor & Francis Group plc, London, UK

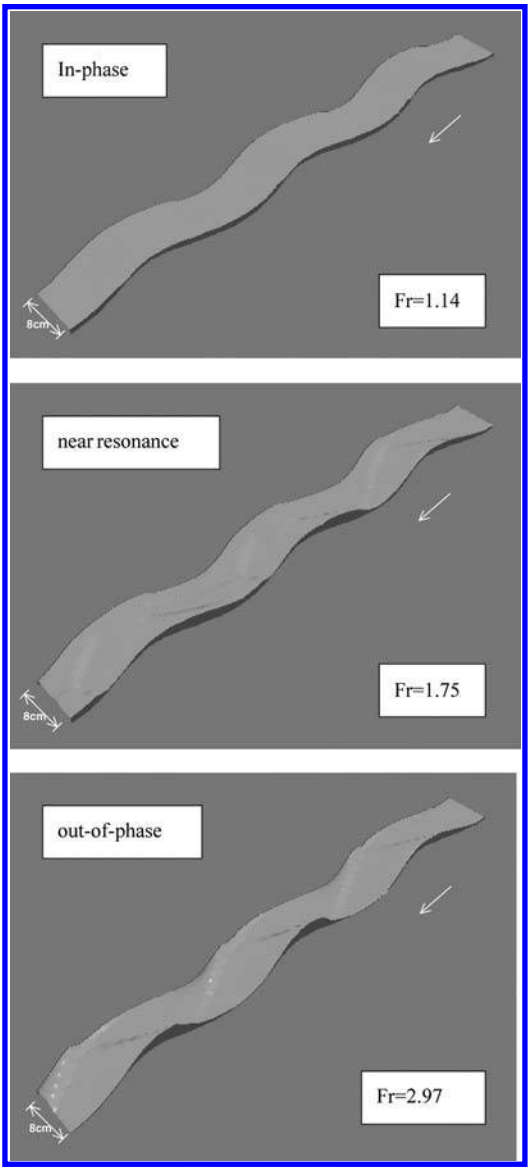


Figure 17. Change of flow pattern with the increase of channel slope (Flume B).

flume B under constant discharges. Here, the uniform flow depth is calculated by the following equation with a value of roughness coefficient as 0.0095 and plotted.

$$h_0 = \left(\frac{nq}{I_0^{1/2}} \right)^{3/5} \tag{28}$$

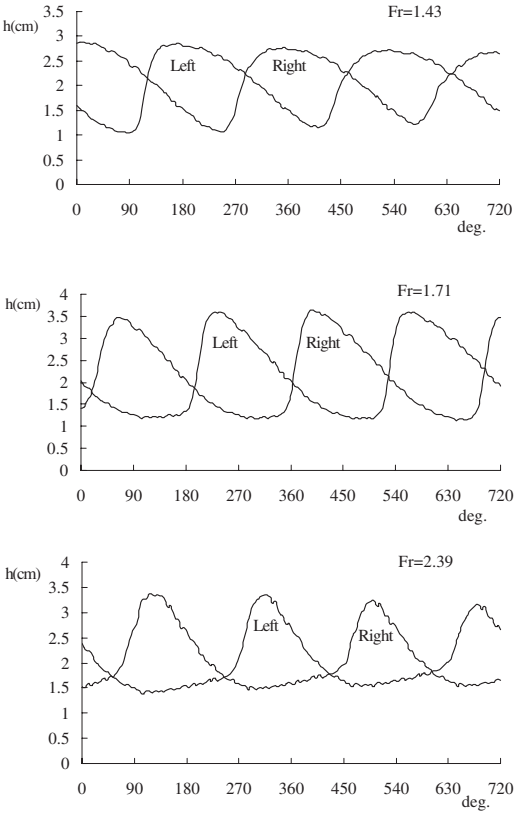


Figure 18. Water surface variations along the right side wall in Flume D.

This figure indicates that the flow resistance increases with the increase of bottom slope and decreases when the slope increases beyond the resonance relation (in this case beyond slope = 1/17).

6 CONCLUSIONS

In this paper, the fundamental flow characteristics of high velocity flows in a sinuous open channel were investigated numerically. It was shown that the flow characteristics can be classified into out-of-phase and in-phase using the resonance relation between water surface and channel meandering based on the solutions of the linearized shallow flow equations. We also showed that a typical water surface profile with hydraulic jump is observed in the central part of flume at the resonance condition. It was found that the flow resistance increases with the increase of bottom slope and decreases when the slope increases beyond the resonance relation.

Copyright © 2006 Taylor & Francis Group plc, London, UK

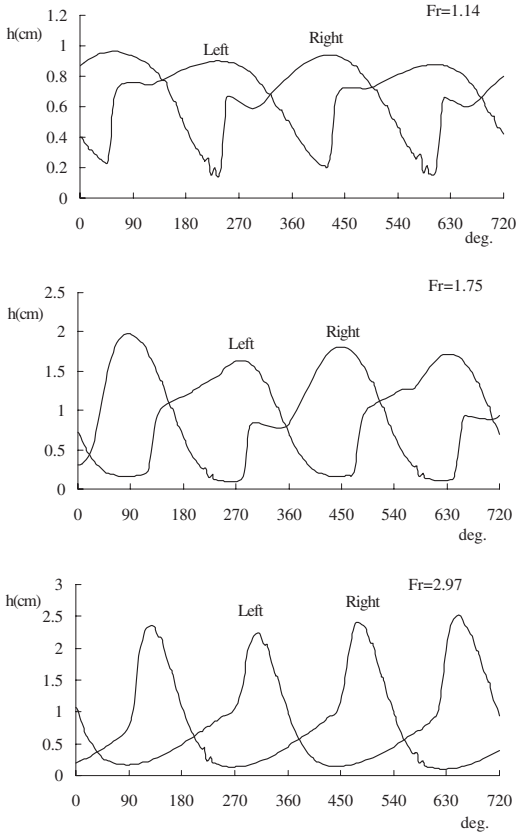


Figure 19. Water surface variations along the right side wall in Flume B.

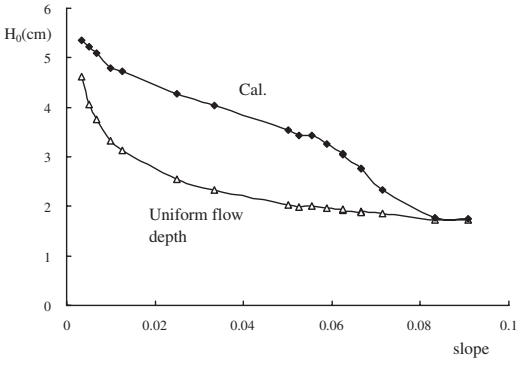


Figure 20. Increase of flow resistance with the increase of bottom slope using Flume B.

REFERENCES

Blondeaux, P. and Seminara, G., 1985, A unified bar-bend theory of river meanders, *J. Fluid Mech.*, 157, 449–470.

Engelund, F., 1974, Flow and bed topography in channel bends, *Proc. ASCE, Jour. Hydraulic Division*, Vol. 100, HY11, 1631–1647.

Hasegawa, K., 1980, The effect of plane and bed forms of channels upon the meander development, *Proc. of JSCE*, No. 296, 143–152.

Hosoda, T., 1999, Fundamental properties of high velocity flows in a continuously meandering channel, *Ann. Jour. of Hydraulic Eng., JSCE*, Vol. 43, 311 (in Japanese).

Ikeda, S., Parker, G. and Sawai, K., 1981, Bend theory of river meandering, Part 1 Linear development, *Jour. of Fluid Mech.*, Vol. 112, 363–377.

Kimura, I. and Hosoda, T., 1997, Fundamental properties of flows in an open channel with a rectangular dead zone, *Journal of Hydraulic Engineering, ASCE*, Vol. 123, No. 2, 98–107.

Nagata, N., Hosoda, T., and Muramoto, Y., 2000, Numerical analysis of river channel processes with bank erosion, *Journal of Hydraulic Engineering, ASCE*, Vol. 126, No. 4, 243–252.

Copyright © 2006 Taylor & Francis Group plc, London, UK

Smoothly limited finite-volume modelling of rapidly varying river flows

T. Krámer & J. Józsa
Budapest University of Technology and Economics, Budapest, Hungary

ABSTRACT: The Barth-Jespersen (BJ) reconstruction procedure is a well established method to provide oscillation-free, higher-order accuracy to Godunov-type schemes on general unstructured meshes. Their scalar limiter is, however, known to suffer from poor convergence to steady-state with nonsmooth solutions, such as those that occur in rapidly varying river flows. In order to improve convergence, a general smoothing procedure applicable to unstructured limiters is introduced in this paper. In essence, the reconstruction gradually reverts to unlimited gradients for small oscillations in the solution thus reducing the adverse interaction between the limiter and numerical noise. Popular limiters – minmod, superbee, van Leer and van Albada – are also brought to the same BJ formulation so as to suit them to general unstructured meshes and smoothing. The advantage of the new, smoothed BJ limiter is demonstrated by solving a steady, two-dimensional transcritical channel flow problem.

1 INTRODUCTION

A wide variety of rapidly varying open channel flows are successfully simulated using Godunov-type finite-volume schemes. A major advantage of these schemes is their shock capturing capability, which makes them suitable to modelling transcritical flow problems involving hydraulic structures or steep slopes. Much progress has been made recently along this line towards robust, higher-order, two-dimensional modelling in the presence of natural bathymetries.

Limiters used to suppress numerical oscillations are key ingredients of such higher-order schemes. They were originally developed for structured grids. Since then, unstructured mesh techniques have been gaining widespread use, largely because they can be adapted flexibly to complicated boundaries and varying resolution. It is straightforward to formulate the finite-volume framework on general unstructured meshes, where the cell orientation and the number of cell faces may vary arbitrarily. Barth and Jespersen (1989) successfully generalised monotonic polynomial reconstruction to unstructured meshes by introducing a divergence- and a least-squares-based gradient scheme and a multidimensional scalar limiter. Yet the Barth-Jespersen limiter is known to suffer from poor convergence to steady-state due to the overreacted limiting of small amplitude noise. Furthermore, the scalar limiter is stricter than necessary because it affects all components of the gradient uniformly.

The main difficulty with unstructured meshes is to translate directionality and cell neighbour information of proven structured methods. Research focused primarily on triangular meshes: for example Jawahar and Kamath (2000) presented an area-weighted multidimensional method that couples gradient calculation and limiting, but their method is not evidently extensible to arbitrary meshes. To address the diffusive character of the scalar limiter without any presumption on mesh topology, some researchers (Hubbard 1999, Rider and Kothe 1997, Berger et al. 2005) limit the slope in a truly multidimensional fashion at the cost of a multiply constrained, data-dependent minimization problem at each cell and timestep. To cure the convergence problem, van Albada et al. (1982) makes the limiter insensitive to noise by smoothly switching it off as the amplitude of the extremum decreases below a small threshold, thus reverting to the unlimited reconstruction. Venkatakrishnan (1995) interprets Spekreijse's structured limiter concept (Spekreijse 1987) within the Barth-Jespersen limiter, which allows him to implement a smooth limiter similar to that of van Albada.

Finding a non-diffusive and convergent limiter suited to arbitrary meshes was motivated in this paper by the implementation of an adaptive MUSCL-type solver for free-surface flows. The two-dimensional, solution-adaptive quadtree mesh of this model is dynamically restructured during the simulation to describe rapid flow variations, such as hydraulic jumps, with high resolution. We have implemented the technique of Barth-Jespersen and find it robust for unsteady problems, but when the same solver is used in steady-state simulations, nonsmooth solutions are sometimes difficult to achieve with good convergence. Following the procedure of Venkatakrishnan

Copyright © 2006 Taylor & Francis Group plc, London, UK

(1995) in this paper, popular limiters – minmod, monotonized-centered, superbee, van Leer and van Albada – are extended to general unstructured meshes and introduce a simple smoothing technique to improve convergence to steady-state. Results obtained for a transcritical flow in an L-shaped channel with the smoothed version of the Barth-Jespersen limiter demonstrate the merits of the method.

2 FLOW SOLVER

2.1 *Governing equations*

Flow is modelled by the inviscid, Reynolds-averaged shallow water equations, which read (Chaudhry 1993):

$$\frac{\partial}{\partial t}\int_A \mathbf{u}\,\mathrm{d}A + \oint_S \left(\mathbf{f}n_x + \mathbf{g}n_y\right)\mathrm{d}S = \int_A \mathbf{s}\,\mathrm{d}A, \tag{1}$$

where t = time; A and S = area and boundary of the cell, respectively; $\mathbf{n}$:(n_x, n_y) = outward unit normal vector to S, expressed with its horizontal Cartesian components (x, y). The flow state vector $\mathbf{u}$, the flux vectors $\mathbf{f}$, $\mathbf{g}$, and the vector of source terms $\mathbf{s}$ are defined as follows:

$$\mathbf{u} = \begin{bmatrix} \eta \\ p \\ q \end{bmatrix}, \quad \mathbf{f} = \begin{bmatrix} p \\ \frac{p^2}{h} + \frac{g}{2}h^2 \\ \frac{pq}{h} \end{bmatrix},$$
$$\mathbf{g} = \begin{bmatrix} q \\ \frac{pq}{h} \\ \frac{q^2}{h} + \frac{g}{2}h^2 \end{bmatrix}, \quad \mathbf{s} = \begin{bmatrix} 0 \\ -gh\frac{\partial z_b}{\partial x} - \frac{\tau_{bx}}{\rho} \\ -gh\frac{\partial z_b}{\partial y} - \frac{\tau_{by}}{\rho} \end{bmatrix}, \tag{2}$$

where η = surface elevation; $\mathbf{q}$:(p, q) = horizontal volume flux; g = acceleration due to gravity; h = total flow depth; z_b = bottom elevation; $\boldsymbol{\tau}_b$:(τ_{bx}, τ_{by}) = bed shear stress; ρ = density of water. Bottom shear stress is expressed using the Manning formula, $\boldsymbol{\tau}_b = \rho g n^2 h^{-1/3}\,\mathbf{v}|\mathbf{v}|$, where n = Manning coefficient; $\mathbf{v}$ = horizontal depth-averaged velocity.

2.2 *Adaptive quadtree mesh*

Quadtree-based hierarchical meshes are well suited to solution-adaptation, as they can be conveniently created and modified according to the desired local level of detail and solution accuracy. Although neighbours can be identified on a quadtree mesh without having to store cell-edge connectivity information explicitly, the finite volume solver treats it as an arbitrary, unstructured Cartesian mesh. As the simulation progresses, the mesh is refined dynamically based on the estimated truncation error of the velocity

$$\frac{A_i}{n_j}\sum_j \left|\mathbf{v}_j - \left[\mathbf{v}_i + \nabla\mathbf{v}_i \cdot \left(\mathbf{r}_j - \mathbf{r}_i\right)\right]\right|, \tag{3}$$

where $j \in$ neighbours of cell i; n_j = number of neighbours; $\mathbf{r}_i$ and $\mathbf{r}_j$ = position vector to the centre of the respective cell; $\nabla\mathbf{v}_i$ = velocity gradient estimated as for the MUSCL reconstruction (see Section 3). The error indicator is weighted by the cell area A_i to find weaker features in coarser mesh areas of the flow once the stronger features have been sufficiently resolved. To ensure a smooth variation of mesh density, adjacent cell sizes never differ by more that a factor of two. The adaptation procedure is described in more detail elsewhere (Krámer and Józsa 2005, Krámer and Józsa 2006).

2.3 *A Godunov-type scheme*

According to Godunov-type finite-volume methods, the integrals in Equation (1) are discretised around the control volume as

$$A\frac{\partial \mathbf{u}}{\partial t} + \sum_{edges}\left(\hat{\mathbf{f}}n_x\Delta y + \hat{\mathbf{g}}n_y\Delta x\right) = A\mathbf{s}, \tag{4}$$

where Δx and Δy = extents of the boundary edge. The numerical fluxes $\hat{\mathbf{f}}$ and $\hat{\mathbf{g}}$ that arise from a local Riemann problem at each cell edge are approximated in this work by the HLLC Riemann solver (Fraccarollo and Toro 1995). The bed slope source term $-gh\nabla z_b$ is treated similarly to the procedure of Bradford and Sanders (2002), without the second-order flux correction.

The extension of the first-order Godunov scheme to second-order spatial and temporal accuracy is achieved by the MUSCL-Hancock method. With this method, the flow variables are reconstructed at the edges with a piecewise linear distribution in each cell, and time integration is performed explicitly in two stages using a non-conservative predictor step followed by a conservative corrector step (Mingham and Causon 1998). For cell i, the linear reconstruction at its edge e is

$$\mathbf{u}_{e,i} = \mathbf{u}_i + \Phi_i\nabla\mathbf{u}_i \cdot (\mathbf{r}_e - \mathbf{r}_i), \tag{5}$$

where $\mathbf{u}_{e,i}$ and $\mathbf{u}_i$ = flow state vector at the edge and at the cell centre, respectively; Φ_i = Barth-Jespersen-type limiter; $\nabla\mathbf{u}_i$ = gradient of $\mathbf{u}$ approximated at the cell centre; $\mathbf{r}_e$ and $\mathbf{r}_i$ = position vector to the edge midpoint and the cell centre, respectively. In general a different flow state is reconstructed on the two sides of an edge, i.e., for an edge between cells i and j, $\mathbf{u}_{e,i} \neq \mathbf{u}_{e,j}$.

Copyright © 2006 Taylor & Francis Group plc, London, UK

2.4 *Boundary conditions*

The flow state $\mathbf{u}_{in}$ on the inner side of a boundary edge is reconstructed from the interior as usual using Equation (5), except that the gradient in Equation (6) is determined from a closed path that connects only the centroids of inner neighbours (de Zeeuw and Powell 1993). Boundary conditions are assigned to the flow state $\mathbf{u}_{out}$ on the outer side. In supercritical state, η_{out} and $q_{\perp,out}$ are set to the prescribed values at the inflow boundary, and free outfall conditions are used at the downstream boundary: $\eta_{out} = \eta_{in}$, $q_{\perp,out} = q_{\perp,in}$, $q_{||,out} = q_{||,in}$, where $q_\perp$ and $q_{||}$ = volume flux component perpendicular and parallel to the boundary edge. A slip wall boundary condition is prescribed along closed boundaries: $\eta_{out} = \eta_{in}$ and $q_{\perp,out} = -q_{\perp,in}$.

3 MUSCL RECONSTRUCTION

3.1 *Gradient calculation*

The gradient $\nabla \mathbf{u}_i$ is calculated in each cell using surrounding cell-averaged values with a method suited to meshes with arbitrary topology (de Zeeuw and Powell 1993). To this end, a closed path connecting surrounding cell centroids is determined around the cell of interest and the gradient is expressed numerically using the divergence theorem:

$$\nabla \mathbf{u}_i \approx \frac{1}{2A_{path}} \sum_{edges} S(\mathbf{u}_p + \mathbf{u}_n)\mathbf{n}, \tag{6}$$

where $2A_{path} = \sum (x_n - x_p)(y_n + y_p)$ is twice the area enclosed by the path around cell i; S, $\mathbf{n}$ = length and outward unit normal of an edge, respectively. The summation is over all edges of the path, and subscripts p and n refer to the starting and ending cell centres of an edge. The order in which the cell centres are visited is indifferent, but the selection of which cells to connect matters. Here we choose a compact path which connects immediate neighbours, and, unlike in References (Barth and Jespersen 1989, de Zeeuw and Powell 1993), the cell where $\nabla \mathbf{u}$ is calculated is never included in the path and the diagonal neighbours only when a connected edge is on a boundary (Fig. 1).

3.2 *The Barth-Jespersen slope limiter*

Using the slope determined by Equation (6) directly when reconstructing the conserved variables by Equation (5) creates new extrema and therefore corrupts non-smooth solutions with artificial oscillations. To avoid this, Barth and Jespersen (1989) proposed limiting $\nabla \mathbf{u}$ by a factor Φ so that the linearly reconstructed $\mathbf{u}$ satisfies monotonicity requirements, by making no assumption on the directionality or the number

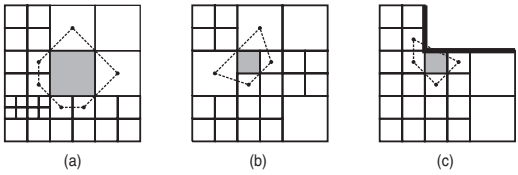


Figure 1. Selection of the closed path for gradient calculation using the divergence theorem.

of neighbours. First we compute $u_{min} = \min(u_i, u_{nbr})$ and $u_{max} = \max(u_i, u_{nbr})$ with all surrounding cell-centered u_{nbr} values, then we seek the maximum admissible limiter that ensures that the flow variable $u_{e,i}$ extrapolated from cell i to the midpoint of each of its edges is bounded:

$$u_{min} \le u_{e,i} \le u_{max} \tag{7}$$

Note that this constraint is more relaxed than the one that requires the reconstructed function $u(\mathbf{r})$ to be bounded at every point within the cell. The monotonicity principle is formulated for each edge as

$$\Phi_e = \begin{cases} \min\left(1, \frac{u_{max}-u_i}{u_{e,i}-u_i}\right) & \text{if } u_{e,i} - u_i > 0, \\ \min\left(1, \frac{u_{min}-u_i}{u_{e,i}-u_i}\right) & \text{if } u_{e,i} - u_i < 0, \\ 1 & \text{if } u_{e,i} - u_i = 0, \end{cases} \tag{8}$$

and the final limiter is determined using $\Phi = \min(\Phi_e)$. In Equation (8), the state at the edge is extrapolated with the unlimited gradient, $u_{e,i} = u_i + \nabla \mathbf{u}_i \cdot (\mathbf{r}_e - \mathbf{r}_i)$.

On regular grids, the Barth-Jespersen (BJ) limiter reduces to the *monotonised-centered* limiter (which is called limited Fromm scheme, double-minmod and MUSCL limiter by some authors). We next follow the procedure of Venkatakrishnan (1995) in order to find the unstructured equivalent of well known limiters. Some of these forms were already derived by Berger et al.(2005), their function $w(f)$ is equivalent to $\Phi(y)$ with $f = y/4$. The analysis is shown in 1D for a sequence of grid indexes $i-1, i, i+1$, whose u values are monotonically increasing or decreasing (otherwise Φ would be 0). Without loss of generality, we assume $u_{min} = u_{i-1}$ and $u_{max} = u_{i+1}$ and consider the reconstruction of the flow variable $u_{i+0.5}$ on the left side of the edge $i + 0.5$ and $u_{i-0.5}$ on the right side of the edge $i - 0.5$. The BJ limiter is in that case

$$\begin{aligned} \Phi_i &= \min(\Phi_{i+0.5}, \Phi_{i-0.5}) \\ &= \min\left[1, \frac{u_{i+1}-u_i}{u_{i+0.5}-u_i}, \frac{u_{i-1}-u_i}{u_{i-0.5}-u_i}\right], \end{aligned}$$

Noting that $u_{i\pm0.5} - u_i = \pm (u_{i+1} - u_{i-1})/4$ and introducing

$$y_i = (u_{i+1} - u_i) / (u_{i+0.5} - u_i),$$

Copyright © 2006 Taylor & Francis Group plc, London, UK

$$\Phi_{BJ}(y) = \min(1, y, 4-y), \tag{9}$$

the reconstruction becomes

$$u_{i\pm0.5} = u_i \pm \frac{1}{4}\Phi_{BJ}(y_i)(u_{i+1} - u_{i-1}),$$

We have brought $\Phi(y)$ to a form similar to the common ψ form of limiters that modulate the one-sided difference on structured grids (Spekreijse 1987):

$$u_{i+0.5} = u_i + \frac{1}{2}\psi(r_i)(u_i - u_{i-1})$$

$$u_{i-0.5} = u_i - \frac{1}{2}\psi(1/r_i)(u_{i-1} - u_i)$$

where

$$r = (u_{i+1} - u_i)/(u_i - u_{i-1}).$$

The Φ and ψ limiters are applied independently on the local flow direction, therefore the following symmetry conditions must hold: $\Phi(y) = \Phi(4-y)$ and $\psi(r) = \psi(1/r)$. The relationship between Φ and ψ can be shown to be

$$\psi(r) = \frac{1}{2}(r+1)\min\left[\Phi\left(\frac{4r}{r+1}\right), \Phi\left(\frac{4}{r+1}\right)\right],$$

$$\Phi(y) = \frac{2+|y-2|}{2}\psi\left(\frac{2-|y-2|}{2+|y-2|}\right),$$

and $r = y/(4-y)$. Additionally, the reconstruction reverts to uniform if u_i is a local extremum, therefore $\psi(r) = 0$ for $r < 0$ and $\Phi(y) = 0$ for $|y-2| > 2$. Now we are ready to express commonly used limiters, *minmod, superbee, van Leer* and *van Albada*:

$$\psi_{MM}(r) = \min(1, r),$$

$$\psi_{SB}(r) = \min[\max(1, r), 2r, 2],$$

$$\psi_{VL}(r) = \frac{2r}{r+1},$$

$$\psi_{VA}(r) = \frac{r^2 + r}{r^2 + 1}$$

in the $\Phi(y)$ formulation:

$$\Phi_{MM}(y) = \frac{1}{2}\min(y, 4-y),$$

$$\Phi_{SB}(y) = \min\left(1 + \frac{1}{2}|y-2|, 2 - |y-2|\right),$$

$$\Phi_{VL}(y) = \frac{y(4-y)}{4},$$

$$\Phi_{VA}(y) = \frac{y(4-y)}{(y-2)^2 + 4}.$$

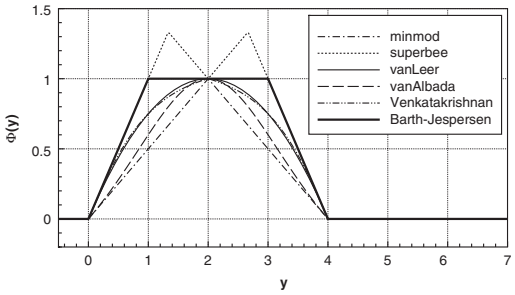


Figure 2. The limiters in $\Phi(y)$ form.

Lastly, the limiter proposed by Venkatakrishnan (1995) is also amenable to a form symmetric about $y = 2$:

$$\Phi_{VKN}(y) = \frac{(|y-2|-3)^2 - 1}{(|y-2| - \frac{5}{2})^2 + \frac{7}{4}}.$$

The $\Phi(y)$ limiters are plotted in Figure 2.

All limiters satisfy $\Phi(2) = 1$, which is required for second-order accuracy. The more diffusive limiters are situated closer to the minmod limiter, and the overcompressive character of the superbee limiter for $y \in (1, 3)$ is also apparent from the figure. The two continuously differentiable limiters (van Leer and van Albada) are convenient in implicit schemes based on a Newton solver.

It is now straightforward to use the new $\Phi(y)$ limiters with the original Barth-Jespersen limiter on unstructured grids: we replace Equation (8) with the more general form:

$$\Phi_e = \begin{cases} \Phi\left(\frac{u_{max} - u_i}{u_{e,i} - u_i}\right) & \text{if } u_{e,i} - u_i > 0, \\ \Phi\left(\frac{u_{min} - u_i}{u_{e,i} - u_i}\right) & \text{if } u_{e,i} - u_i < 0, \\ 1 & \text{if } u_{e,i} - u_i = 0, \end{cases} \tag{10}$$

In the solver presented here, each state variable is reconstructed with its own limiter. For the solution of the Euler equations, it was found preferable (de Zeeuw and Powell 1993) to first calculate Φ_k for each state variable u_k in a cell, then reconstruct all variables in that cell with a common Φ_{min} that is the lowest of the three Φ_k.

3.3 *Smoothing the limiter*

The new limiter is smoothly forced to the unlimited scheme in near-uniform flow regions with a device analogous to that used by van Albada et al. (1982) and Venkatakrishnan (1995). To start, the differences in

Copyright © 2006 Taylor & Francis Group plc, London, UK

the denominator and nominator in Equation (10) are determined separately, denoted by $\Delta_e = u_e - u_i$ and

$$\Delta_m = \begin{cases} u_{max} - u_i & \text{if } \Delta_e > 0, \\ u_{min} - u_i & \text{if } \Delta_e < 0, \\ 1 & \text{if } \Delta_e = 0, \end{cases}$$

respectively. Instead of taking the quotient Δ_m/Δ_e, a smoothed y value is calculated using a small, non-vanishing tolerance ε^2,

$$y' = \frac{\Delta_m \Delta_e + 2\varepsilon^2}{\Delta_e^2 + \varepsilon^2}$$

and Φ_e is evaluated with this modified y'. The modification prevents the clipping of smooth extrema and, more importantly, the wild behaviour of the limiter caused by small numerical fluctuations in near-uniform areas. In fact, if $\Delta_m^2, \Delta_e^2 \ll \varepsilon^2$, then $y' \to 2$ and $\Phi_e(y') \to 1$, that is, we revert to the unlimited slope.

To visualise the effect of smoothing, we fix ε and Δ_e to the same value ($= 1$), and let Δ_m hence y' vary. In this case, the dependence between the non-smoothed y and the smoothed y' is linear,

$$y'(y) = \frac{y + 2\varepsilon^2/\Delta_e^2}{1 + \varepsilon^2/\Delta_e^2},$$

and this has the horizontal stretching effect on $\Phi[y'(y)]$ (Fig. 3). Note that the nonsmooth limiters all revert to the Godunov scheme with zero slope at $y = 0$, whereas the smoothed limiters admit between 50–100% of the unlimited slope there. Smoothing would be of course barely noticeable if ε had a much lower magnitude than the local variation of u. Referring back to Figure 2, $\Phi(y) \le \Phi_{BJ}(y)$ holds for all nonsmooth limiters except the superbee, consequently these limiters also satisfy the boundedness criterion (Eq. 7). Now, if we return to Figure 3, we see that the smoothed $\Phi(y')$ curves exceed the nonsmooth $\Phi_{BJ}(y)$ (denoted by $\varepsilon^2 = 0$ in the legend) for some range of y. In fact, this reflects that the smoothed limiters do not strictly enforce monotonicity.

Next, we fix $\Delta_m = 0.5$ and $\Delta_e = 1$ and plot the functional relationship of y' and $\Phi(y')$ to ε^2 (Fig. 4). As expected, the shape of $y'(\varepsilon^2)$ greatly determines the shape of $\Phi[y'(\varepsilon^2)]$. For low ε^2, the smoothing has no effect and $y' \to y = 1/2$. Only when ε^2 approaches Δ_e^2 and Δ_m^2 does the smoothing become effective. Again, the smoothed scheme reverts to the full, unlimited slopes for large ε^2.

Originally, van Albada et al. (1982) considered setting ε^2 locally proportional to $(\Delta l)^3$, where Δl is the diameter of the circle inscribed into the particular control volume. Wang (2000), who applied Venkatakrishan's limiter on quadtree meshes, found that it was

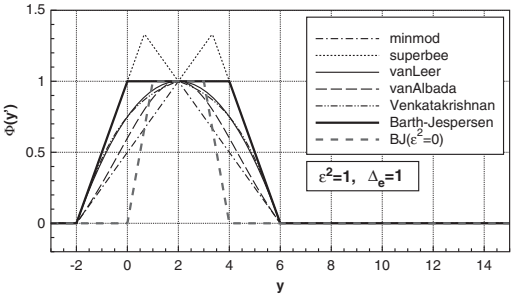


Figure 3. Effect of smoothing the Φ limiters with $\varepsilon^2 = 1$ and $\Delta_e = 1$. The nonsmoothed BJ limiter is also shown.

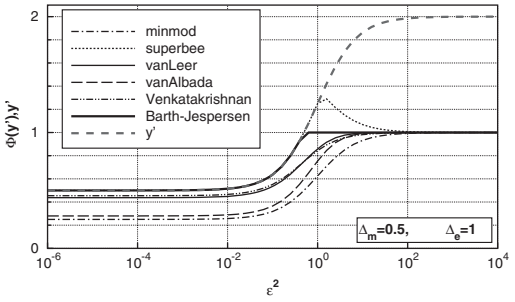


Figure 4. Variation of y' and $\Phi(y')$ to the smoothing parameter ε^2. The differences were fixed to $\Delta_m = 0.5$ and $\Delta_e = 1$.

impossible to find a satisfactory proportionality constant $K = \varepsilon^2/(\Delta l)^3$ that would work well for small and large cells simultaneously and basically set ε^2 constant for each state variable regardless of the local mesh scale. We will pursue the same approach here and set ε^2 a global constant.

4 RESULTS: TRANSCRITICAL FLOW IN A BEND

Steady transcritical flow in a sharp channel bend is modelled in order to highlight the effect of limiter smoothing on convergence. The dimensions of the L-shaped channel as well as the boundary conditions are shown in Figure 5. The prescribed inflow is supercritical with a Froude number of $v/\sqrt{gh} = 3.813$, therefore the normal discharge and the depth are both specified: $q = 0.085\ \mathrm{m^2/s}$, $h = 0.037\ \mathrm{m}$. The bottom is horizontal and its roughness is characterised by a Manning's $n = 0.011\ s/m^{1/3}$. The outfall is free.

The streamlines and the water surface in Figures 6–8 (determined on a fine, adaptively refined mesh with 120,000 active cells) show that the flow separates in the inner corner, recirculates along the top channel wall and makes a sudden transition to subcritical state

Copyright © 2006 Taylor & Francis Group plc, London, UK

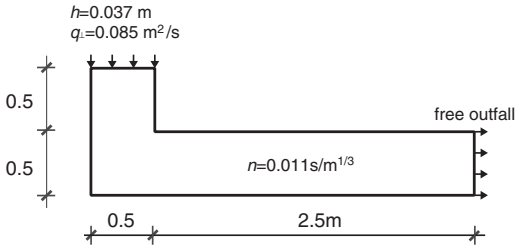


Figure 5. Definition of the steady transcritical flow problem in a 90-degree bend.

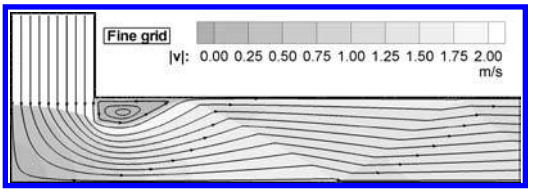


Figure 6. Velocity magnitude and flowlines shown for the reference solution.

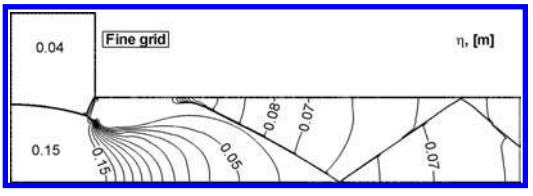


Figure 7. Water surface. Reference solution, contour interval = 0.01 m.

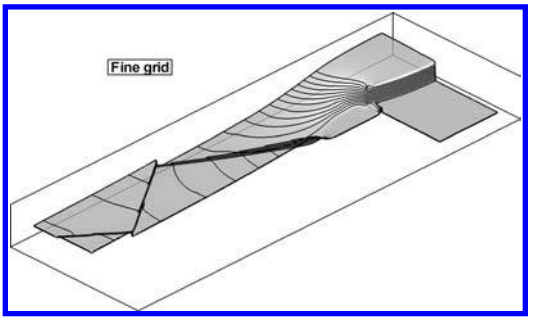


Figure 8. Shaded axonometric view of the water surface. Reference solution, contour interval = 0.01 m.

through a standing hydraulic jump. In the straight downstream reach, the flow turns gradually back to supercritical and a reflecting shock wave develops. The modelled problem was chosen so that it is similar to the unsteady dam break experiment of Soares Frazão and Zech (2002). A qualitative comparison

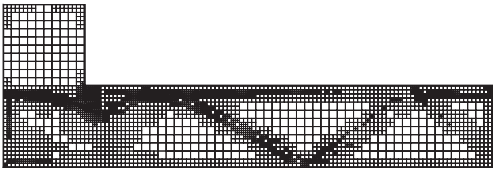


Figure 9. Final adapted mesh consisting of 3500 cells.

reveals the same flow features than in their physical and numerical experiments. Altogether, the genuinely multidimensional character of the flow field, the sharp discontinuities and the arbitrary number of neighbours of the adapted grid provide a good test bed for the smoothed limiters.

The steady-state solution is obtained by explicit time integration. To accelerate the calculation, a near-steady-state solution is first obtained on a uniform, coarse grid with 0.05 m cell size in the first 25 s of model time, then the mesh is adapted to the error indicator in five steps at 1 s interval. The adaptation is limited by the maximum active cell count of 3500 and minimum cell size of 0.00625 m. After the adaptation cycles, the simulation is continued to the final time of 50 s. As the final mesh in Figure 9 confirms, the indicator based on the velocity reconstruction error (Eq. 3) captured the shocks and led to the refinement of the mesh at these places for improved accuracy.

The simulation was repeated for a wide range of values of tolerance ε^2. From the different variants of Φ, only results with the Barth-Jespersen limiter (Eq. 9) are presented. The timestep was dynamically adjusted to yield a maximum Courant-Friedrich-Lewy (CFL) number of 0.8 with local time stepping. The computer program was compiled with 64-bit floating point arithmetic and ran on a desktop PC.

We tracked the L_2-norm of the summed relative residual, defined as

$$\Delta_2 \mathbf{u} = \frac{1}{3}\sum_{k=1}^{3} \frac{\sum_{i \in cells} \left(u_{k,i}^{n} - u_{k,i}^{n-1}\right)^2 A_i}{\sum_{i \in cells} \left(u_{k,i}^{n-1}\right)^2 A_i},$$

where $u_{k,i} \in [\eta_i, p_i, q_i]^T$ are the flow variables for cell i, the upper index n and $n-1$ stand for two successive iteration steps and the inner summations are performed over the whole mesh. The evolution of the residual is plotted for five values of ε^2 in Figure 10 against the number of iterations (time steps).

Residuals decrease rapidly in the startup stage for all schemes but stall at a $\Delta_2 \mathbf{u} = 10^{-3}$ prior to the adaptation, except for the choice $\varepsilon^2 = 10^{-4}$. When viewing the computed flow field, the stalled convergence manifests itself by oscillations in the recirculating zone of bounded, but relatively large amplitude.

Copyright © 2006 Taylor & Francis Group plc, London, UK

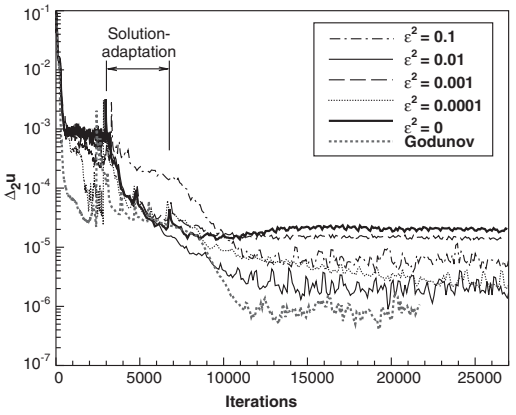


Figure 10. Convergence histories for different values of tolerance ε^2 and for the Godunov scheme ($\Phi = 0$).

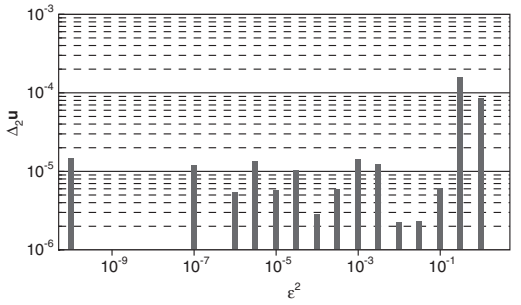


Figure 11. Final value of the summed relative residual vs. the tolerance ε^2.

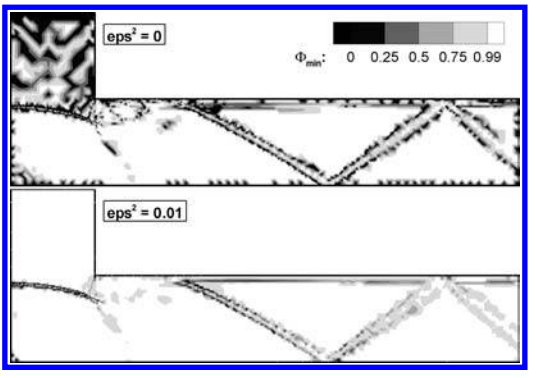


Figure 12. Distribution of Φ using the original BJ limiter (top, $\varepsilon^2 = 0$) and the smoothed BJ limiter (bottom, $\varepsilon^2 = 0.01$).

Solution-adaptation then clearly lowers the residuals by approximately two orders of magnitude. In the later stages of the simulation, limiter smoothing did improve convergence compared to the original BJ limiter ($\varepsilon^2 = 0$, represented by the continuous thick curve) except for the two strongest smoothings ($\varepsilon^2 > 0.1$). Overall, the relationship between ε^2 and the convergence quality is complicated.

Figure 10 also reports the residuals obtained with a first-order Godunov scheme (shown with a thick dotted curve). Due to its excessively diffusive character, the resulting steady-state flow solution lacks the sharp features past the bend. This had the consequence that the adaptive mesh refinement was less concentrated on the standing shocks and more cells of medium size were distributed, affording a larger average timestep and fewer iterations after the adaptation cycles. The Godunov scheme does not use any limiter (it is equivalent to setting $\Phi = 0$ uniformly), so it is insensitive to small-scale oscillations. Nevertheless, convergence stalled at 10^{-6} which is still greater than machine zero and may be attributed the Riemann formulation. This observation allows us to consider the smooth limiter with $\varepsilon^2 = 0.01$ as one that eliminates most of the convergence deterioration caused by MUSCL reconstruction.

Besides the convergence history, the final value of the residual (Fig. 11) also lacks a clear trend with respect to ε^2. Selecting $\varepsilon^2 = 10^{-2}$ or 10^{-4} reduces the residual by almost an order of magnitude compared to the original BJ limiter. Our computational experiments showed that this optimum is not universal: using Roe's approximate Riemann solver with entropy fix instead of HLLC yielded poorer convergence in general and the optimum was with $\varepsilon^2 = 10^{-3}$.

A comparison of the distribution of Φ_{min} for $\varepsilon^2 = 0$ and $\varepsilon^2 = 0.01$ in the last step of the simulation (Fig. 12) shows that smoothing reduces both the extent and the strength of limiting. While the smoothed limiter is active only at the shocks (and near the upper horizontal wall for the transverse flux), the original limiter is also active in the supercritical reach at the inlet. This is an area of near-uniform flow, where machine-level noise produces small extrema and triggers the limiter if these extrema exceed the level set by ε^2. The disturbance propagates downstream and is amplified at the sensitive slip discontinuity between the supercritical main flow and the recirculating eddy. This is reflected in the bumpy water surface of the eddy computed with $\varepsilon^2 = 0.01$ (Fig. 13). In spite of being formally non-monotone, the smoothed limiter yields apparently oscillation-free solutions. For $\varepsilon^2 = 1$, the smoothed limiter becomes so tolerant of oscillations that these visually disrupt the flow field near shocks, though excessive smoothing does not result in improved convergence, which is contrary to expectations.

Similar results were obtained with the van Leer and the Venkatakrishnan limiter (Φ_{VL} and Φ_{VKN}, respectively), whereas the minmod limiter (Φ_{MM}) converged

Copyright © 2006 Taylor & Francis Group plc, London, UK

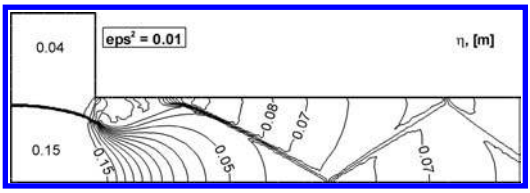


Figure 13. Water surface. Solution using a smoothed limiter ($\varepsilon^2 = 0.01$), contour interval = 0.01 m.

to one order of magnitude less. The poorer performance of the minmod limiter in this case is likely caused by the discontinuity of $d\Phi/dy$ at $y = 2$, i.e., in linearly varying flow field.

5 CONCLUSIONS

We have implemented Barth & Jespersen's (BJ) reconstruction technique into a MUSCL-type solver of the shallow water equations on an adaptive quadtree mesh. Without smoothing, convergence stalled for the steady transcritical flow problem in an L-shaped channel. Hampered convergence associated with slope-limited finite-volume schemes has long been known in the aerodynamic modelling community and was recognised to be due to the interference between small parasitic oscillations and the limiter that is triggered by those oscillations. A simple cure applicable to unstructured meshes is Venkatakrishnan's smooth limiter. We followed the same lines in deriving the smoothed equivalent of popular limiters in the framework of BJ's reconstruction. Among these, the BJ, van Leer and van Albada limiters have the benefit that they are also differentiable for $y' = 2$ (i.e., for linearly varying flow variables) in contrast to Venkatakrishnan's limiter.

The new smoothed BJ limiter is easy to implement and with the optimal ε^2 smoothing parameter, it improves convergence to near the same level as the first-order scheme, one order of magnitude better than the original BJ limiter. The limiter is, however, not as robust as expected, since the convergence history displayed high sensitivity to the value of ε^2. Numerical experiments not reported in this paper indicated that the convergence history is also highly sensitive to the choice of the base limiter, approximate Riemann solver and mesh density.

Further development of the presented technique should consider the analysis of the approximate Riemann solver's role in the scheme's convergence.

REFERENCES

Barth, T. J. & D. C. Jespersen (1989). The design and application of upwind schemes on unstructured meshes. In *27th Aerospace Sciences Meeting*, Reno, Nevada, pp. 12. AIAA. Paper 89-0366.

Berger, M. J., M. J. Aftosmis & S. C. Murman (2005). Analysis of slope limiters on irregular grids. In *43rd Aerospace Sciences Meeting*, Reno, Nevada, pp. 22. AIAA. Paper 2005-0490.

Bradford, S. F. & B. F. Sanders (2002). Finite-volume model for shallow-water flooding on arbitrary topography. *Journal of Hydraulic Engineering* 128:289–298.

Chaudhry, M. H. (1993). *Open channel flow*. Englewood Cliffs, NJ: Prentice Hall.

de Zeeuw, D. & K. G. Powell (1993). An adaptively refined cartesian mesh solver for the Euler equations. *Journal of Computational Physics* 104:56–68.

Fraccarollo, L. & E. F. Toro (1995). Experimental and numerical assessment of the shallow water model for two-dimensional dam-break type problems. *Journal of Hydraulic Research* 33(6):843–864.

Hubbard, M. E. (1999). Multidimensional slope limiters for MUSCL-type finite volume schemes on unstructured grids. *Journal of Computational Physics* 155:54–74.

Jawahar, P. & H. Kamath (2000). A high-resolution procedure for Euler and Navier-Stokes computations on unstructured grids. *Journal of Computational Physics* 164:165–203.

Krámer, T. & J. Józsa (2005). An adaptively refined, finitevolume model of wind-induced currents in Lake Neusiedl. *To appear in Periodica Polytechnica, Ser. Civil Engineering* 49.

Krámer, T. & J. J'ozsa (2006). Solution-adaptivity in modelling complex shallow flows. *Submitted to Computers and Fluids*.

Mingham, C. G. & D. M. Causon (1998). High-resolution finite-volume method for shallow water flows. *Journal of Hydraulic Engineering* 124:605–614.

Rider, W. J. & D. B. Kothe (1997). Constrained minimization for monotonic reconstruction. In *Proc. 13th AIAA Computational Fluid Dynamics Conference*, Snowmass, Colorado, pp. 955–964. AIAA. Paper 97-2036.

Soares Frazão, S. & Y. Zech (2002). Dam break in channels with 90° bend. *Journal of Hydraulic Engineering* 128:956–968.

Spekreijse, S. (1987). Multigrid solution of monotone second-order discretizations of hyperbolic conservation laws. *Mathematics of Computation* 49:135–155.

van Albada, G. D., B. van Leer, & W. W. Roberts (1982). A comparative study of computational methods for cosmic gas dynamics. *Astronomy and Astrophysics* 108:76–84.

Venkatakrishnan, V. (1995). Convergence to steady state solutions of the Euler equations on unstructured grids with limiters. *Journal of Computational Physics* 118:120–130.

Wang, Z. J. (2000). A fast nested multi-grid viscous flow solver for adaptive Cartesian/Quad grids. *International Journal for Numerical Methods in Fluids* 33:657–680.

Copyright © 2006 Taylor & Francis Group plc, London, UK

Large eddy simulation of fully-developed turbulent flow through submerged vegetation

T. Stoesser, C. Liang, W. Rodi, G.H. Jirka
Institute for Hydromechanics (IfH), University of Karlsruhe, Germany

ABSTRACT: Large Eddy Simulations (LES) are performed for an open channel flow through submerged vegetation with a water depth (h) to plant height (h_p) ratio of $h/h_p = 1.5$ according to the experimental configuration of Fairbanks and Diplas (1998). Fairbanks and Diplas measured longitudinal and vertical velocities as well as turbulence intensities along several verticals in the flow and the data are used for the validation of the simulations. The code MGLET is used to solve the filtered Navier Stokes equations on a Cartesian non-uniform grid. In order to represent solid objects in the flow, the immersed boundary method is employed. The computational domain is idealized with a box containing four submerged circular cylinders and periodic boundary conditions are applied in both longitudinal and transverse directions. The predicted streamwise as well as vertical mean velocities are in good agreement with the LDA measurements. Furthermore, good agreement is found between calculated and measured streamwise *r.m.s* velocities. Large-scale flow structures of different shape are present in the form of vortex rolls above the vegetation tops as well as von Karman type vortices generated by flow separation at the cylinders. In this paper the mean and instantaneous flow field is analyzed and further insight into the complex nature of flow through vegetation is provided based on Large Eddy Simulation.

1 INTRODUCTION

Both aquatic and riparian vegetation have become central to river and coastal restoration schemes, the creation of flood retention space and coastal protection projects. Aquatic and riparian plants obstruct the flow and reduce the mean flow velocities relative to non-vegetated regions, and the additional drag exerted by plants influences strongly the mean and instantaneous flow field as well as transport processes and system morphology. The flow through partially-vegetated channels or submerged vegetation is characterized by significant velocity gradients (both laterally and vertically) and strong secondary currents, which result in shear layer formation between the canopy and the flow region above the vegetation. A greater understanding of the interaction of flow with vegetation will improve our ability to accurately model flow and sediment transport through vegetation. Hence, both conceptually- and physically-based representations of vegetation-flow interactions are sought with the objective to reduce modelling uncertainty in engineering practice.

Most research activities on vegetation effects in the benthic and riparian environment have been devoted to laboratory flumes of simple cross-section, and many researchers (for example: Kouwen *et al*., 1969; Tsujimoto *et al.* 1992; Dunn *et al.,* 1996; Nepf and Vivoni, 1999 to name only a few) have observed that the mean streamwise velocity profile within an emergent or submerged vegetated layer (irrespective of whether the vegetation is rigid or flexible) no longer follows the universal logarithmic law. In the surface flow layer above a submerged vegetation zone, researchers (for example Kouwen *et al*. 1969) have generally assumed that the logarithmic law prevails. However, detailed studies of flow-vegetation interaction and the consequences on the instantaneous flow field are rare.

Presently, steady Reynolds Averaged Navier Stokes (RANS) models are the most practical approaches for high-Reynolds-number-fluvial hydraulics applications despite the rapid advancements in computational power and numerical algorithm development. These steady RANS models allow the resolution of the time-averaged turbulent flow field by adding a subgrid force to the RANS and turbulence transport equations to account for vegetative drag effects. For multi-dimensional flow problems, such methods were used by Shimizu and Tsujimoto (1994), Lopez and Garcia (1997), and Fischer-Antze et al. (2001) together with a k-ε turbulence closure approach to study the mean flow through submerged vegetation. Neary (2003) employed the k-ω model as turbulence closure and

Copyright © 2006 Taylor & Francis Group plc, London, UK

reported results very similar to the studies using a k-ε model. Naot *et al.* (1996) and Choi and Kang (2001) used a Reynold's Stress model (RSM) accounting for the anisotropy of turbulence, to simulate the flow through rigid submerged vegetation elements. However, within the surface-layer region there was only minor improvement in the computed mean velocity, turbulent intensity and Reynolds stress profiles for the RSM relative to the k-ε or k-ω model.

Mean flow features resolved by the steady RANS models include: **(a)** the suppression of the streamwise velocity profile in the vegetated zone, **(b)** the inflection of the velocity profile at the top of the vegetation zone, and **(c)** the vertical distribution of the turbulent shear stress, with its maximum value at the top of the vegetation zone. However, although mean velocities were predicted with satisfying accuracy, RANS models have been less successful at correctly predicting streamwise and vertical turbulence intensities, because these models cannot account for organized large-scale unsteadiness and asymmetries (coherent structures) resulting from turbulent flow instabilities. These coherent structures include: **(a)** the transverse and secondary vortices in the form of rolls and ribs (Finnegan, 2000), which occur at the top of the vegetation layer as a result of a Kelvin-Helmholtz instability due to the inflection of the streamwise velocity profile (Figure 1a), and **(b)** 3D vortices produced by the complex interaction of the approach flow with the stem (e.g trailing or necklace vortices) and the enforced vortex shedding in the wake of the stem due to flow separation (Figure 1b).

Recently, modeling techniques that directly resolve large-scale, organized, unsteady structures in the flow and advanced numerical techniques for simulating flows around multiple flexible bodies were introduced for the simulation of such or similar flow problems, e.g. URANS simulations by Paik et al. (2003) or Large Eddy Simulations by Cui and Neary (2002). Such techniques elucidate the large-scale coherent structures described above, their important role in vegetative resistance, and the interaction and feedback between the region within and outside the vegetation layer. The Large Eddy Simulation of flow through and above vegetation is not new and finds its origins in boundary-layer meteorology. To our knowledge, the first LES for flow over vegetation were presented by Deardoff (1972) in which the atmospheric boundary-layer over a wheat field was simulated. Further LES in boundary-layer meteorology were for the flow and the turbulent structures above forests, a flow problem that has been studied extensively with LES (e.g. Moeng, 1984, Shaw and Shumann, 1992, Kanda and Hino, 1993, Dwyer *et al.*, 1997). The advantage of LES lies in the fact that a highly resolved temporal and spatial picture of the flow field can be obtained. The vertical distribution of Reynolds stresses and turbulent fluctuations

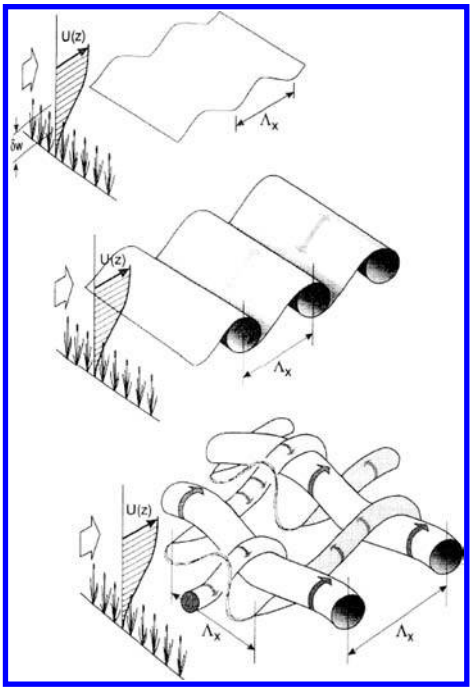


Figure 1a. Kelvin-Helmholtz instabilities resulting in ribs and rolls above vegetation layers (from Finnegan 2000).

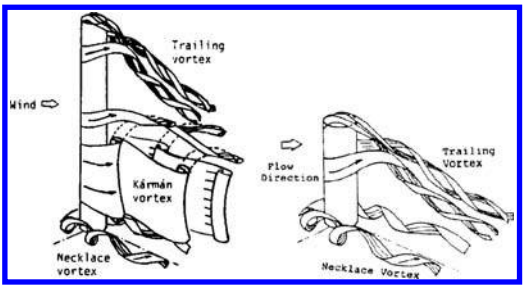


Figure 1b. Vortices originating at tall and short cylinders (from Kawamura et al, 1984).

as calculated with LES were found to be in good agreement with laboratory and field observations. These simulations show the enormous potential of LES in accurately predicting the flow and its associated time-dependent structures.

In this paper we present Large-Eddy simulations of turbulent channel flow through a matrix of cylinders. The flow around the individual cylinders is fully resolved by a high resolution grid and the cylinder-matrix can be regarded as an idealized vegetation layer. The time-averaged velocity field as well as turbulence quantities are presented and compared with laboratory measurements. Moreover, large-scale structures are shown to occur above and within the vegetation layer.

Copyright © 2006 Taylor & Francis Group plc, London, UK

2 NUMERICAL METHOD

The LES code MGLET, originally developed at the Institute for Fluid Mechanics at the Technical University of Munich (Tremblay et al., 2000), was used to perform the Large Eddy Simulations. The code solves the filtered Navier-Stokes equations discretised with the finite-volume method and is based on a staggered Cartesian grid. Convective and diffusive fluxes are approximated with central differences of second order accuracy and time advancement is achieved by a second order, explicit Leapfrog scheme. The Poisson equation for coupling the pressure to the velocity field is solved iteratively with the SIP method of Stone (1968). The subgrid-scale stresses appearing in the filtered Navier-Stokes equations are computed using the Lagrangian dynamic approach of Meneveau *et al.* (1996). The no-slip boundary condition is applied on the surface of the cylinders and the immersed boundary method (e.g. Verzicco, 2000) is employed. This method is a combination of applying body forces in order to block the cells that are fully inside the cylinder geometry with a Lagrangian interpolation scheme of third order accuracy, which is used for the cells that are intersected by the cylinder surfaces to maintain the no-slip condition.

3 FLOW CONFIGURATION

The geometry and the Re number of 15000, based on the channel depth and bulk velocity, are chosen analogous to experimental laboratory investigations undertaken by Fairbanks and Diplas (1998). This allows a comparison between LES and experiments and hence a validation of the LES code as well as the model approximations for the subgrid scale stresses and the treatment of the individual cylinders with the immersed boundary method. In order to investigate the flow through vegetation, Fairbanks and Diplas placed rigid cylinders in a staggered arrangement into a rectangular flume and carried out detailed LDA measurements at the six verticals within the flow as indicated in Figure 2. The Reynolds number based on the bulk velocity u_{bulk} and the cylinder diameter D, Re_D, is approximately *800*. The ratio of cylinder height h_p to water depth is $h_D/h = 2/3$ and the computational box, which is the shaded area indicated in Figure 2, contained four submerged cylinders. The domain spans *20D* in streamwise, *10D* in spanwise and *18D* (which is the full water depth) in vertical direction, respectively. Several simulations with different grid resolutions were carried out, however, in this paper we will only present the results from the finest grid. The grid consisted of $612 \times 308 \times 141$ grid points in streamwise, spanwise and vertical directions, respectively, which sums to a total of approximately

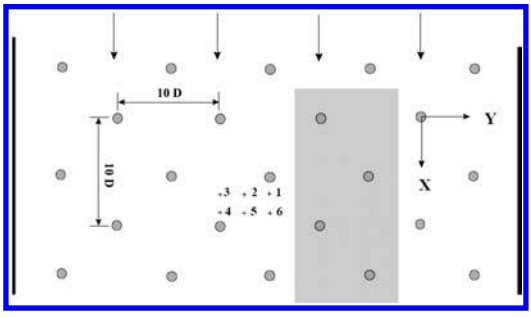


Figure 2. Flow Configuration indicating the positions of the 6 measurement verticals and the computational box.

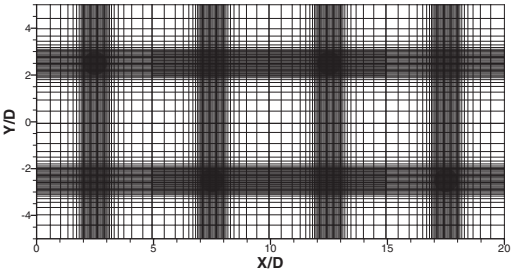


Figure 3. Computational grid for the Large Eddy Simulations (only every 4th grid line is shown).

27 Million grid points. The grid spacings in terms of wall units in streamwise and spanwise direction were $\Delta x^+ = \Delta y^+ \approx 40-60$ in the areas between the cylinders and $\Delta x^+ = \Delta y^+ \approx 1$ near the cylinder surface. In the vertical direction the grid was stretched likewise and values of $\Delta z^+ \approx 60$ near the water surface and $\Delta z^+ \approx 1$ near the top of the cylinders and near the channel bed were obtained. Figure 3 shows the grid in a horizontal plane indicating the refinement of the grid towards the cylinders (note that only every 4th grid line is plotted). Periodic boundary conditions were applied in the streamwise and spanwise directions. At the channel bed the no-slip condition is used and the free surface was set as a frictionless rigid lid and was treated with the symmetry condition. The flow was established over a period of approximately 50 flow through time and circa 80 flow throughs was taken as averaging period. The calculations are still ongoing at the time of the writing and the latest results will be presented at the conference.

4 RESULTS AND DISCUSSIONS

4.1 *Time-averaged flow field*

In Figures 4 and 5, the time-averaged flow field in two selected longitudinal planes (position is indicated in the sketch in the upper right corner) is presented. Due

Copyright © 2006 Taylor & Francis Group plc, London, UK

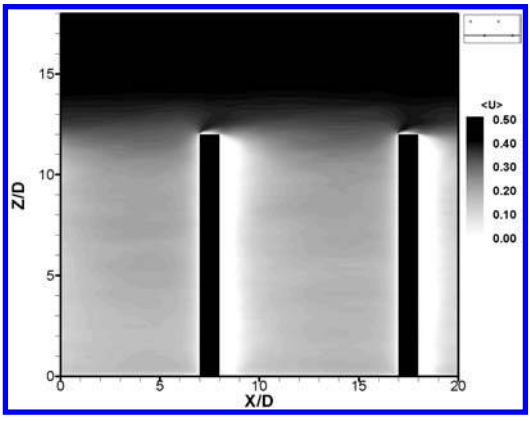


Figure 4. Distribution of time-averaged streamwise velocity in a plane through cylinders (see sketch in the upper right corner).

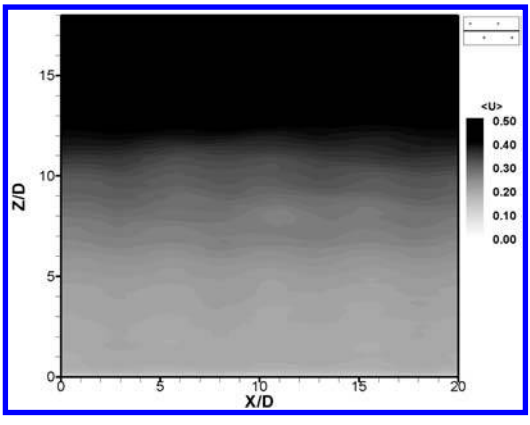


Figure 5. Distribution of time-averaged streamwise velocity in a longitudinal plane midway between cylinders (see sketch in the upper right corner).

to flow separation at several locations on the cylinder walls, e.g. on the top and the rear of the cylinder, the flow develops a number of recirculation zones, due,. The retardation of the flow in the vegetation layer is clearly visible and prevails over the whole width of the channel. Above the cylinders the flow accelerates, causing a strong shear layer. The mean flow field exhibits a wavy shape from the top of the cylinders to the free surface which can be attributed to standing waves forming above the recirculation bubble on the top of the cylinder. In the vegetation layer the velocities are almost constant, though slightly higher in planes where no cylinders are present, except in the rear of the cylinders were recirculation over the whole cylinder height occurs.

Figure 6 presents the comparison of LES with the measurements along the six selected verticals in the flow for time-averaged streamwise velocities. Overall, a good match between the computed and measured quantities could be achieved. Especially the well known vertical distribution of streamwise velocities of the flow through vegetation was reproduced and exists irrespective of the position of the profile. At position #1, which is directly behind the cylinder, the LES underestimates somewhat the streamwise velocities in the vegetation layer. However, this is the region where the highest turbulence occurs, and a longer averaging period is required to obtain a smooth vertical distribution of velocity. Along the Position #6, which is also behind the cylinder but further downstream, the match between measured and computed velocities is very good. Equally good is the agreement at the positions in front of the cylinder (#3 and #4) and along the positions between the cylinders (#2 and #5). Also noticeable is the velocity bulge near the channel bed, resulting from the near bed necklace vortex around the cylinder, which is predicted to a very satisfying degree (see e.g. Positions #1 and #6).

The above mentioned coherent flow structures affect significantly the turbulence intensity distributions along the six verticals. In Figure 7 measured and computed streamwise turbulence intensities are compared. Similar to the comparison of mean velocities, the match between computed and measured *r.m.s* values is very good. As can be seen clearly, the peak in the turbulence intensities appears in the vicinity of the vegetation tops (indicated by the green line). This is the area of highest vertical shear where most of the turbulence production occurs. This region is regarded as the interface between the upper part of the flow and the vegetation layer where momentum transfer between these layers occurs. It should be noted that for a smooth distribution of *r.m.s* velocities a longer averaging time is needed.

Figures 8 and 9 present the distribution of the kinetic energy in two selected longitudinal planes (indicated in the sketch in the upper right corner). In the plane where the cylinders are present (Figure 8), two significant regions of high turbulence can be identified. The highest values of kinetic energy occur in the small recirculation bubble on the top of the cylinder. A second region of high turbulence is the area were the trailing vortex penetrates into the vegetation layer and interacts with the von Karman vortices (see Figure 11) that are shed from the cylinders. In longitudinal planes between the cylinders (Figure 9) the above mentioned shear layer between the vegetation layer and the region above it with elevated levels of kinetic energy is clearly visible and extents between $Z/D = 8 - Z/D = 15$.

4.2 *Instantaneous flowfield*

Figure 10 presents instantaneous streaklines originating at different positions in the flow. All typical

Copyright © 2006 Taylor & Francis Group plc, London, UK

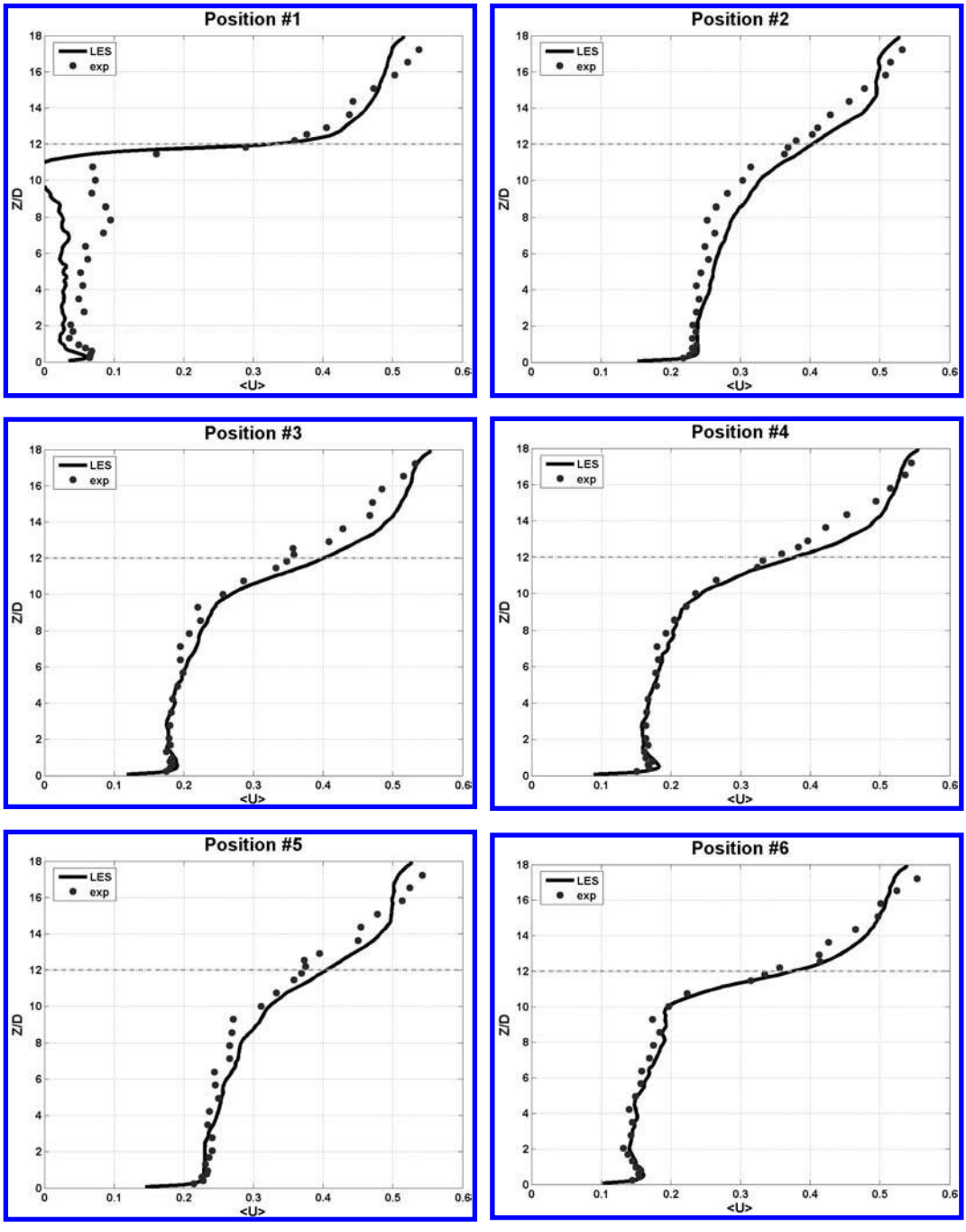


Figure 6. Distribution of mean streamwise velocity $<U>$ along the six measurement positions #1 to #6.

features of the flow through and above a vegetation layer can be identified. Near the channel bed the necklace vortices cause a more or less strong disturbance of the near bed flow. Near the bottom of the second cylinder (from the left) a necklace vortex, also known as the horseshoe vortex, is visualized and strong vertical accelerations are present. In the middle part of the vegetation layer the von Karman vortices dominate the

Copyright © 2006 Taylor & Francis Group plc, London, UK

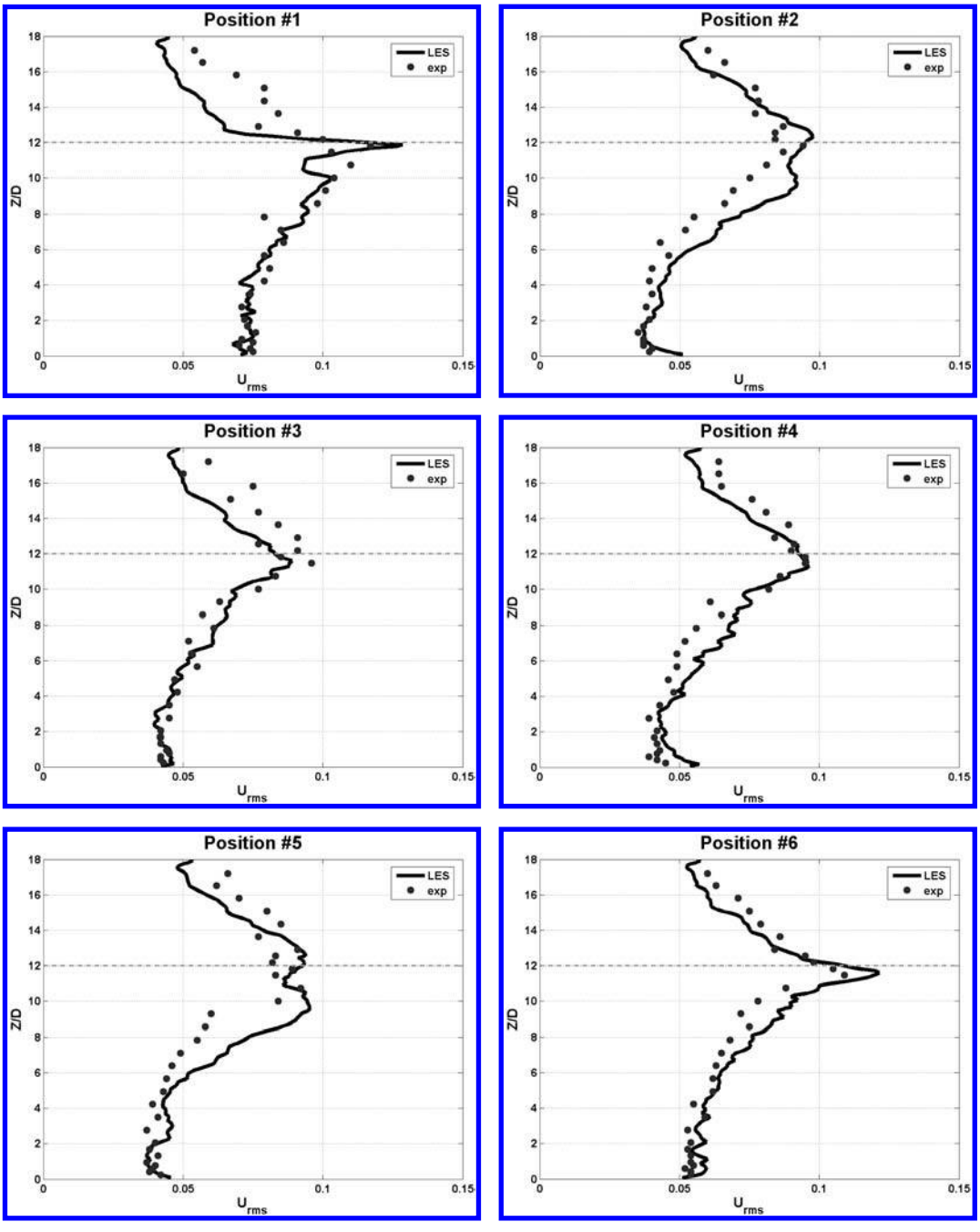


Figure 7. Distribution of streamwise turbulence intensities U_{rms} along the six measurement positions #1 to #6.

flow and instantaneous flow separation occurs. However, the vertical acceleration is fairly small. Near the top of the vegetation layer, the trailing vortices spinning from the top of the cylinder and penetrating the flow within the vegetation layer, is visible. At this instant in time a trailing vortex is present at each of the cylinder tops. Further above the cylinders the flow is characterized by the organized structures in

Copyright © 2006 Taylor & Francis Group plc, London, UK

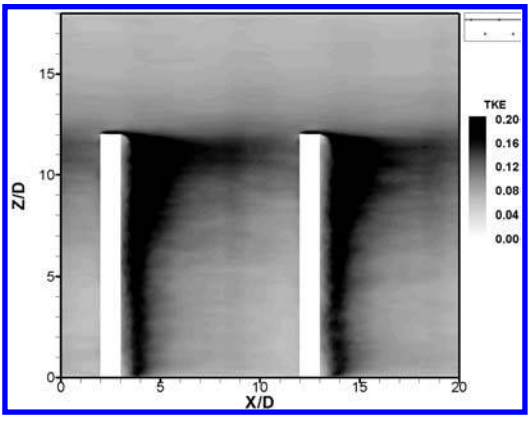


Figure 8. Distribution of time-averaged kinetic energy in a longitudinal plane through cylinders (see sketch in the upper right corner).

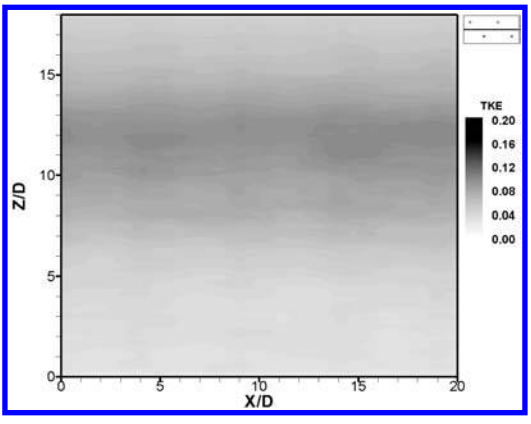


Figure 9. Distribution of time-averaged kinetic energy in a longitudinal plane midway between cylinders (see sketch in the upper right corner).

forms of ribs and rolls, which causes up and downward movement of the flow.

In Figure 11 two dominant flow structures present in the vegetation layer and above the cylinders are visualized. The red isosurfaces of instantaneous pressure fluctuation p' illustrate von Karman vortices shed from the cylinders as a result of alternating flow separation. The vortices travel downstream until they are destroyed by either the trailing vortex that penetrates from the upper region or by interaction with the following cylinder. The upper flow structure, here also visualized by the blue isosurfaces of instantaneous pressure fluctuation, can be identified as vortex rolls that are generated by the shear layer between the vegetation layer and the region above. As can be seen clearly, these two different structures are independent of each other due to the fact

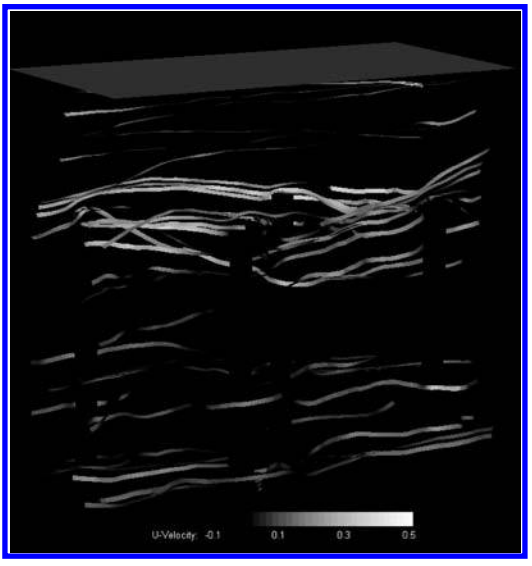


Figure 10. Instantaneous streamtraces colour-coded with instantaneous streamwise velocity.

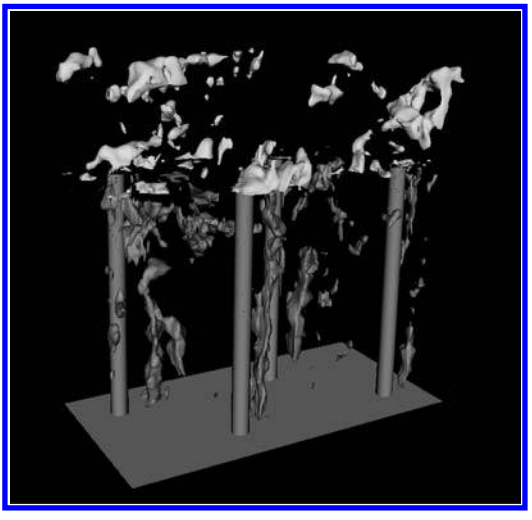


Figure 11. Instantaneous isosurfaces of pressure fluctuations p' visualizing vortex rolls (light grey) and von Karman vortices (dark grey).

that their origin is different. As was shown previously, another flow structure that is responsible for flow interaction is the trailing vortex that disturbs the flow within the vegetation layer transporting momentum from the upper layer of the channel into the vegetation layer and is also responsible for momentum exchange between these two layers as the large-scale ribs and rolls.

Copyright © 2006 Taylor & Francis Group plc, London, UK

5 CONCLUSIONS

In this paper we have presented the results of a Large Eddy Simulation of open channel flow through and above a matrix of cylinders. The time averaged data of the simulations were compared to LDA measurements from laboratory experiments of the same flow. The well known distribution of streamwise velocities was reproduced and the comparison along the six measurement verticals showed good agreement of calculated values with measured data. Furthermore, turbulence intensities were compared and again a good match between computed and measured quantities was found. In addition to the mean flow field the instantaneous flow field was investigated. A strong shear layer develops above the vegetation layer that is responsible for the formation of coherent flow structures being present in the form of vortex rolls. Within the vegetation layer, vortex shedding from the cylinders occurs and von Karman vortices are present. Near the channel bed, the presence of the necklace vortex was confirmed. Also confirmed was the trailing vortex originating at the cylinder tops. It was found that the latter vortex as well as large-scale flow structures in form of ribs and rolls are the main mechanism for flow interaction between the upper part and the vegetation layer.

ACKNOWLEDGEMENTS

This work is part of the research project funded by the German Research Foundation (DFG) under project number Ro 558/29-1. The computations were carried out on the high performance computer HP XC6000 of the computing center at the University of Karlsruhe.

REFERENCES

Choi S-U, & Kang H. (2001). Reynolds Stress Modeling of Vegetated Open Channel Flows. XXIX IAHR Congress Conference Proceedings. Beijing, China. Theme D. Vol 1. 264–269.

Cui, J. & V.S. Neary (2002). Large eddy simulation (LES) of fully developed flow through vegetation. IAHR's 5th International Conference on Hydroinformatics, Cardiff, UK, July 1–5, 2002.

Dunn, C., Lopez F., & Garcia, M.H. (1996). Mean flow and turbulence in a laboratory channel with simulated vegetation. Hydraul. Engr. Series No. 51, UILU-ENG-96-2009, UIUC.

Dwyer, Michael J, Patton, Edward G, Shaw, & Roger H. (1997). Turbulent Kinetic Energy Budgets from a Large-Eddy Simulation of Airflow Above and Within a Forest Canopy. Boundary Layer Meteorology., No. 1: 23–44.

Fairbanks, J.D. & Diplas, P. (1998): Turbulence characteristics of flows through partially and fully submerged vegetation, Wetlands Engineering and River Restoration Conf., March 22–27, Denver, Colorado, USA.

Finnigan, J. (2000). Turbulence in Plant Canopies. Annual Review of Fluid Mechanics, Vol. 32, 519–571.

Fischer Antze, T, Stoesser, T, Bates, PB, & Olsen, NR. (2001). 3D Numerical Modelling of Open-Channel Flow with Submerged Vegetation. IAHR Journal of Hydraulic Research 39: 303–310.

Kanda, M., & Hino, M. (1994). Organized Structures in Developing Turbulent Flow within and above a Plant Canopy, Using a LES. Boundary-Layer Meteor., 68, 237–257.

Kawamura, T., Hiwada, M., Hibino, T., Mabuchi, I., & Kamuda, M. (1984). Flow around a finite circular cylinder on a flat plate. Bulletin of the JSME 27 (232), 2142–2151.

Kouwen N, Unny TE, & Hill HM. (1969). Flow Retardance in Vegetated Channels. Journal of Irrigation and Drainage Division, ASCE 95: 329–342

Kouwen, N. & T.E. Unny (1973). Flexible roughness in open channel. J. of Hydraulic Div., ASCE, Vol. 99, HY5, pp. 713–728.

Lopez, F. & M. Garcia (2001). Mean flow and turbulence structure of open-channel flow through non-emergent vegetation. ASCE J. Hydraulic Engrg., 127(5), 392–402.

Meneveau, C., Lund, T.S. & Cabot, W.H. (1996): A Lagrangian dynamic subgrid-scale model of turbulence, Journal of Fluid Mechanics, 319, pp. 353–385.

Moeng, C.H. (1984). A large-eddy-simulation model for the study of planetary boundary-layer turbulence. Journal of the Atmospheric Sciences, Vol. 41, pp 2052–2062.

Naot, D, Nezu, I, & Nakagawa, H. 1996. Hydrodynamic Behavior of partly vegetated open-channels. ASCE J. Hydraulic Engrg., 122 (11): 625–633.

Neary, V.S. (2003). Numerical solution of fully-developed flow with vegetative resistance. Journal of Engineering Mechanics. 129(5), 558–563.

Nepf, H.M. & Vivoni, E.R. (1998). Drag and Diffusivity in Emergent Vegetation. ASCE Wetlands Engineering and River Restoration Conference. Denver, CO.

Paik, J., Jones, S. C., & Sotiropoulos, F. (2003). DES and URANS of Turbulent Boundary Layer on a Concave Wall. The proceedings of the 3rd International Symposium on Turbulent and Shear Flow Phenomena, Sendai, Japan, June 2003.

Shaw, R.H., & Schumann, U. (1992). Large-Eddy Simulation of Turbulent Flow above and within a Forest. Boundary-Layer Meteor., 61 (1–2), 47–64.

Shimizu, Y. & T. Tsujimoto (1994). Numerical analysis of turbulent open-channel flow over vegetation layer using a k-turbulence model. J. of Hydroscience and Hydraulic Engrg., JSCE, Vol. 11, No. 2, pp. 57–67.

Stone, H.L. (1968). Iterative Solution of Implicit Approximation of Multi-dimensional Partial Differential Equations. SIAM J. Numerical Analysis. No. 3.

Tremblay, F., Manhart, M. & Friedrich, R. (2000): LES of flow around a circular cylinder at a subcritical Reynolds number, EUROMECH Colloquium 412, October, 4–6, Munich, Germany.

Verzicco, R., Mohd-Yusof, J., Orlandi, P., & Haworth, D. (2000). Large Eddy Simulation in Complex Geometric Configurations Using Boundary Body Forces. AIAA , Vol. 38 (3), pp. 427–433.

Copyright © 2006 Taylor & Francis Group plc, London, UK

Experimental characterization and visualization of mass exchange process in dead zones in rivers

W. Brevis
Departamento de Ingeniería Civil, Universidad de Chile, Chile

Y. Niño
Departamento de Ingeniería Civil, Universidad de Chile, Chile

J. Vargas
Departamento de Ingeniería Civil, Universidad de Concepción, Chile

ABSTRACT: This paper summarizes the results of experimental measurements performed to characterize mass exchange at different depth levels between a simplified dead zone and an open-channel. In the analyzed case the flow in the flume was subcritical, an the dead zone was modelled as a lateral rectangular cavity with aspect ratio, length to width, of 2. It was possible to establish that mass transfer is mainly due to the engulfing process associated to a Kelvin-Helmholtz instability at the channel-cavity interface and that the influence of the gradient of concentration is not important as the one-dimensional Transient Storage Model assumes. The flow within the cavity was dominated by a two gyre system. It was observed that the main gyre modulates the interfacial instability and that there is a marked variation of mass exchange with depth.

1 INTRODUCTION

The presence of large scale recirculation zones in rivers modify the characteristics of the mass transport process in rivers. Normally a difference between the concentration curves measured and modelled by the classical advection-dispersion equation is observed. In order to improve the results several researchers, Chapra and Runkel (1991), De Smedt, et al. (2005), Czernuszenko and Rowinski (1997) have used a first-order model exchange (Transient Storage Model, TSM) between two conceptual zones, a dead zone and a main flow zone. The TSM considers that the exchange process between both zones depends on the concentration gradient and a mass exchange coefficient. However, even with this model the skewness of the observed concentrations does not appear to be decreasing as the theory predicts, (Nordin and Troutman, 1980). On the other hand, even though there is a good fit between the observed and modelled concentrations the information of the real process obtained from its parameters is not enough to understand the physical processes occurring in the recirculation zones and its effects on river mass transport. Equations 1 and 2 show the mass balance equations for main channel and dead zone respectively. In the main channel the model assume that the solute concentration changes because of the advection-dispersion processes and the first order exchange with the dead zone. In the former zone, the model assume that the concentration change is only due to the first order exchange with the main flow.

$$\frac{\partial C}{\partial t}+\frac{Q}{A}\frac{\partial C}{\partial x}=\frac{1}{A}\frac{\partial}{\partial x}\left(AD_L\frac{\partial C}{\partial x}\right)+\alpha\left(C_S-C\right) \tag{1}$$

$$\frac{\partial C_S}{\partial t}=-\alpha\frac{A}{A_S}\left(C_S-C\right) \tag{2}$$

Where C is the solute concentration in the main channel $[M/T]$, Q is the volumetric flow $[L^3/T]$, A the cross sectional areaof the main channel $[L^{-2}]$, D_L the longitudinal dispersion coefficient $[L^2/T]$, C_s the solute concentration in the storage zone $[M/T]$, A_s the cross sectional area in the storage zone $[1/L^2]$, α the mass exchange coefficient $[1/T]$, t time$[T]$, x the longitudinal coordinate $[L]$.

The simplest way to model a real dead zone is by means of a rectangular side-cavity, which is similar to harbours, groyne fields and bottom depressions. There are many investigations related with the flow inside cavities, for example according to Shen and Floryan (1985) in cavities with aspect ratio, length to width, 2 is possible to observe a primary and a secondary gyre. Garrison and Rogers (1994), using concentration determination by image analysis and changing upstream conditions close to the cavity, concluded that

Copyright © 2006 Taylor & Francis Group plc, London, UK

the instabilities generated at the interface are fundamental for mass exchange. As a result of experiments in a cavity located at the bottom of a Odell-Kovasznay channel, Strang and Fernando (2004) conclude that there is an increment of turbulent kinetic energy at the cavity-channel interface, and for cavities with aspect ratio equal or greater than 2, the mass exchange is intermittent. Uijtewaal et al. (2001) who did experiments on river groynes, show that this exchange process can be interpreted as a first-order behaviour and McCoy et al. (2005) using *Large Eddy Simulation* (LES) conclude that this exchange process is three-dimensional and changes with depth.

Muto et al. (2000), as a conclusion of experiments in open-channel side cavities with aspect ratio 1 and 3, show that the mass exchange for large aspect ratio cavities is also mainly due to instabilities on the dominant internal flow. For the same case and based on experimental and 2-D numerical results, Kimura and Hosoda (1997) point out the characteristics of the structures of the interface. These structures can be decomposed into two components due to seiching and shear instability respectively; during one seiche, cycle-velocity variations caused by instability are amplified to the large scale vortex selectively by the interaction between seiche and instability components.

This work presents a characterization of the mass transfer in a rectangular dead zone with aspect ratio, length to width, of 2. Based on the similar patterns of flow in the previous cited investigations and with the aim to describe in a proper way the mass exchange process, a high flow depth was used for this experiments, but even with this assumption the results are comparable with real river cases Le Coz et al.). This study was conducted over different depth levels. The Flow structure was obtained by means of *Particle Tracking Velocimetry* (*PTV*) and spatially-averaged concentration curves and visualizations by means of *Laser Induced Fluorescence* (*LIF*).

2 PREVIOUS OBSERVATIONS IN THE CHILLAN RIVER

In order to understand the influence of transient storage in mass transport, a tracer study was performed in a reach of the Chillán river, Chile. The reach, a sequence of pools and riffles with presence of lateral recirculation zones and a gravel bed, was 1.2 km long, with a flow discharge of 2.7 m^3/s (subcritical regime) and a mean width of 18 m.

The tracer used was Rhodamine WT and the instantaneous injection of the dye was made far enough of the first sample station in order to ensure that the mixing process was completely in the cross-section. Four sample stations (E) were used in this field test. The associated concentration response curves to each station are shown in figure 1. As can be seen the curves

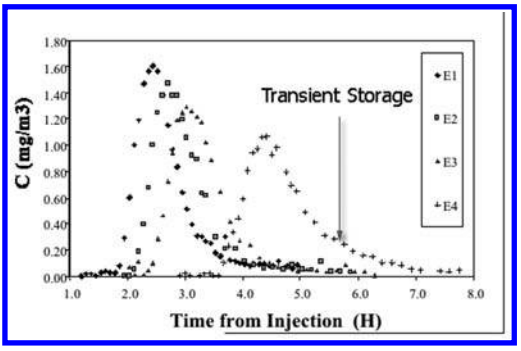


Figure 1. Concentration response curves in the Chillán river.

Table 1. Exchange coefficient observed in the Chillán river.

$SR_1, E_1 - E_2$ [1/s]	$SR_2, E_2 - E_3$ [1/s]	$Sr_3, E_3 - E_4$ [1/s]
2.33e-5	7.46e-5	5.02e-5

present long tails which is due to the effect of transient storage, i.e recirculation zones and hyporreic flow. Using this measurements, the solution obtained by De Smedt et al. (2005) for the TSM model and an optimization algorithm, it was possible to obtain the value of the exchange coefficent α for the sub-reaches (SR) formed between the sample stations. This values are presented in table 1. The exchange coefficient obtained corresponds to a mean value of the effects of the recirculation zones and hyporreic flow over each sub-reach. These value are small but the total effect over mass transport is clearly observed in the curves showed in 1. From this models it is not possible to understand the importance of the recirculation zones in mass transport and due to this experimental research was developed in the laboratory.

3 DESCRIPTION OF THE EXPERIMENTS

In order to understand the physical processes occurring in a recirculation zone, experiments were conducted in a laboratory flume 1200 cm long, 30 cm width, 30 cm deep and a longitudinal slope of 0.001. A width reduction of 10 cm was set along one side of the flume and the cavity was located 300 cm upstream from the end of the flume. A schematic representation of the experimental set-up can be seen in figure 2. The hydraulic condition for the experiments, depth (H), flow discharge (Q), mean velocity (U), hydraulics radius (R), Reynolds number ($Re = \frac{U H}{\nu}$) and Froude number (Fr) are summarized in table 2.

In order to describe the flow and mass transfer ocurring in the cavity, Particle Tracking Velocimetry

Copyright © 2006 Taylor & Francis Group plc, London, UK

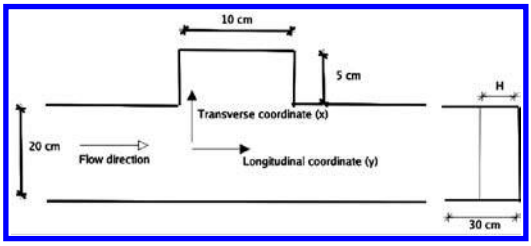


Figure 2. Schematic representation of the experimental set-up.

Table 2. Experimental conditions.

H	Q cm^3	U cm/s	R cm	Re	Fr
10.7	7800	36.45	5.16	39000	0.36

results (*PTV*) and Laser Induced Fluorescence (*LIF*) were employed. Both systems were composed by a 400 MW two-colour laser beam and by a 30 HZ digital camera. In the case of PTV, acrylic particles were employed and tracked by the implementation in Matlab of a dynamic, binary, spatial cross-correlation algorithm between two sequential images (Hassan et al., 1992). Based on the results obtained by David et al. (2002), the Inverse Weighting Method with a Gaussian Adaptive Window, was used for velocity interpolation. For LIF a green-fluorescent dye was injected instantaneously over the entire cross-section of the flume and to avoid variations in ambient light conditions a dark chamber was built in the channel work area. The response curve at each level was obtained using a previously determined calibration curve. It was found that in the used concentration range, there was a linear relation between the tracer concentration and the graylevel intensities. It was assumed that the dispersion process was not relevant for the determination of the response curves in the cavity, i.e. there was no presence of tracer in the channel after the cavity reaches the spatially average peak concentration.

4 GENERAL CHARACTERISTICS OF FLOW STRUCTURE AND MASS TRANSFER

4.1 *Particle tracking velocimetry results (PTV): flow structure*

PTV measurements were carried out to characterize the flow structure at heights of 20, 60 and 100 mm over the channel bottom. 1000 pairs of frames were averaged in order to get a description of the mean flow properties inside the cavities. In Figures 3, 4, and 5, the mean velocity and streamlines are presented. Two main zones are distinguished, a primary gyre located at

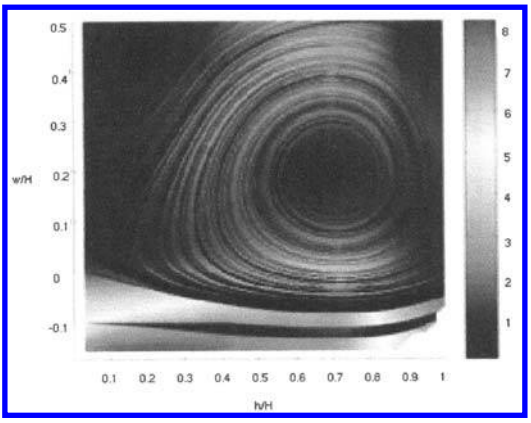


Figure 3. Streamlines over mean velocity 100 mm.

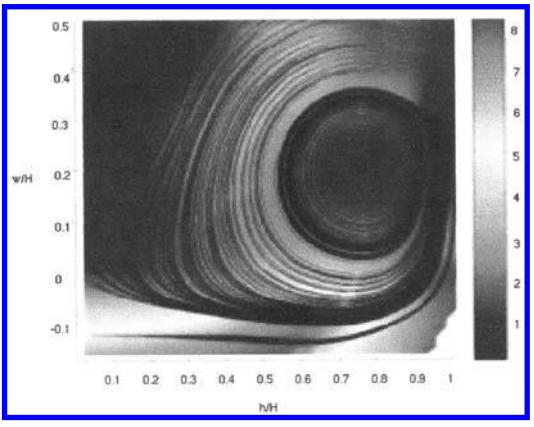


Figure 4. Streamlines over mean velocity 20 mm.

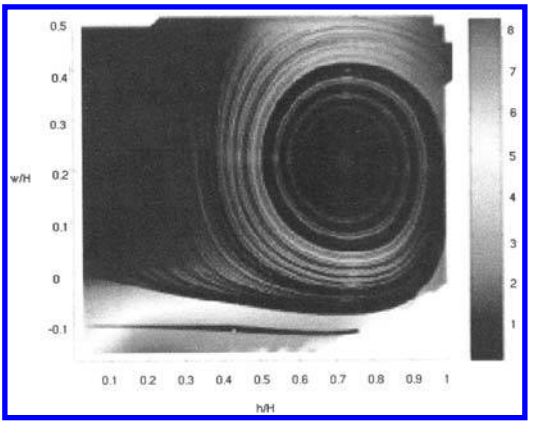


Figure 5. Streamlines over mean velocity 20 mm.

the downstream section of the cavity and a secondary gyre located at the upstream internal corner of the cavity which disappears at 20 mm. From video analysis it was possible to observe an oscillation of the primary

Copyright © 2006 Taylor & Francis Group plc, London, UK

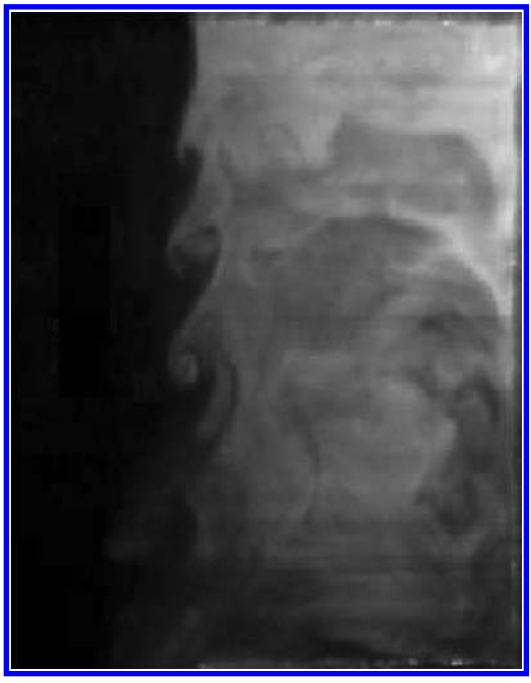


Figure 6. Kelvin-Helmholtz instability at Channel-Cavity interface. The figure show the complete cavity area.

gyre. In general, the velocity magnitude does not suffer important changes and the maximum is at the most six times lower than the main channel flow mean velocity.

4.2 *Laser induced fluorescence (LIF): general observations*

Because of the strong velocity gradient located at the channel-cavity interface, a Kelvin Helmholtz instability is formed. These structures are responsible for the mass exchange between cavity and channel (Garrison and Rogers (1994), Uijtewaal et al. (2001)). This kind of structure depends on the velocity difference between cavity and channel. This means that differences in the vertical flow structure in the channel could affect, in theory, mass exchange. In general, Kelvin-Helmholtz instability allows the exchange from cavity to channel by means of convective patterns called Kelvin billows, and from channel to cavity by means of the engulfing process, these coherent structures will be described below.

From video analysis the velocity of the Kelvin billow was estimated. The advection of these structures was approximately 3 times lower than channel mean velocity, independent of the vertical position, but their frequency of generation changes with elevation: $\simeq$1.1 s at 100 mm, $\simeq$0.7 s at 60 mm, and $\simeq$0.7 s 20 mm.

An intermittent relation between shear layer and primary eddy (shear layer perturbations) has been

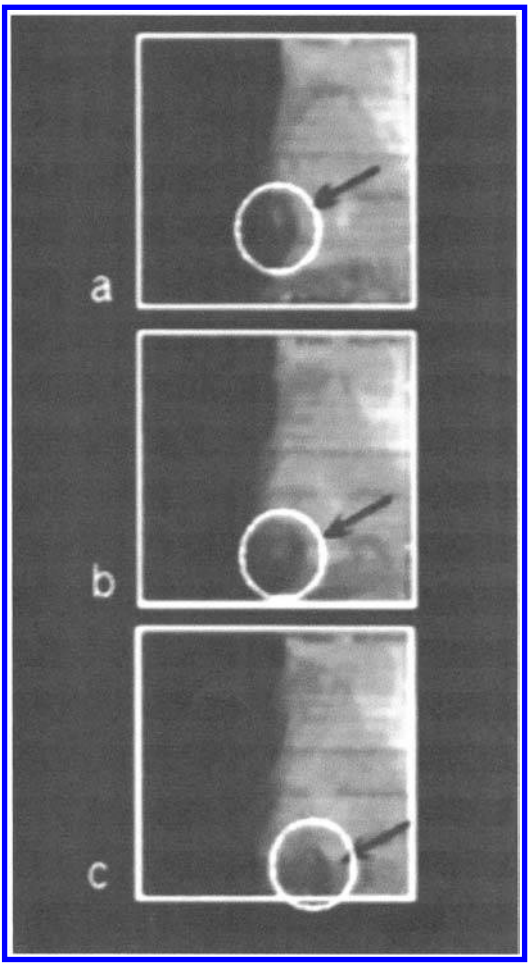


Figure 7. Engulfing process. The picture shows the total cavity area: (a) The Kelvin billow is transported downstream. (b) The billow hits the downstream corner of the cavity. (c) A new volume of water is directly incorporated into the cavity.

observed previously by Strang and Fernando (2004) and Uijtewaal et al. (2001) and they point out that this is the most important mechanism to improve exchange. According to Uijtewaal et al. (2001) the flow is far from stationary and the large turbulence structures in the mixing layer play a prominent role in the exchange process, which is validated by the present experiments. The diffusion process, that occurs preferably in the billows, is fast but does not allow a high volume of exchange in comparison with the observed volume associated to the engulfing process. Figures 8, 9, 10 show the fast diffusion mechanism occurring on Kelvin billows. These figures describe the movement of the upstream billow in figure 11. Due to the camera definiton was not possible to obtain a better resolution for these images. Because of this an investigation

Copyright © 2006 Taylor & Francis Group plc, London, UK

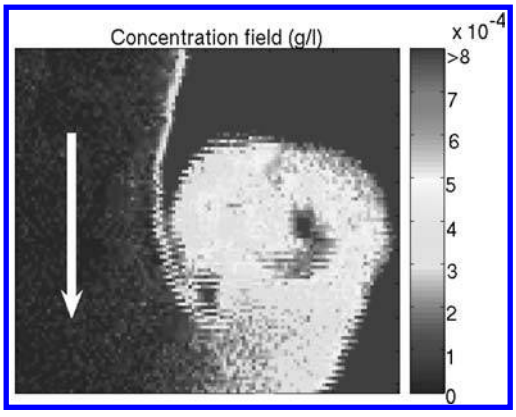


Figure 8. Mixing in Kelvin-Helmholtz instability at 60 mm (t = 0 s). Detail of the upstream billow shown in figure 11.

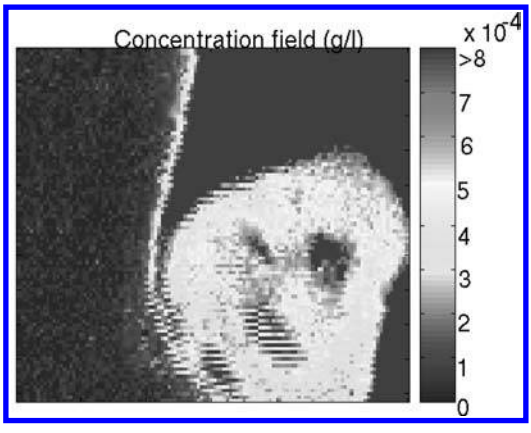


Figure 9. Mixing in Kelvin-Helmholtz instability at 60 mm (t = 0.066 s).

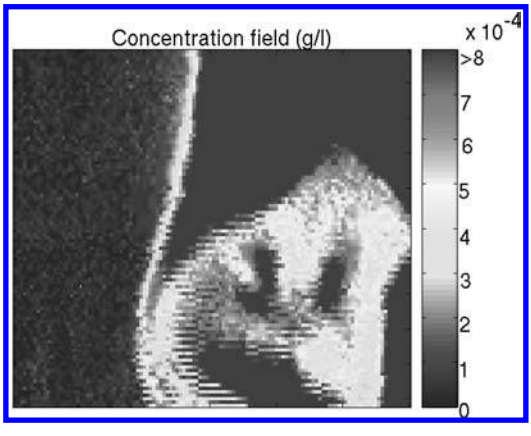


Figure 10. Mixing in Kelvin-Helmholtz instability at 60 mm (t = 0.133 s).

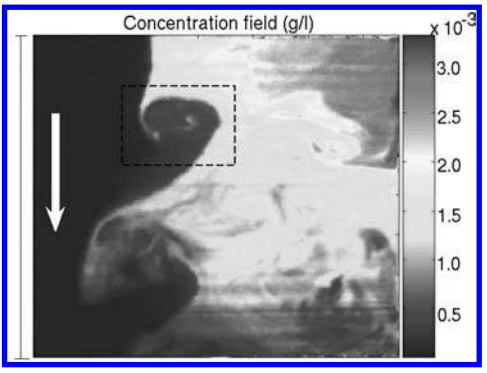


Figure 11. Instantaneous Concentration field at 60 mm. The figure shows the complete cavity area.

conducted to quantify the exchange of these structures will be performed in a future work.

An instantaneous distribution of concentration in the cavity is shown in Figure 11, in this figure it is possible to observe that in the region of the secondary gyre there is an internal recirculation zone of high concentration compared to the concentration in the primary gyre.

4.3 *Engulfing process*

This process is mainly responsible of mass inflow to the cavity. When Kelvin billows are transported, they hit the downstream corner, surrounding fluid that is incorporated into the cavity. The dynamic is presented in figure 7. This process takes relevance when a perturbation acts over the shear layer. In that case the size and direction of the Kelvin billows changes producing a pulse of fluid that is taken inside the cavity.

5 CONCENTRATION RESPONSE CURVES IN THE CAVITY

Using LIF measurements, a mean concentration (spatially averaged over the area) in the cavity was calculated at 5 depth-levels, 20, 40, 60, 80 and 100 mm over the channel bottom. The results are presented in Figure 12, where it can be observed that the lowest exchange takes place at 40 and 20 mm, a medium exchange at 60 and 80 mm and the highest exchange at 100 mm. A similar observation was obtained by Wallast et al. (1999) who compared the exchange integrated over the entire depth with that estimated only at the surface level. They point out that this is due to secondary flow and three-dimensional structures in the flow. The similitude of the mean concentration curve inside the cavity with the previously concentration response curve measured in the Chillán river, shows that the effect of the secondary gyre in the averaged

Copyright © 2006 Taylor & Francis Group plc, London, UK

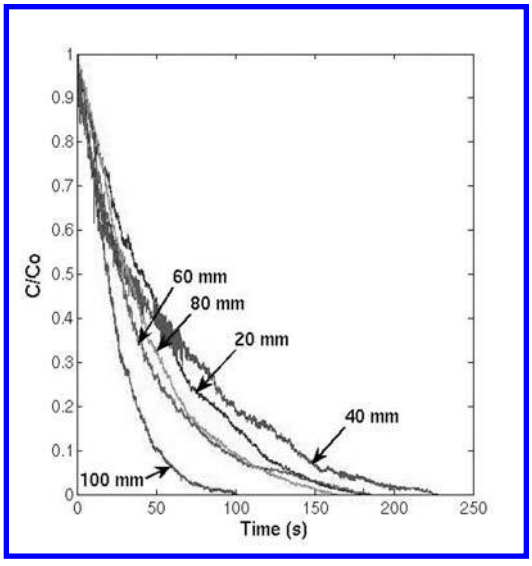


Figure 12. Spatially-averaged concentration response curves in the complete cavity area for 20, 40, 60, 80 and 100 mm over channel bottom.

cavity concentration is the same effect of dead zones over open-channel flows.

5.1 *Evolution of the exchange coefficient with depth*

It is clear from LIF analysis that mass exchange between main channel and cavity do not depend importantly on the concentration gradient, but on the coherent structures formed at the channel-cavity interface. Maybe, due to that assumption the TSM does not allow a physical understanding of the influence of recirculation zones. However, the averaged concentration curves show a first order decay and can be calculated by fitting concentration modelled by equation 3 to experimental data.

$$C(t) = C_0 e^{kt} \tag{3}$$

Where C $[M/L^3]$ is the cavity concentration, C_0 $[M/L^3]$ the initial concentration, k $[1/T]$ the exchange coefficient and t, the time.
Because of the variation of the internal velocity in the cavity with the longitudinal coordinate, the shear velocity (U_*) in the channel flow was used as velocity scale. The spanwise length of the cavity (H) was used as length scale. Using this variables a dimensionless exchange coefficient can be defined as:

$$K = \frac{kH}{U_*} \tag{4}$$

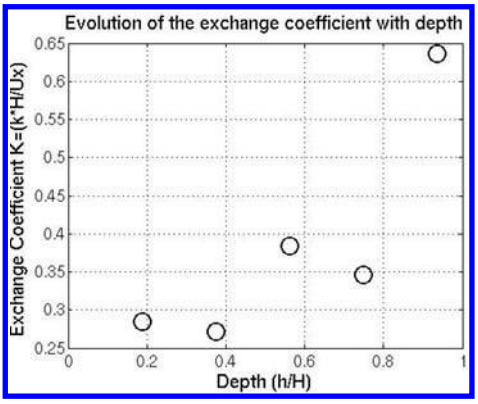


Figure 13. Dimensionless exchange coefficient at different depth levels.

Table 3. Exchange coefficient at different depth levels (1/s).

20 mm	40 mm	60 mm	80 mm	100 mm
0.0187	0.0178	0.0252	0.0227	0.0418

The dimensionless exchange coefficient calculated for each level is presented in figure 13. The corresponding dimensional value for exchange coefficient at each level is presented in Table 3. Clearly, the exchange coefficient increases towards the surface, indicating that the highest mass exchange takes place near the surface.

6 REGIONS ANALYSIS

In order to understand the influence of the primary and secondary gyres on mass transfer, the cavity was divided in two regions: a high velocity region and a low velocity one. The low velocity region was defined arbitrarily as the zone located at the upstream end of the cavity with velocities lower than 1 cm/s. The definition for levels at 40 and 80 mm was obtained by interpolation of the adjacent levels. The low and high velocity regions definition for each level are shown in Figure 14.

6.1 *Peak concentrations in the high and low velocity regions*

Figure 15 shows the influence of low and high velocity regions on mass exchange. The local peak concentration was made dimensionless by means of the maximum mean concentration in the cavity. At the 20 mm level, the low and high velocity regions have almost the same behavior than the complete cavity.

Copyright © 2006 Taylor & Francis Group plc, London, UK

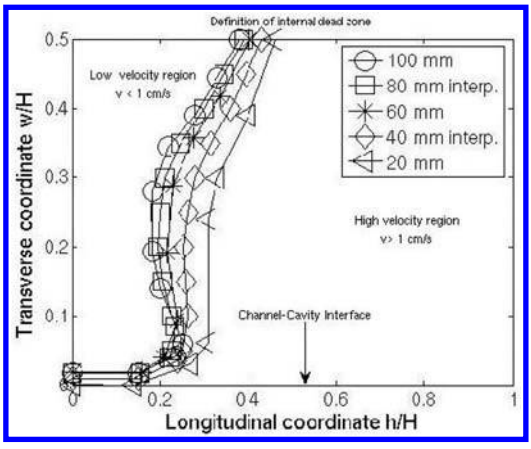


Figure 14. Definiton of low and high velocity regions.

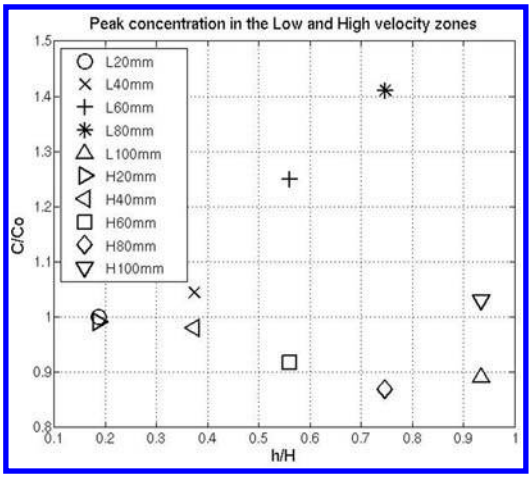


Figure 15. Peak concentrations in low and high velocity regions.

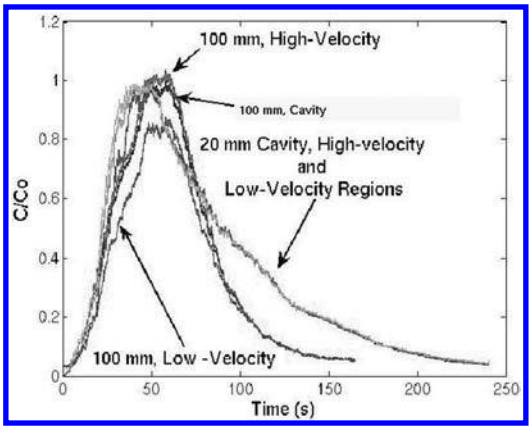


Figure 16. Concentration response curves at 20 and 100 mm. The figure show the concentration curves for each of the three analyzed areas: the complete cavity area, the low velocity region and the high velocity region.

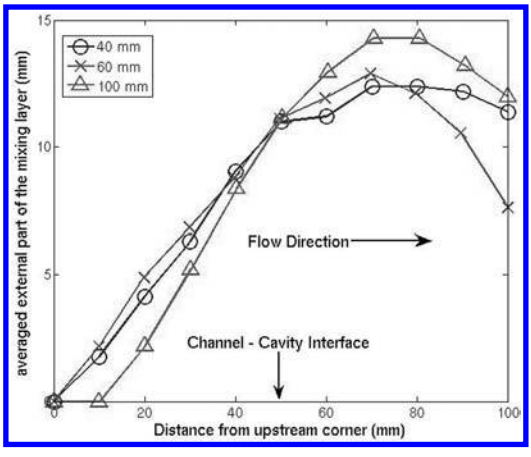


Figure 17. Mixing layer growth out of the cavity.

This is because of the disapearance of the secondary gyre at that level. From 40 mm to 80 mm the importance of the internal recirculation zone (secondary gyre) increases, but at the 100 mm level the primary gyre has the same behavior as the cavity, but the concentration in the low velocity zone is somewhat lower. This situation can partly explain the higher mass exchange obtained at the 100 mm (where also the generation of billows is higher), and as a consequence a three-dimensional characterization of flow structure is needed in order to explain this behavior.

As an example, concentration response curves for the three analyzed regions (the complete cavity, the low velocity region and the high velocity region) at 20 and 100 mm are presented in Figure 16.

7 GROWTH OF THE MIXING LAYER OUT OF THE CAVITY

In order to clarify the differences in mass exchange between the 100 mm level and the others ones, an averaged estimation of the mixing layer structures outside the cavity was developed with the aim of finding possible differences in the billows size. The calculation of the external mixing layer growth was obtained using an over-exposition of the images frames in a period of 20 (s) for the levels located at 40, 60 and 100 mm over channel bottom. Figure 17 shows that mixing layer growth is similar in all the cases, but slightly greater extension of this structure is observed near the surface. The decrease in size in the downstream corner is due to the influence of the primary gyre (main inflow zone).

Copyright © 2006 Taylor & Francis Group plc, London, UK

8 CONCLUSION

Based on *Particle Tracking Velocimetry* (PTV) and *Laser Induced Fluorescence* (LIF) results, it is concluded that the flow structure inside the cavity stays almost constant across the water column, with the exception of the plane located at 20 mm. There are two main regions dominated by a primary and secondary gyre, respectively. The main source for turbulent mass exchange is located at the channel-cavity interface, where Kelvin-Helmholtz instabilities are generated. These structures are responsible for the main mass exchange process from channel to cavity: the engulfing process. The exchange from cavity to channel is carried out by means of the Kelvin-Helmholtz structures, but mainly by intermittent instabilities in the flow inside the cavity that change the size of the Kelvin billows.

The concentration response curves showed a marked variation of exchange with depth. The mean concentration curves show that the exchange process is higher at 100 mm and lower for the range located between 20 and 80 mm levels. The over-exposition images obtained for mixing layer growth characterization show that there are no important differences in billow sizes at different levels, although there is a tendency for the maximum size of them to be close to the surface. The internal recirculation zone which disappears at the 20 mm level, increases its mass retention with depth, but decreases this retention at the 100 mm level. As a conclusion a three-dimensional characterization of the flow structure must be done in order to understand the behavior observed in this study. These experiments must be conducted parallel to surface oscillation measurements in order to better understand the three-dimensional effect of perturbations in the mixing layer.

ACKNOWLEDGEMENTS

This work was supported by the University of Chile. Funding was provided by Fondecyt Project N. 1040494 and the Scholarship Programme of the National (Chilean) Commission of Science and Technology Research, CONICYT.

REFERENCES

Chapra, S. and R. Runkel (1999). Modeling impact of storage zones on stream dissolved oxygen. *Journal of Environmental Engineering 125*, 415–419.

Czernuszenko, W. and P. Rowinski (1997). Properties of the dead-zone model of longitudinal dispersion in rivers. *Journal of Hydraulics Research 35*, 491–504.

David, L., A. Esnault, and D. Calluaud (2002). Comparison of interpolation techniques for 2d and 3d velocimetry. *11th. International Symposia on Aplication of Laser techniques to Fluid Mechanics, Lisboa, Portugal.*

De Smedt, F., W. Brevis, and P. Debels (2005). Analytical solution for solute transport in streams with transient storage in dead zones. *Journal of Hydrology 315*, 25–39.

Garrison, B. and C. Rogers (1994). An experimental study of enhanced fluid transfer mechanism between a channel and a cavity. *Physics of fluids 6*, 421–423.

Hassan, Y., T. Blanchat, and S. Ch. (1992). Piv flow visualization using particle tracking techniques. *Measurement Science Technology 3*, 633–642.

Kimura, I. and T. Hosoda (1997). Fundamental properties of flows in open channel with dead zone. *Journal of Hydraulic Engineering 123*(2), 98–107.

Le Coz, J., W. Brevis, Y. Nino, A. Paquier, and N. Riviere. Open-channel side-cavities: a comparison of field and flume experiments. *Submitted to RiverFlow 2006, Lisbon, Portugal*.

McCoy, A., G. Constantinescu, and L. Weber (2005). Coherent structures and mass exchange processes in channel flow with spanwise obstruction. *A ser presentado en el ERCOFTAC International Symposium on Engineering Turbulence Modeling and Measurements, Sardina, Italy.*

Muto, Y., H. Imamoto, and T. Ishigaki (2000). Velocity measurements in a straight open channel with a rectangular embayment. *Proccedings 12th APD-IAHR Bangkok Thailand.*

Nordin, C. and B. Troutman (1980). Longitudinal dispersion in rivers: The persistens of skewness in observed data. *Water Resources Research 16*, 123–128.

Shen, C. and J. Floryan (1985). Low reynolds number flow over cavities. *Physics of Fluids 28*, 3191–3202.

Strang, E. and H. Fernando (2004). Shear-induced mixing and transport from a rectangular cavity. *Journal of Fluids Mechanic 520*, 23–49.

Uijtewaal, W. D. Lehmann, and A. Mazijk (2001). Exchange process between a river and its groyne fields: Model experimets. *Journal of Hydraulic Engineering 127*, 928–936.

Wallast, W. Uijtewaal, and A. Mazijk (1999). Exchange process between groyne field and main stream. *Proceedings 28th IAHR Congress*, Graz.

Copyright © 2006 Taylor & Francis Group plc, London, UK

Coherent structure of horizontal eddies in meandering compound open-channel flow by using multi-layer scanning PIV

M. Sanjou, I. Nezu, T. Doi & H. Quang
Dept. of Civil Eng., Kyoto University, Kyoto, Japan

ABSTRACT: It is necessary to investigate coherent eddy structure in meandering compound open-channel flows for predicting the transport and distribution of suspended sediments in actual rivers. However, in previous studies, flow-visualization techniques such as PIV and PTV, have not sufficiently been applied to such flows, and thus, there is almost no detailed information of coherent turbulence in meandering compound open-channel flows. Therefore, in this study, we conducted innovative flow-visualization measurements by using a multi-layer scanning PIV system, and analyzed instantaneous velocity vectors on horizontal planes at several different elevations simultaneously. As the results, the vortex-existing probability and space-time correlations between the different elevations were revealed in meandering compound open-channel flows.

1 INTRODUCTION

Two-stage free-surface flows can be often observed in rivers in flood, and they consist of the inbank and overbank areas. Since such a compound open-channel flow causes significantly the inflectional instability near the junction region between the main-channel and flood-plains, the coherent horizontal vortices are generated and advected downstream. These eddies induced mass and momentum exchanges significantly between the high-speed inbank flow and the low-speed overbank flow, and thus, such compound open-channel flows have been studied intensively in river management and hydraulic engineering.

With an innovative development of measurement instruments, turbulent structures have been revealed even quantitatively in the past decade. For example, Tominaga & Nezu (1991) have conducted some accurate turbulence measurements with a laser Doppler anemometer (LDA), and they revealed the distributions of primary velocity and secondary currents in compound open-channel flows. Nadaoka & Yagi (1998) developed a two-dimensional (2-D) LES model in order to investigate the developing and merging processes of coherent horizontal eddies in the compound open-channel flows. Nezu *et al.* (2004) have developed a dual-layer PIV system and revealed the unsteady motion of 3-D vortex-tube structure in a depth-varying compound open-channel flow. As mentioned above, there are a lot of previous studies that offer the detailed information on the hydrodynamic properties, turbulence structure and coherent motions.

On the other hand, actual rivers generally have many bending and meandering sections. Several researchers had a great interest in meandering compound open-channel flows. For example, Fukuoka *et al.* (1997) have measured all three components of velocities by using an electromagnetic velocimetry (EMV) in a large-scale laboratory flume with two-stage meandering zone in order to examine the birth and decay processes of secondary currents. Shiono & Muto (1998) conducted some turbulence measurements in a meandering compound open-channel flow by using LDA. They revealed the distributions of secondary currents, primary velocity and turbulence in the fully-developed bend regions. Wormleaton, *et al*. (2005) have measured the velocity distributions, depth variations and sediment transport under the overbank condition in meandering large-scale channels with graded sand bed.

Recently, Nezu *et al.* (2005a) highlighted the channel-transition zone from the straight toward meandering compound open-channel flow. They investigated experimentally the developing process of secondary currents and turbulence structure along the curved main-channel by using 3-D EMV.

However, detailed information of 3-D structure of horizontal vortices in meandering compound open-channel flows is not available sufficiently, because it is difficult to conduct simultaneous measurements with a lot of LDAs. Therefore, in the present study, we tried to conduct the innovative multi-layer PIV measurements for both of the inbank layer and overbank layer in the meandering compound open-channel flows.

Copyright © 2006 Taylor & Francis Group plc, London, UK

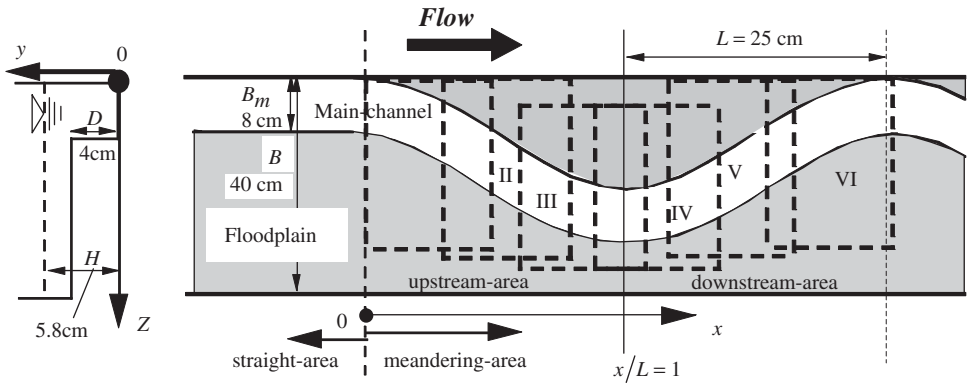


Figure 1. Coordinate system in measurement area.

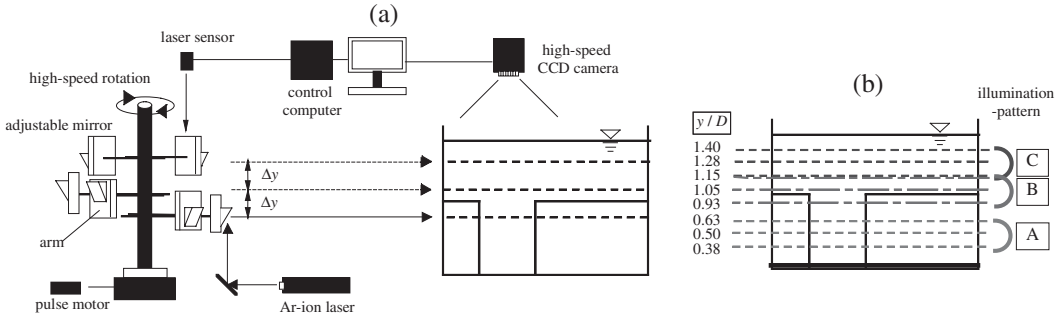


Figure 2. Multi-layer PIV system and illumination patterns of LLS.

2 EXPERIMENTAL PROCEDURES

2.1 *Hydraulic condition and coordinate system*

Figure 1 shows the coordinate system of a glass-made flume, in which the streamwise flow shape of the main-channel is defined as a sine curve, i.e., the sine-generated curve from the straight channel, $x \geq 0$; x is the streamwise coordinate (Fig. 1). The curved side walls are made of transparent 1 mm thick acrylic board in order to project the laser light sheet even into the inbank layers, i.e., $y/D \leq 1$, (see Fig. 1). L is a half of the streamwise length, and y and z are the vertical and spanwise directions; $y = 0$ is at the main-channel bottom-bed and $z = 0$ at the left-side bank of the floodplain. B is the width of the present flume and B_m is the width of the main-channel. D is the floodplain height and H is the main-channel depth.

U, V and W are the time-averaged velocity components in the streamwise, vertical and spanwise directions, respectively. u, v and w are the corresponding turbulent fluctuations. The time-series of horizontal components of velocities, i.e., (u, w), were obtained by PIV measurements, in which six illuminated areas (I–XI) were shown for close-up pictures as shown in Fig. 1

The sinuosity $s \equiv L_s/L$ was chosen to be 1.09 and 1.22 in the present experiments that are in the same order of magnitude as observed in actual rivers. The bend effects are of course larger with an increase of the meandering sinuosity.

2.2 *Measurement instrument*

Figure 2(a) shows the present multi-layer illumination system. In this specially designed beam rotation instrument, three laser-light sheets (LLS) that have different adjusted elevations were projected into the tilting flume by using a rotating beam splitter, which was developed originally for the present study. This beam splitter has three pairs of two arms including with adjustable plane mirrors. PIV analysis of each illuminated layer was conducted on the basis of two set digital images illuminated by the neighboring same elevated mirrors. 2W Ar-ion laser light was projected into the flume as three different elevated LLSs at the almost same time as shown in Figure 2(a).

In this study, these total six arms with each mirror were placed with a constant angle span of $60° = 360°/6$. The speed of the beam rotation was 10 Hz, and thus the time lag of the neighboring LLS was

Copyright © 2006 Taylor & Francis Group plc, London, UK

Table 1. Hydraulic condition.

U_m(cm/s)	D(cm)	H(cm)	H/D	B(cm)	B_m(cm)	s
7.8	4.0	5.8	1.45	40	8.0	1.09 1.22

$1/(6 \times 10) \cong 0.0167$ sec. The seeding particles, which have a diameter of 100 μm and are made of Nylon 12(specific density is 1.01), were uniformly scattered in the circulating water of the flume. The distance Δy between the neighboring LLSs was adjusted accurately as $\Delta y = 5$ mm (Fig. 2). The digital images on the horizontal planes at different elevations were taken simultaneously by a high-speed CCD camera (maximum flame rate: 250 Hz) which was placed above the free surface. As the results, 3-D flow volume, in which LLS were projected, was measured by the PIV method. When more laser light sheets are split and projected, more detailed 3-D PIV is available; the maximum number of the beam splitters is 16 in the present system.

2.3 *Hydraulic condition*

Table 1 shows the hydraulic condition, in which U_m is the bulk-mean velocity in the straight channel region. Two kinds of sinuosities were chosen in order to examine the meandering effects. Figure 2(b) shows the measured patterns of the present multi-layer PIV. We chose three patterns of LLS illumination, i.e., the pattern A ($y/D = 0.38$, 0.50, 0.63) for the inbank layers, the pattern B ($y/D = 0.93$, 1.05, 1.17) for the inbank and overbank layers, and the pattern C ($y/D = 1.15$, 1.28, 1.40) for the overbank layers.

3 RESULTS AND DISCUSSIONS

3.1 *Horizontal distribution of time-averaged velocity components*

First of all, we have to inquire into the horizontal distribution of the time-averaged velocity components (U, W) in the whole measured area indicated in Fig. 1.

3.1.1 *Streamwise velocity*

Figure 3 shows the all component of horizontal distributions of the time-averaged streamwise velocity $U(x, z)$ at eight measured elevations of $y/D = 0.38$, 0.50, 0.63, 0.93, 1.05, 1.15, 1.28 and 1.40, in which the sinuosity was $s = 1.22$. These results were obtained from overlapping the six illuminated areas (I-XI) shown in Figure 1 The streamwise and spanwise coordinates were normalized by L and B_m, respectively. We consider the distributions into two kinds of layers, i.e., the overbank layer ($y/D > 1.0$), and the inbank layer ($y/D \leq 1.0$) in the following way.

Overbank layer

In the straight region, there is a noticeable velocity gradient $\partial U/\partial z$. In particular, a remarkable velocity shear is generated by the high-speed fluid over the main-channel and the low speed fluid on the right-hand side floodplain at $y/D = 1.05$ and 1.15. In the cross-flow area ($x/L = 0.0 - 0.4$), a high-speed stream crosses over the main-channel and attains the maximum at the left-hand side junction. It should be noticed that the high-speed stream zone is observed clearly on the left-side floodplain from $x/L = 0.4$ to 1.2. This is the inbank flow in the straight channel is accelerated due to the up-step impinging effect. In the counter cross-flow region from $x/L = 1.2$ to 1.8, this high momentum fluid is advected over the main-channel with a gradual deceleration. In contrast, we can see the low-speed stream along the right-side junction in the counter cross-flow region ($x/L = 1.0 - 1.5$) at $y/D = 1.15$, 1.28 and 1.40. This result indicates an existence of significant velocity shear $\partial U/\partial z$ in the same manner as observed in the straight channel section. It is therefore inferred that the horizontal vortex may be generated violently in the meandering compound region.

Inbank layer

In the straight region ($x/L < 0$), there is a parabolic profile due to the both side walls. In the cross-flow region ($x/L = 0.5$), we can see that a maximum stream is affected by the meandering boundary walls, that is to say, the maximum region is shifted toward the left-side junction. Of particular significance is that the high-speed zone is seen near the left-side junction of the inner curve. This property is caused by secondary currents as pointed out by some previous researchers, e.g., Fukuoka *et al.*(1997).

3.1.2 *Spanwise velocity current*

Figure 4 shows the distributions of the time-averaged spanwise velocity $W(x, z)$ at $y/D = 0.38$, 0.63 and 1.15, in which $s = 1.22$.

Overbank layer

At the cross-flow region of $x/L = 0.5$, there is a positive zone near the left-side junction. In contrast, at the counter cross-flow region of $x/L = 1.0 - 1.5$, there is a negative zone near the right-side junction.

Inbank layer

There is a positive zone in the cross-flow region, whereas a negative zone in the counter cross-flow region. These values are much larger than the overbank values. It is therefore found that there is much greater effects of the meandering boundary on the inbank layers. These maximum values are distributed in the wider range of the meandering main-channel area.

3.1.3 *Vertical velocity component*

Unfortunately, the vertical velocity component $V(x, z)$ which is associated significantly with secondary

Copyright © 2006 Taylor & Francis Group plc, London, UK

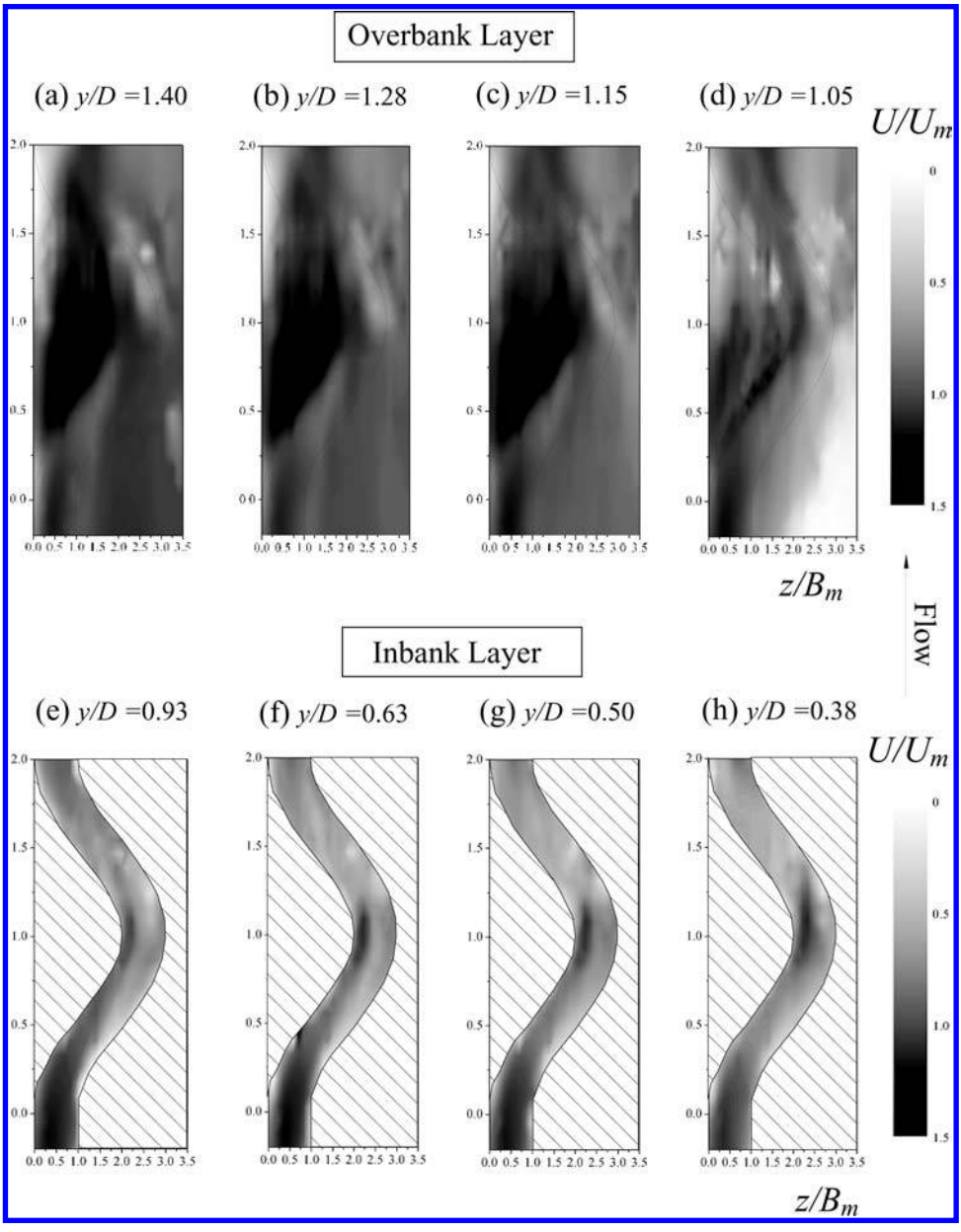


Figure 3. Horizontal distributions of streamwise velocity component ($s = 1.22$).

currents, cannot be measured directly by a single-camera based PIV. In order to overcome these difficulties, we tried to evaluate the time-averaged vertical velocity V by using the following continuity equation:

$$\frac{\partial V}{\partial y} = -\left(\frac{\partial U}{\partial x} + \frac{\partial W}{\partial z}\right) \quad (1)$$

, in which $V = 0$ is given at the free-surface boundary. The validity of this evaluation technique of V was examined by Nezu *et al.* (2005b) who compared them with LDA measurements.

Figure 5 shows the horizontal distributions of $V(x,z)$ at $y/D = 0.38$, 0.63 and 1.15 in the case of $s = 1.22$. Similar positive and negative patterns are seen in these layers, although maximum vales are

Copyright © 2006 Taylor & Francis Group plc, London, UK

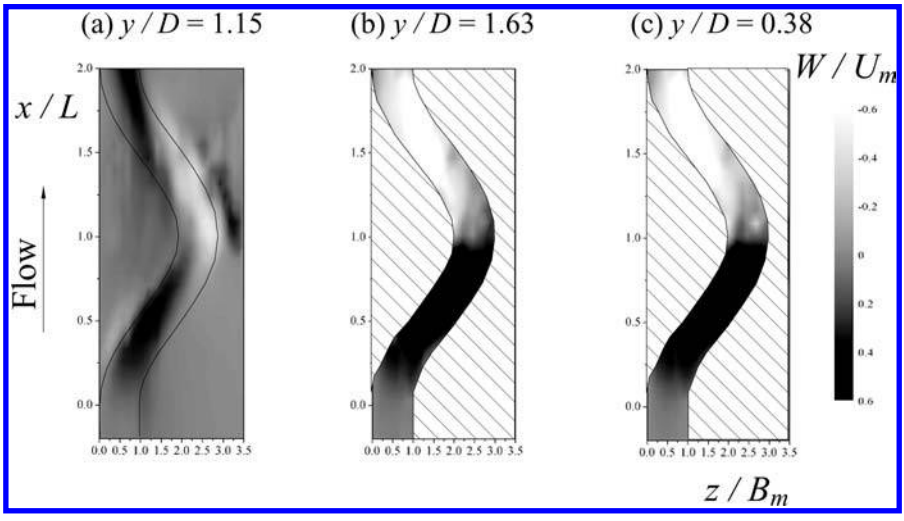


Figure 4. Horizontal distributions of spanwise velocity component ($s = 1.22$).

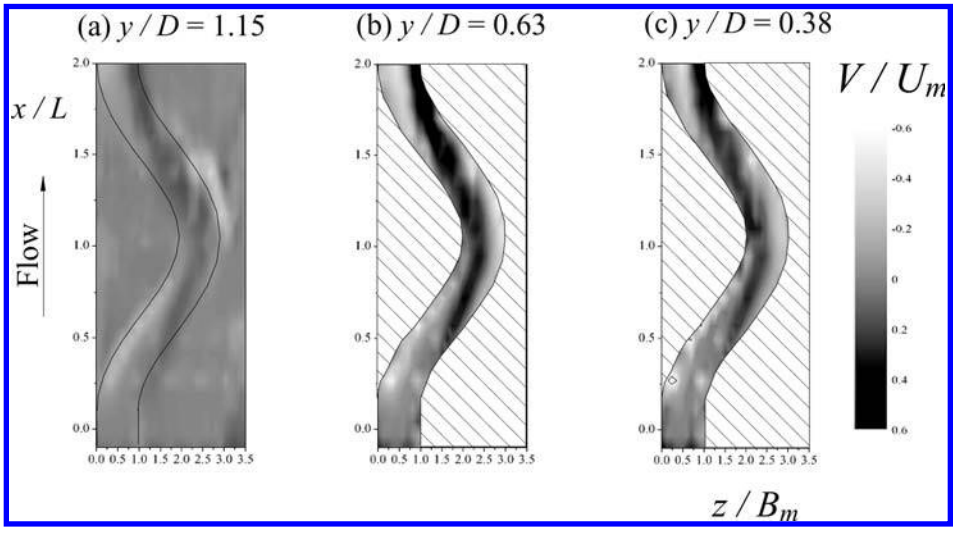


Figure 5. Horizontal distributions of vertical velocity component ($s = 1.22$).

much larger in the inbank layers ($y/D = 0.38$ and 0.63) than in the overbank layer($y/D = 1.15$). In the cross-flow region from $x/L = 0.5$ to 1.0, an upward flow ($V > 0$) appears in the center-line of the main-channel, whereas, a downward flow ($V < 0$) is observed near the left-side floodplain junction. These upward and downward flows correspond to the typical rotational direction of secondary currents as shown in Figure 6. It is therefore said that the present multi-layer PIV system can measure reasonably the existence of secondary currents peculiar to the meandering compound open-channel flows. In the counter cross-flow region from $x/L = 1.5$ to 2.0, there is a strong upward-flow ($V > 0$) zone from the main-channel center-line to the

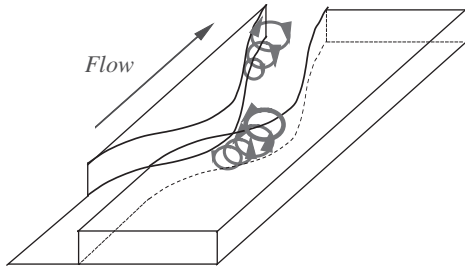


Figure 6. Typical sketch of secondary currents in meandering compound open-channel flow (see Shiono & Muto (1998) and Nezu *et al.* (2005a).

Copyright © 2006 Taylor & Francis Group plc, London, UK

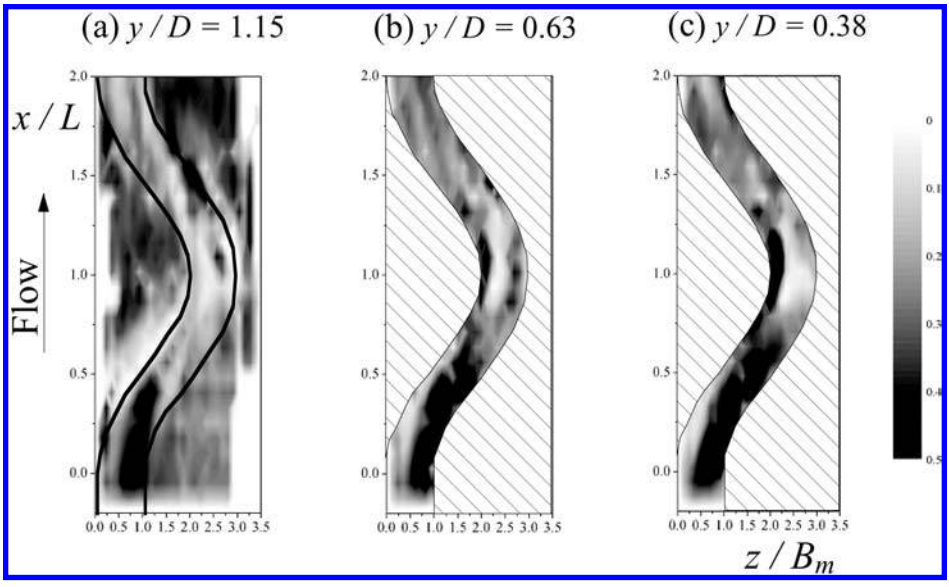


Figure 7. Vortex-existing probability function ($s = 1.22$).

right-side junction, whereas a downward-flow ($V < 0$) zone is observed clearly from the main-channel centerline up to the left-side junction. The downward-flow zone increases in the streamwise direction, and this property is consistent well with the development process of secondary currents in the meandering compound open-channel flows, as pointed out by Shiono & Muto (1998) and Nezu *et al.* (2005a).

3.2 *Vortex-existing probability and time-averaged vorticity*

There are several mathematical methods in order to detect the vortex core in shear flows. One of them is the delta method introduced by Chong & Perry (1990). Fujita & Kumashiro(2005) have recently applied it to backward step flows. The eigenvalues σ of velocity gradient tensor $(\partial \tilde{u}_i/\partial x_j)$ are considered in this method. The eigenvale equation in 2-D flow is given by

$$\sigma^2 - P\sigma + Q = 0 \tag{2}$$

in which,

$$P \equiv \frac{\partial \tilde{u}_i}{\partial x_i} \quad \text{and} \quad Q \equiv \frac{1}{2}\left(\left(\frac{\partial \tilde{u}_i}{\partial x_i}\right)^2 - \left(\frac{\partial \tilde{u}_i}{\partial x_j}\frac{\partial \tilde{u}_j}{\partial x_i}\right)\right) \tag{3}$$

$\tilde{u}_i$ is the instantaneous velocity component, i.e., $\tilde{u}_i \equiv U_i + u_i$. Complex eigenvalues will occur when the discriminant $\Delta \equiv P^2 - 4Q$ is negative, and it corresponds the existence of vortex core.

Figure 7 shows the distribution of the vortex-existing probability Pr defined as follows:

$$Pr \equiv \frac{n_{vor}}{n} \tag{4}$$

n_{vor} is the total count of sampling frame data number in which $\Delta < 0$ and n is the total sampling frame number.

Overbank layer

A stream-like large distribution of the vortex-existing probability Pr appears near the right-side junction in the straight section. This property seems to correspond to the convection of typical horizontal eddies generated by the shear instability between the main-channel and floodplain. The horizontal eddy developed near the right-side junction seems to cross over the meandering main-channel in the cross-flow region. This eddy disappears on the left-side floodplain due to small velocity shear $\partial U/\partial z$. It should be noticed that there is no horizontal eddy in the main-channel from the cross region to the first bend apex ($x/L = 0.5 - 1.0$). In the counter cross-region, a new vortex structure is generated significantly, which may be independent with a horizontal eddy observed in the straight channel region. This renewaly developing vortex is advected downstream near the curving right-side junction.

Inbank layer

In the straight channel region, a large distribution of Pr is seen near the right-side junction as observed in the overbank layer.

Figure 8 shows the distributions of the time-averaged vertical component of vorticity, Ω_y, in the case of $s = 1.22$. Ω_y is defined as

$$\Omega_y \equiv \frac{\partial U}{\partial z} - \frac{\partial W}{\partial x} \tag{5}$$

The signature of vorticity means the rotational direction of the eddy structure. The positive value

Copyright © 2006 Taylor & Francis Group plc, London, UK

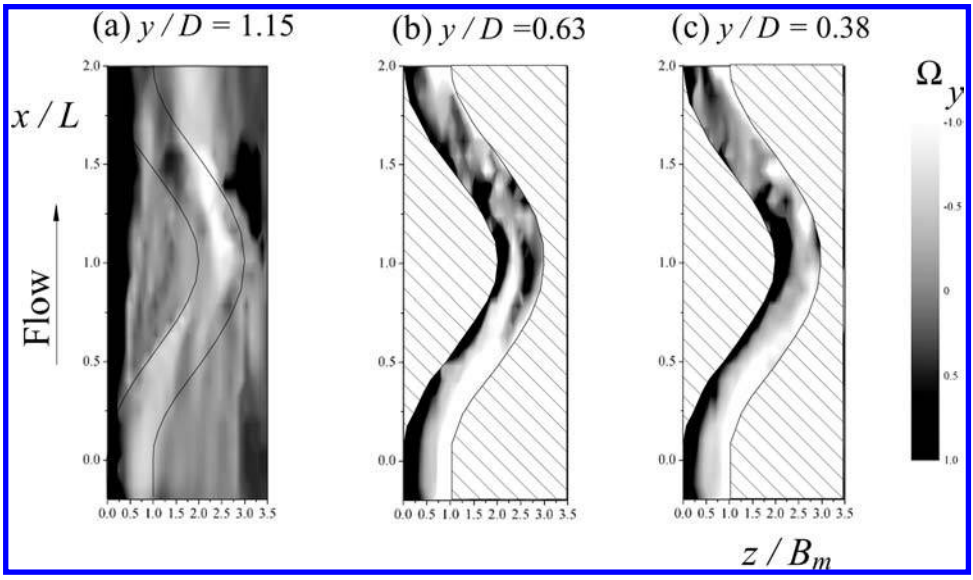


Figure 8. Time-averaged vorticity distribution ($s = 1.22$).

corresponds to the counter clock-wise direction, whereas, the negative value corresponds to the clock-wise direction.

Overbank layer

A large positive zone of $\Omega_y > 0$ appeared along the left-side wall, $z/B_m = 0$. This may not be any eddy structure but the side-wall shear $\partial U/\partial z$ because the vortex-existing probability is very small in this region shown in Figure 7. In the straight section, there is a negative region from the main-channel center-line to the right-side junction. This is the typical horizontal eddy which has a clock-wise rotation. In the counter cross-flow region, there is a negative zone ($\Omega_y < 0$) at $y/D = 1.15$. Therefore, it is found that a renewaly generated vortex has a clock-wise direction in the counter cross-flow region.

Inbank layer

There are strong positive and negative distributions near the curved boundary walls, and thus it is found that the great velocity shear $\partial U/\partial z$ exist even in the inbank layers.

3.3 *Spanwise distribution of velocity*

Figure 9 shows the spanwise profiles of $U(z)$ and $W(z)$ at $y/D = 1.28$ in the upstream region from $x/L = 0.0$ to 1.0, in which the sinuosity s is varied. We consider these distributions in comparison with $s = 1.09$ and 1.22.

Streamwise velocity

In the entrance of meandering area, $x/L = 0.0$, there is a significant difference of U between the

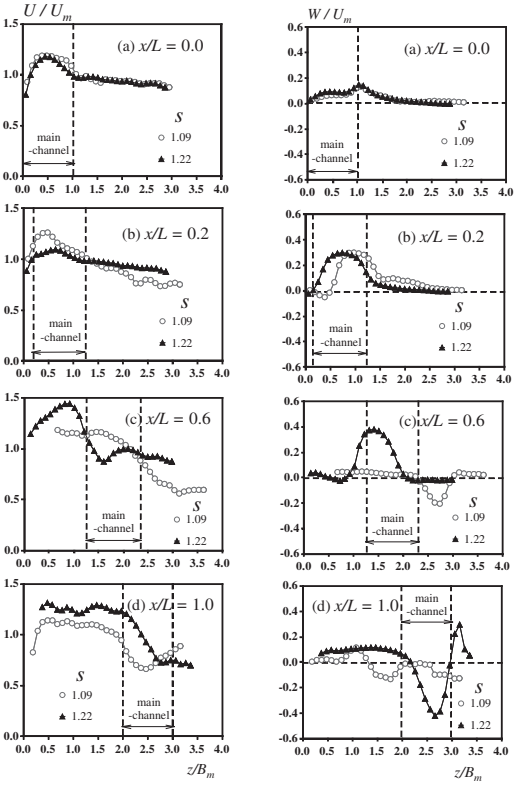


Figure 9. Lateral profiles of the streamwise and spanwise velocities at $y/D = 1.28$ (left hand side: U, right hand side: W).

Copyright © 2006 Taylor & Francis Group plc, London, UK

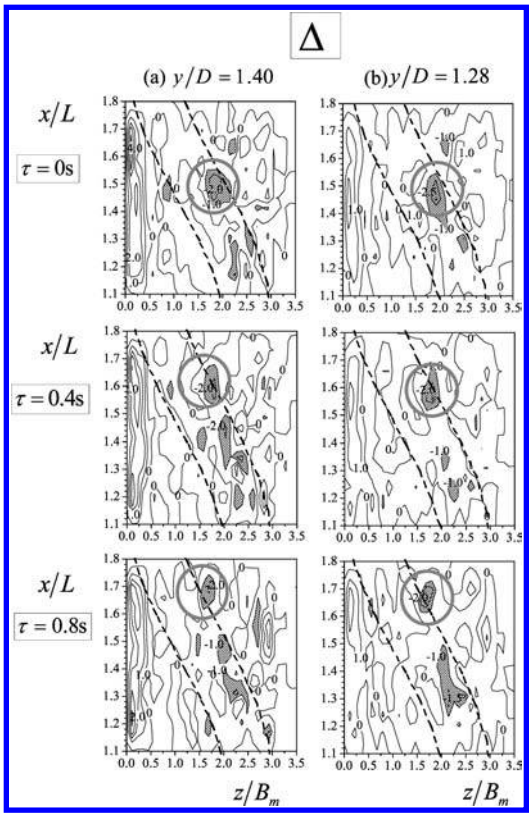


Figure 10. Time-variations of instantaneous delta-value.

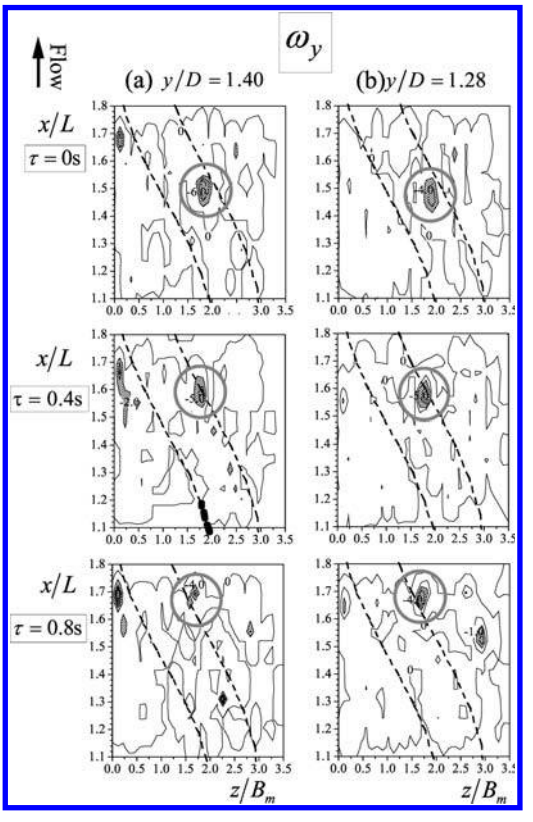


Figure 11. Time-variations of instantaneous vorticity.

main-channel and the right-side floodplain, and the inflectional point appears near the junction in the both cases of $s = 1.09$ and 1.22. At $x/L = 0.2$, the lateral variation becomes smaller, and the main-channel velocity decreases significantly in the case of $s = 1.22$. At $x/L = 0.6$ of the counter cross-flow section, the direction of streamwise flow is changed largely because it flows along the sine generated curve. Therefore a remarkable local decrease appears in the velocity U. Of particular significance is that $U$is accelerated much greatly on the left-side floodplain due to the up-step impinging effect in the case of $s = 1.22$. However, these trends are not seen in the case of $s = 1.09$, and there is one inflectional point as observed in $x/L = 0$. At $x/L = 1.0$, U decreases from the left-side junction to the right-side junction, and one inflectional point appears in the main-channel which correspond to the renewal eddy generation in the counter cross-flow zone.

Spanwise velocity

In the straight section of $x/L = 0$, a small positive zone appears at the right-side junction of $z/B_m = 1.0$. At $x/L = 0.2$, W becomes larger due to the bending effect for both $s = 1.09$ and 1.22. At $x/L = 0.6$, the peak position of W is shifted toward to the left-side junction in the case of $s = 1.22$. In contrast, in the case of $s = 1.09$, W is very small in the main-channel and negative zone is observed on the right-side floodplain. This may be caused by the meandering effect of the downstream region. At $x/L = 1.0$, it is found that there are large negative-value zone in the main-channel in the case of $s = 1.22$.

3.4 *Time-variations of instantaneous eddy structure*

We highlight the visualization area V, in which the coherent horizontal vortex is renewaly generated. Figure 10 shows the instantaneous delta-value Δ at the elevations of $y/D = 1.28$ and 1.40. The time delay of τ was set to be 0.4 sec each. The shadow zone indicates the eddy existing region that is defined as $\Delta < -1.0$. It is observed clearly in both the elevations that the horizontal eddy is convected downstream over the main-channel. The time-dependent position of vorticity core seems to be almost same at $y/D = 1.28$ and 1.40.

Figure 11 shows the distributions of the instantaneous vorticity ω_y, which corresponds to Figure 10.

Copyright © 2006 Taylor & Francis Group plc, London, UK

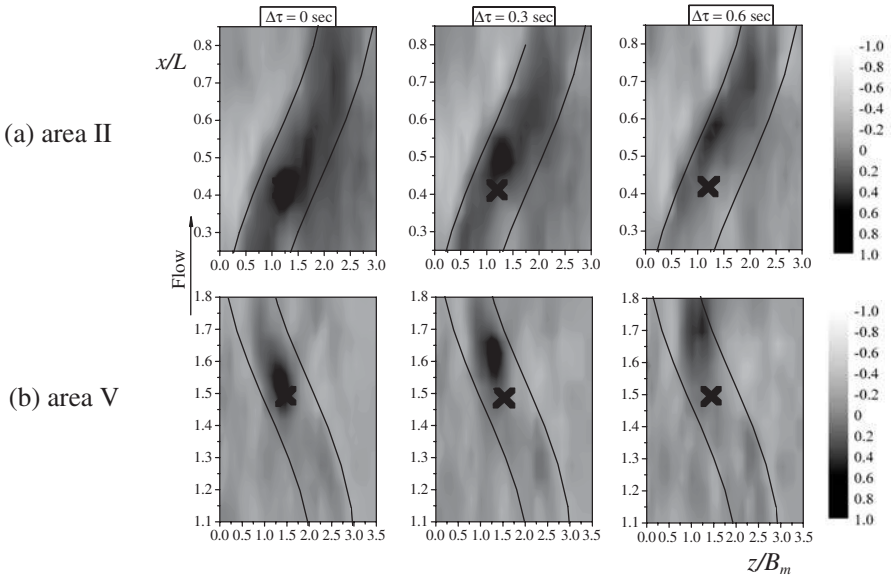


Figure 12. Distribution of space-time correlation function C_{ww} (reference elevation: $y/D = 1.28$, movable elevation: $y/D = 1.40$).

The shadow zone indicates $\omega_y < -2.0$ (1/sec). At the elevations of $y/D = 1.28$ and 1.40, there is a high negative region near $x/L = 1.4$ when $\Delta\tau = 0$. It should be noticed that the time-variation of peak vorticty position corresponds well with the distribution of Δ shown in Figure 10. Therefore, these results suggest strongly that a clock-wise eddy is convected downstream as 3-D tube-like structure in the counter cross-flow region.

3.5 *Space-time correlation analysis*

In order to detect the coherent motion in the meandering compound open-channel flow, the space-time correlation analysis was conducted for the instantaneous spanwise velocity component $\tilde{w}$, because its component is affected significantly by the meandering boundary. A space-time correlation C_{ww} is given by

$$C_{ww} = \frac{\overline{w_0 \times w_{0+\Delta}}}{w_0' \times w_{0+\Delta}'} \tag{6}$$

in which, the subscript 0 denotes a reference point, i.e., (x_0, y_0, z_0, t) and $0 + \Delta$ denotes a movable point $(x_0 + \Delta x, y_0 + \Delta y, z_0 + \Delta z, t + \Delta\tau)$. $w' \equiv \sqrt{\overline{w^2}}$ is the turbulence intensity and the over-bar means the time-averaged operator.

Figures 12(a) and (b) show the horizontal distribution of C_{ww} between the overbank layers of $y/D = 1.28$ and 1.40 as a function of the time delay $\Delta\tau$. "x" means the reference position. Figure (a) and (b) shows the results of the area II and V, respectively. The reference point "x" was chosen to be the center-line of the main-channel curve at $y/D = 1.28$, i.e., $(x_0/L, z_0/B_m) = (0.42, 1.22)$ for the area II and (1.50, 1.37) for the area V.

In the area II, the large peak zone is observed near the reference point at $\Delta\tau = 0$. The peak correlation region moves downstream almost straightly. In the area V, the same trend as the area II is also observed. These results infer that the coherent structure is convected downstream in a vortex-tube manner as indicated in Figures 10 and 11.

Finally, we explain the correlation property between the inbank and overbank layers. Figures 13 (a) and (b) shows the time-dependent distributions of C_{ww} between the overbank of $y/D = 1.05$ and the inbank of 0.93. The horizontal position of reference point was chosen in the same manner as Figure 12. In the area II, the peak correlation is seen near the reference point as well as observed in Figure 12. It should be noted that C_{ww} increases with an increase of $\Delta\tau$. This may be because the spanwise velocity fluctuation of the overbank layer are transported significantly to the inbank layer by the strong downward flow as sketched in Figure 6. In the area V, a weak peak correlation is also recognized near the reference point. This peak correlation moves downstream with a lateral shift toward the left-side junction due to the meandering effects.

4 CONCLUSIONS

In this study, the multi-layer PIV measurements were conducted in meandering compound open-channel

Copyright © 2006 Taylor & Francis Group plc, London, UK

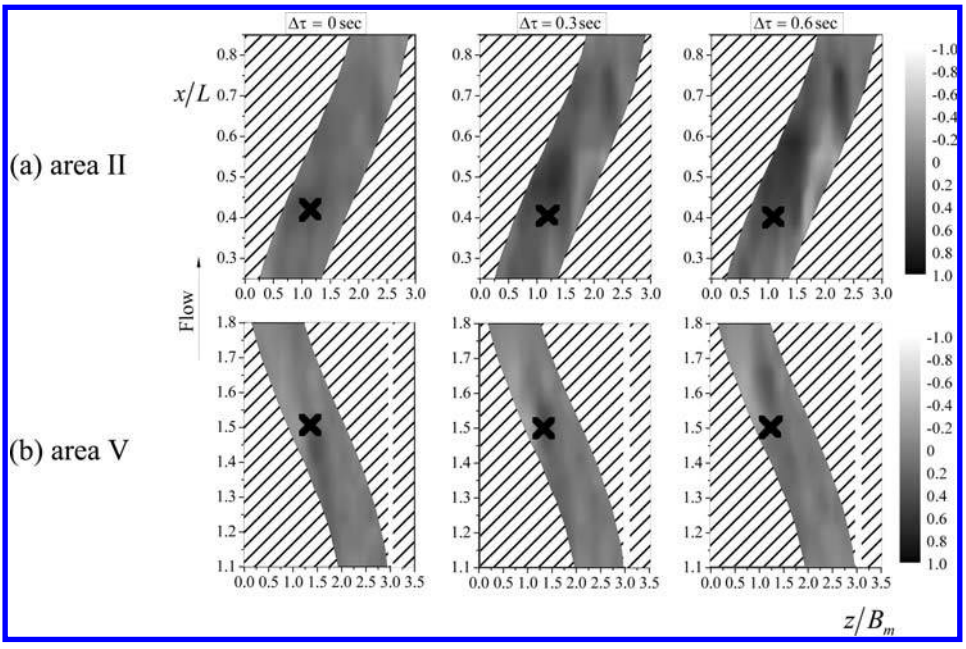


Figure 13. Distribution of space-time correlation function C_{ww} (reference elevation: $y/D = 1.05$, movable elevation: $y/D = 0.93$).

flows in order to reveal the meandering property of coherent eddy structure. The results obtained in the present study are as follows:

1) The typical horizontal eddy, which is developed in the straight-channel zone, crosses over the meandering main-channel and disappears on the floodplain due to the weak velocity shear.
2) A renewal horizontal vortex is generated significantly in the counter cross-flow region.
3) The space-time correlation analysis revealed that there are strong correlations in turbulent fluctuations near the horizontal vortices. These vortices are convected downstream with a 3-D tube-like structure.

ACKNOWLEDGEMENTS

The present study was conducted under the financial support from Hattori Hokokai in Japan, and we thus acknowledge this.

REFERENCES

Chong, M.S. and Perry, A.E. 1990. A general classification of three-dimensional flow fields, *Phys. Fluids*, A, 2(5): 765–777.

Fukuoka, S., Ohgushi, H., Kimura, D. and Hirao, S. 1997. Hydraulic characteristics of the flood flow in a compound meandering channel, *J. of Hydraulic, Coastal and Envir. Eng.*, JSCE, No.579/II-41: 83–92.(in Japanese).

Fujita, I and Kumashiro, S. 2005. Flow structure of open-channel flow with a backward-facing step with a slope, *J. of Applied Mech.* JSCE 8: 765–772.(in Japanese).

Nadaoka, K. and Yagi, H. 1998. Shallow-water turbulence modeling and horizontal large eddy computation of river flow, *J. of Hydraulic Eng.*, ASCE 124, No.5: 493–500.

Nezu, I., Sanjou, M., Doi, T. and Quang, H. 2005a. Velocity distribution and secondary currents in meandering compound open-channel flow with floodplains, *Proc. of 31th IAHR Conference, Seoul,* 10pages on CD-ROM.

Nezu, I., Sanjou, M., and Kamiya, A. 2005b. Development of multi-layer laser-scanning PIV and applications to hydraulic engineering, *Proc. of 31th IAHR Conference, Seoul,* 10pages on CD-ROM.

Nezu, I., Sanjou, M. and Goto, K. 2004. Transition process of coherent vortices in depth-varying unsteady compound open-channel flows, *Shallow Flows(ed. G.H.Jirka& W.S.J. Uijttewaal), Balkema*: 251–258.

Shiono, K. and Muto, Y. 1998. Complex flow mechanisms in compound meandering channels with overbank flow, *J. of Fluid Mech.* 376: 221–261.

Tominaga, A. and Nezu, I. 1991. Turbulent structures in compound open-channel flow, *J. of Hydraulic Eng.*, ASCE 117: 21–41.

Wormleaton, P.R., Hey, R.D., Sellin, R.H.J., Bryant, T., Loveless, J. and Catmur, S.E. 2005. Behavior of meandering overbank channels with graded sand beds, *J. of Hydraulic Eng.*, ASCE 131: 665–681.

Copyright © 2006 Taylor & Francis Group plc, London, UK

Large eddy simulation of turbulent structure in meandering compound open-channel flow

M. Sanjou & I. Nezu
Dept. of Civil Eng., Kyoto University, Kyoto, Japan

ABSTRACT: Horizontal eddies are often observed in compound open-channel flows. The hydrodynamic properties of such coherent voritices were intensively studied by a lot of researchers, because these eddies have significant relations with momentum exchanges between a main-channel and floodplains. However, little attention has been given to the meandering properties of the horizontal eddies developed in a straight open-channel. Therefore, in the present study, a large eddy simulation was conducted in the transition region between the straight and meandering floodplain flows. As the results, coherent eddy structure and correlation properties were investigated numerically in such a complex open-channel flow.

1 INTRODUCTION

Compound open-channel flows are composed of main-channel and floodplains, and we can see them in many actual rivers. In such two-stage flows, the primary velocity distribution has notable inflectional points near the junction between the main-channel and floodplains, and consequently, periodical horizontal vortices are produced due to inflectional shear instability. These eddies promote largely the turbulent transport of various scalars such as suspended sediment in the spanwise direction and furthermore, secondary currents also play a significant role on such a scalar transport associated with coherent eddies. it is, therefore, important in river engineering to reveal these turbulent structure in compound open-channel flows.

Until now, many researchers have studies these interesting topics intensively by using not only measured data but also numerically calculated ones. Recently, various calculation techniques and turbulence models are applied to simulations of compound open-channel flows.

For example, Naot *et al*.(1993) have calculated the compound open-channel flows by using an algebraic stress model (ASM), and they reproduced reasonably the hydrodynamic properties such as the cross-sectional distributions of primary velocity and secondary currents. In particular, their ASM simulations could present the time-averaged motion of the secondary currents which govern significantly turbulence characteristics and momentum transfer between main-channel and floodplains. In order to explain the influences of secondary currents on the mixing solute properties, Lin & Shiono (1995) have developed a 3-D turbulence modeling. Simoes & Wang (1997) have calculated the concentration properties of solutes by using some algebraic eddy viscosity models involved with a buoyancy effect. Nadaoka & Yagi (1998) have developed a depth-averaged 2-dimensional LES model in order to examine the horizontal vortices in compound open-channel flows, and they reproduced the originating, developing and merging processes of these coherent eddies. Sofialidis & Prinos (1999) revealed numerically the effects of floodplain roughness in compound open-channel flows by using an anisotropic $k-\omega$ model.

As mentioned above, although a lot of studies have been conducted about numerical simulations of compound open-channel flows, most of them have focused on rectangular compound straight-channel flows. However, natural river flows have many bending and meandering sections, where typical secondary currents are generated by centrifugal force, i.e., Prandtle's 1-st kind of secondary currents, and quite different from those observed in straight channels, i.e., Prandtle's 2-nd kind of them. Meandering compound open-channel flows observed in rivers in flood have complicated momentum exchanges between the curved lower main-channel flow and the straight overbank flow. Shiono & Muto (1998) have conducted some turbulence measurements in such a meandering compound open-channel flow with a laser Doppler anemometer (LDA), and they revealed the distributions of secondary currents, primary velocity and turbulence in the fully-developed bend region. However, detailed information on the channel-transition effects from the straight to meandering sections is not yet available in meandering compound open-channel

Copyright © 2006 Taylor & Francis Group plc, London, UK

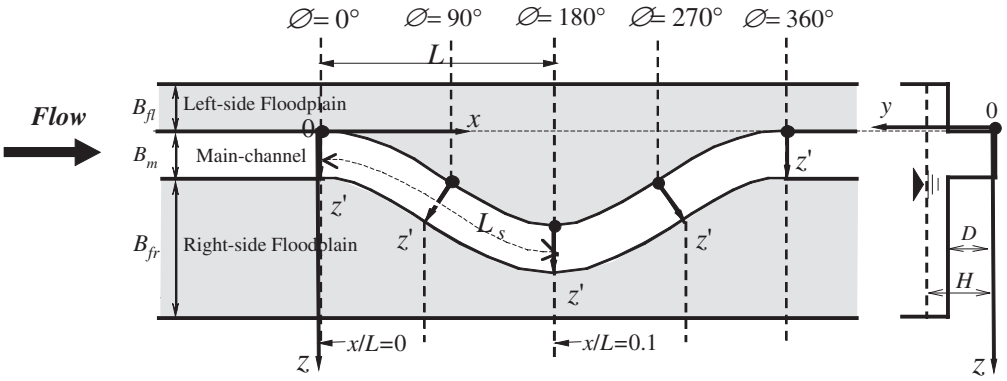


Figure 1. Coordinate system in meandering compound open-channel flow.

flows. In particular, it is very important to investigate the meandering properties of the horizontal eddies generated in the straight channel region, because they are significantly associated with the sediment transport and bed deformation.

Therefore, we highlighted the channel transition effects on the horizontal coherent vortices and tried to reveal them numerically by using a LES. First of all, the examinations of this simulation models were conducted mainly for the primary velocity distributions and secondary currents by comparison with the measured data. Next, the meandering properties of horizontal eddies were examined by using the instantaneous velocity vectors and the space-time correlation analyses.

2 CALCULATION METHOD

2.1 *Basic equations*

The filtered continuity equation and N-S equation are described as follows:
(continuity equation)

$$\frac{\partial\langle\hat{u}_i\rangle}{\partial x_i}=0 \qquad (i=1,2,3) \tag{1}$$

(N-S equation)

$$\frac{\partial\langle\hat{u}_i\rangle}{\partial t}+\langle\hat{u}_j\rangle\frac{\partial\langle\hat{u}_i\rangle}{\partial x_j}=F_i-\frac{\partial\langle\hat{p}\rangle}{\partial x_i}+\frac{\partial}{\partial x_i}(-\tau_{ij}+2\nu\langle\hat{D}_{ij}\rangle) \tag{2}$$

$$F_i=(g\sin\theta,-g\cos\theta,0) \tag{3}$$

$$D_{ij}\equiv\frac{1}{2}\left(\frac{\partial\hat{u}_i}{\partial x_j}+\frac{\partial\hat{u}_j}{\partial x_i}\right) \tag{4}$$

in which, the bracket <> denotes the filtering operation in space and the over hat means the instantaneous components. τ_{ij} is the SGS stress tensor calculated by the standard Smagorinsky model as follows:

$$\tau_{ij}=-2\nu_e\langle D_{ij}\rangle \tag{5}$$

When the local SGS variances are assumed to be isotropic, the SGS eddy viscosity ν_e is given by

$$\nu_e=(C_s\Delta)^2\left(2\langle D_{ij}\rangle\langle D_{ij}\rangle\right)^{1/2} \quad \text{and} \quad \Delta=(\Delta_1\Delta_2\Delta_3)^{1/3} \tag{6}$$

in which C_s is the Smagorinsky constant and $C_s=0.15$ was chosen in this study. $\Delta$is the SGS filter which corresponds with the local grid scale.

The third-order upwind difference scheme was used for convection term and second-order Adams-Bashforth method was adopted for time differentiation.

The computational grids are a boundary-fitted ones and the number of the calculated grids was chosen to be 400, 20 and 80 for the streamwise, vertical and spanwise directions, respectively. The boundary conditions are as follows; the non-slip at the side and bed walls, the free-slip at the water surface and the cyclic boundary condition at the entrance and exit of the calculating region.

2.2 *Calculation case*

The present calculation case was chosen to be the same hydraulic condition as used by Nezu *et al.* (2005) who measured all three components of velocity with electromagnetic velocimetry (EMV). Figure 1 shows the coordinate system in the present study. The streamwise flow shape of the meandering main-channel was defined as a sine generated curve. L is a half wave length of the curved-shaped main-channel (see Fig. 1). L_s is the along-curve length from the meandering entrance to the first bend apex. The EMV measured data used for the comparison with the present LES calculation were the values obtained at five sections.

Copyright © 2006 Taylor & Francis Group plc, London, UK

Table 1. Calculation case.

D (cm)	B_m (cm)	B_{fl} (cm)	B_{fr} (cm)	H (cm)	H/D	Q (l/s)	U_m (cm/s)	S
5.0	20.0	20.0	60.0	7.0	1.4	7.47	24.9	1.09

These streamwise positions were given as a function of ϕ. Here, ϕ is a phase angle of the sine curve, in which $\phi = 0°$, 90°, 180°, 270° and 360° were considered to compare the LES simulations (Fig. 1). $\phi = 0°$ is the meandering entrance section, i.e., the channel transition from the straight to meandering ones, $\phi = 90°$ is the cross section of the curved lower-flow and the straight overbank-flow. $\phi = 180°$ is the first bend apex, $\phi = 270°$ is the counter cross section and $\phi = 360°$ is the second bend apex. y and z are the vertical and spanwise directions; $y = 0$ is on the main-channel bottom-bed and $z = 0$ at the left-side bank of the floodplain. z' is the spanwise coordinate across the main-channel, and $z' = 0$ is at the junction position between the main-channel and the left-side floodplain. In this study, U, V and W are the time-averaged velocity components in the streamwise (x), vertical (y) and spanwise(z)directions, respectively. u, v and w are the corresponding turbulent fluctuations.

We calculated one example of the hydraulic case of the meandering compound open-channel flow that was measured by Nezu *et al.* (2005). Table 1 shows the hydraulic condition, in which D is the floodplain height, $B_{\rm m}$, $B_{\rm fl}$ and $B_{\rm fr}$ are the main-channel, left-side floodplain and right-side floodplain widths, respectively. H is the main-channel depth, $U_{\rm m}$ is the bulk-mean velocity and $s \equiv L_s/L$ is the sinuosity of the meandering main-channel.

3 RESULTS AND DISCUSSIONS

3.1 *Secondary currents*

Figure 2 indicates the descriptions of the time-averaged velocity vectors (V, W) at the typical five sections, in which the right-hand side is the calculated data by LES and the left-hand side is the measured results by EMV. At the straight section of $\phi = 0°$, the present LES model is able to reproduce the upward flows from the junction edge toward the free-surface. This is a typical secondary flow pattern in straight compound open-channel flows measured with LDA by Tominaga & Nezu (1991), although they are not seen clearly in the EMV data due to its accuracy limitation. At the cross-section of $\phi = 90°$, which is the cross section between both the inbank and overbank flows, a strong eddy structure is observed and it seems to be generated by high-speed overbank flows. This measured data suggests that the inbank secondary flows are convected toward the overbank region on floodplain. The present LES reproduces these flow patterns. This secondary eddy near the right junction of floodplain is developing in the streamwise direction, and consequently, it attains the same length scale as the main-channel width $B_{\rm m}$ at the apex section of $\phi = 180°$, and this direction is contrary to that of secondary currents generated by centrifugal force observed in bend channels with no overbank flows. It is therefore considered that these secondary currents are peculiar to the meandering overbank flows. At the counter cross section of $\phi = 270°$, we can see the secondary current eddy which has a counter rotation to that observed at $\phi = 90°$. It is found that this eddy also develops in the streamwise direction and becomes largest at $\phi = 360°$. It is concluded that the present simulation model can calculate the secondary currents and their rotational directions, developing properties reasonably, although there are some discrepancies.

3.2 *Distributions of streamwise velocity*

Figure 3 shows the contour lines distribution of streamwise velocity U_s along the main-channel curve (Fig. 1) at the five sections that are the same positions as indicated in Figure 2. The values of U_s are normalized by the maximum velocity $U_{\rm max}$ at the straight section. It should be noted in this figure that the distribution of U_s is deformed largely due to the effects of secondary currents mentioned before. In the straight section of $\phi = 0°$, bulge features are observed near the both-side junctions, that are generated by strong upward flows as shown by Tominaga & Nezu (1991).

In the curved region ($0° < \phi \leq 360°$), we can see more remarkable bulges that are peculiar to the meandering compound open-channel flows. They are observed significantly near the right-hand side junction of $\phi = 90°$ and $\phi = 180°$, and near the left-hand side one of $\phi = 270°$ and $\phi = 360°$, respectively. Such bulge features correspond to the directions of secondary flows cross over the main-channel. The variations of U_s observed in the laboratory experiment are surely recognized in the calculated LES data, and thus the accuracy of present model is fairly reasonable. In the following sections, the significant eddy properties in the meandering region are predicted numerically, which have not unfortunately been revealed yet in previous studies.

3.3 *Vector descriptions of horizontal eddies*

Figure 4 shows an example of instantaneous velocity vectors which are indicated in a movable coordinate

Copyright © 2006 Taylor & Francis Group plc, London, UK

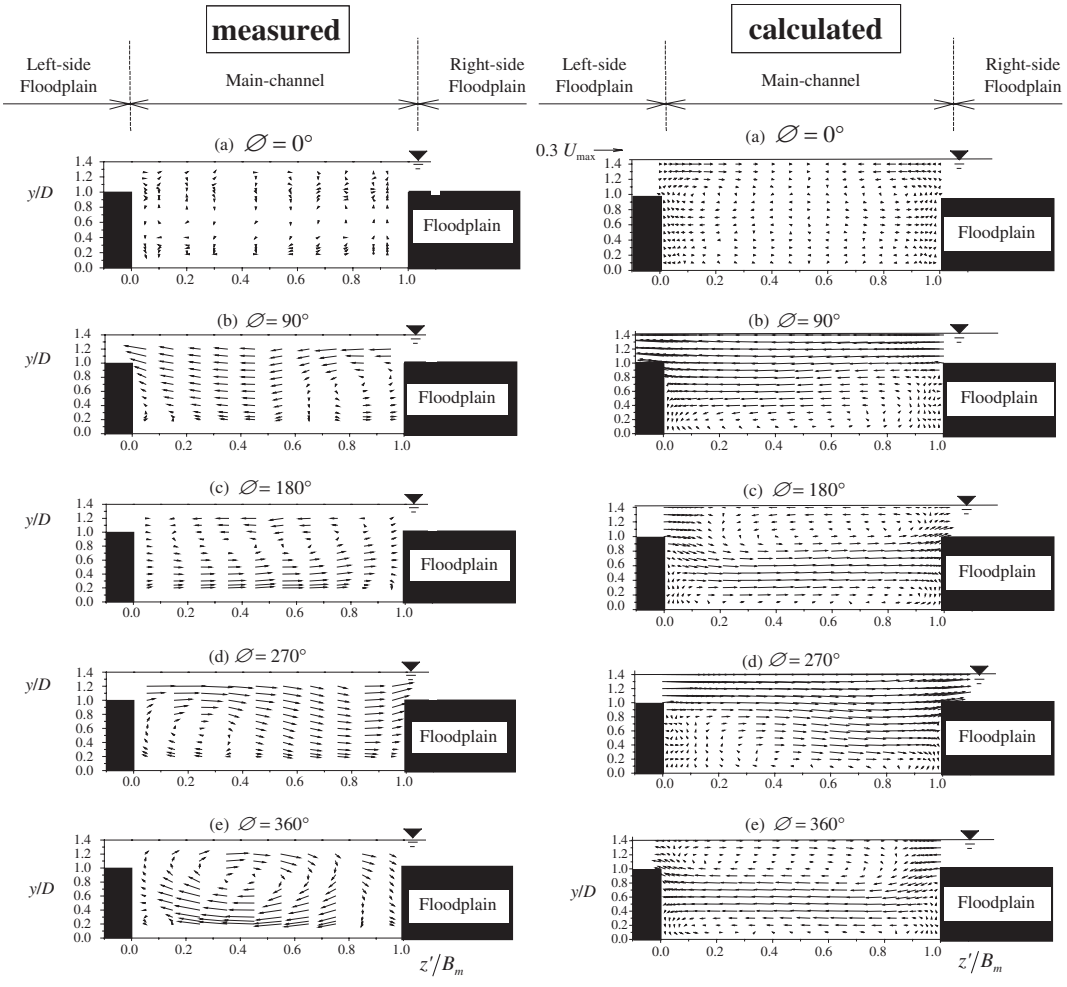


Figure 2. Distribution of the time-averaged secondary currents.

reference with the bulk-mean velocity U_m in the straight flow section. The elevation of flow in Figure 4 was the free-surface one ($y = H$), i.e., the free-surface flow pattern. It is found from these flow vectors that the counter-rotating twin eddy structures appear near the both sides of the main-channel junctions. These are typical large-scale horizontal vortices that have been visualized in compound open-channel flow, e.g., by Sellin (1964), Ikeda & Kuga (1997), Nezu *et al.* (2004), and they are generated periodically by a shear instability of streamwise velocity, as pointed out by Ikeda & Kuga (1997). The present LES reproduces reasonably such a pair of horizontal vortices in the straight compound channel flow.

Figure 5 shows the lateral profile of the spanwise Reynolds stress $-\overline{uw}$ at the meandering entrance of $x/L = 0$, in which the result is normalized by the difference of the maximum to minimum values, i.e., $-\overline{uw}_{\max - \min}$. There are the positive and negative peaks near the right-hand side and left-hand junctions, respectively, and they correspond to a pair of counter-rotating eddies shown in Figure 4. It is found that the momentum exchanges between the main-channel and floodplains are caused significantly by horizontal eddies.

Figure 6 shows the time-variations of these horizontal eddies in the meandering regions, in which instantaneous velocity vectors are indicated at $t = 0.45$s and 0.75s after the results of Figure 4 ($t = 0.0$s). At $t = 0.45$s (, i.e., the just arrival time in the channel-transition section), the vortex pair transported from the upstream side is still observed, in contrast at $t = 0.75$s,

Copyright © 2006 Taylor & Francis Group plc, London, UK

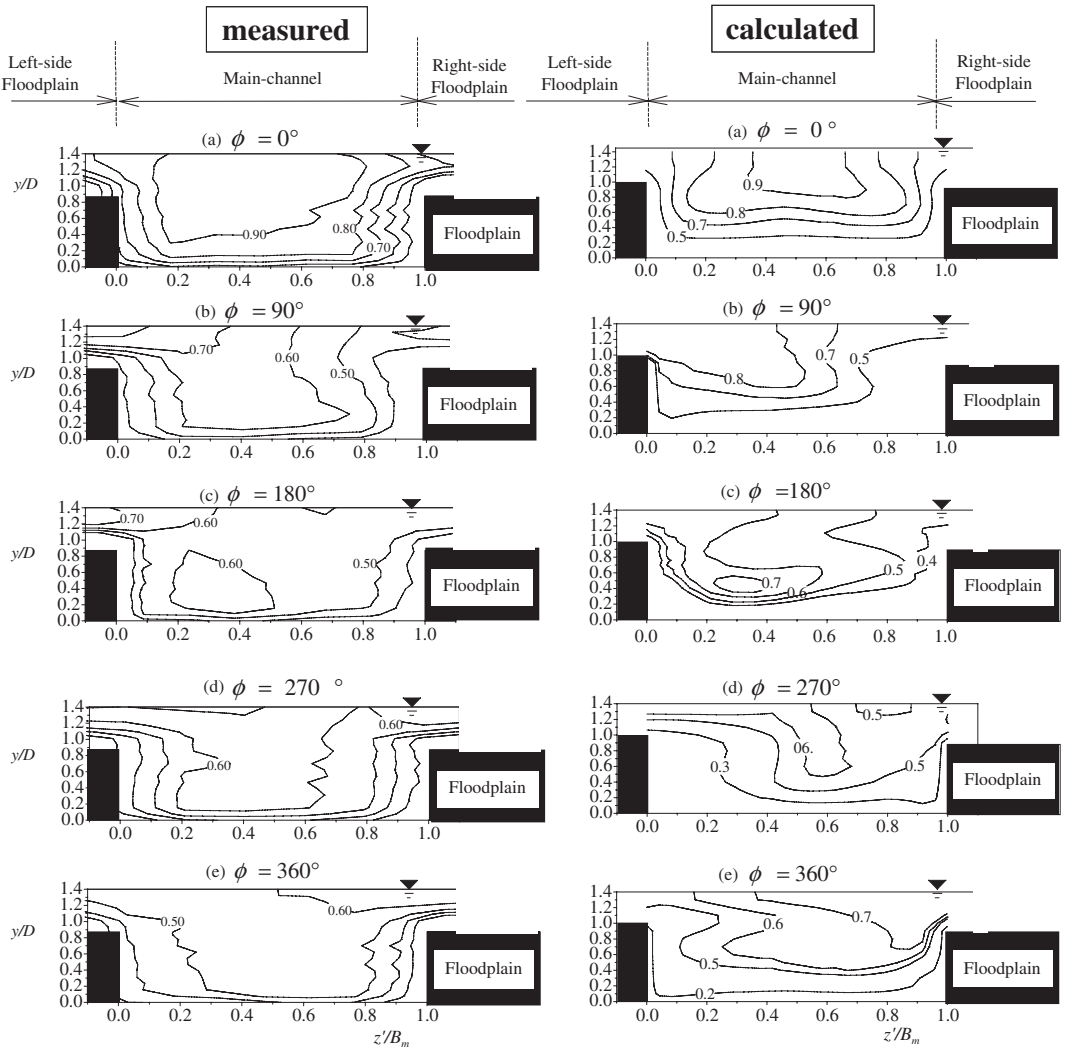


Figure 3. Distributions of the time-averaged streamwise velocity.

the right-side eddy which appeared at $t = 0.45$s in the inner side of main-channel curve, is not visualized clearly. In the following section, this meandering property is examined on the basis of the space-time correlation analyses.

3.4 *Space-time correlation analysis*

In order to visualize the horizontal vortices, it is needed that a movable coordinate is introduced in the instantaneous velocity vector fields. However, such a visualization for eddy detection depends strongly on the subtracted velocity value of the reference, and unfortunately we cannot evaluate the time-variations of vortex form and its core position reasonably. To overcome these difficulties, the unsteady motions of meandering eddies are revealed by using the space-time correlation analysis. Although, the vorticity distribution is often used to detect the eddy structure in the vector field, there may be some numerical errors due to sparse grids. So, we defined the following instantaneous value ϖ, which is the product between streamwise and spanwise velocity components.

$$\varpi \equiv u \times w \tag{7}$$

Copyright © 2006 Taylor & Francis Group plc, London, UK

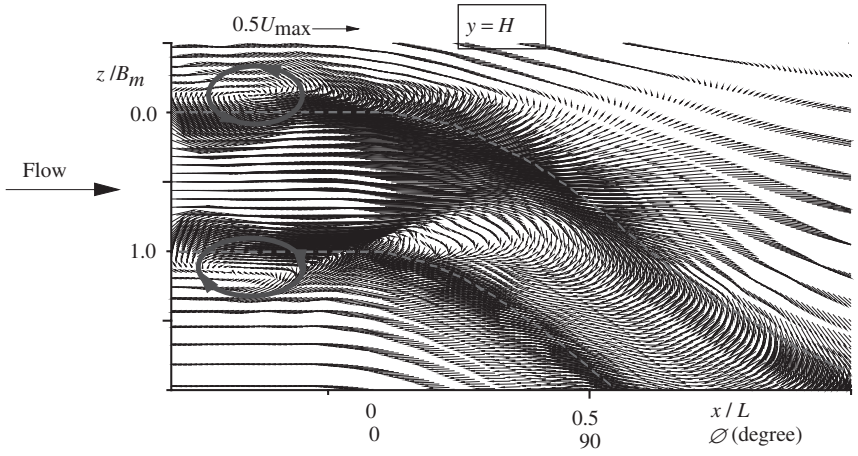


Figure 4. Example of the instantaneous horizontal vortices in the straight channel region.

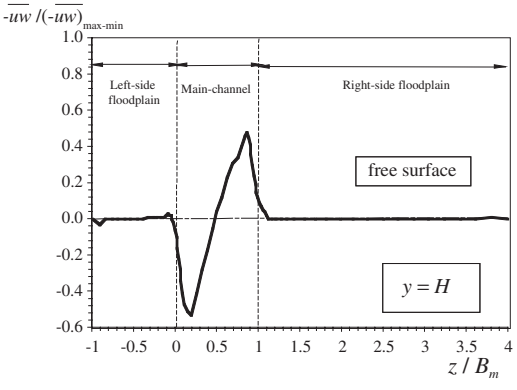


Figure 5. Lateral profile of the spanwise Reynolds stress.

A space-time correlation function $C_{\varpi\varpi}$ is given by

$$C_{\varpi\varpi} \equiv \frac{\overline{(\varpi_o - \overline{\varpi}_o)\times(\varpi_{o+\Delta} - \overline{\varpi}_{o+\Delta})}}{\varpi_o{}'\times\varpi_{o+\Delta}{}'} \tag{8}$$

in which, subscript o denotes a reference point, i.e., (x_o, y_o, z_o, t) and $o+\Delta$ denotes a movable point $(x_o+\Delta x, y_o+\Delta y, z_o+\Delta z, t+\tau)$. $\varpi' \equiv \sqrt{\overline{\varpi\times\varpi}}$ is the standard deviation for normalization and the overbar means the time-averaged operator.

Figure 7 shows the horizontal distributions of $C_{\varpi\varpi}$ as an increases of time-delay τ. Two reference points, that correspond to the twin eddy structure observed in Figure 4, are chosen at the channel-transition section of $x/L = 0$ and $\phi = 0°$. The lateral positions of these reference points are $z'/B_m = 0.15$ and 0.8, respectively, and the elevation is $y/D = 1.1$ above the floodplain height. A maximum correlation region for the left-side eddy moves downstream with an increases of the time-delay,

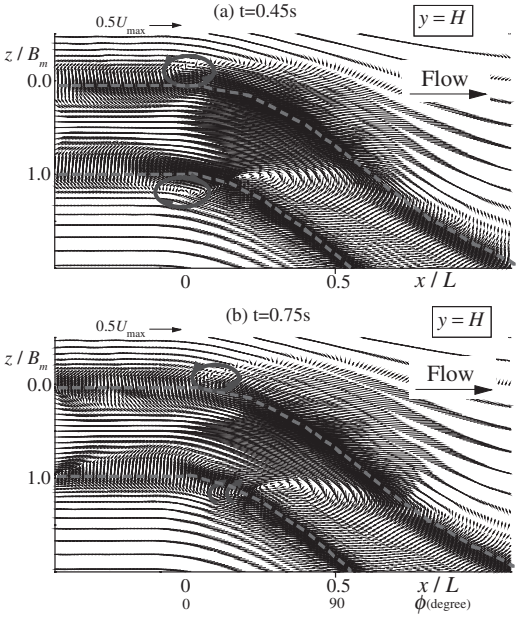


Figure 6. Time-variations of instantaneous velocity vectors.

and it suggests that the left-side eddy is convected almost straightly with streamswise direction. On the other hand, the right-side eddy crosses over the meandering inbank main-channel and moves to the left side floodplain in the apex section of $x/L = 1.0$.

3.5 *Meandering properties of horizontal eddies*

It is suggested from Figure 7 that the right-side eddy which crosses over the main-channel has a more complicated meandering property than the left-side eddy.

Copyright © 2006 Taylor & Francis Group plc, London, UK

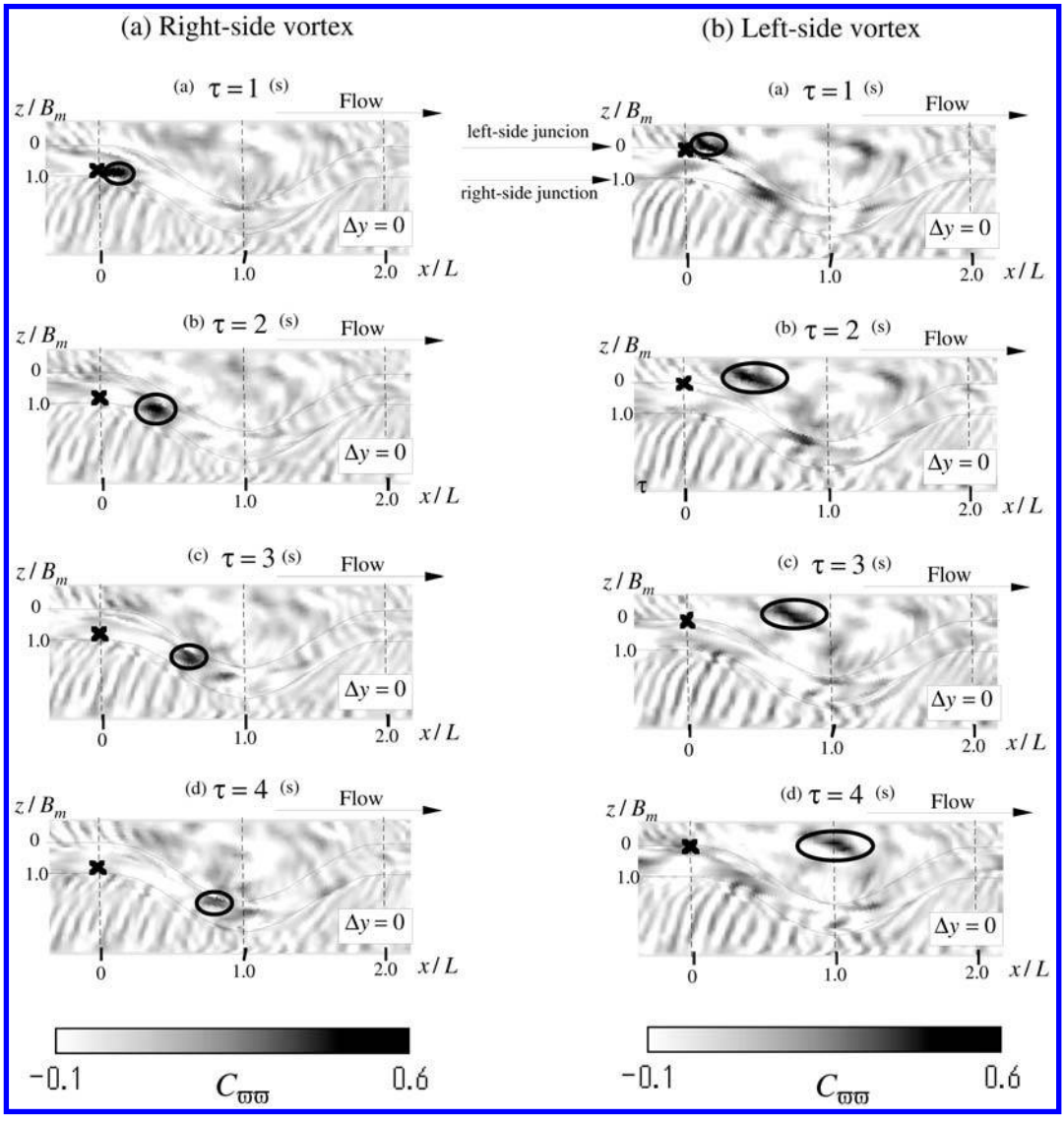


Figure 7. Distributions of space-time correlation function for the right-side and left-side vortices.

The trajectory of the right-side eddy is examined by using the results of correlation analysis. The trajectory is given by connecting the maximum positions of the space-time correlation function $C_{\varpi\varpi}$. Figure 8 shows the trajectories of right-side eddy at several elevations, in which the reference height is fixed at $y/D = 1.1$ and the time-spacing of these plots chosen to be just 1s. This figure indicates clearly that horizontal eddy crosses over the curved main-channel at all elevations. Whereas, we can also see the noticeable property that the horizontal eddy is transported more straightly nearer the free surface, because the curving effects of main-channel become smaller farther from the bottom-bed. This means that the right-side eddy has the complicated tube-like 3-D structure which is inclined with both of the streamwise and spanwise directions. It is comparatively difficult to measure such a 3-D vortex characteristics by experimental methods, e.g. LDA and PIV, and thus the present turbulence simulation is very useful in order to predict and reveal 3-D coherent structure in complex boundary flows.

Copyright © 2006 Taylor & Francis Group plc, London, UK

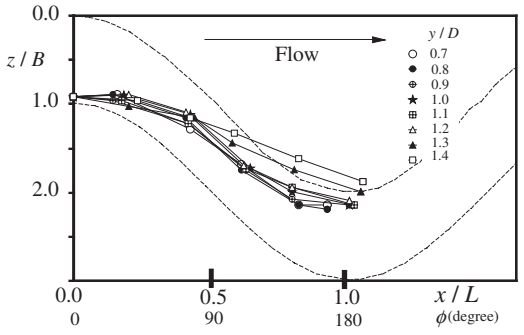


Figure 8. Trajectory of meandering horizontal vortices.

4 CONCLUSIONS

In the present study, 3-D LES was conducted in compound free surface flow included with the transition section from the straight to meandering channels. The present LES model was examined by comparison with the measured EMV data and the meandering characteristics of horizontal eddies were considered numerically. The main findings are as follows:

1) The calculated results of the secondary currents and velocity distributions were compared with those measured by EMV. The calculated patterns of secondary currents, such as magnitude distribution and rotational directions, are the same trend as observed in the measured data.
2) The present simulation could reproduce a pair of counter-rotating horizontal vortices near the junction between the main-channel and the floodplains. This finding was also recognized from the spanwise distributions of the Reynolds stress in which there are two peaks of positive and negative values.
3) The space-time correlation analysis was conducted by using the present data in order to evaluate the trajectories of the coherent vortex core. It is found from this result that the tube-like vortex, which has a strong correlation vertically, was convected along the meandering line.

ACKNOWLEDGEMENTS

The present study was conducted under the financial support from Hattori Hokokai in Japan, and we thus acknowledge this.

REFERENCES

Ikeda, S. and Kuga, T. 1997. Laboratory Study on Large Horizontal Vortices in Compound Open Channel Flow, *J. of Hydraulic, Coastal and Envir. Eng.,* JSCE, No.558/II-38: 91–102. (in Japanese)

Lin, B. and Shiono, K. 1995. Numerical Modeling of Solute Transport in Compound Channel Flows, *J. of Hydraulic Res.*, IAHR, 33, No.6: 773–788.

Nadaoka, K. and Yagi, H. 1998. Shallow-water Turbulence Modeling and Horizontal Large Eddy Computation of River Flow, *J. of Hydraulic Eng.*, ASCE, 124, No.5: 493–500.

Naot, D., Nezu, I. and Nakagawa, H. 1993. Hydrodynamic Behavior of Compound Rectangular Open-channel Flows, *J. of Hydraulic Eng.*, ASCE, 119: 390–408.

Nezu, I., Sanjou, M., Doi, T. and Quang, H. 2005. Velocity Distribution and Secondary Currents in Meandering Compound Open-channel Flow with Floodplains, *Proc. of 31th IAHR Congress, Seoul*, on CD-ROM.

Nezu, I., Sanjou, M. and Goto, K. 2004. Transition Process of Coherent Vortices in Depth-varying Unsteady Compound Open-channel Flows, *Shallow Flows (ed. G.H.Jirka & W.S.J. Uijttewaal), Balkema*, 251–258.

Sellin, R.H.J. 1964. A Laboratory Investigation into the Flow in the Channel of a River and that over Floodplain, *La Houille Blanche*, No.7:. 22–26.

Shiono, K. and Muto, Y. 1998. Complex Flow Mechanisms in Compound Meandering Channels with Overbank Flow, *J. of Fluid Mech.*, 376: 221–261.

Simoes, F.J.M. and Wang, S.S.Y. 1997. Numerical Prediction of Three-dimensional Mixing in a Compound Open Channel, *J. of Hydraulic Res.*, IAHR, 35, No.5: 619–642.

Sofialidis, D. and Prinos, P. 1999. Numerical Study of Momentum Exchange in Compound Open Channel Flow, *J. of Hydraulic Eng.*, ASCE, 125: 152–165.

Tominaga, A. and Nezu, I. 1991. Turbulent Structures in Compound Open-channel Flow, *J. of Hydraulic Eng.*, ASCE, 117: 21–41.

Copyright © 2006 Taylor & Francis Group plc, London, UK

Emergence of large-scale coherent structures in a shallow separating flow

Harmen Talstra, Wim S.J. Uijttewaal & Guus S. Stelling
Environmental Fluid Mechanics Section, Faculty of Civil Engineering and Geosciences, Delft University of Technology, the Netherlands

ABSTRACT: In rivers, the phenomenon of flow separation past obstacles often gives rise to large-scale coherent structures. This study focuses on quasi-2d coherent structures associated with shallow flow separation (vortex shedding). New insights about the physical mechanism governing vortex shedding have been obtained from large-scale Particle Image Velocimetry (PIV) experiments on a Shallow Lateral Expansion (SLE) with a variable inflow width. Analysis of the acquired data stresses the crucial role of the secondary circulation cell, which is often present in shallow separation geometries. A sufficiently developed secondary circulation cell is significantly contributing to vortex shedding. Moreover, the interaction between primary and secondary circulation cells causes a "scale jump" in the horizontal length scale of the shed vortices. An analysis of Reynolds' stresses and the downstream development of conditional averaged eddies does clearly show this jump. Since the scale jump is essentially due to interaction of discrete horizontal eddies, 3D Large Eddy Simulations (LES) are performed in analogy with the measured PIV geometries. The obtained LES data will be used to develop a depth-averaged flow model that will reproduce the discrete horizontal eddy interaction in an accurate way, thus enabling researchers and engineers to predict vortex shedding in river geometries.

1 INTRODUCTION

1.1 *Background and objectives*

The present study focuses on a combination of two classes of turbulent flows. The first class is that of a shallow free-surface flow: geometries with vertical length scales much smaller than the horizontal scales (typical aspect ratio 5% or less), in which most of the large-scale turbulence may be considered as quasi two-dimensional. Both production and dissipation of turbulent kinetic energy are greatly influenced by the presence of bottom friction: see e.g. Uijttewaal & Booij (2000) and Van Prooijen (2004). The second class is that of a separating flow: due to an adverse pressure gradient the main flow separates from a wall, inducing a zone of flow recirculation and possibly the presence of a street of vortices which are shed from the separation point. Both classes come together in many rivers and coastal flow geometries. Shallow separating flows are abundant in nature as well as in man-made environments.

In practice, large-scale coherent structures resulting from a separating shallow flow frequently turn out to cause problems regarding e.g. navigation and bed erosion, the latter combined with settling of sediment in undesirable places. These effects are well-known from rivers normalized by long series of groynes, or harbour entrances becoming less accessible due to large-scale eddies and loss of navigable depth. Since many shallow flows accommodate a variety of functions and interventions in flow systems may have unexpected or unwanted effects, improving the understanding and modelling approach of large-scale coherent structures is of practical relevance. In this study, therefore, an attempt is made to visualize experimentally the emergence and behaviour of individual coherent structures shed from a separation point. This experimental information is being used to validate and inspire further development of numerical models of shallow separation flow geometries.

1.2 *General visualisation of shallow separation*

Figure 1 shows the effect of separation on a shallow channel flow past an obstacle, visualised by the injection of dye. In this case, the separation gives rise to a primary and secondary recirculation cell ("bubble"). In literature, the maximum streamwise recirculation zone length (reattachment length) for this type of lateral expansions is often estimated at approximately 8 times the obstacle size (see Babarutsi, Nassiri & Chu, 1996). At the interface between main flow and recirculation zone, lateral exchange of momentum and dissolved matter takes place due to the presence of a mixing layer and large-scale coherent structures (see e.g. Nassiri & Babarutsi, 1997). The presence of recirculations makes the flow behaviour quite different

Copyright © 2006 Taylor & Francis Group plc, London, UK

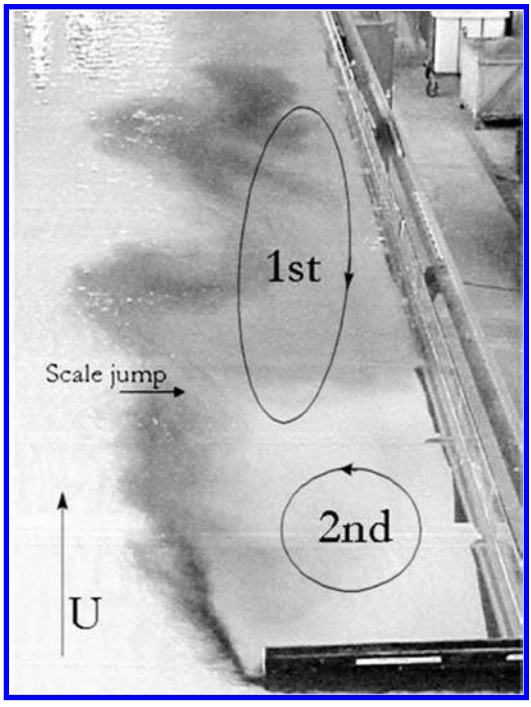


Figure 1. Large-scale structures in a shallow separating flow, visualised by dye. Shown are: direction of the main flow (U), primary bubble (1st), secondary bubble (2nd) and location of the spatial "scale jump" in downstream development of the vortex street.

from that of a plane mixing layer due to a lateral velocity difference only.

In their experimental study on groyne fields, Uijttewaal, Lehman & Van Mazijk (2001) point out a qualitative difference between mixing layer vortices and "vortex shedding". The latter phenomenon is largest in scale and is associated with the presence of a secondary recirculation cell, while the first phenomenon is associated with lateral shear. It is an open question, however, whether there is indeed a difference in physical mechanism for both types of eddies.

From the experiments which are described in this paper, it is visually observed that, indeed, a distinction can be made between the two mechanisms. As soon as a sufficiently well-developed secondary bubble appears, the initial mixing layer changes character and much larger eddies are shed than before. This effect can be associated with the term "vortex shedding". It is observed, however, that the largest eddy scales are emerging not from the separation point, but from a point some distance downstream – approximately at the interface between primary and secondary bubble. At this point, a "scale jump" in vortex sizes is visible. The location of this jump is important, because there is a strong suggestion of positive interaction between the large eddies and the primary bubble ("vortex merging"), while these eddies tend to remain small while passing the secondary bubble slightly upstream. This implies that "vortex shedding" is *not* a distinct mechanism of eddy generation at the separation point, but merely an internal flow feature associated with interaction of existing eddies having the same vorticity sign. This interpretation makes vortex shedding here a typical quasi-2d turbulence phenomenon.

2 DESCRIPTION OF PIV EXPERIMENTS

2.1 *Experimental setup*

In order to study the dynamics of individual large-scale vortices, physical flow experiments have been carried out in a wide and shallow free-surface flume, using the measurement technique of Particle Image Velocimetry (PIV). Because it is desired to study the mere vortex shedding phenomenon with as least geometrical information as possible, the experimental setup has been chosen to be a Shallow Lateral Expansion (SLE). This geometry involves only three length scales: the inflow width, the outflow width and a uniform depth. The SLE is well-known from literature (e.g. Babarutsi, Ganoulis & Chu, 1989), but mostly only with respect to time-averaged quantities rather than individual eddy dynamics. Moreover, it is common practice to take an inflow width equal to 50% of the outflow width, thus effectively reducing the number of length scales to two. In the present study, the inflow width is explicitly chosen to be varied to 3 different values. This yields 3 distinct cases which are object of detailed PIV analysis; the number of qualitative experiments carried out by visual observation, however, is 18 because also depth and discharge have been varied.

The experiments are carried out in a shallow flume with a length of 20.00 m and an outflow width b_2 of 2.00 m. Bottom and wall conditions are hydraulically smooth. In all three PIV experiments, the water depth h is 9.2 cm. The width b_1 of the inflow section is either 0.50, 1.00 or 1.50 m. The three cases are respectively referred to as the 1:4, 2:4 and 3:4 case. The discharge of the first 2 cases being 0.027 m^3/s, the average depth-based Reynolds' number is $Re = 13500$. The discharge of the wide 3:4 case is increased to 0.048 m^3/s ($Re = 24000$) in order to keep the entrance velocity sufficiently high and comparable to the 2:4 case. On the other hand, the 1:4 case discharge is not decreased in order to prevent the recirculation zone from laminarizing. See Figures 2 and 3 for an overview of the experimental geometry and the expected time-averaged flow pattern.

2.2 *Measurement tools*

Floating black polypropylene tracer particles with a diameter of 1.5 mm, contrasting with the white flume

Copyright © 2006 Taylor & Francis Group plc, London, UK

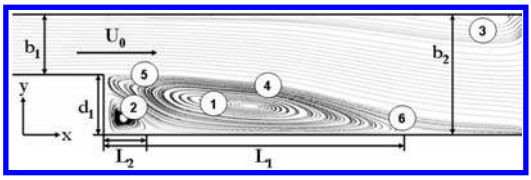


Figure 2. Shallow Lateral Expansion (SLE) with time-averaged streamlines, obtained by a HLES computation. Location of expected flow features: 1) primary bubble, 2) secondary bubble, 3) effect of intermittent opposite bubble, 4) mixing layer, 5) induction of vortex shedding, 6) reattachment point.

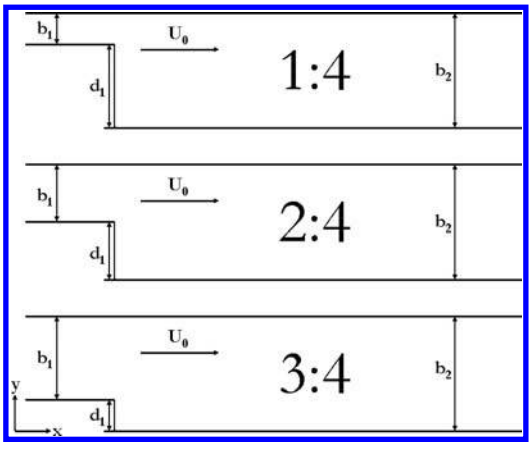


Figure 3. Overview of the 3 PIV geometries (1:4, 2:4 and 3:4).

bottom, are used to visualize the surface velocity field. With a sampling frequency of 10 Hz (2:4 and 3:4 cases) or 15 Hz (1:4 case), instantaneous velocity fields of size $1.50 \times 1.50\,\mathrm{m}^2$ are obtained by a 1 Mpixel digital camera and the PIV algorithm of Davis (version 6.2). Every set of 2 subsequent camera frames is cross-correlated by the algorithm, using an interrogation window overlap of 75%. The results are samples of 2d surface velocity fields on a rectangular co-located grid with a spacing of 2.4 cm in both x- and y-direction. The sample sizes are respectively 7000 frames (2:4 and 3:4 case) and 10500 frames (1:4 case), both accounting for a measurement duration of 700 s.

Because the spatial domain of the camera image is limited to $1.50 \times 1.50\,\mathrm{m}^2$ by resolution requirements, series of samples have to be linearly fit together in order to cover the entire relevant flow area. Therefore, each sample has an overlap of approximately 20% with neighbouring recording areas. The 1:4, 2:4 and 3:4 case data series are consisting of respectively 8, 6 and 4 samples, visualizing the greater part of the vortex shedding areas in downstream direction (Figure 4).

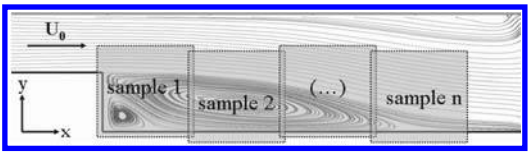


Figure 4. Location of the series $1.50 \times 1.50\,\mathrm{m}^2$ PIV samples.

2.3 *Large eddy visualisation using vector potentials*

A topic requiring special attention is the way in which large-scale eddies within the PIV samples can be detected and visualized. Although a simple look at the velocity vector field often shows these large eddies immediately, it is not always easy to define a straightforward detection algorithm.

Bonnet et al. (1998), Scarano et al. (1999) and Adrian et al. (2000) all give extensive overviews of commonly used identification methods for coherent structures, e.g. based on vorticity, swirling strength or spatial correlations with a "mask eddy". The drawback of the latter method is the spatial inflexibility of the results and their slight dependence on the mask eddy length scale which is chosen *a priori*; the former methods have the disadvantage that, like all gradient-based methods, they tend to enhance the dominance of the small length scales within the velocity signal, rather than the large scales.

In this study, the *vector potential* of a velocity field is used to detect large eddies. The use of vector potentials is quite common within the context of electromagnetism but not within fluid dynamics, in spite of the great mathematical analogy between both scientific fields. Yet, vector potentials are very elegant in use because they allow large vortex scales to be determined directly from instantaneous flow kinematics. They very much resemble the concept of 2d stream functions, but are computed in a different way in order to make a correction for the non-solenoidality of a 2d plane within a 3d velocity field. Vector potentials can be constructed by solving the Poisson equation for each component of the vorticity, using homogeneous Neumann boundary conditions. See the *Appendix* for a full mathematical explanation of construction and relevance of vector potentials.

Each local maximum or minimum of a vector potential function uniquely identifies a large eddy core of positive, resp. negative vorticity sign. The shape of the eddy is given by the surrounding isolines. Within the instantaneous vector potential fields, the permanently present primary and secondary recirculation cells are by far dominant; when the time-averaged pattern is subtracted from instantaneous patterns, however, the result is the visualisation of a straight streamwise line of large vortices being shed from the separation point.

Copyright © 2006 Taylor & Francis Group plc, London, UK

3 RESULTS

3.1 *Visual observations: general flow features*

In order to explore the parameter space of relevant experimental cases, over 30 different flow cases were observed merely visually, using dye and the same black tracer particles as described before. Every flow case was running for about 2 hours and was used to gain insight in the occurring flow features: over-all flow patterns, bubble sizes and large eddy length scales. Water level, discharge and inflow-outflow width ratio were varied in such a way that the flow remained sufficiently turbulent and fully subcritical. In the end, 18 flow cases were concluded to be suitable for mutual comparison.

Table 1 shows the primary and secondary recirculation cell sizes, scaled by the lateral expansion width d_1, for the 2 different discharges (q) and 3 width ratios predefined in Section 2.1. The 18 water depth values are varying for each case because of the practical difficulty to get these exactly equal. The primary bubble size is defined by the reattachment length (L_1) and the secondary bubble size by the x-location of the secondary separation point along the wall (L_2), both taking the expansion's lower left corner as the origin. Both water depth (h) and bubble sizes are made dimensionless by the lateral expansion width.

Table 1. Primary and secondary recirculation cell sizes for 18 different flow cases; visual observations.

		Flow parameters		Recirculation sizes	
No.	Geometry	q [m^3/s]	h/d_1* [-]	L_1/d_1* [-]	L_2/d_1* [-]
1	1:4 case	0.027	0.052	7.2	2.2
2	1:4 case	0.027	0.064	7.6	2.2
3	1:4 case	0.027	0.075	8.4	3.6
4	1:4 case	0.048	0.073	8.8	2.2
5	1:4 case	0.048	0.084	8.8	2.6
6	1:4 case	0.048	0.107	8.8	3.2
7	2:4 case	0.027	0.059	8.4	2.7
8	2:4 case	0.027	0.078	8.4	2.7
9	2:4 case	0.027	0.108	10.2	1.8
10	2:4 case	0.048	0.071	9.6	2.7
11	2:4 case	0.048	0.092	9.6	2.4
12	2:4 case	0.048	0.124	10.2	1.8
13	3:4 case	0.027	0.090	6.0	2.4
14	3:4 case	0.027	0.162	6.6	2.4
15	3:4 case	0.027	0.226	6.6	1.8
16	3:4 case	0.048	0.118	6.6	1.8
17	3:4 case	0.048	0.194	7.2	1.5
18	3:4 case	0.048	0.256	7.2	1.5

* Length scales are made dimensionless by expansion width d_1.

First, the general impression is that the dimensionless reattachment length L_1/d_1 tends to decrease for decreasing dimensionless depth, compared to the maximum deep water limit known from literature. This limit is estimated to lie between 7.0 and 8.0 (the latter number is proposed by Babarutsi, Ganoulis & Chu, 1989). The values found in the 3:4 case seem to confirm this. It is however striking that the values observed in the 1:4 and 2:4 cases exceed this limit, even up to values 9.0 and over, although the reattachment point is usually slightly oscillating. This exceedance may be explained by the hydraulically smooth wall conditions of the present experimental setup, which often are not reached in practice. Also, the relatively large size and the high Reynolds number of this setup may play a role of importance (the experiments of e.g. Babarutsi et al. were carried out on an approximately 3 times smaller scale and with larger values of roughness).

Second, the secondary bubble sizes L_2/d_1 in the 2:4 and 3:4 cases show a pattern opposite to that of the reattachment length: as the relative shallowness increases, the secondary separation point moves further downstream. This can be understood by the primary bubble becoming weaker: as the primary recirculation flow decreases in discharge and energy, it will break away sooner from the solid wall because of the local adverse pressure gradient which previously brought the secondary bubble into being. Hence, with increasing shallowness, the primary bubble is eaten up from two sides, sometimes even to the point that the primary and secondary bubble become comparable in size. The secondary zone of the 1:4 case, on the contrary, is enhanced together with the primary zone. It is observed that, in these cases, the secondary bubble has grown too big to maintain itself within such shallow conditions, and hence breaks up in two or more intermittent structures. In some cases, even a small "tertiary bubble" in the lower left corner is observed.

Third, because of its large relative shallowness (small value of h/d_1), the 1:4 case shows an intermittent bubble opposite to the primary recirculation. The presence of this opposite bubble depends strongly on the passing by of large vortices shed from the separation point. These vortices are able to entrain so much main flow fluid into the mixing layer that the main flow separates from the opposite continuous wall. This feature is however intermittent and is located too close to the outflow boundary to be studied in an accurate way. In the 2:4 and 3:4 cases, it is absent.

Finally, the most important flow feature to be described is the vortex shedding phenomenon. Flow patterns can be described in good detail because of the abundance of tracer particles. Striking is the stability of the near-field mixing layer, in spite of both its small width and the presence of a very strong lateral shear due to the secondary bubble which is almost touching the main flow. The small coherent structures emerging from the separation point seem to be almost immune to their neighbourhood. As soon as the mixing layer approaches the primary bubble, however, the

Copyright © 2006 Taylor & Francis Group plc, London, UK

structures appear to be boosted significantly, both in energy and spatial scale ("scale jump").

This can be explained from the positive interaction between vorticity cores in both mixing layer and primary zone, i.e. the effect of "vortex merging". This effect is well-known from quasi two-dimensional flow theory and can be associated with the suppression of the vortex stretching term in the vorticity equation. The boosted eddies are penetrating to a large extent in both main flow and primary bubble, and are able to exchange a lot of mass and momentum. (This, too, may be an explanation for the remarkably large reattachment lengths that are found in the 1:4 and 2:4 cases.) The zones in between two large shed vortices are observed to be areas of considerable shear. The flow is stretched in streamwise direction here, as well as compressed in spanwise direction. Also, secondary flow in vertical direction is affecting these zones, in contrast with the large vortex cores which appear to be predominantly two-dimensional.

In the 3:4 case the scale jump effect is much weaker, if not absent. In this geometry the secondary bubble zone is relatively deep (largest value of h/d_1). Therefore the bubble remains small and does not touch the main flow. The influence of the primary bubble, hence, is reaching all the way upstream to the separation point, resulting in a smoother and less dramatic mixing layer development. From that point of view, it is not surprising that the reattachment lengths found in the 3:4 case answer better to the expected maximum limit than the 1:4 and 2:4 cases.

In the 1:4 case, the scale jump effect is present but weaker than in the 2:4 case, which contains the most obvious jump. This is explained by a limited influence of the secondary bubble in the 1:4 case, because it tends to break up in separate structures as mentioned above (which is visible in Figure 5a).

Based on the 18 flow cases described above, a representative geometry is selected for detailed PIV analysis. Only the inflow-outflow width ratio remains variable (hence 3 cases). Dimensions and other figures of this geometry have been described in Section 2.1.

3.2 *PIV data analysis: time statistics*

All recorded PIV time series have a sampling period of 700 s, which is equivalent to about 30–70 consecutive large eddies shed from the separation point. In this section, over-all time statistics are shown for the 3 measured flow cases. For each case, neighbouring measurement recording areas were fit together by linear interpolation in the overlapping areas.

Figures 5a to 5i show the contour plots of time-averaged flow quantities: stream function, spanwise turbulent kinetic energy and horizontal Reynolds' stresses of the 1:4, 2:4 and 3:4 cases respectively. The stream functions show that, in the 3:4 case, the

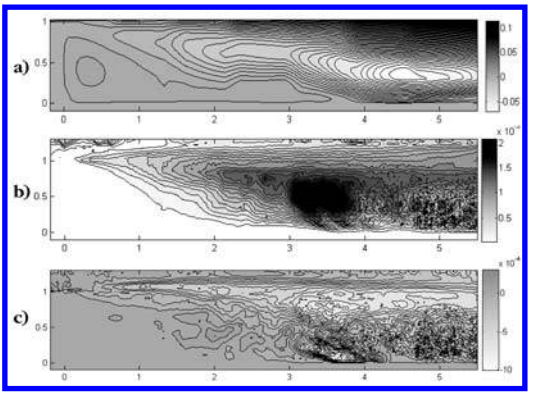


Figure 5a–c. Time-averaged flow quantities of the 1:4 case: a) time-averaged stream function ψ [m^2/s], b) spanwise turbulent kinetic energy $\langle u'^2 \rangle$ [m^2/s^2], c) horizontal Reynolds' stresses $\langle u'v' \rangle$ [m^2/s^2].

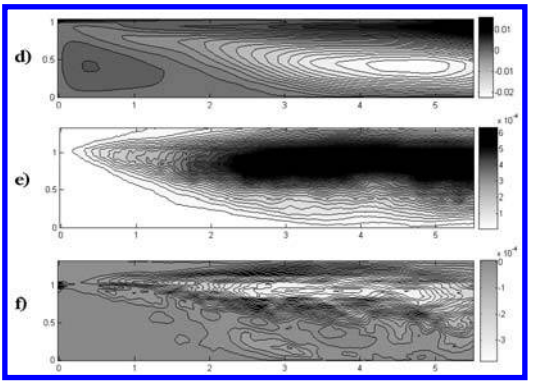


Figure 5d–f. Time-averaged flow quantities of the 2:4 case: d) time-averaged stream function ψ [m^2/s], e) spanwise turbulent kinetic energy $\langle u'^2 \rangle$ [m^2/s^2], f) horizontal Reynolds' stresses $\langle u'v' \rangle$ [m^2/s^2].

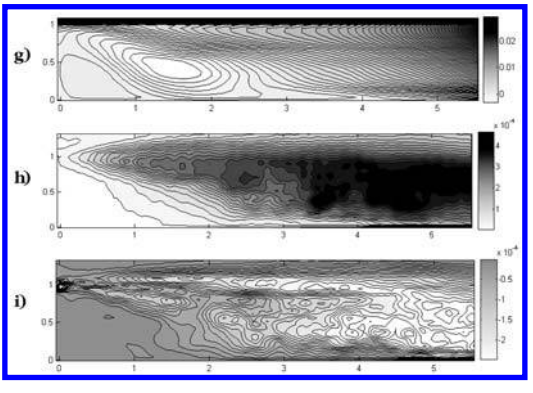


Figure 5g–i. Time-averaged flow quantities of the 3:4 case: g) time-averaged stream function ψ [m^2/s], h) spanwise turbulent kinetic energy $\langle u'^2 \rangle$ [m^2/s^2], i) horizontal Reynolds' stresses $\langle u'v' \rangle$ [m^2/s^2].

Copyright © 2006 Taylor & Francis Group plc, London, UK

secondary bubble is indeed less developed than in the other 2 cases, resulting in a deviant vortex shedding behaviour. Please note the tendency of the 1:4 secondary bubble to break up in two parts.

Reynolds' stress values can be seen as time-averaged indicators for the presence of large-scale coherent structures (velocity correlations). Therefore, it is telling that in the 1:4 and 2:4 cases, the scale jump is visible in the Reynolds' stress contours. In these cases, the negative peak of the Reynolds' stress suddenly widens and deepens from a certain point downstream, while the 3:4 case does not show this behaviour. Furthermore, it is striking that the components of the turbulent kinetic energy show a quite linear development, while the Reynolds' stress contours are more discontinuous. This can be understood by the fact that the velocity variance contains only temporal and local information, whereas the velocity covariance is also pointing towards the spatial structure of the flow field. Apparently, the development of the shed vortices in terms of total energy is pretty continuous, comparable to that of a plane mixing layer; but downstream from the scale jump location, the kinetic energy distribution does shift towards larger length scales. This suggests that the scale jump effect is spatial rather than temporal.

Figure 6 shows the development of the lateral turbulent kinetic energy downstream from the separation point for each of the 3 cases. As expected, no jump is visible here. Examining the downstream development of the associated temporal power density spectra yields the same result. On the other hand, one will expect to find such a jump in the spatial power density spectrum development. Unfortunately, the horizontal dimensions of the PIV camera samples are too limited to allow for reliable spatial spectra.

From the computed Reynolds' stresses a turbulent length scale (Prandtl mixing length) can be defined using a simple mixing length approach. Figure 7 shows the downstream development of this mixing length λ for the three PIV cases. The 2:4 shows the clearest jump. It is however not surprising that this method yields eddy sizes which are almost an order of magnitude too small, because we are using time-averaged statistics of an intermittent phenomenon.

For both reasons mentioned above, spatial vortex scale development can best be examined by conditional averaging of the intermittent shed vortices. Results of this averaging operation are described in the next section.

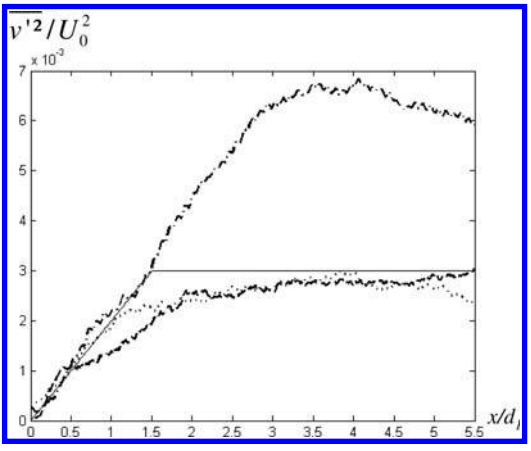


Figure 6. Development of the lateral turbulent kinetic energy downstream from the separation point, normalized by the squared mean inflow velocity. Dashed line: 1:4 case, dash-dot line: 2:4 case, dotted line: 3:4 case, continous: trend line. The downstream distance is scaled by the lateral expansion width. The 2:4 case vortex shedding is containing the largest amount of turbulent kinetic energy relative to the energy of the mean flow. The 1:4 and 3:4 case are quite comparable.

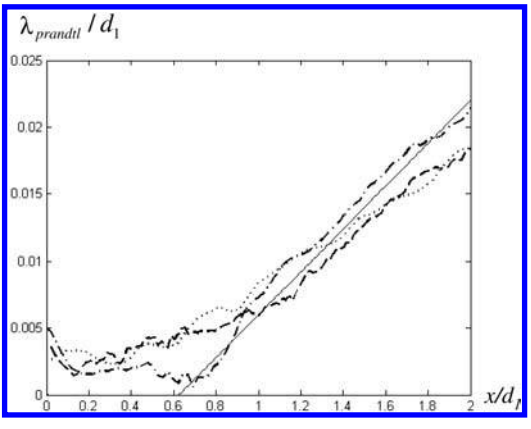


Figure 7. Development of the Prandtl mixing length λ downstream from the separation point, based on measured Reynolds' stresses. Dashed line: 1:4 case, dash-dot line: 2:4 case, dotted line: 3:4 case, continous: trend line downstream of the scale jump location (approximately $x/d_1 = 0.8$). Both the downstream distance and the mixing length are scaled by the lateral expansion width. The 2:4 case shows the most pronounced scale jump behaviour.

3.3 *PIV data analysis: conditional averages*

The location of the conditional averages is the line along which the relevant large eddies are found: the straight streamwise "shadow line" downstream of the separation point. For each point on this line where PIV data are located, the cross section of the flow is checked for the presence of a large eddy. This is done by searching local minima in the vector potential time series *relative* to the mean flow pattern (the latter is needed because otherwise only the primary and

Copyright © 2006 Taylor & Francis Group plc, London, UK

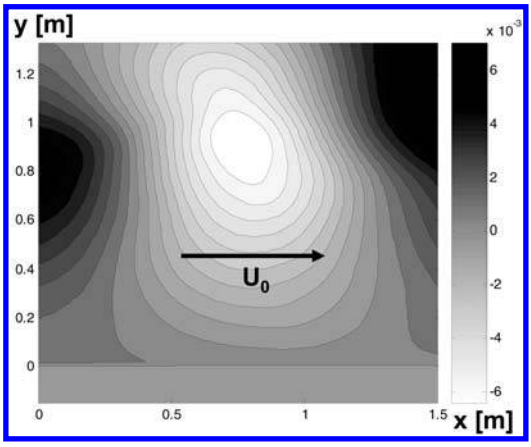


Figure 8. Typical example of a conditionally averaged shed vortex (in the far field of the 2:4 case), visualised by a vector potential field. The computed streamlines agree very well with the associated vector field. The local minimum in the centre of the picture identifies a clockwise large eddy with a diameter of approximately 0.8 m.

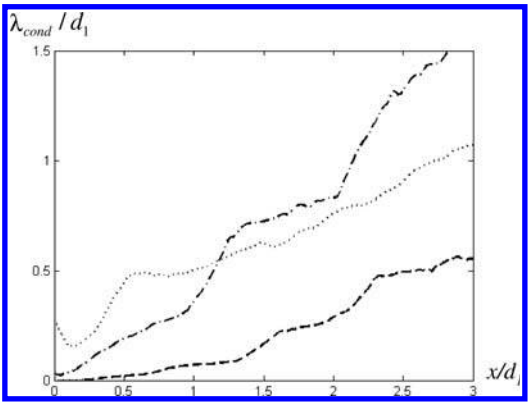


Figure 9. Development of the dominant large eddy scales λ_{cond} downstream from the separation point, based on conditional averaging. Dashed line: 1:4 case, dash-dot line: 2:4 case, dotted line: 3:4 case. The 2:4 case shows the largest eddy scales relative to the lateral expansion width d_1, which is understandable because of the large relative energy of the large-scale turbulence in this case (see also Figure 6).

secondary bubble would be found). After that, statistical operations can be performed on the conditional vortex samples. Figure 8 gives an illustration of the procedure in which the large eddies are detected by means of vector potentials.

In principle, conditional averaging can be done for every point within the measured flow domain. Near the edges of the recording domains, however, the conditional averaged flow fields show biases because of the difficulty to determine a local minimum near a boundary. Therefore, the fitting of neighbouring data recording areas is problematic for conditional averaged quantities. The over-all patterns and trends, however, remain sufficiently clear.

The conditionally averaged spanwise velocity signal (again relative to the mean velocity) is suitable for determining local large eddy length and time scales. Please note that vector potential quantities are used only for performing the conditional averaging process itself and for large eddy detection, but are not suitable as an object of any further data statistics. For determining eddy scales, it is better to return to the velocity signal itself.

The spanwise velocity makes a zero crossing at the location of conditionally averaged eddy cores. An eddy length scale can be defined as the distance between the centroid locations of the vortex velocity profiles left and right of such a zero-crossing; this scale can be computed using first order moments of the signal. A more robust approach, however, is determining the dominant time scales of conditionally averaged vortices and multiplying these by the propagation speed of the large eddy core, thus obtaining an "eddy wave length" (the real eddy size is about 50% of this wave length). The latter approach is much less sensitive to noise and boundary biases, because the obtained PIV data allow for much better temporal than spatial statistics.

Figure 9 shows the computed length scales of the dominant eddies caused by vortex shedding, as a function of x, for each of the 3 PIV cases. Both axes are scaled by the lateral expansion width d_1. Unlike the scales shown in Figure 7, the conditionally averaged eddy sizes do have the correct order of magnitude (of the order of d_1). It is obvious that the 1:4 and 2:4 cases do show a spatial scale jump downstream of the point $x/d_1 = 1.0$, whereas the 3:4 case eddy size development is more linear.

3.4 *Discussion*

In literature, as pointed out in Section 1.2, a distinction can be found between a shallow mixing layer on the one hand and the phenomenon of vortex shedding on the other hand. The latter phenomenon is seen as an extra effect *additional* to a mere mixing layer, typical for shallow separating flows, while a mere mixing layer is considered to be a more general feature of shallow shear flows. With respect to this, e.g. Jirka (2001) treats both types of shallow-flow turbulence separately and speaks of two different mechanisms: respectively the mechanisms of *topographical forcing* (due to flow separation) and *internal transverse shear instabilities* (due to a lateral flow velocity difference). The reason why both mechanisms differ, however, sometimes remains an open question.

The observed phenomenon of the "scale jump" due to a well-developed secondary recirculation cell is a very helpful tool to explain why shallow flow

Copyright © 2006 Taylor & Francis Group plc, London, UK

separation yields large vortices that have a character different from mixing layer vortices. Both vortex types are initially induced by lateral shear, but in a shallow separation geometry, the presence of *permanent* recirculation cell vorticity greatly influences the spatial eddy development. Hence, it can be concluded that in a separation geometry the influence of solid wall friction (inducing recirculations) is never negligible, while a plane mixing layer theoretically does not have walls at al. With that respect, a shallow separation flow is always intrinsically a combination of free turbulence and wall turbulence, whereas a mere mixing layer problem has a free turbulence character to a much larger extent.

The geometry-dependency of shallow separation problems, however, puts also a limit to the amount of conclusions that can be drawn from the current experiments. In practice, many shallow separation geometries do not contain a sufficiently developed secondary bubble (for example due to the presence of downstream obstacles like groynes), so that a less pronounced scale jump effect should be expected there. Also, the local wall and bottom roughness as well as the presence of non-vertical sidewall slopes (which are almost always there in the case of groynes) will play a huge role in most river engineering problems in reality. It is not easy to say how especially the presence of wall slopes will influence the scale jump behaviour. It is not unthinkable that, in the case of groyne fields, scale jump locations will lie so close to a separation point that large eddies seem to be shed directly from the groyne tip.

Therefore, it will be worthwhile to repeat the current experiments replacing the vertical-wall lateral expansions by several real-life groyne geometries, maintaining the level of detail in which the large-scale vortices are detected. However, introducing wall slopes and more associated geometrical parameters will cause the experiments to be less generic in terms of length scales, which will make it more difficult to draw general conclusions from them.

In terms of engineering applications, the current experiments strongly suggest that any attempt to prevent scale jumps from occurring will yield more favourable river flow conditions, thus preventing the well-known navigation and sedimentation problems to a large extent. It is possible to do this by changing shallow separation geometries in an effective way. Especially changing river groyne shapes could be a great asset to river engineers. If groyne shapes can be modified in such a way that they will "shelter off" most of the secondary bubble regions from the main river, this may yield a considerable reduction of the effective lateral shear. A very concise pilot experiment, executed within the same experimental setup as described in this paper, does indeed show that a strong reduction of the vortex shedding intensity is feasible.

4 CONCLUSIONS AND OUTLOOK

Detailed PIV experiments have been performed on a Shallow Lateral Expansion with a variable inflow width. The hypothesis seems to be confirmed that the vortex shedding phenomenon is caused by the presence of a sufficiently developed secondary recirculation cell. A new element of information, however, is that the emergence of large-scale shed vortices is not caused by the flow separation itself, but by interaction of initially induced mixing layer vortices with the primary and secondary recirculation areas. This vortex interaction can be interpreted as a typical feature of shallow (quasi two-dimensional) flows. Also, the location of this large vortex emergence (*scale jump*) does not coincide with the separation point. The decomposition of "mixing layer vortices" and "vortex shedding" opens a perspective of effective manipulation of large eddies in real-world shallow flow situations by changing the geometry with respect to the secondary recirculation cell.

Further analysis of the vortex shedding phenomenon is currently done by performing a series of full 3D Large Eddy Simulations (LES), in full analogy with the three examined PIV geometries. This type of analysis seems to be rewarding because, like PIV data, LES data allow for not only flow statistics but also a very detailed look at the discrete horizontal vortices that are responsible for the observed typical vortex shedding behaviour in shallow flows. Moreover, conditional averaging of large horizontal eddies is an option for LES data analysis too. Although the general flow and turbulence features shown by the already performed LES simulations look quite reasonable, a detailed analysis of the vortex shedding process is not yet available. The obtained LES data will be used to develop and inspire a more concise shallow flow model, possibly fully depth-averaged, yet able to reproduce horizontal eddy interaction in rivers accurately. Meanwhile, examining the vortex shedding process in more various shallow separating flow geometries by detailed physical experiments - thus verifying the proposed scale jump hypothesis – will remain a subject of further research.

ACKNOWLEDGEMENT

This research is supported by the Dutch Technology Foundation STW, applied science division of NWO and the Technology Programme of the Ministry of Economic Affairs.

REFERENCES

Adrian, R.J., Christensen, K.T. & Liu, Z.-C. 2000. Analysis and interpretation of instantaneous turbulent velocity fields. *Experiments in* Fluids, Vol. 29: 275–290.

Copyright © 2006 Taylor & Francis Group plc, London, UK

Babarutsi, S., Ganoulis, J. & Chu, V.H. 1989. Experimental investigation of shallow recirculating flows. *Journal of Hydraulic Engineering,* Vol. 115, No. 7: 906–924.
Babarutsi, S., Nassiri, M. & Chu, V.H. 1996. Computation of shallow recirculating flow dominated by friction. *Journal of Hydraulic Engineering*, Vol. 122, No. 7: 367–372.
Bonnet, J.P., Delville, J. et al. 1998. Collaborative testing of eddy structure identification methods in free turbulent shear flows. *Experiments in Fluids*, Vol. 25: 197–225.
Jirka, G.H. 2001. Large scale flow structures and mixing processes in shallow flows. *Journal of Hydraulic Research*, Vol. 39, No. 6: 567–573.
Nassiri, M. & Babarutsi, S. 1997. Computation of dye concentration in shallow recirculating flow. *Journal of Hydraulic Engineering*, Vol. 123, No. 9: 793–805.
Prooijen, B.C. van. 2004. *Shallow Mixing Layers.* Delft, Ph.D. Thesis Delft University of Technology.
Scarano, F., Benocci, C. & Riethmuller, M.L. 1999. Pattern recognition analysis of the turbulent flow past a backward facing step. *Physics of Fluids*, Vol. 11, No. 12: 3808–3818.
Uijttewaal, W.S.J. & Booij, R. 2000. Effects of shallowness on the development of free-surface mixing layers. *Physics of Fluids*, Vol. 12, No. 2: 392–402.
Uijttewaal, W.S.J., Lehmann, D. & Van Mazijk, A. 2001. Exchange processes between a river and its groyne fields: model experiments. *Journal of Hydraulic Engineering,* Vol. 127, No. 11: 928–938.

APPENDIX: ABOUT VECTOR POTENTIALS

Given a 3d solenoidal velocity vector field:

$$\vec{u} = (u, v, w), \text{ with } \nabla \cdot \vec{u} = 0 \text{ and } \nabla \times \vec{u} = \vec{\omega} \qquad \text{(i)}$$

For such a vector field, a vector potential $\vec{\psi}$ exists such that

$$\vec{u} = \nabla \times \vec{\psi}, \qquad \text{(ii)}$$

for $\nabla \cdot \nabla \times \vec{\psi} = 0$ by definition. Please note that $\vec{\psi}$ is determined apart from an arbitrary gradient field $\nabla\phi$, because $\vec{\psi}' = \vec{\psi} + \nabla\phi$ is also satisfying (ii).

The vorticity $\vec{\omega}$ now can be written as

$$\vec{\omega} = \nabla \times (\nabla \times \vec{\psi}) = \nabla(\nabla \cdot \vec{\psi}) - \nabla^2 \vec{\psi} \qquad \text{(iii)}$$

Because $\vec{\psi}$ has a degree of freedom, it can be chosen such that $\vec{\psi}$ is also solenoidal. In that case, expression (iii) for the vorticity reduces to a Poisson equation:

$$\vec{\omega} = -\nabla^2 \vec{\psi} \qquad \text{(iv)}$$

The wonderful thing about the Laplacian operator in this expression is that it operates on each vector component separately. Therefore, if only one component of the vorticity is known (which is ω_z in this study, for only u and v are known in the horizontal PIV-plane), yet the full z-component of the vector potential can be constructed. On the vector field edges, it is sufficient to use homogeneous Neumann boundary conditions for solving the Poisson equation.

Taking the curl of the constructed ψ_z should yield in turn the original velocity field (u,v). The latter, of course, does only make sense if the vorticity component ω_z is the dominant component within 3d context. This condition is obviously satisfied in case of a shallow quasi-2d flow with large eddies in the horizontal plane. In that case, taking the curl of the vector potential is practically equivalent to:

$$u = \partial\psi_z / \partial y \quad \text{and} \quad v = -\partial\psi_z / \partial x, \qquad \text{(v)}$$

which shows that ψ_z very much resembles a 2d stream function of (u,v), except for the fact that an important correction has been made to circumvent the nonsolenoidality of the (u,v)-plane.

In fact, computing a vector potential is a way to *integrate* the associated velocity field, showing large-scale rotation patterns in the end. On the contrary, computing a vorticity means taking a *derivative* of that velocity field, effectively showing small-scale rotation patterns. This can be understood by considering a velocity signal being a sum of spatial periodical signals (Fourier components). Taking derivatives of the total signal implies multiplying each component i by its wave number k_i, thus enhancing the dominance of the high wave numbers (small scales). Integrating the signal, however, will lead to a division by k_i, hence focussing on the low wave numbers (largest scales). This explains why experimental vorticity data are often very noisy while, on the other hand, vector potential data are quite smooth and hence much easier to handle.

Each local maximum or minimum of a vector potential function identifies a vortex core of positive respectively negative vorticity sign. The function isolines are very well parallel to the original vector field. It may be concluded that vector potentials are a most suitable tool for identifying large eddies.

Copyright © 2006 Taylor & Francis Group plc, London, UK

A.2. Flood propagation and channel/floodplain interactions

Copyright © 2006 Taylor & Francis Group plc, London, UK

Finite element hydrodynamic modeling in a river

Kun-Yeun Han
Department of Civil Engineering, Kyungpook National University, Daegu, Korea

Chang-Hyun Baek
River Information Center, Seoul, Korea

Joon-Woo Noh
Korea Institute of Water and Environment, Daejon, Korea

ABSTRACT: The main objective of this study is to develop efficient and accurate 3D finite element model for hydrodynamic channel flow simulation. To establish governing equation considering turbulent flows, the fundamental 3D Navier-Stokes equation is modified as Reynolds equation. In the governing equation turbulent flow characteristics are expressed using the Smagorinsky scheme in horizontal plan and the Mellor-Yamada scheme for vertical direction. The proposed model adopted the Streamline Upwind/Petrov Galerkin scheme for weighting function in model formulation and moving boundary condition to overcome the limitations of fixed grid. For model validation, the proposed 3D finite element model has been applied for U typed channel flow and compared with the results of existing model to show a good agreement between two models. The simulation results using this model successfully describe 3D flow characteristics for various channel flows with consideration of turbulent flows. Adopting moving boundary conditions in describing water surface variations it is possible to obtain stable and accurate numerical solutions.

1 INTRODUCTION

For hydrodynamic analysis of the channel flow, various numerical schemes have been developed and advanced. Numerous numerical models which solve 2 dimensional shallow water equations are also available for 2-dimensional flow analysis. One of the representative 2-dimensional models is SMS.

In the computation of the channel flow, multi-dimensional numerical analysis is necessary. Especially more accurate numerical analyses are desirable in identifying the flow patterns, pollutant propagations, and sediment transport in the complex channel geometries such as flows in the vicinity of the hydraulic structures, in channel bends, at the points of tributary inflows, and in stratified estuaries. However, to simulate averaged flow characteristics, most of the developed models are depth integrated or laterally averaged. Thus they have limitations in describing the velocity distributions from water surface to channel bed with turbulent flows. To overcome such problems it is necessary to develop 3-dimensional numerical models to differentiate flow characteristics at the water surface and nearby the channel bed. Despite recently advanced computational devices, development of 3-dimensional flow simulation models is very limited.

The main objective of this study is to develop a finite element model which is applicable to simulate 3-dimensional channel flows in complex geometries. The channel flow analysis model proposed in this study is developed by applying the Streamline Upwind/Petrov-Galerkin scheme as a weighting function for the finite element formulation which is combined with the kinematic free-surface conditions. The developed 3-dimensional finite element model employs the Smagorinsky scheme and the Mellor-Yamada scheme to describe the turbulent viscosity in horizontal and vertical direction respectively.

2 REYNOLDS EQUATION

2.1 *Reynolds separation scheme*

In general, analytical solution for the fundamental 3 dimensional Navier-Stokes equations is not available except for particular symmetry conditions. Even such solutions are only limited for laminar flow condition without variations in velocity and pressure fields. For these reasons, it is necessary to introduce Reynolds separation scheme to differentiate the turbulence resulted from fluctuations in the flow regime

Copyright © 2006 Taylor & Francis Group plc, London, UK

due to channel roughness, hydraulic structures, and geometric complexities.

Deriving time average procedure for all variables in Navier-Stokes equations, following Reynolds equations is given as

Momentum equation

$$\rho\left(\frac{\partial \bar{u}}{\partial t}+\bar{u}\frac{\partial \bar{u}}{\partial x}+\bar{v}\frac{\partial \bar{u}}{\partial y}+\bar{w}\frac{\partial \bar{u}}{\partial z}\right)=\Gamma_x-\frac{\partial \bar{P}}{\partial x}+\left(\frac{\partial \bar{\tau}_{xx}}{\partial x}+\frac{\partial \bar{\tau}_{xy}}{\partial y}+\frac{\partial \bar{\tau}_{xz}}{\partial z}\right)$$

$$\rho\left(\frac{\partial \bar{v}}{\partial t}+\bar{u}\frac{\partial \bar{v}}{\partial x}+\bar{v}\frac{\partial \bar{v}}{\partial y}+\bar{w}\frac{\partial \bar{v}}{\partial z}\right)=\Gamma_y-\frac{\partial \bar{P}}{\partial y}+\left(\frac{\partial \bar{\tau}_{yx}}{\partial x}+\frac{\partial \bar{\tau}_{yy}}{\partial y}+\frac{\partial \bar{\tau}_{yz}}{\partial z}\right)$$

$$\rho\left(\frac{\partial \bar{w}}{\partial t}+\bar{u}\frac{\partial \bar{w}}{\partial x}+\bar{v}\frac{\partial \bar{w}}{\partial y}+\bar{w}\frac{\partial \bar{w}}{\partial z}\right)=\Gamma_z-\frac{\partial \bar{P}}{\partial z}+\left(\frac{\partial \bar{\tau}_{zx}}{\partial x}+\frac{\partial \bar{\tau}_{zy}}{\partial y}+\frac{\partial \bar{\tau}_{zz}}{\partial z}\right) \quad (1)$$

Viscosity

$$\bar{\tau}_{xy}=\mu\left(\frac{\partial \bar{u}}{\partial y}+\frac{\partial \bar{v}}{\partial x}\right)-\rho\overline{u'v'} \qquad \bar{\tau}_{xx}=2\mu\frac{\partial \bar{u}}{\partial x}-\rho\overline{u'u'}$$

$$\bar{\tau}_{xz}=\mu\left(\frac{\partial \bar{u}}{\partial z}+\frac{\partial \bar{w}}{\partial x}\right)-\rho\overline{u'w'} \qquad \bar{\tau}_{yy}=2\mu\frac{\partial \bar{v}}{\partial y}-\rho\overline{v'v'}$$

$$\bar{\tau}_{xy}=\mu\left(\frac{\partial \bar{v}}{\partial z}+\frac{\partial \bar{w}}{\partial y}\right)-\rho\overline{v'w'} \qquad \bar{\tau}_{zz}=2\mu\frac{\partial \bar{w}}{\partial z}-\rho\overline{w'w'} \quad (2)$$

where x, y, z are Cartesian coordinates, u, v, w are velocity components in x, y, z direction respectively, ρ is density of fluids, P is pressure, Γ_x, Γ_y, Γ_z is body force per unit mass.

2.2 *Turbulence closure*

Based on the Boussinesq assumption, turbulent stress is given in terms of averaged velocity which can be expressed as Equation 3. In this study eddy viscosity ν_t is computed using the Smagorinsky scheme for 2-dimensional horizontal direction, and the Mellor-Yamada scheme is adopted to compute ν_t along the vertical direction.

$$\tau_{ij}=-\rho\overline{u_i'u_j'}=\rho\nu_t\left(\frac{\partial u_i}{\partial x_j}+\frac{\partial u_j}{\partial x_i}\right)=\varepsilon_{ij}\left(\frac{\partial u_i}{\partial x_j}+\frac{\partial u_j}{\partial x_i}\right) \quad (3)$$

(1) Turbulent stress in horizontal direction

Proposed by Smagorinsky, this scheme assumes that the element size and velocity variation to determine the eddy viscosity. The turbulent stress in 2-dimensional horizontal direction is written as follows

$$\nu_t=(C_s\Delta x)^2\sqrt{S_{ij}S_{ij}} \quad (4)$$

where $S_{ij}=\left(\frac{\partial u_i}{\partial x_j}+\frac{\partial u_j}{\partial x_i}\right)$, Δx is element size, C_s is Smagorinsky constant which ranges between 0.1 and 0.24.

(2) Turbulent stress in vertical direction

In the stratified homogeneous flow, since eddy viscosity of vertical direction varies considerably with flow depth, the proposed model employed the Mellor-Yamada scheme in order to consider such processes.

Determination of the eddy viscosity requires 2 computational steps. In the 1st step, the vertical eddy viscosity is computed assuming stabilized homogeneous flow condition. The vertical eddy viscosity coefficient $E_{xz}=E_{yz}$ at such stable condition is given as follows

$$E_{xz}=E_{yz}=\rho S_m l_m q_t \quad (5)$$

where S_m is a coefficient derived from the experiment conducted by Mellor and Yamada, l_m is the mixing length, and q_t is the variation of turbulent velocity.

3 GOVERNING EQUATIONS FOR 3-DIMENSIONAL FLOW

3.1 *Basic equation*

By assuming that the acceleration term in vertical direction is much less than that in horizontal direction, the complete 3 dimensional equation is composed of 2 momentum equations and integrated continuity equation as follows

$$\rho\left\{\frac{\partial u}{\partial t}+u\frac{\partial u}{\partial x}+v\frac{\partial u}{\partial y}+w\frac{\partial u}{\partial z}\right\}+\rho g\left(\frac{\partial h}{\partial x}+\frac{\partial a}{\partial x}\right)-\Gamma_x$$
$$-\frac{\partial}{\partial x}\left(\varepsilon_{xx}\left(\frac{\partial u}{\partial x}\right)\right)-\frac{\partial}{\partial y}\left(\varepsilon_{xy}\left(\frac{\partial u}{\partial y}+\frac{\partial v}{\partial x}\right)\right)-\frac{\partial}{\partial z}\left(\varepsilon_{xz}\left(\frac{\partial u}{\partial z}\right)\right)=0 \quad (6)$$

$$\rho\left\{\frac{\partial v}{\partial t}+u\frac{\partial v}{\partial x}+v\frac{\partial v}{\partial y}+w\frac{\partial v}{\partial z}\right\}+\rho g\left(\frac{\partial h}{\partial y}+\frac{\partial a}{\partial y}\right)-\Gamma_y$$
$$-\frac{\partial}{\partial x}\left(\varepsilon_{yx}\left(\frac{\partial u}{\partial y}+\frac{\partial v}{\partial x}\right)\right)-\frac{\partial}{\partial y}\left(\varepsilon_{yy}\left(\frac{\partial v}{\partial y}\right)\right)-\frac{\partial}{\partial z}\left(\varepsilon_{yz}\left(\frac{\partial v}{\partial z}\right)\right)=0 \quad (7)$$

$$\int_a^{a+h}\left(\frac{\partial u}{\partial x}+\frac{\partial v}{\partial y}\right)dz+u_s\frac{\partial(a+h)}{\partial x}+v_s\frac{\partial(a+h)}{\partial y}+\frac{\partial h}{\partial t}-u_b\frac{\partial a}{\partial x}-v_b\frac{\partial a}{\partial y}=0 \quad (8)$$

where h is depth, a is channel bed elevation, u_s, v_s, u_b, v_b are Cartesian velocity components at water surface and channel bed respectively.

The main dependent variables are the horizontal velocity components u, v and flow depth h. Thus, the computation of w is separately conducted.

Copyright © 2006 Taylor & Francis Group plc, London, UK

3.2 *Moving boundary condition*

In the 3-dimensional numerical modeling, it is necessary to consider spatial channel bed changes as well as temporal flow depth variations simultaneously. However, due to the numerical difficulties many finite element models utilize fixed computational mesh adapting sigma modification (King, 1982) or revised sigma modification (King, 1985). Although such methods may have advantages in solution converge, they also have some limitations in describing momentum conservation and water surface velocity. If the numerical difficulties are manageable, employing the moving boundary condition system is considered as ideally best to overcome such problems.

Assuming that (ξ, η, ς, τ') is moving the coordinate system, using chain rule to relate with fixed basic coordinate system in differentiation, and applying $\frac{\partial t}{\partial \xi} = \frac{\partial t}{\partial \eta} = \frac{\partial t}{\partial \varsigma} = 0$, $\tau' = 0$ with respect to time associated with velocity component u gives

$$\frac{\partial u}{\partial t} = \frac{\partial u}{\partial \tau'} - \frac{\partial x}{\partial \tau'}\frac{\partial u}{\partial x} - \frac{\partial y}{\partial \tau'}\frac{\partial u}{\partial y} - \frac{\partial z}{\partial \tau'}\frac{\partial u}{\partial z} \tag{9}$$

Since z component is to compute the free surface variation, Equation 9 is modified as following equation,

$$\frac{\partial}{\partial t} = \frac{\partial}{\partial \tau'} - \frac{\partial z}{\partial \tau'}\frac{\partial}{\partial z} \tag{10}$$

and entire differentiated functions are revised in the same manner.

4 3-DIMENSIONAL FINITE ELEMENT EQUATION

4.1 *Construction of finite element mesh*

Using rectangular cubic isoparameter with a total 20 of nodal points, the velocity fields are assigned to entire 20 nodal points and 8 of them are used to define the flow depth.

In general, applying interpolation function the velocity and flow depth are expressed as discrete form as

$$\tilde{u} = \sum_{i=1}^{n} N_i u_i, \quad \tilde{v} = \sum_{i=1}^{n} N_i v_i, \quad \tilde{w} = \sum_{i=1}^{n} N_i w_i, \quad \tilde{h} = \sum_{i=1}^{n} M_i h_i \tag{11}$$

where N_i is 3rd order interpolation function of 20 nodal points for flow velocity, M_i is 3rd order interpolation function of 8 nodal points for flow depth, $\tilde{u}$, $\tilde{v}$, $\tilde{w}$, $\tilde{h}$ are finite element approximation of u, v, w, h, and u_i, v_i, w_i, h_i are node values of u, v, w, h.

To achieve the benefit of computational efficiency, the model is constructed to have base element, and surface element. The base element is applicable for volume integration, and 3 different types of surface elements allow for boundary integration.

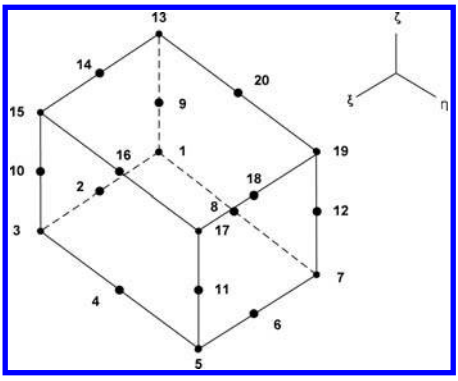


Figure 1. Three dimensional element.

4.2 *Streamline Upwind/Petrov-Galerkin scheme*

Since the Standard Galerkin method yields nonlinear instabilities during numerical simulation of the convection-dominated flow, selective upwind scheme is introduced to remove excessive fluctuation term associated with $2\Delta x$ wave length to overcome such problem. Although upwind scheme is essential for analysis of the convection dominated flow with high Reynolds number, the application is limited because nonlinearity occurs that is related with 2nd order differentiation. To avoid such numerical difficulties this model applies upwind weighting function shown in following equation only for the convection term.

$$W_i = N_i + \frac{\alpha \bar{l}}{2|V|}\left(u\frac{\partial N_i}{\partial x} + v\frac{\partial N_i}{\partial y} + w\frac{\partial N_i}{\partial z}\right) \tag{12}$$

Where W_i is weighting function, $\bar{l}$ is element length in flow direction, $\alpha = \coth \gamma/2 - 2/\gamma$, and $\gamma = Re|V|\bar{l}$ is element Reynolds number.

4.3 *Finite element equation*

Applying integration by parts to viscosity and depth terms, the governing equation can be summarized as following weighted residual form

$$\begin{aligned} f_u = {} & \int W^T \cdot \rho\left(u\frac{\partial u}{\partial x} + v\frac{\partial u}{\partial y} + w\frac{\partial u}{\partial z}\right) + N^T \cdot \rho\left(\frac{\partial u}{\partial t} - \frac{\partial z}{\partial t}\frac{\partial u}{\partial z} - \Omega v\right) \\ & + N_x^T \cdot \left(\varepsilon_{xx}\frac{\partial u}{\partial x} - \rho g h\right) + N_y^T \cdot \varepsilon_{xy}\left(\frac{\partial u}{\partial y} + \frac{\partial v}{\partial x}\right) + N_z^T \cdot \left(\varepsilon_{xy}\frac{\partial u}{\partial z}\right) \\ & + N^T \cdot \left(\rho g\frac{\partial a}{\partial x} - \Gamma_x\right) dV \end{aligned} \tag{13}$$

$$\begin{aligned} f_v = {} & \int W^T \cdot \rho\left(u\frac{\partial v}{\partial x} + v\frac{\partial v}{\partial y} + w\frac{\partial v}{\partial z}\right) + N^T \cdot \rho\left(\frac{\partial v}{\partial t} - \frac{\partial z}{\partial t}\frac{\partial v}{\partial z} + \Omega u\right) \\ & + N_x^T \cdot \varepsilon_{yx}\left(\frac{\partial u}{\partial y} + \frac{\partial v}{\partial x}\right) + N_y^T \cdot \left(\varepsilon_{yy}\frac{\partial v}{\partial y} - \rho g h\right) + N_z^T \cdot \left(\varepsilon_{yz}\frac{\partial v}{\partial z}\right) \\ & + N^T \cdot \left(\rho g\frac{\partial a}{\partial y} - \Gamma_y\right) dV \end{aligned}$$

Copyright © 2006 Taylor & Francis Group plc, London, UK

and for the continuity equation

$$f_c = \int_b M^T \cdot \left[\int_b^{+h} \left(\frac{\partial u}{\partial x} + \frac{\partial v}{\partial y} \right) dz + u_s \frac{\partial (a+h)}{\partial x} + v_s \frac{\partial (a+h)}{\partial y} + \frac{\partial h}{\partial t} - u_b \frac{\partial a}{\partial x} - v_b \frac{\partial a}{\partial y} \right] dA \quad (14)$$
$$= \int M^T \cdot \left(\frac{\partial u}{\partial x} + \frac{\partial v}{\partial y} \right) dV + \int_b \underline{M}^T \cdot \left[u_s \frac{\partial (a+h)}{\partial x} + v_s \frac{\partial (a+h)}{\partial y} + \frac{\partial h}{\partial t} - u_b \frac{\partial a}{\partial x} - v_b \frac{\partial a}{\partial y} \right] dA$$

where W^T is SU/PG weighting function, N^T is the weighting function that is identical to the shape function, and $\underline{M}^T$ is the weighting function for surface element. The wind stress and friction is applied for boundary stress of Γ_x, Γ_y.

5 MODEL APPLICATION

3-dimensional numerical analysis for free surface flow problem is very complicate since it is related with nonlinear characteristics, boundary conditions, physical and numerical instabilities. Through various validation procedures it is necessary to investigate the effect of such factors with computational feasibility, and the proposed model is applied to simulate various types of channel flows to evaluate stability, accuracy, as well as applicability of the model. Model simulation is conducted to identify 3-dimensional flow characteristics for U type channel flows, a confluent channel flow with 90° tributary, and a meandering channel flow with large sinuosity ratio. Then simulation results are compared with existing numerical model RMA-10, also with the experimental results.

5.1 *U-typed channel flow*

Flow field analysis in channel bend is hydraulically important since it yields secondary flow and is 3-dimensional turbulent flow to generate secondary flow. Flow simulation is conducted for the channel with the following configurations: the channel width is 0.3 m, the straight reach of upstream and downstream is 1m respectively, and inner radius of channel bend is 0.15 m. Figure 2 shows 3-layered finite element mesh to have 9,445 node numbers with 3,303 elements. With 0.3 m of flow depth as downstream boundary condition, 0.07 $m^3 s^{-1}$ is assigned for upstream boundary condition.

Along the lines of 1-1(outer side), 2-2(center side), and 3-3(inner side) computed water depth are compared with RMA-10 model, and at (A-A section), (B-B section), and (C-C section) 3 cross sectional velocities and water depth are collected to find velocity and

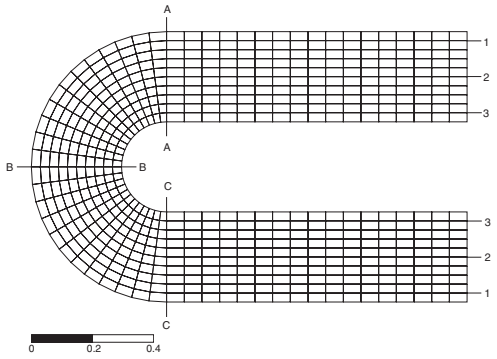


Figure 2. Computational grid for U-type shape channel.

water depth characteristics. During the simulation, it requires 12 times of iteration to obtain the converged solution. Figure 3 & 4 respectively show horizontal velocity distributions in each layer and velocity vectors at each cross section. Figure 3 shows that as the flow approaches channel bend, the inner side horizontal velocity is greater than the outer side and vice versa as it passes channel bend. Shown in Figure 4, the cross sectional velocity vectors move from outer side to inner side at the inlet of channel bend and vice versa at the outlet of channel bend with flow circulation due to opposite flow direction of the surface and the channel bed.

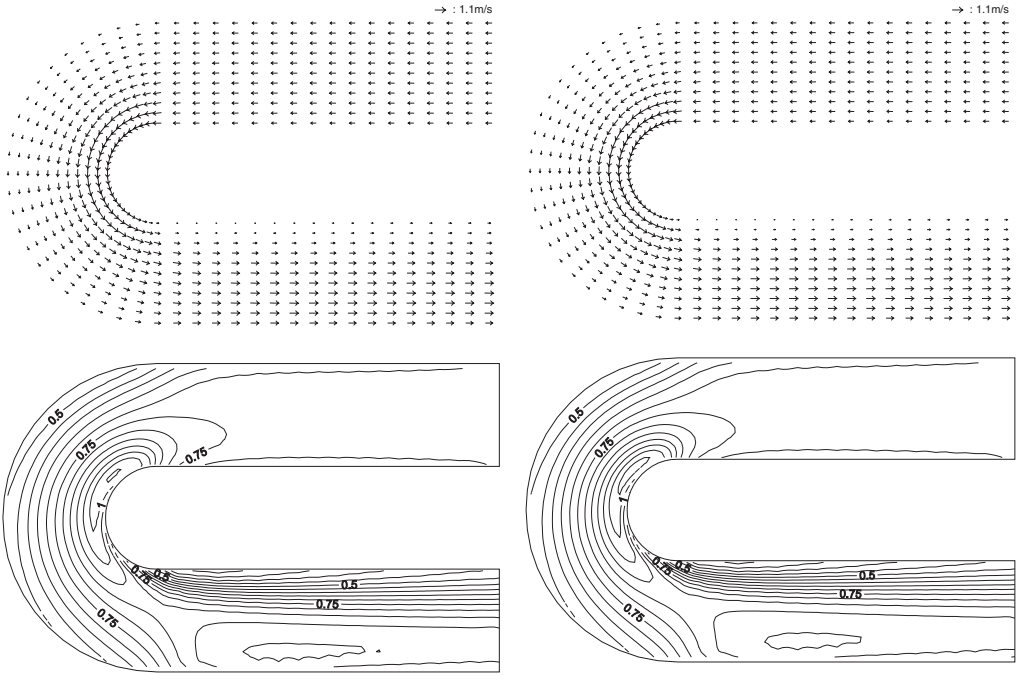
5.2 *Channel with tributary inflow*

The analysis of channel flow with tributary inflow is very important for river mechanics and environmental hydraulics. With simple geometric configuration, since the hydrodynamic of the channel confluence is very complicated, such flow condition is broadly applied for model validation. In this study the proposed model has been applied for the channel given in Figure 5.

The width of both main and tributary channel is given as 0.914 m. With the 9.144 m long tributary, from the confluence the main channel length is 10.973 m toward upstream and 6.401 m in downstream. It is composed of 3 layers to have total 5,859 node number and 2,072 element number. Numerical simulation is conducted for two cases with the definition of following terms: Q_m is flow rate of main channel, Q_b is flow rate of tributary channel, H is downstream water depth, and q^* is a ratio of the flow rate of main channel to total flow rate (Q_m/Q).

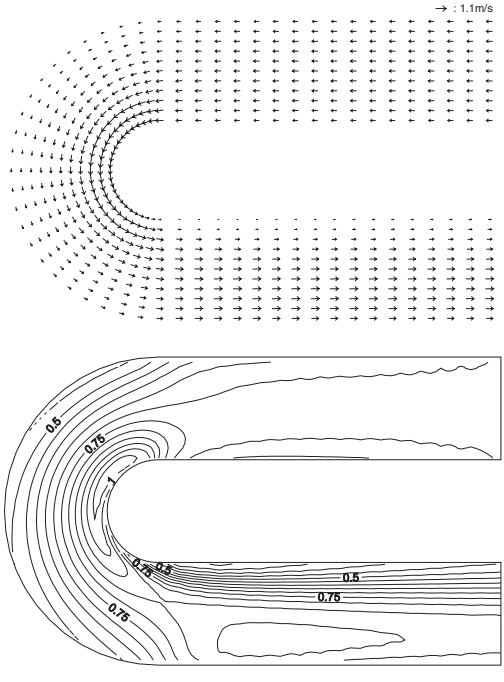
Model validation focuses comparison with water depth using the experimental results conducted by Shumat (1998). Figure 6 shows the simulation results applying two different flow conditions. The numeric values are dimensionless water level which is normalized by downstream water level. In both cases

Copyright © 2006 Taylor & Francis Group plc, London, UK



(a) Surface plane

(b) Mid plane



(c) Bed plane

Figure 3. Velocity distribution in horizontal plan.

Copyright © 2006 Taylor & Francis Group plc, London, UK

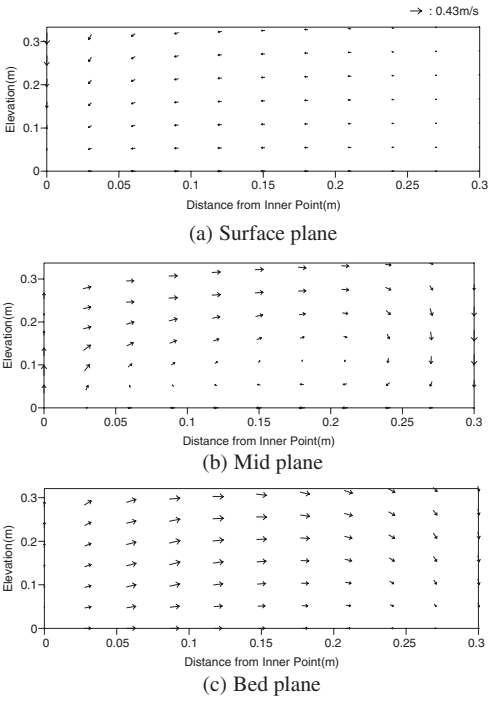


Figure 4. Cross sectional velocity distribution.

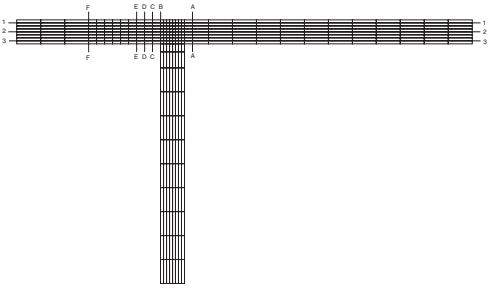


Figure 5. Construction of the finite element mesh.

numerical results well describe flow characteristics at channel confluence to show a good agreement with Shumat's experimental results.

Water surface and channel bed velocity distributions are given in Figure 7 to describe flow characteristics due to flow rate changes. Figures 8 and 9 show cross-sectional velocity distributions for two different flow conditions between the reach from A-A section right before tributary inflow to F-F section 3.656 m away after tributary inflow. Tributary inflow alters cross sectional velocity distribution; especially $q^* = 0.25$ with 2nd flow condition, flow circulation is more evident after D-D section since tributary inflow is greater than the main channel flow.

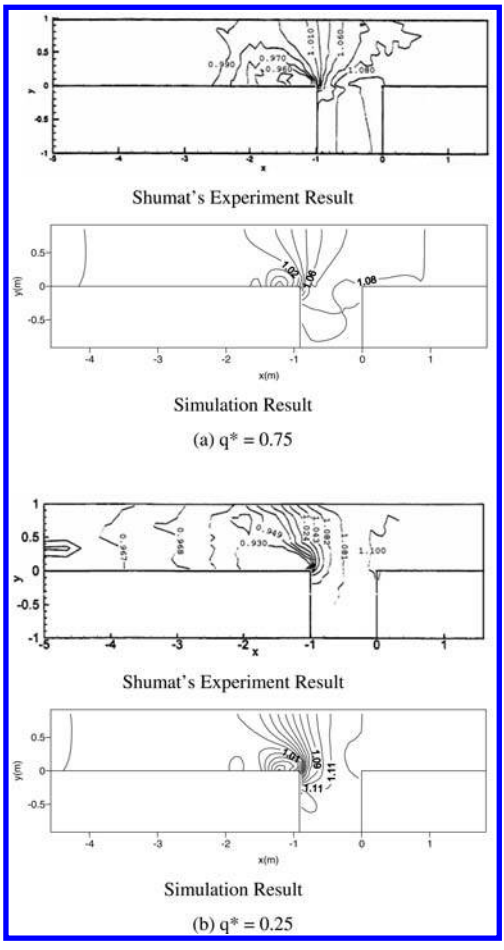


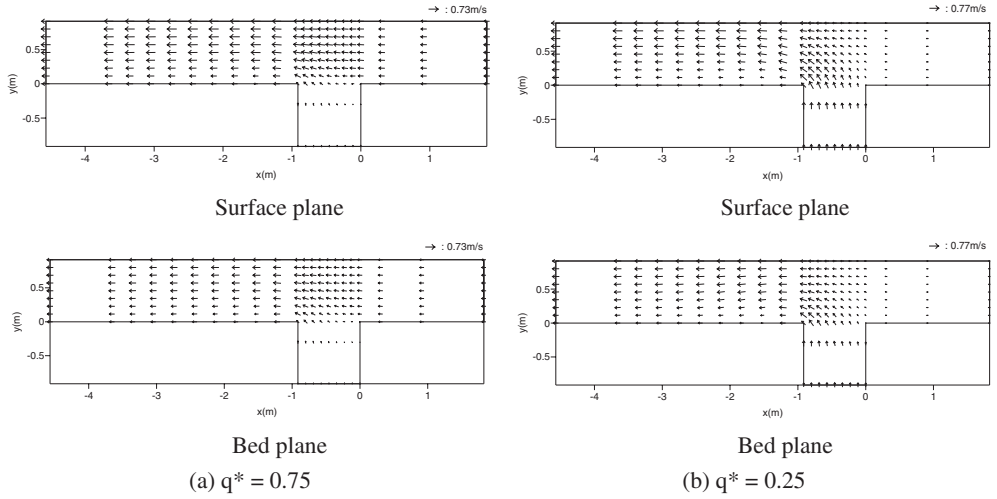
Figure 6. Comparison of water level.

6 CONCLUSIONS

In this study, 3-dimensional finite element model has been developed to simulate hydrodynamics of the channel flow based on the Streamline Upwind/Petrov-Galerkin scheme. Turbulent flow is considered using the Smagorinsky scheme for horizontal plan and Mellor-Yamada scheme in vertical direction. Moving boundary condition is applied for element modification with water surface variations to describe 3-dimensional flow characteristics more accurately. The conclusions of this study can be summarized as follows.

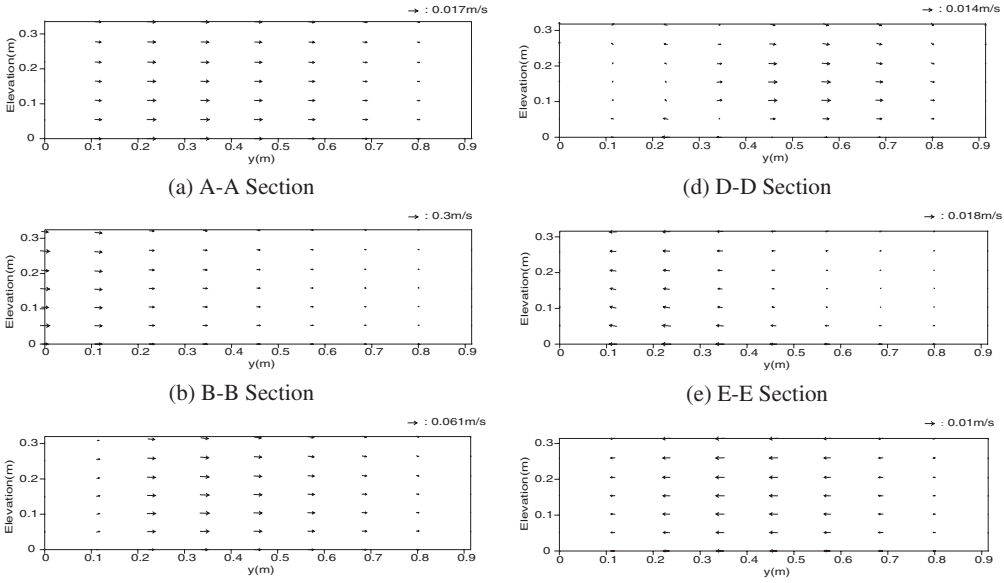
For 3-dimensional channel flow to establish governing equations considering turbulent flow, fundamental 3D Navier-Stokes equation is modified using the Reynolds equation. To describe characteristics of the turbulent flow the Smagorinsky scheme has

Copyright © 2006 Taylor & Francis Group plc, London, UK



(a) q* = 0.75 (b) q* = 0.25

Figure 7. Velocity Distribution of Horizontal Plane.



(a) A-A Section (d) D-D Section

(b) B-B Section (e) E-E Section

(c) C-C Section (f) F-F Section

Figure 8. Velocity Distribution of Cross Section(q* = 0.75).

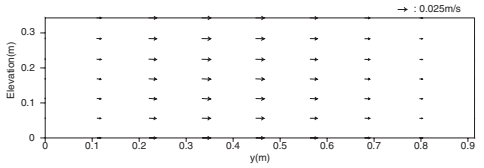
been employed for the horizontal direction, and the Mellor-Yamada scheme for the vertical direction.

3-dimensional finite element model is proposed employing the Streamined Upwind/Petrov Galerkin scheme as weighting function and moving boundary condition to improve the limitations of fixed element.

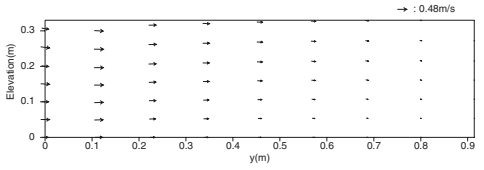
The proposed 3-dimensional finite element model has been evaluated through the application of U typed channel flow, and 3-dimensional velocity and water depth distributions were compared with the results of existing model. Also for the channel flow with tributary inflow it is compared with Shumat's experimental results to show a good agreement with computational results.

The advantage of the proposed model is to simulate 3-dimensional flow characteristics more accurately for various channel flows with consideration of turbulent flows. By adopting moving boundary conditions in describing water surface variations, it is possible to obtain stable and accurate numerical solutions. Further

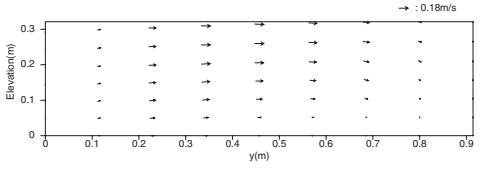
Copyright © 2006 Taylor & Francis Group plc, London, UK



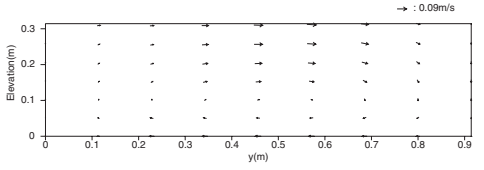
(a) A-A Section



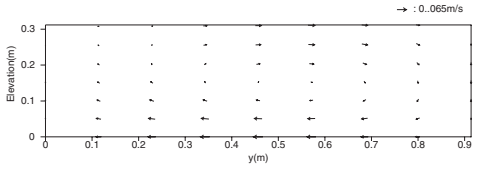
(b) B-B Section



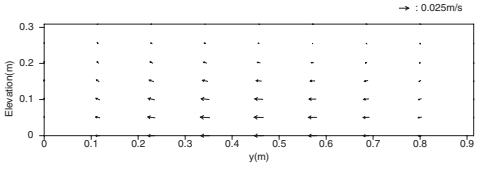
(c) C-C Section



(d) D-D Section



(e) E-E Section



(f) F-F Section

Figure 9. Velocity Distribution of Cross Section ($q^* = 0.25$).

development of the proposed model will focus on the simulation of pollutant propagation and sediment transport.

ACKNOWLEDGEMENTS

This research was supported by a grant (2-3-2) from Sustainable Water Resources Research Center of 21st Century Frontier Research Program.

REFERENCES

Alam, M.M. and Bhuiyan, M.A. (1995). "Collocation finite element simulation of dam-break flows." *Journal of Hydraulic Engineering*, ASCE, Vol. 121, No. 2, pp. 118–128.

Berger, R.C. (1993). "A finite element scheme for 'shock capturing," *TechnicalReport HL-93-12*, U.S. Army Engineer Waterways Experiment Station, Vicksburg, MS.

Berger, R.C., and Stockstill, R.L. (1995). "Finite-element model for high-velocity channels," *Journal of Hydraulic Engineering*, Vol. 121, No. 10, pp. 710–716

Boe, O. (1993). "A monotone Petrov-Galerkin method for quasi-linear parabolic differential equations." *SIAM Journal on Scientific Computing*, Vol. 14, pp. 1057–1071.

Bradford, S.F. and Katopodes, N.K. (2000). "The anti-dissipative, non-monotone behavior of Petrov-Galerkin upwinding." *International Journal for Numerical Methods in Fliuds*, Vol. 33, pp. 583–608.

Davies, A.M. and Lawrence, J. (1994). "A three-dimensional model of the M4 tide in the Irish Sea : The importance of open boundary conditions and influence of wind." *Journal of Geophsical Rsearch*, Vol. 99, No. C8, pp. 16197–16227.

Hicks, F.E. and Steffler, P.M. (1992). "Characteristic dissipative Galerkin scheme for open channel flow." *Journal of Hydraulic Engineering*, ASCE, Vol. 118, No. Katopodes, N.D. (1984). "Two-dimensional surge and shocks in open channels." *Journal of Hydraulic Engineering Eng*, ASCE, Vol. 110, No. 6, 1984, pp. 794–812.

King, I.P. (1976). "Finite element models for unsteady flow routing through irregular channels." *Finite Element in Water Resources*, C.A. Brebbia, et al., eds., Pentech Press, London, pp. 4.165–4.184

Kistler, S.F. and Scriven, L.E. (1983). "Coating flow theory by finite element and asympotic analysis of the Navier-Stokes systems." *International Journal of Numerical Methods in Fluids*, Vol. 8, No. 12, pp. 354–375.

Mayerle, R. and Toro, F.M. (1995). "Verification of a three-dimensional numerical model simulation of flow in the vicinity of spur dikes." Journal of Hydraulics Research, Vol. 33, No. 2, pp. 243–256.

Silva, A.M.F (1995). Turbulent flow in sine-generated meandering channels, Ph.D Thesis, Queen's University.

Thomas, T.G., Leslie, D.C., and Williams, J.J.R. (1995). "Free surface simulations using a conservative 3D code." *Journal of Computational Physics*., Vol. 116, pp. 52–68.

Wambersie. O. and Crochet, M.J. (1992). "Transient finite element method for calculating Steady State Three-Dimensional Free Surfaces." *International Journal for Numerical Methods in Fluids*, Vol. 14, pp. 343–360.

Copyright © 2006 Taylor & Francis Group plc, London, UK

Fourth order balanced WENO schemes for shallow water equations

V. Caleffi & A. Valiani
Dipartimento di Ingegneria, Universitá degli Studi di Ferrara – Ferrara (IT)

ABSTRACT: Two WENO schemes, fourth-order accurate in space and time, for the numerical integration of shallow water equations with bottom slope source term, are presented. Spatial accuracy is achieved using WENO reconstructions of the free-surface elevation and of the specific discharge. In the first Central WENO model, based on staggered grids, time accuracy is achieved using a Runge-Kutta (RK) scheme coupled with its Natural Continuous Extension (NCE). In the second Upwind WENO model, time accuracy is obtained using a Strong Stability Preserving Runge-Kutta method, SSPRK(5,4). Original source term treatment, satisfying the *C-property*, i.e. the property of exactly preserving the quiescent flow, is used in both the models. Such a treatment involves the spatial integration of the source term, which is analytically manipulated in order to take advantage from the regularity of the free surface elevation, usually smoother than the bottom elevation. The source term treatment in the Central scheme involves also an original evaluation of the point-values of the flux gradient, coupled with the source term. Several standard one-dimensional test cases are used to verify the high-order accuracy, the C-property, and the good resolution properties of both the models. Both the schemes are reliable for the application to real problems characterized by very irregular bottoms.

1 INTRODUCTION

In recent years, high resolution methods for conservation laws have been extensively applied to shallow water equations to solve problems in fluid mechanics and hydraulic engineering (Toro 1992). More recently, to increase the computational efficiency, the use of coarse grids and high-order accuracy are pursued. In this context, an important contribute are WENO (Weighted Essentially Non Oscillatory) schemes (Liu et al. 1994; Jiang & Shu 1996).

Inside WENO class, two principal approaches can be distinguished. The classical one is the Upwind approach, (Godunov 1959; Shu 1997), in which the eigensystem is extensively used. The main advantage of this method is its strong physical basis, which allows to obtain a good resolution and the maximum reduction of unphysical oscillations near the shocks. The alternative approach is the Centered scheme family, whose origin is the first order Lax-Friedrichs (Lax 1954) staggered method. The eigensystem is ignored by these schemes.

Several works on SWE are recently devoted to the consistent numerical treatment of source term due to bed slope, to allow the application of WENO methods to engineering problems. A recent work by Vuković & Sopta (2002), devoted to the numerical integration of the shallow water equations, applies, in a WENO context, the idea of balancing the momentum flux with the source term. Such a method has been introduced by Bermudez & Vázquez-Cendón (1994) and then improved by Vázquez-Cendón (1999). In Vuković & Sopta (2002), the *C-property* is satisfied, but the complexity of the method is relevant.

High accuracy and well-balancing are also obtained by Črnjarić-Ž ic et al. (2004) using both Finite Volume WENO and Central WENO schemes. In particular, Črnjarić-Ž ic et al. (2004) apply their schemes not only to SWE but also to de Saint-Venant, cross section averaged, open-channel flow equations, where source terms depend on the channel geometry. Good results are also obtained adopting the DFB method, i.e. the Divergence Form for the Bed slope source term, due to Valiani & Begnudelli (2006). In the original paper is shown an enormous increasing in stability for several appropriate test cases, both in one and two dimensions.

The original contribution of the present work regards the proper numerical treatment of bed slope source term for high accuracy, well-balanced, WENO methods. The novel approach is presented in the Central WENO and in the Upwind WENO context and involves three different aspects of the schemes: the WENO reconstructions are formulated according to the Surface Gradient Method (Zhou et al. 2001), i.e. the free-surface elevation is used instead of the flow depth; the numerical approximation of the point-values of the flux derivative and of the source term considered as

Copyright © 2006 Taylor & Francis Group plc, London, UK

a whole is defined to obtain the balancing between the flux gradient and the source term themselves and the preserving of high accuracy; the cell-integral of the source term is defined to obtain high accuracy and well-balancing. The designed scheme assures the fulfillment of the following conditions: the full achievement of fourth-order spatial and time accuracy; the satisfaction of the exact C-property; the prevention of spurious oscillations when complex and irregular bed configuration occurs.

In this paper only simple one-dimensional flow is considered, in order to verify the introduced novelties over simple, well established test cases. However, the strength of the present method consists of a large applicability in a broad range of engineering problems such as river flows, debris flows, mud flows, real world dam break waves, flood waves, etc. See (Valiani et al. 2004) and the references therein. For example it is simple to extend the present concepts to the movable bed case, see also (Valiani et al. 2004) for preliminary examples, and to 2D problems.

2 CENTRAL WENO MODEL

This numerical model is developed starting from the explicit fourth-order Central WENO scheme proposed by Levy et al. (1999), which is suitable for the numerical integration of homogeneous systems of conservation laws. To avoid any ambiguity in the discrete description of the bed profile in staggered schemes – due to the use of two different, coupled grids – the destaggering procedure presented in (Jiang et al. 1998) is applied. In this work the scheme is extended in order to treat the one-dimensional SWE with the geometrical source term, $u_t + f_x = s$. These equation stands for:

$$\frac{\partial}{\partial t}\begin{bmatrix} h \\ vh \end{bmatrix} + \frac{\partial}{\partial x}\begin{bmatrix} vh \\ gh^2/2 + v^2 h \end{bmatrix} = \begin{bmatrix} 0 \\ ghs_0 \end{bmatrix}, \tag{1}$$

where: $u(x,t)$ is the vector of conservative variables; $f(u(x,t))$ is the flux vector; $s(x,u(x,t))$ is the source term relative to the bottom slope. t is the time, x is the space, $h(x,t)$ is the flow depth, $v(x,t)$ is the vertically averaged velocity, g is the gravity, $s_0 = -\mathrm{d}z/\mathrm{d}x$ is the bottom slope and $z(x)$ is the bottom elevation.

An uniformly spaced grid $x_j = j\Delta x$, and a staggered grid $x_{j+1/2} = (j+1/2)\Delta x$ are defined. Each computational step is characterized by a time interval Δt^n, which is selected in order to assure the stability of the numerical scheme (Levy et al. 1999). t^n is the time level of the known variables, while $t^{n+1} = t^n + \Delta t^n$ is the time level of the unknown variables. Denoting: $I_j = [x_{j-1/2}, x_{j+1/2}]$ the j-th cell, centered around the grid point x_j; $\bar{u}_j^n$ the corresponding cell-averaged solution at time t^n; $\bar{s}_j$ the cell-averaged source term, the integration of Equation (1) over $[x_j, x_{j+1}] \times [t^n, t^{n+1}]$ gives:

$$\Delta\bar{u}_{j+1/2} = -\frac{1}{\Delta x}\int_{t^n}^{t^{n+1}} [f_{j+1} - f_j] + \bar{s}_{j+1/2}\,\mathrm{d}t, \tag{2}$$

with $\Delta\bar{u}_{j+1/2} = \bar{u}_{j+1/2}^{n+1} - \bar{u}_{j+1/2}^{n}$ and $f_j = f(u(x_j,t))$. Equation (2) describes the updating in time of the solution from the cell-averages on the original grid to the cell-averages on the shifted grid. In the non-staggered version of central WENO schemes (Jiang et al. 1998) an additional step is added and the updated solution $\bar{u}_{j+1/2}^{n+1}$ is projected back on the original grid, obtaining $\bar{u}_j^{n+1}$. To discretize Equation (2), it is necessary to design (Levy et al. 1999; Xing & Shu 2005): a reconstruction of the variables to evaluate the cell-averaged values on the staggered grid, starting from cell-averaged values over the non-staggered grid and *vice versa*; a well-balanced spatial integration of the source term; a reconstruction of the variables to determine the point-values in the cell-centers; a well-balanced reconstruction to evaluate the point-value flux derivatives coupled with the source term.

2.1 *Time integration*

The grid staggering is particularly useful because time integrals are evaluated in the cell-centers of the non-staggered grid, where the solution can be considered smooth. Such a condition allows to adopt standard numerical techniques for the time integral approximation (Shu 1997; Jiang et al. 1998; Levy et al. 1999). In particular, to achieve the fourth-order integration in time of Equation (2), a Simpson's quadrature rule is selected (Levy et al. 1999):

$$\Delta\bar{u}_{j+\frac{1}{2}} = \frac{\Delta t^n}{\Delta x}\sum_{l=1}^{3} N_l \left[f_j^{n+\beta_l} - f_{j+1}^{n+\beta_l} + \Delta x\, \bar{s}_{j+\frac{1}{2}}^{n+\beta_l} \right] \tag{3}$$

with:

$$\begin{aligned} \bar{s}_{j+1/2}^{n+\beta_l} &= \tfrac{1}{\Delta x}\textstyle\int_{x_j}^{x_{j+1}} s(x, t^n + \beta_l \Delta t^n)\,\mathrm{d}x \\ f_j^{n+\beta_l} &= f(\hat{u}(x_j, t^n + \beta_l \Delta t^n)) \end{aligned} \tag{4}$$

$N = [1/6, 2/3, 1/6]^{\mathrm{T}}$ are the weights and $\beta = [0, 1/2, 1]^{\mathrm{T}}$ are the nodes of the quadrature; $\hat{u}$ is the estimated point-value solution, see (Levy et al. 1999).

The approximation of the point-values at time t^{n+1}, appearing in Equation (3), is performed using a fourth-order Runge-Kutta scheme expressed by:

$$\begin{aligned} \hat{u}^{n+1} &= \hat{u}^n + \Delta t^n \sum_{i=1}^{4} b_i k^{(i)}, \\ \hat{u}^{(i)} &= \hat{u}^n + \Delta t^n \sum_{j=1}^{i} a_{ij} k^{(j)}, \end{aligned} \tag{5}$$

where $b = [1/6, 1/3, 1/3, 1/6]^{\mathrm{T}}$; a is a matrix of zeros with the exception of the elements $a_{2,1} = a_{3,2} = 1/2$

Copyright © 2006 Taylor & Francis Group plc, London, UK

and $a_{4,3}=1$; $k^{(i)}$ are the Runge-Kutta fluxes. For the considered balance law (1), $k^{(i)}$ is a numerical evaluation of $(-f_x+s)$, computed starting from the point-values $\hat{u}^{(i)}$. The Runge-Kutta fluxes computation is performed using an original approach described in Section 2.2.2, which allows the satisfaction of the C-property.

The evaluation of the point-value at time $t^{n+1/2}$, appearing in Equation (3), is obtained using the Natural Continuous Extension procedure (Zennaro 1986; Levy et al. 1999) inside RK method:

$$\hat{u}^{n+1/2}=\hat{u}^n+\Delta t^n\sum_{i=1}^{4}B_i k^{(i)}, \qquad (6)$$

with: $B=[5/24,1/6,1/6,-1/24]^{\mathrm{T}}$.

2.2 *WENO reconstructions*

Following the SGM Method (Zhou et al. 2001) the free-surface level $\eta=h+z$ is chosen as the basis for the WENO reconstruction. This choice provides accurate point-values estimate of the conservative variables at cell-centers and the achievement of the well-balancing between flux gradient and bottom slope source term. The vector of reconstructed variables $\mu=[\eta,hv]^{\mathrm{T}}$ is introduced.

2.2.1 *Cell-averages and point-values*

The updating of the solution from time t^n to time t^{n+1}, see Equation (3), requires the evaluation of the staggered cell-averages, $\bar{u}^n_{j+1/2}$; the time integration procedure, described in Section 2.1, Equation (5), requires the evaluation of the point-values $\hat{u}^n_j$, starting from the cell-averaged values $\bar{u}^n_j$. The procedure to achieve these purposes is summarized in the following three steps (Levy et al. 1999; Qiu & Shu 2002; Shu 1997):

1. The cell-averaged values $\bar{\mu}_j$ are computed using $\bar{\mu}_j=\bar{u}_j+[\bar{z}_j,0]^{\mathrm{T}}$.
2. The proper reconstruction is a piecewise function over the mesh I_j:

$$T(x)=\sum\nolimits_j R_j(x)\,\chi_j, \qquad (7)$$

where χ_j are the characteristic functions of the intervals I_j and $R_j(x)$ are suitable polynomials of degree 2. Once $T(x)$ is given, $\bar{\mu}_{j+1/2}$ is computed using:

$$\bar{\mu}_{j+1/2}=\int_{x_j}^{x_{j+1}}T(x)\mathrm{d}x= \\ =\int_{x_j}^{x_{j+1/2}}R_j(x)\mathrm{d}x+\int_{x_{j+1/2}}^{x_{j+1}}R_{j+1}(x)\mathrm{d}x, \qquad (8)$$

whilst the point-value is $\hat{\mu}_j=T(x_j)=R_j(x_j)$.
3. Cell-averaged values, $\bar{u}^n_{j+1/2}$, and point-values, $\hat{u}^n_j$, are given by $\bar{u}^n_{j+1/2}=\bar{\mu}^n_{j+1/2}-[\bar{z}_{j+1/2},0]^{\mathrm{T}}$ and $\hat{u}^n_j=\hat{\mu}^n_j-[\hat{z}_j,0]^{\mathrm{T}}$, respectively.

To define the reconstruction $T(x)$, the fulfillment of *conservation, accuracy* and *non-oscillation* requirements must be imposed (Caleffi et al. 2006; Levy et al. 1999; Qiu & 2002) and consequently, the following steps may be performed.

Three sets of three cells (*stencils*) $\mathcal{P}_{j+k}=\cup_{l=-1}^{l=+1}I_{j+k+l}$, with $k=-1,0,1$, are selected. The cell I_j belongs to each of them. Three polynomials of degree 2, $P_{j+k}(x)$, with $k=-1,0,1$, are introduced. Each polynomial is associated with a corresponding stencil $\mathcal{P}_{j+k}$. The cell-average of $P_{j+k}(x)$ on each cell of the stencil $\mathcal{P}_{j+k}$ is equal to the cell-average of the conservative variables, i.e.:

$$\frac{1}{\Delta x}\int_{I_{j+k-i}}P_{j+k}(x)\mathrm{d}x=\bar{\mu}_{j+k-i}, \qquad (9)$$

with $k=-1,0,1$ and $i=-1,0,1$. The coefficients of each polynomial $P_{j+k}(x)$ are uniquely determined by Equation (9).

To satisfy the non-oscillatory requirement, the polynomial $R_j(x)$ is written as a convex combination of the three polynomials $P_{j+k}(x)$, using suitable variable *weights*, w_j^k $(k=-1,0,1)$:

$$R_j(x)=\sum_{k=-1}^{1}w_j^k\,P_{j+k}(x). \qquad (10)$$

To compute w_j^k, the *linear weights*, C_k, and the *index of smoothness* function, IS_j^k, are introduced (Qiu & Shu 2002). The linear weights are chosen such that the reconstruction satisfies the accuracy requirement, where the solution is smooth (see Table 1), while the index of smoothness function allows the optimal weighting of polynomials $P_{j+k}(x)$ in Equation (10), where the solution is discontinuous. Several expressions can be used to quantify the index of smoothness inside the stencil (Liu et al. 1994; Jiang & Shu 1996). In this work the L^2*-norm* of the polynomial derivatives, $P^{(l)}_{j+k}(x)$ on the cell I_j, is selected, as suggested in (Jiang & Shu 1996). The final expressions for the weights is:

$$w_j^k=\frac{\alpha_j^k}{\sum_{l=-1}^{l=1}\alpha_j^l}\quad\text{with}\quad\alpha_j^k=\frac{C_k}{\left(\epsilon+IS_j^k\right)^p}, \qquad (11)$$

where ϵ and p are empirically selected constants. The dimensional nature of ϵ and p parameters implies that

Table 1. Linear weights – Central model.

	C_{-1}	C_0	C_{+1}
$\bar{u}^n_j\Rightarrow\bar{u}^n_{j+1/2},\hat{u}^n_j$	3/16	5/8	3/16
$\hat{K}_j\Rightarrow k_j$ and $\hat{\eta}_j\Rightarrow\hat{\eta}'_j$	1/6	2/3	1/6
$\hat{\xi}_j\Rightarrow\bar{\xi}_{j+1/2}$		1/2	1/2

Copyright © 2006 Taylor & Francis Group plc, London, UK

universal values of these quantities *do not* exist, and problem-dependent values must be chosen. A detailed analysis has shown that this choice must be devoted to minimize numerical diffusion due to the staggering.

2.2.2 *Reconstruction of Runge-Kutta fluxes*

The fourth-order evaluation of Runge-Kutta fluxes, necessary in Equation (5), is performed by an original approach obtained modifying the reconstruction of flux derivative point-values introduced in classical Central WENO schemes (Levy et al. 1999). This approach, inspired also by the work of Črnjarić-Žic et al. (2004), allows the C-property achievement.

The key element is the introduction of a proper cell function $K_j(x, u(x,t))$ defined by:

$$K_j(x,u(x,t)) = \\ = \begin{bmatrix} (vh)_j - (vh) \\ \left(v^2h + \frac{g(\eta-z)^2}{2}\right)_j - \left(v^2h + \frac{g(\eta-z)^2}{2}\right) \end{bmatrix} + \\ + \begin{bmatrix} 0 \\ 1/2g\left((\eta_j - z)^2 - (\eta_j - z_j)^2\right) \end{bmatrix} \quad (12)$$

and satisfying the two analytical relations:

$$\left.\frac{\partial K_j}{\partial x}\right|_{x=x_j} = k_j = (-f_x + s)_j \quad (13)$$

and, for quiescent flow (i.e. $vh = 0$ and $\eta =$ constant):

$$K_j(x) = 0 \qquad \forall x. \quad (14)$$

Naming $T(x)$ the reconstruction of K_j, defined by an equation formally identical to (7), the Runge-Kutta fluxes on the grid x_j should be approximated by $T'(x_j)$, i.e. $k_j \approx T'(x_j)$. This is a direct consequence of relation (13). The fulfillment of (14) assures the well-balancing between the flux gradient and the source term, as explained in (Caleffi et al. 2006).

The polynomials $R_j(x)$ are defined imposing *accuracy* and *non-oscillation* requirements (see 2.2.1). Let us consider three polynomials $P_{j+k}(x)$ of degree 2, related to the stencils $\mathcal{P}_{j+k}$. Their coefficients are univocally determined by imposing the passage of $P_{j+k}(x)$ through the three point-values of K_j, computed on the cell-centers of the respective stencils:

$$P_{j+k}(x_{j+k+l}) = K_j(x_{j+k+l}, \hat{u}^{(i)}_{j+k+l}), \quad (15)$$

with $k = -1, 0, 1$ and $l = -1, 0, 1$. The polynomial $R_j(x)$ is written as a linear convex combination of the three polynomials $P_{j+k}(x)$, using suitable weights, w_j^k (see Equation (10)). Such weights are computed using Equations (11), with a specific set of linear weights (see Table 1). The computation of the linear weights is performed as in classical Central WENO schemes, see (Qiu & Shu 2002).

2.3 *Source term spatial integration*

The novel technique for the numerical integration in space of the source term, appearing in Equation (4), is described in this Section. This integration must be performed at time t^n, $t^{n+1/2}$ and t^{n+1}.

The first step consists of the analytical manipulation of the second component of bed slope source term integral introducing the function $\xi(x) = gz\mathrm{d}\eta/\mathrm{d}x$, using the relation $h = \eta - z$ and a simple integration by parts:

$$s^{[2]}_{j+1/2} = \frac{1}{2}g\left[z^2_{j+1} - z^2_j\right] - g\left[\eta_{j+1}z_{j+1} - \eta_j z_j\right] + \\ + \int_{x_j}^{x_{j+1}} \xi(x)\mathrm{d}x. \quad (16)$$

The two forms are analytically equivalent but, from the numerical point of view, they may be different. In the classical formulation the integration involves the bed spatial derivatives, while in the latter case the integration involves the free surface spatial derivatives. In the case of irregular bottom, the latter formulation must be preferred, because the spatial derivative of the free surface elevation is more regular than the spatial derivative of the bed elevation, even if the solution is discontinuous (Caleffi et al. 2006).

The discretization of the first two terms of the RHS in Equation (16) does not present difficulties, because they can be exactly computed from the point-values z_j and $\hat{\eta}_j$; only the last term requires an *ad hoc* numerical treatment. This procedure is here summarized.

At each time, t^n, $t^{n+1/2}$ and t^{n+1}, the source term integration needs the reconstruction of free-surface point-value derivatives $\hat{\eta}'_j$, starting from free-surface point-values $\hat{\eta}_j$. A WENO reconstruction similar to that described in Section 2.2.2, in which the function $\eta(x)$ is used instead of $K_j(x, u(x,t))$. The point-values $\hat{\xi}_j = (gz\mathrm{d}\eta/\mathrm{d}x)_j = gz_j\hat{\eta}'_j$ are then computed.

Now, the computation of the integral appearing in Equation (16) is based on a CWENO reconstruction of the function $\xi(x)$. This approach is extensively described in (Caleffi et al. 2006) and is here just sketched.

By introducing $M_{j+1/2}(x)$, suitable polynomials of degree 2, the $\xi(x)$ reconstruction on the staggered grid $I_{j+1/2}$ can be written as:

$$L(x) = \sum_j M_{j+1/2}(x)\chi_{j+1/2}. \quad (17)$$

The cell-averaged values, $\bar{\xi}_{j+1/2}$, on the staggered grid $I_{j+1/2}$ are expressed by:

$$\bar{\xi}_{j+\frac{1}{2}} = \frac{1}{\Delta x}\int_{x_j}^{x_{j+1}} L(x)\,\mathrm{d}x = \frac{1}{\Delta x}\int_{x_j}^{x_{j+1}} M_{j+\frac{1}{2}}(x)\,\mathrm{d}x. \quad (18)$$

Copyright © 2006 Taylor & Francis Group plc, London, UK

In this reconstruction, Equation (18) plays the same role of Equation (8) in the staggered cell-averaged variable reconstruction. Notwithstanding this, their structures are quite different. In the case of Equation (18) the staggered cell-average (related to cell $I_{j+1/2}$) involves only one polynomial cell-reconstruction (related to cell $I_{j+1/2}$), whilst in the case of Equation (8) the staggered cell-average involves two polynomial cell-reconstructions (related to cells I_j and I_{j+1}).

The reconstruction $L(x)$ is carried out in order to achieve the fourth-order accuracy and to satisfy the non-oscillation requirement described in 2.2.1, and it is obtained adopting this procedure. On each cell of the staggered grid $I_{j+1/2}$, two stencils of three adjacent cell of the non-staggered grid x_j, are selected, $\mathcal{N}_{j+m}$, with $m=0,1$. Such stencils are centered with respect to the cell boundaries of the cell $I_{j+1/2}$:$\mathcal{N}_{j+m} = \cup_{l=-1}^{l=+1} I_{j+m+l}$. Two polynomials of degree 2, $N_{j+m}(x)$, with $m=0,1$, associated to the stencils $\mathcal{N}_{j+m}$, are defined. Considering the cell-center point-values $\hat{\xi}_{j+m+l}$, with $l=-1,0,1$, related to the stencils $\mathcal{N}_{j+m}$, the coefficients of $N_{j+m}(x)$ are determined solving the system:

$$N_{j+m}(x_{j+m+l}) = \hat{\xi}_{j+m+l} \tag{19}$$

with $m=0,1$ and $l=-1,0,1$. Considering Equation (17) and applying WENO method, $L(x)$ reconstruction on the staggered grid $I_{j+1/2}$ is given by a convex combination of the previously defined polynomials $N_{j+m}(x)$:

$$M_{j+1/2}(x) = \sum_{m=0}^{1} w_j^m N_{j+m}(x), \tag{20}$$

where w_j^m, with $m=0,1$ are two suitable weights, depending on the smoothness of the solution. Linear weights are defined in order to satisfy the proprieties of *convexity* and *symmetry*, described in (Caleffi et al. 2006). From these two conditions an univocal set of coefficients is obtained, whose values are reported in Table 1. Linear weights assure the achievement of the prescribed fourth-order spatial accuracy, too. *Accuracy* condition is *a posteriori* verified (Caleffi et al. 2006). To complete the description of this reconstruction, appropriate weights w_j^m must be defined. Referring to (Section 2.2.1), w_j^m depends on solution regularity over $\mathcal{N}_{j+m}$, whose indicator are the indices of smoothness IS_j^m (Caleffi et al. 2006). Non linear weights are computed using Equation (11). Once $\bar{\xi}_{j+1/2}$ is computed, the second component of the cell-averaged source term can be written as:

$$\begin{aligned} \bar{s}_{j+1/2}^{[2]} &= \frac{g}{2\Delta x}\left(z_{j+1}^2 - z_j^2\right) + \\ &- \frac{g}{\Delta x}\left(\hat{\eta}_{j+1} z_{j+1} - \hat{\eta}_j z_j\right) + \bar{\xi}_{j+1/2}. \end{aligned} \tag{21}$$

The first component of the same cell-averaged source terms is always zero.

3 UPWIND WENO MODEL

The here presented model is developed starting from the Finite Volume WENO scheme, fourth-order accurate in space and time, presented in (Shu 1997), which is extended to allow its application to SWE (1). In particular, the spatial integration of the source term is performed using the same original approach described in Section 2.3. Notwithstanding the great differences between Central and Upwind WENO schemes, the versatility of the proposed method allows its application to both models.

Now, the spatial discretization is based on a single grid, uniformly spaced, defined by $x_j = j\Delta x$, while the time discretization is based on an adaptive time interval Δt^n, which preserves the stability of the numerical scheme (Spiteri & Ruuth 2002). Integrating the Equation (1) over $[x_{j-1/2}, x_{j+1/2}]$ the following semi-discrete expression is achieved:

$$\left.\frac{\mathrm{d}\bar{u}}{\mathrm{d}t}\right|_j = -\left[f_{j+1/2}^* - f_{j-1/2}^*\right] + \bar{s}_j = \mathcal{L}(\bar{u}, x, t) \tag{22}$$

where $f_{j+1/2}^*(\hat{u}_j^R, \hat{u}_{j+1}^L)$ is a numerical flux, computed using the Approximate Riemann Solver HLL due to Toro Toro (1992), which is a function of the right point-value , $\hat{u}_j^R$, related to the cell I_j, and of the left point-value, $\hat{u}_{j+1}^L$, related to the cell I_{j+1}. Equation (22), coupled with an appropriate ODE solver, is used to update the solution from the time level t^n to the time level t^{n+1}, after the definition of a WENO reconstruction for the point-value solution (in correspondence of both the cell boundaries and of the cell-centers) and of a well-balanced spatial integration of the source term.

3.1 *Time integration*

To avoid unphysical oscillations and to guarantee high accuracy and high computational efficiency the SSPRK(5,4) is selected (Spiteri & Ruuth 2002). This method is summarized by the following equations:

$$\begin{aligned} \bar{u}_j^{(0)} &= \bar{u}_j^n \\ \bar{u}_j^{(i)} &= \sum_{k=0}^{i-1}\left(\alpha_{ik}\bar{u}_j^{(k)} + \Delta t \beta_{ik}\mathcal{L}\left(\bar{u}^{(k)}\right)\right) \\ \bar{u}_j^{n+1} &= \bar{u}_j^{(s)} \end{aligned} \tag{23}$$

with $i=1,\ldots,s$ and $s=5$. For the values of the α_{ik} and β_{ik} coefficients and for the details of the method see (Spiteri & Ruuth 2002).

3.2 *WENO reconstructions*

The SGM technique (Zhou et al. 2001) is used also in this model. In this Section the reconstructions of the cell-boundary point-values, $\hat{u}_j^R$ and $\hat{u}_j^L$, necessary for the numerical flux evaluation, and of the cell-center free-surface derivatives, $\hat{\eta}_j'$, necessary for the

Copyright © 2006 Taylor & Francis Group plc, London, UK

Table 2. Linear weights – Upwind model.

	C_{-1}	C_0	C_{+1}
$\bar{\mu}_j \Rightarrow \hat{\mu}_j^R$	1/10	6/10	3/10
$\bar{\mu}_j \Rightarrow \hat{\mu}_j^L$	3/10	6/10	1/10
$\bar{\mu}_j \Rightarrow \hat{\mu}'_j$	5/24	14/24	5/24
$\hat{\xi}_j \Rightarrow \bar{\xi}_j$	1/4	1/2	1/4

source term spatial integration, are presented. Both the reconstructions start from the cell-averages $\bar{u}_j$.

The reconstruction of $\hat{u}_j^R$ is subdivided in three steps, see also Section 2.2.1:

1. $\bar{\mu}_j$ are computed using $\bar{\mu}_j = \bar{u}_j + [\bar{z}_j, 0]^{\mathrm{T}}$.
2. The polynomials of order 2, $R_j(x)$, are introduced and the pursued, piece-wise parabolic, reconstruction $T(x)$ is again formally defined by Equation (7). Consequently, the point-value of the reconstructed variable on the right boundary of the cell I_j is computed using:

$$\hat{\mu}_j^R = T\left(x_j + \Delta x/2\right) = R_j\left(x_j + \Delta x/2\right). \tag{24}$$

3. $\hat{u}_j^R$ is computed using $\hat{u}_j^R = \hat{\mu}_j^R - [\hat{z}_{j+1/2}, 0]^{\mathrm{T}}$.

Three stencils, $\mathcal{P}_{j+k} = \bigcup_{l=-1}^{l=+1} I_{j+k+l}$ with $k = -1, 0, 1$, are selected. On each stencil a polynomial of order 2, $P_{j+k}(x)$, is defined; its coefficients are univocally determined solving the system (9). The polynomials $R_j(x)$ are convex combination of the polynomials $P_{j+k}(x)$ – see Equation (10) – in which the weights, w_j^k, are computed using Equation (11). The necessary linear weights are summarized in Table 2. The reconstruction of the left cell boundary point-values, $\hat{u}_j^L$, is achieved using the same procedure in which the only difference are the linear weights (see Table 2). Finally, using the same reconstruction with another set of linear weights (Table 2), the estimate of the derivatives of the free-surface elevation in the cell-center is performed considering the first component of $\mu'_j = T'(x_j) = R'_j(x_j)$.

3.3 *Source term spatial integration*

The same technique presented in the Central WENO context (Section 2.3), is here applied to the Upwind WENO scheme. Now the Equation (16) is written focusing the attention on the cell I_j instead of the staggered cell $I_{j+1/2}$:

$$\begin{aligned} s_j^{[2]} &= \frac{1}{2} g \left[z_{j+\frac{1}{2}}^2 - z_{j-\frac{1}{2}}^2 \right] + \\ &- g \left[\eta_{j+\frac{1}{2}} z_{j+\frac{1}{2}} - \eta_{j-\frac{1}{2}} z_{j-\frac{1}{2}} \right] + \int_{x_{j-\frac{1}{2}}}^{x_{j+\frac{1}{2}}} \xi(x) \mathrm{d}x. \end{aligned} \tag{25}$$

The first two RHS terms of Equation (25) can be computed exactly; only the last term requires further elaborations. The first step is the evaluation of the cell-center point-values of the function $\xi(x)$, i.e. $\hat{\xi}_j = (gz\mathrm{d}\eta/\mathrm{d}x)_j = gz_j\hat{\eta}'_j$. Then, a new piece-wise reconstruction is introduced:

$$L(x) = \sum_j M_j(x)\chi_j, \tag{26}$$

where $M_j(x)$ are polynomials of order 2. The averaged value of $\xi(x)$ on the cell I_j may be computed using:

$$\bar{\xi}_j = \frac{1}{\Delta x} \int_{x_{j-\frac{1}{2}}}^{x_{j+\frac{1}{2}}} L(x)\mathrm{d}x = \frac{1}{\Delta x} \int_{x_{j-\frac{1}{2}}}^{x_{j+\frac{1}{2}}} M_j(x)\mathrm{d}x. \tag{27}$$

The polynomial $M_{j+1/2}(x)$, used in the Central scheme and described in Section 2.3, results from the convex combination of *two* polynomials N_{j+m} with $m = 0, 1$. In the reconstruction (26), the polynomial $M_j(x)$ is obtained using a convex combination of *three* polynomials $N_j^m(x)$, with $m = -1, 0, 1$. In both cases the symmetry of the reconstructions is preserved, because the union of the cell stencils involved in the $M_{j+1/2}(x)$ and in the $M_j(x)$ definitions are symmetric with respect to $I_{j+1/2}$ and to I_j, respectively. Moreover, in order to avoid the use of negative weights and the associated computational difficulties (Qiu & Shu 2002), $M_j(x)$ is build using polynomials $N_j^m(x)$ of different order, following the principle defined for the *Compact* WENO reconstructions (Levy et al. 2000). In particular, one central polynomial of order two $\mathcal{N}_j^0 = \bigcup_{l=-1}^{l=+1} I_{j+l}$, and two lateral polynomials of order one, $\mathcal{N}_j^{-1} = \bigcup_{l=-1}^{l=0} I_{j+l}$ and $\mathcal{N}_j^{+1} = \bigcup_{l=0}^{l=+1} I_{j+l}$, are used. On each stencil a corresponding polynomial is defined and the coefficients are given by solving the systems:

$$\begin{aligned} N_j^{-1}(x_{j+l}) &= \hat{\xi}_{j+l} \qquad l = -1, 0 \\ N_j^{0}(x_{j+l}) &= \hat{\xi}_{j+l} \qquad l = -1, 0, 1 \\ N_j^{+1}(x_{j+l}) &= \hat{\xi}_{j+l} \qquad l = 0, 1 \end{aligned} \tag{28}$$

The three polynomials are successively combined through the relation:

$$M_j(x) = \sum_{m=-1}^{m=+1} w_j^m N_j^m(x) \tag{29}$$

The weights w_j^m are given by Equation (11), with the appropriate linear weights summarized in Table 2. Once computed the averaged-values $\bar{\xi}_j$, the cell-averages of the source term on the cell I_j, can be easily computed, see also the Equation (21).

Copyright © 2006 Taylor & Francis Group plc, London, UK

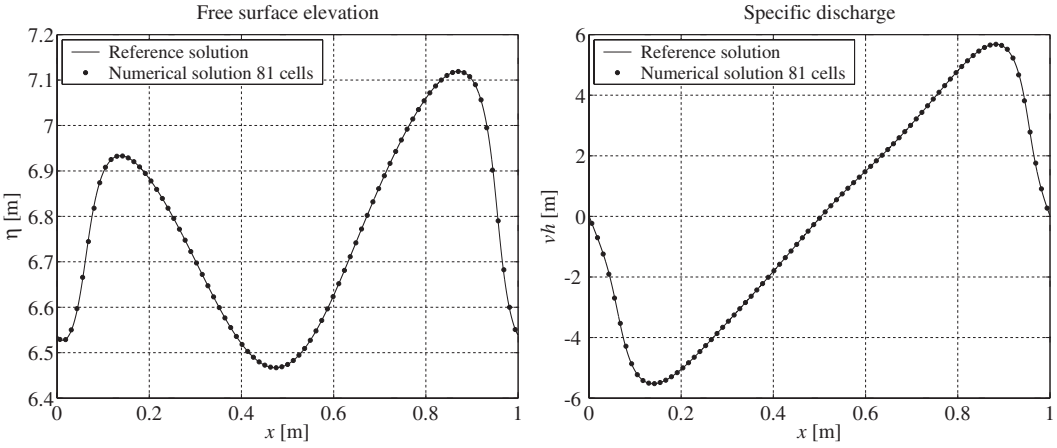


Figure 1. Unsteady flow over a sinusoidal bump: solution at t = 0 : 1 [s].

Table 3. Unsteady flow over a sinusoidal bump – accuracy analysis – free surface elevation.

Cells	L^1	Order	L^2	Order	L^∞	Order
Central WENO						
81	7.2854E–04		1.9615E–03		9.7843E–03	
243	1.3648E–05	3.6205	5.0621E–05	3.3288	4.0506E–04	2.8987
729	1.1443E–07	4.3522	4.3949E–07	4.3205	4.2323E–06	4.1519
2187	1.2328E–09	4.1240	4.5753E–09	4.1552	4.3143E–08	4.1743
Upwind WENO						
81	6.2594E–04		1.6883E–03		8.6696E–03	
243	9.8940E–06	3.7751	3.7513E–05	3.4651	2.9141E–04	3.0883
729	5.9615E–08	4.6529	2.4402E–07	4.5832	2.2102E–06	4.4435
2187	1.3688E–09	3.4352	2.0010E–09	4.3724	1.4581E–08	4.5704

4 APPLICATIONS

4.1 *Unsteady flow over a sinusoidal bump*

The fourth-order space and time accuracy of both the schemes, achieved in smooth regions of the solution, is verified using the test case proposed in (Xing & Shu 2005). Bottom profile is defined by $z(x) = \sin^2(\pi x)$; initial conditions are:

$$\begin{aligned} h(x,0) &= h_0 + e^{\cos(2\pi x)}; \\ vh(x,0) &= \sin(\cos(2\pi x)); \end{aligned} \tag{30}$$

with $h_0 = 5$ m and $x \in [0, 1]$ m. Periodic boundary conditions are assumed. This problem can not be solved analytically and therefore a numerical solution, computed on a very fine mesh of 19683 cells, is adopted as the reference solution. In this test case, $\epsilon = 10^{-6}$ and $p = 2$ are assumed. Figure 1 shows the free surface and the specific discharge after 0.1 s of simulation, computed using the Central WENO model. Results obtained using the Upwind WENO model are very similar and therefore are not reported. It is clear the good agreement between the reference solution and the numerical solution obtained using the coarser grid. In Table 3 the accuracy analysis results, computed considering 81, 243, 729, and 2187 cells are shown. The selected number of cells assures the spatial overlapping of the point-values of the computed solutions with the point-values of the reference solution, simplifying the computation of the norms (Caleffi et al. 2006). For any norm, the fourth-order accuracy is achieved for both the models, confirming that the accuracy of the schemes agrees with the expected one. Similar results are obtained on the specific discharge.

4.2 *C-property test case*

The purpose of this test case, proposed by Xing & Shu (2005), is to verify the achievement of the C-property over non-flat bottom. The bottom profile is described by $z(x) = 5e^{-0.4(x-5)^2}$ m, with $0 \le x \le 10$ m. A constant free surface elevation, $\eta = 10$ m, and a

Copyright © 2006 Taylor & Francis Group plc, London, UK

constant zero discharge are the initial conditions. The quiescent flow must be preserved. A simulation is carried out until $t = 0.5$ s, using a mesh of 200 cells, L^1, L^2 and L^∞ norms of the errors of the water depth are computed (Caleffi et al. 2006). The results, obtained using the double precision floating-point arithmetics in numerical computation, are summarized in Table 4. The differences between the numerical solution and the reference solution, in terms of water depth, are due to round-off errors, see also (Xing & Shu 2005). Similar results are obtained in terms of specific discharge.

4.3 *Steady discontinuous flow over a parabolic bump*

The purpose of this test case is the validation of the source term treatment for the simulation of steady discontinuous flows over a bump (Valiani et al. 2002; Caleffi et al. 2003). This is a classical test problem for transcritical flows. The spatial domain is a 25 m long channel, discretized with 200 cells. The bottom elevation is described by the following function:

$$z(x) = \begin{cases} 0.2 - 0.05(x-10)^2 \text{m} & 8 \le x \le 12 \text{ m} \\ 0 & \text{otherwise,} \end{cases} \quad (31)$$

characterized by a discontinuous first derivative in $x = 8$ m and $x = 12$ m. ϵ and p are set equal to 10^{-6} and 2, respectively. The flow is transcritical and a steady shock is located over the bump. The upstream specific discharge is 0.18 m^2/s and the downstream water surface elevation is set to 0.33 m. The initial free surface elevation is 0.33 m and the initial discharge is everywhere zero.

Table 4. C-property analysis – water depth norms.

	h		
Model	L^1	L^2	L^∞
Central WENO	3.50E–15	1.45E–15	8.88E–16
Upwind WENO	7.51E–11	2.42E–11	9.94E–12

Figures 2 and 3 show the good agreement between the numerical and the analytical solution. The test gives satisfying results in terms of shock resolution and of upstream and downstream water levels reconstruction using both models. The shock position is accurately captured, especially by the Upwind model. Only few numerical point-values of flow discharge do not agree well with the analytical solution, but these points are located at the shock position. Also in this case the Upwind model gives smaller error. The results obtained in this severe test case, in which numerical difficulties due to the discontinuous bottom slope and to the discontinuous nature of the solution coexist, support the reliability of the novel source term technique proposed herein.

4.4 *Pulse over a bump*

This quasi-stationary test case, due to LeVeque (1998), is selected in order to test the capability of the scheme in computing an unsteady flow over a smooth bottom profile. It consists of the simulation of the convection of a pulse, initially 0.1 m long and 10^{-3} m height. The pulse moves in a 1 m long domain initially interested by a quiescent flow characterized by a depth of 1 m. The duration of the simulation is 0.7 s. The bottom profile is described by the following equation:

$$z(x) = \begin{cases} \frac{\left[\cos\left(10\pi\left(x-\frac{1}{2}\right)\right)+1\right]}{4} \text{ m} & \left|x-\frac{1}{2}\right| < 0.1\text{m} \\ 0 & \text{otherwise} \end{cases} \quad (32)$$

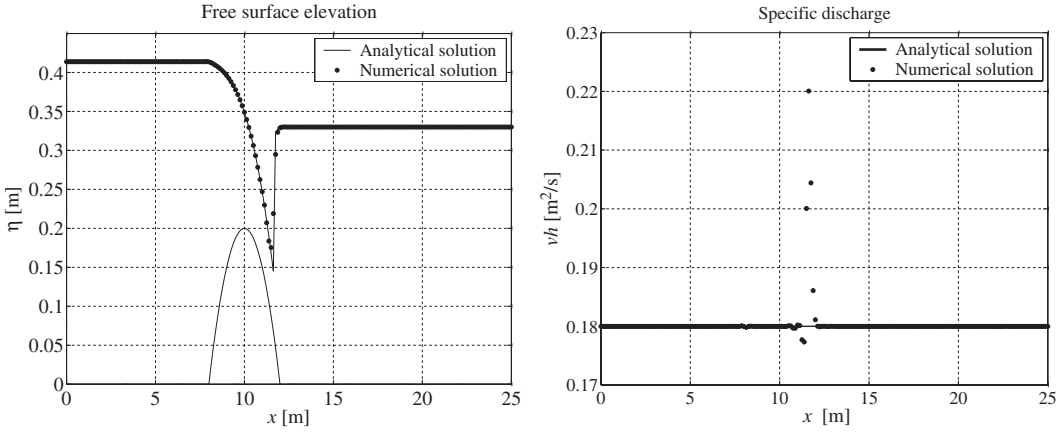


Figure 2. Parabolic bump-transcritical flow test case – Central WENO.

Copyright © 2006 Taylor & Francis Group plc, London, UK

In this case numerical diffusion is minimized using $\epsilon = 10^{-12}$ and $p = 2$, see (Xing & Shu 2005).

The solutions obtained using 100 and 250 cells are compared with the reference solution obtained using 4000 cells. Moreover, the gravity is set to $1\,\mathrm{m/s^2}$ in order to allow a direct comparison with the results obtained by LeVeque (1998). An overall good behavior of the scheme is shown. In particular, it may be noted the absence of perturbations where the bottom elevation is nonzero and this proves the good balancing between source term and flux gradient in unsteady problems. The results obtained using the Upwind model are affected by a greater diffusivity with respect to the results obtained using the Central model. On the other hands, there is not unphysical perturbations over the bump in the results of both models and this is a further proof of the good balancing between flux gradient and source term.

5 CONCLUSIONS

WENO schemes are versatile and efficient tools for the numerical integration of systems of balance laws and can be fruitfully applied to different engineering problems. In particular, applications to the de Saint-Venant open-channel equations and to the movable bed hydraulics show the great potential of these methods. Several aspects of the river mechanics and of the real world hydraulics can be addressed, because the WENO schemes' structure is particularly suitable for the correct modeling of source terms, secondary currents and sediment transport phenomena, which are fundamental keys in the numerical simulation of river evolution. In this work, two original well-balanced schemes, belonging to the family of Central and Upwind WENO schemes respectively, are presented. These schemes are suitable for the integration of the SWE with the

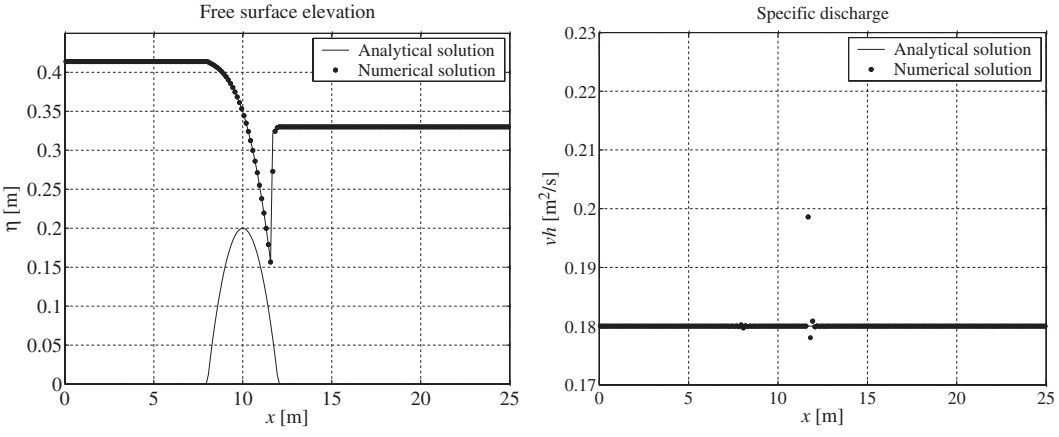


Figure 3. Parabolic bump-transcritical flow test case – Upwind WENO.

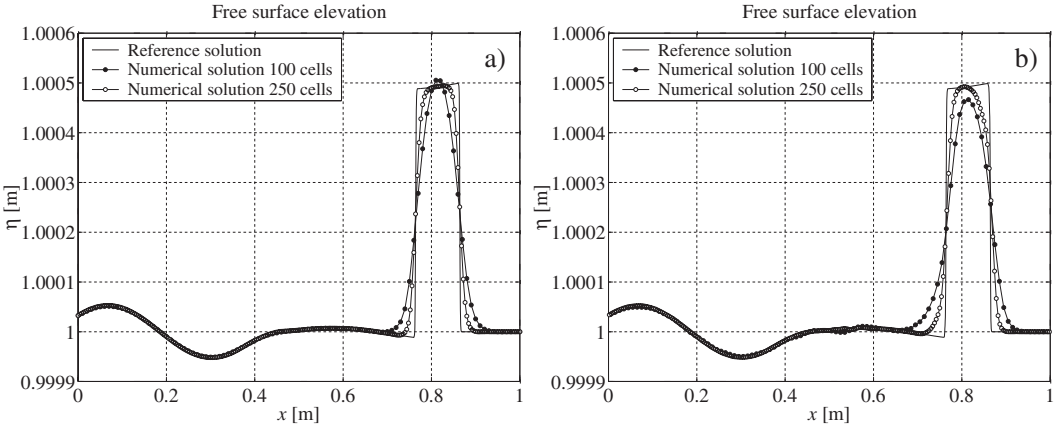


Figure 4. Pulse over a bump: (a) Central WENO Scheme; (b) Upwind WENO Scheme.

Copyright © 2006 Taylor & Francis Group plc, London, UK

source term due to bottom slope. In particular, attention is focused on a new approach for the source term treatment, which allows the fulfillment of the C-property, preserving the fourth-order accuracy in space and time. This approach can be easily applied to the different WENO schemes. Several test cases are used to verify time and space accuracy, the achievement of the C-property and the shock resolution of both models.

REFERENCES

Bermudez, A. & M.E. Vázquez-Cendón (1994). Upwind methods for hyperbolic conservation laws with source terms. *Comput. & Fluids 23*(8), 1049–1071.

Caleffi, V., A. Bernini, & A. Valiani (2006). Fourth-order balanced source term treatment in central WENO schemes for shallow water equations. *J. Comput. Phys.* In press.

Caleffi, V., A. Valiani, & A. Zanni (2003). Finite volume method for simulating extreme flood events in natural channels. *J. Hydr. Res. 41*(2), 167–177.

Godunov, S.K. (1959). A difference scheme for numerical computation of discontinuous solution of hydrodynamic equations. *Math. Sbornik 43*, 271–306.

Jiang, G.-S., D. Levy, C.-T. Lin, S. Osher, & E. Tadmor (1998). High-resolution nonoscillatory central schemes with nonstaggered grids for hyperbolic conservation laws. *J. Num. Anal. 35*(6), 2147–2168.

Jiang, G.-S. & C.-W. Shu (1996). Efficient implementation of Weighted ENO schemes. *J. Comput. Phys. 126*(1), 202–228.

Lax, P.D. (1954). Weak solutions of nonlinear hyperbolic equations and their numerical computations. *Com. Pure and Appl. Math. 44*, 21–41.

LeVeque, R.J. (1998). Balancing source terms and flux gradients in high-resolution Godunov methods: The quasi-steady wave-propagation algorithm. *J. Comput. Phys. 146*(1), 346–365.

Levy, D., G. Puppo, & G. Russo (1999). Central WENO schemes for hyperbolic systems of conservation laws. *Math. Model. Num. Anal. 33*(3), 547–571.

Levy, D., G. Puppo, & G. Russo (2000). Compact central WENO schemes for multidimensional conservation laws. *J. Sci. Comp. 22*(2), 656–672.

Liu, X.-D., S. Osher, & T. Chan (1994). Weighted Essentially Non-Oscillatory schemes. *J. Comput. Phys. 115*(1), 200–212.

Qiu, J. & C.-W. Shu (2002). On the construction, comparison, and local characteristic decomposition for high-order central WENO schemes. *J. Comput. Phys. 183*(1), 187–209.

Shu, C.-W. (1997). Essentially non-oscillatory and weighted essentially non-oscillatory schemes for hyperbolic conservation laws. ICASE Technical Report 97–65, Langley Research Center, Virginia, USA.

Spiteri, R.J. & S.J. Ruuth (2002). A new class of optimal high-order Strong-Stability-Preserving time discretization methods. *J. Num. Anal. 40*, 469–491.

Toro, E. (1992). Riemann problems and the WAF method for solving the two-dimensional shallow water equations. *Philosophical Transactions of the Royal Society A338*, 43–68.

Črnjarić-Žic, N., S. Vuković, & L. Sopta (2004). Balanced finite volume weno and central weno schemes for the shallow water and the open-channel flow equations. *J. Comput. Phys. 200*(2), 512–548.

Valiani, A. & L. Begnudelli (2005). Divergence Form for Bed slope source term (DFB) in shallow water equations. *J. Hydr. Eng.* In press.

Valiani, A., V. Caleffi, & A. Bernini (2004). Central WENO schemes for shallow water movable bed equations. In *12th International Conference on Transport and Sedimentation of Solid Particles*, Volume 2, Prague, Czech Republic, pp. 651–658. Institute of Hydrodynamics, Academy of Sciences of the Czech Republic.

Valiani, A., V. Caleffi, & A. Zanni (2002). Case study: Malpasset dambreak simulation using a 2D finite volume method. *J. Hydr. Eng. 128*(5), 460–472.

Vázquez-Cendón, M.E. (1999). Improved treatment of source terms in upwind schemes for the shallow water equations in channels with irregular geometry. *J. Comput. Phys. 148*(2), 497–526.

Vuković, S. & L. Sopta (2002). ENO and WENO schemes with the exact conservation property for one-dimensional shallow water equations. *J. Comput. Phys. 179*(2), 593–621.

Xing, Y. & C.-W. Shu (2005). High order finite difference weno schemes with the exact conservation property for the shallow water equations. *J. Comput. Phys. 208*(1), 206–227.

Zennaro, M. (1986). Natural Continuous Extension of Runge-Kutta methods. *Math. Comput. 46*, 119–133.

Zhou, J.G., D.M. Causon, D.M. Ingram, & C.G. Mingham (2001). The surface gradient method for the treatment of source terms in the shallow-water equations. *J. Comput. Phys. 168*(1), 1–25.

Copyright © 2006 Taylor & Francis Group plc, London, UK

Two-dimensional numerical simulation of flood propagation in presence of buildings

C. Costanzo & F. Macchione
University of Calabria, LAMPIT (Laboratorio di Modellistica Numerica per la Protezione Idraulica del Territorio), Dipartimento di Difesa del Suolo, Rende, Cosenza (Italy)

ABSTRACT: At present, in numerical simulation of flood propagation, a two-dimensional approach is used in the study of inundations affecting areas with complex geometry like the city zones with various kinds of constructions. In this paper different simulations have been carried out in order to investigate the performance of the different numerical techniques of the treatment of the presence of buildings. In order to do that, a test presented in the literature, representing of a flood propagation over a simplified urban area, has been simulated. The upwind finite volume HLLC scheme has been implemented. The obtained results are compared with experimental data in order to evaluate the accuracy of the numerical solutions.

1 INTRODUCTION

Numerical models are useful tools to investigate and predict possible flooding scenarios, which can then be used to formulate suitable flood hazard mitigation measures. In this context, over the last few years, various works on the numerical modelling of inundated urban areas have been performed. In particular, the importance of the interaction between flood flows and the complicated geometries of structures such as road networks, trees, etc., to predict the behaviour of flood flows has been recognized. A two-dimensional approach in numerical simulation of flood propagation is more and more used in the study of inundations affecting areas with a complex geometry like the city zones.

In particular, the research is devoted to integrating the shallow water equations with numerous numerical methods among which currently the one most applied is the Finite Volume method and the shock capturing schemes based on it. However their application to areas with complex topography is not much so common in the literature.

The irregular bathymetry may cause numerical errors, due to incorrect treatment of the source term, present in the equations. Hence, apart from the obvious need for accuracy, it is especially important to integrate the source term in agreement with the flux functions.

Gallati & Braschi (1990) applied a simplified form of the 2D depth-averaged equation to simulate the flood propagation through the city centre of Florence (Italy), Hervouet et al. (2000) modified the shallow water equations introducing a porosity coefficient to represent constriction effects and the volume occupied by obstacles and a specific law of friction for vertical structures. Porosity is also present in Defina et al. (1994) and in Guinot & Soares-Frazão (2006). Haider et al. (2003) used a two dimensional model to simulate the catastrophic flood in the city of Nîmes. Shige-eda & Akiyama (2003) investigated the hydrodynamic force acting on structures. Mignot et al. (2004) tested the ability of a 2D code to model a flood in an urban area.

In the European IMPACT project tests have been devoted to study flow characteristics in urban areas and the capabilities of different numerical models to represent them accurately.

In this paper, simulations have been carried out in order to investigate the performance of the different numerical techniques of the treatment of the presence of buildings such as representing them as solid wall boundaries, as an abrupt bottom variation or as an increase in flow resistance already used by other authors in the IMPACT project (Murillo et al. 2004). In order to do that, a test presented in literature has been simulated. This test represents the flood propagation over a simplified urban area. The upwind finite volume HLLC scheme has been implemented and the influence of the mesh size on numerical results has been investigated. Moreover, in this work, the application of the technique of introducing a porosity coefficient in the shallow water equations has been analyzed, in order to simulate the inundation on a coarse grid with the cell size greater than the dimension of a building, as often happens in real cases. The obtained results are compared with experimental

Copyright © 2006 Taylor & Francis Group plc, London, UK

data in order to evaluate the accuracy of the numerical solutions.

2 GOVERNING EQUATIONS

Two-dimensional shallow water equations in conservative form are:

$$\frac{\partial \mathbf{U}}{\partial t}+\frac{\partial \mathbf{f}}{\partial x}+\frac{\partial \mathbf{g}}{\partial y}=\mathbf{S} \tag{1}$$

where:

$$\mathbf{U}=\begin{pmatrix} h \\ hu \\ hv \end{pmatrix}; \quad \mathbf{f}=\begin{pmatrix} hu \\ hu^2+gh^2/2 \\ huv \end{pmatrix} \tag{2, 3}$$

$$\mathbf{g}=\begin{pmatrix} hv \\ huv \\ hv^2+gh^2/2 \end{pmatrix}; \quad \mathbf{S}=\begin{pmatrix} 0 \\ gh\left(S_{0x}-S_{fx}\right) \\ gh\left(S_{0y}-S_{fy}\right) \end{pmatrix} \tag{4, 5}$$

in which t is time; x, y are the horizontal coordinates; h is the water depth; u, v are the depth-averaged flow velocity in x- and y-directions; g is the gravitational acceleration; S_{0x}, S_{0y} are the bed slopes in x- and y-directions; S_{fx}, S_{fy} are the friction slopes in x- and y-directions, which can be calculated from Strickler's formula.

Equation (1) is discretized with the finite volume method as follows:

$$\mathbf{U}_{i,j}^{n+1}=\mathbf{U}_{i,j}^{n}-\frac{\Delta t}{\Omega_{i,j}}\sum_{r=1}^{4}[\mathbf{f},\mathbf{g}]_r\cdot\mathbf{n}_r\,\Delta L_r+\Delta t\mathbf{S}_{i,j}^{n} \tag{6}$$

where $\mathbf{U}_{i,j}$ is the average value of the flow variables over the control volume $\Omega_{i,j}$ at a given time, $\mathbf{n}$ is the unit normal vector and L is the length of each boundary.

2.1 *Computation of flux and source terms*

In the proposed approach the flux term $[\mathbf{f},\mathbf{g}]_r\,\mathbf{n}_r$ (Eq. 6) is estimated with a Harten - Lax – van Leer Riemann solver (Harten et al. 1983), that, when applied to the two dimensional equations, gives the following expression for the numerical flux across the edge of the computational cell Ω_L on the left and Ω_R on the right:

$$[\mathbf{f},\mathbf{g}]_r\cdot\mathbf{n}_r=\begin{cases}[\mathbf{f},\mathbf{g}]_L\cdot\mathbf{n}_r & if \;\; s_L\geq 0\\ [\mathbf{f},\mathbf{g}]^*\cdot\mathbf{n}_r & if \;\; s_L\leq 0\leq s_R\\ [\mathbf{f},\mathbf{g}]_R\cdot\mathbf{n}_r & if \;\; s_R\leq 0\end{cases} \tag{7}$$

where:

$$[\mathbf{f},\mathbf{g}]^*\cdot\mathbf{n}_r=\frac{s_R([\mathbf{f},\mathbf{g}])_L\cdot\mathbf{n}_r-s_L([\mathbf{f},\mathbf{g}])_R\cdot\mathbf{n}_r+s_Ls_R(\mathbf{U}_R-\mathbf{U}_L)}{s_R-s_L} \tag{8}$$

As Equations (7–8) depend on the value of wave speeds s_L and s_R, it is necessary to introduce approximate expressions of these variables. The wave speed estimators used in this work are obtained by the application of the two-rarefaction Riemann solver theory (Toro 2001):

$$\begin{aligned} s_L&=\min\left([u,v]_L\cdot\mathbf{n}_r-\sqrt{gh_L},u^*-\sqrt{gh^*}\right)\\ s_R&=\max\left([u,v]_R\cdot\mathbf{n}_r+\sqrt{gh_R},u^*+\sqrt{gh^*}\right)\end{aligned} \tag{9}$$

with:

$$\begin{aligned} u^*&=\frac{1}{2}\left([u,v]_L+[u,v]_R\right)\cdot\mathbf{n}_r+\sqrt{gh_L}-\sqrt{gh_R}\\ \sqrt{gh^*}&=\frac{1}{2}\left(\sqrt{gh_L}+\sqrt{gh_R}\right)+\frac{1}{4}\left([u,v]_L-[u,v]_R\right)\cdot\mathbf{n}_r\end{aligned} \tag{10}$$

The third component of the normal flux vector is computed in order to account for the influence of intermediate wave, characterized by a speed s_m calculated as in Fraccarollo & Toro (1995) $s_m=u^*$:

$$\begin{aligned} [f_3,g_3]_r\cdot\mathbf{n}_r&=[f_1,g_1]_r\cdot\mathbf{n}_r\,v_L \quad if \;\; s_m\geq 0\\ [f_3,g_3]_r\cdot\mathbf{n}_r&=[f_1,g_1]_r\cdot\mathbf{n}_r\,v_R \quad if \;\; s_m<0\end{aligned} \tag{11}$$

The source term vector is decomposed into two different parts which are treated separately: the bottom variation $\mathbf{S}_b=[0;\, ghS_{0x};\, ghS_{0y}]$ and the friction term $\mathbf{S}_f=[0;\, -ghS_{fx};\, -ghS_{fy}]$, $\mathbf{S}=\mathbf{S}_b+\mathbf{S}_f$.

The bottom variation $\mathbf{S}_b$ has been discretized in upwind manner in such a way that steady-state conditions are satisfied (Brufau et al. 2002):

$$\tilde{\mathbf{S}}_{br}=\sum_{m=1}^{3}\beta^m\tilde{\mathbf{e}}^m \tag{12}$$

where $\tilde{\mathbf{e}}^m$ are the eigenvectors of the approximate Jacobian matrix and coefficients β^m are calculated as:

$$\begin{aligned} \beta^{1-,3-}&=\pm\frac{1}{2\tilde{c}}\left(1-\frac{|\lambda_1|}{\lambda_1}\right)\left(\mathbf{S}_b^{(2)}n_x+\mathbf{S}_b^{(3)}n_y\right)\\ \beta^{2-}&=\frac{1}{\tilde{c}}\left(1-\frac{|\lambda_2|}{\lambda_2}\right)\left(-\mathbf{S}_b^{(2)}n_y+\mathbf{S}_b^{(3)}n_x\right)\end{aligned} \tag{13}$$

in which $\tilde{c}=[0.5\,g\,(h_r\text{-}h_l)]^{0.5}$ is the wave celerity; λ_1 and λ_2 are the eigenvalues of the Jacobian matrix.

In order to avoid numerical instability due to the presence of the friction term and a thin water depth, a semi-implicit treatment is applied by computing the matrix $\partial\mathbf{S}_f/\partial\mathbf{U}$ and introducing an implicit coefficient θ. After algebraic manipulations, the Equation (6) becomes:

$$\Delta\mathbf{U}_{i,j}=\frac{\left[-\frac{\Delta t}{\Omega_{i,j}}\sum_{r=1}^{4}[\mathbf{f},\mathbf{g}]_r\cdot\mathbf{n}_r\,\Delta L_r+\Delta t\mathbf{S}_{f}{}_{i,j}^{n}\right]}{\left[\mathbf{I}-\Delta t\theta\left(\frac{\partial\mathbf{S}_f}{\partial\mathbf{U}}\right)^n\right]}+\Delta t\mathbf{S}_{b_{i,j}}^{n} \tag{14}$$

Copyright © 2006 Taylor & Francis Group plc, London, UK

In this work coefficient θ is set to 0.5.

3 NUMERICAL TEST CASES

To demonstrate the capability of the scheme to simulate the inundation of an urban area with complicated geometries, the benchmark test problems from the European IMPACT project have been simulated. The IMPACT-Investigation of Extreme Flood Processes and Uncertainty project is a study program undertaken by a European research team. In order to compare various numerical methods, the program established a number of test cases and commissioned experimental studies. The project was divided into five technical work packages among which a package labelled "WP3" deals with flood propagation.

In the present work, the comparisons between numerical results and the experimental data of the "Model city flooding experiment" (Alcrudo et al. 2003) have been performed. This test is representative of a flood on a simplified urban area formed by a group of buildings. Various cases are considered by modifying, from one test to the other, the width of the valley, the buildings arrangement (either aligned or staggered) and the numerical techniques in order to simulate the influence of the buildings on flows.

3.1 *Description of physical model*

The experiments were performed using a scale model (1:100) of the Italian Toce river valley at ENEL-CESI (Italy). The model is 7 m long and 3.5–5 m wide depending on the location. In order to analyze the influence of buildings only, some tests were carried out in a modified valley model, narrowed by two masonry walls aligned to the model's main axis with the meandering river bed filled up.

The buildings are formed by cube blocks of 0.15 m sides positioned in either an aligned or a staggered manner. The number of the buildings varied from 20 (Fig.1) to 14 (Fig.2). Water levels were measured by means of 10 gauges fixed in space in all the performed experiments.

The following configurations were performed:

- two different positions of the blocks (aligned and staggered);
- two bathymetric configurations (original Toce river valley and modified narrowed geometry).

3.2 *Numerical conditions*

In the numerical simulations the computational domain was divided in structured quadrangular cells of 0.05×0.05 m except in the analysis of the influence of meshing size.

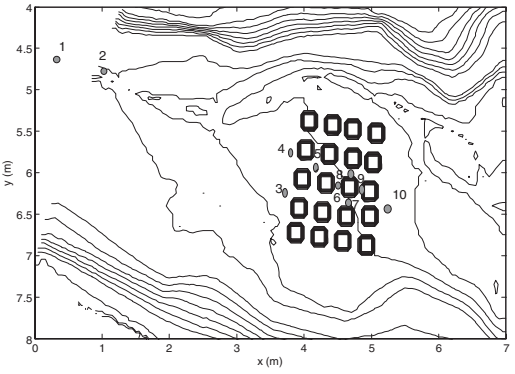


Figure 1. The original model city area with aligned buildings.

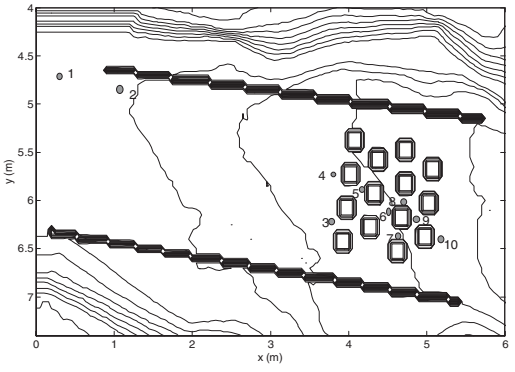


Figure 2. The modified bathymetry with staggered buildings.

In all cases the initial state of the valley was considered dry. The discharge and the water level versus time at probe number 1 were set as upstream conditions. Furthermore, the inflow angle was considered equal to $-23.5°$, as suggested by Alcrudo et al. (2003).

The used hydrograph has a peak of $0.060\ m^3/s$. In the downstream section, critical condition was considered. Strickler's roughness coefficient on the valley is set to $k = 61\ m^{1/3}/s$ and the stability condition is ensured by the Courant-Friedrichs – Lewy condition with a coefficient set to 0.6.

In order to compare the performance of each test, at each gauge j, the norm $L^{(j)}$ was computed as follows:

$$L^{(j)} = \sqrt{\sum_{i=1}^{n_s} \left(h_{si} - h_{n_i}\right)^2 \Big/ \sum_{i=1}^{n_s} h_{s_i}^2} \qquad (15)$$

where: n_s is the number of experimental values; h_{si} is the experimental water depth at gauge j; h_{ni} is the

Copyright © 2006 Taylor & Francis Group plc, London, UK

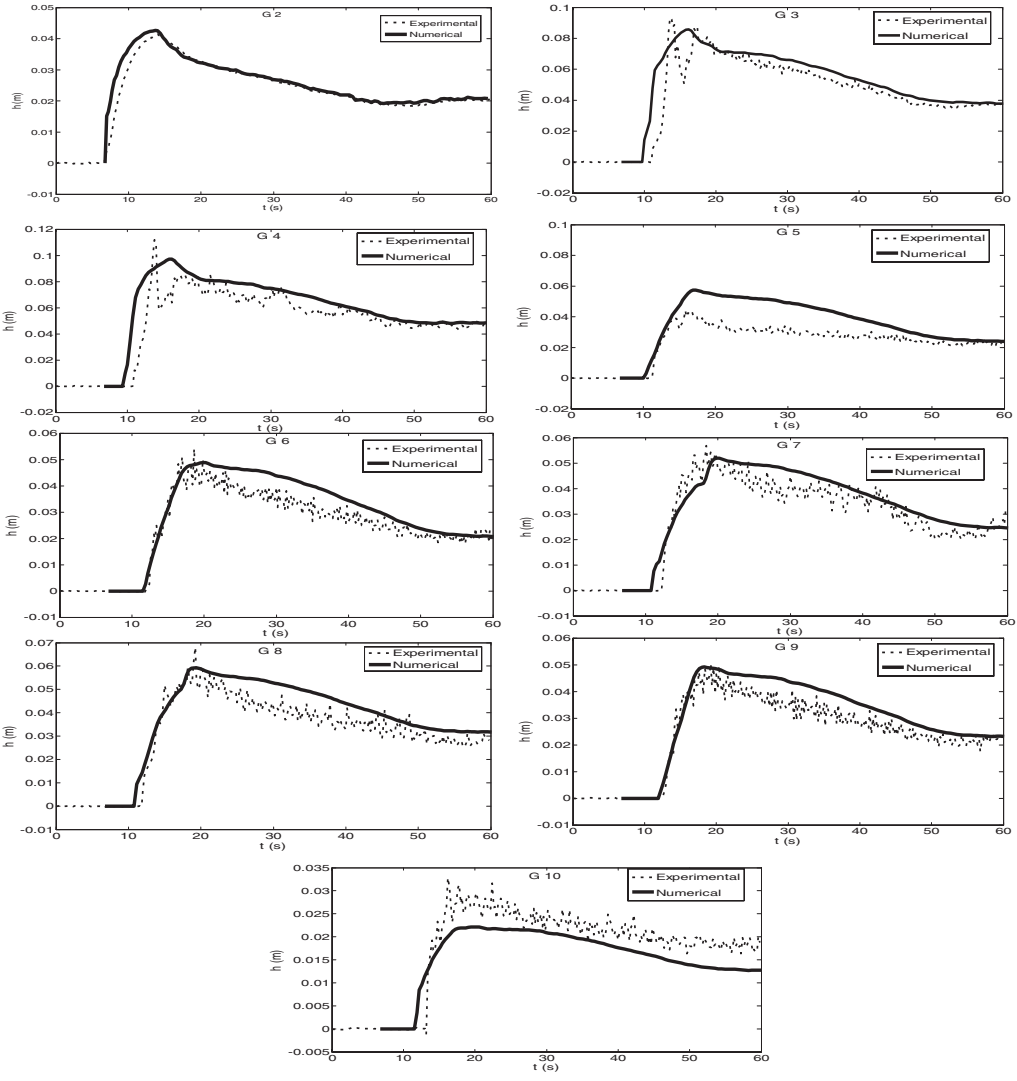


Figure 3. Test 1a: Comparison of the numerical results with the experimental data at various gauges.

computed water depth at gauge j. In particular, the mean value L_m was considered as:

$$L_m = \sum_{j=1}^{P} L^{(j)} / P \tag{16}$$

where P is the number of the gauges.

3.3 *Test 1a and test 1b: Flood propagation on modified bathymetry with aligned and staggered buildings*

These tests simulate the propagation of the inflow hydrograph with a maximum value of 0.060 m^3/s, on the modified bathymetry with the aligned (test 1a) and the staggered (test 1b) position of the buildings. In both cases the effects of the buildings on the flow wave were considered as solid wall conditions on the contours of the same. Figures 3–4 show the comparison between numerical values with observed ones, for the test 1a and the test 1b respectively. The numerical results are in overall good agreement with the experimental data.

At the inlet gauge, number 2, the numerical results are similar to the observed ones which indicates the correctness of the upstream boundary condition. This aspect is also present in the other test cases performed. In both cases, at gauge 10, differences are found due

Copyright © 2006 Taylor & Francis Group plc, London, UK

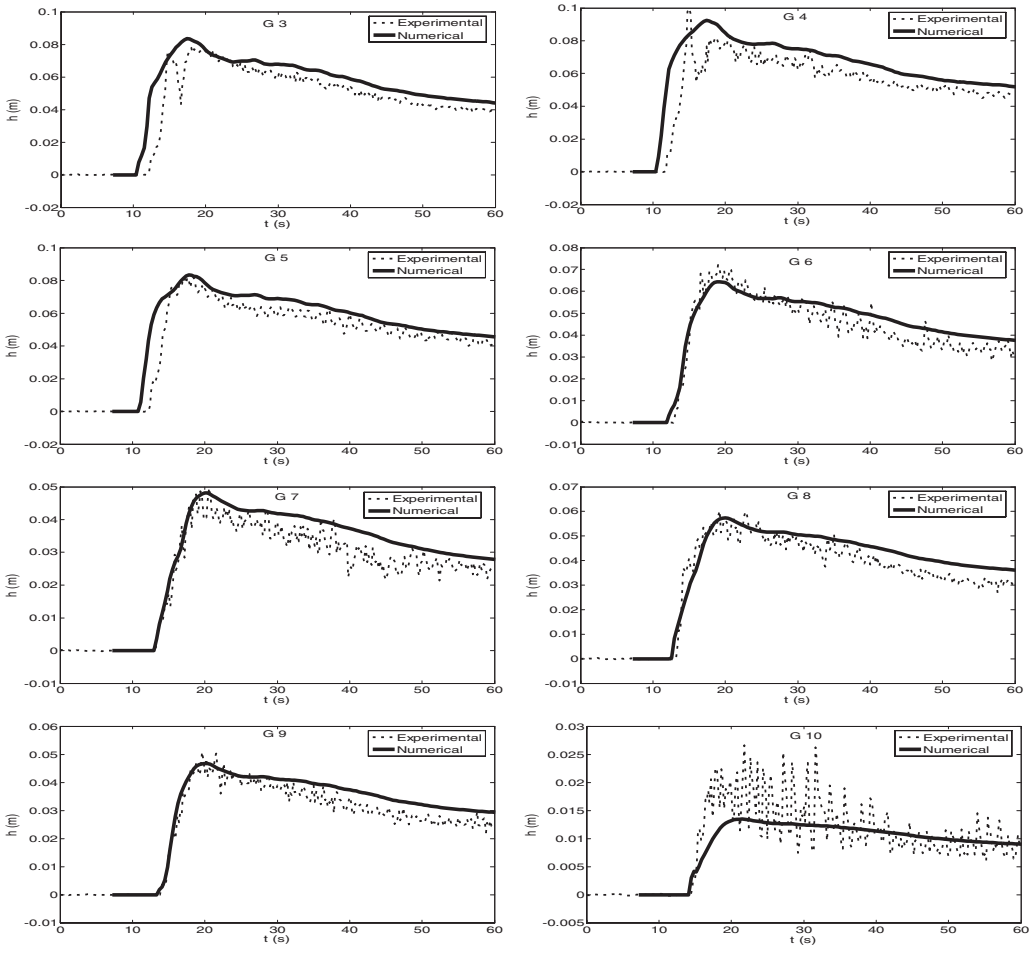


Figure 4. Test 1b: Comparison of the numerical results with the experimental data at various gauges.

to a rapid change of the flow regime at this point and to the downstream conditions, which are considered as critical conditions in all cases. The arrival times are slightly in advance, as are the numerical results obtained by other authors that have carried out the same tests (Murillo et al. 2004). The value of norm L was calculated, at each gauge, to compare numerical solutions with the experimental data in both test cases. As shown in Figures 5–6, L proves to be an acceptable value at all gauges and its mean value is about 0.23 for test case 1a and about 0.18 for test case 1b.

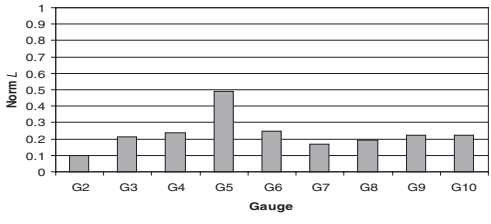


Figure 5. Test 1a: Norm values L at gauges.

3.4 *Test 2a and test 2b: Flood propagation on original bathymetry with aligned and staggered buildings*

The propagation of the hydrograph of the previous test cases was also performed on the original bathymetry of Toce river valley.

The numerical results are compared with the experimental ones in the case where the buildings are aligned (Fig. 7) and in the case where they are staggered (Fig. 8). As can be seen, the numerical results are in good agreement with the observed data.

For test 2a the most significant differences are at gauge 5 as in the previous test case 1a. Figures 9–10

Copyright © 2006 Taylor & Francis Group plc, London, UK

show the values of norm L for test cases 2a and 2b. The mean value of the norm is about 0.20 for both tests.

3.5 *Numerical techniques to simulate the influence of the buildings on the flow wave*

The most important aspects regarding simulations of urban flooding are the correct description of the flow and its interaction with buildings.

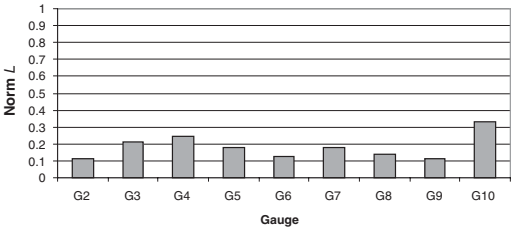


Figure 6. Test 1b: norm values L at gauges.

Different approaches have been implemented to simulate the propagation of the flood on the channelled bathymetry with the staggered position of the buildings. The first approach, used in test 1b, consists in representing the blocks as solid wall boundaries with the normal flow set equal to zero. The second approach is to simulate the influence of the blocks as an abrupt bottom variation.

The final technique is to reproduce the influences of the buildings as an increase in flow resistance assuming Strickler's coefficient equal to 2 $m^{1/3}/s$ on the cells which include the buildings and equal to 61 $m^{1/3}/s$ on the rest. This value of the roughness coefficient in the locations of the buildings is in a range of values commonly used by other authors to simulate flood propagation over an urban area (Alcrudo 2004; Mignot et al. 2004).

In Figure 11 the numerical solutions of the three techniques are compared to the experimental data. The numerical results based on the set of the solid wall conditions appear, as in the previous tests, in agreement

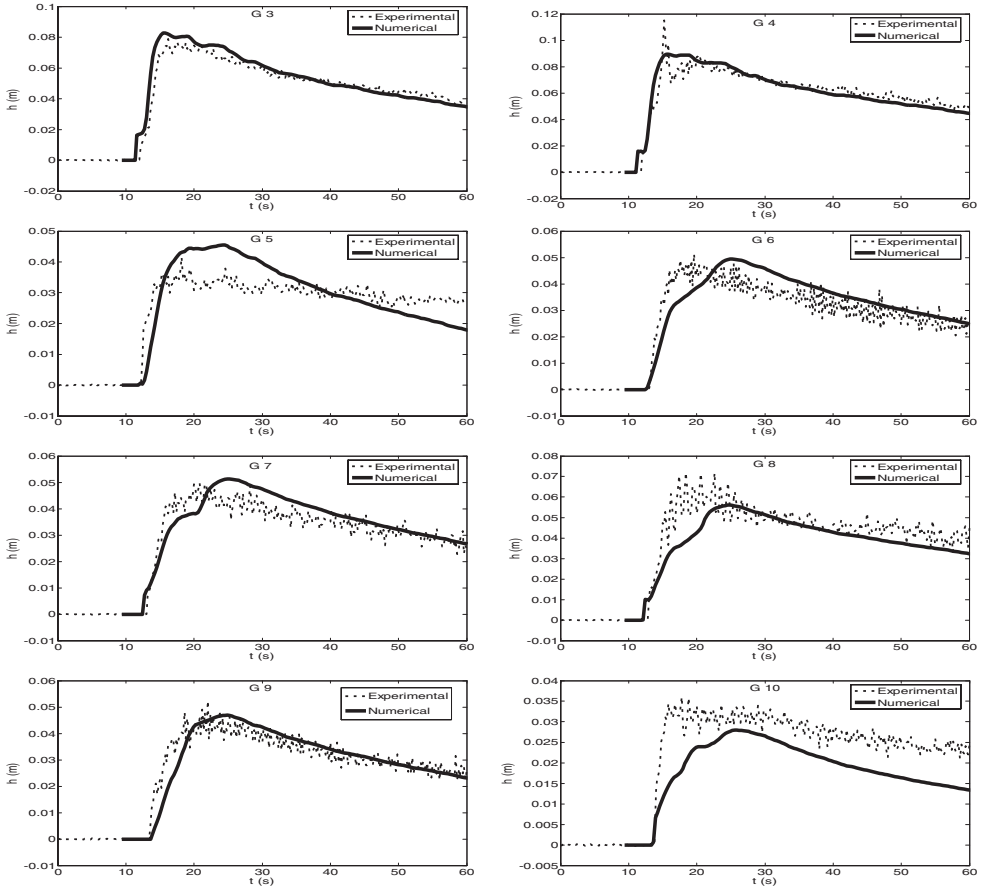


Figure 7. Test 2a: Comparison of the numerical results with the experimental data at various gauges.

Copyright © 2006 Taylor & Francis Group plc, London, UK

with the observed data. The higher differences are in the use of the bottom variation that simulates the recession limb lower than the observations. As observed by other authors, this approach is strictly dependent on the grid size (Alcrudo 2004), so a more refined grid is required. The use of the high friction to simulate the influence of the buildings on the flow wave is the simpler method to implement, although it does not provide a localised description of the flow, but rather an averaged analysis of the event. Moreover, the choice of the proper friction coefficient influences the numerical results, as is possible to note in Figure 12, where, at gauge 6, numerical solutions obtained by using a Strickler's coefficient equal to $2\,m^{1/3}/s$ are compared with those obtained using a Strickler's coefficient set $10\,m^{1/3}/s$.

In all tests, the numerical norm $L$was computed at all gauges (Fig. 13) and the mean values are 0.18 for the use of solid wall boundaries, 0.30 for the use of bottom variation and 0.21 for the use of the high friction coefficient.

3.6 *Influence of mesh size*

The accuracy of the numerical solutions is dependent on the meshing size. Frequently, in real cases it is

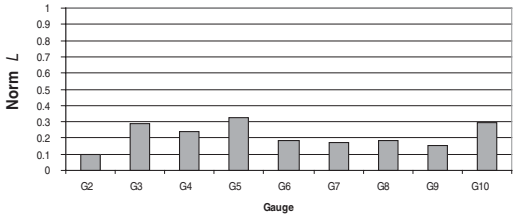


Figure 9. Test 2a: Norm values L at gauges.

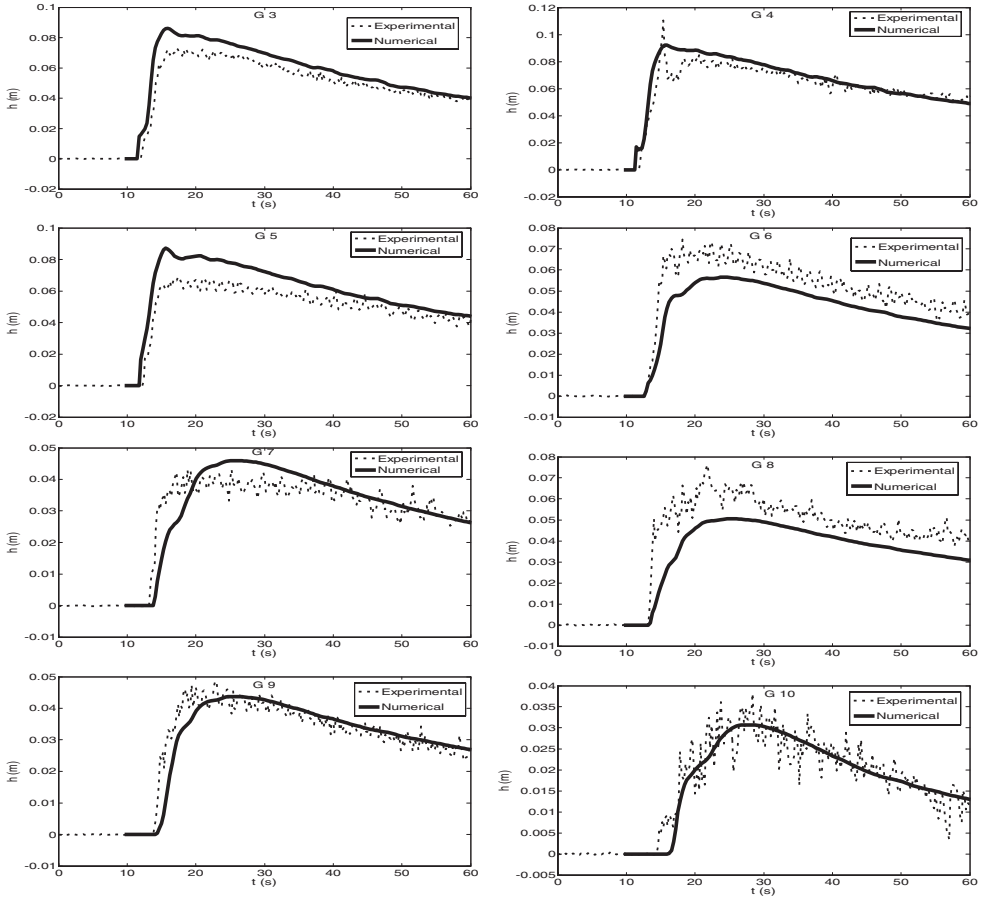


Figure 8. Test 2b: Comparison of the numerical results with the experimental data at various gauges.

Copyright © 2006 Taylor & Francis Group plc, London, UK

not possible to discretize the domain in a mesh fine enough to describe the single building due to the heavy computational requirements and to the relatively low resolution of the original data used.

To analyze the influence of grid size on the computations, the simulation of the flood propagation on the channelled bathymetry with the buildings in a staggered position and mesh size of 0.15 m was performed.

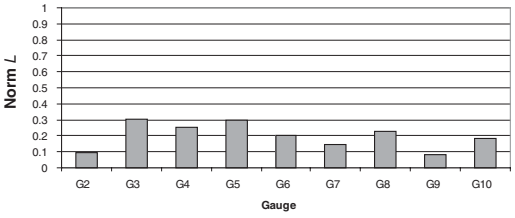


Figure 10. Test 2b: Norm values L at gauges.

Subsequently, a 0.25 m discretized structured mesh size was implemented (Fig.14). In latter case, the mesh size was greater than the single block, so in order to obtain better results, a new technique was used.

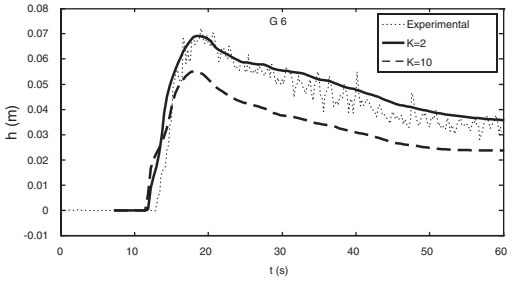


Figure 12. Comparison between numerical solutions using different Strickler's friction coefficients k and experimental data.

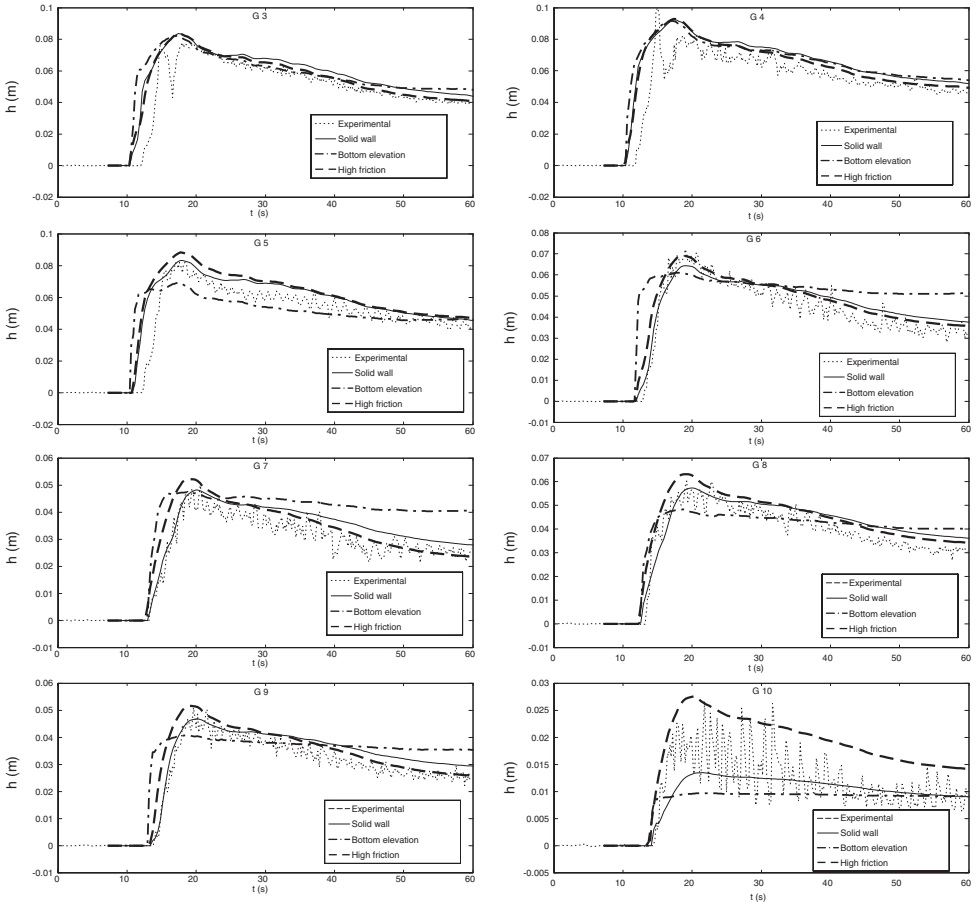


Figure 11. Comparison between numerical solutions of the different techniques to simulate the influence of the buildings on the flow with experimental data.

Copyright © 2006 Taylor & Francis Group plc, London, UK

The shallow water equations were modified by introducing a porosity coefficient φ, that is the ratio between the cell surface area subject to flood and the total cell surface area. Equations 1–6 were modified as follows:

$$\frac{\partial \varphi \mathbf{U}}{\partial t} + \frac{\partial \varphi \mathbf{f}}{\partial x} + \frac{\partial \varphi \mathbf{g}}{\partial y} = \mathbf{S} \tag{17}$$

$$\mathbf{U}_{i,j}^{n+1} = \mathbf{U}_{i,j}^{n} - \frac{\Delta t}{\varphi_{i,j}\Omega_{i,j}} \sum_{r=1}^{4} \varphi [\mathbf{f}, \mathbf{g}]_r \cdot \mathbf{n}_r \Delta L_r + \frac{\Delta t}{\varphi_{i,j}} \mathbf{S}_{i,j}^{n} \tag{18}$$

The source terms are also modified by introducing the difference in pressure, caused by the variation of the porosity, in the term of bottom variation $\mathbf{S}_b$ and a head loss term, caused by a rapid variations in the geometry, in the friction term $\mathbf{S}_f$.

Along the x axis, but in an equivalent way to the y axis, they become (Guinot & Soares-Frazão 2006):

$$S_{bx} = -g\varphi h \frac{\partial z}{\partial x} + g \frac{h^2}{2} \frac{\partial \varphi}{\partial x} \tag{19}$$

$$S_{fx} = -g\varphi h \frac{u\sqrt{u^2+v^2}}{K^2 h^{4/3}} - g\varphi h s_x u \sqrt{u^2+v^2} \tag{20}$$

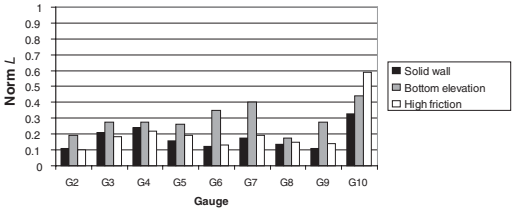


Figure 13. Norm values L with different techniques to simulate the influence of the buildings on the flow at gauges.

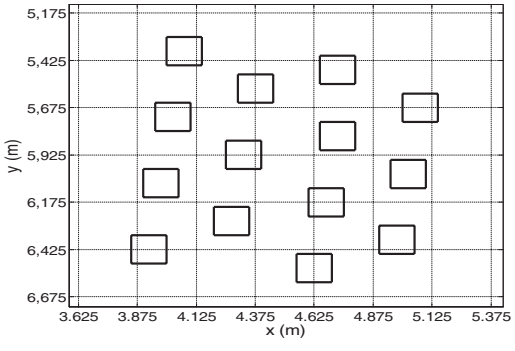


Figure 14. Details of the coarse mesh grid 0.25 m.

where z is the bottom elevation and s_x is a coefficient introduced in order to take into account the head losses of the urban discontinuity calculated by Borda's formula as in Guinot & Soares-Frazão (2006).

In this simulation, the porosity coefficient is set equal to 1 in the whole domain except in the cells that include buildings in which it varies from a value of 0.64 to 0.98 depending on the location of each building (Fig. 14).

The use of a coarse mesh led to less accurate results; the adopted modification to the original equations, on the other hand, provided results similar to those obtained by finer mesh (Fig. 15). The highest differences are found at gauges 5 and 10.

Also in these tests the norm values were computed at all gauges (Fig. 16). The mean value of the norm was about 0.19 for both the cell sizes of 0.15 m and 0.25 m.

4 CONCLUSIONS

In this paper different simulations have been carried out in order to investigate the performance of a number of numerical techniques to assess the presence of buildings in flood simulations. The obtained results prove that the approach based on considering flow interactions with structures such as solid wall boundaries, is the most accurate.

The use of the bottom elevation approach led to less accurate solutions, while the technique to reproduce the influence of buildings as an increase in flow resistance, assuming a high friction coefficient, is closely connected to the choice of the proper coefficient.

The effects of meshing size on numerical results were also analyzed. In order to simulate the propagation on a coarse mesh, the original shallow water equations were modified by introducing a porosity coefficient. In this case, the obtained numerical solutions are similar to those computed on the finer mesh by the solid wall approach.

The results computed by the first order HLLC scheme do not show physical anomalies and they are similar to those obtained with high order schemes used within IMPACT project.

Further studies are in progress in order to simulate real inundation events over urban areas.

ACKNWOLEDGMENTS

The authors thank G. Testa and D. Zuccalà (ENEL-CESI) for providing experimental data.

This work was supported in part by the Italian Ministry of Education, University and Research (MIUR) in the PRIN 2005 funding program.

Copyright © 2006 Taylor & Francis Group plc, London, UK

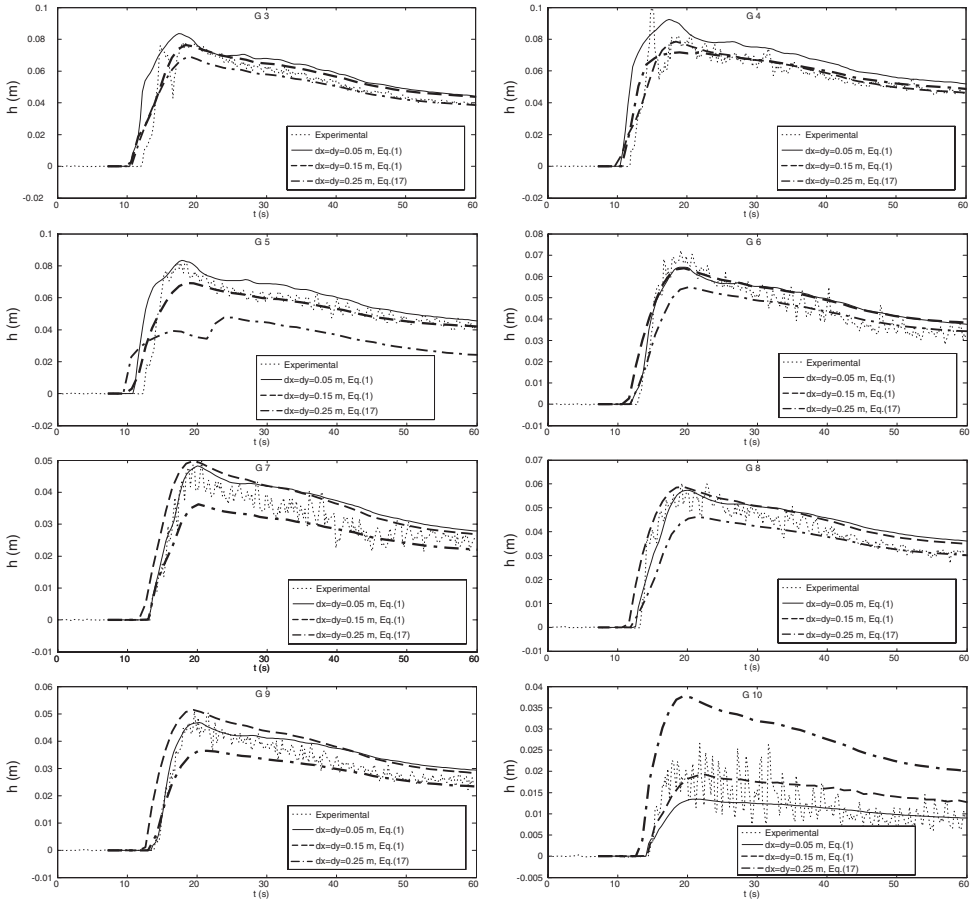


Figure 15. Comparison between numerical solutions using different meshing sizes (0.05 m, 0.15 m, 0.25 m) and different equations (Eq. (1), Eq (17)) with experimental data.

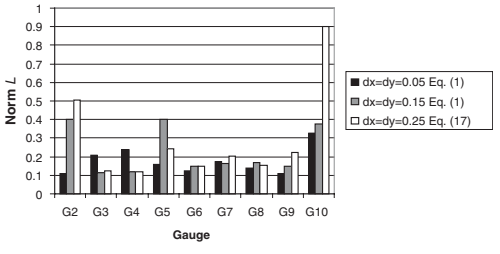


Figure 16. Norm values L with different meshing sizes and equations at gauges.

REFERENCES

Alcrudo F., García P., Brufau P., Murillo J., Garcia D., Mulet J., Testa G. & Zuccala D., 2003. The Model City Flooding Experiment. EC *Contract EVG1-CT-2001-00037 IMPACT investigation of extreme flood processes and uncertainty*. Proceedings of the 3rd Project Workshop, Louvain-La-Neuve, Belgium, 5–7 November 2003.

Alcrudo, F. 2004. Mathematical modelling techniques for flood propagation in urban areas. *IMPACT project technical report*. Available at www.impact-project.net

Brufau P., Vazquez-Cendon M. E. & García-Navarro P., 2002. A numerical model for the flooding and drying of irregular domains. *International Journal for Numerical Methods in Fluids*. Wiley 39:247–275.

Defina, A., D'Alpaos, L. & Mattichio B., 1994. A new set of equations for very shallow water and partially dry areas-suitable to 2D numerical domains. Proceedings Specialty Conference *Modelling of Flood Propagation over Initially Dry Areas*. Molinaro P. & Natale L. eds. Milano, Italy, 29 June–1 July, 1994.

EC Contract EVG1-CT-2001-00037 *IMPACT investigation of extreme flood processes and uncertainty*. Available at www.impact-project.net

Fraccarollo L. & Toro E. F., 1995. Experimental and numerical assessment of the shallow water model for two-dimensional dam-break type problems. *Journal of Hydraulic Research* 33 (6) 843–863.

Copyright © 2006 Taylor & Francis Group plc, London, UK

Gallati, M. & Braschi, G., 1990. Simulation of the inundation of large areas of complex topography caused by heavy floods. in: *HYDROSOFT 90*, *Proceedings of the International Conference on Hydraulic Engineering Software Applications.* Blain E.& Ouazar D. eds. Computational Mechanics Publications, Lowell, MA: 117–126.

Guinot, V. & Soares-Frazão, S., 2006. Flux and source term discretization in two-dimensional shallow water models with porosity on unstructured grids. *International Journal of Numerical Methods in Fluids*, Vol. 50 (3): 309–345.

Haider, S., Paquier, A., Morel, R. & Champagne, J.-Y., 2003. Urban flood modelling using computational fluid dynamics. *Water and Maritime Engineering*, 155 (WM2): 129–135.

Harten A., Lax P. & van Leer B., 1983. On upstream differencing and Godunov-type schemes for hyperbolic conservation laws. *SIAM Review*, 25: 35–61.

Hervouet, J.-M., Samie, R. & Moreau, B., 2000. Modelling urban areas in dam-break flood wave numerical simulations. Proceedings of *RESCDAM* workshop. Seinäjoki, Finland: Finnish Environment Institute.

Mignot, E., Paquier, A. & Rivière, N., 2004. How a 2-D code can simulate urban flood situations. In *River Flow 2004,* Greco, Carravetta & Della Morte eds., vol. 2: 1031–1039.

Murillo, Mulet, J, Brufau, P., García-Navarro, P. & Alcrudo, F., 2004. The model city flooding experiment benchmark.Analysis of modellers results and conclusions. *IMPACTt project technical report*. Available at www.impact-project.net

Shige-eda, M. & Akiyama, J., 2003. Numerical and Experimental Study on Two-Dimensional Flood Flows with and without Structures. *Journal of Hydraulic Engineering*, ASCE, Vol. 129, No. 10: 817–821

Toro E.F., 2001. *Shock–Capturing Methods for Free Surface Shallow Flows*. Wiley, Chichester.

Copyright © 2006 Taylor & Francis Group plc, London, UK

A practical approach to estimating the flow capacity of rivers – Application and analysis

C. McGahey & P.G. Samuels
Water Management Department, HR Wallingford Ltd., Howbery Park, Wallingford, Oxon, United Kingdom

D.W. Knight
School of Engineering, University of Birmingham, Edgbaston, Birmingham, United Kingdom

ABSTRACT: In 2001, the Environment Agency of England and Wales commissioned a Targeted Programme of Research (Evans *et al*, 2001) into reducing uncertainty in conveyance estimation, with the intention of bridging the gap between the advances in scientific knowledge over the past three decades and the calculation approaches adopted in United Kingdom industry practice. The key output was the Conveyance Estimation System (CES) software, which incorporates a methodology (Mc Gahey & Samuels, 2003) for estimating conveyance in a range of channel types and flow conditions, including straight, skewed and meandering plan form shape; simple, two-stage and multi-thread channels; and a variety of vegetation and substrate covers (Defra/EA, 2003; Mc Gahey & Samuels, 2004). In this paper, the CES methodology is applied to fourteen river sites from England, Northern Ireland, New Zealand, Ecuador and Argentina, illustrating reasonable model predictions over a broad application range. Discharge and lateral velocity predictions are compared to observed data, with emphasis on practical application, calibration technique and effects of scale. Consideration is given to the relative magnitude of the equation terms with depth, for example, the role of boundary friction, lateral shear and secondary flows, and how these relate to the observed flow structure and the local site characteristics.

1 INTRODUCTION

Rivers and their associated floodplains form the natural system for the transmission of flood flows. Knowledge of river water levels is essential to flood risk management tasks such as flood risk mapping, strategic planning, scheme design, flood warning and emergency evacuation and channel maintenance. In 2001, the Environment Agency of England and Wales commissioned a Targeted Programme of research into reducing uncertainty in conveyance estimation. The key output was the Conveyance Estimation System (CES) software, which provides a practical methodology for estimating flow capacity in rivers, based on the aggregation and extension of previous laboratory derived approaches for application to natural channels. An essential method requirement was the ease of application to rivers of any scale that may be characterised by irregular cross-section shapes, a variety of surface materials, plan form sinuosity and channel braiding.

Previous approaches to calculating flow capacity can broadly be divided into five categories:

1 *Hand calculation methods* commonly termed Single and Divided Channel Methods where the channel cross-sectional is treated as a single unit or divided into more than one flow zone respectively. These include, for example, the methods of Manning (1889), Lotter (1933), Yen & Overton (1973), Ervine & Baird (1982), Lambert & Myers (1998) and Ackers (1991).
2 *Dimensional Analysis* approaches where the dimensionless channel properties such as relative roughness and Froude or Reynolds' Number are evaluated for scale models and assumed similar for the prototype (e.g. Rameshwaran & Willets, 1999).
3 *Additional energy losses due to bends*, for example, the Soil Conservation Service (SCS) and Linearised SCS methods and the work of Chang (1984).
4 *Energy 'loss' methods* which assume that the energy transfers within each flow zone (e.g. main channel or floodplain region) are proportional to the square of the local flow velocity and they are mutually independent and hence the principle of superposition can be applied. Well known methods include those of Ervine & Ellis (1987), James & Wark (1992) and Shiono *et al* (1999).
5 *Reynolds Averaged Navier-Stokes (RANS)* approaches, which are based on the depth-integration

Copyright © 2006 Taylor & Francis Group plc, London, UK

of the RANS equations for flow in the streamwise direction. Significant research contributions include Shiono & Knight (1988), Wark (1993), Abril & Knight (2004), Spooner & Shiono (2003) and Bousmar & Zech (2004).

These previous conveyance approaches have largely focused on experimental channels, which are prismatic, symmetrical and comprise rectangular or trapezoidal cross-section shapes. Although they provide useful quantifiable parameters for estimating discharge such as width ratios, relative depth, relative roughness and main channel side slopes, they are less useful when applied to rivers with irregular, asymmetrical shapes that may be characterised by distributed roughness or channel braiding. The CES methodology utilizes the 'as surveyed' river cross-sections and the observed local roughness features, while incorporating the aforementioned parameter definitions as a guide to understanding and quantifying the energy transfer mechanisms, and hence deriving more universally applicable parameters. This paper demonstrates the broad application range of the CES methodology, through application to fourteen river sites from five countries. An analysis of the relative magnitude of the CES equation terms, i.e. energy transfers due to hydrostatic pressure, boundary friction, lateral shearing and secondary circulations, is undertaken for inbank, main channel overbank and floodplain flow conditions.

2 METHODOLOGY

The methodology is based on the depth-integration of the Reynolds-Averaged Navier-Stokes equations,

$$ghS_o - \frac{\varphi}{8h^2} f q^2 + \frac{\partial}{\partial y}\left[\lambda h \left(\frac{f}{8}\right)^{1/2} q \frac{\partial}{\partial y}\left(\frac{q}{h}\right)\right] = \alpha\Gamma + (1-\alpha) C_{uv} \frac{\partial}{\partial y}[h] \quad (1)$$

where g = gravitational acceleration (ms^{-2}); q = streamwise unit flow rate (m^{2}s); h = local depth normal to the channel bed (m); S_o = reach-averaged longitudinal bed slope; y = lateral distance across the channel cross-section (m); φ = projection of the boundary shear stress onto the plane due to choice of Cartesian coordinate system; and α = function of the reach-averaged sinuosity. Equation 1 has four calibration coefficients: the local friction factor f, the dimensionless eddy viscosity λ, the secondary flow parameter Γ and the coefficient of meandering C_{uv}. The total flow rate, Q (m^{3}s^{-1}), is hence evaluated from,

$$Q = \int_0^b q\, dy \quad (2)$$

where b = the total channel width (m). The fourteen river sites are all located in straight reaches, and thus Equation 1 can be simplified to,

$$ghS_o - \frac{\varphi}{8h^2} f q^2 + \frac{\partial}{\partial y}\left[\lambda h \left(\frac{f}{8}\right)^{1/2} q \frac{\partial}{\partial y}\left(\frac{q}{h}\right)\right] - \Gamma = 0 \quad (3)$$

(1) (2) (3) (4)

where Term 1 is the hydrostatic pressure, Term 2 is the boundary friction, Term 3 is the turbulence due to vertical interfacial shearing and Term 4 represents the secondary circulations due to turbulence in straight channels. The key difference between Equation 3 and the Shiono & Knight (1988) Method (SKM) is the evaluation of f and Γ in natural channels. Here, f is derived from a local unit Manning roughness n_l, which is converted to an equivalent roughness size, k_s, and then the Colebrook-White Law is incorporated to evaluate the lateral distribution of f at each flow depth (Mc Gahey & Samuels, 2004). The dimensionless eddy viscosity is derived from (Abril & Knight, 2004),

$$\lambda = \lambda_{mc}\left(-0.2 + 1.2 D_r^{-1.44}\right) \quad (4)$$

where λ_{mc} = main channel dimensionless eddy viscosity; and D_r = local relative depth given by h/h_{max}. Here, λ_{mc} is taken as 0.24 for rivers after Elder (1959). The secondary flow model Γ, which is based on the work of Abril & Knight (2004), is adapted to incorporate a transitional model Γ_{trans} for asymmetric channels and channels with floodplains at different bed elevations. The main channel inbank, overbank and floodplain formulae are given by (Abril & Knight, 2004),

$$\Gamma_{mci} = 0.05 H \rho g S_o; \quad \Gamma_{mco} = 0.15 H \rho g S_o;$$

$$\Gamma_{fp} = -0.25 H \rho g S_o \quad (5a\text{-}c)$$

where ρ = fluid density (kg m^{-3}). For asymmetric channels or channels with floodplains situated at different bed elevations, the secondary flow model in the main channel transitional region is given by (Mc Gahey, 2006),

$$\Gamma_{mc(trans)} = \frac{(\Gamma_{mco} - \Gamma_{mci})}{(Z_H - Z_L)}(h_l - Z_L) + \Gamma_{mci} \quad (6)$$

where Z_H and Z_L = bed elevation of the higher and lower floodplains respectively (mAD); and h_l = water surface level for the given depth of flow (mAD).

A further difference is that the CES solution technique is based on the continuity of the unit flow rate q rather than the depth-averaged velocity as previously used in the SKM approach. This is due to the strong continuity properties of q with variations in depth, for example, across a vertical face or 'step' in an engineered channel cross-section (Samuels, 1989; Knight *et al*, 2004). The approximation to the solution of Equation 3 is generated by the Finite Element Method (Defra/EA, 2003b).

Copyright © 2006 Taylor & Francis Group plc, London, UK

3 DESCRIPTION OF DATA SETS

The methodology is applied to fourteen data sets from England, Northern Ireland, New Zealand, Ecuador and Argentina. These are summarized in Table 1, including information on bankfull flow rate Q_{bf}, bankfull depth h_{bf}, main channel width b_{mc} and the bed slope S_o. These data sets cover a range of channel types and scales, notably:

1 *Cross-section shape*: the river sections are all irregular in shape and they include simple (*), compound (**) and asymmetrical (***) shapes (Tab. 1) as well as a range of aspect ratios (b/h).
2 *Channel cover*: the bed, bankside and floodplain ground material includes silt, gravel, cobbles and, small and large boulders well as different vegetation types such as grass, heavy weed growth and fallen trees (Tab. 2).
3 *Longitudinal bed slope*: the data includes steep mountain rivers such as the Cuenca and Tomebamba as well as more gentle gradients such as the Severn and the Trent.
4 *Scale*: This includes a range of flow rates and channel sizes, where Q_{bf} ranges from 420 m^3s^{-1} in the Colorado to a mere 7 m^3s^{-1} in the Heathcote and similarly, h_{bf} varies from 1 through to 6 m. The main channel widths vary from 70 m in the Colorado to 6 m in the Blackwater and the floodplain widths vary from 500 m in the Dane to 30 m in the Main.
5 *Channel braiding*: The Torridge and the Blackwater are characterised by high banks or 'levees' with low adjacent floodplains, which provide an effective channel braiding.

Table 1. Summary of data sets.

Data set	Q_{bf} (m^3s^{-1})	h_{bf} (m)	b_{mc} (m)	S_o $\times 10^{-3}$
England				
1. **River Severn, Montford Bridge (Knight, 1989)	184	5.75	35	0.195
2. ***River Trent, North Muskham (Knight, 1989)	392	6.2	55	0.17–0. 74
3. ***River Trent,Yoxall (Knight, 1989)	~70	2.1	30	1
4. ***River Torridge, Torrington	187	2.78	28	1.45
5. **River Blackwater, Ower	~12	2	6	1.6
6. **River Dane, Rudheath (Ervine & MacLeod, 1999)	~90	5	26	0.5–1.1
Northern Ireland				
7. **River Main, County Antrim (Myers & Lyness, 1990)	~17	0.95	14	2.97
New Zealand				
8. *River Heathcote, Sloan Terrace (Hicks & Mason, 1998)	~6.5	1.75	9	0.62–0.35
9. *River Ngunguru, Drugmores Rock (Hicks & Mason, 1998)	~30	~2.5	20	3.7–6.4
10. *River Waiwakaiho (Hicks & Mason, 1998)	~35 @2 m	–	35	9.1–17.6
Ecuador				
11. *River Cuenca, Ucubamba (Abril & Knight, 2004)	~160	2.3	40	15
12. *River Tomebamba, Monay (Abril & Knight, 2004)	~28	1.53	25	17.6
Argentina				
13. *River Colorado, Patagonia (Tarrab, pers. comm.)	~420	3.6	60	1.3
14. *River La Suela, Cordoba (Tarrab, pers. comm.)	~65	2.14	25	0.9–1.8

* = Simple; ** = Compound; *** = Asymmetrical.

Table 2. Summary of roughness cover for each channel.

River	Roughness description
1. Severn	Grass-covered floodplains
2. Trent, Mus.	Fine gravel & alluvial silts on bed, trees & bushes on floodplain
3. Trent,Yox.	Gravel bed, summer in-channel weed growth, grass & bushes on floodplains
4. Torridge	Trees on berm
5. Blackwater	Vertical sheet piling, fallen trees
6. Dane	Thick channel edge growth, less dense over floodplain
7. Main	Coarse gravel bed, quarry stone side slopes, heavy weed growth on berms
8. Heathcote	Angular cobbles, gravel, mud & silt on channel bed, long bankside grass
9. Ngunguru	Gravel & cobbles on bed, grazed grass & scattered brush on banks
10. Waiwakaiho	Large boulders (d_{50} ~2 m), sparse scrub
11. Cuenca	Small boulders (d_{50} ~1 m)
12. Tomebamba	Large boulders (d_{50} ~1.3 m)
13. Colorado	Clay bed, rock banks
14. La Suela	Alluvial with sparse bankside vegetation

Copyright © 2006 Taylor & Francis Group plc, London, UK

4 VELOCITY AND DISCHARGE PREDICTION

Discharge and velocity predictions have been made for the fourteen river sites. The calibration philosophy is based on the bed friction only. The input local unit roughness n_l, from which the friction factor f is derived (Mc Gahey & Samuels, 2004), is varied in order to reduce the overall percentage difference Λ (%) between the predicted Q_{CES} and measured flow rates Q_{data} i.e.

$$\Lambda = \frac{\sum_{i=1}^{n} \left| \frac{Q_{data} - Q_{CES}}{Q_{data}} \right|_i}{n} 100 \qquad (7)$$

where n is the number of data points for comparison. The standard deviation ς is given by,

$$\varsigma = \sqrt{\frac{\sum_{i=1}^{n} \left[\left(\frac{Q_{data} - Q_{CES}}{Q_{data}} \right)_i - \overline{\left(\frac{Q_{data} - Q_{CES}}{Q_{data}} \right)_i} \right]^2}{n}} \qquad (8)$$

For a given channel cross-section, the unit roughness n_l is provided for a 1m depth of flow, and the depth-variation of roughness is introduced through the Colebrook-White Law. Once Λ has been minimised i.e. the overall flow predictions are reasonable for the full depth-range, the lateral distribution of n_l is refined in order to best predict the lateral depth-averaged velocity distributions at each depth of flow. This is based on visual inspection of the predicted and measured velocities. The velocity results are shown for three of the sites, selected to illustrate an example of a simple, compound and asymmetrical braided channel. Figures 1, 2 and 3 show the depth-averaged velocity predictions for the River Colorado, the River Severn and the River Trent at Yoxall and the calibrated n_l values are given in Table 3.

The River Colorado tends to under-predict the high velocities at large flow depths and slightly over-predict the velocities at lower depths. This is most likely a short-coming in the use of the Colebrook-White formulation for establishing the variation of roughness with depth for this wide channel, where bed generated turbulence has a dominant role and the channel banks have less influence. The River Severn data is captured reasonably well, other than the very high velocities in the centre region of the channel. This may indicate that the CES model is over-representing lateral shearing through a large main channel dimensionless eddy viscosity λ_{mc} value of 0.24 in rivers, resulting in an increased retarding effect of the slower floodplain flow on the main channel flow. The River Trent data includes measurements for two depths of flow. The predictions here are considered reasonable given that

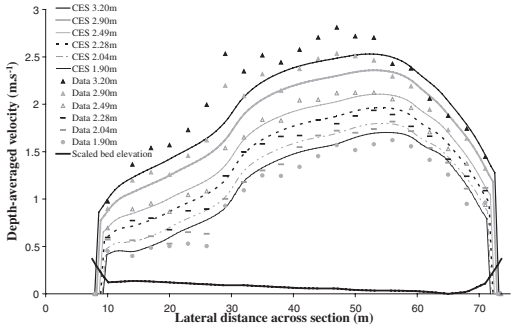


Figure 1. Depth-averaged velocity predictions for different flow depths in the River Colorado, Patagonia.

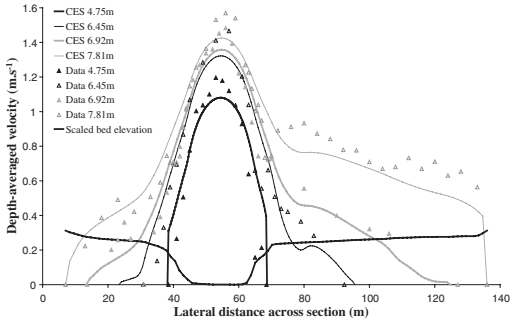


Figure 2. Depth-averaged velocity predictions for different flow depths in the River Severn at Montford Bridge.

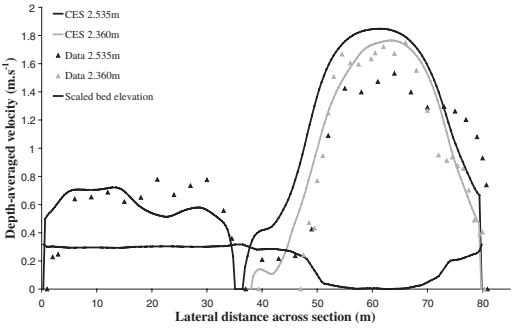


Figure 3. Depth-averaged velocity predictions for two flow depths in the River Trent, Yoxall.

the measurements indicate an overall velocity reduction in the main channel for a larger flow depth. For the braided flow depth, the predicted floodplain velocities are supported by the measurements.

In general, the measured velocities are reasonably well-predicted throughout the depth range for the three rivers.

Figure 4 provides a comparison of the predicted flow rates Q_{CES} to the measured flow rates Q_{data} for

Copyright © 2006 Taylor & Francis Group plc, London, UK

Table 3. Summary if unit roughness values, overall percentage flow difference and standard deviation.

River	Calibrated n_l			Λ (%)	ς
	Left fp	Mc	Right fp		
1. Severn	0.050	0.027	0.028	7.9	17.0
2. Trent, Mus.	–	0.030	0.030	6.6	10.8
3. Trent,Yox.	0.015	0.032	–	13.3	17.9
4. Torridge	0.035	0.029	–	4.8	5.5
5. Blackwater	0.100	0.061	0.100	4.2	5.8
6. Dane	0.082	0.033 0.150*	0.082	14.7	23.1
7. Main	0.075	0.030	0.045	5.6	7.6
8. Heathcote	–	0.031	–	6.8	7.9
9. Ngunguru	–	0.068	–	3.5	48.9
10. Waiwakaiho	-	0.250	–	34.1	37.1
11. Cuenca	–	0.065	–	14.5	16.3
12. Tomebamba	–	0.165	–	8.3	7.9
13. Colorado	0.048*	0.028	0.048*	4.0	4.3
14. La Suela	0.048*	0.032	0.040*	10.9	13.3
Average				9.9	

* channel side banks.

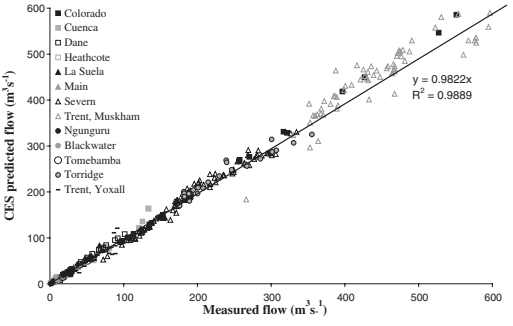


Figure 4. Predicted and measured flow rates for the thirteen river sites.

all the river sites. A perfect match between the model prediction and the data would yield a gradient of 1.0 i.e. $Q_{CES} = Q_{data}$. A least squares regression line gives an R^2 value of 0.9889, indicating a 'good' fit, and a gradient, i.e. Q_{CES}/Q_{data}, of 0.9822. The latter is just less than 1.0, suggesting the CES tends to marginally under-predict the flow rate. Figures 4 and 5 demonstrate the range of scales for which the CES predictions are appropriate, from small rivers such as the Heathcote, with flow rates of $7\,m^3s^{-1}$, through to larger rivers such as the Severn, with flow rates in the range 200 to $300\,m^3s^{-1}$, and finally to much large rivers such as the Trent and the Colorado, with flow rates upwards of $400\,m^3s^{-1}$. The data shows an increasing degree of scatter with increasing flows. This is not surprising since there is more uncertainty associated with river measurements taken at high flows, for example,

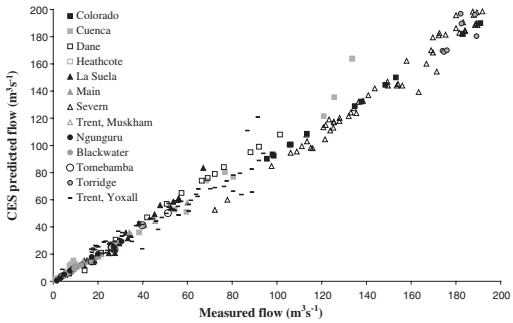


Figure 5. Predicted and measured flow rates for the thirteen river sites (flow rates $<200\,m^3s^{-1}$).

drowned gauge sites, and further to this, the empirically derived model coefficients and models such as Equations 4 and 5 for λ and Γ were largely based on laboratory measurements.

Table 3 provides the overall percentage difference Λ for each data set, giving an average value for the fourteen data sets of 9.9%. This value is inflated by the large contributions of the Trent at Yoxall, the Dane, the Waiwakaiho and the Cuenca. For the Trent, this is not surprising considering the aforementioned trend in the measured velocity data, where greater flow depths have lower velocities. In addition, there is more uncertainty associated with the floodplain measurements, which are beyond the range of the main channel cableway span, and are therefore based on four overbank gauge points. The Dane is characterised by dense seasonal vegetation, and as the high and low flows are typically measured in different seasons, the vegetation characteristics will be different. This seasonal variation is not incorporated in the roughness representation. The Waiwakaiho and the Cuenca are steep mountain rivers with large boulders, and the existing CES methodology does not incorporate a model for boulder roughness. Mc Gahey (2006) demonstrates the improvement in the CES predictions for mountain rivers through application of the Ramette (1992) approach to evaluate the lateral distribution of f with flow depth. Without these four river sites, the average percentage difference is reduced to 6.2%, suggesting a reasonable performance of the CES methodology to at least ten river sites.

Table 3 also includes the standard deviation ς for each site. These values tend to be larger than the overall percentage difference Λ, as the expected or mean value is zero i.e. $Q_{CES} - Q_{data}$, and thus any variation on this mean has a large value relative to zero. The Ngunguru has the largest ς despite the small value of Λ, indicating a high degree of scatter in the data. The Waiwakaiho has a large ς, which is not unexpected considering Λ is a similar order of magnitude. Likewise, the large ς values for the Dane and the Trent

Copyright © 2006 Taylor & Francis Group plc, London, UK

also reflect the large Λ values. For the remaining sites, the standard deviation ς is small and corresponds to the average percentage difference, Λ. This indicates a reasonable model performance in predicting each measured value within each data set, as these measurements are reasonably well-distributed about the CES predicted values.

5 RELATIVE MAGNITUDE OF EQUATION TERMS

Quantifying the relative magnitude of the four principal equation terms in Equation 3 is useful in understanding which flow processes have a dominant role, how these mechanisms change with the depth of flow and what channel properties influence these changes. For example, in wide rectangular channels with no vegetation there may be less lateral mixing than in a heavily vegetated irregular-shaped channel. Essential to this is identifying where the relative contributions are the result of a prescribed model within the CES methodology, for example, a change in the role of the secondary flow term between inbank and overbank flow (Equation 5a-c), compared to external predetermined input parameters such as longitudinal bed slope, channel shape and roughness. The average contributions from the different terms are considered for inbank, main channel overbank and floodplain regions. The river cross-sections and flow depths which are considered are shown in Figures 6 to 16.

Figure 17 provides the relative magnitude of Terms 1 to 4 in Equation 3 for inbank flow conditions in seven rivers.

The averages values are 45% hydrostatic pressure, 43% boundary shear; 9%, vertical interfacial shear and 2% secondary circulations. The large contribution from Term 1 and 2 is not unexpected, as these these constitute the primary balance of forces in the absence of any lateral momentum transfers. Without Terms 3 and 4, Equation 3 would simplify to the well known

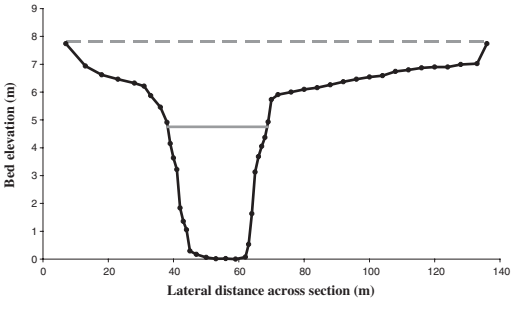


Figure 6. River Severn, Montford.

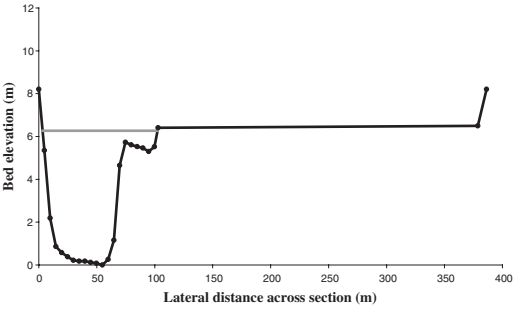


Figure 7. River Trent, North Muskham.

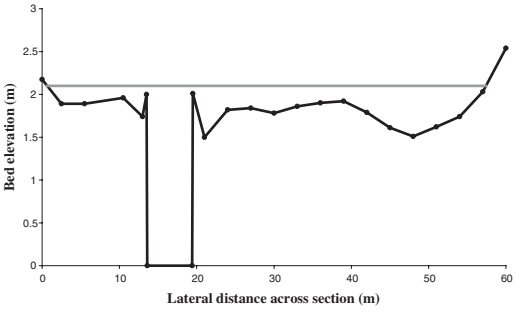


Figure 8. River Blackwater, Ower.

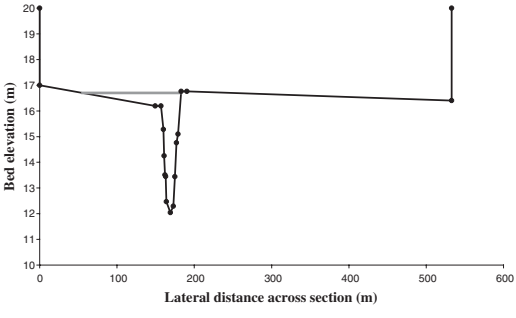


Figure 9. River Dane, Rudheath.

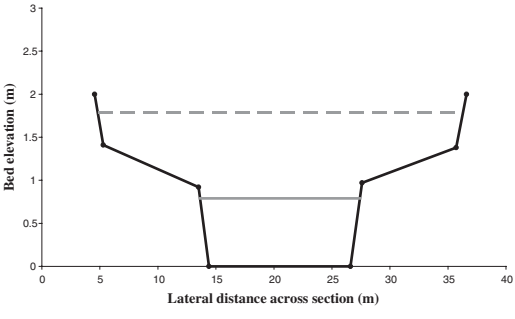


Figure 10. River Main, County Antrim.

Copyright © 2006 Taylor & Francis Group plc, London, UK

Darcy-Weisbach equation. The Term 3 contribution is more variable, indicating different degrees of lateral shear. In wide shallow channels, the side-walls have less influence on the channel centre and the flow is therefore dominated by bed generated turbulence. The velocity gradient is therefore approximately zero in the channel centre, and the Term 3 contribution is small. In narrow deep channels, the side-walls play a larger role, and there is a greater degree of lateral shearing. Figure 18 provides a plot of the percentage lateral shearing versus aspect ratio where the data trend corroborates this reasoning.

The Colorado, the Main, the Waiwakaiho and the Tomebamba all have modest lateral momentum transfers. This is partly due to the large aspect ratios, and partly that the channels have little vegetation and where there is vegetation or boulders there is limited information on the exact location, resulting in the use of average cross-section input unit roughness n_l values. The Heathcote and Ngunguru have a greater degree of lateral shearing which may be explained by the large roughness features which enhance the lateral velocity gradients. The Heathcote has vegetation on the banks and angular cobbles on the channel bed

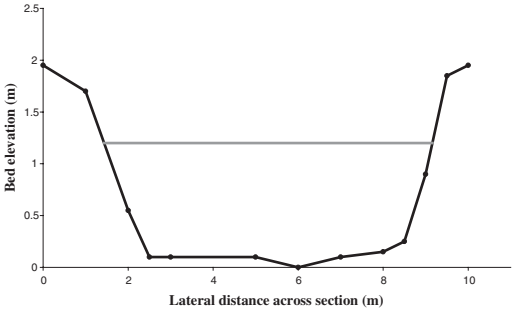


Figure 11. River Heathcote, Sloan Terrace.

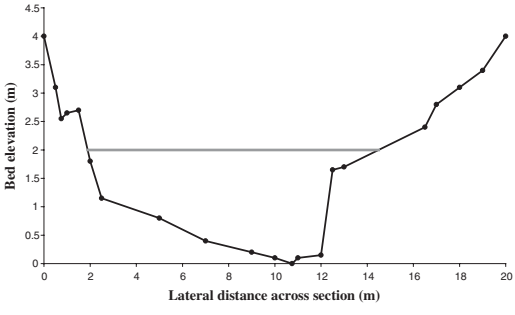


Figure 12. River Ngunguru, Drugmores Rock.

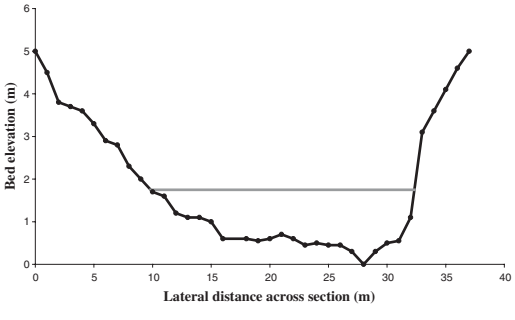


Figure 13. River Waiwakaiho, SH3.

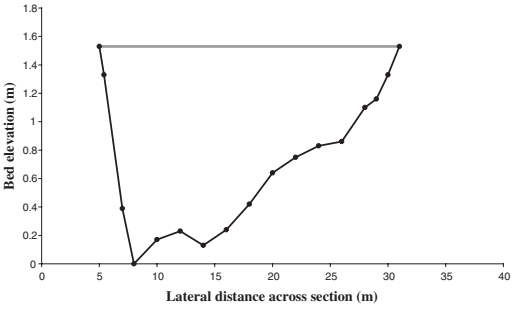


Figure 14. River Tomebamba, Monay.

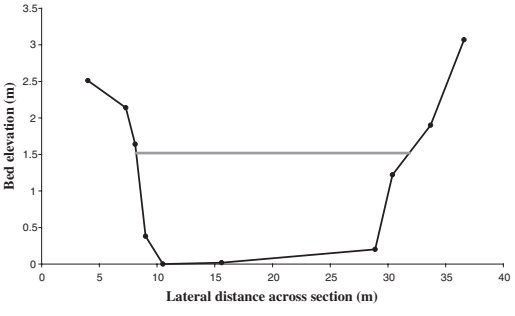


Figure 15. River La Suela, Cordoba.

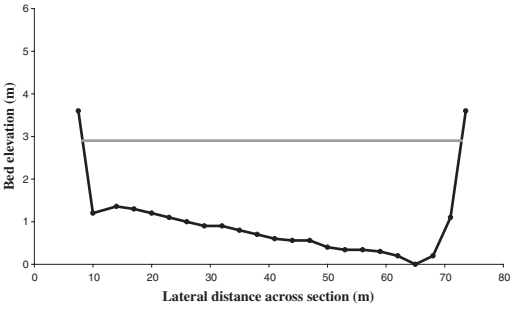


Figure 16. River Colorado, Patagonia.

Copyright © 2006 Taylor & Francis Group plc, London, UK

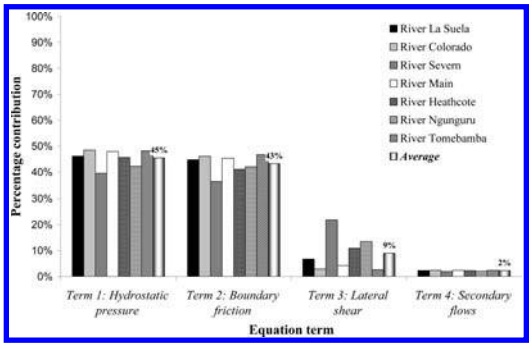


Figure 17. Relative magnitude of equation terms for inbank river flow.

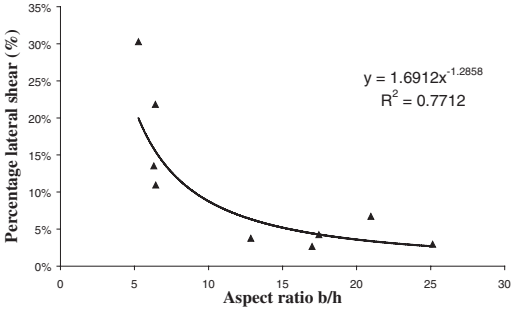


Figure 18. Variation of the percentage lateral shear (Term 3) with aspect ratio.

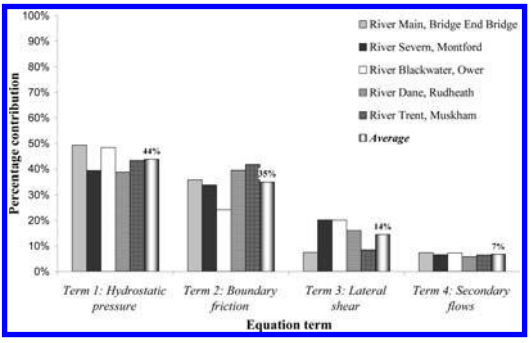


Figure 19. Relative magnitude of equation terms for main channel flow in two-stage rivers.

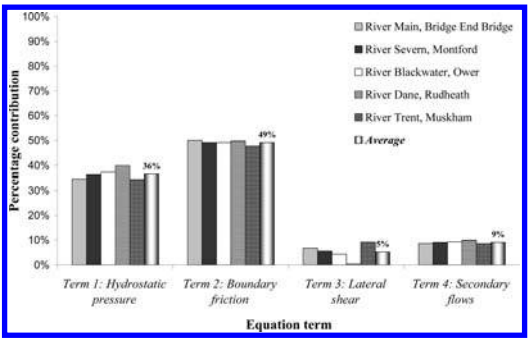


Figure 20. Relative magnitude of equation terms for floodplain flow in two-stage rivers.

and the Ngunguru is characterised by gravel and small cobbles.

Secondary circulations have a small role in inbank flow, which is reflected in the low, empirically derived '0.05' coefficient in Equation 5a, and hence through the small contribution of Term 4.

Some of the rivers differ from the more general trend, for example, the River Severn has a low hydrostatic pressure term and a high degree of lateral shear relative to the other sites. The former may result from incorporating a representative reach-averaged longitudinal slope based on measured water levels for at high flow depths, whereas in reality the surface water slope at Montford Bridge varies substantially with depth (Knight, 1989a). The latter may be attributed to the dense channel vegetation.

Figure 19 provides the relative magnitude of Terms 1 to 4 in Equation 3 for main channel overbank flow conditions in five rivers. The averages values are 44% hydrostatic pressure, 35% boundary shear; 14%, vertical interfacial shear and 7% secondary circulations.

The Severn and the Dane have small hydrostatic pressure contributions, which may be related to the high degree of lateral shearing present in the deep narrow main channel regions. As with the inbank case, the Main has substantially less lateral shearing, than for example, the Severn, as there is less vegetation present and the conveyance is therefore largely geometry driven.

The Blackwater has a noticeably small boundary friction contribution. This is most likely related to the cross-section geometry, in that the irregular geometry results in local steep velocity gradients and hence large lateral momentum transfers. This is reflected in the high lateral shear contribution, which off-sets the boundary friction term in balancing the hydrostatic pressure.

The secondary flow contribution for all sites is more than double that of the inbank flow sites, reflecting the larger '0.15' value in Equation 5b.

Figure 20 provides the relative magnitude of Terms 1 to 4 in Equation 3 for the floodplain flow conditions. The averages values are 36% hydrostatic pressure, 49% boundary shear; 5%, vertical interfacial shear and 9% secondary circulations.

The average hydrostatic pressure term is substantially smaller for floodplain flow, which may be attributed to the lower floodplain flow depths and the high boundary friction due to the presence of dense

Copyright © 2006 Taylor & Francis Group plc, London, UK

floodplain vegetation. The most variable contribution is the vertical interfacial shear. This is approximately zero for the Dane, which may be explained by the low floodplain depths. Conversely, the Trent has the highest lateral shear, which results from the steep velocity gradient at the floodplain main channel interface coupled with the relatively short floodplain width i.e. the inundated floodplain extent is not sufficiently wide to achieve a constant lateral velocity gradient.

The average secondary flow contribution is large, reflecting the large value of the prescribed CES model coefficient in Equation 5c.

6 CONCLUSIONS

A practical approach to estimating the flow capacity of rivers has been demonstrated for fourteen rivers sites from five different countries, where the unit roughness n_l was the only calibration parameter. The depth-averaged velocity predictions compared reasonably well to the measured data for a simple, compound and asymmetrical river example over a range of flow depths. The predicted Q_{CES} and measured Q_{data} flows for fourteen river sites showed a least squares regression fit of 0.9889, which is close to an ideal fit of 1.0. The ratio of Q_{CES} to Q_{data} was 0.9882, suggesting that the CES is more likely to slightly under-predict than over-predict the measured flow values. The average percentage difference Λ between the measured and predicted flows for all sites was 9.9%, demonstrating the effectiveness of the model over a range of scales and channel types. This value may be reduced to 6.2% if the mountainous rivers with large boulders are excluded. The CES methodology is therefore a useful approach for application in river engineering practice, as it incorporates models and parameters that can readily be applied to natural channels, over a range of scales, with irregular geometries, roughness features and channel braiding.

An analysis of the relative magnitude of the four terms in Equation 3 was undertaken for inbank, overbank and floodplain flow. As expected, the hydrostatic pressure and the boundary shear terms were large and they constituted the primary force balance. The boundary friction term was ~10% higher in the floodplain region due to low flow depths and greater vegetation roughness. The lateral shearing term was the most variable. For inbank flows, the variations were shown to be closely related to the aspect ratio. For overbank flow, this was dependent on the floodplain flow depths, where for low or very high floodplain depths, the floodplain flow has less retarding influence on the main channel flow. For main channel overbank flow, the degree of lateral shearing is linked to vegetation growth. The secondary flow contributions are generally small relative to the other equation terms, with a larger contribution in compound channels.

This analysis is useful in practice as it enables practitioners to focus their attention on particular river features. For example, river surveys should ideally include detailed descriptions of the exact cross-section location and nature of vegetation features. It further draws attention to the importance of the main channel dimensionless eddy viscosity λ_{mc} value as well as the rule applied in Equation 4, which may not always be appropriate in describing the lateral shearing in two-stage rivers.

7 RECOMMENDATIONS

The CES methodology has been demonstrated for fourteen river sites, all located in straight river reaches. For further testing, it is recommended that a targeted data acquisition programme is implemented, where the data collection focuses on straight and meandering two-stage natural channels, and measurements include discharge, water level, depth-averaged velocities and, where possible, turbulence measurements.

The methodology incorporates the Colebrook-White Law to evaluate the lateral distribution of the friction factor for each depth of flow. For mountain streams with boulders, an alternative formulation, such as the method of Ramette (1992) is proposed.

The importance of the lateral shearing term in two-stage channels is highlighted. Thus, further investigation of the applicability of Equation 4 for the lateral distribution of the dimensionless eddy viscosity λ in two-stage rivers is advocated.

ACKNOWLDEGEMENTS

This paper draws upon the Targeted Programme of research commissioned by the Environment Agency (EA) of England and Wales as project W5A-057 under the joint the Department for Environment, Food and Rural Affairs (Defra)/EA Flood and Coastal Defence R&D Programme. We wish to thank Dr Mervyn Bramley, the Agency Project Manager for his encouragement and support. The views expressed in this paper are, however, personal and the publication does not imply endorsement by either the EA or Defra. The Authors wish to acknowledge Professor Boris Abril and Miss Leticia Tarrab for their contributions to data.

REFERENCES

Abril, J.B. & Knight, D.W. 2004. Stage-discharge prediction for rives in flood applying a depth-averaged model. *Jnl. of Hydraulic Research,* IAHR. 42(6): 616–629.

Ackers, P. 1991. Hydraulic design of straight compound channels. SR Report 281. *HR Wallingford*, UK, 1&2: 1–130 & 1–140.

Copyright © 2006 Taylor & Francis Group plc, London, UK

Bousmar, D. & Zech, Y. 2004. Velocity distribution in non-prismatic compound channels. *Proc. ICE*, Water Management, 157: 99–108.

Chang, H.H. 1984. Regular meander path model, *Jnl. of Hydraulic Eng.* ASCE, 110(10): 1398–1411.

Defra/EA, 2003. Reducing uncertainty in river flood conveyance. Roughness Review. Project W5A-057, *HR Wallingford*, UK.

Defra/EA, 2003b. Reducing uncertainty in river flood conveyance. Interim Report 2 – Review of Methods for Estimating Conveyance. Project W5A- 057, *HR Wallingford*, UK.

Elder, J.W. 1959. The dispersion of marked fluid in a turbulent shear flow. *Jnl. Fluid Mechanics*, 5(4): 544–560.

Ervine, D.A. & Baird, J.I. 1982. Rating curves for rivers with overbank flows. *Proc. ICE Part 2: Research and Development*, 73: 465–472.

Ervine, D.A. & Ellis, J. 1987. Experimental and computational aspects of overbank floodplain flow. *Trans. of the Royal Society of Edinburgh:* Earth Sciences. 78: 315–475.

Ervine, D.A. & MacLeod, A.B. 1999. Modelling a River Channel with Distant Floodbanks, *Proc. Institution Civil Engineers Water, Maritime and Energy*. 136: 21–33.

Evans, E.P., Pender, G., Samuels, P.G. & Escarameia, M. 2001. Reducing Uncertainty in River Flood Conveyance: Scoping Study. R&D Technical Report to Defra/Environment Agency. Project W5A-057. *HR Wallingford Ltd*. UK.

Hicks, D.M. & Mason, P.D. 1998. Roughness Characteristics of New Zealand Rivers. *NIWA*. Christchurch. 1–329.

James, C.S. & Wark, J.B., 1992, Conveyance estimation for meandering channels SR 329, pp 1–91, HR Wallingford, UK.

Knight, D.W. 1989. River Channels and Floodplains, Final Report *for Severn Trent Water Authority*. April, 1–100.

Knight, D.W., Omran, M. & Abril, J.B., 2004, Boundary conditions between panels in depth-averaged flow models revisited. *Proc. of the 2nd Intl. Conf. on Fluvial Hydraulics: River Flow 2004*, 1: 371-380, Naples, 24–26 June.

Lambert, M.F. & Myers, W.R.C. 1998. Estimating the discharge capacity in straight compound channels. *Proc. ICE Jnl. for Water, Maritime and Energy*, Paper 11530, 130: 84–94.

Lotter, G.K. 1933. Considerations on hydraulic design of channels with different roughness of walls. *Trans. All-Union Scientific Research Institute of Hydraulic Eng*., Leningrad, 9: 238–241.

Manning, R. 1889. On the flow of water in open channels and pipes. *Trans. ICE of Ireland*. 20: 161–207.

McGahey, C. 2006. A practical approach to estimating the flow capacity of rivers. PhD thesis, *Open University*, Milton Keynes, UK.

McGahey, C. & Samuels, P.G. 2003. Methodology for conveyance estimation in two-stage straight, skewed and meandering channels. *Proc. XXX IAHR Congress*, Thessaloniki, C1: 33–40.

Mc Gahey, C. & Samuels, P.G. 2004. River roughness – the integration of diverse knowledge. *Proc. 2nd International Conference on Fluvial Hydraulics*. River Flow 2004. Naples. 24–26 June. 1: 405–414.

Myers, W.R.C. & Lynness, J.F. 1990. Flow resistance in rivers with floodplains. Final Report on research grant GR/D/45437. *University of Ulster*. UK.

Rameshwaran, R. & Willets, B.B. 1999. Conveyance prediction for meandering two-stage channel flows. *Proc. ICE Jnl. for Water, Maritime and Energy*, Paper 11765, 136: 153–166.

Ramette, M. 1992. Hydraulique et morphologie des. rivières: quelques principes d'etude et applications. Compagnie Natinale du Rhone, Formatione Continue, France.

Shiono, K. & Knight, D.W. 1988. Two-dimensional analytical solution for a compound channel. Proc. 3rd Intl. Symposium on Refined Flow Modelling and Turbulence Measurements. *Universal Academy Press*. 591–599.

Shiono, K., Muto, Y., Knight, D.W. & Hyde, A.F.L., 1999, Energy losses due to secondary flow and turbulence in meandering channels with overbank flow. *Jnl. of Hydraulic Research*, IAHR, 37(5): 641–664.

Spooner, J. & Shiono, K. 2003. Modelling of meandering channels for overbank flow. *Proc. ICE Jnl. for Water, Maritime and Energy*, 156: 225–233.

Yen, C.L. & Overton, D.E. 1973. Shape effects on resistance in floodplain channels. *Jnl. of the Hydraulics Division*, ASCE, 99(1): 219–238.

Copyright © 2006 Taylor & Francis Group plc, London, UK

Diffusion wave based modeling of flood inundation based on sub-grid connectivity

D. Yu & S.N. Lane
Department of Geography, University of Durham, Science Laboratories, South Road, Durham

ABSTRACT: We now routinely model flood inundation using reduced complexity models. Traditionally, these have involved both depth-averaging and width-averaging of the mass and momentum equations. Strictly, this assumption is only valid when the flow is shallow and the topographic forcing term is dominant and it still leaves the problem of discretisation and solution, given the strong sensitivity to topographic resolution. In this paper, we present and validate an alternative sub-grid formulation that introduces an explicit representation of finer resolution topographic. This approach uses high-resolution topographic data to develop explicit parameterization of sub-grid-scale topographic variability to represent both the volume of a grid cell that can be occupied by the flow and the effect of that variability upon the timing and direction of the lateral fluxes. This approach is found to give significantly better prediction of fluvial flood inundation in urban areas than traditional calibration of sub-grid-scale effects using Manning's *n*.

1 INTRODUCTION

Fluvial flood modelling in urban areas requires explicit representation of small-scale topographic variation in order to capture the correct patterns of flux near structural elements (e.g. walls, buildings and railroads, etc). However, previous studies (e.g. Horritt & Bates, 2001; Yu and Lane, 2006) demonstrated the severe sensitivity of this type of model to mesh resolution in urban areas and the poor performance of spatially uniform parameterisation using an effective roughness parameter (Manning's *n*). Even using a wetting parameter (following Bradbrook et al., 2004) to reduce the effects of artificial numerical diffusion across the floodplain, strong model sensitivity to mesh resolution was found. Much of this is related to the effects of changing mesh resolution upon topographic information content. Figure 1 shows a hypothetical grid cell set (1a) and an associated coarsened set (1b). The average blockage of the cell in each of 1a and 1b is the same. However, the distribution of sub grid blockages is different. If we consider a cell with water in it, to the left of the coarsened cell (shown in italic) then, in 1a, there should be no inundation. However, averaging as per 1b will lead to inundation when it shouldn't do when water levels to the left of the cells are between 0.15 m and 0.20 m. Thus, with the coarser resolution, and even with the standard wetting treatment used by Bradbrook et al. (2004) and Yu and Lane (2006), water will diffuse more readily across the coarser mesh, leading to a more rapid diffusion of flood inundation extent. It

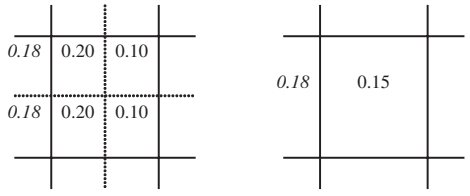


Figure 1. A schematic illustration of the effects of averaging a high resolution topographic dataset (1a) to a lower resolution (1b) in relation to a wave of water moving from the left (elevation shown in italic) and topographic data (non-italic in 1a) subject to averaging (non-italic in 1b). Solid lines are the coarsened mesh cell boundaries. Dotted lines are the sub grid cell boundaries.

may be argued that if the model is only being used to determine inundation extent, the timing is not important. However, Yu and Lane (2006) showed that, for an unconfined floodplain or a large flood on a confined floodplain, the maximum inundation extent was significantly greater for coarser mesh resolutions. This arises because deeper water diffuses too quickly. This may especially be the case in urban areas where the structural complexity of the surface is affected quite significantly by averaging from fine to coarser mesh resolutions. Roughness parameterisation will not deal with this effect fully: even with very high values of the roughness parameter, diffusion will occur across a grid cell in the scenario shown in Figure 1b, even if it is meant not to.

Copyright © 2006 Taylor & Francis Group plc, London, UK

Given the above, this paper seeks to develop a method for sub-grid scale topographic representation with an explicit treatment of the effects of structural elements upon the floodplain upon both blockage and flux. We believe this to be a major contribution to the improved representation of urban flooding noted by Wheater (2002).

2 THEORETICAL DERIVATION OF A SUB-GRID SCALE TOPOGRAPHIC TREATMENT

Bradbrook et al. (2004) and Yu and Lane (2006) review the basis of the model that is modified to provide a sub-grid scale topographic representation in this paper and so it is not covered further. This paper only covers the sub-grid scale topographic representation.

2.1 *Cell blockage effects*

Consider a cell and its sub-grid cells in the configuration shown in Figure 2. The cell is composed of four sub-grid cells with bed elevation e1, e2, e3 and e4 (Figure 2a). These are shown schematically in 1D in Figure 2b. Without a sub-grid scale topographic representation, the elevation of the cell (E) can be calculated simply as the average of the four sub-grid cells. The relationship between water surface elevation and the volume of water that can be stored within the cell without considering the sub-grid topography (i.e. Figure 2a) is a simple linear one, taking the form:

$$V_{ij} = w^2\left(H_{ij} - \frac{1}{N_{ij}}\sum_{k=1}^{N_{ij}} e_k\right) \quad (1)$$

where w is the grid resolution, and H_{ij} is the water surface elevation in cell ij, N_{ij} is the number of sub-grid cells in grid cell ij and e_k is the bed elevation of each sub-grid cell.

However, (1) needs to be modified to represent the actual volume storage effect (Fig. 2b), as (Equation 1) will under-estimate the true volume of storage for $\min(E_{ij}) < H_{ij} < \max(E_{ij})$. Under-estimation of storage volume will lead to over-estimation of water levels, and this partly explains why the effects of mesh coarsening will be amplified in a diffusion type model. In the case of a 2×2 set of cells being averaged to a single cell, the peak under-estimation of volume (or over-estimation of water level) is at $H_{ij} = E_{ij}$ and this diminishes to zero for $H_{ij} = \max(E_{ij})$. This allows us to develop a first approximation of the relationship between water volume (V_{ij}) and water surface elevation (H_{ij}) taking into account sub-grid scale topography:

$$V_{ij} = \frac{w^2}{N_{ij}}\left(N_{ij}^k H_{ij} - \sum_{k=1}^{N_{ij}^k} e_k\right) \quad (2)$$

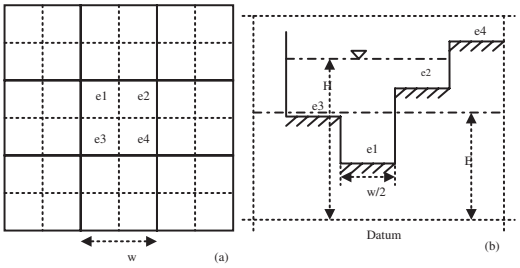


Figure 2. Schematic view of the sub-grid topography. 2a shows the model with its sub-grid cells; e1, e2, e3 and e4 are sub-grid cell bed elevations; w is the resolution of the model grid. 2b shows the four elevations unwrapped onto a 1D plain; H is the sub-grid water surface elevation; B is the bed elevation of the model cell which is equal to the average of its sub-grid cell elevations.

where e_k is the bed elevation of the sub-grid cell k, w is the width of the grid cell which contains N_{ij} sub-grid cells and N_{ij}^k is the number of sub-grid cells within the grid cell that are wet. When the cell is fully wet, $N_{ij}^k = N_{ij}$ and (Equation 2) reduces to (Equation 1).

In a forward differencing scheme, fluxes into and out of cell ij would be determined to give V_{ij}. However, this still leaves two unknowns in (Equation 2), H_{ij} and N_{ij}^k. Thus, N_{ij}^k from the previous time step is taken, used to determine H_{ij}. If H_{ij} exceeds e_{k+1} then N_{ij}^k is increased by one and (Equation 2) is re-evaluated. This continues until H_{ij} no longer exceeds e_{k+1}. A final check is then undertaken to make sure that H_{ij} also exceeds e_k. If not, N_{ij}^k is reduced by one and (Equation 2) is re-evaluated. With the water surface elevation as the dependent variable, the difference between these two scenarios is calculated as:

$$\frac{V_{ij}}{w^2}\left(\frac{N_{ij}}{N_{ij}^k} - 1\right) + \frac{1}{N_{ij}N_{ij}^k}\left(N_{ij}\sum_{k=1}^{N_{ij}^k} e_k - N_{ij}^k\sum_{k=1}^{N_{ij}} e_k\right) \quad (3)$$

(Equation 3) is the general result illustrated above for the case of 2×2 cells: as the water volume increases, the difference in water surface elevation for the two cases decreases, resulting in no difference once all the sub-grid cells are wet, i.e., the number of wet sub-grid cells is equal to the total number of grid cells ($N_{ij} = N_{ij}^k$).

First, when the water surface elevation is less than the average value of the sub grid-scale elevations, but higher than the minimum sub grid-scale elevation, (Equation 2) allows inundation, whereas (Equation 1) does not. Once the water surface is higher than the average sub grid-scale elevation, (Equation 1) will allow inundation. Thus, the peak error with (Equation 1) is when the water surface elevation equals the

Copyright © 2006 Taylor & Francis Group plc, London, UK

average sub grid-scale elevation. The error reduces as the water surface continues to rise until the cell is fully wet when the error is zero. The reverse will occur during the falling limb. Thus, the error due to (Equation 1) is associated with the wetting and drying process in which cells wet up more quickly and dry more slowly than would be the case if (Equation 1) alone were adopted. Second, the sub grid-scale topography has implications for the rate of rise of the water surface within a grid cell. When the cell is wet under (Equation 1), but still partially wet under (Equation 2) (i.e. when the water surface elevation is greater than the average value of the sub grid-scale elevations but less than the maximum value), then the water surface rise within the cell will be more rapid than predicted under (Equation 1).

Third, given that both of these effects determine the rate at which water levels rise, and that diffusion models are based upon the evaluation of water level differences between adjacent cells, the representation in (Equation 2) may affect the way in which water diffuses across the floodplain. With a coarser mesh, when wetting starts, there should already have been flow into (and storage within) the cell. This will have implications for outflow fluxes, with potentially more rapid diffusion of a flood wave than under (Equation 1). However, if the cell is partially wet, then flux cannot occur across all grid cell faces. Thus it is also necessary to look at a sub grid-scale treatment for cell fluxes (see below).

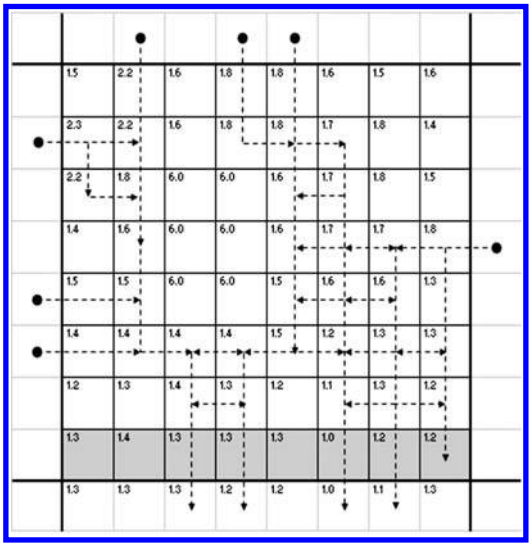


Figure 3. Evaluate the porosity of the bottom side (shaded sub-grid cells) of a model cell with a 1:8 sub-grid ratio through sub-grid connectivity. Numbers in each sub-grid cell are the water surface elevations. Dotted lines with arrows are flow paths and dots are connected flow sources for the sub-grid cells to be evaluated. Five sub-grid cells along this side of the model cell are internally connected to the other three sides and seven sub-grid cells are externally connected in the example. Porosity of this side of the model cell is thus 1/2.

2.2 *Cell flux effects*

We represent cell flux effects using a porosity type treatment which has proved to be a powerful means of representing sub grid scale topographic effects in river flows (e.g. Olsen & Stokseth, 1995; Lane & Hardy, 2002; Lane et al., 2002; Lane et al., 2004) and for representation of wetting and drying processes in depth-averaged hydrodynamic models of floodplain inundation (e.g. Bates, 2000; Bates & Hervouet, 1999). Consider two adjacent grid cells labelled 1 and 2. The first step is to establish a set of rules that determine when flux can occur across the common face of cell 1 and 2, and this has to be done in both directions (i.e. for flux from cell 1 to 2 and from cell 2 to 1). A porosity term is set based upon the percentage of cells that will be able to flux from cell 1 to 2, which varies as a function of water surface elevation. The porosity of each side of the cell is determined by: (i) the internal sub-grid cell connectivity of each sub-grid cell along this side; and (ii) the external sub-grid cell connectivity of each sub-grid cell along this side. Consider the porosity of the bottom side of a model cell with a $1:8$ sub-grid ratio as shown in Figure 3. First, each sub-grid cell along this side is evaluated to check whether it is connected to the other three sides of the model cell (top, left and right sides in Fig. 3). This is based upon the water surface elevation of the sub-grid topography. Dotted lines are the connectivity paths for the sub-grid cells. No rules are defined as to the external connectivity of the sub-grid cells along the connected sides. Second, if a sub-grid cell is connected to the other three sides based on (i), this cell is further evaluated to check whether its water surface elevation exceeds that of its adjacent sub-grid cell. If a sub-grid cell is evaluated to meet (i) and (ii), it is accounted as a connected cell.

If the number of sub grid-scale cells along a common face is l, there will always be $l-1$ values of porosity between zero (no flux across that face) and one (flux across all of the face), and the values of porosity will be multiples of $1/l$. In Figure 3, five sub-grid cells are internally connected to the other three sides and seven externally through the bottom side. Among these, four cells meet both (i) and (ii). Thus, porosity of the bottom side is ½. Flux from this side out to the bottom side is calculated by Manning Equation and further scaled by the porosity of this side explicitly.

One additional correction is introduced. As the flux is a non-linear function of water depth (from the Manning equation), then we need to make sure that the correct water depth is used in the evaluation of flux.

Copyright © 2006 Taylor & Francis Group plc, London, UK

This is done by determining an effective depth for the flux, based upon:

$$d_e = \sqrt[3/5]{\frac{\sum_{i=1}^{n} d_i^{5/3}}{n}} \quad (4)$$

where n is the number of sub-grid cells that are wet along the outflow side of the modelling cell and d_i is the effective depth of the individual sub-grid wetted cells along the outflow wall of the modelling cell. If flux occurs across one sub grid cell face, then the flux evaluated using (4) with the porosity scaling gives the same flux as if a mesh set at the sub grid scale resolution was being adopted. This is not the case when more than one sub grid scale flux occurs because of the non linear form of the depth-flux relationship in the Manning equation. However, provided the topographic variability within fluxing sub grid scale cells is small then the error is small, and the weighting used in (4) further reduces this error.

2.3 *Summary*

In summary, this sub grid cell treatment should represent a simple method for improving the representation of structurally complex topography within two-dimensional diffusion wave modelling. In particular, it should reduce the dependence upon mesh resolution noted by Yu and Lane (2006), especially in dynamic rather than steady state solutions. It differs from the wetting and drying parameter developed by Bradbrook et al. (2004) and used by Yu and Lane (2006) in that the wetting and drying parameter represents an empirical means for dealing with mesh resolution effects whereas the approach used here is explicitly grounded in rules that are locally evaluated in relation to information on the sub grid scale topography in a particular grid cell. In the next section, we evaluate the effects of this development upon sensitivity to mesh resolution within a flood inundation model.

3 MODEL TESTING

This approach described above was assessed using the same flood event as described in (Yu & Lane, 2006). Topographic data processing, validation data and the approach for establishing the connectivity between the river channel and floodplain are described in that paper and are not further covered here. Model time steps and inflow data were also set up in the same way. The model was run using four different spatial resolutions: 4 m, 8 m, 16 m; and 32 m. First, the approach in Section 2 is tested by running the 32 m simulation with different sub-grid ratios (4 m, 8 m and 16 m) using an artificial inflow hydrograph for five hours. Inflow for each bank cells is set constantly at $0.01/m^3s^{-1}$ throughout the simulation. This guarantees the same amount of flux on the floodplain for each simulation. The purpose of these simulations is to investigate the effect of using different orders of sub-grid ratio (32 m: 4 m, 32 m: 8 m and 32 m: 16 m). The inundation extents are compared with the 4 m simulation using the original wetting approach (Bradbrook et al., 2004) at each time step for the whole simulation. Model performance is assessed using a measure of fit (F) for wet cells to compare the model predicted inundation extent with the validation dataset (e.g. Horritt and Bates, 2001; Horritt and Bates, 2002). In terms of a contingency matrix, F is defined by:

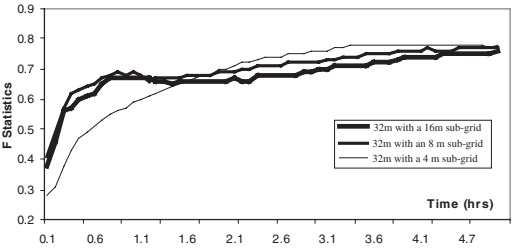


Figure 4. F statistics over time for simulations of different sub-grid coarsens ratios, using 4 m results as reference.

$$F_i = \frac{n_{ii}}{n_{i+} + n_{+i} - n_{ii}} \quad (5)$$

where n_{ii} is the number of cells both observed and predicted as wet, n_{i+} is the number of cells observed as wet, and n_{+i} is the number of cells predicted as wet. The F Statistics for wet cells obtained from simulations of different sub-grid ratios are shown in Figure 4.

The F statistic in Figure 4a suggests that the effect of the higher- order sub-grid treatment is more pronounced during the initial wetting process (first 1.5 hrs). However, the lower-order sub-grid treatment seems to perform better than the higher-order ones later in the simulation. In general, 32 m simulations using 4 m and 8 m sub-grids produce better resemblance to the 4 m results during the initial wetting process, compared with a 16 m DEM as sub-grid. This is an interesting finding as we would expect that a simulation with high-order sub-gird topography ratio will produce better results when compared with the 4 m simulation. However, we don't really know how the original 4 m simulation and 32 m simulation with 4 m sub-grid perform with regard to what happens in the real world. Indeed, for this type of model, others (e.g. Bates & Anderson, 2001) haves suggested that surface velocity might be a more reliable way for model validation. It is clear from these simulations that, there is no immediate benefit of using high orders of sub-grid ratios if the initial wetting process is not going to be examined with real world data.

Copyright © 2006 Taylor & Francis Group plc, London, UK

Given the above, we restricted consideration of sub-grid treatments to a coarsening ratio of 2 : 1 (i.e. we used the sub grid-scale treatment to represent the effects of coarsening: a 4 m mesh to 8 m; an 8 m mesh to 16 m; and a 16 m mesh to 32 m) and apply this approach using the real hydrograph for the flood event. At this point, we used $n = 0.04$ throughout. As with Yu and Lane (2006) the focus of model testing combines both validation and verification. For the purposes of validation, we use the at-a-point in time data at c. 300 hours in the November 2000 flood (see Fig. 2b in Yu & Lane, 2006). Following Yu and Lane (2006), we use a method adopted from remote sensing (Congalton & Green, 1999) to assess model predictions. This sets up model output as a contingency table and calculates the overall accuracy, F (following Bates & Horritt, 2002) Kappa and conditional Kappa from these data (Table 1). As noted by Yu and Lane (2006), reliance upon data from single time periods can give a misleading assessment of model performance, especially where, as in this case, we are interested in reproducing the correct diffusion of inundation through time. Thus, we also undertake verification, and compare the original 8 m, 16 m and 32 m simulations with the 8 m, 16 m and 32 m sub grid model simulations as well as the default 4 m simulation. We also consider the original and sub grid models with different values of n to compare the effectiveness of using n to represent sub grid scale topographic effects with the explicit sub grid treatment. As the focus is the sub grid treatment, we hoped to reduce dependence upon high values of n. Thus, in the first instance, we used $n = 0.04$, 0.06, 0.08 and 0.1; but also undertook simulations with much higher values of n; 1.0 and 10.0; following the findings of Yu and Lane (2006).

4 RESULTS

4.1 *Inundation patterns through time*

Figures 5, 6 and 7 show the first 40 hours of model simulation, with and without the sub grid-scale treatment. It is clear that, in all cases, there is a significant reduction in the rate of inundation diffusion with the sub grid-scale treatment. Figure 5a shows inundation of the confined floodplain by 30.5 hours with the original treatment. With the sub grid treatment, this increases to 40 hours (Fig. 5b), and it is clear that the sub grid treatment has a major impact upon the timing of inundation. The conclusions made regarding the effects of the 8 m sub grid-scale treatment (Fig. 5) are mirrored in the 16 m and 32 m treatments. Flow diffuses much more rapidly in the 16 m (original) case than in the 16 m (sub grid-scale) case (Fig. 6), with almost complete inundation at 30 hours (original case) compared with 36 hours (sub grid-scale). The 32 m (original) case results in extensive inundation within the first

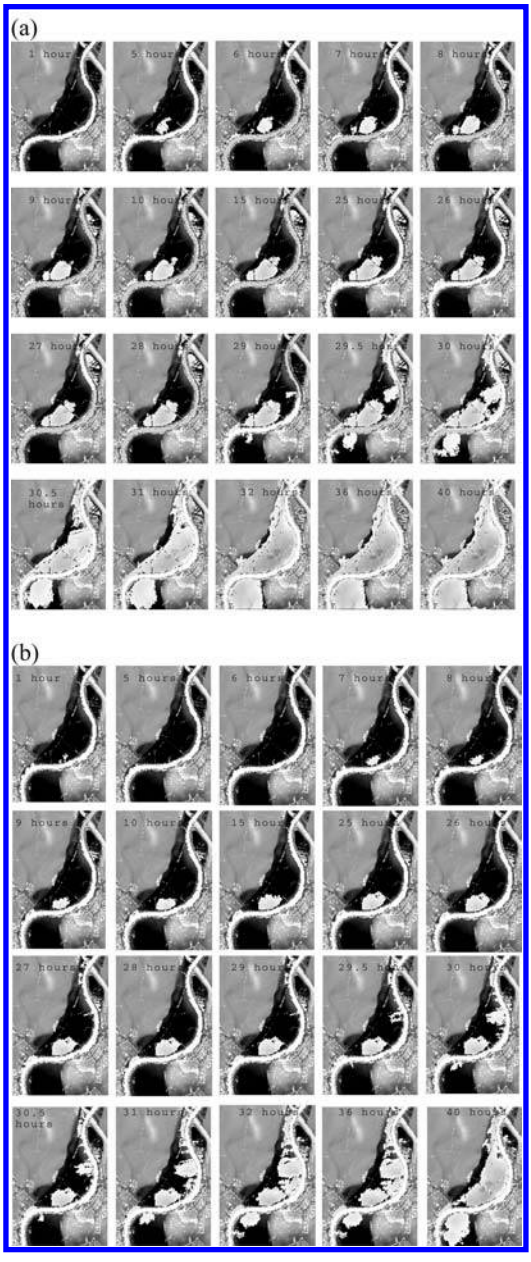


Figure 5. Comparison of the time series inundation extents during the wetting process in the first 40 hours for (a) the original diffusion model; and (b) the sub-grid treatment model; using an 8 m resolution DEM.

10 hours of simulation whereas the 32 m (sub grid-scale) case does not have inundation until c. 31 hours. It seems that, for the first part of the hydrograph, the sub grid-scale treatments delay the inundation process.

Copyright © 2006 Taylor & Francis Group plc, London, UK

Figure 8 shows the effects of the sub grid-scale treatment upon inundated area with $n = 0.04$. This shows that not only do the sub grid-scale treatments reduce the speed of inundation (Figs 5–7) but also the maximum inundation area for all mesh resolutions at all time periods. The original hydrograph had multiple water level peaks. With the 32 m mesh resolution mesh, inundated area responded rapidly to fluctuations in water level, with multiple flood peaks evident in the

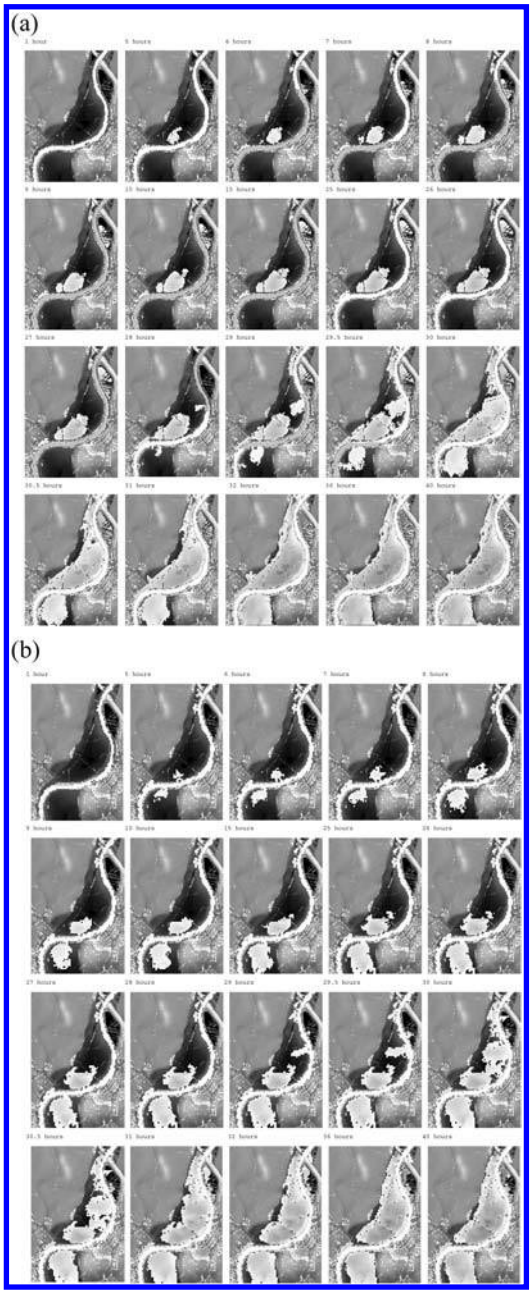


Figure 6. Comparison of the time series inundation extents during the wetting process in the first 40 hours for (a) the original diffusion model; and (b) the sub-grid treatment model; using a 16 m resolution DEM.

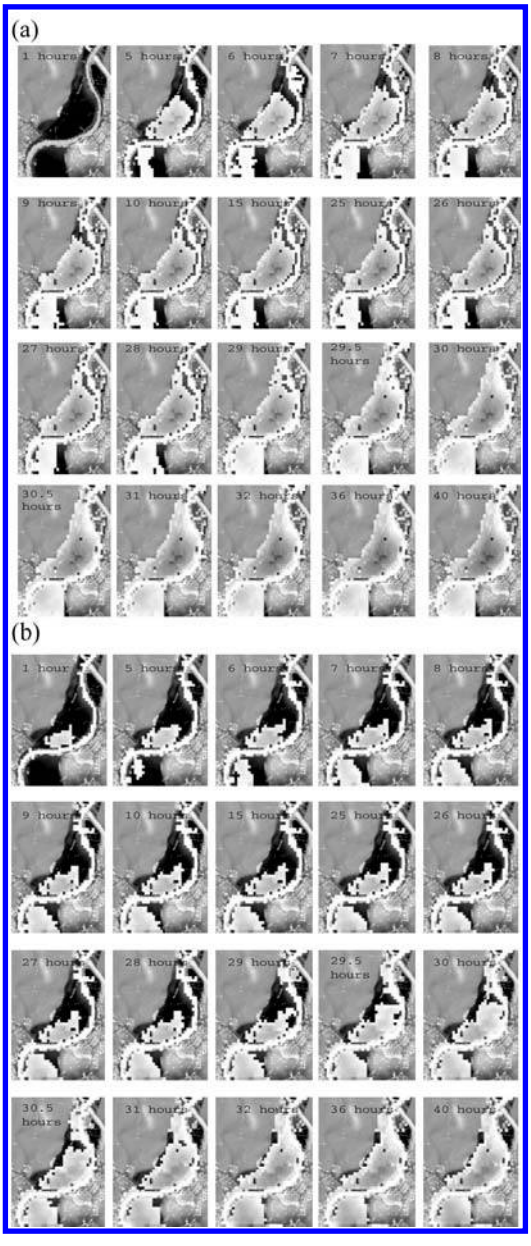


Figure 7. Comparison of the time series inundation extents during the wetting process in the first 40 hours for (a) the original diffusion model; and (b) the sub-grid treatment model; using a 32 m resolution DEM.

Copyright © 2006 Taylor & Francis Group plc, London, UK

inundated area. In the absence of a sub grid-scale treatment, these fluctuations are present in both the 16 m and the 8 m inundated area records. With the sub grid treatments, the inundated area is much less responsive, with response only evident between the third and the fourth water level peak in all sub grid treatments. The sub grid treatments also reduce the total inundation area at all time periods. The differences are quite substantial, especially for the coarsest mesh resolution.

The obvious question that emerges from the above simulations is whether or not the reduced speed of flood wave inundation and the reduced flood inundation extent that is obtained with the sub grid-scale treatment is an improvement over the original diffusion wave formulation. This is addressed with respect to the remotely-sensed validation data and the original 4 m simulation in the next two sections.

4.2 *Model validation*

Table 1 shows the results of the accuracy assessment with the four mesh resolutions simulated and with the three sub grid scale treatments applied to the three coarser mesh resolutions. Table 1 confirms, that as the mesh is coarsened from 8 m to 32 m, all of the accuracy statistics suggest progressively poorer model performance. However, there is an anomaly in that the 4 m resolution only gives the best results for overall accuracy, and performs significantly less well in term of the F statistic. In all cases, Table 1 shows that the sub grid scale treatment improves the level of agreement over the original case. For the 8 m mesh resolution, the improvements in overall accuracy, Kappa and F are small. However, the conditional Kappa improves substantially. The sub grid scale treatment has a progressively greater effect at coarser mesh resolutions with large improvements in F and conditional Kappa at 16 m and in all accuracy statistics at 32 m. Given the discussion in Yu and Lane (2006) of the problems of these types of accuracy measures, reliance on absolute values, from at-a-point in time data, must be treated with caution. What matters here is that, in every case, the sub grid-scale treatment improves the level of agreement as compared with the original diffusion model.

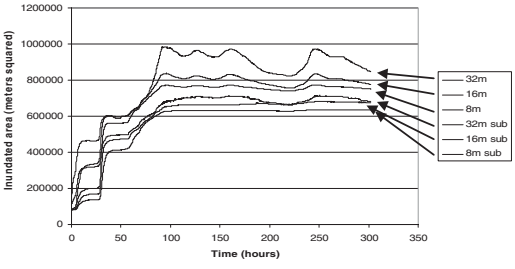


Figure 8. Predictions of inundated area against time for the first 300 hours of model simulation for three mesh resolutions with both default treatments and sub grid-scale treatments.

4.3 *Model verification*

In order to extend the assessment of model performance to a larger number of time steps, accuracy statistics (overall accuracy, Kappa and conditional Kappa) were determined for the first 60 hours by comparing a range of mesh resolutions, with and without sub grid-scale treatments, to the 4 m case (Fig. 9). In all cases, n was held constant at 0.04. The overall accuracy statistic reduces through time (Fig. 9a), reflecting the fact that this statistic is strongly dependent upon the initial number of dry cells used in the comparison and, at the start of a flood event, that both the 4 m and the coarsened mesh and sub grid-scale treatments will both have a larger number of dry cells.

However, Figure 9a shows that use of the sub grid-scale treatment improves agreement with the 4 m case, as judged by overall accuracy. Use of the Kappa

Table 1. Accuracy assessment based upon comparison of model predictions with different mesh resolutions and with and without the sub-grid treatment. The validation data are based upon remotely-sensed imagery obtained at 300 hours during the hydrograph shown in Yu and Lane (2006).

	4 m	8 m	16 m	32 m	8 m sub grid scale treatment	16 m sub grid scale treatment	32 m sub grid scale treatment
Overall accuracy	86.6	87.3	83.4	71.3	88.1	85.6	81.0
Kappa	73.6	75.5	69.6	50.7	76.8	73.5	67.0
F	76.4	78.5	75.0	61.3	80.0	80.4	75.0
Conditional Kappa for wet areas only	66.2	74.0	63.2	40.9	89.5	78.4	65.3

Copyright © 2006 Taylor & Francis Group plc, London, UK

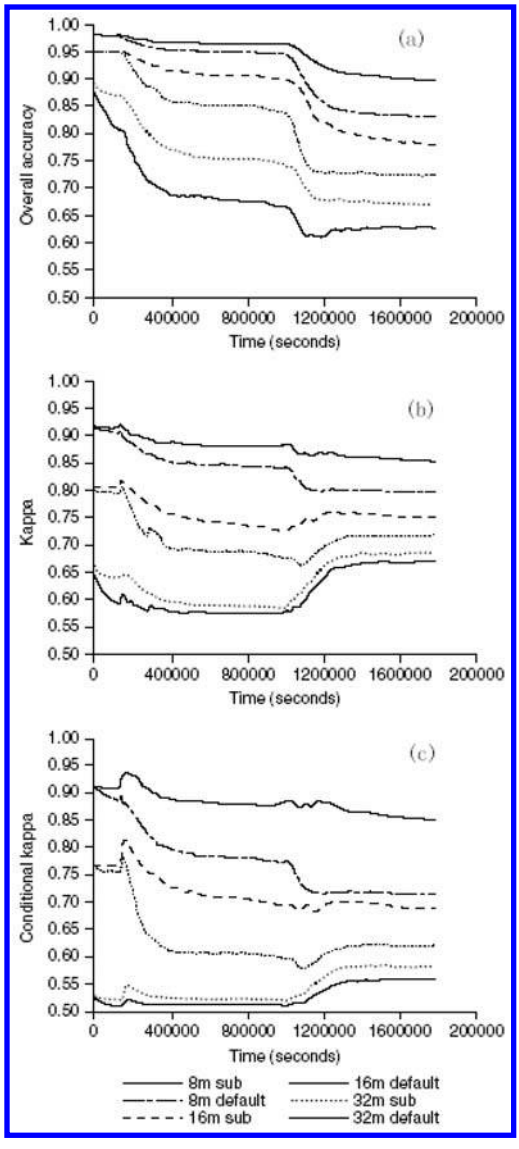


Figure 9. Accuracy statistics (overall accuracy, Kappa and conditional Kappa for wet cells only) determined for model simulations at 32 m, 16 m and 8 m, with and without a sub grid treatment. These are determined as a function of time, taking the 4 m solution without a sub grid treatment as 'true' for verification purposes.

statistic, rather than the overall accuracy, reduces bias in contingency table analyses (Congalton & Green, 1999), although it does not remove completely the dry-bias effect in flood inundation model assessments. Figure 9b confirms that the 32 m and 16 m simulations are more degraded as compared with the 4 m predictions than the 8 m degradation as compared with the 4 m predictions. The sub grid-scale treatments are then most effective in the 8 m case and least effective in the 32 m case. A much more reliable accuracy measure is provided by a conditional Kappa statistic which, in this case, restricts the analysis of the contingency table to only those cells that are predicted as wet. Figure 9c shows the conditional kappa and demonstrates that the sub grid-scale treatment results in a substantial improvement in model accuracy in the 8 m case as compared with the 4 m simulation. It appears that, in all cases, using the sub grid-scale treatment with the 8 m resolution mesh results in a significant improvement in model accuracy, however judged, but that this improvement is reduced at coarser mesh resolutions. This is not surprising as we are only using sub grid-scale topographic data from the 2×2 cells at the next finer resolution (e.g. the 32 m simulations make use of a 16 m DEM). It should be noted that, for the conditional Kappa results (Fig. 9c), accuracy of the 32 m sub grid treatment with respect to the 4 m simulation approaches that of the 16 m no sub grid treatment towards the latter half of the simulation and the 16 m sub grid treatment approaches that of the 8 m no sub grid treatment.

4.4 *Comparison of calibration using Manning's n with sub grid-scale treatment*

The above two sections showed a significant improvement in model predictions through adopting the sub grid-scale treatment in terms of reproducing the time-dependent change in flood inundation. This section compares a more traditional approach to representing sub grid-scale topographic variability based upon calibration using Manning's n by using a sub grid-scale treatment. This is undertaken in terms of both: (1) the inundated area versus time plots; and (2) accuracy statistics, as compared with the 4 m data, reported in the above section. As reported by Yu and Lane (2006), Figure 10a shows that for the 8 m case, there is relatively low sensitivity to Manning's n until $n >> 0.1$. Whereas the sub grid-scale treatment almost exactly recovers the inundation area versus time plot with $n = 0.04$, with $n = 1.0$, the area-time curve almost lies on the 4 m line, but deviates significantly after c. 140000 s. The area-time plot is not recovered as well with the 16 m (Fig. 10b) and 32 m (Fig. 10c) sub grid-scale treatments, although they are still a significant improvement on all values of n without a sub grid-scale treatment. In particular, whilst the area may be correctly estimated with calibration through n alone at certain times during the simulation (e.g. with $n = 10.0$ and a 32 m mesh resolution at c. 120000 s), even with high values of n (> 1.0), the inundated extent exceeds the 4 m inundated extent by the end of the time period.

Copyright © 2006 Taylor & Francis Group plc, London, UK

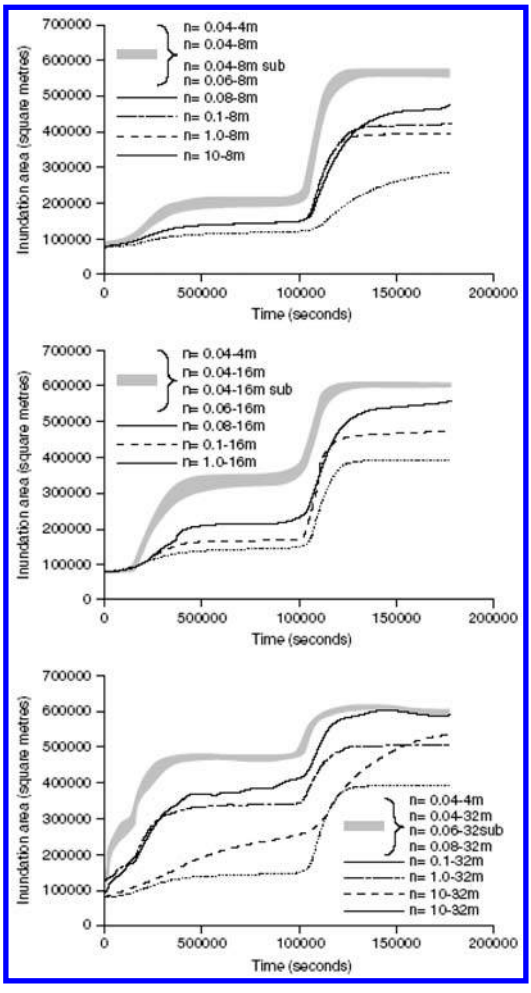


Figure 10. Plots of inundation area versus time for the first 60 hours of simulation, with different mesh resolutions and values of *n*.

5 DISCUSSION

A number of key points emerge from the above results. First, and most importantly, the results show that the sub grid treatment is effective in reducing simulation dependence upon mesh resolution. The sub grid treatment reduced the speed of inundation in the early part of the flood wave (Figs 5–7) and also the maximum inundated area for all mesh resolutions at all time periods (Fig. 8) with a markedly reduced sensitivity of inundated area to water level fluctuations in the main channel. Second, the model used only the immediately finer DEM in parameterising the sub grid treatment (i.e. the 2 × 2 DEM cells in the finer DEM). This was reflected in the comparisons with the 4 m simulations, where degradation to 8 m, with a sub grid treatment, produced the best accuracy statistics through time. It was also reflected in the inundation-time plots, where the 16 m and 32 m sub grid treatments were progressively less effective in reducing inundated area through time back to the 4 m plots. Using a 16 m DEM (i.e. with 8 m sub grid data) and a 32 m DEM (i.e. with 16 m sub grid data) progressively degraded the accuracy statistics derived with respect to the 4 m data. Further research should explore whether using sub grid topographic data with 4 × 4 cells (in this case with 32 m and 16 m meshes) and 8 × 8 (in this case with a 32 m mesh) cells results in accuracy assessment results that approach the 8 m sub grid treatment.

Third, and as expected, the effective value of *n* required to reproduce the 4 m data reduces as mesh resolution is fined. It should be emphasised that this questions the extent to which field estimated values of *n* can be used to parameterise a model such as this. It reinforces the point that *n* is an effective parameter, not only in relation to the sub grid-scale topographic variability but also in relation to decisions being made about how to discretise a model. Any guidance that is provided to assist with roughness specification for floodplain flow should be oriented towards the role of roughness and mesh resolution in the calibration process as well as to how it should relate to the surface of the floodplain under consideration.

However, these simulations (Fig. 10) also showed that *n* alone was not effective in reproducing the inundation-time plot and, although there were some time periods when using very high values of *n* gave a reasonable estimation of inundation for a short period of time, the shape of the area-time plots with high values of *n* with coarser mesh resolutions was often very different to that found with finer mesh resolutions. Introduction of the sub grid treatments was more effective than *n* perturbation in recovering the inundated area-time plot. However, use of the sub grid treatment in turn changed the interaction between model predictions and *n*. In general terms, the model became more sensitive to *n*. This is not surprising as implicit in the sub grid treatment developed here is incorporation of the effects of sub grid scale depth variability, which given the form of the Manning equation will result in greater sensitivity to *n*. The combination of *n* calibration with the sub grid treatment resulted in the best accuracy statistics, aided by a generally increased sensitivity to *n*. This suggests that combining the sub grid treatment with optimisation of *n* may produce optimal model predictions on a coarse mesh but, and more importantly, coarser mesh predictions with the sub grid treatment are more reliable at reproducing the 4 m patterns than those without. This is regardless of whether or not any optimisation using *n* is undertaken.

The obvious question is whether or not all of this matters in terms of applying diffusion wave models to

Copyright © 2006 Taylor & Francis Group plc, London, UK

floodplains that are complex, such as those found in urban areas. The prime effect of changing mesh resolution is to change the timing of flood inundation. The sub grid treatments result in better model validation (Table 1). When taken in combination, this suggests that if the timing of inundation is not right, then it may be difficult to get the inundated area right, whether at the peak flow, or some other point on the hydrograph. This is an important point for any situation where the floodplain is not laterally-confined in relation to the water level associated with the peak inundation extent.

6 CONCLUSION

This paper has described a treatment for representation of the effects of topographic variability at the sub mesh scale. This is based upon explicit representation of sub grid-scale topographic effects through treatment of both sub grid blockage and flux effects. Results suggest that, when using a coarser mesh, this treatment is much more effective than optimization using Manning's n, in terms of both: (1) validation data derived from aerial imagery at a single point on the falling limb of the hydrograph; and (2) recovering the inundated area-time plot obtained with a finer resolution mesh. As the ease with which topographic data are measured and processed is progressively increased, this type of approach should allow diffusion wave models to be applied over very long river reaches whilst still making use of the high resolution of topographic data that can now be acquired.

REFERENCES

Bates, P.D. 2000. Development and testing of a sub grid-scale model for moving-boundary hydrodynamic problems in shallow water. Hydrological Processes. 14: 2073–1088.

Bates, P.D. & Anderson, M.G. 2001. Validation of hydraulic models. Model Validation: Perspectives in Hydrological Science. Anderson, M.G. and Bates, P.D. Chichester, John Wiley and Sons.

Bates, P.D. & Hervouet, J-M. 1999. A new method for moving–boundary hydrodynamic problems in shall water. Proceedings of the Royal Society of London, Series A. 455: 3107–3128.

Bradbrook, K.F., Lane, S.N., Waller, S.G. and Bates, P.D. (2004). "Two dimensional diffusion wave modelling of flood inundation using a simplified channel representation." International Journal of River Basin Management 2(3).

Congalton, R.G. & Green, K. 1999. Assessing the Accuracy of Remotely Sensed Data: Principles and Practice. Boca Raton: Lewis Publishers.

Horritt, M.S. & Bates, P.D. (2001). "Effects of spatial resolution on a raster based model of flood flow." Journal of Hydrology 253: 239–249.

Horritt, M.S. 2002. Evaluating wetting and drying algorithms for finite element models of shallow water flow. International Journal for numerical methods in engineering 55: 835–851.

Olsen, N.R.B. & Stokseth, S. (1995). "Three-Dimensional numerical modelling of water-flow in a river with large bed roughness." Journal of Hydraulic Research 33(4): 571–581.

Lane, S.N. & Hardy, R.J. (2002). Porous rivers: a new way of conceptualising and modelling river and floodplain flows. Transport Phenomena in Porous Media II. Ingham, D. B. and Pop, I. Oxford, Pergamon: 425–449.

Lane, S.N., Reid, S.C. R.M. & Westaway, D.M. 2004. Hicks Remotely sensed topographic data for river channel research: the identification, explanation and management of error. In: R.E.J. Kelly, N.A. Drake, S.L. Barr Spatial Modelling of the Terrestrial Environment. Wiley; 2004:157–174.

Lane, S.N., Hardy, R.J., Elliott, L. and Ingham, D.B. (2002). "High-resolution numerical modelling of three-dimensional flows over complex river bed topography." Hydrological Processes 16(11): 2261–2272.

Wheater, H.S. 2002. Progress in and prospects for fluvial flood modeling. Philosophical Transactions of the Royal Society of London: Series A, 360 (1796): 1409–1431.

Yu, D. & S.N. Lane (2006). Urban fluvial flood modelling using a two-dimensional diffusion wave treatment, part 1: Mesh resolution effects. Hydrological Processes 20: 1541–1565.

Copyright © 2006 Taylor & Francis Group plc, London, UK

Experiments on the flow in a enlarging compound channel

D. Bousmar
Hydraulic Research Laboratory, Ministère de l'Equipement et des Transports, Châtelet and, formerly, Fond National de la Recherche Scientifique, Belgium.

S. Proust
Hydrology-Hydraulics Research Unit, CEMAGREF, Lyon, France

Y. Zech
Civil and Environmental Engineering, Université catholique de Louvain, Louvain-la-Neuve, Belgium

ABSTRACT: The paper presents an experimental investigation of the flow in a compound channel with symmetrically enlarging floodplains. These results complement previous work on symmetrically narrowing floodplains. Both these data sets enable a better understanding of the mass and momentum transfer occurring in non-prismatic compound channels, without facing the complexity of a fully meandering geometry. The new experiments show that, in this diverging geometry: (1) the flow expends on the floodplains with a significant shift in the downstream direction, with the discharge on the floodplains significantly lower than their conveyance capacity in a prismatic compound channel with the same cross section; (2) the lateral distribution of velocities presents a large gradient from the interface between subsections to the floodplain lateral bank; and (3) in some large discharge cases, the flow behaves like a jet, with the maximum velocity filament oscillating from one main-channel bank side to the other, and recirculation zones developing on the floodplains.

1 INTRODUCTION

Flow modelling in a river flooding overbank is challenging for the engineer. Compound channels present a complex flow behaviour that affects significantly the conveyance prediction. In a prismatic compound channel, the flow velocity is generally larger in the main channel than on the floodplain, thanks to a larger flow depth and a lower flow resistance. A shear layer develops at the interface between both subsections and transfers momentum from main channel to floodplains, reducing accordingly the total channel conveyance. In non-prismatic channels, due to the geometrical changes, a mass transfer appears between subsections that increases the momentum transfer.

Both these effects have to be modelled when attempting to predict stage-discharge curves or water surface profile and flooded areas for a flooding river.

The flow interaction in a prismatic compound channel has been investigated intensively, with large experimental campaigns in the last 20 years. Improved modelling methods resulted from this laboratory work (e.g. Ackers, 1993; Shiono & Knight, 1991; Bousmar & Zech, 1999). Flow in non-prismatic channels was also investigated in laboratory flumes, focusing mainly on meandering compound channels. Similarly, improved modelling methods were proposed (e.g. James & Wark, 1992; Greenhill & Sellin, 1993; Ervine et al., 2000).

Unfortunately, apart from the Exchange Discharge Model (EDM) developed by Bousmar & Zech (1999), and to a certain extend the method by Ervine et al. (2000), the methods dedicated to prismatic channels can not be applied to non-prismatic geometries, and, reciprocally, the methods dedicated to non-prismatic channels are not usable in prismatic channels.

In an attempt to bridge this gap between prismatic and non-prismatic channel modelling, Bousmar et al. (2004a) have designed experiments where the floodplains width reduces symmetrically, highlighting mass-transfer effects, without the influence of meanders. This paper presents the results of a mirror set-up, where both floodplains are symmetrically enlarging.

2 PREVIOUS WORK

Most of the experimental work on non-prismatic compound channels has been devoted to meandering geometries. The main characteristics of such flows

Copyright © 2006 Taylor & Francis Group plc, London, UK

were already highlighted by Toebes & Sooky (1967): (1) a shear layer develops in a horizontal interface between main channel and floodplains, at the bankfull level; (2) large rolling motion, or helical secondary circulation, develops in the main channel in the cross-over region; and (3) the total head loss increases significantly when compared to an equivalent prismatic geometry. These observations were later confirmed and completed by further works (e.g. Sellin et al., 1993; Lambert & Sellin, 1996; Shiono & Muto, 1998).

A simpler geometry was investigated by Elliott & Sellin (1990) and Jasem (1990) with a prismatic main channel skewed to a prismatic floodplain. This situation reproduces adequately the flow in the cross over region of a meandering channel: similar horizontal shear layer and rolling motion are observed.

Experiments focusing more on the mass and momentum transfer mechanisms than on the full complexity of a meandering channel were performed by Bousmar (2002) and Bousmar et al. (2004a): symmetrically narrowing floodplains force flow from the floodplains to the main channel (Fig. 1a–b). Thanks to the symmetry, no centrifugal effect is observed as in meandering geometries. On the other hand, horizontal shearing and helical secondary currents were reproduced. The additional head loss due to the mass transfer was estimated. Its value was in several cases as large as the friction loss. Additional investigations were done using digital imaging to record surface velocities (Bousmar et al., 2004b). The horizontal turbulent structures that develop in prismatic channels were shown to stretch in the converging reach, and their influence on the momentum transfer mechanism decreased rapidly.

Lastly, an asymmetric geometry with a more abrupt convergence was also investigated (Rivière et al., 2002; Proust, 2005; Proust et al., 2006). Larger mass transfer and head loss resulted from the higher convergence angle (22°). The analysis also showed that the head presented distinct evolutions in each subsection. Similar investigations were also initiated for groynes perpendicular to the bank, considered as a limit for the progressive convergence and divergence cases explored in this paper (see e.g. Rivière et al., 2004; Proust, 2005).

3 EXPERIMENTAL SETUP

The experiments were performed in a 10 m long, 1.2 m wide compound channel flume, at the Université catholique de Louvain, Belgium. The bed slope was set up at $S_0 = 0.99 \times 10^{-3}$. The flume bottom was shaped with a symmetrical cross-section made of coated plywood. A main channel, 400 mm wide and 50 mm deep, was flanked by two floodplains 400 mm wide. Movable vertical plywood banks were used to modify

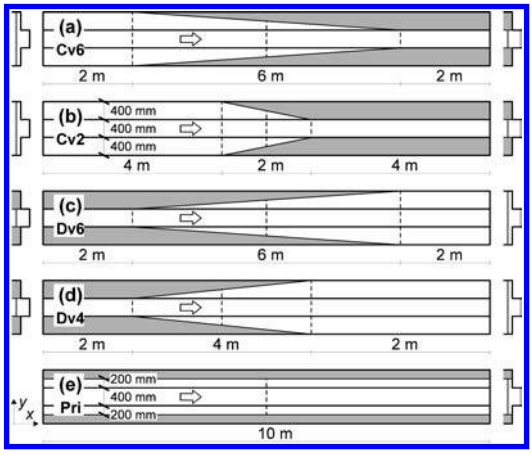


Figure 1. Configuration of the experimental flume: (a–b) Converging; (c–d) Diverging; and (e) Prismatic geometries.

Table 1. Geometries and discharges Q tested.

		Q (l/s) for $H^* =$ [2]		
Series	Geometry	0.2	0.3	0.5
Cv6[1]	Converging angle =,3.8° (6 m narrowing reach)	10.0	10.0 12.0	 12.0 16.0 20.0
Cv2[1]	Converging angle = 11.3° (2 m narrowing reach)	10.0	10.0 12.0	 12.0 16.0 20.0
Dv6	Diverging angle = 3.8° (6 m enlarging reach)	12.0	12.0 16.0 20.0	 16.0 20.0
Dv4	Diverging angle = 5.7° (4 m enlarging reach)	12.0	12.0 16.0 20.0	 16.0 20.0
Pri[1]	Prismatic (floodplain 200 mm)	9.9	13.4	27.6

[1] See Bousmar et al. (2004a).
[2] At $x = 5$ m for Cv6, Cv2 and Dv6; at $x = 4$ m for Dv4.

floodplains width, in order to reproduce progressive narrowing (Fig. 1a-b) or enlargement (Fig. 1c–d).

For selected discharges, the downstream tailgate was adjusted to fix the water level to given values at mid-length of the converging/diverging reach. The flow conditions investigated by Bousmar et al. (2004a) and in this paper are summarized in Table 1, where $H^* = (H - h_f)/H$ = relative flow depth; H = total flow depth in main channel; and h_f = bank full depth. As will be discussed below, using such given values of H^* at mid convergence/divergence enables useful comparison of velocity and discharge distributions between

Copyright © 2006 Taylor & Francis Group plc, London, UK

the different geometries and with the reference prismatic case (Fig. 1e).

Water levels were recorded using an automatic point gauge mounted on a trolley. Velocities were measured with a 4 mm diameter Pitot tube, and velocity directions were recorded with a home-made flag-type element. Additional local velocity measurements were obtained with a Nortek NDV acoustic Doppler probe, but results are influenced by the large size of the probe compared to the actual flow depth. The total discharge was measured with an electromagnetic flowmeter. Lastly, some surface velocity measurements were performed using tracers and digital imagery. Details on this method are available in Bousmar et al. (2004b).

4 EXPERIMENTAL RESULTS

4.1 *Flow description*

Figure 2 shows the water surface profile recorded for all Dv6 and Dv4 series. These profiles appear grouped, as the flow depth is fixed at mid-length of the diverging reach ($x = 5$ m for Dv6, $x = 4$ m for Dv4). In all cases, the flow depth increases gradually in the diverging reach, as the section is enlarging and the mean velocity is decreasing. In the upstream prismatic reach (isolated main-channel), the flow depth is generally decreasing (M2 profile) as the depth at the entrance of the non-prismatic reach is lower than the uniform depth for the given discharges. As will be depicted below, the Froude number was in some cases close or even locally larger than 1.

At the junction of prismatic and non-prismatic reaches, surfaces waves (cross-waves) were generated by the non-smooth transition. These waves are particularly visible for the larger discharge ($Q = 20$ l/s), with significant scattering of the water level measurements. Transverse water surface profiles were also recorded, but did not revealed significant transverse surface gradient compared to the cross-waves amplitude.

Depth-averaged velocity U_d distributions are given on Figure 3 for several Dv4 cases. As expected from the water profile analysis, the maximum velocity is decreasing in the downstream direction, as the cross-section area increases. The depth-averaged velocity is almost constant across the main-channel width, and decreases linearly on the floodplain, from the main-channel bank to the floodplain bank. This gradient corresponds to a progressive intrusion of the flow on the floodplain: as depicted by Figure 4 where almost uniform transverse velocity is observed on the floodplains.

For the lower discharge ($Q = 12$ l/s, Fig. 3a–b), a progressive growth of the floodplain velocity is

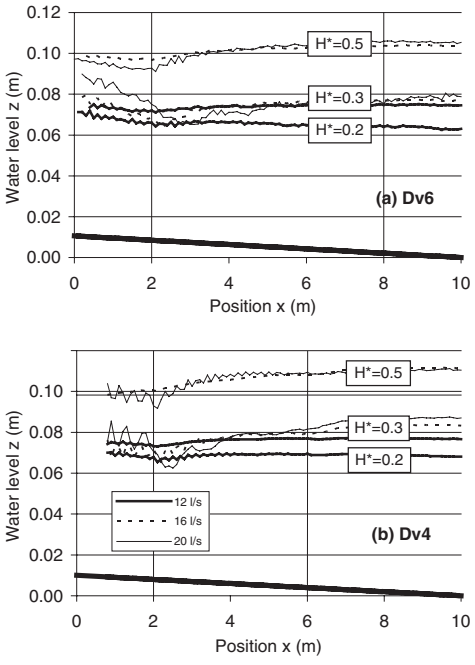


Figure 2. Water surface profiles. (a) Dv6; and (b) Dv4 series.

observed in the downstream prismatic reach, from $x = 6$ m to $x = 8$ m, as a result of this transverse flow. For larger discharges (Fig. 3c–d), this growth is masked by a significant asymmetry of the flow, that will be discussed in the next paragraph.

The uniformity of the depth-averaged velocity observed in the main channel is also observed for the local longitudinal velocity component (Fig. 4a–c). The analysis of the transverse velocity component (Fig. 4d–f) indicates that the helical secondary current cells observed in the main channel of prismatic and converging geometries (flow from bank to axis at water surface and from axis to bank at bottom) do not appear for the diverging case.

Although the transverse velocity components were not measured for all the Dv6 experiments, the distribution of longitudinal velocity for Dv6/03/16 case (Fig. 5) tends to indicate the existence in that case of a secondary current cell with reverse rotating direction when compared to the converging case. Low velocity water seems to move upward from the main channel axis, as shown by the local velocity minimum at the surface.

To conclude this first analysis, based on time and depth-averaged velocities, the velocity distributions of all the diverging series are compared at mid-length of the diverging reach. For this purpose, normalised velocities are obtained by dividing the velocities U_d

Copyright © 2006 Taylor & Francis Group plc, London, UK

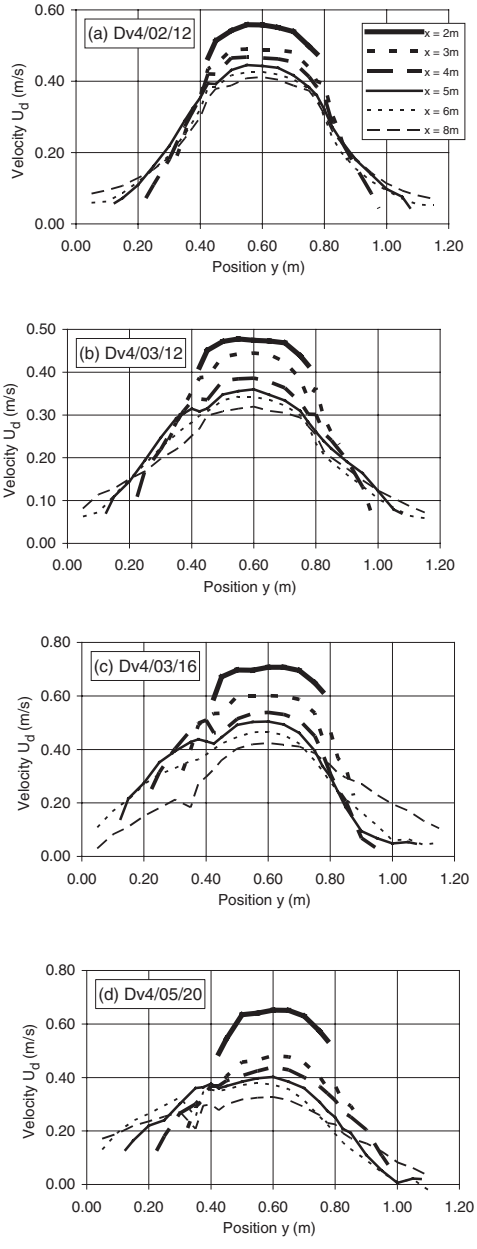


Figure 3. Depth-averaged velocity distributions. (a) Dv4/02/12; (b) Dv4/03/12; (c) Dv4/03/16; and (d) Dv4/05/20.

by the total discharge Q. Figure 6 shows that the velocity distribution is almost the same in the main channel for a given flow depth $H*$. Differences are observed on the floodplains, partly due to a flow asymmetry, but also, for the larger discharge ($Q = 20$ l/s), to a lower floodplain velocity. Lastly, the main channel velocities are more uniform for Dv4 series than for Dv6: this could indicate lower secondary currents for the shorter diverging reach, where the mass transfer could be too large for such currents to fully develop.

4.2 *Dynamic behaviour of the flow*

Flow asymmetry has been highlighted from the depth-averaged velocity distributions. An improved description of this asymmetry can be obtained from digital imaging. Using automatic tracking of surface tracers, the local surface velocities can be computed from the video sequence (see e.g. Bousmar et al., 2004b). Considering the almost constant velocity profile on a vertical (Fig. 4a–c), the ratio between surface and depth-averaged velocities was computed where the latter were available. This ratio was then interpolated on the whole flow field and the depth-averaged velocity field obtained accordingly from the surface recording.

Figure 7 shows the so-computed velocity field for Dv4 series. The main features observed in the velocity distribution in given cross-section (Fig. 3) are also confirmed when considering the whole velocity field: (a) an almost uniform velocity in the main channel; (b) a linear gradient on the floodplain; and (c) a flow asymmetry for the larger discharges.

The analysis of the whole flow field enables a better description of this asymmetry. The main channel flow tends to behave as a jet in an enlarging channel. Instabilities appear and the maximum velocity filament oscillates from one main channel bank to the other. In almost all the cases, recirculation areas develop intermittently, mainly on the right floodplain ($y > 0.8$ m). Such a recirculation causes a delay to the flow expansion on the floodplain and the growth of time-averaged floodplain velocity.

Although instabilities cause the flow to be asymmetric, it remains more stable than a classical jet flow. Indeed, the maximum velocity is confined by the main channel banks. Moreover, the maximum floodplain velocity is generally on the left floodplain. This permanent asymmetry is expected to be due to slight geometry unevenness. Modifying the tailgate horizontality by 0.5° enabled to force the maximum velocity to the other bank.

For the Dv6 series, such jet behaviour was not observed. The opening angle $2\alpha = 7.6°$ was probably low enough to avoid recirculation development. Tentative tests were also attempted with a Dv2 series (2 m diverging reach, $2\alpha = 22.6°$). In that case the recirculation development and the oscillations of the jet were so high that time-averaged measurement of water level and velocities was too tedious. The Dv4 series was thus preferred as being more stable.

Copyright © 2006 Taylor & Francis Group plc, London, UK

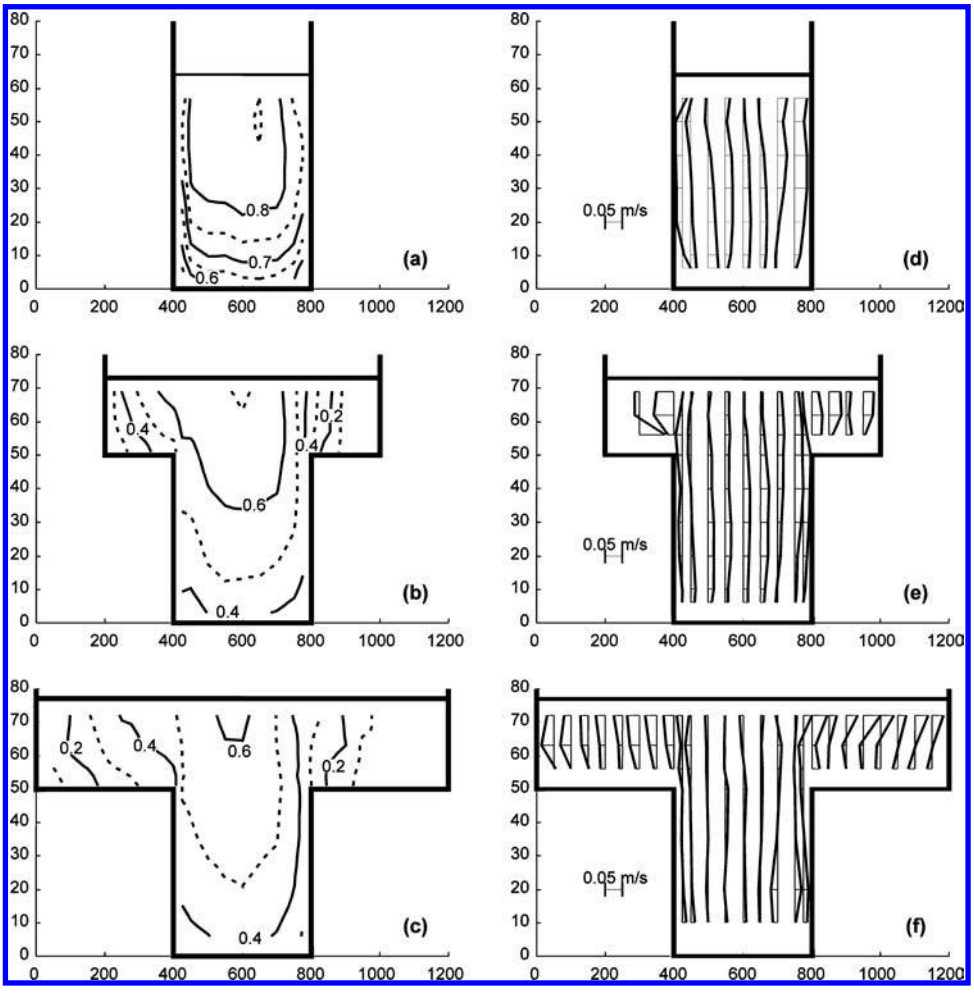


Figure 4. Velocity distribution in a $y-z$ section, Dv4/03/16 case. (a–c) Longitudinal velocity components (m/s); (d–f) transverse velocity components (m/s); (a, d) $x = 2$ m; (b, e) $x = 4$ m; and (c, f) $x = 6$ m.

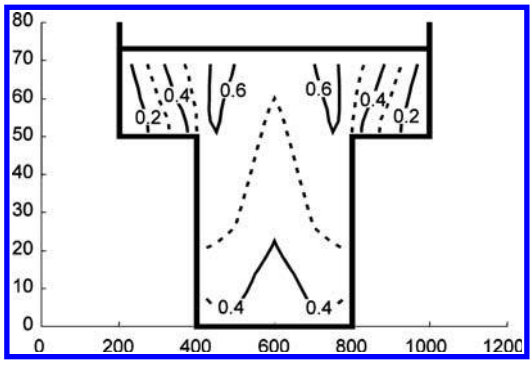


Figure 5. Longitudinal velocity components distribution (m/s) in a $y-z$ section, Dv6/03/16 case, $x = 5$ m.

It is also interesting to point out that the intensity of the oscillation and the asymmetry of the flow increase with the Froude number at the inlet of the diverging reach. This Froude number increases with increasing discharge Q and decreasing flow depth H^*. The larger Froude number is obtained for the Dv4/03/20 case. Figure 8 shows the local Froude number field computed from the depth-averaged velocity obtained by digital imaging. Supercritical Froude number are even observed on the floodplains close to the main-channel banks near the inlet of the diverging reach, where the velocities are the largest and the flow depth the lower. In this area, a small roll, similar to a longitudinal hydraulic jump, was visually observed on the floodplain but was not large enough to be recorded accurately.

Copyright © 2006 Taylor & Francis Group plc, London, UK

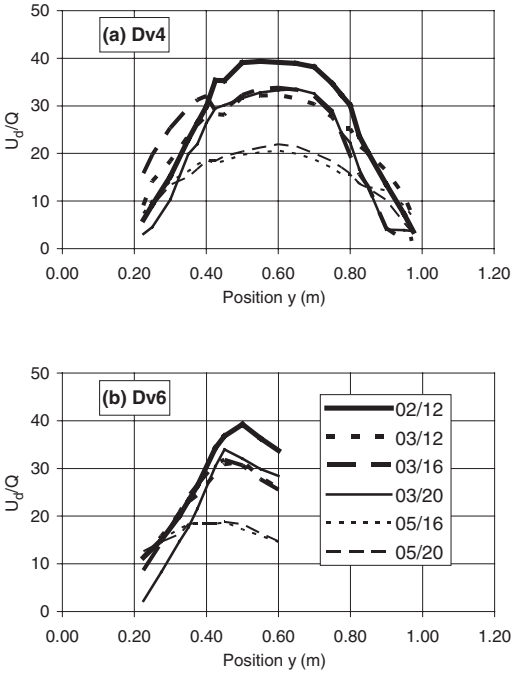


Figure 6. Depth-averaged velocity at mid-length of the diverging reach, normalised by the total discharge. (a) Dv4, $x = 4$ m; and (b) Dv6, $x = 6$ m.

4.3 *Discharge distribution*

The progressive flow expansion out of the main channel is interestingly represented by the discharge distribution between subsections. Figure 9 shows the floodplain discharge expressed as a ratio of the total discharge. This depicts clearly the progressive intrusion of the flow to the floodplain. The discharge distribution is clearly not yet in equilibrium 2 m downstream of the diverging reach ($x = 8$ m), and it can be expected that a much longer prismatic reach would be required to obtain equilibrium (Bousmar et al., 2005).

For $H^* = 0.5$, both cases ($Q = 16$ and 20 l/s) give a similar discharge distribution. For $H^* = 0.3$, the distribution for $Q = 20$ l/s differs from the two other cases, probably due to larger recirculation development. The effects of the recirculation and of the flow asymmetry are clearly depicted by Figure 10: the left and right floodplain discharges present large differences. In some case (Dv4/05/20), almost all the floodplain discharge is conveyed on a unique floodplain, with $Q_{fpl} = 90\%\ Q_{fp}$; where Q_{fpl} = left floodplain discharge.

With the subsection discharge values, it is also possible to compute specific energy $E = z + U_d^2/2g$, or head, for the total cross section and for separate

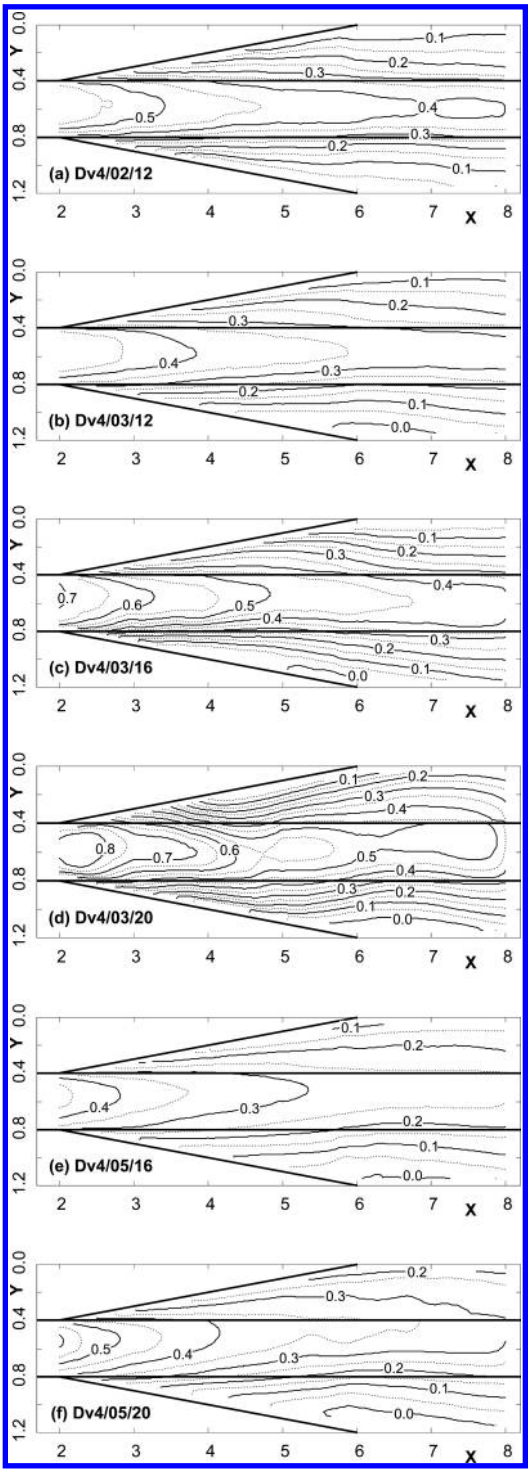


Figure 7. Depth-averaged velocity field, obtained from digital imaging.

Copyright © 2006 Taylor & Francis Group plc, London, UK

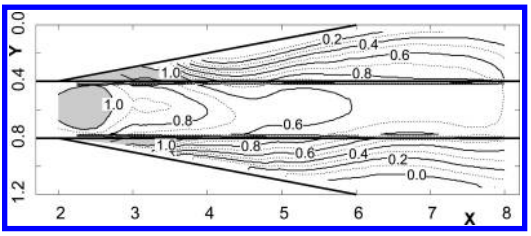


Figure 8. Local Froude number field, obtained from digital imaging. Dv4/03/20 case.

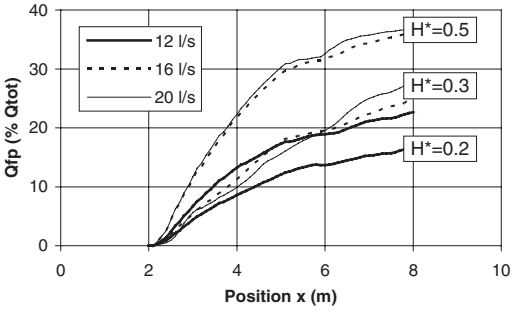


Figure 9. Discharge distribution, Dv4 series: floodplain discharge as a ratio of total discharge.

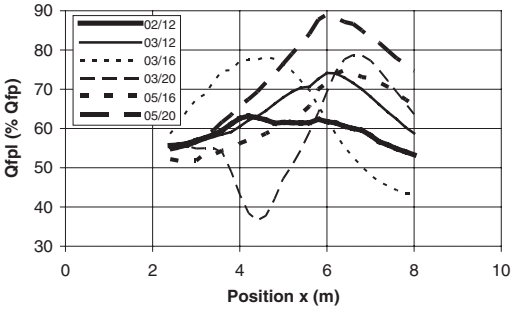


Figure 10. Discharge distribution, Dv4 series: left floodplain discharge as a ratio of floodplain discharge.

subsections. Typical energy profiles are given by Figure 11. In all the cases, the total energy decreases in the downstream direction, due to friction and momentum transfer generated head losses. The main channel energy also decreases, but slower. This indicates that a part of the total energy is used for accelerating the floodplain flow: the floodplain energy profiles are indeed growing from upstream to downstream, thanks to the momentum transferred by the flow from main channel to floodplain.

Figure 12 shows that the maximum turbulent shear stress in the xy plane is indeed observed at the interface between subsections, where this momentum transfer takes place.

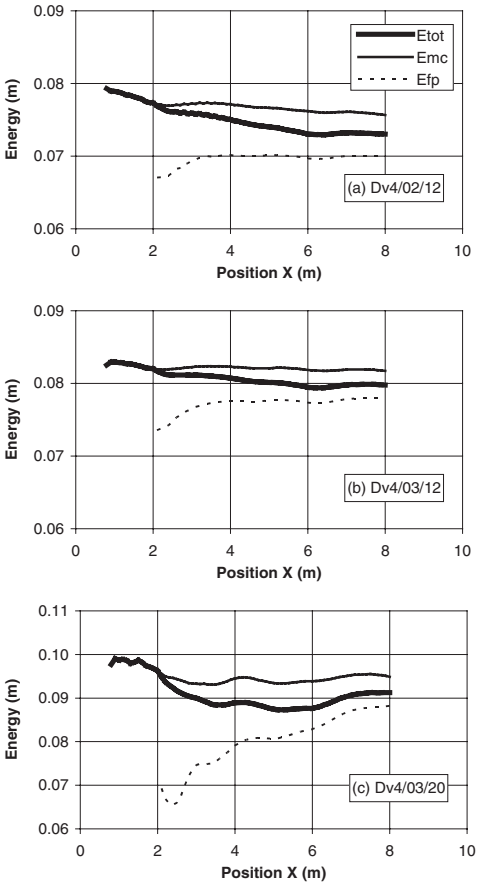


Figure 11. Specific energy profile (whole channel, main channel, floodplains). (a) Dv4/02/12; (b) Dv4/03/12; and (c) Dv4/03/20.

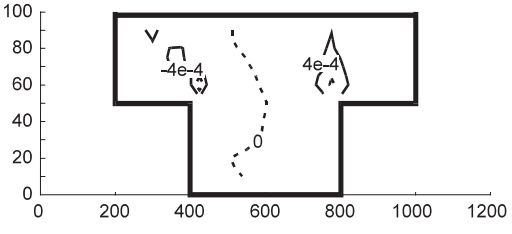


Figure 12. Turbulent shear stress $\overline{u'v'}$ distribution in a $y-z$ section, NDV measurements, DV4/05/20 case.

5 COMPARISON WITH CONVERGING CHANNEL EXPERIMENTS

As depicted in the previous paragraphs, the flow in a symmetrically diverging channel presents significant

Copyright © 2006 Taylor & Francis Group plc, London, UK

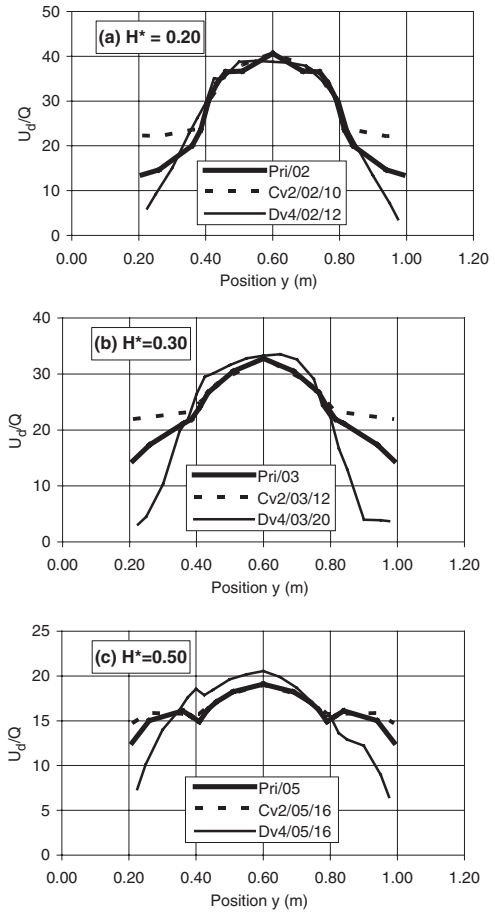


Figure 13. Typical depth-averaged velocity distribution at mid-length of the diverging/converging reach, normalised by the total discharge. (a) $H^* = 0.2$; (b) $H^* = 0.3$; and (c) $H^* = 0.5$.

differences with the flow in a symmetrically converging channel, but also some interesting similarities, mainly in the momentum transfer mechanisms.

Figure 13 shows typical velocity distributions, normalised by the total discharge, for converging and diverging geometries at given flow depth, together with the reference prismatic case (Pri series). The different flow behaviours are clearly depicted:

– In the prismatic case, the flow is dominated by a turbulent momentum transfer. A shear layer develops at the interface between subsections and generates a mild velocity gradient in both main channel and floodplain.
– In the converging case, the flow is dominated by mass transfers between subsections. Due to the floodplain width reduction and to the consecutive flow acceleration, the velocity is almost uniform across the floodplain. The main channel presents a velocity gradient, due to intrusion of slower floodplain flow through the interface (see also Fig. 15).
– In the diverging case, the flow is also dominated by the mass transfer. No inflow influences the main channel velocity distribution, which is almost uniform. On the other hand, a significant velocity gradient is observed on the floodplains. Moreover, as the flow is expanding, instabilities and asymmetry can be observed.

These observations are confirmed and complemented by the corresponding discharge distribution, as depicted on Figure 14. The floodplain discharge in the converging cases is generally slightly larger than for the corresponding prismatic geometry, with discharge distribution in equilibrium, due to a delay in the mass transfer towards the main channel.

On the contrary, the floodplain discharge is lower for the diverging cases. This downstream shift in the discharge distribution is due to the delay in the intrusion of the flow towards the floodplains. When

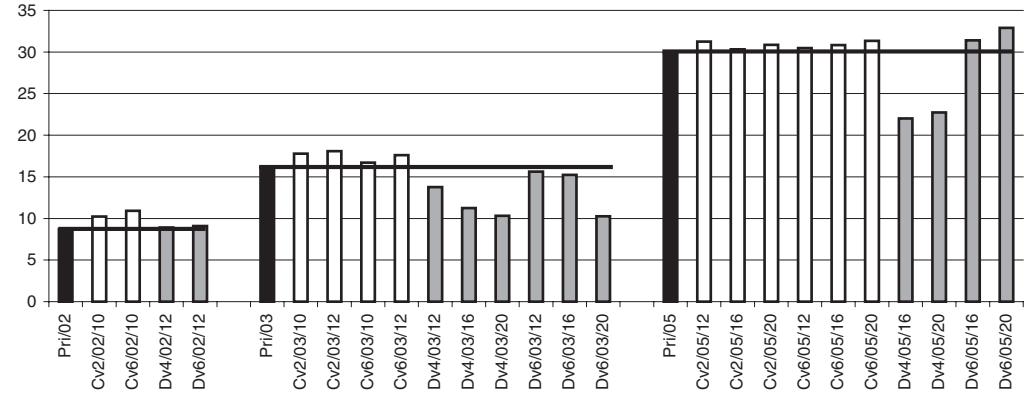


Figure 14. Discharge distribution: floodplain discharge Q_{fp} as a ratio of total discharge Q (%), at mid-length of the converging/diverging reaches.

Copyright © 2006 Taylor & Francis Group plc, London, UK

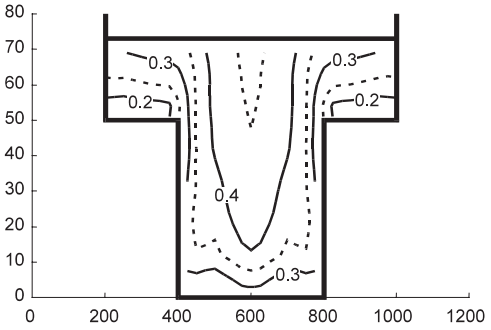


Figure 15. Longitudinal velocity component (m/s) distribution in a $y-z$ section, Cv2/03/12 case, $x = 5$ m.

compared to the converging cases, this delay is here larger, as the flow expansion induces asymmetry and even recirculation development that reduces the floodplain conveyance.

6 CONCLUSIONS

An experimental investigation of the flow in a compound channel with symmetrically enlarging floodplain has revealed the main features of such a flow: the distribution of velocity in the main-channel is almost uniform, while it presents a linear gradient on the floodplains. The floodplain discharge remains significantly lower than the actual conveyance capacity on a long distance. The flow also presents a significant asymmetry: the maximum velocity filament oscillate in the main channel and recirculation zones develop on the floodplains.

The experiments show that momentum is transferred from the main channel to the floodplains with the flow through the interface between these subsections. This transfer causes a decrease in the total head available in the section, and an increase of the local head in the floodplains.

As the momentum transfer between subsections also relies on mass transfer, the diverging geometry flow behaviour presents mirror characteristics with the mirror converging case: (1) the transverse velocity gradient is located on the floodplain and not in the main channel; (2) the discharge on the floodplains is lower and not larger than their conveyance capacity in a prismatic compound channel with the same cross section; and (3) the secondary current cells either disappear or present an inversed rotation direction.

ACKNOWLEDGEMENT

Travel costs for this collaborative research program were partly supported by the Tournesol programme grant 02947VM funded by EGIDE, France and CGRI, Communauté française de Belgique.

REFERENCES

Ackers, P. 1993. "Flow formulae for straight two-stage channels", *Journal of Hydraulic Research, IAHR*, 31(4), 509–531.

Bousmar, D. 2002. *Flow modelling in compound channels. Momentum transfer between main channel and prismatic or non-prismatic floodplains*, PhD Thesis, Université catholique de Louvain, Belgium.

Bousmar, D. & Zech, Y. 1999. "Momentum transfer for practical flow computation in compound channels", *Journal of Hydraulic Engineering, ASCE*, 125(7), 696–706.

Bousmar, D., Wilkin, N., Jacquemart, J.-H. & Zech, Y. 2004a. "Overbank flow in symmetrically narrowing floodplains", *Journal of Hydraulic Engineering, ASCE*, 130(4), 305–312.

Bousmar, D., Denis, B. & Zech, Y. 2004b. "Coherent flow structures in a converging compound channel", *River Flow 2004, Proc. 2nd Int. Conf. on Fluvial Hydraulics, Napoli, Italy, June 2004*, Balkema, Leiden, The Netherlands, 1, 423–430.

Bousmar, D., Rivière, N., Proust, S., Paquier, A., Morel, R. & Zech, Y. 2005. "Upstream discharge distribution in compound channel flumes", *Journal of Hydraulic Engineering, ASCE*, 131(5), 408–412.

Elliott, S.C.A & Sellin, R.H.J. 1990. "SERC flood channel facility: skewed flow experiments", *Journal of Hydraulic Research, IAHR*, 28(2), 197–214.

Ervine, D.A., Babaeyan-Koopaei, K., & Sellin, R.H.J. 2000. "Two-dimensional solution for straight and meandering overbank flows", *Journal of Hydraulic Engineering, ASCE*, 126(9), 653–669.

Greenhill, R.K. & Sellin, R.H.J. 1993. "Development of a simple method to predict discharges in compound meandering channels", *Proc. Institution of Civil Engineers, Water Maritime and Energy*, 101(1), 37–44.

James, C.S. & Wark, J.B. 1992. *Conveyance estimation for meandering channels*, Report SR 329, HR Wallingford Ltd, Wallingford, UK.

Jasem, H.K. 1990. *Flow in two-stage channels with the main channel skewed to the flood plain direction*, PhD Thesis, University of Glasgow, UK.

Lambert, M.F. & Sellin, R.H.J. 1996. "Velocity distribution in a large-scale model of a doubly meandering compound river channel", *Proc. Institution of Civil Engineers, Water, Maritime and Energy*, 118(1), 10–20.

Proust, S. 2005. *Ecoulements non-uniformes en lits composés: effets de variations de largeur du lit majeur*, PhD Thesis, INSA Lyon, Lyon, France, http://www.lyon.cemagref.fr/doc/these/proust/, (in French).

Proust, S., Rivière, N., Bousmar, D., Paquier, A., Zech, Y. & Morel, R. 2006. "Flow in compound channel with abrupt floodplain contraction", *Journal of Hydraulic Engineering, ASCE* (in press).

Rivière, N., Proust, S., Bousmar, D., Paquier, A., Morel, R. & Zech, Y. 2002. "Relevance of 1D flow modelling for compound channels with a converging floodplain", *River Flow 2002, Proc. Int. Conf. on Fluvial Hydraulics, Louvain-la-Neuve, Belgium, September 2002*, Swets & Zeitlinger, Lisse, The Netherlands, 1, 187–195.

Copyright © 2006 Taylor & Francis Group plc, London, UK

Rivière, N., Proust, S. & Paquier, A. 2004. "Recirculating flow behind groynes for compound-channel geometries", *River Flow 2004, Proc. 2nd Int. Conf. on Fluvial Hydraulics, Napoli, Italy, June 2004*, Balkema, Leiden, The Netherlands, 1, 437–442.

Sellin, R.H.J., Ervine, D.A. & Willetts, B.B. 1993. "Behaviour of meandering two-stage channels", *Proc. Institution of Civil Engineers, Water, Maritime and Energy*, 101, 99–111.

Shiono, K. & Knight, D.W. 1991. "Turbulent open channel flows with variable depth across the channel", *Journal of Fluid Mechanics*, 222, 617–646.

Shiono, K. & Muto, Y. 1998. "Complex flow mechanisms in compound meandering channels with overbank flow", *Journal of Fluid Mechanics*, 376, 221–261.

Toebes, G.H. & Sooky, A. 1967. "Hydraulics of meandering rivers with floodplains", *Journal of the Waterways and Harbour Division, ASCE*, 93(2), 1053–1066.

Copyright © 2006 Taylor & Francis Group plc, London, UK

Stage-discharge modelling in mobile bed compound channel

D. Bousmar
Hydraulic Research Laboratory, Ministère wallon de l'Equipement et des Transports, Châtelet, Belgium

S. Atabay
Arup, UK

D.W. Knight
University of Birmingham, UK

Y. Zech
Civil and Environmental Engineering, Université catholique de Louvain, Louvain-la-Neuve, Belgium

ABSTRACT: Compound channel experiments with a mobile bed in the main-channel show that, under some bed-forms development conditions, the main-channel velocity decreases and can even become lower than the floodplain velocity. This results in a reversal of the momentum transfer between main-channel and floodplains. Most of the compound-channel discharge formulae have been developed for rigid bed data and are not suitable in such conditions. In this paper, the Exchange Discharge Model (EDM) is modified to account also for such a reverse momentum transfer. The improved EDM formula is tested against existing experimental data. The data are therefore re-analysed to express mobile bed roughness as a function of the main-channel discharge and to re-assess floodplain roughness parameter. EDM results match satisfactorily stage-discharge curves and also discharge distribution between subsections. Particularly, the reversal of the velocity gradient is adequately captured.

1 INTRODUCTION

During overbank flow, a strong momentum transfer is observed between main-channel and floodplains, due to the velocity difference and the shear layer between both subsections. This effect can significantly reduce the channel conveyance. When a mobile bed is considered in the main-channel, the flow complexity is further increased: the transport capacity is affected by the momentum transfer, and the bed-forms development affects the flow resistance. It has been observed in laboratory flumes that, under some bed-forms development conditions, the main-channel velocity decreases and can even become lower than the floodplain velocity. This results in a reversal of the momentum transfer.

Other situations exist where such a reversal of the velocity gradient can be observed, e.g. (a) in a main-channel with large vegetation development (algae, bushes, etc.) while the floodplain resistance to flow is lower (meadow); or (b) in the cross-over area of a meandering channel where, due to the large sinuosity of the main-channel, the flow path are no more parallel between subsections.

This reversal of the momentum transfer obviously affects the channel conveyance estimation. Compound-channel discharge formulae were generally developed for prismatic compound channels (e.g. Ackers 1993). They were not tested for such particular flow conditions and will probably perform poorly. In this paper, one of these methods, namely the Exchange Discharge Model (EDM, Bousmar & Zech 1999) is modified to account also for this effect. Since the EDM explicitly models the momentum transfer, this modification will be straightforward, as shown below.

The improved EDM formula is tested against existing experimental data of Atabay (2001). The data is therefore re-analysed to express mobile bed roughness as a function of the main-channel discharge and to re-assess floodplain roughness parameter. Consequently, it is possible to test the EDM against overbank flow data sets without any particular parameter fitting.

Copyright © 2006 Taylor & Francis Group plc, London, UK

2 THEORETICAL DEVELOPMENT

2.1 *Traditional methods*

For an inbank flow, the stage-discharge relationship, or the head loss for a given discharge at a given flow depth, can classically be expressed using the Manning equation:

$$Q = \frac{AR^{2/3}}{n} S_0^{1/2} \quad \text{or} \quad S_f = \left(\frac{Q}{AR^{2/3}/n} \right)^2 = \left(\frac{Q}{K} \right)^2 \qquad (1)$$

where Q = discharge; A = section area; R = hydraulic radius; n = Manning roughness coefficient; S_0 = channel slope; S_f = friction slope; and K = section conveyance. When applied to compound cross-sections, the so-called Single Channel Method (SCM) tends to underestimate the discharge for a given flow depth, due to the sudden decrease of the hydraulic radius at bank level.

Alternatively, to account for the velocity discrepancy between main channel and floodplains, each subsection discharge Q_i can be estimated separately using (1), and the total discharge is obtained by addition

$$Q = \sum_i Q_i = \sum_i \frac{A_i R_i^{2/3}}{n_i} S_0^{1/2} = \sum_i K_i S_0^{1/2} \qquad (2)$$

where subscript i refers to a given subsection. The so-called Divided Channel Method (DCM) improves the flow prediction, but the discharge is now overestimated, as the momentum transfer effect is not accounted for.

To improve further the modelling, several corrections of the DCM were proposed. Ackers (1993) developed empirical formulae to correct the computed discharge. Lambert and Myers (1998) proposed an alternative way to divide the channel in subsections, using a weighting between various discharge computations. Bousmar and Zech (1999) attempted to model explicitly the momentum transfer and developed the EDM. The development of this method is summarised in the next paragraph.

2.2 *EDM governing equations*

Each subsection of a compound channel can be considered as a single channel submitted to a lateral flow per unit length q_l. The conservation of mass may be written

$$\frac{\partial A}{\partial t} + \frac{\partial Q}{\partial x} = q_l = q_{in} - q_{out} \qquad (3)$$

where q_{in} = inflow discharge; and q_{out} = outflow discharge.

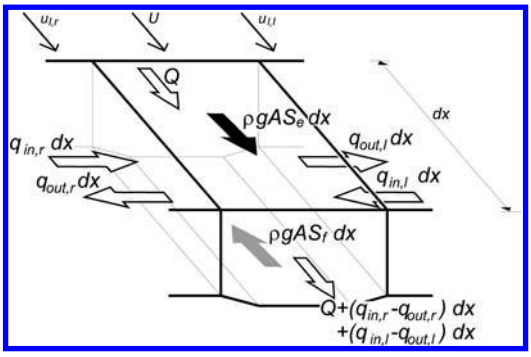


Figure 1. Momentum equilibrium for a compound channel subsection.

The momentum equation for a unit length also accounts for the lateral flow (Fig. 1)

$$\frac{\partial}{\partial t}(\rho AU) = -\frac{\partial}{\partial x}\left(\rho AU^2\right) + \rho q_{in} u_l - \rho q_{out} U + \rho g A\left(S_0 - S_f\right) - \rho g A \frac{\partial H}{\partial x} \qquad (4)$$

where ρ = density of water; g = gravity constant; $U = Q/A$ = mean velocity; H = water depth; and u_l = velocity of the lateral inflow in the direction of the main flow. It is noticeable that inflow and outflow convey different momentum since their initial velocities are not the same.

Assuming steady flow, subtracting the continuity equation (3) multiplied by U from (4), replacing the sum of bed slope and depth gradient by the water level gradient $\partial z/\partial x$, and dividing by gA, the momentum equation reduces to

$$S_e = -\frac{\partial}{\partial x}\left(z + \frac{U^2}{2g}\right) = S_f + \frac{q_{in,r}\left(U - u_{l,r}\right) + q_{in,l}\left(U - u_{l,l}\right)}{gA} = S_f + S_a \qquad (5)$$

where the lateral flow has been divided into right-side r and left-side l inflow; S_e = total head loss per unit length; and S_a = additional loss due to lateral inflow, i.e. momentum transfer effect.

The lateral flows represent turbulent exchange and geometrical transfer (Fig. 2). The turbulent exchange discharge, q^t, is the mass of fluid which oscillates between main channel and floodplain, due to the large vortical structures that develop in the shear layer at the interface, and may be modelled using a mixing length. It is proportional to the velocity difference between

Copyright © 2006 Taylor & Francis Group plc, London, UK

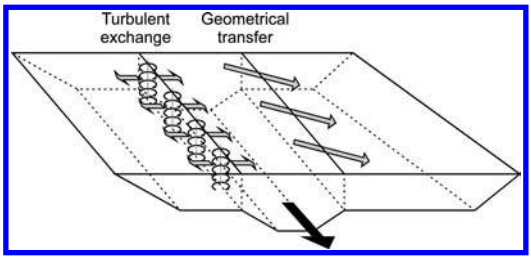


Figure 2. Flow exchange at interfaces between main channel and floodplains.

subsections $|U_c - U_f|$ and to the interface area per unit length $(H - h_f)$, where c and f stands for main channel and floodplain, respectively; and h_f is the bank level:

$$q^t_{cf} = q^t_{fc} = \psi^t \left|U_c - U_f\right| \left(H - h_f\right) \tag{6}$$

where $\psi^t = 0.16 =$ proportionality factor (determined using experimental data). Because turbulent exchange is an oscillating discharge, the lateral inflows q^t_{cf} from main channel to floodplain and the dual inflow q^t_{fc} are equal. Accordingly, the turbulent exchange does not affect the conservation of mass (3) but has a significant effect on the momentum balance (5).

The geometrical transfer, q^g, corresponds to the floodplain conveyance variation due to a non-prismatic geometry or to a gradually varied flow in a prismatic geometry

$$q^g_{fc} = \psi^g \kappa_{fc} \frac{dK_f}{dx} S_{ff}^{1/2}; \; q^g_{cf} = \psi^g \kappa_{cf} \frac{dK_f}{dx} S_{ff}^{1/2} \tag{7}$$

where κ_{fc} and κ_{cf} take the appropriate values, respectively (0, 1) for $dK_f/dx > 0$, i.e. increasing floodplain conveyance, with a transfer from main channel to floodplain; and $(-1, 0)$ for $dK_f/dx < 0$, i.e. decreasing floodplain conveyance, with a reverse transfer. A proportionality factor $\psi^g = 0.50$ has also been included.

Using the momentum equation (5) to correct the friction equation (1), and assuming that the head loss S_e is the same in all subsections, the subsection discharge is given by

$$Q_i = \frac{A_i R_i^{2/3}}{n_i} S_{fi}^{1/2} = K_i S_{fi}^{1/2} = K_i \left(\frac{S_e}{1+\chi_i}\right)^{1/2} \tag{8}$$

where $\chi_i = S_{ai}/S_{fi}$. The total discharge is obtained by addition of subsection discharges.

2.3 *EDM extension*

The practical evaluation of (8) requires the estimation of χ_i values, using (5), (6) and (7). Combining these expressions together, gives

$$\begin{aligned}
\chi_1 &= \frac{1}{gA_1}\left[\psi^t (H-h_1)\left|\frac{R_2^{2/3}}{n_2}\left(\frac{1+\chi_1}{1+\chi_2}\right)^{1/2} - \frac{R_1^{2/3}}{n_1}\right| + \psi^g \kappa_{21}\frac{dK_1}{dx}\right]\cdot\left[\frac{R_1^{2/3}}{n_1} - \frac{R_2^{2/3}}{n_2}\left(\frac{1+\chi_1}{1+\chi_2}\right)^{1/2}\right] \\
\chi_2 &= \frac{1}{gA_2}\left\{\left[\psi^t (H-h_1)\left|\frac{R_2^{2/3}}{n_2}\left(\frac{1+\chi_1}{1+\chi_2}\right)^{1/2} - \frac{R_1^{2/3}}{n_1}\right| + \psi^g \kappa_{12}\frac{dK_1}{dx}\right]\cdot\left[\frac{R_2^{2/3}}{n_2}\left(\frac{1+\chi_1}{1+\chi_2}\right)^{1/2} - \frac{R_1^{2/3}}{n_1}\right]\left(\frac{1+\chi_2}{1+\chi_1}\right)\right. \\
&\quad + \left[\psi^t (H-h_3)\left|\frac{R_2^{2/3}}{n_2}\left(\frac{1+\chi_3}{1+\chi_2}\right)^{1/2} - \frac{R_3^{2/3}}{n_3}\right| + \psi^g \kappa_{32}\frac{dK_3}{dx}\right] \\
&\quad \left.\cdot\left[\frac{R_2^{2/3}}{n_2}\left(\frac{1+\chi_3}{1+\chi_2}\right)^{1/2} - \frac{R_3^{2/3}}{n_3}\right]\left(\frac{1+\chi_2}{1+\chi_3}\right)\right\} \\
\chi_3 &= \frac{1}{gA_3}\left[\psi^t (H-h_3)\left|\frac{R_2^{2/3}}{n_2}\left(\frac{1+\chi_3}{1+\chi_2}\right)^{1/2} - \frac{R_3^{2/3}}{n_3}\right| + \psi^g \kappa_{23}\frac{dK_3}{dx}\right]\cdot\left[\frac{R_3^{2/3}}{n_3} - \frac{R_2^{2/3}}{n_2}\left(\frac{1+\chi_3}{1+\chi_2}\right)^{1/2}\right]
\end{aligned} \tag{9}$$

where subscript 2 stands for the main channel; subscripts 1 and 3 stands for the floodplains; and h_1 and $h_3 =$ main-channel bank level on floodplain 1 and 3 side, respectively.

The system of equations (9) defines the values of the ratios χ_i in an implicit form, and as a function only of water depth, geometry and roughness. An analytical solution of (9) for straight symmetrical uniform flow is given by Bousmar (2002), and Bousmar and Zech (1999) proposed a numerical solution procedure for the general case. When developing these solutions, it was assumed that the main channel velocity was larger than the floodplain velocity. This hypothesis enabled the absolute values in (9) to be replaced by the difference in brackets without any sign change. Solving equation (9) implied the extraction of the roots of quadratic equations. The hypothesis on the velocity gradient enabled one again to select the appropriate root.

In the present work, the solutions of (9) were developed for the case where the floodplain velocity is larger than main channel one. This implies a sign change when replacing the absolute values in (9) by brackets. The tests for selecting the appropriate roots when

Copyright © 2006 Taylor & Francis Group plc, London, UK

developing the solutions also change. For the sake of conciseness, these developments for the general numerical solution procedure are given in an appendix. At least, the same roots can be selected, and only few minor changes are required to obtain a general solution, applicable for both cases. This new solution will now be applied to mobile bed test cases, and the reversal of the momentum transfer direction will be highlighted.

3 EXPERIMENTAL DATA

3.1 *Experimental setup*

The experiments were performed at the University of Birmingham, UK, in a non-tilting 22 m long flume, with a test length of 18 m, moulded into a compound channel, and a bed slope $S_0 = 2.024 \times 10^{-3}$ (Atabay 2001). The flume was 1213 mm wide, and configured into a two-stage channel with a 398 mm wide rectangular main channel and two 407.3 mm wide smooth floodplains at an elevation $h_f = 50$ mm above the main channel bed. Adjustable sidewalls created either an asymmetric compound channel, or an extended rectangular channel isolated from floodplains. Rigid boundaries were constructed from smooth PVC sheets, both for the floodplain and the main channel. For experiments with a mobile-bed, the PVC sheets constituting the bed of the main channel were replaced by sand. The sand was well graded, with a d_{35} & d_{50} sizes of 0.80 mm & 0.88 mm respectively. The flume had three different water supply pipelines, 150 mm, 100 mm and 50 mm in diameter, and discharges were measured by a Dall tube, a Venturi meter and an electro magnetic flow meter respectively.

At the end of the flume a series of three adjustable tailgates were located to produce uniform flow conditions in the 18 m-test length. When uniform flow conditions had been reached, water surface profiles were measured using pointer gauges, also giving the average flow depth and hence mean velocity. In order to obtain local and zonal resistance coefficients the distributions of depth-averaged velocity, U_d, and boundary shear stress were measured for every discharge, using a Novar-Nixon miniature propeller current meter, and a 4.77 mm diameter Preston tube, respectively. It should be noted that measurements were only taken on the rigid bed. Accordingly, no local data are available for the main channel in the loose boundary experiments.

Table 1 summarises the test cases that will be used in this paper. All results are given in Atabay (2001), excepted the LIS series (Ayyoubzadeh, 1997). See also www.flowdata.bham.ac.uk.

3.2 *Results*

The stage-discharge curves for all the test cases are plotted on Figure 3. For a given flow depth, the discharge increases when the floodplain section area contributes to the conveyance: the discharge is higher for the symmetrical channel than for the asymmetrical one; and for the asymmetrical channel than for the isolated main channel. A larger discharge is also obtained for the rigid bed cases than for the mobile bed ones. The bed forms observed in the latter case induce a larger flow resistance.

Table 1. Experimental test cases.

Series	Geometry	Main channel	Discharge (l/s)
RIS	Isolated main channel	Rigid bed	01–30
ROA	Asymmetric overbank	Rigid bed	12–50
ROS	Symmetric overbank	Rigid bed	12–55
LIS	Isolated main channel	Loose bed	01–22
LOA	Asymmetric overbank	Loose bed	11–27
LOS	Symmetric overbank	Loose bed	12–45

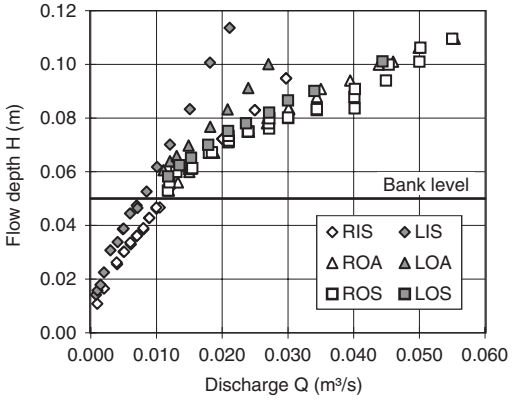


Figure 3. Experimental results: stage-discharge curves.

Figure 4 shows typical depth-averaged velocity distributions for rigid and mobile bed cases. In the rigid bed case, the classical flow behaviour of a compound channel is observed: for the lower discharges, the velocity is significantly larger in the main channel than on the floodplain, generating the shear layer that has been discussed above. When the discharge increases, the floodplain velocity increases faster than the main channel one, as the flow depth also increases, and the velocity gradient decreases.

In the mobile bed case, the flow distribution is obviously affected by the main channel flow resistance. The main channel velocity remains almost unchanged for increasing discharge and flow depth, probably due to bed form development. On the other hand, the floodplain velocity increases rapidly and become even larger than in the main channel. This generates the reversal of the momentum transfer direction discussed previously. A similar behaviour is observed for the bed shear stress distribution.

Copyright © 2006 Taylor & Francis Group plc, London, UK

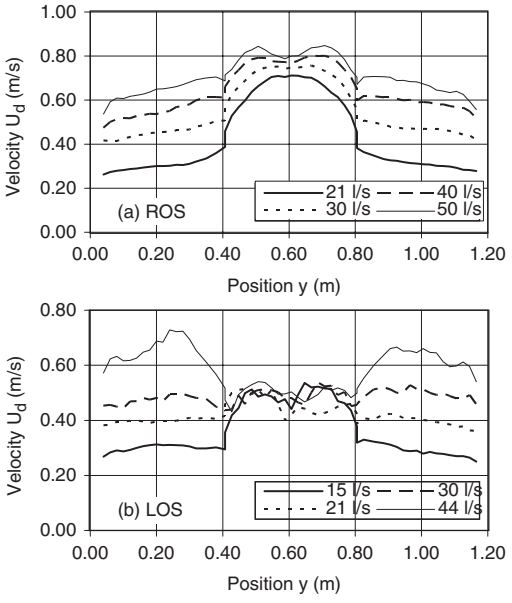


Figure 4. Depth-averaged velocity distribution: (a) ROS series; and (b) LOS series.

The discharge distribution between main channel and floodplain is similarly affected by the main channel flow resistance (Fig. 9). In the rigid bed case, the portion of the total discharge flowing on the floodplain increases with flow depth, but remains always lower than in the main channel. In the mobile bed case, the floodplain discharge becomes larger than the main channel one. A more detailed discussion of all the experimental results can be found in Atabay (2001).

3.3 *Flow resistance*

3.3.1 *Global, zonal and local friction factor*

The resistance, or friction, factor can be defined in different ways for a compound channel: (a) the global resistance factor defined by applying a friction law like (1) to the whole cross-section; (b) the zonal resistance factor defined on a subsection; and (c) the local friction factor obtained by using the local bed shear stress and velocity values. In a single rectangular channel, these three definitions give almost the same friction factor values, depending mainly on the bed material roughness. In a compound channel, significant differences are observed.

The global friction factor encompasses all the head loss occurring in the section, including the effect of the momentum transfer on the channel conveyance. When computed as a Manning roughness coefficient, it presents a sudden drop at bankfull depth to compensate for the reduction in hydraulic radius. The zonal friction factors also encompass momentum transfer

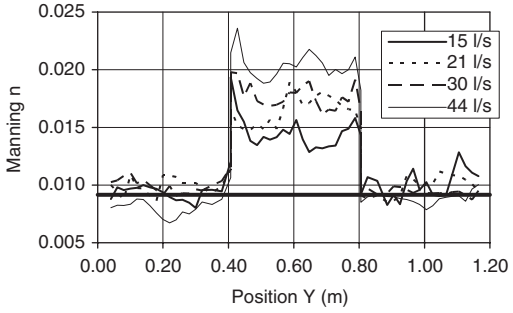


Figure 5. Local Manning roughness coefficient estimated from bed shear stress and velocity measurements. LOS series.

effects. A detailed discussion on the values of these factors obtained from the experimental data can be found in Atabay (2001) and in Atabay and Knight (1999).

In the present analysis, the local friction factor is preferred. As it does not include momentum effects, this factor can be estimated a priori, either from inbank stage-discharge measurements, or from roughness tables. It is then expected that, using the EDM with these a priori determined friction factor, purely predictive modelling could be performed.

3.3.2 *Rigid bed friction factor*

The Manning roughness coefficient n for rigid bed can be estimated from the RIS series (isolated main channel). The best fit between experimental data and a stage-discharge curve computed using (1) is obtained for $n = 0.00916$ s/m$^{1/3}$.

For confirmation, the local roughness value can also be computed from the local bed shear stress τ_b and the local depth-averaged velocity U_d

$$n = \sqrt{\frac{\tau_b H^{1/3}}{\rho g U_d^2}} \tag{10}$$

Typical values of n computed for the LOS series are shown on Figure 5. The values on the rigid floodplains are close to the value computed for inbank flow, while the main channel values are larger, due to the bed forms on the mobile bed.

3.3.3 *Mobile bed friction factor*

The Manning roughness coefficient n_b for the mobile bed can be estimated from the LIS series (isolated main channel), using a wall correction. Figure 6 shows the roughness coefficient as a function of the discharge. The main channel discharge has been selected as abscissa instead of the flow depth, as it is expected that it will be more representative of the transport capacity of the channel and thus of the possible bed forms development for compound channel experiments.

Copyright © 2006 Taylor & Francis Group plc, London, UK

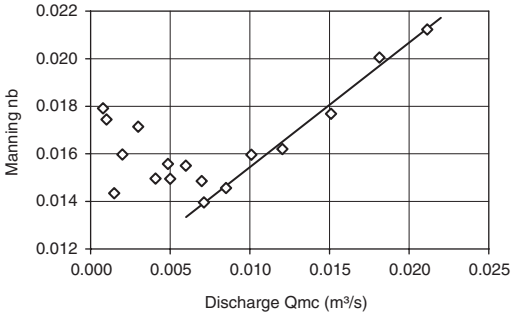


Figure 6. Manning roughness coefficient. LIS series.

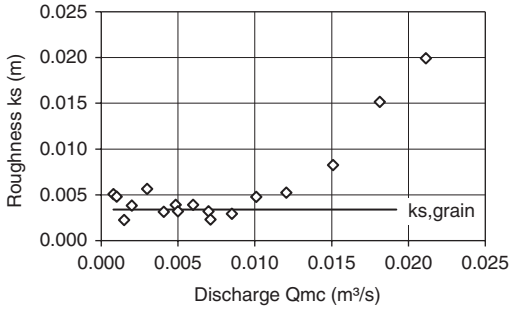


Figure 7. Nikuradse k_s for LIS series.

For a discharge lower than $Q_{mc} = 8$ l/s (i.e. bankfull discharge in compound channel geometries), the Manning n_b value is rather scattered, but tends to decrease. For larger discharge, it varies linearly with the discharge:

$$n_b = 0.0102 + 0.5237\, Q_{mc} \tag{11}$$

Expressing the roughness coefficient as the equivalent roughness of Nikuradse k_s enables a better understanding of its behaviour. The equivalent roughness can be decomposed as

$$k_s = k_{s,grain} + k_{s,form} \tag{12}$$

where $k_{s,grain} = 3\ d_{90}$ = sand roughness; and $k_{s,form}$ = form roughness, due to dune development (Van Rijn, 1982). Figure 7 shows k_s and $k_{s,grain}$ values computed for the LIS series (with $d_{90} = 1.13$ mm). No bed forms were observed for discharges lower than 8 l/s: for these discharges, the roughness is only due to grain roughness, with some experimental scattering for the lower discharge, where flow depths are difficult to record accurately. For larger discharges, bed forms develop and the roughness increases, as already observed in Figure 6 for the Manning n_b. More details on the bed forms development are given by Tang and Knight (2001, 2006).

4 VALIDATION OF EDM

4.1 *Discharge prediction*

Stage-discharge curves and discharge distribution were computed with the EDM using the roughness coefficients estimated in § 3 from inbank measurements, without any further parameter fitting. For the mobile bed cases, the solution is obtained iteratively: after assuming a main-channel bed roughness value n_b, a first computation is done, giving the main channel discharge value Q_{mc}. The roughness n_b is then corrected using (11), and the computation is repeated until it converges (usually in less than 5 iterations).

Figures 8 and 9 show the computed stage discharge curves and discharge distributions, respectively, together with SCM and DCM calculations. The stage-discharge predictions are globally better using EDM than SCM and DCM, although the three methods are not so distinct for the mobile bed cases. Indeed, in this case, the larger main-channel roughness influences all three calculations significantly.

Again, the discharge distributions computed with EDM are closer to the experimental data than those computed with DCM or SCM. However, larger discrepancies are observed between EDM and data for floodplain discharge at the lower flow depths for rigid bed cases. This could be partly due to measurement inaccuracy for these discharges, as a 13 mm diameter propeller was used at the level $z = 0.4\,H$, for local H values lower than 20 mm on floodplains. This problem does not appear in the mobile bed cases, where the floodplain velocities were larger.

4.2 *Momentum transfer analysis*

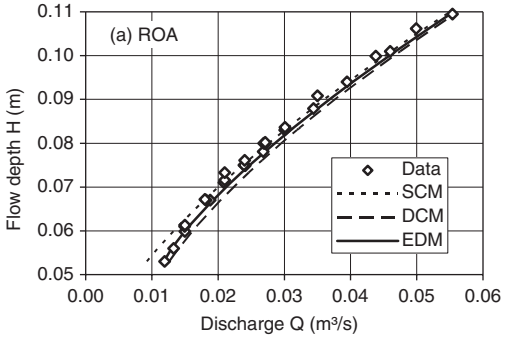
The intensity of the actual momentum transfer through the vertical interface between main channel and floodplain can be estimated from experimental data by computing the apparent shear force ASF_v. This apparent shear force is computed as the force required to equilibrate the momentum balance between water slope and bed shear stress (Atabay, 2001):

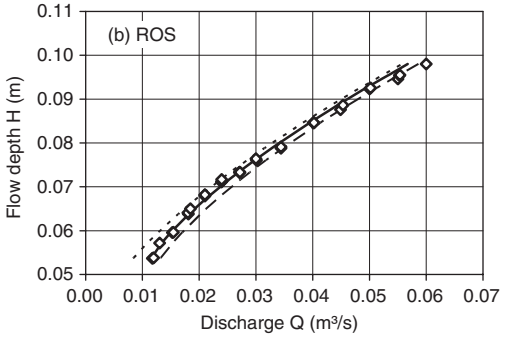
$$-\rho g A_c \frac{\partial z}{\partial x} = \int_{P_c} \tau_b dP + ASF_v \tag{13}$$

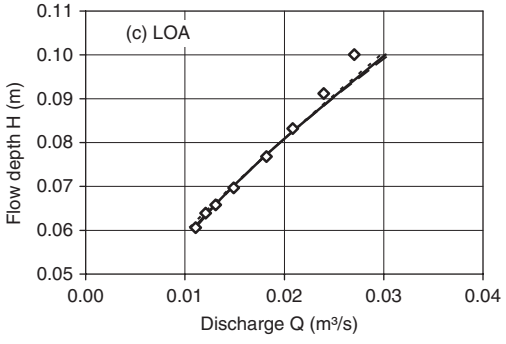
where P_c = main-channel wetted perimeter.

Whereas for rigid-bed experiments, ASF_v was always positive, indicating a momentum transfer from main channel to floodplain, Figure 10 shows that its value become negative for $H > 0.080$ m. This sign change corresponds to the momentum transfer reversal. It occurs when the main channel roughness has increased in such a way that the lateral velocity gradient is reversed, as shown in Figure 4.

Copyright © 2006 Taylor & Francis Group plc, London, UK







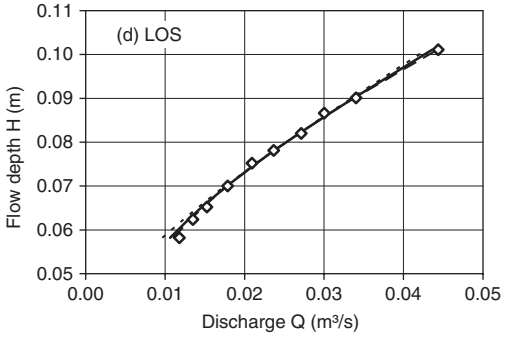
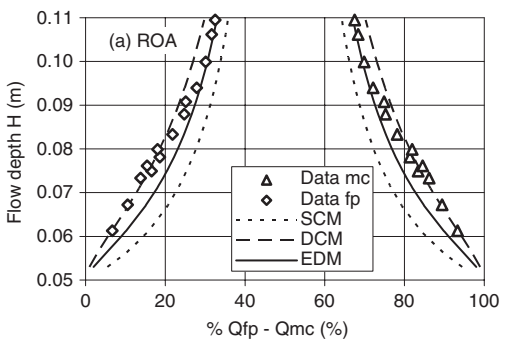
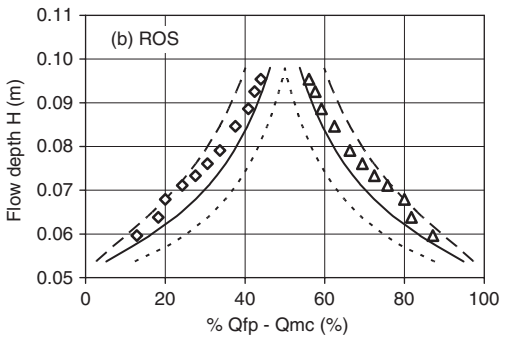
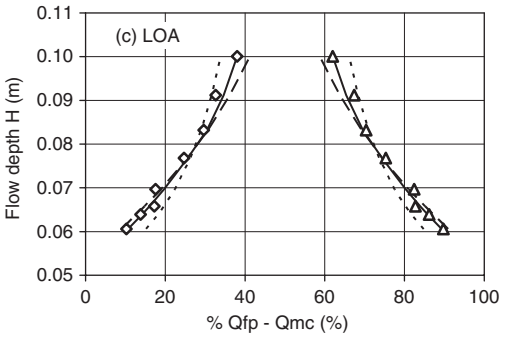


Figure 8. Stage-discharge relationship. Experimental data and computation. (a) ROA; (b) ROS; (c) LOA; and (d) LOS.







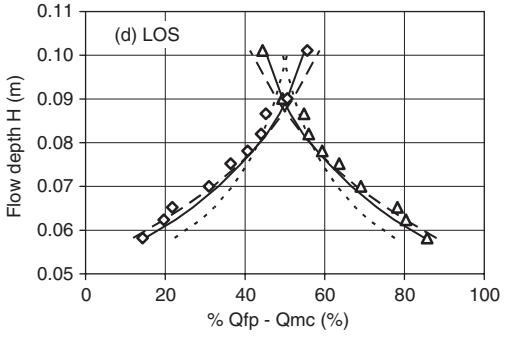


Figure 9. Discharge distribution. Experimental data and computation. (a) ROA; (b) ROS; (c) LOA; and (d) LOS.

Copyright © 2006 Taylor & Francis Group plc, London, UK

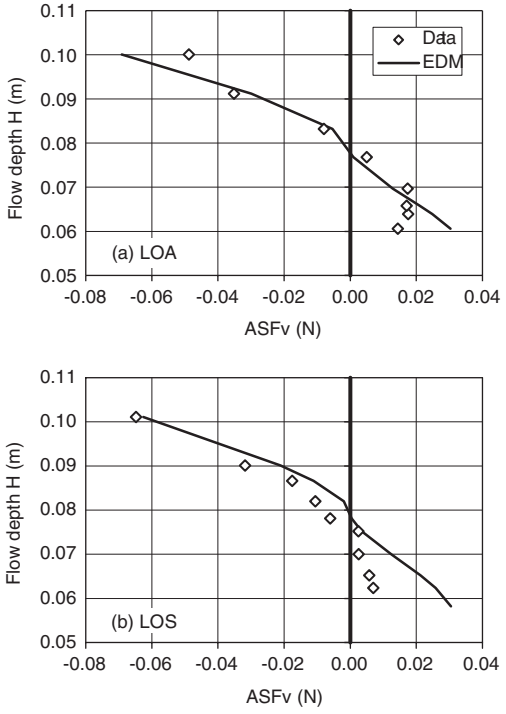


Figure 10. Apparent shear force ASF_v. Experimental data and EDM computation. (a) LOA; and (b) LOS (in this later case, ASF_v is estimated for one interface).

In the EDM, the apparent shear force acting on the interface is modelled explicitly through the additional head loss due to exchange discharges

$$ASF_v = \rho g A_c S_{ac} \tag{14}$$

where S_{ac} expression is given by (5), while its value is computed using the χ_i ratio (see § 2.3).

Figure 10 shows a very good agreement between experimental and EDM-computed values of ASF_v. Not only is the sign reversal modelled, but also the actual values. This result is obtained without any further parameter fitting: the used value of $\psi^t = 0.16$ was calibrated by Bousmar & Zech (1999) for an independent set of data. This last comparison indicates that EDM models adequately the physics of the momentum transfer. It also explains why EDM gets good results for stage-discharge and discharge distribution modelling.

5 CONCLUSIONS

The analysis of compound channel experiments with a mobile bed shows that a reversal of the momentum transfer between main channel and floodplain can be observed. This reversal occurs when large bed forms develop in the main channel and increase its flow resistance. The existing compound channel flow formulae were not tested for such situation.

In this paper, the EDM was modified to account also for such a situation. The mathematical developments show that only minor changes are necessary for such an adaptation, by adding a sign test in the numerical solution.

The EDM was then tested using existing mobile-bed compound-channel experimental data. The data from inbank measurements were re-analysed, in order to determine a priori roughness coefficients. These coefficients were then used for compound channel computations with EDM, without any further parameter fitting.

The EDM gives better results than SCM and DCM, when compared to observed stage-discharge curves and discharge distribution between subsections. It also represents satisfactorily the apparent shear force values, with a sign change at the same flow depth. This confirms that EDM models adequately the actual physics of the momentum transfer between the subsections of a compound channel.

APPENDIX: COMPUTATION OF χ_i RATIOS

To obtain a numerical solution of the system (9), three auxiliary variables are defined:

$$X_i = (1+\chi_i)^{1/2}, \quad i = 1,2,3 \tag{15}$$

For a larger velocity in main channel than on floodplain, the following conditions had to be satisfied (Bousmar & Zech, 1999):

$$\frac{1}{X_1}\frac{R_1^{2/3}}{n_1} \le \frac{1}{X_2}\frac{R_2^{2/3}}{n_2} \text{ and } \frac{1}{X_3}\frac{R_3^{2/3}}{n_3} \le \frac{1}{X_2}\frac{R_2^{2/3}}{n_2}$$
$$0 < X_1 \le 1;\ 1 \le X_2 \text{ and } 0 < X_3 \le 1 \tag{16}$$

where $X_i \le 1$ and ≥ 1 imply velocity increase and decrease respectively, due to momentum transfer, as in (8). When the momentum transfer is reversed, with larger velocity on the floodplain than in the main channel, the conditions (16) become

$$\frac{1}{X_1}\frac{R_1^{2/3}}{n_1} \ge \frac{1}{X_2}\frac{R_2^{2/3}}{n_2} \text{ and } \frac{1}{X_3}\frac{R_3^{2/3}}{n_3} \ge \frac{1}{X_2}\frac{R_2^{2/3}}{n_2}$$
$$1 \le X_1;\ 0 < X_2 \le 1 \text{ and } 1 \le X_3 \tag{17}$$

Equations (9) can be seen as quadratic equations respectively for X_1 and X_3 : extracting the roots and selecting the appropriate ones (fortunately, the same roots X_{1+} and X_{3+} satisfy the conditions given by (16)

Copyright © 2006 Taylor & Francis Group plc, London, UK

or (17), according to the velocity gradient), after simplifications, the following expressions for X_1 and X_3 as functions of X_2 can be obtained:

$$X_1 = \frac{1}{2} X_2 \frac{1}{X_2^2 + \frac{\sigma_1 \psi^t (H - h_1)}{g A_1} \left(\frac{R_2^{2/3}}{n_2} \right)^2} \cdot \left(2 \frac{\sigma_1 \psi^t (H - h_1)}{g A_1} \frac{R_1^{2/3}}{n_1} \frac{R_2^{2/3}}{n_2} - \frac{\psi^g \kappa_{21} dK_1/dx}{g A_1} \frac{R_2^{2/3}}{n_2} + \left\{ \left[4 \frac{\sigma_1 \psi^t (H - h_1)}{g A_1} + \left(\frac{\psi^g \kappa_{21} dK_1/dx}{g A_1} \right)^2 \right] \left(\frac{R_2^{2/3}}{n_2} \right)^2 + 4 X_2^2 \right. \right.$$
$$\left. \left. \cdot \left[1 - \frac{\sigma_1 \psi^t (H - h_1)}{g A_1} \left(\frac{R_1^{2/3}}{n_1} \right)^2 + \frac{\psi^g \kappa_{21} dK_1/dx}{g A_1} \frac{R_1^{2/3}}{n_1} \right] \right\}^{1/2} \right)$$

$$X_3 = \frac{1}{2} X_2 \frac{1}{X_2^2 + \frac{\sigma_3 \psi^t (H - h_3)}{g A_3} \left(\frac{R_2^{2/3}}{n_2} \right)^2} \cdot \left(2 \frac{\sigma_3 \psi^t (H - h_3)}{g A_3} \frac{R_3^{2/3}}{n_3} \frac{R_2^{2/3}}{n_2} - \frac{\psi^g \kappa_{23} dK_3/dx}{g A_3} \frac{R_2^{2/3}}{n_2} + \left\{ \left[4 \frac{\sigma_3 \psi^t (H - h_3)}{g A_3} + \left(\frac{\psi^g \kappa_{23} dK_3/dx}{g A_3} \right)^2 \right] \left(\frac{R_2^{2/3}}{n_2} \right)^2 + 4 X_2^2 \right. \right.$$
$$\left. \left. \cdot \left[1 - \frac{\sigma_3 \psi^t (H - h_3)}{g A_3} \left(\frac{R_3^{2/3}}{n_3} \right)^2 + \frac{\psi^g \kappa_{23} dK_3/dx}{g A_3} \frac{R_3^{2/3}}{n_3} \right] \right\}^{1/2} \right) \quad (18)$$

where $\sigma_i = \text{sign}(R_2^{2/3}/n_2 - R_i^{2/3}/n_i)$. For a velocity larger in the main channel than on the floodplain, $\sigma_i = 1$, and the solution is the same as that developed by Bousmar & Zech (1999).

Using these expressions in equation (9), it is possible to get a single function of X_2 that has to be equal to zero:

$$F(X_2) = 0 = F\left(\frac{X_1}{X_2}, \frac{X_3}{X_2}, X_2 \right) =$$
$$1 - X_2^2 + \frac{1}{g A_2} \left\{ \left[\sigma_1 \psi^t (H - h_1) \left(\frac{R_2^{2/3}}{n_2} \frac{X_1}{X_2} - \frac{R_1^{2/3}}{n_1} \right) + \psi^g \kappa_{12} \frac{dK_1}{dx} \right] \left[\frac{R_2^{2/3}}{n_2} \frac{X_1}{X_2} - \frac{R_1^{2/3}}{n_1} \right] \left(\frac{X_2}{X_1} \right)^2 \right.$$
$$\left. + \left[\sigma_3 \psi^t (H - h_3) \left(\frac{R_2^{2/3}}{n_2} \frac{X_3}{X_2} - \frac{R_3^{2/3}}{n_3} \right) + \psi^g \kappa_{32} \frac{dK_3}{dx} \right] \left[\frac{R_2^{2/3}}{n_2} \frac{X_3}{X_2} - \frac{R_3^{2/3}}{n_3} \right] \left(\frac{X_2}{X_3} \right)^2 \right\} \quad (19)$$

as X_1/X_2 and X_3/X_2 are defined as functions of X_2 by equations (18). The value of X_2 can finally be found using a Newton-Raphson resolution of equation (19), with an initial value of $X_2 = 1$. Getting the value of X_2 as a function of the cross-section geometrical parameters, allows one to obtain the values of the χ_i ratios from the X_i definition (15).

ACKNOWLEDGEMENT

The first author is grateful to FNRS, Belgium, for funding a short stay at Birmingham University in 2004, where this work was initiated.

REFERENCES

Ackers, P. 1993. "Flow formulae for straight two-stage channels", *Journal of Hydraulic Research, IAHR*, 31(4), 509–531.

Atabay, S. 2001. *Stage-discharge, resistance, and sediment transport relationships for flow in straight compound channels*, PhD Thesis, University of Birmingham, UK.

Atabay, S. & Knight, D.W. 1999. "Stage discharge and resistance relationships for laboratory alluvial channels with overbank flow". In Jayawardena, Lee and Wang (eds), *River Sedimentation, Proc. 7th intern. symp. on River Sedimentation, Hong-Kong, Dec. 1998*, Balkema, 223–229.

Ayyoubzadeh, S.A. 1997. *Hydraulic aspects of straight compound channels flow and bedload sediment transport*, PhD Thesis, University of Birmingham, UK.

Bousmar, D. 2002. *Flow modelling in compound channels. Momentum transfer between main channel and prismatic or non-prismatic floodplains*, PhD Thesis, Université catholique de Louvain, Belgium.

Bousmar, D. & Zech, Y. 1999. "Momentum transfer for practical flow computation in compound channels", *Journal of Hydraulic Engineering, ASCE*, 125(7): 696–706.

Lambert, M.F. & Myers, W.R. 1998. "Estimating the discharge capacity in straight compound channels", *Proc. Institution of Civil Engineers, Water, Maritime and Energy*, 130(2), 84–94.

Tang, X. & Knight, D.W. 2001. "Analysis of bed form dimensions in a compound channel", *Proc. 2nd IAHR Symposium on River, Coastal and Estuarine Morphodynamics*, September, Obihiro, Japan, 555–563.

Tang, X. & Knight, D.W. 2006. "Sediment transport in river models with overbank flows", *Journal of Hydraulic Engineering, ASCE*, (in press).

van Rijn, L.C. 1982. "Equivalent roughness of alluvial bed", *Journal of the Hydraulics Division, ASCE*, 108(10), 1215–1218.

Copyright © 2006 Taylor & Francis Group plc, London, UK

Performance of several hybrid numerical schemes to determine flooding extent

I. Villanueva & N.G. Wright
School of Civil Engineering, University of Nottingham, United Kingdom

ABSTRACT: Several hybrid approaches that combine 1D modelling for the main river and 2D modelling for the flood plains are discussed and compared. These range from a commercial quasi-2D or storage cell model approach, a 2D raster based approach based in the Manning equation, and a complete 2D shallow water equation solver in explicit and implicit version, based in Riemann solvers with finite volume and alternating direction formulations. The latter includes a multi-processor version which allows studies at small mesh resolutions or large extents.

Two basic scenarios are used for comparison, a typical rural one with a 15 km river length where the terrain data and validation are obtained from remote sensing, and an urban one where only the terrain data is acquired from remote sensing.

Results will show the ease of implementation of the models, their time steps, induced mass error and prediction accuracy and capability. The influence of the grid size resolution is also reported.

Conclusions for predicting flood plain inundation with various models are drawn and future research directions are discussed.

1 INTRODUCTION

Due to global warming long term weather forecasts are predicting more water cycle disruptions, in particular the raising of sea levels, the increase of tropical sea water temperatures which increases the number of intense hurricanes and storms, and an increase in the number of extreme rains generating flash floodings are forecasted. Although the general distribution of these extreme events around the world is still uncertain due to the many climate models and assumptions, average trends are predicted, (Hadley Centre, Meteorological Office).

Flooding prediction studies require a large amount of terrain and hydraulic data to be collected, although modern techniques like remote sensing LIDAR are collecting the majority easier and faster, many other related problems arise, (Wright et al. 2006), for reported manipulations and extractions of Digital Surface Model from Digital Terrain Models and obtaining Manning or friction coefficient maps.

One of the main objectives of this paper is to assess about use of different numerical techniques in order to predict flooding effects depending on the time scale and spatial extent, and according to the characteristics of the provided digital terrain models, working with standard computers or specialized ones.

2 REVIEW OF MODELS

A basic introduction to currently used hydraulic models of floods is given in (Kutija 2002), or classically (Cunge et al. 1980), ranging from steady state ones to hydrodynamic in one- and two-dimensions.

All the studied models covered here are time dependent or allowed for the study of transient states. Steady state models are now not normally used due to the ready availability of one-dimensional complete models which are fast enough in common Pc's for practical applications (Burguete and Garcia-Navarro 2004). Complete 2D models are also increasingly practical (Villanueva and Wright 2006b).

2.1 *Basic equations*

The 1D and 2D shallow water equations or mass and momentum conservation are applied here. A complete definition and description of their properties can be found (Cunge et al. 1980) and (Weiyan 1992), in conservative formulation are:

$$\frac{\partial U}{\partial t} + \nabla \overline{F}\,(U) = H \qquad (1)$$

With U the main variables related to water depth and discharge, F their flows, and H their source terms.

Copyright © 2006 Taylor & Francis Group plc, London, UK

Being a non-linear coupled system of first order PDE's of hyperbolic nature, (Toro 2001).

Different approaches to solve these equations are commented on the following sections.

2.2 *One-dimensional complete single*

These models are used in cases where the valley cross sections have a complete U shape and no flood plains exist or if any, the water surface level is kept the same across the main river and its flood plain. That approach does not deal with different velocity profiles, although some attempts have been made in the past to complete it (Cunge et al. 1980), in the vast majority of the flood modelling within the UK or in relatively flat lands this approach is incomplete, mainly during the filling and drying of the floodplains.

2.3 *One-dimensional complete plus storage cell model*

If the one-dimensional model for the main river is linked to flood plains using spill boundaries between river and flood plain or between flood plains, a quasi-2D model is defined. Flood plains are considered as reservoirs or storage cells, with typical dimensions for width and length of a few hundreds of meters.

As an example of this modelling, a figure of the studied area of Upton upon Severn (15 kms river length) with the commercial scheme Mike11 is covered in Figure 2, showing the 1D H-Q points, link channels and connected storage cells.

The main advantage of this model is its fast delivery of results once it is built, the main disadvantage is its large pre-processing data time and lack of correct propagation times over the floodplains. It continues to be the most used in consultancy.

This model is time consuming to calibrate, as it relies on many geometrical parameters (spill-weirs), but can be efficient if propagation times of flooding are not required and only maximum flooding extents are needed.

In particular the modeller has to be concerned with the storage cells shape and size while working in the post-processing of output data with GIS systems, because it could be possible that the GIS application can extrapolate water depths and flooding extents, resulting in non mass conservative approaches during the mapping display.

2.4 *Cartesian vs unstructured meshes, hybrid modelling*

From the mathematical point of view an unstructured mesh fits better with a terrain model, and leads to a more detailed and accurate solution for the conservation laws, but it is also highly time consuming if the mesh is fine and generally it requires interpolation techniques for the bathymetry or areas under water where no data are available. With the final practical objective of covering large flooding prone areas with millions of cells the authors have selected a structured Cartesian grid. Latest technical advances in shallow water modelling with unstructured meshes have been reported recently (Murillo et al. 2006).

The idea of hybrid 1D-2D modelling through spill line connections, maintains 1D river reach areas with low demand in computing cost and input data with more demanding ones, the 2D, which is in line with the practical availability and compilation of data in a whole catchment, and the idea of recycling and upgrading older 1D-models and quasi-2D with 2D models partially.

Separating the domains through spilling lines is a consistent approach with the shallow water equations, but also a non realistic one because it ignores the momentum exchange, turbulence and non-hydrostatic pressure distribution by the overtopping of embankments, a process which should be covered through a 3D modelling technique.

It can be summarised that it is desirable for a good mathematical performance and consistency to use a 2D unstructured mesh, but realistic topographic data, computational costs for large domains, and an engineering sense still lead to the use of hybrid models and Cartesian grids.

The following sections contain further techniques which take advantage of Cartesian grids and hybrid modelling.

2.5 *One-dimensional complete plus raster based model*

This model being more exigent in computational cost than the previous one, avoids the phase of assigning, drawing and linking the storage cells through weirs. It also gives wrong propagation times along the floodplains, because it does not consider the momentum equation but instead generates a water surface profile parallel to the bed slope which gives more information than the simple storage cells which act like a system of reservoirs.

In the raster based approach the water depth is calculated according to the discharge between cells (assuming the uniform flow Manning equation):

$$Q_{i+1/2} = \frac{H_{flow}^{5/3}}{n}\left(\frac{\partial Z}{\partial x}\right)^{1/2} \tag{2}$$

With $H_{flow} = max(Z_i, Z_{i+1}) - max(Zb_i, Zb_{i+1})$, being Zb the terrain bottom, h the water depth and $Z = Zb + h$. The Manning friction coefficient is n.

This method was proposed by Estrela and Quintas (Estrela and Quintas 1994), and Bates and de Roo (Bates and Roo 2000) used it to develop LISFLOOD-FP which has been used in many studies.

Copyright © 2006 Taylor & Francis Group plc, London, UK

This model does not require the careful drawing and output data checking needed with storage cells, it is easy and robust to implement as a bespoke technique, being always mass conservative as it is not coupled to any momentum equation. However it requires additional calibration techniques for obtaining correct propagation times. In the version calibrated in the work reported here its time step is determined by the finite volume scheme or an alternating direction scheme, in both cases with velocities $(u, v) = 0$.

2.6 *One-dimensional complete plus two-dimensional complete*

2.6.1 *Riemann solvers*

In order to solve the complete system of shallow water equations, approximate Riemann solvers, in particular the Roe one under the Godunov approach, (Toro 2001) and (Guinot 2003), have been considered as a robust and powerful tool for the prediction of shallow water flows in one- and two-dimensional approximations. See for instance (Alcrudo and Garcia-Navarro 1993), (Zhao et al. 1996), (Anastasiou and Chan 1997), (Erduran et al. 2002), (Brufau et al. 2004) and (Burguete and Garcia-Navarro 2004) for river modelling, or (Hubbard and Dodd 2002) for coastal modelling.

Both the two-dimensional complete model and the one-dimensional complete model referred in this paper use a Riemann solver. The one-dimensional complete plus storage cell scheme described in section 2.3 uses the Abbott-Ionescu scheme (DHI 2005), and the raster based one in 2D (section 2.5) uses a single, uncoupled equation under the Godunov approach.

Both the two-dimensional complete model and the one-dimensional complete approximate Roe Riemmann solvers have been calibrated against laboratory tests proposed by the CADAM group (Concerted Action on Dambreak Modelling), (Villanueva and Wright 2005b). A short technical definition follows.

2.6.2 *Explicit formulation*

The most used schemes are the explicit ones due to the ease of implementation. For the augmented 2D system with 3 components (h, u, v), in Cartesian grid, the definition is:

$$U_{i,j}^{n+1} = U_{i,j}^{n} - \frac{\Delta t}{\Delta x}\left[F_{i+1/2,j}^{*} - F_{i-1/2,j}^{*}\right] - \frac{\Delta t}{\Delta y}\left[G_{i,j+1/2}^{*} - G_{i,j-1/2}^{*}\right] + \Delta t H_{i,j}^{n} \quad (3)$$

Reference (Villanueva and Wright 2006a) describes in detail the flows and source terms considered, and the implementation of the Alternating Direction scheme (AD) which allows slighty larger time steps than the FVM implementation.

2.6.3 *Implicit formulation*

An implicit approach has also been tested, using an Alternating Direction technique in X-Y (ADI), it discretizises the system as follows in 1D:

$$\frac{U_i^{n+1} - U_i^n}{\Delta t} + \frac{1}{\Delta x}\left[\theta(F_{i+1/2}^{*n+1} - F_{i-1/2}^{*n+1})\right] + \frac{1}{\Delta x}\left[(1-\theta)(F_{i+1/2}^{*n} - F_{i-1/2}^{*n})\right] = \theta H_i^{n+1} + (1-\theta) H_i^n \quad (4)$$

With θ the implicit parameter of the system. When $\theta = 0$ it is the explicit Euler scheme, if $\theta = 1$ it is the implicit Euler scheme, and if $\theta = 0.5$ it is the trapezoidal method (second order accurate in time). The system is approximated to obtain a tri-diagonal system in every single dimension:

$$AA_i \Delta U_{i-1}^n + BB_i \Delta U_i^n + CC_i \Delta U_{i+1}^n = RHS_i \quad (5)$$

2.6.4 *Multi-processor approach*

The idea of dividing the 2D domain in equal size sub-domains, according to the number of processors is the simplest to implement. This division for a 2D Cartesian grid is easy to generate and robust using MPI libraries, in particular the SENDRECV blocking communications between neighbours. See EPCC MPI introduction course, (MacDonald et al. 2005).

3 DIFFERENT SCENARIOS

3.1 *Rural river flood: Upton upon Severn*

This scenario and the propagation times of the hydrograph peaks represent a flat or slow flooding, which allows the comparison of many of the described techniques.

The 1D model covers 31 cross sections distributed at 500 meters intervals along 15 Kms of river length. The complete LIDAR Digital Terrain Model (DTM) covers a surface of 74 square Kms. For the 18 m grid study this consist of a reduced grid of $213 \times 482 \approx 102\,K$ cells.

The simulation covers approximately 14 days, and the calibration is made with an available ASAR image at approximately t = 700000 seconds (raising limb of second hydrograph peak), see Figure 1.

Results with Mike11, quasi-2D, a commercial one-dimensional complete plus storage cell model which uses the network displayed in Figure 2, took 12 minutes to complete with a 2.66 GHz processor. The predicted

Copyright © 2006 Taylor & Francis Group plc, London, UK



Figure 1. ASAR image (yellow) available for calibration at t = 700000 secs in yellow, the red lines are the embankments which separate main river from the flood plains. The provided image is cut upstream.



Figure 2. Network structure of the Mike11 quasi-2D model, with cross sections, h-q points, link channels and storage cells.

flooding extent is displayed over the ASAR image at Figure 3.

As reported by Villanueva and Wright in (Villanueva and Wright 2005a) and in more detail in this paper, a 18 m resolution 2D grid is a feasible one with a common desktop for this flooding event which covers a couple of weeks time and a dozen of kilometres river length, with results in less than 24 hours computational time using a shock-capturing explicit first order scheme like the complete 1D-2D TRENT-AD.

The tables below compare the performance of all the bespoke and proposed models, where there are 860 2D cells connected to the 31 1D river cross sections.

Table 1. Computational cost indicators (CFL and medium time step) for the set of complete 2D numerical schemes (TRENT) and raster-based approach (LISFLOOD or LF).

Scheme	CFL	Medium Δt(s), dl = 18 m
TRENT-FVM	0.9	1.21
TRENT-AD	0.9	2.43
TRENT-ADI	1.5	4.02
LF-FVM	0.9	1.21
LF-AD	0.9	2.41

A Manning friction value of 0.035 was used for the main river and 0.03 for the flood plains.

In summary the computed water volume over the flood plains is in a similar range for all bespoke

Copyright © 2006 Taylor & Francis Group plc, London, UK

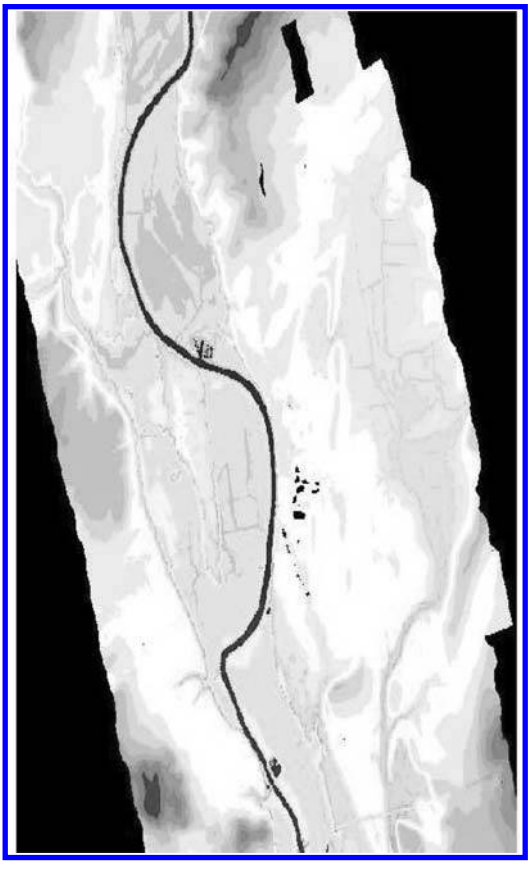


Figure 3. Predicted flooding extent with Mike11 storage-cell model (blue) over ASAR image (yellow).

Table 2. Computational cost for the set of complete 2D numerical schemes (TRENT) and raster-based approach (LISFLOOD or LF). LISFLOOD is around 3 times faster in both versions, FVM and AD. 102 Kcells.

Scheme	Cost, hours : minutes, at 2.8 GHz
TRENT-FVM	38 : 46
TRENT-AD	22 : 25
TRENT-ADI	non-optim
LF-FVM	12 : 33
LF-AD	8 : 24

schemes, (differences less than 10% at 18 m resolution), so for this particular slow flood case, with no need to predict velocities the raster LISFLOOD-AD scheme outputs 2D information in less than 9 hours. It is noticeable that the differences in the maximum flooding extent are less significant than the maximum 10% difference in volume peaks as the surface considered is over 33 squared Kilometers.



Figure 4. Detailed 2D complete FVM flood extent prediction (blue) over ASAR imagery (yellow). Notice that it is only shown the 2D domain result, and the main channel flood is not displayed for the sake of clarity of the hybrid methodology.

Figure 4 shows the flooding extent from TRENT-FVM at the calibration time compared with the ASAR image. All the hybrid models that include a 2D grid produced similar maximum flooding extent and gave better performance than the 1D storage-cell (Figure 3). These methods also have the advantage that the required input data processing is lower. For this particular case the complete 2D models with shock-capturing properties are considered expensive and the raster one feasible with a common desktop.

The implicit scheme (ADI) allowed a time step CFL coefficient of 1.5 for this case, which makes it inefficient, as it sweeps twice in every X and Y direction a value bigger than 2 is needed to make it efficient.

Copyright © 2006 Taylor & Francis Group plc, London, UK

Table 3. Computational cost indicators for the explicit complete 2D numerical schemes (TRENT) and raster-based approach (LISFLOOD or LF), using a grid computing facility with 36 processors, at a resolution of 3 m simulating first quarter of hydrograph (maximum extent), 3.7 Mcells.

Scheme	Cost, hours, dl = 3 m, at 2.2 GHz
TRENT-FVM	282
LF-FVM	156

With flat bottom test cases it has reached a value of 2.5, keeping its property of shock-capturing.

The 2D complete model in FVM formulation, within a multi-processor version has been used in a 3 m resolution grid, in order to check the computational cost of a highly accurate model. This was also done for the raster-based method in a FVM formulation.

The original 3 m DSM had Nx = 1278 columns, and Ny = 2892 rows, the domain division creates $4 \times 9 =$ 36 subdomains with Nxr = 320, Nyr = 322 each.

The times are shown in the table below for 300000 seconds simulation (maximum hydrograph peak).

Showing that the waiting communication times among processors reduces the rate TRENT/LF to 2:1 against the single processor version which was 3:1, although the results could vary because the numerical code needs to be optimized and another sub-domains sizes can be studied. Predicting the same range of water volume for the flood, the advantage of using a small mesh size of 3 m will be reported in future publications, or the developed systematic could be useful for larger meshes with bigger grid size.

3.1.1 *Grid independence*

As shown in (Villanueva and Wright 2006b), the raster based approach is more sensitive to grid size, whereas the complete 2D is more appropiate as it maintains propagation times and maximum values independently. Figures 5 and 6 display the grid dependence for dl = 9, 18, 27 and 54 m for each model. The complete model has more divergences during the drying processes or decreasing limbs.

Further research is expected to determine the influence of different resolutions in the terrain slopes and surface wetting, although global results in (Villanueva and Wright 2006b) seem to show that the complete 2D model keeps the most important values (times and maximums) at different resolutions.

3.1.2 *Drying process*

Subsequent ASAR images are available for the Upton upon Severn event, but their fitting with numerical predictions require a complete description of the whole drainage system, and the incorporation of infiltration processes. Further the drying process is more sensitive to uncertainties in embankment heights than the wetting, see a more complete description in (Wright et al. 2006).

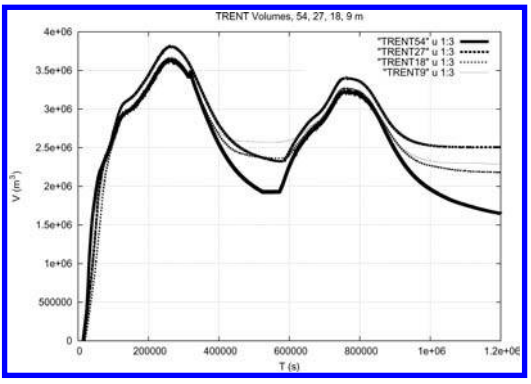


Figure 5. Water volume evolution over one selected floodplain at Upton upon Severn, for TRENT model, dl = 54, 27, 18, 9 m.

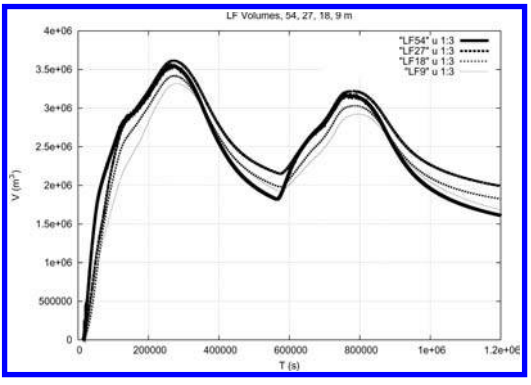


Figure 6. Water volume evolution over one selected floodplain at Upton upon Severn, for LF model, dl = 54, 27, 18, 9 m.

3.2 *Urban tidal flood: London Thames Embankment*

Given the nature of the Upton upon Severn flooding, flat and slow hydrograph in the main river and flooding covering more than 14 days, the use of a raster-based scheme is complete enough for the prediction of flooding extent. For more transient states where propagation times are more important such as the case of an urban flooding, the following study has been included.

A fictitious breach is open in the embankment close to the Thames Barrier in Greenwich, and the induced tidal flow propagates across the floodplain. The experiment is well described in (Tarrant et al. 2006) as scenario C.

An explicit formulation is preferred, due to the nature of the terrain model, which includes streets and

Copyright © 2006 Taylor & Francis Group plc, London, UK

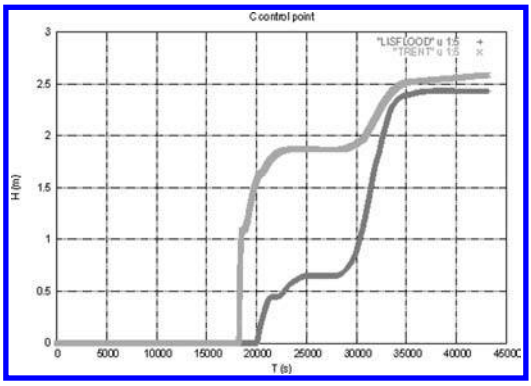


Figure 7. Water depth in C control point at London Thames Barrier, 600 meters away from the breach, red = raster (LISFLOOD) vs green = 2D complete (TRENT).



Figure 8. Maximum flooding extent for both models at London Thames Barrier, red = raster over green = 2D complete.

buildings in an industrial area close to the docks, and because the tidal cycle only covers a few hours.

Figure 7 shows water depth for the raster-based versus 2D complete formulation at a selected point and Figure 8 shows the final flooding extent.

The 2D complete approach propagates the water front faster and higher than the raster one, but in the end they converge, indicating that the LISFLOOD simplification is accurate for long term and final steady states but not for transient ones, at least in urban floods, where there are many reflections between buildings.

To simulate 3 tidal cycles took 70 minutes, with a 2.66 GHz processor for a 10 m resolution grid (184 Kcells) with the 2D complete model and 3 times less with the raster based one.

4 CONCLUSIONS

Practitioners still have reservations about using more complex models than the quasi-2D or storage cells, but their use and efficiency is wide spread in the scientific community. The work presented here tries to show that these models (2D) are feasible with current computers to certain resolutions. They require more technically educated users, but they can save time in the input processing of data, and their output gives much more information. This work also confirms that their coupling with commonly available digital surface models from remote sensing (like LIDAR) is effective.

It is becoming evident that increasing numbers of flood simulations are going to be carried out. The authors support the idea of using flexible programming tools in computer facilities such as multi-processors or grid/cluster computing systems, along with GNU compilers like gcc, mpich and Linux systems. These will provide reliable and high performance tools for fullfilling targets.

Further publications from the research group will cover in detail the London Thames Embankment area with other schemes and other scenarios.

ACKNOWLEDGEMENTS

The authors acknowledge the provision of data by the Environment Agency for England and Wales and the financial support of the Engineering and Physical Sciences Research Council under the research project GR/S17154/01 and under grant GR/S76304/01 “A Flood Risk Management Research Consortium”. Our research partners in the above are acknowledged for their support and useful discussions: Heriot-Watt University, University of Bristol, ESSC and Newcastle University.

REFERENCES

In *http://www.hrwallingford.co.uk/projects/CADAM/*. Concerted Action on Dambreak Modelling.

Climate change, rivers and rainfall. In *http://www.metoffice.com/research/hadleycentre*. Hadley Centre, Meteorological Office.

Alcrudo, F. and P. Garcia-Navarro (1993). A high-resolution godunov-type scheme in finite volumes for the 2d shallow-water equations. *International Journal for Numerical Methods in Fluids 16*, 489–505.

Anastasiou, K. and C. Chan (1997). Solution of the 2d shallow water equations using the finite volume method on unstructured triangular meshes. *International Journal for Numerical Methods in Fluids 24*, 1225–1245.

Bates, P. and A. D. Roo (2000). A simple raster-based model for floodplain inundation. *Journal of Hydrology 236*, 54–77.

Brufau, P. et al. (2004). Zero mass error using unsteady wetting-drying conditions in shallow flows over dry irregular topography. *International Journal for Numerical Methods in Fluids 45*, 1047–1082.

Burguete, J. and P. Garcia-Navarro (2004). Improving simple explicit methods for unsteady open channel and river flow.

Copyright © 2006 Taylor & Francis Group plc, London, UK

International Journal for Numerical Methods in Fluids 45, 125–156.

Cunge, J. et al. (1980). *Practical aspects of computational river hydraulics.* Pitman London.

DHI (2005). Mike 11 user manual. Danish Hydraulic InstituteWater and Environment.

Erduran, K. et al. (2002). Performance of finite volume solutions to the shallow water equations with shock-capturing schemes. *International Journal for Numerical Methods in Fluids 40*, 1237–1273.

Estrela, T. and L. Quintas (1994). Use of a gis in the modelling of flows on floodplains. In *2nd International Conference on River Flood Hydraulics.*

Guinot, V. (2003). *Godunov-type Schemes, an introduction for engineers*. Elsevier.

Hubbard, M. and N. Dodd (2002). A 2d numerical model of wave run-up and overtopping. *Journal of Coastal Engineering 47*, 1–26.

Kutija, V. (2002, October). Hydraulic modelling of floods. In *Palaeofloods, Historical Floods and Climatic Variability: Applications in Flood Risk Assessment*. PHEFRA.

MacDonald, N. et al. (2005). Writing message passing parallel programs with mpi. In *Course Notes*. EPCC Edinburgh.

Murillo, J. et al. (2006). Extension of an explicit finite volume method to large time steps (cfl $\geq$ 1): application to shallow water flows. *International Journal for Numerical Methods in Fluids 50*, 63–102.

Tarrant, O. et al. (2006). 2d floodplain modelling in the tidal thames, addressing the residual risk. Subm. *CIWEM Water and Environment Journal*.

Toro, E. (2001). *Shock-Capturing Methods for Free-Surface Shallow Flows*. John Wiley and Sons.

Villanueva, I. and N. Wright (2005a, June). The integration of one- and two-dimensional riemann-based models for predicting flood inundation and levels from remotely-sensed data. In *Proceedings on the Third International Symposium in Flood Defence.*

Villanueva, I. and N. Wright (2005b). Report on validation of trent solver, part 1: laboratory tests. *On http://www.nottingham.ac.uk/∼evzngw.*

Villanueva, I. and N. Wright (2006a). An integrated one- and two-dimensional model for flood inundation using riemann-based methods and remotely sensed data. *Subm. International Journal for Numerical Methods in Fluids.*

Villanueva, I. and N. Wright (2006b). Integration of 1d and 2d riemann and storage cell models for predicting flooding. *Accep. in ICE Journal on Water Management.*

Weiyan, T. (1992). *Shallow water hydrodynamics.* Elsevier Oceanography series.

Wright, N. et al. (2006). The use of remotelysensed data for modelling flood inundation. *Subm. to Journal of Hydraulic Engineering.*

Zhao, D. et al. (1996, December). Approximate riemann solvers in fvm for 2d hydraulic shock wave modeling. Journal of Hydraulic Engineering 122(12).

Copyright © 2006 Taylor & Francis Group plc, London, UK

Roughness coefficient for flood plains with macro roughness elements

I. Aydin
Assoc. Prof., Civil Eng. Dept., Middle East Technical University, Ankara, Turkey

M.A. Kokpinar
Research Engineer, State Hydraulic Works, Technical Research and Quality Control Dept., Hydraulics Lab., Yücetepe, Ankara, Turkey

M. Ustaomer
Graduate Student, Civil Eng. Dept., Middle East Technical University, Ankara, Turkey

ABSTRACT: Manning's roughness coefficient for flood plains with macro roughness elements is experimentally investigated in an 18 m long and 1 m wide laboratory channel. Velocity field was measured in the main and flood plain channels. Total discharge was obtained both from weir measurement and from integration of measured velocity field. Four different surface patterns including smooth and various arrangements of macro roughness elements were considered. Prismatic concrete volumes were placed as macro roughness elements on the flood plains. Wall shear stresses were determined from measured velocity profiles using logarithmic wall functions. Energy slope was determined from the total tractive force obtained by integration of wall shear stresses. Finally, Manning's roughness coefficient was determined from the Manning's formula applied to main channel and the flood plain channels. It is found that the roughness coefficient on the flood plain channels may increase more then two folds when about 2% of the flow volume in the flood plain is occupied by the macro roughness elements.

1 INTRODUCTION

The cross-section of rivers in nature can be thought as compound channels consisting of one deep main channel and one or two flood plains. In dry seasons flood plains may be used for agricultural purposes. In narrow valleys flood plains may extend to settled areas including houses and small sized buildings. Flood plains with large scale obstructions show increased resistance to flow and may cause unexpected increases in the flow depth. Estimation of the discharge capacity or flow depth during seasonal floods over the flood plains with macro sized roughness elements is of crucial importance to prevent life losses.

Throughout the average velocity and discharge capacity analyzes in singly cross-sectioned channels from Manning's or Chezy's equations; it is enough to use the overall hydraulic radius. However, in case of compound channels, as the depth of water increases, the sudden change of cross-section immediately above the main channel will lead to errors due to sudden decrease in hydraulic radius of the channel. Free surface flow calculations in compound channels require special attention on roughness variations over the cross-section to predict the flow resistance accurately.

Compound channels can be analyzed by subsections as flood plains and main channel. The hydraulic radius in flood plains are greater than that of main channels which results significantly higher velocities in the main channel compared to flood plains. Difference between the velocities causes lateral momentum transfer at the interface from fast flowing main channel to the flood plain, which shows itself as apparent shear stress at this interface. The effect of apparent shear stress reduces the discharge capacity of the compound channel significantly. Essentially the methods used to determine the discharge capacity for regular shaped cross-sectional channels may lead either underestimation of discharge capacity which will risk settlement on flood plains, or may lead to overestimation of discharge capacity resulting in over design and waste of resources.

Significant research has been undertaken in hydraulics of compound channels to understand the mechanics of flow and to obtain more accurate methods of discharge estimation. In this study, the flood plain Manning roughness coefficient is determined for the cubic macro roughness elements. Experiments have been performed to measure the flow depths and velocity distributions for different macro roughness

Copyright © 2006 Taylor & Francis Group plc, London, UK

densities on the flood plains. Measured velocity data is used to estimate the boundary resistance by employing the universal wall functions.

2 LITERATURE REVIEW

Considerable research has been carried out in compound channel hydraulics both experimentally and numerically. Large amount of experimental work was devoted to prediction of momentum exchange between the main channel and the flood plains. A variety of roughness types were also studied.

Yen and Overton (1973) tried to determine the lines that divide the cross-section into subsections at which the shear stress is zero. These lines are not included as a part of a wetted perimeter in flow computation when they are used as division lines. Since little information exists as to the location of these interface planes as they are affected by geometry and flow depth, laminar flow cases were solved to gain quantitative insight.

Myers and Elsawy (1975) studied the effect of the interaction mechanism on shear stress distribution in compound channels. The asymmetric shape was chosen to prevent any compensating effect and to simulate rivers having one flood plain. They revealed that the presence of the interaction between channel and flood plain significantly alters the values and the distribution of shear.

Myers (1978) used a Preston tube to measure shear stress distribution around the periphery of a compound channel, consisting of a deep section and one flood plain. Measurements were made with full cross-section flow and with flow confined to main channel. The results were used to quantify the momentum transfer due to interaction between the main channel flow and that its flood plain. Lateral momentum transfer throughout the main channel and flood plain was compared under isolated and interacting conditions.

Rajaratnam and Ahmadi (1979) studied experimentally interaction between the main channel and flood plain flows for a symmetric flood plain for smooth boundaries. Their results demonstrated the transport of the longitudinal momentum from the main channel to the flood plain. They found that the velocity profiles in the flood plain, and in the main channel above the level of the flood plain to be approximately similar if viewed with respect to the undisturbed flood plain velocity. Also empirical correlations have been found for the velocity and length scales. A possible method to estimate the loss in the flow capacity of the compound cross-section due to the interaction was indicated.

Rajaratnam and Ahmadi (1981) presented the results of an experimental study on the interaction between the flow in a wide main channel and the flood plain. This interaction region was shown to resemble a shear layer with some control exercised by the bed shear stress. The length of this interaction region as well as the reduction and increase of bed shear stress in the main channel and flood plain respectively, in dimensionless forms, was correlated with the ratio of the depth of flow to the depth of the main channel.

Wormleaton et al. (1982) performed a series of laboratory tests to measure the boundary shear stress in a compound channel. From these results, they calculated apparent shear stress across three different assumed main channel-flood plain interface plains (vertical, horizontal and diagonal). A statistical relationship for the apparent shear stress on the vertical interface was derived. The accuracy of the different discharge calculation methods was shown to be independent upon the assumptions on the magnitude of the apparent shear stress on the particular interface chosen. An apparent shear stress ratio was proposed which was found to be useful in selecting the best method of discharge calculation.

Knight and Demetriou (1983) performed experiments concerning the discharge characteristics; the boundary shear stress and boundary shear force distributions in a compound section. Equations were presented giving the shear force on the flood plains as a percentage of the total shear force in terms of two dimensionless parameters. Equations were also given for the proportion of the total flow which occurs in the various sub-areas. The division of flow based on linear portion of the areas is shown to be inadequate on account of the interaction between the main channel and flood plain flows.

Knight and Hamed (1984) presented experimental results concerning the boundary shear force distributions in a compound section comprising of one rectangular main channel and two symmetrically disposed flood plains. The flood plains were roughened progressively in six steps so that the influence of differential roughness between the flood plains and the main channel on the lateral momentum transfer process could be studied. Equations were presented giving the shear force on the flood plains as a percentage of the total shear force in terms of four dimensionless parameters. Supplementary equations were also presented giving the apparent shear force on vertical, horizontal and diagonal interfaces within the cross-section. The influence of momentum transfer between sub-areas on the vertical and lateral distribution of longitudinal velocity was also assessed.

Tominaga et al. (1989) investigated the three-dimensional turbulent structure, including turbulence driven secondary currents in an asymmetric compound open-channel. In this study, accurate measurements in fully developed compound open-channel flows were conducted by means of a fiber-optic Laser Doppler anemometer, and then the secondary currents, turbulence intensities and the Reynolds stresses were measured. Moreover, the effects of channel

Copyright © 2006 Taylor & Francis Group plc, London, UK

geometry and bed roughness on turbulent structure were examined.

Wormleaton and Merrett (1990) performed experiments for discharge and boundary-shear stress distribution in symmetric compound channel with flood plain sections of varying widths and roughness. These were used to assess the performance of several standard discharge calculation methods, which assume different locations of the interface between main channel and flood plain sub-areas. It was shown that these methods can produce large errors in total end, more particularly, component discharges. A modified form of the standard discharge calculation method was discussed, which made a more realistic allowance for interaction at the main channel-flood plain interface. It is achieved by the φ-indices method to characterize momentum transfer between adjacent sub-areas, into the calculation. This modified method was shown to be considerably more accurate than the standard methods in the calculation of total and component discharges. A tentative regression equation was presented for calculating φ-indices from easily identifiable cross-sectional characteristics.

Myers and Brennan (1990) demonstrated the effects of momentum transfer from main channel sections. Flow resistance relationships for the compound section, main channel and flood plains were presented in terms of Manning's and Darcy-Weisbach resistance coefficients and compared with that of simple channel sections.

Stephenson and Kolovopoulos (1990) discussed different methods for the apparent shear stresses between a main channel and its flood plains. The methods discussed include the simplistic method of considering the entire hydraulic cross-section as one, dividing the cross-section into independent sections, trying to find an interface with zero shear stress, or allowing for the shear stresses from a momentum balance. Based on evaluation of alternative steady state models, it was concluded that the area method is the most promising for computation of discharge and that the Prinos et al. equation (1985) gives accurate results for apparent shear stresses at the main channel-flood plain interface.

Smart (1992) studied the stage-discharge discontinuity in composite flood channels. From the experiments it was concluded that the increase in Manning's roughness coefficient was related to the ratio of flood plain drag to main channel driving force. The higher the ratio, the effective Manning's resistance coefficient for the main channel increases.

Kayatürk (1997) studied experimentally the interface Manning roughness coefficient in an artificially roughened compound channel to take into account the apparent shear stress occurring at the interface of the main channel and the flood plain. Associated with this roughness coefficient, a method is proposed to estimate the discharge in the compound channels.



Figure 1. Experimental set-up.

Myers and Lyness (1997) examined the ratios of total discharge to the bank-full discharge and main channel discharge to flood plain discharge and concluded that of the compound channel have homogeneous roughness, the ratios depend on geometry only.

Bousmar and Zech (1999) presented a 1-D model of compound channel flows called as the exchange discharge model. The interactions between main channel and flood plain are taken into account as a momentum transfer proportional to the product of the velocity gradient at the interface by the mass discharge exchanged through this interface due to turbulence. The momentum transfer formulated in this model as an additional head loss enabled practical water-profile computations.

Thornton et al. (2001) studied a predictive expression to permit the estimation of the apparent shear stress at the boundary of a main channel and flood plain as a function of the bed shear stress, average velocity, and depth in both main channel and flood plain and the blockage caused by the flood plain.

3 EXPERIMENTAL STUDY

The experimental part of this study was conducted in the Hydraulic Research Laboratory of General Directorate of State Hydraulic Works of Turkey (DSI). Experiments were made in a 18 m long compound channel made of concrete (Fig. 1).

Water is supplied from a constant head tank and discharge is adjusted by the valve on the supply pipe. At the entrance to the compound channel there is a sharp-crested rectangular weir to measure the discharge into the system. Dimensions of the channel cross-section are shown in Fig. 2.

Cubic concrete volumes shown in Fig. 3 are used to represent the macro roughness elements. Different arrangements of roughness elements were considered

Copyright © 2006 Taylor & Francis Group plc, London, UK

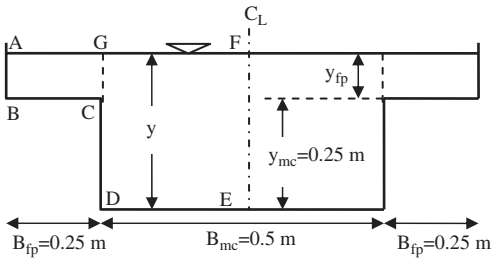


Figure 2. Dimensions of the channel cross-section.

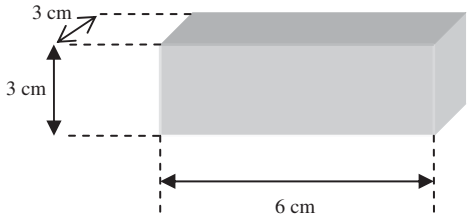


Figure 3. Dimensions of macro-roughness elements.

and each case is named as a roughness pattern. In total, four roughness patterns were used. Pattern-1 is concrete surface with no macro roughness elements. Pattern-2, Pattern-3 and Pattern-4 are as shown in Fig. 4.

AMCA type pitot-tube is used to collect the velocity data in the channel cross-section at about 7.3 m downstream of the entrance section. The velocity distribution is assumed to be symmetrical about the vertical axis (E-F) at centerline of the main channel and velocity data is taken only over the symmetrical half of the channel cross-section. Grid of velocity measuring points for Exp.1 are shown in Fig. 5.

Considering two different discharges with the four different roughness patterns, 8 sets of experiments were conducted. Data describing the experimental cases are given in Table 1. Q_w is the weir discharge, Q_i is the discharge obtained from integration of the measured velocity field over the cross-section, y is water depth, Q_{mc} is the discharge in the main channel, and Q_{fp} is the discharge in one flood plain. The differences between the weir and integral values of the total discharge are less than 5%. Integrated values of discharge will be used in the following analyses. Contourlines of velocity on the symmetrical half of the channel is shown for Exp. 1 in Fig. 6.

4 ANALYSIS

4.1 *Determination of wall shear stresses*

Wall resistance must be determined to express the force balance in the flow direction. Measured velocity

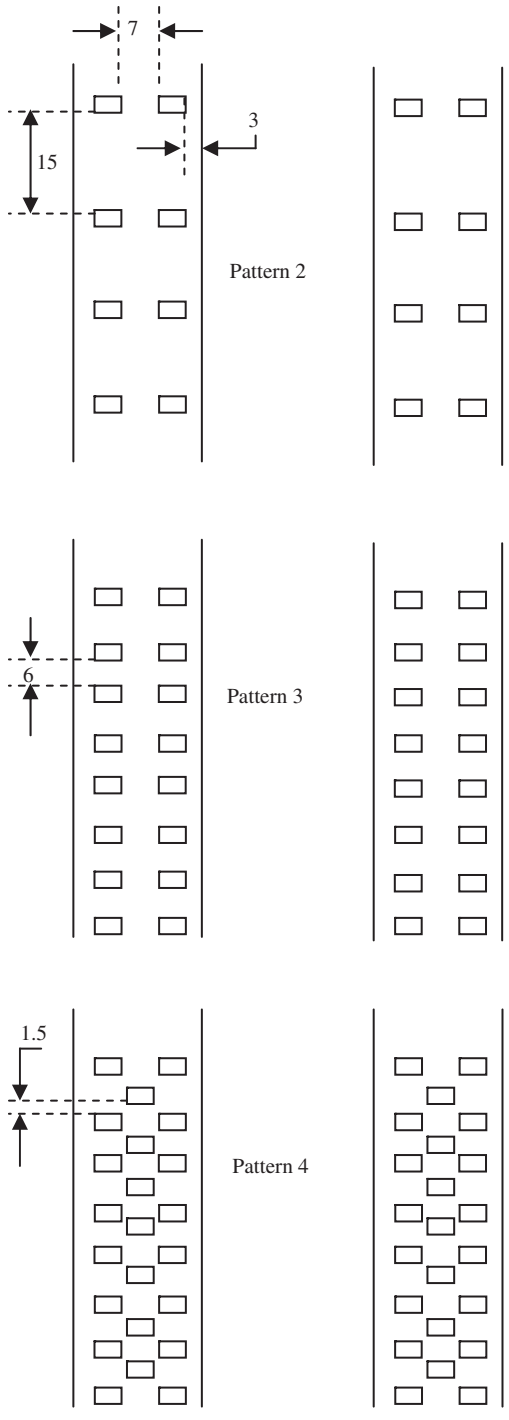


Figure 4. Plan views of macro roughness elements on the flood plains for Patterns 2, 3 and 4. (Dimensions are in cm).

Copyright © 2006 Taylor & Francis Group plc, London, UK

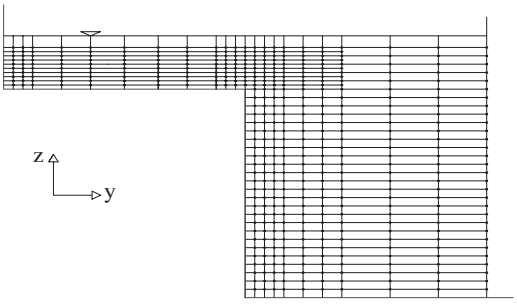


Figure 5. Velocity measurement points in Exp.1.

Table 1. Experiments conducted in this study.

Exp. No.	Rough. Pattern	Q_w (m^3/s)	Q_i (m^3/s)	y (m)	Q_{mc} (m^3/s)	Q_{fp} (m^3/s)
1	Pattern 1	0.180	0.181	0.314	0.077	0.013
2	Pattern 2	0.180	0.180	0.327	0.082	0.008
3	Pattern 3	0.180	0.188	0.337	0.084	0.010
4	Pattern 4	0.180	0.187	0.333	0.085	0.008
5	Pattern 1	0.200	0.209	0.333	0.086	0.018
6	Pattern 2	0.200	0.207	0.361	0.088	0.016
7	Pattern 3	0.200	0.209	0.367	0.088	0.017
8	Pattern 4	0.200	0.209	0.362	0.090	0.015

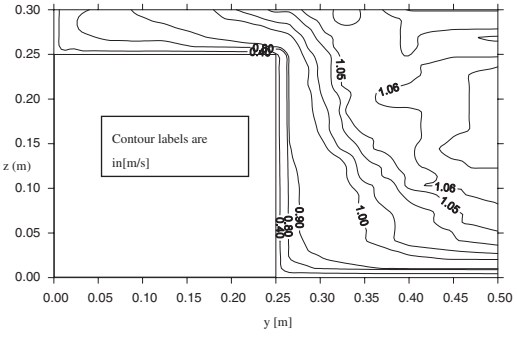


Figure 6. Velocity contour lines for Exp.1.

data is utilized to evaluate the wall shear stresses. It is assumed that the measured velocity all along the wetted perimeter (except the flood plain covered by macro roughness elements) obey the logarithmic wall functions. The law of the wall is written as

$$U^+ = \frac{1}{\kappa}\ln(\eta^+) + D - E \quad (1)$$

$$U^+ = u/U_* \quad (2)$$

$$\eta^+ = \eta U_* / \nu \quad (3)$$

$$U_* = \sqrt{\tau_w/\rho} \quad (4)$$

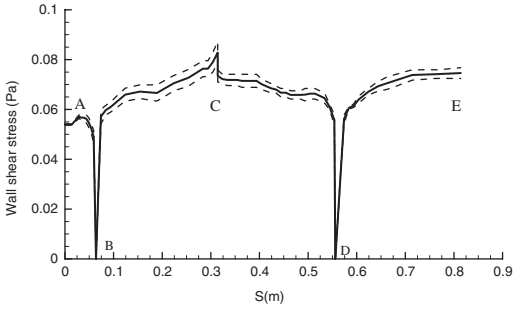


Figure 7. Wall shear stress distributions for Exp. 1.

where U^+ is dimensionless velocity, u is point velocity, η is distance normal to the wall, U_* is the shear velocity, τ_w is the wall shear stress, ρ is fluid density, ν is kinematic viscosity of the fluid, $\kappa = 0.41$, $D = 5.3$, and E is a parameter dependent on surface roughness. After Schlichting (1979),

$$E = \frac{1}{\kappa}\ln(\varepsilon^+) - 3.0 \quad (5)$$

$$\varepsilon^+ = \varepsilon U_* / \nu \quad (6)$$

where ε is the equivalent sand roughness height. Equation 1 is valid in the first 20% of the boundary layer for $\eta^+ > 70$. Only a single point velocity data in the vicinity of the wall is enough to determine the shear velocity from Equation 1 and therefore the wall shear stress provided that the limitations for the existence of the equation are not violated. The wall shear stress along portions of the wetted perimeter without macro roughness elements will be determined by using the wall function method described above. In Exp. 1 and Exp. 5 there are no macro roughness elements in the channel, therefore, the wall function method is applicable for the complete perimeter of the cross-section. Wall shear stress distribution for Exp. 1 is shown in Fig. 7 as function of distance s along the wetted perimeter. Distance s starts from the free surface of the left flood plain (point A in Fig. 2) and ends at the mid point of the channel along the symmetry line (point E). The dashed lines show the wall shear stresses obtained from the first and the second measurement points of velocity next to the wall and the solid line is the average of them which is used in the analysis.

4.2 *Channel slope*

The wall shear stress integrated along the wetted perimeter is equated to the component of gravity force acting in the flow direction.

$$\int_A^E \tau_w \, ds = \frac{\gamma A S_e}{2} \quad (7)$$

Copyright © 2006 Taylor & Francis Group plc, London, UK

where γ is specific weight of water, A is flow area and S_e is the energy slope. For uniform flow conditions S_e obtained from Equation 7 must be equal to the channel bottom slope. The channel slopes obtained from data of Exp. 1 and Exp. 5 are 0.00221 and 0.00223 respectively. The average value $S_e = 0.00222$ is used in the computations.

4.3 *Force balance in the flood plain*

The compound channel (Fig. 2) is divided into main and sub-channels through the vertical interface C-G. Momentum conservation can be applied to the main channel and the flood plain separately. However, the friction force acting along the interface C-G must be known. Macro roughness elements are placed along the horizontal line B-C of the flood plain only. Therefore, the wall shear stresses in all experimental cases can be determined by the wall function method except when the line B-C is covered by the macro roughness elements. The equilibrium of forces acting on the left half main channel in the flow direction can be expressed as

$$\frac{\gamma A_m S_e}{2} - \int_C^E \tau_w \, ds - F_{int} = 0 \tag{8}$$

where A_m is the flow area of the main channel, F_{int} is the friction force acting on the interface line C-G between the main channel and the flood plain. A similar expression for the flood plain would be

$$\gamma A_{fp} S_e - \tau_{fp} P_{fp} + F_{int} = 0 \tag{9}$$

where A_{fp} is the effective flow area of the flood plain, τ_{fp} is the average wall shear stress in the flood plain, P_{fp} is the wetted perimeter (from A to C) of the flood plain. The effective flow area of the flood plain is obtained by subtracting the roughness area (normal to flow direction) averaged for unit length of the channel from the cross-sectional area of the flood plain. Friction force at the interface, F_{int}, is in the direction of the flow augmenting the gravity component. Equation (9) can be re-written in terms of effective energy slope, S_{fp}, in the flood plain which is increased due to the friction at the main channel interface.

$$\gamma A_{fp} S_{fp} - \tau_{fp} P_{fp} = 0. \tag{10}$$

Combining Equation 9 and Equation 10 and solving for S_{fp} gives

$$S_{fp} = S_e + \frac{F_{int}}{\gamma A_{fp}} \tag{11}$$

Manning's equation can now be applied to the flood plain to determine the equivalent roughness coefficient for the flood plain.

$$(n_{fp})_{eq} = \frac{A_{fp} R_{fp}^{2/3} S_{fp}^{1/2}}{Q_{fp}} \tag{12}$$

The roughness coefficient for the macro roughness elements, n_{mr}, is determined from

$$n_{mr} = \left[\frac{(n_{fp})_{eq}^2 (y_{fp} + B_{fp}) - y_{fp} n_c^2}{B_{fp}} \right]^{1/2} \tag{13}$$

where n_c is the Manning's roughness coefficient for the concrete side wall of the flood plain.

Table 2. Results of the momentum analysis.

Exp. No	F_{int} (N)	S_{fp} –	n_{mr} –	V_r –
1	0.3672	0.00456	0.0113	1.000
2	0.4495	0.00469	0.0267	0.964
3	0.5608	0.00500	0.0263	0.945
4	0.4588	0.00469	0.0287	0.914
5	0.3548	0.00396	0.0113	1.000
6	0.7541	0.00506	0.0249	0.975
7	0.8166	0.00519	0.0254	0.959
8	0.7209	0.00502	0.0259	0.936

4.4 *Results and discussions*

Data of Exp. 1 and Exp. 5 are used to determine the Manning's roughness for the concrete surface without macro roughness elements. The equivalent sand roughness height is taken as $\varepsilon = 0.0005$ m and the corresponding Manning's value is obtained as $n_c = 0.0117$. This value is obtained directly from Eq. 7 by a single channel treatment.

Data of experiments 2, 3, 4 and 6, 7, 8 are utilized to determine the Manning's roughness for the corresponding macro roughness patterns by the compound-composite channel procedure described through equations 8∼13. The macro roughness is assumed to depend on volume ratio defined as the ratio of volume of flow area in the flood plain averaged for unit length of the channel divided by volume of flood plain without macro roughness elements. The friction force at the interface, the modified energy slope for the flood plain, Manning's roughness for the macro roughness elements and the volume ratio are shown in Table 2.

Roughness values obtained for Exp. 1 and Exp. 5 are very close to the value obtained from single channel solution. Manning's n for flood plain (n_{mr}) is shown as function of volume ratio in Fig.8. Roughness increases more than twice when macro elements are introduced on the flood plain. Dependence of n_{mr} over the volume ratio is very weak or not clear due to less number of data available.

Copyright © 2006 Taylor & Francis Group plc, London, UK

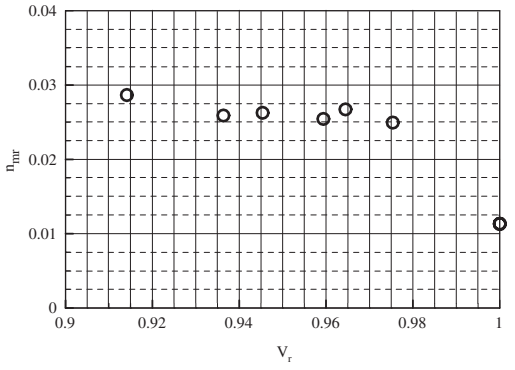


Figure 8. Roughness coefficient for macro roughness elements as function of volume ratio.

5 CONCLUSIONS

Manning's roughness for macro roughness elements on the flood plains of compound channels is investigated through laboratory experiments. The arbitrariness in determination of Manning's roughness for macro roughness elements may be reduced by use of effective flow area for the flood plains in the Manning's equation. More experimental data is necessary to set-up a functional dependence of Manning's n on geometric characteristics of macro roughness elements.

REFERENCES

Bousmar, D., and Zech, Y., 1999. "Momentum Transfer for Practical Flow Computation in Compound Channels", Journal of Hydraulic Engineering, Vol. 125, No. 7, pp.696–706.

Kayatürk, U., 1997. "Interface Manning Roughness Coefficient for Compound Channels", M. S. Thesis, METU, Ankara, Turkey.

Knight, D. W., and Demetriou, J. D., 1983. "Flood Plain and Main Channel Flow Interaction", Journal of Hydraulic Engineering, Vol. 109, No. 8, pp.1073–1092.

Knight, D. W., and Hamed, M.E., 1984. "Boundary Shear in Symmetrical Compound Channels", Journal of Hydraulic Engineering, Vol. 110, No. 10, pp.1412–1430.

Myers R. C., and Elsawy, E. M. 1975. "Boundary Shear in Channel with Flood Plain", Journal of Hydraulics Division, Vol. 101, No. Hy7, pp.993–1025.

Myers W. R. C., 1978. "Momentum Transfer in a Compound Channel", Journal of Hydraulic Research, vol. 16, No. 2, pp.139–150.

Myers W. R. C., and Brennan, E. K., 1990. "Flow Resistance in Compound Channels", Journal of Hydraulic Research, Vol. 28, No. 2, pp.141–155.

Myers, R. C., and Lyness, J. F., 1997. "Discharge Ratios in Smooth and Rough Compound Channels", Journal of Hydraulic Engineering, Vol. 123, No. 6, pp.182–188.

Prinos, P., Townsend, R., and Tavoularis, S., 1985. "Structure of Turbulence in Compound Channel Flows", Journal of Hydraulic Engineering, Vol. 111, No. 9, pp.1246–1261.

Rajaratnam, N., and Ahmadi, R., 1979. "Interaction between Main Channel and Flood Plain Flows", Journal of Hydraulic Division, Vol. 105., No. HY5, pp.573–588.

Rajaratnam, N., and Ahmadi, R., 1981. "Hydraulics of Channels with Flood Plains", Journal of Hydraulic Research, Vol. 9., No. 1, pp.43–59.

Schlichting, H., 1979. "*Boundary Layer Theory*", McGraw Hill Book Company, New York.

Smart, G. M., 1992. "Stage-Discharge Discontinuity in Composite Flood Plains", Journal of Hydraulic Research, Vol. 30, No. 6, pp.817–833.

Stephenson, D., and Kolovopoulos, P., 1990. "Effects of Momentum Transfer in Compound Channels", Journal of Hydraulic Engineering, Vol. 116, No. 12, pp.1512–1522.

Tominaga, A., Nezu, I., Ezaki, K., and Nakagawa, H., 1989. "Three-dimensional Turbulent Structure in Straight Open Channel Flows", Journal of Hydraulic Research, Vol. 27, No. 1, pp.149–173.

Thornton, C., Abbot, S. R., Morris, C. E., Fischenich, J.C., 2001. "Calculating Shear Stress at Channel-Overbank Interfaces in Straight Channels with Vegetated Flood Plains", Journal of Hydraulic Engineering, Vol. 126, No. 12, pp.929–936.

Wormleaton, P. R., Allen, J., and Hadjipanos, P., 1982. "Discharge Assessment in Compound Channel Flow", Journal of the Hydraulics Division, vol. 108, No. HY9, pp.975–994.

Wormleaton, P. R., and Merrett, D.J., 1990. "An Improved Method of Calculation for Steady Uniform flow in Prismatic Main Channel-Flood Plain Sections", Journal of Hydraulic Research, Vol. 28, No. 2, pp.157–174

Yen, C., and Overton, D. E., 1973. "Shape Effects on Resistance in Flood plain Channels", Journal of the Hydraulics Division, Vol. 99, No. HY1. pp.219–238.

Copyright © 2006 Taylor & Francis Group plc, London, UK

Discretization of the friction term in the shallow water equations

J. Murillo, J. Burguete, P. Brufau & P. Garcia-Navarro
Fluid Mechanics CPS, University of Zaragoza, Spain

ABSTRACT: The numerical simulation of unsteady open channel flows is very commonly performed using the one-dimensional or two-dimensional shallow water models. Friction is one of the relevant forces included in the momentum equation. The friction term participates in the Saint Venant mathematical model as a non-linear sink of momentum. The system is a set of partial differential equations that requires numerical resolution in almost all cases of interest. Therefore, a complete analysis of the role played by friction in an open channel flow model does involve the question of the numerical simulation as well as those of the mathematical modeling. Few previous works have treated in detail the consequences of the discretization of the friction term. The most commonly reported procedure is the pointwise discretization of the term independently of the methodology used for the rest of the system, for simplicity reasons. The numerical stability conditions are revisited in cases of dominant friction terms. Usual numerical stability conditions are based on the prevalence of convective terms and may not be sufficient in cases of high roughness. In many cases, the experience indicates that a spatial grid refinement and a time step size reduction becomes necessary to achieve stable solutions. A new condition, complementary to the basic Courant-Friedrichs-Lewy condition, is used. As the condition leads to a requirement on the spatial grid size it will be shown efficient only in 1D cases. The implicit upwind discretizaton of the friction terms will be shown the best option when dealing with high roughness unsteady problems in two dimensions.

1 INTRODUCTION

The one-dimensional shallow water model involves cross sectional averaging of the original flow equations if not only trivial situations have to be handled. One of the main consequences of such cross sectional average is that the viscous flow boundary condition at solid walls and bottom is transformed into a drag/friction force source term. The form of this friction force term is closely related to the underlying turbulence model. Actually, the presence of the wall roughness term is the only trace of the flow turbulence in the mathematical model.

To model friction, empirical or semi-empirical methods have traditionally been applied. Chezy's model, proposed in the 18th century, was one of the first. Later, in the 19th century, Darcy (Darcy, 1858) and Gauckler-Manning (Gauckler, 1867), (Manning, 1890) proposed analogous models. These three models, despite their very early origin, are still widely used nowadays to compute the effect of roughness in Hydraulics. They are all based in an empirical coefficient dependent on the surface roughness as well as on the flow characteristics, and can be found in tabular form in many references as, for instance, (Chow, 1959).

The friction term participates in the Saint Venant mathematical model as a non-linear sink of momentum. The system is a set of partial differential equations that requires numerical resolution in almost all cases of interest. Therefore, a complete analysis of the role played by friction in an open channel flow model does involve the question of the numerical simulation as well as those of the mathematical modeling. Few previous works have treated in detail the consequences of the discretization of the friction term. The most commonly reported procedure (Huang & Song 1985), (Garcia-Navarro et al., 1999), is the pointwise discretization of the term independently of the methodology used for the rest of the system, for simplicity reasons. A different option is also considered in this work and their ability to produce conservative solutions is compared in a case of steady open channel flow with analytical solution.

Finally, the interaction between a dominant friction term in the equations and stability constraints is investigated. Usual numerical stability conditions are based on the prevalence of convective terms and may not be sufficient in cases of high roughness. In many cases, the experience indicates that a spatial grid refinement and a time step size reduction becomes necessary to achieve stable solutions. Liggett and Cunge (Liggett & Cunge, 1997), proposed a time step limit dictated by the friction coefficient, starting from the analysis of the linearized equations. Even though this criterion may help controlling stability in some cases, it is not a

Copyright © 2006 Taylor & Francis Group plc, London, UK

reliable condition in general cases of flow over rough, irregular beds. A more general condition leading to a requirement on the spatial grid size will be derived and tested in a real case.

2 1D DISCRETIZATION OF THE FRICTION TERM

In a general conservative form, the 1D shallow water equations can be expressed

$$\frac{\partial \mathbf{u}(x,t)}{\partial t} + \frac{d\mathbf{F}(x,\mathbf{u})}{dx} = \mathbf{H}(x,\mathbf{u}) \tag{1}$$

where **U** is the vector of conserved variables, **F** the vector of fluxes and **H** the vector of source terms. The justification of the particular form of (1) can be found in (Burguete & Garcia-Navarro, 2001). Our interest is led by the numerical modelling of one-dimensional shallow water flows of practical application in Hydraulics such as river flows. In that case

$$\mathbf{u} = \begin{pmatrix} A \\ Q \end{pmatrix}, \quad \mathbf{F} = \begin{pmatrix} Q \\ \frac{Q^2}{A} + gI_1 \end{pmatrix}, \quad \mathbf{H} = \begin{pmatrix} 0 \\ g\left[I_2 + A\left(S_0 - S_f\right)\right] \end{pmatrix}$$

where Q is the discharge, A is the wetted cross section, g is the acceleration of gravity and S_0 is the bed slope. The rest of the terms account for pressure forces and for friction forces, with S_f associated to wall friction and represented by the empirical Manning law.

2.1 *Unified discretization*

The conservative form of the system of differential equations (1) can be solved by means of a conservative scheme. The following vector is defined for convenience:

$$\mathbf{G}_{i+(1/2)} = \left(\mathbf{H} - \frac{\delta \mathbf{F}}{\delta x}\right)_{i+(1/2)}$$

$$\mathbf{H}_{i+(1/2)} = \begin{pmatrix} 0 \\ g\left[\frac{\delta I_1}{\delta x} - \overline{A}\left(\frac{\partial z_s}{\partial x} + \overline{S_f}\right)\right] \end{pmatrix}_{i+(1/2)} \tag{2}$$

with z_s the water surface level and using the notation $\delta f_{i+(1/2)} = f_{i+1} - f_i$ and $\overline{f} = (f_{i+1} + f_i)/2$. The unified discretization of the friction term consists of discretizing flux, friction and other source terms in the equation in a similar form. A general conservative scheme with unified discretization can be expressed as (Burguete & Garcia-Navarro, 2001), (Burguete & Garcia-Navarro, 2004);

$$\left(1 - \theta \Delta t \mathbf{K}_i^n\right) \Delta \mathbf{u}_i^n = \Delta t \left(\mathbf{G}_{i-(1/2)}^L + \mathbf{G}_{i+(1/2)}^R\right) \tag{3}$$

where $\mathbf{K} = \partial \mathbf{H}/\partial \mathbf{U}$ is the source term Jacobian, $\theta \in [0,1]$ is a coefficient controlling the implicitness of the source term and $\mathbf{G}^{L,R}$ represents the wave discretization particular to each numerical scheme. See (Burguete et al., 2006) for more details.

2.2 *Pointwise discretization*

Due to the form of the friction source term, it is common to find applications using a pointwise discretization. In this case, the source term is split in two terms, one of them involving only the friction term:

$$\mathbf{H} = \mathbf{R} + \mathbf{S} \tag{4}$$

with

$$\mathbf{R} = \begin{pmatrix} 0 \\ -gAS_f \end{pmatrix}, \quad \mathbf{S} = \begin{pmatrix} 0 \\ g\left(I_2 - AS_0\right) \end{pmatrix} \tag{5}$$

Defining now the vector:

$$\mathbf{G}_{i+(1/2)} = \left(\mathbf{S} - \frac{\delta \mathbf{F}}{\delta x}\right)_{i+(1/2)} \tag{6}$$

A conservative scheme is then applied to all the terms except the friction term that is added as:

$$\left(1 - \theta \Delta t \mathbf{L}_i^n\right) \Delta \mathbf{u}_i^n = \Delta t \left(\mathbf{R}_i^{n+\theta} + \mathbf{G}_{i-(1/2)}^L + \mathbf{G}_{i+(1/2)}^R\right) \tag{7}$$

where $\mathbf{L} = \partial \mathbf{S}/\partial \mathbf{U}$ is the Jacobian of the non-frictional source terms.

Even though this discretization is widespread and recommended in several works (Huang & Song 1985), (Garcia-Navarro et al., 1999) due to its simplicity and the possibility to use a fully implicit discretization of the friction term, it can be shown that it produces the unbalance of the friction term and the rest of the terms in the equation in steady state.

Explicit numerical schemes applied the solve the unsteady Saint-Venant equations are said to be numerically stable if the time step and grid size chosen are linked by the Courant-Friedrichs-Lewy condition:

$$\Delta t \leq \frac{\Delta x}{|u| + c} \tag{8}$$

with $u = Q/A$ the average flow velocity and $c = \sqrt{gA/B}$ the critical celerity, where B is the cross

Copyright © 2006 Taylor & Francis Group plc, London, UK

sectional top width. This is a stability condition based on the advective character of the equations.

The friction source term in the Saint-Venant equations is often one of the dominant terms, especially river flow or surface irrigation applications, and it is essential to establish a stability conditions that takes them into account. Despite a few earlier efforts in this sense, as (Liggett & Cunge, 1997) for instance, we believe that stability conditions of the Saint-Venant equations with important friction terms has not been adequately addressed.

Two particular stability conditions will also be analyzed for the non-linear case. Even though they are not general, they can be useful to throw some light on the conditions that must be fulfilled in order to avoid instabilities due to the friction term.

3 1D STABILITY CONSTRAINTS

One of the traditional forms to analyze the stability of a numerical scheme is to study the amplification of the small perturbations that it produces. Using the Gauckler-Manning model and assuming uniform base flow for simplicity and a sinusoidal form can be chosen for the perturbation, in the particular case of long waves ($k \to 0$) a particular condition can be obtained since the a notable simplification is enabled:

$$\left|1 - \Delta t \frac{2gS_f}{u}\right| \leq 1 \tag{9}$$

where,again, the normal flow condition has been used ($S_0 = S_f$). The following restriction, independent of the grid size is obtained:

$$\Delta t \leq \frac{u}{gS_f} \tag{10}$$

The detailed derivation is in (Burguete et al., 2006). Note that, contrary to the standard Courant-Friedrichs-Lewy condition (8), the present stability condition restricts the time step size independently of the spatial step. Thus, instabilities due to the friction term are most likely in coarse grids. This condition was already considered by Liggett and Cunge (Liggett & Cunge, 1997).

On the other hand, a non-linear stability analysis assuming flat bottom and surface levels leads (see (Burguete et al., 2006)) to the evidence that the stability conditions disappear when using an implicit discretization of the source term. Therefore, the implicit treatment ($\theta = 1$) of the friction term is recommended in case of using a coarse mesh in presence of strong roughness.

Finally, the analysis of the stability constraint in presence of friction and adverse slope provides the result that the grid size appears to be limited by the hydraulic radius and the roughness in order to enforce stability on the numerical solution. All the details can be found in (Burguete et al., 2006). If the Gauckler-Manning friction model is used:

$$\Delta x \leq \frac{2R^{\frac{4}{3}}}{gn^2} \tag{11}$$

where R is the hydraulic radius and n is the Manning roughness coefficient. It is easy to show that always, when the CFL condition holds, this condition is stronger than previous time step restrictions for subcritical flow.

4 2D ANALYSIS

When performing a two-dimensional modelling of the flow, it has been previously stated (Brufau et al. 2004) that a pointwise explicit discretization of the friction term produces numerical oscillations when roughness is high. Furthermore, at the wetting/drying fronts, characterized by small values of water depth, this term dominates over any other influence. To avoid friction-driven oscillations, the following conditions must be ensured:

$$\begin{aligned}
&(hu)_i^{n+1} \geq 0, \quad \text{if } (hu)_i^n > 0 \\
&(hu)_i^{n+1} \leq 0, \quad \text{if } (hu)_i^n < 0 \\
&(hv)_i^{n+1} \geq 0, \quad \text{if } (hv)_i^n > 0 \\
&(hv)_i^{n+1} \leq 0, \quad \text{if } (hv)_i^n < 0
\end{aligned} \tag{12}$$

It is easy to show that a pointwise implicit discretization of the friction terms leads to:

$$\begin{aligned}
(hu)_i^{n+1} &= \frac{(hu)_i^*}{1 + g\Delta t\,(S_{fx}/u)_i^*} \\
(hv)_i^{n+1} &= \frac{(hv)_i^*}{1 + g\Delta t\,(S_{fy}/v)_i^*}
\end{aligned}$$

where the superscript $*$ stands for the frictionless updated values and that inconditionally holds 12. On the other hand, it is straightforward to see (Murillo, 2006) that a pointwise explicit discretization of the friction terms leads to a conditional stability where:

$$\Delta t \leq \min\left(\frac{1}{g\,(S_f/|\mathbf{u}|)_i^*}\right)$$

involving the modulus of (S_{fx}, S_{fy}). Finally, it is not difficult to see that an explicit upwind discretization

Copyright © 2006 Taylor & Francis Group plc, London, UK

of the friction terms is compatible with 12 provided that

$$\Delta t \leq \min\left(\left(\frac{gn^2\,|\tilde{\mathbf{u}}_\mathbf{k}|\,d_n l_k}{\min(A_i,A_j)\tilde{h}_k^{4/3}}\right)^{-1}\right)_{k=1,Nedge}$$

where i and j are the labels of the cells separated by every edge k and the $\tilde{h}, \tilde{u}$ variables are evaluated at the average state between them, l_k is the length of edge k and d_n is the distance between cell centers measured normal to the edge.

5 1D EXAMPLES

MacDonald (MacDonald et al., 1997) proposed a series of theoretical steady open channel flow test cases with analytical solution. In all of them sloping bed and friction term are considered. The steady Saint-Venant equations

$$Q = \text{const.}$$
$$\frac{\partial}{\partial x}\left(\frac{Q^2}{A} + gI_1\right) = g\left[I_2 + A(S_0 - S_f)\right] \qquad (13)$$

Given a constant discharge and an analytical water depth function, the steady solutions can be found from the momentum equation:

$$S_0 = S_f + \frac{1}{gA}\left[-gI_2 + \frac{\partial}{\partial x}\left(\frac{Q^2}{A} + gI_1\right)\right] \qquad (14)$$

where S_f is modelled via the Gauckler-Manning friction law. Then, the channel bed form can be obtained.

One of these test cases has been chosen to show the influence of the discretization of the friction term on the quality of the solution. A subcritical flow in a channel of rectangular cross section 10 m wide and 150 m long is assumed. The steady discharge is 20 m^3/s and the bed material is characterized by a friction Manning coefficient 0.03 $sm^{-\frac{1}{3}}$. The water depth is defined by the function:

$$h = 0.8 + 0.25\exp\left[-\frac{135}{4}\left(\frac{x-75}{150}\right)^2\right] \qquad (15)$$

The water depth and surface water level longitudinal profiles are displayed in Figure 1 and Figure 2 for this test case.

Figure 3 and Figure 4 show the numerical results obtained using the first order upwind scheme and both the unified and pointwise methods for the friction term. It can be seen that only the unified method is able to provide a right balance and a perfect conservation in the steady discharge.

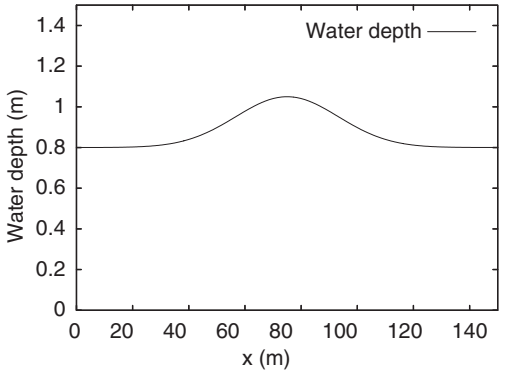


Figure 1. Analytical depth in the MacDonald's test case.

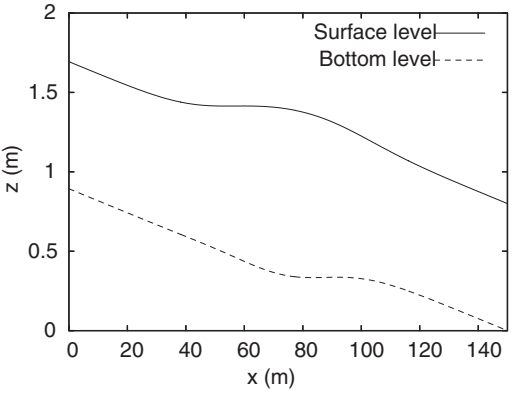


Figure 2. Surface and bottom levels in the MacDonald's test case.

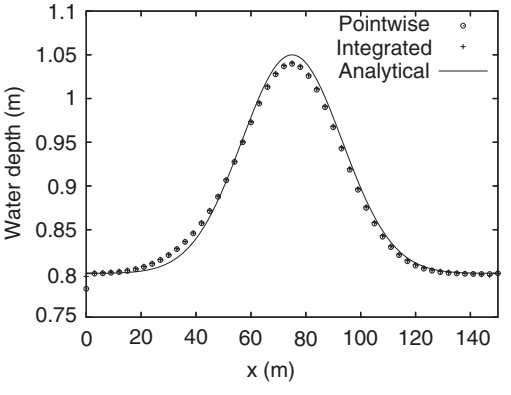


Figure 3. Depth with pointwise and unified treatment of the friction term in the MacDonald test case. The first order upwind scheme was used on a 50 cell grid.

Copyright © 2006 Taylor & Francis Group plc, London, UK

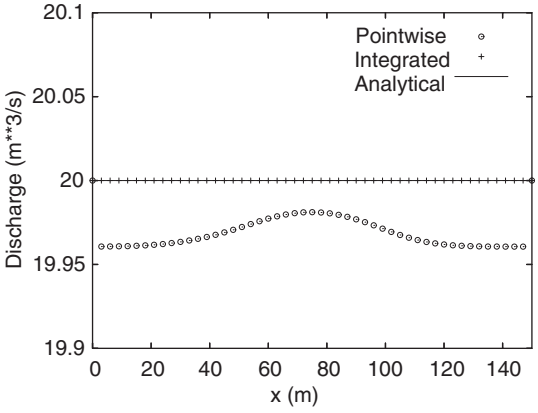


Figure 4. Discharge with pointwise and unified treatment of the friction term in the MacDonald test case. The first order upwind scheme was used on a 50 cell grid.

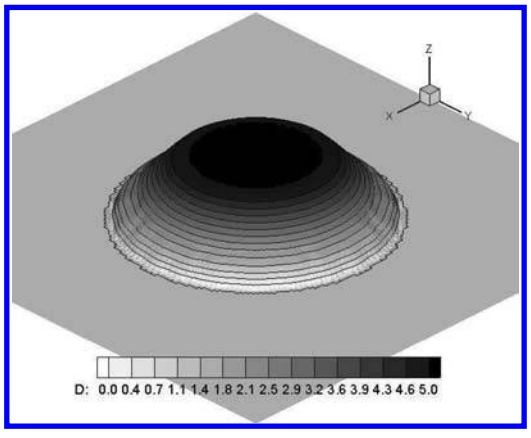


Figure 5. Water level at t = 20s in the 2D radial dam break test case. Implicit pointwise discretization of the friction terms.

6 2D EXAMPLE

A radial dam break flow is used as two-dimensional example. In a flat 4000 m × 4000 m closed domain, the following initial conditions are assumed:

$$r = \sqrt{x^2 + y^2} \leq 800m \quad h = 5m, u = 0, v = 0$$

$$r = \sqrt{x^2 + y^2} > 800m \quad h = 0.01m, u = 0, v = 0$$

The Manning roughness coefficient is $n = 0.03$. 51200 triangular cells have been used to generate Figures 5 and 6. They show the shape of the water level after 20 seconds and correspond to computations where, respectively, a pointwise implicit discretization and an upwind explicit discretization of the friction terms

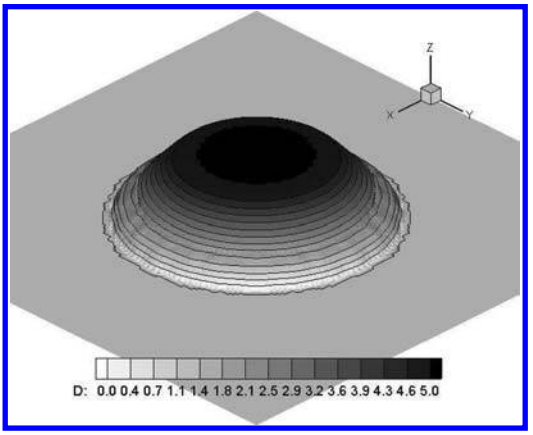


Figure 6. Water level at t = 20 s in the 2D radial dam break test case. Explicit upwind discretization of the friction terms.

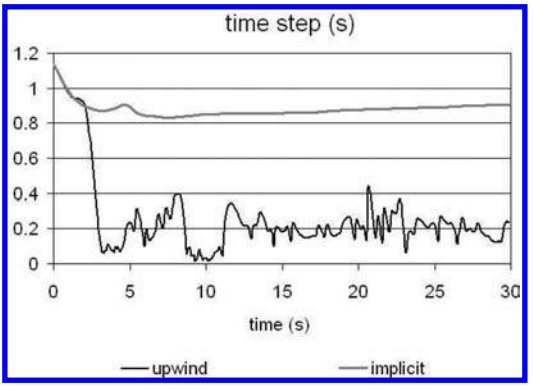


Figure 7. Time evolution of the time step size in the 2D radial dam break test case comparing pointwise implicit and upwind explicit discretization of the friction terms.

have been used. The results are almost identical and both stable. However, the computational cost of such stability is different as Figure 7 shows, where the variations in time of the time step size compatible with stability has been plotted for each method.

7 1D RIVER FLOW APPLICATION

Neila River flows through a mountain region of central Spain. It is highly irregular in shape and steep (with average slope around 20% in some reaches). The base flow is very low (around $1\,m^3/s$) and the stony but vegetated river bed is associated to a high friction factor $n = 0.05\,sm^{-\frac{1}{3}}$. A reach of 18 Km has been characterized by means of 48 cross sections.

The physical conditions of steep slope, low base discharge and high roughness make this river a challenging test case for the numerical schemes to be able

Copyright © 2006 Taylor & Francis Group plc, London, UK

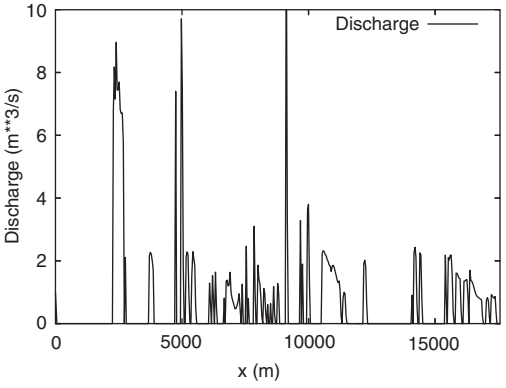


Figure 8. Neila river test case. Discharge using $\Delta x = 40\,m$ and CFL = 0.25.

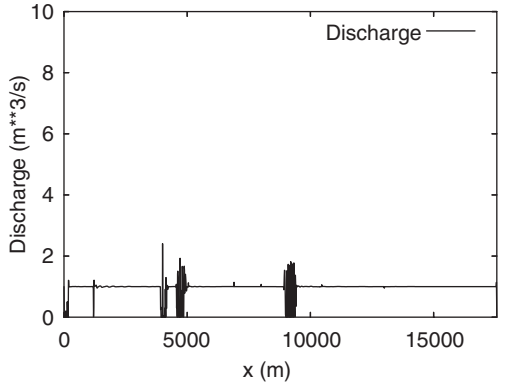


Figure 9. Neila river test case. Discharge using $\Delta x = 10\,m$ and CFL = 0.25.

to produce a stable solution. The water depth in the base flow steady profile can be as low as 4 *cm* in some parts producing, from the stability condition (11) the following requirement:

$$\Delta x \leq 1.1m \tag{16}$$

Figures 8–19 display the results obtained using the first order upwind scheme to convergence to the base flow steady state with dry bed initial conditions. The scheme has been provided with a semi-implicit unified discretization of the friction term. Several spatial grid and time step sizes have been evaluated to estimate their influence in the numerical results. In all cases, the following water depth threshold value, derived from (11) was imposed

$$h_i^n \leq \left(\frac{gn^2\Delta x}{2}\right)^{\frac{3}{4}} \Rightarrow Q_i^n = 0 \tag{17}$$

This condition is necessary to stabilize the solution since it avoids irrealistic growing tendencies in the

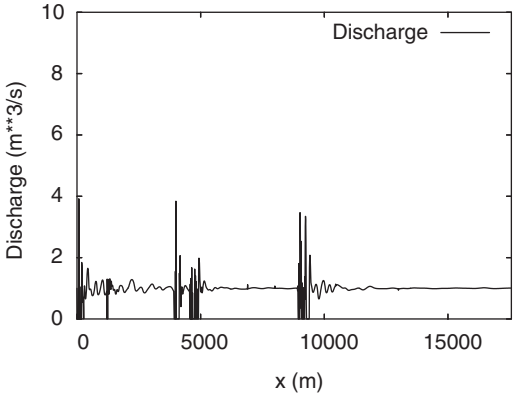


Figure 10. Neila river test case. Discharge using $\Delta x = 10\,m$ and CFL = 0.02.

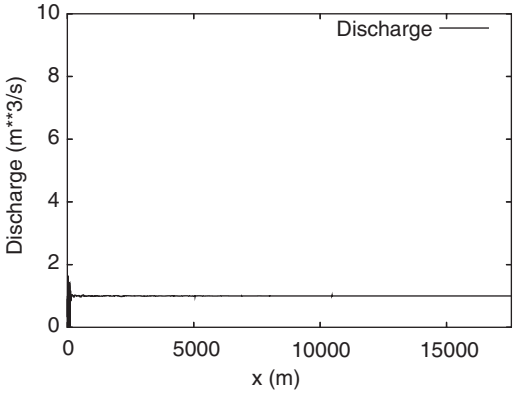


Figure 11. Neila river test case. Discharge using $\Delta x = 2\,m$ and CFL = 0.25.

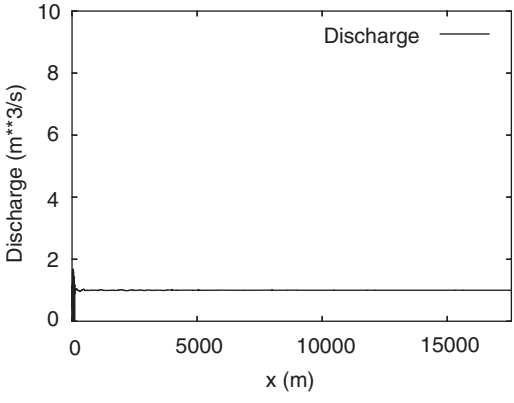


Figure 12. Neila river test case. Discharge using $\Delta x = 2\,m$ and CFL = 0.02.

Copyright © 2006 Taylor & Francis Group plc, London, UK

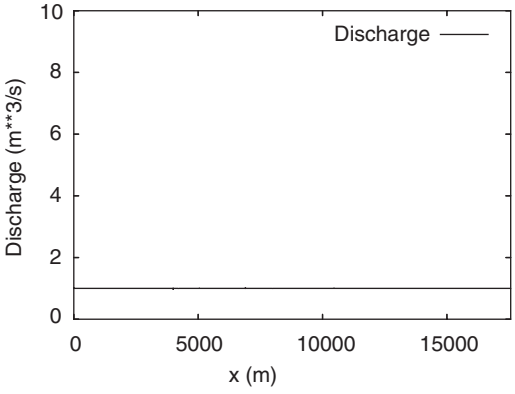


Figure 13. Neila river test case. Discharge using $\Delta x = 1\,m$ and CFL = 0.9.

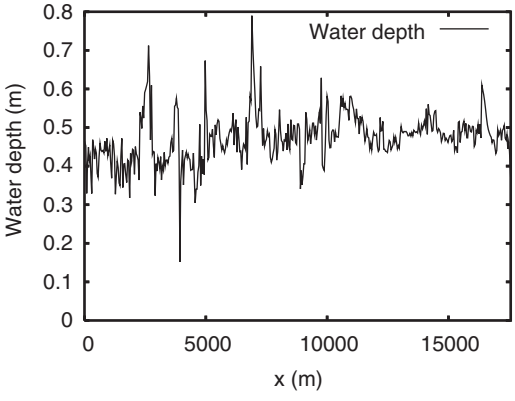


Figure 14. Neila river test case. Water depth using $\Delta x = 40\,m$ and CFL = 0.25.

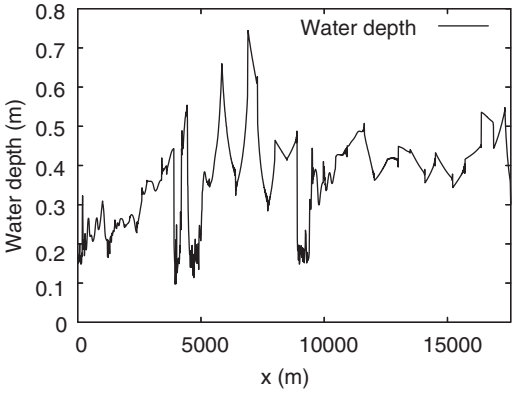


Figure 15. Neila river test case. Water depth using $\Delta x = 10\,m$ and CFL = 0.25.

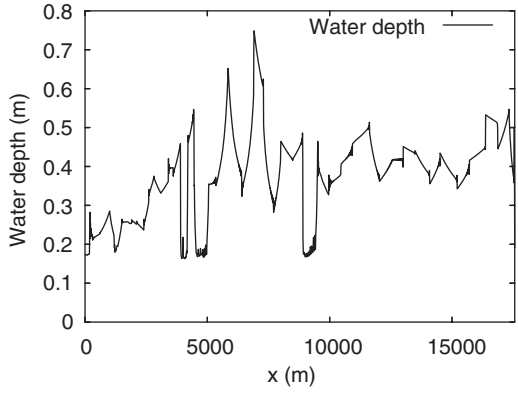


Figure 16. Neila river test case. Water depth using $\Delta x = 10\,m$ and CFL = 0.02.

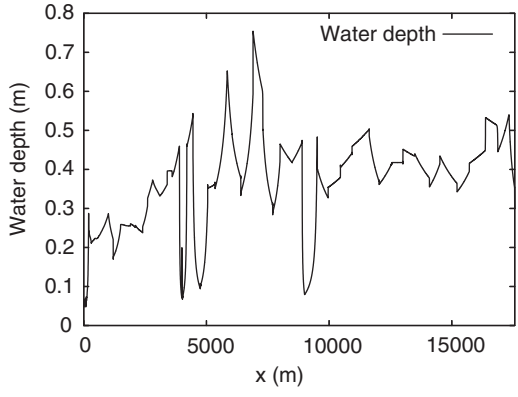


Figure 17. Neila river test case. Water depth using $\Delta x = 2\,m$ and CFL = 0.25.

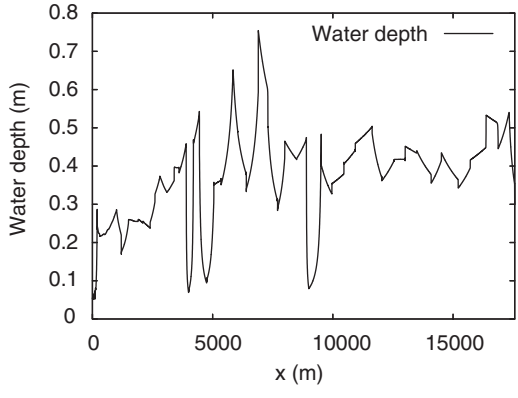


Figure 18. Neila river test case. Water depth using $\Delta x = 2\,m$ and CFL = 0.02.

Copyright © 2006 Taylor & Francis Group plc, London, UK

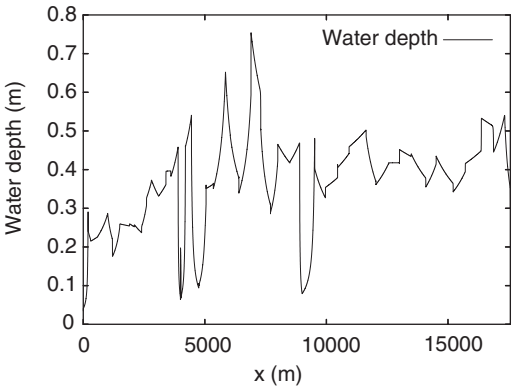


Figure 19. Neila river test case. Water depth using $\Delta x = 1\,m$ and CFL = 0.9.

discrete friction terms. It stops water at depth values less than the limit imposed leading, for coarse grids, to some kind of pulses in the flow during the transient calculation that spoil the quality of the solution.

It was found that $\Delta x = 1\,m$, following (16), is the only grid size ensuring smooth, continuous and steady discharge results. As the grid size is increased above the friction stability limit, and despite the semi-implicit discretization of the friction term, the numerical solutions become eventually unstable. The traditional remedy of trying to reduce the instabilities by decreasing the time step size does not work since, using in $\Delta x = 2\,m$ the time step given by CFL = 0.25 or CFL = 0.02 in the grid $\Delta x = 10\,m$, did not improve the stability of the solution due to the inadequacy of the space discretization.

8 CONCLUSIONS

The unified discretization of the friction term allows for a perfect balance between source terms and flux derivatives at the discrete level, enabling a better quality solution than the pointwise discretization of the friction term at steady state.

The stability constraints linked to important values of the friction terms have been analyzed both in 1D and 2D. The main options considered are to apply a pointwise implicit, a pointwise explicit and an upwind explicit discretization. A new roughness-related numerical stability condition has been derived for the case of upwind explicit discretizations. It restricts the size of the spatial grid as a function of the water depth and the bed roughness. It has been tested in simulations of a real river flow case showing that, for low discharges in very rough river beds, it becomes necessary to restrict the spatial grid size under the prescribed limit to be able to reach stable numerical solutions. For 2D calculations, it is excessively restrictive and the preferable option is to apply an implicit pointwise discretization.

REFERENCES

Brufau, P., Garcia-Navarro, P. & Vazquez-Cendon M.E. (2004) Zero mass error using unsteady wetting-drying conditions in shallow flows over dry irregular topography. International Journal for Numerical Methods in Fluids, 45, 1047–1082.

Burguete, J. & Garcia-Navarro, P. (2001) Efficient construction of high-resolution TVD conservative schemes for equations with source terms: application to shallow water flows. International Journal for Numerical Methods in Fluids, 37, 209–248.

Burguete, J. & Garcia-Navarro, P. (2004) Improving simple explicit methods for unsteady open channel and river flow. International Journal for Numerical Methods in Fluids, 45, 125–156.

Burguete, J. & Garcia-Navarro, P. (2004) Implicit schemes with large time step for non-linear equations: application to river flow hydraulics. International Journal for Numerical Methods in Fluids, 46, 607–636.

Burguete, J., Garcia-Navarro, P. & Murillo, J. (2006) Analysis of the friction term in the one-dimensional shallow water model. Journal of Hydraulic Engineering, ASCE, under revision.

Chow, V.T. (1959). Open channel hydraulics. McGraw-Hill International, New York.

Cunge, J.A., Holly, F.M. Jr. & Verwey A. (1980) Practical aspects of computational river hydraulics. Pitman.

Darcy, H.P.G. (1858). Recherches expérimentales relatives aux mouvements de l'eau dans les tuyaux. Mémoires Présentées à l'Académie des Sciences de l'Institut de France, 14, 141.

Garcia-Navarro, P., Fras, A. & Villanueva, I. (1999) Dam-break flow simulation: some results for one-dimensional models of real cases. Journal of Hydrology, 216, 227–247

Gauckler, P.G. (1867) Etudes thoriques et pratiques sur l'coulement et le mouvement des eaux. Comptes Rendus de l'Acadmie des Sciences, Paris.

Huang J. & Song, C.C.S. (1985) Stability of dynamic flood routing schemes. ASCE Journal of Hydraulic Engineering, 111, 1497–1505.

Liggett, J.A., & Cunge, J.A. (1997) Numerical methods of solution of the unsteady flow equations, ahmood K, Yevjevich V (eds). Water Resources Publications. Unsteady Flow in Open Channels.

MacDonald, I., Baines, M.J., Nichols, N.K. & Samuels, P.G. (1997) Analytical benchmark solutions for open-channel flows. ASCE Journal of Hydraulic Engineering, 123, 1041–1045.

Manning, R. (1890). On the flow of water in open channels and pipes. Institution of Civil Engineers of Ireland.

Murillo, J. (2006) Two-dimensional Finite volume numerical models for unsteady free surface flows, solute transport and erosion/deposition processes. PhD Thesis.

Strickler, A. (1923) Beitrge zur Frage der Geschwindigkeitsformel und der Rauhligkeitszahlen fr Strme, Kanle und Geschlossene Leitungen. Mitt. des Eidgenössischen Amtes für Wasserwirtschaft: Bern, vol. 16.

Copyright © 2006 Taylor & Francis Group plc, London, UK

Numerical simulations on the Paraná de las Palmas River

Juan M. Viscardi & Alfonso Pujol
Post Graduate School in Port Engineering, Faculty of Engineering ,University of Buenos Aires

Volker Weitbrecht & Gerhard H. Jirka
Institute for Hydromechanics (IfH), University of Karlsruhe

Nils R. Olsen
Department of Hydraulic and Environmental Engineering, Norwegian University of Science and Technology

ABSTRACT: The Paraná de las Palmas River is one of the lower branches of the Paraná River system and part of the most important waterway in Argentina, transporting 80% of the Argentinean agricultural export products. The complex and unpredictable flow patterns, especially in the river bends, lead to a limitation of the maximum vessel Length-Over-All (LOA) of 230 m, which has a significant influence on economic aspects of navigation in this region. Because most of the navigation problems occur in the river bends, extensive 3-D ADCP (Acoustic-Doppler-Current-Profiler) velocity measurements have been carried out to analyze the flow pattern in different locations where the navigational problems are most severe. Unsteady 1-D simulations have been performed using HEC-RAS to describe the behavior of the river and to get appropriate boundary conditions which were used then to conduct 3-D RANS (Reynolds-Averaged-Navier-Stokes) simulations using a CFD numerical code in a 3 km river stretch with strong curvature. In the result section the 3-D simulations are compared with the field measurements.

1 INTRODUCTION

Knowledge of the complex flow pattern in the river bends of the Paraná de las Palmas river is important to analyze the shipping conditions in these river stretches and has been an important objective during recent years.

The reason for the pronounced non-homogeneous flow field derives from the characteristics of this river stretch. Compared with European navigable rivers the cross-sectional shape of the Paraná de Las Palmas River is much more compact, with width to depth ratios between 8 to 44. This is an indicator for the existence of strong three-dimensional secondary motions including upwelling effects and spiral motions, especially in the bends. Another particularity of the river is the significant tide influence on water surface elevation and discharge over the complete river stretch of 132 km.

A natural bend in the Paraná de las Palmas river leading to the most difficult flow field is the San Antonio bend of approximately 3 km length (Figure 1).

Different studies were made to predict the flow pattern on this bend. A physical model was developed in the year 1991 (Loschacoff, C. and Hopwood A.J.) and different field studies were done during last years. Drifters were used in October 2003. Three ADCP campaigns were carried out during 2003 and 2004.

This paper presents new contribution to this topic using numerical simulations. 3-D RANS (Reynolds-Averaged-Navier-Stokes) simulations with the standard k-ε model through San Antonio bend using a numerical code called SSIIM, Simulation on Sediment movements In water Intakes with Multiblock option (Olsen N.R.B. 2005).

The aim of this paper is to demonstrate the potential of this numerical model as a research tool for large rivers like the Paraná de las Palmas river with respect to different aspects, such as navigation, environmental quality and the relationship between fluvial behavior and tidal influence.

Neither sediment transport processes nor wind influence are discussed on this paper. Sediment transport processes will be studied in the future using SSIIM but results are not ready for publication yet.

2 THE RIVER

The Paraná de las Palmas river is located at the eastern part of the province of Buenos Aires and is a branch of

Copyright © 2006 Taylor & Francis Group plc, London, UK

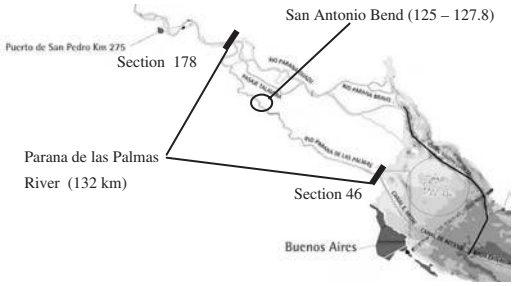


Figure 1. Scheme of the Paraná de las Palmas river and its zone.

the Paraná Inferior River (PIR) discharging its water in the Rio de la Plata estuary (RdeP). It has a length of 132 km and is part of the most important waterway in Argentina, between the section 46 (RdeP) and section 178 (PIR), corresponding to river kilometres.

In Figure 1, the complete river and the zone of study are presented.

The main characteristics of this river can be summarized as: an average discharge of 4200 m^3/s, a typical width of 400 m, a water depth varying from 10 m to 46 m, and a slope of approximately 0.001%. The mean horizontal flow velocity is about 1 m/s.

The study site, San Antonio bend, is a 3 km highly sinuous section of the river situated between section 125 and section 127.8.

2.1 *San Antonio bend*

The plan configuration of San Antonio bend consists of two consecutive bends curving in opposite direction connected by a short 300 m straight reach. A geomorphologic analysis about the variation in the river bed during the last five years was done based on recent topographic surveys.

Changes in bed levels were not significant and therefore, a fixed geometry bed has been used to study the velocity pattern without sediment transport calculations. Erosion processes in the left margin of the river was observed only in two cross-sections by this analysis. This process of erosion is due to the recirculations in the flow field, but was not sufficiently important to be included in this first part of the study. In Figure 2, one cross-section of the bed geometry during the last five years is shown.

The grain size distribution along the bend can be inferred using two studies at different points near the San Antonio bend, one located 7.8 km upstream and the other 8.0 km downstream. Both samples were taken from the upper sediment layer. In Figure 3, the measured grain size distributions at these two points are shown. A bed sediment sample obtained from the hopper of a Trailing Suction Hopper Dredge

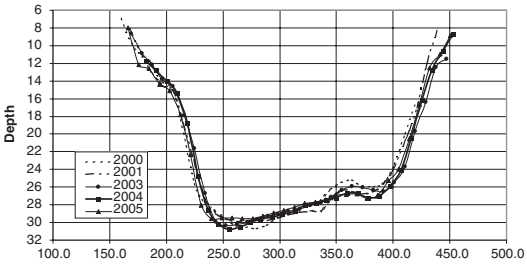


Figure 2. Cross-section surveys of the last five years showing the stability of the bed geometry.

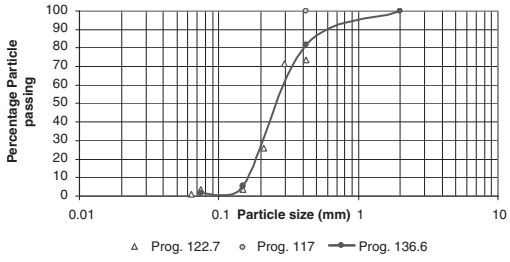


Figure 3. Particle grain size distribution of bed material near San Antonio bend.

three kilometre upstream of San Antonio bend is also included in the plot.

These three curves plotted in Figure 3 show that the material can be classified as small sand with a $d_{50} = 0.26$ mm and $d_{90} = 0.48$ mm.

Extensive 3-D ADCP (Acoustic-Doppler-Current-Profiler) velocity measurements using 2 second time intervals between vertical instantaneous samplings while the equipment is crossing the river, have been carried out to analyze the flow pattern in cross-sections every 100 m.

These measurements were done using the minimum possible time not to have great changes in the flow pattern due to changes in levels and discharges by the tide influence. A plan view of the San Antonio bend with the cross-sections where ADCP surveys have been done is shown in Figure 4. This campaign represents 8 hours of measurements including all the tidal changes.

3 NUMERICAL SIMULATION

In the following the adopted numerical methods are given followed by a description of the model setup including geometry, grid and a roughness development.

3.1 *Methods*

The SSIIM (Olsen, 2005) program solves the Navier-Stokes equations with the k-ε turbulence model on a

Copyright © 2006 Taylor & Francis Group plc, London, UK

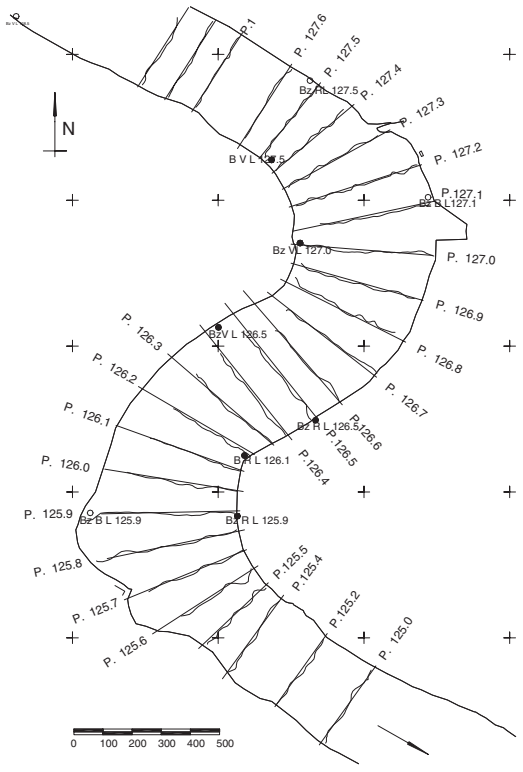


Figure 4. Plan view of the bend, location of the cross-sections measured with ADCP and current direction.

three-dimensional non-orthogonal grid. A control volume method is used for the discretization, together with the power-law scheme (POW) or the second order upwind scheme (SOU). The SIMPLE method (Patankar, 1980) is used for the pressure coupling.

The program uses the Reynolds-Averaged-Navier-Stokes equations for a non-compressible and constant density flow as follow:

$$\frac{\partial U_i}{\partial t} + U_j \frac{\partial U_j}{\partial x_j} = \frac{1}{\rho}\frac{\partial}{\partial x_j}\left(-P\delta_{ij} - \rho\overline{u_i u_j}\right) \quad (1)$$

where U is the velocity, t is time, P is the pressure, δ is the Kronecker delta which is 1 if $i = j$ and 0 if $i \neq j$.

The Navier-Stokes equations for turbulent flow are solved to obtain the water velocity using an implicit solver. The k-ε model is used for calculating the turbulent shear stress. The gravity term is not included in the standard algorithms. The criteria employed to establish the convergence of the iterative algorithm was the reduction of all normalized residuals to at least 10^{-3}. The computation of the water surface was obtained using a free surface algorithm based on the pressure or using a rigid lid approach.

Table 1. Aspect ratios for the final grid.

Cell numbers				Aspect ratios			
Total	i	j	k	$D_{i/j}$	$D_{j/k}$ bank*	$D_{i/k}$ bank*	$D_{i/k}$ max. depth
184500	225	41	20	1.25	135.7	169.6	5.5

*"Bank" implies that depths are small, leading to large distortion ratios.

The results shown in this paper are based on the use of the SOU scheme in the discretization of the convective terms.

3.2 *Model setup*

The geometry of the San Antonio river bed was specified using cross-sectional field surveys of 10-3-2005. In these surveys, cross-sectional profiles were obtained every 200 m in longitudinal direction and a spatial resolution of 9 m in lateral direction from section 125.0 to section 127.8.

The geometry was transferred using a linear interpolation to the numerical grid.

3.2.1 *Numerical grid*

SSIIM uses a non-orthogonal, non-staggered grid to represent the geometry of the river bed. The final grid had 184500 cells, divided in 225 cells in a streamwise direction, 41 cells in a lateral direction and 20 cells in a vertical direction.

The grid cells are approximately 10 m in the lateral direction and 12.5 m in the streamwise direction. This resolution is more than sufficient taking into consideration that the main flow pattern is the goal of this work, and most of the available measurement data have a streamwise resolution of 100 or 200 m only.

For vertical resolution the cells were distributed at every 5% of depth, giving a cell every 2.3 m in vertical in the deepest zones and every 0.07 m near the bank.

The first cell near the bottom was defined to cover 30% of depth all around the first 20 m from the banks and 10% of the depth in vertical profiles cases inside these limits. This change in the size of the first cell elevation was defined to maintain a reasonable ratio between the length of the first cell and the roughness height.

Expansion ratios (in all cases near 1) and aspect ratios were also taken into account to define the grid. The maximum aspect ratios for the final grid are presented in Table 1.

In order to optimize the grid with respect to accuracy and computing time, six different grids were compared. The final grid was selected from which the coarser grid was needed to obtain approximately the same results when the number of cells was doubled.

Copyright © 2006 Taylor & Francis Group plc, London, UK

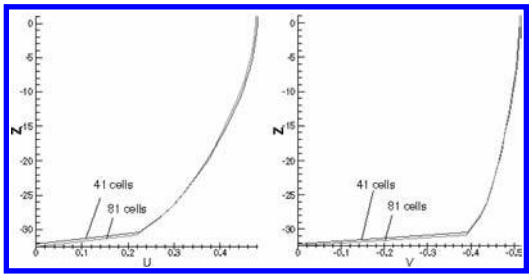


Figure 5. East (U) and North (V) horizontal components of the velocities in (m/s) using different grids.

To define the vertical and lateral resolution, a comparison of results was used. In the streamwise direction the aspect ratio was taken into account.

In Figure 5, comparison of the vertical profiles of the horizontal velocity components of different grids using 41 cells (final grid) and 81 cells (364500 cells) in the lateral direction are shown.

Figure 5 shows that increased resolution leads to negligible changes. In the same way, a resolution in vertical direction of 20 cells was enough to obtain similar results.

Once resolutions in vertical and lateral direction were optimized, the longitudinal resolution was adopted to have an aspect ratio of 1.3. A surface plan view of the final grid is shown in Figure 6.

3.2.2 *Bottom roughness*

One difficulty of numerical modeling of natural river bends is that the distribution of the roughness height along the bed is not usually known. The particle size distribution at the river bed, shown in Figure 3, results in a Manning roughness coefficient value of 0.011. This is unrealistically small and it means that bed forms have a dominating influence on the roughness.

The spatial resolution of the grid is much larger than grain size and the available survey data in cross-sections every 200 m do not have sufficient accuracy to represent bed forms. Therefore, bed form resistance has to be included into the bed roughness. This leads to much greater values of Manning coefficients than if the coefficients were based on the sediment particle size.

Due to this problem, a detailed study of the bed roughness was carried out from three different approaches.

First, the roughness along the bends has to be in the same order of magnitude or smaller than the roughness coefficient obtained for the 1-D numerical model, since the value used in the 3-D numerical model reflects all morphological heterogeneities inside the geometry.

As explained above, the roughness has to include the effect of bed forms. For that purpose, the effective roughness was approximated using Van Rijn's method

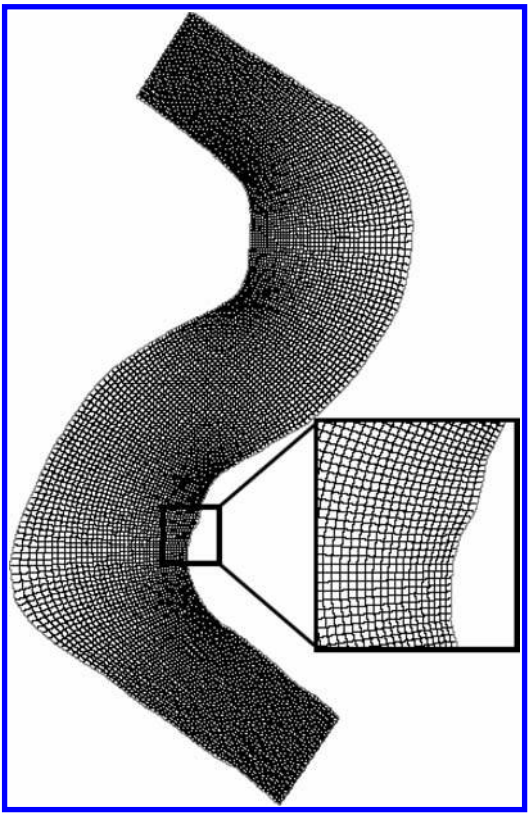


Figure 6. Plan view of the final grid.

(Van Rijn 1984) where the hydraulic roughness of a movable bed surface is caused by grain roughness ($k_{s,grain}$) and by form roughness ($k_{s,form}$) and is linked to the following parameters: particle diameter, D_{50}, flow depth, d, transport stage parameter, T, and bed form steepness, Δ/λ. With T defined as:

$$T = \frac{(u_*')^2 - (u_{*cr})^2}{(u_{*cr})^2} \quad (2)$$

where $u_*' = (g^{0.5}/C')\overline{u}$ is the bed shear velocity and u_{*cr}' is the critical bed shear velocity according to Shields.

The particle size distribution shown in Figure 3 and three representative cross-sections of San Antonio bend with the maximum ($d = 43.2$ m), minimum ($d = 13.3$ m) and average ($d = 23.3$ m) hydraulic depths were used for this analysis.

Dunes were obtained as a result of those three representative cross-sections. The bed form height, Δ, was calculated using Van Rijn formula (1984).

$$\frac{\Delta}{d} = 0.11\left(\frac{D_{50}}{d}\right)^{0.3}\left(1 - e^{-0.5T}\right)(25 - T) \quad (3)$$

Copyright © 2006 Taylor & Francis Group plc, London, UK

Table 2. Different roughness obtained by three different approaches.

Approach	Hydraulic property		Roughness	
	Hydr. radius (m)	Depth (m)	Height (m)	Manning n ($s/m^{1/3}$)
HEC-RAS			–	0.038
Van Rijn	13.3	13.3	0.267	0.031
prediction	26.8	23.3	0.226	0.030
	60.2	43.2	0.041	0.026
SSIIM			0.448	0.034
prediction			0.236	0.030
			0.024	0.021

And the bed form steepness was calculated from:

$$\frac{\Delta}{\lambda} = 0.015\left(\frac{D_{50}}{d}\right)^{0.3}\left(1-e^{-0.5T}\right)(25-T) \quad (4)$$

Finally the hydraulic roughness was computed as:

$$k_s = 3D_{90} + 1.1\Delta\left(1-e^{-25\frac{\Delta}{\lambda}}\right) \quad (5)$$

Table 2 shows Manning coefficients obtained for these three representative sections with their depths, d, and hydraulic radius, R_h.

In a third step, the particle size distribution of the river bed was used as input information to the SSIIM morphological module, such that the roughness height was obtained for all of the cells at the bottom as a numerical solution. SSIIM uses the Van Rijn (1984) procedure to obtain the roughness height and the following equation to convert Manning n, into a roughness height of the bed, k_s:

$$\frac{1}{n} = \frac{26}{k_s^{1/6}} \quad (6)$$

The law of the wall for rough boundaries is used as given by Schlichting and Gersten (1979).

$$\frac{U}{u_*} = \frac{1}{\kappa}\mathrm{Ln}\left(\frac{30y}{k_s}\right) \quad (7)$$

where k_s is the roughness height.

In Figure 7, the variation of roughness heights in the complete river reach obtained using SSIIM is shown. Manning's coefficients are in the range between 0.034 and 0.021.

Results obtained by the three different approaches are summarized in Table 2.

In Table 2 it may be observed that the Manning's coefficients obtained are in a range from 0.038 to 0.021.

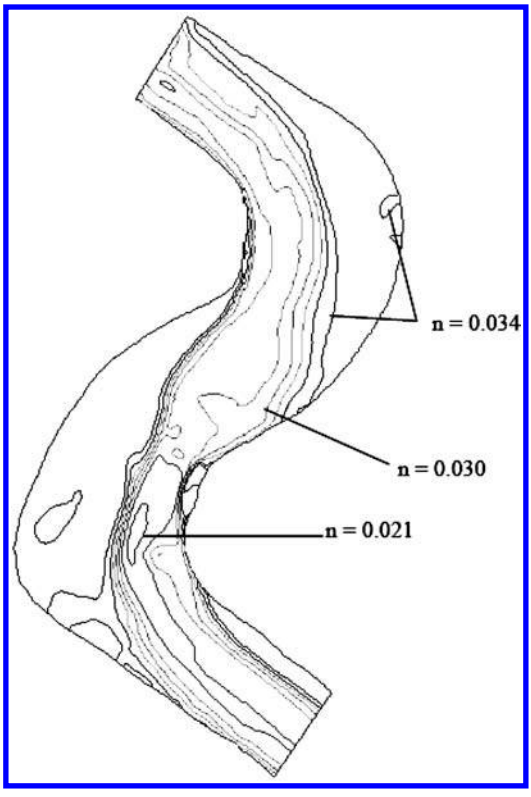


Figure 7. Variation of roughness height all around the bed. Contours show corresponding Manning coefficient values.

The higher limit was obtained in a 1-D approach where all morphological heterogeneities are taken into account inside the parameter.

In a 2-D approach using Van Rijn's formula and three representative cross-sections with constant hydraulic depths and hydraulic radius, Manning n values ranged from 0.031 to 0.026.

For a 3-D calculation, results present a perfect match with the 2-D prediction, but in this case, the range of Manning n values is higher with a variation between 0.034 to 0.021. These changes in limits may be explained since 3-D calculation take into account all different depths present in the geometry of the reach. The lower limit for the Manning n coefficient, $n = 0.021$, corresponds to the deepest zones and the higher limit, $n = 0.034$, to zones of smaller depths than those used in the Van Rijn prediction.

As explained above, all of the Manning n coefficients obtained maintain a logical concordance among approximations and show that roughness heights for San Antonio bend can be estimated using Manning coefficients in a range from 0.034 to 0.025. The three methods provide some confidence in the roughness calibration procedure.

Copyright © 2006 Taylor & Francis Group plc, London, UK

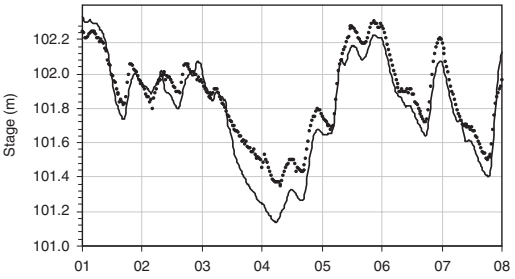


Figure 8. Measured (dotted line) and calculated levels (continuous line) for an unsteady run of 7 days (February-2004).

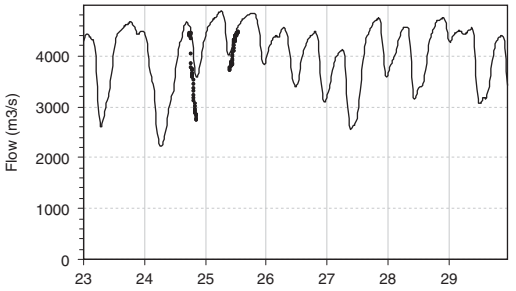


Figure 9. Measured (dotted points) and calculated discharge (continuous line) in a one week period (November-2003).

Different runs using constant Manning values of 0.034, 0.029 and 0.025 were performed. They showed that the influence of the roughness in the case under study is small compared to the expected uncertainties and do not influence the final conclusions.

Therefore, further refinement of the bed roughness does not appear to have any significant effect on the numerical results.

3.2.3 *Boundary conditions*

The definition of appropriate upstream and downstream boundary conditions in the case of a tidal influenced river, is a crucial task.

To understand the behavior of the Paraná de las Palmas river between section 89.0 and section 141.6, an unsteady 1-D numerical model using HEC-RAS 3.1.3 was performed for two different time windows each consisting of seven days.

In Figure 8, the water levels obtained with HEC-RAS compared with measured water levels from a tide gauge during one week of February 2004 are shown.

From Figure 8 it may be seen the tides influence in a section 60 km upstream of the RdeP estuary with mean water level changes of approximately 110 cm in four days and 20–30 cm daily due to this influence.

The maximum error between the predicted levels with HEC-RAS and the measured values is about 0.28 m and the average error is about 0.10 m. These errors are acceptable if they are compared with the geometry of the section where the tide gauge is located: 400 m width, 42 m depth.

The error represents 0.37% of the maximum depth in section 105.8. and did not produce changes in the general behavior of the Paraná de las Palmas River.

In Figure 9, an unsteady behavior of the flow obtained from the numerical model (continuous line) during one week in November 2003 in one cross-section of San Antonio bend is presented. This figure shows the strong variation in discharge with time. Values between 2200 m^3/s and 5000 m^3/s were predicted by the model. These values are compared with discharges in the same time period obtained by integrating the measured ADCP velocities. As may be seen, discharge variations are well represented by the numerical results.

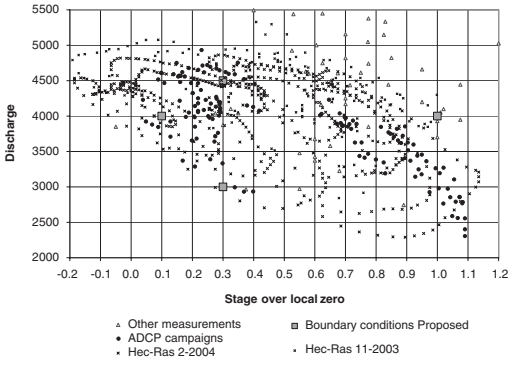


Figure 10. Possibilities for different boundary conditions.

In order to find appropriate discharge and water level boundary conditions for the steady 3-D simulations, historical measurements, ADCP measurements and results of the 1-D numerical model were used as plotted in Figure 10.

Figure 10 shows that is impossible to obtain a rating curve for the Paraná de las Palmas river, due to the influence of the semi-diurnal tide in the RdeP estuary.

Therefore, four different combinations (indicated by the larger squares in Figure 10) were selected with the objective of studying the influence of discharge changes and of level changes on the flow pattern. That means a quasi-steady simulation. Influence of the tidal wave and its celerity are not taken into account.

4 RESULTS AND DISCUSSION

Four different numerical runs were carried out using four different upstream discharge boundary conditions and downstream stage boundary conditions to obtain a quasi-steady simulation.

Results from the numerical model and measured velocities are presented below in the form of vector

Copyright © 2006 Taylor & Francis Group plc, London, UK

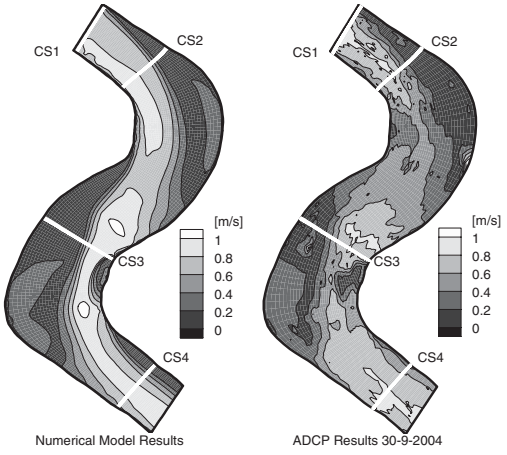


Figure 11. Plan view of the streamwise horizontal velocities near the surface; left: numerical model; right: ADCP measurements on 30-9-2004.

plots and contour plots of the streamwise horizontal velocity distribution, for a plan view and at different cross-sections. Also, a transverse velocity field is shown at some cross-sections.

Results shown in this paper correspond with the use of a Second Order Upwind (SOU) scheme in the discretization of the convective terms using an implicit solver, and with the use of a uniform roughness Manning $n = 0.025$.

The numerical simulation was done with fixed values of Q and H. It has to be noted that the measured velocities represent values obtained during a time period of 8 hours and are influenced by tidal changes.

4.1 *Results of the reference case*

With the four cases defined as boundary conditions, a reference case of study was defined with a Discharge 4000 m^3/s – Relative height (h_r) 1.0 m. This height is related to a local zero in San Antonio bend.

A plan view contour plot of the streamwise horizontal velocity components near the water surface is presented in Figure 11. For easier comparison the ADCP results have been interpolated to the numerical grid.

Figure 11 shows that the highest flow velocities are located at the inner banks of the bends in a range of 0.6 m/s to 1.0 m/s. On the outer banks of the bends, recirculation zones covering the complete water depth are present, which are more clearly visible in the vector plots in Figure 16.

In Figures 12 to 15 the streamwise horizontal calculated velocities are compared with the ADCP results in four different cross-sections corresponding to the indicated cross-sections in Figure 11. The cross-sections (CS) were chosen to represent time windows where the

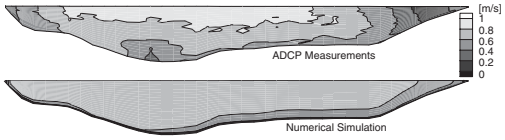


Figure 12. Comparison between measurements on 30-9-2004 with $Q = 3722\ m^3/s$, $h_r = 1$ m (upper picture) and calculated (lower picture) streamwise velocities at cross-section (CS 1) close to the inflow boundary.

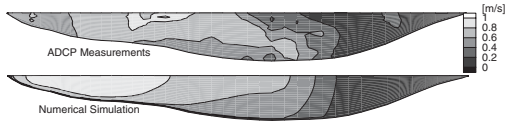


Figure 13. Comparison between measurements on 30-9-2004 with $Q = 3456\ m^3/s$, $h_r = 1.07$ m (upper picture) and calculated (lower picture) streamwise velocities at CS 2.

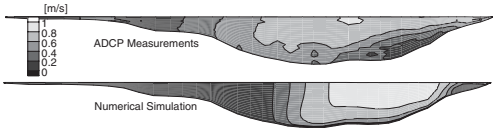


Figure 14. Comparison between measurements on 30-9-2004 with $Q = 3820\ m^3/s$, $h_r = 0.98$ m (upper picture) and calculated (lower picture) streamwise velocities at CS 3.

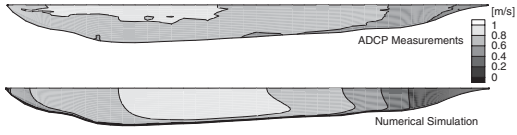


Figure 15. Comparison between measurements on 30-9-2004 with $Q = 3901\ m^3/s$, $h_r = 0.80$ m (upper picture) and calculated (lower picture) streamwise velocities at CS 4.

ADCP measurements are governed by approximately the same boundary conditions than those used for the numerical simulation.

Figures 12 and 13 show that the numerical model is not able to predict the flow field accurately close to the inflow boundary, but 400 m downstream of the inflow boundary, the simulated flow field represents the measured flow field with reasonable accuracy.

A plan view of the vector field near the water surface is given in Figure 16, where only one every four vectors is plotted in streamwise direction and one every two vector is plotted in lateral direction. The measured flow velocities are interpolated to the numerical grid.

The same cross-sections 1 to 4 used to show the streamwise horizontal velocity are now used to show the transverse velocity fields in Figures 17 to 20.

Figures 17 and 18 show the development of the secondary currents with increasing distance from the inflow boundary.

Copyright © 2006 Taylor & Francis Group plc, London, UK

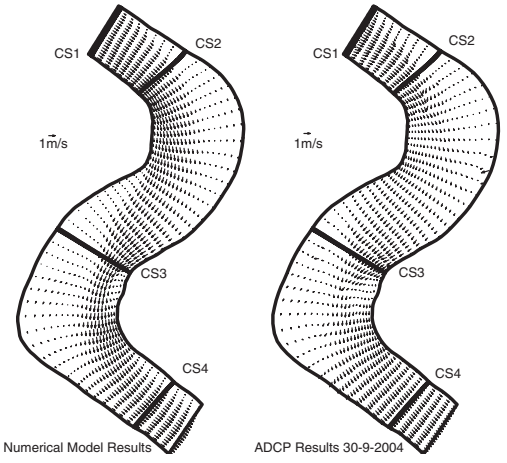


Figure 16. Comparison of the calculated (left picture) and measured (right picture) velocity vector fields.

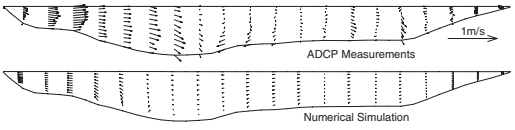


Figure 17. Comparison between measurements on 30-9-2004 with $Q = 3722\,m^3/s$, $h_r = 1\,m$ (upper picture) and calculated (lower picture) secondary current velocities at CS 1 close to the inflow boundary.

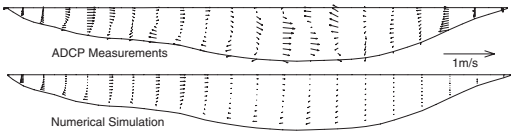


Figure 18. Comparison between measurements on 30-9-2004 with $Q = 3456\,m^3/s$, $h_r = 1.07\,m$ (upper picture) and calculated (lower picture) secondary current velocities at CS 2.

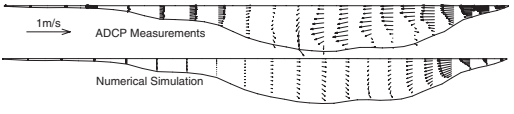


Figure 19. Comparison between measurements on 30-9-2004 with $Q = 3820\,m^3/s$, $h_r = 0.98\,m$ (upper picture) and calculated (lower picture) secondary current flow velocities in CS 3.

Both comparisons, cross-sectional view and plan view indicate that the main flow field including the recirculation zones are well represented by the numerical simulation.

Slight variations can be observed in the areas given by the numerical results for the higher streamwise

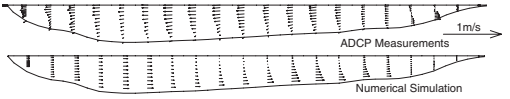


Figure 20. Comparison between measurements on 30-9-2004 with $Q = 3901\,m^3/s$, $h_r = 0.80\,m$ (upper picture) and calculated (lower picture) secondary current flow velocities in CS 4.

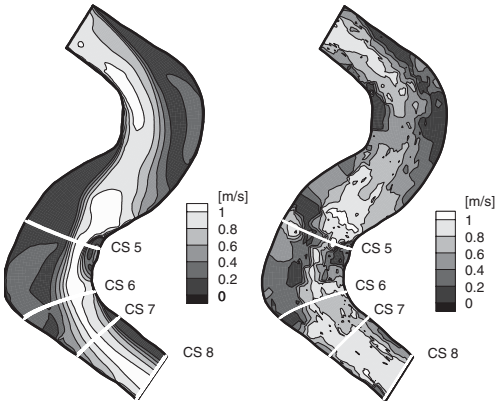


Figure 21. Plan view of the streamwise horizontal velocities near surface; left: numerical model; right: ADCP measurements on 4-2-2004.

horizontal velocities compared with measurements, in all cases the numerical results present larger areas for these velocities.

More discrepancies can be seen in the case of secondary currents, but the scale of these velocities are too small to take these discrepancies into consideration here.

4.2 *Influence of tidal changes*

Additional simulations have been performed with different boundary conditions in order to analyze the influence of the tidal changes on the main flow field.

4.2.1 *Discharge 4500 m³/s – relative height 0.3 m*

In Figure 21 a simulation where the discharge has been increased to $4500\,m^3/s$ and the water surface level at the outflow boundary has been reduced to 0.3 m is compared with measurements of another ADCP campaign made during February 2004.

Compared to the calculated reference case in Figure 11 no strong changes in the mean flow field can be observed.

The larger flow rate leads to higher flow velocities, but the recirculation zones and the secondary currents are only slightly affected.

In Figures 22 to 25 the streamwise flow pattern results is compared with measurements at different cross-sections. Again, cross-sections were chosen to

Copyright © 2006 Taylor & Francis Group plc, London, UK

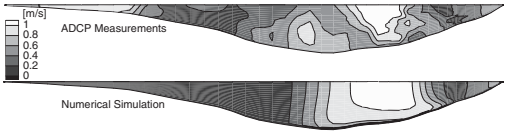


Figure 22. Comparison between measurements on 4-2-2004 with $Q = 4652\,\mathrm{m^3/s}$, $h_r = 0.22\,\mathrm{m}$ (upper picture) and calculated (lower picture) streamwise velocities at CS 5.

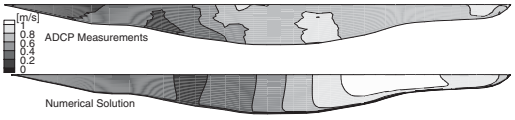


Figure 23. Comparison between measurements on 4-2-2004 with $Q = 4559\,\mathrm{m^3/s}$, $h_r = 0.18\,\mathrm{m}$ (upper picture) and calculated (lower picture) streamwise velocities at CS 6.

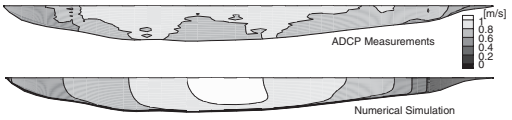


Figure 24. Comparison between measurements on 4-2-2004 with $Q = 4479\,\mathrm{m^3/s}$, $h_r = 0.16\,\mathrm{m}$ (upper picture) and calculated (lower picture) streamwise velocities at CS 7.

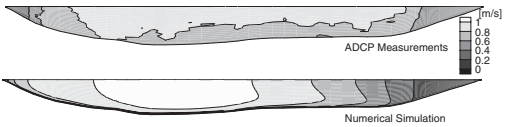


Figure 25. Comparison between measurements on 4-2-2004 with $Q = 4557\,\mathrm{m^3/s}$, $h_r = 0.15\,\mathrm{m}$ (upper picture) and calculated (lower picture) streamwise velocities at CS 8.

represent time windows where the ADCP measurements were governed by boundary conditions close to those used for the numerical simulation.

The comparison between measured and calculated velocities in Figures 21 to 25 shows good agreement with respect to the mean flow pattern.

However, in all cases, regions of high flow velocities are predicted by the numerical simulation that are less pronounced in the measurements, leading to the conclusion that the influence of the increase in discharge is less important than predicted by the model. That means that the importance of the high discharge influence is not so big in reality as is predicted by the numerical resolution.

4.2.2 *Discharge 4000 m^3/s – relative height 0.1 m*

In Figures 26 and 27 a simulation where the discharge has been maintained in $4000\,\mathrm{m^3/s}$ and the water surface level at the outflow boundary has been reduced to $h_r = 0.1\,\mathrm{m}$ is compared with results of the reference

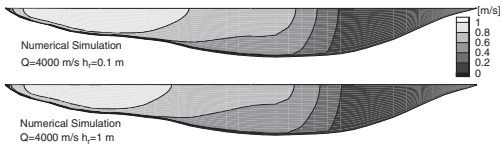


Figure 26. Results using different boundary levels conditions for Relative Height 0.1 m (upper picture) and the reference case (lower picture) at CS 1.

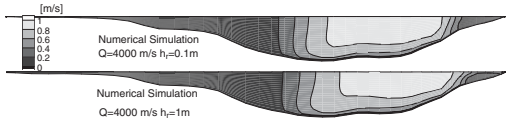


Figure 27. Results using different boundary levels conditions for Relative Height 0.1 m (upper picture) and the reference case (lower picture) at CS 3.

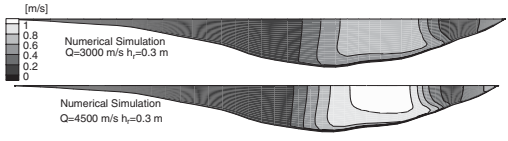


Figure 28. Results using different boundary Discharge conditions for $Q = 3000\,\mathrm{m^3/s}$ (upper picture) and $Q = 4500\,\mathrm{m^3/s}$ (lower picture) at CS 5.

case. As is shown in these Figures, the influence of the levels on the mean flow pattern is not as important for the main flow velocity field as the discharge.

4.2.3 *Discharge 3000 m^3/s – relative height 0.3 m*

In Figure 28 a simulation where the discharge has been changed from 4500 to $3000\,\mathrm{m^3/s}$ and the water surface level at the outflow boundary has been maintained as $h_r = 0.3\,\mathrm{m}$ is compared. It can be seen that the influence of the discharge on the mean flow pattern is important for the calculated main flow velocity field, as was already shown in Figures 22 to 25.

4.3 *Influence of changing bottom roughness*

In order to analyze the influence of locally changing roughness height on the mean flow field, an additional simulation has been performed using local roughness heights calculated by SSIIM. According to Table 2 the Manning n values vary in a range of 0.021 to 0.034. A comparison with the velocity field results using constant roughness shows that this differentiation is of minor importance. The main flow patterns are only slightly affected by the changing roughness bed.

In Figure 29, a plan view of streamwise velocity at surface for both cases is presented.

The same cross-sections 1 and 3 used before are now used to compare results using different roughness height values all across the bend and results using a constant Manning n value of 0.025.

Copyright © 2006 Taylor & Francis Group plc, London, UK

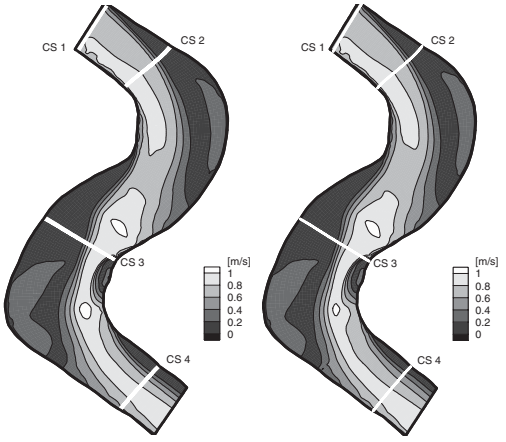


Figure 29. Plan view of the streamwise horizontal velocities at surface. With constant roughness height (left picture) and with variable roughness height (right picture).

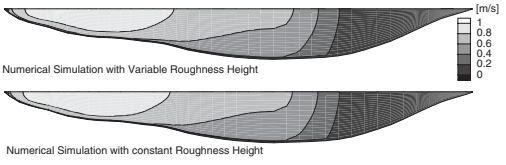


Figure 30. Streamwise horizontal velocity results using variable roughness height (upper picture) and constant roughness height (lower picture) for CS 1.

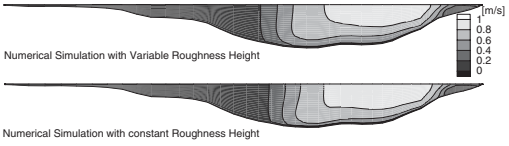


Figure 31. Streamwise horizontal velocity results using variable roughness height (upper picture) and constant roughness height (lower picture) for CS 3.

Results show that in this range of Manning *n* values, there is no significant sensitivity to calibration and a constant value of Manning *n* can be used all around the bed to obtain the mean flow velocity field.

5 CONCLUSIONS AND RECOMMENDATIONS

It could be shown that 3-RANS simulations using SSIIM are a suitable approach for analyzing the complex mean flow pattern in the river bends of the Paraná de las Palmas river, and their effects on navigation. The main characteristics of the flow field that control the shipping conditions in a 3 km river stretch in the so called San Antonio bend could be represented with sufficient accuracy. It seems to be possible to transfer the numerical model, implemented with SSIIM, to different sections of the Paraná de Las Palmas River to determine the behavior of the mean flow at different discharge and water level conditions.

The use of a quasi-steady simulation using different upstream boundary condition discharge and levels at downstream boundary conditions is an adequate approach to represent the regime variations.

The comparison of the results between the four simulations with different boundary conditions show that the influence of the water levels on the mean flow pattern is less important than the influence of the changing discharge, but changes in discharge lead to an overestimation of the flow changes compared to the measured changes.

In the present case, a distance of 400 m from the upstream boundary to the first bend is long enough to reproduce fully developed 3-D recirculating motions in the bend. The approach length is 10 times the depth of the cross-section CS 2 where the first bend starts. In the present case where the water depths are larger, the results are independent of the use of free surface computations or a rigid lid approach that reduces the computational time.

The implementation of a numerical model using SSIIM and its calibration has a relatively low cost and reduced computational effort. The overall effort appeared to be lower than for a physical model, Large-Eddy-Simulations or field measurements for determining the mean flow patterns.

The use of unsteady calculations in the present case is of lesser importance, but can be employed in the future to look at more advanced problems, such as sediment transport. In order to get better comparison between steady computations and unsteady flow measurements (tidal changes), the measured flow fields in the future should be conditioned with respect to the tidal cycle. Furthermore, a comparison between the use of first and second order schemes especially in the recirculation zones would be useful.

ACKNOWLEDGEMENTS

This work is the result of an exchange visitor program between the Institute of Hydrodynamics (IfH), University of Karlsruhe, and the Post Graduate School in Port Engineering, Faculty of Engineering, University of Buenos Aires, during which the first author stayed in IfH.

The authors would like to thank Thorsten Stößer, Dominic von Terzi and John Fenton for their help during the investigation.

REFERENCES

Babarurutsi S. and Chu V.H. 1998. *Modeling transverse Mixing Layer in Shallow Open Channel Flows.* Journal of Hydraulic Engineering. A.S.C.E. Vol. 124. N° 7: 718–727.

Copyright © 2006 Taylor & Francis Group plc, London, UK

Celik I.B. *Procedure for estimation and Reporting of Discretization Error in CFD Applications*. Mechanical and Aerospace Engineering Depart. West Virginia University.

Hardly R.J., Lane S.N., Lawless M.R., Best J.L., Elliot L. and Ingham D.B. 2005. *Development and testing of a numerical code for treatment of complex river channel topography in three-dimensional CFD models with structured grids*. Journal of Hydraulic Research. I.A.H.R. Vol. 43. N° 5: 177–199.

Loschacoff C. and Hopwood A.J. 1991. *Modelo de Navegación de la Vuelta de San Antonio, Informe Final.* LHA-088-06-91. Instituto Nacional del Agua. Buenos Aires. Argentina.

Nezu L. 2005. *Open-Channel Flow Turbulence and its research Prospect in the 21st Century.* Journal of Hydraulic Engineering. A.S.C.E. Vol. 131. N° 4: 229–246.

NPARC Alliance CFD Verification and validation Web Site. *Uncertainty and error in CFD Simulations*. Glenn Research Center, N.A.S.A.

Olsen N.R.B. 2005. *Computational Fluid Dynamics in Hydraulic and Sedimentation Engineering*. Department of Hydraulic and Environmental Engineering. The Norwegian University of Science and Technology.

Olsen N.R.B. 2005. *A three dimensional numerical model for Simulation on Sediment movements In water Intakes with Multiblock option (SSIIM)*. Department of Hydraulic and Environmental Engineering. The Norwegian University of Science and Technology.

Patankar S.V. 1980. *Numerical heat transfer and fluid flow*. Mc. Graw-Hill book company.

Rodriguez J.F., Bombardelli F.A., García M.H., Frothingham K.M., Rhoads B.L. and Abad J.D. 2004. *High-resolution Numerical Simulation of Flow Through a Highly Sinuous River Reach*. Water resources management 18. The Netherlands. Kluwer Academic Publishers.

Schlichting H. and Gersten K. 1999. *Boundary layer theory*. Bochum: Springer.

Selim Y.M. and Ferreira da Silva A.M. 2001. *Fluvial Processes.* Monograph. Delft. I.A.H.R.

Sinha S.K., Sotiropoulos F. and Odgaard A.J. 1998. *Three-dimensional numerical model for flow through natural rivers*. Journal of Hydraulic engineering. A.S.C.E. Vol. 124. N° 1: 13–24.

Tominaga A., Nagao M. and Nezu I. 1999.*Flow structures and momentum transport processes in curved open channels with vegetation.* Proc. 28th. I.A.H.R. Congress. Austria.

U.S. Army Corps of Engineers. 1994. *Engineering and Design – Hydraulic Design of Flood Control Channels*. EM 1110-2-1610. Jun 30th 1994. Engineer Manuals. U.S.A.C.E.

Van Rijn L.C. 1984. *Sediment Transport, Part I: Bed Load Transport*. Journal of Hydraulic Engineering. Vol. 110. N° 10: 1431–1456.

Van Rijn L.C. 1984. *Sediment Transport, Part II: Suspended Load Transport*. Journal of Hydraulic Engineering. Vol. 110. N° 12: 1613–1641.

Van Rijn L.C. 1984. *Sediment Transport, Part III: Bed Forms and Alluvial Roughness*. Journal of Hydraulic Engineering. Vol. 110. N° 12: 1733–1755.

Copyright © 2006 Taylor & Francis Group plc, London, UK

Selection of interface plane in the assessment of discharge in two stage meandering and straight compound channels

Kanhu Charan Patra & K.K. Khatua
National Institute of Technology, Rourkela, Orissa, India

ABSTRACT: An investigation concerning the distribution of shear stress in the main channel and floodplain of meandering and straight compound channels are presented. Discharge in meandering compound channels is strongly dependant on the interaction between flow in the main channel and that in the floodplain. The usual practice in one dimensional analysis is to separate a compound section into subsections using 'divided channel method' through the assumed interface planes running from the main channel–floodplain junctions. Discharge for each subsections are calculated using Manning's equation and added up to get the total discharge of the compound section. If the assumed interface is wrong the resultant discharge becomes erroneous. The apparent shear force at the assumed interface plane gives an insight into the magnitude of flow interaction between the main channel and the adjacent floodplains basing on which the merits of the selection of the interface plains for discharge estimation are decided. Alternative uses of the traditional vertical interface plane for separation of compound channels are proposed. A set of smooth and rough sections is studied with aspect ratio varying between 2 and 5. The discharge results are compared with the results of variable-inclined interface method.

1 INTRODUCTION

Almost all natural rivers meander. In fact straight river reaches of lengths exceeding ten times its width are rather rare. Meandering is a degree of adjustment of water and sediment laden river with its size, shape, and slope such that a flatter channel can exists in a steeper valley. During floods, part of the discharge of a river is carried by the main channel and the rest is carried by the floodplains located to its sides. Once a river stage overtops its banks, the cross sectional geometry of flow undergoes a steep change. The channel section becomes compound and the flow structure for such section is characterized by large shear layers generated by the difference of velocity between the main channel and the floodplain flow. Due to different hydraulic conditions prevailing in the river and floodplain, mean velocity in the main channel and in the floodplain are different. Just above the bank-full stage, the flow in the main channel exerts a pulling or accelerating force on the flow over floodplains, which naturally generates a dragging or retarding force on the flow through the main channel. This leads to the transfer of momentum between the channel section and the floodplain. At the junction region between the main channel and that of the floodplain, Sellin (1964) and Knight and Demetriou (1983) indicated the presence of artificial banks made of vortices, which acted as a medium for transfer of momentum. At low depths over floodplain, transfer of momentum takes place from the main channel flow to the floodplain leading to the decrease in the main channel velocity and discharge, while its floodplain components are increased. As the depth of flow in the floodplain increases beyond a limiting depth, transfer of momentum does not takes place between the main channel and the floodplain. And at still higher depths over floodplains the process of momentum transfer reverses, the floodplain supplies momentum to the main channel. Due to the continuous stream wise variation of radius of curvature, the velocity and flow parameters are considerably more complex in a meandering channel than in a straight channel. The flow geometry in a meandering channel is in the state of either development or decay or both.

In the laboratory the mechanism of momentum transfer between the deep river section and shallow floodplain was first investigated and demonstrated by Zheleznvakov (1965) and Sellin (1964). While calculating discharge in compound channels, a method based on 'divided sections' is usually employed. Imaginary interface planes running from the junction between the main channel and floodplain are used to separate the main channel from the floodplain of the compound section. Momentum transfer between these subsections does not take place, when the shear stress at this fluid boundary is found to be zero. Yen and

Copyright © 2006 Taylor & Francis Group plc, London, UK

Overton (1973) used isovel plots to locate interface planes of zero shear. The data showed that the angle of inclination to the horizontal of the interface plane increased with depth over floodplain.

Following the previous work of Wormleaton et al. (1982), Knight and Demetriou (1983), Knight and Hamed (1984), and Myers (1987) on straight compound channels, with one to four types of geometries and smooth to six types of boundary roughness, the present study is aimed at understanding the general nature of the interaction between the main channel and the floodplain flows in meandering compound sections and propose suitable methods to calculate discharge in such channels.

Wright and Carstens (1970) observed that the calculation of discharge using the 'divided channel method' for compound sections compared well with the observed values although segment discharges varied up to $\pm 10\%$. They included the interface length in the wetted perimeter of the main channel subdivision only, as they considered that the slower flowing floodplain flow exerted a drag on the faster flowing main channel flow. Discharge assessment for compound sections between straight reaches also have been presented by Knight and Demetriou (1983), Knight and Hamed (1984), Wormleaton et al. (1982, 1985), Ackers (1993) covering smooth and rough boundaries.

There are limited reports covering investigation of a meandering channel with floodplains. Toebes and Sooky (1967) carried out laboratory experiments on two composite channel sections and showed that a nearly horizontal fluid boundary located at the junction between the main channel and floodplain would be more realistic than a vertical fluid boundary along the banks of the meandering channel in dividing the compound channel for discharge calculation. Using the data of the Flood Channel Facility at HR Wallingford, Greenhill and Sellin (1993) reported a method of estimation of discharge of meandering compound channels using Manning's equation and by extending the conventional divided channel method. The method assumed a fully developed shear layer at the interface between the main channel and the floodplain flows. For low over bank flow or for a very wide main channel, the method was found to give inaccurate results. Patra (1999), and Patra and Kar (2000) proposed a variable interface plane of separation of compound channel for a better estimate of discharge in meandering and straight compound river sections. The percentages of total flow carried by the main channel and floodplain of a compound section in terms of four dimensionless channel parameters were suitably modeled. The effect of flow interaction between the floodplain and main channel for various depths of flow over floodplain was adequately taken care.

Review of the literature show that investigators propose alternatives interface planes to calculate the total discharge carried by a compound channel section. Either including or excluding the interface length in the wetted perimeter does not make sufficient allowance for discharge calculation for all depths of flow over floodplain. It results either overestimate or underestimate of the discharge results. The work presented in this paper is based on a series of six channel sections with depth ratio between floodplain to main channel flow up to 0.404. In one series of experiment all the surfaces of main channel and floodplains are roughened uniformly.

2 EXPERIMENTAL SETUP

Experimental data from six series of channels are presented in this paper. Summary of experiments conducted are given in Table 1. The ratio α between overall width B and main channel width b are varied from 2.13 to 5.25 for the six sets (series A to I) of observations, of which the series I is symmetrical, the series A (Fig. 1a) is made with two unequal floodplains attached to both sides of the main channel, and the rest are asymmetrical channels with floodplain attached to one side only. The channel sections are made from Perspex sheets for which the roughness of floodplain and main channel are identical. All surfaces of the channels of series F and G are roughened with rubber beads of diameter 4 mm at 12-mm center to center. All observations are made at the section of maximum curvatures (bend apex) of the meandering channels. Plan forms of the types of meandering experimental channels with floodplains are shown in Fig. 1 .Though all the surfaces of the channel series D, F and G are roughened with rubber beads of diameter of 4 mm @ 12 mm center to center, no significant change is observed between the two types of channel in respect of flow characteristics and bed shear stresses.

Boundary shear stress is measured using locally fabricated Preston micro pitot tube in conjunction with a water manometer. Details of the experimental setup and procedure concerning the flow and velocity observations in meandering channels with floodplains are reported earlier (Patra 1999, Patra and Kar 2000). Experiments are conducted utilizing the facilities available at the Water Resources and Hydraulic Engineering Laboratory of the Civil Engineering Department of the IIT Kharagpur, India.

3 THEORETICAL CONSIDERATIONS

The vertical, horizontal, and diagonal plains of separation of compound channel are represented by the interface lengths aa_1, aa, and aa_2 respectively where as the interface plane aa_3 is a variable and is located by measuring the angle θ that it makes with the vertical

Copyright © 2006 Taylor & Francis Group plc, London, UK

Table 1. Summary of experimental runs for meandering channel with floodplains.

Experiment series/ Run no (1)	Nature of channel surface (2)	Bed slope (3)	Top width B (cm) (4)	Main channel width b (cm) (5)	Main channel depth h (cm) (6)	Depth of lower main channel (cm) (7)	$\alpha =$ B/b (8)	$\beta = (H-h)/H$ (9)	Sinuosity S_r (10)	Amplitude/ width ratio (R) (11)	Shape of the compound channel section (12)
A.1	Smooth	0.0061	52.5	10	11.6	10	5.25	0.137	1.22	0.178	
A.2	Smooth	0.0061	52.5	10	14.9	10	5.25	0.328	1.22	0.178	
A.3	Smooth	0.0061	52.5	10	16.8	10	5.25	0.404	1.22	0.178	
C.4	Smooth	0.004	21.3	10	12.19	10	2.13	0.180	1.21	(−)0.481	
C.5	Smooth	0.004	21.3	10	13.81	10	2.13	0.275	1.21	(−)0.481	
C.6	Smooth	0.004	21.3	10	15.24	10	2.13	0.343	1.21	(−)0.481	
D.7	Smooth	0.004	41.8	10	12.19	10	4.18	0.1796	1.21	0.245	
D.8	Smooth	0.004	41.8	10	14.08	10	4.18	0.2898	1.21	0.245	
F.9	Rough	0.004	21.3	10	12.22	10	2.13	0.181	1.21	(−)0.481	
F.10	Rough	0.004	21.3	10	13.71	10	2.13	0.270	1.21	(−)0.481	
F.11	Rough	0.004	21.3	10	15.24	10	2.13	0.343	1.21	(−)0.481	
G.12	Rough	0.004	41.8	10	12.49	10	4.18	0.209	1.21	0.245	
G.13	Rough	0.004	41.8	10	14.23	10	4.18	0.301	1.21	0.245	
G.14	Rough	0.004	41.8	10	15.84	10	4.18	0.369	1.21	0.245	
I.15	Smooth	0.00278	138	44	29.5	25	3.136	0.1525	1.043	0.072	
I.16	Smooth	0.00278	138	44	30.7	25	3.136	0.1857	1.043	0.072	
I.17	Smooth	0.00278	138	44	31.6	25	3.136	0.2089	1.043	0.072	

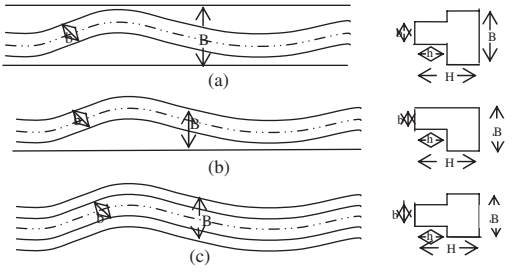


Figure 1. Plan forms of meandering experimental channels with floodplains.

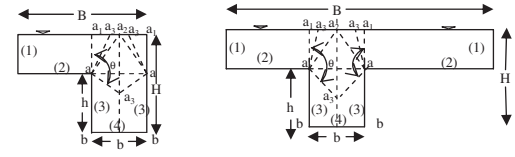


Figure 2. Notations.

plane aa_1 (Fig. 2). Various boundary elements of the compound channels are labeled from 1–4 in Fig. 2. Label (1) denotes the vertical wall(s) of floodplain with length $[2(H-h)]$ and label (2) denotes floodplain bed(s) with length $(B-b)$. Label (3) denotes the two main channel walls and the bed of the main channel is represented by label (4).

3.1 *Shear force on the assumed interface planes*

The measured shear stresses were integrated over the respective lengths of each of the boundary elements (labeled 1–4 in Fig. 2), to obtain the boundary shear force per unit length for the elements. The sum of the boundary shear forces for all beds and walls of the compound channel was used as a divisor to calculate the shear force percentages carried by the boundary elements. The shear force percentage carried by the flood plains is represented as $\%S_{fp}$, and for the main channel it can be taken as $\%S_{mc}$.

The shear force percentages carried by the floodplain with depth ratio β for all the compound channels of varying geometries ($\alpha = 2.13$ to 5.25) are given in col. (3) of Table 2. The total shear force carried by the floodplain beds and walls are very important because the apparent shear force acting on the assumed boundaries originating from the junction between floodplain

Copyright © 2006 Taylor & Francis Group plc, London, UK

Table 2. Shear force and discharge results for meander channels with floodplains.

Experiment Series	Observ. Discharge (cm^3/sc)	% S_{fp}		Apparent Shear Force Results								Discharge Results (cm^3/sec)				
		Exp.	Calc.	%ASF_v		%ASF_D		%ASF_H		%ASF_{VI}		Meth.-I Vert. interf.	Meth.-II Diag. Interf.	Meth.-III Horiz. Interf.	Meth.-IV Variable Interf.	Meth.-V Modified Interf-
				Calc.	Exp.	Calc.	Exp.	Calc.	Exp.	Calc.	Exp.					
(1)	(2)	(3)	(4)	(5)	(6)	(7)	(8)	(9)	(10)	(11)	(12)	(13)	(14)	(15)	(16)	(17)
A.1	3960	64.1	66.2	14.6	13.6	12.5	11.5	20.6	18.5	2.1	0.01	4458	4291	4157	3973	3800
A.2	14000	67.0	68.9	5.3	4.4	1.9	0.9	-3.1	-5.0	2.0	0.07	14132	14018	14244	14039	13857
A.3	19500	67.4	71.2	4.0	2.1	0.3	-1.6	-6.9	-10.7	3.8	0.00	19620	19686	20321	19524	19385
C.4	5800	29.0	28.5	5.8	6.1	2.1	2.3	-3.4	-2.9	-0.5	0.03	6057	5945	5809	5800	5823
C.5	8450	34.8	37.7	7.0	5.6	1.8	0.3	-6.9	-9.9	3.0	0.10	8563	8488	8524	8482	8298
C.6	11200	38.0	42.7	7.4	5.0	1.3	-1.2	-9.9	-14.7	4.9	0.06	11245	11207	11490	11302	10986
D.7	5800	592	55.0	9.3	11.4	6.5	8.5	7.2	11.4	-4.1	0.09	6091	6006	5861	5878	5709
D.8	8450	59.9	593	5.7	6.0	1.9	2.2	-3.8	-3.1	-0.6	0.03	8471	8455	8517	8589	8362
F.9	5500	27.1	28.6	5.8	5.1	2.1	1.3	-3.4	-4.9	1.6	0.04	5738	5634	5507	5509	5517
F.10	8200	34.4	37.4	7.0	5.5	1.8	0.3	-6.7	-9.7	2.9	0.00	8319	8242	8263	8227	8056
F.11	10900	36.1	42.7	7.4	4.1	1.3	-2.1	-9.9	-16.6	6.6	-0.05	10944	10907	11182	10949	10692
G.12	5500	55.9	55.9	8.0	8.0	4.9	4.9	3.5	3.4	0.1	0.02	5693	5628	5521	5525	5414
G.13	8200	56.0	59.7	5.4	3.6	1.6	-0.3	-4.5	-8.3	3.8	0.07	8213	8202	8281	8239	8122
G.14	10900	60.0	62.8	4.4	3.0	0.2	-1.2	-8.2	-11.0	2.9	0.09	10918	10927	11252	11083	10921
I.15	94535	37.1	40.1	7.8	6.3	4.9	3.4	4.0	1.0	3.1	-0.02	110807	104717	100068	99456	103801
I.16	103537	42.8	42.8	7.3	7.3	3.9	3.9	1.2	1.2	0.1	0.03	117395	110867	106413	105861	110984
I.17	108583	46.1	44.6	6.9	7.6	3.3	4.0	-0.6	0.82	-1.4	0.02	120793	114185	110127	109835	114829

and main channel can be determined once this quantity is known. Following the previous work of Knight and Demetriou (1983), Patra and Kar (2000) proposed a general equation for the percentage of shear force carried by the floodplains of meandering compound channels as

$$\%S_{fp} = 48(\alpha - 0.8)^{0.289}(2\beta)^{m}[1 + \alpha \mathrm{Re}^{-1325\beta\delta}]\{1 + 1.02\sqrt{\beta}\log\gamma\} \quad (1a)$$

where the exponent m can be calculated from the relation

$$m = \frac{1}{0.75\, e^{0.38(\alpha - R)}} \quad (1b)$$

in which R = ratio of the amplitude ε of the meandering channel to the top width B of the compound section the values of which are given in col. (11) of Table 1, δ = aspect ratio of the main channel b/h, and γ = the ratio of Manning's roughness n of the floodplain to that for the main channel. For a straight channel the value of R is zero. A zero value of R reduces equations (1a) and (1b) to the form of Knight and Hamed (1984) and for channels with equal surface roughness in the floodplain and main channel ($\gamma = 1$), equation (1) further reduces to the form proposed by Knight and Demetriou (1983). Using (1) the calculated percentage of total shear force carried by the floodplains is given in Table 2 (column 4). Patra and Kar (2000) have reported the adequacy of equation (1).

Once the shear force carried by the floodplain is known, the apparent shear force acting on the imaginary interface of the compound section can be calculated. These apparent shear forces may then be used to get an idea of the momentum transfer between the different subsections of the compound channel. For any regular prismatic channel under uniform flow conditions the sum of boundary shear forces acting on the main channel wall and bed together with an 'apparent shear force' acting on the interface plane between main channel and floodplain must be equal to the resolved weight force along the main channel.

$$\rho g A_{mc} S = \int_{mc} \tau dp + ASF_{ip} \quad (2)$$

in which g = gravitational acceleration, ρ = density of flowing fluid, S = slope of the energy line, A_{mc} = area of the main channel defined by the interface plane, $\int_{mc} \tau dp$ = shear force on the surfaces of the main channel consisting of two vertical walls and bed, and ASF_{ip} = apparent shear force of the imaginary interface plane. Because the boundary shear stress carried by the compound section (ρgAS) is equal to 100%, where A is the total cross section of the compound channel, the percentage shear force carried by the main channel surfaces can be calculated as

$$\% S_{mc} = 100 \frac{\int_{mc} \tau dp}{\rho gAS} = 100 \frac{\rho g A_{mc} S}{\rho gAS} - 100 \frac{ASF_{ip}}{\rho gAS} \quad (3)$$

But since $\%S_{mc} = 100 - \%S_{fp}$; and $100(ASF_{ip}/\rho gAS)$ = percentage of shear force on the assumed interface, substituting the values, the apparent shear force on the interface plane can be calculated as

$$\% ASF_{ip} = 100 \frac{A_{mc}}{A} - \{100 - \% S_{fp}\} \quad (4)$$

in which $\%ASF_{ip}$ = percentage of shear force in the interface plane. Having computed $\%S_{fp}$ through (1), it is easy to evaluate (4) for the assumed interface plane. For example, for vertical interface between the boundary of the floodplain and main channel shown by the

Copyright © 2006 Taylor & Francis Group plc, London, UK

lines aa_1 in Fig. 2, the value of A_{mc} is the area marked by a_1abbaa_1, which when substituted in (4), yields $\%ASF_{ip}$. Similarly for horizontal or diagonal interfaces, A_{mc} can be estimated from the areas marked as aabb or a_2abbaa_2, respectively, in Fig. 2. These apparent shear forces can be expressed as percentages of the total channel shear force using the following relations:

$$\%\,ASF_V = \frac{50}{[(\alpha-1)\beta+1]} - \frac{1}{2}\{100 - \%\,Sfp\} \quad (5a)$$

$$\%\,ASF_D = \frac{25(2-\beta)}{[(\alpha-1)\beta+1]} - \frac{1}{2}\{100 - \%\,Sfp\} \quad (5b)$$

$$\%\,ASF_H = \frac{100\,(1-\beta)}{[(\alpha-1)\beta+1]} - \{100 - \%\,Sfp\} \quad (5c)$$

in which $\%S_{fp}$ can be calculated from (1). Percentages of apparent shear force for the assumed vertical, horizontal, and horizontal interface planes from series A to I are given in Table 2 (columns 5 to 10). The table compares the measured shear force percentages carried by the floodplains in each case along with the computed values using equations (1) and (5).

For the assumed vertical interface plane the shear force is always positive for the ranges of α and β tested. A positive value indicates transfer of momentum from the main channel to the floodplain at the assumed plane indicating the floodplain flow retarding the main channel flow. This apparent shear stress is higher than the bed-shear stress at low floodplain depths and reduces gradually as β increases. For example, for channel series A.1 the apparent shear stress is 4.2% per unit length of the interface plane while the bed shear stress of the main channel per unit length of wetted perimeter is 1.2% of the total shear stress. This follows a similar trend for all channels for the runs C.1, D.1, E.1, F.1, and I.1. For the diagonal and horizontal interface planes it can be observed that the apparent shear force is positive at low depths and changes sign as depth increases indicating that at higher depths over floodplain there is transfer of momentum from the floodplain to the main channel. A smaller value of apparent shear stress renders the interface plane more suitable, but a large negative value of apparent shear stress at higher depths makes the interface plane unsuitable for separating the channel into hydraulically homogeneous zones for calculating discharge of compound channels by the divided channel method. However, none of the above methods explain a boundary for which there is no transfer of momentum for all depths.

3.2 *A variable-inclined interface plane*

Patra and Kar (2000) proposed a method of selecting the interface plane for meandering channel for which the apparent shear stress is found to be nearly zero. This variable plane of separation can be located by an angle θ it makes with the vertical line aa_1 (Fig. 2), and in radians it is expressed as

$$\theta = (\alpha - R\beta)(1-\beta)^{\beta}(5.25\beta)^{0.075}\,e^{-\beta(\alpha-R)} \quad (6)$$

The angle is dependent on the depth of flow over the floodplain, the flowing out width of the floodplain, and the amplitude of the meandering channel. The adequacy of this interface plane for separating the main channel from floodplain for calculating discharge by divided channel method are explained by Patra (1999), and Patra and Kar (2000). Once the angle θ is known (from 6) the area of the main channel A_{mc} representing the area a_3abbaa_3 in Fig. 2 can easily be estimated. For regular and prismatic channels under uniform flow conditions, the apparent shear force percentage of this plane can be obtained from the equation given as

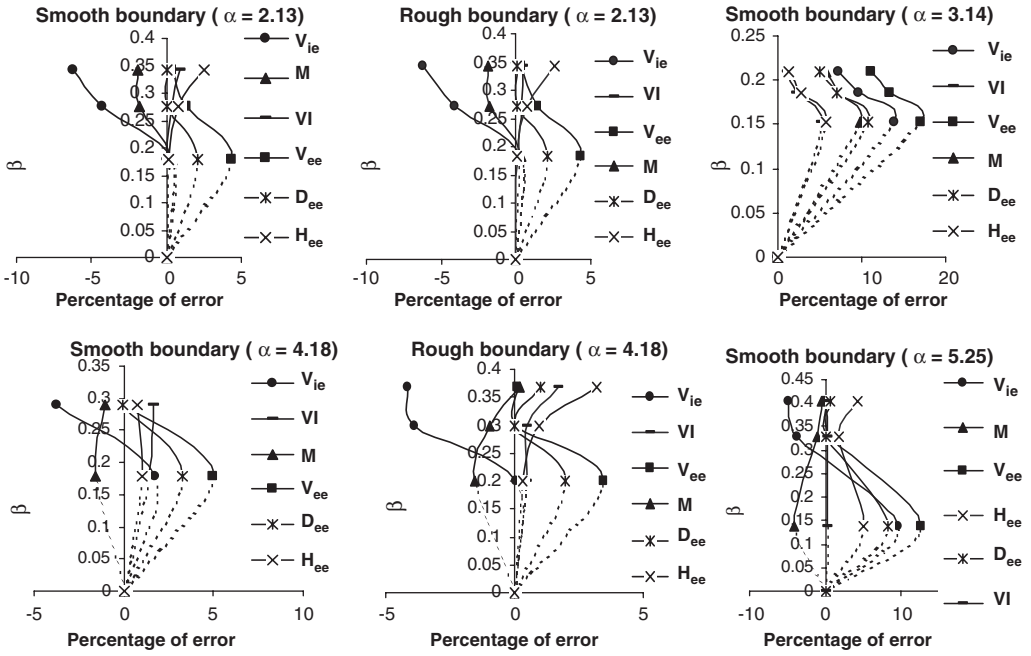
$$\%ASF_{VI} = \frac{100\,A_{mc}}{bH[(\alpha-1)\beta+1]} - \{100 - \%Sfp\} \quad (7)$$

where $\%ASF_{VI}$ = apparent shear force on the variable-inclined interface as percentage of total, b = width of main channel, and H = depth of flow over the main channel. Using (6) and (7) Patra and Kar (2000) had shown that (col. 11–12 of Table 2) the calculated shear force percentage at the variable interface are almost zero for all the channels shown in Table 1. Considering all 17 runs, the standard error between the measured and the estimated apparent shear force using the variable plane of interface is found to be 3%.

4 DISCHARGE RESULTS

Easily located vertical, horizontal or diagonal interface planes running from the main channel floodplain junctions are mostly used to separate a compound channel section into subsections. Discharges for each subsection are calculated using Manning's equation and added to get the total discharge of the compound section. To identify an accurate, simple, but practicable way of calculating discharge for meandering compound channels the cross section of the compound channel is divided into subsections by the preceding four easily identifiable interface planes running from the floodplain-main channel junction. In all the cases, the interface length is not included in the wetted perimeter. Discharge results for the channel sections using the above four interface planes are given in Table 2 (col.13–16). The percentage of error between the observed and calculated discharge results of Table 2 for the four interface planes are shown in Fig. 3. It can be seen in the figure that the error percentage is comparatively less for the variable-inclined interface plane. The error percentage increases gradually to a maximum for the vertical interface through

Copyright © 2006 Taylor & Francis Group plc, London, UK



V_{ee} = Interface Excluded from MC and FP, V_{ie} = Interface Included in MC and Excluded from FP, M = Modified Vertical Interface, VI = Variable Interface Plane, H_{ee} = Horizontal Interface Excluded both from MC and FP, D_{ee} = Diagonal Interface Excluded both from MC and FP

Figure 3. Error percentages between calculated and observed discharges for various interface planes.

horizontal and diagonal planes. Excluding the interface length in the wetted perimeter overestimates the discharge capacity of the channel even at higher depths of flow for the ranges of β tested. This is quite in agreement with the results given by Wormleaton and Hadjipanos (1982).

A look into the apparent shear force at the vertical interface (col. 5, Table 2) shows that there is always transfer of momentum across this interface and therefore what adjustments are to be made to take care of the momentum transfer or shear force acting at this plane has been the subject of present research. In this paper alternative uses of the vertical interface planes are tested to give an insight to the flow processes and to propose the best discharge results.

5 ALTERNATIVE VERTICAL INTERFACE METHODS

5.1 *Interface plane included to the main channel perimeter*

The effect of momentum transfer at low depths of flow over floodplain ($\beta < 0.4$) is to decrease the velocity and discharges of main channel while its floodplain components are increased. It is argued that the interface length $(H - h)$ should be included to the main channel perimeter only to take care of the momentum transfer so that the overestimation of the discharge is checked. Therefore in this method the interface length $(H - h)$ is added to the main channel boundary only. Resulting discharge errors for the compound channels are shown as curves V_{ie} in Fig. 3.

5.2 *Modified vertical interface method*

The vertical interface plain is neither shear free nor the apparent shear at this surface is equal to boundary shear of main channel surface or of the floodplain surface. Myer (1975), Wormelaton et al. (1982), and Knight and Demetriou (1983) have shown that apparent shear in the vertical, horizontal or diagonal interface is many times greater than the boundary shear stress in main channel or floodplain at low floodplain depths. Therefore either excluding or including the interface length to the main channel/floodplain boundary does not fully take care of the interaction effect. It has been shown convincingly that failure to allow for the existence of such mechanism results in erroneous compound channel analysis.

Wormelaton et al. (1982) have shown that the total dragging force on the main channel due to floodplain

Copyright © 2006 Taylor & Francis Group plc, London, UK

at the interfaces must be equal to the accelerating force on floodplain due to the main channel. Therefore the wetted perimeter of the main channel needs to be increased suitably to take care of the net dragging force on the main channel. Similarly the wetted perimeter of the floodplain needs to be reduced by subtracting a suitable length of interface to account for the accelerating force on the floodplain due to the pulling of the main channel water. Net force at the assumed vertical interface should balance each other. Let X_{mc} be the interface length for inclusion in the main channel wetted perimeter and X_{fp} the length of interface length to be subtracted from the wetted perimeter of floodplain. By assuming the channel to be regular, prismatic, and flow under uniform conditions the sum of the boundary shear forces acting on the main channel plus the shear force on the assumed interface must be equal to the weight component of water of the main channel and is written as

$$(P_{mc}\tau_{mc} + X_{mc}\tau_{mc}) = \rho g A_{mc} S \tag{8a}$$

Similarly for the floodplain, equation (8a) is expressed as

$$(P_{fp}\tau_{fp} + X_{fp}\tau_{fp}) = \rho g A_{fp} S \tag{8b}$$

where P_{mc} = the wetted perimeter of the main channel, P_{fp} = the wetted perimeter of the floodplain, A = the area of cross section of the compound channel section = $A_{mc} + A_{fp}$, A_{mc} and A_{fp} = the area of cross sections of main channel and floodplain subsections respectively, τ_{mc} and τ_{fp} = the mean boundary shear stress in main channel and floodplain per unit length, and S = the longitudinal slope of the channel. Again for a compound section, the total boundary shear must be equal to the weight component of flowing fluid along longitudinal direction and is written as

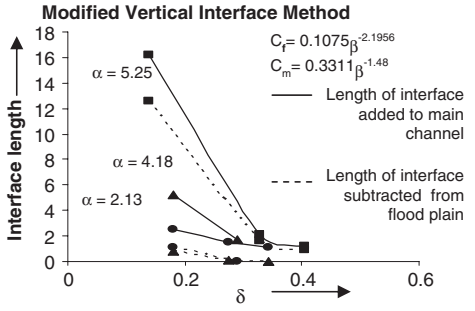
$$\left(P_{mc}\,\tau_{mc} + P_{fp}\tau_{fp}\right) = \rho g A S \tag{9}$$

Since $\rho g A_{mc} S + \rho g A_{fp} S = \rho g A S$, the sum of weight components represented by (8a and 8b) must be equal to the weight component represented by (9) from which we get

$$X_{mc}\,\tau_{mc} = -X_{fp}\,\tau_{fp} \tag{10}$$

Equation (10) shows that the shear force on the main channel arising out of the assumed vertical interface must be equal and opposite to that considered for the floodplain by the divided channel approach. At the assumed vertical interface plane the term $X_{mc}\tau_{mc} = -X_{fp}\tau_{fp}$ is taken as the apparent shear force ASF_{ip}. Now from equation (8a) a general expression for X_{mc} for any interface is written as

$$X_{mc} = \frac{\rho g A_{mc} S - \tau_{mc} P_{mc}}{\tau_{mc}} \tag{11}$$



C_m= Interface length added to main channel = eq 16/(H-h);
C_f= Interface length subtracted from floodplain = eq 17/ (H-h)

Figure 4. Variation of interface length with β.

And for the vertical interface equation (11) is simplified to

$$X_{mcV} = \frac{100\ P_{mc}}{(100 - \%\,S_{fp})\{1 + (\alpha - 1)\beta\}} - P_{mc} \tag{12}$$

Following the above steps, the equivalent decrease in length of floodplain wetted perimeter for any interface can be written similar to (11) as

$$X_{fp} = P_{fp}\left[\frac{100}{\%\,S_{fp}}\left(\frac{A_{mc}}{A} - 1\right) - 1\right] \tag{13}$$

And for vertical interface, equation (13) is written as

$$X_{fpV} = P_{fp} - \frac{100\,(\alpha - 1)\beta}{(\%\,S_{fp})\{1 + (\alpha - 1)\beta\}} P_{fp} \tag{14}$$

where the percentage of shear force ($\%S_{fp}$) carried by the floodplains can be calculated from equation (1).

Knowing $\%S_{fp}$ and channel geometries parameters the interface lengths X_{mcV} and X_{fpV} are calculated. Next the discharge for main channel and floodplain are calculated using Manning's equation given as

$$Q = \frac{\sqrt{S_f}}{n} A_{mc}^{5/3}\left(P_{mc} + X_{mc}\right)^{-2/3} + A_{fp}^{5/3}(P_{fp} - X_{fp})^{-2/3} \tag{15}$$

The lengths in terms of $(H - h)$ times X_{mcV} and X_{fpV} are plotted against β in Fig. 4. The percentage of error between observed and calculated discharges for all the channels are shown as curves M in Fig. 3.

5.3 *Validation of the methods for straight channel*

The methods are tested with experimental data of Knight and Demetriou (1983) for the three types of straight compound channels ($\alpha = 2$, 3, and 4). The three channels give similar results as in the case of meandering sections. The results of Knight and Demetriou (1983) are presented in Fig. 5. Curves H_{ee} and D_{ee} are plotted in the same figure for comparison.

Copyright © 2006 Taylor & Francis Group plc, London, UK

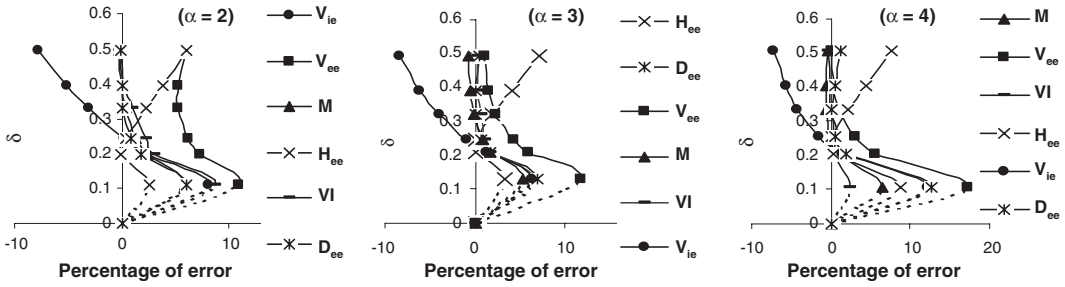


Figure 5. Error percentages between calculated and observed discharges for various interface planes for the channel of Knight and Demetriou (1983).

6 RESULTS AND DISCUSSIONS

Errors in the percentage of discharge between observed and computed values of the compound channel sections are found to be the maximum (up to 17%) for β values between 0.13 and 0.2 when the interface plane is not included in the wetted perimeter of both main channel and floodplains. The error percentage curves then decreases to a minimum when $\beta \approx 0.4$. This shows that momentum transfer is maximum at $\beta = 0.15 - 0.2$ and the transfer of momentum across the vertical boundary is complete at around $\beta = 0.4$.

When an interface length equal to the depth of floodplain is included in the main channel only of the compound section, the error in discharge between observed and computed values are found to be less than the method excluding it (up to 14%). However, at higher depths of flow over floodplain ($\beta > 0.2$), large negative values of discharge errors are obtained (up to -8%) indicating that when the momentum transfer between main channel with that of floodplain is nearly complete at these depths, the method gives inaccurate results.

Modified vertical interface method gives good results of discharge estimates for the compound channels having low α values and for β up to 0.2. But for channels with narrow flood plains carrying flow at higher depths or for wider channels ($\alpha = 5.25$) carrying lower depths of flow, the method gives higher percentages of errors in discharges (up to -5%). From the plots between β and the length of interface added to main channel and subtracted from floodplain the lengths of interfaces are modeled as interface length added to main channel is given as

$$C_m \times (H\text{-}h) \text{ where } C_m = 0.3311\beta^{-1.48} \quad (16)$$

Interface length subtracted from floodplain is given as

$$C_f \times (H\text{-}h) \text{ where } C_f = 0.1075\beta^{-2.19563} \quad (17)$$

The Variable Inclined Interface plane method proposed by Patra and Kar (2000) is based on the theoretical background of locating interface plane of zero shear. The method gives good results but is not as straight forward as the above vertical interface planes.

7 CONCLUSIONS

The following conclusions can be made from the above discussions:

1. Either by including or excluding the length of interface equal to the depth of floodplain to the wetted perimeter of the main channel or to the floodplain does not make sufficient allowance for discharge calculation for all depths of flow over floodplain. These methods either overestimate or underestimate the discharge results.
2. By balancing the magnitudes of shear force at the vertical interface (named as Modified Vertical Interface Method) gives better discharge results (maximum error up to $+9\%$ and -4% respectively at $\beta = 0.15$. This is an improved method of discharge estimation for compound sections. However the method lacks in giving good results for the main channel and the floodplains subsection discharges.
3. The Variable Inclined Interface plane method proposed by Patra and Kar (2000) is based on the theoretical background of locating interface plane of zero shear. The method gives good discharge results but involves more steps in identifying the interface plane and the subsequent discharge estimation.

NOTATIONS

The following symbols are used in this paper:

A = total cross-sectional area of compound channel;
B = top width of compound channel;
b = width of main channel;
C_m = Interface length added to main channel using equation $16/(H - h)$;

Copyright © 2006 Taylor & Francis Group plc, London, UK

C_f = Interface length subtracted from floodplain using equation $17/(H-h)$;
g = gravitational acceleration;
H = depth of flow in main channel;
h = height of main channel up to floodplain bed;
m = exponent used in Eq. (1a);
n = Manning's roughness factor;
R = ratio of amplitude of compound channel to top width B;
S_f = energy slope line;
s_r = sinuosity of meander channel = (ls/lc);
α = width ratio = B/b;
β = relative depth = $(H-h)/H$;
γ = ratio of floodplain roughness to main channel roughness;
δ = ratio between main channel width to its depth (b/h);
ε = amplitude of meander channel;
ρ = density of flowing liquid;
τ = boundary shear stress;
$\int_{mc} \tau\, dp$ = shear force on surfaces of main channel;
$\%ASF$ = percentage of total channel shear force carried by assumed interface planes;
$\%ASFH$ = ASF on horizontal interface (aa) as percentage of total shear force;
$\%ASFip$ = ASF on an interface plane as percentage of total shear force;
$\%ASFV$ = ASF on vertical interface (aa_1) as percentage of total shear force;
$\%ASFVi$ = ASF on variable-inclined interface (aa_3) as percentage of total shear force;
ASF_{IP} = apparent shear at the interface;
P_{mc} = the wetted perimeter of the main channel,
P_{fp} = the wetted perimeter of the floodplain,
A = the area of cross section of the compound channel section and
A_{mc} = are the area of main channel
A_{fp} = flood plain subsections respectively,
τ_{mc} = the mean boundary shear stress in main channel per unit length longitudinally
τ_{fp} = mean boundary shear stress in flood plain per unit length longitudinally
S = the longitudinal slope of the channel.
τ_{av} = is the average shear stress in the assumed vertical interface whose interface length is $l_v = H - h$
$\%S_{fp}$ = the percentage of shear force carried by the floodplains
$\%S_{mc}$ = the percentage of shear force carried by the floodplains
Q = Calculated discharge.
X_{mc} = Length of interface added to main channel subsection
X_{fp} = Length of interface subtracted from flood plain subsection
X_{mcv} = Length of vertical interface added to main channel subsection
X_{fpv} = Length of vertical interface subtracted from flood plain subsection.

REFERENCES

Ackers, P.1993. "Flow Formulae for Straight Two Stage Channels," *Journal of Hydraulic Research*, IAHR Vol.31, No.4, pp. 509–532.

Greenhill, R.K. & Sellin, R.H.J. 1993. "Development of a Simple Method to Predict Discharge in Compound Meandering Channels", *Proc. of Instn. Civil Engrs Wat. Merit. and Energy*, 101, paper10012, march, pp. 37–44.

Knight, D.W. & Demetriou, J.D. 1983. "Flood Plain and Main Channel Flow Interaction", *Journal of Hyd. Engg., ASCE* Vol.109, No.8, pp. 1073–1092.

Knight, D.W. & Hamed, M.E. 1984. "Boundary Shear in Symmetrical Compound Channels", *Journal of the Hydr. Eng., ASCE,* Vol.110, No.HY10, Paper 19217, pp. 1412–1430.

Myers, W.R.C. & Elsawy. 1975. "Boundary Shear in Channel With Floodplain", *Jr. of Hydr. Division, ASCE*, Vol.101, HY7, pp. 933–946.

Myers, W.R.C. 1987. "Velocity and Discharge in Compound Channels", *Jr. of Hydr. Engg., ASCE,* Vol.113, No.6, pp. 753–766.

Patra, K.C. 1999. "Flow interaction of Meandering River with Flood plains", *Thesis Presented to the Indian Institute of Technology,* Kharagpur, at Kharagpur, in partial fulfillment of the requirements for the Degree of Doctor of Philosophy.

Patra, K.C. & Kar, S.K. 2000. Flow interaction of Meandering River with Flood plains, *Journal of Hydr. Engineering, ASCE*, Vol.126, No.8, pp. 593–603.

Sellin, R.H.J. 1964. "A Laboratory Investigation into the Interaction Between Flow in the Channel of a River and that of its Flood Plain", *La Houille Blanche*, No.7, pp. 793–801.

Toebes, G.H. & Sooky, A.A. 1967. "Hydraulics of Meandering Rivers with Flood plains", *Journal of the waterways and Harbor Div., Proc. of ASCE*, Vol.93, No.WW2, May, pp. 213–236.

Wright & Carstens. 1970. "Linear momentum flux to over bank sections", *Journal of Hydr. Division., ASCE*, Vol.96, NoHY9, pp. 1781–1793.

Wormleaton, et al. 1982. "Discharge Assessment in Compound Channel Flow", *Journal of the Hydr. Division, ASCE*, Vol.108, No.HY9, pp. 975–994.

Wormleaton & Hadjipanos, P. 1985. "Flow Distribution in Compound Channels", *Journal of the Hydr. Engg., ASCE*, Vol.111, No.7, pp. 1099–1104.

Yen, C.L. & Overton, D.E. 1973. "Shape Effects on Resistance in Floodplain Channels", *Journal of Hydr. Division., ASCE,* Vol.99, No.1, pp. 219–238.

Zheleznyakov, G.V. 1965. "Interaction of Channel and Floodplain Streams", *Proc. 14th Congress of IAHR,* 5, Paris, France, pp. 144–148.

Copyright © 2006 Taylor & Francis Group plc, London, UK

Mathematical modelling and analysis of river flows in transitional waters

M. Santos
ESTIG – Polytechnic Institute of Beja, Portugal

J. Hipólito
IST – Technical University of Lisbon, Portugal

ABSTRACT: River flows in transitional regions, between inland surface waters and coastal waters, suffer the effects of downstream boundary tides that may enhance several river events or phenomena like floods and erosions among others. The purpose of this paper is to present the study carried out to analyse the influence of tides in the river subcritical flows. So, based on the complete 1-D Saint-Venant equations and using the implicit Preissmann finite-difference method, a mathematical model was developed to simulate one-dimensional unsteady flows in rivers, with irregular and variable cross-sections. The model was applied to the Sado river, more precisely, to a reach of this Portuguese river, right upstream Alcácer do Sal city, in which the fluvial flows are influenced by the tide and during flood events has caused important damage, either human or material. Discharge rating functions on the last section of the river reach were analysed and are described. The correlations between some of the rating functions and the results of the model are quite good. The contributions to the friction slope value of each one of its dynamic components in the last downstream spatial step are also presented.

1 INTRODUCTION

The influence of tides in the flow of tidal rivers may be very important in several river events or phenomena that might occur like floods and erosions located near fluvial structures. However, this type of flow has not been a much explored subject in the existent related bibliography, especially in what concerns the analysis of the discharge in river sections influenced by the tide effects.

Thus, this paper presents the study carried out to analyse the impact of tides in the flow of tidal rivers. The mathematical formulation of the problem was done using the complete 1-D Saint-Venant equations and for its solution the implicit Preissmann finite-difference method was used. In this way a computational model was developed to simulate one-dimensional unsteady flows in rivers, with irregular and variable cross-sections, and with the downstream boundary affected by the tide effects.

In this analysis the important aspect of the interaction between the flood plain and the in bank flow, recently referred by some authors (for example Shiono and Knight 1991, Ackers 1993, Tominaga et al. 1995, Lyness et al. 1997, Bousmar and Zech 1999), as well as the consideration of flow velocity coefficients were left apart.

The tributaries discharges, as well as the salinity effects on flow dynamics, were also left apart.

An application of the referred computational model was carried out to the Sado River, more precisely, to a reach of this Portuguese river, right upstream Alcácer do Sal city, in which the fluvial flows experiment the tide influence and during flood events has caused important damage, either human or material, in the neighbourhood, particularly in that town.

The purpose of this application was to achieve several flow computational simulations in the considered river reach relatively to some flood events, with the intention of studying the fluvial flow influenced by the tide in what concerns its characteristics in terms of discharge, water depth, flow velocity and Froude number. Another intention was the analysis of the relationship between the water depth and the discharge in the last section of the river reach in study.

To illustrate some of the results obtained during the study phase of the work it is only presented in this paper the flow simulation for a flood event, in which the maximum value of the discharge is 2820 m^3/s.

2 MATHEMATICAL MODELLING

The mathematical modelling of the problem in study is based on the complete Saint-Venant equations, which are usually used to represent the unsteady open channel flows that occur in rivers.

Copyright © 2006 Taylor & Francis Group plc, London, UK

In this manner, the one-dimensional unsteady flows in rivers, with arbitrary shape cross-sections which may vary along their length, assuming also that the water density is constant and the flow velocity coefficients are the unit, may be described by the variables water depth, h, and discharge, Q, at any given river cross-section. These dependent variables define the water motion along the river course and in time, i.e. as a function of two independent variables: the space, x and the time, t.

So, the mathematical formulation of the problem leads to the following two partial differential equations, namely the continuity equation and the dynamic equation, both expressed under their matrix form, as it can be seen for example in Chaudhry (1993), Cunge et al. (1980) and Santos (2004):

$$\frac{\partial \mathbf{U}}{\partial t} + \frac{\partial \mathbf{F(U)}}{\partial x} = \mathbf{S(U)} \tag{1}$$

where

$$\mathbf{U} = \begin{bmatrix} A \\ VA \end{bmatrix} \tag{2}$$

$$\mathbf{F(U)} = \begin{bmatrix} VA \\ V^2 A + gA\bar{h} \end{bmatrix} \tag{3}$$

$$\mathbf{S(U)} = \begin{bmatrix} 0 \\ gA(S_0 - J) + gI_2 \end{bmatrix} \tag{4}$$

where $A\bar{h} = I_1$ and $\bar{h}$ is the depth of the flow area centre of gravity.

The symbols that appear in those equations have the following significance:

$A = A(x,t)$ – wetted cross-sectional area,

$Q = VA$ – water discharge through the cross-section, where $V = V(x,t)$ is the uniform cross-sectional velocity,

t – time (independent variable),

x – distance in the flow direction (independent variable),

g – acceleration due to gravity,

I_1, I_2 – cross-sectional moment integrals, which are calculated with the following expressions:

$$I_1 = \int_0^{h(x)} [h(x) - \eta]\sigma(x,\eta)\,d\eta \tag{5}$$

$$I_2 = \int_0^{h(x)} [h - \eta]\left[\frac{\partial \sigma}{\partial x}\right]_{h=h_0} d\eta \tag{6}$$

h – water depth in the considered river cross-section,

$\sigma(x,\eta)$ – width of the cross-section where the water depth is η,

S_0 – bed slope in the x-direction,

J – energy line slope in the x-direction (friction slope); according to the Manning-Strickler formula the friction slope is given by the expression below:

$$J = \left(\frac{Q}{KAR^{2/3}}\right)^2 = \left(\frac{nQ}{AR^{2/3}}\right)^2 \tag{7}$$

where

R – hydraulic radius,

$n = 1/K$ – Manning coefficient.

To solve the problem two computer programs were developed, namely: one for the computation of the fundamental geometric and hydraulic characteristics of the river cross-sections (Geohid_Sectransv model) and the other interrelated with the previous for the computation of the flow variables using the implicit Preissmann finite-difference method (Esquema_Implícito model).

Thus the computation of the flow through the Esquema_Implícito model is based on the numerical discretization of the Preissmann scheme, according to the following expression, as it can be seen for example in Chaudhry (1993) and Santos (2004):

$$\begin{aligned} &\mathbf{U}_i^{j+1} + \mathbf{U}_{i+1}^{j+1} + 2\frac{\Delta t}{\Delta x}\left[\theta\left(\mathbf{F}_{i+1}^{j+1} - \mathbf{F}_i^{j+1}\right) + (1-\theta)\left(\mathbf{F}_{i+1}^{j} - \mathbf{F}_i^{j}\right)\right] + \\ &+ \Delta t\left[\theta\left(\mathbf{S}_i^{j+1} + \mathbf{S}_{i+1}^{j+1}\right) + (1-\theta)\left(\mathbf{S}_{i+1}^{j} + \mathbf{S}_i^{j}\right)\right] = \mathbf{U}_i^{j} + \mathbf{U}_{i+1}^{j} \end{aligned} \tag{8}$$

where

i – cross section index,

j – time instant index,

θ – weighting coefficient in the finite difference approximations of functions and their space derivatives $(0,5 < \theta \leq 1)$,

Δx – spatial step,

Δt – temporal step.

It is important to remark another aspect of this study which consisted in the analysis for the last downstream spatial step of the contributions to the friction slope value of each one of its dynamic components.

Thus, according to Santos (2004), based on the Manning-Strickler resistance law, the continuity equation and the dynamic equation expressed in terms of the water depth and the flow velocity variables, the friction slope may be given by the expression presented below:

$$J = S_0 - \left(1 - \frac{V^2}{c^2}\right)\frac{\partial h}{\partial x} + \frac{V}{c^2}\frac{\partial h}{\partial t} + \frac{V^2}{gA}\left.\frac{\partial A}{\partial x}\right|_{h=cte} - \frac{1}{g}\frac{\partial V}{\partial t} \tag{9}$$

One of the flow computational model explorations that is also important to refer was carried out with the intent of its application to the analysis of the discharge rating function on the last section of the river reach in

Copyright © 2006 Taylor & Francis Group plc, London, UK

study. So the results obtained with the computational model were confronted and criticized face to those which were estimated using the kinematic, diffusive and dynamic wave theories with constant parameters which are described below.

In the study of the discharge rating function, taking into account the above referred contributions to the friction slope, further simplifications were considered:

– the contribution of the component

$$\left.\frac{\partial A}{\partial x}\right|_{h=cte} \tag{10}$$

was disregarded, which is equivalent to consider the final river reach approximately prismatic;

– the contribution of the component

$$\frac{\partial V}{\partial t} \tag{11}$$

was disregarded, thus allowing an explicit formulation for the discharge,

$$Q = Q\left(h, \frac{\partial h}{\partial x}, \frac{\partial h}{\partial t}\right) \tag{12}$$

In this way, considering:

$$\xi = 1 - \frac{V^2}{c^2} \tag{13}$$

$$\eta = \frac{V}{c^2} \tag{14}$$

where c is the wave celerity, the expressions that were tried to estimate the discharge, according to the wave theories and where ah^b stands for the conveyance of the channel in the last section, are the following:

$$\hat{Q} = sgn\left(S_0 - \xi\frac{\partial h}{\partial x} + \eta\frac{\partial h}{\partial t}\right) \times a h^b \sqrt{\left|S_0 - \xi\frac{\partial h}{\partial x} + \eta\frac{\partial h}{\partial t}\right|} \tag{15}$$

for the dynamic wave theory, named dynamic wave (2nd. analysis),

$$\hat{Q} = sgn\left(S_0 - \frac{\partial h}{\partial x} + \eta\frac{\partial h}{\partial t}\right) \times a h^b \sqrt{\left|S_0 - \frac{\partial h}{\partial x} + \eta\frac{\partial h}{\partial t}\right|} \tag{16}$$

where $\xi = 1$, for the dynamic wave theory, named dynamic wave (1st. analysis),

$$\hat{Q} = sgn\left(S_0 - \frac{\partial h}{\partial x}\right) \times a h^b \sqrt{\left|S_0 - \frac{\partial h}{\partial x}\right|} \tag{17}$$

where $\xi = 1$ and $\eta = 0$, for the diffusive wave theory,

$$\hat{Q} = sgn(S_0) \times a h^b \sqrt{|S_0|} \tag{18}$$

where $\xi = 0$ and $\eta = 0$, for the kinematic wave theory.

In these mathematical formulations *a, b,* ξ and η are considered constant parameters to be estimated by the least squares approximation, using the Preissmann weighting scheme to approach the derivatives.

3 APPLICATION TO A REAL CASE STUDY

The Esquema_Implícito model with $\Delta t = 1800$ s and $\theta = 0{,}6$ was applied to a reach of approximately 24 km of the Sado River right upstream of Alcácer do Sal city, in which thirteen cross-sections spaced at a distance of about 2 km were considered (Figure 1).

The main reasons because this real case study was chosen are that the fluvial flow in the referred river reach experiments the tide influence and during some flood events has caused important damage, either human or material.

Although during the study phase of the work several flows were simulated in the considered river reach, in this paper only the flow simulation for a flood event, in which the maximum value of the discharge is 2820 m^3/s, is presented to illustrate some of the results obtained.

Figure 2 shows the hydrograph considered in this simulation for the upstream boundary (section P1).

To characterize the downstream boundary condition the flow water depth induced by the tide was considered (section P13 in Figure 3).

It should be remarked that for all the simulations that were realized the flow regime was subcritical all over the length of the river reach in study.

Figures 2 to 4 show the results obtained through the computational model application to the referred flood event in what concerns the characteristics of

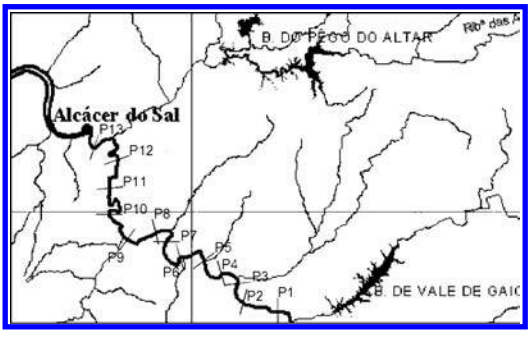


Figure 1. Location of the thirteen cross-sections considered in the river reach in study (adapted from "Plano da Bacia Hidrográfica do Rio Sado" 2002).

Copyright © 2006 Taylor & Francis Group plc, London, UK

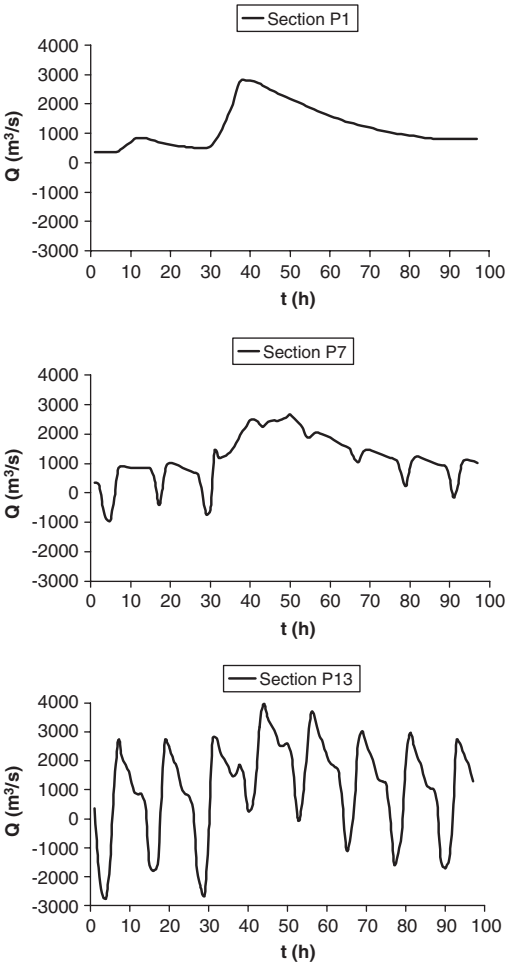


Figure 2. Variation in time of the discharge at the sections P1, P7 and P13 of the river reach in study (estimated flood event).

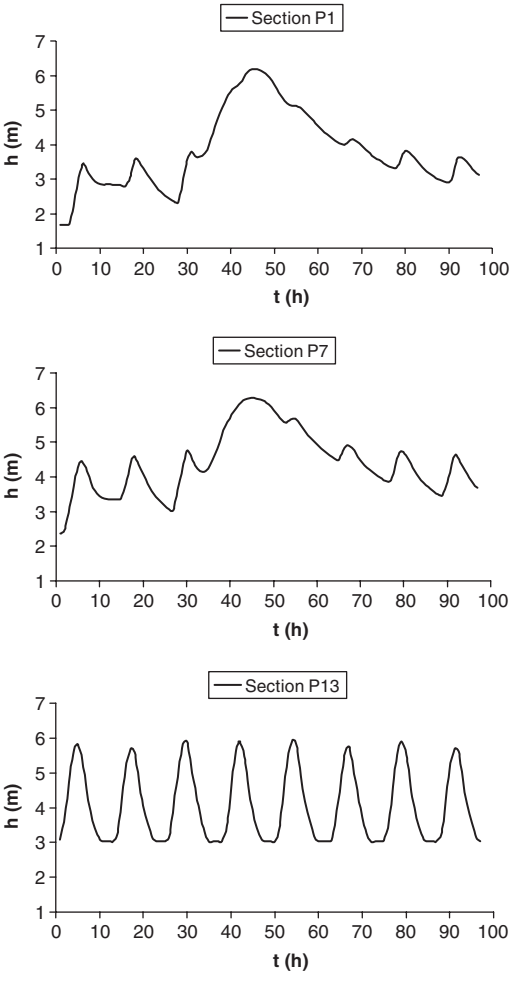


Figure 3. Variation in time of the water depth at the sections P1, P7 and P13 of the river reach in study (estimated flood event).

the fluvial flow influenced by the tide expressed in terms of the variations in time of the discharge, the water depth and the flow velocity in the sections P1, P7 and P13 of the considered river reach. These figures show that there is an inversion of the flow due the tide influence in the fluvial flow and that there is an attenuation of this influence from downstream (section P13) to upstream (section P1), which is more evident upstream the section P7 because this is the narrowest cross-section considered in the river reach in study.

From the analysis of the Figures 5 and 6, where the temporal evolution of discharge and water depth (Figure 5) and the temporal evolution of flow velocity and water depth (Figure 6) in the last section of the considered river reach are shown, it is possible to conclude that the maximum values of the discharge, the water depth and the flow velocity do not occur simultaneously. This fact can lead to increased velocity values which may enhance the "normal" expected erosion near fluvial structures that might exist in the considered river reach.

Those figures also show that the maximum discharge is about one and an half times larger than the maximum discharge that enters upstream of the river reach in study, although the average velocities in absolute value are less than 1 m/s, they can correspond in some places to very large maximum flow velocity values, that, as it was already said, may put in danger the security of some fluvial structures that might exist in the referred river reach.

Copyright © 2006 Taylor & Francis Group plc, London, UK

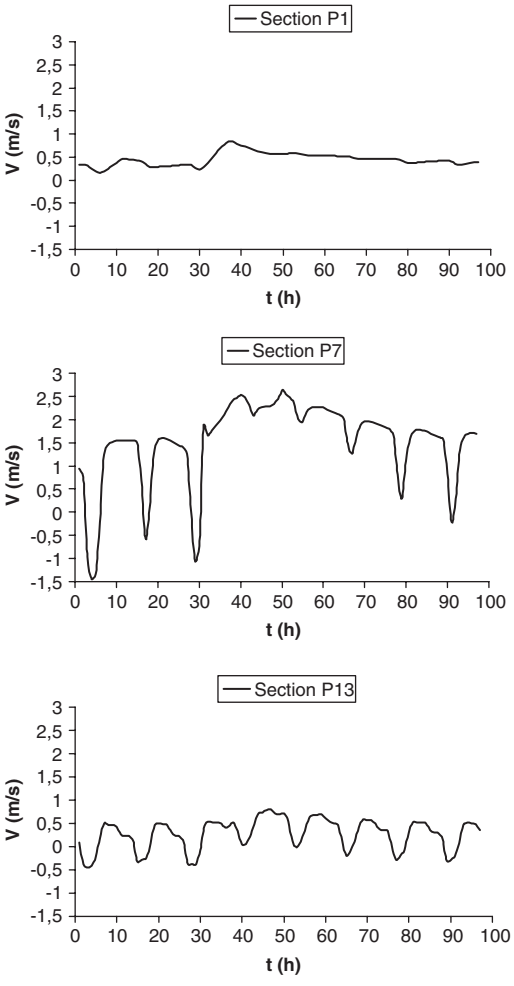


Figure 4. Variation in time of the flow velocity at the sections P1, P7 and P13 of the river reach in study (estimated flood event).

Although the hysteresis is a well known phenomenon when connected to floods in non tidal rivers, when related to tide induced phenomena the cyclical behaviour occurs in an inverse order. That is the maximum water depth occurs in the first place, followed by the maximum discharge and after those by the maximum flow velocity.

Figures 7 to 9 with different ordinate scales show the results obtained in the analysis for the last downstream spatial step of the contribution to the friction slope value of each one of its dynamic components normalized through their division by S_0. The analysis of those figures lead to the conclusion that in the referred last spatial step, with the exception of S_0/S_0, the normalized dynamic component of the friction slope that contributes the most for the variation of its value is

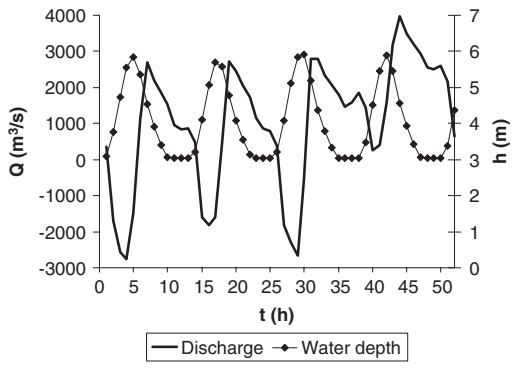


Figure 5. Discharge and water depth hydrographs in the last section of the river reach in study (estimated flood event).

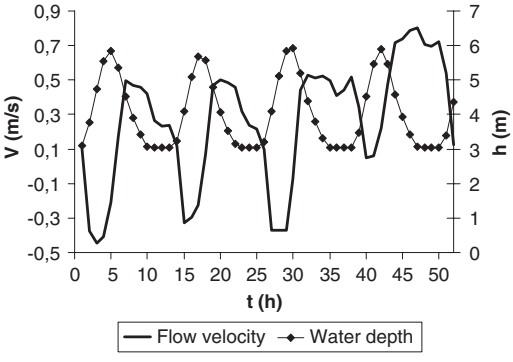


Figure 6. Flow velocity and water depth hydrographs in the last section of the river reach in study (estimated flood event).

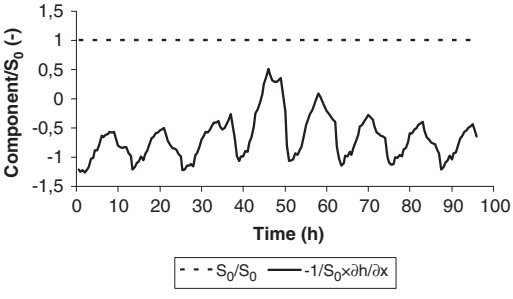


Figure 7. Contribution of the friction slope dynamic components S_0/S_0 and $-1/S_0 \times \partial h/\partial x$ to its value in the last downstream spatial step (estimated flood event).

$-1/S_0 \times \partial h/\partial x$ and that the contribution of the remainder normalized dynamic components have practically no significance in the value of that non dimensional parameter.

Figures 10 to 13 illustrate the results obtained with the calculations of the discharge rating function

Copyright © 2006 Taylor & Francis Group plc, London, UK

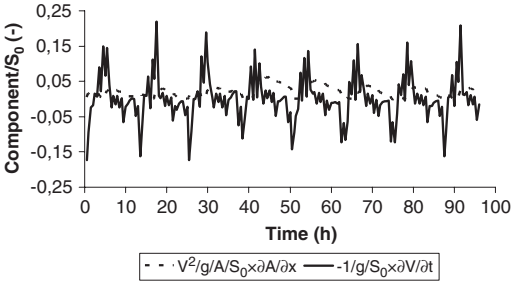


Figure 8. Contribution of the friction slope dynamic components $V^2/g/A/S_0 \times \partial A/\partial x$ and $-1/g/S_0 \times \partial V/\partial t$ to its value in the last downstream spatial step (estimated flood event).

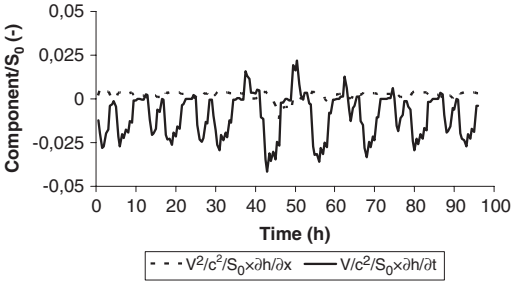


Figure 9. Contribution of the friction slope dynamic components $V^2/c^2/S_0 \times \partial h/\partial x$ and $V/c^2/S_0 \times \partial h/\partial t$ to its value in the last downstream spatial step (estimated flood event).

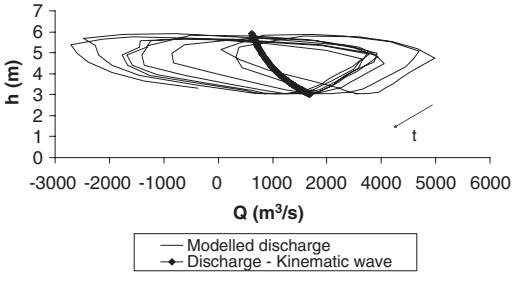


Figure 10. Discharge rating function in the last section of the river reach in study obtained with the flow computational model and the mathematical formulation of the kinematic wave (estimated flood event).

effectuated using the flow computational model and the four presented mathematical formulations based on the kinematic, diffusive and dynamic wave theories. The analysis of the cited figures shows that the kinematic wave theory as expected is not at all appropriate to study the flow in tidal rivers, particularly to study the discharge rating function on a river cross-section influenced by the tide effects. Contrarily, the other wave theories are very adequate for the above referred studies.

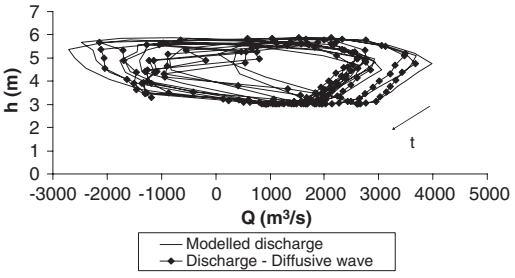


Figure 11. Discharge rating function in the last section of the river reach in study obtained with the flow computational model and the mathematical formulation of the diffusive wave (estimated flood event).

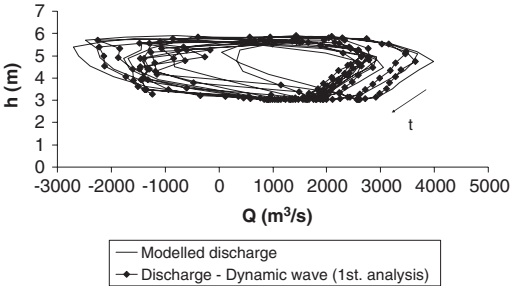


Figure 12. Discharge rating function in the last section of the river reach in study obtained with the flow computational model and the mathematical formulation of the dynamic wave: 1st. analysis (estimated flood event).

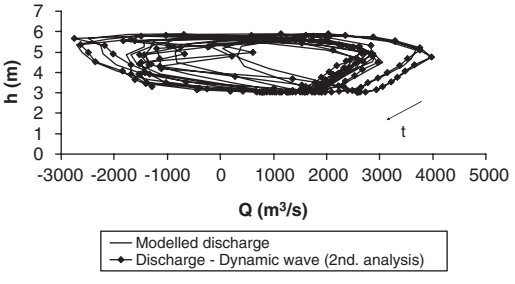


Figure 13. Discharge rating function in the last section of the river reach in study obtained with the flow computational model and the mathematical formulation of the dynamic wave: 2nd. analysis (estimated flood event).

Effectively the correlations between the discharge rating functions modeled and estimated through the diffusive and the dynamic wave theories are quite good. Another result that should be noted from this study is that in tidal rivers the relation between the water depth and the discharge presents great and complex hysteresis and it can be verified that there is more dispersion of the discharges for higher water depths.

Copyright © 2006 Taylor & Francis Group plc, London, UK

4 CONCLUSION

From the analysis of the results obtained in this study it is possible to verify that the tide may represent an important disturbance factor relatively to possible flood wave propagations in tidal rivers.

For the considered flood event, it was shown that there is inversion of the river flow due the tide influence in the fluvial flow and that there is an attenuation of this influence from downstream to upstream of the river reach in study.

In what concerns the last cross-section of the referred river reach in study it is important to note that the maximum discharge may be more than one and an half time larger than the maximum discharge that enters upstream of that river reach and occurs for water depths which are not maximum, which can consequently correspond to very large maximum flow velocity values. In this way, these phenomena can lead to a large increase of the erosions near some fluvial structures that might exist in the considered river reach and can therefore put in danger their security.

One of the aspects of the realized study that is important to refer is the analysis for the last downstream spatial step of the contribution to the friction slope value of each one of its different dynamic components. Thus in the referred last downstream spatial step the dynamic component which contains the partial spatial derivative of the water depth is the one that more contributes for the variation of the friction slope value.

Another part of this study that should be remarked is the flow mathematical model exploration that was done with the intent of its application to the discharge rating function analysis on the last section of the considered river reach. Effectively the correlations between the discharge rating functions obtained with the flow computational model and those which were estimated through the realized adjustment studies based on the diffusive and dynamic wave theories were quite good. Contrarily the kinematic wave theory is not at all appropriate to study the flow in tidal rivers, particularly to study the discharge rating function on a river cross-section influenced by the tide effects.

It is also important to note that in tidal rivers the relation between the water depth and the discharge presents great and complex hysteresis and it can be verified that there is more dispersion of the discharges for higher water depths.

REFERENCES

Ackers, P. 1993. "Flow formulae for straight two-stage channels", *Journal of Hydraulic Research, IAHR,* 31 (4), 509–531.

Bousmar, D. and Zech, Y. 1999. "Momentum transfer for practical flow computation in compound channels", *Journal of Hydraulic Engineering, ASCE,* 125 (7), 696–706.

Chaudhry, M.H. 1993. *Open-Channel Flow.* New Jersey: Prentice Hall: Englewood Cliffs.

Cunge, J.A., Holly, F.M. and Verwey, A. 1980. *Practical Aspects of Computacional River Hydraulics*. London: Pitman Publishing Limited.

Lyness, J.F., Myers, W.R.C. and Wark, J.B. 1997. "The use of different conveyance calculations for modelling flows in a compact compound channel", *Journal of the Institution of Water and Environmental Management*, 11 (5), 335–340.

Ministério do Ambiente e do Ordenamento do Território 2002. "Plano da Bacia Hidrográfica do Rio Sado". Decreto Regulamentar Nº. 6/2002, *Diário da República* Nº. 36 de 12-2-2002, Série I – B (in Portuguese).

Quintela, A.C. 1993. *Hidráulica*. 4.ª Edição. Lisboa: Fundação Calouste Gulbenkian (in Portuguese).

Santos, M.I.M. 2004. *Estudo dos Efeitos da Maré no Escoamento em Rios Sujeitos à sua Influência. Aplicação ao Rio Sado*. M.Sc. in Hydraulics and Water Resources. Lisboa: Instituto Superior Técnico, Universidade Técnica de Lisboa (in Portuguese).

Santos, M.I.M. and Hipólito, J.R. 2005. "Computational modelling of river flows influenced by tide effects", *Proceedings of the Third International Conference on River Basin Management (River Basin Management III)*, Sept. 6–8, Bologna, Section 1: Hydraulics and hydrology, 55–64.

Santos, M.I.M. and Hipólito, J.R. 2006. "Efeitos da Maré Fluvial na Propagação de uma Onda de Cheia", *Actas do 8º. Congresso da Água*, 13–17 Março, Figueira da Foz (in Portuguese).

Santos, M.I.M. and Hipólito, J.R. 2006. "Analysis of the Effects of Tides in the Flow of Tidal Rivers", *American Institute of Hydrology – 2006 Annual Meeting & International Conference Proceedings* (accepted for publication).

Shiono, K. and Knight, D.W. 1991. "Turbulent open channel flows with variable depth across the channel", *Journal of Fluid Mechanics*, 222, 617–646.

Tominaga, A., Liu, J., Nagao, M. and Nezu, I. 1995. "Hydraulic characteristics of unsteady flow in open channels with flood plains", *Proc. 26th Congress of IAHR, Hydra 2000*, London, 1, 373–378.

Yevjevich, V. 1975. *Unsteady Flow in Open Channels*. Vol. I. Fort Collins: K. Mahmood and V. Yevjevich, Water Resources Publications.

Copyright © 2006 Taylor & Francis Group plc, London, UK

Modelling the distribution of boundary shear stress in open channel flows

M. Omran
Arup, Solihull, UK

D.W. Knight
The University of Birmingham, Department of Civil Engineering, Birmingham, UK

ABSTRACT: Determining the boundary shear stress in open channel flows is not a straightforward procedure due to the poor simulation of the secondary flow currents. The Shiono and Knight Method (SKM) overcomes this problem by linking the secondary current term to the position and rotational direction of the secondary current cells. This novel approach makes the SKM a simple two-dimensional tool capable of predicting the depth-averaged velocity and the boundary shear stress distributions accurately for both inbank and overbank flows.

1 INTRODUCTION

The boundary shear stress distribution in open channel flow is important when dealing with sediment transport, dispersion, river habitat, bank protection and other practical river engineering problems. Modelling the boundary shear stress in straight prismatic channels is not an easy task due to the pattern of longitudinal secondary flow cells that occur in the flow. These cells are highly dependent on the nature of the anisotropic turbulence and they are controlled by both the shape of the cross-section and the heterogeneity of the roughness distribution around the wetted perimeter. See Knight et al (1982 & 1994) for further details and the various data sets that are available for different geometries and flow conditions (e.g. at www.flowdata.bham.ac.uk).

The complexity in determining the boundary shear stress distribution can be revealed when adopting a depth-averaged approach for modelling flow in straight channels. Even when the distribution of the depth-averaged velocity is modelled with acceptable accuracy, the corresponding computed boundary shear stress might not necessarily match the experimental data. This paper investigates different philosophies for modelling the secondary flow cells based on the Shiono and Knight Method (SKM). The obtained results are compared to a variety of experimental data for validation.

2 SUMMARY OF THE SHIONO AND KNIGHT METHOD

The Shiono and Knight Method (SKM) is based on a depth-averaged form of the streamwise Reynolds Averaged Navier-Stokes (RANS) equations, expressed for steady uniform flow in a prismatic channel by the following equations:

$$\rho g H S_0 - \frac{1}{8}\rho f U_d^2\left(1+\frac{1}{s^2}\right)^{1/2} + \frac{\partial}{\partial y}\left[\rho\lambda H^2\left(\frac{f}{8}\right)^{1/2} U_d \frac{\partial U_d}{\partial y}\right] = \frac{\partial}{\partial y}\left[H(\rho(UV)_d\right] \quad (1)$$

$$U_d = \frac{1}{H}\int_0^H U dz \; ; \; \tau_b = \left(\frac{f}{8}\right)\rho U_d^2 \; ; \; \bar{\tau}_{yx} = \rho\bar{\varepsilon}_{yx}\frac{\partial U_d}{\partial y} \; ; \; \bar{\varepsilon}_{yx} = \lambda U_* H \; ; \; \frac{\partial H(\rho UV)_d}{\partial y} = \Gamma \quad (2)$$

$$\tau_b\left(1+\frac{1}{s^2}\right)^{1/2} = \rho g H S_o + \frac{\partial}{\partial y}\left\{H\bar{\tau}_{yx}\right\} - \Gamma \quad (3)$$

where (3) is a simplified form of (1) in terms of stress, and ρ = fluid density, g = gravitational acceleration, H = depth, S_o = channel bed slope, f = Darcy-Weisbach friction factor, U_d = depth-averaged streamwise velocity, s = channel side slope (1:s, vertical: horizontal), λ = dimensionless eddy viscosity, U = streamwise velocity, V = transverse velocity, y = lateral co-ordinate, z = co-ordinate normal to bed, τ_b = local boundary shear stress, $\bar{\tau}_{yx}$ = depth-averaged Reynolds stress, $\bar{\varepsilon}_{yx}$ = depth-averaged eddy viscosity, U_* = shear velocity and Γ = transverse gradient of secondary flow term. The depth-averaged parameters of velocity, Reynolds stress and secondary flow are governed by the coefficients f, λ and Γ, concerned with bed friction, lateral shear and secondary

Copyright © 2006 Taylor & Francis Group plc, London, UK

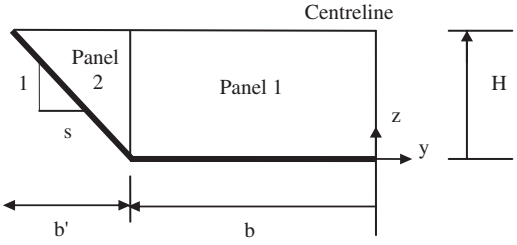


Figure 1. Typical cross-section of trapezoidal channel, with side slopes 1:s.

flow/vorticity respectively. Further details of the SKM, and its application, can be found in Shiono & Knight (1991), Knight & Shiono (1996) and Knight *et al.* (2004).

3 ILLUSTRATION OF A PROBLEM IN THE DISTRIBUTION OF BOUNDARY SHEAR STRESS

Yuen (1989) performed experimental studies measuring the depth-averaged velocity, U_d, and boundary shear stress, τ_b, simple trapezoidal channels with homogeneous roughness. These data are used to illustrate the difficulty associated with modelling the lateral distribution of boundary shear stress. Experimental 16 of Yuen (1989) corresponds to a simple trapezoidal channel with $s = 1$ and $b = 0.075$ m. The SKM was used to model this channel by dividing the cross-section into two domains, one for the side slope region and another for the flat bed, as shown in Figure 1.

Throughout the modelling in this paper, the friction factors used were obtained by applying Darcy-Weisbach equation, $f = 8\tau_b/\rho U_d^2$, to the experimental data. Constant 'standard' values for λ were imposed in all the panels, $\lambda = 0.07$, to make the calibration simple, and only the Γ values were adjusted to match the experimental depth-averaged velocity data. Some guidance on the selection of parameter values is given in Knight & Chlebek (2006) for inbank flows in rectangular channels and in Abril & Knight (2004) for overbank flows in compound channels.

When no experimental data are available, the user has to specify a roughness value in the form of Manning's n for example, from which the friction factor can be computed using $f = 8n^2\, gR^{-1/3}$. Some guidance or empirical equations are required for the Γ term since it is difficult to calibrate it due to the lack of measured data despite knowing its sign from Figure 6.

Figure 2 shows that despite the fact that the analytical U_d distribution was modelled accurately, when compared with the experimental data, the corresponding τ_b distribution was poor, notably in the corner

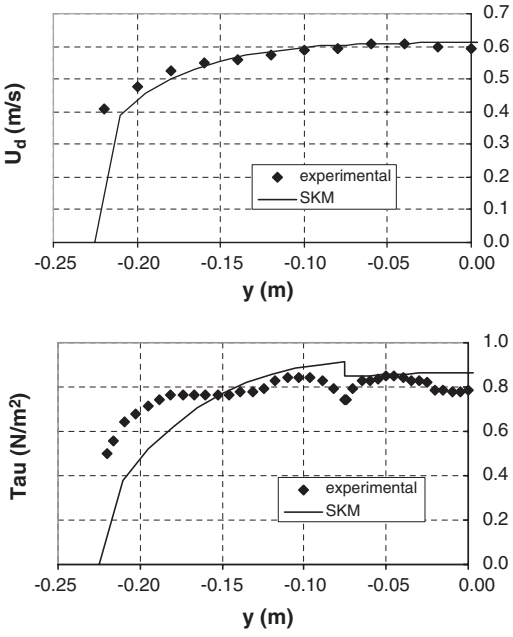


Figure 2. Analytical U_d and τ_b distributions for a simple trapezoidal channel [experiment 16, Yuen, (1989)].

region, at the channel centreline and at the edge of the channel. This distribution was obtained with parameter values of $f_1 = 0.0185$, $f_2 = 0.020$, $\lambda_1 = \lambda_2 = 0.07$, $\Gamma_1 = 0.5$ & $\Gamma_1 = -0.2$.

According to Knight *et al.* (2006), the inadequacy in the τ_b distribution is directly related to the fact that the model as it stands does not incorporate the secondary current cells and their effects.

4 PROPOSED PHILOSOPHY FOR MODELLING SECONDARY CURRENT CELLS IN SIMPLE TRAPEZOIDAL CHANNELS

Tominaga *et al.* (1989) performed experimental studies to determine the pattern of secondary current cells in simple trapezoidal channels. They observed three majors cells, as illustrated in Figure 3. The rotations and approximate positions of these cells were also observed by Knight & Patel (1985a&b) Melling & Whitelaw (1976), Rhodes (1991), Rhodes & Knight (1994), and Yuen (1989).

Figure 4 shows two typical distributions for the longitudinal and transverse velocities. In the former, U, is always positive, with larger values near the free surface than the bed, while in the latter, V, is only a small fraction of U and alters sign depending on the rotational direction of the secondary cell. Hence, at the location corresponding to the centreline position of

Copyright © 2006 Taylor & Francis Group plc, London, UK

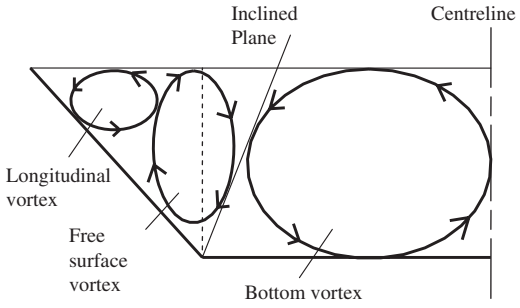


Figure 3. Secondary flow cells in half a trapezoidal channel (after Tominaga *et al*., 1989).

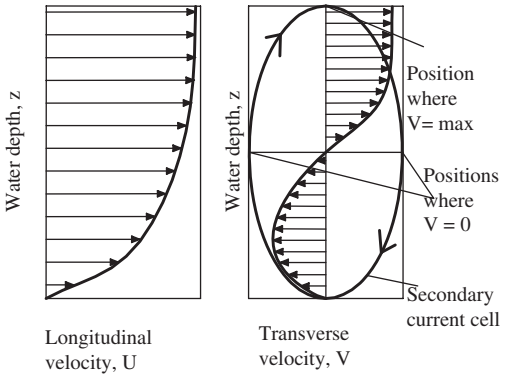


Figure 4. Vertical distribution of the longitudinal and transverse velocities.

a secondary cell, the depth-averaged value of the term UV, $(UV)_d$, can be either positive or negative. As a consequence, as illustrated in Figure 5, $(UV)_d$ at the centreline position of the secondary current cell has a maximum positive value for clockwise rotating cells and a maximum negative value if the cell is rotating in a counter-clockwise direction. It should be noted that at the edge of the secondary current cell, $V = 0$, as previously illustrated in Figure 4, hence at this position, $(UV)_d = 0$. It therefore follows that $(UV)_d$ varies from zero at the edge of the secondary cell to a maximum positive or negative value at the centreline of the cell (depending on the rotational direction) before reaching zero again at the other edge. Knight *et al.* (2006) assumed that the variation of $(UV)_d$ is linear for simplicity.

The philosophy of the SKM is based on using a constant Γ value for each panel, and therefore each time the sign of Γ changes an additional panel is required. As a consequence, Figure 5 shows that half a simple trapezoidal channel should be divided into at least four panels to account for the secondary current cells; two

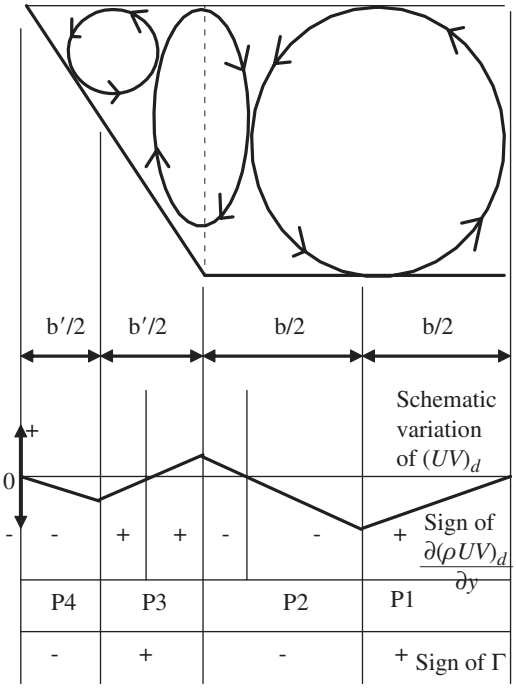


Figure 5. Four panel approach and signs of secondary current term.

of them over the flat bed region and the other two over the side slope domain.

Experiment 16 from Yuen (1989) was then re-modelled by dividing the channel into four panels, following the pattern of Figure 5. Figure 6 shows that the analytical boundary shear stress distribution (marked 'constant f') is better near the channel centreline and near the walls, but that discontinuities in τ_b obviously still remain. These discontinuities are an inevitable consequence of adopting a depth-averaged approach, since changing f between panels is to introduce abrupt changes in τ_b. To overcome this problem, Knight *et al*. (2006) proposed varying f linearly by adopting a common f value at panel interfaces, and then varying f linearly within each panel to match these values. This resulted in a smoother τ_b distribution, as can be seen in Figure 6.

Although the distribution of τ_b in Figure 6 matches the experimental data quite well, the dip in the corner region (at $y = -0.76$ m) is not simulated at all. This arises because of the steep lateral gradients in flow parameters in this region, which then have to be modelled by the insertion of an additional pair of panels, as shown by Knight et al. (2006). However, apart from this minor defect, it is apparent that the SKM with 4 panels is sufficiently sensitive enough to be able to predict the lateral distribution of boundary shear stresses with reasonable accuracy.

Copyright © 2006 Taylor & Francis Group plc, London, UK

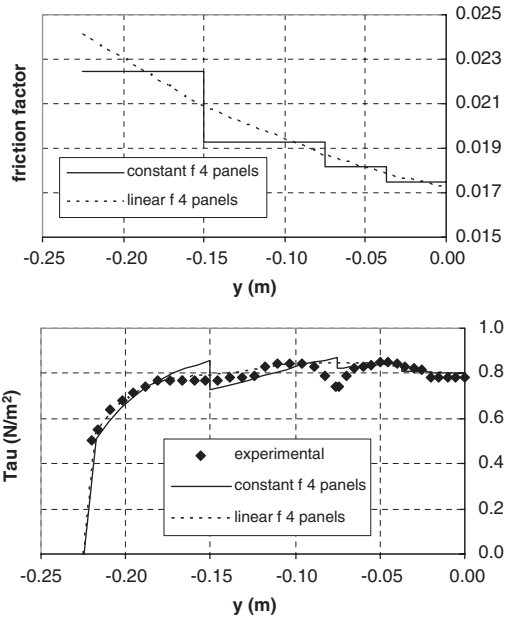


Figure 6. (a) Constant and linear friction factor variation with 4 panels, and (b) corresponding boundary shear stress distributions (experiment 16, Yuen, 1989).

5 EFFECT OF THE SECONDARY CURRENT TERM Γ ON THE DISTRIBUTION OF BOUNDARY SHEAR STRESS

Figure 7 shows that panels 2 and 3 might be composed of two regions each, on account of two different flow cells having some effect in each panel. In panel 2, both regions have a negative sign for Γ, while the two regions in panel 3 have a positive sign for Γ. Previously it was assumed that the same value of Γ could be used in both regions of panel 2 resulting in a single panel with constant negative Γ value. The same assumption was made for panel 3 resulting in one panel with a constant positive Γ value. This section investigates the effect on the analytical solution if these assumptions were not made. In fact, Figure 7 shows that two extra panels, P2a and P3a need to be created by splitting panels 2 and 3 respectively. As a result, panels P2 and P2a will both have negative values of Γ with different magnitudes and panels P3 and P3a will have positive Γ with different values. This will result in six different panels, three in each domain of the simple trapezoidal channel. The same equation of f is used to represent the variation of the friction factor in panels P2 & P2a, this also applies to panels 3 and 3a.

Experiment 08 from Yuen (1989) was used to compare the results of these two philosophies. Experiment 08 corresponds to a simple trapezoidal channel with $H = 0.08$ m, $b = 0.075$ m and $s = 1$. Figure 8 (a)

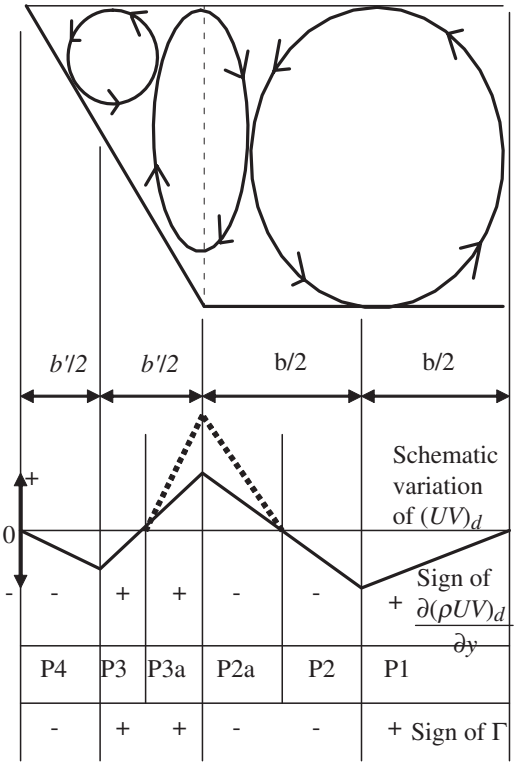


Figure 7. Six panel approach and signs of secondary current term.

shows the analytical results for U_d obtained from both approaches. A small difference of only 0.3% exists between the two. This was expected since U_d is generally well predicted by different approaches and is the reason why the main focus is on predicting the τ_b distribution. Figure 8 (b) shows the shear stress distributions obtained by the two approaches. The differences in the results computed by the two philosophies are again small, and the mean stress differs by less than 1%.

6 EFFECT OF ASSUMING PAIRED VALUES FOR THE SECONDARY CURRENT CELLS

The possibility of allocating a single Γ value for each secondary current cell is now investigated, based on dividing the channel into six panels, as already indicated by Figure 7. In this way, the user will only need to input three values for Γ since $\Gamma_1 = -\Gamma_2$, $\Gamma_{2a} = -\Gamma_{3a}$ and $\Gamma_3 = -\Gamma_4$.

Experiment 03 from Tominaga *et al.* (1989) was used to compare the results of this approach and of the one adopted in section 4. It corresponds to a simple trapezoidal channel with $H = 0.0905$ m, $b = 0.1$ m and s = 1.035. To check the effects on assuming paired

Copyright © 2006 Taylor & Francis Group plc, London, UK

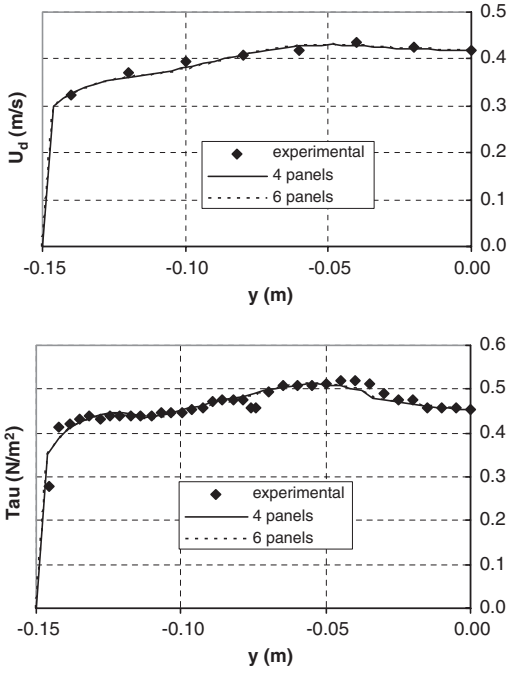


Figure 8. Lateral distributions of U_d & τ_b, based on 4 or 6 panels.

values for the secondary current term Γ, the same experiment was simulated using 6 panels and the same variation of f was used. The Γ term for the bottom vortex was given a value of 0.38, the one for the free surface vortex was 0.30 and the one for the longitudinal vortex was 0.15.

Figure 9 (a) shows the U_d distribution obtained by adopting the paired value approach, as well as the results using just 4 panels. It can be seen that there is not much difference between both approaches when it comes to the U_d distributions, and the difference in the total discharge was only 0.4%. In both approaches, the modelled results match the experimental data well.

7 APPLICATION OF THE MODELLING PHILOSOPHY TO SIMPLE TRAPEZOIDAL CHANNELS

In order to test the analytical model further, trapezoidal channel data from various sources were selected, in which the $2b/H$ values varied from 1.0 to 30. For cases with $2b/H \leq 2.2$, the half width of the channel was divided into four panels and not six, in order to illustrate that in most circumstances, four panels were quite adequate for modelling the τ_b distributions effectively using the SKM.

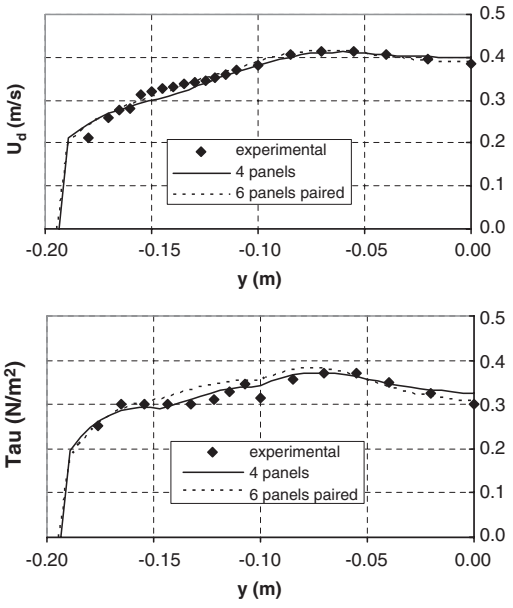


Figure 9. Effect of assuming paired values for the secondary current cells.

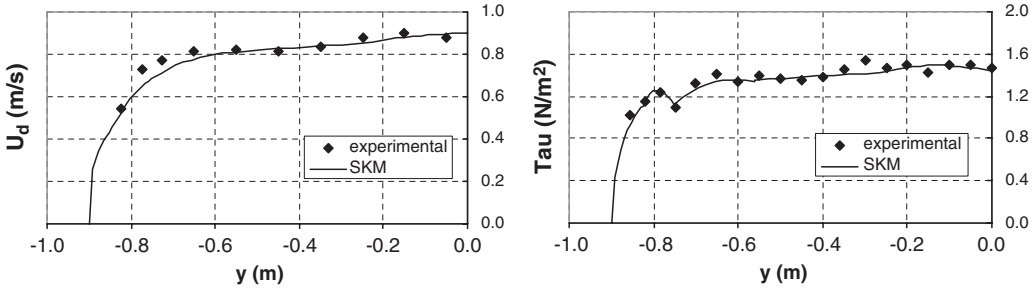
For cases with $2b/H \geq 4.0$, five panels were used to represent the half width of the channel. The friction factor was varied linearly between the panels based on the values adopted at panel interfaces. The λ term was again assumed to be constant at $\lambda = 0.07$ for all panels, while the Γ term was calibrated following the sign convention of Figure 5 so that the analytical U_d results matched the experimental results. Figure 10 shows that accurate distributions of U_d & τ_b were obtained.

8 MODELLING PHILOSOPHY FOR STRAIGHT OVERBANK CHANNELS

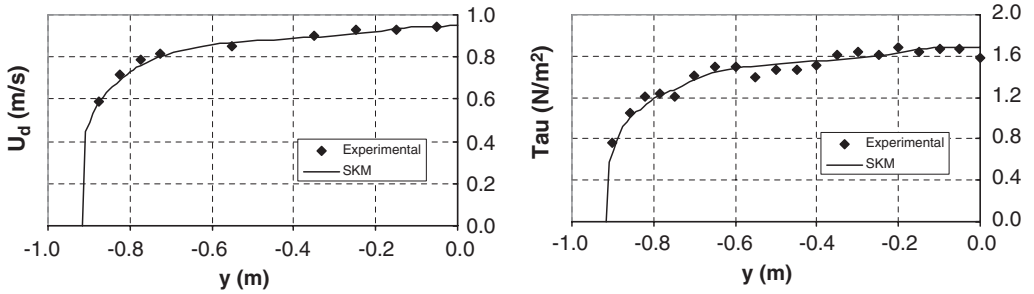
Shiono & Knight (1990 & 1991) computed the secondary current flow contribution based on experimental data obtained from the Flood Channel Facility (FCF). This computation was limited to series that corresponded to compound channels with main channel side slopes of $s = 0$, 1 & 2.

In series 02, with $s = 1$, the half width of the main channel was 0.75 m and of the floodplain 3.15 m, both measured from the channel centreline. The bankfull level was set at 0.15 m. Figure 11 shows the variation of $-(\rho UV)_d$ across the channel for different relative depths. It shows that in the main channel $-(\rho UV)_d$ decreases almost linearly up to the interface between the main channel and the floodplain. On the floodplain, $-(\rho UV)_d$ was found to increase approximately linearly. Hence, this figure suggests that Γ, the lateral

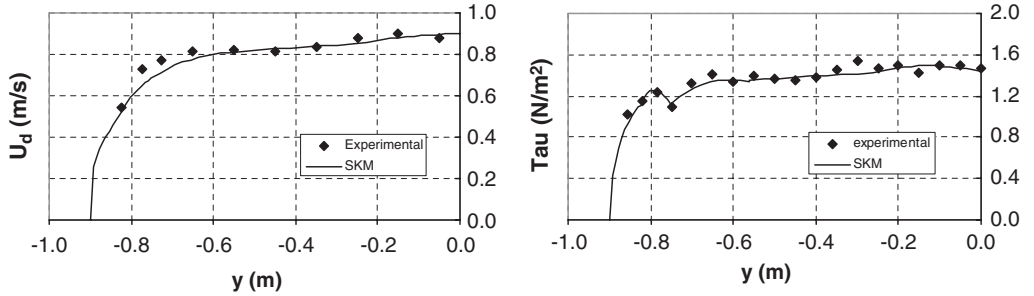
Copyright © 2006 Taylor & Francis Group plc, London, UK



(a) FCF IB04150 b = 0.75 m, s = 1, H = 0.150 m, f_1 = 0.0149, f_2 = 0.0162, f_3 = 0.0166, f_4 = 0.0219, f_5 = 0.0431, Γ_1 = -0.08, Γ_2 = 0.20, Γ_3 = -0.04, Γ_4 = 0.05, Γ_5 = -0.30



(b) FCF 0402 b = 0.75 m, s = 1, H = 0.166 m, f_1 = 0.0152, f_2 = 0.0155, f_3 = 0.0165, f_4 = 0.0166, f_5 = 0.0213, Γ_1 = -0.12, Γ_2 = 0.15, Γ_3 = -0.01, Γ_4 = 0.05, Γ_5 = -0.50



(c) Yuen 13 b = 0.075 m, s = 1, H = 0.100 m, f_1 = 0.0169, f_2 = 0.0167, f_3 = 0.0195, f_4 = 0.0263 Γ_1 = 0.55, Γ_2 = -0.15, Γ_3 = 0.15, Γ_4 = -0.42

Figure 10. Application of the modelling philosophy.

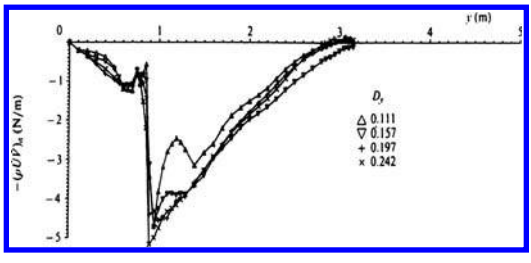


Figure 11. Lateral variation of secondary current term, $-(\rho UV)_d$, for FCF Series 02 (after Shiono & Knight, 1991).

gradient of $(\rho UV)_d$, is positive in the main channel and negative on the floodplain.

FCF experimental depth-averaged velocity and boundary shear stress data are available, from which the friction factors can be back-calculated using the Darcy-Weisbach equation. Abril & Knight (2005) showed that the SKM is not very sensitive to the variation of λ across the channel for wide channels and proposed that a constant value of $\lambda_{mc} = 0.07$ be used in the main channel flat bed region, together with equation (4) to compute λ elsewhere across the channel. The Γ term was calibrated, assuming it is positive in

Copyright © 2006 Taylor & Francis Group plc, London, UK

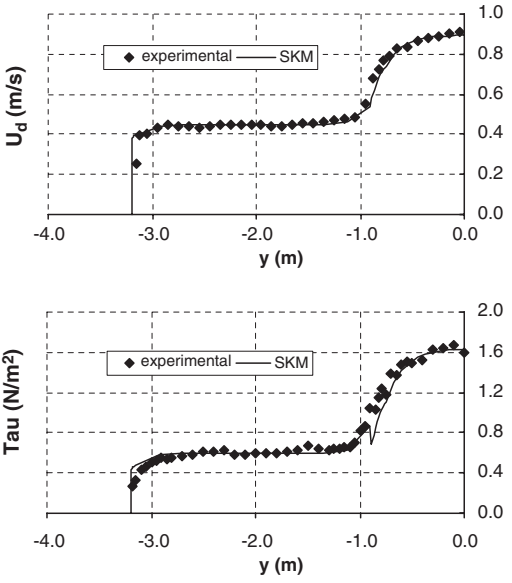


Figure 12. FCF 0205, $f_1 = f_2 = 0.0163$, $f_3 = f_4 = 0.0238$ $\Gamma_1 = \Gamma_2 = 0.35$, $\Gamma_3 = \Gamma_4 = -0.11$.

the main channel and negative on the floodplain, so that the analytical U_d matched the experimental data.

$$\lambda = \lambda_{mc}\left(-0.2 + 1.2Dr^{-1.44}\right) \quad (4)$$

Figure 12 shows that the analytical results match the experimental data for both the U_d and the τ_b distributions. It should be noted that the f and Γ values for the side slope regions in the main channel and floodplain were assumed to be identical to the ones of the corresponding flat bed domain. This comes from the fact that the side slope regions are small compared to the flat bed domains; hence such an assumption facilitates the work of the modeller without affecting the outcomes greatly.

9 CONCLUSIONS

- Secondary flow effects are accounted for in the SKM by specifying the number, position and strength of the cells for a particular flow, and then ascribing an appropriate value for Γ. The values of Γ have been shown to alternate in sign laterally, dependent on the sense of direction of the secondary flows, commensurate with the derivative of the term $H\rho(UV)_d$ with respect to y.
- The number of secondary current cells is found to depend on the channel aspect ratio, $2b/H$.
- For $2b/H \leq 2.2$, the number of secondary current cells in a simple trapezoidal channel was found to be equal to three, with two located over the side slope region and one over the flat bed region.
- For $2b/H \geq 4.0$, the number of secondary current cells in a simple trapezoidal channel was found to be equal to four, with two located over the side slope region and two over the flat bed region.
- Good results for both U_d and τ_b distributions have been obtained for different sets of data, when the proposed method is used with a linear variation of the friction factor across the section.
- The assumption that the maxima, minima and zero values of $(\rho UV)_d$ are aligned is valid and has a little impact on the analytical approach. As a result, the modeller can input four values of Γ, in the four panel case, instead of six values and obtain very much the same accuracy.
- Using paired values of Γ for adjacent panels reduces the accuracy but this simpler calibration philosophy is clearly sufficient to obtain a reasonable first estimate of the τ_b distribution.
- The SKM is able to predict accurately the depth-averaged velocity and the boundary shear stress distribution for overbank channels with a positive and negative value of Γ for the main channel and floodplain respectively.

ACKNOWLEDGEMENTS

The first author acknowledges the financial support from the Lebanese National Council for Scientific Research (LNCSR) and the University of Birmingham.

REFERENCES

Abril, J.B., and Knight, D.W. (2004). Stage-discharge prediction for rivers in flood applying a depth-averaged model. *Journal of Hydraulic Research*, *IAHR*, 42 (6), 616–629.

Knight, D.W., Patel, H.S., Demetriou, J.D. and Hamed, M.E (1982), "Boundary shear stress distributions in open channel and closed conduit flows", *Proceedings of Euromech 156 – The Mechanics of Sediment Transport* [Eds B. Mutlu Sumer & A. Muller], Istanbul, July, A.A. Balkema, Rotterdam, Netherlands, 33–40.

Knight, D.W., and Patel, H.S. (1985a). Boundary shear stress distributions in rectangular duct flow. *Proc. 2nd Int. Symp. on Refined Flow Modelling and Turbulence Measurements*, Iowa, USA, Sept., Hemisphere Publishing Co., I22-1 to I22-10.

Knight, D.W., and Patel, H.S. (1985b). Boundary shear stress distributions in smooth rectangular duct. *Journal of Hydraulic Engineering*, *ASCE*, Vol. 111, No. 1, Jan. 29–47.

Knight, D.W., Yuen, K.W.H. and Alhamid, A.A.I. (1994), Boundary shear stress distributions in open channel flow, in *Physical Mechanisms of Mixing and Transport in the Environment* (Eds K. Beven, P. Chatwin & J. Millbank), J. Wiley, Chapter 4, 51–87.

Copyright © 2006 Taylor & Francis Group plc, London, UK

Knight, D.W. and Shiono, K. (1996). River channel and floodplain hydraulics, in *Floodplain Processes,* (Eds Anderson, Walling & Bates), Chapter 5, J Wiley, 139–181.

Knight, D.W., Omran, M., and Abril, J.B. (2004). Boundary conditions between panels in depth-averaged flow models revisited. *Proc. 2nd Int. Symp. on River flow, IAHR*, Naples, Italy, Jun., 473–483.

Knight, D.W., & Chlebek, J. (2006), A new perspective on sidewall correction procedures, based on modelling the depth-averaged velocity and boundary shear stress in rectangular channels, *RiverFlow 2006*, September, Lisbon, Portugal.

Knight, D.W., Omran, M., and Tang, X. (2006). Modelling depth-averaged velocity and boundary shear in trapezoidal channels with secondary flows. *Journal of Hydraulic Engineering, ASCE* (In press).

Melling, A., and Whitelaw, J.H. (1976). Turbulent flow is a rectangular duct. *Journal of Fluid Mechanics*, (78), Part 2, 289–315.

Rhodes, D.J. (1991). An experimental investigation of the mean flow structure in wide ducts of simple rectangular and compound trapezoidal cross section, examining in particular zones of high lateral shear, *PhD thesis,* The University of Birmingham.

Rhodes, D.G., and Knight, D.W. (1994). Velocity and boundary shear in a wide compound duct. *Journal of Hydraulic Research*, 32, 743–764.

Shiono, K. and Knight, D.W. (1990). Mathematical models of flow in two or multi stage straight channels, *Proc. Int. Conf. on River Flood Hydraulics*, (Ed. W.R. White), Wallingford, September, J. Wiley & Sons, Paper G1, 229–238.

Shiono, K. and Knight, D.W. (1991). Turbulent open channel flows with variable depth across the channel, *Journal of Fluid Mechanics*, Vol. 222, 617–646 (and Vol. 231, October, p 693).

Tominaga, A., Nezu, I., Ezaki, K., and Nakagawa, H. (1989). Turbulent structure in straight open channel flows. *Journal of Hydraulic Research,* IAHR, 27(1), 149–173.

Yuen, K.W.H. (1989). A study of boundary shear stress, flow resistance and momentum transfer in open channels with simple and compound trapezoidal cross sections. *PhD thesis*, The University of Birmingham.

Copyright © 2006 Taylor & Francis Group plc, London, UK

A methodology for computing non-uniform flows in compound channels

S. Proust[1], D. Bousmar[2], N. Rivière[3], A. Paquier[1], Y. Zech[4]
[1] *Hydrology-Hydraulics Research Unit, CEMAGREF, Lyon, France*
[2] *Hydraulic Research Laboratory, Ministère wallon de l'Equipement et des Transports, Châtelet, Belgium*
[3] *Laboratoire de Mécanique des Fluides et d'Acoustique, Lyon, France*
[4] *Civil and Environmental Engineering Dept, Université catholique de Louvain, Louvain-La-Neuve, Belgium*

ABSTRACT: This paper focuses on numerical modelling of non-uniform flows in prismatic and non-prismatic compound channels. A new 1D computation methodology is presented which is called "Independent Subsections Method" (ISM). While conventional 1D models solve the momentum or energy equation on the overall cross-section area, the ISM treats the flow dynamics in the main channel and the floodplains separately. It solves an ordinary differential equations system which calculates the water level and mean velocity in the floodplains and the main channel, simultaneously. This method accounts explicitly for lateral mass exchanges, interfacial shear stress and associated momentum transfer between subsections. ISM simulations of water level and subsection velocities are in agreement with experimental data for four different geometries: straight compound channel; slightly narrowing floodplains; abrupt floodplain contraction; and skewed floodplain boundaries.

1 INTRODUCTION

Flooding rivers usually present flow-width variations that give rise to non-uniform flows in non-prismatic compound geometries. These flows are characterized by turbulent exchanges due to the velocity difference between the flows in the main channel and floodplains, and by mass transfer and associated momentum exchange between subsections. Turbulence and mass transfer induce noteworthy additional head loss that reduces the overall channel conveyance and affects the discharge distribution across the channel.

Non-uniform flows in non-prismatic compound channels were physically described in the case of meandering two stage channels (e.g. Sellin et al. 1993) or skewed floodplains boundaries (e.g. Elliott & Sellin 1990, Sellin 1993). For these flow configurations, the total channel width is constant and accordingly, the subsections flow-depths are nearly invariable in the longitudinal direction. Other experiments focused on non-uniform flows with channel width variations: over bank flows in symmetrically narrowing floodplains (Bousmar 2002, Bousmar et al. 2004); flows in compound channel with abrupt floodplain contraction (Proust 2005, Proust et al. 2006) or with symmetrically enlarging floodplains (Proust 2005, Bousmar et al. 2006).

Various one-dimensional methods were developed to cope with the modelling problems of such gradually varied flows. Every 1D model incorporates a specific approach for the modelling of the momentum exchange at the interface between the main channel and the floodplains. The classical Divided Channel Method (DCM) used in HEC-RAS (USACE) ignores the momentum transfer through subsections boundaries (Brunner 2001). The Debord Formula used in the program Talweg-Fluvia (Cemagref) gives an empirical correction of the DCM that merely models the turbulent transfer (Nicollet & Uan 1979), in a same way as in the flow formulae proposed by Ackers (1993). The Exchange Discharge Model (EDM), developed by Bousmar and Zech (1999) and implemented in the program Axeriv (Université Catholique de Louvain), accounts for both mass and turbulent exchanges.

However, using these three 1D programs for non-uniform flows with width variations leads to moderate errors on the floodplain water depth values (maximum relative error of 25%) but significant errors, up to 100%, on the discharge distributions (Proust 2005, Proust et al. 2006). Accordingly, when simultaneous prediction of both water levels and mean velocity in the flood plain is needed, e.g. for the evaluation of vulnerability in urbanized flood plains or sediment transport in natural floodplains and for the science of habitat hydraulics, these 1D approaches seem to be less relevant.

The computation of backwater surface profile using a 1D energy equation (e.g. in HEC-RAS & Axeriv)

Copyright © 2006 Taylor & Francis Group plc, London, UK

or a 1D momentum equation (in Talweg-fluvia) on the overall cross-section area is less appropriate when significant mass and momentum transfers are observed.

Another 1D approach consists in separating the flow dynamics in the main channel and floodplains. It was first proposed by Yen (1985) for flows in straight compound channels: the author proposed a "quasi-one-dimensional" backwater computation method. This method releases several constraining 1D-assumptions and boundary conditions which are imposed by the conventional 1D models. To the authors knowledge, it was unfortunately not compared to experimental data.

This paper presents the extension of this method to non-prismatic compound channels and its validation against laboratory experiments. A new differential equations system with a specific treatment of the interfacial exchanges is proposed. The results of this method are then compared to experimental data in four different flow configurations: non-uniform flows in straight compound channels (Bousmar et al. 2005), flows with abrupt floodplain contraction (Proust et al. 2006), with slightly narrowing floodplains (Bousmar et al. 2004), and with skewed floodplain boundaries (Sellin 1993).

2 THE INDEPENDENT SUBSECTIONS METHOD

2.1 *Flow equations*

The flow dynamics in the main channel and the floodplains can be separated by writing a 1D momentum equation in each subsection. These equations are linked together by lateral mass discharges and momentum exchange terms acting at the interface between two adjacent subsections. An additional equation ensures the mass conservation on the overall cross-section area.

The compound channel considered here consists of rectangular main channel and floodplains whose width can vary. Subscripts "mc", "lfp", and "rfp" are used for mean values of hydraulic parameters in the main channel, the left flood plain and the right flood plain, respectively. Moreover, water level Z across the compound channel is supposed constant, as $Z_{mc} = Z_{rfp} = Z_{lfp}$.

For such a compound channel, the 1D momentum equations can be simplified for the three subsections (Proust 2005) as:

$$\left(1-\frac{U_{lfp}^{\ 2}}{gh_{lfp}}\right)\frac{dh_{lfp}}{dx} = S_o - Sf_{lfp} + \frac{U_{lfp}^{\ 2}}{gB_{lfp}}\frac{dB_{lfp}}{dx} + \ldots + \frac{\tau_{lfp}.h_{lfp}}{\rho g A_{lfp}} + \frac{q_{lfm}\left(2U_{lfp} - U_{int.lfp}\right)}{gA_{lfp}} \quad (1)$$

$$\left(1-\frac{U_{rfp}^{\ 2}}{gh_{rfp}}\right)\frac{dh_{rfp}}{dx} = S_o - Sf_{rfp} + \frac{U_{rfp}^{\ 2}}{gB_{rfp}}\frac{dB_{rfp}}{dx} + \ldots + \frac{\tau_{rfp}.h_{rfp}}{\rho g A_{rfp}} + \frac{q_{rfm}\left(2U_{rfp} - U_{int.rfp}\right)}{gA_{rfp}} \quad (2)$$

$$\left(1-\frac{U_{mc}^{\ 2}}{gh_{mc}}\right)\frac{dh_{mc}}{dx} = S_o - Sf_{mc} + \frac{U_{mc}^{\ 2}}{gB_{mc}}\frac{dB_{mc}}{dx} + \ldots + \frac{\tau_{lfp}.h_{lfp}}{\rho g A_{mc}} + \frac{\tau_{rfp}.h_{rfp}}{\rho g A_{mc}} \ldots - \frac{q_{lfm}\left(2U_{mc} - U_{int.lfp}\right)}{gA_{mc}} - \frac{q_{rfm}\left(2U_{mc} - U_{int.rfp}\right)}{gA_{mc}} \quad (3)$$

where x = longitudinal direction; h = subsection flow depth; U = subsection mean velocity; U_{int} = longitudinal velocity at the interface; B = subsection width; A = subsection area; S_o = bed slope; S_f = subsection friction slope; τ = shear stress at the interface in the x direction.

Besides, q_{rfm} (resp. q_{lfm}) is the lateral mass discharge per unit longitudinal length between the right floodplain (resp. the left floodplain) and the main channel, being positive from a floodplain to the main channel.

The friction slope S_f is calculated with classical Manning's formula applied to a subsection.

The continuity equations in both floodplains are:

$$\frac{dQ_{lfp}}{dx} = -q_{lfm} \qquad \frac{dQ_{rfp}}{dx} = -q_{rfm} \quad (4)$$

and the mass conservation on the overall cross-section area writes:

$$\frac{dQ_{mc}}{dx} = q_{lfm} + q_{rfm} \quad (5)$$

where the sum of the subsection discharges, Q_{mc}, Q_{frm} and Q_{flm} is the total discharge Q.

The Independent Subsections Method consists thus in solving the set of equations (1), (2), (3) and (5), with closure equations defining the interface shear stress τ and velocity U_{int}.

2.2 *Momentum transfer modeling*

2.2.1 *Turbulent transfers*

Yen (1985) proposed to relate the interfacial side shear stress τ to the velocity gradient in the lateral direction y across the channel, assuming a constant eddy viscosity ν_t. But Wilson et al. (2002) showed that this assumption leads to overestimate turbulent diffusion and therefore to reduce the velocity difference between flows in the main channel and the floodplains.

Copyright © 2006 Taylor & Francis Group plc, London, UK

Table 1. Calibration of turbulent exchange coefficient Ψ^t for uniform flows (h_r is the relative water depth).

UCL flume		LMFA flume	
h_r [−]	Ψ^t [−]	h_r [−]	Ψ^t [−]
0.09	0.0173	0.2	0.0164
0.18	0.0200	0.3	0.0165
0.27	0.0167		
0.41	0.0159		

Other Authors preferred to evaluate the interfacial shear on the subsection boundary by using a mixing length model in the horizontal plane. This model was validated by Ervine & Baird (1982) from experimental data collected by Myers (1978), Rajaratnam & Ahmadi (1981), Ghosh & Jena (1971) and Sellin (1964), by Lambert & Sellin (1996) and by Bousmar (2002). Finally, the mixing length model included in the Exchange Discharge Model was retained (Bousmar & Zech 1999). The side shear stress τ on the two interfaces are modelled by:

$$\left|\tau_{lfp}\right| = \rho \Psi^t \left(U_{mc} - U_{lfp}\right)^2 \quad (6)$$

$$\left|\tau_{rfp}\right| = \rho \Psi^t \left(U_{mc} - U_{rfp}\right)^2 \quad (7)$$

where Ψ^t = a constant coefficient of turbulent exchange.

The Ψ^t value was calibrated using six uniform flows data set, varying relative water depth $h_r = h_{fp}/h_{mc}$. The uniform flows experiments were conducted in two different compound channel flumes (see §3), at the Laboratoire de Mécanique des Fluides et d'Acoustique, Lyon, France (LMFA) and at the Université catholique de Louvain, Belgium (UCL). Results of calibration are reported on Table 1.

Coefficient Ψ^t values are in the range 0.016 to 0.020. They are quite stable in both compound channel flumes. In the sequel, ISM simulations were done with $\Psi^t = 0.020$.

2.2.2 *Mass transfers*

In Equation (1), (2) and (3), $U_{int.lfp}$ is the x-component velocity of lateral mass discharge q_{lfm} (left interface) and $U_{int.rfp}$ is related to q_{rfm} (right interface). Consequently, the momentum transfer due to mass exchange strongly depends on the interfacial velocities values.

Determination of these velocities relies on experimental observations. For flows in compound channels with floodplain(s)-width decrease, the longitudinal velocity of water entering the main channel is very close to the floodplain mean velocity, as observed for symmetrical narrowing floodplains (Bousmar et al. 2004) and abrupt floodplain contraction (Proust et al. 2006). In that case, interfacial velocities can be modelled by:

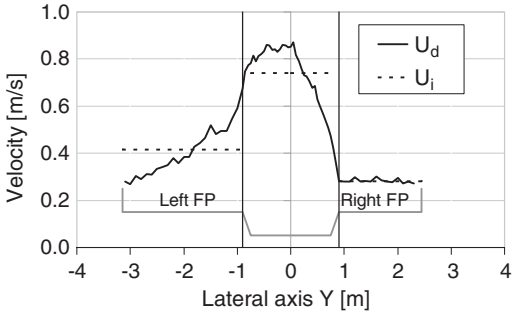


Figure 1. Typical transverse profile of depth-averaged velocity U_d and subsection velocity U_i for skewed floodplain boundaries (skew angle = 9.2°, $h_r = 0.15$).

$$\begin{aligned} U_{int.lfp} &= U_{lfp} \\ U_{int\,rfp} &= U_{rfp} \end{aligned} \quad (8)$$

Conversely, for flows in compound channels with floodplain(s)-width increase, the longitudinal velocity of water leaving the main channel is very close to the main channel mean velocity (Proust 2005, Bousmar et al. 2006). It comes:

$$\begin{aligned} U_{\text{int.}lfp} &= U_{mc} \\ U_{\text{int}\,rfp} &= U_{mc} \end{aligned} \quad (9)$$

For flows in the Flood Channel Facility (FCF) at HR Wallingford, UK, with skewed floodplains boundaries (see Figure 3 and Sellin 1993), both phenomena are observed simultaneously, since the left floodplain is enlarging and the right one is narrowing. Figure 1 shows a typical transverse profile of depth-averaged velocity for a skew angle of 9.2° and a relative water depth h_r of 0.15. In that case, the interfacial velocities are adequately modelled by:

$$\begin{aligned} U_{int.lfp} &= U_{mc} \\ U_{int\,rfp} &= U_{rfp} \end{aligned} \quad (10)$$

Accordingly, the interfacial velocities in ISM are modelled depending on the mass transfer direction for each interface.

2.3 *Differential equations system*

Equations (5), (1), (2) and (3) can be written as an ordinary differential equation system (11), where coefficients a_1, a_2, a_3, a_4, b_1, b_2,c_1, c_4, d_1, d_2 and d_4 are

Copyright © 2006 Taylor & Francis Group plc, London, UK

non-linear functions of velocities U_{lfp}, U_{rfp}, U_{mc}, water depth h_{fpl}, geometrical parameters and subsection manning roughness (Proust 2005).

$$\begin{cases} a_1 \dfrac{dh_{lfp}}{dx} + a_2 \dfrac{dU_{lfp}}{dx} + a_3 \dfrac{dU_{mc}}{dx} + a_4 \dfrac{dU_{rfp}}{dx} = e_1 \\ b_1 \dfrac{dh_{lfp}}{dx} + b_2 \dfrac{dU_{lfp}}{dx} = e_2 \\ c_1 \dfrac{dh_{lfp}}{dx} + c_4 \dfrac{dU_{rfp}}{dx} = e_3 \\ d_1 \dfrac{dh_{lfp}}{dx} + d_2 \dfrac{dU_{lfp}}{dx} + d_4 \dfrac{dU_{rfp}}{dx} = e_4 \end{cases} \quad (11)$$

The differential equations system (11) can also be expressed in matrix form:

$$\begin{bmatrix} a_1 & a_2 & a_3 & a_4 \\ b_1 & b_2 & 0 & 0 \\ c_1 & 0 & 0 & c_4 \\ d_1 & d_2 & 0 & d_4 \end{bmatrix} \cdot \begin{bmatrix} \dfrac{dy(1)}{dx} \\ \dfrac{dy(2)}{dx} \\ \dfrac{dy(3)}{dx} \\ \dfrac{dy(4)}{dx} \end{bmatrix} = \begin{bmatrix} e_1 \\ e_2 \\ e_3 \\ e_4 \end{bmatrix} \quad (12)$$

where $y(1) = h_{lfp}$; $y(2) = U_{lfp}$; $y(3) = U_{mc}$; and $y(4) = U_{rfp}$. It should be noticed that $h_{lfp} = h_{rfp} = h_{mc} - h_b$, with $h_b =$ the bank full flow depth in the main channel.

Equation (12) is equivalent to:

$$\frac{dY}{dx} = F(Y) \qquad \text{with} \qquad Y = \begin{pmatrix} y(1) \\ y(2) \\ y(3) \\ y(4) \end{pmatrix} \quad (13)$$

The Independent Subsections Method consists thus in solving both flow depth and subsection velocities simultaneously. The MATLAB solving procedure ODE45 for ordinary differential equations was used: it is based on a Runge-Kutta explicit scheme of 4th or 5th order.

For subcritical flows, the ISM is solved iteratively: the upstream experimental discharge distribution and a tentative upstream water level are given. The downstream water level results from the computation. The upstream level is then adjusted until the suitable downstream level is obtained.

3 EXPERIMENTAL DATA

The ISM was tested in seven different flow geometries. Hydraulic and geometrical parameters of flow configurations are reported in Table 2, where variations of floodplains-widths B_{lfp} and B_{rfp} and relative water depth h_r between upstream and downstream boundaries are exposed. For non-prismatic reaches, the angle between floodplains walls and main channel axis (longitudinal direction x) is noted α.

Experiments on non-uniform flows in straight compound channels were performed in the laboratory flumes of LMFA and UCL. Non-uniform flows result from a non-equilibrated upstream discharge distribution at the inlet of the flume. The floodplain discharge is too large and a mass transfer towards the main channel occurs along the flume (Bousmar et al. 2005).

Experiments in compound channel with narrowing floodplains were conducted in the UCL flume (Bousmar et al. 2004). Two different geometries were explored: a linear decrease of floodplains-width on 6 meters long ($\alpha = 3.8°$) or 2 meters long ($\alpha = 11.3°$).

Flows in compound channel with abrupt floodplain contraction were obtained in the laboratory of Compagnie Nationale du Rhône (CNR, Figure 2). An obstacle was set on the floodplain, presenting a strong convergence of length 3.5 m and of projected width 1.43 m perpendicularly to the main flow direction (mean angle $\alpha = 22°$). The flow was studied on a 4.5 m length (Proust et al. 2006).

The last data set is the skewed channel geometry studied in the FCF. A prismatic main channel is skewed to prismatic floodplain, with an angle $\alpha = 5.1°$ or 9.2°), while the overall channel width remains constant (Figure 3).

Mass transfers are observed on the one hand, from the right floodplain to the main channel, and on the other hand, from the main channel to the left floodplain (Elliott & Sellin 1990, Sellin 1993). The velocity distribution both in the main channel and over the two floodplains are thus distorted by the cross-flow (Figure 1).

4 ISM SIMULATIONS

In the investigated geometries, three types of ISM simulations were carried out: (1) ignoring the momentum transfer; (2) taking merely into account a modelling of turbulent exchanges; (3) accounting for the total momentum transfer (mass & turbulence). Modifications of dynamical equations for cases (1) and (2) are detailled in Proust (2005).

Afterwards, simulations (1) are labelled "bed friction" on figures, as the bed friction is the only dissipation source; labels "Turb. Transfer" and "Turb. & Mass transfers" are used for simulations (2) and (3), respectively.

4.1 *Non-uniform flows in straight compound channel*

As mentioned in §3, the upstream discharge distribution creates mass transfer from the floodplains towards the main channel. Typical profile of computed and

Copyright © 2006 Taylor & Francis Group plc, London, UK

Table 2. Hydraulic and geometrical parameters of non-uniform flows.

Total discharge Q [l/s]	Relative flow depth h_r [−]	Main channel width B_{mc} [m]	Left floodplain width B_{lfp} [m]	Right Floodplain width B_{rfp} [m]	Length of studied reach L [m]
Straight compound channels (UCL)					
8	0.09	0.4	0.4	0.4	14
10	0.18				
14	0.27				
24	0.41				
Straight compound channels (LMFA)					
17.3	0.2	0.4	–	0.8	8
24.7	0.3				
36.3	0.4				
Abrupt floodplain contraction – $\alpha = 22°$					
150	0.23–0.14	0.8	–	2.2–0.77	4.5
260	0.42–0.33				
Narrowing floodplains – $\alpha = 3.8°$					
10	0.22–0.12	0.4	0.4–0	0.4–0	8
10	0.28–0.26				
12	0.30–0.21				
12	0.48–0.49				
16	0.49–0.47				
20	0.50–0.42				
Narrowing floodplains – $\alpha = 11.3°$					
10	0.22–0.12	0.4	0.4–0	0.4–0	6
10	0.28–0.26				
12	0.30–0.22				
12	0.48–0.48				
16	0.48–0.46				
20	0.49–0.42				
Skewed floodplains boundaries – $\alpha = 5.1°$					
261	0.148	1.8	1.75–2.65	2.05–1.15	10
353	0.243				
725	0.408				
Skewed floodplains boundaries – $\alpha = 9.2°$					
254	0.146	1.8	0.8–2.25	3–1.55	9
356	0.243				
711	0.408				
1132	0.5				

measured floodplain discharge are given on Figure 4; where Q_{fp} = sum of Q_{lfp} and Q_{rfp}.

When the total momentum transfer is considered, ISM reproduces satisfactorily the discharge distribution evolution. Conversely, ignoring both mass and turbulent exchanges in the momentum transfer leads to a 20 % underestimation of the floodplain discharge at the downstream end of the studied reach.

Comparison between "Turb. & Mass transfers" and "Turb. transfer" curves, also indicates that turbulence has a predominant role in the momentum transfer. Similar results were obtained for the other straight channel cases (Proust 2005). A correct modelling of the turbulent transfer is necessary to obtain the proper discharge distribution when the flow tends to uniformity (in the downstream part of the reach).

When the relative flow depth increases, the weight of the momentum transfer terms in the ISM reduces: for $h_r = 0.27$, ignoring the momentum transfer just induces a 9% underestimation of Q_{fp}.

Variations of the computed and experimental flow depths are not represented here, as they are less than 1.5 *mm* between upstream to downstream boundaries.

Eventually, it was observed that equations of mass conservation (Equations 4 and 5) and bed friction terms control the ISM system close to the upstream

Copyright © 2006 Taylor & Francis Group plc, London, UK



Figure 2. Compound channel flume of the Compagnie Nationale du Rhône with abrupt floodplain contraction.

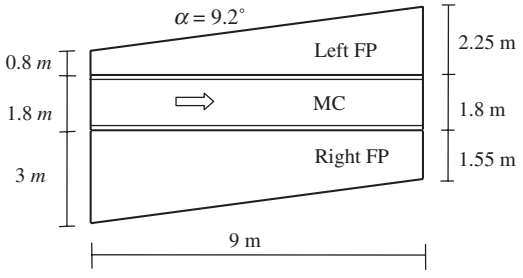


Figure 3. Plan view of compound channel with skewed floodplains boundaries ($\alpha = 9.2°$).

boundary ($x < 2$ m), while bed friction and turbulent transfer govern the flow in the downstream part of the flume.

4.2 *Symmetrical narrowing floodplains*

For flows in compound channels with narrowing floodplains, ISM simulations of $\{h_{lfp};\ U_{lfp};\ U_{rfp};\ U_{mc}\}$ accurately match the experimental data for the ten flow configurations where the relative flow depth h_r varies in the range [0.50; 0.22]. For these flows depths, accounting for the momentum transfer has practically no influence on the ISM results.

For lower h_r [0.22; 0.12], the momentum transfer influences more significantly the results, as shown on Figure 5 for the case: $\alpha = 11.3°$, $Q = 10\,l/s$. Considering the whole momentum transfer, the floodplain discharge Q_{fp} is computed with a maximum relative error of -13% (resp. 0%) at station $x = 4\,m$ (resp. $x = 5m$). Conversely, the floodplain discharge rate is underestimated of 44% (resp. 38%) at these two stations, when neglecting both mass and turbulence in the momentum transfer. Figure 5 also shows that mass exchanges have far more influence than turbulence in the momentum transfer, contrarily to non-uniforms flows in compound channels.

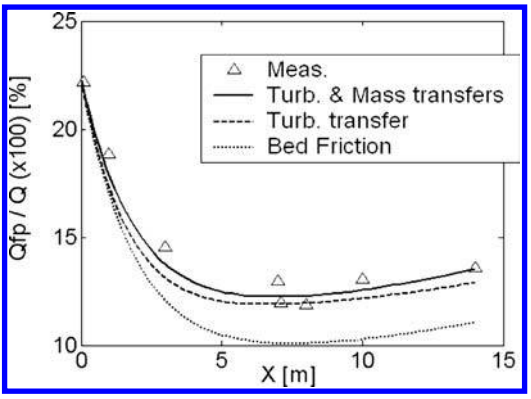


Figure 4. Longitudinal profile of discharge rate in both floodplains Q_{fp} (as percentage of the total discharge Q) – UCL flume, $Q = 10$ l/s, $h_r = 0.18$.

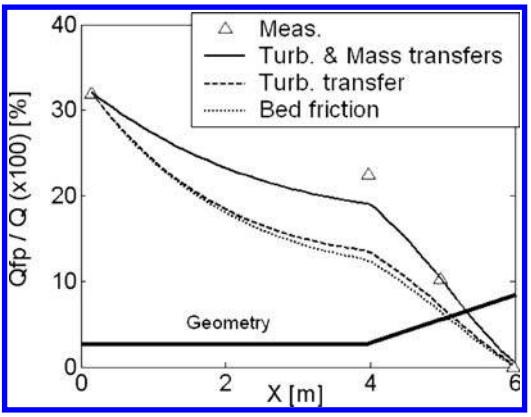


Figure 5. Longitudinal profile of discharge rate in both floodplains Q_{fp} (percentage of the total discharge Q) – Narrowing floodplains, $\alpha = 11.3°$, $Q = 10\,l/s$, $h_r \in [0.22; 0.12]$.

Finally, errors on the floodplains flow depth in the converging reach are less than 4% for the ISM with the whole momentum transfer, and grow up to 23% when considering only bed friction (Figure 6).

ISM simulations clearly demonstrate that momentum transfer due to mass exchanges has to be taken into account for the low over bank flows, when attempting to model flow depth and discharge distribution in such a geometry.

4.3 *Abrupt floodplain contraction*

In this particular geometry, the mass transfers become severe and the flow is clearly three-dimensional (Proust et al. 2006). However, ISM still predicts correctly both water surface and floodplain velocity profiles (see Figures 7 and 8, for $Q = 150\,l/s$). The

Copyright © 2006 Taylor & Francis Group plc, London, UK

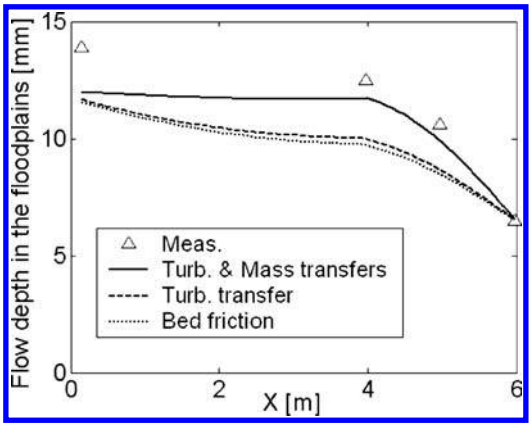


Figure 6. Water surface profile – Narrowing floodplains, $\alpha = 11.3°$, $Q = 10\,l/s$, $h_r \in [0.22; 0.12]$.

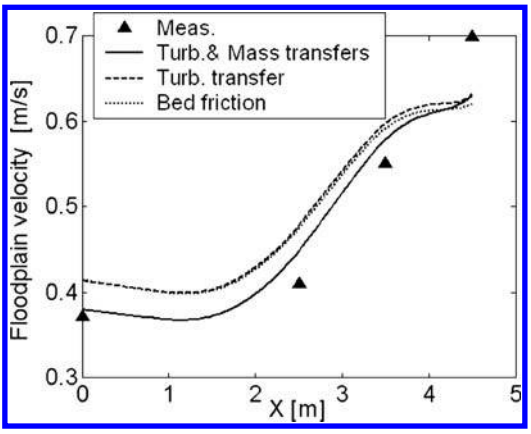


Figure 8. Floodplain velocity profiles – ISM calculation against experimental data.

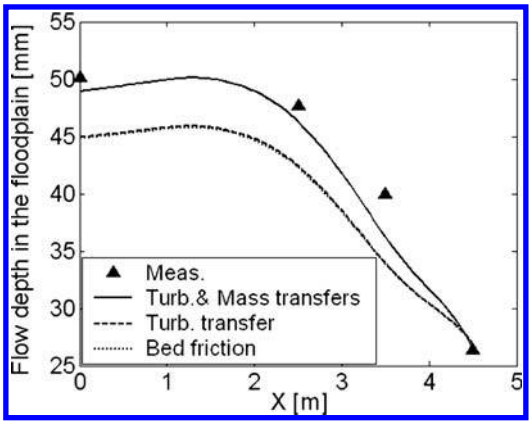


Figure 7. Longitudinal water surface profiles – ISM calculation against experimental data. CNR flume, $Q = 150\,l/s$, $h_r \in [0.23; 0.14]$.

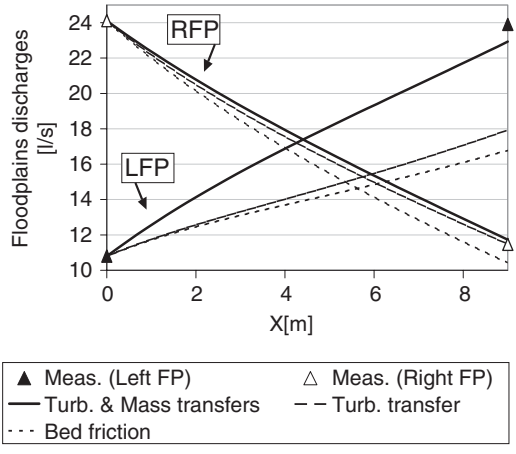


Figure 9. Discharge profiles in both floodplains (Left floodplain & right floodplain) – ISM calculation against experimental data in the Flood Channel Facility, $Q = 254\,l/s$, $h_r = 0.146, \alpha = 9.2°$.

flow depth h_{fp} and velocity U_{fp} are computed with a maximum relative error of -8% and -10%, respectively.

Accounting for the turbulence transfer does not influence the computations, when compared to results with only the bed friction, while considering the momentum transfer due to mass exchange significantly reduces prediction errors, notably on the flow depth. Such an observation confirms the above conclusions for the narrowing floodplains cases.

4.4 *Skewed floodplains boundaries*

ISM computes each floodplain discharge with a maximum error of -7% for the seven flow configurations investigated (see Tab. 2). It also reproduces the observed flow depth profile, with no variation between the upstream and downstream boundaries (variations of computed flow depth are less than 1 *mm*).

For flows with relative water depths $h_r = 0.4$ and 0.5, using ISM with or without the momentum transfer does not modify the simulations.

From $h_r = 0.25$ to 0.15, influence of momentum transfer appears only in the enlarging floodplain, i.e. the left floodplain (Figure 9). In this latter, ISM simulations only considering the bed friction induces a -30% underestimation of discharge Q_{lfp}.

Moreover, this influence seems to be mainly related to mass transfer: this last result is consistent with experimental momentum balances obtained by Elliott and Sellin (1990). They showed that influence of

Copyright © 2006 Taylor & Francis Group plc, London, UK

turbulent transfer rapidly decreases when momentum related to mass transfer between subsections increases.

The asymmetry of the momentum effect of mass transfers between the narrowing right floodplain and the enlarging left one was explored in Proust (2005). Comparison of flows in symmetrical narrowing floodplains (see §4.2) and flows in symmetrical enlarging floodplains (Bousmar et al. 2006) shows that the relative weight of momentum due to mass exchanges is three times larger in the enlarging reaches, for a same angle α. For skewed geometries, this asymetry could be expected from the observation of the gradients of depth-averaged velocities U_d over the two floodplains (Figure 1): nil on the converging floodplain and marked on the enlarging one.

5 1D SIMULATIONS ON THE OVERALL CROSS-SECTION

Three 1D programs were tested in the compound channel with abrupt floodplain contraction (Proust et al. 2006): HEC-RAS (USACE), Talweg-Fluvia (Cemagref) and Axeriv (UCL). All these programs predict water profiles and discharge distribution between subsections.

HEC-RAS solves the Bernoulli equation on the overall cross-section area. It neglects the momentum transfer by using the DCM. However, it accounts for contraction losses by an empirical equation (Brunner 2001). It should be noticed that contraction losses were built to adjust the water surface profile. They do not depend on subsection discharges and hence, do not deal with discharge distribution.

Talweg-Fluvia solves the 1D-momentum equation on the whole cross-section. It accounts for the turbulent exchange through the Debord formula which modifies the conveyance on the whole cross-section by empirical coefficients (Nicollet & Uan 1979). The momentum transfer due to mass exchanges is not considered. The bed friction slope and the discharge distribution in a specific reach are thus the same as the ones obtained for a uniform flow having the same hydraulic radius and averaged velocity.

Axeriv solves the Bernoulli equation on the whole cross-section. The bed friction slope is computed by Manning's formula using the DCM approach. It models the momentum transfer with the Exchange Discharge Model. The EDM accounts for both mass and turbulent exchanges in the momentum transfer. It calculates additional head losses due to the momentum effect in the subsections and the total cross-section (Bousmar & Zech 1999).

Last but not least, the three codes assume the equality of subsection head loss gradients.

Figure 10 shows the measured and computed water surface profiles. The downstream boundary condition

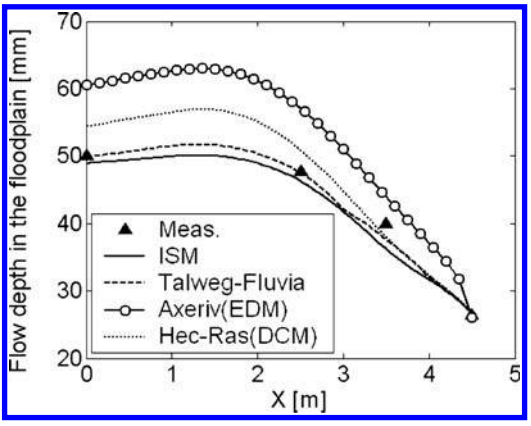


Figure 10. Longitudinal flow depth profile (in the floodplain) – calculation against experimental data: CNR flume, abrupt floodplain contraction, Q = 150 l/s.

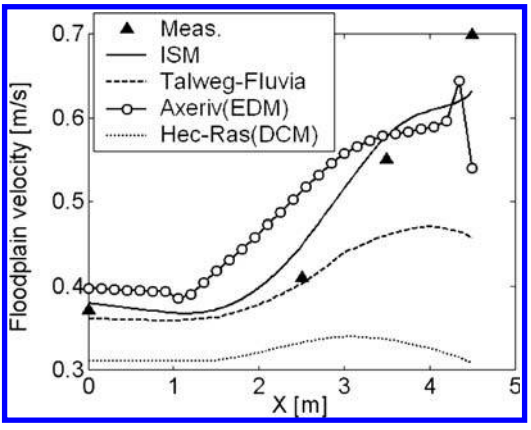


Figure 11. Floodplain velocity profiles – calculation against experimental data: CNR flume, abrupt floodplain contraction, Q = 150 l/s.

used for the computations is the experimental water level, averaged across the total channel width. Computed and measured floodplain velocities are given on Figure 11.

These results show that a 1D-equation defined on the total cross-section can not simultaneously predist both flow depth and mean velocity in the floodplain satisfactorily. The floodplain flow depths are computed with maximum relative errors of +9%, −5.2%, +20% for HEC-RAS, Talweg-Fluvia and Axeriv, respectively, while errors on the floodplain velocity are respectively −57%, −36%, −25%.

Several causes for the poor quality of these results can be identified:

– Incorrect (or missing) estimation of momentum transfer due to mass exchange.

Copyright © 2006 Taylor & Francis Group plc, London, UK

– Incorrect estimation of the lateral mass discharge.
– Assumption of a downstream discharge distribution equal to the distribution in an equivalent uniform flow, which induces erroneous momentum transfer estimations in the EDM.
– Assumption of equal head loss gradients in all subsections.
– Impossibility for HEC-RAS to obtain the actual discharge distributions by calibrating the contraction loss coefficient.

The computed errors on h_{fp} and U_{fp} in the ISM simulations were −8% and −10%, respectively. The comparison of these results with the classical 1D methods clearly demonstrates that: (1) lateral mass discharge and momentum transfer have to be explicitly modelled by separating the flow equations in the subsections; (2) mass transfers have to be modelled by starting the computation from the upstream boundary where the observed discharge distribution is imposed.

ISM also enables to reproduce different head loss gradients in the main channel and the floodplain as physically observed (Proust et al. 2006).

6 CONCLUSIONS

The Independent Subsection Method was developed for modelling non-uniform flows in prismatic or non-prismatic compound channels. The flow dynamics in the main channel and the floodplains are separated by writing a 1D momentum equation in each subsection. An additional equation ensures the mass conservation on the overall cross-section. The ISM solves thus a differential equations system that calculates both flow depth and subsection velocities simultaneously.

The ISM explicitly models lateral mass discharges and momentum transfer between the subsections due to both mass and turbulent exchanges. The closure equations defining the interface shear stress and interfacial velocity are based on a mixing length model in the horizontal plane and experimental observations, respectively.

ISM simulations are compared to experimental data in four flow configurations: non-uniform flows in straight compound channels, flows with abrupt floodplain contraction, with slightly narrowing floodplains, and with skewed floodplain boundaries. The ISM reproduces correctly both water surface and discharge distribution profiles whatever the strength of mass transfers. Results show that turbulent exchanges are predominant in the momentum transfer for non-uniform flows in prismatic geometry. Conversely, the momentum transfer is mainly controlled by mass exchanges in non-prismatic channels.

The ISM is also compared to three conventional 1D methods for the abrupt floodplain contraction case. The prediction of the flow depth and mean velocity in the floodplain is far more accurate with ISM than with the classical 1D methods. These results clearly show that: (1) the computation of backwater surface profile on the total cross-section is no more relevant when mass transfers are significant; (2) lateral mass discharge and momentum transfer have to be explicitly modelled by separating the flow equations in the subsections.

ACKNOWLEDGEMENTS

S. Proust, D. Bousmar, and N. Rivière travel costs were supported by the Tournesol programme grant 02947VM funded by EGIDE, France and CGRI, Communauté française de Belgique.

REFERENCES

Ackers, P. 1993. “Flow formulae for straight two-stage channels.” *Journal of Hydraulic Research*, 31(4), 504–531.

Bousmar, D. 2002. *Flow modelling in compound channels/ Momentum transfer between main channel and prismatic or non-prismatic floodplains*, Ph-D thesis, Université catholique de Louvain, Louvain, 306 p.

Bousmar, D., and Zech, Y. 1999. “Momentum transfer for practical flow computation.” *Journal of Hydraulic Engineering*, 125(7), 696–706.

Bousmar, D., Proust, S. and Zech, Y. 2006. “Experiments on the flow in a enlarging compound channel”, *submitted to River Flow 2006*.

Bousmar, D., Rivière, N., Proust, S., Paquier, A., Morel, R., and Zech, Y. 2005. “Upstream discharge distribution in compound-channel flumes.” *Journal of Hydraulic Engineering*, ASCE, 131(5), 408–412.

Bousmar, D., Wilkin, N., Jacquemart, J. H., and Zech, Y. 2004. “Overbank flow in symmetricaly narrowing floodplains.” *Journal of Hydraulic Engineering*, 130(4), 305–312.

Brunner, G. W. 2001. *Hec-Ras, River Analysis system – Hydraulic Reference Manual*. CPD-69, USACE, Inst. for Water Resources, Hydrologic Engineering Center, Davis CA, USA.

Elliott, S. C. A., and Sellin, R. H. J. 1990. “SERC Flood channel facility skewed flow experiments.” *Journal of Hydraulic Research*, 28(2), 197–214.

Ervine, D. A., and Baird, J. I. 1982. “Rating curves for rivers with overbank flow.” *Proc., I.C.E.*, Part II, 73, 465-472.

Ghosh, S. N., and Jena, S. B. 1971. “Boundary shear distribution in open compound channel.” *Proc. Instn Civ. Engrs*, 417–430.

Lambert, M. F., and Sellin, R. H. J. 1996. “Discharge prediction in straight compound channels using the mixing length concept.” *Journal of Hydraulic Research*, 34(3), 381–394.

Myers, W. R. C. 1978. “Momentum transfer in a compound channel.” *Journal of Hydraulic Research*, 16(2), 139–150.

Nicollet, G., and Uan, M. 1979. “Ecoulements permanents à surface libre en lit composés.” *La Houille Blanche*(1), 21–30.

Proust, S. 2005. *Ecoulements non-uniformes en lits composés: effets de variations de largeur du lit majeur*, PhD

Copyright © 2006 Taylor & Francis Group plc, London, UK

Thesis, n° 2005-ISAL-0083, INSA Lyon, Lyon, France, 362 p (in French), http://www.lyon.cemagref.fr/doc/these/proust/index.shtml.

Proust, S., Rivière, N., Bousmar, D., Paquier, A., Zech, Y. and Morel, R. 2006. "Flow in compound channel with abrupt floodplain contraction", *Journal of Hydraulic Engineering*, ASCE (in press).

Rajaratnam, N., and Ahmadi, R. M. 1981. "Hydraulics of channels with flood plains." *Journal of Hydraulic Research*, 19(1), 43–60.

Sellin, R. H. J. 1964. "A laboratory investigation into the interaction between the flow in the channel of a river and that over its flood plain." *La Houille Blanche*(7), 793–802.

Sellin, R. H. J. 1993. "SERC Flood Channel Facility: experimental data – Phase A – Skewed Floodplain Boundaries." Department of Civil Engineering, University of Bristol, Bristol, UK.

Sellin, R. H. J., Ervine, D. A., and Willets, B. B. 1993. "Behaviour of meandering two-stage channels." *Proc. Institution of Civil Engineers, Water, Maritime and Energy*, 101, 99–111.

Wilson, C., Bates, P. D., and Hervouet, J. M. 2002. "Comparison of turbulence models for stage-discharge rating curve prediction in reach-scale compound channel flows using two-dimensional finite element methods." *Journal of Hydrology*, 257(1-4), 42–58.

Yen, B. C., Camacho, R., Kohane, R., and Westrich, B. 1985. "Significance of flood plains in backwater computation." *Proc. 21st Congress of IAHR*, 3, 439–445.

Copyright © 2006 Taylor & Francis Group plc, London, UK

A coupled 1D to 2D model for flood plain simulation

Varvara Roubtsova, Georges Tchamen, Joseph Abdo & Rene Kahawita
Ecole Polytechnique de Montreal, Montreal, Canada

ABSTRACT: The computation of flood wave propagation is generally computed on the basis of either one-dimensional or two-dimensional models. The exclusive use of a one-dimensional model to simulate the phenomenon can lead to significant errors in mapping the flood plain contours whereas a fully two-dimensional model requires significant computer resources. The approach taken in this project is to use a one-dimensional model in areas where the river is confined laterally by its banks and couple it seamlessly to a simplified two-dimensional model in areas where the topography delineates a flood plain. The advection-diffusion equation is also implemented in the two-dimensional formulation so that the spread of a pollutant plume resulting from the flooding of a toxic source may be simulated. One advantage of the simplified two-dimensional scheme is that regions of wetting and drying are handled without any difficulty. The scheme has been tested on two cases with good results.

1 INTRODUCTION

The computation of flood wave propagation in a river containing flood plains is generally computed on the basis of either one-dimensional or two-dimensional models. The exclusive use of a one-dimensional model to simulate the phenomenon can lead to significant errors in the computation of flood wave propagation times, maximum water levels and discharge since an essentially two-dimensional system is being modeled as a one-dimensional system. To avoid these errors, some 1D models use 'off bank channel storage' terms to avoid participation of the flood plain in the main flow momentum equations. The other choice, which is formally 'correct', is of course to use a fully two-dimensional model; unfortunately this solution frequently requires significant computer resources especially if a flood of long duration and large-scale extent is being studied. Furthermore, a situation confronted quite frequently is a river that is confined to its banks for most of its trajectory but then opens onto a shallow flood plain in certain regions. Consequently, the approach taken in this project is to use a one-dimensional model in laterally confined areas of the river, and couple it seamlessly to a simplified two-dimensional model in areas where the topography delineates a flood plain. Recently, some similar approaches have been proposed [Paquier & Sigris (1997)], some commercial numerical models use a similar technique. The strategy used in the SOBEK model from Delft Hydraulics [Verwey (2001), Dhondia & Stelling (2002)] for example, is to use a one dimensional channel and completely integrate its mesh into the two dimensional mesh of the flood plain. These two meshes are coupled through the continuity equations which are discretized and solved using an implicit finite difference technique. The TUFLOW model strategy is similar to the one presented here in that the two dimensional mesh only covers the area of the flood plain, and not the one dimensional channel. However, the 2D mesh used in TUFLOW is of the finite difference type.

In the present paper, the complete St. Venant formulation is used in the one-dimensional component of the model, numerical solutions being obtained with a Riemann solver using a TVD (Total Variation Diminishing) algorithm. The two-dimensional component is based on a reduced set of the St. Venant equations, which requires that the Froude numbers on the flood plain are small. In fact the approximation made is that invoked for the diffusion analogy for flood wave propagation.

2 THEORETICAL DEVELOPMENT

2.1 *The 1-D approach*

The one-dimensional component is based on the TVD based KIMBULA model developed at Hydro-Quebec. For completeness a brief development of the model will be presented here.

The 1-D approach to the unsteady flow of water is governed by the St-Venant equations with additional

Copyright © 2006 Taylor & Francis Group plc, London, UK

inflows or outflows. Written in conservation law form they are:

$$\frac{\partial \mathbf{U}}{\partial t}+\frac{\partial \mathbf{F}(\mathbf{U})}{\partial x}=\mathbf{G},$$

$$\mathbf{U}=\begin{bmatrix}A\\Q\end{bmatrix},\quad \mathbf{F}(\mathbf{U})=\begin{bmatrix}Q\\\frac{Q^2}{A}+gI_1\end{bmatrix}$$

$$G=\begin{bmatrix}q\\gI_2+gA(S_0-S_f)\end{bmatrix}$$

where

$$S_f=\frac{Q^2n^2}{A^2R^{\frac{4}{3}}}$$

$$R=\frac{A}{P}$$

$$I_1=\int_0^h(h-\eta)b\,d\eta$$

$$I_2=\int_0^h(h-\eta)\frac{\partial b}{\partial x}\,d\eta$$

A is the area of the wetted cross- section;
Q is the discharge;
g is the gravitational acceleration;
S_0 is the local bed slope;
S_f is the local friction slope;
P is the wetted perimeter;
n is the Manning's roughness coefficient;
I_1 is the hydrostatic pressure force term;
I_2 is the pressure force term due to longitudinal width variation;
h is the water depth;
η is the integration variable indicating distance from the bed;
$b(x, \eta)$ is the river width at height η from the bed;
q is the unit bank flow discharge (positive or negative).

2.2 *The 2-D approach*

The development of the two dimensional component uses the reduced form of the full Saint-Venant Equation. (The diffusion equation approximation).

$$\frac{\partial H}{\partial t}+\frac{\partial}{\partial x}\left(k\cdot\frac{\partial H}{\partial x}\right)+\frac{\partial}{\partial y}\left(k\cdot\frac{\partial H}{\partial y}\right)=0 \qquad (1)$$

Here H is the water surface elevation and k the 'diffusion coefficient' is defined in equation (7). Equation (1) is valid when the magnitude of the inertial terms in the momentum equations is negligible. In this case, the momentum equations reduce to:

$$\frac{\partial H}{\partial x}=-S_{fx} \qquad (2)$$

$$\frac{\partial H}{\partial y}=-S_{fy} \qquad (3)$$

with

$$S_{fx}=\frac{N^2\cdot\sqrt{u^2+v^2}}{h^{4/3}}\cdot u \qquad (4a)$$

$$S_{fy}=\frac{N^2\cdot\sqrt{u^2+v^2}}{h^{4/3}}\cdot v \qquad (4b)$$

It is possible to verify the following identity:

$$\left(\frac{\partial H}{\partial x}\right)^2+\left(\frac{\partial H}{\partial y}\right)^2=\frac{N^4}{h^{8/3}}\cdot\left(u^2+v^2\right)^2 \qquad (5)$$

and the relations:

$$uh=-\left(\frac{h^{\frac{7}{3}}}{N^2\cdot\sqrt{u^2+v^2}}\right)\cdot\frac{\partial H}{\partial x}=k\cdot\frac{\partial H}{\partial x} \qquad (6a)$$

$$vh=-\left(\frac{h^{\frac{7}{3}}}{N^2\cdot\sqrt{u^2+v^2}}\right)\cdot\frac{\partial H}{\partial y}=k\cdot\frac{\partial H}{\partial y} \qquad (6b)$$

where

$$k=-\frac{h^{\frac{7}{3}}}{N^2\cdot\sqrt{u^2+v^2}}=-\frac{h^{\frac{5}{3}}}{N\cdot\varphi(\nabla H)} \qquad (7)$$

If $\varphi(\nabla H)$ is defined with the help of identity (5):

$$\varphi(\nabla H)=\left[\left(\frac{\partial H}{\partial x}\right)^2+\left(\frac{\partial H}{\partial y}\right)^2\right]^{\frac{1}{4}} \qquad (8)$$

Consequently, it appears that (1) is simply the continuity equation

$$\frac{\partial H}{\partial t}+\frac{\partial uh}{\partial x}+\frac{\partial vh}{\partial y}=0 \qquad (9)$$

combined with (6a) and (6b).

Copyright © 2006 Taylor & Francis Group plc, London, UK

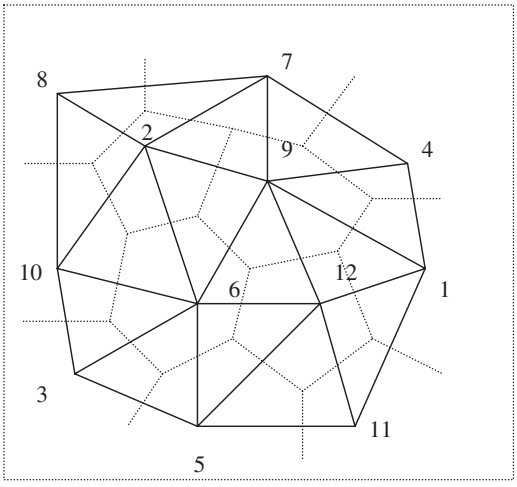


Figure 1. The 2-D area.

Referring to Figure (1), which depicts adjacent computational cells in two space dimensions, the velocity at the interface between a cell and its surrounding neighbors may be computed from the Manning relation. The water surface elevation and depth are defined at the center of the cell while the velocities are defined at the interface between two cells. The cells are fixed and may be dry or wet. Clearly, a horizontal water surface will generate zero velocities and thus result in a zero exchange of volume between cells as expected. Using a simple time-stepping scheme, at each time step Δt, the volume of water exchanged between the cells is computed and their water surface elevations adjusted in consequence using volume conservation. For purposes of computation, each cell is treated as a control volume having constant depth and constant water surface elevation. In order to treat the possibility of a pollutant source (example: a warehouse storing toxic chemicals) being flooded and releasing a pollutant plume, an implementation of the two-dimensional advection-diffusion equation has also been incorporated in the formulation and has been illustrated by an example.

3 1 TO 2D IMPLEMENTATION

Coupling between the 1D and 2D models is achieved by means of mass transfer between the two models. The momentum transfer is driven by difference in water surface elevations.

Before this can be accomplished, it is necessary to develop the mesh over the computational domain:

- A series of one dimensional geometrical cross sections that cover the main channel is established;

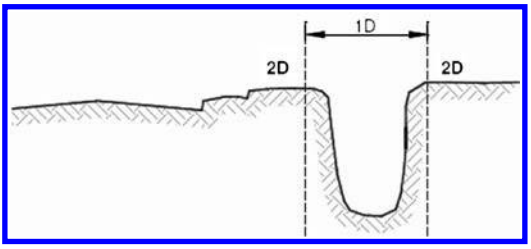


Figure 2. 1D/2D linkage at the cross section level.

- For each 1D cross section, the threshold level above which water flow into the flood plain is established (see figure 2);
- A 2D triangular mesh is generated to cover the flood plain.

An equation of the type (6a & 6b) is used to compute the mass transfer between the channel and the flood plain at the boundaries between the two domains.

4 TESTS

Validation Test for the Two-dimensional Component:

A test computation was performed in a rectangular channel of width 100 m, length 100 m with a constant slope of 0.0005. The Manning's coefficient was set to 0.033. Downstream water surface elevation was 3 m and the upstream discharge 100 m^3/s. Initially the computational domain is dry. The analytical solution is [*Goutal & Rissoan 2000*]:

$$\frac{\partial h}{\partial x} = \frac{S_0 - \dfrac{q^2}{\left(\dfrac{1}{n}\right)^2 h^{10/3}}}{1 - \dfrac{q^2}{gh^3}} \qquad (10)$$

where

S_0 is the slope,

n is the Manning's coefficient,

q is the unit lateral discharge as defined previously,

Equation (10) was integrated numerically using the Runge-Kutta formula.

Comparison with the numerical solution is shown in Figure (3)

In order to demonstrate an application of the model to a real world case, the simulation of a flood in the Eastmain river valley in Quebec, Canada was undertaken. The upstream boundary condition imposed on the 1D component was the inflow hydrograph shown in Figure (4). A constant water surface elevation of 1.5 m was imposed at the downstream border. Initial conditions were simply a constant discharge for the 1D component while the 2D computational area was dry.

Copyright © 2006 Taylor & Francis Group plc, London, UK

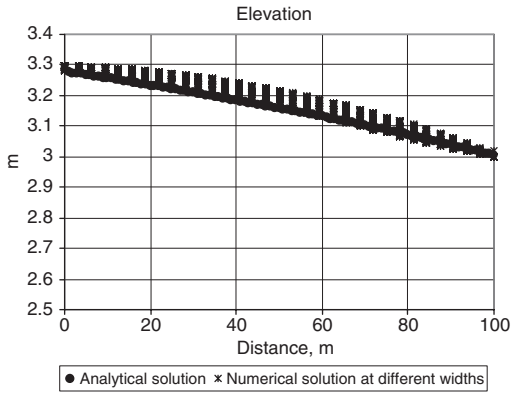


Figure 3. Longitudinal variation of water surface elevation.

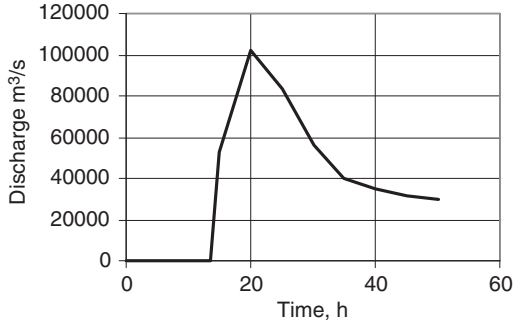


Figure 4. The upstream hydrograph.

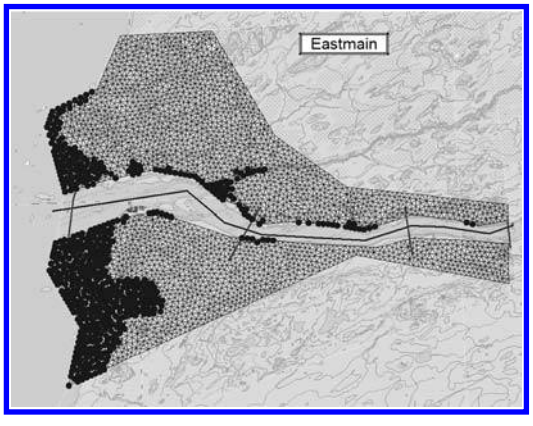


Figure 5. The inundation limits.

Figure (5) indicates the extent of flooding (dark areas) and closely follows the topographic input.

The model was used on a further test case, a region in Quebec where the EDF (Eléctricité de France) TELEMAC two-dimensional model had been used.

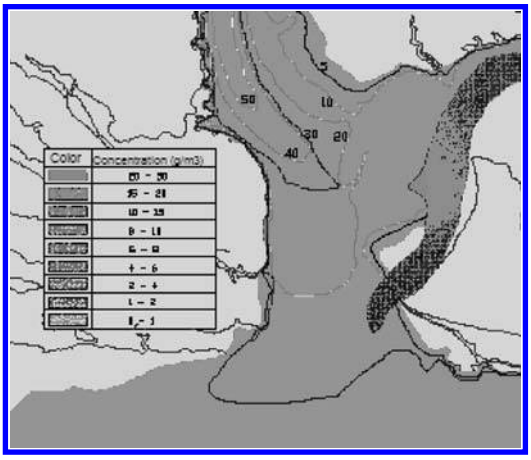


Figure 6. Flood contour lines at 1.5 h.

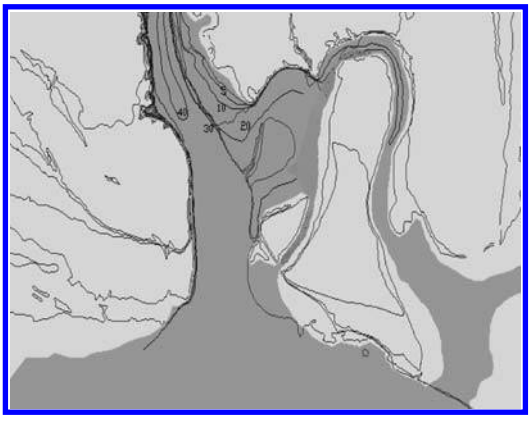


Figure 7. Flood contour lines at 4 h.

The TELEMAC model uses a finite element formulation on a triangular mesh and integrates the full St. Venant shallow water wave equations with no approximations being made. In this case study, the limits of flooding in a large urban area due to a dambreak far upstream was investigated. The present model was implemented a small distance upstream of the urban area where the inertial effects may have been attenuated since the site of the dam failure was over a hundred kilometers upstream. Boundary conditions for the one-dimensional component were obtained from the results of the TELEMAC model. (However, it must be re-iterated that the model is not intended to simulate the surge wave propagation following a dambreak) To assess the pollutant dispersion component of the model a fictitious source of pollution was introduced. Figures (6) to (8) indicate the extent and limit of flooding at 1.5, 4 and 5.5 hours after the arrival of the flood wave

Copyright © 2006 Taylor & Francis Group plc, London, UK

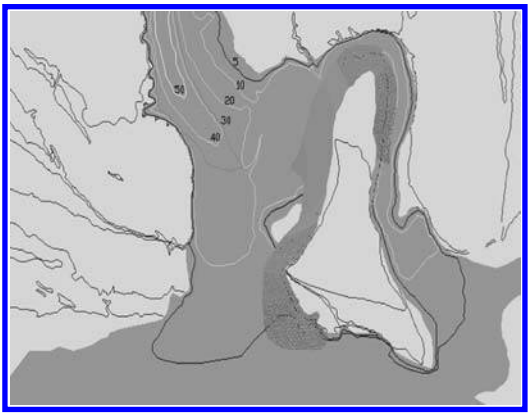


Figure 8. Flood contour lines at 5.5 h.

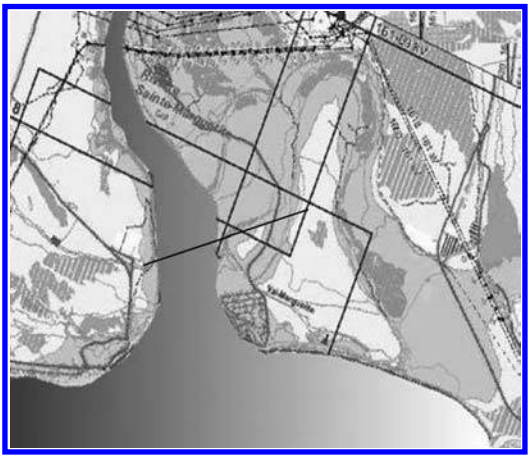


Figure 9. Flood contour lines at 5.5 h Results with TELEMAC model.

(grey areas). The dispersion and spreading of the pollutant plume especially in figure 6 (dark areas) is also clearly seen. Figure 8 when compared to Figure (9) (TELEMAC Results) show excellent agreement on the areas flooded. Computational time for the present model was extremely low.

5 CONCLUDING REMARKS

The model is quite robust and provides good results. It is expected that attempts to model higher velocity flows will result in degradation in quality of the results For flows with low local Froude Numbers good results may be expected.

REFERENCES

Goutal N., & Rissoan C., (2000), Validation Manual for the MASCARET model Version 5, Electricité de France, Service Environement et Production, Group Hydraulique Fluviale rapport HP-73/2000/041/A.

Paquier A., & Sigrist, B., (1997), "Computing a Flood Event by coupling 1D and 2D models", Saint-Venant Symposium, Paris, 13–20.

Verwey, A., (2001), "Latest developments in floodplain modelling – 1D/2D integration", Conference on hydraulics in civil engineering, Hobart – Australia, 7 pages.

Dhondia, J.F., & Stelling, G.S., (2002), "Application of one dimensional-two dimensional integrated hydraulic model for flood simulation and damage assessment", Hydroinformatics 2002, 12 pages.

Gillam, P., Jempson M., & Rogencamp, G., 2005, "The importance of combined 2D/1D modelling of complex floodplains – Tatura case study, Fourth Victorian Flood Management Conference. Shepperton – Victoria, Australia. 11 pages.

Copyright © 2006 Taylor & Francis Group plc, London, UK

1D complex modelling with lateral exchanges coupling two reaches

N. Goutal, C. Cheviet & G. Duvivier
Electricité de France R&D, Chatou, France

ABSTRACT: This paper presents a 1D complex modelling with lateral exchanges coupling two reaches. This study has been performed in the general context of re-assessment of the design values for all French nuclear power plants in case of extreme flood (probability less than 10^{-3}). The main features of the 1D hydrodynamic system Mascaret developed by EDF R&D and used for this study are presented. Then the developments performed to take into account the linking by the lateral exchanges are explained. In the last part of this paper, we present the main results of this study.

1 INTRODUCTION

On the 27th of December, 1999, a severe storm occurred in France and generated a lot of damages (buildings, forests…). It passed very close to a Nuclear Power Plant (NPP) located along the estuary of La Gironde (South West of France). The extreme storm surge and waves due to the storm led to a partial flooding of the NPP, without any impact on safety.

This event was extreme enough to lead EDF (Electricité de France, French utility) to review the methodology of protection against floods and re-assess the design values for all the French NPP (19 in all). 1D and 2D numerical hydraulic models have thus been built.

We will deal here with the complex hydraulic study done for a French plant situated near a regulated river, combining 1D and 2D simulations. We will focus mainly on the 1D part of the study, which necessitated specific developments.

1D hydrodynamic simulations were performed with the software Mascaret developed by EDF R&D – LNHE (National Laboratory of Hydraulics and Environment). After a general description of the software and its main features, we will present a general description of the study and the frame of the study. The fourth chapter will focus on the developments performed to deal properly for this study, on the presentation of the results and leads to the conclusion and the prospects.

2 SOFTWARE MASCARET

The Mascaret system is a one dimensional hydraulic simulation tool solving the shallow water equations, developed by EDF R&D. Three modules are available: a module for steady subcritical flows, a module for unsteady subcritical flows and a module for unsteady sub- and supercritical flows. In this paper, we focus on the features of the third module.

2.1 *Resolution of the shallow water equations*

The shallow water equations can be written as follows:

$$\begin{aligned} &\frac{\partial A}{\partial t}+\frac{\partial Q}{\partial x}=Q_a; \\ &\frac{\partial Q}{\partial t}+\frac{\partial}{\partial x}\left(\beta\frac{Q^2}{A}\right)+gA\frac{\partial y}{\partial x}+S_f=0 \end{aligned} \qquad (1)$$

where $A(y,t)$ = cross-sectional area (m^2); Q_a = lateral discharge; g = gravitational acceleration (m/s^2); $y(x,t)$ = water surface elevation (m); $Q(x,t)$ = discharge (m^3/s); x = longitudinal axis (m); t = time (s); $S_{f=}$ friction slope, expressing the resistance opposed by the river bed to the flow (m^3/s^2); and β = adimensional coefficient expressing the variation of the velocity in the section. This coefficient is taken into account in case of compound channel, i.e. when floodplains are treated as effective flow areas containing water that is actively being conveyed. We have:

$$\beta=\frac{A}{Q^2}\int u^2 dA \qquad (2)$$

Shallow water equations are solved using an explicit finite volume scheme: the Roe scheme. Details on the numerical scheme and the numerical treatment of source terms can be found in (Goutal & Maurel, 2002). We can notice that the time discretisation of the

Copyright © 2006 Taylor & Francis Group plc, London, UK

flux terms and of the source terms are explicit. So, the time step has to respect the following condition called Courant-Friedrich-Levy (CFL) condition.

$$\max\left(\frac{|u+c|\Delta t}{\Delta x}\right) < 1 \quad (3)$$

where u = water velocity (m/s); c = wave celerity (m/s); Δt = time step (s) and Δx = space step (m).

2.2 *Main features*

The module used offers a large range of modelling possibilities like:

- propagation of dam break waves over a dry bed
- modelling of branched or looped networks
- 2D modelling of the confluence
- modelling of compound channel and progressive integration of the floodplains in the active flow area when embankments are overtopped
- modelling of singularities in the geometry when the stage/discharge relationship is unknown
- modelling of storage basins to take into account ineffective flow areas.

Some of these features will be useful for our study. They are detailed just below.

2.3 *2D modelling of confluences*

The confluence between reaches is modelled by a 2D automatically built grid (see Figure 1), made of 4n cells (where n is the number of reaches joining together) leaning on the last cross section of each reach. In the 2D grid, the shallow water equations are solved using the same explicit volume scheme as for the 1D solution.

More details about this modelling and the coupling between 2D and 1D grids are available in the reference manual (Goutal & Maurel, 1996a) (Goutal & Maurel, 1996b).

2.4 *Weirs in the geometry*

With the software Mascaret, it is possible to model a weir directly in the geometry, i.e. to describe the geometry of the weir by the evolution of the bed level. This feature is very useful when the stage/discharge relationship is unknown. However, to obtain good results it is necessary to have a very fine grid around the weir.

2.5 *Storage basins*

Ineffective flow areas can be treated as interconnected storage basins, for each of which the relation between storage volume and water surface elevation is known or assumed. The flow calculation between the basins is based on continuity of volume for each basin and

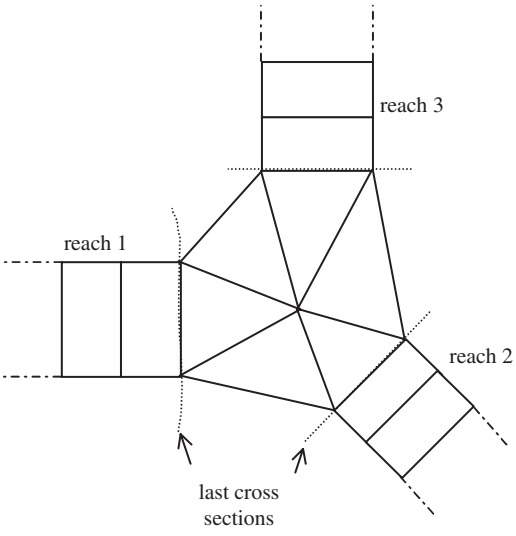


Figure 1. 2D modelling of a confluence.

non-inertial flow laws between basins. Continuity of volume V_j in a floodplain basin j is expressed as:

$$\frac{\partial V_j}{\partial t} = \sum_{i=1}^{n} Q_{ij} \quad (4)$$

where $V_j = V_j(y_j, t)$ volume of water in basin j (m^3); $Q_{ij}(t)$ = discharge from basin i to basin j or from river's cross section i to basin j (m^3/s); n = number of connections leading to basin j; t = time (s).

Discharge Q_{ij} is function of water levels in two adjacent basins or in the river and the basin j. These functions represent basic hydraulic features such as: weirs, sills, siphons, short channels.

For more details about this modelling see the reference manual (Rissoan, 2002).

The following features have been used : complex network with a 2D modelling of the confluence, interaction with lateral storage basins through specific hydraulic links, compound beds.

3 STUDY PRESENTATION

3.1 *Presentation*

The study that we will present here has been undertaken in order to assess the flooding risk for a French nuclear power plant situated near a regulated river.

From East to West, we can note (see conceptual scheme on Figure 2):

- The main river, flowing from South to North, bypassed by a channel. A dam is located at the upstream end, just after the beginning of the regulated channel,

Copyright © 2006 Taylor & Francis Group plc, London, UK

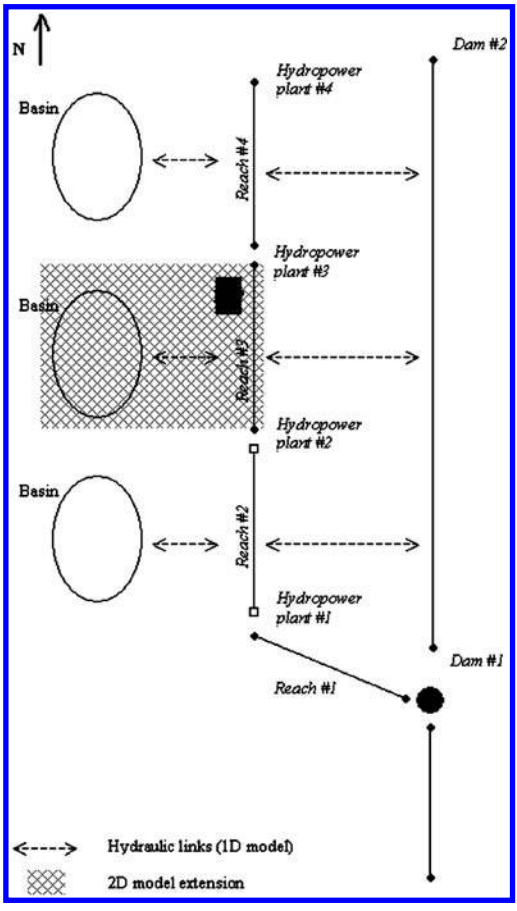


Figure 2. Conceptual scheme.

– A part of floodplain, which is in fact an island,
– The regulated channel, with four hydropower plants delimiting four reaches. At the downstream end, the flow coming from the channel comes back to the river,
– A plain (West end of the model), where the NPP is located (close to the 3rd hydropower plant).

A cross-sectional graph (Figure 3) shows the main topographical features of the study.

In case of flood, the flow is evacuated through the main river because the discharge in the regulated channel is limited. If the flood is not extreme, there is no overflowing of the main river and consequently no links between the regulated reaches and the main river. In this case, the 1D software Mascaret is used with its "standard" release. The model has been calibrated with such a flow.

In case of extreme flood (probability $< 10^{-3}$), the river and the channel are connected through lateral exchanges due to the main river overflowing (it has never been observed in reality). Lateral hydraulic exchanges between the two branches, above the floodplain, are taken into account through specific links (see the next paragraph), whereas the western flood plain is roughly modeled with 3 storage basins linked to the regulated reach. In a second step, in order to obtain the water elevation near the NPP, a 2D code (TELEMAC (Hervouet, 2003)) has been used to model the plain (water potentially flowing towards the NPP). The flow input in the 2D model comes from the flow rate overtopping the dykes on the left bank of the channel (flow rates are recovered from the 1D model using schematic basins in place of the western plain).

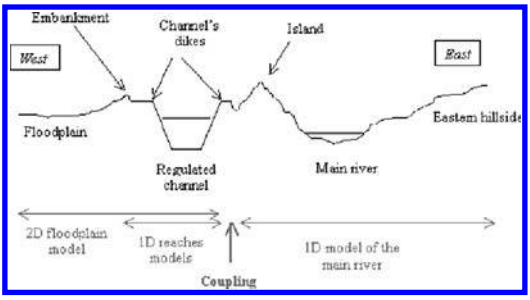


Figure 3. Topographical cross-section.

4 DEVELOPMENTS FOR THIS STUDY AND RESULTS

In order to enable the coupling of the main river with the 3 regulated reaches involved (#2 to #4, see conceptual scheme on Figure 2), new developments have been performed which allow the water transfer between the 3 regulated reaches and the main river. The lateral water transfers are taken into account in the continuity equations written for each reach and for the main river.

4.1 *Water transfer between the main river and the 3 reaches*

As explained previously, the main river is separated from the 3 reaches by an island which is like a "natural" dike with a varying crest elevation. In case of flood, this dike is not submerged. But in case of extreme flood, this dike can be overtopped and consequently, there is a lateral transfer flow between the main river and the 3 reaches (see the hydraulic exchanges schematically drawn on Figure 4).

The water can flow from the main river to the 3 reaches and the discharge in the reaches 2, 3 and 4 influences the water level downstream the reach 4. With such an extreme discharge, a water transfer becomes possible between the regulated reaches and the main river (such extreme conditions have never been observed in reality since the channels' building).

Copyright © 2006 Taylor & Francis Group plc, London, UK

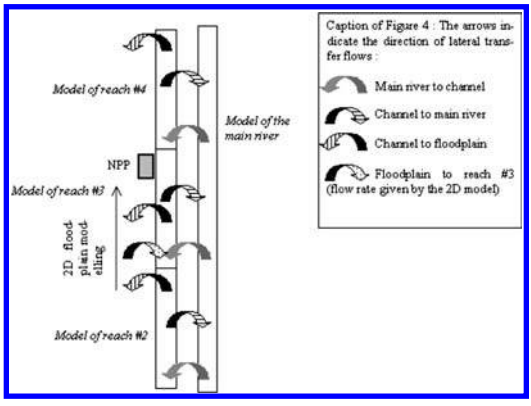


Figure 4. Hydraulic exchanges inside the 1D model.

So, there is a feedback on the main river water level. The different reaches and the main river are coupled through these water transfers.

The other kind of flow transfer is observed from the reaches 2, 3 and 4 to the flood plain situated on the West of the regulated reaches (Fig. 4). This case is easier to deal with because the water level in the flood plain has no influence on the hydraulic state in the 3 reaches.

Now, we are going to write the 1D shallow water equations for the different reaches and the main river and the coupling terms which model the water transfer. These terms will be taken into account only in the continuity equations. The influence on the momentum equations is neglected.

4.2 *Shallow water equations in the main river*

$$\begin{aligned} &\frac{\partial A_{mr}}{\partial t}+\frac{\partial Q_{mr}}{\partial x}=Q_{output}(A_{mr},x)+Q_{input}(A_{reach},x) \\ &\frac{\partial Q_{mr}}{\partial t}+\frac{\partial}{\partial x}\left(\beta\frac{Q_{mr}^{\ 2}}{A_{mr}}\right)+gA_{mr}\frac{\partial y_{mr}}{\partial x}+S_f=0 \end{aligned} \quad (5)$$

where A_{mr} = hydraulic section of the main river (m^2); Q_{mr} = total discharge in the main river (m^3/s); Q_{output} = output lateral discharge due to the overflow (m^3/s) (note that it depends on the water level in the main river); and Q_{input} = lateral discharge due to the flow transfer from the reach 2, 3 and 4 to the main river (m^3/s) (note that it depends on the water level in the regulated reaches).

4.3 *Shallow water equations in the different reaches*

$$\begin{aligned} &\frac{\partial A_{ri}}{\partial t}+\frac{\partial Q_{ri}}{\partial x}=Q_{input}(A_{mr},x)+Q_{output}(A_{ri},x) \\ &\frac{\partial Q_{ri}}{\partial t}+\frac{\partial}{\partial x}\left(\beta\frac{Q_{ri}^{\ 2}}{A_{ri}}\right)+gA_{ri}\frac{\partial y}{\partial x}+S_f=0 \end{aligned} \quad (6)$$

where A_{ri} = hydraulic section of the reach i (m^2); Q_{ri} = total discharge in the reach i (m^3/s); Q_{input} = input lateral discharge due to the overflow (m^3/s) (note that it depends on the water level in the main river); and Q_{output} = lateral discharge due the flow transfer from the reaches 2, 3 and 4 to the main river (m^3/s).

The coupling between the shallow water equations written in the different reaches and in the main river is performed through the source terms (lateral discharge) and this coupling is a strong one due to the feedback of the output-input discharge of the reaches on the hydraulic state of the main river and vice-versa.

This coupling through the source terms has been implemented in the finite volume scheme used to solve the 1D shallow water equations with source terms in the continuity equation.

4.4 *Discretised shallow-water equations in the main river and in the regulated reaches*

Thanks to a finite volume formulation with explicit time discretisation, the shallow water equations can be written as follows (see § 4.5 and 4.6).

We assume that:

- the domain computation is discretised with N finite cells C_i
- the time interval [0,T] is discretised in n sub intervals $[t_n,t_{n+1}]$.

(a) Discretised shallow-water equations in the main river:

For each cell C_i, $i = 1,N$

$$\frac{W_{mr,i}^{n+1}}{\Delta t}=\frac{W_{mr,i}^{n}}{\Delta t}+F_{mr,i+1/2}^{n}-F_{mr,i-1/2}^{n}+TS_i^n+TS_{mr}(W_{mr},W_j)$$

where $(W_{mr})=(A_{mr},Q_{mr})$; F = numerical flux at the interface between two cells; TS = source terms; and TS_{mr} = source terms due to the coupling between the main river and the regulated reaches.

(b) Discretised shallow-water equations in the different reaches

For each cell C_i, $i = 1,N$ and each reach j:

$$\frac{W_{j,i}^{n+1}}{\Delta t}=\frac{W_{j,i}^{n}}{\Delta t}+F_{j,i+1/2}^{n}-F_{j,i-1/2}^{n}+TS_i^n+TS_j(W_{mr},W_j)$$

where $(W_j)=(A_j,Q_j)$; F = flux at the interface between two cells; TS = source terms; TS_j = source terms due to the coupling between the main river and the regulated reaches.

For more details on the finite volume scheme and the discretisation of the source terms, the reader can report to the reference (Goutal & Maurel, 1996a). In this case, we will focus only on the numerical coupling

Copyright © 2006 Taylor & Francis Group plc, London, UK

of the two hydraulic systems by the source terms in the continuity equation.

To deal with this coupling, we have different possibilities:

– to use an implicit discretisation of the source terms. So in this case, we have to solve the global system: the global state is composed with the hydraulic states in the main river and in the different reaches. It will be necessary to re-write an important part of the software.
– to use an explicit time discretisation of the source terms as it is done for the "classical" source terms and the flux terms in the Mascaret software. Consequently, the two hydraulic systems are no more numerically coupled. But, the main drawback of this method is linked to the choice of the time step which must not be too large in order to obtain the stability of the numerical scheme

We retained the second solution for the main following reasons: the explicit time discretisation is in good agreement with the original finite volume numerical scheme of the software Mascaret; so the coupling source terms are discretised in the same way as the classical source terms in the continuity equation. As we have to respect the CFL condition due to the explicit discretisation of the flux terms and of the source terms, the coupling through the source terms is not a supplementary constraint on the time step for this study where the source terms due to the lateral exchanges are not too stiff.

In the case of implicit scheme for the shallow-water equations, the time step will be larger and we will have to iterate in order to obtain the convergence of the uncoupled system.

4.5 *Results*

These specific developments allowed us to simulate the extreme hydraulic behaviour corresponding to the design conditions.

An example of the results is shown on Figure 5: the maximum surface level along reach #3 corresponds to the sloping line, whereas the right bank elevation is bold-plotted (geometrical shape) and the maximum island elevation is the thin line rapidly varying. We can see on this figure some zones where the maximum surface level exceeds the island elevation : lateral transfers from the main river to the regulated reach occur in these places (the main ones are located by horizontal segments).

Another kind of result that can be given is the hydrograph of overflows, from the main river to reach #3 for example on Figure 6. This hydrograph represents the water quantities passing in transit through the coupling terms specifically written for this study.

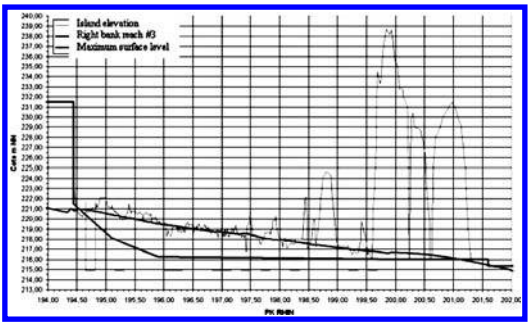


Figure 5. Maximum surface level for an extreme flood along the reach #3.

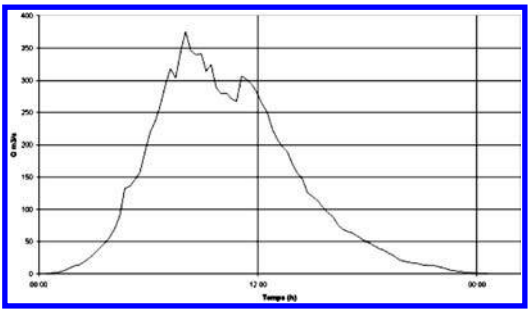


Figure 6. Hydrograph of overflow from the main river to reach #3.

4.6 *2D model implementation*

A two-dimensional model, based on TELEMAC-2D hydro-informatic software (Hervouet, 2003), has been built in order to represent the flow path in the western floodplain, towards the power plant.

The extension of this model can be seen on Figure 2 and on Figure 3 (on the left of the cross section).

The 1D and 2D models were not numerically coupled, but simply connected by giving the 1D results as a boundary condition for the 2D model.

Thus, the flow input in the 2D model comes from the flow rate overtopping the dykes on the left bank of the channel (flow rates are recovered from the 1D model using schematic basins in place of the western plain).

5 CONCLUSION AND PROSPECTIVES

The developments implemented in the 1D Mascaret hydro-informatic software and presented in this article enabled us to simulate complex extreme flows with lateral exchanges between a regulated channel and the main river.

Copyright © 2006 Taylor & Francis Group plc, London, UK

This complex case study raises the need of linking different models (1D-1D as well as 1D-2D) and consequently the necessity for a more general frame for models' interoperability.

The next step will be the development of the 1D model as a linkable model in order to improve the possibility of data exchange between different 1D-1D models and 1D-2D models and to make easier the coupling between different models.

REFERENCES

Goutal N., 2001. Validation d'une modélisation avancée pour le noyau transcritique du système Mascaret. EDF – LNH HP-76/2001/037. pp. 33–42. French.

Goutal N. & Maurel F., 1996a. Note de principe de la version 4.1 du code Mascaret. EDF – LNH HE-43/96/075. pp. 41–46. French.

Goutal N. & Maurel F., 1996b. Note de validation de la version 4.1 du code Mascaret. EDF – LNH HE-43/96/076. French.

Goutal N. & Maurel F., 2002. A finite volume solver for 1D shallow-water equations applied to an actual river. International journal for numerical methods in fluids. 38: 1–19.

Hervouet J.M., 2003. Hydrodynamique des écoulements à surface libre. French.

Lencastre A., 1995. Hydraulique générale. Eyrolles. pp. 334–335. French.

Rissoan C., 2002. Résolution d'un ensemble de casiers dans le système Mascaret : note de principe. EDF – LNHE HP-76/2002/012. French.

Copyright © 2006 Taylor & Francis Group plc, London, UK

A.3. Dam-break and highly unsteady open-channel flow

Copyright © 2006 Taylor & Francis Group plc, London, UK

A marching in space and time solver for the complete 2D shallow water equations: Application to real test cases

C. Aricò, C. Nasello & T. Tucciarelli
Dipartimento di Ingegneria Idraulica ed Applicazioni Ambientali, Università di Palermo, Palermo, Italy

ABSTRACT: A novel methodology for the solution of the 2D shallow water equations is proposed and applied to both synthetic and experimental tests. The algorithm is based on a fractional step decomposition of the original system in a convective and in a diffusive component. In the case of existing scalar potential of the velocity field, the convective component is solved using a Marching in Space and Time (MAST) procedure, that solves a sequence of small systems of ODEs, one for each computational cell, according to the decreasing value of the scalar potential. If inertial terms are not neglected in the momentum equations and the exact potential does not exist, it is shown that a second MAST procedure has to be applied, to solve again the ODEs according to the increasing value of a new function, called approximated potential. For this last case, results of numerical tests are compared with: 1) results of a classical ideal dam-break case proposed in literature and 2) lab data of a dam-break experiment carried out by Fraccarollo and Toro (1995).

1 INTRODUCTION

Saint Venant (SV) equations (or shallow water equations) are usually applied and numerically solved for the simulation of unsteady shallow water flows (Saint Venant, 1871). Both explicit and implicit numerical methods can be used for the solution. Even though implicit schemes are stable for CFL numbers greater than 1, they lead to the solution of large non linear algebraic systems, and the computational effort grows very quickly along with the number of elements. Implicit Preissman schemes show also other limitations, especially for simulations of transcritical flows (Meselhe et al., 1997).

For these reasons, during the last years, Authors have proposed explicit schemes. Several Finite Volume Godunov methods have been proposed for the 'non viscous' form of the SV equations, where source term in the momentum equation is zero (Alcrudo and Garcìa-Navarro, 1993; Mingham and Causon, 1998).

A fractional time step procedure (Toro, 1997) can be applied for the solution of the shallow water equations when source terms cannot be neglected. The corresponding non homogeneous form of the governing equations is solved in two sequential steps. During the first step, the homogeneous problem (without the source term) is solved. In the second step a set of ordinary differential equations including source terms are solved sequentially, one after the other. A similar approach is simple, but often produces bad solutions, especially in stationary cases (LeVeque, 1998).

In the last decade many Authors have developed Godunov-type schemes for the solution of balance laws, including source terms. The main focus of these schemes is the balance between the numerical flux and the source term, when the same numerical discretization is applied. Bermudez and Vazquez-Cendon (1994), using a "Q" scheme with 1st spatial approximation order and upwind discretization of both flux and source terms, introduced the notion of exact conservative property in order to preserve quiescent state. Hubbard and Garcìa-Navarro (2000) extended this approach the a 2nd order MUSCL scheme with flux limiter. Upwinding the source term is computationally expensive, because source term has to be projected on a basis of eigenvectors. LeVeque (1998) introduced a Riemann problem inside the cell for balancing the source term and the flux gradient; the method preserves steady and quasi-steady flow conditions. Vukovic and Sopta (2002) and Zic et al. (2004) developed one of the first version of higher order schemes (ENO and WENO), where numerical flux terms balance the source terms.

The main limitation of these numerical methods proposed for balance laws is that they have been developed for specific forms of the source terms and miss generality.

Copyright © 2006 Taylor & Francis Group plc, London, UK

In the present paper a new numerical scheme is proposed for the solution of the SV equations. The governing equation system is initially split in a convective component and in a diffusive component.

The convective system is solved applying a MArching in Space and Time (MAST) procedure, where the convective fluxes are solved using an Eulerian approach and the computational cells are required to be ordered and solved according to a decreasing scalar potential value. MAST procedure has been recently applied for the solution of the pure convective transport problem (Bascià and Tucciarelli, 2004; Aricò and Tucciarelli, 2006), the 1D and 2D shallow water problem with irrotational flow field (Tucciarelli and Termini, 2000; Noto and Tucciarelli, 2001) and the 1D shallow water problem with a mono-oriented flow (Tucciarelli, 2003).

The correction step computes the diffusive corrective fluxes by means of the solution of a linear system, that has the order of the cell number, but is sparse, symmetric and well conditioned.

The potential is defined as a scalar whose gradient is opposite to the flux direction. Because the flow field computed solving the SV equations has not a scalar potential, an approximated potential has to be used, along with a second correction step that is aimed to compute the rotational fluxes. This approximated potential is defined according to the flow direction inside each element at the beginning of the time step.

2 THE SV EQUATIONS

2D SV equations can be written as:

$$\frac{\partial h}{\partial t}+\frac{\partial p}{\partial x}+\frac{\partial q}{\partial y}=0 \tag{1}$$

$$\frac{\partial q}{\partial t}+\frac{\partial}{\partial x}\left(\frac{p^2}{h}\right)+\frac{\partial}{\partial y}\left(\frac{pq}{h}\right)+ +gh\frac{\partial h}{\partial x}+gh\left(\frac{\partial z}{\partial x}+\frac{n^2 p\sqrt{p^2+q^2}}{h^{10/3}}\right)=0 \tag{2}$$

$$\frac{\partial q}{\partial t}+\frac{\partial}{\partial y}\left(\frac{q^2}{h}\right)+\frac{\partial}{\partial x}\left(\frac{pq}{h}\right)+ +gh\frac{\partial h}{\partial y}+gh\left(\frac{\partial z}{\partial y}+\frac{n^2 q\sqrt{p^2+q^2}}{h^{10/3}}\right)=0 \tag{3}$$

where x and y are the spatial coordinates, t is the time, g is the gravitational acceleration, p and q are the x and y components of the flow per unit width in x and y directions, h is the water depth, z is the ground level and n is the Manning friction coefficient.

The unknowns in the system (1)–(3) are the water depth h and the two flow rates components p and q.

3 INTEGRAL FORM OF THE SV EQUATIONS

Integration in space of eqs. (1), (2) and (3), as well as application of the Green's theorem provides:

$$\frac{\partial h}{\partial t}\sigma_e+\sum_{j=1,3}F_{e,j}=0 \tag{4}$$

$$\frac{\partial p}{\partial t}\sigma_e+\sum_{j=1,3}M^x_{e,j}+R^x_e=0 \tag{5}$$

$$\frac{\partial q}{\partial t}\sigma_e+\sum_{j=1,3}M^y_{e,j}+R^y_e=0 \tag{6}$$

where σ_e is the element area and the source terms R^x_e, R^y_e are defined as:

$$R^x_e=\sigma_e gh\left(\frac{\delta H_e}{\delta x}+\frac{n^2 p_e\sqrt{p_e^2+q_e^2}}{h_e^{10/3}}\right) \tag{7}$$

$$R^y_e=\sigma_e gh\left(\frac{\delta H_e}{\delta y}+\frac{n^2 q_e\sqrt{p_e^2+q_e^2}}{h_e^{10/3}}\right) \tag{8}$$

where H_e is the element water level. Volume fluxes $F_{e,j}$ and moment fluxes $M^x_{e,j}, M^y_{e,j}$ are given respectively by:

$$\begin{aligned}&F_{e,j}=p_e\left(y^e_{jp}-y^e_j\right)-q_e\left(x^e_{jp}-x^e_j\right),\\ &M^x_{e,j}=F_{e,j}\frac{p_e}{h_e},\quad M^y_{e,j}=F_{e,j}\frac{q_e}{h_e}.\end{aligned} \tag{9}$$

where subindex jp indicates the node following node j in couterclockwise direction and $(x^e_{jp}-x^e_j)$ and $(y^e_{jp}-y^e_j)$ represent the projections in $x(y)$ direction of the element side connecting nodes j and jp.

4 FRACTIONAL STEP DECOMPOSITION

Assume that a scalar value ϕ^k_e, called approximated potential, is assigned at the beginning of each time step to each element of the domain. After integration in time, prediction step of system (4)–(9) is defined as:

$$\frac{h^{k+1/3}-h^k}{\Delta t}\sigma_e+\frac{1}{\Delta t}\sum_{j=1,3}\int_{\Delta t}F^p_{e,j}dt=0 \tag{10}$$

$$\frac{p^{k+1/3}-p^k}{\Delta t}\sigma_e+\frac{1}{\Delta t}\left(\sum_{j=1,3}\int_{\Delta t}M^{px}_{e,j}dt+\int_{\Delta t}R^{px}_e dt\right)=0 \tag{11}$$

Copyright © 2006 Taylor & Francis Group plc, London, UK

$$\frac{q^{k+1/3}-q^{k}}{\Delta t}\sigma_e+\frac{1}{\Delta t}\left(\sum_{j=1,3}\int_{\Delta t}M_{e,j}^{py}dt+\int_{\Delta t}R_e^{py}dt\right)=0 \tag{12}$$

where:

$$\begin{aligned}R_e^{px}&=\sigma_e gh\left(\frac{\delta H_e^k}{\delta x}+\frac{n^2 p_e\sqrt{p_e^2+q_e^2}}{h_e^{10/3}}\right)\\ R_e^{py}&=\sigma_e gh\left(\frac{\delta H_e^k}{\delta y}+\frac{n^2 q_e\sqrt{p_e^2+q_e^2}}{h_e^{10/3}}\right)\end{aligned} \tag{13}$$

and

$$\begin{aligned}&F_{e,j}^{p}=max\left(0,p_e\left(y_{jp}^e-y_j^e\right)-q_e\left(x_{jp}^e-x_j^e\right)\right),\\ &M_{e,j}^{px}=F_{e,j}^{p}\frac{p_e}{h_e},\quad M_{e,j}^{py}=F_{e,j}^{p}\frac{q_e}{h_e}\end{aligned} \tag{14}$$

if $\phi_e^k\geq\phi_{ep}^k$ and ep is the index of the element sharing the jth side of element e,

$$\begin{aligned}&F_{e,j}^{p}=min\left(0,p_{ep}\left(y_{jp}^e-y_j^e\right)-q_{ep}\left(x_{jp}^e-x_j^e\right)\right),\\ &M_{e,j}^{px}=F_{e,j}^{p}\frac{p_{ep}}{h_{ep}},\quad M_{e,j}^{py}=F_{e,j}^{p}\frac{q_{ep}}{h_{ep}}\end{aligned} \tag{15}$$

otherwise.

Correction prediction system is defined as:

$$\frac{h^{k+2/3}-h^{k+1/3}}{\Delta t}\sigma_e+\frac{1}{\Delta t}\sum_{j=1,3}\int_{\Delta t}F_{e,j}^{c}dt=0 \tag{16}$$

$$\frac{p^{k+2/3}-p^{k+1/3}}{\Delta t}\sigma_e+\frac{1}{\Delta t}\left(\sum_{j=1,3}\int_{\Delta t}M_{e,j}^{cx}dt\right)=0 \tag{17}$$

$$\frac{q^{k+2/3}-q^{k+1/3}}{\Delta t}\sigma_e+\frac{1}{\Delta t}\left(\sum_{j=1,3}\int_{\Delta t}M_{e,j}^{cy}dt\right)=0 \tag{18}$$

$$\begin{aligned}&F_{e,j}^{c}=\min\left(0,p_{ep}\left(y_{jp}^e-y_j^e\right)-q_{ep}\left(x_{jp}^e-x_j^e\right)\right),\\ &M_{e,j}^{cx}=F_{e,j}^{c}\frac{p_{ep}}{h_{ep}},\quad M_{e,j}^{py}=F_{e,j}^{c}\frac{q_{ep}}{h_{ep}}\\ &\text{if }\ \phi_e^k\geq\phi_{ep}^k,\end{aligned} \tag{19}$$

$$\begin{aligned}&F_{e,j}^{c}=\max\left(0,p_e\left(y_{jp}^e-y_j^e\right)-q_e\left(x_{jp}^e-x_j^e\right)\right),\\ &M_{e,j}^{cx}=F_{e,j}^{c}\frac{p_e}{h_e},\quad M_{e,j}^{cy}=F_{e,j}^{c}\frac{q_e}{h_e}\end{aligned} \tag{20}$$

otherwise.

Diffusive correction system is defined as:

$$\frac{h^{k+1}-h^{k+2/3}}{\Delta t}\sigma_e+\frac{1}{\Delta t}\sum_{j=1,3}\int_{\Delta t}F_{e,j}^{d}dt=\frac{1}{\Delta t}\sum_{j=1,3}\int_{\Delta t}F_{e,j}dt \tag{21}$$

$$\frac{p^{k+1}-p^{k+2/3}}{\Delta t}\sigma_e+\frac{1}{\Delta t}\int_{\Delta t}R_e^{dx}dt=\frac{1}{\Delta t}\int_{\Delta t}R_e^{px}dt \tag{22}$$

$$\frac{q^{k+1}-q^{k+2/3}}{\Delta t}\sigma_e+\frac{1}{\Delta t}\int_{\Delta t}R_e^{dy}dt=\frac{1}{\Delta t}\int_{\Delta t}R_e^{py}dt \tag{23}$$

where index d states that $F_{e,j}^{d}$, R_e^{dx}, R_e^{dy} are computed as $F_{e,j}$, R_e^{x}, R_e^{y} defined in eqs. (7), (8) and (9), but using the water heads and the flow rates of the final correction steps. Initial condition of the convective correction system are the final values of the prediction system and initial values of the diffusive correction system are the final values of the convective correction system. Spatial piezometric gradient $\partial H^k/\partial x$ is assumed constant (in time) in all the systems. Observe that summing all the terms of eqs. (10)–(23), eqs. (4)–(9) are found again. After simple manipulations, eigenvalue analysis provides that characteristic polynomial in both the prediction and the convection correction systems have only one root $\lambda_x=u_x$ and $\lambda_y=u_y$; this implies that both the systems represent simple convection and the characteristic surface, with vertex in a generic x, y, t point, degenerates into a line.

Characteristic polynomial of the diffusive correction system has real and opposite in sign eigenvalues $\lambda_x=\lambda_y=\pm\sqrt{gh}$. This implies that convective fluxes are missing and upwinding techniques are not required to solve the problem with standard finite volume techniques.

5 THE APPROXIMATED SCALAR POTENTIAL

Fractional step methodology provides accurate results only if the solution of the prediction step is close to the corrected one; otherwise, the computation of the spatial gradients at different time levels can strongly affect the solution. In our case, to minimize the variable change in the convective correction step, it is important to choose an approximated potential with a gradient flux opposite in sign, as much as possible, to the water flux along the element sides. If an exact potential exists and this condition is always attained, convective correction system vanishes and the following condition holds:

$$h_e^{k+2/3}=h_e^{k+1/3}\quad p_e^{k+2/3}=p_e^{k+1/3}\quad q_e^{k+2/3}=q_e^{k+1/3} \tag{24}$$

Copyright © 2006 Taylor & Francis Group plc, London, UK

In order to find a good approximated potential, define flux Fl_j^e trough the jth side of element e according to the following rule:

$$Fr_j^e = p_e\left(y_{jp}^e - y_j^e\right) - q_e\left(x_{jp}^e - x_j^e\right) \tag{25}$$

$$Fl_j^e = Fr_j^e \quad \text{if} \quad \left|Fr_j^e\right| \geq \left|Fr_{jm}^{em}\right| \tag{26}$$

$$Fl_j^e = -Fr_{jm}^{em} \quad \text{if} \quad \left|Fr_{jm}^{em}\right| > \left|Fr_j^e\right| \tag{27}$$

where em is the index of the element sharing with element e the side following the jth node in counterclockwise direction and jm is the index of the node of element em preceding the same side in the same direction. ϕ_e and ϕ_{em} indicate the potential values in cells e and em at the beginning of the time step.

An approximated potential can be found as the solution of the following Linear Programming (LP) problem:

$$\text{Min } CT = \sum_{e=1,N}\sum_{j=1,3}\left|Fl_j^e\right|\lambda_j^e \tag{28}$$

$$\text{s. t.} \begin{cases} \left(\phi_e - \phi_{em}\right)Sign\left(Fl_j^e\right) - 1 + \lambda_j^e \geq 0 \\ \lambda_j^e \geq 0 \end{cases} \tag{29}$$

where $Sign(Fl_j^e) = 1$ if $Fl_j^e \geq 0$ and $Sign(Fl_j^e) = -1$ if $Fl_j^e < 0$.

A fast solution can be obtained starting each search, at each time level, with the same basis of the previous optimal solution and initializing the auxiliary variables with:

$$\lambda_j^e = \max\left(0, 1 - \left(\phi_e - \phi_{em}\right)Sign\left(Fl_j^e\right)\right) \tag{30}$$

Even if the flow rates are consistent with the potential gradient at the beginning of the time step, they can change sign along the time step integration. For this reason, the solution of a new convective correction system is required also in the 1D cases, where an easy solution of problem (28)–(29) with zero optimal objective function can always be found.

5.1 *Solution of the prediction and the convective correction systems*

In both the prediction and the convective correction systems (10)–(15) and (16)–(20) unresolved integrals appear. Because both systems represents non linear convection, it is possible to change the integral equations in ordinary differential equations and find efficiently a fast solution using a variable step Runge-Kutta method with adaptive stepsize control (Press et al., 1988). For prediction, as example, the corresponding ODEs system is:

$$\frac{dh_e}{dt}\sigma_e + \sum_{j=1,3} F_{e,j}^p(t) = 0 \tag{31}$$

$$\frac{dp_e(t)}{dt}\sigma_e + \sum_{j=1,3}\left(M_{e,j}^{px}(t) + R_e^{px}(t)\right) = 0 \tag{32}$$

$$\frac{dq_e(t)}{dt}\sigma_e + \sum_{j=1,3}\left(M_{e,j}^{py}(t) + R_e^{py}(t)\right) = 0 \tag{33}$$

Terms $F_{e,j}^p$, $M_{e,j}^{px}$, $M_{e,j}^{py}$ can represent fluxes either leaving or entering the element.

Assuming a first order approximation of all the variables, we assume that the leaving fluxes are function of the element variables, and the entering ones are function of the variables in the neighbour element, as shown in eqs. (14), (15). This allows to solve sequentially the ODEs systems after ordering the elements according to a decreasing value of the approximated potential. In this case, in fact, the entering fluxes will be either given by the mean value leaving from neighbour elements with higher potential, or by the assigned boundary value, where:

$$F_{e,j}^p = BF_{e,j}, \quad M_{e,j}^{px} = BM_{e,j}^x, \quad M_{e,j}^{py} = BM_{e,j}^y \tag{34}$$

if j is the local index of a boundary side with entering flux ($BF_{e,j} \leq 0$). For the solution of the convective correction step the opposite order has to be followed, starting from the elements with lower and ending to the elements with higher potential. In this case boundary fluxes are assumed to be zero.

After the single system of element e is solved along the time step, the mean leaving fluxes have to be estimated. The mean volume flux through each side can be estimated by partitioning the total mean leaving flux, obtained from the mass balance in the element and equal to:

$$\frac{1}{\Delta t}\sum_{out}\int F_{e,out}^p dt = \frac{1}{\Delta t}\sum_{in}\int F_{e,in}^p dt - \frac{h_e^{k+1/3} - h_e^k}{\Delta t}\sigma^e \tag{35}$$

where subindex *in* and *out* indicate the incoming and leaving fluxes. Partition can be done adopting for the mean values the same ratio computed for the final ones. Due to non linearity of the source terms, the same methodology cannot be applied for the estimation of the mean values of the leaving momentum fluxes.

After integration, the mean $M_{e,j}^{px}, M_{e,j}^{py}$ values are given by:

$$\begin{aligned} &\frac{1}{\Delta t}\sum_{out}\int M_{e,out}^{ex} dt = \frac{1}{\Delta t}\sum_{in}\int M_{e,in}^{ex} dt + \\ &-\frac{p_e^{k+1/3} - p_e^k}{\Delta t}\sigma^e - \frac{1}{\Delta t}\int R_e^{px} dt \\ &\frac{1}{\Delta t}\sum_{out}\int M_{e,out}^{ey} dt = \frac{1}{\Delta t}\sum_{in}\int M_{e,in}^{ey} dt + \\ &-\frac{q_e^{k+1/3} - q_e^k}{\Delta t}\sigma^e - \frac{1}{\Delta t}\int R_e^{qy} dt \end{aligned} \tag{36}$$

where the mean values of the source terms have to be numerically estimated. Because the ODEs integration

Copyright © 2006 Taylor & Francis Group plc, London, UK

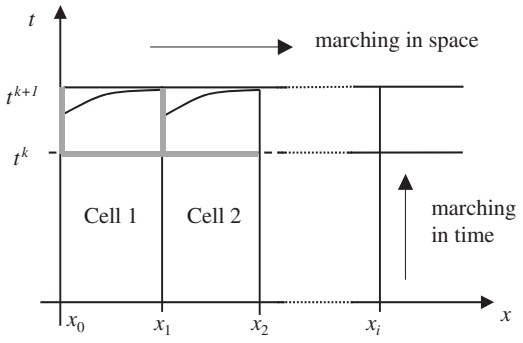


Figure 1. The core of the MAST procedure.

adopts a variable integration step, it is more convenient to assume for the source terms a third order polynomial interpolation, where the initial and final values are known along with the corresponding time derivatives. This computation is not due in the convective correction step, where the source terms are missing. Application of the mass balance can be easily proved to guarantee the local and global mass conservation. Observe that it is possible to solve sequentially the ODEs systems, without any restriction on the size of the time step, because the characteristic line of the convective problem is oriented according to the velocity direction. This is equivalent, after solution of cell 1 from time t^k to time t^{k+1}, to "translate" the boundary condition (thick segment in figure 1) at the interface between cell 1 and 2, to get the initial value of the characteristic curve carrying on the solution of cell 2 and so on through all the computational domain. Because of this, the method can be classified, other than "*marching in time*", also "*marching in space*".

5.2 *Computation of the gradients for the convective systems*

In each element *e*, water depth gradients are computed according to the bottom elevation gradient and to the element location with respect to the boundary. One of the following cases can be selected:

1. At least one side is part of the boundary and its volume flux is positive (leaving flux), or two sides are impervious. In the first case there is no need to compute the water depth gradient and in the second case this one is assumed opposite to the bottom elevation gradient.
2. There are not boundary sides. In this case convective gradient computation is split in two steps. In the first step second order gradient approximation is computed (see for example Mohamadian et al., 2005). If the node *jx* with maximum *y*-coordinate follows node *jn* with minimum *y*-coordinate in counterclockwise direction, it is:

$$\frac{\partial h}{\partial x} \approx \frac{(y_{jx} - y_{jn})h_{jn}}{2\sigma_e} + \frac{(y_{jx} - y_{jm})h_{jx} + (y_{jm} - y_{jn})h_{jm}}{2\sigma_e} \quad (37)$$

where h_n, h_x and h_m are the water depth at the elements next in counterclockwise direction to the nodes *jn*, *jx* and *jm*. In the other case, it is:

$$\frac{\partial h}{\partial x} \approx \frac{(y_{jx} - y_{jm})h_{jm} - (y_{jm} - y_{jn})h_{jn}}{2\sigma_e} + \frac{(y_{jx} - y_{jn})h_{jx}}{2\sigma_e} \quad (38)$$

Second order gradient component in the *y* direction can be computed in a similar way.

Once gradient direction is computed, its norm is estimated according to its first order downstream value, in order to avoid spurious oscillations. If ξ and η are respectively the coordinate along the gradient and its orthogonal left-handed directions, derivative along ξ is given by:

$$\frac{\partial h}{\partial \xi} = \frac{(\eta_{jx} - \eta_{jn})(h_{jn} - h_e)}{\sigma_e} \quad (39)$$

$$\frac{\partial h}{\partial \xi} = \frac{(y_{jx} - y_{jm})h_{jm} + (y_{jm} - y_{jn})h_{jn}}{\sigma_e} + \frac{(y_{jx} - y_{jn})h_e}{\sigma_e} \quad (40)$$

according to the maximum and minimum node coordinate in the η direction. Once the components along the ξ-η coordinate system are computed, they are mapped again in the original *x*-*y* system.

3. One side *j* is an impervious boundary. In this case, the boundary side is chosen as the water level gradient direction, oriented toward the triangle with larger water depth and the derivative along the side direction is given by:

$$\frac{\partial h}{\partial \xi} = \frac{A_e(h_e - h_f)}{\sigma_e} \quad (41)$$

where A_e is the height of element *e* with respect to its impervious side and h_f is the water depth of the triangle, close to element *e* and with smaller water level.

4. One side *j* is a boundary side with entering flux and the other two sides are internal. In this case the gradient direction is computed using a second order approximation along the direction of the boundary side and a first order approximation

Copyright © 2006 Taylor & Francis Group plc, London, UK

along the orthogonal one. Once again, after gradient direction is computed, its norm is estimated according to a first order scheme, applied to the derivative computed along the chosen direction.

5.3 *Boundary conditions for the prediction system*

Boundary terms of eqs. (31)–(33) at time level $k + 1/3$ depend on the flux sign and on the Froude number F_r of the velocity component orthogonal to the boundary side inside the element.

One of the following cases can be selected:

1. Flux through the boundary side is entering the domain. In this case the following equalities hold:

$$BF_{e,j} = bp_{e,j}\left(y^e_{jp} - y^e_j\right) - bq_{e,j}\left(x^e_{jp} - x^e_j\right),$$
$$BM^x_{e,j} = BF_{e,j}\frac{bp_{ej}}{h^k_e}, \quad M^{py}_{e,j} = BF_{e,j}\frac{bq_{ej}}{h^k_e} \qquad (42)$$
$$\text{if } F_r \le 1$$

$$BF_{e,j} = bp_{e,j}\left(y^e_{jp} - y^e_j\right) - bq_{e,j}\left(x^e_{jp} - x^e_j\right),$$
$$BM^x_{e,j} = BF_{e,j}\frac{bp_{e,j}}{bh_{e,j}}, M^y_{e,j} = BF_{e,j}\frac{bq_{e,j}}{bh_{e,j}} \qquad (43)$$

   if $F_r > 1$,

   where $bh_{e,j}$, $bp_{e,j}$ and $bq_{e,j}$ are the assigned boundary water depths and flow rate per unit width components;

2. Flux through the boundary side is leaving the domain. In this case water depth gradient is not known and prediction (or correction) system is replaced, for element e and in both the prediction and the convective correction system, with the hypothesis of neglecting the flow rate and momentum local changes in the same elements. This is equivalent to say that the leaving volume and momentum fluxes are equal to the entering ones. From the previous hypothesis, we obtain:

$$h^{k+1/3}_e = h^k_e, \quad p^{k+1/3}_e = \frac{MT^x_e}{FT_e}h^k_e, \quad q^{k+1/3}_e = \frac{MT^y_e}{FT_e}h^k_e \qquad (44)$$

$$FT_e = -\sum_{j=1,3} min\left(0, F^{k+1/3}_{em,jm}\right),$$
$$MT^x_e = -\sum_{j=1,3} min\left(0, F^{k+1/3}_{em,jm}\right)\frac{p^{k+1/3}_{em}}{h^{k+1/3}_{em}}$$
$$MT^y_e = -\sum_{j=1,3} min\left(0, F^{k+1/3}_{em,jm}\right)\frac{q^{k+1/3}_{em}}{h^{k+1/3}_{em}} \qquad (45)$$

   with the same meanings specified for eqs. (25)–(27).

5.4 *Solution of the diffusive system*

Diffusive system (21)–(23) is simplified by changing the integral mean values with the fully implicit time discretization and linearizing the source terms. This provides a diffusive effect, that goes to zero along with the size of the source terms and the diffusive fluxes. This size is proportional to the time step, as can be observed in eqs. (22) and (23). According to these hypothesis, the same momentum equations can be written in the form:

$$p^{k+1}\left(\frac{1}{\Delta t} + \frac{g\,n^2\left(\sqrt{p^2+q^2}\right)^{k+2/3}}{\left(h^{7/3}\right)^{k+2/3}}\right) + gh^{k+2/3}\frac{\partial h}{\partial x} =$$
$$gh^{k+2/3}\frac{\partial h^k}{\partial x} + \left(\frac{gn^2 p\sqrt{p^2+q^2}}{h^{7/3}}\right)^{k+2/3} + \frac{p^{k+2/3}}{\Delta t} \qquad (46)$$

$$q^{k+1}\left(\frac{1}{\Delta t} + \frac{g\,n^2\left(\sqrt{p^2+q^2}\right)^{k+2/3}}{\left(h^{7/3}\right)^{k+2/3}}\right) + gh^{k+2/3}\frac{\partial h}{\partial y} =$$
$$gh^{k+2/3}\frac{\partial h^k}{\partial y} + \left(\frac{gn^2 q\sqrt{p^2+q^2}}{h^{7/3}}\right)^{k+2/3} + \frac{q^{k+2/3}}{\Delta t} \qquad (47)$$

that is:

$$p^{k+1}_e = -elem_e\frac{\partial h^{k+1}_e}{\delta x} + cost^x_e + p^{k+2/3}_e,$$
$$q^{k+1}_e = -elem_e\frac{\partial h^{k+1}_e}{\delta y} + cost^y_e + q^{k+2/3}_e$$
$$elem_e = \frac{g\left(h^{10/3}_e\right)^{k+2/3}\Delta t}{\left(h^{7/3}_e\right)^{k+2/3} + \Delta t\,g\,n^2\left(\sqrt{p^2_e+q^2_e}\right)^{k+2/3}} \qquad (48)$$
$$cost^x_e = elem_e\frac{\partial h^k_e}{\partial x} \quad cost^y_e = elem_e\frac{\partial h^k_e}{\partial y}$$

where variables with index $k + 2/3$ are known from the solution of the convective correction system. Substituting eqs. (48) in eq. (21), the following equation is obtained:

$$\frac{h^{k+1}_e - h^{k+2/3}_e}{\Delta t}\sigma_e + \sum_{j=1,3}\delta^e_{j,jp}F^{k+1}_{e,j} = 0 \qquad (49)$$

where diffusive fluxes are discretized as:

$$F^{k+1}_{e,j} = -elem_e\frac{h^{k+1}_{ep} - h^{k+1}_e}{\sigma_e}L^2_{e,j} + \quad \text{if } F^k_{e,j} \ge 0 \qquad (50)$$
$$cost^x_e\left(y^e_{jp} - y^e_j\right) + cost^y_e\left(x^e_{jp} - x^e_j\right)$$

Copyright © 2006 Taylor & Francis Group plc, London, UK

$$F_{e,j}^{k+1} = -elem_{ep}\frac{h_{ep}^{k+1} - h_e^{k+1}}{\sigma_{ep}} L_{e,j}^2 + \cos t_{ep}^x \left(y_{jp}^e - y_j^e\right) + \cos t_{ep}^y \left(x_{jp}^e - x_j^e\right), \quad \text{if } F_{e,j}^k < 0 \quad (51)$$

$L_{e,j}$ is the length of the jth side of element e, $\delta_{j,jp}^e = 1$ if the jth and jpth nodes of element e are shared by the elements e and ep (internal nodes), $\delta_{j,jp}^e = 0$ if not (boundary nodes). After computation of the new water depths h_e^{k+1}, the flow rates per unit width can be computed with Eqs. (48) estimating the convective gradients $(\partial h_e^{k+1}/\partial x, \partial h_e^{k+1}/\partial y)$ as already explained in section 5.2.

5.5 *Boundary conditions of the diffusive system*

At the beginning of each time steps, elements with one boundary side j and positive (leaving) flux are selected. The Froude number $fr_{c,j}$ of the flux per unit length is computed as:

$$fr_{c,j} = \frac{p_e\left(y_{jp} - y_j\right) - q_e\left(x_{jp} - x_j\right)}{L_{e,j}\, h^{3/2}\sqrt{g}} \quad (52)$$

If $fr_{c,j} > 1$, zero diffusive flux is assigned, that is $F_{e,j}^{k+1} = 0$. If $fr_{c,j} \le 1$ two possibilities exist. If the assigned boundary water depth is smaller than the critical depth corresponding to the specific flow rate, that is:

$$bh_{e,j} \le \left(\frac{p_e^2 + q_e^2}{g}\right)^{1/3} \quad (53)$$

a total flux corresponding to the critical depth is assigned to the element boundary side, that is:

$$F_{e,j}^{k+1} = \sqrt{g}\left(h_e^{k+2/3}\right)^{3/2} L_{e,j} - F_{e,j}^{k+2/3} \quad (54)$$

If inequality $fr_{c,j} \le 1$ does not hold, boundary water depth is assigned to element e, along with the corresponding Dirichlet condition and diffusive flux is computed a posteriori by means of eq. (49).

6 TEST CASES

6.1 *Test 1. Rectangular partial dam-break*

It is assumed that in the centre of a 200 m × 200 m square area a partial dam-break takes place instantaneously. The breach is 75 m long and extremes are 30 m from the left bank and 95 m from the right bank (see figure 2). Initial water depth is 10 and 5 m respectively upstream and downstream the breach. Zero slope and friction factors are assumed.

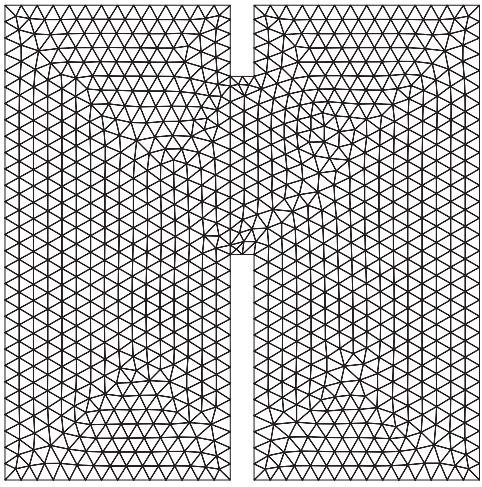


Figure 2. Computational mesh for test 1.

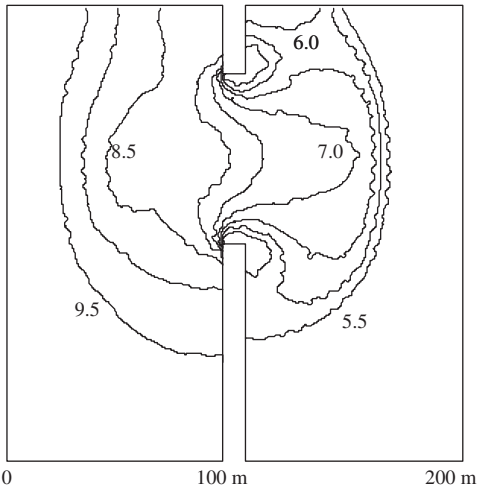


Figure 3. Contour depths; $\Delta t = 0.1$ s.

Immediately after the breach opening, water is released, forming a positive wave that propagates downstream and a negative wave that spreads upstream.

An unstructured triangular mesh with 1962 elements has been used for numerical simulations (see figure 2); the mean value of element area is approximately 25 m^2. Elevation contours are shown in figure 3 at the simulation time $T = 7.2$ s; a time step Δt equal to 0.1 s has been used, with a corresponding 0.57 maximum value of the CFL number. Figure 4 shows the elevation contours at the same simulation time T, but obtained with a Δt equal to 0.6 s; the corresponding maximum value of the CFL number is 3.08. These

Copyright © 2006 Taylor & Francis Group plc, London, UK

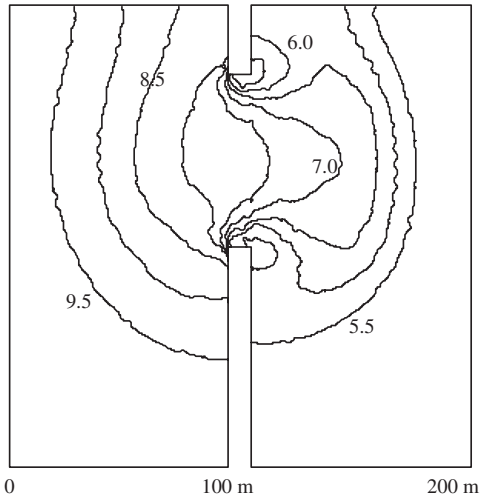


Figure 4. Contour depths; $\Delta t = 0.6$ s.

results show the stability of the proposed method with regard to the time step size. Using a Pentium 4 processor, for $\Delta t = 0.6$ s CPU time for the two convection systems is approximately 0.21 s, while CPU time for the diffusive system is 0.0156 s.

The general shape of the surface and the waves fronts computed for both Δt values appear in good agreement with numerical results given by other explicit numerical methods previously proposed (Glaister, 1993; Fennema and Chaudry, 1990; Mingham and Causon, 1998; Hubbard, 1999; Wang et al., 2003). In these models, either regular quadrilateral mesh with an equivalent element area, or unstructured triangular mesh have been used and the maximum size of the time step is limited by the Courant-Friedrichs-Levy condition.

6.2 *Test 2. 2D dam-break experiment by Fraccarollo and Toro (1995)*

The experimental flume, shown in figure 5, is a flat dry area, 2 m wide and 3 m long. After the first meter, a vertical wall forms a reservoir, filled up to 0.6 m (see Fraccarollo and Toro, 1995). Both the walls and the bottom are covered with the same material, corresponding to a Manning coefficient of 0.0095 s/m$^{1/3}$. The width of the movable gate, symmetrically centred, is 0.40 m. The flood-plain boundaries are all open.

Numerical results have been compared with the measured and the computed ones by Fraccarollo and Toro (1995) and with the results computed by Gottardi and Venutelli (2004).

Fraccarollo and Toro (1995) applied a WAF (Weighted Averaged Flux) scheme (Toro, 1989), a 2nd order conservative, shock capturing Godunov-type

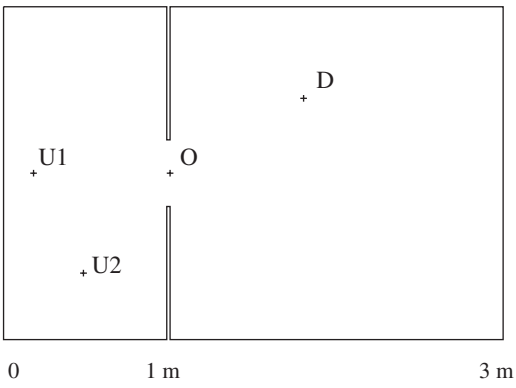


Figure 5. Experimental flume of Fraccarollo and Toro (1995).

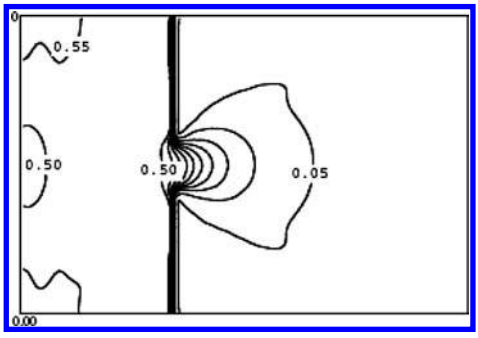


Figure 6a. Water depths by Gottardi and Venutelli (2004).

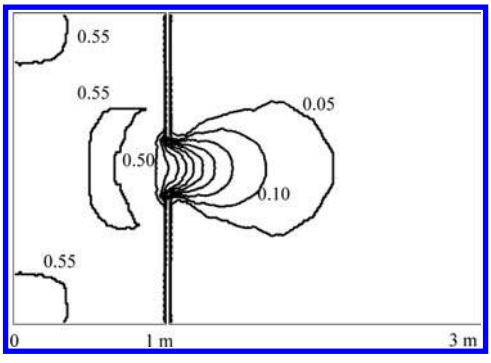


Figure 6b. Water depths computed by the MAST scheme.

scheme. The Authors discretized the domain by means of a regular mesh of 150×50 points along x and y directions respectively, with a corresponding element area 8.E-04 sm.

Gottardi and Venutelli applied an explicit 2nd order central scheme, initially proposed by Kurganov and Tadmor (2000); integration in time has been

Copyright © 2006 Taylor & Francis Group plc, London, UK

performed by means of a 3rd order TVD-Runge-Kutta scheme. They discretized the domain using a regular quadrilateral mesh with side Δx equal to 0.02 m.

For numerical simulations with the MAST scheme a regular mesh with equilateral triangles has been used; total elements number is 8606 with area 8.E-04 sm.

In figures 6a and 6b the contour plot of the water depths are shown for the proposed model and the one by Gottardi and Venutelli at the simulation time $T = 0.5$ s. Maximum value of the CFL number in the reference scheme is 0.5; in the proposed scheme a time step 0.01 s has bees assumed, with a corresponding maximum value of CFL number approximately equal to 3. Numerical results are similar, in spite of the different approximation orders, mesh and time step size.

CPU time for computation of the two convective systems is about 1.4 s and for diffusive system is 0.0625 s.

In figures 7a–7d numerical results are compared for a simulation time $T = 10$ s with data measured at some points and reported in figure 5: "O" ($x = 1$ m, $y = 1$ m), "U1"($x = 0.18$ m, $y = 1$ m), "U2" ($x = 0.48$ m , $y = 0.4$ m) and "D"($x = 1.802$ m, $y = 1.45$ m). Numerical results are in good agreement with the experimental ones. Observe the difference between measured and numerical results for small times at point "O". After the sudden opening of the gate a strong rarefaction wave moving in upstream direction is originated. As in the 1D case, water depth at the gate location (point "O" in the specific case) drops to a local minimum value (about 4/9 of the initial depth) after the opening of the gate. This is analogous to the 1D solution by Ritter (1992) in a horizontal and frictionless channel. After the minimum is reached, a rising stage follows, due to the contribute of the lateral propagation and 2D effects.

Inside the reservoir, Fraccarollo and Toro (1995) measured also the static pressure values at the bottom. In fact, according to the hydrostatic hypothesis, these data represent an indirect measure of the water depths. Pressure measures are reported in meters of water column. For measurement points "U1" and "U2" pressures and water levels values are very close each other and only water levels are reported in figures 7b and 7c; at point "O", as expected, the are some discrepancies between measured and hydrostatic pressures, because of some 3D effects. Observe that at point "O" numerical results are in better agreement with the pressure measures.

In figure 8, numerical results computed by the proposed schemes are compared with numerical results by Fraccarollo and Toro (1995) for the measure point "O". Model results are in good agreement, even if the proposed schemes shows some diffusive effect missing in the results of Fraccarollo and Toro (1995), because of the higher approximation order of the reference scheme with respect to proposed one.

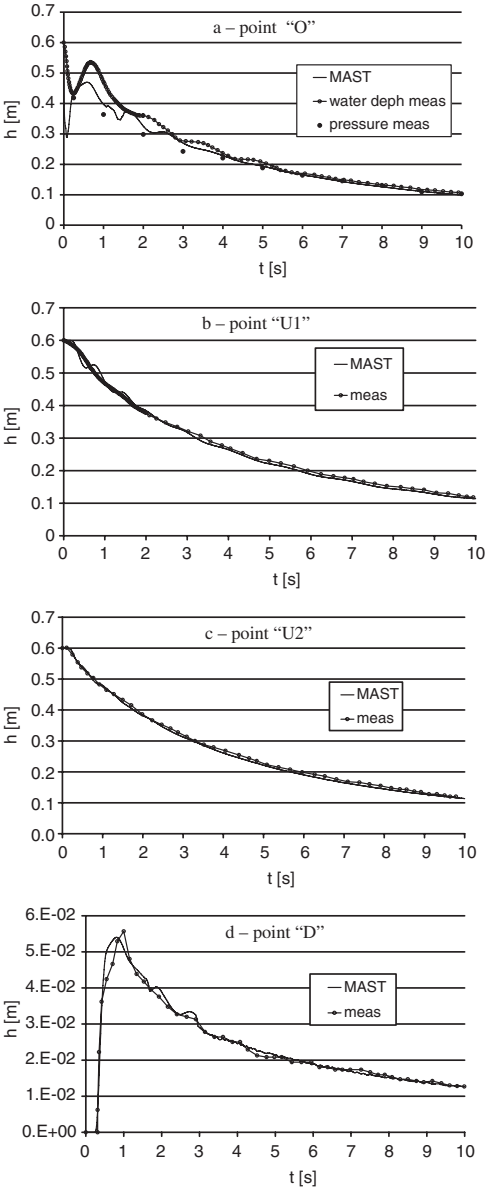


Figure 7. Comparison between experimental data and numerical results computed by the MAST scheme.

The delay between measured and computed data for point "O" is likely due to the small time required for the real opening of the gate (about 0.1 s).

7 CONCLUSIONS

A novel procedure has been proposed for the numerical solution of the 2D shallow water equations.

Copyright © 2006 Taylor & Francis Group plc, London, UK

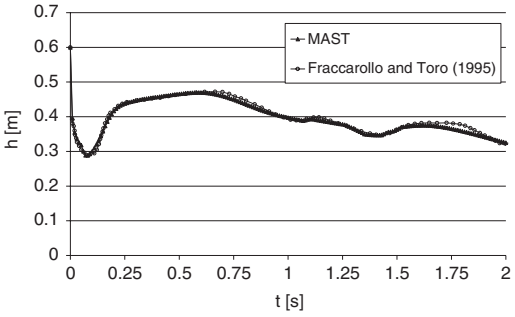


Figure 8. Comparison between numerical results at measure point "O".

In the MAST algorithm, the solution is found in each time step solving three different sub-problems. The main advantage of the algorithm is that the first and the second non linear sub-problem can be solved locally element after element, without any stability restriction on the size of the time step. The computational time of the third problem has been always the smaller one in all the performed simulations. The larger CPU is actually dedicated to the computation of the approximated potential. The use of a bad approximated potential leads to a poor solution, because the spatial gradients are computed at different time levels in each sub-problem and the good performance of the fractional step approach is based on the quality of the prediction step. A promising research is actually in progress in order to find a good compromise between the quality of the approximated potential and the required computational burden.

REFERENCES

Alcrudo F. and Garcìa-Navarro P. A high-resolution Godunov-tipe scheme in finite volume for the 2D shallow water equations. *Int. J. Num. Meth. Fluids*, vol. 14 (1993), pp. 489–505.

Aricò C. and Tucciarelli T. "MAST solution of advection problems in irrotational flow fields". In press for *Adv. Wat. Res*.

Bascià A. and Tucciarelli T. An explicit unconditionally stable numerical solution of the advection problem in irrotational flow fields. *Wat. Res.*, Vol. 40(6), (2004).

Bermudez A. and Vazquez-Cendon M. E. Upwind methods for hyperbolic conservation laws with source terms. *Comput. Fluids*, vol. 23(8) (1994), p. 1049.

De Saint Venant B. Thèorie de mouvement non-permanant des eaux avec application aux crues des rivières et à l'introduction des marèes dans leur lit. *Acad. Sci. Paris C. R*., 73 (1871), pp. 148–154, 237–240.

Fennema R. J. and Chaudhry M.H. Explicit methods for 2-D transient free-surface flows. ASCE *J. Hydr. Eng*., vol. 116 (1990), pp. 1013–1034.

Fraccarollo L. and Toro E. F. Experimental and numerical assessment of the shallow water model for two-dimensional dam-break type. *J. Hydr. Res*., vol. 33(6), pp. 843–864.

Glaister P. Flux difference splitting for open channel flows. *Int J. Num. Meth. Fluids*, vol. 16 (1993), pp. 629–654.

Gottardi G. and Venutelli M. Central scheme for dam – break flow simulation. *Adv. Wat. Res*., vol. 27 (2004) p. 259–268.

Hubbard M. E. Multidimensional slope limiters for MUSCL-type Finite Volume schemes on unstructured grids. *J. Comp. Phys.*, vol. 155 (2000), pp. 54–74.

Hubbard M. E. and Garcìa-Navarro P. Flux difference splitting and the balancing of the source terms and flux gradients. *J. Comp. Phys*., vol. 165(89) (2000), pp. 89–125.

Kurganov A. and Tadmor E. New high-resolution central schemes for nonlinear conservation laws and convection-diffusion equations. *J. Comp. Phys.* vol. 160 (2000), pp. 241–282.

LeVeque R. J. Balancing flux terms and flux gradients in high-resolution Godunov methods: the quasi steady wave propagation algorithm. *J. Comp. Phys*., vol. 146(1) (1998), p. 346.

Meselhe E. A., Sotiropoulos F. and Holly F. H. Numerical simulation of transcritical flow in open channels. ASCE *J. Hydr. Eng.*, vol. 123(9) (1997), pp. 774–783.

Mingham C. G. and Causon D. M. High-resolution finite-volume method for shallow water flows. *ASCE J. Hydr. Eng.*, vol. 124(6) (1998), pp. 605–614.

Mohamadian A., Le Roux D. Y., Tajrishi M. and Mazaheri K. A mass conservative scheme for simulating shallow ?ows over variable topographies using unstructured grid. *Adv. Wat. Res*., vol. 28 (2005), pp. 523–539.

Noto V. and Tucciarelli T. DORA Algorithm for network flow models with improved stability and convergence properties. ASCE *J. Hydr. Eng.*, vol. 127(5) (2001), pp. 380–391.

Press, W. H., Flannery, B. P., Teukolsky, S. A., and Vetterling, W. T. (1988). *Numerical Recipes*, Cambridge University Press, Cambridge, U.K.

Ritter A. Die Fortplanzung der wasserwellen. *Zeitschrift des Vereines Deutscher Ing.,* vol. 36(33) (1992), pp. 947–954.

Toro E. F. A weighted averaged flux method for hypebolic conservation laws. *Proc. R. Soc. Lond*. A423 (1989), pp. 401–418.

Toro E. F. *Riemann solvers and numerical methods for fluid dynamics. A practical introduction*. Springer 1st ed., (1997).

Tucciarelli T. A new algorithm for a robust solution of the fully dynamic Saint-Venant equations. *J. Hydr. Res*., vol. 41(3) (2003), pp. 239–246.

Tucciarelli T. and Termini, D. Finite-element modeling of floodplain flows. ASCE *J. Hydr. Eng*., vol. 126(6) (2000), pp. 416–424.

Vukovic S. and Solpa L. ENO and WENO schemes with exact conservation property for one – dimensional shallow water equations. *J. Comp. Phys*., vol. 179 (2002), pp. 593–621.

Wang J., He Y. and Ni H. Two-dimensional free surface flow in branch channels by a finite-volume TVD scheme. *Adv. Wat. Res*., vol. 26 (2003), pp. 623–633.

Zic N. C., Vukovic S. and Solpa L. Balanced finite volume WENO and central WENO schemes for the shallow water and the open-channel flows equations. *J. Comp. Phys*. vol. 200 (2004), pp. 512–548.

Copyright © 2006 Taylor & Francis Group plc, London, UK

An application of BGK numerical method to tidal flow

Deng Jiaquan
Pearl River Hydraulic Research Institute, Ministry of Water Resources, Guangzhou, China

ABSTRACT: Based on the Bhatnagar-Gross-Krook (BGK) Boltzmann theory for molecule motions, numerical method for open channel flows is formulated and a second-order two-dimensional numerical model for unsteady flows is established. This new method has many advantages comparing to traditional methods which based on Saint-Venant equations and it satisfies the entropy condition and thus prevents unphysical oscillations in computations. The high accuracy and efficiency of this method have been proved. This paper demonstrates the main procedures of the formulation of the method and its application to tidal flows in the Macao water area. The computational results show a good agreement between the computed and measured field data.

1 INTRODUCTION

It has been show that numerical method based on the Bhatnagar-Gross-Krook (BGK) Boltzmann theory for molecule motions has many advantages comparing to traditional methods which based on Saint-Venant equations (Xu, 1995, 1996, Deng, 2000). This method satisfies the entropy condition and thus prevents unphysical oscillations in computations. Its high accuracy and efficiency of this method have been proved. However, molecule motion computations are different from natural river flow computations where irregular river bed slopes exist. For considering this, Xu (2002) proposed a harmonious scheme based on the molecule theory by including the effect in the fluxes terms. This paper uses Xu's method to consider the effect of the bed slope in the proposed two-dimensional BGK model. To improve the accuracy of the proposed numerical model, the water level, instead of the water depth, is used in this study to reconstruct initial data. Based on finite volume method and BGK Boltzmann equation, this paper demonstrates the main procedures of the formulation of the two-dimensional irregular grid BGK numerical model and its application to tidal flows in the Macao water area which has a tidal confluence and complicated boundary.

2 TWO-DIMENSIONAL BGK SCHEME ON IRREGULAR GRIDS

2.1 *BGK Boltzmann equation and basic relationships*

Two-dimensional BGK Boltzmann equation can be written as follows (Deng, 2000)

$$\frac{\partial f}{\partial t}+c_x\frac{\partial f}{\partial x}+c_y\frac{\partial f}{\partial y}+\frac{F_x}{m}\frac{\partial f}{\partial c_x}+\frac{F_y}{m}\frac{\partial f}{\partial c_y}=\frac{q-f}{\tau} \quad (1)$$

where f is molecule speed distribution function, is time, c_x and c_y are molecule speeds in x and y direction; F_x and F_y are external force acting on the molecule in x and y direction; is the molecule mass, q is molecule speed distribution function at equilibrium state, τ is the collision time between molecules.

For two-dimensional water flows, there are following basic relationships between the equilibrium molecule speed distribution function q and water depth h and velocities u and v in x and y direction(Deng, 2000):

$$\int_{-\infty}^{\infty}\int_{-\infty}^{\infty}qdc_xdc_y=h,\quad \int_{-\infty}^{\infty}\int_{-\infty}^{\infty}c_xqdc_xdc_y=hu,$$
$$\int_{-\infty}^{\infty}\int_{-\infty}^{\infty}c_yqdc_xdc_y=hv \quad (2)$$

$$\int_{-\infty}^{\infty}\int_{-\infty}^{\infty}c_xc_yqdc_xdc_y=huv,$$
$$\int_{-\infty}^{\infty}\int_{-\infty}^{\infty}c_x^2qdc_xdc_y=hu^2+\frac{gh^2}{2} \quad (3)$$

According to the conservation laws for the mass and the momentum, the collision function on the right-hand side of equation (1) obeys following conditions(Deng, 2000)

$$\int_{-\infty}^{\infty}\int_{-\infty}^{\infty}\frac{q-f}{\tau}dc_xdc_y=0,\quad \int_{-\infty}^{\infty}\int_{-\infty}^{\infty}c_x\frac{q-f}{\tau}dc_xdc_y=0,$$
$$\int_{-\infty}^{\infty}\int_{-\infty}^{\infty}c_y\frac{q-f}{\tau}dc_xdc_y=0 \quad (4)$$

Copyright © 2006 Taylor & Francis Group plc, London, UK

2.2 *BGK-based model for water flows*

Multiplying equation (1) with $(1, c_x, c_y)^T$ and integrating it by using relationships (2) to (4), we can obtain the following two-dimensional water flow BGK-based model:

$$\frac{\partial U}{\partial t}+\frac{\partial F}{\partial x}+\frac{\partial G}{\partial y}=S \tag{5}$$

where $U=(h, uh, vh)^T$,

$$F=\left(\int_{-\infty}^{\infty}\int_{-\infty}^{\infty}c_x f dc_x dc_y,\ \int_{-\infty}^{\infty}\int_{-\infty}^{\infty}c_x^2 f dc_x dc_y,\ \int_{-\infty}^{\infty}\int_{-\infty}^{\infty}c_x c_y f dc_x dc_y\right)^T$$

$$G=\left(\int_{-\infty}^{\infty}\int_{-\infty}^{\infty}c_y f dc_x dc_y,\ \int_{-\infty}^{\infty}\int_{-\infty}^{\infty}c_x c_y f dc_x dc_y,\ \int_{-\infty}^{\infty}\int_{-\infty}^{\infty}c_y^2 f dc_x dc_y\right)^T,$$

$$S=\left(0, gh(S_{0x}-S_{fx}), gh(S_{0y}-S_{fy})\right)^T.$$

F and G are momentum fluxes in x and y directions respectively. S is source term (external forces).

2.3 *BGK model on irregular grids*

Based on the finite volume method, the increments of the conservative variables in the control volume in time Δt should be equal to the product of Δt and the sum of the fluxes on volume surfaces and the source term, i.e.,

$$A(U_i^{n+1}-U_i^n)=\Delta t\left[-\int_{\partial\Omega}(Fn_x+Gn_y)ds+AS\right] \tag{6}$$

where A is the control volume area n_x and n_y are direction derivatives in x and y directions respectively. The fluxes can be written as

$$\begin{aligned}Fn_x+Gn_y&=F\frac{\Delta y}{\Delta s}-G\frac{\Delta x}{\Delta s}\\&=F\cos\theta+G\sin\theta=T^{-1}F(T(\theta)U)\end{aligned} \tag{7}$$

where θ is the angle between volume surface and y coordinate.

$$\text{coordinate. } T(\theta)=\begin{bmatrix}1&0&0\\0&\cos\theta&-\sin\theta\\0&\sin\theta&\cos\theta\end{bmatrix},$$

$T^{-1}=T^T$, $U_N=TU=(h, hu_\xi, hv_\eta)^T$, $\xi-\eta$ is local coordinate.

Thus, the finite volume equation can be written as

$$A_i\left(U_i^{n+1}-U_i^n\right)=\Delta t\left[-\sum_{j=1}^{m}\left(T_j^{-1}F_{N_j}s_{i_j}\right)+S_iA_i\right] \tag{8}$$

2.4 *Fluxes computation*

Molecule motion computations are different from natural river flow computations where irregular river bed slopes exist. For considering this, Xu (2002) proposed a harmonious scheme based on the molecule theory by including the effect in the fluxes terms. This paper uses Xu's method to consider the effect of the bed slope.

When computing natural river flows, the effect of the river bed slope on the equilibrium molecule distribution function should be considered. For two-dimensional case (Xu, 2002, Deng, 2000),

$$\left(\frac{1}{\sqrt{\pi gh}}e^{-\frac{[(c_x-S_{0x}(t-t^n))-u]^2}{gh}}\right)\left(\frac{1}{\sqrt{\pi gh}}e^{-\frac{[(c_y-S_{0y}(t-t^n))-v]^2}{gh}}\right)h$$

Using Taylor expansion (ignoring higher order of $t-t^n$), we have

$$\begin{aligned}q(x, y, c_x, c_y, t)=&\left[\left(\frac{1}{\sqrt{\pi gh}}e^{\frac{-(c_x-u)^2}{gh}}\right)\left(\frac{1}{\sqrt{\pi gh}}e^{\frac{(c_y-v)^2}{gh}}\right)h\right]\\&\times\left[1+\frac{2}{gh}\left(\alpha S_{0x}(c_x-u)(t-t^n)+\beta S_{0y}(c_y-v)(t-t^n)\right)\right]\end{aligned} \tag{9}$$

where α and β are coefficients for considering the effect of ignoring higher order of $t-t^n$.

Thus, the molecule distribution function in the control volume can be expressed as (Xu, 2002)

$$\begin{aligned}f(x_{i+\frac{1}{2}}, y_j, t)=&\kappa_1\Big\{H(c_x)q^n_{i+\frac{1}{2}^-,j}+[1-H(c_x)]q^n_{i+\frac{1}{2}^+,j}\\&-t\Big\{H(c_x)\left[\left(c_x\frac{\partial q}{\partial x}-\frac{2}{gh}\alpha S_{0x}(c_x-u)(t-t^n)\right)\right.\\&\left.+\left(c_y\frac{\partial q}{\partial y}-\frac{2}{gh}\beta S_{0y}(c_y-v)(t-t^n)\right)\right]^n_{i+\frac{1}{2}^-,j}\\&+[1-H(c_x)]\left[\left(c_x\frac{\partial q}{\partial x}-\frac{2}{gh}\alpha S_{0x}(c_x-u)(t-t^n)\right)\right.\\&\left.+\left(c_y\frac{\partial q}{\partial y}-\frac{2}{gh}\beta S_{0y}(c_y-v)(t-t^n)\right)\right]^n_{i+\frac{1}{2}^+,j}\Big\}+\kappa_2\bar{q}^n_{i+\frac{1}{2},j}\\&+\kappa_3\left(\frac{\partial\bar{q}}{\partial t}\right)^n_{i+\frac{1}{2},j}+\kappa_4\left[\left(c_y\frac{\partial\bar{q}}{\partial y}-\frac{2}{gh}\beta S_{0y}(c_y-v)(t-t^n)\right)\right]^n_{i+\frac{1}{2},j}\\&+[1-H(c_x)]\left(c_x\frac{\partial\bar{q}}{\partial x}-\frac{2}{gh}\alpha S_{0x}(c_x-u)(t-t^n)\right)^n_{i+\frac{1}{2}^+,j}\\&+H(c_x)\left(c_x\frac{\partial\bar{q}}{\partial x}-\frac{2}{gh}\alpha S_{0x}(c_x-u)(t-t^n)\right)^n_{i+\frac{1}{2}^-,j}\Big]\end{aligned} \tag{10}$$

Copyright © 2006 Taylor & Francis Group plc, London, UK

where H is Heaviside function and

$$\kappa_1 = e^{-\frac{t}{\tau}}, \quad \kappa_2 = 1 - e^{-\frac{t}{\tau}}, \quad \kappa_3 = \tau\left(\frac{t}{\tau} - 1 + e^{-\frac{t}{\tau}}\right),$$
$$\kappa_4 = \tau\left(-1 + e^{-\frac{t}{\tau}}\right) + te^{-\frac{t}{\tau}}.$$

From integrations of (8), and by considering

$$erfc(0) = 1, \exp(0) = 1, \quad \frac{\partial(b+h)}{\partial x} = 0, \quad \frac{\partial(b+h)}{\partial y} = 0,$$

we can obtain

$$\alpha_1, \beta_1 = \frac{3}{4}, \quad \alpha_2, \beta_2 = 1 \text{ and } \alpha_3, \beta_3 = \frac{5}{4}.$$

Thus, by substituting (10) into (5) we can obtain the solutions for considered variables.

3 DATA RECONSTRUCTION

Since the variation of the water level is relatively small, it is used to reconstruct the initial data, instead of the water depth.

$$\begin{cases} \begin{pmatrix} \eta \\ hu \\ hv \end{pmatrix}^n = \begin{pmatrix} \eta \\ hu \\ hv \end{pmatrix}^n_{i,j} + \underbrace{\frac{\partial}{\partial x}\begin{pmatrix} \eta \\ hu \\ hv \end{pmatrix}^n_{i,j}}_{x-slope}(x - x_i) + \underbrace{\frac{\partial}{\partial y}\begin{pmatrix} \eta \\ hu \\ hv \end{pmatrix}^n_{i,j}}_{y-slope}(y - y_i) \\ h = \eta - B \end{cases} \quad (11)$$

4 APPLICATION OF BGK NUMERICAL METHOD TO TIDAL FLOWS

4.1 *Computed water area and hydrological data*

The proposed numerical method is applied to the tidal flow in the Macao water area which is quite complicated due to the confluence and irregular boundaries. The computed scope includes the Hongwan waterway (west to Maliuzhou stage), the Qianshan waterway (north to the Wanzhai stage), the Shizimen waterway (south to the Hongqi stage) and the Macao Bay (east to the Waigang stage) (see Fig. 1).

Hydrological data used in the computation was measured on March 28, 1997. Computational boundaries are: water levels are given at Mangzhou and Hongqi stages; discharges are given at Wanzhai and Waigang stages. The computed results are compared with measured data at two stages Maliuzhou and Shizimen which are located in the computed water area.

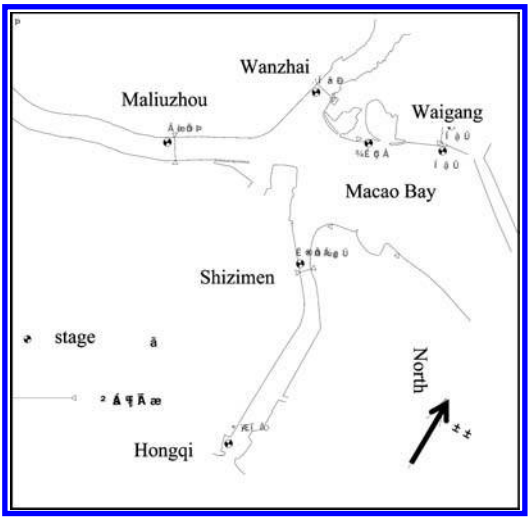


Figure 1. Computed Macao water area.

Table 1. Computed and measured tidal levels unit: m.

Stage	Tidal level	Measured	Computed	Error
Maliuzhou	Highest	0.52	0.57	0.05
	Lowest	−0.78	−0.77	0.01
	Average	−0.06	−0.04	0.02
	Tidal range	1.30	1.34	0.04
Shizimen	Highest	0.49	0.52	0.03
	Lowest	−0.82	−0.84	0.02
	Average	−0.11	−0.13	0.02
	Tidal range	1.31	1.36	0.05

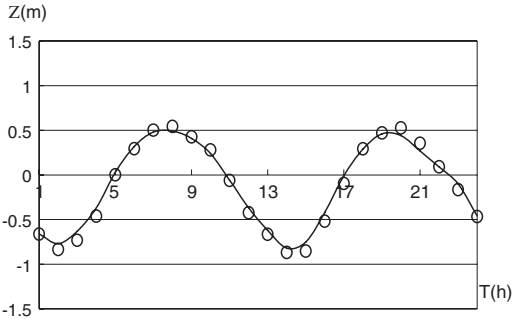


Figure 2. Computed and measured (solid line) tidal level at Shizimen.

4.2 *Comparison between computed results and measured data*

Tidal levels: Table 1 shows the computed and measured water levels at Maliuzhou and Shizimen stages. Fig. 2 and Fig. 3 show the processes of the tidal levels both for computed and measured results. These show

Copyright © 2006 Taylor & Francis Group plc, London, UK

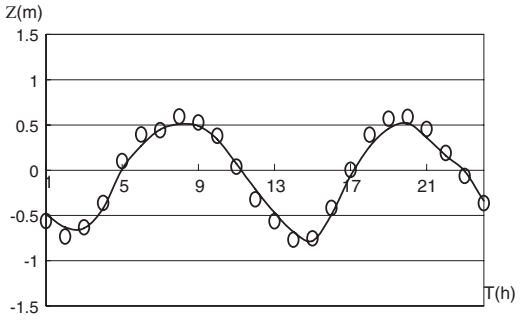


Figure 3. Computed and measured (solid line) tidal level at Maliuzhou.

Table 2. Computed and measured tidal velocities unit: m/s.

Stage	Velocity	Measured	Computed	Error
Maliuzhou	Flood average	0.35	0.34	−0.01
	Ebb average	0.33	0.29	−0.04
Shizimen	Flood average	0.32	0.29	−0.03
	Ebb average	0.43	0.38	−0.05

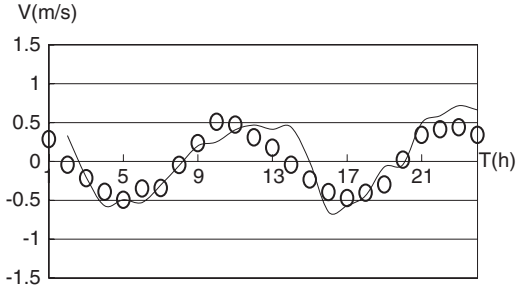


Figure 4. Computed and measured (solid line) tidal velocity at Shizimen.

a good agreement between computed and field measured water levels. The maximum error for the high and low tidal levels is within 0.05 m.

Tidal flow velocities and flow directions: Table 2 shows the computed and measured tidal flow velocities at Maliuzhou and Shizimen stages. Fig. 4 and Fig. 5 show the processes of the tidal flow velocities both for computed and measured results. These show a good agreement between computed and field measured tidal flow velocities. The maximum error for the tidal flow velocities during the flood and ebb tides periods is within 0.05 m/s.

Figures 6 and 7 show the processes of the tidal flow directions both for computed and measured results. These show a good agreement between computed and field measured tidal flow directions.

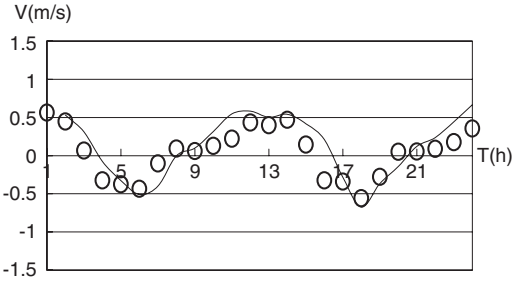


Figure 5. Computed and measured (solid line) tidal velocity at Maliuzhou.

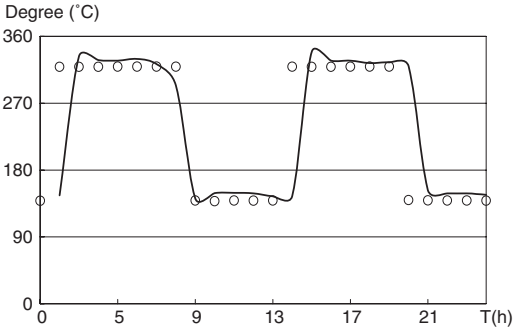


Figure 6. Computed and measured (solid line) flow directions at Shizimen.

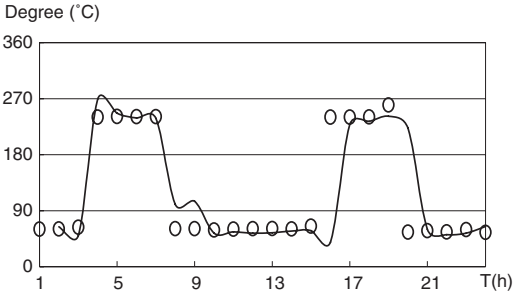


Figure 7. Computed and measured (solid line) flow directions at Maliuzhou.

Figures 8 and 9 show the computed tidal flow fields in the confluence area which agree with measured tidal flow fields well.

5 CONCLUSIONS

Based on finite volume method and BGK Boltzmann equation, this paper proposed a new numerical model for computing two-dimensional practical river or tidal flows with irregular bed slopes. This new method

Copyright © 2006 Taylor & Francis Group plc, London, UK

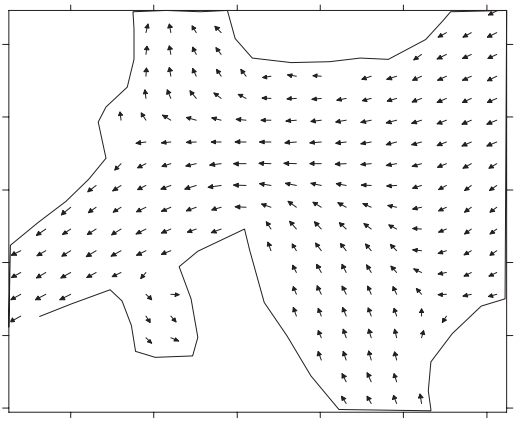


Figure 8. Computed flow field in confluence area (flood tide).

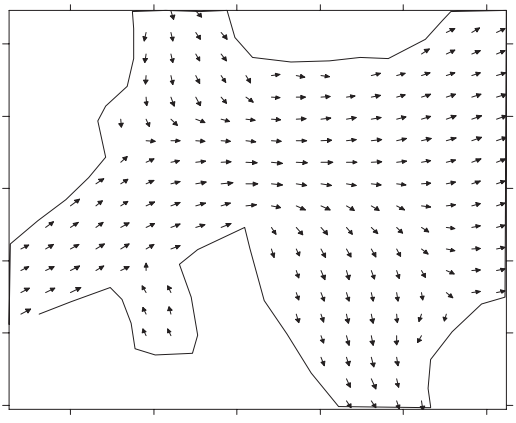


Figure 9. Computed flow field in confluence area (ebb tide).

employs two-dimensional irregular net grids and considers the effect of the bed slope on the molecule distribution function. It suits for any kind of river or estuaries boundary. The application of the new method to model the tidal flow in the Macao water area show this two-dimensional irregular grid BGK numerical model can well simulate the flows with complicated boundaries.

REFERENCES

Deng Jiaquan. 2000. BGK Boltzmann models for free-surface water flows and contaminant transport. *Ph.D. thesis*. The Hong Kong university of science and technology.

Xu, K., Martinelli, L. and Jameson, 1995. A. Gas-kinetic finite volume methods, flux-vector splitting and artificial diffusion. *J. Comput. Phys.*, 120,. 48–65.

Xu, K., Kim, C., Martinelli, L. and Jameson, 1996. A. BGK-based schemes for the simulation of compressible flow. *IJCFD.* 7, 213–235.

Xu, K., A well-balanced gas-kinetic scheme for the shallow water equations with source terms. *J. Comput. Phys*., 178, 2002. 533–562.

Copyright © 2006 Taylor & Francis Group plc, London, UK

A robust implementation of Riemann solvers for one-dimensional free surface flow simulation in natural rivers

G.W. Tchamen & T.T. Quach
Hydro-Quebec, Montreal, Canada

R. Kahawita
Ecole Polytechnique, Montreal, Canada

ABSTRACT: This paper presents the development and validation of a robust numerical scheme of Riemann solver category applied to one-dimensional free surface flow simulation modelled by the Saint-Venant equation set. The scheme presented here is based on a discharge equation in non-conservation form coupled with a matrix transformation that converts the discharge evolution into a velocity evolution that proves to be more robust. The resulting scheme has all the positive attributes of Riemann solvers such as stability through transcritical flow regimes, ability to resolve hydraulic jumps, stability and accuracy with respect to dry bed calculations and robustness in front of rapidly varying flows such as dam-breaks. Most importantly, the present scheme is able to treat large variations in river geometry allowing the use of space steps of the order of hundreds or thousands of meters. The resulting model that uses explicit time steps is so fast on current machines that the incorporation of complicated implicit algorithms is unnecessary.

1 INTRODUCTION

The last fifteen years or so have seen a rapid rise in the use of Riemann solvers as the numerical method of choice, to treat problems in fluvial hydraulics. This is due to their robust properties in being able to handle transcritical flows with shocks, theoretically the sole restriction being compliance with the well-known Courant-Friedrichs-Levy criterion for the time step.

On a practical basis however, all these numerical algorithms exhibit stability problems when applied to natural rivers that may have highly variable geometries in the longitudinal direction. This necessitates the utilization of a very fine mesh, resulting in a significant increase in computational times. It will be shown in this paper that the so called 'conservation' form of the equation set, favoured by most authors because of its suitability for evaluation of the surface flux expressions in the basic equations, is the cause for the deterioration in robustness. Using the strictly conservation form of the governing equations in one dimension results in the appearance of a series of terms dependant on geometric properties of the watercourse. The order of magnitude of their variation may be many times higher than the order of magnitude of the terms that are essentially functions of the flow variables. The alternate non-conservation form of the equations corresponding to an equation for fluid velocity in place of fluid discharge is known to exhibit difficulties in predicting hydraulic jumps.

The scheme presented here uses a linearization around local wetted area or volume to apply a Roe's Riemann solver technique to the original discharge form of the Saint-Venant equations. An additional step that transforms problem variable from discharge to velocity brings more stability, with respect to large space step, to the overall scheme.

Three test cases where analytical solutions are available have been used for validation purposes and to assess model performance. The real case simulation of the filling of a headrace tunnel, some reaches of which have a sixty-degree slope is presented. Two other real cases applied to Canadian rivers are shown, one is the case of a dam break during the passage of the probable maximum flood over a river basin located in northern Canada, and the second is the propagation of a dam break wave in a river in North-Eastern Canada.

2 GOVERNING EQUATIONS

2.1 *Basic one-dimensional Saint-Venant system*

The one dimensional Saint-Venant Equation set constitutes the mathematical basis of the following analysis. This mathematical model is valid for all free surface

Copyright © 2006 Taylor & Francis Group plc, London, UK

flow for which the assumptions of moderate bed slope and negligible vertical acceleration are valid. It is described by the following pair of equations for one space dimension (Cunge et al, 1980):

$$\frac{\partial A}{\partial t} + \frac{\partial Q}{\partial x} = 0 \tag{1.a}$$

$$\frac{\partial Q}{\partial t} + \frac{\partial (VQ)}{\partial x} + gA\frac{\partial H}{\partial x} + gAS_f = 0 \tag{1.b}$$

Equation (1.a) is derived on the basis of mass conservation principle, and (1.b) is based on the principle of momentum conservation.

To complete the description if the system (1) above, it is necessary to define its different variables:

t = designates the time.
x = designates the coordinate position measured along the river bed axis.
A = A(x,t) is the wetted area.
Q = Q(x,t) is the discharge .
V = V(x,t) is the mean velocity; V = Q/A.
H = H(x,t) designates the water surface elevation with respect to reference.
S_f = is the friction term. In practice, the well known Manning Equation is used to express this term.

$$S_f = \frac{N^2|V|}{R^{4/3}} \bullet V$$

R = A/P is the hydraulic radius, with P being the wetted perimeter. N = is the Manning friction coefficient.

The system (1) cannot be written under strict conservation form, i.e.

$$\frac{\partial U}{\partial t} + \frac{\partial F(U)}{\partial x} = 0 \tag{2}$$

Riemann solvers are usually developed on the basis of such conservation forms. This is the reason why most implementations of Riemann solver for Saint-Venant model have used a slightly modified version of (1) which is written under the following quasi conservation with a source term:

$$\frac{\partial U}{\partial t} + \frac{\partial F(U)}{\partial x} = G \tag{3}$$

Where

$$U = \begin{bmatrix} A \\ Q \end{bmatrix}, \qquad F(U) = \begin{bmatrix} Q \\ \left(\frac{Q^2}{A}\right) + g \cdot I_1 \end{bmatrix}, \tag{4a}$$

$$G(U) = \begin{bmatrix} 0 \\ g \cdot A \cdot (S_0 - S_f) + I_2 \end{bmatrix} \tag{4b}$$

The relation which permits the original equation set (1) to be written under the form (4) is the following one:

$$g \cdot A \cdot \frac{\partial H}{\partial x} = \frac{\partial I_1}{\partial x} - I_2 - g \cdot A \cdot S_0 \tag{5}$$

With

$$I_1 = g \int_{Z_f}^{H} A(x,\xi)\, d\xi \tag{6}$$

$$I_2 = g \int_{Z_f}^{H} \frac{\partial A(x,\xi)}{\partial x}\, d\xi \tag{7}$$

And

$$S_0 = -\frac{\partial Z_f}{\partial x} \tag{8}$$

2.2 *Hydraulic head conservation system*

The following system can be derived from the original system (1):

$$\frac{\partial A}{\partial t} + \frac{\partial (V \cdot A)}{\partial x} = 0 \tag{9a}$$

$$\frac{\partial V}{\partial t} + \frac{\partial \left(\frac{V^2}{2}\right)}{\partial x} + g\frac{\partial H}{\partial x} = -g \cdot S_f \tag{9b}$$

This system (9) can be written under matrix form for frictionless flows:

$$\frac{\partial W}{\partial t} + \frac{\partial E(W)}{\partial x} = H \tag{10}$$

With

$$W = \begin{bmatrix} A \\ V \end{bmatrix}, \qquad E(W) = \begin{bmatrix} V \cdot A \\ \left(\frac{V^2}{2}\right) + g \cdot H \end{bmatrix} \tag{11a}$$

$$H(W) = \begin{bmatrix} 0 \\ -g \cdot S_f \end{bmatrix} \tag{11b}$$

For frictionless flows ($S_f = 0$), the system (9) respects the conservation form.

Note that when the flow variables A, Q and V are differentiable, it possible to write the following identity

$$\partial U = \begin{bmatrix} \partial A \\ \partial Q \end{bmatrix} = \begin{bmatrix} \partial A \\ V \cdot \partial A + A \cdot \partial V \end{bmatrix}$$

Copyright © 2006 Taylor & Francis Group plc, London, UK

That is

$$\partial U = \begin{bmatrix} 1 & 0 \\ V & A \end{bmatrix} \begin{bmatrix} \partial A \\ \partial V \end{bmatrix} = K \bullet \partial W$$

This relation can also be verify between the equation presented above:

$$(1) = K \bullet (9)$$

The inverse of this relation is a corner stone of the proposed scheme (see equation 16).

In fact, systems (1) and (9) are equivalent for regular flows, i.e. flows without discontinuities. For flow with discontinuities like hydraulic jumps, the solutions of the two systems are not identical (see Hervouet 2003, or Tchamen 2006). In this case, it is recommended that the solution of the system (1) be retained.

There have been a number of propositions to applied Riemann solvers to the original Saint-Venant equation set. The first propositions (Alcrudo & Garcia-Navarro 1992, Glaister 1988) did not apply to general river geometry case, but rather to frictionless prismatic channel. Later, it has been realized that for general river with arbitrary geometry, a coherent integration of geometric and friction source terms is vital for the overall stability and accuracy of the numerical scheme. Number of works (Bermudez 1995, Goutal and Maurel 2002) has focused on the technique design to integrate those source terms in a way that is coherent with the Riemann solver applied to the homogeneous part of the equation set.

Although these proposals seem to have effectively addressed the challenge of source term integration and work rather well for simple cases that possess analytical solutions, or even for flows in rivers with mild geometric variation, there is a degradation in robustness when applied to rivers with very irregular geometries.

3 A RIEMANN SOLVER FOR THE NON CONSERVATION EQUATION SET (1)

The Riemann solver proposed in the present paper is an implementation of the Roe scheme (Roe 1981, Tchamen 2006) applied to the original set of equation (1).

Figure 1 shows a schematisation of the partition of the physical domain (a river valley) by means of a finite number of geometrical cross sections (S_i, i = 1 to N). A cell associated to the dependent variable $W_i = [A_i, V_i]^T$ is delimited by the two consecutive cross sections S_i and S_{i+1}.

The proposed new scheme is a six step procedure.

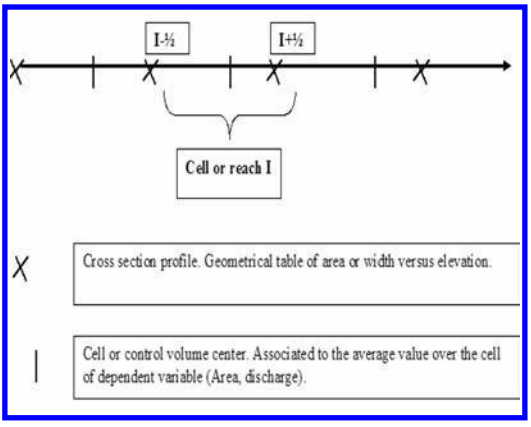


Figure 1. Schematization of domain discretization.

3.1 *Variable transformation*

This is the simplest step. It corresponds of the transformation of the variable W in the scheme into the corresponding variable U for the Riemann problem.

$$U = \begin{bmatrix} A \\ Q \end{bmatrix} = \begin{bmatrix} A \\ V \cdot A \end{bmatrix} = \begin{bmatrix} 1 & 0 \\ 0 & A \end{bmatrix} \bullet \begin{bmatrix} A \\ V \end{bmatrix} = N \bullet W$$

Here, N is the transformation matrix:

$$N = \begin{bmatrix} 1 & 0 \\ 0 & A \end{bmatrix}$$

3.2 *Riemann flux for U variable*

This is one of the most important steps of the present scheme. It corresponds to the now classical Roe's formula (Roe 1981), to evaluate the Riemann flux through the interface between two neighbouring cells, applied to the original equation set (1).

$$F_{I+1/2} = F_{I+1/2}(U_I, U_{I+1}) = \frac{1}{2}\left[F(U_I) + F(U_{I+1}) - |J_{I+1/2}| \bullet \Delta U\right] \quad (12)$$

It is necessary here to underline two main points in the application of this formula.

a) **Local linearization for flux formulation.** Original equation set (1) is not in conservation form. The proposal here is to write it in the following form

$$\frac{\partial U}{\partial t} + \frac{\partial F^P(U)}{\partial x} = G$$

Copyright © 2006 Taylor & Francis Group plc, London, UK

$$\text{With } F^P(U)=\begin{bmatrix} Q \\ (V\cdot A)+A_P\cdot(g\cdot H)\end{bmatrix}$$
$$\text{And } G(U)=\begin{bmatrix} 0 \\ A\cdot g\cdot S_f\end{bmatrix} \quad (13)$$

This means that the linearization is performed around the point P which represents the cell over which the equation set is integrated.

b) **Choice of variable.** In the above formula, the variable to $U=[A,Q]^T$ represents the cell average of the area and discharge respectively, as it is generally understood, but for the jump $\Delta U=\begin{bmatrix} A_{I+1}-A_I \\ Q_{I+1}-Q_I\end{bmatrix}$ in the numerical viscosity $|J_{I+1/2}|\bullet\Delta U$, it is proposed that the classical jump be replaced by a modified one:

$$\Delta U^{CS}=\begin{bmatrix} A_{I+1}^{CS}-A_I^{CS} \\ Q_{I+1}-Q_I\end{bmatrix}$$

Where :

A_I^{CS}, A_{I+1}^{CS} are cross section areas corresponding respectively to water surface elevations H_I and H_{I+1}. This choice is made so that for an initially still horizontal water surface, $H_I=H_{I+1}$, the jump ΔU^{CS} is null and so is the Riemann flux at the interface.

With the above modification, in place of the standard Roe flux (12), the following modified formula is used:

$$F_{I+1/2}^P=F_{I+1/2}^P(U_I,U_{I+1})=\frac{1}{2}\left[F^P(U_I)+F^P(U_{I+1})-|J_{I+1/2}|\bullet\Delta U^{CS}\right] \quad (14)$$

In (14), the point P may represent I or I+1 depending whether the integration is performed over the first or the second of these cells. Clearly, from (13), there is no symmetry:

$$F_{I+1/2}^I\neq F_{I+1/2}^{I+1}$$

3.3 *Temporal variation: U variable*

This step corresponds to the discrete representation of Equation set (1) without friction integrated over a cell I:

$$\Delta_t U^{n+1}=\left(U_I^{n+1}-U_I^n\right)$$
$$\Delta_t U^{n+1}=\frac{\Delta t}{\Delta X^I}\cdot\left[F_{I+1/2}^I-F_{I-1/2}^I\right] \quad (15)$$

3.4 *Evolution of W variable*

Evolution of W variable is realized on the basis of equation (15) together with the following transformation relation:

$$\partial W=\begin{bmatrix}\partial A \\ \partial V\end{bmatrix}$$
$$\partial W=\begin{bmatrix} 1 & 0 \\ -V/A & 1/A\end{bmatrix}\bullet\begin{bmatrix}\partial A \\ \partial Q\end{bmatrix}=T\bullet\partial U \quad (16)$$

Using (15) and (16), it is easy to derive the following relation for the evolution of W:

$$W_I^{n+1}=W_I^n-\frac{\Delta t}{\Delta X^I}\cdot\begin{bmatrix} 1 & 0 \\ \dfrac{-V_I^n}{A_I^n} & \dfrac{1}{A_I^n}\end{bmatrix}\bullet\left[F_{I+1/2}^I-F_{I-1/2}^I\right] \quad (17)$$

3.5 *Friction term*

The friction term is integrated in a separate fractional step method with an implicit algorithm which is known to preserve the stability of the overall procedure (Tchamen and Kahawita, 1998).

The equation to integrate is:

$$\frac{\partial W}{\partial t}=H(W)=\begin{bmatrix} 0 \\ -g\cdot S_f\end{bmatrix}$$
$$\frac{\partial W}{\partial t}=-\begin{bmatrix} 0 & 0 \\ 0 & C_f\end{bmatrix}\bullet W=-K\bullet W \quad (18)$$

Where

$$S_f=\frac{N^2}{R^{4/3}}|V|\cdot V,\qquad C_f=g\cdot\frac{N^2}{R^{4/3}}|V|$$
$$K=\begin{bmatrix} 0 & 0 \\ 0 & C_f\end{bmatrix} \quad (19)$$

Implicit integration of (18) results in

$$W_I^{n+1}=\begin{bmatrix} 1 & 0 \\ 0 & \left(1+\Delta t\cdot C_f^n\right)\end{bmatrix}^{-1}\bullet W_I^n$$
$$=\begin{bmatrix} 1 & 0 \\ 0 & \dfrac{1}{\left(1+\Delta t\cdot C_f^n\right)}\end{bmatrix}\bullet W_I^n \quad (20)$$

3.6 *Update of the cell mean water elevation*

This is a geometric operation which is done for every cell by using the updated cell average area A_I^{n+1} and the

Copyright © 2006 Taylor & Francis Group plc, London, UK

boundary cross section profiles. In fact the algorithm in charge of this step should determine the water level corresponding to the volume $VOL_I^{n+1} = A_I^{n+1} \cdot \Delta X_I$, with the geometry of the cell specified by the mean of the two boundary cross section profiles.

The cell mean water surface level is used in step 2 (Riemann flux).

4 THEORETICAL TEST CASES

The results of three theoretical tests which were proposed within the framework of the European CADAM [Concerted Action on Dam break Modeling] Project by Goutal & Maurel (1997) as validation cases for numerical models designed to simulate dam break flows.

4.1 *Initially quiescent pool of water within a pond of irregular bathymetry*

The purpose of this test is to verify correct treatment of the gravity term, which means that an initially horizontal water surface should remain unchanged in the absence of any inflow or outflow.

Figure 2a and 2b indicate that the chosen bathymetry and channel width is quite irregular. Figure 2c presents the water level after 1000 seconds of simulated time while Figure 2d shows the velocities at the same time. Clearly, no spurious velocity has been generated by the proposed scheme and water surface remains horizontal.

4.2 *Transcritical flow over a hump*

The second test takes place in a frictionless straight channel of rectangular cross section presenting a parabolic hump in the bed elevation. The geometry of this channel may be described by:

- for $X \leq 8$ and $X \geq 12$, $Z_f = 0$
- for $8 \leq X \leq 12$, $Z_f = 0.2 - 0.05(X-8)^2$

A steady state flow is established over this channel, with subcritical regime upstream which goes supercritical over the bump before returning to subcritical regime after going through an hydraulic jump, by imposing a constant specific discharge of $q = 0.18\ m^2/s$ at the entrance, and a constant depth of $H = 0.33$ m at the outlet.

Figure 3a and 3b show respectively the simulated water level and velocity profile against the analytical solution. It appears that the profile simulated on the basis of the system of head conservation (plus sign line), could not detect the hydraulic jump.

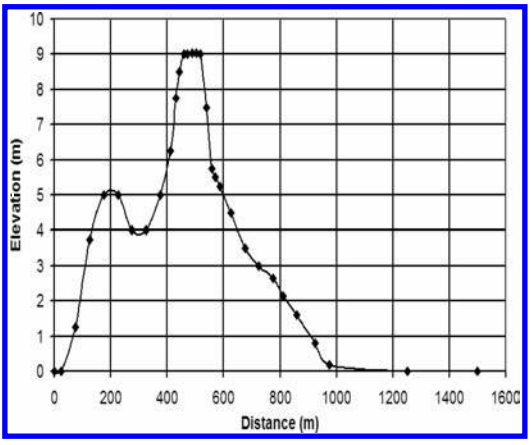


Figure 2a. Theoretical test 1. Bottoms profile.

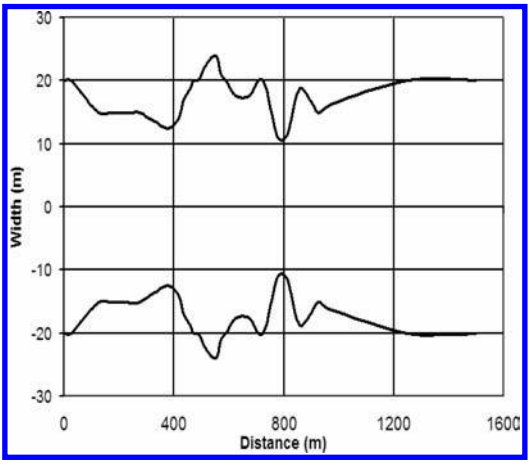


Figure 2b. Theoretical test 1. Profile of channel width.

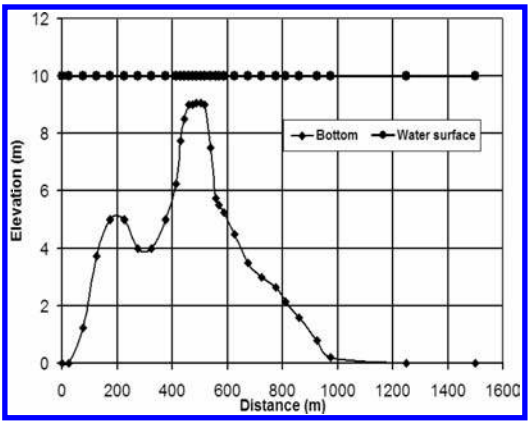


Figure 2c. Theoretical test 1. Water surface profile after 1000 seconds.

Copyright © 2006 Taylor & Francis Group plc, London, UK

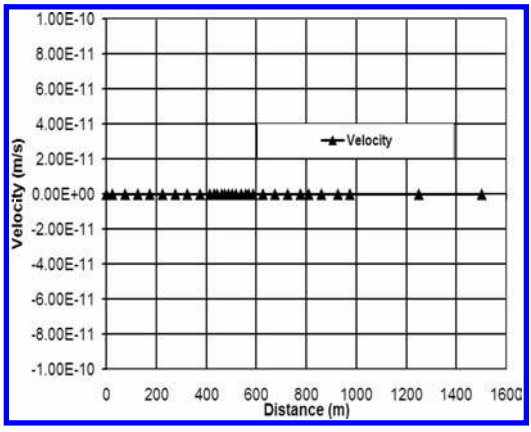


Figure 2d. Theoretical test 1. Velocity profile after 1000 seconds.

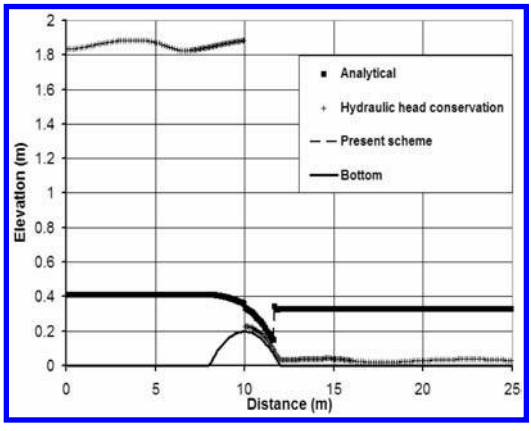


Figure 3a. Theoretical test 2. Water surface profile.

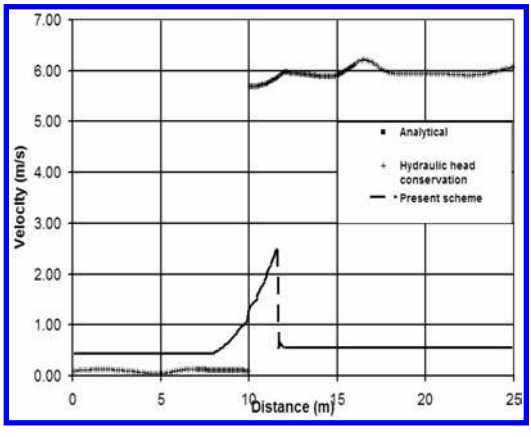


Figure 3b. Theoretical test 2. Velocity profile.

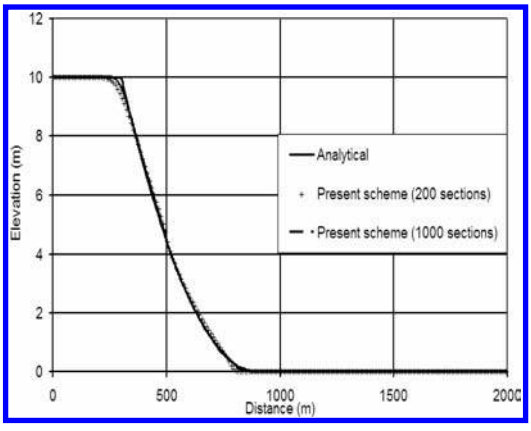


Figure 4a. Theoretical test 3. Water surface profile 20 seconds after dam break.

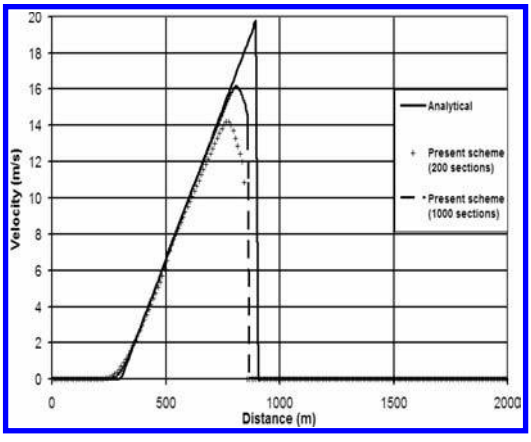


Figure 4b. Theoretical test 3. Velocity profile 20 seconds after dam break.

4.3 *Dam break over a frictionless channel with downstream dry bed*

This test corresponds to the theoretical dam break cases in a prismatic rectangular channel on a horizontal bed. The dam is located at approximately mid reach of the channel and separates a reservoir upstream, having a depth of 10.0 m, from a dry bed downstream.

Figure 4a and b compare respectively the longitudinal water surface profiles and velocities between the numerical and analytical solutions. The resolution of the advancing surge front improves with a finer mesh.

5 APPLICATION TO REAL CASES

5.1 *Filling a headrace tunnel*

For this particular case, the challenge for the numerical scheme is the presence of a mid section inclined

Copyright © 2006 Taylor & Francis Group plc, London, UK

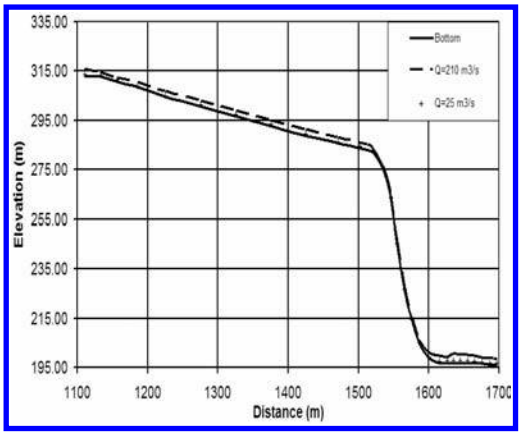


Figure 5a. Practical test 1. Bottom and water surface profiles.

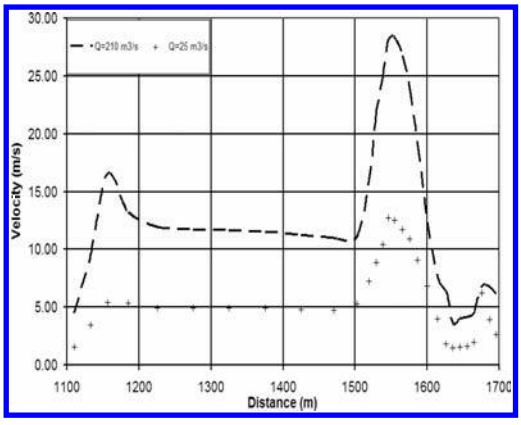


Figure 5b. Practical test1. Longitudinal profile of velocity.

tunnel which presents a sixty degree angle with the horizontal plane. The longitudinal bottom profile is shown in Figure 5a. The tunnel is approximately 1700 meters long, 17 meters wide and 17 meters in height. The tunnel is bounded upstream by a water intake. The opening of the intake vane controls the discharge into the tunnel. The tunnel is bounded downstream by a turbine group.

Two discharge scenarios in the tunnel have been simulated in order to select safe operation with regard to coarse debris entrainment.

Figure 5a and 5b show respectively longitudinal profiles of water surface and mean velocity for discharge values of 25 m^3/s and 210 m^3/s. It is seen that for the 210 m^3/s discharge, velocity values are greater than 6 m/s beyond 1600 m which corresponds to the base of the inclined reach and the entrance to the penstocks. Numerical tests have indicated that the present scheme is capable of treating velocities > 25 m/s in the tunnel.

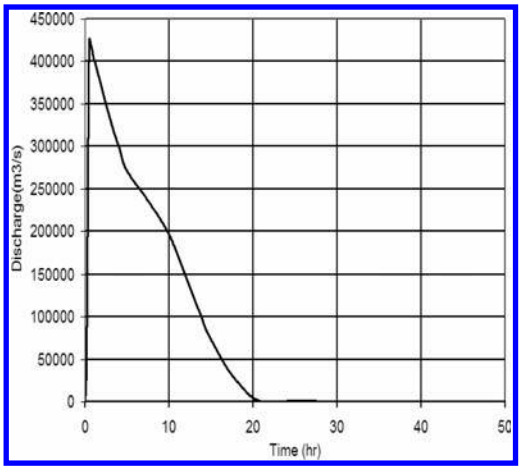


Figure 6a. Practical test 2. Hydrograph of SM3 dam breaking.

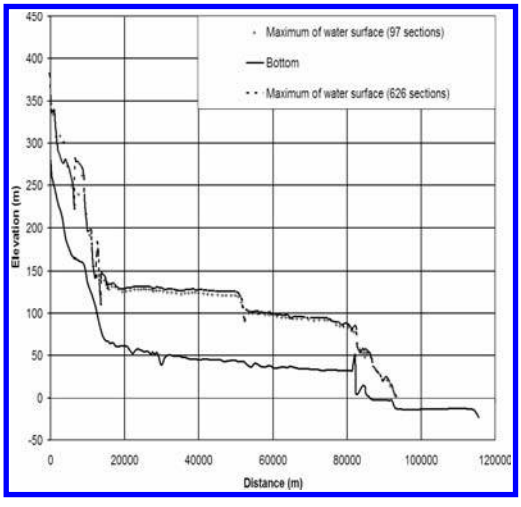


Figure 6b. Practical test 2. SM3 dam breaking. Longitudinal profile of maximum height.

5.2 *Sunny day dam failure in a river in Eastern Canada river*

The examples indicated here correspond to an actual river dam combination located in northeast Quebec, Canada. The failure scenario is completely fictitious, although judged realistic from an engineering risk analysis point of view.

The dam which is more than 100 meters in height would generate a formidable hydrograph, with a peak discharge exceeding 400 000 m^3/s as shown in Figure 6a. Figure 6b shows the longitudinal profile of maximum height over the downstream valley of the

Copyright © 2006 Taylor & Francis Group plc, London, UK

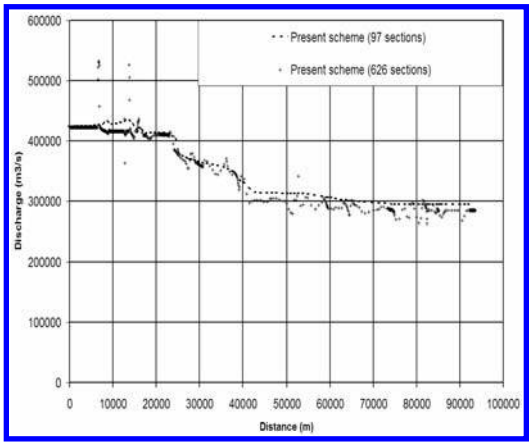


Figure 6c. Practical test 2. SM3 dam breaking. Longitudinal profile of maximum discharge.

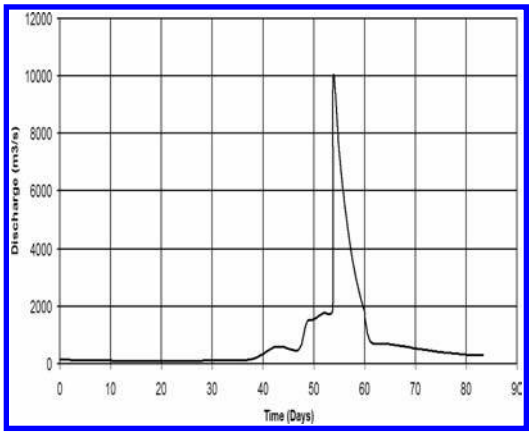


Figure 7a. Practical test 3. Hydrograph of Bourque dam breaking during probable maximal flood.

river with an irregular bottom. Figure 6c presents he longitudinal profile of maximum discharge.

Clearly, the present scheme is capable of handling extreme hydraulic flows in a numerically stable manner. Computational space steps ~ 1 km, were used although it is obvious that for accuracy purposes, it may be necessary to use a finer grid locally.

5.3 *Dam break during passage of probable maximum flood*

This represents a typical scenario that is studied to evaluate dam resistance against extreme flood events in the context of dam safety analyses. The principal challenge is to simulate the propagation of a flood in a natural river valley over a long time period of say two to three months while expending a reasonable amount of computational time. The key for the model is the

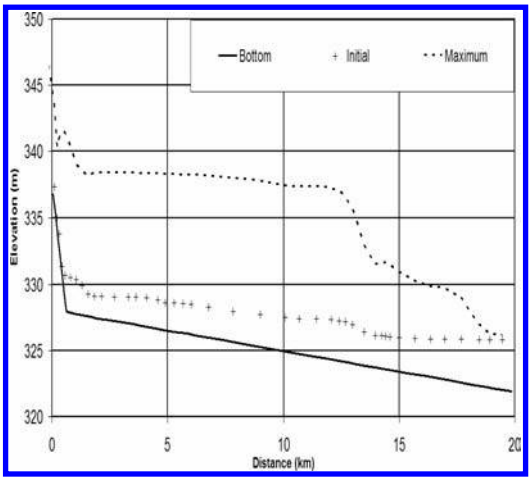


Figure 7b. Practical test 3. Bourque dam breaking. Longitudinal profile of maximum height.

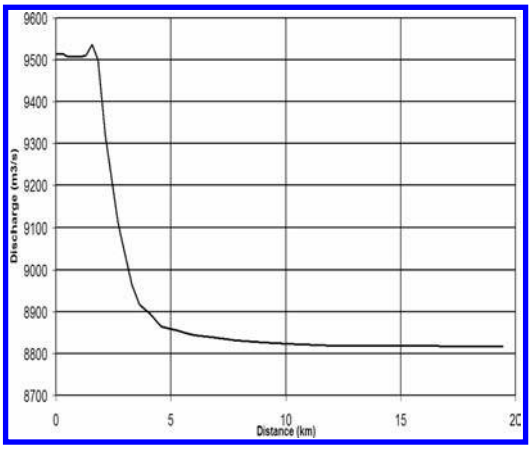


Figure 7c. Practical test 3. Bourque dam breaking. Longitudinal profile of maximum discharge.

speed of its numerical algorithm and the robustness necessary to handle space steps of several hundreds of meters.

In this example as well, a real river situated in northern Quebec Canada forms the basis of the study. The Probable Maximum Flood (PMF) has been synthesised from the standpoint of the site hydrology. Figure 7a indicates the outflow hydrograph expected if dam failure occurred during the flood peak.

Figure 9b shows the envelope of maximum water surface elevations expected along the 20 km downstream valley. Figure 7c shows the longitudinal profile of maximum discharge. The calculation for this scenario was performed with a 2 GHZ Pentium 4 in under 5 minutes.

Copyright © 2006 Taylor & Francis Group plc, London, UK

6 CONCLUSIONS

A new numerical scheme belonging to the class of Riemann solvers has been proposed for one dimensional Saint-Venant Equations. The novelty of this scheme resides on a local linearization, of the gravity term, which avoid to have to deal with various source terms which depends on river geometry and may be complicated to evaluate numerically. This scheme also innovates in adding an stabilizing step which transforms dependent variable from discharge to velocity.

Validation of the scheme has been carried by simulating theoretical test cases proposed in CADAM workshop. The scheme has also been applied to simulate dam break and extreme flood flows on natural river valleys. The scheme proved to accurately approximate analytical solution when they exist, but more importantly, for real case on natural river valleys, it shows great robustness which permits the use of space step of several hundred of meter. For practical cases, the scheme is so fast that it can be used for real time simulation.

REFERENCES

Alcrudo, F. & Garcia-Navarro, P. 1992. Flux difference splitting for 1-D open channel flow equations. *International Journal for numerical Methods in Fluids.* 14. 1009–1018.

Bermudez, A. & Vasquez, M.E. 1994. Upwind methods for hyperbolic conservation laws with source terms, *Computers and fluids*. 23(8).1049–1071.

Cunge, J. A. & Holly, F. M. & Vervwey, A. 1980. *Practical Aspects of River Computational Hydraulics*. London: Pitman.

Hervouet, J.M. 2003. *Hydrodynamique des écoulements à surface libre. Modélisation numérique avec la méthode des éléments finis.* Paris : Presses de l'école nationale des ponts et chaussées.

Glaister, P. 1988. Approximate Riemann Solution of the Shallow-Water equations, *Journal of Hydraulic Research*. 26(3). 293–306.

Goutal, N. & Maurel, F. 1997. Description of the test cases, *Proceedings of the 2nd workshop on Dam-Break wave simulation*. Chatou/Paris : EDF-DER. 7–28.

Goutal, N. & Maurel, F. 2002. A finite volume solver for 1D shallow-water equations applied to an actual river. *International Journal for Numerical Methods in Fluids*. 38, 1–19.

Roe, P.L. 1981. Approximate Riemann Solver, Parameter Vectors and Difference Schemes. *Journal of Computational Physics*. 43. 357–372.

Tchamen, G.W. 2006. *Sur l'utilisation des schémas de Riemann pour la solution des équations de Saint-Venant.* PhD thesis. Montreal : École Polytechnique. Scheduled for March 2006.

Tchamen, G.W., Kahawita, R. 1998. Modelling wetting and drying effects over complex topography. *Hydrological processes*. 12. 1151–1182.

Copyright © 2006 Taylor & Francis Group plc, London, UK

1-Dimensional numerical analysis of tsunami in river

H. Yasuda
Civil Engineering Research Institute for Cold Region, Sapporo, Japan

ABSTRACT: The aim of the paper is to develop a 1-dimensional numerical model of tsunami in river and to apply it to Tokachi-oki earthquake tsunami on September 2003 in Hokkaido, Japan. The computational results of arrival time and water level at each wave gauge agree well with the observed data a high accuracy of less than 10%. Although the actual status of results of field survey is still unknown before the computation, the observed results were explained by the numerical analysis.

1 INTRODUCTION

Tsunamis cause tremendous damage to coastal areas, but they also have the potential to run up rivers and cause damage on a similar scale several kilometers upstream from the mouth. For example, after the 2003 Tokachi-oki Earthquake, a tsunami ran up multiple rivers on the Pacific coast of Hokkaido, Japan, making us strongly recognize that phenomena and realize its potential destructiveness. Although tsunami runup in rivers has been identified as a danger, it has drawn relatively little academic attention, partly because there are few records of the phenomenon.

At the front of a tsunami wave that enters a river, it is possible for the vertical acceleration to exceed the gravitational acceleration and for there to be a deviation from the hydrostatic pressure. When this phenomenon occurs, the wave characteristics totally change. The structural stability that is maintained as long as there is hydrostatic pressure is disrupted and the wave transforms into a new state of structural stability. This phenomenon has a clear bifurcation point between the two states. When a tsunami intrudes into a river channel and exceeds this bifurcation point, a wave number dispersion phenomenon called soliton dispersion, which is accompanied by a water level increase that is not seen under the condition of hydrostatic pressure, occurs at the wave front and an undular bore forms. In the tsunamis from the 1986 Nihonkai-chubu Earthquake(Tsuji, Y. et al. 1991) and 2003 Tokachi-oki Earthquake(Yasuda, H. et al. 2004) and in the 2004 Indian Ocean Tsunami(Tanaka, H. et al. 2006), soliton dispersions are known to have occurred when the tsunamis intruded into rivers. So far, neither the basic characteristics of tsunami waves in rivers, including the scale of water level increase with soliton dispersion at the wave front, nor specific behaviors of tsunami runup have been fully clarified.

Studies on tsunamis in river channels have been conducted by Iwasaki et al. (1977), Goto et al. (1981), Tsuji et al. (1991) and others. All these were based on shallow-water theory, except the studies by Tsuji et al., which employed the KdV-Burgers equation. This is why there has not been sufficient discussion on the undulant nature of wave fronts in undular bore phenomena. Nonetheless, it is of great significance, especially from the viewpoint of fluvial hydraulics, to discuss soliton dispersion at the wave front and the possibility and scale of water level increases even in cases that do not necessarily involve soliton dispersion but occur under non-hydrostatic pressure conditions.

Partial differential equations describing motions of tsunami runup in rivers completely agree, within a limited range, with the shallow-water equation applied to analyses of unsteady flow in rivers. Here, "limited range" means the range where hydrostatic pressure is acting. This means that if one is to perform an analysis of wave number dispersion phenomena based on long-wave equations, a non-linear dispersive wave theory (the Boussinesq equation(1872)) should be applied, because wave number dispersion phenomena do not appear when hydrostatic pressure is acting. Yasuda et al. (2003) pointed out that the non-linear dispersive wave equation is essential for analyses of undular bores running upstream and forming steep wave fronts, as shallow-water equations underestimate the maximum height of undular bores. Yasuda et al. (2005) subsequently conducted a numerical simulation on tsunami runup in river channels using the non-linear dispersive wave equation as the governing equation, and they identified some basic characteristics, such as maximum intrusion distance, maximum water level and its locations of occurrence.

This paper gives a one-dimensional analysis method to describe tsunami runup in rivers and discusses its applicability through a simulation of tsunami intrusion

Copyright © 2006 Taylor & Francis Group plc, London, UK

from the 2003 Tokachi-oki Earthquake into rivers on the Pacific coast.

2 MATHEMATICAL MODELS

2.1 *Governing equations*

In this study, similarly to the analysis by Yasuda et al. (2005), when Ursell number, U_r, is of the order of one, an integral of the Peregrine equation (Peregrine, D.H. 1967) is derived:

$$\frac{\partial q}{\partial t}+\frac{\partial}{\partial x}\left[\frac{q^2}{D}\right]+gD\frac{\partial \eta}{\partial x}=\frac{h^2}{3}\frac{\partial^3 q}{\partial t x^2}-\frac{C_f}{D^2}|q|q \qquad (1)$$

where q is the flow flux, t is the time coordinate, D is the water depth, x is the coordinate for the flow direction, g is the gravitational acceleration, η is the water level, h is the initial water depth, C_f is the bed resistance coefficient. This integral is applied as an equation of non-linear dispersive wave theory, where:

$$\frac{\partial \eta}{\partial t}+\frac{\partial q}{\partial x}=0 \qquad (2)$$

is the corresponding continuity equation. Furthermore, in consideration of application to generalized cross-sections of river channel, the integral of the Peregrine equation is expanded as:

$$\frac{\partial Q}{\partial t}+\frac{\partial}{\partial x}\left[\frac{Q^2}{A}\right]+gA\frac{\partial \eta}{\partial x}=\frac{R^2}{3}\frac{\partial^3 Q}{\partial t x^2}-\frac{C_f}{AD}|Q|Q \qquad (3)$$

where Q is the discharge of the river, A is the cross-sectional area of the flow and R is the hydraulic radius. The continuity equation is rewritten as:

$$\frac{\partial \eta}{\partial t}+\frac{1}{B}\frac{\partial Q}{\partial x}=0 \qquad (4)$$

where B is the width of water surface. The shallow-water equations that express flow flux in a generalized cross section are Eqs. (1) and (3), with the first term in the right-hand side omitted for each equation.

For the influence of bed shear force on tsunami, it was decided to apply an expression with a bed resistance coefficient determined by the relationship between water depth and bed material diameter, as shown in the second terms in the right-hand side of Eqs. (1) and (3). C_f is written as:

$$C_f=\frac{1}{\phi^2} \qquad (5)$$

where ϕ is the flow velocity coefficient determined according to small-scale bed morphology. This C_f and the frequently used Manning's roughness coefficient, n, have a relationship of $n^2=C_f h^{1/3}/g$ via a Manning's uniform-flow equation.

2.2 *Method of numerical analysis*

In non-linear dispersive wave equations like the Peregrine equation, time derivative terms are included not only in local terms but also in dispersion terms; therefore, it is necessary to use an implicit scheme to obtain appropriate solutions. Moreover, for equations with physical dispersive, application of a difference scheme that has a numerical dispersion term (i.e., a dominant truncation error term) will also be reflected in the results. In selecting a difference scheme, it is necessary to consider the truncation error characteristics. When considering computational efficiency and expansion to two-dimensional computation and other phenomena, a two-step mixed finite-difference method (Goto, C. 2003) that combines the staggered Leap-Frog method and the Thomas algorithm to allow for efficient implicit computation would be appropriate. In this study, it was decided to apply the two-step mixed finite-difference method that we used in a previous study(2005).

When applying the two-step mixed finite difference method to Eq. (3), the linear long-wave equation is explicitly solved by the Leap-Frog method in the first step as:

$$\frac{1}{\Delta t}\left[Q^*_{i+1/2}-Q^j_{i+1/2}\right]+\frac{gD}{\Delta x}\left[\eta^{j+1/2}_{i+1}-\eta^{j+1/2}_{i}\right]=0 \qquad (6)$$

In the second step, the convection term and the dispersion term are discretized and solved to fit tridiagonal matrices as:

$$\begin{aligned}&\frac{1}{\Delta t}\left[Q^{j+1}_{i+1/2}-Q^*_{i+1/2}\right]\\&+\frac{1}{4\Delta x}\left[\left\{\left(\frac{Q}{A}\right)^j_{i+3/2}Q^{j+1}_{i+3/2}-\left(\frac{Q}{A}\right)^j_{i-1/2}Q^{j+1}_{i-1/2}\right\}\right.\\&\left.+\left\{\left(\frac{Q}{A}\right)^j_{i+3/2}Q^{j}_{i+3/2}-\left(\frac{Q}{A}\right)^j_{i-1/2}Q^{j}_{i-1/2}\right\}\right]\\&=\frac{1}{3}\left(R^j_{i+1/2}\right)^2\frac{1}{\Delta t\Delta x^2}\\&\left[\left(Q^{j+1}_{i+3/2}-2Q^{j+1}_{i+1/2}+Q^{j+1}_{i-1/2}\right)\right.\\&\left.-\left(Q^{j}_{i+3/2}-2Q^{j}_{i+1/2}+Q^{j}_{i-1/2}\right)\right]\end{aligned} \qquad (7)$$

where Q^* is the intermediate value of $Q^{j+1}_{i+1/2}$ given by linear theory, and i and j are discretization steps for space and time, respectively.

Copyright © 2006 Taylor & Francis Group plc, London, UK

In a previous study, the author conducted a numerical simulation in which a smooth function was used to express the incident tsunami at the mouth of a river with a uniform bed slope. In that simulation, the convection term was discretized by the second-order central difference (Eq.7)). In this two-step mixed finite-difference method, there are two main truncation error terms. One is the third-order derivative term that appears in the process of the Leap-Frog difference and in discretization of the convection terms in the second step; this term causes numerical dispersion. The other is the fourth-order derivative term that appears in the process of discretization of the dispersion term; this term causes numerical viscosity. In such computation, computational instability will be of less concern if appropriate intervals for division of space and time are given.

This study takes a different approach, focusing on computation for a river with the generalized cross section, where changes in forms, such as the form of incident wave of tsunami and those of longitudinal and transverse river sections, cause unwanted high-frequency components. The scheme shown in Eq. (7), having a small numerical viscosity, if used in the computation of this study eventually results in having crucial instability because once high-frequency components are generated they do not readily attenuate but instead remain in the computational domain.

As one can see from the fact that theoretical solutions to a diffusive partial differential equation for $u(x,t)$ with a $2n$-th derivative term are given by

$$u = \exp[-k^{2n}\epsilon t]\exp[\mathbf{i}kt] \tag{8}$$

the higher order of the even-order derivative terms, the more effective is that term in suppressing higher-frequency components. Here, ϵ is the diffusion coefficient, k is the wave number and $\mathbf{i}$ is the imaginary unit. To implement stable computation while maintaining physical dispersion, a difference scheme that includes a truncation error term of higher even-order and focuses on suppressing high-frequency components should be adopted. One effective scheme that meets these conditions is the third-order upwind difference that has a fourth derivative term as the main truncation error term. In this case, in consideration of forming the tridiagonal matrix, the convection term can be discretized as:

$$\begin{aligned}\frac{1}{6\Delta x}\Bigg[&\psi_1\left\{\left(\frac{Q}{A}\right)^j_{i+5/2}Q^j_{i+5/2}\right\}\\ &+\psi_2\left\{\left(\frac{Q}{A}\right)^j_{i+3/2}Q^{j+1}_{i+3/2}+\left(\frac{Q}{A}\right)^j_{i+3/2}Q^j_{i+3/2}\right\}\\ &+\psi_3\left\{\left(\frac{Q}{A}\right)^j_{i+1/2}Q^{j+1}_{i+1/2}+\left(\frac{Q}{A}\right)^j_{i+1/2}Q^j_{i+1/2}\right\}\\ &+\psi_4\left\{\left(\frac{Q}{A}\right)^j_{i-1/2}Q^{j+1}_{i-1/2}+\left(\frac{Q}{A}\right)^j_{i-1/2}Q^j_{i-1/2}\right\}\\ &+\psi_5\left\{\left(\frac{Q}{A}\right)^j_{i-3/2}Q^j_{i-3/2}\right\}\Bigg]\end{aligned} \tag{9}$$

where $\psi_1 \sim \psi_5$ are upwind-coefficients determined depending on whether $Q^j_{i+1/2}$ is positive or negative.

Here, to compare the characteristics of Eqs. (7) and (9), numerical simulation was conducted (Figure 1). The incident condition for the simulation is that only 1/4 period of sine wave is incident at the beginning, followed by a constant water level. As one can tell from the figure, the equations agree very well except for a very small difference in phase at the end of the dispersed wave train.

Regarding computation of the shallow-water equation, the Leap-Frog method was applied to terms other than the convection term, and the first-order upwind difference scheme was applied to the convection term. In computation of the convection term in this equation, it is of course possible to enhance the accuracy by introducing the implicit scheme, such as was introduced for computation of the non-linear dispersive wave equation, or by applying difference schemes of higher-order accuracy. However, application of higher-accuracy schemes to such computation would present the possibility of water level overestimation resulting from the numerical Gibbs oscillation at the wave front, which is caused by the numerical dispersion of the Leap-Frog scheme and becomes more evident when the forward tilting of the tsunami wave is promoted. To avoid this, a first-order upwind difference scheme was applied, as it is expected to show appropriate

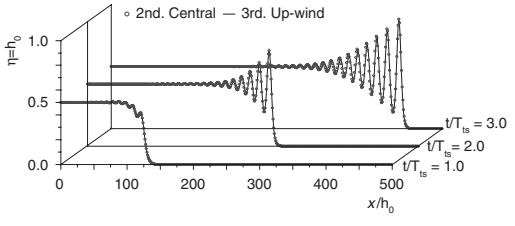


Figure 1. Comparison between second-order central difference and third-order upwind difference scheme in numerical analysis of Soliton dispersion phenomenon. (The third-order upwind difference scheme has a very slight delay in the phase of the wave train, relative to the second-order centered difference scheme, but the two agree very well in terms of wave front.)

Copyright © 2006 Taylor & Francis Group plc, London, UK

numerical viscosity in numerical analyses of the same phenomena.

3 SIMULATIONS

3.1 *Tsunami runup in rivers on the Pacific Coast of Hokkaido from the 2003 Tokachi-oki Earthquake*

The tsunami generated by the Tokachi-oki Earthquake of September 2003 was confirmed to have intruded into the Tokachi, Kushiro, Saru and Mu rivers on the Pacific coast of Hokkaido (Figure 2). An undular bore from tsunami runup was videotaped in the Tokachi River by Japan's Self Defense Forces. The average channel bed slopes of these four rivers are about 1/5,000, 1/7,500, 1/750 and 1/1,000, respectively.

Water level fluctuations indicating tsunami intrusion were clearly observed. On the Tokachi River, the fluctuations were observed approximately 9.5 km in stream centerline distance from the mouth; in the Kushiro River, they were observed approximately 8 km from the mouth, where the channel suddenly narrows. On the Mu and the Saru Rivers, which have steeper channel bed slopes than the two rivers mentioned above, water level fluctuations believed to be caused by the tsunami were observed at the gauging stations nearest to the respective river mouths.

In this study, tsunami runup was simulated for the Tokachi River (Figure 3), based on the analysis method described in the previous sections. Figure 4 shows time waveforms of water level at 10-minute intervals up to four hours after the earthquake. These records were obtained at the Ohtsu, Tabikorai and Dousuiro (the flood way to connect branch to Tokachi River) gauging stations, where significant water level fluctuations

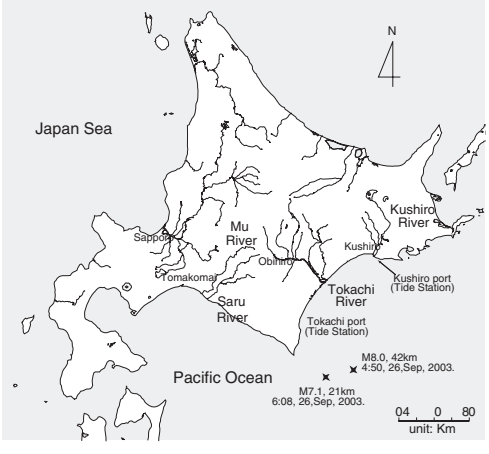


Figure 2. Map of Hokkaido Island and rivers affected by tsunami.

indicated the passage of tsunamis. Within four hours after the occurrence of earthquake, six tsunami waves with a period of 30–40 minutes arrived at the mouth of the Tokachi River. These waves ran up about 7 km from Ohtsu to Tabikorai in about 20 minutes. The time varied depending on the wave height at arrival at the mouth.

The water level gauges at the Ohtsu, Tabikorai and Dousuiro gauging stations have a measuring precision that allows them to detect water level fluctuations of around 2 cm, which is the magnitude of wind waves. They obtain water level measurements every second and output 15-sec averages at 10-minute intervals. It should be noted that although these observed values are highly reliable in terms of each output, they may not be able to fully express continuous waveforms (e.g., wave gradients) due to the observation intervals. This point should be borne in mind when using these observation values.

3.2 *River channel morphology*

The section for analysis was 20 km in stream centerline distance of the Tokachi River from the mouth. However, due to bends and other factors there are sections

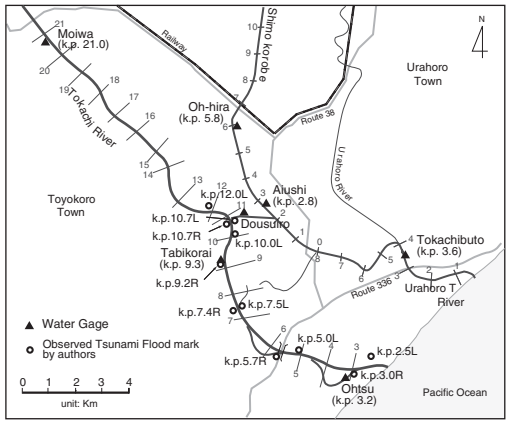


Figure 3. Location map of Tokachi River.

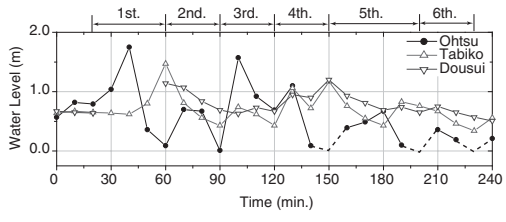


Figure 4. Water level records at 10-minute intervals for the four hours after the occurrence of earthquake. (*interpolated value, since the records did not have values for 0 m and below)

Copyright © 2006 Taylor & Francis Group plc, London, UK

where there is a large difference between the distance indicated by kilometer post (KP) and the stream centerline distance. Therefore, all longitudinal distances in this paper are expressed as stream centerline distances. Figure 5 shows an overview of longitudinal profile for this section of the Tokachi River: The average channel bed gradient is about 1/5,000 and the bed material diameter for this section is approximately 1 to 6 mm. The locations of Ohtsu, Tabikorai and Dousuiro gauging stations are shown in the upper frame of Figure 5. As for the transverse distances, the distance between the embankments of the subject section is about 1,000 m and the low-flow channel width is about 300 m.

It should be noted that hydraulic radius, R, is assigned as a coefficient of the dispersion term in the first term of the right-hand side of Eq.(3). In an non-uniform flow computation with a flow rate increasing by 500 m^3/s, R and average water depth showed close agreement at any flow rate. Therefore, it is considered reasonable to apply R to the computation of this term.

3.3 *Initial conditions*

3.3.1 *Estimation of bed morphology*

Generally, small-scale bed morphology is estimated based on a relationship between the dimensionless tractive force, τ^*, and the flow velocity coefficient, ϕ. As a result of applying this relationship, the section was roughly classified as having a flat bed with little changes from sediment movement. Here, the flow velocity coefficient is

$$\phi = 6 + 2.5 \ln\left(\frac{D}{2.5 d_s}\right) \tag{10}$$

as indicated by Engelund & Hansen (1967), where d_s is the average grain diameter of bed material.

3.3.2 *Estimation of initial flow rate*

Initial flow rate was estimated by an non-uniform flow computation in which the input flow rate increase was set at 20 m^3/s so that water levels at the time of earthquake occurrence could be most appropriately simulated for the Tabikorai, Dousuiro and Moiwa gauging stations. Calculated values and measured values at each observation point have the closest agreement at the flow rate of 220 m^3/s. In this non-uniform flow computation, the water level at the Ohtsu gauging station at the occurrence of earthquake was given as the water level at the downstream end of the section for analysis.

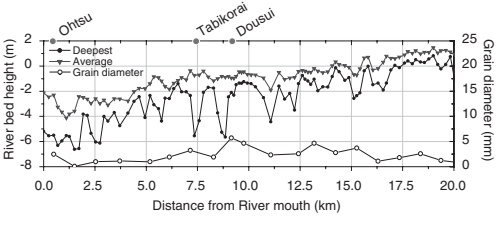


Figure 5. Longitudinal morphology and longitudinal distribution of average grain diameter in the Tokachi River.

3.4 *Boundary conditions*

Boundary conditions for the upstream end were decided as follows: Precipitation records for multiple points along the Tokachi River revealed that although there was some precipitation in the catchment during the 24 hours before and the 24 hours after the earthquake, the rainfall was a small amount of about 30 mm; therefore, its influence on river flow rate was assumed to be negligible. Based on this, the flow rate at the upstream end was set in steady state at 220 m^3/s, which is the value obtained in the estimation above.

Next, for the boundary conditions at the downstream end, the water level observed at the Ohtsu gauging station at 10-minute intervals (the solid black line in Figure 4) was used after interpolation according to Δt. The reasons for using the Ohtsu values are the following: First, the Ohtsu gauging station is about 0.7 km from the mouth. Second, the non-uniform flow computation revealed that the water surface gradient of the section near the mouth that includes the Ohtsu gauging station was very small. The water level data routinely measured at Ohtsu Fishing Harbor at the mouth of Tokachi River did not include the values at the time of tsunami intrusion; therefore, we needed to interpolate the values missing from the Ohtsu gauging station values.

3.5 *Computational conditions*

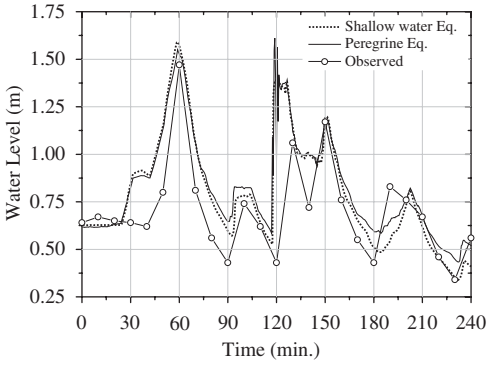
Simulations were performed for a period of four hours from the occurrence of earthquake, during which tsunami intrusion was clearly detected. A spatial discrete interval, Δx, was set at 2 m to avoid aliasing errors and to attain satisfactory description of dispersed wave trains. Meanwhile, time discrete intervals, Δt, were set at 0.02 sec and 0.0002 sec, respectively, for the shallow-water equation and non-linear dispersive wave equation.

4 APPROPRIATENESS OF SIMULATIONS, AND DISCUSSION

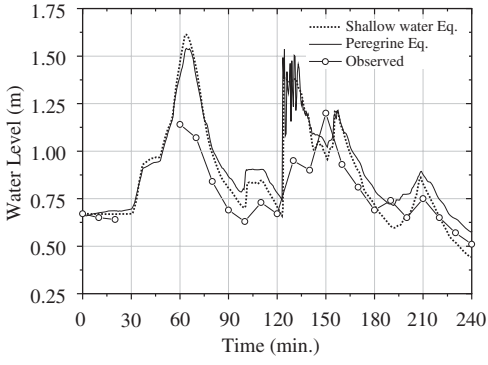
4.1 *Comparison of water level: observed and simulated*

To confirm the appropriateness of the simulations, observed values were compared with the results of numerical computation based on the shallow-water equation and non-linear dispersive wave equation. As

Copyright © 2006 Taylor & Francis Group plc, London, UK



(a) Tabikorai gauging station (stream centerline distance: 7.5 km, KP9.3)



(b) Dousuiro gauging station (stream centerline distance: 9.0 km, KP10.8)

Figure 6. Water level: observed (at 10-minute intervals) and simulated. (Observed values and calculated values of the same time points were compared. Average difference within the simulated period shows a tendency of overestimation of slightly less than 10% for the shallow-water equation and about 15% for the non-linear dispersive wave equation.)

seen in Figures 6 (a) and (b), it can be said that simulations based on either of the governing equations successfully reproduced the arrival time of tsunami at each observation point. Water levels were reproduced with relatively high accuracy, although there was a tendency for calculated values to slightly exceed observed ones. It was also revealed by the computation based on the non-linear dispersive wave equation that only the third wave formed a clear undular bore.

In the first and third waves, differences were seen in some cases between the recorded and calculated water levels. The differences were attributed to the following.

In the third wave, the difference between the recorded and calculated water levels was the greatest 130 minutes after the earthquake at both the Tabikorai and Dousuiro gauging stations. Because the shallow-water equation cannot describe the soliton dispersion phenomena (the apparent soliton dispersion at the wave front is actually caused by truncation error), reasons for such a difference can be hypothetically explained by considering the calculation results of the non-linear dispersive wave equation: Calculation results shown in Figure 6 indicate that both points saw the passage of the third tsunami wave, which was the only wave with a clear soliton dispersion at the wave front. Considering that the third wave passed through the observation points in the form of undular bore, it is assumed that the water level gauges captured the values at the troughs of the undular bore. This is why a great difference eventually appears between the calculation results and the water level records.

In the calculated water level values for the first wave, the highest and lowest points of the wave are overestimated by about 0.20 m. However, the causes of that overestimation have not been identified.

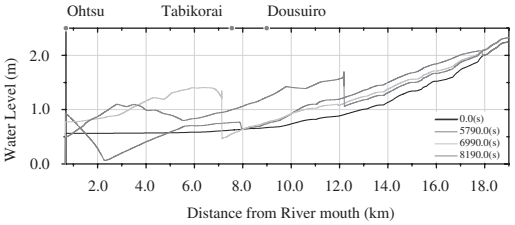
4.2 *Spatial waveforms*

As mentioned in the section above, based on simulations performed in this study the third wave is assumed to have generated a significant soliton dispersion. Figure 7 show computed spatial waveforms of this third wave for every 30 minutes. Figure 7(a) is based on the shallow-water equation, Figure 7(b) on the non-linear dispersive wave equation with the convection term discretized by a second-order central difference, and Figure 7(c) on the non-linear dispersive wave equation with the convection term discretized by a third-order upwind difference.

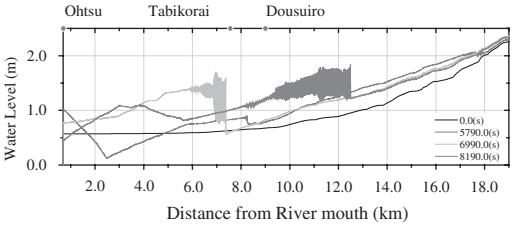
In Figure 7(a), waveforms at $t = 6990$ and 8190 sec seem to represent slightly soliton dispersion at the wave front. However, these are thought to be high-frequency components (the so-called numerical Gibbs oscillation), caused by numerical dispersion from the Leap-Frog method, which did not attenuate due to numerical viscosity associated with the first-order upwind difference.

In contrast to the waveforms in Figure 7(a), the waveforms at $t = 6990$ and 8190 sec in Figure 7 (b) and (c) show wave number dispersion, where the amplitude decreases with increasing distance from the wave front. The length of the section from the wave front to the end of the train gradually increases as the tsunami wave runs upstream. The authors lacked data on the length of the section with this soliton dispersion, and knowledge on the breaking limits for soliton dispersion, so it was not possible to determine whether Figure 7 (b) or (c) is more physically appropriate. Nonetheless, the results in Figure 7 (c) are thought to appropriately reflect the effects of physical dispersion terms alone, because Figure 1 show that second-order central and third-order upwind difference scheme are

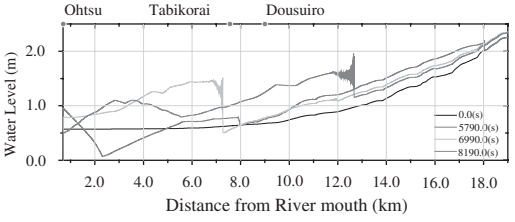
Copyright © 2006 Taylor & Francis Group plc, London, UK



(a) Shallow-water equation



(b) Non-linear dispersive wave equation (central difference, second-order accuracy)



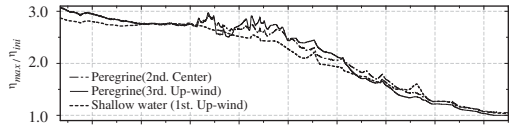
(c) Non-linear dispersive wave equation (upwind difference, third-order accuracy)

Figure 7. Spatial waveforms of the third wave (every 30 minutes).

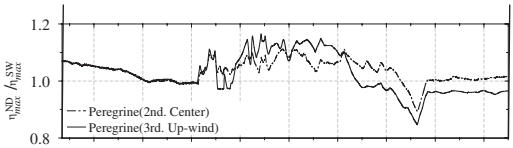
little difference in the numerical simulation on soliton dispersion under ideal conditions, and moreover, intervention of numerical dispersion terms derived from Staggered Leap-Frog scheme can be better controlled by fourth-order numerical viscosity derived from third-order upwind difference.

4.3 *Maximum rate of water level increase and length of river section where wave number dispersion occurs*

A study was made on maximum rates of water level fluctuation associated with tsunami intrusion into rivers and on rates of water level increase at each point caused solely by wave number dispersion phenomena. The results are shown in Figure 8. In Figure 8(a), η_{ini} is the initial water level, η_{max} is the maximum water level; in Figure 8 (b), η_{max}^{ND} is the maximum water level obtained from the calculated values of the non-linear



(a) Maximum rate of water level increase



(b) Rate of water level increase associated with wave number dispersion phenomena

Figure 8. Maximum rate of water level increase and the section where wave number dispersion phenomena occurred.

dispersive wave equation and η_{max}^{SW} is that obtained from the shallow-water equation.

First, according to Figure 8 (a), the attenuation rate of tsunami wave height was not very great up to about 6 km from the mouth, but beyond this point the attenuation rate seems to be greater. This figure shows the results from the shallow-water equation and the nonlinear dispersive wave equation, and by looking at the latter, one can tell that a significant wave number dispersion phenomenon was generated after the tsunami wave arrived at the point about 6 km upstream of the mouth. Furthermore, although the amplitude of the wave train with high wave number caused by the wave number dispersion phenomenon was gradually attenuated, it was maintained 15 km and further upstream from the mouth.

As one can see from Figure 8(b), water level increases associated with wave number dispersion phenomena occur in a section over several kilometers. The rate of water level increase is at least 10% under either difference scheme and around 15% under a third-order upwind difference where interference of the numerical dispersion term is small.

4.4 *Discussions on actual phenomena based on simulation results*

4.4.1 *Flood channel inundation*

Yasuda et al. (2004) conducted a trace survey and an analysis of water level records for the runup of this tsunami in this river. Based on the survey and analysis they discussed the possibility of the tsunami reaching the flood channel. Figure 9 shows the relationship between the maximum water level envelope and the elevation of the flood channels. According to this figure, it is highly likely that flood channel

Copyright © 2006 Taylor & Francis Group plc, London, UK

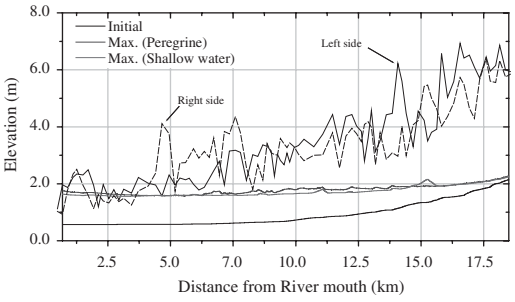


Figure 9. Relationship between maximum water level and flood channel height.



Figure 10. Videotaped undular bore in Tokachi river at 3.2 km upstream from the mouth on 6:30, 26th Sep., 2003 by Japan's Self Defense Force.

inundation took place on the right bank side and on a part of the left bank up to at least 3.7 km (KP 6.0) from the mouth. These results agree well with results obtained in the trace survey, although according to the figure there is no flood channel inundation on the right bank near 3.2 km (KP 5.7) whereas vegetation knocked down in the upstream direction was confirmed in the trace survey and there is no inundation on the left bank at 5.6 km (KP 7.5) where inundation traces were also confirmed.

4.4.2 *Using video footage to verify computation results*

An undular bore formed by tsunami runup was videotaped in the Tokachi River by Japan's Self Defense Forces about 100 minutes after the occurrence of the earthquake, at the point around 3.2 km (KP5.7) upstream of the mouth (Figure 10). As one can tell from Figure 6 and other data, this is the third wave. The numerical analysis shows that a rapid forward inclination of the wave front of the third wave takes place to form an undular bore near a point 5.0 km from the mouth about 108 minutes after the earthquake. The

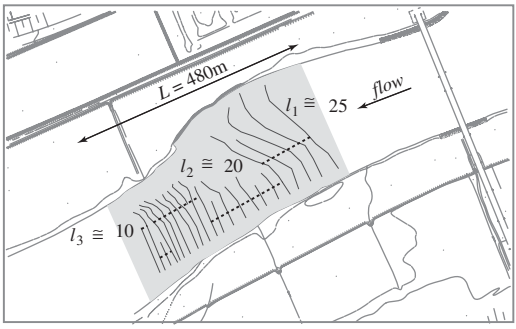


Figure 11. Wavelengths of soliton wave trains videotaped on the Tokachi River.

discrepancy can be interpreted as follows: When passing Ohtsu, the third wave has slightly greater steepness than the measured steepness, but this is not reflected in the observed value due to the 10-minute observation intervals. Since the wave steepness obtained from water level records at Ohtsu and used as the boundary conditions is less than the observed steepness, undular bore formation appears further upstream in calculations than in the observations.

Wavelengths of the videotaped soliton wave train were measured (Figure 11). The video frame that most clearly captured the tsunami was selected, and from there, wave crests of the tsunami wave were mapped on a plane (the solid lines on water surface in Figure 11) and distances between the crest lines were measured on the dotted lines in Figure 11. Distances between the wave crests of the wave group located most upstream, l_1, were about 25 m with some variations, those for l_2 were about 20 m and those for l_3 were about 10 m. As mentioned earlier, the calculated appearance positions of the soliton wave trains were farther upstream than the position observed in the video. In a comparison of distances between the wave crests, however, the values measured as shown in the figure and the calculated values showed close agreement. Nonetheless, there is room for further examination on the validity of the individual soliton waves in the wave train obtained by the non-linear dispersive wave equation.

5 CONCLUSIONS

One-dimensional analysis for tsunami runup in rivers was presented, and its appropriateness was confirmed by using it to reproduce actual phenomena. The results show that although this is a simple analysis method, calculated values and measured values agree well in terms of arrival time, maximum water level and other values. Questions remain regarding certain details, but the study clarifies that water level increases associated with wave number dispersion phenomena occur

Copyright © 2006 Taylor & Francis Group plc, London, UK

over a long section and on a considerable scale. In numerical analyses of these phenomena, the non-linear dispersive wave equation should be applied as the governing equation, and numerical computation should be performed based on careful consideration of calculation efficiency and characteristics of truncation errors. Continuous discussions are needed on the influence of sharp bends and meso-scale bed morphology on the phenomena and on cases of large finite amplitudes.

ACKNOWLEDGEMENTS

The author would like to thank the Hokkaido Development Agency of the Ministry of Land, Infrastructure and Transport and its Obihiro Development and Construction Department for supporting this study and providing valuable reference materials, including water level records and river channel morphology data.

REFERENCES

Boussinesq, J. (1872). Théorie des ondes et des remous qui se propagent le long d'un canal rectangulaire horizontal, en communiquant an liquide contenu dans ce canal de vitesses sensiblement pareilles de la surface anfond. *Liouvilles J. Math. 17*, 55–108.

Engelund, F. and Hansen, E. (1967). *A Monograph on Sediment Transport in Alluvial Stream, Teknisk Forlag, Copenhagen, Denmark*, 62p.

Goto, C. (2003). Evaluation on truncation error of 2-step mixed finite-difference method with linear dispersive wave theory. *Annual Report ofTsunami Engineering, DCRC, Tohoku University 20*, 13–22 (in Jananease).

Goto, C., and Shuto, N. (1981). 2-dimensional numerical analysis of tsunami runup. *Annual Journal of Coastal Engineering, JSCE, 28*, 64–68 (in Jananease).

Iwasaki, T., Abe, T., and Hashimoto, K. (1977). Study on characteristic of tsunami in river. *Annual Journal of Coastal Engineering, JSCE, 24*, 74–77 (in Jananease).

Peregrine, D.H. (1967). Long waves on a beach. *J. Fluid Mech. 27*, 815–827.

Tanaka, H., Nakagawa, H., Ishino, K., Yano, S., Nawarathna, B., Yasuda, H., Watanabe, Y., and Hasegawa, K. (2006). Filed investigation of disasters in sri lankan rivers caused by sumatra earthquake tsunami. *Annual Journal of Hydrulics Engineering, JSCE, 50*, (in Jananease with English Abstract).

Tsuji, Y., Yanuma, T., Murata, I., and Fujiwara, C. (1991). Tsunami ascending in rivers as an undular bore. *Natural Hazards 4*, 257–266.

Yasuda, H. and Watanabe, Y. (2005). Numerical study on the propagation of tsunami in rivers. *Annual Journal of Hydrulics Engineering, JSCE, 49*, 1327–1332 (in Jananease with English Abstract).

Yasuda, H., Watanabe Y., and Fujima K. (2004). Report on river-runup of tsunami generated by the tokachi-oki earthquake on 26 september, 2003. *Journal of Hydraulics, Coastal and Environment Engineering, JSCE*, (No.768/II–68), 209–218 (in Jananease with English Abstract).

Yasuda, H., Yamada, T., and Goto, C. (2003). Experimental and numerical study on hydraulic bore generated by gate-operation. *Journal of Hydraulics, Coastal and Environment Engineering, JSCE*, (No.733/II– 63), 89–105 (in Jananease with English Abstract).

Copyright © 2006 Taylor & Francis Group plc, London, UK

Analytical solutions of laminar and turbulent dam break wave

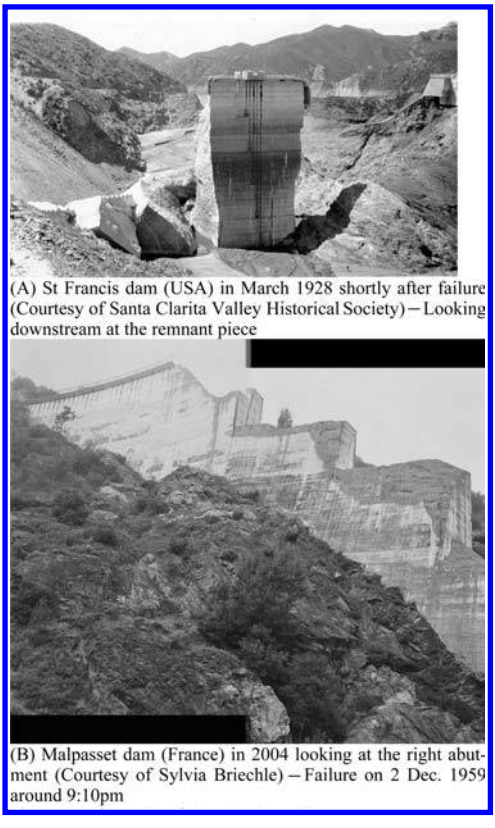
H. Chanson
Civil Engineering, The University of Queensland, Brisbane, Australia

ABSTRACT: Modern predictions of dam break wave rely often on numerical predictions validated with limited data sets. Basic theoretical studies were rare during the past decades. Herein simple solutions of the dam break wave are developed using the Saint-Venant equations for an instantaneous dam break with a semi-infinite reservoir in a wide rectangular channel initially dry. New analytical equations are obtained for both turbulent flow and laminar flow motion on horizontal and sloping inverts with non-constant friction factor. The results are validated by successful comparisons between theoretical results and several experimental data sets. The theoretical developments yield simple explicit analytical expressions of the dam break wave with flow resistance. The results compare well with experimental data and more advanced theoretical solutions. The developments are simple, yielding nice pedagogical applications of the method of characteristics for horizontal and sloping channels. These analytical solutions may be used to validate numerical solutions, while the simplicity of the equations allows some extension to more complex fluid flows (e.g. non-Newtonian fluids).

1 INTRODUCTION

Dam break waves have been responsible for numerous losses of life (e.g. Fig. 1). Figure 1 illustrates two tragic accidents. Related situations include flash flood runoff in ephemeral streams, debris flow surges and tsunami runup on dry coastal plains. In all cases, the surge front is a sudden discontinuity characterised by extremely rapid variations of flow depth and velocity. Dam failures motivated basic studies on dam break wave, including the milestone contribution by Ritter (1892) following the South Fork (Johnstown) dam disaster (USA, 1889). Physical modelling of dam break wave is relatively limited despite a few basic experiments (Table 1). In retrospect, the experiments of Schoklitsch (1917) were well ahead of their time, and demonstrated that Armin von Schoklitsch (1888–1968) had a solid understanding of both physical modelling and dam break processes.

For the last 40 years, there have been substantial efforts in dam break research, in particular with the European programs CADAM and IMPACT, and some American programs. These efforts were associated with the development of numerous numerical models and a few physical model studies. But, at a few exceptions, there has been no new theoretical developments since the basic works of Dressler (1952) and Whitham (1955) for horizontal channel and Hunt (1982,1984) for sloping channel. There have been also contradictory arguments on flow fundamentals. For example, some measurements highlighted a boundary layer region in the surging wave leading edge



(A) St Francis dam (USA) in March 1928 shortly after failure (Courtesy of Santa Clarita Valley Historical Society) – Looking downstream at the remnant piece

(B) Malpasset dam (France) in 2004 looking at the right abutment (Courtesy of Sylvia Briechle) – Failure on 2 Dec. 1959 around 9:10pm

Figure 1. Photographs of dam break accidents.

Copyright © 2006 Taylor & Francis Group plc, London, UK

Table 1. Experimental studies of dam break wave.

Reference	Slope deg.	Experimental configuration
Turbulent flows		
Schoklitsch (1917)	0	$D \leq 0.25$ m, $W = 0.6$ m $D \leq 1$ m, $W = 1.3$ m
Dressler (1954)	0	$D = 0.055$ to 0.22 m, $W = 0.225$ m Smooth invert, Sand paper, Slats
Cavaillé (1965)	0	$L = 18$ m, $W = 0.25$ m $D = 0.115$ to 0.23 m, Smooth invert $D = 0.23$ m, Rough invert
Montuori (1965)	0.06	Casino I powerplant raceway $L = 13.6$ km, $W = 1.95$ m
Estrade (1967)	0	$L = 13.65$ m, $W = 0.50$ m $D = 0.2$ & 0.4 m, Smooth & Mortar $L = 0.70$ m, $W = 0.25$ m $D = 0.3$ m, Smooth & Rough invert
Lauber (1997)	0	$L < 3.6$ m, $W = 0.5$ m, $D < 0.6$ m Smooth PVC invert
Laminar flows		
Debiane (2000)	0	$L < 0.66$ m, $W = 0.3$ m, $D = 0.055$ m Glucose syrups ($12 \leq \mu \leq 170$ Pa.s)
Thixotropic flows		
Chanson et al. (2006)	15	$L = 2$ m, $W = 0.34$ m, $D < 0.08$ m Bentonite suspensions.

*D: initial reservoir height; L: channel length; W: channel width.

(e.g. Mano 1984, Davies 1988, Fujima and Shuto 1990, Chanson 2005c) while others obtained quasi-ideal vertical velocity distributions (Estrade 1967, Wang 2002, Jensen et al. 2003). Most studies were restricted to Newtonian fluids, but a few (e.g. Piau 1996, Chanson et al. 2006), while air entrainment at the shock leading edge was nearly always ignored (Chanson 2004a).

This study describes simple analytical solutions for instantaneous dam break wave based upon the method of characteristics. The solutions are developed for initially-dry horizontal and sloping channels with either laminar or turbulent motion assuming non-constant friction coefficient. Results are compared with several data sets obtained in large-size facilities. It is the aim of this work to provide simple explicit solutions of dam break wave problems that are easily understood by students, young researchers and professionals.

2 DAM BREAK WAVE ON A HORIZONTAL CHANNEL

2.1 *Presentation*

A dam break wave is the flow resulting from a sudden release of a mass of fluid in a channel. For one-dimensional applications, the continuity and momentum equations yield the Saint-Venant equations:

$$\frac{\partial d}{\partial t} + \frac{A}{B}\frac{\partial V}{\partial x} + V\frac{\partial d}{\partial x} + \frac{V}{B} * \left(\frac{\partial A}{\partial x}\right)_{d=constant} = 0 \quad (1)$$

$$\frac{\partial V}{\partial t} + V\frac{\partial V}{\partial x} + g\frac{\partial d}{\partial x} + g\,(S_f - S_o) = 0 \quad (2)$$

where d is the water depth, V is the flow velocity, t is the time, x is the horizontal co-ordinate with $x = 0$ at the dam, S_o is the bed slope ($S_o = \sin\theta$), θ is the angle between invert and horizontal with $\theta > 0$ for downward slopes, and S_f is the friction slope (Liggett 1994, Viollet et al. 2002, Chanson 2004b).

The Saint-Venant equations cannot be solved analytically usually because of non-linear terms that include the friction slope:

$$S_f = \frac{f}{2}\frac{V^2}{g\,D_H} \quad (3)$$

where D_H is the hydraulic diameter and f is the Darcy-Weisbach friction factor that is a non linear function of Reynolds number and relative roughness.

For a prismatic rectangular channel, Equations (1) and (2) yield:

$$\frac{\partial d}{\partial t} + \frac{\partial (d\,V)}{\partial x} = 0 \quad (4)$$

$$\frac{\partial V}{\partial t} + V\frac{\partial V}{\partial x} + g\frac{\partial d}{\partial x} + \frac{f}{2}\frac{V^2}{D_H} = g\,S_o \quad (5)$$

2.1.1 *Ideal fluid flow solution*

For a frictionless dam break in a wide horizontal channel, the analytical solution of Equations (4) and (5) yields Ritter solution (Ritter 1892):

$$U = 2\sqrt{g\,D} \quad (6)$$

$$\frac{x}{t\sqrt{g\,D}} = 2 - 3\sqrt{\frac{d}{D}} \quad (7)$$

where U is the wave front celerity (Fig. 2). Equation (7) was first derived by Barré de Saint Venant (1871).

Equations (6) and (7) give the wave front celerity and instantaneous free-surface profile at any instant $t > 0$. The flow velocity everywhere may be derived from the method of characteristics.

2.1.2 *Real fluid flow solution*

Let us consider an instantaneous dam break in a rectangular, prismatic channel with bed friction and for a semi-infinite reservoir. The turbulent dam break flow

Copyright © 2006 Taylor & Francis Group plc, London, UK

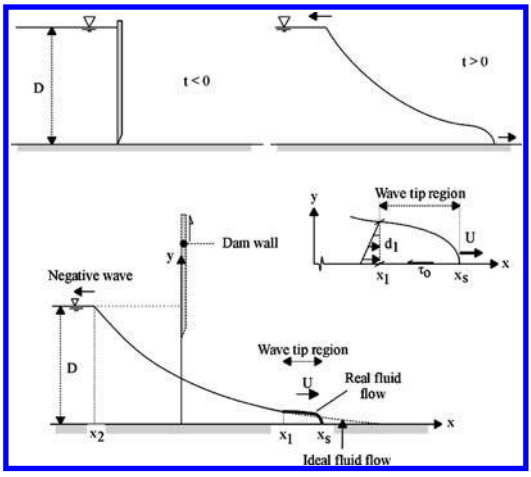


Figure 2. Sketch of dam break wave in a horizontal channel.

is analysed as an ideal-fluid flow region behind a flow resistance-dominated tip zone (Fig. 2). Whitham (1955) introduced this conceptual approach that was used later by other researchers (e.g. Piau 1996, Debiane 2000), but these mathematical developments differ from the present simple solution.

In the wave tip region ($x_1 \leq x \leq x_s$, Fig. 2), the flow velocity does not vary rapidly in the wave tip zone (Dressler 1954, Estrade 1967, Liem and Kongeter 1999). If the flow resistance is dominant, and the acceleration and inertial terms are small, the dynamic wave equation (Eq. (5)) may be reduced into a diffusive wave equation. Assuming that the flow velocity in the tip region is about the wave front celerity U, Equation (5) yields:

$$\frac{\partial d}{\partial x} + \frac{f}{8}\frac{U^2}{g\,d} = 0 \qquad \text{Wave tip region} \qquad (8)$$

In the ideal fluid flow region behind the friction-dominated tip region, Equations (4) and (5) are used with $f = 0$.

Chanson (2005a,b) solved analytically Equations (4), (5) and (8) assuming a constant Darcy friction factor in the wave tip region. In the following paragraphs, the method will be extended to non-constant friction factor.

The solutions involve the conservation of mass. That is, the mass of fluid in motion ($x_2 \leq x \leq x_s$) must equal the initial mass of fluid at rest ($x_2 \leq x \leq 0$):

$$\int_{x_2}^{x_s} d\,dx = -x_2\,D \qquad \text{at any time t} \qquad (9)$$

In Equation (9), right handside term, the negative sign indicates that the negative wave propagates upstream (Fig. 2) and that $x_2 < 0$.

2.2 *Solution for turbulent flow motion ($S_o = 0$)*

For turbulent motion, the flow resistance may be approximated by the Altsul formula first proposed in 1952:

$$f = 0.1\left(1.46\frac{k_s}{D_H} + \frac{100}{Re}\right)^{1/4} \qquad (10a)$$

where k_s is the equivalent sand roughness height, Re is the Reynolds number ($Re = \rho V D_H/\mu$), and ρ and μ are the fluid density and dynamic viscosity respectively. Equation (10) is a simplified expression that satisfies the Moody diagram and which may be used to initialise the calculations with the Colebrook-White formula (Idelchik 1969, Chanson 2004b).

Assuming that Equation (10) holds in unsteady flows, and for a wide channel (i.e. $D_H \approx 4\,d$), it may be rewritten as:

$$f = \frac{1}{\left(\frac{d}{D}\right)^{1/4}} G^{1/4} \qquad (10b)$$

where the dimensionless term G equals:

$$G = 3.65\text{ E-}5\,\frac{k_s}{D} + \frac{2.5\text{ E-}3}{Re_D\,\frac{U}{\sqrt{g\,D}}} \qquad (11)$$

and $Re_D = \rho\sqrt{g\,D^3}/\mu$ is a dimensionless Reynolds number defined in terms of the initial reservoir height D and fluid properties.

The integration of Equation (9) gives the shape of the wave front:

$$\frac{d}{D} = \left(\frac{9}{32}G^{1/4}\left(\frac{U}{\sqrt{g\,D}}\right)^2\frac{x_s - x}{D}\right)^{4/9} \qquad \text{Wave tip region} \qquad (12)$$

for turbulent dam break wave.

Combining Equations (4), (5), (8), (9) and (12), the flow properties at the transition between the wave tip and ideal-fluid regions are:

$$\frac{d_1}{D} = \left(\frac{9}{32}G^{1/4}\left(\frac{U}{\sqrt{g\,D}}\right)^2\frac{x_s - x_1}{D}\right)^{4/9} \qquad (13)$$

$$\frac{x_1}{t\sqrt{g\,D}} = \left(\frac{3}{2}\frac{U}{\sqrt{g\,D}} - 1\right) \qquad (14)$$

Copyright © 2006 Taylor & Francis Group plc, London, UK

The conservation of mass (Eq. (9)) yields an explicit relationship between the wave celerity U and time t:

$$\frac{\frac{32}{13}\left(1 - \frac{1}{2}\frac{U}{\sqrt{g\,D}}\right)^{7/2}}{G^{1/4}\left(\frac{U}{\sqrt{g\,D}}\right)^{2}} = \sqrt{\frac{g}{D}}\,t \qquad (15)$$

as well as the location of the wave leading edge:

$$\frac{x_s}{D} = \left(\frac{3}{2}\frac{U}{\sqrt{g\,D}} - 1\right)\sqrt{\frac{g}{D}}\,t + \frac{32}{9}\frac{1}{G^{1/4}\left(\frac{U}{\sqrt{g\,D}}\right)^{2}}\left(1 - \frac{1}{2}\frac{U}{\sqrt{g\,D}}\right)^{9/2} \qquad (16)$$

The instantaneous free-surface profile is then:

$$\frac{d}{D} = 1 \qquad x \le x_2 \qquad (17a)$$

$$\frac{d}{D} = \frac{1}{9}\left(2 - \frac{x}{t\sqrt{g\,D}}\right)^{2} \qquad x_2 \le x \le x_1 \qquad (17b)$$

$$\frac{d}{D} = \left(\frac{9}{32}G^{1/4}\left(\frac{U}{\sqrt{g\,D}}\right)^{2}\frac{x_s - x}{D}\right)^{4/9} \qquad x_1 \le x \le x_s \qquad (17c)$$

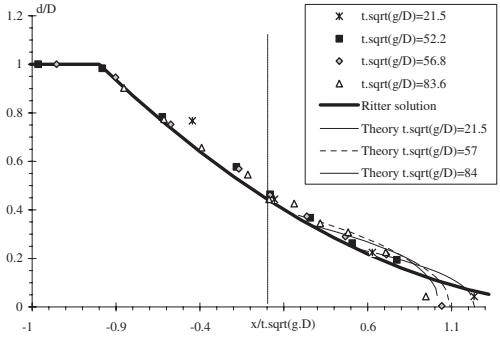
$$\frac{d}{D} = 0 \qquad x_s \le x \qquad (17d)$$

where G is defined in Equation (11).

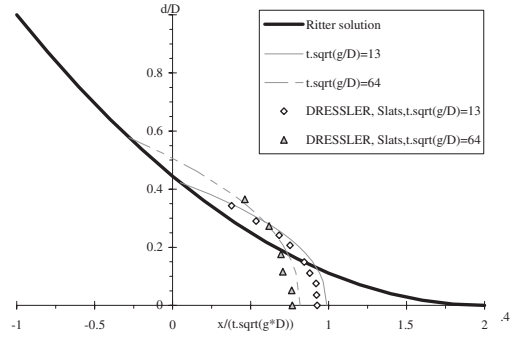
Equation (15) gives the wave front celerity at any instant t (t > 0), Equations (16) and (17) provide the entire free-surface profile, and the flow velocity may be deduced everywhere.

The analytical solution was compared systematically with several experimental studies (Table 1). Figure 3 shows some examples illustrating the good agreement between theory and experiments. Figure 3 shows instantaneous free-surface profiles for different types of invert and different times from dam break. The comparative analysis suggested that the results were sensitive to the choice of the equivalent sand roughness height k_s and that its selection must be based upon a match with instantaneous free-surface profiles. Alternate comparisons with wave front celerity or location data are approximate and often unsuitable.

Present results were also compared successfully with the analytical solutions of Dressler (1952), Whitham (1954) and Chanson (2005b). The differences were small and much smaller than experimental uncertainties.



(A) Experiments of Cavaillé (1965) with smooth invert



(B) Experiments of Dressler (1954) with slats - Calculations assuming $k_s/D = 0.2$

Figure 3. Instantaneous free-surface profiles: comparison between the present theory and experiments (turbulent flow motion).

2.3 *Solution for laminar flow motion ($S_o = 0$)*

In very viscous fluids, the flow motion is laminar and the resistance must be estimated accordingly. Some researchers argued that the flow resistance in unsteady flows may differ from classical steady flow estimates and they suggested that the friction factor may be estimated as: $f = \alpha\,64/Re$ where α is a correction coefficient and $\alpha = 1$ for steady flows (e.g. Aguirre-Pe et al. 1995, Debiane 2000). For a wide channel (i.e. $D_H \approx 4\,d$), the Darcy friction factor in the wave tip region becomes:

$$f = \frac{16\,\alpha}{Re_D\,\frac{U}{\sqrt{g\,D}}\,\frac{d}{D}} \qquad (18)$$

The integration of Equation (8) yields the shape of wave tip region for a laminar flow motion:

$$\frac{d}{D} = \sqrt[3]{6\,\alpha\,\frac{\mu\,U}{\rho\,g\,D^2}\,\frac{x_s - x}{D}} \qquad (19)$$

Copyright © 2006 Taylor & Francis Group plc, London, UK

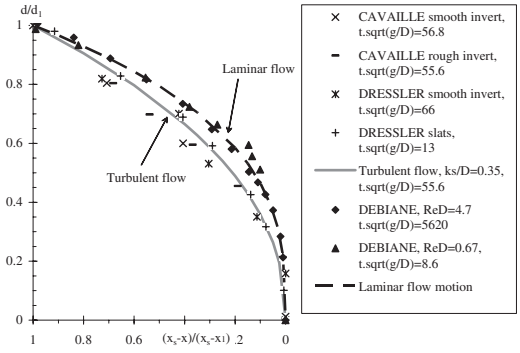


Figure 4. Dimensionless free-surface profiles in the wave tip region – Comparison between Equations (12) and (19), and experimental data (Laminar flow: Debiane 2000, Turbulent flow: Dressler 1954, Cavaillé 1965).

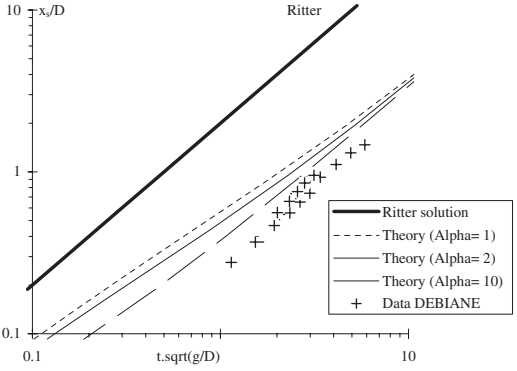


Figure 5. Dimensionless wave front location in laminar dam break flow motion – Comparison between Equations (21), ideal fluid flow solution and experiments (Debiane 2000).

Equation (19) is compared with experimental data and with Equation (12) in Figure 4. Equation (19) was found to be in qualitative agreement with experimental data by Tinney and Bassett (1961), Aguirre-Pe et al. (1995) and Debiane (2000), and the analytical solution of Hunt (1994).

Figure 4 presents the dimensionless water depth d/d_1 as function of the dimensionless distance $(x_s - x)/(x_s - x_1)$ where the subscripts s and 1 refer respectively to the wave leading edge and to the transition between ideal fluid and wave tip regions. Note the good agreement between Equations (12) and (19) and their corresponding experimental data. The results suggest further that the wave front is comparatively steeper in a laminar dam break wave than in turbulent flow motion.

For a rectangular horizontal channel, the integration of the continuity equation within the boundary conditions gives a simple expression of the wave front celerity:

$$\frac{1}{8\,\alpha}\,Re_D\,\frac{\left(1 - \frac{1}{2}\frac{U}{\sqrt{g\,D}}\right)^5}{\frac{U}{\sqrt{g\,D}}} = \sqrt{\frac{g}{D}}\,t \qquad (20)$$

while the location of the wave leading edge is:

$$\frac{x_s}{D} = \left(\frac{3}{2}\frac{U}{\sqrt{g\,D}} - 1\right)\sqrt{\frac{g}{D}}\,t + \frac{1}{6\,\alpha}\,\frac{Re_D}{\frac{U}{\sqrt{g\,D}}}\left(1 - \frac{1}{2}\frac{U}{\sqrt{g\,D}}\right)^6 \qquad (21)$$

The instantaneous free-surface profile is:

$$\frac{d}{D} = 1 \qquad x \le x_2 \qquad (22a)$$

$$\frac{d}{D} = \frac{1}{9}\left(2 - \frac{x}{t\sqrt{g\,D}}\right)^2 \qquad x_2 \le x \le x_1 \qquad (22b)$$

$$\frac{d}{D} = \sqrt[3]{6\,\alpha\,\frac{\mu\,U}{\rho\,g\,D^2}\,\frac{x_s - x}{D}} \qquad x_1 \le x \le x_s \qquad (22c)$$

$$\frac{d}{D} = 0 \qquad x_s \le x \qquad (22d)$$

The characteristic locations x_1 and x_2 are given by:

$$\frac{x_1}{\sqrt{g\,D}\,t} = \left(\frac{3}{2}\frac{U}{\sqrt{g\,D}} - 1\right) \qquad (23)$$

$$\frac{x_2}{t\sqrt{g\,D}} = -1 \qquad (24)$$

A comparison with experimental results is restricted by a lack of detailed measurements. Debiane (2000) presented a rare set of experimental data performed in a 3 m long 0.3 m wide channel using glucose-syrup solutions of dynamic viscosities between 12 to 170 Pa.s. Figures 4 and 5 show some comparison between theory and experiments during the early stages of the dam break. Figure 5 presents a comparison in terms of dimensionless wave front location in horizontal channel. Experimental data are compared with Equation (21) for three values of α and with an ideal dam break (Ritter solution).

Experiments with very viscous solutions showed a trend similar to theoretical calculations (Present study, Piau and Debiane 2005) (Fig. 4). But the data gave consistently a slower wave front propagation as observed in Figure 5. Debiane experienced some experimental difficulties (Debiane 2000, pp. 161–163). The gate opening was relatively slow and could not be considered to be an instantaneous dam break. Some fluid

Copyright © 2006 Taylor & Francis Group plc, London, UK

remained attached to the gate while other portions were projected away. Sidewall effects were also observed for the most viscous solutions ($\mu = 170$ Pa.s) including some fluid crystallisation next to the walls at the shock front. Debiane's comments underlined the difficulties associated with physical modelling, but his advice is nonetheless useful for future experiments.

3 DAM BREAK WAVE ON A SLOPING CHANNEL

3.1 *Presentation*

The above development were obtained for a horizontal channel ($S_o = 0$). They may be extended to situations with some initial flow motion and to sloping invert. The former development was discussed by Chanson (2005a) and the latter case is discussed below.

For an ideal fluid flow, the friction slope is zero and Ritter solution may be extended using a method of superposition (Peregrine and Williams 2001, Chanson 2005a). For a mild, constant slope, the solution of the Saint Venant equations is:

$$\frac{d}{D} = \frac{1}{9}\left(2 + \frac{1}{2}\sqrt{\frac{g}{D}}\,S_o\,t - \frac{x}{t\sqrt{g\,D}}\right)^2 \qquad -1 \leq \frac{x}{t\sqrt{g\,D}} \leq 2 + \frac{1}{2}\,S_o\sqrt{\frac{g}{D}}\,t \tag{25}$$

$$\frac{V}{\sqrt{g\,D}} = \frac{2}{3}\left(1 + S_o\sqrt{\frac{g}{D}}t + \frac{x}{t\sqrt{g\,D}}\right) \qquad -1 \leq \frac{x}{t\sqrt{g\,D}} \leq 2 + \frac{1}{2}\,S_o\sqrt{\frac{g}{D}}\,t \tag{26}$$

where the bed slope S_o is positive for a downwards lope. The celerity of the wave leading edge is:

$$\frac{U}{\sqrt{g\,D}} = 2 + S_o\sqrt{\frac{g}{D}}\,t \tag{27}$$

For a channel inclined upwards (e.g. beach face), the wave front stops ($U = 0$) at: $t = -2\sqrt{D/g}S_o$.

3.2 *Solution for turbulent flow motion*

Considering a turbulent flow down a constant slope, the momentum equation in the wave tip region becomes:

$$\frac{\partial d}{\partial x} + \frac{f}{8}\frac{U^2}{g\,d} = S_o \qquad \text{Wave tip region} \tag{28}$$

where the Darcy friction factor f satisfies Equation (10). The complete integration yields a complicated

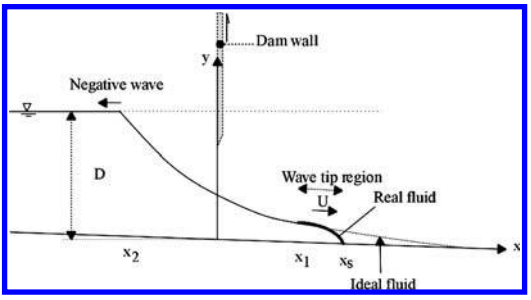


Figure 6. Definition sketch of dam break wave in a sloping channel.

result that is presented in the Appendix. A Taylor series expansion of the solution gives the earlier result:

$$\frac{d}{D} = \left(\frac{9}{32}\,G^{1/4}\left(\frac{U}{\sqrt{g\,D}}\right)^2\frac{x_s - x}{D}\right)^{4/9} \qquad \text{Wave tip region} \tag{12}$$

where the dimensionless term G is:

$$G = 3.65\text{ E-}5\,\frac{k_s}{D} + \frac{2.5\text{ E-}3}{Re_D\,\frac{U}{\sqrt{g\,D}}} \tag{11}$$

and $Re_D = \rho\sqrt{g\,D^3}/\mu$. Equation (12) implies that both acceleration, inertial and gravity terms are small in the wave tip region. The assumption is valid on mild slope and more generally for $S_f \gg S_o$. Equation (12) was successfully compared with field observations in the Casino I powerplant tunnel by Montuori(1965).

Using Equation (12), the integration of the conservation of mass (Eq. (9)) yields an explicit relationship between the wave front celerity U and the time since dam break t:

$$\frac{32}{13}\frac{\left(1 + \frac{1}{2}\sqrt{\frac{g}{D}}\,S_o\,t - \frac{1}{2}\frac{U}{\sqrt{g\,D}}\right)^{7/2}}{G^{1/4}\left(\frac{U}{\sqrt{g\,D}}\right)^2} = t\sqrt{\frac{g}{D}} \tag{29}$$

while the location of the wave front is:

$$\frac{x_s}{D} = \left(\frac{3}{2}\frac{U}{\sqrt{g\,D}} - \sqrt{\frac{g}{D}}\,S_o\,t - 1\right)\sqrt{\frac{g}{D}}\,t + \frac{32}{9}\frac{\left(1 + \frac{1}{2}\sqrt{\frac{g}{D}}\,S_o - \frac{1}{2}\frac{U}{\sqrt{g\,D}}\right)^{9/2}}{G^{1/4}\left(\frac{U}{\sqrt{g\,D}}\right)^2} \tag{30}$$

Copyright © 2006 Taylor & Francis Group plc, London, UK

The instantaneous free-surface profile at any instant $t > 0$ is:

$$\frac{d}{D} = 1 \qquad x \le x_2 \quad (31a)$$

$$\frac{d}{D} = \frac{1}{9}\left(2 - \frac{x}{t\sqrt{g\,D}}\right)^2 \qquad x_2 \le x \le x_1 \quad (31b)$$

$$\frac{d}{D} = \left(\frac{9}{32} G^{1/4} \left(\frac{U}{\sqrt{g\,D}}\right)^2 \frac{x_s - x}{D}\right)^{4/9} \qquad x_1 \le x \le x_s \quad (31c)$$

$$\frac{d}{D} = 0 \qquad x_s \le x \quad (31d)$$

while the characteristic location x_1 satisfies:

$$\frac{x_1}{D} = \left(\frac{3}{2}\frac{U}{\sqrt{g\,D}} - \sqrt{\frac{g}{D}} S_o\, t - 1\right)\sqrt{\frac{g}{D}}\, t \quad (32)$$

Equations (29), (30), (31) and (32) define the entire free-surface at a given instant. Note that, in Equation (29), the time t appears in both right and left handside terms. Equation (29) is hence non-linear.

3.3 *Solution for laminar flow motion*

The same reasoning may apply to a laminar flow motion. The exact solution in terms of wave front celerity is:

$$\frac{1}{8\,\alpha}\frac{\rho\sqrt{g\,D^3}}{\mu}\frac{\left(1 + \frac{1}{2}\sqrt{\frac{g}{D}} S_o\, t - \frac{1}{2}\frac{U}{\sqrt{g\,D}}\right)^5}{\frac{U}{\sqrt{g\,D}}} = \sqrt{\frac{g}{D}}\, t \quad (33)$$

The wave front location is given by:

$$\frac{x_s}{D} = \left(\frac{3}{2}\frac{U}{\sqrt{g\,D}} - \sqrt{\frac{g}{D}} S_o\, t - 1\right)\sqrt{\frac{g}{D}}\, t + \frac{\frac{4}{f}}{\frac{U^2}{g\,D}}\left(1 + \frac{1}{2}\sqrt{\frac{g}{D}} S_o\, t - \frac{1}{2}\frac{U}{\sqrt{g\,D}}\right)^4 \quad (34)$$

The instantaneous free-surface equations are:

$$\frac{d}{D} = 1 \qquad x \le x_2 \quad (35a)$$

$$\frac{d}{D} = \frac{1}{9}\left(2 + \frac{1}{2}\sqrt{\frac{g}{D}} S_o\, t - \frac{x}{\sqrt{g\,D}\,t}\right)^2 \qquad x_2 \le x \le x_1 \quad (35b)$$

$$\frac{d}{D} = \sqrt[3]{6\,\alpha \frac{\mu\, U}{\rho\, g\, D^2}\frac{x_s - x}{D}} \qquad x_1 \le x \le x_s \quad (35c)$$

$$\frac{d}{D} = 0 \qquad x_s \le x \quad (35d)$$

The location of the transition between ideal fluid and wave tip regions is:

$$\frac{x_1}{D} = \frac{3}{2}\frac{U}{\sqrt{g\,D}} - S_o\sqrt{\frac{g}{D}}\, t - 1 \quad (36)$$

Note also that the expression of the wave front celerity (Eq. (33)) is a non-linear equation.

3.4 *Remarks*

The writer was alerted that Takahashi (1991) and Toro (2001) presented some related developments for dam break wave down a sloping chute.

4 DISCUSSION

The present theoretical solutions are based upon a few key assumptions. These include (a) $V(x,t) = U(t)$ in the wave tip region and (b) some discontinuity in terms of $\partial d/\partial x$, $\partial V/\partial x$ and bed shear stress at the transition between wave tip and ideal fluid flow regions (i.e. $x = x_1$). Turbulent flow data tended to support the first approximation (a). For example, the data of Estrade (1967), Lauber (1997) and Liem and Kongeter (1999). The experimental results showed little longitudinal variations in velocity in the wave tip region. Further the comparisons between present diffusive wave solutions and experimental results were successful for a fairly wide range of experimental data obtained independently (Fig. 4). Such comparisons constitute a solid validation. Whitham (1955) and Dressler (1952) produced two very different analytical solutions with and without a discontinuity at the transition between ideal flow region and wave tip region (e.g. Fig. 7) Figure 7 illustrates differences in longitudinal bed shear stress distributions between the different theoretical models. Yet all theories gave close results in terms of wave front celerity and instantaneous free-surface profiles and good agreement with experimental data. All these suggest little effects of some discontinuity at $x = x_1$, although the physics of a constant Darcy friction factor is questionable!

Copyright © 2006 Taylor & Francis Group plc, London, UK

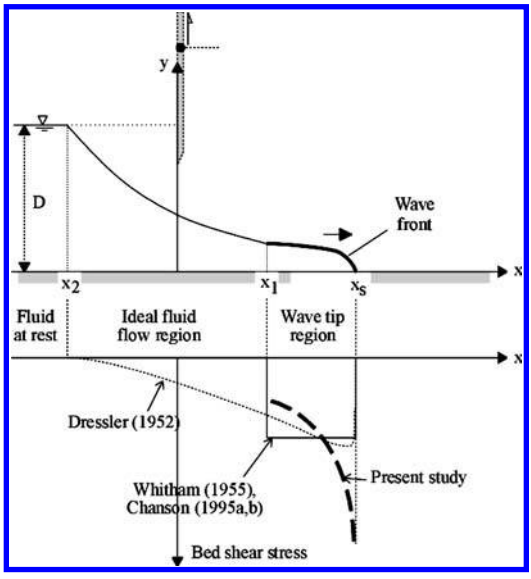


Figure 7. Sketch of longitudinal bed shear stress in turbulent dam break wave for the theoretical models of Dressler (1952), Whitham (1955), Chanson (2005a,b) and present study.

Ultimately, a practical question is: which is the best theoretical model for turbulent dam break wave? Dressler's (1952) method is robust, but the treatment of the wave leading edge is approximate: "*To handle the tip region accurately, some type of boundary-layer technique would be necessary* […] *but no results are yet available.* […] *In the absence of more satisfactory boundary layer results, we will apply* […] *approximate considerations to obtain some data about the wavefront*" (Dressler 1952, pp. 223–224). Whitham's (1955) method is also a robust technique, but the results are asymptotic solutions. Both the model of Chanson (2005a,b) with constant friction factor and present results provide complete explicit solutions of the entire flow field. The velocity field and water depths are explicitly calculated everywhere. Note that the methods of Dressler, Whitham and Chanson (2005a,b) assume a constant friction factor, and the results are sensitive to the selection of the flow resistance coefficient value. In contrast, the present method requires only the selection of an equivalent roughness height. In practice, the selection of a suitable analytical model is linked with its main application. For example, for pedagogical purposes, the writer believes that Chanson's (2005a,b) model based upon a constant friction coefficient in the wave tip region is nicely suited to introductory courses and young professionals because of the explicit and linear nature of the results.

The new developments shown herein present substantial advantages over previous works. The theoretical results yield simple explicit analytical expressions for real-fluid flows that compares well with experimental data and more advanced theoretical solutions. They cover a wide range of applications that include linear and turbulent flows, horizontal and sloping channels. The proposed solutions are simple pedagogical applications, linking together the ideal fluid flow equations yielding Ritter solution, with a diffusive wave equation for the wave tip region. These explicit results may be used to validate numerical solutions of the method of characteristics applied to dam break wave problem. The development may be also extended to a wider range of practical applications including non-Newtonian fluids (e.g. Chanson and Coussot 2005).

5 SUMMARY AND CONCLUSION

New analytical solutions of dam break wave with bed friction are developed for turbulent and laminar flow motion with non constant friction factors. For each development, the dam break wave flow is analysed as a wave tip region where flow resistance is dominant, followed by an ideal-fluid flow region where inertial effects and gravity effects are dominant. In horizontal channels, turbulent flow solutions were validated by successful comparisons between several experimental data sets obtained in large-size facilities and theoretical results in terms of instantaneous free-surface profiles, wave front location and wave front celerity. The former comparison with instantaneous free-surface data is regarded as the most accurate technique to estimate the flow resistance and relative roughness, hence the best validation technique. A new analytical solution of dam break wave with laminar flow motion is also presented. The shape of the wave front compared well with experimental observations. The results were further extended to sloping channels.

These simple theoretical developments yield explicit, non-linear expressions that compare well with experimental data. The simplicity of the equations will allow some extension of the method to more complex geometries, flow situations and broader applications, including non-Newtonian fluids, sheet flow and beach swash.

It must be acknowledged that the present approach is limited to semi-infinite reservoir, rectangular channel and quasi-instantaneous dam break. Further experimental data with very viscous fluids and non-Newtonian fluid flows are also needed.

6 APPENDIX

Let us consider an instantaneous dam break wave in an initially dry inclined channel. In the

Copyright © 2006 Taylor & Francis Group plc, London, UK

friction-dominated tip region, the dynamic wave equation becomes:

$$\frac{\partial d}{\partial x} + \frac{f}{8}\frac{U^2}{g\,d} = S_o \qquad \text{Wave tip region} \qquad \text{(A-1)}$$

where the Darcy friction factor satisfies the Altsul formula:

$$f = \frac{1}{\left(\frac{d}{D}\right)^{1/4}} G^{1/4} \qquad \text{(A-2)}$$

and the dimensionless term G is:

$$G = 3.65\ \text{E-5}\,\frac{k_s}{D} + \frac{2.5\ \text{E-3}}{Re_D\,\frac{U}{\sqrt{g\,D}}} \qquad \text{(A-3)}$$

Equation (A-1) may be rewritten in dimensionless form as:

$$\frac{\partial d'}{\partial x'} + \frac{X}{d'^{5/4}} = S_o \qquad \text{(A-4)}$$

where $d' = d/D$, $x' = x/D$ and

$$X = \frac{0.1}{8}\left(\frac{1.46}{4}\frac{k_s}{D} + \frac{100}{4}\frac{\nu}{U\,D}\right)^{1/4} \frac{U^2}{g\,D}$$

with $\nu = \mu/\rho$ is the kinematic viscosity.

The boundary conditions are $d' = 0$ at the leading edge ($x' = x'_s$). For a non-zero slope, the exact solution of Equation (A-4) is:

$$S_o\,(x_s' - x') = 0.020034\left(\frac{X}{S_o}\right)^{4/5} - d' - \frac{4}{5}\left(\frac{X}{S_o}\right)^{4/5} \text{Ln}\left(\left(\frac{X}{S_o}\right)^{1/5} - d'^{1/4}\right) - \frac{2\sqrt{2\,(5+\sqrt{5})}}{5}\left(\frac{X}{S_o}\right)^{4/5} \text{ArcTan}\left(\frac{(-1+\sqrt{5})\left(\frac{X}{S_o}\right)^{1/5} + 4\,d'^{1/4}}{\sqrt{2\,(5+\sqrt{5})}\left(\frac{X}{S_o}\right)^{1/5}}\right) - \frac{2\sqrt{10-2\sqrt{5}}}{5}\left(\frac{X}{S_o}\right)^{4/5} \text{ArcTan}\left(\frac{(1+\sqrt{5})\left(\frac{X}{S_o}\right)^{1/5} + 4\,d'^{1/4}}{\sqrt{10-2\sqrt{5}}\left(\frac{X}{S_o}\right)^{1/5}}\right) - \left(\frac{1}{\sqrt{5}} - \frac{1}{5}\right)\left(\frac{X}{S_o}\right)^{4/5} \text{Ln}\left(\left(\frac{X}{S_o}\right)^{2/5} - \frac{-1+\sqrt{5}}{2}\left(\frac{X}{S_o}\right)^{1/5} d'^{1/4} + \sqrt{d'}\right) + \left(\frac{1}{\sqrt{5}} + \frac{1}{5}\right)\left(\frac{X}{S_o}\right)^{4/5} \text{Ln}\left(\left(\frac{X}{S_o}\right)^{2/5} + \frac{1+\sqrt{5}}{2}\left(\frac{X}{S_o}\right)^{1/5} d'^{1/4} + \sqrt{d'}\right) \qquad x_1 \le x \le x_s \qquad \text{(A-5)}$$

REFERENCES

Aguirre-Pe, J., Plachco, F.P., and Quisca, S. (1995). "Tests and Numerical One-Dimensional Modelling of a High-Viscosity Fluid Dam-Break Wave." *Jl of Hyd. Res.*, IAHR, Vol. 33, No. 1, pp. 17–26.

Barré de Saint Venant, A.J.C. (1871). "Théorie et Equations Générales du Mouvement Non Permanent des Eaux Courantes." *Comptes Rendus des séances de l'Académie des Sciences*, Paris, France, Séance 17 July 1871, Vol. 73, pp. 147–154.

Cavaillé, Y. (1965). "Contribution à l'Etude de l'Ecoulement Variable Accompagnant la Vidange Brusque d'une Retenue." *Publ. Scient. et Techn. du Ministère de l'Air*, No. 410, Paris, France, 165 pages.

Chanson, H. (2004a). "Unsteady Air-Water Flow Measurements in Sudden Open Channel Flows." *Experiments in Fluids*, Vol. 37, No. 6, pp. 899–909.

Chanson, H. (2004b). "The Hydraulics of Open Channel Flows: An Introduction." *Butterworth-Heinemann*, Oxford, UK, 2nd edition, 630 pages.

Chanson, H. (2005a). "Applications of the Saint-Venant Equations and Method of Characteristics to the Dam Break Wave Problem." *Report No. CH55/05*, Dept. of Civil Engineering, The University of Queensland, Brisbane, Australia, May, 135 pages.

Chanson, H. (2005b). "Analytical Solution of Dam Break Wave with Flow Resistance. Application to Tsunami Surges." *Proc. 31th Biennial IAHR Congress*, Seoul, Korea, B.H. Jun, S.I. Lee, I.W. Seo and G.W. Choi Editors, Theme D1, Paper 0137, pp. 3341–3353.

Chanson, H. (2005c). "Air-Water and Momentum Exchanges in Unsteady Surging Waters: an Experimental Study." *Experimental Thermal and Fluid Science*, Vol. 30, No. 1, pp. 37–47.

Copyright © 2006 Taylor & Francis Group plc, London, UK

Chanson, H., and Coussot, P. (2005). "Fluid Dynamic Treatment of Thixotropic Debris Flows and Avalanches." *Proc. 31th Biennial IAHR Congress*, Seoul, Korea, B.H. JUN, S.I. LEE, I.W. SEO and G.W. CHOI Editors, Theme D.5, Paper 0039, pp. 5654–5666.

Chanson, H., Jarny, S., and Coussot, P. (2006). "Dam Break Wave of Thixotropic Fluid." *Jl of Hyd. Engrg.*, ASCE, Vol. 132, No. 3, pp. 280–293.

Davies, T.R.H. (1988). "Debris Flow Surges - A Laboratory Investigation." *Mitteilungen der Versuchsanstalt fur Wasserbau, Hydrologie und Glaziologie*, No. 96, ETH-Zurich, Switzerland, 122 pages.

Debiane, K. (2000). "Hydraulique des Ecoulements Laminaires à Surface Libre dans une Canal pour des Milieux Visqueux ou Viscoplastiques: Régimes Uniformes, Graduellement Varié, et Rupture de Barrage." *Ph.D. thesis*, University of Grenoble I, Rheology Laboratory INPG-UJF-CNRS, France, 273 pages.

Dressler, R.F. (1952). "Hydraulic Resistance Effect upon the Dam-Break Functions." *Jl of Research, Natl. Bureau of Standards*, Vol. 49, No. 3, pp. 217–225.

Dressler, R. (1954). "Comparison of Theories and Experiments for the Hydraulic Dam-Break Wave." *Proc. Intl Assoc. of Scientific Hydrology Assemblée Générale*, Rome, Italy, Vol. 3, No. 38, pp. 319–328.

Estrade, J. (1967). "Contribution à l'Etude de la Suppression d'un Barrage. Phase Initiale de l'Ecoulement." *Bulletin de la Direction des Etudes et Recherches*, Series A, Nucléaire, Hydraulique et Thermique, EDF Chatou, France, No. 1, pp. 3–128.

Fujima, K., and Shuto, N. (1990). "Formulation of Frictions Laws for Long Waves on a Smooth Dry Bed." *Coastal Engineering in Japan*, Vol. 33, No. 1, pp. 25–47.

Hunt, B. (1982). "Asymptotic Solution for Dam-Break Problems." *Jl of Hyd. Div.*, Proceedings, ASCE, Vol. 108, No. HY1, pp. 115–126.

Hunt, B. (1984). "Perturbation Solution for Dam Break Floods." *Jl of Hyd. Engrg.*, ASCE, Vol. 110, No. 8, pp. 1058–1071.

Hunt, B. (1994). "Newtonian Fluid Mechanics Treatment of Debris Flows and Avalanches." *Jl of Hyd. Engrg.*, ASCE, Vol. 120, No. 12, pp. 1350–1363.

Idelchik, I.E. (1969). "Mémento des Pertes de Charge." *Eyrolles Editor*, Collection de la direction des études et recherches d'Electricité de France, Paris, France.

Jensen, A., Pedersen, G.K., and Wood, D.J. (2003). "An Experimental Study of Wave Run-up on a Steep Beach." *Jl of Fluid Mech.*, Vol. 486, pp. 166–188.

Lauber, G. (1997). "Experimente zur Talsperrenbruchwelle im glatten geneigten Rechteckkanal." ('Dam Break Wave Experiments in Rectangular Channels.') *Ph.D. thesis*, VAW-ETH, Zürich, Switzerland.

Liem, R., and Kongeter, J. (1999). "Application of High-Speed Digital Image Processing to Experiments on Dam Break Waves." *Proc. CADAM Meeting*, Zaragossa, Spain, pp. 399–411.

Liggett, J.A. (1994). "Fluid Mechanics." *McGraw-Hill*, New York, USA.

Mano, A. (1994). "Boundary Layer Developed near Surging Front." *Coastal Engineering in Japan*, Vol. 37, No. 1, pp. 23–39.

Montuori, C. (1965). "Introduction d'un Débit Constant dans un Canal Vide." *Proc. 11th IAHR Biennial Congress*, Leningrad, Russia, Vol. 3, paper 3.55, pp. 1–7 &9 plates.

Piau, J.M. (1996). "Flow of a Yield Stress Fluid in a Long Domain. Application to Flow on an Inclined Plane." *Jl of Rheology*, Vol. 40, No. 4, pp. 711–723.

Piau, J.M., and Debiane, K. (2005). "Consistometers Rheometry of Power-Law Viscous Fluids." *Jl of Non-Newtonian Fluid Mech.*, Vol. 127, pp. 213–224.

Peregrine, D.H., and Williams, S.M. (2001). "Swash Overtopping a Truncated Plane Beach." *Jl of Fluid Mech.*, Vol. 440, pp. 391–399.

Ritter, A. (1892). "Die Fortpflanzung der Wasserwellen." *Vereine Deutscher Ingenieure Zeitswchrift*, Vol. 36, No. 2, 33, 13 Aug., pp. 947–954 (in German).

Schoklitsch, A. (1917). "Über Dambruchwellen." *Sitzungberichten der Königliche Akademie der Wissenschaften, Vienna*, Vol. 126, Part IIa, pp. 1489–1514.

Takahashi, T. (1991). "Debris Flow." *IAHR Monograph*, Balkema Publ., Rotterdam, The Netherlands.

Tinney, E.R., and Bassett, D.L. (1961). "Terminal Shape of a Shallow Liquid Front." *Jl of Hyd. Div.*, Proceedings, ASCE, Vol. 87, No. HY5, pp. 117–133.

Toro, E.F. (2001). "Shock Capturing Methods for Free-Surface Shallow Flows." *John Wiley*, New York, USA.

Viollet, P.L., Chabard, J.P., Esposito, P., and Laurence, D. (1998). "Mécanique des Fluides Appliquée. Ecoulements Incompressibles dans les Circuits, Canaux et Rivières, autour des Structures et dans l'Environnement." *Presses des Ponts et Chaussées*, Paris, France, 367 pages.

Wang, Z.Y. (2002). "Initiation and Mechanism of Two Phase Debris Flow." *Proc. Conf. on Flood Defence'2002*, Ed. WU et al., Science Press, New York, pp. 1637–1648.

Whitham, G.B. (1955). "The Effects of Hydraulic Resistance in the Dam-Break Problem." *Proc. Roy. Soc. of London*, Ser. A, Vol. 227, pp. 399–407.

Internet resources

"Fluid Mechanics and Hydraulic Engineering of Dam Break Wave. From the Dam Busters to Self-Flowing Concrete Testing." *Internet resource*. (http://www.uq.edu.au/∼e2hchans/dam_brk.html)

Photographs of dam break accidents (http://www.uq.edu.au/∼e2hchans/photo.html)

"Sabo check dams. Mountain protection systems in Japan." *Internet resource*. (http://www.uq.edu.au/∼e2hchans/sabo.html)

Copyright © 2006 Taylor & Francis Group plc, London, UK

Efficient implicit upwind schemes for river flow simulation with or without shocks

J. Burguete, P. Garcia-Navarro, P. Brufau & J. Murillo
Fluid Mechanics, CPS, University of Zaragoza, Spain

ABSTRACT: In this work, first order upwind implicit schemes are considered. The traditional tridiagonal scheme is rewritten as a sum of two bidiagonal schemes in order to produce a simpler method better suited for unsteady transcritical flows. On the other hand, the origin of the instabilities associated to the use of upwind implicit methods for shock propagations is identified and a new stability condition for non-linear problems is proposed. This modification produces a robust, simple and accurate upwind semi-explicit scheme suitable for discontinuous flows with high *CFL* numbers.

The performance of the proposed technique will be shown in the solution of an ideal dam-break test case and in a realistic flood routing problem, where stable and accurate solutions will be presented using *CFL* values up to 100.

1 INTRODUCTION

Implicit schemes are well known for the property of allowing numerical stability in the resolution of partial differential equations in presence of time steps not restricted by the Courant-Friedrichs-Lewy condition. Therefore, they have traditionally been the most attractive methods in CFD for steady or gradually unsteady flows. Computational Hydraulics has been a field of frequent search for accurate and robust implicit schemes. Some research has been recently oriented to the development of new implicit techniques able to deal with transcritical flows in order to overcome deficiencies found in previous implicit methods. The results from the mentioned schemes are however characterized by a limitation in the allowable time step size in cases of unsteady and discontinuous flow. It is usually found that *CFL* values bigger than 3 lead to instabilities in the resolution of moving front waves. This is due to a poor treatment of the linearization of the implicit flux terms, which are often locally evaluated. In this work, first order upwind implicit schemes are considered. The traditional tridiagonal scheme is rewritten as a sum of two bidiagonal schemes in order to produce a simpler method better suited for unsteady transcritical flows. On the other hand, a new stability condition for non-linear problems is used that produces a robust, simple and accurate upwind semi-explicit scheme suitable for discontinuous flows with high *CFL* numbers. The performance of the proposed technique will be shown in the solution of unsteady realistic flood routing and dam-break problems, where stable and accurate solutions will be presented using high *CFL* values.

2 MATHEMATICAL MODEL

We are interested in solving as efficiently as possible 1D hyperbolic systems with source terms. In a general conservative form

$$\frac{\partial \mathbf{u}(x,t)}{\partial t} + \frac{d\mathbf{F}(x,\mathbf{u})}{dx} = \mathbf{H}(x,\mathbf{u}) \tag{1}$$

where $\mathbf{u}$ is the vector of conserved variables, $\mathbf{F}$ the vector of fluxes and $\mathbf{H}$ the vector of source terms. Our interest is led by the numerical modelling of one-dimensional shallow water flows of practical application in Hydraulics such as river flows. In that case

$$\mathbf{u} = \begin{pmatrix} A \\ Q \end{pmatrix}, \quad \mathbf{F} = \begin{pmatrix} Q \\ \frac{Q^2}{A} + gI_1 \end{pmatrix}, \quad \mathbf{H} = \begin{pmatrix} 0 \\ g\left[I_2 + A\left(S_0 - S_f\right)\right] \end{pmatrix}$$

where Q is the discharge, A is the wetted cross section, g is the acceleration of gravity and S_0 is the bed slope. The rest of the terms account for pressure forces and for friction forces, with S_f associated to wall friction and represented by the empirical Manning law (Cunge et al., 1980).

Copyright © 2006 Taylor & Francis Group plc, London, UK

From the equations in conservative form (1), it is possible to pass to an associated non-conservative form

$$\frac{\partial \mathbf{u}(x,t)}{\partial t} + \mathbf{J}(x,\mathbf{u}) \frac{\partial \mathbf{u}(x,t)}{\partial x} = \mathbf{H}'(x,\mathbf{u}) \tag{2}$$

where $\mathbf{J} = \frac{\partial \mathbf{F}}{\partial \mathbf{u}}$ is the Jacobian matrix of the original system and $\mathbf{H}' = \mathbf{H} - \frac{\partial \mathbf{F}}{\partial x}$. In shallow water equations

$$\mathbf{H}' = \begin{pmatrix} 0 \\ gA\left(S_0 - S_f - \frac{dh}{dx} + \frac{1}{B}\frac{dA}{dx}\right) \end{pmatrix}$$

$$\mathbf{J} = \begin{pmatrix} 0 & 1 \\ c^2 - u^2 & 2u \end{pmatrix}$$

with h the depth, $u = Q/A$ the fluid velocity, $c = \sqrt{gA/B}$ the velocity of the infinitesimal surface waves and B the top width.

It is now convenient to develop the characteristic form of the equations given the importance it has for the correct formulation of upwind schemes and boundary conditions. This form is obtained from a diagonalization of the Jacobian in (2). Calling $\mathbf{P}$ and $\mathbf{P}^{-1}$ the matrices that make $\mathbf{J}$ diagonal, and Λ the resulting diagonal matrix

$$\mathbf{J} = \mathbf{P}\Lambda\mathbf{P}^{-1}, \quad \Lambda = \mathbf{P}^{-1}\mathbf{J}\mathbf{P}$$

The matrix Λ is formed by the eigenvalues of $\mathbf{J}$, and $\mathbf{P}$ is constructed with its eigenvectors. Let $\mathbf{w}$ be the set of variables (characteristic variables) that verify

$$d\mathbf{u} = \mathbf{P}d\mathbf{w}, \quad d\mathbf{w} = \mathbf{P}^{-1}d\mathbf{u}$$

Then,

$$\frac{\partial \mathbf{w}(x,t)}{\partial t} + \Lambda(x,\mathbf{w}) \frac{\partial \mathbf{w}(x,t)}{\partial x} = \mathbf{P}^{-1}(x,\mathbf{w})\,\mathbf{H}'(x,\mathbf{w}) \tag{3}$$

In the one-dimensional shallow water model, the above matrices are

$$\mathbf{P} = \begin{pmatrix} 1 & 1 \\ u+c & u-c \end{pmatrix}, \quad \Lambda = \begin{pmatrix} u+c & 0 \\ 0 & u-c \end{pmatrix}$$

3 NUMERICAL SCHEMES

The most common definition of a conservative scheme follows the structure (Toro, 1997, p. 171)

$$\Delta\mathbf{u}_i^n = \Delta t \left[\mathbf{H}_i^* - \frac{1}{\delta x}\left(\mathbf{F}_{i+\frac{1}{2}}^* - \mathbf{F}_{i-\frac{1}{2}}^*\right)\right] \tag{4}$$

where $\mathbf{H}^*$ is the numerical source at cell i and $\mathbf{F}_{i+\frac{1}{2}}^*$ is the numerical flux at cell interface $i+\frac{1}{2}$. They represent a suitable approximation of the true source and flux terms in the equation. Δ will be used for time increment $\Delta f_i^n = f_i^{n+1} - f_i^n$, and δ represents spatial increment $\delta f_{i+\frac{1}{2}} = f_{i+1}^n - f_i^n$. Schemes so defined will be conservative since they cancel the contributions of the flux at the grid interfaces, being the global variation of the conserved variables due only to the source terms and to the fluxes at the boundaries.

A numerical flux $\mathbf{F}_i^T$ can also be defined at the grid nodes (Burguete & García-Navarro, 2001). The difference in this flux between two nodes can be decomposed into parts affecting the two nodes. Schemes so built follow

$$\delta\mathbf{F}_{i+\frac{1}{2}}^T = \mathbf{F}_{i+1}^T - \mathbf{F}_i^T = \delta\mathbf{F}_{i+\frac{1}{2}}^R + \delta\mathbf{F}_{i+\frac{1}{2}}^L$$

$$\Delta\mathbf{u}_i^n = \Delta t \left[\mathbf{H}_i^* - \frac{1}{\delta x}\left(\delta\mathbf{F}_{i+\frac{1}{2}}^R + \delta\mathbf{F}_{i-\frac{1}{2}}^L\right)\right] \tag{5}$$

This also leads to conservative schemes since this form can be shown to be equivalent to (4) (Burguete & García-Navarro, 2001).

In addition, and following evidences from previous works (Glaister, 1988), (Bermúdez & Vázquez-Cendón, 1994), (García-Navarro & Vázquez-Cendón, 2000), (Burguete & García-Navarro, 2001), we consider a non-pointwise contribution of the source terms

$$\mathbf{H}_{i+\frac{1}{2}}^T = \mathbf{H}_{i+\frac{1}{2}}^R + \mathbf{H}_{i+\frac{1}{2}}^L$$

so that the following formulation for the conservative scheme is proposed

$$\Delta\mathbf{u}_i^n = \Delta t \left[\left(\mathbf{H} - \frac{\delta\mathbf{F}}{\delta x}\right)_{i-\frac{1}{2}}^L + \left(\mathbf{H} - \frac{\delta\mathbf{F}}{\delta x}\right)_{i+\frac{1}{2}}^R\right] \tag{6}$$

Conservative schemes can also be derived from the non-conservative form of the equations (2) (Burguete & García-Navarro, 2001). The advantage is that the latter form tends to be simpler to deal with than the conservative form. We need to establish the conditions under which schemes derived in this way are equivalent to the conservative scheme (6) derived from the conservative equations. First of all, the following equality must hold at the discrete level

$$\mathbf{G}_{i+\frac{1}{2}} \equiv \left(\mathbf{H} - \frac{\delta\mathbf{F}}{\delta x}\right)_{i+\frac{1}{2}} = \left(\mathbf{H}' - \mathbf{J}\frac{\delta\mathbf{u}}{\delta x}\right)_{i+\frac{1}{2}} \tag{7}$$

Note that this equality requires a non-pointwise treatment of source terms and is an extension of the

Copyright © 2006 Taylor & Francis Group plc, London, UK

Roe's average (Roe, 1981). In shallow water this average is (García-Navarro & Vázquez-Cendón, 2000)

$$\tilde{u}_{i+\frac{1}{2}} = \frac{Q_{i+1}/\sqrt{A_{i+1}} + Q_i/\sqrt{A_i}}{\sqrt{A_{i+1}} + \sqrt{A_i}}, \quad \tilde{c}_{i+\frac{1}{2}} = \sqrt{g\frac{A_{i+\frac{1}{2}}}{B_{i+\frac{1}{2}}}}$$

From (7) it follows that two equivalent forms of building conservative schemes with non-pointwise source terms are possible (Burguete & García-Navarro, 2001). Defining $\mathbf{G}$ as

$$\mathbf{G}_{i+\frac{1}{2}} \equiv \left(\mathbf{H} - \frac{\delta \mathbf{F}}{\delta x}\right)_{i+\frac{1}{2}} \tag{8}$$

the form (6) is achieved, whereas defining this term like

$$\mathbf{G}_{i+\frac{1}{2}} \equiv \left(\mathbf{H}' - \mathbf{J}\frac{\delta \mathbf{u}}{\delta x}\right)_{i+\frac{1}{2}} \tag{9}$$

with the restriction (7), the non-conservative form of the conservative scheme is derived. In any case

$$\Delta \mathbf{u}_i^n = \Delta t \left(\mathbf{G}_{i-\frac{1}{2}}^L + \mathbf{G}_{i+\frac{1}{2}}^R\right) \tag{10}$$

where the decomposition in left and right parts is to be defined according to every particular numerical scheme.

Conservative schemes based in the characteristic form of the equations are the basis for the wave decomposition of upwind schemes. From (3) it is possible to rewrite

$$\frac{\partial \mathbf{w}}{\partial t} = \mathbf{P}^{-1}\left(\mathbf{H}' - \mathbf{J}\frac{\partial \mathbf{u}}{\partial x}\right) = \mathbf{P}^{-1}\mathbf{G}$$

Then, a discrete wave decomposition into left and right moving contributions can be done (Burguete & García-Navarro, 2001)

$$\left(\mathbf{P}^{-1}\mathbf{G}\right)_{i+\frac{1}{2}} = \left(\Omega^L \mathbf{P}^{-1}\mathbf{G}\right)_{i+\frac{1}{2}} + \left(\Omega^R \mathbf{P}^{-1}\mathbf{G}\right)_{i+\frac{1}{2}}$$

being Ω^L and Ω^R diagonal matrices to be defined in every particular numerical scheme. In order to ensure the conservative character of the scheme, they have to obey

$$\left(\Omega^L + \Omega^R\right)_{i+\frac{1}{2}} = \mathbf{I} \tag{11}$$

Multiplication by $\mathbf{P}$ gives the final form for the discretization in terms of the conserved quantities

$$\Delta \mathbf{u}_i^n = \Delta t\left[\left(\mathbf{P}\Omega^L \mathbf{P}^{-1}\mathbf{G}\right)_{i-\frac{1}{2}} + \left(\mathbf{P}\Omega^R \mathbf{P}^{-1}\mathbf{G}\right)_{i+\frac{1}{2}}\right] \tag{12}$$

Note that this discretization requires again a non-pointwise formulation of the source terms, being equally possible (8) or (9) for $\mathbf{G}$. Both options can be inserted into the general form of the conservative schemes (10) by definition of:

$$\mathbf{G}^{L,R} = \mathbf{P}\Omega^{L,R}\mathbf{P}^{-1}\mathbf{G} \tag{13}$$

3.1 *Tridiagonal upwind scheme*

Upwind schemes are based on the idea of approximating the spatial derivatives by non-centered differences biased in the sense of propagation of information in the physical problem. In order to construct a first order scheme, suitable for left and right moving propagation velocities, the following wave decomposition can be made:

$$\mathbf{F}_i^T = \mathbf{F}_i^{n+\theta}, \quad \delta \mathbf{F}_{i+\frac{1}{2}}^L = \left(\delta \mathbf{F}^+\right)_{i+\frac{1}{2}}^{n+\theta}$$

$$\delta \mathbf{F}_{i+\frac{1}{2}}^R = \left(\delta \mathbf{F}^-\right)_{i+\frac{1}{2}}^{n+\theta}$$

leading to:

$$\Delta \mathbf{u}_i^n = \Delta t\left[\left(\mathbf{G}^+\right)_{i-\frac{1}{2}}^{n+\theta} - \left(\mathbf{G}^-\right)_{i+\frac{1}{2}}^{n+\theta}\right] \tag{14}$$

where $\mathbf{G}^-$, $\delta \mathbf{F}^-$ and $\mathbf{J}^-$ are associated to negative velocities, and $\mathbf{G}^+$, $\partial \mathbf{F}^+$ and $\mathbf{J}^+$ to positive velocities and the notation $f^{n+\theta} = \theta f^{n+1} + (1-\theta) f^n$ is used. From (12), the following wave decomposition is assumed for this scheme in order to select the appropriate influence region in every case.

$$\Omega^L = \Omega^+ = \frac{1}{2}\left[\mathbf{I} + \Lambda^{-1}|\Lambda|\right],$$

$$\Omega^R = \Omega^- = \frac{1}{2}\left[\mathbf{I} - \Lambda^{-1}|\Lambda|\right]$$

$$\mathbf{J}^{\pm} = \mathbf{P}\Omega^{\pm}\mathbf{P}^{-1}\mathbf{J}, \quad \delta \mathbf{F}^{\pm} = \mathbf{P}\Omega^{\pm}\mathbf{P}^{-1}\delta \mathbf{F},$$

$$\mathbf{G}^{\pm} = \mathbf{P}\Omega^{\pm}\mathbf{P}^{-1}\mathbf{G} \tag{15}$$

A linear analysis of the homogeneous equations shows that the stability condition is

$$(1-2\theta)CFL \leq 1 \tag{16}$$

with $CFL = \max|a^k|\Delta t/\delta x$ the Courant-Friedrichs-Lewy (CFL) number and a^k the eigenvalues of the Jacobian, being unconditionally stable if $\theta \geq \frac{1}{2}$. This linear analysis also shows that the scheme is Total variation Diminishing (TVD) if (Burguete & García-Navarro, 2005)

$$CFL \leq \frac{1}{1-\theta} \tag{17}$$

being this condition more restrictive. The scheme is unconditionally TVD if $\theta = 1$.

With non-linear equations this scheme requires to involve $\mathbf{F}^{n+1}$ and $\mathbf{H}^{n+1}$, which represents a difficulty.

Copyright © 2006 Taylor & Francis Group plc, London, UK

In order to avoid this problem, a linearization can be made (Burguete & García-Navarro, 2005).

Using the wave decomposition (15), the conservative scheme in characteristic form (12) can be expressed

$$\theta\frac{\Delta t}{\delta x}\left(\mathbf{J}^{-}\Delta\mathbf{u}\right)^{n}_{i+1}+\left[1-\theta\Delta t\left(\mathbf{K}-\frac{\mathbf{J}^{+}}{\delta x}+\frac{\mathbf{J}^{-}}{\delta x}\right)\right]^{n}_{i}\Delta\mathbf{u}^{n}_{i}$$
$$-\theta\frac{\Delta t}{\delta x}\left(\mathbf{J}^{+}\Delta\mathbf{u}\right)^{n}_{i-1}=$$
$$\Delta t\left[\left(\mathbf{G}^{+}\right)^{n}_{i-\frac{1}{2}}-\left(\mathbf{G}^{-}\right)^{n}_{i+\frac{1}{2}}\right] \qquad (18)$$

with $\mathbf{J}^{\pm}=\mathbf{P}\Omega^{\pm}\mathbf{P}^{-1}\mathbf{J}$. It is worth noting that it is simpler to make the upwind treatment of the source terms in the explicit operator keeping a pointwise discretization for $\mathbf{K}$ in the linearized implicit operator.

The numerical scheme, as described in (14) or in the linearized version (18), is unable to deal with transonic problems of the type subcritical to supercritical flow, requiring in these cases the introduction of an artificial viscosity (Harten & Hyman, 1983). Therefore, the quantities $\mathbf{G}^{\pm}$ will be redefined to cope with the mentioned transitions as

$$\left(\mathbf{G}^{\pm}\right)^{n}_{i+\frac{1}{2}}=\left(\mathbf{P}\Omega^{\pm}\mathbf{P}^{-1}\mathbf{G}\pm\nu\frac{\delta\mathbf{u}}{\delta x}\right)^{n}_{i+\frac{1}{2}} \qquad (19)$$

This linearized implicit scheme was developed (Yee, 1987) in the context of Gas Dynamics and succesfully used for steady problems. The performance for steady problems is highly sensitive to the *CFL* used during the transient phase. When shocks are present in the solution of a non-linear equation and a high time step is used, the propagation velocities (eigenvalues in the system case) can change strongly between the two time levels. The implicit linearized methods are not unconditionally stable in these cases because the linearization involves the evaluation of the Jacobian at time level *n*. In the references the test cases presented confirm this behaviour.

3.2 *Bidiagonal scheme*

The scheme built as in (18) leads, in general, to a linear block tridiagonal system of equations. In order to work with a simpler block bidiagonal system and to avoid spurious errors in the transcritical points, the original scheme (18) can be altered. The following modification by splitting the increments due to positive and negative propagations was proposed (Burguete & García-Navarro, 2005)

$$\mathbf{F}^{T}_{i}=\mathbf{F}^{n}_{i}+\theta\left(\mathbf{J}^{+}\Delta\mathbf{u}^{+}+\mathbf{J}^{-}\Delta\mathbf{u}^{-}\right)^{n}_{i}$$
$$\delta\mathbf{F}^{L}_{i+\frac{1}{2}}=\left(\delta\mathbf{F}^{+}\right)^{n}_{i+\frac{1}{2}}+\theta\delta\left(\mathbf{J}^{+}\Delta\mathbf{u}^{+}\right)^{n}_{i+\frac{1}{2}}$$
$$\delta\mathbf{F}^{R}_{i+\frac{1}{2}}=\left(\delta\mathbf{F}^{-}\right)^{n}_{i+\frac{1}{2}}+\theta\delta\left(\mathbf{J}^{-}\Delta\mathbf{u}^{-}\right)^{n}_{i+\frac{1}{2}}$$

and the original scheme is transformed in a two-step block bidiagonal system:

$$\left[1-\theta\frac{\Delta t}{\delta x}\left(\mathbf{J}^{-}\right)\right]^{n}_{i}\left(\Delta\mathbf{u}^{-}\right)^{n}_{i}+\theta\frac{\Delta t}{\delta x}\left(\mathbf{J}^{-}\Delta\mathbf{u}^{-}\right)^{n}_{i+1}=$$
$$=\Delta t\left(\mathbf{G}^{-}\right)^{n}_{i+\frac{1}{2}}$$
$$\left[1+\theta\frac{\Delta t}{\delta x}\left(\mathbf{J}^{+}\right)\right]^{n}_{i}\left(\Delta\mathbf{u}^{+}\right)^{n}_{i}-\theta\frac{\Delta t}{\delta x}\left(\mathbf{J}^{+}\Delta\mathbf{u}^{+}\right)^{n}_{i-1}=$$
$$=\Delta t\left(\mathbf{G}^{+}\right)^{n}_{i-\frac{1}{2}}$$
$$\left(1-\theta\Delta t\mathbf{K}^{n}_{i}\right)\Delta\mathbf{u}^{n}_{i}=\left(\Delta\mathbf{u}^{+}+\Delta\mathbf{u}^{-}\right)^{n}_{i} \qquad (20)$$

When dealing with scalar equations with no source terms, this discretization is always identical to the classical tridiagonal scheme except for transcritical points. Hence, the stability (16) and TVD (17) conditions, deduced for linear cases, are equally valid for this scheme.

Despite the improvement achieved by the splitting phylosophy in transcritical flow points, this scheme is still not able to cope with high *CFL* numbers in presence of moving shocks.

3.3 *Semi-explicit NDA first order upwind scheme*

In a different approach the scheme (20) can be improved by means of a locally defined spatial weighting parameter. A wave decomposition like (Burguete & García-Navarro, 2005)

$$\mathbf{F}^{T}_{i}=\mathbf{F}^{n}_{i}+\frac{\delta x}{\Delta t}\left(\xi^{+}\Delta\mathbf{u}^{+}-\xi^{-}\Delta\mathbf{u}^{-}\right)^{n}_{i}$$
$$\delta\mathbf{F}^{L}_{i+\frac{1}{2}}=\left(\delta\mathbf{F}^{+}\right)^{n}_{i+\frac{1}{2}}+\frac{\delta x}{\Delta t}\delta\left(\xi^{+}\Delta\mathbf{u}^{+}\right)^{n}_{i+\frac{1}{2}}$$
$$\delta\mathbf{F}^{R}_{i+\frac{1}{2}}=\left(\delta\mathbf{F}^{-}\right)^{n}_{i+\frac{1}{2}}-\frac{\delta x}{\Delta t}\delta\left(\xi^{-}\Delta\mathbf{u}^{-}\right)^{n}_{i+\frac{1}{2}}$$

Produces the following numerical scheme

$$\left(1+\xi^{-}\right)^{n}_{i}\left(\Delta\mathbf{u}^{-}\right)^{n}_{i}-\left(\xi^{-}\right)^{n}_{i+1}\left(\Delta\mathbf{u}^{-}\right)^{n}_{i+1}=$$
$$=\Delta t\left(\mathbf{G}^{-}\right)^{n}_{i+\frac{1}{2}}$$
$$\left(1+\xi^{+}\right)^{n}_{i}\left(\Delta\mathbf{u}^{+}\right)^{n}_{i}-\left(\xi^{+}\right)^{n}_{i-1}\left(\Delta\mathbf{u}^{+}\right)^{n}_{i-1}=$$
$$=\Delta t\left(\mathbf{G}^{+}\right)^{n}_{i-\frac{1}{2}}$$
$$\left(1-\theta\Delta t\mathbf{K}^{n}_{i}\right)\Delta\mathbf{u}^{n}_{i}=\left(\Delta\mathbf{u}^{+}+\Delta\mathbf{u}^{-}\right)^{n}_{i} \qquad (21)$$

It is worth noting that this definition of the parameters ξ modifies the wave decomposition of the implicit

Copyright © 2006 Taylor & Francis Group plc, London, UK

operator in a manner very similar to the introduction of the artificial viscosity applied in the explicit operator to correct the sub-super transitions. This suggests that the physical meaning of these parameters is analogous and that the ξ's represent an implicit artificial viscosity.

From a non-linear analysis based on a scalar equation, (Burguete & García-Navarro, 2005), the set of parameters ξ will be calculated as

$$\xi_i^{\pm} = \max\left[\pm\frac{\Delta t}{\delta x}a_{i\mp\frac{1}{2}}^{\pm} - 1, \xi_{i\mp1}^{\pm} - 1, 0\right] \tag{22}$$

In those cases of transition from subcritical to supercritical flow, an artificial viscosity needs also to be included and (19) must be applied. It can be easily verified through a detailed non linear analysis (Burguete & García-Navarro, 2005), that the artificial viscosity also modifies the set of parameters ξ as

$$\xi_i^{\pm} = \max\left[\pm\frac{\Delta t}{\delta x}a_i^{\pm} - 1, \xi_{i\mp1}^{\pm} - 1, 0\right] \tag{23}$$

3.4 *Boundary conditions*

A correct numerical model for unsteady flow problems must be based not only on a numerical scheme with good properties but also on an adequate procedure to discretize the boundary conditions. The theory of characteristics provides clear indications about the number of necessary external boundary conditions to define a well posed problem. When a characteristic curve defined in the $x-t$ plane enters the computational domain, the influence region associated to it is exterior to the domain and therefore one external boundary condition is required. This kind of boundary conditions is also called physical boundary conditions. On the other hand, when the characteristic curve leaves the domain, the influence region belongs to the computational domain and the information linked to that characteristic curve depends exclusively on the interior points. This kind of boundary conditions are also called numerical boundary conditions.

All the methods proposed in the past to discretize the numerical boundary conditions generate error in the global mass conservation. In this work, a method based on the integral form of the mass conservation equation extended to the full domain (global mass conservation) is also considered. The technique can be adapted to any conservative numerical scheme used for the interior points leading to a machine accuracy global mass conservation in all steady or unsteady situations.

4 EXAMPLES

4.1 *Ideal dam-break wave*

The unsteady flow induced by an ideal dam-break is the most widely used test case for numerical schemes

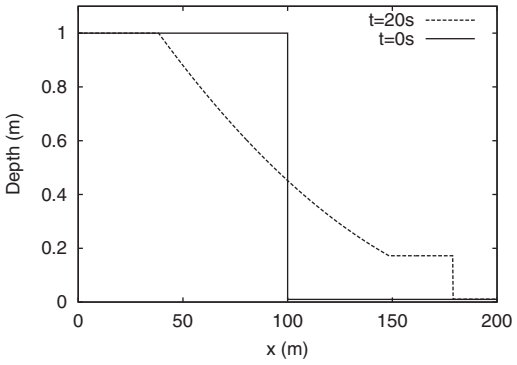


Figure 1. Initial conditions for the water surface ($t = 0$) and exact water surface solution at $t = 20$s for the ideal dam-break problem.

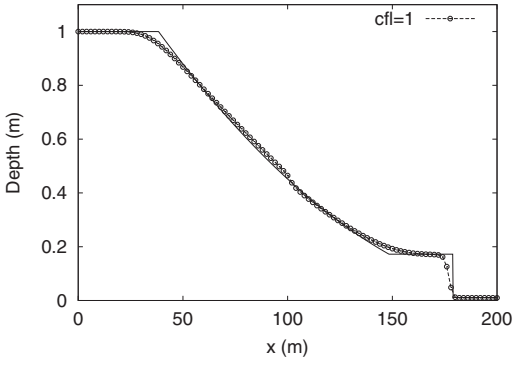


Figure 2. Water depth profiles for the dam-break test case. NDA semi-explicit. $CFL = 1$.

of the kind considered here. The initial conditions defining this nonlinear problem, as well as the exact solution are plotted in Figure 1. Implicit methods are particularly affected by the discontinuous character of the initial conditions and are usually reported to fail for most applications using *CFL* values above 3 or 4. In the example presented here an initial depth ratio of 100 was used. The numerical solutions are displayed for comparison on Figures 2, 3 and 4 together with the exact solution (Stoker, 1957). They show the solution obtained with the NDA semi-explicit method using $CFL = 1$, $CFL = 10$ and $CFL = 100$ respectively. In the case of $CFL = 100$ the numerical solution is obtained in only one time step and shows a strong dependence on the discontinuous initial conditions. The stability limit for the bidiagonal implicit scheme in this case is shown in Figure 5 after one time step of calculation (approximately corresponding to $CFL = 6$). The oscillation shown makes a second time step impossible. It is worth to note that the solution is even more accurate at low *CFL* values in this example

Copyright © 2006 Taylor & Francis Group plc, London, UK

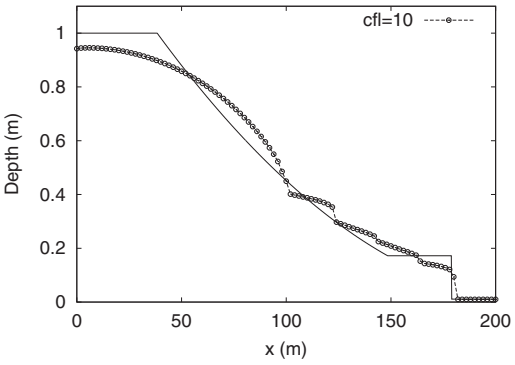


Figure 3. Water depth profiles for the dam-break test case. NDA semi-explicit. $CFL = 10$.

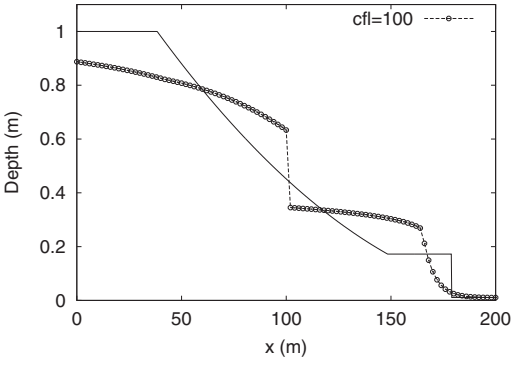


Figure 4. Water depth profiles for the dam-break test case. NDA semi-explicit. $CFL = 100$.

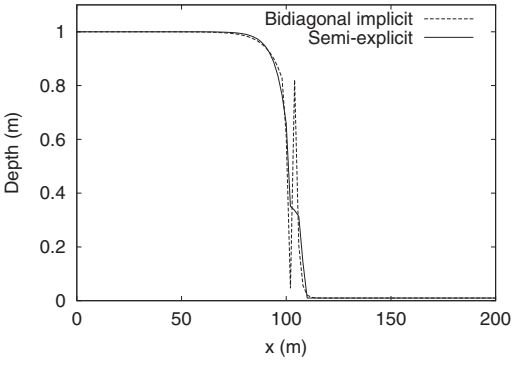


Figure 5. Water depth profiles for the dam-break test case after one step time calculation ($CFL \approx 6$).

than using the bidiagonal implicit. The stability of the NDA scheme with $CFL = 100$ contrasts again with the strange shape of the solution at the first time steps. In order to follow how the solution of this example evolves in time, Figures 6 and 7 show the water depth at times $t = 60\,s$ and $t = 150\,s$ in a longer domain. The

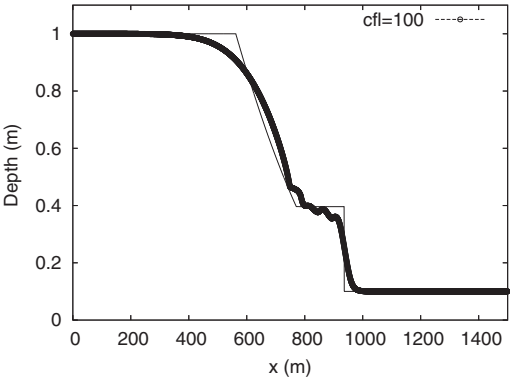


Figure 6. Analytical and numerical solution of the dam-break case using the NDA semi-explicit scheme with $CFL = 100$ in a longer domain at $t = 60\,s$.

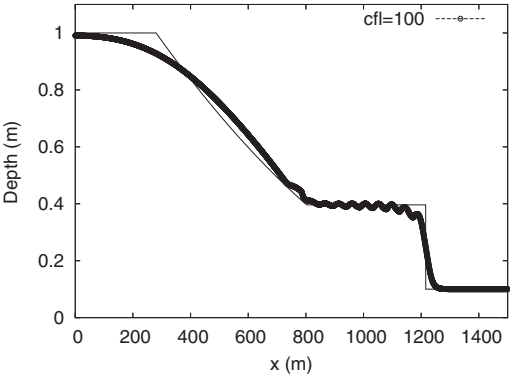


Figure 7. Analytical and numerical solution of the dam-break case using the NDA semi-explicit scheme with $CFL = 100$ in a longer domain at $t = 150\,s$.

main shape of the wave is well reproduced despite small oscillations.

4.2 *Flood wave in a river*

The river reach used for the simulation belongs to the lower part of the Ebro river and therefore has very mild average slope and low water velocities. The river cross section is highly variable in shape along the axis of the river and presents an irregular tendency in the bottom level variation leading to adverse and important slopes in some parts.

The total length of the simulated reach is around $11400\,m$. Geometric data were available at 49 cross sections. The Manning coefficient was assumed uniform and equal to $0.03\,sm^{-1/3}$.

A first run supplied the initial condition for the flooding simulation. This first run started from dry bed and introduced an upstream constant discharge of $Q = 200\,m^3/s$ until convergence.

Copyright © 2006 Taylor & Francis Group plc, London, UK

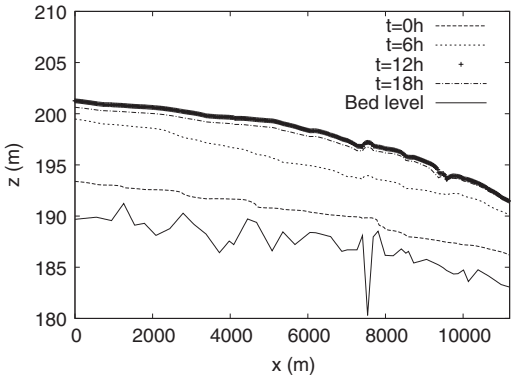


Figure 8. Water surface at base flow ($t = 0$), and at times $t = 6\,h$, $12\,h$ *(peak inflow) and* $18\,h$ using the NDA semi-explicit scheme with CFL = 1.

Unsteady shallow water flow over dry beds is at present one of the topics of research in computational hydraulics. Our approach consists of a calculation of the front position as it advances over a computational mesh covering all the physical domain and in which there are both wet and dry cells at the same time. The set of equations we are solving are written in terms of wetted cross section size and average velocity. The information concerning the original velocity profile is therefore reduced to a friction source term which takes into account the wall tangential stress and other viscous effects. The option chosen in this work is based on the empirical correlation proposed by Strickler in 1923 for the Manning coefficient in rivers,

$$n = 0.041 d_{50}^{1/6}$$

Given an estimation for the global or local Manning coefficient, the above relation supplies the order of magnitude of the mean diameter of the bed material d_{50}. In our model, this value is used as the minimum water depth required at the front position to allow front advance. For water depths below that value, water is forced to stop and accumulate.

Using the converged steady state as initial condition, the flood was represented by means of an upstream hydrograph, used as upstream boundary condition. The shape of this hydrograph was simplified making it triangular and only the peak discharge, $Q = 5300\,m^3/s$, corresponded to the estimated maximum discharge for the flood event of return period equal to 500 years. The downstream boundary condition was set to critical flow in all cases.

From the numerical point of view, 400 nodal values were used and different values for the *CFL* number. Figures 8, 9, 10 and 11 show the results obtained with the NDA semi-explicit scheme with $CFL = 1$ and $CFL = 100$, leading to CPU times of around $90\,s$, $2\,s$ respectively for the 36 hours simulated event on a

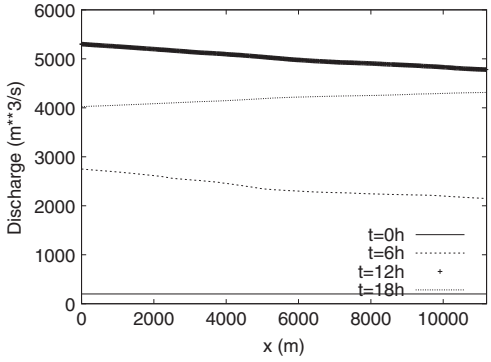


Figure 9. Discharge profile at base flow ($t = 0$), and at times $t = 6\,h$, $12\,h$ (peak inflow) and $t = 18\,h$ using the NDA semi-explicit scheme with CFL = 1.

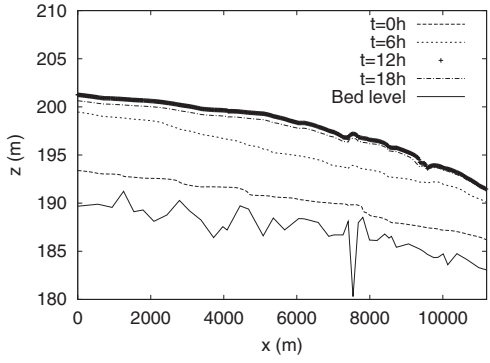


Figure 10. Water surface at base flow ($t = 0$), and at times $t = 6\,h$, $12\,h$ (peak inflow) and $t = 18\,h$ using the NDA semi-explicit scheme with CFL = 100.

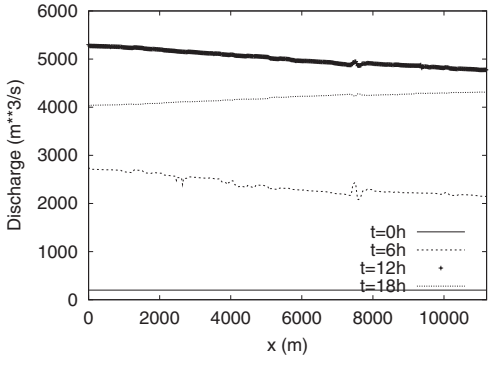


Figure 11. Discharge profile at base flow ($t = 0$), and at times $t = 6\,h$, $12\,h$ (peak inflow) and $t = 18\,h$ using the NDA semi-explicit scheme with CFL = 100.

1 GHz Pentium III PC. For the sake of comparison in this real test case, the same simulation was performed with the bidiagonal implicit upwind schemes. The results are presented in Figures 12 and 13 with

Copyright © 2006 Taylor & Francis Group plc, London, UK

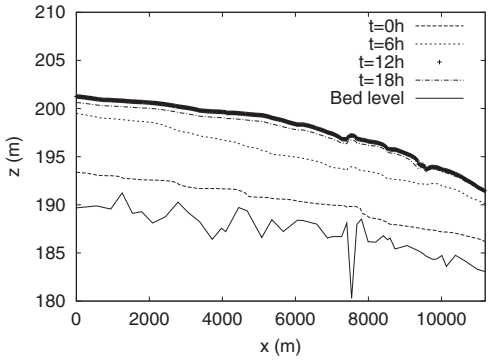


Figure 12. Water surface at base flow ($t = 0$), and at times $t = 6\,h$, $12\,h$ (peak inflow) and $t = 18\,h$ using the bidiagonal implicit scheme with CFL = 5.

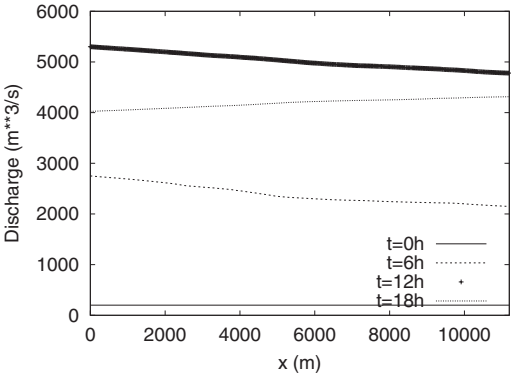


Figure 13. Discharge profile at base flow ($t = 0$), and at times $t = 6\,h$, $12\,h$ (peak inflow) and $t = 18\,h$ using the bidiagonal implicit scheme with CFL = 5.

$CFL = 5$ (CPU time $= 10\,s$) for the bidiagonal implicit. Higher values of the *CFL* number were not possible for stable solutions using this scheme.

The water depth and discharge profiles plotted and displayed correspond to the hypothesis of vertical walls at the left and right points of every supplied cross section, that is, no lateral water loses are assumed. A control over the global volume conservation of the numerical results gives accuracy to machine precision in all cases. The results are remarkably similar and almost independent of the CFL (time step) used in this transient flow problem.

5 CONCLUSIONS

Conservative implicit methods belonging to the family of linearized upwind schemes have been presented. They are in general suitable for the numerical treatment of a variety of hydraulic problems. Among them, the basic linearized scheme is restricted to low *CFL* values for the simulation of unsteady transcritical flow with shocks. Two modifications of this scheme have been derived introducing the idea of splitting the scheme in a superposition of negative and positive wave influences: a bidiagonal implicit and a semi-explicit scheme.

The performance of the implicit schemes has been tested in a dam-break problem arising from the shallow water equations and in a transient river flow example.

Both the bidiagonal implicit and the semi-explicit schemes are able to handle unsteady problems involving transcritical shocks. However, only the NDA semi-explicit can handle these problems with no stability restriction on the *CFL*.

REFERENCES

Bermúdez A. & Vázquez-Cendón M.E. (1994). Upwind methods for hyperbolic conservation laws with source terms. Computers and Fluids, 23(8), 1049–1071.

Burguete J. & García-Navarro P. (2001). Efficient construction of high-resolution TVD conservative schemes for equations with source terms: application to shallow water flows. Internal Journal for Numerical Methods in Fluids, 37, 209–248.

Burguete J. & García-Navarro P. (2005) Implicit schemes with large time step for non-linear equations: Application to river flow hydraulics. International Journal for Numerical Methods in Fluids, 2, 1–9.

Burguete J., García-Navarro P. & Murillo J. (2006). Numerical boundary conditions for globally conservative methods to solve the shallow-water equations and applied to river flow. International Journal for Numerical Methods in Fluids, (in press).

Cunge J.A., Holly F.M. & Verwey A. (1980). Practical Aspects of Computational River Hydraulics. Pitman, London, U.K.

García-Navarro P. & Vázquez-Cendón M.E. (2000). Some considerations and improvements on the performance of Roe's schemes for 1D irregular geometries on numerical treatment of the source terms in the shallow water equations. Computers and Fluids, 126, 26–40.

Glaister P. (1988). Approximate Riemann solutions of the shallow water equations. Journal of Hydraulic Research, 26, 293–306.

Harten A. & Hyman J.M. (1983). Self adjusting grid methods for one-dimensional hyperbolic conservation laws. Journal of Computational Physics, 50, 235–269.

Roe P.L. (1981). Approximate Riemann solvers, parameter vectors, and difference schemes. Journal of Computational Physics, 43(2), 357–372.

Stoker J.J. (1957). Water waves. Interscience Publishers, New York.

Toro E.F. (1997). Riemann Solvers and Numerical Methods for Fluid Dynamics. Springer-Verlag, Berlin.

Yee H.C. (1987). Construction of explicit and implicit symmetric TVD schemes and their applications. Journal of Computational Physics, 68, 151–179.

Copyright © 2006 Taylor & Francis Group plc, London, UK

Numerical and experimental modelling of the generation and propagation of waves caused by landslides into reservoirs and their effects on dams

Rita Fernandes de Carvalho & José Simão Antunes do Carmo
University of Coimbra, Portugal

ABSTRACT: Slope failures may occur on the margins of reservoirs, and they give rise to water level variations in the reservoir. In this work, the generation of water waves in dam reservoirs by landslides and their effect on dams was investigated by means of laboratory measurements and two mathematical models. The experimental work was done in a channel of dimensions 12 m × 1 m × 1 m, on which a variable slope bank and a dam 10 m away were built. The waves were generated by the falling of calcareous blocks and the time history of the surface elevation was measured at several points. The waves overtopping and breaking on the dam were also measured using a video camera to obtain the time history of the surface elevation above the crest. The hydrodynamic force on the dam was measured using four pressure transducers. The experimental work was complemented by numerical simulations using two mathematical models, one based on Boussinesq-type equations and another on the 2D Reynolds-averaged Navier-Stokes equations coupled with a Volume-Of-Fluid (VOF) method for treating arbitrary free surfaces. There was a fair agreement between the numerical solutions and the experimental results. It was concluded that the approach described in the present study, using both physical and numerical modeling, is promising for future studies on dam safety.

1 INTRODUCTION

Dam safety is a significant issue in dam engineering and the study of causes and consequences of dam failure is now mandatory for authorities responsible for the operation of many existing dams. Dam failure may be caused by natural accidents or human action. Singh (1996) summarises the main causes of dam failure as follows:

i) 30% floods exceeding spillway capacity;
ii) 37% foundation problems (seepage, piping, excess pore pressures, fault movement, settlement);
iii) 10% (slides (earth, rock, glacier, avalanches), and
iv) 23% improper design and construction, inferior quality of material, acts of war, lack of operation and maintenance.

The high costs associated with the building of a dam, as well as the material and human losses which would result from a break imply that careful studies of natural accidents and their consequences should be made, both at the project and regular operations stages.

Reservoirs in mountainous terrain are vulnerable to landslides activated by earthquakes. Reservoir slope stability studies are needed if it is feared that landslides into the reservoir may either reduce its volume available for storage or produce a tidal wave that may overtop the dam and cause flooding downstream. Overtop of the dam could cause the instability of the downstream slope due to the erosion and the unloading suction effect of the water. A breach at the dam crest may be initiated, which could also cause the failure of the dam. The integrated study of the phenomena related with natural accidents must be considered in the project phase of a dam, especially when the construction site is placed in a high risk seismic activity zone, or when a geological study of the banks indicates the existence of a potential landslide area. These slides may occur at a considerable distance from the reservoir and travel to it as a flow or avalanche, via a tributary valley.

Dynamic loading from earthquakes increases the shear stresses in a slope and may initiate slope failures. Heavy rains also act like a process accelerator.

In 1963, at the Vajont reservoir, the whole of the disturbed mountain-side slid downhill with such momentum that it crossed the river gorge (99 m wide) and rode 135 m up the other side of the valley. More than 25×10^7 m^3 had moved, at a speed of about 24 ms^{-1}. This sliding lasted for 20 seconds, produced a seismic shock that was recorded throughout Europe, and sent a huge wave over the dam which, however, survived. The wave levelled five villages in the valley below and killed more than 2500 people. After

Copyright © 2006 Taylor & Francis Group plc, London, UK

the Vajont disaster, the International Commission On Large Dams – ICOLD advised to the risk of slope failure on the margins of dam reservoirs, and these concerns were included in the regulations for the safety of dams. Measures such as carrying out geological, seismic and geo-technical studies of the region as well as studies of structural safety in normal and break scenarios, are included in existing Portuguese legislation ("Regulations for Dam Security", appendix to Portuguese Legislation DL (Dec Lei) No 11/90). Such precautions are also a motivation for the implementation of a study programme involving all problems under consideration.

In order to identify and characterize the main causes and consequences, to the valley downstream, after a dam overtopping or even its failure, a characterization of the waves generated is essential.

The characteristics of the wave packets generated by landslides are dependent of the following factors:

i) the sliding mass volume;
ii) the sliding mass velocity at the moment of impact, that will be dependent on the out of balance forces/moments, which will be influenced by the dynamic properties of soil, by the soil brittleness and by topographic effects;
iii) the size, or volume, and the reservoir depth.

Experimental studies of impulse waves generated by landslides composed by granular rockslide were presented in Fritz *et al*. (2004). According to these studies, four wave types were determined: weakly, nonlinear oscillatory, nonlinear transition and solitary wave. Fritz *et al*. (2004) proposed several empirical formulas to predict the wave characteristics, based on three fundamental dimensionless parameters: slide Froude number, $F = v_s/\sqrt{gh_0}$, where v_s is the slide velocity, h_0 is the initial reservoir water level and g the acceleration due to gravity; dimensionless slide volume, $V = V_s/(bh_0^2)$ where V_s, is the slide volume and b is the slide width and dimensionless slide thickness, $S = s/h_0$, where s is the slide thickness.

In this work, the wave generations by a block sliding over inclined planes as well as the overtopping and hydrodynamic force on a dam placed downstream were studied using laboratory experiments and two different numerical models. The experimental work was performed in a channel with dimensions $12\,\text{m} \times 1\,\text{m} \times 1\,\text{m}$, where the time history of the surface elevation was measured at several points as well as the hydrodynamic pressures on the dam. These measurements were complemented with the evaluation of sliding and overtopping over the dam using a video camera. The laboratory experiments were complemented with numerical simulations obtained using two numerical models, one based on the Boussinesq equations and another on the 2D Reynolds-averaged Navier-Stokes equations with a VOF approach fortreating arbitrary free surfaces. The Boussinesq model is less computationally intensive and can treat larger domains, whereas the VOF model can treat more complicated phenomena, such as wave overturning and breaking.

The rest of this paper is organised as follows. In the following section, the characterization of the physical processes resulting from landslides and parameters for the laboratory setup are described. In section 3, the numerical models and the installation are described. Section 4 contains a summary of the numerical and experimental results obtained. In section 5, the main conclusions are presented.

2 CHARACTERIZATION OF THE PROCESSES AND MODELLING FACILITIES

2.1 *Characterization of landslides on banks*

The risk evaluation of a slope failure into a reservoir should at first be evaluated using geological information complemented with remote sensing techniques. Concerning the geological information, the lithology, the geomorphology, the geological structure and the stress on the existing or potential shear zones are extremely important in the threshold of failure movements on slopes. Only a detailed field survey can provide the evaluation of the local geological characteristics prone to slope instability in the margins of reservoirs. The geological information must be analysed together with the water level fluctuations in the reservoir and correlated with other external factors promoting slope instability, like rain, water or earthquakes.

On areas prone to slope failure, the size of the sliding mass and the potential for fast slope movements should be investigated. The rate of displacement is a function of the pos failure brittleness and of soil dynamic properties.

Concerning brittle soil slide induced, whatever causes the initial failure of the slide ceases to be in equilibrium and moves to a new flatter position. Failures of slopes on high plasticity clays, showing positive rate effects, have a contained failure, the strength increases with velocity and the slide decelerates. The rate of displacement is low and the movement may last over a long period of time, instead of seconds as it will have been predicted if the dynamic properties of the soil were not considered (Lemos, 1991; Lemos & Coelho, 1991, and Lemos *et al.*, 1994). It is of interest to note that the reduction of static shear resistance with displacement is a function of the velocity and not a displacement due to of the interference of the rate of displacement in the clay particle alignment. When the slide comes into rest it will be in equilibrium with its slow residual strength operating.

Copyright © 2006 Taylor & Francis Group plc, London, UK

Slide in a granular soil with a neutral rate effect, initiated by any external force, the drop from peak to constant volume shear strength is accompanied by volume expansion. The brittleness increases with the initial density and structural bonding. When the gravity and friction forces are no longer in balance, the sliding mass accelerates and may reach a considerable velocity, as it happens in the more plastic clays, due to the increase in the viscous component of the shear resistance.

Failures of slopes on low plasticity clays show negative rate effects, with high losses of shear resistance beyond a critical fast displacement rate; if the critical displacement rate is not exceeded, the behaviour is similar to the one described above, for the positive rate effect. However, if the critical displacement rate is exceeded, the slide accelerates and a fast movement can result as the slide develops momentum, which carries it beyond the equilibrium point. As pointed out, above the drastic reduction to the fast residual strength needs free water access to the shear zone.

2.2 *Physical modelling*

It is impossible to take into account all aspects involved on the process of landslides. For practical reasons, the landslide was reproduced in the laboratory installation by calcareous mass falling sliding over a bank placed on a channel 1 m wide. The bank was made using acrylic glass, with dimensions 10 mm × 2.51 m × 0.992 m, supported by a metallic structure which allows the slope variation between 30° and 45°. At the bank, 0.95 m and 1.05 m away from the bottom, a gate was placed for sustain calcareous material. The gate was also made by acrylic glass with dimensions 10 mm × 0.98 mm × 0.51 m and moving in two U gutters, connected in a guide pulley system to a counter balance. The falling of the counter balance provokes the ascension of the gate, and so the falling of the material. Figure 1 shows a view of the bank and the mechanism that permits the falling of the material over the bank.

Falling masses were simulated by several calcareous blocks, with dimensions 7 cm × 8 cm × 10 cm, with density $\rho_s = 2.3755$, porosity $\eta_{por} \approx 0.40$, and friction angle determined experimentally. Some blocks were cut for adjusting the gate. Two positions of the gate were considered for avoiding two different high falls, and two different sets of blocks were considered. Figure 2 illustrates the two sets of material composed by:

i) volume 1 → a volume of 0.0814 m^3 corresponding to a mass of 193.29 Kg and a friction slope $\phi \approx 23.83°$;
ii) volume 2 → a volume of 0.168 m^3 corresponding to a mass of 400.85 Kg and a friction slope $\phi \approx 26.02°$.



Figure 1. Bank, gate, guide pulley system and counter balance.

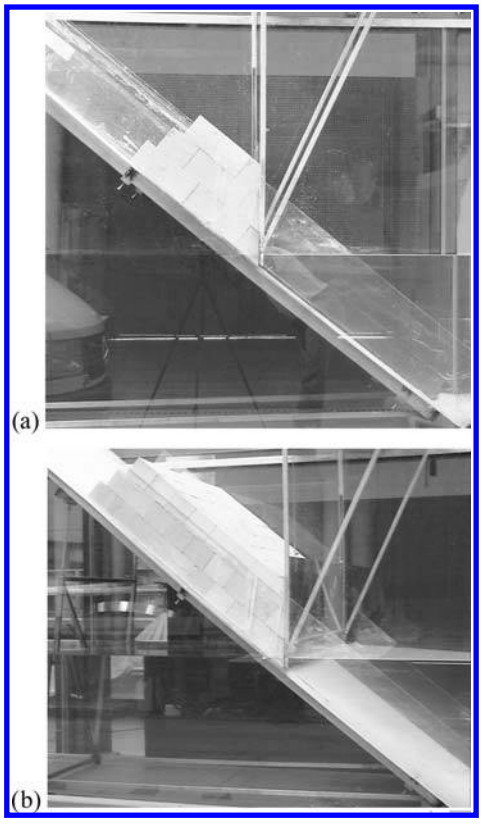


Figure 2. Bank and slide mass: (a) Volume 1; (b) Volume 2.

Copyright © 2006 Taylor & Francis Group plc, London, UK

Table 1. Centroid position for different experiments.

Gate position [cm]	Slide slope [°]	Mass [kg]	Centroid height [cm]
51.5	30.7	0.0814	74.15
61.5	30.7	0.0814	84.16
51.5	30.7	0.1687	85.08
51.5	39.5	0.0814	76.60
61.5	39.5	0.0814	86.60
51.5	39.5	0.1687	89.97

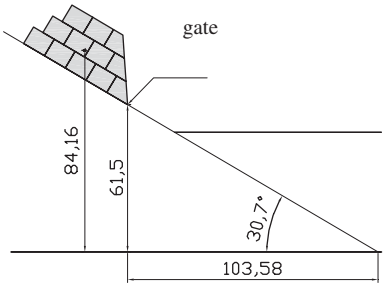


Figure 3. Mass centre at: position gate n° 1 and bank angle n°1.

For both volumes, mass centers were calculated for the two positions at the bank (61.5 cm and 71.5 cm), and for two different angles (30.7° and 39.5°). Table 1 illustrates the different parameters tested, and Figure 3 illustrates the mass center position for position 1 of the gate and for angle 1 of the bank.

3 GENERATION, PROPAGATION AND IMPACT OF WAVES CAUSED BY LANDSLIDES

3.1 *Numerical approach*

The results of two distinct numerical models, based on different mathematical formulations, were compared with physical data obtained at five probes installed into the reservoir.

The first model is based on the Reynolds-averaged Navier-Stokes equations governing the motion of the mean 2D incompressible flows in the $x-z$ plane, in which the free surface is described using a refined Volume-Of-Fluid (VOF) method. The internal obstacles are described by means of the Fractional Area-Volume Obstacle Representation (FAVOR) algorithm.

The mass and momentum conservation equations (Navier-Stokes equations) are:

$$\nabla.(\theta\,\vec{u}) = 0 \tag{1}$$

$$\frac{\partial \vec{u}}{\partial t} + \frac{1}{\theta}\nabla.(\theta\,\vec{u}\otimes\vec{u}) = -\frac{1}{\rho}\nabla p + \\ + \frac{1}{\theta}\nabla.\left[\theta(\nu+\nu_T)\left\{\nabla\vec{u} + (\nabla\vec{u})^T\right\}\right] + \vec{g} \tag{2}$$

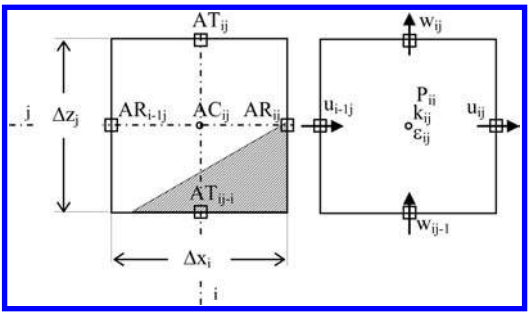


Figure 4. Definition of geometric and dependent variables in a typical mesh cell.

where $\vec{u} = (u(x,z,t),\ w(x,z,t))$ is the mean velocity vector, $p = p(x,z,t)$ is the mean pressure, ν is the coefficient of kinematic viscosity, ν_T is the eddy viscosity, $\vec{g} = (g_x, g_z)$ is the body force term and $\theta = \theta(x,z)$ is the porosity function whose value is "0" for a point inside an obstacle and "1" for a point that can be occupied by the fluid. If $\theta = \theta(x,z) = 1$ for all points of the domain, equations (1) and (2) reduce to the usual Navier-Stokes equations.

Since the position of the free surface is not known a-priori its configuration has to be determined as part of the solution. The fluid configuration can be described in terms of the VOF-function $F = F(x,z,t)$ whose value is 1 for a point occupied by the fluid and zero elsewhere. The equation governing the time evolution of F is:

$$\frac{\partial F}{\partial t} + \frac{1}{\theta}\nabla.(\theta\,\vec{u}) = 0 \tag{3}$$

which states the lagrangian invariance of F in an Eulerian representation.

The governing equations were discretized using a finite difference staggered grid system of rectangular cells (control volume) with variables width Δx_i and height Δz_j. The porosity function θ is defined at the horizontal and vertical faces of each control volume using the mesh-wide arrays AT and AR and at the centre of the control volume using another array AC. This forms the basis of the FAVOR method that allows the treatment of curved boundaries in cartesian meshes without stair-step instabilities. The arrangement of the geometric and dependent variables in a typical mesh cell is illustrated in Figure 4.

The main computational cycle by which the dependent variables are updated from u^n, w^n, p^n, F^n, at time level $n\,\Delta t$ to $u^{n+1}, w^{n+1}, p^{n+1}, F^{n+1}$, at time $(n+1)\,\Delta t$ consists of the following steps:

Step 1: A provisional velocity field $\vec{u}^* = (u^*, w^*)$ is computed using the discretized momentum equation with the advanced-time pressure p^{n+1} replaced by p^n. This provisional velocity field is not div-free since

Copyright © 2006 Taylor & Francis Group plc, London, UK

p^{n+1} is not yet known (it is important to treat the advection term accurately – in the computer code, this term was approximated using the SMART scheme to obtain the interpolated values at the four cell faces E, W, N and S (see Darwish and Moukalled, 1996);
Step 2: The advanced-time velocity $\vec{u}^{n+1} = (u^{n+1}, w^{n+1})$ and pressure p^{n+1} are computed using a pressure-velocity iterative scheme based in a cell by cell pressure-velocity relaxation scheme so that $\vec{u}^{n+1}$ is discretely div-free;
Step 3: The advanced-time fluid configuration F^{n+1} is computed at all cells of the domain using a special discretization of eq. (3) for maintaining the sharpness of the interface and conserving total fluid volume (Hirt & Nichols, 1981 and Rider & Kothe, 1998).

The details of the can be found in Carvalho (2002).

To describe a properly posed problem, initial and boundary conditions for eqs. (2)–(5) must be specified. The inflow boundary is very important to reproduce the physical wave.

The second model solves an extension of the modified Boussinesq equations, which are considered a suitable mathematical model for obtaining the characteristics of a wave caused by a landslide and its propagation within the reservoir. These equations may be derived from the fundamental equations of the Fluid Mechanics relating to a three-dimensional and quasi-irrotational flow of a viscous fluid. The set of equations thus obtained can be solved numerically using, for example, a finite element method for spatial discretization of the partial differential equations (Antunes do Carmo *et al*., 1993; Antunes do Carmo, 1995; Antunes do Carmo & Seabra Santos, 1996). Similarly, an equation can be developed to calculate the pressure field exerted on the upstream face of the dam during the approach and possible overtopping of the wave (Antunes do Carmo, 1996). The complete set of 1D equations is written:

$$\frac{\partial h}{\partial t} + \frac{\partial (h\bar{u})}{\partial x} = 0$$
$$\frac{\partial \bar{u}}{\partial t} + \bar{u}\frac{\partial \bar{u}}{\partial x} + g\frac{\partial (h+\xi)}{\partial x} - \frac{(H-\xi)^2}{3}\frac{\partial^3 \bar{u}}{\partial x^2 \partial t} + $$
$$+ (H-\xi)\frac{\partial^2 \bar{u}}{\partial x \partial t}\frac{\partial \xi}{\partial x} + \frac{H-\xi}{2}\frac{\partial \bar{u}}{\partial t}\frac{\partial^2 \xi}{\partial x^2} - \nu\frac{\partial^2 \bar{u}}{\partial x^2} - \frac{\tau(\xi)}{h} = 0 \quad (4)$$

as well as the following equation to obtain the dynamic pressure on the upstream face:

$$\frac{1}{\rho}p(z) = g(\eta - z) + (\eta - z)\frac{\partial \xi}{\partial x}\frac{\partial \bar{u}}{\partial t} + (\eta - z)\frac{\partial^2 \bar{u}}{\partial x \partial t}\left(\frac{\eta - z}{2} + H - \xi\right)$$

where h is the total water depth, H the initial water level, $\bar{u}$ the horizontal mean velocity and ξ the bed elevation; $\tau(\xi)$ represents bottom shear stress and $\eta = h - H + \xi$.

Grouping terms containing $\bar{u}$-derivatives in time in this equations system, we can re-write an equivalent form of system (4) in the form (5). It is easy to show that after substituting the third equation in the second one of system (5), we again find the final equation system (4).

$$\frac{\partial h}{\partial t} + h\frac{\partial \bar{u}}{\partial x} + \bar{u}\frac{\partial h}{\partial x} = 0$$
$$\frac{\partial \bar{r}}{\partial t} = -\bar{u}\frac{\partial \bar{u}}{\partial x} - g\frac{\partial (h+\xi)}{\partial x} + \nu\frac{\partial^2 \bar{u}}{\partial x^2} - \frac{\tau(\xi)}{h}$$
$$\bar{u} - \frac{(H-\xi)^2}{3}\frac{\partial^2 \bar{u}}{\partial x^2} - (H-\xi)\frac{\partial (H-\xi)}{\partial x}\frac{\partial \bar{u}}{\partial x} - $$
$$- \frac{H-\xi}{2}\frac{\partial^2 (H-\xi)}{\partial x^2}\bar{u} = \bar{r} \quad (5)$$

Schematically, the last set of equations can be written as (6) and a finite element method was utilized to obtain the solution of this equation system.

$$-\frac{\bar{u}_i^n}{4\Delta x}h_{i-1}^{n+1} + \left[\frac{1}{\Delta t} + \frac{1}{2}\left(\frac{\partial \bar{u}}{\partial x}\right)_i^n\right]h_i^{n+1} + \frac{\bar{u}_i^n}{4\Delta x}h_{i+1}^{n+1}$$
$$= \left[\frac{1}{\Delta t} - \frac{1}{2}\left(\frac{\partial \bar{u}}{\partial x}\right)_i^n\right]h_i^n - \bar{u}_i^n\frac{1}{2}\left(\frac{\partial h}{\partial x}\right)_i^n$$
$$h_i^{n+\theta} = (1-\theta)h_i^n + \theta\, h_i^{n+1}$$
$$\bar{r}_i^{n+1} = \bar{r}_i^n - \left[\bar{u}_i^n\left(\frac{\partial \bar{u}}{\partial x}\right)_i^n + g\left(\frac{\partial h}{\partial x} + \frac{\partial \xi}{\partial x}\right)_i^{n+\theta} - \nu\left(\frac{\partial^2 \bar{u}}{\partial x^2}\right)_i^n + \left(\frac{\tau}{h}\right)_i^n\right]\Delta t$$
$$\left[-\frac{(H-\xi)^2}{3\Delta x^2} + \frac{(H-\xi)}{2\Delta x}\frac{\partial (H-\xi)}{\partial x}\right]_i \bar{u}_{i-1}^{n+1} +$$
$$+\left[1 + \frac{2(H-\xi)^2}{3\Delta x^2} - \frac{H-\xi}{2}\frac{\partial^2 (H-\xi)}{\partial x^2}\right]_i \bar{u}_i^{n+1} +$$
$$+\left[-\frac{(H-\xi)^2}{3\Delta x^2} - \frac{(H-\xi)}{2\Delta x}\frac{\partial (H-\xi)}{\partial x}\right]_i \bar{u}_{i+1}^{n+1} = \bar{r}_i^{n+1}$$
$$\bar{u}_i^{n+\theta} = (1-\theta)\bar{u}_i^n + \theta\, \bar{u}_i^{n+1} \quad (6)$$

The numerical procedure used to compute the solution of equation system (4) (values of the variables h and u at time $t + \Delta t$) is based on the following numerical scheme, itself based on the last equation system (5), for the variables h, r and $\bar{u}$ (Antunes do Carmo *et al.*, 1993; Antunes do Carmo & Seabra Santos, 1996):

Step 1; The first equation allows us to predict the values of variable h ($h_p^{t+\Delta t}$) utilizing a semi-implicit scheme, considering the known values of h and u at time t in the whole domain.
Step 2; The second equation allows the explicit prediction of the values of variable r ($r_p^{t+\Delta t}$), considering the values of $h^{t+\theta\,\Delta t} = (1-\theta)h^t + \theta\, h_p^{t+\Delta t}$, u and r^t, known for the whole domain.

Copyright © 2006 Taylor & Francis Group plc, London, UK

Step 3; The third equation allows us to obtain the values of variable u at time $t + \Delta t$ ($u^{t+\Delta t}$) utilizing a semi-implicit scheme, considering the predicted values of r ($r_p^{t+\Delta t}$) in the whole domain.
Step 4; The first equation allows us to compute the depth h at time $t + \Delta t$ ($h^{t+\Delta t}$), taking into account the values of variables h^t and $u^{t+\theta\,\Delta t} = (1-\theta)u^t + \theta\, u^{t+\Delta t}$ known for the whole domain.
Step 5; The second equation allows us to compute the values of variable r at time $t + \Delta t$ ($r^{t+\Delta t}$), taking into account the values of variables r^t, $h^{t+\theta\,\Delta t} = (1-\theta)h^t + \theta\, h^{t+\Delta t}$ and $u^{t+\theta\,\Delta t} = (1-\theta)u^t + \theta\, u^{t+\Delta t}$ known for the whole domain.

3.2 *Experimental data*

Data on the characteristics of waves formed when large masses of soil and/or rock fall into the reservoir were collected in the laboratory installation consisting by a channel where the bank, a reservoir and a dam were placed. The dimensions were settled considering non-dimensional characteristics equivalent to prototype disturbances. The reservoir water level varied between 0.30 m and 0.55 m.

The movement and the impact velocity of the mass into the water are essential to characterize the wave generation and the inflow condition for the numerical simulations (Carvalho & Carmo, 2006). The movement was filmed using a video-camera. The images were subsequently analyzed to obtain an estimate of the submerged mass and volume as a function of time, that is $M = f(t)$. This knowledge was required to solve equation (7), which describes the movement of the sliding block:

$$M\frac{dv_s}{dt} = Mg\sin\alpha - M_w g\frac{\rho_s}{\rho_w}\sin\alpha - Mg\cos\alpha\tan\phi - \frac{1}{2}C_x\rho_w A V^2 \qquad (7)$$

where M is the mass of the sliding block, M_w is the submerged mass, v_s is the slide mass velocity, α is the bank slope, ϕ is the friction slope, ρ_s is the density of slide mass, ρ_w is the water density, C_x is the drag coefficient for the slide, A is the slide mass section, t is the time and g is the acceleration due to gravity. For solving eq. (7), a 4th Runge-Kutta method was used.

An equipment based on a three laser pointed on the channel was also tested, but due to the channel glass characteristics, the measures were not trustable.

Between the bank and the dam, five probes (HR Wallingford wave probe monitors 0.6 m) were positioned at 2, 4, 6 and 8 m away from the bank for measuring the water level. A probe more closed to the mass slide impact was desirable, but the probe could not be secure.



Figure 5. Physical model, including the sliding slope, the water mass (reservoir) and one of the five gauges.

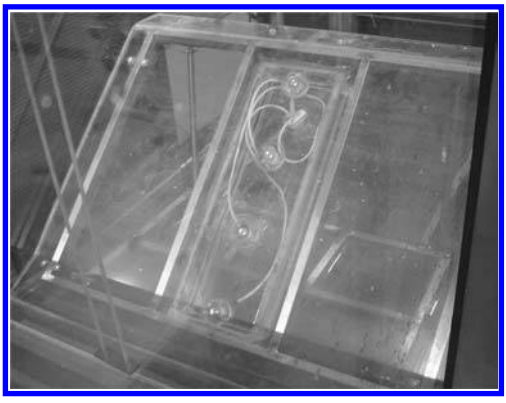


Figure 6. Dam with the four pressure gauges installed.

The wave impact and reflection on the upper face of the dam were also obtained in the laboratory experiments. This was done by measuring both the wave height and the pressure exerted on the wall. Figure 5 shows the physical model, including the sliding slope, the water mass (reservoir) and the first gauge, placed 2 m after the bank, and Figure 6 shows the dam with the four pressure transducers installed.

4 RESULTS

4.1 *Experimental essays*

The laboratory study of the wave characteristics and the hydrodynamic effects caused by landslides was based on a test matrix that included 18 different conditions. The relevant parameters governing the wave generation consist of: mass of the sliding block, the still water level in the reservoir, the slide velocity, the slide mass, the slope and the initial position of the sliding block. The four parameters were varied as follows:

i) slide slope, $\alpha = 30.7°$ and $39.5°$;
ii) reservoir water level, $h_0 = 0.50$ m and 0.55 m;

Copyright © 2006 Taylor & Francis Group plc, London, UK

Table 2. Experimental essays plan.

Name	Slide slope [°]	Reservoir water level [m]	Slide volume [m^3]	Centroid height [m]
E01	30.7	0.5	0.0814	0.74
E02	30.7	0.5	0.0814	0.84
E03	30.7	0.5	0.1687	0.85
E04	30.7	0.55	0.0814	0.74
E05	30.7	0.55	0.0814	0.84
E06	30.7	0.55	0.1687	0.85
E07	39.5	0.5	0.0814	0.77
E08	39.5	0.5	0.0814	0.87
E09	39.5	0.5	0.1687	0.90
E10	39.5	0.55	0.0814	0.77
E11	39.5	0.55	0.0814	0.87
E12	39.5	0.55	0.1687	0.90
E13	30.7	0.5	0.1687	0.95
E14	30.7	0.4	0.1687	0.95
E15	30.7	0.3	0.0814	0.95
E16	30.7	0.3	0.0814	0.84
E17	39.5	0.3	0.0814	0.74
E18	39.5	0.3	0.0814	0.84

Table 3. Wave types.

Name	Wave type	$F = v_s/\sqrt{gh_0}$ Nonlinear (nl)	4–7.5S Oscillatory (osc)	6.6–8S Transition (tran)	8.2–8S Dissipative (diss)
E01	n.l.	0.3	0.40	2.76	4.36
E02	osc.	0.5	0.40	2.76	4.36
E03	n.l.	0.3	0.40	2.76	4.36
E04	nl	0.4	0.73	3.11	4.71
E05	nl	0.5	0.73	3.11	4.71
E06	nl	0.4	0.73	3.11	4.71
E07	osc.	0.9	0.40	2.76	4.36
E08	osc.	1.0	0.40	2.76	4.36
E09	osc.	0.9	0.40	2.76	4.36
E10	osc.	0.9	0.73	3.11	4.71
E11	osc.	0.9	0.73	3.11	4.71
E12	osc.	0.9	0.73	3.11	4.71
E13	osc.	0.5	0.40	2.76	4.36
E14	osc.	0.5	0.50	1.80	3.40
E15	tran.	0.8	−2.00	0.20	1.80
E16	tran.	0.8	−2.00	0.20	1.80
E17	tran.	1.2	−2.00	0.20	1.80
E18	tran.	1.3	−2.00	0.20	1.80

iii) slide volume $V = 0.0814\,\text{m}^3$ and $0.1687\,\text{m}^3$;
iv) centroid slide mass position.

Table 2 shows the different parameter values chosen for the 18 experiments.

For the 18 experiments, the position of the sliding block was calculated using eq.(7) and the images processed form the video recordings. The time history of the water level and pressure on the upper face of the dam were also measured simultaneously using software that permits real time visualization on the computer.

4.2 *Wave generation – wave type*

Based on wave type classification proposed by Noda (1970) and used by Fritz *et al.* (2004), the fundamental parameters were calculated. Table 3 shows the predicted wave types for the 18 essays.

The slide Froude number was determined by the following expression deduced taking into account the energy balance between the positions before and after the slide:

$$v_s = \sqrt{2g\Delta z \sin(\alpha - \phi)} \tag{8}$$

where v_s is the slide velocity when the centroid arrives to the water surface, Δz is the height between the position of the centroid before and after the slide fall, g is the acceleration due to gravity, α is de slide slope and ϕ is the friction slope. The velocity was compared with the calculated values obtained through eq. (7) and in the majority of the essays, it was observed an acceptable proximity of the maximum slide velocity, except for the lower slide slopes and smaller centroid heights. Figure 7 shows the variation of the slide mass velocity during the fall calculated by eq. (7).

Figure 7 illustrates the importance of the chosen parameters. The initial water level position, for small bank angles, is not so important (slide mass velocity variation during the fall is similar in E01-E03 and E04-E06). For the higher angle, the maximum velocity difference become visible (E08 and E11). For the slide mass volume, similar results could be observed (E01 and E03). However, the slide mass volume variation could not be analyzed dissociated from the centroid initial position. This parameter is very important both in the initial and maximum slide mass velocity (see E01 and E02, E07 and E08, E10 and E11 or E16 and E17). The slide slope is also very influent in the maximum slide mass velocity (see E01 and E07). In particular, when the initial water level is low, this parameter causes large slide initial velocity (see E16 and E17). Concerning the velocity variation, the following ascending variation could be observed: parabolic (E01–E12), linear (E13–E17) and sinusoidal (E18). Sudden descending variations were verified due to the reservoir water level, which is not large enough to decelerate the slide mass.

4.3 *Wave characteristics and propagation*

The knowledge of the wave amplitude and celerity is very important for the risk prediction and hazard prevention, i.e. for efficient activation of emergency

Copyright © 2006 Taylor & Francis Group plc, London, UK

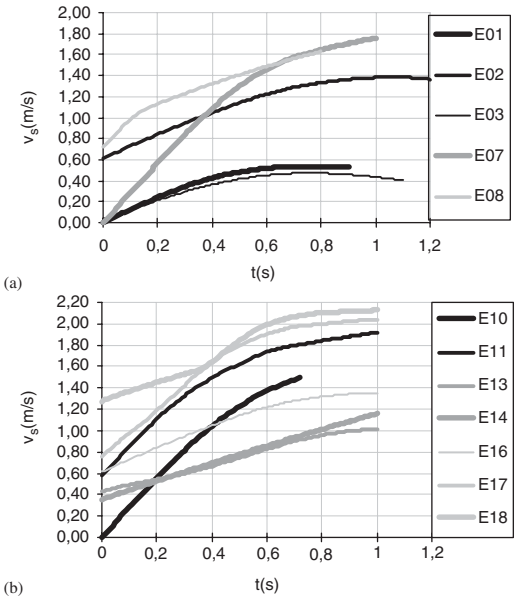


Figure 7. Variations of the slide mass velocity during the fall: (a) essays E01, E02, E03, E07 and E08; (b) E10, E11, E13, E14, E16, E17 and E18.

plans. In most of the tests, the maximum wave amplitude was attained by the first wave. However, in gauge number 4, placed 8 m far from the bank, the amplitude of the second wave exceeded that of the leading wave in tests E10 and E11.

The maximum positive wave amplitude was observed in E03 and E13, the minimum was observed in E04. These results show the strong dependence of the phenomena on the mass (volume) of the sliding mass and the initial water level. In terms of the dimensionless parameter a_c/h_0, the maximum wave amplitude was observed in E17 (0.46) due to the greater velocity which is in turn due to the higher bank slope and minor water level. This result agrees with the formula proposed by Fritz *et al*. (2004):

$$\frac{a_C}{h_0} = 0.25\left(\frac{v_s}{\sqrt{gh_0}}\right)^{1.4}\left(\frac{s}{h_0}\right)^{0.8} \quad (9)$$

The maximum negative wave amplitude was observed for E10 and E11 and the minimum for E16, where the wave shows solitary characteristics.

The minimum wave length L is observed in E05, which corresponds to the greater wave steepness a_c/L. E08 presents the maximum wave length and the minimum wave declivity (0.02). The value of L/h_0 is maximum in E18 and minimum in E05. It was obtained: $4.55 < L/h_0 < 12.28$ and $0.02 < a_c/L < 0.05$. All values are less than 0.06, the limit of breaking. However, it can't be negligible that the first wave amplitude values were obtained at the first gauge placed 2 m after the bank.

For non linear waves, celerity is strongly dependent on the relative amplitude, a_c/h_0, wave length, L, and initial water level, h_0. Propagation velocity decreases with the amplitude and wave length. According to Boussinesq theory, the following expression for the solitary wave velocity is valid: $c_{c1}/\sqrt{gh_0} = 1 + a_{c1}/(2h_0)$, where 1 refers to the first wave. According to Fritz et al (2004), velocities 30% greater than those calculated by eq. (10) were observed. In the present study values in the range $0.9 < c_{c1}/\sqrt{gh_0} < 1.2$ for the first wave and $0.6 < c_{c1}/\sqrt{gh_0} < 1.0$ for the second one were obtained. All values of a_c/h_0 are greater than 0.03, all values of a_c/L are greater than 0.006 and the Ursell number is always greater than 1, which confirms the waves nonlinearity characteristics. Figure 8 shows a comparison between numerical results and laboratory data of the reservoir water level variations in essay E14 at 2, 4, 6 and 8 m from the slide mass falling point.

Figure 8 shows a good agreement between both models. However, after the second wave the numerical solutions show a lag in time relative to the experimental results. The results for other simulations were similar. It can be concluded that the numerical models:

i) underestimate the negative amplitude of the first wave in E10 and E11;
ii) overestimate positive and negative amplitudes in E16 and E18;
iii) in general,the VOF model produced better agreement with the laboratory measurements;
iv) the numerical solutions are very sensitive to the inflow condition: small variations in the velocity function could produce remarkable amplitude differences.

4.4 *Wave impact on dam*

Hydrodynamic pressures on the upper dam face were measured by pressure transducers. Figure 9 illustrates pressure data measured at the four transducers placed on the face of the dam and the time history of the water level at gauge 5, placed 10 m far from the slide mass falling point (just close to the beginning of the upper dam face, where the pressure transducers were installed).

An instability was observed when the wave is reflected upstream at the upper face of the dam. It also could be noted that the negative wave amplitude is greater on the pressure transducer placed close to the free surface. These could not be perceptible by the gauge measures and should be studied in more detail.

Other experimental and numerical results are under development.

Copyright © 2006 Taylor & Francis Group plc, London, UK

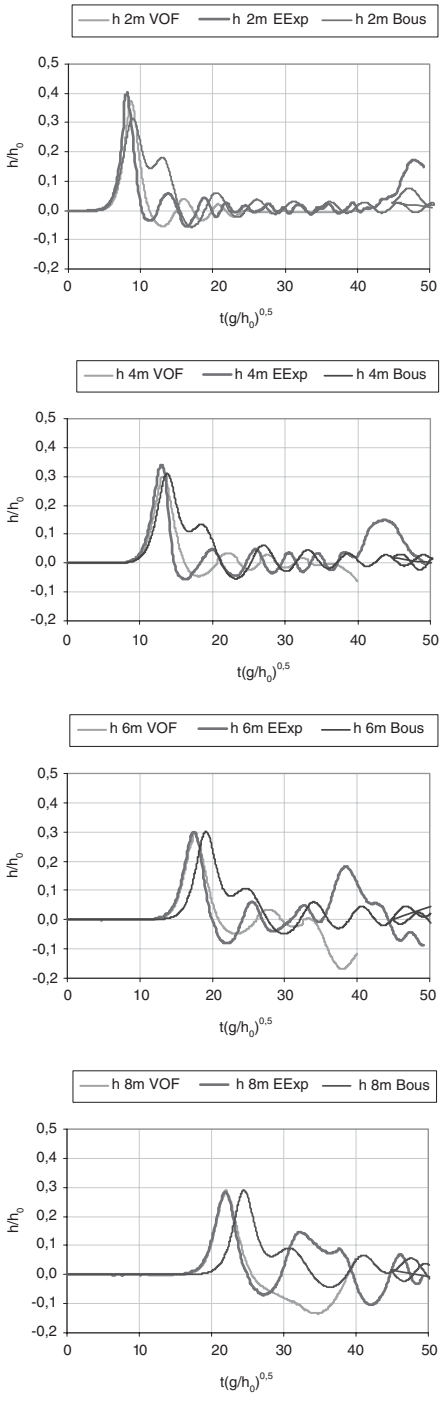


Figure 8. Variations of the reservoir water level in essay E14 at 2, 4, 6 and 8 m from the slide mass falling point. Comparisons between data obtained in laboratory and numerical results of two numerical approaches (section 3.1).

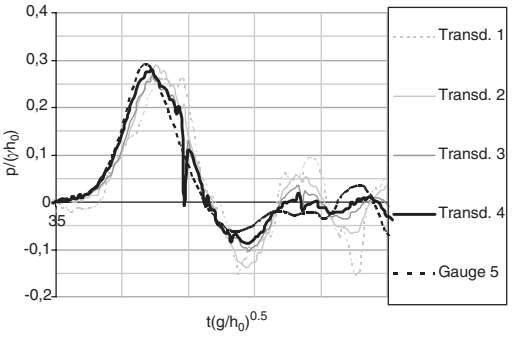


Figure 9. Reservoir water level variations (Gauge 1 placed 10 m far from the slide mass falling point) and pressure transducers 1, 2, 3 and 4 from up to down on the upper face of the dam (see Figure 6): Essay E03.

5 CONCLUSIONS

Data on the wave characteristics formed when large masses of soil or rock fall into a reservoir were presented. The wave propagation and its impact on a dam were examined by means of laboratory measurements and numerical models with different approaches.

Numerical results showed a fair agreement with experimental data. It could be concluded that numerical simulations are strongly dependent on the definition of the inflow boundary condition, which in turn depends on the velocity variation of the sliding mass.

More experiments are needed to improve and detail the measurements that lead to the slide mass velocity function during the fall, to allow a better numerical solution.

However, this work permitted to conclude that:

- different velocity diagrams (inflow boundary condition): nearly linear, sinusoidal and parabolic were produced;
- different types of waves are formed depending on the relevant parameters governing the wave generation: mass of the sliding block, still water level in the reservoir, sliding velocity, slide mass, bank slope and initial position of the sliding block;
- numerical results can predict fair accurately the wave formed by landslide, mainly the amplitude and length of the first wave;
- hydrodynamic pressure appeared on the upstream face of the dam.

In general, more essays results are essential to support correlation and develop formulas able to predict the wave amplitude and velocity propagation. It could also be pointed that the amplitude of the first wave should be measured closer to the slide mass impact.

Copyright © 2006 Taylor & Francis Group plc, London, UK

ACKNOWLEDGEMENTS

This work forms part of a research project entitled "Dam breaks: a study of the natural and technological causes and a modelling of the associated hydrodynamic and sedimentary issues", funded by the FCT – the Portuguese Foundation for Science and Technology – under the POCTI/ECM/2688/2003 project. The authors wish to acknowledge to M. Joaquim Cordeiro experiment from LHRHA-DEC-FCTUC and students Paula Canetas and André Pestana which give contributions related to the experimental work in the laboratory.

REFERENCES

Antunes do Carmo, J.S., Seabra Santos, F.J. & Barthélemy, E., 1993. Surface Waves Propagation in Shallow Water: A Finite Element Model. *International Journal for Numerical Methods in Fluids*, Vol. 16, 447–459.

Antunes do Carmo, J.S. 1995. *Contribuição para o Estudo dos Processos Morfodinâmicos em Regiões Costeiras e Estuarinas*. PhD Thesis in Sciences of Engineering, University of Coimbra, April, 225 p.

Antunes do Carmo, J.S., 1996. As cheias: fenómenos naturais e causas de ocorrências excepcionais. Revista *Cadernos de Geografia*, Faculdade de Letras da Universidade de Coimbra, N° 15, 85–99. ISBN 0871-1623.

Antunes do Carmo & Seabra Santos, F.J., 1996. On breaking waves and wave current interaction in shallow water. A 2DH finite element model. International Journal for *Numerical Methods in Fluids*, Vol. 22, 429–444.

Carvalho, R.F. 2002. "Acções hidrodinâmicas em estruturas hidráulicas: Modelação computacional do ressalto hidráulico", Tese de Doutoramento, Faculdade de Ciências e Tecnologias da Universidade de Coimbra, Coimbra.

Carvalho, R.F. & Antunes do Carmo, J.S. 2006. "Ondas provocadas por deslizamentos de taludes em albufeiras", 8° Congresso da água, APRH, Figueira da Foz.

Darwish & Moukalled, 1996. "The Normalized Weighting Factor Method: A novel technique for accelerating the convergence of high-resolution convective schemes". *Numerical Heat Transfer*, Part B, Vol.30, 217–237.

Fritz H. M., Hager, W. H. and Monor, H.-E., 2004. "Near Field Characteristics of Landslide Generated Impulse Waves". *Journal of Waterway, Port, Coastal, and Ocean Engineering*, pp. 287–300.

Hirt & Nichols, 1981. "Volume of Fluid (VOF) Method for the Dynamics of Free Boundaries". *J. Comp. Phys*. 39, 201–225.

Lemos, L.J.L. 1991. Shear strength of shear surfaces under fast loading. Proceedings of the Tenth European Conference on Soil Mechanics and Foundation Engineering, Associazione Geotecnica Italiana, Vol. 1, 137–142.

Lemos, L.J.L. & Coelho, P.A.L.F., 1991. "Displacements of slopes under earthquake loading. Second International Conference on Geotechnical Engineering and Soil Dynamics, Shamsher Prakash, University of Missouri-Rolla, Rolla, Missouri, Vol. II, 1051–1056.

Lemos, L.J.L., Gama, A. M. P. & Coelho, P. A. L. F., 1994. Displacements of cohesive slopes induced by earthquake loading. *Proceedings of the Thirteenth International Conference on Soil Mechanics and Foundation Engineering*, New Delhi. Vol. 3, 1041–104.

Noda, E., 1970. "Water waves generated by landslides", *J. Waterw., Port, Coastal, Ocean Div.*, Am. Soc. Civ. Eng., 96(4), 835–855.

Rider & Kothe, 1998. "Reconstructing Volume Tracking". *J. Comp. Physics* 141, 112–152.

Singh, V.P., 1996. "Dam Break Modelling Technology". Kluwer Academic Publishers, Dordrecht.

Copyright © 2006 Taylor & Francis Group plc, London, UK

High-order finite volume modelling of one-dimensional flows

L. Cozzolino & D. Pianese
Department of Hydraulic and Environmental Engineering, Federico II University, Naples, Italy

ABSTRACT: In this paper, a numerical model is presented, aiming at the accurate solution of the one-dimensional Shallow-water Equations with bed slope source terms. The numerical model, which is fully third-order precise in time and space, is based on the Spectral Volume Method, and makes use of the HLL approximate Riemann solver to evaluate the fluxes at the interfaces between the cells. The source terms are treated, in the context of the HLL solver, in an upwinded fashion. A number of numerical experiments are reported, showing the promising capabilities of the model to solve real-world problems with complicate topographies.

1 INTRODUCTION

The numerical solution of the one-dimensional flow equations is useful to model a variety of physical phenomena such as tidal flows at river estuaries, flood propagation through natural and artificial channel networks, bore wave propagation, etc. Since these equations are non linear, they admit the formation of discontinuities in the flow field even in case of smooth initial conditions: such discontinuities are also encountered in the case of propagation of the flood on an initially dry bed.

Moreover, the momentum equation is characterized by the presence of a geometrical source term, due to gravity, which balances the advective fluxes when a steady-state condition is attained. The numerical solution of the Shallow-water Equations with source terms has to take into account this fact, in order to avoid spurious oscillations of the numerical solution and instability of the algorithm, even in the case of water-at-rest solutions. The numerical schemes which preserve the steady state conditions, and that balance the fluxes with the source terms, independently of the grid mesh, are called *well-balanced* (Greenberg & Leroux, 1996). A number of well-balanced schemes for the solution of Shallow-water Equations, which are at most second-order accurate, can be found in literature (see for example Gosse, 2000, Jin, 2001).

Of course, the preservation of any possible steady-state condition is quite a restrictive requirement, and attention has been focused on numerical schemes which satisfy the water-at-rest condition: these schemes have demonstrated to improve the numerical solution for more general cases. The schemes that satisfy the water-at-rest condition exactly or within a fixed order of accuracy are said to satisfy the *C-property* (Bermúdez & Vázquez, 1994, Bermúdez et al., 1998). In this context, a number of different approaches have been considered (see Xing & Shu, 2005, for a brief review): among others, the upwinding of source terms has proven to be very effective (Bermúdez & Vázquez, 1994, Hubbard & García Navarro, 2000).

Modelling long-term flow transients in shallow-water bodies is a challenging task: the current numerical models, which are usually second-order accurate in time and space, have demonstrated their ability to correctly manage special situations as fast transients following dam-break phenomena, but they show excessive numerical dissipation when applied to the case of long transients. In the context of the Finite Volume Method, a number of high-order schemes for the solution of the one- and two-dimensional Shallow-water Equations with source terms have been presented. Kurganov and Levy (2002) have considered a central-upwind scheme with a third-order approximation of the fluxes and a second-order approximation of the source terms: the scheme behaved better than a fully second-order scheme, of course. Črnjarić-Žic et al. (2004) have proposed a Finite Volume WENO scheme with upwind treatment of source terms: their approach allows for the use of non-uniform grids, but the proposed treatment of the central part of geometrical source terms degrades the theoretical accuracy of the scheme (as confirmed by their convergence experiments). The same authors propose a Central WENO scheme, on staggered grids: it respects the theoretical accuracy, but is not suitable for non-uniform grids. Noelle et al. (2005) extended the original source-terms treatment by Audusse et al. (2004) to the third-order theoretical accuracy, and they used a fifth-order WENO approximation for the fluxes. Their convergence experiments seem to show that their scheme is

Copyright © 2006 Taylor & Francis Group plc, London, UK

fifth order accurate. Ortega (2005) proposed a third-order ENO scheme for the fluxes and a second-order integration rule for the source terms: the convergence experiments in steady-flow conditions confirmed that the accuracy order of the scheme was less than three.

Continuing the work started in Cozzolino & Pianese (2005), in this paper a new Finite Volume numerical model is described, aiming at the solution of the one-dimensional Shallow-water Equations with bed-slope source terms, with the third-order of accuracy. Following Alouges et al. (1999), source terms are treated in an upwind fashion, just like the advective fluxes. The concept of Spectral (Finite) Volume (Wang, 2002) is used for the space discretization of the equations, and the fluxes are calculated by means of the HLL approximate Riemann solver. Runge-Kutta's algorithm is applied to solve the set of ODE's obtained after the space discretization.

2 THE NUMERICAL METHOD ADOPTED

2.1 *Shallow-water equations and the finite volume method*

The 1D Shallow-water Equations are a system of hyperbolic partial differential equations which can be written, in vector form, as

$$\frac{\partial \vec{U}}{\partial t} + \frac{\partial \vec{F}(\vec{U})}{\partial x} = \vec{S}(x, \vec{U}) \tag{1}$$

The symbols in Equation 1 have the following meanings:

$$\vec{U} = \begin{pmatrix} h & hU \end{pmatrix}^T \tag{2}$$

is the vector of the conserved quantities h (water height) and hU (discharge per unitary width), where U is the velocity;

$$\vec{F} = \begin{pmatrix} hU & hU^2 + \frac{1}{2}gh^2 \end{pmatrix}^T \tag{3}$$

is the vector of the fluxes, and

$$\vec{S} = \begin{pmatrix} 0 & -gh\frac{dz_b}{dx} \end{pmatrix}^T \tag{4}$$

is the vector of the source terms, where z_b represents the bed elevation.

If the computational domain is subdivided into N finite volumes, Equation 1 can be spatially integrated in each of these elements, obtaining

$$\frac{d\vec{U}_i}{dt} = \vec{L}_i(\vec{U}), \quad i = 1...N \tag{5}$$

where

$$\vec{L}_i(\vec{U}) = -\frac{1}{\Delta x_i}\left[\vec{F}^*_{i+\frac{1}{2}} - \vec{F}^*_{i-\frac{1}{2}}\right] + \frac{1}{\Delta x_i}\int_{x_{i-\frac{1}{2}}}^{x_{i+\frac{1}{2}}} \vec{S}\,dx \tag{6}$$

and

$$\vec{U}_i = \frac{1}{\Delta x_i}\int_{x_{i-\frac{1}{2}}}^{x_{i+\frac{1}{2}}} \vec{U}\,dx \tag{7}$$

is the vector of the cell-averaged values of the quantities conserved in the finite volume i, whose left and right boundaries have abscissas $x_{i-1/2}$ and $x_{i+1/2}$ respectively, and lengths $\Delta x_i = x_{i+1/2} - x_{i-1/2}$. The numerical source terms are evaluated from the cell-averaged values z_{bi} of the bed elevation z_b in each of the finite volumes.

If the quantities on the right-hand side of Equation 5 (numerical fluxes and numerical source term) depend on the averaged values $\vec{U}_i$ of the conserved quantities, then the Equation 5 represents a system of ordinary differential equations which can be properly integrated in time (method of lines).

2.2 *HLL Riemann solver*

Since the Shallow-water Equations are a system of non linear hyperbolic equations, discontinuities in the flow field can also develop in the case of continuous initial conditions, and numerical fluxes F^* between two cells must account for this.

Here, the approximate Riemann solver HLL is adopted (Toro, 1999):

$$\vec{F}^* = \alpha\vec{F}_L - \beta\vec{F}_R + \gamma(\vec{U}_R - \vec{U}_L) \tag{8}$$

where $\vec{F}_L$ and $\vec{F}_R$ are the physical fluxes, while $\vec{U}_L$ and $\vec{U}_R$ are the conserved quantities, on the left and right sides of each interface, respectively. In Equation 8 the following positions have been made:

$$\alpha = \frac{s_R}{s_R - s_L}; \quad \beta = \frac{s_L}{s_R - s_L}; \quad \gamma = \frac{s_R s_L}{s_R - s_L} \tag{9}$$

and the wave speeds s_L and s_R can be evaluated as in Fraccarollo & Toro (1995).

The conserved quantities at each interface can be calculated, from the averaged values of the quantities conserved in each finite volume, by means of proper polynomial reconstruction. In the present case, the variables h, hU and $\varsigma = z_b + h$ (water surface elevation) have been chosen for the reconstruction (Audusse et al., 2004), implying that the bottom elevation reconstruction changes at each time step, according to the water surface elevation and water depth reconstruction.

Copyright © 2006 Taylor & Francis Group plc, London, UK

After that the reconstruction of the conserved quantities has been accomplished, the physical fluxes and the wave speeds can be evaluated on both sides of each interface.

2.3 *Upwinding of source terms*

Bermúdez & Vázquez (1994) have shown that the upwinding of source terms in the Shallow-water Equations can enforce the respect of the *C-property*: in their original method, the source terms are integrated on a mesh that is staggered with respect to the original finite volume mesh, and then they are projected onto the eigen-vectors of Roe's Jacobian, in the context of Roe's approximate Riemann solver. Following this approach, the numerical source term can be regarded as the sum of two cell-interface contributions. Delis (2003) applied a first-order method, in the context of HLL-E approximate Riemann solver, again by projecting the integral of the source terms onto the eigen-vectors of Roe's Jacobian: this approach doubles the number of wave speeds to be calculated.

Hubbard & García-Navarro (2000) extended the scheme by Bermúdez & Vázquez (1994) to the second-order precision in time and space. They remarked that, in the context of slope-limited schemes, a central source-term has to be introduced to the interfaces source term contributions in order to enforce the equilibrium with the advective fluxes. Ortega (2005) explicitly added the primitive of the source terms to the fluxes, and this sum was reconstructed by means of a third-order ENO-Roe reconstruction. However, the formal order of precision of the algorithm was degraded because of the quadrature rule used to compute the source term integrals. Črnjarić-Žic et al. (2004) proposed a Finite Volume scheme with WENO reconstruction of the conserved variables: the proposed treatment of the central part of geometrical source terms degraded the theoretical accuracy of the scheme.

Here, the original idea by Alouges et al. (1999) is applied. The geometrical source terms can be rewritten in divergence form

$$\vec{S} = \frac{\partial}{\partial x}\int_{x_a}^{x} \vec{S} dx = -\frac{\partial \vec{B}}{\partial x} \tag{10}$$

and then added to the divergence of fluxes. Equation 1 can be rewritten as

$$\frac{\partial \vec{U}}{\partial t} + \frac{\partial \vec{H}}{\partial x} = 0 \tag{11}$$

where

$$\vec{H} = \vec{F} + \vec{B} = \vec{F} - \int_{x_0}^{x} \vec{S} dx \tag{12}$$

and the following numerical flux can be defined:

$$\vec{H}^{*} = \alpha \vec{H}_L - \beta \vec{H}_R + \gamma\left(\vec{U}_R - \vec{U}_L\right) \tag{13}$$

Since at each interface one has, by construction,

$$\alpha - \beta = 1 \tag{14}$$

we can write

$$\begin{aligned} &\left[\alpha \vec{H}_L\right]_{i+\frac{1}{2}} - \left[\beta \vec{H}_R\right]_{i+\frac{1}{2}} - \left[\alpha \vec{H}_L\right]_{i-\frac{1}{2}} + \left[\beta \vec{H}_R\right]_{i-\frac{1}{2}} = \\ &= \left[\alpha\left(\vec{H}_R - \vec{H}_L\right)\right]_{i-\frac{1}{2}} - \left[\beta\left(\vec{H}_R - \vec{H}_L\right)\right]_{i+\frac{1}{2}} + \\ &+ \left(\vec{H}_L\right)_{i+\frac{1}{2}} - \left(\vec{H}_R\right)_{i-\frac{1}{2}} \end{aligned} \tag{15}$$

Finally, the following equation holds:

$$\begin{aligned} &\vec{H}^{*}_{i+\frac{1}{2}} - \vec{H}^{*}_{i-\frac{1}{2}} = \left[\gamma\left(\vec{U}_R - \vec{U}_L\right)\right]_{i+\frac{1}{2}} + \\ &- \left[\gamma\left(\vec{U}_R - \vec{U}_L\right)\right]_{i-\frac{1}{2}} + \left[\alpha\left(\vec{H}_R - \vec{H}_L\right)\right]_{i-\frac{1}{2}} + \\ &- \left[\beta\left(\vec{H}_R - \vec{H}_L\right)\right]_{i+\frac{1}{2}} + \left(\vec{H}_L\right)_{i+\frac{1}{2}} - \left(\vec{H}_R\right)_{i-\frac{1}{2}} \end{aligned} \tag{16}$$

which is the HLL version of the slope-limited Roe scheme proposed by Hubbard & García-Navarro (2000). Recalling that

$$-gh\frac{\partial z_b}{\partial x} = \frac{1}{2} g \frac{\partial h^2}{\partial x} - gh\frac{\partial \varsigma}{\partial x} \tag{17}$$

one has:

$$\begin{aligned} &\Delta x_i \frac{d(hU)_i}{dt} = -\left[\gamma(hU_R - hU_L)\right]_{i+\frac{1}{2}} + \\ &+ \left[\gamma(hU_R - hU_L)\right]_{i-\frac{1}{2}} - \left(\alpha h U_L^2\right)_{i+\frac{1}{2}} + \left(\beta h U_R^2\right)_{i+\frac{1}{2}} + \\ &+ \left(\alpha h U_L^2\right)_{i-\frac{1}{2}} - \left(\beta h U_R^2\right)_{i-\frac{1}{2}} - \alpha_{i-\frac{1}{2}} \int_{x^{-}_{i-\frac{1}{2}}}^{x^{*}_{i-\frac{1}{2}}} gh\frac{\partial \varsigma}{\partial x} dx + \\ &+ \beta_{i+\frac{1}{2}} \int_{x^{-}_{i+\frac{1}{2}}}^{x^{*}_{i+\frac{1}{2}}} gh\frac{\partial \varsigma}{\partial x} dx - \int_{x^{*}_{i-\frac{1}{2}}}^{x^{-}_{i+\frac{1}{2}}} gh\frac{\partial \varsigma}{\partial x} dx \end{aligned} \tag{18}$$

If the bed is continuous (not necessarily smooth), the following condition holds

$$z_{bi+\frac{1}{2}} = \left(\varsigma_R - h_R\right)_{i+\frac{1}{2}} = \left(\varsigma_L - h_L\right)_{i+\frac{1}{2}} \tag{19}$$

and it is easy to show that

$$\int_{x^{-}_{i+\frac{1}{2}}}^{x^{*}_{i+\frac{1}{2}}} gh\frac{\partial \zeta}{\partial x} dx = g\left[\frac{h_L + h_R}{2}\left(\varsigma_R - \varsigma_L\right)\right]_{i+\frac{1}{2}} \tag{20}$$

Copyright © 2006 Taylor & Francis Group plc, London, UK

The last integral, on the right-hand side of Equation 18, can be evaluated by means of a proper quadrature formula. Here, the approach by Noelle et al. (2006) is used:

$$\int_{x_{i-\frac{1}{2}}^{+}}^{x_{i+\frac{1}{2}}^{-}} gh\frac{\partial \zeta}{\partial x}dx = \frac{2g}{3}(h_1+h_2)(\zeta_2-\zeta_1)+ \\ +\frac{2g}{3}(h_2+h_3)(\zeta_3-\zeta_2)-\frac{g}{6}(h_1+h_3)(\zeta_3-\zeta_1) \tag{21}$$

where the following positions have been made:

$$\begin{cases} h_1=(h_R)_{i-\frac{1}{2}}; \quad h_2=(h_C)_i; \quad h_3=(h_L)_{i+\frac{1}{2}} \\ \zeta_1=(\zeta_R)_{i-\frac{1}{2}}; \quad \zeta_2=(\zeta_C)_i; \quad \zeta_3=(\zeta_L)_{i+\frac{1}{2}} \end{cases} \tag{22}$$

and the quantities with the subscript C are evaluated at the centres of the finite volumes. It can be demonstrated that Equation 21 is a fourth-order approximation of the integral over a finite volume of the central part of the source terms (Press et al., 1992): of course, it is only a third-order approximation of the cell-averaged value of the source term in the finite volume.

In spite of its form, which resembles a discretization of the non-conservative equation

$$\frac{\partial hU}{\partial t}+\frac{\partial\left(hU^2\right)}{\partial x}=-gh\frac{\partial \zeta}{\partial x} \tag{23}$$

the Equation 18 is a conservative discretization of the second component of the Equation 1. In fact, in the case where bed-slope source terms are absent, one has

$$-gh\frac{\partial \zeta}{\partial x}=-gh\frac{\partial h}{\partial x} \tag{24}$$

and some algebra demonstrates that

$$-\alpha_{i-\frac{1}{2}}\int_{x_{i-\frac{1}{2}}^{-}}^{x_{i-\frac{1}{2}}^{+}} gh\frac{\partial \zeta}{\partial x}dx+\beta_{i+\frac{1}{2}}\int_{x_{i+\frac{1}{2}}^{-}}^{x_{i+\frac{1}{2}}^{+}} gh\frac{\partial \zeta}{\partial x}dx+ \\ -\int_{x_{i+\frac{1}{2}}^{+}}^{x_{i+\frac{1}{2}}^{-}} gh\frac{\partial \zeta}{\partial x}dx=-\left(\alpha g\frac{h_L^2}{2}\right)_{i+\frac{1}{2}}+\left(\beta g\frac{h_R^2}{2}\right)_{i+\frac{1}{2}}+ \\ +\left(\alpha g\frac{h_L^2}{2}\right)_{i-\frac{1}{2}}-\left(\beta g\frac{h_R^2}{2}\right)_{i-\frac{1}{2}} \tag{25}$$

2.4 *Spectral (Finite) Volume Method*

In order to reach high-order accuracy in space, proper reconstruction of the conserved variables has to be accomplished in each control volume, starting from the cell-averaged values: here, the relatively recent *Spectral (Finite) Volume Method* (Wang, 2002) has been adopted. This method, which was originally developed in the context of gas-dynamics, was applied to the solution of the Shallow-water Equations by Choi et al. (2004) too. However, in their application, they neglected the bed-slope source terms.

The computational domain has been subdivided into *NS* non–overlapping domains named *Spectral Volumes*, whose lengths are

$$\Delta x_i=x_{i+1/2}-x_{i-1/2}; \quad i=1,2...,NS \tag{26}$$

To reach the k-th order of accuracy, each of the Spectral Volumes has been again subdivided into k Finite Volumes, whose lengths are

$$\Delta x_{i,j}=x_{i,j+1/2}-x_{i,j-1/2}; \quad i=1,2...,NS; j=1,2...k \tag{27}$$

If $u_{i,j}$ is the cell-averaged value of the conserved variable in the finite volume $C_{i,j}$, there exists only one polynomial reconstruction $p_i(x)$ of degree $(k-1)$ in the spectral volume S_i that ensures

$$\int_{x_{i,j-\frac{1}{2}}}^{x_{i,j+\frac{1}{2}}} p_i(x)dx=u_{i,j}\Delta x_{i,j} \tag{28}$$

for each control volume $C_{i,j}$. Given the reconstruction $p_i(x)$, it is easy to show that the reconstructed values of the variable u at the interfaces of the finite volumes are a linear combination of the cell-averaged values $u_{i,j}$: the coefficients of this linear combination depend only on the computational mesh, thus they can be precalculated and stored in memory. The finite volumes in each spectral volume are not equally spaced, in order to reduce the spurious oscillations at the boundaries of each spectral volume (Wang & Liu, 2004). Here, the Gauss-Lobatto points

$$\frac{x_{i,j+1/2}-x_i}{\Delta x_i}=-\frac{1}{2}\cos\left(\frac{j\pi}{k}\right); \quad j=0,1,...,k \tag{29}$$

have been used to collocate the interfaces between the control volumes, where x_i is the mid point of the spectral volume S_i.

We observe that the compactness and linearity of the reconstruction scheme leads to an efficient treatment of boundary conditions, and savings in CPU requirements. Moreover, the method is suitable for non-uniform grids, and its extension to quadrilateral

Copyright © 2006 Taylor & Francis Group plc, London, UK

and triangular non-structured meshes is possible. The Spectral (Finite) Volume Method permits to attain very high-order precision in space: Choi et al. (2004) presented schemes up to the eighth order for the solution of the Shallow-water Equations without source terms. Here, third-order precision in space is attained by making use of $k = 3$ control volumes for each spectral volume.

Once that the reconstructed variables are known on both sides of the cell interfaces, limitation of data is accomplished where needed. Aiming at this, the TVBM limiter by Cockburn & Shu (1989) is used, in order to avoid accuracy degeneration near extrema, which is consequent to the use of a total variation diminishing limiter. The TVBM limiter depends on a constant M to be tuned, namely an upper bound to the absolute value of the second-order derivative of the solution at local extrema: for a system of equations, a different value of the constant M can be used for each of the variables.

To determine the interface value of the flow depth, the following algorithm has been applied (Audusse et al., 2004), after the polynomial reconstruction and limitation of ς and h: first, the bed elevation value

$$z_b^* = \max\left(\varsigma_{L,i,j+1/2} - h_{L,i,j+1/2}; \varsigma_{R,i,j+1/2} - h_{R,i,j+1/2}\right) \quad (30)$$

is determined at each interface; then the water depths

$$\begin{cases} h_{R,i,j+1/2} = \max\left(\varsigma_{R,i,j+1/2} - z_b^*, 0\right) \\ h_{L,i,j+1/2} = \max\left(\varsigma_{L,i,j+1/2} - z_b^*, 0\right) \end{cases} \quad (31)$$

are chosen for the computations.

After the reconstruction and limitation of the conserved variables at the boundaries of each control volume, the value at the centre can be calculated by means of the following third-order approximation

$$u_{C\,i,j} = \frac{-u_{R\,i,j-1/2} + 6u_{i,j} - u_{L\,i,j+1/2}}{4} \quad (32)$$

2.5 *Time evolution*

To solve Equation 5, for each of the control volumes, the third-order optimal Runge-Kutta scheme is used, namely (Gottlieb & Shu, 1998):

$$\begin{cases} \vec{U}_{i,j}^{(1)} = \vec{U}_{i,j}^{n} + \Delta t \vec{L}_{i,j}\left(\vec{U}^{n}\right) \\ \vec{U}_{i,j}^{(2)} = \dfrac{3\vec{U}_{i,j}^{n}}{4} + \dfrac{\vec{U}_{i,j}^{(1)}}{4} + \dfrac{\Delta t}{4}\vec{L}_{i,j}\left(\vec{U}^{(1)}\right) \\ \vec{U}_{i,j}^{n+1} = \dfrac{\vec{U}_{i,j}^{n}}{3} + \dfrac{2\vec{U}_{i,j}^{(2)}}{3} + \dfrac{2\Delta t}{3}\vec{L}_{i,j}\left(\vec{U}^{(2)}\right) \end{cases} \quad (33)$$

where $\vec{U}^n$ is the vector of the conserved variables at the time level t^n, and $\Delta t = t^{n+1} - t^n$ is the time step. Finally, the spatially averaged value of the conserved variables in the spectral volume S_i can be calculated at each time step by means of

$$\vec{U}_i = \frac{\sum_{j=1}^{k} \Delta x_{i,j} \vec{U}_{i,j}}{\Delta x_i} \quad (34)$$

2.6 *C-property*

It is easy to demonstrate that the proposed scheme satisfies the *C-property* exactly. In fact, in the case of water-at-rest, Equation 18 reduces to

$$\begin{aligned} \Delta x_i \frac{d(hU)_i}{dt} = &-\alpha_{i-\frac{1}{2}} \int_{x_{i-\frac{1}{2}}^{-}}^{x_{i-\frac{1}{2}}^{+}} gh\frac{\partial \varsigma}{\partial x} dx + \\ &+ \beta_{i+\frac{1}{2}} \int_{x_{i+\frac{1}{2}}^{-}}^{x_{i+\frac{1}{2}}^{+}} gh\frac{\partial \varsigma}{\partial x} dx - \int_{x_{i-\frac{1}{2}}^{+}}^{x_{i+\frac{1}{2}}^{-}} gh\frac{\partial \varsigma}{\partial x} dx \end{aligned} \quad (35)$$

Starting from the rest conditions, the water surface elevation is uniform in the computational domain and equal to ς_o: the polynomial reconstruction ensures that the values of ς reconstructed at the centre and at the interfaces of each control volume are equal to ς_o. This implies that the source terms at the right-hand side of Equation 35, as calculated by means of Equations 20 and 21, are null, and the fluid does not accelerate. Significantly, the scheme chosen for the integration in time does not alter this equilibrium, which is satisfied at each of the inner steps of the Runge-Kutta algorithm (Equation 33).

3 NUMERICAL EXPERIMENTS

3.1 *Introduction*

In this section, a number of numerical experiments are presented, in order to verify the accuracy properties of the numerical scheme proposed, as well as its capability to preserve water-at-rest states, by using classical tests very often reported in the literature.

3.2 *Verification of the C-property*

The first test aims to verify if the numerical scheme proposed satisfies the *C-Property*. A channel, $L = 1500$ m long, with rectangular cross-section of unitary width, has a complicate bottom topography

Copyright © 2006 Taylor & Francis Group plc, London, UK

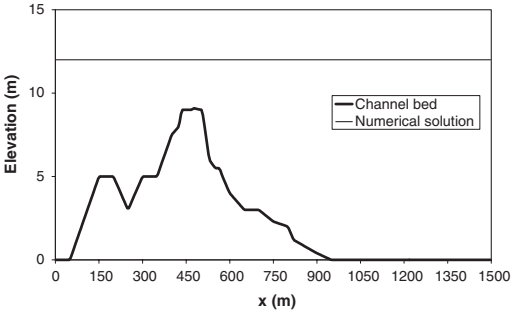


Figure 1. Quiescent flow test-case: water surface elevation, t = 1000 s.

(Figure 1), inspired to that of the test-case proposed by Goutal & Maurel (1997).

The quiescent initial conditions are $\varsigma_o = 12$ m, and $(hU)_o = 0$ m^2/s. The upstream and downstream boundaries of the channel are open and the physical boundary condition $(hU)_u = 0$ m^2/s is imposed upstream, while $\varsigma_d = 12$ m is imposed downstream. In spite of the complicate bottom topography, the analytical solution is of quiescent water, which is maintained indefinitely.

The results shown in Figure 1 ($t = 1000$ s) have been calculated, in double precision, on a uniform grid of 300 spectral volumes ($\Delta x = 5$ m), with time step $\Delta t = 0.02$ s. The limiting parameters used in the test are $M_h = 50$, $M_\varsigma = 50$, $M_{hU} = 0$.

Significantly, the error for the water surface elevation is of the order of the machine epsilon, and it has not been reported here. The L_∞ error norm (maximum absolute error) for the specific discharge hU is $3.67 \cdot 10^{-13}$ m^2/s, while the L_1 error norm (which is proportional to the average absolute error, if the grid is uniform) is $1.15 \cdot 10^{-13}$ m^2/s. Since after 50000 time steps the errors are very small, and not far from the level of round-off, it remains confirmed that, if the exact *C-Property* is satisfied, the water-at-rest solutions can be respected with good precision, and numerical stability is ensured.

3.3 *Convergence test*

In order to verify the accuracy of the numerical model, a convergence test has been accomplished, considering a subcritical flow over a bump. A horizontal channel is considered, $L = 25$ m long and 1 m wide, where a parabolic bump of height $H = 0.2$ m is present. The topography of the channel is defined as follows (see Figure 2):

$$z_b(x) = \begin{cases} 0; & x \le 8 \\ 0.2 - 0.05(x-10)^2; & 8 < x < 12 \\ 0; & x \ge 12 \end{cases} \qquad (36)$$

Table 1. hU errors and numerical orders of accuracy.

Number of spectral volumes	L_1 error		L_∞ error	
	error	order	error	order
25	$3.5 \cdot 10^{-5}$		$2.8 \cdot 10^{-4}$	
50	$4.6 \cdot 10^{-6}$	2.92	$4.1 \cdot 10^{-5}$	2.76
100	$6.1 \cdot 10^{-7}$	2.91	$5.3 \cdot 10^{-6}$	2.95
200	$7.6 \cdot 10^{-8}$	3.01	$7.0 \cdot 10^{-7}$	2.94
400	$9.6 \cdot 10^{-9}$	3.01	$8.9 \cdot 10^{-8}$	2.98
800	$1.2 \cdot 10^{-9}$	2.94	$1.3 \cdot 10^{-8}$	2.79

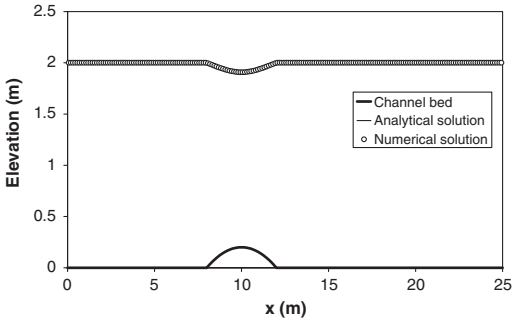


Figure 2. Subcritical flow over a bump: water surface elevation, t = 300 s.

A steady-state condition is considered where the specific discharge flowing through the channel is $hU = 4.42$ m^2/s, and a downstream boundary condition $\varsigma = 2$ m is imposed. In this case, the flow is subcritical, and an analytical solution exists, which can be found by means of the Bernoulli Theorem.

The test has been repeated for different grids, considering a number of spectral volumes ranging from 25 to 800, and keeping the Courant number constant, with time steps ranging from 0.05 s to 0.0015625 s. The limiter parameters were $M_h = 50$, $M_\varsigma = 50$, $M_{hU} = 0$ in all the convergence tests. The L_1 and L_∞ error norms are shown in Table 1, with the order of accuracy, for the specific discharge hU. It can be clearly seen that the third order of accuracy is attained by the numerical scheme.

In Figure 2 are compared the exact and calculated water surfaces elevations for the case of 200 spectral volumes ($\Delta x = 0.125$ m, $\Delta t = 0.00625$ s) at $t = 300$ s: it is apparent that the numerical solution is in close agreement with the analytical one.

In Figure 3 the specific discharge error is plotted for the 200 spectral volumes test, showing the good conservation properties of the scheme proposed.

3.4 *Transcritical flow without shock*

In this test the bed-topography of the channel is the same as in the preceding case. A steady-state condition

Copyright © 2006 Taylor & Francis Group plc, London, UK

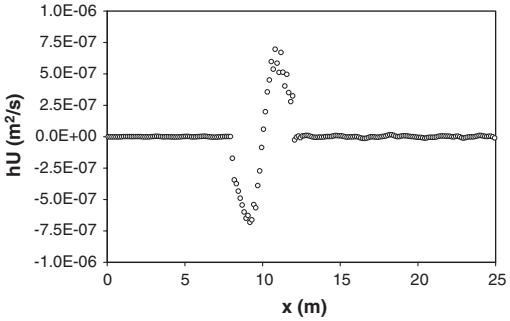


Figure 3. Subcritical flow over a bump: specific discharge error, t = 300 s.

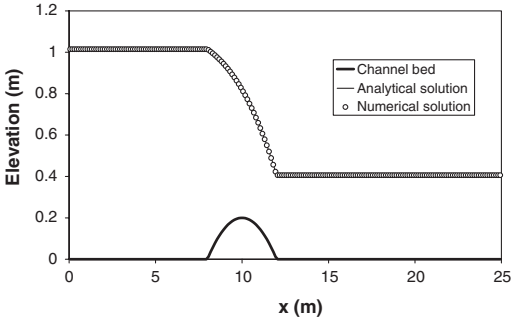


Figure 4. Transcritical flow over a bump: water surface elevation, t = 300 s.

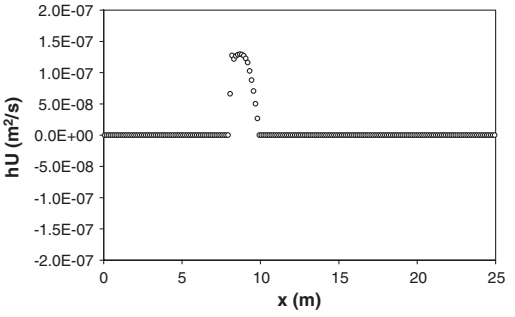


Figure 5. Transcritical flow over a bump: specific discharge error, t = 300 s.

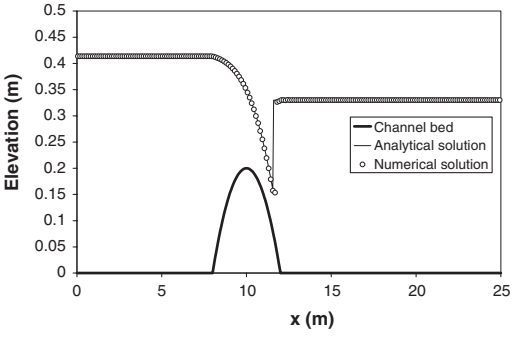


Figure 6. Transcritical flow over a bump with shock: water surface elevation, t = 300 s.

is considered where the specific discharge flowing through the channel is $hU = 1.53\,\mathrm{m}^2/\mathrm{s}$, and a downstream boundary condition $\varsigma = 0.66\,\mathrm{m}$ is imposed, which influences the flow until the condition downstream is supercritical. An analytical solution exists, which can be found by means of the Bernoulli Theorem, corresponding to a transition of the flow from subcritical to supercritical conditions, passing over the bump. For this test, a grid of 200 spectral volumes has been considered ($\Delta x = 0.125\,\mathrm{m}$), with time step $\Delta t = 0.005$ s. Again, the limiting parameters $M_h = 50$, $M_\varsigma = 50$, $M_{hU} = 0$ were used. The analytical water surface elevation and the numerical solution at time $t = 300$ s are compared in Figure 4, showing very good agreement.

The error at time $t = 300$ s, with reference to the specific discharge, is plotted in Figure 5, confirming good conservation properties of the scheme.

3.5 *Transcritical flow with shock*

The same bed topography and computational grid as in the preceding case has been used. A steady-state condition is considered where the specific discharge flowing through the channel is $hU = 0.18\,\mathrm{m}^2/\mathrm{s}$, and a downstream boundary condition $\varsigma = 0.33\,\mathrm{m}$ is imposed. An analytical solution exists, which can be determined by coupling the Bernoulli Theorem with the Rankine-Hugoniot condition, corresponding to a transition from subcritical to supercritical flow, passing over the bump, and again from supercritical to subcritical flow downstream of the bump: the second transition implies the formation of a stationary shock. The time step used for the test is $\Delta t = 0.001$ s, while the limiting parameters used are $M_h = 20$, $M_\varsigma = 20$, $M_{hU} = 0$.

The analytical water surface elevation and the numerical solution, at time $t = 300$ s, are compared in Figure 6, again showing good agreement.

The presence of the stationary shock is a challenging feature of the flow to be modelled, and conservation errors are expected to appear in the numerical solution. The specific discharge at time $t = 300$ s is plotted in Figure 7, showing that the major conservation errors influence a little number of cells. The results shown compare favourably with those available in literature (Delis, 2003, Xing & Shu, 2005).

Copyright © 2006 Taylor & Francis Group plc, London, UK

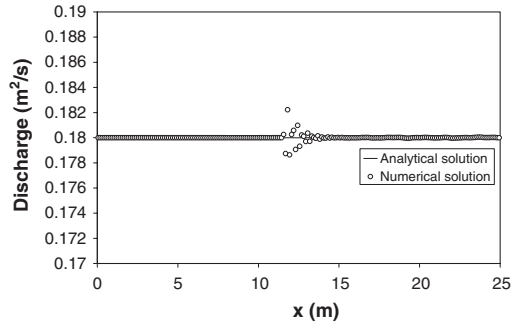


Figure 7. Transcritical flow over a bump with shock: specific discharge error, t = 300 s.

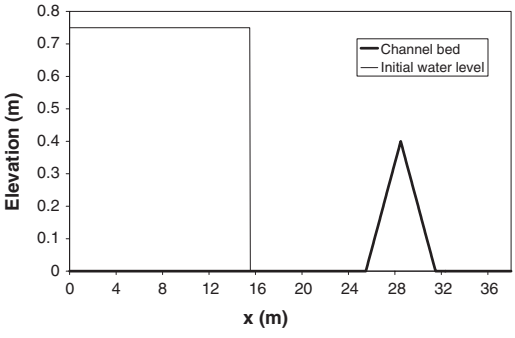


Figure 8. Dam-break over a triangular bump: initial condition.

3.6 *Dam-break experiment*

In this test, the results of the numerical model are compared with the experimental data of the laboratory dam-break performed by Hiver at the Recherches Hydrauliques Lab. Chatelet, together with the Universitè Libre de Bruxelles (Alcrudo & Soares Frazão, 2000).

The experimental set-up consisted of a 38 m long channel, of rectangular cross section, with 0.75 m constant width, where a gate divided a 15.5 m long reservoir from the dry bottom portion of the channel. A symmetric triangle-shaped bump, 6 m long and 0.40 m high, was located 10 m downstream of the gate. The end of the channel consisted of a free outlet. The Strickler roughness coefficients 80 $m^{1/3}/s$ and 90 $m^{1/3}/s$ were evaluated for the bed and for the vertical walls, respectively. The initial conditions consisted of 0.75 m of water in the reservoir (see Figure 8): the sudden removal of the gate permitted to reproduce the instantaneous failure of a dam. Seven gauges (G2, G4, G8, G11, G12, G13, G20) were collocated at different distances from the gate (see Table 2), in order to measure the water depth variations during the transient consequent to the dam failure.

Table 2. Gauge positions.

Gauge	abscissa (m)
G2	17.5
G4	19.5
G8	23.5
G10	25.5
G11	26.5
G13	28.5
G20	35.5

In order to perform this numerical test, the friction losses source term S_f was added to the bed-slope source term in Equation 4, obtaining the following source term vector:

$$\vec{S} = \begin{bmatrix} 0 & gh\left(-\frac{dz_b}{dx} - S_f\right) \end{bmatrix}^T \tag{37}$$

The Gauckler-Strickler formula was used for the evaluation of the punctual friction slope, with Strickler coefficient equal to 80 $m^{1/3}/s$. Again, the bed slope source term was evaluated by means of the upwind approach, while a pointwise approach was used for the friction slope: in order to attain third-order precision, the Simpson rule was used to approximate the integral

$$g\int_{x_{i,j-\frac{1}{2}}}^{x_{i,j+\frac{1}{2}}} hS_f\,dx = \frac{g\Delta x_{i,j}}{6}\left[\left(hS_f\right)_1 + \left(4hS_f\right)_2 + \left(hS_f\right)_3\right]_{i,j} \tag{38}$$

where the addends at the right hand side of Equation 38 were evaluated at the boundaries (hS_{f1} and hS_{f3}) and at the centre (hS_{f2}) of each control volume.

A tolerance ε was defined to handle possible instabilities at the wetting front, due to the evaluation of the friction terms where the water depth is very small: in particular, the slope friction was not evaluated in the cells with water depth smaller than ε, where the cell velocity was set to zero. No other special treatment was adopted in order to deal with the wetting/drying fronts. The computational domain was subdivided in 760 spectral volumes (each 0.05 m long), and the following parameters were used for the calculations: $\Delta t = 0.005$ s, $M_h = 0$, $M_\varsigma = 0$, $M_{hU} = 0$, $\varepsilon = 0.001$ m.

In Figure 9 a comparison is made between the experimental data at the gauge G4 and the numerical results. It can be seen that the numerical model fairly predicts the wave arrival time, as well as the maximum water level at the gauge. The successive waves reflected by the bump are reproduced less accurately with respect to the arrival time.

The results related to the gauge G10 are shown in Figure 10. Again, the numerical model fairly predicts the first and second wave arrival time, as well as the wave receding stage, with a slight over-prediction

Copyright © 2006 Taylor & Francis Group plc, London, UK

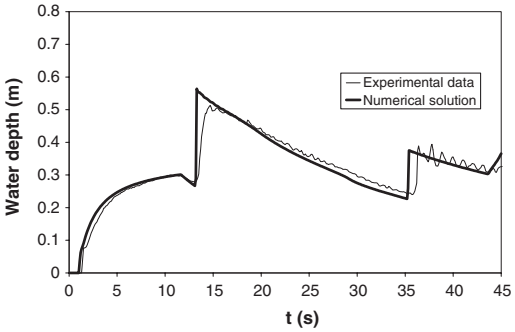


Figure 9. Dam-break over a triangular bump: gauge G4.

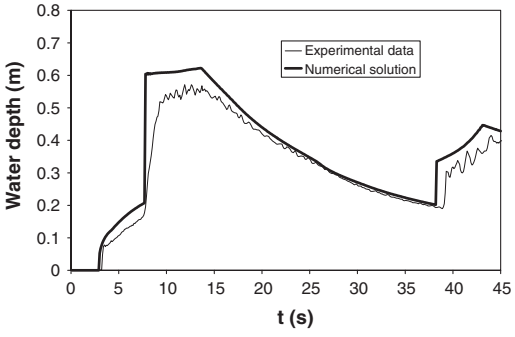


Figure 10. Dam-break over a triangular bump: gauge G10.

of the maximum water level at the gauge. The third wave time arrival is under-predicted. The results can be compared with those presented by Zhou et al. (2004), where a HLL Riemann solver is used, coupled with the Surface Gradient Method for the treatment of source terms: the comparison shows a better behaviour of the model presented here.

Interestingly, the main discrepancies between the numerical solution that has been proposed here and the experimental data are shared with other numerical models available in literature (Brufau et al., 2002, Črnjarić-Žic et al., 2004): this fact addressesthe importance of real water effects (turbulence, three-dimensional effects) which can not be well reproduced by the one-dimensional Shallow-water Equations mathematical model.

The inspection of the plot related to the Gauge G13 (Figure 11), located on the top of the bump, where the three-dimensional effects are expected to have a major influence on the flow behaviour, seems to confirm the last observations.

4 CONCLUSIONS

A Spectral Volume model aiming at the accurate solution of the Shallow-water Equations with bed-slope

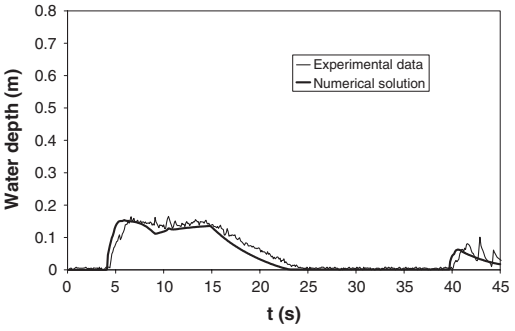


Figure 11. Dam-break over a triangular bump: gauge G13.

source terms has been presented. The special treatment of the source terms, which can be decomposed in interface (upwind) contributes, and a central contribute, ensures the full order of accuracy of the method. A number of tests have been presented, in order to verify the capability of the model to manage complicate topographies, both in steady and in transient conditions, as well as its capability to enforce the respect of the *C-Property*. The third-order accuracy of the model was confirmed by the convergence test carried out: in the case that a higher order of approximation is required, different quadrature formulas for the source terms can be used, which make use of the variables reconstructed at proper quadrature points by means of the methods considered above.

The use of the Spectral Volume Method, which allows to attain very high orders of precision, can be extended from one- to two-dimensional problems, in the context of triangular and quadrilateral unstructured grids, which are preferable when dealing with natural geometries; moreover, the extension of the method presented here to the solution of the Open-channel flow Equations can be considered, introducing not only the bed-slope source term, but also the source terms arising from slight cross-section variations along the channel: these topics will be the object of future communications.

REFERENCES

Alcrudo, F. & Soares Frazão S. 2000, Conclusions from the 1st CADAM Meeting – Wallingford, UK. In S. Soares Frazão, M. Morris and Y. Zech (eds.), *Concerted Action on DAm-break Modelling*. Université Catholique de Louvain. (CD-ROM).

Alouges, F., Ghidaglia, J.-M. & Tajchman, J. 1999, On the interaction of upwinding and forcing for nonlinear hyperbolic systems of conservation laws. *preprint 9907 Centre de Mathématiques et de Leurs Applications*.

Audusse, E., Bouchut, F., Bristeau, M.-O., Klein, R. & Perthame, B. 2004, A fast and stable well-balanced scheme

Copyright © 2006 Taylor & Francis Group plc, London, UK

with hydrostatic reconstruction for Shallow-water flows. *SIAM J. Sci. Comput.*, 25(6): 2050–2065.

Bermúdez, A., Dervieux, A., Desideri, A. & Vázquez, M.E. 1998, Upwind schemes for the two-dimensional shallow water equations with variable depth using unstructured meshes. *Comput. Methods Appl. Mech. Engrg.*, 155: 49–72.

Bermúdez, A. & Vázquez, M.E. 1994, Upwind methods for hyperbolic conservation laws with source terms. *Comp. & Fluids*, 23(8): 1049–1071.

Brufau, P., Vázquez-Cendón, M.E. & García-Navarro, P. 2002, A numerical model for the flooding and drying of irregular domains, *Int. J. Num. Meth. Fluids*, 39(3): 247–275.

Choi, B.J., Iskandarani, M., Levin, J. & Haidvogel, D.B. 2004, A spectral finite-volume method for the shallow water equations. *Month. Weath. Rev.*, 132(7): 1777–1791.

Cockburn, B. & Shu, C.-W. 1989, TVB Runge-Kutta local projection discontinuous Galerkin finite element method for conservation laws II: General framework. *AMS Math. Comp.*, 52(186): 411–435.

Cockburn, B. & Shu, C.-W. 2001, Runge-Kutta discontinuous Galerkin methods for convection-dominated problems. *J. Sci. Comput.*, 16(3): 173–261.

Cozzolino, L. & Pianese, D. 2005, Finite volume modelling of water quality changes in Shallow-water bodies (Paper C22-2). In Gye-Byong-Ho Jun, Sang-Il Lee, Il Won Seo and Gye-Woon Choi (eds.), *Proc. Of the XXXI IAHR Congress., Seoul, 11–16 September 2005*. (CD-ROM).

Črnjarić-Žic, N., Vuković, S. & Sopta, L. 2004, Balanced finite volume WENO and central WENO schemes for the shallow-water and open channel flow equations. *J. Comp. Phys.*, 200(2): 512–548.

Delis, A.I. 2003, Improved application of the HLLE Riemann solver for the shallow water equations with source terms. *Comm. Numer. Math. Engng.*, 19(1): 59–83.

Fraccarollo, L. & Toro, E.F. 1995, Experimental and numerical assessment of the shallow water model for two-dimensional dam-break type problems. *IAHR J. Hydr. Res.*, 33(6): 843–864.

Gosse, L. 2000, A well-balanced flux-vector splitting scheme designed for hyperbolic systems of conservation laws with source terms. *Comp. & Math. With Appl.*, 39: 135–159.

Gottlieb, S., & Shu, C-W. 1998, Total Variation Diminishing Runge-Kutta schemes. *AMS Math. Comp.*, 67(221): 73–85.

Goutal, P. & Maurel, F. 1997, Technical Report IIE-13/97/016A. *EDF – Département Laboratoire National d'Hydraulique, Groupe Hydraulique Fluviale*.

Greenberg, J.M & Leroux A.Y. 1996, A well-balanced scheme for the numerical processing of source terms in hyperbolic equations. *SIAM J. Num. Anal.*, 33(1): 1–16.

Guinot, V. & Soares Frazão, S. 2006, Flux and source term discretization in two-dimensional shallow water models with porosity on unstructured grids. *Int. J. Num. Meth. Fluids*, 50(3): 309–345.

Hubbard, M.E. & García-Navarro, P. 2000, Flux difference splitting and the balancing of source terms and flux gradients. *J. Comp. Phys.*, 165(1): 89–125.

Jin, S. 2001, A steady-state capturing method for hyperbolic systems with geometrical source terms. *Math. Model. Num. Anal.*, 35(4): 631–645.

Kurganov, A. & Levy, D. 2002, Central-upwind schemes for the Saint-Venant system. *Math. Modell. Num. Anal.*, 36(3): 397–425.

Noelle, S., Pankratz, N., Puppo, G., & Natvig, J.R. 2006, Well-balanced finite volume schemes of arbitrary order of accuracy for shallow water flows. *J. Comp. Phys.*, 213(2): 474–499.

Ortega, G.H. 2005, *Numerical simulation of shallow water equations and some physical models in image processing*. PhD Thesis, Universitat Pompeu Fabra, Barcelona.

Press, W.H., Teukolsky, S.A., Vetterling, W.T. & Flannery, B.P. 1992, *Numerical Recipes*. Cambridge: Cambridge University Press.

Toro, E.F. 1999, *Riemann solvers and numerical methods for fluid dynamics*. Berlin: Springer-Verlag.

Wang, Z.J. 2002, Spectral (finite) volume method for conservation laws on unstructured grids. *J. Comp. Phys.*, 178(1): 210–251.

Wang, Z.J. & Liu, Y. 2004, Spectral (finite) volume method for conservation laws on unstructured grids III: one dimensional systems and partition optimization. *J. Sci. Comp.*, 20(1): 137–157.

Xing, Y. & Shu, C.-W. 2005, High order finite difference WENO schemes with the exact conservation property for the shallow water equations. *J. Comp. Phys.*, 208(1): 206–227.

Zhou, J.G., Causon, D.M., Mingham C.G. & Ingram, D.M. 2004, Numerical prediction of dam.break flows in general geometries with complex bed topography. *ASCE J. Hyd. Engrg.*, 130(4): 332–340.

Copyright © 2006 Taylor & Francis Group plc, London, UK

Nonparallel spatial stability of shallow water flow down an inclined plane of arbitrary slope

P. Bohorquez & R. Fernandez-Feria
E.T.S.Ingenieros Industriales, Universidad de Málaga (Spain)

ABSTRACT: Roll waves are known to occur in the frictional flow of a thin layer of water down an inclined solid surface. For a layer of constant depth, the formation of these waves on a solid plane with small slope angle have been explained as a hydrodynamic instability occurring above a critical Froude number by analyzing the temporal stability of the constant velocity flow. Here we analyze the linear, spatial stability of the shallow-water flow down an inclined plane of arbitrary slope including the first order effects of the gradients of both the velocity and the water depth. For constant water depth (parallel case) we reproduce previous results of the temporal stability analysis. Then we apply the nonparallel stability formulation to the kinematic wave approximation of the shallow-water flow down an inclined plane of arbitrary slope and characterize, analytically, the frequency and the wavelength of the most unstable waves as a function of the Froude number, slope angle, velocity and velocity gradient. We find important qualitative differences with respect to the parallel (constant depth) case. These stability results are used to discuss the numerical solution to the nonlinear shallow-water flow equations for the dam-break problem on an inclined surface of arbitrary slope. A good agreement between the waves resulting from the numerical simulations and the predictions of the stability analysis is found.

1 INTRODUCTION

A thin layer of water flowing down an inclined surface may undergo, in some circumstances, a transition to an oscillatory movement where a train of surface waves propagates downstream. The amplitude of these waves increases, and eventually break into the form of a train of hydraulic bores at quite regular intervals, as they propagate downstream. These so-called roll waves where first scientifically observed in open channel flows by Cornish in 1904 (Cornish 1934), and have been subsequently documented in many man-made and natural shallow water flows (Kenyon 1998; Chanson 2004). The presence of these waves is generally undesirable from the hydraulic engineer point of view because they can produce overflow from the channel sides and because excessive intermittency at the outlet. Therefore the interest in determining with precision the conditions under which they appear.

Since the early work of Jeffreys (1925), these roll waves are known to be originated by inertial instabilities of the turbulent shallow water flow in a channel. Particularly, this author analysed the linear, temporal stability of the St. Venant one-dimensional model for the uniform flow over a plane, including a drag term proportional to the square of the velocity, and found the instability condition $Fr > 2$, where Fr is the Froude number (see below for its definition). Subsequently, Dressler (1949) confirmed this stability result and constructed finite-amplitude roll waves by piecing together smooth solutions separated by discontinuous shocks. Experiments by Brock (1967) showed the formation of roll waves for $Fr > 2$. Further linear stability results for the uniform turbulent flow down open inclined channel include both temporal (Brock 1967; Whitham 1974; Berlamont and Vanderstappen 1981) and spatial stability analysis (Di Cristo and Vacca 2005). All these stability results do not modify Jeffrey's basic finding that the uniform flow becomes unstable for $Fr > 2$.

In this work we consider the spatial stability analysis of the shallow water flow with friction down an inclined plane. The two features introduced here that have not been considered before are that the basic flow is valid for arbitrary slope of the channel, and that nonparallel effects accounting for the slow streamwise variations of both the basic flow and the perturbation are taken into account. Earlier stability analysis of the shallow water flow down an open inclined channel used the St. Venant one-dimensional shallow-water equations, valid for small slopes of the channel (Stoker 1957; Whitham 1974). Recently, Bouchut et al. (2003) and Keller (2003) have generalized these shallow water equations for arbitrary slopes of the bottom of the channel. But, for a constant (but arbitrary) slope, the equations are formally the same as the St. Venant

Copyright © 2006 Taylor & Francis Group plc, London, UK

equations, provided that appropriate variables are used (Savage and Hutter 1991). Therefore, this generalisation to an arbitrary slope of the inclined plane does not modify, as we shall see, the basic Jeffreys's stability result. However, we find that the inclusion of nonparallel effects in the stability analysis qualitatively modify the stability properties of the flow. Therefore, the critical parameters at which roll waves are predicted in a non-uniform flow may be substantially different from those in an uniform flow.

The structure of the paper is as follows. In the next section we formulate the spatial stability problem. We consider non-parallel effects for a general non-uniform flow down an inclined plane of arbitrary slope. Then we reproduce the known stability results for a uniform flow when non-parallel effects are neglected, but for arbitrary slope of the channel. Detailed stability properties of non-uniform flows, when non-parallel effects are included, are given for the case when the kinematic wave approximation (Whitham 1974) is used for the basic flow. These stability results are then compared with the outcome of some numerical simulations for the dam-break problem on an inclined surface of arbitrary slope, and with some available experimental results. Finally, some conclusions are drawn in the last section.

2 FORMULATION OF THE PROBLEM

We consider here the one-dimensional flow over a constant slope bed. In the shallow-water approximation, the dimensionless equations for the mass conservation and momentum in the direction of the flow can be written as [see Fig. 1]

$$\frac{\partial \eta}{\partial t} + \frac{\partial \eta U}{\partial X} = 0\,, \tag{1}$$

$$\frac{\partial U}{\partial t} + U\frac{\partial U}{\partial X} + \cos\theta \frac{\partial \eta}{\partial X} = \sin\theta - \frac{s_f}{\eta}\,, \tag{2}$$

where θ is the angle between the bed and the horizontal, t is the time, X is the coordinate along the bed, η is the depth of the water measured along the coordinate Y perpendicular to the bed, U is the depth-averaged velocity component along X, and s_f is a dimensionless bed friction (see below). All the magnitudes in these equations have been non-dimensionalized with respect to a length scale η_0, corresponding to some initial depth, and a velocity scale $U_0 \equiv \sqrt{g\eta_0}$, where g is the acceleration due to gravity. Equations (1)–(2) are formally the same as the classical St. Venant equations for the shallow-water in a channel with small angle of inclination θ (Stoker 1957). However, it can be shown (Savage and Hutter 1991; Bouchut et al. 2003; Keller 2003) that these equations, written in the present coordinates X and Y (see Fig. 1), are valid for *any* slope

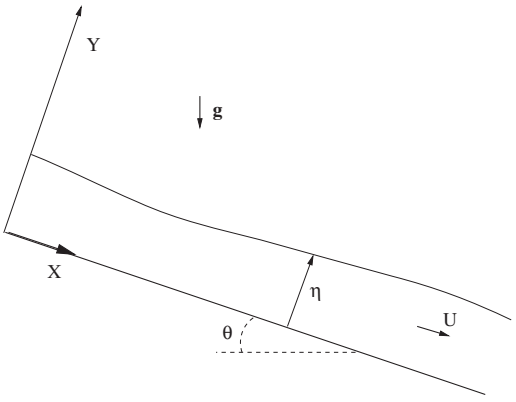


Figure 1. Sketch of coordinates and variables.

$\tan\theta$ of the *constant-slope* bed, not just for small channel slope, provided that the characteristic length scale of the flow in the direction of the coordinate X is much greater than the characteristic length scale in the Y direction.

To compute the friction term, $s_f \equiv (\tau_b/\rho U_0^2)$, where τ_b is the bed shear stress and ρ the fluid density, we shall use the Darcy-Weisbach friction factor f, so that s_f may be written as

$$s_f = \frac{f}{8}|U|U\,. \tag{3}$$

The factor f is a function of the local Reynolds number, based on the velocity U and the hydraulic diameter of the channel, and the relative height roughness of the bed. However, to simplify the present analysis we shall assume that the friction factor f is constant in what follows.

Here we shall analyse the spatial stability of a flow governed by Eqs. (1)–(2). To that end, if $\eta = H(X,t)$ and $U = V(X,t)$ is a solution to these equation, the perturbed flow is decomposed, as usual, as the sum of the basic flow solution plus a small perturbation, $\eta'(X,t)$ and $U'(X,t)$,

$$\eta = H + \eta', \quad U = V + U', \tag{4}$$

where the (non-dimensional) perturbations satisfy

$$|\eta'| \ll H, \quad \text{and} \quad |U'| \ll V\,. \tag{5}$$

We shall also assume that the streamwise variation of the basic flow is small,

$$\left|\frac{\partial H}{\partial X}\right| \ll 1\,, \quad \left|\frac{\partial V}{\partial X}\right| \ll 1\,. \tag{6}$$

Substituting (4) into (1)–(2), taking into account that $[H, V]$ is a solution to the equations, and neglecting

Copyright © 2006 Taylor & Francis Group plc, London, UK

second order terms in both the small perturbations and the streamwise derivatives of the basic flow, one is left with the following set of linear equations for the perturbations:

$$\frac{\partial \eta'}{\partial t} + \frac{\partial H U'}{\partial X} + \frac{\partial V \eta'}{\partial X} = 0, \tag{7}$$

$$\frac{\partial U'}{\partial t} + \frac{\partial V U'}{\partial X} + \cos\theta \frac{\partial \eta'}{\partial X} + \frac{f V^2}{8H}\left(\frac{2U'}{V} - \frac{\eta'}{H}\right) = 0. \tag{8}$$

The perturbation $\mathbf{s} \equiv [\eta'(X,t), U'(X,t)]^T$, where the superscript T denotes transposed vector, is decomposed in the standard form

$$\mathbf{s}(X,t) = \mathbf{S}(X)\boldsymbol{\chi}(X,t), \tag{9}$$

where the complex amplitude

$$\mathbf{S}(X) \equiv \begin{pmatrix} F(X) \\ G(X) \end{pmatrix} \tag{10}$$

depends only on the streamwise coordinate. In accordance with (6), we shall assume that $|d\mathbf{S}/dX| \ll 1$. The other part of the perturbation is of exponential form and describes the wave-like nature of the disturbance,

$$\boldsymbol{\chi}(X,t) = \exp\left[\int_{X_i}^{X} a(X')dX' - i\omega t\right], \tag{11}$$

where X_i is an initial or reference value of the coordinate X. The non-dimensional, complex wavenumber a is defined as

$$a(X) \equiv \gamma(X) + i\alpha(X). \tag{12}$$

The real part $\gamma(X)$ is the local exponential growth rate, and the imaginary part $\alpha(X)$ is the local wavenumber. A non-dimensional frequency ω has also been defined in (11).

Substituting (9)–(12) into (7)–(8), the resulting set of two linear equations may be written in the matrix form

$$\mathbf{A}\cdot\mathbf{S} + a\mathbf{B}\cdot\mathbf{S} + \mathbf{B}\cdot\frac{d\mathbf{S}}{dX} = 0, \tag{13}$$

where

$$\mathbf{A} = \begin{pmatrix} -i\omega + V_X & H_X \\ -\frac{fV^2}{8H^2} & -i\omega + V_X + \frac{fV}{4H} \end{pmatrix}, \tag{14}$$

$$\mathbf{B} = \begin{pmatrix} V & H \\ \cos\theta & V \end{pmatrix}, \tag{15}$$

and $H_X \equiv \frac{\partial H}{\partial X}$, $V_X \equiv \frac{\partial V}{\partial X}$.

The retained terms in (13) account for two different non-parallel effects on the stability of the perturbations: the effect of the non-parallelism of the basic flow and of the amplitude of the perturbations, and the effect of the history, or convective evolution, of the perturbations. This last effect is described by the d/dX terms of the stability equation. All these effects are negligible in the parallel limit of uniform basic flow with uniform perturbations.

As it stands there is some ambiguity in the partition of the perturbations (9) into two functions of the coordinate X. To close the problem one has to enforce an additional normalization condition which puts some restriction on the streamwise variation of the perturbation amplitude (Bertolotti et al. 1992). We shall perform here a local spatial stability analysis (Fernandez-Feria 2000): Given a *real* frequency ω, Eq. (13) and its X-derivative will be solved locally for each location $X = X_0$ with the *normalization* condition $[da/dX]_{X=X_0} = 0$. This condition will restrict, as required, the downstream variation of the perturbation amplitude (eigenfunction), yielding, for each $X = X_0$, the local growth rate and the wavenumber (or the phase speed of the disturbance). To that end, the eigenfunction $\mathbf{S}$ is expanded in a Taylor series about $X = X_0$, where only two terms are retained to be consistent with the approximation made in Eq. (13):

$$\mathbf{S}(X) \simeq \mathbf{S}(X_0) + (X - X_0)\left.\frac{d\mathbf{S}}{dX}\right|_{X=X_0} \equiv \mathbf{S}_0 + (X - X_0)\mathbf{S}_1. \tag{16}$$

This expansion is now substituted into (13) and its X-derivative to obtain two equations for $\mathbf{S}_0$ and $\mathbf{S}_1$ ($|\mathbf{S}_1| \ll |\mathbf{S}_0|$). Using the local normalization condition $[da(X)/dX]_{X=X_0} = 0$, one has a set of four homogeneous linear equation that may be written as

$$\mathbf{F}\cdot\boldsymbol{T} = \mathbf{0}, \tag{17}$$

where

$$\mathbf{F} = \begin{pmatrix} \mathbf{A} + a\mathbf{B} & \mathbf{B} \\ \mathbf{C} + a\mathbf{D} & \mathbf{E} + a\mathbf{B} \end{pmatrix}, \quad \boldsymbol{T} \equiv \begin{pmatrix} \mathbf{S}_0 \\ \mathbf{S}_1 \end{pmatrix}, \tag{18}$$

$$\mathbf{C} = \begin{pmatrix} 0 & 0 \\ -\frac{fV}{4H^3}(HV_X - VH_X) & \frac{f}{4H^2}(HV_X - VH_X) \end{pmatrix}, \tag{19}$$

$$\mathbf{D} = \begin{pmatrix} V_X & H_X \\ 0 & V_X \end{pmatrix}, \tag{20}$$

$$\mathbf{E} = \begin{pmatrix} -i\omega + 2V_X & 2H_X \\ -\frac{fV^2}{8H^2} & -i\omega + 2V_X + \frac{fV}{4H} \end{pmatrix}. \tag{21}$$

For a given basic flow, and given ω and $X = X_0$ (for simplicity, in the above expressions, and in what

Copyright © 2006 Taylor & Francis Group plc, London, UK

follows, we write X for the local value X_0), the homogeneous equation (17) constitutes an eigenvalue problem for the complex eigenvalue a and the complex eigenfunction $\boldsymbol{T}$. That is to say, the homogeneous equation (17) has nontrivial solutions only when the determinant of $\mathbf{F}$ vanishes, yielding a dispersion relation of the form

$$D(a,\omega;\theta,f,V,H,V_X,H_X)=0, \tag{22}$$

that determines the eigenvalue a.

One is interested in looking for convective instabilities propagating towards $X>0$, i.e. in the same direction as the basic flow. Thus, for a given positive value of the real frequency ω, one is interested in modes whose eigenvalue a has both its real and imaginary parts positive. According to (11)–(12), this ensures that the perturbation grows exponentially as it propagates towards increasing $X(\gamma>0)$, with phase velocity directed downstream (i.e. $c_{ph}\equiv\omega/\alpha>0$). As a matter of fact, one has to consider the sign of the group velocity,

$$c_g\equiv\frac{\partial\omega}{\partial\alpha}, \tag{23}$$

instead of the sign of the phase velocity c_{ph}, in order to determine the propagation direction of the perturbations. But, as we shall see, the sign of c_g always coincide with the sign of c_{ph} in all the cases considered below (all the instabilities found are convective instabilities, with both c_g and c_{ph} positive). On the other hand, the frequency range of study can be reduced to just non-negative values because the real and imaginary parts of the linear operator $\mathbf{F}$,

$$\mathbf{F}(\omega,\alpha,\gamma)\equiv\mathbf{F}_{\Re}(\gamma)+i\mathbf{F}_{\Im}(\omega,\alpha), \tag{24}$$

have the property

$$\mathbf{F}(a,\omega)=\overline{\mathbf{F}}(\overline{a},-\omega), \tag{25}$$

where $\overline{(\cdot)}$ denotes the complex conjugate, and both $\mathbf{F}_{\Re}$ and $\mathbf{F}_{\Im}$ are real functions. Thus, if a is the eigenvalue corresponding to the real frequency ω, $\overline{a}$ is also an eigenvalue of the problem, corresponding to the frequency $-\omega$. So that one has to consider only non-negative values of ω to fully analyse the linear stability of the flow.

3 RESULTS

3.1 *Parallel flow: Roll waves*

Before undertaking the non-parallel stability analysis of a non-uniform flow down an open inclined channel, it is convenient to consider first the simplest case of an uniform flow, thus reproducing previous stability results. This analysis will also serve as a reference for better understanding the results given in the next section.

For an uniform and steady basic flow, $H=constant$ and $V=constant$, one has $d\mathbf{S}/dX\equiv\mathbf{S}_1=0$ in (17)–(18). In fact, the second equation in (17) becomes unnecessary, and the linear stability equation is just (13) with $d\mathbf{S}/dX=0$. The dispersion relation (22) reduces then to

$$\det(\mathbf{A}+a\mathbf{B})=0, \tag{26}$$

with $H_X=V_X=0$ in (14).

For an uniform and steady basic flow, the solution to (1)–(3) relates the constant values of H and V by

$$H=\frac{fV^2}{8\sin\theta}. \tag{27}$$

It is convenient to use the Froude number

$$Fr\equiv\frac{V}{c}=\frac{V}{\sqrt{H\cos\theta}}=\sqrt{\frac{8}{f}\tan\theta}, \tag{28}$$

instead of the friction factor f, where $c=\sqrt{H\cos\theta}$ is the non-dimensional wave speed for small surface perturbations. Substituting (27)–(28) into (26), one obtains the following dispersion relation for the complex eigenvalue a and the real frequency ω:

$$a^2V^2\left(1-\frac{1}{Fr^2}\right)+a(3\sin\theta-2\omega Vi)-\omega^2-\frac{2\sin\theta\omega}{V}i=0. \tag{29}$$

The number of parameters may be reduced to just one, the Froude number, if one makes the following changes of variables valid for $\sin\theta\neq0$:

$$e\equiv\frac{aV^2}{\sin\theta},\quad w\equiv\frac{\omega V}{\sin\theta}, \tag{30}$$

so that (29) reduces to

$$e^2(1-\varrho)+e(3-2wi)-w^2-2wi=0, \tag{31}$$

where, for convenience, we use the inverse of the square of the Froude number,

$$\varrho\equiv\frac{1}{Fr^2}. \tag{32}$$

The new growth rate σ and wavenumber ϵ are defined as [see (12)]

$$e\equiv\sigma+i\epsilon,\quad \sigma=\frac{\gamma V^2}{\sin\theta},\quad \epsilon=\frac{\alpha V^2}{\sin\theta}. \tag{33}$$

Copyright © 2006 Taylor & Francis Group plc, London, UK

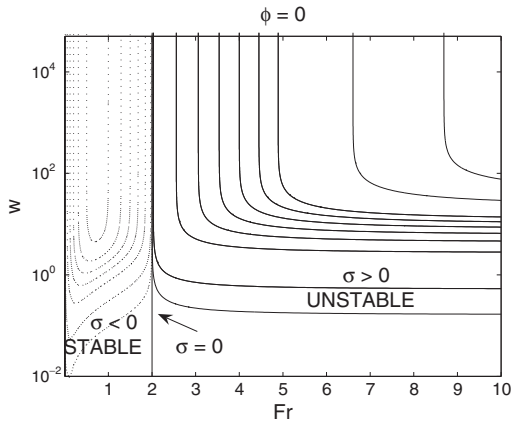


Figure 2. Contour lines for constant growth rate in the (w,Fr) plane for the parallel flow case. Continuous lines: $\sigma = 0, .001, .01, .2, .4, .6, .8, 1, 1.2, 2, 3$. Dashed lines: $\sigma = -.001, -.01, -.05, -.1, -.15, -.2, -.25$.

The neutral curve for instability, corresponding $\sigma = 0$, may be easily obtained by substituting $e = i\epsilon$ into (31). The imaginary and real parts of the resulting equation yield, respectively,

$$\epsilon = \frac{2}{3}w \quad \text{and} \quad \varrho = \frac{1}{4}. \tag{34}$$

The flow is stable ($\sigma < 0$) for $\varrho > \varrho_c = 1/4$, while it is (convectively) unstable ($\sigma > 0$) for any value of the frequency w if $\varrho < 1/4$. This obviously reproduces Jeffreys (1925) instability condition $Fr > 2$: any perturbation is unstable above the critical Froude number 2. In addition, one obtains that the phase velocity of the neutrally stable waves,

$$c_{ph} \equiv \frac{\omega}{\alpha} = \frac{wV}{\epsilon} = \frac{3}{2}V, \tag{35}$$

is three times larger that the surface wave speed c for the critical $Fr = 2$, $c = V/Fr = V/2$.

Figure 2 depicts the neutral curve in the plane (Fr, w), which is just the vertical line $Fr = 2$, together with some contour lines for constant growth rate σ. This figure qualitatively explains why Brock (1967) did not observed the formation of roll waves for Froude numbers below 3.5, approximately, in his experiments for an uniform flow in an inclined channel. For Fr close to the critical value $Fr_c = 2$ the growth rate is so small that a extremely long channel would be required for the developments of the waves (note that for $Fr < 3.5$, $\sigma < 0.5$, approximately).

To finish this section it is worth to mention that for a horizontal channel ($\sin\theta = 0$), Eq. (29) does not yield unstable solutions (i.e., solutions with $\sigma > 0$ together with $\epsilon > 0$).

3.2 *Nonparallel flow: Kinematic wave approximation*

We now turn to the general nonparallel stability formulation (17). In order to obtain some quantitative results, but without recurring to any particular basic flow, we shall consider here the 'kinematic wave approximation' to the shallow-water flow equations (Lighthill and Whitham 1955; Whitham 1974), which have proved to be very useful for approximating the long time behavior of the flow down an open inclined channel (Hunt 1983).

In the kinematic wave approximation, one neglects the left hand side of Eq. (2) and, after using the friction law (3), obtains the same relation (27) between H and V. But now, H and V are not constant, they must satisfy the continuity equation (1) and the initial and boundary condition of the particular problem under consideration. Substituting (27) into the left hand side of Eq. (2) and using (1), one obtains the following condition for the validity of this approximation:

$$\left|\frac{\partial H}{\partial X}\right| \ll \left|\frac{\sin\theta}{\cos\theta - \frac{2}{f}\sin\theta}\right|, \tag{36}$$

which in the case $f \ll 2\tan\theta$ may be simplified to $|\partial H/\partial X| \ll f/2$.

With this approximation, one can eliminate the dependence on H and on H_X of the dispersion relation (22) by using (27) and its derivative with respect to X:

$$H = \frac{fV^2}{8\sin\theta}, \quad H_X = \frac{fVV_X}{4\sin\theta}. \tag{37}$$

In addition, the explicit dependence on the angle θ and on the local flow velocity V can be eliminated from the dispersion relation by using the same change of variables (30) together with

$$\phi \equiv \frac{V_X V}{\sin\theta}. \tag{38}$$

Thus, taking the determinant of **F** (18) and using the above notation, the dispersion relation may be written as

$$D(e, w; \varrho, \phi) \equiv d_0 + d_1\phi + d_2\phi^2 + d_3\phi^3 + d_4\phi^4 = 0, \tag{39}$$

where

$$d_0 \equiv \left[e^2(\varrho - 1) + w^2 + 2iew + (2iw - 3e)\right]^2, \tag{40}$$

$$\begin{aligned} d_1 \equiv 2\big[&3iw^3 + 2e^3(\varrho - 1)^2 + 4ew^2(\varrho - 2) \\ &+7ie^2w(\varrho - 1) - 13e^2(\varrho - 1) - 12w^2 \\ &+2iew(5\varrho - 12) + (12e - 11iw)\big], \end{aligned} \tag{41}$$

Copyright © 2006 Taylor & Francis Group plc, London, UK

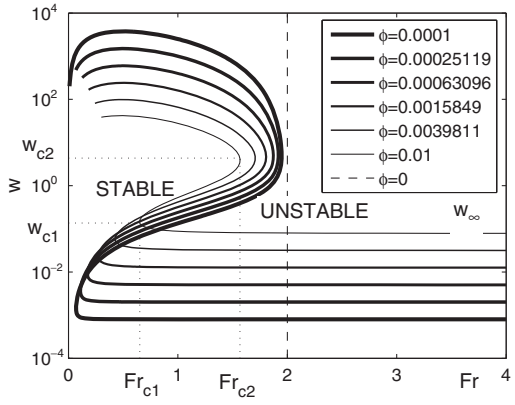


Figure 3. Neutral curves ($\sigma = 0$) for different values of $\phi > 0$ (as indicated).

$$d_2 \equiv -13w^2 + 8e^2(\varrho - 1)^2 + 4iew(4\varrho - 5) + 36 - 2[iw(27 - 4\varrho) + e(22\varrho - 25)], \quad (42)$$

$$d_3 \equiv -4[3iw + 2e(\varrho - 1) + 2(3\varrho - 5)], \quad (43)$$

$$d_4 \equiv 4, \quad (44)$$

and where use has been made of the Froude number (28) and (32). In the new variables, the validity condition (36) for the kinematic wave approximation reads

$$|\phi| \ll \left| \frac{2}{4\varrho - 1} \right|. \quad (45)$$

The neutral curves for instability, corresponding to vanishing real part of $e(\sigma = 0)$ in (39), depend on w, ϱ (or Fr), and ϕ. Figure 3 shows these neutral curves in the (Fr, w) plane for several values of $\phi > 0$. As it is observed, there exists marked differences with the neutral curve for the parallel flow case $\phi = 0$. Firstly, the flow is always stable for very small frequencies [for $w < w_\infty(\phi)$], independently of the Froude number. Secondly, the minimum, or critical, Froude number for instability, $Fr_{c1}(\phi)$, corresponding to the frequency $w_{c1}(\phi)$, is always less that 2 when $\phi > 0$. This critical Froude number tends to zero as ϕ decreases, though the frequency range around w_{c1} for which the flow is unstable is small, vanishing as $\phi \to 0$. As in the parallel case, the flow is unstable for almost any frequency when $Fr > 2$ (except for very small frequencies, as commented on above). In fact, there exists another critical value of the Froude number, $Fr_{c2}(\phi) < 2$, corresponding to the frequency $w_{c2}(\phi)$, above which the flow is always unstable provided that the frequency is not too small ($Fr_{c2} \to 2$ and $w_\infty \to 0$ as $\phi \to 0$). For high frequencies the stability region shrinks to disappear for very high w, the larger the smaller ϕ. But these very high frequencies, like the very small ones $w < w_\infty$, are too extreme to be physically meaningful. Thus, the two pairs of critical values (Fr_{c1}, w_{c1}) and (Fr_{c2}, w_{c2}) are the most significant physical results. Figures 4 and 5 show these critical values (together with w_∞) as functions of $\phi(>0)$.

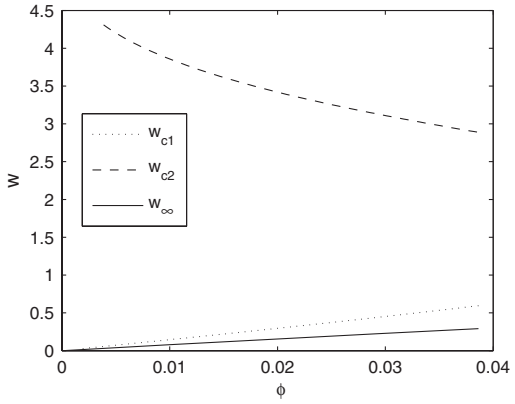


Figure 4. w_{c1}, w_{c2}, and w_∞ as functions of ϕ.

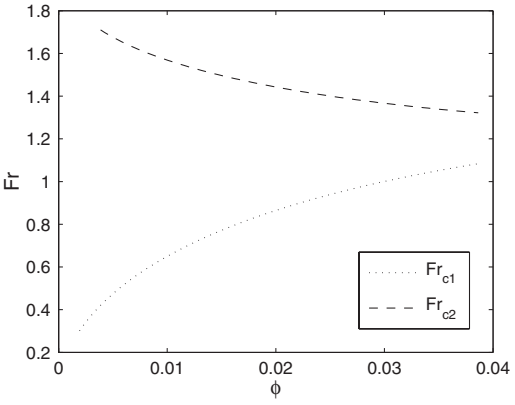


Figure 5. Fr_{c1}, and Fr_{c2} as functions of ϕ.

To have an idea of the most unstable frequencies, Fig. 6 shows contour lines of constant growth rate σ for a particular value of ϕ. It is observed that, though the critical Fr is much smaller than 2 for low frequencies, the growth rate for $Fr < 2$ is always quite small (except for very high, unrealistic frequencies). This explains why we have to use a very long channel and leave the flow evolve during a quite long time in our numerical simulations of the next section to observe the formation of roll waves for $Fr < 2$.

In all the numerical computations we have made where roll waves are formed in a nonuniform flow (some of them reported in the next section for the

Copyright © 2006 Taylor & Francis Group plc, London, UK

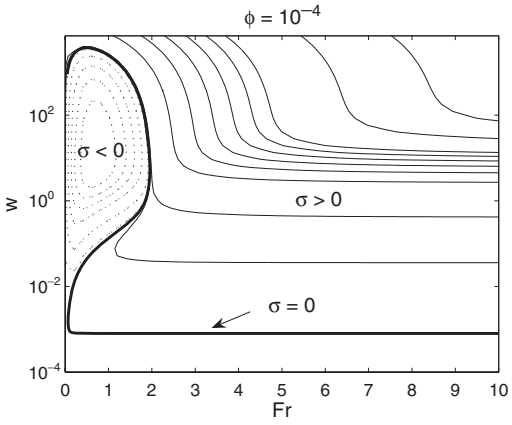


Figure 6. Contour lines of constant growth rate in the (w, Fr) plane for $\phi = 10^{-4}$. Continuous lines: $\sigma = 0$, .001, .01, .2, .4, .6, .8, 1, 1.2, 2, 3. Dashed lines: $\sigma = -.001, -.01, -.05, -.1, -.15, -.2$.

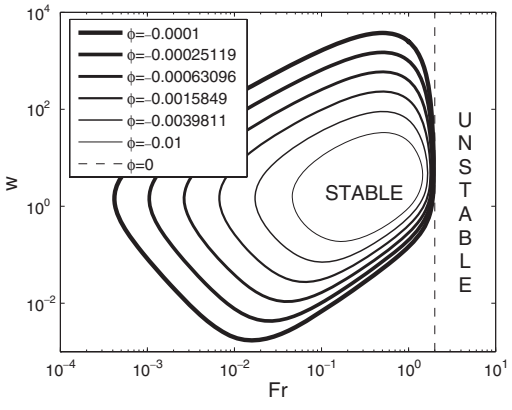


Figure 7. Neutral curves ($\sigma = 0$) for different values of $\phi < 0$ (as indicated).

dam-break problem on an inclined channel), the waves develop in regions of the flow where the kinematic wave approximation applies and where $\phi > 0$, i.e. in regions where the velocity (and the height) increases downstream. Nonetheless, we include here the stability results for $\phi < 0$ for completeness. Figure 7 shows the neutral curves in the (Fr, w) plane for several values of $\phi < 0$, while Fig. 8 depicts contour lines of constant growth rate σ for a particular value of $\phi < 0$.

As in the cases with $\phi > 0$, the flow may be unstable for $Fr < 2$ and the stability properties are very sensitive to the non-uniformities of the flow: with very small values of $|\phi|$, the region of instability changes dramatically with respect to the parallel flow case. However, the growth rates for $Fr < 2$ are very small, except for

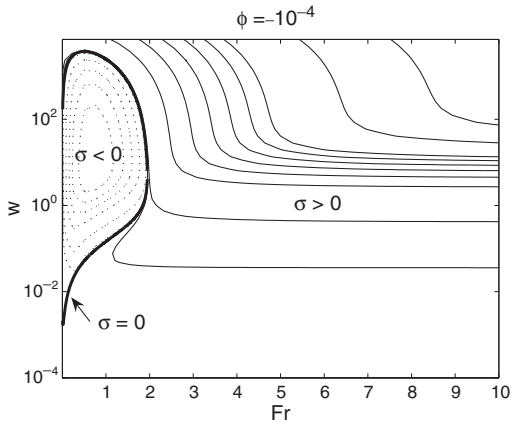


Figure 8. As in Fig. 6, but for $\phi = -10^{-4}$.

very high unrealistic frequencies (Fig. 8), as it also occurs for $\phi > 0$. There are, nonetheless, some important differences between $\phi > 0$ and $\phi < 0$. First, for $\phi < 0$ there no exists the frequency w_∞, and the flow is always unstable as $w \to 0$. In fact, the stable region in the (Fr,w) plane is closed, so that the flow is unstable for any frequency when Fr is very small (Fig. 7). However, for these very small values of the Froude number the kinematic wave approximation is no longer valid because condition (45) implies

$$Fr \gg \sqrt{\frac{4|\phi|}{2+|\phi|}} \simeq \sqrt{2|\phi|}\,. \tag{46}$$

This applies for both $\phi < 0$ and $\phi > 0$. This restriction, together with the very small growth rates for $Fr < 2$ in both cases, explain why it is difficult to observe the development of roll waves when $Fr < 2$, in spite of the fact that the critical Froude number for instability can be much smaller than 2 for both positive and negative values of ϕ.

4 COMPARISON WITH NUMERICAL RESULTS FOR THE DAM-BREAK PROBLEM

As an example on the formation of roll waves in a nonuniform flow, we have considered the dam-break problem in an inclined channel (Fernandez-Feria 2006; Bohorquez and Fernandez-Feria 2006). Actually, our interest in the present stability problem originated from the observation of roll waves in some numerical simulations for that non-uniform flow problem. Basically, a finite mass of water like that sketched in the inset of Fig. 9 is released at $t = 0$ on an inclined plane of angle θ. The equations (1)–(2)are solved numerically by using a high-resolution TVD finite-volume

Copyright © 2006 Taylor & Francis Group plc, London, UK

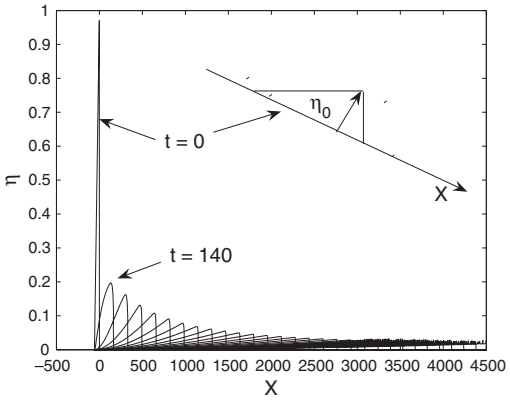


Figure 9. Water depth $\eta(X)$ for different instants of time in the dam break problem for $\theta = 1°$ and $Fr = 2.5$. The different curves are for $t = 0$, 140, 288, 454,638, 841, 1061, 1298, 1550, 1817, 2097, 2392, 2699, 3018, 3349, 3691, 4045, 4409, 4784, 5167, 5542, 5901, 6267, 6637, 7012, 7394, 7779, 8172, 8568, 8966. Also included is a sketch of the initial configuration of the dam-break problem.

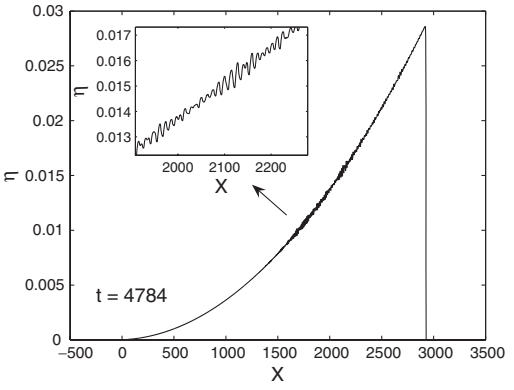


Figure 10. $\eta(X)$ for $t = 4784$ (from Fig. 9).

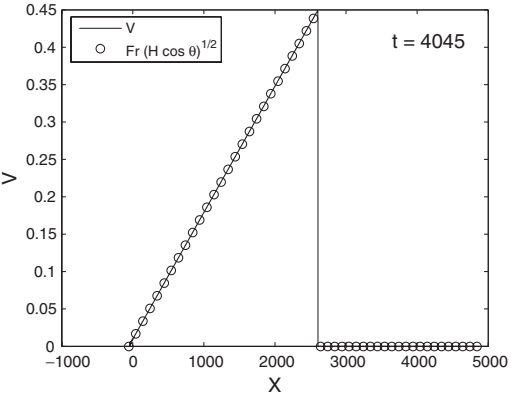


Figure 11. Comparison between the numerical results for the velocity (line) and the kinematic wave approximation (circles), for the flow depicted in Fig. 9 at $t = 4045$.

method like that described in Burgete and Garcia-Navarro (2001) (see the above mentioned references for the details of the formulation of the problem and the numerical method used). We have started a systematic search for the instabilities and the formation of roll waves in that flow, and we present here some preliminary results.

We have not found the spontaneous formation (i.e., with the only forcing of the round-off numerical noise) of roll waves in our numerical simulations for Froude numbers less than 2. This is explained by the small growth rate of the unstable perturbations when Fr is less than, approximately, 2 (see Figs. 6 and 8), so that a very long channel is needed for the roll waves to develop. In fact, we have observed perturbations growing downstream for $Fr < 2$ when disturbances with much higher amplitude than the numerical noise are introduced upstream. But these waves never reach the stage of a roll wave for $Fr < 2.5$ with the channel lengths used so far. In any case, to our knowledge, no roll waves have been documented before from experimental observations for Froude numbers less than approximately 3.5, whence the interest of the numerical results given below.

Figure 9 shows the evolution of the water depth η for several instants of time after the break of the dam in a channel with $\theta = 1°$ and for $Fr = 2.5$ (a sketch of the initial configuration is also shown in the figure). For $t \simeq 4400$, the instability in the free surface begins to be appreciated in the numerical simulations, originated just from numerical noise, as it is clearly evident in Fig. 10 for $t = 4784$. For these instants of time, the kinematic wave approximation is already valid in all the flow domain (in fact, it is very accurate; see Fig. 11), so that one may use the stability results obtained in the last section. Eventually, the amplitude of the instability waves grows to reach the stage where the free surface has the aspect of the classical roll waves (see Fig. 12).

The frequency of the initial waves developed after the instability of the flow can be obtained by plotting the velocity perturbation at a given location as a function of time. Figure 13 is such a plot for $X = 2342$, starting from $t = 4400$, the instant at which one begins to observe numerically the formation of the instability waves at the surface. The velocity perturbation, $U' = U - V$, has a frequency $\omega \simeq 0.1924$, which remains almost constant for a long period of time. Taking into account that during the period of time considered in Fig. 13 V and its gradient vary, in the location considered, in the ranges $0.28 < V < 0.37$ and $1.9 \times 10^{-3} < \phi < 3.3 \times 10^{-3}$, respectively, that

Copyright © 2006 Taylor & Francis Group plc, London, UK

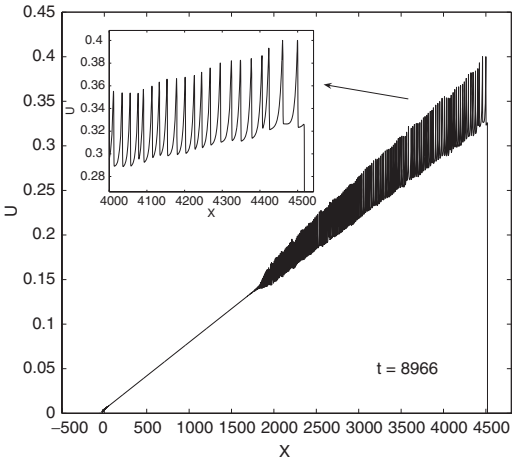


Figure 12. $U(X)$ at $t = 8966$ for the flow depicted in Fig. 9.

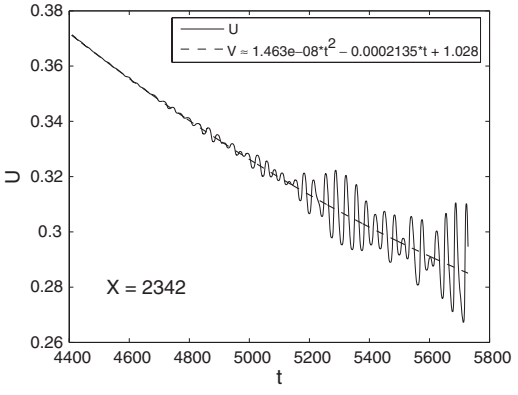


Figure 13. $U(t)$ at $X = 2342$ for the flow depicted in Fig. 9. Also shown is an extrapolation of the mean velocity without perturbation, $V(t)$ (dashed line).

frequency corresponds to $3.1 < w < 4.1$, approximately. For these values of w, ϕ and Fr, the stability analysis predicts that the eigenvalue $e = \sigma + \epsilon i$ ranges between $0.1136 + 2.163i$ and $0.1591 + 2.8922i$ ($0.0203 + 0.3687i$ and $0.0253 + 0.4814i$ in terms of $a = \gamma + \alpha i$). This corroborates, first, that the growth rate σ cannot be too small in order to observe the instabilities in the numerical simulations (σ is larger that 0.1, which in Fig. 6 only occurs if Fr is sufficiently larger than 2, if the frequency w is not too large). On the other hand, the wavelength $\lambda = 2\pi/\alpha$ given by the stability analysis ranges between 13 and 17, approximately. This agrees quite well with the wavelength in the numerical simulation, which from the inset in Fig. 10 can be estimated as the ratio between the space domain length to the number of crests to be $370/27 \approx 14$.

5 CONCLUSIONS

We have analysed the spatial stability of the shallow-water flow in an inclined surface of arbitrary slope. We have developed a local analysis that takes into account the effect of the local gradients of both the velocity and the water depth. In particular, we have considered the kinematic wave approximation, that is shown to be a very good approximation to any non-uniform and non-steady frictional flow for sufficiently long times. The stability results depend only on two dimensionless parameters: the Froude (Fr) number and a parameter ϕ characterizing the local gradient of the water depth. Since the stability analysis is a spatial one, we have characterized the frequency ranges in the parameter space (Fr,ϕ) for which instabilities develop. The main result is that the stability properties of the flow change qualitatively (substantially) when the non-parallelism of the shallow-water flow is taken into account. In particular, instabilities can be present for Froude numbers smaller than 2 in some frequency ranges that depends on ϕ (for a parallel, constant-depth flow, the instability condition is $Fr > 2$). However, the growth rate for the unstable modes is so small when $Fr < 2$ that, without artificially disturbing the initial flow, we have not observed the formation of roll waves in our numerical simulations for the dam-break problem in a inclined surface when $Fr < 2$. We have been able to simulate numerically the formation of roll waves in the dam-break problem in an inclined surface for $Fr = 2.5$. The instability waves, and the subsequent roll waves, develop from just the numerical round-off noise at this Froude number, and for larger values of Fr. This is also a relevant finding because, to our knowledge, there are no previous observations of roll waves in physical experiments for Fr less than approximately 3.5, due to the above mentioned fact that the growth rate of the perturbations is very small when Fr is close to its critical value for instability. Finally, we find that the reported numerical results compare very well with the predictions of the stability analysis.

REFERENCES

Berlamont, J. E. and N. Vanderstappen (1981). Unstable turbulent flow in open channels. *J. Hydraul. Div. 107*, HY4, 427–449.

Bertolotti, F. P., T. Herbert, and P. R. Spalart (1992). Linear and nonlinear stability of the blasius boundary layer. *J. Fluid Mech. 242*, 441–474.

Bohorquez, P. and R. Fernandez-Feria (2006). Transport of suspended sediment under the dam-break flow on an inclined bed of arbitrary slope. *J. Hydr. Res., submitted*.

Copyright © 2006 Taylor & Francis Group plc, London, UK

Bouchut, F., A. Mangeney-Castelnau, B. Perthame, and V. J. P. (2003). A new model of Saint Venant and Savage-Hutter type for gravity driven shallow water flows. *C. R. Acad. Sci. Paris, Ser. I 336*, 531–536.

Brock, R. R. (1967). Development of roll waves in open channels. Technical report, W. M. Keck Lab. of Hydraul. and Water Resources, California Inst. of Tech., Report KH-R-16.

Burguete, J. and P. Garcia-Navarro (2001). Efficient construction of high-resolution TVD conservative schemes for equations with source terms: application to shallow water flows. *Int. J. Numer. Meth. Fluids 37*, 209–248.

Chanson, H. (2004). *The hydraulics of open channel flow: an introduction*. Elsevier, Amsterdam.

Cornish, V. (1934). *Ocean waves and kindred geophysical phenomena*. Cambridge University Press.

Di Cristo, C. and A. Vacca (2005). On the convective nature of roll waves instability. *J. Appl. Math. 2005:3*, 259–271.

Dressler, R. F. (1949). Mathematical solution of the problem of roll waves in inclined open channels. *Commun. Pure Appl. Maths. 2*, 149–194.

Fernandez-Feria, R. (2000). Axisymmetric instabilities of Bodewadt flow. *Phys. Fluids 12*, 1730–1739.

Fernandez-Feria, R. (2006). Dam-break flow for arbitrary slopes of the bottom. *J. Engng. Math., in press (published online)*.

Hunt, B. (1983). Asymptotic solution for dam break on a sloping channel. *J. Hydraulic Eng. 109*, 1698–1706.

Jeffreys, H. (1925). The flow of water in an inclined channel of rectangular section. *Phil. Mag. 49*, 793–807.

Keller, J. B. (2003). Shallow-water theory for arbitrary slopes of the bottom. *J. Fluid Mech. 489*, 345–348.

Kenyon, K. E. (1998). Roll wave theory. *Phys. Essays 11*, 531–540.

Lighthill, M. J. and G. B. Whitham (1955). On kinematic waves: I. Flood movement in long rivers; II. Theory of traffic flow on long crowed roads. *Proc. Roy. Soc. A, 229*, 281–345.

Savage, S. B. and K. Hutter (1991). The dynamics of avalanches of granular materials from initiation to run-out. *Acta Mech. 86*, 201–223.

Stoker, J. J. (1957). *Water waves*. Interscience.

Whitham, G. B. (1974). *Linear and nonlinear waves*. Wiley, New York.

Copyright © 2006 Taylor & Francis Group plc, London, UK

Dam-break flow experiments in simplified city layouts

S. Soares-Frazão
Fonds National de la Recherche Scientifique and Department of Civil and Environmental Engineering, Université catholique de Louvain, Belgium

B. Spinewine, A. Duthoit, J.F. Deswijsen & Y. Zech
Department of Civil and Environmental Engineering, Université catholique de Louvain, Belgium

ABSTRACT: Inundation following the breaking of a dam or a dyke are likely to occur in areas that are not subject to common river floods. In urban districts, the flow route is dictated by the layout of buildings and streets rather than by a natural river thalweg. This paper presents a study of transient flow in simplified representations of urban districts, under the circumstances of a dam-break wave, or any rapid wave following a flash flood. An experimental study was conducted on three different configurations: (i) a square city layout of 5 × 5 buildings aligned with the flow direction, (ii) a single crossroad and (iii) a square city layout of 5 × 5 buildings not aligned with the main flow direction. Measurements were obtained by means of water level gauges and digital imaging techniques. Those measurements form a complete data set that is used to validate a numerical model based on 2D shallow-water equations.

1 INTRODUCTION

Flooding of urbanised areas constitutes a major threat for populations, especially if they are not prepare to cope with the situation. This is likely to occur when the inundation happens following unexpected or uncommon events such as the breaking of a dam or a dyke, or a flash flood after a heavy rainfall. Several examples can be found in the last years events: frequent flooding in Barcelona, Spain, inundation of Nîmes, France, in 1988 following a heavy rainfall of huge intensity and the recent flooding of New-Orleans (2005) in the United States following the breaking of several protecting dykes.

In urban districts, the flow route is dictated by the layout of buildings and streets rather than by a natural river thalweg. This induces complex flow features, and water levels in the streets higher than what would have happened without the presence of the city.

This type of flow have been studied experimentally by some authors, but generally under steady flow conditions, either subcritical or supercritical. Nanía et al. (2004) presented an experimental study of supercritical flow in a crossroad, with the aim of deriving one-dimensional relationships to predict the dividing flow in crossings. A similar study was conducted by Rivière & Perkins (2004). The propagation of inundation both through the streets and through the subway network in a detailed representation of an urban area was studied by Ishigaki et al. (2003).

Experiments under dam-break flow conditions were conducted by Soares-Frazão et al. (2004), to investigate the influence of the presence of a single building in the valley.

Those experiments are generally conducted with the objective of providing valuable data sets to calibrate and validate numerical models aimed at simulating flows in urban district, for the design of flood defence structures or emergency plans.

This paper presents dam-break flow experiments in three different idealised city layouts: (i) a square city layout of 5 × 5 buildings aligned with the flow direction, (ii) a single crossroad and (iii) a square city layout of 5 × 5 buildings not aligned with the main flow direction. Measurements were obtained by means of water level gauges and digital imaging techniques. Finally, numerical results obtained with a two-dimensional finite-volume model are compared to the experiments.

2 EXPERIMENTAL SET-UP

The experimental set-up is located in the laboratory of the Civil and Environmental Engineering Department of the Université catholique de Louvain, in Belgium. The channel is 36 m long and 3.6 m wide, with a partly trapezoidal cross section as indicated in Figure 1. A gate is located between two impervious blocks in order to simulate a breach in a dam or a dyke. The initial water level in the reservoir is 0.40 m and there is a thin

Copyright © 2006 Taylor & Francis Group plc, London, UK

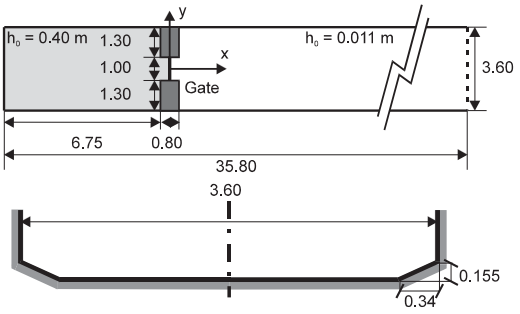


Figure 1. Experimental set-up: channel dimensions (m).

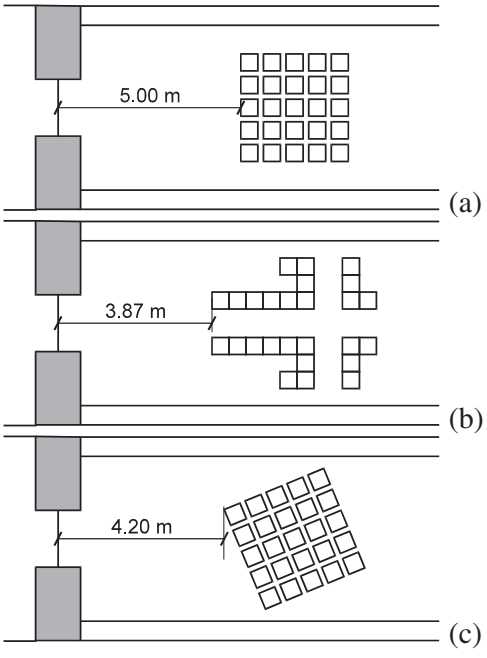


Figure 2. Simplified urban district layouts: (a) aligned case, (b) single street crossing and (c) skew case.

layer of 0.011 m water in the channel. The Manning friction coefficient for the channel is 0.01 $sm^{-1/3}$. The flow following the rising of the gate is thus typically two-dimensional as it expands in the downstream part of the channel.

Three different layouts of simplified urban district were studied in the channel (Deswijsen & Duthoit, 2005), as sketched in Figure 2: (i) a square city layout of 5×5 buildings aligned with the flow direction (Figure 2a), (ii) a single crossroad (Figure 2b) and (iii) a square city layout of 5×5 buildings making an angle of 22.5° with the main flow direction (Figure 2c).

The buildings consist in impervious wooden blocks of $0.3\,m \times 0.3\,m$. The buildings are fixed on the channel bed using a no-slip material and heavy weight inside the blocks. This system allows an easy repositioning of the blocks in order to simulate a wide range of city layouts. The single crossroad for example is set up by placing the individual buildings next to each other as sketched in Figure 2b.

In the square city layouts (aligned and not aligned with the flow direction), the streets are 10 cm wide, while for the single crossroad, the street is 50 cm wide. This latter test was designed to observe in more details the complex flow features in the crossroads.

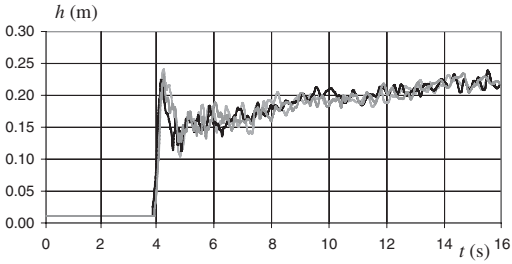


Figure 3. Reproducibility of the experiment. Gauge located inside the skew urban district ($x = 4.649$ m, $y = -0.548$ m).

3 FLOW DESCRIPTION

3.1 *Measurement devices*

Several measurement devices were used to characterise the flow. First, the water level evolution was measured at different locations by means of water level gauges. Those water level measurements (about 40 different gauge locations in each case) can be combined thanks to the reproducibility of the experiment in order to observe water profiles in the streets. Figure 3 illustrates the reproducibility of the results by means of four series of measurements at a gauging point located at the entrance of the skew urban district.

The surface velocity field was obtained using digital imaging techniques (Capart et al., 2002, Spinewine et al., 2003) to track the movement of tracer particles on the free surface. Again, thanks to the reproducibility of the experiment, several locations could be imaged and combined, which allows to identify particular features of the flow such as re-circulation for example.

In this particular case of rapid transient flow, surface-velocity measurement give valuable information on the depth-averaged velocity field. Indeed, it was observed (Soares-Frazão et al., 2004) that under rapid transient flow conditions, the velocity profile in a vertical plane was close to a uniform profile, as the flow had no time to adapt to a fully developed profile.

Copyright © 2006 Taylor & Francis Group plc, London, UK



Figure 4. Hydraulic jump upstream from the urban district in the aligned case.

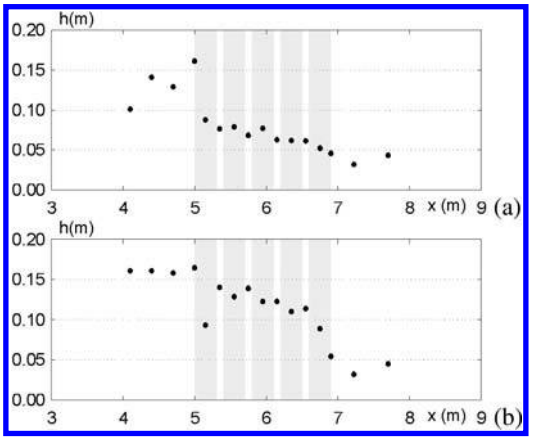


Figure 5. Experimental water profile in the left central street: (a) $t = 5$ s and (b) $t = 10$ s.

3.2 *The aligned case*

Flow observations show that after the violent impact of the wave against the buildings, the flow rises before entering the streets. A hydraulic jump forms upstream (Fig. 4), with the consequence that the water level is locally higher than without buildings. Immediately downstream from the city, a wake zone is observed. Then, further downstream, the flow slowly recovers the structure it would have had without the presence of the city (Soares-Frazão et al., 2004).

Looking at the water profile in the left central street (located at $y = 0.2$ m) obtained from the gauge measurements, we can see that after 5 s (Fig. 5a) the hydraulic jump has formed following the reflection of the flow against the buildings, and that the water depth in the urban district is still low. Then, after 10 s (Fig. 5b), the upstream hydraulic jump is still present but the water level has significantly raised in the streets. The flow in the urban district has evolved from supercritical to subcritical. Figure 6 shows the measured velocity vectors in the left central street after 5 s (Fig. 6a) and 10 s (Fig. 6b). Combining the

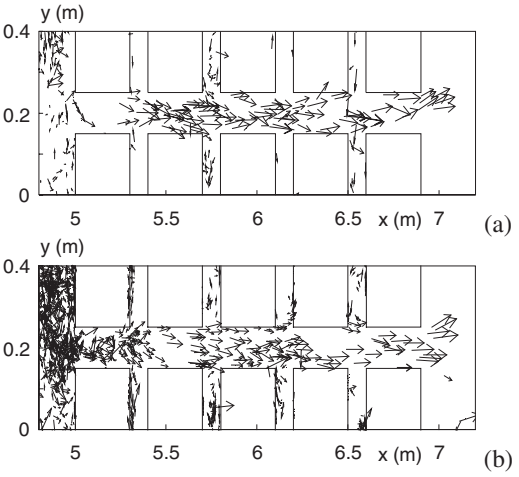


Figure 6. Velocity vectors in the left central street: (a) $t = 5$ s and (b) $t = 10$ s.

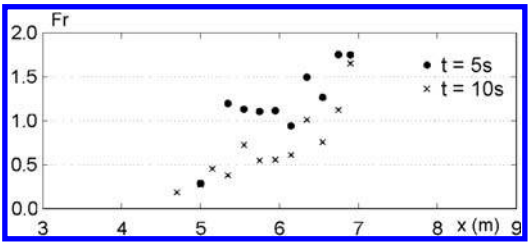


Figure 7. Estimated Froude number in the left central street.

water depth measurements with the velocity measurements, an estimate of the local Froude number can be obtained. This is illustrated in Figure 7, and confirms the change from supercritical to subcritical flow in the upstream part of the urban district. At the exit of the urban district, the flow accelerates and is supercritical.

3.3 *The single crossroad*

This test case is a kind of "zoom" on the previous situation. Indeed, in the previous aligned case, complex interactions appeared at each crossroad between the rapid flow in the longitudinal streets and the slow flow in the transversal direction. However, the scale of this first series of experiments did not allow detailed measurements of those interactions.

When the dam-break wave hits the main street of the system, a hydraulic jump forms and the flow is divided in three parts: a main flow through the central street, and lateral flow on both sides of the channel. Those latter waves will later enter the crossroad through the lateral streets and merge with the main axial flow.

Copyright © 2006 Taylor & Francis Group plc, London, UK

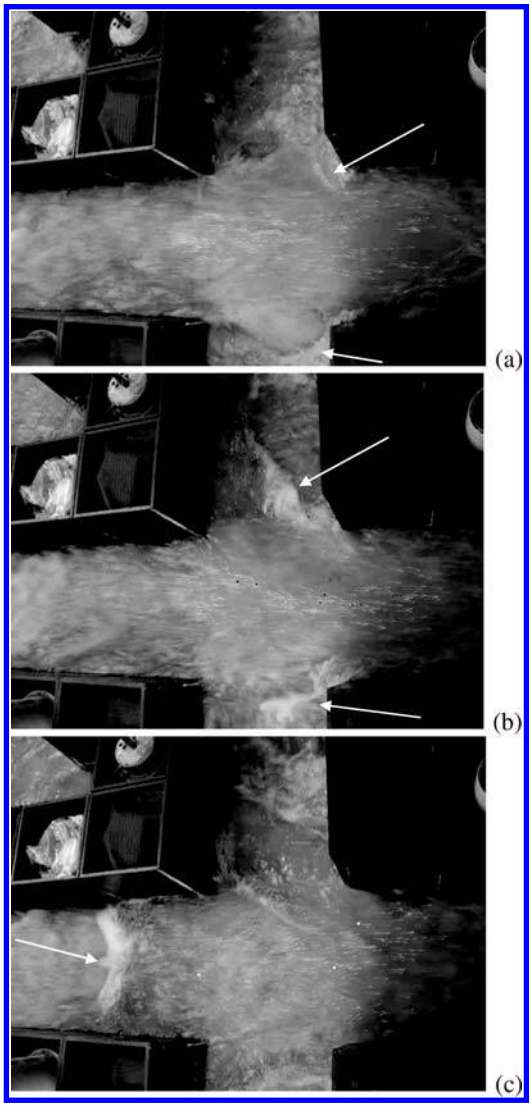


Figure 8. Formation and evolution of the hydraulic jump in the single crossroad (a) $t = 4.5$ s, (b) $t = 5$ s, (c) $t = 7$ s.

The formation and evolution of the hydraulic jump in the crossroad are illustrated in Figure 8 by means of pictures of the flow combined with velocity vectors issued from the digital imaging measurements. When the slow flow from the lateral streets comes up with the rapid main flow in the central street (Fig. 8a), hydraulic jumps form in the lateral streets (Fig. 8b, marked by arrows) and re-circulating flows can be observed. As the flow in the lateral streets increases, the hydraulic jumps are pushed towards the crossroad and merge, then starts to recede in the upstream direction in the central street (Fig. 8c, marked by an arrow).

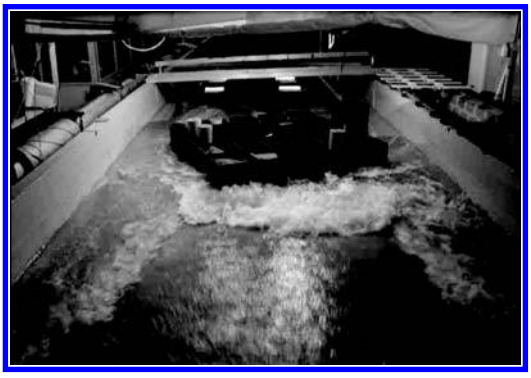


Figure 9. Upstream hydraulic jump in the skew case.

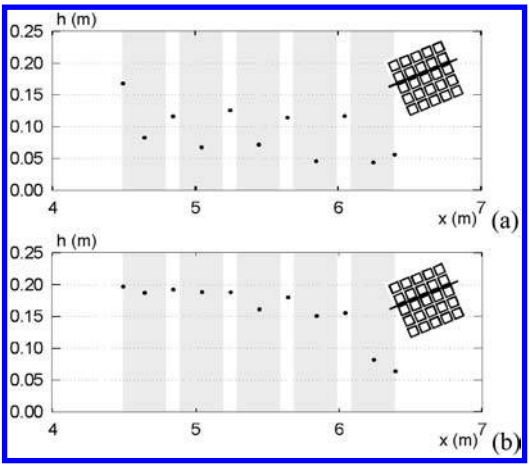


Figure 10. Water profile through the urban district in the skew case: (a) $t = 4$ s and (b) $t = 9$ s.

3.4 *Not aligned (skew) square city*

In this test case, the square urban district is now rotated by an angle of 22.5° and the streets are thus no more aligned with the main flow direction.

Like in the aligned case, a hydraulic jump forms upstream from the buildings (Fig. 9). As the flow enters the urban district through the front side and through the left side, the hydraulic jump is not symmetric as in the previous case.

Complex interactions occur at each crossroad and the urban district is progressively filled with water. Figure 10a shows the measured water depths after 4 s. The experimental data in Figure 10a show a much more important scatter than in the aligned case (Fig. 4). This highlights the complexity of the flow in this case, where the interactions at the crossroads lead to more local reflections in the streets during the first times of inundation of the urban district. After 9 s, when the urban district is completely flooded (Fig. 10b), the flow

Copyright © 2006 Taylor & Francis Group plc, London, UK

stabilises towards a profile similar to the one obtained in the aligned case, i.e. a progressive decrease of the water depth along the urban district. The main difference relies in the absence of any hydraulic jump inside the urban district, as was observed in the aligned case.

Due to difficulties of lightening the scene but also mainly due to imperfect distribution of tracers in the skew streets with the available devices, data obtained with the digital imaging technique were found not be completely usable at this stage. Only water level results will thus be presented in this paper.

4 NUMERICAL MODEL

Fast transient free-surface flows are usually simulated using the two-dimensional shallow-water equations. Those equations are solved using a shock-capturing finite-volume scheme, which means that the scheme is able to represent discontinuities such as hydraulic jumps. The scheme is briefly presented here. More details can be found in Soares-Frazão and Zech (2002).

4.1 *Two-dimensional shallow-water equations*

In two-dimensional conservative vector form, the Saint-Venant shallow-water equations stating mass and momentum conservation read (Abbott, 1979)

$$\frac{\partial \mathbf{U}}{\partial t} + \frac{\partial \mathbf{F}(\mathbf{U})}{\partial x} + \frac{\partial \mathbf{G}(\mathbf{U})}{\partial y} = \mathbf{S} \qquad (1a)$$

with the variables defined as

$$\mathbf{U} = \begin{pmatrix} h \\ uh \\ vh \end{pmatrix}, \quad \mathbf{F} = \begin{pmatrix} uh \\ u^2h + gh^2/2 \\ uvh \end{pmatrix} \qquad (1b,c)$$

$$\mathbf{G} = \begin{pmatrix} vh \\ uvh \\ v^2h + gh^2/2 \end{pmatrix}, \quad \mathbf{S} = \begin{pmatrix} 0 \\ gh\left(S_{0x} - S_{fx}\right) \\ gh\left(S_{0y} - S_{fy}\right) \end{pmatrix} \qquad (1d,e)$$

In equation 1, h is the water depth, uh and vh the unit discharge in the x- and y-direction respectively, S_{0x} and S_{0y} the bed slope in the x- and y-direction respectively and S_{fx} and S_{fy} the components of the friction slope, computed using Manning's formula and considering that friction only applies for the channel bed.

4.2 *Finite-volume scheme*

The finite-volume scheme is built upon an integral form of equation 1, yielding the generalised expression for non-Cartesian grids (Toro, 1997):

$$\mathbf{U}_i^{n+1} = \mathbf{U}_i^n - \frac{\Delta t}{\Omega_i} \sum_{j=1}^{nb} \mathbf{T}_j^{-1} \mathbf{F}_j^* \left(\bar{\mathbf{U}}_j\right) L_j + \mathbf{S}_i \, \Delta t \qquad (2)$$

where Ω_i is the cell-base area, L_j the j-interface length and nb the number of cell interfaces (3 for triangular cells). The vectors $\bar{\mathbf{U}}$ and $\mathbf{F}(\mathbf{U})$ express $\mathbf{U}$ and $\mathbf{F}$ in terms of normal and tangential velocity components, u_n and v_t, attached to the considered interface, using a transformation matrix $\mathbf{T}$, where n_x and n_y are the components of the outwards unit vector normal to the interface:

$$\bar{\mathbf{U}} = \mathbf{T}\,\mathbf{U} = \begin{pmatrix} 1 & 0 & 0 \\ 0 & n_x & n_y \\ 0 & -n_y & n_x \end{pmatrix} \begin{pmatrix} h \\ uh \\ vh \end{pmatrix} = \begin{pmatrix} h \\ u_n h \\ v_t h \end{pmatrix} \qquad (3)$$

The flux normal to the interface becomes:

$$\mathbf{F}\left(\bar{\mathbf{U}}\right) = \begin{pmatrix} u_n h \\ u_n^2 h + gh^2/2 \\ u_n v_t h \end{pmatrix} \qquad (4)$$

The problem is thus solved by computing the mass and momentum fluxes in the direction normal to each interface, and then combining those fluxes to obtain the mass and momentum balance over each cell.

The normal fluxes are computed using Roe's scheme adapted to the shallow water equations (Alcrudo & Garcia-Navarro, 1993), taking into account the wave propagation celerity of the system.

4.3 *Discretisation of the urban district*

An unstructured triangular mesh is used to discretise the computational domain, with a higher density of triangles around the urban area to increase the results accuracy (Fig. 11).

The buildings are impervious blocks, and their limits are represented as impervious boundary conditions in the model (closed walls).

In this way, wave reflections against the buildings are accounted for in a way conform to the physics. The mesh used for each urban district layout is shown in Figure 10: 53591 elements in the aligned case, 15649 elements for the single crossroad and 14667 elements in the skew case.

5 COMPARISON WITH THE EXPERIMENTS

For each configuration of the urban district, the water level and velocity predictions by the numerical model will be compared respectively to the water level measured by means of the water level gauges and to the velocity measured by means of the digital imaging technique.

Copyright © 2006 Taylor & Francis Group plc, London, UK

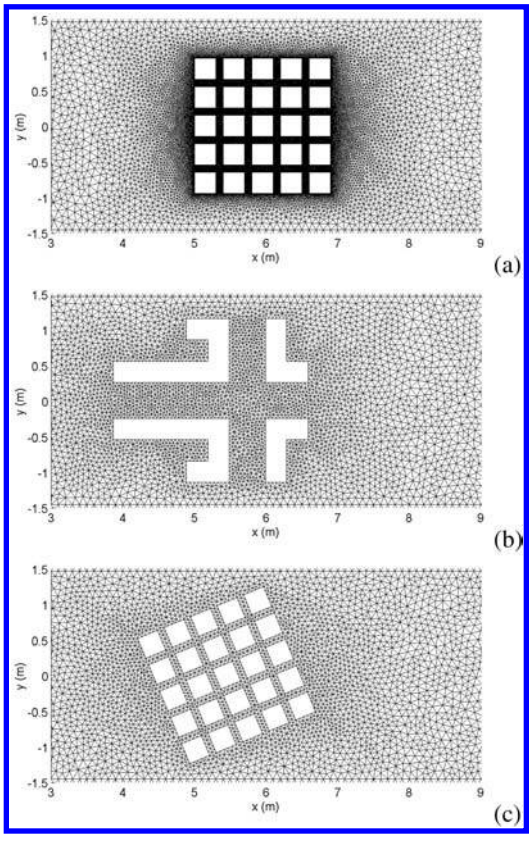


Figure 11. Computational mesh for (a) the aligned case, (b) the single crossroad and (c) the skew case.

The velocity data will be used either under the form of a surface-velocity field showing the magnitude and direction, or under the form of velocity magnitude, for example to compare the velocity in a particular street of the urban district.

From the water level evolution in time measured at each gauging point, data is extracted at a given time to form a water profile. To account for the important variability of the water level in time that can be observed in the experimental data sampled at a rate of 200 measurements per second, an averaged is performed over a time step of 0.05 s. This means that the water level at time t is represented by the averaged measured water level over the period $[t - 0.025\ \text{s};\ t + 0.025\ \text{s}]$.

A similar averaging procedure is used for the velocity measurements issued from the digital imaging technique. To obtain an equivalent "point" measurement of the velocity at a position (x, y), data is averaged in space over a square box of 0.05 m around (x, y) and in time over a time step of 0.1 s.

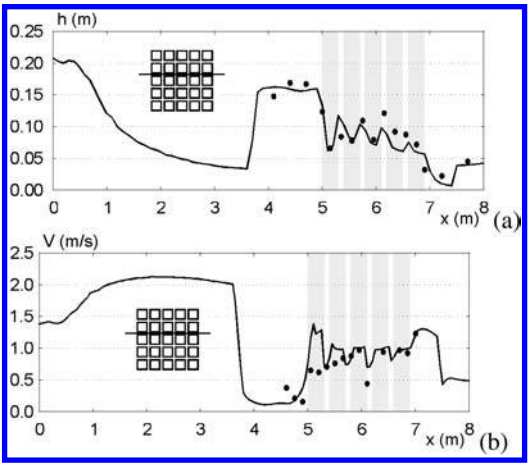


Figure 12. Water level (a) and velocity profiles (b) in a central street at $t = 6$ s. Comparison between experimental data (points) and numerical results (continuous line).

5.1 *The aligned case*

As shown in Figure 11, the mesh used to represent the urban district is quite refined, such that there is an average of 10 triangles over the width of each street. This level of refinement allows the resolution of details of the flow, including two-dimensional features in the street and in the crossroads. However, the corresponding computational time is important.

Simulations were also undertaken using a coarser mesh of 14341 elements, with only 2 triangles over the width of each street. Using such a mesh implicitly indicates that the flow in the streets is considered as being mainly one-dimensional. It appeared that this coarse mesh was insufficient to accurately represent the water profile (Deswijsen & Duthoit, 2005).

Longitudinal flow profiles in a street close to centre of the urban district are shown in Figures 12 and 13. The exact location of the profile is indicated. Figure 12 shows results after 6 s with the water level profile in Figure 12a and the velocity profile in Figure 12b. Similar results at time $t = 8$ s are shown in Figure 13.

The numerical model reproduces well the observed flow features. Especially, the hydraulic jump at entrance of the urban district is well reproduced. This was not the case when using a coarse mesh with only 2 triangles over the width of the streets: the hydraulic jump was completely missed, as illustrated in Figure 14.

However, the agreement is better for the water level than for the velocity, which tend to be overestimated in the numerical model. This might be due to momentum exchanges and losses in the crossroads that are not properly taken into account by the numerical model. Indeed, the flow is complex at the streets interactions, as illustrated in Figure 8 for the single crossroad: the

Copyright © 2006 Taylor & Francis Group plc, London, UK

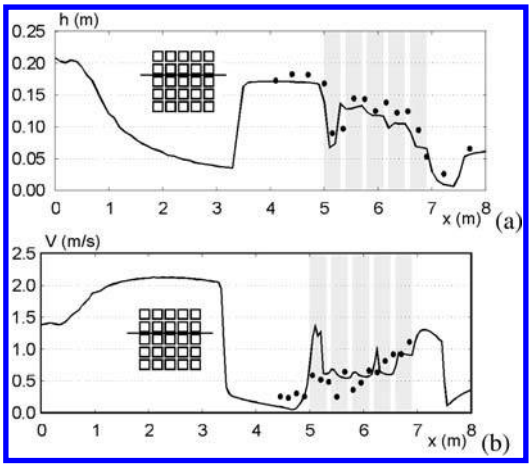


Figure 13. Water level (a) and velocity profiles (b) in a central street at $t = 8$ s. Comparison between experimental data (points) and numerical results (continuous line).

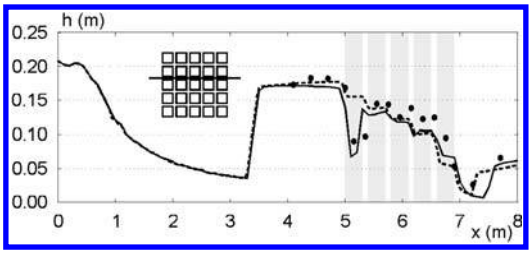


Figure 14. Water level in a central street at $t = 8$ s. Comparison between experimental data (points) and numerical results (continuous line for the fine mesh, dotted line for the coarse mesh).

hydrostatic pressure assumption of the model does probably not hold there, and three-dimensional effects including re-circulation in the vertical plane occur.

Moreover, it must be recalled that the velocity is measured at the surface, which is certainly not representative of the depth-averaged velocity in the case of a complex velocity profile in re-circulation areas.

5.2 *The single crossroad*

As already mentioned, this case can be considered as a zoom on the previous test case, with the aim of better describing the flow in the crossroads. The computational mesh of 15649 elements is such that the main street is discretised with 10 triangles on the width, corresponding to the mesh refinement used in the previous case.

5.2.1 *Water and velocity profiles*

Experimental and computed water level and velocity profiles at $t = 9$ s are shown in Figure 15. The hydraulic

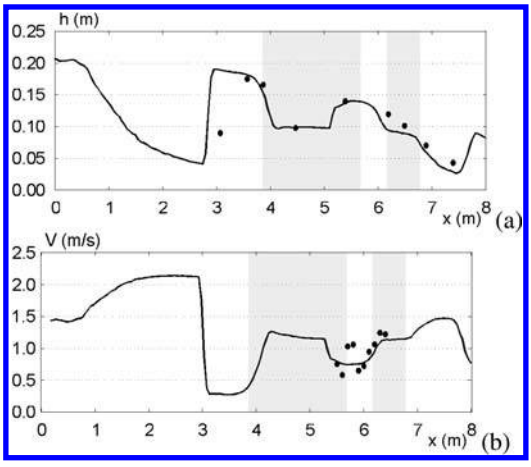


Figure 15. Water level (a) and velocity (b) profiles in the main street at $t = 9$ s. Comparison between experimental data (points) and numerical results (continuous line).

jump at the entrance of the main street can be clearly identified. This jump propagates in the upstream direction. The overall agreement of the computations with the measurements is good. The velocity reduction in the crossroad is well predicted.

5.2.2 *Velocity field and water surface*

The computed water depth and velocity field in the crossroad are shown at different times in Figure 16, corresponding to the three stages of the formation of the hydraulic jump illustrated in Figure 8. The grey-scale map used in the water surface plots is such that dark regions correspond to a high water depths (around 0.15 m), and clear regions to shallow water depths (around 0.02 m).

Comparing Figure 19 and Figure 8, it can be observed that the complex flow features are well reproduced by the numerical model. The shape of the hydraulic jump growing from the lateral streets is well reproduced.

5.3 *The skew urban district*

In this case, the square urban district is rotated by an angle of 22.5° and is thus no more aligned with the flow direction. However, the streets can still be considered as "longitudinal" and "transversal" (Fig. 2c).

The computational mesh used in this case is similar to the coarse mesh used in the aligned case, with only 2 triangles over the width of the streets. Again, like for the experiments, more in-depth analysis is in progress to obtain a complete characterisation of the flow in this skew case. However, the preliminary analysis with the coarse mesh and only water level data already provides interesting information, presented in the next section.

Copyright © 2006 Taylor & Francis Group plc, London, UK

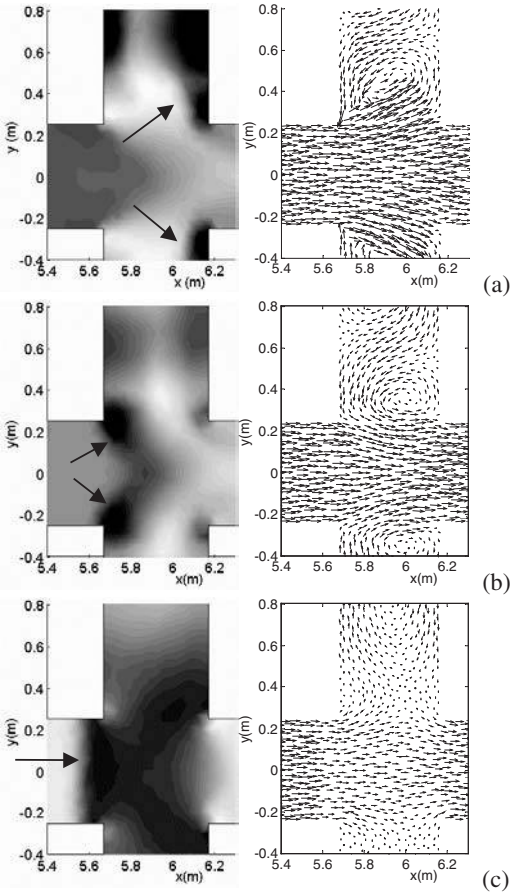


Figure 16. Computed water depth and velocity field at times (a) $t = 4.5$ s, (b) $t = 5$ s, (c) $t = 7$ s.

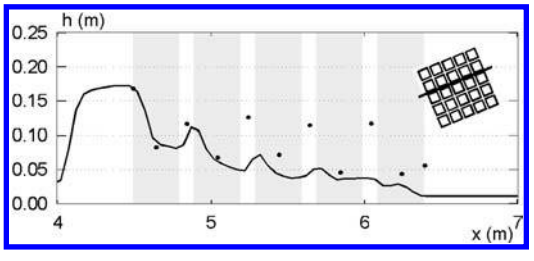


Figure 17. Water level profile in a longitudinal street at $t = 4$ s. Comparison between experimental data (points) and numerical results (continuous line).

5.3.1 *Water level profiles*

Water level profiles are illustrated for the fast transient period of the flow in Figure 17 ($t = 4$ s) and after stabilisation of the flow in Figure 18 ($t = 9$ s).

The overall agreement of the computed results with the experimental data is good. The progressive decrease of the water depth along the urban district is well reproduced, although the water depth is slightly underestimated in the numerical model. This is expected to be improved by refining the mesh in the streets, like in the aligned case.

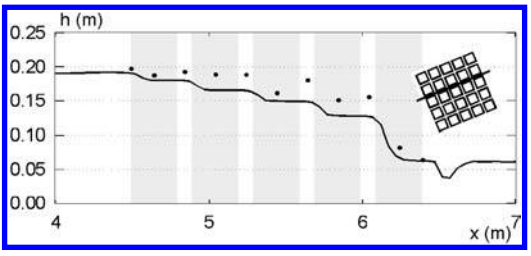


Figure 18. Water level profile in a longitudinal street at $t = 9$ s. Comparison between experimental data (points) and numerical results (continuous line).

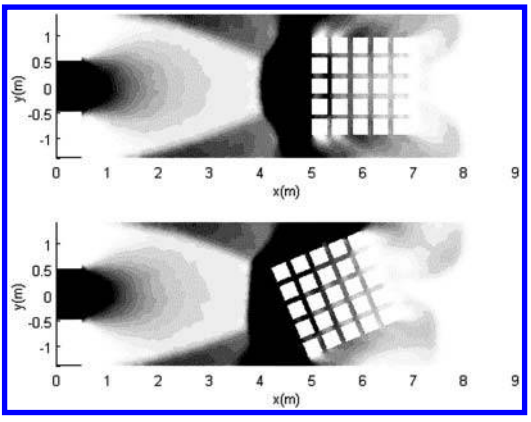


Figure 19. Computed map of the water depth at $t = 3$ s for (a) the aligned case and (b) the skew case.

5.3.2 *Comparison with the aligned case*

As it was shown in the previous sections that the numerical model is able to reproduce well the main features of the observed flow, only numerical results will be used here to highlight the particular features linked to the orientation of the urban district.

In the initial stage of the inundation of the urban district, the distribution of water in the streets logically depends on their orientation. This is illustrated in Figure 19, comparing computed results after 3 s in the aligned and skew case. The upstream hydraulic jump is also influenced by the orientation of the urban district.

After 10 s, when the flow reaches a quasi steady state, i.e. when the urban district is filled with water, the water level maps tend to be closer to each other (Fig. 20). This trend is confirmed by the longitudinal profiles in Figure 21.

Copyright © 2006 Taylor & Francis Group plc, London, UK

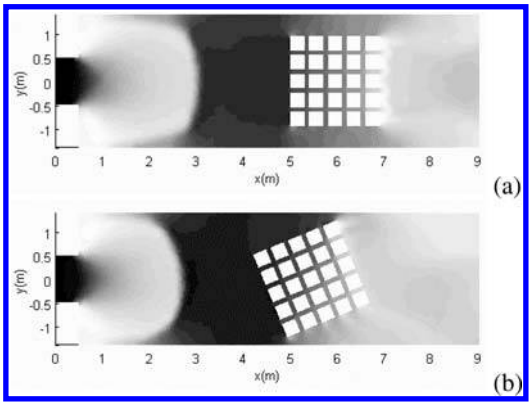


Figure 20. Computed map of the water depth at $t = 10$ s for (a) the aligned case and (b) the skew case.

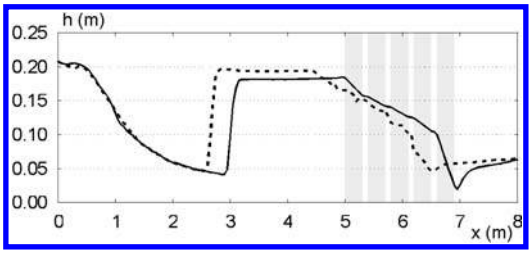


Figure 21. Computed water profile at $t = 10$ s for the aligned case (continuous line) and the skew case (dotted line).

6 CONCLUSIONS

Three dam-break flow experiments in idealised urban districts have been presented. The first one concerned an aligned configuration, for which the analysis could be deepened by investigating the flow behaviour in a single crossroad. Then, by rotating the urban district, some ideas of the influence of the orientation of the streets could be given.

A two-dimensional finite-volume scheme is used to solve the shallow-water equations describing this type of flow. It was successfully validated against the experimental measurements, which allows its use in further analysis of different flow configurations close to the ones studied here.

A particularly interesting conclusion arises from the observation that after the complete inundation of the urban district, the flow profile is not much dependent on the orientation of the streets. This observation introduces the idea of considering the urban district like a porous media inducing mass storage and momentum losses, regardless of its exact shape and orientation. This assumption of course has to be further investigated.

Some tentative developments were undertaken to include this concept of "urban porosity" in the shallow-water equations (Guinot & Soares-Frazão, 2006). They now have to be validated against this new experimental data set.

REFERENCES

Abbott, M.B. 1979. *Computational Hydraulics*. Pitman, London

Alcrudo, F. & Garcia-Navarro, P. 1993. A High-Resolution Godunov-Type Scheme in Finite Volumes for the 2D Shallow-Water Equations. *Int. J. Numer. Methods in Fluids*, 16, 489–505.

Capart, H., Young, D.L. & Zech, Y. 2002. Voronoï imaging methods for the measurements of granular flows. *Experiments in Fluids* 32 (1): 121–135.

Deswijsen, J.F. & Duthoit, A. 2005. *Ecoulement consécutif à une rupture de barrage en milieu urbain idéalisé: étude expérimentale et numérique* (in French). Diploma final work, Université catholique de Louvain, Belgium.

Guinot, V. & Soares-Frazão, S. 2006. Flux and source term discretization in two-dimensional shallow-water models with porosity on unstrucrured grids. *Int. J. Numer. Methods in Fluids*, 50, 309-345.

Ishigaki, T., Toda, K. & Inoue, K. 2003. Hydraulic model tests of inundation in urban area with underground space, *30th IAHR Congress,August 2003, Greece, Theme B*, pp.487–493.

Nanía, L.S., Gómez, M. & Dolz J. 2004. Experimental study of the dividing flow in steep street crossings. *J. Hydraul. Research* 42(4):406–412.

Rivière, N. & Perkins, R.J. 2004. Supercritical flow in channel intersections, *Proc. River Flow 2004 Int. Conf. Fluvial Hydraulics, Naples* (2):1073-1078.

Spinewine, B., Capart, H., Larcher, M. & Zech, Y. 2003. Three-dimensional Voronoï imaging methods for the measurement of near-wall particulate flows. *Experiments in Fluids* 34 (2): 227–241.

Soares-Frazão, S. & Zech, Y. 2002. Dam-break in channels with 90° bend, *Journal of Hydraulic Engineering, American Society of Civil Engineers (ASCE)* 128 (11): 956–968.

Soares-Frazão, S., Noël, B. & Zech, Y. 2004. Experiments of dam-break flow in the presence of obstacles, *Proc. River Flow 2004 Int. Conf. Fluvial Hydraulics, Naples* (2):977–982.

Toro, E.F. 1997. *Riemann solvers and numerical methods for fluid dynamics.* Springer, Berlin, Germany.

Copyright © 2006 Taylor & Francis Group plc, London, UK

A.4. Vegetated beds and flow resistance

Copyright © 2006 Taylor & Francis Group plc, London, UK

Evolution of mixing layers in turbulent flow over submersed vegetation: Field experiments and measurement study

A. Sukhodolov & T. Sukhodolova
Institute of Freshwater Ecology and Inland Fisheries, Berlin, Germany

ABSTRACT: Submersed plants interact with river flow and create complex flow patterns that absorb wakes behind stands and internal boundary layers developing over plant canopies on the general pattern of the open-channel flow. Recent laboratory investigations suggested the usage of mixing layer analogy for flow inside and on the upper edge of canopies. This field study explores applicability of mixing layer analogy in a natural stream. A series of field experiments was completed in a lowland river. In these experiments detailed measurements of flow characteristics were made over a patch of *Sagittaria Sagittifolia* implanted in a certain order on the river reach. Density of canopies varied among the experimental runs. Analysis of obtained data confirmed efficiency of mixing layer analogy and provided insight into spatial evolution of mixing layers in the natural stream. The results are compared to the canonical and shallow mixing layers and discrepancies between those layers are discussed.

1 INTRODUCTION

Aquatic vegetation exposed to flowing waters in fluvial systems experiences physical forces imposed by flow and alters the surrounding flow via resistance forces. These interactions affect transport and mixing processes in natural streams and hence are of great importance for ecology of river ecosystems. Until recently the effect of vegetation on flow has been of primary interest only in respect to complex roughness characteristics imposed by vegetation on the river channel. Customary logarithmic law stemming from perturbed boundary layer approximation was used as an analytical framework for flows over vegetative canopies (Kouwen & Unny 1973; Murota et al. 1984; Stephan & Gutknecht 2002). However, recent laboratory studies with scaled model vegetation (Ghisalberti & Nepf 2002) have indicated that flow within and just above a canopy behaves more like a mixing layer rather than a boundary layer.

A free mixing layer belongs to the family of free-turbulence flows that also includes free wakes and free jets. The qualifier *free* stresses the fact that these turbulent flows are maintained by internal velocity gradients and their evolution is independent of solid boundaries (Monin & Yaglom 1971; Brown & Roshko 1974). Canonical free mixing layers evolve in coflowing liquids of different densities or flows of different mean velocities, for instance downstream a splitter plate, Figure 1.

The available quantitative methods describing evolution of free shear flows are based on similarity

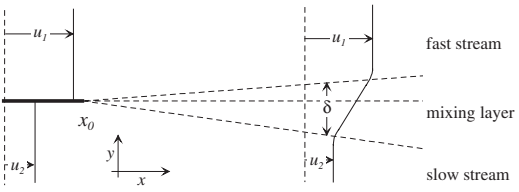


Figure 1. A sketch of evolution of a canonical free mixing layer downstream a splitter plate (after Tukker 1997).

hypotheses that impose scaling relationships (Monin & Yaglom 1971) $L(x) \sim x^m$ and $U(x) \sim x^{-n}$, where L and U are characteristic length and velocity scales of turbulence, m and n are the scaling exponents. In canonical free mixing layer the characteristic length scale is the width of layer δ and characteristic velocity scale is velocity difference $\Delta u = u_1 - u_2$. The scaling exponents in mixing layer take values of 1 and 0, respectively (Brown & Roshko 1974)

$$\frac{\partial \delta}{\partial x} = \alpha \lambda \tag{1}$$

$$\lambda = \frac{\Delta u}{u_1 + u_2} = \frac{\Delta u}{2u_c} \tag{2}$$

where α is spreading coefficient which value for canonical mixing layers was determined experimentally, $\alpha = 0.18$, λ is velocity ratio, and u_c is the mean velocity. Mean velocity profile in mixing layers has

Copyright © 2006 Taylor & Francis Group plc, London, UK

been shown to comply with hyperbolic tangential distribution (Michalke 1965)

$$\frac{u}{u_s} = 1 + \tanh\left(\frac{2y}{L}\right) \tag{3}$$

where $u_s = \Delta u/2, L = \gamma\delta$ is characteristic length scale, and γ is a coefficient. Canonical mixing layer model assumes well defined flow upstream of the layer origin and equations (1)–(3) are supposed to be valid at distances relatively far from the origin.

Conditions similar to those of the canonical flow can be attained in the atmospheric flows over terrestrial vegetation, for instance over woods of considerable area (Raupach et al. 1996). However in rivers macrophytes form patches variable in size and locality with well defined margins and spatially separated by areas of free flowing water (Sand-Jensen & Pedersen 1999; Sukhodolov & Sukhodolova 2005). Therefore in natural streams the areas over which spatially uniform mixing layers develop may be relatively small and the flow is thus permanently evolving. For that reason the knowledge on spatial dynamics of mixing layers in natural streams with submersed vegetation is particularly valuable.

Another important difference between terrestrial and freshwater vegetation is flexibility and buoyancy of the later. These properties of submersed plants make the characteristics of submersed canopies dependable upon the bulk characteristics of the flow – mean velocities and depth. The relationships between elastic deformations and buoyancy of plant species, and flows drag and lift are extremely complex and generally unknown – what makes prediction of deflected canopy height and projected area of plants uncertain.

Because of difficulties to carry out detailed field studies of mixing layers over submersed vegetation in natural stream the research was hitherto carried out in the laboratory facilities with a simulated vegetation (Ghisalberti & Nepf 2002). Some preliminary data about velocity and turbulence intensity distributions over the patches of macrophytes were obtained by Sand-Jensen & Pedersen (1999). Their pioneering study presents an excellent qualitative picture but unfortunately lacks the quantitative analysis and is insufficient in detail for examining the evolution of mixing layers.

The goals of the present study were: (1) to investigate the dynamics of the flow over submersed vegetation in a natural stream; (2) to explore the applicability of mixing layer analogy and spatial evolution of mixing layers over macrophytes patches; (3) to examine complex relationships between density of plant canopies, flow velocity and deflected height of canopies. To achieve these goals a field-scale experimental study has been carried out in a straight reach of a lowland river. The design of the study included an original methodic combining field measuring study traditional for natural conditions with an experimentation aimed at exploring wider range of governing flow variables characteristic of laboratory investigations. Therefore the study besides the focus of its own program provides a valuable link between contemporary field and laboratory methods. This paper presents the first results of the study and concentrate on the details of experimental procedures, analysis of spatial patterns of mean velocity and Reynolds stresses distributions, attempts to generalize the findings, and also briefly discusses further research on this study.

2 FIELD EXPERIMENTS

2.1 *Experimental river reach*

Field experiments were performed in the lowland river Spree near the village Freienbrink, 10 km east of Berlin, Germany. In the study reach the channel is straight with stone armored banks and with a bed covered by sands of about 1 mm in diameter. Detailed information about river reach morphology, morphodynamic processes and seasonal dynamics of submersed vegetation cover on the reach is provided by previous investigations (Sukhodolova et al. 2004; Sukhodolov & Sukhodolova 2005). The study was completed in July 2005. Hydraulic and morphometric characteristic of the bulk river flow and experimental conditions are presented in Table 1.

Table 1. Bulk characteristic of the flow during field measurements.

Run	Q, m^3/s	U, m/s	H, m	h, m	S, $\times 10^5$	ρ, kg/m^3	Fr,	Re, $\times 10^{-5}$	$\sqrt{gHS}$, cm/s
1	5.08	0.18	1.23	1.65	8.98	0.132	0.06	2.18	3.2
2	5.10	0.18	1.24	1.65	9.13	0.048	0.06	2.19	3.3
3	5.24	0.18	1.27	1.68	9.15	0.014	0.06	2.29	3.3
4	5.09	0.18	1.24	1.64	9.57	0.000	0.06	2.19	3.4

where Q is water discharge, U mean flow velocity, H is mean depth on the reach, h is depth at the experimental vegetative patch, S is water slope, ρ is density of vegetative cover (dry weight of plans per volume of the canopy), Fr is Froude number, and Re is Reynolds number.

Copyright © 2006 Taylor & Francis Group plc, London, UK

2.2 *Experimental program*

The main purpose of the experimental program was to obtain the spatial patterns of flow characteristics over a patch of submersible plants. Experimentation was attained by means of control provided on the properties of the vegetation patch – its composition, location, and density of the canopy. Measurements of instantaneous velocities were taken on the verticals distributed along the longitudinal axis of the patch. Experimental run typically consisted of ten vertical profiles and a stationary point. After completion of each particular experimental run the canopy density was progressively reduced by factor of four preserving uniformity and the pattern of plants distribution and a next run was commenced.

The patch of rectangular shape 4×8 m in dimesion was created artificially in the central part of the river reach. It was composed of uniformly distributed submerged macrophytes *Sagittaria Sagittifolia*. The plants of approximately the same dimensions (leaves length 1.6 m, number of leaves 12, and the diameter near the root of 20 mm) were gathered over the river reach and manually implanted, Figure 2. The aluminum rods of 20 cm in length were fixed by wires at roots of individual plants before implanting. The rods were completely buried into the riverbed together with roots of the plants enabling firm plantation in the river flow. Positioning of plants was assisted with the aluminum guides spanned by marks on 20 cm intervals. The plants were distributed uniformly on a chess board pattern, Figure 3. A week later after macrophytes implanting, the control observation indicated that plants accommodated completely to the new locations and produced fresh rhizomes.

2.3 *Measuring systems and equipment*

The acoustic Doppler velocimeter (ADV) was used to measure velocities in this study. The device is capable of remotely sensed three-component sampling of velocities at frequency of 25 Hz. To mount ADV probes customary manufactured mounting equipment was employed. This equipment consists of an adjustable T-shaped platform designed for accurate positioning and easy traversing of velocimeters probes along the flow, Figure 4. During measurements 3 synchronized ADV probes were operated by a portable computer set on a floatable platform equipped with a shelter for an operator, Figure 4. The ADV probes (5-cm distance from the tip to the sampling volume, on 1-m cable) were attached to the ends of 2-m long aluminum rods positioned in the vertical directions by elevating nodes. A pair of orthogonal cylindrical bubble levels was used to align the rods along vertical axis. The third ADV probe was set upside down on the riverbed at a stationary location in the upstream part of the vegetation patch, Figure 5. The T-shaped platform was firmly secured to the riverbed by 6 taglines. Vegetation naturally grown around the artificial patch was preserved and this way provided conditions typical for surrounding flow environment over natural vegetation patches, Figure 5.

Surveys of riverbed morphology and measurements of free surface slope were performed with a laser total station Elta R55. Local river depth was measured with standard hydrometrical wading rods. Bed material was collected manually with a handy sampler.

To measure the deflected height of the vegetative canopy *in-situ* a purposely developed underwater video system UVS-RAY was employed in this study. The system consists of a digital camera Olimpus

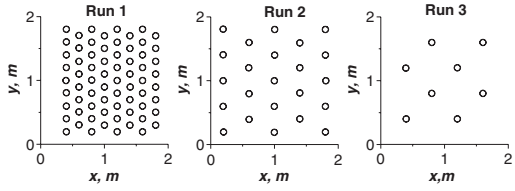


Figure 3. Patterns of spatial distributions of plants in the field experiments.

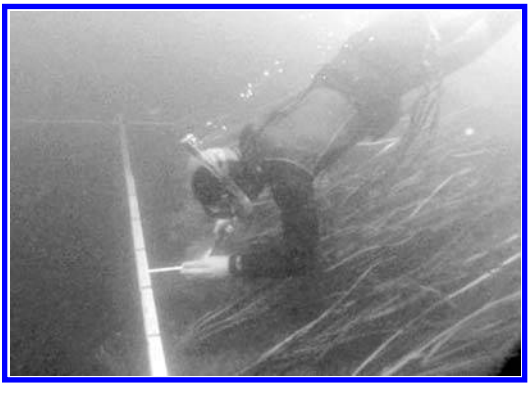


Figure 2. Implanting macrophytes *Sagittaria Sagittifolia* in the experimental patch by divers.



Figure 4. Mounting and operating platforms.

Copyright © 2006 Taylor & Francis Group plc, London, UK

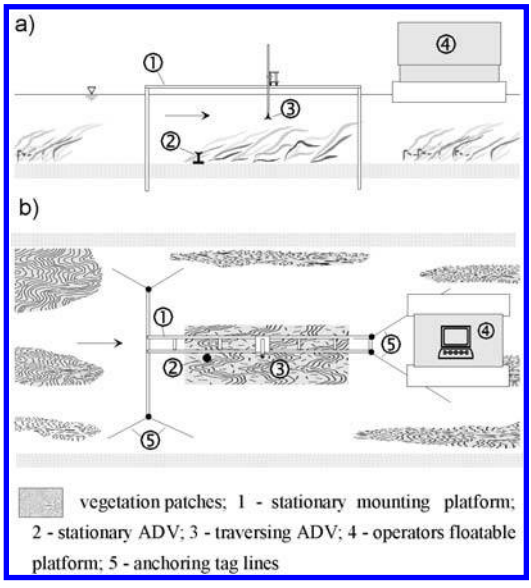


Figure 5. Schematic view of the experimental setup.

C-5060 with a wide angle lens converter WCON-07 mounted in an underwater housing IKELITE and an underwater lighting system Werner Videolight 100. The camera was installed on a platform aligned with a wire screen. The mesh of the screen (10 cm) provides a reference coordinates enabling further processing of the obtained digital video records. Two examples of underwater pictures taken with UVS-RAY are shown in Figure 6.

2.4 *Measurements*

Instantaneous 3-D velocities were measured at seven points uniformly distributed over each vertical profile. Records were taken at 25 Hz sampling rate and over 300 s sampling periods for each point. To prevent crossing of ADV sampling volume by plant leaves the plants adjacent to probes were removed. As laboratory studies indicate (Ghisalberty & Nepf 2002; Ikeda & Kanazawa 1996) that removal of up to four plants had produced no significant effect on the flow.

Video recording of the underwater canopy was performed for each experimental run after velocity measurements. Video records were taken over 50 second for each of five frames juxtaposed longitudinally on the right hand side of the experimental vegetative patch. At the last frame (downstream edge of the canopy, Figure 6b) video recording was taken synchronously with ADV records during 300 s periods.

Water surface levels and the slope of free surface of the flow were measured prior and after velocity measurements on each vertical. Fluctuations of water level were within 3–5 mm which was negligible small in comparison with the mean depth of the flow. The

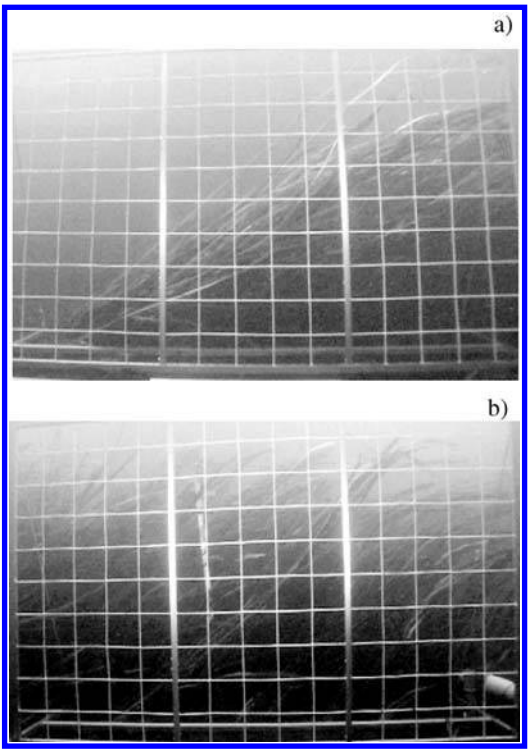


Figure 6. Side view of the experimental patch of macrophytes, Run 1, (a) – upstream edge and (b) downstream edge.

plants removed in the course of reduction of the canopy density were collected, dried and later weighted to determine a biomass density of the canopy.

2.5 *Data processing*

Time series of velocity measurements were processed with a versatile commercial software package ExploreV 1.5, Nortek AS, Norway. The software provides interactive graphical environment enabling fast and comprehensive data treatment. It allows editing, clipping, filtering of row data, stationarity, spectral, cross-spectral and other advanced methods of analysis including the data processing on a spatial grid.

With the use of ExploreV measured time series were inspected visually to identify possible problems, such as spikes, trends or abrupt discontinuities in the time series. Frequency distributions of the velocity data were also examined to identify outliers. Examination of these distributions is especially valuable for determining errors associated with large spikes resulting from interruption of the acoustic signal by large pieces of debris moving through the sampling volume. Spikes always generated velocity values more than 3 standard deviations from the mean (3σ). These spikes were removed and replaced with values generated by linear

Copyright © 2006 Taylor & Francis Group plc, London, UK

interpolation between adjacent data using a 3σ filter in the time series option of ExploreV. In all cases this post-processing procedure did not greatly affect the values of means, producing changes of only few mm/s.

Video records were converted into a sequence of digital images in the format JPEG with the specialized software DVD Create. JPEG images were imported into GRAPHER 6 software and the boundaries between free flow and macrophytes were digitalized. The physical coordinates of the boundaries were computed using calibration screen marks (Figure 6) and averaged over the sequence of the frames to obtain double time-spatial averages of variable canopy boundaries.

3 RESULTS AND ANALYSIS

3.1 *Mean velocities*

Distribution of measured mean flow velocities over the vegetative stand of plants is shown in Figure 7. Density of the vegetative canopy is decreasing on this plot from (a) to (c), plot 7d corresponds to a zero density. The boundaries of the layers of the flow are depicted in accordance with a definitional scheme of the canonical mixing layers (Figure 1).

The data in Figure 7a obviously indicate a flow pattern resembling at first glance the canonical mixing layer, Figure 1. However, there are noticeable distinctions between these mixing layers. First, in the canonical mixing layer velocity difference Δu is constant along the whole lengths of the flow domain while measurements indicate systematic growths of Δu in the streamwise direction. The second difference is the direction of mixing. In the canonical flow faster stream accelerates the slower flow and therefore the mixing layer appears progressively transversely distorted toward the slower flow. Figure 1 indicate the opposite – the domain occupied by the faster flow progressively decreases toward free surface of the flow. With the decrease of vegetation density the lower boundary of the layer is decreasing and at lowest density the mixing layer hits the riverbed. Obviously that at low density of vegetation the flow behaves much like perturbed boundary layer rather than mixing layer.

3.2 *Reynolds stresses*

Measured spatial patterns of the principal component of the Reynolds stresses tensor $-\overline{u'w'}$ are shown in Figure 8. Dashed lines on this plot are also marking the boundaries of the mixing layers. However for Reynolds stresses the boundaries were determined differently. Intersects of zero or nearly zero values of Reynolds stresses with vertical axis were considered to represent the boundaries of the layers. Comparison with the flow without vegetation indicates the applicability of this approach. Although principal features of the mixing layers conjectured from velocity distributions apply to those inferred from Reynolds stresses, there were some quantitative differences. In general, Reynolds stresses display somewhat broader layers than velocity distributions. The difference can be accounted for the fact that Reynolds stresses manifest subtle mechanisms that are smeared in velocity gradients.

Measured distributions of the Reynolds stresses also indicate that at far downstream distances of the mixing layer origin the maximum of Reynolds stresses practically coincide with the upper margin of the vegetative canopy, Figure 8. This observation supports an analytical treatment of the overlaying flow as a perturbed boundary layer.

3.3 *Velocity difference*

A principal feature of the canonical mixing layers is that they display constant velocity difference along the whole flow domain. This feature of course is not expected to hold in shear flows developing in vegetative canopies and therefore the behavior of the velocity difference is important for understanding the evolution of the flow. The velocity differences normalized by mean velocity of the layer u_c are shown in Figure 9.

Two types of changes in the velocity difference can be observed in Figure 9. In runs 1 and 2 the velocity difference increases at the beginning of the mixing layers and then, at distances larger than 3 m from the upstream margin of the vegetative patch, the differences stabilize and remain practically constant over the downstream part of the patch. When the density of plants is low (experimental run 3) the velocity difference decreases at downstream distances close to origin and then gently increases at far downstream, Figure 9.

3.4 *Mixing layer widths*

Mixing layers widths determined for certain verticals from velocity and Reynolds stresses distributions are summarized in Figure 10. Figure 10a shows mixing layers widths δ_v obtained from velocities (Figure 7), and Figure 10b the values δ_s from Reynolds stresses (Figure 8). For comparison Figure 10 represents spatial dynamics in the canonic mixing layer with a constant velocity difference and spreading coefficient $\alpha = 0.18$, reported in many literature sources (Brown & Roshko 1974; Tukker 1997). Dashed lines in Figure 10 indicate the spatial dynamics in the far field of the boundary layer $\delta \sim x/\ln x$ (Tennekes & Lumley 1972).

It can be seen from Figure 10 that measured mixing layer widths agree with equation (1) quite closely at distances shorter than 4 m and systematically deviate at far downstream. The departure from (1) obviously depends on the density of vegetative cover and the experimental data exhibit convergence to the behavior typical for the boundary layers. Such convergence should be naturally expected as with the decreasing

Copyright © 2006 Taylor & Francis Group plc, London, UK

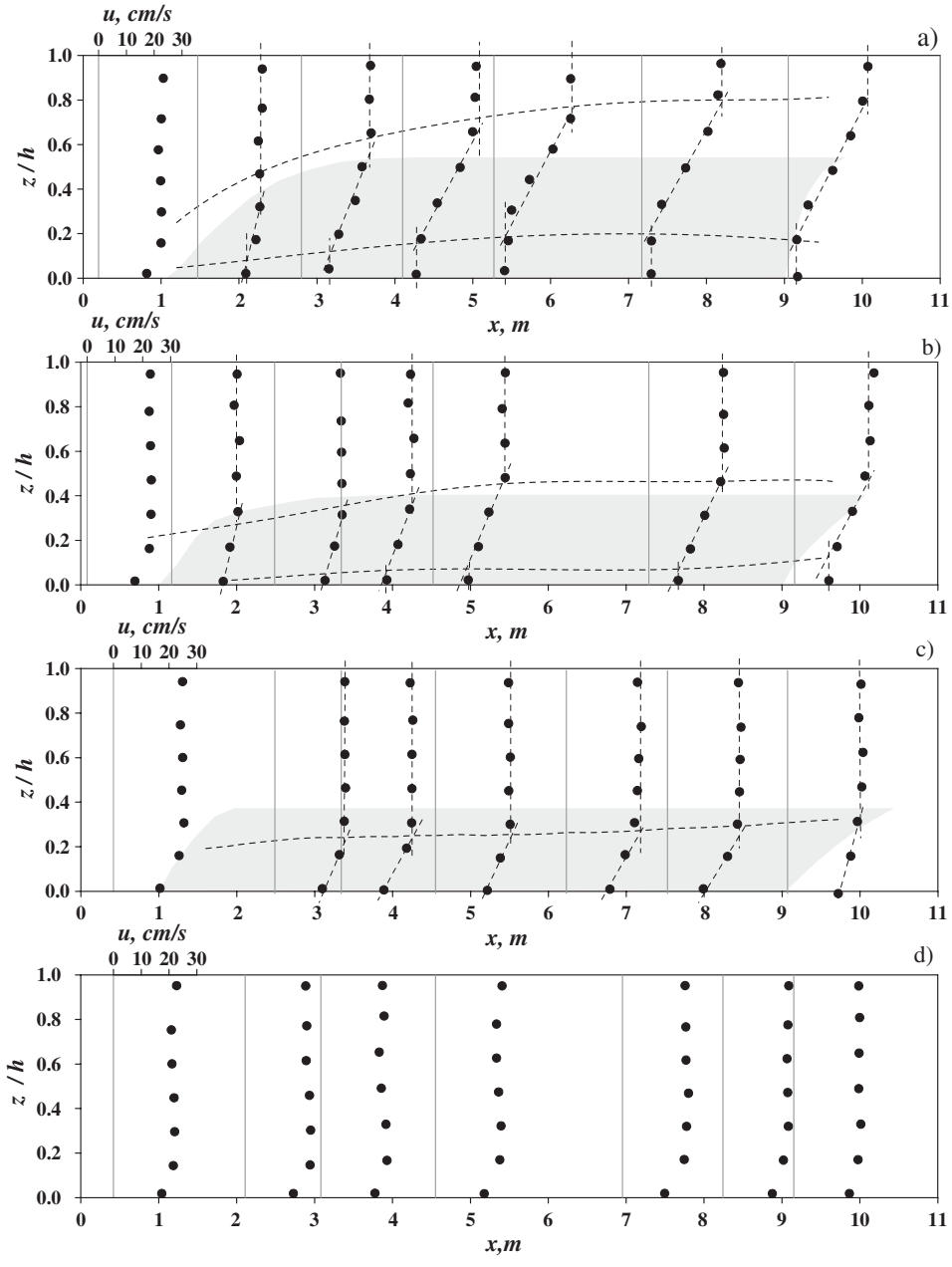


Figure 7. Vertical profiles of mean streamwise velocity as a function of position over the experimental vegetative patch: a) run 1; b) run 2; c) run 3, and d) run 4 (dashed lines mark the boundaries of the flow layers).

density of vegetation the lower boundary of the mixing layer converges to the riverbed.

3.5 *Vertical velocity distribution*

The data on mixing layer widths were used to normalize measured mean streamwise velocities in accordance with equation (3). The vertical positions of measuring points were centered in respect to the mixing layer centerline z_c and scaled with the local width of the mixing layer. Velocity deviations from mean inside the mixing layer were normalized with velocity difference across the flow, Figure 11.

Copyright © 2006 Taylor & Francis Group plc, London, UK

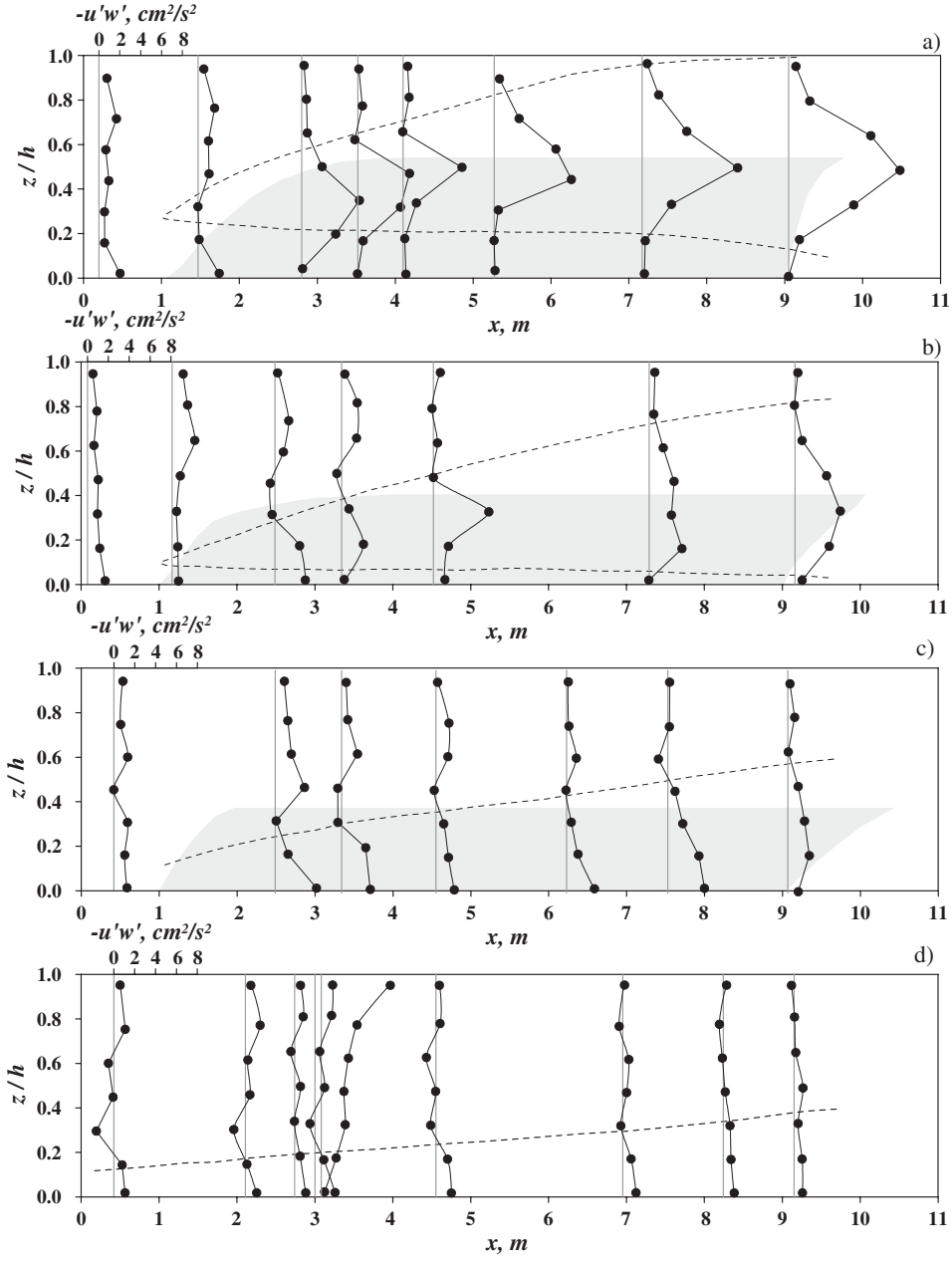


Figure 8. Vertical profiles of Reynolds stresses as a function of position over the experiemntal vegetative patch: a) run 1; b) run 2; c) run 3, and d) run 4 (dashed lines mark the boundaries of the flow layers).

Normalized data indicate a collapse at a certain curve characteristic for mixing layers, Figure 11. Comparison of this pattern with the universal dimensionless profile indicates a reasonable agreement for runs 1 and 2, Figure 11a,b. In run 3 the data systematically deviated from equation (3). Vertical velocity distribution measured in far downstream of the vegetative patch indicate only minor scatter around (3) while in the near field of the patch origin the scatter was significantly larger. This scatter is most probably attributed

Copyright © 2006 Taylor & Francis Group plc, London, UK

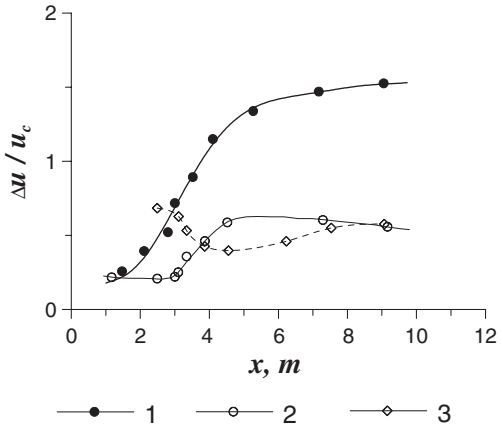


Figure 9. Downstream variation of velocity difference across mixing layers (numbers indicate experimental runs).

to the stochastic instability of field conditions of measurements rather then physically explainable flow behavior.

3.6 *Effect of vegetation density*

In previous sections it was clearly shown that flow characteristics and also reconfiguration abilities of vegetation depend on the vegetation density. To quantify the effect of vegetation a simple dimensionless analysis suggests

$$\frac{\Delta u}{u_c} = f_1\left(\frac{\rho}{\rho_0}\right), \text{ and} \tag{4}$$

$$\frac{h_l}{h} = f_2\left(\frac{\rho}{\rho_0}\right) \tag{5}$$

where h_l is average height of the macrophytes in a patch, ρ_0 is density of water. At first approximation empirical functions f_1 and f_2 can be obtained using a standard least square method, Figure 12. The following relations were established

$$\frac{\Delta u}{u_c} = 0.44\exp\left(0.87\frac{\rho}{\rho_0}\times 10^4\right) \tag{6}$$

$$\frac{h_l}{h} = 0.35\exp\left(0.33\frac{\rho}{\rho_0}\times 10^4\right) \tag{7}$$

Both velocity difference and the average height of macrophytes in a patch decay exponentially with the decrease of vegetation density. Although the applicability of least squares method to a data set of only few points may seem unreasonable, we think that derived equations are valuable because they are still today the only relations representing basic parameters for natural conditions.

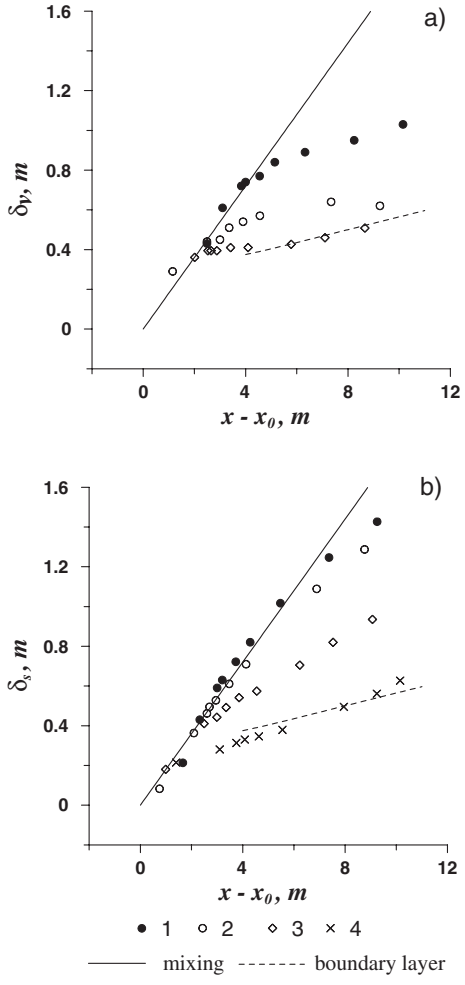


Figure 10. Downstream evolution of the mixing layers.

4 DISCUSSION AND CONCLUSIONS

This field-scale experimental study was performed to investigate spatial evolution of the mixing layers in a river with submersed vegetation. In this study the patch of natural uniformly distributed submersed plants was placed in the experimental river reach, and a series of accurate measurements of instantaneous velocities provided the spatial distributions of basic characteristics of turbulence. Obtained experimental data were compared with the evolutionary models of the canonical mixing layers. Variation of vegetation density in the experimental program provided possibility for investigating the effect of vegetation density on evolution of the flow over submersed vegetation. The study has revealed noticeable similarities and principal differences between canonical mixing layers and

Copyright © 2006 Taylor & Francis Group plc, London, UK

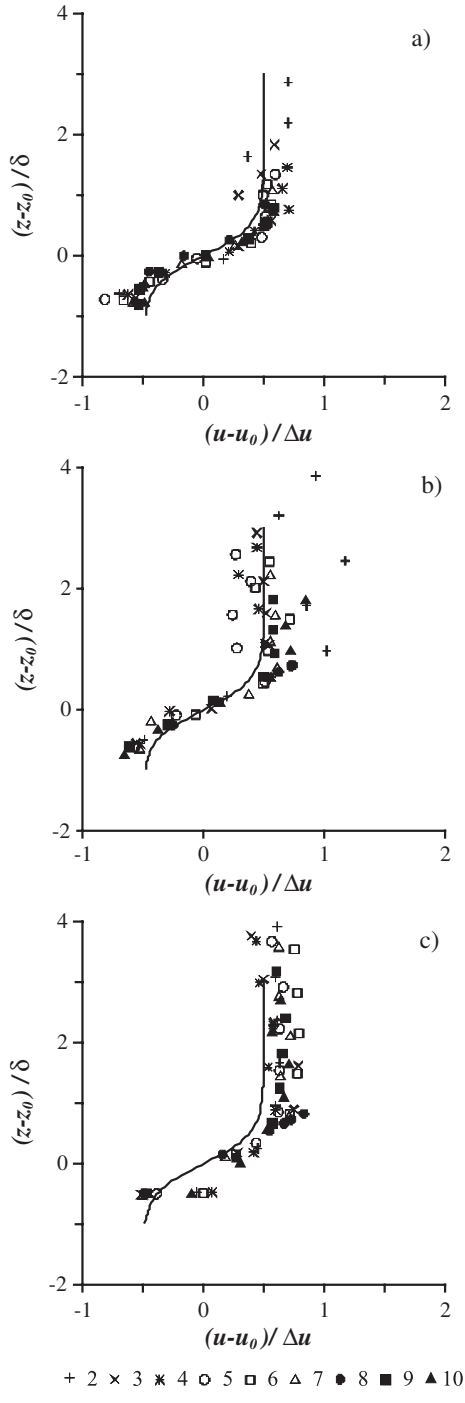


Figure 11. Vertical distribution of mean streamwise velocity component: a) run 1; b) run 2; and c) run 3.

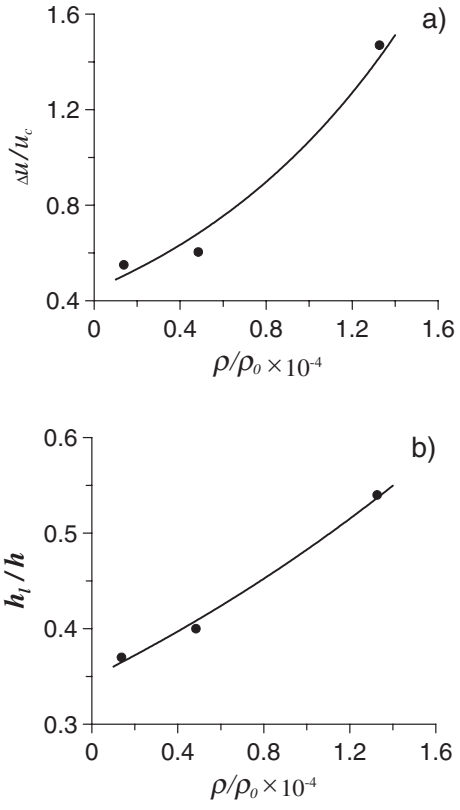


Figure 12. Velocity difference (a) and average height of vegetation in a patch as the functions of vegetation density.

the flow over submersed vegetation. A principal difference between the canonical mixing layer and the flow over submersed vegetation in a river is the evolution of the velocity field. In contrast to the canonical mixing layer with a constant velocity difference between the mixing flows, the flow over submersed vegetation maintains the velocity difference along a certain distance at near field of the vegetative patch origin. As the upper boundary of the flow reaches the free surface of the flow the mixing layer attains nearly constant velocity difference. The width of the developed mixing layer over submersed vegetation is thus controlled by two vertical length scales – the local river depth, and the penetration depth which strongly depends on the density of the vegetation cover.

As the velocity difference is variable, this experimental observation invalidates the applicability of the model (1), and (2). Adequate representation of the mixing layer will require formulation of dynamical relation for spreading coefficient as a function of spatial distance and density of vegetative cover. Similar solutions were applied in the models of shallow mixing

Copyright © 2006 Taylor & Francis Group plc, London, UK

layers where velocity difference was decreasing with the distance (Tukker 1997).

Vertical distribution of the streamwise mean velocity component in the form of hyperbolic tangent equation (3) was compared to the normalized measured velocity distributions. In general this comparison revealed applicability of equation (3) to describe velocity distributions in natural streams with vegetation. However, the results of the study also suggest that density of vegetative canopies should be also taken into consideration.

The conclusions of the study summarize as follows. The flows developing over submersed vegetative patches in natural streams behaves differently than in the canonical free turbulent mixing layers and mixing layers in shallow open-channel flows. At the same time these flows are shown to attain some self-similarity as the vertical velocity profiles can be scaled with the reasonable accuracy to reveal self-similar solution in the form of hyperbolic tangent function. This function was shown to describe satisfactory the velocity profiles in the canonical mixing layers, in the shallow mixing layers in open-channel flows, and in the developed laboratory flows over model submersed vegetation. In this study we propose simple empirical formulae relating main parameters of the flow and the average height of submerged plants in the patches to the dimensionless macrophytes density. Further studies required to explore the applicability of mixing layer model to describe flow over natural vegetative patches with non-uniform distribution of plants.

Although from a formal point of view, the flow in natural streams cannot be considered as free flow because its spatial evolution is limited by the free-surface of the river, this flow behaves as free flow over substantial domain and thus the term *mixing layer* should be preserved for classification purposes. However, certain specification for the term is required and by our opinion it should be qualified as a free-surface limited vertical mixing layer.

ACKNOWLEDGEMENTS

The authors acknowledge the help of Rüdiger Biskupek and Henrik Zwadlo in the construction of field equipment. Heinz Bungartz is thanked for assistance with organization of the field campaigns. Anna Sukhodolova and Mischael Thiele provided logistics support during measurements and Ruslan Andronov helped with underwater video recording. The research was supported in parts by Deutsche Forschungsgemeinschaft (BU 1442/1-1, SU 405/2-1) and by Collaborative Programme of NATO (ESP.NR.EV 981608).

REFERENCES

Brown, G.L. & Roshko, A. 1974. On density effects and large structure in turbulent mixing layers. *Journal Fluid Mech.* 64: 775–816.

Ikeda, S. & Kanazawa, M. 1996. Three-dimensional organized vorticies above flexible water plants. *Journal of Hydraulic Eng.*122(11): 634–640.

Ghisalberti, M. & Nepf, H. 2002. Mixing layers and coherent structures in vegetated aquatic flows. *Journal of Geophysical Research*107(C2): doi: 10.1029/2001JC000871.

Kouwen, N. & Unny, T.E. 1973. Flexible roughness in open channels. *Journal of Hydraulics Div.* ASCE, 99(HY5): 713–728.

Michalke, A. 1965. On spatially growing disturbances in an inviscid shear layer. *Journal Fluid Mech.* 23: 521–544.

Monin, A.S. & Yaglom, A.M. 1971. *Statistical Fluid Mechanics. Mechanics of Turbulence.* 1, Cambridge: MIT Press.

Murota, A., Fukuhara, T. & Sato, M. 1984. Turbulence structure in vegetated open channel flows. *Journal of Hydroscience and Hydraulic Eng.* 2(1): 47–61.

Raupach, M.R., Finnigan, J.J., & Brunet, Y. 1996. Coherent eddies and turbulence in vegetation canopies: the mixing-layer analogy. *Boundary-Layer Meteorology* 78: 351–382.

Sand-Jensen, K. & Pedersen, O. 1999. Velocity gradients and turbulence around macrophyte stands in streams. *Freshwater Biology* 42: 315–328.

Stephan, U. & Gutknecht, D. 2002. Hydraulic resistance of submerged flexible vegetation. *Journal of Hydrology* 269: 27–43.

Sukhodolov, A. & Sukhodolova, T. 2005. Morphodynamics and hydraulics of vegetated river reaches: a case study on the Müggelspree in Germany. In: *River, Coastal and Estuarine Morphodynamics.* G. Parker, & M.H. Garcia (eds.), V1: 229–236.

Sukhodolova, T., Sukhodolov, A. & Engelhardt, C. 2004. A study of turbulent flow structure in a partly vegetated river reach. In: *River Flow 2004.* M. Greco, A. Carravetta, & R. Della Morte (eds.), V1: 469–478.

Tennekes, H. & Lumley, J.L. 1972. *A First Course in Turbulence.* Cambridge: MIT Press.

Tukker, J. 1997. *Turbulence Structures in Shallow Free-Surface Mixing Layers*. Report 97-2, Delft: Delft University of Technology Press.

Copyright © 2006 Taylor & Francis Group plc, London, UK

A new 1D-numerical model for flexible vegetated channels

D. Velasco, A. Bateman & V. Medina
Hydraulic, Maritime and Environmental Engineering Department, Technical University of Catalonia (GITS-UPC), ETSCCPB, Av/ Gran Capitan s/n, Barcelona, Spain

ABSTRACT: This paper suggests a simple new numerical scheme for calculating the vertical velocity profile, turbulent shear stress distribution and canopy deflection for flow in vegetated channels. The scheme is derived from the simplified, steady Reynolds equation (momentum balance) and its vertical integration. This study includes an experiment that compares and calibrates the numerical model to flume data. Fourteen runs were performed in a laboratory flume, of which nine involved natural grass (cultivated barley) and five involved plastic plants (PVC). Turbulent diffusion coefficient, mixing length, and a resistance equation (drag coefficient *Cd* vs. Reynolds number) were the input parameters for the numerical model. Parameters with physical meaning were calibrated. This scheme offers a low computation time and good estimation of plant deflection and velocity and stress profiles.

1 INTRODUCTION

When we study fluvial hydrosystems, we must not focus only on the various isolated elements involved in the process (water, sediment, vegetation and fauna). Rather, we must deepen our knowledge of their common relationships. We aim to study the effect of flexible vegetation on flow. The presence of flexible canopy (grass, bushes and reeds) in the riverbed and along the banks changes flow resistance and, in consequence, river hydrodynamics. Many authors (Kouwen, 1969 and Nepf, 1999) have experimented with plastic and natural canopy in their laboratories to obtain empirical relationships. The complexity of physical model studies and the popularization of numerical schemes in hydraulics have led to the development of applications focused on flow through vegetation. Three different lines of numerical research have been followed. First, well-known 3D turbulent schemes have been applied to special geometric boundaries to simulate obstruction due to vegetation. López and García (2001) and Fischer-Antze (2001) adjusted the two-equation κ-ε closure model to flow through vertical rigid cylinders. These simulations are quite well adjusted. Cui and Neary (2002) compared the numerical results of Reynolds-averaged Navier-Stokes (RANS) and large eddy simulation (LES) in order to reproduce the particular anisotropy generated in flow through rigid, submerged cylinders. Finally, Choi and Kang (2004) used Reynolds stress modeling (RSM) to improve mean and turbulent field results. High-accuracy numerical schemes will be developed in the future, but the high computational cost is still a disadvantage in terms of their practical application to large-scale hydraulic problems. A second group of researchers (Klopstra, 1997 and Carollo, 2002) has developed analytical expressions for adjusting velocity profiles $U(z)$ in very specific conditions, but the input parameters involved in the problem are hard to estimate. The third line of research is very interesting because it considers the flexural properties of vegetation and calculates the reduction in relative depth h/k due to stem bending. Kutija and Hong (1996) developed this line of research based on very simple turbulent models applied to the 1D Reynolds momentum equation. They calculated deflected plant height k using a function that reproduces the elastic behavior of a vertical beam or cantilever loaded by drag forces. Unfortunately, no data was available to verify the model with flexible vegetation, and the only data used in the calibration were from Tsujimoto's test with rigid cylinders.

This paper tries to improve this third line of research. We develop a new integrated momentum balance scheme for calculating the velocity and turbulent stress profile that includes a mechanical stem-deflection subroutine. We then verify and calibrate the results with our experimental data, which were measured in a flume covered with flexible vegetation.

Copyright © 2006 Taylor & Francis Group plc, London, UK

2 GOVERNING EQUATIONS

The numerical model is based on integrated momentum conservation equations, Eqs. (1) to (4), which are obtained from the vertical integration of the Reynolds x-equation. Let us now recognize and separate four different zones in the flow. The resulting equations are written as Eqs. (1) to (4):

$$0 = \underbrace{\rho.g.So.(h-z)}_{\tau_G(z)} + \tau_{xz}(z) \qquad \text{ZONE 1. external region, } h > z > k$$

$$0 = \rho.g.So.(h-z) + \tau_{xz}(z) + \tau_{Cd}(z) \qquad \text{ZONE 2. internal region, } k \geq z > p$$

$$0 = \rho.g.So.(h-z) + \tau_{Cd}(z) \qquad \text{ZONE 3. shearless region, } p \geq z > \delta_o$$

$$0 = \rho.g.So.(h-z) - \nu.\frac{\partial U(z)}{\partial z} + \tau_{Cd}(z) \qquad \text{ZONE 4. laminar region, } \delta_o \geq z$$

(1),(2),(3),(4)

Zone 1, the "external region", corresponds to heights z from h to k, above the canopy, and thus has no drag forces. Integral Eq. (1) shows how the gravity shear term is uniquely balanced to turbulent shear stress τ_{xz}. Maximum turbulent stress is located, then, at $z = k$. Zone 2, the "internal region", is located below $z = k$. It is characterized by the presence of canopy. The vertical integration of drag forces f_{cd} from the top of canopy k to height z is the amount of shear stress that is absorbed by the plant (τ_{cd}). This vegetative stress is defined in Eq. (5), where C_d = drag coefficient, B = plant width and a = stem spacing. From Eq. (2), we can deduce that gravity shear stress is balanced by both vegetative and turbulent stress. Hence, turbulent stress τ_{xz} is reduced at $z < k$ and, if τ_{cd} is equal to gravity shear τ_G, then turbulent stress τ_{xz} disappears (see Fig. 1). This means that the momentum absorption capability of the canopy is greater than the hydraulic gravity shear. Zone 3 is delimited by height $z = p$, which is called the penetration depth (Nepf, 1999). This zone is called the "shearless region" because the turbulent stress τ_{xz} is negligible (Eq. (3)). In this region, there is no vertical momentum exchange, but turbulence is completely developed; the flow is governed by drag forces that balance the gravity shear completely.

$$\tau_{Cd}(z) = \int_z^k f_{cd}(z)dz = \int_z^k \frac{1}{2}.\rho.C_d(z).\frac{B(z)}{a^2}.U^2(z).dz \qquad (5)$$

The vertical computational domain is uniformly discretized with a Δz step, as shown in Fig. 2, and all of the variables are calculated at these nodes. Water depth (h), undeflected plant height (h') and deflected plant height (k) are denoted as *ih, ihp* and *ik* indexes respectively. Finite-difference approximations (forward differences) are used in the explicit method when vertical velocity U profiles are computed, and first order integral methods (Simpson's rule) are applied in integral operations. Because the scheme is explicit, the number of nodes must be considerable.

Two different boundary conditions must be set in the computational domain: 1) $\tau_{xz} = 0$ at the water surface ($z = h$), and 2) $\partial\tau_{xz}/\partial z = 0$ in the shearless region ($0 < z < p$). The application of the former to the Reynolds equation in the x direction leads to an expression that can be used to explicitly estimate velocity U. Thus, at the very first node of calculation, and for the entire shearless zone ($z_i < p$), velocity U_o is determined by

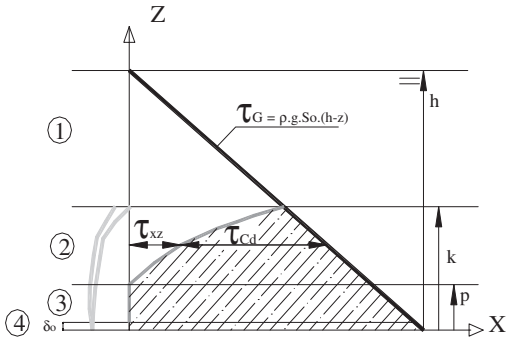


Figure 1. Shear balance scheme for high vegetative momentum absorption capability.

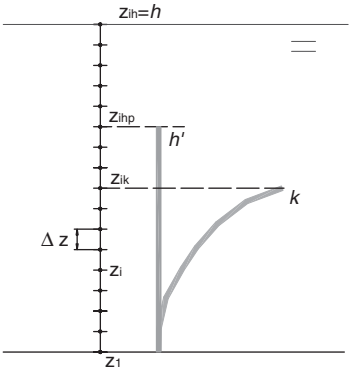


Figure 2. Vertical discretization scheme.

$$U_o = \left(\frac{2.g.So.a^2}{C_{d,o}.B_o}\right)^{1/2} \qquad (6)$$

where drag coefficient $C_{d,o}$ and plant width B_o correspond to node 1. This velocity boundary condition is critical because the general method is based on the hypothesis that the shearless region (Zone 3 in Fig. 1) is developed.

In order to relate Reynolds turbulent stresses to velocity gradients, we used Von Karman's turbulent mixing-length theory. This one-equation turbulence closure reflects momentum diffusion in a very simple way and could be considered a low-accuracy method. However, for the purposes of this work, the results are quite good as a first approach to the problem of

Copyright © 2006 Taylor & Francis Group plc, London, UK

turbulence. The turbulence mixing-length equation is expressed as follows:

$$\tau_{xz} = \rho l^2 . \left|\frac{\partial U}{\partial z}\right| . \frac{\partial U}{\partial z} \tag{7}$$

where ρ = water density and l = mixing length. Various theories on vertical profiles of mixing length $l(z)$, with and without vegetation, are found in the literature. We finally adopted Eq. (8) to estimate the variation of mixing length l as a function of depth. The integral scale L is analogous to the popular mixing-length l of the Von Karman turbulence closure equation because both concepts reflect a characteristic eddy scale. The diffusion mechanism is therefore not very different. We analyzed the vertical distribution of integral scale L from experimental profiles and concluded that, despite the dispersion of the estimated data, a linear tendency above $z = p$ was estimated. Eq. (8) describes the proposed distribution of mixing-length l:

$$\begin{cases} l(z) = l_o + \kappa' . (z - p) & \text{for } z > p \\ l(z) = l_o & \text{for } z \le p \end{cases} \tag{8}$$

where l_o is the mixing length in the shearless zone and κ' is a diffusion coefficient. Numerical parameters l_o (bed mixing length) and κ' (diffusion coefficient) are unknown and must be calibrated, but the advantage is that both of them have a particular physical meaning.

The intrinsic effects of secondary currents and the turbulent anisotropy of flow over vegetated covers are introduced in the model by a simple preliminary approach. The experimental data show the effective reduction of the energy slope ($So_{max\ shear}$), so we propose using a secondary current factor α_{sc}, defined as $\alpha_{sc} = S_{o,max\ shear}/S_o$, where S_o=channel slope (in uniform flow conditions). The value of α_{sc} is always less than one. As a turbulent parameter, it must also be calibrated.

Finally, the drag stress term τ_{cd} in the governing equations (2) and (3) is estimated using Eq. (5). The numerical integral is expressed as Eq. (9):

$$\tau_{Cd}(z_i) = \frac{\rho}{2.a^2} . \int_{z_i}^{z_{ik}} C_{d,j} . B_j . U_j^{\,2} . dz \tag{9}$$

where C_{dj}, B_j and U_j are the drag coefficient, plant width and velocity respectively at node j.

Special care must be taken in the estimation of drag coefficients C_{dj} because they are closely related to the resistance to flow over vegetated covers. The value of C_d is very sensitive to changes in the flow turbulence regime, which is governed by the obstacle or stem Reynolds number $Re_d (= U.B/\nu)$, where ν = water kinematic viscosity. Therefore, a resistance

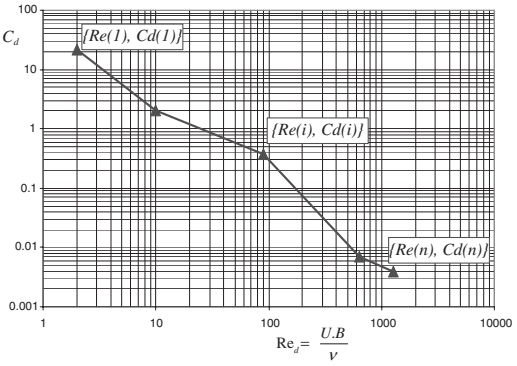


Figure 3. Estimation of the Cd(Red) law as a linear approximation between a series of discrete points {Red(i), Cd(i)} in a log-log graph.

function of the type $C_d(Re_d)$ is added to the model to take this important factor into account and Re_d is calculated at every computational node i as Eq. (10):

$$Re_{d,i} = \frac{U_i . B_i}{\nu} \tag{10}$$

Unfortunately, the classical resistance laws $C_d(Re_d)$ of 2D rigid bodies that have been widely studied in the past are not applicable to the heterogeneous shape of stems and leaves. New relationships must be researched. In order to further the fitting-optimization procedure, the estimation of the $C_d(Re_d)$ law was introduced as a linear approximation between a series of discrete points {Re_d (i), C_d (i)}, for i = 1,n, in a log-log graph. Fig. 3 shows the proposed resistance law as a function of a series of n = 5 points.

The numerical estimation of drag coefficient C_d at node i is based on the previous calculation of $Re_{d,i}$ by Eq. (10) and the application of the linear discrete function $C_{di,} = \Psi_n(Re_{d,i})$. This C_{di} value is included as drag in Eq. (9).

3 DESCRIPTION OF THE NUMERICAL PROCEDURE

3.1 *General iterative scheme*

This numerical model aims to create an iterative succession of well-balanced flow solutions that can generate the final stabilization or convergence of the deflected plant height k. Fig. 4 shows the computational flowchart. At each iteration i, the deflected plant height k^i is calculated and, as a consequence of the geometric change, a new flow solution $U^i(z), \tau^i_{xz}(z)$ is obtained. At this point, the plant deformation is recalculated using the aforementioned flow conditions and a new deflected plant height k^{i+1} is incorporated at iteration $i + 1$. The computation finishes when

Copyright © 2006 Taylor & Francis Group plc, London, UK

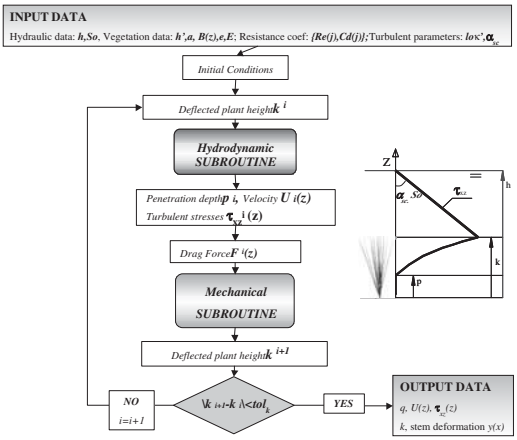


Figure 4. General flowchart.

a convergence in $\{k^i\}$ is a set ($\backslash k^{i+1} - k^i \backslash < tol_k$). The flow solution is then considered dynamically and mechanically balanced.

The input data consists of hydraulic variables: water depth h, energy slope So and the vegetation's geomechanical properties (undeflected plant height h', plant spacing a, vertical distribution of plant width $B(z)$, thickness of stems e, stiffness modulus E, the resistance law $\{Re(j),Cd(j)\}$ and three turbulence parameters [bed mixing-length lo, diffusion coefficient κ' and secondary currents factor α_{sc}]). The results of the model (output data) are unit discharge q, velocity $U(z)$, Reynolds stresses $\tau_{xz}(z)$, deflected plant height k and stem deformation $y(x)$.

The model can estimate the unit discharge q given an initial water depth h and an energy slope So, which is equivalent to solving the flow resistance equation for any kind of vegetation. Friction factors (the Darcy-Weisbach f or the Manning n) can easily be deduced from the hydraulic results.

The general scheme is very simple in its conception, but the most important and critical part is the creation of adequate modules to calculate velocity profiles and stem deformation. The hydrodynamic subroutine calculates flow profiles $\{U^i(z),\tau_{xz}(z)\}$ for a particular plant height k and the mechanical subroutine estimates the deflected plant height k as a function of drag forces $F(z)$. The next section briefly explains the numerical methods used in these two subroutines.

3.2 *Description of the hydrodynamic subroutine*

The numerical strategy used to estimate well-balanced velocity profiles is based on a predictor-corrector technique for Reynolds stresses τ_{xz}. and a minimization function. Fig. 5 shows a flowchart and a schematic diagram with predicted τ_{xz} and corrected τ_{xz} profiles.

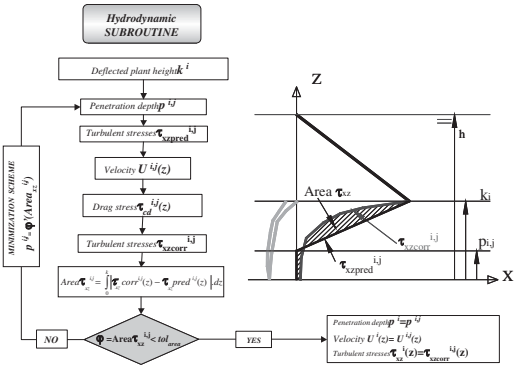


Figure 5. Flowchart of the hydrodynamic subroutine.

Based on a constant deflected plant height k^i (the input of this subroutine), a penetration depth $p^{i,j}$ is proposed and a linear distribution of turbulent stresses $\tau_{xz,pred}{}^{i,j}(z)$ is then predicted (as seen in Fig. 5). Eqs. (6) and (7) are then used to calculate the velocity profile $U^{i,j}(z)$ and Eq. (9) is used to estimate drag stresses $\tau_{cd}{}^{i,j}(z)$. Then, the corrected $\tau_{xz,corr}{}^{i,j}(z)$ profile is balanced using Eqs. (1), (2) and (3). The area between the predicted and corrected stress profiles is then calculated using Eq. (11).

The value of $Area\tau_{xz}{}^{i,j}$ is then related to the penetration depth $p^{i,j}$, and a positive function is defined as $\varphi(p) = Area\tau_{xz}(p)$. Under this scheme, the minimization of function φ implies a well-balanced solution in the $\tau_{xz,corr}(z)$ and $U(z)$ profiles. An iterative, first-order minimization method is applied to $\varphi(p)$ and the solution (penetration depth p^i, velocity $U^i(z)$ and stresses $\tau_{xz}{}^i(z)$) is sent to the main program. The accuracy of the solution basically depends on the definition of function $\varphi(p)$ (existence and uniqueness of an absolute minimum). The analysis of this function shows that the search method's behavior and efficiency are sufficient.

$$Area\,\tau_{xz}{}^{i,j} = \int_0^k \left|\tau_{xz,corr}{}^{i,j}(z) - \tau_{xz,pred}{}^{i,j}(z)\right| dz \qquad (11)$$

3.3 *Description of the mechanical subroutine*

This subroutine consists of a numerical code that reproduces load-deformation processes in a stem. Each canopy element is modeled as a vertical, isolated beam or cantilever in order to simplify the structural problem. The forces on the stem are imported from the hydrodynamic subroutine and are applied to every calculation node in order to obtain an approximation $y(x)$ of stem deformation. Classical, analytical expressions of deformation on beams are not valid here, because they are only derived for small deformation conditions. Natural canopy elements bend easily in river floods.

Copyright © 2006 Taylor & Francis Group plc, London, UK

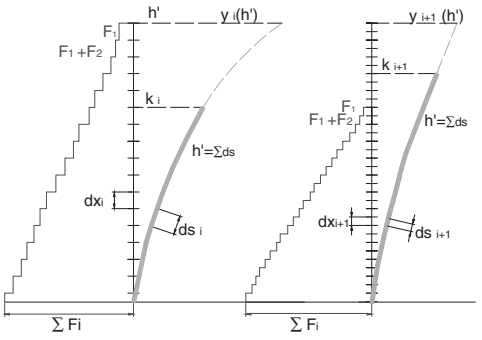


Figure 6. Numerical discretization and iteration process for the mechanical subroutine (large deformations).

Brushes and aquatic species also bend easily in normal flows. The deformation of the top of the canopy is often of the same order as the deflected plant height ($y(h') \cong k$). In the simulation, large deformations are required to adequately estimate the vertical deflected plant height k.

A discretization of the beam elasticity equation is applied in the stem (x is adopted as the vertical, longitudinal direction of the stem) and an explicit forward finite-difference scheme is computed to solve the transversal deformation profile y(x), as in Eq. (12):

$$\frac{\partial^2 y}{\partial x^2} = -\frac{Mf}{E.I} \tag{12}$$

where $y =$ transversal deformation, $Mf =$ moment (N.m), $E =$ stiffness modulus (N/m^2) and $I =$ cross area inertial modulus (m^4). The large deformation hypothesis conserves total stem length h'. The vertical load distribution (drag forces) must then be redistributed to reach equilibrium. A general iterative scheme is established in $\{y_i(x), k_i\}$ to converge to the deflected plant height k. The deformation profile $y_i(x)$ is calculated from Eq. (12) and the total stem length is measured along the deformed stem to define the deflected plant height k_i. New nodes are defined according to k_i. A new distribution of forces F is used. Then, $y_{i+1}(x)$ and k_{i+1} are calculated. Fig. 6 presents a diagram of the iterative procedure. The convergence into the solution is fast enough (less than 15 iterations, in general). In calculating large deformations, the additional bending due to second-order moments in the beam must be taken into account. New moments Mf' appear in the beam due to non-orthogonality between loads F and the longitudinal direction of the deformed beam(s). This effect is introduced as follows: 1) first-order moments Mf are used and a deformed profile $y(x)$ is obtained; 2) secondary moments Mf' are calculated from derivatives $y'(x)$ and vertical distances; and 3) a new calculation of the beam is performed for the total moments $Mf + Mf'$. The final result is a decrease from the first-order calculations in the deflected plant height k and an increase in the bending curvature (observed in real elastic materials). Fig. 7 demonstrates the importance of including secondary moments in order to more accurately reproduce the bending of elastic stems.

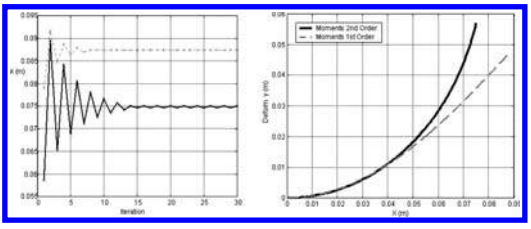


Figure 7. Comparison of computational stem deformation with (solid line) and without (dashed line) the calculation of secondary moments.

4 MODEL VERIFICATION

In this study, we were able to calibrate and verify the model in an accurate, controlled way due to a previous experimental study. Our own data was vitally important. Although the tests were limited in number (a greater variety of plant density and shapes would be desirable), we obtained detailed measurements.

To calibrate the mechanical subroutine, we performed load-deformation tests in the laboratory under strictly controlled conditions. We tested PVC cylinders with well-known geomechanical properties to check that the large deformation hypothesis and numerical algorithm were acceptable. We directly measured or estimated the geomechanical properties of the canopy (both PVC palms and natural barley stems), including length, average width and thickness, stiffness modulus E and inertial modulus I. These properties were introduced as input data in the mechanical model. The results were quite good for all load steps. Although the bending-stem curvatures were hard to reproduce (due to the heterogeneity of real stem properties), we assumed the discrepancies and finally accepted the model. Limitations were present for larger deformations ($k/h' < 0.6$). The adjustment between the measured and calculated deformation profiles presented the lowest accuracy (Fig. 8). The error on k was 12%.

The numerical results of the integrated model were compared to experimental data in order to verify the accuracy of the method. Fig. 9 shows two examples. First, the experimental data obtained by Tsujimoto (1990) was adjusted for flow through rigid cylinders. Run A11 involved vertical cylinders 4.59 cm tall and 1.5 mm in diameter, arranged in a staggered pattern with 2 cm spacing. The second run in Fig. 9 used data from our tests (barley cover). The flexible barley stems were 18 cm tall. The spacing between

Copyright © 2006 Taylor & Francis Group plc, London, UK

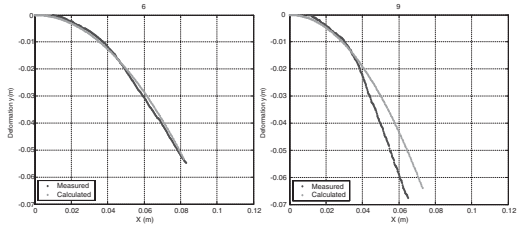


Figure 8. Comparison between measured and calculated deformations of a barley stem (length h′ = 0.125 m) for increasing loads.

stems was $a = 6.7$ mm and the submergence ratio was h/k = 1.83. The vertical distribution of plant width $B(z)$ was defined as a constant for cylinders and was variable for barley (calculated from a frontal image). The drag coefficients $C_d(z)$ were set as a unique value for cylinders ($C_d = 1.5$). For barley, the experimental values of $C_d(z)$ obtained from the barley test were used in the numerical model.

Computational input parameters such as mixing length lo, momentum diffusion constant κ', and the secondary current factor α_{sc} were adjusted for each run. For Tsujimoto's run they were $lo = 2.5$ mm, $\kappa' = 0.17$ and $\alpha_{sc} = 1.0$. For the barley run with TN-h′ = 0.18 m, the parameters were $lo = 10$ mm, $\kappa' = 0.08$ and $\alpha_{sc} = 0.78$. Fig. 9 shows very good agreement between the measured and calculated velocity profiles, and the velocity profile curvatures were reproduced quite well.

Calibrating the general model involved a significant amount of work. A particular set of general computational parameters needed to be found to fit all different tests. The list of unknown parameters included drag coefficient points, $\{Re(j), Cd(j)\}$, j = 1,5, mixing length lo, momentum diffusion constant κ', and the secondary current factor α_{sc}. A multi-parameter optimization technique was applied to fourteen runs with vegetation (T3 and TN runs) in which the canopy was deflected and totally submerged. The measured data used in the optimization routine was the unit discharge q_{mea} (m^3/m/s) and the velocity profiles $U_{mea}(z)$. Some discrepancies were obtained between the measured unit discharge q_{mea} and the vertical integral of $U_{mea}(z)$ due to 3D flow characteristics. Both measurements were integrated in the optimization function. This function Φ was defined as a quadratic function of the difference between the calculated output data and the measured data. A first-order, intelligent-conjugate-gradients technique was used to find the minimum of Φ. Table 1 shows the optimal adjusted parameters.

These parameters are consistent with the physical measurements, but some comments must be made about the resistance law. The values of adjusted $Re(j)$ and $Cd(j)$ are shifted with respect to measured data, as shown in Fig. 10. Adjusted drag coefficients C_d are lower than measured C_d. This shift is probably due to a numerical diffusion in the model.

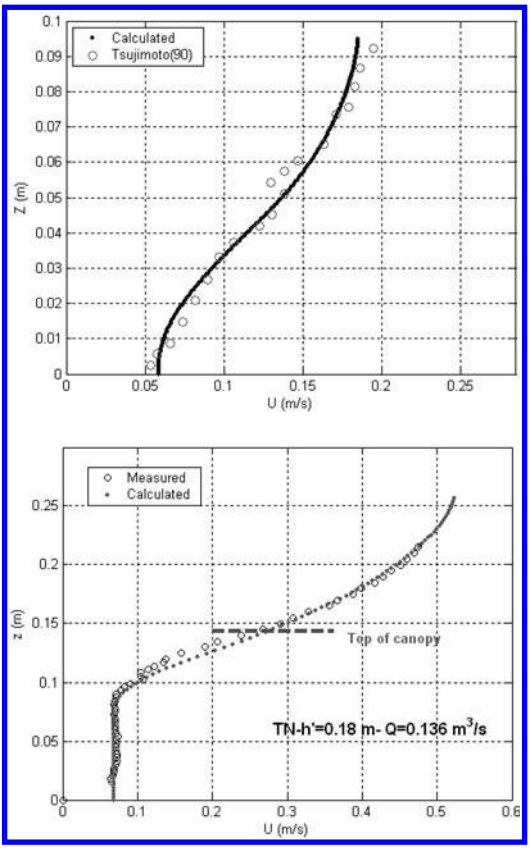


Figure 9. Comparison between measured and calculated velocity profiles. Top: run A11 for vertical rigid cylinders from Tsujimoto's experiments (1990). Bottom: flexible barley run (TN-h′ = 0.18 m) from our own experiments.

Table 1. Adjusted parameters of the drag coefficient law and turbulence parameters.

Resistanece law		Turbulent parameters		
Re	C_d	lo (*m*)	κ'	α_{sc}
2	22.5	0.01	0.04	0.54
10	3.14			
90	0.37			
632	0.009			
1275	0.004			

5 NUMERICAL RESULTS

This section discusses the results of the model calibration. Fig. 11 shows four different runs and compares

Copyright © 2006 Taylor & Francis Group plc, London, UK

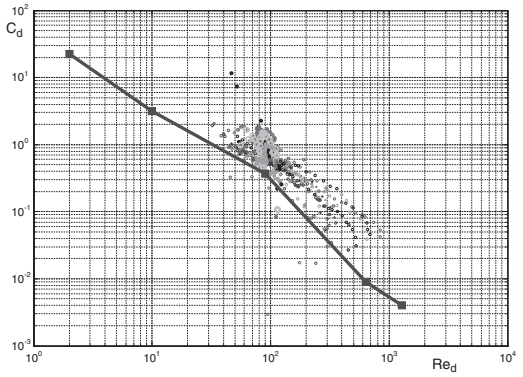


Figure 10. Optimally adjusted resistance law (Cd vs. Red) compared to experimental data (circles).

experimental data to computed data. Velocity $U(z)$ and Reynolds turbulent stress $\tau_{xz}(z)$ profiles are presented. In general, velocities and shear are both well adjusted. Very good agreement is observed for the penetration depth p, and the shearless zone is well defined in terms of velocity and shear. Velocity U_o in this zone is calculated as a uniform profile and agreement with measured U_o is sufficient. We therefore conclude that the proposed velocity boundary condition (Eq. (6)) is efficient. In Zone 2 (internal zone $p < z < k$), the calculated stress τ_{xz} shows some deviation from the measured data, but vegetative momentum absorption seems to be accomplished. The top of the canopy in the figure (circle) corresponds to the peak of calculated stress ($\tau_{xz,max}$) and approximately agrees with the peak of measured τ_{xz}. In the external zone ($z > k$), the slope of calculated τ_{xz} does not fit the data. However, the effects of secondary currents are simulated, which is a major goal of the numerical model and the calibration study. The calculated velocity $U(z)$ reproduces the gradients in the internal zone quite well, but there is some discrepancy close to the free surface.

Figure 12 shows the calculated *Re* and C_d vertical profiles and compares them to the experimentally measured profiles. The obstacle Reynolds number shows good agreement both for natural and artificial plants (plant shape controls *Re* distribution). However, as mentioned above, the numerical drag coefficients are lower than the experimental C_d. This effect is very important in the artificial plants (T3 runs), as shown in the figure.

Lower drag coefficients should translate into a reduction in drag stresses (see Eq. (9)). However, the final balance of momentum is well adjusted. This discrepancy should be reviewed in the future by verifying the adjusted parameters through new tests with a range of vegetation configurations (the influence of spacing a) and submergence ratios. The next step in the results analysis is mass conservation. In Fig. 13, the

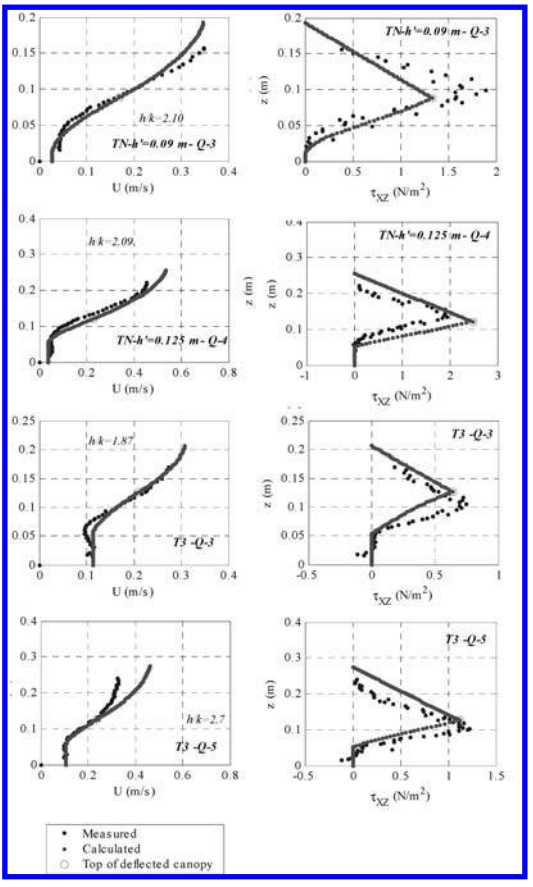


Figure 11. Comparison between calculated and measured U(z) and τ_{xz}(z) profiles.

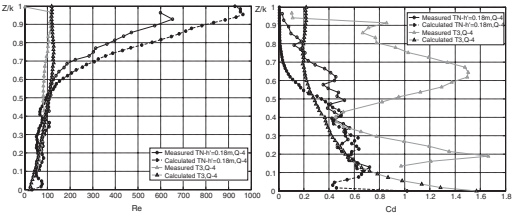


Figure 12. Measured and calculated Re and Cd vertical profiles.

water discharge (an output of the numerical model) is compared to the experimental discharge. For all fourteen tests, the comparison between the calculated unit discharge q_{calc} (m^2/s) and the measured q_{mea} shows a certain dispersion. The average estimation error is 14.8%, but the experimental error between q_{mea} and the vertical integral of experimental $U_{mea}(z)$ was set at 10%. We conclude that the data on discharge q is not much more accurate than typical laboratory work

Copyright © 2006 Taylor & Francis Group plc, London, UK

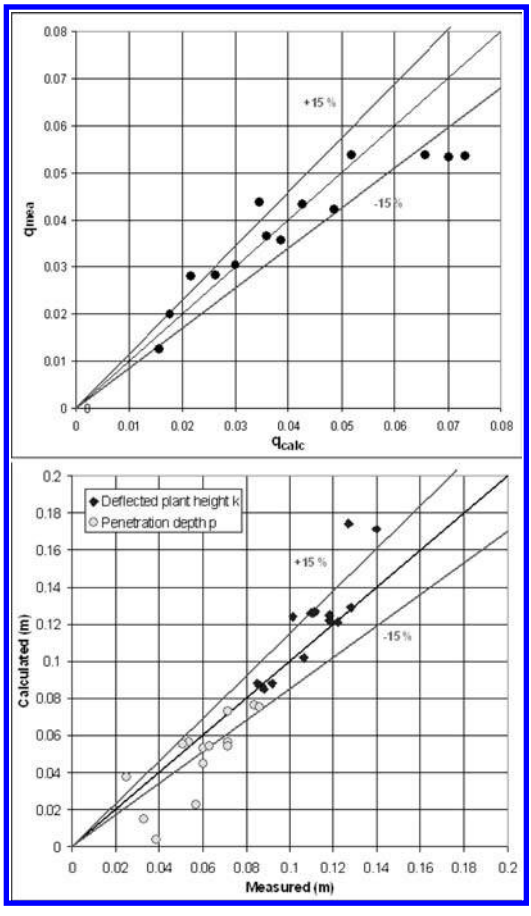


Figure 13. Numerical results for unit discharge q (top) and deflected plant height k and penetration depth p (bottom).

involving vegetation covers. Figure 13 also shows the results for deflected plant height k and penetration depth p. Some dispersion of data is detected, but the estimations are generally in an error range of 15%. More experiments are needed to check that the calculated deflected plant is adjusted to reality (especially in large deformation conditions, $h'/k > 0.6$).

6 LIMITATIONS OF THE MODEL

The integrated vegetation model is very useful for reproducing vegetative covers in both emergent and submerged plant conditions. Due to its low computational cost, this model can easily be incorporated into any general 1D or 2D hydraulic code to estimate friction factors in riverbeds and floodplains. However, the numerical code has certain limitations. The governing equations are only defined for the existence of a shearless zone, so vegetation must be able to absorb the total gravity shear τ_G. This model is therefore recommended for high-to-medium plant density (high A_o/a ratio). The model should be modified for flooding scenarios in which the canopy is totally prone, friction factors are low and an effective shear stress is acting on the river bed. Furthermore, the model introduces real convective currents in the flow through canopy (α_{sc} factor) but it is still hard to evaluate for different flow conditions. Finally, a more intense experimental campaign is needed to verify the proposed drag coefficient law $C_d(Re_d)$ for new plant shapes and configurations.

7 SUMMARY AND CONCLUSIONS

This paper presents an experimental and numerical study that provides deeper knowledge of resistance to flow through flexible vegetation. A numerical model was computed to simulate vertical velocity profiles and plant deflection. The scheme was derived from the simplified, steady Reynolds equation, which was vertically integrated above and along the deflected plant height k. A mechanical module was computed to estimate large elastic deformation in stems. Mixing-length theory was used in a turbulence closure equation for the hydrodynamic subroutine. We proposed an iterative convergence scheme for plant deformation k as a function of balanced drag forces. Finally, the well-balanced vertical velocity profile $U(z)$ was calculated using a simple, explicit finite-difference scheme.

In the experimental chapter, two different experimental flumes were used. Both natural (barley) and artificial (PVC strips) vegetative covers were fixed on the channel bed. Vertical velocity profiles U and turbulent shear stress τ_{xz} (obtained using ADV measurement techniques) provided valuable experimental data on every flow and vegetative configuration. Fourteen experimental runs were performed to verify and calibrate the numerical model. Turbulent diffusion coefficients, mixing length and a resistance equation (drag coefficient C_d vs. Re_d) were the input parameters of the model. Parameters with physical meaning were calibrated. A multi-parameter minimization algorithm was used to adjust the computed profiles to the experimental data. Finally, the parameters were estimated. In theory, these computational parameters should be universal and independent of vegetation shape and configuration. In practice, the uniqueness of this set of general parameters should be verified in the future using different species of vegetation.

This integrated model offers a low computation cost and a reasonable estimation of plant deflection, velocity and stresses. Vertical profiles are obviously less accurate than any 3D-turbulent scheme. However, the approximation errors are quite small and would therefore be easily dealt with in a general floodplain

Copyright © 2006 Taylor & Francis Group plc, London, UK

calculation. This quick model is therefore very suitable and fast enough to be included in a future general 1D or 2D hydraulic model as a resistance function for vegetation.

ACKNOWLEDGMENTS

This research was supported by a *UPC per la recerca* grant (Technical University of Catalonia) and projects REN2000-1013/HID and BTE2002-0375. We are especially grateful to Prof. J.M. Redondo, who was very helpful in the initial phase of the experimental work.

NOTATION

The following symbols are used in this paper:

a	= Spacing between plants
A_o	= Frontal area of plant
b	= Channel width
B	= Average plant width
C_d	= Drag coefficient
E	= Stiffness modulus
h	= Water depth
h'	= Undeflected plant height
I	= Second-order geometrical momentum
k	= Deflected plant height
l	= Mixing length
L	= Integral scale
M	= Density of vegetation (plants/m^2)
Mf	= Moment
p	= Penetration depth
q	= Unit discharge ($= Q/b$)
Q	= Discharge
Re	= Reynolds number ($= U.h/\nu$)
Re_d	= Obstacle Reynolds number ($= U.B/\nu$)
R_h	= Hydraulic radius
S_f	= Energy slope
$S_{omax\ shear}$	= Experimental energy slope obtained from the τ_{xz}, vertical profile
S_o	= Geometric slope
U, V, W	= Longitudinal, transversal and vertical mean velocities respectively
u', v', w'	= Longitudinal, transversal and vertical velocity fluctuations respectively
u^*	= Shear velocity
α_{sc}	= Secondary current factor
γ	= Specific weight of water
κ	= Von Karman universal diffusion constant
κ'	= Diffusion coefficient
ν	= Kinematic viscosity
ρ	= Water density
$\tau_{xz}, \tau_{xy}, \tau_{yz}$	= Reynolds stresses
τ_{cd}	= Vegetative drag stress
τ_*	= Bed shear stress

REFERENCES

Carollo, F., Ferro, V. 2002. Flow Velocity Measurements in Vegetated Channels. *ASCE Journal of Hydraulic Engineering*, Vol. 128, 664–673.

Cui, J., Neary, V.S. 2002. Large eddy simulation (LES) of fully developed flow through vegetation. *Hydroinformatics 2002: Proceedings of the 5th International Conference on Hydroinformatics*, Cardiff, UK.

Chen, C. 1976. Flow resistance in broad shallow grassed channels. *ASCE Journal of the Hydraulics Division*, Vol. 102, No. HY3, 307–322.

Choi, S., Kang,. H. 2004. Reynolds stress modeling of vegetated open-channel flows. *Journal of Hydraulic Research,* Vol. 42, No. 1, 3–11.

Dunn, C., López, F. 1996. Mean flow and turbulence in a laboratory channel with simulated vegetation. *Civil Engineering Studies, Hydraulic Engineering Series*, No. 51. University of Illinois, Urbana-Champaign.

Finnigan, J. 2000. Turbulence in plant canopies. *Annu. Rev. Fluid Mech.*, Vol. 32. 519–571.

Fischer-Antze, T., Stoesser T., Bates, P. 2001. 3D numerical modelling of open-channel flow with submerged vegetation. *Journal of Hydraulic Research*, Vol. 39, No. 3. 303–310.

Ikeda, S., Kanazawa, M. 1996. Three-dimensional organized vortices above flexible water plants. *ASCE Journal of Hydraulic Engineering,* Vol. 122, No. 11, 634–640.

Klopstra, D., Barneveld, H.J. 1997. Analytical model for hydraulic roughness of submerged vegetation. *Proceedings of the 27th Congress of the IAHR*, San Francisco (USA).

Kouwen, N. Unny, T.E, Hill, H.M. 1969. Flow retardance in vegetated channels. *ASCE Journal of Irrigation and Drainage Division*, Vol. 95, No. IR2, 329–342.

Kouwen, N. Unny. T.E. 1973. Flexible roughness in open channels. *ASCE Journal of the Hydraulics Division,* Vol. 99, No. HY5, 713–727.

Kouwen, N. Li, R. 1980. Biomechanics of vegetative channel linings. *ASCE Journal of the Hydraulics Division*, Vol. 106, No. HY6, 1085–1103.

Kouwen, N. 1992. Flow resistance in vegetated waterways. *ASCE Journal of Irrigation and Drainage Engineering*, No. 5, 733–743.

Kutija, V., Minh Hong, H.T. 1996. A numerical model for assessing the additional resistance to flow introduced by flexible vegetation. *Journal of Hydraulic Research*, Vol. 34, No. 1, 99–114.

López, F., García, M.H. 2001. Mean flow and turbulence structure of open-channel flow through non-emergent vegetation. *ASCE Journal of the Hydraulics Division*, Vol. 127, No. HY5, 392–402.

Naot, D., Nezu, I., Nakagawa, H., 1996. Hydrodynamic behavior of partly vegetated open channels. *ASCE Journal of Hydraulic Engineering*, Vol. 122, No. 11, 625–633.

Nepf, H.M. 1999. Drag, turbulence and diffusion in flow through emergent vegetation. *Water Resources Res*. 35(2).

Nepf, H.M., Vivoni, E. 2000. Flow structure in depth-limited, vegetated flow. *Journal of Geophysical Research*, Vol. 105.

Nezu, I., Nakagawa, H. 1993. Turbulence in open channel flows. *Monograph series IAHR*. Ed. Balkema.

Copyright © 2006 Taylor & Francis Group plc, London, UK

Nezu, I., Onitsuka, K. 2001. Turbulent structures in partly vegetated open-channel flows with LDA and PIV measurements. *Journal of Hydraulic Research*, Vol. 39, No. 3. 629–642.

Petryk, S., Bosmajian, G. 1975. Analysis of flow through vegetation. *ASCE Journal of the Hydraulics Division*, Vol. 101, 871–884.

Raupach, M.R., Thom, A.S. 1981. Turbulence in and above plant canopies. *Annual Review of Fluid Mechanics*. 97–129.

Rodi, W. Turbulence Models and their application in hydraulics. *Monograph, IAHR*, Delft, The Netherlands.

Rouse, H. 1946. Elementary mechanics of fluids. *Dover Publications*.

Tsujimoto, T., Kitamura, T. 1990. Velocity profile of flow in vegetated-bed channels. *KHL Progressive Report*, Hydraulic Laboratory, Kanazama University, Japan.

Velasco, D., Bateman A. 2003. An open channel flow experimental and theoretical study of resistance and turbulent characterization over flexible vegetated linings. *Flow, Turbulence and Combustion*, No. 70. FTAC Special Issue: Fluxes and Structures in Fluids. Kluwer Publications, 69–88.

Wu, F.C., Shen, H.W., 1999. Variation of roughness coefficients for unsubmerged and submerged vegetation. *ASCE Journal of Hydraulic Engineering*, Vol. 125, No. 9, 934–942.

Copyright © 2006 Taylor & Francis Group plc, London, UK

Steady 1D water surface model of natural rivers with vegetated floodplain: An application to the Lower Biebrza

D. Świątek, J. Kubrak, J. Chormański
Warsaw Agricultural University, Warsaw, Poland

ABSTRACT: A steady 1D flow model for water surface calculation, based on the energy equation, was developed for natural rivers with vegetated floodplains. The friction slope was determined by the friction law of Darcy-Weisbach. The total Darcy-Weisbach friction factor for each cross section was calculated according to type of vegetation and flow interaction between main channel and vegetated areas. The model was applied to the Biebrza River, situated in the north-eastern part of Poland, flowing through the last extensive, fairly undisturbed river-marginal peatland in Europe. A 41 km long reach of the Lower Biebrza River, which basin covers 350 km^2, was selected for the study. The floodplains are covered by mosaic pattern vegetation. There are reeds, sedges, grasses, bushes as well as trees and scrubs. Three steady flow cases were computed. Two of them, when water levels are low, were compared to measured data. The absolute roughness values in the main channel were calibrated by the measurement in conditions where the water levels were less than bankfull levels. In the next case, when water was on the floodplains, the Digital Elevation Model of the floodplain constructed with the use of GIS techniques was coupled with calculated water level for spatial flood extent in the valley. Result was verified with the help of the processed Landsat satellite image. Water levels produced by the model correlated well with the measured data and the processed satellite image. Elaborated model can be also useful for water surface assessment in lowland rivers with floodplains and vegetation.

1 INTRODUCTION

Many studies were carried out in the past to investigate the hydraulic impact of natural roughnesses such as bank and flood plain vegetation or bed roughnesses of different textures on the overall flow field (see e.g. Rouve 1987, Kubrak & Nachlik 2003). The flow processes in channels with local flood berm vegetation between main channel and flood plains are very complex. The ability to model water level between the instream and floodplain is fundamental for assessing the quality of aquatic habitat for riverine biota, particularly floodplain vegetation and waterbirds. Precise hydraulic modelling of these relationships is difficult because of the lack of appropriately scaled information to describe floodplain topography and surface roughness. Non-uniform flow occurring in a lowland river with gradual changes in its free surface elevation is termed gradually varied.

Existing methods for water level calculation are, to varying degrees, unreliable for compound channel hydraulics. Therefore, more accurate methods are needed for calculation of water levels in these channels. The steady gradually-varied flow model was used for estimation of water profiles in the reach of the Biebrza River.

2 NUMERICAL MODEL DEVELOPMENT

2.1 *The steady flow model*

The water profile in steady gradually-varied flow was calculated using the standard step method. This method is characterized by dividing the river with compound cross sections into short reaches and carrying the computation step by step from one end of the reach to the other. Problem is formulated as follows: For a given discharge the river stage H_2 is known at one section (2) downstream and it is required to calculate the stage H_1 at the adjacent section (1) upstream. At both sections a plan of the waterway is available, from which values of cross section area, wetted perimeter, mean velocity, perimeter of vegetation, etc., may be determined for any given stage.

The equation for H_1 calculation is conduced from equating the total heads at two end sections:

$$\alpha_1 \frac{V_1^2}{2g} + H_1 = \alpha_2 \frac{V_2^2}{2g} + H_2 + \frac{1}{2}(J_1 + J_2)\Delta L \quad (1)$$

where H_1, H_2 = water surface elevation at the two end sections; J_1, J_2 = friction slopes at the two end sections, V_1, V_2 = mean velocities; and α_1, α_2 = energy

Copyright © 2006 Taylor & Francis Group plc, London, UK

coefficients at the two end sections; ΔL = length of the river reach.

For a trial value of unknown stage H_1 the values V_1, α_1, J_1 were calculated. The same values were calculated at section 2 by given stage H_2. The test of trial process is whether this value of H_1 is equal to the one previously calculated; if not, a further trial value must be taken.

The discharge of steady flow in the river was expressed as the product of the velocity and the water area. For the mean velocity calculation Darcy-Weisbach formula was used. Velocities, friction factors and the components of discharge in the main channel and on the floodplains were calculated using momentum transfer between the main channel and the floodplains were included in the model using Pasche method (Pasche 1984).

2.2 *Determination of friction factors*

Physically, the composite roughness along the wetted perimeter of the compound cross section modifies the velocity distribution across the cross section. A detailed examination on the effects of varying wall roughness and cross sectional geometry would require three-dimensional analysis of the flow. Pasche (1984) proposed the one-dimensional analysis of steady flow in compound cross section of the lowland river based on the Darcy-Weisbach formula.

According to observed velocity distribution the compound cross section is divided into sections with vertical interfaces into the main channel and neighbouring floodplains. The heights of these interfaces are taken into consideration at calculation of wetted perimeter of the main channel. Mean velocity of the flow in each section is calculated according to the Darcy-Weisbach equation, which results from the momentum balance in part of cross section:

$$v = \sqrt{\frac{8gRJ}{\lambda}} \tag{2}$$

where λ = average dimensionless friction factor of flow in given part of section, g = gravitational acceleration [m/s^2], J = hydraulic slope [-], R = hydraulic radius [m].

For the velocity calculation in each section proper evaluation of the friction factor λ is necessary. The resistance of flow in parts of channel sections overgrown by vegetation depends on both vegetation and bed roughness. The friction factor for this area, according to the concept issued by Einstein and Banks (Indlekofer 1981), is the following sum:

$$\lambda = \lambda_s + \lambda_v \tag{3}$$

where λ = average friction factor in part of cross-section [-], λ_s = friction factor caused by channel bed roughness [-], λ_v = friction factor for submerged vegetation [-].

The resistance of flow caused by the roughness of the scarp and the channel bed is calculated from the formula given by Colebrook-White:

$$\frac{1}{\sqrt{\lambda_s}} = -2.03 \log\left(\frac{2.51}{Re\sqrt{\lambda_s}} + \frac{k_s}{14.84\,R}\right) \tag{4}$$

where λ_s = friction factor of not overgrown part of channel [-], k_s = bed roughness of channel [m], Re = the Reynolds number for part of cross-section.

As it results from the Colebrook-White law, the friction factors of flow depend on the Reynolds number and on relative roughness k_s/R. The influence of the Reynolds number on friction factors decreases along the increase of its value and of relative roughness of channel sides. In natural channels the relative roughness is also considerable that the influence of the Reynolds number may be neglected without any harm to the precision of calculations. Therefore Rickert (1988) recommends to apply the equation (4) for practical calculations in the following form:

$$\frac{1}{\sqrt{\lambda_s}} = -2.03 \log\left(\frac{k_s}{14.84\,R}\right) \tag{5}$$

The friction factor of scarps and of channel bed with k_s roughness is then calculated from transformed formula (5).

The friction factors for high vegetation λ_v were the object of investigations by Kaiser (1984), Lindner (1982) and Pasche (1984). For areas with trees the λ_v factor is calculated on the basis of resistances caused by submerged vegetation and is related to the area of the whole floodplain:

$$\lambda_v = \frac{4h_p d_p}{a_x a_y} C_{WR} \cos\alpha \tag{6}$$

where h_p = height of submerged part of trees [m], d_p = trees diameter [m], α = the angle of slope of the bed in transverse direction to direction of flow, C_{WR} = dimensionless drag coefficient for submerged part of the trees.

The drag coefficient C_{WR} depends on the ratio of the V_i flowing velocity to the average velocity V_v of the flow going through tree-overgrown areas, and the height of waves formed on the surface of the water flowing around the trees:

$$C_{WR} = \left(1.1 + 2.3\frac{d_p}{a_y}\right)\left(\frac{V_i}{V_v}\right)^2 + 2\left(\frac{1}{1 - d_p/a_y} - 1\right) \tag{7}$$

Copyright © 2006 Taylor & Francis Group plc, London, UK

Pasche (1984) gave an empirical formula on the relative velocity of water flowing against the tree, and Rickert reduced it to the following form:

$$\left(\frac{V_i}{V_v}\right)^2 = 0.6 + 0.5log\left(\frac{a_x}{a_y}\right) \quad (8)$$

where a_x, a_y = distance between plants along the flow and transversal.

The way of calculation of flow intensity in the floodplain with trees is exemplified below. Calculation of the flow rate in a floodplain requires definition of the width of this area. For this aim we need calculation of the length a_{NL} and the width a_{NB} of the Karmann path of the round-the-tree flow.

$$a_{NL} = 128.87 C_{W\infty} d_p \left(1 + \frac{g\, a_{NL} J}{V_T^2/2}\right)^{-2.143} \quad (9)$$

$$a_{NB} = 0.24\, a_{NL}^{0.59} (C_{W\infty} d_p)^{0.41} \quad (10)$$

where a_{NL}, a_{NB} = the length and the width of the Karmann path formed at a single plant submerged [m].

The drag coefficient $C_{W\infty}$ is determined for a single tree at ideal two-dimensional flow. Its variability for different forms of the turbulent flow was given by Lindner (1982) in the equations:

$$C_{W\infty} = 3.07 Re_p^{-0.1680} \quad \text{for} \quad Re_p = \frac{V_v d_p}{\nu} < 800 \quad (11)$$

$$C_{W\infty} = 1.0 \quad \text{for} \quad 800 \le Re_p \le 8000 \quad (12)$$

$$C_{W\infty} = 1.2 \quad \text{for} \quad 8000 < Re_p < 10^5 \quad (13)$$

where Re_p = the Reynolds number for a single plant [-], ν = viscosity of water [m^2/s].

The calculations are conducted at the assumption of the V_T value, and of $V_T > V_v$, due to the occurrence of velocity V_T in the formula (9) for cross-section interfaces. Then the coefficient of overgrowing is calculated:

$$\Omega = \left(0.07 \frac{a_{NL}}{a_x}\right)^{3.29} + \left(\frac{a_{NB}}{a_y}\right)^{0.95} \quad (14)$$

The dimensionless velocity in interfaces is calculated from the formula:

$$C_T = -3.27 log\, \Omega + 2.85 \quad (15)$$

The width of the area of main channel flow influence on flows in floodplains is calculated from the formula:

$$b_m = \frac{h_T}{\lambda_v (0.068 e^{0.56 C_T} - 0.056)} \quad (16)$$

where h_T = depth of interfaces between main channel and floodplain [m]; c_T = dimensionless velocity in interfaces.

At calculation of the discharge in the main channel, the interface of the floodplain from the main channel is treated as the rough wall with roughness of channel k_T and friction factor λ_T. In reality these resistances are made by intensive cyclical impulses of mass and momentum in transverse direction to the main flow, as well as by associated high turbulence strains and whirls on the surface of water in round-the-tree flows. The roughness in the interfaces is calculated from the formula:

$$k_T = 0.854\, R_{hy,T}\, \Omega \left(1.7 \frac{2b_m}{b_k}\right)^{1.07} \quad (17)$$

where $R_{hy,T}$ = hydraulic radius concerning the resistance by the interface [m]; b_m = width of the zone of influence of the area with trees on the area without trees [m]; b_k = main channel width [m].

The occurrence of different roughness and friction factors in the main channel requires calculation of the average friction factor and the distribution of the hydraulic radius of the main channel according to the concept by Einstein assuming the equality of average velocity in every sub-domain of the main channel:

$$R_{hy,i} = \frac{\lambda_i}{\lambda} R_{hy,F} \quad (18)$$

where λ_i = friction factor of part-section with hydraulic radius; R_i, $R_{hy,F}$ = hydraulic radius of the main channel calculated with account of the length of interfaces h_T.

The calculation of the hydraulic radius for different roughness in cross-sections is conducted using the iterative method. The hydraulic radius in the interface $R_{hy,T}$ is calculated from the formula (18), then the equivalent height of roughness in the interface k_T from the formula (17) and the friction factor λ_T from the formula (5) for k_T.

The average friction factor in the whole main channel λ is calculated with consideration to the friction factors in the flow bed λ_s and λ_T in the interface cross-section:

$$\lambda = \frac{2\lambda_T h_T + \lambda_s l_s}{2h_T + l_s} \quad (19)$$

The average velocity of main channel flow is calculated from the Darcy – Weisbach formula (2), and the velocity V_T in the interface between the main channel and its floodplain from the formula:

$$V_T = C_T \sqrt{\frac{\lambda_v}{8}} V_F \quad (20)$$

Copyright © 2006 Taylor & Francis Group plc, London, UK

The velocity V_T calculated from the equation (20) is usually different from the one assumed at the beginning of a_{NL} calculation (9); therefore the wholeness of calculations should be repeated, accepting the calculated value V_T according to formula (20) as the next approximation.

2.3 *Pre-processing programs*

The pre-processing programs were developed to create an input of complex data to steady state simulation. The first program is a graphical interface, which inserts measured coordinate points of cross-sections to the data and assigns vegetation parameters to segments of cross-sections. A computed channel is divided into components with different resistance parameters on the floodplains and in the part of the main channel.

The second program enables to the input of boundary conditions and distances between cross-sections along a main-channel and floodplains. It is capable of interpolating the cross-sections geometry with a selected space step.

The vegetation parameters are transferred to interpolated cross-sections from downstream part for each line segment between two adjacent measured cross-sections. Vegetation components ranges or resistance parameters for any interpolated cross-section may be changed by using a graphical editor.

3 APPLICATION: THE LOWER BIEBRZA

3.1 *Research area*

The elaborated model was applied to a 41 km long reach in the Lower Biebrza Basin, between two gauges: Osowiec in upstream and Burzyn in downstream. The Lower Biebrza Basin is a river-marginal peatland, located in the north-eastern Poland. The flood phenomenon occurs regularly in this river system and is not constrained by any man-made structures. The Biebrza Lower Basin forms a natural valley with numerous oxbows, organic saturated soils and natural vegetation, which generates problems during field measurements and consequently makes a process of calibration and verification of numerical model very difficult.

3.2 *Topographical data*

The Digital Elevation Model (DEM) of the Lower Basin was elaborated with GIS techniques as a representation of the floodplain morphology. The DEM was generated by the ArcInfo TOPOGRIDTOOL procedure during an interpolation process. This interpolation method is based upon the ANUDEM program developed by Hutchinson (1996) specifically designed for the creation of a hydrologically correct DEM.

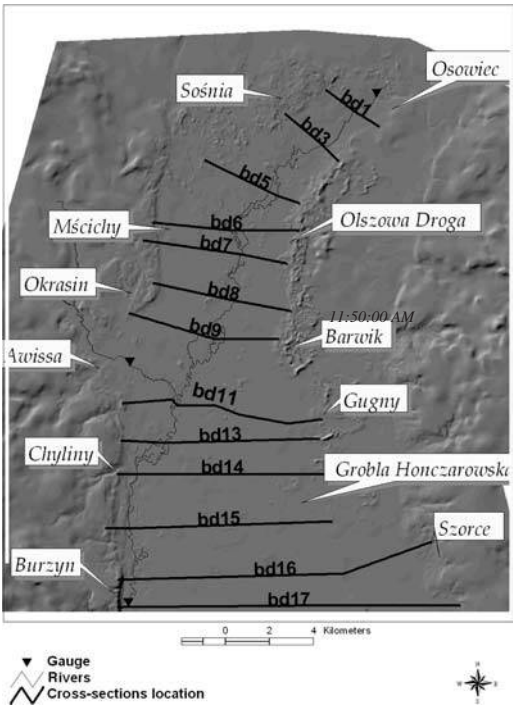


Figure 1. DEM of the Lower Biebrza Basin and cross sections location.

Wise (2000), evaluated the TOPOGRID routine as one of the best available algorithms for DEM generation. The main data source for the model generation was a set of contour lines in the digital form, with an accuracy of 1:25,000 scale topographic maps. Additionally, the point elevation data was digitized from the topographic maps and measured in the field. In order to improve the interpolation process and obtaining the DEM which correspond to numerical model, the valley cross-sections were included in data source. The DEM was created with cell resolution of 25 m (Figure 1). Next, interpolation errors were identified and corrected. Then, three valley cross-sections were measured in selected location which included different types of valley for the purpose of model verification. The survey compared with DEM gave the root mean square error (RMSE) of 0.35 m. According to the verification results, it is concluded that, the constructed DEM seems to be good enough for spatial mapping of flood.

3.3 *Hydraulic data*

Cross-sections, in the number of 13 (Figure 1, Table 1), were established at the distance of 2–6 km from each other along the river, from Osowiec downstream to Burzyn, to for describe the geometry of the river channel and valley geometry.

Copyright © 2006 Taylor & Francis Group plc, London, UK

Table 1. Distance between the measured cross-sections.

Cross-section name	Distance along the river [km]	Distance between cross-sections [km]		
		Left floodplain	Channel	Right floodplain
BD1	0.00			
BD3	2.38	2.17	2.38	2.04
BD5	7.36	2.98	4.98	3.35
BD6	11.61	1.59	4.25	2.45
BD7	14.37	1.32	2.76	1.03
BD8	17.44	2.10	3.07	2.04
BD9	19.98	1.85	2.54	1.83
BD11	26.73	3.12	6.75	3.60
BD13	29.94	1.69	3.21	1.80
BD14	33.23	1.40	3.29	1.56
BD15	36.12	2.44	2.89	2.50
BD16	38.87	2.34	2.75	2.34
BD17	41.23	1.27	2.36	1.27

The river bed elevations were measured by manual sounding, the neighbourhood of river banks was leveled and points situated in floodplain were calculated from Digital Elevation Model and topographic maps for each cross section. Close to the river, the cross sections were measured in the field by coupling the traditional leveling survey with Differential GPS (DGPS) techniques. Then, the reference points – one for each cross section – were measured by the DGPS technique with post-processing differential correction, using 12 channel L1 single-frequency GPS receiver MX 9400N Leica receivers. The DGPS was found as a very useful and time saving method for coordinates and altitude measurements, and were often the only possible method in such a remote area with dense vegetation, numerous oxbows, and limited number of reference points (Chormański et al. 2000). At these points the levelling was done giving the shape of the valley close to the river on both sides of the river channel. The measured part of cross-sections varied from 50 to 500 meters depending on the height and the density of floodplain vegetation. Then, the cross-sections were extended to the edge of the valley by capturing elevation every 100 meters from DEM and topographic maps (Chormański et al. 2002) (Figure 1).

The water level of the Biebrza River was measured between Osowiec and Burzyn by use of dual frequency GPS (L1/L2) TOPCON Legacy E GPS receivers with RTK DGPS techniques. The water level was measured from a motorboat each 200–400 m. This technique provides us with horizontal accuracy of ±1–2 cm and vertical accuracy of 2–3 cm (Chormanski et al. 2003).

3.4 *Floodplain vegetation data*

The vegetation parameters of Biebrza floodplains used in calculations were determined on the basis of vegetation inventory in the Lower Biebrza Basin, vegetation map and PHARE aerial photos. Every part of a cross-section has one bottom roughness parameter. Water flow resistance in flowing round high vegetation such as bushes or trees is calculated on the basis of supplementary average vegetation diameter d_p and supplementary distances between plants in direction of water flow a_x, and transversal to it a_y. Resistances of totally flooded vegetation are characterized by roughness height of flexible and stiff vegetation k_s determined on the basis of vegetation map, shape of particular vegetation types and parameters suggested by Ritterbach (1991) for different types of vegetation. The vegetation types and parameters of Biebrza floodplains are presented in Table 2.

Table 2. Vegetation hydraulic parameters (k_s, a_x, a_y).

Name of plant	k_s [m]	d_p [m]	a_x [m]	a_y [m]
Meadow	0.3–0.4			
field under cultivation	0.2–0.3			
tall sedge communities	0.4–0.5			
reed rushes	1–1.2			
Glycerietum maximae rushes	1–1.2			
Phalaridetum arundinaceae rushes	1–1.2			
willow shrubs	0.3	0.045	0.16	0.16
alder swamp forest	0.8–1.6	0.175	1.54	1.5

3.5 *Simulation results*

Three steady flow cases were computed and compared to measured data. Two of them were calculated for conditions when water level is less than bankfull. They were refered to discharges $Q_a = 8.8\,m^3/s$ and $Q_b = 12.9\,m^3/s$ at Burzyn gauge, where an over bank discharge is $40.1\,m^3/s$. The next case was a flood event with discharge $Q_c = 168\,m^3/s$. Because for the flood condition the water level was measured only in a lower part of valley, the Digital Elevation Model of the floodplain constructed with GIS techniques was coupled with calculated water level for spatial flood extent and a result was verified with the help of the processed Landsat satellite image. In the computation the discharge at the cross-section BD1 was used as the upper boundary condition and the water level at the Burzyn gauge (BD17) determined the lower boundary condition. Because an average distance between measured cross-sections is about 3.4 km the interpolated cross-sections were added with a space step 0.5 km.

There is a significant difference in discharge rates between the upper (BD1 cross-section) and the lower

Copyright © 2006 Taylor & Francis Group plc, London, UK

Table 3. Discharge rate distribution along the river.

Cross-section name	Distance along the river [km]	Q [m^3/s]
BD1	0.00	100.9
BD3	2.38	104.5
BD5	7.36	111.9
BD6	11.61	118.3
BD7	14.37	122.4
BD8	17.44	127.1
BD9	19.98	130.9
BD11	26.73	146.4
BD13	29.94	151.2
BD14	33.23	156.1
BD15	36.12	160.5
BD16	38.87	164.6
BD17	41.23	168.0

Table 4. Calibrated roughness values of an analyzed reach.

Distance from BD1 [km]	k_s [m]
BD1	0.1
BD3	0.005
BD5	0.2
BD6–BD8	0.02
BD9	0.1
BD11	0.005
BD13	0.5
BD14	0.01
BD15	0.15
BD16–BD17	0.03

part of a river (BD17 cross-section). This is mainly due to the lateral inflow from a subcatchment during the flood event. The lateral discharge inflow, Q_{Wissa}, from the Wissa tributary was added 14.5 km upstream of Burzyn. Next, the uniform lateral inflow $Q_{in} = Q_{BD17} - Q_{BD1}$ was imposed along the river section (Table 3).

This solution is obviously a rough approximation of the actual situation, as it does not account for the spatial variation of the lateral inflow. A more realistic approach to this issue needs to be elaborated in further study. The roughness values in the main channel were calibrated by the measurement of a water level at the discharge rate 8.8 m^3/s and by the use of formulas (3), (5). The Table 4 presents the calibrated roughness values for the main channel. The rough recognition of geometry of an analysed strongly meandering reach, where an average distance between measured cross-sections is 3.4 km, is a reason of a very high value of roughness factors for some cross-sections.

The calculated water levels from the simulation are presented in Figure 2 and Figure 3. In order to objectively evaluate the model performance, the most commonly employed error measure, such as the root mean square error (*RMSE*) was computed for each

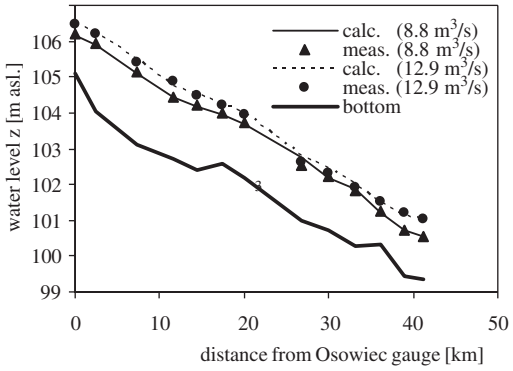


Figure 2. Calculated and measured water levels for low discharges.

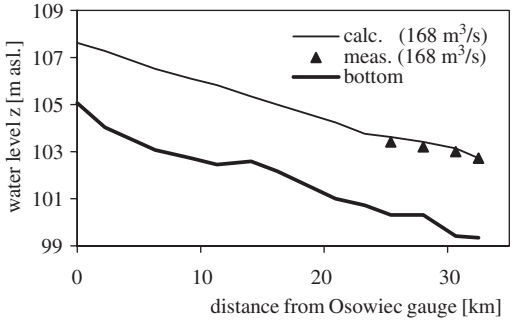


Figure 3. Calculated and measured water levels for a flood event (Q = 168 m^3/s).

Table 5. The RMSE for calculated steady state for different discharges.

Q_{Burzyn} [m^3/s]	RMSE [m]
8.8	0.07
12.9	0.09
168	0.19

case and summarized in Table 5. The *RMSE* can be defined as:

$$RMSE = \sqrt{\frac{\sum_{i}^{N}\left(W_{m_i} - W_{p_i}\right)^2}{N}} \qquad (21)$$

where W_m = the measured water level; W_p = the computed water level; and N = the number of cross-sections.

The RMSE is varied from 0.07 m for the low discharge rate to 0.19 m for the flood condition.

Although the main channel roughness heights were calibrated at the lowest discharge rate, the error at high over bank water level is acceptable.

Copyright © 2006 Taylor & Francis Group plc, London, UK

The second calibration of the main channel roughness factor for data of water level during flood event, should improve the model accuracy. Unfortunately, there were collected water level data partly in the lower part of the valley and they are not enough to an appropriate calibration at a high discharge rate.

The Digital Elevation Model was coupled with calculated water level for spatial flood extent in the valley. Calculated water stages by hydraulic model in cross-sections were interpolated into water surface elevation model and next mapped in whole floodplain by analyzing of the difference between water level and DEM in GIS software ArcView GIS. Result was verified with help of the processed Landsat satellite image.

The image was geometrically corrected, and next, processed by use of selected ratios and transformations: moisture ratio 7/5, NDVI and PC1 (Chormanski 2003). The moisture ratio 7/5 is a simple division of two middle infrared bands: TM7 by TM5. The second, the Normalized Difference Vegetation Index (NDVI), is computed by dividing the difference of the near-IR (TM4) and visible red (TM3) by the sum of them. The PC1 is a first component of the principal component analysis (PCA). Finally, the supervised classification by maximum likelihood method was performed on these new developed image bands. The high classification accuracy equal to 93% was obtained during verification on the basis of 796 points with known cover type, for the March 2002 flood (Chormanski 2003). Next, result was reclassified for flooded, inundated by snowmelt and groundwater seepage and dry classes. Identification of inundated and flooded classes is done based on observed vegetation types. It was assumed that areas flooded by river water correspond to distinguished classes as follows: deep open water, shallow open water, inundated tall sedges and reeds, inundated alder forest, inundated meadow. Consequently, flooding caused inundation is determined, but somewhere these could be found far a way from the river channel as isolated areas (e.g. a class of shallow open water on areas where vegetation was cut). Then, a number of inundation areas, which are isolated from the flooded area were eliminated from flooding results. Water levels produced by model correlated well with measured data and processed satellite image.

The processed image was used for verification of the spatial extent of maximum river flood generated by hydraulic model. Comparison of the inundated area generated by hydraulic model coupled with DEM with one obtained by remote sensing method shows very good correctness (Figure 4). The flooded area calculated by model is equal to 76.36 sq km and flooded area determined by remote sensing is equal to 66.42 sq km, which give as difference of 13%. This difference comes partly from DEM quality, which is not perfect when we cannot generate it based on direct measurements and use topographic maps instead. They come partly from

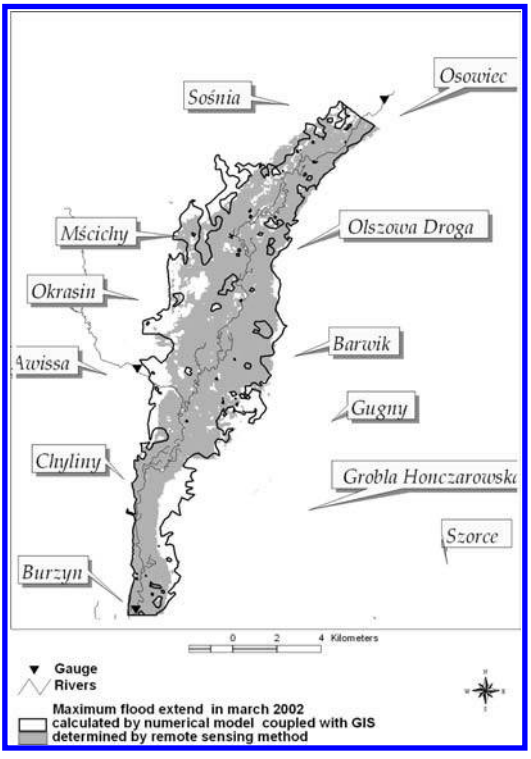


Figure 4. Comparison of the maximum flood extend in march 2002 calculated by model and obtained from Remote sensing analysis.

simplification of the classification procedure used for such a satellite image processing.

The lower Biebrza River is strongly meandering (Table 1, Figure 1) and when water is on the floodplains a reach length is significantly shorter than total river distance when water is below a bankfull level. The weighted reach length L is calculated from a following expression:

$$L = \frac{L_{lf} Q_{lf} + L_{ch} Q_{ch} + L_{rf} Q_{rf}}{Q_{lf} + Q_{ch} + Q_{rf}} \tag{22}$$

where L_{lf}, L_{ch}, L_{rf} = reach length between two adjacent cross-section in the left floodplain, main channel and right floodplain, respectively; Q_{lf}, Q_{ch}, Q_{rf} = arithmetic average of the discharge rate between two adjacent cross-section in the left floodplain, main channel and right floodplain, respectively

The Figure 3 shows, that at a discharge rate 168 m^3/s, the river length was a 78% of a total reach length.

The variation of friction factors of a main channel for different discharges is presented in Figure 5. It decreases at a high discharge and a range of a variation depends on channel dimensions.

Copyright © 2006 Taylor & Francis Group plc, London, UK

The components of the discharge on the floodplains and the main channel are shown in the Figure 6, giving an overview of water conveying. The high variation of distribution of total discharge to floodplains and main channel along a river as well as in eachcross-section are caused by significant differences in cross-sectional areas, water depths and type of vegetation.

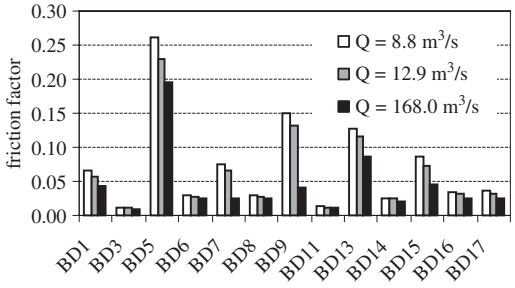


Figure 5. Variation of friction factors for different discharges.

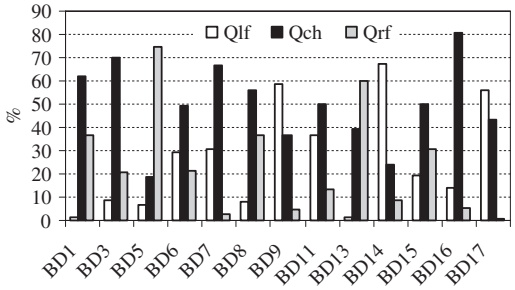


Figure 6. Percentages of discharge rate on the floodplains and in the main channel.

The discharges, velocities, water depths and areas in cross-section BD14 (Figure 7 and Table 6) were analysed as an example.

There are following seven types of vegetation below water level 103.12 m: 1 – alder swamp forest, 2 – tall sedge communities, 3 – meadow, 4 – tall sedge communities, 5 – main channel vegetation, 6 – Glyceretum maximae rushes, 7 – meadow. The depths of the imaginary boundaries are 0.24 m (area 2 – area 1), 1.19 m and 0.85 m for main channel and left and right floodplains respectively (Figure 7). The flow velocity in the interface between the alder swamp forest and the sedge community is 0.05 m/s. The left floodplain conveyed up to 67%, the main channel 24% and the right floodplain 9% of total discharge. The velocity is varying from 1.56×10^{-2} m/s to 1.42×10^{-1} m/s and

Table 6. Computed water widths B, areas A, water depths h and discharges Q for each parts of cross-section BD14.

Area number	B [m]	A [m^2]	h [m]	Q [m^3/s]
1	328	50.7	0.15	0.8
2	1420	724	0.51	50.4
3	392	279	0.71	32.0
4	120	143	1.19	20.4
5	33.6	81.1	2.41	37.3
6	27.8	20.4	0.73	2.2
7	446	167	0.37	11.5

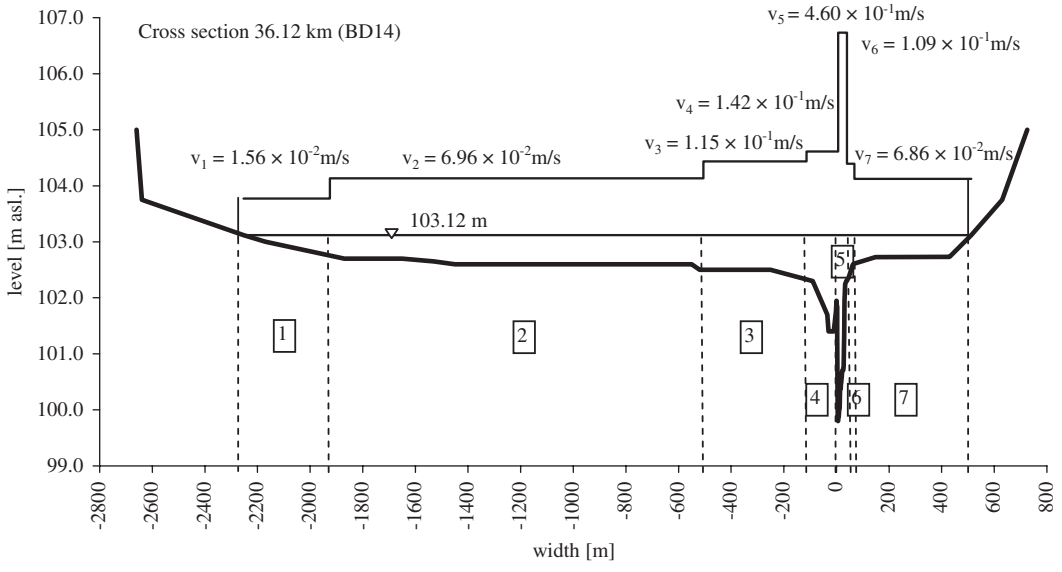


Figure 7. The vegetation division of the cross-section BD14 and computed velocities.

Copyright © 2006 Taylor & Francis Group plc, London, UK

from 6.86×10^{-2} m/s to 1.09×10^{-1} m/s on the left and right floodplains respectively.

The main channel velocity (4.6×10^{-1} m/s) is significantly higher than over banks velocities, but the channel area is only 9% and 43% of left and right floodplains areas. The field monitoring has confirmed that the left floodplain in this cross-section is conveyed a flow in a distance over 2 km from a river bank during very high discharges.

4 CONCLUSIONS

The developed model enables a solution for steady flow problems for natural rivers with floodplains and different vegetation. It may be used as a tool to estimate new water surface level for renaturalized rivers, especially for flood condition, as well as to ensure suitable conditions for habitat diversity in projects of environmental flood management.

The model was used to a reach of the Lower Biebrza. The results showed a good reproduction of recorded water levels. Analysis of the spatial extend of flood calculated by model coupling with GIS shows good correlation with inundation detected by remote sensing, although significant part of inundation in Lower Basin is cased by snowmelt and groundwater seepage. Contrary to the traditional approach, where floodplains are considered as storage areas, the proposed model computes velocities, discharges and friction factors for each specified part dependently on type of vegetation on floodplains and in the main channel. The floodplains convey a significant part of a total discharge rate.

The Lower Biebrza case shows that for strongly meandering lowland rivers, which feature varying cross-sections and an irregular longitudinal profile, the field data such as geometry of sections should be measured at short distances along a river.

REFERENCES

Bousmar, D. 2002. *Flow modelling in compound channels. Momentum transfer between main channel and prismatic or non-prismatic floodplains*. Thesis presented for the degree of Doctor in Applied Sciences.

Chormanski, J., Okruszko, T., Kardel, I., Siłakowski, M. 2000. Field data collection and management using GPS and GIS. In W. Mioduszewski & M. Wassen (eds), *Some aspects of Water Management in the valley of Biebrza River* : 87–100. Falenty : IMUZ Press.

Chormański, J., Okruszko, T., Wassen, M.J., Skąpsi, J. 2002. Surface water system analysis. Flood extent measurements and topography of the valley. In W. Mioduszewski & E.P. Querner (eds), *Hydrological system analysis in the valley of Biebrza River* :39–57. Falenty : IMUZ Press.

Chormański, J. 2003: *Methodology for the flood extent determination in the Lower Biebrza Basin*. Warsaw Agricultural University. Ph.D. Thesis.

Chormański, J., Kowalewski, K., Mazippus, M. 2003: Application of GPS techniques for water stage measurements and river slope calculation in wetland area of Upper Biebrza. In S. Ignar, P. Nowakowski, T.Okruszko (eds), *Measurements techniques and data assessment in wetlands hydrology*: 53–60. Warsaw : Warsaw Agricultural University Press.

DVWK220 1991. Hydraulische Berechnung von Flieβgewässern. Hamburg.

Hutchinson, M.F. 1996. A locally adaptive approach to the interpolation of digital elevation model. *Third International Conference/Workshop on Integrating GIS and Environmental Modeling, Santa Fe, NM, 21–26 January 1996*. Santa Barbara, CA: National Center for Geographic Information and Analysis http://www.ncgia.ucsb.edu/conf/SANTA_FE_CD-ROM/sf_papers/hutchinson_michael _dem/local.html.

Indlekofer, H. 1981. Überlagerung von Rauhigkeitseinflüssen beim Abfluß in offenen Gerinnen. *Mitt. Institut für Wasserbau und Wasserwirtschaft* 37: 105–145.

Kaiser, W. 1984. *Fließwiderstandsverhalten in Gerinnen mit durchströmten Ufergehölzzonen*. Thesis presented for the degree of Doctor in Applied Sciences TH Darmstadt.

Kubrak, J. & Nachlik, E. 2003. *The basics for the hydraulic calculation of the capacity of rivers*. Warsaw: Warsaw Agricultural University Press.

Lindner, K. 1982. Der Strömungswiderstand von Pflanzenbeständen. *Mitteilungen aus dem Leichtweiss - Institut für Wasserbau der TU Braunschweig* 75: 102–123.

Pasche, E. 1984. *Turbulenzmechanismen in naturnahen Fließgewässern und die Möglichkeit ihrer mathematischen Erfassung*. Thesis presented for the degree of Doctor in Applied Sciences. RWTH Aachen.

Rickert, K. 1988. Hydraulische Berechnung naturnaher Gewässer mit Bewuchs. *DVWK-Fortbildung* 13: 59–83.

Rouvé, G. 1987. Hydraulische Probleme beim naturnahen Gewässerausbau Ergebnisse aus Schwerpunktprogramm. *Anthropogene Einflüsse auf hydrologische Prozesse.* Band 2.

Ritterbach, E. 1991. *Wechselwirkungen zwischen Auenökologie und Fließgewässerhydraulik und Möglichkeiten der integrierenden computergestützten Plannung*. Mitteilungen für Wasserbau und Wasserwirtschaft. Achen: Rheinish-Westfälische Technische Hochschule Press.

Wise, S. 2000. Assessing the quality for hydrological applications of digital elevation models derived from contours. *Hydrol. Process.* 14: 1909–1929.

Copyright © 2006 Taylor & Francis Group plc, London, UK

Experimental investigation of flow characteristics in vegetated channels

F.G. Carollo & V. Ferro
Dipartimento di Ingegneria e Tecnologie Agro-Forestali – Facoltà di Agraria – Università di Palermo – Viale delle Scienze – Palermo – Italy

D. Termini
Dipartimento di Ingegneria Idraulica ed Applicazioni Ambientali – Universitá di Palermo – Viale delle Scienze – Palermo – Italy

ABSTRACT: Vegetation altering hydrodynamic conditions of an open channel flow controls the exchanges of sediment, nutrients and contaminants. In this paper the local flow characteristics in a straight flume with grass-like vegetation bed is studied. A 2D-ADV is used to measure the local flow velocities, for different vegetation concentrations by varying the discharge and the flume slope. The influence of both vegetation concentration and depth/vegetation height ratio on the measured velocity and turbulence intensity profiles is analyzed. All measured velocity distributions are S-shaped and exhibit a three zones profiles with an inflection point at a water depth quasi-equal to the bent vegetation height. The analysis of turbulence intensity distributions highlights that the peak value of turbulence intensity occurs at the same water depth of the inflection point. A theoretical velocity profile allowing to describe the flow both inside and above the vegetation and based on the classical Prandtl's mixing length approach is presented.

1 INTRODUCTION

Vegetation affects fluvial processes and is a key in current river management and river hydraulics.

The main difficulty to analyze the effects of vegetation on hydrodynamic characteristics of flow is that vegetation is flexible in varying degrees and it oscillates in the flow changing position. Thus, in vegetated channels, a large variation in depth of flow and in hydraulic roughness have to be encountered. In general, large-scale roughness conditions may occur when depth of flow is less than or equal to vegetation height; small-scale roughness conditions migth occur when flow depth is greater than vegetation height. But, because of temporal changing of roughness due to natural vegetative growth, tillage practices and dynamic response of vegetation to the flow, the hydrodynamic conditions could change continuously. In other words, flow in a vegetated channel is essentially a movable boundary problem since roughness elements are deformed by the flow within the channel.

In accordance with Palmer (1945) essentially three flow conditions could be experienced by vegetation: 1) low flow, with the flow passing through stems without bending and submerging them (erect vegetation position); 2) intermediate flow, with complete submergence of the vegetation, that is bent and flattened towards the bed (waving position); 3) high flow, forcing vegetation to a prone or nearly prone position.

Velocity profiles measured by Eastgate (1969) over Kikuyu grass bed showed that local mean longitudinal velocity, u, varies in proportion to the logarithm of the distance, y, from the channel bed. Kouwen et al. (1969) presented velocity profiles observed in a laboratory flume in which artificial flexible vegetation (strips of styrene) was fixed and found that the logarithm velocity profile adequately represents flow conditions above a flexible plastic cover.

The analysis of Gourlay (1970) established that for slopes less than 0.05 three layers can be distinguished in the experimental velocity profiles: 1) a layer of virtually constant low velocity within the grass near the bed in which the velocity can be assumed proportional to the shear velocity u^*; 2) a layer of rapidly increasing velocity within the upper part of the vegetation elements; 3) a layer of less rapidly increasing velocity above the grass. For slopes greater than 0.05 the layers 2) and 3) merged together and the profiles presented a two layer appearance.

Thus, indicating with k_v the bent vegetation height, the velocity distribution above flexible roughness can

Copyright © 2006 Taylor & Francis Group plc, London, UK

be defined by the following logarithm law (Kouwen et al. 1969):

$$\frac{u}{u^*} = \frac{u_{kv}}{u^*} + \frac{1}{k} ln\left(\frac{y}{k_v}\right) \quad (1)$$

in which k = the von Karman's constant and u_{kv} = the longitudinal flow velocity at distance k_v from the bed (slip velocity).

From a theoretical point of view, the logarithmic velocity profile (1) is applicable above a reference distance from the bed which would be the level where the bottom layer of constant velocity matches with the shear layer above it. This reference level could be either within the vegetated layer or at the top of the vegetation depending on the flow regime (erect, waving, prone). Because of measurement difficulties, reliable measurements of flow velocity through the vegetated boundary region are somewhat limited. For practical applications Kouwen & Unny (1973) suggested a reference level equal to the vegetation height.

Temple (1986) suggested a two layers velocity distribution: for y values less than bent vegetation height k_v, the velocity through the vegetation is assumed constant and is only dependent on vegetation characteristics and energy slope; for $y > k_v$, the velocity profile is dependent on momentum transfer in the form of the turbulent shear. In this last case, Temple (1986) obtained a generalized velocity profile using the Prandtl's mixing length approach and assuming a mixing length proportional to $y - k_v$.

Ikeda & Kanazawa (1996) carried out experiments in an open channel flow with artificial filaments on the bed. The analyses of the vertical distributions of longitudinal velocity component, measured using a two component Laser Doppler Velocimeter, allowed to highlight some peculiar aspects on flow velocity behavior. The Authors observed that the temporally averaged velocity profile has an inflection near the top of the vegetation layer. Furthermore, both the longitudinal component of the turbulence intensity and the shear stress have the maximum value at the top of the vegetation layer and decrease toward the free surface and the bottom.

Many theoretical and experimental investigations have been performed in order to analyze also the turbulence structure of open-channel flow (Nezu & Rodi 1986; Lemmin & Rolland 1997, Shvidchenko & Pender 2001).

Referring to a two-dimensional uniform flow and a small-scale roughness condition, the turbulence structure has been analyzed considering three different regions (Nezu & Nakagawa 1993): 1) the near to the bed region and for $y^+ = yu^*/\nu < 50$ (in which ν = the kinematic viscosity) where the production of turbulent energy exceeds its dissipation rate; 2) the near to the free surface region, i.e. for $y/h \geq 0.6$ (in which h is the flow depth) where the energy dissipation exceeds the turbulent energy production; 3) the intermediate region where the turbulence energy is transported from the bed toward the free surface and an equilibrium between the energy production and its dissipation exists.

The attention of many researches has been devoted to the study of the turbulence structure in the inner region, where the so-called bursting phenomena evolve (Kline et al. 1967, Corino & Brodkey 1969, Jackson 1976; Cantwell 1981). They consist in coherent and organized motions whose growth and breakdown occur periodically.

Experimental investigations (Grass 1971) revealed that a sequence of bursts appears both in smooth and in rough beds. For an hydraulically smooth regime, bursting occurs because of the viscous sublayer instability; in rough turbulent regime bursts are generated inside the cavities between the elements forming the bed roughness. The instantaneous vertical velocity profiles associated with a complete bursting sequence (lift-up, oscillation, ejection and sweep motion), show an inflection point, due to the vortex ejection, where the vertical distribution of the turbulence intensity shows a maximum.

Recently, Shvidchenko & Pender (2001) observed the turbulent structure of the flow in a gravel bed channel. The experiments were conducted by using a visualization technique and measuring the flow velocity by an Acoustic Doppler Velocimeter (ADV). On the basis of their measurements, the authors confirmed the formation of an ordered sequence of long-term large-scale vortices moving downstream with the same velocity as the mean flow and producing a motion of fluid toward both the bed (sweep) and the free surface (ejections), involving the whole flow depth. The longitudinal turbulence intensity decreases progressively as the distance from the bed increases, with the exception of the thin layer close to the wall, where the viscous effects exceeded the turbulent fluctuations (Nezu & Nakagawa 1993).

Very few studies analyze the turbulence structure in vegetated channels and, presently, there are no models readily available for predicting the distribution of turbulence intensity.

Experimental runs carried out in a laboratory flume with flexible bottom vegetation (Kutija & Hong 1996; Ikeda & Kanazawa 1996), investigated some peculiar characteristics of flow turbulence structure. The measurements carried out by Ikeda & Kanazawa (1996) revealed also in this case the generation of periodic organized vortices whose center is located slightly above the top of the vegetation layer. The intermittent motion of these coherent structures has been, in turn, considered responsible of the flexible vegetation oscillation. The form of the vortex was elliptical with the long axis inclined downwards toward the front.

Copyright © 2006 Taylor & Francis Group plc, London, UK

The analysis of collected measures highlighted that at the bent vegetation heigth, where velocity profile has an inflection point, the flow becomes unstable, rolling up into discrete vortices and the turbulence intensity assumes the highest value.

In this paper velocity measurements, obtained by a two-dimensional (2D) Acoustic Doppler Velocimeter (ADV) in a rectangular laboratory flume with a bottom grass vegetation, are used to establish the influence of the vegetation concentration and the depth/vegetation height ratio on the velocity profile and turbulence intensity profile.

The velocity measurements are used to test a new velocity profile reproducing the typical shape of the velocity distribution and having a single equation to represent the flow conditions both inside and above the vegetation.

2 EXPERIMENTAL APPARATUS

The experimental runs were carried out in a rectangular straight laboratory channel of Dipartimento di Ingegneria Idraulica ed Applicazioni Ambientali at the University of Palermo. The flume had a sloping bed and was 0.60 m wide and 14,4 m long (Figure 1). The channel banks were of transparent glass.

In a reach of the channel (measurement reach), located at 7.9 m from the entrance channel section and 3 m long, the bed was covered by a turf layer The turf layer was produced sowing a soil layer having a thickness of 5 cm, and then the obtained vegetated plot was installed into the measuring reach. The grass bed was a mixture of stable *Loietto* (50%), *Festuca rubra* (40%) and *Poa pratensis* (10%).

Three values of the vegetation concentration, δ(280, 377, 440 stems/dm^2) were used for the experimental runs. The concentration, estimated as the number of stems per unit area, was measured in a reference area 0.6 m wide and 1.0 m long as explained in a previous work (Carollo et al. 2002). The visual bent vegetation height, k_v, (i.e. the vegetation heigth in presence of flow observed through the transparent walls) and the non-submerged vegetation height (i.e. the vegetation height in absence of flow), H_v, were estimated as the mean of three measurements by three decimal rules fixed to flume wall.

The turf layer was jointed with the flume bed by two plane chutes (50 cm long and 5 cm height) that bounded the experimental reach. The reference level was set coincident with the upper soil surface where the plants were rooted, at 5 cm above the flume bed.

The water depth h was measured by an hydrometer in four cross-sections (the first was at 90 cm downstream from the beginning of turf reach and the following three cross-sections had a relative distance of 40 cm), in order to verify the occurrence of quasi-uniform flow conditions in the middle part of experimental reach.

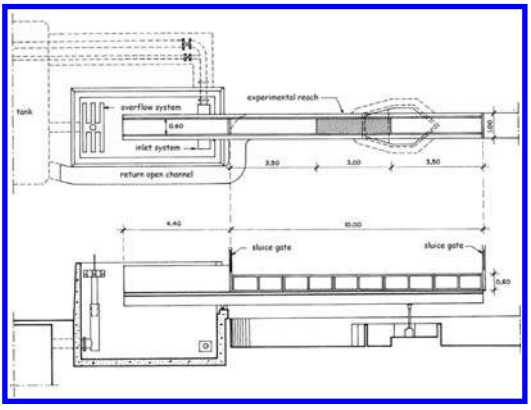


Figure 1. Layout of experimental installation.

Table 1. Characteristic data of experimental runs.

Run	h [cm]	s [%]	Q [l/s]	H_v [cm]	δ [stem/dm^2]	k_v [cm]
1	11.9	1.0	37.6	11.0	310	4.8
2	13.5	1.0	30.1	20.0	440	8.0
3	14.6	0.2	30.1	20.0	440	8.0
4	14.0	0.2	26.9	20.0	440	8.2
5	12.5	1.0	26.9	20.0	440	7.7
6	17.8	0.2	77.6	20.0	440	7.0
7	16.8	1.0	77.6	20.0	440	6.6
8	19.9	0.2	105.9	20.0	440	6.3
9	18.3	1.0	105.9	11.5	440	5.9
10	12.8	0.2	26.9	11.5	280	7.0
11	19.0	0.2	77.6	11.5	280	5.4
12	21.7	0.2	105.9	11.5	280	4.9
13	24.5	0.2	135.0	11.5	280	4.7
14	27.2	0.2	170.8	11.5	280	4.5
15	27.7	0.2	188.7	5.9	337	3.8
16	27.2	0.2	189.2	3.5	337	3.1

Sixteen runs were carried out in order to analyze the influence of the depth/vegetation height ratio h/k_v and of the stem concentration δ on velocity and turbulence intensity profiles. For a given stem concentration, the influence of depth/vegetation height ratio was examined by varying the discharge and the flume slope s.

For each run, Table 1 lists water depth h, flume slope s, discharge Q, non-submerged vegetation height H_v, stem concentration δ and bent vegetation height k_v.

For all runs, the vegetation was submerged. Runs 1–14 were carried out with a vegetation which was always prone; while for runs 15 and 16 ($H_v = 5.9$ and 3.5 cm) the vegetation was cut (original vegetation height equal to 10 cm) for obtaining more rigid stems having a quasi-erect configuration.

Copyright © 2006 Taylor & Francis Group plc, London, UK

The local flow velocities were measured by using a 2D, side-looking probe, Acoustic Doppler velocimeter (ADV) (Kraus et al. 1994) in five verticals of a cross-section located in the middle of the measuring reach. The measurements positions were located at a distance of the wall equal to 4 cm, 7 cm, 14 cm, 22 cm and 30 cm (axial vertical).

The 2D-ADV acoustic sensor was connected to a signal conditioning module. It was mounted on a rigid stem 40 cm long and was composed of one transmitting transducer and two receiving transducers. The three transducers were in the same plane and aligned along the x axis set coincident with the main flow direction. The intersection of the receiving and the transmitting beams defined the barycentre of the sampling volume (0.25 cm^3) localized at 5 cm from the axis of the acoustic sensor along the transverse direction. The accuracy of measures was greater than ±0,25% or ±0,25 cm/s (Carollo et al. 2002).

Eighty velocity and turbulence intensity distributions were measured. For each measurement point, the turbulence intensity u' was calculated by the following relationship:

$$u' = \sqrt{\frac{\sum_{i=1}^{N}(u_i - u)^2}{N}}, \quad (2)$$

in which u_i = the local instantaneous longitudinal flow velocity, N = the number of samplings.

For each measurement point the maximum sampling rate of 25 Hz was used. The number of samplings was set equal to the minimum value required to determine a constant local mean velocity u. The tests, carried out for different values of δ, h and y, showed that 700 local velocity samplings were sufficient to obtain a stable estimate of u.

3 ANALYSIS OF EXPERIMENTAL DISTRIBUTIONS

3.1 *Flow velocity profiles*

The measured longitudinal flow velocities have been normalized by the shear velocity u^* and plotted against the relative water depth $Y = y/h$. The shear velocity has been estimated by Clauser method (Kironoto & Graf 1995). As an example, in Figure 2 a velocity profile measured in the axial vertical during run 8 is shown.

The analysis of the eighty measured velocity distributions highlighted that for each velocity profile three zones, marked by two relative depths Y_1 and Y_2, can be identified (Figure 2):

1. zone I, obtained for relative depth values $Y < Y_1 < k_v/h$, is characterized by very small flow velocities.

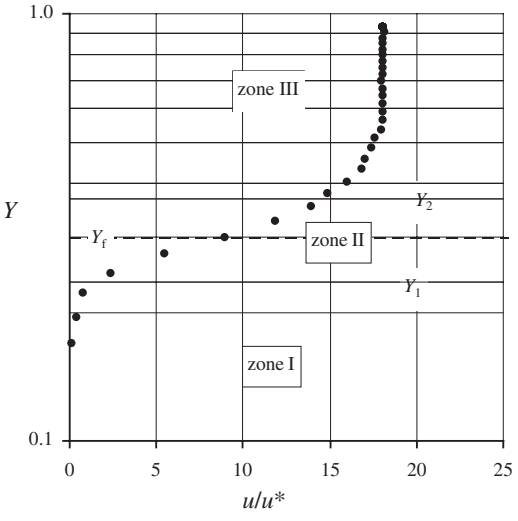


Figure 2. Localization of three different zones into measured velocity profile.

In contrast to the findings of Gourlay (1970), for $Y < Y_1$, the measured flow velocities do not assume a constant value, but show an increasing vertical velocity gradient;

2. zone II is obtained for $Y_1 \leq Y \leq Y_2$. Here the logarithm velocity profile can be fitted to the measured velocities;
3. zone III, for distances $Y > Y_2$. This zone is characterized by positive vertical velocity gradients which are progressively decreasing until to become null near the free surface, where the measured velocity distribution follows a vertical profile.

In the zone I the velocity profile has the concavity turned toward the bottom and tends asymptotically to the vertical axis. In the zone II the velocity values rapidly increase, and the velocity gradient along the vertical assumes its maximum value. In other words, even if a logarithm velocity profile can be fitted, the shape of the experimental velocity distribution clearly shows that an inflection point, located at a distance from the bed equal to y_f, occurs in the zone II ($Y_f = y_f/h < Y_2$).

Within the zone III the part of the velocity profile below the free stream zone shows a concavity turned toward the free surface. This confirms that the inflection point is located inside the zone II.

Carollo et al. (2002) suggested to estimate Y_1 and Y_2 by the following equations:

$$Y_1 = 0.865\frac{k_v}{h} \quad (3a)$$

$$Y_2 = 0.15 + 0.865\frac{k_v}{h} \quad (3b)$$

Copyright © 2006 Taylor & Francis Group plc, London, UK

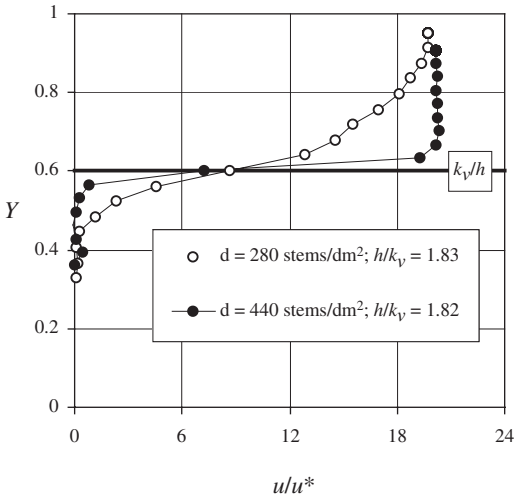


Figure 3. Velocity profiles for different values of vegetation concentration.

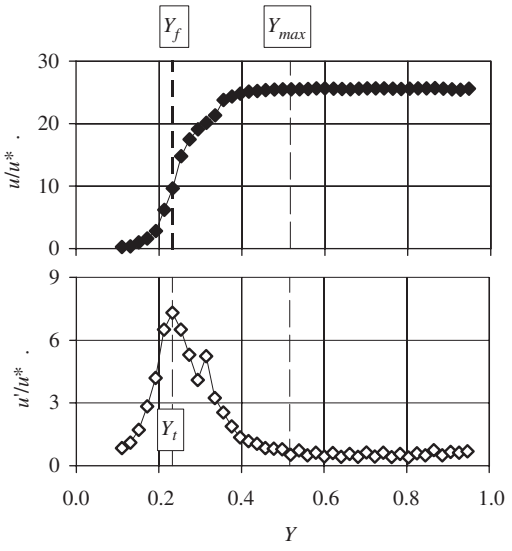


Figure 4. Comparison between a measured turbulence intensity distribution and the corresponding velocity profile.

that satisfy the boundary conditions for $k_v/h \rightarrow 0 Y_1 = 0$ (in absence of vegetation the zone I does not exist) and $Y_2 = 0.15$ (in absence of vegetation the superior limit of the logarithm profile, Y_2, coincides with the superior limit of the "inner region").

According to the eqs. (3) the location of the logarithm distribution zone (zone II) strongly depends on the non-dimensional vegetation height k_v/h, but the thickness of this velocity distribution zone, equal to $0.15\,h$, does not depend on vegetation height.

Since the measured velocity profiles showed that the depths Y_1 and Y_2 do not vary with the stem concentration δ, the location of the three velocity distribution zones does not depend on δ.

The experimental runs showed that for decreasing values of the stem concentration, the flow velocity increases inside the vegetation and decreases above it (Figure 3), and the thickness of the vertical velocity profile in zone III decreases. Thus, decreasing the stem concentration decreases the curvature of the velocity profile both inside and above the vegetation.

3.2 *Turbulence intensity distribution*

In order to analyze the distribution of the turbulence intensity, the values of u', estimated at each measurement point according by (q), have been normalized by the shear velocity u^* and plotted against Y.

The distributions of the normalized turbulence intensity have been compared with the distributions of the local mean velocity. As an example the comparison of the distributions measured in the axial vertical of run 13 is reported in Figure 4.

Some peculiar characteristics of the vertical profile of both turbulence intensity and velocity are highlighted in this figure:

1. the turbulence intensity profile shows a peak value at a relative water depth Y_t corresponding to the relative depth Y_f: for $Y < Y_t$ the turbulence intensity increases rapidly; for $Y > Y_t$ the turbulence intensity decreases until $Y = Y_{max}$, being Y_{max} the relative water depth in which the maximum value of velocity is reached; then, i.e. for $Y > Y_{max}$, the turbulence intensity assumes a constant low value;
2. approaching the free surface the decrease in vertical velocity gradient coincides with the decrease in turbulence intensity. Furthermore when the vertical velocity gradient is close to zero the turbulence intensity becomes constant. For $Y < Y_t$ the turbulence intensity increases with Y, as well as the vertical velocity gradient.

During the experiments a strong oscillation of stems was observed. The vegetation stems were bent with different inflection degrees and oscillated in the flow changing position and producing a variation of the bent vegetation height. In accordance with Ikeda & Kanazawa (1996), it has been observed that the motion of the flexible vegetation is strongly related to the high velocity gradient and to the inflection of the velocity profile occurring at the top of vegetation layer. The flow instability causes a vortex generation and the generated vortices move downstream just above the vegetated layer producing the wavy motion of the flexible stems, known as monami (Ghisalberti & Nepf, 2002).

Copyright © 2006 Taylor & Francis Group plc, London, UK

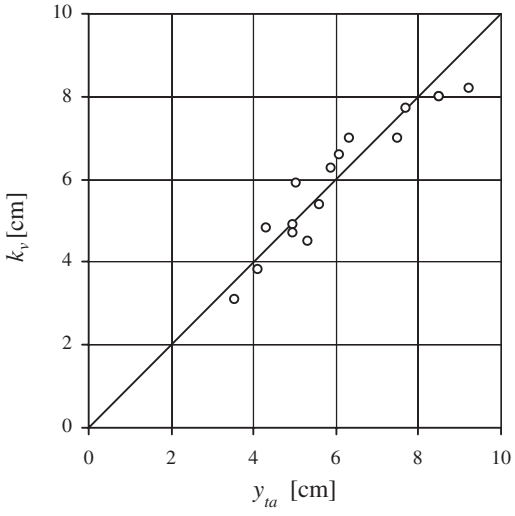


Figure 5. Comparison between mean depth at which maximum turbulence intensity is located and visual vegetation height.

The cyclic presence and absence of vegetation stems in the region where monami appears determines a strong variability on instantaneous longitudinal velocities. This variability produces a peak value of the normalized turbulence intensity u'_{max}/u^*. Therefore, the peak value of u'_{max}/u^* appears at the same distance from the bed where the number of changes (presence–absence of vegetation stems) is maximum.

These observations support the idea that the relative water depth Y_t, where the peak of turbulence intensity occurs, can be considered as a local estimate of the relative distance of the top of the bent vegetation layer from the bed.

In Figure 5 the bent vegetation height k_v is compared with the average y_{ta} of the depths y_t corresponding to the five measurement verticals. In spite of the dispersion due to measurement discontinuity (intervals of 5 mm along the water depth were used) and to the errors due to the visual estimation, the pairs (y_{ta}, k_v) place around the bisector line. Thus, the maximum turbulence intensity is located approximately at the depth of the top of the bent vegetation.

Figure 6 shows, for all measurement verticals, the comparison between the pairs (Y_t, Y_1), (Y_t, Y_2) and corresponding eqs. (3), in which k_v/h has been replaced with Y_t. It is evident that the top of vegetation is located into zone II of velocity profile.

For a given vegetation concentration ($\delta = 280$ stems/dm^2), Figure 7 shows the trend of the normalized turbulence intensity for different relative vegetation roughness k_v/h. Figure 7 clearly highlights that the normalized turbulence intensity presents a peak

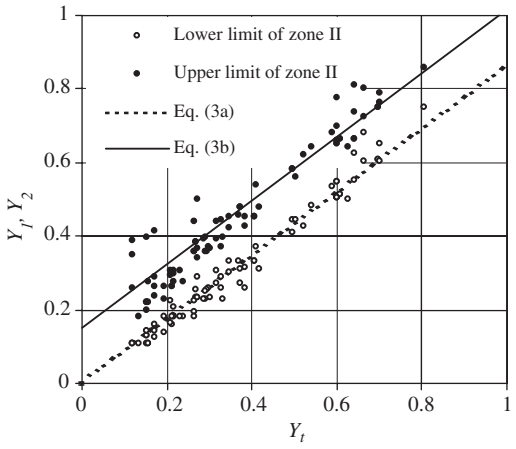


Figure 6. Comparison between pairs (Y_t, Y_1) and eq. (3a) and between pairs (Y_t, Y_2) and eq. (3b).

value for $Y = Y_t$. This trend of the normalized turbulence intensity is very similar to that observed in non-vegetated bed channels (Grass 1971); but the peak value, u'_{max}/u^*, is higher than that one ($u'_{max}/u^* < 3.6$) obtained in non-vegetated beds (Blinco & Partheniades 1971; Wang et al. 1993; Nezu & Nakagawa 1993). Furthermore, it seems clear from Figure 7 that the relative vegetation roughness (k_v/h), strongly affects the turbulence intensity distribution. Taking into account that the relative depth Y_t increases with the relative roughness, the whole turbulence intensity profile is shifted toward the free surface.

For a given k_v/h, vegetation concentration increasing induces a reduction of turbulence intensity. Analogous result was found in gravel bed channels (Carollo et al. 2005) where the turbulence intensity is damped by boulder concentration increasing.

3.3 *Proposed analytical velocity profile*

On the basis of the experimental observations discussed in previous sections, the following velocity profile equation has been derived (Carollo et al. 2002):

$$\frac{u}{u^*} = b_o + b_1 \arctan\left(\frac{Y - a_1}{a_2}\right) \tag{4}$$

The relationship (4) has been theoretically deduced applying the mixing length approach and a new expression of the mixing length l:

$$l = \left[k_1 (y - k_v)^2 + l_0\right]\sqrt{\frac{\tau}{\tau_{max}}} \tag{5}$$

Copyright © 2006 Taylor & Francis Group plc, London, UK

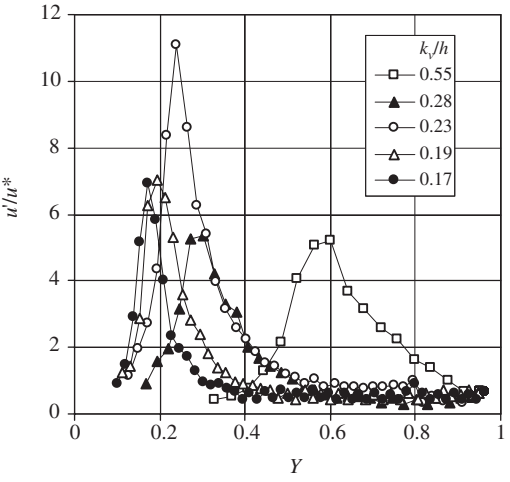


Figure 7. Turbulence intensity distributions measured in the axial vertical and corresponding to different values of the relative roughness.

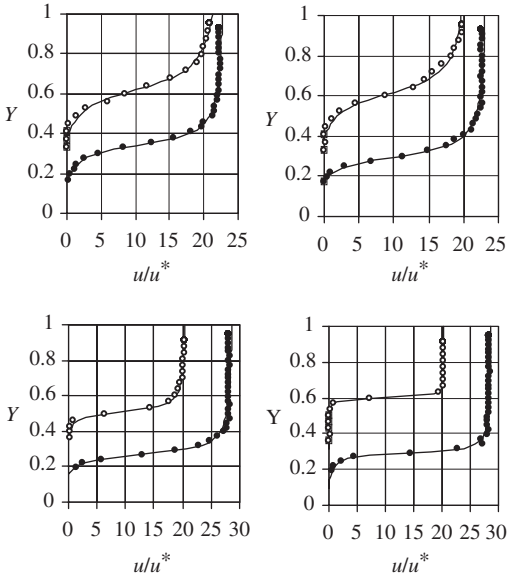


Figure 8. Examples of fitting of eq. (4) to measured profiles.

where k_l = numerical constant, τ_{max} = the maximum shear stress which is located at $y = k_v$, l_0 = the mixing length at $y = k_v$.

The coefficients a_1 and b_0 of eq. (5) have a physical meaning since they represent the coordinates Y and u/u^*, respectively, of the inflection point while b_1 and a_2 are parameters linked to the coefficients k_l, l_o and τ_{max} of eq. (6) (Carollo et al. 2002). The parameters a_1, a_2, b_0, b_1,have also a geometrical meaning: a_1 and b_0 produce respectively the vertical and the horizontal translation of the profile, a_2 modifies its steepness, and b_1 determines the distance between the two vertical asymptotes.

The velocity profile (5) is an analytical function characterized by two vertical asymptotes:

– when $Y \to +\infty$: then $u/u^* \to b_0 + b_1\pi/2$;
– when $Y \to -\infty$: then $u/u^* \to b_0 - b_1\pi/2$.

Substantially, the u/u^* values calculated by eq. (5) for $Y = 1$ and $Y = 0$ are quasi-equal to the asymptotes for $Y \to +\infty$: and $Y \to -\infty$, respectively. The velocity profile (4) reaches the maximum velocity u_{max} at $Y = 1$.

The eq. (5) fits very well to the empirical velocity profiles both near the bed and the free surface, as Figure 8 shows for some distributions chosen as examples. Furthermore, eq. (5) locates almost exactly the position of its inflection point ($a_1 = Y_f$) at Y_t (Figure 9).

3.4 *Relative turbulence intensity distribution*

The experimental turbulence intensity profile can also be analyzed using the ratio u'/u named relative turbulence intensity (Laufer 1951; Blinco & Partheniades 1971; Nezu & Nakagawa 1993).

Excluding a zone very near the bed ($Y < 0.003$ for the smooth bed) in which viscous effects are dominant, Blinco & Partheniades (1971) showed that for a given roughness condition the relative turbulence intensity decreases with the relative depth. Increasing of roughness (from smooth to rough bed) produces an increase of the relative turbulence intensity values.

As an example, Figure 10 shows the pairs $(Y, u'/u)$ corresponding to four experimental runs. Along the relative turbulence intensity profiles three regions, marked by two relative water depths $Y_1' < Y_t$ and $Y_2' > Y_t$, can be identified:

1) for $Y_1' < Y < Y_2'$ the relative turbulence intensity exponentially decreases with the distance from the bed;
2) for $Y < Y_1'$, i.e. for water depth close to the bed, both the flow velocities and the turbulence intensity values are very small and their ratio can increase or decrease with the bottom distance depending on which variable (u or u') is prevalent;
3) for $Y > Y_2'$ the variability of the relative turbulence intensity is not appreciable and for $Y > Y_{max} u'/u$ takes a constant value.

This behavior of the relative turbulence intensity can be explained analyzing both the instantaneous turbulence distribution and the flow velocity profile. In fact, the experimental runs showed that for $Y > Y_2'$ the measured values of both the turbulence intensity u'

Copyright © 2006 Taylor & Francis Group plc, London, UK

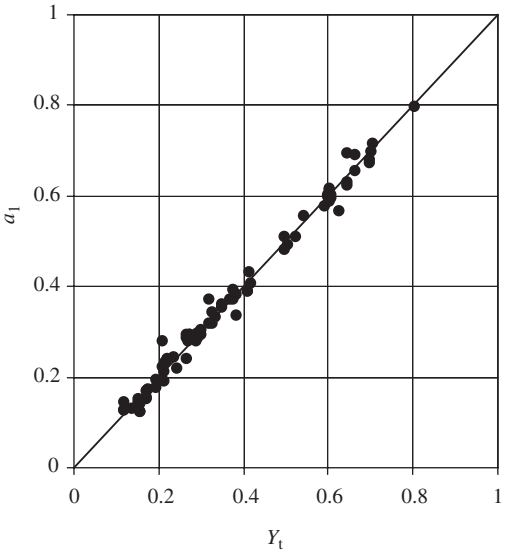


Figure 9. Comparison between relative depths Y_t, and the relative depth a_1 at which the inflection point of theoretical profile (5) is located.

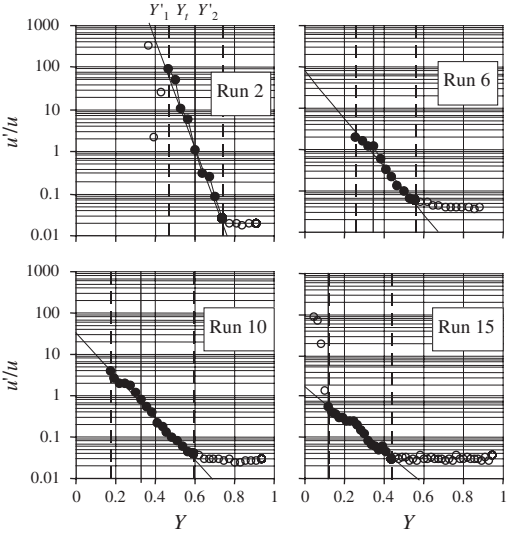


Figure 10. Relative turbulence intensity profiles measured in four experimental runs.

and the local flow velocity u are quasi-constant and that those values become constant for $Y = Y_{max}$.

In the range $Y'_1 < Y < Y'_2$ two different trends of u' and u with Y determine the same exponential-type trend of the relative turbulence intensity profile: for $Y_t < Y < Y'_2$ both the decrease in u' and the increase in u with Y determine a decreasing ratio u'/u; for

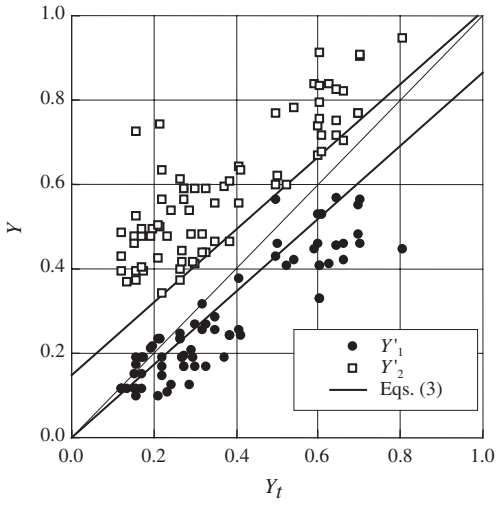


Figure 11. Localization of three different zones into measured velocity profile.

$Y'_1 < Y < Y_t$ both u' and u increase with Y but the ratio u'/u follows the same exponential trend established in the range $Y_t < Y < Y'_2$.

Thus, in contrast to the turbulence intensity distribution u'/u^*, no angular discontinuity can be observed at the top of the vegetation layer, i.e. at $Y = Y_t$.

The behavior of the relative turbulence intensity profile observed in the range $Y'_1 < Y < Y'_2$ is very similar to that observed by Blinco & Partheniades (1971), who found a decrease in u'/u above the viscous sub-layer both in smooth and in rough bed.

The analysis of all measured relative turbulence intensity profiles showed that at $Y = Y_t$ the relative intensity u'/u assumes values ranging from 0.3 to 1; when $Y = Y'_2$ the value of u'/u ranges from 0.02 to 0.06. These extreme values are very similar to those observed by Blinco & Partheniades (1971) near the bed ($u'/u = 0.4$–0.6) and near the free surface ($u'/u = 0.05$). Close to the bed (for $Y < Y'_1$) the relative turbulence intensity u'/u moves away from the exponential decreasing trend; this result can be justified, according to Blinco & Partheniades (1971), taking into account that the viscous effects become dominant.

In Figure 11 the relative depths Y'_1 and Y'_2 are plotted versus Y_t, assumed, as aforesaid, as a measure of the relative local bent vegetation height. The relative depth values Y'_2 fall beyond the bisector line while the relative depths Y'_1 fall below this line. This result confirms that the top of the vegetation layer falls inside the region $Y'_1 = Y = Y'_2$. According to Figure 11, the values of the relative depths Y'_1 and Y'_2 increase with the relative roughness k_v/h, so that when $k_v = 0$, i.e. without bed vegetation, $Y'_1 = 0$ and the reference plane coincides

Copyright © 2006 Taylor & Francis Group plc, London, UK

with the bed; if the vegetation becomes emergent it means that $k_v/h = 1$ and, thus, $Y_2' = 1$.

The eqs. (3) are also represented in Figure 11, clearly demonstrating that $Y_1' \leq Y_1$ and $Y_2' \geq Y_2$; in other words the region $Y_1' = Y = Y_2'$ of the relative turbulence intensity profile, contains the zone II of the velocity profile (Figure 2).

4 CONCLUSION

The flow velocity measurements carried out in a straight flume with grass-like vegetation bed highlighted that all measured velocity distributions are S-shaped. Three zones can be identified along the velocity profiles: zone I, inside the vegetation, characterized by very small velocities; zone II in which the logarithm velocity profile can be fitted to the measured velocities; zone III characterized by positive vertical velocity gradients, progressively decreasing until to become null near the free surface. Inside zone II an inflection point at a water depth quasi-equal to the bent vegetation height occurs. The localization of zone II (logarithm zone) is influenced by the depth/vegetation height ratio, but no relevant influence of the stem concentration has been observed. The stem concentration affects the shape of the velocity profile: decreasing the stem concentration the flow velocity increases inside the vegetation and decreases above it.

The analysis turbulent intensity distributions show a peak value at a relative water depth Y_t. The comparison, for each measurement vertical, with the corresponding measured velocity profiles has clearly shown that the inflection point occurs at a relative water depth coincident with Y_t.

These observations support the idea that the relative water depth where the peak of turbulence intensity occurs could be considered as a local estimate of the relative distance of the top of the bent vegetation layer from the bed.

On the basis of the aforementioned characteristics a new velocity profile has been presented. It has been theoretically deduced applying the mixing length approach and a new expression of the mixing length. The proposed velocity profile fits very well the experimental data both near the bed and near the free surface and allows to locate correctly the position of the flex point.

Finally, the analysis of the relative turbulence intensity distributions have shown that in contrast to the turbulence intensity distributions, no angular discontinuity can be observed at the top of the vegetation layer, i.e. at the relative water depth Y_t. Furthermore, in accordance with the experimental results obtained by Blinco & Partheniades (1971) above the viscous sub-layer both in smooth and in rough bed, these distributions show a decrease in relative turbulence intensity inside a region, delimited by two relative water depths Y_1' and Y_2', containing the zone II of the velocity profile.

This peculiar trend of the relative intensity distributions stimulates to keep up the work toward the verification of the experimental observations presented in this paper for different kind of vegetation concentration and stiffness characteristics.

REFERENCES

Blinco, P. H. & Partheniades, E. 1971. Turbulence characteristics in free surface flows over smooth and rough boundaries. *Journal of Hydraulic Research* 9: 43–69.

Cantwell, B. J. 1981. Organized motion in turbulent flow. *Ann. Rev. Fluid Mech*. 13: 457–515.

Carollo, F. G., Ferro, V. & Termini, D. 2002. Flow velocity measurement in vegetated channels. *Journal of Hydraulic Engineering* 128(7): 664–673.

Carollo, F. G., Ferro, V. & Termini, D. 2005. Analyzing turbulence intensity in gravel bed channel. *Journal of Hydraulic Engineering* 131(12): 1050–1061.

Corino, E. R. & Brodkey, R. S. 1969. A visual investigation of the wall region in turbulent flow. *Journal of Fluid Mechanics* 37: 1–30.

Eastgate, W. I. 1969. Vegetated stabilization of grassed waterways and dam bywashes. *Water Research Foundation of Australia* 16.

Ghisalberti, M. & Nepf, H. M. 2002. Mixing layer and coherent structures in vegetated acquatic flows. *Journal of Geophysical Reseach* 107(2):3–1–3–11.

Gourlay, M. R. 1970. *Discussion of* Flow resistance in vegetated channels. by N. Kouwen, T. E. Unny & Hill, H. M. *Journal of Irrigation and Drainage Division* 96(3): 351–357.

Grass, A. J. 1971. Structural features of turbulent flow over smooth and rough boundaries. *Journal of Fluid Mechanics* 50: 233–255.

Ikeda, S., Kanazawa, M. 1996. Three dimensional organized vortices above flexible water plants. *Journal of Hydraulic Engineering* 122(11): 634–640.

Jackson, R. 1976. Sedimentological and fluid-dynamic implications of the turbulent bursting phenomenon in geophysical flows. *Journal of Fluid Mechanics* 77: 531–560.

Kironoto, B. A., Graf, W. H. 1994. Turbulence characteristics in rough uniform open-channel flow. *Water, Maritime and Energy* 106(4): 333–344.

Kline, S. J., Reynolds, W. C, Schraub, F. A. & Runstadler, P. W. 1967. The structure of turbulent boundary layers. *Journal of Fluid Mechanics* 30: 741–773.

Kouwen, N. & Unny, T. E. 1973. Flexible roughness in open channels. *Journal of Hydraulic Division* 99(5): 713–728.

Kouwen, N., Unny, T. E. & Hill, H. M. 1969. Flow retardance in vegetated channels. *Journal of Irrigation and Drainage Division* 95(2): 329–342.

Kraus, N. C., Lohrmann, A. & Cabrera, R. 1994. New acoustic meter for measuring 3D laboratory flows. *Journal of Hydraulic Engineering* 120(3): 406–412.

Kutija, V. & Hong, H. T. M. 1996. A numerical model for assessing the additional resistance to flow introduced by flexible vegetation. *Journal of Hydraulic Research* 34(1): 99–114.

Copyright © 2006 Taylor & Francis Group plc, London, UK

Laufer, J. 1951. Investigation of turbulent flow in a two dimensional channel. *National Advisory Committee for Aeronautics* NACA, Tech. Report 1053.

Lemmin, U. & Rolland, T. 1997. Acoustic Velocity profiler for laboratory and Field Studies. *Journal of Hydraulic Engineering* 123(12): 1089–1097.

Nezu, I. & Nakagawa, H. 1993. *Turbulence in open-channel flows*. Rotterdam: Balkema.

Nezu, I. & Rodi, W. 1986. Open-channel flow measurements with a Laser Doppler Anemometer. *Journal of Hydraulic Engineering* 112(5): 335–355.

Palmer, V. J. 1945. A method for designing vegetated waterways. *Agricultural Engineering* 26(12): 516–520.

Shvidchenko, A. B. & Pender, G. 2001. Macroturbulent structure of open-channel flow over gravel beds. *Water Resources Research* 37(3): 709–719.

Talmon, A. M., Kunen, J. M. G., & Ooms, G. 1986. Simultaneous flow visualization and Reynolds-stress measurement in a turbulent boundary layer. *Journal of Fluid Mechanics* 163: 459–478.

Temple, D. M. 1986. Velocity distribution coefficients for grass-lined channels. *Journal of Hydraulic Engineering* 112(3): 193–205.

Wang, J., Dong, Z., Chen, C., & Xia, Z. 1993. The effects of bed roughness on the distribution of turbulent intensities in open channel flow. *Journal of Hydraulic Research* 31(1): 89–98.

Copyright © 2006 Taylor & Francis Group plc, London, UK

A two-dimensional lattice model for describing the open channel flow with vegetation

F.J. Jiménez-Hornero & J.V. Giráldez
Department of Agronomy, University of Córdoba, Spain

A.M. Laguna
Department of Applied Physics, University of Córdoba, Spain

S.J. Bennett
Department of Geography, University at Buffalo, State University of New York, Buffalo, New York, USA

C.V. Alonso
National Sedimentation Laboratory, ARS, USDA, Oxford, Mississippi, USA

ABSTRACT: A 2D lattice Boltzmann model (LBM) is proposed for describing the turbulent shallow water flow in a vegetated channel. The flow turbulence is taken into account by means of the standard Smagorinsky subgrid-scale model. The drag stress exerted by the flow on the vegetation as well as the frictional effects of the channel bed and walls are included in the LBM main equation. The simulated results are compared to the experimental cross-stream profiles of flow velocity obtained when considering a flume with alternate vegetation zones in which a meandering flow pattern is developed. In addition, a study about the influence of the distance between these vegetated areas on the flow turbulent structures is also reported.

1 INTRODUCTION

Many field and laboratory experiments have been devoted to describe the interaction among flow, sediment transport and riparian vegetation. The effect of both the emergent or submerged and rigid or flexible vegetation on the flow velocity and turbulent structure has been analyzed among others by Nepf (1999), Nezu & Onitsuka (2001), López & García (2001), Wilson & Horritt (2002), Righetti & Armanini (2002), Bennett et al. (2002) and Bennett (2004). Some works have studied the drag coefficient of vegetation (e.g. Fathi-Maghadam & Kouwen, 1997; Wu et al., 1999; James et al., 2004; Lee et al., 2004; Armanini et al., 2005). López & García (1998) explored the sediment transport in vegetated channels and Tsujimoto (1999) measured the efficiency of the vegetation trapping and sorting sediments.

The complex interactions between flow, sediment and vegetation have been simulated with different models. Among others, Wu & Wang (2004) and Wu et al. (2005) proposed a depth-averaged two-dimensional k-ε model for describing the flow in vegetated open channels combining it with a sediment transport model. López & García (2001) used vertical two-dimensional models to characterize turbulent flow with vegetation effect. Su & Li (2002) developed a large eddy simulation (LES) model to simulate the hydrodynamic behavior of turbulent flow in an open channel with a domain of vegetation. Choi & Kang (2004) applied the Reynolds stress model to open channel flows with vegetation.

In order to complement the models previously mentioned, new alternatives are always opportune. The lattice model approach (e.g. Succi, 2001) is a numerical tool developed to simulate fluid dynamics that has recently raised great interest. The kinematic viscosity is easily fitted and the fluid-solid interactions are implemented in a simple way. In addition, the LES method is straightforwardly included in that model producing a code that can be parallelized.

The objective of this work is to verify whether the lattice model approach is suitable to reproduce the flow patterns in the presence of alternate vegetated zones. With this aim, a lattice model is proposed including the effects of the channel bed and walls friction as well as the drag exerted by the stream on the vegetation. The model is calibrated using the experimental

Copyright © 2006 Taylor & Francis Group plc, London, UK

results reported by Bennett et al. (2002). After that, the influence of the distance between vegetated zones on the flow turbulent structures is analyzed.

2 THE LATTICE MODEL

The lattice model is a numerical approach developed to simulate fluid dynamics (e.g. Chen & Doolen, 1998; Wolf-Gladrow, 2000 §5). In that model, the reality is transformed into a regular lattice where particles move and interact with each other following simple rules. The lattice model used in this work is the known as BGK. Chen et al. (1992) and Qian et al. (1992) firstly presented it in an independent way. This model is based on a simplification of the lattice Boltzmann model, using the relaxation time parameter proposed by Bathnagar, Groos & Krook (1954) in the context of collisions of gas molecules. To honor the latter authors the model was named lattice BGK.

2.1 *The lattice BGK model equation*

In this approach the fluid particles move in a regular lattice in which each node is linked to its neighbors following a vicinity model that is chosen depending on the complexity of the phenomenon to be simulated. To calculate the fluid velocity field in two dimensions the vicinity model *d2q9* is used (Fig. 1), with $d=2$ meaning the number of dimensions and $q=9$ the number of particles considered. In this case there are eight moving particles and one at rest. The interactions of the particles keep up the mass and momentum (Rothman & Zaleski, 1997 §6.1; Chopard & Droz, 1998 §3.5).

The probability of finding a particle in a link i that connects a node with one of its neighbors, is represented by the independent variable f_i which varies continuously between 0 and 1 according to the hypothesis of Boltzmann molecular chaos. The main mesoscopic equation of the lattice BGK model for a node $\mathbf{r}$ at time t is (e.g. Succi, 2001 §5.1):

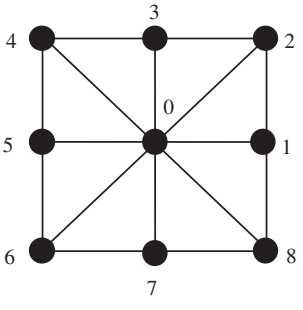


Figure 1. The vicinity model *d2q9* used in simulations done with the proposed lattice BGK model; d and q denote the number of dimensions and particles (eight moving and one at rest), respectively.

$$f_i(\mathbf{r}+\mathbf{c}_i,t+1) = \frac{1}{\eta} f_i^{eq}(\mathbf{r},t) + \left(1-\frac{1}{\eta}\right) f_i(\mathbf{r},t) + \frac{1}{c_s^2} t_i c_{i\alpha} F_\alpha(\mathbf{r},t) \quad (1)$$

where t is the time. $\mathbf{c}_i$ is the velocity of a particle in the link i and f_i^{eq} is the local equilibrium function. The relaxation time parameter, η, represents the difference between f_i and f_i^{eq} while t_i are weighting factors associated with the lattice directions. The parameter c_s is selected according to the vicinity model chosen and F_α is the component of the external stress in the α direction. Equation (1) reproduces a hydrodynamic behavior if f_i^{eq} is expressed as:

$$f_i^{eq} = \rho t_i \left[1+\frac{c_{i\alpha}u_\alpha}{c_s^2}+\frac{1}{2}\left(\frac{c_{i\alpha}u_\alpha}{c_s^2}\right)^2-\frac{u_\alpha u_\alpha}{2c_s^2}\right], \; i\in[1,8]$$
$$f_0^{eq} = \rho t_0\left(1-\frac{u_\alpha u_\alpha}{2c_s^2}\right), \quad i=0 \quad (2)$$

where $\rho(\mathbf{r},t)$ and $\mathbf{u}(\mathbf{r},t)$ stand for the fluid density and velocity, respectively. In Equation (2), the Einstein's summation convention has been adopted (i.e. $u_\alpha u_\alpha = \sum_\alpha u_\alpha u_\alpha$) and k_α is the component of any vector $\mathbf{k}$ in the α dimension.

The fluid density and velocity are deduced from f_i in the following way:

$$\rho(\mathbf{r},t) = \sum_{i=0}^{q-1} f_i(\mathbf{r},t)$$
$$\mathbf{u}(\mathbf{r},t) = \frac{\sum_{i=0}^{q-1} f_i(\mathbf{r},t)\mathbf{c}_i}{\rho(\mathbf{r},t)} \quad (3)$$

The relaxation time parameter allows the identification of the kinematic viscosity, υ

$$\upsilon = c_s^2\left(\eta-\frac{1}{2}\right) \quad (4)$$

In the case of the simulation of turbulent flows is possible to use the LES method combined with the lattice model as Hou et al. (1996) suggested. In this situation, a spatially-dependent kinematic viscosity $\overline{\upsilon}$, also known as effective viscosity, made up of the original viscosity υ and an eddy viscosity υ_t has to be considered:

$$\overline{\upsilon} = \upsilon + \upsilon_t \quad (5)$$

Copyright © 2006 Taylor & Francis Group plc, London, UK

The eddy viscosity has been used in many approaches like the Smagorinsky eddy viscosity model (Smagorinsky, 1963; Pope, 2000 §13.4; Succi, 2001 §9.5), where υ_t is defined as

$$\upsilon_t = C_{smg}^2 |S| \tag{6}$$

where $|S|$ is the magnitude of the strain-rate tensor $S_{\alpha\beta}$, with the spatial components α and β and the external parameter C_{smg} called the Smagorinsky constant. The spatially-dependent relaxation time, $\overline{\eta}$, is related to the original and eddy relaxation times, η and η_t, respectively, from (4) as:

$$\overline{\eta} = \frac{\overline{\upsilon}}{c_s^2} + \frac{1}{2} = \frac{\upsilon + \upsilon_t}{c_s^2} + \frac{1}{2} = \eta + \frac{\upsilon_t}{c_s^2} = \eta + \eta_t \tag{7}$$

After some operations the expression for $\overline{\eta}$ is derived:

$$\overline{\eta} = \frac{1}{2}\left(\eta + \sqrt{\eta^2 + 2C_{smg}^2 \frac{C_2}{C_4}\frac{\sqrt{Q}}{\rho c_s^2}}\right) \tag{8}$$

where Q is the scalar product of the non-equilibrium momentum flux tensor, $Q = \Pi_{\alpha\beta}\Pi_{\alpha\beta}$, with

$$\Pi_{\alpha\beta} = \sum_i c_{i\alpha} c_{i\beta} \left(f_i - f_i^{eq}\right) \tag{9}$$

Finally, η is replaced by $\overline{\eta}$ in (1). To simulate a turbulent flow with the lattice BGK and Smagorinsky models it is necessary to fit empirically C_{smg}, usually between 0.1 and 0.4, depending on the configuration of the flow. This is the main drawback of the use of the Smagorinsky subgrid scale stress model.

2.2 *The external stress in the lattice BGK model*

The external stress can be easily included in the lattice BGK model equation (e.g. Zhou, 2002a; 2002b). In the model proposed for describing the flow in an open and vegetated straight channel, the external stress consists of the bed and wall shear stresses due to friction, τ_b and τ_w, respectively, and the drag exerted on vegetation, D_f. For the spatial direction α, F can be expressed as

$$F_\alpha(\mathbf{r},t) = -\left[\tau_{b\alpha}(\mathbf{r},t) + \tau_{w\alpha}(\mathbf{r},t) + D_{f\alpha}(\mathbf{r},t)\right] \tag{10}$$

The shear stress due to bed friction is included in the lattice BGK model by means of the expression (11) (e.g. Julien, 1994 §6.2)

$$\tau_{b\alpha} = C_b(1-\chi_b)u_\alpha\sqrt{u_\beta u_\beta} \tag{11}$$

Where χ_b is the fraction of bed occupied by the vegetation in the zones where it is placed. For the vegetated area shown in Fig. 2, χ_b is derived from

$$\chi_b = 2N\phi^2/\vartheta^2 \tag{12}$$

with N as the number of vegetation elements, ϕ as the diameter of each vegetation element and ϑ as the diameter of the semi-circular vegetated area. Otherwise, $\chi_b = 0$. C_b is a non-dimensional bed friction coefficient that is calculated from

$$C_b = \frac{g n_b^2}{h^{1/3}} \tag{13}$$

where g is the acceleration of gravity, n_b is the roughness coefficient of Manning at the bed and h is the flow depth that is equal to the vegetation height, h_v, in case of emergent vegetation.

The shear stress in the channel walls is considered as (e.g. Zhou, 2001)

$$\tau_{w\alpha} = C_w(1-\chi_w)u_\alpha\sqrt{u_\beta u_\beta} \tag{14}$$

where C_w is a non-dimensional friction coefficient calculated from (13) replacing n_b by the Manning's roughness coefficient at the walls, n_w. In this work $n_b = n_w$ is assumed. χ_w is the fraction of the channel wall area covered by the vegetation elements in the zone where they are placed. For the vegetated area shown in Fig. 2, $\chi_w = \phi/b_v$, with ϕ as the diameter of each vegetation element. Otherwise, $\chi_w = 0$.

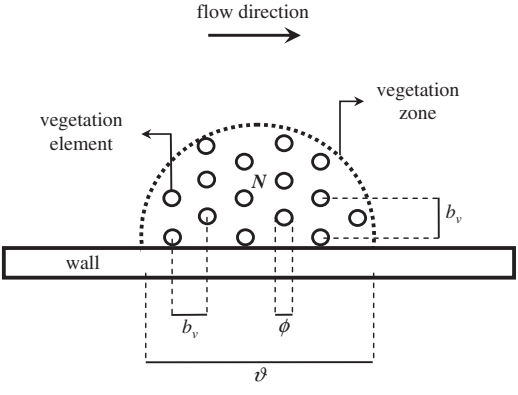


Figure 2. Scheme used for explaining the calculation of the projected area of the vegetation in the streamwise direction, A_v. The vegetated zone is a semi-circle with a diameter ϑ containing N similar emergent vegetation elements (open circles) in a staggered arrangement with a diameter ϕ separated between them by a distance b_v.

Copyright © 2006 Taylor & Francis Group plc, London, UK

Finally, the drag stress exerted by the flow on vegetation is (e.g. Shao, 2000 §5.2)

$$D_{f\alpha} = \frac{1}{2} C_d A_v u_\alpha \sqrt{u_\beta u_\beta} \tag{15}$$

with C_d as a non-dimensional drag coefficient related to the flow and vegetation characteristics (e.g. Alonso, 2004). A_v represents the relationship between the projected area of the vegetation elements in the streamwise direction, A_{nv}, and the area of the vegetated zone where they are placed, A_{vz}, both projected in the streamwise direction such that

$$A_v = \frac{A_{nv}}{A_{vz}} \tag{16}$$

For the scheme shown in Fig. 2, it can be obtained that $A_{nv} = N\phi\mu h$ with μ being a non-dimensional shape factor of vegetation related to its irregularity and flexibility and $A_{vz} = h\vartheta/2$, resulting $A_v = 2N\phi\mu/\vartheta$.

2.3 *Boundary conditions*

In the lattice BGK model simulations done in this work, the flow is determined assigning the spatially averaged velocity u_0 at the inlet of the computational domain in such a way that if α is the flow direction and β its normal, $u_\alpha = u_0$ and $u_\beta = 0$. Periodic boundary conditions are applied at the outlet.

Because of considering the shear stress in channel walls, the boundary condition applied at these places has to be different from the common bounce-back rule used in lattice BGK models for simulating solids. As Zhou (2001) observed, there is a large velocity gradient near a solid boundary for turbulent flows due to wall friction. This can not be correctly simulated with no-slip boundary condition. Although there are other alternatives for dealing with this kind of boundaries such as diffuse reflection (e.g. Sofonea & Sekerka, 2005), the semi-slip boundary condition proposed by Zhou (2001) is adopted. It consists of a combination of the shear stress (14) with the specular reflection. That boundary condition has been implemented according to Zhang et al. (2002) at the places marked as channel wall in the computational domain.

3 LABORATORY EXPERIMENTS PERFORMED BY BENNETT ET AL. (2002)

The experiments on the flow in the presence of alternate emergent vegetation zones done by Bennett et al. (2002) were conducted using a tilting recirculating flume of $L = 16.5$ m in length and $w = 0.6$ m in width. Its scheme is shown in Fig. 3. The flow discharge, P, was kept constant at $0.0042\ \mathrm{m^3 s^{-1}}$. Flow depths were measured over a longitudinal section excluding the vegetation zones and these data were used to calculate the spatially averaged flow depth h and velocity u_0.

A total of six alternate vegetation zones were placed along the length flume spaced a distance $\lambda = 4.8$ m each other, λ was the so-called meander wavelength (Fig. 3). The shape of the vegetated areas was semicircular with a diameter of $\vartheta = 0.6$ m. The emergent vegetation was simulated by Bennett et al. (2002) using wooden dowels of $\phi = 3.2 \times 10^{-3}$ m in diameter and 70×10^{-3} m in height. For a determined vegetation density, VD, a number of dowels, N, were placed perpendicularly to the plywood flume floor in a staggered

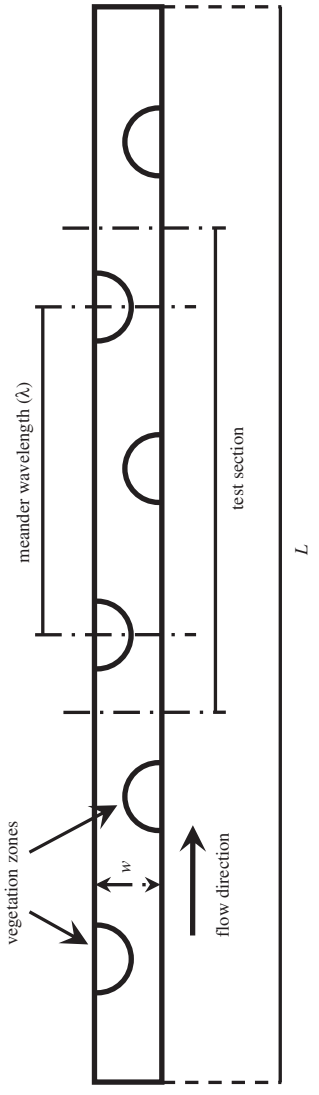


Figure 3. Scheme of the experimental channel used by Bennett et al. (2002) to study the turbulent flow structures provoked by emergent vegetation placed in alternate zones.

Copyright © 2006 Taylor & Francis Group plc, London, UK

arrangement with spacing b_v to maximize the flow resistance (Fig. 2). The definition of vegetation density (17), expressed in m^{-1}, adopted by Bennett et al. (2002) was the proposed by López & García (1997) as the ratio between the sum of the frontal areas of the vegetation divided by the volume of fluid (depth water over an area encompassing one meander wavelength λ)

$$VD = \frac{N\phi h}{w\lambda h} \tag{17}$$

Bennett et al. (2002) used the Particle Image Velocimetry (PIV) to characterize the surface flow field for the test area marked in Fig. 3. The experimental results in some cross sections of the flume, obtained by Bennett and co-workers with $VD = 2.739\,m^{-1}$ ($u_0 = 0.196\,m\,s^{-1}$, $h = 0.036\,m$), were reported in Wu & Wang (2004).

4 RESULTS

The experimental results of Bennett et al. (2002) were taken into account to calibrate the proposed lattice model. A computational domain of 516×20 square cells was used with the scale factors $\Delta r = 0.03\,m$ and $\Delta t = 0.011302\,s$, for the length and time, respectively. The relaxation parameter $\eta = 0.50004$ and $C_{smago} = 0.2$ were taken. The parameters C_b and C_w were calculated from (13) considering $n_b = n_w = 0.015\,m^{-1/3}s$. The value of the Manning's roughness coefficient was not reported by Bennett (2001) and Bennett et al. (2002). The value adopted here for the flume plywood corresponds to the suggested by Chow (1959) for laminated wood. Regarding to the vegetated zones, χ_b, χ_w and A_v were deduced from the experimental arrangement of the simulated vegetation elements described by Bennett et al. (2002). The shape factor was assumed $\mu = 1$. The drag coefficient C_d had to be obtained from calibration by comparing the simulated and the surface flow velocities measured by Bennett et al. (2002) and reported in Wu & Wang (2004). Table 1 summarizes the values of the parameters used for simulating the effects of the considered vegetation density.

Figure 4 shows the time-averaged surface flow pattern over 100 samples each one taken every 1000

Table 1. Values of the parameters used in the lattice BGK model for the simulation of the experimental results described by Bennett et al. (2002) for the vegetation density $VD = 2.739\,m^{-1}$.

$C_b = C_w$	χ_b	χ_w	C_d	A_v
0.00709	0.09973	0.355	3.15	37.397

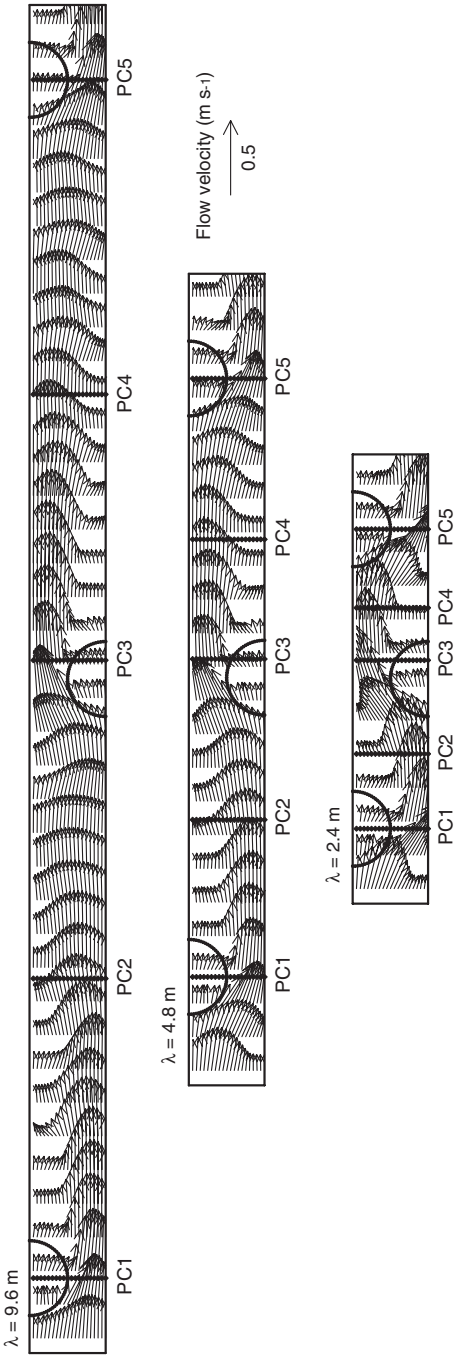


Figure 4. Time-averaged surface flow patterns simulated with the proposed lattice BGK model for the test section (Fig. 3) considering different values of meander wavelength (λ). The vegetation zones are represented by semi-circles. The vertical lines *PCi*, $i \in [1,5]$ mark the places where the time-averaged surface flow velocities were considered.

Copyright © 2006 Taylor & Francis Group plc, London, UK

time-steps considering several values of λ. The simulated effect of the vegetation for $\lambda = 4.8$ m was similar to the described by Bennett et al. (2002). The flow was influenced by the emergent vegetation. It decelerated in the leeward of the vegetation zones and accelerated in the opposite regions. In the same way that Bennett et al. (2002) reported, the flow was diverted away from the vegetation zone toward the other bank until it encountered the next vegetation zone downstream where it diverted again toward the opposite bank.

In the case of $\lambda = 2.4$ m the flow keeps the same pattern described before but, as is shown in Fig. 4, it is greatly perturbed due to the nearness of the vegetated zones. When $\lambda = 9.6$ m, the variation in the time-averaged surface velocity is lower compared to the two previous cases with decelerated areas of $\approx \lambda/4$ in distance downstream the vegetation obstacles.

Some of the effects of vegetation on turbulent flow structure are shown in Fig. 5 when different values of λ are considered. They correspond to the snapshots obtained after 75×10^3 time steps (≈ 14 minutes of real time) of simulation. For the case of $\lambda = 4.8$ m, the turbulent structures reproduced by the lattice model are comparable to those described by Bennett (2004). The flow decelerated upstream, within and downstream near the vegetation areas while it accelerated around the vegetated zones apices. Bennett (2004) also described a mixing layer created downstream of the vegetation zone and associated with small-scale and large scale vortices. Both of them are clearly visible in the flow pattern simulated with the proposed model. The small-scale vortices were located near and downstream of the vegetation zone apex, while the large-scale vortices were placed further. The direction of rotation was toward the vegetation zone and their shape was elliptical being in agreement with the description done by Bennett (2004). As can be appreciated in Fig. 5, the small-scale vortices appear for all the values of λ. However, the large-scale vortices only are reproduced in the cases of $\lambda = 4.8$ and 9.6 m, being fully developed in the last case. For $\lambda = 2.4$ m, the proximity of the vegetated zones avoid the presence of these turbulent structures.

In the test area cross sections denoted by *PCi*, $i \in$ [1,5] in Fig. 4, the time-averaged surface flow velocity was considered. Figure 6 shows the experimental data taken using PIV by Bennett et al. (2002), reported in Wu & Wang (2004), and the results obtained with the proposed lattice BGK model for $\lambda = 4.8$ m. As can be appreciated, the simulated results were in good agreement with the measurements. The surface velocities reproduced by the model when $\lambda = 9.6$ m are similar to those obtained for $\lambda = 4.8$ m in the corresponding cross sections. However, the differences are notable in the case of $\lambda = 2.4$ m. This fact is a consequence of the strong influence of the vegetated zones on the flow in this case.

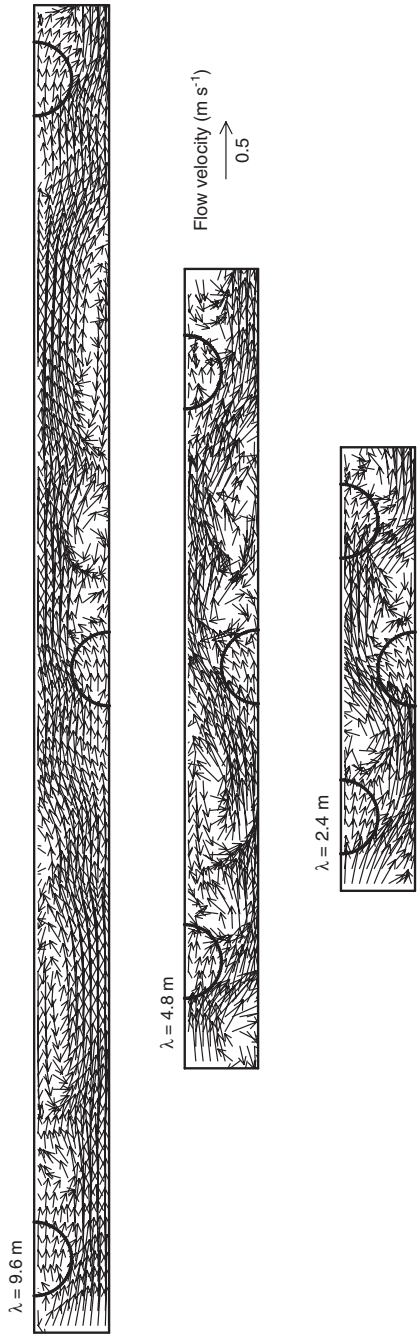


Figure 5. Flow pattern snapshots obtained from the lattice BGK model simulations in the test section of Fig. 3 after 75×10^4 time steps (≈ 14 minutes of real time) considering different values of meander wavelength (λ). The simulated turbulent flow structures agree with those described by Bennett (2004) for $\lambda = 4.8$ m.

Copyright © 2006 Taylor & Francis Group plc, London, UK

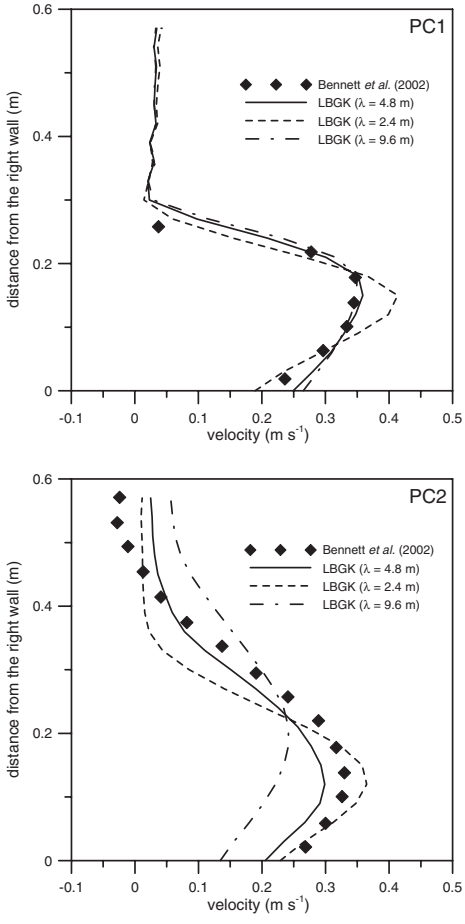


Figure 6. Experimental surface flow velocities (symbols) measured by Bennett et al. (2002) and reported in Wu & Wang (2004) for $\lambda = 4.8$ m and the results (solid lines) simulated with the lattice model in the sections PC1 and PC2 marked in Fig. 3. The dash and dash-dot lines correspond to the simulations done for $\lambda = 2.4$ and $\lambda = 9.6$ m, respectively.

5 CONCLUSIONS

The proposed lattice BGK model has shown to be a suitable alternative for describing the water flow in presence of emergent vegetation arranged in alternate zones along an experimental flume. The simulated time-averaged flow pattern and the surface flow velocities agree with the experimental results obtained by Bennett et al. (2002). The effects of vegetation on the turbulent flow structure reproduced by the lattice model, including accelerated and decelerated zones and small-scale and large-scale vortices, are similar to those described by Bennett (2004). In addition, the model simulates in an acceptable way the influence

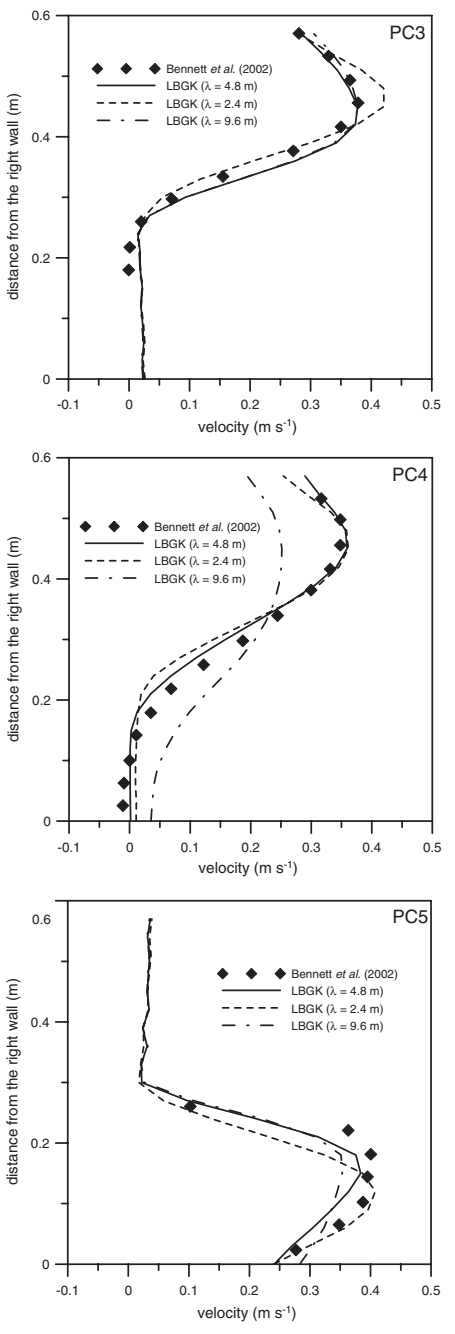


Figure 6. (cont.). Experimental surface flow velocities (symbols) measured by Bennett et al. (2002) and reported in Wu & Wang (2004) for $\lambda = 4.8$ m and the results (solid lines) simulated with the lattice model in the sections PC3, PC4 and PC5 marked in Fig. 3. The dash and dash-dot lines correspond to the simulations done for $\lambda = 2.4$ and $\lambda = 9.6$ m, respectively.

Copyright © 2006 Taylor & Francis Group plc, London, UK

of the distance between vegetated zones on the open channel flow.

The main advantageous features of the numerical model introduced in this work are: (a) the Smagorinsky subgrid scale stress model for simulating the flow turbulence can be straightforwardly included; (b) a simple slip boundary condition is used for the treatment of solid walls overcoming the drawbacks of applying at these locations the standard non-slip boundary condition in turbulent flows; (c) the frictional effects of the channel bed and walls and the drag exerted on the vegetation are added in the lattice model as external stresses, permitting to consider the vegetation density influence on the flow in an easy way.

The above mentioned characteristics make the lattice BGK model a promising tool for being applied to simulate different river restoration techniques.

ACKNOWLEDGMENTS

The authors gratefully acknowledge the support of the Spanish Government Project AGL2005-05326/AGR. F.J. Jiménez-Hornero wishes to thank the support of Consejería de Innovación, Ciencia y Empresa, Junta de Andalucía (Ayudas para facilitar el Retorno de Investigadores a Centros de Investigación y Universidades de Andalucía).

REFERENCES

Alonso, C.V. 2004. Transport mechanics of stream-borne logs. In S.J. Bennett & A. Simon (eds), *Riparian Vegetation and Fluvial Geomorphology, Water Science and Application Service* 8: 59–69. Washington: American Geophysical Union.

Armanini A., Righetti, M. & Grisenti, P. 2005. Direct measurement of vegetation resistance in prototype scale. *Journal of Hydraulic Research* 43: 481–487.

Bathnagar, P., Gross, E.P. & Krook, M.K. 1954. A model for collision processes in gases. I. Small amplitude processes in charged and neutral one-component systems. *Physical Review B* 94: 511–525.

Bennett, S.J. 2004. Effects of emergent riparian vegetation on spatially averaged and turbulent flow within an experimental channel. In S.J. Bennett & A. Simon (eds), *Riparian Vegetation and Fluvial Geomorphology, Water Science and Application Service* 8: 29–41. Washington: American Geophysical Union.

Bennett, S.J. Pirim, T. & Barkdoll, B.D. 2002. Using simulated emergent vegetation to alter stream flow direction within a straight experimental channel. *Geomorphology* 44: 115–126.

Chen, S. & Doolen, G. 1998. Lattice Boltzmann method for fluid flows. *Annual Review of Fluid Mechanics* 30: 329-364.

Chen, S. Wang, Z., Shan, X. & Doolen, G. 1992. Lattice Boltzmann computational fluid dynamics in three dimensions. *Journal of Statistical Physics* 68: 379–400.

Choi, S.U. & Kang, H.S. 2004. Reynolds stress modeling of vegetated open-channel flows. *Journal of Hydraulic Research* 42: 3–11.

Chopard, B. & Droz, M. 1998. *Cellular Automata Modeling of Physical Systems*. Cambridge: Cambridge University Press.

Chow, V.T. 1959. *Open-channel Hydraulics*. New York: McGraw-Hill.

Fathi-Maghadam, M. & Kouwen, N. 1997. Nonrigid, nonsubmerged, vegetative roughness on floodplains. *Journal of Hydraulic Engineering-ASCE* 123: 51–57.

Hou, S., Sterling, J. Chen, S. & Doolen, G.D. 1996. A lattice subgrid model for high Reynolds number flows. *Fields Institute Communications* 6: 151–166.

James, C.S., Birkhead, A.L., Jordanova, A.A. & O'Sullivan, J.J. 2004. Flow resistance of emergent vegetation. *Journal of Hydraulic Research* 42: 390–398.

Julien, P.Y. 1994. *Erosion and Sedimentation.* Cambridge: Cambridge University Press.

Lee, J.K., Roig, L.C. Jenter, H.L. & Visser, H.M. 2004. Drag coefficients for modeling flow through emergent vegetation in the Florida Everglades. *Ecological Engineering* 22: 237–248.

López, F. & García, M. 1997. Open-channel flow through simulated vegetation: turbulence modeling and sediment transport. *Wetlands Research Program Technical Report WRP-CP-10*. Vicksburg: Water-ways Experimental Station.

López, F. & García, M. 1998. Open-channel flow through simulated vegetation: Suspended sediment transport modelling. *Water Resources Research* 34: 2341–2352.

López, F. & García, M.H. 2001. Mean flow and turbulence structure of open-channel flow through non-emergent vegetation. *Journal of Hydraulic Engineering-ASCE* 127: 392–402.

Nepf, H.M. 1999. Drag, turbulence, and diffusion in flow through emergent vegetation. *Water Resources Research* 35: 479–489.

Nezu, I. & Onitsuka, K. 2001. Turbulent structures in partly vegetated open-channel flows with LDA and PIV measurements. *Journal of Hydraulic Research* 39: 629–642.

Pope, S.B. 2000. *Turbulent Flows*. Cambridge: Cambridge University Press.

Qian, Y.H., D'Humieres, D. & Lallemand, P. 1992. Lattice BGK models for Navier-Stokes equation. *Europhysics Letters* 17: 479–484.

Righetti, M. & Armanini, A. 2002. Flow resistance in open channel flows with sparsely distributed bushes. *Journal of Hydrology* 269: 55–64.

Rothman, D.H. & Zaleski, S. 1997. *Lattice-gas Cellular Automata. Simple Models of Complex Hydrodynamics*. Cambridge: Cambridge University Press.

Shao, Y. 2000. *Physics and Modelling of Wind Erosion*. Dordrecht: Kluwer Academic Publishers.

Smagorinsky, J. 1963. General circulation experiments with the primitive equations: I. the basic equations. *Monthly Weather Review* 91: 99–164.

Sofonea, V. & Sekerka, R.F. 2005. Boundary conditions for the upwind finite difference Lattice Boltzmann model: Evidence of slip velocity in micro-channel flow. *Journal of Computational Physics* 207: 639–659.

Su, X.H. & Li, C.W. 2002. Large eddy simulation of free surface turbulent flow in partly vegetated open channels.

Copyright © 2006 Taylor & Francis Group plc, London, UK

International Journal for Numerical Methods in Fluids 39: 919–937.

Succi, S. 2001. *The Lattice Boltzmann Equation for Fluid Dynamics and Beyond*. Oxford: Oxford University Press.

Tsujimoto, T. 1999. Fluvial processes in streams with vegetation. *Journal of Hydraulic Research* 37: 789–803.

Wilson, C.A.M.E. & Horritt, M.S. 2002. Measuring the flow resistance of submerged grass. *Hydrological Processes* 16: 2589–2598.

Wolf-Gladrow, D.A. 2000. *Lattice-gas Automata and Lattice Boltzmann Models*. Berlin: Springer-Verlag.

Wu, F.C. Shen, H.W. & Chou, Y.J. 1999. Variation of roughness coefficients for unsubmerged and submerged vegetation. *Journal of Hydraulic Engineering-ASCE* 125: 934–942.

Wu, W. & Wang, S.S.Y. 2004. A depth-averaged two-dimensional numerical model of flow and sediment transport in open channels with vegetation. In S.J. Bennett & A. Simon (eds), *Riparian Vegetation and Fluvial Geomorphology, Water Science and Application Service* 8: 253–265. Washington: American Geophysical Union.

Wu, W. Shields., F.D. Jr. Bennett, S.J. & Wang, S.S.Y. 2005. A depth-averaged two-dimensional model for flow, sediment transport, and bed topography in curved channels with riparian vegetation. *Water Resources Research* 41: W03015, doi:10.1029/2004WR003730.

Zhang, X. Crawford, J.W. Bengough, A.G. & Young, I.M. 2002. On boundary conditions in the lattice Boltzmann model for advection and anisotropic dispersion equation. *Advances in Water Resources* 25: 601–609.

Zhou, J.G. 2001. An elastic-collision scheme for lattice Boltzmann methods. *International Journal of Modern Physics C* 12: 387–401.

Zhou, J.G. 2002a. A lattice Boltzmann model for the shallow water equations. *Computer Methods in Applied Mechanics and Engineering* 191: 3527–3539.

Zhou, J.G. 2002b. A lattice Boltzmann model for the shallow water equations with turbulence modelling. *International Journal of Modern Physics C* 13: 1135–1150.

Copyright © 2006 Taylor & Francis Group plc, London, UK

Depth-averaged flow in presence of submerged cylindrical elements

F. Huthoff
Water Engineering and Management, University of Twente, The Netherlands
HKV Consultants, Lelystad, The Netherlands

D.C.M. Augustijn & S.J.M.H. Hulscher
Water Engineering and Management, University of Twente, The Netherlands

ABSTRACT: The hydraulic resistance of vegetation can play a major role in the hydrodynamics of rivers with extensive natural floodplains. Vegetation penetrates the flow field and thereby causes drag that, in addition to the flow resistance at the bed level, causes energy losses and slows down the flow. Here, these flow processes are studied in an idealized form by treating vegetation as cylindrical roughness elements with homogeneous geometrical dimensions. Based on scaling considerations of the forces involved, depth-averaged flow velocities within the resistance layer and in the free flowing layer above the roughness elements are estimated. This yields a new description of the overall average flow field, which is entirely determined by measurable geometrical boundaries. We tested the new relation against laboratory flume experiments and found very good agreement ($R^2 = 0.98$). The new description even showed realistic results when the depth of flow is of similar size as the height of the roughness elements themselves. This result demonstrates its superiority over commonly used wall-roughness methods.

1 INTRODUCTION

Submerged vegetation directly influences the discharge capacity in rivers, floodplains or irrigation channels. As a result, the hydraulic resistance of vegetation has been extensively studied in the past decades (for overview see Green 2005). While the hydraulic resistance of solid boundaries with small scale irregularities is quite well understood, situations in which resistance elements are of similar sizes as flow depths still pose large problems (e.g. Smart et al. 2002, Stone and Shen 2002). Especially near the roughness tops, the general form of the most representative velocity profile is still a matter of debate (e.g. Nikora et al. 2004). In case of vegetation, this is further complicated by the natural variability in plant dimensions or streamlining effects.

Laboratory flume studies with natural vegetation have resulted in several empirical flow resistance equations (e.g. Huntington et al. 1992, Copeland 2000). A drawback of these resistance relations is that it is not possible to attribute the relative importance of different flow processes to overall energy losses. General application is therefore difficult, especially in situations that differ much from the original experiments.

More general insight into the hydraulic resistance of vegetation can be achieved by ruling out effects that are due to streamlining effects of leaves and natural variability. Natural vegetation is then replaced by an idealized form: rigid cylindrical stems. Examples hereof can be found in flume studies (e.g. Meijer and van Velzen 1998 or Stone and Shen 2002) and detailed numerical flow models (e.g. Uittenbogaard 2003, Neary 2003). While numerical flow models have shown to represent flow characteristics realistically, the computational effort makes them of limited use for large-scale river applications. Therefore, more simplified solutions are desired that describe the mean flow field in terms of the cylinder characteristics and flow depth.

Stephan and Gutknecht (2002) suggest that the mean deflected plant height is a suitable measure for vegetation resistance. However, Klopstra et al. (1997) claim that a roughness height analogy underestimates vegetative resistance and developed a method that takes into account drag due to individual stems (cylinders) and turbulent mixing. Through depth-integration of the vertical velocity profile an analytical expression for the mean velocity was derived. Unfortunately, the expression is still quite complex and the necessary turbulence closure parameter is poorly understood. Consequently, there are still difficulties in its practical application.

In the current work, flow over vegetation is described by an average-velocity model where distinct flow characteristics are attributed to two separate flow

Copyright © 2006 Taylor & Francis Group plc, London, UK

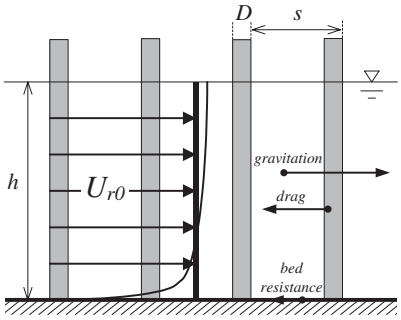


Figure 1. The depth-averaged velocity U_{r0} is the result of the balance between the gravitational force (i.e. gravity-driven flow, because of channel with bed slope i), the drag force and the bed resistance. The individual stems have a diameter D [m] and a separation s [m] ($s = 1/\sqrt{m}$, m = surface density [m^{-2}]).

layers. These two regions will be referred to as the surface layer and the resistance layer (see also Figure 2). General scaling assumptions are made, which avoid the necessity of integration over depth and the associated complications of depth-dependence of turbulence intensities. Even though specifics of natural vegetation are neglected, its accurate description of flow through an array of cylindrical stems gives confidence in applications that involve vegetative hydraulic resistance.

2 FLOW THROUGH VEGETATION

When a flow field is penetrated by vegetation, turbulent vortices are created in the wake behind the protruding stems (e.g. Akilli and Rockwell 2002). Consequently, in addition to the resistance at the bed, drag effects around the individual plant stems cause the flow to slow down. By replacing the vegetation with a homogeneous field of identical cylindrical stems, the water movement is represented by a bulk force balance (e.g. Baptist 2005):

$$\underbrace{\rho g h i}_{\text{gravitation}} = \underbrace{\tfrac{1}{2}\rho C_D m D h U_{r0}^2}_{\text{stem drag}} + \underbrace{\rho f U_{r0}^2}_{\text{bed resistance}} \qquad (1)$$

where the individual stems, with diameter D [m] and bed surface density m [m^{-2}], exceed the flow depth h [m] (see Figure 1). Furthermore, C_D [-] is the drag coefficient, i [-] the slope of the channel, and f [-] is the bed resistance function. The separation between individual cylinders s is entirely determined by their bed surface density m:

$$s = \frac{1}{\sqrt{m}} \qquad (2)$$

Also, the stem diameter D and the stem surface density m can be combined to give a new length scale. Together with the drag coefficient we introduce b, the *drag length*:

$$b = \frac{1}{C_D m D} \qquad (3)$$

By using (3), the average velocity U_{r0} [m/s] may be written as:

$$U_{r0} = U_{r0}^* \sqrt{\frac{1}{1 + \frac{2b}{h} f}} \qquad (4)$$

where U_{r0}^* is the average flow velocity in the resistance layer if no bed resistance effects were present (i.e. when $f = 0$).

$$U_{r0}^* = \sqrt{2bgi} \qquad (5)$$

The average flow velocity U_{r0} can now be determined if the bed resistance function f is specified. For turbulent flows, several functions for f exist (see e.g. Yen 2002). A commonly used relation for turbulent rough flow was proposed by Strickler (1923), here given in a dimensionally homogeneous form:

$$\sqrt{f} = \frac{\sqrt{ghi}}{U} = \tfrac{1}{8}\left(\frac{k_S}{h}\right)^{1/6} \qquad (6)$$

where Strickler's roughness height k_S [m] reflects the size of the irregularities on the bed and U the associated depth-averaged velocity. Considering that k_S is usually much smaller than the flow depth h, the contribution of bed resistance is often negligible in the force balance (1) and, consequently, the average velocity in the resistance layer U_{r0} is practically equal to U_{r0}^*.

Kadlec (1990) warns of the possibility that within the resistance layer flow velocities could reduce to yield a laminar flow field. In that case, the resistance function f is inversely proportional to the Reynolds number (see e.g. Yen 2002).

3 SUBMERGED VEGETATION

3.1 *The resistance layer*

Whenever cylindrical elements become submerged, the flow in the surface layer has a higher average velocity because in this layer no drag due to the stems is experienced. The energy losses in the surface layer are then entirely due to a shear stress near the top of the resistance layer, which balances the gravitational force that drives the flow. Subsequently, the shear stress between surface and resistance layer (i.e. the *interface*

Copyright © 2006 Taylor & Francis Group plc, London, UK

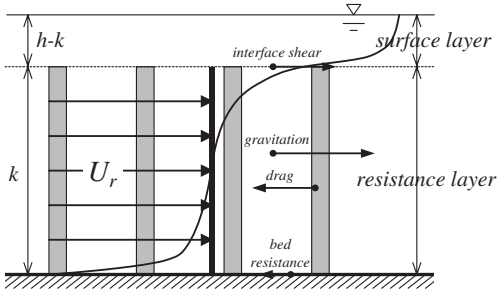


Figure 2. The depth-averaged velocity U_r in the layer occupied by the cylindrical stems (i.e. in the *resistance layer*) in the case that the stems are submerged.

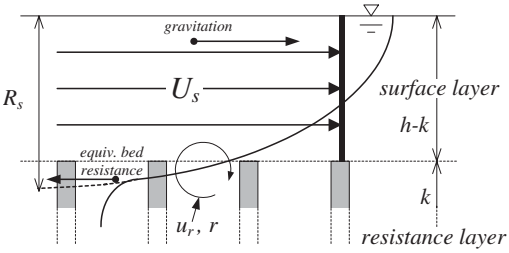


Figure 3. The depth-averaged velocity in the surface layer U_s. Two hydraulic radii are also shown: R_s reflects the depth of the surface layer with respect to an artificial rough bed and r (the *spacing hydraulic radius*) reflects the roughness height of the artificial rough bed.

shear) also causes the flow in the top of the resistance layer to speed up (see Figure 2). With an extra component due to the surface layer, the force balance (1) modifies to:

$$\underbrace{\rho g(h-k)i}_{\text{interface shear}} + \rho g k i = \frac{\rho k {U_r}^2}{2b} + \rho f {U_r}^2 \qquad (7)$$

The two contributions on the left-hand-side of (7) are due to the gravitational force that acts on the surface and in the resistance layer, respectively. The drag force acts over a depth k, as opposed to the total flow depth h in case of (1), where the cylindrical stems were not submerged. As a result, the average velocity in the resistance layer U_r becomes:

$$\frac{U_r}{U_{r0}} = \sqrt{\frac{h}{k}} \quad (h \geq k) \qquad (8)$$

where U_{r0} is the average velocity in the resistance layer if no free flowing layer above the cylindrical stems were present (equation (4)). Inserting the bed resistance function f as given in (6) into (7), yields for U_{r0}:

$$U_{r0} = U^*_{r0} \sqrt{\frac{1}{1 + \frac{b}{32k}\left(\frac{k_S}{h}\right)^{1/3}}} \qquad (9)$$

In earlier works, results similar to the square root law in (8) have been found. Smart et al. (2002) point out that with increasing relative roughness, a conceptual drag coefficient model would lead to a square-root law of the flow resistance. Baptist et al. (2006) used dimensionally aware genetic programming (Keijzer and Babovic 2000) and also found a square root dependence with respect to the relative flow depth h/k.

3.2 *The surface layer*

Based on physical principles and scaling assumptions, the well-known Strickler equation (6) can be derived for the case of rough channel flow (see Gioia and Bombardelli 2002). The main principles behind the derivation are: (i) a simple force balance; (ii) scaling of turbulent velocity fluctuations to the average flow velocity; and (iii) the concept of a constant energy dissipation rate when large turbulent flow patterns (i.e. eddies) break up into smaller ones (known as *Kolmogorov scaling*). Here we will follow the same line of reasoning to describe depth-averaged flow over submerged rigid cylinders (i.e. for the surface layer; see Figure 3).

3.2.1 *Shear stress in the surface layer*

In steady flow over a rough bed, the shear stress at the top of the bed τ_k balances the gravitational pull on the water volume above the bed. In analogy, for the surface layer this gives an expression for the shear stress (R_s is the hydraulic radius of the surface layer):

$$\tau_k = \rho g R_s i \qquad (10)$$

Furthermore, from the Reynolds averaged Navier-Stokes equation it follows that the (Reynolds) shear stress at any location in a (2D) flow field is determined by the magnitude of fluctuations in the velocity field (e.g. Pope 2000):

$$\tau_{xz} = \rho \overline{v_x v_z} \qquad (11)$$

where v_z and v_x are velocity fluctuations perpendicular and parallel to the direction of the average flow field. The overbar denotes time-averaging of these fluctuations. Gioia and Bombardelli (2002) argue that for the shear stress near the bed, v_x is associated with the characteristic velocity in the surface layer and that the perpendicular component is related to turbulent eddies that dominate between the roughness elements. The average velocity in the surface layer is U_s and the velocity associated with the dominating eddies near the artificial rough bed is denoted by u_r. Following

Copyright © 2006 Taylor & Francis Group plc, London, UK

Gioia and Bombardelli the shear stress at the artificial bed (i.e near the top of the resistance layer, see Figure 3) scales as:

$$\tau_{xz} \propto \rho U_s u_r \tag{12}$$

Together with the force balance (10) this yields:

$$\rho g R_s i \propto \rho U_s u_r \tag{13}$$

To find a relation for the average velocity in the surface layer U_s an independent expression for u_r needs to be found. For that purpose, energy considerations of the turbulent flow field are used.

3.2.2 *Turbulent energy and Kolmogorov scaling*

In the Kolmogorov view on turbulent flow, turbulent energy is created through external forcing at the largest scale of the system (energy containing range) and is dissipated to successively smaller scales until eventually viscosity damps the smallest flow patterns (viscous dissipation). The rate of dissipation of turbulent kinetic energy per unit mass is denoted by ε [m^2/s^3] and, at large scales, is independent of molecular viscosity. For the energy input at the largest scale (the energy containing scale), a scaling expression for ε is composed of representative geometrical parameters (hydraulic radius R_s) and the representative flow velocity (U_s), based on dimensional analysis (e.g. Pope 2000).

$$\varepsilon \propto \frac{U_s^3}{R_s} \tag{14}$$

Furthermore, if we assume that:

- the turbulence intensity at the artificial rough bed is a result of the energy cascade to smaller scales;
- eddies of size r and velocity u_r dominate the flow field near the artificial rough bed;

then the dissipation rate should also scale as:

$$\varepsilon \propto \frac{u_r^3}{r} \tag{15}$$

Now ε is related to the characteristic velocity u_r and the spacing hydraulic radius r that bounds the extent of the dominant local eddies. The characteristic velocity in the resistance layer can be related to the average velocity in the surface layer as (using (14) and (15)):

$$u_r \propto U_s \left(\frac{r}{R_s}\right)^{1/3} \tag{16}$$

Expression (16) can now be inserted into relation (13). This yields a scaling expression for the average velocity in the surface layer:

$$U_s \propto \left(\frac{R_s}{r}\right)^{1/6} \sqrt{g R_s i} \tag{17}$$

Note that relation (17) reduces to the Manning/Strickler equation (Manning 1889, Strickler 1923) if the total relative flow depth is large (R_s large) and the spacing hydraulic radius is small (r becomes an equivalent roughness height). Also, using expression (16) and (17) a scaling equation for the characteristic velocity at the top of the resistance layer (u_r) can be established:

$$u_r \propto \left(\frac{r}{R_s}\right)^{1/6} \sqrt{g R_s i} \tag{18}$$

To specify the hydraulic radii R_s and r in terms of geometrical quantities, we will analyze the two scaling expressions (17) and (18) for their behaviour in certain limiting cases (*asymptotic analysis*).

3.2.3 *Asymptotic behaviour of hydraulic radii*

Scaling the average velocity in the surface layer U_s (17) to the velocity U_{r0} (9) yields the dimensionless velocity function:

$$\frac{U_s}{U_{r0}} \propto \sqrt{1 + \frac{b}{32k}\left(\frac{k_S}{h}\right)^{1/3}} \frac{R_s^{2/3}}{(2b)^{1/2} r^{1/6}} \tag{19}$$

For most practical cases the bed resistance can be neglected ($k_S << h$). Therefore, (19) reduces to:

$$\frac{U_s}{U_{r0}} \approx \frac{U_s}{U_{r0}^*} \propto \frac{R_s^{2/3}}{(2b)^{1/2} r^{1/6}} \tag{20}$$

We now assume that both U_s and u_r scale to the relative depth of the surface layer $(h-k)/\ell$, where ℓ is an unknown scaling length to be determined empirically. By making U_s and u_r dimensionless through division with U_{r0} we define the following power law asymptotics:

$$\frac{U_s}{U_{r0}} \propto \left(\frac{h-k}{\ell}\right)^{\gamma} \tag{21}$$

$$\frac{u_r}{U_{r0}} \propto \left(\frac{h-k}{\ell}\right)^{\eta} \tag{22}$$

The power law expressions (21) and (22), with constant γ and η, express *complete similarity* between the considered dimensionless velocities and the relative flow depths of the surface layer (as opposed to *incomplete similarity* when γ and η are variable, see Barenblatt 1996). According to (21) and (22) U_s and u_r allow different rates of convergence, but both eventually vanish when the surface layer disappears. The latter observation immediately limits the validity of the assumptions that lead to (21) and (22): the average flow velocity in the surface layer should always be larger than the flow

Copyright © 2006 Taylor & Francis Group plc, London, UK

velocity in the resistance layer (U_{r0}), even if the surface layer is extremely shallow. Essentially, power laws (21) and (22) no longer give realistic results when values below unity are found (i.e. when the depth of the surface layer, $h-k$, becomes smaller than ℓ). Nevertheless, we continue with (21) and (22), realizing their limitations, and later on evaluate implications for practical application.

Solving for R_s and r by combining (21) and (22) with (17) and (18) yields:

$$R_s \propto 2b\left(\frac{h-k}{\ell}\right)^{\eta+\gamma} \tag{23}$$

$$r \propto 2b\left(\frac{h-k}{\ell}\right)^{4\eta-2\gamma} \tag{24}$$

Next, the two unknowns in the power law η and γ are determined by investigating the expected behaviour in the case that the water depth becomes much larger than the roughness height. Experimental observations (e.g. Manning 1889, Strickler 1923) have shown that when the depth of flow is much larger than the roughness height, then the flow hydraulic radius can be replaced by the flow depth h. For these conditions, the spacing hydraulic radius r as it appears in relation (17) reflects a roughness height and is independent of depth. Thus:

- If $h >> r$ then $R_s \sim h$
- If $h >> r$ then $r \sim$ constant

A priori it is not quite clear which parameter, or combination of parameters, r should scale to when h becomes much larger than k, but as long as r is not dependent on the depth h then the power law for r in (24) should vanish:

$$h^{4\eta-2\gamma} \sim 1 \Rightarrow 4\eta - 2\gamma = 0 \tag{25}$$

The hydraulic radius in the surface layer scales with h; therefore the power law in (23) should behave as:

$$h^{\eta+\gamma} \sim h \Rightarrow \eta + \gamma = 1 \tag{26}$$

Solving for η and γ by combining expression (25) and (26) yields $\eta = 1/3$ and $\gamma = 2/3$. As a result, the power law expressions for R_s and r become:

$$R_s \propto 2b\left(\frac{h-k}{\ell}\right) \tag{27}$$

$$r \propto 2b = \frac{2}{mDC_D} = \frac{2s^2}{C_D D} \tag{28}$$

It was mentioned earlier that r reflects the extent of the largest eddies near the artificial bed. This means that when the separation between roughness elements s is equal to the dynamic diameter of the cylinders (i.e. $C_D D$) then the largest eddies are bounded by s. However, when the diameter of the elements are significantly smaller than the spacing between elements, then (28) shows that r exceeds s. In effect, relation (28) tells us that whenever the spacing between elements is large as compared to the size of the elements themselves, then the eddies are not confined to the space in between the roughness elements.

Expressions (27) and (28) are inserted into the scaling expressions for the average velocity in the surface layer (19), and we arrive at:

$$\frac{U_s}{U_{r0}} \propto \left(\frac{h-k}{\ell}\right)^{2/3} \tag{29}$$

This is the new scaling expression for the average velocity in the surface layer. Basic assumptions that lead to this result were (i) similarity between velocities and relative flow depths (power laws (21) and (22)) and (ii) correspondence with Manning's equation at large flow depths. A specification of the unknown scaling length ℓ in terms of measurable geometric parameters follows from comparison with laboratory experiments.

4 COMPARISON TO DATA FROM FLUME EXPERIMENTS

4.1 *Average velocities in the two flow layers*

The experimental data used in this section is adopted from laboratory flow studies as performed at the *De Voorst* WL|Delft Hydraulics facility in 1996 (Meijer and van Velzen 1998, Meijer 1998, also reported in Baptist 2005). Based on four flow experiments without artificial vegetation, the roughness height k_S of the flume bed was determined to be $k_S = 2.3 \pm 0.6$ mm. In the results presented here, this value for k_S is used for computing U_{r0} (equation 9).

Further data from these studies comprise 48 flow experiments with homogeneously distributed cylindrical stems that all have the same diameter D of 8 mm. Flow depths h and cylinder heights k were varied between the experimental runs (three values for k were used: 0.45, 0.9 and 1.5 [m]). Half of the experiments were carried out with a surface density of $m = 256$ cylindrical stems per square meter, and the other half with a surface density of $m = 64$ [m^{-2}]. Flow velocities were measured at different depths 0.10 [m] apart. Using linear interpolation the average flow depth for the surface and the resistance layer were estimated separately. From the measured average velocities in the resistance layer, local Reynolds numbers were calculated ($Re \sim 3 \cdot 10^4 - 4 \cdot 10^4$) and, subsequently, the drag coefficients C_D for the circular cylinders. Standard works on fluid mechanics report that in such a flow

Copyright © 2006 Taylor & Francis Group plc, London, UK

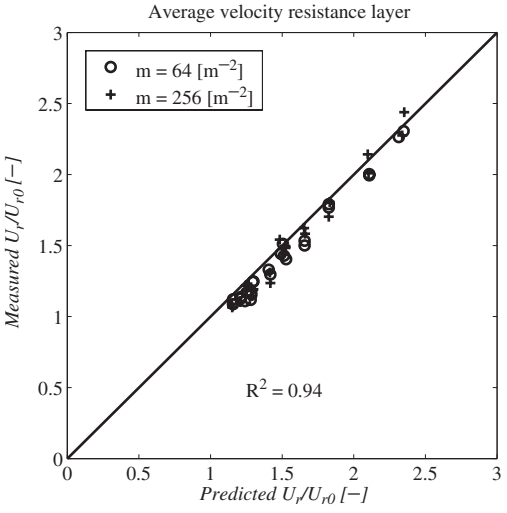


Figure 4. The proposed scaling relation for the depth-averaged velocity U_r in the resistance layer (relation (8), on horizontal axis) as compared to results from laboratory flume experiments (m = number of cylindrical stems per m^{-2} on the bed surface).

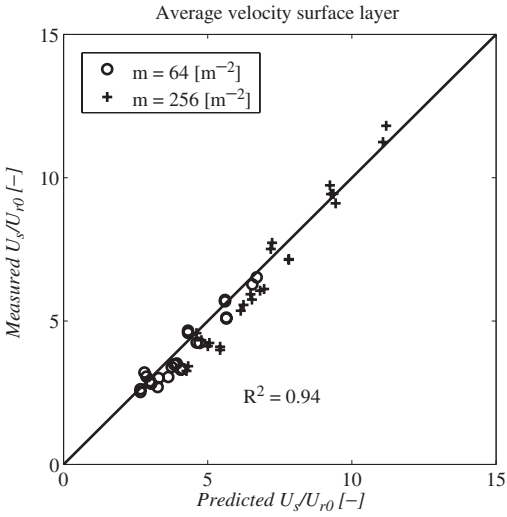


Figure 5. The depth-averaged velocity U_s in the surface layer; the proposed relation (30) (on horizontal axis) vs. measured flow velocities.

regime the drag coefficient remains fairly constant with a value of nearly 1 (e.g. Schlichting 1979).

Figure 4 shows the measured average velocities in the resistance layer as compared to the predictions of relation (8). Although for slow flows the velocities are slightly overestimated, by using relation (8) overall agreement with data is very good ($R^2 = 0.94$).

For the specification of the unknown scaling length ℓ in relation (29), several combinations of available length scales were attempted (D, s, b and combinations of these). It turns out that for $\ell = s$ the proposed scaling law gives best agreement with laboratory data (see Figure 5). The correlation coefficient is again $R^2 = 0.94$, in which we have chosen the coefficient of proportionality equal to unity. Apparently, the spacing between the roughness elements is a suitable measure of the extent to which the flow in the surface layer influences the flow field in the resistance layer. Based on this finding, it seems natural to assume that ℓ may never exceed the height of the cylinders k. By imposing a limit of height k on the scaling length ℓ, we propose the following scaling expression for the average velocity in the surface layer:

$$\frac{U_s}{U_{r0}} = \left(\frac{h-k}{\min(s,k)}\right)^{2/3} \tag{30}$$

In section 3.2.3 it was argued that expression (29), or (30), is no longer valid when the flow depth $(h-k)$ is close to or smaller than the scaling length ℓ (i.e. $\ell = \min(s,k)$). However, in the considered experimental data the flow depth $(h-k)$ goes down to less than three times ℓ, and still expression (30) performs well (see Figure 5).

4.2 *A two-layer scaling model for the entire flow depth*

The average flow velocity for the entire flow depth U_T can be found by adding the weighted average flow velocities of the resistance and the surface layer (U_r and U_s, respectively):

$$\frac{U_T}{U_{r0}} = \frac{k}{h}\frac{U_r}{U_{r0}} + \frac{h-k}{h}\frac{U_s}{U_{r0}} \tag{31}$$

By making use of scaling relations (8) and (30), the expression for the average velocity over the entire flow depth (31) becomes:

$$\frac{U_T}{U_{r0}} = \sqrt{\frac{k}{h}} + \frac{h-k}{h}\left(\frac{h-k}{\min(s,k)}\right)^{2/3} \tag{32}$$

In the previous section the validity of (30) was addressed for cases when the depth of the surface layer $(h-k)$ becomes small. Significant errors in (30) are expected when $(h-k)$ becomes close to or smaller than ℓ. However, relation (31) shows that in such cases the average velocity in the surface layer (U_s) only contributes little to the *overall* average velocity (U_T). Therefore, errors in (30) due to shallowness of the surface layer only have a minor impact on the total depth-averaged velocity U_T.

Copyright © 2006 Taylor & Francis Group plc, London, UK

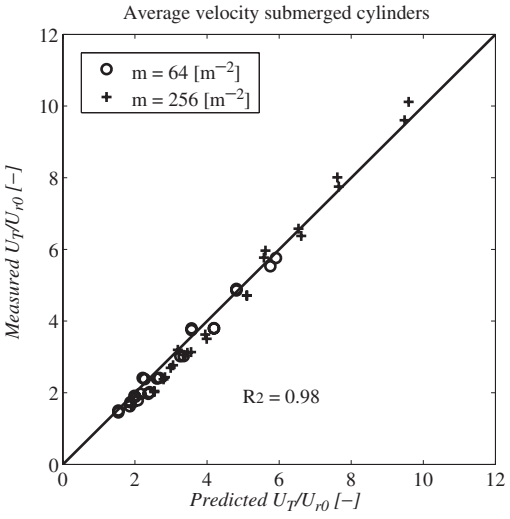


Figure 6. The depth-averaged velocity U_T over the entire flow depth (relation (32), on horizontal axis) vs. measured average velocities.

In Figure 6, the predictions of relation (32) are shown in comparison to the measured average flow velocities (interpolation between flow velocities measured at different depths). The combined performance of the velocity scaling expressions (8) and (30) is even better than found before, yielding a correlation coefficient of $R^2 = 0.98$.

5 CONCLUSIONS

For open channel flow over rough surfaces, several suitable relations exist that relate the average flow velocity to a roughness height that reflects the resistance of the bed. However, when the bed is covered with large roughness elements such as vegetation, or cylindrical elements, these methods are theoretically no longer valid. In this paper, a two-layer scaling model is proposed that treats the flow field above and in between the roughness elements separately, and, when combined, gives a description of the depth-averaged velocity of the entire flow field. When comparing the newly derived description to results from flume experiments, very good agreement is found (correlation coefficient $R^2 = 0.98$). The scaling length ℓ, that completes the velocity relation in the surface layer, is found to be well represented by the spacing between the cylindrical stems. It is expected that this is no longer the case when the height of the cylinders is smaller than the distance between them. Further investigations with different geometrical properties of the cylinders, and different spatial distributions, should be carried out to substantiate this claim.

The difficulty of describing flow over vegetation is primarily due to flow characteristics near the top of the vegetation, as reflected in the scaling length ℓ that is necessary to describe the flow in the surface layer. The flow field in between the resistance elements is satisfactorily described by drag forces. However, for the surface layer energy losses are due to the turbulent patterns, for which in a bulk flow description a representative closure parameter is required. In the used experimental data set, vegetation was represented by homogeneously distributed identical rigid stems, and the turbulent length scale was adequately described by one geometrical length scale from *within* the resistance layer. Future work will be focussed on the characteristics of such a scaling length when geometric variability between the resistance elements exist. Eventually, the aim is to describe flow over natural vegetation, which involves further complications as stem flexibility, or leaves and side branches that individual plants may have.

NOTATION

ρ	[kg/m^3]	Water density
g	[m/s^2]	Gravitational acceleration
i	[–]	Bed slope of channel
h	[m]	Flow depth
k	[m]	Height of cylinders
C_D	[–]	Drag coefficient
m	[m^{-2}]	Bed surface density of cylinders
D	[m]	Diameter of cylinders
s	[m]	Separation between cylinders
b	[m]	Drag length
f	[–]	Bed resistance function
k_S	[m]	Strickler's roughness height
U_r	[m/s]	Depth-averaged flow velocity in resistance layer (general)
U_{r0}	[m/s]	As U_r, for $h < k$
U^*_{r0}	[m/s]	As U_{r0}, neglecting bed resistance
U_s	[m/s]	Depth-averaged flow velocity in surface layer
U_T	[m/s]	Depth-averaged flow velocity over total flow depth
u_r	[m/s]	Characteristic eddy-velocity near top of resistance elements
R_s	[m]	Hydraulic radius of surface layer
r	[m]	Spacing hydraulic radius
ℓ	[m]	Unknown scaling length
ε	[m^2/s^3]	Energy dissipation rate
v	[m/s]	Velocity fluctuation

ACKNOWLEDGEMENTS

This research is supported by the Technology Foundation STW, applied science division of NWO and

Copyright © 2006 Taylor & Francis Group plc, London, UK

the technology programme of the Ministry of Economic Affairs (the Netherlands). Earlier stages of this research were carried out with the support of the German Federal Institute of Hydrology (Bundesanstallt für Gewässerkunde). Furthermore, we gratefully thank Francisco Fontanele Araujo from the Department of Applied Physics at the University of Twente for his critical views and comments.

REFERENCES

Akilli, H. and D. Rockwell (2002). Vortex formation from a cylinder in shallow water. *Physics of Fluids 14*(9), 2957–2967.

Baptist, M. J. (2005). *Modelling Floodplain Biogeomorphology*. Ph. D. thesis, Delft University of Technology.

Baptist, M. J., V. Babovic., J. Rodriguez Uthurburu., M. Keijzer., R. E. Uittenbogaard., A. Mynett, and A. Verwey (2006). On inducing equations for vegetation resistance. *Journal of Hydraulic Research*. (subm.).

Barenblatt, G. I. (1996). *Scaling, selfsimilarity, and intermediate asymptotics*, Volume 14 of *Cambridge Texts in Applied Mathematics*. Cambridge University press.

Copeland, R. R. (2000). Determination of flow resistance coefficients due to shrubs and woody vegetation. Technical report, U.S. Army Engineer Research and Development Center, Vicksburg, MS, USA.

Gioia, G. and F. A. Bombardelli (2002). Scaling and similarity in rough channel flows. *Physical Review Letters 88*(1), 14501–14504.

Green, J. C. (2005). Modelling flow resistance in vegetated streams: review and development of new theory. *Hydrological Processes 19*, 1245–1259.

Huntington, S. W., E. Whitehead., P. Brown, and P. Hollindrake (1992). The hydraulic roughness of vegetated channels. Technical Report SR 305, HR Wallingford, Wallingford, England.

Kadlec, R. H. (1990). Overland flow in wetlands: vegetation resistance. *Journal of Hydraulic Engineering 116*(5), 691–706.

Keijzer, M. and V. Babovic (2000). Genetic programming within a framework of computeraided discovery of scientific knowledge. In D. Whitley, D. Goldberg, E. Cantu Paz, L. Spectro, I. Parmee, and H. G. Beyer (Eds.), *Proceedings of the Genetic and Evolutionary Computation Conference*, Las Vegas, NV, USA. Morgan Kaufman.

Klopstra, D., H. J. Barneveld., J. M. van Noortwijk, and E. H. van Velzen (1997). Analytical model for hydraulic roughness of submerged vegetation. In *Managing Water: Coping with scarcity and abundance*, Proceedings of the 27th IAHR Congress, San Fransisco, CA, USA, pp. 775–780.

Manning, R. (1889). On the flow of water in open channels and pipes. *Transactions of the Institution of Civil Engineers of Ireland 20*, 161–207.

Meijer, D. G. (1998). Modelproeven overstroomde vegetatie. Technical Report PR121, HKV Consultants, Lelystad, The Netherlands.

Meijer, D. G. and E. H. van Velzen (1998). Prototypescale flume experiments on hydraulic roughness of submerged vegetation. Technical report, HKV Consultants, Lelystad, The Netherlands.

Neary, V. S. (2003). Numerical solution of fully-developed flow with vegetative resistance. *Journal of Engineering Mechanics 129*(5), 558–563.

Nikora, V., K. Koll., I. McEwan., S. McLean, and A. Dittrich (2004). Velocity distribution in the roughness layer of rough bed flows. *Journal of Hydraulic Engineering 130*(1), 1036–1042.

Pope, S. B. (2000). *Turbulent Flows* (3rd ed.). Cambridge University press.

Schlichting, H. (1979). *Boundary Layer Theory* (7th ed.). New York: McGrawHill.

Smart, G. M., M. J. Duncan, and J. M. Walsh (2002). Relatively rough flow resistance equations. *Journal of Hydraulic Engineering 128*(6), 568–578.

Stephan, U. and D. Gutknecht (2002). Hydraulic resistance of submerged flexible vegetation. *Journal of Hydrology 269*, 27–43.

Stone, B. M. and H. T. Shen (2002). Hydraulic resistance of flow in channels with cylindrical roughness. *Journal of Hydraulic Engineering 128*(5), 500–506.

Strickler, A. (1923). Beitrage zur Frage der Geschwindigkeitsformel und der Rauhigkeitszahlen für Ströme, Kanäle und geschlossene Leitungen. Mitteilungen des Amtes für Wasserwirtschaft 16, Eidg. Department des Innern, Bern, Switserland.

Uittenbogaard, R. (2003). Modelling turbulence in vegetated aquatic flows. In *International workshop on riparian forest vegetated channels: hydraulic, morphological and ecological aspects*, Trento, Italy.

Yen, B. C. (2002). Open channel flow resistance. *Journal of Hydraulic Engineering 128*(1), 20–39.

Copyright © 2006 Taylor & Francis Group plc, London, UK

Turbulent structure and dispersive properties in vegetated canopy open-channel flows

I. Nezu, M.Sanjou & T. Okamoto
Dept. of Civil Eng., Kyoto University, Kyoto, Japan

ABSTRACT: It is very important in river environment as well as in hydraulic engineering to investigate the hydrodynamic properties in vegetated canopy rivers, in which velocity distributions are largely changed in not only vertical but also spanwise directions. In particular, it is necessary to reveal such dispersive properties of velocity components, since the velocity dispersion has significant relations with turbulent transport and generation of turbulence due to the vegetation wakes. Therefore, in this study, turbulence measurements were conducted intensively in the vegetated open-channel flows by using two-component laser Doppler anemometer (LDA), and consequently, the turbulent structure and dispersive effects were revealed experimentally.

1 INTRODUCTION

A large amount of aquatic plants are observed in actual rivers and they have significant effects on hydrodynamic characteristics such as the velocity distributions, turbulence and coherent structure, as well as mass and momentum exchanges between the vegetated and non-vegetated zones. Of particular significance is that the importance of river vegetation has recently been recognized not only for water management but also for river environment, and it is therefore needed to reveal a coherent property of turbulence which has a vital influence on scalar transports, such as dissolved oxygen, chemical materials and suspended sediment in water.

In particular, open-channel flows with submerged vegetation may somewhat be similar to air flows over the forest and crop fields. Some meteorologists have studied intensively these canopy flows by field measurements and laboratory experiments. For example, Raupach *et. al* (1979, 1981) have tried to measure the canopy roughness flows in a wind tunnel by using hot-wire anemometers, and revealed the roughness effects on the velocity profiles and turbulence characteristics. Shaw *et. al* (1990) have conducted the field measurements with a sonic anemometer and pressure sensor in canopy flows of deciduous forest, and they showed a strong linear relationship between the deviations of velocity and pressure. Meyers & Baldocchi(1991) have also measured canopy flows in pine forest, and examined turbulent kinetic energy (TKE) budget, shear stress and vertical profiles of high order moments. These results have revealed that the turbulent energy is generated more largely by the velocity shear than by the vegetation wake except for around vegetation edge. Raupach *et. al* (1991) have compared their experimental data of wind tunnel canopies with some field data measured by the other researchers, and showed the relation between the velocity profiles and vegetation density. Furthermore, they have investigated a large-scale coherent structure by using two-point velocity correlation function and conditional analysis. Finnigan (2000) has reviewed the aerodynamic characteristics and turbulence in plant canopies on the basis of the recently measured and calculated data, and as the results, an interesting analogy between the canopy flow and the plane mixing layer was proposed. There are also some numerical studies on forest canopy flows. Dwyer *et al.* (1997) have calculated the TKE budget in air shear layers above and within a forest by LES. The noticeable advantage of such a numerical simulation is that the pressure transport term is evaluated directly, whereas it is very difficult to measure it experimentally. They predicted numerically the vertical profiles of the pressure diffusion transport and other terms in TKE.

As mentioned above, there are a lot of knowledge and valuable data in air flows over and within the vegetation canopies. In contrast, the vegetated rivers and open-channel flows have recently been investigated. For example, Neph *et al*. (2000) have conducted some turbulence measurements in vegetated open-channel flows with both of a laser Doppler anemometer (LDA) and an acoustic Doppler velocimetry(ADV). They highlighted a relation between the water depth and turbulence structure, and pointed out that the generation of wake turbulence is strongly associated with the relative water depth. Poggi *et al*. (2004) have also

Copyright © 2006 Taylor & Francis Group plc, London, UK

measured the vegetated open-channel flows by using LDA. They classified the whole flow depth region into three layers, i.e., the first is the lower layer in which sweep and ejection events are dominant, the second is the middle layer in which K-H waves are generated by the inflectional instability and the third is the upper layer which is similar to the boundary layer. They showed the relation between the energy cascade of spectrum and the vegetation density.

Although the friction law and resistance of vegetation have in the past decades been investigated intensively, a lot of uncertainties remain concerning the coherent structure, dispersive effects and turbulent energy transport properties. Therefore, we highlighted these important topics in the present study, and conducted accurate turbulence measurements with LDA in vegetated canopy open-channel flows in order to investigate dispersive properties and turbulence structure by varying the vegetation density.

2 EXPERIMENTAL PROCEDURES

2.1 *Measurement system*

Figure 1 shows the experimental setup and the coordinate system. The experiments were conducted in a 10 m long and 40 cm wide tilting flume. The elements of vegetation model were composed of non-flexible strip plates. These vegetation elements were attached vertically on the flume bed, as seen in Fig. 1. The size of this element is 50 mm height, 8 mm width and 1 mm thick, as shown in Fig. 2. H is the water depth and h is the vegetation height. B_v and L_v are the neighboring vegetation spacings in the spanwise and streamwise directions, respectively. x, y and z are the streamwise, vertical and spanwise coordinates. The vertical origin, $y = 0$, is chosen as the channel bed. The time-averaged velocity components in each directions are defined as U, V and W and the turbulent fluctuations are defined as u, v and w, respectively.

In order to measure two components of instantaneous velocity, i.e., $\tilde{u} \equiv U + u$ and $\tilde{v} \equiv V + v$, within and above the canopy vegetations, two-component fiber-optic LDA (DANTEC) system was used as shown in Fig. 1. This probe was located at 7 m downstream from the channel entrance. The four laser beams of 2W Ar-ion laser were projected into within the canopy layer as well as over the canopy vegetation. We could successfully measure the velocity profiles in the whole flow region from the bottom-bed to the water surface, including within the canopy vegetation, because the laser beams were not blocked by any vegetation strips.

2.2 *Hydraulic condition*

Table 1 shows the hydrodynamic conditions. Three kinds of experiments were conducted, i.e., case A, B and C, in which only the vegetation density λ was varied. U_m is the bulk mean velocity, $Re \equiv U_m H/\nu$ is the Reynolds number, $Fr \equiv U_m/\sqrt{gH}$ is the Froude number and U_* is the friction velocity.

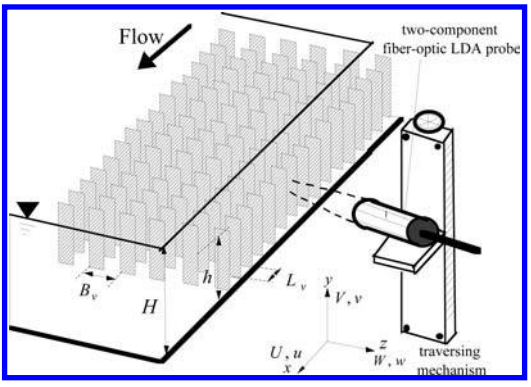


Figure 1. Experimental setup and coordinate system.

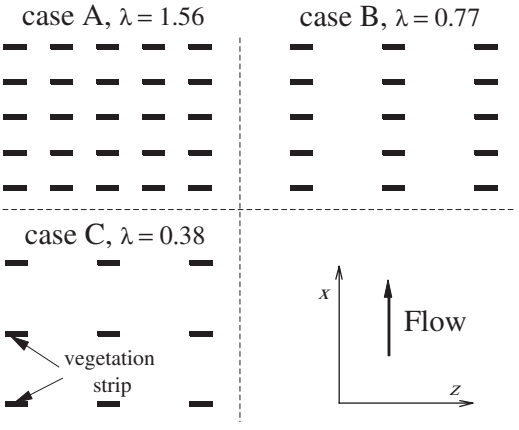


Figure 2. Allocation patterns of vegetations (top-view).

Table 1. Hydrodynamic conditions.

Case	λ	U_m(cm/s)	H (cm)	h (cm)	Re	Fr	U_* (cm/s)
A	1.56						2.8
B	0.77	12.0	15.0	5.0	18000	0.10	2.5
C	0.38						2.3

The combinations of B_v and L_v were selected as three patterns to examine the effects of the vegetation density as shown in Fig.2. The vegetation density λ is defined as follows:

$$\lambda \equiv \sum_i A_i / S \tag{1}$$

A_i is the frontal square of the vegetation strip and S is the referred bed area of $40 \times 40\,cm^2$. In this study, the

Copyright © 2006 Taylor & Francis Group plc, London, UK

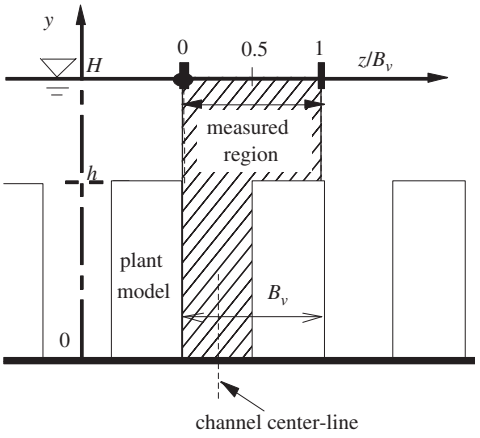


Figure 3. Measured region within and above vegetations (case A).

largest vegetation density is $\lambda = 1.56$(caseA), the middle density is $\lambda = 0.77$(caseB) and the sparsest density is $\lambda = 0.38$(caseC). In order to examine the lateral variations of velocity components and their dispersive properties, LDA measurements were conducted along eight vertical traversing lines between the neighboring plants, $0 \le z/B_v \le 1.0$, as shown in Fig. 3.

To reveal the effects of vegetation on turbulent structure, it is of essential importance to consider the horizontal space averaging in the time-averaging N-S equations (RANS), as pointed out by Raupach *et al.* (1991) and Finnigan(2000). A hydrodynamic value Φ is defined as follows:

$$\Phi \equiv \langle \Phi \rangle + \Phi'' \tag{2}$$

in which the angle bracket $\langle\rangle$ denotes the horizontal space averaging, and the double prime denotes the deviation from the space-averaged quantity.

3 RESULTS AND DISCUSSIONS

3.1 *Lateral profiles of streamwise velocity*

Figures 4(a) and (b) show the spanwise distributions of streamwise mean velocity $U(z)$ at several elevations within and above canopy for the different vegetation densities of $\lambda = 0.38$ and 1.56, respectively. The velocity is normalized by the space-averaged velocity $\langle U(y) \rangle$. It is found clearly that the streamwise velocity is varied significantly in the spanwise direction within the canopy, i.e., $y/h \le 1$, due to the local deceleration behind the vegetation, i.e., we call the "vegetation wake area". This trend is more remarkable in the denser vegetation. In contrast, over the canopy ($y/h > 1$), the lateral variations become smaller with an increase of

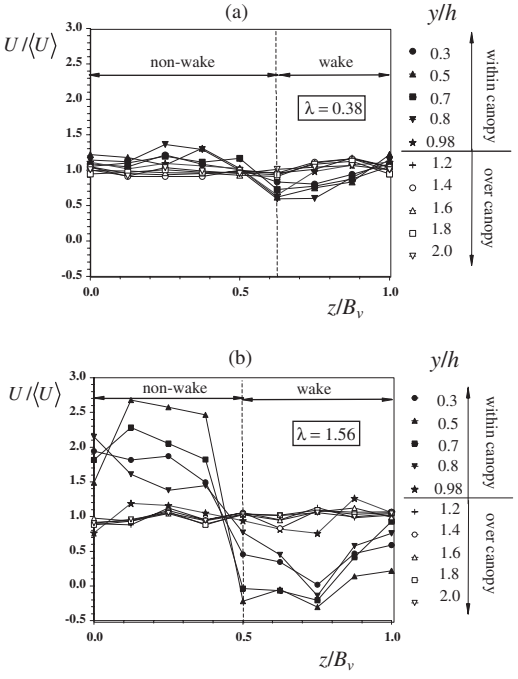


Figure 4. Lateral profiles of the streamwise velocity.

y/h, because the local effects of vegetations become negligibly small. From this viewpoint, it is suggested strongly that the velocity profiles may have a universal function over the canopy in a wide range of vegetation density as mentioned later.

3.2 *Space-averaged velocity profiles*

Figure 5 shows the vertical profiles of space-averaged streamwise velocity $\langle U(y) \rangle$, which is normalized by the vegetation-edge velocity $U_h \equiv \langle U(h) \rangle$. This figure reveals that the typical drag effects of vegetation decelerate the streamwise velocity more largely in the canopy layer of $y/h \le 1$ as the vegetation density becomes larger. Consequently, a significant inflectional point appears near the canopy edge$y/h = 1$, the feature of which is consistent with that of plant canopy flows, as reviewed by Finnigan(2000). Furthermore, a second peak, i.e., the counter-gradient velocity profile, is observed near the bottom-bed, which may be caused by three-dimensional dynamics of wakes.

In order to evaluate the inflectional velocity strength reasonably, the shear length scale L_s is defined as

$$L_S \equiv \frac{U(h)}{(\partial U / \partial y)_{y=h}} \tag{3}$$

Copyright © 2006 Taylor & Francis Group plc, London, UK

in the same manner as used by Raupach *et al.* (1996). They pointed out that L_s has a significant relation with the wave length of coherent eddies observed in mixing layers and canopy flows. Figure 6 shows the relation between L_s and λ, in which previous field plant data of Raupach *et al.* (1996) are also plotted for a comparison. L_s is in good correlation with vegetation density, and it is found obviously that the present flume value of L_s become smaller with an increase of λ, which is consistent with plant data reviewed by Raupach *et al.* (1996).

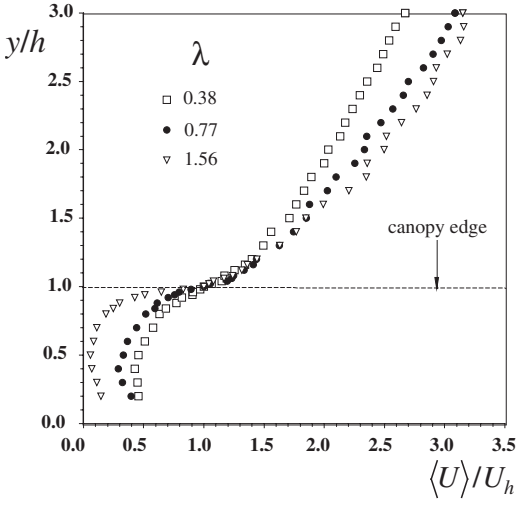


Figure 5. Vertical profiles of the horizontal averaged streamwise velocity.

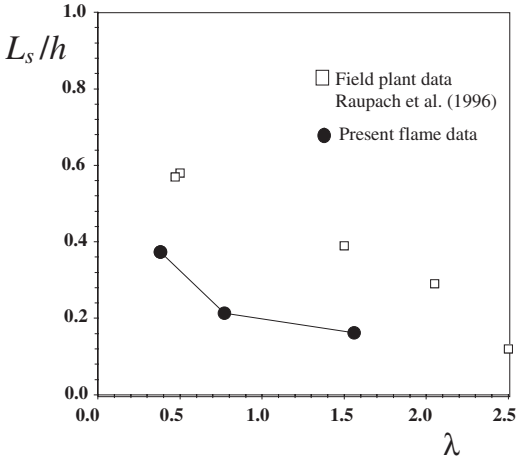


Figure 6. Relation between the shear length-scale and vegetation density.

3.3 *Reynolds stress and friction velocity*

Figure 7 compares the vertical profiles of horizontal averaged Reynolds stress, $-\langle\overline{uv}\rangle/U_*^2$, in the different vegetation density of $\lambda = 0.38, 0.77$ and 1.56. The friction velocity U_* was evaluated here as the peak value of the Reynolds stress, which is consistent with the method of plant canopy flows as reviewed by Finnigan (2000). The following theoretical equation derived from 2-D equation of motion is also included in Fig. 7.

$$-\left\langle\overline{uv}\right\rangle/U_*^2 = 1-(y-h)/(H-h) \tag{4}$$

It should be noticed that there are almost no differences among the vegetation densities over the canopy region of $y/h > 1$ and also that the normalized Reynolds stress coincides well with Eq. (4). In contrast, within the canopy, $y/h \leq 1$, the values of $-\langle\overline{uv}\rangle/U_*^2$ decrease toward the flume bed, irrespective of vegetation density. This trend is the most remarkable in the densest case due to the vegetation effect. The friction velocity U_* evaluated from Eq. (4) is also indicated in also Table 1. The results suggest that the bed friction becomes larger with an increase of the vegetation density.

3.4 *Logarithmic law*

We found that vegetations have much more significant effects on the space-averaged velocity and Reynolds stress within the canopy rther than over the canopy. Therefore, a universal formula may be applied to the velocity profiles over the canopy. Previous studies of

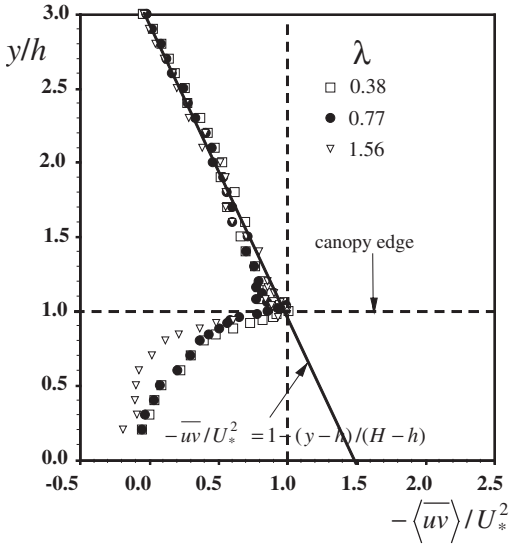


Figure 7. Distribution of the horizontal averaged Reynolds stress.

Copyright © 2006 Taylor & Francis Group plc, London, UK

plant flows have suggested the following log-law in the inner layer roughness wall and vegetation boundaries, e.g., see Jackson (1981)

$$\langle U\rangle/U_* = \frac{1}{\kappa}\ln\left(\frac{y-d}{y_o}\right) \tag{5}$$

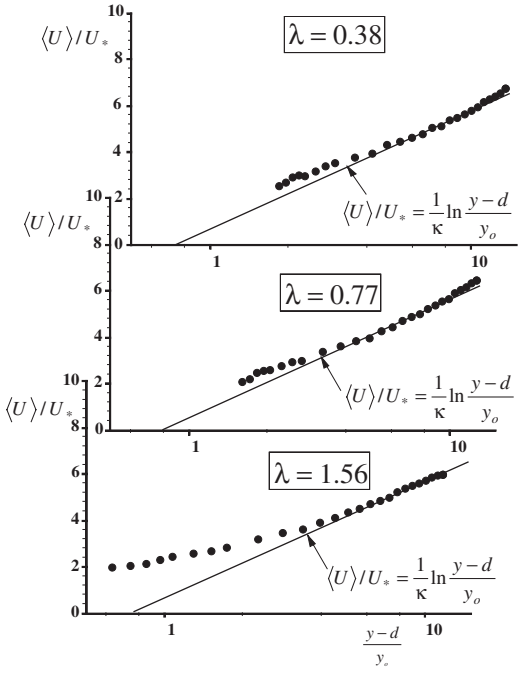


Figure 8. Horizontally averaged streamwise velocity normalized by the friction velocity.

in which d and y_o are the displacement thickness and roughness height, respectively. The von Karman constant κ was used as the standard value in the open-channel flows, i.e., $\kappa = 0.412$. Figure 8 shows the space-averaged velocity profiles over the vegetation canopies, in which the logarithmic law of (5) is also included. The measured values are in good agreement with the log-law for all vegetation densities. Figure 9 shows the relation between d and λ, which includes the field data and the wind-tunnel data obtained by previous researchers shown in Table 2. The detailed information is available in Raupach *et al*. (1996). It is found that d becomes slightly larger as the vegetation density is denser, and this property is also observed in a wide range of vegetation types. Figure 10 shows the relation between y_o and λ. Although the various data

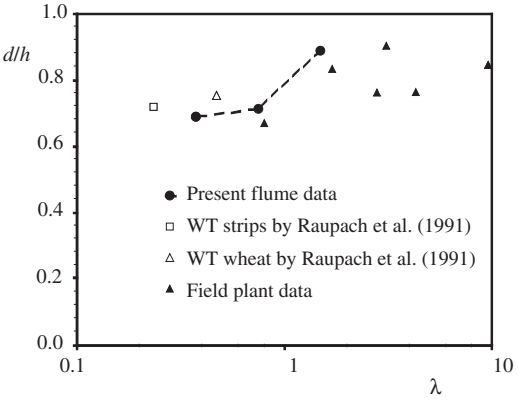


Figure 9. Relation between the displacement thickness and the vegetation density.

Table 2. Measured canopy flows in previous studies

	Case	Vegetation type	h (m)	λ	γ_0/h	d/h	$U(h)/U_*$
Field data	a	Tree	9	0.06	0.05	–	–
(air flows)	b	Trees	9	0.21	0.09	–	–
	c	Early Wheat	0.4	0.10	0.04	–	–
	d	Late Wheat	1.0	0.25	0.05	–	–
	e	Pines	13	2.3	0.03	–	–
	f	Vineyard:rows along wind	0.9	0.04	0.03	–	–
	g	Vineyard:rows across wind	0.4	0.22	0.30	–	–
	h	Forest	10	2.8	0.05	0.76	3.8
	i	Forest	22	3.1	0.03	0.9	2.9
	j	Forest	15.5	4.3	0.06	0.76	3.3
	k	Forest	4.5	0.8	0.10	0.67	2.9
	l	Forest	23	1.7	0.05	0.83	3.1
	m	Forest	11.5	9.6	0.03	0.84	3.4
Laboratory data	WT	Strips (Raupach *et. al* 1991)	0.06	0.23	0.14	0.72	3.3
(air flows)	WT	Wheat (Raupach *et. al* 1991)	0.05	0.47	0.09	0.75	3.6
Laboratory data	present-A	Strips	0.05	1.56	0.15	0.89	2.08
(water flows)	present-B	Strips	0.05	0.77	0.17	0.71	2.10
	present-C	Strips	0.05	0.38	0.17	0.68	2.51

Copyright © 2006 Taylor & Francis Group plc, London, UK

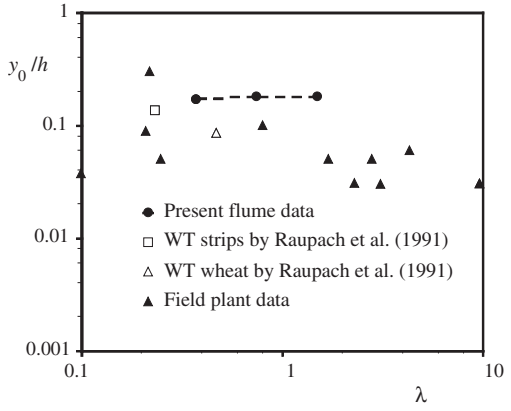


Figure 10. Relation between the roughness height and the vegetation density.

are somewhat scattered, the present values are in the same order as the wind-tunnel (WT) ones, in which the strip-type vegetations were also used.

3.5 *Conditional analysis*

It is inferred from the inflectional profiles of velocity shown in Figure 5 as well as the Reynolds stress profiles shown in Figure 7 that coherent eddies are generated by the velocity shear near the vegetation edge, and consequently, they cause large momentum exchanges between the low-speed flow within the canopy and the high-speed flow over the canopy. In order to evaluate these properties quantitavely, the quadrant conditional analysis was conducted for the instantaneous Reynolds stress $-u(t)v(t)$. The quadrant Reynolds stress RS_i is defined as follows:

$$RS_i = \left(\overline{uv}\right)^{-1} \lim_{T\to\infty} \frac{1}{T} \int_0^T uvI_i\,dt \quad (i=1,2,3,4) \qquad (6)$$

If (u, v) exists in a quadrant i, then $I_i = 1$, otherwise $I_i = 0$. Each quadrant of (u, v) corresponds to the following coherent events:

$i=1$ $(u>0, v>0)$: outward interaction
$i=2$ $(u<0, v>0)$: ejection
$i=3$ $(u<0, v<0)$: inward interaction
$i=4$ $(u>0, v<0)$: sweep

Figure 11 indicates the vertical profiles of RS_i in the non-wake region between the neighboring elements ($z/B_v = 0.25$ in the case A, $z/B_v = 0.375$ in the cases B and C). It is found that RS_2 is larger than RS_4 near the free-surface and thus, the ejection event is pronounced in the same manner as observed in boundary layers. In contrast, RS_4 is much larger than RS_2 within the canopy, and the sweep event is more dominant.

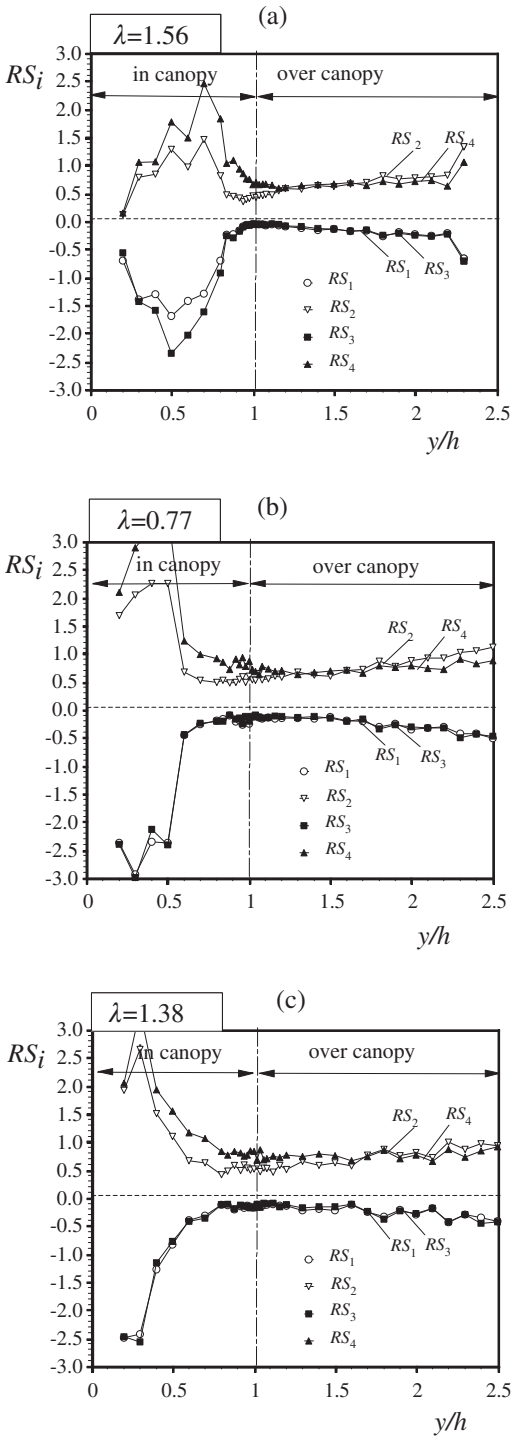


Figure 11. Distribution of the conditional Reynolds stress (non-wake region).

Copyright © 2006 Taylor & Francis Group plc, London, UK

It should be noticed that the coherent sweep motion transports the high-speed fluid from the outer canopy toward the inner canopy region. Of particular significance is that RS_2 and RS_4 attain the peak value closer to the bottom-bed with a decrease of the vegetation density λ, and it suggests strongly that the high-speed sweep motion is more inrushed toward the channel-bed in sparser canopy flows.

3.6 *Distributions of third-order moments*

The sweep and ejection events are related with skewness which is the third-order moments, because the skewness means the deviation from the Gaussian (the skewness is zero), as pointed out by Nakagawa & Nezu (1977). The skewness factors of $u(t)$ and $v(t)$ are defined as follows:

$$S_u \equiv \overline{u^3}/u'^3, \quad S_v \equiv \overline{v^3}/v'^3 \tag{7}$$

Figure 12 shows the variations of S_u and S_v, $\Delta RS \equiv (RS_4 - RS_2)$ which means the difference of sweeps to ejections. S_u and S_v are close to zero over the canopy, whereas these values vary largely within the canopy. Of particular significance is that S_u has a large positive peak and S_v has a large negative peak within the canopy. These results suggest that coherent motions are generated predominantly near the just edge and within the canopies. The values of ΔRS are positive ones within the canopy, and the distribution of ΔRS is similar to that of S_u. From these findings, it is considered that the coherent events such as sweeps and ejections are related significantly with the third-order moments.

3.7 *Spectral analysis*

Figure 13 shows some examples of the power frequency spectrum $F_u(f)$ of the streamwise fluctuations $u(t)$ in the within-canopy layers ($y/h \leq 1$) and the over-canopy layers ($y/h > 1$), in which each figure is shifted up by 10^3 to avoid confusions, and the spectrum is normalized by the frequency f and the turbulent intensity. In the over-canopy layers, the spectral distributions obey the Kolmogoroff's $-5/3$ power law (the spectral gradient in Figure 13 is not $-5/3$ but $-2/3$ due to the multiplying by f.) in the inertial subrange ($1 < f < 10$ Hz). However, within the canopy, the spectral distribution fits to the $-5/3$ power law in a narrower range($1 < f < 5$ Hz), and the spectrum increases in the high frequency range of $f > 10$ Hz. This suggests that there may be a turbulence energy supply caused by the wake eddies generated behind the vegetation elements. This property is more remarkable nearer the bottom bed, whereas the spectral profile nearer the free surface is closer to that of boundary layers since the

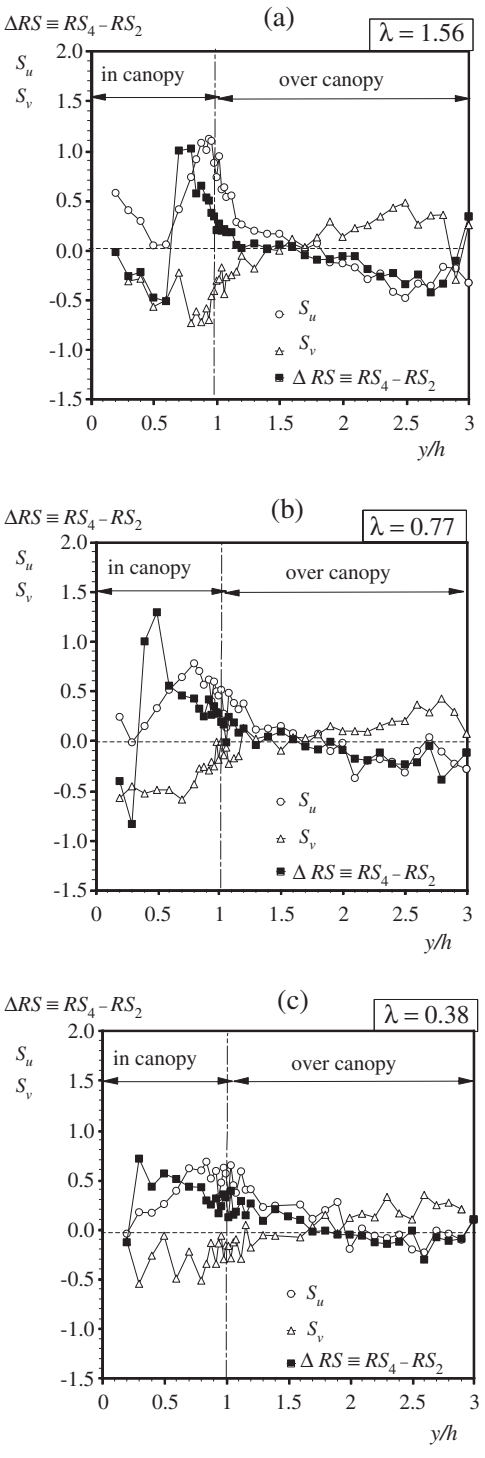


Figure 12. Skewness factors of u and v, and the difference of RS_i (non-wake region).

Copyright © 2006 Taylor & Francis Group plc, London, UK

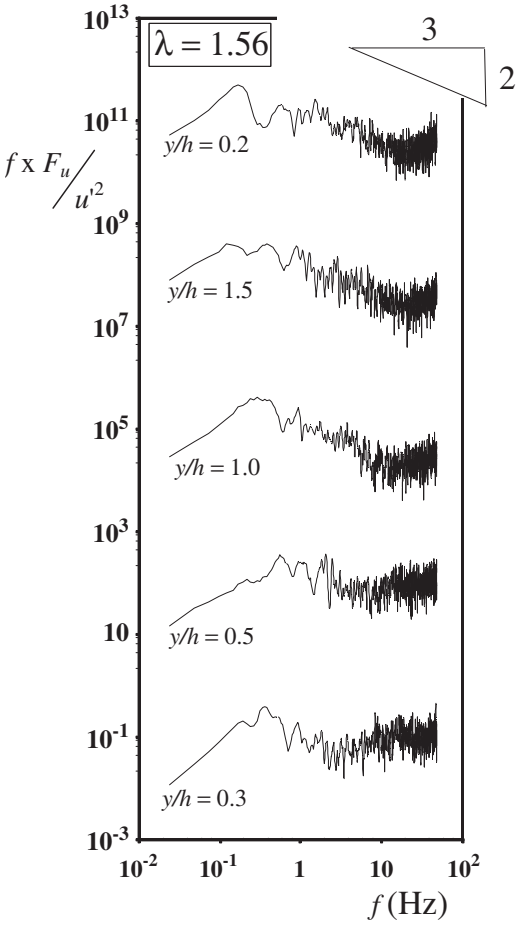


Figure 13. Spectrum distribution ($\lambda = 1.56$ and $z/B_v = 0.25$).

effects of coherent motions are smaller farther from the vegetation layer.

3.8 *TKE budget*

It is found from the present study that the lateral variations of turbulence characteristics are very small over the vegetation canopy, whereas, they are, however, varied largely within the canopy. It is therefore suggested strongly that there are significant dispersive influences due to space-averaging of Eq. (2) in vegetated open-channel flows. In this section, we highlight the despersive effects on the generation of turbulent energy. The turbulent kinetic energy (TKE) is given by

$$k \equiv \frac{1}{2}(u'^2 + v'^2 + w'^2) \tag{8}$$

Since the spanwise velocity component $w(t)$ was not measured in the present study, k was approximately given by:

$$k \cong \frac{1}{2}(u'^2 + 2v'^2) \tag{9}$$

The horizontally averaged TKE equation is reduced to

$$\frac{\partial k}{\partial t} = \langle G_s \rangle + G_w + \langle T_t \rangle + T_d + \langle T_p \rangle + \langle T_v \rangle - \langle \varepsilon \rangle \tag{10}$$

as pointed out by Raupach *et al.* (1996). Each term in the right-hand side of (10) means the sink and source of the turbulent kinetic energy, and it is given by, respectively,

$$\text{(shear generation)} \quad \langle G_s \rangle = -\langle \overline{uv} \rangle \frac{\partial \langle U \rangle}{\partial y} \tag{11}$$

$$\text{(wake generation)} \quad G_w = \left\langle \overline{u_i u_j}'' \frac{\partial U_i''}{\partial x_j} \right\rangle \tag{12}$$

$$\text{(turbulence transport)} \quad \langle T_t \rangle = -\frac{\partial}{\partial y}\langle \overline{vk} \rangle \tag{13}$$

$$\text{(dispersive transport)} \quad T_d = -\frac{\partial}{\partial y}\langle V''k'' \rangle \tag{14}$$

$$\text{(pressure transport)} \quad \langle T_p \rangle = -\frac{\partial}{\partial y}\langle \overline{vp} \rangle \tag{15}$$

$$\text{(viscous diffusion)} \quad \langle T_v \rangle = -\nu \frac{\partial^2}{\partial y^2}\langle k \rangle \tag{16}$$

The first and second terms in the right-hand side of (10) imply the turbulence generation rate. $\langle G_s \rangle$ is the horizontally averaged shear generation caused by the velocity gradient $\partial U/\partial y$, which is generally dominant near the wall region in boundary layers and open-channel flows. On the other hand, G_w is the wake generation which implies the energy transport from the mean flow toward turbulence field by the wakes behind the vegetation elements. Of particular significance is that G_w is introduced by the space-averaging operation of (2), and its term does not appear at all in the standard TKE (local) equation of (10). To avoid differential errors when the measured data are used in (11), Raupach *et al* (1986) have given the following approximate equation.

$$G_w \cong -\langle U \rangle \frac{\partial \langle \overline{uv} \rangle}{\partial y} \tag{17}$$

Copyright © 2006 Taylor & Francis Group plc, London, UK

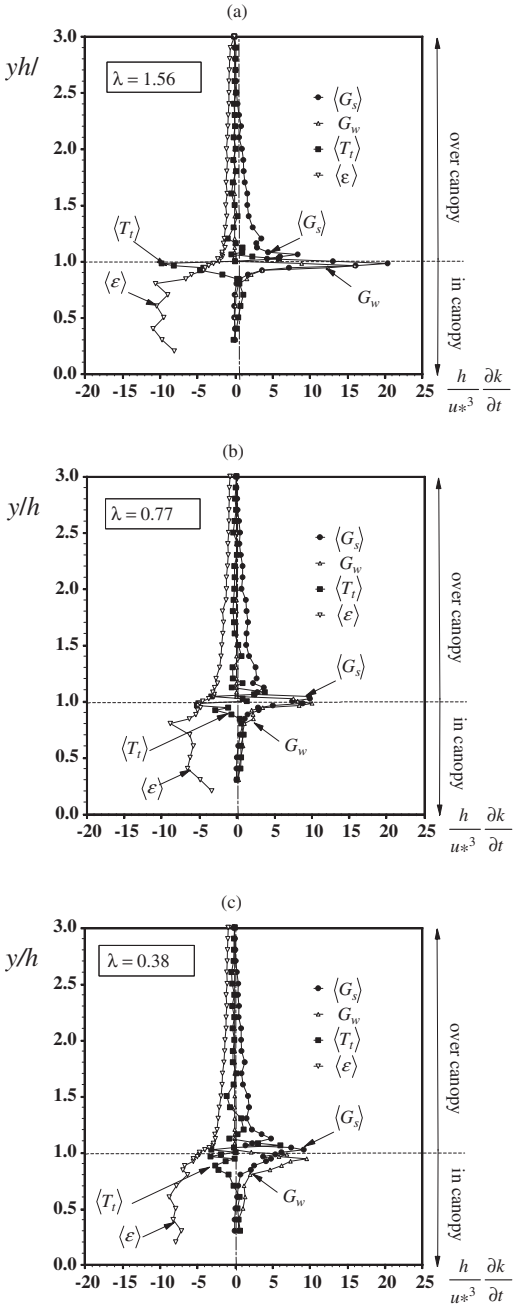


Figure 14. Turbulent kinetic energy budget.

$\langle T_t \rangle$, T_d, $\langle T_p \rangle$, $\langle T_v \rangle$ and $\langle \varepsilon \rangle$ imply the 'turbulence transport', the 'dispersive transport', the 'pressure transport', the 'viscous diffusion' and the 'space-averaged energy dissipation'. The local dissipation of ε was evaluated by applying the Kolmogoroff's $-5/3$ power law to the sectrum distributions in the whole depth region ($0 < y < H$). Unfortunately, $\langle T_p \rangle$ could not be evaluated directly because the pressure was not measured in the present study. T_d and $\langle T_v \rangle$ were assumed to be negligibly small.

Figure 14 shows the vertical distributions of $\langle G_s \rangle$, G_w, $\langle T_t \rangle$ and $\langle \varepsilon \rangle$. $\langle G_s \rangle$ has a peak value near the vegetation edge and this corresponds to the Reynolds stress profiles shown in Fig. 7. It is also found that G_w decreases toward the vegetation bed. Of particular significance is that G_w is comparable with or larger rather than the shear generation $\langle G_s \rangle$. This suggests that the wake generation plays an important role on the turbulence generation within the canopy.

$\langle T_t \rangle$ has negative values near the edge within the canopy. This implies that the significant energy loss is caused by strong downward sweeps which transport high-speed momentum toward the inner vegetation layer. As the results, we can observe a positive distribution of $\langle T_t \rangle$ around the middle canopy layer ($y/h \cong 0.5$). Since these fluctuations are much dissipated into heat, $\langle \varepsilon \rangle$ becomes more dominant within the canopy layer.

4 CONCLUSIONS

The hydrodynamic properties and dispersive effects were investigated in the vegetated open-channel flows on the basis of LDA measurements in the whole depth region from the bottom-bed to the free surface. In particular, it was found that the vegetation density correlates strongly with the turbulent structure. The main findings obtained in the present study are as follows:

1) The mean velocity profile has an inflectional point near the vegetation edge, which causes the significant shear instability. The measured shear length-scale decreases with an increase of the vegetation density.
2) The mean velocity profile is affected by the vegetation within the canopy, and it is decelerated largely with an increase of the vegetation density. On the other hand, it obeys the universal formula, i.e., the log-law over the canopy in which the plant elements do not greatly affect the fluid.
3) It is found from the skewness distributions that there are noticeable coherent structures within the canopy, and the significant momentum exchange occurs between the within-canopy and the over-canopy. The conditional quadrant analysis revealed that the sweep event is greater than the ejection event near the canopy edge.
4) The spectrum obeys the Kolmogoroff's $-5/3$ power law in the inertial subrange within and above the canopy. However, it should be noticed that the high-frequency spectrum becomes larger as compared

Copyright © 2006 Taylor & Francis Group plc, London, UK

with the low-frequency one within the canopy vegetation. This may be caused by the wake turbulence behind the vegetation elements.

5) The TKE budget was examined in order to reveal the dispersive contributions of turbulence due to vegetations. Of particular significance is that the turbulent fluctuations are generated strongly near the vegetation edge and the wake generation is comparable or larger than the shear generation. Furthermore, it is demonstrated significantly that the coherent motion such as sweeps transports the turbulent energy into the canopy layer.

ACKNOWLEDGEMENTS

The financial support to the present study was awarded from the government [Grand-in-Aid for Scientific Research (B) No.15360265; Representative: I. Nezu], and it is hereby acknowledged.

REFERENCES

Dwyer, M.J., Patton, E.G. and Shaw, R.H. 1997. Turbulent Kinetic Energy Budgets from a Large-Eddy Simulation of Airflow above and within a Forest Canopy, *Boundary-Layer Meteorology* 84: 23–43.

Finnigan J. 2000. Turbulence in Plant Canopies, *Annu. Rev. Fluid Mech.* 32: 519–572.

Jackson, P.S. 1981. On the Displacement Height in the Logarithmic Velocity Profile, *Journal of Fluid Mech.* 111: 15–25.

Meyers, T.P. and Baldocchi, D.D. 1991. The Budgets of Turbulent Kinetic Energy and Reynolds Stress within and above a Deciduous Forest, *Agricultural and Forest Meteorology* 53: 207–222.

Nakagawa, H. and Nezu. I. 1977. Prediction of the Contributions to the Reynolds Stress from the Bursting Events in Open-channel Flows, *J. of Fluid Mechanics* 80: 99–128.

Nepf, H. M. and Vivoni, E. R. 2000. Flow Structure in Depth-limited, Vegetated Flow, *J. of Geophysical Res.* 105: 28547–28557.

Poggi, D., Porpotato, A. and Ridolfi, L. 2004. The Effect of Vegetation Density on Canopy Sub-layer Turbulence, *Boundary-Layer Meteorology* 111: 565–587.

Raupach, M.R., Thom, A.S. and Edwards, I. 1979. A Wind-Tunnel Study of Turbulent Flow close to Regularly Arrayed Rough Surface, *Boundary Layer Meteorology*, 18: 373–393.

Raupach, M. R. and Thom, A.S. 1981. Turbulence in and above Plant Canopies, *Ann. Rev. Fluid Mech*.13: pp. 97–129.

Raupach, M.R., Coppin, P.A. and Legg, B.J. 1986. Experiments on Scalar Dispersion within a Model Plant Canopy, Part I: The Turbulence Structure, *Boundary Layer Meteorology* 35: 21–52.

Raupach, M. R., Antonia, R. A. and Rajagopalan, S. 1991. Rough-wall Turbulent Boundary Layers, *Appl. Mech. Rev.* 44: 1–25.

Raupach, M. R., Finnigan, J.J. and Brunet, Y. 1996. Coherent Eddies and Turbulence in Vegetation Canopies: The Mixing-layer Analogy, *Boundary Layer Meteorolog*. 78: 351–382.

Shaw, R. H., Pawu, K. T., Zhang, X, J., Gao, W., Denhartog, G. and Neumann, H. H. 1990. Retrieval of Turbulent Pressure Fluctuations at the Ground Surface beneath a Forest, *Boundary-Layer Meteorology* 50: 319–338.

Copyright © 2006 Taylor & Francis Group plc, London, UK

Influence of aquatic plants on the flow resistance and the hydraulic capacity of vegetated rivers

L. De Doncker, P. Troch & R. Verhoeven
Hydraulics Laboratory, Ghent University, Belgium

K. Bal & P. Meire
Ecosystem Management Research Group, University of Antwerp, Belgium

ABSTRACT: Vegetation growth drastically influences water levels and flow patterns in lowland rivers. Rise of the water level can have consequences for the surrounding areas and varying velocity patterns can influence the morphology of the river. The universities of Ghent and Antwerp are carrying out research in the river Aa, the Grote Kaliebeek and the Desselse Nete (Antwerp, Belgium) in order to better understand the natural phenomena involved and to come to a more accurate determination of the different parameters. Field measurements are carried out to collect data on discharge, stage and amount and variation of aquatic weed growth. The variation of the friction factor (Manning coefficient), influenced by the varying amount of vegetation, is determined as a function of time and distance. Following a seasonal cycle, flow resistance increases with plant growth in spring, reaches a maximum in early summer and then decreases slowly to the minimum in winter. Knowledge of the variation of the biomass in the time will lead to appropriate use of roughness coefficients in modelling surface flow in rivers.

1 INTRODUCTION

1.1 *Scope*

Vegetation growth influences water levels and flow patterns in lowland rivers. The mowing of vegetation in order to meet the requirements of protecting riparians against summer floods is directly opposing the need for a sound environment and a well balanced ecosystem. Studies aiming at finding a solution for both these problems by limited but well-considered mowing and at the same time guaranteeing safe evacuation of floods should lead to a better river ecosystem management.

The universities of Ghent (UG) and Antwerp (UA) are conducting scientific research in de river Aa in Belgium.

This fundamental study on exchange processes in river ecosystems is multidisciplinary. The overall research aim is to study the diverse physical and biological processes in margins and inundation areas of water courses and their interactions with regard to the exchange of water, dissolved compounds and particulate matter. In a first phase, the influence of the vegetation on the flow resistance in the stretch will be investigated, using both field measurements and hydraulic surface water modelling.

1.2 *Importance of the roughness coefficient*

Knowledge of the movement of water is essential as water flow is the driving factor for all other water related processes. Measurements of discharge and water level give an idea of the actual situation, but hydraulic modelling allows to represent parameter influence and future prospects. Hydraulic modelling becomes more and more important with respect to water resources management, strategic planning and crises management.

A hydraulic model tries to provide reliable information on some aspects of the real situation. The numerical model is used to simulate the actual behaviour of the river, but it is also an important tool to produce a forecast of possible floodings, peak discharges, low water levels, etc. in the future. For that, a representative model is necessary. The topography of the river and river banks is determined, discharges and water levels are registered. A parameter of main importance is the roughness of the river channel and the banks. This roughness cannot be measured. It can be determined by empirical formulas (e.g. Cohan) which include the bed material, presence of vegetation in the river, meandering, etc. However, the large variability of the coefficients leaves too many degrees

Copyright © 2006 Taylor & Francis Group plc, London, UK

of freedom to allow an accurate determination of the roughness coefficient. Another methodology is to use pictures which represent a comparable situation or to use graphs and tables (Hydrologic Engineering Center, US Army Corps of Engineers 2004).

As this approach also does not guarantee accurate values for the Manning coefficient, a calculation of the roughness starting from measurements is recommended. The assumptions made are: first, the bottom slope and the cross sections are supposed to be constant, so sediment transport and transformation of the channel bed are not included. Further, the friction factor or roughness coefficient (expressed by the Manning coefficient n) is set as a constant value in the channel and at the banks. The flow is regarded in a 1-dimensional way, with uniform velocity over the cross section. The Manning coefficient n can be calculated in two ways: first, when uniform flow is supposed, the energy slope is equal to the bottom slope and n is obtained from the Manning equation. Further, when the Bresse equation is used, also here steady state flow is assumed and the roughness coefficient n is calculated from the energy slope.

Several measurement campaigns allow to determine the variation of the roughness coefficient (friction factor or Manning coefficient n [$m^{-1/3}s$]) as a function of time, type and density of vegetation, hydraulic parameters, etc. and to evaluate flow pattern changes in the vicinity of vegetation patches. During these measurement campaigns, velocity and discharge measurements are performed in multiple cross-sections in presence of and after careful local removal of vegetation in the measurement section. Removing the vegetation allows for determining species and vegetation density as well as for studying the influence of plants on flow distribution and patterns.

1.3 *Calculation of the Manning coefficient*

The most widely used expression to analyse open channel flow is the Manning equation, which was named after the Irish engineer Robert Manning in 1891 (Dyhouse et al. 2003). The formula is commonly used to express the roughness, particularly with respect to vegetated channels. The expression is based on the Chezy equation (first found relationship to calculate velocity in a channel) and close to the resistance equation proposed by Ganguillet and Kutter in 1869 (Dyhouse et al. 2003), which was a first try to introduce the roughness of the channel, all of them using the assumption of uniform flow (Dyhouse et al. 2003). The Manning equation [metric units] is:

$$n[m^{-1/3}s] = \frac{S_f^{1/2}R^{2/3}}{U} = \frac{S_f^{1/2}A^{5/3}}{QP^{2/3}} \quad (1)$$

where U [m/s] is the mean channel velocity, R[m] is the hydraulic radius, S_f [-] is the slope of the energy grade line and n [$m^{-1/3}s$] Manning's roughness coefficient.

In this study, the Manning coefficient is calculated according to three different approaches, in the following mentioned as 'Approach 1', 'Approach 2' and 'Approach 3'. 'Approach 1' calculates the roughness coefficient directly using Manning's equation (Eq. 1). Second way (Approach 2) of calculating the Manning coefficient is by using the numerical model HEC-RAS solving the complete Saint-Venant equations (in steady state conditions, which correspond with Bresses equation). Fitting allows to determine the roughness value. 'Approach 3' is similar to 'Approach 2' but is using a simplified geometry (constant cross-section and bottom slope) to evaluate the accurateness of the model.

1.4 *The river Aa*

The catchment basin of the river Aa is situated in the region of Antwerp in Belgium and is hydrographically part of the Nete basin. More than 40% of the water in the Nete basin is carried by the river Aa. The river Aa flows into the Kleine Nete near the city of Grobbendonk. The well of the river Aa is found near the communities of Merksplas and Turnhout. It passes through Turnhout, Gierle, Gielen, Poederlee and Vorselaar, it has a total length of 36.8 km and a drainage area of about 23,700 ha. The study area is focused on the downstream part of the Aa, on a reach controlled by 2 weirs over a distance of 1.4 km.

As a comparison, also measurements in the Grote Kaliebeek and the Desselse Nete, in the same region as the river Aa, are carried out.

1.5 *Research*

This paper discusses the influence of aquatic plants on the flow resistance and the hydraulic capacity of the river Aa. First of all, the study area is introduced, then the measurement of flow characteristics and the results of the measurement campaigns are presented. In particular, research on the importance of the roughness factor, expressed by the Manning coefficient, is carried out. The interaction of vegetation and Manning coefficient is shown. Finally, results of other rivers in the neighbourhood of the river Aa are presented.

2 MEASUREMENTS OF FLOW CHARACTERISTICS

2.1 *Hydraulic measurements*

The discharge measurements are carried out by UG. Two teams have determined the discharges from a bridge and from a boat. First of all, the flow is measured at the up- and downstream end of the stretch of the

Copyright © 2006 Taylor & Francis Group plc, London, UK

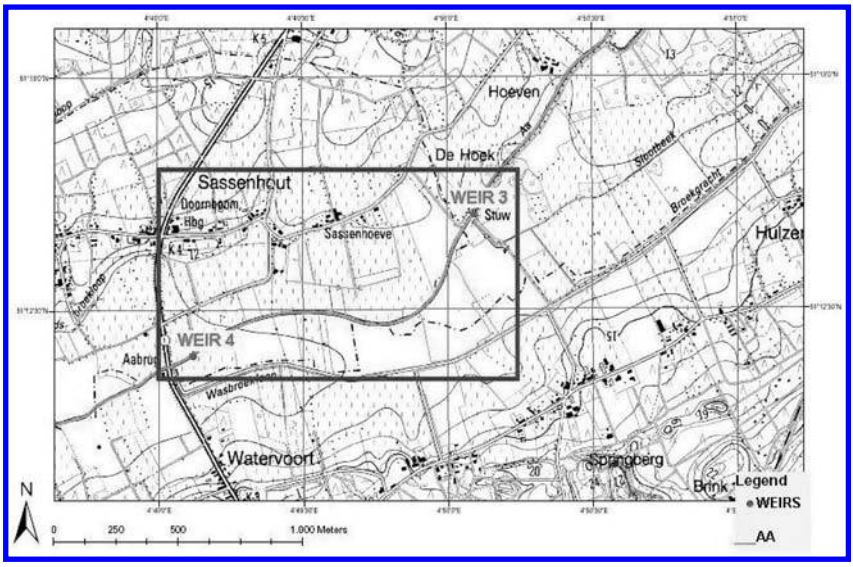


Figure 1. Study area of the river Aa, Poederlee, province of Antwerp, Belgium.

river Aa. In the sections also the biomass is determined by UA.

Two systems are used for measuring the velocity of the water. First of all, flow measurements have been carried out using hydrometric propellers (Type: OTT, C31 Universal Current Meter). This instrument is designed for flow metering in combination with a cable suspended from a bridge or boat. The rotation rate of the calibrated propeller is proportional to water velocity. The velocity is determined with a counter unit by counting the time for a present number of revolutions of the propeller. Knowing the dimensions of the river channel and the measured velocities, the flow is calculated using the principal of integration of the velocities over the cross section (2):

$$Q[m^3/s] \quad = \quad \sum U * \Delta A \qquad (2)$$

with Q = discharge [m^3/s], U = velocity [m/s], Δ A = part of the wetted cross section to which U is attributed [m^2].

The sections are divided into several vertical parts. For each of these verticals (for example, each half a meter), the velocity of the water is measured on different depths, so that the velocity profile is known over the entire water column. The result of the measurements is an overview of velocities over the section. Integration of the values over the wetted area gives an average velocity over the cross section.

When the amount of vegetation is substantial, use of the propellers is difficult. Then, an electromagnetic instrument (type: OTT, Nautilus C2000/SENSA Z300 and Valeport, Type 801) is applied to measure the velocities. Advantage of these devices is that they can be used in vegetated rivers. There are no moving parts which can interfere with the macrophytes, the device is wear-resistant and maintenance free.

Measurements are not carried out according standards as these suppose a Prandtl Von Karman velocity profile, which is not seen in vegetated rivers.

Next to the velocity measurements to calculate the discharge, also the water levels are registered.

2.2 *Measurement campaigns*

To collect accurate and relevant data for calibrating the model, hydraulic measurements are carried out. Monthly, the discharge was measured upstream and downstream the selected stretch of the river Aa. Also water levels are registered to calculate the energy slope and to check the influence of the aquatic plant growth on the water stage.

The studied stretch of the river Aa is situated between two weirs. A gauge is fixed upstream and downstream the stretch. During the measurements, the water level is read off the gauge regularly, with an accuracy of 0.5 cm. The water height is measured while carrying out the discharge measurements in particular sections. Also, the water level upstream and downstream the weir is registered continuously by the Hydrological Information Centre (HIC) of Flanders Hydraulics Research.

Further more, some intensive measurement campaigns are organised. Measurements of hydraulic characteristics (as discharge and water level) and of groundwater seepage and leakage are carried out. Also biomass and water quality information is collected. This multidisciplinary project asks for coherent

Copyright © 2006 Taylor & Francis Group plc, London, UK

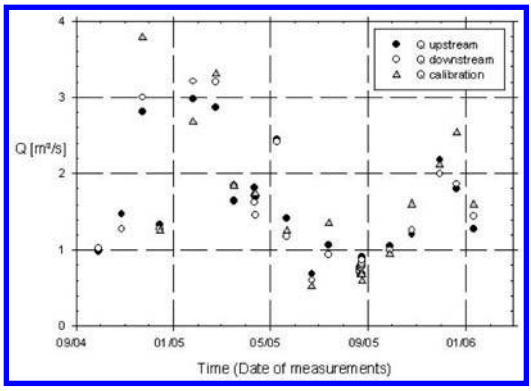


Figure 2. Measured discharge values Q in both upstream and downstream sections as a function of time.

collection of data. In 2005, the campaigns were organised in April and August.

2.3 *Data processing*

Up- and downstream discharge values in the channel are given in Figure 2. For each of the monthly measured values, the discharge upstream (black dots) and the discharge downstream (white dots) is indicated. The small difference between both values is due to groundwater inflow/outflow, to little tributary inflow between the sections and to inaccuracy of the measurements. Next to that, also the calculated discharge based on the calibration formula of the downstream weir, is added (triangles). In general, there is good agreement between this value and the others. The calibration value of November '04, July '05 and December '05 are higher, but it is not obvious what is the reason for that. Probably, a vegetation patch disturbs the free flow over the weir. Together with the discharges, the up- and downstream water stages are registered. The measured discharges and stages are used for the calculation of the roughness coefficient of the stretch.

The Hydrological Information Centre (HIC) of Flanders Hydraulics Research has registered the water levels and the discharge in the studied stretch during 2004. Using these values, the length of the stretch ($L = 1400$ m), a constant wetted cross section ($A = 13\ m^2$) and a constant wetted perimeter ($P = 16$ m), the Manning coefficient n can be calculated with the Manning equation (cf. Eq. (1)). Curves are presented in Figure 3.

First of all, it can be seen that the highest discharges occur during the winter period. During summer, the energy slope (i.e. the difference between the water level upstream and downstream) is bigger. The Manning coefficient is increasing from May until full summer, reaches the highest values in August and is decreasing from October to November. This trend accompanies the vegetation growth in spring and summer. Maximum values of the Manning coefficient in 2004 (according this approximative calculation method) are up to 0.3 which is lower than the values recorded for 2005 (Figure 4).

3 MANNING COEFFICIENT FOR BOTTOM ROUGHNESS

3.1 *Variation of the Manning coefficient*

In this section, the relation of the Manning coefficient to other variables is presented.

The three calculation methods (cf. section 1.3) for the Manning coefficient are applied in the stretch of the river Aa. Calculations are carried out separately for both the discharges measured up- and downstream.

For each of the monthly measurements, the roughness coefficient is plotted in Figure 4. The different calculation methods are indicated with a different symbol. Using the same calculation approach, the Manning coefficient based on the upstream discharge value and on the downstream discharge are comparable.

For the measurements of November, January and February, differences in the Manning coefficient are negligible. The spreading range is biggest for the measurements of September, May and June. During winter, the presence of vegetation remains rather constant, while during spring and summer, the Manning coefficient increases rapidly with the amount of vegetation.

Using an incorrect Manning coefficient while modelling flows in rivers can imply large deviations. As can be seen, during spring, Manning coefficients are up to 10 times higher then the values during winter.

From this, a seasonal trend is observed in the value of the Manning coefficient with low values appearing in January, February (winter), a slight increase in March and April and a fast rise in May and June. Then, the resistance remains high during summer. During winter, the amount of vegetation is decreasing, yielding lower flow resistance and a decreasing roughness coefficient. In summer, the effect is the other way round.

Comparing Figure 2 and Figure 4 for the same measuring period (September to July) shows that lower discharges correspond with higher Manning coefficients (cf. Figure 5). A larger amount of vegetation in the stretch, reduces the cross sections open to flow so that less water can pass in a given time period, which is the definition of discharge.

Figure 5 shows the relation between the discharge and the Manning coefficient. The discharge is calculated upstream and downstream in the stretch of the river Aa. The Manning coefficient is calculated with the numerical model Hec-Ras. As can be seen, higher Manning coefficients correspond with lower

Copyright © 2006 Taylor & Francis Group plc, London, UK

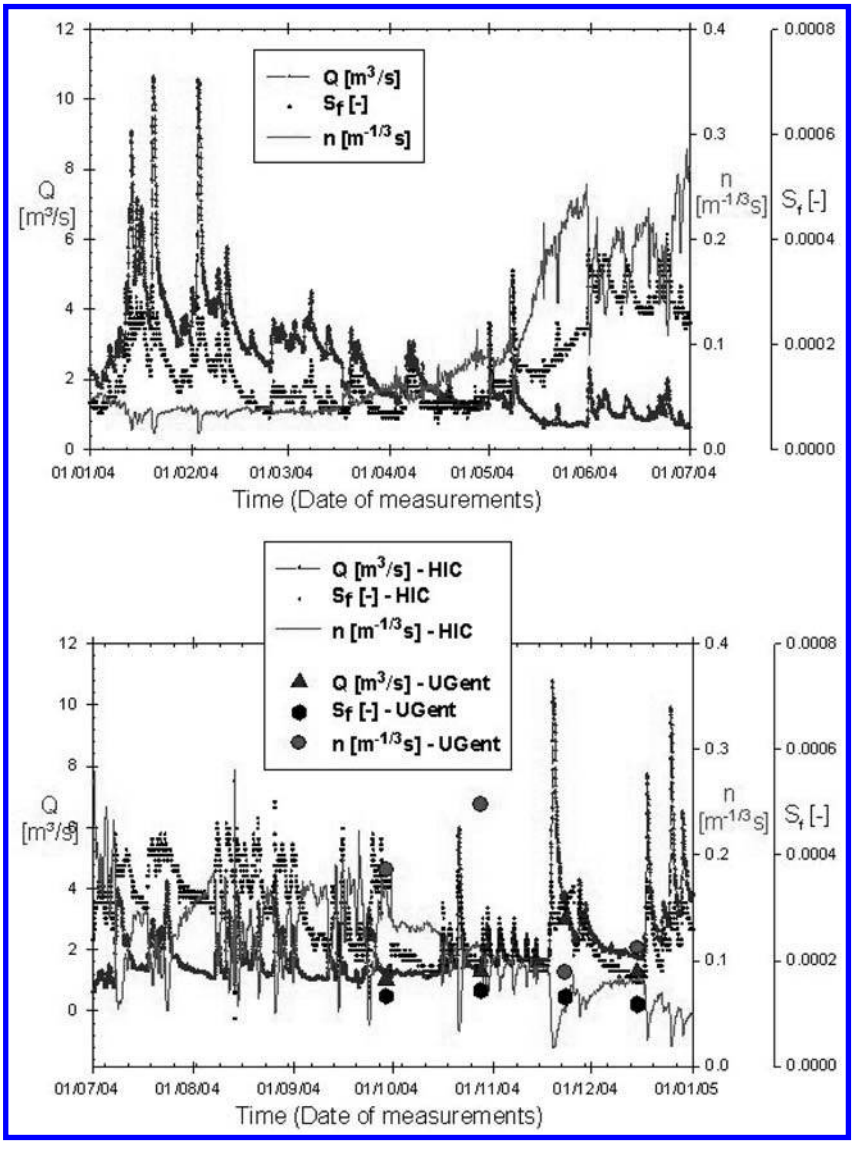


Figure 3. The discharge Q, the energy slope S_f and the Manning coefficient n, for the measurements of 2004 (HIC) (January–July) and (July–December).

discharges. Discharges are varying between 0.6 and 3.2 m^3/s. Manning values ranges between 0.05 and 0.5 $m^{-1/3}s$. The trend follows Eq. (1) and the same for upstream and downstream measured discharges.

Figure 6 shows the relation between the Manning coefficient and the upstream velocity. The trend is added and represents an exponentional path. Higher Manning coefficients correspond with lower velocities. Upstream velocities are varying between 0.04 and 0.022 m/s. This conclusion can also be connected to the aquatic weed growth; the more plants in the water, the more roughness in the river and the lower the velocities. In a cross section where the channel is obstructed by a wealthy plant growth, there is a higher resistance to water flow.

In Figure 7, the upstream and downstream water levels are plotted as a function of the Manning coefficient. Although there is no clear trend, it becomes evident that in general higher Manning coefficients (due to more aquatic plant growth) correspond to higher water levels. If a part of the cross section is obstructed by vegetation the water level will be higher.

Copyright © 2006 Taylor & Francis Group plc, London, UK

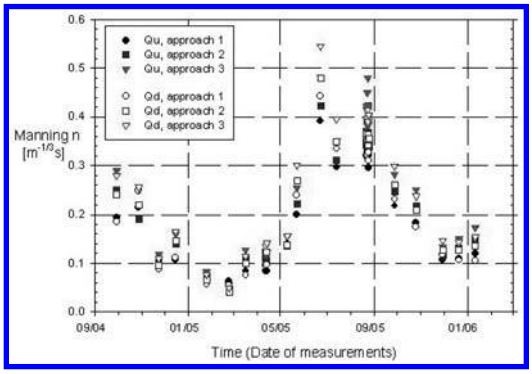


Figure 4. Manning coefficient n for the upstream (Qu) and downstream (Qd) value of Q: comparison of the values calculated using three approaches: Manning's equation given by Eq. 2 (1), fitting based on the Saint-Venant equations (HEC-RAS)(2), and fitting using an average section (3).

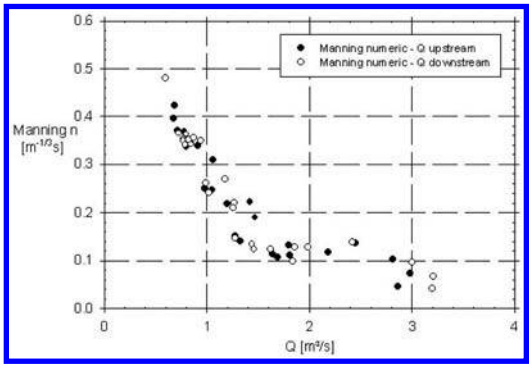


Figure 5. Relation between Manning coefficient n and upstream and downstream discharge Q.

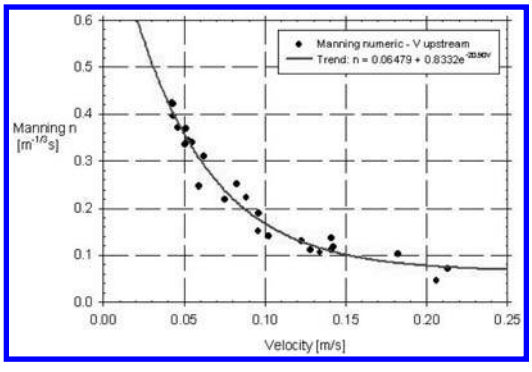


Figure 6. Relation between Manning coefficient n and upstream velocity.

In Figure 8, the Manning coefficient calculated with the numerical model Hec-Ras is plotted together with the measured wetted cross section A, upstream the stretch. The upstream wetted cross section of the Aa

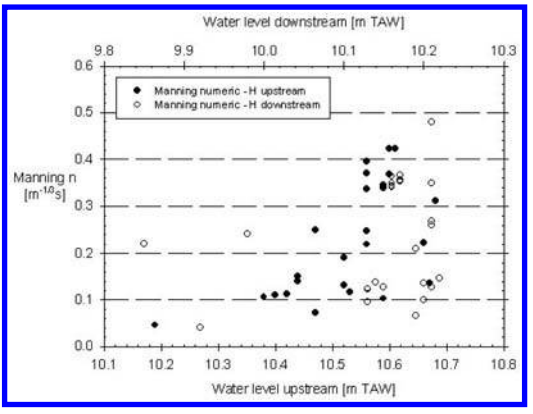


Figure 7. Relation between Manning coefficient n and water level.

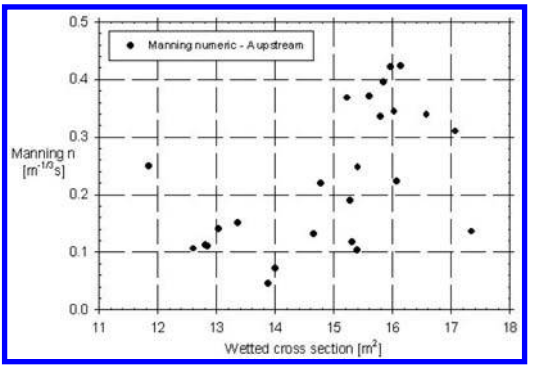


Figure 8. Relation between Manning coefficient n and upstream wetted cross section.

varies between about 12 and 17.5 m^2. The relation between wetted cross section and Manning coefficient is not clear, but in general lower wetted cross sections are corresponding to lower Manning coefficients. Because of a wealthy vegetation growth in the river, water levels will be higher and so, the wetted cross section is larger. More vegetation growth is also corresponding to a higher Manning coefficient.

Due to vegetation and the related influence of backwater, the energy slope along the stretch may vary substantially. Figure 9 shows a simulated situation in the stretch of the river Aa with a length of 1.4 km. Two cases are considered: a Manning coefficient of 0.046 $m^{-1/3}s$, which was calculated from the Manning formula (Eq. 1) and the measurements of February and a Manning coefficient of 0.423 $m^{-1/3}s$ (June).

First remark is that the Manning coefficient is 9 times higher in the month of June when there is a wealthy vegetation. Starting from the same downstream water level and using a discharge of 1 m^3/s, the upstream water level is calculated for both values of the

Copyright © 2006 Taylor & Francis Group plc, London, UK

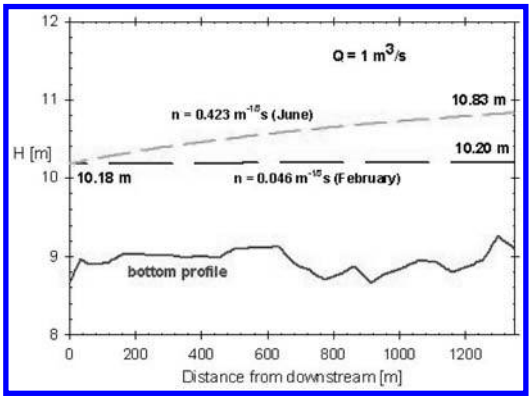


Figure 9. Influence of backwater of the Manning coefficient on the water level for a given discharge.

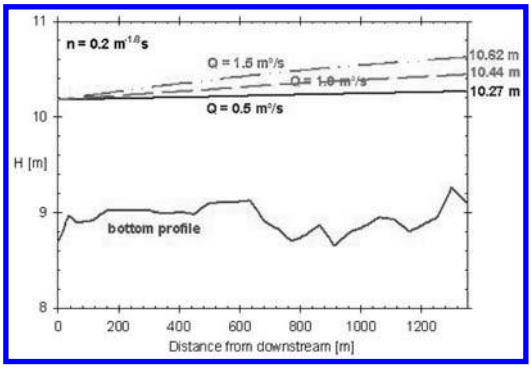


Figure 10. Backwater influence of the Manning coefficient on the discharge for a given amount of vegetation.

Manning coefficient. In June, an upstream water level of 10.83 m is calculated, while 10.20 m is obtained in February, which is a difference of more than 60 cm due to the presence of vegetation.

Because of the better water quality, the organic matter in the rivers has decreased and the clearness of the water has increased. Next to that, the agricultural activities in the neighbourhood of the river Aa bring fertilizers into the water. These factors are responsable for the explosive growth of the aquatic plants, resulting in a rise of the water level up to 60 cm.

Figure 10 shows the influence of the discharge on the energy slope S_f. For three different values of the discharge, the water surface profile is calculated. The Manning coefficient does not change. It seems that tripling the discharge results in an increase of the water level of 0.35 m. So, the impact of the vegetation on Sf is much bigger (Figure 9) and explains why a dangerous situation may occur with regard to inundation during summer floods.

Tables 1 and 2 compare the measured values by Ghent University, the registered values of the Flanders

Table 1. Comparison of the results measured by UG and the values calculated by Hec-Ras, the first row are the upstream values, the second row are the downstream values.

		Measured UG			Hec-Ras
Date	Time	Q [m^3/s]	H [m]	n (ap.1) [$m^{-1/3}s$]	n (ap.2) [$m^{-1/3}s$]
29/09/04	11:40–13:05	0.98	10.485	0.194	0.250
29/09/04	14:20–15:20	1.02	9.995	0.186	0.242
28/10/04	14:00–15:40	1.47	10.520	0.214	0.190
28/10/04	14:50–16:30	1.27	9.850	0.248	0.220
23/11/04	10:40–12:05	2.81	10.590	0.095	0.103
23/11/04	13:36–15:00	3.00	10.130	0.089	0.096
15/12/04	10:20–12:00	1.33	10.440	0.108	0.140
15/12/04	13:10–14:50	1.28	10.220	0.112	0.146

Table 2. Comparison of the results registered by HIC and the values calculated by Hec-Ras, the first row are the upstream values, the second row are the downstream values.

		Registered HIC			Hec-Ras
Date	Time	Q [m^3/s]	H [m]	n (ap.1) [$m^{-1/3}s$]	n (ap.2) [$m^{-1/3}s$]
29/09/04	11:40–13:05	1.366	10.495	0.153	0.250
29/09/04	14:20–15:20	1.378	10.016		0.242
28/10/04	14:00–15:40	2.04	10.584	0.089	0.190
28/10/04	14:50–16:30	2.23	10.222		0.220
23/11/04	10:40–12:05	3.196	10.591	0.062	0.103
23/11/04	13:36–15:00	3.301	10.163		0.096
15/12/04	10:20–12:00	1.755	10.443	0.083	0.140
15/12/04	13:10–14:50	1.713	10.214		0.146

Hydraulics Lab (HIC) and the values calculated with the numerical model Hec-Ras. The tabulated data are also shown in Figure 3. As can be seen, the measurements of October do not give a corresponding result. For the others, the discharges registered by HIC are higher. These discharges are registered downstream the stretch (downstream weir 4) while Ghent University measures between the two weirs. Differences can be due to that adaption. For the measurements of October, there were problems with the downstream measurements. Seeing the other values, a higher discharge would be more realistic. Furthermore, the Manning coefficients based on the HIC-values are calculated with an average wetted cross-section and an average wetted perimeter, which does not correspond with the natural situation. The same calculations have been carried out by using Hec-Ras (and based on the measurements of Ghent University) to have a more accurate result. The Hec-Ras results for the Manning coefficient agree more with the values calculated from the measurements of Ghent University (with the

Copyright © 2006 Taylor & Francis Group plc, London, UK

Manning equation) than with the registered values of HIC. All the calculations are based on the water levels measured (UG) or registered (HIC) at the same time.

Because of the higher discharges registered by HIC, the Manning coefficients, calculated with these values, are lower. The values of the discharge and the water level are important for the calculation of the Manning coefficient. Errors on the measurements can be the cause of large deviations in the calculations. So, measurements have to be carried out with the most care and precision. In November and December, the downstream discharge is also calculated with the formula of the calibrated weir. Therefore, the water height over the flap of the weir is measured. Results are values of 3.79 m^3/s (November) and 1.25 m^3/s (December), which are in the same range of the measured and registered values.

This comparison illustrates the importance of accurate information on hydraulic data with regard to the determination of the friction factor as a key-value in numerical modelling.

3.2 *Biomass influence*

A positive correlation between the biomass and the Manning coefficient was found by Brooker (1978) and mentioned in (Viaene and Vereecken 2001). The biomass in fact, is the amount of vegetation in the channel and is expressed in g/m^2 (horizontal surface). During peak growth of the vegetation (April–June), the biomass as well as the Manning coefficient are inversely proportional to the flow velocity in the water course (Viaene and Vereecken 2001), which is also clearly illustrated in Figure 6.

Presence of vegetation decreases the section and increases the roughness and by this also the water level for the same discharge value. Absence of an univocal correlation between discharge and water level at a gauge is attributed to seasonal changes in the amount of vegetation, quantitatively represented by the biomass.

The evolution of the Manning coefficient is related to the amount of vegetation (Figure 11). Starting from the measurements in January, the amount of macrophytes is determined. As can be seen, more biomass results in a higher Manning coefficient. An exponentional curve is fitted to the values in Figure 11.

For low values of the biomass (less then 100 g/m^2), the Manning coefficient is varying between 0.04 and 0.14 $m^{-1/3}/s$. This variation is due to different discharges. As can be seen on Figure 5, lower discharges correspond with higher Manning coefficients.

It becomes evident again that the Manning coefficient is strongly increasing in spring, due to explosive vegetation growth (Figure 12). During summer, the roughness reaches a peak value. After dying out of the plants, also the Manning coefficient is decreasing. This cycle is almost the same for each year. A sudden fall in the roughness during the vegetation period can be due to the wash away or flattening of a vegetation patch with large discharges. By this the discharge influences the roughness coefficient. The roughness decreases when the discharge increases. Hence, the variation of the Manning coefficient is influenced by discharge and vegetation.

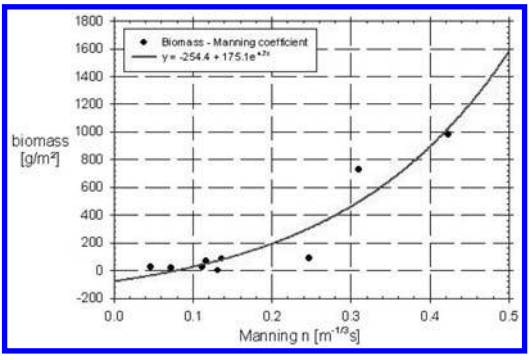


Figure 11. Relation between Manning coefficient n and biomass.

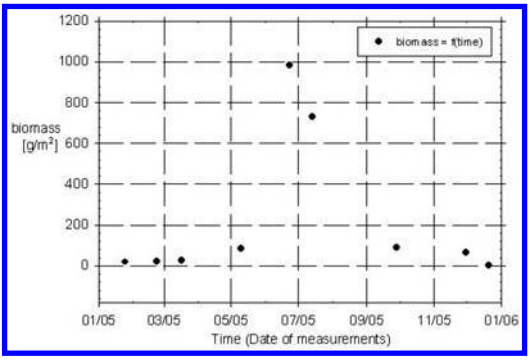


Figure 12. The measured biomass in the river Aa as a function of time.

3.3 *Manning coefficients in other rivers*

The relation between the measured biomass and the Manning coefficient n is investigated here. The calculated Manning coefficients and the dry biomass for the river Aa, the study area, are compared with values of the Desselse Nete and the Grote Kaliebeek.

The Desselse Nete is a river in the upstream part of the Nete basin. The river has still its meandering characteristics contrary to other rivers in the basin which have been straightened during the years.

The Kaliebeek is the largest tributary of the river Aa. This river is coming into the river Aa, near the border of Tielen and Poederlee (province of Antwerp, Belgium). The Grote Kaliebeek (originating in Oud-Turnhout) and the Kleine Kaliebeek (originating in Kasterlee)

Copyright © 2006 Taylor & Francis Group plc, London, UK

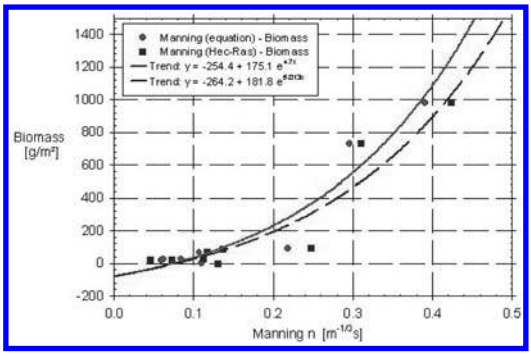


Figure 13. Relation between biomass and Manning coefficient for the river Aa.

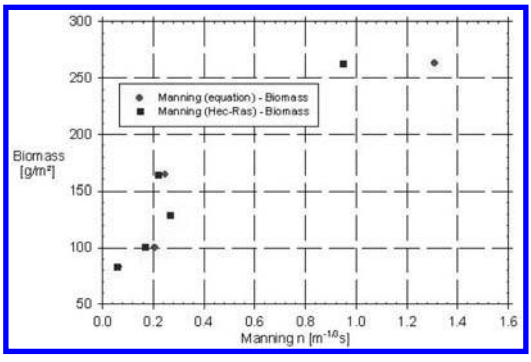


Figure 14. Relation between biomass and Manning coefficient for the Grote Kaliebeek.

are coming together near Tielen. From there, the river is known as the Kaliebeek.

For the river Aa and the Desselse Nete, an exponential trend is found. For the Grote Kaliebeek, the trend is less clear.

For rivers, the Manning coefficient is calculated using both the numerical model Hec-Ras and the Manning equation (Eq. (1)).

Figure 13 presents the exponential trend, found in the river Aa, study area, for both approaches of the calculation of the Manning coefficient.

As can be seen from Figure 14, for the Grote Kaliebeek, no exponentional trend is found. The data are collected in the period from May till the end of September. A stretch of 170 m is selected to measure the energy slope for the calculation of the Manning coefficient. For higher biomass, extremely high values of the Manning coefficients are registered. The biomass in the Grote Kaliebeek, is only a quarter of the biomass found in the river Aa, and nevertheless the Manning coefficients are higher (up to 1). An explanation could be found in the difference in wetted cross-section where the cross-section of the river

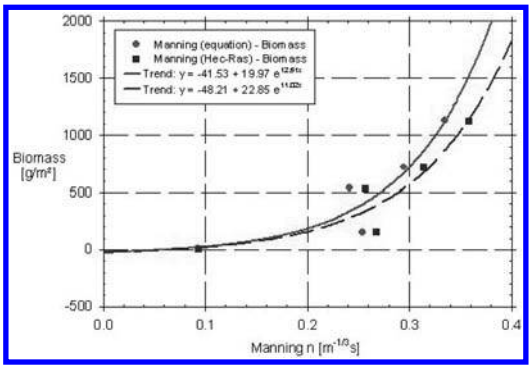


Figure 15. Relation between biomass and Manning coefficient for the Desselse Nete.

Aa is much bigger then the cross-section of the Grote Kaliebeek.

Figure 15 shows the results for the Desselse Nete. Biomasses higher then 1,000 g/m^2 are found. The data are representing regular measurements in the period from June till the end of September. A stretch of 200 m is selected to measure the energy slope for the calculation of the Manning coefficient. For the Desselse Nete, Manning coefficients as well as biomass can be found in the same range as in the river Aa.

4 CONCLUSIONS

An accurate and reliable numerical model must be based on the input of accurately determined parameters. Some of them are rather easy to determine, but others, like the Manning coefficient, vary as a function of time.

A correct prediction, based on numerical modelling, asks for correct calibration data. Good knowledge of the variation of the Manning coefficient n as a function of time, distance and water stage is needed. Therefore, it is necessary to carry out measurements on a regular basis and to collect hydraulic information all over the year. A numerical model based on a Manning coefficient measured once a year, may introduce large errors in the calculation results, since this roughness coefficient can change up to a factor ten from winter to summer conditions.

In this paper, the link between the amount of vegetation, the discharge, the velocities in the cross sections, the water level and the roughness coefficient has been put to evidence.

The relation between the biomass variation and the variation of the friction factor is obvious and should be further investigated.

Predicting vegetation growth in a river, in combination with information on discharges can lead to a

Copyright © 2006 Taylor & Francis Group plc, London, UK

better estimation of the Manning coefficient and by this to more reliable results of numerical modelling.

ACKNOWLEDGEMENTS

This research is funded by the FWO (Fund for Scientific Research) – Flanders (G.0306.04).

Thanks to Mr. Martin Van Daele and Mr. Stefaan Bliki for their assistance with the discharge measurements. Also thanks to the Hydrological Information Centre of Flanders Hydraulics Research (HIC, Mr. E. Cornet) for providing the discharge and water level data of the river Aa.

REFERENCES

Chow, V. T. (1959). *Open Channel Hydraulics*.

Chow, V. T., D. R. Maidment and L. W. Mays (1988). *Applied Hydrology*.

Dyhouse, G., J. Hatchett and J. Benn (2003). *Floodplain Modeling using Hec-Ras*. ISBN 0-9714141-0-6.

Green, J. C. (2005a). Effect of macrophyte spatial variability on channel resistance. *Advances in Water Resources*. Will be published.

Green, J. C. (2005b). Modelling flow resistance in vegetated streams: review and development of new theory. *Hydrological Processes* (19), 1245–1259.

Hydrologic Engineering Center, US Army Corps of Engineers (2004). *HEC-RAS River Analysis System, Version 2.1.4*. Hydrologic Engineering Center, US Army Corps of Engineers. http:\\www.hec.usace.army.mil.

Jarvela, J. (2004). *Flow resistance in environmental channels: focus on vegetation*. Water resources publications, Helsinki University of Technology.

Kouwen, N. (2003, February). Using vegetation properties to predict flow resistance and erosion rates. In *Vegetated channels: hydraulic, morphological and ecological aspects*, Trento, Italy. International workshop on riparian forest.

N.N. Meandering rivers, online lecture. Technical report. http://www.pitt.edu/cejones/ Geology1020/06MeanderingRivers.pdf.

Querner, E. (1993). *Aquatic weed control within an integrated water management framework*. Ph. D. thesis, Agriculture University Wageningen. ISBN 90-5485-122-8.

Viaene, P. and H. Vereecken (2001). Stromingsweerstand tengevolge van waterplanten. Technical report, Flanders Hydraulics. Rapport Ministerie van de Vlaamse Gemeenschap, Departement Leefmilieu en Infrastructuur, Administratie Milieu, Land-en Waterbeheer, Afdeling Water, Model 566.

Copyright © 2006 Taylor & Francis Group plc, London, UK

Experimental study of flexible and rigid vegetation in an open channel

M. Ben Meftah, F. De Serio, D. Malcangio & A.F. Petrillo
Department of Water Engineering and Chemistry, The Technical University, Bari, Italy

M. Mossa
Department of Environmental Engineering and Sustainable Development, The Technical University, Bari, Italy

ABSTRACT: In this paper, the effect of a rigid and flexible submerged vegetation, with a characteristic low density, on a transversal current was analyzed. Different configurations as vegetation type, flow depth and velocity were investigated in the laboratory flume. 3D velocity components and turbulence characteristics, such as turbulence intensity and Reynolds stresses, were conducted at different measurement points by the Acoustic Doppler Velocimeter (ADV) system. The velocity and turbulence profiles and distributions were plotted in horizontal and transversal sections, in order to quantify the effect of the two kinds of vegetation on the crossflow. The results showed a local behavior, due to the particular low vegetation density that do not allow to consider the flow field homogeneous at the stem scale. Besides, flow velocity deceleration and turbulence increase were stronger under the top of the rigid vegetated layer than in the case of flexible stems.

1 INTRODUCTION

The fact that a solid element, whatever it is in type and shape, creates a disturb to a crossflow is well established in the scientific word (e.g. Sumner et al. 1999, Kang 2003, Silvestrini & Lamballais 2004). The interest on a similar phenomenon, instead, is always high because of it is easy to find it ordinarily in nature, e.g. in river flows, and so in problems connected to natural channel management and restoration, which require engineering interventions.

The most common obstacle that crosses the current is the vegetation, which presence has been regarded both positively, e.g. for its fundamental ecological functions in the riverine environment and because it reduces the risk and effect of erosion, and negatively, e.g. for the effects of the hydraulic cross section reduction which hinders flow capacity and increases the river bed roughness. Nevertheless, current environmental river engineering prefers to conserve natural riverbank and floodplain vegetation.

Flow resistance of natural open channels, in particular the effect of flexible and rigid vegetation, is a well-established key of research in literature, from the past (e.g. Chow 1959, Barnes 1967) till nowadays (e.g. Ghisalberti & Nepf 2002, Järvelä 2004, Carollo et al. 2005). All the works concur that the main characteristics that define the hydraulic behavior of a single vegetation element are (i) its diameter, (ii) its height compared with the flow depth and then the possibility to be submerged under the flow surface or emergent, (iii) its shape and flexibility that distinguishes the case of flexible elements from that of rigid ones, and (iv) its plane distribution, that is its density. The contribution of different vegetation considered as roughness types to the total flow resistance depends strongly on the combination of the vegetative elements and presents considerable variability in time and space (Järvelä 2002a,b). For example, in nature during the growing season, leaves on willows contribute more to the total drag rather than the bottom grasses, while, in winter, when the willows are leafless, the last ones are likely to dominate the total flow resistance (Järvelä 2004).

The hydraulic behavior of rigid elements is similar to that of a fixed bed formed by elements of known geometry in large-roughness conditions (Petryk & Bosmajian 1975, Stone & Shen 2002). The flexible vegetation instead exhibits four different configurations, depending on the current speed: (i) erect, (ii) gently swaying, (iii) strong, coherent swaying (monami) and (iv) prone (Grizzle et al. 1996, Nepf & Vivoni 2000). For each configuration, different values of the inflection degree, i.e. the ratio between the bent vegetation height h_s and the vegetation height in the absence of current h_v, occur. For low values of flow velocity, the behaviors of the flexible elements is comparable with that of rigid vegetation.

Most efforts to study vegetal effects on a current have concentrated on analyzing submerged vegetation. In this case, according to El-Hakim & Salama

Copyright © 2006 Taylor & Francis Group plc, London, UK

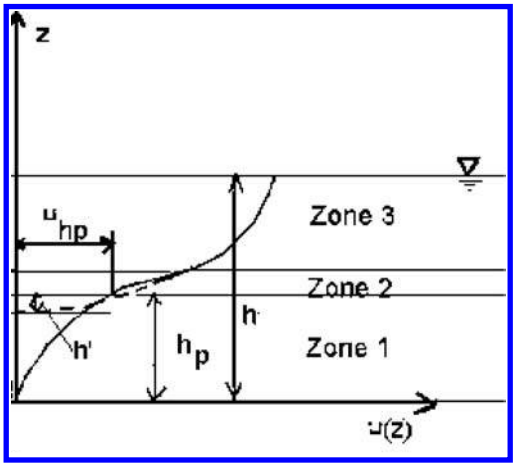


Figure 1. Classification of flow layers and the corresponding velocity profile in the case of totally submerged vegetation (adapted from El-Hakim & Salama 1992).

(1992), three different flow layers can be distinguished, as shown in Figure 1. Zone 1 refers to flow inside the canopy. The thickness of this layer is h_p, which denotes the deflected height of vegetation h_s in the case of flexible plants, while for stiff plants it coincides with the elements height h_v that is not influenced by the flow velocity. In Zone 3 the velocity distribution is assumed to be logarithmic, but the zero point of the velocity is assumed to be inside the vegetation (see broken line in Figure 1). The variable h' is called the shift of the zero point from h_p in the logarithmic velocity distribution, whereas u_{hp} is the velocity at the top of vegetation, where the profile present an inflection point and both the turbulent shear stress and the turbulence intensity assume the maxima values (Carollo et al. 2002). The confined region of shear containing the inflection point is called Zone 2, which can be considered a mixing and transition layer between the two zone described above. The distinction of these regions is more and more evident in the case of submerged flexible vegetation and, in general, with increasing vegetation density, defined as the number of vegetal elements per base area, due to the reduction of the momentum exchange between the two zones 1 and 3 (Kowen & Li 1980).

For large part, research on vegetated open channels has focused on flow resistance due to vegetation, in particular on the determination of the friction factor and the drag coefficient in the flow resistance law, by means of analytical flow models (e.g. Kutija & Hong 1996, Righetti & Armanini 2002, Stoesser et al. 2003) and laboratory flumes (Kowen & Unny 1973, Fathi-Maghadam & Kowen 1997, Wu et al. 1999, Kowen & Fathi-Maghadam 2000).

Traditionally, empirical approach to estimate flow resistance are often based on relating Manning's *n* to some parameters selected to describe the flow conditions, but nowadays the assessment of the resistance coefficient is still difficult to carry out. Moreover, most of works consider the vegetation as a wide turf and consequently the bed-friction coefficient is taken as the average of the local values, uniformly constant for all the channel. Less is known about the local effect of the vegetation when it is characterized by a very low concentration. Indeed, in this conditions, it is not possible to consider the flow field homogeneous and so assign constant values to parameters such as the resistance index, the bed-friction velocity and/or the drag force, for the whole canal.

The rood topic of the present work is the investigation of the hydrodynamic effects of both rigid and flexible vegetation on a crossflow, in terms of velocity and turbulence distribution. The research is limited to the case of relatively low current velocities and flow depths higher than the height of vegetation, which was identical for both the rigid and flexible type. Emphasis is put on assigning a minimal density to the artificial plants, as it is expected that in non-uniform, bed-friction conditions in the channel a local analysis is needful for better understanding the phenomenon. Therefore, to capture spatial variability within the array, multiple measurement points were set between each two consecutive elements on the three principal directions. The analysis of measurement data produces a good estimation of the different behavior of the current for the separate presence of the two kinds of vegetation reproduced in the laboratory flume.

2 EXPERIMENTAL METHODS

Experiments were carried out in a re-circulating glass-wall flume 8 m long, 0.3 m wide and 0.4 m deep, located at the Mediterranean Agronomic Institute (IAM) of Bari, Italy. Flow was released from a head tank (1.2 m × 1 m × 1.4 m) equipped with stilling grid and lateral weir, which ensured a smooth access of the water to the flume and maintained a constant head upstream. Two movable gates made in Plexiglas were constructed respectively at the upstream and downstream ends of the flume, to allow the passage of different discharges with different corresponding channel flow depths. At the downstream end of the flume, the flow was intercepted by a stilling reservoir (2 m × 1 m × 1 m) tooled up with four vertical grids to stabilize water and with a triangular weir (V-notch sharp crested weir) for measuring the flow discharge. The water head above the weir crest, on which depends the regression function of the discharge, was measured by an electrical hydrometer. Water disposal regained the pumping reservoir through the closed hydraulic circuit.

For rigid vegetated channel experiments, the plants were simulated by means of metallic cylinders with

Copyright © 2006 Taylor & Francis Group plc, London, UK

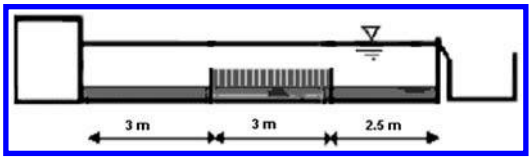


Figure 2. Schematic long-view of the laboratory flume (not to scale).



Figure 3. Photographs of the laboratory flume with rigid (left) and flexible (right) artificial vegetation.

rough lateral surface, while the flexible model array was constructed from commercial broom head. Both kinds of artificial vegetation were mounted in 3 m plywood board, perforated uniformly with holes of 3 mm, that is the diameter of the rigid elements, D, whereas, in the case of flexible vegetation, 8 single elements of the broom head with a diameter 0.4 mm each one were stacked. The three-meter long test area of each vegetation was located around the halfway of the flume (Fig. 2), but for all the channel length same boards were stuck on the bottom in order to obtain a uniform bed roughness. The stems were spaced along the longitudinal and transversal direction by a distance equal respectively to $\Delta x = 10$ cm and $\Delta y = 6$ cm, i.e. the stem density $\lambda_1 = \Delta S^{-2}$ was kept constantly equal to 400 stems/m^2 (Fig. 3). The height of the rigid elements, h_v, was equal to 10 cm and coincided with the flexible vegetation height in the absence of current.

The analyzed configurations differed in the artificial vegetation material, as described above, and in the two flow depths in the flume, $H = 21$ cm and $H = 30$ cm, which corresponded the mean current velocity $U_{C1} = 0.28$ cm/s and $U_{C2} = 0.19$ cm/s, respectively. For all the configurations, the vegetation was taken submerged, allowing us to observe the particular behavior of the crossflow at the top of the stems, depending on the relative submergences considered ($H/h_v = 2.1$ and $H/h_v = 3.0$). The bent height, h_s, of the flexible vegetation was estimated as the average of ten measurements by means of decimal rules fixed to the flume wall. Corresponding to the two given values of the water depth H, h_S was respectively 9.5 cm and 9.2 cm.

The mean velocity components (U, V, W) and the rms turbulence intensities (u′, v′, w′) along the stream-wise (x), lateral (y) and vertical (z) directions, respectively, together with the average Reynolds stresses ($-u'v'$, $-u'w'$, $-v'w'$) on the corresponding coordinate planes, were measured by means of the three-dimensional Acoustic Doppler Velocimetry (ADV) system. Exactly, the origin of the axial coordinate system for the measurements was located at the beginning of the vegetated channel area, in the central section of the channel, with the depth (z) defined as zero at the bottom and positive upwards, and the x-axis positive downstream. Mean and turbulent velocity statistics were estimated from 3000 records sampled at 25 Hz, with a measurement error for each record equal to ± 0.15 mm/s. The distribution of the stems was chosen so as to facilitate the measurements with the ADV probe.

3 RESULTS AND DISCUSSION

3.1 *Velocity field*

In order to study the variations of the velocity distribution at the local scale around both rigid and flexible individual element, several analysis of the velocity component data into the flume have been carried out, along longitudinal and horizontal sections.

Profiles of the time-averaged longitudinal velocity, U(z), are shown in Figure 4 for both kinds of stem (flexible in Fig. 4a and rigid in Fig. 4b), at different longitudinal distances from the plants. In particular, the vertical velocity profiles were measured at six different positions located at the centerline of the flume, in order to neglect the influence of the walls, around the stem fixed at the coordinate $x = 120$ cm. A deep analysis of Figure 4 shows the presence of two regions of flow motion, correspondingly inside and above the submerged vegetation. Exactly, for distance z from the bottom less than h_v or h_s, the current is subject to a strong slow motion due to the presence of the close element. Near the top of the vegetation, both the local velocity and its gradient increase progressively, producing at the vertical profile an evident inflection point and the typical S shape, as reported in literature (e.g. Kowen et al. 1969). Upon the vegetation, the velocity gradient decreases with z, with the concavity directed upward. These differences decrease as we move away upstream or downstream from the stem, and are particular evident for rigid elements. Differently, the six profiles plotted around the flexible plant do not present the same flat individual pattern, for each x-position, as the rigid case. Moreover, the velocity corresponding to the coordinate $x = 120$ cm, where is located the flexible stem plant, is not completely cancelled, as the flow escapes through the branches of the plastic plant. Thus, it is evident from Figure 4, (i) how local the impact of the flow on the vegetation is, in reference

Copyright © 2006 Taylor & Francis Group plc, London, UK

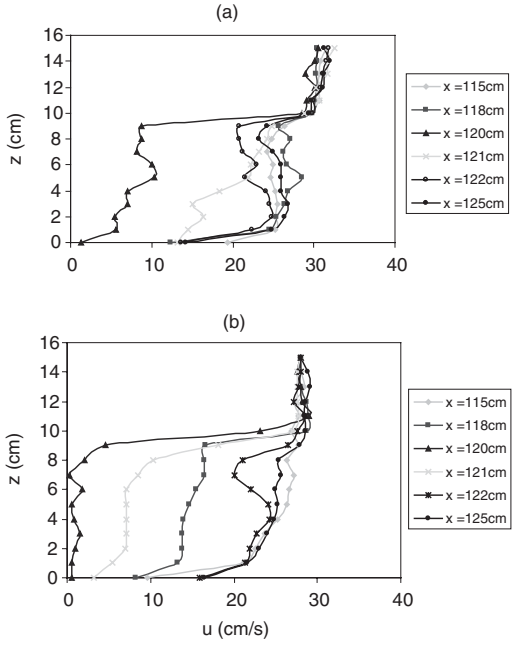


Figure 4. Vertical U-velocity profiles for water depth H = 21 cm in presence of (a) flexible and (b) rigid vegetation.

to the distance from a single stem, and (ii) how different the flow behavior is with the presence of rigid and flexible plants. Same results have been obtained for the configurations with flow depth equal to 30 cm.

To better highlight the local effect of the artificial vegetation on the crossflow, velocity data have been processed and plotted on horizontal planes at different levels. For the sake of brevity, hereafter there will be discussed results relating to a single plane distant from the channel bottom 5 cm and to the single configuration with flow depth of the cross section H = 30 cm, for both rigid and flexible plants. This is the case of Figure 5, which represents the distribution of the U-velocity component normalized by the mean velocity of the current, U_a, at z/H = 0.17, i.e. at the middle height of the stems, in the flume with flexible (Fig. 5a) and rigid (Fig. 5b) vegetation. Dashed contours, which represent values of $U/U_a \leq 0.5$, are localized around the vegetation stems. It should be meant that artificial vegetations delay the flow motion of about the 50% in a area confined to the location of each element. Nevertheless, the different kind of material sees to it that the shape of this area and so the preferred direction of the mutual interference between two consecutive arrays of stems is quite different for the two configurations. In fact, the isovel contours around the rigid plants are not circular but elliptical with major axis parallel to the longitudinal direction, which reveals the anisotropy of vegetation stem effects

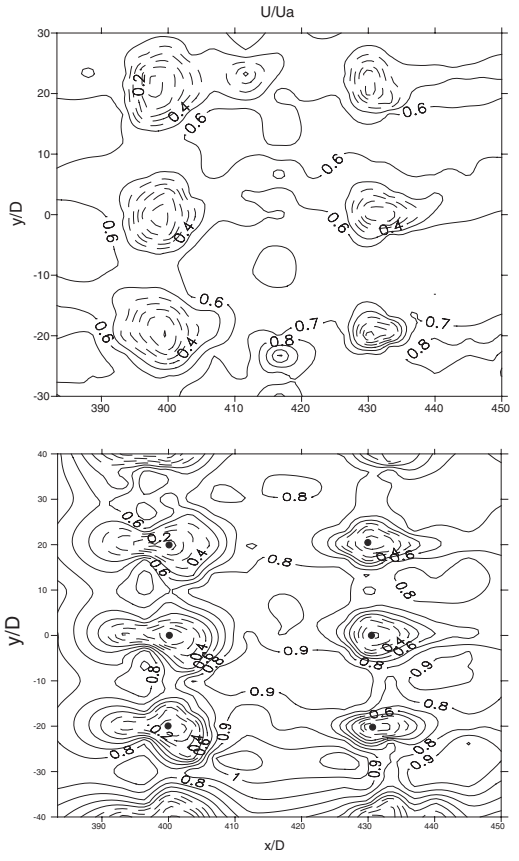


Figure 5. Distribution of the normalized velocity U/U_a in presence of (a) flexible and (b) rigid vegetation. Top view (z/H = 0.17). Black solid circles represent the rigid vegetation stems.

over the hydrodynamic flow distribution. Moreover, considering the continue contours representing values of $U/U_a \geq 0.5$, Figure 5 highlights that the flow pattern is strongly modified, i.e. the current is particularly delayed, by the presence of the flexible elements for all the depth analysed (Fig. 5a), while with rigid cylinders the normalized flow velocity at the middle longitudinal section of two arrays reach the value 1 or slightly large, which mean the negligence of the vegetation stem effects as long as going away from it (Fig. 5b). As a first justification of this different behavior, it must be taken into consideration that both the geometry of the vegetation elements and the turbulence characteristics of the flow affect the hydrodynamic resistance and the size of the vortical wakes generated downstream of the single element (Carollo et al. 2005). In the specific case of the flexible vegetation, because of at each measured location the element is constituted by a group of branches, which tend to open moving

Copyright © 2006 Taylor & Francis Group plc, London, UK

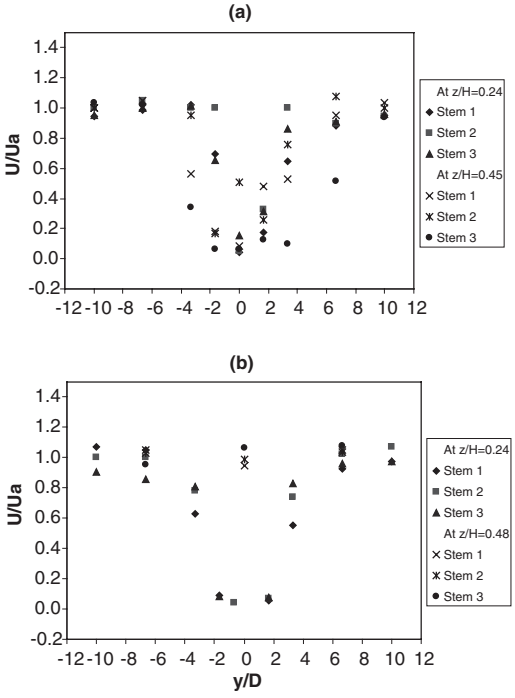


Figure 6. Similarity distribution of streamwise flow velocity U/U_a at $x = 120$ cm (water depth $H = 21$ cm) for three transversal aligned (a) flexible and (b) rigid stems, at two different levels.

upwards, it is understandable why the velocity is closed to zero value for a wide x and y range.

In order to study the different behavior of the flow velocity distribution around the vegetation stems, the values of U/U_a at $x/D = 400$, i.e. immediately beyond a row of plants, have been plotted against y/D, as shown in Figure 6, where the origin ($y/D = 0$) corresponds to the centre of each stem. Both flexible and rigid elements indicated by 1 are located in the axial symmetric longitudinal and transversal section, while stems 2 and 3 are positioned respectively on the right and the left side of stem 1 looking downstream. Data plotted in Figure 6 referred to the configuration with the water depth in the channel $H = 21$ cm. In each diagram, three of the six horizontal profiles of U/U_a correspond to the plane at the middle height of the vegetated zone ($z = 5$ cm), while the second level analysed is different for the flexible and rigid vegetations, as for the first one it coincide with the bent height h_s of the elements ($z = 9.2$ cm), which is less than the fixed height of the rigid stems ($z = 10$ cm). Nevertheless, the aim of the research in this stage has been the investigation of the particular hydraulic path of the flow inside the vegetated zone and just on its top, and the detection of the different behavior due to the particular kind of plants. A comparison of Figures 6a–6b demonstrates that the normalized U-velocity component profiles at $z = 5$ cm obtained around the flexible elements match those related to the rigid ones, with minimum velocity values close to zero in the y/D range between −2 and 2, i.e. just in proximity of each stem, while for larger absolute values of y/D the velocity tends to rich the average value of the current in the flume in absence of vegetation. Contrariwise, at the top of vegetations, the flow pattern is quite different. When the presence of the rigid elements seems to not disturb the current, which velocity values keep constant along the whole transversal section, the flexible vegetation branches make the horizontal velocity profiles more irregular but still similar to the Gaussian curve. Thus, it can be concluded that, halfway between two consecutive stems along the transversal direction, flow patterns in the vegetated area are similar to those of simple open-channel without vegetation, independently of the kind of vegetation. On the contrary, at the top of vegetations, only for the rigid stems, flow resistance disappears and velocity distribution fells to be uniformly similar to the current average value.

3.2 *Turbulence characteristics*

Aquatic plants convert mean kinetic energy into turbulent kinetic energy at the scale of the plant stems (rigid vegetation) and branches (flexible vegetation). This energy transfer, linked to wake generation, affects vegetative drag and turbulence intensity. Drawing on this physical link, turbulence intensity and Reynolds-stresses distributions have been obtained, with the intention of highlighting the influence of different kind of vegetation on the turbulence behavior of the current.

Representative profiles of the rate u'_{rms}/u, with u'_{rms} and u respectively the fluctuation root-mean square and the average of the instantaneous streamwise velocity at the same measurement points, are shown in Figure 7. The two plots refer to the same submerged condition for the flexible and rigid stems, but consider two different water depth of the flume. Profiles for both the considered cases stress a significant discontinuity of the normalized streamwise turbulence in a region near the top of the elements, characterizing the generation of a horizontal shear layer. However, a different behavior is recognizable for the two kinds of artificial vegetations. For the rigid rods, values of u'_{rms}/u peak just below the rod top, as data have been collected 1 cm beyond the element, maintaining same maximum magnitude independently of the hydraulic flume conditions. On the contrary, the maximum streamwise turbulence occurs above the element tops for the flexible canopy situation, particularly when the relative submergence H/h_s is small. Moreover, the influence of the submergence on the turbulent current path in presence of flexible vegetation appears visibly comparing

Copyright © 2006 Taylor & Francis Group plc, London, UK

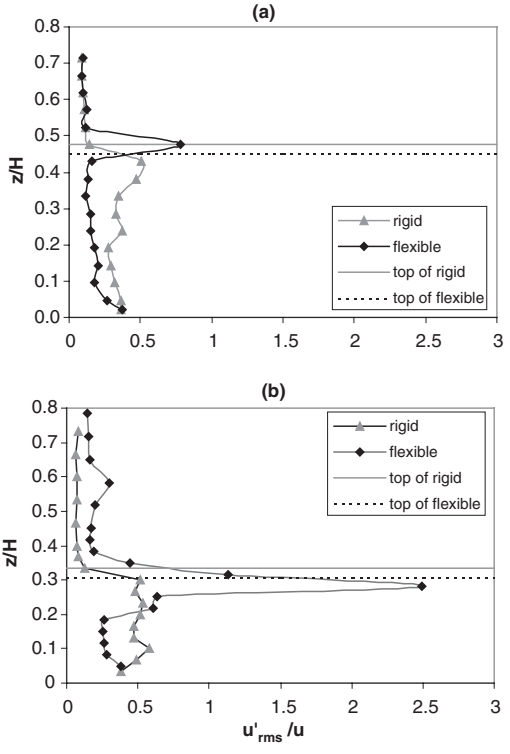


Figure 7. Representative profiles of the normalized, streamwise turbulence intensity u'_{rms}/u for rigid and flexible stems at x/D = 403.3 along the central longitudinal axis and with water depth (a) H = 21 cm and (b) H = 30 cm.

Figures 7a, b. A relatively higher magnitude of turbulence takes place within the flexible canopy when the water depth is H = 30 cm than the case of a lower level of flow depth. This last result is in agreement with findings for both single flexible rod and frond canopy by Wilson et al. (2003) that reveal a lowering of the peak with the decreasing of the flow depth. Same outcomes were pointed out in previous works about open channel flow of intermediate and small submergence of gravel beds (e.g. Bayazit 1976, Nezu & Nakagawa 1993). They found that the maximum turbulence intensity decreases considerably with decreasing submergence, justifying this phenomenon with the damping effect of large scale eddies, i.e. coherent structures like sweeps and ejections. For small and intermediate relative submergence, coherent structures cannot develop their whole size due to the limited flow depth or due to the too large roughness elements. These factors are assumed to lead to the damping of turbulent intensities (Stephan & Gutknecht 2002).

Thus, these observations indicate that also for flexi ble plant covered bed, the maximum value of turbulence intensity u'_{rms}/u is expected to increase with

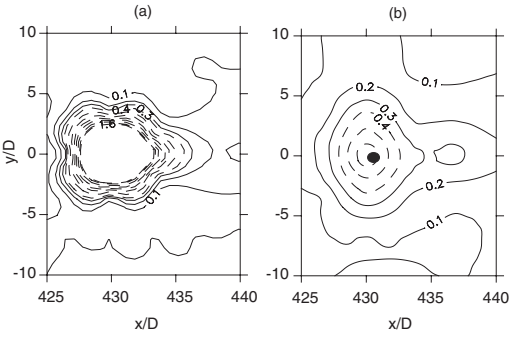


Figure 8. Distribution of the normalized, streamwise turbulence intensity u'_{rms}/u in presence of (a) flexible and (b) rigid vegetation. Top view (z/H = 0.17). Black solid circles represent the rigid vegetation stem.

increasing relative submergence H/h_s, as obtained in the present work.

To better understand the different behavior of the flow in the open channel due to the existence of two kind of plants, Figure 8 shows a representative horizontal map of the relative streamwise turbulence intensity at z/H = 0.17, i.e. at the middle height of the stems. Dashed contours represent values of $u'_{rms}/u \geq 0.40$ and are located in the proximity of both the rigid and flexible rods, where the turbulence intensities reach their maximum values. Nevertheless, high values of the turbulence intensity appear in a wider area surrounding the flexible stem than the rigid one, with the aptitude of turbulence spreading more intensely in the longitudinal direction.

In Figure 9, the vertical Reynolds stresses measured at the same two longitudinal positions (Figs 9a, b) in the channel with flexible and rigid vegetations have been plotted, with the aim of underlining the different spatial behavior of the turbulent current due to the distinct geometry of the rods. The shear stresses have been normalized by the friction velocity of the flume without vegetation but under the same flow condition (i.e. discharge and water depth). It is well know that, in open channel flow and for a value of z/H < 0.2, flow is sensitive to the bed shear stress effects (Nezu & Nakagawa, 1993). Therefore, the average bed shear stress, in this region and according to Prandtl's theory, can be estimated as follows

$$\overline{\tau_b} = \rho \frac{1}{z} \int - u' w' dz \qquad (1)$$

and thus

$$\overline{U^*} = \sqrt{\frac{\overline{\tau_b}}{\rho}} \qquad (2)$$

where ρ is the flow density. In general, for a channel with vegetation canopy, bed shear stress depends

Copyright © 2006 Taylor & Francis Group plc, London, UK

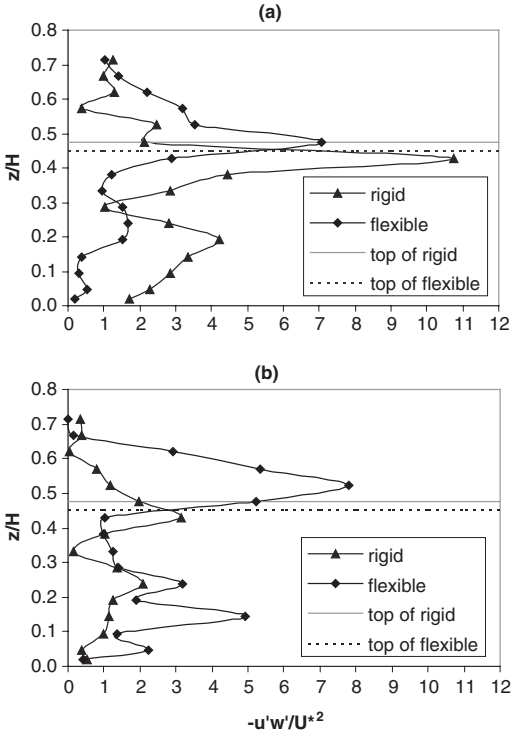


Figure 9. Representative profiles of the normalized, vertical Reynolds stress $-u'w'/U^{*2}$ for rigid and flexible stems along the central longitudinal axis at (a) x/D = 403.3 and (b) x/D = 483.3. Flow depth H = 21 cm.

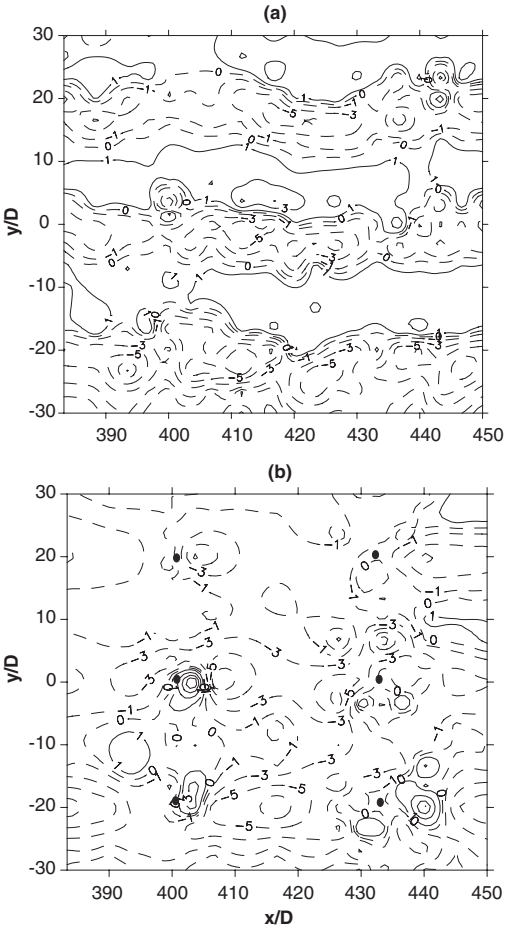


Figure 10. Distribution of the normalized, transversal Reynolds stress $-u'v'/U^{*2}$ in presence of (a) flexible and (b) rigid vegetation. Top view (z/H = 0.24). Black solid circles represent the rigid vegetation stems.

strongly by the presence of vegetation and then the friction velocity should be different from that one found in non vegetated channel. For our case study, the vegetation density was not very elevated to allow to uniform shear distribution. Thus, the friction velocity of the channel without vegetation has been considered more significant as parameter to utilise. Figure 9a shows that immediately beyond the artificial plants the magnitude of the dimensionless stress $-u'w'/U^{*2}$ presents a maximum in a layer close to the top of the elements, as observed in previous Figure 7, with higher value beyond the rigid element. Again, the eight plastic rods fixed in each measurement point shift the Reynolds stress peak to a higher level in the flow, above the canopy, than the single rigid element. This suggests that the plastic stems at their top inhibit the momentum exchange between the interior of the canopy and the overlying surface flow by confining the lower layer, and induce additional turbulence, which shifts the maximum turbulent stresses to a level above the top of the canopy and above the maximum value of the stress register ed for the rigid vegetation. To same results Wilson et al. (2003) came with their work about rod canopy and fronds canopy. What emerges from a comparison between Figures 9a and b is that the turbulent shear layer penetrates a relatively larger horizontal area of the flexible vegetation than the rigid one. So, although the shear generated turbulence 1 cm be-yond the flexible plants is reduced possibly due to the inhibition of the vertical momentum exchange by the greater surface area of the several plastic rods than the single rigid element, opposite outcome is reached at a middle distance between two consecutive stems (Fig. 9b). At this position, the influence of the rigid vegetation on the current seems to disappear, while the effect of the flexible stems is still attending.

As final analysis, Figure 10 shows the transversal Reynolds stress distribution normalized by the velocity friction of the channel, $-u'v'/U^{*2}$, in the

Copyright © 2006 Taylor & Francis Group plc, London, UK

horizontal plane at z/H = 0.24. Dashed contours represent the zero or negative values of stress, whereas the solid ones represent the positive values. In addition, it can be observed two different bitmapped areas, which show a distribution of a stress ranges between −1 and 1. The bitmapped area with more black concentration represents a stress values ranges between 0 and 1. In contrast, the bitmapped area with less black concentration illustrates the stress distribution between −1 and 0. Examining Figure 10a, white areas, of both positive and negative stresses, are located, approximately, along the longitudinal direction, with the only positive contours aligned to the flexible vegetation stems. In contrast, for the rigid rods showed in Figure 10b, a larger amount of white positive areas is located between two longitudinal arrays of stems, with connection in the transversal direction. Regularity of stress distribution between flexible stems depends upon emplacement of the last ones, which well transfer the effect of vegetation on flow patterns. Positive, vertical turbulent stresses correspond to development of positive velocity gradients, $\partial u/\partial z/ > 0$, whereas negative ones correspond to negative gradients, $\partial u/\partial z/ < 0$. As a result, alternate of positive and negative vertical stresses (velocity gradients), along longitudinal direction, as shown in Figure 10a, confirms the development of clock and anti-clock primary vortexes.

4 CONCLUSIONS

An experimental study has been conducted to explore the effect of two types of vegetation, i.e. rigid and flexible, on the flow velocity field and the turbulence structures. Metallic cylinders with rough lateral surface were used to simulate rigid plants, while commercial broom head acted as surrogate of the flexible vegetation. Additionally, artificial plants were submerged in all test runs, with same plant structures, stem lengths and plant densities. Particularly, the vegetation density has been selected with the aim of demonstrating that in non-uniform, bed-friction conditions in the channel, a local analysis is needful for better understanding the phenomenon. The paper also provides insight into the effect of different kinds of submerged plants on momentum transfer and addresses the issue of considering their effects on the current dependent on the relative submergence.

The measured velocity field shows lower magnitude in the vegetated layer than that in the surface-flow layer. This difference decreases as we move away upstream or downstream from the stem. As a first remark, this result can be justified by the particularly low vegetation density chosen for the experimental work. Moreover, it can be seen that near the top of the vegetation, both the local velocity and its gradient increase progressively, producing at the vertical profiles an evident inflection point. In particular, velocity profiles for the rigid plants show higher gradient than the case of flexible vegetation.

In addition to dictating the mean flow patterns, the presence of different vegetations also impacts turbulence structures. At the top of both vegetation kinds, a peak of turbulence intensity occurs, showing the largest value in the case of flexible plants. Finally, alternate of the positive and negative, transversal Reynolds stress distribution, between stems, implies the formation of clock and anti-clockwise vortices.

REFERENCES

Barnes, H.H. 1967. Roughness characteristics of natural channels. *US Geological Survey Water-Supply paper 1849*.

Bayazit, M. 1976. Free surface flow in a channel of large relative roughness. *J. Hydraul. Res.* 14(2): 115–126.

Carollo, F.G., Ferro, V. & Termini, D. 2002. Flow Velocity Measurements in Vegetated Channels. *J. Hydraul. Eng.* 128(7): 664–673.

Carollo, F.G., Ferro, V. & Termini, D. 2005. Flow Resistance Law in Channels with Flexible Submerged Vegetation. *J. Hydraul. Eng.* 131(7): 554–564.

Chow, V.T. 1959. *Open channel hydraulics*. New York: McGraw-Hill.

El-Hakim, O. & Salama, M.M. 1992. Velocity Distribution Inside and Above Branched Flexible Roughness. *Journal of Irrigation and Drainage Engineering* 118(6): 914–927.

Fathi-Maghadam, M. & Kowen, N. 1997. Nonrigid, nonsubmerged, vegetative roughness on floodplains. *J. Hydraul. Eng.* 123(1): 51–57.

Ghisalberti, M. & Nepf, H.M. 2002. Mixing layers and coherent structures in vegetated acquatic flows. *J. Geophys. Res.* 107(C2): 1–11.

Grizzle, R.E., Short, F., Newell, C., Hoven, H. & Kindblom, L. 1996. Hydrodynamically induced synchronous waving of seagrasses: 'Monami' and its possible effects on larval mussel settlement. *J. Exp. Mar. Biol. Ecol.* 206: 165–177.

Järvelä, J. 2002a. Flow resistance of flexible and stiff vegetation: a flume study with natural plants. *J. Hydrol.* 269: 44–54.

Järvelä, J. 2002b. Determination of flow resistance of vegetated channel banks and floodplains. In D. Bousmar & Y. Zech (eds), *River Flow 2002*: 311–318. Lisse: Swets & Zeitlinger.

Järvelä, J. 2004. Determination of flow resistance caused by non-submerged woody vegetation, *Intl. J. River Basin Management* 2(1): 61–70.

Kang, S. 2003. Characteristics of flow over two circular cylinders in a side-by-side arrangement at low Reynolds numbers. *Phys. Fluids* 15(9): 2486–2498.

Kowen, N., Unny, T. & Hill, A. 1969. Flow retardance in vegetated channels. *Proc. Journal of Irrigation and Drainage Engineering* 95(2): 329–342.

Kowen, N. & Unny, T. 1973. Flexible roughness in open channels. *J. Hydraul. Div.* 99(5): 713–728.

Kowen, N. & Li, R.M. 1980. Biomechanics of vegetated channel linings. *J. Hydraul. Div.* 106(6): 1085–1103.

Copyright © 2006 Taylor & Francis Group plc, London, UK

Kowen, N. & Fathi-Maghadam, M. 2000. Friction factors for coniferous trees along rivers. *J. Hydraul. Eng.* 126(10): 732–740.

Kutija, V. & Hong, T.M.H. 1996. A numerical model for assessing the additional resistance to flow introduced by flexible vegetation. *J. Hydraul. Res.* 34(1): 99–114.

Nepf, H.M. & Vivoni, E.R. 2000. Flow structure in depth-limited, vegetated flow. *J. Geophys. Res.* 105(C12): 28547–28557.

Nezu, I. & Nakagawa, H. 1993. *Turbulence in Open Channel Flows*. Rotterdam: Balkema.

Petryk, S. & Bosmajian, G. 1975. Analysis of flow trough vegetation. *J. Hydraul. Div., Am. Soc. Civ. Eng.* 101(7): 871–884.

Righetti, M. & Armanini, A. 2002. Flow resistance in open channel flows with sparsely distributed bushes. *Journal of Hydrology* 269: 55–64.

Silvestrini, J.H. & Lamballais, E. 2004. Direct numerical simulation of oblique vortex shedding from a cylinder in shear flow. *International Journal of Heat and Fluid flow* 25: 461–470.

Stephan, U. & Gutknecht, D. 2002. Hydraulic resistance of submerged flexible vegetation. *J. Hydrol.* 269: 27–43.

Stoesser, T., Wilson, C.A.M.E., Bates, P.D. & Dittrich, A. 2003. Application of a 3D numerical model to river with vegetated floodplains. *J. Hydroinformat.* 5(2): 99–112.

Stone, B.M. & Shen, H.T. 2002. Hydraulic resistance of flow in channels with cylindrical roughness. *J. Hydraul. Eng.* 128(5): 500–506.

Sumner, D., Wong, S.S.T., Price, S.J. & Paydoussis, M.P. 1999. Fluid behaviour of side-by-side circular cylinders in steady cross-flow. *J. Fluids Struct.* 13: 309–330.

Wilson, C.A.M.E., Stoesser, T., Bates, P.D. & Batemann Pinzen, A. 2003. Open Channel Flow through Different Forms of Submerged Flexible Vegetation. *J. Hydraul. Eng.* 129(11): 847–853.

Wu, F-C., Shen, H.W., Chou, Y-J. 1999. Variation of roughness coefficients for unsubmerged and submerged vegetation. *J. Hydraul. Eng.* 125(9): 934–942.

Copyright © 2006 Taylor & Francis Group plc, London, UK

Longitudinal dispersion in vegetated channels

E. Murphy
Department of Civil and Environmental Engineering, Massachusetts Institute of Technology, Cambridge, Massachusetts, USA

M. Ghisalberti
School of Environmental Systems Engineering, University of Western Australia, Crawley, Western Australia, Australia

H.M. Nepf
Department of Civil and Environmental Engineering, Massachusetts Institute of Technology, Cambridge, Massachusetts, USA

ABSTRACT: Vegetation is ubiquitous in rivers, strongly influencing both water conveyance and mass transport. The plant canopy influences both mean and turbulent flow structure, thereby affecting both advection and dispersion. In this paper, we focus on the longitudinal dispersion coefficient. Traditionally, it has been modeled by drawing analogy to rough boundary layers, even in the presence of dense vegetation. This approach is inappropriate in many cases, as the vegetation provides a significant dead zone, which may trap scalars and augment dispersion. This paper describes a new theoretical model for longitudinal dispersion in a vegetated channel. The flow is divided into two regions: (i) a shear layer above the canopy where flow is fast; and (ii) a relatively quiescent zone within the vegetation, where flow and mixing may be greatly diminished. Experimental results are shown to support the theoretical arguments posed in the derivation of the model.

1 INTRODUCTION

In fluvial systems, the primary impact of submerged vegetation is an increase in flow resistance and subsequent reduction in conveyance capacity (Kouwen et al. 1969; Stephan & Gutknecht 2002; Stone & Shen 2002, and references therein). However, recent work has shown in more detail how submerged vegetation dramatically alters the mean and turbulent structure of the flow (Ikeda & Kanazawa 1996; Ghisalberti & Nepf 2004; Poggi et al. 2004). In particular, the velocity profile is far from logarithmic over the full depth, so that traditional treatments of longitudinal dispersion in open channels cannot be directly applied to vegetated channels. While dispersion in flows with emergent vegetation has been studied (Nepf et al. 1997; White & Nepf 2003; Lightbody & Nepf 2006), the effects of submerged vegetation on dispersion have not to date been fully investigated.

The coefficient of longitudinal dispersion (K_x) describes the growth rate of the longitudinal variance (σ_x^2) of a tracer cloud in a shear flow, according to

$$K_x = \frac{1}{2}\frac{d\sigma_x^2}{dt}. \tag{1}$$

After sufficient time, σ_x^2 increases linearly with time, such that K_x is constant. Prior to this time, known as the Fickian limit, differential advection will dominate and the rate of increase in the variance will not necessarily be linear.

In a flow dominated by vertical shear, K_x is given by

$$K_x = -\frac{1}{H}\int_0^H u'' \int_0^z \frac{1}{D_z}\int_0^z u'' dz\, dz\, dz \tag{2}$$

(Fischer et al. 1979), where H is the flow depth, u'' is the deviation from the depth-averaged velocity, $\langle U \rangle$, and D_z is the vertical diffusivity. In an infinitely-wide straight channel with a logarithmic velocity profile, it can be shown analytically that $K_x = 5.93 u_{*H} H$ (Elder 1959). Here, u_{*H} denotes the friction velocity, determined from the relationship

$$u_{*H} = \sqrt{gSH} \tag{3}$$

where S is the surface slope. Elder's analytical prediction is comparable to dispersion coefficients observed in very wide ($w_c/H \sim O(10)$, where w_c is the channel width), straight, rough-bottomed laboratory channels (Fischer 1973). However, these conditions do

Copyright © 2006 Taylor & Francis Group plc, London, UK

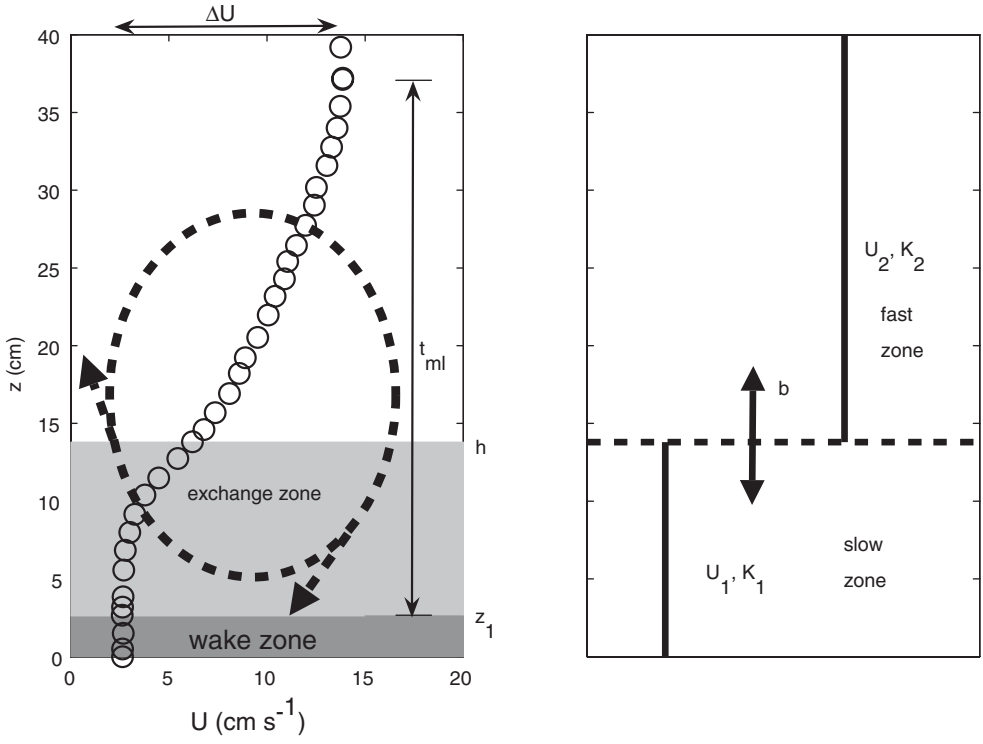


Figure 1. (a) The vertical profile of velocity (U), shown here for Run H (Table 1), resembles a mixing layer. The shear layer does not penetrate fully to the bed, separating the canopy into an upper ("exchange") zone ($z_1 < z < h$) with rapid vertical exchange and a lower ("wake") zone ($0 < z < z_1$) with greatly reduced turbulent velocity and length scales. The diffusivity in the exchange zone is typically an order of magnitude greater than the assumed value in the wake zone (D_w). (b) shows a schematic of the two zone model for the same run. The channel depth is divided into a fast overflow region of thickness ($H - h$) and and a layer of slow flow within the canopy ($0 < z < h$).

not hold in all fluvial systems. For example, lateral nonuniformities such as bends and dead zones can result in significant lateral shear and dramatically increased dispersion (Day 1975; Nordin & Troutman 1980; Davis et al. 2000). Likewise, the drag imparted by submerged vegetation generates velocity profiles and rates of vertical mixing that differ significantly from those in a logarithmic boundary layer (Ghisalberti & Nepf 2005), invalidating several assumptions behind Elder's analysis. Now that there is a greater mechanistic understanding of vegetated flows (to be described in §2), there is a new potential for the prediction of dispersion in vegetated channels. In this paper, we propose a simple model for shear dispersion in vegetated channels and validate it experimentally.

2 TWO-ZONE MODEL FOR VEGETATED CHANNELS

As first presented by Raupach et al. (1996), flows near the top of submerged vegetation most closely resemble mixing layers, rather than boundary layers (Fig. 1a). A mixing layer is a confined region of shear (of size t_{ml}) that separates two regions of approximately constant velocity. The total shear across the layer is denoted by ΔU. Much as in a free-shear-layer, the shear layer produced in vegetated flow is characterized by a street of coherent Kelvin-Helmholtz (K-H) vortices that dominate vertical transport between the canopy and overlying layer (Ikeda & Kanazawa 1996; Ghisalberti & Nepf 2005). These coherent structures do not always grow to encompass the entire flow depth (Nepf & Vivoni 2000). Consequently, as shown in Figure 1a, the canopy is often separated into an upper region of rapid vortex-driven transport (the "exchange zone") and a lower region with greatly reduced mixing (Nepf & Vivoni 2000). Denoting the canopy height as h and the bottom of the shear layer as z_1, the exchange zone spans $z_1 < z < h$. Vertical transport in the lower region (termed the "wake zone", $0 < z < z_1$) is dominated by stem-wake turbulence, with significantly smaller length and velocity scales than the shear-layer vortices. Consequently, the diffusivity in the wake zone

Copyright © 2006 Taylor & Francis Group plc, London, UK

(D_w) is typically an order of magnitude lower than that in the exchange zone (Ghisalberti & Nepf 2005). Nepf et al. (2006) showed that the penetration of shear ($h - z_1$) into a vegetation canopy is inversely proportional to the drag coefficient (C_D) and a canopy density parameter (a),

$$(h - z_1) \approx 0.2(C_D a)^{-1}. \tag{4}$$

Here, a describes the projected frontal area of the vegetation per unit volume and can be related to the familiar leaf area index (LAI) (Nepf & Vivoni 2000, and references therein).

The diminished velocity and turbulence in the canopy layer make it distinct from the overflowing water.We therefore propose a two-zone model for the vegetated channel, as shown in Figure 1b. Constant velocities (U_1 and U_2) are assumed for each zone. K_1 and K_2 are the independent dispersion constants in the slow and fast zones, respectively. Scalar transport across the boundary between the two layers is characterized by the layer exchange coefficient, b, which has dimensions T^{-1}.

This approach is similar to transient storage, or dead zone models, which were developed to explain observations of persistently skewed concentration distributions in natural channels (Day 1975; Nordin & Troutman 1980; van Masijk & Veling 2005). These observations have led to widespread consensus that an accurate analysis of longitudinal dispersion must explicitly consider the effects of "dead", or "slow" zones (Valentine & Wood 1977; Chikwendu & Ojiakor 1985). A plethora of multi-layer models have emerged (Thacker 1975; Smith 1981; Chikwendu & Ojiakor 1985; Chikwendu 1986a; Roberts & Strunin 2004, and references therein), attempting to characterize the effect of transverse variability in pipe and open channel hydraulics. The basis for most of these analyses involves the application of coupled advectiondispersion equations to each region of the flow.

Following Chikwendu's (1986b) approach, in our two-zone model the longitudinal dispersion coefficient at large times is given by

$$K_x = \frac{(\frac{h}{H})^2(\frac{H-h}{H})^2(U_2 - U_1)^2}{b} + (\frac{h}{H})K_1 + (\frac{H-h}{H})K_2. \tag{5}$$

This form highlights three different processes that contribute to dispersion in channels containing submerged vegetation. The first term of (5) represents dispersion that arises from inefficient exchange between the fast zone ($h < z < H$) and the slow zone ($0 < z < h$). In other words, scalars trapped in the slow zone are held up relative to the mass in the fast zone, increasing the spread in the longitudinal direction. For simplicity, we allow

$$(U_2 - U_1) = \beta_1 \Delta U, \tag{6}$$

where β_1 is an $O(1)$ scale constant. Also, we will show in §4 that $\Delta U \sim u_{*H}$. Next, the exchange coefficient, b, is determined by the magnitude of z_1/h. If $(z_1/h) \simeq 1$, vortex penetration is so limited that incanopy diffusion controls exchange between the layers, such that

$$b \simeq \frac{D_w}{h^2}. \tag{7}$$

However, if $(z_1/h) \ll 1$, canopy exchange is driven by the K-H vortices. Scaling arguments and experiments by Ghisalberti & Nepf (2005) show that vortexdriven exchange yields an exchange coefficient

$$b = \frac{\Delta U}{40h}. \tag{8}$$

Physical laboratory constraints, such as flume size, allowed a maximum experimental value of $z_1/h = 0.6$ to be obtained here. For most of the experiments, $z_1/h \ll 1$, such that this regime is the primary focus of the study.

The second term in (5) represents dispersion in the slow zone. K_1 is the dispersion coefficient that would be obtained for $0 < z < h$, if this region were detached from the flow above. Here, K_1 is assumed to be equivalent to the dispersion constant in an emergent canopy, which is a function of vegetation density, Reynolds number and bulk drag coefficient (White & Nepf 2003). The additive effect of vertical velocity shear could potentially be included by evaluation of (2) but this is likely to be insignificant. The contribution of K_1 to the overall dispersion is generally expected to be small, except in the limit as $H \to h$, and is therefore excluded from the model hereafter.

The third term in (5) contains K_2, which represents the longitudinal dispersion in the fast zone due to large-scale velocity shear in this region. Above the canopy, the velocity profile reverts to a logarithmic profile for $z > h$, with a virtual bottom boundary near $z = h$ (Kouwen et al. 1969; Nepf & Vivoni 2000; Carollo et al. 2002). Thus, Elder's simple analytical expression is expected to hold in the region $h < z < H$, yielding

$$K_2 = 5.9u_*(H - h) \tag{9}$$

where u_* is obtained from

$$u_* = \sqrt{gS(H - h)}. \tag{10}$$

Although the analysis of Nepf & Vivoni (2000) suggests that $z = z_1$ is a more appropriate choice for the lower limit to the logarithmic profile, simplicity and practical applicability of the model dictate the use of $z = h$.

Copyright © 2006 Taylor & Francis Group plc, London, UK

It should be mentioned that (5) is consistent with well-established dispersion theory for boundary layers, as it reduces to (9), with $u_* = u_{*H}$, in the limit of $H/h >> 1$. Similarly, in the limit of emergent vegetation ($H/h \rightarrow 1$), $K_x = K_1$.

Bearing the preceding arguments in mind, we can begin to simplify the slow zone model, given by (5). The exchange term is first simplified by substitution of (8), (6) and the scaled ratio $\beta_2 = \Delta U/u_{*H}$. As discussed previously, the slow zone dispersion term containing K_1 is dropped. Finally, K_2 is replaced by the right hand side of (9), yielding

$$K_x = 40\beta_1^2\beta_2\left(\frac{h}{H}\right)^2\left(\frac{H-h}{H}\right)^2 hu_{*H} + 5.9\frac{(H-h)^2}{H}u_* \quad (11)$$

For convenience, we combine the constants in the first term into a single parameter, β. Then, we divide through by $u_*(H-h)$ and rearrange, allowing us to obtain a nondimensional coefficient of longitudinal dispersion given by

$$\frac{K_x}{u_*(H-h)} = \beta\left(\frac{h}{H}\right)^3\left(\frac{H-h}{H}\right)^{1/2} + 5.9\left(\frac{H-h}{H}\right), \quad (12)$$

Alternatively, normalization by $u_{*H}H$ gives

$$\frac{K_x}{u_{*H}H} = \beta\left(\frac{h}{H}\right)^3\left(\frac{H-h}{H}\right)^2 + 5.9\left(\frac{H-h}{H}\right)^{5/2}, \quad (13)$$

which may be preferable for practical application.

3 METHODS

Experiments were conducted in a 24-m-long × 38-cmwide × 58-cm-deep, glass-walled recirculating flume (Fig. 2). The flow rate in the flume was controlled by a Weinman 3G-30P14 pump, with a capacity that ranged from 600 cm^3/s to 15,000 cm^3/s. A Signet flow gauge, with ± 200 cm^3/s accuracy, provided estimates of flow rate. A number of measures were taken to ensure smooth inlet conditions. A dense, 0.5-m-long array of emergent wooden dowels was used to break up turbulence. A mat of rubberized coconut fiber extended throughout the cross-section of the flume, to further dampen the turbulent inlet jet. Honeycomb flow-straighteners eliminated swirl, providing unidirectional flow in the downstream direction.

The model plant canopy consisted of maple cylinders (diameter, $d = 6$ mm), inserted in a random configuration into perforated Plexiglas boards, which covered the entire length of the flume. The dimensionless density (ad) represents the solid volume fraction within the canopy. It was varied between 0.015 and 0.048, within a range representative of dense aquatic meadows, as cited in Ghisalberti & Nepf (2004). Two canopy heights were employed, 7 cm and 14 cm.

Velocity measurements were taken by a two dimensional (2-D) laser Doppler velocimeter (LDV). Velocity profiles for runs A-I were measured by acoustic Doppler velocimeters, as reported in Ghisalberti & Nepf (2004). A 300 mW blue-green argon-ion laser was used in conjunction with a Dantec 58N40 flow velocity analyzer (FVA) unit. Vertical profiles, taken at mid-width in the flume, consisted of five-minute records at spacings of between 0.5 cm and 2 cm, depending on the precision required. All measurements were taken sufficiently far downstream of the start of the canopy such that the flow was fully developed (ie. $\partial/\partial x = 0$). The velocity statistics were temporally averaged and the standard Reynolds decomposition applied, yielding components of mean flow speed and turbulent fluctuation in the x- (longitudinal) and z- (vertical) directions,

$$u = U + u' \quad (14)$$

and

$$w = W + w'. \quad (15)$$

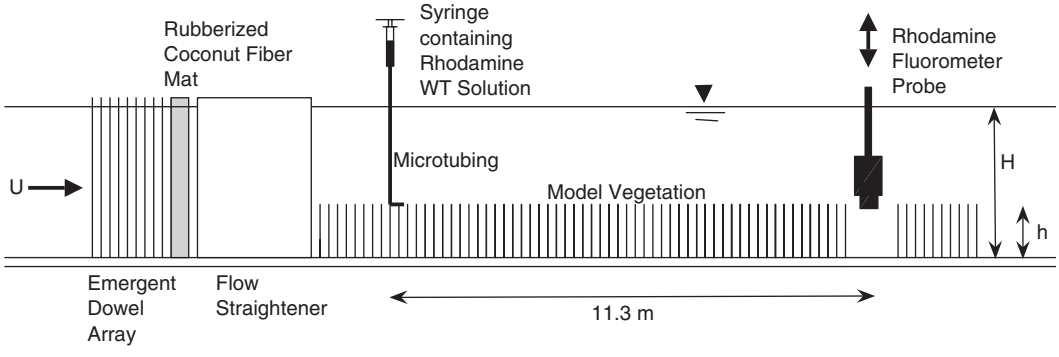


Figure 2. Experimental setup (not shown to scale).

Copyright © 2006 Taylor & Francis Group plc, London, UK

The LDV probe was aligned such that $W = 0$, since unidirectional mean flow was assumed. Reynolds' stress ($-\overline{u'w'}$) profiles were used to determine the distribution of momentum flux, which peaked near the top of the canopy in all cases and decayed towards the bed and free surface.

Twenty-seven different flow scenarios were investigated, with varying values of discharge, Q, and canopy density, ad. The water depth to canopy height ratio, H/h, was also varied between 1 and 4.25 to model vegetation conditions ranging from emergent to thoroughly submerged. The water depth Reynolds number ($Re_H = \langle U \rangle H/\nu$, where angle brackets denote depth-averaging) was between ~1,900 and 41,000 for the experiments. These values of Re_H are consistent with those observed in natural vegetated channels (Leonard & Luther 1995). The stemdiameter Reynolds number ($Re_d = U_1 d/\nu$) is more relevant to dispersion in the slow zone, and values within the experimental range $Re_d \sim 20$–580 correspond well to field conditions.

Tracer experiments were conducted by releasing a small pulse of fluorescent dye at the top of the canopy, 6 m downstream of the leading edge. This longitudinal position was observed to be well within the region of fully developed flow, determined by measured velocity profiles. The tracer consisted of a mixture of Rhodamine WT dye and isopropyl alcohol, with the latter added to render the solute neutrally buoyant in the flume. The dye was injected manually with a 60 ml syringe, through micro-tubing (1 mm inner diameter) that was glued to the top of a dowel at mid-width and oriented parallel to the mean flow. Care was taken to match the injection speed with the local water velocity, to limit near-field mixing effects. The duration of the injection was minimized, to mimic a pulse, and subsequent leakage of tracer into the flow was eliminated by withdrawal of the syringe.

The depth-averaged concentration of dye was measured as a function of time, at a location 11.3 m downstream of the injection point. This was done using a Rhodamine fluorometer, with a sampling rate of 8 Hz. In all cases, the travel time of the tracer cloud from its point of injection to the probe was much greater than the time taken to introduce the dye mixture. This confirmed that the initial condition closely resembled an instantaneous release. The fluorometer was mounted at mid-width in the flume on a pulley system that allowed smooth, precise maneuvering in the vertical plane. As the tracer cloud advected by, the fluorometer was repeatedly raised and dropped at timed intervals, so that the entire water depth was sampled. It was necessary to ensure that the velocity of the probe greatly exceeded the mean Lagrangian velocity of the solute, such that the resulting measurements approached depth-averaged concentration records. Experimental runs were terminated when it was evident that tracer mass in the leading edge of the cloud had fully recirculated around the flume. Each tracer experiment was repeated five times, to reduce random error.

The temporal variance, σ_t^2, of the measured concentration-time distributions was calculated using the method of moments (Aris 1956),

$$\sigma_t{}^2 = \frac{M_2}{M_0} - \left(\frac{M_1}{M_0}\right)^2. \tag{16}$$

M_i denotes the ith temporal moment of the distribution, obtained from

$$M_i = \int_{-\infty}^{\infty} t^i C(t) dt. \tag{17}$$

The velocity, U_c, of the tracer center of mass can be expressed as

$$U_c = X/\mu \tag{18}$$

where X is the distance between the point of injection and the fluorometer (11.3 m), μ, the mean arrival time of the solute cloud, is obtained from the relationship

$$\mu = M_1/M_0. \tag{19}$$

Combining results from five realizations of each experiment yielded ensemble-averaged values of U_c and σ_t. The "frozen cloud" approximation (Fischer et al. 1979, pp. 137) was then applied, meaning that the tracer mass was assumed not to disperse appreciably, as it passed the fluorometer. The spatial variance could then be inferred from the mean Lagrangian velocity of the tracer,

$$\sigma_x^2 = \sigma_t^2 U_c^2 \tag{20}$$

and longitudinal dispersion coefficients were estimated from $K_x = \sigma_x^2/2\mu$, an approximation of (1). Here, it was assumed that X was sufficiently large, in all cases, for the solute to have reached a Fickian dispersive regime. Fischer (1973) proposed that a "reasonable practical criterion" for this to be true, is that the dimensionless time scale for cross-sectional mixing

$$\tilde{t} = t\frac{\langle D_z \rangle}{H^2} \tag{21}$$

should be greater than 0.4. However, preliminary investigations using a numerical random walk model (Murphy, unpubl.) indicate that acceptance of this standard may result in up to 40% underprediction of K_x for tracer experiments in vegetated flows. In fact, errors of less than 10% in K_x may require a minimum of $\tilde{t} \simeq 1.2$, similar to Chatwin's (1972) stricter requirement of $\tilde{t} \geq 1.0$. There are potentially two reasons for this: (i) the depth average D_z in (21) underestimates

Copyright © 2006 Taylor & Francis Group plc, London, UK

the contribution from zones of significantly reduced diffusivity (this is a resolution issue, as discussed by Thacker (1975)), and (ii), concentration measurements at a single location dictate the approximation of (1) by $\sigma_x^2/2\mu$, which will remain an inaccurate predictor of K_x until some time after the onset of a Fickian regime. These subjects will be dealt with in greater detail, in a forthcoming publication.

4 RESULTS

Flow parameters for twenty-five of the twenty-seven experiments are listed in Table 1 (many of the parameters do not apply to conditions of emergent vegetation, so two runs with $H = h$ were omitted). The first eight rows in the table correspond to runs of the same letter in Ghisalberti & Nepf (2004).

The concentration-time distribution for run *A5* is shown in Figure 3. Note that individual realizations are consistent with the average, implying that five repetitions adequately describe each experiment. A nonzero skewness coefficient (also shown in Figure 3) reveals a slight deviation from Gaussian form that agrees with observations in natural channels (Nordin & Troutman 1980). The statistics of all temporal concentration distributions are presented in Table 2, along with the dispersion coefficients obtained from (1). In all cases, $Pe = U_c X/K_x >> 1$, where Pe is the longitudinal dispersion Péclet number. This confirms the prevalence of advection-dominated flow (Levenspiel & Smith 1957), validating the frozen cloud assumption, made in §3.

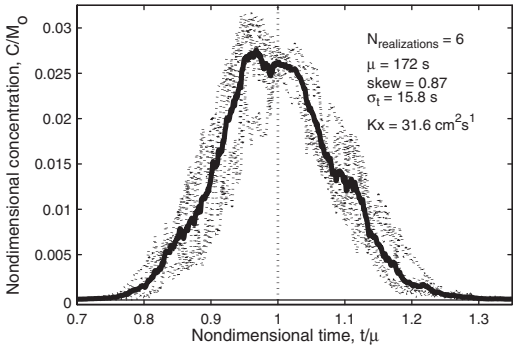


Figure 3. The collapse of the concentration-time curves for run A5. The ensemble average (solid line) is superimposed on the individual realizations (dotted curves). The time and concentration axes have been normalized by the mean arrival time (μ) and the total recovered mass of the solute (M_0), respectively. Normalization of the concentration data eliminates, so far as is possible, non-uniformities across realizations caused by slight differences in the masses of tracer injected (White & Nepf 2003).

Table 1. Summary of experimental conditions and flow parameters.

Run	Q $\times 10^{-2}$ cm^3 s^{-1}	h (cm)	H (cm)	a (cm^{-1})	S $\times 10^5$	U_1 (cm s^{-1})	U_2 (cm s^{-1})	ΔU (cm s^{-1})	$h - z_1$ (cm)	Re_d	Re_H $\times 10^{-4}$
A	48	14.0	46.7	0.025	0.99	1.6	3.7	3.2	12.7	78	1.5
B	17	14.0	46.7	0.025	0.18	0.5	1.5	1.3	9.1	30	0.6
C	74	14.0	46.7	0.034	2.50	2.0	5.5	4.9	10.9	102	2.1
D	48	14.0	46.7	0.034	1.20	1.4	3.8	3.5	12.3	66	1.4
E	143	14.0	46.7	0.040	7.50	4.2	10.6	9.5	11.6	210	4.1
G	48	14.0	46.7	0.040	1.30	1.4	3.7	3.3	10.3	66	1.4
H	143	14.0	46.7	0.080	10.00	3.3	11.1	11.0	11.2	162	4.1
I	94	14.0	46.7	0.080	3.40	2.1	7.2	7.4	9.8	102	2.7
A6	17	7.0	29.8	0.025	0.30	0.6	1.6	1.6	5.8	17	0.4
B6	94	7.0	29.8	0.025	8.04	3.3	8.4	7.0	7.0	152	2.2
C6	48	7.0	29.8	0.025	2.42	1.7	4.4	3.7	3.4	83	1.1
A1	17	7.0	23.6	0.025	1.06	0.7	1.6	1.4	7.0	30	0.3
B1	94	7.0	23.6	0.025	11.57	4.3	10.2	9.1	7.0	207	2.0
C1	48	7.0	23.6	0.025	4.27	2.2	5.1	4.8	5.1	111	1.0
A2	17	7.0	14.0	0.025	1.73	1.3	2.9	2.4	7.0	75	0.3
B2	94	7.0	14.0	0.025	48.66	7.8	15.5	11.8	7.0	461	1.7
C2	48	7.0	14.0	0.025	30.05	5.0	10.6	7.8	7.0	283	1.1
A3	17	7.0	10.5	0.025	12.44	2.5	5.4	5.5	2.9	136	0.4
C3	48	7.0	10.5	0.025	66.61	6.9	14.7	14.6	7.0	395	1.0
A5	17	7.0	8.8	0.025	28.35	2.8	5.3	3.2	3.9	163	0.3
C5	48	7.0	8.8	0.025	134.04	9.9	18.7	12.6	7.0	582	1.1
C6D	48	7.0	29.8	0.080	2.03	0.8	4.6	5.3	7.0	26	1.1
C2D	48	7.0	14.0	0.080	36.64	3.0	9.3	9.5	7.0	142	0.9
A2D	17	7.0	14.0	0.080	4.74	1.0	3.4	3.4	5.3	46	0.3
A3D	17	7.0	10.5	0.080	23.19	2.0	5.2	4.6	5.4	101	0.3

Copyright © 2006 Taylor & Francis Group plc, London, UK

Figure 4 shows that $u_* = \sqrt{gS(H-h)} \simeq \sqrt{-\overline{u'w'|h}}$ for the entire range of H/h. This is not surprising, given that the very definition of a shear velocity is $u_* \equiv \sqrt{\tau_o/p}$, where τ_0 is the shear stress at the bottom

Table 2. Statistics derived from temporal moment analysis of concentration distributions.

Run	μ (s)	σ_t (s)	Pe	K_x (cm^{2}s^{-1})	ε_{Kx}* (cm^{2}s^{-1})
A	390	89.1	39	85	±20
B	1220	231	58	19	±7
C	252	58.4	37	140	±20
D	356	80.3	40	90	±20
E	137	34.1	32	290	±35
G	382	81.0	45	75	±12
H	123	35.2	25	420	±70
I	192	48.6	31	210	±60
A6	729	140	55	32	±5
B6	141	21.1	89	100	±10
C6	252	38.9	84	60	±6
A1	567	100	65	35	±8
B1	96.8	13.0	111	120	±9
C1	192	26.6	104	64	±9
A2	332	48.3	95	41	±12
B2	60.7	5.9	210	100	±30
C2	117	12.1	189	58	±3
A3	234	29.2	129	42	±6
C3	89.4	8.7	211	68	±3
A5	172	15.8	236	32	±4
C5	70.3	5.9	281	65	±9
C6D	289	62.2	43	103	±9
C2D	128	19.0	91	110	±10
A2D	326	52.3	77	51	±9
A3D	231	33.8	93	60	±2

* The uncertainty in K_x shown here is based on the root mean square of the measured variances. The values given do not contain any information about the closeness of the approximation, $K_x = 0.5\ \frac{\partial \sigma_x^2}{\partial t} \approx \frac{\sigma_x^2}{2\mu}$, discussed in §3. This is considered in an upcoming publication.

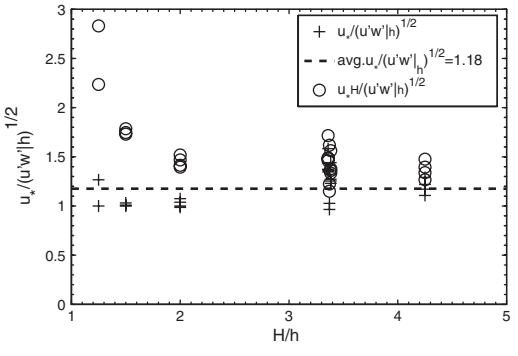


Figure 4. The relationship between the friction velocities, $u_* = \sqrt{gS(H-h)}$ and $u_{*H} = \sqrt{gSH}$, and the square root of the Reynolds stress evaluated at the top of the canopy. Shown for the range of experimentally observed H/h values.

of a logarithmic layer (Kundu & Cohen 2002, pp. 552). As such, this confirms the suitability of the choice of u_* as the characteristic velocity scale for dispersion in the fast zone, rather than u_{*H}, which is seen to vary considerably over a range of H/h conditions (Fig. 4). For thoroughly submerged vegetation ($H/h > 4-5$), the flow approaches a rough boundary layer, and $u*$ and u_{*H} are equally valid velocity scales for dispersion. However, as $H \to h$, the use of u_{*H} becomes increasingly inappropriate, since this parameter cannot accurately capture information about dispersion within the vegetated region, and overpredicts the shear stress at the bottom of the logarithmic layer.

The scaled ratio $\Delta U/u_{*H}$ is reasonably constant (see Figure 5), as anticipated in §2. The same data shows that $\Delta U \sim 6.3u_*$ is just as statistically accurate over the entire range of data. However, we see that in the transition from $H/h = 2$ to $H/h = 1$, the region in which the two zone model is most sensitive to the exchange term of (5), $\Delta U/u_*$ increases significantly. Thus u_{*H} is the more consistent scale for ΔU. This is because u_{*H} captures the total shear across the mixing layer, including the contribution from the region $z < h$, which is not necessarily negligible.

The velocity measurements in Table 1 show that $\beta_1 = (U_2 - U_1)/\Delta U$ is constant (0.68 ± 0.05). Furthermore, Figure 5 shows that $\beta_2 \simeq 4.5$, so given these values we would expect $\beta \simeq 83$. The least-squares best fit of (12) to the experimental data is shown in Figure 6 and yields (with 95% confidence) a value of $\beta = 93 \pm 11$, which agrees with our expectations, within uncertainty.

5 DISCUSSION

Figure 6 shows that the two layer model accurately captures the variation of the longitudinal dispersion coefficient with H/h. We see that as $H/h \to \infty$, velocity shear in the logarithmic fast zone dominates

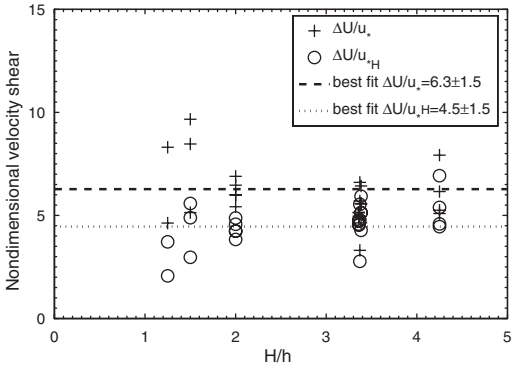


Figure 5. The ratio of total shear to friction velocity and best fit averages ± standard deviations.

Copyright © 2006 Taylor & Francis Group plc, London, UK

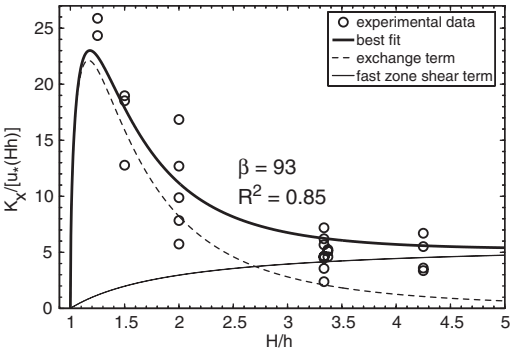


Figure 6. Least squares fit of equation (12) to experimental dispersion coefficient data. The contributions of the first (dash curve) and second (dash dot curve) terms in (5) are shown. The solid curve represents their sum.

dispersion. At this limit, the contribution from inefficient exchange between the layers is negligible, because the slow zone occupies only a small portion of the flow depth. At around $H/h = 2.7$, the two processes are of equal importance. As H/h decreases from this value, fast zone shear dispersion drops off gradually, while layer exchange becomes increasingly important, until a maximum is reached at $H/h \simeq 1.2$. This point also corresponds to a peak in the overall dispersion, as shown by the solid line in Figure 6. The exchange term then drops to zero from here, as $H/h \to 1$. At $H/h = 1$, neither process contributes to dispersion. There will be some contribution from stem-scale shear dispersion in emergent canopies but, as discussed in §2, the relatively low importance of this effect makes its inclusion here unwarranted, especially since $H/h = 1$ is relatively uncommon in rivers.

Increasing scatter in the data as $H/h \to 1$ in Figure 6 may be explained by an expected variability in the exchange coefficient, given by (8). This relationship was determined by Ghisalberti and Nepf (2005) for vegetated flows in which the free surface had negligible effect on the shear layer hydrodynamics. Nepf and Vivoni (2000) showed that this will not be the case when $H/h \leq 2$, as the turbulence length scales at the top of the canopy become confined by the water depth. Figure 5 shows that $(\Delta U/u_*) \simeq (\Delta U/\sqrt{-\overline{u'w'}})$ increases as $H/h \to 1$, meaning that turbulence transport is reduced relative to velocity shear in this limit. This is consistent with diminished eddy length scales for $H/h \leq 2$, as described in Nepf and Vivoni (2000). As discussed in the beginning of this section, this range of H/h corresponds to that in which the contribution of the exchange term in (5) is a maximum, so further investigation of this parameter is critical for improvement of the model.

The convenience of this model lies in the simplicity of the terms in (12) and (13). H, h, u_* and u_{*H} are all easily measured or calculated parameters. Neither the bulk drag coefficient, C_D, nor the canopy density, ad, are explicitly included in the formulation but are instead absorbed into the exchange term and friction velocity, u_*. This is advantageous for a number of reasons. Firstly, there is much about the mechanics of C_D that is still not fully understood (Nepf 1999) and so it is preferable to not need to estimate it. The advantage of including ad implicitly, is that (i), estimating the density of vegetation is often cumbersome and inaccurate, and (ii), u_* is a parameter that is familiar to hydraulic engineers, which increases the compatibility of the model with existing theory.

It should be noted that this model is based on observations and theory for dense canopies and may not extend fully to systems containing sparse vegetation, where plant spacing $\sim O(h)$ or greater.

6 CONCLUSIONS

A theoretical framework for evaluating the longitudinal dispersion coefficient in vegetated flows is proposed. A two-zone model is presented in terms of easily measured parameters, such as the water depth, the overflow friction velocity, u_*, and the height of the vegetation. The model shows good agreement with experimental observations. Three contributory processes are identified: large-scale shear dispersion above the canopy, inefficient exchange between the vegetated layer and the overflow, and stem-scale dispersion within the vegetation. The first two will generally dominate, with the latter only playing an important role in the limit of emergent vegetation. A transition from exchange-driven dispersion to logarithmicshear dispersion is observed at $H/h \simeq 3$.

Further improvement of the model's performance will require a careful examination of the time scales and processes governing exchange between the canopy and the overflow.

ACKNOWLEDGEMENTS

This material is based upon work supported by the National Science Foundation under Grant No. EAR-0309188. Any opinions, findings, and conclusions or recommendations expressed in this material are those of the author(s) and do not necessarily reflect the views of the National Science Foundation. The first author was supported by a Fulbright/Marine Institute Scholarship (2004–2005).

REFERENCES

Aris, R. 1956. On the dispersion of a solute in a fluid flowing through a tube. *Proc. R. Soc. Lond. A235*: 67–77.

Copyright © 2006 Taylor & Francis Group plc, London, UK

Carollo, F., Ferro, V., & Termini, D. 2002. Flow velocity measurements in vegetated channels. *J. Hydraul. Eng. 128*(7): 664–673.

Chatwin, P. 1972. The cumulants of the distribution of a solute dispersing in solvent flowing through a tube. *J. Fluid Mech. 51*(1): 63–67.

Chikwendu, S. 1986a. Application of a slow-zone model to contaminant dispersion in laminar shear flows. *Int. J. Engng. Sci. 24*(6): 1031–1044.

Chikwendu, S. 1986b. Calculation of longitudinal shear dispersivity using an N-zone model as $N \rightarrow \infty$. *J. Fluid Mech. 167*: 19–30.

Chikwendu, S. & Ojiakor, G. 1985. Slow-zone model for longitudinal dispersion in two-dimensional shear flows. *J. Fluid Mech. 152*: 15–38.

Davis, P., Atkinson, T., & Wigley, T. 2000. Longitudinal dispersion in natural channels: 2. the roles of shear flow dispersion and dead zones in the River Severn, U.K. *Hydrol. Earth System Sci. 4*(3): 355–371.

Day, T. 1975. Longitudinal dispersion in natural channels. *Water Resour. Res. 11*(6): 909–918.

Elder, J. 1959. The dispersion of marked fluid in turbulent shear flow. *J. Fluid Mech. 5*: 544–560.

Fischer, H. 1973. Longitudinal dispersion and turbulent mixing in open-channel flow. *Annu. Rev. Fluid Mech. 5*: 59–78.

Fischer, H., List, E., Koh, R., Imberger, J., & Brooks, N. 1979. *Mixing in inland and coastal waters*. San Diego, CA: Academic Press.

Ghisalberti, M. & Nepf, H. 2004. The limited growth of vegetated shear layers. *Water. Resour. Res. 40, W07502, doi:10.1029/2003WR002776*.

Ghisalberti, M. & Nepf, H. 2005. Mass transport in vegetated shear flows. *Env. Fluid Mech. 5*(6): 527–551.

Ikeda, S. & Kanazawa, M. 1996. Three-dimensional organized vortices above flexible water plants. *J. Hydraul. Eng. 122*(11): 634–640.

Kouwen, N., Unny, T., & Hill, H. 1969. Flow retardance in vegetated channels. *J. Irrig. Drain. Div. ASCE 95*(2): 329–342.

Kundu, P. & Cohen, I. 2002. *Fluid mechanics*. San Diego, CA: Academic Press.

Leonard, L. & Luther, M. 1995. Flow hydrodynamics in tidal marsh canopies. *Limnol. Oceanogr. 40*(8): 1474–1484.

Levenspiel, O. & Smith, W. K. 1957. Notes on the diffusion-type model for the longitudinal mixing of fluids in flow. *Chem. Engng. Sci. 6*: 227–233.

Lightbody, A. & Nepf, H. 2006. Prediction of velocity profiles and longitudinal dispersion in emergent salt marsh vegetation. *Limnol. Oceanogr. 51*(1): 218–228.

Murphy, E. Longitudinal dispersion in vegetated aquatic systems. Unpublished data.

Nepf, H. 1999. Drag, turbulence, and diffusion in flow through emergent vegetation. *Water. Resour. Res. 35*(2): 479–489.

Nepf, H., Ghisalberti, M., & White, B. 2006. A scale constraint for shear-layers generated in canopies and other obstructed flow. *Env. Fluid Mech.*, Submitted.

Nepf, H., Mugnier, C., & Zavistoski, R. 1997. The effects of vegetation on longitudinal dispersion. *Estuar. Coast Shelf S. 44*: 675–684.

Nepf, H. & Vivoni, E. 2000. Flow structure in depth-limited, vegetated flow. *J. Geophys. Res. 105*(C12): 28547–28557.

Nordin, C. & Troutman, B. 1980. Longitudinal dispersion in rivers: The persistence of skewness in observed data. *Water Resour. Res. 16*(1): 123–128.

Poggi, D., Porporato, A., Ridolfi, L., Albertson, J., & Katul, G. 2004. The effect of vegetation density on canopy sublayer turbulence. *Bound.-Layer Meteorol. 111*: 565–587.

Raupach, M., Finnigan, J., & Brunet, Y. 1996. Coherent eddies and turbulence in vegetation canopies: the mixinglayer analogy. *Bound.-Layer Meteorol. 78*: 351–382.

Roberts, A. & Strunin, D. 2004. Two-zone model of shear dispersion in a channel using centre manifolds. *Q. Jl. Mech. Appl. Math. 57*(3).

Smith, R. 1981. A delay-diffusion description for contaminant dispersion. *J. Fluid Mech. 105*: 469–486.

Stephan, U. & Gutknecht, D. 2002. Hydraulic resistance of submerged flexible vegetation. *J. Hydrol. 269*: 27–43.

Stone, B. & Shen, H. 2002. Hydraulic resistance of flow in channels with cylindrical roughness. *J. Hydraul. Eng. 128*(5): 500–506.

Thacker, W. C. 1975. A solvable model of "shear dispersion". *J. Phys. Oceanogr. 6*: 66–75.

Valentine, E. & Wood, I. 1977. Longitudinal dispersion with dead zones. *J. Hydraul. Div. A.S.C.E. 103*: 975–990.

van Masijk, A. & Veling, E. 2005. Tracer experiments in the Rhine Basin: Evaluation of the skewness of observed concentration distributions. *J. Hydrol. 307*: 60–78.

White, B. & Nepf, H. 2003. Scalar transport in random cylinder arrays at moderate Reynolds number. *J. Fluid Mech. 487*: 43–79.

Copyright © 2006 Taylor & Francis Group plc, London, UK

Turbulent characteristics of flows through emergent vegetation

P.M. Rowiński & A. Mazurczyk
Institute of Geophysics Polish Academy of Sciences, Warsaw, Poland

ABSTRACT: The results of experimental studies, aimed at the recognition of turbulence structure in channels with the simulated riparian woody vegetation, are discussed in the paper. The study embraces the experiments performed in a compound channel with high vegetation occurring on floodplains and in another channel with specially designed vegetated side pocket. The emphasis is put on the investigations of the influence of vegetation on turbulence characteristics. The analyses include vertical distributions of local mean velocities, turbulent intensities, bed shear stresses, autocorrelation functions and velocity spectra. Relevant temporal and spatial scales of turbulence are also evaluated. The logarithmic law does not apply to the vegetated areas and other methodology has to be checked to describe mean velocities. Also the turbulence characteristics are very strongly affected by the vegetation and particularly by wake vortices generated behind all vegetation rods. Recognition of their pattern is therefore crucial for understanding of momentum and mass transfer through vegetated areas.

1 INTRODUCTION

There is no doubt, that turbulence is a key factor determining the character and intensity of mass and momentum transport in rivers. A great deal of research has been recently devoted to the experimental studies of turbulence in vegetated channels (e.g. Baptist 2005; Ghisalberti and Nepf 2002; Tsujimoto &Kitamura 1992; Velasco et al. 2003). Khublaryan et al. (2004) as the main reason of that interest name the development of macrophytes which depends on the processes of turbulent mass exchange in a vegetated channel, on sediment transport and redeposition, oxygen regime of the environment and so on. All those processes are obviously influenced by turbulence structure. This list may be easily extended to the problems of the flow resistance, diffusion of matter, heat transfer, bed formation, development of various bed forms etc.

Nowadays, occurrence of vegetation on river floodplains is advisable due to its environmental functions, but brings additional complexity of hydraulic processes (Nepf 1999). We are, however, still lacking a comprehensive theory allowing to describe the turbulence structure in vegetated channels and the experimental studies in that direction are highly demanded.

Present study aims at the description of the selected properties of a turbulent flow field through emergent vegetation. To this end, flume experiments were used with model vegetation consisting of regular arrays of stiff vertical cylinders with variation in cylinder spacing employed. Different flow geometries were considered. More detailed description of the turbulence structure will be given elsewhere.

2 EXPERIMENTAL SETUP

2.1 *Laboratory channels' description*

Experiments were performed in two channels of different geometries. First part of investigations was carried out in the Hydraulic Laboratory of the Department of Hydraulic Structures, Faculty of Environmental Science at the Warsaw Agriculture University (further named WAU channel). In a straight open channel 16 m long and 2.10 m wide with symmetrical trapezoidal cross-section (Fig. 1) emergent aluminum pipes of 0.8 cm diameter were evenly placed in an uniform pattern ($m = 42$ trees/m^2) on two floodplains. They were representing stems of riparian trees. It was also assumed that the whole branch systems of trees were above water level and the effects like bending or waving of branches were not considered. The bed slope was 0.0005 and the water surface was kept almost parallel to the bed. Water level was constant – 28 cm in the main channel, 12 cm on the floodplains. Turbulence studies in that channel were already discussed in a previous publication but that study was based on 1D measurements with use of a special programmable electromagnetic velocity meter (Rowiński et al. 2002).

Second part of investigations was conducted in the Institute for Hydraulic Engineering at Braunschweig Technical University in Germany in a two-stage

Copyright © 2006 Taylor & Francis Group plc, London, UK

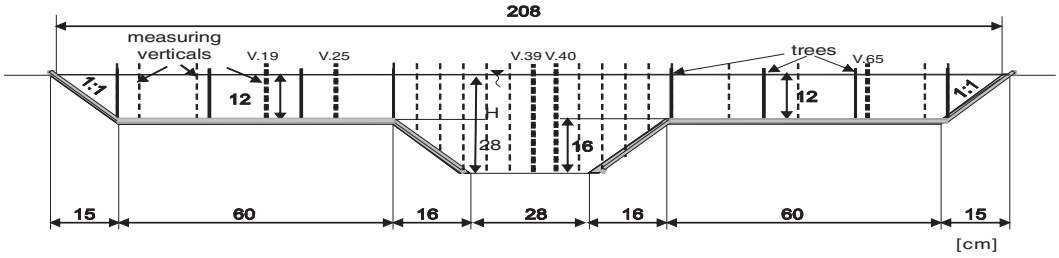


Figure 1. Cross-section of the laboratory channel in Warsaw (WAU).

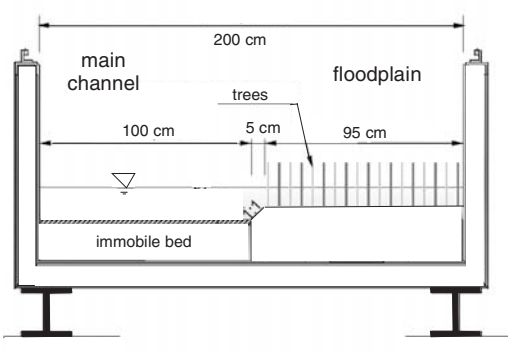


Figure 2. Cross-section of the laboratory channel in Braunschweig (BTU).

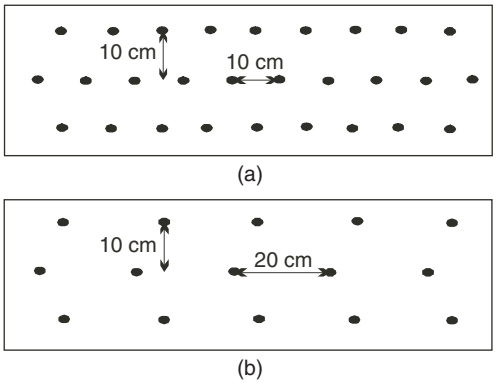


Figure 3. Two densities of sticks on floodplain in BTU (a) 95/m^2 and (b) 45/m^2.

laboratory channel with length of 30 m, width of 2 m, with 1 m wide one-side floodplain (Fig. 2) and the regulated bed-slope (0–1,5%) (Specht 2002). It will be further denoted as BTU channel. A 9-m-long side-pocket (angle 45°) was constructed on the floodplain. Plastic, rigid sticks with diameter of 1 cm were evenly placed in a floodplain-pocket (Fig. 3).

The experiment was carried out under steady-state conditions. The tests were run for the discharge 100 l/s and different arrangements of simulated trees (two sticks' densities and a case with no vegetation were considered) (Fig. 3). The slope was fixed at 0.0009.

2.2 *Measuring equipment*

Instantaneous velocities were measured with use of a three-component acoustic Doppler velocity meter (ADV) manufactured by Sontek Inc. ADV works on pulse-to-pulse coherent Doppler techniques in relatively high temporal resolution (Lohrmann et al. 1994). ADV proved to yield a good description of the turbulence characteristics when certain conditions related to the flow itself and the configuration of the instrument are satisfied (Garcia et al. 2005). The measurements were conducted with maximum frequency 25 Hz.

Buffin-Bélanger & Roy (2005) report, that for the most turbulent statistics sufficient record length for the measurements is 60–90 s. In cases of our experiments even longer time series (120–360 s) were recorded to provide reliability of data and constancy of higher order velocity moments.

2.3 *Measuring setup*

In case of WAU compound channel one cross-section in the middle of the flume was selected for measurements (Fig. 1). It consisted of 23 verticals – six on each floodplain and eleven in the main channel.

The velocities in BTU channel were measured at 12 cross-sections, but for the purpose of this study only the results from the middle cross-section – dividing the pocket into halves – will be presented.

3 RESULTS AND ANALYSIS

3.1 *Mean and friction velocities*

In a compound channel the velocity field is three dimensional (Knight et al 1994), but local longitudinal mean-time velocities give us the most insight into the flow structure. As shown on the contour map of isovels (Fig. 4) velocities in the main channel were definitely higher than on the floodplains and the

Copyright © 2006 Taylor & Francis Group plc, London, UK

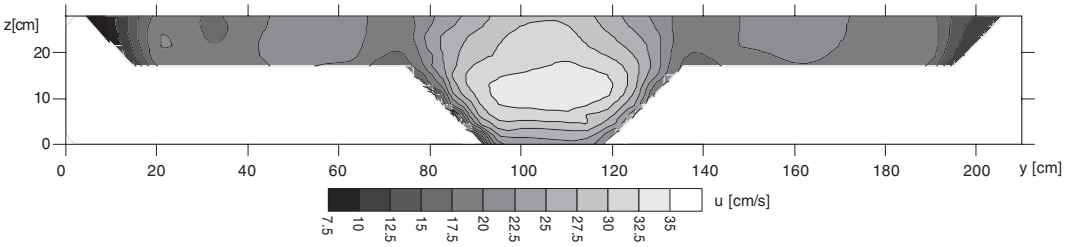


Figure 4. Contour lines for longitudinal mean-time velocities (WAU).

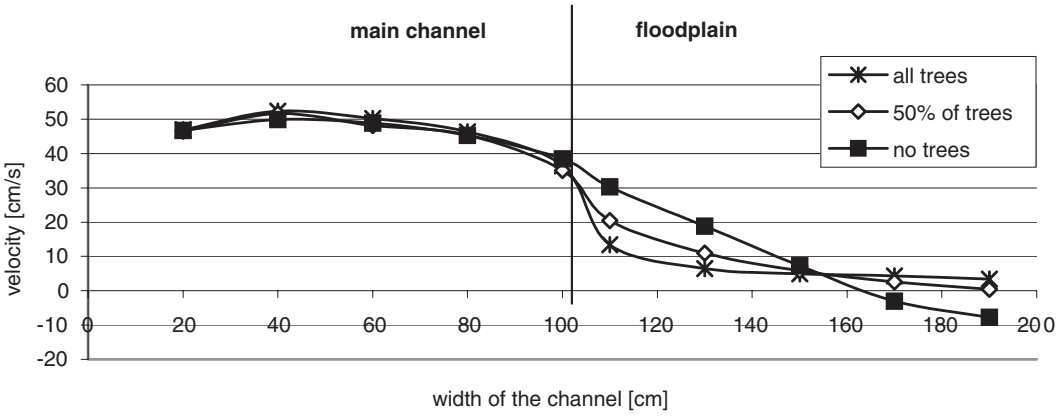


Figure 5. Transverse distributions of longitudinal mean-time velocities for two densities of trees and a case without vegetation (BTU).

flow could be easily divided into separate parts: two floodplain-flows with maximum velocity about 20 cm/s and the main-flow with velocities about two times higher. The main channel-floodplain interaction zone is rather small and velocities on the floodplains vary hardly crosswise.

The studies at BTU allowed for the investigations of the effect of vegetation density on the mean velocity field. Two densities of rods were considered, the occurrence of denser vegetation not only significantly lowered the mean-time velocities on the floodplain, but also constrained the mixing of water from the main channel and floodplain. Denser vegetation reduced visibly the size of the interaction zone (Fig. 5). Negative values of mean velocities in Fig. 5 are the results of the created secondary currents caused by the geometry of the side pockets (Mazurczyk 2004).

The investigations of the vertical distributions of longitudinal mean velocities are of particular importance. In vegetation-free areas one may expect that traditional approach pertaining to logarithmic or exponential distributions should apply. In vegetated areas flow is resisted not only by the boundary shear but also by drag exerted through the flow depth and therefore velocities are expected to be much more uniformly distributed over the flow depth. Fig. 6 presents examples of vertical distributions of mean velocities for both considered channels. In case of the main channel (WAU lab) the longitudinal velocities in the inner region ($z/H < 0.2$) to some degree fulfill the log-law equation (Nezu, Nakagawa 1993):

$$\frac{\overline{u}}{u_*} = \frac{1}{\kappa}\ln\left(\frac{zu_*}{\nu}\right) + A \qquad (1)$$

where $\overline{u}$ = mean-time longitudinal velocity, u_* = shear velocity, z = distance from the bed, κ = universal von Karman constant ($\kappa = 0.41$), ν = kinematic viscosity of water, A = integral constant. The main channel WAU is rather narrow and some interactions with the floodplains occur. Therefore the integral constant A varied in larger range (from 4.2 to 6) than suggested in literature.

In vegetated areas almost uniform vertical longitudinal velocity distributions are observed (Fig. 6). Various attempts to find simple mathematical formulae for vertical velocity distributions have recently been undertaken (Baptist 2005; Khublaryan et al. 2004; Rowiński and Kubrak 2002). The model proposed by Rowiński and Kubrak (2002) proved to provide good agreement with measured data. That model takes into consideration the forces acting on the volumetric element surrounding rods simulating

Copyright © 2006 Taylor & Francis Group plc, London, UK

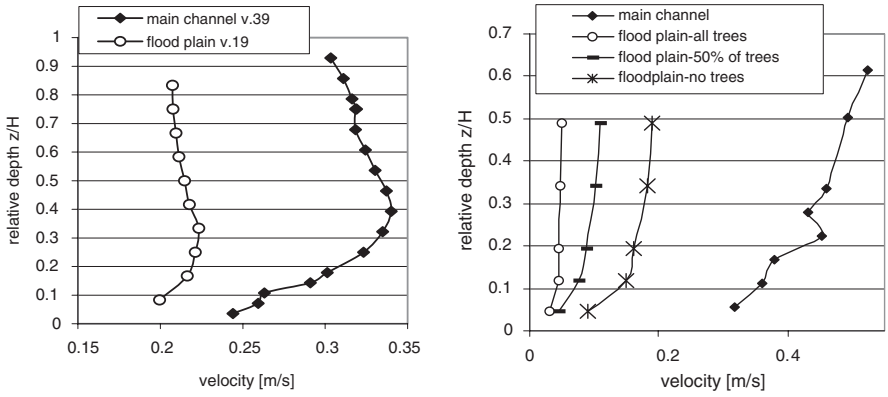


Figure 6. Examples of vertical profiles of longitudinal velocities in WAU (left) and BTU (right).

riparian trees. In the model a mixing length hypothesis was used but with the modification that the mixing length is a linear function of the distance from the bed up to a given level and further it is fairly constant due to the eddy generation by vegetation elements only. All the mentioned models account for flow resistance by means of a friction velocity or bed shear stress. Evaluation of bed shear stresses in vegetated channels is another still open research question.

3D measurements of turbulent velocities provide an opportunity to compare different methods of the evaluation of friction velocity. The detailed study of this kind has been recently given in (Rowiński et al 2005). In principle at the points in the centre of floodplains, friction velocities obtained by means of the near-bed Reynolds stress method and 1D iterative procedure, described in the mentioned paper of Rowiński and Kubrak (2002), provide similar results. The disadvantage of the near-bed Reynolds stress method is that it pertains to the detailed measurements of fluctuating velocities which in practice is rarely available. The method based on the bulk velocities, however, is relevant only at sufficiently large distance from the main channel and the sloping banks to neglect the effect of transverse momentum transport. Friction velocities on the vegetated floodplains varied in the range from 1 to 1.36 cm/s at WAU laboratory.

3.2 *Statistical properties of turbulence*

Second, third and fourth order statistics are frequently used to characterize turbulent velocity field. Particularly, the information on turbulent intensities is very important – these values have a direct impact on mass, momentum and energy transfer in the channel.

The relative turbulent intensities in three directions by definition are:

$$\sigma_x = \sqrt{\overline{u'^2}}\ /\bar{u} \quad \sigma_y = \sqrt{\overline{v'^2}}\ /\bar{u} \quad \sigma_z = \sqrt{\overline{w'^2}}\ /\bar{u} \qquad (2)$$

where u′, v′, w′ = fluctuating components and $\bar{u}$ = mean-time longitudinal velocity in the Reynolds decomposition of the instantaneous point velocity.

It has been observed that turbulence intensities in longitudinal direction are generally much larger than those in the vertical and transverse directions – turbulence is not isotropic in that areas. In the surface boundary layers (in the main channels in both WAU and BTU) their values are much smaller than in the vegetated areas. In principle, vegetation generates turbulence along whole verticals by creation of a wake behind a row of parallel rods. As can be seen in Fig. 7 larger density of vegetation creates larger turbulent intensities. The further increase, however, of the density of vegetation may cause damping of the magnitudes of root-mean squared velocities, similarly as in the atmospheric flows within plant canopies (e.g. Poggi et al. 2004). This condition was not checked in the present study. High relative turbulence intensities in flows through vegetation, often (especially in BTU) exceeding the value of 0.3, cause methodological problems. In such situations Taylor's frozen eddy hypothesis is violated and we may not assume that the properties of the eddies remain unchanged by the time they pass the sensor.

Taking the whole cross-section into consideration (case of WAU), one can observe that the calculated values are visibly higher above the slope between the main channel and the floodplain. Remarkable increase of intensities appear also near the sloping bank of the floodplains and in the main channel-floodplain interaction zones (Fig. 8).

Turbulent kinetic energy defined as:

$$k = 0.5\sqrt{u'^2 + v'^2 + w'^2} \qquad (3)$$

at selected verticals is shown in Fig. 9. The turbulent kinetic energy is produced by shear and wakes. In principle shear production converts mean kinetic energy to turbulence and at the same time wakes are

Copyright © 2006 Taylor & Francis Group plc, London, UK

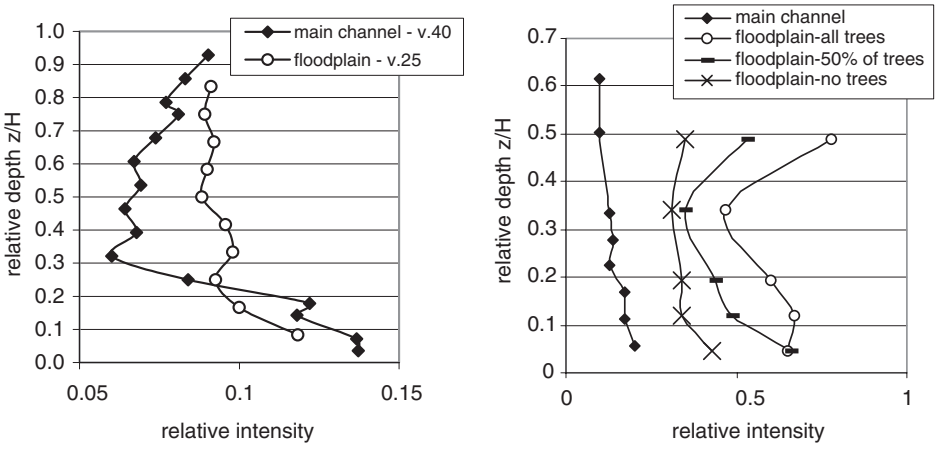


Figure 7. Vertical distributions of relative turbulence intensities in longitudinal direction in WAU (left) and BTU (right).

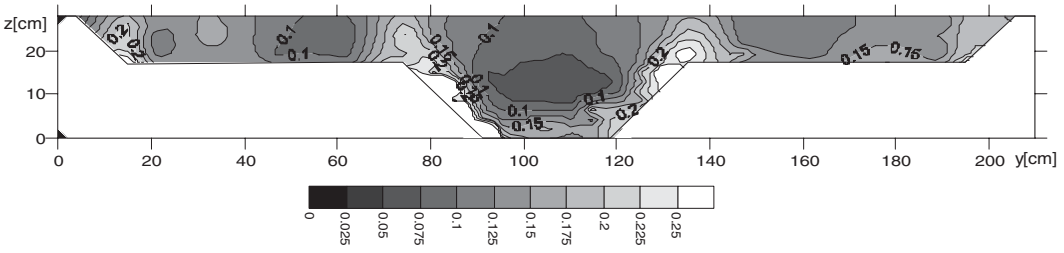


Figure 8. Contour map of relative turbulence intensities in longitudinal direction in WAU.

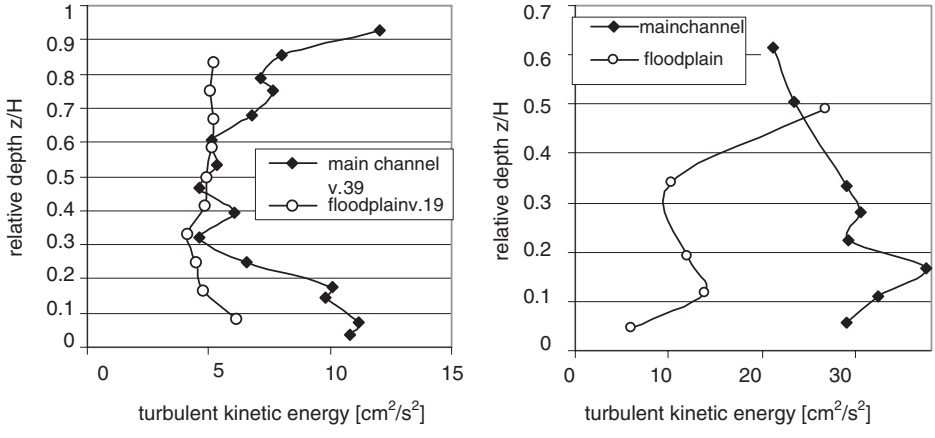


Figure 9. Vertical distributions of turbulent kinetic energy in WAU (left) and BTU (right).

created as an effect of work against form drag. This is characteristic of turbulence in vegetated areas only and has very important consequences. Firstly it makes the vertical distributions of kinetic energy much more uniformly distributed, which is particularly evident in case of WAU. One may also suspect that this additional work against form drag may cause disturbances in the inertial subrange of the turbulence cascade which may bring about the deviation from the "−5/3" power law in the energy spectra – it will be shown further in the

Copyright © 2006 Taylor & Francis Group plc, London, UK

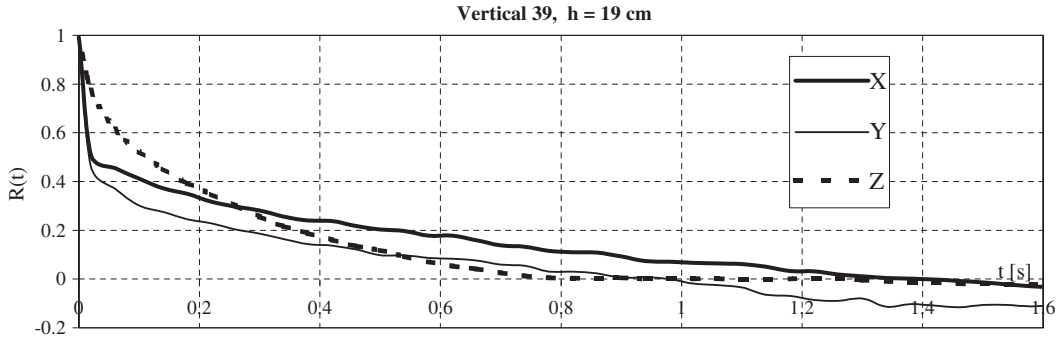


Figure 10. Autocorrelation functions of three velocity components 19 cm above the bed in the middle-profile in the main channel (WAU).

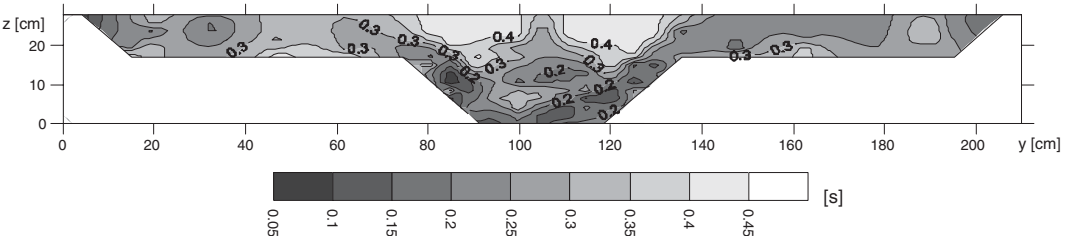


Figure 11. Contour map of time scales of turbulence in streamwise direction [s] – WAU channel.

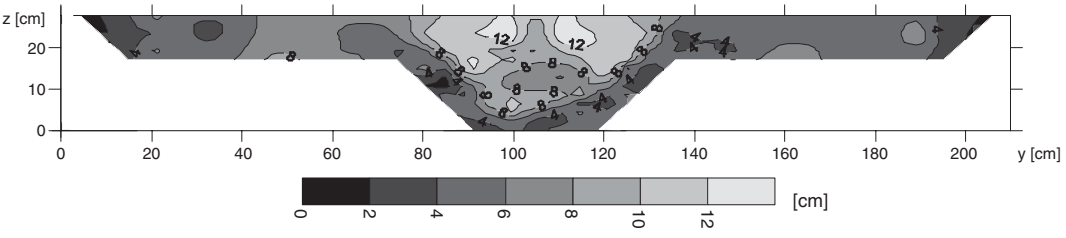


Figure 12. Contour map of spatial scales of turbulence [cm] – WAU channel.

paper. But this expectation is not confirmed in our study.

3.3 *Scales of turbulence*

Autocorrelation functions R(t) were used for the evaluation of macro time-scales of turbulence. Those functions exhibit very similar forms of decaying curves with an alteration of the domains of the positive and negative values (e.g. Fig. 10). The values of the time scale of turbulence T (the eddies' period), calculated as:

$$T = \int_0^\infty R(t)dt \qquad (4)$$

range over floodplains from 0.4 to 0.54 s and in the main channel from 0.2 to 0.46 s in WAU (Fig. 11). Taking into account a very rough approximation of spatial scales, by means of the Taylor hypothesis of "frozen turbulence" (which is not justified at few points at WAU channel with large turbulent intensities) one obtains the following. The distributions of the sizes of eddies do not reveal any stable regularity. But they have the tendency to decrease towards the channel bed within the main channel and to be rather uniformly distributed at verticals within floodplains (Fig. 12). The relative lengths of eddies are bigger on the floodplains and achieve values of 0.5 to 1 of the flow depths on the floodplains, whereas in the main channel the sizes of largest eddies do not exceed the value of 0.5 of the total water depth.

Copyright © 2006 Taylor & Francis Group plc, London, UK

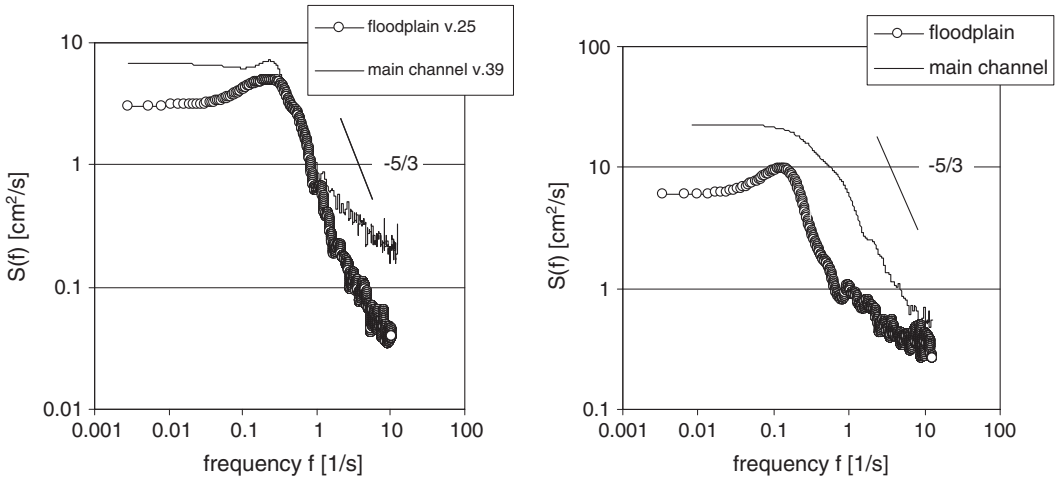


Figure 13. Frequency spectra for selected points in WAU at water depth z = 21 cm (left) and BTU at z = 9 cm (right).

3.4 *Frequency spectra*

Characteristic one-side frequency spectra at the selected measuring points are shown in Fig. 13. Those spectra are presented for both vegetation-free areas and for flows within emergent vegetation to reveal the basic differences.

There is easily distinguishable peak in the low frequency region corresponding to time periods analogous to the periods of motion of the macro turbulent eddies. The movement of large scale eddies is most likely the reason of the low-frequency flow velocity fluctuations.

For the eddies smaller than the energy containing eddies and much larger than dissipative eddies, turbulence is controlled solely by the dissipation rate and the size of the eddy. In this subrange the energy power spectrum should fulfill "−5/3" power law (Nezu & Nakagawa 1993). The inertial subranges can be easily indicated in both main channels of WAU and BTU and in most situations in vegetated areas.

4 CONCLUSIONS

Large scale turbulence structure has been investigated in two different channels with the simulated vegetation occurring on floodplains. The effect of vegetation is considerably high and it influences most of the turbulence characteristics in the channel. Particularly evident is the additional energy supply causing that turbulent intensities and turbulent kinetic energy become more uniformly distributed at verticals. It is also reflected in the frequency spectra at low frequencies. To complement the picture one should also provide a detailed study of Reynolds stresses together with their decomposition into four quadrants, providing the information on outward interactions, ejections, inward interactions and sweeps. Such information will be provided in a separate publication.

ACKNOWLEDGEMENTS

This study was supported by the Polish Ministry of Education and Science – grants no 2 P04D 026 29 and 2 P06S 028 29.

REFERENCES

Baptist, M. 2005. Modelling floodplain biogeomorphology. Delft University Press. P. 195.

Buffin-Bélanger, T., Roy, A.G. 2005. 1 min in the life of a river: selecting the optimal record length for the measurement of turbulence in fluvial boundary layers, *Geomorphology 68*: 77–94.

Garcia, C.M., Cantero, M.I., Nino, Y., Garcia, M.H. 2005. Turbulence Measurements with Acoustic Doppler Velocimeters, *Journal of Hydraulic Engineering, December 2005:* 1062–1073.

Ghisalberti, M., Nepf, H.M. 2002. Mixing layers and coherent structures in vegetated aquatic flows, *Journal of Geophysical Research, 107, C2:* 3-1-3-11.

Khublaryan, M.G., Frolov, A.P., Zyryanov, V.N. 2004. Modeling Water Flow in the Presence of Higher Vegetation, *Water Resources, 31, 6*: 617–622.

Knight, D.W., Yuen, K.W.H., Al-Hamid, A.A.I. 1994. Boundary shear stress distributions in open channel flow, *Mixing and Transport in the Environment*, Eds. K.J. Beven, P.C. Chatwin and J.H. Millibank, John Wiley & Sons: 51–87.

Lohrmann, A., Cabrera, R., Kraus, N. 1994. Acoustic-Doppler Velocimeter (ADV) for Laboratory Use. *Fundamentals and Advacements in Hydraulic Measurements and Experimentation; Proc., Buffalo*, New York: 351–365.

Mazurczyk, A. 2004. Horizontal velocity distributions in a compound channel with a vegetated floodplain, *24th International School of Hydraulics, Hydraulic problems in*

Copyright © 2006 Taylor & Francis Group plc, London, UK

Environmental Engineering (ed. W. Majewski), Jastrzębia Góra: 211–218.

Nepf, H.M. 1999. Drag, turbulence and diffusion in flow through emergent vegetation, *Water Resour. Res. 35(2)*: 479–489.

Nezu, I., Nakagawa, H. 1993. Turbulence in open-channel flows, Rotterdam: Balkema.

Poggi, D., Porporato, A., Ridolfi, L., Albertson, J.D., Katul, G.G. 2004. The effect of vegetation density on canopy sub-layer turbulence, *Boundary-Layer Meteorology, 111*: 565–587

Rowiński, P.M., Aberle, J., Mazurczyk, A. 2005. Shear velocity estimation in hydraulic research. *Acta Geophysica Polonica 53 (4):* 567–583.

Rowiński, P.M., Czernuszenko, W., Kozioł, A.P., Kubrak, J. 2002. Properties of a streamwise turbulent flow field in an open two-stage channel, *Archives of Hydro-Engineering and Environmental Mechanics* 49, 2: 37–57.

Rowiński P.M., Kubrak J., 2002, A mixing-length model for predicting vertical velocity distribution in flows through emergent vegetation. *Hydrol. Sci. J.* 46 (6): 893–904.

Specht, F.J. 2002. Einfluss von Gerinnebreite und Uferbewuchs auf die hydraulisch-sedimentologischen Verhältnisse naturnaher Fließgewässer, TU Braunschweig, ISBN 3-89720-606-4 [doctor thesis].

Tsujimoto, T., Kitamura, T. 1992. Experimental study on flow with vegetation zone in the middle of open channel, KHL Progressive Report, Hydraulics Laboratory, Kanazawa University: 47–66.

Velasco, D., Bateman, A., Redondo, J.M., Demedina, V. 2003. An open channel flow experimental and theoretical study of resistance and turbulent characterization over flexible vegetated linings, Flow, *Turbulence and Combustion, 70*: 69–88.

Copyright © 2006 Taylor & Francis Group plc, London, UK

Longitudinal dispersion in a lowland river with submersed vegetation

T. Sukhodolova, A. Sukhodolov, H-P. Kozerski & J. Köhler
Institute of Freshwater Ecology and Inland Fisheries, Berlin, Germany

ABSTRACT: Aquatic plants increase hydraulic resistance, modify transport and mixing processes. To assess quantitatively the impact of vegetation on these processes field tracer studies were performed on the Müggelspree river. Analysis of obtained data indicated that in early spring, when vegetation is absent and water discharges are relatively high, the volume of dead zones is small but their retention time is large. During the vegetation period the volume of dead zones increases with the increase of biomass but the retention time of dead zones decreases two orders of magnitude. In early spring the dead zones are represented predominantly by recirculation zones formed by flow separation on banks irregularities. In vegetative period the dead zones are formed by blocking effect of submersible and emergent vegetation occupying substantial part of the river cross-section though penetration time of these dead zones is comparable with the time scales of wakes evolving behind the plant canopies.

1 INTRODUCTION

Aquatic plants, or macrophytes, colonize lowland rivers and produce considerable biomass – a source of fine particulate organic material utilized by invertebrates (Cushing & Allan 2001). However their role in ecosystems is generally associated with the effect on river flow and habitats of many species of the aquatic life (Carpenter & Lodge 1986). A quantitative assessment of the effects of macrophytes represents therefore a challenging task for ecologists, river practitioners, and the community of hydrodynamic scientists (Denny 1988; Nepf 1999; Righetti & Armanini 2002).

Macrophytes form patchy patterns composed of stands variable in dimension and locality, having well defined margins leading to the development of significant gradients in flow velocities. Within the stands the flow is reduced due to the shading by stems and leaves of plants and hence the mixing processes are modified.

Mixing processes, in form of one-dimensional approach suitable for practical purposes in river studies, were for long time treated in frame of classical Fickian theory (Fischer 1966; Day 1975; Czernuszenko 1990; Sukhodolov et al. 1997). However, because of grooving evidence for inconsistency between field observations and the theory an alternate, model with dead zones, was proposed (Pedersen 1977; Valentine & Wood 1977; Runkel and Chapra 1993; Czernuszenko & Rowinski 1997). The advantage of using longitudinal dispersion model with dead zones is that the model is capable to describe complex asymmetric distributions of tracer concentrations in flows with stagnant or recerculating zones. Although the model vividly represents a convenient tool for studies in natural streams with vegetation, there has been relatively little reported in the literature about this aspect of the model application.

The purpose of this paper is to report the results of the field tracer studies exploring mixing processes and seasonal dynamics of these processes in a river reach with vegetation. Analysis of the data was completed using longitudinal dispersion model with dead zones there and the results are compared to the predictions of the Fickian theory.

2 THEORETICAL BACKGROUNDS

Longitudinal dispersion with dead zones combines two fundamental physical mixing processes, turbulent diffusion and advection, and constitutes of differential equations describing mass conservation for stream and dead zone segments (Czernuszenko & Rowinski 1997)

$$\frac{\partial C}{\partial t}+U\frac{\partial C}{\partial x}-D\frac{\partial^2 C}{\partial x^2}=\frac{\varepsilon}{T}\left(C_d-C\right) \quad (1)$$

$$\frac{\partial C_d}{\partial t}=\frac{\left(C-C_d\right)}{T} \quad (2)$$

where C and C_d are cross-sectionally averaged in-stream concentration and dead zone solute concentration, t is time, x is distance, U is mean flow velocity, ε is spatial average dead zone volume fraction $\varepsilon = A_d/A$, A_d is spatial average of dead zone cross-sectional area, A is cross-section area of the stream,

Copyright © 2006 Taylor & Francis Group plc, London, UK

T is dead zone time scale called also dead zone penetration time, and D is dispersion coefficient.

The system (1) and (2) transforms to the classical advection-dispersion equation when $\varepsilon \to 0$ and $T \to \infty$. To solve dead zone balance equations (1) and (2) one needs to specify boundary and initial conditions (Czernuszenko et al. 1997)

$$C_d(x,0) = C(x,0) = 0, \quad 0 < x < \infty \tag{3}$$

$$C(0,t) = C_0(t), \quad \lim_{x\to\infty} C(x,t) = 0 \tag{4}$$

Although hitherto analytical solutions of the boundary value problem (1)–(4) have been not found, the temporal moments of the concentration distributions were proposed recently (Czernuszenko & Rowinski 1997)

$$\mu_1 = \bar{t} = \frac{2D}{U^2} + \frac{x}{U}(1+\varepsilon) \tag{5}$$

$$\mu_2 = \sigma_t^2 = \frac{8D^2}{U^2} + \frac{x}{U}\frac{2D}{U^2}(1+\varepsilon) + 2\frac{x}{U}\varepsilon T \tag{6}$$

$$\mu_3 = Sk \times \sigma_t^3 = 2\frac{x^2 D}{U^4}(1+\varepsilon)^2\varepsilon + 64\frac{D^3}{U^6} + \tag{7}$$

$$\frac{x}{U}\left[12\frac{D^2}{U^4}(1+\varepsilon)^2 + 4\varepsilon T(\varepsilon+2) + 6\varepsilon T^2\right]$$

where μ_i, $i = 1, 2, 3$ are central moments of the temporal concentration distribution. The first moment characterizes the transport rate of the mass center of the concentration distribution and sometimes, specifically in freshwater biology, called stream retention time. The second moment characterizes the spreading rate of the solution cloud and the third one is representing the shape of the cloud and can be normalized with the second moment to obtain skewness coefficient.

Analysis of experimental and numerical studies of the boundary value problem (1)–(4) show that equations (5)–(7) adequately represent spatial evolution for temporal moments of concentration distribution (Czernuszenko et al. 1997). The temporal moments for the classical longitudinal dispersion model, exactly the same as presented by Nordin & Troutman (1980), can be obtained considering asymptotical behavior of the system (1) and (2). The moments (6)–(7) can be used to determine parameters of the dead zone model U, D, ε and T from results of tracer studies by means of nonlinear optimization procedure similar to the methods of moments in the classical dispersion model.

3 FIELD TRACER STUDIES

3.1 *Experimental river reach*

Tracer experiments were carried out during May–August 2005 on the downstream part of the river Spree

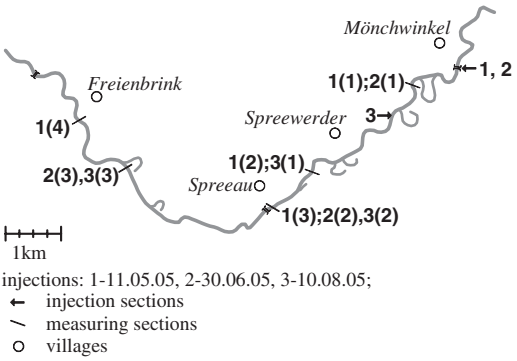


Figure 1. Experimental river reach on the Müggelspree river.

(Müggelspree) in Germany. The Spree river is a typical lowland river about four hundred kilometers in length, running from Lusatian mountains through several shallow lakes to Berlin, were it joins the Havel river. The Spree river is crossed by the Oder – Spree canal near Fürstenwalde where the river is completely intercepted by the canal. Therefore the source of the lower part of the river – Müggelspree – is located at the outlet of the canal near the village Grosse Tranke. The river reach between the bridge near the village of Mönchwinkel and the bridge at autobahn Berliner Ring was selected as the experimental river reach for this study (Figure 1).

The river channel on there is canalized slightly sinuous in plane with a trapezoidal shape of the cross-section. The banks are protected with a rip-rap of cobbles. The river within experimental river reach has only minor tributaries with discharge of few liters per second and the distributed groundwater inflow is small.

3.2 *Equipment and measurements*

Field measurement program included observations of downstream changes of the instantaneously injected tracer cloud and a set of hydrometric and morphologic measurements. The concentration of the tracer, flow rate and cross-sectional profiles of the riverbed elevations were measured in each experiment. Solution of uranin was used as the tracer in these studies. The solution was injected from a bridge as a surface line across the channel. Each injection consisted of 400 g of uranin AT dissolved in about 700 L of river water. The time of injection was within of 20 s and can be considered as instantaneous. Solution of uranin AT dye is ecologically harmless and allowed for scientific purposes in natural environments. However, because of sensitivity to the sun light, uranin solution exposed to the bright light decays relatively rapidly. To prevent considerable loses of the tracer the experiments were performed during the night time.

Copyright © 2006 Taylor & Francis Group plc, London, UK

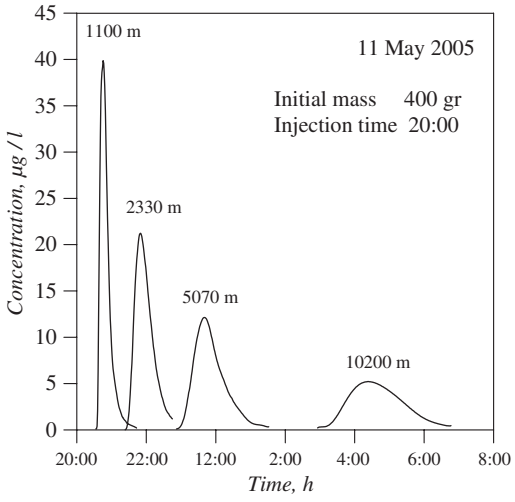


Figure 2. Examples of measured concentration curves.

Table 1. Hydraulic and morphometric characteristics.

No.	Date, month	Q, m^3/s	B (width), m	h (depth), m
1	11.05	9.0	25	1.06
2	30.06	2.8	23	0.87
3	10.08	7.5	27	1.54

The concentrations of the tracer cloud were determined using a back scat fluorometer (Haardt, Germany). Examples of concentration distribution are shown in Figure 2. A summary of hydraulic and morphological variables for the field tracer studies is presented in Table 1.

4 RESULTS AND ANALYSIS

4.1 *Evaluation of parameters*

Determination of model parameters was achieved by solving optimization problem in respect to the central moments (5) and (7)

$$\lim_{u,D,\varepsilon,T}\left\{F(u,D,\varepsilon,T)=\sum_{i=1}^{3}\sum_{k=1}^{N}\left[\mu_{i\,m}(x_k)-\mu_i(x_k)\right]^2\right\} \quad (8)$$

where F is the criterion function, k is the number of measured sections of the tracer cloud. This method to determine the parameters of the dead zone model may be less accurate than solving the optimizing problem by fitting measured concentration curves with the numerical solutions of boundary value problem (1)–(4). However, accurate numerical solution would require detailed information on the flow and river channel geometry for the entire river reach. In the absence of that information the performance of the moments method (8) is expected to be the same as for advanced techniques (Czernuszenko et al. 1997).

Table 2. Parameters of the dead zone model.

No.	U, m/s	D, m^2/s	ε	T, min
1	0.34	11.5	0.01	29.1
2	0.14	8.0	0.03	0.08
3	0.18	18.0	0.15	2.50

Parameters of the longitudinal dispersion model evaluated with optimization technique (8) are summarized in Table 2. Comparison of measured and predicted values for central moments of concentration distributions are shown in Figure 3. It can be seen from this figure that the analytical solutions (5)–(7) approximate spatial distributions of measured moments quite accurately. Specifically two first moments prescribed with deviations less then 5%. The scatter of the measured data about theoretical prediction (7) for the third central moment is about 20%. This scatter is explained by the sensitivity of numerical estimates of the third moment to the imperfections of measuring procedures. Thus, because of limited number of fluorometers some units were moved to downstream sections and the tails of concentration curves were cut on non-zero value. There were also errors associated with calibration procedures for the devices.

The results of tracer studies indicate substantial reduction of mean flow velocities of the flow during the vegetative period (Table 2). At the same time the data reveal a systematic increase in the values of dead zone volume and decrease of penetration times.

4.2 *Comparison with Fickian model*

To understand better the effect that dead zones cause on the mixing and transport processes it is useful to compare experimental data with predictions from classical model of longitudinal dispersion: $\varepsilon = 0$, $T = \infty$ in equation (1). Assuming instantaneous injection of the tracer, the downstream evolution of dimensionless maximal concentration is described as (Sukhodolov et al. 1997)

$$\frac{2A\sqrt{\pi\, DB/U}\, C_{\max}}{M} = \frac{1}{\sqrt{x/B}} \quad (9)$$

where $A = hB$ is cross-section area, and M is mass of injected tracer. Tracer studies in natural streams (Sukhodolov et al. 1997) indicate that equation (9) is satisfied quite accurately for the distances $x/B > 70$. Comparison of scaled measured maximal

Copyright © 2006 Taylor & Francis Group plc, London, UK

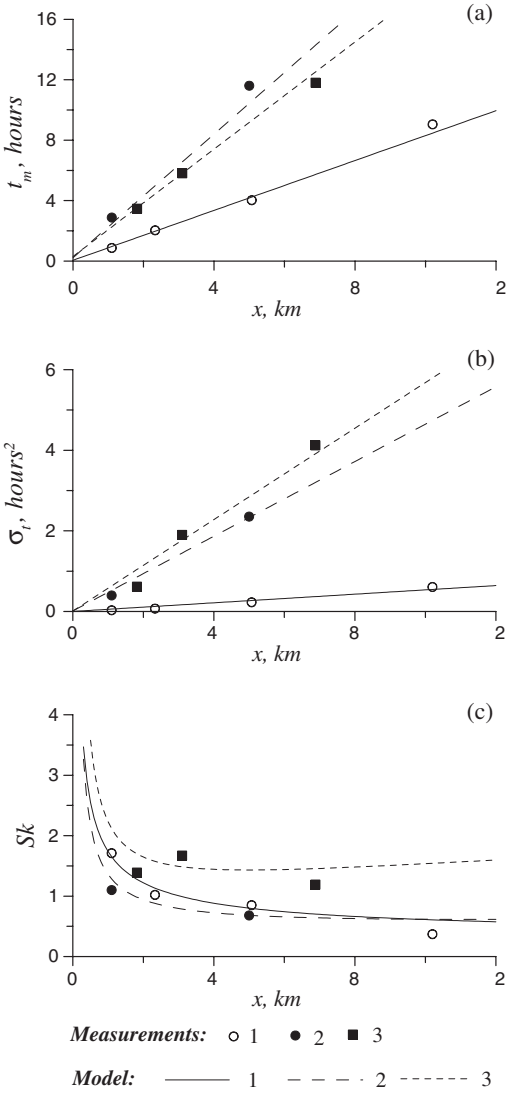


Figure 3. Downstream evolution of the central moments for concentration clouds; (a) retention time on the river reach, (b) variance of tracer cloud, and (c) skewness (numbers correspond to the experiment number in Table 1, 2).

concentrations of uranin with the predictions from relation (9) is demonstrated in Figure 4. It can be seen from this figure that measured data deviate systematically from (9) at distances $x/B > 70$ and the deviation magnitude increases with distance.

Dimensionless form for the variance of the tracer cloud is obtained from the definition of the dispersion coefficient

$$D = \frac{U^3\sigma_t^2}{2B}\frac{1}{x/B}, \quad \frac{U^3\sigma_t^2}{2DB} = x/B \qquad (10)$$

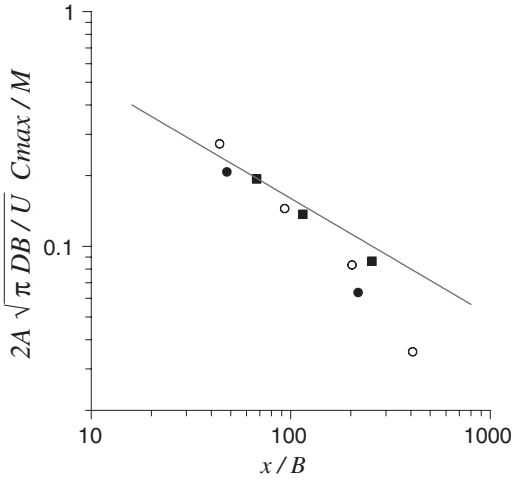


Figure 4. Decay of dimensionless maximal concentrations along the experimental river reach (the symbols are the same as in Figure 3).

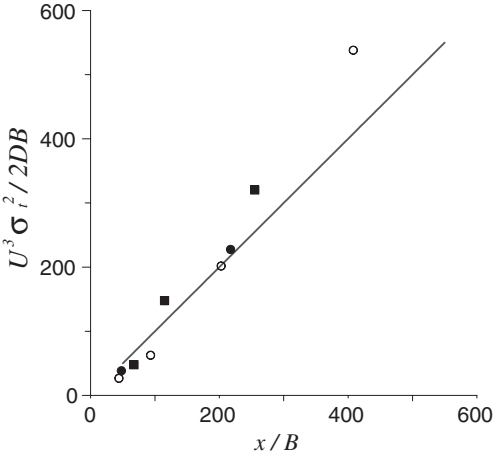


Figure 5. Decay of dimensionless maximal concentrations along the experimental river reach.

Measured downstream growths of the tracer cloud and its comparison with the linear relation (10) are shown in Figure 5. Systematic deviation from the classical dispersion process (10) is also evident at this plot. The size of the tracer cloud is evolving at higher rate than linear and, hence, equation (10) significantly underestimates variance of the distribution.

Relationship for skewness in Fickian model was obtained by Sukhodolov et al. (1997) in the form

$$Sk \sim \left(\frac{Uh}{D}\right)^{-1/2}\left(\frac{x}{B}\right)^{-1/2} \qquad (11)$$

Copyright © 2006 Taylor & Francis Group plc, London, UK

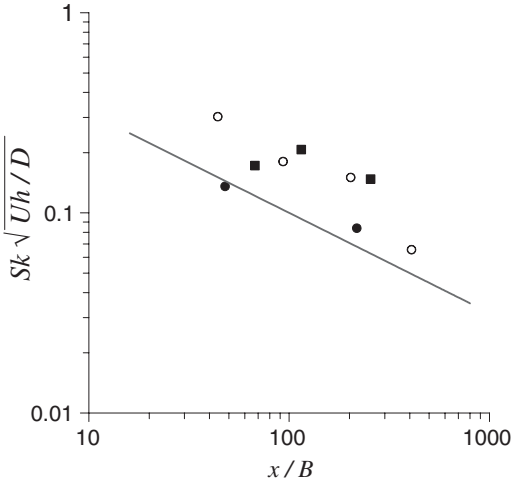


Figure 6. Variation of dimensionless skewness coefficients along the experimental river reach.

Measured data for skewness normilazed in accordance with (11) are plotted in Figure 6. The data reveal systematic deviations from (11) indicating that only in the channel free of vegetation the trend similar to Fickian model was observed. In vegetated channel the skewness was approaching constant state along the river reach.

4.3 *Dispersion coefficients*

In general form the longitudinal dispersion coefficient can be represented as

$$D = \frac{1}{2}\frac{\overline{dx'^2}}{dt} = \int_0^\infty \overline{U'(t)U'(t+\tau)} \qquad (12)$$

where x' is deviation of a liquid particle from its mean position, U' is deviation of the instantaneous longitudinal velocity of the particle from its average velocity, and τ is time shift. Neglecting the effect of turbulence in comparison with dispersion stipulated by non-homogeneous mean velocity field and performing simple transformations in (12), yields

$$D = \sigma_u^2 T_L \qquad (13)$$

where σ_u^2 and T_L are variance and time Lagrangian scale of mean velocity field. From physical considerations and based on dimensional analysis the Lagrangian scales can be related to Eulerian scales as (Sukhodolov et al. 1997)

$$\overline{\sigma_u^2} = \alpha^2 U^2 \qquad (14)$$

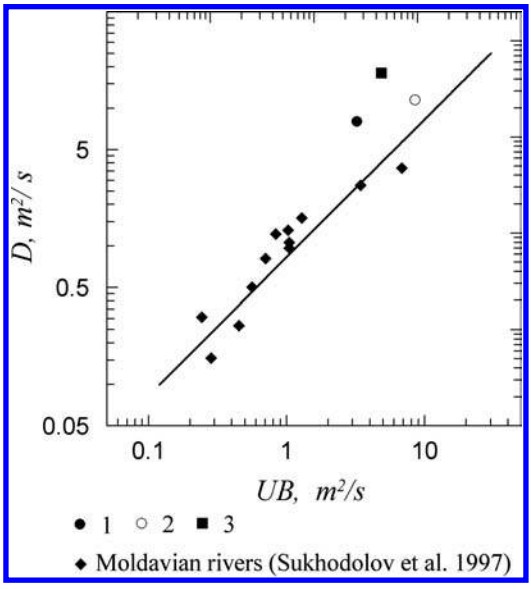


Figure 7. Relation between flow parameters and dispersion coefficient.

$$T_L = \beta\frac{B}{U} \qquad (15)$$

Substituting (14) and (15) into (13) one obtains

$$D = \alpha^2 \beta U B \qquad (16)$$

Coefficient α characterizes the degree of heterogeneity of mean velocity field in the river channel. Field tracer studies completed on small Moldavian rivers without vegetation provided the value 0.83 for the multiple parameter $\alpha^2\,\beta$.

Measured values of the dispersion coefficient and the values computed from flow parameters according to (16) are shown for comparison in Figure 7. The data of tracer studies completed in small rivers of Moldova are also indicated in this plot (Sukhodolov et al. 1997). Close correspondence between measured and predicted value of the dispersion coefficient can be reported for the flow without vegetation (point 1). In vegetated channel measured values of the dispersion coefficient were significantly higher than those predicted with equation (16).

4.4 *Dynamics of vegetative cover*

Depending on the weather and flow conditions on the watershed and in the river the in-stream vegetation begins to grow in the Müggelspree in April–May. The maximum in vegetation cover is observed in July–August and it gradually disappears in October–November. Observations of seasonal evolution of

Copyright © 2006 Taylor & Francis Group plc, London, UK

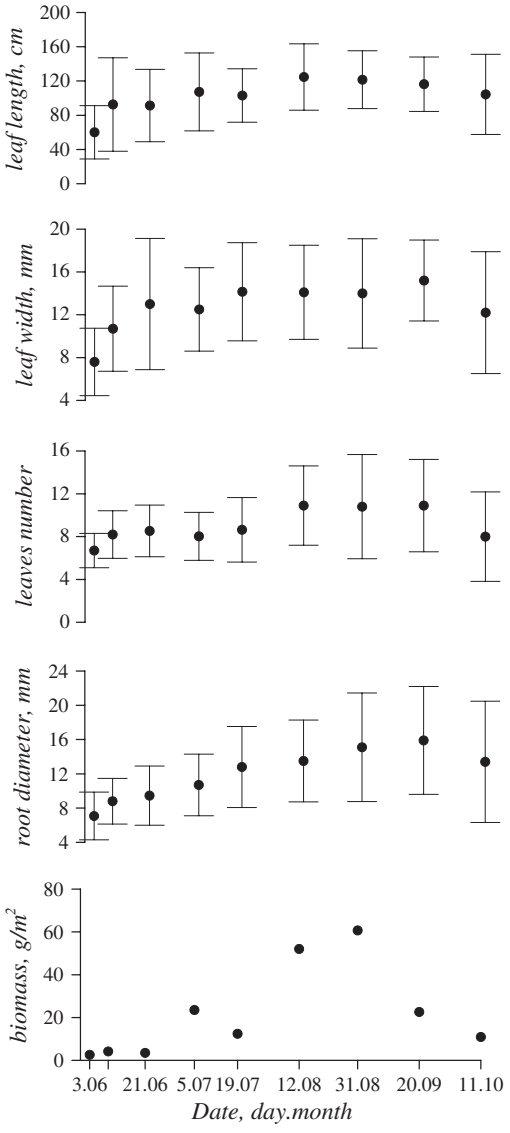


Figure 8. Dynamics of vegetation cover characteristics in the Müggelspree river near Freienbrink (observations during summer 2004).

Sagittaria Sagittifolia, a dominant submersible species in the Müggelspree river were performed near the village of Freienbrink (Figure 1). Patches of vegetation initially appear there as narrow ($2 \div 3$ m in width), elongated (length up to a 100 m) strips that widen and merge during the vegetative period. Noteworthy, the plants forming patches get their maximum characteristics quite fast – practically during the first three weeks and change non-significantly during the rest of vegetative period, Figure 8. At the same time the plants biomass grows quite monotonously and reaches its maximum at the end of summer. Some deviations are due to the spatial non-uniformity of the vegetative cover in the area of plants harvesting. Although the most characteristics of individual plants remain practically constant during the vegetation period, the diameter of plants near the root increases $1.5 \div 2$ times. This characteristic indicates rigidity of the plants and therefore controls bending angle.

5 DISCUSSION AND CONCLUSIONS

In this study the effect of submersible vegetation on longitudinal transport and mixing of dissolved substances in a lowland river is investigated. Tracer technique was employed in field measurements to quantify the spatial evolutions of the tracer cloud. Three sets of measurements were performed during the vegetative period. Obtained data were analyzed using longitudinal dispersion model with dead zones and allowed to examine temporal changes of the parameters. Performance of the dead zone model was compared to the classical Fickian model.

The results of the study indicate that downstream evolution of temporal moments of concentration curves is accurately predicted by the model of longitudinal dispersion with dead zones. Comparison of measured temporal moments with predictions of the classical Fickian theory of longitudinal dispersion indicated unacceptable large discrepancies.

Specific parameters of the dead zone model, dead zone volume and penetration time, exhibited a distinct behavior during the vegetative period. As might be expected, the relative volume of dead zone was increasing from 1% in May to 15% in August. Correspondently, the grows of biomass (dry weight per area of the river channel) indicated increase from 5 to 60 g/m^2. However, the penetration time – characteristic time scale of tracer residence in the dead zone decreased from 30 minutes to 2.5.

Phenomenologically the observation can be explained only by metamorphoses of dead zone. In early spring the dead zones are represented predominantly by recirculation zones formed because of flow separation on banks irregularities (Figure 9). Although these dead zones have considerable dimensions and retention times about 30 minutes, they are sparsely distributed on the river reach and respectively their relative volume is small. In vegetation period the dead zones are formed by blocking effect of submersible and emergent vegetative canopies occupying substantial part of the river cross-section though the penetration time of these dead zones is comparable with the time scales of wakes developing behind the plant canopies and ranges from 5 s to 3 minutes.

Theoretical analysis indicates that dispersion coefficient value is depending linearly on the mean velocity

Copyright © 2006 Taylor & Francis Group plc, London, UK



Figure 9. A dead zone at the left bank of the Müggelspree river near Monchwinkel.

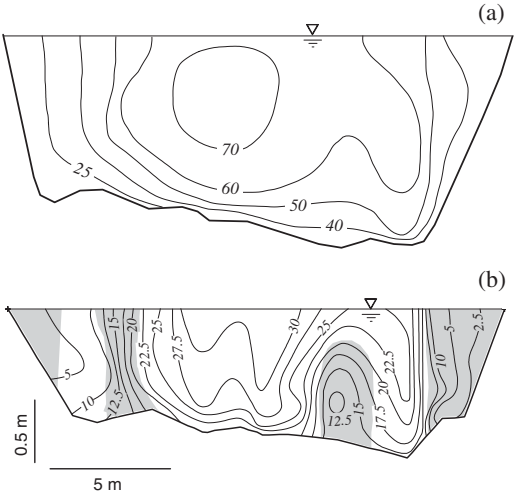


Figure 10. Downstream velocity isovels (cm/s) in the vegetation-free cross-section in May (a), and in the cross-section with vegetation (shaded areas) in July (b).

and the river width (16). Although mean velocity decreased two times in August as compared to non-vegetated conditions in May, dispersion coefficient values increased 1.6 times (Table 2, Figure 7). This observation can be explained by increasing non-uniformity of the mean velocity field because of vegetation. The results of our previous investigations of river turbulence on the reach (Sukhodolov et al. 1998; Sukhodolova et al. 2004; Sukhodolov & Sukhodolova 2005) provide qualitative estimates for the degree of non-homogeneity of the flow in vegetated channel. Figure 10 shows isovels of mean velocity field measured in the cross-section of the Müggelspree near the village of Freienbrink. Despite the large differences in discharge, plot (a) corresponds to 13.4 m^3/s while plot (b) to only 3.25 m^3/s, the maximal difference in the mean velocities are still nearly the same – about 20–25 cm/s. At the same time because of non-uniformity of the vegetative cover the differences in mean velocities observed in much larger areas across the flow making the dispersion mechanism more effective.

This case study provides valuable quantitative information about transport and mixing processes in natural environment subjected to intensive influence of the biological component of the fluvial ecosystem. We hope that results of the study will facilitate complex multidisciplinary investigations and understanding of flow-biota interactions.

ACKNOWLEDGEMENTS

Dr. Heinz Bungartz is thanked for assistance with organization of field campaigns. The research was supported in parts by Deutsche Forschungsgemeinschaft (BU 1442/1-1, SU 405/2-1) and by Collaborative Programme of NATO (ESP.NR.EV 981608).

REFERENCES

Carpenter, S.R. & Lodge, D.M. 1986. Effects of submersed macrophytes on ecosystem processes. *Aquatic Botany* 26: 341–370.

Cushing, C.E. & Allan, D. 2001. *Streams. Their Ecology and Life.* San Diego: Academic Press.

Czernuszenko, W. 1990. *Dispersion of pollutants in flowing surface waters.* Encyclopedia of Fluid Mechanics V10, Gulf Publishing Company, Houston.

Czernuszenko, W. & Rowinski P. 1997. Properties of the dead-zone model of longitudinal dispersion in rivers. *J. Hydr. Res.* 35(4): 491–504.

Day, T.J. 1975. Longitudinal dispersion in natural channels. *Water Resour. Res.* 11(6): 909–918.

Denny, M.W. 1988. *Biology and the Mechanisms of the Wave-Swept Environment.* Princeton: Princeton University Press.

Fischer, H.B. 1966. A note on the one-dimensional dispersion model. *Air and Water Pollution, An Internatioanl Journal* 10: 443–452.

Nepf, H.M. 1999. Drag, turbulence, and diffusion in the flow through emergent vegetation. *Water Res. Research* 35(2): 479–489.

Pedersen, F.B. 1977. Prediction of longitudinal dispersion in natural streams. Series Paper 14, Institute of Hydrodynamics and Hydraulic Engineering, Techical University of Denmark, Lyngby.

Righetti, M. & Armanini, A. 2002. Flow resistance in open channel flows with sparsely distributed bushes. *Journal of Hydrology* 269: 55–64.

Runkel, R.L. & Chapra, S.C. 1993. An efficient numerical solution of the transient storage equations for solute transport in small streams. *Water Resour. Res.* 29(1): 211–215.

Sand-Jensen, K. & Pedersen, O. 1999. Velocity gradients and turbulence around macrophyte stands in streams. *Freshwater Biology* 42: 315–328.

Copyright © 2006 Taylor & Francis Group plc, London, UK

Stephan, U. & Gutknecht, D. 2002. Hydraulic resistance of submerged flexible vegetation. *Journal of Hydrology* 269: 27–43.

Sukhodolov, A.N., Nikora, V.I., Rowinski, P.M. & Czernuszenko, W. 1997. A case study of longitudinal dispersion in small lowland rivers. *Water Env. Res.* 69(7): 1246–1253.

Sukhodolov, A. & Sukhodolova, T. 2005. Morphodynamics and hydraulics of vegetated river reaches: a case study on the Müggelspree in Germany. In: *River, Coastal and Estuarine Morphodynamics.* G. Parker and M.H. Garcia (eds.), V1: 229–236.

Sukhodolova, T., Sukhodolov, A. & Engelhardt, C. 2004. A study of turbulent flow structure in a partly vegetated river reach. *Proceedings of the second international conference on fluvial hydraulics River Flow 2004* Vol. 1: 469–478.

Sukhodolov, A., Thiele, M. & Bungartz, H. 1998. Turbulence structure in a river reach with sand bed. *Water Resour. Res.* 34(5): 1317–1334.

Valentine, E.M. & Wood, I.R. 1977. Longitudinal dispersion with dead zones. *Journal of the Hydraulics Division,* ASCE 103(HY9): 975–990.

Copyright © 2006 Taylor & Francis Group plc, London, UK

Effects of aquatic and bank-side vegetation on hydraulic performance of small streams

V. Nikora
University of Aberdeen, Engineering Department, Aberdeen, Scotland, UK

S. Larned, K. Debnath, G. Cooper & M. Reid
National Institute of Water and Atmospheric Research, Christchurch, New Zealand

N. Nikora
Christchurch City Council, Christchurch, New Zealand

ABSTRACT: We consider effects of bed and bank-side vegetation on hydraulic resistance of small streams, and develop simple quantitative relationships for predicting and quantifying these effects using the normalized plant characteristics. We conducted two field studies to explore effects of submerged aquatic and bank-side vegetation on stream hydraulics. In the first study, we examined the effects of aquatic plant biomass, stature and architecture on hydraulic conditions in five small streams representing a range of channel dimensions, flows and aquatic plant assemblages. In the second field study, we created experimental floods in a small stream to examine the effects of submerged bank-side vegetation on hydraulic conditions. The results of the studies and the relationships presented in the paper may be used to provide initial estimates of resistance coefficients for hydraulic modelling, predicting effects of aquatic weed management and bank-side planting on flood levels, and designing naturalisation and enhancement projects for small streams.

1 INTRODUCTION

Understanding of flow-vegetation interactions is important for both engineering (e.g., flood level estimates) and ecological (e.g., stream restoration) applications. In-stream (aquatic) and bank-side (terrestrial) vegetation are common in stream channels and have significant physical, biological, and biophysical functions. Interactions between flow and vegetation are complex and depend on environmental factors and plant characteristics such as mean flow velocity, turbulence, sediment transport, channel morphology, water temperature, plant morphology, age, size and spatial distribution of plant patches (e.g., Howard-Williams 1991). Flow conditions affect the roles of plants as suspended sediment filters, sinks for dissolved nutrients and contaminants, and habitat for other stream biota. On the other hand, plant structure and abundance affect flow depth, flood conveyance, sediment transport capacity, and other hydraulic and hydrologic parameters. Hereafter, we use the term aquatic plants to refer to vascular plants, bryophytes and macroalgae that occur on stream beds and require submergence. The term bank-side plants is used to refer to vascular terrestrial plants that occur on stream bank slopes, and which tolerate temporary submergence during high flow events.

The goals of the project reported in this paper were to examine vegetation effects on hydraulic resistance, and develop simple quantitative relationships for predicting and quantifying these effects using the plant characteristics with the greatest explanatory power. These relationships may be used to provide initial estimates of resistance coefficients for hydraulic modeling, which can be further calibrated by matching the observed and computed hydraulic parameters (e.g., Darby 1999). To progress with these goals, two field studies were completed to explore effects of submerged aquatic and bank-side vegetation on stream hydraulics. In the first study, we examined the effects of aquatic plant biomass, stature and architecture on hydraulic performance of five small streams representing a range of channel dimensions, flows and aquatic plant assemblages. In the second study, we created experimental floods in an urban small stream to identify the effects of submerged bank-side vegetation on hydraulic resistance. In this second study

Copyright © 2006 Taylor & Francis Group plc, London, UK

we focused on the effects of two bank-side vegetation parameters: planting density and general plant morphology. Most studies of flow-vegetation interactions have been conducted using artificial plants in laboratory conditions and the use of natural plants is generally limited to grasses (e.g., Yen 2002). In our studies, we maximized naturalness by conducting field experiments using naturally-occurring aquatic plants, and bank-side plants fabricated from natural plant materials.

Hydraulic resistance of stream channels is quantified using various resistance coefficients. In our study we used the most popular: Manning's n, Chezy's C, and Darcy-Weisbach's friction factor f, which are defined as

$$n = \frac{R^{2/3} S^{1/2}}{U},\quad C = \frac{U}{(RS)^{1/2}},\quad f = \frac{8u_*^2}{U^2} \text{ or } \sqrt{\frac{8}{f}} = \frac{U}{u_*} \quad (1)$$

where R = hydraulic radius; U = cross-sectional mean velocity; S = energy slope; $u_* = (gRS)^{1/2}$ = shear velocity; and g = gravity acceleration. Manning's n, Chezy's C, and Darcy-Weisbach's f are interrelated as $n = R^{2/3}S^{1/2}/U = R^{1/6}(f/8g)^{1/2} = R^{1/6}/C$. Although a wide range of theoretical and conceptual approaches are currently in use (e.g., Kouwen et al 1969; Petryk & Bosmajian 1975; Wu et al. 1999; Stephan & Gutknecht 2002; Yen 2002; Jarvela 2002, 2005; Wilson et al. 2003; Carrolo et al. 2005; Green 2005), there is a general agreement that resistance coefficients such as Manning's n, Chezy's C, and Darcy-Weisbach's f may be expressed as the following function of dimensionless arguments:

$$R_C = F(\mathrm{Re}, Fr, N, K, d, B, M, G, J, D, P) \quad (2)$$

where R_C = resistance coefficient (i.e., Manning's n, Chezy's C, or Darcy-Weisbach's f); F represents a function; Re, Fr, N, and K = flow parameters (Reynolds number, Froude number, non-uniformity/unsteadiness parameter, and relative submergence, respectively); d, B, and M = dimensionless parameters for bed material, bed form, and channel form (e.g., sinuosity), respectively; and G, J, D, and P = dimensionless parameters for vegetation (geometry, flexibility/stiffness, area/volume density, and patchiness, respectively). The form of the function F and its arguments are long-standing problems in hydraulic research, and they remain unclear today. In our study, we focused mainly on the effects of aquatic and bank-side vegetation on hydraulic performance of small streams (keeping other parameters similar), and development of quantitative relationships for predicting these effects. Below we present results for in-stream vegetation, then for bank-side vegetation, and conclude with a brief discussion of how our findings lend support to models of hydraulic resistance in vegetated channels.

2 EFFECTS OF AQUATIC VEGETATION

2.1 *Experimental sites and methodology*

For the first study, we selected approximately straight reaches at five small streams in Christchurch, New Zealand, covering a range of flow widths, depths, and plant species (Table 1). The aquatic plants at these stream reaches form elongated patches that cover 40–100% of the bed. At each site, five measurement campaigns were conducted over 6 months from summer to winter (January to June 2004). The same measurement cross-sections were used for each date/campaign with the following parameters measured.

1. Water levels at a reference cross-section every 20–30 min during the campaign, to monitor stationarity of hydraulic conditions.
2. 'Instant' water levels on both banks at five cross-sections for obtaining water surface slopes. The distance between cross-sections was 1–2 channel widths. Measurements were made using a Spectra-Physics Laserplane laser level and a custom-built hydrostatic measurement device. These data, together with cross-sectional areas and velocities, were used for calculating energy slopes following a standard procedure (e.g., Graf and Altinakar 1998).
3. Water discharge Q at a cross-section with minimum vegetation cover, which could be outside the experimental site.
4. Bed/bank elevation z_b, flow depth, height of the vegetation canopy h_c, plant species, and plant lengths l_p at 5 to 15 evenly spaced verticals (locations) in each of the five cross-sections.
5. Areal ρ_{Aw} and volumetric ρ_{Vw} biomass densities at each cross-section. To determine biomass densities, one vertical was selected at random along each cross-section, and all visible plant material was collected from a 0.085 m^2 area around the vertical. At the laboratory, the material was dried to constant weight (60°C for 3–4 days). Areal dry biomass density was defined as the ratio of dry weight to sampling area. Volumetric dry biomass density was defined as the ratio of dry weight to sampling volume, i.e., to the product of sampling area and canopy height. Corresponding wet densities were estimated from wet-dry weight conversion factors for each species. The above measurements were supplemented by measurements of plant volumes for estimating 'vegetation porosity', as the ratio of the fluid volume to the total sampling volume within the vegetation canopy.
6. Six-point vertical profiles of mean velocities and velocity standard deviations were made at two locations at each cross-section, using a Sontek Flow-Tracker acoustic Doppler velocimeter. For most velocity profiles, two points were measured

Copyright © 2006 Taylor & Francis Group plc, London, UK

Table 1. Ranges of site-averaged parameters and dominant aquatic vegetation at experimental sites, Christchurch, New Zealand.

Site	Width (m)	Mean depth (m)	Flow rate (m^3/s)	Mean velocity (m/s)	Shear velocity (m/s)	Dominant vegetation types
Cross Stream (Elmwood Park)	2.0–2.2	0.12–0.31	0.054–0.104	0.14–0.25	0.047–0.070	*Myriophyllum sp.*, filamentous green algae
Snellings Drain (Clare Park)	1.7–1.8	0.12–0.14	0.009–0.014	0.03–0.07	0.024–0.083	Filamentous green algae, *Callitriche sp.*
Cashmere Stream (Hoon Hay Valley Rd)	3.5–3.8	0.37–0.58	0.107–0.258	0.06–0.16	0.031–0.063	Elodea canadensis, *Nitella hookeri*
Avon River (Harakeke Street)	4.5–5.0	0.42–0.62	0.339–0.404	0.13–0.17	0.016–0.027	*Nitella hookeri*, filamentous green algae
Wairarapa Stream (Wairarapa Tce)	8.0–8.1	0.34–0.40	0.343–0.361	0.11–0.13	0.014–0.018	*Myriophyllum sp.*, *Riccia sp.*

inside the vegetation canopy, one point at the vegetation-flow interface, and three points above the canopy. The duration of each measurement was 40 s. The measurement points within and above the canopy were evenly spaced. During very low flows, the number of measurement points in a profile was reduced.

Vegetation parameters obtained from the field data were patch-averaged and site-averaged. Both averages were then used to explore vegetation effects on flow resistance factors such as Manning's n, Chezy's C, and Darcy-Weisbach's friction factor f. Site averages included both vegetated and unvegetated areas of the stream bed.

2.2 *Dependence of resistance coefficients on aquatic vegetation parameters*

During the 6-month study, Manning's n, Chezy's C, and Darcy-Weisbach's f varied by an order of magnitude or more among sites and seasons (Fig. 1). Froude $Fr = U/(gH)^{1/2}$ and Reynolds $Re = (UH/\nu)$ numbers for each site indicate that flows were subcritical and fully turbulent, except for Snellings Drain ($\mathrm{Re} = 1000-5000$, Table 1), where flow may have been transitional from laminar to turbulent at lower water discharge. In the formulas above, H = site-averaged channel depth, and ν = fluid viscosity. Vegetation porosity during all measurement campaigns was higher than 0.98 and, therefore, effects of water displacement by plants on computation of hydraulic parameters could be neglected.

The key physical parameters of vegetation, assumed to influence hydraulic resistance and measured in our study, were relative roughness h_c/H, plant inclination factor l_p/h_c, areal vegetation cover W_c/W, and site-averaged relative roughness $[h_c(W_c/W)]/H = (W_c h_c/WH)$ [or relative submergence $H/[h_c(W_c/W)] = (WH/W_c h_c)$], where h_c and l_p = patch-averaged canopy height and plant length, respectively, obtained by averaging plant heights and lengths measured within all vegetation patches within an experimental site; W = site-averaged channel width, W_c = site-averaged cover of a cross-section by vegetation, and the site-averaged canopy height is defined as $h_c(W_c/W)$. Correlations between the resistance coefficients n, C, f and $U/u_* = \sqrt{8/f}$, and the preceding normalised vegetation parameters were generally high ($r^2 > 0.80$), except for plant inclination l_p/h_c ($r^2 = 0.15 - 0.33$). Among the vegetation parameters, the site-averaged relative roughness ($W_c h_c/WH$) had the highest predictive power (Figs 1a-1c), in agreement with results of field studies of vegetated rivers and canals in the Netherlands and Britain (Kouwen et al. 1969; Watson 1987; Green 2005).

Figures 1a to 1c show that the relationships $n = F(h_c W_c/HW)$, $C = F(h_c W_c/HW)$, and $f = F(h_c W_c/HW)$ can be best approximated by exponential functions $n = n_b \exp(\gamma_n h_c W_c/HW)$, $C = C_b \exp(\gamma_C h_c W_c/HW)$, and $f = f_b \exp(\gamma_f h_c W_c/HW)$, where subscript '$b$' indicates resistance coefficients in the absence of vegetation when $(h_c W_c/HW) \to 0$, and γ_n, γ_C, γ_f are coefficients ($r^2 = 0.89 - 0.91$). Exponential approximation suggests that a non-linear combination of bed surface and vegetation components in the overall hydraulic resistance is more likely than their linear superposition. The data from different sites and measurement campaigns collapse around the same lines in plots for Manning's n, Chezy's C, and Darcy-Weisbach's friction factor f (Fig. 1). This indicates that values of n_b, C_b, and f_b were approximately the same among sites, in agreement with visual observations that the bed surfaces were topographically similar. Figure 1d shows a plot for $\sqrt{8/f} = U/u_* = F(HW/h_c W_c)$ where the data is best approximated by a semi-logarithmic relationship. This is in agreement with the preceding exponential approximations for resistance coefficients, as, after re-arrangement, the

Copyright © 2006 Taylor & Francis Group plc, London, UK

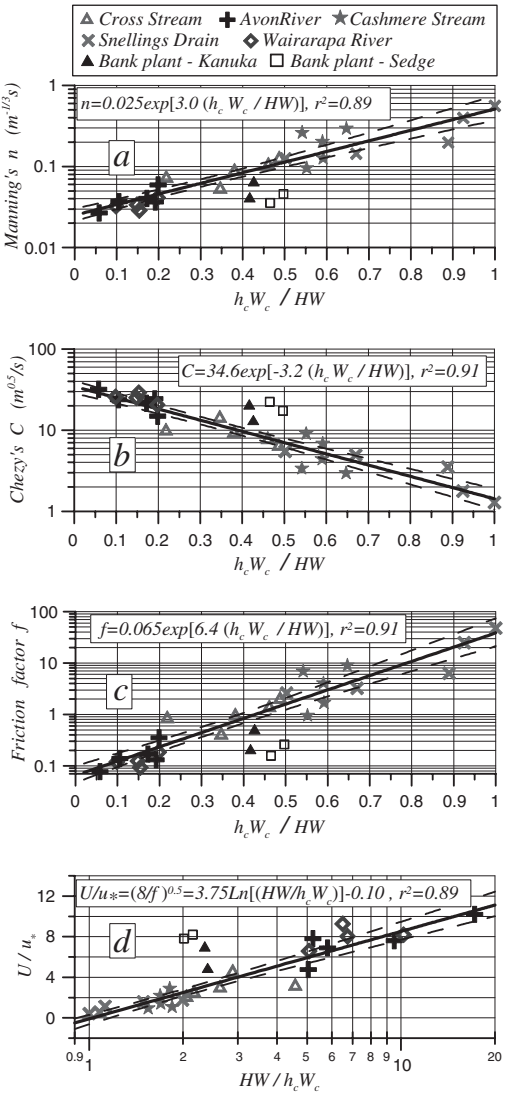


Figure 1. Relationships between resistance parameters n, C, f, and U/u_* and site-averaged relative submergence HW/h_cW_c for aquatic (in-stream) and bank-side vegetation. The regression approximations are shown by solid lines; 95% confidence intervals are shown with dashed lines.

semi-logarithmic equation for $U/u_* = F(HW/h_cW_c)$ produces curves for n, C, and f that appear exponential.

The plant inclination factor l_p/h_c had little explanatory power in the current study, although it has been considered useful for characterising hydraulic resistance in some vegetated streams (e.g., Kouwen & Unny 1973). This is partly because plant characteristics and flow conditions both changed between

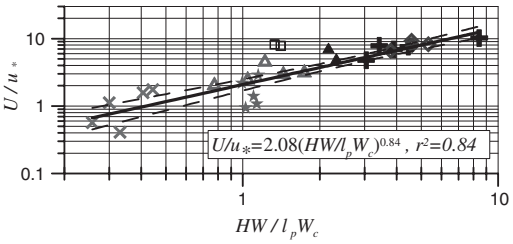


Figure 2. Relationships between resistance parameter U/u_* and site-averaged parameter HW/l_pW_c for aquatic (in-stream) and bank-side vegetation. Symbols are as in Figure 1. The regression approximation is shown by solid line; 95% confidence intervals are shown with dashed lines.

measurement dates at each site. As a result, the ratio l_p/h_c stays approximately constant during plant growth and, therefore, the parameter l_pW_c/HW provides nearly as good description of vegetation effects as h_cW_c/HW, with slightly reduced squared correlation coefficients in the exponential relationships for n, C, and f ($r^2 = 0.60 - 0.70$). Compared to the semi-logarithmic form of $U/u_* = C_1 \ln(HW/h_cW_c) + C_2$, the relationship $U/u_* = F(HW/l_pW_c)$ is slightly better approximated by a power function (Fig. 2).

Areal and volumetric biomass densities had little explanatory power compared to the relative vegetation parameters h_cW_c/HW and l_pW_c/HW described above. Between the two, areal density performed slightly better ($r^2 = 0.46 - 0.50$) than volumetric density ($r^2 = 0.25 - 0.26$).

3 EFFECTS OF BANK-SIDE VEGETATION

3.1 *Experimental sites and methodology*

For the second field study, we selected a straight reach of Milns Drain in Christchurch. The site had good access to municipal water supplies, which we used to generate experimental flood flows with substantial bank submergence. Site preparation for the flood experiments consisted of: (1) cutting the long grass on the drain bank-sides short; (2) filling the drain channel with gravel to raise the water level so bank submergence could be achieved at lower flow rates; (3) inserting baffles of plastic film into the gravel at 1 m intervals to reduce water flow in the gravel fill; (4) lining some depressions of the stream banks with fine gravel to smooth the bank surface; (5) building a temporary weir downstream of the working section to control flow levels and the water surface curve; and (6) assembling a piping system to supply water from an adjacent drain. The experimental reach was 60 m in length with a 50 m working section. The channel had a 60 cm wide rectangular cross-section with approximately 45° bank slopes above the drain channel

Copyright © 2006 Taylor & Francis Group plc, London, UK

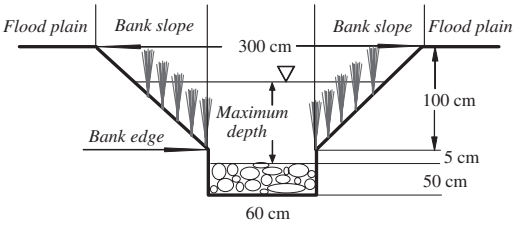


Figure 3. Cross-section of the experimental site of Milns Drain. Maximum flow depth shown in the sketch corresponds to the 'flood' level.

(Fig. 3). Water from three sources, a fire hydrant, a local water main, and an adjacent drain, was pumped into the drain 15 m upstream of the working section. Using water from three independent sources enabled us to precisely control discharge in the experimental reach.

The effects of bank-side vegetation on the hydraulic conditions and vice versa were assessed by comparing flow characteristics in the presence and absence of semi-artificial bank plants. We manufactured replicate bank plants using natural plant materials cable-tied to wire anchors. This approach allowed us to rapidly install and remove hundreds of plants between experimental runs, and to control planting density and spatial arrangement. Two native plant species were used that have contrasting architectures, *Kunzea ericoides* (kanuka) and *Carex* sp. (sedge). Kanuka and sedges are common stream bank plants in New Zealand, and both are frequently used in New Zealand stream enhancement and re-vegetation projects. Kanuka is a shrub with stiff divaricating branches and small (<1 cm length) leaves. Sedges are grass-like plants that form tussocks and have long (>10 cm length), unbranched, flexible leaves (Fig. 4).

We established six cross-sections and made hydraulic measurements in the absence of bank-side vegetation first. Then kanuka or sedge plants were installed on both bank slopes by inserting the wire anchors into the bank soil until flush with the soil surface. The hydraulic measurements were then repeated at the same cross-sections. Each plant species was used in two experimental runs, one at high plant density ($33.3\ m^{-2}$) and one at low density ($8.33\ m^{-2}$). The same spatial arrangement was used for both plant species and both densities (Fig. 5). Planting areas were strips 35–40 cm wide and 50 m long on each bank slope (Fig. 3).

The following experimental runs were conducted:

1. No bank-side vegetation, water surface at the bank edge.
2. No bank-side vegetation, water surface 30-cm above the bank edge.
3. Kanuka, high density, water surface 30-cm above the bank edge.

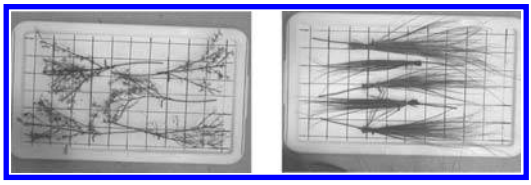


Figure 4. Semi-artificial plants used in the bank-side vegetation study. Left: Kanuka (*Kunzea ericoides*). Right: sedge (*Carex* sp.).

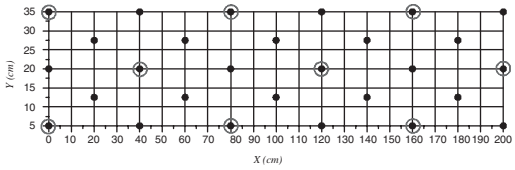


Figure 5. Spatial patterns of the semi-artificial plants. Dots: – high density, dots in circles: – low density. Y-axis shows distance above lower bank edge (see Fig. 3).

4. Kanuka, low density, water surface 30-cm above the bank edge.
5. Sedge, high density, water surface 30-cm above the bank edge.
6. Sedge, low density, water surface 30-cm above the bank edge.

Water level was kept constant during experimental runs 2 to 6 so that all changes in hydraulic resistance could be measured by changes in flow rate. The experimental protocol was similar to that described in section 2.1. The key parameters for each experimental run are listed in Table 2. The symbols used are the same as above, with one addition, the parameter N_A, which is the number of individual plants per unit area of stream bank.

3.2 *Dependence of resistance coefficients on bank-side vegetation parameters*

The most notable results of the bank-side vegetation study concern the effects of vegetation density N_A and species (i.e., plant architecture) on hydraulic resistance. Figure 1 compares effects of both species of bank-side vegetation with those of aquatic vegetation described in section 2. In the absence of bank-side vegetation, the resistance coefficients are comparable with those obtained for sites with low aquatic plant cover in the first study. The total roughness n of the channel with submerged banks and no bank-side vegetation is higher than that for the bankflow conditions (Table 2). The values in Figure 1 indicate that, at the same site-averaged submergence, the effects of bank-side vegetation are small compared to those of aquatic vegetation. For our field experiments, the increase in

Copyright © 2006 Taylor & Francis Group plc, London, UK

Table 2. Hydraulic and bank-side vegetation parameters.

Run*	Q (m^3/s)	U (m/s)	u_* (m/s)	Fr	Re	f	C ($m^{0.5}/s$)	n ($m^{-1/3}s$)	N_A (m^{-2})	h_c (m)	l_p (m)
1	0.016	0.29	0.035	0.38	17490	0.11	26.4	0.024	0	0.009	0.016
2	0.157	0.31	0.034	0.20	77980	0.10	28.6	0.028	0	0.032	0.063
3	0.115	0.21	0.052	0.13	55255	0.48	12.8	0.063	33.3	0.117	0.145
4	0.135	0.26	0.041	0.16	66124	0.20	20.0	0.040	8.33	0.105	0.131
5	0.130	0.25	0.045	0.16	63560	0.26	17.3	0.046	33.3	0.130	0.215
6	0.133	0.26	0.036	0.17	65478	0.16	22.4	0.036	8.33	0.121	0.225

*Notes on experimental runs. 1: No bank-side vegetation, water surface at bank level; 2: No bank-side vegetation, water surface 30 cm above bank level; 3: Kanuka, high density, water surface 30 cm above bank level; 4: Kanuka, low density, water surface 30 cm above bank level; 5: Sedge, high density, water surface 30 cm above bank level; 6: Sedge, low density, water surface 30 cm above bank level. Values of h_c and l_p for runs 1 and 2 are for background grass.

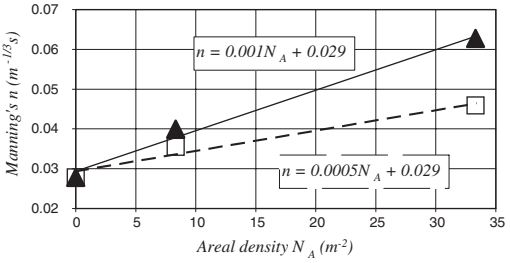


Figure 6. Dependence of Manning's n on stream-bank plant species and density (▲ Kanuka, and □ Sedge).

roughness from an unvegetated state to a vegetated state is greater for aquatic vegetation on stream beds than for submerged terrestrial vegetation on stream bank sides (Fig. 1).

Figure 6 illustrates how plant density and differences between a rigid branching shrub (kanuka) and a flexible unbranched sedge influence hydraulic resistance. One may predict that bank slope roughness due to kanuka should be higher compared to that due to sedges, and both should be higher than bank slope roughness without plants (i.e., bare soil or grass only). Figure 6 agrees with this prediction and provides quantitative measures of bank slope planting effects on hydraulic resistance. The data suggest that Manning's n increases nearly linearly with plant density N_A. Kanuka and sedges represent two extremes in flexibility and architecture, so quasi-linear relationships between n and N_A may be postulated for a wide range of plant forms. Free terms in the relationships shown in Figure 6 represent the background roughness n_b without implanted plants on the bank sides. However, the relationships in Figure 6 are based on very limited field data and should be treated with caution.

4 DISCUSSION

Our results support two promising models, which represent two mainstream directions in studying hydraulic resistance in vegetated channels. The first model was suggested by Kouwen et al. (1969) who derived the relationship:

$$\sqrt{8/f} = \frac{U}{u_*} = C_1 \ln\left(\frac{A}{A_p}\right) + C_2 \quad (3)$$

where A = total cross-sectional area of the flow; A_p = part of the total cross-sectional area occupied by vegetation; C_1 and C_2 = coefficients depending on vegetation properties. Relationship 3 was originally derived using the logarithmic formula for velocity distribution above vegetation canopy uniformly covering the bed. Subsequent tests (e.g., Kouwen et al. 1969; Kouwen & Unny 1973) showed that for a range of hydraulic conditions this equation approximates experimental data reasonably well. The ratio A/A_p was originally considered for a straight section with a bed uniformly covered by vegetation. While typical for laboratory set-ups, such vegetation patterns are rarely seen in streams. For patchy vegetation cover, the ratio A/A_p can be interpreted as a site-averaged relative submergence, i.e., $A/A_p = (WHL/W_c h_c L) = (WH/W_c h_c)$ where L = reach length. Note that the reversed ratio A_p/A is known in the literature as the blockage factor (e.g., Kouwen et al. 1969; Green 2005). We believe that interpretation of A_p/A as the site-averaged relative roughness is more appropriate hydraulically. Figure 1 showing a plot for $\sqrt{8/f} = U/u_*$ demonstrates that our data closely match Kouwen et al.'s (1969) model equation 3. Theoretical justification of this equation, which is usually attributed to the logarithmic velocity distribution above vegetation canopies (Kouwen et al. 1969), may require revision. Indeed, although our direct velocity measurements showed deviation from the logarithmic profiles due to vegetation patchiness, the data can still be very well approximated by equation 3. We contend that an alternative derivation of relationship 3 that does not invoke the logarithmic formula is likely to be more plausible, because vertical velocity distributions in natural vegetated channels may not be logarithmic.

Copyright © 2006 Taylor & Francis Group plc, London, UK

The second model was recently proposed by Carollo et al. (2005). Based on similarity considerations, Carollo et al. (2005) derived a relationship:

$$\sqrt{8/f} = \frac{U}{u_*} = A_o\left(\frac{H}{h_c}\right)^{\alpha_1}\left(\frac{u_* h_c}{\nu}\right)^{\alpha_2}\left(\frac{l_p}{h_c}\right)^{\alpha_3} \quad (4)$$

where A_o = coefficient depending on vegetation density; and α_i = empirical exponents. Equation 4 was derived for straight channels with beds uniformly covered by vegetation, as was equation 3. Carollo et al. (2005) showed that equation 4 provided a better fit to their flume data than equation 3. In section 2.2 we pointed out that the relationship $\sqrt{8/f} = U/u_* = F(HW/l_pW_c)$ is better approximated by a power function than by the semi-logarithmic formula $U/u_* = C_1 \ln(HW/l_pW_c) + C_2$ suggested by Kouwen et al. (1969). This result agrees well with Carollo et al.'s (2005) model. For low vegetation density Carollo et al. (2005) found that $U/u_* \propto (H/h_c)^{\alpha_1}(l_p/h_c)^{\alpha_3}$ with $\alpha_1 = 1.168$, $\alpha_3 = -0.861$, and $\alpha_2 = 0$. If we neglect the small difference between the exponents α_1 and $|\alpha_3|$, and assume $\alpha_1 \approx -\alpha_3 \approx 1$ then we may obtain $U/u_* \propto (H/l_p)^{\alpha}$ with $\alpha \approx 1$. Figure 2 shows that $U/u_* \propto (HW/l_pW_c)^{\alpha}$ with $\alpha = 0.84 \approx 1$. Thus, our data suggest that Carollo et al.'s (2005) model may be applicable to field conditions with patchy vegetation if, instead of H/l_p, a site-averaged parameter $H/[l_p(W_c/W)] = HW/l_pW_c$ is used.

Our aquatic plant data cover the entire range of possible values of site-averaged relative submergence (HW/h_cW_c) and (HW/l_pW_c) with different plant patch mosaics. However, no dependence on dominant plant species or patch mosaic patterns is apparent in Figures 1 and 2. The good fit for all sites to single curves, regardless of plant species composition, suggests that the general physical parameters for vegetation h_c/H, W_c/W, h_cW_c/HW, and l_pW_c/HW should be dominant roughness descriptors for hydraulic resistance. However, the bank-side vegetation data show that plant stature and architecture may be important factors, which should be studied at a wider range of parameters.

5 CONCLUSIONS

In this paper we examined the effects of aquatic (in-stream) and bank-side vegetation on hydraulic resistance over a range of stream dimensions and vegetation types, and suggested simple quantitative relationships for predicting and quantifying these effects using the site-averaged relative roughness (or submergence) and plant density. Effects of dominant aquatic plant species and their patch patterns were not significant. The data on aquatic plants from all sites collapsed around single curves, suggesting that the site-averaged physical parameters of vegetation may be the primary determinants of hydraulic resistance in vegetated streams, not species-specific parameters. Our results on aquatic plants support the applicability of both Kouwen et al.'s (1969) and Carollo et al.'s (2005) models, which can be extended for conditions of patchy vegetation, subject to selection of appropriate site-averaged vegetation measures. Compared to aquatic vegetation, the effects of bank-side vegetation at the same site-averaged relative roughness (or submergence) were smaller. For both aquatic and bank-side plants, plant shoot length was nearly as good a roughness descriptor as canopy height. This suggests that the plant length to canopy height ratio may be less important than previously assumed.

ACKNOWLEDGEMENTS

This study was partly funded by the Foundation for Research Science and Technology (New Zealand, contract CO1X0308), the Christchurch City Council (CCC), and the University of Aberdeen. The authors are grateful to CCC staff members O. Southen, and K. McCombs for help with site selection and technical and logistical support. A. Davey, M. Gee, S. Miller, C. Mohlmann, D. Sutherland and J. Sykes helped with field measurements, preparation of bank plants and laboratory analyses. R. Spigel, G. Smart, and an anonymous reviewer provided useful suggestions and comments on earlier drafts.

REFERENCES

Carollo, F.G., Ferro, V. & Termini, D. 2005. Flow resistance law in channels with flexible submerged vegetation. *J. Hydraul. Eng., ASCE* 131(7): 554–564.

Darby, S.E. 1999. Effects of riparian vegetation on flow resistance and flood potential. *J. Hydraul. Eng., ASCE* 125(5): 443–454.

Graf, W.H. & Altinakar, M.S. 1998. *Fluvial Hydraulics. Flow and transport processes in channels of simple geometry*. John Wiley & Sons, Chichester. 681 p.

Green, J.C. 2005. Modelling flow resistance in vegetated streams: review and development of new theory. *Hydrol. Process.* 19: 1245–1259.

Howard-Williams, C. 1991. Dynamic processes in New Zealand land – water ecotones. *New Zealand Journal of Ecology 15*: 87–98.

Jarvela, J. 2002. Flow resistance of flexible and stiff vegetation: a flume study with natural plants. *J. Hydrol,* 269: 44–54.

Jarvela, J. 2005. Effect of submerged flexible vegetation on flow structure and resistance. *J. Hydrol.* 307: 233–241.

Kouwen, N., Unny, T.E. & Hill, H.M. 1969. Flow retardance in vegetated channels. *J. Irrig. Drain. Eng., ASCE* 95(IR2): 329–342.

Kouwen, N. & Unny, T.E. 1973. Flexible roughness in open channels. *J. Hydraul. Eng., ASCE* 99(HY5): 713–728.

Copyright © 2006 Taylor & Francis Group plc, London, UK

Petryk, S. & Bosmajian, G. 1975. Analysis of flow through vegetation. *J. Hydraul. Div., ASCE* 101: 871–884.
Stephan, U., & Gutknecht, D. 2002. Hydraulic resistance of submerged flexible vegetation. *J. Hydrol.* 269: 27–43.
Watson, D. 1987. Hydraulic effects of aquatic weeds in UK rivers. *Regul. River.* 1: 211–227.
Wilson, C.A.M.E., Stoesser, T., Bates, P.D. & Pinzen, A.B. 2003. Open channel flow through different forms of submerged flexible vegetation. *J. Hydraul. Eng., ASCE* 129(11): 847–853.
Wu F.-C., Wen S.H., & Chou, Y.-J. 1999. Variation of roughness coefficients for unsubmerged and submerged vegetation. *J. Hydraul. Eng., ASCE*, 125(9): 934–942.
Yen, B.C. 2002. Open channel flow resistance. *J. Hydraul. Eng., ASCE* 128(1): 20–39.

Copyright © 2006 Taylor & Francis Group plc, London, UK

Interaction of vegetation, current and sedimentation

S. Schneider, F. Nestmann & B. Lehmann
Institute for Water and River Basin Management, Universität Karlsruhe, Germany

ABSTRACT: The incorporation of vegetation in stream restoration in urban areas is not just since the implementation of the European Water Framework Directive a desirable purpose for a healthy ecosystem. But vegetation causes conveyance loss, induces sediment problems and increases flooding. Because of these hydraulic and sediment uncertainties, hydraulic engineers have been reluctant to incorporate vegetation into designs of river restoration projects.

Therefore recommendations for the design and maintenance of riparian vegetation in nature-orientated water bodies, especially for urban areas are required. These recommendations are derived from the combination of a newly developed rating matrix with analysis of a hydraulic model. The hydraulic model identifies the interaction of dense vegetation and sedimentation, while the rating matrix calculates the flow velocity under considerations of vegetation succession.

1 INTRODUCTION

The European Water Framework Directive (WFD) has its main focus on enhancing water bodies. One of the aims is to achieve a diverse river ecosystem. Especially in urban areas the improvement of degraded waterways into nature-orientated rivers poses the challenge for hydraulic engineers and landscape and city planner.

The paper deals with the incorporation of vegetation in stream restoration and flood control projects. Hydraulic engineers have long been reluctant to incorporate different types of vegetation into designs since vegetation could cause conveyance loss, induce sediment problems, increase flooding, and disrupt normal channel-floodplain interactions. The tools generally used for evaluating open channel flow do not typically allow for consideration of the varied effects of vegetation.

Healthy riparian vegetation is of great value for an ecosystem; it stabilises stream banks, provides shade that prevents excessive water temperature fluctuations, performs a vital role in nutrient cycling and water quality, improves aesthetic and recreational benefits, and is immensely productive as wildlife habitat (Fischenich 2001).

The ability to predict or account for impacts associated with gradual developing vegetation on streams and flood control projects is hampered by the lack of recommendations for nature-orientated water bodies. Additionally, recommendations derived from hydraulic and numerical models regarding the maintenance of vegetation along river banks must play a more important role in guaranteeing flood water security even if the river restoration was done years ago.

The purpose of this paper is to investigate, how the growth of shrubs and trees influences flow velocities and sedimentation processes in cross sections.

2 METHOD

Vegetation increases flow resistance, changes backwater profiles and modifies sediment transport (Yen, 2002). In urban river restoration projects vegetation may be natural or planted to improve aesthetics, habitat or prevent erosion (Fischenich 2001). A prosperous river restoration which ensures flood security implies thought about the objective design of plants in cross sections.

Therefore hydraulic losses and flow resistance due to mixing plant arrangement were calculated with a rating matrix (see Figure 1) enhanced for practical use by Lehmann (2005). The interaction of vegetation and sedimentation rate is studied in a large-scale hydraulic model.

2.1 *Numerical rating matrix*

Resistance to flow is typically characterised by a roughness coefficient. Evaluating flow resistance caused by vegetation has generated a multitude of studies. Chow (1959) describes a roughness coefficient, where different aspects of flow resistance are

Copyright © 2006 Taylor & Francis Group plc, London, UK

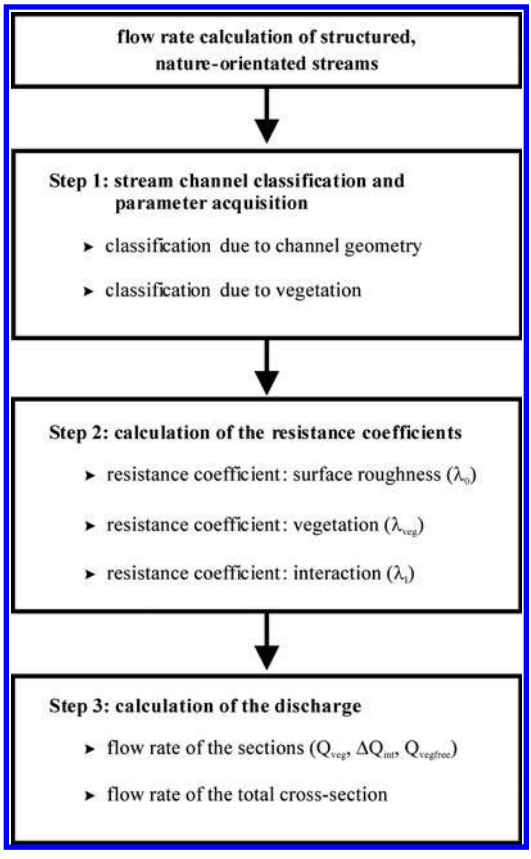


Figure 1. Principle of the rating matrix (Lehmann 2005).

combined. The effects of tall non-submerged vegetation on flow resistance were investigated by Li & Shen (1973). Petryk & Bosmajian (1975) estimated Manning values as a function of hydraulic radius and vegetation density for rigid vegetation in a group. Lindner (1982) presented an equation to compute the drag coefficient for a single plant arranged in a group. Pasche (1984) determined the computed drag coefficient of Lindner through an iterative process including experimental results with rigid cylinders.

The method used in the described rating matrix is based on the turbulence-theoretical equation of Pasche (1984) with modifications of Schumacher (1995), Oplatka (1998), Gerstkrasser (2000), Stephan (2002) and Schnauder (2004). Calculating flow rates for structured, nature orientated rivers is the aims of the presented rating matrix (see Figure 1).

Natural and near-natural rivers and streams are characterised by irregular cross-sections with a wide diversity in occurring roughness coefficients. At first geometric data have to be analysed to enter the hydraulic calculation. Therefore spatial surveying data

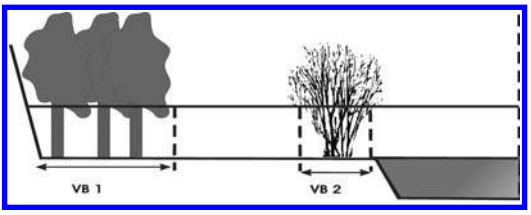


Figure 2. Simplified cross sections divided into vegetated (VB) and none vegetated section (Schneider 2005).

are abstracted (see Figure 2) into simplified geometric data to ensure the comparability of geometric and shaping parameters.

The sectional roughness coefficient and the resulting flow velocities are computed in step 2. Step 3 calculates the sectional flowing discharge to determine the flow rate of the total cross-section.

The challenge of the discharge calculation is the determination of the resistance coefficients. Therefore the cross section needs to be divided into areas where the resistance factor is either dominated by vegetation or by interaction and vegetation or by surface roughness.

The resistance coefficient caused by surface roughness (λ_O) is according to Keulegan (1938):

$$\lambda_0 = 8 * \left(2{,}5 * \ln\left(\frac{r_{hy}}{k_s} \right) + Br \right)^{-2} \quad (1)$$

with

$$Br = \begin{cases} 3{,}25 & for\ h/k_s \leq 4 \\ 0{,}1875 * (h/k_s) + 3{,}25 & for\ 4 < h/k_s < 20 \\ 6{,}25 & for\ h/k_s \geq 20 \end{cases} \quad (2)$$

Where λ_O = is resistance coefficient due to surface roughness; r_{hy} = hydraulic radius (m); k_s = equivalent sand roughness (m); Br coefficient (-); h = flow depth in observed section (m).

The resistance coefficient caused by vegetation is defined as:

$$\lambda_{ges,veg} = \lambda_0 + \lambda_{veg} \quad (3)$$

with

$$\lambda_{veg} = \frac{4 * c_D * h * d_{veg}}{a_x * a_y} * \cos(\alpha) \quad (4)$$

Due to missing c_D-value for vegetated area the c_D-value has to be calculated by iteration. Starting the iteration process the c_D-value (4) is firstly defined as 1.0 to calculate a flow velocity of the vegetated area (5).

$$v_{veg} = \frac{1}{\sqrt{\lambda_{ges,veg}}} * \sqrt{8 * g * r_{hy} * I} \quad (5)$$

Copyright © 2006 Taylor & Francis Group plc, London, UK

This v_{veg} needs to be verified by the following formula:

$$c_D = c_{W\infty} \cdot \left(1 + 1{,}9 \cdot \frac{d_{veg}}{a_y} \cdot c_{W\infty}\right) \cdot \left(\frac{v_{veg}}{v_m}\right)^2 + \Delta c_w \qquad (6)$$

with

$$\left(\frac{v_{veg}}{v_m}\right)^2 = 1{,}15 \cdot \left(\frac{a_{NL}}{a_x}\right)^{-0{,}48} + 0{,}5 \cdot \left(\frac{a_{NB}}{a_y}\right)^{1{,}1} \qquad (7)$$

and

$$c_{w\infty} = \begin{pmatrix} 3{,}07 \cdot \mathrm{Re}_{veg}^{-0{,}168} & für & \mathrm{Re}_{veg} < 800 \\ 1{,}0 & für & 800 \le \mathrm{Re}_{veg} < 8000 \\ 1{,}2 & für & 8000 \le \mathrm{Re}_{veg} < 10^5 \end{pmatrix} \qquad (8)$$

and

$$\Delta c_W = \frac{2}{Fr^2} \cdot \left(1 - y^*\right) \qquad (9)$$

with

$$\frac{y^* \cdot \left(y^{*2} - 1\right)}{2 \cdot \left(y^* - \frac{a_y}{a_y - d_{veg}}\right)} \overset{!}{=} Fr^2 \qquad (10)$$

a_{NL} and a_{NB} are calculated according to Pasche (1984). The iteration finishes at:

$$\left|1 - \frac{c_D}{c_D'}\right| \approx 0 \qquad (11)$$

Where $\lambda_{ges,veg}$ = total resistance coefficient of section with vegetation; λ_{veg} = resistance coefficient due to vegetation; I = slope; c_D = drag coefficient due to vegetation; h hydraulic flow depth in section (m); d_{veg} = average equivalent vegetation diameter (m); a_x = equivalent distance in flow direction (m); a_y = equivalent distance cross flow direction of vegetation elements (m); α = angle of inclination of section wall (only at triangular approximation); Re = Reynolds number; Δc_W = resistance coefficient due to the influence of a cylinder to surface waves; y^* = relative flow depth in front of and behind a rigid cylinder (m).

The calculation of the resistance coefficients in vegetated sections (VB, see Figure 2) presumes a close-by approximation of nature-vegetation.

Vegetation parameters are determined according to the recommendations of DVWK (1991). Firstly a control area (A_{pro}) within the vegetation area has to be defined. The control area typically has a size of 1–5 m^2. Inside this control area (A_{pro}) the equivalent vegetation parameter has to be determined. The vegetation parameter depends on the type of vegetation and the amount of branches and trees. To calculate the vegetation parameter one has to choose between the following equations:

– Control area dominated by shrubs

$$a_x = a_y = \sqrt{\frac{A_{pro}}{n_R}} \qquad (12)$$

– Control area dominated by trees

$$a_x * a_y = \frac{A_{pro}}{n_B} \qquad (13)$$

and

$$a_x = C * a_y = \sqrt{\frac{A_{pro}}{n_B \cdot C}} \qquad (14)$$

– Control area with trees and shrubs

$$a_x = a_y = \sqrt{\frac{A_{pro}}{n_E}} \qquad (15)$$

with

$$n_E = n_B + n_R \qquad (16)$$

$$n_R = \frac{n_{R,tree}}{A_{pro,tree}} * A_{pro} \qquad (17)$$

Where A_{pro} = control area (m^2); $A_{pro,tree}$ = control area trees only (m^2); n_R = number of all branches and rods within the control area; n_B = number of trees within the control area; n_E = number of all elements of vegetation within the control area; $n_{R,tree}$ = number of all elements of vegetation within the control area of trees only; C = factor, describing the dependence between a_x and a_y.

The resistance coefficient dominated by the interaction process also has to be calculated by iteration according to Schumacher (1995) and Pasche (1984).

Afterwards these three calculated resistance coefficients enter the computation of the total flow discharge for the regarded cross section (see Figure 1).

The verification of the model is based on observed nature data. Measured natural vegetation data regarding the amount of branches per m^2, the distances between the trees in and vertical to the flow direction and the average diameter of the branches (see Table 1) were recorded.

The recording of actual branch number and – diameter takes place at the height of 75% of the plant size respectively at the maximum water level. In average the control area was 1.5 m^2 for counting shrub branches and 12 m^2 for control areas, planted

Copyright © 2006 Taylor & Francis Group plc, London, UK

with trees, to calculate the required average distance parameters.

2.2 *Physical model*

In addition to the theoretical hydraulic disquisition the recommendations for nature-orientated design and maintenance of rivers and flood plains in urban areas are derived from carried out qualitative analysis of a hydraulic model.

The researched question is dominated by a gravity-depending flow involving free water surface. Therefore the main objective was to achieve an equality of the Froude number:

$$Fr_N = Fr_M \Leftrightarrow \frac{v_N}{\sqrt{g \cdot \ell_N}} = \frac{v_M}{\sqrt{g \cdot \ell_M}} \tag{18}$$

A scale model uses the method of direct (physical) simulations of hydraulic phenomena in the same medium as in nature. The scaling laws define conditions that must be satisfied to achieve the desired similarity between the model and nature. The ratio of a variable in nature to the corresponding variable in the model describes the scaling factor l_r. Creating dynamic similarity can be observed as long as the geometric similarity and the kinematic similarity is given. The geometric similarity is represented by:

$$\ell_r = \frac{\ell_N}{\ell_M} \tag{19}$$

The kinematic similarity represents the similarity of motions:

$$t_r = \frac{t_N}{t_M}; \quad v_r = \frac{\ell_N / t_N}{\ell_M / t_M} = \frac{\ell_r}{t_r}; \quad a_r = \frac{\ell_N / t_N^2}{\ell_M / t_M^2} = \frac{\ell_r}{t_r^2} \tag{20}$$

and the dynamic similarity represents the similarity of forces:

$$F_r = \frac{F_N}{F_M} \tag{21}$$

Where Fr_N = Froude number in nature, Fr_M = Froude number in model; g = gravity; ℓ_r = scaling factor; ℓ_N = length in nature; ℓ_M = length in model; t_r = time scaling factor; t_N = time span in nature; t_M = time span in model; v_r = velocity scaling factor; a_r = acceleration scaling factor; F_r = force scaling factor; F_N = force in nature; F_M = force in model.

The application of a very large and complex model (scale 1:6) with a moveable channel bed and a controllable detritus enabled a very demonstrative documentation of the current-detritus-interaction. This eventually affects the dynamics of the water body morphology by sedimentation and erosion processes.

The physical model experiments were carried out at the Theodor-Rehbock-Wasserbaulaboratorium in Karlsruhe utilising a large, partly glass-walled flume of 60 m length, 2.5 m width and 0.8 m depth. The design of the flume is characterised by a moveable bed with an additional feeding of fine particles for simulating sedimentation process.

A river stretch of 180 m in nature of the River Enz in Pforzheim, Germany, provided the basis for the design. The scaling factor was chosen to be 1:6. The represented river stretch of the River Enz is characterised by an armoured layer with an average diameter of 150 mm in nature LFU (2003), therefore according to the geometric scale factor the channel bottom had to be build up of gravel with an average grain diameter of 25 mm.

The challenge of this hydraulic model is the task of simulating fine sand sedimentation. Fine sand, downscaled according to the scaling factor, tends to coagulate. The result is an interruption of the dynamic simulation of the hydraulic model. Hence for the fine sand bed load simulation polystyrol-granulate was used with a density of $\rho_{PS} = 1300\ kg/m^3$. From this it follows that, under the terms of the dynamic similarity the size of the polystyrol-granulate is according to Kobus (1978):

$$\frac{d_{K_M}}{d_{K_N}} = \sqrt[3]{\frac{\rho_{K_N} - \rho_w}{\rho_{K_M} - \rho_w}} \tag{22}$$

The used polystyrol-granulate had a size of 2.5 mm. Where d_{KM} = diameter of sediment in model; d_{KN} = diameter of sediment in nature; ρ_{KN} = density of sediment in nature, ρ_{KM} = density of sediment in model, ρ_W = density of water.

With a constant addition of the polystyrol-granulate the discharge was set to 400 l/s. This represents a flood event with a 5 year return period. As long as the geometrical similarity is achieved the time scale in a Froude model is defined as:

$$t_r = \sqrt{l_r} \tag{23}$$

Difficulties arise out of the limited downscaling of fine sand. The interruption of the geometrical similarity of the fine sand material demanded a so-called "historical experiment". This is an imitation of the natural sedimentation behaviour and was in this case set to two hours according to Dorer (1984). The shorter identified time scale factor in the experiment than in the equation is due to the lesser density and the bigger size of the used granules.

Plenty of materials are used for simulating trees and shrubs in hydraulic models. Most of them are made out of different plastic or metal materials, however research compares these materials to natural behaviour are still missing. Therefore the use of flexible locust, broom-bristled and young willow branches were preferred for the simulation of bank vegetation.

Copyright © 2006 Taylor & Francis Group plc, London, UK

Experiments were conducted with homogenous and mixed plant groupings. Altogether 11 different vegetation arrangements were studied, varying in plant density, spacing and size. Different vegetation arrangements (see Figure 3) along the stream bank were studied: collective shrubs stocks (see Fig. 4); tall forbs with young flexible shrubs; influence of branches cut near the bottom; dense woody vegetation; arrangements of shrubs in two lines varying in density and diagonal arranged shrubs (see Figure 3). An overview of the vegetation arrangement design is given in Figure 3.

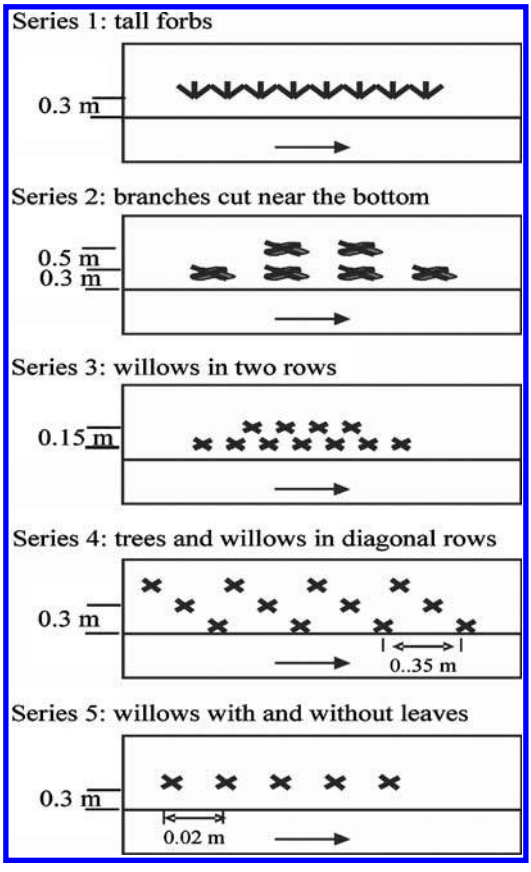


Figure 3. Overview of the vegetation arrangements in the hydraulic model.



Figure 4. Ideal vegetation for equivalent vegetation parameters calculation. (Bernhart).

3 EXPERIMENTAL RESULTS AND INTERPRETATION

3.1 *Numerical rating matrix*

One of the challenges is the abstraction of actual vegetation data into equivalent vegetation parameters. Vegetation simulation in hydraulic models is typically arranged in geometrical forms, with uniform distances between tree trunks (see Figure 4). In nature the density of plants per m^2 varies. Finding tall forbs near a collective of shrubs and trees is no curiosity (see Figure 5).

Branch numbers recorded in control areas vary according to the age of the shrubs. In average there could be found up to 50 rods per m^2 of one year old willows. The diameter of these branches is about 0.01 m. The resulting flow velocity, influenced by the willow roots, would be 0.27 m/s according to the rating matrix. The input-parameters of the presented results were set to $I = 0.002$, $r_{hy} = 3.0$ m, $h = 3.0$ m and $k_s = 2.0$. The diameter of the branches increases due to the growth of the plant. The average branches number per m^2 decreases. A three to five year old willow has less than half the number of branches per m^2 than a one year old willow, but three times the diameter of the branches.

Nevertheless the resulting flow velocity and therefore the discharge capacity in flood plains dominated by shrubs remains almost constant. Older willows grow in diameter; however the branch density is reduced. (see Table 1).

In sections dominated by trees the flow velocity can increase to more than double the amount as in sections dominated by willows. Trees with only a density of 1 tree/m^2 are typical for areas, where the maintenance has been very intensive in the first years after the



Figure 5. Typical plant arrangements in nature. (Schneider).

Copyright © 2006 Taylor & Francis Group plc, London, UK

Table 1. Variations of vegetation arrangements and the corresponding flow velocity according to the rating matrix.

Vegetation			v_{veg} [m/s] for $k_s = 2$
Arrangement of shrubs			
50 branches/m^2	a_x	0,14	0,27
	a_y	0,14	
	d_{veg}	0,01	
30 branches/m^2	a_x	0,18	0,23
	a_y	0,18	
	d_{veg}	0,02	
20 branches/m^2	a_x	0,22	0,23
	a_y	0,22	
	d_{veg}	0,03	
10 branches/m^2	a_x	0,32	0,25
	a_y	0,32	
	d_{veg}	0,05	
Arrangement of trees			
1,5 trees/m^2	a_x	0,81	0,55
	a_y	0,81	
	d_{veg}	0,06	
1 tree/m^2	a_x	1,00	0,42
	a_y	1,00	
	d_{veg}	0,15	
8 trees/15 m^2	a_x	1,37	0,56
	a_y	1,37	
	d_{veg}	0,15	

planting. Hence this is typically for planted floodplain vegetation and reveals that river restoration projects with planted vegetation increase the reduction of flow velocity. Natural developed vegetation is characterised by less dense vegetation.

3.2 *Physical model*

The influence of the vegetation density on the sedimentation rate was observed.

Series 1: Tall forbs and high grass
A high sedimentation rate of fine sand can be observed between these types of riverine vegetation. High grass and tall forbs act like a sieve that filters the fine sand, increases the sedimentation rate and decreases the discharge capacities of the cross-section. Hence tall forbs and high grass should be carefully used.
Series 2: Branches cut near the bottom
This situation is typical for vegetation maintenance during higher water level especially in late fall or early spring time. Cutting of branches near the bottom causes high sedimentation rates in these areas.
Series 3: Willows in two rows
In this case the row placed at the flood plain side, showed a higher sedimentation rate than the row at the riverside. Additionally the hydraulic model revealed that the denser the flood plain row the higher the sedimentation rate.

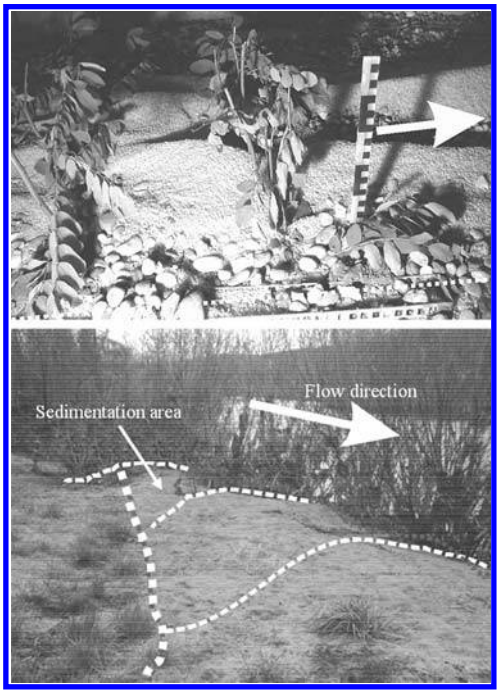


Figure 6. Sedimentation of sand caused by vegetation in the hydraulic model (top) and in nature (bottom). (Lehmann).

Series 4: Trees and willows in diagonal rows
This trail showed a very high sedimentation rate inside the vegetation arrangement (see Figure 4). The reduction of the sedimentation rate can be induced by removing willows in a line parallel to the flow direction. While removing willows in lines upright to the flow direction leads to an additional reduction of the small sedimentation rate.
Series 5: Old and young willows in one row with and without leaves
This type of riverine vegetation is a typical situation along streams in urban areas. The analysis showed that creating gaps in the row after several meters leads to an additional reduction of the sedimentation rate. Willows arranged in one row with gaps cause almost no sedimentation. The influence of leaves on the sedimentation rate is negligible; however it increases slightly when young flexible willows are very densely planted. Nevertheless these are the recommended vegetations arrangements in flood plain areas, where no sedimentation is allowable.

Summarising the hydraulic model research, it could be stated that collective shrubs stocks, dense woody vegetation and diagonally arranged shrubs cause sedimentation of fine sand within and behind vegetated sections (VB) where flow velocities are low. The dimensions of the sedimentation zone within

Copyright © 2006 Taylor & Francis Group plc, London, UK

reduced current velocities caused by vegetation could be calculated with the approach of Pasche (1984). Dense vegetation causes a reduction of flow velocity which increases the sedimentation rate. Due to this fact it is to recommend that in those dense vegetation arrangements the maintenance has to be enhanced.

4 CONCLUSION

To achieve a transfer from theory to practice it is necessary to define requirements of nature-orientated water body management in urban areas to help hydraulic engineers in their planning phase. The focus of finding practical recommendations for river management has to be laid on the interaction of current flow, morphology and vegetation along the stream banks.

The newly developed rating matrix for the estimation of the characteristics of discharge in nature-orientated streams is the result of a study of existing practical problems. The matrix enables the engineers to choose the appropriate rating method and ask for the appropriate parameters e.g. vegetation parameters. Additionally, the rating matrix helps to teach the hydraulic engineers the significance of their chosen parameters. Hence, a possibility is given to simulate the developing vegetation along the river banks by plain parameters. The rating matrix can calculate the influence of vegetation on the flow characteristics. The typical application area ranges from streams to smaller rivers with vegetated banks and flood plains.

Derived recommendations from the hydraulic model regarding the arrangement of the vegetation and the maintenance of that vegetation along the river banks should play a supplementary role especially during the planning of the restoration, the maintenance and for landscape planning aspects.

REFERENCES

Bollrich, G. (1989). Technische Hydromechanik Band 2. 2.Aufl., Berlin: VEB Verlag für Bauwesen

Bollrich, G. (2000). Technische Hydromechanik Band 1. 5.Aufl., Berlin: Verlag Bauwesen

Chow (1959). Open-channel hydraulics. MrGraw-Hill, New York

Dorer (1984). Ähnlichkeit bei Flussbaulichen Modellen. Heft 54, Mitteilung der Bundesanstalt für Wasserbau Karlsruhe.

DVWK (1991). Hydraulische Berechnung von Fließgewässern. Merkblätter 220, Deutscher Verband für Wasserwirtschaft und Kulturbau e.V.

Fischenich & Copeland (2001). Environmental Considerations for Vegetation in Flood Control Channels. Technical Report ERDC/CHL TR-01-16, US Army Engineer Research and Development Center, Vicksburg, MS.

Freeman et al. (2000). Determination of resistance due to shrubs and woody vegetation. Technical Report ERDC/CHL TR-00-25, US Army Engineer Research and Development Center, Vicksburg, MS.

Gerstkrasser (2000). Ingenieurbiologische Bauweisen an Fließgewässern, Grundlagen zu Bau, Belastbarkeit und Wirkungsweisen. Heft 52, Universität für Bodenkultur Wien (Doctoral thesis).

Keulegan, G.H. (1938). Laws of turbulent flow in open channels. Research Paper 1151 (Journal of Research, National Bureau of Standards, 21).

Kobus, H., Abraham, G. (1978). Wasserbauliches Versuchswesen. DVWW Mitteilungsheft Nr. 4, Essen : DVWW

Lehmann (2005). Empfehlungen zur naturnahen Gewaesserentwicklung im urbanen Raum – unter Berueckichtigung der Hochwassersicherheit. Heft 230. Mitteilung des Instituts für Wasser und Gewaesserentwicklung, Karlsruhe (Doctoral thesis)

Li & Shen (1973). Effect of tall vegetations on flow and sediment. J. Hydr. Div. ASCE, 99(5), 793–814

Lindner (1982). Der Strömungswiderstand von Pflanzenbeständen. Mitteilung 75, Leichtweiss-Institut für Wasserbau, TU Braunschweig. (Doctoral thesis)

Oplatka (1998). Stabilität von Weidenverbauungen an Flussufern. Heft 156, Mitteilungen der Versuchsanstalt für Hydrologie und Glaziologie der Eidgenössischen Technischen Hochschule Zürich

Pasche (1984). Turbulenzmechanismen in naturnahen Fließgewässern und die Möglichkeit ihrer mathematische Erfassung. Aachen (Mitteilungen des Institut für Wasserbau und Wasserwirtschaft RWTH Aachen, Heft 24)

Petryk Bosmajian (1975). Analysis of flow through vegetation. J. Hydr. Div. ASCE, 101(7), 871–884

Schnauder (2004). Strömungsstrukturen und Impulsaustausch in gegliederten Gerinnen mit Vorlandvegetation. Heft 224, Mitteilung des Instituts für Wasser und Gewaesserentwicklung, Karlsruhe (Doctoral thesis)

Schumacher (1995). Zur Durchflussberechnung gegliederter, naturnah gestalteter Fließgewässer. Heft 127, Mittlung des Instituts für Wasserbau und Wasserwirtschaft der TU Berlin

Stephan (2002). Zum Fließwiderstandsverhalten flexibler Vegetation. Band 180, Wiener Mitteilungen.

Yen (2002) Open Channel Flow Resistance. J. Hydr. Eng., 128(1), 20–39.

Copyright © 2006 Taylor & Francis Group plc, London, UK

A.5. Interaction with structures

Copyright © 2006 Taylor & Francis Group plc, London, UK

Large-scale motion induced by turbulent plunging jets in pools created by scouring of the riverbed

Pedro Manso, Anton Schleiss, Jean-Louis Boillat & Erik Bollaert
Ecole Polytechnique Fédérale de Lausanne (EPFL), Laboratory of Hydraulic Constructions (LCH)
Lausanne-Switzerland

ABSTRACT: Plunging jets are a common feature in fluvial systems occurring in waterfalls, weirs and dams. The erosive process generated by jet impact in the river bed is of interest for hydraulic engineers, as well as the diffusion, mixing and aeration processes. Experimental investigations were carried out to study the interaction between the diffusion of plunging jets and the geometry of the pool created by scouring of the riverbed. Circular jets with quasi-prototype velocities up to 30 m/s were produced to study jet diffusion in flat and laterally confined pools. The influence of laterally confining the diffusion of the jet was investigated by systematically testing several cylindrical confinements with diameters D_c of 5.6, 11 and 16.7 times the jet diameter D. Dynamic pressure measurements at 1 kHz were performed at the plunge pool bottom. Particular flow patterns such as surface oscillations inside the confined region, intermittent ejections, pool surface oscillations and ring vortices, were observed and documented for $D_c/D = 16.7$. The lateral confinement tested enhanced the development of the jet, changing the flow pattern in the pool and the impact pressures at the pool bottom. The origin of important recirculation currents that may lead to bank erosion was directly related with the water level above the river bed, being preferable to have deep confined pools than shallow confined or flat pools.

1 INTRODUCTION

The impact of a turbulent shear layer generated by the diffusion of plunging jets may scour the riverbed downstream of water releasing structures, weirs or waterfalls. Large recirculation currents may as well create undesirable erosion of the riverbanks. The turbulent mixing and air entrainment in the pool by plunging jets represent a major interest for water quality, since they contribute to the processes of degradation of organic matter and dilution of pollutants. These phenomena are directly related with the type of macro-turbulent flow in the pool, which often depends on its geometry. Riverbed and bank erosion have been observed in nature and real-size facilities, as well as investigated in reduced-scale laboratory facilities. Jet diffusion and impact loads in plunge pools have mainly been studied in pools with flat bottom (Cola 1966; May and Willoughby 1991; Ervine et al. 1997; Bollaert and Schleiss 2003). However, pool geometry may considerably differ in practice, as a function of the joint set patterns and the degree of fracturing of the rock mass (Figure 1). Extensive experimental work with idealized scour geometries using quasi-prototype velocity jets and aeration conditions have been performed by Manso (2006). The understanding of the physical processes governing the interaction between the pool flow patterns and jet diffusion may help engineers inferring the behaviour of a given plunge pool and providing adequate solutions for the mitigation of scour and bank erosion induced by recirculation currents. This paper presents results of experimental investigations with plunging jets in laterally confined plunge pools using near-prototype jet velocities and aeration conditions. Due to the difficulties of performing direct measurements of pool flow characteristics under such extreme conditions of air concentration and high Reynolds numbers, the approach consisted in measuring dynamic wall pressures. The analysis of the fluctuating characteristics of bottom pressures allows presenting evidence of the main flow features. This

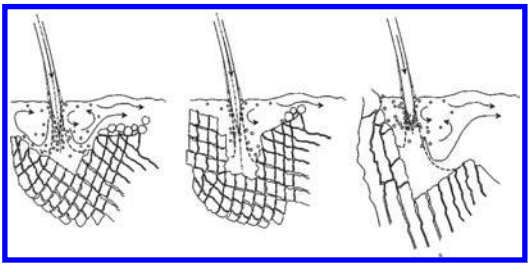


Figure 1. Three different plunge pool configurations.

Copyright © 2006 Taylor & Francis Group plc, London, UK

analysis is correlated with direct observations of the flow motion.

2 EXPERIMENTAL WORK IN TYPIFIED SCOUR GEOMETRIES

The plunge pool is simulated by means of a round flat basin with variable pool depth – Figure 2. Modular steel cylinders were prepared to simulate lateral confinements of $D_c/D = 5.6$, 11 and 16.7 with a relative height of $t/D = 2.8$ (Figure 3). These lateral confined pools corresponds to intermediate stages of development of a plunge pool. The experimental work herein presented aims at documenting the flow field inside the pool by means of interpretation of wall pressure measurements. Systematic and extensive measurements of the flow field are yet unfeasible due to instrumentation limitations. The jet outlet is cylindrical with a nozzle diameter of 0.072 m and is 70 cm higher than the pool bottom. The facility produces jets with velocities up to 30 m/s, a maximum Reynolds number of 1.87×10^5 and a rather uniform velocity profile (Manso 2006). The 300 mm diameter upstream conduit supplies a maximum discharge of 120 l/s by means of a 63 m high head pump. Tests were performed for jet velocities ranging from 7.4 to 29.5 m/s.

The initial pool depth Y varies from 7.5 to 67 cm for aerated (plunging) jet conditions (about 1D to 9.3D) and 82 or 87 cm for non-aerated jet conditions (Y/D ratios of 11.4 and 12.1) for which the jet outlet is submerged. By increasing the pool depth, the travel length in the air is reduced. For a typical turbulence intensity of 4% the degree of jet break-up are $L/L_b = 0.02$ for Y/D = 9.3 and $L/L_b = 0.44$ for Y/D = 1.04. All tested jets are undeveloped at entry in the plunge pool. At entry in the pool, the jet entrains air in near-prototype conditions. Jet diffusion is axisymmetrical. Dynamic pressures at impact on the pool are representative of prototype conditions. From tests with pools with flat bottom (Manso 2006), impact conditions correspond to the impact of the jet core for $Y/D < 5.6$ (i.e. shallow pools) and to the impact of a fully developed jet for $Y/D > 9$ (i.e. deep pools). For the intermediate

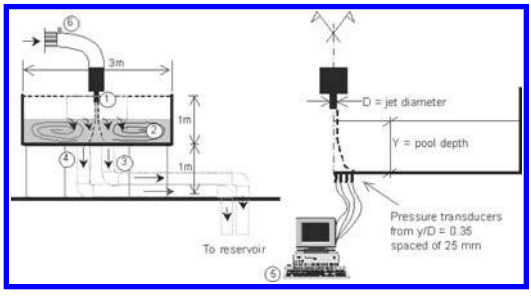


Figure 2. Schematic representation of the experimental facility: 1) cylindrical jet outlet ($D = 0.072$ mm), 2) cylindrical basin, 3) and 4) outflow system, 5) Digital Acquisition system for pressure transducers, which are at the pool bottom respectively at 25, 50, 75, 95, 150 and 200 mm from the jet axis, 6) air vent and honeycomb grid; x and y are the vertical and horizontal co-ordinates, respectively.

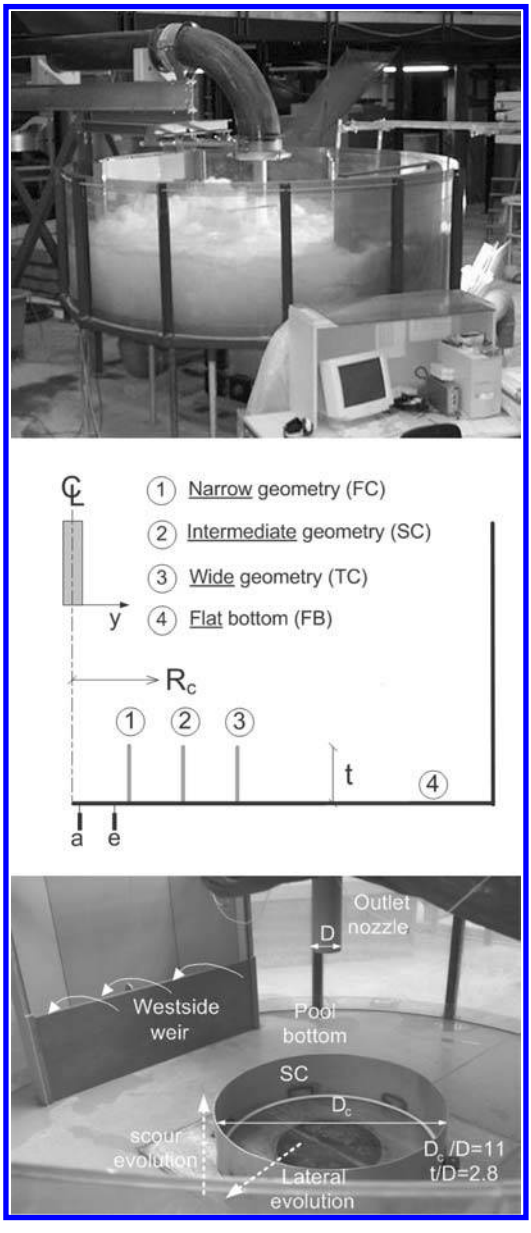


Figure 3. Experimental facility: top) photo of highly aerated pool flows; middle) cross-section of basin; bottom) photo of the "intermediate" geometry. The lateral confinements have diameters D_c of 40, 80 and 120 cm and a height t of 20 cm.

Copyright © 2006 Taylor & Francis Group plc, London, UK

range of pool depths, the impact conditions are highly dependent on the boundary conditions (i.e. transitional pools).

Pressure measurements were performed with micro piezoresistive transducers type KULITE XTM-190-17BAR-A (pressure range 0–17 bar absolute, 3 mm diameter diaphragm) flush-mounted on the pool bottom. Ergodic sampling was guaranteed with 3-min runs for an acquisition rate of 1 kHz. Selected data from measurement stations at $y/D = 0.35$ (point a) and $y/D = 2.08$ (point e) are presented hereafter.

3 FLOW BEHAVIOUR IN LATERALLY CONFINED POOLS

After impact on the pool bottom, the plunging jet divides into wall jets. In pools with flat bottom, large eddies are formed around the falling jet. The flow is highly aerated, disabling visualisation of the flow behaviour inside the pool. When the jet outlet is submerged, an external observer can see through the pool. In laterally confined pools, the wall jets are deflected upwards. After piercing through the water surface, they generate plunging jets of much less velocity (and momentum) than the main jets. These lateral plunging jets also entrain air into the pool. For deep pools and velocities between 7.5 and 20 m/s, good observation conditions are still found; for higher velocities, the air entrained by the laterally plunging jets reduces visibility starting from the surface.

For relative pool depths $Y/D \leq 5.6$ (i.e. shallow pools), the confinements generate geyser-like flow ejections. The lateral confinements deflect the bottom wall jet upward in the direction of the pool surface. For increasing pool depths, the upward flow is hindered by increased submergence and the ejections are reduced to a surface boil. This was observed for all the three lateral confinements tested.

The best visualisation conditions were obtained with the $D_c/D = 16.7$ wide confinement. For low velocities, there is little air in the outer pool region and the flow features inside the confinement are perceptible. For $Y/D = 4.2$, periodic surface waves (oscillations) are observed between the confinement and the falling jet with an estimated frequency of ≈1 Hz. The impact of these oscillating waves with the falling jets is clearly visible, leading to upward ejections (Figure 4, top). With regular frequency, these ejections reach heights of approximately four times the jet's diameter. For deeper pools, i.e. $Y/D > 4.2$, the surface oscillations are observed over the entire pool (Figure 4, bottom). The peaks and nodes of the pool surface oscillations rotate slowly clockwise in plan view. The amplitude of the oscillations is approximately twice the jet's diameter. The time series of the pressure signal obtained at $y/D = 2.08$ confirmed the presence of pressure head oscillations of ≈15 cm occurring with a frequency of 1–2 Hz.

For deep pools with $Y/D = 9.3$ and 11.4, the jet outlet is either intermittently submerged or permanently submerged, respectively. The formation of a ring vortex between the falling jet (in the centre) and the upward deflected jet (along the perimeter of the confinement) is clearly visible due to the presence of trapped air bubbles from initial pool filling (Figure 5). When jet velocity is reduced, pool currents fade out and the air bubbles go up by buoyancy. When the outlet is initially submerged, no air is entrained in the pool by the jet. Only a small quantity of air is entrained at

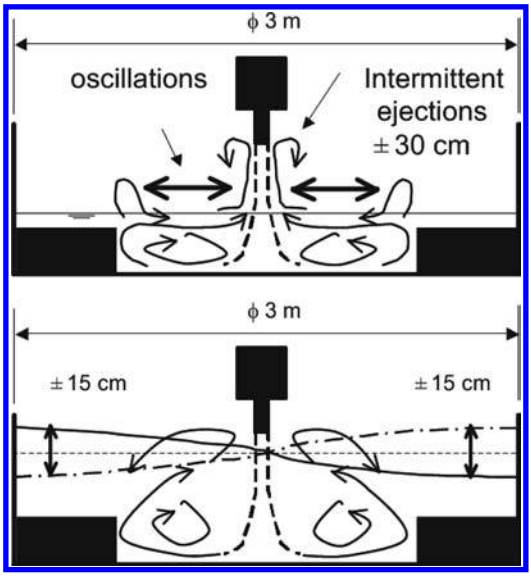


Figure 4. Schematic representation of: top) oscillations inside the confinement with intermittent ejections; bottom) pool surface oscillations.

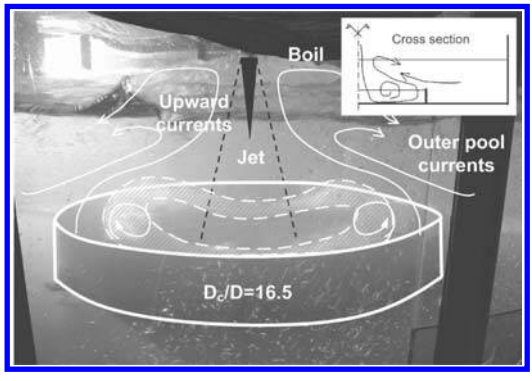


Figure 5. Main flow features inside pool with $D_c/D = 16.7$, submerged nozzle ($Y/D = 11.4$) and $V = 12.33$ m/s. Entrapped air bubbles can be seen in the ring vortex.

Copyright © 2006 Taylor & Francis Group plc, London, UK

Table 1. Selected statistics of pressure fluctuations at $y/D = 0.35$ in wide pools, $D_c/D = 16.7$. The Strouhal number is defined as $St = f\lambda/V$ where $\lambda = t$.

Y/D	V_0 [m/s]	σ [bar A]	p'^+ [bar A]	p'^- [bar A]	z_{max}	z_{min}	K	C_s	Comments
4.2	9.82	0.082	1.435	0.772	3.0	−5.0	1.58	−1.07	Oscillations in
	12.28	0.151	1.839	0.730	2.7	−4.6	0.52	−0.95	confinement with f ≈ 2.5 Hz
	14.74	0.206	2.367	0.836	3.4	−4.0	0.48	−0.93	Ejections with f ≈ 1 Hz
	17.19	0.240	2.791	0.808	3.1	−5.2	1.82	−1.24	
5.6	9.82	0.109	1.480	0.836	2.9	−3.0	−0.82	0.01	Pool surface oscillations,
	12.28	0.197	1.842	0.859	2.6	−2.4	−1.18	0.10	with f ≈ 1 Hz
	14.74	0.253	2.270	0.885	2.6	−2.9	−0.88	−0.20	
6.9	9.82	0.085	1.412	0.762	4.8	−2.9	0.28	0.68	Pool surface oscillations
	12.28	0.156	1.802	0.722	4.0	−3.0	−0.29	0.49	with f ≈ 1 Hz
	14.74	0.192	2.187	0.748	4.5	−3.0	0.07	0.64	
9.3	9.82	0.054	1.300	0.834	5.6	−3.0	0.39	0.58	Visible ring vortex
	12.28	0.086	1.565	0.836	5.4	−3.0	0.41	0.62	with f ≈ 1–4 Hz
	14.74	0.121	1.836	0.799	5.3	−3.3	0.35	0.61	Energy peaks at
	17.19	0.163	2.431	0.836	6.6	−3.2	0.41	0.62	70–110 Hz
	19.65	0.214	2.711	0.834	5.4	−3.3	0.32	0.58	for increasing velocities

the surface through the boil. The ring vortex is saddle-like; its peaks and nodes rotate clockwise in plan view. It is a low pressure and low velocity flow region. For the range of jet velocities allowing visual observations (9.8–19.6 m/s), the vortex rotating frequency was estimated between 1 and 4 Hz. The vortex also expands and contracts in the radial direction. For $V > 19.6$ m/s, visual observation becomes difficult due to increased air entrainment through the surface boil. Depending on the ratio D_c/D, the upward currents may influence the development of the plunging jet and the dissipation of energy before impact on the bottom: the larger the confinement the lower the interference is. For large values of the tailwater depth (i.e. $h = Y - t$), the upward currents are pushed to the centre by the recirculation currents, increasing friction with the plunging jet and hindering the penetration of air bubbles in the pool. In this case, the deeper the confined region in comparison with the total depth Y, the lower the risk of formation of intense recirculation currents.

4 EVIDENCE OF FLOW FEATURES

4.1 *Turbulent pressures*

All the three lateral confinements change the pressure fluctuations at the pool bottom compared to the flat reference case. For transitional and deep pools, the energy content, i.e. σ^2, is reduced. Despite the reduction, more energy can be concentrated at frequencies corresponding to undesirable flow phenomena. As an example, macro-turbulent pool flows may produce air-water ejections that may affect ancillary structures located in the banks downstream of dams. Or, in case of fully fractured rock, the close matching with the resonating frequencies of rock fissures conjugated with a dynamic uplift may lead to loosening of blocks and their displacement in the pool.

Selected statistical properties of 3-min data sets simultaneous to the previous mentioned observations are presented in Table 1. A few conclusions can be drawn:

- the energy of pressure fluctuations is larger in shallow confined pools than in deep confined pools, as well as the maxima and minima of the pressure fluctuations.
- the skewness C_s is negative whenever core impact occurs and positive when developed jet impact conditions are obtained, in good agreement with previous findings in pools with flat bottom (Manso 2006). In other words, the analysis of extreme events shows that the probability distribution of pressure fluctuations is negatively skewed for shallow pools (i.e. the Gaussian variable $|z_{min}| < z_{max}|$) and positively skewed for deep pools.
- for a given pool depth Y/D the sign of the skewness and (excess) kurtosis K parameters are a function of jet velocity, meaning that jet diffusion and flow pattern are also a function of jet velocity and, of course, of pool geometry.

4.2 *Spectral distribution: influence of pool depth*

The breakdown of energy generated by different turbulent scales is described in terms of power spectra for points "a" and "e". Each spectrum is obtained from 3 runs of 65'536 points sampled at 1 kHz, divided in 64 blocks with 50% overlapping using Welch's periodogram method and a Hamming window. Spectra of turbulent fluctuations present three main features from low to high frequencies (Chassaing 2000): (1) the production zone, related to the mean characteristics of

Copyright © 2006 Taylor & Francis Group plc, London, UK

the energy source (the jet), (2) the energy redistribution zone from large eddies at low frequencies to progressively smaller vortexes (cascade of energy) and (3) the dissipation or viscous zone, where the energy of the small turbulent structures (high frequencies) is dissipated by viscosity. The transition from the redistribution to the dissipation zone is known as the inertial sub-range, where the slope of the spectra follow a $f^{-5/3}$ slope. In the reference case of pools with flat bottom, core impact conditions correspond to constant sloped spectra at approximately f^{-1} in a log-log scale, and developed impact conditions to a double sloped spectra that falls into dissipation for higher frequencies with slopes steeper than $f^{-5/3}$ (Bollaert and Schleiss 2003). The present facility generates core impact conditions for pools with $Y/D \leq 5.6$ and $17 < V < 30$ m/s (Manso 2006). Figure 6 presents spectra obtained in the wide pool with a jet velocity of 12.3 m/s and a wide range of pool depths. Spectra estimates are also divided by the variance σ^2 plotted against the Strouhal number defined as $St = f\lambda/V$, i.e. taking the scour depth t for length scale λ. The plots show traces of the visually observed phenomena at low frequencies, as well as the energy redistribution and decay for higher frequencies.

A detailed analysis of the computed spectra for an intermediate jet velocity of 14.7 m/s at points "a" and "e" shows that (Figure 7):

- At $y/D = 0.35$ ("a"), the oscillations inside the confinement occur for $Y/D = 4.2$ and 5.6. The peaks in spectral energy at 1–3 Hz are related to the ejections and pool surface oscillations. For $Y/D > 4$, the spectra are typical of developed jet impact conditions. The transition to the dissipation range occurs between 20 and 40 Hz. Disregarding the low-frequency disturbances, the spectra have a rather mild slope for $f < 25$ Hz. For $Y/D = 2.8$, the core impacts the bottom. In general, the oscillations disappear with increasing submergence, i.e. Y/D.
- At $y/D = 2.08$ ("e"), the oscillations inside the confinement are also visible for $Y/D = 4.2$. The spectra for $Y/D = 8.3$ shows rather "incipient" developed jet impact conditions. The spectra for $Y/D = 6.9$ and 9.3 are similar. Compared to results closer to the axis of the jet, these spectra have in general lower energy. Several spectra have less energy at lower frequencies than at high frequencies. The energy content at high frequencies is similar to that of spectra reflecting the impact of the turbulent shear layer of develop jets. The low energy at low frequencies shows that there are no major sources of turbulent energy at lower frequencies (apart from the oscillations for $Y/D = 4.2$) or, in other words, the kinetic energy of the flow is mainly in the mean field and in turbulent scales with high frequencies. In this case, the pressure transducer is under the influence of a bottom wall jet, developing close to solid boundary under the impact of turbulent shear layer.

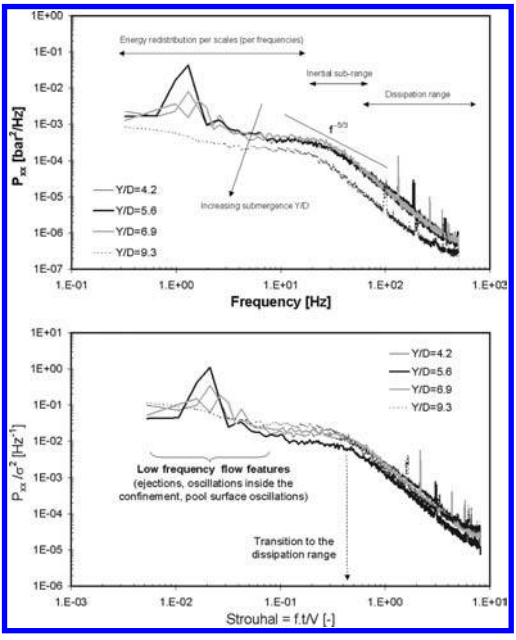


Figure 6. Spectral density functions for wide pools, $D_c/D = 16.7$, $t/D_c = 0.17$, $V = \mathbf{12.3\ m/s}$ and different pool depths Y/D. The bottom picture is dimensionless and the Strouhal number is defined in terms of the scour depth "t".

- The non-dimensional plots show that several spectra almost match, save those for $Y/D = 8.3$. This is a particular case, for which flow in the experimental set-up generated strong recirculation currents reduced considerably the "effective" pool level; this is considered an artifact of the facility but the results were nevertheless included for completion and comparison. Full matching of dimensionless spectra is herein interpreted as corresponding to similar flow conditions. For developed impact conditions, most spectra at $y/D = 0.35$ match, save the one for core impact (Y/D = 2.8) and the particular case of $Y/D = 8.3$ for which flow conditions are anyway different. At $y/D = 2.08$, spectra match in pairs: one for $Y/D \leq 4.2$, i.e. shallow pools, and another for $Y/D = 6.9$ and 9.3 for which there is already larger energy at lower frequencies due to enhanced development of the turbulent shear layer of the plunging jet.

4.3 *Spectral distribution: influence of the velocity*

Power spectra for $Y/D = 4.2$ (i.e. shallow pools) have been computed for all the velocities tested and are presented in Figure 8 for points "a" and "e" (Fig. 3). At $y/D = 0.35$ (point "a"), low frequency oscillations of about 1–4 Hz are identified for $V = 12.3$ to 17.2 m/s.

Copyright © 2006 Taylor & Francis Group plc, London, UK

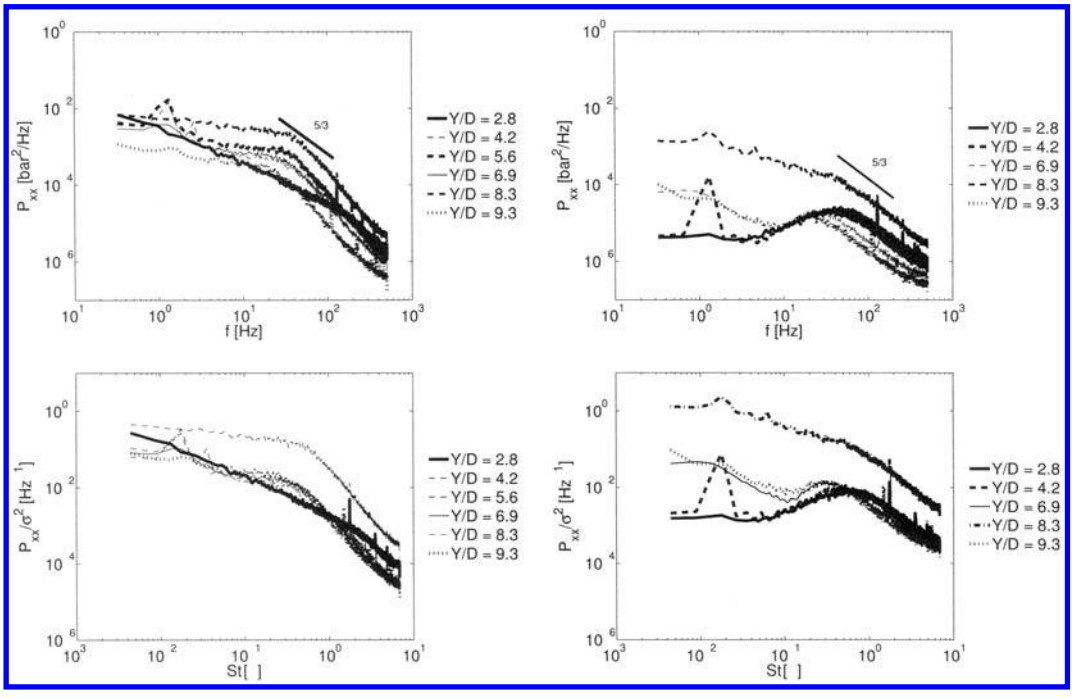


Figure 7. Spectral density functions for wide pools, $D_c/D = 16.7$, $t/D_c = 0.17$, $V = \mathbf{14.7\ m/s}$ and different pool depths Y/D: left) y/D = 0.35; right) y/D = 2.08. Strouhal number defined in terms of the scour depth "t".

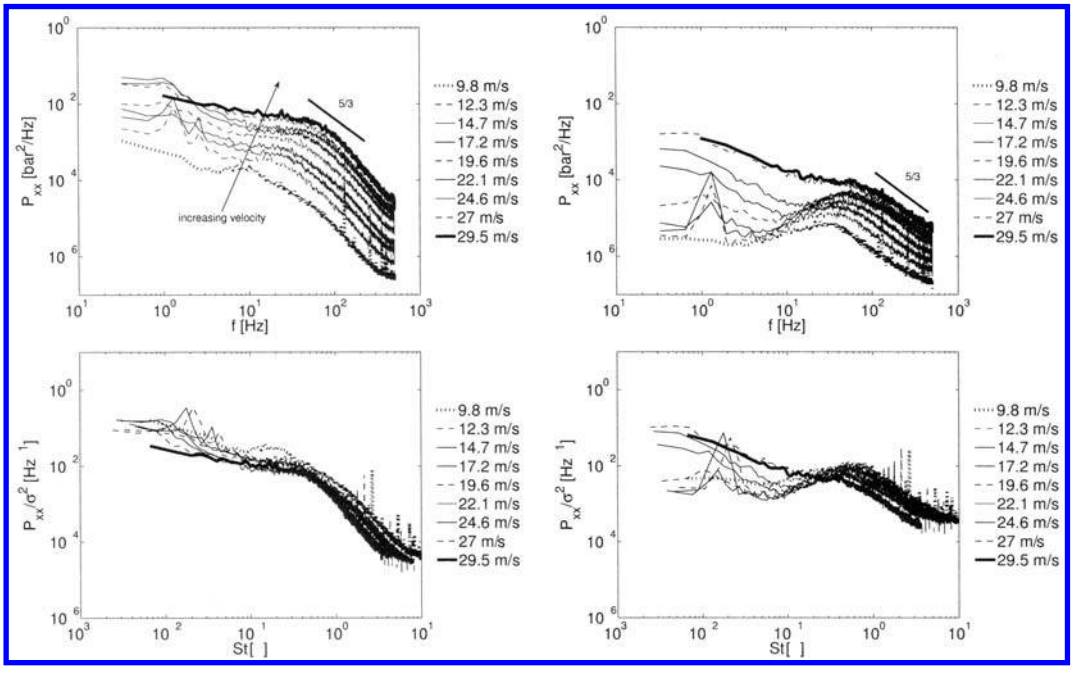


Figure 8. Spectral density functions for wide pools, $D_c/D = 16.7$, $t/D_c = 0.17$, **with** $Y/D = \mathbf{4.2}$ and different jet velocities: left) y/D = 0.35; right) y/D = 2.08. Envelope cases are highlighted.

Copyright © 2006 Taylor & Francis Group plc, London, UK

All spectra correspond to the impact of developed jets. At $y/D = 2.08$ (point "e"):

- low frequency oscillations are also observed at about 1 Hz for $V = 12.3$ to 17.2 m/s;
- all spectra for $V \leq 24.6$ m/s show much less energy up to 40–50 Hz than those for $V = 27$ and 29.5 m/s. Beyond these frequencies, all spectra have a similar decay;
- for $f > 50$ Hz, the spectra decay with a slope $\leq -5/3$ and thus is not clear if the dissipation range is attained.
- The reduction of spectral energy for $f < 40$–50 Hz is related to the formation of a bottom wall jet. The bottom wall jet does not have the same spectral energy of the impacting turbulent shear layer (TSL). For $V = 27$ and 29.5 m/s, the TSL impacts the bottom at $y/D = 2.08$. For $V = 12.3$ to 17.2 m/s, the surface oscillations are superposed to the wall jet.

In deep pools (e.g. $Y/D = 9.3$) no major change in the main flow features with jet velocity can be identified from the spectra.

The mentioned low-frequency flow patterns can also be clearly identified in dimensionless spectra for $Y/D = 4.2$ (Figure 8, bottom row) for Strouhal numbers of ≈ 0.01 defined in terms of t or 0.03 if the Strouhal number is defined in terms of the distance from the jet axis to the confinement R_c. According to Figures 6, 7, 8, the spectra enter the energy dissipation range for $St \geq 0.3$.

5 TYPICAL SCALES OF FLOW FEATURES

5.1 *Surface oscillations and ejections*

The frequency of pool oscillations *inside* the confinement f_δ can be defined as:

$$f_\delta = f(R_c, \frac{Y}{D}, V_i, ..) \quad (1)$$

In the present case, pool oscillation were only observed for $Y/D < 5.6$. The amplitude δ of oscillations over the *entire* pool is:

$$\delta = f(R_c, \frac{Y}{D}, V_i, \forall, d/s, ..) \quad (2)$$

where $\forall$ is the total volume of the pool and d/s stands for downstream conditions. In the present case, such oscillations are observed for $5.6 < Y/D < 9.3$.

5.2 *Developed flow impact conditions*

In most practical situations, core jet impact is limited to the very early stages of scour or spillway operation. Confining laterally the free diffusion of plunging jets modifies the flow pattern in the pool. This is reflected in the impact pressures at the pool bottom. Pressure fluctuations spectra show developed jet impact conditions for pool depths as shallow as $Y/D = 4.2$. For $Y < R_c$ core impact conditions are observed, but few tests were performed in these conditions. For $Y = 4 - 5.6$D, core impact conditions could occur for very large pools, i.e. $R_c > 8$D. For $Y > 5.6$ the core of the jet vanishes independently of the value of R_c.

For wide confined pools (TC), developed jet conditions are obtained starting from Y = 4.2D, which is $\approx R_{tc}/2$. In this case, developed impact conditions are obtained for:

$$Y \geq 0.5R_{tc} \quad \text{i.e Y} \geq 4.2\text{D} \quad (3)$$

In narrow pools (FC) developed impact conditions were obtained in all tests and thus:

$$Y \geq 2.8D = R_{fc} \quad \text{i.e Y} \geq 2.8\text{D} \quad (4)$$

However, for intermediate confined pools (SC) core impact is obtained for Y = 2.8D (i.e. $R_{sc}/2$). Therefore, to obtain developed jet impact conditions:

$$Y \geq 0.5R_{sc} \quad \text{i.e Y} \geq 2.8\text{D} \quad (5)$$

Two envelope expressions are derived:

$$Y \geq R_c \quad \text{for } 2.8\text{D} \leq R_c \leq 5.6\text{D} \quad (6)$$

and

$$Y \geq 0.75R_c \quad \text{for } R_c \geq 5.6\text{D} \quad (7)$$

It should be stressed that $Y = 0.75 \times 5.6\text{D} = 4.2\text{D}$ is less than the core development length in pools with flat bottom with the turbulent jets generated in the present experimental set-up.

5.3 *Induced currents and cells*

The most relevant current patterns identified in the cases of shallow and deep laterally confined pools are:

- the shear eddy, between the turbulent shear layer (TSL) and the confinement;
- the upward currents generated by the reflection of the bottom wall jets on the pool boundaries;
- the pool recirculation currents, that set in motion the volume of water *outside* the scour hole.

The shear eddy (or dissipation cell) was also described by (Puertas-Agudo 1994) based on visualisation of the flow structure during experiments. The shear cell is the most important of the three phenomena regarding impact pressures. For very narrow confinements, the shear cell does not develop and the deflected upward currents oppose directly to jet momentum. Depending on the direction of these upward currents and on their proximity to the diffusion region, they can

Copyright © 2006 Taylor & Francis Group plc, London, UK

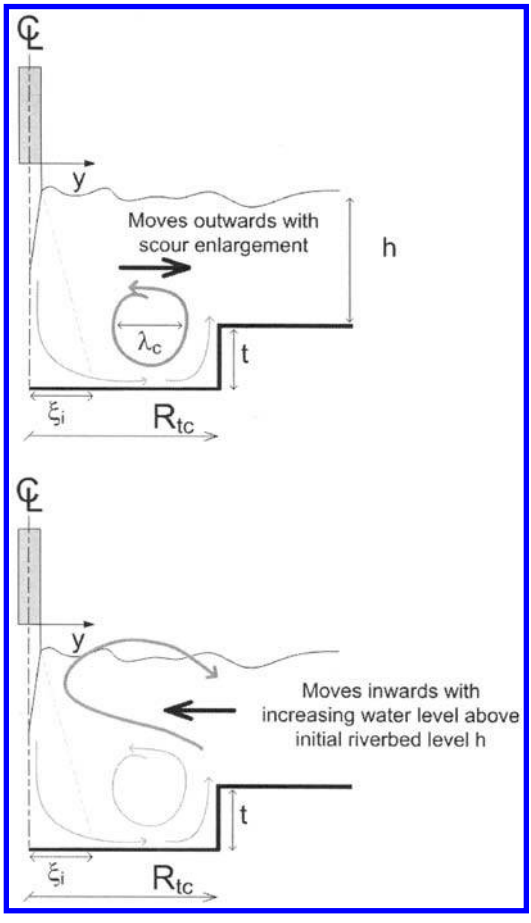


Figure 9. Shear eddy and recirculation currents behaviour. Dotted line corresponds to the theoretical shear layer in free jet diffusion of turbulent rough jets.

also hinder air bubble penetration in the pool. When the scour region is enlarged, this cell is created in between the jet and the upward currents – Figure 9. If scour keeps enlarging, the cell grow and is pushed outwards, remaining closer to the confinement than to the jet axis.

The pool circulation currents are highly relevant for back erosion but are generally overlooked in the definition of impact pressures and thus in the scour process. In fact, depending on the tailwater level h, these currents push the upward currents radially inwards and contribute to enhance dissipation and hinder air entrainment. For particular situations combining pool geometry, jet velocity and pool depth the generated circulation flow reduced the tailwater level locally at the plunging section. This was observed in the present facility for pools with flat bottom and $Y/D = 8.3$. The local reduction of pool depth generated impact pressures quite similar to those obtained for $Y/D = 6.9$. For the aforementioned reasons, circulation currents play an important role in the riverbed scour process, as well as in the bank erosion process.

5.4 *Definition of the length scale of the shear cell*

The observations of large-scale flow features (TC pool) allowed identifying the presence of a dissipation shear cell between the plunging jet and the upward currents. The location of this cell varies with the degree of confinement D_c/D, whereas its size is mainly function of a characteristic flow depth, either the scour depth t in confined geometries, or the pool depth Y in wide flat geometries. Its frequency varies with jet velocity, due to the influence of jet velocity on the definition of the interaction between the upward currents and the recirculation currents.

Despite the absence of direct velocity field measurements, some characteristics of such cells can be defined.

The width of the turbulent shear layer (TSL) at impact on a flat bottom is assumed $\xi \approx$ Y/3, according to several authors (Cola 1966; Beltaos and Rajaratnam 1974).

In the present set-up, the turbulent shear layer impacts the bottom between 1.4D (for $Y = 2.8$D) and 2.8D (for a maximum pool depth of 9.3D), assuming a diffusion spreading angle of 14° in pools with flat bottom. The ξ is maximum 3D. Hence, any narrow pool (FC) interferes directly with the TSL. The space between the axis and the confinement is shared between the "confined" shear layer and the upward currents.

The observation of the shear cell in wide pools (TC, in submerged jet conditions and for $t/D = 2.8$ only) allows estimating the cell's dimension $\lambda_c < R_{tc}/2$. In these conditions $Y = 11$D and $R_{tc} = 8.3$D. Therefore, $\lambda_c < 4.2D$ if assumed circular. From visual interpretation of the flow field, $\lambda_c <$ Y/2. The bundle of air bubbles that allowed visualisation did not exceeded 20 cm (i.e 2.8D).

For intermediate pools (SC, $R_c = 5.6D$) and for $t/D = 2.8$, the jet core impacts the bottom only for the minimum Y/D, i.e. $\xi = 0.33(2.8\text{D}) = 1.4$D. For all the other pool depths Y/D, developed jet impact conditions are registered. One can consider that:

- with a TSL width of 1.8D for $Y = 4.2$D and a shear cell of 2.8D, the upwards currents can still occupy 1.4D and have little influence over the plunging jet. This is good agreement with the results.
- with a TSL width of 2.8D for $Y = 9.3$D, λ_c is lower than 2.8D. In this case two possibilities can be considered: either λ_c is 2.8D or the TSL has to be smaller.

Copyright © 2006 Taylor & Francis Group plc, London, UK

The previous analysis of the narrow, intermediate and wide confinements suggests that the y-length scale of the shear eddy, when existing, is of about 2.8D. This corresponds to $R_{sc}/2$ or $R_{tc}/4$. The x-length scale (vertical) is likely related with t, i.e. the depth of scour below initial riverbed. In fact, for $Y > t$ (i.e. $h \neq 0$) the recirculation currents in the region outside of the confined zone may influence λ_c. This can be visually observed in TC pools ($t/D = 2.8$) with $Y/D = 9.3/11.4$.

The length scale of the shear cell λ_c is thus defined as:

$$\text{if} \quad R_c = t \quad \text{and} \quad R_c > 2.8D \quad \text{and} \quad h \geq t \quad \Rightarrow \quad \lambda_c \approx t \qquad (8)$$

For pools that are *deeper than wider*, i.e. $R_c <$ t:

$$\text{if} \quad R_c > 2.8D \quad \text{and} \quad Y > 1.5t \quad \text{or} \quad Y \geq D_c \quad \Rightarrow \quad \lambda_c \approx R_c/2 \qquad (9)$$

assuming Cola's hypothesis for the impinging zone (i.e. 0.33Y). For pools that are *wider than deeper*, i.e. $R_c >$ t:

$$\text{if} \quad 4D < Y \leq 1.5R_c \quad \text{and} \quad R_c > 4.2D \quad \Rightarrow \quad \lambda_c \approx t \qquad (10)$$

For pools with flat bottom, λ_c is estimated based on Cola's statement that the centre of gravity of the cells is at 0.25Y. In these conditions:

$$\text{if} \quad Y > 5.6D \quad \Rightarrow \quad \lambda_c \approx 0.50Y \qquad (11)$$

However, in the present set-up, the outflow is controlled by side weirs. They define the pool level Y and influence the large recirculation currents in pools with flat bottom. (Puertas-Agudo 1994) observed $\lambda_c < 0.50Y$ due to the same "weir" effect.

5.5 *Evolution of the Strouhal number with scour depth*

The dimensions and frequency of the shear cell can be used to define a characteristic Strouhal number per pool geometry. The rotation frequency of the shear cell can be computed by:

$$\hat{f} = \frac{U_r}{\pi \lambda_c} \qquad (12)$$

where U_r is the rotation velocity, i.e. the velocity necessary to do one revolution of $\pi\lambda_c$ (perimeter) in a given period T. The Strouhal number corresponding to this turbulent flow pattern can be defined as:

$$St_2 = \frac{U_r}{\pi V} \qquad (13)$$

which is similar to the expression proposed by (Ervine et al. 1997). The rotation velocity is assumed as the velocity of the plunging jet at the entry of the impinging region (i.e. 0.25Y). This depth corresponds to the x-coordinate of the centre of the cell (Cola 1966; Puertas-Agudo 1994).

Based on these assumptions, the characteristic frequencies of shear cells are presented in Table 2. For the wide (TC) deep pool, the estimated frequencies range from 10 to 30 Hz, and are in agreement with the visual observations. The results are very sensitive to the U_r assumptions. Since there is no centreline velocity decay law available for each pool geometry, U_r values were obtained from the mean pressure values measured at stagnation (i.e. y/D = 0.35).

Rotating frequencies are estimated between 10–30 Hz in deep pools and 10–65 Hz in shallow pools. This is in good agreement with the indications from the spectral analysis. For several other geometries, the rotation frequencies obtained were lower than 20 Hz with St_2 not exceeding 0.16 (Manso 2006), with larger t/D ratios and combining different D_c/D geometries to compose stepped conical plunge pools.

Table 2. Characteristic cell frequencies, based on estimates of λ_c and U_r.

Pool	Y/D	Y [m]	h [m]	R_c [m]	t [m]	V [m/s]	λ_c [m]	U_r [m/s]	f [Hz]	St_2 [-]
FB	4.2	0.30	0.30	–	–	29.5	0.15	29.5	63	0.32
				–	–	10	0.15	10	21	0.32
	9.3	0.67	0.67	–	–	29.5	0.34	20	19	0.22
				–	–	10	0.34	8	8	0.25
SC1	4.2	0.30	0.10	0.4	0.2	29.5	0.20	15	24	0.16
						10	0.20	6	10	0.19
	9.3	0.67	0.47	0.4	0.2	29.5	0.20	18	29	0.19
						10	0.20	5	8	0.16
TC1	4.2	0.30	0.10	0.6	0.2	29.5	0.20	20	32	0.22
						10	0.20	8	13	0.25
	9.3	0.67	0.47	0.6	0.2	29.5	0.20	11	18	0.12
						10	0.20	3	5	0.10

Copyright © 2006 Taylor & Francis Group plc, London, UK

5.6 *The role of the shear eddy in energy dissipation*

Energy dissipation is done by jet diffusion through the pool and impact in the river bottom. In laterally confined pools the direct contact between the plunging jet and the upward currents enhances dissipation in the water column. If a shear eddy cell is formed, it will also contribute to the dissipation process. As the scour is enlarged, the eddy cell moves away from the jet, exposing the riverbed to higher mean pressures.

5.7 *The role of the shear eddy in abrasion*

Abrasion is a scouring process complementary to fracture propagation in rock and rock block displacement by dynamic uplift. When blocks are ejected, they join the pool flow. If the shear eddy has sufficient momentum to keep them in motion, blocks act as a rotating "mill stone" on the pool boundaries. Rock blocks get smaller in size, until they are light enough to be washed away by the flow. If the blocks are oversized compared with the eddy's momentum, they will rather hinder any rotational movement in the confined region.

6 CONCLUSIONS

The diffusion of plunging jets in laterally confined plunge pools has been studied experimentally and compared with diffusion in pools with flat bottom. Dynamic pressures were sampled at the pool bottom. Point statistics and a limited number of multi-point description of the spatial turbulent pressure field are dsicussed in this paper. The analysis of pressure distributions, spectral energy content and the visualisation of large-scale flow features show that:

- the geometry of the plunge pool is a key element in the definition of the mean and turbulent character of dynamic impact pressures on the pool boundaries;
- the flow patterns induced by the interaction of the turbulent shear layer with the pool geometry considerably alter jet diffusion and air bubble penetration in non-flat pools, compared to the most-documented case in literature of pools with flat bottom;
- confining laterally the evolution of plunge pool enhance dissipation in the water column, reduce impact pressures and ultimately reduce scour potential; and,
- wall pressure measurements can be used to infer characteristics of the turbulent flow field with high air content in the pool.

The presented analysis is part of a broad research in rock scour by high-velocity plunging jets. The thorough analysis of the key physical processes involved in jet diffusion in a highly aerated water pool, jet impact in solid boundaries and the scouring potential of the corresponding dynamic loads, is a basic requirement for the further development of comprehensive modelling tools of the scouring process.

ACKNOWLEDGEMENT

The research was funded by the OFEN (Switzerland) and the FCT grant SFRH/BD/6894/2001 (Portugal).

REFERENCES

Beltaos, S. and N. Rajaratnam (1974). Impinging circular turbulent jets. *Journal of the Hydraulics Division 100*(10), 1313–1328.

Bollaert, E. and A. Schleiss (2003). Scour of rock due to the impact of plunging high velocity jets. Part 2: Experimental results of dynamic pressures at pool bottoms and in one- and two-dimensional closed end rock joints. *Journal of Hydraulic Research 41*(5), 465–480.

Chassaing, P. (2000). *Turbulence en Mécanique des fluides – Analyse du phénomène en vue de sa modélisation à l'usage de l'ingénieur (in French).* POLYTECH. Toulouse: Cépaduès-Editions.

Cola, R. (1966). Diffusione di un getto piano verticale in un bacino d'acqua d'altezza limitata. *L'Energia Elettrica* (11), 649–664.

Ervine, D. A., H. R. Falvey, and W. Withers (1997). Pressure fluctuations on plunge pool floors. *Journal of Hydraulic Research 35*(2), 257–279.

Manso, P. A. (2006). *The influence of pool geometry and induced flow patterns on rock scour by high-velocity plunging jets.* Ph. D. thesis, EPFL Thesis No. 3430.

May, R. W. P. and I. R. Willoughby (1991). Impact pressures in plunge basins due to vertical falling jets. In *Reports SR242*. HR-Wallingford.

Puertas-Agudo, J. (1994). *Hydraulic criteria for the design of energy dissipation basins in arch dams with free crest overfall (in Castillan).* Ph. D. thesis, Universitat Politècnica de Catalunya.

Copyright © 2006 Taylor & Francis Group plc, London, UK

Numerical investigation of the turbulent flow around a bridge abutment

A. Teruzzi & F. Ballio
Politecnico di Milano, Milano, Italy

S. Salon
OGS, Trieste, Italy

V. Armenio
Università degli studi di Trieste, Trieste, Italy

ABSTRACT: Bridge failures are frequently related to phenomena of local erosion at piers and abutments; literature on this topic does not provide fully satisfactory formulations to evaluate the scour depth. Since a detailed definition of the flow can improve the comprehension of the phenomenon, a numerical study on the turbulent flow around an obstacle archetypal of an abutment is presented. The turbulent flow characteristics are investigated by means of Large Eddy Simulation, obtaining results both on the averaged flow characteristics as on the instantaneous ones. The averaged flow around the obstacle is structured as a highly three-dimensional system of vortex structures; instantaneous structures are characterized by high vortex intermittency. The shear and normal stress distributions on the bottom-wall are analyzed in comparison with experimental observations relative to erosion phenomena. The numerical simulations are consistent with experimental observations on flow characteristics around an abutment in flat-bed condition and provide details on its three-dimensional features and instantaneous behavior.

1 INTRODUCTION

As documented in literature works (see for example Cardoso & Bettess 1999) local scour at piers or abutments is one of the most frequent cause of bridge failure. The erosion phenomenon is the result of the interaction between a complex three-dimensional turbulent flow and the river bed; since the definition of the flow features can improve the comprehension of the localized erosion phenomenon, in this work a study on the flow around an obstacle archetypal of an abutment is presented.

Several literature works on erosion problems propose various parametric formulas to evaluate maximum scour depth at bridge piers or abutments (see Melville & Coleman 2000 and literature therein cited), but the resulting values from the different formulations are very scattered, as showed in Cardoso & Bettes (1999), and therefore not really satisfactory in bridge design. In order to explain the dependency of the scour depth from the control parameters of the system, a comprehension of the erosion mechanism (the sediment-flow interaction) at the sediment scale could be useful. For such an approach it is relevant to define the flow field characteristics (in terms of velocities, vortexes, stresses, etc.) and the associated sediments motion features (as velocities, directions, mass-rate intensities, etc.).

In this work the turbulent flow characteristic aspects are investigated, and particularly a Large Eddy Simulation study of the turbulent flow around a trapezoidal obstacle on a flat-bed is presented. Examples of literature experimental results for similar configurations can be found in Ahmed & Rajaratnam (2000) and in Barbhuiya & Dey (2003) with flat-bed condition and with developed scour hole respectively. The literature results from experiments around abutments are averaged in time and do not describe the turbulent nature of the flow. A general description of the principal (averaged) vortex structures can be found in Melville & Coleman (2000), where the principal vortex is identified as the main responsible for the erosion process.

Numerical and experimental results of a turbulent flow field around an abutment in flat-bed configuration are presented in Chrisohoides et al. (2003) where a URANS model is used for numerical simulations. Their results are consistent with the description of an highly three-dimensional flow near the abutment, recognizing a complex system of multiple vortexes in front of the obstacle.

Copyright © 2006 Taylor & Francis Group plc, London, UK

In this work the LES technique permits to define in details both the averaged flow characteristics as well as the instantaneous ones for the flow field around a trapezoidal obstacle; the attention is particularly focused on the area in front of the obstacle, correspondent to the region where the maximum scour depth is observed in erosion experiments. Results describing the three-dimensional flow structures are presented, as well as the shear and normal stress patterns on the walls. The latter variables are directly correlated to the scour process, and are therefore analyzed in comparison with observations of erosion experiments.

2 NUMERICAL MODEL

The turbulent flow results presented in this work are obtained by means of Large Eddy Simulations (LES). LES method is intermediate between RANS and DNS; it resolves the large, energy carrying scales and models the dissipative small ones, supposed isotropic.

The SGS stresses are evaluated by the generalized coordinates dynamic Lagrangian mixed model proposed in Armenio & Piomelli (2000), which in Cartesian frameworks can be written as:

$$\tau_{ij} = \overline{\bar{u}_i \bar{u}_j} - \overline{\bar{u}_i}\,\overline{\bar{u}_j} - 2C\bar{\Delta}^2 \left|\bar{S}\right| \bar{S}_{ij} \qquad (1)$$

where the overbar indicates the filtering operation, $\bar{u}$ are the velocity resolved components, $\bar{S}_{ij}$ is the resolved strain-rate tensor, $\bar{\Delta}$ is a term related to the filtering dimension and C is the model coefficient. The first two terms and the last one in (1) represent respectively the scale similar (Bardina et al. 1980) and the eddy viscosity part (Smagorinsky 1963). In the used dynamic Lagrangian model the coefficient C is evaluated during the simulation, using the energy content of the small resolved scales (Germano et al. 1991), and averaged over flow path lines (Menevau et al. 1996), since in the presented geometry there is not homogeneity directions over which averaging can be operated. Particulars on the model implementation, specifically on the formulation in curvilinear coordinates, can be found in Armenio & Piomelli (2000).

3 GEOMETRY AND PARAMETERS

The numerical simulations are carried out in a duct with rectangular cross-section and a near wall trapezoidal obstacle (representing an abutment). A sketch of the duct and obstacle geometry and of the coordinate system is presented in Figure 1. With reference to quantities indicated in Figure 1, the duct and obstacle dimension are: $B = 2.5\,h$, $L = 13.5\,h$, $b = 0.5\,h$, and $\alpha = 45°$.

The Large Eddy Simulations are carried out setting no-slip boundary condition on the duct and obstacle walls; the inlet condition is a series of cross-section velocity fields previously obtained from a developed and constant mass-rate turbulent flow in a straight rectangular duct, with same dimensions and flow-rate of the present case, but without the obstacle. The Reynolds number based on the duct height and bulk velocity at the inlet cross-section is equal to 7000. The number of grid points is $256 \times 64 \times 96$ respectively in the x-, y- and z-direction. The grid points are clustered in the y- and z-direction near the walls in order to assure that the viscous sub-layer is directly resolved; moreover the grid spacing along the x-direction is reduced in the obstacle region, since the complexity of the flow field in this area requires a higher definition.

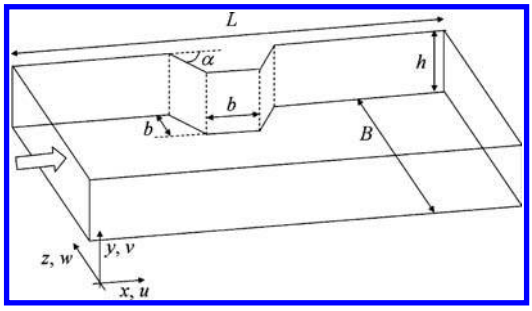


Figure 1. Sketch of duct geometry and coordinate system (not in scale).

The simulations are carried out with a constant time step corresponding to a Courant number close to 0.4. The mean quantities presented in section 4 are obtained by averaging on about 10 large eddy turn over time (LETOT) and over the two symmetric parts of the duct separated by the (x, z) half height plane, therefore all the averaged results are defined on the half duct.

4 RESULTS

4.1 *Flow field around the obstacle*

The numerical simulations allow the definition of the flow field around the trapezoidal obstacle in detail, and specifically to obtain information on its complex three-dimensional and turbulent characteristics.

The vortex structures are identified for the instantaneous and mean flow fields by the Q-criterion. In Figure 2 the results obtained for the averaged flow show a system of vortices in front of the obstacle and the vortex sheet detaching from the edge of the obstacle. Upstream the obstacle different structures can be identified: a corner vortex (indicated with I), with axis parallel to the y-direction, which is bended horizontally in proximity of the bottom wall and eventually joined to a horizontal vortex (II), thus creating a big structure rounding the obstacle (III), parallel to the (x, z)-wall; finally, a longitudinal vortex can

Copyright © 2006 Taylor & Francis Group plc, London, UK

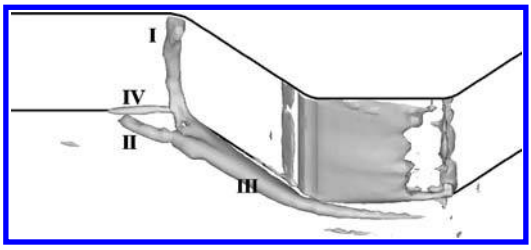


Figure 2. Vortex structures of the averaged flow (half duct).

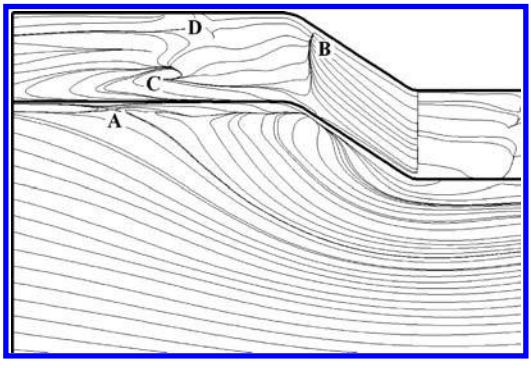


Figure 3. Stream-traces of the averaged flow on the (x, y)- and (x, z)-wall (half duct).

be observed in the corner between the (x, y)- and (x, z)-wall (IV). In Figure 2 the directions of the vorticity vectors associated to the described structures are qualitatively shown.

More details on the three-dimensional structures are provided by the shear stress traces on the walls. Figure 3 shows the stream-traces of the averaged flow on the (x, y)- and (x, z)-wall, revealing the flow topology resulting from the interaction between the incoming boundary layer and the adverse pressure gradient due to the obstacle. The averaged flow is probably affected by not fully developed statistics, since non-zero velocity component v on the symmetry plane are present. An enlarged schematic of shear lines topology is shown in Figure 4.

The trace of the circulation in front of the obstacle due to the (main) horizontal vortex II is clearly detectable on the (x, y)-wall (focus/node C). On the upstream wall of the obstacle an attachment line exits from node B directed vertically downwards; it eventually continues upstream on the bottom, connecting node B to the saddle A. Node B, as well as its counterpart on the lateral wall, i.e. the saddle D, are the direct consequence of the presence of vertical vortex I. Notice that saddle D should lay on the symmetry plane: we already discussed that the incomplete symmetry of the flow is due to incomplete convergence of the mean values.

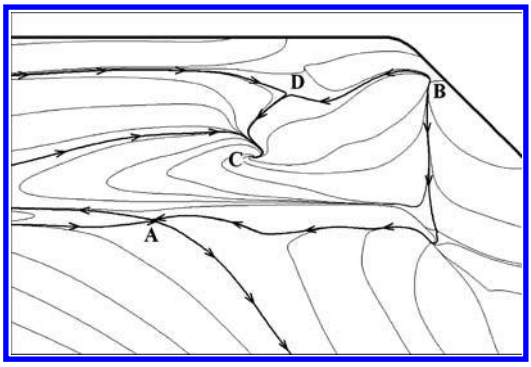


Figure 4. Sketch of topology (half duct).

The singular attachment line B-A (and its continuation A-C, partially not visible in the figures) delimitates the domain where the flow is pushed towards the lateral vertical wall by the vortices I and IV, while the outer streamlines directly follow the main path around the obstacle. Fluid particles within the "inner" domain enters either vortex I or vortex II, and are consequently transported in the outer region where the two vortices merge together and are stretched by the main flow.

The vortex sheet detaching from the abutment edge is basically two-dimensional, coherent with a 2D separation – reattachment pattern.

The averaged flow results are coherent with classics literature schemes about flow around abutments, but add details in the description of the backflow in front of the obstacle, particularly on the near (x, y)-wall region (not experimentally easy to investigate). Indeed the corner vortices I and IV, associated to the specific topology of this flow, are a distinguishing element with respect to the flow over symmetrical bodies (see for example results around bridge piers).

The analysis of the instantaneous values can provide significant additional information to be considered for the comprehension of the sediment-fluid interaction; indeed the river bed sediments interact with the intermittent turbulent flow, which characteristics are not necessarily revealed by the averaged features.

The instantaneous stream-traces on the walls near the obstacle give qualitative information on the instantaneous flow, particularly they reveal that some highlighted elements of the mean flow are permanent in the instantaneous one, while others are very intermittent. On the (x, y)-wall the instantaneous flow fields are very complex and, as expected, there is not symmetry with respect to the duct center plane, so the flow topology is not easily readable and referable to the main characteristics highlighted in the averaged flow. On the (x, z)-wall the saddle is not easily recognizable and very intermittent in time and position.

Figure 5a, b show an example of instantaneous stream-traces respectively on the (x, y)- and (x, z)-wall

Copyright © 2006 Taylor & Francis Group plc, London, UK

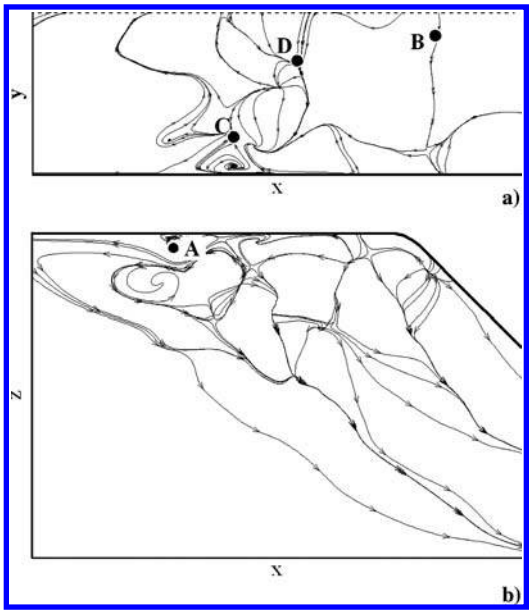


Figure 5. Instantaneous stream-traces: a) on the (x, y)-wall, b) on the (x, z)-wall (half duct).

(only the half part of the (x, y)-wall is reproduced). The position of the described singular points in the averaged flow are indicated, to highlight the differences between instantaneous and averaged topology.

In the instantaneous fields, the vortex system is quite different from the averaged one (see some examples of instantaneous vortexes in front of the obstacle in Fig. 6); several elongated vortexes in the flow direction can be recognized in all the analyzed time steps, while a very intermittent corner structure parallel to the y-axis is sometime present (see Fig. 6b). Typical detaching rolls are always recognizable at the obstacle edge, while the upstream vortex organization change significantly in time, see Figure 6a, b, c.

The evolution in time of the topological features and the differences between instantaneous and averaged flow emphasize the complexity in time and space of the flow obtained from simulations, which is representative of the one interacting with sediments around an abutment.

4.2 *Stresses*

Large Eddy Simulations of this study are representative of the flow around an abutment in a flat-bed river, that is at the beginning of the scour processs. In Oliveto & Hager (2002) the scour maximum depth evolution in time is analyzed; the authors observe that at abutments the scour starts at the edge of the obstacle, progressively moving towards the vertical wall as scour develops, so that the erosion process tends to

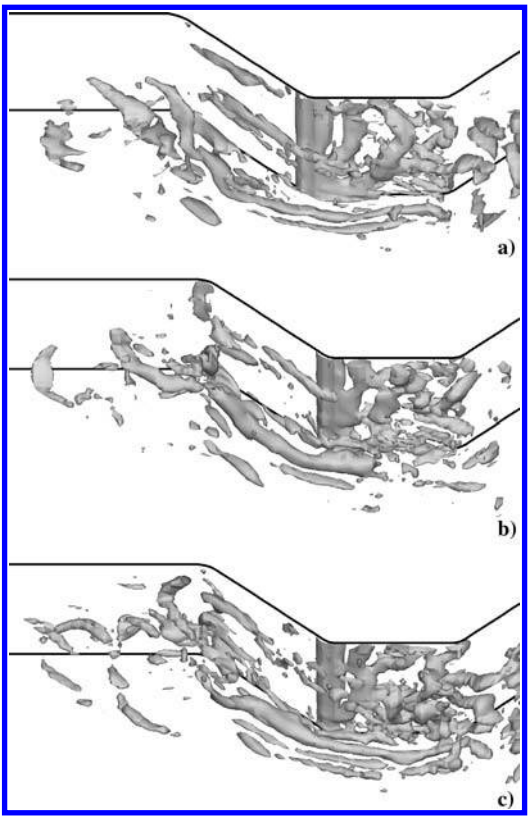


Figure 6. Examples of instantaneous vortex structures (half duct).

interest all the region upstream the abutment. Similar consideration were made in Teruzzi (2002). The experimental works of Molinas et al. (1998) and of Rajaratnam & Nwachukwu (1983) indicate that the maximum shear stress at the bed lies near the abutment edge. In the numerical simulations of Chrisohodes et al. (2003) the maximum shear velocity is localized in a similar position (they used an abutment geometry without edge).

The averaged results of stress distribution near the obstacle on the (x, z)-wall are presented in Figures 7, 8 and 9. Figure 7 shows the time-averaged shear stress module on the (x, z)-wall divided by $\bar{\tau}$, that is the mean shear stress in a straight duct with same dimension and Reynolds number of the present one; upstream and to the side of the obstacle there is a large region with shear stress higher than $3\bar{\tau}$, with a maximum of about $13\bar{\tau}$ at the obstacle.

Results of Figure 7 indicate that the region where the shear stresses exceed the mean value of the far field is concentrated in the edge region and in the wake, while no stress amplification is detectable in the proximity of the vertical wall. In a situation where the mean

Copyright © 2006 Taylor & Francis Group plc, London, UK

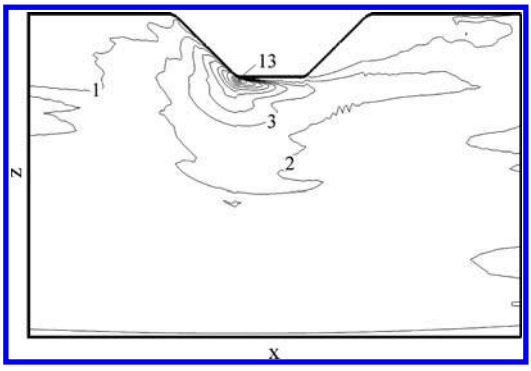


Figure 7. Averaged shear stress module on the (x, z)-wall, normalized by $\bar{\tau}$.

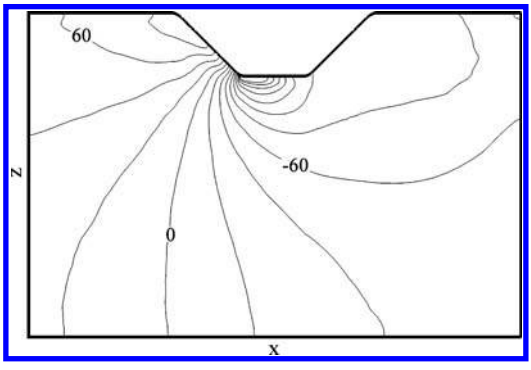


Figure 8. Averaged pressure on the (x, z)-wall, normalized by $\bar{\tau}$.

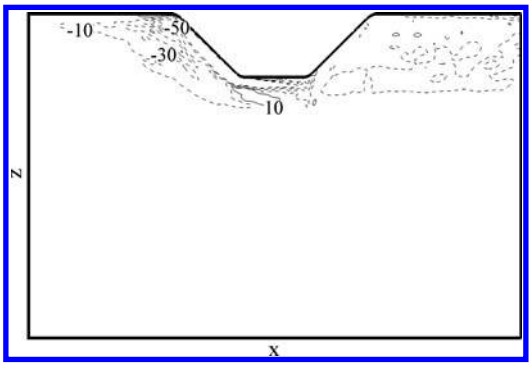


Figure 9. Averaged pressure gradient along the y-axis, normalized by $\bar{\tau}$ and h (dashed lines when negative).

value $\bar{\tau}$ is close to the incipient condition for grain motion, this result would indicate that the sediment motion could commence at the abutment edge (consistently with literature observation) but at the same time that no sediment transport and therefore no scour could be expected close to the vertical wall. The mean

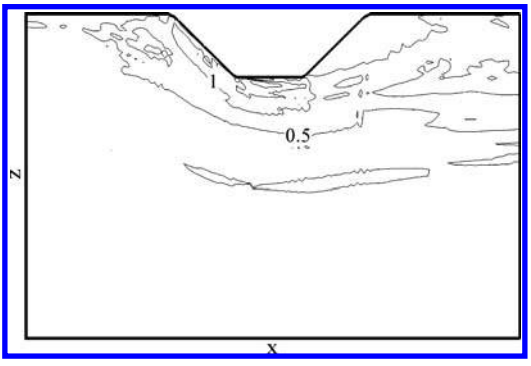


Figure 10. Shear stress module *rms*, normalized by $\bar{\tau}$.

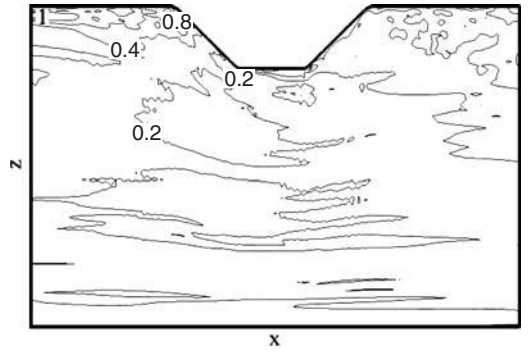


Figure 11. Variation coefficient of shear stress module.

shears are not able to explain the experimental experience of authors, which indicates that in the first instant of scour some sediment motion can be observed in the corner region.

The pressure distribution can play a role in the erosion process; in Figures 8 and 9 the normalized averaged pressure and its gradient along y-direction on the (x, z)-wall are respectively presented. The pressure minimum in Figure 8 lies at the obstacle edge, coherently with the maximum shear in this position. Maximum pressure values are positioned on the vertical wall, in front of the abutment, as a result of the blocking effect of the obstacle. It is possible that the pressure gradient can be an additional active factor for the scour process in the proximity of the edge, but this is hardly true in proximity of the vertical wall. In this area, however, the averaged vertical pressure gradient (Fig. 9) is particularly intense, so that, depending on the grain size, an uplift pressure effect can play a significant role on particle entrainment.

Due to the turbulent character of the flow, a relevant role in the erosion is played by the instantaneous quantities, specifically by the instantaneous shear stresses; indeed, in regions where the averaged shear stress module does not exceed the (average) critical value, grain

Copyright © 2006 Taylor & Francis Group plc, London, UK

movements can be explained by fluctuating components, which as indicated by statistics are higher than those of a flow over the standard plane-bed configuration for which incipient motion conditions are defined. From the detailed data of the Large Eddy Simulations it is possible to obtain τ', the *rms* of the shear stress module on the (x, z)-wall, which is showed in Fig. 10, normalized by $\bar{\tau}$. In Figure 11 the variation coefficient is plotted, where τ' values are normalized versus the local mean stress. Values of τ' have the same order of magnitude of $\bar{\tau}$, with maxima of about 1.5 $\bar{\tau}$ along the upstream face of the abutment; highest values of variation coefficient can be observed upstream the obstacle (in the corner and near the separation) revealing region where the instantaneous fluctuations of the shear stress module are of the same order of magnitude than the averaged ones. On the contrary near the obstacle edge the fluctuating terms are about 10% of the averaged shear stresses.

Results for the fluctuating components of shear stresses together with those for vertical pressure gradients may explain the erosion capacity of the flow field in the corner region, where mean shear stresses do not exceed those in the far field; on the contrary, for flat-bed conditions (beginning of the erosion process), mean shear values can be easily pointed as the prevailing scour agent in the edge region, coherently with previous literature observations.

5 CONCLUSIONS

In this work a Large Eddy Simulation study of the turbulent flow around an obstacle, archetypal of a bridge abutment, is presented, with aim to improve knowledge on the local scour phenomenon. Data from numerical simulations enables a detailed description of the turbulent flow field and stresses in the near obstacle region.

The flow field results are consistent with previous literature description of a complex highly three-dimensional system of vortex structures in front of the abutment. The instantaneous flow field analysis reveals high intermittency of the flow field characteristics and particularly of the flow structures organization in front of the obstacle. Maximum mean shear stress values are concentrated in a relatively small area at the abutment upstream edge, where the maximum scour capacity is typically located. Mean values alone are presumably not sufficient to explain the scour capacity in the corner region, close to the vertical wall: in this area fluctuating components as well as local pressure gradients may have an important role, so that standard sediment-fluid interaction models (incipient motion thresholds and transport equation) may be inadequate to describe the phenomenon.

The coherence of our results with observations from flume experiments gives value to the hypothesis that the studied flow field is representative of the phenomenon in spite of the wall boundary condition on the upper surface.

REFERENCES

Ahmed, F. & Rajaratnam, N. 2000. Observations on flow around bridge abutment. *Journal of Engineering Mechanics* 126(1): 51–59.

Armenio, V. & Piomelli, U. 2000. A Lagrangian mixed subgrid-scale model in generalized coordinates. *Flow, Turbulence and Combustion* 65: 51–81.

Barbhuya, A.K. & Dey, S. 2003. Vortex flow field in a scour hole around abutments. *International Journal of Sediment Research* 18(4): 310–325.

Bardina, J., Ferziger, J.H. & Reynolds, W.C. 1980. Improved subgrid scale models for large eddy simulation. AIAA paper, *13th Fluid and Plasma Dynamics Conference, Snowmass, 14–16 July 1980*. New York: AIAA.

Cardoso, A.H. & Bettess, R. 1999. Effects of time and channel geometry on scour at bridge abutments. *Journal of Hydraulic Engineering* 125(4): 388–399.

Chrisohoides, A., Sotiropoulos, F. & Sturm, T.W. 2003. Coherent structures in flat-bed abutment flow: computational fluid dynamics simulations and experiments. *Journal of Hydraulic Engineering* 129(3): 177–186.

Germano, M., Piomelli, U., Moin, P. & Vabot, W.H. 1991. A dynamic subgrid-scale eddy viscosity model. *Physics of Fluids A* 3(7): 1760–1765.

Melville, B.W. & Coleman, S.E. 2000. *Bridge scour*. Highlands Ranch, Colorado: Water Resources Publications.

Menevau, C., Lund, T.S. & Cabot, W.H. 1996. A Lagrangian dynamic subgrid-scale model of turbulence. *Journal of Fluid Mechanics* 319: 353–358.

Molinas, A., Kheireldin, K. & Wu, B. 1998. Shear stress around vertical wall abutments. *Journal of Hydraulic Engineering* 124(8): 822–830.

Oliveto, G. & Hager, W.H. 2002. Temporal evolution of clear-water pier and abutment scour. *Journal of Hydraulic Engineering* 128(9): 811–820.

Rajaratnam, N. & Nwachukwu, B.A. 1983. Flow near groin-like structures. *Journal of Hydraulic Engineering* 109(3): 463–480.

Smagorinsky, J. 1963. General circulation experiments with the primitive equations. I. The basic experiment. *Monthly Weather Review* 91–99.

Teruzzi, A. 2002. Erosione localizzata e generalizzata in corrispondenza delle spalle dei ponti. Studio sperimentale. *Degree thesis*, Politecnico di Milano.

Copyright © 2006 Taylor & Francis Group plc, London, UK

The shallow flow around a single groyne under submerged and emerged conditions

A. Kadota & K. Suzuki
Department of Civil & Environmental Engineering, Faculty of Engineering, Ehime University, Matsuyama, Ehime, Japan

W.S.J. Uijttewaal
Environmental Fluid Mechanics Section, Faculty of Civil Engineering and Geosciences, Delft University of Technology, Delft, Netherlands

ABSTRACT: The effects of submergence and emergence on the mean flow and coherent flow structures around single groyne were experimentally discussed in the present study. In order to investigate the flow pattern around the single groyne, a scaled and schematized model was implemented and experiments were conducted by means of surface flow visualization technique and Particle Tracking Velocimetry (PTV). The results show the differences of the location and distribution of gyres generated downstream of the groyne, distribution of large scale turbulence around groyne tip and its downstream evolution.

1 INTRODUCTION

Groynes have been used for the stabilization of banks and for creating a navigation channel by confining the cross-sectional area, especially for large European rivers such as the River Rhine and the River Elbe. Therefore, studies on shallow flows and transport phenomena in groyne fields, have paid attention to the appropriate design for bank protection and obtainment of enough depth in the main channel as well as the proper environment for ecosystems. Also suitably designed groynes have been constructed all over Japan after the technical knowledge of the design was transferred from the Netherlands two centuries ago (however, a few groynes are date back to the 16th century in local region and they were empirically constructed).

Studies on flow patterns and transport process around groyne-like structures have recently and significantly developed as growth of experimental and computational techniques. Chen & Ikeda (1997), Kimura & Hosoda (1997), Uijttewaal et al. (2001), Weitbrecht & Jirka (2001) have studied the flow pattern of gyres and mixing layer with respect to the aspect ratio (length and distance between groynes). As for the exchange process between the main stream and the embayment, Altai & Chu (1997), Uijttewaal et al. (2001), Weitbrecht & Jirka (2001) have performed experimental studies by using dye concentration analysis. In addition to the above studies, scouring process were studied earlier by Garde et al. (1961), Gill (1972), Kuhnle et al. (2002) considering flow dynamics around the groyne tip. Furthermore, there are also some studies focusing on the suitable groyne design depending on purpose. Hentschel & Anlauf (2002) proposed an ecologically optimized design and Klaassen et al. (2002) proposed permeable pile groynes to reduce the turbulence level. Uijttewaal et al. (2002) also investigated the advantages and disadvantages of the various groyne designs to manipulate low turbulence level around the mixing layer. There are a few studies on field investigation by Sukhodolov et al. (2002) and Muto et al. (2004).

There are several studies on flow patterns around groynes as described in the above. However, a few studies focus on variations of water level, especially for submerged and emerged conditions. A typical Japanese river is characterized by large and sudden variations in discharge due to big amounts of rainfalls. As a result the groynes are often in submerged as well as emerged conditions. The present study, therefore focuses on the effects of submergence and emergence on the mean flow and coherent flow structures around a single groyne. Experiments were conducted with a scaled and schematized model of an existing Japanese groyne by means of surface flow visualization technique and Particle Tracking Velocimetry (PTV). This method is preferred because there are large velocity differences in the horizontal plane between the outside and inside of the dead zone behind the groyne. 2D-PTV codes were programmed in this study with inclusion of suitable ideas to make the calculation faster by using advantages of FFT and Direct Correlation



Photo 1. Typical groyne in Hiji River (NAGE at Watariba, located 18 km from rivermouth).

methods because many large images had to be processed. Furthermore, analytical techniques of proper orthogonal decomposition (POD) and space-time correlation are applied to reveal the coherent structures and their advection process, respectively. The experimental setup, analytical procedure and the differences of flow structure between the submerged and the emerged conditions around the groyne are explained and discussed in the following.

2 GROYNE IN HIJI-RIVER

One of the characteristics of Japanese-rivers is the large variation of discharge due to occasionally large rainfalls, so that the groynes are often in submerged and emerged conditions.

The study site is the Hiji River, located at Ozu City, in Ehime prefecture at north-west side of Shikoku Island, Japan (catchment area: 1,210 km^2, length: 103 km, annual rainfall: 1,800 mm). The Hiji River is famous for its many tributaries and narrow rivermouth resulting in frequent flooding. According to the investigation by the River Bureau of the Japan Ministry of Land, Infrastructure and Transport (http://www.mlit.go.jp/river/), 67 groyne-like structures (namely, flow-controlling structures) have been constructed from 16th century in the main Japanese rivers managed by the ministry. The groynes in Hiji River were constructed in 17th century (8 groynes still remain) and have a special name 'Nage' (Photo 1). They were used for creating a navigation channel and for protecting the bank. Due to the frequent flooding, the Nages are often in submerged and emerged conditions so that it is needed to investigate the detailed structure of flow pattern around the Nage for both conditions.

3 EXPERIMENTS AROUND SINGLE GROYNE

3.1 *Experimental setup and scaling model*

Experiments were conducted by means of surface flow visualization technique in laboratory of the Environmental Fluid Mechanics section of the Faculty

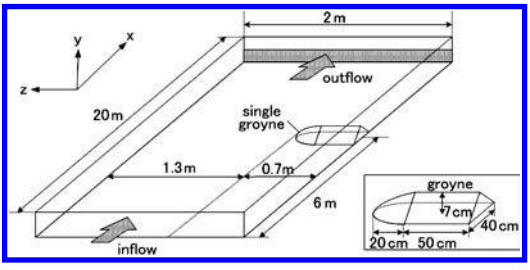


Figure 1. Experimental flume and groyne model.



Photo 2. Overview of area around groyne (Target area is indicated by square).

of Civil Engineering and Geosciences at Delft University of Technology, The Netherlands. Experimental flume is in 2 m wide and 20 m in length as shown in Figure 1.

One of typical groynes in Hiji River as indicated in Photo 1, was selected for this experiment and it is located at 18.8 km upstream from river mouth. Photo 2 shows an overview of area around the groyne. It is seen that there is a scouring area downstream of the groyne. It is considered that the scouring might be caused by submerged flow due to flooding. Furthermore, there is deposition at the downstream side of the scouring area. Because the water body around the deposition

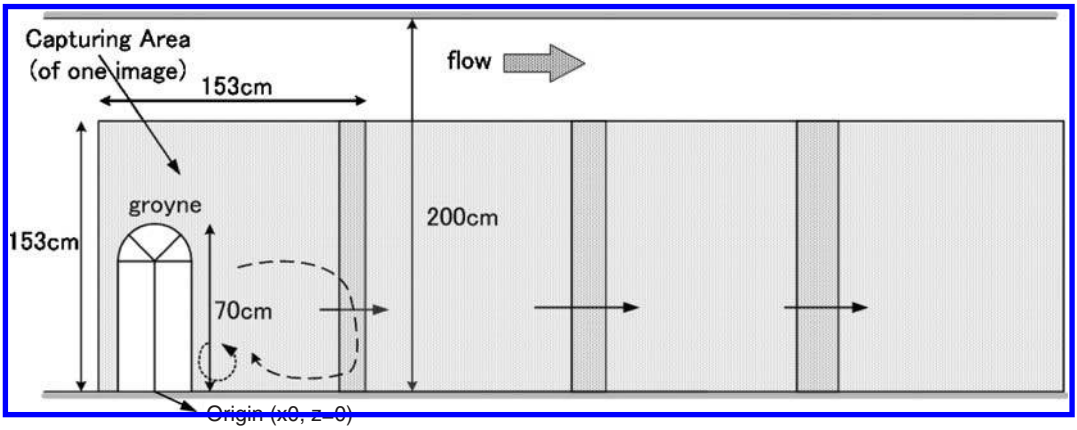


Figure 2. Capturing areas (4 sections shot with overlap).

is circulating and its velocity is low the sediments are transported and deposited from scouring area and mainstream. It is also considered that the sediment deposition in this area from mainstream can occur even in emerged condition as seen in Photo 2.

As for the scaling of the groyne model, it is estimated as ~0.342 considering the ratio of the length of groyne (41~48 m) to the river width (130 m). Therefore, scaling of the groyne model with this ratio was used with a length of 70 cm, width of 40 cm (at base) and a height of 7 cm as seen in Figure 1.

3.2 *Experimental conditions*

The groyne in the Hiji River will be submerged at 800 m^3/s discharge which corresponds to a water level of 2.8 m. Experimental conditions are determined by Froude similarity so that the Froude number becomes Fr ~ 0.2 using data of the Ozu water-level measuring point. Therefore, the discharges are determined as close as possible by considering the limitations of flow visualization technique providing an estimated value of about $Q = 20$ liters/sec for both the submerged and emerged conditions. Then the flow depths are also determined as $h = 8.5$ and 6.0 cm for submerged and emerged conditions, respectively.

3.3 *Image recording process*

Image recording was conducted by using a digital camera (Redlake ES1.0) and image acquisition software (Video Savant). The image size is 1018 times 1008 pixels for stream-wise and lateral directions, respectively. One recording section covers an area of 153 cm by 153 cm. Frequency of recording is 9.67 Hz, and capturing areas are shown in Figure 2. Because large scale vortices are generated near the tip of the groyne, long time series of recording were necessary. In order to obtain an impression of downstream development of the flow, 4 sections were recorded separately with some overlapping.

3.4 *Image processing and PTV analysis*

In the present study, the Particle Tracking Velocimetry (PTV) method is adopted and implemented in order to calculate velocities fast and accurately. The interrogation window size needs to be chosen carefully, because of the large velocity differences between outside and inside of dead zone behind the groyne. PTV results are used for calculating turbulence statistics and for visualizing flow pattern, respectively. Before applying the algorithm, some image pre-processing was done such as subtracting the background, removing noise, binarization and labeling of particle images.

There are a number of algorithms for the PTV analysis to determine the displacement of the particle image. One of them is an FFT algorithm which is fast in comparison with an alternative method of Direct Correlation. However, interrogation window size is limited to 16, 32, 64 and 128 pixels. On the other hand, Direct Correlation algorithm can use flexible interrogation window size or flexible search range but it takes a lot of time and the size of the interrogation area must be determined after the overall flow velocity is known. Therefore in this study, a 2D-PTV code was programmed with inclusion suitable ideas to make the calculation faster by using advantages of FFT and Direct Correlation methods as described below.

A flowchart of the code is explained in Figure 3. In this flowchart, the FFT algorithm is used for estimating the 1st temporal velocity. In this algorithm, the target particle is set at center position of interrogation window of the 1st image (step 1). In this step, it is better to set the size of the interrogation window to a large value to obtain a rough estimate of the overall velocity (64pix times 64pix are applied in this case). The cross-correlation function is calculated (at step 2) by using

the 1st interrogation window and the same-size and the same-position interrogation-window of 2nd image (i.e. 2nd inter-rogation window). After the calculation of the cross-correlation function, a displacement is seen between the peak and the center positions of cross-correlation area as seen in Figure 3. This displacement can be associated with the displacement of the target particle and its surroundings which correspond to the velocity (step 3). At this step, the problem remains regarding accuracy, because the velocity can vary over the large interrogation window. To cope with this disadvantage, in the subsequent step a direct correlation method is applied by using the now available overall velocity. The search range of the interrogation window in the direct correlation method is flexibly determined by dividing the overall velocity into an x and y component (step 4). The size of search range is adjusted to the overall velocity (step 5). This means a reduction of useless search area resulting in a procedure for a fast correlation calculation. The accurate velocity vector is calculated by direct correlation method under suitable search range (at step 6). Verification was done by comparing vectors with result from Lavision Flow Master by using a strong-vortex image by Stanislas et al. (2003). The images recorded in these experiments were processed by the above mentioned procedure with satisfactory results.

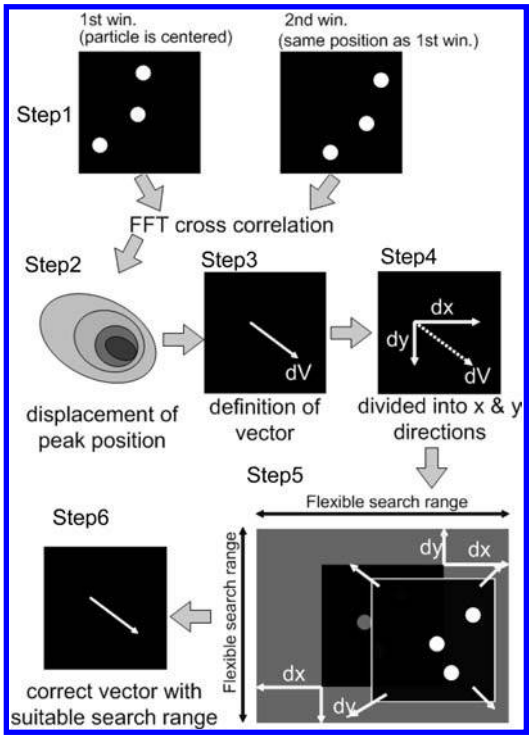


Figure 3. Flowchart of PTV code (by FFT & D.Corr Method with flexible search range).

3.5 *Statistical analysis for mean & coherent flows*

An important problem is how to estimate the turbulence statistics such as mean velocity, turbulence intensity, Reynolds stress etc., because PTV vectors are scattered according to the distribution of the particles. There are various options for the calculation of turbulence statistics. One is to use the information of all individual vectors the other is to use only the vectors interpolated on a regular grid. With the ensemble averaging method, some areas (or volumes) are determined in whole area. If vector exists in an area for one certain time, the vector is counted. Then, all vectors existing in the area are summarized and mean velocity is calculated. On the other hand, the 2nd method is to estimate the mean velocity by summarizing the interpolated vectors. In this study, the interpolated vectors in normal grid are applied to estimate the turbulence statistics because there might be deficit of vector point and series of interpolated vector profile are used in POD analysis as described in the following.

Here we try to obtain an impression of the fluctuating pattern and its coherent structures by applying POD (proper orthogonal decomposition). This method was proposed by Lumey (1967) and used to educe those turbulent structures that containing most of the energy (i.e. coherent flow structure). POD decomposes a signal onto a basis of non-specified functions chosen to represent the energy of the signal in the fewest number of modes. The calculus of variations reduces this maximization problem to the solution of a Fredholm integral equation of the first kind.

$$\int R_{uu}(x,x')\phi_u^{(n)}(x')dx' = \lambda_u^{(n)}\phi_u^{(n)}(x) \tag{1}$$

where, $\phi_u^{(n)}(x)$ is the Eigenfunctions and $\lambda_u^{(n)}$ is the Eigenvalue. Superscript n is the number of the Eigenfunction (i.e., number of mode). The above equation is explained by using stream-wise instantaneous velocity u as an example. In this equation, $R_{uu}(x,x')$ is the cross correlation of u velocities in the separated points (x,x').

$$R_{uu}(x,x') = \langle u(x)u(x')\rangle \tag{2}$$

where, $\langle\rangle$ denotes ensemble averaging. If the coordinate x is discrete, equation (1) reduces to an Eigenvalue problem as follows;

$$R_{uu}(x_i,x_j)\phi_u^{(n)}(x_j)\Delta x = \lambda_u^{(n)}\phi_u^{(n)}(x_i) \tag{3}$$

where Δx is the distance between points (x, x'). By solving the above equation, $\lambda_u^{(n)}$ and $\phi_u^{(n)}(x)$ are obtained. On the other hand, the instantaneous velocity $u(x,t)$ is presented as the summation of Eigenfunctions $\phi_u^{(n)}(x)$ with corresponding amplitudes $\alpha_u^{(n)}$.

$$u(x,t) = \sum_{n=1}^{\infty} a_u^{(n)}(t)\phi_u^{(n)}(x) \tag{4}$$

Because of the orthogonal expansion, the coefficient $a_u^{(n)}$ can be presented as follows;

$$a_u^{(n)}(t) = \int u(x,t)\phi_u^{(n)}(x)dx \tag{5}$$

As for Eigenfunction $\phi_u^{(n)}(x)$,

$$\int \phi_u^{(n)}(x)\phi_u^{(m)}(x)dx = \delta_{nm} \tag{6}$$

On the other hand, $R_{uu}(x,x')$ corresponds to the summation of Eigenfunctions.

$$R_{uu}(x,x') = \sum_{n=1}^{\infty} \lambda_u^{(n)} \phi_u^{(n)}(x)\phi_u^{(n)}(x') \tag{7}$$

Therefore, from the relation of equations (2),(5) and (6), the following equation is obtained.

$$\left\langle a_u^{(n)} a_u^{(m)} \right\rangle = \lambda_u^{(m)} \delta_{nm} \tag{8}$$

By means of the above relations, the ensemble averaged squared velocity of signal u is obtained as the summation of Eigenvalues:

$$\left\langle u^2(x,t) \right\rangle = \sum_{n=1}^{\infty} \lambda_u^{(n)} \left\{\phi_u^{(n)}(x)\right\}^2 \tag{9}$$

$$E_u = \int \left\langle u^2(x,t) \right\rangle dx = \sum_{n=1}^{\infty} \lambda_u^{(n)} \tag{10}$$

where E_u is the turbulent kinetic energy. Therefore, the maximum Eigenvalue corresponds to the maximum energy. Lumley (1981) mentioned that Eigenfunctions with the maximum, the 2nd or 3rd largest Eigenvalue are dominant in their contribution to the turbulent kinetic energy. It is implicitly assumed that large-energy flow structures can be associated with the large-amplitude Eigenfunctions.

In addition to the POD analysis, a space-time correlation analysis is applied in order to see how this technique can be used to estimate the advection of flow structures. For example, the space-time cross-correlation C_{uw} of stream- and span-wise velocities (u,w) is defined as follows;

$$C_{uw}(x,\Delta x;z,\Delta z,t,\tau) = \frac{\overline{u(x,z,t)w(x+\Delta x,z+\Delta z,t+\tau)}}{u'(x,z,t)w'(x+\Delta x,z+\Delta z,t+\tau)} \tag{11}$$

where, x and z are the fixed points, defined near the tip of the groyne in this study. Δx and Δz are distances between 2 separated points, t and τ are the time and the delay time, respectively.

4 RESULTS AND DISCUSSIONS

4.1 *Mean flow profiles*

Figures 4(a) and 4(b) show the mean vector fields for the emerged and submerged conditions, respectively. In addition, Figures 5(a) and 5(b) also show the streamlines corresponding to Figure 4. Obviously the mean flow patterns as observed at the free surface are completely different. The confinement of the cross-sectional area results for both cases in an increased velocity in the main stream, whereas in the submerged case the flow over the groyne attains a high velocity. The latter rapidly disappears as a result of flow separation in the vertical plane and associated vertical velocities. These three-dimensional effects make the interpretation of the flow pattern for the submerged case difficult. The emerged groyne induces a virtually

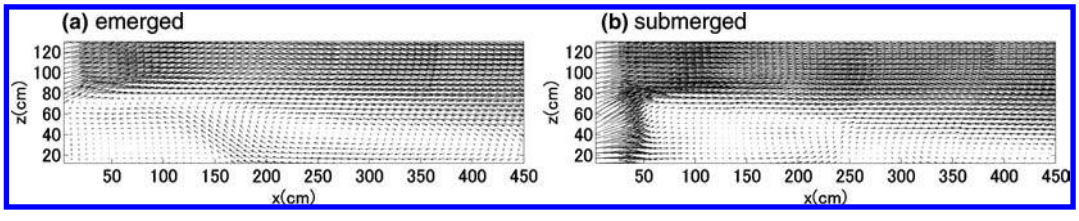


Figure 4. Mean vector profiles (U,W).

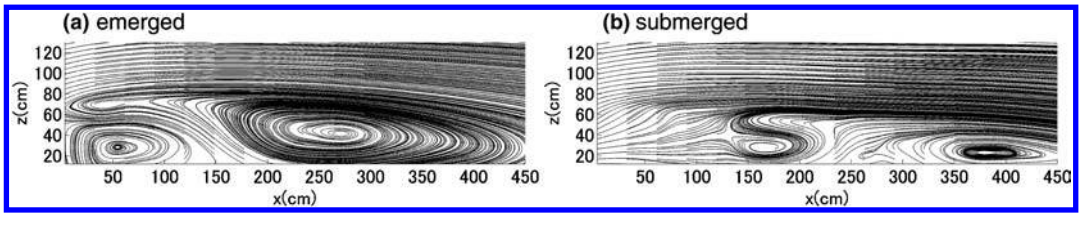


Figure 5. Streamlines.

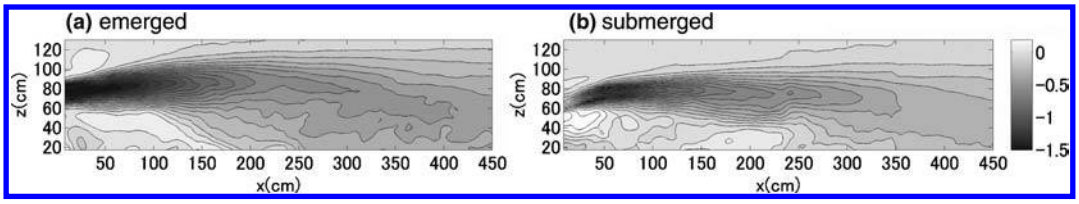


Figure 6. Mean vorticity.

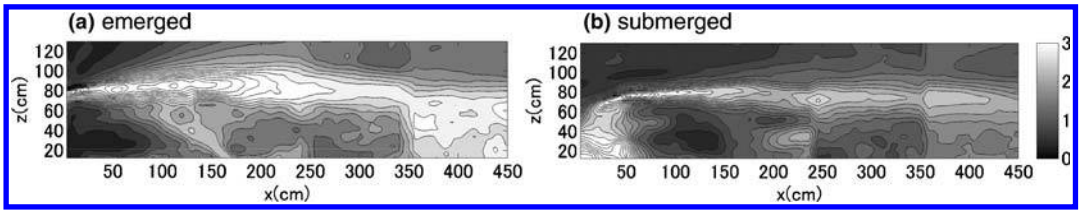


Figure 7. Stream-wise component of turbulence intensity u_{rms}(cm/sec).

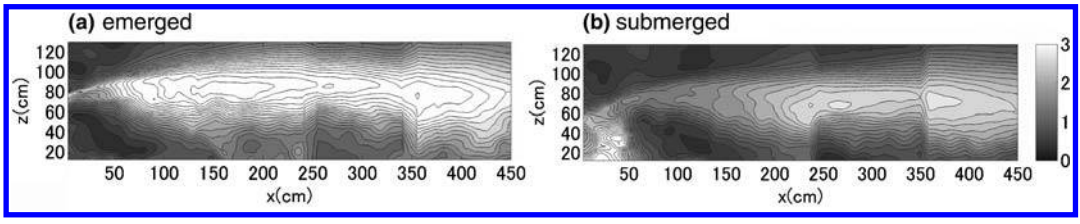


Figure 8. Span-wise component of turbulence intensity w_{rms}(cm/sec).

two-dimensional circulation pattern with the main primary gyre rotating in the clockwise direction. The much smaller secondary gyre receives its momentum from the primary gyre and rotates therefore anti-clockwise. At the location where the secondary gyre touches the main stream a narrow shear layer is found bridging a high velocity difference. Observation of the submerged case reveals 2 m downstream of the groyne the flow has become rather uniform over the vertical resulting in a small but also weak clockwise gyre. The complex streamlines seen in figure 5(b) in the range $x = 1.5$–2.0 m are due to three-dimensional time varying patterns.

It looks as through the overall disturbance of the main flow pattern due to the groyne is much smaller in the submerged case. In view of bank and bed protection the submerged groyne gives rise to small velocities near the bank except for the overflow location at the root of the groyne. Furthermore the three dimensional effects in the first two meters downstream are expected to have consequences for the stability of the bed. These effects could as well be responsible for the relatively low bed level just downstream of the groyne, as seen in photo 2.

Figures 6(a) and 6(b) show the contours of mean vorticity for the emerged and submerged conditions, respectively. In accordance with the vector field and streamlines, the large vorticity is concentrated in the shear layer downstream of the groyne tip following the contour of the interface with the stagnant zone. The emerged case exhibits a relatively wide area containing strong vorticity, reflecting the large portion of water that is substantially deflected by the groyne.

Regarding the turbulence properties, turbulence intensities in stream-wise and span-wise directions (u_{rms}, w_{rms}), and Reynolds stress profiles ($-\overline{uw}$) are shown in Figures 7, 8 and 9, respectively. As seen in these figures, the area most affected by turbulent fluctuations is the mixing layer where the horizontal shear is the source from which large-scale fluctuations emerge.

The area of streamwise fluctuations is narrow when compared with the spanwise fluctuations for both cases. Maximum values are found farther downstream in the submerged case, clearly at the location where the main gyre starts developing. As for $x < 2.5$ m, the horizontal motion is affected more by the small-scale three-dimensional turbulence. In the 0.5 m just downstream of the submerged groyne the turbulence intensities are enhanced as a result of the vertically separated flow.

The maximum momentum transfer (maximum Reynolds stress) is found in the mixing layer at 2 m downstream of the separation point at the location

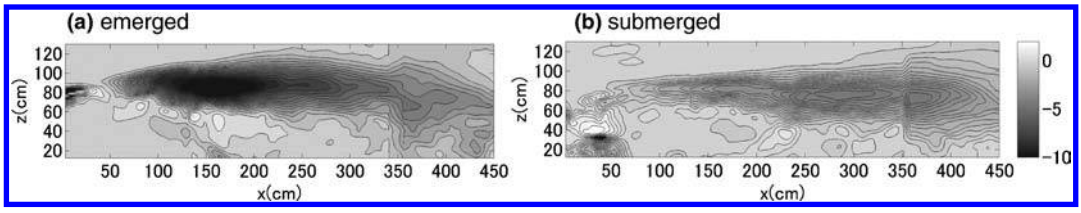


Figure 9. Reynolds stress $-\overline{uw}(\mathrm{cm}^2/\mathrm{sec}^2)$.

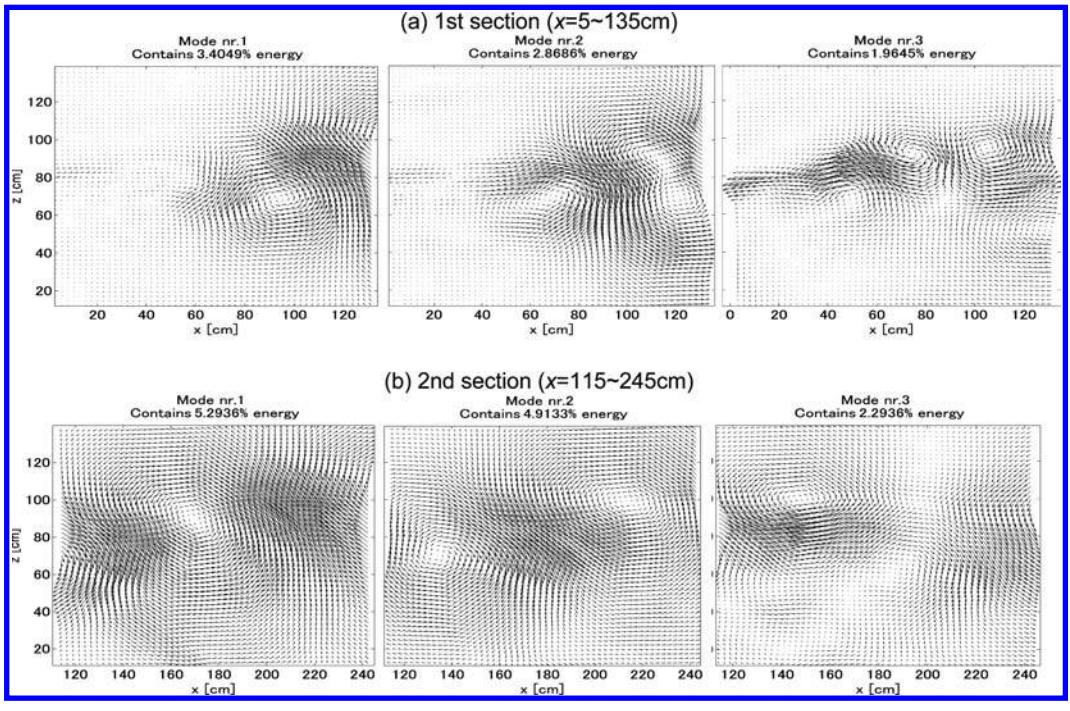


Figure 10. POD-decomposed flow-patterns under emerged condition.

where the primary gyre is in touch with the mixing layer. Apparently the high shear velocity and high vorticity as found close to the separation point do not result in an efficient transfer of momentum. The mixing length scale needed for that is found farther downstream. This holds for both the submerged and emerged cases.

4.2 *Coherent flow structures*

Figures 10(a) and 10(b) show the decomposed patterns under emerged conditions by using the POD method for the 1st capturing section ($x = 5 \sim 135$ cm) and the 2nd capturing section ($x = 115 \sim 245$ cm), respectively. Each figure is arranged with respect to the energy level of the mode number (up to 3). The decomposed pattern with the 1st mode can be interpreted as typical fluctuating pattern with the most energy content. As seen in the POD decomposed pattern of Figure 10, one typical pattern of circulating fluctuation is dominant with a relatively large scale along the high shear layer with highest energy (mode 1). This pattern indicates a kind of typical fluctuation in the region of high turbulence intensities as seen in Figures 7(a) and 8(a). These decomposed patterns reveal typical fluctuations that can not be seen in *rms* profiles. As for modes 2 and 3, the decomposed patterns are smaller than mode 1 and two or more typical fluctuation patterns are detected. In the 2nd section of Figure 10(b), the decomposed pattern with highest energy grows to larger scales up to a doubling of the pattern size when compared with all modes of Figure 10(a). It can be considered that the fluctuation pattern around this area expands in horizontal direction with the development of the shear layer.

Figures 11(a) and 11(b) also show the typical fluctuation pattern under submerged conditions which are

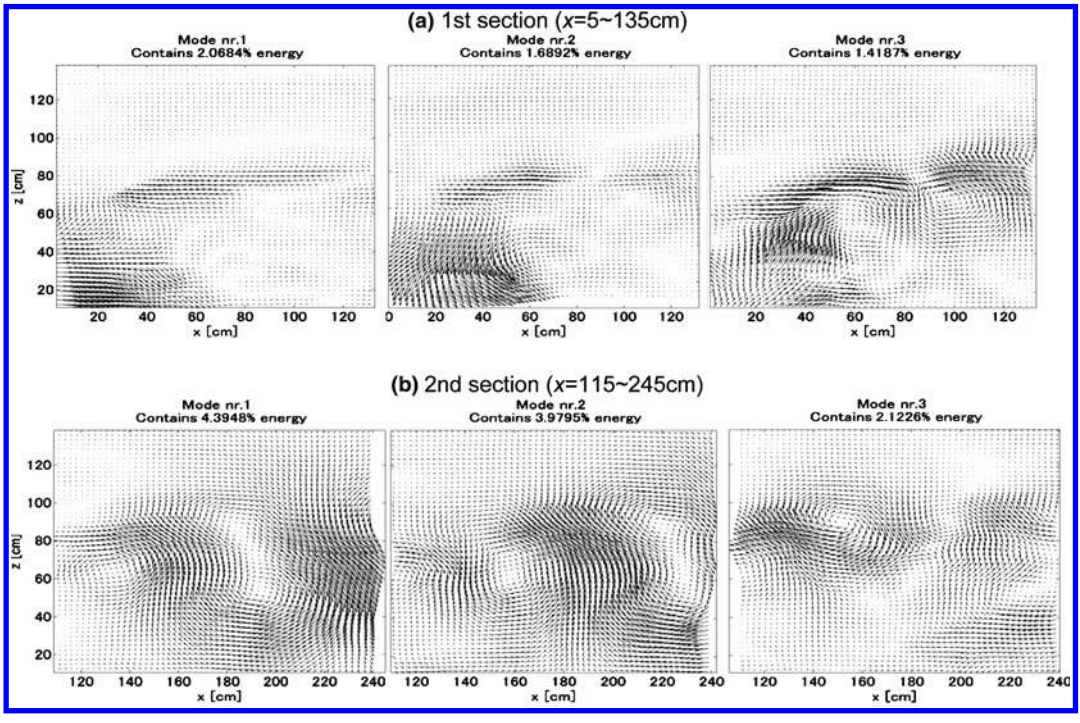


Figure 11. POD-decomposed flow-patterns under submerged condition.

decomposed by using the POD method similar as with Figure 10. As seen in Figure 11(a), two separate patterns near groyne are dominant and show the highest energy content (mode 1). In this region, high values of turbulence intensities are located near the tip of groyne and in the stagnant zone independently, as seen in Figures 7(b) and 8(b) and they are corresponding to the decomposed patterns. As for Figure 11(b) of the 2nd section, two of those typical fluctuating patterns are also seen in mode 2 and 3 but these are located slightly nearer to the right side of channel, which corresponds also to the region of high turbulence intensity. In addition, these patterns are located in the far field downstream of the groyne and shifted downstream due to the flow over the groyne showing the difference with emerged condition.

Consequently, a detailed fluctuating pattern can be revealed by means of POD analysis that is not possible to understand from mean profiles such as turbulence intensities (u_{rms}, w_{rms}).

An alternative way to analyze the large scale motion in the flow is displayed in Figures 12(a) and 12(b) where the contours are shown for the space-time correlation *Cuu* in the first capturing section ($x = 3 \sim 131$ cm), in accordance with Equation (11) for emerged and submerged conditions. The 2D autocorrelation function of the u-velocities is discussed in this section because it is expected that the conditions at the separation point will have a dominant effect on the downstream flow pattern. Therefore, the fixed point (indicated as dotted point in these figures) for the space-time correlation C*uu* is defined at neighborhood of groyne tip (i.e., $x_{fix} = 24.9$ cm, $y_{fix} = 67.9$ cm) for both conditions. The delay time τ is shown above each figure. It can be seen that the streamwise fluctuations at the fixed point are positively correlated to the main stream (white blob) and negatively with the stagnant zone (black).

The large correlation areas are advected downstream whereas, for the emerged case a lateral displacement is seen for especially the positively correlated area. It appear that the more uniform advection is found for the submergence on the groyne. These properties are corresponding to the near field pattern as seen in Figures 5.

Figures 13(a) and 13(b) show the contours of space-time correlation *Cuw* in the second capturing section ($x = 114 \sim 242$ cm) for the emerged and submerged conditions, respectively. The cross correlation between u-velocities at the fixed point and w-velocities at the distant point are discussed in this section because it is considered that the dominant stream-wise flow generated upstream from the groyne is entrained into span-wise direction through the shear layer. Therefore, the fixed point in this section is defined in the mixing layer (i.e., $x_{fix} = 136.0$ cm, $y_{fix} = 67.9$ cm).

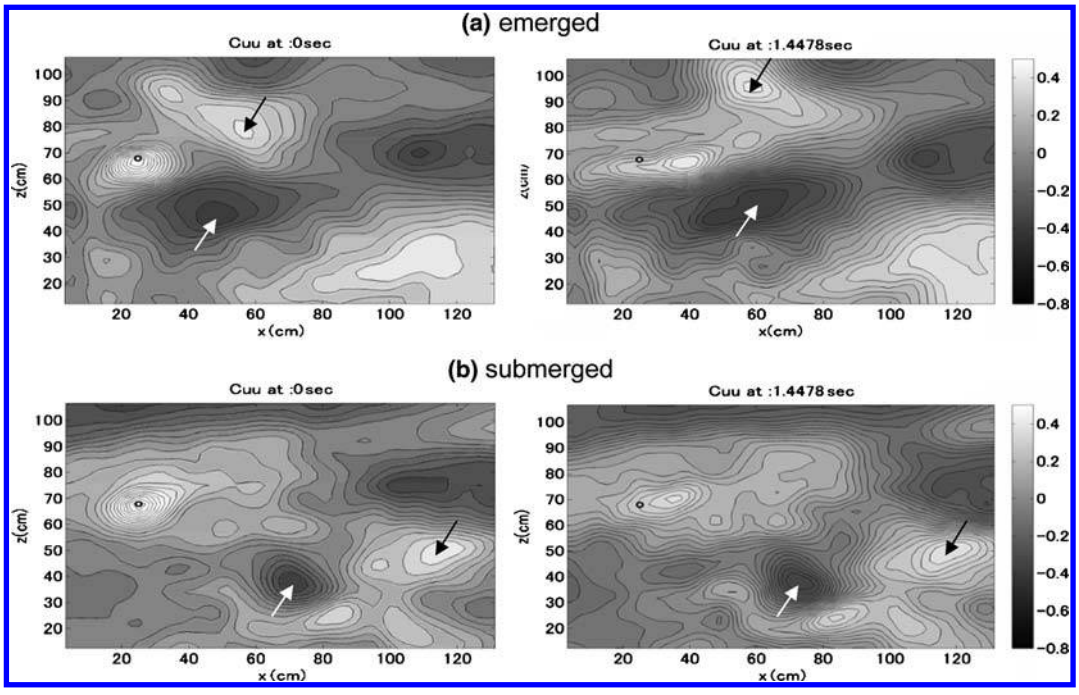


Figure 12. Space-time correlation *Cuu* in 1st capturing section ($x = 3 \sim 131$ cm).

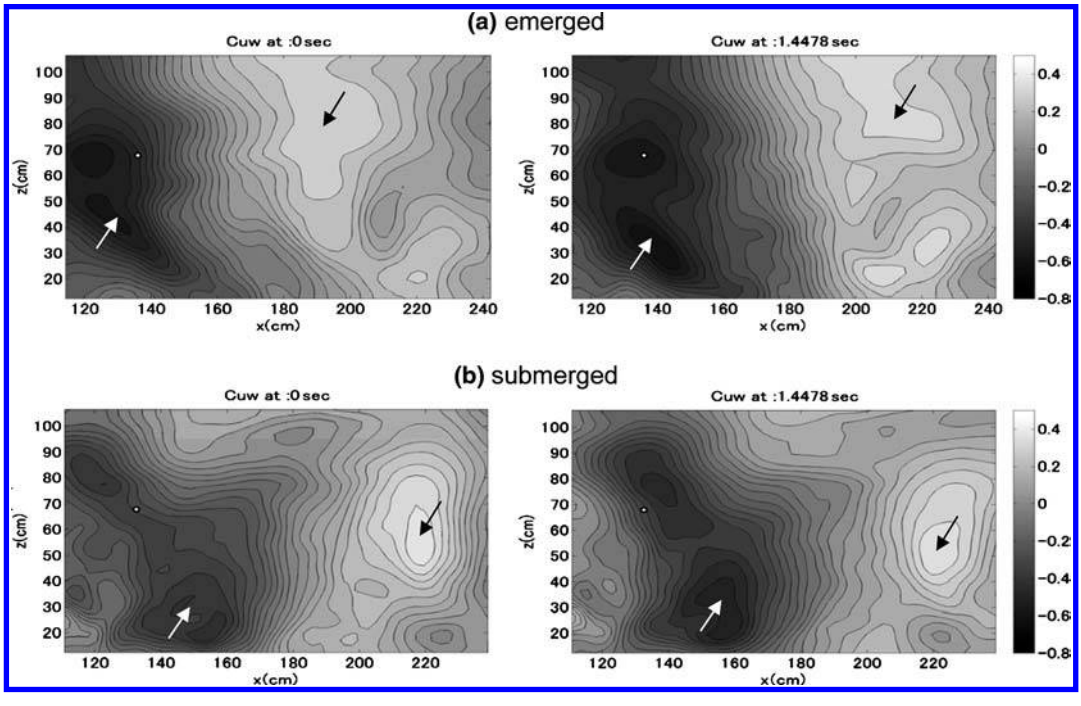


Figure 13. Space-time correlation *Cuw* in 2nd capturing section ($x = 114 \sim 242$ cm).

The negative correlation is found on the left side of the graphs whereas the positive correlation is found on the right hand side. It shows the typical distance over which the lateral velocity component changes sign thereby indicating the size of the coherent structure that contributes to the momentum transfer by the mixing layer.

5 CONCLUSIONS

In the present study, it is described that the groyne in Japan plays an important role for controlling the flow, navigation and protecting river bank. Due to big amounts of sudden rainfall, the groynes are often subjected to submerged and emerged flow conditions.

By taking account of such conditions, the effects of submergence and emergence on the mean flow and coherent flow structures around single groyne were experimentally investigated.

In order to analyze the flow pattern around the single groyne, a scaled and schematized model was implemented and experiments were conducted by means of surface flow visualization technique and Particle Tracking Velocimetry (PTV). For the PTV velocity determination an algorithm was implemented with a flexible search range making use of both FFT and Direct Correlation methods.

Furthermore, differences between submerged and emerged cases are discussed. The results show the difference in location where the main flow characteristics are seen in profiles of mean statistics, POD and space-time correlation for emerged and submerged flows. The most important differences are found in the area downstream of the groyne. The submerged case shows a clear separation zone in the vertical plane whereas the circulation associated with the emerged case lies predominantly in the horizontal plane. Further downstream the overall flow pattern looks quasi two dimensional with a clear circulation in the horizontal plane. The disturbance due to the submerged groyne appears much smaller than that due to the emerged groyne. Apart from the direct neighborhood of the groyne the submerged groyne is sufficiently shielding the bank from the high-velocity main stream.

The results of the POD and the spatial correlation analyses are clearly seen for the fluctuating pattern and large-scale motion, respectively. However, they are not effective answers so far. A further analysis is required. This includes also other techniques like conditional averaging and spectral analysis. The successful application of the PTV-technique has resulted in a dataset that is very useful for such analyses.

ACKNOWLEDGEMENT

The present study is a joint project with the Environmental Fluid Mechanics Section, Delft University of Technology, Netherlands, and was supported by Ehime University Fellowship 2005. The authors would like to give great appreciation to Profs H. Nakagawa and I. Nezu who recommended for study at Delft University. The staff members of the Institute for Hydromechanics at Karlsruhe University in Germany, are gratefully acknowledged for their hospitality.

REFERENCES

Altai, W. and Chu V.H. (1997): Retention time in a recirculating low, Proc. XXVI IAHR congress, San Francisco, pp. 9–14.

Chen, F-Y. and Ikeda, S. (1997): Horizontal separation flows in shallow open channels with spur dikes, J. Hydroscience and Hydr. Engrg. JSCE 15(2), 15–30.

Garde, R.J., Subramanya, K. and Namburdripad, K.D. (1961): Study of scour around spur dikes, J. Hydr. Div. ASCE 87(HY6), 23–37.

Gill, M.A. (1972): Erosion of sand beds around spur-dikes, J. Hydr. Div. ASCE 98(HY9), 1587–1602.

Hentschel, B. and Anlauf, A. (2002): Ecological optimization of groynes in the Elbe river, New insights in the physical and ecological process in groyne fields, van Mazijk and Weibrecht eds., 121–133.

Kimura, I. and Hosoda, T. (1997): Fundamental properties of flows in open channels with dead zone, J. Hydr. Engrg. ASCE, 123(2), 98–107.

Klaassen, G.J., Douben, K. and van der Wal, M. (2002): Novel approaches in river engineering, Proc. Int. Conf. on Fluvial Hydraulics, Bousmar and Zech eds., Balkema, The Netherlands, 27–43.

Kuhnle, R.A., Alonso, C.V. and Shields, F.D. (2002): Local scour associated with angled spur dikes, J Hydr. Engrg. ASCE 128(12), 1087–1093.

Lumley, J. L.(1967): Atmospheric Turbulence and Radio Wave Propagation (ed. Yaglom A. M. and Tatarsky V. I.), Nauka, Moscou, pp. 166–178.

Lumley, J. L.(1981): Transition and Turbulence (ed. Meyer R. E.), Academic, pp. 215–241.

Muto, Y., Baba, Y. and Fujita, I. (2002): Velocity measurements in rectangular embayments attached to a straight open channel, Proc. Int. Conf. on Fluivial Hydraulics, Bousmar & Zech eds., Balkema, The Netherlands, 1213–1219.

Sukhodolov, A., Uijttewaal, W.S.J. and Engelhardt, C. (2002): On the correspondence between morphological and hydrodynamical patterns of groyne fields, J. Earth Surf. Process Landforms, 27, 289–936.

Uijttewaal, W.S.J., Berg, M.H. and Wal, M. van der (2002): Experiments on physical scale models for submerged and non-submerged groynes of various types, Proc. Int. Conf. on Fluvial Hydraulics, Bousmar and Zech eds., Balkema, The Netherlands, 377–383.

Uijttewaal, W.S.J, Lehmann, D. and Mazijk, A. van (2001): Exchange process between a river and its groyne fields: model experiments, J. Hydr. Engrg. ASCE, 127(11), 928–936.

Weitbrecht, V. and Jirka, G.H.J. (2001): Flow patterns and exchange processes in dead zones o rivers, Proc. 29th IAHR congress, Beijing, China, theme B, pp. 439–445.

Diverse riverbed figuration by using skew spur-dike groups

A. Tominaga
Nagoya Institute of Technology, Nagoya, Japan

D. Matsumoto
Graduate student, Nagoya Institute of Technology, Nagoya, Japan

ABSTRACT: Continuous spur dikes were often used to create diverse riverbed configuration with riffles and pools. In order to control sediment transport by using spur dikes, the effects of orientation were investigated. A spur-dike group was composed of three submerged spur dikes. Those spur-dike groups were set on both sidewalls alternately and the velocity distributions were measured. Then the flow structures were calculated by using a simple 3-D numerical model. The overriding flow on a spur dike was deflected to the direction normal to the spur-dike longitudinal line. In upstream-skew spur-dike groups, large scour holes were observed in front-edge regions of spur dikes and deposition regions were formed beside the sidewalls. In downstream-skew spur-dike groups, front regions of spur dikes and sidewall regions were largely scoured. In a range of the present experiments, the upstream-skew spur-dike group can produce the most dynamically varied bed formation. On the other hand, the downstream-skew spur-dike group tends to erode the sidewall region. These bed configurations were well related with the characteristic 3-D flow structures around submerged spur dikes.

1 INTRODUCTION

Spur dikes are often used for protecting levee from erosion during flood in middle and lower reaches of alluvial rivers. On the other hand, they provide diversity of flow to ecological surroundings by creating riverbed configurations with riffles and pools. In order to design adequate installation of spur dikes for this purpose, it is necessary to predict and control the flow structures and sediment transport around spur dikes. Several researchers have studied resistance characteristics such as the roughness and the deflection effects of submerged spur-dikes (e.g. Gill 1972, Klingeman et al. 1984, Fukuoka et al. 1998). In some cases, detailed flow structures around spur dikes around spur dikes were made clear on fixed bed (e.g. Rajaratnam and Nwachukwu 1983, Chen and Ikeda 1996). In cases of movable bed, research interests were concentrated on characteristics of local scour around spur dikes (e.g. Elawady et al. 2001 and Rahman and Muramoto 1997). Three-dimensional flow structures around submerged spur dikes have been clarified in regard to the relative height and the orientation angle (e.g. Elawady et al. 2000 and Tominaga et al. 2003). However, there are few examples evaluating the functions of spur dikes for providing diverse riverbed configuration.

Numerical simulations have become a powerful tool for predicting flow structures and sediment transport around spur dikes with complex design items (Kimura et al. 2002, Zhang et al. 2005). It is necessary to accumulate experimental data for developing numerical models that can predict three-dimensional flow structures and bed deformation.

We have studied flow structures over submerged spur dikes with different orientation by using PIV method (Tominaga and Tamoto 2003). We found that the orientation of submerged spur dike changes flow structures extremely and affect on sediment transport around them.

In this study, the flow structures and bed deformation were investigated in open channels with continuous spur-dike groups used to create diverse riverbed configurations. We concentrated on the effects of orientation on the riverbed configuration. A three-dimensional numerical model was adopted to predict such complex flow structures.

2 EXPERIMENTAL PROCEDURE

The experiments were conducted in a 13 m long and 0.6 m wide rectangular flume. As the method of creating diversity in straight open channels, a spur-dike group was composed of three submerged spur dikes and those spur-dike groups were set on both sidewalls alternately. The placements of spur dikes are shown in

Copyright © 2006 Taylor & Francis Group plc, London, UK

Figure 1. The projection length, the interval length of each spur dike and the interval length of each group were uniformly set. The spur-dike model was made of 18 mm thick plywood. The distance between spur dikes was 22.5 cm and the angle of skew spur dikes was 45° to the streamwise direction. The projection length of the spur dike was arranged to 15 cm in all cases as shown in Figure 1. The height of the spur dike was 4 cm. The first spur dike was located at 5.8 m downstream from the entrance and the origin of stream wise axis was set at the upstream root of the first spur dike. The distance between alternate groups was 75 cm, and the fronts of spur-dike groups were located at $x = 0$ cm and 150 cm along the right bank and at $x = 75$ cm and 225 cm along the left bank. The experiments for a single group setting were preliminarily performed to clarify basic characteristics of bed deformation related to the orientation. The present placements of spur-dike groups were arranged based on the scour pattern in the case of single-group experiments.

The hydraulic conditions of experiments are shown in Table 1. In all cases, the discharge Q was 0.0125 m^3/s and the water depth h was adjusted to 8 cm at the section 4.5 m downstream from the channel entrance by controlling the downstream weir. As to the coordinates, x is the streamwise direction, y is the cross-stream direction and z is the vertical direction. Two components of the velocity (u and v) were measured by using an I-type electromagnetic velocimeter.

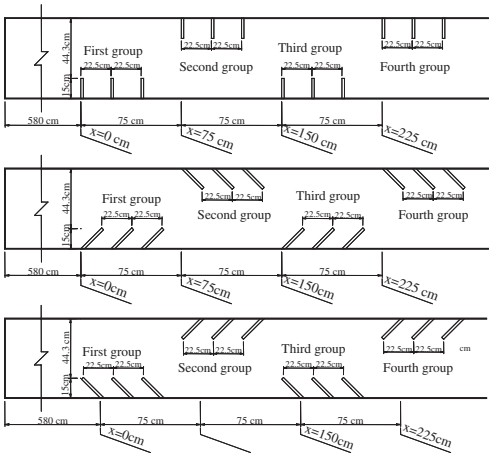


Figure 1. Placements of spur dike groups (Upper: Case A, normal spur dike, Middle: Case B, downstream-skew spur dike, Lower: Case C, upstream-skew spur dike).

Experiments were conducted in fixed and movable bed conditions. In cases of movable bed conditions, sand grains of 0.4 mm mean diameter were paved on the bed with 110 mm thickness from 4.5 m to 10.5 m in the streamwise direction. Sand feeding was not made because the moving bed conditions were static. After 1 hour from the flow start, bed configurations were measured by using a bed form visualizing equipment. At this moment, the bed deformation was not completely established, but it was recognized as almost stable state. The velocity was measured on this deformed bed, which was solidified by using cement.

3 NUMERICAL SIMULATION METHOD

The flow over a submerged spur dike becomes three-dimensional situation dominated by steep local currents. In practical sense, it is meaningful to consider a possibility for predicting fundamental flow structures by a low-order turbulence model. In this study, the streamwise component of the following Reynolds equation and continuity equation were solved numerically by using a zero-equation turbulence model.

$$\frac{\partial U_i}{\partial t} + \frac{\partial U_i U_j}{\partial x_j} = -\frac{1}{\rho}\frac{\partial p}{\partial x_i} + \frac{1}{\rho}\frac{\partial \tau_{ij}}{\partial x_j} \tag{1}$$

$$\frac{\partial U_i}{\partial x_i} = 0 \tag{2}$$

where U_i is the mean velocities, p is the pressure and ρ is the water density. τ_{ij} is the Reynolds stress components and these are expressed by an eddy viscosity model.

$$\frac{\tau_{ij}}{\rho} = \nu_t\left(\frac{\partial U_i}{\partial x_j} + \frac{\partial U_j}{\partial x_i}\right) \tag{3}$$

where ν_t is the eddy viscosity. This eddy viscosity is given as follows, by assuming the log-law and linear distribution of the shear stress.

$$\begin{aligned} 0 \le \frac{z}{h} \le 0.8 \quad &: \quad \nu_t = \kappa u_* z\left(1 - \frac{z}{h}\right) \\ 0.8 \le \frac{z}{h} \quad &: \quad \nu_t = 0.16\kappa u_* h \end{aligned} \tag{4}$$

Table 1. Experimental conditions.

Discharge Q (lit/s)	Flow depth h(cm)	Channel width B(cm)	Energy gradient Ie	Mean velocity U_m(cm/s)	Froude number Fr	Reynolds number Re
12.5	8.0	59.3	0.00038	23.4	0.265	14400

Copyright © 2006 Taylor & Francis Group plc, London, UK

where u_* is the friction velocity, h is the water depth and κ is the Karman constant ($\kappa = 0.41$).

The equations are discretized by a finite volume method with hybrid scheme and solved by the SIMPLE algorithm. The numbers of calculation grids are 206 in x-direction, 33 in y-direction and 21 in z-direction. The minimum grid lengths are $\Delta x = 5$ mm, $\Delta y = 10$ mm and $\Delta z = 4$ mm near the wall. A block masking method for a rectangular coordinate system is used to express spur dikes. As to the boundary conditions, the near-wall velocity is assumed to comply with the log-law that covers rough boundaries. The water depth h is modified according to the pressure p at a free surface control volume and the vertical coordinate z is rearranged dividing the water depth h proportionally. A water depth is fixed at the downstream end and a constant discharge is given at the upstream end. The water depth change was approximately 4 mm in the longitudinal direction.

4 FLOW STRUCTURES AROUND SPUR-DIKE GROUPS ON FIXED BED

The effects of spur-dike orientation were considered by measuring velocity distributions on fixed bed and comparing them with calculated ones. Figures 2 and 3 show velocity vectors on x-y plains of $z = 1.5$ cm and 6.5 cm in the normal case comparing the measured values with calculated ones. The calculated velocity vectors show good agreements with the measured ones on the plain of $z = 1.5$ cm even though the simple numerical model was used. Spur dikes generate the flow deflection and make the main flow meander slightly. The flow between spur dikes forms circulating motion. Separated zones behind spur-dike groups were remarkably narrowed compared with the single-group case. On the plain of $z = 6.5$ cm, the calculation also shows good reproducibility in accelerating and decelerating processes over spur dikes. A mild meandering is seen in these figures.

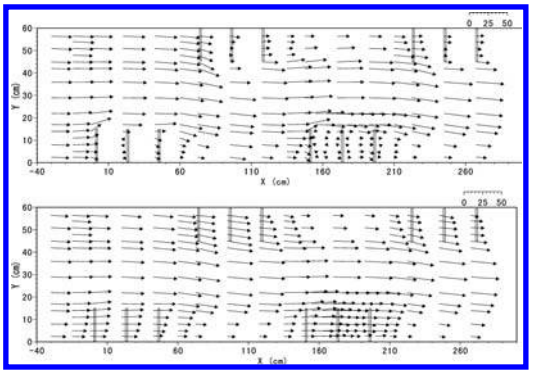


Figure 2. Measured velocity vectors in normal case (Upper: $z = 1.5$ cm, Lower: $z = 6.5$ cm).

Figures 4 and 5 show velocity vectors on x-y plains in the upstream-skew case. Though the skew spur dike was expressed by rectangular grids, the calculated values well reproduce the characteristics of experimental results. On the plain of $z = 1.5$ cm, a deceleration in

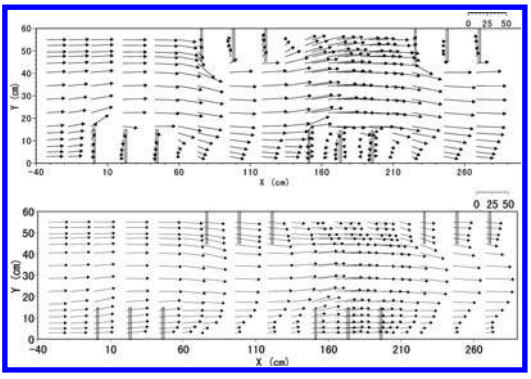


Figure 3. Calculated velocity vectors in normal case (Upper: $z = 1.5$ cm, Lower: $z = 6.5$ cm).

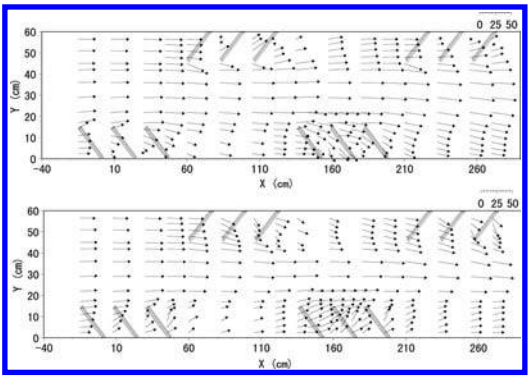


Figure 4. Measured velocity vectors in upstream-skew case (Upper: $z = 1.5$ cm, Lower: $z = 6.5$ cm).

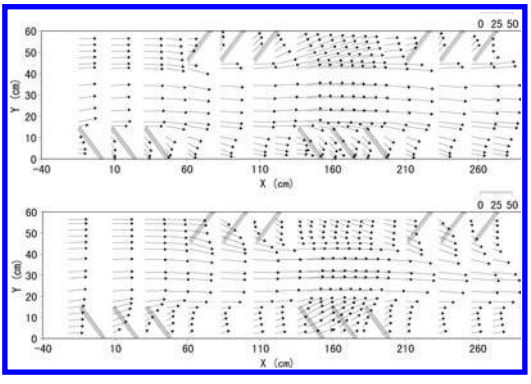


Figure 5. Calculated velocity vectors in upstream-skew case (Upper: $z = 1.5$ cm, Lower: $z = 6.5$ cm).

Copyright © 2006 Taylor & Francis Group plc, London, UK

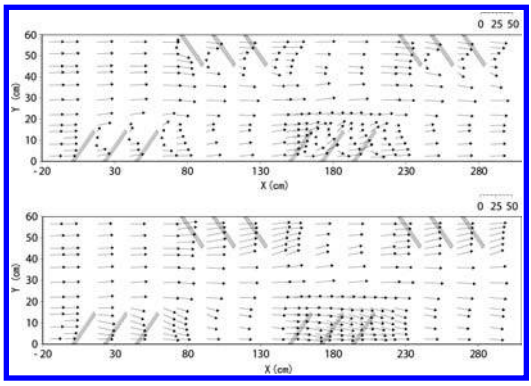


Figure 6. Measured velocity vectors in downstream-skew case (Upper: $z = 1.5$ cm, Lower: $z = 6.5$ cm).

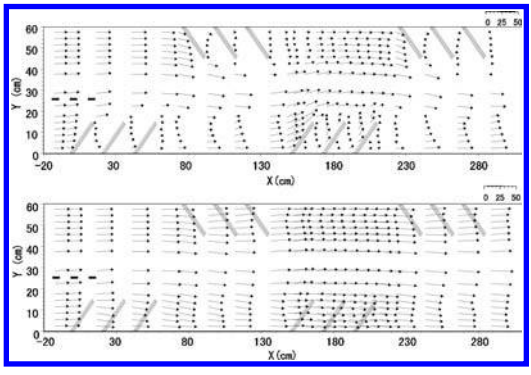


Figure 7. Calculated velocity vectors in downstream-skew case (Upper: $z = 1.5$ cm, Lower: $z = 6.5$ cm).

front of spur dikes was remarkable and the flow was angled toward the sidewall along the skew spur dike. As a result, the separated circulation does not appear and the flow toward the sidewall becomes significant in the interval zone behind the spur-dike group. On the contrary, the flow is deflected toward the center over the spur-dike group on the plain of $z = 6.5$ cm. This deflecting flow pattern is well reproduced by the present calculation. The primary velocity is decreased but the lateral velocity is not so varied through the process of going over the spur-dike group. Therefore, the angle of the velocity vector to the streamwise direction becomes larger on the last spur dike than on the head one. The flow toward the center maintains in the interval area between spur-dike groups. The flow in the sidewall region within the top line of spur-dike groups is decelerated uniformly and the velocity in the center region becomes relatively larger.

Figures 6 and 7 show velocity vectors on x-y plains in the downstream-skew case. The calculated values reasonably reproduce the characteristics of experimental results as well as the other cases. On the plain of

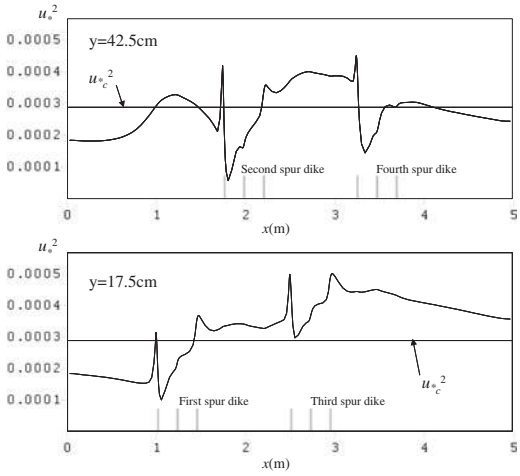


Figure 8. Streamwise distributions of calculated bed shear stress in normal case (Upper: $y = 42.5$ cm, Lower: $y = 17.5$ cm).

$z = 1.5$ cm, a deceleration at the top of a spur dike was remarkable but the flow near the spur-dike root is not so decelerated. The flow is angled toward the center in zones behind spur-dike groups. As a result, high-speed flows appear at both the sidewall and the center region. The calculated result shows a good agreement in the center region and the interval region of the sidewall, but the velocity inside the spur-dike group is underestimated. On the plain of $z = 6.5$ cm, the flow is angled toward the sidewall through the process of going over the spur-dike group. However, the velocity on the spur-dike group is rather accelerated in contrast to the upstream-skew case. The flow toward the sidewall remains in the interval region between spur-dike groups. As a whole, the main flow is distributed to the sidewalls and the velocity redistribution becomes uniform in the lateral direction. This outward deflected and uniformly distributed flow pattern is well reproduced by the present calculation.

Next, we consider the bed shear stress distributions on the fixed bed in order to predict the bed deformation by using the calculated results. Figures 8–10 show streamwise distributions of the bed shear stress divided by the density (square of the friction velocity) along the lines of 2.5 cm away from the top of a spur dike lines. The critical friction velocity, u_{*c}^2, corresponding to the sand used in the movable-bed experiment is indicated in this figure. The bed shear stress increases near the top of a spur dike. This may be a trigger of a scour around the top of a spur dike. Behind the head spur dike, it decreases rapidly especially in the normal and the downstream-skew cases. As to the effects of middle and last spur dikes, the bed shear stress increases at the top of a spur

Copyright © 2006 Taylor & Francis Group plc, London, UK

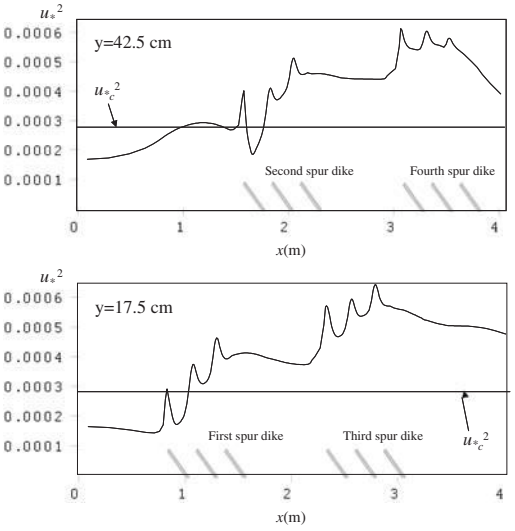


Figure 9. Streamwise distributions of calculated bed shear stress in upstream-skew case (Upper: $y = 42.5$ cm, Lower: $y = 17.5$ cm).

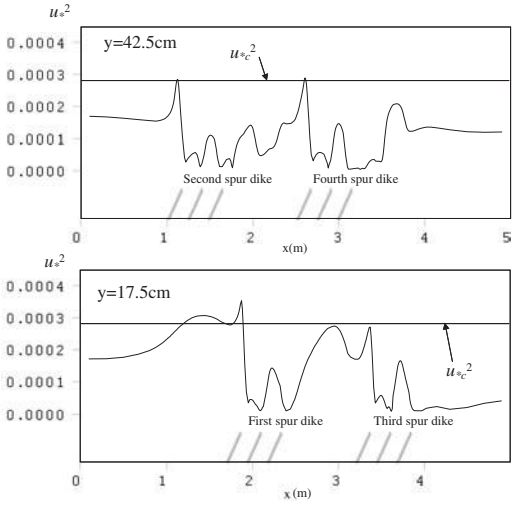


Figure 10. Streamwise distributions of calculated bed shear stress in downstream-skew case (Upper: $y = 42.5$ cm, Lower: $y = 17.5$ cm).

dike in the normal and upstream-skew cases. The second peak does not appear and the third peek comes near the first peek in the normal case. Three peeks appear increasingly from the first to the third in the upstream-skew case. Reversely, the bed shear stress decreases at the top of a spur dike and increases behind it in the downstream-skew case. The average shear stress remarkably decreases behind the head spur dike and increases behind the last spur dike in this case. The bed shear stress increases incrementally from the first group to the third in the normal and upstream-skew cases. The increasing rate is larger in the upstream-skew case since the main flow is accelerated due to the concentration of the main flow to the center region. While it decreases so much behind the head spur dike of the fourth group in the normal case, it does not so decrease in the upstream-skew case. Since the bed shear stress exceed the critical tractive force downstream from the first group, a local increase or decrease of the bed shear stress are related to the scour and the deposition in a movable bed. In the downstream-skew case, the maximum bed shear stress in front of the head spur dike does not change in the downstream direction and it does not exceed the critical tractive force. So, bed deformations are not expected along these lines in this case. However, they are not directly linked to the bed formation because the sand-feeding rate from the upstream side is different by location.

5 BED DEFORMATION BY SPUR-DIKE GROUPS

At first, we compare the effects of the spur-dike orientation on bed deformation for single group setting. Figure 11 shows the photographs of the bed configurations for three cases of orientation. The deference of the scour pattern is remarkable responding to the orientation. There is a deep scour at the top and deposition at the root of a spur dike in the upstream-skew case. On the contrary, there is a scour at the root and deposition at the top in the downstream-skew case. In the normal case, the bed form shows intermediate pattern.

Figure 12 shows the contours of the bed elevation for the single placement cases. As to the scour around the head spur dike of the normal case, a deep scour hole is produced centering on the top and is followed by a scour along the spur dike. Scours around the middle and last spur dikes become smaller at the top. In the interval region between spur dikes, front scours are not observed but small depositions appear in a central area. Scour holes propagate with undulation to the opposite bank at the angle of about 20°. The deposition line is observed behind this scour line in parallel.

In the upstream-skew case, a circular scour hole is generated centering on the top of the head spur dike. This scour is deepest and widest among three cases. The scour at the top area becomes smaller toward the middle and the last spur dike. Of particular significance is that a remarkable deposition occurs at a root region. This deposition height becomes larger toward downstream and exceeds the crest height at the last spur dike. The propagation angle of scour holes is about 17° that is smaller than the normal case. Deposition line starts from the root of the last spur dike parallel to the scour line.

Copyright © 2006 Taylor & Francis Group plc, London, UK

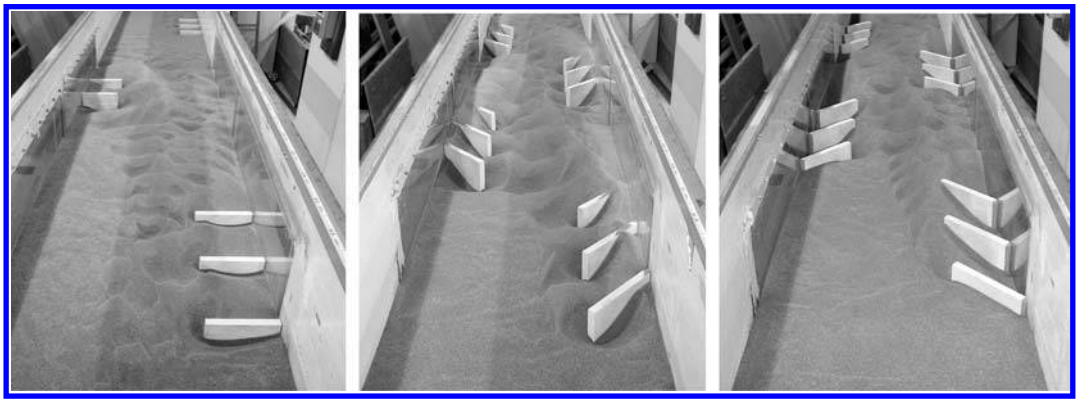


Figure 11. Photograph of bed configuration (Left: normal case, Middle: upstream-skew case, Right: downstream-skew case).

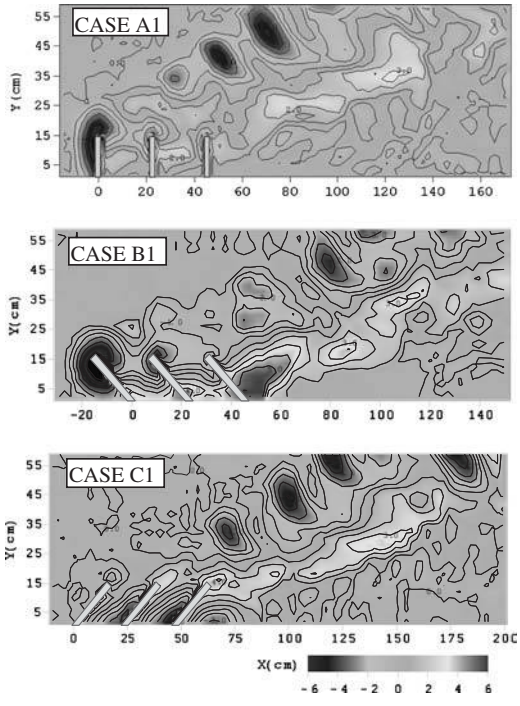


Figure 12. Contours of bed elevation of single placement (Upper: normal case, Middle: upstream-skew case, Lower: downstream-skew-case).

In the downstream-skew case, there is no scour in front of the head spur dike but a small scour hole is observed at the tip of the head spur dike. However, deep scour holes appear centering on the root of the middle and the last spur dike. It is likely to deposit at the top of the middle and the last spur dike and a small deposition line follows downstream skewing toward the opposite side. The scour propagation is also observed upstream of this deposition line.

The observed bed configurations in the spur dike region are well connected to the flow structures obtained by the PIV experiments (Tamoto et al. 2003). Figures 13 and 14 show their results of velocity vectors in the upstream- and downstream-skew spur dike. The most important feature is that flow direction passing over a spur dike becomes perpendicular to a spur-dike orientation. In the upstream-skew case, the center-oriented overflow comes down at the top of the second spur dike. This causes a strong downflow in the top region (right of Fig. 13). Then a strong inward flow is created near the bed (left of Fig. 13). Lastly, a backward upflow occurs in the root region (middle of Fig. 13). This flow sequence brings sands toward the sidewall and blowing up near the sidewall makes a large deposition behind the root of a spur dike.

In the downstream-skew case, the sidewall-oriented overflow comes down at the root of the second spur dike. This causes a strong downflow in the root region (middle of Fig. 14). Then a strong outward flow is created near the bed (left of Figure 14). Since the flow is strongly deflected by the first spur dike, the flow running through the top of the second spur dike becomes weak. In the top region, a small downflow is observed (right of Fig. 14). This flow structure makes a deep scour in front of a spur dike. It brings sands outward and may make small deposition at the top region.

By combining three spur dikes as a group structure, these effects of orientation are likely to be strengthened. The distance between the first group and the second group was determined to adjust the head of the second group to the center of scour hole at the opposite sidewall in the normal case. In the skew cases, this position is shifted downstream, but we did not change this distance for comparison.

Figure 15 shows the contours of bed elevation for the cases of four-groups setting. The characteristics of scour and deposition around the first group are almost similar to the single-placement case reflecting the effects of the orientation of spur dikes. However,

Copyright © 2006 Taylor & Francis Group plc, London, UK

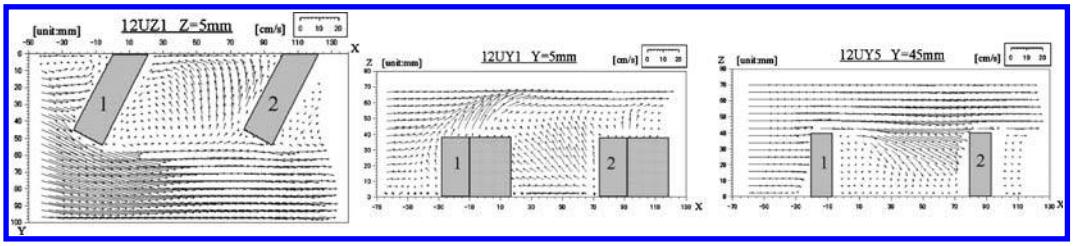


Figure 13. Velocity vectors in horizontal and vertical plains in upstream-skew case by Tamoto et al. 2003 (left: horizontal plain near the bed, middle: vertical plain near the sidewall, right: vertical plain near the top line of spur dikes).

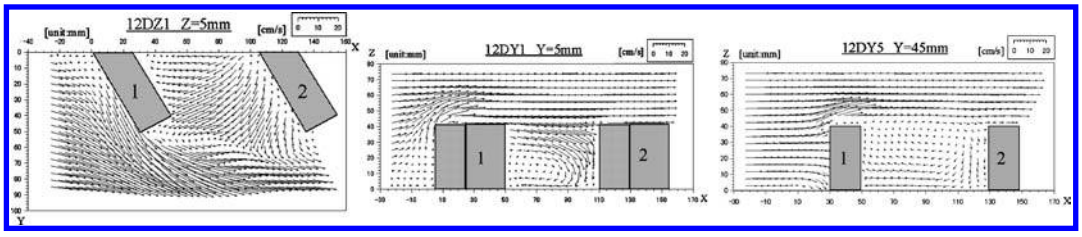


Figure 14. Velocity vectors in horizontal and vertical plains in downstream-skew case by Tamoto et al. 2003 (left: horizontal plain near the bed, middle: vertical plain near the sidewall, right: vertical plain near the top line of spur dikes).

the scour around the head spur dike is reduced and the following deposition area is narrowed in all cases. This reduction of bed deformation around the first group of alternate placement may be caused by the change of bed shear stress distribution from the single placement case.

In the normal case, the scour-hole propagation from the head of the first group reaches just at the head spur dike of the second group. This condition makes the maximum scour depth at this region. The similar scour holes are generated at the head spur dikes of the third and fourth group but the scour propagation does not appear along the line connecting head spur dikes. At the middle and the last spur dikes in a group structure, scour holes are small in all the groups. In the center region of this case, the scour and deposition are cancelled out and bed the deformation tends to be underdeveloped.

In the upstream-skew case, deep scour holes occur at the top of spur dikes from the second to the fourth group. Deep scour regions are generated along the top line from the head to the last spur dike. The scour propagation line observed in the single-group case shown in Figure 12 does not match the head scour of the second group. Therefore, the scour propagation line is pushed away from the opposite side to the center and it forms small scour area along the centerline of the channel. High deposition regions are widely produced spreading from the root of the last spur dike toward the center. In this way, the upstream-skew spur-dike groups can make dynamic riverbed deformation with riffle and pool.

In the downstream-skew case, deep scour holes appear in front of the middle and the last spur dikes in all the groups. The scour depth becomes larger from the middle to the last spur dike. The sidewall scour holes are generated behind the last spur dike and these scour depth increase as going downstream. Deposition areas appear from the top of the last spur dike to the downstream region in parallel to the streamwise direction. The scour propagation observed in the single-group case shown in Figure 8 does not appear in this alternate placement case. There is no significant bed deformation in the center region outside the spur-dike area.

Next, velocity distributions on the dynamically deformed bed were investigated in the upstream-skew case. Figure 16 shows the velocity vectors on the horizontal plains of $z = 1.5$, 4.0 and 6.5 cm. On the plain of $z = 1.5$ cm, the velocity could not be measured at some measuring points because of deposition. The flow inside the spur-dike region is steered toward the sidewall along the spur-dike wall in the same manner as the fixed-bed case. The main flow in the center region shows meandering feature that is a little more significant than the fixed bed case. On the plain of $z = 4$ cm, inflows toward the sidewall are observed in front of the middle and the last spur dikes. The flow overriding on a deposition area is observed in the interval regions of the spur-dike groups. This flow is bended toward the sidewall in these interval regions. On the plain of $z = 6.5$ cm, the flow deflected toward the center is observed over the spur-dike group in the same manner as the fixed-bed case. However, overriding flow

Copyright © 2006 Taylor & Francis Group plc, London, UK

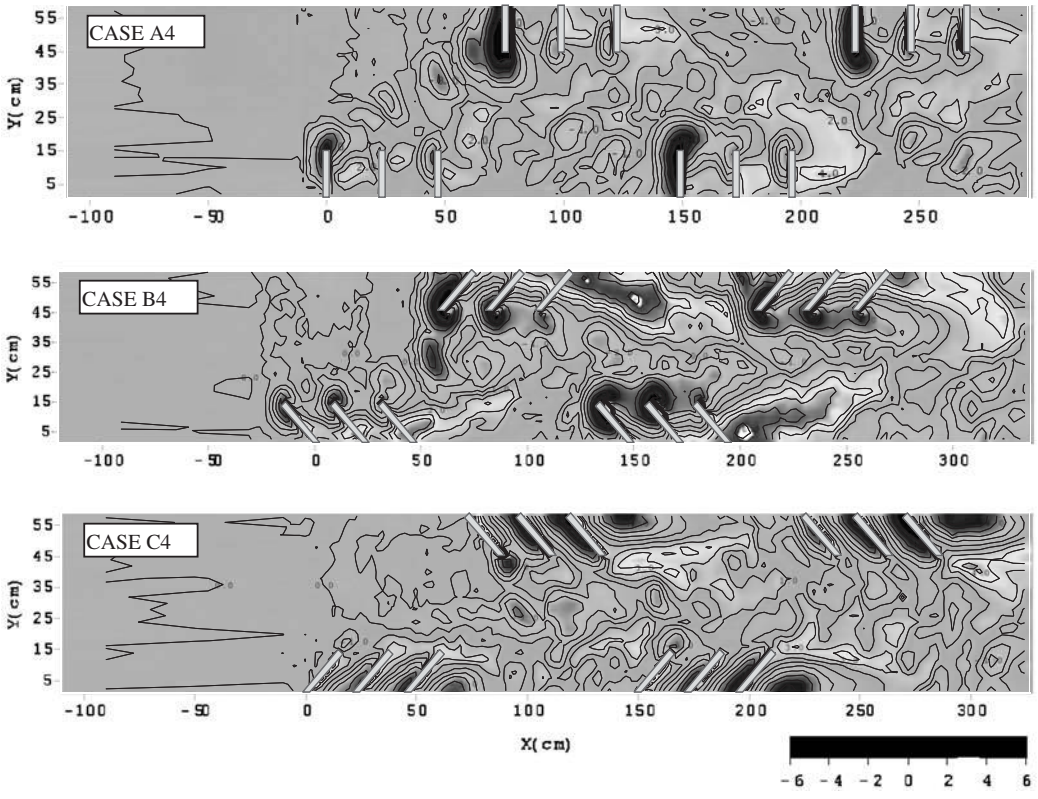


Figure 15. Contours of bed elevation of alternate placement (Upper: normal case, Middle: upstream-skew case, Lower: downstream-skew case).

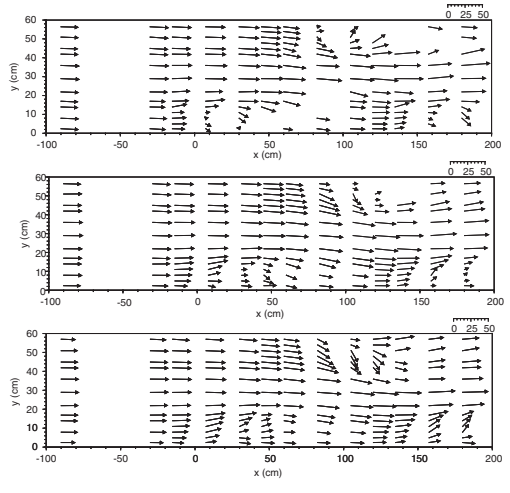


Figure 16. Velocity vectors after bed deformation in upstream-skew case (Upper: $z = 1.5$ cm, Middle: $z = 4$ cm, Lower: $z = 6.5$ cm).

toward the sidewall is observed on the deposition area behind the spur-dike group while the flow deflected toward the center is dominant in the fixed-bed case in this interval region.

6 CONCLUSIONS

It is found that the orientation of a submerged spur dike affects the flow and the bed deformation enormously. The overriding flow on submerged spur dikes generates characteristic flow structures and creates typical bed configurations. An upstream-skew spur dike angles the flow toward the sidewall near the bed and transport sands to the root of a spur dike. The overflow is deflected toward the center, decelerating the sidewall region and accelerating the center region. These sequent flow structures cause deep scours along the top line of the spur dikes and high deposition along the sidewall behind them. A downstream-skew spur dike accelerates the sidewall region and a downflow in front of the spur dike makes deep scour. In this case, the bed deformation in the center region becomes

Copyright © 2006 Taylor & Francis Group plc, London, UK

mild. The group-structure placement of skew spur dikes strengthens the characteristic effects of each spur dike and has a possibility to make diverse river configurations. In particular, the alternate arrangement of upstream-skew spur-dike groups is satisfactory to make riffles and pools in a straight river course. These fundamental flow structures can be reasonably predicted by using the present simple 3-D numerical model. It is expected to develop a numerical simulation model of bed deformation with 3-D flow prediction in the next step.

REFERENCES

Chen, F. and Ikeda, S. 1996, "Experimental study on horizontal separation eddies in open-channel flow with groins", *Annual Journal of Hydraulic Engineering*, JSCE, vol.40: 787–792 (in Japanese).

Elawady, E., Michiue, M. and Hinokidani, O. 2000, "Experimental study of flow behavior around submerged spur-dike on rigid bed", *Annual Journal of Hydraulic Engineering*, JSCE, vol.44: 539–544.

Elawady, E., Michiue, M. And Hinokidani, O. 2001, "Movable Bed Scour Around Submerged Spur-Dikes", Annual *Journal of Hydraulic Engineering*, vol.45: 373–378.

Fukuoka, S., Nishimura, T., Okanobu, M. and Kawaguchi, H. 1998, "Flow and bed topography around groins installed in a straight channel", *Annual Journal of Hydraulic Engineering*, JSCE, vol.42: 997–1002 (in Japanese).

Gill, M. A., 1972, "Erosion of sand beds around spur dikes", *J. Hydraulics Division*, ASCE, vol.98, No.9: 1587–1602.

Kimura, I., Hosoda, T. and Onda, S. 2002, Prediction of 3D Flow Structures Around Skewed Spur Dikes by Means of a Non-linear k-ε Model, *River Flow 2002*, 1: 65–73.

Klingeman, P.C., Kehe, S.M. and Owusu, Y.A. 1984, "Streambank erosion and channel scour manipulation using rockfill dikes and gabions", *WRRI Report for Project No.373909*, Oregon State Univ.: 1–169.

Peng, J., Kawahara, Y., and Tamai, N. 1997, "Numerical analysis of three-dimensional turbulent flows around submerged groins", *Proc. 27th IAHR Congress*, San Francisco, Vol.A: 244–249.

Rahman, M. M. And Muramoto, Y. 1999, "Prediction Of Maximum Scour Depth Around Spur-Dike-Like Structures", *Annual Journal of Hydraulic Engineering*, vol.43: 623–628.

Rajaratnum, N. and Nwachukwu, B.A. 1983, "The study of flow near groin-Like structures", *J. Hydraulic Engineering*, ASCE, vol.109, No.3: 463–480.

Tominaga, A., Ijima, K. and Nakano, Y. 2001, "Flow Structures around Submerged Spur Dikes with Various Relative Height", *Proc. of 29th IAHR Congress,* Theme D, vol.1: 421–427.

Tamoto, N., Tominaga, A. and Ijima, K. 2003, "Flow structures in continuous spur dike zone with orientation angle", *Proc. of 30th IAHR Congress*, C-2: 325–332.

Zhang, H., Nakagawa, H., Ishigaki, T., Muto, Y. and Baba, Y. 2005, Three-dimensional mathematical modeling of local scour, *Journal of Applied Mechanics, JSCE*, vol.8: 803–812.

Copyright © 2006 Taylor & Francis Group plc, London, UK

Turbulence analysis of vertical slot fish pass by in situ measurements and CFD modelling

B. Sokoray-Varga, S. Baranya & J. Józsa
Budapest University of Technology and Economics, Budapest, Hungary

ABSTRACT: Turbulence features in a operating vertical slot fish pass were explored first by means of analyzing in situ ADV data. The mean velocity field, its vorticity and important turbulence parameters were quantified. The swirling character of the flow was made visible, and the vertical velocity component proved to play an important role at places. As to turbulence features, the Eulerian space-scale provided valuable information on the dominant eddy size in the flow, expected to contribute to the detailed flow structure dependent analysis of the swimming performance of fish in various fish pass facilities. The order of magnitude of this eddy size was found quite close to the one of the fish migrating there. As a future design tool, a first implementation of the 3D k-ε SSIIM model was carried out and provided promising primary results. The CFD model could reasonably reproduce the important elements and overall complexity of the mean flow field, typical to vertical slot fish pass arrangements.

1 INTRODUCTION

In fluvial systems to make the stream-wise passage for fish possible at the presence of various man-made transversal obstructions such as damming is a more and more required element of the so-called good ecological status. In fact, transversal hydraulic structures controlling water level or discharge usually present insurmountable obstacles in themselves severely violating ecological continuity of the system where a number of fish species used to migrate according to specific rules. To minimize these negative effects a number of fish pass facilities have been conceived and successfully implemented well suited to the given local conditions.

One of the most popular solutions to the problem is the vertical slot fish pass. In such facilities the difference insurmountably large for fish between headwater and tailwater free surface levels is dissipated in a distributed way. In fact, it occurs in a series of pools interconnected by vertical slots, in portions small enough for the fish to cope with when migrating (see e.g. Wu et al. 1999). The design of such hydraulic facilities is usually performed by considering rather global hydrodynamic and ecological parameters, whereas suitability depends a lot on the flow features at a wide range of scales: pool- wide patter, large turbulence eddies and fine scale turbulence. Laboratory experimental studies have significantly contributed to answer such questions as presented by Wu et al. (1999) and Pea et al. (2003).

Moreover, important conclusions can be also drawn from measurements carried out on operating fish passes. However, in the ideal case an efficient design tool would be a CFD model validated for existing conditions and flexible enough to investigate different geometry and flow regime variants. The results of the first steps toward such an approach are presented in this paper, where in situ ADV (Acoustic Doppler Velocimetry) turbulence measurements and related 3D CFD modelling carried out in an operating vertical slot fish pass in Hungary are analysed.

2 FLOW PATTERN AND TURBULENCE ASPECTS IN VERTICAL SLOT PASSES

The upstream reach of the fish pass is a rectangular channel divided by baffles into a number of pools as usual for the vertical slot type of arrangement (Fig. 1). It continues then in a strongly irregular, meandering, landscape-friendly reach (Fig. 2).

When migrating up the stream, the fish swims basically in countercurrent. While passing through the series of pools the fish keeps on moving up the stream. As is known, in a pool of a vertical slot fish pass two rather distinct regions in flow pattern can be detected (Fig. 3). One of them is a direct flow region a jet-like, though often curved, high speed flow interconnecting the slots. The other is a large recirculation region, indirectly driven by the jet, and characterized by relatively small velocities (see e.g. Wu et al. 1999, Pena et al. 2003). After passing through the high velocity zone at the slot, the fish is assumed to leave the direct flow region and continue their way for a while in the recirculation region, in the zone just adjacent to the main

Copyright © 2006 Taylor & Francis Group plc, London, UK



Figure 1. View of the vertical slot reach of the fish pass.

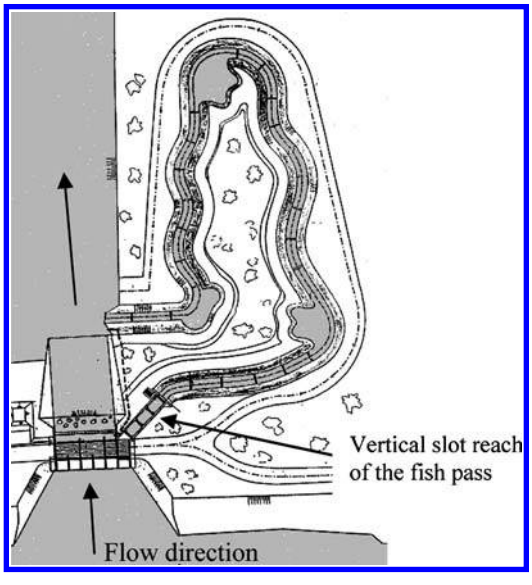


Figure 2. Plan view of the fish pass.

stream. In this way the two kinds of region in flow pattern enable them to find opportunities for a rest in the recirculation regions after swimming through the fast flowing zones, especially the one straight at the slot.

In a vertical slot fish pass the flow usually becomes highly turbulent even given calm conditions in the river

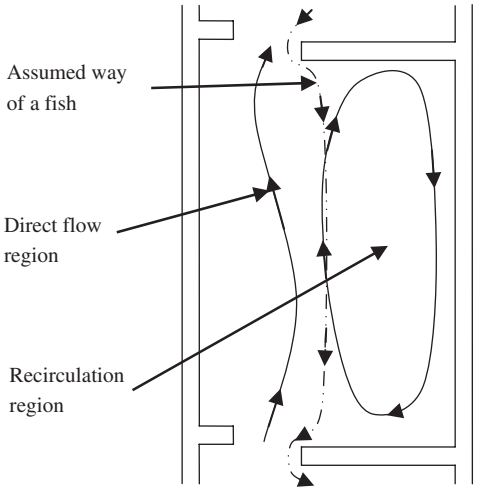


Figure 3. The two different regions in the flow pattern.

straight upstream. Hydro-biological investigations on the hydrodynamic impact on the swimming performance of fish have pointed out its scale-dependence (Nikora et al. 2003). In fact, turbulent eddies of scales smaller, comparable or much larger than fish size have certainly various impact on the motion of a fish (Fig. 4). In this paper we present a primary quantification of such parameters by evaluating the 3D ADV measurements carried out in an operating fish pass, supporting the evaluation also by CFD analysis. The aim is to contribute to the better understanding of fish pass hydrodynamics and to the embedded various flow features and structures with possibly different relevance on the swimming performance of fish (as sketched in Fig. 4). In fact, turbulent eddies much smaller than the size of the fish, are not expected to have significant impact on short term swimming. In turn, eddies with a scale comparable or somewhat larger than the size of a fish can present direct dynamic loading in terms of rolling, pitching and yawing. Eddies much larger than the fish will, of course, also have a considerable impact but mainly as a macroscale part of the advective flow pattern, with relatively slow space-time variation.

3 IN SITU FLOW MEASUREMENTS

In the upstream reach of the study fish pass the pools are generally characterized by high speed flow and complex turbulence conditions. In order to capture the essential of turbulence in such field conditions, the Vector ADV of Nortek was applied, providing 3D velocity vectors in a small (around 1 cm^3) sampling volume at 16 Hz as a default sampling rate in time, which can be set up to 64 Hz (for more details see Nortek AS 2001).

Copyright © 2006 Taylor & Francis Group plc, London, UK

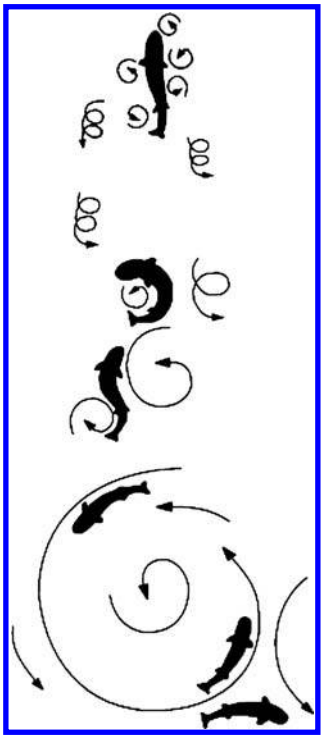


Figure 4. The fish in flow with various characteristic turbulent eddy sizes (after Odeh et al. 2002).

The field measurements took place in the downstream part of the 3rd pool of the vertical slot fish pass in the two cross-sections (A and B) as presented in Figure 5, at points shown in Figure 6. In both cross-sections the measurements included 5 verticals with 6 points in each, forming a regular raster. During the measurement period the flow conditions were practically steady, with a discharge estimated to 0.6 m^3/s and mean depth to 0.90 m (in the measurement region). Velocities were measured at each selected location for 2 min at a sampling rate of 16 Hz, considered sufficient to capture all the important scales. The local coordinate system was a pool longitudinal axis aligned one as seen in Figure 5, with z pointing upward.

As one single ADV was available, only, the velocity time series obtained in situ subsequently were assumed as samples of stationary flow conditions. They served then to estimate both the large scale mean pattern and the turbulent space-time structure of the flow.

4 FLOW MEASUREMENT ANALYSIS

As usual the measured instantaneous spatial velocity vector

$$\mathbf{v}(t) = u(t)\cdot\mathbf{i} + v(t)\cdot\mathbf{j} + w(t)\cdot\mathbf{k} \qquad (1)$$

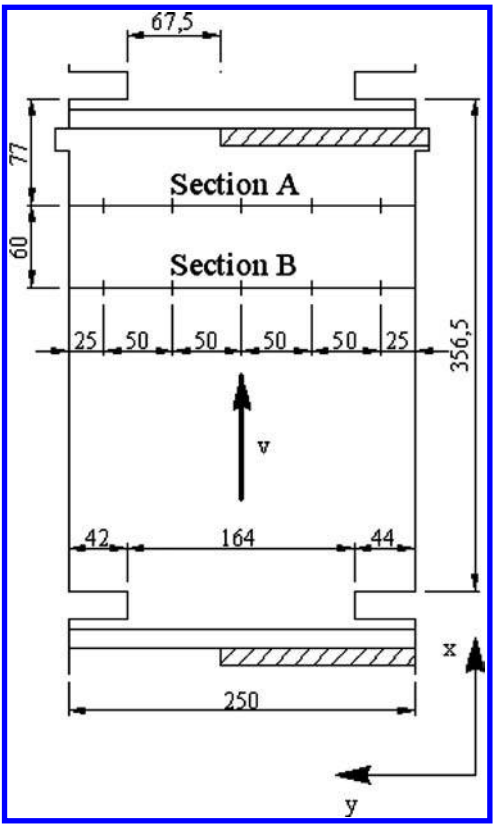


Figure 5. Plan view of the pool and the measurement sections (dimensions indicated in cm).

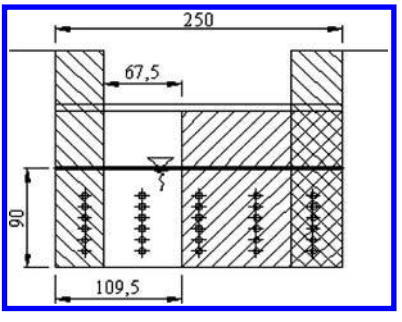


Figure 6. The measuring points in the selected cross-sections (dimensions indicated in cm).

was handled according to the Reynolds decomposition

$$\begin{aligned} u(t) &= U + u'(t), \\ v(t) &= V + v'(t), \\ w(t) &= W + w'(t), \end{aligned} \qquad (2)$$

Copyright © 2006 Taylor & Francis Group plc, London, UK

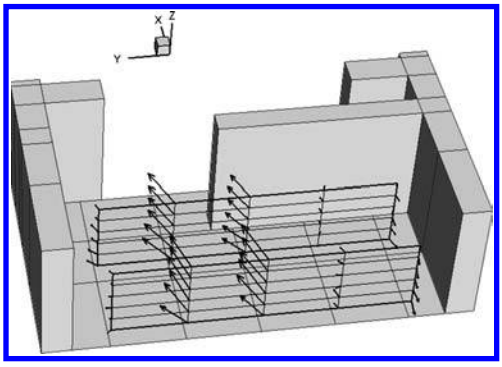


Figure 7. Layout of the measurement points with mean velocity vectors.

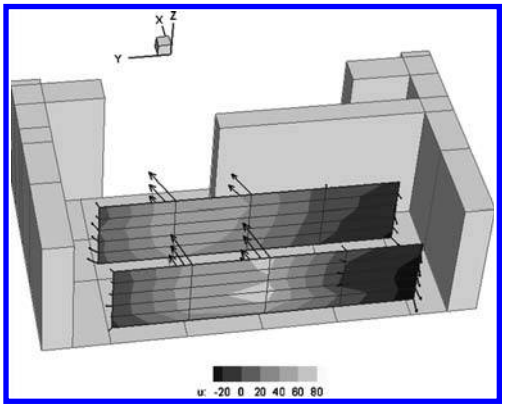


Figure 8. Measured mean velocity vectors and the distribution of the x-component of the mean velocity in cm/s.

where $u(t)$, $v(t)$, $w(t)$ are instantaneous velocity components in x, y, and z direction, respectively, U, V and W are their Reynolds-averaged mean values and $u'(t)$, $v'(t)$ and $w'(t)$ the instantaneous fluctuation around the mean.

The results of the time series analysis are displayed in the measurement cross-sections mostly as appropriately interpolated fields using Tecplot. In the figures one looks downstream. Note that the colour scales are different from figure to figure.

Figure 7 shows the mean velocity vectors which show the mean spatial structure of the flow even in themselves, making it possible to distinguish the jet region and the much slower recirculation zone adjacent to that. Symptoms of swirling can also be seen.

In Figure 8 the cross-sectional distribution of the x-wise velocity component is displayed putting a light onto the direct through-flow, the slow recirculation flow region and the highly sheared zones. The highest velocities in the direct through-flow region exceed

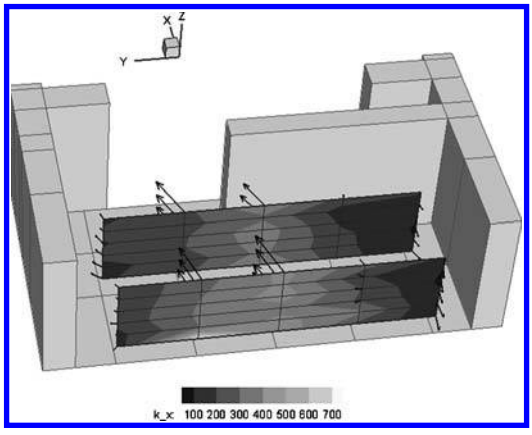


Figure 9. Distribution of the x-component of the turbulent kinetic energy in cm^2/s^2.

0.80 m/s. It can also be seen that curved contracting way the main stream approaches the outlet slot. In the recirculation region the velocities go up to 0.30 m/s at most.

The variance of the fluctuation components u', v' and w' provided the estimation of the turbulent kinetic energy. The cross-sectional distribution of its component in the x-direction

$$k_x = \frac{1}{2}(\overline{u'^2}) = \frac{S_u^2}{2}, \tag{3}$$

which shows in Figure 9 that the largest values develop in the shear layer between the jet and the recirculation region, well known as turbulence production zone.

The autocorrelation function $\rho(\tau)$ of the fluctuation terms having calculated, one could estimate the

$$T_{EI} = \int_0^\infty \rho(\tau)\mathrm{d}\tau \tag{4}$$

Eulerian integral time scale T_{EI} (usually sufficient to integrate as far as the first zero point), and also the

$$L_{EI} = U \cdot T_{EI} \tag{5}$$

integral length scale by assuming the Taylor hypothesis. This is considered as an order of magnitude estimation of the energy containing dominant eddy size (see e.g. Bedford 1993). The cross-sectional averaged value of these length scales calculated for the measurement points in all the three directions are summarized in Table 1.

As was mentioned before, the eddy size is expected to be a good indicator of its impact rate on the swimming fish. The obtained average values are somewhat different in the different directions but have got the

Copyright © 2006 Taylor & Francis Group plc, London, UK

Table 1. Averaged Eulerian integral length scales in cm.

	x-direction	y-direction	z-direction
Section A	20	12	11
Section B	28	20	13

Table 2. Alternative Eulerian integral length scales in cm.

	x-direction	y-direction	z-direction
Section A	15	9	7
Section B	21	11	7

same order of magnitude. In fact, these values fall just in the range of the fish size observed to use regularly the fish pass. Moreover, one should also note that the bottom of the pool is roughened by large rip-rap with an approximate size close to what was found as characteristic eddy size.

As is known, much better eddy size estimate could be obtained from Lagrangian autocorrelation functions but such measurements are difficult to perform in situ. The Taylor hypothesis looses its validity especially in regions with mean velocity close to zero. As an alternative, the standard deviation of the fluctuation was also used as characteristic velocity scale providing

$$L'_{EI} = T_{EI} \cdot \sqrt{\overline{u'^2}} \,. \tag{6}$$

The calculated cross-sectional averaged values of L'_{EI} are summarized in Table 2.

The nearly stationary conditions made it possible to evaluate some further large scale features of the flow. Though the measurement were carried out in two cross-sections, only, the x-component of the

$$\boldsymbol{\omega} = \frac{1}{2}\left(\frac{\partial w}{\partial y} - \frac{\partial v}{\partial z}\right)\cdot \mathbf{i} + \frac{1}{2}\left(\frac{\partial u}{\partial z} - \frac{\partial w}{\partial x}\right)\cdot \mathbf{j} + \\ + \frac{1}{2}\left(\frac{\partial v}{\partial x} - \frac{\partial u}{\partial y}\right)\cdot \mathbf{k} = \frac{1}{2}\nabla \times \mathbf{v} = \frac{1}{2} rot\mathbf{v} \tag{7}$$

total vorticity vector could be, nevertheless, estimated as

$$(rot\mathbf{v})_x = \left(\frac{\partial w}{\partial y} - \frac{\partial v}{\partial z}\right)\cdot \mathbf{i} \tag{8}$$

by appropriate finite difference approximation. The calculated vorticity fields can be seen in Figure 10. As was already expected from the velocity vector field, one can distinguish two large swirling structures, one on the left hand side presenting clockwise, and another one on the right hand side presenting anti-clockwise rotation.

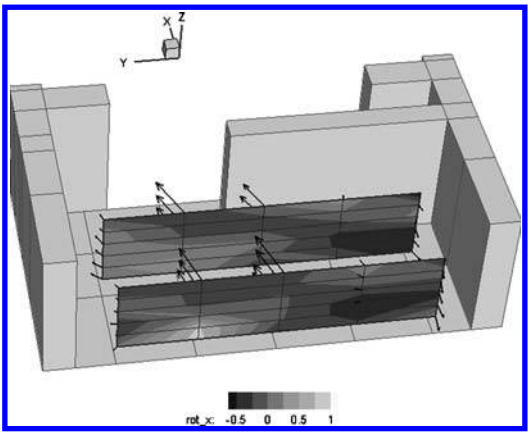


Figure 10. Cross-sectional distribution of the x-component of the vorticity vector in 1/s.

5 CFD MODELLING

In order to make steps toward an efficient future design tool, a 3D turbulence CFD model was implemented to the investigated part of the study fish pass. The primary goal was to reproduce realistic 3D flow patterns verified by the measured ones and get a more refined insight to the complexity of the flow.

5.1 *Applied CFD code*

The numerical model used in this study is the CFD code called SSIIM (Olsen 2002). It solves the Reynolds-averaged Navier-Stokes equations with the two-equation k-ε turbulence closure (see e.g. Rodi 1984) in three dimensions for non-hydrostatic conditions.

The Reynolds-averaged Navier-Stokes equations are written in a compact form as follows:

$$\frac{\partial U_i}{\partial t} + U_j \frac{\partial U_i}{\partial x_j} = \frac{1}{\rho}\frac{\partial}{\partial x_j}\left(-P\delta_{ij} - \rho \overline{u'_i u'_j}\right), \tag{9}$$

where U = time-averaged velocity, u' = velocity fluctuation, P = pressure, x_j = Cartesian space co-ordinates, δ_{ij} = Kronecker delta, ρ = fluid density.

The eddy viscosity concept with k-ε turbulence closure is used to model the Reynolds stress terms as follows:

$$-\rho \overline{u'_i u'_j} = \rho \nu_T \left(\frac{\partial U_i}{\partial x_j} + \frac{\partial U_j}{\partial x_i}\right) - \frac{2}{3}\rho k \delta_{ij} \tag{10}$$

where ν_T = eddy viscosity coefficient, k = turbulent kinetic energy.

Copyright © 2006 Taylor & Francis Group plc, London, UK

In the model, in which ε represents the rate of turbulent energy dissipation, a transport equation is solved both for k and ε as a result of which the eddy viscosity coefficient can be evaluated as

$$\nu_T = c_\mu \frac{k^2}{\varepsilon} \tag{11}$$

where $c_\mu = 0.09$.

The governing equations are solved in a finite volume context by using the SIMPLE method (Patankar 1980) on a three-dimensional, non-orthogonal curvilinear structured grid.

5.2 *Applied mesh and boundary conditions*

In the CFD model three pools of the investigated fish pass were included resulting in 13 m total length and 2.50 m width. A mesh with 260×50 cells provided 0.05×0.05 m horizontal resolution, whereas in the vertical 7 layers were used with decreasing spacing toward the bottom where strong gradients were expected to occur in the flow variables.

Velocity measurements carried out by means of the ADV provided the discharge close to 0.60 m^3/s. This value was applied then as upstream boundary condition. As downstream water level 0.90 m was prescribed.

Equations 9 and 10 are valid inside the fluid flow in the free turbulence zone, whereas next to the boundaries the flow characteristics are calculated from the following boundary layer formula (Schlichting 1979):

$$\frac{U}{u_*} = \frac{1}{\kappa} \ln\left(\frac{30y}{k_s}\right), \tag{12}$$

where U = velocity parallel to boundary, u_* = friction velocity, κ = von Karman constant, y = distance of the investigated point from the wall, k_s = roughness height. Since the investigated fish pass was constructed from concrete with relatively smooth surface, a Strickler parameter equal to 40 $m^{1/3}/s$ and roughness height corresponding to that was adopted all along the pool boundary surface. As the bottom is covered by large stones, to take into account this fact a simple first approach was to define regularly placed solid cubes 0.2 m size in the mesh, represented by the two lowest model layers as a sort of macro-roughness (see Fig. 11).

5.3 *Model results*

Steady-state velocity patterns were calculated and compared to field measurement results. Using a reference system identical to the one applied in the previous chapter, in Figure 11 the distribution of the

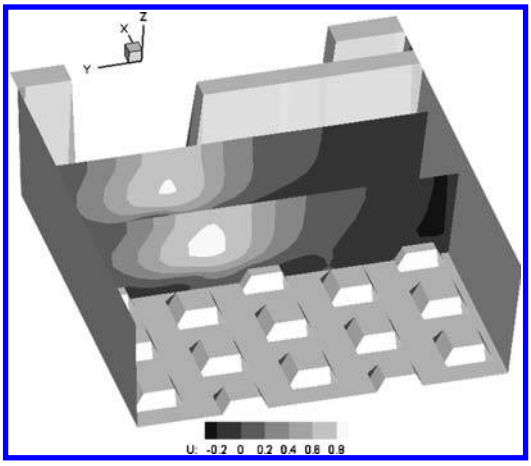


Figure 11. Distribution of the x-component of the Reynolds-averaged velocity in the measurement cross-sections in m/s.

Reynolds-averaged x-wise velocities is plotted in the two measurement cross-sections. Fairly good agreement can be observed with measured data (see Fig. 8), which means that the roughness conditions could be reasonably approximated in the CFD model (note that close to the side walls and to the free surface field velocity data could not be gathered).

A path-line representation of the flow using the surface layer velocity field provides a good insight into the modelled pattern as is seen in Figure 12. Both the direct through-flow and the large recirculation region (even on the left hand side of the jet) accompanied with some further, smaller corner eddies develop in a way close to what was measured in situ.

In Figure 13 four representative path-lines show the strong three-dimensionality of the flow. Indicating the elevation in grey-scale, one can see how a neutrally buoyant particle moves both horizontally and vertically, resulting locally in up- or downwelling in the large recirculation region. For instance the particle entering the domain on the right-hand side close to free surface carries out three loops before leaving the domain close to bottom. On the left-hand side the opposite occurs, namely the particle arriving into the pool close to bottom first rises then is entrained into the main through-flow. The other two particles released well in the jet will go through remaining all along in it with little change in elevation.

The velocity vector field in the layer just below the crest level of the bottom cubes is given in Figure 14 and provides some further explanation to the motion of particles discussed above. In the direct through-flow region relatively high velocities develop, whereas close to the vertical walls of the pool vectors point in general opposite to the main steam.

Copyright © 2006 Taylor & Francis Group plc, London, UK

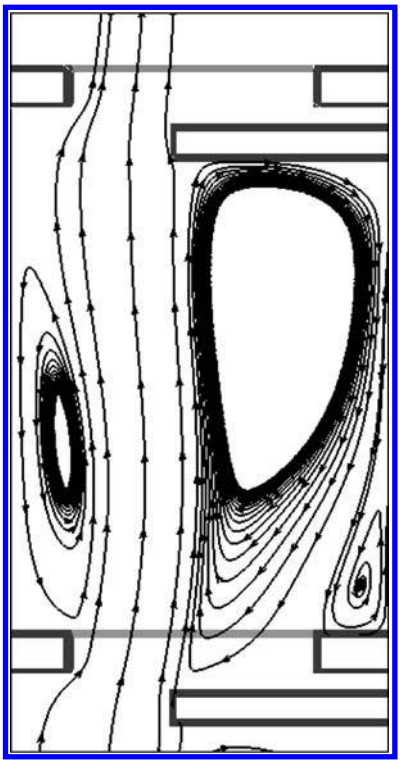


Figure 12. Path-lines in the near-surface layer.

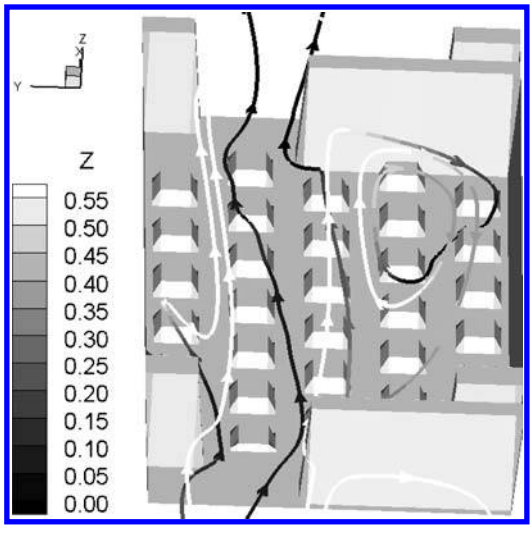


Figure 13. Visualization of characteristic path-lines and their elevation.

Velocity vectors taken close to the measurement cross-sections are displayed in Figure 15 both in the near-surface layer (black) and in a lower layer, nevertheless, well above the crest level of the bottom

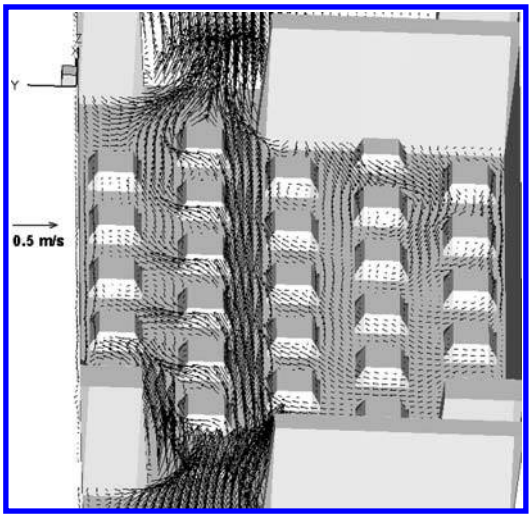


Figure 14. Velocity vector field close to the bottom.

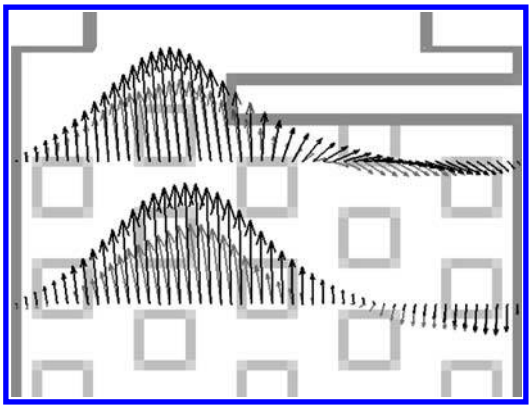


Figure 15. Velocity vectors close to free surface (black) and above the crest level of the bottom cubes (grey) in the two measurement cross-sections.

cubes. One can clearly see the character of the spanwise distribution of the velocity similar to the one observed in the nature. Moreover, based on the flow directions one can also see the swirling character of the main stream again in a sense identical to the observed one. The recirculation region can also be identified with its strong three-dimensionality close to the downstream wall, all that underlining the necessity of the 3D modelling approach.

As to the free surface variation, steep slope zones obviously appear in the vicinity of the narrow slots (Fig. 16). There the change of the water level is some centimetres within a short distance, seemingly also reasonably captured by the applied CFD model.

Copyright © 2006 Taylor & Francis Group plc, London, UK

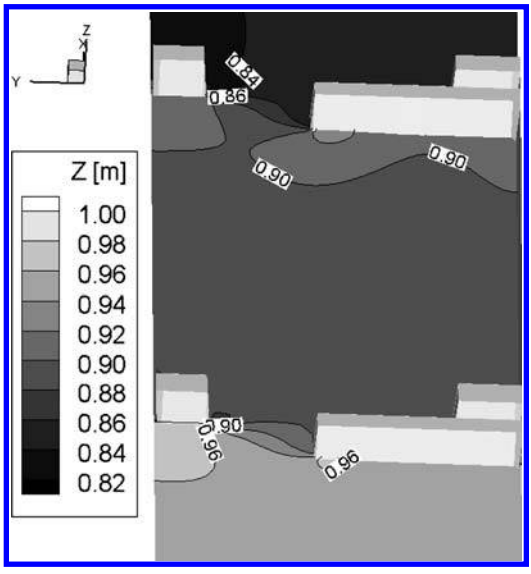


Figure 16. Modelled free surface with local steep slopes.

6 DISCUSSION AND CONCLUSIONS

Turbulence features in an operating vertical slot fish pass were explored by means of analyzing ADV data. In quasi-stationary flow conditions the mean velocity field, its vorticity as well as a number of important turbulence parameters could be quantified. The vorticity field made the swirling character of the flow even more visible. The vertical component of the velocity, often neglected in laboratory scale model studies, proved to play an important role at places.

As to turbulence features, what was shown in a novel way is the importance of the estimation not only of the kinetic energy, but also further parameters such as the Eulerian integral time- and space-scale. The latter can provide valuable information on the dominant eddy size in the flow thus contributing to the detailed flow structure dependent analysis of the swimming performance of fish in various fish pass facilities. Interestingly, the order of magnitude of this eddy size was found quite close to the one of the fish migrating there. Of course, further research is needed to investigate the above mentioned impact in details, and also the role of the large scale bottom roughening in there development.

Future design or improvement of the operation of existing fish passes could, nevertheless, best carried out by mean of 3D CFD turbulence models once suitably validated in existing conditions, including preferably a number of geometry set-up and flow regime. A first implementation of the 3D k-ε SSIIM provided promising primary results to reach this goal. The CFD model could reasonably reproduce the important elements and overall complexity of the mean flow field, typical to vertical slot fish pass arrangements.

A next step in CFD modeling will be the more realistic representation of the large scale bottom roughening including also a parameter sensitivity study on it, moreover, the numerical estimation of the local dominant eddy size by using the calculated turbulent kinetic energy and dissipation rate fields. Reasonable fitting of the latter with the ones observe in nature would really enhance the robustness of the CFD model in fish pass design.

ACKNOWLEDGEMENTS

The research was partially supported by OTKA Grant T030792 on “Measurement and parameterization of spatial characteristics of free surface flows”. The authors wish to thank N. R. B. Olsen and N. Ruether for all their valuable support in implementing SSIIM in the project.

REFERENCES

Bedford, K. W. 1993. Diffusion Dispersion and sub-grid parametrization. *Coastal, Estuarial and Harbour Engineer's Reference Book*. London: Chapman & Hall.

Nikora, V. I., Aberle, J., Jowett, I. G., Biggs, B. J. F., Sykes J. R. E. 2003. On turbulence effects on fish swimming performance. *Procedings of XXX IAHR Congress* Theme C, Vol. II. Thessaloniki: IAHR.

Nortek AS 2001. Vector Operation Manual. Nortek, Norway.

Odeh, M., Noreika, J. F., Haro A., Maynard A., Castro-Santos, T., Cada G. F. 2002. Evaluation Of The Effects Of Turbulence On The Behavior Of Migratory Fish. Final Report Report to Bonneville Power Administration.

Olsen, N. R. B. 2002. A three-dimensional numerical model for simulation of sediment movements in water intakes with moving option. User's Manual, Department of Hydraulic and Environmental Engineering, The Norwegian University of Science and Technology, Trondheim, Norway.

Patankar, S. V. 1980. Numerical heat transfer and fluid flow. McGraw-Hill Book Company, New York.

Pena, L., Teijeiro, T., Puertas, J. 2003. Experimental study of depth-discharge equations and velocity patterns on vertcal slot fishways. *Procedings of XXX IAHR Congress* Theme C, Vol. II. Thessaloniki: IAHR.

Rodi, W. 1984. Turbulence models and their application in hydraulics. State-of-the-art paper, IAHR Experimental and Mathematical Fluid Dynamics.

Schlichting, H. 1979. Boundary layer theory. McGraw-Hill.

Wu, S., Rajaratnam, N., Katopodis, C. 1999. Structure of flow in vertical slot fishway. *J. Hydr. Eng.*, ASCE, Vol. 125, No.4.

Copyright © 2006 Taylor & Francis Group plc, London, UK

Stability analysis of turbulent water jets onto both rigid and mobile beds

C. Adduce, M. la Rocca & P. Mele
Dipartimento di Scienze dell'Ingegneria Civile, Università degli Studi RomaTre, Roma, Italy

ABSTRACT: A laboratory-theoretical investigation on the stability of jets developing downstream of a drop structure is presented. Two series of laboratory experiments were performed with both a mobile and a flat rigid bed downstream of the drop. The discharge and the downstream water depth were varied and two kinds of jet flow were observed developing downstream of the drop: a surface wave jet and an oscillating jet. The oscillating jet is an unstable flow configuration. Both velocity and free surface flow measurements were performed. Starting from laboratory measurements, a mathematical model, which investigates the stability of the surface wave jet both over a flat and a scoured bed, was developed. The modified De Saint-Venant equations, i.e. with correction terms accounting for the curvature of the streamlines, were obtained from the theoretical velocity and pressure profiles. The stability of the surface wave jet is affected by the presence of the scoured bed, which weakens its stability properties.

1 INTRODUCTION

When the main stream interact with hydraulic structures as drops, gates, spillways, a jet flow may develop. Several investigations, performed with a flat rigid bed or a mobile bed, (Adduce and Mele, 2004; Chatterjee, et al., 1994; Dey and Westrich, 2003; Farhoudi and Smith, 1985; Gijs and Hoffmans, 1998; Hassan and Narajanan, 1985; Kurniawan, et al., 2001; Wu and Rajaratnam, 1998; Fritz and Hager, 1998; Ohtsu and Yasuda, 1991b) observed this kind of flow. If the jet flow develops over a mobile bed, it may endanger the structures' stability, because it may produce a deep scour hole.

Different kinds of jet flow, related both to different hydraulic conditions and hydraulic structures' geometry, were observed (see Ohtsu and Yasuda, 1991a, Ohtsu and Yasuda, 1991b; Hager, 1992; Wu and Rajaratnam, 1998; Fritz and Hager, 1998).

Three flow conditions were observed for submerged overflow structures, with the downstream water depth higher than the structure's height: (a) plunging flow, also referred to impinging flow, with a submerged main flow and a surface roller; (b) surface wave (breaking or not breaking) flow, with the main flow along the free surface and a bottom recirculation zone; (c) surface jet flow, similar to the surface wave flow, but with a nearly horizontal free surface (see Wu and Rajaratnam, 1998; Fritz and Hager, 1998; Bukreev, 2001). A transition condition between the "surface state" (surface wave flow) and the "bottom state" (plunging flow) was observed by Bukreev (2001).

The aim of the present paper is to investigate, by both laboratory experiments and a mathematical model, the influence of the bed geometry on the surface wave jet stability. Jet flow was produced by the interaction of the main flow with a drop structure, followed by a rigid apron. Two series of laboratory experiments were performed in order to develop surface wave jets (U1, U2, U3) and oscillating jets (T1, T2,T3), downstream of the drop, followed by a mobile bed. The jet-sediments interaction produced a scoured bed. The same experiments were repeated with a fixed horizontal bed (tests U1FB, U2FB, U3FB, T1FB, T2FB,T3FB).

A mathematical model, following the work by Montes and Chanson (1998) was developed, starting from the analytical determination of the velocity and pressure fields in presence of a surface wave flow. Such velocity and pressure fields, unlike Montes and Chanson (1998), were obtained accounting for a scoured bed. A comparison between the theoretical and the measured velocity profiles was performed, in order to have an idea of the validity of the theoretical model. A modified version of the De Saint-Venant equations, i.e. with correction terms accounting for the curvature of the streamlines, was developed and used to perform a stability analysis of the surface wave jet, both with a flat and a scoured bed. The result of this analysis is that a scoured bed weakens the stability properties of the surface wave flow.

The paper is set out as it follows: the experimental apparatus is described in section 2; the laboratory experiments are presented in section 3; the

Copyright © 2006 Taylor & Francis Group plc, London, UK

mathematical model is described in section 4; a comparison with laboratory measurements is shown in section 5. The conclusions of the work are presented in section 6.

2 EXPERIMENTAL APPARATUS

Laboratory experiments were performed at the Hydraulics Laboratory of RomaTre University, in a 17 m long, 1 m high and 0.8 m wide flume of rectangular cross section. Scouring tests were carried out in a 0.3 m high, 0.8 m wide and $L = 3$ m long sediment recess section, made by raising artificially the flume bed. An uniformly graded sand characterized by $d_{50} = 0.7$ mm and a density $\rho_s = 2650\ kg/m^3$, was used to fill the sediment recess section in order to have a mobile bed. All the scouring tests were conducted in clear water scour conditions. A trapezoidal drop of height $D_p = 0.15$ m followed by a rigid apron of length $L_p = 0.5$ m was positioned upstream of the test section, as it is shown in Figure 1. A control gate, positioned at the end of the flume, was used to change the downstream water depth. The water level in the flume was measured using a resistive point gage of accuracy ± 0.10 mm. The water discharge at the inlet was controlled by an inlet valve and measured by an electromagnetic flowmeter. For a detailed description of the experimental apparatus see Adduce (2004).

At the end of the experiment, velocity measurements were performed by an Ultrasonic Doppler Velocity Profiler (UDVP). The Ultrasonic Doppler Velocity Profiler, first developed for medical studies on blood flow Willemetz (1990), is today used to perform measurements both in transparent (Ito et al., 2001; Hurther, 2001; Rolland, 1994) and optically opaque fluids and high temperature fluids (Eckert & Gerberth, 2002), giving spatiotemporal velocity information. The UDVP consists of a piezoelectric probe, which works both as emitter and receiver of a signal consisting of ultrasonic bursts traveling across the fluid and backscattered by the targets, i.e. small air bubbles or particles, moving with the flow. For a detailed description of the UDVP technique, see Willemetz (1990, 2001). The UDVP probe measures profiles of the velocity component parallel to the probe axis. In order to measure the profiles of the horizontal and the vertical velocity components three probes with the same emitting frequency were used, following the technique showed in Longo et al. (2001) and Adduce (2004). Two probes were tilted with respect to the vertical direction of an angle of 20°, while a third probe was positioned parallel to the vertical direction. Velocity measurements were performed along the flume centerline.

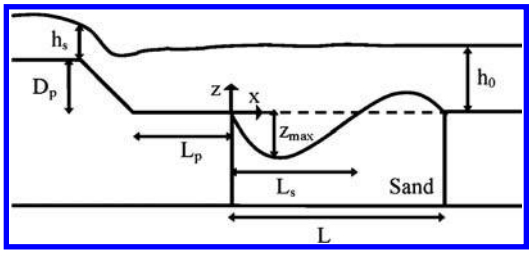


Figure 1. Definition sketch of the test section in the x-z plane.

3 LABORATORY EXPERIMENTS

Two series of laboratory experiments were performed with both a mobile (scouring experiments) and a flat rigid bed downstream of the drop. The discharge and the downstream water depth were varied and two kinds of jet flow were observed developing downstream of the drop: a surface wave jet and an oscillating jet. The oscillating jet is an unstable flow configuration. For a detailed description of the different kind of jet flow see Bukreev (2001) and Adduce (2004).

Before starting each scouring experiment, the level of the mobile sand bed, positioned in the sediment trap, was set to the same height of the fixed bed. In order to avoid the undesirable scour of the sediment bed, the control gate was completely closed and the flume slowly filled with the water pumped from the laboratory water reservoir by an auxiliary pumping device. The water discharge was then slowly increased, starting from zero, and set to the desired experimental value, paying attention to avoid any movement of the sand bed. The experiment started when the downstream water depth was set to the desired experimental value by opening the control gate. The water discharge was kept constant for the entire duration of the experiment.

Two series of scouring experiments were run, as it shown in Table 1: series U (surface wave jet) and series T (oscillating jet). We stopped the experiments when the measured maximum scour depth, plotted versus logarithm of time was sensibly constant (Adduce et al.,

Table 1. Experimental parameters for the experiments with a scoured bed: Q, discharge; h_s, water depth over the drop; h_0, downstream water depth over the rigid bottom; z_{max}, maximum scour depth.

Run	Q (l/s)	h_s (cm)	h_0 (cm)	z_{max} (cm)
T1	30.00	4.20	18.57	4.0
T2	34.04	4.45	18.86	5.6
T3	38.64	4.80	19.34	10.8
U1	31.01	4.80	19.88	5.1
U2	33.10	5.00	20.36	5.5
U3	37.40	5.20	20.78	6.2

Copyright © 2006 Taylor & Francis Group plc, London, UK

Table 2. Experimental parameters for the experiments with a rigid flat bed: Q, discharge; h_s, water depth over the drop; h_0, downstream water depth over the rigid bottom.

Run	Q (l/s)	h_s (cm)	h_0 (cm)	z_{max} (cm)
T1FB	30.00	4.20	18.57	–
T2FB	34.04	4.45	18.86	–
T3FB	38.64	4.80	19.34	–
U1FB	31.01	4.80	19.88	–
U2FB	33.10	5.00	20.36	–
U3FB	37.40	5.20	20.78	–

2004, Adduce, 2004). For the present experiments the maximum scour depth did not increase with the logarithm of time after about 6 hours, as a consequence the duration of scouring experiments was set to 10 hours. For a detailed description of the scouring process due to different kinds of jets see Adduce (2004).

The considered values of the experimental parameters: water discharge (Q), water depth over the drop (h_s), water depth downstream of the sediment trap (h_0) and maximum scour depth measured along the flume centerline (z_{max}), are shown in Table 1.

The series U and T were repeated with the same hydraulics parameters, but with a flat rigid bed, in order to investigate the influence of the bed geometry on the jet stability. The experimental parameters used for the experiments performed with a flat rigid bed are shown in Table 2.

Figure 2a-c shows the comparison between the scoured bed, measured at the end of the run and the theoretical scoured bed used in the mathematical model and which will be defined in the following of the paper.

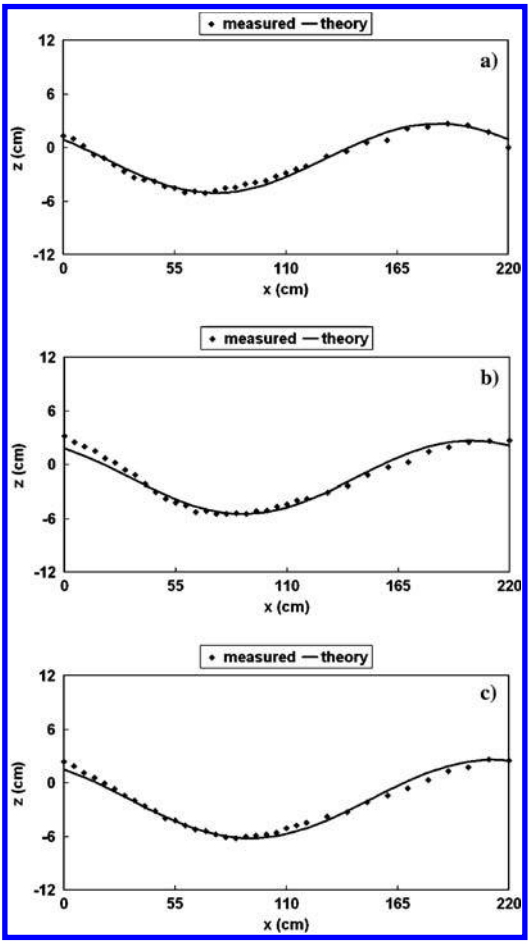


Figure 2. Comparison between measured and theoretical scour profiles: a) Run U1; b) Run U2; c) Run U3.

4 STABILITY ANALYSIS OF A SURFACE WAVE JET

The stability analysis is performed starting from the motion equations considered in the streamline centered s-n system of reference (Rouse, 1938). The quantities required for the description of the phenomenon are defined in Figure 3a. Moreover we assume that the considered motion condition occurs in the plane s-n. Let $\boldsymbol{V}$ be the velocity vector, defined as $\boldsymbol{V} = V(s,n)\boldsymbol{e}_s$, being V the modulus, $\boldsymbol{e}_s$ the unit vector tangent to the instantaneous streamline, s the coordinate on it and n the coordinate along the direction normal to the instantaneous streamline.

The equations of motion are:

$$V\frac{\partial V}{\partial s} = -\frac{1}{\rho}\frac{\partial p}{\partial s} - g\frac{\partial z}{\partial s} - \frac{1}{\rho}\frac{\partial \tau}{\partial s} \tag{1}$$

$$\frac{V^2}{R} = -g\frac{\partial}{\partial n}\left(z + \frac{p}{\rho g}\right) \tag{2}$$

where R is the radius of curvature of the instantaneous streamline. The term $(1/\rho)\partial\tau/\partial s$ accounts for head losses.

As a consequence, equation (1) gives the modified Bernoulli equation

$$z + \frac{p}{\rho g} + \frac{V^2}{2g} + \frac{\tau}{\rho g} = const \tag{3}$$

Inserting equation (3) in (2), the following equation for the determination of V is obtained

$$\frac{V^2}{R} = V\frac{\partial V}{\partial n} + \frac{1}{\rho}\frac{\partial \tau}{\partial n} \tag{4}$$

which is the same obtained by Montes and Chanson (1998), but the term $(1/\rho)\partial\tau/\partial n$, which accounts for the variation of the tangential stress along the n coordinate.

Copyright © 2006 Taylor & Francis Group plc, London, UK

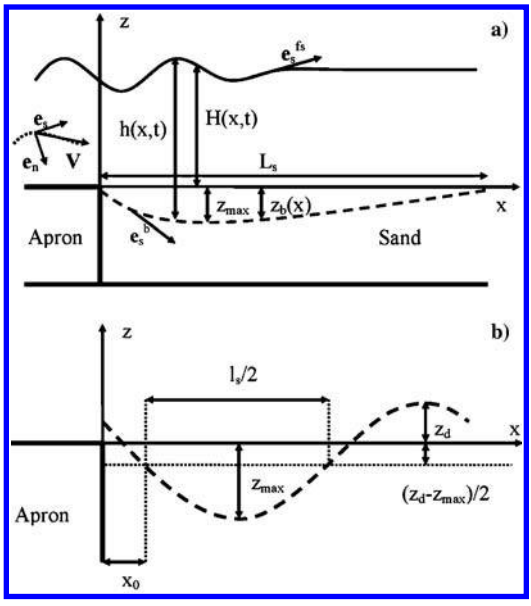


Figure 3. Definition sketch for the mathematical model.

Now, adopting the geometrical hypothesis of Montes and Chanson (1998), introducing the dimensionless variable η, defined as:

$$\eta = \frac{z - z_b(x)}{h(x,t)} \tag{5}$$

and expressing the geometrical quantities as known functions of the respective bottom and free surface quantities, equation (4) becomes:

$$\left[a_1\eta^k + a_2(1-\eta)^k\right]V^2 + V\frac{dV}{d\eta} + \frac{1}{\rho}\frac{d\tau}{d\eta} = 0 \tag{6}$$

being k a positive constant of order unity (Montes and Chanson, 1998). The coefficients appearing in equation (6) account for the curvature of the streamlines and are defined as:

$$a_1 = -\frac{hH''}{\left[1+(H')^2\right]}, a_2 = -\frac{hz_b''}{1+(z_b')^2} \tag{7}$$

Where

$$H(x,t) = z_b(x) + h(x,t) \tag{8}$$

and

$$H' = \frac{\partial H}{\partial x},\ z_b' = \frac{dz_b}{dx},\ H'' = \frac{\partial^2 H}{\partial x^2},\ z_b'' = \frac{d^2 z_b}{dx^2} \tag{9}$$

In order to obtain velocity profiles from equation (6) it is necessary to describe the behavior of the stress along the coordinate η. In this work it is assumed that inside of the region where the flow is expanding (upstream of the abscissa of maximum scour depth x_{sd}) the term which accounts for the curvature of the streamlines is not negligible with respect to the other two, while inside of the region where the flow is accelerating (downstream of the abscissa of maximum scour depth), the term which accounts for the curvature of the streamlines in equation (6) is less important than the other two terms. As a consequence equation (6) assumes the following different expressions, respectively upstream and downstream of the abscissa of maximum scour depth:

$$\begin{cases} \left[a_1\eta^k + a_2(1-\eta)^k\right]V^2 + V\dfrac{dV}{d\eta} + \dfrac{1}{\rho}k\left[\tau_{fs}\eta^{k-1} + \tau_b(1-\eta)^{k-1}\right] = 0 \quad (x \le x_{sd}) \\ V\dfrac{dV}{d\eta} + \dfrac{d}{d\eta}\left\{\left(kh\eta\sum_i\left[-\dfrac{(-1)^i}{i!}\left(\dfrac{hu_*}{\nu A}\eta\right)^i\right]\right)^2\dfrac{1}{h}\dfrac{dV}{d\eta} + \nu\right\}\dfrac{1}{h}\dfrac{dV}{d\eta} = 0 \quad (x > x_{sd}) \end{cases} \tag{10}$$

For $x \le x_{sd}$ the following law is adopted for the stress

$$\tau\ \tau = \tau_{fs}\eta^k + \tau_b(1-\eta)^k \tag{11}$$

being τ_{fs}, τ_b the tangential stresses respectively on the free surface and on the bottom. The former can be neglected, while the latter can be expressed as:

$$\tau_b = \rho u_*^2 = \rho g\frac{U^2 n_m^2}{h^{1/3}} \tag{12}$$

being U the depth averaged velocity and n_m the Manning's coefficient.

For $x \ge x_{sd}$ the tangential stress is described by means of an eddy viscosity model, due to the fact that the motion tends to become more regular, based on the mixing length hypothesis (Rodi, 2000; Nezu and Nakagawa, 1993):

$$\tau = \frac{\rho}{h}\left[l_m^2\frac{dV}{d\eta} + \nu\right]\frac{dV}{d\eta} \tag{13}$$

It is assumed that $dV/d\eta$ is always positive for $x \ge x_{sd}$ and that l_m the mixing length is given by the following polynomial approximation of the Van Driest expression (Rodi, 2000; Nezu and Nakagawa, 1993):

$$l_m = kh\eta\sum_i\left[-\frac{(-1)^i}{i!}\left(\frac{hu_*}{\nu A}\eta\right)^i\right] \tag{14}$$

where $k = 0.43$ is the Von Karman constant, ν the kinematic viscosity of the water, A a damping factor, which

Copyright © 2006 Taylor & Francis Group plc, London, UK

for open channel flows is equal to 26 (Nezu and Rodi, 1986), and

$$u_* = n_m \sqrt{\frac{g}{h^{\frac{1}{3}}}} U \tag{15}$$

the friction velocity.

The general solution of equations (10) can be expressed as a power series

$$V(x,\eta) = U(x) f(\eta) = U(x) \sum_i \alpha_i \eta^i \tag{16}$$

whose coefficients α_i $(i = 2, 3, \ldots)$ are defined by means of recurrence relations, as functions of the coefficients α_0, α_1, obtained substituting the solution (16) in the differential equations (10) and equating terms with the same power of η. Two boundary conditions are necessary in order to define the coefficients α_0, α_1 as functions of the flow characteristics. Such boundary conditions are the following:

$$\begin{cases} U = \int_0^1 V d\eta \Rightarrow \int_0^1 f d\eta = \sum_{i=0}^{N} \frac{\alpha_i}{(i+1)} = 1 \\ \left.\frac{dV}{d\eta}\right|_{\eta=\frac{d_{50}}{h}} = h \frac{u_*}{\kappa d_{50}} \end{cases} \tag{17}$$

The derivation of the first boundary condition is straightforward. The second boundary condition is derived imposing that the velocity profile has the same inclination of the logarithmic profile in correspondence of the bottom: i.e. for $\eta = h/d_{50}$. Once the analytical expression (16) of V is completely determined, the expressions of the horizontal and vertical velocity components as well as the pressure can be obtained. In particular this latter is given by:

$$p = \rho g h (1-\eta) + \rho h \int_\eta^1 \left(a_2 (1-\xi)^k + a_1 \xi^k \right) V^2 d\xi \tag{18}$$

where the hydrostatic and dynamic pressure contributions are distinguishable.

In Figure 4a-d a comparison between the measured and predicted velocity profiles of the horizontal velocity component at four different locations, $x = 5$ cm (Figure 4a), $x = 65$ cm (Figure 4b), $x = 105$ cm (Figure 4c) and $x = 165$ cm (Figure 4d), respectively, for test U1 is shown. The agreement between measured and predicted velocity profiles is good, showing the validity of the assumed hypothesis.

Velocity components and pressure (18) depend on $z_b(x)$, $h(x,t)$, $U(x,t)$, $H(x,t) = z_b(x) + h(x,t)$, as well as on the Manning's coefficient. In this work $z_b(x)$ is obtained by interpolating experimental data, while

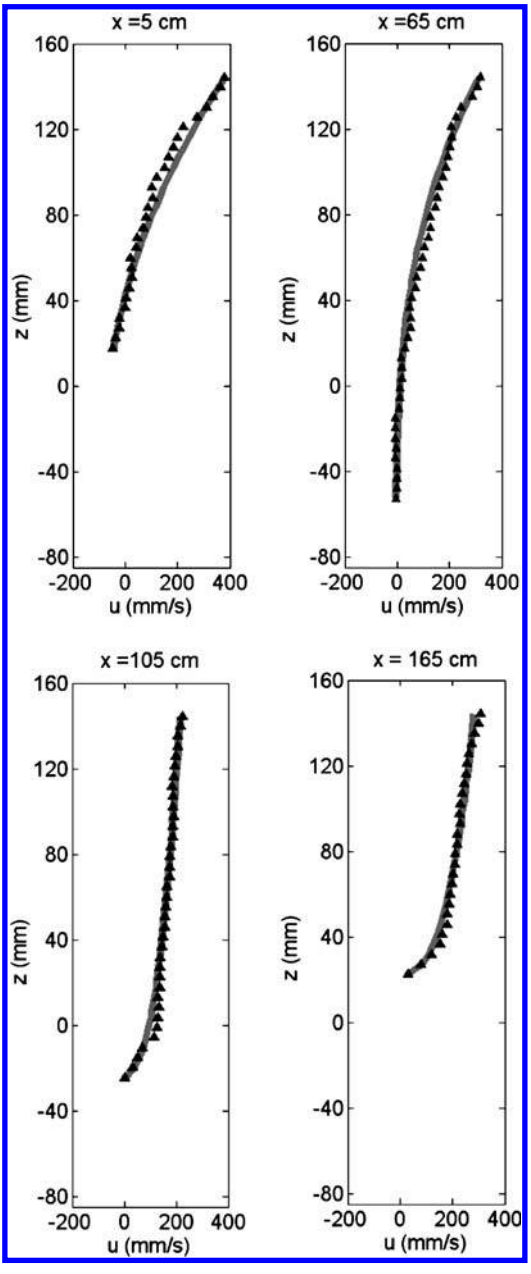


Figure 4. Comparison between measured and predicted profiles of the u velocity component at four different locations for test U1.

the Manning's coefficient is calculated as (Marchi and Rubatta, 1980):

$$n_m = \frac{(2d_{50})^{\frac{1}{6}}}{24\sqrt{g}} \tag{19}$$

Copyright © 2006 Taylor & Francis Group plc, London, UK

At last evolution equations for $h(x,t)$, $U(x,t)$ can be obtained depth –averaging the mass and momentum balance equation. The result is:

$$\begin{cases} \dfrac{\partial h}{\partial t} + \dfrac{\partial Uh}{\partial x} = 0 \\ \dfrac{\partial U}{\partial t} + g\dfrac{\partial}{\partial x}\displaystyle\int_0^1 \left(\frac{V^2}{2g} + h\eta + z_b + \frac{p}{\rho g} \right) d\eta = -g n_m^2 \frac{U|U|}{\Re^{4/3}} \end{cases} \quad (20)$$

where n_m, and $\Re$ are, respectively, the Manning's coefficient and the hydraulic radius, defined in the usual way for open channel flow with a mobile bed (Garde and Ranga Raju, 1977, Marchi and Rubatta, 1980). Equations (20) are the classic De Saint Venant equations for free surface flows, in which curvature effects connected to the free surface and bottom profiles have been accounted for. At last, the unknown functions $h(x,t)$ and $U(x,t)$ are defined as the sum of a base flow and an unsteady perturbation with a known dependency on time:

$$\begin{cases} h(x,t) = h_0(x) + h_1(x)e^{\gamma t} \\ U(x,t) = U_0(x) + U_1(x)e^{\gamma t} \end{cases} \quad (21)$$

It is supposed that the perturbations are small quantities with respect to those of the base flow. Then, after having substituted expressions (21) in equations (20), quadratic and higher order perturbation terms nonlinear terms are discarded. Imposing that the expressions (21) satisfy equations (20), a linear, homogeneous differential system is obtained for the evolution of the perturbation flow, given the base solution $h_0(x)$, $U_0(x)$. The parameter γ, which can be considered as an eigenvalue of such linear and homogeneous differential problem, gives information on the stability of the base solution: if the real part of γ is positive, perturbations imposed on the base solution will tend to destroy the base solution and then this latter is considered unstable. On the contrary, if the real part of γ is negative, perturbations imposed on the base solution will tend to decrease with time and the base solution is considered stable. Of course, such conclusions are considered valid in the framework of a linear stability analysis: i.e. they are valid in the early stage of the perturbations.

5 COMPARISON WITH LABORATORY MEASUREMENTS

Base flow is assumed to be known and given by the following interpolating expressions for $H_0(x)$, $z_b(x)$, obtained by laboratory measurements of free surface and bottom profiles:

$$H_0(x) = h_d + \eta \sin\left(\frac{2\pi x}{l_0} \right) \quad (22)$$

$$z_b(x) = \frac{z_d - |z_{\max}|}{2} - \left(\frac{z_d + |z_{\max}|}{2} \right) \sin\left(\frac{2\pi(x - x_0)}{l_s} \right) \quad (23)$$

l_0 and η are respectively the measured wavelength and amplitude of the free surface undulations, defined respectively as the distance between the first two crests of the free surface and half the distance between first crest and first throat over the eroded bed. With reference to Figure 3b, z_{max} is the maximum scour depth, z_d is the dune height, x_0 is the abscissa where the scour depth is equal to

$$z_b(x_0) = \frac{z_d - |z_{\max}|}{2} \quad (24)$$

and l_s is the scour hole wavelength defined in Figure 3b. With such a definition of the bottom wavelength, the expression (23) best fits the scour profile, as it is possible to see in Figure 2a-c. As a consequence the mean velocity profile $U_0(x)$ is given by:

$$U_0(x) = \frac{Q}{b h_0(x)} = \frac{Q}{b[H_0(x) - z_b(x)]} \quad (25)$$

Q being the discharge, considered constant with respect to time.

The experimental configurations considered, both for a flat and a scoured bed, are shown in Table 3, where Fr_d is the downstream Froude number, defined as:

$$Fr_d = \frac{Q}{b h_0 \sqrt{g h_0}} \quad (26)$$

Table 3. Experimental configurations: Fr_d, downstream Froude number; l_0, measured wavelength of the free surface undulations; η_0, measured amplitude of the free surface undulations; l_s, scour wavelength.

Run	Fr_d	l_0 (m)	η_0 (m)	l_s (m)	Stability
T1	0.15	0.12	0.0045	2.2	Unstable
T2	0.17	0.15	0.0030	2.0	Unstable
T3	0.18	0.18	0.0020	2.8	Unstable
U1	0.14	0.35	0.0030	2.2	Stable
U2	0.15	0.25	0.0040	2.3	Stable
U3	0.16	0.35	0.0035	2.9	Stable
T1FB	0.15	0.20	0.0029	–	Stable
T2FB	0.17	0.25	0.0034	–	Stable
T3FB	0.18	0.20	0.0031	–	Stable
U1FB	0.14	0.25	0.0054	–	Stable
U2FB	0.15	0.25	0.0144	–	Stable
U3FB	0.16	0.25	0.0139	–	Stable

Copyright © 2006 Taylor & Francis Group plc, London, UK

The stability of the experimental configurations can be performed by adopting the following expression for the perturbation flow:

$$\begin{cases} h_1(x) = a\,Cos\left(\frac{2\pi}{l_0}x\right) + b\,Sin\left(\frac{2\pi}{l_0}x\right) \\ U_1(x) = c\,Cos\left(\frac{2\pi}{l_0}x\right) + d\,Sin\left(\frac{2\pi}{l_0}x\right) \end{cases} \quad (27)$$

by substituting them in the correspondent linear, homogeneous differential system and by averaging this latter with respect to x. At last, imposing a suitable solvability condition, an algebraic, fourth order equation is obtained for γ. The real part of this latter gives indications on the stability of the base flow.

Figure 5a-f and Figure 6a-f, in which the horizontal axis represents the wavelengths of the surface wave jet, the vertical axis the downstream Froude number, show the results of the stability analysis. Both in Figure 5a-f and Figure 6a-f lines separate the unstable from the stable region: the stability region is on the right of the lines. The six stable and unstable experimental configurations are represented in the diagrams by diamonds.

Horizontal lines limit the area over which it is physically possible to have a hydraulic jump for the experimental conditions considered. So the stability diagram is divided into three regions: the stable region on the right, the unstable region on the left and the no hydraulic jump region in the lower part.

The presence of a scoured bed weakens the surface wave jet stability properties. As a matter of fact, in Figure 6a-f, relative to the comparison of the stability diagrams with flat bottom (Figure 6a-c) and with scoured bed (Figure 6d-f), the stability characteristics of the oscillating jet are modified passing from the flat bed to the scoured bed both because the stability areas increase and because the characteristics of the free surface undulations (amplitude and wavelength) change, i.e. the experimental point changes its position. So the transitional jet becomes stable if the bed is flat.

The comparison of the free surface undulations amplitudes of tests U1-U3 and U1FB-U3FB, shown in Table 3, highlight how the presence of a scoured bed increases the dissipation. The increased dissipation is due to the expansion of the flow in presence of a scoured bed.

In conclusion, the stability analysis of the modified De Saint-Venant equations (20) gave good results, because, starting from the experimental values of discharge, downstream water depth, free surface undulations amplitude, length and maximum scour depth, it was able to highlight stability and instability areas to which experimental points belong.

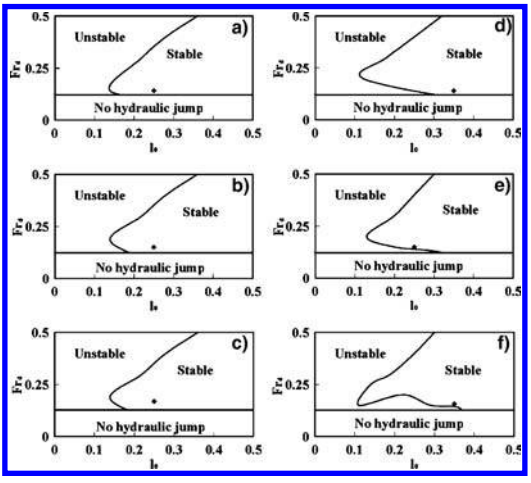


Figure 5. Stability diagrams for tests: U1FB (a), U2FB (b), U3FB (c), U1 (d), U2 (e), U3 (f).

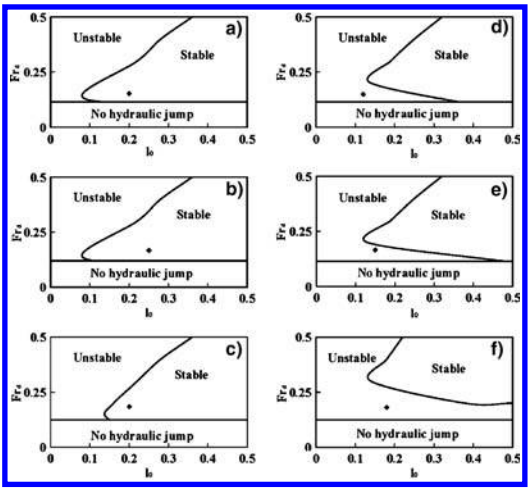


Figure 6. Stability diagrams for tests: T1FB (a), T2FB (b), T3FB (c), T1 (d), T2 (e), T3 (f).

6 CONCLUSIONS

The dependence of turbulent jets stability on bed geometry is investigated by both a laboratory and a theoretical study. Jet flow was produced by the interaction of the main flow and a drop, followed by a rigid apron. Two series of laboratory experiments were performed with both a mobile and a flat rigid bed downstream of the drop. The discharge and the downstream water depth were varied and two kinds of jet flow were observed: a surface wave jet and an oscillating jet. The oscillating jet is an unstable flow configuration. Both velocity and free surface flow measurements

Copyright © 2006 Taylor & Francis Group plc, London, UK

were performed. Starting from those laboratory measurements, a mathematical model, which investigates the stability of the surface wave jet both over a flat and a scoured bed, was developed. A mathematical model, derived starting from the momentum equation, in the s, n coordinate system, permitted to obtain analytical expressions for the horizontal and vertical velocity component and for the pressure. The stability analysis of the surface wave jet both on a flat and a scoured bed, performed by a modified version of De Saint-Venant equations allows the classification of the experimental configuration under consideration. The mathematical model was able to reproduce velocity profiles in different location along the scour, revealing the validity of the assumptions made. The comparison between the analysis of the surface wave flow on flat and scoured bed highlighted the influence of the scoured bed on the stability of the surface wave flow. The scoured bed weakens the stability properties of the surface wave flow, so that stable configurations with a flat bed are unstable with a scoured bed. Moreover, the presence of the scour increases the dissipation: as a matter of fact larger surface wave amplitudes are found with a flat bed than a scoured bed. This fact is easily explained by the expansion of the flow occurring with the scoured bed.

REFERENCES

Adduce, C. 2004. *Local scour downstream of a turbulent jet*. Ph.D. Thesis, University of Rome "Roma Tre", Rome, Italy, 20 October 2004.

Adduce, C. and Mele, P. 2004. Local scour by submerged turbulent jets, *International Conference on Hydroscience and Engineering 2004*, Brisbane, Australia, May 31–June 3.

Bukreev, V.I. 2001. Undular jump in open-channel flow over a sill, *J. App. Mech. Tech. Phy.*, 42(4), 596–602.

Chatterjee, S.S. Ghosh, S.N. & Chatterjee, M. 1994. Local scour due to submerged horizontal jet. *Journal of Hydraulic Engineering*, 120 (8), 973–992.

Dey, S. & Westrich, B. 2003. Hydraulics of submerged jet subject to change in cohesive bed geometry. *Journal of hydraulic engineering, ASCE*, 129 (1), 44–53.

Farhoudi, J. & Smith, K.V.H. 1985. Local scour profiles downstream of hydraulic jump. *Journal of Hydraulic Research*, 23 (4), 343–358.

Fritz, H.M. & Hager, W.H. 1998. Hydraulics of embankment weirs. *Journal of Hydraulic Engineering, ASCE*, 124(9), 963–971.

Garde, R.J., and Ranga Raju, K.G. 1977. *Mechanics of sediment transport and alluvial stream problems*. Wiley, New York, US.

Gijs J., and Hoffmans, J.C.M. 1998. Jet Scour in equilibrium phase, *J. Hydraul. Eng*., 124(4), 430–437.

Hager, W.H. 1992. *Energy dissipators and hydraulic jumps*. Dordrecht: Kluwer Academic.

Hassan, N.M.K.N. & Narayanan, R. 1985. Local Scour Downstream of an Apron. *Journal of Hydraulic Engineering, ASCE*, 111 (11), 1371–1385.

Hurther D. 2001. 3-D Acoustic Doppler velocimetry and turbulence in open-channel flow, Ph.D. Thesis, EPFL, Lausanne, Switzerland.

Ito T., Tsuji, Y. Nakamura, H. Kukita. Y. 2001. Application of ultrasonic velocity profile meter to vortex shedding and empirical eigenfunctional analysis, *Experiments in Fluids*, 31, 324–335.

Kurniawan, A. Altinakar, M.S. & Graf, W. H. 2001. Flow pattern of an eroding jet, *International Association for Hydraulics and Research Congress*; *Proc. intern. symp., Beijing*.

Longo, S., Losada, I.J. Petti, M. Pasotti, N. & J.L. Lara (2001), Measurements of breaking waves and bores through a USD velocity profiler, Technical Report UPR/UCa_01_2001, University of Parma, Italy and Ocean & Coastal Research Group Laboratory, University of Cantabria, Spain.

Marchi, E. & Rubatta, A. 1980. *Meccanica dei fluidi. Principile applicazioni idrauliche*, UTET, Bologna, Italy.

Montes, J.S. & Chanson, H. 1998. Characteristics of undular hydraulic jumps: Experiments and analysis, *J. Hydr. Eng.* 124(2),192–205.

Nezu. I. & Nakagawa, H. 1993. *Turbulence in open-channel flow,* IAHR-AIRH Monograph Series, A.A. Balkema Publishers, Rotterdam, The Netherlands.

Nezu, I. & Rodi, W. 1986. Open-channel flow measurements with a laser Doppler anemometer, *Journal of Hydraulic Engineering*, ASCE, 112, 335–355.

Ohtsu, I. & Yasuda, Y. 1991a. Hydraulic jump in sloping channels, *Journal of Hydraulic Engineering*, 117(7), 905–921.

Ohtsu, I. & Yasuda, Y. 1991b. Transition from supercritical to subcritical flow at an abrupt drop, *Journal of Hydraulic Research*, 29(3), 309–328.

Rodi, W. 2000. *Turbulence models and their application in Hydraulics,* IAHR-AIRH Monograph Series, A.A. Balkema Publishers, Rotterdam, The Netherlands.

Rolland, T. 1994. *Development d'une instrumentation Doppler ultrasonore adaptée à l'étude hydraulique de la turbulence dans les canaux*, PhD thesis, EPFL, Lausanne, Switzerland.

Rouse, H. 1938. *Fluid Mechanics for Hydraulic Engineering*, McGraw Hill, New York, US.

Schoklitsch, A. (1932), Kolkbildung unter Überfallstrahlen, Die Wasserwirtschaft, 24, 341–343.

Willemetz, J.C. 1990. *Etude Quantitative de l'Hémodynamique de Vaisseaux Profonds par Echographie Doppler Ultrasonore*, PhD thesis, EPFL, Lausanne, Switzerland.

Willemetz J.C. 2001. DOP 2000 Users manual.

Wu, S. & Rajaratnam, N. 1998. Impinging jet and surface flow regimes at drop. *Journal of Hydraulic Research*, 36(1), 69–74.

Copyright © 2006 Taylor & Francis Group plc, London, UK

Investigation of the velocity and pressure fluctuations distributions inside the turbulent horseshoe vortex system around a circular bridge pier

G. Kirkil, G. Constantinescu & R. Ettema
Civil & Environmental Engineering Department, IIHR-Hydroscience & Engineering The University of Iowa, M. Stanley Hydraulics Laboratory, Iowa City, IA

ABSTRACT: Large eddy simulation with a dynamic sub-grid scale model is used to study the spatio-temporal structure of the horseshoe vortex (HV) system around a bridge pier of circular section in a shallow channel with a flat bed. It is found that the structure of the turbulent HV system varies considerably in space and time, though, typically, a relatively stable, necklace like vortical structure (primary vortex) is present around the upstream face of the cylinder and oscillates randomly. The simulation captures the presence of bimodal aperiodic chaotic oscillations inside the HV system region, as well as the sharp increase in the resolved velocity fluctuations and pressure fluctuations observed in previous experimental investigations of high Reynolds number junction flows. It is observed that in the bimodal region the histogram of the velocity fluctuations displays a double-peak shape for all the velocity components except the one along the core of the primary HV.

1 INTRODUCTION

Natural river channels are subject to continuous change in geometry due to the interaction between the flow and the erodible boundaries. In particular, the study of scour associated phenomena at bridge piers and abutments (Melville, 1997) is a problem of paramount importance for bridge designers due to the fact that scouring of the river bed takes place near these structures. As a consequence, the resulting weakening of the bridge foundation during flood events is the main cause of bridge failure. Despite a great deal of studies (see for instance Melville, 1997) which focused mainly in predicting the dimensions of the scour hole and maximum scour depth, a clear understanding of the mechanisms that govern the interaction of the approach flow with the bridge abutment and the river bed is still lacking. We think that a better understanding of the flow structure in the scour region and, more generally, of the flow physics of junction flows, will be useful toward developing new methods to predict the scour around bridge piers.

A wide range of turbulent scales are present around the bridge pier and control the transport process. Regardless of the exact form of the pier, one the main mechanisms (Dargahi, 1989, Simpson, 2001) that drives the formation and future evolution of the scour hole is the formation of a necklace like vortical structure, commonly known as the horseshoe vortex (HV) system. Thus, to understand the scour mechanism, one has first to be able to qualitatively describe the structure of the coherent vortices part of the HV system in the different flow regimes and to quantitatively characterize its effect on the flow and the river bed, near the pier base. In this paper we are interested in studying the HV system at the start of the scouring process (flat bed conditions) in the case of a pier with a circular section. A similar investigation of the flow under equilibrium scour conditions was described in Kirkil et al. (2005).

The separation of the upstream boundary layer and the formation of a separation (stagnation) line on the bottom surface around the pier are a consequence of the adverse pressure gradients induced by the presence of the pier. These streamwise adverse pressure gradients are also the main cause of the formation of necklace vortices around the upstream part of the pier base. These horseshoe vortices are a consequence of the reorganization of the boundary-layer vorticity downstream of the separation line. The primary HV has the same sense of rotation as the vorticity in the upstream boundary layer. The HV will stretch around the pier and fold around the upstream part of it, very close to the bottom, partly because of the spanwise pressure gradients. Consequently, the sides of the vortex lines will become oriented in the streamwise direction, with the vorticity being of opposite sign in the two sides (legs). The main necklace vortices entrain higher velocity fluid from the outer layer along the upstream face of the pier toward the bed in what is generally called the downflow. As a result of the interactions between the downflow, the bed and the HV

Copyright © 2006 Taylor & Francis Group plc, London, UK

system, the drag around the upstream side of the pier is increased. In the case of an incoming turbulent flow, the location, size and intensity of the HV eddies are observed to be highly varying in time, to produce high turbulence and pressure fluctuations (Simpson, 2001, Dargahi, 1989) and to induce high bed shear stresses.

Recent experimental investigations (Devenport & Simpson, 1990, Rife et al., 1992, Chen et al., 2000, Wei et al., 2001) using Particle Image Velocimetry (PIV) and Laser Doppler Velocimetry (LDV) techniques have increased considerably our understanding of the intricate structure of the horseshoe vortex system, especially in the symmetry plane. Dargahi (1989) used hydrogen-bubble techniques and hot film anemometry to investigate the turbulent HV system in front of a circular bridge pier. He observed that vortices were shed from the separation region, similar to the case of a laminar HV system. The turbulent HV system was found to contain, at most times, several primary vortices rotating in the same direction and a number of bed-attached vortices rotating in opposite direction. Measurements of the mean flow-fields around a surface mounted cylinder in an open channel with a flat bed ($Re_D \sim 10^5$) were reported by Graf & Yulistiyanto (1998). The mean components of the velocity and turbulent stresses were measured using an Accoustic Doppler Current Profiler (ADCP), both upstream and downstream the cylinder. The mean extent of the HV region was estimated, but no attempts were done to visualize the coherent structures inside the HV system or downstream the cylinder. Chen et al. (2000) investigated the flow past cylinders of different shapes at $Re_D = 32{,}000$ and observed that, in average, the turbulent HV system is characterized by the formation of a large primary vortex that oscillates chaotically around a mean position.

One of the most interesting phenomena associated with the turbulent HV system is the presence of bimodal aperiodic chaotic oscillations which are one of the main causes of the observed sharp increase of the velocity fluctuations, turbulence production, Reynolds stresses and pressure fluctuations inside the HV region (Devenport & Simpson, 1990, for a Rood wing, and Olcmen & Simpson, 1994, for the case of an elliptic nose NACA tail wing). This phenomenon which consists of the flow in the HV region switching between two modes at times intervals whose probability density function is likely Markovian was observed first by Devenport & Simpson (1990) in the study of the flow past a surface mounted wing shaped cylindrical body at very high Reynolds numbers ($Re_D \sim 10^6$, where D corresponds to the maximum thickness of the wing). In the bimodal region, the histogram of velocity fluctuations was observed to display a double-peak shape. The switching was observed to take place at a relatively low frequency compared to the oscillation (passage frequency) of the vortices inside the HV system. In a related study of the flow past the Rood wing, Rife et al. (1992) measured the mean frequency (f) of the velocity fluctuations associated with the bimodal oscillations at around St $(= fD/U) = 0.05$, where the maximum width of the wing was used as the length scale (D) and U is the mean velocity. This suggests that the low-frequency oscillations are not produced by the coherent structures in the HV region, but rather due to fluctuations in the momentum in the outer part of the boundary layer that are recirculated as they impinge on the wing nose. It is however believed that the bimodal aperiodic large-scale horseshoe vortex phenomenon is a common feature of junction flows in the turbulent regime, provided that the surface mounted body is blunt enough.

Despite the new information obtained from recent experimental studies, a detailed quantitative description of the HV system around the base of a circular pier is still not available. Eddy-resolving numerical simulations like Large Eddy Simulation (LES) which obtain the whole three-dimensional (3D) fields as part of the time-accurate solution have the advantage of allowing an in-depth investigation of the HV system at an arbitrary number of polar planes or in other relevant sections, at no additional cost. They also allow direct estimation of the spatio-temporal distribution of the bed-shear stress and pressure fluctuations in its immediate vicinity. As pointed out by Simpson (2001) in his review of junction flows, LES appear to be the best suited numerical technique to capture the details of the HV dynamics, due to the large range of energetic scales and associated frequencies that are present in the HV region. It is very doubtful that unsteady RANS methods, even with second order closures, will be able to accurately capture the flow physics in the bimodal flow region.

2 NUMERICAL METHOD AND SIMULATION SETUP

A recently developed massively parallel LES flow solver (Mahesh et al., 2004) is used in the present work. The algorithm, that was developed for unstructured grids, is non-dissipative (central-differences schemes are used to discretize all operators in the governing equations, including the convective terms and no filtering of the resolved velocity field is used), yet robust at high Reynolds numbers on highly skewed meshes. Discrete energy conservation was found essential to ensure this behavior. The dynamic Smagorinsky model is used to account for unresolved turbulence effects.

Figure 1 shows a sketch of the computational domain with the convention used to identify the vertical sections cutting at a certain polar angle ϕ relative to the free stream velocity. The y axis is perpendicular to the channel bed. The physical domain extends

Copyright © 2006 Taylor & Francis Group plc, London, UK

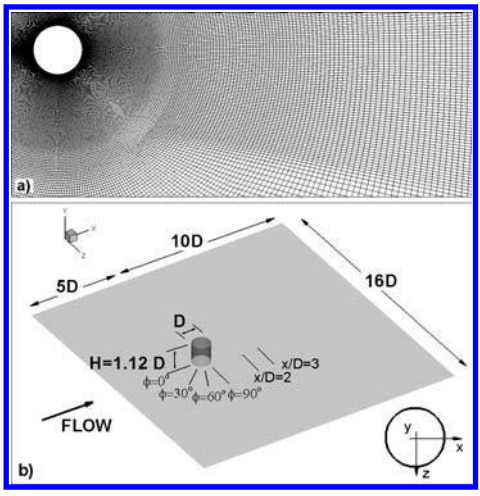


Figure 1. Computational domain; a) detail view of the mesh in a horizontal plane; b) sketch showing main dimensions of the computational domain.

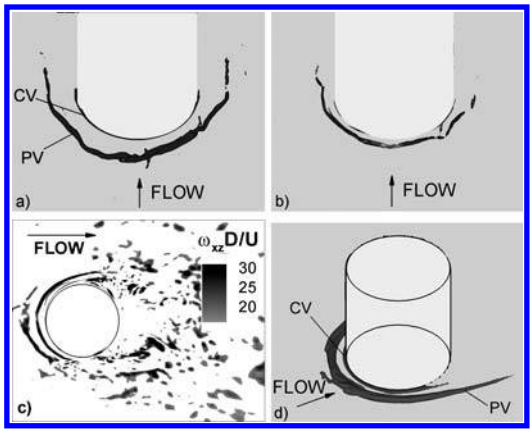


Figure 2. Instantaneous and mean structure of the horseshoe vortex system; a) and b) visualizations of the instantaneous structure using Q-isosurfaces at two different time instants; c) instantaneous in-plane vorticity contours in y/D = 0.04 plane; d) visualization of the primary mean horseshoe vortex and corner vortex using Q-isosurfaces.

5D upstream of the cylinder and 10D downstream, where the length scale D is the cylinder diameter. The depth of the channel, H, is constant and equal to 1.12D. The lateral extent of the domain is 16D. The cylinder Reynolds number is $Re_D = UD/\nu = 16{,}000$, where U is the mean channel velocity and ν is the molecular viscosity. To enhance the generality of the results presented in the paper at a particular value of the Reynolds number, all the variables are nondimensionalized with the cylinder diameter, D, and the mean channel velocity, U. The inflow conditions, which contain realistic turbulence fluctuations, are obtained from a separate LES simulation in a periodic channel of identical section, at the same channel Reynolds number. The LES velocity fields are then fed in a time-accurate way through the inflow section. The grid density is varied throughout the domain such that a very dense mesh is generated in the HV region, in the detached shear layers and inside the turbulent wake. The unstructured mesh contains over 4 million cells distributed using a paving technique that allows maintaining a high quality of the mesh while varying substantially the mean size of the elements among the different regions. Near the solid surfaces, the first layer of cells is situated at about one wall unit, $\Delta y^+ (= \Delta y.u_\tau/\nu) = 1$, (the non-dimensional friction velocity u_τ/U is conservatively assumed to be equal to 0.04) from the solid surfaces. Typical computational cell dimensions in the HV region away from the walls and inside the detached shear layers are 4-20 wall units. A detail view of the free surface mesh around the cylinder is shown in Figure 1a. The time step was 0.002 D/U. The simulation was run on 24 processors of a Xeon PC Cluster with Myrinet.

3 RESULTS

The degree of intermittency of the HV eddies was found to be high and the overall structure of the HV system was observed to change significantly in time. However, at most times the presence of a large primary vortex (PV) that oscillates and changes his coherence randomly was observed. The simulation also captured the presence of several secondary coherent unsteady vortices, part of the HV system. For instance, the Q criterion is used in Figures 2a and 2b to educe the main coherent structures in the region around the base of the pier in two instantaneous solutions. The common feature of the results in Figures 2a and 2b is the presence of a relatively large necklace vortex (PV) along with a small corner vortex (CV) right at the junction between the cylinder and the bed. Though the PV is present in both frames, its position relative to the cylinder and extent in the polar direction is found to vary significantly. In Figure 2a, the PV covers the region defined by polar angles in the interval $-90° < \phi < 90°$, while in Figure 2b the PV is present only in the region $-90° < \phi < 45°$ and is located closer to the cylinder. More details about the instantaneous vortical content of the HV region is given by snapshots of the in-plane instantaneous vorticity $(\sqrt{\omega_x^2 + \omega_z^2})$ contours, plotted in a plane parallel to the bed situated at y/D = 0.04 (Figure 2c). At that particular instant of time, the PV is present in the region defined by $-90° < \phi < 70°$. Additionally, a secondary necklace structure is visible at negative polar angles upstream the PV. In fact, animations show that the HV region is populated by necklace like eddies whose extent in

Copyright © 2006 Taylor & Francis Group plc, London, UK

the polar direction is highly variable in time. Random formation and shedding of small necklace "new" vortices from the separation region is observed. Some of these vortices will merge with the primary vortex that is being stretched, and form a "new" primary vortex, others will loose their coherence rapidly. Some of them can move over the PV before merging with it or, in some cases, two secondary vortices may oscillate around each other and, eventually, merge together. The overall scenario observed for the evolution of the HV system in our simulation is very close to that observed by Kim et al. (1991) who studied the turbulent HV system in front of a wing shaped body (Rood wing) for $16{,}500 < \mathrm{Re_D} < 62{,}000$.

However, when the instantaneous flowfields are averaged, only the PV and CV structures are present. This is evident in Figure 2d where the vortical structure of the mean flow is visualized using Q isosurfaces. Q is defined as the second invariant of the velocity gradient tensor and regions of positive Q are considered as vortical regions (Jeong & Hussain, 1995). One should observe that the legs of the PV eddy educed using the Q criterion are not exactly parallel with the mean flow direction. An indication of the decay of the intensity of PV at high polar angles and then in the leg region is given by the fact that the PV has the largest cross section in the $\phi = 0°$ plane. The cross section is decaying with the increase in the absolute value of the polar angle.

To visualize the position of the mean HV system relative to the cylinder, one can also look at the distributions of the turbulent kinetic energy (tke) and pressure fluctuations in various polar planes along with the flow patterns shown by 2D streamlines. This was done in Figures 3a ($\phi = 0°$) and 3b ($\phi = 45°$) using the pressure fluctuations. The region characterized by high pressure fluctuations correlates well with the main vortex in the 2D streamline plot (compare Figures 3b and 3c). The 2D streamlines in Figure 3c also show the presence of a bottom attached vortex just upstream of the PV and of the corner cortex CV. This vortex was also observed to form in experimental visualizations of the flow in turbulent HV system around the circular pier (Dargahi, 1989).

Clearly the turbulence inside the HV region dominates the surrounding turbulence. The ratio between the largest pressure fluctuations inside this region and that of the surrounding flow is close to ten, in agreement with the experimental measurements of Devenport & Simpson (1990) obtained at a much higher Reynolds number. It is unlikely that the high tke and pressure fluctuations levels in the HV region are produced only by turbulence mixing. Related to the variation of the intensity of the PV as it wraps around the cylinder, a detailed analysis of the flow in different polar sections (similar to the two frames in Figure 3) confirmed that the intensity of the pressure

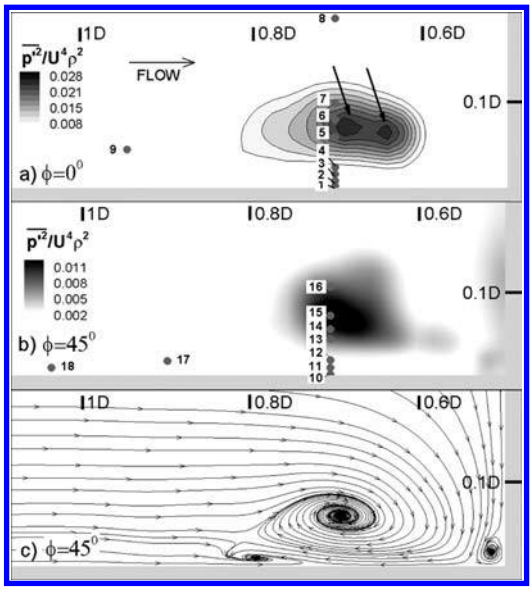


Figure 3. Visualization of the primary vortex in the mean flow; a) mean pressure fluctuations, $\phi = 0°$plane; b) mean pressure fluctuations, $\phi = 45°$plane; c) mean 2D streamlines, $\phi = 45°$ plane.

fluctuations and tke decays with the absolute value of the polar angle (see also distributions of vertical velocity fluctuations in Figure 13). Moreover, until $\phi = 70°$, the PV vortex gets closer to the cylinder (see also vertical velocity fluctuations distributions in Figure 3). The average position of PV is between $r/D = 0.6$ and $r/D = 0.8$, where the radius is measured from the center of the cylinder. Also, it is worth mentioning the fact that in Figure 3a the distribution of the r.m.s. pressure fluctuations has two areas of relatively high values in the HV region. We are going to see that this double peak distribution is induced by the oscillations of the PV between the two modes identified by Devenport & Simpson (1990). Interestingly, the pressure fluctuations levels inside the CV are higher in the $\phi = 45°$ plane compared to the $\phi = 0°$ plane though the double peak distribution is not present.

Another way to visualize the instantaneous structure of the flow in the HV region and to investigate the reason why the double peak structure is present in the pressure fluctuations distributions (Figure 3a), vertical velocity fluctuations (Figure 13) and turbulent kinetic energy distributions (not shown) at low polar angles is to examine the distributions of the out-of-plane instantaneous vorticity and 2D streamlines in different polar planes around the cylinder and at different time instants. This was done in Figure 4, where the structure of the HV system in the $\phi = 0°$ plane at different time instances was visualized. It was observed that at some time instances the PV was situated closer

Copyright © 2006 Taylor & Francis Group plc, London, UK

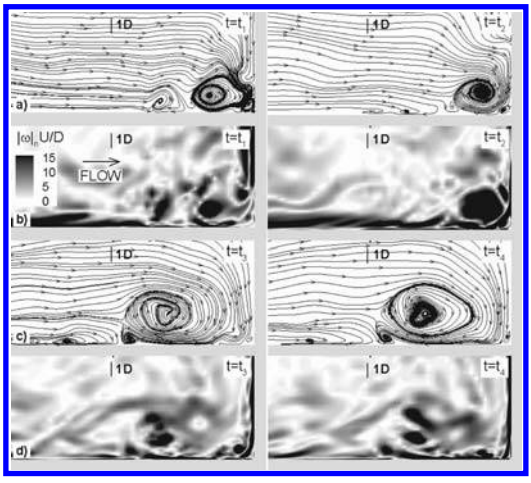


Figure 4. Instantaneous out-of-plane vorticity contours and 2D streamlines in $\phi = 0°$ plane at different time instants; a) and b) zero-flow mode (t_1, t_2); c) and d) backflow mode (t_3, t_4).

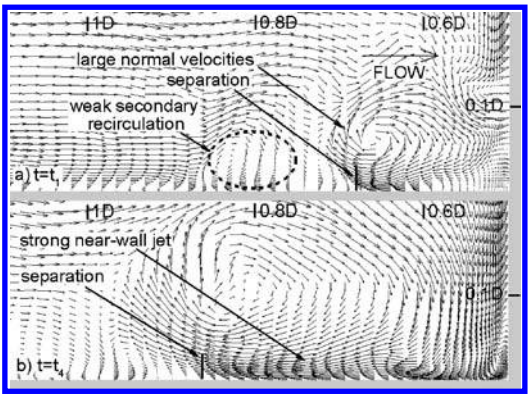


Figure 5. Velocity vectors in the $\phi = 0°$ plane at two time instances corresponding to the HV system being in a) zero-flow mode (t_1); b) backflow mode (t_4).

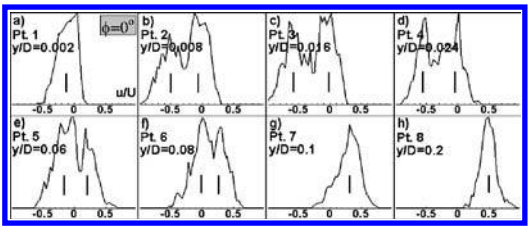


Figure 6. Histograms of probability density function of u-velocity along a vertical line cutting the HV region in $\phi = 0°$ plane at; (a) pt. 1 (y/D = 0.002); (b) pt. 2 (y/D = 0.008); (c) pt. 3 (y/D = 0.016); (d) pt. 4 (y/D = 0.024); (e) pt. 5 (y/D = 0.06); (f) pt. 6 (y/D = 0.08); (g) pt. 7 (y/D = 0.1); (h) pt. 8 (y/D = 0.2). Positions of the points are shown in Fig. 3a.

to the cylinder and its coherence was relatively high. A unique, relatively circular, patch of vorticity appeared to be associated with the PV. Two time instances when the HV system had these characteristics which, according to Devenport & Simpson (1990), correspond to the zero-flow mode are shown in Figures 4a and 4b. At the opposite range, in terms of the observed states of the HV region, the overall size of the PV appears to be sensibly larger, its shape is elliptical, its coherence is lower as the positive vorticity distribution within the HV region is much more diffused (less compact) and the center of this region is situated at a larger distance from the cylinder. These states are associated with what is called the backflow mode (Figures 4c and 4d). Observe also the sheet of negative vorticity beneath the PV which is much longer in the frames corresponding to the backflow mode. This sheet of negative vorticity is in fact due to the presence of a near-wall jet of variable intensity in that region. The jet is clearly visualized in the in-plane velocity vector plots in Figure 5b when its intensity is at its highest (backflow mode). In the same figure, separation from the bed is taking place at about 0.35D–0.4D from the face of the cylinder. In contrast to that, in Figure 5a corresponding to the case when the HV system is in the zero-flow mode, the intensity of the jet flow is much smaller, separation takes place at only 0.2D from the cylinder and the normal velocities above the separation region are larger. Additionally, a weak recirculation region is observed upstream of the jet separation region, consistent with the experiments of Devenport & Simpson (1990).

The formation of the backflow mode is thought to be due to entrainment of patches of high-velocity low-vorticity fluid from the free-stream flow that get entrained in the HV regions via the downflow. The unsteady reversed jet-like flow beneath the HV region increases its momentum and also forces the PV to move away from the cylinder. As this large but not very coherent necklace vortex system gets stretched around the cylinder, its cross section gets smaller, the intensity of the jet like flow beneath it decreases, the PV becomes more compact and moves closer to the cylinder face. During this time, in which the HV is in the zero-flow mode, the flow becomes more stable until a new patch of free-stream flow is injected in the HV region or the interactions between the main necklace vortex with the secondary vortices are strong enough to destabilize the flow and produce again a larger, less compact vortex. Devenport & Simpson (1990) also associated the zero-flow mode with the injection of a patch of rotational low-momentum fluid from the outer region of the boundary layer inside the HV region.

More evidence and explanation of the existence of the two modes and their effect on the flow in the HV region is given by analysis of the probability density function (pdf) plots of the velocity components.

Copyright © 2006 Taylor & Francis Group plc, London, UK

This information is shown in Figures 6 to 8 for the streamwise, vertical and spanwise components on a vertical line intersecting the mean PV vortex (position of the points 1 to 8 is shown in Figure 3a) in the $\phi = 0°$ plane. The pdf's of the streamwise and vertical velocities are shown in Figures 9 and 10 (position of the points 10 to 16 is shown in Figure 3b) in the $\phi = 45°$ plane. Additionally, the pdf's of the streamwise and vertical velocities at two points situated outside the HV region (points 17 and 18 in Figure 3b) are shown in Figure 11. In the $\phi = 0°$ plane, the bimodal behavior of the pdf's for the streamwise u-velocity starts from $y/D = 0.008$ (Point 2) and continues up to $y/D = 0.08$ (Point 6) inside the mean primary vortex. Close to the bed ($y/D = 0.002$) and above the PV region ($y/D > 0.1$) the bimodal behavior is absent. The bimodal distribution is also observed for the vertical velocity component, but the bimodal region in the same section is shifted upwards ($0.02 < y/D < 0.15$). In agreement with the findings of Davenport & Simpson (1990), no bimodal region is detected in the pdf's of the spanwise (along the core of the PV) velocity component in the $\phi = 0°$ plane (Figure 8). In the $\phi = 45°$ plane, a bimodal region is observed for all three Cartesian velocity components (this is normal, as none of them is oriented along the core of the vortex), but the size of the bimodal region appears to shrink ($0.01 < y/D < 0.06$ for u and $0.02 < y < 0.06$ for v). As expected, outside

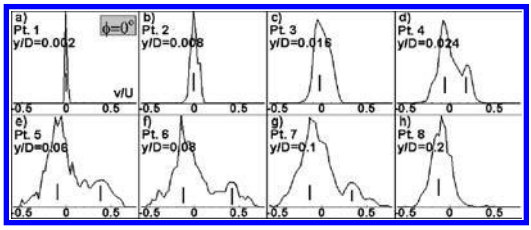


Figure 7. Histograms of probability density function of v-velocity along a vertical line cutting the HV region in $\phi = 0°$ plane at; (a) pt. 1 ($y/D = 0.002$); (b) pt. 2 ($y/D = 0.008$); (c) pt. 3 ($y/D = 0.016$); (d) pt. 4 ($y/D = 0.024$); (e) pt. 5 ($y/D = 0.06$); (f) pt. 6 ($y/D = 0.08$); (g) pt. 7 ($y/D = 0.1$); (h) pt. 8 ($y/D = 0.2$). Positions of the points are shown in Fig. 3a.

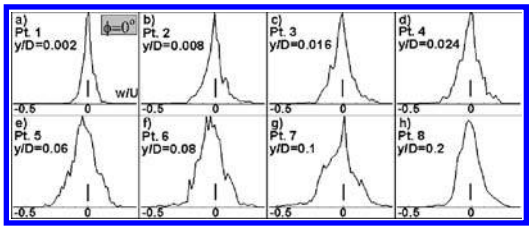


Figure 8. Histograms of probability density function of w-velocity along a vertical line cutting the HV region in $\phi = 0°$ plane. (a) pt. 1 ($y/D = 0.002$); (b) pt. 2 ($y/D = 0.008$); (c) pt. 3 ($y/D = 0.016$); (d) pt. 4 ($y/D = 0.024$); (e) pt. 5 ($y/D = 0.06$); (f) pt. 6 ($y/D = 0.08$); (g) pt. 7 ($y/D = 0.1$); (h) pt. 8 ($y/D = 0.2$). Positions of the points are shown in Fig. 3a.

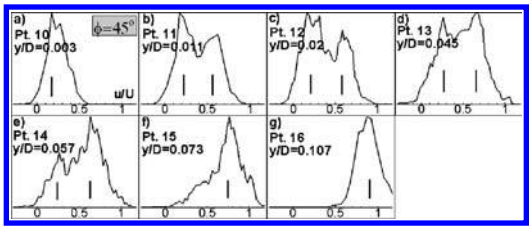


Figure 9. Histograms of probability density function of u-velocity along a vertical line cutting the HV region in $\phi = 45°$ plane. (a) pt. 1 ($y/D = 0.003$); (b) pt. 2 ($y/D = 0.011$); (c) pt. 3 ($y/D = 0.02$); (d) pt. 4 ($y/D = 0.045$); (e) pt. 5 ($y/D = 0.057$); (f) pt. 6 ($y/D = 0.073$); (g) pt. 7 ($y/D = 0.107$). Positions of the points are shown in Fig. 3b.

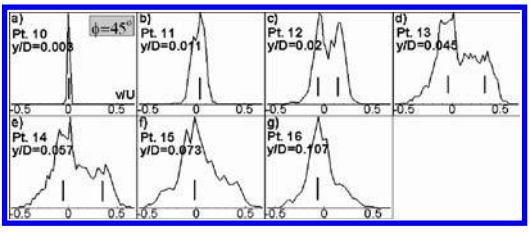


Figure 10. Histograms of probability density function of v-velocity along a vertical line cutting the HV region in $\phi = 45°$ plane. (a) pt. 1 ($y/D = 0.003$); (b) pt. 2 ($y/D = 0.011$); (c) pt. 3 ($y/D = 0.02$); (d) pt. 4 ($y/D = 0.045$); (e) pt. 5 ($y/D = 0.057$); (f) pt. 6 ($y/D = 0.073$); (g) pt. 7 ($y/D = 0.107$). Positions of the points are shown in Fig. 3b.

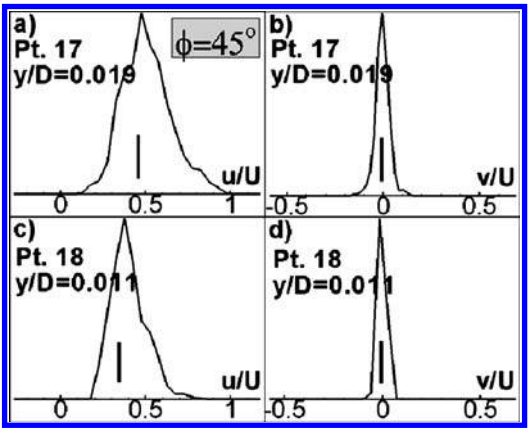


Figure 11. Histograms of probability density function of u-velocity and v-velocity at two points outside the HV region in $\phi = 45°$ plane; (a) pt. 17 ($y/D = 0.019$); (b) pt. 17 ($y/D = 0.019$); (c) pt. 18 ($y/D = 0.011$); (d) pt. 18 ($y/D = 0.011$). Positions of the points are shown in Fig. 3b.

Copyright © 2006 Taylor & Francis Group plc, London, UK

the HV region, the pdf's of the velocity components have a single peak (Gaussian) shape (Figure 11).

The time intervals corresponding to successive mode switching was computed at several points in the bimodal region. It was observed that the most common time between events corresponds to a non-dimensional time interval of about 2.96D/U which is comparable to the most probable residence time (~4.14D/U) calculated by Davenport & Simpson (1990) in their study of flow around a cylindrical wing body at Reynolds numbers larger than one million.

A range of energetic frequencies around St(= fD/U) = 0.1 – 0.18 was present in the resolved velocity and pressure spectra (not shown). This band of low frequencies does not appear to be related to the oscillation of the primary vortex or to the shedding of secondary vortices from the separation region toward the PV which take place in a higher frequency band ($0.3 < St < 0.6$) but rather with the bimodal oscillations. The lower frequency range is consistent with results obtained by Rife et al. (1992) who measured the mean frequency of the velocity fluctuations associated with the bimodal oscillations at around St = 0.05 (the maximum width of the wing was used as the length scale). Power spectra determined from the present simulation show the presence of an inertial resolved range until St ~ 40. The predicted spectral information appear to be consistent with that from the experimental study of the flow past a circular pier at $Re_D = 39{,}000$ of Dargahi (1989). The Strouhal number range corresponding to the energetic frequencies in the velocity spectra was measured between 0.058 and 1.15. The lower part of the range is likely to be associated with the bimodal oscillations. The spectra measured by Wei et!al. (2001) at $Re_D \sim 10{,}000$, when the initially laminar boundary layer is becoming turbulent in the HV region, contained a range of energetic frequencies in the interval St = 0.15 to 0.95. In their experiments the cylinder section was square. Taking into account the different conditions between the aforementioned experiments and our simulation, our results look reasonable.

More information about the effect of the scillation of the PV vortex between the backflow mode and the zero-flow mode is given by the distributions of the velocity fluctuations in a horizontal direction corresponding to the local polar angle ("polar" direction) in that section (Figure 12) and by the vertical velocity

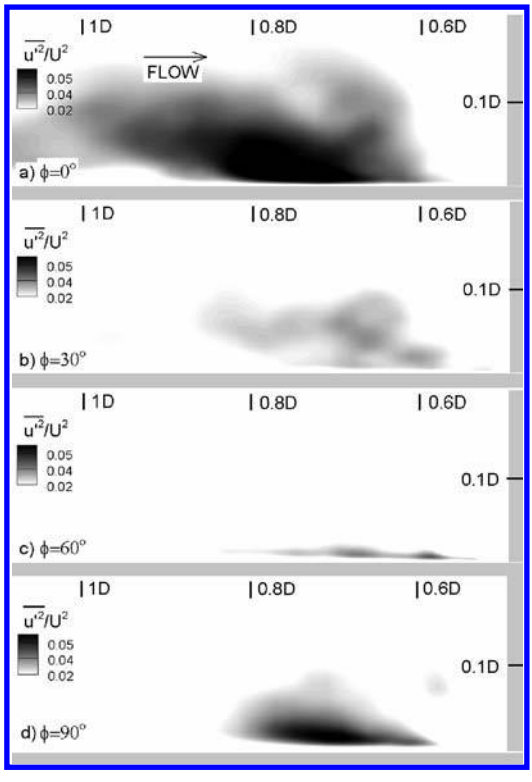


Figure 12. Distribution of velocity fluctuations in a horizontal direction oriented after the local polar angle ("polar" direction); a) $\phi = 0°$ (streamwise fluctuations) b) $\phi = 30°$; c) $\phi = 60°$; d) $\phi = 90°$ plane.

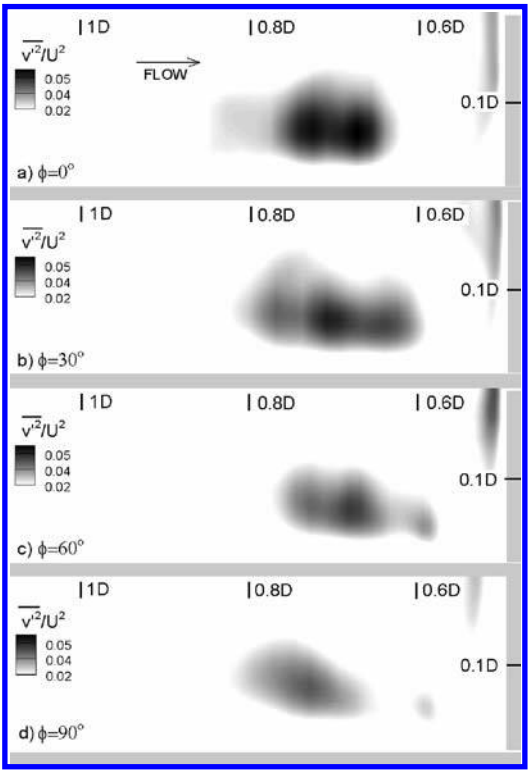


Figure 13. Distribution of vertical velocity fluctuations; a) $\phi = 0°$; b) $\phi = 30°$; c) $\phi = 60°$; d) $\phi = 90°$ plane.

Copyright © 2006 Taylor & Francis Group plc, London, UK

fluctuations (Figure 13) in the $\phi = 0°$, 30°, 60°, 90° planes.

The regions of high vertical velocity fluctuations in Figure 13 correlate very well with the mean position of the PV vortex. The double peak structure is still present even in the $\phi = 60°$ frame of Figure 13. The change in the overall shape of the core of the PV with the polar angle from strongly elliptical in the symmetry plane to relatively circular in the legs is due precisely to the decay of the intensity of the mode switching phenomenon with the polar angle. The resolved velocity fluctuations in the "polar" direction are peaking much closer to the floor in the region in which the intensity of the intermittent reversed wall-attached jet is highly variable in time (e.g., see Figure 12a in which the "polar" direction is streamwise oriented), as the flow switches between the two modes. So, the high velocity fluctuations in regions characterized by a low magnitude of the polar angle are directly associated with the mode switching and to a lesser degree due to locally high values of the small scale turbulence in that region. The decay of the velocity fluctuations in the "polar" direction with the polar angle (for $|\phi| < 60°$) is much sharper compared to that observed for the vertical fluctuations.

Observe also the relatively high vertical velocity fluctuations very close to the cylinder face due to modulations in the intensity of the downflow by the eddies transported in the outer flow. These eddies are being stretched as they are projected toward the bed and can strongly interact with the PV. The velocity fluctuations inside the CV are relatively low.

The distribution of the total tke production in the symmetry plane (Figure 14a) clearly shows that in the HV region and, in particular, in the sub-region associated with the chaotic mode switching, the turbulence energy production is high. The elongated patch of high positive production ($-0.88 < x/D < -0.68$, x measured from the center of the cylinder) contains two peaks, again corresponding approximately to the positions of the PV in the two extreme modes. A very elongated region, in which the production is negative, is observed close to the bottom wall, between the upstream face of the cylinder ($x/D \sim -0.53$) and $x/D \sim -0.65$. It is interesting to notice that these features of the distribution of the total production term in the symmetry plane are very similar to those of the measured tke production in front of a wing shaped body at much higher Reynolds numbers by Devenport & Simpson (1990). Figures 14a, 14b and 14c show the distributions of the main terms contributing to the total production $-2\overline{u'^2}\partial U/\partial x(D/U^3)$, $-2\overline{v'^2}\partial V/\partial y(D/U^3)$ and $-2\overline{u'v'}\partial U/\partial y(D/U^3)$, respectively. Consistent with the high intensity of the streamwise velocity fluctuations recorded in the region corresponding to the intermittent wall attached jet (see Figure 12a) and with the deceleration of the backflow in the positive

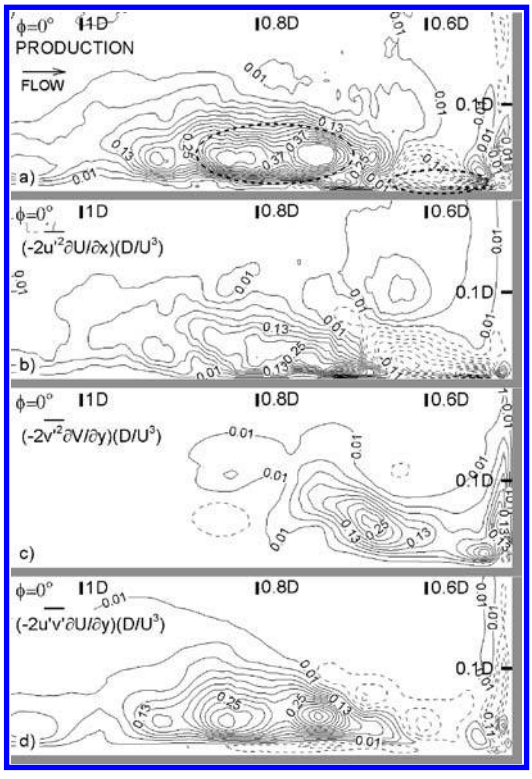


Figure 14. Contours of the turbulent production terms in the turbulent kinetic energy equation, $\phi = 0°$ plane; a) total production; b) $-2\overline{u'^2}\partial U/\partial x(D/U^3)$; c) $-2\overline{v'^2}\partial V/\partial y(D/U^3)$; d) $-2\overline{u'v'}\partial U/\partial y(D/U^3)$.

x direction, as the jet loses streamwise momentum, a region of high positive $-2\overline{u'^2}\partial U/\partial x(D/U^3)$ values is observed beneath the mean PV. In between the extremity of this region and the upstream face of the cylinder, another region of relatively high negative values of this term is present. In this region the backflow accelerates before moving beneath the center of the PV. The production term associated with the vertical Reynolds stress shows high positive levels in a region closer to the cylinder that corresponds to the PV being in the zero flow mode. Interestingly, the maximum values are comparable to the ones recorded for the other main two terms. Finally, the primary Reynolds shear stress production term $-2\overline{u'v'}\partial U/\partial y(D/U^3)$ shows a two positive peak distribution, similar to the total production term. The first peak is situated just upstream of the patch of fluid characterized by high values of $-2\overline{v'^2}\partial V/\partial y(D/U^3)$. The large values of the primary shear stress in the region of high $-2\overline{u'v'}\partial U/\partial y(D/U^3)$ values are due mostly to the bimodal large-scale flow oscillations. The large mean streamwise velocity gradient in the normal direction is mostly due to the

Copyright © 2006 Taylor & Francis Group plc, London, UK

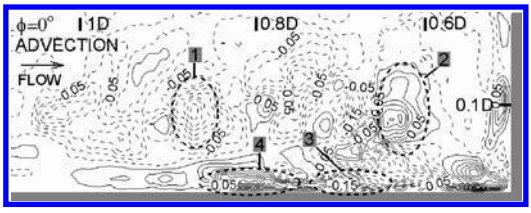


Figure 15. Contours of the total advection term in the turbulent kinetic energy equation, $\phi = 0°$ plane.

position of the patch close to the center of the PV. The contributions from the other production terms were found to be small in the symmetry plane.

The contours of the total advection term in the tke equation (Figure 15) show a more complex distribution. Two areas of positive tke advection and two areas of negative tke advection are observed in the symmetry plane around the mean position of the PV. The relative positions of these regions relative to the PV are very similar to the ones observed by Devenport & Simpson (1990) in the symmetry plane upstream of a wing shaped body. The regions of high absolute value of advection do not coincide with the approximate position of the PV as it switches between the two modes because the advection does not depend on the values of the Reynolds stresses that, as we have seen, are strongly amplified in the PV region. The region 1 of high negative advection in Figure 15 covers part of the upstream side of the mean PV and extends upstream into the separating boundary layer. The negative values of the advection in this region are due primarily to the strong variation of the normal Reynolds stresses in the streamwise direction, as they are transported toward the pier. In region 2, situated immediately downstream the mean PV, the advection values are positive but the absolute values are not as high as those present in region 4. In this region the incoming flow, deflected by the presence of the PV, is starting moving downwards into the downflow. In region 2 the vertical velocity fluctuations are observed to vary significantly in both the streamwise and vertical directions (Figure 13a). The elongated patch of high negative values situated close to the bed, slightly to the right of the PV center, is denoted as region 3 in Figure 15. This region corresponds to the upstream part of the near wall jet flow beneath the PV and is characterized by a sharp increase in the streamwise velocity fluctuations in the upstream direction (see Figure 12a). As the mean jet velocity is oriented in the streamwise direction away from the cylinder, the most important contribution comes from the term $-U\partial\overline{u'^2}/\partial x(\mathrm{D/U^3})$. Region 4, in which high positive values of the advection term are observed, is situated near the bed but slightly upstream of the PV and of region 3. The positive values in this region correspond to a gain of turbulence energy. This area corresponds to the deceleration and separation regions of the near bed jet flow in which the streamwise velocity fluctuations are decaying in the streamwise direction as we go away from the cylinder. Additionally, due to the detachment of the jet from the bed, the peak in the streamwise fluctuations is moving away from the bed, in the direction of the jet flow, and a non-zero mean vertical velocity component is present. Thus, the contribution from $-V\partial\overline{u'^2}/\partial y(\mathrm{D/U^3})$ can be significant. Finally, a region of high positive advection produced by the interaction of the downflow with the bed surface is present near the junction between the cylinder and the bed ($-0.65 < \mathrm{x/D} < -0.5$). This region was outside the measurement window in the experiments of Devenport & Simpson (1990).

4 CONCLUSIONS

The present numerical investigation shows that the structure of the turbulent HV system that develops in front of the upstream face of a circular pier varies considerably with the polar angle around the cylinder. The bimodal velocity probability phenomenon observed to occur in front of surface mounted bluff bodies at much higher Reynolds numbers (Simpson, 2001) was found to be present in the flow around a circular bridge pier at a moderate Reynolds number ($\mathrm{Re_D} = 16{,}000$). In agreement with Devenport & Simpson (1990), the bimodal structure was found to be present only in the velocity components perpendicular to the core of the PV. This bimodal structure of the HV region is induced by the oscillations of the PV between two modes. In the first one, called the zero-flow mode, the PV is more compact and situated closer to the upstream face of the pier. In the second one, called the backflow mode, patches of high-momentum low-vorticity fluid from the outer flow are entrained in the downflow and from there into the HV region. As a result, the coherence of the PV is lower, its size is sensibly larger and its center is situated farther from the pier. The injection of high momentum outer flow is also the cause for the formation of a relatively high streamwise momentum near wall jet that is present beneath the PV and eventually detaches upstream of it. During the zero-flow mode the near wall jet is still present, but its momentum is much lower.

The HV system was found to strongly modify the turbulence structure upstream the pier nose mainly because of the amplification in the levels of the turbulent velocity and pressure fluctuations in the HV region. Most of this amplification in the region corresponding to the mean PV was shown to be related to the bimodal aperiodic chaotic mode switching phenomenon that is especially strong at polar angles smaller than 45° and eventually disappears in the legs

Copyright © 2006 Taylor & Francis Group plc, London, UK

of the horseshoe vortices. The low frequency oscillations of the PV between the zero-flow mode and the backflow mode and the variations in the intensity of the intermittent wall-attached jet beneath it, induce high bed shear stress values. Additionally, relatively large pressure fluctuations are present in the immediate vicinity of the bed, beneath the HV system. These flow features can significantly accelerate the sediment entrainment in the case of a movable bed and explain the efficiency of the HV system in removing sediment during the scouring process. The region of bimodal flow was also shown to be one of large turbulence production. Additionally, it was found that the production terms associated with the normal Reynolds stresses were comparable to the one due to the primary shear stress similar to the findings of Devenport & Simpson (1990) for a highly turbulent flow in front of a wing shaped body. The tke advection was shown to be concentrated in several regions around the mean position of the PV, consistent with the measurements of Devenport & Simpson (1990).

An analysis of the interactions between the horseshoe vortices (in particular, their legs) with the detached shear layers and between the vortex tubes that populate these detached shear layers and the bed, which may explain scour/deposition phenomena near the downstream face of the cylinder and past it, will make the object of a future paper.

REFERENCES

Chen, G., Du, X. D., & Wei, Q. D. 2000. The effects of cylinder shape on the primary horseshoe vortex of juncture flow. *9th Symposium on Flow Visualization*, Paper 54: 1–9.

Dargahi, B. 1989. The turbulent flow field around a circular cylinder. *Experiments in Fluids*, 8: 1–12.

Devenport, W. J. & Simpson, R. L. 1990. Time-dependent and time-averaged turbulence structure near the nose of a wing-body junction. *Journal of Fluid Mechanics*, 210: 23–55.

Graf, W. H. & Yulistiyanto, B. 1998. Experiments on flow around a cylinder, the velocity and vorticity fields. IAHR *Journal of Hydraulic Research*, 36(4): 637–653.

Jeong, J. & Hussain, F. 1995. On the identification of vortex. *Journal of Fluid Mechanics*, 285: 69–94.

Kim, S. A., Walker, D. A. & Simpson, R. L. 1991. Observation and measurements of flow structures in the stagnation region of a wing-body junction, *VPI&SU Report No. VPI-E-91-20, Virginia Polytechnic Institute and State Univ., Blacksburg, VA*.

Kirkil, G., Constantinescu, G. & Ettema, R. 2005. The Horseshoe Vortex System around a Circular Bridge Pier on Equilibrium Scour Bed. ASCE-EWRI *World Water and Environmental Resources Congress, May 2005, Alaska.*

Mahesh, K., Constantinescu, S.G., & Moin, P. 2004. A numerical method for large eddy simulation in complex geometries, *Journal of Computational Physics*, 197: 215–240.

Olcmen, M. S. & Simpson, R. L. 1994. Influence of wing shapes on surface pressure fluctuations at wing-body junctions. *AIAA Journal*, 32: 6–15.

Rife, M. C., Davenport, W. J. & Simpson, R. L. 1992. An experimental study of the relationship between the velocity and pressure fluctuations in a wing-body junction. *VPI&SU Report No. VPI-AOE-188, Virginia Polytechnic Institute and State University, Blacksburg, VA*.

Simpson, R. L. 2001. Junction flows, *Annual Review of Fluid Mechanics*, 33: 415–443.

Wei, Q. D., Chen, G. & Du, X. D. 2001. An experimental study on the structure of juncture flows. *Journal of Visualization*, 3(4): 341–348.

Copyright © 2006 Taylor & Francis Group plc, London, UK

The scour-hole problem due to sluice gates: Quadrant analysis of the turbulence characteristics in the presence of Görtler vortices

I. Albayrak & U. Lemmin
Laboratory of Environmental Hydraulics (LHE), Ecole Polytechnique Fédérale de Lausanne, Switzerland

ABSTRACT: Turbulence characteristics and their effect on the erosion capacity of a wall jet issuing from a sluice gate are experimentally investigated. From a loose bed experiment the Görtler number was calculated and an instability analysis was to carried out. In the present case, the Görtler number and the curvature parameter are well above their critical values, and longitudinal vortices occur along the concave scour hole. These Görtler vortices make the wall jet unstable and strongly contribute to suspend the bed sediment particles by increasing the wall shear stress. With surface particles fixed, a scour- hole bed of equivalent roughness was created and intensive instantaneous velocity measurements using a 3D Acoustic Doppler Velocity Profiler (ADVP) at several positions along the channel axis were carried out. A quadrant analysis in the streamwise and transversal planes shows that all along the scour hole, ejection and sweep events dominate turbulence in the inner layer of the wall jet and contribute to Reynolds shear stress more than outward and inward interactions. Above $0.6y/y_{1/2}$, outward and inward interactions slightly dominate.

1 INTRODUCTION

Extensive research on the dynamics of wall jets issuing from a sluice gate has been carried out in relation to local scour, heat, mass and momentum transfer and engineering applications. Wall jets can cause significant local scour downstream of hydraulic structures, and local scour on a large scale can lead to failure of structure foundations.

The turbulence characteristics of wall jets are closely related to their erosion capacity and sediment transport. A plane turbulent wall jet and a wall jet along a concave surface have different turbulence structures. Therefore, their effect on local scour and sediment transport are different. The occurrence of counter-rotating longitudinal Görtler vortices changes the turbulence structure of the wall jet along a concave surface (Kobayashi et al, 1983) and increase the sediment transport rate above the critical Görtler number (Hopfinger et al., 2004).

The existence of Görtler vortices was first shown experimentally by Gregory and Walker (1956) on the basis of flow visualizations and by Tani (1962) on the basis of direct in-flow measurements. The critical conditions of Görtler instability were given by Tani (1962) and Kobayashi & Fujisawa (1980, 1983) on a stability diagram of turbulent wall jets relating the curvature parameter and velocity ratio. A detailed study of Görtler instability is found in Floryan (1991) who experimentally and theoretically investigated its mechanism, and linear and nonlinear stages of this instability.

An experimental and numerical study investigating the local scour downstream of a sill followed by a rigid apron was carried out by Adduce et al. (2004). They proposed a 1D mathematical model simulating the local scour downstream of a sill and showed a good agreement between the measured scour profiles and the predictions with the model.

Görtler vortices and their contribution to the sediment erosion along a concave surface were studied experimentally by Hopfinger et al. (2004). They found that streamwise Görtler vortices play an important role in sediment transport by creating turbulence.

The primary purpose of this study is to investigate experimentally turbulence characteristics and their effect on the erosion capacity of a wall jet issuing from a sluice gate. The non-linear behavior of the counter-rotating streamwise Görtler vortices which make the wall jet unstable along the scour hole and lift up bed sediment particles was studied in relation to instability analysis based on Görtler numbers and flow events that are responsible for the initiation and transport of sediment motion. An experimental investigation of the conditionally sampled covariance events $u'w'$ in the streamwise direction and $v'w'$ in the across stream plane is reported in this paper. This was accomplished by performing intensive instantaneous velocity

Copyright © 2006 Taylor & Francis Group plc, London, UK

measurements using the 3D Acoustic Doppler Velocity Profiler (ADVP) developed by Lhermitte and Lemmin (1994) and Rolland and Lemmin (1997) at several points in a fixed scour hole. The velocity measurements were complemented with video data taken with a non intrusive digital video camera with 25 frames per second to record the bed profile and to visualize and count the counter-rotating streamwise vortices. In the first part of this paper, the experimental set-up, procedure and instrumentation are described. In the second part, the instability analysis in terms of Görtler number and a quadrant analysis of the instantaneous velocity data obtained with the ADVP in relation to the local erosion potential of the counter-rotating streamwise vortices are presented.

2 EXPERIMENTAL SETUP, INSTRUMENTATION AND PROCEDURE

Experiments were conducted in a re-circulating horizontal flume with a rectangular cross-section and glass side walls as shown schematically in Figure 1a. The flume is 17 m long, 0.5 m wide and 0.8 m deep. Figure 1b shows the fixed concave scour hole, the configuration of the wall jet and the definition of the parameters used here. In order to obtain a 3.8 m long, 0.35 m deep test section at a distance of 5 m from the inlet of the flume, the upstream and the downstream ends of the flume were raised by inserting rigid panels. The test section was filled with uniformly graded sand of average grain diameter $d_{50} = 2$ mm. Firstly, a loose bed experiment was conducted in order to calculate the Görtler number and to carry out an instability analysis of the counter-rotating streamwise vortices. After the loose bed experiment, the surface particles in the 0.2 m radius scour hole were fixed to create a scour hole bed of equivalent roughness. The sluice gate from which the wall jet issues was located 4.9 m from the inlet, and the gate opening was $b_0 = 5$ cm for all experiments reported here. The downstream water depth was kept constant during the experiments $h_2 = 22.4$ cm. In order to maintain the initial jet velocity, $U_0 = \sqrt{2g\Delta h}$, the upstream water depth, h_1, was controlled. The slope of the channel was zero. The Acoustic Doppler Velocity Profiler (ADVP) was used to measure the three

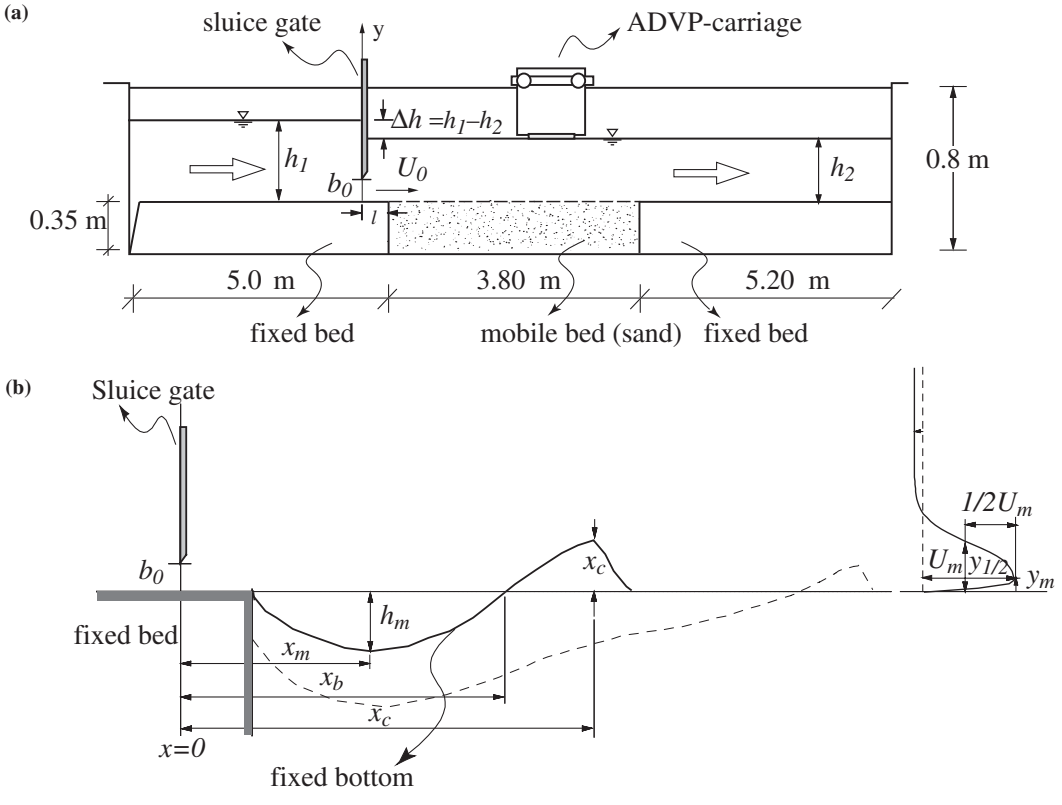


Figure 1. (a) Schematic diagram of the hydraulic flume and test section. (b) the scour hole dimensions. Solid line: the fixed score-hole shape (t = 100 sec); dashed line: long-term asymptotic state of the bottom profile.

Copyright © 2006 Taylor & Francis Group plc, London, UK

velocity components simultaneously across the water depth at 12 different streamwise sections along the centerline of the flume.

The high space and time resolution of the ADVP measurements allowed us to correctly evaluate the turbulence information and establish a correlation between velocity components without any specific requirements for the flow condition. In the present study, the ADVP system was multistatic. The system consists of a central beam emitter and four wide-angle receivers placed around the center providing one redundancy to eliminate the signal noise and to control the quality of the velocity data (Hurther and Lemmin, 2000). The spatial and temporal resolution of the ADVP system presented here are equal to $\cong$3 mm and 0.032 s, respectively. The duration of the velocity measurement at each position in the scour hole is over 600 s.

The instantaneous water surface and bed profile were recorded by using a digital camera with 25 frames per second. The recorded video data were treated by computer using such software as i-movie and graphic solutions by Adobe.

The flow conditions (Table 1) for the tests conducted here are identical with those defined in an earlier study (Hopfinger et al., 2004). First, the mobile bed was covered with a thin plate which had no influence on the flow conditions and on the onset of scouring. The upstream and downstream water levels were then adjusted to obtain $\Delta h = 2.6$ cm. As soon as the plate was withdrawn from the channel at t = 0s, the scouring progressed rapidly. The scouring progress was filmed with the camera starting at t = 0s. The scour hole reached a quasi-steady-state depth $h_s = h_m$ in time $t = t_s$. Figure 1b shows the characteristic dimensions of the scour hole shape. The sediment streaks in the scour hole and their variation across the channel were observed with a second video camera looking downstream. In the first run, for time t = 100s, the deepening rate was large (short-time regime) and the Görtler vortices were clearly visible from the recorded video data. The instability analysis was made with the method reported in Hopfinger et al. (2004). The calculated Görtler number (Table 1) was found to be above the critical value. To study the turbulence characteristics of the wall jet along the concave scour hole and the counter-rotating streamwise Görtler vortices, a second run was conducted. In the second run, the experiment was stopped at t = 100s and the scour hole was fixed using a chemical glue. All velocity measurements and analyses presented here were carried out in the fixed concave scour hole (run 3).

3 MEAN FLOW CHARACTERISTICS

The mean 2D velocity vectors measured with the 3D ADVP at 12 measurement sections of the scour-hole (large curvature) are presented in Figure 2. Jet entrainment and return flow occur early on, and the wall jet

Table 1. Summary of the experimental conditions and the calculated Görtler numbers.

Test	b_0 (m) $\times 10^{-2}$	l (m) $\times 10^{-2}$	Δh (m) $\times 10^{-2}$	U_0 [ms^{-1}]	n, number of streaks observed	R (m)	G_T	t_s, quasi-steady state(s)
Run 1	5	10	2.6	0.71	~6	0.205	2.86	240
Run 2	5	10	2.6	0.71	~6	0.205	2.86	NA
Run 3 (fixed bed)	5	10	2.6	0.71	~6	0.205	2.86	NA

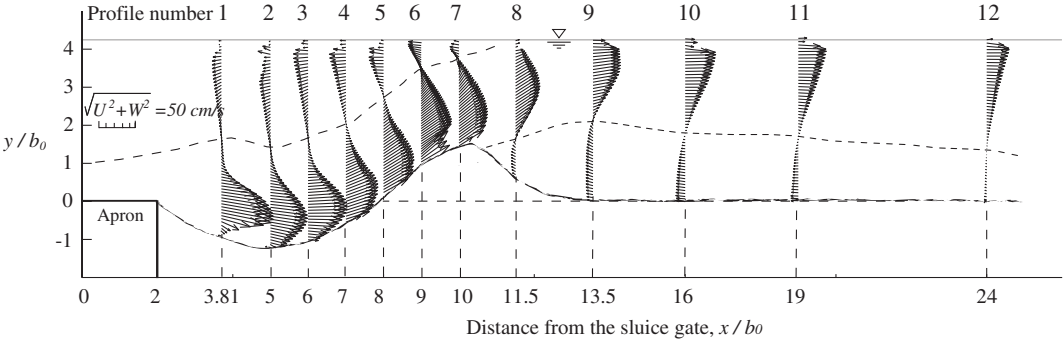


Figure 2. The mean 2D dimensional velocity distributions.

Copyright © 2006 Taylor & Francis Group plc, London, UK

passing over the apron attaches to the scour hole bed at around x/b = 3.81. The wall jet remains attached to the fixed sediment surface until point x/b = 10 where the flow separates. A second return flow zone between x/b = 11.5 and x/b = 24 occurs near the wall as clearly seen in Figure 2.

4 INSTABILITY ANALYSIS

Counter-rotating streamwise Görtler vortices may develop in a concave boundary layer owing to centrifugal instability. Based on observed erosion by these vortices, the corresponding control parameter for this instability, the Görtler number, was calculated according to the method suggested by Hopfinger et al. (2004). We observed that the sediment streaks lifted up by the streamwise vortices appeared and disappeared randomly and their values varied with time as reported by Hopfinger et al. (2004). From the high quality images recorded with the video camera (Fig. 3) in the loose bed experiment (run 1), the radius of curvature, R, and the wave length λ of the sediment streaks, were determined for the time around 100 s. The number of streaks, n, was counted in each video frame (Fig. 3) and the wavelength, λ, and the wave number, α, were calculated as:

$$\lambda = B/n, \qquad \alpha = 2\pi\lambda \tag{1}$$

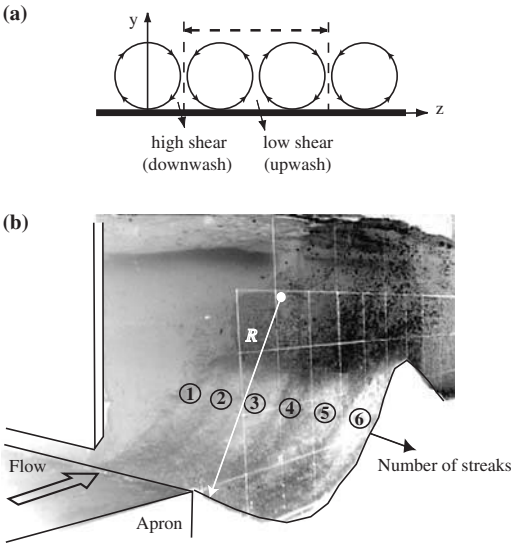


Figure 3. (a) The pattern of streamwise streaks, (b) Longitudinal sediment streaks formed by Görtler vortices for run 1.

The number of streaks, n, given in Table 1 is a mean value of several pictures. For the laminar boundary layer, the Görtler number is:

$$G = \mathrm{Re}_\theta \left(\frac{\theta}{R}\right)^{1/2} \tag{2}$$

where θ is a viscous length scale which is equal to $(\nu x/U)^{1/2}$ or to the momentum thickness. R is the radius of curvature and $\mathrm{Re}_\theta = U\theta\nu$. In the present study, the flow is turbulent and of the wall-jet type. Thus we calculated the Görtler number for turbulent boundary layers on a concave wall as given by Hopfinger et al. (2004).

$$G_T = \frac{U_m}{\nu_T}\sqrt{\frac{\theta}{R}} \approx 31\sqrt{\frac{\theta}{R}} \tag{3}$$

where U_m is the maximum local velocity and ν_T is the eddy viscosity. The calculated Görtler number for the present study is 2.86, well above the critical value. Figure 4 shows the experimental value presented here on the Görtler number-wave number diagram of Tani (1962). In both the loose and fixed bed experiments for R = 0.205 m, the Görtler vortices are not steady. They tend to move about in a seemingly random manner, i.e. they come together, separate, appear and disappear. As mentioned by Hopfinger et al. (2004), the stronger vortices, which can carry a sediment load, survive long enough to carry the particles up the bed slope.

Another instability criterion based on the linear stability theory is found in Kobayashi et al. (1983). The stability diagram of turbulent wall jets relating the curvature parameter and the velocity ratio $\beta = U_\infty/U_m$, where β is a ratio of the free stream velocity U_∞ outside of the wall jet to the maximum velocity U_m was given. The present wall jet corresponds to $\beta = 0$ assuming $U_\infty = 0$. The curvature parameter $y_m/R = 0.22$, is well above the critical

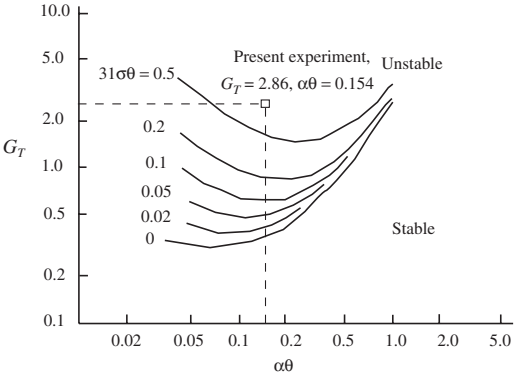


Figure 4. Dimensionless wave number, $\alpha\theta$, versus the Görtler number (Tani, 1962). The present experiment is indicated with the square symbol.

Copyright © 2006 Taylor & Francis Group plc, London, UK

curvature parameter 0.05. Since the theoretical analysis includes some approximations, we expect that longitudinal vortices will occur in the present case. The fact that a strong increase of turbulence in the present experiment occurred shows the existence of longitudinal vortices caused by centrifugal instability.

Both theoretical and experimental instability analysis show that in the present case, the Görtler number and the curvature parameter are well above their critical values and longitudinal vortices occur along the concave scour hole.

5 CONTRIBUTION OF THE GÖRTLER VORTICES TO SEDIMENT TRANSPORT

The action of the wall jet issuing from the sluice gate creates a scour hole. Total shear stress is a key element for sediment erosion and transport. The critical value of shear stress for the initiation of sediment motion is given by the following relationship:

$$\theta = \frac{U_f^2}{g(s-1)d} \tag{4}$$

in which U_f = friction velocity, g = acceleration by gravity and s = the particle specific gravity. The quantity θ is a Shields parameter based on the particle size d. The Shields parameter can be written in terms of bed shear stress by:

$$\tau_{crit} = \tau_b / g(s-1)d \tag{5}$$

where τ_b is the bed shear stress. The critical value of the Shields parameter for the initiation of motion over an almost flat bed is $\tau_{crit} = 0.035$ (Graf 1971). The total effective shear stress consists of the shear stress due to the boundary-layer turbulence τ_t and Görtler vortices τ_G and is expressed by

$$\tau_b = \tau_t + \tau_G \tag{6}$$

$$\tau_t = \rho(c_f/2)U_m^2 \text{ and } \tau_G = \rho(c_{fG}/2)U_m^2 \tag{7}$$

where c_f and c_{fG} are the friction coefficients for the boundary-layer turbulence and the Görtler vortices, respectively. For the present experiment, $c_f = 0.014$, $c_{fG} = 0.014$ and $\tau_b \approx 0.007(1+4)\,\rho U_m^2$ were obtained with the expression under the same experimental conditions and Görtler number at location x/b = 7 ($x \approx 1.7(x_m - l)$) presented in Hopfinger et al. (2004). The measured value of the shear stress in the wall region of the turbulent wall jet at x/b = 7 is ρ 0.0066 N/m^2 and is almost the same as the value calculated with the expression, $\tau_b \approx 0.007(1+4)\,\rho U_m^2$. These results agree well with the experiments by Kobayashi & Fujisawa (1983) and Hopfinger et al. (2004). The measured effective shear stress, τ_b, which is active and responsible in sediment transport, is well above the critical value and shows a remarkable mobilizing force in the scour process. Görtler instability increases the shear stress at the locations corresponding to downwash induced by the counter-rotating streamwise vortices and decrease at locations corresponding to upwash (Floryan, 1991). From the present observations, in the downwash region, the vortices easily moved sediment at the wall by increasing the wall shear stress and eventually lifted up sediment to the main body of the flow in the upwash regions by forming ridges on the bottom. The process repeated itself as time progressed. Thus, Görtler vortices play an important role in local erosion and sediment transport.

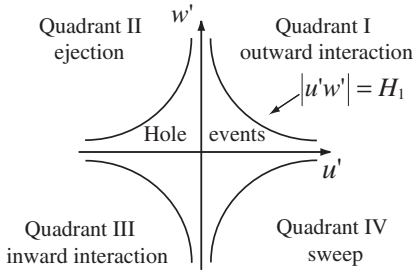
6 THE QUADRANT ANALYSIS OF THE INSTANTANEOUS VELOCITY

Two different sets of coherent structures are found in turbulent boundary layers. The inner layer is governed by the eddy structure, whereas in the outer flow, large-scale structures control the entrainment into the boundary layer. Most of the production of Reynolds stress and turbulent energy occurs in the inner layer and is related to wall eddies involved in a sequence of events called the 'bursting process'. The bursting phenomenon in turbulent flows was discovered by Kline et al. (1967). The bursting process may be composed of cycles of sweeps ($u' < 0, w' > 0$) and ejections ($u' > 0, w' > 0$), and inward ($u' < 0$, $w' < 0$) and outward ($u' > 0$, $w' > 0$) interactions (Fig 5; modified from Nezu and Nakagawa, 1993). Blackwelder & Kaplan (1976) showed that two counter-rotating streamwise vortices form and act to pump low-speed fluid away from the wall, forming the low speed streaks and consequently an inflexional velocity profile. This causes an instability similar to that found in the boundary layers. Oscillations within this instability terminate in a rapid ejection of fluid away from the wall. This motion has a rapid timescale and is called 'burst'. The growth and breakdown of streamwise vortices via the Görtler instability mechanism are similar to those found in transitional and turbulent flow fields (Bippes, 1972).

The flow events in the bursting process are responsible for the onset of sediment motion. The sweeps cause the initiation of bedload motion on the stream bed, whereas the ejections are primarily responsible for the particles' suspended motion. Nelson et al. (1995) showed that the outward interactions also contribute to bedload transport.

Copyright © 2006 Taylor & Francis Group plc, London, UK

(a) Longitudinal section (w_1)



(b) Transversal section (w_2)

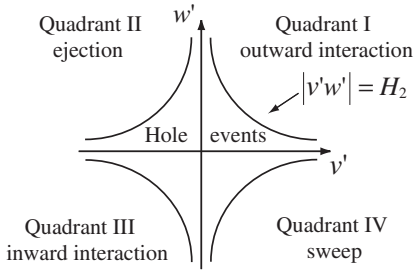


Figure 5. Schematic division of events in the (a) longitudinal and (b) transversal planes.

7 THEORETICAL ASPECTS OF THE CONDITIONAL STATISTICS OF RELATIVE COVARIANCES

In this section, the contribution of bursting events to Reynolds stress will be presented. u', w', v' are the zero mean fluctuating longitudinal, vertical and transversal velocity components, respectively. The normalized velocity fluctuations are:

$$\hat{u} = u'/\sqrt{\overline{u'^2}}\ , \hat{w} = w'/\sqrt{\overline{w'^2}} \text{ and } \hat{v} = v'/\sqrt{\overline{v'^2}} \qquad (8)$$

In Figure 5, the covariance terms for the different planes of the relative shear stress are $w_1 = u'w'/\overline{u'w'}$ and $w_2 = v'w'/\overline{v'w'}$. The joint probability functions of $\hat{u}$, $\hat{w}$ and $\hat{v}, \hat{w}$ are denoted by $p(\hat{u}, \hat{w})$ and $p(\hat{v}, \hat{w})$, respectively (8). The detailed mathematical expressions are found in Nakagawa and Nezu (1977). The following equations are given:

$$\begin{aligned} p_{k,2}(w_k) &= p_G(w_k) + \varphi_k^{-}(w_k) \\ p_{k,4}(w_k) &= p_G(w_k) - \varphi_k^{-}(w_k) \end{aligned} \quad (w_k > 0) \quad k = 1,2$$

$$\begin{aligned} p_{k,1}(w_k) &= p_G(w_k) + \varphi_k^{+}(w_k) \\ p_{k,3}(w_k) &= p_G(w_k) - \varphi_k^{+}(w_k) \end{aligned} \quad (w_k < 0) \qquad (9)$$

where the index a in $p_{k,a}$ denotes the quadrant in the kth plane, with the longitudinal plane (1) and transversal plane (2).

From (9), the time fraction $T_{k,a}(H_k)$ and the contribution to the Reynolds stress $RS_{k,a}(H_k)$ corresponding to each event are presented as a function of the threshold levels H_k by the following expressions:

$$T_{k,a}(H_k) = \begin{cases} \int_{H_k}^{\infty} p_{k,a}(w_k)dw_k & k=1,2 \quad a=2,4 \quad H_k \geq 0 \\ \int_{-\infty_k}^{H_k} p_{k,a}(w_k)dw_k & k=1,2 \quad a=1,3 \quad H_k \leq 0 \end{cases}$$

$$RS_{k,a}(H_k) = \begin{cases} \int_{H_k}^{\infty} w_k p_{k,a}(w_k)dw_k & k=1,2 \quad a=2,4 \quad H_k \geq 0 \\ \int_{-\infty_k}^{H_k} w_k p_{k,a}(w_k)dw_k & k=1,2 \quad a=1,3 \quad H_k \leq 0 \end{cases} \qquad (10)$$

As shown in Figure 5, the contributions to the Reynolds stress can be associated with five events. Event 5 is called the 'hole event' term when $|w| < H.T_{k,5}$ and $RS_{k,5}$ are given by

$$T_{k,5} = 1 - \sum_{a=1}^{4} T_{k,a}(H_k) \qquad k = 1,2$$

$$T_{k,5} = 1 - \sum_{a=1}^{4} T_{k,a}(H_k) \qquad k = 1,2 \qquad (11)$$

8 RESULTS AND DISCUSSION

Figure 6 presents the experimental quadrant fractional contributions of the relative covariance term w_1 calculated from (9) at section x/b = 7 in the fixed scour hole. As seen from Figure 6, in the inner layer of the wall jet ($y/y_{1/2} \leq 0.5$), ejections and sweeps contribute more than outward and inward interactions and that ejection events show significantly larger values than other events. Coherent structures, ejections and sweeps, are the main turbulent energy producers. The contributions of inward and outward interactions are less in the inner layer, but are more important than other events in the outer layer. This result is consistent with a near-wall turbulence model suggested by Kastrinakis et al. (1977) in which ejections from low-speed streaks occur between pairs of intense counter rotating streamwise vortices.

The time fraction of the hole events $T_{1,5}$ is shown in Figure 6. It is clearly seen that the variation of $T_{1,5}$ in the inner layer is weak. For $H_1 = 10$, the time fraction of the hole events is more than 90%. The contribution to event generation is less than 10%. In this case, the

Copyright © 2006 Taylor & Francis Group plc, London, UK

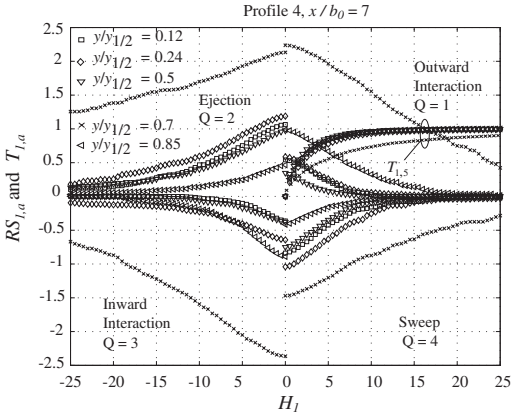


Figure 6. Fractional contributions to Reynolds stress versus threshold level H_1 and time fraction occupied by the hole events $T_{1,5}$ for profile 4 in the longitudinal plane.

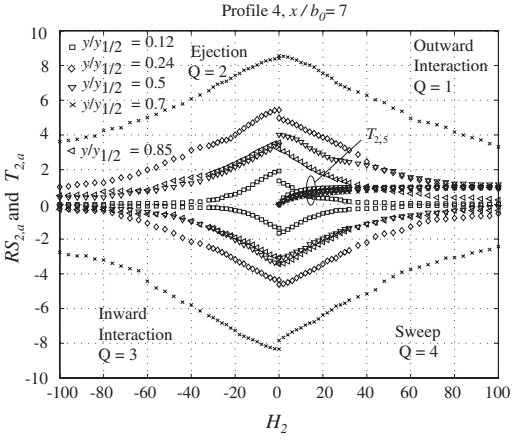


Figure 7. Fractional contributions to Reynolds stress versus threshold level H_2 and time fraction occupied by the hole events $T_{2,5}$ for profile 4 in the transversal plane.

sweep event decreases rapidly with H_1 and only the ejection event contributes to the Reynolds stress. The time occupied by this event is very short. The ejection event manifests itself in the form of a very sharp pulse as indicated by Nakagawa & Nezu (1977). This indicates that the nonlinear growth of Görtler vortices continues, that they approach each other, form a pair, and lift up some sediment (In next section, the nonlinear development of Görtler vortices will be shown). In the outer layer ($y/y_{1/2} > 0.5$), the negative contribution to Reynolds stress appears and the outward interaction shows slightly larger values than the inward interaction.

For the covariance events w_2 in the transversal plane of the turbulent wall jet, the same quantities as in Figure 6 are presented in Figure 7. We can observe for $T_{2,5} \approx 0.90$ that near the wall, $y/y_{1/2} = 0.12$, the contribution of ejection events is slightly greater than that of sweep events. However, it can be seen that in general the contribution of all events in a bursting cycle is nearly equal and symmetrical, independent of the threshold level H_2 and depth. Hurter et al. (2000) observed a similar distribution of all events in the transversal plane in the boundary layer of open-channel flow.

In order to compare quantitatively the time fraction, $T_{1,a}$ occupied by all quadrants in the longitudinal plane, Figure 8 illustrates their profiles over the depth for the threshold level $H_1 = 0$. In profile 4, it is clearly seen that the time occupied by ejection and sweep events within a bursting cycle in the inner layer is higher than that of the outward and inward interactions, whereas in the outer layer, the outward and inward interactions occupy more time. In the wall region of all profiles in the scour hole, the sweep events occupy more time than other events and the magnitude of the fraction of

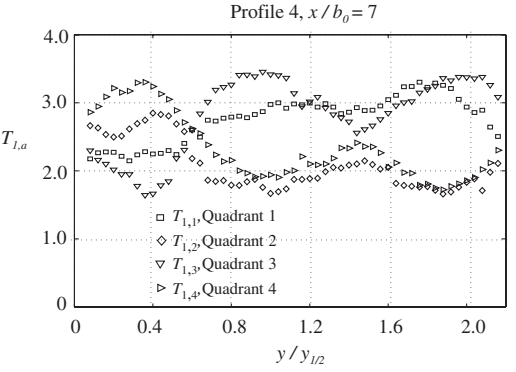


Figure 8. Distributions of the time fraction occupied by each event with $H_1 = 0$.

time $T_{1,a}$ satisfies the relation sweep > ejection > outward interaction ≅ inward interaction. These results agree well with those obtained by Nagakawa and Nezu (1977).

9 OBSERVATION OF STRUCTURAL FLOW FEATURES IN A WALL JET ALONG A SCOUR HOLE

Figure 9a shows a close up of the 2D velocity vectors of profile 4 for the time between t = 40s and 42s. Flow patterns such as ejections, sweeps, upwellings and downwellings in the water column are presented with the Reynolds shear stress distribution corresponding to the same time interval. The ejection events can be seen in Figure 9a in the wall region at t = 40.10, 40.60,

Copyright © 2006 Taylor & Francis Group plc, London, UK

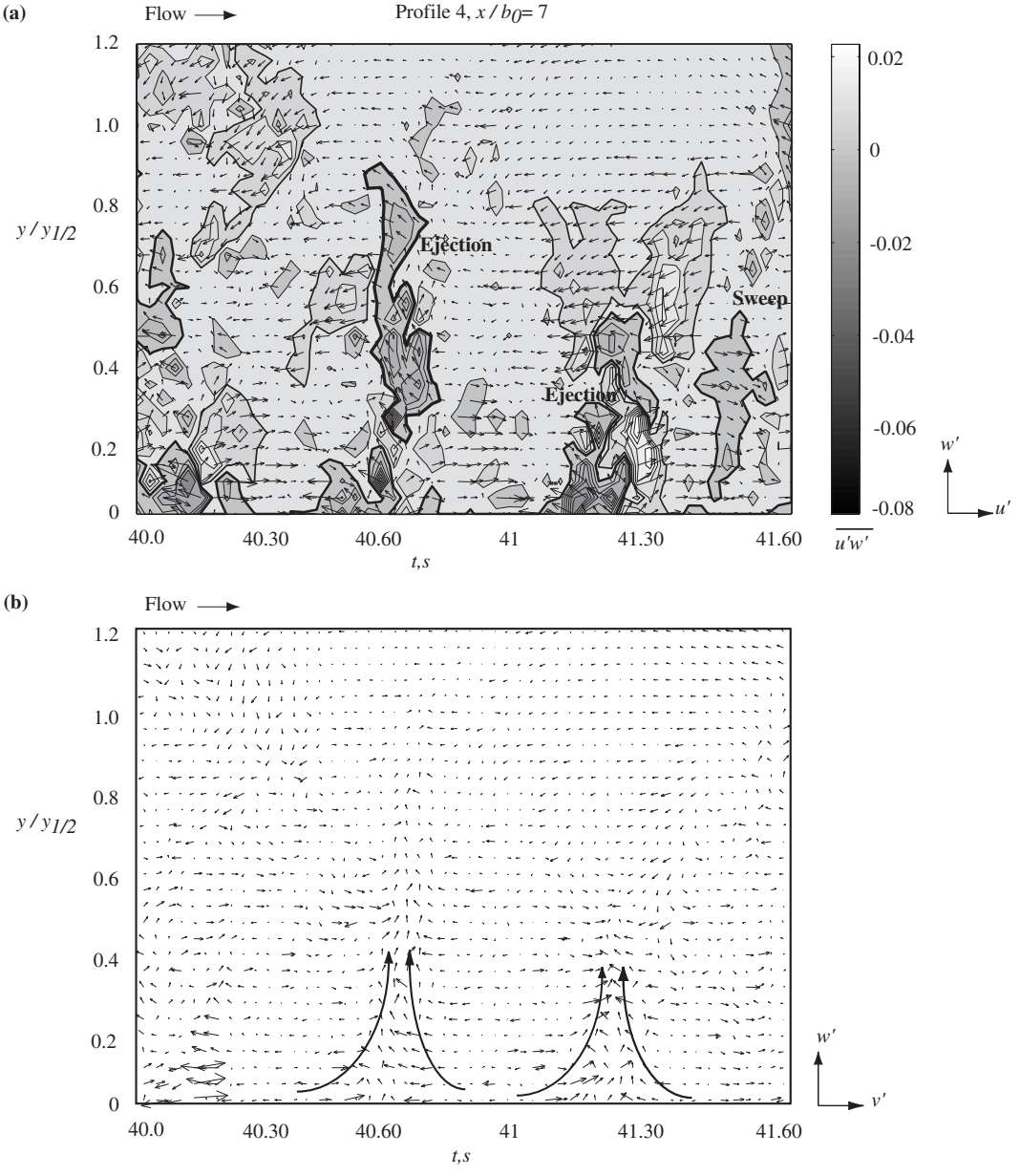


Figure 9. 2D velocity vectors of profile 4 for the time between t = 40s and 42s in longitudinal plane (a) and transversal plane (b).

41.30. For t = 40.60, the coherent shear stress structure (ejection) extends up to $y/y_{1/2} = 0.9$. A sweep event at t = 41.50s at $y/y_{1/2} = 0.3$, can be seen in Figure 9a. From the Reynolds shear stress map, it is seen that the contribution of the high-shear layer such as an ejection event to the Reynolds shear stress is significant. In the outer layer, the inward and outward events are found dominant at several locations (in Fig. 9a, at t = 40.30s at $y/y_{1/2} = 1$, at t = 41.60s at $y/y_{1/2} = 0.5$).

As can be seen in Figure 9b, there is a clear indication of streamwise vortices at t = 40.60 and 41.30. The matching between u′-w′ and v′-w′ flow field patterns is quite remarkable. Between two counter-rotating Görtler vortices, an outward event in the transversal

Copyright © 2006 Taylor & Francis Group plc, London, UK

plane occurs at t = 40.60s corresponding to the ejection event in the longitudinal plane. At the center of the Görtler vortices ($y/y_{1/2} = 0.40$), the transversal velocity is zero and the vertical velocity is at a maximum near the bed. This spanwise pattern of the Görtler vortices agrees well with those observed by Petitjeans et al. (1997).

10 CONCLUSION

This study experimentally investigated turbulence characteristics and their effect on the erosion capacity of a wall jet issuing from a sluice gate. It was demonstrated that due to the curvature of the scour-hole bed, Görtler vortices occur on the upslope side of the hole. In the present case, the Görtler number and the curvature parameter are well above their critical values, and between six and seven longitudinal vortices occur along the concave scour hole. These Görtler vortices make the wall jet unstable. They also strongly contribute to the suspension of the bed sediment particles by significantly increasing the wall shear stress.

With surface particles fixed, a scour- hole bed of equivalent roughness was created and intensive instantaneous velocity measurements using a 3D Acoustic Doppler Velocity Profiler (ADVP) at several positions along the channel axis were carried out. The mean velocity profiles indicate that the jet remains attached to the wall all along the scour hole. Recirculation occurs in the layers above the wall jet. A quadrant analysis in the streamwise and transversal planes shows that all along the scour hole, ejection and sweep events dominate turbulence in the inner layer of the wall jet and contribute to Reynolds shear stress more than outward and inward interactions. Above 0.6 $y/y_{1/2}$, outward and inward interactions slightly dominate. Ejections in the longitudinal direction correlate with upwash zones between the Görtler vortices.

ACKNOWLEDGEMENT

We are grateful for the financial support that was provided by the Swiss National Science Foundation, grant 200020-100383, for this study. We thank to anonymous reviewer for his careful reading and his constructive comments.

REFERENCES

Adduce C. et al. 2004. Numerical and experimental investigation of local scour downstream of a sill. *River Flow 2004*. 615–620.

Bippes H. and Görtler H. 1972. Dreidimensionale Störungen in der Grenzschicht an einer konkaven Wand. *Acta Mech*. 14: 251–267.

Blackwelder R. F. and Kaplan R. E. 1976. On the wall structure of the turbulent boundary layer. *J. Fluid Mech.* 76: 89–112.

Floryan J. M. 1991. On the Görtler instability of boundary layers. *Prog. Aerospace Sci.* 28: 235–271.

Graf W. H. 1971. *Hydraulics of Sediment Transport*. McGraw-Hill.

Gregory N. and Walker W. S. 1956. The effect on transition of isolated surface excrescences in the boundary layer. *ARC Repl.*, R&M No. 2779: 1–10.

Hopfinger E. J. et al. 2004. Sediment erosion by Görtler vortices: the scour-hole problem.*J. Fluid Mech.*520:327–342.

Hurter D. and Lemmin U. 2000. Shear stress statistics and wall similarity analysis in turbulent boundary layers using a high resolution 3-D ADVP. *J. Oceanic Engineering (IEEE)* 25: 446–457.

Kastrinakis et al. 1977. On the mechanism of boundary turbulence shear flows. *Lecture notes in physics,* 75: 190–204.

Kobayashi R. and Fujitsawa N. 1980. Taylor-Görtler instability of turbulent wall jets along concave surfaces. *J. Appl. Mech., Trans. ASME* 47: 671–672.

Kobayashi R. and Fujitsawa N. 1983. Turbulence measurements in wall jets along strongly concave surfaces *Acta Mech.* 47: 39–52.

Lhermitte R. and Lemmin U. 1994. Open-channel flow and turbulence measurements by high resolution Doppler sonar. *J. Atmos. Oceanic Technol.* 11: 1295–1308.

Nakagawa H. and Nezu I. 1977. Prediction of the contribution to the Reynolds stress from bursting events in open-channel flows. *J. Fluid Mech.* 80: 104–143.

Nelson J. et al. 1995. Role of near-bed turbulence structure in bed load transport and bed form mechanics. *Water Resourses Research.* 31: 2071–2086.

Nezu I. Nakagawa H. 1993. Turbulence in open-channel flows. *IAHR Monograph series.*

Petitjeans P. et al. 1997. Mass and momentum transport in longitudinal vortical structures in liquid: example of Görtler vortices. *Exp. in Fluids* 23: 388–394.

Rolland T. and Lemmin U. 1997. A two-component acoustic velocity profiler for use in turbulent open-channel flow. *J. Hydr. Res.* 33: 545–561.

Tani I. 1962. Production of longitudinal vortices in a boundary layer along a curved wall. *J. Geophys. Res.* 67: 3075–3080.

Copyright © 2006 Taylor & Francis Group plc, London, UK

Temporal flow evolution of sediment embedded circular bridge piers

Jens Unger & Willi H. Hager
VAW, ETH Zurich, Zurich, Switzerland

ABSTRACT: Bridge hydraulics has become an important issue in river engineering given the importance of bridges as a basic infrastructure. Many of the current research works investigate empirically the temporal advance of scour depth. In contrast, this paper presents some major results on the flow characteristics around a circular cylindrical bridge pier mounted in a mobile sediment bed resulting from an experimental study conducted at Versuchsanstalt für Wasserbau, Hydrologie und Glaziologie VAW during the past four years. The internal flow features were investigated by a newly developed *Particle Image Velocimetry* setup. This installation allows for a quasi 3-dimensional visualization of the velocity field around a bridge pier by means of horizontal and vertical planes. The main characteristics of the down-flow, the horseshoe vortex system and the tailwater vorticity field were detected from the non-intrusive and instantaneously measured velocity fields; additionally the bed-shear stresses were calculated in the scour region. This work, therefore, provides novel insight into the complex and fascinating two-phase flow around circular bridge.

1 INTRODUCTION

A common reason for bridge failure is the collapse of its foundation. The acting hydraulic load causes local erosion around the sediment embedded bridge pier or abutment. This so-called scour is able to endanger the stability of the complete bridge construction. Therefore, a number of bridge scour research projects are presently conducted all over the world. Most of these focus the prediction of the maximum scour depth and scour extension, generally as a function of time for steady hydraulic conditions, e.g. Breusers & Raudkivi (1991), Hoffmans & Verheij (1997), Melville & Coleman (2000) or Oliveto & Hager (2005). In contrast, the governing internal flow features of the scour process have received comparatively little attention. A limiting factor so far was the available experimental technique. The standard instrumentation was mainly intrusive, thus appreciably disturbing the flow and consequently the scour process.

Melville & Raudkivi (1977) conducted an early research work on the flow characteristics in scour holes. They investigated the flow field around a circular bridge pier using four vertical plans at 0°, 30°, 60° and 90° relative to the approach flow direction, by using a DISA hot-film anemometer in addition to the hydrogen-bubble technique. All experiments were confined to clear water scour conditions and a fixed sediment bed for two conditions: (1) The initially flat bed and (2) the 'equilibrium' scour hole. The main results concern the flow patterns, the turbulence intensity distribution and the boundary shear stress distribution in the scour region. Based on this work numerous studies were realised to refine the specific flow structures. Thus, Qadar (1981) investigated the interaction between the horseshoe vortex and the scour hole. In addition, Dargahi (1989) detected the simultaneous presence of various vortices above a fixed smooth bed at the leading pier front. The down-flow characteristics in front of the pier were observed by Ahmed & Rajaratnam (1998) and Sarker (1998) by means of a Preston tube and *Acoustic Doppler Velocimetry* (ADV), respectively. A more detailed study was presented by Graf & Yulistiyanto (1998) and expanded by Graf & Istiarto (2002). Therein, an ADV Profiler was used to measure instantaneous velocity components in a defined profile of the flow field around a circular bridge pier for fixed and mobile bed configurations, respectively. These works refer to the flow pattern up- and downstream of the bridge pier, the longitudinal distribution of bed-shear stresses in the axis of symmetry and the turbulent kinetic energy. Barbhuiya & Dey (2004) obtained similar results in a semicircular pier arrangement placed at the channel sidewall.

All these studies use intrusive and non-instantaneous velocity-measuring methods. As stated, this technique disturbs the turbulent flow field considerably and does not allow recording the highly unsteady flow patterns in the horseshoe vortex system due to the point-wise

Copyright © 2006 Taylor & Francis Group plc, London, UK

velocity readings. The present research work aims at a detailed temporal description of the flow patterns around bridge piers using *Particle Image Velocimetry* (PIV), a non-intrusive and instantaneous measuring technique. The knowledge of these coherent plane flow structures allows determining the bed-shear stresses rather than a point-wise description of the flow.

2 EXPERIMENTAL SETUP

2.1 *Physical model*

The hydraulic model tests were conducted in the VAW scour channel, with a maximum discharge of $Q = 130$ l/s and a maximum water depth of 0.40 m. The rectangular channel had a width of $B = 1$ m, and a length of 13 m with a working section of some 5 m. A detailed description of this scour channel is provided by Hager et al. (2002). Two sediments were used: (1) an almost uniform sediment with a median sediment size of $d_{50} = 1.14$ mm and a sediment non-uniformity of $\sigma = (d_{84}/d_{16})^{1/2} = 1.18$, and (2) a sediment mixture with $d_{50} = 5.00$ mm and $\sigma = 2.29$. The semicircular pier models had diameters of $D = 0.457$ and 0.260 m. The plexiglass pier was always attached to the glassed channel sidewall, to visualize both the flow characteristics around the bridge pier and inside the scour hole. Preliminary tests demonstrated that this configuration has only a minor effect on the flow field with regard to the boundary layer development along the glass wall (Unger 2006, Unger & Hager 2006). The present research considered only clear water scour conditions with no notable sediment transport in the approach flow region. Consequently the threshold Froude number $\mathrm{F}_t = V_o/V_t$ varied between $0.60 \leq \mathrm{F}_t \leq 1.05$, with V_t as threshold velocity and V_o as approach flow velocity. The discharge varied in a range of $0.025 \leq Q \leq 0.110$ m^3/s resulting in a densimetric Froude number $\mathrm{F}_d = V_o/(\mathrm{g}' d_{50})^{1/2}$ between 1.83 and 3.22, with $\mathrm{g}' = [(\rho_s - \rho)/\rho]\mathrm{g}$ as the reduced gravitational acceleration, ρ as the fluid density and ρ_s as the sediment density. Table 1 summarizes the experimental conditions of the present research.

To initiate an experiment, the sediment bed was set horizontally by using a grading mechanism. After the half cylinder was positioned at the glass wall, the pump was started and the discharge slightly increased to the test value, thereby carefully inhibiting sediment entrainment around the pier. Next, the water level was slowly lowered, using the flap gate in the tailwater. Once the first particle moved, the time was set to $t = 0$ and the water depth was further reduced to the test value. Normally the water and the sediment surface topographies and the velocity vector field were measured at times $t = 60$, 180, 360, 600, 1200, 2400, 3600, 7200, 14440, 28800 and 86400 s, therefore from 1 minute to 1 day after sediment entrainment.

2.2 *Instrumentation*

Two different measurement techniques were employed, namely (1) a combined surface measuring unit consist of a Laser Distance Sensor (LDS) plus an Ultra Sonic Sensor (USS) and (2) a large-scale Particle Image Velocimetry (PIV) setup to measure instantaneously the unsteady and highly turbulent plane flow field. The combined LDS/USS unit was mounted on a movable high precision carriage allowing for displacements in all three space directions. The accuracy of the simultaneous sediment- and water surface readings was ± 0.5 mm.

Figure 1 shows a sketch of the planar PIV-setup. It provides instantaneous velocity vector fields both in horizontal sections around the pier and in vertical sections parallel to the mean flow direction. For the plan view observations, the nearly horizontal water surface was covered with a thin plexiglass-plate to inhibit optical problems with surface waves. Given that the approach Froude number varied typically between 0.2 and 0.5, hydrodynamic effects can be neglected (Unger & Hager 2005). A flashed Xenon-stroboscope ① was used to illuminate the light sheet layer. This plane was spanned by a fiber-optic line-converter ⑤, which was linked to the stroboscope with a fiber bundle ④. The Programmable Timing Unit (PTU) ③ was the key element for timing the PIV system. The PTU received the external Transistor – Transistor – Logical (TTL) start trigger from the CCD camera ②

Table 1. Test conditions of Unger (2006).

Nr.	d_{50} [mm]	D [m]	Q [m^3/s]	h_o [m]	F_d [–]	$\mathrm{F}_{di,\beta}$ [–]	F_t [–]	$\mathrm{R}_D \times 10^{-5}$ [–]
A1	5.00	0.457	0.050	0.096	1.83	1.69	0.53	2.36
A2	5.00	0.457	0.050	0.072	2.44	1.62	0.74	3.14
A3	5.00	0.457	0.080	0.132	2.13	1.78	0.59	2.74
A4	5.00	0.457	0.080	0.091	3.09	1.68	0.91	3.98
A5	5.00	0.457	0.110	0.190	2.04	1.87	0.54	2.62
A6	5.00	0.457	0.110	0.125	3.09	1.76	0.87	3.98
B1	5.00	0.260	0.050	0.080	2.20	1.87	0.66	1.61
B2	5.00	0.260	0.050	0.058	3.03	1.78	0.95	2.22
B3	5.00	0.260	0.080	0.133	2.11	2.02	0.59	1.55
B4	5.00	0.260	0.080	0.090	3.12	1.90	0.92	2.29
B5	5.00	0.260	0.110	0.160	2.42	2.07	0.65	1.77
B6	5.00	0.260	0.110	0.130	2.97	2.01	0.83	2.18
C1	1.14	0.457	0.050	0.150	2.46	1.79	0.74	1.51
C2	1.14	0.457	0.050	0.120	3.07	1.74	0.95	1.89
C3	1.14	0.457	0.070	0.190	2.71	1.86	0.79	1.67
C4	1.14	0.457	0.070	0.160	3.22	1.81	0.96	1.98
C5	1.14	0.457	0.025	0.080	2.30	1.63	0.76	1.41
C6	1.14	0.457	0.025	0.065	2.83	1.58	0.97	1.74
D1	1.14	0.260	0.050	0.166	2.22	2.03	0.66	0.78
D2	1.14	0.260	0.050	0.126	2.92	1.95	0.90	1.02
D3	1.14	0.260	0.070	0.231	2.23	2.12	0.63	0.78
D4	1.14	0.260	0.070	0.182	2.83	2.05	0.83	0.99
D5	1.14	0.260	0.025	0.088	2.09	1.84	0.68	0.73
D6	1.14	0.260	0.025	0.064	2.88	1.75	0.98	1.01

Copyright © 2006 Taylor & Francis Group plc, London, UK

and controlled its exposure in synchronisation with the stroboscope flash. The first flash was sent out just before the interline transfer of the CCD sensor started and the second flash was released thereafter. Each pair of this double frame single exposure images allowed for a velocity vector calculation by cross-correlation. With a frame rate of 60 Hz of the progressive scan monochrome CCD camera the time resolution of the PIV system was 30 Hz. The used seeding particles had a diameter of 0.5 mm and were mixed with water in a container ⑥ prior to injection ⑧ by a pump ⑦ (Unger 2006).

3 EXPERIMENTAL RESULTS

3.1 *Flow in vertical plane*

Figure 2 shows the temporal evolution of the vertical flow field in the channel axis, parallel to the mean flow direction, as streamline plots, for times $t = 60$, 180, 600 and 2400 s (run D6). At time $t = 60$ s no scour has yet occurred in the pier symmetry plane, because the sediment entrainment starts at an angle of about $\phi = 75°$ from pier symmetry axis. The streamlines in the approach flow region $x/h_o < -2.50$ are nearly parallel such that the flow is not affected by the presence of the pier and the vertical velocity profiles have a standard logarithmic distribution. It was demonstrated that the effect of the pier on the upstream flow field extends to approximately a distance of $x = -(h_o D^2)^{1/3}$ measured from the leading pier front (Unger 2006). For run D6, a distance $x/h_o = -2.60$ results, therefore. Closer to the pier, in the region $-2.50 < x/h_o < -1.50$, the flow is decelerated but conserves a logarithmic velocity profile. Toward the pier, the flow is strongly deflected in the vertical direction, resulting in an up-flow toward the water surface and a down-flow toward the sediment surface due to the presence of a stagnation point. The up-flow develops into a relatively small surface recirculation, whereas the down-flow is deflected in the transverse channel direction. Close to the sediment bed in the region $-1.50 < x/h_o < -0.50$, a so-called initial vortex develops, additionally (Fig. 2a).

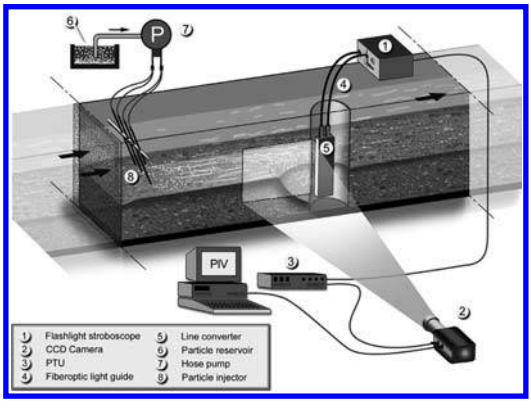


Figure 1. Scheme of the PIV-setup.

At time $t = 180$ s the scour has migrated from the pier side to the symmetry plane, without an appreciable change of the flow in the approach flow region as compared to $t = 60$ s. From the scour hole boundary a vertical flow deflection toward the instantaneous sediment surface is observed. Furthermore, the down- and up-flows, the surface recirculation and the stagnation point have established. In contrast to $t = 60$ s, the initial vortex has disappeared by now. Thus, the down-flow is deflected in the transverse channel direction along the scour surface. The scour hole then continuously deepens and the horseshoe vortex system is developed. At time $t = 600$ s it consists in the initial stage of a single vortex located directly above the rim in the scour hole. At $t = 2400$ s this vorticity field is divided into a primary horseshoe vortex plus one or even more secondary vortices. Both, the primary- and the secondary horseshoe vortices rotate clockwise. Note that the approach flow, the down- and up-flows, the stagnation point as well as the surface recirculation essentially conserve their structure, independent from the scour hole development.

Due to the large hydraulic load of run D6, the evolution of the different flow patterns is relatively fast. For

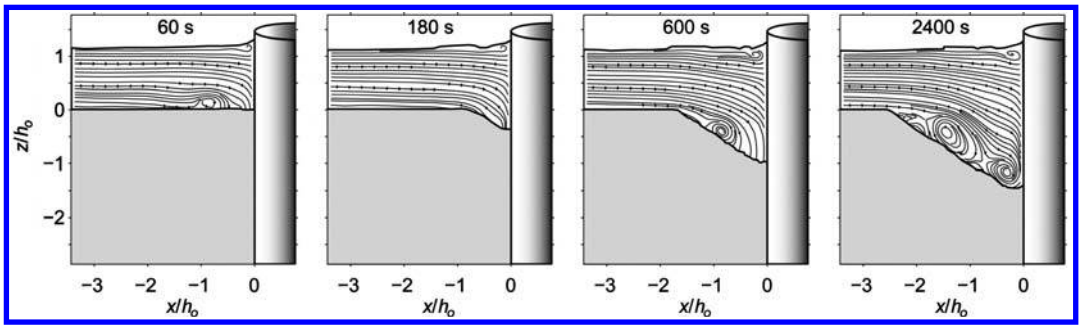


Figure 2. Streamline plots at various times for run D6.

Copyright © 2006 Taylor & Francis Group plc, London, UK

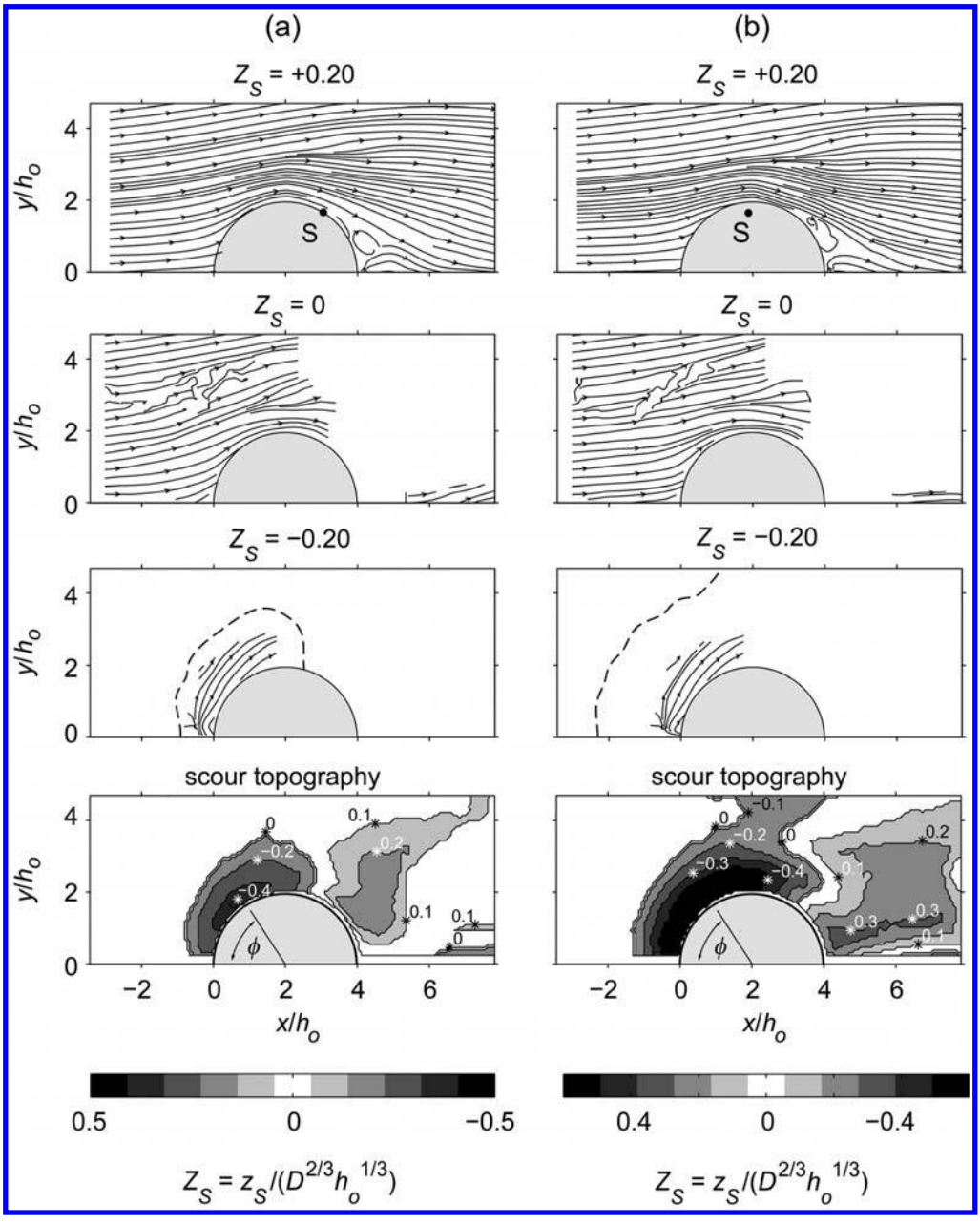


Figure 3. Horizontal streamline plots and scour topography in various planes for run D6 at times t = (a) 60 s and (b) 180 s; (- - -) scour extension

hydraulic conditions with smaller values of F_d and F_t this progress requires much more time (Unger 2006).

3.2 *Flow in horizontal plane*

Figure 3 refers to the analogous flow fields as shown in Figure 2 at identical times t in three horizontal planes, namely (1) at $Z_S = z_S/(D^2 h_o)^{1/3} = +0.20$ corresponding to approximately an elevation $z_s = h_o/2$ above the original sediment surface, (2) at the original sediment surface $Z_S = 0$ and (3) inside the scour hole at $Z_S = -0.20$. The plots for $Z_S = -0.20$ additionally show the instantaneous scour boundary as a dashed

Copyright © 2006 Taylor & Francis Group plc, London, UK

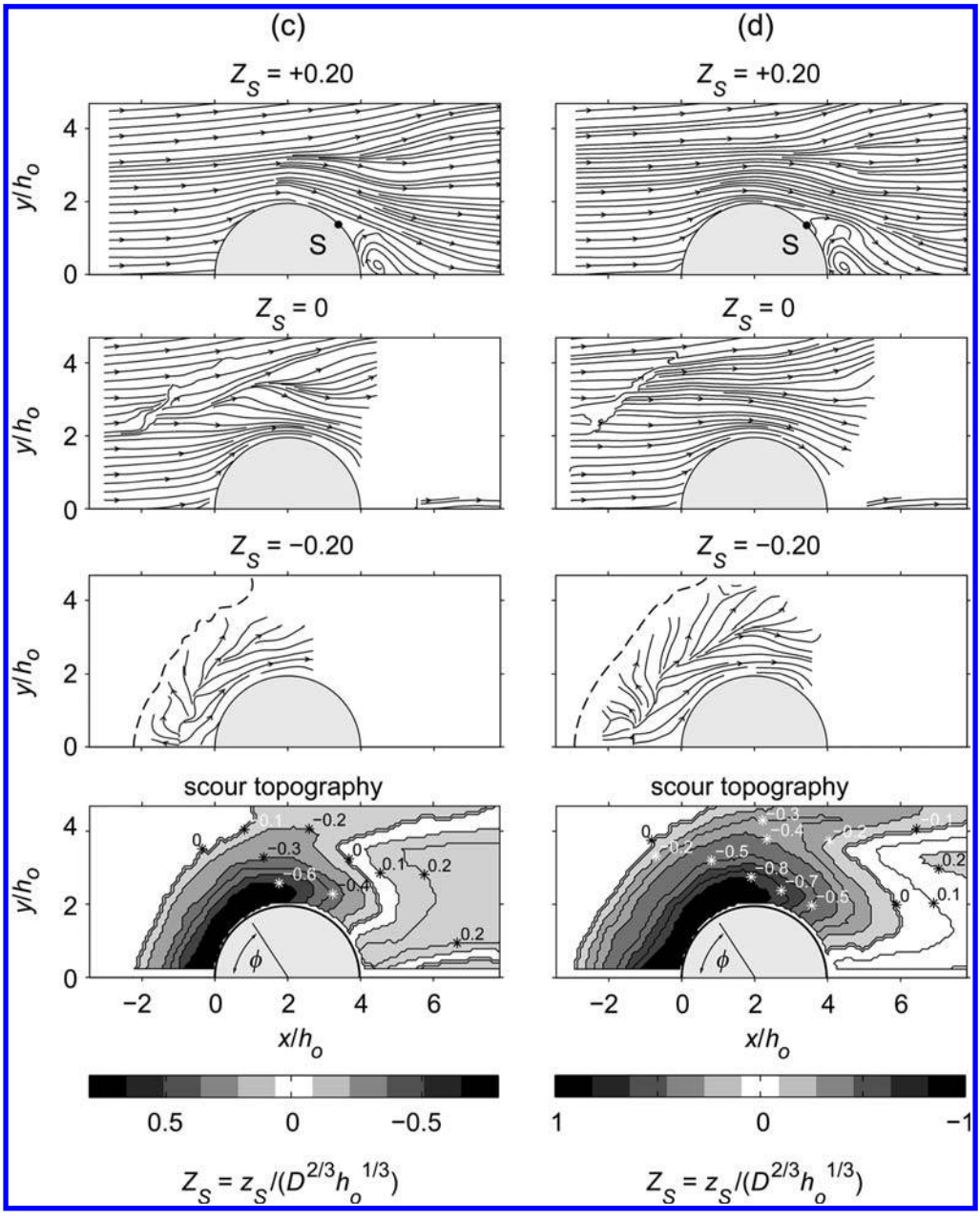


Figure 3. Continued. $t =$ (c) 600 s and (d) 2400 s; (- - -) scour extension.

line. Finally, the dimensionless scour topography with the same scaling is plotted for each time.

At depth $Z_S = +0.20$ the flow field is similar for all times. Upstream from the pier, the flow is relatively uniform, as reflected by the parallel and constantly spaced streamlines. Closer to the pier, from $x/h_o \cong -2.00$, the flow is deflected in the transverse channel direction y and accelerated, with the maximum velocity at an angle of $\phi = 75°$, resulting there in sediment entrainment. Simultaneously, the pressure along the pier decreases to its minimum at $\phi = 75°$. Beyond this region at an angle of $90° \leq \phi \leq 120°$ the flow separates from the pier due to the well-known pressure increase (Schlichting & Gersten 1997). The

Copyright © 2006 Taylor & Francis Group plc, London, UK

position of the separation point S is subject to turbulent fluctuations and eventually migrates in the region $90° \leq \phi \leq 120°$ as specified above. Downstream of the separation point is the turbulent wake zone consisting of highly unsteady vortices. These vortices are transported downstream by the mean flow and dissipated by turbulence production. The flow beyond the downstream plot end is redistributed and relatively uniform.

The flow of the plane $Z_S = 0$ is more complex than at $Z_S = +0.2$. Whereas upstream of the pier in the region $y/h_o < -2$ only minor differences are visible, the instantaneous scour circumference generates a separation line. Up to $\phi = 150°$ and for $Z_S \leq 0$ the flow does not separate from the pier and the flow is attached to it as with the Coanda effect. This phenomenon is discussed below.

Consider now the flow field in the horizontal plane $Z_S = -0.20$ (Fig. 3). At times $t = 60$ and 180 s a source flow develops at the pier front, due to the down-flow. The source flow is deflected in the transverse channel direction along the pier perimeter. This is in agreement with the vertical flow fields shown in Figure 2, containing no recirculation in the scour hole. During the next two time steps $t = 600$ and 2400 s an attached node line is developed in the scour, with the origin at $y/h_o = 0$ and $x/h_o \cong -1.00$ and -1.20, respectively. This singularity extends from the pier periphery along the scour hole in a constant distance of $\sim 1.00 \cdot D/4$ and $\sim 1.20 \cdot D/4$, respectively. As observed in the vertical planes, this structure is an indication for the existence of a vortex system (Fig. 2). The horseshoe vortex in Figure 2 is of spatial structure, surrounding the pier like a thick cord, therefore.

Figure 3 shows in addition the temporal evolution of the scour topography. The scour zone starts at an angle of $\phi \cong 75\circ$ for $t = 60$ s. The sediment deposition zone in this early stage is close to the pier immediately downstream from the scour zone. With increasing time, the scour zone migrates toward the pier front and expands laterally. At $t = 600$ s, the maximum scour depth has reached the pier front, and the sediment deposition zone has successively migrated downstream beyond the pier end. In the further scour process, the maximum scour depth and the scour expansion increase logarithmically with time (Melville & Coleman 2000, Oliveto & Hager 2002).

4 DISCUSSION OF RESULTS

4.1 *Principle flow features*

From the previously presented results pertaining to run D6, and the detailed analysis of the experimental program (Table 1), four principle flow phases around a cylindrical bridge pier may be identified. Figure 4 shows these phases schematically in the vertical plane of the pier symmetry axis.

As mentioned, sediment entrainment and scour activity starts always at roughly $\phi = 75°$, due to the locally high velocities in this region. During *phase* 1, the pier front has not yet undergone any scour. Upstream of the pier the mean flow is relatively uniform with a logarithmic velocity distribution. Toward the pier front, the flow is first decelerated and upon reaching it deflected (Fig. 4a). The stagnation point at the pier front divides the approach flow into two parts, (1) the *up-flow* toward the water surface and (2) the *down-flow* toward the instantaneous sediment surface. Unger (2006) demonstrated, that the geometric position of the stagnation point remains constant with time and may be described with a linear function of the reference length $z_R = (D^2 h_o)^{1/3}$ and the median sediment size d_{50}. Near the water surface the up-flow generates constantly a small *surface recirculation*. Its diameter, geometric position and vortex strength are also time-independent and depend on the densimetric Froude number F_d and the ratio z_R/d_{50}, respectively.

Close to the sediment surface a relatively small non-scour inducing *initial vortex* results from the down-flow in *phase* 1. During *phase* 2 this initial vortex disappears, and the down-flow close to the simultaneous sediment surface is completely deflected in the transverse channel direction. The relative time T_0 relating to the start of phase 2 depends mainly on threshold Froude number F_t describing the entrainment of sediment in the approach flow channel. Further, the flow around the pier is decelerated and thereby increasing the scour surface from $\phi = 75°$ mainly in the upstream direction.

The characteristic *horseshoe vortex system* develops eventually in *phase* 3. It consists first of a scour inducing *primary vortex*, to where the maximum scour depth migrates in the pier symmetry axis. Due to the continuous scour depth progress the discharge section increases resulting in a smaller flow velocity along the pier side, associated with a reduction of the scour advance in the lateral scour hole region.

In *phase* 4 the effect of the primary horseshoe vortex increases. The vortex diameter expands and one or more *secondary vortices* are generated. Both the primary and the secondary vortices rotate clockwise and induce additional small opposite-rotating vortices. The main horseshoe vortex generates the typical rim in the scour hole upstream from the pier. The high bed-shear stresses generated by this vortex result in a continuous deepening of the scour hole. When the slope of the scour hole attains its critical value avalanches slide toward the pier and the sediment is transported downstream. This process is repeated periodically and causes the main scour advance during phase 4.

A detailed description of the horseshoe vortex and the down-flow is given by Unger (2006). Therein,

Copyright © 2006 Taylor & Francis Group plc, London, UK

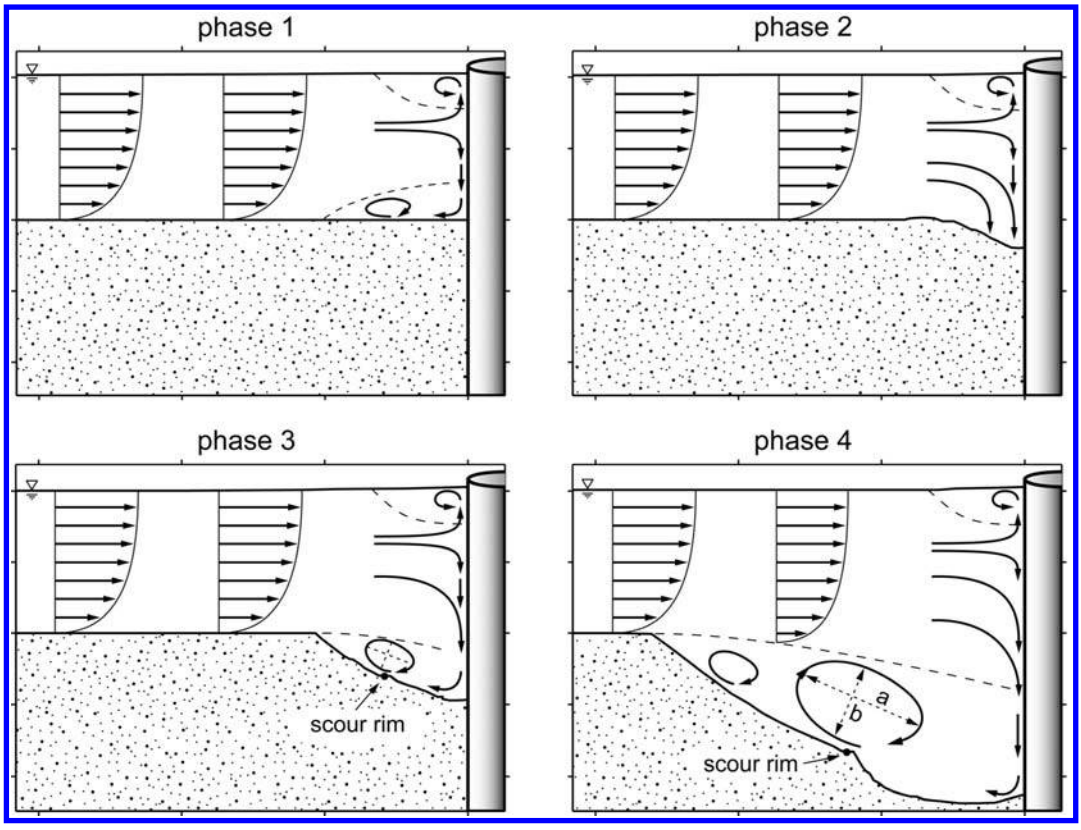


Figure 4. Principle vertical flow features around a circular bridge pier in the pier symmetry axis. *Phase* 1: initial vortex, *Phase* 2: flow deflection in transverse channel direction, *Phase* 3: scour evolution inducing horseshoe vortex system and *Phase* 4: fully developed horseshoe vortex system with one primary and several secondary vortices.

general velocity profiles are derived as a coupled square and exponential function. It is demonstrated that the maximum vertical down-flow velocity component reaches up to $0.75 \cdot V_o$ depending mainly on the ratio z_R/d_{50}. By means of normalization with the instantaneous scour depth the velocity profile function of the down-flow remains constant with time, in contrast to the velocity distribution through the centre of the primary horseshoe vortex. Here the maximum velocity governing the induced shear stress increases logarithmically with time and its geometric position moves toward the instantaneous sediment surface.

Figure 5 shows a sketch of the principal flow features in the horizontal plane. The arrows represent typical streamlines along the instantaneous sediment surface, and the flow separation zones in the wake of the pier are limited with dashed lines. In *phase* 1, the scour just started at roughly $\phi = 75°$, the sediment deposition zone being close to the pier. Upstream from the pier the flow is first decelerated and then deflected in the transverse channel direction, associated with a flow acceleration. Simultaneously the pressure along the pier periphery decreases up to the minimum value at $75° \leq \phi \leq 115°$ resulting further downstream in the flow separation zone due to the pressure increase. With a pier Reynolds numbers $R_D = (V_o D)/\nu$ between $5 \cdot 10^4$ and $3.5 \cdot 10^6$ (with ν as kinematic viscosity) for the present experiments, the geometric position of the pressure minimum and the separation point are subject to turbulent fluctuations. The reason is the permanent switch of laminar and turbulent separation linked with the possible turbulent re-attachment or a fully turbulent wake flow (Schlichting & Gersten 1997, Achenbach 1968). Downstream from the separation point S extends the turbulent wake zone. Because of the increased scour surface, the separation point in *phase* 2 migrates downstream along the pier perimeter. Note, that the plotted arrows represent streamlines along the instantaneous sediment topography of the scour hole, such that no migration of the separation point above the original sediment elevation was observed. The wake zone reduces due to migration of

Copyright © 2006 Taylor & Francis Group plc, London, UK

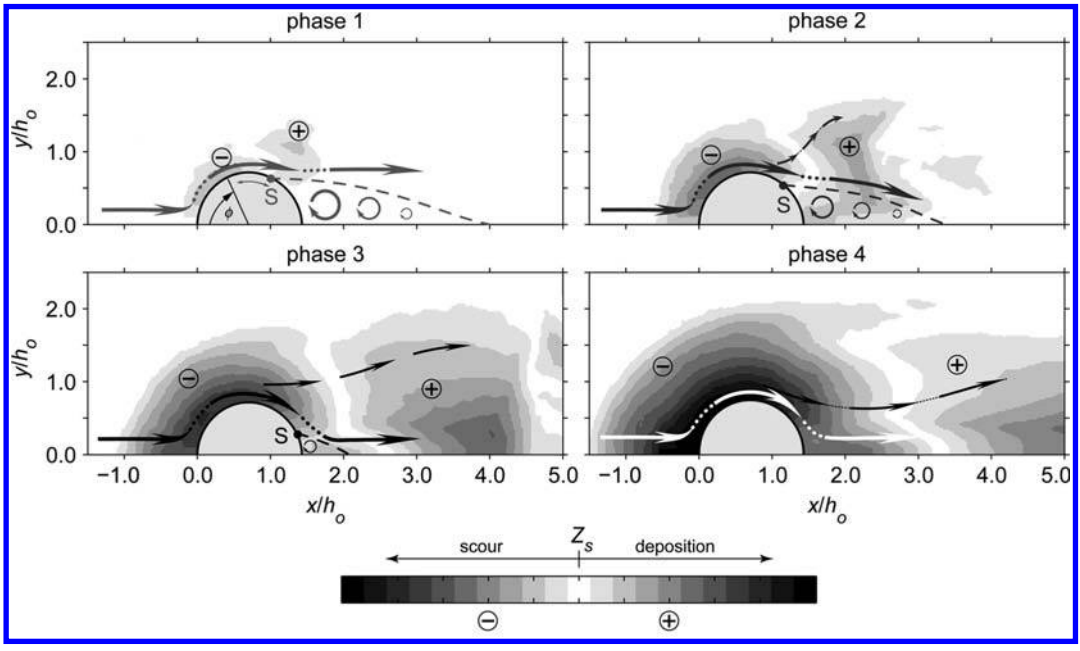


Figure 5. Principle horizontal flow features around a circular bridge pier close to the instantaneous sediment surface (see Figure 4).

the separation point. Additionally the flow separates near the pier side, due to the sediment deposition zone downstream of the pier.

In *phase* 3 the flow below $Z_S = 0$ follows practically along the entire pier perimeter and is similar to a Coanda flow, because: (1) Due to the continuous scour hole enlargement the pressure along the pier surface close to the instantaneous sediment surface increases. Consequently, the pressure gradient decreases and the flow separates at a larger angle ϕ, and (2) the special scour topography in this region effects the flow like a curved training wall. Additionally, due to the sediment deposition, the flow separation is much smaller because of the continuous downstream migration of this zone.

Finally, in *phase* 4, the flow below $Z_S = 0$ is completely attached to the pier perimeter. Because of the large and deep scour hole the flow velocity around the pier decreases and the scour advance decelerates, therefore. The main scour activity is concentrated to the pier front zone resulting from the fully developed main horseshoe vortex.

4.2 *Bed-shear stresses*

The estimation of a bed-shear stress from experimental data is a difficult task. Given that the direct experimental measurement techniques are limited both for laminar and turbulent flows, the available velocity distributions were used to approximate the effective bed-shear stresses. A detailed analysis confirmed the modified mixing layer concept (Unger 2006). Based on the velocity components v_x and v_z close to the instantaneous sediment surface, the velocity $v_{par} = (v_x^2 + v_y^2)^{1/2} \cdot \cos\alpha$ parallel to the bed was calculated with α as the instantaneous angle of the scour hole above the velocity vector considered. The bed-shear stress τ was subsequently computed as,

$$\tau = \rho\kappa^2 z_{par}^2 \left(\frac{\mathrm{d}v_{par}}{\mathrm{d}z}\right)^2 \tag{1}$$

with $\kappa = 0.40$ as the von Kármán constant and z_{par} as the normal distance of the instantaneous sediment surface to the origin of v_{par}. The critical (subscript c) bed-shear stress τ_c for entrainment is,

$$\tau_c = \rho V_*^2 \tag{2}$$

Here, V_* is the critical shear velocity determined according to Hager & Oliveto (2002) as

$$V_* = 1.08 D_*^{1/12} \left(\frac{R_{ho}}{d_{50}}\right)^{1/6} \left(\mathrm{g}' d_{50}\right)^{1/2} \tag{3}$$

Herein, $D_* = (g'\nu^2)^{1/3}/d_{50}$ is the dimensionless sediment size and $R_{ho} = Bh_o/(2h_o + B)$ the hydraulic radius of the approach flow. A similar method to estimate the bed-shear stresses inside the scour hole was

Copyright © 2006 Taylor & Francis Group plc, London, UK

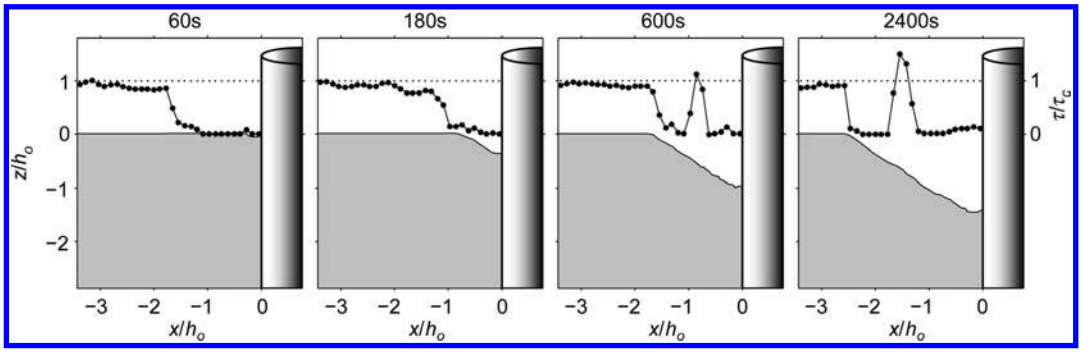


Figure 6. Relative bed-shear stresses τ/τ_c in the pier symmetry axis for run D6.

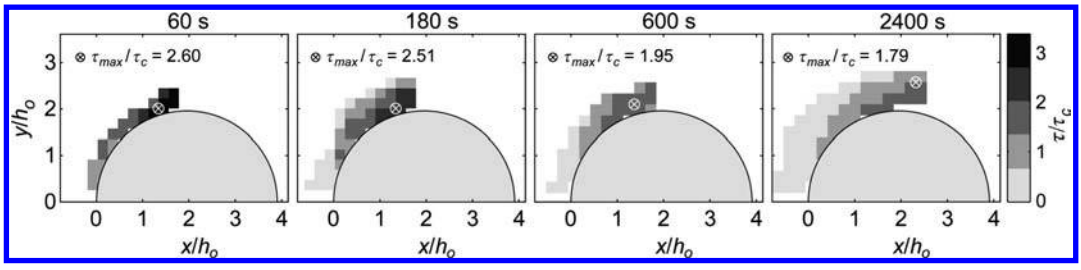


Figure 7. Relative bed-shear stresses τ/τ_c in the horizontal plane closest to the instantaneous scour surface for run D6.

also used by Barbhuiya & Dey (2004), Dargahi (1989), Graf & Istiarto (2002) and Graf & Yulistiyanto (1998).

The computed bed-shear stresses for the vertical flow field are shown in Figure 6 for the times considered in Figs. 2 and 3. In the approach flow region upstream from the instantaneous scour hole the relative bed-shear stress τ/τ_c is roughly constant and close to the critical value of $\tau/\tau_c = 1$. This is in agreement with the flow threshold Froude number $F_t = 0.98$. At time $t = 60$ s, corresponding to *phase* 1, the relative bed-shear stress reduces rapidly from $x/h_o \cong -1.5$ to the leading pier front, due to flow deceleration. Therefore, the initial vortex in phase 1 induces only minor shear stresses. At time $t = 180$ s corresponding to *phase* 2 this sudden bed-shear stress reduction migrates downstream to the starting point of the scour hole. In p*hase* 3 at $t = 600$ s, the horseshoe vortex develops, resulting in a relative bed-shear stress peak $\tau/\tau_c > 1$ directly below the horseshoe vortex centre. Finally in *phase* 4 at time $t = 2400$ s this peak increases and migrates upstream. Thus, the scour progress in the pier front zone is mainly governed by the primary horseshoe vortex. Directly at the starting point of the scour hole the relative bed-shear stress reduces in all four phases rapidly to $\tau/\tau_c = 0$ from the approach flow value τ_o.

The sediment close to the scour perimeter *slides* into the scour hole instead of being entrained from where it is transported downstream by the horseshoe vortex. Figure 6 demonstrates that bed-shear stresses are $\tau/\tau_c > 1$ in the vertical streamwise plane only after the formation of the primary horseshoe vortex and below the centre of it.

Figure 7 shows the corresponding horizontal bed-shear stress distribution close to the instantaneous scour surface and its maximum value τ_{max}/τ_c. The bed-shear stress was computed in the same manner as previously. Note that the calculated bed-shear stresses result from velocity vectors at the currently lowest elevation (here at $Z_S = -0.20$). Due to the particular scour topography, the velocity field and the resulting bed-shear stress distribution cover only the region close to the pier perimeter, and no general horizontal bed-shear stress distribution is available so far.

At scour beginning during *phase* 1, the maximum relative bed-shear stresses of $\tau/\tau_c \cong 3$ are located at $\phi \cong 75°$ to 90°, as previously described. In the whole region $0° \leq \phi \leq 90°$ the bed-shear stresses reach values $\tau/\tau_c > 1$, so that the scour at the pier side develops fast associated with the migration of the maximum depth toward the pier front. During *phase* 2 the bed-shear stress distribution is similar to phase 1. In the further progress, the bed-shear stresses decrease continuously in the observed scour region. Simultaneously the maximum bed-shear stresses migrate downstream along the pier perimeter. For $t = 600$ s, thus in *phase* 3, the computed bed-shear stress data near the pier front attain values $\tau/\tau_c < 1$, whereas bed-shear stresses $\tau/\tau_c > 1$ result besides the pier for $\phi > 45°$. In *phase* 4

Copyright © 2006 Taylor & Francis Group plc, London, UK

this decrease continues so that the scour deepening migrates downstream of the pier to $\phi > 90°$. The scour progress upstream from the pier is mainly related to the primary horseshoe vortex. Because of the localized observational region, the resulting shear stresses from this vortex are not included in Figure 7. Unger (2006) gives a generalized approach to compute directly the induced bed-shear stresses.

5 CONCLUSIONS

A large scale Particle Image Velocimetry (PIV) setup as a non-intrusive and simultaneously velocity measuring technique was successfully applied to bridge pier scour to obtain further insight into the temporal evolution of the flow features and the scour process. This contrasts most of the previous studies on the fascinating flow features around a circular bridge pier, arranged in a mobile sediment bed using point-wise and intrusive instrumentation. The present experimental observations contribute to pier scour experimentally and to the validation of numerical simulations concerning scour hydraulics. Using the instantaneous velocity fields the main flow patterns may be described from a spatial point of view.

The presence of a cylindrical pier results in flow deflection with the following main features: (1) stagnation point, (2) up-flow with a (3) surface recirculation and (4) down-flow close to the leading pier front, besides (5) the initial vortex upstream of the pier that eventually develops into (6) the horseshoe vortex system. In the horizontal planes (7) separation from the pier sides, (8) a wake zone downstream of the pier and (9) several singularities inside the scour were observed. The temporal evolution of these characteristics was described with 4 main phases in terms of the governing hydraulic and geometric parameters. Finally, an approach to predict the bed-shear stresses was attempted, based on the velocity field close to the instantaneous sediment surface. This paper gives a compact overview on some fundamental findings of a scour research project, therefore.

ACKNOWLEDGEMENT

The first author acknowledges the financial support from the Swiss National Science Foundation, Contract Number NF 2-77095-01.

NOTATIONS

B	channel width
D	pier diameter
d_{50}	median sediment size
F_d	$= V_o/(g' d_{50})^{1/2}$ densimetric particle Froude number in the approach flow
F_{di}	$= V_i/(g' d_{50})^{1/2}$ densimetric particle Froude number for general sediment entrainment
$F_{di,\beta}$	$= V_{i,\beta}/(g' d_{50})^{1/2}$ densimetric particle Froude number for sediment entrainment at the pier
F_t	$= V_o/V_t$ threshold Froude number
g	gravitational acceleration
g′	$= [(\rho_s - \rho)/\rho]g$ reduced gravitational acceleration
h_o	approach flow depth
Q	discharge
R_D	$= (V_o D)/\nu$ pier Reynolds number
T_0	relative time to horseshoe vortex formation
t	time
V_i	inception velocity
V_o	approach flow velocity
V_t	threshold velocity
v_{par}	velocity parallel to instantaneous sediment surface
v_x, v_y, v_z	velocity components
z_{par}	normal distance to instantaneous sediment surface
z_R	$= (D^2 h_o)^{1/3}$ reference length
z_S	local scour depth
Z_S	$= z_S/(D^2 h_o)^{1/3}$ normalized depth
α	local scour hole angle
ρ	fluid density
ρ_S	sediment density
σ	$= (d_{84}/d_{16})^{1/2}$ sediment non uniformity
ϕ	angle of the flow direction relative to channel axis
ν	kinematic viscosity
τ_0	bed-shear stress
τ_0	bed-shear stress in the approach flow
τ_c	critical bed-shear stress

REFERENCES

Achenbach, E. (1968). Distribution of local pressure and skin friction around a circular cylinder in cross-flow up to $Re = 5 \cdot 10^6$. *Journal of Fluid Mechanics* 34(4): 625–639.

Ahmed, F., Rajaratnam, N. (1998). Flow around bridge piers. *Journal of Hydraulic Engineering* 124(3): 288–300.

Barbhuiya, A.K., Dey, S. (2004). Measurement of turbulent flow field at a vertical semicircular cylinder attached to the sidewall of a rectangular channel. *Flow Measurement and Instrumentation* 15(2): 87–96.

Breusers H.N.C., Raudkivi A.J. (1991). *Scouring*. IAHR Hydraulic Structure Design Manual 2. Balkema: Rotterdam.

Dargahi, B. (1989). The turbulent flow field around a circular cylinder. *Experiments in Fluids* 8(1): 1–12.

Graf, W.H., Istiarto, I. (2002). Flow pattern in the scour hole around a cylinder. *Journal of Hydraulic Research* 40(1): 13–20.

Copyright © 2006 Taylor & Francis Group plc, London, UK

Graf, W.H., Yulistiyanto, B. (1998). Experiments on flow around a cylinder: The velocity and vorticity fields. *Journal of Hydraulic Research* 36(4): 637–653.

Hager, W.H., Oliveto, G. (2002). Shields' entrainment criterion in bridge hydraulics. *Journal of Hydraulic Engineering* 128(5): 538–542.

Hager, W.H., Unger, J., Oliveto, G. (2002). Entrainment criterion for bridge piers and abutments. In D. Bousmar & Y. Zech (eds.), *River Flow* 2002. Louvain-la-Neuve 2: 1053–1058.

Hoffmans, G.J.C.M., Verheij, H.J. (1997) *Scour manual*. Balkema: Rotterdam.

Melville, B.W., Coleman, S.E. (2000). *Bridge scour*. Water Resources Publication: Highlands Ranch, CO.

Melville, B.W., Raudkivi, A.J. (1977). Flow characteristics in local scour at bridge piers. *Journal of Hydraulic Research* 15(4): 373–380.

Oliveto, G., Hager, W.H. (2002). Temporal evolution of clear-water pier and abutment scour. *Journal of Hydraulic Engineering* 128(9): 811–820.

Oliveto, G., Hager, W.H. (2005). Further results to time-dependent local scour at bridge elements. *Journal of Hydraulic Engineering* 131(2): 97–105.

Qadar, A. (1981). The vortex scour mechanism at bridge piers. *Proc. ICE - Research and Theory* 71(3): 739–757.

Sarker, M.A. (1998). Flow measurement around scoured bridge piers using Acoustic-Doppler Velocimeter (ADV). *Flow Measurement and Instrumentation* 9(4): 217–227.

Schlichting, H., Gersten, K. (1997). *Grenzschicht-Theorie*. Springer-Verlag: Berlin (in German).

Unger, J. (2006). Strömungscharakteristika um kreiszylindrische Brückenpfeiler – Anwendung von Particle Image Velocimetry in der Kolkhydraulik. *PhD thesis* 16557. ETH: Zurich.

Unger, J., Hager, W.H. (2005). Spatial and temporal scour features of circular bridge piers. 31. *IAHR Congress* Seoul: 5122–5131.

Unger, J., Hager, W.H. (2006). Riprap failure at circular bridge piers. *Journal of Hydraulic Engineering* 132(4): 354–362.

Copyright © 2006 Taylor & Francis Group plc, London, UK

A numerical model for local scour at piers according to the unit stream power approach

M.E. Cunninghame & N.P. Armitage
Department of Civil Engineering, University of Cape Town, Rondebosch, South Africa

ABSTRACT: Local scour threatens the integrity of river bridges and fluvial structures. A numerical model for local scour hole evolution at a circular pier using incremental manual channel bed deformation was investigated. The three-dimensional flow field was computed in Fluent 6.2 by solution of the steady Reynolds-Averaged Navier Stokes equations using the k-ε model for turbulent closure. The bed geometry was then manually adjusted in proportion to the applied unit stream power to simulate scour and deposition. This procedure of flow field computation and bed deformation was repeated to simulate scour hole evolution. A slope correction factor was applied to the critical stream power required for incipience in the scour hole. The numerical model shows promise for simulation of local scour hole evolution although automated bed deformation procedures and alternative slope correction formulae must be developed.

1 INTRODUCTION

Local scour threatens the integrity of river bridges and fluvial structures. In a recent study of scour damage in South Africa, Armitage *et al.* (2005) found that local scour is evident at approximately 60% of scour-damaged bridges in the country.

Accurate and consistent methods are needed to predict local scour. Empirical formulae are inconsistent in their predictions of maximum scour depth (Johnson 1995) and each has a limited range of application. Physical models are time consuming and therefore expensive. Numerical models have undergone rapid development in the past decades. Olsen & Melaaen (1993) developed a non-transient, three-dimensional (3D), finite volume code which computed changes in channel bed elevation from the sediment concentration in bed-adjacent cells to simulate scour and deposition processes. Olsen & Kjellesvig (1998) developed this model further to incorporate time dependence and an adaptive grid to model temporal scour hole evolution. More recently, Nagata *et al.* (2002) investigated automated procedures for local scour hole evolution using stochastic models to describe sediment transport processes. Although reasonable agreement with physical model data was obtained, it was noted that the model required further development.

The objective of this study was to investigate a numerical model for simulating temporal scour hole evolution. Development of a clear-water local scour hole in uniform, quartzitic sand at a circular pier, studied by means of a physical model by Ahmed (1995), was simulated numerically. The commercial CFD code FLUENT V6.2 was used to compute the flow field and the unit stream power model was applied to predict patterns of scour and deposition. The channel bed deformation was computed as a function of the scour potential at the channel bed and the incremental bed adjustments were implemented manually.

2 THEORETICAL BACKGROUND

2.1 *Numerical model for flow computation*

The flow field was computed by solution of the steady Reynolds-Averaged Navier-Stokes (RANS) equations using the k-ε model for turbulent closure. The general form of the RANS equations is as follows (White 1991):

$$\rho\frac{D\mathbf{u}}{Dt}=\rho\mathbf{g}-\nabla p+\frac{\partial}{\partial x_j}\left[\mu\left(\frac{\partial u_i}{\partial x_j}+\frac{\partial u_j}{\partial x_i}\right)+\delta_{ij}\lambda div\mathbf{u}\right] \qquad (1)$$

where ρ is the fluid density; $\mathbf{u}$ is the velocity vector; t is time; $\mathbf{g}$ represents gravitational acceleration; p is the pressure; μ is the fluid viscosity; u_i is the velocity component in the x_i direction; and λ is Lamé's constant.

The k-ε turbulence model was selected as it offers a reasonable compromise between accuracy and computational cost and has been widely used and validated

Copyright © 2006 Taylor & Francis Group plc, London, UK

(Versteeg & Malalasekera 1995). The k-ε model has been successfully applied to modelling open channel flow and local scour by numerous investigators (e.g. Ali & Karim 2002, Nagata *et al.* 2002, Olsen & Melaaen 1993, Richardson & Panchang 1998, Salehi Neyshabouri *et al.* 2003). The transport equations for the turbulent kinetic energy k and dissipation rate ε are (Rodi 1984):

$$\frac{\partial}{\partial t}(\rho k)+\frac{\partial}{\partial x_i}(\rho k u_i)=\frac{\partial}{\partial x_j}\left[\left(\mu+\frac{\mu_t}{\sigma_k}\right)\frac{\partial k}{\partial x_j}\right]+G_k+G_b-\rho\varepsilon-Y_M+S_k \quad (2)$$

$$\frac{\partial}{\partial t}(\rho\varepsilon)+\frac{\partial}{\partial x_i}(\rho\varepsilon u_i)=\frac{\partial}{\partial x_j}\left[\left(\mu+\frac{\mu_t}{\sigma_\varepsilon}\right)\frac{\partial \varepsilon}{\partial x_j}\right]+C_{1\varepsilon}\frac{\varepsilon}{k}(G_k+C_{3\varepsilon}G_b)-C_{2\varepsilon}\rho\frac{\varepsilon^2}{k}+S_\varepsilon \quad (3)$$

where σ_k and σ_ε are the respective turbulent Prandtl numbers for k and ε; and G_k and G_b represent the generation of turbulent kinetic energy due to mean velocity gradients and buoyancy respectively. The turbulent viscosity μ_t is computed by combining k and ε as follows:

$$\mu_t=\rho C_\mu\frac{k^2}{\varepsilon} \quad (4)$$

The constant terms in Equations 2, 3 and 4 have the standard values (Rodi 1984): $C_{1\varepsilon}=1.44$, $C_{2\varepsilon}=1.92$, $C_\mu=0.09$, $\sigma_k=1.0$ and $\sigma_\varepsilon=1.3$.

2.2 *Unit stream power theory*

According to stream power theory, energy is expended by the flow in doing work on sediment particles to initiate and maintain sediment motion. The conservation of energy for a fluid element may be stated as follows (Versteeg & Malalasekera 1995):

$$\rho\frac{Di}{Dt}=-pdiv\mathbf{u}+div(k_T\,gradT)+\Phi+S_i \quad (5)$$

where i is the internal energy; k_T is a conduction coefficient; T is the fluid temperature; and S_i accounts for external energy sources. The dissipation function, Φ, accounts for work done by viscous stresses, τ_{ij}, in the energy equation (Eq. 5) and is an expression of the applied unit stream power, P_t (W/m^3), in three dimensions (Armitage 2002). P_t is defined as:

$$P_t\equiv\Phi=\tau_{ij}\frac{\partial u_i}{\partial x_j} \quad (6)$$

For an incompressible, Newtonian fluid, P_t may be expressed in terms of velocity components u, v and w in the respective x, y and z directions as follows:

$$P_t=\mu\left[2\left(\left(\frac{\partial u}{\partial x}\right)^2+\left(\frac{\partial v}{\partial y}\right)^2+\left(\frac{\partial w}{\partial z}\right)^2\right)+\left(\frac{\partial u}{\partial y}+\frac{\partial v}{\partial x}\right)^2+\left(\frac{\partial u}{\partial z}+\frac{\partial w}{\partial x}\right)^2+\left(\frac{\partial v}{\partial z}+\frac{\partial w}{\partial y}\right)^2\right] \quad (7)$$

This 3D unit stream power model is suitable for describing sediment transport in a numerical model as local velocity components are computed throughout the domain in the solution process. For local scour, this complete 3D description is also more accurate than that of 1D and 2D models linking sediment transport to mean velocities (Rooseboom 1975, Yang & Song 1979), which are often a poor reflection of flow conditions near the channel bed.

2.3 *Critical unit stream power for incipient motion*

Armitage (2002) analysed a large set of experimental incipient motion data consisting of 529 data points from eight researchers to establish the boundary between scour and deposition. Armitage proposed that the critical unit stream power required for incipient motion, P_{tc}, is some fraction, η, of that required for particle suspension, P_r. Incipient motion begins with rolling and sliding of sediment particles. These modes of motion are sustained by less energy or stream power than that required for particle suspension. The critical unit stream power is thus (Armitage 2002):

$$P_{tc}=\eta P_r \quad (8)$$

where η is a function of the nature of the boundary layer, that is, whether the boundary layer is laminar, transitional or turbulent. For rough turbulent boundaries $\eta=1/67$. If ρ_s is the sediment particle density and v_{ss} is the particle settling velocity, P_r is given by:

$$P_r=(\rho_s-\rho)gv_{ss} \quad (9)$$

For incipient motion on sloping channel beds, a slope correction factor, ψ, for the longitudinal and transverse bed slopes, β and γ respectively, must be incorporated. If ϕ is the sediment angle of repose and the bed slope angles are taken as positive measured downwards from the horizontal plane, ψ is given by (Chiew & Parker 1994):

$$\psi=\sqrt{\cos\beta\left(1-\frac{\tan\beta}{\tan\phi}\right)\cos\gamma\left(1-\frac{\tan^2\gamma}{\tan^2\phi}\right)}^{1/2} \quad (10)$$

For rough turbulent boundaries, the critical unit stream power required for incipience on a sloping channel bed, $P_{tc,\beta\gamma}$, is related to that required on a horizontal bed, $P_{tc,0}$, as follows:

$$P_{tc,\beta\gamma}=\psi^3P_{tc,0} \quad (11)$$

3 MODEL DESCRIPTION

The numerical model was based on a physical laboratory model studied by Ahmed (1995) for clear-water local scour of uniform, cohesionless quartzitic sand at a 64 mm diameter circular pier. The sand had a median diameter of 0.88 mm and an angle of repose of 35°.

Copyright © 2006 Taylor & Francis Group plc, London, UK

The bed was subject to a steady flow of 50 l/s with an approach depth of 182 mm and Froude Number of 0.17. An equilibrium clear-water local scour hole with a maximum depth of 54 mm near the upstream face of the pier was established after 220 hours in the physical model.

The finite volume commercial CFD code, Fluent V6.2, was used to solve the flow field in three dimensions using the k-ε model with default constants for turbulent closure. The stratified flow of air and water through the computational domain was modelled using the Volume of Fluid (VOF) method (Hirt & Nichols 1981) to track the free surface. Logarithmic velocity distributions for uniform open channel flow as well as values of k and ε were specified as boundary conditions at the upstream and downstream domain boundaries. The height of wall adjacent cells was chosen such that $y^+ \approx 30$. The wall unit, y^+, is defined as follows:

$$y^+ = \frac{u_* y}{\nu} \tag{12}$$

where y is the distance from the boundary to the wall-adjacent cell centre and ν is the kinematic fluid viscosity. The shear velocity, u_*, in Equation 12 is defined in terms of the bed shear stress τ_0 as:

$$u_* = \sqrt{\frac{\tau_0}{\rho}} \tag{13}$$

A steady solution was computed to give the initial distribution of the applied unit stream power on the channel bed prior to the commencement of scour. It was found that the maximum applied power, $P_t = 17\ \mathrm{W/m^3}$, did not exceed the critical value for incipience of $29\ \mathrm{W/m^3}$, suggesting that no scour would take place (Fig. 1). It is suspected that the error lies in the fact that the power dissipation function (Eq. 7) is very sensitive to the depth at which it is computed near the channel bed as velocity gradients are very high in this region.

A critical stream power of $P_{tc,0} = 5\ \mathrm{W/m^3}$ was simply assumed to facilitate development of the model. This simply implies that scour commences at a lower intensity of particle motion.

The scour potential, Ω ($\mathrm{W/m^3}$), was calculated as the difference between the applied stream power P_t computed by the solver and the assumed critical stream power, corrected for bed slope where applicable, as follows:

$$P_{tc,\beta\gamma} = \psi^3 P_{tc,0} \tag{14}$$

$$\Omega = P_t - \psi^3 P_{tc,0} \tag{15}$$

The critical scour potentials at which scour and deposition would commence, Ω_{scour} and Ω_{depo} respectively, were then chosen. Therefore,

$$\text{if } \Omega > \Omega_{scour}\text{, scour occurs} \tag{16}$$

$$\text{if } \Omega < \Omega_{depo}\text{, deposition occurs} \tag{17}$$

The vertical adjustment, Δy, applied to each node at which scour or deposition would occur was calculated as a function of the difference between the computed and critical scour potentials. Relaxation factors C_{scour} and C_{depo} for scour and deposition respectively, were introduced to convert the difference in scour potential into a vertical node movement. These factors were calibrated to limit the adjustment of the vertical coordinate of any node to a maximum of 5 mm at any one adjustment. The bed adjustment algorithm can therefore be summarised as follows:

$$\text{if } \Omega > \Omega_{scour}\text{, then } \Delta y = -C_{scour}(\Omega - \Omega_{scour}) \tag{18}$$

$$\text{if } \Omega < \Omega_{depo}\text{, then } \Delta y = +C_{depo}(\Omega - \Omega_{depo}) \tag{19}$$

The linear adjustments described by Equations 18 and 19 were applied in the first four adjustments.

It was found that with further adjustment, the channel bed became undulating with sharp peaks and troughs. For the fifth and sixth bed adjustments, functions of the form:

$$\Delta y \propto \sqrt{\Omega - \Omega_{scour}} \tag{20}$$

were employed in an attempt to generate a "smoother" channel bed within and around the scour hole. The following functions were thus applied in these final two adjustments:

$$\text{if } \Omega > \Omega_{scour}\text{, then } \Delta y = -C_{scour}\sqrt{\Omega - \Omega_{scour}} \tag{21}$$

$$\text{if } \Omega < \Omega_{depo}\text{, then } \Delta y = +C_{depo}\sqrt{\Omega - \Omega_{depo}} \tag{22}$$

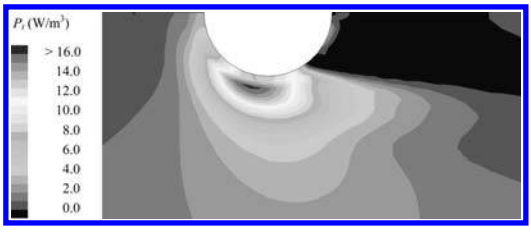


Figure 1. Initial distribution of applied stream power on the flat channel bed prior to scour.

4 RESULTS

The local scour hole generated by six manual bed adjustments is shown in Figures 2 a–f. Shaded plots of P_t are superimposed on the scour hole bathymetry. The colour scale is the same as that in Figure 1. Local scour commenced at the pier sides at approximately 70 to 80 degrees to the symmetry planealong the channel centreline.

Copyright © 2006 Taylor & Francis Group plc, London, UK

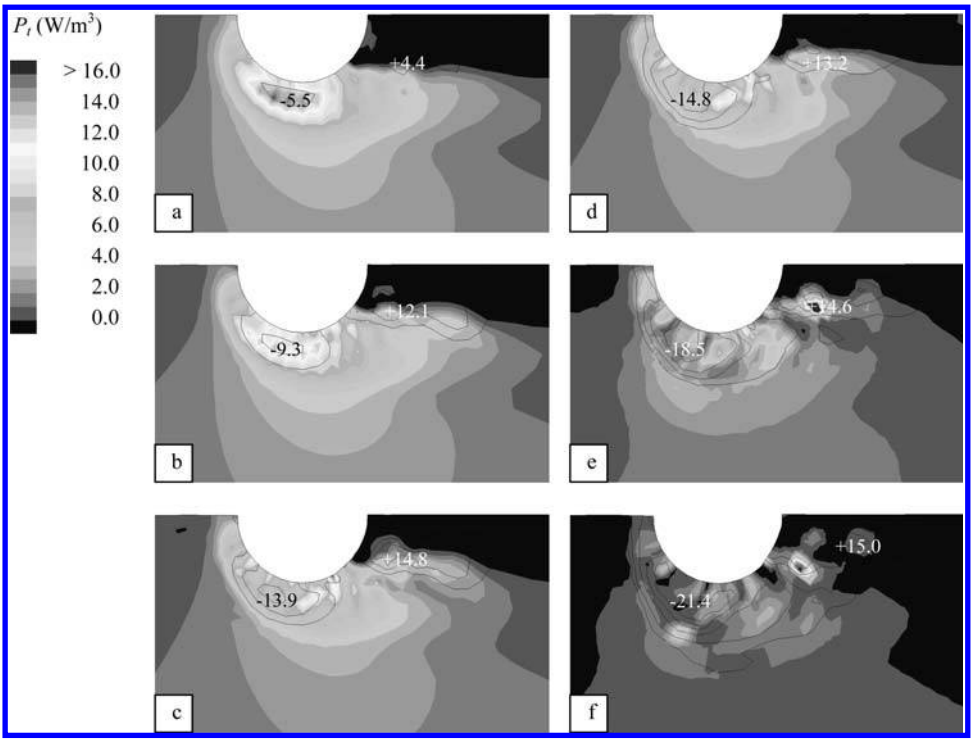


Figure 2. Distribution of applied stream power at the channel bed during manual bed adjustment. (Contour lines indicate bed elevation in mm; contour interval = 4 mm).

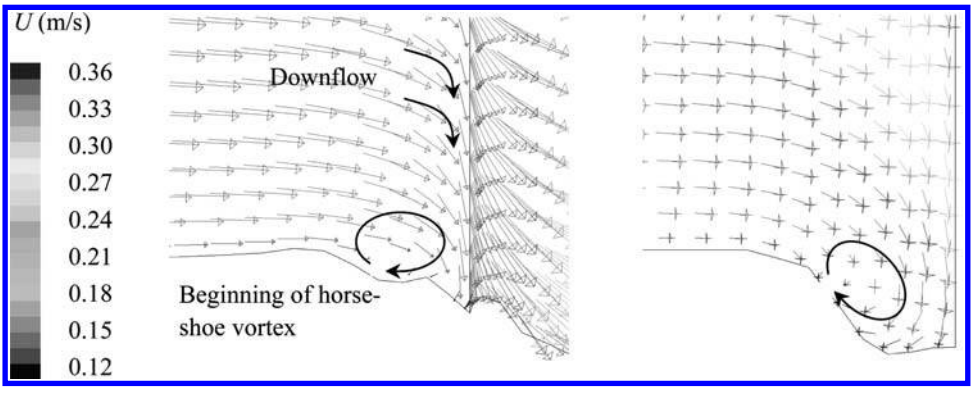


Figure 3. Initial development of the horseshoe vortex at the upstream face and at the side of the pier at 60 degrees to the channel centreline, after bed adjustment 4.

During the adjustment process, the scour hole migrated upstream to extend around the upstream face of the pier although the maximum scour depth remained at the side of the structure.

The initial development of small lateral scour holes and migration of the scour hole around the upstream face of the pier correspond to the temporal patterns of local scour hole development observed in physical models (Breusers & Raudkivi 1991, Dargahi 1990, Graf 1998).

The maximum downflow velocity at the upstream face of the pier, v_{max}, increased steadily during the bed deformation process with the evolution of the scour hole. Prior to scour, $v_{max} = 0.34U$, where U is the mean approach velocity, was computed by the model. After the 6th adjustment, $v_{max} = 0.42U$ was

Copyright © 2006 Taylor & Francis Group plc, London, UK

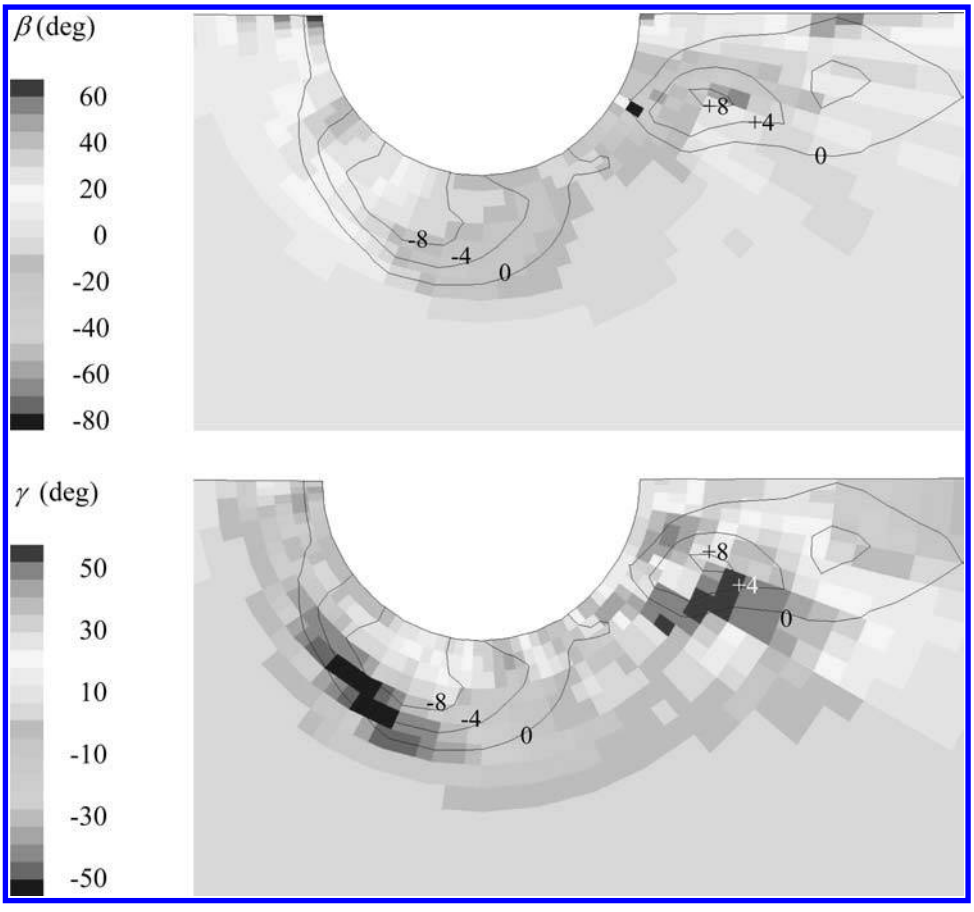


Figure 4. Distribution of streamwise (β) and transverse (γ) slope angles on the channel bed after adjustment 4 ($\phi = 35°$, depth contours shown in mm).

computed. These values correspond well with the theoretical value $v_{max} = 0.4U$ given by Raudkivi (1998) for a flat channel bed, that is, prior to the commencement of scouring. The initial development of the horseshoe vortex around the base of the pier is evident and shown in Figure 3 for the 4th adjustment as an example. The mesh near the channel bed is, however, not fine enough to resolve this clearly.

Accurate modelling of downflow at the upstream face of the pier and the horseshoe vortex in the scour hole around the pier base is essential for local scour simulation as the horseshoe vortex is a most influential mechanism in the local scouring process (Graf & Isitiarto 2002, Hoffmans & Verheij 1997).

The manual bed adjustments used to generate the scour hole of Ahmed (1995) were stopped after the sixth adjustment as the process is extremely tedious when undertaken manually and the slope correction formula (Eq. 10) became undefined at an increasing number of nodes with subsequent adjustments.

Figure 4 shows that the angle between the bed and velocity vectors near the channel bed exceeded the sediment angle of repose of 35° in many regions. At the first adjustment, ψ was undefined at 3 nodes but by the 6th adjustment, ψ could not be computed and was therefore estimated at 40 nodes on the channel bed. The chosen slope correction formulation does not allow computation when $|\beta| > \phi$. Dey *et al.* (1995) studied the flow fields in clear-water local scour holes and noted that the slope of the scour hole sides attain a "dynamic angle of repose" which exceeds ϕ by 10 to 20%.

5 CONCLUSIONS

A numerical model, employing incremental bed adjustment based on the unit stream power theory, was investigated for simulation of the temporal development of a local scour hole at a circular pier.

Copyright © 2006 Taylor & Francis Group plc, London, UK

The model shows promise for application to local scour problems.

The method of incremental bed adjustment until the unit stream power model indicates that an equilibrium hole has developed is a useful technique for generating local scour holes. This method is an alternative to time-accurate simulation of clear-water scour hole development, which would require a substantial amount of computing power as time scales for local scour are long. It is, however, necessary for the investigated procedure to be automated, allowing smaller vertical bed deformations to be used at each adjustment.

The initiation of scouring and early patterns of scour hole development predicted by the numerical model correspond well with the characteristics of local scour holes observed in physical models. A lateral scour hole initiated at the side of the pier and then migrated upstream. The numerical model produced good predictions of the flow patterns around the pier and within the scour hole. The downflow at the upstream face of the pier and formation of the horseshoe vortex around the pier base were evident. Correct representation of these features in the numerical model is most important as the development of downflow at the upstream pier face and the horseshoe vortex at the base are highly influential in the scouring process.

It is felt that a numerical model for local scour, such as that investigated, can be implemented in a general, commercial CFD code such as Fluent. Underestimation of the applied stream power on the channel bed requires attention in future use of the stream power model. In addition, alternative slope correction formulae or algorithms, which facilitate computation even when the bed slope exceeds the sediment angle of repose, must be developed for implementation in an automated bed adjustment model. The dynamic angle of repose should be accounted for. It may also be necessary to write in additional code to control the mesh quality as the bed deforms.

ACKNOWLEDGEMENTS

The authors wish to thank Dr Chris Meyer and Danie de Kock for support in numerical modelling; and the Harry Crossley Foundation and Water Research Commission of South Africa for financial support.

REFERENCES

Ahmed, F. 1995. Flow and erosion around bridge piers. PhD thesis, University of Alberta, Canada.

Ali, K.H.M. & Karim, O. 2002. Simulation of flow around piers. *J. Hydr. Res.* 40(2): 161–174.

Armitage, N.P. 2002. A unit stream power model for the prediction of local scour. PhD dissertation, University of Stellenbosch, South Africa.

Armitage, N.P., Cunninghame, M.E. & Kabir, A. 2005. Local scour in rivers: The extent of the problem in South Africa; The state of the art of numerical modelling. *Water Research Commission of South Africa*, Report No. 565, Pretoria, South Africa.

Breusers, H.N.C. & Raudkivi, A.J. 1991. *Scouring: IAHR Hydraulic Structures Design Manual 2*. Rotterdam: Balkema.

Chiew, Y.-M. & Parker, G. 1994. Incipient motion on non-horizontal slopes. *J. Hydr. Res.* 32(5): 649–660.

Dargahi, B. 1990. Controlling Mechanism of Local Scouring. *J. Hydr. Engrg* 116(10): 1197–1214.

Dey, S., Bose, S.K. & Sastry, G.L.N. 1995. Clear Water Scour at Circular Piers: A Model. *J. Hydr. Engrg* 121(129): 869–876.

Graf, W.H. 1998. *Fluvial Hydraulics: Flow and transport processes in channels of simple geometry*. UK: John Wiley & Sons.

Graf, W.H. & Isitiarto, I. 2002. Flow pattern in the scour hole around a cylinder. *J. Hydr. Res.* 40(1): 13–20.

Hirt, C.W. & Nichols, B.D. 1981. Volume of fluid (VOF) method for the dynamics of free boundaries. *J. Computational Physics* 39: 201–225.

Hoffmans, G.J.C.M. & Verheij, H.J. 1997. *Scour Manual*. Rotterdam: Balkema.

Johnson, P.A. 1995. Comparison of pier-scour equations using field data. *J. Hydr. Engrg* 121(8): 626–629.

Nagata, N., Hosada, T., Nakato, T. & Muramoto, Y. 2002. 3D Numerical simulation of flow and local scour around a cylindrical pier. *J. Hydroscience & Hydraulic Engineering* 20(1): 113–125.

Olsen, N.R.B. & Kjellesvig, H.M. 1998. Three-dimensional numerical flow modelling for estimation of maximum local scour depth. *J. Hydr. Res.* 36(4): 579–590.

Olsen, N.R.B. & Melaaen, M.C. 1993. Three-dimensional calculation of scour around cylinders. *J. Hydr Engrg* 119(9): 1048–1054.

Raudkivi, A.J. 1998. *Loose Boundary Hydraulics*. 4th Ed. Rotterdam: Balkema.

Richardson, J.E. & Panchang, V.G. 1998. Three-dimensional simulation of scour-inducing flow at bridge piers. *J. Hydr. Engrg* 124(5): 530–540.

Rodi, W. 1984. Turbulence models and their application in hydraulics. State of the art review, second edition revised, *IAHR Section on Fundamentals of Division II: Experimental and Mathematical Fluid Dynamics*. Rotterdam: IAHR.

Rooseboom, A. 1975. Sediment Transport in Rivers and Reservoirs. D.Eng dissertation, University of Pretoria, South Africa.

Salehi Neyshabouri, A.A., Ferreira da Silva, A.M. & Barron, R. 2003. Numerical simulation of scour by a free falling jet. *J. Hydr. Res.* 41(5): 533–539.

Versteeg, H.K. & Malalasekera, W. 1995. *An Introduction to Computational Fluid Dynamics: The Finite Volume Method.* Essex: Longman Group Limited.

White, F.M. 1991. *Viscous Fluid Flow*. Second edition. New York: McGraw-Hill Inc.

Yang, C.T. & Song, C.C.S. 1979. Theory of minimum rate of energy dissipation. *J. Hydr. Div.* 105(HY7): 769–784.

Copyright © 2006 Taylor & Francis Group plc, London, UK

Conservative scheme for flow numerical modeling of submerged bridges

M. Catella & G. Bechi
Department of Civil Engineering, Florence University, Florence, Italy

ABSTRACT: A one-dimensional numerical model to study river hydrodynamics of submerged bridges in open-channel flow is presented. The St. Venant equations, written in a conservative form, are solved by employing a finite volume method. The resulting scheme has been extensively tested under unsteady flow conditions by reproducing various open channel and bridge geometries both ideal and real, with non-uniform grids and without any interpolation of topographic survey data and including subcritical, supercritical and transcritical flows with and without shocks. The proposed model provides a great versatility, stability and robustness moreover capturing transcritical sections and conserving mass.

1 INTRODUCTION

The prediction of flood wave propagation in a natural channel is an important feature in hydraulic engineering analysis and in the design for river man-agement and civil protection. Moreover one of the major challenging problem on this subject is the analysis of the river hydrodynamic behavior at bridge sites.

Several studies have been performed in recent years both on local flow and scouring processes around piers or abutments (Umbrell et al., 1998; Biglari & Sturm, 1998; Ahmed & Rajaratnam, 1998; Ahmed & Rajaratnam, 2000).

Nowadays the topic of bridge backwater has become more of a concern (Naudascher & Medlarz, 1983; Hunt et al., 1999; Martín-Vide & Prió, 2005). In the past, flooding caused by bridge constrictions was considered a serious hazard, due to the lack of accurate computational methods of the backwater amount (Kaatz & James, 1997).

Usually, numerical schemes employ local boundary conditions to relate the characteristics of flow upstream and downstream the bridge faces, where the hypothesis of small two dimensional effects disappoint. As mentioned by Natale et al. (2004), some numerical models, such as ISIS (Rosu & Ahmed, 1999) and TEVERE (Natale et al., 1999), are able to reproduce only subcritical flow regime. Others, such as MIKE 11 (DHI, 2000), simulate both subcritical and supercritical flows. Nevertheless transcritical flow conditions are treated by reducing the inertial term influence as the Froude number grows, neglecting them if the Froude number becomes greater than one.

Under low flow condition, the water depth on both sides of the bridge is sufficiently lower than the gate opening height and thus free-surface flow condition is established. Pressure flow condition occurs whenever the water surface elevation exceeds the bottom elevation of the bridge deck's structural members. When the approaching flow begins to overtop the bridge deck, the deck behaves like a broad-crested weir. Under this condition, the flow changes from exclusively submerged pressurized flow under the bridge to a combination of weir and submerged pressurized flow (Umbrell et al., 1998).

The objective of the present analysis is to focus on the bridge hydrodynamic modeling under submerged conditions.

Free-surface flow under a bridge with piers and abutments is modeled by means of the water continuity and momentum equations, by considering a loss of wetted cross sectional area and an increase in wetted perimeter.

Furthermore, this study does not address the special problem of weir flow over the bridge deck.

2 GOVERNING EQUATIONS

Consider a system of orthogonal Cartesian axis (x, y, z) with unit vectors ($\bar{i}, \bar{j}, \bar{k}$). The vertical z-axis is positive in the upwards direction and the horizontal x-axis, corresponding to the projection of the thalweg line on the plan $z = 0$, is positive downstream. Considering weak values of bottom slope, channel cross sections are assumed to be orthogonal to the x-axis. As usual in the one-dimensional scheme the flow is straighten in the plan.

The control volume V at the *jth* cell is defined by the channel reach included between two vertical cross sections j and $j + 1$ orthogonal to the x-axis. The control surface S is then compounded respectively by the

Copyright © 2006 Taylor & Francis Group plc, London, UK

upstream cross section S_j, the downstream cross section S_{j+1}, the wetted surface S_l, delimited by S_j and S_{j+1}, and the water free surface S_{pl}.

The momentum equation applied to the control volume V and projected on the horizontal x-axis, reads:

$$\rho \frac{\partial}{\partial t} \int_{x_j}^{x_{j+1}} Q dx + S_{tj+1} - S_{tj} + \int_{S_l} (p\bar{n} - \bar{\tau}) \cdot \bar{i} dS_l = 0 \qquad (1)$$

where $\rho =$ water density; $Q =$ liquid discharge; $p =$ pressure; $\bar{n} =$ unit vector outward normal to S; $\bar{\tau} =$ shear stress (viscous + turbulent); and $\bar{S}_{tj}$ is the momentum function defined as follows:

$$\bar{S}_{tj} = \int_{S_j} (p + \rho v^2) \bar{i} dS \qquad (2)$$

Particular attention is posed to the treatment of the source terms of the Equation (1) related from one hand to the hydrostatic pressure acting on the wetted surface S_l and on the other hand to the shear stress. Following Catella & Solari (2005), Equation (1) reads:

$$\begin{aligned} &\frac{\partial}{\partial t} \int_{x_j}^{x_{j+1}} Q dx + \left[\beta \frac{Q|Q|}{A} + gI_1 \right]_{x_j}^{x_{j+1}} + \\ &- g\left[A_{j+1}(h_m - z_{gj+1}) - A_j(h_m - z_{gj}) \right] + \\ &+ \frac{\Delta x_j}{2} \left[B_{j+1} \left(\frac{Q|Q|}{(CA)^2} \right)_{j+1} + B_j \left(\frac{Q|Q|}{(CA)^2} \right)_j \right] = 0 \end{aligned} \qquad (3)$$

where $\beta =$ Boussinesq velocity distribution coefficient; $A =$ wetted cross sectional area; $g =$ gravitational acceleration; $I_1 =$ first moment of the wetted cross section with respect to the free surface; $h_m =$ average elevation of the water surface within the jth cell; $z_g =$ center mass elevation of the wetted cross section; $\Delta x_j =$ distance between the vertical cross sections j and $j+1$; $B =$ wetted perimeter; and $C =$ dimensionless Chézy coefficient.

The integral form of the continuity equation under the assumption of no lateral inflow or outflow is:

$$\frac{\partial}{\partial t} \int_{x_j}^{x_{j+1}} A dx + [Q]_{x_j}^{x_{j+1}} = 0 \qquad (4)$$

Introducing the usual discretization:

$$\frac{\partial}{\partial t} \int_{x_j}^{x_{j+1}} G dx \cong \frac{G_m^{n+1} - G_m^n}{\Delta t^n} \Delta x_j \qquad (5)$$

(where G is an arbitrary variable, G_m its average value within the $j_t h$ cell and n the time step index) we obtain a $2(N-1)$ equations system function of $2(N-1)$ variables A_m and Q_m average values of the wetted cross sectional area A and the liquid discharge Q in each $N-1$ cells defined by a N grid points approximation of the entire reach length. The N grid points are generally provided by topographic surveys at not equidistant discrete locations x_j.

The assignment of the $2N$ variables A and Q to the N grid points from the $2(N-1)$ average values within each cell follows a criterion based on the Froude number of the average flow of the upstream and downstream cells between the interface to assign.

3 NUMERICAL SCHEME

The solution of the present equations system is conducted by following a decoupled procedure.

Firstly, by assuming a fixed-bed, the solution of water continuity and momentum equations is conducted by applying an explicit two steps predictor-corrector conservative scheme based on a finite volume method (Catella & Solari, 2005).

The proposed technique, composed by a sequence of two sub-steps in which the spatial derivatives are taken in the same directions, reads:

$$\mathbf{U}_j^p = \mathbf{U}_j^n - \frac{\Delta t^n}{\Delta x_j} [\mathbf{F}_{j+1}^n - \mathbf{F}_j^n] + \Delta t^n \mathbf{S}(\mathbf{U}^n, x) \qquad (6)$$

$$\mathbf{U}_j^c = \mathbf{U}_j^n - \frac{\Delta t^n}{\Delta x_j} [\mathbf{F}_{j+1}^p - \mathbf{F}_j^p] + \Delta t^n \mathbf{S}(\mathbf{U}^p, x) \qquad (7)$$

where the superscripts p and c indicate the predictor and the corrector steps, while $\mathbf{U}$, $\mathbf{F}$ and $\mathbf{S}$ are the vectors of conserved variables, fluxes and source terms, respectively.

The solution at the new time level $n+1$ is then evaluated as an average between the two sub-steps:

$$\mathbf{U}_j^{n+1} = 0.5 \cdot \left(\mathbf{U}_j^p + \mathbf{U}_j^c \right) \qquad (8)$$

In the present model Q is always assigned by allocating Q_m to the downstream intercell starting from the inflow boundary condition. To assign A, a criterion based on the Froude number of the average flow of the upstream and downstream cells across the interface to assign is applied in addition to an appropriate boundary condition at the upstream or downstream edge of the channel. In particular, if the average flows in the jth and $j+1th$ cells are both subcritical, A at the $j+1th$ intercell takes the value of A_{mj+1}, in the opposite case, both supercritical, the value of A_{mj}. In the case of transcritical flows, if the average flows in the jth and $j+1th$ cells are subcritical and supercritical respectively, A at the $j+1th$ intercell takes the critical value, in the opposite case, supercritical and subcritical respectively, a criterion based on the momentum

Copyright © 2006 Taylor & Francis Group plc, London, UK

function of the flows in the upstream and downstream cells across the interface to assign is applied.

For the stability of the present explicit scheme, the Courant-Friederich-Lewy number N_{CFL} must satisfy the following condition:

$$N_{CFL} = \Delta t \cdot \frac{\max_i \left[\left| \frac{Q}{A} \right|_i \right] + \max_i \left[\sqrt{\frac{g \cdot A}{\alpha \cdot b}}_i \right]}{\min_i [\Delta x_i]} < 1 \quad 1 \le i \le N \tag{9}$$

where $\alpha =$ Coriolis velocity distribution coefficient.

4 BRIDGE HYDRAULIC ANALYSIS

Consider a horizontal girder bridge with a determined gate opening height a and without any cross section constriction or enlargement. Under these assumptions the pressure flow under the bridge can be approximated to the pressure flow under a vertical sluice gate.

In mild slope channels, upstream the bridge the water surface elevation increases due to the presence of the obstruction generating a backwater profile. Downstream, depending on the opening height of the gate, different regimes may be present. If the opening height is higher than the critical depth a submerged outflow occurs. While, if the opening height is lower than the critical depth a hydraulic jump may occur. In this latter case, the hydraulic jump may be submerged (Fig. 1) or not (Fig. 2) if the conjugate depth corresponding to the gate opening multiplied by the contraction coefficient is lower or higher than the downstream water depth, respectively.

In steep slope channels, a transition from supercritical to subcritical regime takes place upstream the obstacle, being the water depth just upstream the bridge always greater than the critical depth. Assuming no downstream control on water surface elevation, the water depth tends to the normal depth downstream the bridge. If the gate opening height is higher or lower than the normal depth, the water profile extends between the critical and the normal depth or below the normal depth, respectively (Figs. 3–4).

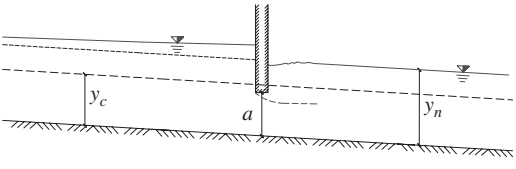


Figure 1. Sketch of water surface profile affected by a bridge in a mild slope channel: submerged jump case.

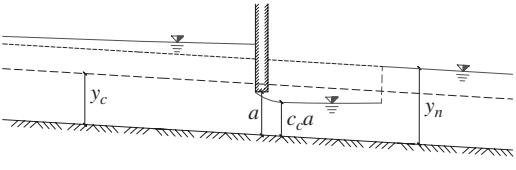


Figure 2. Sketch of water surface profile affected by a bridge in a mild slope channel: non-submerged jump case.

The water surface profile through a pressurized bridge is estimated by following a two step computational procedure.

Firstly, before analyzing the bridge, the solution of water continuity and momentum equations is conducted by applying the explicit two steps predictor-corrector conservative scheme based on a finite volume method (see Chapter 2). Secondly, the bridge analysis is initiated.

In the present model, the hydraulic analysis of pressurized bridge requires the definition of a minimum of three cross sections. The entrance and the exit cross sections are located immediately upstream and downstream the bridge faces, respectively. While, the third cross section is located downstream the bridge reasonably close to the exit section to ensure the applicability of the momentum theorem.

First, the type of water surface profile in the exit cross section should be calculated.

If a supercritical flow regime is found in the third cross section a free outflow occurs.

Vice versa a submerged or non-submerged jump (i.e. submerged or free outflow) may occur downstream of the gate if the flow depth of the *vena contracta* is higher or lower than the conjugate depth of the downstream undisturbed subcritical flow, respectively.

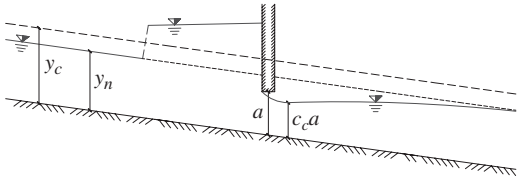


Figure 3. Sketch of water surface profile affected by a bridge in a steep slope channel: the gate opening height is lower than the normal depth.

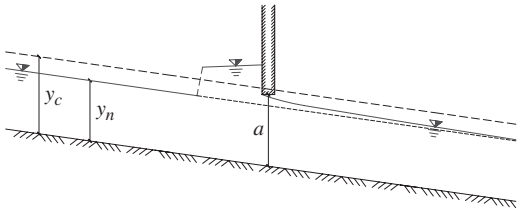


Figure 4. Sketch of water surface profile affected by a bridge in a steep slope channel: the gate opening height is higher than the normal depth.

Copyright © 2006 Taylor & Francis Group plc, London, UK

At the occurrence of a submerged outflow, the wetted cross sectional area A at the exit cross section takes the average value of A_m within the downstream cell delimited between the exit and the third cross section. Otherwise, if a free outflow occurs, A takes the value of the contracted area $c_c\hat{A}$, where c_c is the contraction coefficient and $\hat{A}$ is the area of the gate opening. Note that the flow depth of the *vena contracta* is located at the exit bridge cross section.

Next, the flow depth at the entrance cross section should be estimated. Due to the short length of the reach, information can be assumed to propagate instantaneously inside the bridge. Thus the water levels upstream and downstream the bridge can be evaluated by applying steady flow relationships. Besides, the upstream flow depth can be calculated by assuming a constant liquid discharge throughout the bridge faces and by applying the Bernoulli equations between the entrance and the exit cross sections:

$$y_0 + \alpha\frac{Q^2}{2gA_0^2} = c_c a + \hat{\alpha}\frac{Q^2}{2g(c_c\hat{A})^2} + \Delta E \tag{10}$$

where the subscript 0 indicate the entrance cross section and ΔE is the specific energy loss.

In free outflow case the specific energy loss is assumed to be negligible ($\Delta E = 0$), while in the case of submerged outflow the specific energy loss is defined by:

$$\Delta E = \xi\frac{\left(\hat{\alpha}\dfrac{Q}{c_c\hat{A}} - \alpha_0\dfrac{Q}{A_0}\right)^2}{2g} \tag{11}$$

where $0 < \xi \leq 1$ is the local head-loss coefficient between the entrance and the exit cross sections.

Note that the assumption of energy conservation in the vicinity of the obstacle only holds if the induced flow curvatures are small.

5 HYSTERESIS BOUNDARY REGION

In the present model, pressure flow conditions are achieved whenever water surface elevation of the undisturbed flow exceeds the bottom elevation of the bridge deck ($y_0 = a$). Therefore, the height of the gate opening corresponds to the upper limit of water depth defining the detachment threshold between free-surface and pressurized flows. Following Defina & Susin (2003) the water depth upper limit can be written in terms of dimensionless parameters as follows:

$$\frac{a}{y_c} = F_0^{-2/3} \tag{12}$$

where y_c = critical depth; $F_0 = U_0/\sqrt{gy_m\alpha^{-1}}$ is the Froude number of the undisturbed flow immediately upstream the bridge and y_m is the average flow depth of the equivalent rectangular cross section characterized by the same wetted cross sectional area and water surface width.

Hence, when the undisturbed flow depth becomes slightly higher than the gate opening height a pressurized flow is obtained and a backwater effect is established. Starting from this flow state, if the water depth starts to go down under the gate opening height two different scenarios can be drawn. In subcritical flow regime a decrease in water depth under the gate height reestablishes an undisturbed free-surface flow. While in supercritical flow regime the hysteresis effect of the hydraulic jump significantly affects the hydraulic phenomenon.

The hysteresis occurrence in a supercritical flow regime approaching an obstacle has been widely investigated both experimentally and theoretically (Muškatirović & Batinić, 1977; Baines, 1984; Austria, 1987; Lawrence, 1987; Baines & Whitehead, 2003; Defina & Susin, 2003). In open channel flow, when a transition between supercritical and subcritical flow occurs, an hysteretic behavior is observed in a particular range of values of the governing variables (Austria, 1987). Hysteresis or multiple equilibria correspond to situations where two different flow states may exist for the same external steady conditions (Baines, 1984), and the actual regime depends on the previous history of the flow (Muškatirović & Batinić, 1977; Defina & Susin, 2003).

In particular, the hysteretic behavior of the flow under a vertical sluice gate or a girder bridge concerns the possibility that, for a given height of the gate opening, a supercritical approaching flow may either continue undisturbed or undergo a supercritical to subcritical transition upstream the gate (Defina & Susin, 2003).

The lower limit of water depth defining the detachment threshold between pressurized and free-surface flows in supercritical regime can be evaluated by applying the Bernoulli equation between the undisturbed flow upstream the bridge and the *vena contracta*. Again, following (Defina & Susin, 2003) the water depth lower limit can be written in terms of dimensionless parameters as follows:

$$\left(\frac{a}{y_c}c_c\right) + \frac{1}{2}\left(\frac{a}{y_c}c_c\right)^{-2} = \frac{1}{2}\left(-1+\sqrt{1+8F_0^2}\right)F_0^{-2/3} + \frac{2F_0^{4/3}}{\left(-1+\sqrt{1+8F_0^2}\right)^2} \tag{13}$$

Therefore if the water depth increase over the upper limit or decrease under the lower limit a pressure or a free-surface flow is established respectively. In subcritical regime upper and lower limit of water depth

Copyright © 2006 Taylor & Francis Group plc, London, UK

are both defined by Eq. (12), while in supercritical regime upper and lower limit are obtained by mean of Eqs. (12) and (13) respectively defining the boundaries of the hysteresis region.

The present numerical scheme is able to predict for the same range of parameters both an undisturbed supercritical flow and a flow with a stationary hydraulic jump upstream the bridge and to compute the proper flow state by including the past history of the flow.

6 APPLICATIONS

To analyze the performance and the reliability of the present numerical algorithm devoted to describe the flow regimes throughout the bridge, several schematic test cases are conducted under unsteady flow conditions including subcritical, supercritical and transcritical flows with and without shocks.

In all the following numerical tests a 1000 m long and 25 m wide rectangular channel is employed. In particular, an intermediate reach of the Vezza Creek (North Tuscany) is taken as a prototype to find out an average channel width, a roughness coefficient and the flood hydrograph. Thus, the inflow liquid discharge corresponds to a 50 years return period flood hydrograph (see Fig. 5). The hydrograph lasts 9 hours and the discharge values range between 34.5 m^3/s and 366.5 m^3/s.

In the computations the channel is outlined by 100 cells ($\Delta x = 10$ m), N_{CFL} is set equal to 0.9 and the value of the Manning coefficient is set equal to 0.029 $s/m^{1/3}$. Note that the solutions are not affected by the N_{CFL} values, therefore the chosen time step size is very close to the maximum allowed by numerical stability.

Moreover in the following tests, to make plain the problem, the contraction coefficient c_c is always set equal to 1, thus the contracted area is equal to the area of the gate opening.

Note that no changes must be introduced in the numerical scheme to model bridge in natural irregular geometries.

In mild slope channels the bottom slope is 0.001, while in steep slope channel the bed slope is 0.01.

In subcritical flow, the discharge at the upstream side and the normal flow depth at the downstream side are imposed as boundary conditions. In supercritical flow, the liquid discharge and the normal depth are specified as upstream boundaries.

All the girder bridges are characterized by horizontal low chord and no constrictions. In single bridge cases the structure is delimited by two cross sections located at $x = 490$ m and $x = 500$ m, respectively. In two bridges in series cases, the structures are characterized by different gate opening heights and each one is still delimited by two cross sections.

6.1 *Mild slope channel tests*

Firstly the single bridge test case is conducted. The gate opening height is set equal to 2 m. The evolution of the water level profiles at different time instants are reported in Figure 6. Figure 6 shows that the theoretical behavior is correctly reproduced. Upstream a continuous backwater profile is formed. When simulation time is about 2 hours, pressure-flow condition is established. As the water surface continues to rise, the pressurized flow under the bridge increases as the degree of submergence increases. Downstream, submerged outflows always occur, since the conjugate depth of the downstream undisturbed subcritical flow is lower than the flow depth of the *vena contracta* $c_c a$ at all times. In Figure 7, discharge values versus water depths are plotted at the entrance and the exit cross sections, respectively, pointing out the backwater effect triggered by the bridge.

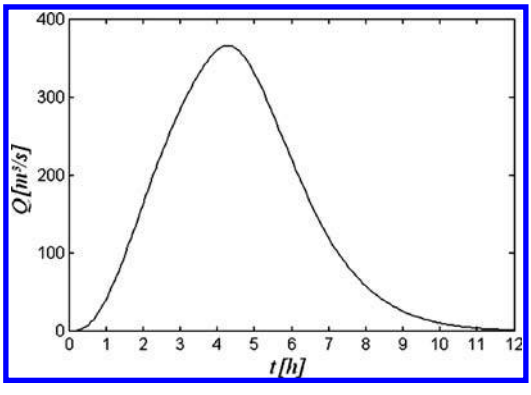


Figure 5. Liquid discharge hydrograph for return period of 50 years.

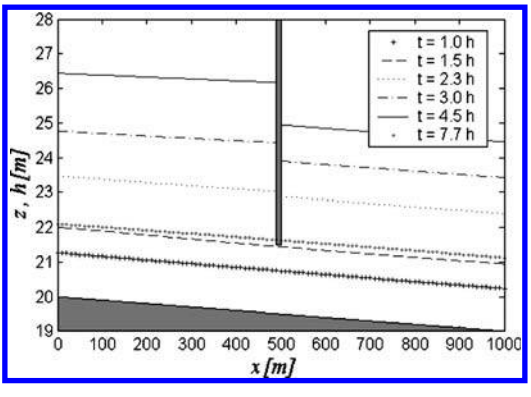


Figure 6. Single bridge test case in a mild slope channel: temporal sequence of water surface level. Bed level and bridge structure are sketched in solid grey.

Copyright © 2006 Taylor & Francis Group plc, London, UK

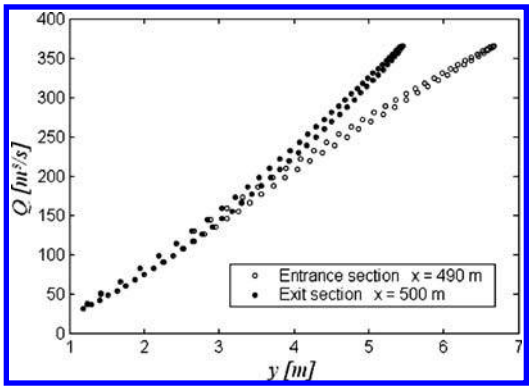


Figure 7. Single bridge test case in a mild slope channel: discharge versus water depth values. Results are plotted at two different river stations (entrance and exit cross sections).

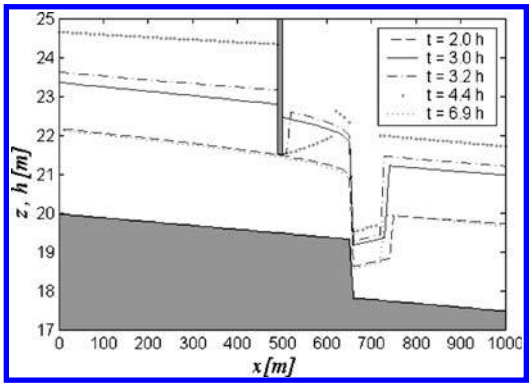


Figure 8. Single bridge and dam test case in a mild slope channel: temporal sequence of water surface level. Bed level and bridge structure are sketched in solid grey.

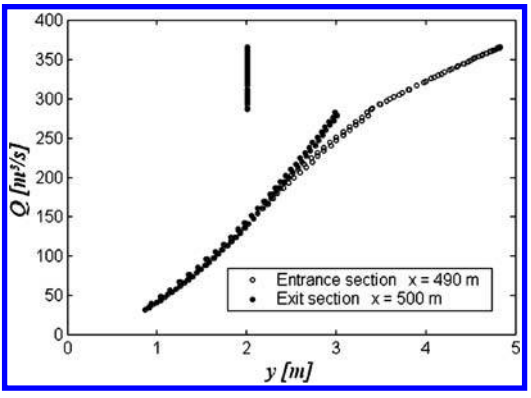


Figure 9. Single bridge and drop test case in a mild slope channel: discharge versus water depth values. Results are plotted at two different river stations (entrance and exit cross sections).

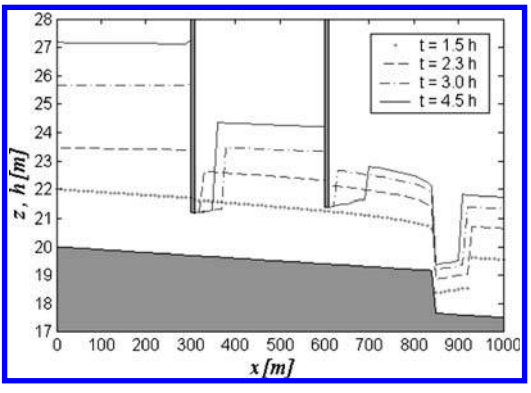


Figure 10. Two bridges in series test case in a mild slope channel: temporal sequence of water surface level. Bed level and bridge structures are sketched in solid grey.

Secondly a single bridge test case with a downstream control on water depth is analyzed. Bridge and channel geometries are the same of the previous test, to which a 1.5 m high drop located 150 m downstream the exit cross section is added. The flow is therefore influenced by the water level above the drop. The water surface profile develops between the normal and the critical depths dropping in the downstream direction. Hence, at time equal about 3.2 hours, the outflow, which is submerged, changes into free and a hydraulic jump occurs (see Fig. 8). In spite of the previous test case, the free outflow is allowed due to the lower values assumed by the flow momentum quantities in the channel reach between the two inline structures. As water surface continues to rise, the supercritical reach length downstream the bridge increases as the degree of submergence increases. In Figure 9, discharges versus water depths are reported just upstream and downstream the bridge. The submerged to free outflow transition induces a suddenly abrupt reduction of the water level. In fact until the outflow is free, the water depth at the exit cross section is set equal to the gate height.

Next two bridges in series are modelled in order to investigate their mutual interaction. The entrance cross sections are located at $x = 300$ m and $x = 600$ m, respectively. The first gate opening height is set equal to 1.5 m, while the second one is set equal to 2 m. A 1.5 m high drop located $x = 840$ m is added. The temporal sequence of the water level profile during the flood hydrograph is reported in Figure 10. Figure 10 shows that, due to the drop control on water depth, a free outflow begins downstream the first bridge at time equal to about 2.3 hours, while the second structure is still characterized by a submerged outflow. The smaller is the gate opening height, the earlier is the beginning of the outflow transition. The resulting hydraulic jump,

Copyright © 2006 Taylor & Francis Group plc, London, UK

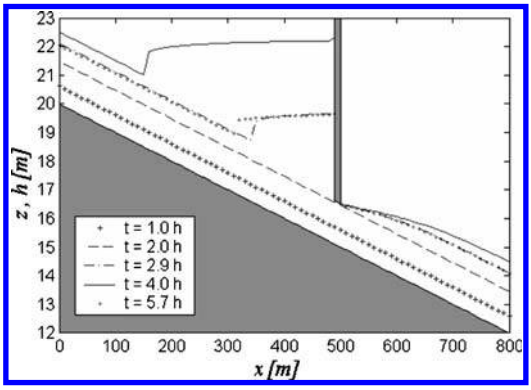


Figure 11. Single bridge test case in a steep slope channel: temporal sequence of water surface level. Bed level and bridge structures are sketched in solid grey.

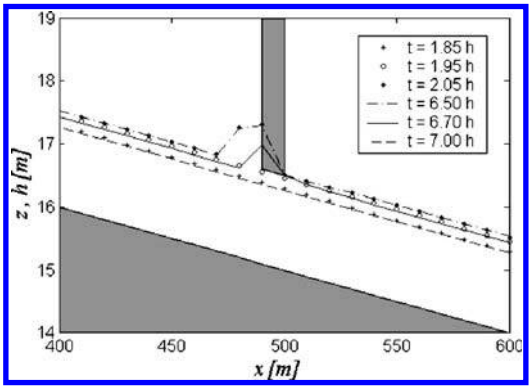


Figure 12. Hysteretic behavior of the flow: under the same range of parameters both an undisturbed supercritical flow and a flow with a stationary hydraulic jump upstream the bridge are computed.

located between the two structures, starts to migrate downstream. The supercritical reach length, immediately downstream the first bridge, rather than increases as the submergence degree increases, is bordered downstream by the rising backwater effect. Besides, at the edge of the rising part of the flood hydrograph, the hydraulic jump moves upstream toward the exit section of the first bridge.

6.2 *Steep slope channel tests*

Firstly a single bridge test case is conducted again. The gate opening height is set equal to 1.5 m. In Figure 11, the sequence of water level profiles at different time instants are plotted, showing that also in this flow regime the theoretical behaviour is correctly reproduced. During the rising part of the hydrograph, once the water surface elevation exceeds the gate opening height, the flow passes abruptly from a supercritical flow regime to a subcritical one. Therefore the water depth upper limit defining the detachment threshold between free-surface and pressurized flows is equal to 1.5 m ($Q = 165.0\,m^3/s$). As the water surface continues to rise, the hydraulic jump propagates in the upstream direction. During the falling part of the hydrograph the jump location moves back towards the bridge. Note that in these latter flow conditions, the subcritical reach length is characterized by a greater extension as emerged by the comparison between the two water profiles plotted in Figure 11 at times equal to 2.9 h and 5.7 h, respectively. Moreover the pressurized flow still endures despite the water surface level becomes lower than the gate opening height due to the hysteretic behavior of the flow. As Figures 12–13 point out, the numerical model is able to reproduce the hysteresis phenomenon, which is developed under a particular range of values of the governing variables due to the occurrence of a transition between

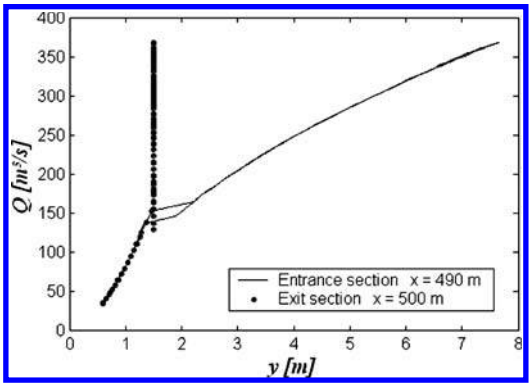


Figure 13. Single bridge test case in a steep slope channel: discharge versus water depth values. Results are plotted at two different river stations (entrance and exit cross sections).

supercritical and subcritical flows. In the present test case, lower limit of water depth defining the detachment threshold between pressurized and free-surface flows is about 1.42 m ($Q \cong 145.2\,m^3/s$). Downstream free outflow occurs at all times.

Finally two bridges in series are modelled in order to investigate their mutual interaction in supercritical flow regime. The entrance cross sections are located at $x = 400$ m and $x = 700$ m, respectively. The first gate opening height is set equal to 2.0 m, while the second one is equal to 1.5 m. The water level profile sequence during the flood hydrograph is reported in Figure 14. Figure 14 shows that the backwater effect induced by the downstream bridge rises and moves upstream as the discharge increases. Thus a submerged outflow downstream the first bridge for high discharge values is established.

Copyright © 2006 Taylor & Francis Group plc, London, UK

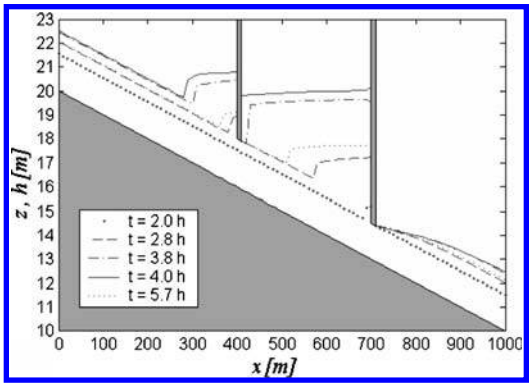


Figure 14. Two bridges in series test case in a steep slope channel: temporal sequence of water surface level. Bed level and bridge structures are sketched in solid grey.

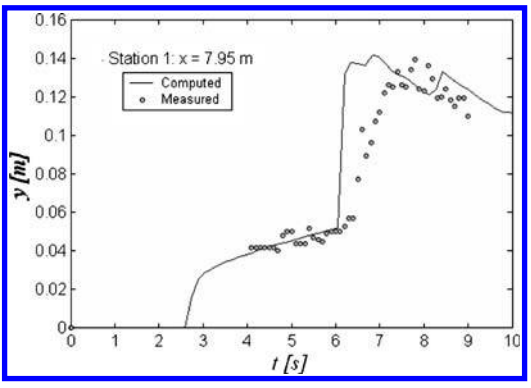


Figure 15. Comparison between computed (line) and measured (marker) water depths as a function of time at $x = 7.95$ m.

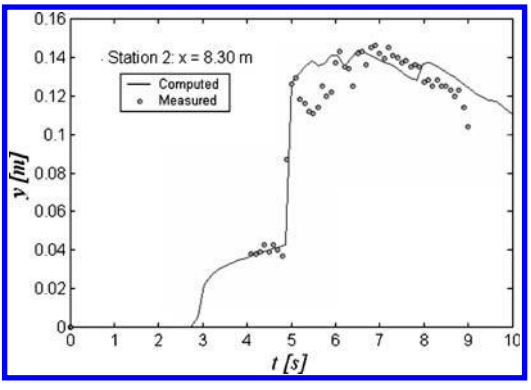


Figure 16. Comparison between computed (line) and measured (marker) water depths as a function of time at $x = 8.30$ m.

7 APPLICATION TO AN EXPERIMENTAL TEST CASE

The numerical scheme is here applied to simulate the propagation of a shock wave impacting two consecutive sluice gates.

To verify the bridge hydraulic modeling, the numerical scheme is applied to reproduce the experimental activity carried out by Natale et al. (2004) in the Hydraulic Laboratory of Pavia University.

The channel is 9.3 m long, 0.48 m wide with rectangular cross section and horizontal bed. A removable dam is located at $x = 3.36$ m.

Two vertical sluice gates were positioned at $x = 8.40$ m and $x = 9.30$ m. The gate opening heights were 0.04 m and 0.02 m for the upstream and the downstream gate, respectively.

In the computations the rectangular channel is described by 186 cells ($\Delta x = 0.05$ m), N_{CFL} is set equal to 0.1 and the Manning coefficient is set equal to 0.008 s/m$^{1/3}$. No difference in the solution appears by using different N_{CFL} values.

Initially, the water depth upstream the dam was equal to 0.20 m, while the bed was dry downstream.

At $t = 0$ s, the dam was suddenly removed and dam-break waves propagated upstream and downstream along the channel.

In Figures 15–16 the water level hydrographs at two different cross sections located at $x = 7.95$ m and $x = 8.30$ m are plotted, respectively.

The proposed numerical model shows a very good agreement between computed and measured water depths at the cross section closest to the upstream sluice gate (Fig. 16).

A good agreement is also achieved in the comparison between numerical and laboratory results obtained in Station 1. Even if Figure 15 shows a slightly overestimation of the computed values between 6.0 s and 7.0 s resulting from the hydraulic jump modeling. In fact, the present numerical scheme spreads the hydraulic jump extension over two cross sections only, where the conjugate water depths of the jump occur. Therefore, while the jump is moving upstream, in Station 1 either the supercritical flow depth or the subcritical flow depth due to backwater is possible.

8 CONCLUSIONS

A one-dimensional numerical model to study submerged bridge hydrodynamics is presented.

The St. Venant-Exner equations are solved by employing a finite volume method.

The governing equation system is solved in the following unknowns: wetted cross sectional area and liquid discharge of the average flow in each cell. The assignment of these unknowns along the river intercells is based on a Froude number criterion of the

Copyright © 2006 Taylor & Francis Group plc, London, UK

upstream and downstream average cell flow across the node point.

The main characteristic of the present method is the employment, as conservative variables of the governing equations, of average quantities within each cell independently from the adopted spatial grid.

The present model is extended to simulate the river hydrodynamics of submerged bridges by employing local boundary conditions to relate the characteristics of flow upstream and downstream the bridge faces.

The numerical scheme is able to model the bridge backwater, free and submerged outflows and the hysteretic behavior of the flow in the transition between supercritical and subcritical regime upstream the bridge deck's structural member. In particular, the backwater amount at the entrance cross section is computed by an energy balance between the upstream and downstream faces of the bridge.

The scheme is successfully applied to various unsteady benchmark problems including subcritical, supercritical and transcritical flows modeling single or multiple bridges and involving downstream control on water surface elevation. The good agreement between model results and experimental data reveals the suitability of the adopted methodology.

Since the extraordinarily conceptual and algorithm simplicity, the proposed model provides a great versatility, stability and robustness.

ACKNOWLEDGMENT

The authors wish to acknowledge Prof. Enio Paris for his help and his valuable comments and suggestions.

REFERENCES

Ahmed, F. & Rajaratnam, N. 1998. Flow around Bridge Piers. *Journal of Hydraulic Engineering* 124(3): 288–300.

Ahmed, F. & Rajaratnam, N. 2000. Observations on Flow around Bridge Abutment. *Journal of Hydraulic Engineering* 126(1): 51–59.

Austria, P.M. 1987. Catastrophe model for the forced hydraulic jump. *Journal of Hydraulic Research* 25(3): 269–279.

Baines, P.G. 1984. A unified description of two-layer flow over topography. *Journal of Fluid Mechanics* 146: 127–167.

Baines, P.G. & Whitehead, J.A. 2003. On multiple states in single-layer flows. *Physics of Fluid* 15(2): 298–307.

Biglari, B. & Sturm, T.W. 1998. Numerical Modeling of Flow around Bridge Abutments in Compound Channel. *Journal of Hydraulic Engineering* 124(2): 156–164.

Catella, M. & Solari, L. 2005. Conservative scheme for numerical modeling of flow in natural geometry. *Proc., XXXI Int. Congress, Int. Association for Hydraulic Research, Seoul, Korea*.

Defina, A. & Susin, F.M. 2003. Hysteretic behavior of the flow under a vertical sluice gate. *Physics of Fluids* 15(9): 2541–2548.

DHI, Mike 11. A modelling system for Rivers and Channels, Reference Manual, 2000.

Hunt, J., Brunner, G.W. & Larock, B.E. 1999. Flow Transitions in Bridge Backwater Analysis. *Journal of Hydraulic Engineering* 125(9): 981–983.

Kaatz, K.J. & James, W.P. 1997. Analysis of Alternatives for Computing Backwater at Bridges. *Journal of Hydraulic Engineering* 123(9): 784–792.

Lawrence, G.A. 1987. Steady flow over an obstacle. *Journal of Hydraulic Engineering* 113(8): 981–991.

Martín-Vide, J.P. & Prió, J.M. 2005. Backwater of arch bridges under free and submerged conditions. *Journal of Hydraulic Research* 43(5): 515–521.

Muškatirović, D. & Batinić, B. 1977. The influence of abrupt change of channel geometry on hydraulic regime characteristics. *Proc., 17th Int. Congress, Int. Association for Hydraulic Research, Baden-Baden, Federal Republic of Germany*.

Naudascher, E. & Medlarz, H.J. 1983. Hydrodynamic loading and backwater effect of partially submerged bridges. *Journal of Hydraulic Research* 21(3): 213–231.

Natale, A., Savi, F. & Ubertini, L. 1999. Probability of inundation of Rome. *Proc., IASTED International Conference on Modelling and Simulation, Philadelphia, USA*.

Natale, A., Petaccia, G. & Savi, F. 2004. Il deflusso di onde a fronte ripido attraverso singolarità idrauliche. *Proc., 29° Convegno di Idraulica e Costruzioni Idrauliche, Trento, Italia* (in Italian).

Rosu, C. & Ahmed, M. 1999. Toce River dam-break test case. A comparison between the ISIS numerical model and the physical model. *Proc., 4th CADAM meeting, Milan, Italy*.

Umbrell, E.R., Young, G.K., Stein, S.M. & Jones, J.S. 1998. Clear-Water Contraction Scour under Bridges in Pressure Flow. *Journal of Hydraulic Engineering* 124(2): 236–240.

Copyright © 2006 Taylor & Francis Group plc, London, UK

Turbulent flow field modeling as an aid to the analysis of scour and for a protection scheme

R. Aragão & V.S. Srinivasan
Department of Civil Engineering, Federal University of Campina Grande, Campina Grande, Paraíba, Brazil

K. Suzuki & A. Kadota
Department of Civil and Environmental Engineering, Ehime University, Matsuyama, Ehime, Japan

ABSTRACT: Bridge scour is one of the main causes of bridge failure and to determine the scour hole depth due to a given flood and adopt countermeasures, it is important to know the scouring mechanisms. Scouring is marked by a complex three-dimensional flow around the piers, which can be modeled using the Navier-Stokes equations and a turbulence model, such as the k-ε model. A model of this type was applied to analyze the scouring around and downstream of the piers of Shimanto River Bridge (Japan). Considering the true shape of the piers (two cylinders joined by a collar) and the shape of the scour hole around the piers several situations were simulated. The results show that for a certain flow condition the collar works as a shield against the downward flow found at the upstream face. Based on the flow field within the scour hole, a riprap protection could be recommended.

1 INTRODUCTION

When a unidirectional flow approaches an obstacle protruding in a river channel, such as bridge piers, it turns into a three-dimensional one, generating turbulences and vorticities, which contributes to an increase in flow velocity, leading to an increment in the shear stress over the river bed. The shearing dislodges the riverbed material from around the piers easing the entrainment of it by the flow and creating a scour hole. This process is known as bridge scour. The continuous process of scouring may lead to a bridge failure and this fact exerts a strong influence on the bridge design (Melville & Coleman, 2000).

Among the factors influencing the scour the following are the most important: flood frequency, flow velocity, flow depth, pier shape and size, sediment grading, pier alignment relative to the flow, degree of contraction, type of sediment transport (clear water or live-bed scour), and contraction length (Breuseres & Raudkivi, 1991). Some of them can be accessed quantitatively, however, others are difficult to quantify. The most needed information in bridge design is the scour depth caused either by a storm event or for a given design flood. Based on the measurable variables, experiments have been conducted and techniques for measuring scour depth have been developed (Aragão et al., 2005), resulting in a variety of equations for predicting scour depth, usually applied in bridge design (Jain, 1981).

For several years, flume experiments were the only way available for verifying some theories and guidance in bridge design (Johnson, 1995; Jain, 1981; Breusers & Raudkivi, 1991). Then with these, bridges were designed, considering large safety margins to compensate for uncertainties intrinsic in the process of predicting such scour depths. As a drawback, high costs and conservative designs were usually found. Furthermore, those equations give good results only when applied to flume data where the experimental conditions are controlled.

Scour processes involve a three-dimensional approach, not possible to be quantified easily, neither 'in loco' nor through laboratory experiments. In order to describe the flow field in its three-dimensional aspect there exist the continuity equation, the averaged Navier-Stokes equations, and some turbulence closures. However, to achieve the flow field description it is necessary to solve those equations or their simplifications in the time and space domain, which was not easy until few years ago. With the advent of fast digital computers and the development of theories about algorithms for solving complex equations, the simulation of flow field could finally be achieved with success. Here a model involving those equations has been used for analyzing the mechanisms of bridge

Copyright © 2006 Taylor & Francis Group plc, London, UK

scouring, having as a case study, the problem found at the Shimanto River Bridge in Japan. There will be described in the following sections the method used for doing the simulations and the data needed for providing a bases for comparison between the results from the model and those found at the field.

2 SCOURING AROUND BRIDGE PIER

The flow field around a pier is complex and this is further aggravated by the development of the scour hole. Scour at bridge pier is influenced by turbulence and vorticity.

Considering a cylindrical pier as an example, as the flow approaches the cylinder it decelerates, coming to rest at upstream face of the pier. The associated stagnation pressures are high near the surface, where the deceleration is large, and decrease downwards. In response to this downwards pressure gradient, the strength of the downwards flow in front of the cylinder reaches a maximum value just below the bed level when a scour hole is present. This downward flow impinging on the bed is pointed as the main scouring agent (Breusers & Raudkivi, 1991; Melvile & Colleman, 2000). In conjunction with the downward flow action, a horseshoe vortex appears and transports the dislodged material downstream. The separated flow at the upstream face reunites downstream, creating wakes that suck up sediments from the bed and also transport the entrained material (Figure 1).

Over the last century scouring around bridge piers received much attention due to the cost involved in bridge reconstruction and a complete protection against scouring may not be feasible. The results, of the knowledge thus obtained, are translated into formulae that estimate the depth of scour due to a given flood. However, the application of different formulae to a given problem results in different values of scour depths (Johnson, 1995). Hence, these results obtained should be used with certain care.

To be realistic, a scour simulation model should represent the three-dimensional flow field and the sediment transport process adequately. Some attempts have been made but the geometries of the models utilized are very simple. Moreover, theoretical modeling of this process still needs further researches before the mechanism is truly understood. In the present work, the simulation of the flow field as an aid to the analysis of the scouring process is attempted.

3 MODELING OF FLOW FIELD AND TURBULENCE MODEL

3.1 *Simulation of flow field*

Scour appears as a resultant of the interaction between turbulent flow and the movable stream bottom.

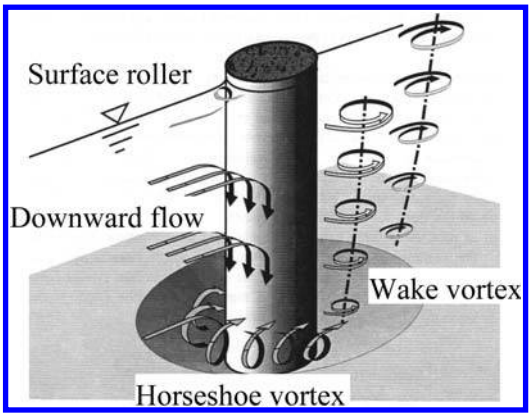


Figure 1. Scouring around a cylindrical pier and its characteristics (*after Melville and Coleman, 2000*).

Therefore, to understand the scour mechanism is primordial to realize first the flow pattern surrounding bridge piers. Flow field simulation consists in obtaining to fluid flow problems with the aid of the computers.

The equations governing the fluid flow problem are the continuity equation (Equation 1), the average Navier-Stokes (Equation 2), and the energy equations. These equations form a system of coupled non-linear partial differential equations. However, in taking an average Navier-Stokes equation for a turbulent flow, some information about fluid motion is lost and hence, an additional term known as Reynolds stress form appears (Rodi, 1980).

$$\frac{\partial \rho}{\partial t} + \frac{\partial \rho u_i}{\partial x_i} = 0 \tag{1}$$

$$\frac{\partial \rho u_i}{\partial t} + \frac{\partial \rho u_i u_j}{\partial x_i} = \frac{-\rho \partial \overline{u_i u_j}}{\partial x_i} - \frac{\partial p}{\partial x_i}, \quad i = 1,2,3;\ j = 1,2,3 \tag{2}$$

$$\overline{-u_i u_j} = \mu_T \left(\frac{\partial U_i}{\partial x_j} + \frac{\partial U_j}{\partial x_i} \right) - \frac{2}{3} \delta_{ij} k \tag{3}$$

where ρ is the local fluid density, t is time, x_i is the position vector in the ith coordinate direction, u_i is the ith fluid velocity component, p is the pressure, τ_{ij} is the Reynolds stress, δ_{ij} is the Kronecker delta function ($\delta_{ij} = 1$ if $i = j$; δ_{ij} if $i \neq j$), k is the specific turbulent kinetic energy described in the next section.

3.2 *Turbulence model*

To recover the lost information, a turbulence model for the Reynolds stress term must be introduced. It is represented in terms of mean flow quantities and some

Copyright © 2006 Taylor & Francis Group plc, London, UK

turbulence parameters. To this end, a variety of turbulence models have been proposed (Hwang & Jaw, 1998). Among them, the two-equation standard k-ε model (Launder & Spalding, 1974) has gained credibility due to its simplicity and the approach used for describing the terms k-ε which employs the Boussinesq eddy viscosity concept (Equation 3) as described in Equation 4, 5, 6, 7:

$$\frac{\partial \rho k}{\partial t}+\frac{\partial \rho u_i k}{\partial x_i}=\mu_t G-\varepsilon+\frac{\partial}{\partial x_i}\left[\left(\mu+\frac{\mu_t}{\sigma_k}\right)\frac{\partial k}{\partial x_i}\right] \quad (4)$$

$$\frac{\partial \rho \varepsilon}{\partial t}+\frac{\partial \rho u_i \varepsilon}{\partial x_i}=\frac{\varepsilon}{k}(C_{\varepsilon 1}\mu_t G-C_{\varepsilon 2}\rho\varepsilon)+\frac{\partial}{\partial x_i}\left[\left(\mu+\frac{\mu_t}{\sigma_\varepsilon}\right)\frac{\partial \varepsilon}{\partial x_i}\right] \quad (5)$$

$$G=-\overline{u_i u_j}\frac{\partial u_i}{\partial x_j} \quad (6)$$

$$\mu_t=\frac{C_\mu \rho \kappa^2}{\varepsilon} \quad (7)$$

where k and ε are the specific turbulent kinetic energy and turbulent kinetic energy dissipation rate, respectively, μ_t is the eddy viscosity coefficient, C_μ is a dimensionless model constant, assumed as equal to 0.09. The values of the empirical constants have been established as $C_{\varepsilon 1}=1.44$, $C_{\varepsilon 2}=1.92$, $\sigma_k=1.0$, and $\sigma_\varepsilon=1.3$ (Hwang & Jaw, 1998). The shear stress was calculated based on the values of μ_t for each node.

Utilizing this turbulence model, the flow field around bridge at the Shimanto River Bridge in Japan, was simulated.

3.3 *Numerical resolution*

Equations 1 to 6 constitute the basic set of partial differential equations used for simulating the three-dimensional flow field. These equations should be discretized and solved individually. However, the dependent variables obey the same generalized conservation principle and, therefore, can be reduced to a single convective-diffuse conservation equation.

To solve the equations mentioned above over the computational domain, the finite-volume discretization concept is used. This implies a division of integral computational domain into a series of small, elementary control volumes (cells) over which the integration is carried out. Curvilinear coordinates (either orthogonal or body-fitted) can be used to define the cells.

Patankar (1980) states the procedure necessary for discretizing the governing equations of the model. It consists in integrating the governing equations over the control volume shown in Figure 2. The volume integrals are converted to surface integral for the control volume using Green's theorem; the individual

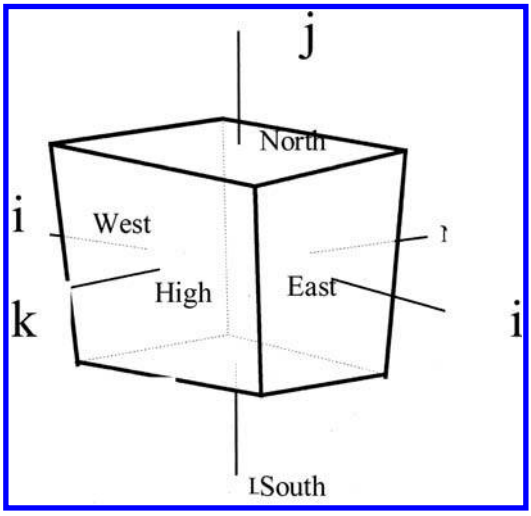


Figure 2. Cell face nomenclature for the model.

fluxes at the face of each cell are then estimated using appropriate interpolation procedures.

The equations described previously are numerically resolved in a general purpose CFD (computational fluid dynamic) package named STORM/CFD 2000 (Simunet Corporation, 2000) which can simulate, over the time and space domain, the fluid flow in various situations. This package also has powerful flow field visualization for a post-processing work.

Before starting the simulations several initial boundary conditions should be provided. Among these conditions, initial flow velocities, geometric arrangement of the elements, and the type of turbulence model to be applied are necessary.

4 CHARACTERISTICS OF THE STUDY SITE

The Shimanto river bridge is located in the south-eastern part of Kochi prefecture (in Shikoku Island, Japan). The bridge site is 9.5 km upstream of the river estuary. The bridge is 508 m in length, and is founded on 13 compound piers (P1 to P13), formed by joining two cylindrical piers, through a concrete collar (Figures 3, 4). Eight of these piers are located inside the main river channel. The span between each pier is about 53.6 m. The riverbed material is of the sand-gravel type whose $D_{50}=20$ mm and $D_{84}=50$ mm (Aragão et al., 2003).

To avoid the scour processes around the piers and between them, some scour control measures were installed, which consisted of a square slab footing (23 m × 23 m), built around the piers, and a concrete block, simulating a pavement, installed between the piers. These countermeasures were flat when constructed, but after successive floods, the slab footing

Copyright © 2006 Taylor & Francis Group plc, London, UK

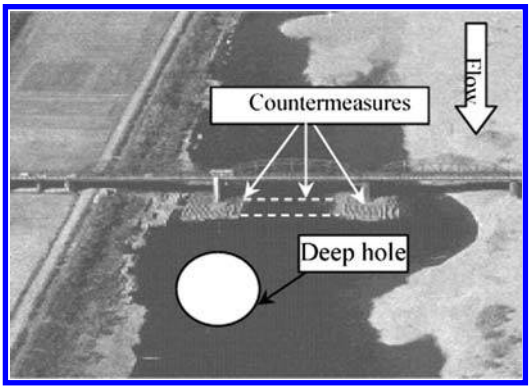


Figure 3. Shimanto River Bridge.

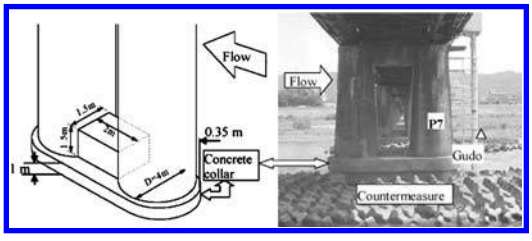


Figure 4. Pier of Shimanto River Bridge (schematic representation and real shape).

deformed and the concrete block subsided, assuming a fan shape. To register the water level, two measuring sections were installed: one upstream of the bridge (Gudo II) and another at the pier 7 (Gudo). Several floods have been registered at the bridge section as a result of heavy rainfall caused either by typhoons or by wet fronts (Aragão et al., 2003).

Over a long period of observation, data on channel cross-section at 23 different river sections as well as on the bed elevation have been collected. Based on those data, a profound scour hole of 10 m deep and located at 30 m, downstream of the bridge (Figure 2) was detected. The causes of this hole are not well known and need to be investigated as otherwise it may enlarge and compromise the bridge structure. In 2001, an underwater video robot was used to verify the riverbed condition around the hole, its deepness and real shape. Those data showed a continuous process of aggradation and degradation along the river, permitting the perception of the contour lines of the area surrounding the bridge (Figure 5), and the calculation of flow velocity ($n = 0.03$) (Table 1).

5 FLOW FIELD MODELING

Based on the bridge characteristics and on the data about the floods observed at the bridge site (Table 1),

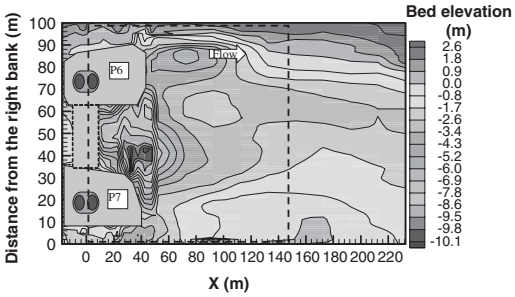


Figure 5. Bed elevation downstream from the Shimanto River Bridge.

Table 1. Floods observed, flow velocity and depth, and Froude number at Gudo section.

Date dd/mm/yy	Q (m^3/s)	T.P.W. (m)	U (m/s)	h (m)	Fr
09/08/63	13,400	10.3	5.0	9.3	0.527
21/08/70	8,700	7.9	4.1	6.9	0.502
29/08/71	9,800	8.5	4.4	7.5	0.509
23/07/72	7,600	7.3	3.9	6.3	0.495
02/09/74	6,400	6.5	3.6	5.5	0.484
16/08/75	8,500	7.8	4.1	6.8	0.501
29/08/82	10,200	8.7	4.5	7.7	0.512
19/08/92	9,400	8.3	4.3	7.3	0.507
16/09/97	10,000	8.6	4.4	7.6	0.510
14/09/01	2,700	3.5	2.1	2.5	0.427
01/09/02	3,100	3.9	2.3	2.9	0.437
19/05/03	5,700	6.0	3.3	5.0	0.477
01/06/03	6,700	6.7	3.6	5.7	0.487

* T.P.W stands for water level (m); U is flow velocity calculated through Manning equation (m/s); h is flow depth (m); Fr is Froude number in which flow depth is the characteristic length.

three-dimensional flow field modeling was attempted. In order to achieve this objective, the model needs specifications regarding the initial boundary conditions such as the initial flow velocity, the geometry of the pier structure and the type of turbulence model, among others. Some of these data can be collected in situ. However, others are closely related to the flow field being simulated. In turn, this will depend on the shape of the scour hole around the piers for a given flood and the velocity that would cause such a scour hole. Such information is also needed over the entire target area where the flow is being simulated.

Considering the real field conditions of the bridge section (Section 4), obtaining these data in real time would be a very costly and time consuming work. Thus, based on the principle of similarity, if model tests could be carried out in a laboratory flume,that would reproduce the observed field conditions, it would be

Copyright © 2006 Taylor & Francis Group plc, London, UK

possible to estimate closely the required input data for the flow field modeling.

With this objective in mind, experiments were conducted in a flume and for this purpose, the riverbed for the model was considered to be fixed and flat. The water flow was modeled by means of a rigid-lid boundary, and the surface was approximated as a slip wall. The main objective in simulating this configuration was to find the probable causes of the scour processes and the role of each factor in preventing or contributing to the scour around the bridge.

Admitting the conditions stated above, flow field modeling was carried out considering the following situations: 1) with a single compound model pier, 2) with two compound model piers, 3) with one scaled compound pier, 4) with two scaled compound piers, and 5) simulation of the flow field with the presence of the deep scourhole downstream of the bridge.

5.1 *Flume experiments*

In order to understand well the mechanisms behind the scouring around the bridge (Figure 5), and to provide the values of the hydraulic variables that would be used as boundary conditions for flow field modeling, flume experiments were considered as a viable option. The initial geometry of the existing countermeasures, and the Froude numbers associated with each flood flow (Table 1) were taken into account. The laboratory installations consisted of the following: a re-circulating flume (20 m × 0.5 m × 0.5 m); model piers with and without bed protection, scaled to 1/100 and 1/200 of the real size; an experimental section formed by a thick sand bed (1.71 m long, 0.5 m wide, and 0.20 m deep) located at 12 m from the inlet of the flume (Figure 6). Uniform sediment mixtures with different median sizes, $D_{50} = 1.42$ mm, and $D_{50} = 0.45$ mm were used and the discharges varied from 5 to 20 l/s (Table 2).

The experiments with one compound pier were conducted under clear-water conditions and with two compound piers, the experiments were conducted under live-bed conditions. Thus, in the latter case, an additional sediment source became necessary. This was achieved by setting the model piers in the middle of the sand bed installed in the flume, so that the sediment from upstream could serve as the incoming sediment load. Later on, the squared area shown by dashed line in Figure 5 was geometrically scaled to 1/200 and the cross-section of the riverbed within this interval was molded by using Styrofoam. This mold was then impressed on the test section (Figure 7), and the river bed was made up with a sand of $D_{50} = 0.45$ mm size. The measurement of flow velocities at different depths within and outside the hole were carried out with a Pitot tube. Following a methodology proposed by Suzuki et al. (1997), a critical diameter Dc for a given u_*,

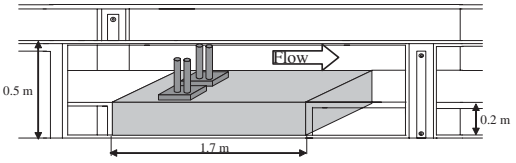


Figure 6. Two compound piers.

Table 2. Conditions of the experiments.

Mixture	Q (l/s)	One*	Two **	Number of runs	
Uniform D_{50} 1.42 mm	5 ∼ 20	D = 4.8 cm	D = 2 cm	One 105	Two 18
Uniform D_{50} 0.45 mm			D = 2 cm	–	9

* One – one compound pier.
** Two – two compound piers.

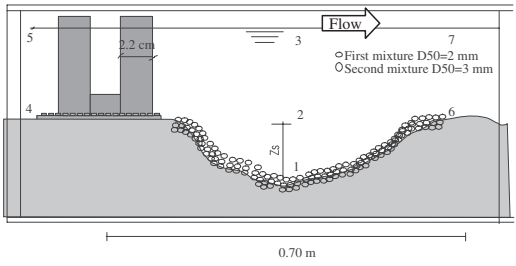


Figure 7. Schematic view of the scour hole protected with the artificial armor coat.

that would resist erosion due to the shear stress caused by the movement of water inside the deep hole was calculated according to Equation 8:

$$D_c = \frac{u_*^2}{sg\tau_c} \tag{8}$$

in which, u_* is the shear velocity; g is the gravitational acceleration, τ_c is a dimensionless critical shear stress (≅0.05), $s = ((\rho_s/\rho)\text{-}1)$, ρ_s is the density of the gravel, ρ is the water density. Sediments with the size equal to Dc was then placed over the target area in three different layers (as indicated in Figure 7) and discharges varying from 8 l/s to 15 l/s were applied.

5.2 *Flow modeling*

5.2.1 *Single compound pier*

To simulate the flow field around just one compound pier, experimental data for the pier of 4.8 cm, flow

Copyright © 2006 Taylor & Francis Group plc, London, UK

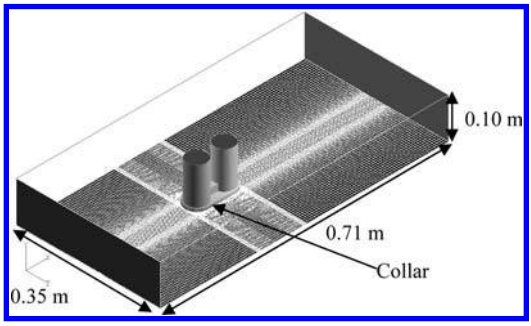


Figure 8. Geometry used for the flow simulation around a compound pier model.

depth of 10 cm for a discharge Q, of 15.8 l/s with a mean flow velocity of 0.31 m/s was chosen. Based on these, the shear velocity was calculated as 0.02 m/s. The attack angle of the flow was set to zero. The flow was assumed to be steady and turbulent for applying the standard k-ε model for turbulence simulation. The bottom was considered non-slippery whose roughness height was 1.4 mm (the D_{50} value of the uniform sand used during the experiments). The mesh associated with this geometry had 148 nodes stream-wise, 72 nodes cross-stream-wise, and 13 nodes depth-wise.

Based on these considerations, the flow field was simulated for two different cases: 1) the flume bed set at the level of the upper face of the collar (Figure 8) and, 2) the flume bed set at the level of the lower face of the collar. The purpose of these two simulations was the following: 1) to verify the flow field conditions at the beginning of the experiment, and 2) to verify the flow field around the collar when the scour hole is already formed.

5.2.2 *Two compound piers*

The flow field was simulated for the case of two compound piers, the scour hole geometry for the model had the dimensions of 1.74 m long, 0.50 m wide, and 0.047 m deep. For this geometry, the associated grid consisted of 164 stream-wise nodes, 171 nodes across the stream and 20 nodes depthwise. Each pier was 0.022 m in diameter. The non-slip bed had a roughness of 1.42 mm, the D_{50} of the first sand mixture (Section 5). To simulate the flow field with this configuration, data from one of the experiments in which flow velocity was 0.3 m/s with an associated discharge of 12.5 l/s, and the shear velocity of 0.021 m/s was utilized. The geometry of the model piers is shown in Figure 9.

5.2.3 *One scaled compound pier*

For the simulation of flow field with the scaled real size of the compound pier, the collar surrounding the piers was omitted (Figure 4), since, the collar is, generally, only exposed after the occurrence of multiples

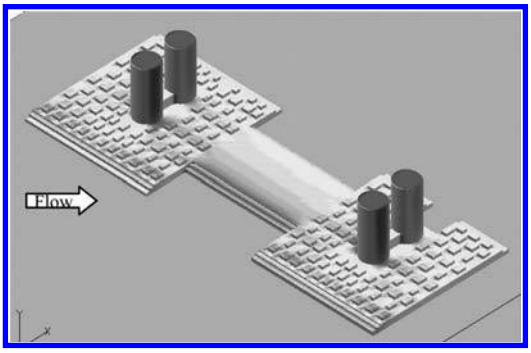


Figure 9. Geometry used for the flow field simulation of the two compound pier models with countermeasures.

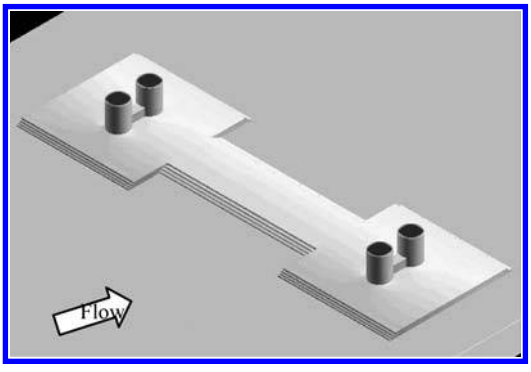


Figure 10. Geometrical pattern used for flow field simulation around two compound piers.

floods or during a very large event. The conditions used for simulation corresponded to: a pier diameter of 4 m, flow depth of 6 m, bed roughness equal to 5 cm (the D_{50} of the riverbed), total length of 200 m, mean flow velocity of 3.8 m/s, and an attack angle of the flow set to zero. These hydraulic conditions led to a shear velocity equal to 0.21 m/s and a flow discharge corresponding to 9,800 m^3/s, at the site observed on 29th August, 1971. The mesh associated with this geometry had 148 nodes along the stream, 72 nodes across, and 13 nodes depth wise.

5.2.4 *Two scaled compound piers*

For this case, the model geometry had the following dimensions: 328 m along the stream, 107.64 m wide, and 6 m in depth. The associated mesh had 323 nodes stream-wise, 220 nodes cross-stream-wise, and 25 nodes depth-wise. The flow conditions comprised of: initial velocity of 3.4 m/s, steady flow, pier diameter equal to 4 m, and a non-slippery bed, whose roughness was equal to 5 cm(D_{50} of the riverbed). These conditions were observed during the flood registered on 31st May, 2003. Figure 10 shows the geometrical pattern used for simulation of the flow field.

Copyright © 2006 Taylor & Francis Group plc, London, UK

5.2.5 *Simulation of the flow field inside the deep scour hole*

In order to verify the predictability of the 3D flow simulation model, the true geometry of the shape of the scour hole (Section 4; Figures 5 and 7) and its related flow conditions were modeled with $Q = 12.5$ l/s and $U = 0.38$ m/s, and Dc = 2.5 mm. The grid had 350 nodes stream-wise, 150 nodes cross-stream-wise, and 25 nodes depth-wise. The other conditions were similar to those stated in the previous section.

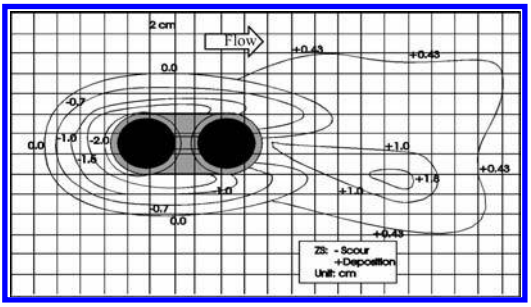


Figure 11. Zs/D vs. Ns for uniform sand and an attack angle = 0.

6 RESULTS AND DISCUSSION

6.1 *Scouring around one compound pier*

In the flume experiments, the resultant bed elevations for $Q = 12.5$ l/s with a mean velocity of 0.30 m/s is shown in Figure 11. It is seen that the scouring occurs not only at the upstream face of the pier, but also propagates downstream (Sections 2 and 3). The bed material removed due to the action of both downward flow and the horseshoe vortex is deposited a little further from the downstream face. At the downstream face the negative pressure caused by the wake vortex also removes the bed material which is entrained and is deposited further downstream from the pier. The scour depth, Zs, was normalized by the pier diameter, D, (Zs/D). In Figure 11, the aggradations are denoted by a plus sign and degradations are marked by a minus sign. Such bed variations are a direct consequence of the increase and decrease in flow velocity caused when the approaching flow meets the compound pier.

During for flow modeling, the first attempt was to simulate the flow field at the beginning of the scour process, when the collar is covered by the bed material. For this situation and considering a ratio of y/h = 0.2, the resultant flow field is presented in Figure 12. Here it is observed a considerable increase in flow velocity at the upstream face, caused by vortices and higher values of this variable at the laterals of the pier, which certainly will cause high scouring. Figure 12 shows areas of negative velocity where the combined effect of the horseshoe and wake vortex works (Figure 13) as an additional scouring agent. Then, from X/D = 7, where the scouring agents loose power and the velocity decreases, deposition occurs.

When the collar surrounding the two cylinders is exposed (Figure 14), the overall velocities around the pier are smaller than those found when the collar is covered (Figure 12) since it works as a shield against the downward flow, reducing its scouring effect. Yet, when the collar is completely uncovered (Figure 14), allowing the flowing water to reach its lower face, the scouring appears stronger than before and a very large amount of material is removed from around the pier, creating a deep hole.

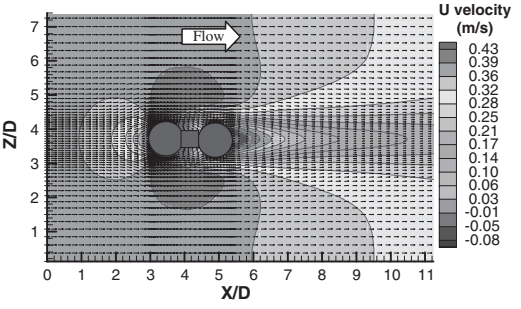


Figure 12. Velocity vectors around the compound pier model and at the scouring initiation.

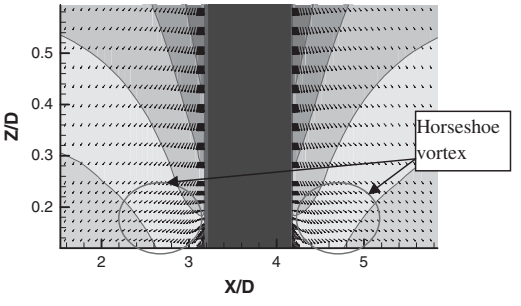


Figure 13. Velocity vectors on the Y-Z plane and at the upstream face of the compound pier model.

Similar results were also observed by Ettema (1980), Dargahi (1990), and Chiew (1992). If this situation takes place at a bridge site, the pier destruction is a matter of time.

The same comment can be extended to the scouring processes around the real sized compound pier. However, for that situation the velocities around the piers are expressively higher, leading to notable bed removal. Measurement campaigns done at the bridge site (Aragão, 2004) showed that for a flood event of Q = 3,500 m^3/s the degradation was around 0.9 m, which is a matter of concern because floods of that

Copyright © 2006 Taylor & Francis Group plc, London, UK

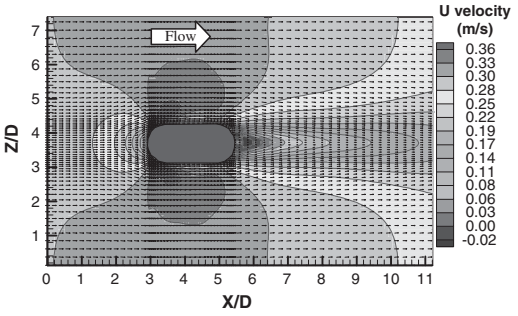


Figure 14. Flow field around the compound pier model after the scouring initiation.

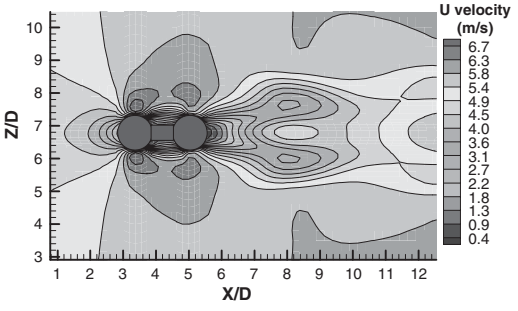


Figure 15. Contour of U velocity around the compound pier.

magnitude or higher are often observed. The simulation showed that for the situation proposed at Section 5.2.3, the velocity at the laterals of the piers reaches almost 6.7 m/s. The wake vortex described by Dargahi (1990), Breusers & Raudikivi (1991), and Graf & Istiarto (1998) are indicated by the negative velocities at the downstream face of the pier (Figure 15). In addition, at X/D = 7 and further downstream, the flow tends to reach the same velocity found upstream of the pier at X/D = 1. This can be translated into a huge amount of turbulent kinetic energy that is generated and is dissipated, mainly at the laterals of the pier in the interval $3.8 < X/D < 4.8$. In other words, a high gradient of energy is dissipated from upstream to downstream, contributing to decrease of energy of transport and scour of the flow.

6.2 *Scouring around two compound piers*

For the boundary condition stated in Section 5.1 the results from the experiments were conducted and the bed variation around the piers represented in Figure 16. In this figure it is observed that past the pavement in between the piers a scouring develops and extends to X/D = 22 from which, the removed material is deposited. It is important to say that the same

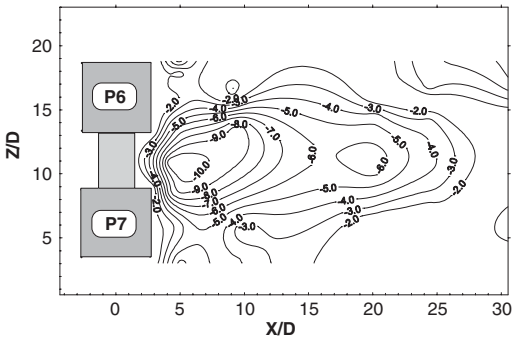


Figure 16. Bed elevation (mm) past the piers (Q = 15 l/s, H = 4 cm, h = 6.8 cm, U = 0.44 m/s).

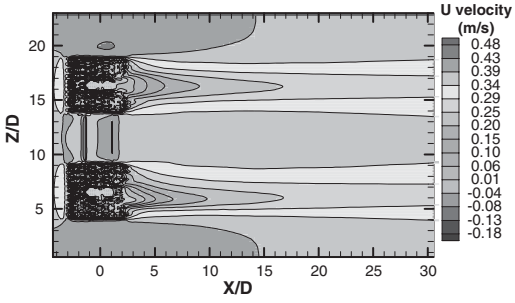


Figure 17. Contour of U velocity around the compound pier model.

behavior was observed when other discharges were applied. In addition, the results show that the deepest point change its location according to the discharges as does the depth of the scour hole, which gets closer to the downstream face of the piers as the discharge increases.

As stated in Section 5.2.3, the hydraulic conditions found during the experiments were applied as the initial values for the flow simulations, resulting in the contour map of U velocity around the piers for y/h = 0.2 as displayed in Figure 16. In this figure it is possible to notice that on the countermeasure, that surrounds the piers, the velocity gets close to zero, but, immediately past such structures, this variable reaches a value of 0.3 m/s. This variation can also be considered an agent for dislodging and entraining the bed material.

As expected, the constriction caused by the piers increased the velocity in the area between them up to 75% more than the initial one. Scour certainly would occur there, but the pavement in between the piers prevented the bed from being removed. Figure 17 also shows a region of high flow velocities starting upstream of the riprap to its downstream edge constituting an effective scour area.

Copyright © 2006 Taylor & Francis Group plc, London, UK

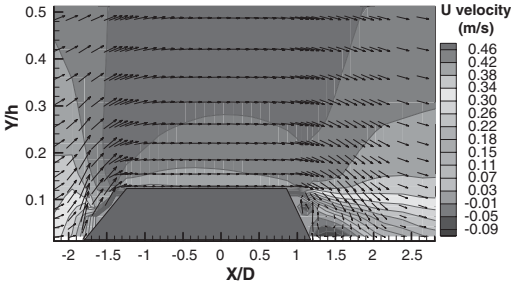


Figure 18. Velocity vectors over the link between the two compound pier models.

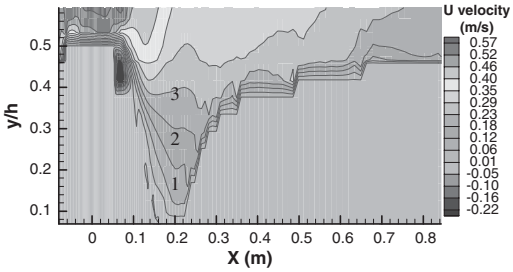


Figure 19. Contour of U velocity along the longitudinal line.

With a high degree of accumulated kinetic energy, due to the constriction, the flow passing over such pavement acts first as a jewt that removes the material and then as an important agent in sediment entrainment as shown in Figure 18. This figure also shows that this jet hits the bottom more than once, constituting an effective scour agent. These aspects of the flow field can only be observed through careful and timeless measurements or though simulation of the flow field.

Considering the similarities between the prototype and the model, the results found for the model piers can be extended to the real sized compound piers (Section 5.2.3). The simulation of this arrangement confirmed these results obtained for the model piers.

For both model piers and the real sized compound piers, the riprap around the piers and between them was decisive in preventing the bridge failure due to the scouring at its foundation. Also, the accumulation of energy and its dissipation streamwise, can explain the degradations and aggradations around the bridge (Figures 16 to 18).

6.3 *Scouring past the piers and simulation of the flow field inside the deep scour hole*

The velocity measurement at three sites, 1, 2, 3, with Pitot tube (Figure 7) resulted in the following values: 1) 0.14 m/s, 2) 0.34 m/s, and 3) 0.38 m/s. The experiments were conducted with three different critical diameters (1 mm, 2 mm, and 3 mm), Section 5.1, allowed to conclude that such a countermeasure not only prevented the target area from being scoured, but also induced the deposition of the bed material from upstream inside the hole. For some runs the aggradation inside the hole was about 2 cm. In addition, for the first Dc (3 mm), the rim of the hole and the areas upstream and downstream of it were preserved. For Dc = 1 mm and 2 mm, the area inside the role was also preserved, however, outside the hole and over the rim, the riprap was removed, proving these sizes could protect the hole, but scouring could be expected somewhere downstream.

The intention of finding a suitable riprap size during the experiment was to transfer such knowledge to the bridge site. Considering the scale factor involved (1/200) and the target area (Figure 5) a Dc = 3 mm means rocks or concrete blocks of 60 cm leading to a very high cost. Then, to allow for cost reduction, feasibility, and safety, Dc = 2.5 mm was also tested and the riprap remained undamaged in this case also.

As for the simulation of flow inside the scour hole downstream from the bridge, the arrangement proposed in Section 5.2.5 provided means to model the flow field around the piers and inside the scour hole (Figure 19). This figure shows the variation of the flow velocity with the flow depth, which in turn agrees with the values measured during the related experiments described above.

Considering the geometrical similarity the model, the bed material of $D_{50} = 2.5$ mm (the critical diameter of the present experiments) and finally that the values simulated at points 1, 2, and 3 are close to those measured, this simulation permits to conclude that the use of flow field modeling for analyzing scour around bridge piers and the related consequences, constitute a valuable tool. In other words, the present model could not only predict the measured values but also, reproduce the variations in flow velocities at different sites locations and outside the scour hole.

7 CONCLUSIONS

In order to analyze the mechanism involved in scouring around bridge piers a 3D turbulent flow modeling has been utilized. The data used as a base for comparison are from the Shimanto River Bridge where advanced scour processes have been identified not only around the bridge foundations, but also downstream from them. Based on the finding from flow modeling and flume experiments and considering similarities it is possible to conclude the following: the bed variation around a compound pier could be explained through the analysis of the flow field; the collar around the pier at times works as a shield against the downward flow. However, if the scouring goes beyond the lower face

Copyright © 2006 Taylor & Francis Group plc, London, UK

of the collar then the scouring is more intense than before. The presence of riprap around two compound piers was decisive in preventing the area from being scoured, but contributed somehow to the excavation of a deep scour hole downstream of the bridge; the mechanism of such a process could only be understood with the flow field modeling. To prevent further scouring inside the deep hole the use of a riprap formed by three layers of a critical diameter was tested and could be recommended.

AKNOWLEDGEMENTS

This study has been supported by the National Council for Research and Technological Development (CNPq) of the Ministry of Sciences and Technology of Brazil, and by the Ministry of Education Culture and Sports of Japan (MONBUKAGAKUSHO). The Ministry of Land, Infrastructure and Transport of Japan, Nakamura city Branch provided the data about the Shimanto River Bridge.

REFERENCES

Aragão, R., Kadota, A, and Suzuki, K. 2003. Local Scour around the Piers of the Shimanto River. *Annual Journal of Hydraulic Engineering*, JSCE, Vol.47, pp. 673–678.

Aragao, R. 2004. *Actual measurement and 3d turbulent numerical analysis on local scour around Shimanto River Bridge*. Dissertation Thesis, Ehime University, Ehime, Matsuyama, Japan. 191p.

Aragão, R., Suzuki, K., Kadota, A., Srinivasan, V.S. and Shingo, I. 2005. Investigation of the localized scouring processes through an integrated approach. *Proceedings of the XXXI IAHR Congress*, Seoul. Korea. 1. 2543–2552.

Breusers, H.N.C. and Raudkivi, A.J. 1991. *Scouring*, Hydraulics Structures Design Manual, No. 2, IAHR, Balkema, 143p.

Chiew, Y.M. 1992. Scour Protection at Bridge Piers. *Journal of Hydraulic Engineering*, ASCE, 118 (9), 1260–1269.

Dargahi, B. 1990. Controlling Mechanism of Local Scouring, *Journal of Hydraulic Engineering*. ASCE, 11 6(10): 1197–1214.

Ettema, R. 1980. *Scour at Bridge Piers*. Report No. 216, School of Engineering, The University of Auckland, Auckland, New Zealand, 527p.

Graf, W.H. and Yulistiyanto, B. 1998. Experiments on Flow around a Cylinder; the Velocity and Vorticity Fields. *Journal of Hydraulic Research*, IAHR, 36 (4), 637–653.

Hwang, R.R. and Jaw, S.Y. 1998. Second-Order Closure Turbulence Models: Their Achievements and Limitations, In *Proceedings of the National Science Council ROC(A),* 22 (6), 703–722.

Jain, S.C. 1981. Maximum Clear-Water Scour around Cylindrical Piers. *Journal of Hydraulic Engineering*, ASCE, 107 (5), 611–625.

Johnson, P. A. 1995. Comparison of pier-scour equations using field data. *Journal of Hydraulic Engineering*, 121 (8), ASCE, 626–629.

Launder, B.E. and Spalding, D.B. 1974. The Numerical Computation of Turbulent Flows, In *Comp. Methods Appl. Mech. Eng.*, 3, 269–289.

Melville, B. W. and Coleman, S. E. 2000. *Bridge Scour*, Water Resources Publication, LLC., The University of Auckland, Auckland, New Zealand, 550p.

Patankar, S.V. 1980. *Numerical heat transfer and fluid flow*. (Org.) Taylor and Francis, 197p.

Rodi, W. 1980. *Turbulence models and their application in hydraulic*. Tech. rep., IAHR, Delft, the Netherlands, pp104.

Simunet Corporation 2000. Storm/CFD2000 basic equations. Alhambra, California. USA. 75p.

Suzuki, K., Yamamoto, H. and Kadota, A. 1998. Mechanism of Bed Load Fluctuations of Sand-Gravel Mixture in a Steep Channel, In *Proceeding of the 11th Congress of the IAHR-APD,* Indonesia, 1, 679–687.

Copyright © 2006 Taylor & Francis Group plc, London, UK

Predictions of turbulent flows around a bridge pier using various numerical models

I. Kimura
Dept. of Civil and Environmental Engineering, Matsue National College of Technology, Matsue, Japan

T. Hosoda & S. Onada
Dept. of Civil Engineering, Kyoto University, Kyoto, Japan

ABSTRACT: Turbulent flow structures around bridge piers are examined numerically using various computational models focusing on vortex shedding and water surface elevations. Four different types of numerical models, namely, two kinds of 2D plane model, a quasi-3D model (a 3D model with hydrostatic assumption) and a full-3D model, are considered. As a turbulence model, a simple 0-equation model with linear and non-linear constitutive equations are used for the 2D plane model and a 2nd order non-linear k-ε model with effects of strain and rotation parameters are applied for the quasi-3D and full-3D models. First, laboratory test is carried out to obtain data for verification. Then, the computations are performed under the same conditions as the laboratory test. The numerical results showed that the 2D and full 3D models could capture well the height of water elevation at the upstream region of the pier though the quasi-3D model under-predicted it. The 2D model overestimated the depth of the hollow behind the pier. The quasi-3D model considerably over-estimated the length of the re-circulation zone.

1 INTRODUCTION

The upstream region of bridge piers in rivers is often become a weak-point of flood control because the water surface is elevated due to the flow resistance caused by the piers. It is therefore important to develop a numerical model, which can predict the flow patterns around piers with practical accuracy from the viewpoint of disaster prevention. In this paper, the turbulent flow structures and water surface variations around bridge piers with square cross-sections are numerically investigated using various numerical models. Four different models, namely, two kinds of 2D (two-dimensional) plane models, quasi-3D model (3D model with hydrostatic assumption) and full-3D model, are applied and the results are compared. As a turbulence model, a simple 0-equation model with linear and non-linear constitutive equations are used for the 2D plane models and a non-linear k-ε model with effects of strain and rotation parameters proposed by Kimura & Hosoda (2003) are applied for the quasi-3D and full-3D models. A laboratory test was carried out prior to the numerical tests in order to obtain data for verifications using a rectangular open flume under the conditions of $\mathrm{Re} = 8400$ and $\mathrm{Fr} = 0.54$. A rectangular cylinder is used as a model of a bridge pier. The computations using a finite volume method were performed in the same conditions as those in the laboratory test and the results were compared focusing on the Karman vortex shedding, a horseshoe-vortex formation and water level distributions around the cylinder.

2 NUMERICAL MODELS

2.1 *Full-3D model (F3D model)*

2.1.1 *Basic equations*

The Reynolds averaged 3D flow equations with contravariant components of velocity vectors on a generalized curvilinear movable coordinate system are used as governing equations. The equations are described as follows.

[Continuity equation]

$$\frac{1}{\sqrt{g}}\frac{\partial V^{\alpha}\sqrt{g}}{\partial \xi^{\alpha}} = 0 \tag{1}$$

[Momentum equation]

$$\frac{\partial V^{i}}{\partial t} + \nabla_j\left[V^{i}(V^{j} - W^{j})\right] + V^{i}\nabla_j W^{j} + V^{j}\nabla_j W^{i} = F^{i} - \frac{1}{\rho}g^{ij}\nabla_j p + \nabla_j\left[-\overline{v^{i}v^{j}}\right] + 2\nu\nabla_j e^{ij} \tag{2}$$

Copyright © 2006 Taylor & Francis Group plc, London, UK

[k equations]

$$\frac{\partial k}{\partial t}+\nabla_j\left[k(V^j-W^j)\right]+k\nabla_j W^j = -g_{il}\overline{v^i v^j}\nabla_j V^i-\varepsilon+\nabla_j\left\{\left(\frac{D_t}{\sigma_k}+\nu\right)g^{ij}\nabla_i k\right\} \quad (3)$$

[ε equations]

$$\frac{\partial \varepsilon}{\partial t}+\nabla_j\left[\varepsilon(V^j-W^j)\right]+\varepsilon\nabla_j W^j = -C_{\varepsilon 1}\frac{\varepsilon}{k}g_{il}\overline{v^i v^j}\nabla_j V^i - C_{\varepsilon 2}\frac{\varepsilon^2}{k}+\nabla_j\left\{\left(\frac{D_t}{\sigma_k}+\nu\right)g^{ij}\nabla_i\varepsilon\right\} \quad (4)$$

where ξ^I = generalized curvilinear coordinate, t = time, V^i = contravariant component of the velocity vector of flows, W^i = contravariant component of the velocity vector of grid motion, p = pressure, ν = molecular dynamic viscosity, ρ = density of water, k = turbulent energy, ε = turbulent energy dissipation rate, g_{ij} and g^{ij} = covariant and contravariant component of metric tensor, $g=\det(g_{ij})$ and F^i = contravariant component of gravity acceleration. ∇^i indicates a covariant differential, for instance,

$$\nabla_i A^k = \frac{\partial A^k}{\partial \xi^i}+A^j\Gamma_{ij}^{\ k} \quad (5)$$

where Γ^k_{ij} = Christoffel symbol described as

$$\Gamma_{ij}^{\ k}=\left\{\begin{matrix}k\\ij\end{matrix}\right\}=\frac{1}{2}g^{km}\left(\frac{\partial g_{jm}}{\partial \xi^i}+\frac{\partial g_{im}}{\partial \xi^j}-\frac{\partial g_{ij}}{\partial \xi^m}\right)=\frac{\partial \xi^k}{\partial x^p}\frac{\partial^2 x^p}{\partial \xi^i \partial \xi^j} \quad (6)$$

To calculate a complex turbulent flow with separation and vortex shedding, a 2nd-order non-linear k-ε model by Kimura & Hosoda (2003) is adopted as a turbulence model. This model has been applied to various flow fields, such as, a flow around a spur dikes (Kimura et al 2004), a flow around a surface-mounted cubic obstacle (Kimura & Hosoda 2000) and a compound open channel flow (Kimura et al 2001). The constitutive equations of the model are described as follows.

$$-\overline{v^{*i}v^{*j}} = D_t S^{ij}-\frac{2}{3}k\delta^i_s g^{sj}-\frac{k}{\varepsilon}D_t\left[\alpha_1 Q_1+\alpha_2 Q_2+\alpha_3 Q_3\right] \quad (7)$$

$$D_t = C_\mu\frac{k^2}{\varepsilon} \quad (8)$$

$$Q_1 = S^{i\alpha}g_{\alpha l}\Omega^{lj}+S^{j\beta}g_{\beta l}\Omega^{li} \quad (9)$$

$$Q_2 = S^{i\alpha}g_{\alpha l}S^{lj}-\frac{1}{3}S^{k\alpha}g_{\alpha m}S^{m\beta}g_{\beta k}\delta^i_l g^{lj} \quad (10)$$

$$Q_3 = \Omega^{i\alpha}g_{\alpha l}\Omega^{lj}-\frac{1}{3}\Omega^{k\alpha}g_{\alpha m}\Omega^{m\beta}g_{\beta k}\delta^i_l g^{lj} \quad (11)$$

$$S^{ij} = g^{j\alpha}\nabla_\alpha V^i + g^{i\alpha}\nabla_\alpha V^j \quad (12)$$

$$\Omega^{ij} = g^{j\alpha}\nabla_\alpha V^i - g^{i\alpha}\nabla_\alpha V^j \quad (13)$$

The model coefficients are essentially not constants but functions of the strain parameter S and the rotation parameter Ω. In this study, all the coefficients are given as functions with one variable M for simplicity as follows (Kimura & Hosoda 2003).

$$\alpha_1=-0.1325 f_M,\quad \alpha_2=0.0675 f_M,\quad \alpha_3=-0.0675 f_M \quad (14)$$

$$f_M=\left[1+0.02M^2\right]^{-1},\quad M=\max[S,\Omega] \quad (15)$$

$$C_\mu=\min\left[0.09, 0.3/(1+0.09M^2)\right] \quad (16)$$

$$S=\frac{k}{\varepsilon}\sqrt{\frac{1}{2}S^{i\alpha}g_{\alpha j}S^{j\beta}g_{\beta i}},\quad \Omega=\frac{k}{\varepsilon}\sqrt{\frac{1}{2}\Omega^{i\alpha}g_{\alpha j}\Omega^{j\beta}g_{\beta i}} \quad (17)$$

Equations (14) and (15) were adjusted through the consideration of the distribution of turbulent intensities in a simple shear flow (Kimura & Hosoda 2000). Equation (16) was tuned to satisfy the realizability constraints in a simple shear flow and possible singular points in both 2D and 3D flows (Hosoda et al 2001).

The standard linear k-ε model is also applied for the comparison of turbulence models. The constitutive equation of the standard model is

$$-\overline{v^{*i}v^{*j}} = D_t S^{ij}-\frac{2}{3}k\delta^i_s g^{sj},\quad D_t = C_\mu\frac{k^2}{\varepsilon} \quad (18)$$

where C_μ is 0.09 (=const.).

2.1.2 *Outline of numerical method*

The differential equations governing the mean-velocities and the turbulence field are solved with the finite volume method on full-staggered grid system. The arrangement of hydraulic variables on a full-staggered grid is shown in Figure 1. The metric tensor and Cristoffel symbol are defined only at grid points to save computer memory and the values at other positions are interpolated at each computational step.

QUICK scheme is applied to the convective inertia terms and the central differencing is used for the diffusion terms in the momentum equations. The hybrid central upwind scheme is applied to the k and ε equations for the computational stability. Adams-Bashforth scheme with second-order accuracy in time is used for time integration in each equation. The basic equations are discretized as fully explicit forms and are solved successively along the time axis step by step. The pressure field is solved using iterative procedure at each time step using SOLA algorithm by Hirt et al. (1975).

Copyright © 2006 Taylor & Francis Group plc, London, UK

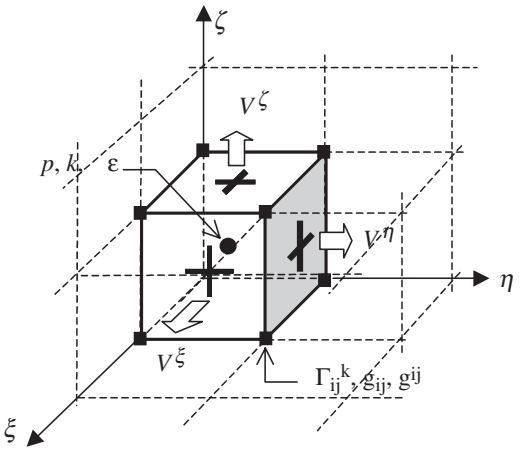


Figure 1. Arrangement of hydraulic variables and metric tensors on full staggered grid (F3D, Q3D models).

2.1.3 *Boundary conditions*

Since the present turbulence model is a high Reynolds number type, the wall function approach is applied as the wall boundary conditions for k and ε. The wall friction is evaluated by the log-law. At the downstream end of the computational domain, the longitudinal gradients of all variables are assumed to be zero. At the boundary inlet, the level of k is chosen to be $(0.02U_0)^2$ (U_0 = averaged velocity). The value of ε at the inlet is determined from the value of k at the inlet and Equation (8) by specifying the ratio $D_t/\nu = 10$ (Bosche & Rodi 1998).

The free surface elevation is solved by the simple relation in Equation (19) since the contravariant components of the velocity vector are used in the basic equations (Takizawa et al. 1992).

$$\Delta h = \sqrt{g_{33}} V^3 \Delta t \tag{19}$$

where Δt = time increment and Δh = surface elevation during Δt. To consider the rapid attenuation of turbulent intensities in the depth-wise direction near the free surface, the eddy viscosity is multiplied by the following dumping function (Hosoda 1990)

$$f_s = 1 - \exp\left(-B\frac{(h-y)\varepsilon_s}{k_s^{3/2}}\right), \quad (B = 10) \tag{20}$$

where sub-s indicates the value at the surface layer. The turbulence dissipation rate at the surface layer is evaluated by the following formula proposed by Sugiyama et al. (1995) to calculate the secondary currents of 2nd kind.

$$\varepsilon_s = \frac{C_{\mu 0}^{3/4} k_s^{3/2}}{0.4\Delta y_s}, \quad (C_{\mu 0} = 0.09) \tag{21}$$

2.1.4 *Initial conditions*

At the beginning of the calculation, U (=velocity in the longitudinal direction (x-direction)) = U_0 (=averaged bulk velocity), V (=velocity in the transverse direction (y-direction) = 0, $k = k_{in}$ and $\varepsilon = \varepsilon_{in}$ (k_{in} and ε_{in} are the values of k and ε at the inlet boundary) are specified over the whole computational domain. In order to avoid the influence of the initial conditions, the numerical results after 50 seconds from the initial conditions are used for the following examinations.

2.2 *Quasi-3D model (Q3D model)*

The momentum equation in the vertical direction can be simplified as the following form when the hydrostatic assumption is assumed.

$$g^{3j}\nabla_j p = \rho F^3 \tag{22}$$

Since the iteration procedure to obtain a pressure field (SOLA) becomes unnecessary under this assumption, the CPU time in the quasi-3D model becomes considerably smaller than that in the full-3D model. The turbulence model in the quasi-3D model is same as that in the Full-3D model.

2.3 *Plane 2D linear model (2D-L models)*

2.3.1 *Basic equations*

Basic equations are depth averaged ones composed of a continuity equation and momentum equations as

$$\frac{\partial h}{\partial t} + \frac{\partial M}{\partial x} + \frac{\partial N}{\partial y} = 0 \tag{23}$$

$$\frac{\partial M}{\partial t} + \frac{\partial uM}{\partial x} + \frac{\partial vM}{\partial y} + gh\frac{\partial h}{\partial x} = gh\sin\theta + \frac{\partial(-\overline{u'^2}h)}{\partial x} + \frac{\partial(-\overline{u'v'}h)}{\partial y} + \nu\left[\frac{\partial}{\partial x}\left(h\frac{\partial u}{\partial x}\right) + \frac{\partial}{\partial y}\left(h\frac{\partial u}{\partial y}\right)\right] \tag{24}$$

$$\frac{\partial N}{\partial t} + \frac{\partial uN}{\partial x} + \frac{\partial vN}{\partial y} + gh\frac{\partial h}{\partial y} = \frac{\partial(-\overline{u'v'}h)}{\partial x} + \frac{\partial(-\overline{v'^2}h)}{\partial y} + \nu\left[\frac{\partial}{\partial x}\left(h\frac{\partial v}{\partial x}\right) + \frac{\partial}{\partial y}\left(h\frac{\partial v}{\partial y}\right)\right] \tag{25}$$

where h = depth; (u, v); depth-averaged velocity; (M, N) = discharge flux (M = hu, N = hv); (τ_{bx}, τ_{by}) = bottom shear-stress; ν = dynamic viscosity; θ = bottom slope of main channel; = depth-averaged Reynolds stress tensors (u_1' = u', u_2' = v') and β = momentum coefficient (1.0 for turbulent flow, 1.2 for laminar flow).

Components of the bottom shear-stress vector are evaluated by

$$\tau_{bx} = f\rho u\sqrt{u^2+v^2}/2; \quad \tau_{by} = f\rho v\sqrt{u^2+v^2}/2 \tag{26}$$

Copyright © 2006 Taylor & Francis Group plc, London, UK

where f = friction factor related to local Reynolds number $Re' \equiv uh/\nu$, evaluated as follows:

$$f = 6/R_e' \quad (R_e' \le 430) \ , \tag{27a}$$

$$\sqrt{2/f} = A_S - \left[1 - \ln\left(R_e' - \sqrt{f/2}\right)\right]/\kappa \quad (R_e' > 430) \tag{27b}$$

where $\kappa = 0.4$, $A_S = 5.5$.

2.3.2 *Turbulence model*

The following linear constitutive equation has been used in usual 0-equation models.

$$-\overline{u_i' u_j'} = \nu_h \left(\frac{\partial u_i}{\partial x_j} + \frac{\partial u_j}{\partial x_i} \right) - \frac{2}{3} k \delta_{ij} \tag{28}$$

where k = depth-averaged turbulent kinetic energy. Neze & Nakagawa (1993) proposed an empirical formula for vertical distribution of k as

$$k/u_*^2 = 4.78 \exp(-2z/h) \tag{29}$$

where z = direction perpendicular to the bottom bed. The depth-averaged turbulent kinetic energy becomes the following formula when equation (29) is integrated from the bottom to the surface.

$$k = \gamma_k u_*^2 , \quad \gamma_k = 2.07 \tag{30}$$

The eddy viscosity coefficient ν_t is given as

$$\nu_t = \alpha h u_* \tag{31}$$

where α is a constant (=0.2).

2.3.3 *Numerical scheme*

The numerical methods in the plane 2D models are similar to those in the F3D and Q3D models, namely, a finite volume method on full-staggered grid with the QUICK scheme for convective terms and the Adams Bashforth method for time integration. The arrangement of hydraulic variables in 2D model is shown in Figure 2.

The friction of walls is evaluated by log-law. The eddy viscosity is multiplied by the following two functions in order to reproduce the velocity profile near walls.

$$f_{d1} = \left[1 - \exp\left(-\frac{1}{C_{vm}} \frac{u_{*w} l_w}{\nu} \right) \right]^2 \tag{32}$$

$$f_{d2} = \begin{cases} 1 & , \quad l_w \ge h \\ \dfrac{l_w}{h}\left(1 - \dfrac{l_w}{h}\right) & , \quad l_w < h \end{cases} \tag{33}$$

where, l_w: distance to wall, u_{*w}: friction velocity at wall and C_{vm}: constant (=50.0).

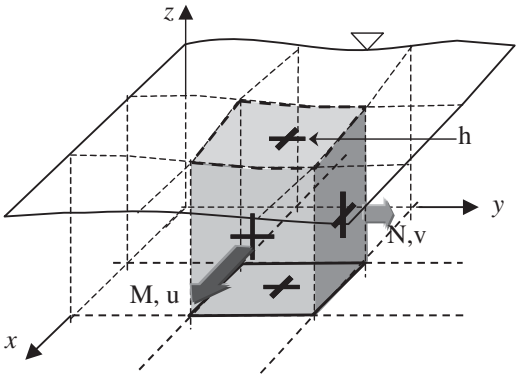


Figure 2. Arrangement of hydraulic variables in plane 2D models (2D-L, 2D-NL models).

2.3.4 *Plane 2D non-linear model (2D-NL model)*

A 2nd order non-linear formula with 0-equation model is adopted in the constitutive equation of the Reynolds stresses in the 2D-NL model as

$$-\overline{u_i u_j} = \nu_t S_{ij} - \frac{2}{3} k \delta_{ij} - \lambda_p \frac{h}{u_*} D_t \sum_{\beta=1}^{3} C_\beta \left(S_{\beta ij} - \frac{1}{3} S_{\beta\alpha\alpha} \delta_{ij} \right) \tag{34}$$

$$S_{1ij} = \frac{\partial U_i}{\partial x_\gamma}\frac{\partial U_j}{\partial x_\gamma}, \quad S_{2ij} = \frac{1}{2}\left(\frac{\partial U_\gamma}{\partial x_i}\frac{\partial U_j}{\partial x_\gamma} + \frac{\partial U_\gamma}{\partial x_j}\frac{\partial U_i}{\partial x_\gamma} \right), \quad S_{3ij} = \frac{\partial U_\gamma}{\partial x_i}\frac{\partial U_\gamma}{\partial x_j} \tag{35}$$

where ν_t is an eddy viscosity coefficient and C_1-C_3 are model coefficients. The model constants, C_1-C_3 are tuned as the following functions of the strain and rotation parameters considering the distributions of turbulence intensities in a simple shear flow.

$$C_1 = 0.4 f_M(M), \quad C_2 = 0, \quad C_3 = -0.13 f_M(M) \ ,$$
$$f_M(M) = (1 + 0.02 M^2)^{-1} \ , \quad M = \max[S, \Omega] \tag{36}$$

$$S = \lambda_p \frac{h}{u_*} \sqrt{\frac{1}{2}\left(\frac{\partial U_i}{\partial x_j} + \frac{\partial U_j}{\partial x_i} \right)^2} \ , \quad \Omega = \lambda_p \frac{h}{u_*} \sqrt{\frac{1}{2}\left(\frac{\partial U_i}{\partial x_j} - \frac{\partial U_j}{\partial x_i} \right)^2} \tag{37}$$

$$\lambda_p = \frac{\alpha}{\gamma_k C_\mu} = 1.07 \tag{38}$$

Though the expression of the eddy viscosity is given in equation (31) like 2D-L model. α in equation (31) is tuned as not a constant but a function of the strain and rotation parameters in this model as

$$\alpha(M) = \min\left[0.2, \ 0.3\gamma_k \lambda_p / (1 + 0.09 M^2)\right] \tag{39}$$

The function above was tuned considering the realizability in the similar way as that in F3D model.

Copyright © 2006 Taylor & Francis Group plc, London, UK

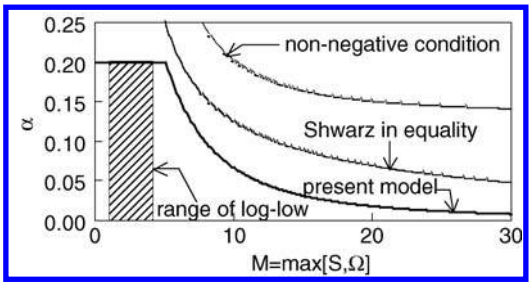


Figure 3. α(M) in the non-linear 0-equation model (2D-NL) and realizability conditions.

Figure 3 shows the function of α(M) together with the realizability conditions.

The other part of the model is same as that in the plane 2D linear (2D-L) model.

3 LABORATORY TEST

A laboratory test was performed to obtain data for assessment of model performance. The experimental flume is a 10 m long, 20 cm wide and 30 cm deep tilting flume. A rectangular wood cylinder of 4 cm × 4 cm in the cross-section and 20 cm in the length is mounted at the center of the bed. The plan and vertical views of the flow field are shown in Figure 4 and the hydraulic conditions are listed in Table 1. The water level and the velocity field around the cylinder are measured using a digital point-gauge and a propeller-type anemometer (diameter of the propeller is 3mm), respectively. The Karman vortex shedding was visualized using aluminum powder.

4 COMPUTATIONAL RESULTS

4.1 *Computational conditions and CPU times*

The computations were performed under the conditions of the preset laboratory test. The numerical grid for all models in a horizontal x-y plane is shown in Figure 5. The computations were performed using PC with CPU: Dual Xeon 2.4 GHz, RAM: 512 MB and Open MP parallel computing. The CPU times for real time of 10(sec) are 1.7(min) in 2D-L model, 2.0(min) in 2D-NL model, 284(min) in Q3D model and 365(min) in F3D model.

4.2 *Time mean flow patterns*

Figure 6 shows the time-mean velocity vectors in a horizontal x-y plane. This figure shows that the lengths of the recirculation zone behind the cylinder in 2D models are not affected by turbulence models.

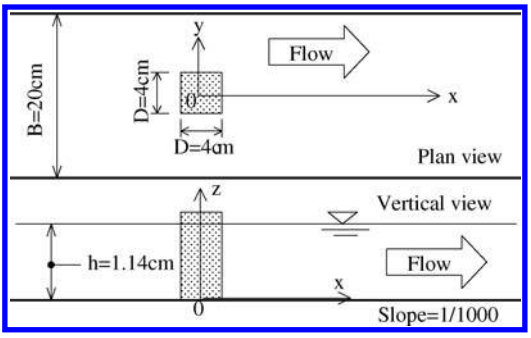


Figure 4. Schematic diagram of the flow domain.

Table 1. Hydraulic parameters in the laboratory test.

h(cm)	U_0(cm/s)	D(cm)	B/D	h/D	Re	Fr
1.14	18.18	4.0	5	0.285	8400	0.54

h: depth, U_0: mean velocity, D; side-length of cylinder B: channel width, Re: Reynolds number (=U_0D/ν), Fr: Froude number.

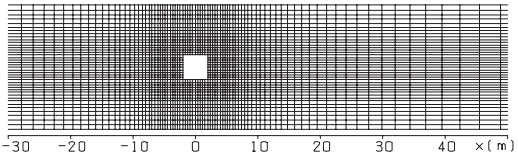


Figure 5. Numerical grid around the cylinder (x-y plane).

Note that the length closely depends on spatial dimensions. The length by the Q3D model yields longest recirculation zone.

Figure 7 shows the time-averaged velocity vectors in a vertical x-z plane along the x-axis at the upstream region of the cylinder by Q3D and F3D models. A vortex in the clockwise direction can be seen in both the results. The vortex means a formation of a horseshoe vortex around the cylinder. A diameter and a velocity of the vortex by F3D model are a little larger than that by Q3D model.

4.3 *Characteristics of vortex shedding*

Figure 8 shows snap shots of plan velocity vectors in the numerical results. This figure shows that all models can generate the Karman vortex shedding and the starting points of the vortex in 2D models locates much nearer to the pier than those in 3D models due to the shorter recirculation zone.

Figure 9 shows the temporal variations of velocities in x-direction (u) in the laboratory test and computational result of 2D-L, 2D-NL and F3D models.

Copyright © 2006 Taylor & Francis Group plc, London, UK

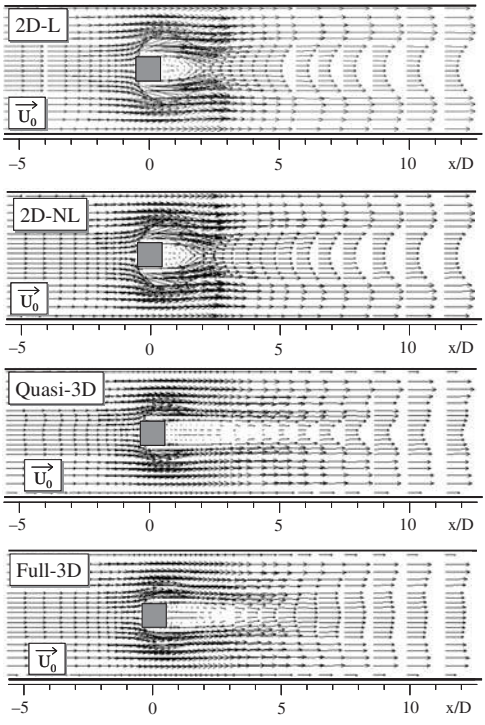


Figure 6. Time mean flow patterns in an x-y plane.

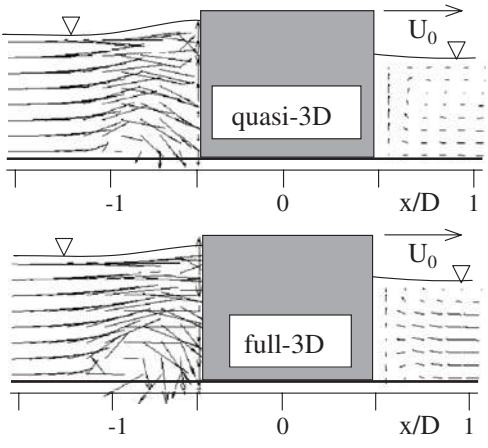


Figure 7. Time-mean flow patterns in a x-z plane (y/D = 0).

The locations of the measurement points are shown in the figure. The Strouhal number of the Karman vortex shedding in the laboratory test is estimated as $St = (fD/U_0) = 0.24$ from this figure. The Strouhal numbers in both 2D and 3D numerical results are in good agreement with the experimental value. The experimental result shows that the period of the oscillation at the centerline (y/D = 0) is larger than that at

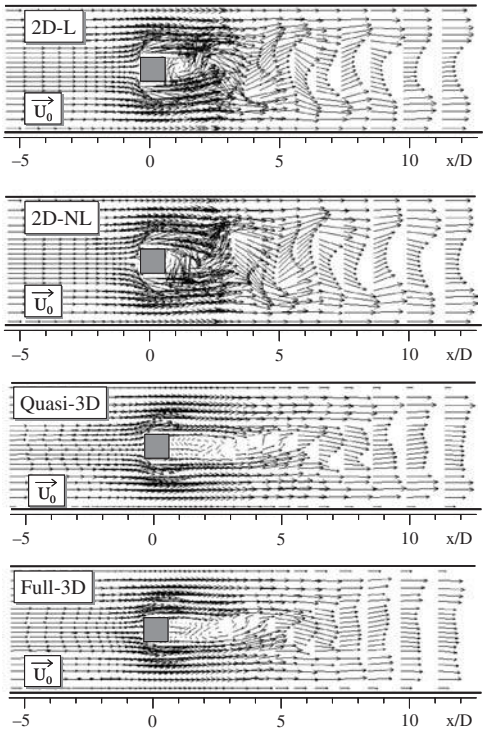


Figure 8. Snap shots of flow patterns in an x-y plane.

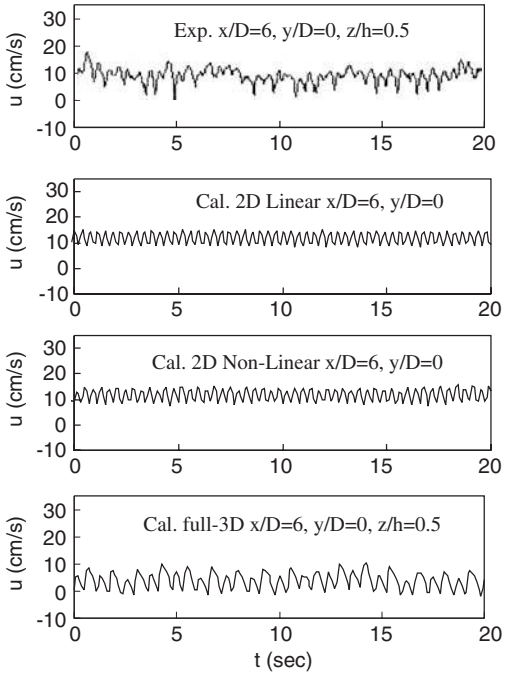


Figure 9 (a). Temporal variation of U (x/D = 6, y/D = 0).

Copyright © 2006 Taylor & Francis Group plc, London, UK

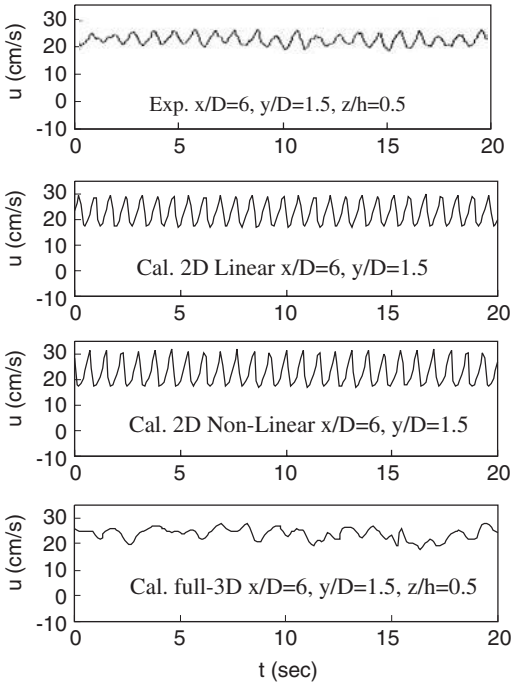


Figure 9 (b). Temporal variation of U (x/D = 6, y/D = 1.5).

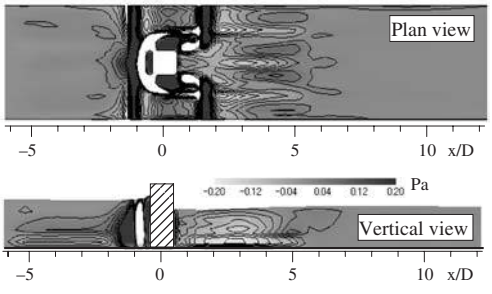


Figure 10. Time-averaged dynamic pressure distribution by the full 3D (F3D) model.

y/D = 1.5. The numerical results with 2D-L, 2D-NL and F3D models can capture this feature though the amplitude at y/D = 1.5 by 2D-L and 2D-NL models are larger than the experimental result. F3D model can capture reasonably both amplitude and period of the oscillation.

4.4 *Dynamic pressure by F3D model*

Figure 10 shows the time mean distribution of the dynamic pressure (=total pressure – hydrostatic pressure) by F3D model. The upper figure shows the profile in the horizontal plane at half the depth and

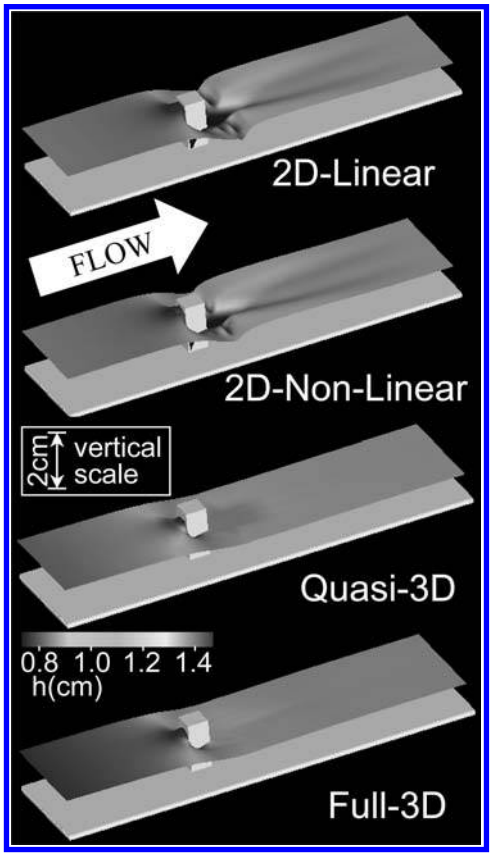


Figure 11. Time-mean surface profiles by different models.

the lower one shows the profile in the vertical section along the x-axis. The vertical scale in the latter one is enlarged 5 times compared with the horizontal scale. The horizontal distribution shows that the dynamic pressure becomes negative along the horseshoe vortex because the flow in the vortex is affected by the centrifugal force. A negative pressure is generated again along separation zones at both the sides of the downstream region of the cylinder. A positive dynamic pressure can be seen between the horseshoe vortex and the cylinder. In the vertical section, a negative dynamic pressure can be seen in large area at upstream region of the cylinder, where the stream pattern forms a saddle point due to the impingement of the flow on the cylinder. The computed pressure field seems to be reasonable considering the 3D flow pattern though the direct comparison with an experiment is not feasible due to the lack of experimental pressure data.

4.5 *Water elevation around the cylinder*

Figure 11 shows the comparison of time-averaged water level distributions by 4 models. This figure

Copyright © 2006 Taylor & Francis Group plc, London, UK

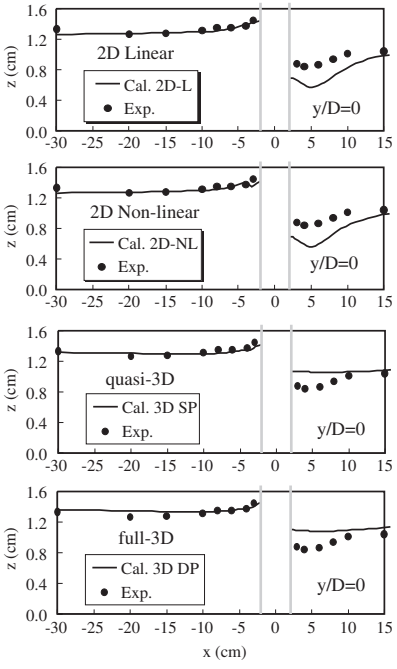


Figure 12 (a). Surface profile in the longitudinal direction at $y/D = 0$.

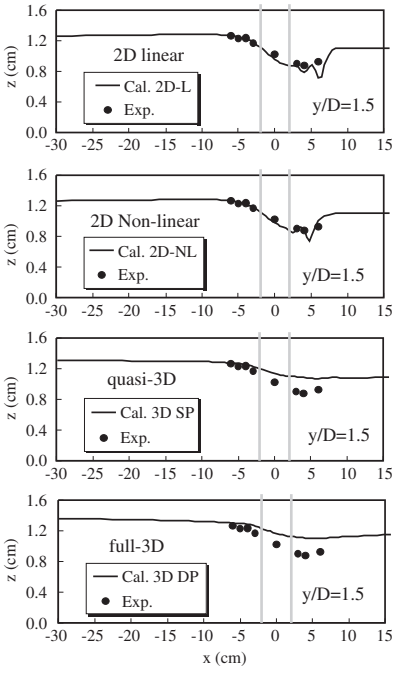


Figure 12 (b). Surface profile in the longitudinal direction at $y/D = 1.5$.

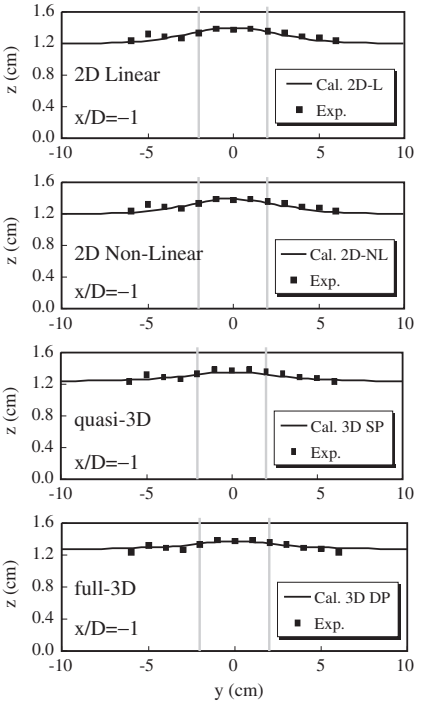


Figure 13 (a). Surface profile in the cross-section at $x/D = -1$.

shows that the hollow of the water surface behind the cylinder becomes deepest by the 2D-NL model and shallowest by the Q3D model.

Figures 12 (a) and (b) shows the computed time-averaged surface profiles in longitudinal directions at $y/D = 0$ and $y/D = 1.5$, respectively together with the experimental results. It is pointed out that all the models can capture well the surface profile at upstream region of the cylinder, on the other hand, the 2D-L and 2D-NL models over-predict the decrease of the depth behind the cylinder and Q3D and F3D models under-predict it. The prediction of the backwater effect is important from the viewpoint of flood control. The maximum depths at upstream region are 1.45 cm in the experiment, 1.45 cm in 2D-L and 2D-NL, 1.42 cm in Q3D and 1.45 cm in F3D models. Therefore, Q3D model slightly under-predicts the depth of the backwater. In the section of $y/D = 1.5$, the results by 2D-L and 2D-NL models are in good agreement with the experimental result though other 2 models predict the profile too flat.

Figure 13 shows the depth profiles along the cross-sections at $x/D = \pm 1.0$. The profiles in all models are in good agreement with the experimental result at $x/D = -1.0$ thought the Q3D model slightly under-predict the water elevation. In the section of $x/D = 1.0$, the effect of turbulence model in 2D model can be seen

Copyright © 2006 Taylor & Francis Group plc, London, UK

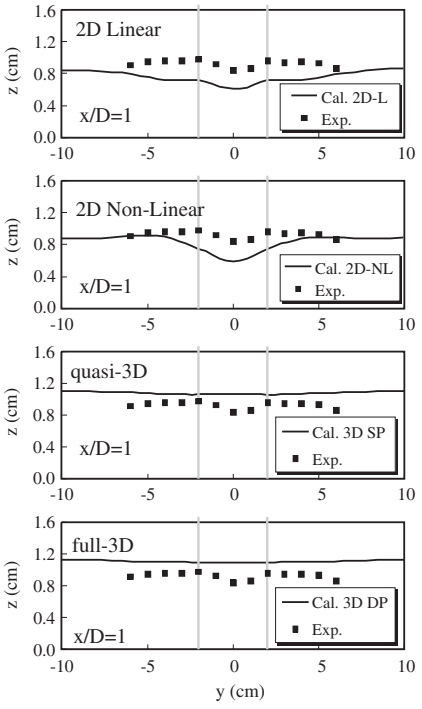


Figure 13 (b). Surface profile in the cross-section at x/D = 1.

clearly, i.e., the 2D-NL model yields better prediction of the cross-sectional water level than 2D-L model.

5 CONCLUSIONS

We investigated the turbulent open channel flow around a rectangular cylinder focusing on the Karman vortex shedding and the water level distributions using 4 different models. The main findings of the results are listed as follows.

1. The length of the recirculation zone behind the pier is generated smaller in plane 2D models than those in 3D models.
2. The fluid oscillation due to the vortex shedding attenuate more rapidly in the full-3D model than that in plane 2D models.
3. The depth variation around the cylinder is overestimated by the plane 2D models and underestimated by quasi-3D model.
4. The non-linear 2D model improved the prediction of water depth distributions compared with the linear 2D model.

ACKNOWLEDGEMENT

The authors are grateful to Yoko Watanabe and Yukari Sumi for assistance on the laboratory tests.

REFERENCES

Bosch, G. & Rodi, W. 1998. Simulation of vortex shedding past a square cylinder with different turbulence models. International Journal for Numerical Methods in Fluids, 28: 601–616.

Hirt, C. W., Nichols, B. D. & Romero, N. C. 1975. SOLA – a Numerical solution algorithm for transient fluid flows. Los Alamos Scientific Report, LA-5852.

Hosoda, T. 1990. Ph.D. Thesis, Kyoto University (in Japanese).

Hosoda, T., Kimura, I. & Shinichiro, O. 2001. Some necessary conditions for a non-linear k-ε model in classified flow patterns with a singular point. Proc. 2nd TSFP, Stockholm, Vol.3, pp.155–160.

Kimura, I. & Hosoda, T. 1999. 3-D Unsteady flow structures around rectangular column in open channels by means of non-linear k-ε model. Proc. of 1st TSFP, Santa Barbara, CA, USA, 1001–1006.

Kimura, I. & Hosoda, T. 2000. Numerical simulation of flows around a surface-mounted cube by means of a non-linear k-ε model. Proceedings of 9th. International Symposium on Flow Visualization, Edinburgh, Scotland, Paper No. 388 (CD-ROM).

Kimura, I. & Hosoda, T. 2003. A non-linear k-ε model with realizability for prediction of flows around bluff bodies. International Journal for Numerical Methods in Fluids, Vol.42, pp.813–837.

Kimura, I., Hosoda, T. & Sakurai, T. 2001. Prediction of flow characteristics in compound open channels by means of a non-linear k-ε model. Proc. 3rd ISEH, Tempe, USA, (CD-ROM).

Kimura, I., Hosoda, T., Onda, S. & Tominaga, A. 2004. Computations of 3D turbulent flow structures around submerged spur dikes under various hydraulic conditions, River Flow 2004, Naples, Italy, Balkema, Vol.1, pp.543–553.

Nezu, I. & Nakagawa, H. 1993. Turbulence in open channel flows. Balkema, Rotterdam, Netherlands.

Sugiyama, H., Akiyama, M. & Matsubara, T. 1995. Numerical simulation of compound open channel flow on turbulence with a Reynolds stress model. Journal of Hydraulic, Coastal and Environmental Engineering, 515/II-31: 55–65 (in Japanese).

Takizawa, A., Koshizuka, S. & Kondo, S. 1992. Generalization of physical component boundary fitted co-ordinate (PCBFC) method for the analysis of free-surface flow, International Journal for Numerical Methods in Fluids, Vol.15, pp.1213–1237.

Copyright © 2006 Taylor & Francis Group plc, London, UK

B. River Morphodynamics and sediment transport

B.1. Mechanics of sediment tansport

Copyright © 2006 Taylor & Francis Group plc, London, UK

Validation of a new model to account for bed slope effect for prediction of equilibrium condition in loose bed channels with significant suspended sediment transport

Jie Zeng, George Constantinescu & Larry Weber
Civil & Environmental Engineering Department, IIHR-Hydroscience and Engineering, The University of Iowa, M. Stanley Hydraulics Laboratory, Iowa City, IA

ABSTRACT: A fully three-dimensional non-hydrostatic model (Zeng et al., 2005a, 2005b, 2006) using RANS models without wall functions and with capabilities to account for bed roughness effects in open channels and river reaches is used to predict the equilibrium flow, suspended and bed load sediment transport, and bathymetry in the S-shaped channel with vertical lateral walls (case CH13) studied experimentally by Onishi (1972). The bed load transport is modeled using a non-equilibrium model. A new procedure is proposed to account in a consistent way for bed slope gravitational force effects not only for the bed load transport component, as was done in the original formulation of the model, but also for the suspended sediment load. The calculations are started with a flat bed. The bed levels, streamwise velocity and suspended sediment concentration profiles are compared with experimental data at several sections. It is found that though the predictions of the streamwise velocity and concentration profiles given by the original and new versions are very similar, the new version of the model yields better agreement with the experimental data for the bed level profiles.

1 INTRODUCTION

In meandering rivers and bended channels the sediment transport and secondary currents in the transverse direction cannot be neglected, as they are responsible for the highly irregular bed profiles observed around regions of high channel curvature. The main characteristic of the bed deformation in these bends is the formation of a point bar near the inner bank and of a pool at the outer part of the bend. The flow, sediment transport and associated bathymetry evolution are determined to a large degree by the helical motion of the water due to the action of the centrifugal forces present in regions of high channel curvature. As a consequence of the action of these forces, a pressure gradient is induced between the inner and outer banks. This pressure gradient is balanced near the free surface by a secondary current which, near the bed, is oriented from the outer toward the near inner bank. The secondary flow modifies the transversal distribution of the streamwise velocity profile, induces a vertical velocity component in the section, and redistributes the magnitude and direction of the bed shear stresses and sediment transport along the bend (Blanckaert and De Vriend, 2004). In particular, the magnitude of the bed shear stress is amplified compared to the values observed in the straight part of the channel. As a consequence, under mobile bed conditions, sediment particles move, near the bed, toward the inner bank where, eventually, they deposit and raise the bed level by forming a point bar. Concomitantly, the mean flow velocity and bed shear stress increase in the region close to the outer bend, erosion is initiated and a pool is created. As the scour develops in the outer region, the transversal slope increases until the force induced by the secondary current against the transversal slope is balanced by the (downwards) component of the gravitational force acting on the particle in the same direction. At this point equilibrium is reached and the bathymetry would not change anymore in time. These conditions are observed to be approximately reached in most curved bends, but there are flows for which such an equilibrium state cannot be reached. Non-local effects due to the redistribution of the flow and sediment motion as one advance downstream in the bend can contribute to the local increase of the transverse bed slope.

One-dimensional (1D) models are clearly not appropriate to predict morphological changes in curved bends due to the presence of highly non-uniform bed profiles in the transverse direction. 2D depth averaged models suffer from similar deficiencies, though to a lesser degree compared to 1D models, especially for prediction of flow and sediment

Copyright © 2006 Taylor & Francis Group plc, London, UK

transport processes in alluvial channels in which regions of strong channel curvature are present. Though empirical corrections are available to incorporate the effects of strong secondary currents and non-equilibrium effects (Duc et al., 2004, Choi et al., 2005, Vasquez et al., 2005), these 2D or quasi 3D models need lots of calibration and introduce additional assumptions on the flow (e.g., related to the inertial adaptation of the secondary flow, radius of the curvature of the streamlines, the presence of linear of quadratic distribution shapes for the velocity components, etc.) which are not always true in a complex application.

To accurately capture the aforementioned effects, full 3D numerical and turbulence models that can account for history effects and can accurately capture the intensity of the secondary currents have to be used. Still, because of the empiricism related especially to the bed load transport modeling, model validation and a certain degree of calibration (though much more reduced than the one required by 2D or quasi 3D models) is necessary even if fully 3D hydrostatic or non-hydrostatic models are employed. In this regard, comparison of computed results with experimental data corresponding to well-controlled laboratory experiments is essential before application of the model to predict flow, sediment and morphological changes in real river reaches. Due to the advances in computational power, the use of fully 3D non-hydrostatic models using advanced RANS closures that include sediment transport capabilities is becoming more common. Recent examples include the work of Wu et al. 2000, Fang and Rodi (2003), Olsen (2003) and Ruther and Olsen (2005).

In the following, the previously developed finite-differences 3D non-hydrostatic model of Zeng et al. (2005a, 2005b, 2006) is applied to calculate the flow, sediment transport and bathymetry at equilibrium conditions in the S-shaped channel studied experimentally by Onishi (1972). The model uses deformable grids in the vertical direction, does not use wall functions, and the RANS closures (the Spalart-Allmaras model is used in this paper) are implemented in versions that can account for roughness effects. This test case is the first application of the model to a meandering channel flow in which the suspended sediment load is comparable to the total load. Thus, the need to consider more carefully some processes that can be neglected when the model is applied to cases when the bed load transport is dominant. The most important one is to account for bed-slope gravitational effects on sloped surfaces for the suspended sediment. The need to do that is clear if we consider the extreme case when the bed load transport can be neglected, and the bathymetry changes are due to the entrainment/deposition of suspended sediment. A new procedure to account for these effects is proposed and tested for the case corresponding to experiment CH13 conducted by Onishi (1972). The main idea is to rewrite the non-equilibrium bed-load transport equation proposed by van Rijn (1987) as an equation for the total sediment load.

2 HYDRODYNAMIC AND SEDIMENT TRANSPORT MODELS

In the present model, the 3D incompressible RANS and turbulence/sediment transport equations are first transformed in generalized curvilinear coordinates. However, the primitive variables (Cartesian velocity components, V_i) for which the momentum equations are solved are left unchanged (partial transformation approach). The continuity and momentum equations are:

$$J\frac{\partial}{\partial \xi^j}\left(\frac{V^j}{J}\right)=0 \tag{1}$$

$$\frac{\partial Q}{\partial t}+A_j\frac{\partial Q}{\partial \xi^j}-J\frac{\partial E_{vj}}{\partial \xi^j}+H=0 \tag{2}$$

where x_i are the Cartesian coordinates and ξ^i are the curvilinear coordinates. In equation (2), $Q=(V_1,V_2,V_3)^T$ is the Cartesian velocity vector; J is the Jacobian $\mathrm{J}=\partial(\xi^1,\xi^2,\xi^3,)/\partial(x_1,x_2,x_3)$, $V^i=V_j\xi^j_{xi}$ are the contravariant velocity components, $\mathrm{A_j}=\mathrm{diag}(V^1,V^2,V^3)$ and $E_{vj}=E^1_{vj},E^2_{vj},E^3_{vj}$ are the vectors containing the viscous and turbulence fluxes and, finally, H is the pressure gradient vector

$$H=\left(\xi^k_{x1}\frac{\partial\Phi}{\partial\xi^k},\xi^k_{x2}\frac{\partial\Phi}{\partial\xi^k},\xi^k_{x3}\frac{\partial\Phi}{\partial\xi^k}\right)^T \tag{3}$$

The governing equations, including the ones solved part of the turbulence and suspended sediment transport models, are non-dimensionalized using a length scale $\mathrm{H_0}$ (water depth at the inlet) and a velocity scale U (bulk velocity in the inlet section) such that formally the Reynolds number ($Re=\mathrm{UH_0}/\nu$) replaces the molecular viscosity ν, and the Froude number ($Fr=U/(\mathrm{gH_0})^{0.5}$) is used to scale the free surface deformations. The modified pressure Φ is defined as $\Phi=p+2/3k$ and the effective piezometric pressure P is defined as $P=p/\rho+z/Fr^2-2/3k$, where p is the pressure, z is the free surface elevation and k is turbulence kinetic energy. The Froude number enters the solution through the free-surface boundary condition assuming that the deformable free surface model is turned on (for more details on this see Zeng et al., 2005a). The velocity components are set equal to zero on all solid surfaces. At the outflow all variables are extrapolated from the interior. The pressure is extrapolated from the interior of the domain on all boundaries except at the free surface.

Copyright © 2006 Taylor & Francis Group plc, London, UK

The eddy viscosity is calculated using the Spalart-Allmaras (SA) model in the simulations discussed in the present paper. In the SA model only one transport equation is solved for the modified viscosity $\tilde{\nu}$ based on which the eddy viscosity is evaluated. At the lateral walls, that are considered smooth in the present simulations, $\tilde{\nu}$ is set equal to zero. To account for bed roughness effects, the distance to the rough walls is redefined (see also Spalart, 2000, Zeng et al., 2005b) as: $d = d_{\min} + 0.03k_s$ where $d_{\min}$ is the distance to the nearest rough wall. At the bed, that is treated as a rough surface, the value of $\tilde{\nu}$ is estimated (Spalart, 2000) by solving $\partial\tilde{\nu}/\partial n = \tilde{\nu}/d$ where n is the wall normal direction. This makes $\tilde{\nu}$ and the eddy viscosity to be formally non-zero at the rough bed. The equivalent bed roughness is estimated using a formula proposed by van Rijn (1984) in the case in which small bed forms are present:

$$k_s = 3d_{90} + 1.1\Delta(1 - e^{-25\psi}) \tag{4}$$

where the first term accounts for the sand grain roughness contribution and the second term represents the bed form contribution. In equation (4), $\psi = \Delta/\lambda$ where Δ and λ are the height and length of the sand waves, respectively. Following van Rijn (1984) and Wu et al. (2000) the length λ is assumed to be $\lambda = 7.3H$ and the parameter ψ is estimated from:

$$\psi = \Delta/\lambda = 0.015(d_{50}/H)^{0.3}\left(1 - e^{-0.5T}\right)(25 - T) \tag{5}$$

in which H is the local water depth, d_{50} and d_{90} are the median and 90% diameters of the bed material, and T is the non-dimensional excess shear stress given by van Rijn (1987).

A fractional step method is used to solve the RANS equations. All terms in the pressure Poisson equation are discretized using second-order accurate central differences. The momentum and turbulence transport equations are discretized using second order accurate upwind differences for the convective terms. All other operators are calculated using second-order central discretizations. All terms are treated implicitly, including the source terms in the transport equations for turbulence quantities ($\tilde{\nu}$). To accelerate the convergence of the resulting system of equations toward steady state (equilibrium), local time-stepping techniques are used. An approximate factorization technique is used to simplify the inversion of the discrete form (left hand side) of the momentum, pressure-Poisson and turbulence transport equations. The equations are solved implicitly using the alternate-direction-implicit (ADI) method. The implementation of the deformable free surface module in which the proper kinematic and dynamic boundary conditions are applied at the top boundary is described in Zeng et al. (2005a).

An advection-diffusion scalar transport equation with an additional settling-velocity source term is solved to determine the local sediment concentration C and the suspended sediment fluxes at the top of the bed load layer for simulations in which the suspended sediment load cannot be neglected. The equation is not solved up to the wall, as are the momentum equations, but rather up to the interface with the bed load layer (δ(x,y)) which typically corresponds to a k = constant surface in the computational grid. In curvilinear coordinated, the equation is:

$$\frac{\partial C}{\partial t} + V^j \frac{\partial C}{\partial \xi^j} - \omega_s \delta_{3i} \frac{\partial C}{\partial \xi^j}\frac{\partial \xi^j}{\partial x_i} - J\frac{\partial}{\partial \xi^j}\left(\frac{g^{ij}}{J}\left(\frac{\nu + \nu_t}{\sigma_c}\right)\frac{\partial C}{\partial \xi^i}\right) = 0 \tag{6}$$

where ω_s is the setting velocity of the sediment, δ_{3j} is the Kronecker delta symbol with $j = 3$ indicating the vertical direction and σ_c is the Schmidt number. Its role is to relate the sediment (turbulent) diffusivity to its (eddy) viscosity. At the free surface, the total vertical flux of suspended sediment is set to zero:

$$\frac{\nu + \nu_t}{\sigma_c}\frac{\partial C}{\partial \xi^j}\frac{\partial \xi^j}{\partial x_3} + \omega_s C = 0 \tag{7}$$

At the interface between the suspended sediment and the bed load layers (z = δ(x,y) such that there is no ovelap between the two layers) situated not far but not necessarily at the reference level z = a, following van Rijn (1987) and Wu et al. (2000), the entrainment rate is assumed to be equal to the one under equilibrium conditions. The total vertical sediment flux at the interface is equal to the net sediment transport (deposition minus entrainment) across the interface.

$$\frac{\nu_t}{\sigma_c}\frac{\partial C}{\partial \xi^j}\frac{\partial \xi^j}{\partial x_3} + \omega_s C = D_b - E_b \tag{8}$$

$$D_b - E_b = \omega_s C - \omega_s C_{b**} \tag{9}$$

where C_{b**} is the equilibrium concentration at z = δ, $D_b = \omega_s C_b$ is the deposition rate and $E_b = \omega_s C_{b**}$ is the entrainment rate at the top of the bed layer. The value of C_{b**} can be calculated assuming Rouse formula to be valid between the reference level where $C = C_{b*}$ (z = a) and the interface between the bed and the suspended load layers (z = δ(x,y)). There is no unique way to choose the reference level a. In some cases it is taken equal to the bed roughness, in other cases it is taken as a percentage of the total depth (see also Lin & Falconer, 1996). At the inlet section a concentration profile needs to be prescribed, while at the sidewalls and outlet a zero gradient boundary condition is imposed.

The empirical formulas proposed by van Rijn (1987) are used in the present study to estimate the

Copyright © 2006 Taylor & Francis Group plc, London, UK

equilibrium concentration at the reference level (C_{b^*}) needed to calculate $C_{b^{**}}$ in (9), the equilibrium bed load transport rate (Q_{b^*}) and the non-equilibrium adaptation length (L_s). The last two variables are needed to close the non-equilibrium bed transport model. In this model, the mass balance equation for the sediment within the bed load layer (van Rijn, 1987), in which the storage term is neglected, is:

$$(1-p')\frac{\partial z_b}{\partial t} - D_b + E_b = -\nabla Q_b = -J_b\left(\frac{\partial}{\partial \xi}\left(\frac{Q_{b\xi}}{J_b}\right)+\frac{\partial}{\partial \eta}\left(\frac{Q_{b\eta}}{J_b}\right)\right) = 0 \quad (10)$$

In the above equation p' is the porosity, J_b is the Jacobian of the geometric transformation in the bed load layer, $(J_b = \partial(\xi,\eta)/\partial(x,y))$, z_b is the bed level above a datum, $Q_{b\xi}$ and $Q_{b\eta}$ are the components of the bed-load transport in the two directions. Then, one assumes that the relation between the bed change due to deposition from the bed load layer is:

$$(1-p')\frac{\partial z_{b_bed_load}}{\partial t} = \frac{1}{L_s}(Q_b - Q_{b^*}) \quad (11)$$

such that the total change in the bed elevation is:

$$(1-p')\frac{\partial z_b}{\partial t} = D_b - E_b + \frac{Q_b - Q_{b^*}}{L_s} \quad (12)$$

The equation for the bed load rate Q_b is derived from equation (10) in which we made the substitution corresponding to the model assumed in equation (12):

$$\frac{(Q_b - Q_{b^*})}{L_s} + \nabla Q_b = 0 \quad (13)$$

One should make the important observation that equation (13) which is solved to determine the bed load Q_b is the same for both the case when the suspended sediment transport module is active and for the case when the suspended sediment transport can be neglected. However, in the first case the total bed elevation change will be partly due to the net entrainment/deposition of suspended sediment at the top of the bed load layer (see equation 10).

To close the model, one has to express $Q_{b\xi}$ and $Q_{b\eta}$ function of Q_b. When the bed becomes sloped, the gravitational force on the particles will resist the shear force to further carry the particles to the upper part of the slope. The sediment transport direction will deviate from the local direction of the bed shear stress. In this study, the relationship of Delft Hydraulics (see Sekine and Parker, 1992) is used:

$$Q_{b\xi}/Q_{b\eta} = \left(\sin\theta_b - \beta\frac{\partial z_b}{\partial l_\xi}\right)\Big/\left(\cos\theta_b - \beta\frac{\partial z_b}{\partial l_\eta}\right) \quad (14)$$

where $\theta_b = \tan^{-1}(\tau_{b\eta}/\tau_{b\xi})$ is the angle between the bed shear stress vector and the streamwise direction, $\beta = \beta^*\,(\tau_c^*/\tau_L^*)^m$, τ_L^* is the nondimensional longitudinal Shield stress $\tau_L^* = \tau_* \cos\theta_b/\rho\, Rgd_{50}$, $R = \rho_s/\rho - 1$ ρ_s is the sediment density, ρ is the water density, the critical shear stress $\tau_c^* = \rho u_{*cr}^2$ is given by Shields diagram, m is a coefficient (m = 1), $\beta^* = \alpha_G/\tau_c^*$, $\partial z_b/\partial l_\xi$, $\partial z_b/\partial l_\eta$ are the streamwise and transverse bed slopes, and α_G is a coefficient typically in the range 0.45–0.7. In the present simulations we used $\alpha_G = 0.6$. The bed load transport rate at the inlet is the only variable needed to be specified. Once z_b is calculated, the grid points between the bed level and the free surface are redistributed vertically based on the new positions of the water surface and bed level elevations.

Before presenting the method to account for bed slope effects for the suspended sediment load component, we will review the main equations that are solved for the three types of possible applications.

In the first type of applications in which the suspended sediment transport can be neglected, D_b and E_b are set to zero in (12). The equations to be solved are (12) and (13) with $Q_{b\xi}/Q_{b\eta}$ given by (14).

In the second type of applications in which the bed load transport can be neglected, first the concentration field C is determined from equation (6) with boundary conditions given by (7) and (8). Then, the deposition and entrainment rates are evaluated using their definition, and the net entrainment/deposition rate is calculated from (9). This value is then introduced in (12) with $Q_b = Q_{b^*} = 0$ to calculate z_b.

In the third type of applications in which both the bed and suspended loads cannot be neglected, the concentration C, deposition and entrainment rates are obtained in the same way as for the second type of applications, Q_b is obtained from (13) and (14) and, finally, z_b is obtained from (12).

In simulations in which the suspended sediment load becomes comparable or larger than the bed load, it is important to account for bed slope effects for the total load Q_T. To do that in our model, we define the total load (considered as a vectorial relationship in the horizontal directions) as simply:

$$Q_T = Q_b + Q_S \quad (15)$$

where Q_S is the suspended sediment load flux in the local water column from the top of the bed layer to the free surface. By taking the divergence of (15) we obtain using the mass conservation equation in the water column corresponding to the suspended sediment domain (between $z = \delta(x,y)$ and free surface) and neglecting the storage term:

$$\nabla Q_T = \nabla Q_b + \nabla Q_S = \nabla Q_b - D_b + E_b \quad (16)$$

Then, we rewrite equation (13) for the total load using equations (15) and (16):

$$\frac{1}{L_s}(Q_T - Q_S - Q_{b^*}) + \nabla Q_T + D_b - E_b = 0 \quad (17)$$

Copyright © 2006 Taylor & Francis Group plc, London, UK

As the new variable in (17) is Q_T, we rewrite (12):

$$(1-p')\frac{\partial z_b}{\partial t} = -\nabla Q_T \tag{18}$$

where use was made of equations (10) and (16). At this point the new model is closed, provided that we are able to estimate Q_S from the concentration field and a formula to split Q_T after the two horizontal directions (ξ, η) is available.

To evaluate Q_S, one simply has to apply the definition to calculate the two components of the flux in the horizontal directions (x,y):

$$Q_{Sx} = \int_s^h \left(uC - \frac{\nu + \nu_t}{\sigma_c}\frac{\partial C}{\partial x} \right) dz' \tag{19}$$

$$Q_{Sy} = \int_s^h \left(vC - \frac{\nu + \nu_t}{\sigma_c}\frac{\partial C}{\partial y} \right) dz' \tag{20}$$

The magnitude of the suspended sediment flux is:

$$Q_S = \sqrt{\left({Q_{Sx}}^2 + {Q_{Sy}}^2 \right)} \tag{21}$$

To introduce bed slope effects directly for Q_T, the same splitting formula (14) is used, but with Q_b replaced by Q_T:

$$Q_{T\xi} / Q_{T\eta} = \left(\sin\theta_b - \beta\frac{\partial z_b}{\partial l_\xi} \right) \Big/ \left(\cos\theta_b - \beta\frac{\partial z_b}{\partial l_\eta} \right) \tag{22}$$

Thus, the divergence operator ∇Q_T can be calculated in curvilinear coordinates (ξ, η). The concentration, and the deposition/entrainment rates are obtained in the same way as in the second type of applications.

3 VALIDATION

The meandering flume experiments for sediment transport conducted by Onishi (1972) are used to estimate the predictive abilities of the original model (Method 1) and of the new version (Method 2) that accounts for bed slope effects for both the suspended and the bed loads, for a test case in which the suspended sediment load is comparable to the bed load.

The curved flume configuration shown in Figure 1 consists of two identical 90^0 bends disposed in opposite directions. The first bend is preceded by a short straight section (4.27 m long) ahead of which sand and water are supplied by a retour circuit. Two straight sections of same length are used to connect the two bends and to extend the exit from the second bend. The channel sidewalls are vertical, the total channel width is 2.34 m and the radius of the bends is 8.54 m. In the test case CH13 that is simulated in the present

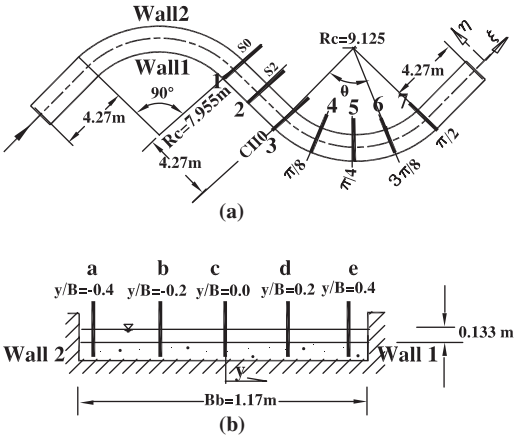


Figure 1. Experimental setup showing location of cross-sections and stations where vertical velocity and concentration profiles were measured. (a) flume layout; (b) cross-section at the start of the experiment.

study, the actual width of the channel was 1.17 m. The inflow water depth was $H_0 = 0.133$ m and the mean inflow velocity was $U = 0.536$ m/s. The corresponding Froude and Reynolds numbers were 0.469 and 71,454, respectively. The experiments were conducted using sand with median diameters of $d_{50} = 0.255$ mm and $d_{90} = 0.355$ mm. The average slope of the water surface was 0.0018. In the experiment, the bed was leveled with an uniform layer of sand. The experiment was carried out continuously for more than 3 days, until equilibrium steady state bathymetry was reached. The bathymetry, mean streamwise velocities and concentration profiles were then measured at selected sections (see Figure 1a) downstream the first 90° bend.

The numerical simulations started with a flat sand bed similar to the experiment and continued until equilibrium flow and bathymetry conditions were reached. The length of the outlet straight reach was increased by 4.5 m to minimize the influence of the outlet boundary conditions on the solution in the downstream part of the channel. To be consistent with the physical experiments in which sediment and water were supplied by a retour circuit system, the calculated distribution of the suspended sediment concentration and the bed load transport rate at the outlet were used to specify the bed load transport rate and mean (laterally averaged) concentration profile at the inlet boundary.

The numerical simulations were carried out using the SA model on a mesh with 320,000 ($90 \times 101 \times 35$) grid points. The first point off the channel sidewalls and bottom was situated at $\Delta n/H_0 \sim 0.00035$, corresponding to a non-dimensional distance of one in wall units ($\Delta n^+ = 1.0$). The value of the bottom roughness calculated using equation (4) was found to be situated well into the fully rough regime ($k_s \sim 0.005$ m

Copyright © 2006 Taylor & Francis Group plc, London, UK

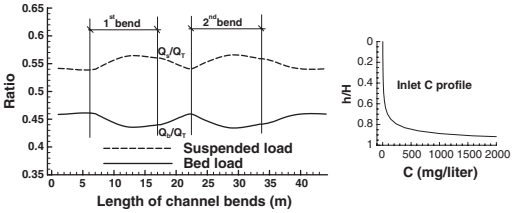


Figure 2. Ratios of suspended sediment and bed loads to total load along longitudinal direction and suspended sediment concentration profile in the inlet section at equilibrium.

corresponding to $k_s^+ \sim 280$ in the initial straight part of the channel). The streamwise velocity distribution at the inlet was taken from a precalculated fully-developed SA solution obtained in a straight channel of identical section to the inflow section. The channel Reynolds number was the same in the preliminary and curved channel simulations. The value of the Schmidt number was equal to 0.7. The reference level corresponding to the depth of the bed load layer was taken equal to $6.0d_{90}$, corresponding to about 1.5% of the water depth at the inflow section. A total of 12 grid points were used in the vertical direction to resolve this region.

Figure 2 shows the variation of the ratio of the cross-section averaged suspended sediment load to the total load in the longitudinal direction. As the results of the two simulations were very close, only Method 2 results are shown. The average value of this ratio for the simulated flow conditions was found to be close to 0.56, confirming the fact that the suspended sediment component plays an essential role in the overall sediment transport process. The largest values of this ratio ($\sim$0.575) are observed to occur toward the middle of the two 90^0 bends. The minimum values ($\sim$0.54) occur at the end of the straight section between the two bends and the near the end of the channel. In the same figure, the width averaged suspended sediment concentration distribution over the depth at equilibrium conditions is shown.

Figure 3 shows the predicted bed levels in seven cross-sections (see Figure 1a) at equilibrium state along with experimental results from two sets of measurements. Overall, most of the predicted bathymetry profiles agree well with the experimental measurements for both simulations. In particular, excellent agreement is observed at section 1 situated just at the entrance into the straight reach between the two bends. At sections 2 and 3 situated in the same straight transition channel, some overprediction of the scour (up to 0.03 m) are observed near $Y = 0.25$ m (Y is the positive/negative distance measured from the center of the channel in a section) and around $Y = 0.5$ m (close to wall 2), respectively. Just after the entrance into the second 90^0 bend (section 4), the water depth

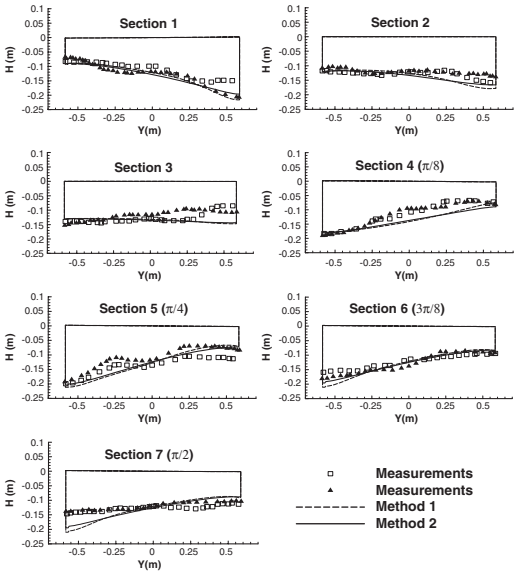


Figure 3. Comparison between predicted and measured bed levels at equilibrium conditions.

is accurately predicted near both sidewalls. However, some overprediction of the scour (up to 0.025 m) is observed to occur in the range $-0.1\,\text{m} < Y < 0.4\,\text{m}$ toward the center of the cross-section. Both simulations predict a decay of the water depth between wall 2 (inner wall for the second bend) and wall 1 at a practically constant slope, while in the experimental data the slope appears to be much smaller toward wall 2. In section 5, situated at the middle of the second bend, the agreement can be considered satisfactory taking into account the scatter between the two sets of experimental data. However, a careful analysis of the experimental profiles shows the presence of a break in the slope of the water depth decay from the inner to the outer wall between $-0.25\,\text{m} < Y < 0\,\text{m}$, where the slope becomes slightly negative. This results in the simulations overpredicting the scour around $Y = 0.25$ m by about 0.02 m. The predictions by the two methods at sections 6 and 7 show some differences especially near the outer wall (wall 1). In particular, at section 6 situated half distance between the middle and the end of the second bend, the agreement is excellent for Method 2. Method 1 overpredicts the scour near the outer wall by about 0.02 m. Same trends are observed at the exit from the second bend (section 7). However, at this location both simulations overpredict the scour in the region situated close to the outer wall by as much as 0.04 m. This is because the simulations predict a longer recovery distance for the bed to become again relatively flat after the exit from the second bend.

Figure 4 shows the streamwise velocity distribution is several representative sections along the S-shaped

Copyright © 2006 Taylor & Francis Group plc, London, UK

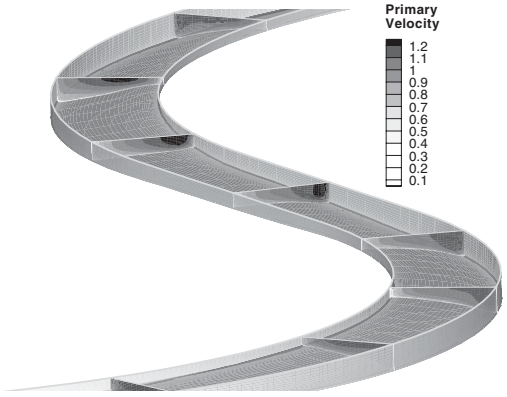


Figure 4. Predicted velocity magnitude contours at representative sections within the channel. Computational mesh is also shown in the same figure.

channel. The main observation is the fact that the bathymetry and the streamwise velocity distribution in equivalent sections in the two bends is not exactly anti-symmetric as one would expect in a meandering channel containing a large number of opposite bends. One can observe that in the middle of the straight channel between the two bends, the region of high streamwise velocity is situated closer to wall 1. This region of high velocity magnitude appears to be smaller and situated closer to the outer wall (wall 1) inside the second bend compared to the position and shape of the corresponding region inside the first bend. Though at the exit from the first bend the flow is far from being symmetric with respect to the center of the channel, at the exit from the second bend the return to symmetry for both the bathymetry and the streamwise velocity distribution in the section is much more noticeable.

Figure 5 shows the streamwise velocity profiles at four stations (Figure 1b) situated in the same seven sections in which the bathymetry profiles were compared. To facilitate comparison, the depth shown on the vertical axis is nondimensionalized by the local water depth. The results from the two methods are very close, so in the following discussion we will refer to them as the simulation results. Only one set of measurements was available for the streamwise velocity. The experimental results indicate a very clear tendency of the flow to divert toward the outer bank of the two channel bends. For instance, the streamwise velocity value away from the bottom is close to 0.6 m/s at station S1b (first number denotes the section number, second letter denotes the relative position inside the section as shown in Figure 1b) near the outer wall of the first bend and close to 0.4 m/s near the inner wall. Same trend is observed in sections 2 and 3 situated inside the straight channel reach connecting the two bends (compare stations S2b with S2e and S3b with S3e). The trend starts being inverted at section 4. At section 7 situated at the exit from the second bend (the corresponding section for the first bend will be S1), the difference between the velocity near the outer and inner walls is comparable to the one observed to occur toward the end of the first bend. The outer wall values are very similar (around 0.65 m/s, compare S1b with S7e) but the values at station b are close to 0.50 m/s compared to 0.4 m/s observed at station S1e. This is however misleading as the station corresponding to S7b is S1d (anti-symmetric with respect to the center of the channel, see Figure 1b). The streamwise velocity values away from the bed are close to 0.5 m/s at station S1d. Still, as already pointed out when discussing Figure 4, the velocity profiles at corresponding sections are not exactly anti-symmetric. The overall agreement between the experiment and simulations is good. The simulations successfully capture the shift of the region characterized by high streamwise velocities from wall 2 to wall 1 over the second bend. At the first three sections situated inside the transition channel, the only noticeable disagreement occurs at stations S3b and S3c. At station S3b the predicted velocities are larger than the measured ones from the bed up to mid channel depth, while at station S3c the opposite is observed. At the entrance into the second bend (section 4) the velocities are underpredicted at station S4e near wall 1 by about 0.07 m/s. Inside the second bend, the simulations tend to overpredict the measurements at stations S5b, S6b and S7b at $Y/B = -0.2$ midway between the inner wall (wall 2) and the center of the section. However, the predictions at the center of the channel in the same sections are quite accurate with the exception of station S5c where the velocities are overestimated near the bed. The predictions at the same sections in the outer bend region are quite accurate.

Figure 6 shows the contours of the predicted bottom shear stress ($\tau/\rho U^2$) inside the channel bend at equilibrium. As expected, a patch of relatively high shear stress values is present at the entrance into the first bend closer to the inner wall. As one moves downstream, the area of high bed shear stress switches toward the deeper outer wall region inside the first bend. Inside the straight transition channel between the two bends the bed shear stress remains high on the wall 2 side showing that the flow is far from being axisymmetric with respect to the center of the channel at the entrance into the second bend. Thus, one should not expect the flow inside the first and second bends to be exactly anti-symmetric. The region of high shear stress switches from wall 2 to wall 1 over the second half of the second bend, as wall 1 becomes the outer wall. The bed shear stress peaks at a distance of about 4 m from the end of the second bend. The bed shear stress values in the region close to wall 1 decay slowly as the flow tries to recover toward a symmetric

Copyright © 2006 Taylor & Francis Group plc, London, UK

variation of the bathymetry and velocity distribution with respect to the axis of the channel in the straight reach at the end of the meandering channel.

Figure 7 shows the suspended sediment concentration profiles at five stations (Figure 1b) inside each of the seven sections (Figure 1a) at which experimental measurements were taken. The predictions of the two methods were found to be very close to each other. The

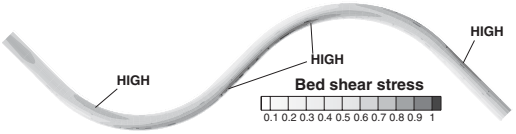


Figure 6. Contours of predicted bottom shear stress (τ/ρ) at equilibrium conditions.

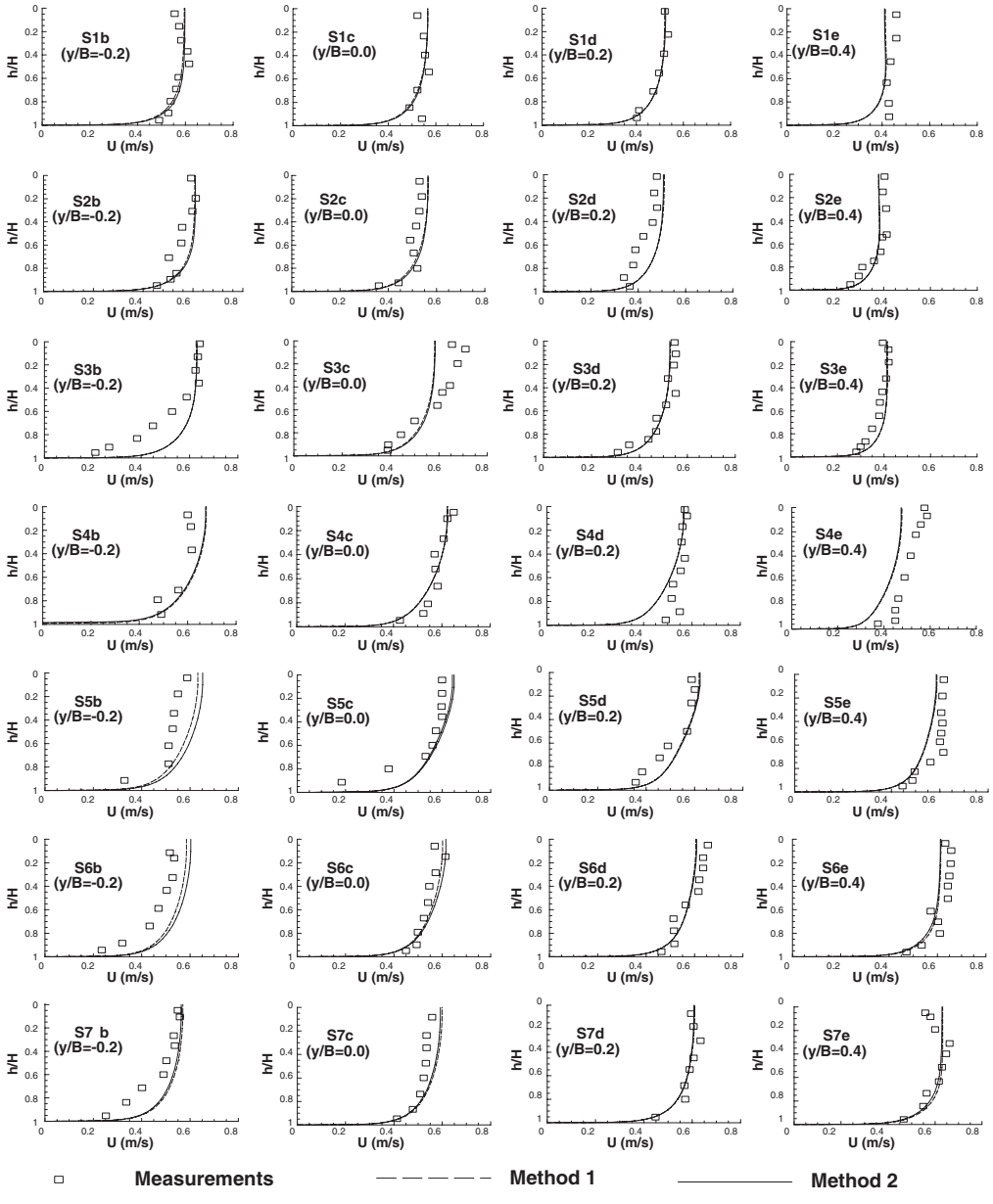


Figure 5. Comparison between predicted and measurement streamwise velocity profiles at equilibrium conditions.

Copyright © 2006 Taylor & Francis Group plc, London, UK

simulation results at most stations are in good agreement with the experiment. This is true especially for stations a and e situated the closest to the two banks. The simulations tend to underestimate the concentration of the suspended sediment in the upper layer, near the free surface, and in the middle layer, especially in the central parts of the sections situated in the second bend (stations b, c and d). For example, the concentration is underestimated away from the bed region at station d between sections 2 and 6 and at station c (mid-distance between the two lateral walls) between sections 2 and 4. However, this trend is not uniform as at some of the stations in the same regions the agreement is quite good (e.g., stations S6c, S7d). Conversely, the suspended sediment concentration in the region situated just above the bed load layer tends to be overestimated by the simulations. One should also mention that the sediment concentration

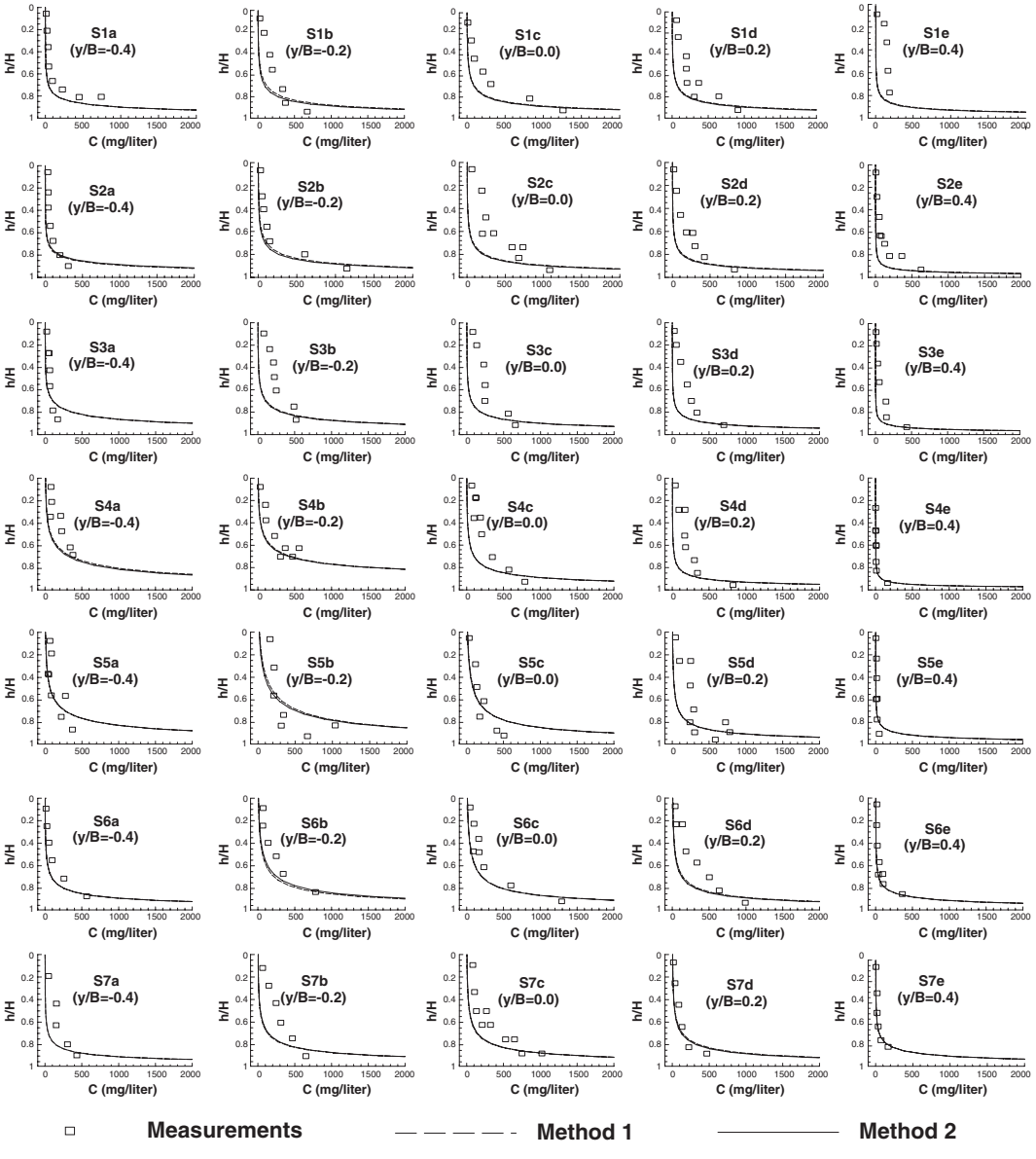


Figure 7. Comparison between predicted and measured suspended sediment concentration profiles at equilibrium conditions.

Copyright © 2006 Taylor & Francis Group plc, London, UK

measurements appear to have lots of scatter and sometimes show unphysical large values of the concentration near the free surface (e.g., see station S5b), so the error bar on the concentration measurements is probably quite high. Unfortunately, Onishi (1972) does not provide an estimation of the measurement errors. Quite probably, the bathymetry prediction errors reflect quite strongly into some of the observed errors in the prediction of the suspended sediment concentration throughout the channel. However, the important thing about the suspended sediment concentration field is that its prediction is accurate enough such that the net influx of sediment at the top of the bed layer is captured with sufficient accuracy such that the predictions of the bathymetry contours at equilibrium conditions are quite accurate.

4 CONCLUSIONS

A fully 3D non-hydrostatic model developed by Zeng et al. (2005a, 2005b, 2006) to predict the flow, free surface deformation, bed load and suspended sediment transport and bed morphology in open channels at equilibrium conditions was tested for the case of the flow in an S-shaped channel studied experimentally by Onishi (1972) in which the suspended sediment load was comparable to the bed load. Additionally, a new formulation of the model capable to account for bed slope gravitational force effects for both the suspended and the bed load components was proposed and tested for the same flow. Comparison of the simulation results with the experiments showed that though both formulations were able to predict reasonably well the bathymetry, streamwise velocity and suspended sediment concentration profiles, the new formulation was able to predict slightly more accurately the bathymetry in the deep regions of the scoured channel, where the original version of the model was found to predict too large bed-slope values. It is expected that the new formulation will be able to give even better predictions compared to the original one in cases in which very large water depth variations (or, equivalently large slopes, especially in the transverse direction) are observed at equilibrium conditions over small distances. Investigation of such a case is under way.

ACKNOWLEDGEMENTS

The authors would like to thank Professor A. Jacob Odgaard at IIHR-Hydroscience and Engineering, The University of Iowa for his insightful advice related to different aspects of this study.

REFERENCES

Blankaert, K. & De Vriend, H.J. 2004, Secondary flow in sharp open-channel bends, *J. Fluid Mech.*, 498, 353–380.

Choi, S.U., Kim, T.B. & Min, K.D. 2005, 2D finite element modeling of bed elevation change in a curved channel, *River and Coastal Estuarine Morphology Conference*, The University of Illinois, Urbana Champaign, Illinois.

Duc, B.M., Wenka, T & Rodi, W. 2004, Numerical modeling of bed deformation in laboratory channels, *J. Hydraulic Engineering*, 130(9), 894–904.

Fang, H. & Rodi, W. 2003, 3D calculations of flow and suspended sediment transport in the neighborhood of the dam for the Three Gorges Project Reservoir in the Yangtze River, *J. Hydraulic Research*, 41(4), 379–394.

Lin B. L. & Falconer, R. 1996, Numerical modeling of three-dimensional suspended sediment for estuarine and coastal waters, *J. Hydraulic Research*, 34(1), 435–455.

Olsen, N.R. 2003, 3D CFD modeling of self-forming meandering channel, *J. Hydraulic Engineering*, 129(5), 366–372.

Onishi, Y, 1972, Effects of meandering on sediment discharges and friction factors of alluvial streams, *Ph.D. Dissertation thesis*, Department of Civil and Environmental Engineering, The University of Iowa, Iowa.

Ruther, N. & Olsen, N.R. 2005, 3D modeling of sediment transport in a narrow 90^0 channel bend, *J. Hydraulic Engineering*, 131(10), 917–920.

Sekine, M. & Parker, G. 1992, Bed load transport on transverse slope, *J. Hydraulic Engineering*, 118(4), 513–535.

Spalart. P.R. 2000, Trends in Turbulence Treatments, *AIAA Paper 2000–2306*, Fluids 2000, Denver.

van Rijn, L.C. 1984, Sediment transport, Part III: Bed forms and alluvial roughness, *J. Hydraulic Engineering*, 110(12), 1733–1754.

van Rijn, L.C. 1987, Mathematical modeling of morphological processes in the case of suspended sediment transport, *Delft Hydraulics Communication* No. 382., The Netherlands.

Vasquez, J.A., Millar, R.G. & Steffler, P.M. 2005, Vertically-averaged and momentum model for alluvial bend morphology, *River and Coastal Estuarine Morphology Conference*, The University of Illinois, Urbana Champaign, Illinois.

Wu, W., Rodi, W. & Wenka, T. 2000, 3D numerical modeling of flow and sediment transport in open channels, *J. Hydraulic Engineering*, 126(1), 4–15.

Zeng, J., Constantinescu, G. & Weber, L. 2005a, A fully 3D non-hydrostatic model for prediction of flow, sediment transport and bed morphology in open channels, *XXXIst International Association Hydraulic Research Congress*, Seoul, Korea, September 2005.

Zeng, J., Constantinescu, S.G. & Weber, L.J. 2005b. Validation of a computational model to predict suspended and bed load sediment transport and equilibrium bed morphology in open channels. *River and Coastal Estuarine Morphology Conference*, The University of Illinois, Urbana Champaign, Illinois.

Zeng, J., Constantinescu, G. & Weber, L. 2006, Prediction of equilibrium flow and bed load transport in a curved bend, *EWRI World Water and Environmental Resources Congress 2006*, Omaha, Nebraska.

Copyright © 2006 Taylor & Francis Group plc, London, UK

A PIV/PTV experiment on sediment transport in a horizontal open channel flow

W.A. Breugem & W.S.J. Uijttewaal
Environmental Fluid Mechanics Section, Delft University of Technology, The Netherlands

ABSTRACT: In this paper, sediment transport in a turbulent open channel flow is studied using a combined PIV-PTV technique. We introduced 350 μm polystyrene particles at three different streamwise locations near the free surface in a $Re = 10,000$ flow. It is shown that a distance of the order $h<u>/v_{rms}$ is needed for the sediment profile to become completely developed. At smaller distances, gradient diffusion modeling cannot be applied. In this situation, the downward transport of sediment is governed by sweeps with a vertical scale of the order of the water depth, whereas ejections are the main contributor to the upward flux of sediment in the fully developed situation. Because of this, the particle streamwise velocity is higher than the fluid velocity when the particles are still adapting, but lower than the fluid velocity in the fully developed situation. Some examples of instantaneous flow structures transporting the particles are shown.

1 INTRODUCTION

The transport of suspended sediment particles is important in geophysical problems as sand is transported in rivers and estuaries. It can as well be important for application in process engineering. Systematic experimental investigations on these processes date back at least half a century (Vanoni, 1946), but the limited understanding of turbulence and experimental difficulties have limited the amount of progress.

In recent years, a great deal of progress has been made in the experimental methods used to study particle laden flows. The use of equipment such as phase-Doppler-anemometry (PDA) and combinations of Particle Tracking Velocimetry (PTV) and Particle Image Velocimetry (PIV) has enabled researchers to determine the velocity of both sediment and fluid separately. These investigations (Kaftori *et al.*, 1995b; Best *et al.*, 1997; Muste & Patel, 1997; Kiger & Pan, 2002; Righetti & Romano, 2004; Nezu & Azuma, 2004; Muste *et al.*, 2005) show that the mean particle velocity is lower than the fluid velocity, which can be attributed to the preferential concentration of particles in regions of low fluid velocity. The only exception is the near-wall region, where particles are faster than the fluid, because they keep their higher velocity due to their inertia while descending in sweeps.

Less agreement exists on the fluctuating particle velocity. Both smaller wall-normal particle velocities were reported (Muste & Patel, 1997; Kiger & Pan, 2002) and larger ones (Kaftori *et al.*, 1995b; Best *et al.*, 1997; Righetti & Romano, 2004) when compared to the fluid wall-normal velocity fluctuations. The streamwise fluctuating particle velocity generally did not differ much from the fluctuating fluid velocity.

Measurements of the sediment concentration profiles, which determine the total sediment transport in combination with the mean sediment velocity, have not lead to identical conclusions. The lack of agreement concerned the Prandtl-Schmidt number β, a measure for the diffusion of sediment compared to streamwise momentum, which is used in analytical formulations for the sediment concentration profile such as the Rouse equation. It has been found to be both higher (Nezu & Azuma, 2004) and lower (Cellino & Graf, 1999) than one, whereas Muste *et al.* (2005) report both smaller and larger values for nylon and sand particles respectively. Nikora & Goring (2002) even found β to vary over the water depth.

From the above, it can be concluded that the knowledge on sediment laden flows is still limited and the experimental data that exist yield contradictory results. Furthermore, all these investigations were done in fully-developed situations, whereas in many practical applications, these conditions are rarely found.

The present paper aims at providing more insight into the mechanics of particle transport. Hereto, an experimental investigation of a particle laden flow in a open channel was performed. Both instantaneous fluid and particle velocities were measured with a combined PIV-PTV technique. Polystyrene particles with a diameter $d_p \approx 350\ \mu m$ were used as pseudosediment

Copyright © 2006 Taylor & Francis Group plc, London, UK

particles. Flow velocities and sediment were chosen such that a direct comparison to a Direct Numerical Simulation (DNS) with particle tracking (used by for example Uijttewaal & Oliemans (1996) for particles in a gas) is feasible. These simulations are currently being performed at the Kramers Laboratory of Delft University of Technology.

The sediment was fed to the flow near the free water surface at different distances from the measurement section, thus providing data on the development of a plume of sediment. This also gives some further insight in the the dispersion process, as the interesting situation arises that the flux due to gravity and turbulent diffusion work in the same direction, thus allowing us to find the turbulence structures that are important for dispersing the sediment.

2 EXPERIMENTAL SETUP

The experiments were performed in an open channel, with a length of 23.5 m a width of 0.495 m and a height of 0.50 m (Fig. 1). The walls and bottom were made of glass in order to have a hydraulically smooth boundary. The water was pumped from a buffer into the flume. At the downstream side, the water level was controlled with an adjustable weir, followed by three pipes allowing the water to return to the buffer. In order to perform the fluid velocity measurements, the water was seeded with 10 μm hollow glass spheres ($\rho = 1100\, kg/m^3$).

As pseudo-sediment, 347 μm ($\sigma = 45\, \mu m$) polystyrene particles were used, which had a density ρ_p of 1035 kg/m^3. We measured a terminal velocity v_T of 2.2 mm/s, which compares well with the theoretical estimate of 2.1 mm/s ($Re_p = v_T d_p/\nu_f = 0.71$). The particles were fed to the channel with a particle feeder that consisted of two vessels. In the first vessel ($V = 80\, l$), a mixer was used to mix the particles with the water, using baffles and a specially adapted bottom shape to obtain a homogeneous mixture. This sediment mixture was pumped into a second smaller vessel, from which it was led into the channel. The concentration of the mixture after it had left the mixing vessel was measured with an infrared turbidity meter (Oslim) with a sample frequency of 10 Hz, in order to check the stationarity of the concentration influx. In order to obtain a constant mixture discharge, the water level in the second vessel was held constant by letting the surplus flow in a third vessel from which the mixture was pumped back to the mixing vessel. The sediment mixture entered the channel through a nozzle with an inner diameter of 1 cm at the channel's centerline and its center located at 0.7 cm below the free surface. The inflow velocity was manually adjusted to the channel velocity. Preliminary tests, in which the mixture flowing from the nozzle was collected for a concentration measurement showed that no demixing occurred in the second vessel and that concentration of the mixture coming from the nozzle was constant and correlated well with the turbidity measurement. Downstream of the weir, the particles were collected in a filter.

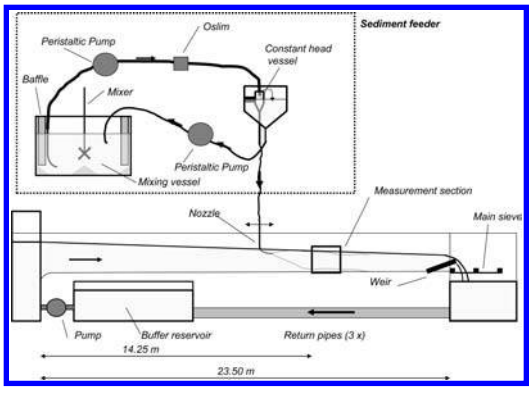


Figure 1. Experimental setup.

The measurement section was located at a distance of 14.25 m from the channel entrance. At this location, a combination of both PIV and PTV was used to measure the velocities of the polystyrene particles and the fluid. A 50 mW double pulsed laser was used to illuminate all particles in the measurement area. A light sheet was made with a cylindrical lens and two spherical lenses and its width was set to 1.0 mm with an adjustable slit. A 1 cm wide glass plate was put on the free surface in a streamlined device to let the laser light penetrate the free surface. Images were recorded with a Kodak Megaplus ES 1.0 $1008 \times 1018\, pix^2$, 15 Hz CCD camera with a 55 mm lens ($f\# = 2.8$). The time between the two image frames was set to 6.0 ms, resulting in particle displacements of about 25 pixel between two frames with the objective to increase the displacements of the relative motion above the experimental accuracy, which is of the order of 0.1 pixel for the algorithms used here. Note that the time between the frames is still significantly smaller than the Kolmogorov timescale (estimated at 50 ms), which means that the error made by approximating the particle movement as a straight line will be small. At the measurement section, a 1 cm wide strip of absorbing fluorescent paint was used in combination with an optical filter in front of the camera, to diminish laser light reflections from the bottom.

Three sets of experimental data were collected. All of these sets were measured at $Re = 10{,}000$ ($Re_* = 508$), which was obtained by setting the centerline velocity to 0.20 m/s and the water depth to 0.050 m. This velocity was chosen to ensure a sufficient amount of sediment in the water column ($u_*/v_T \approx 5$). The only variable that was changed between these sets was the position of the nozzle, which was placed at 80 cm, 175 cm and 375 cm from the measurement section,

Copyright © 2006 Taylor & Francis Group plc, London, UK

i.e. at $x_{in}/h = 16$, $x_{in}/h = 35$ and $x_{in}/h = 75$. During the measurements, it appeared that the discharge from the nozzle in the $x_{in}/h = 16$ case was somewhat lower than in the other cases. The volumetric sediment concentration in the mixing vessel was $1.2\,10^{-2}$. For each set, a sequence of 300 double images was recorded at 15 *Hz* and another sequence of 15×300 double images was recorded at 2 *Hz*. In this second series, the time interval between two velocity measurements (0.5 *s*) was significantly larger than the Eulerian integral timescale, estimated as $h/<u> \approx 0.25\,s$, which means that all velocity measurements in this set are approximately independent. Because of the large number of samples, the measurement period for a set was about one and half hour. Before and after the measurement, the water levels were measured at five different locations in order to check whether the flow was stationary. This showed a variance of less than 0.4% for the water levels at each location and a variance of 2.2% for the u_* determined from the water level slopes. The variance of the Oslim output was about 2% with a trend in the data of less than 3%/*h*, indicating that the sediment concentration that was introduced in the flume was approximately constant in time. For comparison, also four sets of 300 double images were recorded at a frame rate of 2 *Hz* for the flow in the channel, without the nozzle and any sediment input, which we will call the clear water flow (CWF).

The data were processed with a modified version of the method of Kiger & Pan (2000) to discriminate between sediment and tracer particles. This algorithm consists of the following steps.

1. The recorded image is filtered with a median filter with a filter size of 7 pixels. This eliminates the tracer as well as small scale noise from the image. From now on, the resulting image will be called the sediment image.
2. The sediment image is subtracted from the original image. This leads to an image of the tracers. However, some leftovers of the brightest sediment particles are clearly visible in this image.
3. A median filter with a filter width of 7 pixels is applied to the subtracted image in order to determine the location of the sediment particle leftovers and then subtracted from the result of the preceding step. The result is called the tracer image.
4. A PIV algorithm (LaVision, 2002) is applied to the tracer image with first a 64×64 window (50% overlap) and then two 32×32 window (75% overlap) iterations. The results are post-processed with a median filter to eliminate vectors that differ significantly from their neighbours. This leads to 126×126 vectors with distance of 0.37 *mm* (3.76 wall units) between each other. The number of good vectors was on average 98.7%, 93.2%, 95.4% and 95.8% for the respective cases: the clear water flow, $x_{in}/h = 75$, $x_{in}/h = 35$ and $x_{in}/h = 16$. Peak locking was found to be negligible as the histogram of the subpixel displacements did not show any peaks.
5. A PTV algorithm developed by Eindhoven University of Technology (van der Plas *et al.*, 2003) was applied to the sediment image. This algorithm uses the centroid of the particles to determine the particle velocities, where the mean velocity profile of the fluid from the PIV measurements was used as an initial guess for the particle velocities, with a maximal allowed deviation of 8 pixels. Particles on the edge of the measurement area are eliminated, because they generally result from the inability of the median filter to eliminate tracers at the edge of the image. A histogram of the subpixel displacements of the particles showed negligible bias to integer displacements (peaklocking).
6. Errors due to lens distortion were eliminated with a third-order polynomial fit to a picture of a calibration grid.

3 RESULTS

3.1 *Mean quantities*

The mean velocity profile in wall coordinates is shown in figure 2. The friction velocity $u_* = \sqrt{\tau/\rho}$ was determined by fitting the $<u'v'>$ profile in the clear water flow and it was found to be 1.02 *cm/s*. For comparison, the generally accepted law of the wall $u^+ = 1/\kappa\ ln(y^+) + A$ is plotted with $\kappa = 0.41$ and $A = 5.29$, as found by Nezu & Rodi (1986). Our data generally compares well with the law of the wall, but is slightly higher (with a maximum shift of $\pm 0.4\,u_+$). The boundary layer, which develops due to the small glass

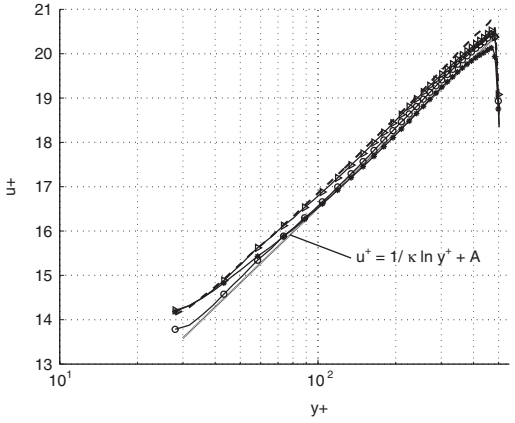


Figure 2. Mean fluid velocity profiles in wall coordinates. $-\circ-$: $x_{in}/h = 75$; $-\triangleright-$: $x_{in}/h = 35$; $-$: $x_{in}/h = 16$; Dashed line: Clear water flow; Dotted line: law of the wall.

Copyright © 2006 Taylor & Francis Group plc, London, UK

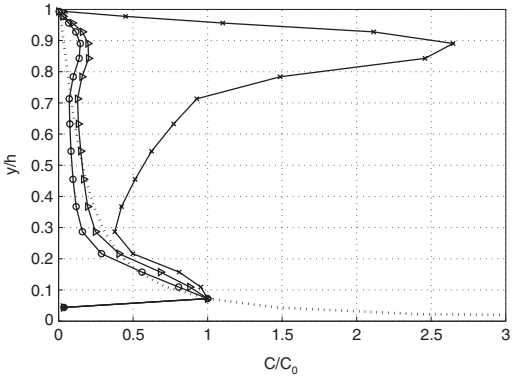


Figure 3. Mean sediment concentration profiles. – ∘ –: $x_{in}/h = 75$; – ▷ –: $x_{in}/h = 35$; – × –: $x_{in}/h = 16$; Dashed lines: Rouse profile.

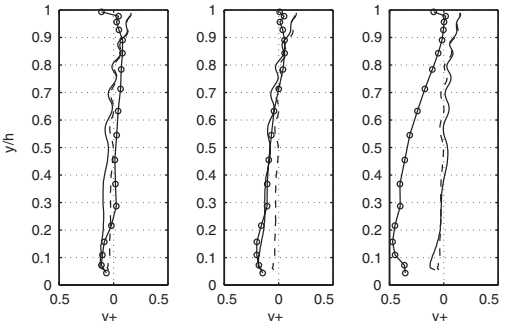


Figure 4. Mean vertical velocity profiles. Left: $x_{in}/h = 75$; Middle: $x_{in}/h = 35$; Right $x_{in}/h = 16$; Particle Velocities: (– ∘ –); Fluid velocity: (solid line); Clear water flow: (Dashed line);

on the water surface can clearly be seen. Its thickness agrees well with the Blasius estimate (as cited in Pope, 2000) $\delta/x \approx 4.9(U_0 x/\nu_f)^{-1/2}$, which gives a thickness of about 2.9–3.8 *mm* (0.06–0.08 *h*).

After the particles were injected, they formed a plume of sediment. Quite soon, the first particles started reaching the channel bottom, where they formed streaky structures similar to those observed previously by Rashidi *et al.* (1990); Kaftori *et al.* (1995a); Niño & García (1996); Kiger & Pan (2002).

The mean sediment concentrations are shown in figure 3. All statistics for the particle phase were interpolated on a grid, that was refined near the water surface, where the concentration gradient is largest (at least for the $x_{in}/h = 16$ case) and near the bottom, where the velocity and turbulence gradients were largest. In order to do so, the upper edge of the ith grid cell y_i was defined by:

$$y_i = \frac{h}{2}\left(\frac{tanh(1.7Z_i)}{tanh(1.7)} + 1\right); \qquad (1)$$

where h is the water depth and $Z_i = -1 + 2i/n$, n is the number of cells. The concentration was determined by counting the number of particles in each grid cell and dividing by the area of the grid cell. The concentrations were normalized with the concentration at $y/h = 0.072$, which is the lowest grid cell where dc/dy was negative as the increasing near-wall sediment concentration is presumably due to the removal of particles attached to the image edge in the data processing. Scaling the $x_{in}/h = 16$ case with a reference concentration near the wall was done for easy comparison with the other cases, but there are no physical reasons for doing so. For comparison, we plot the Rouse distribution:

$$\frac{c(y)}{c(y_0)} = \left(\frac{h-y}{y}\frac{y_0}{h-y_0}\right)^{\frac{w_T}{\beta\kappa u_*}} \qquad (2)$$

with $\beta = 0.7$, and $c(y_0)$ is the concentration at the reference height y_0.

At $x/h = 16$, the sediment is predominantly at the height where it was injected, but already at $x/h = 35$ a concentration profile has developed that is quite similar to the Rouse profile. This is unexpected, as the distance is much shorter than an adaptation length of say $L/h \approx <u>/v_T = 100$ (i.e. the distance a particle travels in the time it needs to settle to the bottom. The influence of the introduction of sediment is still clearly visible in all measured cases at $y/h > 0.8$ (the nozzle was at $0.8 < y/h < 1$).

That the conditions are indeed almost fully developed can be seen from the mean vertical velocity profile (Fig. 4). Note that because the fully developed situation ($x_{in}/h = 75$) is the reference to which we compare, we have placed this situation on the left in each figure. In the $x_{in}/h = 16$ case, the particles have a mean downward velocity of up to $0.5\,u_*$, whereas the vertical fluid velocities are zero up to experimental uncertainty, which for the discrete window shifting PIV algorithms is of the order of 0.1 pixel per frame ($0.08\,u_*$). In the $x_{in}/h = 35$ or 75 cases, the mean vertical particle velocity has reduced to zero too.

The velocity deficit profiles are shown in figure 5, where the centerline velocity Umax is the maximum velocity. We calculated the particle velocity statistics by averaging the velocities of all particles in a grid cell. In this way, concentration weighted statistics are obtained similarly to those used in two-fluid modeling (e.g. Drew, 1983; Simonin *et al.*, 1993; Enwald *et al.*, 1996).

At $x_{in}/h = 16$, the mean particle velocity is up to $0.25\,u_*$ faster than the mean fluid velocity, but in the course of development it decreases to a value that is $0.3\,u_*$ slower than the mean fluid velocity at $x_{in}/h = 75$, which compares well with previous investigations. This phenomenon can be explained by looking a bit deeper in two-fluid modeling theory. The momentum

Copyright © 2006 Taylor & Francis Group plc, London, UK

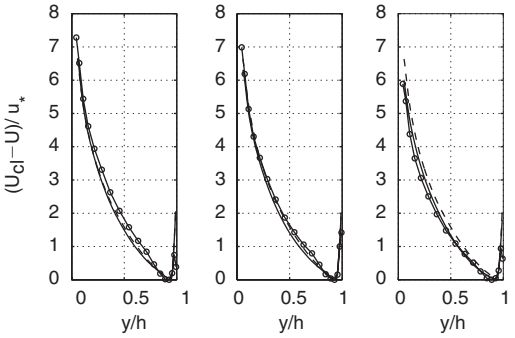


Figure 5. Velocity deficit profiles. Left: $x_{in}/h = 75$; Middle: $x_{in}/h = 35$; Right $x_{in}/h = 16$; Symbols as in figure 4.

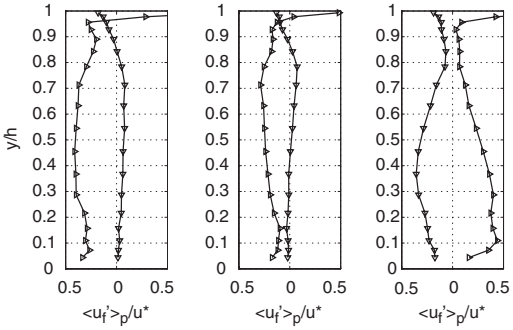


Figure 6. Drift velocity. Left: $x_{in}/h = 75$; Middle: $x_{in}/h = 35$; Right $x_{in}/h = 16$; – ▷ –: streamwise direction – ▽ –: wall normal direction.

equation in the i-direction for the particle phase is (with only Stokes drag working on the particles):

$$\frac{DC < u_{p,i} >_p}{Dt} = \underbrace{-\frac{\partial C < u'_{p,i} u'_{p,j} >_p}{\partial x_j}}_{\text{Particle Reynolds stress contribution}} + \underbrace{\frac{\rho_p - \rho_f}{\rho_p} g_i}_{\text{Buoyancy}} + \underbrace{\frac{C}{\tau_p} < u_{rel,i} >_p}_{\text{Stokes drag}} \quad (3)$$

where D/Dt is the time derivative in a frame moving with the mean particle velocity, τ_p is the particle time scale, C the ensemble averaged concentration, $u_{p,i}$ is the particle velocity, ρ_p and ρ_f the particle and fluid densities, and $<>_p$ and $<>_f$ denote ensemble averaging over the particle and fluid phase respectively. Simonin *et al.* (1993) found that the average of the relative velocity in the i-direction $<u_{rel,i}>_p$ in the drag term of equation 3 can be expressed as:

$$\begin{aligned} < u_{rel,i} >_p &= < u_{p,i} >_p - < u_f >_p \\ &= < u_p >_p - < u_f >_f - < u'_f >_p \end{aligned} \quad (4)$$

Note that $<u_{p,i}>_p$ (the particle velocity averaged over all particles) is equal to the flux of particles divided by the mean concentration. It is clear that the fluctuating fluid velocity seen by the particle $<u'_f>_p$ in principle does not need to be equal to zero. In a homogeneous, stationary situation, equation 3 for the vertical direction reduces to :

$$< u_{p,y} >_p = < u_{f,y} >_f + < u'_{f,y} >_p + \underbrace{\tau_p \frac{\rho_p - \rho_f}{\rho_p} g_y}_{=v_T} \quad (5)$$

Equation 5 physically means that the mean particle velocity (i.e. the flux per unit of concentration) is equal to the settling velocity added to mean vertical fluid velocity and the extra $<u'_f>_p$ term. Simonin *et al.* (1993) called $<u'_f>_p$ the drift velocity and used a gradient diffusion hypothesis for the closure of this term. In fact, the drift term is comparable to the $<c'v'>$ term in traditional advection-diffusion models.

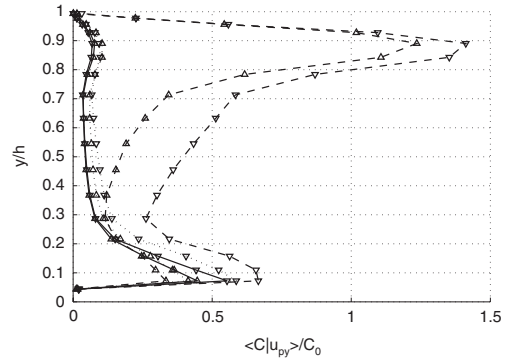


Figure 7. Conditionally averaged concentration profile. Conditioned on upward moving particles: (– △ –); Conditioned on downward moving particles: (– ▽ –). Dashed line: ($x_{in}/h = 16$); Dotted line: ($x_{in}/h = 35$); Solid line: ($x_{in} = 75$).

We determined the drift velocities from our measurements using bicubic interpolation to determine the fluid velocity on the particle location (Fig. 6). This figure clearly shows that at $x_{in}/h = 16$, the vertical fluid velocity seen by the particles is downward, which means that the particles are found more often in sweeps than in ejections, thus in fluid structures where the fluid velocity is higher than the mean streamwise velocity, which is also obvious from figure 6. This result in a larger number of particles moving down than up (Fig. 7). Rather interestingly, the absolute values of the drift velocity in both streamwise and wall normal directions increase in downward direction at

Copyright © 2006 Taylor & Francis Group plc, London, UK

least down to $y/h = 0.3$ for the $x_{in}/h = 16$ case. The explanation for this is that at this short distance, only particles which were in the strongest downward turbulence structures can reach the near wall locations, and therefore only those that have the largest vertical drift velocities. The streamwise velocities in these structures are those from high up in the flow, so they will deviate more from the mean flow here than nearer to the free surface. At $y/h = 0.3$, the concentration gradient changes sign, whereas the vertical drift velocity does not, although it decreases in magnitude. Simonin *et al.* (1993) uses a gradient diffusion hypothesis for modeling the drift velocity:

$$< u'_{f,y} >_p = \frac{-D_{yy}}{C} \frac{\partial C}{\partial y} \tag{6}$$

where D_{yy} is the diffusion coefficient. Using this equation would lead to negative diffusion coefficients for $y/h < 0.3$. Apparently, the sediment flux is still determined by sediment advected from near the free surface in turbulence structures with a vertical scale of the order of the water depth, and the effect of the locally negative concentration gradient (at $y/h < 0.3$) is to slow down the drift velocity, rather than to determine its direction.

An estimation of the Lagrangian integral timescale $T_L \approx L_E/u_{rms}$ (Hinze, 1975) (L_E is the Eulerian integral length scale, which scales with the water depth in the outer layer) gives $T_L \approx 5\,s$ and hence a distance of $<u>_b\, T_L = 1\,m = 20\,x_{in}/h$ would be needed for the long term diffusion in Taylor's (1921) diffusion theory to become completely applicable. For short distances, Taylor (1921) requires that the dispersion $<y'^2>$ scales with $<v'^2> t^2$, which means that the spreading is determined by an advective process. This coincides quite well with our measurements, as in the $x_{in}/h = 35$ case, a stationary situation has developed, where the mean vertical particle velocity is approximately zero. In the $x_{in}/h = 16$ case on the other hand, the situation such a stationary situation has not developed yet.

At $x_{in}/h = 75$, the vertical drift velocity has a value just above zero, but lower than the fall velocity, although according to equation 5, we would expect those to be equal. It is not clear whether our signal to noise ratio is not good enough to resolve velocities of the order of magnitude of the settling velocity or that equilibrium is still not reached and a larger vertical drift velocity still has to develop. For $y/h > 0.85$, the vertical drift velocity is still negative, suggesting that the clearly visible effect of the sediment injection are still present. The streamwise drift velocity in these cases are negative, indicating that the sediment has already started to be preferentially concentrated in ejections rather than in sweeps, which explains the mean streamwise velocity being lower for the particles than for the fluid. Note that the number of upward and downward moving particles in this case is equal except near the bottom (Fig. 7), which is in agreement with Kiger & Pan (2002).

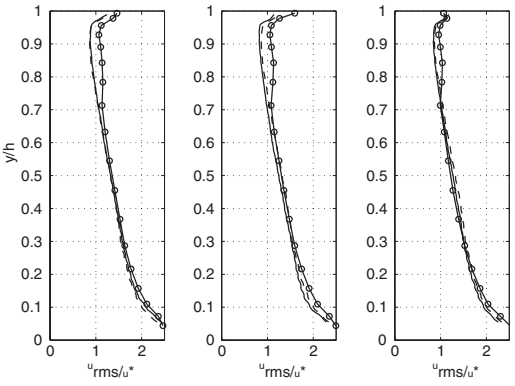


Figure 8. Streamwise turbulence profile. Mean flow profiles. Left: $x_{in/h}/h = 75$; Middle: $x_{in}/h = 35$; Right $x_{in}/h = 16$; Symbols as in figure 4.

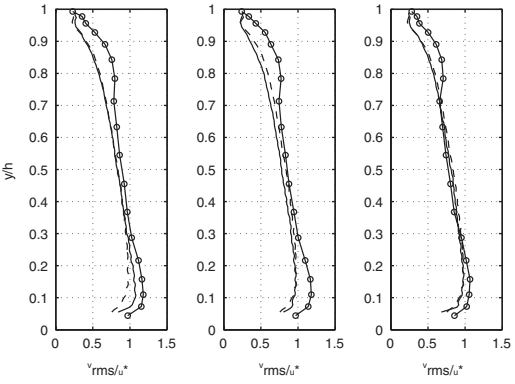


Figure 9. Wall normal turbulence profile. Mean flow profiles. Left: $x_{in}/h = 75$; Middle: $x_{in}/h = 35$; Right $x_{in}/h = 16$; Symbols as in figure 4.

3.2 *Turbulence characteristics*

The fluctuating fluid and particle velocities are shown in figure 8 and 9. Apart from the area affected by the sediment injection ($y/h > 0.8$), the streamwise fluctuating particle velocities do not differ much from the fluctuating fluid velocities, which was also found in previous investigations. In the $x_{in}/h = 35$ and 75 cases, the wall normal fluctuating velocities are slightly larger (5%) than the fluctuating fluid velocities for $0.3 < y/h < 0.8$, but they are substantially larger in the near wall region. In these fluctuations, the influence of the sediment introduction is also clearly visible. Note that particle velocity fluctuations that are larger than fluid velocity fluctuations are in agreement with the

Copyright © 2006 Taylor & Francis Group plc, London, UK

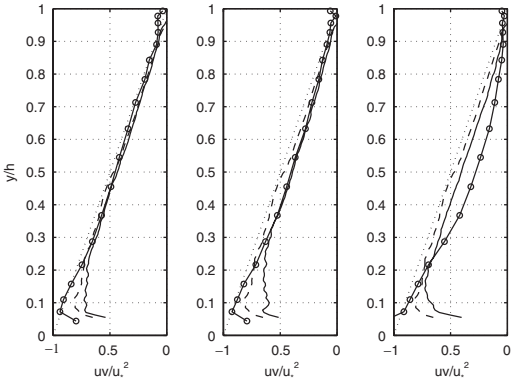


Figure 10. Reynolds stress profile. Mean flow profiles. Left: $x_{in}/h = 75$; Middle: $x_{in}/h = 35$; Right $x_{in}/h = 16$; Symbols as in figure 4.

experiments from Kaftori *et al.* (1995b), who used similar particles as we used, with those from Best *et al.* (1997) and those from Muste *et al.* (2005), but in contradiction with the theory (Hinze, 1975).

The fluid and particle Re-stresses are shown in figure 10. At $x_{in}/h = 16$, the particle Re-stresses are well below the fluid Re-stresses for $y/h > 0.2$ and they clearly do not follow a straight line. During the development to a stationary profile, the particle Restress profile increases and straightens until it becomes equal to the fluid Re-stress profile. The lower Re-stresses at $x_{in}/h = 16$ can possibly be explained by the fact that the particles in this stage are mainly found in sweeps, which although they occur during a larger fraction of time than ejections in the outer layer, their contribution to the Re-stresses is smaller (Nezu & Nakagawa, 1993). Apparently, this is not compensated by the fact that the particles are located in those sweeps that have the largest vertical velocities, especially near the bottom.

3.3 *Instantaneous flow structures*

In order to verify the conclusions that were drawn based on the statistical information obtained in the preceding paragraphs, we now inspect some instantaneous images of both particle and fluid velocity (Fig. 11 and 12) from the 15 *Hz* datasets. In these figures, we subtracted a constant velocity of 0.18 *m/s* (0.9 U_{max}) as was recommended by Adrian *et al.* (2000). This has the advantage compared to using a Reynolds decomposition, that the velocity gradients are not altered. Figure 11 shows an example of particles that are being entrained by a strong ejection, in the $x_{in}/h = 35$ case. Two hairpin vortex heads are visible, one downstream of the ejection rotating in the direction of the shear, and one upstream rotating opposite to the shear. Vortex heads rotating against the direction

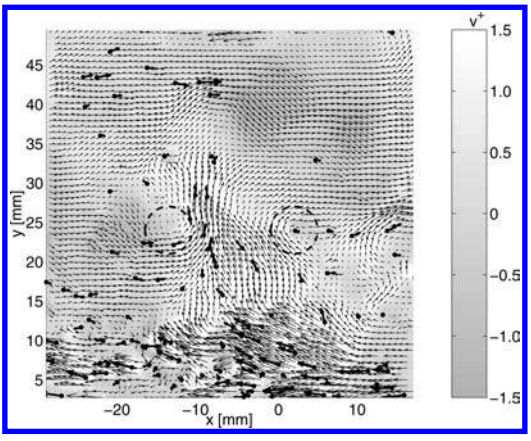


Figure 11. Example of an instantaneously measured flow structure in the $x_{in}/h = 35$ case. Fluid vectors are shown in dark gray, particles in black. Vertical velocities are indicated with gray background colors. Vortex heads are marked with a dashed circle.

of the shear are not rare events, although less common than those rotating in the direction of the shear (Portela, 1997). According to Adrian *et al.* (2001), these vortices originate from the merging of two hairpin vortices. The combined induction of both vortices explains why this is a rather extreme ejection, with a larger wall-normal than streamwise extend.

Although these violent ejections are rather sporadic, it does not automatically mean that they are not important, because a very intermittent character of the sediment fluxes has been noted by Hurther & Lemmin (2003) and Nikora & Goring (2002), who noted flatness factors of $c'v'$ of about 30 and more than 10 respectively (in contrast with 3 for a Gaussian distribution). Note that entrainment by somewhat weaker ejections is encountered frequently in these images.

By examining this ejection event in time (it was visible in four consecutive time frames), it was clearly visible how the structure advected through the measurement frame. The structure did not appear to change significantly during this 0.26 *s* ($O(0.1T_L)$), nor did it seem to move much upward. The particles on the other hand, could clearly be seen to move upward through the structure. This means that during the entrainment process, apparently a flux of sediment is caused by almost static flow structures. This is a clear contrast with the findings of Mutlu Sumer & Deigaard (1981) and Niño & García (1996), who suggest that the velocity structure is moving itself and taking the particles with them, until the flow structure looses coherence. Their explanation is presumably due the use of flow visualization to study the fluid structures as the dye advects in the same way as the sediment particles. Landahl (1993) estimated the viscous timescale T_v for convected disturbances

Copyright © 2006 Taylor & Francis Group plc, London, UK

to decay to be $T_v = (L^2/(v_f(d<u_f>/dy)^2)^{(1/3)}$, which gives timescales in the outer layer of 50–500 s, which is one to two orders of magnitude larger than our estimation of the Lagrangian timescale with $T_{L,i} \approx L_{E,i}/u_i'$ (Philip, 1967; Hinze, 1975). The latter time scale is a measure of how long it takes a particle to cross a structure of size $L_{E,i}$ with a characteristic velocity u_i', which is indeed what we saw happening in the entrainment process. If the structure itself would have moved vertically as well with a velocity of the order of magnitude of the fluid ejection had (and thus as the particles would have except for gravity), this would lead to significantly longer Langrangian time scales. Christensen & Adrian (2002) measured the acceleration of hairpin vortices in a turbulent channel flow and found that although the vortices move upward slowly, this movement is an order of magnitude smaller than the instantaneous vertical velocities.

The preceding compares with the frequent observation (e.g. Squires& Eaton, 1991) in homogeneous turbulence that the integral Eulerian time scale in a frame moving with the mean velocity is larger than the Lagrangian timescale (although not an order of magnitude). The integral time scale in this moving frame is then determined by a combination of the structures drifting away vertically and viscous decay. Yet, statistical data on the three different time scales in channel flow is very rare and it is especially not known how all three time scales vary over the depth. It might be possible that young hairpin vortices near the wall ascend faster, because of their stronger self induction. The DNS that is currently being performed might provide valuable insight into this.

In the $x_{in}/h = 16$ case, mainly sweeps are responsible for transporting the particles downwards. An example is shown in figure 12. The sweep apparently exists because of induction from the hairpin vortex in the lower left part. This explains why sweeps are weaker than ejections, as the latter structures are not only induced by the head of the hairpin vortex, but also by its neck and legs. The sweep can be seen to transport many particles downward, whereas the areas without vertical velocities low in the water column are almost void of particles. Following this structure (as well as others) confirmed that the flow structures moved only very slowly vertically, while the particles were moved through the structure, similar as was found for the ejections. In this case, similar strong ejections as in figure 12 did not result in large entrainment, just because at $x_{in}/h = 16$ less sediment particles were present in the low velocity layer from where the fluid was ejected, and thus decreasing the probability that a large ejection would transport much sediment upward, although some ejections with some particles were found near the bottom, thus explaining the increase of the vertical drift velocity toward zero for $y/h < 0.3$.

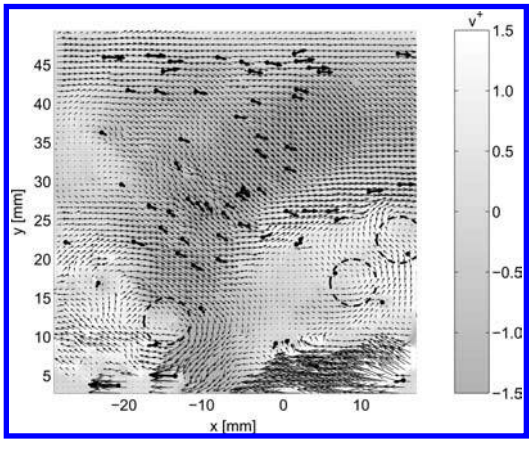


Figure 12. Example of an instantaneously measured flow structure in the $x_{in}/h = 16$ case. Symbols as in figure 11.

4 SUMMARY AND CONCLUSIONS

In this paper, an experiment was performed to measure both the fluid and sediment velocities with a combinated PIV-PTV technique in a turbulent open channel flow, using 350 μm polystyrene particles. The particles where introduced at three different locations upstream from the measurement area and near the free surface. It was found that already at $x_{in}/h = 35$, the sediment concentration developed into a shape similar to the Rouse profile, although the sediment's initial conditions remain visible for a significantly longer distance. After the profile has developed completely, the mean particle velocity is slower than the mean fluid velocity because the particles are found mainly in ejections. At $x_{in}/h = 16$, the sediment concentration has the highest values high in the water column. Here, the particles are found more often in downward going fluid structures (sweeps), which have a streamwise velocity higher than the mean fluid velocity causing the mean particle velocity to be faster than the fluid velocity. The dispersion process at this short distances is mainly affected by advection of sediment from above, rather than by turbulent diffusion and the use of a gradient diffusion hypothesis would lead to a negative eddy diffusion coefficient for $y/h < 0.3$. Note that this still not explains why particles concentrate in a particular turbulence structure.

For all cases, the streamwise fluid and particle turbulence profiles were found to be approximately equal, whereas the particle wall normal turbulence intensities were significantly larger than the fluid ones near the wall ($y/h < 0.3$), but just slightly larger for the outer region of the flow ($0.3 < y/h < 0.8$). In the $x_{in}/h = 16$ case, the particle Reynolds stresses are lower than fluid

Copyright © 2006 Taylor & Francis Group plc, London, UK

Re-stresses in the center of the flow, presumably due to the fact that the particles are located in sweeps, rather than ejections, the latter of which contribute more to the total Reynolds stresses.

Examples of instantaneous flow structures supported the estimation of the Lagrangian integral time scale with $T_l \sim L_E/v_{rms}$ (Hinze, 1975), which is vital for the determination of diffusion coefficients in Taylor's (1921) diffusion theory. Yet, a sound statistical basis is currently lacking as Lagrangian data, both from experiments and simulations, remains scarce. The DNS simulations in combination with particle tracking that are currently being performed at the Kramers Laboratory of Delft University of Technology can provided more insight in this matter.

The implications from this investigation are twofold. First of all, it shows that gradient diffusion modeling of sediment fluxes is especially awkward to predict sediment transport with a scale $L_p < O(h < u > /v_{rms})$. This scale was determined by estimating the distance traveled by the fluid in one Lagrangian time scale, estimated with $T_l \sim h/v_{rms}$. In these cases, it seems necessary to use more advanced models like transport equations for the drift velocity (Simonin *et al.*, 1993), which in the scalar case reduce to the Reynolds flux equations. Secondly, because the large scale turbulence structures, which proved to limit the utility of gradient diffusion models for short Lagrangian timescales, are also present in the fully developed cases, it seems necessary to include large scale transport in order to improve the current modeling of sediment concentrations in fully developed conditions. An example of a modeling approach that incorporates large scale transport processes is given by Nielsen & Teakle (2004).

ACKNOWLEDGEMENT

The financial support from STW, WL|Delft Hydraulics and KIWA Water Research is highly appreciated. We thank Synbra Technology in Etten-Leur for providing us the polystyrene particles.

REFERENCES

Adrian, R.J., Meinhart, C.D., & Tomkins, C.D. 2000. Vortex organization in the outer region of the turbulent boundary layer. *Journal of Fluid Mechanics*, **422**, 1–54.

Adrian, R.J., Balachandar, S., & Liu, Z.C. 2001. Spanwise Growth of Vortex Structures in Wall Turbulence. *KSME International Journal*, **15**(12), 1741–1749.

Best, J., Bennett, S., Bridge, J., & Leeder, M. 1997. Turbulence Modulation and Particle Velocities over Flat Sand Beds at Low Transport Rates. *Journal of Hydraulic Engineering*, **123**(12), 1118–1129.

Cellino, M., & Graf, W.H. 1999. Sediment-Laden Flow in Open-Channels under Noncapacity and Capacity Conditions. *Journal of Hydraulic Engineering*, **125**(5), 455–462.

Christensen, K.T., & Adrian, R.J. 2002. The velocity and acceleration signatures of small-scale vortices in turbulent channel flow. *Journal of Turbulence*, **3**(023), 1–28.

Drew, D.A. 1983. Mathematical modelling of two-phase flow. *Annual Review of Fluid Mechanics*, **15**, 261–291.

Enwald, H., Peirano, E., & Almstedt, A.-E. 1996. Eulerian two-phase flow theory applied to fluidization. *International Journal of Multiphase Flow*, **22**(Suppl.), 21–66.

Hinze, J.O. 1975. *Turbulence*. Second edn. McGraw-Hill.

Hurther, D., & Lemmin, U. 2003. Turbulent particle flux and momentum flux statistics in suspension flow. *Water Resources Research*, **39**(5), 1139, 1–11.

Kaftori, D., Hetsroni, G., & Banerjee, S. 1995a. Particle behavior in the turbulent boundary layer. I. Motion, deposition, and entrainment. *Physics of Fluids*, **7**(5), 1095–1106.

Kaftori, D., Hetsroni, G., & Banerjee, S. 1995b. Particle behavior in the turbulent boundary layer. II. Velocity and distribution profiles. *Physics of Fluids*, **7**(5), 1107–1121.

Kiger, K.T., & Pan, C. 2000. PIV Technique for the Simultaneous Measurement of Dilute Two-Phase Flows. *Journal of Fluids Engineering*, **122**, 811–818.

Kiger, K.T., & Pan, C. 2002. Suspension and turbulence modification effects of solid particulates on a horizontal turbulent channel flow. *Journal of Turbulence*, **3**(019), 1–21.

Landahl, M.T. 1993. Near-Wall Model for Boundary Layer Turbulence. *Applied Scientific Research*, **51**, 435–443.

LaVision. 2002 (February). *FlowMaster Manual. PIV Hardware Manual for Davis 6.2*. Tech. rept. LaVision GmbH.

Muste, M., & Patel, V.C. 1997. Velocity Profiles for Particles and Liquid in Open-Channel Flow with Suspended Sediment. *Journal of Hydraulic Engineering*, **123**(9), 742–751.

Muste, M., Yu, K., Fujita, I., & Ettema, R. 2005. Two-Phase versus Mixed-Flow Perspective on Suspended Sediment Transport in Turbulent Channel Flows. *Water Resources Research*, **41**(10402), 1–22.

Mutlu Sumer, B., & Deigaard, R. 1981. Particle motions near the bottom in turbulent flow in an open channel. Part 2. *Journal of Fluid Mechanics*, **109**, 311–337.

Nezu, I., & Azuma, R. 2004. Turbulence Characteristics and Interaction Between Particles and Fluid in Particle-Laden Open Channel Flows. *Journal of Hydraulic Engineering*, **130**(10), 988–1001.

Nezu, I., & Nakagawa, H. 1993. *Turbulence in Open-Channel Flows*. A.A. Balkema.

Nezu, I., & Rodi, W. 1986. Open-channel Flow Measurements with a Laser Doppler Anemometer. *Journal of Hydraulic Engineering*, **112**(5), 335–355.

Nielsen, P., & Teakle, I.A. 2004. Turbulent diffusion of momentum and suspended particles: A finite-mixing-length theory. *Physics of Fluids*, **16**(7), 2342–2348.

Nikora, V.I., & Goring, D.G. 2002. Fluctuations of Suspended Sediment Concentration and Turbulent Sediment Fluxes in an Open-Channel Flow. *Journal of Hydraulic Engineering*, **128**(2), 214–224.

Niño, Y., & García, M.H. 1996. Experiments on particle-turbulence interactions in the near-wall region of an open

Copyright © 2006 Taylor & Francis Group plc, London, UK

channel flow: implications for sediment transport. *Journal of Fluid Mechanics*, **326**, 285–319.
Philip, J.R. 1967. Relation between Eulerian and Lagrangian Statistics. *Physics of Fluids*, S69–S71.
Pope, S.B. 2000. *Turbulent Flows*. Press Syndicate of the University of Cambridge.
Portela, L.M. 1997. *Indentification and characterization of vortices in the turbulent boundary layer*. Ph.D. thesis, Stanford University.
Rashidi, M., Hetsroni, G., & Banerjee, S. 1990. Particle-turbulence interaction in a boundary layer. *International Journal of Multiphase Flow*, **16**(6), 935–949.
Righetti, M., & Romano, G.P. 2004. Particle-fluid interactions in a plane near-wall turbulent flow. *Journal of Fluid Mechanics*, **505**, 93–121.
Simonin, O., Deutsch, E., & Minier, J.P. 1993. Eulerian Prediction of the Fluid Particle Correlated Motion in Turbulent Two-Phase Flows. *Applied Scientific Research*, **51**(1-2), 275–283.
Squires, K.D., & Eaton, J.K. 1991. Lagrangian and Eulerian statistics obtained from direct numerical simulation of homogeneous turbulence. *Physics of Fluids*, **3**(1), 130–143.
Taylor, G.I. 1921. Diffusion by continuous movements. *Proceedings of the London Mathematical Society*, **xx**, 196–212.
Uijttewaal,W.S.J., & Oliemans, R.V.A. 1996. Particle Dispersion and Deposition in Direct Numerical and Large Eddy Simulations of Vertical Pipe Flows. *Physics of Fluids*, **8**(10), 2590–2604.
van der Plas, G.A.J., Zoeteweij, M.L., Bastiaans, R.J.M., Kieft, R.N., & Rindt, C.C.M. 2003 (April). *PIV, PTV and HPV User's Guide 1.1*. Eindhoven University of Technology. Draft.
Vanoni, V.A. 1946. Transportation of suspended sediment by water. *American Society of Civil Engineers Transactions*, **2267**, 67–133.

Copyright © 2006 Taylor & Francis Group plc, London, UK

Towards a Direct Numerical Simulation (DNS) of particle motion close to river beds

A.E. González & F.A. Bombardelli
Department of Civil & Environmental Engineering, University of California, Davis, CA, USA

Y. Niño
Department of Civil Engineering, University of Chile, Santiago, Chile

ABSTRACT: The Basset force that takes part in the momentum equations for a solid particle moving close to a wall can make the numerical solution of these equations computationally time consuming. Reductions of the computational cost of the Basset term are therefore strongly needed. In this paper, we present and discuss a methodology to deal with the difficulties associated with the Basset force. We use an approximation of the Basset term based on a semi-derivative (fractional mathematics), and we redefine the integration time of the term. These results constitute the first step of a larger project aimed at integrating fluid and particle motion close to a river bed using an Eulerian-Lagrangian approach.

1 INTRODUCTION

The prediction of particle motion close to a rigid or movable wall is an extremely complex task. Depending on the particle size and on flow conditions, particles may either move along the bed by rolling and saltating, or may "fly" in suspension relatively far from the boundary. Recent numerical simulations of sediment transport close to walls have satisfactorily estimated the global amount of material put into motion, and they have provided information on the characteristics of the particle trajectories (Sekine & Kikkawa (1992), Hu & Hui (1996), Niño & García (1998), Schmeeckle & Nelson (2003)). In these studies, the flow field has been specified via either the law of the wall (Niño & García (1998)) or measurements (Schmeeckle & Nelson (2003)).

Very recently, some authors have incorporated aspects of the two-phase flow theory in describing particle-laden flows for industrial applications. Generally speaking, particle-laden flows have been considered as a two-phase system in which the fluid and solid phases obey basic conservation laws coupled through interactions forces.

One of the forces in those two-phase models is the well known Basset force, which highly affects the motion of small particles (Sommerfeld (1992), Sommerfeld (2003), Portela & Oliemans. (2003), Ten Cate et al. (2004)). This force, which represents the "memory" of the particle, requires the calculation of the relative acceleration along the particle trajectory. Depending on the length of the simulation time, the computation of the Basset force could be extremely time consuming. In the event that numerous interacting particles are simulated, the inclusion of the Basset force may render the whole computation inviable. Therefore, any attempt to reduce the computational cost associated with this term will benefit the entire modeling effort.

Based on these ideas, in this paper we focus on methods to reduce the computation time of the Basset force. In section 2, we present the Lagrangian model to track the particles in a turbulent flow, and in section 3, we describe a new method to compute the Basset force (introduced by Tatom in 1988; to the best of our knowledge, not put to work until now), which is based on semi-derivatives. In section 4, we describe a new strategy to evaluate the integration time for the Basset integral. Finally, we discuss the results in section 5.

Our results are relevant for the development of numerical models which integrate fluid and particle motion close to river beds, using Eulerian- Lagrangian approaches.

2 EQUATIONS FOR SEDIMENT PARTICLE SALTATION IN A TURBULENT BOUNDARY LAYER

One of the most recent and complete forms of the governing equations for the motion of a small spherical particle in an unbounded fluid (within the Stokes drag

Copyright © 2006 Taylor & Francis Group plc, London, UK

range) was presented by Mei et al. (1991), based on the equations proposed earlier by Maxey & Riley (1983). The ith component of these equations can be written as:

$$\rho_s\left(\frac{dU_{pi}}{dt}\right)=g_i(\rho_s-\rho)-\frac{18}{d_p^2}\left(U_{pi}-U_{fi}-\frac{1}{24}d_p^2\nabla^2U_{fi}\right)+$$
$$+\frac{9}{d_p}\left(\frac{\rho\mu}{\pi}\right)^{1/2}\int_0^t\frac{d}{d\tau}\left(U_{fi}-U_{pi}+\frac{1}{24}d_p^2\nabla^2U_{fi}\right)\frac{d\tau}{\sqrt{t-\tau}}+$$
$$+\rho C_m\frac{d}{dt}\left(U_{fi}-U_{pi}+\frac{1}{24}d_p^2\nabla^2U_{fi}\right)+\rho\frac{DU_{fi}}{Dt} \qquad (1)$$

where ρ and ρ_s denote fluid and particle density respectively, U_p and U_f indicate the instantaneous particle and fluid velocity, respectively, μ denotes the dynamic viscosity, C_m refers to the added mass coefficient, d_p indicates the particle diameter, g is the acceleration of gravity, t denotes time and τ is a dummy variable for integration. The terms on the right hand side of (1) correspond to the following forces per unit volume: buoyancy, Stokes drag, Basset history force, and forces due to added mass and fluid acceleration, respectively. The operator D(·)/Dt indicates the material derivative using the fluid velocity in the advective term, as opposed to the particle velocity employed in d(·)/dt.

Niño & García (1994) modified the previous expression to consider large particles in a turbulent flow; this turbulent flow was characterized by the log-law expression for the time-averaged velocity. They averaged the velocities over turbulence, neglected second order terms and added lift and Magnus effects on the particle acceleration (González (2006)). They also modified the expression for the drag force to be able to simulate cases of larger Reynolds numbers. Expressions (2) and (3) below provide the dimensionless equations developed by Niño & García to calculate the streamwise and vertical particle velocities (u_p and v_p, respectively), considering the particle diameter as a length scale and the shear velocity u^* as a velocity scale.

$$\frac{du_p}{dt}=\alpha\frac{\sin\theta}{\tau_*}-\frac{3}{4}\alpha C_D\left(u_p-u_f\right)\left|u_r\right|+\alpha C_m v_p\frac{du_f}{dy}$$
$$+\frac{9\alpha}{\sqrt{\pi R_p}\tau_*^{1/4}}\int_0^t\frac{d}{d\tau}\left(u_f-u_p\right)\frac{d\tau}{\sqrt{t-\tau}} \qquad (2)$$

$$\frac{dv_p}{dt}=-\alpha\frac{\cos\theta}{\tau_*}-\frac{3}{4}\alpha C_D v_p\left|u_r\right|+\frac{3}{4}\alpha C_L\left(\left|u_r\right|_T^2-\left|u_r\right|_B^2\right)-$$
$$-\frac{9\alpha}{\sqrt{\pi R_p}\tau_*^{1/4}}\int_0^t\frac{d}{d\tau}v_p\frac{d\tau}{\sqrt{t-\tau}}+\frac{3}{4}\alpha\left|u_r\right|\left(S-\frac{1}{2}\frac{du_f}{dy}\right) \qquad (3)$$

In these equations C_D and C_L denote the drag and lift coefficients, respectively, u_r, u_{rT} and u_{rB} are the relative velocity at the center, top and bottom of the particle, respectively, α is defined as $(1+R+C_m)^{-1}$, R is defined as $(\rho_s/\rho-1)$, τ^* is given by u^{*2}/gRd_p, R_p is given by $(R\,g\,d_p^3)^{0.5}/\nu$ and S is defined as $\Omega\,d_p/u^*$, where Ω is the particle angular velocity. Mathematically, this is an initial-value problem for which initial conditions are needed. After computing the velocities, the positions of the particles are determined by simple integration.

These equations govern the "flight" time between rebounds of the particle against the wall. In fact, gravity acts against turbulence fluctuations and pull the particles downwards. To simulate the rebound against the wall, we employed a stochastic model, following Niño & García (1994). The model assumes a bed formed by uniformly-packed spheres and it computes the particle velocity after the collision by considering coefficients of restitution and friction in addition to the particle velocity immediately before the collision. The angle of contact of the incoming particle and the particle at the bed is treated as a random variable (González (2006)).

Niño & García (1994, 1998) compared the results provided by their saltation model with their own experimental observations, obtaining a good agreement.

3 BASSET FORCE COMPUTATION

The particle trajectory equations presented can be easily integrated using the standard fourth-order Runge-Kutta method. However, the Basset term presents extra difficulties because the denominator in the integrand vanishes when the upper integration limit is enforced. Therefore it is necessary to devise a method to circumvent this problem.

Niño & García (1994) employed a method first suggested by Brush et al. (1964) that consists in dividing this integral in two terms (see Equation 4 below).

$$\int_0^T\frac{\frac{du_{ri}}{dt}}{\sqrt{T-t}}dt=\int_0^{T-\delta t}\frac{\frac{du_{ri}}{dt}}{\sqrt{T-t}}dt+2\sqrt{\delta t}\left(u_j\frac{du_{fi}}{dx_j}-\frac{du_{pi}}{dt}\right) \qquad (4)$$

Tatom (1988) in turn proposed to approximate this term using the Riemman-Liouville integral definition of a semi-derivative. The Basset term is calculated as follows:

$$\int_0^T\frac{\frac{du_r}{dt}}{\sqrt{T-t}}dt=\Gamma\left(\frac{1}{2}\right)\frac{d^{-0.5}\left(\frac{du_r}{dt}\right)}{dt^{-0.5}} \qquad (5)$$

where $\Gamma(\cdot)$ represents the gamma function (Abramowitz & Stegun, 1970). For a general function f(x), the

Copyright © 2006 Taylor & Francis Group plc, London, UK

semi-derivative is calculated using an infinite series, as proposed by Oldham & Spanier (1974):

$$\frac{d^q f}{dx^q} = \lim_{N\to\infty}\left\{\left(\frac{x}{N}\right)^{-q}\frac{1}{\Gamma(-q)}\sum_{k=0}^{N-1}\frac{\Gamma(k-q)}{\Gamma(k+1)}f\left(x-\frac{k\,x}{N}\right)\right\} \quad (6)$$

where q is an arbitrary value. In this case the value of q is equal to -0.5. We have adopted this last methodology in our work with the objective of reducing the computational cost of the Basset term. To the best of our knowledge, this way of computing the Basset term has not been incorporated into particle models so far.

To check the accuracy of this method, a test case was adopted. We picked the following arbitrary function $f(x) = x^3/3$, and we calculated the Basset integral both numerically and analytically. The analytical solution for this expression is given by:

$$\int_0^T \frac{\frac{df(t)}{dt}}{\sqrt{T-t}}dt = \int_0^T \frac{\frac{dt^3}{3dt}}{\sqrt{T-t}}dt = \frac{16}{15}T^{2.5} \quad (7)$$

For an arbitrary value of T equal to 100, the Basset integral presents a value equal to 106,034. This value was considered as a reference value, for error calculations, as follows.

The numerical approximation of the Basset integral depends on the number of terms (N) used in the sum in (6). The value of N was varied between 5 and 50,000 in order to analyze the accuracy of this approximation. The results of the numerical integration of the test function f(t) using the expression (5) are presented in Figure 1. We defined the relative error as the relative difference between the numerical integration and the value obtained from the analytical expression. As expected, the error associated with the numerical approximation decreases as the number of terms (N) increases. A value of N equal to 1,000 appears to be reasonably large for obtaining accurate results. However, the application of this parameter in the particle tracking code must be carefully studied. For a long simulation time, the value of the parameter N could be unmanageable and other strategies should be considered.

The results obtained using the approximation of the Basset term as a semi-derivative were compared with results obtained using the approximation proposed by Brush et al. (1964). Figure 2 shows the relative difference in the calculation of the Basset integral using both methods. The results were obtained for a single particle jump considering $R_p = 53$ and $\tau^* = 0.056$. The results show that the percentage of error between both approximations is less than the 3%. A large portion of this small difference is attributed to the fact that we are comparing the semi-derivative approximation with the first term in Brush et al.'s method (Eq. 4).

Figures 3 and 4 show results in terms of jump length and height. The relative error between both

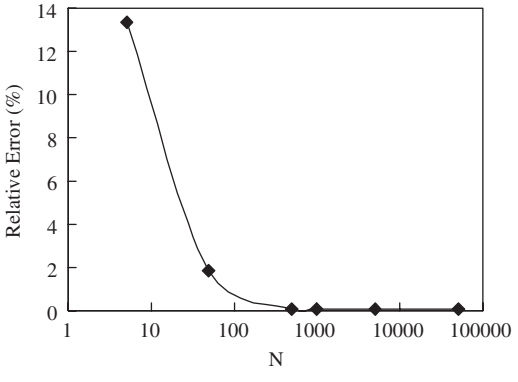


Figure 1. Error associated with the Basset integral approximated as a semi-derivative vs. parameter N. Test function.

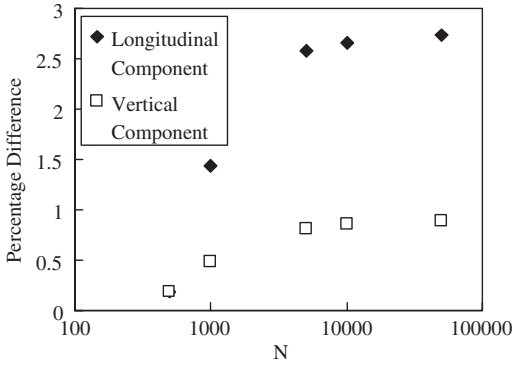


Figure 2. Percentual difference between methods (Brush et al.'s (1964) and semi-derivate) to calculate longitudinal and vertical components of the Basset force. Single jump. $R_p = 53$. $\tau_* = 0.056$.

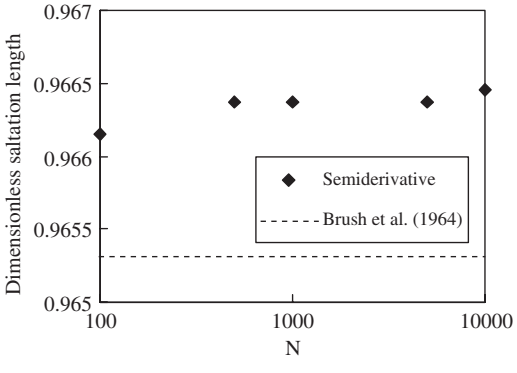


Figure 3. Dimensionless jump length as computed using the semi-derivative method and Brush et al.'s (1964) method. $R_p = 53$. $\tau_* = 0.056$.

Copyright © 2006 Taylor & Francis Group plc, London, UK

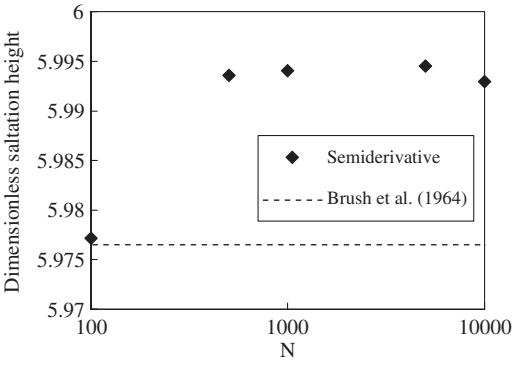


Figure 4. Dimensionless jump height as computed using the semi-derivative method and Brush et al.'s (1964) method. $R_p = 53$. $\tau_* = 0.056$.

approximations is less than 0.5%, which indicates a very good agreement between both methods. In addition to providing a close estimate to the Basset force, this methodology reduces the computational time by 20% as compared with the Brush et al.'s method. (In these computations, the forces of buoyancy, virtual mass, drag and Basset were considered.)

4 MEMORY TIME PERIOD IN THE BASSET FORCE

The integral associated with the Basset force must be performed, by definition, between the beginning of times and the current time of the computation. The integration of the particle relative acceleration along the simulation time requires a large storage capacity that could eventually make the simulation inviable. Since it can be assumed that the collision of the particle with the wall may likely eliminate correlation between velocities in jumps separated by long distances, it seems reasonable to consider that only the most recent events influence the current particle velocity (see Mei (1990)). It is thus reasonable to assume that the effect produced by far away events with respect to the current particle velocity could be disregarded.

Considering the previous argument, a new Basset integral definition is proposed. The approximation of this term is given by the following expression:

$$\int_0^T \frac{\frac{du_{ri}}{dt}}{\sqrt{T-t}}\,dt \approx \int_{T-T_{back}}^{T} \frac{\frac{du_{ri}}{dt}}{\sqrt{T-t}}\,dt \qquad (8)$$

where T_{back} represents the time interval where the history of the particle affects the current particle velocity. There is no formal definition for T_{back}; however this "memory time period" should be related to certain particle time scales and/or flow characteristic times.

The behavior of particles is controlled by the particle time scale τ_p – particle relaxation time- which, from the steady state balance between inertia and the linear Stokes drag, is defined as:

$$\tau_p = \frac{\rho_s d^2}{18\nu} \qquad (9)$$

Large particle characteristic times are associated with large particle sizes and denote large particle inertia (large particles require a large amount of time to modify its trajectory under any flow change). On the other hand, small particle time scales (associated with small particles) indicate that the particle rapidly changes its trajectory under a change of flow conditions.

In order to define a flow characteristic time, it is necessary to study the flow structures that may affect the particle trajectory close to a boundary. The term coherent structure is used to represent a spatial flow pattern that remains identifiable for some period of time, such us ejection and sweep motions. Experiments with sediment particles by Niño & García (1996) indicated that these structures maintain their identity for as long as 60 to 80 wall time units, and extend vertically a distance of about 100 wall units. Using dimensional analysis, a flow characteristic time is defined herein using these concepts:

$$\tau_f = 80\frac{u_*^2}{\nu} \qquad (10)$$

To define the value of T_{back}, two methods are proposed, as explained below.

Model 1

The memory time T_{back} is obtained by choosing the biggest value between the particle relaxation time and the flow characteristic time, and then multiplying it by a factor C.

Model 2

An alternative definition for T_{back} can be obtained by considering the memory time in terms of a number of previous jumps. If N_{back} is the number of jumps considered in the computation of the Basset term, the value of T_{back} is defined from the beginning of the N_{back}^{th} jump.

In order to compare the results obtained from both approximations to T_{back}, the code was run using the semi-derivative approximation for the Basset force for a simulation time equal to 1,000 non dimensional units. In this case only drag, virtual mass, Basset and buoyancy terms were considered. Values for $R_p = 100$ and $\tau_* = 0.056$ were used. Initial conditions for both models were identical. Both approximations are compared in terms of average particle jump height and

Copyright © 2006 Taylor & Francis Group plc, London, UK

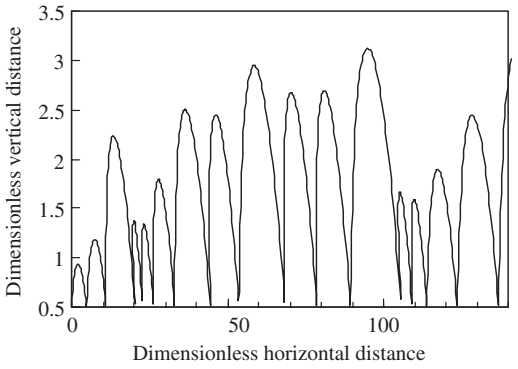


Figure 5. Simulated succession of saltations. $R_p = 100$. $\tau_* = 0.056$.

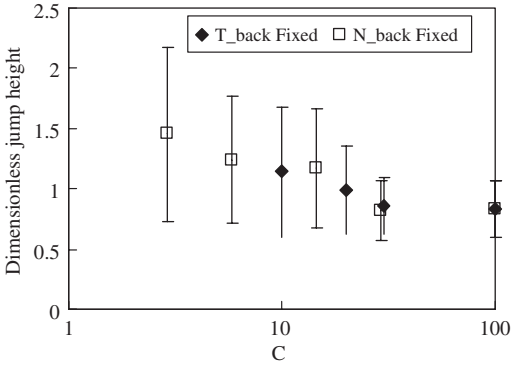


Figure 6. Comparison of the average jump height computed using the semi-derivative approximation for the Basset force. Multiple jumps (stochastic collisions). $R_p = 100$. $\tau_* = 0.056$.

length. These 1,000 time units are equivalent for these flow conditions to approximately 50 particle jumps. In order to compare both results, the results obtained from the second model are presented in terms of an equivalent value of the factor C. The stochastic collision model causes the height and length of each jump to be different, such that statistically- meaningful parameters can be obtained, as it is observed in Figure 5.

Figures 6 and 7 present the results obtained in terms of average jump length and height respectively. The intervals denote the range of jump heights or lengths. The number of times that the particle/flow time is considered in the Basset integral is given by C. We notice that fixing a number of particle or fluid time scales (whichever is larger) gives similar results than using a number of previous steps, clearly indicating that there is a loss of correlation between current and previous jumps. The value of C equal to 100 represents the computation of the Basset term from the beginning of the particle movement (T-T_{back} equal to 0).

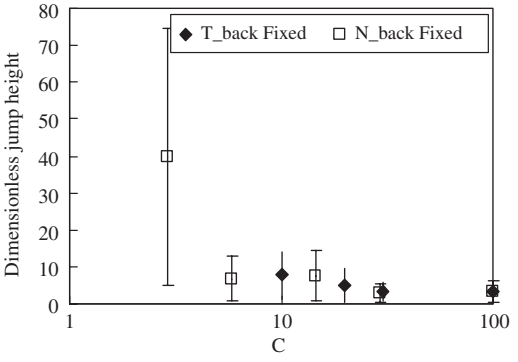


Figure 7. Comparison of the average jump length computed using the semi-derivative approximation for the Basset force. Multiple jumps (stochastic collisions). $R_p = 100$. $\tau_* = 0.056$.

5 FURTHER RESULTS

In order to have a better definition of the necessary number of previous jumps to be considered in the Basset term, a series of additional simulations were performed, covering a wider range of values of R_p and τ^*.

Vojir & Michaelides (1994), Niño & García (1996), Mordant & Pinton (2000), Armenio & Fiorotto (2001) have shown the importance of the Basset force in the definition of the trajectory of small particles. Considering the particle characteristics used by these authors in their analysis, we considered very small particle sizes and flow velocity between 0.07 and 0.5 m/s in our simulations. Electro- chemical forces, that are present in the case of very small particles, have been left outside of the analysis for this paper.

We decided to run the program for a long simulation time (1,000 dimensionless time units) in order to have a significantly large number of jumps to study, independent of the initial conditions of the particle. A *reference* simulation was defined (i.e., calculating the Basset integral from the beginning of the particle motion) which was represented with a value of N_{back} equivalent to 500. The reference simulation provides the value of the Basset integral classically defined, as the integration of the whole particle history. Simulations using values of N_{back} equal to 100, 50, 25, 10 and 5 were compared with the reference simulation to analyze the influence of this parameter in the precision of the Basset integral.

For each parameter of study (particle velocity and jump length and height), we specified an interval consisting of one deviation standard with respect to the average value of the reference simulation (drawn as dashed horizontal lines in each figure). This interval helps to determine the degree of departure of the Basset integral computed with a limited number

Copyright © 2006 Taylor & Francis Group plc, London, UK

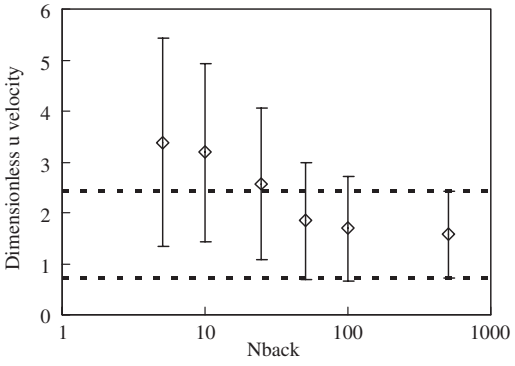


Figure 8. Average dimensionless horizontal velocity u vs. number of jumps in the past (N_{back}). $R_p = 100$. $\tau_* = 0.056$.

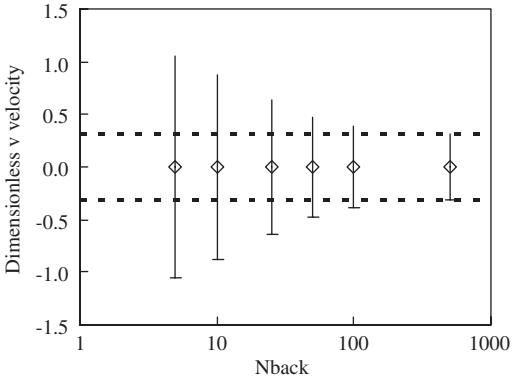


Figure 9. Average dimensionless vertical velocity v vs. number of jumps in the past (N_{back}). $R_p = 100$. $\tau_* = 0.056$.

of previous jumps, as compared with the reference simulation.

To analyze how the value of N_{back} affects value of the Basset integral, the following criterion was established: if the average value of the parameter to study lie inside of the interval defined by the reference simulation (dashed lines) then the value of N_{back} affects the value of the Basset integral little. Therefore, we are interested in defining the minimum value of N_{back} that affects little the value of Basset integral in order to reduce the computation time of the simulation under different particle and flow conditions. Three different simulations were performed, as it is described below.

5.1 *First run*

The first run was performed using a value of R_p equal to 100 and a value of τ_* equal to 0.056. The results are presented in Figures 8 to 11. In each figure, the dotted lines represent the reference range.

Figure 8 shows that for a value of N_{back} equal to 25 the average horizontal velocity is outside of the

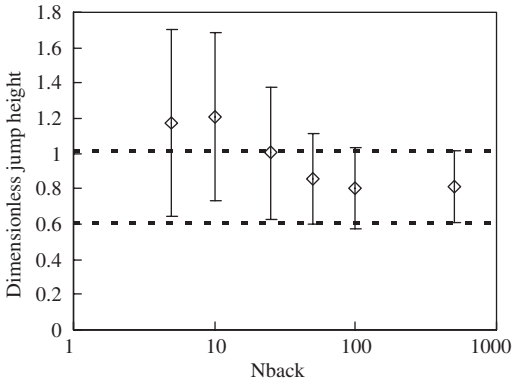


Figure 10. Average jump height vs. number of jumps in the past (N_{back}). $R_p = 100$. $\tau_* = 0.056$.

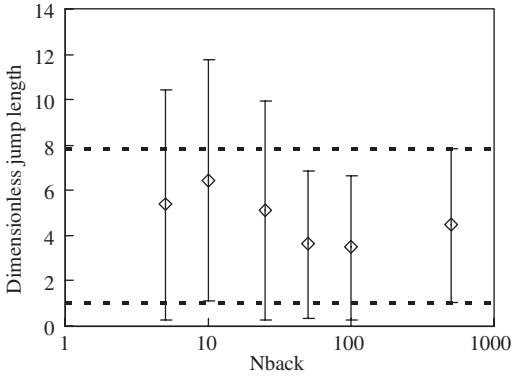


Figure 11. Average jump length vs. number of jumps in the past (N_{back}). $R_p = 100$. $\tau_* = 0.056$.

reference interval. However, all the remaining figures show that for N_{back} equal to 25 the average parameter value is inside this interval. Therefore a values of N_{back} equal to 50 or 75 particle jumps seems appropriate under these conditions.

Another important result is obtained from this simulation: the computational time is reduced in approximately 70% of the original simulation time using a reduced integration time.

5.2 *Second run*

The second run was performed using a value of Rp equal to 100 and a value of τ_* equal to 0.28. Even though the simulation time is large, the total number of jumps obtained for the reference simulation is only 22. The results are presented in Figure 12.

Results depicted in Figure 12 show that for a value of N_{back} equal to 5 the average jump length lays outside the reference interval. It seems that a more appropriate

Copyright © 2006 Taylor & Francis Group plc, London, UK

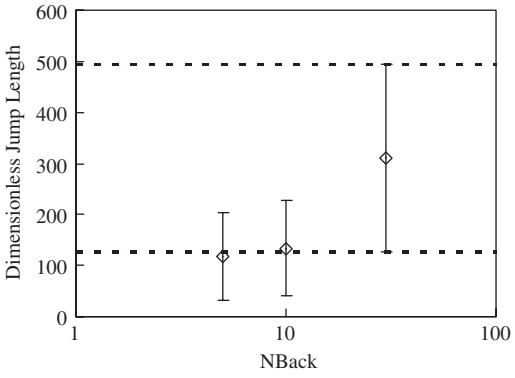


Figure 12. Average jump length vs. number of jumps in the past (N_{back}). $R_p = 100$. $\tau_* = 0.28$.

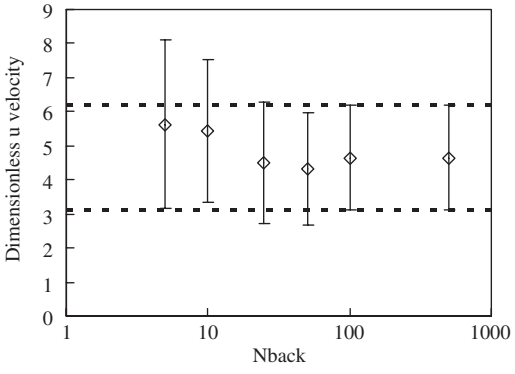


Figure 13. Average dimensionless horizontal velocity u vs. number of jumps in the past (N_{back}). $R_p = 100$. $\tau_* = 0.11$.

value for N_{back} is 10; however the number of jumps simulated does not allow for a conclusive result.

5.3 *Third run*

The third and last run was performed using a value of R_p equal to 100 and a value of τ_* equal to 0.11. The results are presented in Figures 13 to 16.

In Figures 13 to 16, for all the parameters studied, the reference range is large enough to contain all the values of N_{back} evaluated. However, selecting a number of jumps between 10 and 25, it is possible to argue that a satisfactory compromise between computing time reduction and representation of the integral (the physics of the problem) has been achieved.

5.4 *Time reduction*

The simulation time directly depends on the value of N_{back} selected for each simulation: the smaller the value of N_{back}, the smaller the simulation time is.

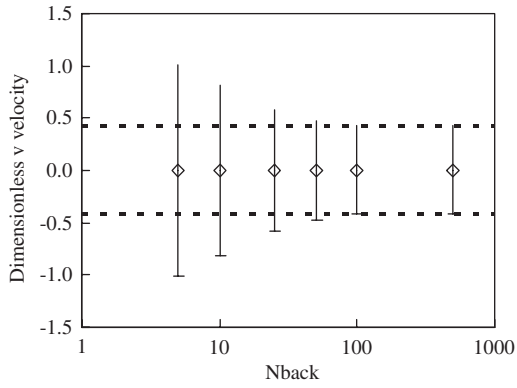


Figure 14. Average dimensionless vertical velocity v vs. number of jumps in the past (N_{back}). $R_p = 100$. $\tau_* = 0.11$.

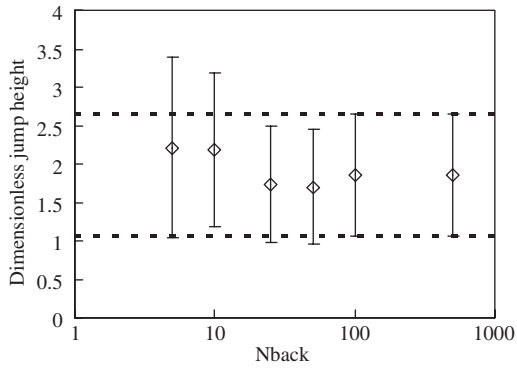


Figure 15. Average jump height vs. number of jumps in the past (N_{back}). $R_p = 100$. $\tau_* = 0.11$.

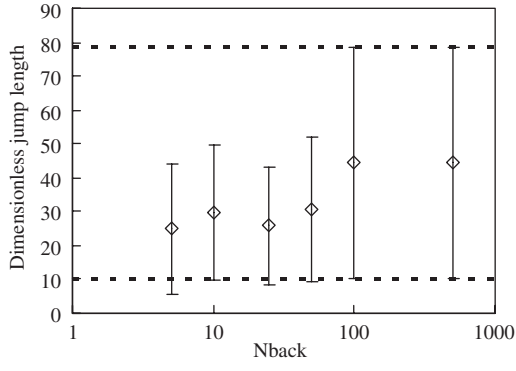


Figure 16. Average jump length vs. number of jumps in the past (N_{back}). $R_p = 100$. $\tau_* = 0.11$.

Figure 17 shows the reduction in time of a simulation of 100 particle jumps using different values of N_{back} compared with the computational time used in the reference simulation.

Copyright © 2006 Taylor & Francis Group plc, London, UK

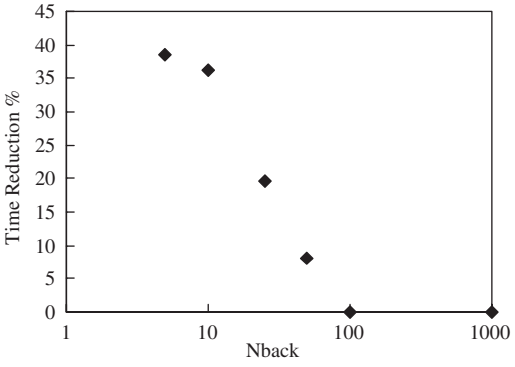


Figure 17. Simulation time decrease, in percentage, vs. N_{back}. The run considers 100 particle jumps.

6 CONCLUSIONS

Computations of particle trajectories in fluids are in general relatively affordable using Lagrangian approaches. However, these calculations could be very time consuming due to the Basset integral, which considers the contribution of the particle history. This term has a relatively large importance for small particles. In this paper we have discussed an alternative to minimize its computational time. The use of a semi-derivative approximation to calculate the Basset integral was found to reduce the computational time by 30%. In addition, this method is simple to implement and it does not require any assumption on the velocity flow field.

In order to reduce further the computational time, we have proposed to reduce the integration time considered in the Basset integral. It has been assumed that only events occurring to the particle in the proximities of the current time are relevant. The concept of T_{back}, the memory time period, has been introduced, i.e., the interval of time where the history of the particle affects the current particle movement.

Two different approaches were devised: to calculate T_{back} considering a fluid-particle characteristic time or considering a determined number of previous jumps in the particle trajectory.

In order to study the minimum number of jumps that affects little the value of the Basset integral, three different simulations were performed. The simulations were performed considering a small particle size (under flow conditions equivalent to 0.07–0.5 m/s).

We concluded that the minimum number of past jumps to be considered in the Basset term varies between 25 and 50, depending on flow conditions. Very importantly, the approximation of the Basset force using the T_{back} concept reduces the computational time of the code, between 70 to 90 percent of the original simulation time.

The results obtained in this paper provide important information for the development of numerical models for particle motion close to the river beds, which is the long term goal of our project.

REFERENCES

Abramowitz, M. & Stegun, I. 1970. *Handbook of mathematical functions*. New York: Dover Publications Inc.

Armenio, V. & Fiorotto, V. 2001. The importance of the forces acting on particles in turbulent flows. *Physics of Fluids*. 13 (8): 2437–2440.

Brush, J.S., Ho, H.W. & Yen, B.C. 1964. Acceleration motion of sphere in a viscous fluid. *ASCE J. Hydraulic Division.* 90: 149–160.

González, A.E. 2006. Study of the influence of Basset force in small particles. Unpublished.

Maxey, M.R. & Riley J.J. 1983. Equation of motion for a small rigid sphere in a nonuniform flow. *Physics of Fluids*. 26: 883–889.

Mei, R. 1990. Particle dispersion in isotropic turbulence and unsteady particle dynamics at finite Reynolds number. *PhD Thesis.* Urbana-Illinois: University of Illinois at Urbana-Champaign.

Mordant, N. & Pinton, J.F. 2000. Velocity measurement of a settling sphere. *The European Physical Journal B.* 18: 343–352.

Niño, Y. & García, M. 1994. Gravel Saltation. 2. Modeling. *Water Resources Research.* 30 (6): 1915–1924.

Niño, Y. & García, M. 1996. Experiments on particleturbulence interactions in the near-wall region of an open channel flow: implications for sediment transport. *J. Fluid Mech.* 326: 285–319.

Niño, Y. & García, M. 1998. Using Lagrangian particle saltation observation for bedload sediment transport modeling. *Hydrol. Process.* 12: 1197–1218.

Oldham, Y. & Spanier, M. 1974. *The fractional calculus*. New York: Academic Press.

Portela, L. & Oliemans, R. 2003. Eulerian-Lagrangian DNSLES of particle-turbulence interactions in wall bounded flows. *Int. J. for Numerical Methods in Fluids*. 43: 1045–1065.

Schmeeckle, M.W. & Nelson, J.M. 2003. Direct numerical simulation of beadload transport using a local, dynamic boundary condition. *Sedimentology* 50: 279–301.

Sekine, M. & Kikkawa, H. 1992. Mechanics of saltation grains II. *ASCE J. of Hydraulic Engineering Division.* 104: 1303–1321.

Sommerfeld, M. 1992. Modelling of particle-wall collisions in confined gas-particle flows. *Int. J. Multiphase Flow*. 18: 905–926.

Sommerfeld, M. 2003. Analysis of collision effects for turbulent gas-particle flow in horizontal channel: Part I: Particle transport. *Int. J. Multiphase Flow*. 29: 675–699.

Ten Cate, A., Dersksen, J., Portela, L. & Van Den Akker, H. 2004. Fully resolved simulations of colliding monodisperse spheres in forced isotropic turbulence. *J. Fluid Mech*. 519: 233–271.

Tatom, F.B. 1988. The Basset term as a semiderivative. *Applied Scientific Research* 45: 283–285.

Vojir, D.J. & Michaelides, E.E. 1994. Effect of the History term on the motion of rigid spheres in a viscous fluid. *Int. J. of Multiphase Flow.* 20 (3): 547–556.

Copyright © 2006 Taylor & Francis Group plc, London, UK

Modelling sorting over the lee face of individual bed forms

Astrid Blom
University of Twente, Water Engineering & Management, The Netherlands

Maarten G. Kleinhans
University of Utrecht, Fac. Geosciences, Dept. Physical Geography, The Netherlands

ABSTRACT: River dunes, alternate bars, and subaqueous deltas are often characterised by a lee face at about the angle of repose. Transport of mixed-size sediment over the crest of such a bed form results in grain size-selective deposition of particles over the lee face. The complex interaction between two different deposition mechanisms, i.e. grain fall from suspension and grain flows at nearly the angle of repose, results in coarse particles preferentially depositing at the lower elevations of the lee face, and fine particles at the upper ones. In this study we develop a simple empirical model describing the sorting of particles over the lee face of a bed form. This lee face sorting model is calibrated and verified on data from flume experiments with deltas and dunes. Field data of lee face sorting over dunes in an ebb-tide dominated mouth bar of the river Teign, UK, are used to validate the model. The lee face sorting model describes the grain size-selective deposition over a lee face well, although the model does not reproduce the deposition of fines from suspended load which slightly modifies the sorting by producing a fine deposit at the base of the bed forms.

1 INTRODUCTION

Migrating river dunes composed of mixed sediment are characterised by various types of sediment fluxes (Kleinhans 2002, Blom et al. 2003): (1) deposition of particles over the lee face; (2) the formation of coarse bed layers underneath migrating dunes; (3) the winnowing of fines from the trough surface and subsurface; and (4) vertical sediment fluxes due to the variability in bed form trough elevations. This paper focusses on the first mechanism, viz. the deposition process on the lee side of individual bed forms and the sediment sorting therein. Erosion of sediment from the stoss side and deposition of the eroded sediment on the lee side make a dune migrate downstream. In dunes and bars, sediment is commonly sorted over the lee face in an upward fining manner (e.g. Bagnold 1941, Allen 1965, Kleinhans 2004). This macroscopic sorting results from various microscopic sorting processes.

First, sediment settles from the bed load and suspended sediment in the flow expansion downstream of the brinkpoint (Fig. 1). Most of the sediment deposits just downstream of the brinkpoint but a smaller amount, notably the finer grades, settle further downstream (Jopling 1965, Jopling 1967). This sediment may be preserved as a toe or bottomset. In this settling process, the deposit is fining in the downstream direction and consequently along the lee slope of the dunes. The grain fall process continues to build up a wedge on the lee side of the dune until the static angle of repose is reached.

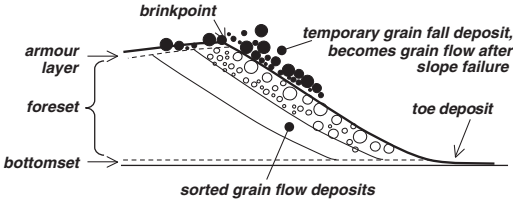


Figure 1. Sorting and definitions in dune deposits. The stoss side of the dune is eroded. The eroded sediment is deposited just downstream of the brinkpoint until the slope fails and the grains flow down the slope and becomes sorted. The toe deposit from settled suspended sediment is sometimes preserved as a bottomset.

Second, when the static angle of repose is exceeded, the slope fails and the remobilised sediment avalanches down the slope as a grain flow (Allen 1965, Hunter and Kocurek 1986). During the grain flows on the lee side, the sediment is sorted such that the larger grains deposit further down the lee slope and smaller grains deposit near the top of the dunes. In subaqueous dunes, mostly the grain flow deposits are preserved

Copyright © 2006 Taylor & Francis Group plc, London, UK

(Kleinhans 2004), so the sorting in grain flows determines the sorting in dunes. This process is only indirectly affected by the flow conditions; it is mostly a process of slope failure of a noncohesive sediment.

When the grain flow commences, kinematic sieving takes place. The mixture dilates because the grains vibrate in the motion. The smaller grains percolate downwards through the increased pores of the dilated mixture. In this process the larger grains are pushed upwards. So, the sorting is coarsening-upwards in the incipient grain flow (Kleinhans 2005). Next, the large grains roll further down the slope than the small grains, because large grains on a bed of small grains roll much more easily than small grains on a bed of large grains (Makse 1997). Hence, the fine sediment of the incipient grain flow deposits near the top of the dune, whereas the coarse sediment deposits further down the slope (Kleinhans 2005).

Experiments with sediment mixtures deposited as laboratory deltas[1] demonstrate that the sorting process can be very efficient: almost no coarse sediment is deposited near the top and almost no fine sediment is deposited near the bottom, except the sediment mixed in from the grain fall. This was found for both well- and poorly sorted mixtures (Kleinhans 2005). Sometimes grain flows do not travel down the whole lee slope at once, but subsequent grain flows re-entrain this sediment and continue the sorting process. Also, protruding large grains from the previous grain flow are dragged down the slope by the next grain flow, which further increases the vertical sorting efficiency (Kleinhans 2005).

A model describing the grain size-selective deposition over the lee face of individual dunes is particularly useful as part of a new type of sediment continuity model for rivers dominated by dunes and sediment mixtures (Blom and Parker 2004, Blom et al. 2006). In a morphodynamic river model, such a sediment continuity model describes the interaction among grain size-selective sediment transport, sorting processes and changes in mean bed level. Hirano (1971) was the first to develop a sediment continuity model for sediment mixtures. Parker et al. (2000) made a step forward by developing a sediment continuity model based on a probability density function of active bed surface elevations rather than discrete and homogeneous bed layers. Blom and Parker (2004) and Blom et al. (2006) have extended the Parker et al.

Blom and Parker (2004) propose a simple empirical model describing the grain size-selective deposition over the lee face of individual dunes. The formulation by itself was not properly calibrated and validated, as Blom et al. (2006) calibrate the complete sediment continuity model, including the sub-model of lee face sorting, upon data from a small number of flume experiments. Although the lee face sorting model acted reasonably well for these flume experiments, the model appeared to behave problematically for situations in which the sediment mixture becomes uniform. Kleinhans (2005) proposes a simple empirical model describing the variation of the arithmetic mean grain size down the lee face of individual bed forms. Yet this model does not satisfy the laws of mass conservation of the various grain size fractions in the mixture. This paper presents an improvement to the Blom et al. (2006) lee face sorting model, which is based on a relatively large set of data on sorting over lee faces of individual bed forms.

2 PARAMETER DEFINITIONS

This section lists the main parameters and definitions used in the present paper. We use the same notation as used by Blom and Parker (2004). The quantity $F_{leeloci}$ denotes the volume fraction content of size fraction i in the sediment deposited at elevation z at the bed form lee face. As we assume the density of the grains not to depend on grain size, grain size distributions based on volume fractions are equal to the measured grain size distributions by weight. The lee sorting function w_i determines to what extent a specific size fraction that is transported over the bedform crest is deposited at a certain elevation of the lee face and is defined as

$$\omega_i = F_{leeloci}/F_{leei} \tag{1}$$

where F_{leei} denotes the volume fraction content of size fraction i in the lee deposit.

A first constraint to the lee sorting function is that integration of the composition of the deposited sediment over the lee face, $F_{leeloci}$, must result in the composition of the lee face deposit, F_{leei}:

$$F_{leei} = \frac{1}{\Delta}\int_{\eta_b}^{\eta_t} F_{leeloci}\, dz \tag{2}$$

where Δ, η_b, and η_t denote bed form height, bed form trough elevation, and bed form crest elevation, respectively. Two other constraints are

$$\sum_i^N F_{leeloci} = 1 \qquad 0 \le F_{leeloci} \le 1 \tag{3}$$

where N denotes the number of grain size fractions. Equation (3) expresses that, at each bed elevation, the total volume fraction content of all size fractions must equal unity and the volume fraction content of each size fraction must be larger than or equal to zero and smaller than or equal to unity.

[1] A delta is here defined as a slope at about the angle of repose over which sediment is deposited when the water depth suddenly and largely increases, due to, for instance, a river flowing into a deep lake or ocean. (2000) sediment continuity model to conditions dominated by dunes.

Copyright © 2006 Taylor & Francis Group plc, London, UK

Table 1. Data sets considered in the development of the lee face sorting model.

Data set	Type bedform	Flume or field	Mixture characteristics	Reference
Calibration				
Klein05a	deltas	flume	natural	Kleinhans (2005)
Klein05b	deltas	flume	artificial	Kleinhans (2005)
Blom03a	dunes	flume	artificial, tri-modal	Blom et al. (2003)
Verification				
Klein02	dunes	flume	natural	Kleinhans (2002)
Termes86	deltas	flume	natural	Termes (1986)
BlomKl	dunes	flume	natural (Rhine)	Blom et al. (2003), Kleinhans (2002)
Validation				
SantKl05	dunes	field	natural	Van Santen and Kleinhans (2005)

Based on earlier analyses of measured sorting profiles (Kleinhans 2004, Kleinhans 2005, and Blom et al. 2003) and following the approach by Blom and Parker (2004), we assume that a size fraction is deposited over this uniformly sloped lee face with its volume fraction content *decreasing or increasing linearly with elevation*, and propose the following form for the lee sorting function, ω_i:

$$\omega_i = (1 + \delta_i z^*) \tag{4}$$

where z^* is a dimensionless vertical co-ordinate relative to the average elevation of the lee face:

$$z^* = (z - \eta_a)/\Delta \tag{5}$$

where η_a denotes mean bed level. By definition, for triangular dunes $z^* = -1/2$ at the lower limit of the lee face and $z^* = 1/2$ at the upper limit of the lee face. The lee sorting parameter δ_i depends on grain size, and Equations (1) and (4) show that it is defined as:

$$\delta_i = \frac{d\omega_i}{dz^*} = \frac{1}{F_{leei}} \frac{dF_{leeloci}}{dz^*} \tag{6}$$

It can be found that (1) together with (4) indeed meets the constraint in (2).

Another important parameter is the arithmetic mean grain size of the lee deposit, ϕ_{mlee}:

$$\phi_{mlee} = \sum_i^N \phi_i F_{leei} \tag{7}$$

where ϕ_i denotes the grain size of size fraction i on ϕ-scale[2]:

$$\phi_i = -^2\log\left(\frac{d_i}{d_{ref}}\right) \tag{8}$$

[2] Equation (8) equals the conventional manner in which the arithmetic mean grain size is calculated. Yet this is the mathematically correct notation, as logarithms cannot be taken of nondimensionless parameters. As a result, the arithmetic grain size (ϕ) is correctly dimensionless.

where d_i denotes grain size, and in which the reference grain size d_{ref} equals 1 mm. The arithmetic standard deviation of the lee deposit, σ_a, and the dimensionless bed shear stress, τ^*, are defined by, respectively

$$\sigma_a^2 = \sum_i^N (\phi_i - \phi_{mlee})^2 F_{leei} \tag{9}$$

$$\tau^* = \tau / [(\rho_s - \rho) g d_{mlee}] \tag{10}$$

where the geometric mean grain size of the lee deposit, d_{mlee}, is given by

$$d_{mlee} = d_{ref}\, 2^{-\phi_{mlee}} \tag{11}$$

and where the bed shear stress, τ, is determined from

$$\tau = \rho\, g\, a\, s \tag{12}$$

where a denotes water depth and s energy slope. Note that in case of the laboratory deltas (Kleinhans 2005, Termes 1986), the shear stress is based on the water depth and energy slope just upstream from the delta face.

3 FLUME AND FIELD DATA

Table 1 lists the data sets applied in the calibration, verification, and validation of the lee face sorting model. The 'Klein05a', 'Klein05b', and 'Termes86' data sets consider sorting over the lee faces of laboratory deltas, while the other data sets consider sorting over the lee faces of dunes. In the data sets natural sediment mixtures are used, except for the 'Klein05b' and 'Blom03a' data sets. All experiments were dominated by bed load transport. The amount of suspended load transport was negligible (data set 'Blom03a', see Blom et al., 2003) to very limited (other data sets).

For all lee faces in the data sets listed in Table 1, Figure 2 shows the following parameters: (1) the geometric mean grain size of the lee deposit, d_{mlee}; (2) the

Copyright © 2006 Taylor & Francis Group plc, London, UK

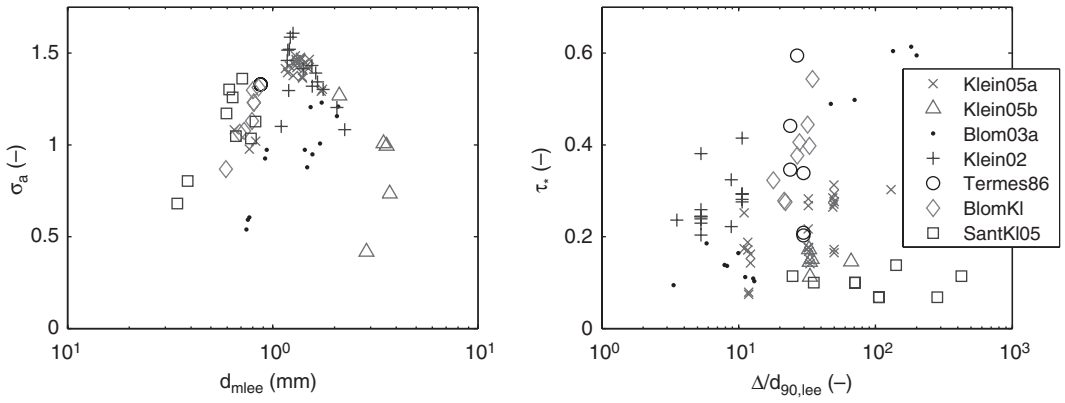


Figure 2. (a) Relation between the geometric mean grain size of the lee deposit, d_{mlee}, and the arithmetic standard deviation of the lee deposit, σ_a. (b) Relation between the ratio of bed form height, Δ, to the d_{90lee} of the lee deposit and the dimensionless shear stress, τ^*. The data sets are listed in Table 1. Each data point denotes one lee face.

arithmetic standard deviation of the lee deposit, σ_a; (3) the ratio of bed form height, Δ, to the d_{90} of the lee deposit[3]; and (4) the dimensionless shear stress, τ^*. For a detailed description of the data sets, we refer to the publications listed in Table 1.

4 MODEL FOR LEE FACE SORTING

In this section we propose a new empirical model for lee face sorting.We now define the relative grain size, ϕ_{rel}, which indicates the difference in the arithmetic grain size of size fraction i and the arithmetic mean grain size of the lee deposit:

$$\phi_{rel} = \phi_i - \phi_{mlee} \tag{13}$$

Figure 3 shows the relation between the relative grain size, ϕ_{rel}, and the lee face sorting parameter, δ_i, for the experimental data used in the calibration phase. The figure confirms that if the grain size on ϕ-scale of size fraction i, ϕ_i, is smaller than the arithmetic mean grain size of the lee deposit ($\phi_i < \phi_{mlee}$), the lee face sorting parameter, δ_i, is negative. In other words, if size fraction i is coarser than the geometric mean grain size of the lee deposit, the size fraction shows a preference to be deposited at the lower elevations of the lee face. The figure also shows that a size fraction finer than the geometric mean grain size of the lee deposit ($\phi_i > \phi_{mlee}$) shows a preference for the upper elevations of the lee face.

Note that for values of the relative grain size larger than unity the scatter is relatively large. This seems to be partly due to the larger probability of these size fractions being deposited from grain fall forming a fine

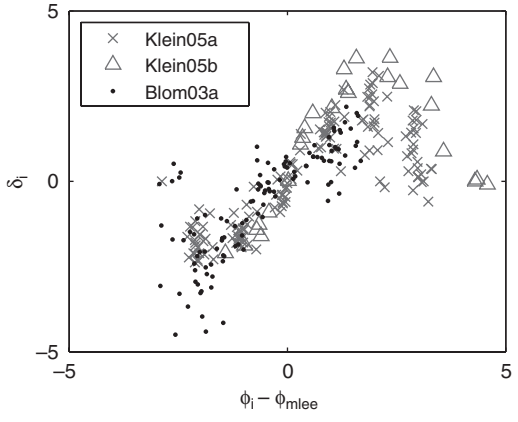


Figure 3. Relation between the relative grain size, ϕ_{rel}, and the lee sorting parameter, δ_i, for the experimental data used in the calibration phase.

toe set, which significantly influences the sorting trend of the size fractions over the lee face. Figure 3 shows that, if the grain size of a size fraction becomes equal to the geometric mean grain size of the lee deposit ($\phi_i = \phi_{mlee}$), the lee face sorting parameter, δ_i, equals about zero, which means that the sorting of this size fraction over the lee face is negligible. In other words, the size fraction will be deposited over the lee face uniformly.

To find out whether the parameter δ_i/ϕ_{rel} is influenced by other factors, Figure 4 shows its relation with (a) the dimensionless shear stress, τ^*, and (b) the arithmetic standard deviation of the lee deposit, σ_a. Although there is experimental evidence that the sorting trend becomes smaller with increasing shear stress due to capture of suspended sediment (Allen 1965, Kleinhans 2005), this does not cause a significant

[3] The d_x denotes the grain size for which x% of the sediment mixture is finer.

Copyright © 2006 Taylor & Francis Group plc, London, UK

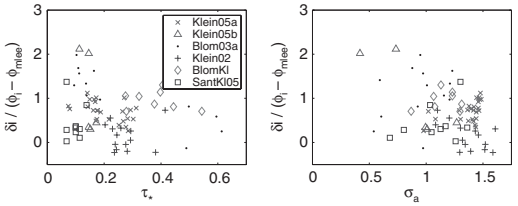


Figure 4. Lack of relation between the ratio of the lee sorting parameter, σ_i, to the relative grain size, ϕ_{rel}, and (a) the dimensionless shear stress, τ^*, and (b) the arithmetic standard deviation of the lee deposit, σ_a, for all data sets listed in Table 1 except 'Termes86'. Here each data point denotes one lee face.

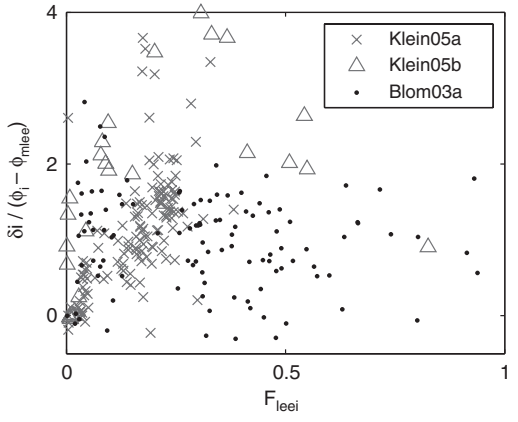


Figure 5. Relation between the ratio of the lee sorting parameter, δ_i, to the relative grain size, ϕ_{rel}, and the volume fraction content of the size fraction in the lee deposit, F_{leei}, for the experimental data used in the calibration phase.

deviation of the general sorting trend (Figure 4a). We therefore neglect the dependency of the lee sorting parameter on shear stress. Figure 4b shows that the arithmetic standard deviation of the lee deposit, σ_a, does not have a clear effect on lee face sorting.

Figure 5 shows the relation between the ratio between the lee sorting parameter δ_i and ϕ_{rel} and the volume fraction content of the size fraction in the lee deposit, F_{leei}. It appears that, besides its effect on the arithmetic mean grain size of the lee deposit (see Eq. (7)), F_{leei} affects lee face sorting also in another way: the ratio of δ_i to ϕ_{rel} appears to approach zero when F_{leei} approaches zero (Fig. 5). This can be understood as follows. If F_{leei} of size fraction i approaches zero, the preference of this size fraction for either upper or lower elevations of the lee face must decrease to zero. In other words, the size fraction will be distributed over elevations uniformly. Otherwise the volume fraction content of this size fraction in the deposit at elevation z^*, $F_{leeloci}$, may become smaller than zero, which is

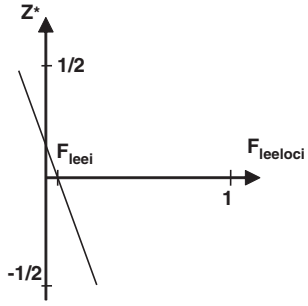


Figure 6. Physically unrealistic variation of the volume fraction content of size fraction i in the lee face deposit at elevation z^**, $F_{leeloci}$, for a relatively coarse size fraction for which the volume fraction content of the size fraction in the lee deposit, F_{leei}, approaches zero. This illustrates the fact that the lee sorting parameter, δ_i, should approach zero when F_{leei} approaches zero.

physically unrealistic. The latter situation is presented in Figure 6.

Summarizing, we have the following requirements for the new lee face sorting model:

- The relation between the lee sorting parameter, δ_i, and the relative grain size, ϕ_{rel}, seems to be more or less linear.
- If the grain size of size fraction i equals the arithmetic mean grain size ($\phi_i = \phi_{mlee}$), then δ_i should approach zero.
- For the range of data considered here, no obvious relation is observed between the lee sorting parameter, δ_i, and bed form height, Δ, between δ_i and the dimensionless shear stress, τ_*, and between δ_i and the standard deviation of the mixture, σ_a.
- If the mixture becomes uniform ($F_{leei} = 1$ and $\phi_i = \phi_{mlee}$.), then δ_i should approach zero.
- If the volume fraction of size fraction i in the lee deposit approaches zero ($F_{leei} = 0$), then δ_i should approach zero.

We now propose the following model for the lee sorting parameter, δ_i, which fulfills the above requirements:

$$\delta_i = a\, F_{leei}^{b}\, (\phi_i - \phi_{mlee'}) \tag{14}$$

In order to have (14) fulfill the constraint given by (3a), an 'adapted' arithmetic mean grain size of the lee deposit, $\phi_{mlee}0$, now needs to be defined:

$$\phi_{mlee'} = \frac{\sum_i^N \phi_i F_{leei}^{(1+b)}}{\sum_i^N F_{leei}^{(1+b)}} \tag{15}$$

As in the next few sections we will compare predictions by the new lee face sorting model to predictions

Copyright © 2006 Taylor & Francis Group plc, London, UK

by the model by Blom et al. (2006), we show their definition of the lee face sorting parameter:

$$\delta_i = \gamma \frac{\phi_i - \phi_{mlee}}{\sigma_a} (\tau_b^*)^{-\kappa} \quad (16)$$

where $\gamma = 0.3$ and $\kappa = 0.5$. The constant γ weights the relative importance of the grain-size term on the right-hand side of (16), while the value of $\cdot$ sets the relative importance of the dimensionless bed shear stress term.

5 MODEL CALIBRATION

For the model predictions, the volume fraction content of size fractions transported over the bed form crest, F_{leei}, is used as input and is determined from the measured sorting profile over the lee face, $F_{leeloci}$, according to (2). For the experimental data used in the calibration phase, we have derived a best fit of Equation (14) for $a = 2.1$ and $b = 0.43$. Now Figure 7 shows the relation between the measured values for the lee sorting parameter δ_i according to (6) and predicted values for δ_i, for the experimental data used in the calibration phase. In the left-hand plot δ_i is predicted according to the lee face sorting model by Blom et al. (2006) (Eq. (16)), and in the right-hand plot according to the new model (Eqs. (14) and (15)). Note that optimal predictions would result in the relation represented by the line.

The mean prediction error e of both models is calculated from:

$$e = 1/M \sum_{1}^{M} \sqrt{((\delta_{i,meas} - \delta_{i,calc})^2)} \quad (17)$$

where M denotes the number of data points. For the Blom et al. (2006) model the mean prediction error e equals 0.91, while for the new model the mean prediction error equals 0.73, which means a significant improvement of the present model with respect to the one by Blom et al. (2006). Note that the predicted sorting of the natural mixtures (data set 'Klein05a') agrees somewhat better with the measured data than the artificial mixtures (data sets 'Klein05b' and 'Blom03a').

Figures 8, 9, and 10 shows the predicted sorting profiles (lines) together with the measured ones (symbols), for a selection of lee sides from the data sets 'Klein05a', 'Klein05b', and 'Blom03a', respectively. The model shows fine results for the natural mixtures in Figure 8, while for the artificial mixtures in Figure 9 the predicted sorting is somewhat smaller than the measured one. The model shows reasonable results for the artificial tri-modal mixtures in Figure 10.

6 MODEL VERIFICATION

Figure 11 shows the relation between the the measured values for the lee sorting parameter δ_i according to (6) and predicted values for δ_i, for the experimental data used in the verification phase (data sets 'Klein02' and 'BlomKl'). Data set 'Termes86' is not included in Figure 11, as measured volume fraction contents of size fractions over the lee faces are not available. Therefore measured values for δ_i cannot be determined.We can see that for data set 'BlomKl' the predicted sorting improves with respect to the model by Blom et al. (2006), while for data set 'Klein02' the predicted sorting is too strong and worse with respect to the model by Blom et al. (2006). The latter is perhaps due to the fact that the height of the dune faces was relatively small with respect to the d_{90} (also see Fig. 2b). In other words, the lee face height was only a few of

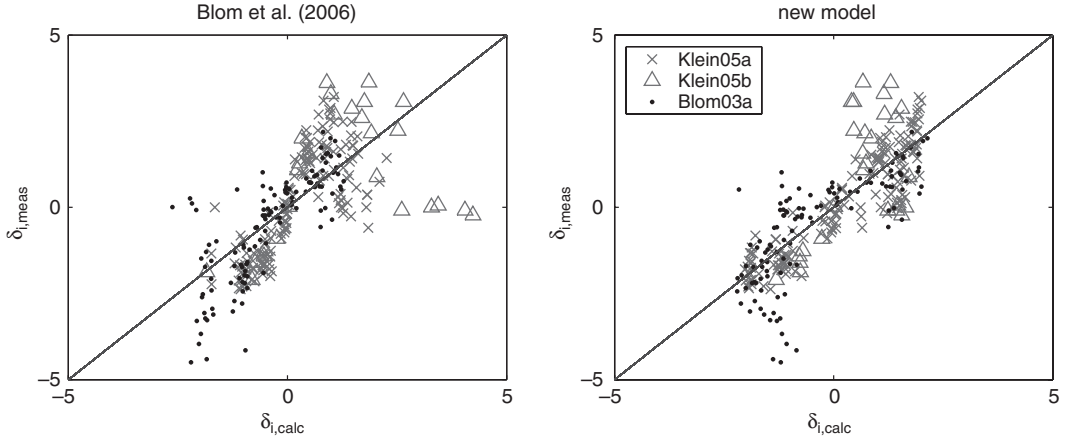


Figure 7. Relation between the predicted and measured values for the lee sorting parameter, δ_i, for the experimental data used in the calibration phase.

Copyright © 2006 Taylor & Francis Group plc, London, UK

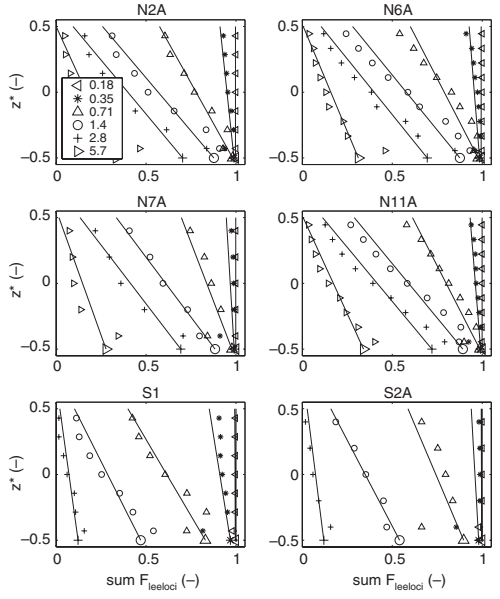


Figure 8. Volume fraction contents of grain size fractions deposited down lee faces of laboratory deltas composed of natural mixtures; selection from data set 'Klein05a' (Kleinhans, 2005). Measured volume fraction contents are indicated by the symbols and computed ones by the lines. The large marker at the lower limit of a line indicates the specific geometric grain size, which is shown in the legend (in mm). The volume fraction content of a specific size fraction is indicated by the difference between two lines or two types of symbols. For instance, the volume fraction content of the 2.8 mm fraction is indicated by the difference between the crosses and the triangles pointing right.

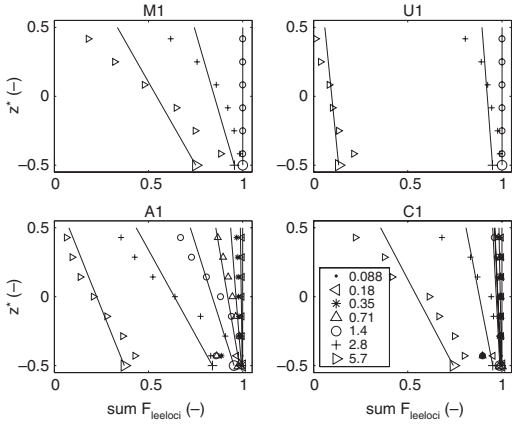


Figure 9. Volume fraction contents of grain size fractions deposited down lee faces of laboratory deltas composed of artificial mixtures; selection from data set 'Klein05b' (Kleinhans, 2005). For explanation of the figure, see the caption of Figure 8.

the d_{90} grains high, which decreased the effectivity of the sorting process.

For the flume experiments conducted by Termes (1986) on sorting down laboratory delta faces, only data on the variation of the d_{10}, d_{50}, and d_{90} over the lee face was available. For the model prediction, the composition of the lee deposit, F_{leei}, was assumed equal to sediment fed at the upstream end of the flume. Figure 12 shows the predicted and measured values for d_{10}, d_{50}, and d_{90} over the lee face. Although the delta height varied between the experiments, the measured data is plotted in a single figure, as dune height does not significantly affect the predicted sorting profile. The predicted sorting profile does not vary between the experiments. For data set 'BlomKl', Figure 13 shows that the measured sorting of size fractions is not always linear. Yet the predicted sorting profiles shows reasonable agreement with the data. For data

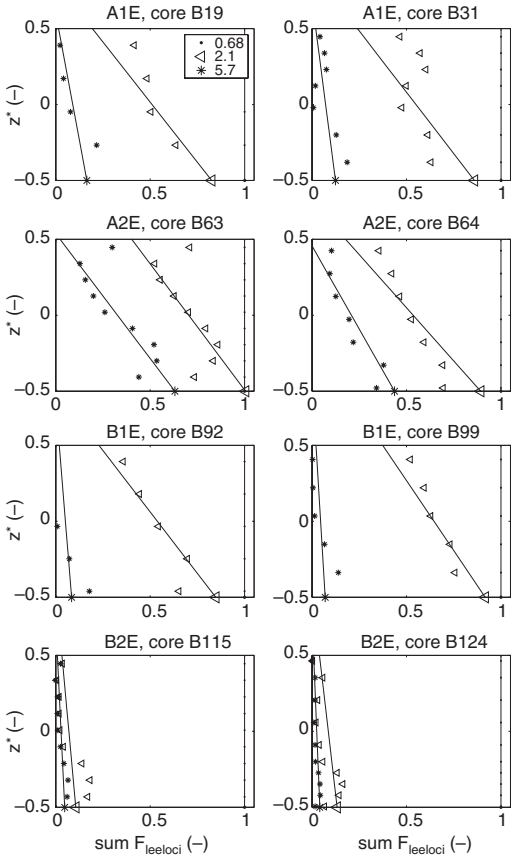


Figure 10. Volume fraction contents of grain size fractions deposited down lee faces of laboratory dunes composed of artificial mixtures; selection from data set 'Blom03a' (Blom et al., 2003). For explanation of the figure, see the caption of Figure 8.

Copyright © 2006 Taylor & Francis Group plc, London, UK

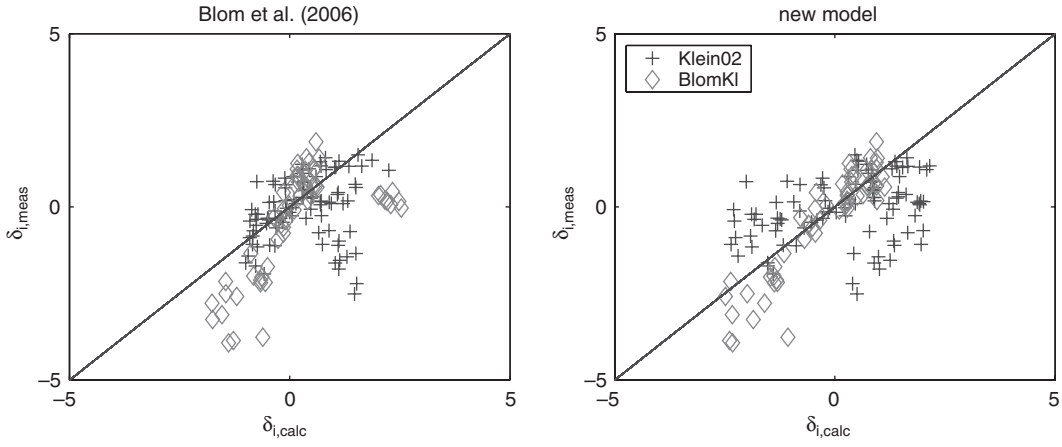


Figure 11. Relation between the predicted and measured values for the lee sorting parameter, δ_i, for the experimental data used in the verification phase.

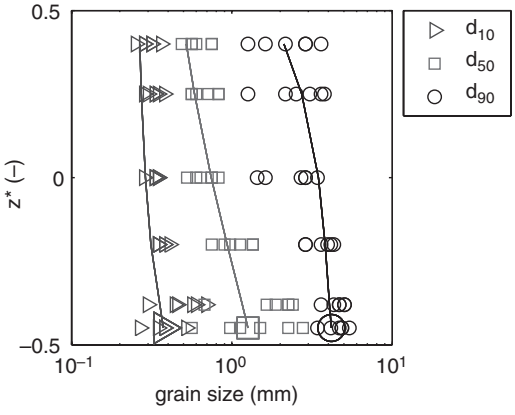


Figure 12. Measured and predicted sorting down lee faces of laboratory deltas. Data set 'Termes86' (Termes, 1986).

set 'Klein02', the predicted sorting is much stronger than the measured one (Fig. 14).

7 MODEL VALIDATION

Data from an ebb-tide dominated mouth bar of the river Teign at Teignmouth, UK (Van Santen and Kleinhans 2005) is used to validate the model (Fig. 15). Although the measured deposition of grain sizes does not always show a linear trend with lee face elevation, the results are quite satisfactory.

8 DISCUSSION

The proposed lee face sorting model (Eqs. (1), (4), and (14)) describes sorting due to grain flows. It

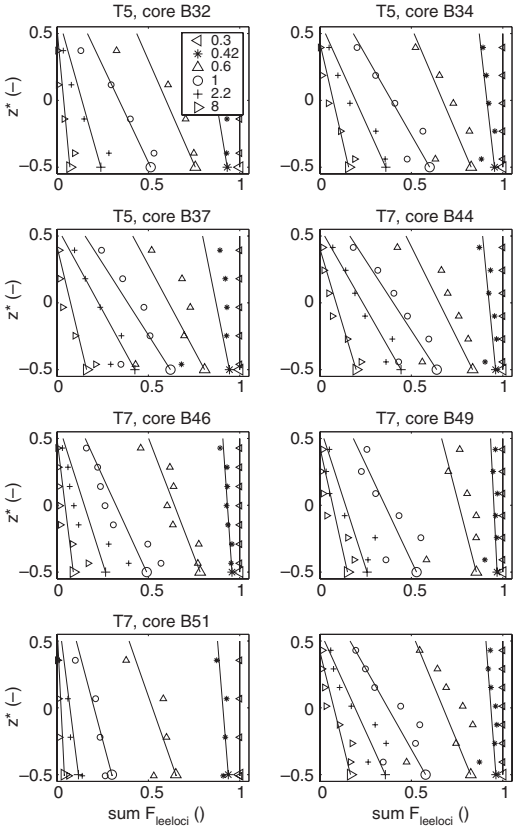


Figure 13. Volume fraction contents of grain size fractions deposited down lee faces of laboratory dunes; selection from data set 'BlomKl99' (Blom et al., 2003, Kleinhans, 2002). For explanation of the figure, see the caption of Figure 8.

Copyright © 2006 Taylor & Francis Group plc, London, UK

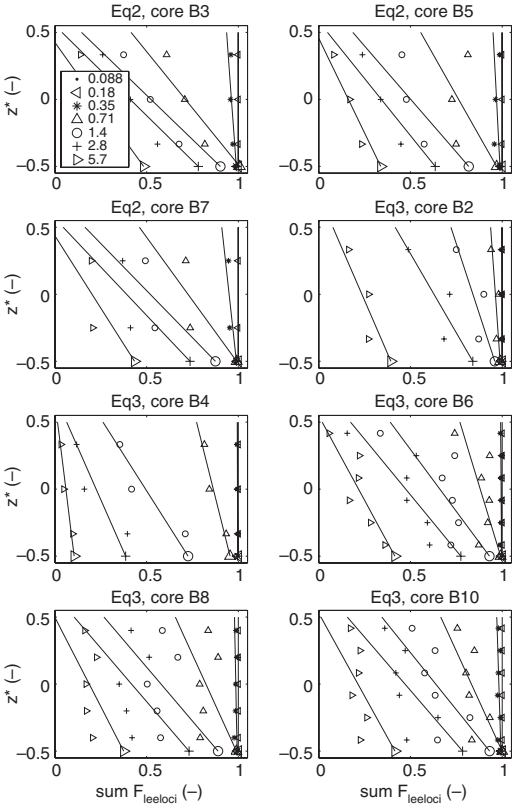


Figure 14. Volume fraction contents of grain size fractions deposited down lee faces of laboratory dunes; selection from data set 'Klein02' (Kleinhans, 2002). For explanation of the figure, see the caption of Figure 8.

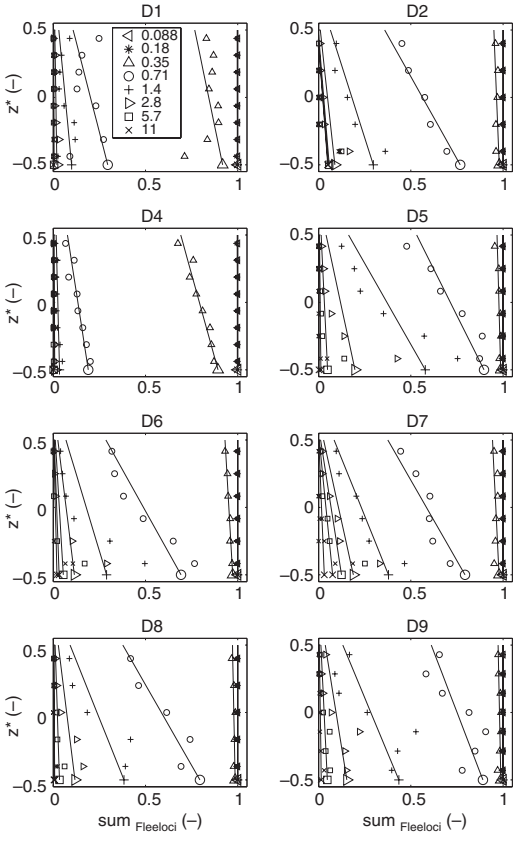


Figure 15. Volume fraction contents of grain size fractions deposited down the ebb-tide dominated mouth bar of the river Teign; selection from data set 'SantKl05' (Van Santen and Kleinhans, 2005). For explanation of the figure, see the caption of Figure 8.

essentially predicts that the sediment is sorted linearly and as efficiently as possible. Of the coarsest sediment, almost nothing is deposited near the top and and a maximum amount near the bottom of the dune, while its deposition rate over the lee face decreases almost linearly with elevation. For the finest finest sediment passing the bed form crest the opposite is valid, as observed most clearly in the deltas of the 'Klein05a' runs (Figs. 8. This efficient sorting breaks down when the grain flow process breaks down. On one end of the spectrum, the grain flow ceases to occur on lee faces with a height smaller than a few times the largest grains, where a lee slope at the angle of repose is difficult to observe anyway. Consequently, in very low dunes and bed-load sheets the sorting is less than perfectly efficient, as observed in the 'Klein02' runs (Fig. 14). The less efficient sorting can also be expected in bed load sheets. On the other end of the spectrum, the lee slope becomes so long that the grain flows do not make it to the bottom of the slope. Instead, they halt at some point and are later rejuvenated by a next grain flow. This situation is expected for very high bars or large and complex deltas, but not for the range of heights of river dunes commonly considered in modelling river morphodynamics.

The present work is limited to conditions with dominant bed load transport. The proposed lee face sorting model describes sorting by grain flows at the angle of repose, which are initiated by the sediment delivered to the brinkpoint of the dune. For the deltas, the water depth over the delta was very small compared to the basin depth. The suspended sediment was therefore strongly decelerated by the flow expansion over the lee side and deposited near the top where it was mixed and sorted into the grain flow. The flow is much deeper, however, over dunes, so that the deceleration is much less important and the grains are suspended over a range of heights. The coarsest sediment will settle fast and deposit near the top, but the finer grades will settle only slowly and mix into the toe and trough

Copyright © 2006 Taylor & Francis Group plc, London, UK

zones (Jopling 1965). In other words, the addition of sediment by grain fall depends on the concentration profile of the suspended sediment, and on the flow expansion over the dune troughs. This process cannot straightforwardly be described by the present lee face sorting model, because it requires a dependence on shear stress for the suspension process, and a dependence on dune height, which depends on water depth (and to some extent on shear stress).

9 CONCLUSIONS

In this study a simple and empirical model for lee face sorting was developed. In the model and in most observations, the deposition of fines over the lee face decreases linearly with elevation (and vice versa for coarse material). The proposed model is suitable for lee faces of dunes and deltas for which the deposition process is dominated by grain flows. If the finer part of the transported sediment is suspended, it may settle on the lower lee face or at the toe. This modifies the sorting profiles to a non-linear shape and may create a fine bottom set in deltas and bars. This process cannot straightforwardly be implemented in the present lee face sorting model, which limits the applicability to conditions in which the lee face deposition is dominated by grain flows (also see Section 1). In the experiments, we found no significant differences in the measured sorting profiles between dunes and deltas except for the finest fractions, indicating that the grain flow sorting process is the same.

For the conditions considered in this analysis, the standard deviation of the mixture and the dimensionless shear stress appear not to affect the sorting profile. For higher values of the shear stress, however, we expect the sorting trend to become smaller with increasing shear stress. The dune height appears not to affect the sorting mechanism. Yet for small values of the ratio of dune height to the d_{90}, (Δ/d_{90lee}) in combination with a relatively high shear stress, which is valid for data set 'Klein02' (see Fig. 2b), the observed sorting trends appear to be significantly smaller than the ones predicted by the new lee face sorting model.

For very small parameters of the volume fraction content of a size fraction in the lee deposit (F_{leei}), the size fraction does not show a preference for certain elevations of the lee face and is distributed over the lee face uniformly. This effect has been incorporated in the present version of the model.

ACKNOWLEDGEMENTS

The authors thank Pim van Santen for granting them permission to use data from a field measurement campaign in the river Teign, UK. The research of the first author is supported by the Technology Foundation STW, applied science division of the Netherlands Organisation for Scientific Research (NWO) and the technology programme of the Ministry of Economic Affairs (VENI grant TCB.6286). The research by the second author is supported by the Netherlands Earth and Life sciences Foundation (ALW) with financial aid from the Netherlands Organisation for Scientific Research (grant ALW-VENI-863.04.016).

REFERENCES

Allen, J. R. L. (1965). Sedimentation to the lee of small underwater sand waves: an experimental study. *J. Geology 73*, 95–116.

Bagnold, R. A. (1941). *The physics of blown sand and desert dunes*. New York: Methuen.

Blom, A. and G. Parker (2004). Vertical sorting and the morphodynamics of bedform-dominated rivers: A modeling framework. *J. Geophys. Res. 109*. F02007, doi:10.1029/2003JF000069.

Blom, A., G. Parker, J. S. Ribberink, and H. J. de Vriend (2006). Vertical sorting and the morphodynamics of bedform-dominated rivers: An equilibrium sorting model. *J. Geophys. Res. 111*. F01006, doi:10.1029/2004JF000175.

Blom, A., J. S. Ribberink, and H. J. de Vriend (2003). Vertical sorting in bed forms: Flume experiments with a natural and a trimodal sediment mixture. *Water Resour. Res. 39*(2). 1025, doi:10.1029/2001WR001088.

Hirano, M. (1971). River bed degradation with armouring. *Transactions Jap. Soc. Civ. Eng. 3*(2), 194–195. Hunter, R. E. and G. Kocurek (1986). An experimental study of subaqueous slipface deposition. *J. Sed. Petrology 56*(3), 387–394.

Jopling, A. V. (1965). Laboratory study of the distribution of grain sizes in cross-bedded deposits. In G. V. Middleton (Ed.), *Primary sedimentary structures and their hydrodynamic interpretation, Spec. Publ., 12*, Oklahoma, USA. Soc. of Econ. Paleontologists and Mineralogists.

Jopling, A. V. (1967). Origin of laminae deposited by the movement of ripples along a streambed: a laboratory study. *J. Geology 75*, 287–305.

Kleinhans, M. G. (2002). *Sorting out sand and gravel: sediment transport and deposition in sand-gravel bed rivers*. Ph. D. thesis, Utrecht University.

Kleinhans, M. G. (2004). Sorting in grain flows at the lee-side of dunes. *Earth Science Reviews 65*, 75– 102. 10.1016/S0012-8252(03)00081-3.

Kleinhans, M. G. (2005). Grain-size sorting in grain- flows at the lee side of deltas. *Sedimentology 52*, 291311. doi: 10.1111/j.1365-3091.2005.00698.x.

Makse, H. A. (1997). Stratification instability in granular flows. *Phys. Rev. E 56*(6), 7008–7016.

Parker, G., C. Paola, and S. Leclair (2000). Probabilistic Exner sediment continuity equation for mixtures with no active layer. *J. Hydraul. Eng. 126*(11), 818– 826.

Termes, A. P. P. (1986). Vertical composition of sediment in a dune. Technical Report R657-XXX, Delft Hydraulics, Delft, the Netherlands.

Van Santen, P. and M. G. Kleinhans (2005). Extreme bedform variation at an active ebb-tidal delta. In *Book of Abstracts, Fluvial Sedimentology VIII, Delft, Netherlands*.

Copyright © 2006 Taylor & Francis Group plc, London, UK

Entrapment of fines in coarse sediment beds

B.G. Krishnappan & P. Engel
National Water Research Institute, Environment Canada, Burlington, Ontario, Canada

ABSTRACT: In this paper, a fine sediment entrapment study using a rotating, circular flume is described. An existing flocculation and settling model was modified for the analysis of the experimental data. An entrapment coefficient, relating the rate of entrapment to the settling rate of sediment at the sediment-water interface, was introduced in this study for the first time. It was applied as one of the boundary conditions to the model and determined through model calibration using the experimental data. The entrapment coefficient obtained in this study was found to depend on the bed material type when the bed sediment was immobile. But, when the bed sediment was mobile, the coefficient depended on both bed material type and bed shear stress. A systematic study is planned to determine the plane bed entrapment coefficient for different bed material types and bulk hydraulic characteristics.

1 INTRODUCTION

Entrapment of fine sediment in coarse river bed substrate impacts on both the roughness characteristics of the river bed and the quality of river habitat. Fine sediment fills the interstitial space and changes the grain size distribution of the material forming the bed layer. It also alters the porosity and permeability of the stream bed, which in turn can have an effect on the ecology in the hyporheic zone. Ecological studies carried out in spawning streams in England and Wales have implicated deposited fines for the decline of salmonid fisheries (Olsson & Persson (1988); Acornley & Sear (1999)). Egg-to-hatching success of salmonids is strongly influenced by the rate of supply of the dissolved oxygen and the rate of removal of carbon dioxide and metabolic wastes, which are governed by the permeability of the spawning beds (Hausel & Coble (1976); Iwomoto et al. (1978); Turnpenny & Williama (1980)). Intra gravel movement and eventual emergence of newly hatched fry or alevins are controlled by the porosity of the spawning beds. Excessive accumulation of fine sediment can block the interstitial pathways, smother the surface of the gravel and cause concretion of the spawning substrate (Philips et al. (1975); Crisp (1993)).

Entrapment of fines in coarse gravel beds has been studied extensively in the laboratory and to a limited extent in the field (Elliott and Brooks (1997a); (1997b); Packman et al. (2000a); (2000b); Fernald et al. (2001); Marion and Bellinello (2002); Packman and Mackay (2003); Zaramella and Packman (2003); Marion et al. (2004)). Laboratory studies have been carried out primarily in straight channels with bed-forms. These studies have led to the formulation of a bed-form induced advective pumping model to calculate the colloid exchange between the water column and the hypoheic zone (Packman et al. (2000); (2004)). In this model, the dynamic head variation along the stream bed, due to the presence of bed-forms, was considered as the driving force for the subsurface flow in the hyporheic zone. Assuming a sinusoidal variation for the dynamic head and using Darcy's law, Elliott and Brooks (1997) derived a theoretical expression for the advective subsurface flow field. The induced advective pore water flow carries the fine sediment through and out of the bed. The net exchange of fine sediment from the stream into the hyporheic zone takes place because of the settling velocity of the sediment particles and the sediment immobilization in the bed due to the filtration effect (Packman et al. (2000)).

The infiltration effect described in the above model depends on the steepness of bed-forms. As the steepness of the bed-forms decreases, the advective flow velocity decreases and becomes zero when the bed is plane. Therefore, the pumping model described above will fail to treat the entrapment of fines under plane bed conditions. Experimental studies of entrapment of fine sediment under plane bed conditions are limited. Therefore, to fill this knowledge gap, a new research program has been initiated at the National Water Research Institute in Burlington, Ontario, Canada. Fine sediment entrapment experiments are being carried out using a rotating circular flume. The experimental data are analyzed using a modified flocculation and settling model that was formulated for predicting the fine sediment transport characteristics in rotating circular flume assemblies

Copyright © 2006 Taylor & Francis Group plc, London, UK

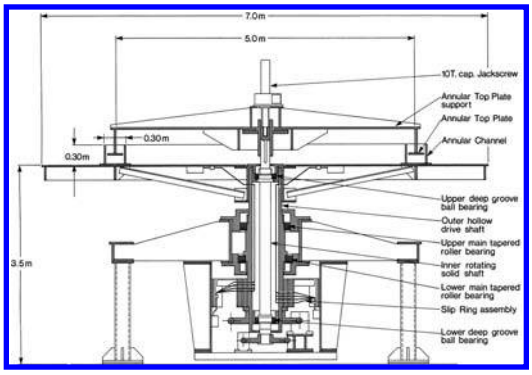


Figure 1. Schematic representation of the rotating circular flume.

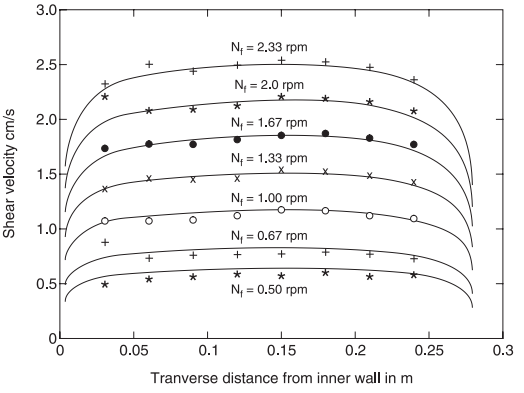


Figure 2. Bed shear stress distributions across the flume.

(Krishnappan & Marsalek (2002)). The details of the experimental program and the model are outlined in this paper.

2 EXPERIMENTAL PROGRAMME

2.1 *Rotating circular flume*

The entrapment experiments are being carried out in a rotating, circular flume. The flume is 5.0 m in mean diameter, 0.30 m wide and 0.30 m deep. It rests on a rotating platform, which is 7.0 m in diameter. A counter rotating top cover (ring) fits inside the flume with close tolerance, (∼1.5 mm gap on either side) and it makes contact with the water surface in the flume. The maximum rotational speeds of the flume and the ring are 3 rpm respectively. Figure 1 shows a schematic view of the flume and the complete details of the flume can be found in Krishnappan (1993).

The flows generated in the flume are nearly two dimensional and the bed shear stress distribution across the width of the flume is fairly uniform as can be seen in Figure 2. In this figure, the bed shear stresses are plotted as a function of transverse distance across the width of the flume with rotational speed, N_f as a parameter. The ring speed, N_R had to be slightly larger than the flume speed in order to minimize the secondary circulations. For the tests shown in this figure, the ratio N_R to N_f was maintained at 1.167. The flume bed surface was smooth and the depth of water in the flume was 0.12 m. The points are measured values and the lines represent predictions from a three dimensional, hydrodynamic model called PHOENICS (Rosten & Spalding (1984)). It can be seen from this figure that the model predictions agree very well with the measured data. The model is used as an operating tool to predict the relationship between the bed shear stress and the rotational speeds of the flume assembly under both smooth and rough bed conditions (Krishnappan & Engel (2004)).

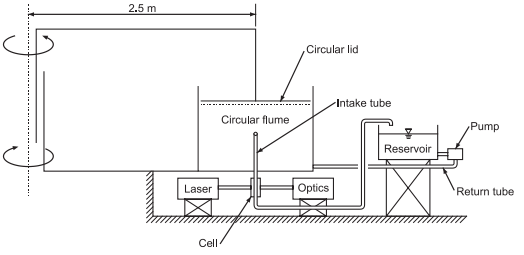


Figure 3. Schematic representation of the arrangement of the Malvern Particle Size Analyzer mounted on the flume.

The flume is equipped with a Malvern Particle Size Analyzer for measuring the size distribution of sediment flocs in suspension. The instrument is placed directly underneath the flume as shown schematically in Figure 3. A short tube connects the sampling point to the sample cell. The sample is drawn through the sample cell continuously by gravity. The sample, after passing through the sample cell, flows into a reservoir from where it is pumped back into the flume. The instrument operates on the principle of diffraction of a laser beam. As the beam crosses the sample in the sampling cell, the light is diffracted by the particles in the sample. The diffraction pattern is then measured using a light sensitive sensor consisting of a series of photodiodes mounted in semi circular arcs. A microprocessor in the instrument converts the diffraction pattern into a particle size distribution using the Fraunhofer diffraction theory (Weiner (1984)).

2.2 *Experimental procedure*

For an entrapment experiment, the flume bed was covered with coarse gravel of a certain size to a certain thickness. The flume was then filled with tap water to a depth of 0.12 m above the top surface of the gravel layer. The flume was operated at a speed high

Copyright © 2006 Taylor & Francis Group plc, London, UK

Table 1. Summary of experimental conditions of the entrapment tests.

Test no.	Bed material size (D_{50}) in mm	Bed shear stress in Pa
1	8	0.3
2	8	0.7
3	1	0.2
4	1	0.4
5	0	0.17
6	0	0.33

enough to keep the injected sediment in suspension for about 20 minutes. During this time, a thick slurry of kaolin was injected into the flume. Care was taken to maintain the water level in the flume by pumping the excess water out. The rate of pumping was equal to the rate of slurry injection, and therefore, the top cover maintained contact with the water surface at all times. After the injection of kaolin, the flume and the ring speeds were lowered to a level commensurate with the desired bed shear stress, and maintained at that level for the duration of the experiment. An experiment lasted about five hours. During this time, the kaolin concentration in the water column and the size distribution of the kaolin particles were monitored at regular intervals of time. The concentration of kaolin was determined by collecting samples, which were then dried and weighed. The size distributions were obtained with the Malvern Particle Size Analyzer. Altogether, six experiments were conducted for three different bed conditions and two different bed shear stresses. These test conditions are summarized in Table 1.

2.3 *Experimental results*

The concentration variation as a function of time for all the six tests is shown in Figure 4. From this figure, one can see that the entrapment of kaolin occurs in both 8 mm gravel and 1 mm sand beds. When comparing the concentration variation of the impervious runs with those for porous beds, one can see that entrapment occurs in plane, porous beds. As expected, it is more pronounced in the 8 mm gravel than in the 1 mm sand. Furthermore, the data in Figure 4 show that the bed shear stress also plays a role in the entrapment of fine sediment in porous beds.

3 THEORETICAL CONSIDERATIONS

The results of the entrapment experiments were analyzed using a mathematical model that was developed for analyzing the fine sediment transport processes in a rotating circular flume (Krishnappan & Marsalek (2002)). According to this model, the motion of the

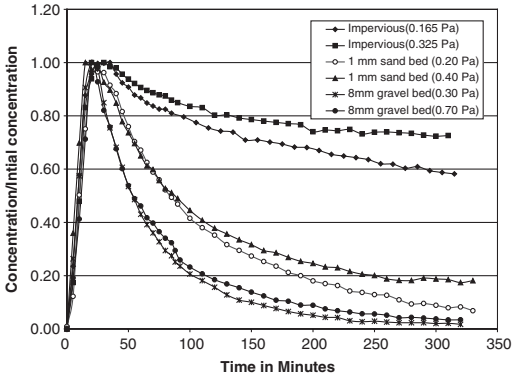


Figure 4. Concentration vs time curves for all the six tests summarized in Table 1.

settling sediment is considered as a two stage process: a transport or a settling stage and a flocculation stage. The model is adopted to examine the entrainment process by incorporating a new boundary condition for the settling stage of the model. Some of the salient features of the model, including the new boundary condition, are discussed here for the sake of completeness.

3.1 *Settling stage*

The governing equation for the settling stage was obtained from mass balance considerations, and assuming that the flow in the rotating flume is uniform in the longitudinal and tangential directions, the one dimensional mass balance equation as shown below was adopted.

$$\frac{\partial C_k}{\partial t} + w_k \frac{\partial C_k}{\partial z} = \frac{\partial}{\partial z}(\Gamma \frac{\partial C_k}{\partial z}) + S \qquad (1)$$

where, C_k is the concentration of kaolin in size fraction k, w_k is the settling velocity of that fraction and Γ is the dispersion coefficient in the vertical direction. The symbol t stands for time axis and the symbol z stands for the coordinate axis in the vertical direction. S is the source/sink term.

The boundary conditions used for the settling stage are as follows:

at the free surface:

$$- w_k C_k - \Gamma \frac{\partial C_k}{\partial z} = 0 \qquad (2)$$

at the bed:

$$- w_k C_k - \Gamma \frac{\partial C_k}{\partial z} = q_e + q_d + q_{entrap} \qquad (3)$$

The free surface boundary condition expresses the balance between the settling flux and the dispersive

Copyright © 2006 Taylor & Francis Group plc, London, UK

flux. In other words, there is no external input of sediment at this boundary. At the bed surface, it is assumed that the settling and dispersive fluxes are balanced by the net amount of sediment exchanged at the sediment-water interface. The sediment exchange at the sediment-water interface can occur in three ways. 1) Sediment can be eroded from the bed because of the shear stress induced by the flow and can be entrained into the water column (q_e). 2) Sediment can settle to the bed and stays at the bed as the deposited sediment (q_d). 3) Sediment can settle to the bed and a portion of the settled sediment gets into the pores of the bed sediment and become unavailable for further erosion and entrainment (q_{entrap}).

The first two components of the sediment exchange at the sediment water interface have been studied extensively in the literature. A number of formulations exist to quantify these components. For example, the erosion rate of fine sediment has been studied by Partheniades (1962); Mehta & Partheniades (1982); Parchure (1984) and Lick (1982) just to name a few. Deposition characteristics of fine sediment have been studied by Krone (1962); Mehta & Partheniades (1975); Lick (1982) among others. In this study, the approach proposed by Krone (1962) has been adopted. According to this approach, net deposition flux was calculated as:

$$q_d = Pw_s C_b \tag{4}$$

where P is a probability parameter which gives a measure of the probability that a floc, settling to the bed, stays at the bed. Krone (1962) proposed a relationship for P as:

$$P = (1 - \frac{\tau}{\tau_{crd}}) \tag{5}$$

where τ is the bed shear stress and τ_{crd} is the critical shear stress for deposition, which is defined as the bed shear stress above which none of the initially suspended sediment would deposit.

The third, entrapment component, is introduced for the first time in this study. It is assumed that this component is directly proportional to the settling flux near the bed and is expressed as:

$$q_{entrap} = \alpha w_s C_b \tag{6}$$

where α is the proportionality constant and is termed as the entrapment coefficient. The entrapment coefficient is expected to be a function of porosity of the gravel substrate, thickness of the gravel bed layer and the permeability of the substrate. It was determined in this study by fitting the model predictions to the measured concentrations in the water column. In other words, it was treated as a calibration parameter and was determined as part of the calibration process.

3.2 *Flocculation stage*

The flocculation stage was modeled on the basis of the coagulation equation (Fuchs (1964)) shown below:

$$\frac{\partial N(i,j)}{\partial t} = -\beta N(i,t)\sum_{j=1}^{\infty} K(i,j)N(j,t) + \frac{1}{2}\beta\sum_{j=1}^{\infty} K(i-j,j)N(i-j,j)N(j,t) \tag{7}$$

where $N(i,t)$ and $N(j,t)$ are number concentrations of particle size classes i and j respectively. $K(i,j)$ is the collision frequency function, which is a measure of the probability that a particle of size i collides with a particle of size j in unit time and β is the cohesion factor, which defines the probability that a pair of collided particles will coalesce and form a new floc. β accounts for the effects of cohesion properties such as the electrochemical properties of the sediment-water mixture, effects of polymers secreted by micro-organisms etc.. In this study, β is treated as an empirical parameter and was determined through the calibration of the model using experimental data.

The first term on the right side of equation (7) gives the reduction of particles in size class i because of flocculation of these particles in size class i with all other size classes. The second term gives the generation of new particles in the size class i because of flocculation of particles in smaller size classes. In this process the mass of particles is assumed to be conserved. Equation (7) was simplified by considering the particle sizes in discrete size classes as shown in Figure 5. In this figure, the continuous particle size space is considered in discrete size ranges. Each range is considered as a bin containing particles of certain size range. For example, r_1 is the geometric mean radius of particles in bin No.1. The particle ranges were selected in such a way that the mean volume of particles in bin i is twice that of the preceding bin. The volume ranges of the various size ranges are shown in Figure 5.

Under this scheme, when particles of bin i flocculate with particles in bin j ($j < i$), the newly formed

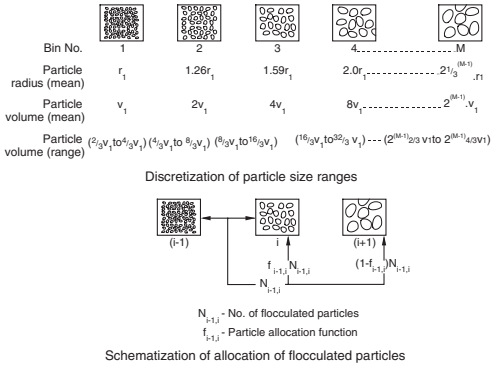


Figure 5. Schematic representation of flocculation stage.

Copyright © 2006 Taylor & Francis Group plc, London, UK

particles will fit into bins i and $i+1$. The proportion of particles going to these bins can be calculated by considering the mass balance of particles before and after flocculation. With this simplification, the coagulation equation can be expressed in discrete form as follows:

$$\frac{\Delta N_i}{\Delta t} = -\sum_{j \le i} \beta K(r_i, r_j) N_i N_j + \sum_{j<i} f_{i,j} \beta K(r_i, r_j) N_i N_j + \sum_{j<i-1} (1 - f_{i,j}) \beta K(r_i, r_j) N_{i-1} N_j \quad (8)$$

where $f_{i,j}$ is the allocation function given by:

$$f_{i,j} = (\rho_{s,i} V_i + \rho_{s,j} V_j - \rho_{s,i+1} V_{i+1}) / (\rho_{s,i} V_i - \rho_{s,i+1} V_{i+1}) \quad (9)$$

where, ρ_s denotes the density of the flocs and V is the volume of the flocs. The density of the flocs is dependent on their size of the flocs, and an empirical relationship proposed by Lau & Krishnappan (1997) was adopted in this study. The form of the relationship is as follows:

$$\rho_s - \rho = \rho_p \exp(-bD^c) \quad (10)$$

where ρ_s, ρ and ρ_p are densities of flocs, water and parent material forming the floc (the last one measured in water, i.e. submerged density) respectively. D is the diameter of the floc and b and c are empirical coefficients to be determined through model calibration. The settling velocity of flocs, needed for the settling stage of the particle motion, was calculated using the above density relation and Stoke's Law. The resulting expression is as follows:

$$w_k = (1.65/18) \exp(-bD_k^c) g D_k^2 / \upsilon \quad (11)$$

where g stands for acceleration due to gravity and υ stands for the kinematic viscosity of water.

The collision frequency function $K(i,j)$ takes different functional forms depending on the collision mechanisms that bring the particles to close proximity. The mechanisms considered in this study include 1) Brownian motion (K_b), 2) Turbulent fluid shear (K_{sh}), 3) Inertia of particles in turbulent flow (K_I) and 4) Differential settling of flocs (K_{ds}). An effective collision frequency function, K_{ef} was calculated in terms of the individual collision functions as follows:

$$K_{ef} = K_b + \sqrt{(K_{sh}^2 + K_I^2 + K_{ds}^2)} \quad (12)$$

The collision frequency functions for the individual collision mechanisms can be found in Valioulis & List (1984).

The break-up of flocs due to turbulent fluctuations of the flow was modelled using a scheme proposed by Tambo & Watanabe (1979). According to this scheme, a "collision-agglomeration" function was introduced as a multiplier to the collision frequency function, K_{ef}. This produced an effective collision frequency that resulted in an optimum floc size distribution for a given level of turbulence. The function proposed by Tambo and Watanabe is as follows:

$$\alpha_R = \alpha_0 (1 - \frac{R}{S+1})^n \quad (13)$$

where R is the number of primary particles contained in a floc and S is the number of particles contained in the biggest floc for the given level of turbulence. The parameters α_0 and n assume values of 1/3 and 6 respectively.

3.3 *Calibration of the model*

3.3.1 *Input parameters*

To model the flocs in different size classes, the initial size distribution of the flocs has to be known as well as the turbulent diffusion coefficient and the collision frequency functions.

The initial size distribution was obtained from the size distribution data measured using the Malvern Particle size analyzer. Typical data obtained for the kaolin used in the present experiments is shown in Figure 6.

The turbulent diffusion coefficient, Γ was assumed to be equal to the momentum diffusivity, which was determined by simulating flow characteristics in the rotating flume using the PHOENICS model (Rosten & Spalding (1984)). The PHOENICS model is a three dimensional hydrodynamic model and it employs the $\kappa - \varepsilon$ turbulence model to close the system of governing equations. From the predictions of flow characteristics, a cross sectional average value of Γ was computed and used in this study.

The collision frequency functions for the different collision mechanisms considered in the flocculation process were calculated using the flow characteristics

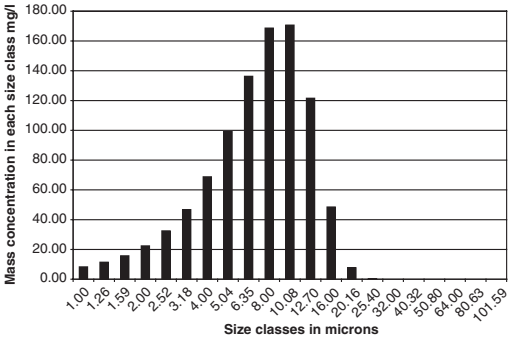


Figure 6. A typical size distribution of kaolin measured at the beginning of an experiment in the present study.

Copyright © 2006 Taylor & Francis Group plc, London, UK

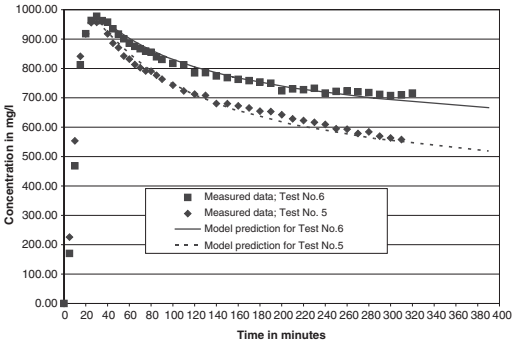


Figure 7. Comparison of model values and the measured data for impervious bed tests.

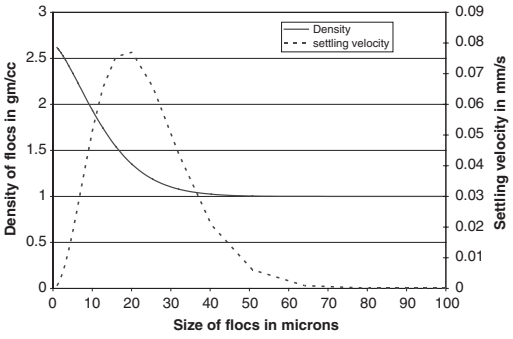


Figure 8. Density and settling velocity of kaolin as predicted by the model.

predicted using the PHOENICS model. The main flow parameter required for this purpose is the turbulent energy dissipation rate ε, which is one of the flow parameters computed in the PHOENICS model.

3.3.2 *Calibration procedure*

The impervious bed tests (i.e. Tests 5 and 6) were used to calibrate the settling and flocculation stage of the model and obtain the settling velocity parameters b and c and the flocculation parameters β. For this case, there is no entrapment in the bed. As a result, the entrapment coefficient $\alpha = 0$. The calibration was carried out using a trial and error procedure. To start the procedure, the values of b and c given by Lau and Krishnappan (1997) were used, and a range of β values were tried in the model, and the size distribution of the sediment flocs were determined. These distributions were then compared with the measured size distributions (not shown in this paper). The β value that gave the closest agreement was chosen. Using this chosen β value, a range of b and c values were tried in the model and the variation of concentration as a function of time was determined. This variation was then compared with the measured data and the set of values that gave the closest match was chosen. The process was repeated until the size distribution predictions and the concentration-time variation predictions agreed well with the measured data. Such a convergence was achieved within a small number of iterations (within five). The values that gave the best fit of the model results to the measured data are: $\beta = 0.2$, $b = 0.02$ and $c = 1.45$. These values are valid only for the kaolin particles tested in this study. The comparison between the computed and the measured values for the two impervious tests are shown in Figure 7.

From Figure 7, one can see that the computed values and the data agree very well for the two impervious bed tests indicating that the model describes the sedimentation process very well. For these tests, the flocculation process is significant. It was not possible to obtain such a fit by using the settling stage alone (i.e. by equating β to be zero).

4 RESULTS AND DISCUSSION

4.1 *Variation of density and settling velocity*

When the calibrated values of b and c are substituted into the density and settling velocity relations (i.e. in Equations 10 and 11), the variation of density and settling velocity as a function of floc size can be determined as shown in Figure 8.

Figure 8 shows that the density of the flocs decreases as a function of floc size, and for flocs greater than about 45 microns, the density of the floc becomes almost equal to that of water. The settling velocity exhibits a complex behaviour. It increases as a function of floc size for lower values of floc size, reaches a maximum value for the floc size of about 20 microns and then decreases with further increase in floc size. There is experimental evidence in the literature to support the above noted dependence of settling velocity of flocs on floc size (see. Petticrew (2005) and Atkinson et al. (2005)).

4.2 *Entrapment coefficient*

The entrapment coefficients were determined by applying the calibrated model to the entrapment experiments (i.e. for tests 1 to 4). In other words, values of β, b and c, obtained from the calibration of the model with impervious conditions were used for these computations. In these applications, the entrapment boundary condition (i.e. Eqn. 6) was adopted and the value of α was adjusted until the measured concentrations agreed with the values obtained with the model. Comparisons of the measured concentrations and the best fit values for Test No. 1 and Test No. 3 are shown in Figures 9 and 10 respectively. These figures indicate that the model agrees with the measured data reasonably well, showing once again that the model

Copyright © 2006 Taylor & Francis Group plc, London, UK

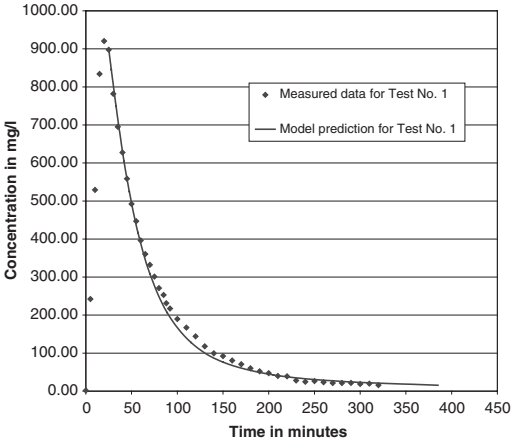


Figure 9. Comparison of model values and measurements for entrapment Test No. 1.

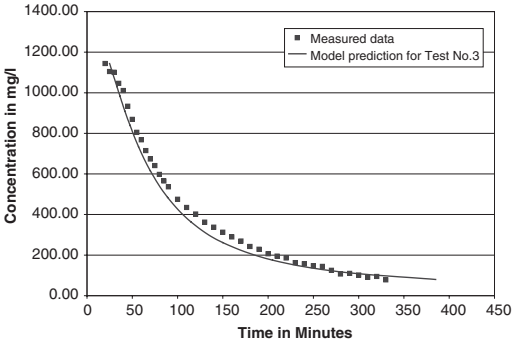


Figure 10. Comparison of model values and measurements of entrapment (Test No. 3).

describes the sedimentation and entrapment processes very well. The agreement for Test No. 2 and 4 was similar to those for Test No. 1 and 3, and hence are not shown here. The entrapment coefficients obtained with the model fit are listed in Table 2. The values for Test No. 1 and 2 are the same (i.e. 0.94), whereas the values for Test 3 and 4 are 0.19 and 0.48 respectively. Higher values for the larger size bed material are expected because of the higher porosity. For the smaller size bed material, the entrapment coefficient is considerably smaller (0.19) because of the lower porosity. However, for Test No. 4, which has the same bed material as Test No. 3, the entrapment value is higher (0.48). This is due to the fact that for Test No. 4, the bed shear stress was larger and, at this bed shear stress, movement of the bed material occurred and bed-forms developed. The increased entrapment rate is due to this bed-form formation.

Presence of bed-forms causes enhanced entrapment because of the advective pumping mechanism that was

Table 2. Entrapment coefficient for all tests.

Test no.	Bed shear stress in Pa	Bed material size (D_{50}) in mm	Entrapment coefficient α
1	0.3	8	0.94
2	0.7	8	0.94
3	0.2	1	0.19
4	0.4	1	0.48
5	0.17	0	0.00
6	0.33	0	0.00

described earlier. The entrapment process under the presence of bed-forms can be considered to consist of two components: one due to the bed-forms and the other due to plane bed. As the plane bed transform into undulating bed, the component due to plane bed could be overshadowed by the component due to bed-forms (advective pumping). More research is needed to unify the two different entrapment processes. Furthermore, additional experiments are needed to fully investigate the dependence of entrapment coefficient on the bed characteristics such as porosity, bed depth and permeability for the case of stationary, plane beds.

Plans are already underway to carry out a comprehensive study. Theory of dimensional analysis will be used to derive the dimensionless parameters determining the entrapment coefficient.

5 SUMMARY AND CONCLUSIONS

Entrapment of fine sediment into coarse gravel substrate was studied using a rotating circular flume. The flume bed was covered with coarse sediment. Two different sizes of sediment were used (median sizes: 8.0 mm and 1.0 mm). A pre-mixed slurry of kaolin was injected into the flume, and the concentration of kaolin in suspension was monitored as a function of time to evaluate the entrapment of kaolin into the coarse sediment substrate. A calibrated flocculation and settling model was used to compute the concentration variation in the flume as a function of time. An entrapment boundary condition was introduced in the model to simulate the fine sediment entrapment in the coarse gravel substrate. The model results compared with the measured data well for both pervious and impervious bed conditions. A systematic study is planned to determine the entrapment coefficient for various bed material types and bulk hydraulic parameters.

ACKNOWLEDGEMENTS

The authors wish to thank Mr. Robert Stephens of the Aquatic Ecosystem Impacts Research Division of Environment Canada for carrying out the entrapment experiments in the rotating circular flume.

Copyright © 2006 Taylor & Francis Group plc, London, UK

REFERENCES

Acornley, R.M. & Sear, D.A. 1999. Sediment transport and siltation of brown trout (*salmo trutta* L.) spawning gravels in chalk streams. *Hydrological Processes*. 13: 447–458.

Atkinson, J.F., Chakraborti, R.K. & Van Benschoten, J.E. 2005. Effects of floc size and shape in particle aggregation. In: Droppo, I., Leppard, G.G., Liss, S.N. & Milligan, T.G. (eds). *Flocculation in Natural and Engineered systems*. CRC Press, pp. 95–120.

Crisp, D.T. 1993. The ability of U.K. salmonid alevins to emerge through a sand layer. *J. Fish. Biol*. 43:656–658.

Elliott, A.H. & Brooks, N.H. 1997a. Transfer of nonabsorbing solutes to a streambed with bedforms: Theory. *Water Resources Research*. 33(1): 123–136.

Elliott, A.H. & Brooks, N.H. 1997b. Transfer of nonabsorbing solute to a streambed with bedforms: Laboratory experiments. Water Resources Research. 33(1): 137–151.

Fernald, A.G., Landers, D.H. & Wingington Jr., P.J. 2000. Water quality effects of hyporheic processing in a large river. In: Wingington, P.J. & Beschta, R.L. (eds). *International conference on Riparian Ecology and Management in multi-land use watersheds*. American Water Resources Association. Middlebury, Va, pp. 167–172.

Fuchs, N.A. 1964. *The Mechanics of Aerosols*. Pergamon, New York, 408 pages.

Hausle, D.A. & Coble, D.W. 1976. Influence of sand in reddson survival and emergence of brook trout (*Salvelinus fontinalis*). *Trans. Am. Fish. Soc*. 1: 57–63.

Iwamoto, R.N., Salo, E,O., Madej, M.A., McComas, R.L. & Rulifson, R.L. 1978. Sediment and Water Quality: A Review of the literature including a suggested approach to water quality criteria with summary of workshops and conclusion and recommendations. *U.S. Environmental Protection Agency.* 910/9-78-048. 151 pages.

Krishnappan, B.G. 1993. Rotating circular flume. *Journal of Hydraulic Engineering*, ASCE. 119(6): 758–767.

Krishnappan, B.G. & Marsalek, J. 2002. Modelling of flocculation and transport of cohesive sediment from an on-stream stormwater detention pond. *Water Research*. 36: 3849–3859.

Krishnappan, B.G & Engel, P. 2004. Distribution of bed shear stress in rotating circular flume. *Journal of Hydraulic Engineering*, ASCE. 130(4): 324–331.

Krone, R.B. 1962. Flume studies of the transport of sediment in estuarial shoaling processes. *Final Report. Hydraulic Engineering laboratory and Sanitary Engineering Research Laboratory*, University of California, Berkeley, California.

Lau, Y.L. & Krishnappan, B.G. 1997. Measurement of size distribution of settling flocs. *NWRI Publication No. 97–223*. National Water Research Institute, Environment Canada, CCIW, Burlington, Ontario, Canada.

Lick, W. 1982. Entrainment, deposition and transport of fine grained sediment in lakes. *Hydrobiologia*. 91: 31–40.

Marion, A. & Bellinello, M. 2002. Effect of bedform geometry on the penetration of nonreactive solutes into a stream bed. *Water Resources Research*. 38(10): 1209, 10-1029/2001WR000264.

Marion, A., Zaramella, M. & Packman, A.I. 2003. Parameter estimation of the transient storage model for stream-subsurface exchange. *Journal of Environmental Engineering*, ASCE. 129(5): 456–463.

Mehta, A.J. & Partheniades, E. 1975. An investigation of the depositional properties of flocculated fine sediments. *Journal of Hydraulic Research*, IAHR. 13: 361–381.

Mehta, A.J. & Partheniades, E. 1982. Resuspension of deposited cohesive sediment beds. *Proc. 18th Coastal Engineering Conference*, Capetown, South Africa. 2: 1569–1588.

Olsson, T.I. & Persson, B. 1988. Effects of deposited sand on ova survival and alevin emergence in brown trout (*salmo trutta* L.). *Arch. Hydrobiol*. 113: 621–627.

Packman, A.I., Brooks, N.H. & Morgan, J.J. 2000a. A physico-chemical model for colloid exchange between a stream and a sand streambed with bed forms. *Water Resources Research*. 36(8): 2351–2361.

Packman, A.I., Brooks, N.H. & Morgan, J.J. 2000b. Kaolinite exchange between a stream and streambed: Laboratory experiments and validation of a colloid transport model. *Water Resources Research*. 36(8): 2351–2361.

Packman, A.I. & Mackay, J.S. 2003. Interplay of stream-subsurface exchange, clay particle deposition and stream bed evolution. *Water Resources Research*. 39(4) 1097, 10-129/2002WR001432.

Packman, A.I., Salehin, M. & Zaramella, M. 2004. Hyporheic exchange with gravel beds: Basic hydrodynamic interactions and bedform induced advective flows. Journal of Hydraulic Engineering, ASCE. 130(7): 647–656.

Parchure, T.M. 1984. Erosional behaviour of deposited cohesive sediment. *Ph.D dissertation*, University of Florida, Gainesville, Florida.

Partheniades, E. 1962. A study of erosion and deposition of cohesive soils in salt water. *Ph.D dissertation*, University of California, Berkeley, California.

Petticrew, E. 2005. The composite nature of suspended and gravel stored fine sediment in streams: A case study of O'neil Creek in British Columbia, Canada. In: Droppo, I., Leppard, G.G., Liss, S.N. & Milligan, T.G. (eds). *Flocculation in Natural and Engineered systems*. CRC Press, pp. 71–93.

Philips, R.W., Lantz, R.L., Claire, L.L. & Moring, W.E. 1975. Some effects of gravel mixtures on emergence of coho salmon and steelhead trout fry. *Trans. Am. Fish. Soc*. 104: 461–465.

Rosten, H.I. & Spalding, D.B. 1984. The PHOENICS Reference manual, *TR/200*, CHAM Ltd., Wimbledon, London.

Tambo, N. & Watqanabe, Y. 1979. Physical aspects of flocculation process-I. Fundamental Treatise. *Water Research*. 13: 429–439.

Turnpenny, A.W. & Williams, R. 1980. Effects of sedimentation on the gravels of an industrial river system. *J. Fish. Biol*. 17: 681–693.

Valioulis, I.A. & List, E.J. 1984. Numerical simulation of a sedimentation basin. 1. Model development. *Environmental Science and Technology*. 18(4): 242–247.

Weiner, B.B. 1984. Particle and droplet sizing using Fraunhofer diffraction. In: Barth, H.G. (ed)). *Modern methods of particle size analysis. Chapter 5*, John Wiley & Sons.

Zaramella, M. & Packman, A.I. 2003. Application of the transient storage model to analyze advective hyporheic exchange with deep and shallow sediment beds. *Water Resources Research*. 39(7), 1198, 10.1029/2002WR001344.

Copyright © 2006 Taylor & Francis Group plc, London, UK

Can a two-layer morphological model compete with common sediment transport formulae?

C. Savary & Y. Zech
Dept. of Civil and Environmental Engineering., Université catholique de Louvain, Louvain-la-Neuve, Belgium

ABSTRACT: In opposition to the common approach based on the Saint-Venant – Exner equations, a two-layer model does not introduce the solid discharge as a closure relation. The solid discharge is one of the main unknowns of the differential system and depends on the expression of the various shear-stresses at each layer interface. Once the corresponding friction coefficients calibrated for one situation, the two-layer model is able to generate the water depth and the solid discharge for any situation. In several versions of the two-layer model, each relying on different assumptions, the sediment transport was calculated for a wide range of Froude numbers. A basic model assuming identical velocity in both the water and the transport layer revealed to be unsatisfactory. Allowing the velocity in the two layers to be distinct leads to good agreement with common sediment transport formulae. Assuming distinct concentrations in the transport layer and in the bed results in still better agreement.

1 INTRODUCTION

In fluvial hydraulics, different sets of equations are used to model the interaction between water and sediment. The most usual are the Saint-Venant – Exner equations (see for example Vreugdenhil & de Vries, 1967; Rahuel, 1988; Correia, 1990; Correia et al., 1991), where a transport layer is not explicitly considered. In this case, two closure equations have to be added to the partial differential equation system, one dealing with the friction slope (e.g. by the Manning relation) and the other providing the solid discharge by any common formula (e.g. by the Meyer-Peter–Müller (1948) relation).

In contrast, the two-layer approach (Capart, 2000) takes explicitly the transport layer in consideration. The model accounts for the solid discharge as a main variable, while the friction is represented by the various shear-stresses at each layer interface. The solid discharge is influenced by the friction coefficients associated to those shear stresses. In uniform flow conditions, the solid discharge calculated by the two-layer model or by the common formulae should be the same, allowing to calibrate the friction coefficients.

Once calibrated for one situation (e.g.: a given bottom slope), using either experimental or theoretical data, the two-layer model is able to generate the water depth and the solid discharge for any situation (e.g.: other bottom slopes), without use of any transport formula. In that sense the method offers an alternative to common transport formulae.

The comparison between common transport formulae and several versions of the two-layer model, each relying on different assumptions, is tested. First, analysis and comparisons are made in the case of a model allowing different mean velocity in the water and the transport layer, but the same sediment concentration in the transport layer as in the fixed bed (Capart & Young, 2002). Then a model (Spinewine, 2005) assuming distinct concentrations in the transport layer and in the bed is tested. A simplified model (Capart, 2000) assuming identical velocity in both layers is tested. For each of those models, the sediment transport (solid discharge, transport layer depth and velocity) is calculated for a wide range of Froude numbers and grain diameters.

2 TWO-LAYER MODEL

To calculate morphodynamic evolution, a two-layer model developed by Capart (2000) and improved by Capart & Young (2002) is proposed. This two-layer numerical scheme is documented in more details in Chen et al. (in press), where it is applied to flows involving water and mud layers. In this paper, a one-dimensional point of view is taken into account. Assuming the shallow-water hydrostatic pressure distribution, the flow is divided in two layers constituted of incompressible fluid. The main variables are the thickness of the water layer h_w and of the transport layer h_s, the velocity in each layer u_w and u_s,

Copyright © 2006 Taylor & Francis Group plc, London, UK

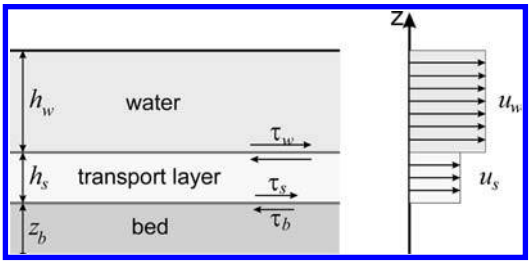


Figure 1. Two-layer model.

respectively, and the level of the interface between the transport layer and the bed z_b (Fig. 1).

The transport layer and the fixed bed are constituted of a water-sediment mixture with a sediment concentration C, assumed as constant in time and in space. The volumetric density of this transport layer is $\rho'_s = (1-C)\rho_w + C\,\rho_s$, where ρ_w and ρ_s are the water and the grain density, respectively. In fact, sediment mobilisation often requires a decrease of concentration (Spinewine, 2005) but, for the sake of simplicity, this is not taken into account in the model here presented. The velocity in the transport layer is allowed to be distinct from the velocity in the water layer, but they are assumed to be uniform in both layers. As only the bed load is modeled, there is no mass and momentum exchange between the transport layer and the water. The only possible mass exchange occurs between the bed and the transport layer. The five-equation system proposed by Capart & Young (2002) results from mass (Equations 1–2) and momentum (Equations 4–5) conservation in each layer and from the definition of the erosion rate e_b (Equation 3).

$$\frac{\partial h_w}{\partial t}+\frac{\partial h_w u_w}{\partial x}=0 \tag{1}$$

$$\frac{\partial h_s}{\partial t}+\frac{\partial h_s u_s}{\partial x}=e_b \tag{2}$$

$$\frac{\partial z_b}{\partial t}=-e_b \tag{3}$$

$$\frac{\partial h_w u_w}{\partial t}+\frac{\partial\left(h_w u_w^2+\frac{1}{2}gh_w^2\right)}{\partial x}+gh_w\frac{\partial(z_b+h_s)}{\partial x}=-\frac{\tau_w}{\rho_w} \tag{4}$$

$$\frac{\partial h_s u_s}{\partial t}+\frac{\partial\left(h_s u_s^2+\frac{1}{2}gh_s^2\right)}{\partial x}+gh_s\frac{\partial\left(z_b+\frac{\rho_w}{\rho_s}h_s\right)}{\partial x}=\frac{\tau_w}{\rho'_s}-\frac{\tau_b}{\rho'_s} \tag{5}$$

where the erosion rate e_b depends on the shear stresses τ_s and τ_b.

$$e_b=\frac{\tau_s-\tau_b}{\rho'_s u_s} \tag{6}$$

The shear stress between the water and the transport layer τ_w and the shear stress applied on the fixed bed τ_s are assumed to follow a Chézy-like friction law:

$$\tau_w=\rho_w C_{f,w}|u_w-u_s|(u_w-u_s) \tag{7}$$

$$\tau_s=\rho'_s C_{f,s}|u_s|u_s \tag{8}$$

where $C_{f,w}$ and $C_{f,s}$ are water and sediment friction coefficients. The resistance shear stress to the flow, exerted by the fixed bed, is expressed by a Mohr–Coulomb relation.

$$\tau_b=\tau_{crit}+tg\varphi(\rho'_s-\rho_w)gh_s \tag{9}$$

where τ_{crit} is the threshold value of τ_s allowing erosion and φ is the repose angle of the soil.

3 UNIFORM FLOW TWO-VELOCITY MODEL

In uniform steady flow conditions, (1) and (2) disappear and (4) and (5) simplify since the partial derivatives $\partial/\partial t = 0$ and $\partial/\partial x = 0$, except $\partial z_b/\partial x = -S_0$:

$$-gh_w\frac{\partial z_b}{\partial x}=gh_w S_0=\frac{\tau_w}{\rho_w} \tag{10}$$

$$-gh_s\frac{\partial z_b}{\partial x}=gh_s S_0=\frac{\tau_b}{\rho'_s}-\frac{\tau_w}{\rho'_s} \tag{11}$$

The sediment transport is in equilibrium, which means that neither erosion nor deposition occurs, thus

$$\tau_b=\tau_s \tag{12}$$

The unit liquid and solid discharges can be defined

$$q_w=u_w h_w \tag{13}$$

$$q_s=u_s h_s \tag{14}$$

Equations (10–14) and (7–9) form a set of 8 uniform-flow equations linking 13 parameters: S_0, q_w, q_s, h_w, h_s, u_w, u_s, τ_w, τ_s, τ_b, τ_{crit}, C_{fw} and C_{fs}. In uniform-flow condition, if five of them are known, the others may be deduced.

It is thus possible to calibrate the two friction coefficients, C_{fw} and C_{fs}, either from measurement or from estimation of only five parameters.

For example, for a given discharge q_w in a channel of slope S_0 with mobile bed whose characteristic diameter is d, the water depth h_w may be deduced from any uniform-flow relation.

If now the solid discharge q_s and the critical shear stress τ_{crit} are computed from any empirical formula, we obtain a set of five parameters (the water depth h_w,

Copyright © 2006 Taylor & Francis Group plc, London, UK

the discharges q_w and q_s, the slope S_0 and the critical shear stress τ_{crit}) required to calibrate C_{fw} and C_{fs}. If experimental data are available, they can be used to deduce the flow parameters h_w and q_s , existent uniform flow and solid discharge relations are no more required.

Once those coefficients are calibrated, one may investigate the behaviour of the two-layer model in other flow conditions by considering various combinations of q_w and S_0. For each combination, it is possible to compute q_s, h_w, h_s,u_w,u_s, τ_{crit}, τ_w, τ_s and τ_b.

To analyse the two-layer model behaviour, an example was computed with the following data: a unit water discharge $q_w = 10\,\mathrm{m^3/s/m}$ in a channel, whose bed is constituted of uniform grains of diameter d varying from 1 to 10 mm; the density $s = \rho_s/\rho_w = 2.65$, and the repose angle of the soil $\varphi = 30°$.

For each diameter, the calibration of C_{fw} and C_{fs} was done for a bottom slope S_0 corresponding to the value of the Froude number $\mathbf{Fr}_w = 2$. The Manning roughness coefficient n may be evaluated from the Strickler formula

$$K = \frac{1}{n} = \frac{26}{d^{1/6}} \tag{15}$$

and the water depth h_w may be deduced from the Manning uniform-flow relation:

$$q_w = \frac{1}{n} h_w^{5/3} S_0^{1/2} \tag{16}$$

The corresponding transport q_s and critical shear stress τ_{crit} are evaluated from Meyer-Peter–Müller formula.

$$q_s = 8\sqrt{g(s-1)d^3}\left(\left(\frac{n_b'}{n_b}\right)^{3/2}\frac{\gamma_w R_b S_0}{(\gamma_s-\gamma_w)d} - 0.047\right)^{3/2} \tag{17}$$

$$\tau_{crit,MPM} = 0.047(\gamma_s-\gamma_w)d_{50} \tag{18}$$

where n_b is the Manning roughness coefficient corresponding to the bed, n_b' is the Manning roughness coefficient taking bed forms into account (if no bed forms occurs, the ratio $n_b'/n_b = 1$), R_b is the hydraulic radius related to the bed, γ_w and γ_s are respectively the water and the bed volumetric weight.

Then, for each diameter, a range of bottom slopes is explored. Using the set of equations (10–14) and (7–9), it is possible to compute the various parameters as a function of the Froude number.

$$\mathbf{Fr}_w = \frac{u_w}{\sqrt{g h_w}} \tag{19}$$

From Figures 2 and 3, it clearly appears that as well the sediment-layer depth h_s as its velocity u_s increase

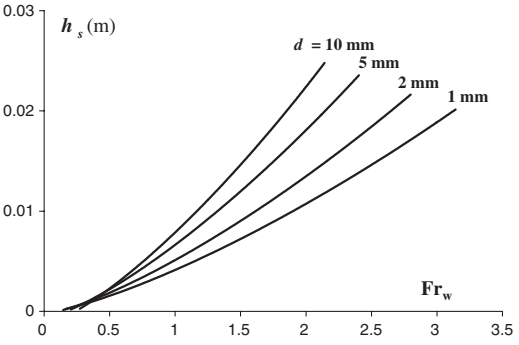


Figure 2. Evolution of the sediment-layer depth h_s (computed with the two-layer model) with Froude number $\mathbf{Fr}_w$ ($d = 1$ to 10 mm) ($q_w = 10\,\mathrm{m^3/s/m}$).

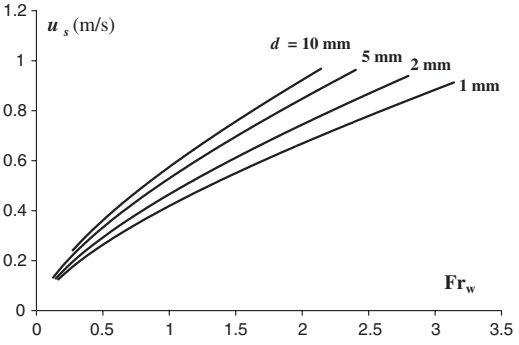


Figure 3. Evolution of the sediment-layer velocity u_s (computed with the two-layer model) with Froude number $\mathbf{Fr}_w$ ($d = 1$ to 10 mm) ($q_w = 10\,\mathrm{m^3/s/m}$).

with increasing Froude number (thus with increasing bottom slope S_0, decreasing water depth h_w, and increasing water velocity u_w). The resulting increase of solid discharge q_s is due, for a part, to the increase of sediment velocity u_s, but mainly to the development in depth of the sediment layer h_s.

Computing the solid discharge from (14) yields a result very close to the Meyer-Peter–Müller formula (Fig. 4). The latter formula was used to calibrate the two-layer model for $\mathbf{Fr}_w = 2$. The three curves on Figure 4 represent three ways to compute q_s for other Froude numbers. One is calculated with the two-layer model, another is obtained applying Meyer-Peter–Müller formula to the water depth h_w calculated with the two-layer model and the last is calculated completely independently with Manning and Meyer-Peter–Müller formulae. That means that the two-layer model and its closure equations (1–9) are at least consistent with the predictions of Meyer-Peter and Müller. As the curves on Figure 4 are quite close, the value of Froude number chosen to calibrate the

Copyright © 2006 Taylor & Francis Group plc, London, UK

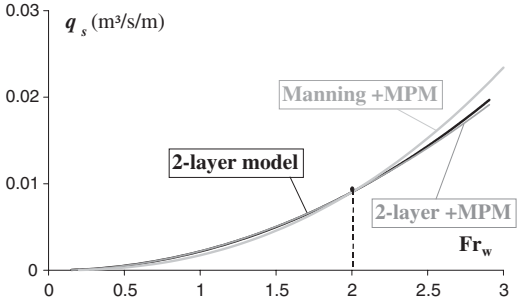


Figure 4. Evolution of solid discharge q_s with Froude number $\mathbf{Fr}_w$: comparison between two-layer model and Meyer-Peter–Müller formula ($d = 1$ mm, $\tau_{crit} = 0.76$ N/m^2, $q_w = 10$ m^3/s/m, $C_{fw} = 0.0016$, $C_{fs} = 0.069$).

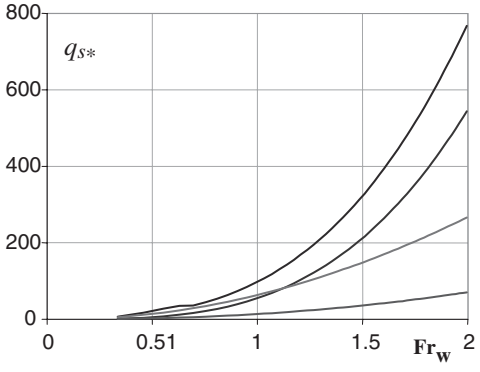


Figure 5. Dimensionless solid discharge in uniform flow conditions – $d = 1$ mm; $q = 10$ m^3/s/m; VR = van Rijn formula (bed load and total load), AW = Ackers-White formula (total load), MPM = Meyer-Peter–Müller formula (bed load).

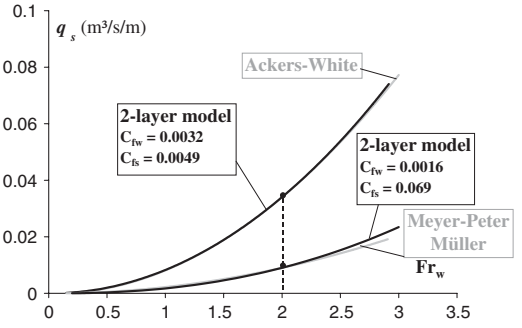


Figure 6. Solid discharge: comparison between two-layer model, Meyer-Peter–Müller formula and Ackers White formula ($d = 1$ mm, $\tau_{crit} = 0.76$ N/m^2, $q_w = 10$ m^3/s/m, $C_{fw} = 0.0016/0.0032$, $C_{fs} = 0.069/0.0049$).

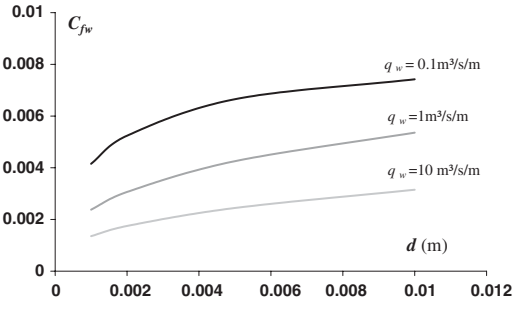


Figure 7. Evolution of the friction coefficient C_{fw} with grain diameter d and water discharge q_w (calibration based on the Meyer-Peter–Müller formula, $\mathbf{Fr}_w = 2$).

friction coefficients is not very important. A Froude number corresponding to the flow is chosen, for example, the mean Froude number in the part of the flow where sediment transport is observed. This consistency is confirmed for other grain diameters ($d = 2$, 5 and 10 mm) and other unit discharges ($q_w = 1$ m^3/s/m), at least if the calibration conditions are not too close to the threshold τ_{crit} under which no transport is expected.

Even if the differences between the common sediment transport formulae are important (Fig. 5), the model seems able to be consistent with several laws.

The Meyer-Peter–Muller relation (17) used to estimate the solid discharge could be replaced by another sediment transport formula like the one proposed by Ackers-White (1980) for example. The calibrated values of the friction coefficientsC_{fs} and C_{fw} depend on the estimation of the solid discharge, which depends in turn on the sediment transport formula used.

If Ackers-White formula is used instead of Meyer-Peter–Muller formula in the previous example ($q_w = 10$ m^3/s/m, $d = 1$ mm; $\rho_s/\rho_w = 2.65$, $\varphi = 30°$, $\mathbf{Fr}_w = 2$), the obtained frictions parameters are significantly different. The calibrated friction coefficients obtained on base of Meyer-Peter–Müller formula are $C_{fw} = 0.0016$ and $C_{fs} = 0.069$, they become $C_{fw} = 0.0032$ and $C_{fs} = 0.0049$ in the case Ackers-White formula is used. For other flow conditions (various slopes for a constant discharge) the solid discharge is calculated by the model and compared with the formulae of Meyer-Peter–Müller and Ackers-White in Figure 6, each computation is in good agreement with the corresponding formula. As the parameters C_{fs} and C_{fw} depend significantly on the chosen formula, it is important to select a formula adapted to the problem, the range of application of the formula has to be respected.

Figures 7 and 8 illustrate the way the friction coefficients C_{fw} and C_{fs} evolve depending on the sediment diameter d and the water discharge q_w. Actually, these figures allow to have a quick idea of which value to

Copyright © 2006 Taylor & Francis Group plc, London, UK

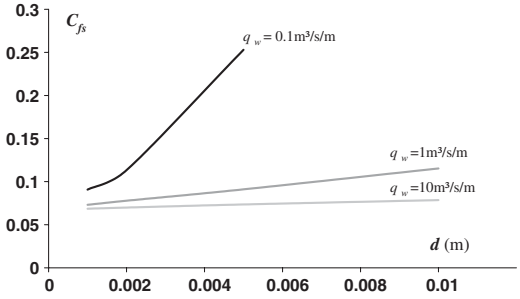


Figure 8. Evolution of the friction coefficient C_{fs} with grain diameter d and water discharge q_w (calibration based on the Meyer-Peter–Müller formula, $\mathbf{Fr}_w = 2$).

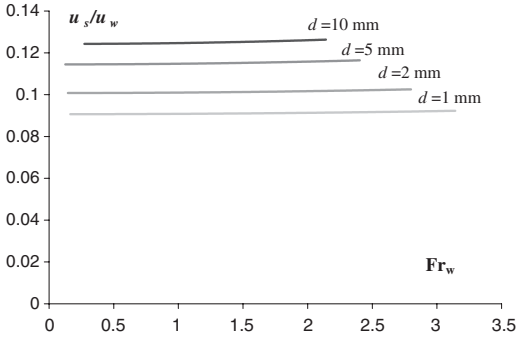


Figure 9. Evolution of the ratio of velocity u_s/u_w in each layer with Froude number $\mathbf{Fr}_w$ (calibration based on the Meyer-Peter–Müller formula, $\mathbf{Fr}_w = 1$).

chose for these coefficients knowing only few parameters of the flow (the grain diameter d and the water discharge q_w). The two coefficients seem to increase with the diameter d and to decrease with the water dischargeq_w. In these figures, the coefficients are calibrated with one specific sediment transport formula for a single Froude number. The important rise of C_{fs} with the diameter for the smallest water discharge ($q_w = 0.1\ m^3/s$) is due to the proximity of the sediment transport threshold. If the grain diameter d is too important and the discharge q_w is too low, the sediment transport is close to zero and the formula is out of its application field.

The ratio of the velocity in each layer u_s/u_w is quite constant with the water Froude number (Fig. 9), only depending on the diameter and the water discharge (Fig. 10). The velocity ratio decreases with the discharge and increases with the diameter to reach asymptotically a near steady value. Once more, when the calibration conditions are too close to the sediment movement threshold ($q_w = 0.1\ m^3/s$, $d > 2$ mm in Fig. 10), the transport formula is no more appropriate.

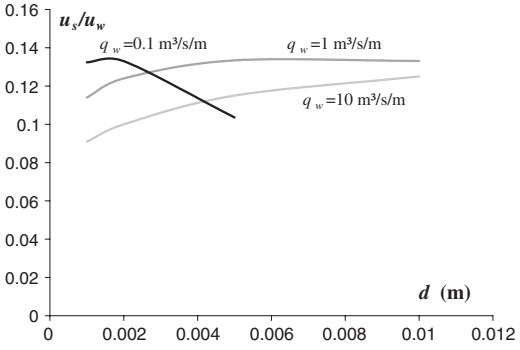


Figure 10. Evolution of the ratio of velocity u_s/u_w in each layer with grain diameter d and water discharge q_w (calibration based on the Meyer-Peter–Müller formula, $\mathbf{Fr}_w = 2$).

These observations underlines the fact the calibration conditions have to be adapted to the flow, avoiding too low sediment transport conditions.

4 TWO-CONCENTRATION MODEL

To take into account different concentrations in the transport layer and in the fixed bed, the source terms of Equations 1–5 are modified (Spinewine, 2005). However, in case of uniform flow, equations 10 and 11 are not modified, as far as ρ_s' is adapted. Thus, the friction coefficients C_{fw} and C_{fs} are calibrated as formerly.

The two models (equal versus distinct concentrations) are compared. In the model assuming identical concentrations, the concentration of the transport layer is set to 0.6 as in the fixed bed, while in the distinct-concentration model, the concentration of the transport layer is set to 0.2, according to Sumer et al. (1996) results.

The parameters are calibrated for $\mathbf{Fr}_w = 1$. For one- and two-concentration model, respectively C_{fw} was found nearly identical (0.0014 vs. 0.00134), while C_{fs}, is significantly distinct (0.068 vs. 0.1166).

Unsurprisingly, the transport layer thickness (Fig. 11) is a little more than 3 times higher in the two-concentration model when the concentration is 0.2 instead of 0.6 in the transport layer. The velocity in the transport layer (Fig. 12) decreases a little in the two-concentration model. The difference in concentration influences mainly the depth of the transport layer. The solid discharge (Fig. 13) remains quite close to Meyer-Peter–Müller predictions for both models. Nevertheless, for large Froude numbers, the solid discharge calculated by the two-concentration model is slightly greater than the predictions by the two other models.

Copyright © 2006 Taylor & Francis Group plc, London, UK

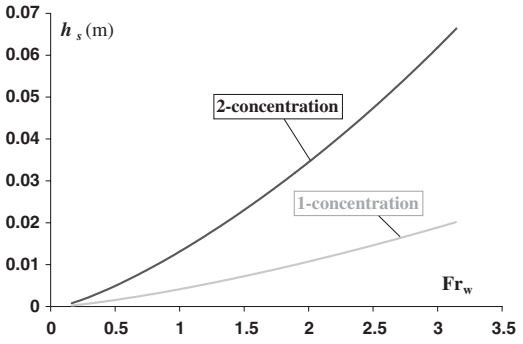


Figure 11. Evolution of the sediment-layer depth h_s with Froude number $\mathbf{Fr}_w$: comparison between the one-concentration model (concentration of the transport layer = 0.6) and the two-concentration model (concentration of the transport layer = 0.2) ($d = 1$ mm, $q_w = 10\,\mathrm{m}^3/\mathrm{s/m}$).

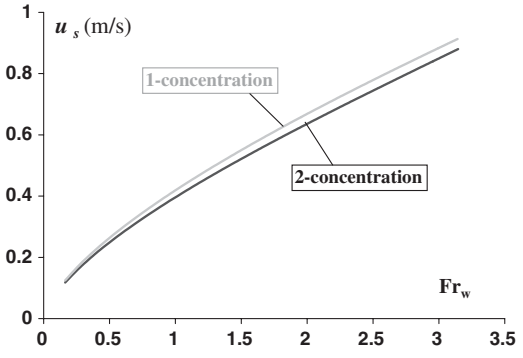


Figure 12. Evolution of the sediment-layer velocity u_s with Froude number $\mathbf{Fr}_w$: comparison between the one-concentration model (concentration of the transport layer = 0.6) and the two-concentration model (concentration of the transport layer = 0.2) ($d = 1$ mm, $q_w = 10\,\mathrm{m}^3/\mathrm{s/m}$).

5 ONE-VELOCITY MODEL

If the velocity in the water layer and in the transport layer is the same, the five-equation system 1–5 reduces to four equations (Capart 2000, Fraccarollo et al. 2003).

We define the total transport depth $h_m = h_w + h_s$, the common velocity $u_m = u_w = u_s$ and a correction factor $r = C\,[(\rho_s - \rho_w)/\rho_w]$ accounting for the additional mass in the sediment layer compared to the water layer ($\rho_s'/\rho_w = 1 + r$).

In uniform steady flow conditions, the four equations simplify

$$g\frac{\partial z_b}{\partial x} = \frac{-\tau_m}{\rho_w(h_m + r h_s)} \tag{20}$$

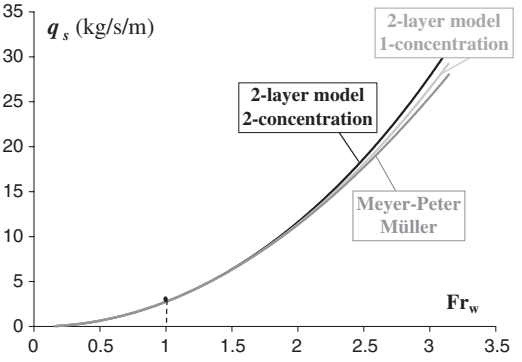


Figure 13. Evolution of sediment transport q_s with Froude number $\mathbf{Fr}_w$ comparison between the one-concentration model (concentration of the transport layer = 0.6), the two-concentration model (concentration of the transport layer = 0.2) and the Meyer-Peter–Müller formula ($d = 1$ mm, $q_w = 10\,\mathrm{m}^3/\mathrm{s/m}$).

The sediment transport is in equilibrium, which means that neither erosion nor deposition occurs; thus Equation 12 reduces to the condition

$$\tau_b = \tau_m \tag{21}$$

where

$$\tau_m = \rho'_s C_{f,m} |u_m| u_m \tag{22}$$

As the velocity is the same in the two layers, there is no friction shear stress τ_w between the two layers.

If we now define the unit liquid and solid discharges

$$q_m = q_w + q_s = u_m h_m \tag{23}$$

$$q_s = u_m h_s, \tag{24}$$

equations (20–24) and (9) form a set of 6 uniform-flow equations linking 10 parameters: S_0, q_m, q_s, h_m, h_s,u_m, τ_m, τ_b, C_{fm} and τ_{crit}. In opposition to the two-velocity model, only one friction coefficient C_{fm} remains. The critical shear-stress τ_{crit} has to be calibrated in the same way as the friction coefficient, if it is estimated with an external expression (Meyer-Peter–Müller for example), the problem is over-determinate and no solution exists.

Identically to the two-velocity model, it is possible to calibrate the friction coefficient C_{fm} and the critical shear-stress τ_{crit} either from measurement or from estimation of only four parameters (S_0, q_w, h_w, q_s).

The calibration of C_{fm} and τ_{crit} was done for a bottom slope S_0 corresponding to the value of the Froude number $\mathbf{Fr}_w = 1$. During the calibration stage, the water depth h_w was estimated with Manning relation and the corresponding sediment transport q_s was evaluated with Meyer-Peter–Müller formula.

Copyright © 2006 Taylor & Francis Group plc, London, UK

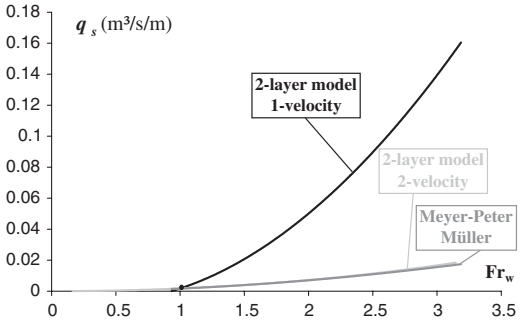


Figure 14. Evolution of sediment transport q_s with Froude number $\mathbf{Fr}_w$ comparison between the one-velocity model, the two-velocity mode and Meyer-Peter–Müller formula ($d = 1$ mm, $q_w = 10\,\mathrm{m}^3/\mathrm{s/m}$).

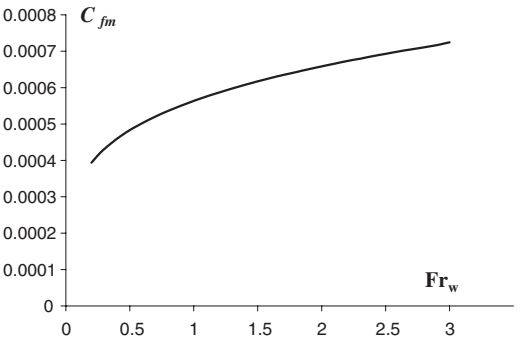


Figure 15. What should be the variation of coefficient C_{fm} with Froude number $\mathbf{Fr}_w$ to make the one-velocity model match Meyer-Peter–Müller ($d = 1$ mm, $q_w = 10\,\mathrm{m}^3/\mathrm{s/m}$).

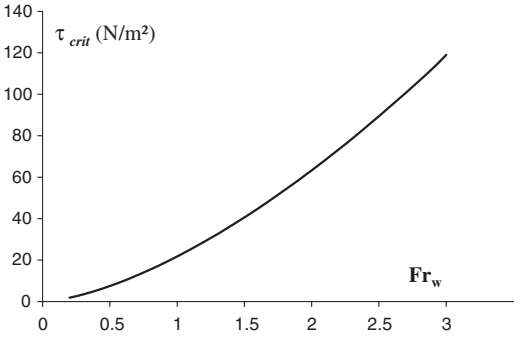


Figure 16. What should be the variation of critical shear stress $\tau_{m,crit}$ with Froude number $\mathbf{Fr}_w$ to make the one-velocity model match Meyer-Peter–Müller ($d = 1$ mm, $q_w = 10\,\mathrm{m}^3/\mathrm{s/m}$).

The solid discharge computed from Equations 20–24, 9 with the calibrated friction coefficient C_{fm} and critical shear stress τ_{crit} is compared with the Meyer-Peter–Müller formula in Figure 14. In case of $\mathbf{Fr}_w > 1$ (supercritical flow), the computed solid discharge highly overestimates the solid discharge calculated by the Meyer-Peter–Müller formula. In case of $\mathbf{Fr}_w < 1$, the computed solid discharge underestimates the Meyer-Peter–Müller formula, too quickly reaching zero with decreasing Froude number. The only Froude number for which the two ways to calculate the solid discharge are identical is $\mathbf{Fr}_w = 1$ corresponding to the calibration point. In opposition with the previous models, no matches with the classical formulae is observed for constant parameters C_{fm} and τ_{crit}.

The velocity in the sediment layer $u_s = u_m$ is overestimated (close to u_w), thus for a given solid discharge the thickness of the transport layer h_s is underestimated. According to (22) and (9), the shear stress applied to the bed τ_m is overestimated and the part of the resistance shear stress τ_b linked to h_s is underestimated. At equilibrium conditions, these two shear stresses have to be equal (21). The deduced critical shear stress τ_{crit} is excessive in comparison with the one proposed by Meyer-Peter–Müller. It explains why the one-velocity model reaches the sediment motion threshold for higher Froude number than the one corresponding to Meyer-Peter–Müller observations. The inappropriate estimation of the shear stresses also explains the overestimation in sediment transport for high Froude numbers.

The values of the parameters C_{fm} and τ_{crit} deduced from the calibration point cannot be extended to other flow conditions. Figures 15 and 16 illustrate how the parameters C_{fm} and τ_{crit} should vary with Froude number (instead of being constant) to match with the Meyer-Peter–Müller formula. This implies the one-velocity model is not able to correctly approach non-uniform flows, except in extreme situations where the assumption of identical velocity in sediment and water holds (e.g.: dam break wave).

This variability of parameters supposed to be constant underlines the expressions of the shear stresses τ_m (22) and τ_b (9) are not appropriate under these assumptions. The correct expression of τ_m (22) should refer to the real velocity $u*$ at the interface between mobile and fixed bed, which is smaller than the mean velocity u_m:

$$\tau_m = \rho_w (1+r) u^{*2} \tag{25}$$

The expression (22) makes use of the assumption $u*^2 = C_{fm}\, u_m^2$ where C_{fm} is a constant. According to the formula of Meyer-Peter–Müller, the shear stress applied to the bed τ_m is expressed

$$\tau_{m,MPM} = \gamma_w R_b S_0\,, \tag{26}$$

which becomes using the Manning formulation

$$\tau_{m,MPM} = \gamma_w n^2 \frac{u^2}{h^{1/3}} = \alpha \frac{u^2}{h^{1/3}} \tag{27}$$

Copyright © 2006 Taylor & Francis Group plc, London, UK

where α g s a constant, or using the Chézy formulation

$$\tau_{m,MPM}=\gamma_w\frac{1}{C^2}u^2=\beta u^2 \quad (28)$$

The variation of the friction coefficient C_{fm} with water Froude number illustrates the difference between Manning and Chézy formulation. To calibrate, the Manning formula is used, but the expression (22) is Chézy-like. The solution to obtain a constant coefficient C_{fm} would be to unify the way to calculate the shear stress applied to the bed both in the model and in the calibration.

However, the main problem remains the important variation of the critical shear stress with the Froude number. Instead being constant the critical shear stress should rise sharply with the Froude number (Fig. 16). As the critical shear stress is set constant, the resistant shear stress τ_b is underestimated for high Froude number inducing too much transport and overestimated for low Froude number. An artificial correction of the critical shear stress depending on the Froude number would allow the model to fit better with the classical formulation of sediment transport as the one proposed by Meyer-Peter–Müller.

6 CONCLUSIONS

More and more often, two-layer approaches are used as an alternative to common sediment-transport models. The purpose of the paper was to check if these models could compete with those common approaches in the simple case of uniform flow.

Using either experimental data or results of classical approach for one situation, a calibration procedure of the friction parameters is proposed.

Models based on different assumptions were compared: distinct velocities or not in the water and the transport layer, distinct concentrations or not in the bed and the transport layer. The one-velocity model appears to fail in matching the common sediment-transport formulae results, while the solid discharge predicted by a two-velocity model is closer to those. Looking more precisely to the thickness and velocity of the transport layer, the model where also the concentration is distinct reveals to be the more appropriate.

Laboratory experiments are required to generalise the above results and to define a range of applicability of the method.

Our experience of the proposed model seems to show a wide applicability in term of solid discharge, while the thickness of the transport layer is sometimes more difficult to interpret in the case of low transport rates.

ACKNOWLEDGEMENTS

The authors would like to thank H. Capart for the access to his two-layer software.

REFERENCES

Ackers P. & White W.R. 1980. Bed material transport: a theory for total load and its verification. International Symposium on River Sedimentation, Beijing, China, March 1980, 249–268.

Capart, H. 2000. Dam-break induced geomorphic flows and the transition from solid- to fluid-like behaviour across evolving interfaces. PhD thesis, Université catholique de Louvain, Louvain-la-Neuve, Belgium.

Capart, H. & Young, D.L. 2002. Two-layer shallow water computations of torrential geomorphic flows. Proceedings of River Flow 2002, Louvain-la-Neuve, Belgium, September 2002, 1003–1012.

Chen, S.-C., Peng, S.-H. & Capart, H. Two-layer shallow water computation of mud flow intrusions into quiescent water. *Journal of Hydraulic Research* (in press).

Correia, L.R.P. (1990). Numerical modelling of unsteady sediment transport, PhD thesis, Ecole Polytechnique Fédérale de Lausanne, Lausanne, Switzerland.

Correia, L.R.P., Krishnappan, B.G. & Graf, W.H. (1991). Laboratory verification of a coupled unsteady flow model. Proceedings of XXIV IAHR Congress, Madrid, Spain, 1991, A471–A480.

Fraccarollo L., Capart H. & Zech Y. 2003. A Godunov method for the computation of erosional shallow water transients. *International Journal for Numerical Methods in Fluids* 41 951–976.

Meyer-Peter, E. & Müller, R. 1948. Formulas for bed-load transport. 2nd IAHR Congress, Stockolm, 1948.

Rahuel, J.L. (1988). Modélisation de l'évolution du lit des rivières alluvionnaires à granulométrie étendue (in French), Institut National Polytechnique de Grenoble, Grenoble, France.

Spinewine B. 2005. Two-layer flow behaviour and the effects of granular dilatancy in dam-break induced sheet flow. PhD thesis, Université catholique de Louvain, Louvain-la-Neuve, Belgium.

Sumer, B.M., Kozakiewicz, A, Fredsoe, J & Deigaard R.1996. Velocity and concentration profiles in sheet-flow layer of movable bed. *Journal of Hydraulic Engineering* 122 (10): 549–558.

Veugdenhil C.B. & de Vries M. (1967). Computation of non-steady bed-load transport by a pseudo viscosity method, Delft Hydr. Lab. Publ. No 45, Delft, The Netherlands.

Copyright © 2006 Taylor & Francis Group plc, London, UK

Wide solid-discharge fluctuations and collective effects in bed-load transport

C. Ancey
École Polytechnique Fédérale de Lausanne, Ecublens, Lausanne, Switzerland

T. Böhm & P. Frey
Cemagref, Domaine Universitaire BP Saint-Martin-d'Hères Cedex, France

M. Jodeau
Cemagref, 3 bis quai Chauveau, Lyon, France

ABSTRACT: Observations in rivers or flumes have shown that for low water discharge, sediment transport is a very intermittent process. To understand the physical origins of the solid-discharge fluctuations, we investigated the motion of coarse spherical glass beads entrained by a steady shallow turbulent water flow down a steep two-dimensional channel with a mobile bed and steady bead supply at the inlet. Flows were filmed from the side by a high-speed camera. We also revisited Einstein's theory on sediment and derived the statistical properties of the key flow variables. Analyzing the autocorrelation functions and the probability distributions of our measurements revealed the existence of long-range correlations. These frequent wide fluctuations stemmed particle entrainment and motion being collective phenomena rather than individual processes, contrary to what is assumed in most theoretical models.

1 INTRODUCTION

The objective of this paper is to characterize and understand the physical origins of wide fluctuations in the solid discharge for sediment transport in gravelbed rivers and mountain torrents. Sediment is assumed to be made up of coarse particles driven by gravity and drag exerted by a water turbulent flow.

Despite substantial progress made over the last two decades in the physical understanding of the motion of coarse particles in a turbulent stream, the ability to compute sediment flux in rivers remains poor. For instance, the sediment flow rates measured in gravel-bed rivers differ within one to two orders of magnitude from the bed-load transport equations (Wilcock 2001; Martin 2003; Barry et al. 2004), even though these equations have been established from flume experiments using regression techniques and are believed to provide a proper evaluation of sediment transport in a well-controlled laboratory environment.

Impediments to a full analytical approach to twophase flows are many: complex interplay between the particles and the carrying fluid, particle exchanges between the bed and the flow, turbulence effects (bed friction, advection of turbulent structures), etc. That is why most models are based on substantial approximations of the interplay between the solid and fluid phases.

Einstein (1950) realized how important it is to account for the episodic nature of particle transport in computing the solid discharge. In Einstein's view, sediment transport does not result from an equilibrium in the momentum transfers between solid and liquid phases (Bagnold's assumption), but rather from the difference between the entrainment and deposition rates. Einstein's stochastic approach raises a number of issues that have received few responses to date. For instance, since particles move sporadically and in different groups, the solid flow rate is made up of a series of pulses and is highly fluctuating, which makes it difficult to define and measure it properly, even under steady flow conditions (Bunte & Abt 2005). Both field and laboratory experiments have revealed that instances in which the instantaneous solid discharge is four times higher than its mean value are frequent (Kuhnle & Southard 1988; Lisle 1989; Böhm et al. 2004). Translated statistically, this observation means that the probability density functions of the transportrate records have a thick tail and depart from the expected Gaussian behavior. This departure can be seen as the hallmark of collective motions (Sornette 2000); if so, this also implies that any mean-field

Copyright © 2006 Taylor & Francis Group plc, London, UK

approximation runs into difficulty since cooperation between particles is not accounted for.

Our idea was to run experiments in an inclined, two-dimensional flume with a continuous particle supply and steady flow rate. This two-dimensional flume is assumed to be the simplest representation of sediment transport on the laboratory scale and presents overwhelming advantages: the boundary conditions can be controlled and most of the flow variables can be measured using image processing. Since a quantitative comparison between theory and experiment is biased by any parameter fitting, we tested Einstein's theory by analyzing the probability distributions and correlations of the signals measured.

2 EINSTEIN'S THEORY REVISITED

Using *ad hoc* arguments, Einstein (1950) derived a bed-load equation, which has been considered as the cornerstone of probabilistic theories of bed-load transport. Taking inspiration from the work done by Lisle et al. (1998) and Papanicolaou et al. (2002), we assume that sediment transport at low flow rates can be described using a birth-death process.

The solid discharge can be defined as the flux of particles through a flow cross-section $\mathcal{S}$. Equivalently, we can define the flow rate $\dot{n} = q_s/v_p$ as the number n of particles in motion within a control volume of length L times their respective velocity u_i

$$\dot{n} = \frac{1}{L}\sum_{i=1}^{n} u_i, \tag{1}$$

(Böhm et al. 2004). In order to compute the discharge equation, we need to establish (i) the number n of particles in motion and (ii) their velocities depending on the control parameters (water discharge q_w, θ, particle radius a, particle density ρ_p.

In order to compute the number of particles in motion, we can draw an analogy with chemical reactions. If the particles resting on the bed surface are denoted by B, the moving particles by M, we can represent the exchanges between the two phases in the following way: $B \rightleftarrows M$: From these equations, we can establish a kinetic equation, which tells us the rate at which exchanges occur between the species B and M. The time variation in the number of moving particles is

$$\frac{dn}{dt} = \frac{n_{b\to m}}{t_b} - \frac{n_{m\to b}}{t_m}, \tag{2}$$

where $n_{b\to m}$ is the number of particles dislodged from the bed and $n_{m\to b}$ is the number of moving particles that are left to rest within the observation window. These population exchanges are associated with the characteristic times t_b and t_m, which are in turn related to the mean times during which a single particle stays

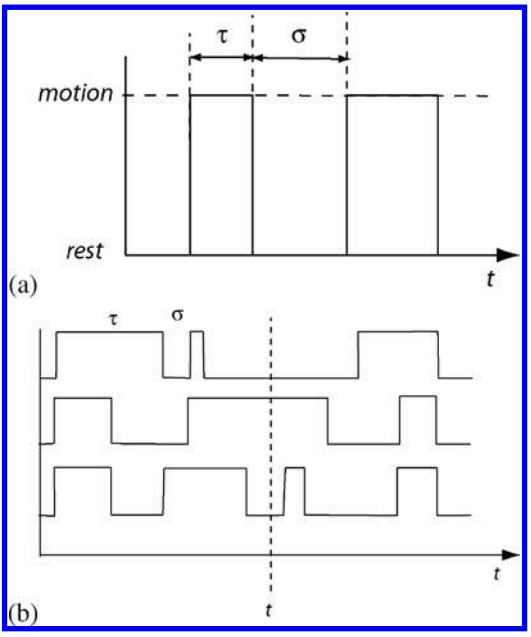


Figure 1. (a) Succession of resting and moving phases for a single particle. (b) The solid discharge is related to the sum of the state variables.

at rest or moves, respectively σ and τ [see Fig. 1(a)]. We can also use Eq. (1) to define the entrainment rate (first term on the right-hand side) and the deposition rate (second on the right-hand side).

Transitions between the moving/resting states occur randomly. Following Lisle et al. (1998) and Papanicolaou et al. (2002), we assume that the particle motion is influenced only by its present state and has a fade memory of its previous states. In other words, the state transitions are governed by a continuous-time Markov process of order 1, with two discrete states (moving/resting). If we further assume that there is time and space invariance in the erosion/deposition process, the Markov transitions occur with constant probability per unit time. For any small time increment δt, we have

$$\text{Prob(moving at time } t+\delta t) = \sigma^{-1}\delta t + o(\delta t),$$
$$\text{Prob(resting at time } t+\delta t) = \tau^{-1}\delta t + o(\delta t),$$

where the characteristic times σ and τ are constant. This two-state Markov process is known as a telegrapher's process (Gardiner 1983). With these assumptions, it can be shown that the resting and moving times are exponentially distributed with means σ and τ, respectively. If $T_{b,i}$ and $T_{m,i}$ represent the durations of the ith periods of rest and motion since observation has started, then $\text{Prob}(T_m) = \tau^{-1}\ \exp(T_m/\tau)$ and $\text{Prob}(T_b) = \sigma^{-1}\ \exp(T_b/\sigma)$; said differently, the waiting time $\Delta t_{b\to r}$ between two entrainments is

Copyright © 2006 Taylor & Francis Group plc, London, UK

exponentially distributed with a mean time equal to σ: $\text{Prob}(\Delta t_{b\to r}) = (\sigma+\tau)^{-1}\exp(\Delta t_{b\to r}/(\sigma+\tau))$. Using the correspondence between the Poisson and exponential distributions, we also deduce that the number of events (deposition/entrainment) that occur per unit time is distributed according to a Poisson distribution: the probability that we observe k entrainments of the same particle within the time interval δt (of any duration) is given by $\text{Prob}(k;\ \delta t) = \nu^k \exp^{-\nu}/k!$, with $\nu = \delta t/\sigma$. The autocorrelation function is $\rho(s) = \exp(-(1/\tau + 1/\sigma)s)$ (Gardiner 1983).

This description is a simplified probabilistic Lagrangian description of a single particle's motion. We generalize it to obtain a Eulerian viewpoint, where we describe the motion of n particles within an observation window. Within our observation window of length $L = 2\lambda a \gg a$ (λ being a free parameter that can take any value), we assume that on average, the particle flux is steady, which means that the particles that leave the window are replaced by other particles coming from upstream. Within this window, there are approximately $N = \lambda$ particles lying over the bed surface, either at rest or in motion. The number n of particles in motion is then the sum of N variables independently distributed and governed by a telegraph process [see Fig. 1(b)]. Since each particle is governed by a telegraph process, the probability of observing it in motion is $\xi = \tau/(\tau+\sigma)$, i.e., it follows a Bernoulli distribution. Now, summing N particles following a Bernoulli distribution leads to a binomial distribution with mean ξN and variance $\xi(1-\xi)N$. We then conclude that with our assumptions, the number n of moving particles is distributed according to a binomial distribution, which means that if ξ stays constant independently of the number of particles N when $L \to \infty$, then the probability distribution of n tends toward a Gaussian distribution. If we further assume that whenever a particle is set in motion, it reaches a fairly constant velocity u_p (Ancey et al. 2003), then using Eq. (1) leads to concluding that the probability distribution of the solid discharge is the binomial distribution Bi, with mean $\xi N u_p$ and variance $\xi(1-\xi)N u_p^2$

$$\text{Prob}(\dot{n}) = \text{Bi}[\xi N u_p,\ \xi(1-\xi)N u_p^2].$$

In the large N limit, this distribution tends to be Gaussian. Since the sum of Poisson-distributed variables also has a Poisson distribution, we infer that the number of deposition/entrainment events per unit time has a Poisson distribution: the probability that we observe k entrainments within the time interval δt is given by

$$\text{Prob}(k;\ \delta t) = \frac{\nu^k}{k!}\exp^{-\nu}, \tag{3}$$

with $\nu = N\delta t/\sigma$. Instead of the Poisson distribution for characterizing the number of events per unit time, we can equivalently use the exponential distribution for specifying the lag times between two events; the mean waiting times between two entrainments within the observation window is $(\sigma+\tau)/N$. The autocorrelation function of N parallel telegrapher's processes is

$$\rho(s) = \exp(-s/\tau_*), \tag{4}$$

with $\tau_* = \sigma\tau/(\tau+\sigma)/N$. It is worth noting that, with our assumptions, the solid discharge and the number of moving particles have the same autocorrelation function.

According to Einstein (1950), the probability of entrainment is the fraction of time $\xi = \tau/(\tau+\sigma)$ that a particle is in a moving state. It also represents, on average, the relative number of particles (i.e., p) that have moved within the observation window for a given time interval (Papanicolaou et al. 2002). Moreover, in Einstein-like theories, particle entrainment results from a loss of stability: when the instantaneous lift and/or drag force exceeds the resisting forces, the particle is dislodged from the bed and starts to roll. By relating the fluid forces to the instantaneous fluid velocity u_f, we can deduce the fluid threshold u_c corresponding to incipient motion (Papanicolaou et al. 2002; Marsh et al. 2004). The probability p is then defined as $p = \xi = \text{Prob}(u_f > u_c)$. Over the time interval t_b, the number of particles that are entrained is then $n_{b\to m} = N_p$, while the number of particles that come to a halt is $n_{m\to b} = n(1-p)$ over the period t_m. In steady flow conditions, Eqs. (2) and (1) lead to

$$q_s = \frac{p}{1-p}\frac{t_m}{t_b}\frac{N}{L}u_p = \frac{p}{1-p}\frac{t_m}{t_b}\frac{u_p}{2a}, \tag{5}$$

which is formally similar to the solid-discharge equation derived by Einstein (1950), except that the solid discharge is now explicitly dependent on the particle velocity.

3 EXPERIMENTAL FACILITIES

3.1 *Overview*

In order to test the influence of fluid velocity (or, equivalently, Shields number) on bed-load transport, we ran six experiments with different flow rates in a twodimensional channel (see Sect. 3.2). The features of each run are summarized in Table 1. The hydraulic conditions are specified using classic dimensionless numbers. The flow Reynolds number is defined as $Re = 4R_h\overline{u}_f/\nu$, where $Rh = Wh/(2h+W)$ denotes hydraulic radius, $\overline{u}_f = q_w/(Wh)$ mean fluid velocity, ν kinematic viscosity of water, and h the time-averaged water depth. The Froude number $Fr = \overline{u}_f/\sqrt{gh}$ varied significantly over the duration of the experiment and along the main stream direction. The mean Fr values are reported in Table 1. The Shields number is defined as $Sh = \rho_f\overline{u}_f^2/((\rho_p-\rho_f)gh)$ and reflects the ratio of the

Copyright © 2006 Taylor & Francis Group plc, London, UK

Table 1. Flow characteristics and time-averaged values of dimensionless numbers characterizing bed load and water flow. The slope is kept constant: $\tan\theta = 10\%$, while the solid discharge at the inlet $\dot{n}_0$ is altered. The notation E10-6 means: $\tan\theta = 10\%$ and $\dot{n}_0 \approx 6$ beads/s. The measured solid discharge within the observation window is denoted by $\dot{n}$. *Re*, *Fr*, and *Sh* are the Reynolds, Froude, and Shields dimensionless numbers. The time-averaged particle velocity in the rolling (saltating, respectively) regime is denoted by $\overline{u}_r$ ($\overline{u}_s$, respectively), while n_r (n_s, respectively) represents the mean number of rolling (saltating, respectively) particles; the variance (Var) of n_r and n_s is provided. We have also reported the autocorrelation time t_e of the rolling-particle number $n_r(t)$.

Experiment	E10-6	E10-7	E10-8	E10-9	E10-16	E10-21
$\tan\theta$ (%)	10.0	10.0	10.0	10.0	10.0	10.0
$\dot{n}_0$ (beads/s)	5.3	6.7	8.0	10.0	15.4	20.0
$q_w = W$ (10^{-3} m^2/s)	4.15	4.42	5.38	5.54	8.19	10.31
h (mm)	10.2	10.6	12.2	12.3	16.6	19.1
$\overline{u}_f$ (m/s)	0.41	0.42	0.44	0.45	0.49	0.54
$\dot{n}$ (beads/s)	5.72	6.85	7.74	9.41	15.56	20.57
Re	4020	4090	4550	4570	5280	5910
Fr	1.29	1.29	1.28	1.30	1.22	1.25
Sh	0.113	0.120	0.135	0.139	0.188	0.216
C_s (%)	2.40	2.69	2.50	2.96	3.30	3.47
$\overline{u}_r$ (m/s)	0.063	0.074	0.065	0.075	0.075	0.072
$\overline{u}_s$ (m/s)	0.28	0.29	0.29	0.29	0.32	0.32
n_r	7.29	6.92	10.37	9.94	16.65	26.69
Var(n_r)	59.13	32.72	55.82	42.61	69.37	119.06
n_s	2.17	2.93	3.39	3.74	6.19	7.52
Var(n_s)	2.40	2.87	3.14	3.30	4.88	5.44
t_e (s)	0.34	0.36	0.23	0.22	0.20	0.18

water driving force to the friction resistance force on the bed (Böhm et al. 2004). The solid concentration is defined as the ratio of the solid and water discharges $C_s = q_s/q_w$. Values reported in Table 1 are low, which indicates that particle flow was dilute. The h/d ratio is low, typically in the range 1.7–3.2.

3.2 *Channel*

Experiments were carried out in a tilted, narrow, glass-sided channel, 2 m in length and 20 cm in height. Figure 2 shows a sketch of the experimental facility. The channel width W was adjusted to 6.5 mm, which was slightly larger than the particle diameter (6 mm). In this way, particle motion was approximately two-dimensional and stayed in the focal plane of the camera. The channel slope $\tan\theta$ was 10%.

3.3 *Channel base and mobile bed*

The channel base consisted of half-cylinders of equal size ($a = 3$ mm), but they were randomly arranged. Disorder was essential, as it prevented slipping of entire layers of particles on the upper bed surface.

3.4 *Solid and water supplies*

Colored spherical glass beads with a nominal diameter $2a$ of 6 mm and a density ρ_p of 2500 kg/m^3 were used. They were injected from a reservoir into the channel using a wheel driven by a direct current motor and equipped with 20 hollows on the circumference, as depicted in Fig. 2. For the experiments presented here, the injection rate $\dot{n}_0$ ranged from 5 to 20 beads per second, with an uncertainty of less than 5%. This corresponded to a solid discharge per unit width q_s/W of $9-38 \times 10^{-5}$ m^2/s. The water supply at the channel entrance was controlled by an electromagnetic flow meter. The discharge per unit width q_w/W ranged from 4 to 10×10^{-3}m^2/s. The hydraulic conditions (velocity profile, bed friction, etc.) have been specified in earlier papers (Ancey et al. 2002; Böhm et al. 2004).

3.5 *Experimental procedures*

Once bed equilibrium was reached, the particles and the water stream were filmed using a Pulnix partial scan video camera (progressive scan TM-6705AN). The camera was placed perpendicular to the glass panes at 115 cm away from the channel, approximately 80 cm upstream from the channel outlet. It was inclined at the same angle as the channel. Lights were positioned in the backside of the channel. An area of $L = 22.5$ cm in length and 8 cm in height was filmed and later reduced to accelerate image processing.

The camera resolution was 640×192 pixels for a frame rate of $f = 129.2$ fps (exposure time: 0.2 ms, 256 gray levels). Each sequence was limited to 8000 images due to limited computer memory; this corresponded to an observation duration of approximately 1 minute.

Copyright © 2006 Taylor & Francis Group plc, London, UK

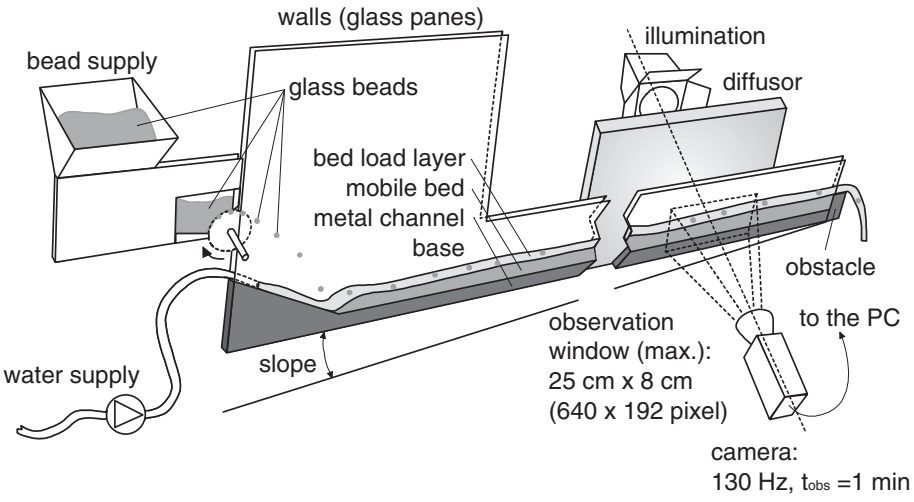


Figure 2. Sketch of the experimental setup.

Each experiment was repeated at least twice in order to spot possible experimental problems and to get an idea of the data scattering. Images were analyzed using the WIMA software, provided by the *Traitement du Signal et Instrumentation* laboratory in Saint- Etienne (France). For more details, the reader can refer to (Böhm 2005).

4 EXPERIMENTAL RESULTS

As we shall see below (Sect. 4.1), the generalized Einstein theory predicts a number of features such as the nearly Gaussian distribution of the solid discharge, the Poissonian character of the occurrence of entrainment/deposition over time, and the exponential decrease in the autocorrelation function of the number of particles moving within the observation window. There are also a number of features that conflict with the fundamental assumptions underpinning this theory. In Sect. 4.2, we will see that the probability distributions of the key variables have much thicker tails than expected. This will be interpreted as the hallmark of cooperation processes between particles when they are entrained or when they move.

4.1 *Solid-discharge time series*

Figure 3 shows the time variations in the solid discharge $\dot{n}$, the number of particles n_r in a rolling regime, the number of particles that passed from a resting state to a rolling state ($r \rightarrow b$) and conversely ($b \rightarrow r$). This diagram represents the results obtained for a mean bed slope of 0.1 and a solid discharge at the flume inlet $\dot{n}_0 = 8$ beads/s (experiment 10-8 in Table 1); these plots are typical of the results that we obtained for other solid discharges $\dot{n}_0$.

Note that in these state transitions [see Fig. 3(d–e)], more than one particle can be involved; because of the limitation of the acquisition rate of our highspeed camera (130 images per second), we could not resolve two events that occurred over very short time intervals. This limitation may pose problems when interpreting the Markovian properties of our time series.

A striking point in Fig. 3 is the wide fluctuations that all the time series exhibit. Typically, the solid flow rate ranged from 0 to 22 beads/s, while the mean flow rate imposed at the inlet was $\dot{n}_0 = 8$ beads/s. For the rolling regime, the fluctuation range was 0–40 beads within the observation window, whereas the mean number was $\overline{n}_r = 9.7$ beads.

As shown in Fig. 4(a), the empirical probability distribution of solid discharge is closely approximated by a Gaussian distribution, although, in places, there are spikes departing from the Gaussian trend. These spikes reflect the existence of a finite number of particles within the observation window (Böhm et al. 2004). This Gaussian behavior is expected since the solid discharge is defined as the product of the number of moving particles and of their velocities [see Eq. (1)]. Indeed, if the particle velocities are sufficiently agitated (resulting in a random velocity distribution) and the number of moving particles within the observation window varies significantly with time, the law of large numbers supports this expectation.

As expected, the autocorrelation functions ρ of the measured signals $\dot{n}(t)$, $n_r(t)$, and $n_s(t)$ are similar. As shown by Fig. 4(b), the typical behavior is the same: (i) we observe a fairly slow exponential decrease, i.e. for short times, we have $\rho(s) \approx \exp(-t/t_e)$ with t_e a

Copyright © 2006 Taylor & Francis Group plc, London, UK

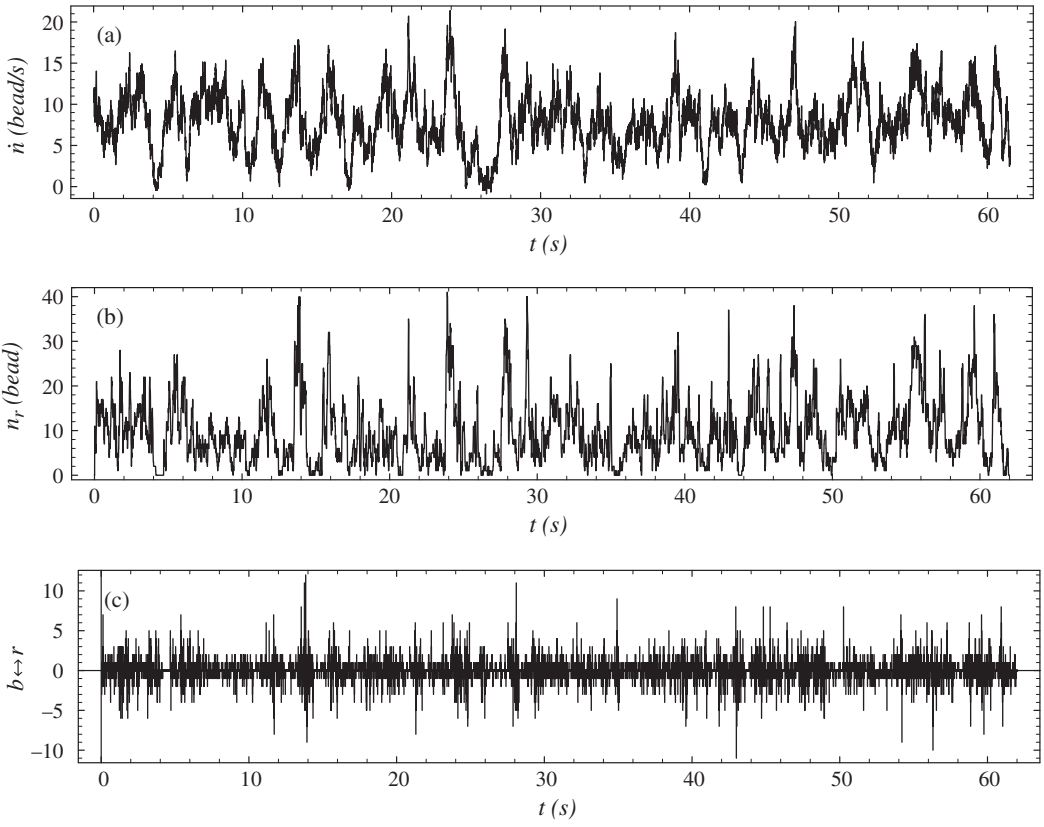


Figure 3. Experiment 10-8: mean solid discharge at the channel inlet $\dot{n}_0 = 8$ beads/s; mean bed slope $\tan\theta = 0.1$. (a) Solid discharge $\dot{n}$ as a function of time. (b) Variation in the number of rolling particles n_r. (c) Exchanges between the bed and the rolling phases: each bar oriented upward indicates the number of beads that passed from the resting state to the rolling regime over a given time interval $\Delta \approx 1/130$ s; downward-oriented bars represent the number of rolling particles coming to a halt.

typical time scale; (ii) the typical time scales t_e related to each signal are very close. For experiment E10-8, we found $t_e \approx 230$ ms. The autocorrelation times for other experiments are reported in Table 1.

In an earlier paper (Böhm et al. 2004), the timescale t_e was interpreted as the typical travel time of the moving particles through the observation window. While this interpretation seems reasonable for the solid discharge, there is at first glance no clear reason why this should be so for the number of rolling/saltating particles. One could call on the following explanation for the similarity in the autocorrelation functions: once a particle experiences a transition into another regime, it moves at approximately the same velocity as the mean phase velocity and hence one expects that the autocorrelation time $n_r(t)$ and $n_s(t)$ is somehow related to a travel time. However, since their mean phase velocity was quite different (see Table 1), their autocorrelation times should also be different.

In Sect. 2, we have also shown that for particle entrainment, the waiting-time distribution should follow an exponential distribution of rate $r = N/(\sigma + \tau)$. A particular problem encountered here in evaluating the parameter r is that we could not resolve successive events when they occurred within a very short time interval (less than the acquisition rate of our camera, i.e. for lag times shorter than $2/130 = 0.015$ s); this means that we should censor the lag-time sample to remove the lowest values if we want to properly evaluate the sample distribution. For the sake of simplicity, however, we did not proceed in this way. Figure 5(a) shows the empirical probability distribution function of the lag times Δt for the different classes of events (entrainment or deposition, transition to a rolling or a saltating regime). We have superimposed the exponential distribution, the coefficient of which has been adjusted using the method of moments on the whole sample. As expected, the exponential distribution is a fairly good representation of the lag-time distribution whatever the type of exchange except at low values of Δt, for which the empirical distribution departs significantly from the exponential

Copyright © 2006 Taylor & Francis Group plc, London, UK

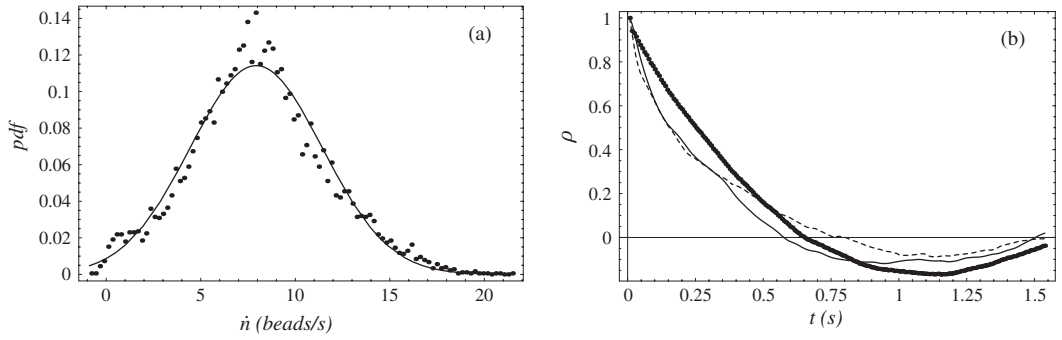


Figure 4. (a) Probability distribution function (pdf) of the solid discharge for experiment E10-8 ($\dot{n}_0 = 8$ beads/s; mean bed slope $\tan\theta = 0.1$): the dots represent the empirical pdf, whereas the solid line is a Gaussian distribution adjusted on the data (mean: 7.93, standard deviation: 3.49). (b) Autocorrelation function for experiment E10-8: the thick dotted line corresponds to the solid discharge $\dot{n}$, the thin solid line to the number of rolling particles n_r, and the dashed line to the number of saltating particles n_s.

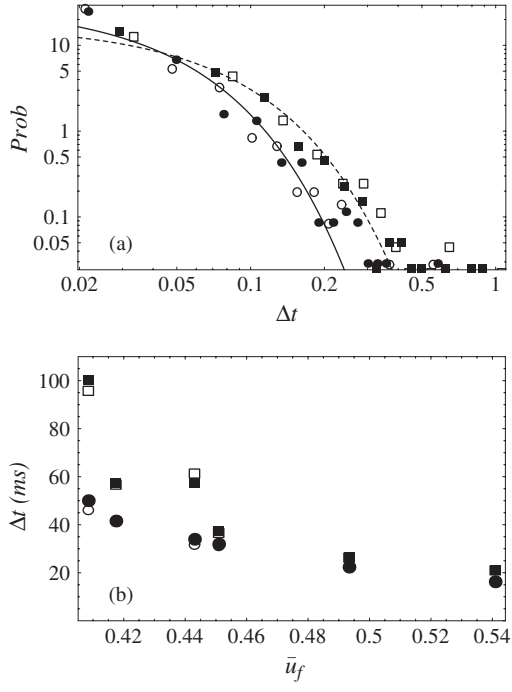


Figure 5. Probability distribution of the time lag Δt between two events (change in state): the filled disks represent the state transition $b \to r$ (entrainment, $\tau_{b\to r}$), while the empty disks represent the state transition $r \to b$ (deposition, $\tau_{r\to b}$); the solid line provides the exponential probability distribution adjusted on the data $b \longleftrightarrow r$ (using the method of moments). The filled boxes represent the state transition $r \to s$, while the empty boxes represent the converse transition $s \to r$; the dashed line is the exponential probability distribution adjusted on the data $r \longleftrightarrow s$. (b) Variation in the lag times $\Delta t_{b\to r}$ (filled disks), $\Delta t_{r\to b}$ (empty disks), $\Delta t_{r\to s}$ (filled boxes), and $\Delta t_{s\to r}$ (empty boxes).

trend. Adjustment provides the following characteristic times for each transition type for experiment E10-8: $\Delta t_{b\to r} = 33.9$ ms, $\Delta t_{r\to b} = 31.7$ ms, $\Delta t_{r\to s} = 57.4$ ms, and $\Delta t_{s\to r} = 61.3$ ms. For all experiments, the mean lag times are reported as a function of the mean fluid velocity in Fig. 5(b).

Up to this point, the generalized Einstein theory is qualitatively consistent with our laboratory experiments. A discrepancy is, however, noticeable. In Sect. 2, we found that the autocorrelation time t_e was $\tau_* = \sigma\tau/(\tau+\sigma)/N$ and the waiting time was $\Delta t_{b\to r} = r^{-1} = (\sigma + \tau)/N$. From these relations, we deduce that the ratio

$$\frac{\tau_*}{\Delta t_{b\to r}} = \frac{\tau/\sigma}{(\tau/\sigma+1)^2} < 1,$$

in contradiction with our experimental results, since for instance for E10-8, we have $\tau_*/\Delta t_{b\to r} = 6.9$. The autocorrelation time is much longer than expected. As we shall see in the next subsection, this result is not fortuitous and illustrates the existence of long-range correlations in the physical processes governing sediment transport.

4.2 *Probability distribution of the number of moving particles*

Analyzing the probability distribution of the number of moving particles is richer than examining that of the solid discharge because the latter combines two sources of fluctuations: the number of particles and their velocities, which makes it difficult to properly interpret them. Here, we will focus on the probability distributions of the number of rolling particles n_r (see Fig. 6).

Figure 6 shows how the probability distribution of n_r changes when the fluid velocity is increased. At low

Copyright © 2006 Taylor & Francis Group plc, London, UK

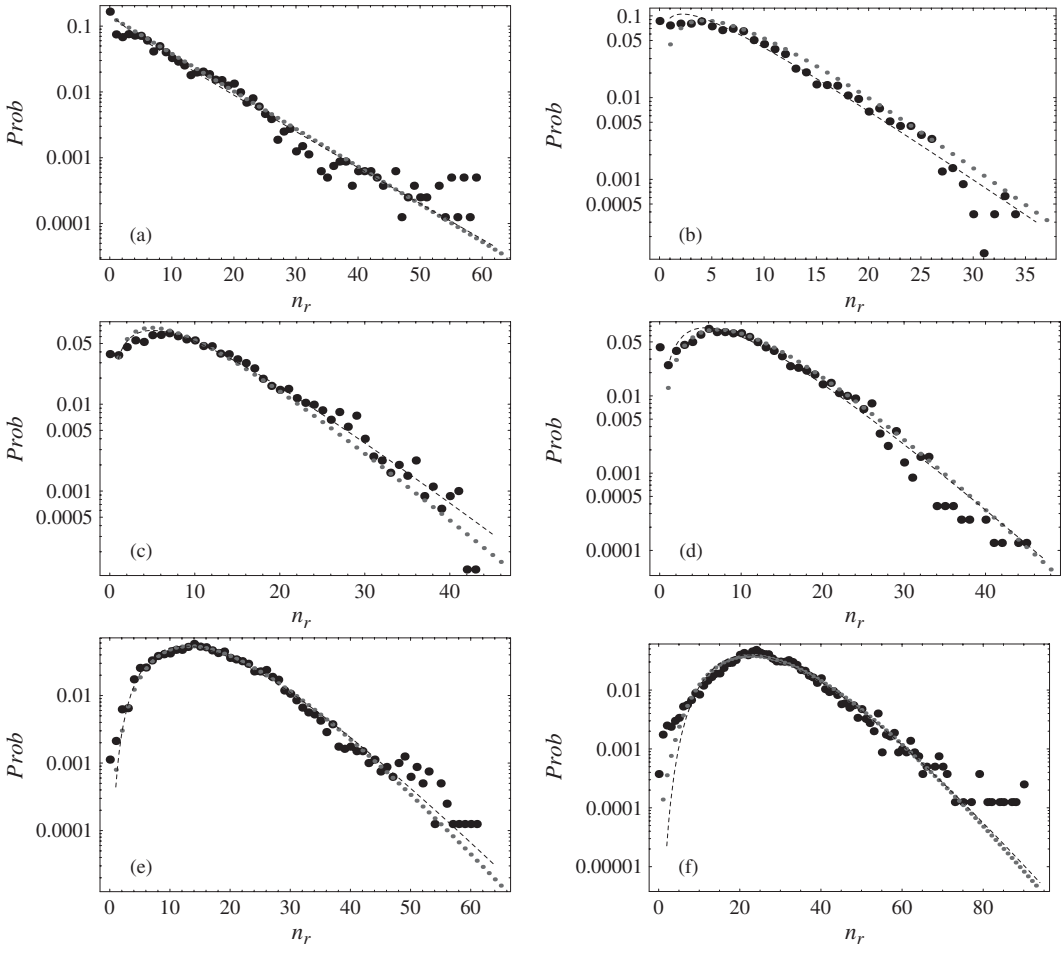


Figure 6. Probability distributions of the number of rolling particles. The dots represent the empirical probability mass functions. The dotted lines represent the negative binomial distribution, while the dashed lines represent the gamma distribution. (a) experiment E10-6, (b) experiment E10-7, (c) experiment E10-8, (d) experiment E10-9, (e) experiment E10-16, (f) experiment E10-21.

fluid velocities, the probability distribution is close to a straight line in a log-linear diagram, revealing a power-like behavior. At higher fluid velocities, the probability distribution takes the shape of an asymmetric bell, with its maximum moving from left to right. At first sight, the prominent impression is that increasing the solid discharge leads to making the probability distribution of n_r more Gaussian.

In the generalized Einstein theory presented in Sect. 2, we inferred that the number of moving particles should be distributed according to a binomial law, with mean ξN and variance $\xi(1-\xi)N$ where N is the density number of particles lying on the bed and $\xi = \tau/(\sigma+\tau)$ is the mean relative time during which a particle is maintained in motion by the stream. A particularity of the binomial law is that its variance must be lower than its mean. For all our experiments, we found that the sample variance exceeded the sample mean. For instance, for experiment E10-8 [see Fig. 6(c)], the mean number of particles is $\overline{n}_r = 10.4$, whereas the variance is $\mathrm{Var}(n_r) = 55.8$. For all probability distributions, the distribution tail is much thicker than expected.

Since thick tails are often associated with collective phenomena (Sornette 2000), it is worthwhile characterizing these distributions more accurately.We found that the negative binomial distribution provides a fairly proper representation of the empirical distribution, as shown in Fig. 6. Small departures are observed in the distribution tail (insufficient number of data) and when $n_r \to 0$. Note that it was not always very easy to distinguish between incipient motion and oscillations of

Copyright © 2006 Taylor & Francis Group plc, London, UK

bed particles and consequently our image-processing algorithm failed at times to count the exact number of moving particles. The small deviations between the theoretical and empirical probability distributions may result from this uncertainty on n_r. Except for the behavior close to the boundaries, the whole trend is well represented by the negative binomial distribution. Instead of a discrete distribution, we can use a continuous probability distribution to approximate the empirical distribution of n_r. A natural candidate is the gamma distribution, which can be fairly well adjusted on data, as shown in Fig. 6.

This observation is of fundamental importance since it conflicts with the assumptions underlying the birthand- death process used in the theoretical derivation. Indeed, if the particles are independent and identical, then one obtains a binomial distribution whatever the model taken for rest/move, provided that the flow is steady and there is bed equilibrium. The only way to obtain a non binomial behavior would be to have (i) unsteady flow conditions or (ii) non identical or dependent particles. Assumption (ii) is the most plausible. Taking a closer look at the resting and moving states showed that on many occasions, particles moved in well-separated groups (Böhm et al. 2004). Collective displacement and entrainment of particles explained why the particles were to some extent dependent and thus why the autocorrelation time was much longer than expected. One might think that aggregate transport was promoted by particle sphericity and equal size. Our observations are, however, well supported by field measurements, which documented similar processes in gravel-bed rivers (Drake, Shreve, Dietrich, & Leopold 1988). The wide range of fluctuations exhibited by laboratory or field measurements (Wilcock 2001; Martin 2003; Barry, Buffington, & King 2004) also confirmed the existence of thick-tailed probability distributions for sediment transport involving irregular particles.

5 CONCLUSION

Our experimental results provided evidence that, although some statistical properties (such as the autocorrelation function of the solid discharge) predicted by Einstein's theory were consistent with our data, the autocorrelation functions of the number of moving particles and their mass distribution functions violated the assumptions underpinning Einstein's theory. Typically, the autocorrelation time was much longer than expected and the mass distribution function had a much thicker tail than predicted using Einstein's arguments. For instance, from the theoretical standpoint, the number of moving particles within any observation window is a random number distributed according to a binomial distribution; in the large-number limit, the theoretical distribution should tend very quickly toward a Gaussian limit. In contrast, our experiments showed that the sample variance outweighed the sample mean and a negative binomial distribution fits the data better. This means that extreme events (i.e., a large number of moving particles) are much more frequent than expected. Furthermore, our experiments showed that the convergence toward the Gaussian limit is slow. At the lowest solid discharges achievable with our system, the probability distribution of the particle number is closer to a power-law distribution. When increasing the solid discharge, the variance/ mean ratio decreases and the probability distribution becomes increasingly bell-shaped.

The present study has many important implications. First, it provides a plausible explanation about the failure of all mean-field theories on bed-load transport, which ignore any cooperation effects between particles. It thus motivates further research with a clear focus on collective effects in entrainment and displacement of coarse particles as a result of fluid action. Second, this work sheds some light in the critical issues concerning bed-load measurement in rivers (Bunte & Abt 2005). Hydraulicians and geomorphologists use various systems (Helley-Smith sampler, bed-load trap) to measure the solid discharge by capturing sediment over a given time interval. The crux of the issues lies in the proper selection of the sampling time (ranging from a few seconds to several minutes), and this dif- ficulty of selecting a proper timescale is illustrated by the large differences among various measurement systems.

REFERENCES

Ancey, C., F. Bigillon, P. Frey, & R. Ducret (2003). Rolling motion of a single bead in a rapid shallow water stream down a steep channel. *Phys. Rev. E 67*, 011303.

Ancey, C., F. Bigillon, P. Frey, R. Ducret, & J. Lanier (2002). Motion of a single bead in a rapid shallow water stream down an inclined steep channel. *Phys. Rev. E 66*, 036306.

Barry, J., J. Buffington, & J. King (2004). A general power equation for predicting bed load transport rates in gravel bed rivers. *Water Resour. Res. 40*, W10401.

Böhm, T. (2005). *Motion and interaction of a set of particles in a supercritical flow*. Ph. D. thesis, Joseph Fourier University.

Böhm, T., C. Ancey, P. Frey, J.-L. Reboud, & C. Duccotet (2004). Fluctuations of the solid discharge of gravity-driven particle flows in a turbulent stream. *Phys. Rev. E 69*, 061307.

Bunte, K. & S. Abt (2005). Effect of sampling time on measured gravel bed load transport rates in a coarsebedded stream. *Water Resour. Res. 41*, W11405.

Drake, T., R. Shreve, W. Dietrich, & L. Leopold (1988). Bed-load transport of fine gravel observed by motion-picture photography. *J. Fluid Mech. 192*, 193–217.

Einstein, H. (1950). The bed-load function for sediment transportation in open channel flows. Technical Report Technical Report No. 1026, United States Department of Agriculture.

Copyright © 2006 Taylor & Francis Group plc, London, UK

Gardiner, C. (1983). *Handbook of Stochastic Methods*. Berlin: Springer Verlag.

Kuhnle, R. A. & J. B. Southard (1988). Bed load transport fluctuations in a gravel bed laboratory channel. *Water Resour. Res. 24*, 247–260.

Lisle, I., C. Rose,W. Hogarth, P. Hairsine, G. Sander, & J. Y. Parlange (1998). Stochastic sediment transport in soil erosion. *J. Hydrol. 204*, 217–230.

Lisle, T. (1989). Sediment transport and resulting deposition in spawning gravels, north coastal California. *Water Resour. Res. 25*, 1303–1319.

Marsh, N., A.Western, & R. Grayson (2004). Comparison of Methods for Predicting Incipient Motion for Sand Beds. *J. Hydraul. Eng. 130*, 616–621.

Martin, Y. (2003). Evaluation of bed load transport formulae using field evidence from the Vedder River, British Columbia. *Geomorphology 53*, 75–95.

Papanicolaou, A., P. Diplas, N. Evaggelopoulos, & S. Fotopoulos (2002). Stochastic incipient motion criterion for spheres under various bed packing conditions. *J. Hydraul. Eng. 128*, 369–390.

Sornette, D. (2000). *Critical Phenomena in Natural Sciences*. New York: Springer.

Wilcock, P. (2001). Toward a practical method for estimating sediment-transport rates in gravel bedrivers. *Earth Surf. Proc. Landforms 26*, 1395–1408.

Copyright © 2006 Taylor & Francis Group plc, London, UK

SETRAC – A sediment routing model for steep torrent channels

D. Rickenmann, M. Chiari & K. Friedl
University of Natural Resources and Applied Life Sciences, Vienna, Austria

ABSTRACT: A sediment routing model for steep torrent channel networks called SETRAC has been developed. SETRAC is the acronym for sediment transport in Alpine catchments. In SETRAC the water runoff is given as input hydrographs at discrete points. A kinematic flow routing of the flood hydrograph is performed in the channel network. Different sediment transport formulae and flow resistance approaches can be selected in SETRAC. The sediment is transferred through the channel network considering a reachwise sediment budget. Initial sediment stock can be assigned for each channel reach. SETRAC is applied to a well documented case study on a flood event with substantial sediment transport which occurred in a torrent catchment in the Austrian Alps. Using a rough correction procedure to account for form roughness losses which reduce the energy slope available for bedload transport, a reasonable agreement has been obtained between simulated and observed sediment loads. Considering the uncertainty of the input data, the results are encouraging.

1 INTRODUCTION

In contrast to studies on lowland gravel-bed rivers, relatively few have been made on sediment transport in steep headwater channels, with stream gradients steeper than about 0.05. Sediment transport dynamics in these channels may be quite different from low-gradient channels. There is often a strong interaction between hillslope processes and the channel network. Sediment transport may be supply limited rather than controlled by the sediment transport capacity under given discharge and channel conditions. Steep headwater streams are characterized by a wide range of sediment sizes and temporally- and spatially-variable sediment sources. Bed morphology and channel structures may be influenced by the presence of large boulders, woody debris and bedrock constrictions. This can result in large variations in channel geometry, streamflow velocity and roughness, and thus the application of theoretical sediment transport equations may be problematic (Gomi & Sidle 2003). Quantitative measurements of sediment and bedload transport in steep streams are very limited (Rickenmann 2001).

Many bedload transport formulas for gravel-bed rivers were developed or calibrated based on experiments in laboratory flumes. Measured transport rates in natural streams may differ substantially from values predicted with such formulas (e.g. Bathurst et al. 1987, Gomez & Church 1989). Also, measured transport rates in gravel-bed rivers and boulder-bed streams may vary by several orders of magnitude at similar (mean) flow conditions (e.g. Bathurst et al. 1987, Gomez 1987, Reid & Laronne 1995, Hegg & Rickenmann 1999, Rickenmann 2001). In very steep streams and at high transport intensities (e.g. "immature" debris-flow conditions) the distinction between bedload and suspended load transport becomes blurred (Takahashi 1987, Rickenmann 1990a).

For boulder-bed channels, which are typical for torrents and mountain streams steeper than a few percent, a two-phase model as described by Beschta (1987) and Bathurst (1987) can provide a conceptual framework for the description of sediment transport behaviour. In "phase 1 transport" there is basically no destruction of the coarse surface layer, and the transported sediment is generally made up the finer fractions (sand and fine gravel); transport rates largely depend on fine material available in pools and behind channel obstructions, or on external sediment supply which can vary by orders of magnitude. In "phase 2 transport" the surface or armour layer is broken up and there is essentially equal mobility of all size fractions, i.e. the size distribution of the bedload is similar to that of the subsurface material. Several studies have applied different bedload transport formulas to field measurements in gravel-bed rivers and tried to assess their performance. For example, Bathurst et al. (1987) compared six bedload transport formulas with field and flume data at bed-slopes up to 0.09, and found that the best predictions were given by Schoklitsch's (1962) equation.

Flow resistance in steep mountain streams with irregular bed topography includes both grain friction

Copyright © 2006 Taylor & Francis Group plc, London, UK

and form drag. Flows are typically characterized by low relative flow depths. Recent investigations and discussions of such flow conditions were made by Aberle & Smart (2003), Bathurst (2002), Lee & Ferguson (2002), and Smart et al. (2002).

For flows in natural streams with values of h/d_c (with coarse grain size $d_c = d_{84}$ or d_{90}) smaller than about 4 to 6 a marked increase in flow resistance has been observed (Pitlick 1992, Rickenmann 1996, Bathurst 2002). Jarrett (1990) reported that flow resistance may be substantially larger and more variable in steep boulder-bed channels at smaller values of relative flow depths, i.e. when the ratio of the hydraulic radius to the medium grain diameter is less than about 5. Bathurst (1993) discussed the development of a roughly S-shaped velocity profile in boulder-bed channels, at relative flow depths h/d_{84} of about 1 to 4. Compared to a logarithmic velocity profile, the flow in the lower zone near the boulders is retarded while there is a higher velocity zone near the flow surface. The additional drag caused by the boulders in this range may be partly responsible for the lower bedload transport "efficiency" as compared to flows with higher relative flow depths (Rickenmann 2001).

In principle two different approaches may be taken to consider sediment routing in steep streams. The first approach consists in using a hydraulic simulation model including sediment transport and accounting for variations in bed geometry due to erosion or deposition. These models typically include the full Saint Venant equations for one- or two-dimensional flow. A sediment transport equation is used in combination with the so-called Exner equation to account for sediment transport and storage effects in the riverbed. Examples are the MORMO model (Schilling & Hunziker 1995) and the FLUMEN model (Beffa 2005); in both models, armouring of the river bed can be considered.

A second group of hydrosedimentologic models considers sediment transfer processes at the catchment scale, including channel sediment transfer with different degrees of details. These models can typically be linked to a rainfall-runoff module and a module to account for sediment transfer from hillslopes into the channel network. Examples are the ETC rainfall-runoff-erosion model (Mathys et al. 2003), and the SHESED model (Wicks & Bathurst 1996).

The objective of this paper is to present the framework of equations to predict flow resistance and sediment transport in steep torrents and to introduce the new sediment routing model for steep torrent channel networks, called SETRAC, where these equations have been implemented. In addition, an application of the SETRAC model is discussed for the case of a flood event in an Austrian torrent which occurred in August 2005 and transported about 30,000 m^3 of debris to the fan area.

2 FLOW RESISTANCE

2.1 *Flow resistance approaches*

For steep streams with gradients larger than about 0.1 there are only few velocity measurements, and in most cases no information is available on flow depth. However, the well known Manning-Strickler equation is also used in torrents, due to the lack of other approaches.

$$v = \frac{1}{n} R^{0.67} S^{0.5} \tag{1}$$

where v is the mean flow velocity, n *is* Manning's roughness coefficient ($1/n = k_{St}$, where k_{St} is Strickler's coefficient of roughness), R is the hydraulic radius and S is the channel gradient.

Due to the lack of flow depth data in steep streams, Rickenmann (1994, 1996) developed a set of empirical equations where the mean flow velocity, the Strickler or Manning's coefficient and the surface width of the flow, respectively, can be expressed as a function of discharge, channel gradient, and a characteristic grain size of the surface bed material. All the equations are dimensionally homogeneous; they are based on more than 300 measurements in torrents and gravel-bed rivers. The equations to estimate Manning's roughness coefficient n are (Rickenmann 1996):

$$\frac{1}{n} = \frac{0.97 g^{0.41} Q^{0.19}}{S^{0.19} d_{90}^{0.64}} \quad for \quad S > 0.008 \tag{2}$$

$$\frac{1}{n} = \frac{4.36 g^{0.49} Q^{0.02}}{S^{0.03} d_{90}^{0.23}} \quad for \quad S < 0.008 \tag{3}$$

where g is the acceleration due to gravity, Q is the discharge and d_{90} is the grain size of the surface bed material for which 90% of the bed material is finer. The equations are based on stream flow velocity observations covering a wide range of flow conditions, including mountain streams with channel gradients of up to 0.2 and relative flow depth as small as about 0.4. The original regression equations were derived using dimensionless parameters. Figure 1 compares the two equations with the field data. For most of the data points, the difference between predicted and observed values is less than about +/−50%.

Alternatively the mean flow velocity can also be expressed as a function of discharge instead of flow depth (Rickenmann 1991, 1994):

$$v = \frac{1.3 g^{0.2} q^{0.6} S^{0.2}}{d_{90}^{0.4}} \tag{4}$$

where q is the flow rate per unit width. Equation (4) was originally proposed by Takahashi (1978) based on

Copyright © 2006 Taylor & Francis Group plc, London, UK

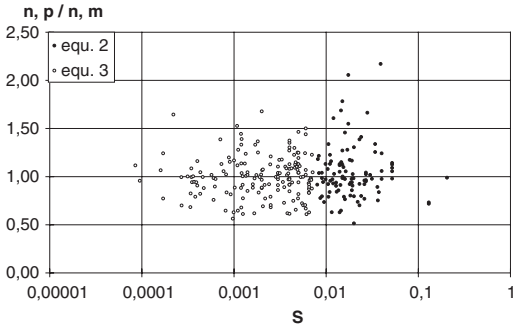


Figure 1. Ratio of predicted to measured Manning roughness coefficient, n_p/n_m, against the slope, S for the equations (2) and (3).

laboratory experiments on debris flows, and successfully applied by Rickenmann (1991) to experimental sediment transporting flows. Like equation (2) and (3) equation (4) is dimensionally homogenous.

Equation (4) was applied to field data by Rickenmann (1996), resulting in a similar scatter between predicted and observed velocities, as when applying equation (2) in combination with equation (1). With $q = vh$ equation (4) can be transformed to:

$$v = \frac{1.93 g^{0.5} h^{1.5} S^{0.5}}{d_{90}} \tag{5}$$

where h is the flow depth.

Another flow resistance equation for steep channels was introduced by Smart & Jäggi (1983). The formula is based on their laboratory data of sediment transporting flows. The increasing flow resistance at low relative flow depths is expressed by:

$$v = 2.5 v^* \left(1 - e^{\frac{-0.05 h_m}{S^{0.5} d_{90}}}\right) \ln\left[\frac{12.3 h_m}{1.5 d_{90}}\right] \quad \text{for } S \le 0.20 \tag{6}$$

where the shear velocity is defined as $v^* = (g h_m S)^{0.5}$, and the expression in the first brackets accounts for increasing flow resistance at low relative flow depths. The mixture flow depth h_m accounts for the space occupied by moving particles. The increase compared to the fluid flow depth, $h_f = q/v$, was found to be important for channel gradients steeper than about 0.1 in the laboratory experiments. In SETRAC, the following empirical relation for the ratio h_f/h_m is used (Rickenmann 1990a):

$$\frac{h_f}{h_m} = 1 - 1.64 S^{0.42} \left(\frac{q_b}{q}\right)^{0.63} \tag{7}$$

where q_b is the bedload transport rate per unit channel width. The experiments for the development of (7) covered channel gradients up to 0.2. To avoid unrealistic extrapolations, the minimum value of h_f/h_m is set as 0.2, which approximately corresponds to the maximum packing density of natural sediment.

2.2 *Flow resistance due to form roughness*

In steep mountain streams with irregular bed topography, form roughness is an important contribution to total grain friction. Flows are typically characterized by low relative flow depths and substantial form drag.

Wong & Parker (in review) proposed an expression for the roughness coefficient n_r associated with skin friction only, in the context of reanalysing the bedload relation of Meyer-Peter & Müller (1948):

$$\frac{1}{n_r} = \frac{23.2}{d_{90}^{1/6}} \tag{8}$$

A similar equation for n_r has also been reported by Jäggi (1984). Following a procedure proposed by Palt (2001), the relative proportion of grain roughness to total roughness can be expressed by dividing (8) by (2):

$$\frac{n_r}{n} = \frac{0.131 g^{0.09} Q^{0.19}}{S^{0.19} d_{90}^{0.47}} \quad \text{for } S > 0.008 \tag{9}$$

In (9) the contribution of form resistance to the total resistance is represented by $(1 - n_r/n)$. A slightly different expression for n_r/n can be obtained by using (8) in combination with the empirical equations for velocity and flow width (equations (2a) and (4) in Rickenmann 1994), resulting in:

$$\frac{n_r}{n} = 0.185 S^{-0.22} \left(\frac{h}{d_{90}}\right)^{0.55} \quad \text{for } S > 0.008 \tag{10}$$

A comparison of (9) and (10) is made in Figure 2 where they are applied to the data set of flow velocity measurements used by Rickenmann (1994, 1996). A large variation of the n_r/n values is observed for channel gradients up to about 0.1. For steeper channels form roughness appears to be more important than grain roughness, based on the limited data available.

The slope of the energy line S can now be partitioned into a fraction S_{red} associated with skin friction only:

$$\frac{S_{red}}{S} = \left(\frac{n_r}{n}\right)^2 \tag{11}$$

Using a similar procedure, Palt (2001) accounted for form losses and found much better agreement with his bedload measurements in Himalayan rivers and

Copyright © 2006 Taylor & Francis Group plc, London, UK

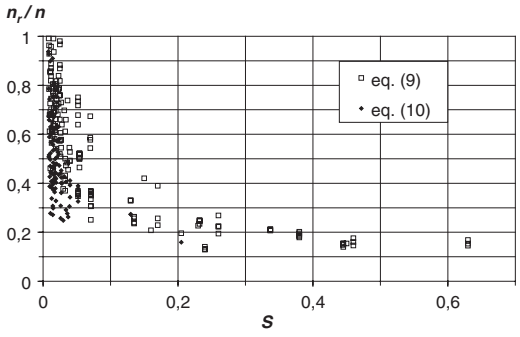


Figure 2. Comparison of two approaches to estimate the proportion of form and grain roughness in steep streams.

the bedload transport data of Meyer-Peter and Müller (1948).

The exponent of 2 in equation (11) is based on the Manning-Strickler equation. However Meyer-Peter & Müller (1948) argued that the exponent in the following equation (12) may be different from 2, and from their experiments they empirically determined a value $a = 1.5$ (Meyer-Peter & Müller 1948), as is also discussed by Wong & Parker (in review). A more general form of equation (11) is therefore:

$$S_{red} = S\left[\frac{n_r}{n}\right]^a \tag{12}$$

where plausible values of a are probably in the range $1 \le a \le 2$.

3 SEDIMENT TRANSPORT

The sediment transport module includes formulae for the determination of the total and grain resistance, the determination of incipient motion conditions in high gradient streams and the calculation of the sediment transport capacity. These interacting components can be combined within SETRAC.

Only a very limited number of bedload transport formulas have been developed for steep gravel bed streams. At ETH Zurich, a total of 252 experiments on bedload transport in gravelbed channels were performed both for gradients of 0.0004 to 0.023 (Meyer-Peter & Müller 1948) and for gradients of 0.03 to 0.20 (Smart & Jäggi 1983, Rickenmann 1990a).

Smart & Jäggi (1983) performed flume experiments to estimate the maximum transport capacity in steep channels:

$$q_b = \frac{4}{s-1}\left(\frac{d_{90}}{d_{30}}\right)^{0.2} qS^{1.6}\left(1-\frac{\theta_{cr}}{\theta}\right)$$

$$\text{for } 0.002 \le S \le 0.20 \text{ and } d_{90}/d_{30} \le 10. \tag{13}$$

where $s = \rho_s/\rho$ is the ratio of solid to fluid density and θ is the dimensionless bed shear stress. They estimated the dimensionless critical shear stress at initiation of bedload transport, θ_{cr}, with:

$$\theta_{cr} = \theta \cos\arctan S\left(1-\frac{S}{\tan\varphi}\right) \tag{14}$$

where ϕ is the angle of response.

For the entire slope range, including a total of 252 experiments, the following dimensionless bedload transport equation was developed (Rickenmann 1991):

$$\Phi_b = 3.1\left(\frac{d_{90}}{d_{30}}\right)^{0.2} \theta^{0.5}(\theta-\theta_{cr})Fr^{1.1}(s-1)^{-0.5} \tag{15}$$

where $\Phi_b = q_b/[(s-1)gdm^3]^{0.5}$ is the dimensionless bedload transport rate, d_m is the mean grain size and the dimensionless shear stress is $\theta = h_m S/[(s-1)d_m]$, and the Froude number is $Fr = v/(gh)^{0.5}$.

For the steep slope range only, i.e. $0.03 \le S \le 0.20$, a slightly more accurate representation of the data on bedload transport is given by the following equation (Rickenmann 1990a):

$$q_b = 12.6\left(\frac{d_{90}}{d_{30}}\right)^{0.2} (q-q_c)S^{2.0}(s-1)^{-1.6} \tag{16}$$

where q_c is the critical discharge for beginning of bedload transport.

Rickenmann (2001) slightly modified equation (15) by setting $Fr = 1$ and transforming it into a form similar to (16).

$$q_b = 3.1\left(\frac{d_{90}}{d_{30}}\right)^{0.2} (q-q_c)S^{1.5}(s-1)^{-1.5} \tag{17}$$

This form facilitates a comparison with other sediment transport formulae specifically developed for streams with gradients steeper than about 0.03. For a typical value of $s = 2.65$ and setting $d_{90}/d_{30} = 1.05$ for a uniform grain size distribution (Smart & Jäggi 1983), a comparison is made between equation (13), (16), and (17) with experimental data from the steep flume studies at ETH Zurich (Figure 3). For this purpose, (13) has been slightly modified to substitute θ_{cr} by q_c (Rickenmann 1990a).

The formulae (16) and (17) can be combined with an equation for the critical discharge.

$$q_c = 0.065(s-1)^{1.67} g^{0.5} d_{50}^{1.5} S^{-1.12} \tag{18}$$

$$q_c = 0.143(s-1)^{1.67} g^{0.5} d_{90}^{1.5} S^{-1.167} \tag{19}$$

Copyright © 2006 Taylor & Francis Group plc, London, UK

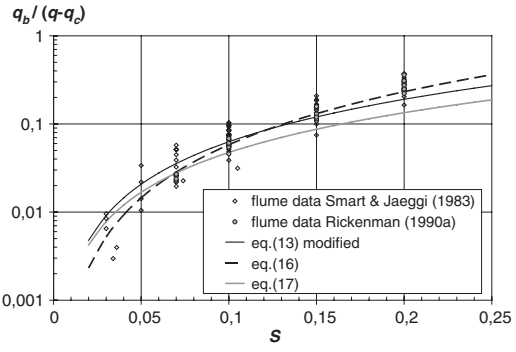


Figure 3. Comparison of bedload transport equations implemented in SETRAC with steep flume data of ETH Zurich.

Equation (18) was proposed by Bathurst et al. (1987) based on field data, and was slightly modified by Rickenmann (1990a). It represents bed conditions without an amour layer. Equation (19) is based on block ramp experiments by Whittaker & Jäggi (1986), and by using d_{90} as characteristic grain size it may be considered to represent the critical discharge required to break up an amour layer in steep streams.

4 SETRAC MODEL

4.1 *Modelling concept*

A one-dimensional sediment routing model for steep torrent channel networks called SETRAC has been developed at the University of Natural Resources and Applied Life Sciences, Vienna (Friedl 2004, Fuchs & Friedl 2002). SETRAC is the acronym for Sediment Transport Model in Alpine Catchments.

The channel network and longitudinal channel profile may be determined by means of a GIS. The channel cross-sections may have irregular shapes, representing a terrestrial bed survey. For the computations, the cross-sections may be represented with different degrees of simplification. A rainfall-runoff model may be used to determine the lateral input into channel sections in SETRAC, or input hydrographs may be defined at discrete points of the channel network.

The model uses a kinematic flow routing of the flood hydrograph through the channel network, neglecting diffusive and convective terms of the full Saint Venant equations.

Typically, the flow resistance approaches (1) or (4) are combined with the sediment transport formulae (16) and (17) and with the critical discharge (18) and (19). The flow resistance approach (6) can be combined with the sediment transport formulae (13) or (15). The flow resistance losses due to form drag (9) and (12) may or may not be taken into account with a sediment transport equation.

4.2 *Graphical user interface*

The SETRAC graphical user interface provides a clearly arranged tool for data handling. The input files can be selected and stored as projects. The channel network and the cross-sections including information about the discretization for calculation can be visualized. The parameters can be set and the formulae for the simulation can be selected. During the simulation the hydrographs and sedigraphs for the outlet and for selected locations can be monitored.

At any point in the channel network, the following output can be generated: Hydrograph and sedigraph as well as a sediment transport diagram showing reaches with erosion, “equilibrium” transport, and deposition of sediment. The longitudinal section can be exported as DXF (to be opened with CAD Software). The results of the simulation can also be stored as ASCII files.

4.3 *Geometric data*

The channel network is represented by nodes, sections and cross-sections. The longitudinal profile and the cross-sections need to be surveyed in the field, because the resolution of DEMs is commonly of the order of 25 m by 25 m. These may not be accurate enough to produce data expected by numerical models in river hydraulics and morphology. Data from laser scan flights or terrestrially scanned DEMs can also be used to generate the input data needed.

The channel geometry has to be defined by points. These points are defined by x and y coordinates and are connected by sections. Each node needs a related cross-section.

The sections include information about how the points are connected and the distance between the points. The reach lengths between the cross-sections should consider the flows in the main channel that can be longer than the thalweg. Initial sediment stock can be assigned for each section.

Cross-sections are defined through a series of points of known elevation, which may include optional floodplains. Bed and bank sediment properties are considered as part of cross-sectional data. The characteristic grain sizes d_{90}, d_{50} and d_{30} are required. The Strickler’s roughness coefficient k_{St} is required for bed, bank and floodplain, if it is not determined by equation (2) or (3). A specify variable hydraulic roughness across the channel bed can also be defined for the bank and the floodplain. For calculation the cross-section is divided into strips to get a representative discretization of the profile. The number of strips depends on the number of points that were recorded in the field. That means the number of strips increases with the complexity of the cross-section (Figs 4 and 5).

Copyright © 2006 Taylor & Francis Group plc, London, UK

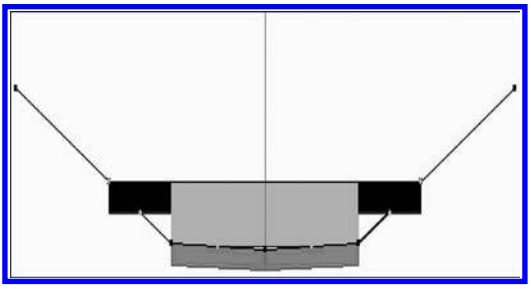


Figure 4. Simple cross-section with approximation by strips.

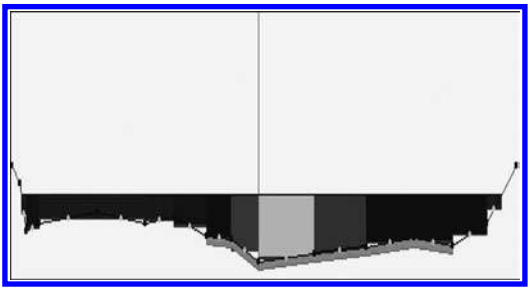


Figure 5. Structured cross-section with approximation by strips.

4.4 *Flow data*

In SETRAC, the water runoff is given as input hydrographs at discrete points. Inflow discharge should be specified as time series.

Sediment can also be fed as sedigraph at nodes (time series).

4.5 *Applications*

The model is designed to calculate sediment transport in steep headwater catchments, i.e. torrent streams. Depending on the formulae set used it can be applied to channel gradients up to 0.63. It can only be used for sediment transport. For steeper channel gradients sediment concentrations comparable to hyperconcentrated flow or debris flows can be achieved. However, debris flows are not explicitly considered.

5 CASE STUDY

For comparison between observed and modeled sediment transport SETRAC is applied to well documented extreme events that occurred in the Austrian Alps. The erosion and deposition of bedload was mapped in the field. The longitudinal profile and representative cross sections were also surveyed. Grain size analyses were made with line by number sampling and evaluated after Fehr (1987).

Table 1. Formulae combinations used for the simulations.

Case	v	n	q_b	q_c	n_r/n	a in (12)
A	(1)	(2)	(16)	(18)	–	–
B1	(1)	(2)	(16)	(18)	(10)	1.0
B2	(1)	(2)	(16)	(18)	(10)	1.5
B3	(1)	(2)	(16)	(18)	(10)	2.0

5.1 *Sessladbach*

After the extreme events from August 2005 several torrents were documented by a team of our University. One oft these torrents is the Sessladbach in Tyrol, Austria (Hübl et al. 2005). The catchment area is about 9.9 km^2 and the main channel is 4 km long. The mean slope is 0.25, the steepest parts are in the middle reaches with channel gradients up to 0.4. The slope of the fan is 0.18. About 32,000 m^3 of sediment were mobilized. The sediment erosion and deposition was mapped in the field in order to be compared with SETRAC calculations.

The input hydrographs needed for SETRAC were generated with the Hydrologic Modelling System HEC-HMS (Version 2.2.2). Data from a precipitation gauge situated in the catchment, which delivers data in one minute resolution, were used. The simulated peak discharge was calibrated with reconstructed values of the peak discharge at several appropriate cross sections. The catchment was separated into four sub catchments. The resulting hydrographs were attached to the related nodes in the SETRAC model. The duration of the whole event was 24 hours with a peak discharge of about 25 m^3/s at the fan apex. No streamflow measurements are available for this channel.

5.2 *Simulation*

Depending on the field investigations, different cases can be computed with SETRAC. If information about sediment stock is available, it is possible to model a so-called supply limited case. That means that sediment can only be eroded if the stock has not been depleted. If there is no information about reach wise sediment availability, a uniform sediment stock in m^3/m can be assumed. If the sediment availability is set at a very high value, the so-called transport limited case can be modeled.

Four simulation runs were computed with the formulae as indicated in Table 1. In the first simulation flow resistance due to form roughness was not considered. The other runs considered a reduced energy Slope according to formulae (8) and (11) with a variation of the exponent a. The exponent was set as 1.0, 1.5 and 2.0. The different cases are described in table 1.

For the discretization in space and time 50 meters and 60 seconds were chosen to limit the discretization error as well as the computing time.

Copyright © 2006 Taylor & Francis Group plc, London, UK

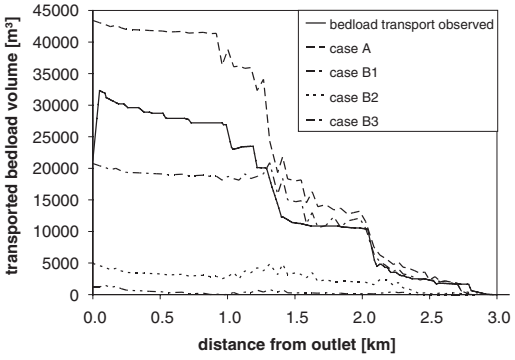


Figure 6. Observed versus simulated bedload transport for the supply limited case.

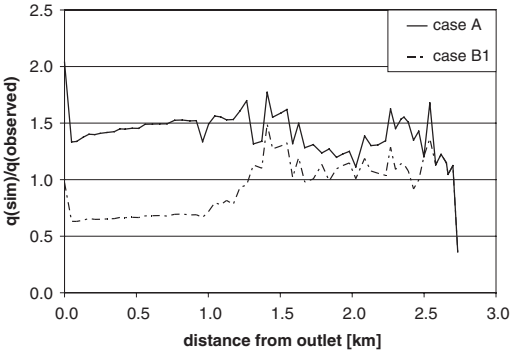


Figure 7. Variation of the ratio between simulated and observed bedload transport for the supply limited case along the torrent channel.

The presented simulation results were computed with SETRAC version V20060127 (Version of 27 January 2006).

Figures 6 and 8 show bedload volumes integrated over the flood duration for any cross-section along the torrent channel.

For the supply limited case (Fig. 6) sediment stock in reaches was considered. The availability varied between 1.0 m^3/m for channel reaches mainly in bedrock and up to 100 m^3/m for channel reaches where intensive erosion was observed. The sediment stock in the reaches was assumed as it might have been estimated by a channel survey before the extreme event occurred. Simulation A slightly overestimates the sediment transport due to the higher availability of sediment. The case B1 also shows a good agreement with the observed sediment transport. The least discrepancies result for the upper and middle reaches of the Sessladbach. The different behaviour of the simulations for A and B1 in the reaches from km 1.0 to km 1.4 may be related to the fact that massive lateral erosion occurred of finer material from the banks and the main channel changed its bed. Changes in the cross-sections geometry can not be modeled with the actual version of SETRAC. On the lowest 100 m of the fan about 10,000 m^3 of sediment were deposited outside of the channel. This two-dimensional problem can not be reproduced by the one-dimensional simulations in SETRAC. Considering the sediment transport simulations along the entire channel, it is found, that for the cases B2 and B3 there is a too strong reduction of the energy slope for the Sessladbach (Fig. 6).

Figure 7 shows the ratio between simulated and observed bedload transport for the supply limited case for the simulation without a reduction of the energy slope and for the simulation considering an exponent $a = 1.0$ in equation (12) for the reduced energy slope.

For the transport limited case (Fig. 8) a constant sediment availability of 100 m^3/m along the entire channel bed was assumed. The simulation A represents

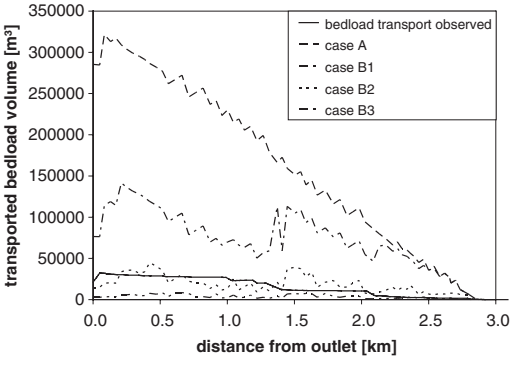


Figure 8. Observed versus simulated bedload transport for the transport limited case.

the transport capacity and clearly overestimates the observed sediment transport by a factor of ten. The best agreement between observed and computed sediment transport was found for B1, whereas B2 and B3 result in a too weak sediment transport. The discrepancy between simulated and observed bedload transport in the reaches from km 2.1 to km 2.4 (Fig. 9) is a result of the "unlimited" availability of sediment. In reality, this reach has a very rough channel bed, and probably a higher critical discharge is necessary for the beginning of motion than estimated by equation (18). This shows the necessity of detailed field investigations on sediment availability for the calculation of sediment transport in torrents.

6 DISCUSSION

To evaluate the performance of a sediment transport model in torrent channels, the observations on bedload transport in steep experimental flumes are taken as a reference condition; these conditions define maximum

Copyright © 2006 Taylor & Francis Group plc, London, UK

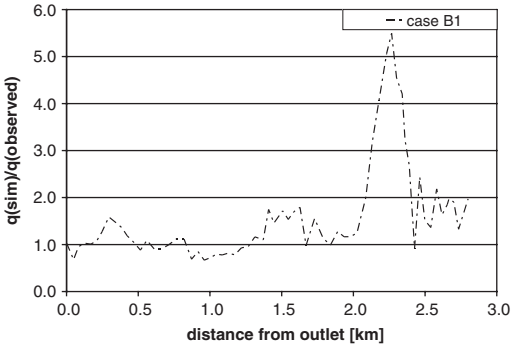


Figure 9. Variation of the ratio between simulated and observed bedload transport for the transport limited case along the torrent channel.

transport rates for the idealized case of rather uniform bed material, essentially no morphological features and hence no significant form roughness effects. Rickenmann (2001) found that observed sediment transport in the steep and small streams was one to three orders of magnitude smaller than values predicted by a sediment transport capacity formula. Apart from limited sediment supply, this discrepancy may be partly due to substantial bedform roughness reducing bedload transport efficiencies. A tendency for over prediction of sediment loads using a bedload transport capacity formula was also found in case studies on sediment transport during flood events in Swiss torrents: Rickenmann (1990b) applied equation (16) and used a relatively high critical discharge to move the coarsest bed particles to obtain reasonable agreement of the calculated sediment load with field observations. For the transport-limited case (i.e. unlimited sediment availability), bedload volumes are overestimated by about a factor of ten for the case study examined with the SETRAC model. Applying two sediment transport models to a river reach with a channel gradient of about 0.02, Rathburn & Wohl (2001) found that predicted bedload discharges were overestimated by up to several orders of magnitude.

7 CONCLUSION AND OUTLOOK

The SETRAC model is a new one-dimensional simulation program for torrent channels. Three flow resistance approaches appropriate for steep channel gradients have been implemented. A formula is established to take into account the effect of flow resistance due to form roughness on sediment transport in channels with stable structures by modifying the energy slope. The extent of the reduction can be related to different roughness structures. These formulae can be combined with different bedload transport equations.

The presented case study of an extreme event in the Austrian Alps demonstrates the models capability to compute sediment transfer in steep headwater torrents. Using a rough correction procedure, a reasonable agreement has been obtained between simulated and observed sediment loads. Considering the uncertainty of the input data, the results are encouraging. Further improvement and validations of the model are necessary and are continuing to develop a reliable software tool for the prediction of sediment transport in torrents.

The SETRAC model will be further developed to take into account both bed armouring effects and transport by size fractions, and to take into account bed level variations during the simulations.

8 NOTATION

The following symbols are used in this paper:

a	variable exponent
d_m	mean grain size (m)
d_{30}	characteristic grain size for which 30% of the sediment is finer by weight (m)
d_{50}	characteristic grain size for which 50% of the sediment is finer by weight (m)
d_{84}	characteristic grain size for which 84% of the sediment is finer by weight (m)
d_{90}	characteristic grain size for which 90% of the sediment is finer by weight (m)
Fr	Froude number
g	acceleration due to gravity (m/s^2)
h	flow depth (m)
h_f	fluid flow depth (m)
h_m	sediment mixture flow depth (m)
k_{St}	Strickler coefficient of roughness (m$^{1/3}$/s)
n	Manning's coefficient of roughness (s/m$^{1/3}$)
n_r	roughness coefficient associated with skin friction only (s/m$^{1/3}$)
Q	discharge (m^3/s)
q	volumetric water or fluid discharge per unit width (m^3/sm)
q_b	volumetric bedload transport rate per unit width (m^3/sm)
q_c	critical flow discharge at the beginning of bedload transport (m^3/sm)
R	hydraulic radius (m)
S	slope of the energy line
S_{red}	component of the energy line related with skin friction
s	ratio between grain and fluid density
v	velocity (m/s)
v^*	shear velocity (m/s)
θ	dimensionless bed shear stress
θ_{cr}	critical value of θ at initiation of motion
ρ	fluid density (kg/m^3)

Copyright © 2006 Taylor & Francis Group plc, London, UK

ρ_s solid density (kg/m^3)
ϕ angle of response
Φ_b dimensionless bedload transport rate

REFERENCES

Aberle, J. & Smart, G.M. 2003: The influence of roughness structure on flow resistance on steep slopes. *J. Hydraul. Res.*, 41(3): 259–269.

Bathurst, J. C., Graf, W. H. & Cao, H. H. 1987. Bed load discharge equations for steep mountain rivers, in *Sediment Transport in Gravel-Bed Rivers*, edited by C. R. Thorne, J. C. Bathurst, and R. D. Hey, 453–477, John Wiley, New York.

Bathurst, J.C. 1987: Measuring and modelling bedload transport in channels with coarse bed materials. In *K. Richards (ed.), River Channels – Environment and Process:* 272–294, Blackwell, Oxford.

Bathurst, J.C. 1993. Flow resistance through the channel network. In K. Beven and M. J. Kirkby (eds), *Channel Network Hydrology*: 69–98, John Wiley, New York.

Bathurst, J.C. 2002. At-a-site variation and minimum flow resistance for mountain rivers. *J. Hydrology,* 269(1–2): 11–26.

Bathurst, J.C., Graf, W.H., Cao, H.H. 1987. Bed load discharge equations for steep mountain rivers. In C.R. Thorne, J.C. Bathurst, and R.D. Hey (eds), *Sediment transport in gravel-bed rivers*: 453–477, J. Wiley & Sons, New York.

Beffa, C. 2005: 2D-Simulation der Sohlenreaktion in einer Flussverzweigung. *Österreichische Wasser- und Abfallwirtschaft*, 42(1–2), 1–6.

Beschta, R.L. 1987. Conceptual model of sediment transport in streams. In C.R. Thorne, J.C. Bathurst, and R.D. Hey (eds), *Sediment transport in gravel-bed rivers*: 387–419, J. Wiley & Sons, New York.

Fehr, R. 1987. Geschiebeanalysen in Gebirgsflüssen. *Mitteilung 92*, Versuchsanstalt für Wasserbau, Hydrologie und Glaziologie, ETH Zurich.

Friedl, K. 2004. Computergestützte Modellierung von Sedimenttransport in alpinen Einzugsgebieten unter Anwendung Geographischer Informationssysteme. *Dissertation an der Universität für Bodenkultur Wien*, Institut für Vermessung, Fernerkundung und Landinformation, Vienna.

Fuchs, H. & Friedl, K. 2002. Ermittlung des Naturraumrisikos in ausgewählten Einzugsgebieten – Entwicklung und Anwendung des Modells SETRAC als Grundlage einer flächendeckenden, dynamisierten, gefahrenorientierten regionalen Raumplanung (Endbericht). Universität für Bodenkultur Wien, Institut für Vermessung, Fernerkundung und Landinformation. *Auftraggeber: Bundesministerium für Land- und Forstwirtschaft, Umwelt und Wasserwirtschaft* (unpublished).

Gomez, B. 1987. Bedload. In A.M. Gurnell and M.J. Clark (eds), *Glacio-fluvial Sediment Transfer:* 355–376, John Wiley, New York.

Gomez, B. & Church, M. 1989. An assessment of bedload sediment transport formulae for gravel bed rivers. *Water Resour. Res*., 25(6): 1161–1186.

Gomi, T. & Sidle, R.C. 2003. Bed load transport in managed steep-gradient headwater streams of southeastern Alaska. *Water Resour. Res.*, 39(12): 1336, doi: 10.1029/2003 WR002440.

Hegg, C. & Rickenmann, D. 1999. Comparison of bedload transport in a steep mountain torrent with a bedload transport formula. In: *Hydraulic Engineering for Sustainable Water Resources Management at the Turn of the Millenium; Proceedings 28th IAHR Congress, 22–27 August 1999, Graz, Austria.* [CD-ROM] Graz, Technical University, 7p.

Hübl, J., Ganahl, E., Bacher, M., Chiari, M., Holub, M., Kaitna, R., Prokop, A., Dunwoody, G., Forster, A., Kerschbaumer, M., Schneiderbauer, S. (2005): Ereignisdokumentation 22./23. August 2005, Tirol, *Band 1: Generelle Aufnahme (5W-Standard). IAN Report 109*, im Auftrag von: BMLFUW, Abt. IV/5 (unpublished).

Jäggi, M. 1984. Abflußberechnung in kiesführenden Flüssen. *Wasserwirtschaft*, 74(5), 263–267.

Jäggi, M., Nigg, U., Teysseire, P. 2004. Die Sedimentkatastrophe von Baltschieder. *Interpraevent Tagungspublikation*, Bd. 3, VII/165–180.

Jarrett, R.D. 1990. Hydrologic and hydraulic research in mountain rivers. *Water Resour*. Bull., 26 (3): 419–429.

Lee, A.J.& Ferguson, R.I. 2002. Velocity and flow resistance in step-pool streams. *Geomorphology* 46(1–2): 59–71.

Lenzi, M.L., Mao, L., Asti, G., Comiti, F., Scussel, G. 2004. Impact of sediment supply on bed load transport in a high-altitude alpine torrent. *Interpraevent Tagungspublikation*, Bd. 1, III/171–182.

Mathys, N., Brochot, S., Meunier, M., Richard, D. 2003. Erosion quantification in the small marly experimental catchments of Draix (Alpes de Haute Provence, France). Calibration of the ETC rainfall–runoff–erosion model. *Catena 50*: 527– 548.

Meyer-Peter, E. & Müller, R. 1948. Formulas for bedload transport. *Proc. 2nd meeting Int. Assoc. Hydraulic Structures Research,* Appendix 2: 39–64, Stockholm, Sweden.

Palt, S.M. 2001. Sedimenttransporte im Himalaya-Karakorum und ihre Bedeutung für Wasserkraftanlagen. *Mitteilung 209*, Institut für Wasserwirtschaft und Kulturtechnik, Universität Karlsruhe.

Pitlick, J. 1992. Flow resistance under conditions of intense gravel transport. *Water Resour. Res.*, 28(3): 891–903.

Rathburn, S.L. & Wohl, E.E. 2001. One-dimensional sediment transport modeling of pool recovery along a mountain channel after a reservoir sediment release. *Regulated Rivers: Research & Management*, 17(3): 251–273.

Reid, I. & Laronne, J.B. 1995. Bedload sediment transport in an ephemeral stream and comparison with seasonal and perennial counterparts. *Water Resour. Res*., 31(3): 773–781.

Rickenmann, D. 1990a. Bedload transport capacity of slurry flows at steep slopes. Versuchsanstalt für Wasserbau, Hydrologie und Glaziologie, ETH Zurich, *Mitteilung* Nr. 103.

Rickenmann, D. 1990b. Debris flows 1987 in Switzerland: Modelling and sediment transport. In O. Sinniger & M. Monbaron (eds), *Hydrology in Mountainous Regions II, Artificial Reservoirs, Water and Slopes (Proceedings of two International IAHS Symposia,* Lausanne, Switzerland, 27 August – 1 September 1990), IAHS Publ. no. 194: 371–378.

Copyright © 2006 Taylor & Francis Group plc, London, UK

Rickenmann, D. 1991. Hyperconcentrated flow and sediment transport at steep slopes. *Journal of Hydraulic Engineering 117(11)*: 1419–1439.

Rickenmann, D. 1994. An alternative equation for the mean velocity in gravel-bed rivers and mountain torrents. *In G.V. Cotroneo & R.R. Rumer (eds), Proceedings ASCE 1994 National Conference on Hydraulic Engineering*, Vol. 1: 672–676, Buffalo N.Y., USA

Rickenmann, D. 1996. Fliessgeschwindigkeit in Wildbächen Gebirgsflüssen. *Wasser, Energie, Luft* 88(11/12): 298–304.

Rickenmann, D. 2001. Comparison of bed load transport in torrents and gravel bed streams. *Water Resources Research*, Vol. 37, No. 12: 3295–3305.

Rickenmann, D. 2005. Geschiebetransport bei steilen Gefällen. Versuchsanstalt für Wasserbau, Hydrologie Glaziologie, ETH Zürich. Versuchsanstalt für Wasserbau, Hydrologie und Glaziologie, ETH Zürich, *Mitteilung Nr. 190*, 107–119.

Schilling, M., Hunziker, R. 1995. Programmpaket MORMO – Grundlagen. In: *"Mathematische Modelle offener Gerinne"*, ÖWAV-Seminar 21. Nov. 1995, Konstruktiver Wasserbau – Landschaftswasserbau, Bd. 17: 91–104.

Schoklitsch, A. 1962. Handbuch des Wasserbaus. 3rd edition, Springer Verlag, Wien.

Smart, G.M. & Jäggi, M.N.R. 1983. Sedimenttransport in steilen Gerinnen. Versuchsanstalt für Wasserbau, Hydrologie und Glaziologie, ETH Zurich, *Mitteilung Nr. 64*.

Smart, G.M., Duncan, M.J., Walsh, J.M .2002. Relatively rough flow resistance equations. *J. Hydraul. Eng.*, 128(6): 568–578.

Takahashi, T. 1987. High velocity flow in steep erodible channels. In *Proceedings 22nd IAHR Congress, Lausanne*, Switzerland, Techn. Session A, 42–53.

Whittaker, J. & Jaeggi, M. (1986): Blockschwellen. Versuchsanstalt für Wasserbau, Hydrologie und Glaziologie, ETH Zürich, *Mitteilung Nr. 91*.

Wicks, J.M. & Bathurst, J.C. 1996. SHESED: a physically based, distributed erosion and sediment yield component for the SHE hydrological modelling system. *J. Hydrology*, 175: 213–238.

Wong, M. & Parker, G. in review. Re-analyses and corrections of bedload relation of Meyer-Peter and Müller using their own database. *Journal of Hydraulic Engineering*.

Copyright © 2006 Taylor & Francis Group plc, London, UK

Influence of sand shape to vertical sorting under uniform flow condition

E. Harada
Dept. of Civil Engineering, Toyota National College of Technology, Eisei-cho, Toyota, Aichi, Japan

H. Gotoh
Dept. of Urban and Environmental Engrg., Kyoto Univ., Yoshida Hnomachi, Sakyo-ku, Kyoto, Japan

ABSTRACT: Generally, sand particles, which are used in Distinct Element Method, are modeled using spheres or circle elements in a movable bed simulation. However, because actual beds are composed of many shapes of sand particles, it is important to investigate the influence of sand shape on characteristics of sediment transport. In this study, numerical simulation was performed for the sorting process under sheetflow conditions using a vertical two-dimensional granular material model based on the Distinct Element Method. Thereby, we investigated the influence of sand shape on the sorting process.

1 INTRODUCTION

Uneven bed form is the key to numerical simulation of sediment transport. From such a perspective, granular material model based on the Distinct Element Method proposed by Cundal & Strack (1979) is an effective tool because the inter-elemental force among particles can be tracked directly. Generally, circle or sphere elements are used in the granular material model because of limited computational capability and the relative ease of handling. On the other hand, numerical simulation, which has treated non-circle or non-sphere elements, has been attempted to support improvements in computer performance. For example, Latham & Munjiza (2002) simulated the collision process of rocks using the elements, with surface details. The resistance against motion of the circular or spherical elements is less than that of actual sand. Furthermore, the pores of the particle arrangement made using circles and spheres differ from those of actual sand. Consequently, in the present study, the vertical sorting process of two shapes and two sizes of elements (squares and circles) were investigated numerically using the improved movable bed simulator code, which was developed by Gotoh & Sakai (1997).

2 OUTLINE OF THE SIMULATION MODEL

2.1 *Distinct element method*

The movable bed was evaluated by the granular material model based on the Distinct Element Method.The motion of each particle was governed by the translational and rotational equations as follows:

$$\rho\left(\frac{\sigma}{\rho}+C_M\right)V_i\frac{d\boldsymbol{u}_{pi}}{dt}=\boldsymbol{F}_{p\,\mathrm{int}}+\boldsymbol{F}_D+\boldsymbol{F}_{gr} \tag{1}$$

$$I_i\frac{d\boldsymbol{\omega}_{pi}}{dt}=\boldsymbol{T}_i \tag{2}$$

$$\boldsymbol{F}_D=\frac{1}{2}\rho C_D S_i\left|\boldsymbol{U}-\boldsymbol{u}_{pi}\right|\left(\boldsymbol{U}-\boldsymbol{u}_{pi}\right) \tag{3}$$

$$\boldsymbol{F}_{gr}=-\rho\left(\frac{\sigma}{\rho}-1\right)V_i\boldsymbol{g} \tag{4}$$

where, $\boldsymbol{F}_{pint}$: vector of the inter-particle force, $\boldsymbol{F}_D$ vector of the drag force, $\boldsymbol{F}_{gr}$: vector of the gravitational force, $\boldsymbol{u}_{pi}$: vector of the i-th particle velocity, C_M: added mass coefficient, $\boldsymbol{U}$: vector of the flow around the i-th particle, V_i: volume of the i-th particle, I_i: moment of inertia of i-th particle, S_i: projection area to the flow direction, T_i: torque acting on the i-th particle, $\boldsymbol{\omega}_{pi}$: angular velocity of the i-th particle, C_D: drag coefficient, σ: density of the particle and ρ: density of the water.

Each inter-particle force was expressed by the spring and dashpot system (see Fig. 1). Between two contacting particles, Voigt model is assumed in both of the normal and tangential directions, to describe the dynamic interparticle relation. The acting forcer between i-th and j-th particles in normal and tangential direction, f_n and f_s, can be written as follows:

$$f_n(t)=e_n(t)+d_n(t) \tag{5}$$

Copyright © 2006 Taylor & Francis Group plc, London, UK

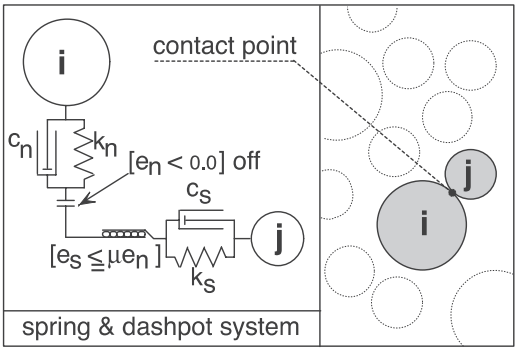


Figure 1. Spring and dashpot system between contacting particles.

$$f_s(t) = e_s(t) + d_s(t) \tag{6}$$

$$e_n(t) = e_n(t - \Delta t) + k_n \cdot \Delta\xi_n \tag{7}$$

$$d_n(t) = c_n \cdot \Delta\dot{\xi}_n \tag{8}$$

$$e_s(t) = e_s(t - \Delta t) + k_s \cdot \Delta\xi_s \tag{9}$$

$$d_s(t) = c_s \cdot \Delta\dot{\xi}_s \tag{10}$$

in which e_n,e_s:forces working on springs, d_n,d_s:forces working on dashpots, $\Delta\xi_n$, $\Delta\xi_s$:displacement of particles during the time Δt(Δt = time step of the calculation), k_n,k_s:spring constants and c_n,c_s:damping coefficients. In this simulation model, particles are non-cohesive, hence the joint, which has no resistance to the tensile force, is assumed in the normal direction. While, in the tangential direction, the frictional force works. To describe this characteristics, the joint, which slips at the limit of the shear stress, is assumed in the tangential direction. These joints can be formulated as follows:

$$f_n(t) = f_s(t) = 0 \quad when \quad e_n(t) < 0 \tag{11}$$

$$f_s(t) = \mu \cdot SING(e_n(t), e_s(t)) \quad when \quad |e_s(t)| > \mu \cdot e_n(t) \tag{12}$$

$$SIGN(a,b) = \begin{cases} |a| & when \quad b \geq 0 \\ -|a| & when \quad b < 0 \end{cases} \tag{13}$$

in which μ:coefficient of friction. The spring constants to the normal (k_n) and the tangential direction (k_s), the damping constants to the normal (c_n) and the tangential (c_s) and the friction coefficient (μ) were determined as the relationship between bottom shear-stress and sediment transport rate could be reproduced in the uniform circle elements bed according to the optimization procedure proposed by Gotoh et al. (2001).

The outline of the optimization procedure is as follows. In the ordinary Distinct Element Method, the condition for the stability for the simple mass-spring system:

$$\Delta t \leq 2\sqrt{m / k_n} \tag{14}$$

in which m:mass of the element, is frequency considered to estimate the time step of the calculation under the given spring constant. Here, the time step of the calculation is determined by considering the natural period, or T, of the simple mass-spring system as follows:

$$\Delta t = T / 20 \ ; \ T = 2\pi\sqrt{m / 2k_n} \tag{15}$$

This relation was proposed by Masuya & Kajikawa (1991), as the more stable condition than the usual stability condition. The relation between the normal and tangential spring constants are given as follows:

$$k_s = \frac{k_n}{2(1+\nu)} \tag{16}$$

in which ν:Poisson rate (=0.3). The critical damping condition for the Voigt model gives the relation between spring and damper constants as follows:

$$c_n = \alpha_{cn} \cdot 2\sqrt{m \cdot k_n} \ ; \ c_s = c_n / \sqrt{2(1+\nu)} \tag{17}$$

When the constants $\alpha_{cn} = 1.0$, this equation is coincide with the standard stability condition of Voigt system. This parameter is tuned to fit the calculated sediment transport rate to the experimental data. For the irregularly arranged particles, $\alpha_{cn} = 1.3$ is the appropriate value.

2.2 *Judgment of contacting elements*

Two kinds of elements' geometric shapes, or circle and square, were used in the present simulation. Hence, three kinds of the judgment of contact conditions between elements: 1) circle–circle, 2) circle–square, 3) square–square are required.

The judgment of contact condition between circle and circle elements is as follows:

$$\frac{d_i + d_j}{2} \geq \sqrt{\left(x_i - x_j\right)^2 + \left(y_i - y_j\right)^2} \tag{18}$$

where, d_i,d_j: diameter of the i-th and j-th elements respectively and (x_i,y_i),(x_j,y_j): coordinate of the center of the i-th and j-th elements respectively(see Fig. 2).

The judgment of contact condition between circle and square elements is defined as the condition that the coordinate of the center of the j-th element is in

Copyright © 2006 Taylor & Francis Group plc, London, UK

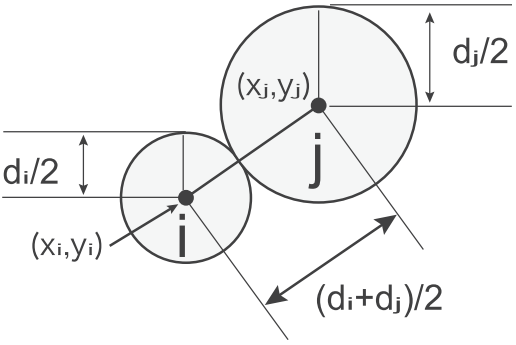


Figure 2. Judgment of contacting elements between circle & circle.

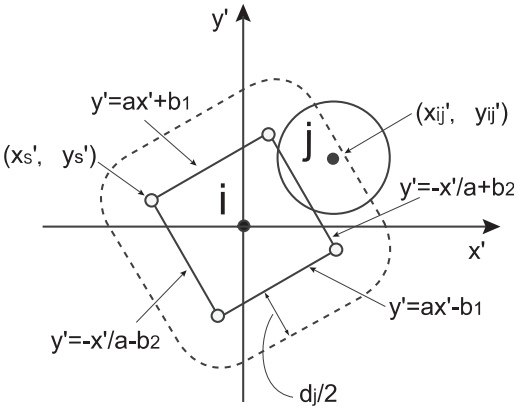


Figure 3. Judgment of contacting elements between circle & square.

the range surrounded the i-th square element in the width of $d_j/2$:

$$\left.\begin{aligned} & ax_{ij}' + b_1 \geq y_{ij}' \geq ax_{ij}' - b_1 \quad and \\ & -x_{ij}'/a + b_2 \geq y_{ij}' \geq -x_{ij}'/a - b_2 \quad and \\ & d_j/2 \geq \sqrt{\left(x_s' - x_{ij}'\right)^2 + \left(y_s' - y_{ij}'\right)^2} \end{aligned}\right\} \tag{19}$$

where, (x'_{ij}, y'_{ij}): relative distance of the coordinate of the center between the i-th square element and the j-th circle element, a, b_1, b_2: parameters defined by the relative position between the circle and square elements and (x'_s, y'_s): four coordinates of the corner of the square element (see Fig. 3). And x'–y' coordinate is thelocal coordinate, the origin of which is the coordinateof the center of the square element.

The judgment of contact condition between square and square elements is defined as the condition that

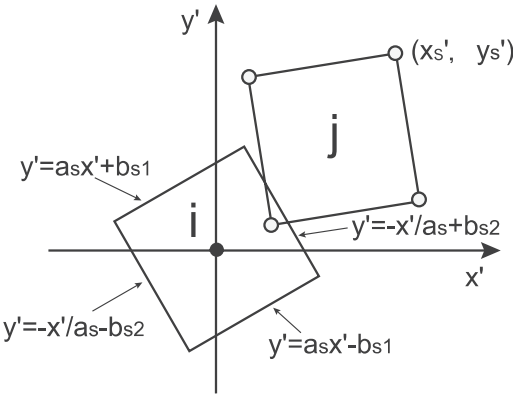


Figure 4. Judgment of contacting elements between square & square.

any corner coordinates of the j-th square is in the i-th square element:

$$\left.\begin{aligned} & a_s x_s' + b_{s1} \geq y_s' \geq a_s x_s' - b_{s1} \quad and \\ & -x_s'/a_s + b_{s2} \geq y_s' \geq -x_s'/a_s - b_{s2} \end{aligned}\right\} \tag{20}$$

where, a_s, b_{s1}, b_{s2}: parameters defined by the relative position between square elements(see Fig. 4).

2.3 *Model of flow phase*

The modeling of the flow phase is necessary for the appropriate evaluation of the driving force acting on sand elements. There are not a few items to modeling of the flow phase in detail, such as turbulent fields and sediment laden flow and so on. Here, we focused on the motion of the elements especially, and the modeling of flow phase was treated simplified.

The mean flow velocity is given by logarithmic law as follows:

$$\frac{U}{u_*} = \frac{1}{\kappa}\ln\left(30.1\frac{y + 0.25d}{k_{sr}}\right) \tag{21}$$

where, u_*: shear velocity, κ: von Karman constant and ksr: roughness (mean diameter). The time series of the flow turbulence is simulated by the simple Monte Carlo method. The fluctuating velocity components of the flow can be written as follows:

$$u(t) = r_u \cdot \sqrt{u^2} \;\; ; \;\; v(t) = r_v \cdot \sqrt{v^2} \tag{22}$$

where, r_u,r_v: random numbers following to the standard Gauss distribution in x and y directions and $\sqrt{u^2}$, $\sqrt{v^2}$: turbulent intensities in x and y directions. The two

Copyright © 2006 Taylor & Francis Group plc, London, UK

series of random numbers satisfy the two dimensional Gauss distribution as follows:

$$f_r(r_u,r_v)=\frac{1}{2\pi}\exp\left(-\frac{r_u^2}{2}\right)\frac{1}{\sqrt{2\pi}\sqrt{1-\gamma^2}} \times\exp\left\{-\frac{(r_v-\gamma\cdot r_u)^2}{2(1-\gamma^2)}\right\} \quad (23)$$

where, γ: cross correlation coefficient of two series of the random numbers. Eq. 10 can be re-written through an simple variable transformation as follows:

$$r_u=\xi_r \;;\; r_v=\gamma\cdot\xi_r+\sqrt{1-\gamma^2}\cdot\zeta_r \quad (24)$$

Turbulent intensities is given by the semi-empirical formulation as follows:

$$\frac{\sqrt{\overline{u^2}}}{u_*}=2.30\exp\left(-\frac{y}{h}\right)\;;\;\frac{\sqrt{\overline{v^2}}}{u_*}=1.27\exp\left(-\frac{y}{h}\right) \quad (25)$$

where, h: water depth, u_*: shear velocity. The cross correlation coefficient of two turbulent velocity components can be related to the Reynolds stress as follows:

$$\gamma=\frac{-\overline{uv}}{\sqrt{\overline{u^2}}\sqrt{\overline{v^2}}}=0.342\left(1-\frac{y}{h}\right)/\exp\left(\frac{2y}{h}\right) \quad (26)$$

The detailed information of modeling of flow is shown in Gotoh & Sakai(1997).

3 VERTICAL SORTING PROCESS

3.1 *Calculated condition*

The model constants using in the granular material model based on the Distinct Element Method were determined by following the optimization procedure proposed by Gotoh et al.(2001). The model constants are as follows: $k_n=314.01$ N/m, $k_s=120.77$ N/m, $c_n=0.66$ Ns/m, $c_s=0.41$ Ns/m and $\Delta t=0.0002$ s. The predicted sediment transport rate shows the good agreement with the previous experiment. Two kinds of geometric shapes and size elements, or circle and square, were used. The calculated conditions are shown in tab. 1. The number in tab. 1 shows the number of the elements, which was determined as correspondence with the total number of elements in each case. And the specific density of all kinds of geometric shapes of elements are the same specific density. And also, both sides of the calculated domain are periodic boundaries to save the calculation time. In addition, the simulation was conducted under the dimensionless bottom shear stress $\tau_*=0.1$ for 95.0 seconds.

Table 1. Calculated condition of case1 & case2.

case No.	D	d	L	l
case1	199	526	–	–
case2	–	–	199	526

[unit : num.]

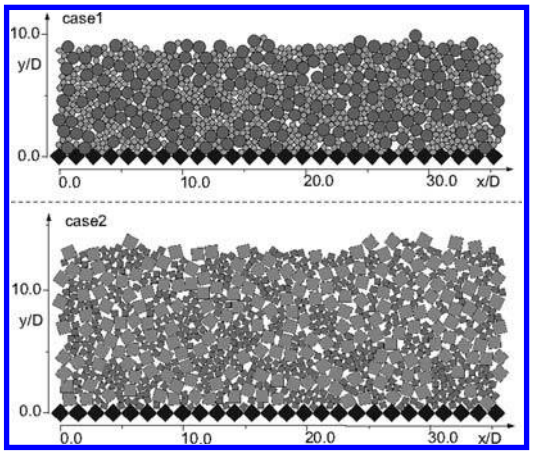


Figure 5. Initial condition of movable bed [upper: case1, lower: case2].

Initial arrangement of both simulations are shown in Fig. 5. The bottom boundary is formed by using large square elements. The calculated total area of the square element is larger than that of the circle element in the same calculated bottom length. Because the square element is squarish shape. Hence, the volume of the square case is larger than the circle case in spite of using the same number of elements in both simulations.

3.2 *Influence of square elements*

The snapshots of both cases are shown in Fig. 6. To show the developing process of the armor coat clearly, the motion of the element in the vicinity of the exchange layer is focused. The active motion of elements are confirmed in both cases. However, the rising process of the large elements to the surface of the sand layer and the descent process of the small elements, or percolation, can be seen in case1, while, such that tendency cannot be seen in case2(see the time $t=20.0$–40.0 s). The difference of the geometric shape between both cases, or the difference of the moving resistance of the square element is larger in comparison with the circle element, would be the cause of that. At the time $t=95.0$ s, the significant armoring around

Copyright © 2006 Taylor & Francis Group plc, London, UK

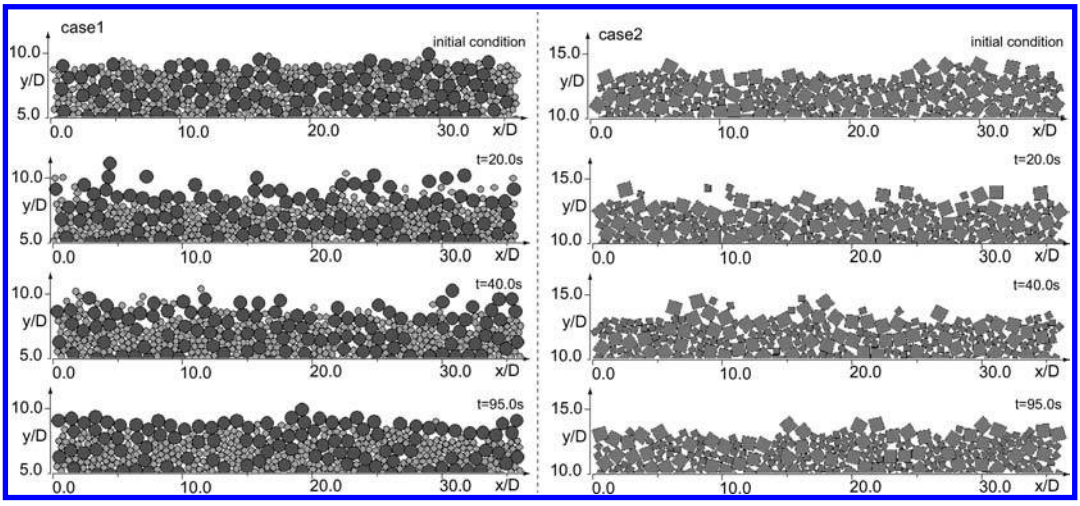


Figure 6. Snapshots of sediment transport around exchange layer in sheetflow regime [left: case1, right: case2].

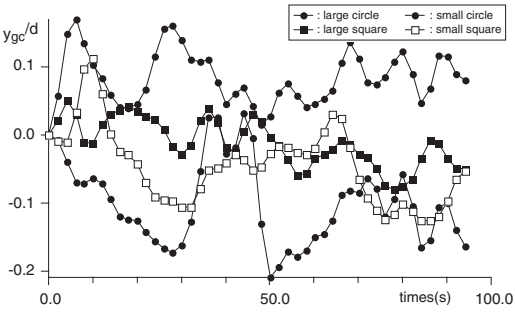


Figure 7. Time series of gravity center in each case.

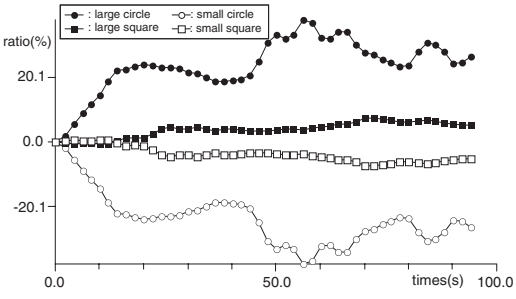


Figure 8. Time series of ratio around exchange layer in each case.

the sand surface is confirmed in case1, while, such a phenomenon isn't confirmed in case2, the effect of the difference geometric shape to the vertical sorting is shown clearly.

Figure 7 shows the time series of the gravity center of each form. And the y-axis indicates the relative gravity center to initial condition of each element. The decrease of the gravity center of the small element and the increase of gravity center of the large element is shown in case1. While, in case2, although the fluctuating of the gravity center is seen, a difference in the small and large elements isn't clear and the gravity center keeps about same level. The effect on the geometric shape of element to the vertical sorting can be confirmed in the time series of the gravity center as well as the snapshots.

Figure 8 shows the time series of the ratio of each element around the exchange layer. And the y-axis shows the relative share to the initial condition. The increase of the share of the large circle and the decrease of the that of the small circle is shown clearly just after the acting of the shear stress. This indicates the developing of the armor coat around the surface of the movable bed. While, only a little difference is seen by the time $t = 20.0$ s in case2. Although, after the time $t = 20.0$ s, slight increase of the share of the large square element is shown, the significant developing process of the armor coat isn't confirmed in comparison with case1.

3.3 *Inner structure of movable bed*

The effect of the geometric shape to the sorting is shown through the snapshots, time series of the gravity center and the time series of the share. To show the inner structure of the movable bed, the distribution of the inter-element force is shown in Fig. 9. The interelement force is represented by using the pass line called stress chain connected between the center of the elements, the direction of which indicates the acting direction of inter-element force, and the level of the inter-element force is in proportion

Copyright © 2006 Taylor & Francis Group plc, London, UK

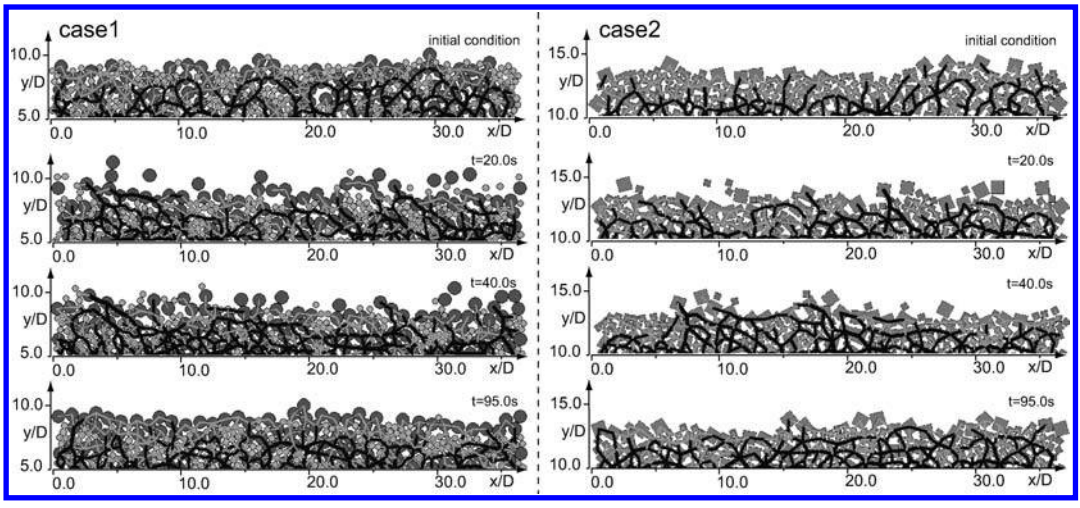


Figure 9. Snapshots of inter element force by stress chain around exchange layer in sheetflow regime [left: case1, right: case2].

to thickness of the pass line. And also, to show the inner structure of the movable bed clearly, the color of the pass line changes according to the level of the inter-element force, or Black line indicates the comparatively high inter-element force, and Gray line indicates the comparatively low inter-element force.

The high inter-element force is distributed in the large area around the surface of the movable bed in case2 in comparison with case1. The difference of the effect of the engagement between elements due to the difference of the geometric shape would be one of the cause. In other words, the moving resistance of the square element is larger than that of circle element because of its squarish shape.

4 CONCLUSIONS

In this study, the influence of sand shape on vertical sorting under uniform flow conditions was investigated from a numerical simulation using the granular material model based on Distinct Element Method. Furthermore, the differences according to the element shape were investigated from the viewpoint of snapshots, the time series of the center of gravity, and the ratio in the exchange layer. Moreover, the inner structure of the movable bed was investigated using the distribution of the inter-elemental forces. Although investigation of the vertical sorting process in consideration of the elements' geometric shape is important, the representation of all geometric shapes of the actual movable bed in the simulation code is extremely difficult. In the near future, the effect of geometric shape should be evaluated in consideration of some indexes.

ACKNOWLEDGEMENTS

This research was supported in part by a grant from Research Foundation for the Electrotechnology of Chubu.

REFERENCES

Cundall, P.A. & Strack, O.D.L. 1979. Discrete Numerical Model for Granular Assenblies. *Geotechnique*, Vol.29: 47–65.

Gotoh, H. & Sakai, T. 1997. Numerical Simulation of Sheetflow as Granular Material. *Jour. of Waterway, Port, Coastal and Ocean Engrg., ASCE*, Vol.123, No.6: 329–336.

Gotoh, H. et al. 2001. Optimization of Parameters in DEM-Based Numerical Movable Bed Simulator. *Jour. of Hydraulic, Coastal and Environmental Engrg., JSCE*, No.691/II-57: 159–164.

Latham, J.P. & Munjiza, A. 1995. Porosity and Packing Simulations of Particles with Any Shape or Size-Dynamic 3D Results. *Proc. 28th ICCE*: 1424–1435.

Masuya, H. & Kajikawa, Y. 1991. Numerical analysis of the collision between a falling rock and a cushion by distinct element method. *Computer Methods and Advances in Geomechanics*: 493–498. Rotterdam: Balkema.

Nezu, I. 1977. Turbulent structure in open channel flows. Ph.D Thesis presented to Kyoto University, Kyoto, Japan.

Copyright © 2006 Taylor & Francis Group plc, London, UK

Investigation of flow hydrodynamics under equilibrium bedload transport conditions using PIV

F. Bigillon, G. Couronné & J.Y. Champagne
Laboratoire de mécanique des fluides et d'acoustique, Lyon, France

A. Recking & P. Frey
Cemagref Grenoble, UR ETNA, Domaine Universitaire Saint-Martin-d'Hères Cedex, France

ABSTRACT: We present results of velocity, turbulence intensities, and Reynolds stress distribution in presence of bed load transport obtained from flume experiments carried out under equilibrium bed load transport conditions. Measurements of those quantities were obtained using Particle Image Velocimetry. They are compared with trends typically found in classical turbulent flow with no sediment load: a logarithmic law, exponential laws, and a linear trend respectively. Our results show a more complex behaviour than the one predicted by classical laws as sediment transport increases. The general trend shows that increasing bed load transport results in lower longitudinal velocities, larger turbulence intensity, and larger Reynolds stress values compared to conditions without sediment load. However, we observe a critical point, corresponding to mid transport rate, for which this general trend fails. This behaviour may be explained by changes in bed roughness and relative flow depths.

1 INTRODUCTION

There is uncertainty regarding the effect of sediment transport on mean flow and turbulence characteristics. In general, increasing sediment transport enhances flow resistance (Song et al. 1998), reduces longitudinal velocities, and increases turbulence intensities (Campbell et al. 2005, Carbonneau & Bergeron 2000). However, recent work suggests that bed load transport can also reduce flow resistance (Recking et al. 2005) and produce higher longitudinal velocities (Campbell et al. 2005). This complex behaviour seems related to the size of sediments (Campbell et al. 2005), bed roughness, and sediment transport itself (Recking et al. 2005, Carbonneau & Bergeron 2000).

Few investigations have been done concerning the effect of bed load transport on flow characteristics. Most of them concern flow resistance and few attempt to describe velocity and turbulence characteristics. This may be due to the difficulty of performing measurements in presence of sediments. In addition, previous work focused on gentle slopes and relatively low transport rates.

In this paper we investigate the effect of bed load transport rate on longitudinal velocity distribution and turbulence characteristics under steep slopes and equilibrium bed load transport conditions. The flume experiments we carried out, as well as the Particle Image Velocimetry (PIV) technique we used to measure flow velocity, are described in section 2. In section 3 we present the results of our flume experiments that are compared with distributions generally found in turbulent flow with no sediment load: a logarithmic law for the velocity, exponential laws for the turbulence intensities, and a linear trend for the Reynolds stress.

2 EXPERIMENTS

2.1 *Experimental setup and conditions*

We conducted experiments in a tilting flume 8.0 m long and 0.05 m wide. The bed of the flume was formed of sediments of mean diameter $d = 2.25$ mm and its sidewalls were made of glass.

Table 1 summarizes the experimental conditions of the tests. The slope S corresponds to the equilibrium slope of the bed and to the channel slope and was set at 3% and 5%. We measured the flow rate q_l with an electromagnetic flow meter and the solid discharge q_s using GDS, a visualisation based technique described in Frey et al. (2003). Sediments concentration, defined as the ratio of solid discharge over flow rate, was between 0 and 4%. We used the visualization method developed by Recking et al. (2005) to obtain the bulk mean flow velocity U_q. The flow depth h_q computed from q_l and U_q, was small enough to have a

Copyright © 2006 Taylor & Francis Group plc, London, UK

Table 1. Experimental conditions of the tests.

Tests	S	q_l [l/s]	q_s [g/s]	U_q [m/s]	h_q [mm]	Fr	Re	u_{q^*} [m/s]
S3T1	0.03	0.1	0	0.3	6.66	1.17	1998	0.043
S3T4	0.03	0.2	0	0.4	10	1.27	3970	0.052
S3T6	0.03	0.4	3.4	0.48	16.7	1.19	8016	0.066
S3T7	0.03	0.6	7.4	0.57	21.3	1.25	12,141	0.074
S5T1	0.05	0.1	0	0.32	6.3	1.29	2016	0.054
S5T2	0.05	0.2	4.2	0.38	10.4	1.19	3952	0.069
S5T3	0.05	0.29	8.2	0.43	13.3	1.19	5719	0.077
S5T4	0.05	0.6	22.5	0.65	18.3	1.53	11,895	0.09
S5T5	0.05	0.74	28.9	0.72	20.5	1.61	14,760	0.095

large channel aspect ratio (i.e. $B/h_q > 3$) that prevented the formation of significant secondary flows. For all tests, the Froude number defined as $Fr = U_q/(gh_q)^{0.5}$ was larger than one, and the Reynolds number defined as $Re = U_q h_q/\nu$, where $\nu = 10^{-6}$ m^2/s is the kinematic viscosity of the water at 20°C, was larger than 2000 so that all flow conditions correspond to supercritical and turbulent flows. We computed the shear velocity u_{*q} as $(gR_hS)^{0.5}$ where R_h is the hydraulic radius.

We performed all tests under equilibrium bed load transport conditions using uniform natural sediments of mean diameter $d = 2.25$ mm and density $\rho_s = 2650$ kg/m^3. To ensure bed load transport equilibrium conditions, we compared the measured solid discharge to the one estimated using Smart & Jaeggi (1983) bed load transport formula. This formula is valid for slopes ranging from 3% to 20% and can be written for uniform sand distribution as:

$$\frac{q_s}{q_l} = 4\frac{S^{1.6}}{s-1}\left(1-\frac{\tau^*_{cr}}{\tau^*}\right) \quad (1)$$

where s is the relative sediment density and τ^* is the dimensionless shear stress defined as:

$$\tau^* = \frac{\rho u_*^2}{(\rho_s - \rho)gd} \quad (2)$$

and ρ is the water density.

Figure 1 represents the solid discharge as a function of the dimensionless shear stress. We observe a good agreement between measured and predicted values (Eq. 1–2), which corroborates that our tests correspond to equilibrium bed load transport conditions.

2.2 *Particle Image Velocimetry measurements*

We measured the instantaneous velocity field along the flume centreline of a test section for different flow conditions specified in Table 1 (Fig. 2). The test section was located 4 m downstream from the entrance, and its

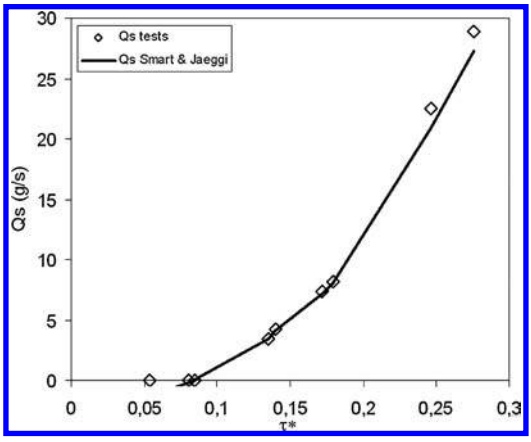


Figure 1. Solid discharge measured from GDS (diamonds) and computed from Smart & Jaeggi formula (solid line).

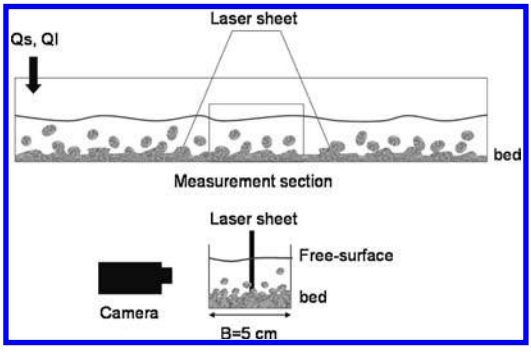


Figure 2. Side view and front view of the experimental setup.

size was about 25 × 25 mm. It was made dark in order to preserve the uniformity of the recording conditions.

We performed the velocity measurements using a PIV system from *Dantec* that includes illumination, image capture, and data acquisition components. We used a dual-pulsed 15 Hz Solo PIV I Nd:YAG laser manufactured by *New Wave Research* for illumination. This laser system gives 15 mJ per pulse over 5 ns pulse width and has a wave length of 532 nm. We used neutral, buoyant particles about 10 μm in diameter as water tracers.

The use of the PIV technique is not typical for the study of sediments laden flows. To utilize it in our experiments we had to solve the following issue. Since sediments do not follow the fluid velocity, we had to eliminate them in the estimation of velocity vectors. To do so, we used fluorescent tracer particles (orange vinyl pigment, water soluble, by Lefranc and Bourgeois, see Nogueira et al. 2003). Those particles when excited by the laser emit light at higher wavelengths

Copyright © 2006 Taylor & Francis Group plc, London, UK

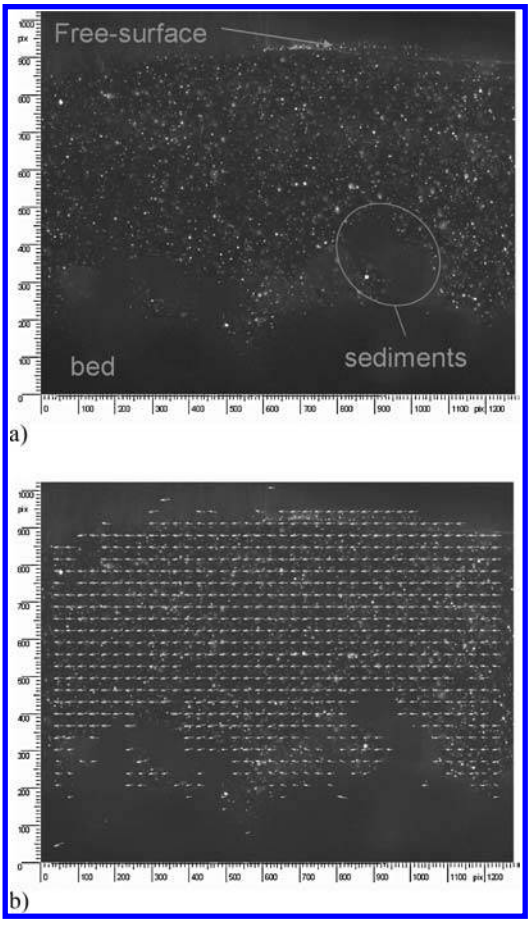


Figure 3. a) PIV image. b) Computed velocity field (test S5T4).

than the laser. We added a 540 nm high pass filter to the camera to capture only signals emitted by tracer particles. As result, sediments are eliminated from images (Fig. 3a).

We captured images using a HighSense camera mounted with an objective Nikkor 60 mm/2.8. The camera resolution was 1024 × 1080 pixels, with each pixel measuring 6.7 μm^2, and a maximum frame rate of 9 Hz. We controlled the camera using *Flowmap* software. We recorded image pairs at 2 Hz and sent them to a PC through a frame-grabber board. We recorded and stored about 800 image pairs for each flow case. We collected four series of 200 image pairs (50 s per realization) over 5 minutes in order to randomly sample the flow. The time between recordings was needed to transfer the images to the computer.

We processed image pairs using a correlation technique available in *Flowmap* software. Each frame was split up into a grid of small interrogation areas of

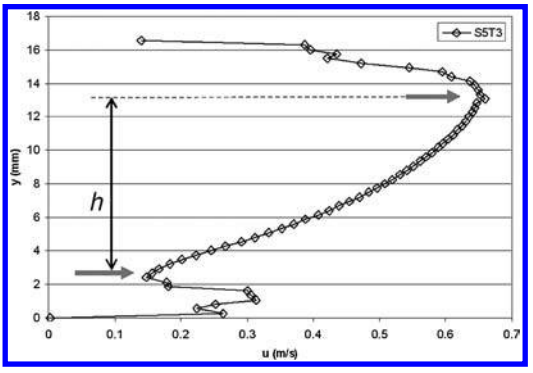


Figure 4. Computation of flow depth from velocity profiles.

32 × 32 pixels with 50% overlap. We computed the mean displacement of the tracer particles in each interrogation area using a two dimensional cross-correlation algorithm. That procedure gave spurious vectors that we eliminated applying sequentially a signal/noise and a range filter to the vectors fields.

2.3 *Difficulties of data analysis*

Figure 3 displays a typical image and the corresponding instantaneous velocity field obtained in the tests using PIV. Figure 3b shows that vectors were eliminated in areas located above the free surface, at the bed, and in regions with sediments. Those locations in Figure 3b coincide with zones in Figure 3a containing few tracers. Figure 3 shows that there were few velocity measurements into the bed load layer. However, velocity measurements were possible over the bed load layer that is in the clear water part of the flow.

As instantaneous velocity fields measured in such conditions were very irregular, data analysis and computation of mean quantities were very difficult. The main difficulty was to determine the average flow depth *h* because of bed load transport and free surface waviness. This quantity was necessary to compare dimensionless vertical profiles between different tests. We chose to compute the flow depth based on the average profile of the longitudinal velocity (Fig. 4). The flow depth was defined between the maximum velocity and the first inflection point encountered moving towards the bed. With this procedure, flow depth corresponded to the clear water flow depth that did not take into account the bed load layer.

3 EXPERIMENTAL RESULTS

This section focuses on the description of the flow located mainly above the bed load layer that does not have sediment load. This part of the flow is denoted as

Copyright © 2006 Taylor & Francis Group plc, London, UK

Table 2. Hydrodynamics of the clear water flow.

Tests	U [m/s]	h [mm]	u_* [m/s]	$y/h(U)$ [−]
S3T1	0.32	6.4	0.039	0.41
S3T4	0.49	13.9	0.051	0.46
S3T6	0.49	15.2	0.053	0.40
S3T7	0.62	15.5	0.053	0.36
S5T1	0.3	7.47	0.053	0.57
S5T2	0.42	12.3	0.064	0.54
S5T3	0.48	10.7	0.061	0.7
S5T4	0.66	13.9	0.066	0.5
S5T5	0.78	15.5	0.068	0.5

clear water flow in the following. The origin of the bed $y = 0$ is located at the bottom of the clear water flow, i.e. at the stationary bed for the tests without bed load, and at the top of the bed load layer for the tests with bed load.

3.1 *Hydrodynamics of the clear water flow*

Table 1 presents the bulk hydrodynamics of the total flow, taking into account the flow in the bed load layer. Table 2 summarizes the hydrodynamics of the flow over the bed load layer calculated using PIV measurements. As bed load transport increases, we observe larger differences in hydrodynamics computed using both methods. In particular, values of flow depth, h, and shear velocity, $u_* = (gR_hS)^{0.5}$, are smaller in the clear water flow than the ones corresponding to the total flow as bed load transport increases. Values of the mean velocity, U, computed from the velocity profile, show that mean velocity for the clear water flow is very close to the mean velocity of the total flow. In general, U is found at y/h in the range 0.4–0.5.

3.2 *Vertical distribution of the longitudinal velocity*

We computed the vertical distribution of the average longitudinal velocity, $u(y)$, using a double-averaging procedure: first we calculated the time (or ensemble) average field, and then the spatial average of time-averaged field in the longitudinal direction.

In general, the vertical distribution of the longitudinal velocity in a fully developed turbulent open channel flow is well represented by a logarithmic distribution (e.g. Bigillon et al. in press). However, there is no evidence that the velocity profile remains logarithmic in presence of bed load transport. Figure 5 shows the vertical distribution of double-averaged longitudinal velocity plotted in a semi-logarithm scale as function of $y^+ = yu_*/\nu$. This figure displays the experimental data as well as the logarithmic velocity distribution obtained for smooth and rough wall

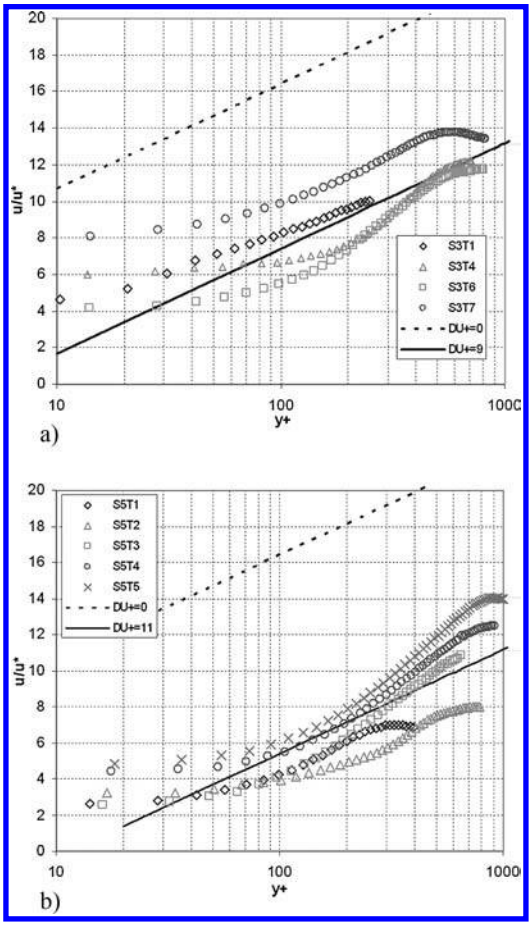


Figure 5. Vertical distribution of the longitudinal velocity above the bed: a) S = 3%; b) S = 5%. Experimental data and distribution computed from Eq. (1).

given by (e.g. Nezu & Nakagawa 1993, Bigillon et al. in press):

$$u^+ = \frac{1}{\kappa} \ln y^+ + B - \Delta U^+ \qquad (3)$$

where $u^+ = u/u_*$, $\kappa = 0.41$ is the von Kármán constant, $B = 4.9$, and ΔU^+ represents the shift of the log-law due to roughness effect. In our study, ΔU^+ is between 7 and 11 for S = 0.03, and between 11 and 13 for S = 0.05. Figure 5 illustrates that velocity profiles have a thin logarithmic zone for values of y^+ between 80 and 200, corresponding to values of y/h smaller than about 0.25. This result corroborates that velocity outside of the bed load layer satisfy a log-law like it was previously found over a sheet-flow (Summer et al. 1996).

Figure 5 indicates a complex behaviour as sediment transport increases. In absence or for small transport rates (tests S3T1, S3T4, S3T6, S5T1, S5T2),

Copyright © 2006 Taylor & Francis Group plc, London, UK

increasing sediment transport shifts velocity profiles towards smaller values of the dimensionless velocity u/u_*. This result was previously found by Carbonneau & Bergeron (2000). It is also consistent with the fact that drag and sediments collision extract kinetic energy from the mean flow. On the other hand, for large transport rates (tests S3T7, S5T3, S5T4, S5T5), the shift occurs towards higher values of the velocity. We think that this complex behaviour is related to roughness effect. When there is not sediment transport, roughness is due to static sediments forming the bed. As sediment transport increases, sediments start moving on the bed which results in a more irregular bed. Thus, the bed appears rougher to the flow that dissipates more energy and slows down compare to case without transport. As sediment transport continues increasing, more sediments move on the bed. The bed load layer becomes more concentrated and, at the limit, turns into a sheet-flow layer. In such condition, the bed appears somehow regular to the clear water flow that consumes less energy and accelerates compared to the mid-transport case. This roughness effect is supported by recent work on flow resistance obtained in the same experimental setup (Recking et al. 2005).

3.3 *Turbulence intensities*

Figures 6–7 display the longitudinal and vertical turbulence intensities, u_{rms}/u_* and v_{rms}/u_*, where u_{rms} and v_{rms} denote the root mean square of velocity fluctuations u' and v' respectively. We computed velocity fluctuations using a classical Reynolds decomposition i.e. by removing the time-averaged velocity field from the instantaneous velocity field.

Figures 6–7 show a very complex behaviour of turbulence in presence of bed load transport. We observe that, in general, higher sediment transport rates enhance longitudinal turbulence intensity as shown in Figure 6. This tendency agrees with previous research (e.g. Campbell et al. 2005) and supports the idea that bed load extracts momentum from the mean flow. However, this trend reverses in tests that correspond to moderate bed load transport (tests S3T4 and S3T6, S5T2 and S5T3) and a ratio of the flow depth to the grain diameter of about 5.

Figures 6–7 demonstrate that turbulence intensities are reasonably well represented by typical exponential laws previously found for smooth and rough beds such as (e.g. Nezu & Nakagawa 1993, Song et al. 1994, Bigillon et al. in press):

$$u^+_{rms} = 2.3\exp(-\frac{y}{h}) \quad (4)$$

$$v^+_{rms} = 1.14\exp(-0.76\frac{y}{h}) \quad (5)$$

However, for tests corresponding to low bed load transport and ratio of the flow depth to the grain diameter smaller than 6 (tests S3T1, S3T4, S5T1, S5T2, S5T3), vertical turbulence intensity is more homogenous (Fig. 7).

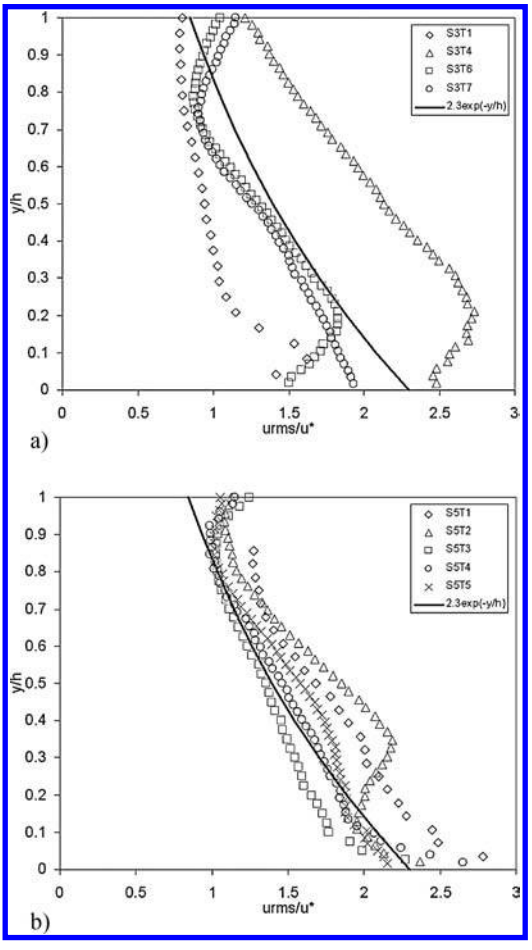


Figure 6. Vertical distribution of the longitudinal turbulence intensities. a) S = 3% b) S = 5%.

3.4 *Reynolds stress*

Figure 8 displays the vertical distribution of the Reynolds shear stress normalized with u_*^2, denoted by $u'v'$, plotted versus y/h.

Reynolds stress profiles indicate that turbulence production is enhanced by increasing bed load transport. This trend is evident for tests preformed with a slope S = 5% (Fig. 8b), but it should be mentioned, however, that the Reynolds stress curve corresponding to test S3T7, is under the one corresponding to test S3T6, contradicting the previous argument. This may be caused by an underestimation of the shear velocity.

Copyright © 2006 Taylor & Francis Group plc, London, UK

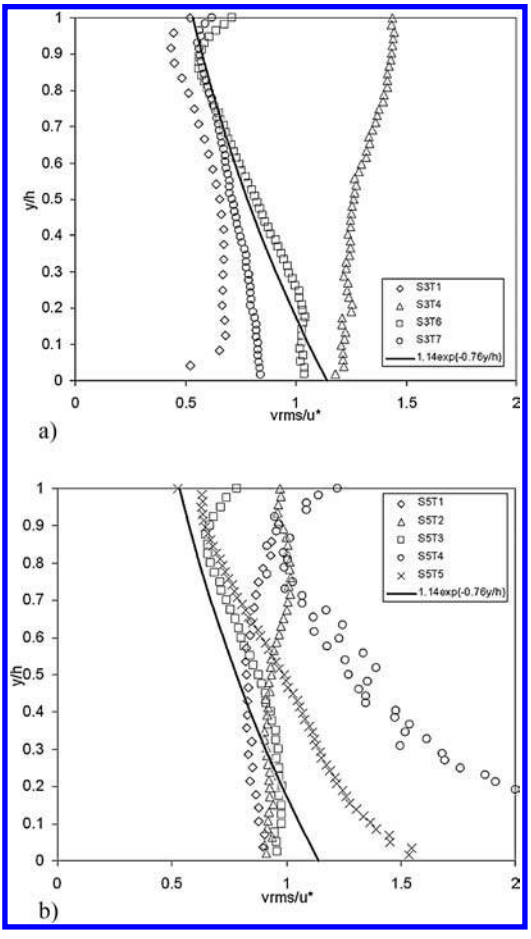


Figure 7. Vertical distribution of the vertical turbulence intensities. a) S = 3% b) S = 5%.

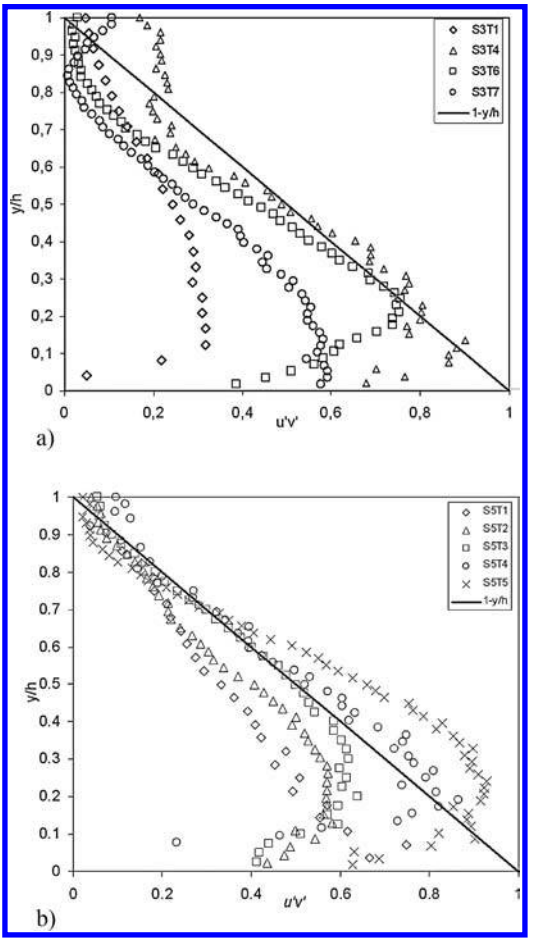


Figure 8. Vertical distribution of the dimensionless Reynolds shear stress $u'v'$: a) S = 3% b) S = 5%.

Reynolds stress profiles present a similar shape for all tests. They demonstrate a linear trend around the one given by (e.g. Bigillon et al. in press):

$$u'v' = 1 - y/h \quad (6)$$

However many tests deviate from (6) and display a different slope. This could be due to secondary currents that yield to different values of the shear velocity than the one estimated by the method described in section 3.1.

As previously found by Campbell et al. (2005), Reynolds stress deviates from a linear trend near the bed. In particular, we observe that the fluid shear stress decreases towards the bed indicating the existence of a roughness sublayer. This layer extends from the top of the bed to the level of maximum Reynolds stress and it is one to two diameters thick in all tests. The existence of this layer demonstrates that additional momentum extraction mechanisms appear in this region. In particular, some shear stress is extracted from the fluid and given to the sediments via drag. At the limit, according to Bagnold hypothesis (e.g. Seminara et al. 2002), the fluid shear stress at the bed should reduce to the threshold value associated with incipient motion.

4 CONCLUDING REMARKS

This study provides new information about the effect of bed load transport on flow velocity and turbulence. We collected velocity measurements using PIV in flume experiments performed under equilibrium bed load transport conditions. PIV data provided instantaneous and average hydrodynamics fields over the bed load layer. Results from our experiments show

Copyright © 2006 Taylor & Francis Group plc, London, UK

that bed load transport has a complex effect on hydrodynamics corroborating previous results (Campbell et al. 2005, Carbonneau & Bergeron 2000). Our data indicate that bed load transport causes opposite effect depending on bed load rate. In general, we observe that increasing bed load transport results in lower longitudinal velocities, larger turbulence intensity, and larger Reynolds stress values compared to conditions without sediment transport. However, an increase of bed load transport results in larger longitudinal velocities and smaller longitudinal turbulence intensity in tests corresponding to moderate sediment transport rates. We think that this behaviour is related to changes in bed roughness and relative flow depths, as it was recently proposed by Recking et al. (2005). Those changes may be related to a transition from a bed load transport to a type of sheet flow transport. Further work is required to develop a better understanding of bed load effect on flow hydrodynamics. Future work should focus on the study of moderate sediment transport conditions for which it seems that the bed load produces sudden changes on hydrodynamics.

BIBLIOGRAPHY

Bigillon, F. Niño, Y. & Garcia, M.H. in press. Measurements of turbulence characteristics in an open-channel flow over a transitionally-rough bed using Particle Image Velocimetry. *Experiments in fluids*.

Carbonneau, P.E. & Bergeron, N.E. 2000. The effect of bed-load transport on mean and turbulent flow properties. *Geomorphology* 35:267–278.

Campbell, L. McEwan, I. Nikora, V. Pokrajac, D. Gallagher, M. & Manes, C. 2005. Bed-load effects on hydrodynamics of rough-bed open-channel flows. *Journal of Hydraulic Engineering* 132(7):576–585

Frey, P. Ducottet, C. & Jay, J. 2003. Fluctuations of bed load solid discharge and grain size distribution on steep slopes with images analysis. *Experiments in fluids* 35:589–597.

Recking, A. Paquier, A. Frey, P. Belleudy, P. & Champagne, J.Y. 2005. Flow resistance: towards a slope-dependant model. *XXXI IAHR Congress, 11–16 September 2005.* Seoul, Korea.

Nezu & Nakagawa 1993. *Turbulence in open channel flows.* IAHR Monograph, Rotterdam: Balkema.

Nogueira, S. Sousa, R.G. Pinto, A.M.F.R. Riethmuller, M.L. & Campos, J.B.L.M. 2003. Simultaneous PIV and pulsed shadow technique in slug flow: a solution for optical problems. *Experiments in Fluids* 35:598–609.

Seminara, G. Solari, L. & Parker, G. 2002. Bed load at low Shields stress on arbitrarily sloping beds: Failure of the Bagnold hypothesis *Water Resources Research* 38(11):1249.

Smart, G. & Jaeggi, M. 1983. Sediment transport on steep slopes, Zurich.

Song, T. Chiew, Y.M. & Chin, C.O. 1998. Effect of bed-load movement on flow friction factor. *Journal of Hydraulic Engineering* 124:165–175.

Song, T. Graf, W.H. & Lemmin, U. 1994. Uniform flow in open-channels with gravel bed. *Journal of Hydraulic Research* 6:861–876.

Sumer, B.M. Kozakiewicz, A. Fredsoe, J. & Deigaard, R. 1996. Velocity and concentration profiles in sheet-flow layer of movable bed. *Journal of Hydraulic Engineering* 122(10):549–558.

Copyright © 2006 Taylor & Francis Group plc, London, UK

The resistance of transported sediment

Graeme Smart
Nat. Inst. of Water & Atmospheric Research, Christchurch, New Zealand

ABSTRACT: In the 1980s the author undertook flume experiments that extended the 1940s Meyer-Peter & Mueller sediment transport data to higher transport rates and to steeper slopes. This paper investigates these data for friction losses associated with sediment transport, by measuring water velocity within the flow mixture and by breaking down the mixture depth into water depth (h_w) + sediment depth (h_s). Interrelationships between the mean fluid velocity, mean sediment velocity, water depth, sediment depth, mixture depth and energy gradient are evaluated. The lag between sediment velocity and water velocity for the steep flume data is shown to be a function of $\sqrt{(gd(\rho_s/\rho - 1))}$, h_s/d, and $(h_w + h_s)/d$. Resistance coefficients that incorporate sediment behavior were introduced and reasonable quantitative predictions of the sediment and water components of the flow were achievable.

1 INTRODUCTION

Correct prediction of the depth of floodwaters is necessary to design riparian structures and to define flood hazard zones. As many floods carry high sediment loads any influence of transported sediment on flow resistance should be understood. Many contemporary flow resistance equations are derived assuming a logarithmic or power law velocity profile above the bed. Where the bed boundary is mobile (Fig. 1) these equations may still be applicable, albeit with altered boundary roughness and/or depth of flow. When there are particles in transport over much of the flow depth (Fig. 2) the theoretical, clear-water velocity profiles may not apply and conventional resistance equations may not be suitable.

This concern is overcome if a simple friction coefficient is used to quantify flow resistance. The problem then becomes one of how to calculate the correct coefficient.

Since the work of Meyer-Peter & Mueller (MPM) in the 1940s there has been debate over friction losses associated with transportation of sediment. Bagnold (1973) described how particle velocity was less than fluid velocity but he encountered problems in quantifying the difference. Muste & Patel (1997) measured the difference to be up to 4% for sand particles in water. More recent studies are described by Cheng (2004). These investigations did not consider sediment sizes larger than sand and Cheng concluded by calling for further research.

In the 1980s, Smart (1984a) undertook sediment transport experiments in an adjustable slope flume in MPM's laboratory, which extended the MPM data to

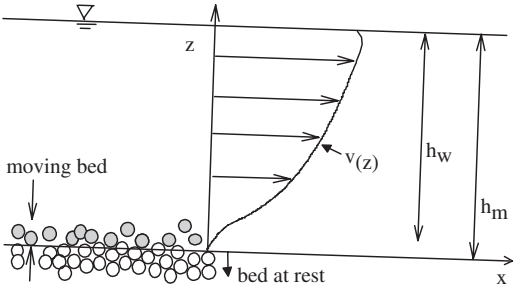


Figure 1. Conditions for application of conventional flow resistance equations, v = water velocity, c = sediment concentration, h_w = depth of water, h_m = depth of mixture.

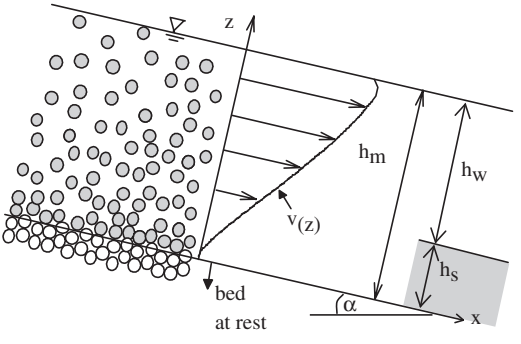


Figure 2. Typical conditions assessed in this investigation, h_s = depth of moving sediment excluding porosity, α = slope angle.

Copyright © 2006 Taylor & Francis Group plc, London, UK

Table 1. Sediment materials used in the steep flume experiments. d = mean particle size, other symbols are defined in the notation section.

Material	ρ_s [kg/m^3]	d [mm]	d_{30} [mm]	d_{90} [mm]
I	2670	4.3	1.3	11.0
II	2670	4.2	3.6	5.2
III	2680	2.0	1.0	4.6
IV	2680	10.5	9.0	12.1

higher transport rates and steeper slopes. The flume was 6 m long, 0.2 m wide and sediment transport data were measured for slopes ranging from 3% to 25%. Four sediment materials were used in the experiments. Their properties are given in table 1.

As part of the experiments the fluid velocity was measured independently from that of the fluid/sediment mixture. This fluid velocity ranged from 0.6–2.8 m/s while the bulk flow velocity ranged from 0.6–2.4 m/s. Until now these measurements have not been fully analyzed. As mean sediment particle velocity can also be calculated from the measurements, the data should provide insight into factors influencing flow resistance in situations similar to the Figure 2 – type conditions. This paper presents these data and analyses interrelationships between the fluid velocity, sediment velocity, flow resistance coefficient, water depth, sediment depth, mixture depth and energy gradient. Potential ways to improve prediction of flow depth in Figure 2 – type conditions are: (a) develop a flow resistance coefficient that incorporates sediment drag or bulking effects or (b) predict water depth and sediment depth separately and add these to give the overall mixture depth.

2 MEASUREMENT METHODS

2.1 *Water and sediment discharge*

The steady water discharges in the experiments were determined from calibrated pressure differentials measured across an orifice plate in the flume supply pipe. Steady sediment discharges were regulated by an upstream conveyor belt and weighed in a collection hopper downstream of the flume. Details of the experimental setup were given by Smart & Jaeggi (1983).

2.2 *Mixture depth*

The depth of the flowing sediment/water mixture (h_m) was read from millimeter scales fixed to the outside of plexi-glass walls on the sides of the flume. At higher sediment transport rates the water surface was fluctuating and the bed surface was mobile, thus making it difficult to define the exact location of the non-mobile bed. For such extreme conditions the mixture depth measurement error could be of the order of ±10 mm.

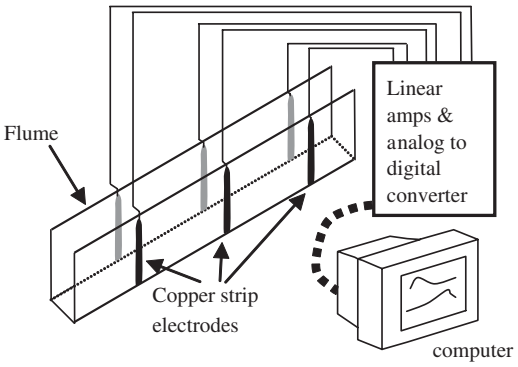


Figure 3. Diagram showing water velocity measurement apparatus.

2.3 *Water velocity*

The velocity of water (v_w) within the sediment/water mixture was recorded by measuring the travel time of salt slugs injected instantaneously into the flow. Water travel time was indicated by monitoring the conductivity between pairs of electrodes mounted on the flume walls as shown diagrammatically in Figure 3.

Each pair of electrodes indicated the conductivity of the water cross-section between them. Slugs of sodium carbonate were injected near the upstream flume end and as these slugs advected and dispersed down the flume the conductivity between the electrodes changed. Mean velocity was defined as the distance between two pairs of electrodes divided by the time difference between the centroids of the peaks in conductivity at each electrode pair. Technical details of the automated velocity measurement setup are given by Smart (1984b). Three pairs of electrodes were used so that the velocity could be determined independently over two reaches of the flume, thus enabling verification of flow uniformity.

3 CALCULATED PARAMETERS

3.1 *Water depth and velocity, sediment depth and sediment velocity*

The mean velocity of the sediment water mixture is:

$$v_m = (q_w + g_s/\rho_s)/h_m \quad (1)$$

where q_w is the measured water discharge divided by the flume width, g_s = measured mass transport rate

Copyright © 2006 Taylor & Francis Group plc, London, UK

per unit width and ρ_s = sediment density. The mean velocity of water over the mixture depth is:

$$v_{mw} = q_w/h_m \quad (2)$$

The depth (h_w) of clear water within the mixture is calculated from the continuity equation:

$$h_w = q_w / v_w \quad (3)$$

where v_w can be measured as described in 2.3 above.

The equivalent sediment depth h_s with no porespace, is:

$$h_s = g_s / (\rho_s v_s) \quad (4)$$

where v_s = sediment velocity along the flume. From conservation of volume, the mixture depth is the sum of the water depth and the sediment depth:

$$h_m = h_s + h_w \quad (5)$$

With mixture depth measured as described in section 2.2, the sediment depth can be calculated using (3) and (5). Eq. (4) then gives the sediment velocity:

$$v_s = g_s / (\rho_s (h_m - h_w)) \quad (6)$$

Using this breakdown of the flow components, in order to predict h_m given q_w, g_s, S and d_m, it will be necessary to calculate v_w and v_s. For low sediment loads v_w should be predictable by the usual clear water resistance equations such as Manning's Eq. or a log law equation. As sediment load increases, v_w may decrease due to the drag of suspended particles.

3.2 *Drag force balance*

For a single suspended sediment particle diameter d, traveling downstream at v_s, the streamwise drag force is $(C_d/2)\ \rho\ (v_w\text{-}v_s)^2\ \pi\ d^2/4$ where C_d is a drag coefficient that depends on particle shape and flow turbulence. The number of identical, spherical, moving particles above area A of bed is $(h_s A)/(\pi\ d^3/6)$. Introducing C_p to correct for differences in the sediment and water velocity profiles and particle interaction, the total streamwise particle drag F_s above the area A of bed is the sum of the drag on individual particles times the number of particles:

$$F_s = 3\ C_d\ C_p\ \rho\ (v_w\text{-}v_s)^2\ \ h_s\ A\ /\ (4\ d) \quad (7)$$

Assuming the weight of suspended particles is eventually supported by the bed, the transfer of particle drag force to the bed can be described using a coefficient of dynamic friction μ and the normal force:

$$F_s = \mu\ (\rho_s\text{–}\rho)\ h_s\ A\ g\ \ \cos\alpha \quad (8)$$

Equating (7) and (8) gives:

$$\mu\ /\ (C_d\ C_p) = .75\ (v_w\text{-}v_s)^2\ \ \rho\ /\ [(\ \rho_s\text{–}\rho\ )\ g\ d\ \cos\alpha] \quad (9)$$

All parameters on the right hand side of (9) can be measured or derived from the flume data allowing calculation of $\mu/(C_d\ C_p)$. Such calculated values will contain any errors introduced by the above assumptions and by measurement inaccuracies. The equation does not differentiate between the case where water moves faster than the sediment and the potential case of sediment moving faster than the water.

3.3 *Energy head loss*

For the uniform flow conditions investigated here the energy loss per unit weight per unit channel length is given by the channel slope (S).

Without sediment load, according to Meyer-Peter & Mueller (1949), the energy gradient required to produce a depth h_w in the flume would be:

$$S_b = v_w^2\ n^2\ /\ h_w^{4/3}, \qquad n = d_{90}^{1/6}/26 \quad (10)$$

where d_{90} is the sediment sieve diameter for which 90% of a sediment sample is finer. As there were no bedforms other than antidunes in the flume, an approximate indication of the energy gradient (S_s) associated with the sediment load component of a mixture (with water depth h_w) is therefore:

$$S_s = S - S_b \quad (11)$$

The relation is approximate because of the different flow structure when sediment is present and the different weight of flow carrying a sediment load compared to flow without a sediment load.

3.4 *Friction coefficient*

Friction coefficients represent a ratio of driving force and frictional resistance force. To modify friction parameters to allow for sediment drag it is necessary to understand the physical composition of friction coefficients like Chézy C or friction factor. The driving force for unit bed area and flow depth h, is the down-slope weight of the flow $\tau_o = \rho\ h\ g\ \sin(\alpha)$ where g = gravitational force per unit mass. The retarding frictional drag force over unit bed area is considered as skin drag: $\tau_b = C_b\ \rho\ v_b^2/2$ where C_b is a bed drag coefficient and v_b is the effective flow velocity at the bed. The effective bed velocity is some function of mean velocity, say $v_b^2 = v^2/(C_a/2)$. Equating the driving and retarding forces gives:

$$v^2/(gh\ \sin\alpha)\ = C_a\ /\ C_b \quad (12)$$

Even at the moderate slopes of these experiments, little error is introduced by assuming $\sin\alpha = S$ and the left side of (12) is seen to be $(v/v^*)^2$ where

Copyright © 2006 Taylor & Francis Group plc, London, UK

$v^* = \sqrt{(ghS)}$. The correspondence between v/v* and friction factor, Manning's n and Chézy C is described by Smart (2002). The right side of (12) is not constant and in rough turbulent flow, the factor C_a/C_b may depend on flow depth, bed roughness height, particle shape and particle packing. When sediment is introduced into the flow the downslope weight component increases and other forces come into play. Sediment weight can be incorporated if v* is redefined as:

$$v^*_{ws} = \sqrt{(g(h_w+(\rho_s/\rho-1)h_s)\,S)} \qquad (13)$$

Various guises of v/v* can be considered and the following friction coefficients are proposed:

$$c_m = v_m/\sqrt{(gh_m\,S)} \quad \text{mixture coef.} \qquad (14)$$

$$c_{mw} = v_{mw}/\sqrt{(gh_m\,S)} \quad \text{mixture water coef.} \qquad (15)$$

$$c_{mg} = v_m/v^*_{ws} \quad \text{mixture coef. using (13)} \qquad (16)$$

$$c_w = v_w/\sqrt{(gh_w\,S)} \quad \text{water coef.} \qquad (17)$$

$$c_s = v_s/\sqrt{(gh_s\,S)} \quad \text{sediment coef.} \qquad (18)$$

3.5 *Wall effect correction*

In the experiments, the flume-width to flow-depth ratio varied from 2.2 to 6.9 and there is no consensus on the best technique for correcting for flow resistance effects associated with drag caused by the flume walls. As the roughness of sediment on the flume bed was an order of magnitude greater than the equivalent roughness height of the smooth flume walls, no sidewall correction is applied to the present data analyses. In the original investigations (Smart & Jaeggi, 1983) it was found that the use of a wall drag correction procedure did not improve the correlation between predicted and measured transport rates.

4 RESULTS

Water velocities were measured in 71 experiments. Inaccuracies in measurement of mixture depth indicated negative, zero or infinite sediment velocities in 6 cases and these data were excluded in the following analyses.

4.1 *Energy head loss*

An indication of the energy gradient associated with the sediment load, as discussed in section 3.3, is given in Figure 4. It appears that for these steep flume experiments up to almost 100% of the available energy may be spent on transporting sediment. Figure 4 shows a log function fits the data reasonably well:

$$(S-S_b)/S = .038*\ln(h_s/d) + 0.90 \qquad (19)$$

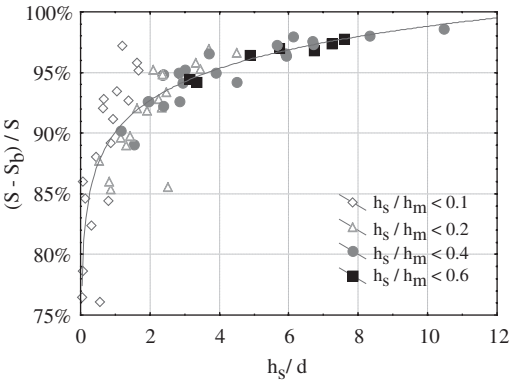


Figure 4. Indication of fraction of energy spent on sediment transport as a function of relative sediment depth. Symbols showing h_s/h_m illustrate the effect of sediment concentration.

but, as explained in section 3.3, this approach is not particularly robust on a theoretical basis.

4.2 *Velocity lag*

Widely used in investigations of fine sediments, the lag between mean sediment velocity and mean water velocity can be misleading where there are coarser particles, especially when these are transported as bedload. In the case of no sediment movement the lag would be 100%.

Figure 5 shows velocity lag as fraction of water velocity. Negative lags occur at moderate slopes indicating that sediment is moving faster than the interstitial water or that there is measurement error. Figure 5 shows the sediment concentration (h_s/h_m) ranges from near zero to more than 50%, indicating that there can be more sediment than water in the flow mixture. Figure 5 shows that the relative velocity lag is a function of the sediment concentration and channel slope.

Further analysis of relative velocity lag is not straightforward and the velocity lag is studied using the drag force balance of Equation (9).

Figure 6 shows calculated values of the parameter $\mu/(C_d\,C_p)$ according to Eq. (9). The main variation in this parameter should come from C_p which relates the effective water velocity moving the sediment to the mean water and sediment velocity. A decrease in C_p is expected as sediment transport rate increases and bedload becomes suspended load.

Figure 6 shows that $\mu/(C_d\,C_p)$ increases with mixture depth to grain size ratio and increases with sediment depth to grain size ratio.

The relation can be described by the equation

$$\mu/(C_d\,C_p) = 0.6\,(h_m/d)\sqrt{(h_s/d)} \qquad (20)$$

Copyright © 2006 Taylor & Francis Group plc, London, UK

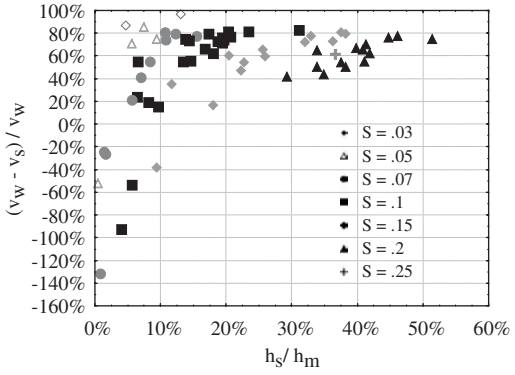


Figure 5. Sediment velocity lag as fraction of water velocity compared with sediment to water volume ratio (h_s/h_m) and channel slope S.

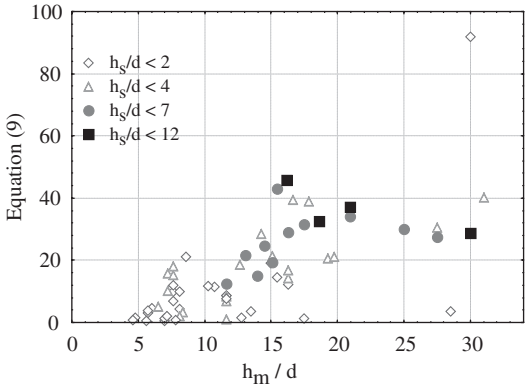


Figure 6. Coefficient of drag force balance (Eq. 9) as a function of relative mixture depth and relative sediment depth.

and, taking into account that measurement errors in ($v_w - v_s$) are squared in calculation of $\mu/(C_d\ C_p)$, the goodness of fit is reasonable as shown in Figure 7.

4.3 *Friction coefficient v/v**

For clear water, the friction coefficient can be explained as a function of the flow depth to roughness height ratio. Parameters explaining the sediment influenced coefficients of equations (13) to (18) are investigated in the following sections. An increase in the coefficient indicates a decrease in flow resistance. Each coefficient was examined for dependence on experimental variables such as relative depth, sediment concentration, d_{90}/d_{30} and energy gradient. Results are not given where no relation was evident. The relations are not applicable when there is no sediment load and were not investigated for slopes flatter than 3%.

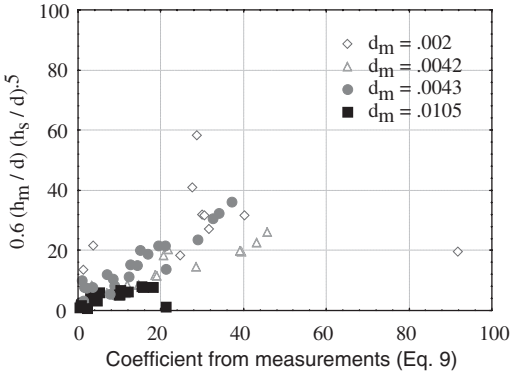


Figure 7. Measured coefficient $\mu/(C_d\ C_p)$ compared with value calculated by Eq. (20).

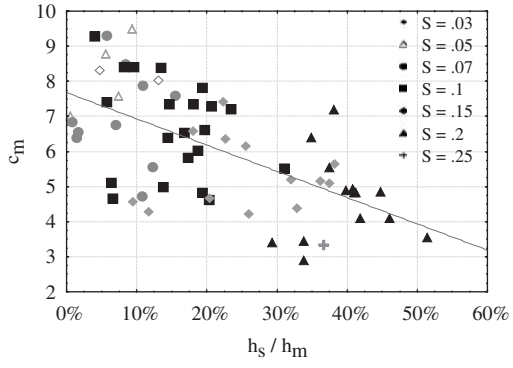


Figure 8. Mixture coefficient c_m decreases with increasing sediment concentration (h_s/h_m).

4.3.1 *Mixture coefficient c_m (Eq. 14)*

Values of c_m in the steep flume experiments, range from around 2.9 for the coarsest sediment to 9.5 for the finest sediment. No straightforward description of c_m in terms of clear water parameters such as $\log(h_m/d_{90})$ was evident. There is a decrease in c_m with increasing sediment concentration as shown in Figure 8. The relation is $c_m = 7.75 - 7.73\ (h_s/h_m)$. Considering $h_s/h_m = 1 - h_w/h_m$ this may be written:

$$c_m = 7.7\ (h_w/h_m) \tag{21}$$

4.3.2 *Mixture water coefficient c_{mw} (Eq. 15)*

The range of c_{mw} values was similar to the c_m range but a stronger relation explaining the decrease in c_{mw} with h_s/h_m was evident. The line fitted to Figure 9 has the equation: $c_{mw} = 7.51–9.15*(h_s/h_m)$ $r^2 = 0.5$.

Re-arranging to a form similar to (21) gives:

$$c_{mw} = 9.15\ (h_w/h_m) - 1.64 \tag{22}$$

A relation is also evident between c_{mw} and $\log(h_m/d_{90})$ as shown in Figure 10. A different log law

Copyright © 2006 Taylor & Francis Group plc, London, UK

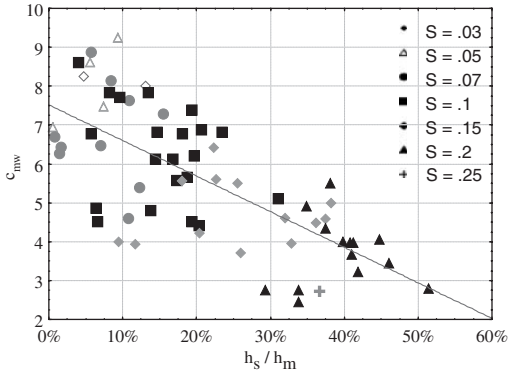


Figure 9. Mixture water coefficient as a function of sediment concentration showing flume slope S.

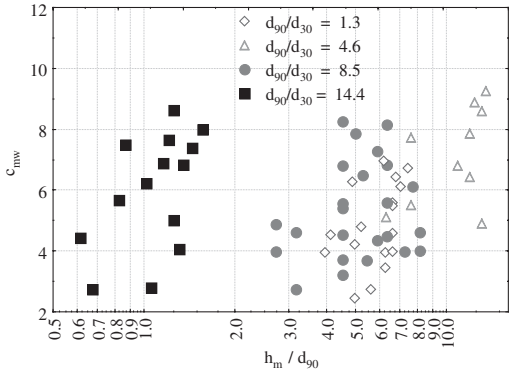


Figure 10. Mixture water coefficient as a function of $\log(h_m/d_{90})$.

is indicated for the sediment with $d_{90}/d_{30} = 14.4$ than for the other sediment types. From the present data set it was not possible to find a variable that improved on the data grouping and a general log law equation could not be found.

4.3.3 *Mixture coefficient corrected for weight c_{mg} (Eq. 16)*

The c_{mg} coefficient behaved similarly to c_m and c_{mw}. A stronger relation explaining the decrease in c_{mg} with h_s/h_m was evident compared to c_m but the correlation was similar to that between c_{mw} and h_s/h_m ($r^2 = 0.5$).

4.3.4 *Water coefficient c_w (Eq. 17)*

The c_w coefficient shows no significant relation to sediment concentration. A relation with log (h_m/d_{90}) was discernable for some sediment materials but it was not possible to formulate a general log law.

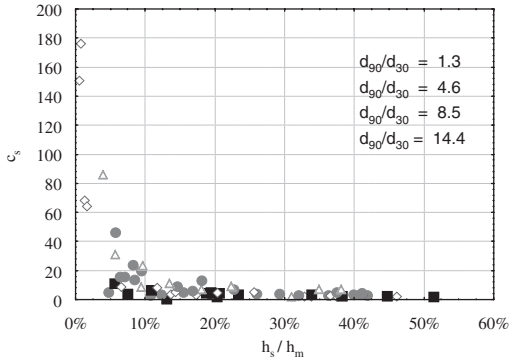


Figure 11. Sediment resistance coefficient c_s as a function of sediment concentration.

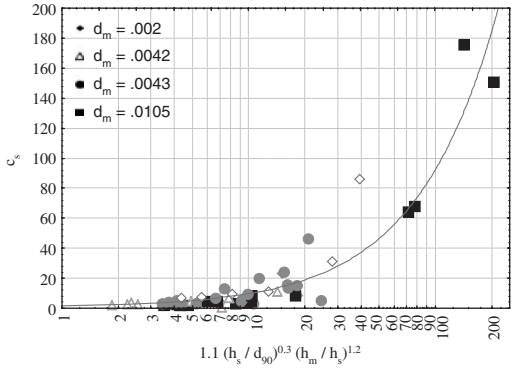


Figure 12. Measured c_s coefficient compared with value calculated by Eq. (23). Line shows $y = x$.

4.3.5 *Sediment coefficient c_s (Eq. 18)*

This coefficient has a large range in values from near 200 to almost zero. The value falls quickly (resistance increases) as sediment moves from bedload to suspended load and concentration increases as shown in Figure 11.

The coefficient can be explained by a relation incorporating relative sediment roughness depth (h_s/d_{90}) and sediment concentration:

$$c_s = 1.1\ (h_s/d_{90})^{0.3} / (h_s/h_m)^{1.2} \qquad (23)$$

The high correlation of this relation ($r^2 = 0.87$) is evident in Figure 12 where the x-axis is given on a log scale to show the spread of low c_s values.

5 DISCUSSION

Recalling that the goal of the investigations is to investigate sediment resistance and improve prediction of flow depth, the results are now analyzed to determine whether this can be achieved.

Copyright © 2006 Taylor & Francis Group plc, London, UK

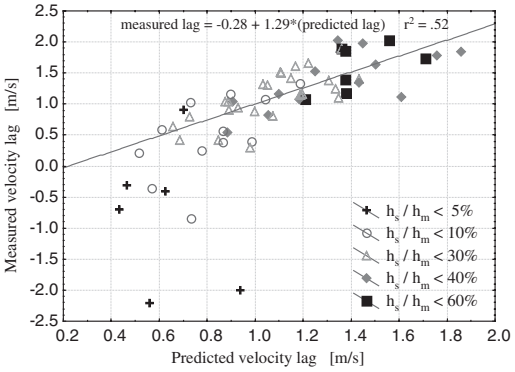


Figure 13. Comparison of predicted and measured velocity lag.

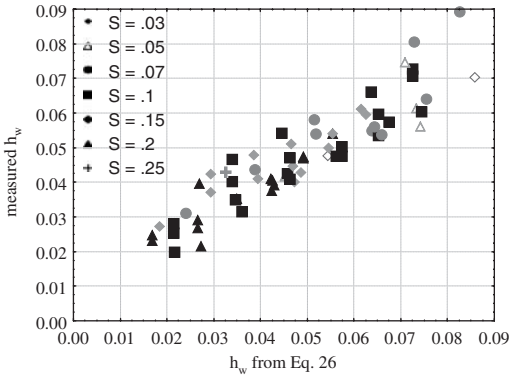


Figure 14. Measured water depths compared with values predicted by Equation (26).

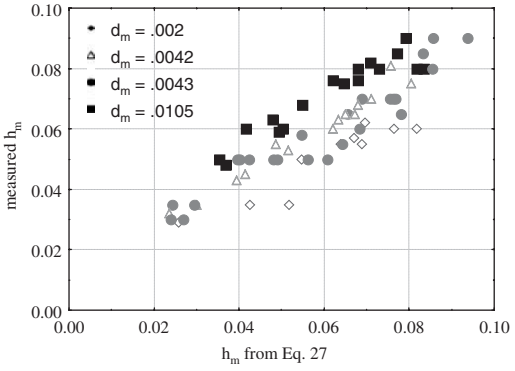


Figure 15. Measured flow mixture depth compared with values predicted by Equation (27).

5.1 *Velocity lag*

Substituting the empirical prediction of the $\mu/(C_d\ C_p)$ coefficient from Eq (20) into the drag force balance equation (9) and using $\cos\alpha = 1$ gives: $v_w - v_s = \pm 0.9\ (h_s/d)^{0.25}\ [(g(\rho/\rho_s - 1)\ h_m]^{0.5}$. The equation does not identify whether sediment velocity lags water velocity or *vice versa*. Figure 13 shows this predicted velocity lag versus measured velocity lag. It appears that, at lower sediment concentrations on moderate slopes, the sediment may travel faster than the water. It was noted during the experiments that some particles were entrained with such vigor that they were ejected through the water surface. This vigorous entrainment by turbulence may explain these high sediment velocities at low transport rates.

Using only positive lags to correct the coefficient for best fit (Figure 13) and grouping logically gives:

$$v_w\text{-}v_s = 1.2(h_s/d)^{0.25}(h_m/d)^{0.5}[(g(\rho/\rho_s)\text{-}1)d]^{0.5} - 0.28 \quad (24)$$

This relation is not applicable when there is low sediment load or no sediment load.

5.2 *Predicting* h_m *from components* $h_w + h_s$

The mixture friction coefficient equation (21), may be written as:

$$h_w = 0.13\ (q_w + g_s / \rho_s\ ) / \sqrt{(g h_m S)} \quad (25)$$

Similarly the mixture water coefficient equation (22), indicates:

$$h_w = 0.11\ (\ q_w / \sqrt{(g h_m S)}) + 0.18\ h_m \quad (26)$$

In comparison with measured data, Equation (26) gives better results. It is shown in Figure 14 compared with the measured values of h_w.

Equating (25) and (26) to eliminate h_w gives:

$$h_m = (0.11\ q_w + 0.72\ g_s / \rho_s\ )^{2/3} /\ (g\ S)^{1/3} \quad (27)$$

This prediction of overall flow depth is shown in Figure 15.

The figure indicates that the reasonable prediction of mixture depth may be improved upon by incorporating a grain size indicator. In the case when there is no sediment transport Equation (27) implies $c_w = c_m = 12$. The form of clear water flow resistance equations (e.g. Keulegan, 1938) implies that this "constant" should be a log or power law function of depth and bed roughness. Further work is therefore required to develop a general purpose equation.

5.3 *Sediment resistance coefficient*

The sediment resistance coefficient of Equation (23) can also be arranged to a form similar to (25) indicating:

$$h_s = .85\ ((g_s / \rho_s)/\sqrt{(g\ h_m\ S)})^{1.67}\ \sqrt{(d_{90} / h_m)} / h_m^{0.67} \quad (28)$$

Copyright © 2006 Taylor & Francis Group plc, London, UK

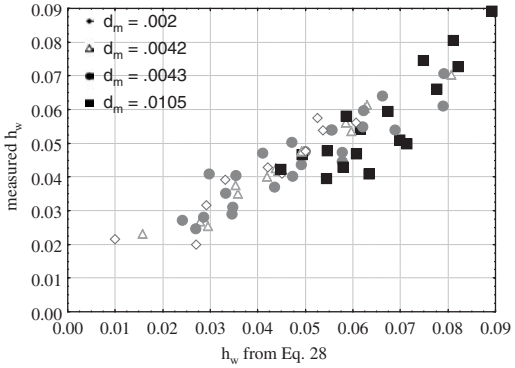


Figure 16. Measured water depths compared with values predicted by $h_w = h_m - (h_s$ from Equation 28).

In Figure 16 this is plotted as h_w $(=h_m - h_s)$ for comparison with previous results.

The goodness of fit is excellent ($r^2 = .84$) and is equivalent to that achieved using c_{mw} (Figure 14).

6 SUMMARY AND CONCLUSIONS

Resistance properties of steep slope flows with high sediment loads were investigated by measuring water velocity within the mixture and by breaking down the mixture depth into water depth + sediment depth. The drag of transported sediment was studied in terms of force balance, from an energy loss perspective and from a velocity lag point of view. The physical meaning of the classical (clear water) friction coefficient v/v* was explained and five variants were introduced to incorporate sediment effects. These conceptual approaches were then investigated with the experimental data.

The questionable energy loss approach indicated that for high sediment loads more than 90% of the available energy may be spent on transporting sediment. The relative energy loss due to sediment could be predicted by Equation (19).

The lag between sediment velocity and water velocity for the steep flume data was shown (Equation 24) to be a function of $\sqrt{(gd(\rho_s/\rho - 1))}$, h_s/d, and h_m/d. Several situations with negative velocity lags were also evident which may indicate vigorous entrainment by turbulence.

For the 5 variants of friction coefficient, predictive equations for c_m, c_{mw} and c_s could be found. These were evaluated by comparing measured and predicted water depth and measured and predicted mixture depth (Figures 14–16). Reasonable quantitative predictions of the sediment and water components of the flow were achievable.

The equations presented above were not verified against independent experiments and consequently they should be used as a starting point for further research rather than as a design tool.

ACKNOWLEDGEMENT

This study was funded by contract CO1X0401 from the Foundation for Research Science and Technology (New Zealand).

7 NOTATION

α	slope angle
A	representative area on channel bed
C_a	coefficient relating v_b to mean velocity
C_b	bed drag coefficient
C_d	particle drag coefficient
c_m	mixture coefficient
c_{mw}	mixture water coefficient
c_{mg}	mixture coefficient using v^*_{ws}
C_p	velocity profile correction factor
c_s	sediment coefficient
c_w	water coefficient
d	mean particle size
d_{30}	particle size for which 30% of bed material is finer
d_{90}	particle size for which 90% of bed material is finer
F_s	streamwise particle drag force
g	gravitational force per unit mass
g_s	sediment mass flowrate per unit flume width
h_m	depth of water & sediment mixture
h_s	depth of sediment load with no porespace
h_w	depth of clear water within flow mixture
n	Manning's roughness coefficient
ρ	density of water
ρ_s	density of sediment
q_w	water discharge per unit flume width
r^2	squared correlation coefficient
S	energy gradient
S_b	energy gradient due to bed roughness
S_s	energy gradient associated with sediment load
μ	coefficient of dynamic friction
v	depth-averaged mean velocity
v_b	effective flow velocity at the bed
v_m	mean velocity of the sediment water mixture
v_{mw}	mean velocity of water over the mixture depth
v_s	mean velocity of sediment within the mixture
v_w	mean velocity of water within the mixture
$v_{(z)}$	velocity at height z above the bed
v^*	shear velocity
v^*_{ws}	shear velocity corrected for weight of sediment

Copyright © 2006 Taylor & Francis Group plc, London, UK

REFERENCES

Cheng, N. 2004. Analysis of velocity lag in sediment-laden open channel flows. *Journal of Hydraulic Engineering, ASCE*, 130(7) 657–666.

Keulegan, G.H. 1938. Laws of turbulent flow in open channels. *Journal of the National Bureau of Standards, USA, Research Paper 1151, 21*: 707–741.

Meyer-Peter, E and Mueller, R. 1949. Eine Formel zur Berechnung des Geschiebetriebs, *VAW Mitteilung no. 16,* Swiss Federal Technical University (ETH) Zurich.

Muste, M. and Patel, V.C. 1997. Velocity profiles for particles and liquid in open-channel flow with suspended sediment. *Journal of Hydraulic Engineering, ASCE*, 123(9) 742–751.

Smart, G.M. and Jaeggi, M. 1983. Sedimenttransport in steilen Gerinnen (in German & English). Mitteilungen der Versuchsanstalt fuer Wasserbau, Hydrologie und Glaziologie, No. 64, VAW, ETH, Zurich.

Smart, G.M. 1984a. Sediment transport formula for steep channels. *Journal of Hydraulic Engineering, ASCE*, 110(3) 267–276.

Smart, G.M. 1984b. On-line velocity measurement by salt conductivity. Hydrosoft '84, Hydraulic Engineering Software (Ed. Brebbia et al.) Elsevier. ISBN 0444 996079

Smart G.M., Duncan M.J. & Walsh J. 2002 "Relatively rough flow resistance equations". *Journal of Hydraulic Engineering, ASCE*, 128(6) 568–578.

Copyright © 2006 Taylor & Francis Group plc, London, UK

Development of a hybrid adaptive neuro-fuzzy system for the prediction of sediment transport

M. Valyrakis & P. Diplas
Civil and Environmental Eng., Virginia Tech, Blacksburg, USA

C.L. Dancey
Mechanical Engineering, Virginia Tech, Blacksburg, USA

T. Akar & A.O. Celik
Civil and Environmental Eng., Virginia Tech, Blacksburg, USA

ABSTRACT: In natural streams, turbulent flow is considered as the forcing mechanism responsible for particle dislodgement. A hybrid approach is presented here for predicting the movement of individual grains. To effectively manage the uncertainties that rise because of the dynamic, non linear and complex nature of the highly interrelated variables of the system, an Adaptive Neuro Fuzzy Inference System (ANFIS) is utilized. This system combines the ability to model human reasoning, by means of fuzzy inference (if-then rules) and linguistic variables with the power of learning and adaptation inherited from neural networks. Thus the tuning of the fuzzy system is performed automatically using experimental data, instead of heuristics, which is a tedious process and requires extensive insight and expertise of the studied phenomenon. The experimental data are obtained via the use of a laser Doppler velocimeter (LDV) for the velocity measurements and visual techniques (video capturing) for identifying grain movement in an existing research flume. The experimental setup involves a mobile spherical particle, which is only allowed to be subjected to small displacements. The total velocity measurements obtained with the LDV signal, are treated as fuzzy input sets while the captured video, supplies the time history of the incidents of displacement of isolated particle representing the fuzzy output set. Different architectures of the model are evaluated, and compared with a previously studied artificial neural network model. The model is capable of good prediction of the dislodgment events.

1 INTRODUCTION

Sediment transport is an environmental problem of high concern to the civil and environmental engineer; either it is related to the bank erosion or deposition, the scour around bridge piers or even the transportation of contaminants and pollution of the downstream ecosystems. To be able to understand such a complex phenomenon, we have to first identify the major underlying factors that significantly affect it. Under that context, the study of the initiation of particle movement in relation to variables which have the greater impact upon it such as the instantaneous local velocity field is considered here. A plethora of researchers have pursued this issue. For instance Papanicolaou et al. (2001) as well as Shvidchenko and Pender (2001) employed a visualization technique to investigate the effect of near bed turbulence in rough beds. Nino et al. (2003) studied both rough and smooth boundaries investigating particle suspension via a theoretically approached threshold of particles motion criterion.

However, the existence of near bed turbulence from which it inherits a highly nonlinear behavior, makes it difficult to be accurately resolved by time deterministic averaging (Shields 1936) or stochastic (Papanicolaou et al. 2002) approximations. The strong non-linearity and chaotic structure of turbulence (Gallavotti 2000) and the hydrodynamic instantaneous forces on which it depends (Einstein & El-Samni 1949), render the above approaches unable to be characterized as universally superior models.

Recently soft-computing techniques such as artificial neural networks (ANNs) and fuzzy inference systems (FIS) have demonstrated a unique ability in dealing successfully with nonlinearity over a wide range of applications and disciplines related to forecasting. Thus the use of such sophisticated algorithms is thought as an appropriate methodology to address the problem of particle entrainment.

In this paper we present a state of the art neuro-fuzzy approach as a predictive tool in an attempt to investigate the dynamics of single particle dislodgement.

Copyright © 2006 Taylor & Francis Group plc, London, UK

The proposed adaptive neuro-fuzzy inference system (ANFIS) is a well established algorithm which combines the features of neural networks such as the data driven process of learning, with the fuzzy logic concept which accounts for imprecision and vagueness in the data.

In the following we present the use of the developed ANFIS model in predicting the initiation of a particle sediment motion. Firstly a discussion of the experimental setup, the algorithm's architecture and preparation of data is provided. Next the results from the analysis are shown along with respective results from a previous ANN model so that a constructive comparison will be drawn. Finally the outcomes of the model are further analyzed complemented by conclusions and evaluation of the model in respect to its performance in computational resources and accuracy.

2 METHODOLOGY

2.1 *ANFIS overview*

Since their discovery ANNs have been used in many applications. Recently their implementation in sedimentation prediction (Ariffin 2004), scour (Azmathullah et al. 2005) and river discharge forecasting (Sahoo & Ray 2006) has been reported. ANNs are data driven algorithmic structures which are able to accurately predict the evolution of a nonlinear system by adapting to it. In contrast to conventional numerical or analytical solutions they do not require a priori knowledge of the system or construction of rigorous approximating relationships. However they are considered as "black boxes" since they are unable to reveal the way the variables interact with each other. On the other hand fuzzy logic is able to provide rules for the underlying dynamics of the studied system dealing also effectively with impreciseness of the utilized data (Zadeh 1973). For this reason ANFIS is thought to integrate the mentioned virtues of both ANNs and FL into a powerful computational hybrid model (Jang 1993). It has successfully been implemented in numerous applications such as fault detection and diagnosis (Awadalah et al. 2005, Kazeminezhad et al. 2005), modeling (Hasiloglu 2004), prediction (Chang and Chang 2006) and signal processing (Valsan et al. 2002). Thus ANFIS has a high potential as a predictive tool for the study of the initiation particles entrainment.

2.2 *ANFIS architecture*

ANFIS has a structure that resembles a multilayer feed-forward ANN, which uses fuzzy inference to map an input to an output space (Sugeno 1995). For instance if we consider a first order Takagi-Sugeno fuzzy inference type, with two inputs (x, y), an output ($f(x)$) and a typical fuzzy rule base of two "If-Then" rules, then we can express them as follows (Jang 1993):

Rule 1: If x is A_1 and y is B_1, Then $f_1 = p_1x + q_1y + r_1$
Rule 2: If x is A_2 and y is B_2, Then $f_2 = p_2x + q_2y + r_2$

where A_i, B_i are values of membership functions for x, y respectively, in the premise (If) part and p_i, q_i, r_i are the linear parameters of the consequent (Then) part. The subscript i is used as a notation for each of the rules.

Each layer of ANFIS has different nodes as described below for the general case of N_{in} number of inputs (x_i, $i = 1, \ldots, N_{in}$), N_{xi} fuzzy numbers (or linguistic labels $A_{i,j}$) for each input and N_R number of rules (Figure 1).

Layer 1: This layer consists of a total of N adaptive nodes ($N = \Sigma N_x$) – one for every linguistic label $A_{i,j}$ – with a membership function ($\mu A_{i,j}$), which maps the input x_i, to a certain output value:

$$O_{i,j}^1 = \mu_{A_{i,j}}(x_i) \tag{1}$$

Widely used are bell shaped functions bounded from zero to one from which the most popular is the Gaussian:

$$\mu_{A_{i,j}}(x) = \exp\left[-\left(\frac{x - c_{i,j}}{2\sigma_{i,j}}\right)^2\right] \tag{2}$$

defined by $c_{i,j}$, $\sigma_{i,j}$ named as premise parameters.

Layer 2: Each node in this layer (Rule node) combines the transmitted signals by using membership functions of different input variables. Thus the output of each node is analogous to the firing strength of the rule it represents. The operator used to combine the signals is the multiplication (AND) T-norm fuzzy operator (Tanaka 1996):

$$O_k^2 = w_k = \prod \mu_{A_{i,j}}(x) \tag{3}$$

meaning that the antecedent part of *kth* rule which involves one membership function $\mu_A(x)$ for each input, is satisfied proportionally to w_k.

Layer 3: In this layer we calculate the ratio of each rules firing strength to the sum of them for all rules. In a way a normalization of the firing strengths for each rule is performed:

$$O_3^k = \overline{w_k} = \frac{w_k}{\sum_{i=1}^{N_R} w_i} \tag{4}$$

where w_k is the normalized firing strength for *kth* rule.

Layer 4: The consequent part of fuzzy reasoning is represented by this layer where the contribution of each of the rules ($k = 1, \ldots, N_R$) in the final output is given by:

$$O_k^4 = \overline{w_k} f_k = \overline{w_k}\left(\sum_{i=1}^{N_R} p_{i,k} x_i + r_k\right) \tag{5}$$

Copyright © 2006 Taylor & Francis Group plc, London, UK

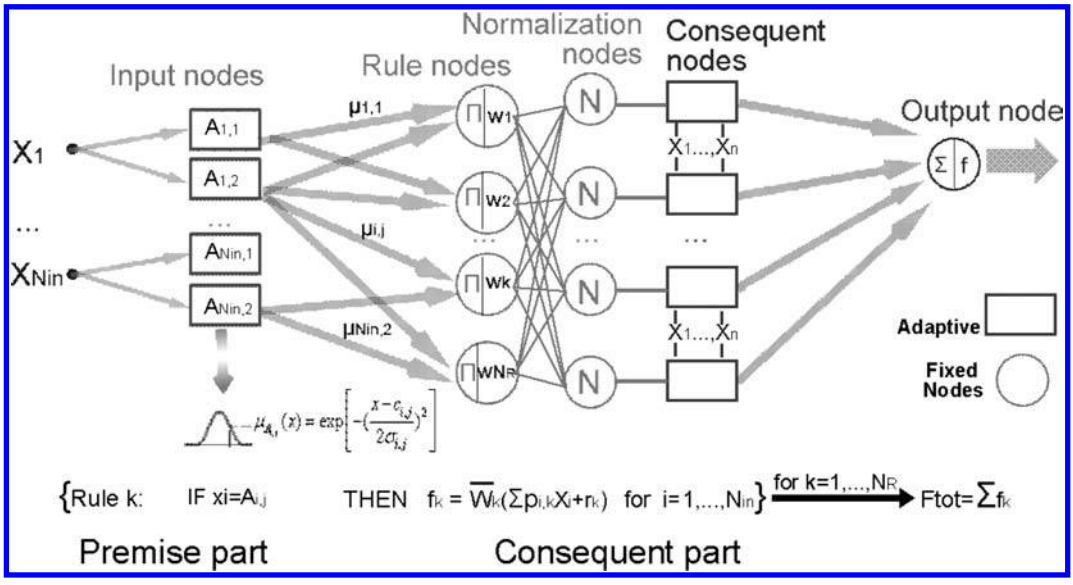


Figure 1. ANFIS architecture for $N_{i,j}$ number of inputs, $N_x = 2$ linguistic labels ($A_{i,j}$) for each input and N_R number of rules.

with $p_{i,k}, r_k$ the consequent parameters as mentioned before.

Layer 5: In the final layer the total output is calculated by adding all the transferred signals from each rule:

$$O^5 = \sum_{i=1}^{N_R} \overline{w}_i f_i \qquad (6)$$

Above we have described the forward pass of the input signal which provides the respective result. The hybrid learning procedure proposed by Jang (1993), involves tuning or calculating the consequent linear parameters $p_{i,k}$, and r_k in the forward pass of the transmitted signal with the least square method. Moreover ANFIS is trained with supervised learning which means that the model adjusts its parameters according to the error, which is the difference of calculated output from the desired output taken from the respective input-output pair. Thus the above error has to be back-propagated to adjust the premise parameters$c_{i,j}$, $\sigma_{i,j}$ with a nonlinear optimization method such as gradient descent.

There exists no guiding rule in defining a priori the model's architecture since it is highly dependent on the nature of the studied problem. In general a complex structure with many nodes attains high accuracy (small training error) but poor generalization ability (higher testing error). In contrast a simple, relatively to the size of the training data set, architecture exhibits the worse approximation and good generalization. Thus in our case a trial and error analysis was undertaken to find the optimum number of parameters that define ANFIS model. The selected architecture is not of high complexity and is limited by the huge size of the data pairs compared to the available computational resources.

The maximum number of lagged variables in the input vector was three representing the local velocities. The number of utilized membership functions determines the granularity (or level of detail) of the model (Zadeh 1997), and in our case did not seem to significantly affect models performance.

2.3 *Experimental setup*

The input to our ANFIS model consisted of laser Doppler velocimetry measurements obtained simultaneously with data from a camcorder which provided the time and duration of particle movement. Similar experiments for the study of initiation of particles motion, have been reported (Smcheeckle et al. 2003, Dancey et al. 2002, Papanicolaou et al. 1999).

The experiments for the initiation of motion of a single spherical particle were performed in a research flume located at the Kelso S. Baker Environmental Hydraulics Laboratory, Virginia Tech. The flume has dimensions of 20.5 m, 0.6 m and 0.3 m for its length, width and depth respectively. A Viton® sphere of 8.0 mm diameter was used as a mobile particle exposed to a fully-rough turbulent open channel flow of average stream-wise local velocity of 0.21 m/sec. The Viton® sphere of 8.0 mm diameter was used as a mobile particle exposed to a fully-rough turbulent open sphere is placed over a bed made of four layers of packed glass beads of the same diameter (Figure 2). The particle's displacement is retained by a fixed pin. Thus

Copyright © 2006 Taylor & Francis Group plc, London, UK

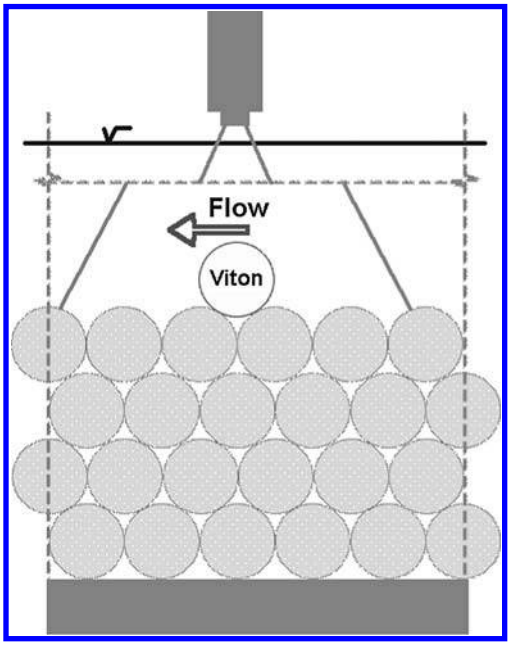


Figure 2. Profile of the study area.

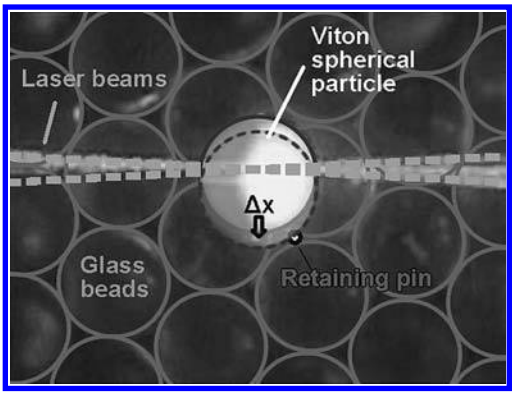


Figure 3. A planar view of the study area. The dashed circle indicates the position of the displaced sphere by Δx.

the particle can only be displaced for a certain small distance (Δx), and then return to its initial position (Figure 3).

Thus only a small dislodgment of the particle from its pocket is allowed, enabling the continuous monitoring of a series of sphere movement events. The particle's displacement events are recorded with a commercial camcorder, mounted on top of the flume above the free surface of the flow (Figure 2). The camera is looking downwards capturing the area of interest at a rate of thirty frames per second. The recorded movie is then digitized in a computer and a digital video file is produced from which the time series of

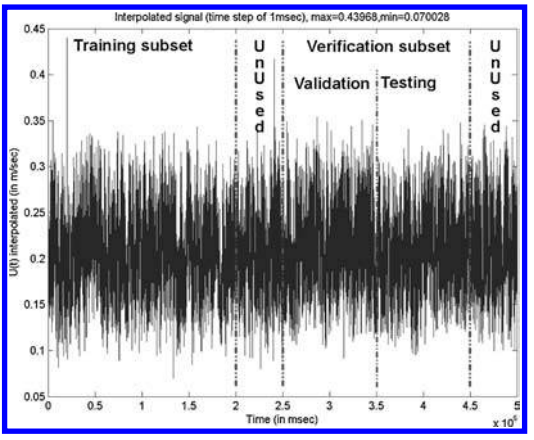


Figure 4. Interpolated values of stream-wise velocity measurements, divided into training and verification input subsets.

those events is manually generated by observation to be used as an output for the ANFIS model.

The time series of velocity measurements were acquired by laser Doppler velocimetry (LDV). A two-component color separated LDV system with frequency-domain signal processing was employed to measure the stream-wise component of velocity. The LDV system was oriented in direct backscatter mode. It was mounted along side of the flume and tilted approximately 4.8 degrees from the horizontal. According to this technique measurements are obtained randomly only when seeding particles cross the measurement area formed by the laser beams (denoted by the green dashed lines in Figure 3). Thus the seeding density and the quality of the seeding material are major factors that significantly affect the experiment's outcome. The seeding material was SiC (silicon carbide) with a mean particle diameter of 4 microns. The stream-wise velocity was measured directly with a sufficient average data rate of approximately 450 measurements per second.

2.4 *Data preparation*

The available LDV measurements are unevenly spaced in the time domain (due to the fact that seeding particles cross the measurement area in randomly distributed time instances), which means that a reconstruction of the time series with a constant instead of a varying time step is required. Thus the data were interpolated (Figure 4), to a constant time step of one millisecond. We also implement a reconstruction of the observed output to the same constant time step (Figure 5). The output data set is built by considering a Gaussian function for each of the observed displacement events, of width (σ) equal to the duration of the displacement.

Copyright © 2006 Taylor & Francis Group plc, London, UK

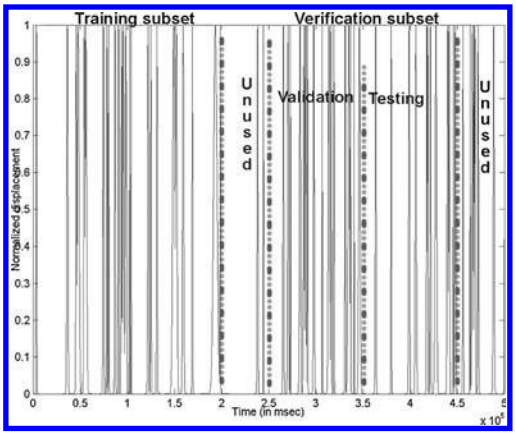


Figure 5. Distribution of displacement events in training and verification output subsets.

Table 1. Characteristics of the chosen subsets.

		Verification set	
	Training set	Validation	Testing
From [msec]	1	250000	350001
To [msec]	200000	350000	450001
Observed events	5	17	12
Data points	200000	100000	100000
Mean	0.2079	0.2163	0.2108
Standard deviation	0.0393	0.0399	0.0377

The available data are divided into two sets which are totally independent. As it can be seen in Figures 4–5, these are the training and verification subsets. The role of the training set is to build the model by tuning the adaptive nodes in the consequent and premise part of each fuzzy rule. The validation subset is utilized to simulate the network and provide a model with good generalization ability. Finally the testing data set is employed to check the model's response to newly fed data. In order to sufficiently train the model without compromising the validation and testing procedure we choose a ratio of length of our data subsets of 2: 1: 1. These data sets must not have any overlapping data points so data from one subset are unseen from the others. Under this context it is ensured that the models performance is not overestimated. The corresponding number of data points and displacement events per subset is shown in Table 1.

When choosing the training input data, it is important to include a wide range of data which will be descriptive of the solution domain. In a different case the model will extrapolate returning probably poor results (Kazabof 1998).

We also calculate the statistical properties of the subsets, which is indicative of their same representative ability. A slight difference between the means of the subsets is eliminated after de-trending our data sets. Removing any existing trend or seasonality improves the effectiveness of the model (Nelson et al. 1999).

We utilize the horizontal component of the instantaneous velocity, assuming that it contains a high degree of information for discovering the dynamics of the phenomenon. Using time delays of this input variable, we construct a lagged in time input vector to predict future values of the dislodgment events:

$$D_{(t+\tau)} = f(U_{(t)}, U_{(t-1)}, \ldots, U_{(t-n+1)}) \quad (7)$$

were $D_{(t+\tau)}$ is the output variable which we want to predict τ steps ahead and $U_{(t-i)}$ is the i input vector representing the stream-wise velocity $i-1$ time steps before the time instant $t \cdot f$ is the transfer function of ANFIS model mapping a sequence of previous observation of inputs $U_{(t-i)}$ to outputs $D_{(t+\tau)}$. The accuracy of the model was found to strongly depend on the size of the time step. Thus a right selection of this variable will provide data sets with "richer information" and better predictability (Mencar 2005). A sensitivity analysis for the effect of the time lag on the reliability of the model was carried, and the results are shown in Figure 8.

Moreover, Abarbanel has proposed that working with a higher embedded dimension than the one of the studied system introduces noise contamination deteriorating the predictability of the forecast model. (Abarbanel et al. 1993). Therefore choosing the appropriate lag time is required so that the input vector will include only useful information. This forecast method is the same as the one implemented by a previously developed time-delay Artificial Neural Network (Valyrakis et al. 2006), which we use to compare the obtained results.

We observe that the optimum lag time for which our model performs relatively better, is at about 150 milliseconds. This is in agreement with the findings of Nelson (Nelson et al. 1995), who used a similar experimental setup and showed that the stream wise velocity measured about 0.1 sec before a sediment grain movement highly correlates with the measured sediment flux (Nelson et al. 1995).

3 RESULTS

3.1 *Performance indices*

To evaluate the overall performance of each of the developed models and be able to compare them, we adopt the accuracy criteria and error metrics which follow (Twomey & Smith 1996).

– Normalized mean squared error (NMSE):

$$NMSE = \frac{\sum_{i=1}^{N}(o_i - t_i)^2}{\sum_{i=1}^{N}(t_i - t_{mean})^2} \quad (8)$$

Copyright © 2006 Taylor & Francis Group plc, London, UK

Table 2. Characteristics of ANFIS and ANN structures.

	Number of input vectors	Number of parameters	Training data size	Time [msec]	Maximum correlation coefficient	Minimum training NMSE	Minimum verification NMSE	Minimum training MAE	Minimum verification MAE
ANN1	2	12	50000	62.78	0.46	0.83	0.82	0.056	0.057
ANN2	4	30	50000	152.67	0.55	0.72	0.75	0.049	0.052
ANN3	4	30	200000	593.29	0.56	0.69	0.71	0.063	0.070
ANN4	6	56	200000	9873.80	0.57	0.67	0.70	0.062	0.069
ANFIS1	2	36	50000	292.33	0.45	0.80	0.84	0.069	0.064
ANFIS2	2	24	200000	4237.14	0.48	0.80	0.78	0.073	0.067
ANFIS3	2	36	200000	5438.39	0.52	0.75	0.74	0.069	0.064
ANFIS4	3	63	200000	9539.40	0.53	0.71	0.71	0.056	0.057

where o_i, t_i are the computed and the observed (target) output the for each (i) of the N data points, while t_{mean} is the mean of the observed values.

– Root mean square error (RMSE):

$$RMSE = \sqrt{\frac{\sum_{i=1}^{N}(o_i - t_i)^2}{N}} \quad (9)$$

– Correlation coefficient (CC):

$$CC = \frac{Cov(o_i, t_i)}{\rho_{o_i}\rho_{t_i}} \quad (10)$$

where ρ_{o_i}, ρ_{t_i} are the standard deviations of the model's output and the target respectively. Their covariance is (11)

$$Cov(o_i, t_i) = \sum_{i=1}^{N}\left[(o_i - o_{mean})(t_i - t_{mean})\right]/N \quad (11)$$

– Mean average error (MAE):

$$MAE = \frac{\sum_{i=1}^{N}(o_i - t_i)^2}{N} \quad (12)$$

All of the above performance indicators are dependent on the residuals (e) of the predicted minus the observed values ($e_{(i)} = o_{(i)} - t_{(i)}$). Generally the smaller the *MAE, NMSE* or *RMSE* metrics are the better the model's accuracy is, while high covariance values indicate the degree to which the predicted results coincide with the observed ones. *MAE* is also dependent on the size of data. This is the reason why for the same model but larger size of data sets (N) we may observe a smaller *MAE* (Table 2).

3.2 *ANFIS simulation results*

All of the simulations were carried out on a 3.20 GHz Pentium®4 processor with 1.25 GB of RAM, running under Microsoft Windows XP v.2002 SP2.

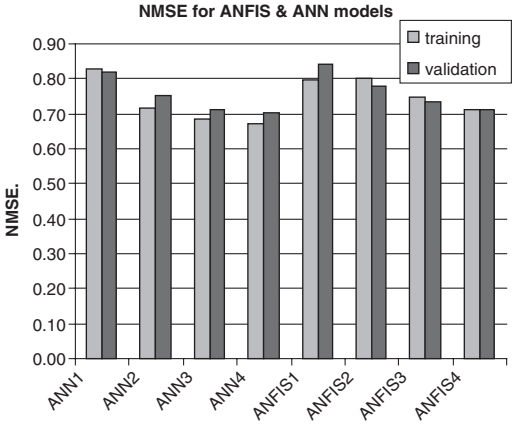


Figure 6. Minimum values of RMS errors for each ANN and ANFIS structure.

The computational code of both ANN and ANFIS was written in Matlab v.6.5, release 13.

We studied four architectures for the ANFIS model, with different size of shifted input vectors or number of membership functions per input variable, in order to assess the sensitivity of our model to that parameter (Table 2). A comparison between the first two models (ANFIS1 and 2) illustrates that the more data utilized the better the obtained accuracy. The same occurs for increasing complexity of the model's architecture as verified from the error indices (Figure 6). However if a certain level of complexity for a given size of data set, is exceeded, the model will not be able to generalize and will be over-trained, by memorizing the training subset. A result of this "over fitting" phenomenon is that the model performs awkwardly in unseen data (Twomey 1996). None of the studied models was over-trained according to Figure 6.

Due to the data size, as the complexity of structure increases, the computational time increases exponentially, with a relatively small improvement in accuracy (Table 2).

Copyright © 2006 Taylor & Francis Group plc, London, UK

Thus there exists a trade off between accuracy and computational effectiveness, which will eventually affect our choice for the optimum model.

The predicted versus the observed values are given for the model with the best performance (Figure 7). To evaluate the generalization ability of the chosen model, we plot the error curves for each of the aforementioned error metrics (Figure 8). The optimum time lag is the one which gives the minimum error for the validation set. Additionally we observe that the randomly initiated membership functions (Figure 9) significantly

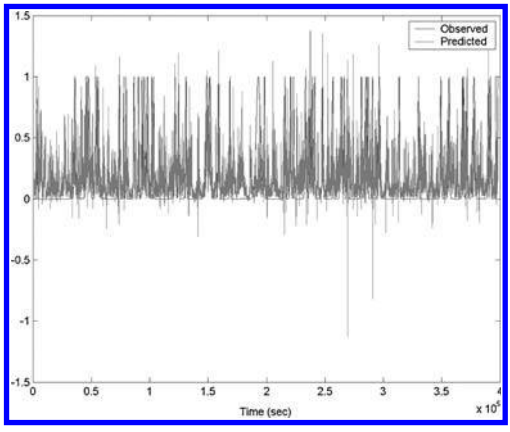


Figure 7. Predicted and observed displacement event values for the minimum validation error of the chosen ANFIS3 architecture (150 msec of time lag).

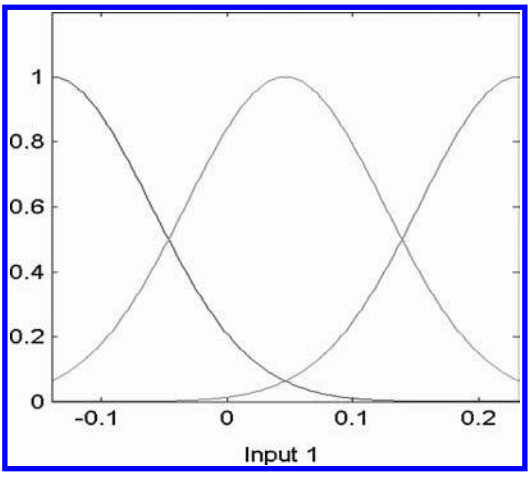


Figure 9. Initial membership functions (same for each of the lagged input vectors of local velocity U_i, in m/sec).

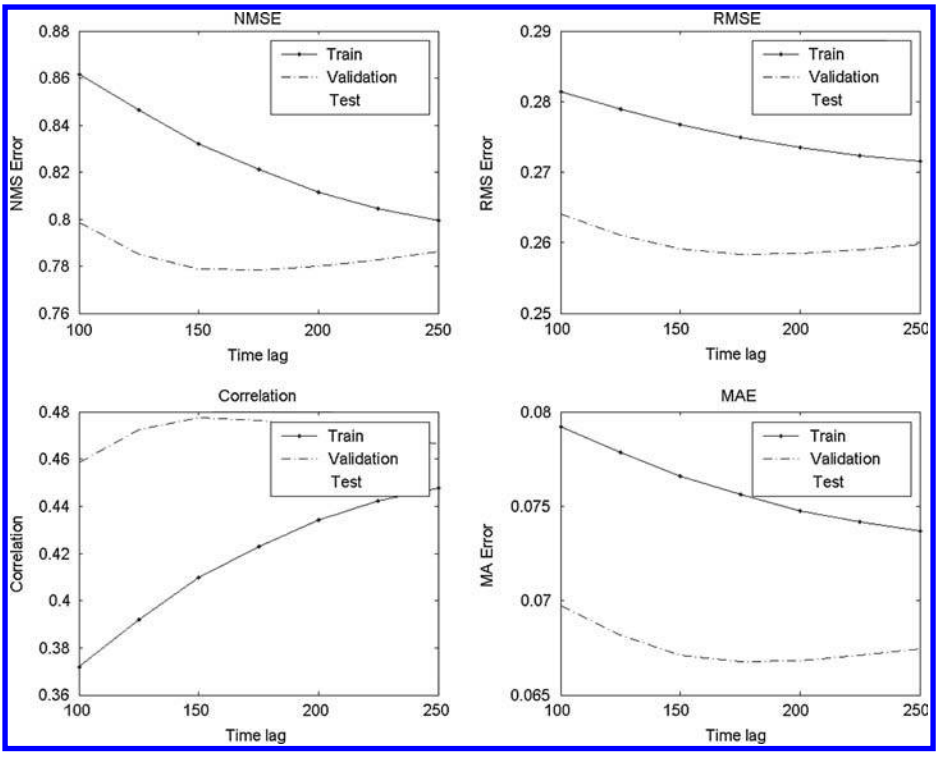


Figure 8. Performance evaluation of ANFIS3 (2 input vectors) for time lag values varying from 100 to 250 msec.

Copyright © 2006 Taylor & Francis Group plc, London, UK

change in shape and position indicating the effect of the training process (Figure 10).

3.3 *ANFIS-ANN comparison*

To better understand the performance of the built ANFIS models, a comparison is made with ANN models with the same forecasting technique and data sets (Table 2). We observe that the ANFIS model is able to make a better prediction for the same size of input vectors. ANFIS models were trained for 50 epochs (Figure 11), while ANNs for 100 training cycles. Figure 11 suggests that training and validation errors do not improve over the training cycles, which means that computational time may be significantly reduced if the model is trained for fewer epochs without loss in accuracy.

However a compelling advantage of ANFIS as opposed to ANNs is that they are more transparent, enabling the derivation of input-output relations for every "If-Then" rule, as described in the model's architecture section. ANFIS can also incorporate expert knowledge in initiating the rule construction or complementing the training procedure, a procedure which may be easily embedded in a later model and might significantly improve its efficiency.

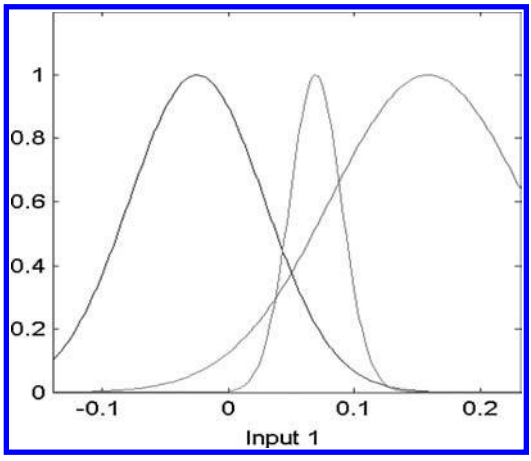


Figure 10. Final membership functions of U_1, for the ANFIS4 model with time lag 150 msec.

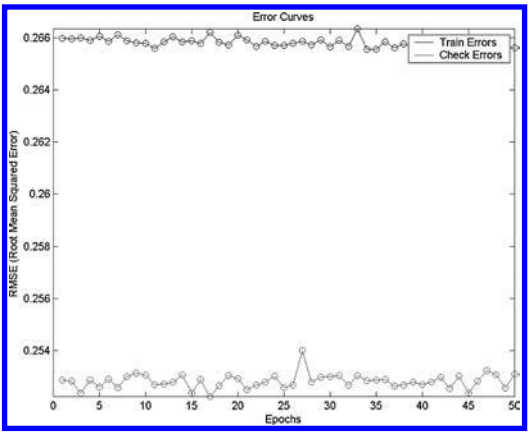


Figure 11. RMSE of ANFIS3 for time lag 150 as a function of training epochs.

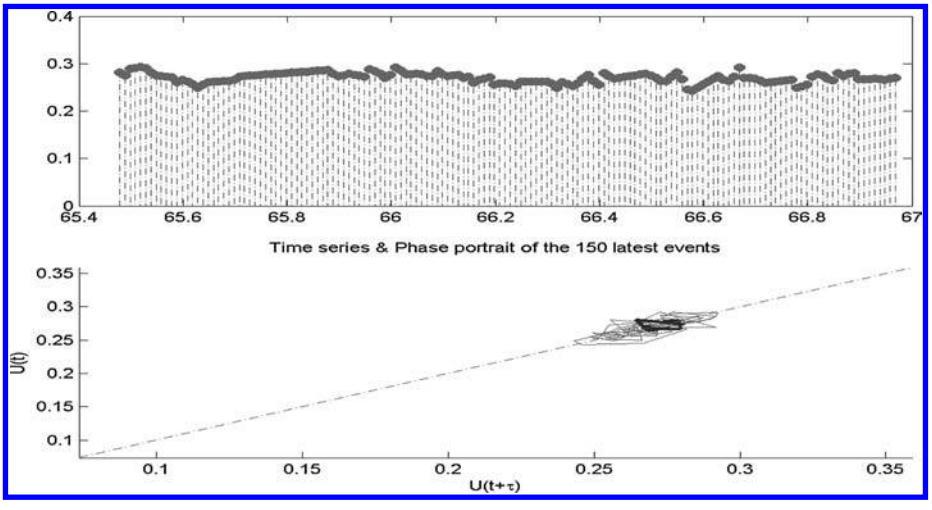


Figure 12. Representation of a sequence of 150 local 1D-LDV measurements (1.5 sec) prior to a dislodgment event: in time (upper plot), and phase space (lower plot).

Copyright © 2006 Taylor & Francis Group plc, London, UK

4 CONCLUSIONS

This study was conducted to illustrate the potential effectiveness of ANFIS with hybrid learning, for the prediction of initiation of particle movement.

The performance of ANFIS was evaluated using standard error measurements which revealed that a right choice of the embedded dimension is necessary for better predictability. The generalization ability and accuracy was assessed by checking the performance indices of the training and testing data subsets.

As data driven methods, their performance is highly depended on the architecture and the quality and quantity of the training data. Thus model performance might have been better if a more complex structure was employed. Furthermore, the relative scarcity of the observed output events (Table 1) may have deteriorated the situation. The performance was found to strongly depend on the way we constructed the output data (using a Gaussian function to resemble the particle's movement in time). Thus better performance may be attained if a more precise technique for obtaining the output is followed.

Moreover if we also utilize the vertical component of the instantaneous velocities we may acquire a better understanding of the system's dynamics.

The magnitude of time lag for which we observe the optimum results, is directly related to the mass of the sediment particle. In a different case the particle's dislodgment events would correlate well with local velocities, with a zero time lag.

Thus we should expect that the length of window in time or time history of velocities required for a certain level of prediction is analogous to the mass of the particle.

Observing the forecasted and output events we can say that the model is able to predict when the particle will move out of its pocket. However this is not always the case since we also observe events of lower magnitude which we may neglect if we set a threshold for when we should consider that the particle fully dislodged or just slightly moved. Using the same concept we could denote that the low level "noise" is due to small vibrations of the particle which however our visualization technique was not able to follow.

ANFIS method would work well in comparison to other averaging techniques since the density of entrainment events is well predicted. However it may be very expensive in computational time.

In general the model predicts a higher possibility of particle entrainment for a sequence of increasing velocities, which is also verified by plotting the phase portrait of the experimental time series just prior to a dislodgment event (Figure 12). This may be accessed if we also plot the piecewise linear relations provided by the model (Figure 13).

In those plots the inputs are mapped to a certain output which is weighted according to the activated rules to return the overall possibility of displacement.

A comparison with a feed-forward artificial neural network (FF-ANN) trained with back-propagation and the same data set, demonstrated that the combination of FIS and learning with NN provided a relative advantage, allowing for rules extraction which facilitates interpretation of the interconnecting relations between them. Although the study is still in an early stage the fusion of ANNs with fuzzy inference systems is quite promising in unveiling the nonlinear interaction of the salient variables which trigger the sediment entrainment in the near bed flow.

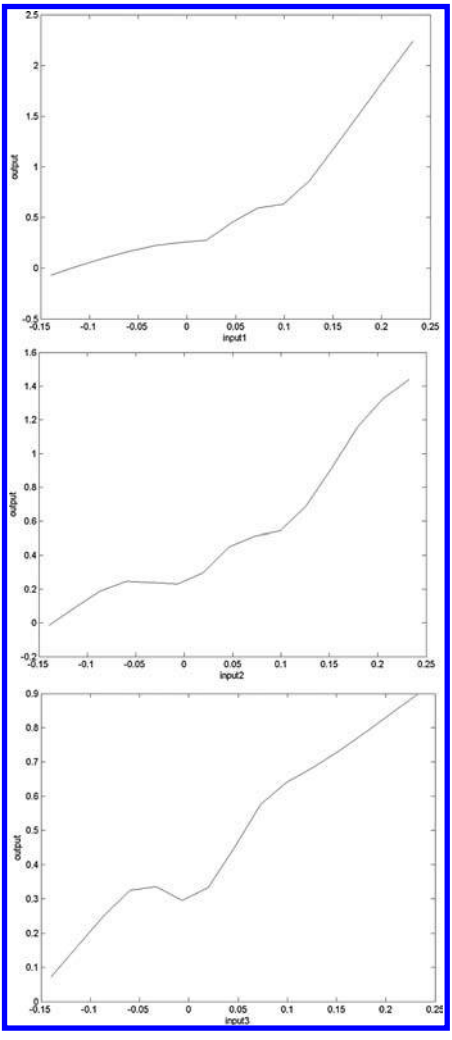


Figure 13. Piecewise linear Input-Output relations for ANFIS4.

Copyright © 2006 Taylor & Francis Group plc, London, UK

In order to access more generic results and rules, we need a plethora of runs with different flow or particle properties, which will be pursued in a future study.

ACKNOWLEDGEMENT

The support of the national Science Foundation (EAR-0439663) is gratefully acknowledged.

REFERENCES

Abarbanel, H.D.I., Brown, R., Sidorowich, J.J. and Lev Sh, T. 1993. "The analysis of observed chaotic data in physical systems." *Reviews of Modern Physics* 65(4): 1331–1392.

Awadallah, M.A., Morcos, M.M., Gopalakrishnan, S. and Nehl, T.W. 2005. "A Neuro-Fuzzy Approach to Automatic Diagnosis and Location of Stator Inter-Turn Faults in CSI-Fed PM Brushless DC Motors." *IEEE transactions on energy conversion* 20(2): 253–259.

Chang, F.-J. and Chang, Y.-T. 2006. "Adaptive neuro-fuzzy inference system for prediction of water level in reservoir." *Advances in Water Resources*(29): 1–10.

Dancey, C.L., Diplas, P., Papanicolaou, A. and Bala, M. 2002. "Probability of Individual Grain Movement and Threshold Condition." *Journal of Hydraulic Engineering* 128(4): 1069–1075.

Einstein, H.A. and El-Samni, E.-S.A. 1949. "Hydrodynamic forces on a rough wall." *Reviews of modern physics* 21(3): 520–523.

Gallavotti, G. 2000. *Foundations of Fluid Mechanics*. Roma.

Hasiloglu, A., Yilmaz, M., b, O.C. and Ekmekci, I. 2004. "Adaptive neuro-fuzzy modeling of transient heat transfer in circular duct air flow." *International Journal of Thermal Sciences* 43: 1075–1090.

Jang, J.-S.R. 1993. "ANFIS : Adaptive Network-Based Fuzzy Inference System." *IEEE Transactions on Systems, Man and Cybernetics* 23(3): 665–685.

Kasabov, N.K. 1998. *Foundations of Neural Networks, Fuzzy Systems, and Knowledge Engineering*, MIT Press.

Mencar, C., Castellano, C. and Fanelli, A.M. 2005. "Deriving Prediction Intervals for Neuro-Fuzzy Networks." *Mathematical and Computer Modelling* (42): 719–726.

Nelson, J.M., Shreve, R.L., McLean, S.R. and Drake, T.G. 1995. "Role of near bed turbulence structure in bed load transport and bed form mechanics." *Water resources research* 31(8): 2071–2086.

Nelson, M., Hill, T., Remus, W. and O'Connor, M. 1999. "Time Series Forecasting Using Neural Networks: Should the Data be Deseasonalized First?" *Journal of Forecasting* (18): 359–367.

Nino, Y., Lopez, F. and Garcia, M. 2003. "Threshold for particle entrainment into suspension." *Sedimentology* 50: 247–263.

Papanicolaou, A.N., Diplas, P., Dancey, C.L. and Balakrishnan, M. 2001. "Surface roughness effects in near-bed turbulence: implications for sediment entrainment." *Journal of Engineering Mechanics* 127(3): 211–218.

Papanicolaou, A.N., Diplas, P., Evaggelopoulos, N. and Fotopoulos, S. 2002. "Stochastic Incipient Motion Criterion for Spheres under Various Bed Packing Conditions." *Journal of Hydraulic Engineering* 128(4): 369–380.

Pollock, D.S.G. 1999. *Time-series analysis, signal processing and dynamics*, Academic Press.

Shvidchenko, A.B. and Pender, G. 2001. "Macroturbulent structure of open-channel flow over gravel beds." *Water resources research* 37(3): 709–719.

Smcheeckle, M.W. and Nelso, J.M. 2003. "Direct numerical simulation of bedload transport using a local, dynamic boundary condition." *Sedimentology* (50): 279–301.

Sugeno, M. 1995. *Industrial Applications of Fuzzy Technology in the World*, World Scientific.

Tanaka, K. 1996. *An introduction to fuzzy logic for practical applications*, Springer.

Twomey, J.M. and Smith, A.E. 1996 B. Validation and Verification. *Artificial Neural Networks for Civil Engineers: Fundamentals and Applications*. Kartam, N., Flood, I. and Garrett, J., ASCE Press.

Valyrakis, M., Diplas, P., Dancey, C.L., Akar, T. and Celic, A.O. 2006. Prediction of particle entrainment using Neural Networks. *Protection and Restoration of the Environment*, Chania, Greece.

Zadeh, L.A. 1973. "Outline of a new approach to the analysis of complex systems and decision processes." *IEEE Transactions on Systems, Man, and Cybernetics* 3(1): 28–44.

Zadeh, L.A. 1997. "Toward a theory of fuzzy information granulation and its centrality in human reasoning and fuzzy logic." *Fuzzy Sets and Systems* (90): 111–127.

Copyright © 2006 Taylor & Francis Group plc, London, UK

Experimental study of bed load on steep slopes

Philippe Frey, Matthieu Dufresne, Tobias Böhm & Magali Jodeau
Cemagref Grenoble, ETNA, Saint Martin d'Hères Cedex, France

Christophe Ancey
Ecole Polytechnique Fédérale de Lausanne, Ecublens, Lausanne, Switzerland

ABSTRACT: An important issue in the study of bed load transport in gravel-bed rivers is related to the physical mechanisms governing the bed resistance and particle motion. In order to better understand the physical processes ruling bed load solid transport at the grain scale, an experimental study of the motion of coarse spherical glass beads entrained by a turbulent and supercritical water flow down a steep channel with a mobile bed was set up. The initial width was 6.5 mm slightly larger than the particle diameter of 6 mm to create a two-dimensional particle flow allowing recording from the side all particles with a high speed camera. The overall aim of this research is to measure the trajectories of all particles and to analyze the fluctuations of the solid discharge as well as the state of movement, rolling or saltation. This paper is focussing on global hydrodynamic and equilibrium solid transport results. The channel inclination ranged from 7.5% to 15% and a doubled width of 12.7 mm was also studied. Data were corrected with the Einstein's method to account for side-wall effects. Non-dimensional solid discharge vs. Shields numbers results are in good agreement with classical incipient motion Shields numbers and compare favorably with two specific semi-empirical bed-load formulae. Those results show that upscaling of data obtained at the particle scale to the reach scale is possible despite the unusual hydraulic configuration of this narrow channel.

1 INTRODUCTION

Despite substantial progress made over the last two decades in the physical understanding of the motion of coarse particles in a turbulent stream, the ability to compute bulk quantities such as the sediment flux in rivers remains poor. For instance, the sediment flow rates measured in gravel-bed rivers differ within one to two orders of magnitude from the bed-load transport equations (Wilcock 2001; Martin 2003; Barry et al. 2004). In order to better understand the physical processes ruling bed-load solid transport at the grain scale, an experimental study of the motion of coarse spherical glass beads entrained by a turbulent and supercritical water flow down a steep channel with a mobile bed was set up. The initial width was 6.5 mm slightly larger than the particle diameter of 6 mm to create a two-dimensional particle flow allowing recording from the side all particles with a high speed camera. The overall aim of this research is to measure the trajectories of all particles and to analyze the fluctuations of the solid discharge as well as the state of movement (rolling or saltation). First the trajectory of a single saltating or rolling particle was analyzed (Ancey et al. 2002; Ancey et al. 2003). Secondly, the aim was to measure the trajectories of all particles and to analyze the fluctuations of the solid discharge as well as the state of movement, rolling or saltation (Boehm et al. 2004; Boehm 2005; Boehm et al. 2006). More recently a doubled width of 12.7 mm was also investigated. The objective of this paper is to present data focusing on global time-averaged hydrodynamic and bed load results. Results will first be discussed for each width taking account of wall effects. Non-dimensioned solid discharge vs. Shields numbers will be analyzed and compared with classical formulae.

2 EXPERIMENTAL FACILITIES AND TECHNIQUES

2.1 *Channel*

Experiments were carried out in a tilted, narrow, glass-sided channel, 2 m in length. Figure 1 shows a sketch of the experimental facility. The channel width W was initially adjusted to 6.5 mm, which was slightly larger than the particle diameter (6 mm). In this way, the particle motion was approximately two-dimensional and stayed in the focal plane of the camera. The channel slope $\tan\theta$ ranged from 7.5% to 15% (i.e., channel representative of steep gravel-bed rivers as

Copyright © 2006 Taylor & Francis Group plc, London, UK

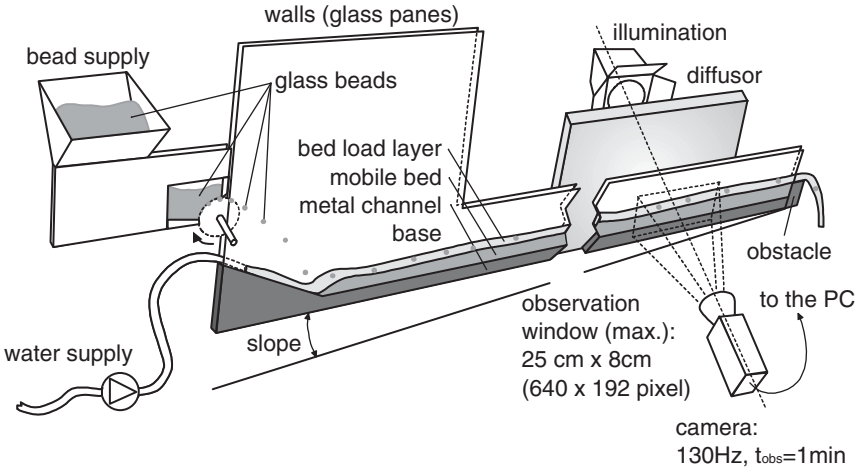


Figure 1. Sketch of the experimental setup.

Table 1. Flow characteristics and time-averaged values of dimensionless numbers characterizing bed load and water flow for width 6.5 mm. Varying parameters: Channel inclination $\tan\theta$ and solid discharge $\dot{n}$. The notation E7-6 indicates: $\tan\theta \approx 7\%$ and $\dot{n} \approx 6$ beads/s. Not all experiments made at $\tan\theta = 10\%$ are reported here, see (Boehm et al. 2004; Boehm 2005) for further information.

Experiment	E7-6	E7-8	E7-9	E10-16	E12-9	E12-16	E12-21	E15-16	E15-21
$\tan\theta$ (%)	7.5	7.5	7.5	10	12.5	12.5	12.5	15.0	15.0
$\dot{n}$ (beads/s)	5.7	7.8	8.7	15.4	9.3	15.2	20.0	15.6	21.5
q_w (10^{-3} m^2/s)	10.00	11.54	13.85	8.19	2.97	3.85	4.46	2.31	2.92
C_s (%)	0.95	1.17	1.16	3.30	5.58	7.02	7.74	11.65	12.23
h (mm)	18.9	20.8	24.9	16.9	7.0	8.2	9.4	4.9	6.7
u_f(m/s)	0.53	0.55	0.56	0.48	0.42	0.47	0.48	0.47	0.44
Re	5860	6230	6400	5280	3760	4360	4600	3680	3830
Fr	1.26	1.26	1.15	1.24	2.20	2.09	1.90	3.72	2.63
h/d	3.16	3.47	4.15	2.82	1.17	1.37	1.56	0.82	1.11
$2h/W$	5.83	6.40	7.65	5.21	2.16	2.53	2.88	1.51	2.05

encountered in mountain areas). In order to test the influence of the channel slope on bed load, 15 experiments with different inclinations and various flow rates (see Table 1) were first set up. The channel base consisted of half-cylinders of equal size ($r = 3$ mm), but they were randomly arranged on different levels, from 0 to 5.5 mm, by increments of 0.5 mm. These levels were generated using a sequence of uniformly distributed random numbers. Disorder was essential as it prevented slipping of entire layers of particles on the upper bed surface, which would have induced artificial erosion conditions. Maintaining disorder in monosized spherical particles is difficult, with severe constraints (Bideau and Hansen 1993), here involving mainly how to create disorder in the packing and the bed thickness. For thick beds (typically, whose thickness exceeded 5–6 particle diameters), a regular, crystalline arrangement was observed along the upper part of the bed. This is expected since it is well-known that the disorder range induced by a defect in a crystalline arrangement of monosized spherical particles is a few particle diameters (Bideau and Hansen 1993). Therefore, in order to be able to control the order in the particle arrangement, we built beds whose thicknesses did not exceed 5 particle diameters. The effects of disorder on bed-load transport features have been presented in another paper (Boehm et al. 2004). An obstacle was set at the channel outlet to enable bed formation and prevent full bed erosion; its height could be adjusted.

More recently, 33 new experiments were performed with a width of 12.7 mm about two bead diameters

Copyright © 2006 Taylor & Francis Group plc, London, UK

Table 2. Flow characteristics and time-averaged values of dimensionless numbers characterizing bed load and water flow at a width of 12.7 mm. Varying parameters: Channel inclination $\tan\theta$ and solid discharge $\dot{n}$. The notation F7-8 indicates: $\tan\theta \approx 7\%$ and $\dot{n} \approx 8$ beads/s. See (Dufresne 2005) for further information.

Experiment	F7-8 to F7-26	F10-8 to F10-25	F12-11 to F12-19	F15-19 and F15-24
$\tan\theta$ (%)	7.5	10	12.5	15
$\dot{n}$ (beads/s)	8.4–25.6	8.2–25.3	11.4–19.4	19.0–24.4
q_w (10^{-3} m^2/s)	5.91–11.50	3.86–6.86	3.13–3.60	2.70–3.06
C_S (%)	1.2–1.7	1.9–3.8	3.2–4.8	6.3–7.1
h (*mm*)	13.7–26.2	9.4–14.3	9.1–11.4	10.4–10.5
u_f (m/s)	0.43–0.60	0.37–0.51	0.30–0.37	0.26–0.29
Re	7490–12210	5850–7540	4800–5600	4080–4630
Fr	1.17–1.34	1.06–1.39	0.91–1.22	0.81–0.92
h/d	2.3–4.3	1.6–2.4	1.5–1.9	1.7–1.8
$2h/W$	2.2–4.1	1.5–2.2	1.4–1.8	1.6–1.7

(see Table 2). In that case, there is no more problems in creating disorder as there is an added widthwise degree of freedom. The first objective was to adapt the image analysis algorithms preparing for studying two-size mixtures. the second objective whose results are reported in this paper was to assess the influence of the width and wall effects of this unusually narrow channel.

2.2 *Solid and water supplies*

Black spherical glass beads with a nominal diameter d of 6 mm and a density ρ_p of 2500 kg/m^3 (provided by Sigmund Lindner GmbH, Germany) were used. They were injected from a reservoir into the channel using a wheel driven by a direct current motor and equipped with 20 hollows on the circumference, as depicted in figure 1. For the experiments presented here, the injection rate $\dot{n}$ ranged from 5 to 26 beads per second, with an uncertainty of less than 5%. This corresponded to a volumic solid discharge per unit width q_s of $7 - 38 \times 10^{-5}$ m^2/s. The water supply at the channel entrance was controlled by an electromagnetic flow meter provided by Krohne (France). The discharge per unit width q_w ranged from 3 to 15×10^{-3} m^2/s. The values for 6.5 mm wide runs (labelled E) are summarized in Table 1 and ranges of values for 12.7 mm wide runs (labelled F) appear in Table 2.

2.3 *Dimensionless numbers*

The hydraulic conditions can be specified using classic dimensionless numbers. In tables 1 and 2, h is the time-averaged flow depth. To make the particle rate $\dot{n}$ more palpable, we express it in beads/s instead of m^3/s. The flow Reynolds number is defined as $\mathrm{Re} = 4R_h\bar{u}_f/\nu$, where $R_h = Wh/(2h+W)$ denotes hydraulic radius, $\bar{u}_f = q_w/h$ fluid velocity (averaged in the y- and z-directions), ν kinematic viscosity of water. The Froude number $\mathrm{Fr} = \bar{u}_f/\sqrt{gh}$ (where g denotes gravity acceleration) varied significantly over the experiment duration and along the main stream direction. The mean Fr values are reported.

The Shields number is defined as the ratio of the bottom shear stress ($\tau_0 = \rho_p g R_h \tan\theta$) to the stress equivalent of the buoyant force of a particle lying on the bottom (Julien 1994): $\tau* = \tau_0/(gd(\rho_p - \rho_f))$. The solid concentration is defined as the ratio of the solid and the water discharge $C_s = q_s/q_w$. The ratio h/d is low, typically in the range 0.8–4. A few aspects of the free-surface line and the bed configuration are shown in the tabulated figure 2 for the experiments in the 6.5 mm wide channel. Figure 3 shows a typical image obtained in the 12.7 *mm* wide channel compared to an image at a width of 6.5 *mm* where trajectories of all beads are two-dimensional. Disorder induced by the doubled width appears quite obviously.

Note that the dimensionless number values differ substantially from the values usually found in the hydraulics literature. The reason is twofold: first we used a short and narrow channel, which led to studying low Reynolds number regimes, whereas in most experiments on bed load transport, one takes care to avoid such regimes; this is the price to pay to have access to the details of particle movements. Since we used coarse particles, particle motion was weakly dependent on the actual value of the flow Reynolds number and turbulence structure. Therefore we think that the small size of the experimental setup is not a handicap. Second we mostly studied supercritical flows because of the steep slopes investigated. However, in a supercritical regime, flow depth was low: on the order of the particle size, meaning that particle motion was affected by the water free surface.

2.4 *Experimental procedures*

The preliminary procedure can be split into three major steps. First of all, a particle bed was built along the

Copyright © 2006 Taylor & Francis Group plc, London, UK

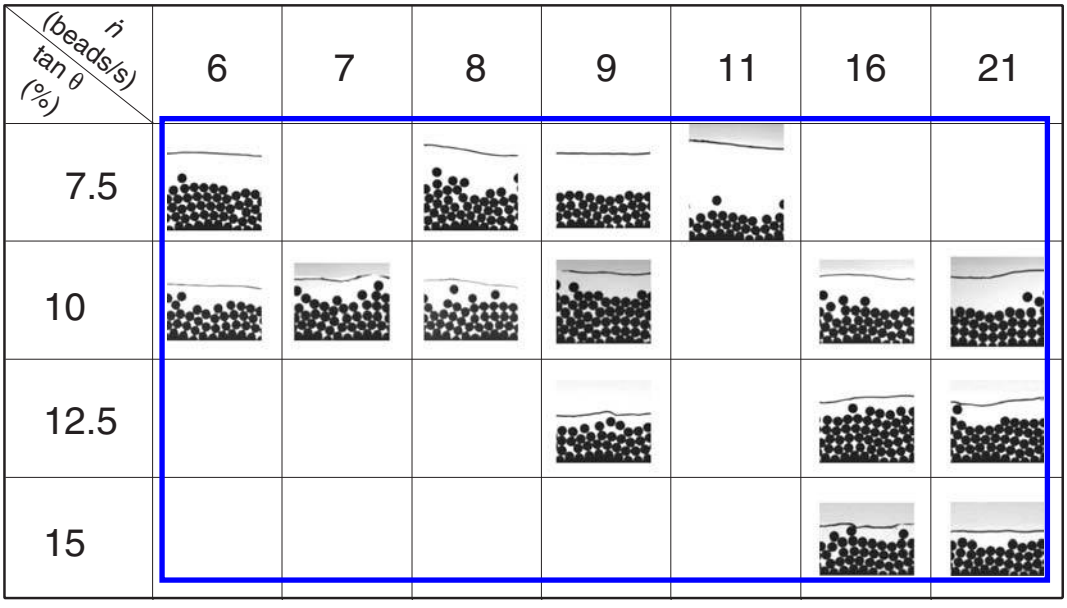


Figure 2. Overview of the experiments conducted for width 6.5 mm at various solid discharges $\dot{n}$ and slopes $\tan\theta$. For each experiment, a detail of one filmed image is shown. See Table 1 for the experimental conditions.

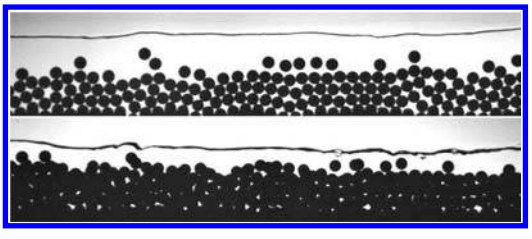


Figure 3. Typical images obtained respectively in the 6.5 *mm* (above) and 12.7 *mm* (below) wide channel.

channel base, which remained stationary on average. To that end, an equilibrium between the water discharge, solid discharge, bed elevation, and channel slope was sought. This equilibrium was reached by using the following procedure:

1. The water discharge q_w was set to a constant value.
2. An obstacle (approximately 20 mm in height) was positioned at the downstream end of the channel. The solid discharge $\dot{n}$ at the channel entrance was set to a constant value. The solid discharge per unit width q_s was calculated by the relation $q_s = \pi d^3 \dot{n}/(6W)$. The first beads supplied by the feeding system were stopped by the obstacle at the channel outlet and started to form a bed. The bed line rose to the level of the obstacle and beads began to leave the channel. After approximately 10 minutes, the system arrived at bed load equilibrium, i.e., there was no more bed deposition or erosion over a sufficiently long time interval.
3. In order to make the bed line parallel with the channel base, the water discharge was then adjusted. After several iterations, we arrived at the configuration of a bed that consisted of two to three almost stationary bead layers along the channel, for which the bed line slope matched the channel base inclination. Average equilibrium conditions were sustained over long time periods, basically as long as 30 minutes.

Once bed equilibrium was reached, the particles and the water stream were filmed using a Pulnix partial scan video camera (progressive scan TM-6705AN). The camera was placed perpendicular to the glass panes at a distance of 115 cm from the channel, approximately 80 cm upstream from the channel outlet. It was inclined at the same angle as the channel. Lights were positioned in the backside of the channel. An area of approximately 25 cm in length and 8 cm in height was filmed and later reduced to accelerate image processing.

The camera resolution was 640×192 pixels for a frame rate of $f = 129.2$ fps (exposure time: 0.2 ms, 256 gray levels). Each sequence was limited to 8000 images due to limited computer memory; this corresponded to an observation duration of approximately 1 minute.

Copyright © 2006 Taylor & Francis Group plc, London, UK

Each experiment was repeated at least twice in order to spot possible experimental problems and to get an idea of the data scattering.

2.5 *Image and data processing*

Images were analyzed using the WIMA software, provided by the *Traitement du Signal et Instrumentation* laboratory in Saint-Etienne (France). Positions of the bead mass centers were detected by means of an algorithm combining several image-processing operations. It compared the filmed images with the image of a model bead and calculated the correlation maxima to obtain the bead positions. Data obtained from the image sequences were analyzed to obtain the particle trajectories. For this purpose, we developed a particle-tracking algorithm. This algorithm compared the bead positions of two consecutive images to determine the trajectory of each bead step by step. Since the particle movement was nearly two-dimensional and the displacement of a particle between two images was always smaller than a particle diameter, the trajectories (approximately 700 per sequence) could be calculated with no significant error. The state of movement of a particle was also defined by considering that each bead was always either in a resting, rolling, or saltating regime (Boehm et al. 2006; Boehm 2005). In this paper image analysis was only used to measure the water depth. Since the experiments involved a mobile bed, the water depth was defined as the difference between the free surface and the bed surface elevation. The water free surface (averaged in the direction perpendicular to the channel walls) was detected using its slim form; missing portions were inter- or extrapolated. For the 6.5 mm width the bed surface profile was taken as the line linking the top points of the uppermost resting or rolling beads. For the width 12.7 mm, a different algorithm was used to derive the bed line combining derivative and morphological operators (Dufresne 2005).

3 RESULTS

3.1 *Analysis of uncorrected data*

A widespread way of representing bed load transport rates for different flow conditions is to plot the dimensionless solid discharge ϕ as a function of the Shields number $\tau*$. The solid discharge was made dimensionless by the definition

$$\phi = q_s/\sqrt{(\rho_p/\rho_f - 1)gd^3},$$

where q_s is the bed load transport rate per unit width, $q_s = \pi d^3 \dot{n}/6W$.

First, the Shields number $\tau*$ was calculated with the global hydraulic radius.

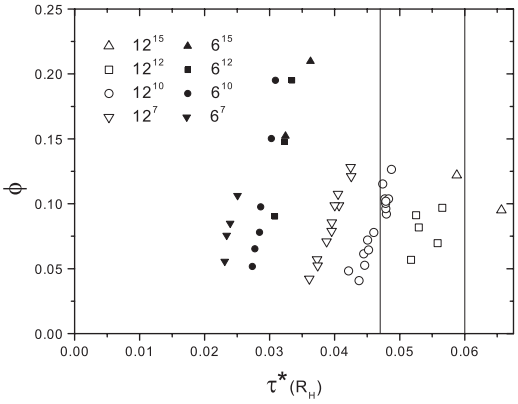


Figure 4. Relations between dimensionless solid discharges and uncorrected Shields numbers. Black lines correspond to incipient motion thresholds: $\tau* = 0.06$ or $\tau* = 0.047$.

Although the dimensionless solid discharge increases with the Shields number on figure 4, most of the values of Shields number are lower than widely accepted incipient motion thresholds ($\tau* = 0.06$ or $\tau* = 0.047$). Moreover experiments at width 6.5 mm and 12.7 mm are separated in two groups and it seems that data are scattered depending on the slope value. A closer look on data within tables shows that the lowest values of $\tau*$ are obtained for the highest values of the aspect ratio $2h/W$. This behavior is then clearly due to side-wall effects.

3.2 *Side-wall correction procedure*

The purpose of this section is to present the method used to calculate a bottom hydraulic radius. The method used is the well-known Einstein's method (Cao 1985).

This method is based on three hypotheses:

- three Darcy–Weisbach equations can be written:

$$\sqrt{\frac{8}{f}} = \frac{u_f}{\sqrt{gR_h sin\theta}} \quad (1)$$

$$\sqrt{\frac{8}{f_b}} = \frac{u_f}{\sqrt{gR_{h_b} sin\theta}} \quad (2)$$

$$\sqrt{\frac{8}{f_w}} = \frac{u_f}{\sqrt{gR_{h_w} sin\theta}} \quad (3)$$

- the energy slope is the same for each area,
- the flow velocity is the same for each area.

With theses hypotheses, we can write the following equations:

$$\frac{f}{R_h} = \frac{f_b}{R_{hb}} = \frac{f_w}{R_{hw}} \quad (4)$$

Copyright © 2006 Taylor & Francis Group plc, London, UK

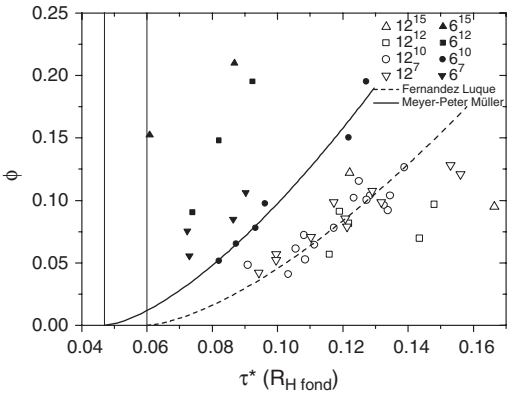


Figure 5. Relations between dimensionless solid discharges and Shields number calculated with the bottom hydraulic radius. Black lines correspond to incipient motion thresholds: $\tau* = 0.06$ or $\tau* = 0.047$.

$$\frac{Re}{f} = \frac{Re_b}{f_b} = \frac{Re_w}{f_w} \tag{5}$$

$$f_b = f + \frac{2h}{W}(f - f_w) \tag{6}$$

f_w is calculated with the following turbulent and smooth formula (Graf and Altinakar 1993):

$$\frac{1}{\sqrt{f_w}} = 2log(Re_w\sqrt{f_w}/4) + 0.32 \tag{7}$$

f_b is then calculated by using *eq.* 6 and knowing f and $2h/W$. R_{h_b} is calculated with the help of eq 4.

It must be stressed that the Einstein's method is usually applied to account for minor side-wall effects. In our case, the $2h/W$ ratio is always above 1 meaning that the water depth is always superior to the width. The side-wall effects are then important and it can be questioned whether the Einstein's method would be relevant in our case. Results are presented on figure 5. By comparing with figure 4, we can see that results are relevant with incipient motion thresholds because all points are above these levels. We notice too that the two groups of points (width 6.5 mm and width 12.7 mm) are nearer than on figure 4. Although more than a mild correction the Einstein's method proved in our case relatively efficient in so far as corrected data appear to agree with classical results.

In addition both the two widely used Meyer-Peter Müller (Meyer-Peter and Muller 1948) and Fernandez Luque semi-empirical formulae (Fernandez Luque and van Beek 1976) are plotted on figure 5. Note that these empirical formulas were established for slopes much lower than in our case, but this should not be a major issue since the physics should remain essentially the same.

Our data lie relatively near incipient motion as our maximum Shields Number is only about three times critical incipient motion Shields Numbers. Although it is well known that empirical formulae do not perform well near the threshold of motion, our data, most surprisingly, relatively agree with those formulae which again shows that the Einstein's method is relevant. A closer look to figure 5 reveals that data for the steepest slopes (12.5% and 15%) agree the least with the formulae. As already discussed, at the lower width, these data have the lowest h/d submergence ratio approaching 1 which means that the free surface acts as a physical barrier truncating the saltation trajectories and forcing most particles to move in the rolling regime. As the saltation of a single particle has been used as a theoretical basis to establish semiempirical bed-load formulae (Bagnold 1973; Wiberg and Smith 1985; Wiberg and Smith 1989; Bridge and Bennett 1992), it is not surprising that those formulae are not in good agreement with data presenting the lowest h/d ratios (Ancey et al. 2005).

4 CONCLUSIONS

In this paper, global time-averaged hydrodynamic and bed load results obtained on an idealized very narrow channel are presented. This channel was primarily designed for studying bed load from a physical viewpoint at the grain scale, the width of the channel being the same as the particle diameter. To analyze results from the fluid mechanics viewpoint and to study the wall effects, a double width was investigated. Nondimensional bed load solid discharges vs. uncorrected Shields numbers appeared quite scattered depending on width and slope but more precisely on the aspect ratio. The classical use of the Einstein's method to account for side-wall effects proved efficient although in our case hypotheses behind this method could be questionable. Corrected results were in good agreement with classical incipient motion Shields numbers and compared favorably with two specific semiempirical bed-load formulae. For steeper slopes with low submergence of the order of the particle diameter more deviation was observed probably because the assumptions underlying the classical bed load formulae do not hold any more.

The experimental set-up was designed to be as simple as possible to gain access to the trajectories of all particles for studying solid discharges fluctuations and motion regimes. In particular analysis of probability distribution functions are thought to help better modelling of bed-load especially near incipient motion. However the crucial question is whether upscaling from the grain scale to the reach scale would be possible with results obtained in this narrow channel. The global results presented in this paper are encouraging

Copyright © 2006 Taylor & Francis Group plc, London, UK

in that perspective. The use of the simple Einstein's correction to account for side-wall effects appears enough to yield results comparable to data obtained with classical large tilting flumes and natural materials. In short, our experimental set-up makes it possible to bridge the gap between the physics and the fluid mechanics approaches in bed load research.

ACKNOWLEDGMENTS

This study was supported by the program ECCO/PNRH of INSU and ANR. We are grateful to the laboratory TSI UMR 5516 of University of Saint Etienne, France (Christophe Ducottet, Nathalie Bochard, Jacques Jay, and Jean-Paul Schon).

REFERENCES

Ancey, C., F. Bigillon, P. Frey, and R. Ducret (2003). Rolling motion of a bead in a rapid water stream. *Phys. Rev. E 67*, 011303.

Ancey, C., F. Bigillon, P. Frey, R. Ducret, and J. Lanier (2002). Saltating motion of a bead in a rapid water stream. *Phys. Rev. E 66*, 036306.

Ancey, C., T. Boehm, P. Frey, M. Jodeau, and J.-L. Reboud (2005). Saltating or rolling stones? In *River coastal and estuarine morphodynamics 2005*, Urbana-Champaign, USA, pp. 641–651. AIRH.

Bagnold, R. (1973). The nature of saltation and of 'bed load' transport in water. *Proc. Roy. Soc. London A 332*, 473–504.

Barry, J., J. Buffington, and J. King (2004). A general power equation for predicting bed load transport rates in gravel bed rivers. *Water Resour. Res. 40*, W10401.

Bideau, D. and A. Hansen (Eds.) (1993). *Disorder and granular media*. Random materials and processes. Amsterdam: North-Holland.

Boehm, T. (2005). *Motion and interaction of a set of particles in a supercritical flow*. Ph. D. thesis, Joseph Fourier University, Grenoble.

Boehm, T., C. Ancey, P. Frey, J.-L. Reboud, and C. Duccotet (2004). Fluctuations of the solid discharge of gravity-driven particle flows in a turbulent stream. *Phys. Rev. E 69*, 061307.

Boehm, T., P. Frey, C. Ducottet, C. Ancey, M. Jodeau, and J.-L. Reboud (2006). Two-dimensional motion of a set of particles in a free surface flow with image processing. *Experiments in Fluids, in press*.

Bridge, J. and S. Bennett (1992). A model for the entrainment and transport of sediment grains of mixed sizes, shapes, and densities. *Water Resour. Res. 28*, 337–363.

Cao, H. (1985). *résistance hydraulique d'un lit de gravier mobile a pente raide; étude éxperimentale*. Ph. D. thesis, Ecole Polytechnique Federale de Lausanne.

Dufresne, M. (2005). Etude exprimentale du transport de particules solides par charriage a forte pente. Master's thesis, Louis Pasteur University, ENGEES, Strasbourg.

Fernandez Luque, R. and R. van Beek (1976). Erosion and transport of bed-load sediment. *J. Hydraul. Res. 14*, 127–144.

Graf, W. and M. Altinakar (1993). *Hydraulique fluviale*, Volume 2. Lausanne: Presses polytechniques et universitaires romandes.

Julien, P.-Y. (1994). *Erosion and Sedimentation*. Cambridge: Cambridge University Press.

Martin, Y. (2003). Evaluation of bed load transport formulae using field evidence from the Vedder River, British Columbia. *Geomorphology 53*, 75–95.

Meyer-Peter, E. and R. Muller (1948). Formulas for bed load transport. In IAHR (Ed.), *2nd meeting*, Stockholm.

Wiberg, P. and J. Smith (1985). A theoretical model for saltating grains in water. *Journal of Geophysical Research (C4) 90*, 7341–7354.

Wiberg, P. and J. Smith (1989). Model for calculating bedload transport of sediment. *J. Hydraul. Eng. 115*, 101–123.

Wilcock, P. (2001). Toward a practical method for estimating sediment-transport rates in gravel bed-rivers. *Earth Surface Processes and Landforms 26*, 1395–1408.

Copyright © 2006 Taylor & Francis Group plc, London, UK

Downstream fining of sediments in the Meuse River

R. Murillo-Muñoz
School of Civil Engineering, University of Costa Rica, San Jose, Costa Rica

Gerrit J. Klaassen
UNESCO-IHE Institute for Water Education, Delft, Netherlands

ABSTRACT: The available information on the river characteristics of the Meuse River in combination with the geological conditions are assessed and analyzed in an attempt to understand the occurrence of a transition from a gravel-bed to a sand-bed river. This transition is characterized by a reduction in D_{50} of the bed material from about 16 to about 2.6 mm whilst the bed slope changes from about 0.5 to 0.10 m/km. From the analysis it is concluded that neotectonic subsidence provides an adequate environment for deposition of coarser sediments triggering the selective transport of particles. The combined action of this selective transport and the abrasion of sediment particles result in an increase of the sand content on the bed material. After some distance a threshold point is reached where the sand content starts to govern the behavior of the sediment mixture; at this point the sand overwhelms the gravel and the river starts to behave as a sand-bed river; consequently the gravel-sand transition is formed.

1 INTRODUCTION

The Meuse River (Maas River) is the second largest river in The Netherlands and it has an international basin that spreads over four countries. It enters The Netherlands in Southern Limburg near Maastricht from where it flows to the North forming the border with Belgium in the reach known as the Common Meuse. In this reach major nature restoration projects are planned (Helmer et al, 1991; Klaassen et al, 1999), which has generated substantial interest in the morphological phenomena occurring in this gravel bed river.

Near the city of Roermond (Figure 1), the Meuse River shows a sharp transition from a gravel-bed to a sand-bed river. Over this transition the D_{50} of the bed material changes from about 16 to about 2.6 mm whilst the slope also decreases from about 0.5 to about 0.10 m/km. Several possible explanations can be proposed for this sudden change on the granulometric composition of the bed material. Most of them centre around three possible causes: abrasion, break down and selective transport. Authors like Holly & Rahuel (1990), Parker (1991a,b), Hoey & Ferguson (1994) among others have studied these phenomena and they reported that downstream fining of sediments is linked to aggradation. However, aggradation has not been observed in the Meuse River in the past; on the contrary, the riverbed seems to have degrade over the last century. This seeming contradiction might be explained by subsidence due to tectonics. Therefore, this contribution explores the role of abrasion, break down, selective transport and subsidence on the observed gravel-sand transition.

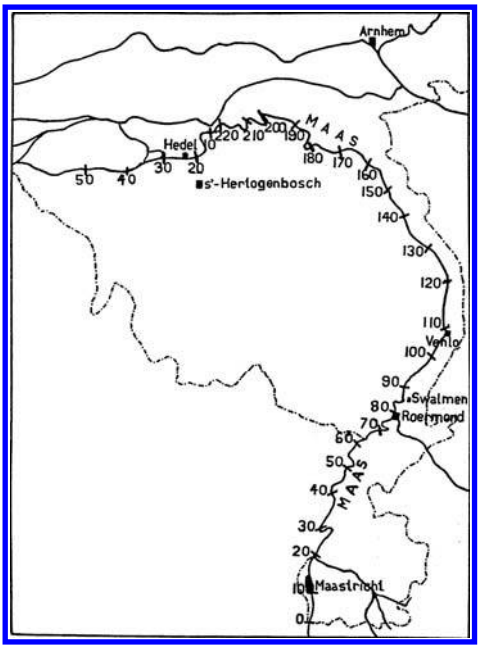


Figure 1. Map of the Meuse River in The Netherlands.

Copyright © 2006 Taylor & Francis Group plc, London, UK

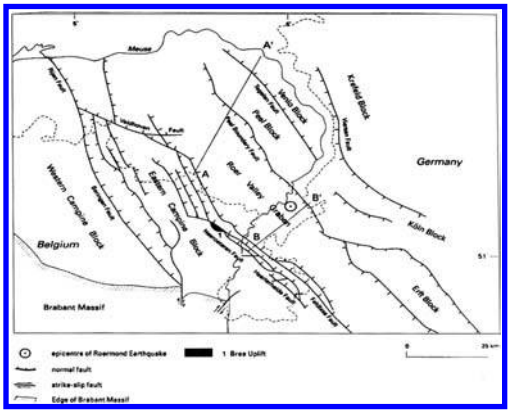


Figure 2. Classification of the different blocks. (Van den Berg, 1996).

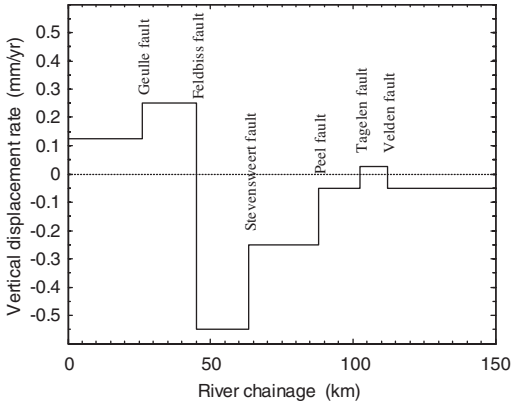


Figure 3. Approximate vertical displacement rates along the Meuse River. (Data from Van den Berg et al, 1994).

2 WATERSHED CHARACTERISTICS

2.1 *Hydrological conditions*

The Meuse River drains an area of about 33,000 km^2 distributed over France (30%), Belgium (40%), Netherlands (18%) and Germany (12%). Available hydrological data includes discharges and water levels from 1911 onwards. The basin response to precipitation is fast, chiefly due to the presence of large tributaries together with relative impervious subsoils in Belgium. On the long term, the yearly average discharge in the Meuse River at Borgharen is about 250 m^3/s. Discharge records go from less than 70 m^3/s in 1976 up to 3047 m^3/s in 1993, indicating that the river has a great variation in its flows.

2.2 *Geological setting*

The watershed of the Meuse covers several geological formations and therefore, it is a complex combination of morphotectonic units. The area of interest is localized in the Lower Rhine Embayment, a tectonic depression localized between the southern North Sea Basin, the uplifting areas of Ardennes and Rhenish Shield and the London-Brabant Massif. This depression is composed of several north-eastward tilted blocks which are determined by a set of faults with NW-SE orientation (Figure 2). These blocks have differential movements between them and Figure 3 shows a schematic representation of the vertical displacement rates of these blocks along the river course. From this figure, it is clear that the movements are not uniform and the Feldbiss fault separates the uplifting blocks from the subsiding blocks.

2.3 *Bed level and bed slope*

Bed levels along the Meuse have changed significantly in the upper part of the river. These changes are due to

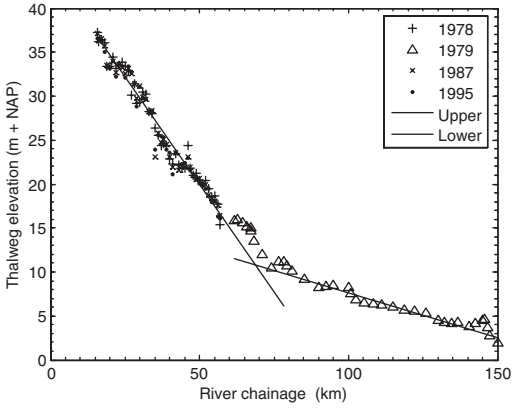


Figure 4. Trend of the thalweg elevation along the Meuse River.

the impressive degradation process that the river has suffered during the last century as a result of training works and subsurface mining. In the area near Maasband this has resulted in degradation of some 5 m while in others reaches the degradation is less severe but still considerable. On the contrary, minimum degradation has been observed in the lower parts of the river, with a number of reaches experiencing some aggradation.

Measured bed levels along the Meuse are shown in Figure 4. From these levels the slope of the river bed is estimated and the resulting lines represent the trend of the bed elevation. The trend of the data in the upper part of the river indicates a slope of 0.5 m/km whilst for the lower reach a value of 0.10 m/km is found. It is possible to observe also that the change in the slope occurs between km 60–80. However, a close inspection of the bed levels indicates that in period 1909–1916 the change in slope was more gradual with a sharper transition near the km 95, where probably the gravel-sand

Copyright © 2006 Taylor & Francis Group plc, London, UK

transition was formed (Murillo-Muñoz, 1998). This suggests that the current location of the transition in the bedslope is probably the results of the intensive degradation process induced by the human interference in the system.

2.4 *Sediment transport rates*

Regarding the sediment transport rates there is great variability of data reported in the literature. Waterloopkundig Laboratorium (1994) reports that the average sediment transport rate of the Meuse River is approximately 35×10^3 m^3/y; but at Linne it is reported to be about 26×10^3 m^3/y, while 19×10^3 m^3/y at Kessel and 70×10^3 m^3/y at Ravenstein are mentioned for the more downstream reach (Gerretsen, 1968).

Furthermore, it has been observed in the Meuse River that the transported sediment load depends on whether or not the armour layer has been mobilized during a previous flood. Klaassen (1986) indicated that if the armour layer remains stable when the smaller floods are passing little sediment is transported. Once the armour layer is mobilized the substratum material is available and the sediment load increases rapidly. This phenomenon has been estimated to occur at discharges higher than 1250 m^3/s (Klaassen, 1981), which coincide with the present estimated bank-full discharge. During the receding part of the flood the armour layer is built up once again but at a lower level, and on top of the eroded layer sediments are deposited. These deposited (and often finer) sediments are available for transport and therefore after a flood period this material can be transported at smaller discharges until the armour layer is exposed again. Hence, the composition of the armour layer and the sediment transport is a function of the magnitude of previous floods (Duizendstra, 1999). A high flood will give a finer armour layer and more eroded sediment on top of the restored armour layer after the flood (Klaassen, 1986).

2.5 *Human interference*

Human impact on the Meuse River is extensive and it includes changes in land use, water withdrawal for irrigation and human consumption, mining, hydropower production as well as extensive river training works for navigation and flood control. At the same time, the sediment supply to the downstream river reaches has been reduced considerable to the extent that the river hardly transports any bed material load across the border; however, the wash load content of the river has increased substantially (Micha & Brolee, 1989). In fact, due to the reduced upstream sediment supply and the degradation of the river over the last century the armouring of the river might have increased. For this, however, no evidence is available. It can be stated that the overall effect of human interference has resulted in the Meuse River being an incised river which only floods occasionally its floodplain. Furthermore, the morphological processes in the Meuse River are extremely slow (de Vries, 1975). The very long morphological time scale implies that the Meuse River responds very slowly to changes and should not be considered to be "in equilibrium". Even without further human interference, for a long period to come the river will continue to adjust to changes in the past.

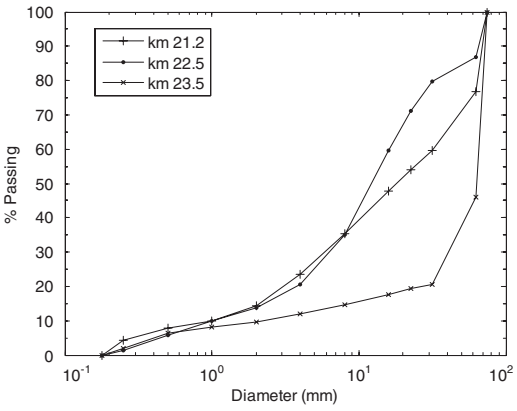


Figure 5. Spatial variation of the bed material in the Meuse River.

3 ANALYSIS OF THE BED MATERIAL CHARACTERISTICS

The Meuse is a gravel-bed river and therefore it is not easy to characterize it by the few statistical parameters often used for other rivers, notably median diameter, standard deviation and D_{50}. Spatial and temporal variation of the deposited sediments is important. In dry periods, the Meuse presents an armour layer while during floods this layer becomes unstable and the underlying material is mobilized. Thus, depending when and where the samples are taken and the frequency of the sampling, the characterization could lead to substantially different results. As an example of such variations, Figure 5 presents the variability of the bed material composition in longitudinal direction. In addition, reworking of the bed material due to training works is extensive making it even more difficult to characterize the bed material by means of a few statistical parameters. The reader should be aware of this large variability.

3.1 *Characteristic parameters*

The variation of the D_{50} in the bed material and its geometric standard deviation are shown in Figures 6 and 7, respectively. It can be observed that until the km 90 the D_{50} approximately is mainly in the coarse gravel range, with an average value of 16 mm shown

Copyright © 2006 Taylor & Francis Group plc, London, UK

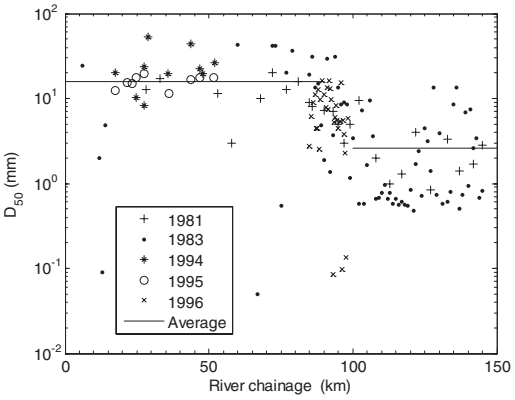


Figure 6. Variation of the D_{50} in the bed material along the Meuse River.

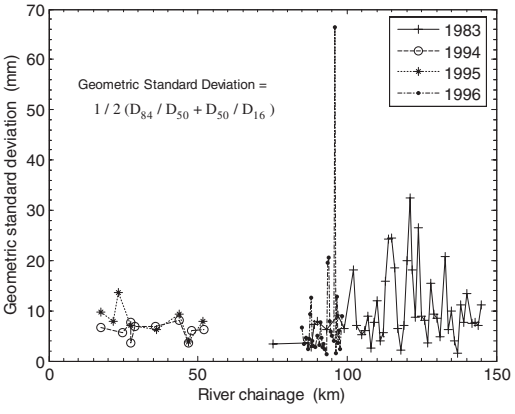


Figure 7. Geometric standard deviation of the bed material samples in the Meuse River.

as a straight line in Figure 6. There are a few points in this reach which are in the medium sand range but they may be due to problems related to the sampling. Furthermore, the Meuse is characterized by armour layers in its upper reaches. This may be linked to the fact that sediment supply is insufficient and that the river is degrading but it can also be explained as a normal phenomena for a gravel-bed river. From about km 105 onwards, the D_{50} is significant smaller and the average value is about 2.6 mm. In this zone, there is a lot of scatter in the data and this is reflected by higher values in the geometric standard deviation (Figure 7), probably produced by sediment bimodality in combination with lateral sorting. Between km 90 and 105 approximately, a gradual transition in the values of D_{50} is observed. An important point is the large values of the geometric standard deviation, especially from km 90 onwards. This implies that the correct collection of samples is particularly important in this reach. It also

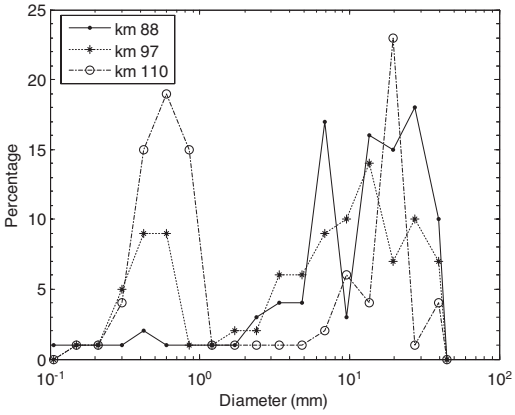


Figure 8. Development of the bimodal composition in the bed material.

indicates the necessity of more samples, which might not reduce the variability but it would improve the estimate of the average value. It may very well be that the large variation is caused by physical phenomena and is inherent to this type of mixed gravel-sand bed river.

3.2 *Bimodal composition of the bed material*

One of the characteristics observed in many transitions from gravel to sand-bed rivers is the development of a bimodal composition of the bed material. The Meuse is no exception; Figure 8 shows the grain size distribution at three locations, the development of a gap in the range of 1–5 mm is clearly observed. The gap in size material has been related to the break down of gravel particles into sand (Yatsu, 1955; Sambrook Smith & Ferguson, 1995).

3.3 *Median diameter*

A bimodal composition of the bed material makes the D_{50} a sensitive parameter in the characterization of the sediments. Especially if the D_{50} is within the flat zone of the granulometric curve (1–5 mm approximately). In such a case of bimodal composition, the median diameter (D_m) is more representative for the bed material. Figure 9 shows the available D_m values. This picture is less complete than Figure 6 but appears to be more consistent. Furthermore, the relation between D_{50} and D_m for the all data ensembles yields a ratio of $D_m/D_{50} = 1.52 \pm 0.42$ mm.

3.4 *Gravel-sand content of the sediments*

The gravel-sand content of the sediments is another way to represent the spatial variation of the sediments. Figure 10 gives the percentage of gravel ($D_j \geq 2$ mm) content along the Meuse River. In this

Copyright © 2006 Taylor & Francis Group plc, London, UK

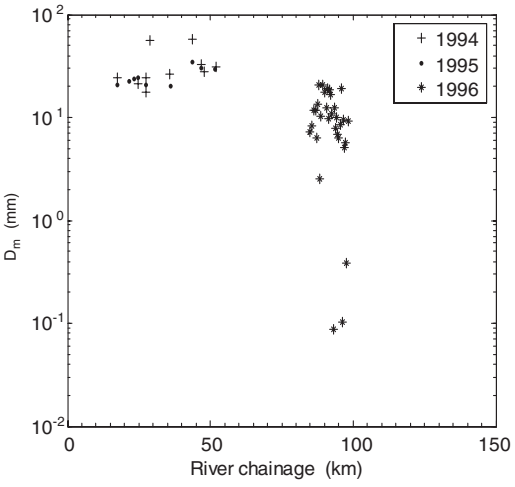


Figure 9. Median diameter of the bed material.

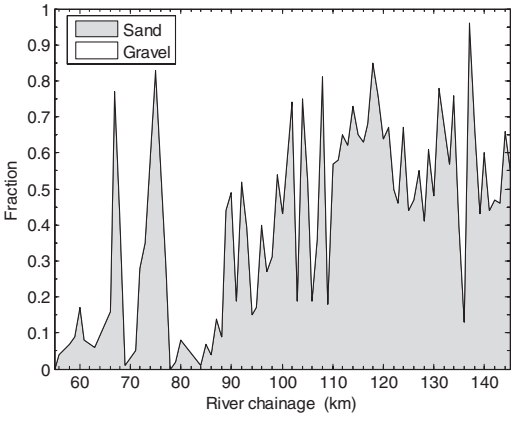


Figure 10. Gravel and sand content along the Meuse River.

figure is possible to notice that the average sand content exceeds the 50% around km 100 approximately, which is also the reach where the gravel-sand transition occurs. Inspection of the spatial variation in D_{16}, D_{50} and D_{84} confirmed such location (Murillo-Muñoz, 1998). In Figure 10, two peaks in the sand content are observed, notably around km 67 and 75. These peaks may be produced by the barrages of Linne and Roermond respectively, which induce sedimentation of sand during low flow conditions.

4 QUALITATIVE ASSESSMENT OF THE DOWNSTREAM FINING

Along the river course the Meuse sediments are subjected to different factors that contribute to the overall fining in downstream direction. These factors are: abrasion, break down of particles, subsidence, and selective transport. In principle also other factors can be considered (like the presence of ancient Rhine deposits and the input of finer sediments from a minor tributary of the Meuse River, notably the Roer River) but in Murillo-Muñoz (1998) it was shown that these have a negligible effect and hence they are not discussed here.

4.1 *Abrasion process*

The abrasion process causes a slow reduction in the particle size and produces mainly sands and silts, thus the sand content and the wash load increase while the total bed load decreases. The rate of reduction depends on the rock type. Van Straaten (1946) provides a general classification of the rock fragments present in the South Limburg area. Van Straaten classified the rocks into four groups and sized them into six fractions. From this work it is possible to infer that the dominant rock group in the gravel fraction corresponds to common sandstones like arkose, quartzite and phyllite; follow by rock fragments containing quartz like gneiss.

Furthermore, Edelman & Van Baren (1935) reported on the mineralogical composition of the Meuse deposits. A re-examination of their findings suggests that the gravel and coarse sand deposits present in the whole area are likely to come from fragments of metamorphic rocks and to a lesser extent from igneous rocks. The metamorphic rock fragments present in the deposits probably come from gneiss and schist. From the above mentioned rocks, the two weaker ones are phyllite and schist; which have similar internal structure and therefore comparable resistance to weathering.

To assess the relevance of abrasion, not only the rock type should be selected but also the particle's velocity should be assessed. Rijkswaterstaat has filmed the movement of the bed-load particles using a video camera attached to a Helley-Smith sampler (Duizenstra et al, 1994). From these movies, it was possible to observe that particles do not move for quite some time but when they move velocities reaching about 1 m/s can occur. If this velocity is considered, the loss of weight over the 15 km of the transition is about 5% using the abrasion rates reported by Abbott & Peterson (1978). This corresponds to a change in particle diameter from 16 to 15.7 mm approximately. Furthermore, if the particle velocity would be as low as 3 cm/s the loss of weight would be about 15%, which corresponds to a reduction of only 0.8 mm in particle diameter. Hence, abrasion per se does not explain the formation of the gravel-sand transition in the Meuse River though it would contribute to the production of sand. Here it is assumed that abrasion occurs only when the particle is moving. However, a particle at rest suffers abrasion by

Copyright © 2006 Taylor & Francis Group plc, London, UK

the blows of other particles, by sandblasting and even by chemical attack. These mechanisms are difficult to incorporate into the available methodologies.

4.2 *Break down of particles*

Break down refers to the breaking of a particle into two or more parts of roughly equal size. It produces a discontinuity in the grain size of the bed-load material but it does not affect the total load. It occurs when the particles reach a certain cut-off diameter and this happens along the river course rather than at certain locations (Parker & Cui, 1998).

The break down of particles mainly depends on the lithology of sediments. In the case of the Meuse River likely sediments are quartzite, sandstone and phyllite. Quartzite has an internal structure, which is compact, with no defined structural planes of weakness and therefore break down is unlikely to occur as principal mechanism of the abrasion process although it will produce big quantities of sand. On the other hand, sandstone particles may have planes of weakness depending on the environment of deposition and the degree of cementing between the grains; thus sandstone might suffer break down. Finally, the elements of phyllite are grouped in plates (or in laminar layer) and therefore the phyllite is more likely to break down and produce fine gravel and sand. However, there are no sufficient field evidences to reject or to accept the break down as an important process in the case of the Meuse River. There is still the evidence of the bimodal composition of the bed material, with a gap in the range of 1–5 mm. Yatsu (1955), Moss (1972) as well as Sambrook Smith & Ferguson (1995) indicate that particles in this range show tendency to break down into smaller sizes. Nevertheless, field surveys are needed to further study the importance of break down in the Meuse River.

4.3 *Tectonic movement, simplified approach*

In the past, the Meuse was a free system. The river meandered within its floodplains and the location of the main channel shifted slowly over time. Thus, if sedimentation of coarse grains occurred only at the main channel the location of the deposited sediments was governed by the meandering process. This process is time dependant and if long-term average conditions are sought, the total deposition width over which sedimentation occurred should be considered, i.e., all locations where the main channel was during a whole meander cycle.

Considering the above, an initial assessment of the relevance of tectonic movements can be made using the sediment mass balance equation expressed in finite differences as (see Figure 11)

$$B\Delta Z\Delta x = -\left(S_d - S_u\right)\Delta t \qquad (1)$$

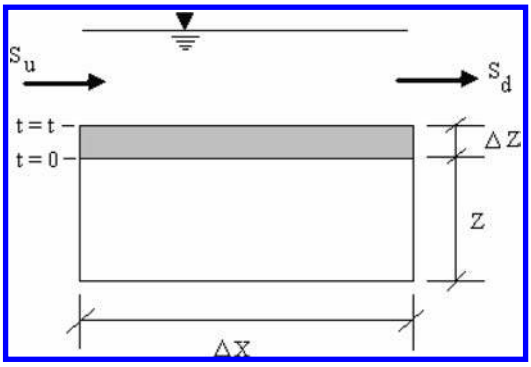


Figure 11. Definition sketch for the sediment mass balance.

where B is the total deposition width, ΔZ the uniform thickness of the deposition layer, Δx the reach length and S the total sediment transport; sub-index u and d refers to upstream and downstream.

Equation 1 does not include the effects of longitudinal sorting. If subsidence is taking place in the reach under consideration it is possible to assume that ΔZ is uniform and equal to the subsidence magnitude over a certain period of time. Hence, the bed level would remain stable and Equation 1 can be written in the following way:

$$S_d = S_u - B\Delta x\frac{\Delta\Gamma}{\Delta t} \qquad (2)$$

where the term $\Delta Z/\Delta t$ was substituted by the subsidence rate $\Delta\Gamma/\Delta t$ in the area. The second term on the right side of Equation 2 represents the volume of material V that is deposited in the reach during the time interval Δt. This volume depends on the length of the subsidence reach, on the rate of subsidence and on the assumed deposition width. Moreover, under the above mentioned assumptions, Equation 2 shows that the sediment transport within the reach of interest depends on the incoming sediment, the deposition width, and the subsidence rate.

If the volume V represents the amount of material deposited on the subsiding reach, and this volume is removed from the coarser fractions of the sediment load entering the reach, the remaining grain size distribution would give an indication of the effects that subsidence has on the sediment composition. Figure 12 presents the results of applying such an idea on an average granulometric curve. Figure 12 shows a fair agreement in the fine part of the curves at km 110. It is also possible to observe that at this location, the bed material already has a bimodal composition with a gap between 1–5 mm. The coarse part of the bimodal composition is not correctly reproduced by this simplified approach, probably because particle break down is not considered and there may be some deposition

Copyright © 2006 Taylor & Francis Group plc, London, UK

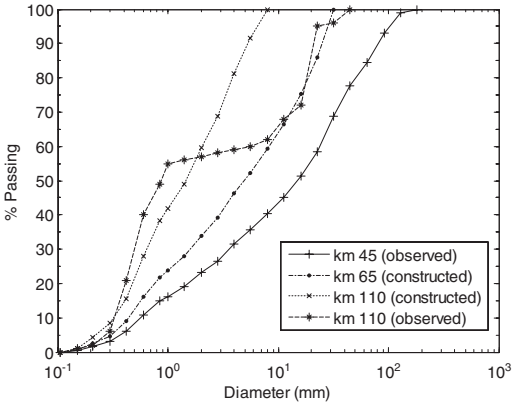


Figure 12. Granulometric composition of the bed material at different locations, B = 750 m, S = 35×10^3 m^3/y (incoming sediment load).

of the finer fractions. In using the above methodology two differential rates of subsidence were considered, the first one between Feldbiss and Stevensweert faults (see Figure 3) at an average rate of 0.6 mm/y and the second one between Stevensweert and Tegelen faults at 0.3 mm/y.

In addition, several combinations of deposition width ($100 \leq B \leq 2500$ m), upstream sediment supply ($15 \leq S \leq 75 \times 10^3$ m^3/y) and granulometric curves were analyzed. The results of this sensitivity analysis indicate that the deposition width should be between 500–750 m in order to properly estimate the observed $D_{50} = 2.6$ mm of lower Meuse reaches. In addition, these results suggest that the agraddation process which accompanies the downstream fining can be effectively counteracted by a similar subsidence rate preserving always the bed elevation and the reduction in size of the bed material. The reduction in size depends on the incoming sediment load and the deposition width, the latter parameter being the more important one.

5 NUMERICAL SIMULATION

In the previous section an individual assessment of the different potential causes was given. The present section presents an assessment in which the processes of abrasion, break down, subsidence and selective transport are combined via a numerical model. The selected model is Acronym5 which was developed by Cui & Parker (1998). This is a 1-dimensional steady state model that computes the long-term profiles by applying on the gravel reach the selective transport approach of Parker (1990) on the full grain size distribution. On the sandy reach only one diameter represents the sediment and the Engelund-Hansen expression is used to predict the sediment load. Acronym5 allows for three types of gravel-sand transition: 1) the gravel can run out; 2) all the gravel can reach the cut-off size and break into sand or 3) the sand can overwhelm the gravel. This last type of transition occurs when the capacity condition for sand transport is reached before the gravel transport has drop to zero, and thus, leaves a residual load of gravel in the sand-bed reach that is typically a very small fraction of the sand load. Further details on the model can be found in Sinha & Parker (1996), Parker & Cui (1998) as well as in Cui & Parker (1998).

5.1 *Model schematization*

Since Acronym5 does not simulate differential vertical movements, only the subsidence area of the Roer Graben Rift system is taken into consideration, i.e. only from km 45 onwards subsidence is modeled. The discharge considered during the simulations is the bankfull discharge, which is approximately 1250 m^3/s and occurs about 1% of the time. The sediment load entering at km 45 is estimated from Wilbers (1996) and corresponds to about 36×10^3 m^3/y. This amount was divided into gravel (80%) and sand (20%) according to the percentage found in Wilkens & Lambeek (1997). The grain size distribution of the gravel load is assumed to be equal to the surface layer distribution at Koeweide (km 46.9) as reported by Van Manen et al. (1994).

The subsidence rate considered is the average between km 45 and 102.5; this average value is 0.5 mm/y. Similarly, an average abrasion coefficient of 2×10^{-5} m^{-1} is used. Moreover, the sinuosity of the Meuse is set at 1.46 and the main channel width at 100 m. For the deposition width a value of 650 m is employed. The grain size cut-off is estimated in 4.8 mm whilst bed porosity at 0.4. Finally, due to limitation of the model the sand diameter in the sandy reach is set at 2 mm instead of the better estimate of 2.6 mm.

5.2 *Results of the simulation*

Results of the application of the model are presented in Figure 13. In this simulation the gravel-sand transition occurs at km 98, which is nearly the middle of the defined transition zone (km 90–105). In this simulation the D_m obtained by the model fairly agrees with the behaviour of the field and average values. The gravel-sand transition occurs because the gravel load drops to almost zero allowing the sand to "overwhelm" the remaining gravel particles.

Important is the fact that the field values shown in Figure 13 are obtained by the relation $D_m = 1.52\, D_{50}$ previously mentioned. Remarkable is the gradual variation of the D_m in the gravel reach due to abrasion. The D_m in the sandy reach is equal to 2 mm due to limitations of the program.

Copyright © 2006 Taylor & Francis Group plc, London, UK

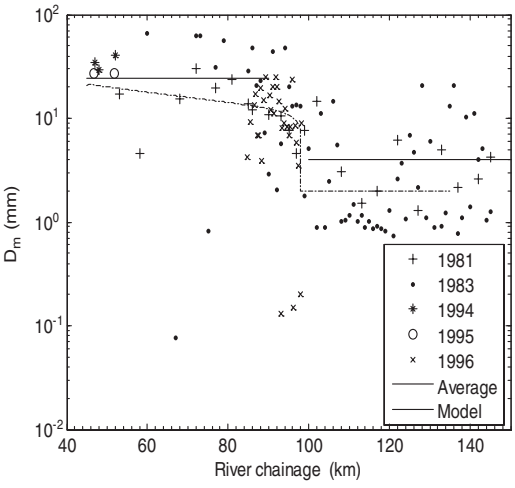


Figure 13. Variation of the median diameter on the Meuse River according to the simulation.

5.3 *Sensitivity analysis*

A sensitivity analysis of the findings indicates that an increment on the subsidence rate moves the location of the transition in upstream while the D_m increases moderately. Conversely, when the subsidence rate is lower the transition moves in downstream direction, but the rate of change in location and in D_m is higher than in the case of higher subsidence rate. In the case of pure abrasion (no subsidence) there is no gravel-sand transition in the area of interest. This case also demonstrates the effect of abrasion in the reduction of the grain diameter. Over 100 km the D_m reduces from 20 to 7 mm, which corresponds to a reduction in volume of 90%, only 10% of the volume remains.

Moreover, changes in the sediment load produce only slight variations on the location of the gravel-sand transition, suggesting that the location is not sensitive to changes in total value of sediment load. On the other hand, the deposition width affects the location of the transition; a reduction of the width moves the location in downstream direction. The deposition width has only a slight effect in the reduction of the grain diameter.

Regarding the abrasion coefficient, a reduction of its value shifts the transition in downstream direction. In the case of pure abrasion (no subsidence), all the available sand is deposited in between gravel grains and there is no sand left at the transition point and therefore, it cannot form. This confirms that although abrasion does not explain completely the presence of the transition, it plays an important role. It provides sand to fill the voids between the gravel particles and thus allows the formation of a transition.

Finally, in all the cases with the exception of pure abrasion and pure subsidence, the transition is formed because the gravel load drops to almost zero allowing the sand to overwhelm the remaining gravel particles. Moreover, the cut-off diameter for break down is not reached in any of the simulations. Thus, according to the simulations break down does not occur in the Meuse River.

5.4 *Effect of river training in the 19th century*

The results previously presented are obtained using a deposition width of 650 m, which was probably the situation when the Meuse River was a free meandering system. However, during the last two centuries the river has been trained and currently the planform of the river is fixed. This makes the deposition width similar to the main channel width, which is 100 m approximately. Simulations using this value suggest that the gravel-sand transition in the Meuse River is probably moving in downstream direction due the reduction of the deposition width. This movement is probably taking place very slowly and because of many human interference in the river and the spatial and temporal variation of the bed material data is difficult to detect in the field.

6 DISCUSSION OF RESULTS

The analysis of the field data reveals that there is an appreciable variability of the bed material characteristics in space and time. The variability in space is amongst others caused by armouring and by lateral and longitudinal sorting. Probably the latter variation occurs at the length scale of bends. Variability in time has two main causes. The passage of floods, which causes instability of the armour layer, generates much sediment and affects the armour layer composition. The second cause is the delayed response of the river system to human interference. This reflects that the river cannot be considered to be in "equilibrium condition"; most probably this condition of non-equilibrium is the result of the many training works, dredging and other human interferences with the Meuse river system since the 19th century. In addition, there might be also changes in lithology that introduce additional difficulties to the bed material characterization. Therefore, to characterize the Meuse River by means of simple statistical parameters is probably too much a schematization and might not represent the real conditions of the river.

The variability of the bed material has implications on the data collection. Specifically, the use of bucket sampling is not advisable since special care should be taken to differentiate between the armour layer and the substratum material. Similarly, separate description of

Copyright © 2006 Taylor & Francis Group plc, London, UK

the banks and channel should be done. Furthermore additional bed material samples are needed, especially in the ranges 50–88 km and 100–150 km. Additionally, the presence of armour layers along the Meuse also requires that field measurements of sediment load should be done not only during flood conditions but also before and after such an event. In particular, after a large flood, substantial quantities of sediments are still transported at lower discharges.

Nevertheless, the changes in the average value of the bed material and the bed slope show that a fairly sudden transition is present. Furthermore, the development in downstream direction of a bimodal bed material composition was confirmed. This bimodal composition is especially appreciable in the gravel-sand transition (km 90–105) and it is likely produced by the break down of particles. The results suggest that the diameter at which the particles are breaking is about 5 mm; this diameter though depends on the lithology of the bed material. Further studies into this aspect are appropriate.

Looking at the abrasion process, the principal rock in the Meuse River deposits is likely to be sandstone. Solely, abrasion does not explain the sudden transition to a sand-bed river; however, the sand content increases in downstream direction due to abrasion and as suggested by the simulations, this increase is important in the development of the transition. On the other hand, break down of particles is probably the dominant process in the development of the bimodal composition of the bed material, but field data should be collected in order to verify this hypothesis.

The vertical tectonic movements (uplift and subsidence) within the basin play an important role in the long-term morphological behavior of the Meuse River. The uplift process in the South Limburg block is likely to encourage an incision of the river bed. Probably the current Meuse terraces are the product of this incision. Conversely, the subsidence in the Roer Graben imposes changes in the river slope and thus, it provides a depositional environment in which the coarser particles can deposit due to selective transport. If deposition and subsidence rates were in equilibrium, the bed level would not change in time but downstream fining would still occur.

In the Meuse River the gravel-sand transition occurs between km 90–105; in this reach the gravel and sand contents are about 50% each. This sand content in the studied case is reached by the selective transport triggered by the subsidence within the Roer Graben as well as the abrasion process. Hence, the gravel-sand transition in the Meuse River is the result of the combined action of selective transport (induced by subsidence) and the abrasion of particles.

However, the transition of the bed slope takes place between km 60–80 and not in the vicinity of the change in D_{50} as expected. If only the surveys of the beginning of the 20th century are considered, the change in slope used to be located near the transition of the grain size. The present location of the bed slope transition is probably the results of the many human interferences that have taken place since the middle of the 19th century.

The width over which deposition is taking place in the subsiding reach was shown to be an important factor in the overall process of the downstream fining. However, its consideration depends on the time scale of the problem; in the case of long-term profiles the deposition width should be considered as the width over which the river has been meandering. This width depends on factors like floods, bank erosion rates and soil type among others. The simplified approach and the numerical simulations suggest that in the case of the Meuse River the representative deposition width is about 650 m. Probably though a more complicate picture should be drawn. During the meandering process the channel is mostly present in a narrow band around the valley axis. Occasionally the meandering extends farther away from this axis. This implies that in the floodplain areas away from the axis conditions are different. There finer material is also stored, and hence these far-away reaches contribute less to the preferential settling of the coarser sediments. The value of 650 m should therefore be considered as the result of a weighting procedure of probability of occurrence of a channel and the effectivity of the selective transport.

The results using a deposition width of 100 m indicate that due to fixation of the planform the gravel-sand transition would shift in downstream direction. This shifting in position could be the explanation of why the field data suggest that the gravel-sand transition is between km 90–105. Perhaps in the past, the transition was arrested near km 90 but since the Meuse River has been trained and its planform fixed, the transition may have moved slowly towards a more downstream location, which could be at this moment, near km 105. This dynamic process is likely to be happening now as well and it might explain some of the scatter in the data. Unfortunately at the present moment, there is no morphological time scale to predict how long the shifting process would take.

Given these results, it is important that abrasion, differential vertical movements and the actual deposition width are incorporated into a potential mathematical model of the Meuse River. This model should not use parameters that are sensitive to the bimodal composition of the bed material. Furthermore, it should be able to distinguish whether the armour layer has been mobilized or not. Finally, it should be realized that a complete numerical model of the Meuse River will never be possible. Too many uncertainties and limitations of the available data as well as the fact that the Meuse is never in "equilibrium condition" preclude this. It seems preferable to concentrate on a model that predicts the present conditions at an acceptable level.

Copyright © 2006 Taylor & Francis Group plc, London, UK

7 CONCLUSIONS

The Meuse River can be characterized as a gravel-bed river upstream of km 90 and as a sand-bed river downstream of km 105. Thus, a gravel-sand transition occurs between km 90–105 where the D_{50} of the bed material changes from about 16 to 2.6 mm. There is also a pronounced and fairly sharp transition in the bed slope. This slope changes from about 0.5 m/km to about 0.10 m/km around km 70.

The gravel-sand transition takes place fairly smoothly as a result of the abrasion process and the action of selective transport triggered by tectonic subsidence. These two mechanisms allow the sand content to increase in downstream direction until the point that it overwhelms the gravel fraction. This phenomenon is well simulated by Acronym5, allowing a better assessment of the relevant processes.

The assumed deposition width plays a major role in the assessment. There is however only limited understanding of this concept as used in this contribution. This deposition width is much larger than the channel width, and although some support is available for this assumption, more studies are needed to clarify the concept and to make a good choice of it based on the meandering characteristics of the river and the lateral sorting on point bars.

In addition, there is a large variability both in space and probably in time of the particle distribution of the bed material in the Meuse River. This variability is linked to the physical processes in the river. Also the transient phenomena induced by human interference in the system since the 19th century might be important on this respect. It is clear however, that the Meuse River shows the development of a bimodal grain size distribution with a gap between diameters of 1–5 mm. Nevertheless there is still not sufficient data and insight to fully characterize the bed material of the Meuse River. More studies may shed additional light on this aspect.

Finally, sediment transport processes in the Meuse River are quite complicated and difficult to understand because of (1) the occurrence of an armour layer in the Common Meuse; (2) the poorly understood effect of floods on the armour layer; (3) the occurrence of the gravel-sand transition; (4) the effects of human interference which has induced transient phenomena and (5) the limited availability of field data on bed material and sediment transport.

ACKNOWLEDGMENTS

The authors gratefully appreciate the comments of Ir. H.D. Duizendstra, Rijkswaterstaat, RIZA. This study was funded by the Ministry of Transport, Public Works and Water Management of Netherlands (Directorate Limburg, Rijkswaterstaat), and administered through RIZA.

REFERENCES

Abbott, P.L, & Peterson, G.L. 1978. Effects of abrasion durability on conglomerate clast populations: examples from cretaceous and eocene conglomerates of the San Diego area, California. *J. Sediment. Petrol.* 48(1): 31–42.

Cui, Y. & Parker, G. 1998. The arrested gravel front: stable gravel-sand transitions in rivers. Part 2: general numerical solution. *J. Hydr. Res.* 36(2): 159–182.

Duizendstra, H.D., Kos, T.J.M & Hal, L.W.J. 1994. Bed load measurements in the Border Mesue from bridges: first results Rijkswaterstaat RIZA, werkdocument 94.059X. Nederland. (in Dutch)

Duizendstra, H.D. 1999. *Sediment transport in the Border Meuse. Transport capacity and supply of sediment*. RWS, RIZA, Werkdocument 99.158X (in Dutch)

Edelman, C.H. & Van Baren, F.A. 1935. La pétrograhpie des sables de la Meuse Néerlandaise. *Mededelingen Landbouwhoogeschool* 39. Wageningen, Nederland.

Gerretsen, J. 1968. *Sediment transport in the Meuse River.* RWS, Dir. Limburg, Studied. Maas, nota 68.8 (in Dutch)

Helmer, W., Klaassen, G.J. & Silva, W. 1991. *Future for a gravel bed river*. RWS, RIZA, Arnhem, nota 91.0007 (in Dutch)

Hoey, T.B & Ferguson, R. 1994. Numerical simulation of downstream fining by selective transport in gravel bed rivers: model development and illustration. *Water Resour. Res*. 30(7): 2251–2260.

Holly, F.M. & Rahuel, J.L. 1990. New numerical/physical framework for mobile-bed modelling. Part II test applications. *J. Hydr. Res*. 28(4): 401–416.

Klaassen, G.J. 1981. *Morphological phenomena Border Meuse River.* Delft Hydraulics, Report R863 Part A (text) and Part B (tables and figures) (in Dutch)

Klaassen, G.J. 1986. *Morphology of armoured river beds. Experiments with flood waves*. Delft Hydraulics, Report M2056, Netherlands (in Dutch with English summary)

Klaassen, G.J., Lambeek, J., Mosselman, E., Duizendstra, H.D. & Nieuwenhuijzen, M.E. 1999. Re-naturalization of the Meuse River in The Netherlands. In P.C. Klingeman et al (eds), *Gravel-Bed River in the Environment: Colorado, Water Resources Publications*, pp. 655–674

Micha, J.C. & Borlee, M.C. 1989. Recent historical changes on the Belgian Meuse. In G.E. Petts, H. Moller, A. L. Roux. (ed.), *Historical Changes of Large Alluvial Rivers: Western Europe, Wiley.*

Moss, A.J. 1972. Technique for assessment of particle breakage in natural and artificial environments. *J. Sedim. Petrology* 42(3): 725–728.

Murillo-Muñoz, R.E. 1998. Downstream fining of sediments in the Meuse River. UNESCO-IHE, M.Sc. Thesis.

Parker, G. 1990. Surface-based bedload transport relation for gravel rivers. *J. Hydr. Res.* 28(4): 417–436.

Parker, G. 1991a. Selective sorting and abrasion of river gravel. I Theory. *J. Hydr. Eng*. 117(2): 131–149.

Parker, G. 1991b. Selective sorting and abrasion of river gravel. II Applications. *J. Hydr. Eng.* 117(2): 150–177.

Parker, G. & Cui, Y. 1998. The arrested gravel front: stable gravel-sand transitions in rivers. Part I: Simplified analytical solution. *J. Hydr. Res.* 36(1): 75–100.

Copyright © 2006 Taylor & Francis Group plc, London, UK

Sambrook Smith, G.H. & Ferguson, R.I. 1995. The gravel-sand transition along river channels. *J. Sedimentary Res.* A65(2): 423–430.

Sinha, S.K & Parker, G. 1996. Causes of concavity in longitudinal profiles of rivers. *Water Res. Res.* 32(5): 1417–1428.

Van den Berg, M.W. 1996. Fluvial sequences of the Maas: a 10 Ma record of neotectonics and climatic change at various time-scales. University of Wageningen. Ph.D. thesis.

Van den Berg, M.W., Groenewoud, W., Lorenz, G.K., Lubberts, P.J., Brus, D.J. & Kroonenberg, S.B. 1994. Patterns and velocities of recent crustal movements in the Dutch part of the Roer Valley rift system. *Geologie en Mijnbouw.* 73(2–4): 157–168.

Van Manen, G.R., Onneweer, J.G. en Van den Berg, J.H. 1994. Spatial variation of sedimentary structure and texture of the bed of the Border Meuse (barrage Borgharen, km 15.5-Maaseik, km 52.7). Report GEOPRO 1994.94. Faculeit Ruimtelijke Wetenschappen, Vakgroep Fysische Geografie, Universiteit Utrecht. Nederland. (in Dutch)

Van Straaten, L.M.J.U. 1946. Studies on gravel in Southern Limburg ; Ph.D. thesis Leiden, Nederland (in Dutch).

Vries, M. de. 1975. A morphological time-scale for rivers. *Proc. XVI Congr. IAHR*, Sao Paolo, Brazil.

Waterloopkundig Laboratorium. 1994. Study flooding problems Meuse River, Report for Rijkswaterstaat

Wilbers, A. 1996. The Border Meuse over the years. A study into the morphological changes of the bed of the Meuse River from 1978 to 1998, Utrecht University, (in Dutch).

Wilkens, D.H. & Lambeek, J.J.P. 1997. Bed load transport measurements Border Meuse. Delft Hydraulics, Rapport Q2354 (in Dutch)

Yatsu, E. 1955. On the longitudinal profile of the graded river. *Transactions of the American Geophysical Union* 36(4): 655–663.

Copyright © 2006 Taylor & Francis Group plc, London, UK

Cohesive sediment removal from a fixed bed

R. Della Morte
Faculty of Engineering, University of Naples, Naples, Italy

C. Mucherino, D. Pianese & F. Pirozzi
Department of Hydraulic and Environmental Engineering, Federico II University, Naples, Italy

ABSTRACT: A few experiments were carried out, in a 1:1 scale laboratory flume, to evaluate, by the acquisition and processing of photographic images, the capability of currents flowing in a stream to remove cohesive sediments deposited on the bed of a river. The results of the experiments, expressed in terms of area and volume eroded, and changes in the concentration of suspended sediments carried by water, were consistent with the physical phenomenon, and congruous with others results already reported in the literature. Considering the goodness of the results obtained by the experiments carried out, it was possible to assert that the procedure adopted for the evaluation of sediment removal is suitable for studying the erosion and transport phenomena involving most kinds of granular or cohesive sediments.

1 INTRODUCTION

Starting from the XIX century, the study of sediment transport in both rivers and channels is a very important topic in hydraulic engineering and a challenging task in the research. Most of the analyses carried out were focused on deposit/erosion phenomena involving granular sediments, whereas there is poor experience on the behaviour of cohesive sediments. Indeed, cohesive sediments exhibit different capability to resist to the flow actions, strongly depending on the composition of sediment itself and, then, on the strength of electrical attraction forces among particles. Besides, it is practically impossible to reproduce these forces in a smaller scale: as a consequence, when a problem arises involving the evaluation of erosion/deposit behaviour of cohesive sediments subject to a flow, it is usually impossible to bring useful information from the literature.

Starting from these considerations, some experiments were carried out at the laboratory of the Department of Hydraulic and Environmental Engineering *Girolamo Ippolito* of the University of Naples *Federico II*, aiming to reproduce, in a 1:1 scale flume, the capability of currents flowing in a natural river (the Bagnoncino Creek, Tuscany, Italy) to remove cohesive sediments deposited on the river bed.

In particular, the cohesive sediments specifically considered in this study were *aluminum hydroxide flocs*, diffusely found on the river bed, with layers up to 0.40 m thick. These flocs were discharged into the river, for a very long time (about 1 year), because of malfunctioning of a few water treatment plants, whose goal was to remove, by adding aluminum salts, the sediments present in the water coming from some tunnel digs and containing high level of suspended solids.

The flocs covered the river bed, at first destroying the fluvial vegetation, and then provoking the disappearance of fish, riparian fauna and vegetation.

As a consequence, in order to evaluate the possibility that the sediments were *naturally* removed, and transported until prefixed "sediment traps" to locate along the creek, it was important to individuate the hydraulic conditions needed to have sediment removal by the currents flowing in the stream.

For this reason, some laboratory activities were carried out to evaluate: i) the capability of flow to remove cohesive sediment from a fixed bed; ii) the mechanic of transport of this kind of sediment; iii) the time required for complete sediment removal.

The experiments have regarded five different aspects: i) the evaluation of the optimal conditions to artificially produce aluminum hydroxide flocs; ii) the massive production of aluminum hydroxide flocs and their subsequent transfer into the laboratory flume; iii) the acquisition of the flow velocity profiles by an Acoustic Doppler Velocimeter Profiler (*ADVP*); iv) the acquisition and processing of photographic images taken during the sediment removal; v) the evaluation of the capability of flows to remove the sediments.

It could be important to observe that the work presented here could be considered of some importance not only because it aims to solve a few specific problems, such as the determination of critical flow

Copyright © 2006 Taylor & Francis Group plc, London, UK

conditions for starting erosion of a given cohesive sediment or the evolution in time of erosive phenomena, but also because it proposes a new kind of laboratory approach, that could be useful even for studying the behaviour of other kinds of cohesive or granular sediments.

2 LABORATORY SET-UP

The experimental work aimed to reproduce natural phenomena that could be observed, both during low discharge periods and in consequence of floods events, in the *Bagnoncino Creek* (Tuscany, Italy), that was interested, a few years ago, by large deposit phenomena of cohesive sediments. Because of the impossibility to know and scale the inter-particles attraction forces originating the flocs, and the strength of links among the flocs themselves, it was decided to try to reproduce, in a 1:1 scale channel, the actual conditions that could be usually observed in a central region of the creek cross-sections. As a consequence, a Perspex channel 18.0 m long, 0.76 m wide and 0.60 m deep, having a fixed slope $i = 0.001$ m/m, was used for the experiments (Fig. 1). To adequately reproduce the field conditions, the bed of the experimental flume was covered with a single layer of stones. The grain size distribution of sediments used in the experiments fitted quite well that of sediments observed at the bottom of the Bagnoncino Creek (Fig. 2). In particular, the d_{50} diameter of the stones used in the experiments was equal to 30 mm.

In the middle of the channel, a removable wood tablet, 0.45 m long and 0.76 m wide, with fixed stones was arranged (Fig. 3). The tablet was covered with aluminum hydroxide flocs produced inside a 1 m^3 tank and then positioned in the channel.

It was decided to produce cohesive sediment into the tank to avoid water contamination in the general laboratory circuit.

2.1 *Procedure used to obtain the optimal chemical dosage for pollutant production*

The first phase of the experiments was focused to establish the optimal conditions to produce aluminum hydroxide flocs. To achieve this purpose, a great number of *Jar-Tests* were carried out, adding in the water samples variable dosages of lime, polyelectrolyte and aluminium chloride and changing the environmental conditions. The procedure used in the tests is made of the following steps: 1) addition of lime in the water (to correct the *pH* value) and its rapid mixing for 10 minutes; 2) addition of the polyelectrolyte solution, and its rapid mixing for at least 10 minutes; 3) addition of powdered aluminium chloride, and its slow mixing until the flocs are done.



Figure 1. View of the experimental channel.

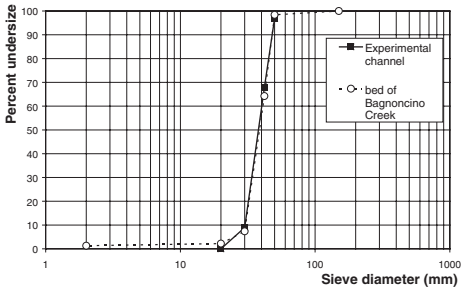


Figure 2. Grain size distribution of the sediments at bed of the Bagnoncino Creek and of the sediment used in the experiments.



Figure 3. Plain view of the removable tablet.

Copyright © 2006 Taylor & Francis Group plc, London, UK

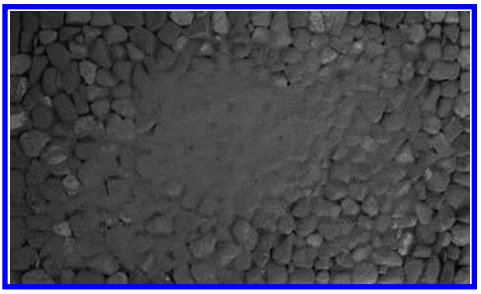


Figure 4. A top view of the contaminant on the table.

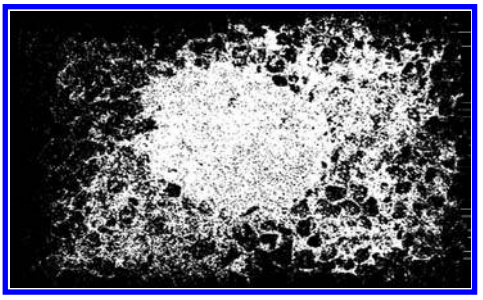


Figure 5. The output of the software.

The optimal conditions resulting from *Jar-Test* were the following: $pH = 9$; lime dose = 0.15–0.25 g/l; polyelectrolyte dose = 0.125 ml/l; aluminium chloride dose = 0.01 g/l.

2.2 *Pollutant production*

As above mentioned, the massive flocs production have taken place in the 1 m^3 tank, using the optimal conditions resulting from *Jar-Tests*. The procedure was carried on until the removable tablet was totally covered with flocs (Fig. 4). In addition, blue of methylene was added to colour the flocs, in order to be able to optically scan the variation of their concentration at bed.

2.3 *The photographic image acquisition*

At the end of the flocs production step, the wood tablet was removed from the tank and positioned at bed of the experimental flume. A digital camera was positioned at the top of the channel and snap shots were taken at regular time steps. Then, the pictures taken during each experiment were processed, by using a specific software, to identify the blue pixels associated with the pollutant presence. Given the dimensions of the pictures, it was possible to calculate both the pollutant quantity on the tablet and its variation in time due to the erosion processes originated from the shear stresses transmitted by the flow. Picture definition and luminosity were essential to be able to correctly process them by using the software. Some problems were encountered due to the presence of light reflections, the non uniformity of the water surface and the non homogeneous luminosity in the room. Thus, a correct alignment of the camera was necessary to avoid errors due to perspective. Furthermore, a black screen was positioned over the entire area to eliminate reflected light.

2.4 *The software*

The software determined the variations in blue from one shot to the following one, by comparing the corresponding pixels on the pictures. The colour information for each pixel is a 24 bit datum, ranging from black (value = 0) to very light blue (value = 255). The area with non zero values was calculated and monitored in time. A software filter was utilized to compare the single pixel datum with the adjacent ones in order to remove isolated black pixels due to light reflections or water waves at the surface, thus obtaining homogeneous areas of contaminant.

Afterwards, the value of each pixel was compared against a threshold value in order to obtain an output with only two colours. All pixels with values below the threshold value became black, and the rest were white. The threshold value falls in the range 25–28, and could be considered low enough to include also dark blue.

It is possible to show that the white area obtained by the procedure proposed perfectly corresponds to the area of the contaminant (Fig. 5).

2.5 *Hydraulic flow characteristics*

An *ADVP* was used to acquire the vertical distribution of mean local velocities along the channel axis. The number of longitudinal sections considered for measurements was 8, 20 cm spaced (Fig. 6). The range of the discharges used in the experiments was 20–85 l/s. Flow depths were also measured by using a point gauge with a *vernier scale*.

For *large-scale roughness* conditions, like those observed during the experiments, the shape of the flow velocity profile is affected by local phenomena developing near the bed. According to the experimental data of Bathurst (1988) and Marchand et al. (1984), velocity profiles could be considered *S-Shaped* when the velocities measured near the free water surface are noticeable greater than the ones measured near the bed.

The particular shape of the velocity profile is due to the existence of two different regions (Bathurst 1988): a *lower zone*, immediately over the boulders, in which the flow is delayed by drag effects due to the coarser elements; an *upper zone*, located above the boulders up to the free water surface, in which a quasi-smooth flow occurs (Morris 1959; Marone 1970).

According to Bathurst (1988), the development of a *S-Shaped profile* can be observed if: i) the value of the depth/sediment ratio is $1 \leq h/d_{84} \leq 4$; and ii) the size distribution of the bed materials is non uniform,

Copyright © 2006 Taylor & Francis Group plc, London, UK

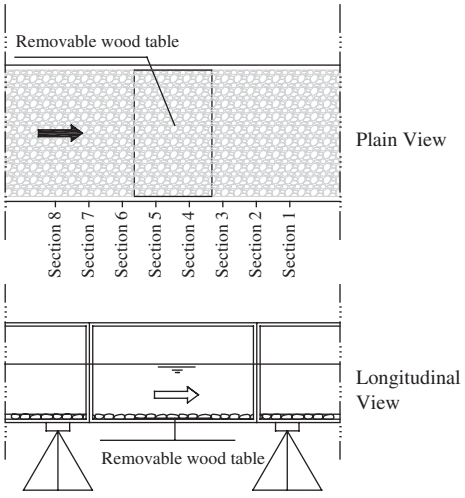


Figure 6. Schematic representation of experimental flume carrying the position of measurement cross-sections.

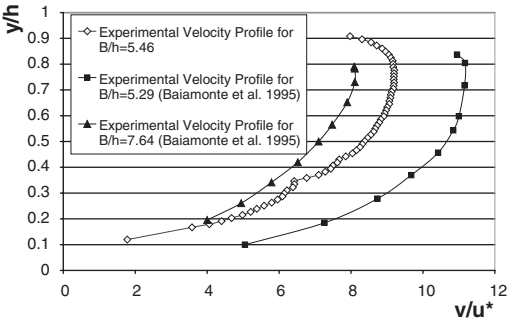


Figure 7. Experimental Velocity Profile in Section 1.

in order to allow the development of the lower zone flow (Baiamonte et al.1995).

In the cases examined, $d_{84} = 45$ mm and $h/d_{84} = 1.9 \div 3.2$.

As a matter of fact, the local velocity profiles were characterized mainly by the presence of a progressive transition to the *S-Shaped* form that is peculiar to gravel bed streams (Baiamonte et al. 1995; Nikora & Smart 1997).

With reference to the experimental data, the velocity profiles show a progressive transition to the *S-Shaped form*. This behaviour is confirmed by the observations.

As an example of experimental results, in Figure 7 is represented the vertical profile of local mean velocity at the cross-section n.1, corresponding to a flow rate $Q = 80$ l/s and a ratio $B/h = 5.46$. For comparison, the experimental results obtained in these conditions are plotted, in dimensionless form, together with those reported, by Baiamonte et al. (1995), for $B/h = 5.29$ and $B/h = 7.64$, respectively.

Table 1. Values of $q = Q/B$, Ks, u_*., τ_o, h

Q (l/s)	q (m^2/s)	K_s (m)	u_* (m/s)	τ_o (N/m^2)	h (m)
20*	0.0263	–	–	–	0.084
30	0.0395	0.055	0.0289	0.8328	0.097
40	0.0526	0.084	0.0495	2.4547	0.107
55	0.0658	0.098	0.0640	4.0956	0.116
60	0.0789	0.068	0.0796	6.3362	0.125
70	0.0921	0.081	0.0881	7.7605	0.134
80	0.1053	0.096	0.0944	8.9087	0.139
85*	0.1118	–	–	–	0.143

*For $Q = 20$ l/s and 85 l/s the velocity profiles are not available.

It seems evident that the vertical profile of local mean velocity is actually *S-Shaped*.

For large-scale roughness, the velocity distribution in the lower zone can be described by the following logarithmic profile:

$$\frac{u(y)}{u_*} = \frac{1}{k}\ln\frac{h}{K_s} + a \tag{1}$$

where y is the distance from the top of the bed, h is the flow depth, u_* is the shear velocity, $u(y)$ is the local mean flow velocity, K_s is the roughness height, $a = 8.48$ is the value frequently used for rough bed, and k is the Von Karman's constant, that can be assumed equal to 0.4 for low concentration field. Note that the values of u_* and K_s in the Eq. (1) are unknown, that have to be determined by experimental data.

Substituting the values of the constants a and k in the Eq. (1), it is possible to write:

$$\frac{u(y)}{u_*} = 5{,}75\log\frac{h}{K_s} + 8{,}48 \tag{2}$$

Referring to the present data, the velocity distribution (2) could be considered valid for $y\,u_*/v \geq 30$ and $y/h < 0.2$.

The best fit of the lower part of the velocity profiles along the channel axis and along each vertical was obtained by using the least square method.

The u_* and K_s values found by using this approach are listed in the Table 1. The K_s values are congruous with the ones reported in literature, included in the range 2-3 d_{50} (Becchi 1978).

The shear stress values τ_o were obtained considering the average of the u_* values, through the expression:

$$\tau_0 = \rho\, u_*^2 \tag{3}$$

where $\rho =$ density of the water at 20° C.

In Figure 8 are reported the τ_o and $q = Q/B$ values, where $B =$ width of experimental channel.

Copyright © 2006 Taylor & Francis Group plc, London, UK

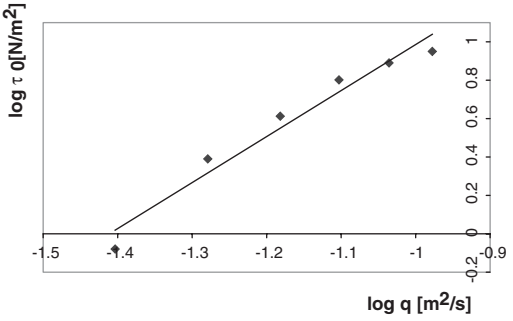


Figure 8. Relationship between τ_o and q.

The experimental relationship obtained between τ_o and q was:

$$\tau_o = 2404.4q^{2.3955} \cong 2400\ q^{2.4} \quad (4)$$

The τ_o values for $Q = 20$ l/s and $Q = 85$ l/s were obtained from the equation (4).

3 EVALUATION OF THE EROSION RATE

By using the technique described before, the erosion process of cohesive sediment vs time was evaluated for discharges $Q = 20$, 40, 55, 70 and 85 l/s (Fig. 9).

It appeared that the resistance to the erosion increases with decreasing bulk density of the pollutant. In fact, the initial erosion rate of sediment at the bed is high and it concerns the first layer, where the bulk density of the contaminant is low. Then, after a time t_c that could be considered to be constant for all the experiments, the erosion rate decreases. This behaviour could be explained considering that the lower layers, after compaction and loss of water, oppose higher resistance to the action of flow.

Vice versa, in the layers near the bed the strength of the flocs might be more and, thus, the erosion could be more difficult.

In the first phase, the erosion could be considered as exponentially decreasing with time, while in the second phase it seems to be linear.

Between the two phases, there is a kind of plateau, that might be explain as a stabilization phase where the flocs, notwithstanding the stresses induced by flow, are not removed. After a few time, the steady action of the flow weakens the links between the flocs (Partheniades 1965), and erosion can start again, though with lower rate.

It appears that the area of contaminant decreases with increasing of the value of discharge and at 85 l/s almost all the contaminant is eroded.

At the discharge $Q = 20$ l/s, the contaminant eroded was very little and, therefore, this condition was taken

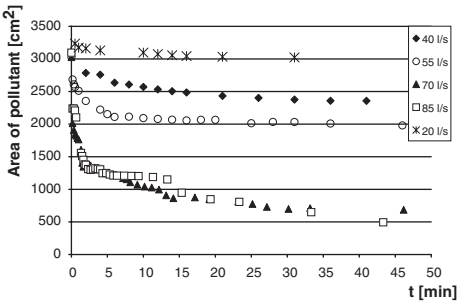


Figure 9. Area of cohesive sediments remaining on the tablet vs time.

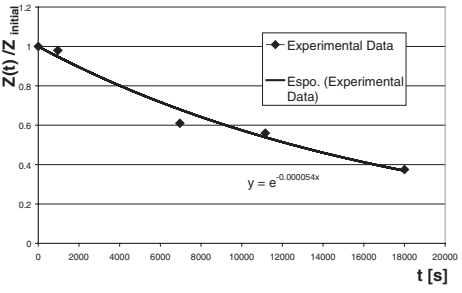


Figure 10. Variation of $Z(t)$ vs time.

as the value of the critical discharge, or condition for the *first breakaway*. The corresponding shear stress value is $\tau_{o,cr} = 0.39$ N/m^2.

To obtain the variation in concentration over time, it was necessary to calculate the volume eroded in time:

$$V(t) = A(t) \cdot Z(t) \quad (5)$$

where $V(t) =$ volume of pollutant eroded in time; $A(t) =$ area of pollutant eroded in time; $Z(t) =$ pollutant thickness.

The following law was chosen to represent the area variation in time:

$$A(t) = \frac{A_0}{(1 + t/t_\alpha)^\beta} \quad (6)$$

where $A_o =$ area of pollutant at the time zero, t_α and β are unknown parameters.

The parameters t_α and β were calculated using the experimental values of $A(t)$ evaluated in the time interval $[t = 0,\ t = t_c = 50$minutes], when the erosion rate is greatest.

According to the experimental results of Winterwerp & Kranenburg (1997), which used suspensions of kaolin, the behaviour of $Z(t)$ was considered to be a decreasing exponential function. The trend considered for following evaluations is represented in Figure 10, where the dimensionless ratio $Z(t)/Z_{initial}$ vs. time is plotted, together with a few experimental values.

Copyright © 2006 Taylor & Francis Group plc, London, UK

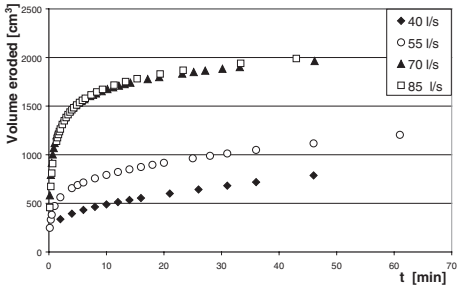


Figure 11. Variation of volume eroded vs. time.

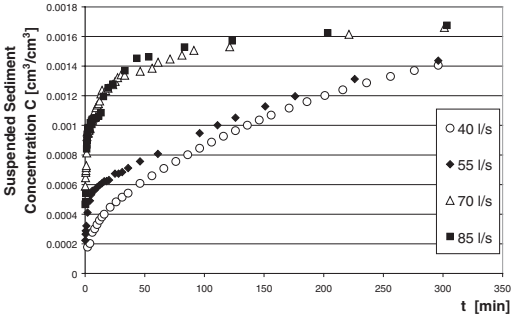


Figure 12. Suspended sediment concentration C vs time.

By comparing these results with those of Winterwerp & Kranenburg (1997), it is possible do observe that the aluminum hydroxide flocs show an erosion rate significantly lower than the kaolin, due to the differences existing in interacting forces between the particles.

In Figure 11, the variation of the calculated volume V vs time is represented for the present data:

The trend is similar to that given by Kuti & Yen (1976) for kaolin.

In order to compare to the results obtained from the experiments with those by Patheniades & Metha (1965) and of Metha & Parchure (1985), it was also evaluated the concentration of eroded material with time (Fig. 12).

It is possible to observe that the suspended sediment concentration increases with time. The rate of increasing is greater in the first phase; then, the curve tends to a constant value, because the shear stress of the flow doesn't overcome the shear stress of the cohesive soil. In particular, for $Q = 70$–85 l/s, at the end of the test, all the contaminant initially present at bed of the flume was eroded.

4 CONCLUSIONS

The main objective of this work was the evaluation of the hydraulic conditions needed to have removal, by currents flowing in a stream, of a specific cohesive sediment (*aluminum hydroxide flocs*), for which seem not available literature data.

The first difficulty was the lack of solidity of the *flocs* considered in the experiments. For this reason, it was not possible to utilize the traditional procedures of measurement. So, a new procedure was used, based on the acquisition and processing of photographic images during sediment removal. The results of area eroded, volume eroded and suspended sediment variation of concentration were consistent with the physical phenomenon and congruous with the results of literature.

However, in order to evaluate in a more rigorous way the cohesive sediment erosion, it is necessary to reproduce a greater number of experiments. Moreover, it can be interesting to repeat the tests with other types of flocs at different time of consolidation to evaluate the relationship between the time of consolidation and the capability of erosion of the flow.

By comparison with the results obtained by other researchers, it is possible to assert that the new procedure proposed, based on the acquisition and subsequent processing of photographic images taken during sediment removal processes, gives solutions consistent with the results reported in literature, and then seems suitable for studying the removal of both cohesive and granular sediments at bed of rivers and channels.

REFERENCES

Baiamonte, G., Giordano, G. & Ferro, V. 1995. Advances on velocity profile and flow resistance law in gravel bed rivers. *Excerpta*; 9: 41–89.

Bathurst, J.C. 1988. Velocity profile in high gradient, boulder bed channels. Proc. International Conference on Fluvial Hydraulics, Budapest.

Becchi, I. 1978. Considerazioni sulla scabrezza dei letti granulari piani (in italian). *L'Energia Elettrica*, 11–12: 493–503.

Ferro, V. & Baiamonte, G. 1994. Flow Velocity Profiles in Gravel-Bed Rivers. Proc. ASCE *Journal of Hydraulic Engineering*; 120, 1: 60–80.

Kuti, E.O. & Yen, C.L. 1976. Scouring of cohesive soils. *Journal of Hydraulic Research*, 14, 3: 195–207.

Marchand, J.P., Jarret, R.D., Jones, L.L. 1984. Velocity profile, watersurface slope, and bedmaterial size for selected streams in Colorado. Open File Report 84773, U.S. Geological Survey.

Marone, V. 1970. Le resistenze al movimento uniforme in un alveo chiuso o aperto di sezione rettangolare e scabrezza definita (in italian). *L'Energia Elettrica*, n. 1.

Morris, H.M. 1959. Design methods for flow in rough conduits, Proc. ASCE, HY7, 85.

Partheniades, E. 1965. Erosion and Deposition of cohesive soils, Proc. ASCE *Journal of the Hydraulics Division Proceedings of the American Society of Civil Engineers*, HY1,91: 105–139.

Winterwerp, J.C. & Kranenburg, C. 1997. Erosion of Fluid Mud Layers. II: Experiments and Model Validation, *Journal of Hydraulic Engineering*, 123,6: 512–519.

Copyright © 2006 Taylor & Francis Group plc, London, UK

Modeling granular sediment transport over water worked gravels within a CFD framework

R.J. Hardy
Department of Geography, Science Site, South Road, Durham, UK

ABSTRACT: A numerical description of the hydraulics and sediment transport processes operating in a fluvial environment is far from complete due to the complex interactions between form, flow and sediment transport. Near bed turbulence determines the dynamics of sediment transport, however an analytical description of turbulent flow and sediment transport is subject to significant errors due to the poor parameterization of physical processes and that mean boundary shear stress is frequently determined from velocity profiles. This paper reports a numerical model that calculates the transport paths of individual granular particles over a natural water worked gravel surface. Surface topography is measured using digital photogrammetry and incorporated into a computational fluid dynamics (CFD) scheme by the application of a porosity algorithm. The predicted hydraulics determines the forces acting on each particle enabling the particle trajectory to be solved by Langrangian transport equations. The methodology demonstrates the importance of including complex topography in the numerical scheme as topographically induced hydraulic acceleration and deceleration affect both the transport mechanism and subsequent trajectory of the particle.

1 INTRODUCTION

A numerical description of the high spatial resolution hydraulics and sediment transport processes operating in a gravel bed river is far from complete due to the complex interactions between form, flow and sediment transport. The heterogeneous structure of the gravel bed determines both the turbulence and sediment transport dynamics and subsequent development of bed forms through a series of complex feedback processes (Clifford et al. 1992; Ashworth, 1996). An analytical description of turbulent flow and sediment entrainment, transport and deposition is subject to significant errors due to the poor parameterisation of physical processes (McEwan & Heald, 2001). One reoccurring limitation is that velocity profiles are frequently used to determine the mean boundary shear stress (McLean et al. 1999) which may be inadequate to describe the effect of bed roughness on flow characteristics (Papanicolaou, 2001). Such averaging obscures the complex, nonlinear interaction of wake decay, boundary-layer development and topographically induced acceleration and deceleration which leads to an inaccurate estimate of boundary stress, particularly skin friction, which is essential in sediment transport. This is especially true for gravel bed rivers which have complex surfaces (Clifford et al. 1992; Butler et al. 2002; Lane et al. 2004), where the flow depth is unusually shallow in relation to the height of the morphological form. In such shallow flows the detailed micro-topography of the bed exerts a significant effect on the flow (Wiberg & Smith, 1991). Moreover, entrainment and motion of sediment grains are driven by fluctuating instantaneous lift and drag forces. These events depend on the flow structures acting on the particle, in as much as they correlate poorly with measurements made upstream of, or over the particle (Nelson et al. 2001). Thus, they are determined by both the particle exposure to the flow and the pocket geometry of the particle.

Granular material can be transported either by: (1) suspension, an advanced stage of transport (Graf 1988) where the particles are rarely in contact with the bed; (2) saltation, the unsuspended transport of particles in the form of consecutive hops within the near bed region which is generally considered the dominant mode of bed load transport (Nino & Garcia, 1994) and; (3) rolling and sliding which occur to a lesser extent mainly near the threshold of entrainment and in between individual saltation events (Bridge & Dominic, 1984). Previous research has indicated that saltation dominates the majority of bed load transport (Sekine & Kikkawa, 1992; Wiberg & Smith 1989) and flume experiments using photogrammetric techniques have been used to understand saltation processes and determined saltation characteristics (e.g. Sekine &

Copyright © 2006 Taylor & Francis Group plc, London, UK

Kikkawa, 1992; Abbot & Francis, 1977; Drake et al. 1988; Nino et al. 1994). Through this processes understanding semi-empirical relationships of saltation characteristics have been calculated (Bagnold 1973; Bridge & Domic, 1984; Bridge & Bennett, 1992), enabling the development of generalised bed load equations. These have been used in the development of numerical models to predict particle saltation in water (Wiberg & Smith, 1989; Sekeine & Kikkawa, 1992). The most frequently used approach has been the application of Langrangian equations to predict particle motion (e.g. Van Rijn, 1984; Wiberg & Smith, 1985, 1989; Nino & Garcia, 1994; Lee & Hsu, 1994; Sekeine & Kikkawa, 1992). These have previously been applied to gain an understanding of the kinematic and geometric characteristics of the particle saltation process, including saltation length, height and particle velocity, which have all agreed well with experimental results.

The reoccurring limitation with all these individual particle based transport models is that the hydraulic representation is calculated by averaged velocity profiles over a homogenous bed. The topographically forced flow introduces a random element into sediment entrainment which in the past has required a probabilistic approach to problem (Grass, 1970).

However, if the complex topography can be included in the numerical model the probabilistic nature of sediment transport may be reduced. Recent research in computational fluid dynamics (CFD) has developed a mass flux scaling algorithm based upon a cell porosity approach (Lane et al. 2004; Hardy et al. 2005) that enables the prediction of both the time averaged hydraulics over a water worked gravel surface (Lane et al. 2004) and the prediction of time dependent flow by the application of Large Eddy Simulation (Hardy & Lane, 2004). The development of this method has allowed an understanding of the way in which a complex gravel-bed surface interacts with the associated 3D flow field. Furthermore it provides a high resolution prediction of the hydraulic forces acting on each individual particle. Here a sediment transport model is described where individual particle motion is mathematically modelled through trajectories based on Langrangian equations driven by hydraulic forces calculated from a CFD scheme.

2 METHODOLOGY

2.1 *The hydraulic scheme*

The numerical solution is three dimensional and based upon a finite volume approach. The incorporation of complex micro-topographies (individual particles) within such a CFD scheme has been problematic to date as the representation of large-scale topographic features has required the application of boundary fitted co-ordinates (BFCs). Here we apply an alternative approach which has recently been developed for incorporating complex river-bed topographies into regular structured meshes, without the need to use boundary fitted co-ordinates (Lane et al. 2004; Hardy et al. 2005). It uses a porosity based method based upon the methodology proposed by Olsen & Stokseth (1995) and involves the use of regular structured grid, in which all control volumes are orthogonal in both computational and Cartesian space, with the bed topography specified using cell porosities. The porosity algorithm for the flow treatment used has previously been reported, demonstrated and validated against Acoustic Doppler Velocimetry (ADV) for the case of time-averaged flow over rough gravel beds (Lane et al. 2004) and digital Particle Imaging Velocimetry (DPIV) data as applied to an irregular arrangement of cuboidal roughness elements (Hardy et al. 2005). The hydraulics calculated using this approach are then applied to drive a sediment transport scheme which is outlined below.

2.2 *The sediment transport scheme*

The model determines the particle transport trajectory and velocity, in a Lagrangian framework, by:

$$\frac{\partial x_p}{\partial t} = U_p \tag{1}$$

where x_p = particle position; and U_p = particle velocity. The particle velocity is calculated by a particle momentum equation:

$$m_p \frac{\partial U_p}{\partial t} = D_p(U - U_p) + m_p g - V_p \nabla_p \tag{2}$$

where m_p = particle mass; D_p = drag function; U = the continuous-phase instantaneous velocity ($U = U_c + U_c'$, where U_c = continuous-phase average velocity; and U_c' = turbulent fluctuation component), g = gravity; V_p = particle volume and; ∇_p = continuous-phase pressure gradient. The drag function (D_p) assumes that the particles are spherical and calculated by:

$$D_p = \frac{1}{2}\rho A_p C_D |U - U_p| \tag{3}$$

where A_p = particle projected area and; C_D = the drag coefficient.

The effect of turbulent fluctuations on a particle's trajectory is calculated with a stochastic turbulence model which applies a Reynolds decomposition approach. The fluctuating component is calculated assuming a normal distribution with a mean of zero and a standard deviation of $\sqrt{2k/3}$, where k is the

Copyright © 2006 Taylor & Francis Group plc, London, UK

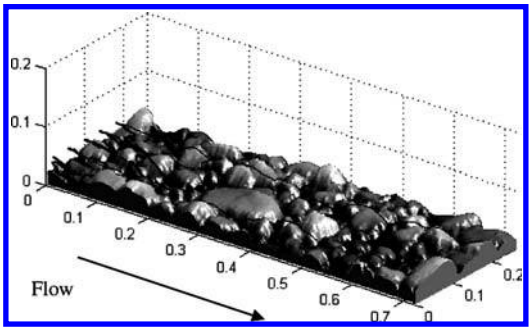


Figure 1. The trajectories for particles with 0.5 mm and 2 mm diameters for a flow velocity of 0.435 ms^{-1}.

turbulence kinetic-energy. The fluctuating component U_c' acts over a time interval which is defined as the minimum lifetime of the local eddy which the particle is traversing (Ludwig et al. 2004).

Interaction with bed topography is presently based upon the application of a restitution coefficient. In this application a value of 0.5 is used as it the mid value of the data of Wiberg and Smith (1985). Finally a stagnation criterion is applied where the particle trajectory will stop being calculated if the particle has fallen into a hydraulically stagnant region which is based on a pre-defined criterion based on zero movement over a number of iterations. The bed topography (through the porosity algorithm) is then modified as it is assumed that the particles have been deposited. At present only spherical particles are considered and the Basset and the Magnus forces are not resolved.

2.3 *Experimental set-up*

The topography and hydraulic predictions used here are based upon unpublished flume experiments. A bulk sample of sediment from the River Wharfe, northern England was placed in the flume and water worked until a stable bed (no sediment transport) was obtained. The surface morphology was measured using digital photogrammetry. Figure 1 shows the final DEM, a 0.76 m by 0.26 m gravel surface with a vertical precision of ±0.002 m. The gravel DEM is incorporated into a computational mesh on a resolution of 0.002 × 0.002 × 0.002 meters (361 × 130 × 100 = 4 693 000 grid cells).

For the experiments a water depth of 0.2 meters was maintained above the bed of the flume. Three different flow conditions were considered with the downstream velocity at 0.4 z/h being 0.155 ms^{-1}, 0.3 ms^{-1} and 0.435 ms^{-1}. Table 1 summarizes the hydraulic conditions used in the study. Velocity measurements were obtained using a two-dimensional digital Particle Imaging Velocimetry (2D DPIV). The DPIV methodology applied here is identical to that applied by Hardy et al. (2005) and is used to provide inlet boundary conditions as well as to validate the hydraulic scheme.

Table 1. The hydraulic condition used in the experiments.

Flow velocity (ms-1)	0.155	0.300	0.435
Flow depth (m)		0.200	
Flume width (m)		0.300	
Froude number (–)	≈0.11	≈0.21	≈0.31
Reynolds number (–)	≈13 000	≈25 000	≈37 000

Particles enter the domain at the inlet at prespecified locations where the initial particle velocity is dependent upon the hydraulic inlet boundary conditions. In each case the particle is assumed to be spherical and quartz (density 2650 kgm^{-2}). Each particle trajectory is tracked until it either leaves the domain through the outlet or is deposited. If the particle is deposited the bed elevation is modified through the porosity algorithm.

3 RESULTS

As discussed above the hydraulic methodology has previously been applied on several different examples. Therefore, in this paper only the sediment dynamics are reported.

Figure 1 demonstrates 10 predicted particle trajectories released from 5 locations for the 0.435 ms^{-1} experiment. Two separate experiments were undertaken, the first with a particle size of 2 mm and the second with a particle size of 0.5 mm. Each particle was assigned an initial velocity associated with the inlet velocity at the x, y, z-location. In this experiment only two particles reach the end of the domain, both 0.5 mm particles, with none of the 2 mm particles traveling more than 0.25 cm (0.36 x/l). The two particles which reach the end of the domain show very similar transport characteristics. The particles are transported by the combination of two processes; initially the particle bounces through a saltation process which then lifts the particle into a skimming flow formed above the largest protruding bed particles. The product of these processes are elongated hydraulically induced hops. For example, 0.4 meters down the domain from the inlet both particles move into separate hollows behind a large clast, the particle bounces on impact with the bed and is then entrained over the clast by a primary vortex (Hunt et al. 1978) and incorporated into a hydraulically skimming flow over the largest bed form. A more classical saltation processes can be observed for the particle at ≈0.2 across the domain where the particle saltates down the bed form. In this case the particle does not rebound high enough in the flow, or the hydraulics are not sufficient, to induce one of the hydraulically induced hops, as observed earlier.

Copyright © 2006 Taylor & Francis Group plc, London, UK

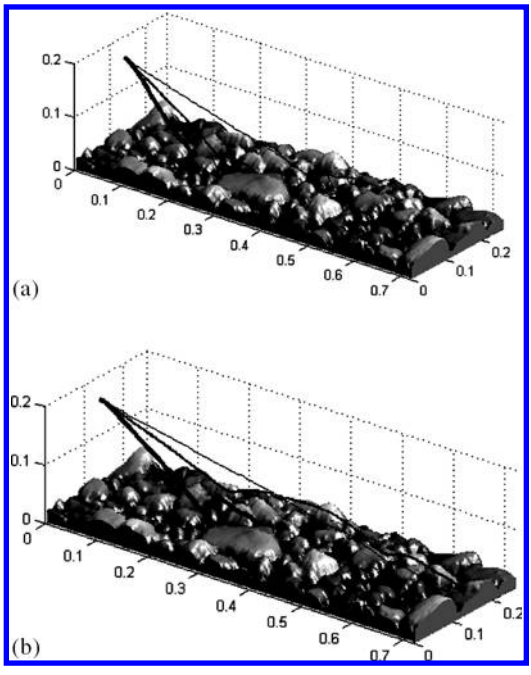


Figure 2. The trajectories for 0.5 mm, 1 mm and 2 mm particles for flow velocity of (a) 0.30 ms^{-1} and (b) 0.435 ms^{-1}.

The 2 mm particles show similar characteristics by entrainment into primary vortices at 0.1 m (0.14 x/l) location where the particles are lifted, with a sharp vertical gradient, up and over the bed form (micro topography). However, these two particles, as with the other 2 mm particles they are deposited in a short space within a hydraulically sheltered region. Although the transport distance is not that significant, the hydraulically induced hop shows the importance of including complex topography within an integrated hydraulic-sediment transport scheme.

Figures 2a & b demonstrate the predicted trajectories from a single point for the 0.5, 1 and 2 mm particles for both the 0.3 and 0.435 ms^{-1} experiments. It is acknowledged that the starting point for the particle is unnaturally high in the flow, however the results in Figure 1 demonstrated that transport distances were not that great if the particle starting point was in the bottom 25% of the flow depth. This starting point was deemed necessary to test the different transport mechanisms. For all 6 particles the initial trajectories are the particles tending towards an equilibrium height with the surrounding hydraulics. Therefore, the transport mechanism is a reflection of the initial conditions. If the 2 mm particles are studied (thick lines), considerable differences between the particle trajectories for 0.435 ms^{-1} and 0.3 ms^{-1} experiment can be observed. As would be expected the particle in the 0.435 ms^{-1} experiment collides with the bed further downstream than the 0.3 ms^{-1} experiment. In both cases the particles fall into hydraulically sheltered regions between large clasts. Both particles have the same restitution coefficient so their outward post collision velocity is of the same order of magnitude. However, the subsequent particle transport mechanism depends dramatically depending on the flow velocity. For the 0.435 ms^{-1} the particle is entrained by a tertiary vortex into a shear flow and over a clast before being deposited within another hydraulically sheltered region. However, in the 0.3 ms^{-1} experiment the hydraulics are not sufficient to induce the hydraulic hop and the particle is forced around the clast, potentially by a horseshoe vortex, in a hydraulically driven saltation process. The particle trajectories for the 1 mm particles show some similarities to the 2 mm particles. For example, the 1 mm particle in the 0.3 ms^{-1} experiment follows a similar mode of transport to the 2 mm particle in the 0.435 ms^{-1} experiment, the particle initially falls in a hydraulically sheltered region and then is transported by a hydraulically induced hop. The particle then falls into another hydraulically sheltered region, rolls back down the slope of the particle and is deposited. However, the 1 mm particle in the 0.435 ms^{-1} experiment takes a completely different transport path, where after an initial collision the bed the particle travels in a long elongated hop ($\approx$0.4 meters) in the skimming flow over the bed. Then after a final collision the particle leaves the domain. For the 0.5 mm particle in the 0.435 ms^{-1} experiment the initial starting point is such that it travels completely out the domain with only minimal contact with the bed at 0.6 m downstream (0.85 x/l). For the 0.5 mm particle in the 0.3 ms^{-1} experiment the particle, after its first contact with the bed is entrained by localised flow structures before being deposited.

The particle trajectories are explored further by dissecting them into the particle height and the particle's vertical (w-) velocity component for the 1 mm and 2 mm particles. These are shown in Figure 3. If the 2 mm particles are considered first both particles can be seen to be falling towards the bed with a vertical velocity of -0.4 ms^{-1} until each particle collides with the bed. At this point, both particles show an instantaneous change in the particle w-component as they bounce off the gravel surface. For the 0.3 ms^{-1} experiment the particle, as observed in Figure 2, is transported around in a confined hydraulically sheltered region, with the particle transport characteristics showing rapid changes in both velocity and transport distance. This is expanded further in Figure 4. The particle in the 0.435 ms^{-1} experiment impacts the bed and there is a dramatic increase in the w-component. This momentum is sufficient to lift the particle into a region where the hydraulic forces are sufficient to continue particle motion downstream. This is in a series of hydraulically induced hops which can be

Copyright © 2006 Taylor & Francis Group plc, London, UK

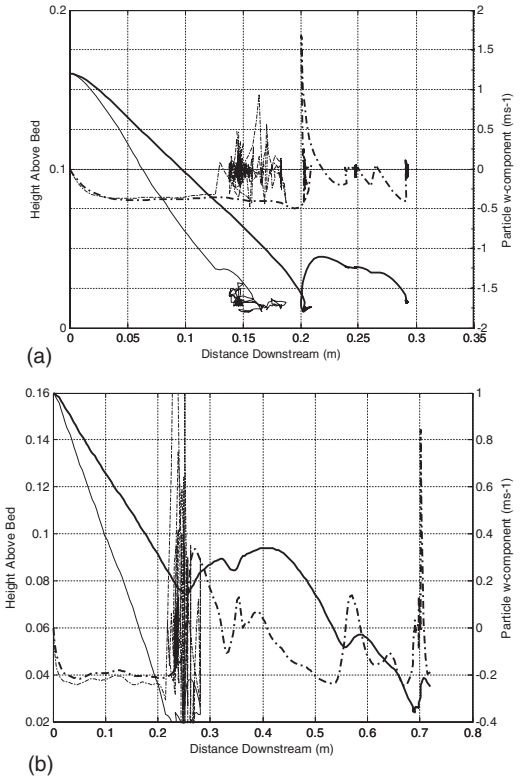


Figure 3. The particle trajectories represented through particle height and particle vertical velocity. Thick lines represent 2 mm particles while the thin lines 1 mm particles. Solid lines represent particle height while dashed lines represent particle velocity. (a) The particle trajectories for the 0.435 ms^{-1} experiment. (b) The particle trajectories for the 0.3 ms^{-1} experiment.

observed in both the height above the bed and in the *w*-velocity component. There is no consistent pattern in the profile of these saltation hops in terms of height above the bed or particle velocity due to the changing local hydraulics. A similar pattern is observed for the 1 mm particle, the particle trajectories for the 0.3 ms^{-1} experiment reflect that of the 2 mm particle and the same is true for the 0.435 ms^{-1} experiment. Although no definite conclusions can be drawn on the pattern of sediment transport from the examination of one particle there possibly could be a change in processes observed in sediment transport between the 0.3 and 0.435 ms^{-1} experiments.

Figure 4 demonstrates some more localised processes of granular sediment transport that has been observed above. The figure shows a view down the DEM from the inlet. The particle is transported in a localised area of low flow and a region of possible deposition in front of a large pebble. However the

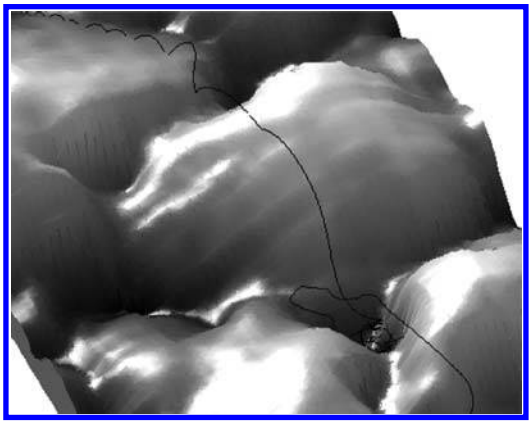


Figure 4. The localized sediment dynamics. The graph shows the particle trajectory from the inlet.

localised hydraulics in front of the particle, a possible suppressed saddle point vortex (Hunt et al. 1978), transport the particle within a confined area until a tertiary vortex (Hunt et al. 1978) entrains the particle into the shear flow over the particle into a hydraulically induced hop. This demonstrates the spatial variability and the processes gradients operating in these environments. It is demonstrated that a spatial difference of millimetres can affect the forces acting on the particle and the possible transport mechanism. Once the particle transported over the large clast the transport mechanism changes to saltation and the particle moves down slope.

4 DISCUSSION

The results demonstrate the importance of microtopography for the generation of localised flow structures, which in turn determine the transport direction of the particles as well as the associated transport mechanisms. In none of the experiments did a particle travel the full length of the experiment by saltation. This is not that surprising due to the difference in size between the transported particles and the particles on the bed. However, transport paths are observed which have similar trajectories to saltating particles although they are driven by different mechanisms. In this transport mechanism the particle collides with the bed and bounces, or local vortex structures lift the particle until it is entrained into a shear layer over an individual particle. They are therefore hydraulically induced. This mechanism can not be defined as saltation, which Bagnold (1973) described as the unsteady suspended transport of particles by fluid flow, in the form of consecutive hops, in which no upward impulses are imparted to the particle other than those attributed to successive contacts between them and the

Copyright © 2006 Taylor & Francis Group plc, London, UK

bed. This implies that hydrodynamic lift is not important in the saltation process and rules out the effect of turbulence as the mechanism to sustain saltation (Nino et al. 1994). However, these results have demonstrated that the saltation process can be re-started by localised hydraulic forces in that after a hydraulically induced hop, the particle can saltate if the bed topography is smooth enough.

The model presented herein provides a new methodology to determine the role of micro-topographical forcing of flow and turbulence in a fluvial environment. The localised interactions have been demonstrated to determine both the transport mechanism and its dynamics.

ACKNOWLEDGEMENT

RJH was funded under NERC fellowship NER/J/S/2002/00663.

REFERENCES

Abbot, J. & Francis, J. 1977. Saltation and suspension trajectories of solid grains in a water stream. *Philos. Trans. R. Soc. London, Ser. A* 284: 225–254.

Ashworth P.J. 1996. Mid-channel bar growth and its relationship to local flow strength and direction. *ESPL*. 21: 103–123.

Bagnold, R.A. 1973. The nature of saltation and of 'bed-load' transport in water. *Proc. of the Roy. Soc. of London, A* 332: 473–504.

Bridge, J. & Bennett, S. 1992. A model for the entrainment and transport of sediment grains of mixed sizes, shapes, and densities. *Water Resour. Res*. 28: 337–363.

Bridge, J. & Dominic, D. 1984. Bed load grain velocities and sediment transport rates. *Water Resour. Res*. 20: 476–490.

Butler, J.B., Lane, S.N. Chandler, J.H. & Porfiri, K. 2002. Throughwater close-range digital photogrammetry in flume and field environments, *Photogramm. Rec*. 17: 419–439.

Clifford, N.J., Robert, A. & Richards, K.S. 1992. Estimation of flow resistance in gravel-bedded rivers: A physical explanation of the multiplier of roughness length. *ESPL* 17: 111–126.

Drake, T., Shreve, R. Dietrich, W., Whiting, P & Leopold, L. 1988. Bedload transport of fine gravel observed by motion picture photography, *J. Fluid Mech*. 192: 193–217.

Graf, W.H. 1988. *Fluvial Hydraulics: Flow and transport processes in channels of simple geometry*. John Wiley and Sons, Chichester.

Grass, A.J. 1970. Initial instability of fine bed sand, *J. of Hydr. Eng. ASCE* 96: 619–632.

Hardy, R.J. & Lane, S.N. 2004. The numerical simulation of time dependent flow structures over water worked gravel. (A2-116). In *River Flow 2004*, Greco M, Carravetta A, Della Morte R. (Eds). Second International Conference on Fluvial Hydraulics Department of Hydraulic and Environmental Engineering Girolamo Ippolito University of Napoli Federico II Naples, Italy. p235–245.

Hardy, R.J., Lane, S.N. Lawless, M.R., Best, J.L., Elliot, L. & Ingham, D.B. 2005. Development and testing of numerical code for treatment of complex river channel topography in three-dimensional CFD models with structured grids. *Journal of Hydraulic Research* 43: 468–480.

Hunt, J.C.R., Abell, C.J., Peterka J.A. & Woo, H. 1978. Kinematic studies of the flow around free or surface mounted obstacles; applying topology to flow visualization. *Journal of Fluid Mechanics* 86: 179–200.

Lane, S.N., Hardy, R.J., Elliot, L. & Ingham, D,B. 2004. Numerical modelling of flow processes over gravelly-surfaces using structured grids and a numerical porosity treatment. *Water Resourc. Res*. 40: W01302.

Lee, H.Y. & Hsu I.S. 1994. Investigation of saltating particle motions, *J. of Hydr. Eng. ASCE*. 120: 831–854.

Ludwig, J.C., Fueyo, N. & Malin, M.R. 2004. The GENTRA User Guide (Version 3.6). Documentation for PHOENICS TR 211. Published by CHAM.

McEwan, I. & Heald, J. 2001. Discrete particle modelling of entrainment from flat uniformly sized sediment beds. *J. Hydr. Eng. ASCE* 127: 588–597.

McLean, S.R., Wolfe, S.R. & Nelson, J.M. 1999. Predicting boundary shear stress and sediment transport over bed forms, *J. Hydr. Eng ASCE* 125: 725–736.

Nelson, J.M., Schmeeckle, M.W. & Shreve, R.L. 2001. Turbulence and particle entrainment. In: *Gravel Bed Rivers V*. M.P. Mosley (Ed). New Zealand Hydrological Society, 221–248.

Nino, Y. & Garcia, M. 1994. Gravel Saltation 2: modelling. *Water Resourc. Res*. 30: 1915–1924.

Nino, Y., Garcia, M. & Ayala, L. 1994. Gravel saltation, 1, Experiments. *Water Resour. Res*. 30: 1907–1914.

Olsen, N.R.B. and Stokseth, S. 1995. Three-dimensional numerical modelling of water flow in a river with large bed roughness. *J. Hydr Res*. 33: 571–81.

Papanicolaou, A.N., Diplas, P., Dancey, C.L. & Balakrishnan, M. 2001. Surface roughness effects in near-bed turbulence: Implications to sediment entrainment. *J. Engin. Mech. ASCE* 127: 211–218.

Sekine, M. & Kikkawa, H. 1992. Mechanics of saltating grains, 2. *J. Hydr. Eng. ASCE* 118: 536–558.

Van Rijn, L.C. 1984. Sediment transport, 1: Bedload transport, *J. Hydr. Eng. ASCE* 110: 1613–1641.

Wiberg, P.L. & Smith, J.D. 1991. Velocity distribution and bed roughness in high gradient streams. *Water Resour. Res*. 27: 825–838.

Wiberg, P. & Smith, J. 1985. A theoretical model for saltating grains in water. *J. Geophys. Res*. 90(C4), 7341–7354.

Wiberg, P. & Smith, J. 1989. Model for calculating bed load transport of sediment, *J. Hydr. Eng*. 115: 101–123.

Copyright © 2006 Taylor & Francis Group plc, London, UK

The beginning of sediment transport – A different approach

R. Aleixo & R. Maia
Departamento de Engenharia Civil, Faculdade de Engenharia da Universidade do Porto Rua, Porto, Portugal

ABSTRACT: The beginning of motion of particles at the bottom of a water channel is a result of a rather complex interaction between the flow and the particles. Using a simplified bed model it is possible to easily study and isolate the interactions between the flow and the bed and to better define the conditions leading to the beginning of bed particles motion. A theoretical approach that takes into account the different parameters such as support angle and turbulence intensity, is presented and compared with the Shields diagram and experimental results. This study is the first phase of a broader research project in course who aims to better understand and explain the beginning of sediment particles motion.

1 INTRODUCTION

Aiming to study the interaction between the flow and the channel bed, a simple model was developed in order to allow a proper description of that interaction in terms of its physics. Some assumptions were made and based on the known results of the boundary layer theory.

This work summarizes the first stage of a broader research project in course at the Hydraulics Laboratory of Faculty of Engineering of Porto University, currently focused at the study of the flow around a single particle, aiming to be used in future work to characterize the interaction between particles.

2 CONCEPTUAL MODEL

The bed model studied consists on a flat and horizontal plate in which a localized two-particles' width bed, with the full transverse length of the water channel was provided, as depicted in Figure 1. Over this bed of particles, at the channel axis, a single particle was placed. The particles that support that single particle will be from now on referred as supporting particles and the single particle will be designated as test-particle. This model consists in a simplification of one presented by (Nezu and Nakagawa 1993).

There are two possible 3D configurations to support the test-particle: a three- or a four-particles bed arrangement. For this analysis the test-particle is assumed to be supported by a four particles bed arrangement with the centres of the five spheres forming a square-based pyramid as shown in Figure 2. It can be shown that the maximum height of the sphere is $h_{1t} = d/\sqrt{2}$ and that the support angle is $\theta = \text{atan}\,\sqrt{2}/2 = 35.26°$ (as depicted on Fig. 2).

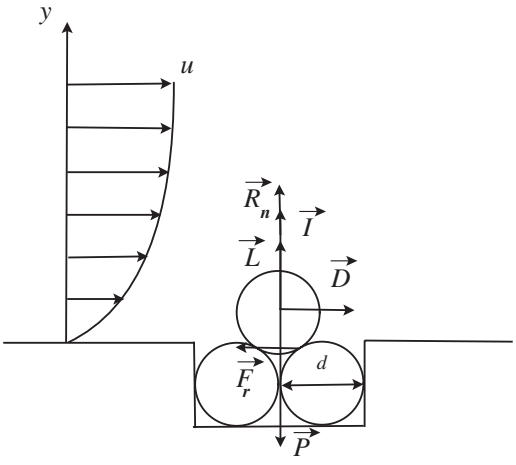


Figure 1. Simplified bed model. A test-particle, with the same diameter as the ones of the bed is immersed on a flow with a velocity profile $u = u(y)$. The forces acting on a particle (referred as test-particle) are the weight $\vec{P}$, the drag $\vec{D}$, the lift $\vec{L}$, the buoyancy $\vec{I}$, the normal reaction $\vec{R}_n$, the friction force $\vec{F}_r$, and d is the particle's diameter.

For this simple model theoretical hypothesis regarding the beginning of motion were assumed:

1. the flow is processed over a flat smooth bed until it reaches the test-particle.
2. the flow is bidimensional and developed, so that the longitudinal component, u, is much larger

Copyright © 2006 Taylor & Francis Group plc, London, UK

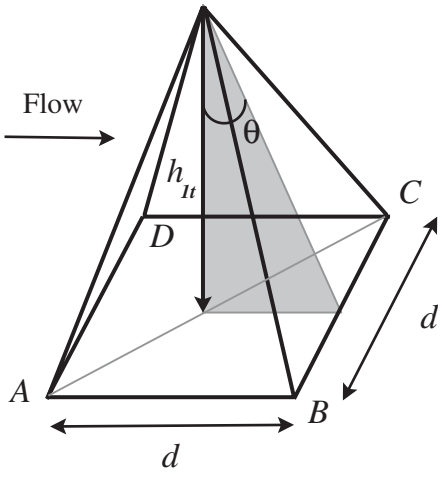


Figure 2. A squared based pyramid results from the four-spheres support arrangement considered in this study, being θ the supporting angle. Flow direction is perpendicular to the segment AD.

than the vertical and transversal components v and w, respectively;

3. the boundary-layer is limited to a narrow region near the bed, so that the test-particle may be considered, in this approach, immersed in a uniform stream, of velocity U_∞;
4. outside the boundary layer, the turbulence intensity profile will be assumed constant (Hinze 1975);
5. the flow is fully established;

2.1 *Analysis of the forces acting on the test-particle*

The forces acting on the test-particle are the following (considering an horizontal plate) are:

– The immersed weight force, $\vec{P} - \vec{I}$:

$$P - I = \frac{\pi}{6}(\rho_s - \rho)gd^3 \tag{1}$$

where $\rho_s =$ density of the particle; $\rho =$ density of the water; $g =$ acceleration of gravity; and $d =$ particle's diameter.

– The drag, $\vec{D}$, and lift, $\vec{L}$, forces (Goldstein 1965):

$$D = \frac{1}{2}\rho U_\infty^2 S C_D \tag{2}$$

$$L = \frac{1}{2}\rho U_\infty^2 S C_L \tag{3}$$

where $U_\infty =$ velocity of the flow far from the bed; $S =$ particle's section exposed to the flow; $C_D =$ the drag coefficient; and $C_L =$ lift coefficient.

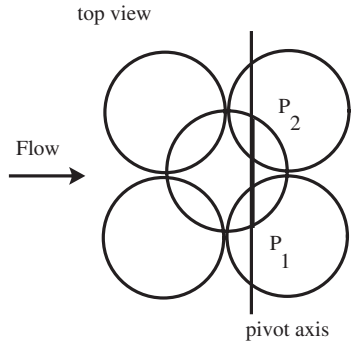


Figure 3. Top view of the particle arrangement and representation of the pivot points (P_1 and P_2) and axis formed by those points. Flow direction is perpendicular to the segment P_1P_2.

– The resistance force, $\vec{F}_r$ which can be expressed as (Halliday et al. 2001):

$$F_r = \mu_e R_n \tag{4}$$

where $\mu_e =$ static friction coefficient; and $R_n =$ normal reaction.

From the equilibrium conditions, $\sum \vec{F} = 0$ and $\sum \vec{M} = 0$, where $\vec{F}$ represents the resultant force and $\vec{M}$ the resulting torque, one obtains respectively for the force balance:

$$\frac{U_\infty^2}{(s-1)gd} = \frac{4}{3C_D}\left(\frac{\mu_e}{1 + \frac{C_L}{C_D}\mu_e}\right) \tag{5}$$

and for the torque balance:

$$\frac{U_\infty^2}{(s-1)gd} = \frac{4}{3C_D}\left(\frac{\tan\theta}{1 + \frac{C_L}{C_D}\tan\theta}\right) \tag{6}$$

where $\theta =$ support angle, as represented in Figure 2; and $s = \rho_s/\rho$. According to observations for the studied case conditions and considering current values of static friction coefficients for glass and *perspex* (0.7 to 0.9), equation (6) was taken as the critical reference in the following analysis.

The first member of equation (6) can be identified as a Froude number, and so the following relation can be written:

$$\mathrm{Fr} = f(C_D, C_L, \theta, \phi) \tag{7}$$

where C_D and C_L are functions of the particle Reynolds number, defined as $Re_p = U_\infty d/\nu$ and of the shear rate defined as $\partial u/\partial y$ (Saffman 1964). For C_D and C_L, formulations corresponding to the situation of a sphere in a shear flow should be used, if available.

Copyright © 2006 Taylor & Francis Group plc, London, UK

In accordance with the model's theoretical hypothesis referred (as 3.) before, it was assumed that C_L was zero (Goldstein 1965), corresponding to, on a first approach, not taking into account lift force effects. That simplification was assumed although having in mind that, accordingly to (Saffman 1964), a sphere in a slow shear flow is submitted to a lift force. Therefore equation (6) can be written:

$$\frac{U_\infty^2}{(s-1)gd} = \frac{4}{3C_D}\tan\theta \tag{8}$$

or, multiplying both terms by the squared shear velocity, $u_*^2 = \tau_w/\rho$:

$$\frac{u_*^2}{(s-1)gd} = \frac{4}{3U_\infty^{+2}C_D}\tan\theta \tag{9}$$

where $U_\infty^+ = U_\infty/u_*$. For turbulent boundary layer flows, and using the skin friction coefficient definition, it is possible to demonstrate that $u_*/U_\infty \approx 1/20$. The left hand side of equation (9) may be identified as the Shields parameter (Shields 1936) and will be denoted by Sh (sometimes referred in the literature by θ or Y), and referred from now on as the Shields number.

The behavior of the C_D can be expressed as a function of the particle Reynolds number (Cliff et al. 1978). Some of those expressions, which are particle Reynolds number range dependent, are:

- for $0.01 \le \mathrm{Re}_p \le 20$:

$$C_D = \frac{24}{\mathrm{Re}_p}\left(1 + 0.1315\mathrm{Re}_p^{0.82-0.05\log\mathrm{Re}_p}\right) \tag{10}$$

- for $20 \le \mathrm{Re}_p \le 260$:

$$C_D = \frac{24}{\mathrm{Re}_p}\left(1 + 0.1935\mathrm{Re}_p^{0.6385}\right) \tag{11}$$

- for $260 \le \mathrm{Re}_p \le 1.5\times10^3$:

$$\log C_D = 1.6435 - 1.1242W + 0,1558W^2 \tag{12}$$

- for $1.5\times10^3 \le \mathrm{Re}_p \le 1.2\times10^4$:

$$\log C_D = -2.4571 + 2.5556W - 0.9295W^2 + 0,1049W^3 \tag{13}$$

with $W = \log \mathrm{Re}_p$.

Taking into account the referred expressions (10 to 13) for the C_D evaluation, equation (9) can be plotted and compared with the Shields diagram (correspondent to granular mixtures), considering the Reynolds number range variation (using $u_* \approx U_\infty/20$), and different support angles (Fig. 4).

For the turbulent regime, $\mathrm{Re}_* > 80$, and considering $\theta = 35.26°$, the Shields number Sh, as calculated by equation (6) is approximately 0.006, which is about 10 times less than the value usual accepted for the Shields

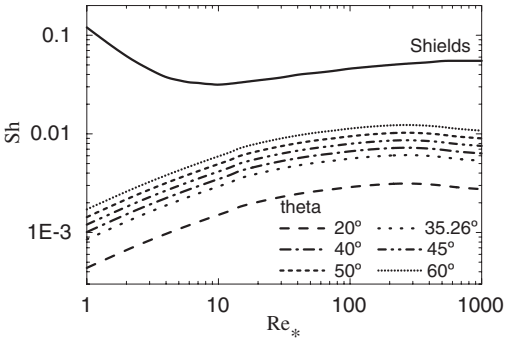


Figure 4. Comparison of Shields diagram with curves obtained for an isolated sphere, for different support angles (theta means θ).

diagram in the same conditions, $Sh \approx 0.06$, (Cardoso 1998). In experiments carried out by (Fenton and Abbott 1977) a value of $Sh \approx 0.01$ was obtained, for large values of Re_*. Moreover, this last result is in good agreement with the ones obtained by (Coleman 1967).

In addition to the previous considerations one should also take into account the existence of turbulence forces, namely a turbulent drag and a turbulent lift. Starting from the definition of drag force, and expressing the velocity in terms of a mean value and of a fluctuation component:

$$D = \frac{1}{2}\rho(u+u')^2 SC_D \tag{14}$$

or:

$$D = \frac{1}{2}\rho(u^2 + 2uu' + u'^2)SC_D \tag{15}$$

Applying the Reynolds average in order to eliminate the term uu' and taking into account the simplified theoretical hypothesis 3 referred before, one has:

$$\overline{D} = \frac{1}{2}\rho(U_\infty^2 + \overline{u'^2})SC_D \tag{16}$$

expressing that the drag force has a contribution from the mean as well as from the fluctuating velocity components and it can be seen that the drag force has a contribution from the mean value of the flow and from the fluctuating component. A similar reasoning is valid for the lift force. It is then possible to individualize drag and lift turbulent forces, $\overline{D_t}$ and $\overline{L_t}$, with:

$$\overline{D_t} = \frac{1}{2}\rho\overline{u'^2}C_D S \tag{17}$$

$$\overline{L_t} = \frac{1}{2}\rho\overline{u'^2}C_L S \tag{18}$$

Copyright © 2006 Taylor & Francis Group plc, London, UK

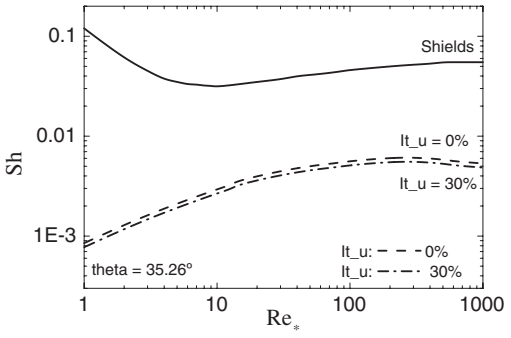


Figure 5. Variation of the Shields number with the turbulence intensity of the longitudinal velocity component (u) on the Shields number, for a support angle of $\theta = 35.26°$ (It_u stands for It_u).

where $u' =$ fluctuation of the longitudinal velocity.

Conducting a similar approach as before (neglecting the lift component), and again from the torque analysis equation (9) turns now into:

$$Sh = \frac{4}{3C_D}\tan\theta \frac{1}{U_\infty^{+2}}\left(\frac{1}{1+It_u^2}\right) \tag{19}$$

where $It_u^2 = \overline{u'^2}/U_\infty^2$, is defined as the turbulence intensity for the u component. If It_u is small compared with unity, equation (19) can be written as:

$$Sh = \frac{4}{3C_D}\tan\theta \frac{1}{U_\infty^{+2}}\left(1-It_u^2\right) \tag{20}$$

The plot of this function is depicted in Figure 5 considering $\theta = 35.26°$ for two different values of It_u. One can observe that the contribution of turbulence, although not relevant, shall be envisaged and taken into account, the most as more turbulent the flow is.

3 EXPERIMENTAL SETUP

The experiments were made on the flume channel of the Hydraulics Laboratory at FEUP. The channel is 0.4 m wide by 0.6 m high and has a length of 17 m.

On this channel a model similar to the one described before (Fig. 1) was built in a *perspex* plate placed on the bottom of the water channel and the 5 mm diameter spherical particles used were made of glass ($\rho_s = 2.65\,\mathrm{kgm^{-3}}$).

In order to measure the mean and turbulent velocities of the flow a one component laser Doppler velocimeter (LDV) system from DANTEC was used. The characteristics of this system are shown in Table 1.

The measurement grid used is depicted in Figure 6 and shows the plant view of the measured profiles.

Table 1. Parameters of the LDV (m.c.v. stands for measurement control volume).

Parameter	Value	Comment
λ	514 nm	wavelength
θ	6.834°	angle of laser beams
δ_x	2.53 mm	major axis of m.c.v.
δ_y	162 μm	minor axis of m.c.v.
D_f	4.318 μm	fringe spacing
f_s	0.6 MHz	frequency shift

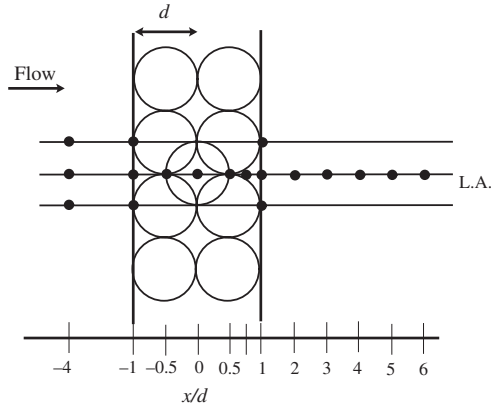


Figure 6. Top view of the measurement grid used in the measurements (L.A. stands for Longitudinal Axis).

4 EXPERIMENTAL RESULTS

In order to determine the conditions for the detachment of the test-particle (hereafter referred as critical conditions) several tests were carried out in order to obtain a narrow band of flow rate values for which the single test particle was removed, hereby referred as critical flow rate, Q_c. It was observed in the laboratory that the obtained interval for the critical flow rate was:

$$Q_c = [15.85;\ 17.25]\ \mathrm{(L/s)} \tag{21}$$

The average flow rate obtained was 16.16 L/s and that was the flow value used as the critical flow case.

4.1 *Studied flow characteristics*

In order to allow the measurement for velocity fields characterisation in the critical condition to be made, the glass sphere was replaced by a steel sphere with the same diameter. The mean and turbulent velocity fields over and close to the test-particle were also characterised for two other flowrate values in the range below the critical one.

Table 2 summarizes the characteristics of the studied flows in terms of flow (Q), Reynolds number

Copyright © 2006 Taylor & Francis Group plc, London, UK

Table 2. Parameters of the flows considered.

Re_h	Height h (m)	Q (L/s)	τ_w (Nm^{-2})
3.1×10^4	0.055	4.04	0.120
7.0×10^4	0.085	10.10	0.224
1.0×10^5	0.120	16.16	0.323

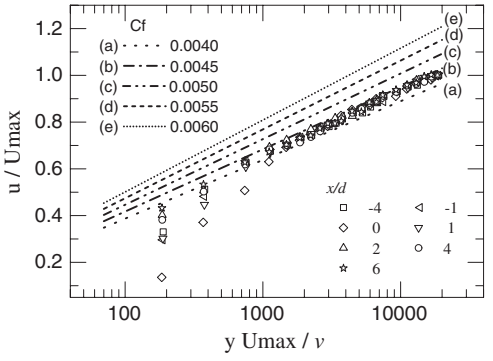


Figure 7. Application of the Clauser method to obtain the shear stress values on different longitudinal sections of the channel for $Re_h = 1.0 \times 10^5$ (take $U_{max} = U_\infty$).

($Re_h = UR_h/\nu$, where R_h is the hydraulic radius, U is the cross sectional mean velocity and ν is the kinematic viscosity) and shear stress (τ_w). The latter was evaluated by applying the Clauser method to the measured velocity profiles.

The flow fields characterization for any of those flows was carried for two situations: one with and the other without the test-particle placed in the flow. The last ones enabled the application of the Clauser's method. In fact, according to (Young 1989) from the log velocity law it is possible to demonstrate that the following relation holds:

$$\frac{u}{U_\infty} = \frac{1}{\kappa}\sqrt{\frac{C_f}{2}}\ln\left(\frac{U_\infty y}{\nu}\right) + \sqrt{\frac{C_f}{2}}\left(B + \frac{1}{2\kappa}\ln\left(\frac{C_f}{2}\right)\right) \quad (22)$$

where $C_f = 2\tau_w/\rho U_\infty^2$ is the skin-friction coefficient, $\kappa = 0.4$ is the von Kármán's constant and B is a constant. Choosing several values of C_f it is possible to determine a family of curves, and choose the one who better fits the obtained experimental data. In Figure 7 the Clauser method is illustrated for the critical condition, $Re_h = 1.0 \times 10^5$.

As it can be seen the obtained values for C_f at different longitudinal sections, for the fitting range, are constant.

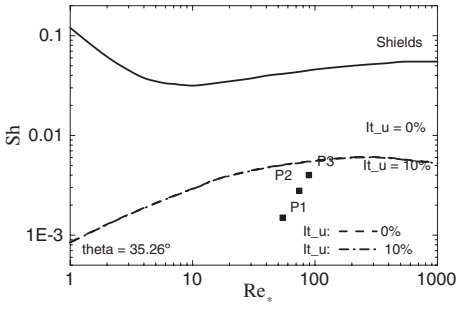


Figure 8. Comparison of the experimental results with the proposed conceptual model. Particle detachment situation corresponds to point P3 (obtained for the critical flow, $Re_h = 1.0 \times 10^5$). Points P1 and P2 correspond to the two other flows considered ($Re_h = 3.1 \times 10^4$ and $Re_h = 7.0 \times 10^4$, respectively).

Table 3. Experimental data points obtained in the channel flume.

Point	Re_h	Re_*	*Sh*	*Sh* (Predicted)
P1	3.1×10^4	54	0.0015	—
P2	7.0×10^4	74	0.0028	—
P3	1.0×10^5	89	0.0040	0.0055

4.2 *Analysis of the conceptual model*

The conceptual model presented in the beginning of this paper is analyzed here in the light of the experiments. Using the flow characteristics (referred on Table 2), the correspondent Shields numbers (*Sh*) and Re_* could be obtained and are plotted in Figure 8 and listed on Table 3.

Comparing those values with the classical Shields diagram, also depicted on Figure 8, it is clear that, even for the determined critical condition, Shields' theory does not predict the beginning of particle motion. This is recognised to be due to the fact that the Shields' criterion was derived considering the erosion of a granular bed of sediments and not only a single particle. Nevertheless the comparison is made since the Shields diagram is one of the important tools to assess the beginning of sediment motion and it is a very widely used reference for granular mixtures. It can be seen that (i) all the experimental points obtained present a consistent and crescent trend and (ii) the point correspondent to the critical flow (P3) is quite close to the line obtained by application of the simplified conceptual model, but still below the predicted critical value.

As referred before, the model assumes that there is no lift force contribution. It can be expected that if lift force is taken into account, the prediction of the critical value may be improved. In fact by considering the lift component, by adopting in equation (6) the

Copyright © 2006 Taylor & Francis Group plc, London, UK

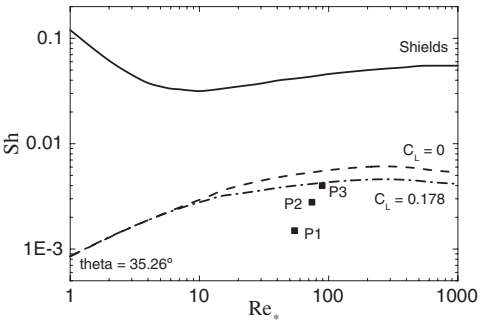


Figure 9. Comparison of the experimental results with the proposed conceptual model considering $C_L = 0$ and $C_L = 0.178$ as proposed by Einstein and Samni. Considering the lift coefficient the conceptual model gives results closer to the experimental ones.

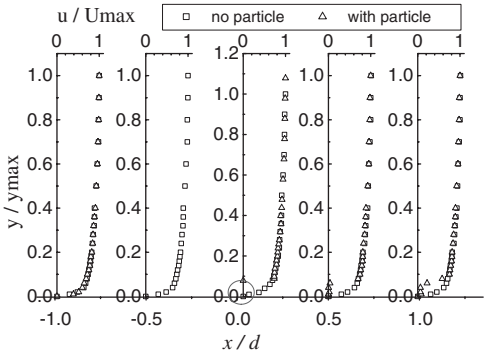


Figure 10. Mean velocity profiles of the u component on the test-particle for $\mathrm{Re}_h = 1.0 \times 10^5$, at the longitudinal axis (take $U_{max} = U_\infty$ and note that the circle is only to indicate the test-particle height).

value of $C_L = 0.178$ proposed by (Einstein and Samni, 1949), a new conceptual model curve may be obtained as depicted on Figure 9.

Figure 9 indicates that by considering the lift contribution the predicted critical values will be still in better agreement with experimental ones, and so the use of formulations for both C_L and C_D on the conceptual model is recommended.

4.3 *Flow field over the test-particle*

The use of the LDV, as referred, allowed to characterize mean velocity and turbulence intensity values on both longitudinal (u) and vertical (v) directions. Those measurements were carried out in the perspective of investigating the influence of the turbulence fluctuations and also the kinetic energy in the detachment process of the particle. Of course, that in addition of the characterization of the flow field for the critical condition case.

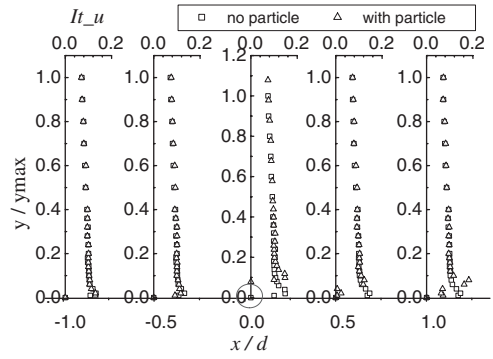


Figure 11. Turbulence intensity for the longitudinal component (u) over the test-particle for $\mathrm{Re}_h = 1.0 \times 10^5$, at the longitudinal axis (take $U_{max} = U_\infty$, It_u = It_u and note that the circle is only to indicate the test-particle height).

The velocity profiles corresponding to the critical condition ($\mathrm{Re}_h = 1.0 \times 10^5$) are depicted in Figures 10 to 13 and compare the behavior of the velocity field with and without test-particle along the longitudinal axis (see Fig 6).

Figure 10 shows that immediately upstream of the test-particle there is a reduction on the value of the longitudinal velocity (u) due to the deceleration of the flow. It is also clearly seen that over the test-particle there is an acceleration of the flow, with a high velocity gradient; on the other hand the wake region is characterized by a low velocity zone (with velocities about zero). The turbulence intensity (Fig. 11) has a similar behavior but, in the wake region the higher values are located at a distance of the wall of about one diameter ($y/d \approx 1$). Over the test-particle turbulence intensity, It_u is about 18% (Fig. 10).

For the v component, due to geometric limitations, it was not possible to make the measurements near the bottom. Nevertheless, it was possible to measure at a distance of 0.75 mm from the top of the sphere. The correspondent results are shown in Figures 12 and 13.

In terms of order of magnitude it can be concluded that the longitudinal mean component, u, is much larger than the correspondent vertical component v. It is also possible to note that the turbulence intensity associated to the vertical velocity component (v) is of the same order of magnitude of the correspondent mean component.

4.4 *Kinetic energy evaluation*

Using the information available from the measured velocity profiles it is possible to determine the kinetic energy of the flow. In order to study the effect of the test-particle on the kinetic energy of the flow an analysis was made concerning sections $x/d = -1$ and $x/d = +1$ (along the axis of the test-particle) by calculating the kinetic energy difference between those

Copyright © 2006 Taylor & Francis Group plc, London, UK

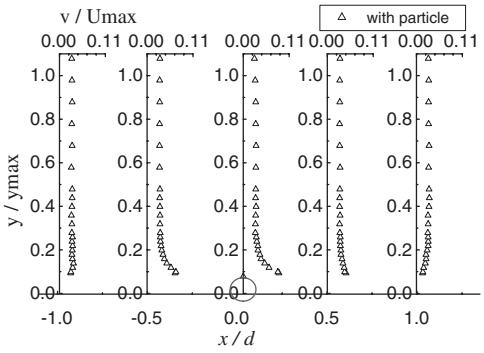


Figure 12. Velocity profiles of the mean v component on the test-particle for $\mathrm{Re}_h = 1.0 \times 10^5$, at the longitudinal axis (take $U_{max} = U_\infty$ and note that the circle is only to indicate the test-particle height).

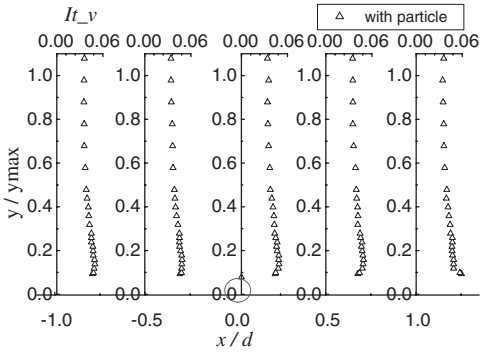


Figure 13. Turbulence intensity for the v component on the test-particle for $\mathrm{Re}_h = 1.0 \times 10^5$, at the longitudinal axis (take $U_{max} = U_\infty$, It_v $= It_v = \overline{v'^2}/U_\infty$ and note that the circle is only to indicate the test-particle height).

sections. The kinetic energy of the flow is given by (Hinze 1975):

$$k = \overline{k} + k' \tag{23}$$

where $\overline{k} = (\overline{u}^2 + \overline{v}^2 + \overline{w}^2)/2$ is the kinetic energy due to the mean components and $k' = (\overline{u'^2} + \overline{v'^2} + \overline{w'^2})/2$ is the kinetic due to the turbulent fluctuations of the flow. Due to experimental limitations the transverse w component was not measured and so the following approximation was made:

$$k \approx \frac{1}{2}(\overline{u}^2 + \overline{u'^2} + \overline{v}^2 + \overline{v'^2}) \tag{24}$$

The difference between the kinetic energy of the flow measured at $x/d = +1$ and at $x/d = -1$ is then given by:

$$\Delta K = K_{+1} - K_{-1} \tag{25}$$

where $K_{+1} =$ total kinetic energy at section $x/d = +1$; and $K_{-1} =$ total kinetic energy at section $x/d = -1$. By

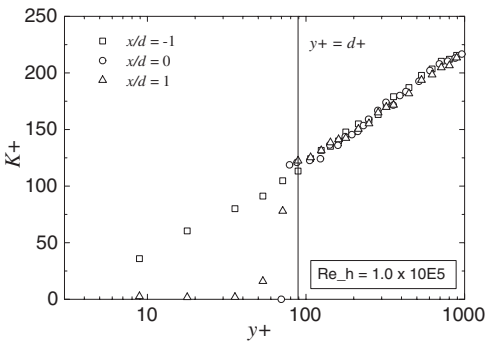


Figure 14. Total non-dimensional kinetic energy profiles measured at $x/d = -1{,}0$, and $+1$ for the critical flow situation. Note that at $x/d = +1$ the total turbulent kinetic energy decreases significantly when compared with the one measured at $x/d = -1$.

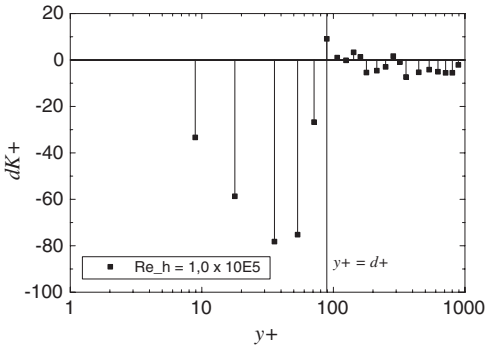


Figure 15. Total non-dimensional kinetic energy difference between profiles measured at $x/d = -1$ and $x/d = +1$ ($dK^+ = \Delta K^+$).

dividing by u_*^2 equation (25) is made non-dimensional, which may be expressed by writing:

$$\Delta K^+ = K_{+1}^+ - K_{-1}^+ \tag{26}$$

Figure 14 shows the profiles of the total non-dimensional kinetic energy in $x/d = -1{,}0$, and $+1$ for the critical flow situation ($\mathrm{Re}_h = 1.0 \times 10^5$) at the longitudinal axis.

The correspondent quantitative changes between the profiles at $x/d = -1$ and $x/d = 1$ are expressed in Figure 15.

In order to characterize the test-particle influence in the kinetic energy longitudinal variations it is possible to define the average kinetic energy between the bed and the particle's top. This averaged value can be expressed in a non-dimensional form as:

$$\epsilon = \frac{1}{d^+}\int_0^{d^+} \Delta K^+ dy^+ \tag{27}$$

Copyright © 2006 Taylor & Francis Group plc, London, UK

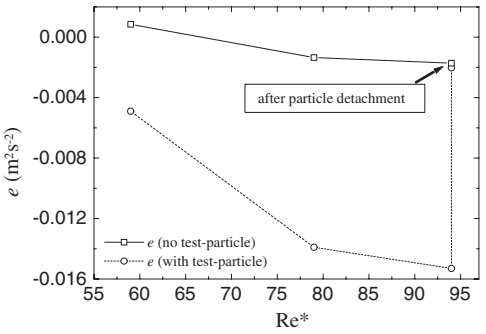


Figure 16. Variation of the e parameter with the shear Reynolds number considering two situations: with no test-particle and with test-particle. It can be seen that the test-particle acts as an energy dissipater.

where $d^+ = u_* d/\nu$ is the non-dimensional height of the particle. ϵ may be interpreted as the mean value of the total kinetic energy difference between the bottom and d^+.

In dimensional form, the average value of the total kinetic energy difference may be expressed by:

$$e = \epsilon u_*^2 \tag{28}$$

On Figure 16 the variation of e is plotted against the variation of the shear Reynolds number Re_* for two cases: one considering the presence of the test-particle in the flow and other not considering it. From the case with test-particle it can be seen that the test-particle acts naturally as a kinetic energy dissipater, and it can be guessed that the particle will be detached if the flow has enough kinetic energy to remove it from its place. Further developments of this energy based method to assess the beginning of sediment motion are to be studied.

5 CONCLUSIONS

A conceptual model for the beginning of motion of a singular test-particle was presented that considers the influence of the drag and of turbulent drag forces.

The improvement of the model by considering the lift force contribution proved to enhance model accuracy, as should be expected. Although the complete form and adequacy of the conceptual model to the full range of shear Reynolds number has still to be validated, the obtained results of the model showed a good agreement with the ones obtained experimentally for the beginning of motion. In order to avoid approximations and use of inadequate data, the values of lift and drag coefficients should be calculated considering the particle Reynolds number and the shear rate ($\partial u/\partial y$) near the wall.

It is known that turbulence is an important mechanism regarding the beginning of sediment motion. The presented model showed also that turbulence intensity contributed to influence particle detachment, but the formulation used, based on time averaged values, did not reveal that effect as mostly significant in current turbulent flows, as it could be expected. Improvements on this model should also be implemented in order to deal properly with the turbulence effects, namely by considering all velocity components, based on laser Doppler anemometry measurements.

Using the velocity profiles it was possible to study the flow field for the critical condition and estimate the kinetic energy of the flow (mean and fluctuation component). It is clear that the test-particle acts as a kinetic energy dissipater and that there is a threshold for which the test-particle is removed. That should be explored in order to better assess the beginning of particles motion.

ACKNOWLEDGMENTS

This work was supported by Fundação para a Ciência e Tecnologia grant, ref. POCTI/ECM/46693/2002.

The authors would also like to thank Professor Maria Fernanda Proença for the help in the LDV measurements.

REFERENCES

Cardoso, A.H. (1998). *Hidráulica Fluvial*. Lisboa: Fundação Calouste Gulbenkian.

Cliff, R., J. Grace, and M. Weber (1978). *Bubbles, Drops and Particles*. New York: Academic Press.

Coleman, N. (1967). A theoretical and experimental study of drag and lift forces actings on a sphere resting on a hypothetical stream bed. *Proc. 12th Congress, IAHR 3*, 185–192.

Fenton, J. and J. Abbott (1977). Initial movement of grains on a stream bed. *Proceedings of the Royal Society 352*, 523–537.

Goldstein, S. (1965). *Modern Developments in Fluid Dynamics vol.2*. New York: Dover Publications Inc.

Halliday, D., R. Resnick, and J. Walker (2001). *Fundamentals of Physics*. New York: John Wiley & Sons.

Hinze, J.O. (1975). *Turbulence*. New York: McGraw-Hill.

Nezu, I. and H. Nakagawa (1993). *Turbulence in Open-Channel Flows*. Rotterdam: A.A. Balkema.

Saffman, P. (1964). The lift on a small sphere in a slow shear flow. *Journal of Fluid Mechanics 22*(2), 385–400.

Shields, A. (1936). *Anwendung der Aenlichkeitsmechanik und der Turbulezforschung auf die Geschiebbewegung*. Ph. D. thesis, Mitteilungen der Preussischen Versuchsanstal fur Wasserbau und Schiffbau, Berlin.

Young, A. (1989). *Boundary Layers*. Oxford: BSP Professional Books.

Copyright © 2006 Taylor & Francis Group plc, London, UK

Marbles in oil, just like a river?

S.M. Cameron, S.E. Coleman & B.W. Melville
The University of Auckland, Auckland, New Zealand

V.I. Nikora
The University of Aberdeen, Aberdeen, Scotland

ABSTRACT: An oil flume in combination with a 100 Hz Particle Image Velocimetry system has been used to study entrainment of 11 mm diameter spherical Nylon particles. The flow field near the bed and around sediment particles holds essential information for studying entrainment mechanics, but measurements in water are often hampered by a lack of adequate resolution, particularly for smaller particle sizes. The higher viscosity of oil compared to water increases length scales, allowing water flows to be modelled with much larger sediment sizes and deeper near-bed flow layers. The 11 mm diameter particles used in the present oil flow experiments are dimensionally equivalent to 0.74 mm diameter quartz particles in water flow. Analysis of the flow field at the instant of bed particle movement indicates that sweep structures (higher than averaged streamwise velocity combined with bed-directed vertical velocity) are the dominant mechanism of entraining particles for the bed geometry and flow regimes studied.

1 INTRODUCTION

Subaqueous granular movement is presently analysed based on the premise that granular material is moved by an average flow property, typically a depth-averaged velocity or an average shear stress exerted by the bulk flow on the surface of the granular mass. This premise, which is inadequate for real (e.g. non-uniform or 3-D) flows, limits understanding, analysis and prediction of granular material motion in nature, numerical modelling of loose-boundary processes being restricted to empirical approximations.

Recent research has focused on relating grain entrainment to local flow conditions, particularly coherent flow structures such as hairpin and funnel vortices. García et al. (1996) used a liquid tracer injected into the flow combined with high-speed photography to visualise a range of particle sizes (0.038–0.53 mm) in both hydraulically smooth and transitional flow regimes (grain Reynolds number $R_* = 0.7$–20) being entrained into suspension. They concluded that ejection events downstream of shear layers are primarily responsible for lifting particles from the bed, even for particles that are immersed within the viscous sub-layer.

Hofland & Booij (2004) used Particle Image Velocimetry (PIV) to measure the flow field over a gravel bed (median sediment size $d_{50} = 17.8$ mm, $R_* = 1200$), with a single moveable light-weight target particle. Their findings suggest that a small-scale ejection creates the initial uplift of the target particle followed by a larger sweep event that dislodges the stone completely. They conclude that sweep events by themselves are less effective than the ejection-sweep combination for moving bed material because the downwards-directed flow associated with sweep events reduces the lift force acting on the particle.

Nelson et al. (2001) found a strong coupling between instantaneous drag force and streamwise flow velocity, but suggest instantaneous lift force is poorly correlated with local velocity either above or in front of the test particle. Horizontal and vertical force components were measured using a force transducer attached to a 19 mm diameter sphere with simultaneous PIV measurements of the flow field. They suggest the optimal conditions for high-lift events are a combination of high velocity (and associated low pressure) over the top of the particle and lower than average velocity (with a high pressure) beneath the particle, maximising pressure differential.

2 DIMENSIONAL ANALYSIS

2.1 *Improving effective measurement resolution*

Resolving the flow field around individual particles, detecting and controlling bed geometry, and

Copyright © 2006 Taylor & Francis Group plc, London, UK

measuring particle movement are all essential for studying particle entrainment at the grain scale. Flows of interest in the $R_* = 5$–50 range (typical sand-size sediments with 0.5–2 mm diameter), where Shields curve describing entrainment shows significant variation with R_*, are difficult to study at the grain scale using conventional techniques due to the small scales involved.

Such flows can be modelled using larger particles by reducing sediment density (effectively decreasing u_* for entrainment) and/or by increasing fluid viscosity ν. Maintaining similarity of the Shields' parameter (θ_c) and the grain-size Reynolds number R_* to ensure correct simulation of particle entrainment under viscous, gravity and fluid shear forces, we can write Equation 1 and Equation 2, which reduce to Equation 3.

$$\lambda_{\theta_c} = \frac{\lambda_{u_*^2}}{\lambda_{(S_s-1)}\lambda_g\lambda_d} = 1 \quad (1)$$

$$\lambda_{R_*} = \frac{\lambda_{u_*}\lambda_d}{\lambda_\nu} = 1 \quad (2)$$

$$\lambda_d = \left[\frac{\lambda_\nu^2}{\lambda_g\lambda_{(S_s-1)}}\right]^{1/3} \quad (3)$$

where λ is the ratio between model and prototype scales, S_s = submerged sediment density, d = particle diameter, g = acceleration due to gravity and u_* = shear velocity. Using oil of higher viscosity than water, the sediment size needs to be increased according to Equation 3 to correctly replicate fluvial sediment processes. Improved resolution of near-boundary flow and entrainment mechanics in this manner using oil flows is the focus of the present study.

3 HIGH-VISCOSITY CONDUITS

3.1 *Previous flumes*

Einstein & Li (1958) and Eckelmann (1974) both used oil flumes to study the viscous sublayer region of turbulent flows. The former study used relatively shallow flows (0.044 m) and high velocities (2 m/s) in a 0.292 m-wide flume to achieve flow Reynolds numbers of around R = 4000. Eckelmann in contrast used comparatively slow flows (0.225 m/s) in a larger 0.5 m-wide and 0.85 m-deep flume with Reynolds numbers around R = 7000. Einstein & Li (1958) used oil with a kinematic viscosity of 66×10^{-6} m^2/s, while Eckelmann used a less viscous paraffin oil with a viscosity of 6×10^{-6} m^2/s, 6 times more viscous than water.

Bechert et al. (1992) constructed an oil flume 11 m long, with a cross section measuring 0.25 m wide by 0.85 m deep. The flume had a racetrack design with two propellers driving the 12×10^{-6} m^2/s white paraffin oil at velocities up to 1.2 m/s, giving flow Reynolds numbers up to R = 45,000. Coleman & Eling (2000) used a small-scale oil flume to study sand-wave generation in laminar flows. Flow depths ranged from 0.038 m to 0.068 m in the 0.1 m-wide flume, with Reynolds numbers typically less than 2000. Both Bechert et al. (1992) and Coleman & Eling (2000) highlight potential problems with air bubble generation, air bubbles tending to remain suspended in the flow, reducing visibility and affecting measuring equipment. Pilotti & Menduni (2001) also studied sediment transport in laminar and hydraulically-smooth turbulent flows using a 2 m long and 0.15 m wide flume, with a maximum flow depth around 0.02 m. The fluid used was a water-glucose solution, with kinematic viscosity adjustable in the range 1×10^{-6} to 281×10^{-6} m^2/s.

3.2 *University of Auckland oil flume*

A new flume has been constructed at The University of Auckland (Figure 1 capable of circulating viscous fluids at flow rates up to 80 litres/second. The glass-sided tilting flume has a width of 0.4 m, maximum fluid depth of 0.2 m and an open-channel section length of 10 m. A tank measuring 1.5 m long, 0.65 m wide and 1.6 m deep collects fluid at the downstream end of the open-channel section, and a twin-screw positive-displacement pump returns the fluid via a 250 mm diameter pipe to the top end of the flume. The oil used is Shell Ondina 15, a white mineral oil with a density of $\rho = 850$ kg/m^3 and a kinematic viscosity of 36×10^{-6} m^2/s at 20°C. The flume is covered at all times to reduce contamination of the colourless and odourless oil. Heating elements in the tank connected to a thermostat allow the oil temperature to be varied between ambient (~20–24°) and 40°C, the kinematic viscosity varying according to Figure 2.

Initial trials with the flume showed that air bubble entrainment would be problematic when higher flow rates were used. The air bubbles were predominantly generated by strong surface turbulence in the collection tank where the flow reaches the end wall. The problem was sufficiently mitigated by installing a series of vanes (running parallel to the flow) in the tank in order to create drag and reduce flow velocity. At the end of the vanes, a double-cup-shaped curved section was installed to turn the flow away from the end wall and back down the sides of the tank, where it was separated from the incoming flow by the outer guide vanes. The writers note that Acoustic Doppler Velocimeters do not function in this oil, possibly because of attenuation of the 16 Mhz signal due to fluid compressibility.

Copyright © 2006 Taylor & Francis Group plc, London, UK

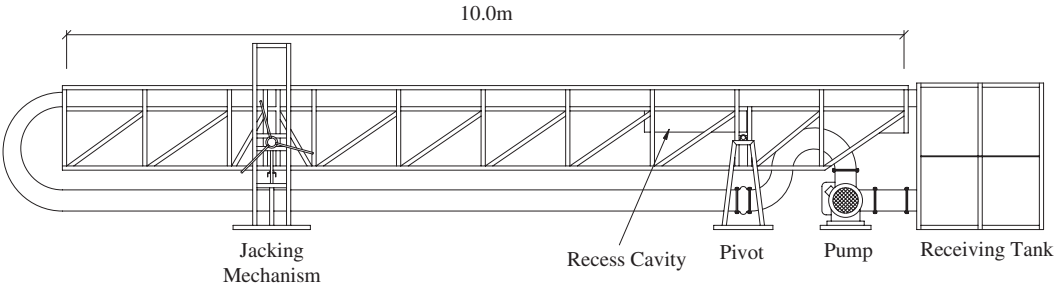


Figure 1. University of Auckland oil flume.

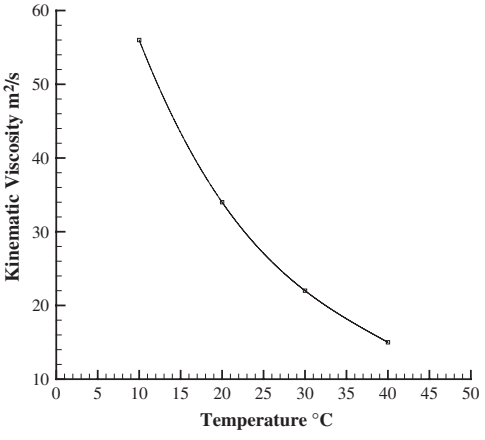


Figure 2. Kinematic viscosity for Shell Ondina 15.

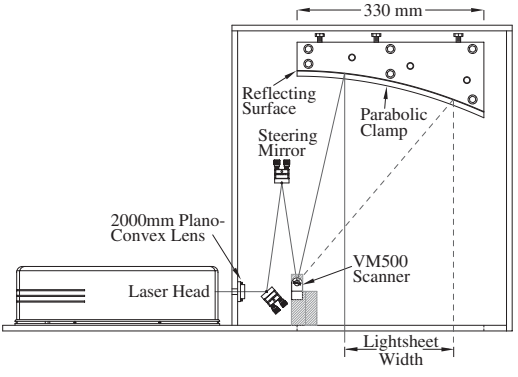


Figure 3. Scanning beam box.

4 PARTICLE IMAGE VELOCIMETRY

Particle Image Velocimetry is a non-intrusive velocity measurement technique where a video camera is used to capture images of small seeding particles added to the flow, the particles typically illuminated by a thin sheet of laser light. The recorded images are broken up into smaller interrogation regions, with particle motion between successive video frames analysed to provide an estimate of velocity at each interrogation region.

Light sheets can be produced by diverging a laser beam with a cylindrical lens when using pulsed lasers, where the light energy is confined to short duration pulses at regular intervals. When using continuous wave lasers however, a diverged light sheet often has insufficient intensity to capture flows of higher velocity, the comparatively longer exposure time required leading to blurring of the particle images. In the case of continuous wave lasers, the available light energy is more efficiently used by scanning the laser beam across the area of interest (Gray et al. 1991), confining the effective exposure time for a seeding particle to the time it takes for the beam width to scan across the particle.

Single-pulsed and double-pulsed lasers have limited flexibility in the range of inter-pulse times that they can produce, essentially limiting the range of flow velocities that can be resolved. This problem is often addressed by using two pulsed lasers, the time between successive laser pulses then easily adjusted to suit the flow conditions. Commonly-available pulsed lasers, however, typically have pulse repetition rates <50 Hz, which can be insufficient to resolve the smaller time scales in turbulent flows. When using a scanning beam system, higher sampling frequencies are possible, while maintaining the flexibility of more costly twin pulsed laser setups.

The University of Auckland PIV system uses the scanning beam technique to generate up to 200 PIV images per second. The beam is scanned using a GSI Lumonics VM500 galvanometer with a 6 mm clear aperture silver-coated mirror in combination with a parabolic mirror as shown in Figure 3. A Miniature Single Axis (MiniSAX) servo amplifier drives the galvanometer, continuously monitoring and updating the mirror position (within an angle of $\pm 10°$ relative to the reference position) to match the command waveform generated by an SC2000 Digital scanning controller, which connects to a computer via an RS-232 serial interface.

Copyright © 2006 Taylor & Francis Group plc, London, UK

The computer-created command waveform is generated using simple control statements such as "Slew 16383 130", which tells the scanner mirror to move to position 16,383 angle units (approximately 10°) over time period 130 time units (approximately 3 ms). A complete waveform is generated by combining a series of commands, which can then be uploaded to the SC2000 controller, where it continuously loops the commands without further interaction with the computer. Commands can also be used to set sync pins on the SC2000 controller to high or low at particular positions in the scan cycle, or the galvanometer can be commanded to wait for a change in state of a sync pin before continuing the scan cycle. These sync pin commands are used in the present system to synchronise the scanning mirror to the camera system.

The camera system consists of a Basler A504k camera, a Coreco X64-CL frame grabber, and Streampix image-capture software. The camera is a 1280 × 1024 pixel, 8bit, monochrome digital camera, with a CMOS sensor capable of capturing a maximum of 500 full resolution images per second. The frame grabber has 128 MB of on-board frame buffer memory and sits on a 64bit/66 MHz PCI bus that supports data rates of up to 528 MB/s. The Streampix software, developed by Norpix, allows image data to be streamed directly to hard disk drives (6 × 18 GB 15 k RPM SCSI drives attached to an Intel SRCU42X PCI-X raid controller for the present system) in the host PC. The present drives, configured as a Raid-0 array, support a sustained transfer rate of 200 MB/s across the entire 108 GB of storage space. When operating at a resolution of 960 × 960 pixels and a frame rate of 200 frames per second (fps), there is sufficient storage space to allow for over 8 minutes of continuous recording.

To capture single-exposure images for cross-correlation, it is necessary to have a single scan of the galvanometer for each camera frame, with the galvanometer retrace positioned between camera exposures. Two synchronisation options are available depending on the time required between successive exposures, which is a function of flow velocity. For interframe times equal to the inverse of the camera frame rate, the "galvanometer master" timing shown in Figure 4a is adopted, which allows for interframe times down to 5 ms (for a maximum video streaming rate of 200 fps). For higher flow velocities, the "camera master" timing shown in Figure 4b is adopted, which uses frame straddling to give an effective interframe time of 2.5 ms.

The "galvanometer master" timing uses a sync pulse generated by the scan controller to trigger the camera. As illustrated in Figure 4a, the position of the galvanometer mirror lags the command waveform by 0.5 ms due the finite torque of the galvanometer and the rotational inertia of the mirror. To compensate for this lag, the sync pulse is delayed from the start of

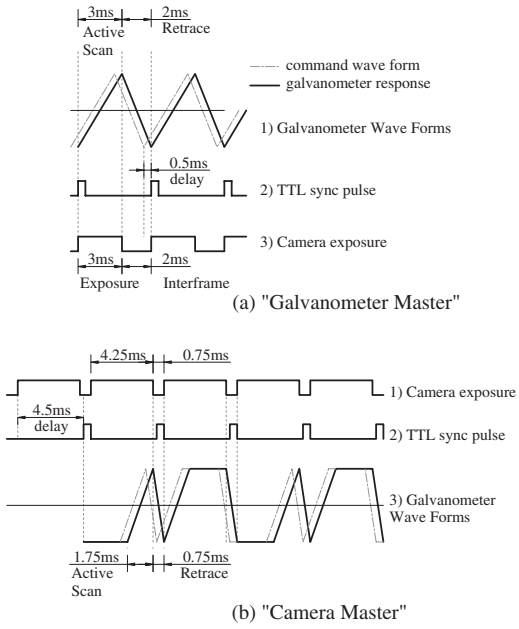


Figure 4. Lightsheet-camera synchronisation options.

the command waveform by 0.5 ms using the built in command set for the scan controller. For the present work, a typical example of this timing (which can be varied to suit the measured flow field) is for the camera to run in an external sync mode, capturing a 3 ms exposure (corresponding to the active scan time of the galvanometer) at each sync pulse.

The "camera master" timing uses a sync pulse generated by the frame grabber to trigger the galvanometer. The camera is set in a 200 fps free-run mode with an exposure time of 4.25 ms. The sync pulse is positioned 4.5 ms after the start of a camera frame or 0.5 ms before the start of the next frame (accounting for the lag of the galvanometer). After receiving the sync pulse, the galvanometer runs a sequence of "idle-active scan-retrace", waits for another sync pulse, and then runs the sequence "active scan-idle-retrace", positioning one active scan at the end of one frame and another at the start of the next. The idle setting corresponds to the galvanometer mirror being parked at either extreme of the scan range where the laser beam is blocked from leaving the scanning beam box (Figure 3). Galvanometer retraces are positioned between camera exposures.

5 PARTICLE-ENTRAINMENT STUDIES

For the present study, the length of the flume is covered in a single layer of 11 mm nominal-diameter glass balls in a hexagonal close packed arrangement and

Copyright © 2006 Taylor & Francis Group plc, London, UK

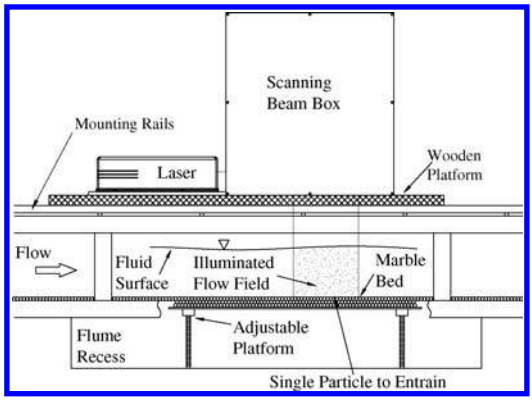


Figure 5. Experimental setup.

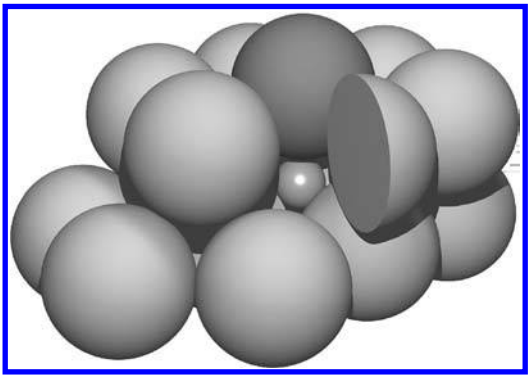


Figure 6. Sphere stacking.

glued to Aluminium sheets along the bed of the flume. Over a length of 1 m in the flume recess (Figure 5), the glass balls are increased to 3 layers deep to more accurately reflect pore flow conditions that might be expected in natural sediments. A removable section 19 ball diameters long, 4 wide and 2 deep in the test section is constructed of precision 11.11 mm black glass spheres. The black glass reduces the reflection and scatter of the laser beam giving more suitable conditions for near-bed PIV measurements. One sphere position in the centre of the removable section is left empty for the target particle of the entrainment experiments to sit. The protrusion of this particle can be adjusted in discreet steps by placing a smaller steel ball into the cavity before placing the target particle on top (Figure 6), the protrusion above the surrounding particles varying according to the diameter of the steel bearing as shown in Table 1. The target particle has a diameter of 11.11 mm and is made of Nylon with a density of 1150 kg/m^3 ($S_s = 1.35$). Equation 3 indicates that entrainment of the 11 mm Nylon particle in the 27×10^{-6} m^2/s oil is equivalent to entrainment of a 0.74 mm quartz ($S_s = 2.65$) sediment in water.

Table 1. Sphere protrusion for different steel-ball diameters.

Steel ball diameter mm	P mm	P_{vb} mm
3.2	1.2	3.4
3.5	1.8	4.0
4.0	2.5	4.7
4.5	3.2	5.4

where: P = protrusion above surrounding particle tops, P_{vb} = protrusion relative to the virtual bed $0.2d$ below particle tops, e.g. Fenton and Abbott (1977).

Each experiment begins by setting the target bed particle at the required protrusion, and adjusting the flume slope to give uniform flow at the expected entrainment flow rate. The flow rate is initially set to just below the threshold level and any transient effects associated with flow rate adjustment allowed to dissipate. The PIV system is then started and the flow rate increased in small increments every 2 minutes until the particle is entrained.

Recorded images are processed using an iterative cross-correlation technique with discrete window shifting. The window-shifting technique, where the location of the second interrogation window is offset with respect to the first, improves correlation peak height, as fewer particles leave the interrogation region between exposures, and permits resolution of larger particle displacements, which are limited to less than half the interrogation region size with basic cross-correlation. Our typical analysis uses a 64×64 pixel interrogation window without window shifting for the first pass, reducing to 32×32 pixel for the second pass with a window shift according to the displacement determined from the first pass.

The position of the target particle is detected at the same time as cross-correlation processing of flow velocities using a technique similar to the intensity-gradient-based Canny Edge Detector (Canny 1986). The first step in the edge-detection process is to apply a Gaussian blur to the source image to reduce background noise (Figure 7a). The horizontal and vertical intensity gradients of the blurred image are then estimated by convolving the image with the Sobel operator defined in two orientations, Gx and Gy (Figure 8), which respond optimally to vertical and horizontal edges respectively. In essence, both orientations of the Sobel operator are swept across all pixels in the image, combining surrounding pixel grey levels to a give a modified value for the central pixel. The absolute magnitude of the intensity gradient (G) and the gradient direction θ can then be approximated at each pixel location using Equations 4 and 5 (Figures 7b, c). Candidate edges, defined by pixels with intensity gradients above a threshold level, are usually several pixels thick

Copyright © 2006 Taylor & Francis Group plc, London, UK

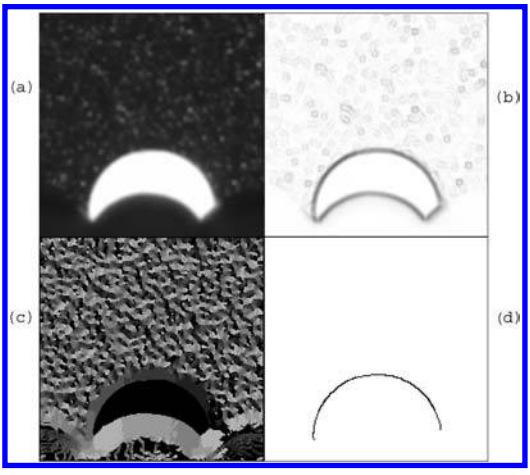


Figure 7. Intermediate steps in the edge-detection process: (a) Gaussian blur, (b) intensity-gradient magnitude, (c) intensity-gradient direction, and (d) non maximum suppression with edge-length filtering.

-1	0	-1
-2	0	-2
-1	0	-1

Gx

-1	-2	-1
0	0	0
-1	-2	-1

Gy

Figure 8. Sobel operator.

due to the applied Gaussian blur and the width of the Sobel operator. The thickness of these edges is reduced using a process called Non Maximum Suppression (NMS), where pixels having intensity gradients that are not a local maximum in the direction perpendicular to the edge are suppressed, reducing candidate edges to one pixel wide. The final step in the edge-detection process is to remove lower particle edges (assessed from the gradient direction) and to trace along all remaining edges, determining their length and selecting the longest as the top edge of the target particle. A parabola is then fitted to the highest 10 rows of pixels on the edge, and the horizontal and vertical coordinates of the peak point calculated.

$$|G| = |Gx| + |Gy| \tag{4}$$

$$\theta = \tan^{-1}\left(\frac{Gy}{Gx}\right) \tag{5}$$

6 RESULTS

For the four protrusions tested (Table 1), double-averaged (in time and space) streamwise velocity ($\langle\bar{u}\rangle$) profiles at threshold conditions are shown in Figures 9

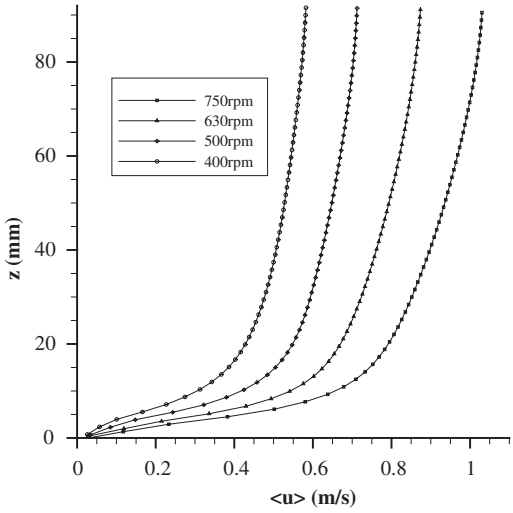


Figure 9. Double-averaged velocity profiles.

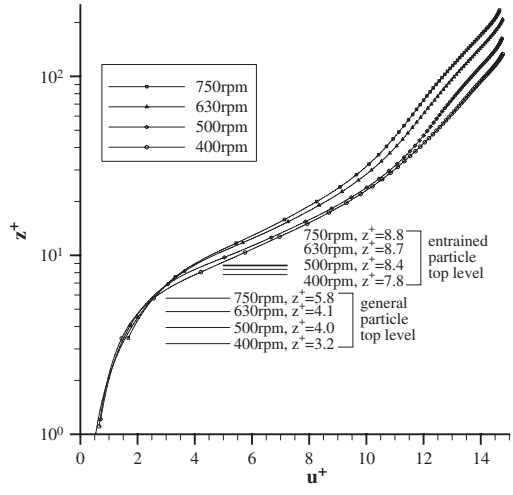


Figure 10. Dimensionless velocity profiles, where: $z^+ = zu_*/\nu$ and $u^+ = \langle\bar{u}\rangle/u_*$

and 10. In each case, the spatial-averaging window used extended over 10 particles, with the vertical origin at the virtual-bed, $0.2d$ below the surrounding particle tops. Below particle tops, $z^+ = zu_*/\nu = 3.2 - 5.8$, averaging was carried out over the fluid volume. Figures 9 and 10 show classic near-bed profiles, with particle tops generally within the laminar sublayer, and the top of the entrained particle at the lower extent of the buffer layer.

Figure 11 illustrates the time-averaged flow patterns for the case of the target particle protruding 3.2 mm above the tops of the surrounding particles ($P_{vb} = 5.4$ mm). Of particular interest is the area of the

Copyright © 2006 Taylor & Francis Group plc, London, UK

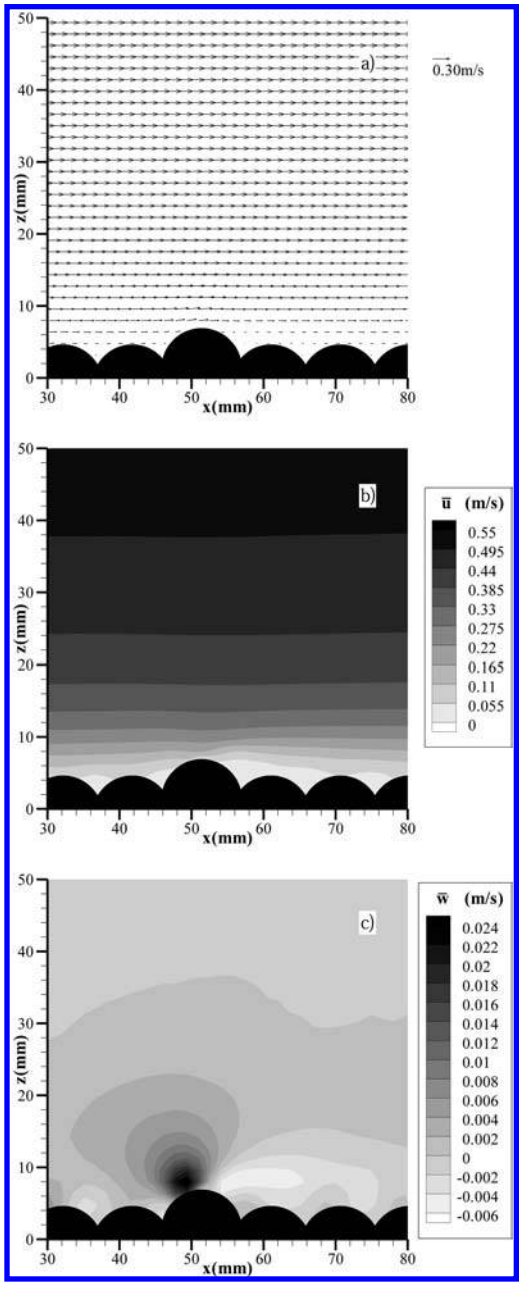


Figure 11. Time-averaged flow field for particle protruding 3.2 mm above tops of surrounding particles ($P_{vb} = 5.4$ mm): (a) velocity vectors, (b) ū contours, (c) and w̄ contours. Bed origin is the image base level.

flow field affected by the protruding particle, extending more than 5 times the protrusion in the upstream and vertical directions and 10 times the protrusion in the downstream direction.

Table 2. Flow properties at threshold protrusion.

Pump rpm	P_{vb} mm	H m	U m/s	R	u_{*c} m/s	u_c/u_{*c}	R_*
750	3.4	0.132	0.91	10690	0.070	10.6	27.7
630	4.0	0.131	0.77	9422	0.059	11.2	24.6
500	4.7	0.129	0.63	7299	0.048	10.8	17.3
400	5.4	0.129	0.50	5793	0.039	10.8	14.4

where: $\nu = 27 \times 10^{-6}\ m^2/s$, P_{vb} = protrusion relative to the virtual bed, H = flow depth, U = depth-averaged velocity, $R = UH/\nu$ = flow Reynolds number, u_{*c} = critical shear velocity, u_c = critical local velocity, $R_* = du_*/\nu$ = particle size Reynolds number.

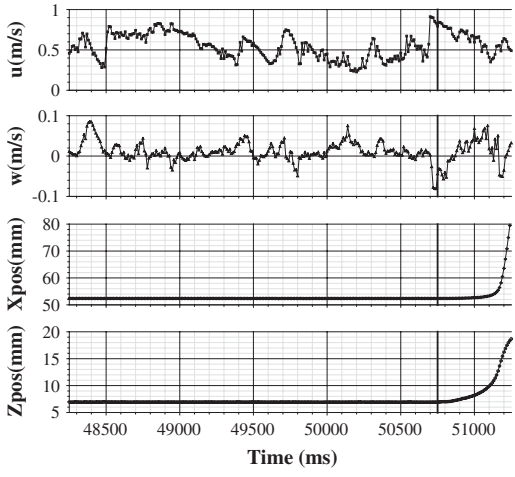


Figure 12. Time series showing velocity components (u & w) and particle position (Xpos & Zpos) for $P_{vb} = 3.4$ mm. Darkened vertical bar at Time = 50,750 ms marks the start of particle movement.

Flow properties for the each of the four tested particle protrusions are summarised in Table 2.

Figure 12 shows time series of streamwise and vertical flow velocities extracted from a point 4.5 mm upstream and 2.5 mm above the top of the target particle, which in this case protrudes 1.2 mm above the tops of the surrounding particles ($P_{vb} = 3.4$ mm). Apparent from the diagram is a period of higher than average streamwise velocity combined with negative vertical velocity (a 4th-quadrant sweep event) peaking just prior to the marked onset of particle motion. The apparent delay (around 50 ms in Figure 12) between peak streamwise velocity and detected particle movement may be accounted for by the upstream/elevated location of the interrogation region and the time it takes for the velocity peak to reach the lower fluid layers closer to the particle. The initial particle displacement between measurement intervals (every 10 ms) is

Copyright © 2006 Taylor & Francis Group plc, London, UK

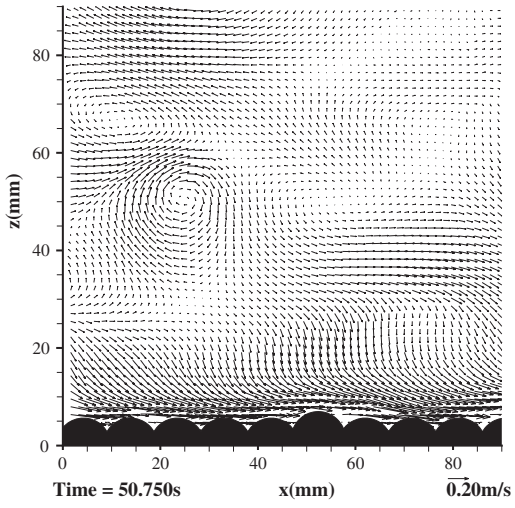


Figure 13. Vectors of $u' = u - \bar{u}$ and $w' = w - \bar{w}$ at the time of entrainment for $P_{vb} = 3.4$ mm. Mean flow is from left to right. 1 mm = 2.6 wall units.

also very small (~0.01 mm) making it difficult to pinpoint the exact, at this fine resolution, moment of the initiation of particle movement.

The u' and w' vector field shown in Figure 13 corresponding to the time of first-detected particle movement (Time = 50,750 ms) for the same experiment as Figure 12 confirms the entraining sweep structure to be present over a bed area greater than the 90 mm window size, and to extend vertically for approximately 10–20 mm (26–52 wall units). The sweep structure may be consistent with down-flow to the side of a streamwise-orientated vortex (e.g. at the outside of the leg of a stretched hairpin-vortex), or between a pair of counter-rotating vortices, but improved interpretation requires full 3d flow-field information, ideally, or in the absence of this, greater numbers of captured particle- entrainment events.

Figures 14 and 15 present velocity time series (aligned with entrainment at Time = 0) averaged over eight repeat runs of the four protrusions tested (Table 2). The series in each figure are offset vertically to aid clarity. These figures highlight a consistent entrainment process, with a positive spike in horizontal velocity and a negative spike in vertical velocity (i.e. a sweep), although the latter is less clear for the entrainments at larger protrusions and lesser R_*.

The path followed by the particle after the initial movement is illustrated in Figure 16a for the case of a 1.2 mm protrusion above the tops of the surrounding particles ($P_{vb} = 3.4$ mm), and in Figure 16b for a 3.2 mm protrusion ($P_{vb} = 5.4$ mm). For the high protrusion case, the particle appears to roll out of the cavity, maintaining contact with the bed until it

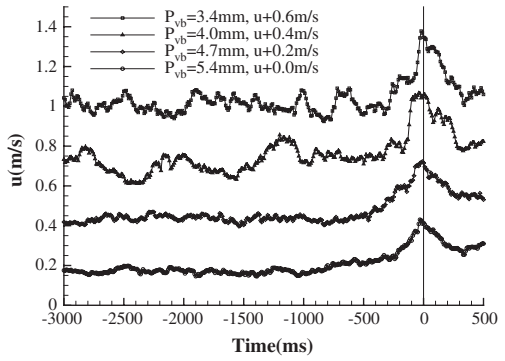


Figure 14. Run-averaged streamwise velocity. Time = 0 corresponds to particle entrainment.

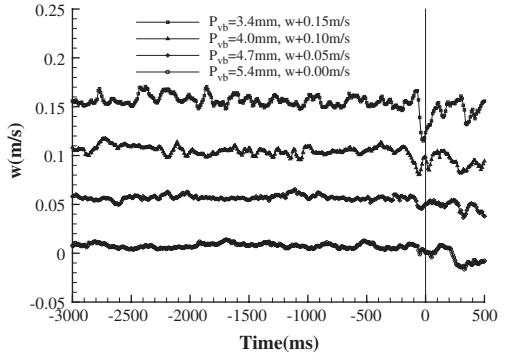


Figure 15. Run-averaged vertical velocity. Time = 0 corresponds to particle entrainment.

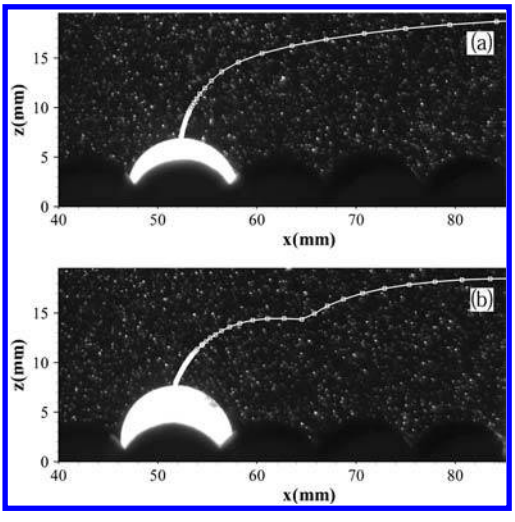


Figure 16. Particle path following entrainment: (a) 1.2 mm protrusion relative to surrounding particles ($P_{vb} = 3.4$ mm), and (b) a 3.2 mm protrusion ($P_{vb} = 5.4$ mm).

Copyright © 2006 Taylor & Francis Group plc, London, UK

bounces off a downstream particle, then gaining elevation and being carried some distance downstream before regaining contact with the bed. The lower protrusion particle, while still rolling out of the cavity, has sufficient lift force and momentum to leave contact with the bed after clearing the cavity.

In future experiments, we plan to extend the current methodology to visualise entrainments over a wide range of grain-size Reynolds numbers by varying particle density, fluid viscosity and particle size. Of particular interest will be whether the sweep structure identified in the experiments to date (Figures 12–15) remains the dominant entrainment mechanism for hydraulically smooth and rough flows. Also of interest is whether particles can be entrained for laminar flows, and implications of this to understanding of entrainment mechanics.

7 CONCLUSIONS

A series of experiments has been conducted in an oil flume to study the flow field near sediment particles leading to particle movement. The higher viscosity of the oil ($\nu = 27 \times 10^{-6}\,\mathrm{m^2/s}$) compared to water ($\nu = 1 \times 10^{-6}\,\mathrm{m^2/s}$) enhances length scales, enabling 0.74 mm quartz sediment in water flows to be modelled with 11 mm diameter nylon particles in the oil, effectively improving measurement resolution for the near-bed flow. A particle image velocimetry (PIV) system employing the scanning-beam technique of light sheet generation was used to measure streamwise and vertical velocities in a 2d slice of the flow field at a frequency of 100 Hz. Experiments focused on the entrainment of a single 11 mm diameter Nylon particle of varying protrusion set in a bed of tightly-packed, co-planar, 11 mm diameter marbles. Time series of near-particle velocity for the four protrusions considered (3.4–5.4 mm above the virtual bed), consistently show a period of high streamwise velocity, often accompanied by downwards flow, immediately prior to entrainment. Flow field vector maps indicate a sweep structure over and around the target particle to be the cause of entrainment. This mechanism is consistent with drag and lift forces both scaling with the square of streamwise velocity. The motion of particles as they are entrained and carried downstream can be tracked from the PIV images using an edge-detection algorithm, potentially enabling measurements of particle velocity and acceleration as it is entrained. Double-averaged (in time and space) streamwise velocity profiles confirm the deepened nature of the near-bed viscous sublayer and buffer regions of the present turbulent flows. Future experiments will extend the same experimental techniques to hydraulically smooth and rough turbulent flows, as well as laminar flows, by varying particle size, particle density and fluid viscosity.

REFERENCES

Bechert, D.W., Hoppe, G., van der Hoeven, J.G., & Makris, R. (1992). The Berlin oil channel for drag reduction research. *Experiments in Fluids 12*, 251–260.

Canny, J.F. (1986). A computational approach to edge detection. *IEEE Transactions on Pattern Analysis and Machine Intelligence 8*(6), 679–698.

Coleman, S.E. & Eling, B. (2000). Sand wavelets in laminar open-channel flows. *Journal of Hydraulic Research 38*(5), 331–338.

Eckelmann, H. (1974). The structure of the viscous sublayer and the adjacent wall region in a turbulent channel flow. *Journal of Fluid Mechanics 65*(3), 439–459.

Einstein, H.A. & Li, H. (1958). The viscous sublayer along a smooth boundary. *Transactions of the American Society of Civil Engineers 123, Paper No. 2922*, 293–313.

Fenton, J.D. & Abbott, J.E. (1977). Initial movement of grains on a stream bed: The effect of relative protrusion. *Proceedings of the Royal Society of London Series A, 352*, 523–537.

García, M., Niño, Y. & López, F. (1996). Laboratory observations of particle entrainment into suspension by turbulent bursting. In P.J. Ashworth, S.J. Bennett, J.L. Best, & S.J. McLelland (eds.), *Coherent Flow Structures in Open Channels*, pp. 63–86. New York: John Wiley and Sons.

Gray, C., Greated, C.A., McCluskey, D.R. & Easson, W.J. (1991). An analysis of the scanning beam PIV illumination system. *Measurement Science and Technology 2*(8), 717–724.

Hofland, B. & Booij, R. (2004). Measuring the flow structures that initiate stone movement. In M. Greco, A. Carravetta, & R. Della Morte (eds.), *River Flow 2004*, Naples, pp. 821–830. Balkema.

Nelson, J.M., Schmeeckle, M.W. & Shreve, R.L. (2001). Turbulence and particle entrainment. In M. Mosley (ed.), *Gravel-Bed Rivers V*, pp. 221–248. Wellington: New Zealand Hyrdrological Society.

Pilotti, M. & Menduni, G. (2001). Beginning of sediment transport of incoherent grains in shallow shear flows. *Journal of Hydraulic Research 39* (2), 115–124.

Copyright © 2006 Taylor & Francis Group plc, London, UK

Bed load fluctuations and channel processes in a braided network laboratory model

Walter Bertoldi, Thomas Amplatz, Stefano Miori, Luca Zanoni, Marco Tubino
Department of Civil and Environmental Engineering, University of Trento, Italy

ABSTRACT: Braided networks are characterized by multiple and different temporal and spatial scales. In order to understand their evolution mechanisms and to improve our predicting ability it is relevant to recognize these scales and to relate them to different channel processes. In this work we present the results of detailed observations performed on a braided network scale model within a 2.9 *m* wide laboratory flume, with movable bed made of a well sorted quartz sand. Measurements comprised the survey of bed topography through laser scanning device, the image analysis of the planimetric configuration and the continuum record of sediment transport rate. We focussed our attention on the fluctuations of the sediment transport rate, which are mainly determined in braided streams by the over-reaction of the sediment flux to the bed morphology. Therefore, they may be seen as an indicator of the inherent unsteadiness of the evolution process of the network.

Previous studies pointed out the presence of various temporal scales, which were related to various processes like bedforms migration and network rearrangement (see for example Ashmore 1988 and Hoey and Sutherland 1991). The Fourier analysis of time series of sediment transport data allowed us to provide a detailed measure of the above scales. In particular, three different timescales could be detected in our experiments. The first scale mainly characterizes the initial stage of network development and it is related to the migration of bars in individual distributaries. The other two scales, which correspond to shorter frequencies, seems to be related to the migration of the nodes (bifurcations and confluences) and to the overall rearrangement of the network, which mainly occurs through the lateral shift of the main channel.

1 INTRODUCTION

The relationship of sediment transport and channel morphology is a key feature of braided networks. As pointed out by Murray and Paola (1994) and Paola (2001), the strongly unsteady character of these systems is inherently related to the over-reaction of the sediment flux to bed changes and to the longitudinal variation of the geometrical properties of the network (total free surface width, number of channels, mean bed elevation, …).

Previous experimental works have highlighted the existence of different spatial scales in braided networks. Suitable indexes have been identified (such as the mean width of the belt, the link length, the braiding index,…) through which a static description of the network can be given (Ashmore 2001). Similarly, bed load fluctuations have been widely documented, along with the occurrence of bed waves with different length-scale, and their relationship with the morphology of the channels has been pointed out (see for example Hoey 1992).

Ashmore (1988) has analyzed bedload fluctuations in a laboratory model of a braided network, showing that the autocorrelation of the sediment transport rate may decay relatively fast (about 30 minutes), though in many experiments a peak was detected at higher lags (from 5 to 10 hours). However, the above phenomenon has not been observed to show a high degree of regularity. Therefore it was not clear whether it could be related to morphological characteristics, though a possible relationship of long scale fluctuations with the aggradation and degradation phases of the whole network has been identified, at least qualitatively.

Analyzing the variability of the sediment transport and the possible relationship with channel morphology, Hoey and Sutherland (1991) have found that a correlation can be established in terms of the capacity of the cross section to store sediments. Consequently the occurrence of bed pulses has been qualitatively referred to the three-dimensional structure of the network. Furthermore, through the analysis of 11 experiments starting from the same initial condition, Warburton and Davies (1994) have attempted to relate

Copyright © 2006 Taylor & Francis Group plc, London, UK



Figure 1. General overview of the laboratory model, flow is from bottom to top (run P7A).

the observed differences in mean bedload transport rate to the braiding index. A weak relationship of braiding intensity and transport rate has been clearly detected only for a timescale of the order of 10 hours, which agrees with the observations of Ashmore (1988).

In this work we have pursued the attempt of defining quantitative relationships of the bed and channel evolutionary processes and the bed load fluctuations measured in a braided network scaled model. Laboratory modelling is a suitable tool to investigate the intrinsic evolutionary scales of braided patterns, since the feeding conditions can be regulated; furthermore, the planimetric and altimetric configuration of branches and the sediment transport flux can be measured with high detail and accuracy. A snapshot of the braided network is given in Figure 1. The records of the outgoing sediment transport flux have been processed through a Fourier transform procedure in order to identify the dominant frequencies of the sediment transport fluctuations. These have been then related to the timescales of the main processes that determine major changes of network morphology, namely the formation and migration of bar fronts, the creation and destruction of bifurcations and confluences, and the shift of the main channels within the braided belt.

The experimental setup and the data analysis procedure are described in the next section, where the dominant frequencies of bed load fluctuations are determined through a Fourier analysis. The resulting timescales are then compared with those typical of the morphological processes occurring in the network.

2 EXPERIMENTAL SET UP AND PROCEDURE

The experiments have been performed on a large laboratory flume, 25 m long and 3.14 m wide, constructed in the Hydraulic Laboratory of the University of Trento. In the flume a 24 m long and 2.90 m wide floodplain of well-sorted quartz sand is set up, characterized by a mean diameter d_s of 0.63 mm and a relative density Δ equal to 1.63. Water and sediment discharges can be automatically regulated by a software, such that both steady and unsteady incoming conditions can be simulated. At the upstream end of the flume the kinetic energy of the incoming flow is dissipated by a 1 m long basin. At the downstream end a chute conveys both the liquid and solid flux in a submerged tank, where the sediment transport rate is measured. The water is recycled by a submerged pump, controlled by an inverter. The sand is supplied by a volumetric sand feeder at the upstream end of the flume through three rotating screws and a diffuser. The open circuit supply system allows one to obtain a precise input, particularly for relatively low sediment rates.

Bed topography has been surveyed by a laser profiler supported by a carriage mounted on a high accuracy rail system. The carriage and the laser are both automatically controlled by software. Bed elevation has been measured on a regular grid, with longitudinal spacing of 10 cm and transverse spacing of 1 cm. Another movable carriage supporting a digital camera located 4 m above the sand bed has been used to provide a regular photographic monitoring of the evolution of the channel planform, through a series of vertical images. Moreover, other digital cameras have been used to get an overall view of the floodplain or to survey specific processes (like node evolution) with higher detail.

The system has been freely run to generate a braided network, subject to a constant water and sediment supply. Each run has been performed starting from a topographic configuration made up by a single straight channel cut on the flat sand surface, which has been initially levelled at a prescribed slope. The geometry of the channel has been selected in order to ensure bankfull conditions, with an initial width to depth ratio equal to 10, i.e. lower than the threshold value for alternate bar growth (see Colombini et al. 1987).

13 experimental runs have been performed, with different values of longitudinal slope S and water discharge Q. The sand has been supplied according to the bed load transport capacity of the channel and ensuring a mass balance between the input and the output. The initial conditions have been chosen in order to reproduce values of the Shields stress typical of gravel bed braided rivers.

In Table 1 the parameters characterizing each run are reported. S is the initial slope, Qs^{IN} is the incoming sediment discharge, b_o is the channel width, D_o is the flow depth, ϑ_o is the Shields parameter, $\Omega = \gamma QS$ is the stream power, where γ is the specific weight of water (the subscript $_o$ denotes the initial reference values of

Copyright © 2006 Taylor & Francis Group plc, London, UK

Table 1. Values of the main parameters characterizing the performed runs.

Run	S	Q [l/s]	*QsIN* [g/min]	bo [m]	do [m]	ϑo	Ω [W/m]	*QsOUT* [g/min]	Duration [h]
P2A	0.007	1.0	46.0	0.160	0.020	0.09	0.069	42.0	70
P3A	0.007	1.0	87.0	0.160	0.020	0.09	0.069	41.0	76
P4A	0.007	1.0	33.2	0.160	0.020	0.09	0.069	41.0	103
P5A	0.007	1.5	76.0	0.185	0.024	0.10	0.103	75.0	52
P6A	0.007	1.2	46.0	0.170	0.021	0.10	0.082	54.0	81
P7A	0.007	0.7	25.6	0.155	0.019	0.09	0.048	29.0	42
P8A	0.007	0.9	33.0	0.140	0.018	0.08	0.062	38.0	84
P9A	0.007	1.1	33.2	0.165	0.021	0.09	0.076	35.9	18
P4B	0.013	0.5	27.6	0.125	0.0128	0.11	0.064	35.6	110
P5B	0.013	0.7	60.5	0.125	0.0158	0.13	0.089	78.3	79
P6B	0.013	0.7	60.5	0.125	0.0158	0.13	0.089	88.6	30
P7B	0.013	1.0	85.8	0.148	0.0179	0.15	0.128	104.7	42
P8B	0.013	1.0	112.3	0.148	0.0179	0.15	0.128	128.9	30
P9B	0.013	0.8	93.2	0.148	0.0153	0.13	0.102	88.2	90

parameters). Moreover Qs^{OUT} is the mean outgoing sediment transport rate.

The total duration of each run has been set depending upon the morphologic activity of the network. It ranged between 30 and 110 hours. During each run we have monitored the solid discharge at the downstream end of the flume, measuring the weight of the sand cumulated in a submerged tank, held up by four load cells.

The acquisition time interval has been set equal to 1–5 minutes. The minimum recording interval is imposed by the accuracy of the load cell and the amount of transported sand. The planimetric configuration of the network has been reconstructed through 15 vertical images that have been then stitched and scaled. The images have been processed to obtain information on the width of the braid belt and of the single channels, the number of branches, their length, the number and position of the morphological active channels, the characteristics of the bifurcations.

3 DATA ANALYSIS

In order to investigate the timescale of the bed load fluctuations we have used a Fourier transform analysis. In spite of the complexity of the signal and of the presence of irregular time fluctuations such analysis has provided reasonably good results.

A first analysis performed on the rough data has highlighted the existence of dominant harmonics, though the signal displayed a high degree of irregularity. Therefore we have decided to pre-process the data and to select suitable, albeit shorter, data record.

The signal has been smoothed with a moving average procedure based on 5, 10 and 30 minutes intervals. Such procedure returned a more clear signal, where the fluctuations with a timescales of the order of few hours have been detected more easily: the Fourier spectrum shows in this case the presence of more distinguishable dominant harmonics.

These fluctuation frequencies have been then checked and more precisely defined by a further step. The Fourier analysis has been carried out on a 'window' of data, that moves along the whole data set. The length of the window, i.e. the number of data on which the Fourier transform has been applied, has been defined as a n-multiple of the timescale previously found. In this way it has been possible to assess the regularity of the signal and to single out ranges of data characterized by a more clear spectrum, where the oscillation can be more easily detected.

The evaluated timescales for a selection of experiments are reported in Figure 3 (only few values are plotted to keep the readability of the figure). The above analysis provides for each run an evaluation of the wavelength of the dominant harmonics, however a general behaviour can hardly be detected. Figure 3 shows the presence of different fluctuations scales, ranging from tens of minutes to few hours. The question then arises whether the occurrence of different timescales can be the results of a non linear interaction among various processes, such to produce a cascade of oscillations. On the other hand, as the sediment transport is intrinsically related to the altimetric and planimetric development of the channels, distinct fluctuations and precise timescales can be determined by the evolutionary scales of the network. In this respect it is worth noticing that theoretical and experimental research on the unit processes of braiding (Bolla Pittaluga et al. 2001) has pointed out the existence of defined timescales of some of the recurring processes.

For example a well known phenomenon is the occurrence of migrating bed waves. According to the

Copyright © 2006 Taylor & Francis Group plc, London, UK

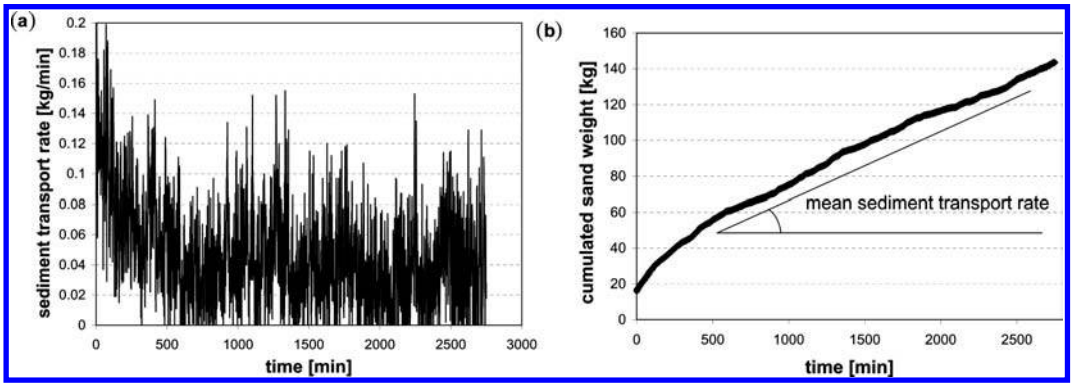


Figure 2. (a) sediment transport rate as a function of time; (b) cumulated weight of transported sand (run P4B).

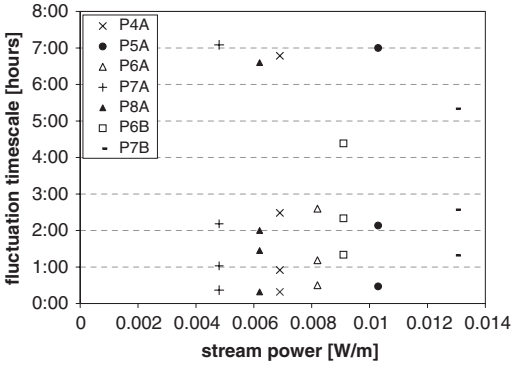


Figure 3. Some examples of different timescales of sediment transport fluctuations.

weakly non linear theory of Colombini et al. (1987) it is possible to determine the migration speed of the alternate bars, that have been invariably observed to form throughout the whole runs. In our experiments, bars have been found to migrate with a period of approximately 30 minutes. Analogous estimates have been obtained in previous experiments where alternate bar developed in a single almost straight channel (see Bertoldi et al. 2005).

The problem of the temporal evolution of a Y-shaped bifurcation has been tackled recently through theoretical (Miori et al. 2006) and experimental works (Bertoldi et al. 2005). They have shown that a bifurcation evolves toward an unbalanced equilibrium configuration, in which the downstream distributaries are characterized by an uneven flow and sediment distribution. Furthermore the process seems to be regulated by an intrinsic timescale, which is typically much smaller than the morphological timescale which is required to adapt to the influence of downstream boundary conditions.

Hence, though the dominant harmonics we have detected can not be accurately resolved, it is reasonable to consider that they reflect different planimetric and altimetric processes that concur in the evolution of the network.

4 BED LOAD TRANSPORT RATE ANALYSIS

Figure 2 shows an example of the measured bed load transport rate (run P4B). In Figure 2(a) the sediment discharge (averaged over 5 minutes interval) is given as a function of time while in Figure 2(b) the cumulated transport rate is reported. The analysis of the bed load transport rate data shows that it is possible to distinguish an initial period in which the sediment transport is more intense. This is due to the higher bed load transport capacity that characterizes the initial straight channel, which decreases when the width and the number of branches increases. The plot of the cumulated sediment transport (Figure 2b) shows that, after the first hours, the total sand weight increases almost linearly, with a constant slope, which changes in each run. In these conditions we can consider the network to be fully developed and in equilibrium with the upstream sand feeding. The mean values and the amplitude of the fluctuations reported in the following plots have been computed with reference to this period of dynamic equilibrium.

In Figure 4 we report the mean sediment transport rate for each experimental run as a function of the stream power. The values follow a power law relationship with an exponent equal to 1.54. Figure 4 also shows the minimum and the maximum transport rate, averaged over an interval of 30 minutes, for each run. The values range from 0 to about 3–4 times the mean value and the amplitude of the fluctuations increases for larger values of the stream power. The high variability highlighted by this analysis, though data are averaged on a quite long interval, points out the complexity and, in some cases, the randomness of field measurements of bed load transport.

Copyright © 2006 Taylor & Francis Group plc, London, UK

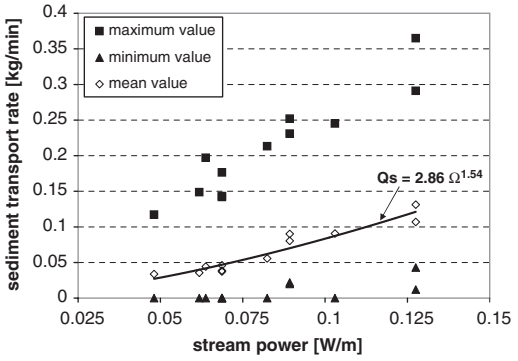


Figure 4. Minimum, mean and maximum sediment transport rate as a function of the stream power for each experimental runs (data are averaged on 30 minutes interval).

In order to compare the data with other experimental results we have introduced two dimensionless parameters, that account for the effect of mean sediment diameter. Both the sediment transport rate and the stream power have been divided by the sediment transport scale and by the flume width B_f as follows:

$$\phi = \frac{Q_s}{B_f\sqrt{g\Delta d_s^3}}, \qquad \omega = \frac{Q \cdot S}{B_f\sqrt{g\Delta d_s^3}}, \tag{1}$$

where g is gravity.

In Figure 5 a comparison between present results and data obtained by Ashmore (1988), Young and Davies (1990), Hoey and Sutherland (1991) and Warburton and Davies (1994) is reported. A similar behaviour is exhibited in all cases, with an average exponent of the power law ranging about 1.8. Some runs display a lower sediment flux, but this could be due to the choice of the flume width B_f as the scale of the experiments, since the active width of each run can not be easily determined in previous works.

As pointed out before, the temporal series display a wide range of fluctuations, characterized by different timescales (see Figures 2a and 3).

In the following plots we report some examples of the bed load transport rate fluctuations and the results of the Fourier analysis in terms of the timescales as a function of the stream power. The main harmonics (reported in Figure 3) can be divided in three groups, with characteristics frequencies and similar amplitudes: a short timescales with a period of 20–30 minutes, two medium fluctuations characterized by a period of 1–2 hours and a longer oscillation with a period ranging about 4 to 8 hours.

The shorter timescale (see Figure 6) is comparable with the autocorrelation time of the sediment transport measures found in previous laboratory investigations (e.g. Ashmore 1988 and Hoey and Sutherland 1991).

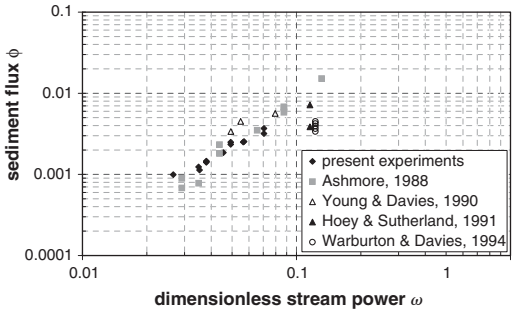


Figure 5. Comparison of mean sediment flux for different experimental works as a function of the dimensionless stream power ω.

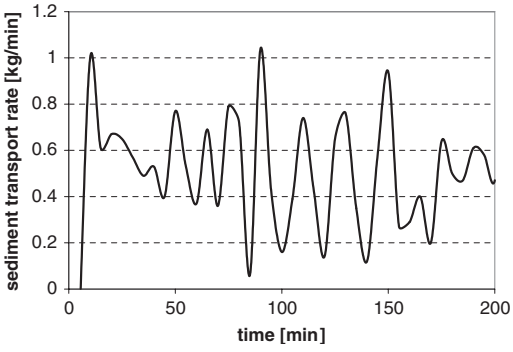


Figure 6. Typical bed load fluctuations determined by the migration of alternate bars (run P4A).

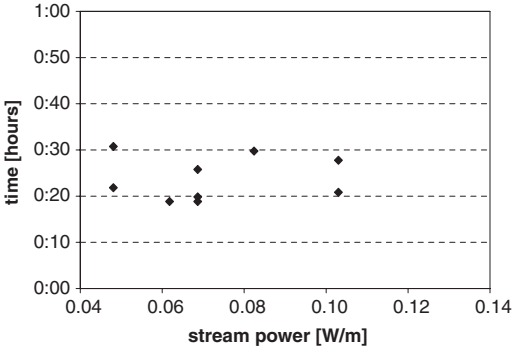


Figure 7. Short term timescale for each experimental runs.

In these series of runs this fluctuation is clearly distinguishable in the first hours, when the planimetric configuration is still characterized by the presence of a single channel, but it is also present during the whole run, superimposed to the other fluctuations.

In Figure 7 we report the computed short timescale for each experimental run. The period is quite constant

Copyright © 2006 Taylor & Francis Group plc, London, UK

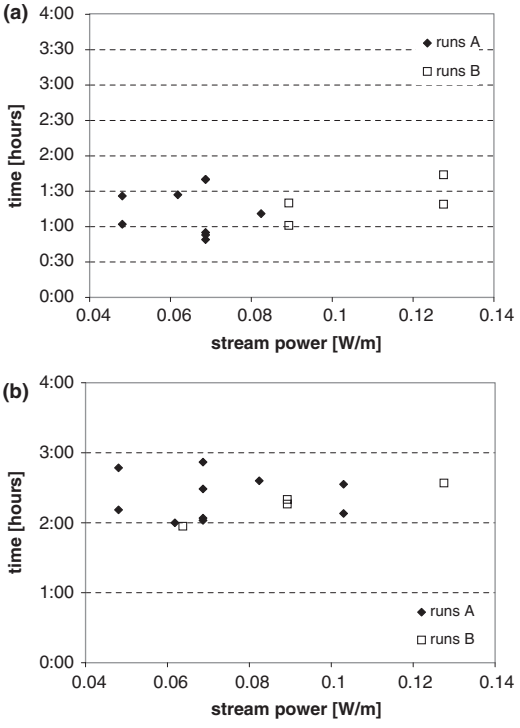


Figure 8. Medium bed load fluctuations timescale evaluated for each run.

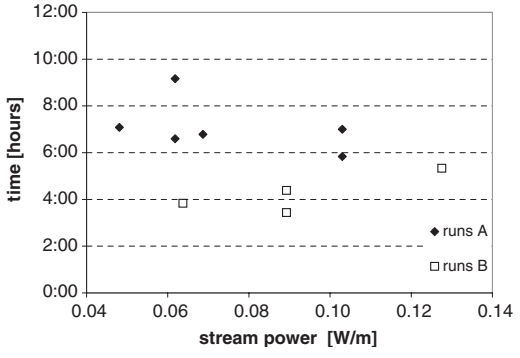


Figure 9. Long bed load fluctuations timescale evaluated for each run.

and does not seem to be strongly affected by the different water and sediment supply.

The two 'medium' timescales range respectively from 1 to 1.5 hours and from 2 to 3 hours. In Figure 8 the obtained values are reported as a function of the stream power Ω. Furthermore Figure 10(a) shows an example of the medium term bed load fluctuations: these oscillations are more clearly detectable on the record of data averaged over 30 minutes interval.

In Figure 10(b) the sediment transport rate is plotted for an interval of about 15 hours. It is possible to notice four subsequent phases of high sediment discharge, characterized by similar frequencies, even if the shape and the amplitude are not regular. This is an example of the long term bed load fluctuations that we have detected through the Fourier analysis. We may notice that the above timescale can be hardly singled out, because of the interference of the other scales on the signal. Figure 9 shows the result of the bed load data records analysis, in terms of the long term dominant harmonic of the Fourier spectrum. This timescale is characterized by a higher variability, since its values range between 4 and 7 hours. This variability can be due to the different configuration of the branches in the runs with a longitudinal slope of 0.7% and 1.3% (see next Section).

5 BED LOAD FLUCTUATIONS AND CHANNEL PROCESSES

In this Section we try to relate the timescales of the bed load fluctuations to the braided network evolution, characterized by the migration of bed forms and by the change in the number and relative position of the branches. The analysis is based both on the detailed topographic data collected in present experiments and on the results of recent investigation carried out on the bifurcation process (see Tubino and Bertoldi 2006).

The short term fluctuations can be related to the formation of migrating bars, that induces regular bed load waves. This phenomenon is more evident in the first phase of the run, when no other channel process influences the sediment transport, but it occurs also when the network is fully developed. In particular we observed the formation of migrating bars when the network is subject to a degrading process. In this case the high erosion rate determines a more intense sediment transport, that gets organized in the form of alternate bars. Moreover, in the degrading phases the network displays a more simple structure, consisting of few branches displaying an almost straight pattern.

The analysis of the vertical images taken on regular intervals allows for an estimate of the migration period of the alternate bars. The measured time step between the transit of two subsequent bars corresponds with high accuracy to the observed short bed load fluctuations timescale. The existence of this short term fluctuation, along with the observation that the correlation time of the sediment transport rate is of the order of 20–30 minutes (Ashmore 1988; Hoey and Sutherland 1991) points out that the movement of sediment in a gravel bed braided stream is generally organized in the form of migrating bars.

The medium and long term oscillations have been related to the planimetric evolution of the network and

Copyright © 2006 Taylor & Francis Group plc, London, UK

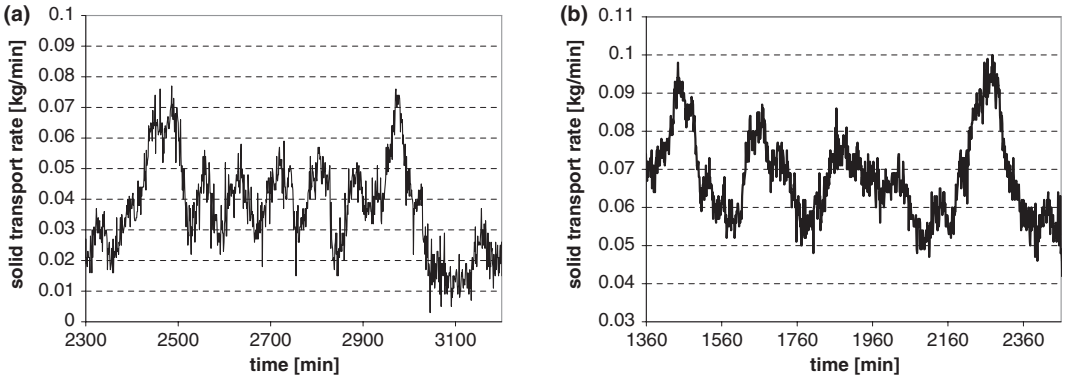


Figure 10. Two examples of medium and long term bed load fluctuations. Data are smoothed on a 30 minutes interval. (a) run P4B, with clear 1.5 hours oscillations; (b) run P5B, shows 3.5 hours oscillations.

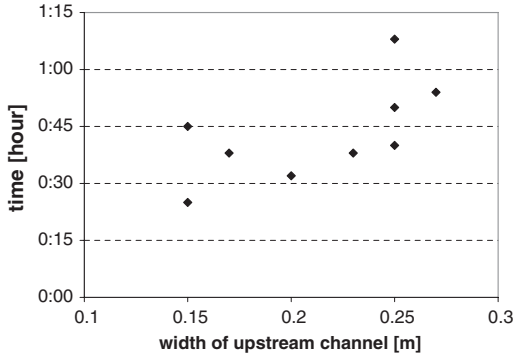


Figure 11. Timescale of bifurcation evolution.

in particular to the processes governing the dynamics of the nodes and of the main branches in the network.

A bifurcation is likely to assume an unbalanced configuration when the upstream channel is characterized by low values of the Shields parameter and relatively high values of the aspect ratio. These conditions are easily found in gravel bed braided networks and, as a consequence, the nodes are subject to a process that leads to the closure of one of the downstream distributaries. A bifurcation undergoing such evolution determines a fluctuation of the sediment transport rate, as far as the bed load capacity of one channel carrying the total discharge is different from that of two branches. In fact, the total sediment discharge of a symmetrical node in which the flow is equally distributed is generally lower than that of a strongly unbalanced bifurcation, with a large part of water and sand flowing in the main branch. Similarly, aggrading phases are associated with a high braiding intensity, whereas degrading periods are characterized by few incised channels.

We have analyzed the evolution of single bifurcations inside the network, measuring the time during which both the distributaries of a newly formed bifurcation are characterized by sediment transport, and consequently can be defined active in a morphodynamic sense. The results of this observation are reported in Figure 11, as a function of the width of the upstream branch. We have found that this scale ranges between 1 and 2 hours, in agreement with the experimental observation on Y-shaped bifurcations of Bertoldi et al. (2005). This timescale is quite close to the medium fluctuations highlighted through the Fourier analysis of the bed load transport rate.

The planimetric timescale of the network can be quantified in a different way taking into consideration the shift of branches inside the network. The lateral evolution of the main channel has been monitored by a detailed photographic survey. We have observed that the channel moves frequently inside the network, changing its position through two different mechanisms. Most of the time the main channel moves slowly, evolving like a weakly meandering channel that increases its axis curvature through the erosion of the outer bank. The second process, which seems to be peculiar of the dynamic rearrangement of braiding systems, is a rapid shift of the position of the main channel, that leads to a markedly different network configuration.

In Figure 12 we give an example of the lateral migration of the main branch just upstream of the downstream tailgate of the flume (run P8A). Experimental data suggest a strong correlation between high sediment transport phases and rapid migration of the main branch. On the other hand, low sediment transport rates are recorded when the active channels move slowly.

We have monitored the transversal location of the main channel in different cross sections along the

Copyright © 2006 Taylor & Francis Group plc, London, UK

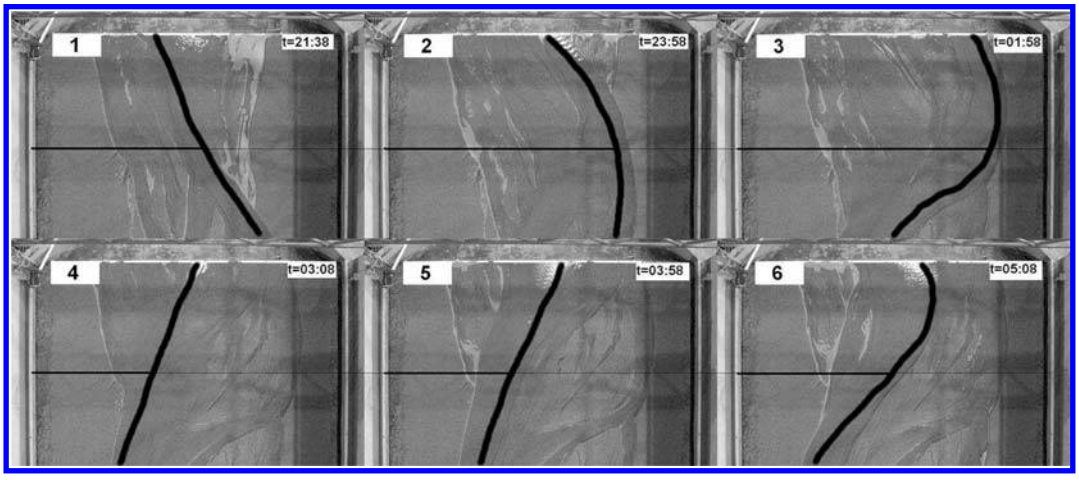


Figure 12. An example of the lateral migration of the main branch, flow is from bottom to top (run P8A).

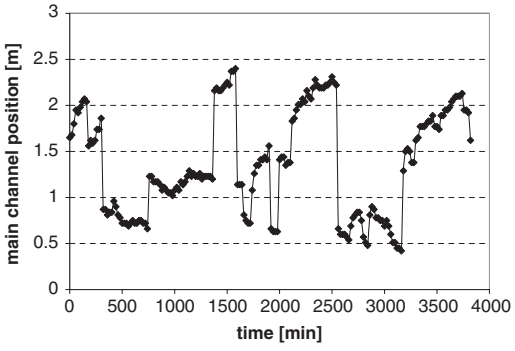


Figure 13. An example of the transversal fluctuations of the main branch (run P8A).

network (an example is reported in Figure 13). The time interval between two subsequent rapid shifts has been analyzed in order to obtain the corresponding timescale. We have found that it can be well represented by a log-normal distribution (reported in Figure 14). In particular we have measured a mean shift interval equal to approximately 100 minutes, that again correspond to the medium bed load fluctuations. The sudden movements of the main channel are actually determined by the modification of the flux distribution in an upstream bifurcation. Moreover, the data in Figure 14 display a not negligible probability of shift characterized by a timescale of 3–4 hours. As a result, the long term oscillations plotted in Figure 9 can be related to the sudden changes that determine a complete rearrangement of the network and the transition of the main branch from one side to the other of the flood plain. This process can be also influenced by the development of an axis curvature in the main channels. The different timescales evaluated for the *A* and the *B* runs (Figure 9) can be explained considering that the runs characterized by a lower value of the longitudinal slope generally showed a higher sinuosity and therefore larger values of the maximum curvature.

6 CONCLUSIONS

In this paper we present the results of an experimental work on braided networks, in which detailed measures of both sediment transport rate and planimetric configuration have been carried out, in order to quantify the characteristic timescales. The main conclusions of the analysis are summarized in the following.

1. Bed load time series show a wide range of fluctuations that can be characterized by few dominant timescales. The variability is not random, but defined modes of oscillation have been recognized, through a Fourier transform analysis of the data records.
2. Three different timescales have been found, that in the model show a period of about 30 minutes, 1–2 hours, 4–7 hours.
3. The shorter fluctuations are determined by the migration of bed forms. They are more clearly visible in the first phase of the runs, when other processes are absent, though we observed the formation and migration of alternate bars during the whole run.
4. The second timescale can be related to the evolution of the bifurcations. The variation of the water and sediment distribution occurring at a node that evolves toward an unbalanced equilibrium configuration affects the sediment transport along the network, determining a sequence of aggrading and degrading phases.

Copyright © 2006 Taylor & Francis Group plc, London, UK

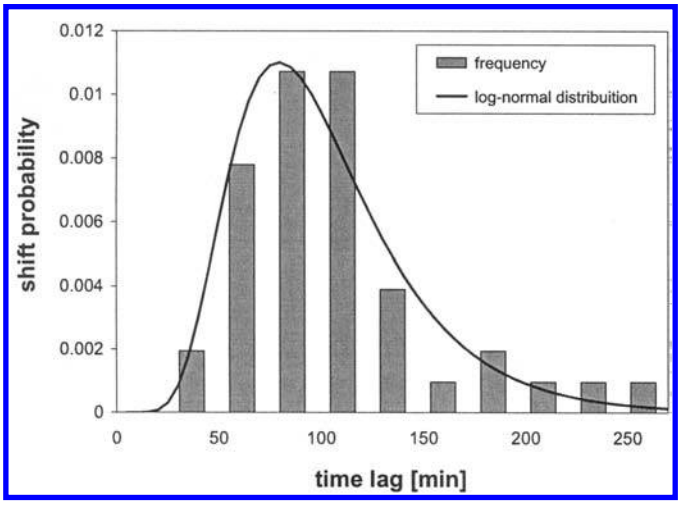


Figure 14. Timescale of the main channel shifts.

5. The longer timescale is controlled by the planimetric rearrangement of the network. We have observed that the main branch shifts its position within the network with a timescale comparable to that of the bifurcation evolution, but longer time lags are possible, in particular when the single channels develop a higher axis curvature.

ACKNOWLEDGMENTS

This work has been developed within the framework of the 'Centro di Eccellenza Universitario per la Difesa Idrogeologica dell'Ambiente Montano – CUDAM' and of the project 'La risposta morfodinamica di sistemi fluviali a variazioni di parametri ambientali – COFIN 2003', co-funded by the Italian Ministry of University and Scientific Research (MIUR) and the University of Trento and of the project 'Rischio Idraulico e Morfodinamica Fluviale' financed by the Fondazione Cassa di Risparmio di Verona, Vicenza, Belluno e Ancona. The authors gratefully acknowledge the fundamental support of Federica Castaman, Alessio Pasetto, Martino Salvaro and the staff of the Hydraulic Laboratory of the University of Trento who helped in the execution of the experimental runs.

REFERENCES

Ashmore, P. (1988). Bed load transport in braided gravel-bed stream models. *Earth Surface Processes and Landforms 13*, 677–695.

Ashmore, P. (2001). *Braiding phenomena: statics and kinetics*, pp. 95–121. in Gravel-bed Rivers V, Mosley M.P. (eds), New Zealand Hydrological Society, Wellington.

Bertoldi,W., A. Pasetto, L. Zanoni, and M. Tubino (2005). Experimental observations on channel bifurcations evolving to an equilibrium state. In *Proceedings of RCEM2005 Conference, Urbana, Illinois, USA, 4–7 October*, pp. 409–419.

Bolla Pittaluga, M., B. Federici, R. Repetto, C. Paola, G. Seminara, and M. Tubino (2001). *The morphodynamics of braiding rivers: experimental and theoretical results on unit processes*, pp. 143–181. in Gravel-bed Rivers V, Mosley M.P. (eds), New Zealand Hydrological Society, Wellington.

Colombini, M., G. Seminara, and M. Tubino (1987). Finite-amplitude alternate bars. *Journal of Fluid Mechanics 181*, 213–232.

Hoey, T. (1992). Temporal variations in bedload transport rates and sediment storage in gravelbed rivers. *Progress in Physical Geography 16 (3)*, 319–338.

Hoey, T. and A. Sutherland (1991). Channel morphology and bedload pulses in braided rivers: a laboratory study. *Earth Surface Processes and Landforms 16*, 447–462.

Miori, S., R. Repetto, and M. Tubino (2006). A one-dimensional model of bifurcations in gravel-bed channels with erodible banks. *Water Resources Research submitted.*

Murray, B. and C. Paola (1994). A cellular model of braided rivers. *Nature 371*, 54–57.

Paola, C. (2001). *Modelling stream braiding over a range of scales*, pp. 11–46. in Gravel bed rivers V, Mosley M.P. (eds), New Zealand Hydrologic Society, Wellington.

Tubino, M. and W. Bertoldi (2006). *Bifurcations in gravel-bed streams.* in Gravel Bed Rivers 6. (in publication).

Warburton, J. and T. Davies (1994). Variability of bedload transport and channel morphology in a braided river hydraulic model. *Earth Surface Processes and Landforms 19*, 403–421.

Young, W. and T. Davies (1990). Prediction of bedload transport rates in braided rivers: a hydraulic model study. *Journal of Hydrology (N.Z.) 29 (2)*, 75–92.

Copyright © 2006 Taylor & Francis Group plc, London, UK

Conceptual model for the bedload layer of gravel bed stream based on laboratory observations

Rui M.L. Ferreira
Instituto Superior Técnico, Lisbon, Portugal

João G.A.B. Leal
Universidade da Beira Interior, Covilhã, Portugal

António H. Cardoso
Instituto Superior Técnico, Lisbon, Portugal

ABSTRACT: A conceptual model for the morphological and textural evolution of gravel bed rivers is proposed. It is composed of conservation and closure equations. The former are drawn from the shallow-water theory, using a multiple layer framework and the continuum hypothesis for each transport layer. The latter specify flow resistance and phenomena pertaining to the dynamics of gravel transport. Special attention is given to the theoretical formulation of the velocity of the bedload layer and to the experimental characterization of the grain and water velocities. For that purpose, new experimental gravel transport data is presented. The proposed formulation envisages the incorporation of sediment dynamics in the overall momentum conservation equation. The model is applied to a simple test case, strong overfeeding imposed at the upstream end of a mild-sloped mobile bed channel. The numerical results of the proposed model are compared with those of a classic de Vries-type model. It is argued that the inclusion of the dynamics of the transported particles represents a major change in the structure of the morphological models, thus justifying further research efforts.

1 INTRODUCTION

The mathematical modelling of the morphological and textural evolution of gravel bed rivers requires a conceptual model composed of conservation equations and of closure equations. The former are generally drawn from the shallow-water theory. The latter specify, among other aspects, flow resistance and phenomena pertaining to the dynamics of gravel transport.

Since the work of Hirano (1971), the physical domain has been idealized as layered system. Earlier modelling attempts would either conceptualize the entire flow depth as a continuum or simply ignore the dynamic effects of the added density by assigning an infinitely small thickness to the bedload layer (de Vries 1965). In order to include the inertia of the transported sediment, the bedload layer can be idealized as a continuum (in the sense of Atkin and Crane (1976) whose density depends on the sediment concentration.

Ferreira (2005), §2, pursuing objectives earlier stated by Ferreira and Cardoso (2000), developed a multiple-layer model for the transport of poorly sorted mixtures. In that model, the continuum hypothesis was embraced and the problem of the velocity lag between water and sediment was explicitly addressed.

In this paper, the continuum multiple-layer model is further explored. The main objectives are: (i) the derivation of an expression for the velocity of the bedload layer, depending on the grain and water velocities; (ii) the development of a conceptual model incorporating the continuum bedload layer; and (iii) the validation of the model using a simple test case. To pursue these objectives, theoretical, experimental and numerical modeling work was carried out. The main theoretical issues are presented in section 2. The conceptual model is presented with emphasis on the idealization of particle-fluid segregation and respective mathematical treatment.

The experimental work is described in section 3. Grave bed experiments under hydraulically uniform conditions and equilibrium transport (capacity conditions) were carried out in a recirculating flume. The velocity of the gravel size fractions was investigated with the help of a particle tracking algorithm. Water velocity at the upper regions of the bedload layer was measured with Laser Doppler annemometry. The results are shown in section 4.

The validation of the model is carried out in section 5. A simple test case, upstream overfeeding upon an uniform subcritical flow, is proposed in order to

Copyright © 2006 Taylor & Francis Group plc, London, UK

identify the differences between the continuum model and the classical de Vries-type model. The discussion of the performance of the model takes place in the last section of the paper.

2 CONCEPTUAL MODEL

2.1 *Description of the physical system*

A conceptual model for the modelling of the morphological and textural evolution of gravel bed rivers can be derived by means of a control volume analysis within the shallow-water framework.

Two flow layers are identified in figure 1. The uppermost layer transports clear water and, possibly, wash load. It is admitted that the bed material is sufficiently coarse so that no suspended sediment is generated locally.

In a confined layer above the bed, termed bedload layer, sediment particles are transported as contact load. The localization of the boundaries of the bedload layer is a matter of convention. The lower boundary is the bed surface. Following a procedure similar to that of Parker et al. (2000), Ferreira (2005), p. 86–87, defined the bed surface as the elevation above the lowest trough for which the percentage of area occupied by solids is 15. As for the upper boundary, it is assumed that the thickness of the bedload layer should scale with the saltation height.

There exists segregation between the sediment particles transported in the bedload layer and the mean flow: the ensemble average of the path-averaged velocity of the sediment particles (see section 4.1) of any given size fraction is lower than the time- and space-averaged velocity of the water in the bedload layer.

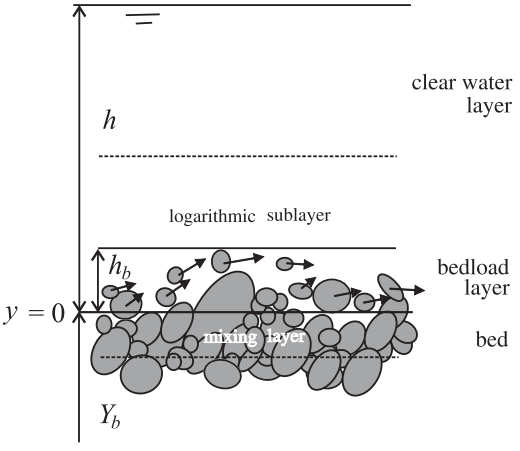


Figure 1. Idealised physical system. The involved variables and parameters are h, the flow depth, h_b, the thickness of the bedload layer, Y_b, the elevation of the bed and y, the vertical co-ordinate.

The upper bed region is the mixing layer (Hirano 1971). The trade-off between the bed and the transport layer is controlled by the dynamics of this layer. Acting like a filter, it controls both the incoming fractions to the bed and the outgoing fractions to the transport layer.

It is hypothesized that the flow is rough turbulent and two-dimensional. Furthermore, Townsend's wall-similarity hypothesis (see Townsend 1976, p. 135–143) is assumed to hold. Hence, there is a region above the bedload layer where the velocity profile is logarithmic and that Reynolds stresses $-\rho^{(w)}\overline{u'w'}$ (where u' and w' stand, respectively, for the fluctuations of the longitudinal and vertical velocity), make up for the totality of the shear stress and are linearly distributed. Above this region, the velocity profile will eventually suffer the effect of the free-surface and deviate from the log-profile.

In the bedload layer, the mean flow interacts with the moving particles and with the wakes of the protruding grains. The structure of the flow is determined by the shape, surface density and arrangement of the roughness elements (protruding grains or clusters or exposed grains) and by the intensity of the bedload transport (Ferreira 2005; Nikora et al. 2001). The overall effect of these interactions to the two-dimensional flow is that of a sink of momentum. As a result, the velocity profile is bound to strongly deviate from the log-law.

Theoretical and experimental results by Nikora et al. (2001) and experimental results by Ferreira (2005), p. 91–92, show that the profile of the time- and space-averaged velocity in the bedload layer should be linear.

2.2 *The continuum approach*

The equation of conservation of the mass of sediment in the bedload layer can be obtained from a control volume analysis for the discrete set of particles actually in motion (details *in* Ferreira 2005, p. 18–41). It reads

$$\partial_t \left(\hat{C}^{(2)} h_b \right) + \partial_x \left(\hat{C}^{(2)} h_b u_b^{(g)} \right) = \phi_{2,3}^{net} \tag{1}$$

where t and x stand for the time and space co-ordinates, h_b is the thickness of the bedload layer, $u_b^{(g)}$ is ensemble average of the path-averaged grain velocity (irrespectively of the class size), $\phi_{2,3}^{net}$ is the vertical net flux of sediment between the bed and the bedload layer and $\hat{C}^{(2)}$ is the depth-averaged concentration. The latter is defined as

$$\hat{C}^{(2)} = \frac{\forall_g^{(2)}}{\forall^{(2)}} \tag{2}$$

where $\forall_g^{(2)}$ is the average volume of the particles moving in any given control volume enclosing the bedload

Copyright © 2006 Taylor & Francis Group plc, London, UK

layer between two vertical cross-sections and $\forall^{(2)}$ is the size of that control volume.

In the wake of de Vries (1965), early mobile bed models would conceptualize the entire flow depth as a continuum or simply ignore the dynamics of the bedload. Under non-equilibrium transport and for sufficiently high sediment concentrations, the inertia of the granular phase, in particular the convective inertia, may play a relevant role in the morphological evolution of the stream. In order to include these inertial terms, the bedload layer can be idealized as a continuum (in the sense of Atkin and Crane 1976) whose density depends on the sediment concentration. The mixture of water and sediment, although idealized as continuous, remains non-homogeneous and fluid-particle segregation must be addressed.

In the continuum approach, the mass flow rate characteristic of the bedload layer must be maintained. It can be defined as $\rho_b q_b$ where $q_b = u_b h_b$ is the total volumetric discharge in the bedload layer, u_b is the layer velocity and $\rho_b = \rho^{(w)}(1 + (s-1)C_b)$ is the layer density. The parameter s is the specific gravity of the bedload grains. The concentration C_b is a flux-averaged layer concentration, defined as

$$C_b = \frac{q_{gb}}{q_b} \tag{3}$$

where q_{gb} is the volumetric bedload discharge.

The idealisation of the physical system within the continuum approach can be seen in figure 2. The layer velocity can be obtained from the integration of the mean longitudinal velocity profile of the water constituent and from the average velocity of grains moving as bedload. The velocity in the clear water layer can also be obtained from the velocity profile. These velocities can be parametrised for the friction velocity, which can be drawn from the $\overline{u'w'}$ profile. Under the shallow-flow hypothesis, the pressure distribution is hydrostatic. It should be noticed (figure 2) that, within the continuum approach, the slope of the pressure diagram must be larger in the bedload layer

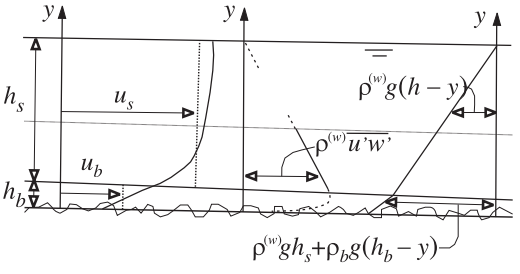


Figure 2. Idealised physical system for the multiple layer approach. The involved previously unspecified variables and parameters are h_s, the thickness of the clear water layer, u_s, the velocity of the clear water layer.

than in the clear water layer due to the greater layer density.

Under the shallow-flow hypothesis and within the continuum paradigm, the equation of conservation of momentum can be obtained for the bedload layer (details *in* Ferreira 2005, p.23–23):

$$\begin{array}{c} \partial_t\left(\rho_b h_b u_b\right) + \\ \partial_x\left(\rho_b u_b^2 h_b + g\left(\frac{1}{2}\rho_b h_b^2 + \rho^{(w)} h_s h_b\right)\right) + \\ g\rho_b h_b \partial_x\left(Y_b\right) = -\tau_b + \tau_s + \rho^{(w)} u_1 \phi_{2,3}^{net} \end{array} \tag{4}$$

In equation (4) the previously unspecified variables ans parameters are τ_b, the bed shear stress, τ_s, the shear stress between the bedload layer and clear water layer and g, the acceleration of gravity. A relation among the variables that describe the discrete system, $u_b^{(g)}$ and $\hat{C}^{(2)}$ (used in equation 1), the fluid velocity and the continuum variables u_b and C_b (employed in equation 4) will be sought next.

2.3 *Bedload layer variables*

The layer velocity can be obtained from mass conservation. The total discharge in the bedload layer is

$$q_b = q_{gb} + q_{wb} = h_b u_b \tag{5}$$

where $q_{gb} = \hat{C}_b^{(2)} h_b u_b^{(g)}$ is the sediment discharge in the bedload layer, $q_{wb} = (1 - \hat{C}_b^{(2)}) h_b u_b^{(w)}$ is the water discharge in the same layer and $u_b^{(w)}$ is the time- and space-averaged flow velocity in the bedload layer. Hence, from the above definitions and from equation (5), the bedload layer velocity can be written as

$$u_b = u_b^{(w)} - \hat{C}^{(2)}\left(u_b^{(w)} - u_b^{(g)}\right) \tag{6}$$

Further elaborating over the relation between the layer velocity and the grain and water velocities, consider a control volume whose length, height and width are, respectively, $u_b^{(w)}\,\mathrm{d}t$, h_b and B, the later being the width of the channel. The size of the control volume is, thus, $\forall^{(2)} = B h_b u_b^{(w)}\,\mathrm{d}t$. Inside the control volume there are N moving particles at a given instant t_0. The number of particles that leave the control volume between t_0 and $t_0 + \mathrm{d}t$ is n. Considering that there is segregation between fluid and sediment and that the particles move slower than the fluid, one has $n \leq N$.

Ensemble-averaging over a large number of control volumes whose length is $u_b^{(w)}\,\mathrm{d}t$ it is obtained

$$\frac{\langle n \rangle}{\langle N \rangle} \cong \frac{u_b^{(g)}}{u_b^{(w)}} \stackrel{def}{=} \frac{1}{\alpha_*} \tag{7}$$

The result expressed in equation (7) requires that the system is ergodic, *i.e.* that the time-averaged velocity

Copyright © 2006 Taylor & Francis Group plc, London, UK

of the particles in the control volume is, in the limit, equal to the ensemble average of the velocities of all particles in the system. Although not strictly necessary, it is also assumed that the moving particles are not organized in bed forms.

Introducing the definition of α_* in equation (6), one obtains

$$u_b = u_b^{(g)} \left(\alpha_* + \hat{C}^{(2)} \left(1 - \alpha_* \right) \right) \tag{8}$$

Equation (8) can be used to re-write the flux of sediment in the bedload layer. It is obtained

$$q_{gb} = \frac{\hat{C}^{(2)}}{\alpha_* + \hat{C}^{(2)} \left(1 - \alpha_* \right)} h_b u_b \tag{9}$$

It is easy to verify that the term $\hat{C}^{(2)}/(\alpha_* + \hat{C}^{(2)}(1-\alpha_*))$ is the flux-averaged concentration of sediment in the bedload layer. For that purpose, let $N \equiv \langle N \rangle$ be the number of moving particles in the control volume and let $n \equiv \langle n \rangle$ be the number of particles that leave the control volume. The bedload becomes

$$q_{gb} = n \forall^{(g)} \tag{10}$$

where $\forall^{(g)}$ is the volume of each particle. The total discharge in the bedload layer is

$$q_b = B h_b \mathrm{d}x - N \forall^{(g)} + n \forall^{(g)} \tag{11}$$

where $\mathrm{d}x = u^{(w)}\, \mathrm{d}t$. The quantities $B h_b \mathrm{d}x - N \forall^{(g)}$ and $n \forall^{(g)}$ are, respectively, the volumes of water and of sediment that leave the control volume during the time interval $\mathrm{d}t$. Introducing equations (10) and (11) in (3), the flux-averaged concentration of sediment becomes

$$C_b = \frac{n \forall^{(g)}}{B h_b \mathrm{d}x - N \forall^{(g)} + n \forall^{(g)}} \tag{12}$$

Introducing the expressions for the volume of sediment and for the total volume, the depth-averaged concentration of sediment in the bedload layer, defined as (2), becomes

$$\hat{C}^{(2)} = \frac{N \forall^{(g)}}{B h_b \mathrm{d}x} \tag{13}$$

Dividing both the numerator and the denominator of equation (12) by $B h_b \mathrm{d}x$, introducing equation (13) and attending to the definition of α_*, equation (7), equation (12) becomes $C_b = \hat{C}_b^{(2)}/(\alpha_* + \hat{C}_b^{(2)}(1-\alpha_*))$, which completes the verification.

For computational convenience, the volume of sediment, per unit bed area, accumulated in the bedload layer, term $\hat{C}_b^{(2)} h_b$ in equation (1), should be written in terms of flux-averaged quantities, for which

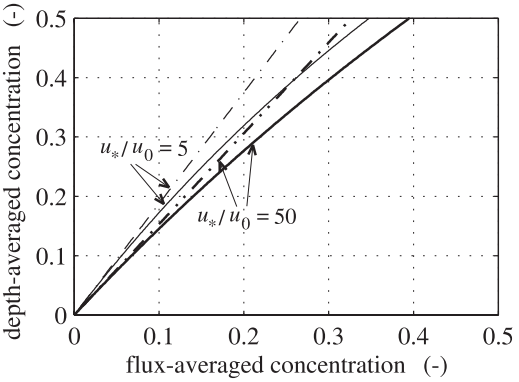


Figure 3. Relation between depth-averaged and flux-averaged concentrations with α_* calculated by equation 14.

purpose α_* must be estimated. The fluid velocity in the bedload layer may be expressed as $u_b^{(w)} = \alpha^{(w)} u_*$ where $\alpha^{(w)} = \alpha^{(w)}(X)$, $X = u_* d_{50}/\nu$ and d_{50} is the median diameter of the bed material. As for the mean velocity of the coarse grains, it will be seen that $u_b^{(g)} = \alpha_c (u_* - u_0)$ where u_0 is a best fit parameter. Hence, from definition (7), one has

$$C_b = \frac{\hat{C}_b^{(2)}}{\alpha_* + \hat{C}_b^{(2)} \left(1 - \alpha_* \right)} \tag{14}$$

Let $\alpha^{(w)} = 7.1$, $\alpha_c = 4.5$ and $u_0 = 0.029\,\mathrm{ms}^{-1}$ (see section 4). Equation (**??**), with α_* calculated by equation (14), can be plotted along with $\hat{C}_b^{(2)} = \alpha_* C_b$. The results can be seen in figure 3.

From figure 3 it is concluded that (i) the depth-averaged concentration of sediment is, for low values of the friction velocity (*eg.* $u_*/u_0 = 5$), about two times the flux-averaged velocity; (ii) the greater the friction velocity (the more intense the bedload) the smaller the difference between the dept-averaged and the flux-averaged velocities and (iii) equation (**??**) is well approximated by

$$\hat{C}_b^{(2)} = \alpha_* C_b \tag{15}$$

provided that the depth-averaged concentrations are less than 0.2; in this case the error between the computed flux-averaged concentrations is less than 10%.

Thus, it will be assumed that the relation between flux- and depth-averaged concentrations on the bedload layer is given by equation (15). Introducing this equation in (1), it is obtained

$$\partial_t \left(\alpha_* C_b h_b \right) + \partial_x \left(C_b h_b u_b \right) = \phi_{2,3}^{net} \tag{16}$$

Equation (16) is the equation of conservation of the total mass of sediment in the bedload layer written in conservative form.

Copyright © 2006 Taylor & Francis Group plc, London, UK

The scope of this study is restricted to flows for which the role of the mixing layer is negligible *eg.* when the bed is composed of well-sorted sediment or if all size fractions are imposed in the bedload. Within this scope, the remaining set of conservation equations is shown next.

2.4 *The complete model*

The complete set of conservation equations comprises (i) the equation of conservation of the total mass

$$\partial_t (h) + \partial_x (hu) = \tfrac{1}{(1-p)} \phi_{2,3}^{net} \tag{17}$$

where u is the mean flow velocity, defined as $(u_b h_b + u_s h_s)/h$; (ii) the equation of conservation of the sediment mass in the bed

$$\partial_t (Y_b) = -\phi_{2,3}^{net} \tag{18}$$

and (iii) the equation of conservation of the momentum of both phases

$$\begin{aligned} &\partial_t (\rho_m hu) + \partial_x \left(\rho^{(w)} u_s^2 h_s + \rho_b u_b^2 h_b + \right. \\ &\left. g \left(\tfrac{1}{2} \rho^{(w)} h_s^2 + \tfrac{1}{2} \rho_b h_b^2 + \rho^{(w)} h_s h_b \right) \right) + \\ &g \left(\rho^{(w)} h_s + \rho_b h_b \right) \partial_x (Y_b) = -\tau_b \end{aligned} \tag{19}$$

where $\rho_m = \rho^{(w)}(1 + (s-1)C)$ is the average flow density and $C = C_b u_b h_b/(uh)$ is the flux-averaged concentration of the entire flow.

The complete system admits 4 unknowns: h, u, Y_b and C_b.

3 EXPERIMENTAL FACILITIES, INSTRUMENTATION EXPERIMENTAL PROCEDURES

The experimental characterization of α_c and $\alpha^{(w)}$, fundamental for the derivation of the layer velocity, is undertaken next.

The experiments were performed in an 11 m long and 40 cm wide prismatic recirculating tilting flume existing in the Laboratory of Fluid Mechanics of the University of Aberdeen. The side-walls are made of glass, enabling visualization and laser measurements. In order to achieve and maintain uniform flow conditions, a manually operated vane was placed at the outlet. A detailed description can be found in Cunningham 2000, pp. 47–55, and Ferreira 2005, pp. 57–59.

Five kinds of measurements were performed: (i) water and sediment discharges; (ii) water depth and bed elevation; (iii) instantaneous flow velocity; and (iv) velocity of the bedload particles.

Two orthogonal components of the instantaneous flow velocity were measured with a DANTEC 55X Modular Laser Doppler Anemometer. The transmitting optics features a 20 mW, monochromatic He-Ne laser. The sampling software enabled the collection of 12000 samples before writing to file. The LDA system was placed at about 6 m from the inlet. The sampling frequency varied with the hydraulic parameters between 200 Hz and 300 Hz.

The flow was recorded on video, with a 25 fps Panasonic video camera with adjustable shutter speed and lenses aperture. The maximum saltation height was accessed by analyzing side-view video footages. The paths and the velocities of individual gravel particles moving in the bedload layer were computed from video footages taken from above (details of the setup *in* Ferreira 2005, pp. 57–66).

Table 1. Summary of the characteristics of the experimental tests.

Name	Q (ls^{-1})	i_0 (–)	h_0 (cm)	u_* (ms^{-1})	$\Phi(\times 1000)$ (–)	Fr (–)
T_0	10.3	0.0014	7.46	0.033	–	0.40
T_1	14.3	0.0014	8.96	0.037	≈0	0.43
T_2	13.2	0.0031	6.75	0.045	0.013	0.60
T_3	18.3	0.0031	8.28	0.051	0.081	0.61
T_4	13.2	0.0023	7.45	0.041	<0.001	0.52
T_5	13.2	0.0055	5.59	0.054	0.564	0.80
T_6	19.2	0.0055	7.24	0.062	4.505	0.79
T_7	13.3	0.0046	5.97	0.050	0.090	0.73
T_8	18.5	0.0046	7.52	0.057	2.175	0.72
T_9	17.3	0.0046	6.99	0.056	1.584	0.75

A total of 10 capacity, subcritical and uniform flow experimental tests were carried. Their main characteristics are shown in table 1. In this table, Q stands for the total discharge, i_0 for the bed slope, h_0 for uniform flow depth, Φ for the non-dimensional sediment discharge and Fr for the Froude number. The friction velocity, u_*, was computed from the linear profile of $\overline{u'w'}$ in the logarithmic sublayer. In order to determine sediment discharge, sediment samples were collected at the flume outlet.

The bed was composed of a gravel mixture with $d_{50} = 5.45$ mm, $d_{90} = 5.45$ mm and $\sigma_g = 5.45$. The sediment grains were transported exclusively as bedload and no appreciable bed forms were registered.

4 EXPERIMENTAL RESULTS

4.1 *Particle velocity*

The velocity of the particles of each size fraction, $u_{b_k}^{(g)}$, was determined with the help of a particle tracking algorithm (described in Ferreira 2005, p. 171–174). Figure 4 shows examples of trajectories of particles detected by the algorithm. The trajectories show an apron-like shape, typical of particles entrained by turbulent sweep events.

Copyright © 2006 Taylor & Francis Group plc, London, UK

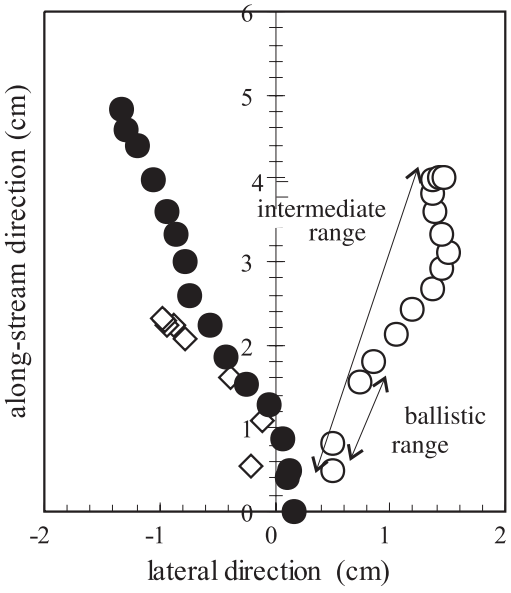


Figure 4. Paths of displaced gravel particles.

A typical path between the initial and the final rest positions encompasses, as seen in figure 4, saltation and rolling or sliding. During saltation, the displacement between two successive positions is larger than the displacement between to successive particle during rolling or sliding.

Nikora et al. (2002) categorized the movement of gravel particles in the bedload layer in three ranges: the ballistic, the intermediate and the global. the velocity histogram in ballistic range is narrow and the mode has a high value; in the intermediate range, the velocity histogram is wide and the mean velocity is much smaller than the peak velocity. The global range includes also the periods of rest that a particle may have in its downstream travel.

Saltation belongs to the to the ballistic range whereas the full particle path between rest positions, containing a succession of saltation, rolling and sliding reaches, pertains to the intermediate range. It is reasonable to assume that, for a given control volume, all types of movement will be present if the set of N moving particles is large enough. Thus, bedload should be defined as the product of the particle velocity, computed in the intermediate range, the depth-averaged sediment concentration and the thickness of the bedload layer, defined as the maximum saltation height.

The velocity of the particles, as defined in this study, is the ensemble average, over a large number of particles, of the path-averaged velocity in the along-stream direction. This definition is thus compatible with the concept of bedload explained above. Considering that the frame rate is constant, the path-averaged velocity is obtained by dividing the total particle displacement (see figure 4) by the time elapsed.

The results, for the size fractions characterized by $d = 1.5$, 2.4, 3.1, 4.0, 5.5 and 6.4 mm, are shown in figure 5. As discussed, the velocities shown in this figure pertain to the intermediate range. This observation will enable the comparison of the present experimental results with those of earlier studies, notably Fernandez Luque and van Beek (1976). Indeed, it is observable in figure 5 that the average velocity of each size fraction follows a linear trend, as was the case of Luque and van Beek's results.

All size fractions can be represented by the linear regression

$$u_b^{(g)} = 4.5\,(u_* - u_0) \tag{20}$$

where $u_0 = 0.029\,\mathrm{ms}^{-1}$.

It is recalled that Fernandez Luque and van Beek (1976) obtained $u_b^{(g)} = 11.5(u_* - 0.7u_{*c})$. Thus, equation (20) is similar to Fernandéz Luque & van Beek's with the conspicuous difference that the slope of the former is smaller than the slope of the latter. It is argued that the difference between both formulas is due to the fact that the measurements performed by Fernandez Luque and van Beek (1976) pertained to the ballistic range; indeed, they measured the velocity of particles during saltation events. Thus, it was considered that the formula proposed by Fernandéz Luque & van Beek would lead to an overestimation of the bedload by overestimating the average particle velocity. It is noted that Niño and Garcia (1994) observed $u_b^{(g)} = \alpha_c u_*$, α_c between 4 and 6, a formula that is in better agreement with equation (20).

4.2 *Water velocity*

The profiles of the time-averaged velocity corresponding to the experimental tests shown in table 1 can be seen in figure 6. These profiles are obtained by ensemble-averaging four distinct sets of time-averaged measurements for each height above the bed. Space averaging was not performed because the bed was mobile – the geometry of the bed would be different for each time-averaged profile. Thus, it is assumed that the ensemble average is equivalent to a space average.

The velocity profile is composed of three regions, described by as many mathematical expressions. In the roughness sublayer, the lower layer of the inner flow region, the velocity profile is approximately linear. In the upper parts of the inner flow region, the profile is logarithmic. In outer flow region the flow is described by a log-wake law (*cf.* Townsend 1976).

Assuming that the bedload layer is contained in the roughness sublayer, the depth-averaged velocity of

Copyright © 2006 Taylor & Francis Group plc, London, UK

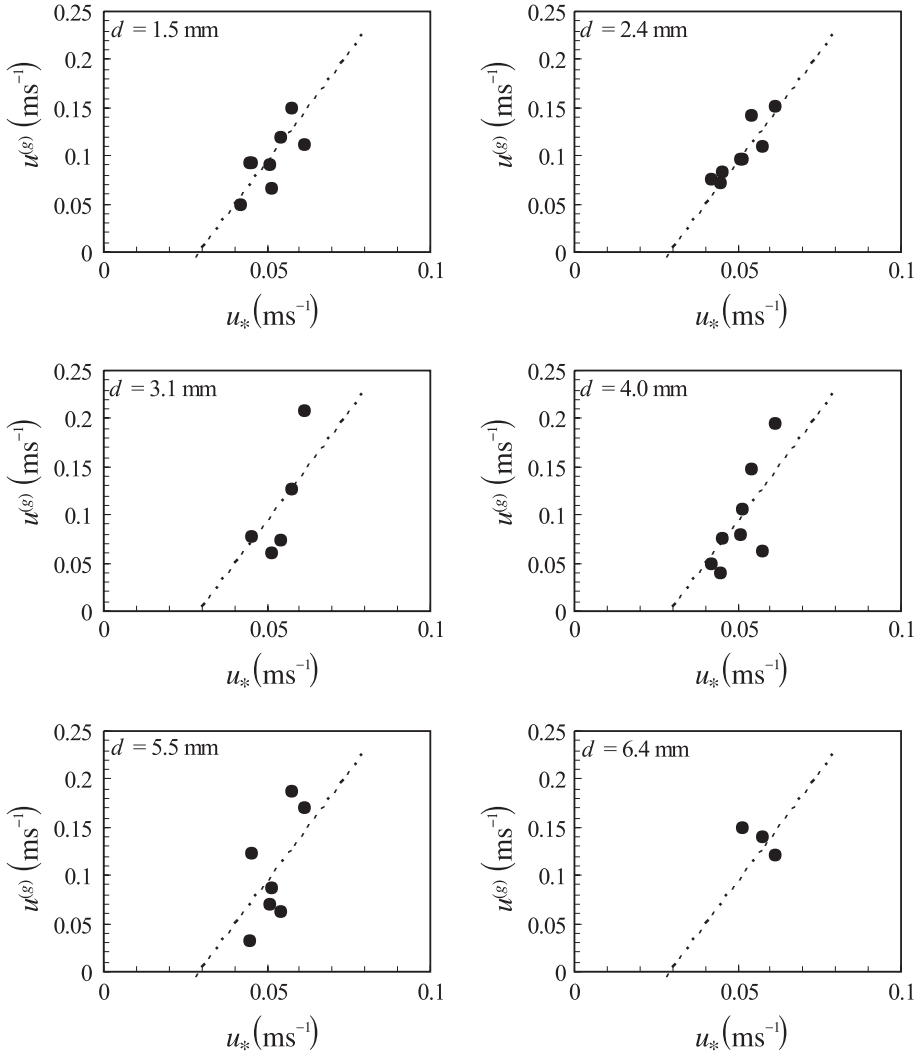


Figure 5. Ensemble average of the path-averaged velocity of the gravel particles of each size fraction (black dots). Dotted line stands for equation (20).

the water in the bedload layer can be estimated from the integration of the linear velocity profile seen in figure 6. Symbolically, it is

$$\frac{u^{(w)}(y)}{u_*} = C_1 \frac{y}{k_s} + C_2 \tag{21}$$

where k_s is the equivalent roughness height. The integration of equation (22) renders

$$\frac{u_b^{(w)}}{u_*} = \int_0^{h_b} \left\{ \frac{u^{(w)}(y)}{u_*} \right\} \mathrm{d}y = \frac{C_1}{2} \frac{h_b}{k_s} + C_2 \tag{22}$$

Ferreira 2005, p. 91, quantified the values of C_1, C_2 and k_s. From the profiles shown in figure 6 it was obtained $C_1 = 4.65$ and $C_2 = 4.49$. The equivalent roughness height was computed from the water-worked bed profiles and related to the mean height of the protruding particles, δ_a. It is assumed that $k_s = 2.5\delta_a$.

The values shown in table 2 suggests that k_s is approximately constant in the range of θ_{50} corresponding to the experimental tests carried out. Thus, let $k_s = 1.90 d_{90}$ where $d_{90} \approx 2.2 d_{50}$ (table 2). Substituting the values of the constants in equation (22) and considering that $h_b/d_{50} = 3$, a frequent value, the

Copyright © 2006 Taylor & Francis Group plc, London, UK

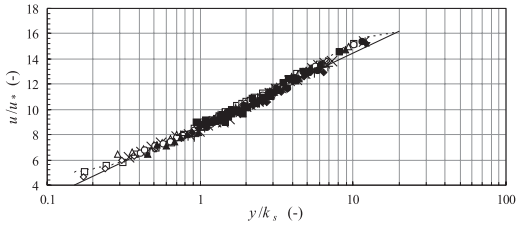


Figure 6. Profiles of the time- and ensemble-averaged fluid velocity.

Table 2. Summary of the characteristics of the experimental tests.

Name	k_s (mm)	d_{50} (mm)	d_{90} (mm)	σ_g (mm)
T_0	7.39	3.29	6.07	1.70
T_1	7.52	3.28	6.04	1.72
T_2	7.22	3.35	6.13	1.73
T_3	7.01	3.39	6.12	1.70
T_4	7.35	3.30	5.96	1.70
T_5	6.86	3.45	6.17	1.67
T_6	5.97	3.50	6.26	1.64
T_7	6.65	3.46	6.24	1.71
T_8	6.24	3.44	6.20	1.69
T_9	6.14	3.43	6.17	1.65

depth-averaged water velocity in the bedload layer becomes

$$u_b^{(w)} = 7.1 u_* \tag{23}$$

Parameter α_* is obtained from equation (7), with $\alpha^{(w)} = 7.1$, $\alpha_c = 4.5$ and $u_0 = 0.029\,\mathrm{ms}^{-1}$. The continuum velocity of the bedload layer is retrieved from equation (8). The remaining closure equations are presented in the context of the model application.

5 APPLICATION – OVERFEEDING AT THE UPSTREAM REACH

5.1 *Test conditions*

Upstream overfeeding can be enforced by supplying sediment at the upstream reach while maintaining sediment recirculation. For that purpose, a conveyor belt with adjustable velocity was installed at the upstream reach of the flume described in section 3.

The bedload discharge was set by adjusting the thickness and the width of the sediment layer in the belt and the velocity of the motor.

The experimental procedure comprises two phases, recirculation and overfeeding. In the first phase, uniform and capacity conditions are obtained by running a recirculation test during 8 hours. Generalized deposition is enforced by imposing, at the upstream reach, a steady sediment discharge. The duration of the overfeed test was 15 hours.

The recirculation phase was characterized by $Q = 0.0138\,\mathrm{m}^3\mathrm{s}^{-1}$, $h_0 = 0.099\,\mathrm{m}$, $i_0 = 0.001$ and $u_* = 0.029\,\mathrm{ms}^{-1}$.

At the end of the recirculation phase, the bed was composed of a mixture of coarse sand and gravel characterized by $d_{50} = 2.02$ mm, $d_{90} = 5.61$ mm and $\sigma_g = 2.79$. The equivalent roughness height was $k_s = 4.61$ mm.

During the recirculation phase sediment transport was incipient. The sediment discharge imposed at the upstream end during the overfeeding phase was $Q_s \approx 2.5\,\mathrm{gs}^{-1}$. The composition of the feeding material was approximately equal to that of the bed surface.

5.2 *Closure equations and solution procedure*

In order to simulate the overfeeding test described in the preceding section, the model requires closure equations for the thickness of the bedload layer, for the bed shear stress and for the vertical flux of sediment between the bed and the bedload layer.

The thickness of the bedload layer, h_b, is addressed first. Since the physical system features no appreciable bed forms, h_b is expected to scale with the saltation height (see discussion in Ferreira 2005, p. 114–115). The later is expected to increase with the bed shear stress and with the bedload discharge. In this study, is is assumed that

$$\frac{h_b}{d_{50}} = 2\frac{10.5\theta_{50}}{1 + 0.2\theta_{50}} \tag{24}$$

The flux of sediment between the bedload layer and the bed is modeled by spatial lag equation, following Phillips and Sutherland (1989). It is proposed

$$\phi_{2,3}^{net} = -\left(C_b h_b u_b - q_b^*\right)/\Lambda \tag{25}$$

where Λ is the adaptation length and q_b^* is the equilibrium (capacity) volumetric bedload discharge. For the latter, a simple monomial equation, in the form of $q_b^* = m(u - \chi)^3$, was employed.

The friction coefficient may be expressed by a Keulegen-type law (Chow 1959, p. 204), given that it is assumed that only grain roughness exists. The particular law employed was

$$C_f = \left(5.75\mathrm{Log}\left(\frac{h}{k_s}\right) + 4.4\right)^{-2} \tag{26}$$

The constants were modified to achieve better matches to the measured values of $(u_*/u)^2$. The Shields parameter, θ_{50}, is computed from the definition $C_f u^2/(\rho^{(w)}(s-1)d_{50})$.

Copyright © 2006 Taylor & Francis Group plc, London, UK

The solution procedure involves the discretization by an explicit 1st order finite volume discretization whose general form is

$$\mathbf{U}_i^{n+1} = \mathbf{U}_i^n - \frac{\Delta t}{\Delta x}\left(\mathbf{F}_{i+\frac{1}{2}}^n - \mathbf{F}_{i-\frac{1}{2}}^n\right) + \Delta t \mathbf{G}_i^n \qquad (27)$$

where $\mathbf{U} = [h \;\; \rho_m uh \;\; \alpha_* C_b h_b \;\; Y_b(1-p)]$ is the vector of conservative dependent variables and $\mathbf{F}$ and $\mathbf{G}$ are, respectively, the corresponding flux and source terms vector (see equations 16, 17, 18 and 19). Inter-cell fluxes are calculated by Godunov's method. The length of the computational space and time steps are, respectively, Δx and Δt.

The proposed test represents a boundary-initial value problem. Initial conditions comprised steady total discharge, constant water depth and equilibrium sediment concentrations. Since the Froude number was smaller than one, two boundary conditions were imposed at the upstream section and one boundary condition was imposed at the downstream end. Constant total and sediment discharge hydrographs were imposed at the upstream end. A stage-discharge hydrograph derived from the proposed friction law was imposed at the downstream end.

5.3 *Comparison between experimental and numerical results*

The imposition of strong overfeeding at the upstream end originates a sediment wave, with steep front, that propagates downstream. Associated to this discontinuity in the bed profile there is necessarily a discontinuity in the water depth (see Ferreira tese Ha Ha) which may be a hydraulic jump should the Froude number of the flow over the sediment wave be larger than one.

The morphologic response of the stream can be seen in figure 7. Profiles of the measured sediment wave and water elevation are shown in this figure, at $t = 2.5$, 5.0, 7.5, 10 and 14 hours. In order to transport the sediment discharge imposed at the upstream reach the stream increases its slope and, hence, its transport capacity. A new equilibrium slope would be obtained at sufficiently large times.

The corresponding profiles obtained by the numerical solution of the model described in the previous sections are shown in figure 7(b), superimposed to the experimental results. In figure 7(a) the results of a de Vries type of model are also shown. Water and bed elevations are made non-dimensional by h_0, the depth of the uniform flow in the recirculation phase. Distances in the longitudinal direction are made non-dimensional by the work length of the flume for this test, $L_0 = 10$ m.

The adaptation length Λ and the parameters m and χ were fitted to achieve best results in the proposed model. The values employed were $\Lambda = 0.4$ m, $m \approx 0.0006\,\mathrm{m^{-1}s^2}$ and $\chi = 0.35\,\mathrm{ms^{-1}}$. The parameter

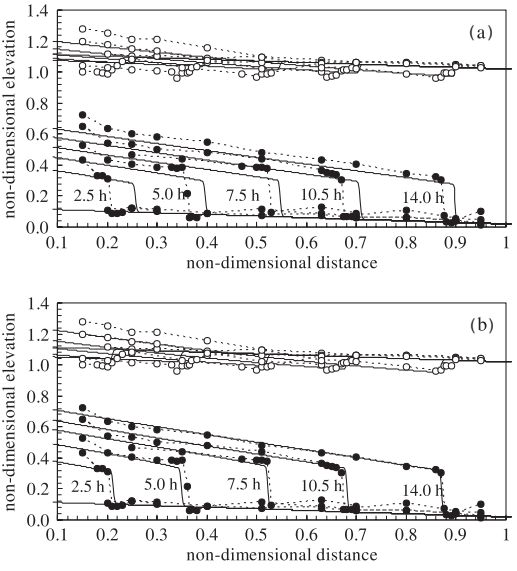


Figure 7. Profiles of the free surface and of the bed. Measured profiles superimposed to calculated profiles by (a) a de Vries type of model and (b) the model described in section 2. Solid thick lines (——) stand for computed bed elevation; thin lines (——) stand for the elevation of the free surface. Dashed lines with black dots (- - ● - -) stand for the measured bed elevation; dashed lines with open circles (- - ○ - -) stand for the measured free surface elevation.

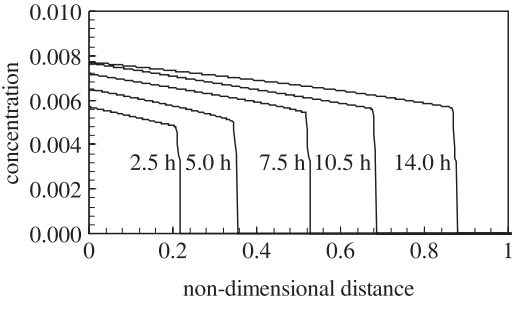


Figure 8. Profiles of the calculated concentrations in the bedload layer.

m acts mainly on the velocity of the wave front while Λ is relevant for the rate of deposition and, hence, for the shape of sediment wave. The same parameters were used in the de Vries-type model. In that model, the adaptation length was used in a lag equation that corrects the equilibrium bedload discharge to simulate non-equilibrium conditions. This procedure, described in Ferreira (1998), p.? - ?, represents an extra computational step, suitable for explicit schemes.

The computed concentrations in the bedload layer are plotted in figure 8. The profiles are monotone

Copyright © 2006 Taylor & Francis Group plc, London, UK

decreasing since, over the sediment wave, the water depth is not constant.

As the new equilibrium slope is attained, the concentration tends to a constant value. This is evident in the vicinity of the upstream reach where the C_b approached a constant value from $t = 10$ h onwards.

6 DISCUSSION AND CONCLUSIONS

The proposed model is based on the shallow-water equations complemented with mass conservation equations for the sediment constituent. It explicitly incorporates the inertia of the transported sediment by dividing the water column in two transport layers, each modeled as continuum, and by assigning the bedload layer a density and a velocity highly dependent on the concentration of sediment.

Should the concentration be zero, the proposed model converges essentially to the clear-water shallow-water equations. The same happens to models similar to that of Vries (1965), since they are obtained by complementing the shallow-water equations with Exner equation. Thus, it is expected that, for small concentrations of transported sediment, both types of models render similar results. Gravel transport is typically associated to small sediment concentrations. It is thus a matter of discussion if the dynamics of the transported sediment are negligible in the overall dynamics of the system or if it should be included in the morphological models.

The differences observed by comparing the results of models that share the equation for capacity bedload discharge must be interpreted as differences resulting from the structure of the models. The coefficients of the laws that describe bedload transport were fitted so that the results of the proposed model would fit the observed morphologic response. As seen in figure 7, the proposed model and the de Vries-type model render quite different solutions for the same transport laws. Hence, it is concluded that the structure of the models is indeed different, even for concentrations as low as those seen in figure 8. Furthermore, the dynamics of the bedload, as idealized in the proposed model, must be relevant for the morphological response of the stream.

While it appears to be clear that joint effect of the convective inertia of the transported sediment and the accumulation of sediment sediment mass in the bedload layer (the terms that are not present in the de Vries-type model), the present study did not address the relative importance of these terms. Furthermore, the application of the model to more realistic test cases requires the specification of the a physically based bedload transport formula applicable to poorly sorted sediment mixtures. Efforts should be undertaken to address experimentally these issues.

ACKNOWLEDGEMENTS

The study was partly funded by the Portuguese Foundation for Science and Technology, project PRAXIS/P/ECM/12040/98. The first author thanks the support and assistance of Prof. Brian Willets and of Mr. Bill Lowson during his stay at the University of Aberdeen.

REFERENCES

Atkin, R.J. and R.E. Crane (1976). Continuum theories of mixtures: Basic theory and historical development. *Q. Jl. Mech. appl. Math. XXIX*(2), 209–244.

Chow, V.T. (1959). *Open Channel Hydraulics*. Reprinted in 1973. New York, USA: McGraw Hill International Edition.

Cunningham, G.J. (2000). *Predicting entrainment of mixed size sediment grains by probabilistic methods*. Ph.D. thesis, University of Aberdeen, Aberdeen, UK.

de Vries, M. (1965). Considerations about non-steady bedload transport in open-channels. In *Proc. of 21th Int. Association for Hydraulic Research (IAHR), Leningrad, URSS*, pp. 3.8.1–3.8.11.

Fernandez Luque, R. and R. van Beek (1976). Erosion and transport of bed-load sediment. *J. Hydraul. Res. 14*(2), 127–144.

Ferreira, R.M.L. (1998). *Mathematical modeling of mobile bed open-channel flows. Comparison between coupled and uncoupled models.* Master's thesis, Instituto Superior Técnico, Lisboa, Portugal (in Portuguese).

Ferreira, R.M.L. (2005). *Morphological evolution of rivers. Conceptual model and Applications*. Ph. D. thesis, Instituto Superior Técnico, Lisboa, Portugal.

Ferreira, R.M.L. and A.H. Cardoso (2000). Modelling the morphologic evolution of graded sediment beds using multiple bed layers and diffusive flux concepts. In *Proc.* 4th *Int. Conf. on Hydroscience and Engineering, Seoul, Korea*. (Ed. in Cd-Rom).

Hirano, M. (1971). River bed degradation with armouring. *Trans. of Japonese Soc. Civ. Eng. 3*(part 2), 194–195.

Nikora, V., D. Goring, I. McEwan, and G. Griffiths (2001). Spatially averaged open-channel flow over a rough bed. *J. Hydraul. Eng. 127*(2), 123–133.

Nikora, V., H. Habersack, T. Huber, and I. McEwan (2002). On bed particle diffusion in gravel bed flows under weak bed load transport. *Water Resourc. Res. 38*(6), 17–1–17–9.

Niño, Y. and M. Garcia (1994). Gravel saltation. 1. experiments. *Water Resourc. Res. 30*(6), 1907–1914.

Parker, G., C. Paola, and S. Leclair (2000). Probabilistic exner sediment continuity equation for mixtures with no active layer. *J. Hydraul. Eng. 126*(11), 819–826.

Phillips, B.C. and A.J. Sutherland (1989). Spatial lag effects in bed load sediment transport. *J. Hydraul. Res. 27*(1), 115–133.

Townsend, A.A. (1976). *The Structure of Turbulent Shear Flows.* (2nd ed.). Cambridge, UK: Cambridge University Press.

Copyright © 2006 Taylor & Francis Group plc, London, UK

Energy dissipation downstream of dams established in alluvial beds

A. Sá Lopes, M.F. Proença & R. Maia
Departamento de Engenharia Civil, Faculdade de Engenharia da Universidade do Porto, Porto, Portugal

ABSTRACT: Energy dissipation behind the hydraulic structure of a mobile dam was experimentally studied with the aid of Laser-Doppler Anemometry (LDA), aiming to optimize the design and length of the dissipation devices, most commonly a stilling basin followed by rock fill alluvial bed protection.

Measurements of the flow field over the rock protection were carried out in order to prevent damages at the foundations of the structure as well as to protect the river bed from erosion, namely due to operational reasons. The characterisation of mean velocity and turbulence intensities were carried out for different flow conditions and different rock fill characteristic dimensions, using a physical model of the Crestuma dam, located in the Douro river.

The obtained results (namely values of bottom shear stress) provide a better insight of the rock fill protection behaviour and can help to achieve a cheaper and safer design of the rock fill protection.

1 INTRODUCTION

Energy dissipation of flood discharges is a very important issue that must be carefully analysed when bearing in mind the design and layout of hydraulic structures, namely dams. The usual formation of a hydraulic jump downstream the weir devices requires adequate protection of the river bed, at locations where energy dissipation occurs and where flow velocities present higher values, especially if the constructions are established in alluvial beds.

Stilling basins concrete slabs followed by rock fill bed protections are one of the most common devices that are used to allow weir discharges to be performed without damaging the construction foundation. Length and characteristics of the protected zone and, specially, the rock fill bed protection depend on flow conditions and have to be carefully defined in order to prevent erosion or scour of the river bed.

Flow velocity and bed shear stress values play an important role in the process and have been the basis for the establishment of different criteria, allowing initiation of movement prediction.

In the present work an experimental study of a physical model of the Crestuma dam was carried out. Flow field definition for different flow conditions and different bed rock protections were made using laser Doppler anemometry technique in order to allow the analysis of velocity flow characteristics in each situation. Rock fill protection behaviour, concerning scour and erosion occurrence, has been studied in relation to flow field type changes.

Bottom shear stress values have been calculated and compared with the literature (Shields diagram) in order to try to explain any possible erosion effects. Two different approaches to Shields diagram have been made, taking into account the existence or not of flow uniformity characteristics of the studied flow. In accordance, two different methods of evaluation of friction velocity values have been applied.

2 THEORETICAL FRAMEWORK

In 1936, Shields described the initial bed grain instability problem based on experimental data. Shields diagram was referred to plane beds with grains of uniform size and was modified in order to take into account the non uniform distribution of the mixtures of different grains and their orientation under flow conditions. The modified Shields diagram (Fig. 1) presents several curves instead of the original one, grading different levels of incipient motion of the particles as referred by Hoffmans et al. (1997).

For a particular situation the critical shear stress value can be obtained through the Shields parameters ψ and D_* definition, assuming:

$$\Psi = \frac{u_*^2}{\Delta g d} \quad and \quad D_* = d\left(\frac{\Delta g}{\nu^2}\right)^{\frac{1}{3}} \tag{1}$$

where Δ = relative density $((\rho_s/\rho) - 1)$; d = particle diameter $(d = d_{50})$; u_* = friction velocity;

Copyright © 2006 Taylor & Francis Group plc, London, UK

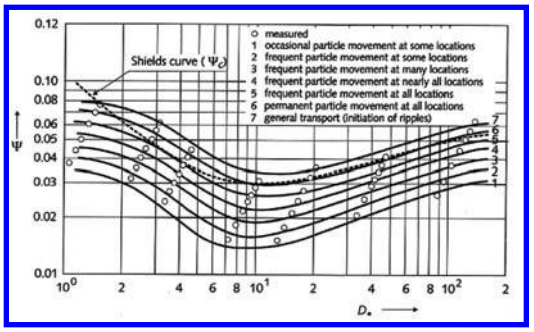


Figure 1. Modified Shields diagram (Hoffmans et al. 1997).

g = acceleration of gravity; ν = cinematic viscosity; ψ = mobility parameter; D_* = dimensionless diameter.

Shields diagram application requires the knowledge of flow and bed sediment characteristics.

Flow uniformity can be checked plotting u/U_{max} versus y'/h on different sections and verifying if the velocity profiles overlap on a single curve with the following law:

$$\frac{u(y')}{U_{max}} = A\ln(\frac{y'}{h}) + B \tag{2}$$

where u = mean flow velocity; y' = vertical distance to the bed flow, corrected according to rough bed situation; U_{max} = maximum velocity profile; h = flow depth; and, A and B constants.

The above equation will not be valid if the following conditions are not fulfilled (Rota criterion 1962, according to Cardoso 1990):

$$\left.\begin{aligned} &\frac{u_*}{U_{max}} = constant \\ &\beta = \frac{\rho hg(-I_0 + \frac{\delta h}{\delta x})}{\tau_0} = constant \\ &\frac{d(\frac{U_{max}\delta_*}{u_*})}{dx} = constant \end{aligned}\right\} \tag{3}$$

where I_0 is the bottom slope, δ_* and τ_0, are the boundary layer momentum thickness and the shear stress values, respectively. For β values: <-1, accelerated flow; $=-1$, uniform flow; >-1, decelerated flow.

Non-uniformity may then concern a set of flows which equilibrium is affected by the upstream flow conditions. Corresponding velocity profiles will vary along the flow.

Friction flow velocity evaluation must be done taking into account the referred flow characteristics.

For uniform flow, the general equation, most commonly used is:

$$u_* = (gRJ)^{\frac{1}{2}} \tag{4}$$

where R is the hydraulic radius and J the energy loss by unit length, that can be given by the Manning-Strickler expression:

$$J = \frac{U^2}{K_s^{\,2} R^{\frac{4}{3}}} \tag{5}$$

where K_s (=1/n) is the Strickler coefficient and U the mean sectional velocity. For uniform flows with small bottom gradient, R may be usually taken as h, the flow depth, and J as I_o, the bottom channel slope.

Regarding non-uniform flows using Saint Venant equations and according to Graf & Song (1995) and Graf & Altinakar (1998) the friction velocity can be given by:

$$u_*^2 = ghI_0 + (-gh\frac{\delta h}{\delta x}(1 - Fr^2)) \tag{6}$$

where I_0 is the bottom channel slope, x the velocity profile coordinate and Fr the Froude number, which is defined as:

$$Fr = \frac{U}{\sqrt{gh}}$$

3 EXPERIMENTAL SET UP

3.1 *Facilities and measuring equipment*

Experiments have been carried out in a water channel of the Hydraulics Laboratory of FEUP. The water channel, with a length of 32,3 m, a width of 1,0 m and a bottom slope of 0,5%, is provided with side windows allowing visual access to the test sections.

The channel is fed from a reservoir located at a higher level, provided with a water level control allowing a constant flow to be delivered to the channel.

Flow measurement values can be controlled, upstream through a flow meter, Sparling Waterhawk series 600, flangeless version, and downstream through a sluice crested weir whose discharge value is obtained measuring the water level by means of a Bestobell Mobrey MSP90 system.

Velocity measurements have been made using a one component fibre optics Laser System from Dantec, working in forward scatter mode.

A 100 MW Argon-Ion laser source, operating in multi-mode was used.

The main characteristics of the Laser Doppler Anemometer system are shown in table 1.

Copyright © 2006 Taylor & Francis Group plc, London, UK

Table 1. Laser Doppler Anemometer characteristics.

Laser wave length	514,5 nm
Half angle of measuring beams in air	3,65°
Shift frequency	0,6 MW
Beam expansion ratio	1,95
Dimensions of control volume in air	
Major axis	2,53 mm
Minor axis	1,62 mm
Fringe spacing	4,04 mm
Frequency shift	0,6 Mw

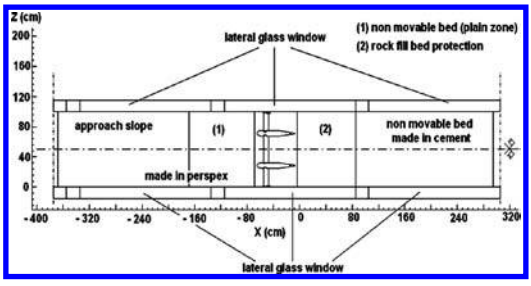


Figure 2. Crestuma model – plant.

The signal from the photomultiplier was band-pass filtered and processed by a TSI 1990c counter, operating in the single measurement per burst mode, with a frequency validation of 1% at 10/16 cycle comparison. A 1400 Dosteck card interfaced the counter with a computer, which provided all statistical quantities, using a purpose's built software.

3.2 *Physical model characteristics and similarity conditions*

In order to perform experimental work a physical model of Douro river Crestuma dam was built.

Crestuma dam is a mobile type dam founded on alluvial bed, whose flow discharges are made through double slicing gates installed on 8 spans of 28 m each and supported by 49 m length and 6 m width piles. The double slicing gates can move independently and allow discharges over or underneath their body or both simultaneously. Flow discharge energy dissipation is achieved on a concrete slab stilling basin with a length of 42 m from gate axis position, followed by the rock fill bed protection with a length of 80 m.

The model was made of perspex using a 1:80 geometric scale. Taking into account that gravitational forces are predominant in this case, the Froude number similarity was used for model construction.

Considering the above mentioned scale and taking into account the width of the water channel of Hydraulics Laboratory (1 m), the portion of Crestuma dam represented by the model includes one central span, two piles and two lateral incomplete spans (approximately half spans) as represented in Figure 2.

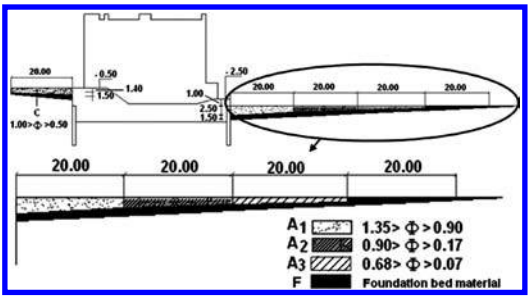


Figure 3. Crestuma dam rock fill bed protection characteristics.

Crestuma rock fill protection has a variable depth and includes different number of layers along its length as shown on Figure 3, where rock fill material dimensions are also indicated.

The concrete slab basin of the plant was modelled on Perspex and the rock fill protection by means of granite and sand grains with specific weights of:

- Granite grains – 26 KN/m^3
- Sand grains – 16 KN/m^3
- Wet sand grains – 18 KN/m^3

The four top layer sections used in the model were 25 cm length each and will be referred as section 1, 2, 3 and 4, corresponding to the above A1, A2, A3 and F designations. Section 4 corresponds to natural foundation bed material.

The bed grain size distribution used for the different sets of experiments corresponds to three different rock fill protection characteristics, A, B and C, as shown on table 2. The rock fill bed protection designated as type A corresponds to the scaled rock fill bed protection used in Crestuma dam. Type B section (increased) dimension was designed taking into account market maximum available dimensions of rock fill to be used in section 1 of the prototype. Type C section 1 element dimensions (the largest of all three) were determined using the following formula proposed by U.S. Corps of Engineers, and used on Crestuma project (LNEC, 1972):

$$d \geq k \frac{U^2}{2g} \frac{\gamma}{\gamma_s - \gamma}$$

where γ and γ_s are respectively the specific weights of water and rock material, k is dependent on flow turbulence and was taken equal to 1, 35.

Sections 2 and 3 element dimensions of types B and C rock protections have been evaluated regarding to grading correspondence to section 1 elements dimension used on type A (Crestuma Project) rock fill protection.

Copyright © 2006 Taylor & Francis Group plc, London, UK

Table 2. Model rock fill bed protection characteristics.

		Rock fill bed protection		
		Type A (cm)	Type B (cm)	Type C (cm)
Section 1	d_{35}	1,32	1,85	2,85
	d_{50}	1,50	2,00	3,00
	d_{65}	1,55	2,15	3,15
	d_{75}	1,60	2,25	3,25
	d_{84}	1,76	2,34	3,34
	d_{85}	1,77	2,35	3,35
	d_{90}	1,81	2,40	3,40
Section 2	d_{35}	0,72	0,85	1,19
	d_{50}	0,80	1,00	1,35
	d_{65}	0,82	1,15	1,52
	d_{75}	0,90	1,25	1,63
	d_{84}	1,36	1,34	1,72
	d_{85}	1,37	1,35	1,74
	d_{90}	1,41	1,40	1,80
Section 3	d_{35}	0,66	0,71	0,95
	d_{50}	0,70	0,75	1,05
	d_{65}	0,75	0,80	1,16
	d_{75}	0,80	0,83	1,22
	d_{84}	1,12	0,85	1,23
	d_{85}	1,17	0,86	1,30
	d_{90}	1,20	0,87	1,33

Table 3. Main flow characteristics.

Flow value (l/s)	11,5	12,2
H_1 (mm)	165	165
y_0 (mm)	58,5	60,5
Froude nb	5,81	5,79
Gate opening (mm)	9	12,5

3.3 *Flow conditions*

As previously mentioned Crestuma gates allow different types of discharges. In the present work flow discharge was considered to be done always by the sections underneath the gates and keeping equal gate openings in all the three spans of the model.

Two different flow values have been considered, 11,5 l/s and 12,2 l/s, which main features are presented on table 3, where H_1 is the upstream water level and y_0 is the downstream water level.

The 11,5 l/s value corresponds to a flow situation where hydraulic jump is formed within the stilling basin slab. A small increase of 6% to 12,2 l/s, on the flow value, led to an hydraulic jump showing much more instable characteristics with an oscillatory behaviour and a tendency to move away from the stilling basin slab.

4 EXPERIMENTAL RESULTS

Taking into consideration the two referred flow conditions and the three different types of rock fill bed protection, four sets of measurements have been carried out.

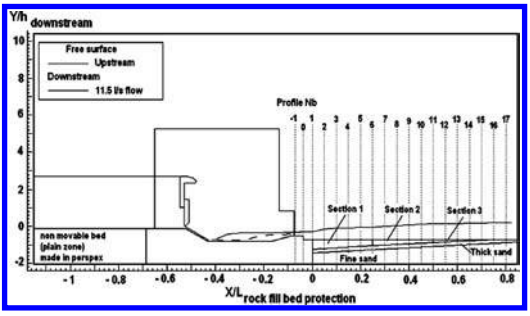


Figure 4. Location of measured profiles.

On each of them, mean and fluctuating velocity profiles have been measured at different flow sections behind the hydraulic structure, as shown on Figure 4.

The first set of experiments concerned a gate flow discharge value of 11,5 l/s and the use of a rock fill bed protection, designated as type A.

Mean and fluctuating values of the horizontal and of the vertical velocity components for the different profiles above referred have been measured and led to the results shown on Figures 5a and 5b. Values of velocities and depth presented are dimensionless taking as reference respectively the horizontal mean sectional velocity and the flow depth values of the stabilized flow on the sections downstream the rock fill bed protection.

As already stated the flow characteristics showed a quite stable hydraulic jump formed within the stilling basin slab. The highest velocity values were observed before entering the rock fill bed protection and no erosion was verified.

The second set of measurements concerned the same type A of rock fill bed protection but a higher gate flow discharge value of 12,2 l/s. Flow characteristics showed a quite unstable and oscillating hydraulic jump moving periodically away from the stilling basin slab.

The consequence of this type of flow gate discharge was the start of the formation of a scour hole on the rock fill bed protection, whose characteristics, concerning dimensions and location, are shown on Figure 6. Scour hole depth values were made dimensionless by considering the ratio to the downstream flow depth value. The scour hole was mostly located in front of the central gate span, along section 1 of the rock fill bed protection. Stabilization of sediment transport occurred, approximately, two hours after the starting of the test.

Mean and fluctuating horizontal velocity component values, after sediment transport stabilization, are presented on Figures 7a and 7b.

Figures 7a and b also represent longitudinal profiles of maximum scour and of maximum deposition,

Copyright © 2006 Taylor & Francis Group plc, London, UK

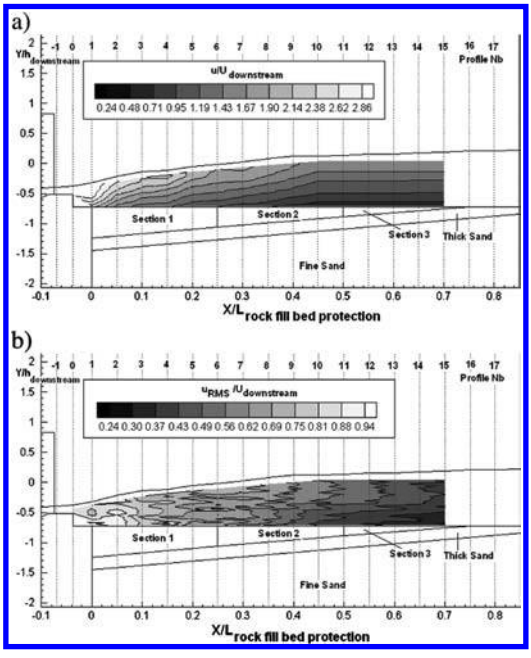


Figure 5. Evolution of the horizontal component values for 11,5 l/s flow and type A rock fill protection: (a) mean velocity and (b) rms (note: dark values are the lowest in range).

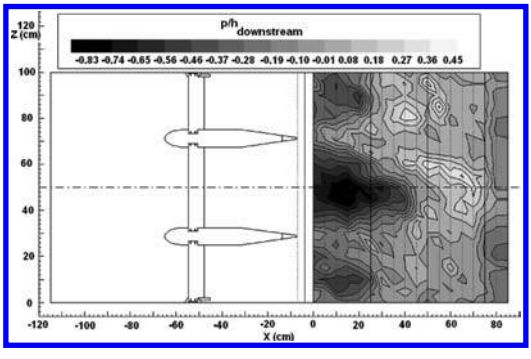


Figure 6. Scour hole caused by a 12,2 l/s gate discharge on type A rock fill bed protection.

the first corresponding to the central channel axis and the other to the pile axis, in accordance with eroded material being transported and deposited downstream, at different transverse rates and locations. The deposition of that material turned the velocity measurement on some downstream profiles impossible because measuring points were out of reach of laser beams. Moreover, only horizontal velocity component could be measured due to the very low flow depth associated with very high flow surface fluctuations and because of LDA system characteristics, namely beam separation at front lens probe.

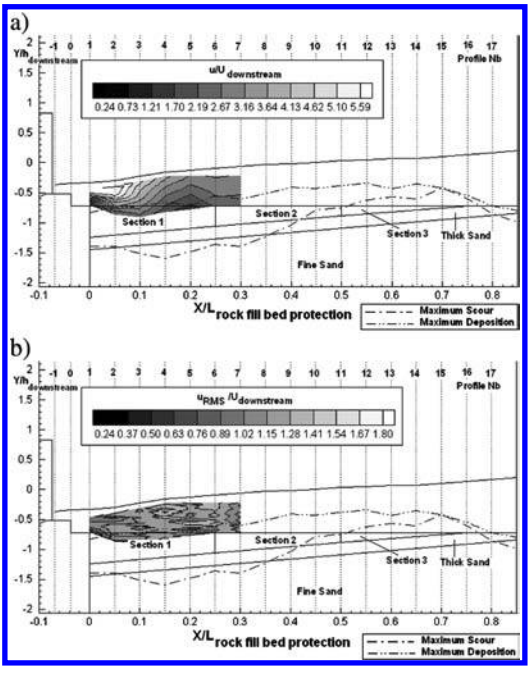


Figure 7. Evolution of the horizontal component values for 12,2 l/s flow and type A rock fill protection: (a) mean velocity and (b) rms (note: dark values are the lowest in range).

A comparison of velocity flow fields of 11,5 l/s and 12,2 l/s flows is presented on Figures 8a and b.

These figures enable to conclude that much higher velocity values and much more important velocity gradient values on the rock fill protection region have been achieved with the 12,2 l/s flow, due not only to the flow velocity values increase, but as well as to the tendency of movement of the hydraulic jump towards downstream.

The third set of experimental measurements was carried out with the same flow gate discharge of 12,2 l/s but using type B rock fill protection.

Scour process did not start immediately. Several oscillations could be noticed on the material of upstream measuring sections (1 and 2) of top layer rock protection during the first 24 h of the test, which have been followed by the formation of the scour hole presented on Figure 9.

The scour hole position moved downstream, in comparison with the situation previously reported for type A rock fill (Fig. 6), and it was now located at the end of section 1 and beginning of section 2 of the rock fill bed protection.

Mean and fluctuating horizontal component velocity measurements have been made before and after the scour hole formation and the results are presented on Figures 10a and 10b.

Copyright © 2006 Taylor & Francis Group plc, London, UK

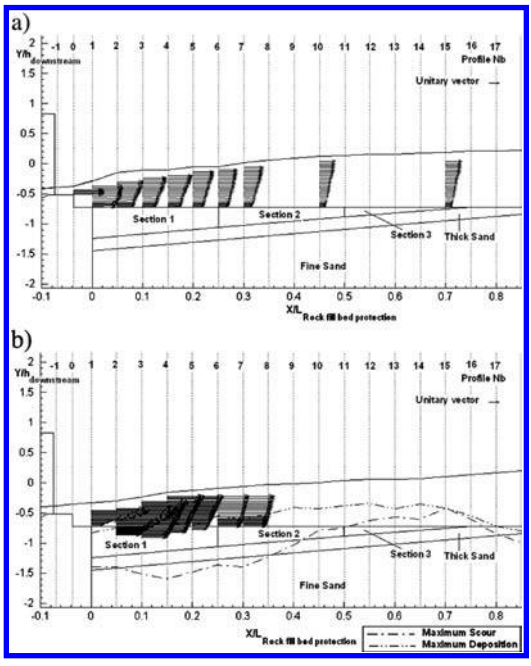


Figure 8. Flow fields for (a) 11,5 l/s and (b) 12,2 l/s gate flow discharges and for type A rock fill bed protection.

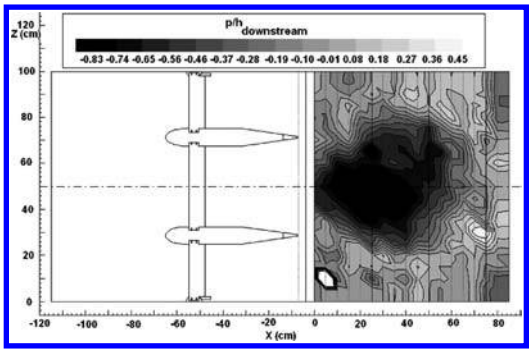


Figure 9. Scour hole caused by a 12,2 l/s gate discharge on type B rock fill protection.

As shown on these figures, the two experiments do show similar mean horizontal component velocity profiles at the beginning of the rock fill protection. Higher differences can be noticed on velocity profiles P5 to P8, corresponding to the end of section 1 and beginning of section 2 of the top rock fill layer protection. The analysis of Figures 11a and 11b, concerning corresponding horizontal component fluctuating velocity values, shows that after scour hole formation the highest fluctuation values have moved towards section 1 zone of bed protection whilst, before

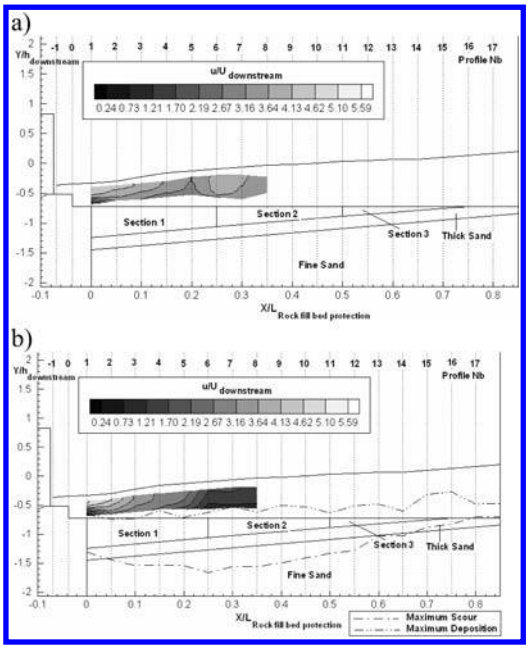


Figure 10. Evolution of horizontal component mean velocity values for 12,2 l/s flow and type B rock fill protection: (a) before and (b) after scour hole formation (note: dark values are the lowest in range).

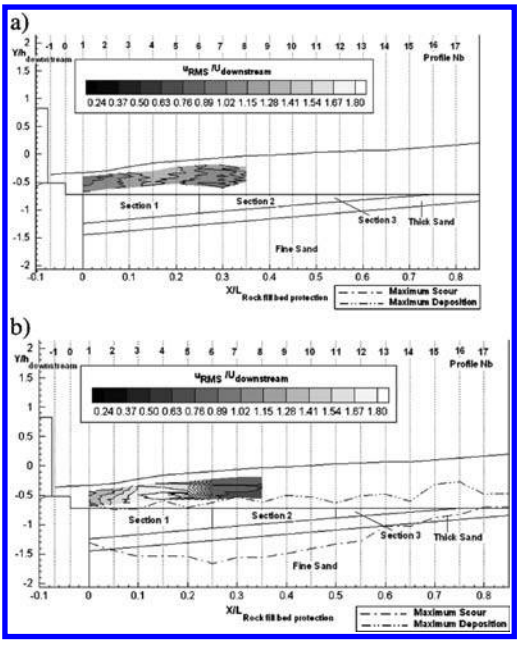


Figure 11. Evolution of horizontal component rms values for 12,2 l/s flow and type B rock fill protection: (a) before and (b) after scour hole formation (note: dark values are the lowest in range).

Copyright © 2006 Taylor & Francis Group plc, London, UK

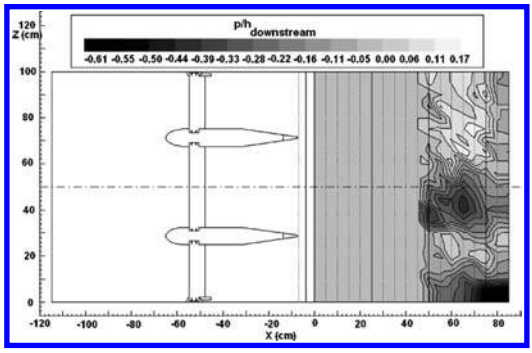


Figure 12. Scour hole caused by a 12,2 l/s gate discharge on type C rock fill bed protection.

erosion was noticed, those values were located by the end of section 1 and beginning of section 2.

The last set of measurements concerned the rock fill bed protection type C and again the use of the same gate flow value of 12,2 l/s.

During the corresponding tests no erosion was noticed on sections 1 and 2 of the rock fill protection. Only slight erosion of the material of section 3 could be observed. Related scour hole characteristics are presented in Figure 12.

Horizontal component mean and fluctuating velocity values are presented on Figures 13a and 13b.

It can be confirmed that mean velocity values are quite similar to the 11,5 l/s flow case. In what concerns fluctuating values, less instability was noticed in this case.

A comparison of the mean flow velocity fields for 12,2 l/s flow regarding rock fill types B (after sour occurrence) and C is made on Figures 14a and b.

This information complements Figure 8b, enabling to compare influence of rock fill protection dimension.

5 RESULT ANALYSIS

The results, earlier presented have been analysed bearing in mind the rock fill bed protection behaviour, concerning its characteristics and flow conditions.

Result analysis has been carried out considering Shields criterion for initiation of movement of gravel particles on a flat bed, using the modified Shields diagram, presented on Figure 1.

The application of Shields diagram and the mobility values calculation required the definition of the friction velocity values. That has been made considering the flows under study either as uniform or as non-uniform flows.

For uniform flows, friction velocity values, u_*, have been directly assessed by using the expressions

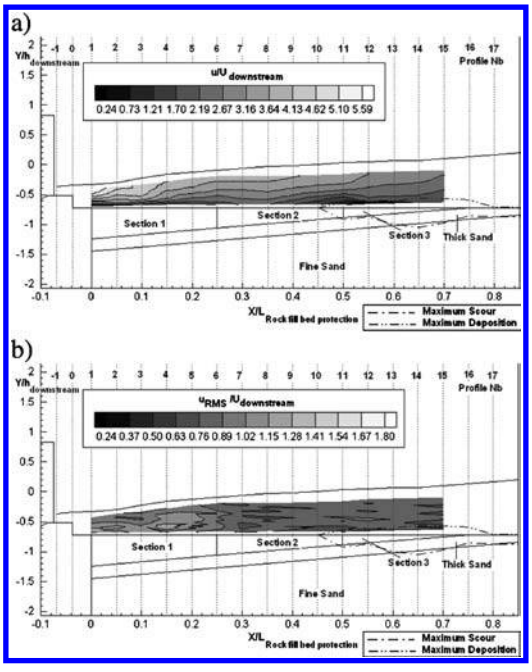


Figure 13. Evolution of horizontal component values for 12,2 l/s flow and type C rock fill protection: (a) mean velocity and (b) rms (note: dark values are the lowest in range).

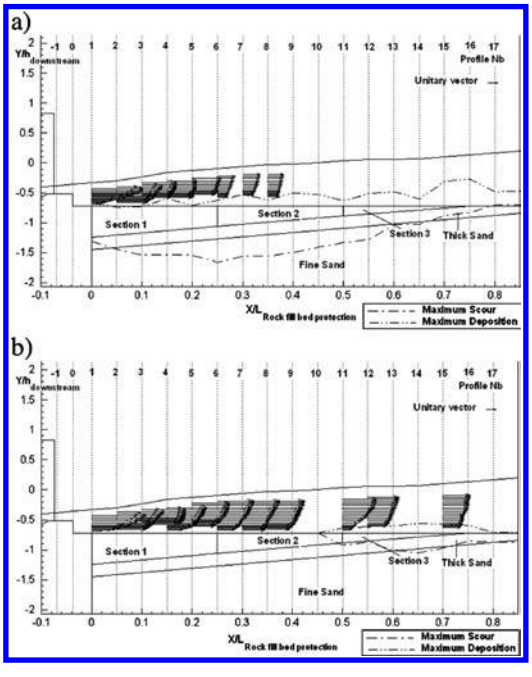


Figure 14. Flow fields for 12,2 l/s flow and (a) type B rock fill protection (after scour occurrence) and (b) type C rock fill protection.

Copyright © 2006 Taylor & Francis Group plc, London, UK

Table 4. Friction velocity values evaluation for 12,2 l/s flow value and type C rock fill protection (uniform flow).

Profile	x (cm)	h (cm)	R (cm)	U (m/s)	J (m/m)	u_* (cm/s)
P1	0	2,4	2,3	0,821	7,49E-02	12,97
P2	5	2,6	2,5	0,758	5,77E-02	11,83
P3	10	3,0	2,8	0,729	4,44E-02	11,11
P4	15	3,4	3,2	0,652	3,04E-02	9,74
P5	20	3,6	3,4	0,599	2,39E-02	8,87
P6	25	3,8	3,5	0,592	1,67E-02	7,62
P7	30	4,0	3,7	0,623	1,74E-02	7,95
P8	35	4,2	3,9	0,630	1,67E-02	7,97
P11	50	4,6	4,2	0,519	9,27E-02	6,21

(4) and (5), and assuming Strickler coefficient as previously referred:

$$K_s = \frac{1}{n}$$

where, according to Chang (1988), n is given by:

$$n = 0{,}0482(d_{50})^{\frac{1}{6}}$$

That allowed bed shear stresses (τ_o) and Shield's parameters (D* and ψ) to be evaluated (based on equation 1) for flow profiles not affected by scour hole formation. Table 4 exemplifies the evaluation of u_* for 12,2 l/s flow, type C rock fill protection. For this same flow and types A and B rock fill bed protection, this method enabled only to evaluate those parameters for the entrance of the rock fill protection area (profile P1). Figure 15 (a, b and c) shows plots of the correspondent obtained values.

According to Figure 15a there will be no movement on the rock fill protection for the 11,5 l/s flow (for type A rock fill protection), being the nearest point to curve 1, of the modified Shields diagram, the one representative of profile P1. This curve corresponds to "occasional particle movement at some locations" (see legend of Figure 1). In fact, during the tests no erosion or scour was noticed, only some rock material instability was remarked.

Figure 15b enabled comparison of Shield diagram plots correspondent to profile P1 for this case (type A), for different flow conditions (Q = 11,5 l/s and 12,2 l/s). The point representative of the 12,2 l/s flow value was now located between curves 6 and 7 of Shields diagram, corresponding to "permanent moving of particles" and "general transport of ripples" situations, as was, in fact, confirmed during the tests.

Figure 15c compares Shield plots correspondent to all the rock fill protection types for 12,2 l/s flow.

For type B protection, where velocity profile P1 was measured before erosion occurrence, the diagram

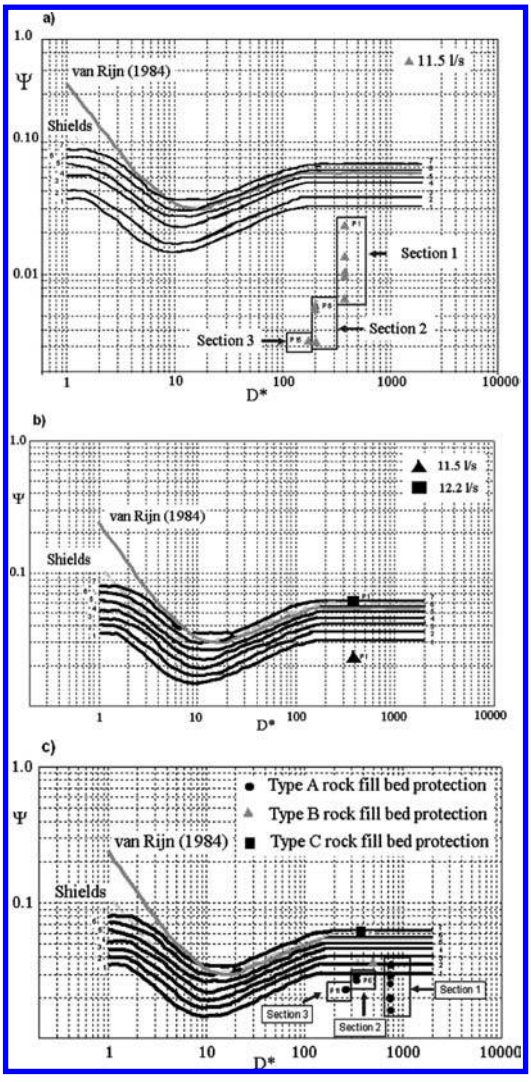


Figure 15. Modified shields diagram for: (a) 11,5 l/s flow and type A rock fill bed protection; (b) 11,5 l/s and 12,2 l/s and type A rock fill protection; (c) 12,2 l/s and types A, B and C rock fill protection (assuming uniform flow case).

indicated the situation of "frequent movement of particles in some locations", which was in agreement with the experimental results.

In which regards C type rock fill bed protection, Shields diagram enabled to conclude that there will be no particle movement of materials except on profile P1 location where there will be the tendency to "occasional to frequent movement of particles". In fact, it should be pointed out that, during the experiments, no erosion events of bed protection on sections 1 and 2 were recorded. However, on section 3, some scour has

Copyright © 2006 Taylor & Francis Group plc, London, UK

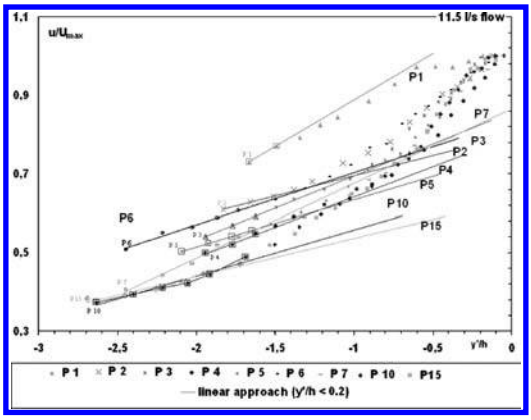


Figure 16. Uniformity flow analysis for 11,5 l/s flow.

Table 5. Rotta criterion parameters evolution for 12,2 l/s flow and for type A, B and C rock fill bed protections: (a) u_*/U_{max}; (b) β; (c) $U_{max}\delta^*/u_*$.

	Rock fill bed protection								
	Type A			Type B			Type C		
Profile	a)	b)	c)	a)	b)	c)	a)	b)	c)
P1	0,102	0,6	9,8	0,103	0,7	7,0	0,118	0,4	5,3
P2	–	–	–	–	–	–	0,121	1,4	4,8
P3	–	–	–	–	–	–	0,123	1,8	4,6
P4	–	–	–	–	–	–	0,119	1,2	5,8
P5	–	–	–	–	–	–	0,116	1,6	7,0
P6	–	–	–	–	–	–	0,101	2,2	8,3
P7	–	–	–	–	–	–	0,103	2,1	7,4
P8	–	–	–	–	–	–	0,105	1,6	6,9
P11	–	–	–	–	–	–	0,089	0,7	13,3

occurred, as it was shown in the previously referred Figure 12.

The above analysis was based on the assumption that the studied flows were uniform flows and thus the representation of their velocity profiles could be made using the logarithmic law defined by the expression (2).

Nevertheless, velocity profiles on the inner region, corresponding to the 11,5 l/s flow case have been plotted, and shown on Figure 16. For inner limit region, the value of $y'/h = 0.2$, often used, was considered. Those profiles enabled to conclude that the flow, was in fact not uniform.

The same conclusion could be withdrawn through Rotta criterion application, using the set of expressions (3) which values are shown on table 5 for the 12,2 l/s flow and the three rock fill bed protections studied, which confirms the non-uniformity of the flow.

Table 6. Friction velocity values evaluation for 12,2 l/s flow value and type C rock fill protection (non-uniform flow).

Profile	x (cm)	h (cm)	u_*^2 (cm^2/s^2)	u_* (cm/s)
P1	0	2,4	173,36	13,17
P2	5	2,6	78,32	8,85
P3	10	3,0	164,60	12,83
P4	15	3,4	66,87	8,18
P5	20	3,6	18,10	4,25
P6	25	3,8	27,37	5,23
P7	30	4,0	19,99	4,47
P8	35	4,2	12,91	3,59
P11	50	4,6	192,73	13,88

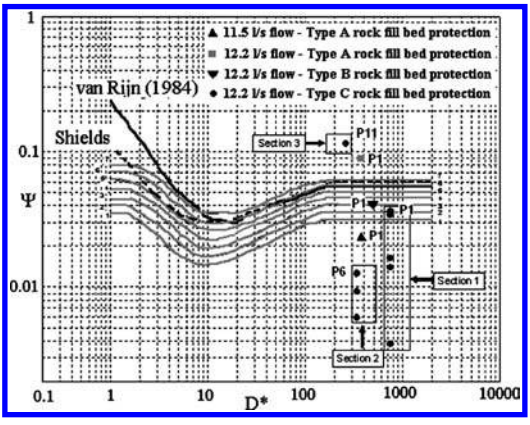


Figure 17. Modified Shields diagram for 11,5 l/s and 12,2 l/s flows and for type A, B and C rock fill bed protections, assuming the non uniform flow case.

Based on the data obtained from the velocity profiles measured and for the different test conditions, velocity friction values have then been recalculated using equation (6). Table 6 presents an example of those calculations for the same case as in table 4: 12,2 l/s flow and type C rock fill protection.

The same procedure has been applied to all the flow values and bed fill protection types and have been on the basis of Shields parameters recalculation for all set of flows and rock fill bed protections, which are shown on Figure 17.

The plotted values considering the non-uniformity conditions show to be in better agreement with the experiments. From the above figure, it can be concluded that for A and B rock type protections movement of materials shall occur, which was confirmed by the experiments, and that for C type only on section 3 of the rock fill protection, profile P11, erosion will occur, in accordance with what was, in fact, reported on experiments and shown on Figure 12. That occurrence could not be confirmed by Shields diagram when considering uniform flow case.

Copyright © 2006 Taylor & Francis Group plc, London, UK

6 CONCLUSIONS

A physical model of Crestuma dam was made and tested for two flow values and for three different types of rock fill bed protections, in order to have a better insight on flow energy dissipation effect on those protections.

Laser Doppler Anemometry was used for flow velocity measurements in order to define the corresponding flow fields on the different test conditions. Velocity profiles measurements at different locations in the stilling basin and in the downstream rock fill bed protection, allowed the definition of the mean and turbulent flow field characteristics corresponding to each one of the different test conditions.

Two different limit flow discharges were studied, enabling the analysis of scour effects on different rock fill bed protections; one close to incipient motion of particles of (type A) rock fill bed protection and the other with scouring effects on the three different studied (growing in dimension, types A, B and C) rock fill types.

Critical shear stress criterion, using modified Shields diagram was applied to analyse the different types of rock fill bed protection behaviour. Subsequently, Shields parameters have been calculated assuming uniformity or non-uniformity behaviour of the flow.

Based on the above criterion scour occurrence was analysed and experimental results compared with the theoretical ones.

It could be concluded that, in general, the non-uniform flow approach led to better results on scour occurrence analysis.

Future work shall be made taking into account other different criteria for initiation of sediments movement in order to compare the obtained results.

ACKNOWLEGEMENTS

The authors are grateful to FCT who funded this work through the project POCTI/ECM/36031/2000 “Energy Dissipation in Hydraulic Structures Established on Mobile Bed”.

REFERENCES

Cardoso, A.H. 1990. *Spatially Accelerating Flow in a Smooth Open Channel, These N.º 813 (1989),* Ecole Polythechnique Fédérale de Lausanne.

Chang, H.H. 1988. Fluvial processes in river engineering. John Wiley & Sons.

Graf, W.H. & Song, T. 1995. Bed-shear stress in non-uniform and unsteady open-channel flows, *Journal for Hydraulic Research*, vol. 33: 699–703.

Graf, W.H. & Altinakar, M.S. 1998. *Fluvial Hydraulics – Flow and Transport Processes in Channels of Simple Geometry*. John Wiley & Sons.

LNEC. 1972. *Estudo hidráulico em modelo reduzido do aproveitamento de Crestuma, 1º Relatório, (Hydraulic Study of Crestuma dam in physical model, 1st Report), Laboratório Nacional de Engenharia Civil, Lisboa.*

Hoffmans, G.J.C.M. & Verheij, H.J. 1997. *Scour Manual,* Rotterdam: Balkema.

Copyright © 2006 Taylor & Francis Group plc, London, UK

B.2. Bed forms and flow resistance

Copyright © 2006 Taylor & Francis Group plc, London, UK

Modelling morphodynamic evolution of river dunes

A.J. Paarlberg, C.M. Dohmen-Janssen & S.J.M.H. Hulscher
University of Twente, Water Engineering & Management, Enschede, The Netherlands

J. van den Berg
University of Twente, Numerical Analysis & Computational Mechanics, Enschede, The Netherlands

A.P.P. Termes
HKV Consultants, Lelystad, The Netherlands

ABSTRACT: River dunes influence the hydraulic roughness and water levels in rivers. Especially during floods the interplay between dunes and the flow field could become significant. Therefore, it is desired to forecast the dimensions of dunes during such extreme and unsteady flood events. At present it is not yet feasible to predict the dimensions of dunes by computing the flow and sediment transport in full detail for operational spatial and temporal scales. In this paper, we present a morphodynamic model that simulates dune development, without computing all details in the flow field. The flow model is based on the 2D-vertical hydrostatic equations, with a constant eddy viscosity over depth. Flow separation and the sediment transport behaviour in the flow separation zone are included in a parameterized way. Results of the morphodynamic model using steady flow conditions, are in general agreement with flume experiments. A next step in the research will be to use forecasted dune dimensions for hydraulic roughness predictions.

1 INTRODUCTION

Water levels during floods in rivers are largely influenced by the flow resistance that results from flow over a dune-covered bed. A flood event itself determines the development of the dunes, leading to a complex interplay of bed formation and flow characteristics.

In current practice, in hydraulic flow models the roughness of the main channel is used as the calibration parameter to match observed water levels. Although the total flow resistance of the river is due to several different sources (e.g. vegetation or groynes), dunes have a large influence on the roughness because of energy dissipation behind steep dunes (e.g. Vanoni and Hwang 1967). During their development, the lee-side of a dune may become so steep that the flow cannot follow the bed surface any longer, forming a flow separation zone. The turbulence (eddies) generated in the flow separation zone slows the flow down. This process is often referred to as form roughness or form drag.

At present, there is still limited knowledge about the effect of dunes on the hydraulic roughness of a river, let alone about their development during floods. In order to understand flow resistance due to dunes, it is necessary to first understand their behaviour. If dune dimensions and their resulting resistance can be predicted as a function of flow conditions and sediment properties, this part of the total flow resistance may be excluded from the calibration of hydraulic models.

Several researchers proposed methods to forecast dune dimensions (e.g. dune length and dune height), based on a range of parameters like flow strength, water depth or sediment size. Part of the proposed methods are empirical (e.g. Julien and Klaassen 1995; Van Rijn 1984), while others are more theoretical (e.g. Kennedy 1969; Onda and Hosoda 2004). All these methods are designed to calculate equilibrium dune dimensions in steady, uniform flow. In that case a unique dune height and dune length exist for each specific combination of flow characteristics and sediment properties.

Observations have shown that changes in flow resistance are out of phase with flood intensity. Maximum dune dimensions occur later than the maximum discharge (e.g. Ten Brinke et al. 1999; Julien et al. 2002). Several researchers tried to include the observed time-lag between dune dimensions and flood intensity in their models to forecast dune dimensions (e.g. Allen 1976; Fredsøe 1979). However, as shown by Wilbers (2004), none of these predictors are able to predict dune dimensions during several floods in the River

Copyright © 2006 Taylor & Francis Group plc, London, UK

Rhine in the Netherlands adequately. Wilbers (2004) developed an empirical calculation method to forecast dune development under unsteady flow conditions, based on a method proposed by Allen (1976). This method is applied with success to three sections of the Rhine branches. However, a major drawback is that the method is not generally applicable. For every situation, initial dune dimensions have to be known and data are required to calibrate empirical coefficients. Furthermore, the method gives only limited insight in the physics behind dune development during floods.

To forecast the behaviour of dunes on a physical basis, the flow and sediment transport resulting from that flow has to be predicted. Yoon and Patel (1996) adopted a k-ω turbulence model enabling a detailed computation of the flow in the separation eddy. Results were shown to be in general agreement with the experimental data. Stansby and Zhou (1998) showed that the computation of the flow in the separation zone improved when a non-hydrostatic pressure (instead of hydrostatic) was applied. Nelson et al. (2005) have shown that a large eddy simulation model with non-hydrostatic pressure, in combination with a sediment transport model taking fluctuations of the bed shear stress on turbulent timescales into account, realistically models dune development. Such approaches require modelling all details in the flow field and especially the complex flow in the flow separation zone. A disadvantage of such methods is that they are complicated and require much computational effort. This becomes a problem when the flow calculation has to be done repeatedly for each bottom update.

As a first step towards predicting flow resistance caused by dunes on large spatial and long temporal scales, we propose a morphodynamic model to forecast dune development under steady flow conditions. We aim to develop the most basic morphodynamic model that still describes the most relevant processes to predict dune development.

Paarlberg et al. (2005) have shown that the morphodynamic model of Hulscher (1996), which is originally developed to simulate offshore sandwaves, can also be used to simulate river dunes in unidirectional flows. This morphodynamic model is numerically implemented by Németh et al. (2006) and Van Den Berg and Van Damme (2005), of which the latter is used in this research.

The numerical model is based on hydrostatic equations, implying that flow separation cannot be treated explicitly. To keep the model appropriate, we present an approach to include flow separation in a parameterized way. Following the approach of Kroy et al. (2002), the idea is to cut off the flow separation zone from flow computations and only compute the flow above this zone. Paarlberg et al. (2005) showed that the shape of the flow separation can be estimated on the basis of general dune dimensions. Although the predicted shape was in agreement with detailed measurements on turbulent flows over dunes, the parameterization was not tested in a morphodynamic model. Therefore, in this paper, the morphodynamic model is extended with a parameterization of sediment transport behaviour in the flow separation zone, and tested against flume data.

2 MODEL FOR GENTLE DUNES

To simulate dune development, flow and sediment transport due to this flow are modelled. A stationairy version of the code described in Van den Berg and Van Damme (2005) is used for computations. This model is based on earlier models by Hulscher (1996) and Németh and Hulscher (2003). In this section the model equations are discussed. Further, the numerical model is applied to a situation with gentle bed-slopes (i.e. streamlined flow without separation).

2.1 *Steady flow model*

Flow is simulated with the hydrostatic two-dimensional vertical (2DV) shallow water equations. The momentum equation in x-direction and the continuity equation read:

$$u\frac{\partial u}{\partial x} + w\frac{\partial u}{\partial z} = -g\frac{\partial \zeta}{\partial x} + A_v\frac{\partial^2 u}{\partial z^2} + gi \tag{1}$$

$$\frac{\partial u}{\partial x} + \frac{\partial w}{\partial z} = 0 \tag{2}$$

The velocities in the x- and z- directions (see Figure 1) are u and w, respectively. The water surface elevation is denoted by ζ, i is the average bottom slope,

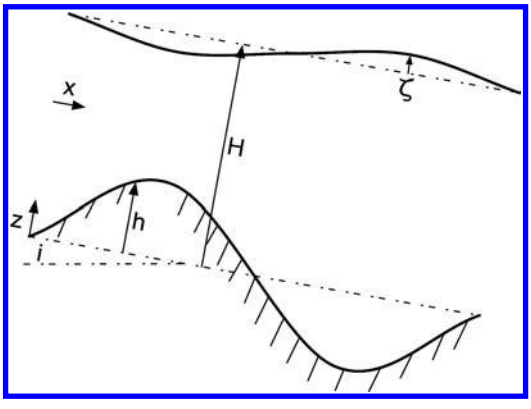


Figure 1. Definitions of H (average height of the water column), $h(x)$ (bottom disturbance) and $\zeta(x,t)$ (surface elevation).

Copyright © 2006 Taylor & Francis Group plc, London, UK

and g and A_v denote the acceleration due to gravity and the vertical eddy viscosity, respectively.

2.2 *Boundary conditions*

Two boundary conditions are imposed at the water surface ($z = H + \zeta$): (*i*) there is no flow through the surface, and (*ii*) there is no shear stress at the surface:

$$u\frac{\partial \zeta}{\partial x} = w \tag{3}$$

$$\frac{\partial u}{\partial z} = 0 \tag{4}$$

The boundary condition at the bed ($z = h$) is that there is no flow through the boundary:

$$u\frac{\partial h}{\partial x} = w \tag{5}$$

As a basic turbulence closure, a constant eddy viscosity is used. In combination with the fundamental property of boundary layers, the no-slip boundary condition leads to an over-prediction of the shear stress at the bed. Soulsby (1990) has made a comparison between different turbulence models for boundary layer flows. He also examined alternatives to the no-slip boundary conditions. It turns out that constant eddy viscosity in combination with a partial slip conditions results in a good representation of the vertical flow structure and the shear stress at the bed level.

The partial slip condition at the bed ($z = h$) is given by:

$$\tau_b = A_v\frac{\partial u}{\partial z} = Su_b \tag{6}$$

where τ_b is the volumetric bed shear stress [m^2/s^2]. The slip parameter S determines the resistance at the bed; $S \to \infty$ would amount to a no slip condition.

Paarlberg et al. (2005) calibrated the values of A_v and S using flume measurements of the actual velocity profile and the bottom shear stress.

2.3 *Sediment transport model and bed behaviour*

Only bedload sediment transport is considered in the model, since this is assumed to be the main transport mechanism behind dune development. A general bed load formula including bed slope effects is applied:

$$q_b = \alpha|\tau_b|^\beta\left[\frac{\tau_b}{|\tau_b|} - \lambda\frac{\partial h}{\partial x}\right] \tag{7}$$

where q_b is the volumetric bed load transport [$m^2\ s^{-1}$]. The proportionality constant α [$s^2\ m^{-1}$] describes how efficiently the sand particles are transported by the bed shear stress (Van Rijn 1993) and strongly determines the time-scale of bed evolution. Parameter β represents the nonlinear dependence of sediment transport on the bed shear stress. The bed slope parameter λ describes the downhill preference of moving sediment. Bed evolution follows from the Exner equation:

$$(1-\epsilon_p)\frac{\partial h}{\partial t} = -\frac{\partial q_b}{\partial x} \tag{8}$$

where ϵ_p is bed porosity (typically $\epsilon_p \sim 0.4$).

2.4 *Results*

The model presented in this section cannot treat flow separation, since the pressure distribution is hydrostatic. However, the model should be able to reproduce the main characteristics of dune development in the case of streamlined flow (no flow separation). Figure 2 shows results of a simulation with an initially small symmetrical bed disturbance and periodic boundary conditions. Used parameter values are specified in Table 1 (see also Paarlberg et al. 2005).

The figure shows that over time the dunes grow in amplitude and migrate in streamwise direction. Further, it can be observed that dune asymmetry (ratio of stoss- and lee-side slope) increases over time. These processes are well known processes in dune development, giving confidence in the used model equations. However, to enable determination of equilibrium dune dimensions the model needs to be extended to enable simulations in cases where flow separation occurs.

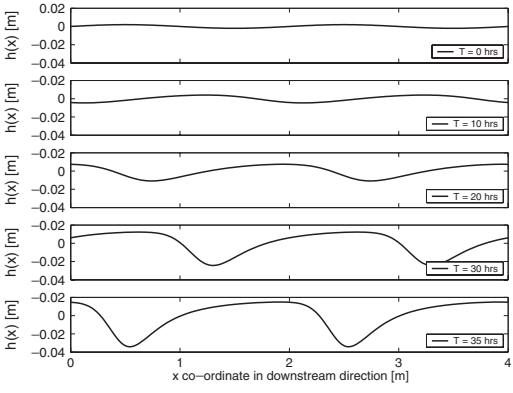


Figure 2. Development of small initial disturbance (2 mm). See Table 1 for model parameter settings. Flow is from left to right. T are flow hours.

Copyright © 2006 Taylor & Francis Group plc, London, UK

Table 1. Parameter values for a model run where no flow separation occurs (Figure 1).

Par.	Description	Value	Dim.
A_v	Eddy viscosity	$1.9 \cdot 10^{-4}$	m^2/s
S	Slip parameter	$1.9 \cdot 10^{-3}$	m/s
g	Acceleration of gravity	9.81	m/s^2
q	Specific discharge	0.038	m^2/s
i	Mean bottom slope	$5.5 \cdot 10^{-4}$	–
H	Average water depth*	0.10	m
α	Prop. constant	0.3	s^2/m
β	Power of τ_b	1.5	–
λ	Slope parameter	0.1	–

* The average water depth may vary during a simulation, as a result of changing bed roughness.

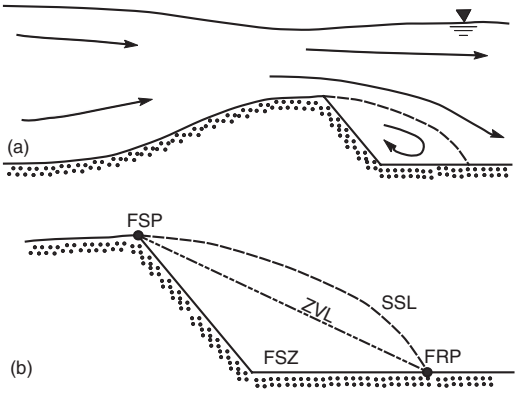


Figure 3. (a) Streamlines and water surface profile over a typical dune shape (vertical exaggeration). (b) Emphasis on the flow separation zone (abbreviations are explained and used in the text).

3 FLOW SEPARATION

3.1 *Process of flow separation*

Flow over a river bed is driven by gravity. Seen in vertical direction the pressure gradient is linear between the watersurface (zero) and the bed ($\rho g h_l i$, with h_l the local water depth) for parallel and non-curved streamlines. This condition holds more or less for slowly accelerating flow over the stoss side of a dune.

If we consider flow over a dune, such as shown in the bottom panel of Figure 2, the pressure gradient in horizontal direction is positive (or adverse) at the lee-side of the dunes due to an increasing local water depth. This adverse pressure gradient is most pronounced in the region close to the bed. Here momentum is lowest, leading to a velocity profile with a $\partial u/\partial z$ of zero near the bottom. Even further downstream on the lee-side, where the adverse pressure gradient is larger, reverse flow is observed. As a result of the reversed flow, a flow separation zone will form behind steep dunes. Here, the location where the flow separates is termed the flow separation point (FSP).

Figure 3 shows flow over a typical dune with presence of a flow separation zone (FSZ). The flow reattaches to the bed at a typical distance of about 6 times the dune height at the flow reattachment point (FRP). The separating streamline (SSL) indicates the boundary between the recirculating flow cell, and the normal flow field. The zero velocity line (ZVL) connects the points where the horizontal velocity is zero. The abbreviations used in this section are included in Figure 3 for later reference.

3.2 *Parameterization of the shape of the flow separation zone*

Paarlberg et al. (2005) propose a parameterization of the shape of the flow separation zone, based on the approach of Kroy et al. (2002). They state that formation and migration of aeolian sand dunes do not very sensitively depend on the details in the FSZ. Since there is flow recirculation in the FSZ, it is assumed that computation of the flow field above the separating streamline is sufficient. Therefore, a parameterization of this separating streamline was developed by Paarlberg et al. (2005).

The main concepts of the parameterization are:

- The shape of separation zone is independent of flow conditions;
- The SSL can be represented by a 3rd order polynomial: $s(x) = s_3(x_*)^3 + s_2(x_*)^2 + s_1(x_*) + s_0$, with $x_* = x - x_s$ and x_s the position of the FSP;
- There is smooth connection at separation point giving s_1 and s_0;
- The (dimensionless) length of the separation zone can be estimated from (see Paarlberg et al. 2005 for determination of coefficients):

$$L_{fsz}/H_{dune} = 0.19\alpha_s + 5.66 \quad (9)$$

  where L_{fsz} the FSZ-length, H_{dune} the dune height at separation and α_s the local bed slope at separation (degrees);
- The angle of the SSL at the FRP is $-25°$ with the average bottom slope.

4 THE MORPHODYNAMIC MODEL

To include flow separation, the numerical model described in Section 2 is extended with the parameterization for flow separation as described in Section 3. Figure 4 shows a schematic representation of the morphodynamic model setup, which will be explained in this section. If there is no flow separation, the left part of Figure 4 is followed which is the model as described

Copyright © 2006 Taylor & Francis Group plc, London, UK

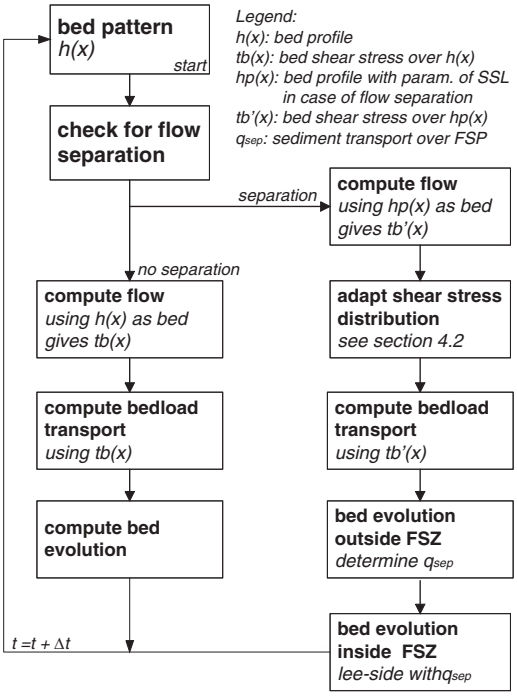


Figure 4. Schematic representation of the morphodynamic model.

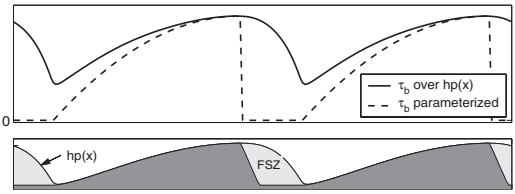


Figure 5. Parameterization of bed shear stress distribution over a dune. The bottom panel gives an arbitrary bed profile with flow separation zones (FSZ) indicted. The top panel gives the computed and parameterized bed shear stress distribution.

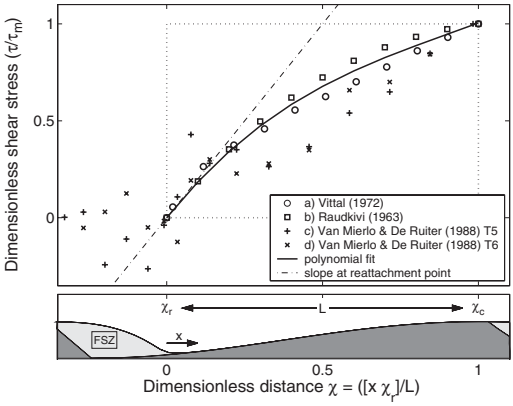


Figure 6. Measured bed shear stress distributions over dunes. For case (a) and (b) the data points are directly taken from reported literature; for case (c) and (d) the values are derived by assuming a logarithmic velocity profile close to the bed. The horizontal axis is scaled by $L = \chi_c - \chi_r$, being the horizontal length between the FRP and the next bedform top. The vertical axis is scaled by the maximum bed shear stress measured at the top (see also Table 2).

in Section 2. When flow separation does occur the model follows the right part in Figure 4.

4.1 *Flow separation criterion in the model*

In the flow solver, no pressure distributions are computed. The criterion for flow separation to occur is based on local bed gradients. Strong (negative) bed gradients result in an increase of adverse pressure gradient. In line with e.g. Kroy et al. (2002) we use the following separation criterion: separation occurs if the local bed gradient exceeds $-14°$ (with the mean bottom slope).

4.2 *Bed shear stress distribution over a dune*

In our approach, flow is computed over the SSL above the FSZ, and over the bed elsewhere. Thus the flow inside the FSZ is not computed explicitly. Figure 5 shows an example of the bed shear stress distribution over two identical dunes with flow separation.

Measurements show that the time-averaged bed shear stress approximates zero in the FSZ (see e.g. Van Mierlo and De Ruiter 1988). Furthermore, if bedload transport is dominant, the sediment flux in the FSZ is close to zero due to flow recirculation in the FSZ. The flow computation over the parameterized bed ($hp(x)$) is used to give a first estimate of the bed shear stress distribution over the dunes. Next, the average bed shear stress (and thus the flux) is set to zero inside the FSZ. This procedure results in two discontinuities in the shear stress distribution over a dune. At the FSP the bed shear stress goes to zero. In Section 4.3 will be shown that this is no problem because of the method used for bed evolution inside the FSZ. However, the discontinuity at the FRP must be resolved. Therefore, we need a parameterization for the distribution of the average bed shear stress over the stoss-side of the dunes.

Figure 6 shows measurements of (dimensionless) bed shear stress distributions over dunes (dune characteristics can be found in Table 2). At the FRP the measured time-averaged bed shear stress is zero, and downstream of the FRP the time-averaged bed shear stress gradually increases until it reaches a maximum at the dune crest. To mimic this behaviour a curve is

Copyright © 2006 Taylor & Francis Group plc, London, UK

Table 2. Measurements that are used to obtain a bed shear stress distribution for the model. General dune and flow characteristics, used scaling parameters for Figure 6, and general flow characteristics are included.

	(a)	(b)	(c)	(d)
λ	0.6	0.39	1.6	1.6
Δ	0.03	0.03	0.08	0.08
L	0.51	0.25	1.16	1.16
τ_m	0.72	0.30	1.12	1.50*
i	$3.5{\cdot}10^{-4}$	$5.3{\cdot}10^{-4}$	$9.4{\cdot}10^{-4}$	$9.4{\cdot}10^{-4}$
H	0.200	0.130	0.290	0.372
q	0.070	0.037	0.099	0.171

λ: Dune length [m]; Δ: Dune height [m]; L: Distance between FRP and next crest position [m]; τ_m: Maximum bed shear stress [N/m^2] (the latter two parameters are used as scaling parameters in Figure 6); i: Average bottom slope [−]; H: Average water depth [m]; q: Specific discharge [m^2/s]; *: measured shear stress was slightly higher due to horizontal section just before top; (a): Vittal (1972); (b): Raudkivi (1963); (c,d): Van Mierlo and De Ruiter (1988).

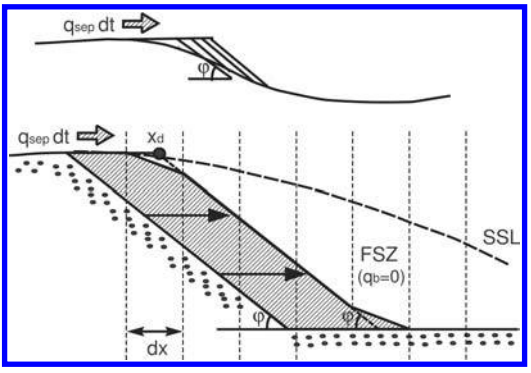


Figure 7. If flow separation occurs, a lee-side with an angle of repose (φ) is formed (top figure). The volumetric sediment transport ($q_{sep}dt$), where dt is the timestep, distributes evenly over the lee-side, as sketched in the lower figure. x_d is the horizontal position where the lee-side starts; dx is the horizontal grid distance. Due to interpolation to the grid in each time step, errors occur, which are compensated in the next time step.

fitted through these measurement points. Since we are interested in the shear stress on the stoss-side of a dune only measurements in the rectangular box in Figure 6 are used. The solid line in Figure 6 is a third order polynomial fit through the data, which fits quite well to the data. Therefore, we choose to approximate the bed shear stress distribution over a dune with a third order polynomial:

$$\tau'(\chi) = \begin{cases} 0 & \text{if } \chi < 0 \text{ (FSZ)} \\ a_3(\chi)^3 + a_2(\chi)^2 + a_1(\chi) + a_0 & \text{if } \chi_r \le \chi \le \chi_c \end{cases} \quad (10)$$

where χ is a dimensionless position along the dune (see Figure 6), and the coefficients $a_0 \ldots a_3$ are calibrated using the measurements. Parameter a_0 equals zero, since the bed shear stress is zero at the reattachment point (χ_r) and for a_1 holds at χ_r:

$$\left.\frac{d\tau'}{d\chi}\right|_{\chi_r} = 2\frac{\tau_m}{L}, \quad L = \chi_c - \chi_r \quad (11)$$

The coefficients a_2 and a_3 are calibrated by imposing smooth connection to the computed bed shear stress (and gradient in bed shear stress) at the crest of a dune.

4.3 *Bed evolution*

Bed evolution in the region outside the FSZ is determined by computing sediment transport and bed level changes by applying Eqs. (7) and (8). Since the time-averaged bed shear stress is set to zero inside the FSZ, there is no sediment transport in that zone. To schematize bed deformation in the FSZ, the material that passes the FSP is assumed to avalanche down the lee-side of the dunes and to be distributed evenly over the lee-side, with a lee-side angle at the angle of repose φ (for natural sand $\varphi \sim 30°$).

When performing this operation numerically, two small errors are made at each numerical timestep: (1) a "truncation error", being the difference between the volume that should be stored behind the dune and the amount that is actually stored; this error is kept within 1×10^{-6} m^2, and (2) a "rounding error" due to interpolation to the grid when the lee-side of the dune is set (this error is of order 1×10^{-5} m^2). The sum of both errors implies that either too few or too much sediment is stored at the lee-side of the dune. This error is computed and corrected in the next morphodynamic update.

As may be observed in Figure 2, using the flow separation criterion discussed in Section 4.1, the position where flow separation occurs for the first time in the model is somewhere halfway the lee-side of the dune. In the model, from this moment onward separation occurs at the crest of the dune, inducing avalanching of sediment over the top. This process occurs fast compared to the overall timescale of dune development (migration of about order 10 m/day, see e.g. Wijbenga and Van Nes 1986), and is illustrated in Figure 7. Effectively, it means that the lee-side does not deform from the moment that it reaches a slope at the angle of repose, and that the distance that the lee-side moves downstream is determined by the sediment volume over the separation point and the dune height.

Copyright © 2006 Taylor & Francis Group plc, London, UK

5 RESULTS WITH FIXED DUNE LENGTH

In this section, the performance of the model from the previous section is presented. The eddy viscosity A_v and slip parameter S remain constant during the simulation. As bedforms develop over time, the roughness of the bed changes. Although the roughness (included in the model via the slip parameter S) is constant in a simulation, the average water depth H is changed to ensure a constant steady discharge. Simulations are made with periodic boundary conditions, putting restrictions on the wave length of simulated dunes (i.e. the dune length will remain constant).

5.1 *Bed evolution*

Simulations start with an initially flat bottom with very small disturbances. These disturbances develop into asymmetric features as shown in Section 2.4. Using the morphodynamic model discussed in the previous section, simulations can now be performed including the effect of flow separation. Parameter settings for the model runs presented here are the same as in Section 2.4. Figure 8 shows the long term evolution of two dunes, leading to typical dune shapes with a lee-side at the angle of repose.

After sufficiently long time, a (dynamic) equilibrium is obtained as shown in Figure 9. The equilibrium is referred to as dynamic because the dunes still migrate in downstream direction, while their height remains constant. The dune height (defined as the vertical distance between crest- and trough elevation averaged over the two dunes) steadily increases, attaining an equilibrium height after about 130 flow hours. The average water depth (H) shows a similar behaviour, as a result of increasing flow resistance due to a growing FSZ.

Determination of the migration velocity of the dunes is not straightforward, because the dune profile deforms, as well. For example, in cases without flow separation, the crest of the dunes migrates faster than the trough. Since simulations initially start with a sinusoidal disturbance in a periodic domain, we choose to apply a fast fourier transform to determine the migration velocity of the Fourier mode most prominently present in the bed. The phase difference between the Fourier components at two subsequent timesteps is translated into an estimate of the migration velocity. Figure 9c shows, apart from the "discontinuity", that the migration velocity decreases with increasing dune height. Larger dunes, with constant dune length, imply lower migration velocities, since more sediment has to be moved.

The discontinuities in Figure 9 are related to our implementation of flow separation. The system suddenly switches from a situation without flow separation to one with flow separation. When this switch

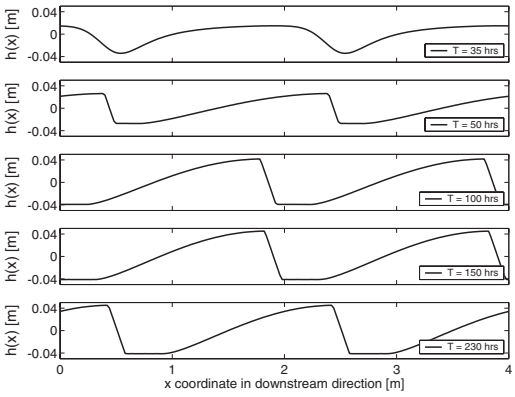


Figure 8. Long term development of two identical dunes. The top panel is the same as the last panel of Figure 2 with a different scale on the y-axis. T are flow hours.

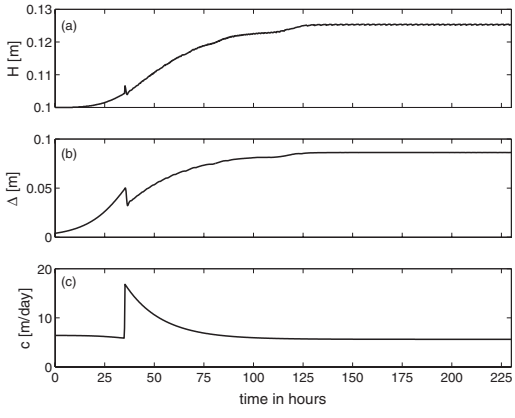


Figure 9. Development of average water depth H (a), dune height Δ (b), and migration velocity (c) over time for the simulation shown in Figure 8. The discontinuity is at the time where flow separation happens for the first time (after about 35 hours).

occurs, the system needs to adapt to the strong changes in bed shear stress distribution over the dunes. After about 35 flow hours, when flow separation occurs, the bed shear stress in the FSZ becomes zero and on the stoss side the bed shear stress gradient increases (i.e. Eq. (10)). From separation onwards, all the sediment transported over the FSP is stored in the FSZ behind the lee-side of a dune. This leads to a situation with a larger migration velocity, compared to a situation where the sediment was redistributed over a sinusoidal dune.

5.2 *Flow field and bed shear stress*

Figure 10 shows the bed velocity, the bed shear stress distribution and the velocity field in equilibrium after

Copyright © 2006 Taylor & Francis Group plc, London, UK

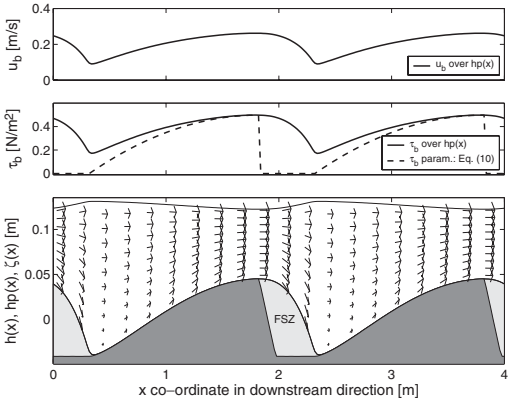


Figure 10. Bed velocity (top), bed shear stress (center) and velocity field (bottom) after 150 flow hours. Dark gray shading is the bed, light gray shade represents the FSZ, over which the flow is computed.

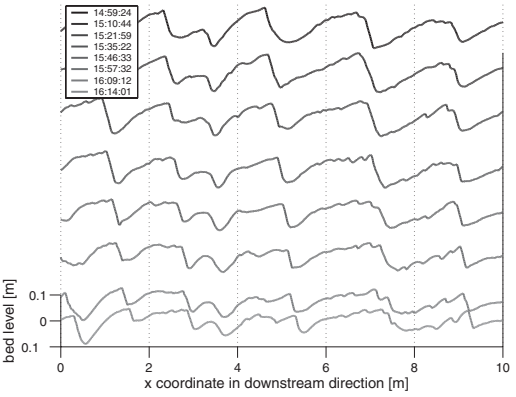


Figure 11. Bed profile measurements for TOW test T14 in equilibrium (Bakker et al. 1986). Test conditions: $q = 0.04\,\mathrm{m^2/s}$, $H = 0.106\,\mathrm{m}$, and $i = 1.06 \cdot 10^{-4}$. Time reads from top to bottom, and scale is indicated on the lower left side of the plot.

150 flow hours. The dunes occupy a considerable height of the water column ($\Delta/H \approx 0.7$ in equilibrium), and also water surface fluctuations are significant. The velocity at the bed increases over the stoss-side. Due to the partial slip condition, velocities near the bed differ from zero. Also we clearly see lower velocities at the bed compared to velocities at the surface.

5.3 *Comparison with measurements*

Between 1973 and 1980 a series of flume experiments with steady flow conditions and uniform sediment were carried out at the Delft Hydraulics Laboratory (Bakker et al. 1986). The measurements were performed in a flume which is 100 m in length and 1.5 m wide.

Figure 11 shows a series of recorded bed profiles for test T14 in equilibrium. The first 10 m of a 30 m long measurement section at the end of the flume are shown. In this experiment, which started with a bed profile resulting from a previous experiment, the following flow conditions hold in equilibrium: a specific discharge $q \approx 0.04\,\mathrm{m^2/s}$, an average water depth $H = 0.106\,\mathrm{m}$, and mean bottom slope $i = 1.06 \cdot 10^{-4}$. The energy slope is kept constant during the experiment by a weir at the downstream end of the flume. These conditions are comparable to the simulation that is performed. In the experiments, an equilibrium was attained after about 250 flow hours. In equilibrium, the average dune height is about 0.05 m, the average length about 1.7 m, and the migration rate is estimated at about 10 m/day. All these characteristics are in general agreement with our simulation, although the dune height seems somewhat over estimated by our simulation model. This may be due to our approximation of constant eddy viscosity over depth, or the imposed constant dune length.

6 DISCUSSION

The proposed model is simple and fast in application, but highly parameterized. Some of the parameters maybe estimated a priori. An estimation of the eddy viscosity A_v can be obtained from a relationship that follows from integration of an parabolic eddy viscosity profile in vertical direction:

$$A_v = \frac{1}{6}\kappa u_* H \tag{12}$$

in which κ is the Von Kármán constant (=0.407), and u_* is the shear velocity ($=\sqrt{gHi}$). Evaluating this equation for an initial water depth of $H = 10\,\mathrm{cm}$ results in $A_v = 1.56 \times 10^{-4}\,\mathrm{m^2/s}$. This is very close to the calibrated value (see Table 1). The slip parameter S is more difficult to estimate, and may depend on grain-size, water depth and energy slope; for now, this remains a parameter for calibration.

The parameter α appearing in the sediment transport relationship is set to 0.3 following Van Rijn (1993). According to Komarova and Hulscher (2000) its value can be estimated with:

$$\alpha = \frac{m}{(s-1)g} \tag{13}$$

where s is the specific grain density (=1.65), and m is an empirical coefficient, which may vary between 5.7 and 12 depending on the rate of sediment transport (Wiberg and Smith 1989). To arrive at a value of $\alpha = 0.3$, m should be about 5. Although this seems a

Copyright © 2006 Taylor & Francis Group plc, London, UK

quite low value, it is considered that the value of α primarily influences the rate of sediment transport and thus the timescale of bed evolution. It has only minor influence on the general bed behaviour.

In the proposed morphodynamic model, we do not account for turbulent fluctuations, and use the average bed shear stress to compute the sediment transport over the dunes. For sure we cannot reproduce all details of the complicated dune development process. However, our goal is to develop an appropriate model to reproduce general dune behaviour. Therefore, we believe that this approach is appropriate for our goals.

In the flow solver, no details of the turbulent flow inside the FSZ are computed. However, it is expected that there is an influence of the energy losses in the FSZ on the remainder of the flow field, since simulated water surface elevations above the FSZ are quite large. This influence is not included in the proposed model. It could be included by changing the boundary condition above the SSL (Eq. (6)) using a characteristic turbulent mixing length, e.g. the vertical distance between the ZVL and the SSL. This would require a depth-dependent eddy viscosity.

At the FRP the time-averaged bed shear stress is close to zero. However, experimental observations show that at the FRP much sediment is brought into transport. This is probably due to large fluctuations of the bed shear stress at the FRP. The influence could be included by imposing a fluctuation on the computed bed shear stress.

In our model, the dune length is assumed constant. However, e.g. Ten Brinke et al. (1999) observed that during dune development dunes do not only grow in amplitude, but their length also increases. Furthermore, a constant dune length has an influence on the model results, since a combination of dune height and dune length determines the steepness of the dunes (and thus influence the sediment transport via the slope parameter). Furthermore, a changing dune length is expected to be related to the influence of flow separation on equilibrium dune dimensions. Therefore, a next step in the model should certainly be to include a variable dune length in the model.

7 CONCLUSIONS

In this paper we present a morphodynamic model to simulate dune development. We focus on modelling processes that are most relevant to get a general idea of dune dimensions under certain flow conditions and sediment characteristics.

In cases where flow separation does not occur (i.e. when dunes have gentle slopes), the basis model qualitatively reproduces well known morphological behaviour: dunes grow in amplitude, migrate in streamwise direction, and become asymmetrical. These processes can be modelled using hydrostatic equations and a simple sediment transport model based on average bed shear stress.

Flow separation plays a key role in dune development. To keep the model appropriately, we follow an approach introduced by Kroy et al. (2002) to determine the shape of the flow separation zone on the basis of general dune dimensions (see also Paarlberg et al. 2005) and effectively cut off the flow separation zone from computations. The flow field is only computed above the flow separation zone and the sediment transport behaviour downstream of the reattachment point and in the flow separation zone, where no flow is computed, is parameterized. In the paper it is shown that the basis model, extended with this parameterization of flow separation is able to simulate dune development to equilibrium conditions, under steady discharge conditions. Moreover, the model is in general agreement with laboratory flume data.

Future work will focus on more detailed calibration and validation of the flow model, and the application of the model to unsteady flow conditions. Furthermore, the morphodynamic model will be extended to include variable dune length during the development process of dunes. When the model is applied to unsteady flood events, the dimensions of the dunes (length, height and steepness) and of the flow separation zone can be used to make predictions of the overall roughness that may be expected. This is very important for water manager to make accurate predictions of water levels.

ACKNOWLEDGEMENTS

This work is supported by the Technology Foundation STW, the applied science division of NWO and the technology programme of the Ministry of Economic Affairs (Project No. TCB.6222).

REFERENCES

Allen, J. R. L. (1976). Computational models for dune time-lag: general ideas, difficulties and early results. *Sedimentary Geology 15*, 1–53.

Bakker, B., A. J. Struijk, and H. Nijdam (1986, February). Flume experiments on dunes under steady flow conditions (uniform sand, $d_m = 0.77$ mm); description of bed forms, volume I-III. TOW rivers R 567 – XIX / M 1314 part VIII, WL | Delft Hydraulics, Delft, The Netherlands.

Fredsøe, J. (1979). Unsteady flow in straight alluvial streams: modification of individual dunes. *Journal of Fluid Mechanics 91, part 3*, 497–512.

Hulscher, S. J. M. H. (1996). Tidal-induced large-scale regular bed form patterns in a three-dimensional shallow water model. *Journal of Geophysical Research 101*, 20727–20744.

Julien, P. Y. and G. J. Klaassen (1995). Sand-dune geometry of large rivers during floods. *Journal of Hydraulic Engineering 121*(9), 657–663.

Copyright © 2006 Taylor & Francis Group plc, London, UK

Julien, P. Y., G. J. Klaassen, W. B. M. Ten Brinke, and A. W. E. Wilbers (2002). Case Study: Bed resistance of Rhine River during 1998 flood. *Journal of Hydraulic Engineering 128*(12), 1042–1050.

Kennedy, J. F. (1969). The formation of sediment ripples, dunes and antidunes. *Ann. Rev. Fluid Mech. 1*, 147–168.

Komarova, N. L. and S. J. M. H. Hulscher (2000). Linear instability mechanics for sand wave formation. *J. of Fluid Mechanics 413*, 219–246.

Kroy, K., G. Sauermann, and H. J. Herrmann (2002). Minimal model for aeolian sand dunes. *Physical Review E 66*(3), 19 pp.

Nelson, J. M., A. R. Burman, Y. Shimizu, S. R. McLean, R. L. Shreve, and M. Schmeeckle (2005). Computing flow and sediment transport over bedforms. In G. Parker and M. H. Garcia (Eds.), *Proceedings of the 4th IAHR Symposium on River, Coastal and Estuarine Morphodynamics, Urbana, Illinois, USA*, Volume 2, pp. 861–872. Taylor & Francis Group, London.

Németh, A. A. and S. J. M. H. Hulscher (2003). Finite amplitude sand waves in shallow seas. In *Proceedings 3rd Symposium on River, Coastal and Estuarine Morphodynamics*, Barcelona, Spain, pp. 435–444. IAHR.

Németh, A. A., S. J. M. H. Hulscher, and R. M. J. Van Damme (2006). Simulating offshore sand waves. *Coastal Engineering 53*, 265–275.

Onda, S. and T. Hosoda (2004). Numerical simulation on development process of dunes and flow resistance. In M. Greco, A. Carravetta, and R. Della Morte (Eds.), *Proceedings of River Flow 2004, Napoli, Italy*, Volume 1, pp. 245–252. Frederico II University of Napoli: Balkema publishers, Leiden, the Netherlands.

Paarlberg, A. J., C. M. Dohmen-Janssen, S. J. M. H. Hulscher, and A. P. P. Termes (2005). A parameterization of flow separation in a river dune development model. In G. Parker and M. H. Garcia (Eds.), *Proceedings of the 4th River, Coastal and Estuarine Morphodynamics conference, Urbana, Illinois, USA*, Volume 2, pp. 883–895. Taylor & Francis Group, London.

Raudkivi, A. J. (1963). Study of sediment ripple formation. *Journal of the Hydraulics Division 89*(6), 15–33.

Soulsby, R. L. (1990). Tidal-current boundary layers. *In: The Sea, Vol. 9. Ocean Engineering Science, B. Le Mehaute and D. Hanes (eds.)*, 523–566.

Stansby, P. K. and J. G. Zhou (1998). Shallow water flow solver with non-hydrostatic pressure: 2D vertical plane problems. *International Journal of Numerical Methods in Fluids 28*, 541–563.

Ten Brinke, W. B. M., A. W. E. Wilbers, and C. Wesseling (1999). Dune growth, decay and migration rates during a large-magnitude flood at a sand and mixed sand-gravel bed in the Dutch Rhine river system. *Spec. Pub., Int. Assoc. Sediment. 28*, 15–32.

Van den Berg, J. and R. Van Damme (2005). Sand wave simulation on large domains. In G. Parker and M. H. Garcia (Eds.), *Proceedings of the 4th conference on River, Coastal and Estuarine Morphodynamics, Urbana, Illinois, USA*, Volume 2, pp. 991–997. Taylor & Francis Group, London.

Van Mierlo, M. C. L. M. and J. C. C. De Ruiter (1988). Turbulence measurements above artificial dunes; Report on measurements. Report Q789, WL | Delft Hydraulics, Delft, The Netherlands.

Van Rijn, L. C. (1984). Sediment transport, part III: Bed forms and alluvial roughness. *Journal of Hydraulic Engineering 110*(12), 1733–1754.

Van Rijn, L. C. (1993). *Principles of sediment transport in rivers, estuaries and coastal seas*. AQUA Publications.

Vanoni, V. A. and L. S. Hwang (1967). Relation between bed forms and friction in streams. *Journal of the Hydraulic Division 93*, 121–144.

Vittal, N. (1972). Flow over triangular roughnesses in open channels. University of Roorkee, India.

Wiberg, P. L. and J. D. Smith (1989). Model for calculating bed load transport of sediment. *Journal of Hydraulic Engineering 115*(1), 101–123.

Wijbenga, J. H. A. and A. R. Van Nes (1986). Flow resistance and bedform dimensions for varying flow conditions; results of flume experiments with flood waves. TOW rivieren R 567 – XXV / M 1314 part XIII, WL | Delft Hydraulics, Delft, The Netherlands.

Wilbers, A. (2004). *The development and hydraulic roughness of river dunes*. Ph. D. thesis, University of Utrecht, Utrecht, The Netherlands.

Yoon, J. Y. and V. C. Patel (1996). Numerical model of turbulent flow over sand dune. *Journal of Hydraulic Engineering 122*(1), 10–18.

Copyright © 2006 Taylor & Francis Group plc, London, UK

Field investigations of sand-gravel bed forms within the Raba River, Poland

Artur Radecki-Pawlik
Agricultural University of Krakow, Poland

Paul A. Carling
Southampton University, UK

Ewa Słowik-Opoka & Leszek Książek
Agricultural University of Krakow, Poland

Richard Breakspeare
Southampton University, UK

ABSTRACT: The paper presents the important, both from practical and theoretical reasons, problem of forming river bed forms within sand-gravel mixtures. In natural rivers, due to the complicated nature of the discharge and changes in the water level, the bed forms are quite complicated structures. These features are changing in length and height and when present they change the hydraulics conditions. Up to now there are few papers concerning gravel bed forms found in rivers. Most of scientific papers focus only on sand riverbed forms. The present paper concentrates on the field measurements of sand-gravel bed forms found in the Raba River in Polish Carpathians. The research focuses here mostly on the geometrical parameters of these bed forms such as height, length, as well as granulometric characteristics of the sediment. Based on *in-site* measurements different hydraulics parameters were also determined. Special attention was given to the roughness coefficient, which is very important from a practical point of view for engineers working with river training works and hydraulics structures.

1 INTRODUCTION

Gravel sub aqueous bed forms (those with a median grain size greater than 2 mm), such as dunes and bed load sheets, which occur on river beds which are composed of sand and gravel mixtures are reported very rarely within the world literature. There is even less information on the hydrodynamic development of such gravel features. Reviewing the literature, equilibrium and non-equilibrium gravel dunes range in length from less than 0.6 m to greater than 100 m. Their heights range from less than 0.1 m to 16 m (Carling 1999). In general terms dunes have lengths that scale primarily with boundary layer thickness or water depth (Best 1996). Height (H) and length (L) data for the gravel dunes reported by some researchers (Carling 1999) are consistent with the H:L function reported by Ashley (1990) for equilibrium dunes developed in sand. Using Ashley's (1990) dune form criteria of height (>0.1 m) and length (>0.6 m) as a general guide it can be shown that gravel dunes have been correctly identified in the number of studies (e.g. Galay 1967, Dinehart 1992 and Carling et al. 2005). As far as gravel bed forms hydrodynamics is concerned, gravel dunes are suppose to develop for a range of Froude numbers up to 0.75. For the non-dimensional mean shear stress $\Theta = 0.25$ they should reach their maximum height and start to reduce in height at Shields parameter value $\Theta = 0.30$ (Carling 1999). The other bed forms which develop on the river bed are ripples. Their length is proportional to the grain size. They have heights up to a few tens of millimeters and lengths less than 0.6 m (Allen 1984). The reports from the literature about ripples which are developed in gravel are controvertible, being based mostly on length:height criteria. However ripples are suppose to develop only in the bed sediments not coarser than about 0.6 mm ($D_{50} < 0.6$ mm) in hydraulic smooth flow ($U * D < 10$) which is not associated with mobile gravel. However Gomez et al. (1989) reported some gravel bed forms which he called ripples, but Carling (1999) suggests that they were bed load sheets. Finally some scientists (e.g. Kuhnle 1986, Iseya and Ikeda 1987) report bedload sheets and define them as low-relief bedforms,

Copyright © 2006 Taylor & Francis Group plc, London, UK

that develop in mixture of coarse sand and gravel (D_{50} from 2 mm to 5 mm).These features are one or two grains in height and share some characteristic of incipient dunes (e.g. Bridge 1993). What is worthy of notice is that no bed load sheets developed in 100% gravels in experiments described by Iseya and Ikeda (1982) as well as Dietrich et al. (1989). At the same time in a mixture of gravel and sand, Whiting et al. (1988) describes bed sheets as stable bed forms, which could grow in thickness giving asymmetric dune like forms up to 0.10 m height, and that such bed forms give the bed instability from which incipient dunes can develop. The main objective of the present work is to understand how riverbed forms developed in the mixture of sand and gravel develop. The study site was in the upland part of the the Raba River below the Dobczyce Water Reservoir and close to the confluence with the Vistula River. The study is important firstly because of the need for a better understanding of the process of formation such features like sand-gravel bed forms. Secondly, dunes are responsible for flow resistance, which is significant, for example, when designing hydraulics structures or calculating flow residence times for water supply or pollutant dispersion. Thirdly, understanding of bed form forming process is important for geologists to interpret how sedimentary rocks were deposited, where ancient sedimentary assemblages are believed to be of alluvial origin.

2 MATERIALS AND METHODS

2.1 *Study location*

The Raba River – Figure 1 – (137 km long with a catchment area of 1537 km^2) is mostly (86%) situated in the Polish part of the Eastern Carpathian Mountains

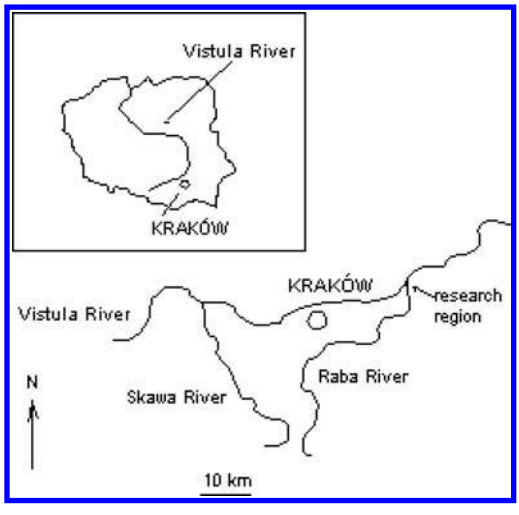


Figure 1. The location of the research region.

(the Wyspowy Beskid and the Zywiecki Beskid) which are Carpathian flysh. Its streambed, along the alluvial part, consists mostly of sandstone and mudstone bed-load pebbles and cobbles (from Magurian nappe). The typical structure of the lower Raba River alluvial plain, from the beginning of the 20th century consists of normally loose pebble gravels, open work pebble gravels, dilated framework pebble gravels, trough cross-stratified and parallel laminated medium to very coarse grained sands, massive find sands and muds (Wyzga 1993). The coarser grains which collect as armour on the river bed, also form a framework, the interstices of which are filled by a matrix of finer sediment. The Raba River, during the spring and early summer floods, experiences frequent bed load movement, which is reflected in many mobile gravel bars which form along the margins and centre of the river channel. The research region of the Raba River (reach 700 m long, close to the Uscie Solne municipality), where the Raba joins the Vistula River, is situated at the border of the uplands (14% of the catchment is situated in Carpathian intramontane and submontane depressions). The river loses here its mountainous character and is alluvial. The river bed sediment here is the mixture of sand and gravel. The river bed usually is characterised by an armour layer where the range of sediment is from 0.4 mm to 50 mm, with sand and gravel moving above it. In low to medium flows the water is very clear making the sediment transport processes visible to the eye. On the armouring layer sand and sand-gravel bedforms appear under certain range of hydraulics conditions. These bedforms are built up with sediment of the range from $D_{50} = 0.5$ mm up to 11 mm. The average slope of the whole Raba River is 0.00443, the slope of the whole lower part of the Raba is 0.00198 whereas the slope of the research reach, at the confluence, is 0.0006. The river channel at the research reach averages 50 m wide. According to Krzanowski (1972) the average annual flow is here 20.86 [$m^3 \cdot s^{-1}$] and the minimum annual flow is 2.71 [$m^3 \cdot s^{-1}$].

2.2 *Methods*

The research location was safely accessible from the Raba River banks on foot under low discharge and from a rubber boat under mean discharge conditions. The location was being visited daily during several sampling periods between 2001 and 2005. The work within the research reach concentrated on surveying the migration of several ripples, dunes and other sand and sand-gravel structures, measuring the water depth and the speed of the flow with a NAUTILUS 2000 magnetic current meter. Velocities of running water were recorded above all characteristic points of the bed-forms: crest, trough, along the stoss and lee slopes and finally above the flat bed. Such

Copyright © 2006 Taylor & Francis Group plc, London, UK

hydraulics parameters as Froude number, Reynolds number, shear velocity, shear stresses and drag coefficient were calculated. For sediment sampling the technique described by Church, McLean and Wolcot (1987) was applied. Samples were collected from a homogeneous body of sub-armour sediment, so as not to combine them with the distinct surface material. The sieving analysis for coarse grains was carried out by hand in the field using round-mesh sieves (Michalik 1990). Fine material was sieved in the laboratory. Water velocity measurements were based on Jarrett's (1990) recommendations regarding the taking of velocity profiles in river cross-sections. Bergeron and Abraham's (1992) methods were then applied to the field data, and shear velocity V_* values were calculated from the velocity profiles obtained near to the river-bed. Finally, shear stress τ values were calculated from:

$$\tau = V_*^2 \rho \quad [\mathrm{N\,m^{-2}}] \tag{1}$$

where:
V_* – shear velocity [m s^{-1}],
ρ – water density [kg m^{-3}].

To calculate various flow resistance coefficients the methods given by Wijbenga (1990) and Przedwojski et al. (1995) were used. The Darcy-Weisbach flow resistance coefficient was obtained from:

$$f = 8\,g\,J\,R / V^2 = 8\,(V_* / V)^2 \tag{2}$$

where: V – average cross-section velocity [m s^{-1}].

The Strickler formula for the roughness is as follows (Sobota 1994):

$$k = \frac{21.1}{\sqrt[6]{d}}, \quad n = \frac{1}{k} \tag{3}$$

where: k – Strickler coefficient, d – the roughness height which could be a grain dimension (e.g., D_{50}) or the height of the bed form [m], n – roughness coefficient.

The roughness given by Chézy with Manning's n could be written as follows (Sobota 1994):

$$C = \frac{1}{n} R_h^{1/6} \tag{4}$$

where: C – Manning coefficient, R_h – hydraulic radius [m], n – roughness coefficient[–].

The equation for roughness according to the findings of Chow (1959), which could be determinated after field measurements, is as follows:

$$n = \frac{(x-1)\,y^{\frac{1}{6}}}{6.78\,(x+0.95)} \tag{5}$$

where: $x = v_{0.8}/v_{0.2}$, y – maximum water depth in the cross section [m], $v_{0.2}$ – velocity value measured at $0.2y$ [m s^{-1}], $v_{0.8}$ – velocity value measured at $0.8y$ [m s^{-1}].

3 RESULTS AND DISCUSSION

For the reasons of brevity all results of investigations and calculations are presented in tabular and graphic manner. Every time the research reach in the field was visited geometrical survey of bedforms were conducted, velocity profiles were obtained close to the bed as well as higher within the flow and sediments samples for granulometric analysis were obtained (Figure 2). Every time after major flooding (it has happened twice during the measuring campaign) a geodetic survey was made to get the river bed altitude details (Figure 3).

Under low discharges (up to 3.9 m^3/sec) we noted that only sand ripples of heights (H) up to tens millimetres were developing and moving along the full width of the research reach, whereas pre-existing sand-gravel bedforms were immobile on the armoured bed.

When the discharge was larger (up to 11.4 m^3/sec) coarser bed load was moving, including overpassing coarser grains over the crests of the sand-gravel features which then began to migrate. Under the latter conditions sand ripples only developed close to the river banks where the flow velocity was lower than in the centre of the channel, whereas sand-gravel barchanoid dunes were developing along the whole width of the channel although predominantly in the centre. Figure 4 presents measured heights (H) of the investigated bedforms against their lengths (L).

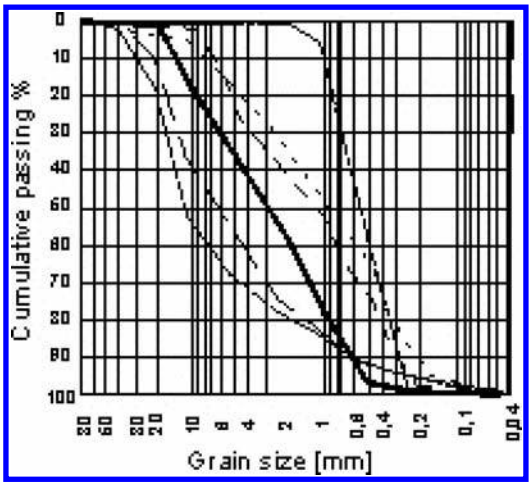


Figure 2. Examples of representative grain-size curves taken from different bedforms.

Copyright © 2006 Taylor & Francis Group plc, London, UK

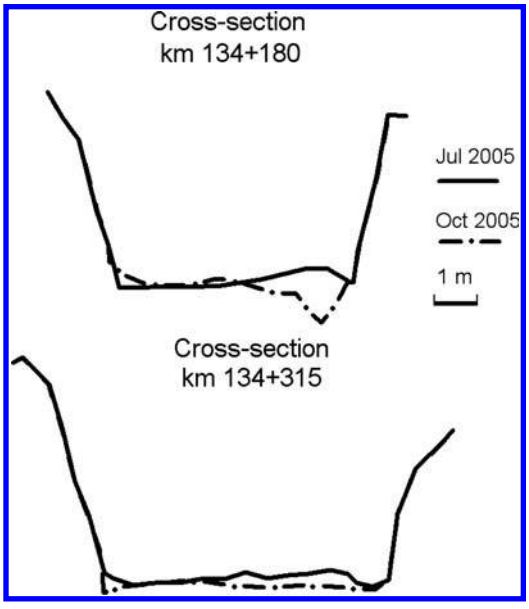


Figure 3. Examples of changes in the riverbed configuration after major flooding.

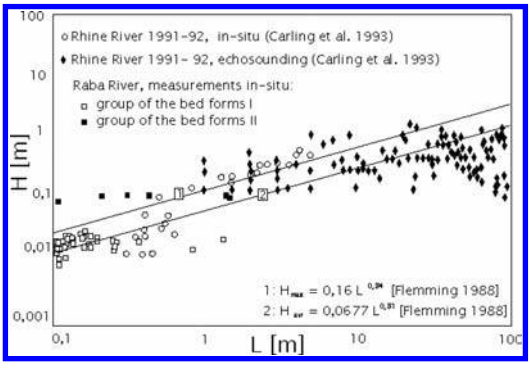


Figure 4. Height-length relation for the Raba River bedforms.

The Raba data are compared with Fleming (1988) central tendency and limit lines as well as with bigger sand dunes found on the bed of the River Rhine (Carling et al., 2000). The Raba data we divided in Figure 3 into two groups: Type 1 with the $1 < D_{50} < 2.4$ mm and $L < 0.6$ m which are here termed bed forms I and the second, Type 2 which are longer with $4 < D_{50} < 11$ mm which are termed bed forms II. The relation between Raba features describes the relation: $H = 0{,}05\,L^{0{,}35}$ ($r^2 = 0.47$; $F_{0.05\ (1;55)} = 3.95$; $\alpha = 0.05$; $n = 57$). The Raba type 1 bedforms are much shorter and smaller than the Rhine features and are also mostly below the upper limit given by Flemming (1988). Type 2 bedforms are steep and lie above Flemming's curve.

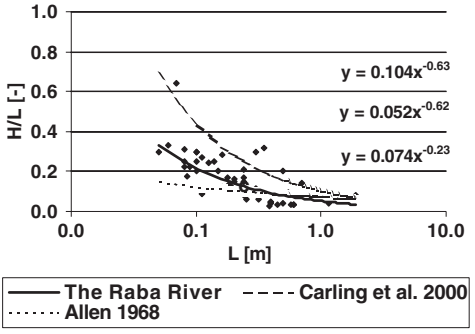


Figure 5. Steepness index (H/L) of the Raba River bedforms against their lengths (L).

Raba bedforms are steeper (Figure 5) then dunes described by Allen (1968) but flatter then the Rhine long sand dunes. Their H/L index $= 0.0518L^{0.622}$ ($r^2 = 0.71$; $F_{0.05\ (1;51)} = 7.24$; $\alpha = 0.05$; $n = 52$).

Also plotted are the geometrical lengths and height of the Raba features against water depth (Figure 6 a, b), they lie close to the Yalin (1964) middle curve as far as their length (L) is concerned but some of them are higher (H) than the maximum limitation. This may be because the higher bedforms has formed under a previous discharge when water depths were greater and have not yet fully readjusted their morphology.

Table 1 presents examples of hydraulics parameters calculated for sand-gravel dunes we found during the investigations. The shear stresses were not sufficient to disrupt the armouring layer of the sediment river bed. However, under the highest measured values coarse sediment movement occurred over the sand-gravel features and intensive sedimentation occurred at the toes of the bedforms. Also the sand ripples were transported, building and then decaying rapidly in different parts of the flat gravel armoured river bed. The smaller features were moving with a celerity of 5 cm/sec and larger with 2 cm/sec.

The Froude number was between 0.238 and 0.678 indicating that they are still in the developing or steady stage, below the transition stage. At the same time the D_{50} shows that they are fine-gravel to medium gravel (Gordon et al. 1992). Table 2 shows the different roughness coefficient values, for different ways of their calculations. As expected, when using the bed form height in the Strickler formula larger values of roughness values are obtained. Given that all the measurements were for low or medium discharges, it is possible that larger dunes would have developed under higher flows and thus a larger n value for discharge calculation, would be required. Consequently a traditional approach to estimating the roughness coefficient values would be inaccurate.

Copyright © 2006 Taylor & Francis Group plc, London, UK

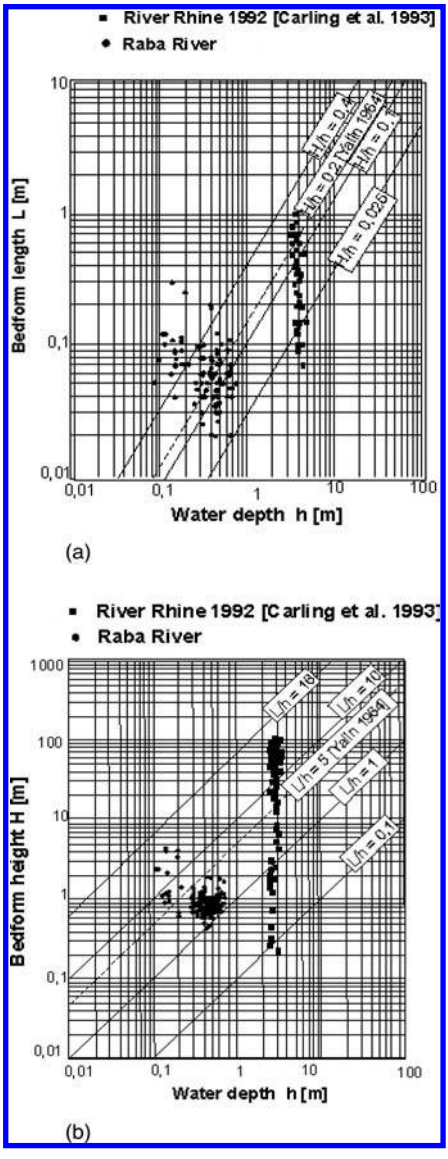


Figure 6. (a,b) Lengths (L) and (b) heights (H) of investigated bedforms against water depth (h).

4 CONCLUSIONS

The following conclusions can be drawn from the analysis of the data:

1. Under the range of low discharges up to 3.9 m^3/sec only sand and very fine sand-gravel bedforms of $1 < D_{50} < 2.4$ mm of heights (H) up to tens millimetres can develop and move, whereas other existed sand-gravel features were preserved, sitting on the armoured bed.

Table 1. Hydraulic parameters of investigated bedforms.

D_{50} [m]	τ [N m^2]	f	Re	Fr
0.0070	1.65	0.00131	170800	0.368
	1.47	0.00127	130000	0.332
	1.12	0.00116	106400	0.410
	1.47	0.00160	100000	0.255
0.0110	1.12	0.00489	64600	0.249
	0.88	0.00187	121500	0.668
	1.35	0.00060	151800	0.439
	2.65	0.00133	225000	0.238
0.0070	1.41	0.00410	100800	0.274
	0.94	0.00170	126400	0.631
	1.29	0.00064	158400	0.490
	1.94	0.00268	171600	0.289
0.0080	1.45	0.00338	97500	0.249
	6.35	0.01481	136000	0.678
	0.38	0.00089	172200	0.571
	2.09	0.00060	220000	0.278

Table 2. Roughness coefficient value (n).

By Strickler			
For D_{50}	For H	By Chezy	By Ven Te Chow
0.01308	0.02200	0.03410	0.04214
0.02018	0.03173	0.01564	0.00193
0.01804	0.02772	0.01622	0.00555
0.01804	0.02200	0.02418	0.01439
0.01308	0.02200	0.04433	0.06215
0.02018	0.03328	0.01583	0.00539
0.01804	0.02772	0.01822	0.00714
0.01804	0.02200	0.02660	0.01289
0.01308	0.02200	0.03499	0.04571
0.02018	0.03762	0.01511	0.00635
0.01804	0.03527	0.01511	0.00412
0.01804	0.02200	0.02046	0.01722

2. When the discharge is growing up to 11.4 m^3/sec the sand-gravel dunes start to develop with $4 < D_{50} < 11$ mm. The movement of sediment along such features is under such discharges very low and mostly the crests are mobilized first.
3. The relation between height (H) and length (L) Raba River bedforms describes the relation: $H = 0.05\,L^{0.35}$ ($r^2 = 0.47$; $F_{0.05\,(1;55)} = 3.95$; $\alpha = 0.05$; $n = 57$). The Raba's bedforms are much shorter and smaller than the features measured at the bed of larger rivers (e.g. the Rhine). They are mostly below the limitation given by Flemming (1988).
4. The Raba bedforms are steeper and flatter then classical dunes described by Allen (1968). Also they are flatter then the features from bigger rivers (e.g.

Copyright © 2006 Taylor & Francis Group plc, London, UK

the Rhine). Their H/L index is: $H/L = 0.0518\,L^{0.622}$ ($r^2 = 0.71$; $F_{0.05\ (1;51)} = 7.24$; $\alpha = 0.05$; $n = 52$).

ACKNOWLEDGEMENTS

Authors would like to thanks the River Water Authority in Krakow for their logistic help they provided, especially to Mr. Stanislaw Kmiec. Also we are thankful for financial support to British Council and Polish Scientific Committee (KBN).

REFERENCES

Allen J.R.L. 1968. Current Ripples. Amsterdam, North Holland, 433 p.

Allen J.R.L. 1984. Sedimentary Structures: Their Character and Physical Basis. Amsterdam, Elsevier, 539 p.

Allen J.R.L. 1985. Loose-boundary hydraulics and fluid mechanics: selected advances since 1961. In Brenchley. P.J., and Williams. B.P.J. eds. *Sedimentology: Recent Developments and Applied Aspects*: Geological Society of London. Special Publication 18, p. 7–28.

Ashley G.M. 1990. Classification of large-scale subaqueous bedforms: a new look al an old problem: *Journal of Sedimentary Petrology*, v. 60, p. 160–172.

Bergeron N.E. and Abrahams A.D. 1992. Estimating shear velocity and roughness length from velocity profiles. *Water Resources Research*, ser. 28, 8, p. 2155–2158.

Best J. 1996. The fluid dynamics of small-scale alluvial bedforms. In Carling P.A. and Dawson M.D., eds. *Advances in Fluvial Dynamics and Stratigraphy,* Chichester, U.K., Wiley, p. 67–125.

Bridge J.S. 1993. The interaction between channel geometry, water flow, sediment transport and depositin in braided rivers. In best J. and Bristow C. *Braided rivers*, Geol. Soc. London, Spec. Publ. 75, p. 13–71.

Carling P.A. 1999. Subaqueous gravel dunes. Journal of sediment research, v. 69, n. 3, p. 534–545.

Carling P.A., Gölz E., Orr H.G. and Radecki-Pawlik A. 2000. The morphodynamics of fluvial sand dunes in the River Rhine near Mainz, Germany. I. Sedimentology and morphology. *Sedimentology*, 47, p. 227–252.

Carling P.A., Radecki-Pawlik A., Williams J.J., Rumble B., Meshkova L., Bell P. and Breakspear R. 2005. The morphodynamics and internal structure of intertidal fine-gravel dunes: Hill Flats, Severn Estuary, UK. *Sedimentary Geology*, Elsevier, 21 p. (in print).

Chow V.T. 1959. Open channel hydraulics. McGraw Hill. New York, London.

Church M.A., McLean J.F. and Wolcot J.F. 1987. River Bed Gravels: Sampling and Analysis. In *Sediment Transport in Gravel-bed Rivers* (ed. by C.R. Thorne), John Wiley and Sons, London, p. 43–87.

Dietrich, W., Kirchner, J., Ikeda H. and Iseya F. 1989. Sediment supply and the development of the coarse surface layer in gravel-bedded rivers. *Nature*, v. 340, p. 215–217.

Dinehart R.L. 1989. Dune migration in a sleep, coarse-bedded stream: Water Resources Research, v. 25, p. 911–923.

Flemming B.W. 1988. Zur klassifikation subaquatischer stomungsiransversaler Transport-korper. *Bochumer Geologische und Geotechnische Arbeiten*, v. 29, p. 44–47.

Galay V.J. 1967. Observed forms of bed roughness in an unstable gravel river. *International Association for Hydraulic Research.* 12th Congress. Proceedings, p. 85–94.

Gomez B., Naff R., Humbbell D. 1989. Temporal variations in bed load transport rates associated with the migrations of bedforms. *Earth Surface Processes and Landforms*, v. 14, p.135–156.

Gordon D.N., McMahon T.A. and Finlayson B.L. 1992. Stream Hydrology. An Introduction for Ecologysts. Wiley and Sons, London.

Ikeda H. 1982. An experimental study of the formation of openwork gravel layers under alluvial flow conditions. *Japanese Geomorphological Union*, Transactions, v. 3, p. 57–65.

Iseya S. and Ikeda H. 1987. Pulsation in bedload transport rates induced by a longitudinal sediment sorting: a flume study of sand and gravel mixtures: *Geografiska Annaler*, v. 69A, p.15–27.

Jarrett R. 1991. Wading measurements of velocity profiles. *Geomorphology*, 4, p. 243–247.

Kuhnle R. 1986. Experimental studies of heavy-mineral transpiration – segregation and deposition in gravel-bed streams. Ph.D, thesis. Cambridge. Massachusetts. Massachusetts Institute of Technology 209 p.

Krzanowski S. 1972. The spatial changes of the average discharge, in Polish. Ph.D. thesis. Agricultural University of Krakow 254 p.

Michalik A. 1990. Bed-load transport investigations in some Polish Carpathians rivers, in Polish. *Zesz. Nauk. AR Kraków* seria Rozpr. Hab., 138, 115 p.

Przedwojski B., Błażejewski R., Pilarczyk K.W. 1995. River training techniques. Balkema, Rotterdam, Brookfield, 487 p.

Sobota J. 1994. Hydraulics, in Polish. AR, Wrocaw, t. I i II.

Vanoni V. 1974. Factors determining bedforms of alluvial streams. American Society of Civil Engineers. Proceedings. *Journal of the Hydraulics Division*, v. 100, p. 363–377.

Whiting P., Dietrich W., Leopold L., Drake T. and Shreye R. 1988. Bedload sheets in heterogeneous sediment. *Geology*, v. 16, p. 105–108.

Whiting P.J. 1996. Sediment sorting over bed topography. In Carling P.A. and Dawson M.R. *Advances in Fluvial Dynamics and Stratygraphy*. Chichester, UK, Wiley, p. 204–228.

Wijbenga J.H. 1990. Flow resistance and bed-form dimensions for varying flow conditions. *Delft Hydraulics.* Part 1–4, Toegepast Onderzoek Waterstaat, A58.

Wyzga B. 1992. Evolution of the fluvial system of the middle and lower Raba in the last 200 years, in Polish. PAN IGiPZ. Ph.D. thesis. Warszawa, 92 p.

Yalin M. 1964. Geometrical properties of sand waves. *Proc. Am. Soc. Civ. Eng*., Raport 90, 119 p.

Copyright © 2006 Taylor & Francis Group plc, London, UK

Semi-empirical model to predict mobile bed evolution in presence of a side overflow

B. Rosier, J.-L. Boillat & A.J. Schleiss
Laboratory of Hydraulic Constructions (LCH), Swiss Fed. Inst. of Technology, Lausanne, Switzerland

ABSTRACT: Side weirs are a widely used device to control flow processes along a channel or river course. The lateral loss of water is responsible for the reduction of sediment transport capacity in the main-channel yielding to aggradation and the formation of a local sediment deposit in the downstream weir alignment. The reduced cross section generates backwater effects and additional contraction and expansion losses. As a consequence, the head over the side weir rises. Accompanied with supplementary roughness induced by the development of bed forms, the design discharge to be diverted over the weir is increased by this flow-sediment transport interaction. Based on a flume study, a semi-empirical model to predict the length and the global longitudinal shape of the aggraded reach as well as the position and height of the maximum bed elevation is developed. The longitudinal shape is fairly well represented by an adapted Maxwell-type distribution function.

1 INTRODUCTION

Within the framework of the multidisciplinary flood protection research project *DIFUSE* (*Di*gues *Fu*sibles et *S*ubmersible*s*, Fuse plugs and overflow dams at rivers), involving governmental offices, private companies and four research institutes, the *Laboratory of Hydraulic Constructions* (*LCH*) investigates the effects of a side overflow on sediment transport in a natural channel. The topic of the present paper constitutes one aspect of this study.

A side weir, also known as a lateral weir, is a free overflow weir set into the side of a channel which allows part of the liquid to spill over the side when the surface of the flow in the main channel rises above the weir crest. Hydraulic structures of this kind find their use in urban drainage systems, irrigation engineering, river restoration, and flood control management.

The flow over a side weir is a typical case of spatially varied flow with decreasing discharge. The main design objective is to estimate the total overflow discharge. The hydraulic behaviour of side weirs has been subject to numerous investigations. A review of literature indicated that the main focus of research within this field is laid on the determination of an appropriate discharge coefficient. Sharp-crested side weirs in a rectangular channel have been studied extensively by Nadesmoorthy & Thomson (1972), Subramanya & Awasthy (1972), Ranga Raju et al. (1979), Hager (1987), Singh et al. (1994), and Borghei et al. (1999).

All contributions have in common that a fixed channel bottom is assumed to describe side overflow intensity, since most studies refer to irrigation or drainage engineering. Especially in natural rivers a mobile bed is present and for the purpose of flood control management its morphological behaviour and aspects of bed load transport have to be taken into account.

The lateral loss of water is responsible for the reduction of sediment transport capacity in the mainchannel by decreasing the bottom shear stress. This yields to an elevation of the mean bed level and the formation of a local sediment deposit in the weir alignment. Consequently, the cross section is reduced and the upstream water level rises and the head over the side weir as well. In addition with supplementary roughness induced by the development of bed forms, the design discharge to be diverted over the side weir is increased in an unforeseen way.

In the present study, a semi-empirical model to describe the interaction between bed morphology and side weir discharge is developed. Based on laboratory experiments, the global longitudinal shape of the aggraded channel reach is modeled using a Maxwellian distribution function. For this purpose, the wavy cross-sectional averaged variation of the bed surface elevation is smoothed using an appropriate moving average. An adequate window length is obtained determining a characteristic periodic longitudinal bed surface elevation. Important parameters of the Maxwell-type distribution function such as location and height of the maximum bed surface elevation and a shape factor are expressed in terms of geometric channel and side weir variables

Copyright © 2006 Taylor & Francis Group plc, London, UK

as well as hydraulic parameters and bed load transport relations.

2 EXPERIMENTAL SETUP

The tests were conducted in a rectangular 2.0 m wide, 30 m long and 1.2 m deep flume. The flume was subdivided longitudinally into two separate channels by a vertical 0.9 m high smooth wall. The first channel, being 1.5 m wide, represents the actual testing facility including the mobile bed ($d_{50} = 0.72$ mm, $d_m = 1.05$ mm) and the side weir on the right bank. The second one, 0.47 m wide, constitutes a lateral channel permitting to evacuate the diverted discharge. A general layout of the experimental setup is shown in Figure 1.

In order to determine the influence of lateral overflow on bed-load transport, the main channel discharge including flood hydrographs, channel slope, length and height of the lateral weir crest, and number of weirs were considered as test parameters. Table 1 gives an overview of the of test series used for analysis in the present paper.

The channel facility originally possesses a horizontal slope. The bottom slope bed for each experiment has been created by adjusting the mobile bed to the requested slope. Once the desired discharge has been introduced to the initially plane bed, sediment was fed into the upstream end of the flume via a conveyer belt. The quantities to be supplied were estimated according to the formula of Smart & Jäggi (1983) and adjusted during the test in order to maintain both, uniform flow and equilibrium transport conditions in the approach channel upstream of the side overflow. The side overflow discharge was determined using a sharp-crested weir located in the evacuation channel (Fig. 2) and equipped with an ultrasonic gauge.

Water depth was recorded continuously in the centreline of the main channel by the use of ultrasonic gauges (Fig. 2). The 2D velocity field was measured with an Ultrasonic Doppler Velocity Profiler (UVP) allowing to obtain instantaneously a 1D-velocity profile over the entire water depth (Metflow 2000). As far as the monitoring of the river bed morphology is concerned, digital photogrammetry has been applied to

Table 1. Overview of test series and parameters studied.

No. of test	No. of weirs n_D	Length of weir crest L_D [m]	Sill height w_D [m]	Flume slope S_0 [%]	Discharge Q_1 [l/s]	Duration t [h:m]
B01	1	3.0	0.10	0.2	131	2:10
B02	1	3.0	0.10	0.2	181	3:20
B03	1	3.0	0.10	0.4	177	2:00
B04	1	3.0	0.10	0.1	98	4:10
B05	1	3.0	0.10	0.2	144	2:08
B06	1	3.0	0.10	0.3	148	2:18
C01	1	6.0	0.09	0.2	160	2:05
C02	1	6.0	0.09	0.2	197	2:00
C03	1	6.0	0.09	0.2	191	2:00
C04	1	6.0	0.09	0.2	179	2:00
C05	1	6.0	0.09	0.2	181	2:00
D03	2	2.5	0.09	0.2	222	2:00
D04	2	2.5	0.09	0.2	182	2:00

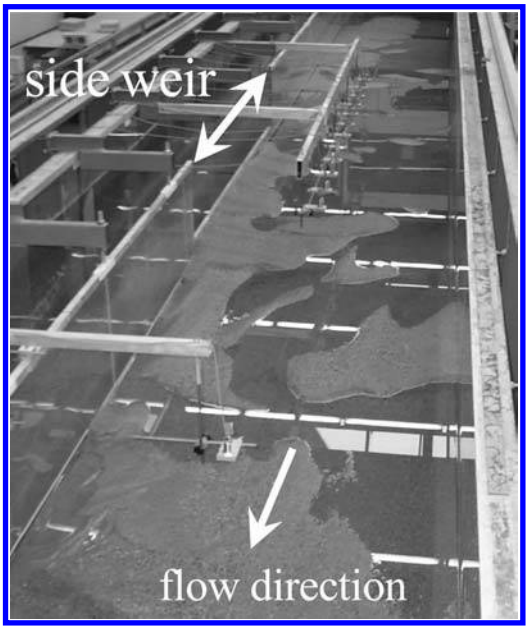


Figure 1. Laboratory setup with main channel, side weir, mobile bed and evacuation channel.

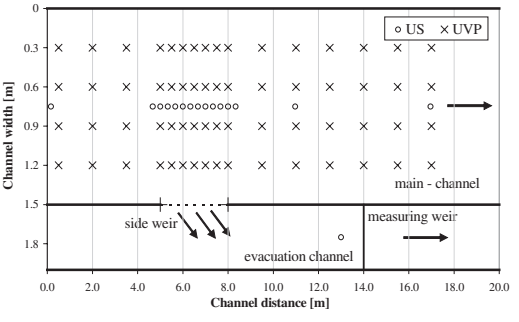


Figure 2. Experimental setup and disposition of water level (US) and velocity (UVP) recordings.

Copyright © 2006 Taylor & Francis Group plc, London, UK

obtain a digital elevation model (DEM) (Rosier et al. 2004).

3 ANALYSIS

3.1 *Variation of mean longitudinal bed surface elevation*

After introducing the flow to the initially flat bed, bed forms rapidly form. In Figure 3, a cut-out of the final bed situation for experiment B01 is shown. Furthermore, longitudinal bed elevation profiles for different lateral wise locations are presented in Figure 4, top). Two profiles are located on the right river bank ($y = 0.30$ m, $y = 0.60$ m), two on the left ($y = 0.90$ m, $y = 1.20$ m) and one in the centreline of the channel ($y = 0.75$ m). In addition, the cross sectional averaged longitudinal profile is presented (denoted "z-mean"). A detailed view of this profile is given in Figure 4 (bottom).

This profile is used to determine a characteristic periodic variation for the mean longitudinal bed surface elevation (in the following denoted as ω) which will serve later on as the moving window length to smooth the wavy profile.

The variation of the mean bed surface elevation has been determined manually by searching the profile record for the presence of lee slopes (Coleman & Melville, 1994). For a detected lee slope within a bed profile, the location of the corresponding ω-value was taken as being given by the upstream trough of the same bed feature. The trough elevation for the ω-bed feature was defined as the minimum bed elevation occurring between the location of the present one and that of the subsequent (downstream) one.

Similarly, the crest elevation was defined as the maximum bed elevation occurring between the location of the present ω-value and that of the previous (upstream) feature. The ω-length is determined as the longitudinal difference between two troughs.

Once ω-lengths are determined for the entire bed profile, mean values (ω_{mean}) for each test series are calculated. In Figure 5, averaged ω-lengths as well as hydraulic and geometric parameters are combined.

The corresponding Equation 1 is found to represent the mean ω-lengths for the entire data set in the best way. The R^2-value of Equation 1 is 0.97.

$$y = \frac{\omega_{mean}}{L_D} = 0.0025x^2 + 0.049x \quad (1)$$

where L_D = side weir length, Q_1 = upstream discharge, $y_1 - w_D = h_1$ = side weir head at the upstream weir corner, y_1 = water depth at the upstream weir corner, w_D = side weir crest height, g = acceleration due to gravity and S_0 = bottom slope (Fig. 6).

In this context it has to be mentioned that the side weir length for test series D is assumed to be

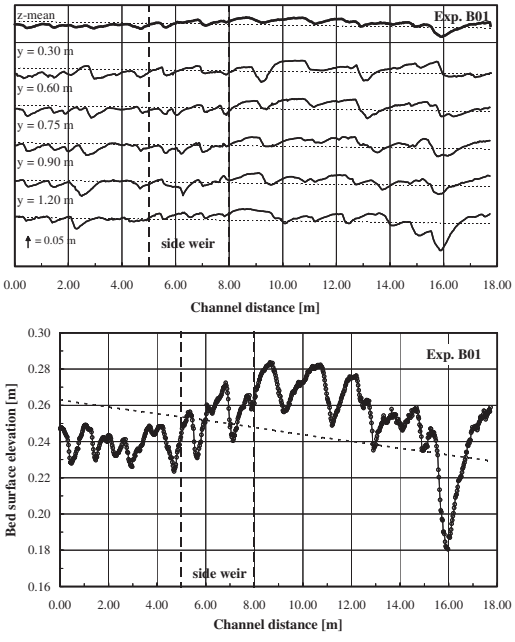


Figure 4. Top: Longitudinal bed surface profiles for different lateralwise locations and cross sectional averaged profile, denoted "z-mean". Bottom: Detailed view of the z-mean profile. The dotted lines represent the initially flat bed.

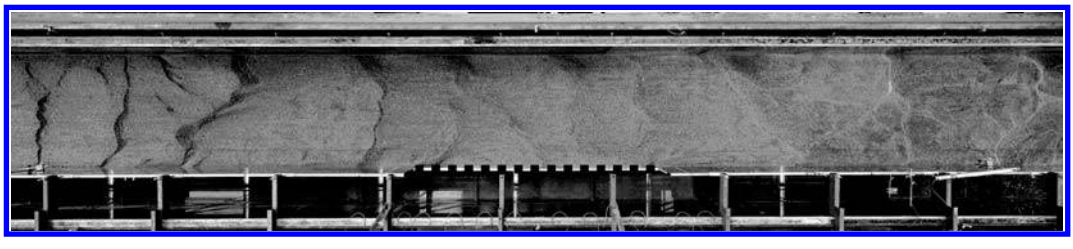


Figure 3. Cut-out ($x = 0.5$ m to $x = 12.5$ m) of the final bed morphology for experiment B01. The dotted line represents the side weir position. Flow is from left to right.

Copyright © 2006 Taylor & Francis Group plc, London, UK

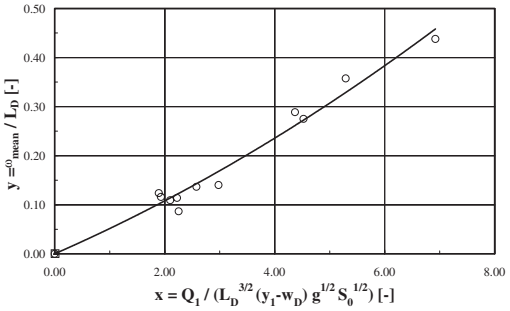


Figure 5. Combination of hydraulic and geometric parameters to describe the mean variation of the bed surface elevation ω_{mean}.

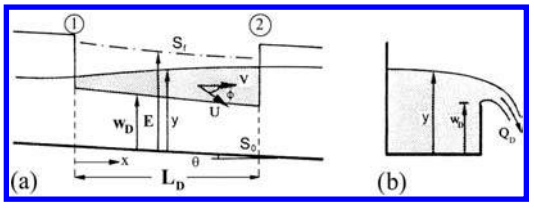


Figure 6. Definition sketch: (a) longitudinal section; (b) cross section (from Hager 1987, modified).

$L_D = 2 \times 2.5 = 5.0$ m, since the short 1.0 m long separation wall between the two weirs reveals no significant importance.

The data analysis further shows that a window length for the moving average of $\omega^* = 3.50$ m turns out to yield satisfying results. To obtain ω^* from Equation 1, the right term has to be multiplied by L_D ($\omega_{mean} = y\ L_D$) and a factor of 4.542, thus $\omega^* = 4.542 y\ L_D = 4.542 \omega_{mean}$.

3.2 *Shape of deposit*

In most of the experiments, the shape of the sedimentary deposit is characterized by a rather steep stoss slope and a milder lee slope. This type of shape is similar to the shape of flood hydrographs. Furthermore, the main parameters describing the deposit are the maximum bed elevation z_{max}, the corresponding position of the maximum bed elevation x_{max}, its volume and shape.

With regard to these aspects, a feasible and satisfying approach for the parameterisation of the deposit is represented by the Maxwell distribution function. This function is a probability distribution with applications often found in physics and chemistry (e.g. heat and gas transfer) as well as in hydrology to parameterize flood hydrographs (see above paragraph). The function is rather simple and straightforward since it is composed of only three dimensionless variables. In addition to that, it offers an analytical solution and is

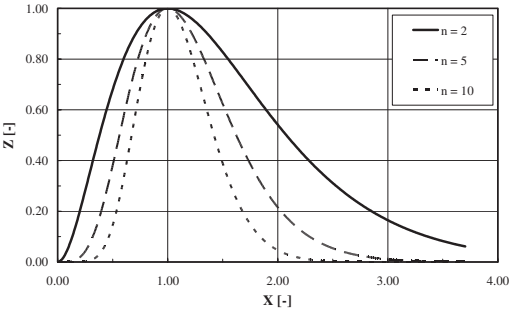


Figure 7. Dimensionless shape of the aggraded channel reach for different n-values.

continuous and derivable. An advantageous property is, in contrast to e.g. a Gaussian distribution, its boundedness. Another reason for having chosen this kind of function is the fact that it fits the experimental results in the best way.

Introducing the dimensionless parameters referring to the peak values (z_{max}, x_{max})

$$X = \frac{x}{x_{max}}, \quad Z = \frac{z}{z_{max}} \tag{2}$$

the aggraded channel reach can be described by the following Maxwell distribution function:

$$Z(X) = \left(X\ e^{1-X} \right)^n \tag{3}$$

In Equation 3 n represents the "shape parameter" of the deposit. In Figure 7, the function $Z(X)$ is presented for different n-values. It can be observed that the shape of the deposit becomes more peaked with increasing n. Furthermore, by definition, the maxima of both, X and Z, are located at 1.00.

3.3 *Data processing for determination of deposition shape*

Once the moving average according to section 3.1 is determined, the characterisation of the aggraded channel reach is assessed using the Maxwell-type distribution function introduced in section 3.2.

The procedure to obtain the Maxwell distribution function from the moving average is exemplarily described for experiment B01.

In a first step, the starting and ending point of the aggraded channel reach has to be identified. These points do not compulsory coincide with the initial bed although this should theoretically be the case and would be desirable. For the present data set, slight erosion or aggradation upstream or downstream, respectively, might be encountered in some experiments (e.g. in Figure 8 (top), the starting point of the

Copyright © 2006 Taylor & Francis Group plc, London, UK

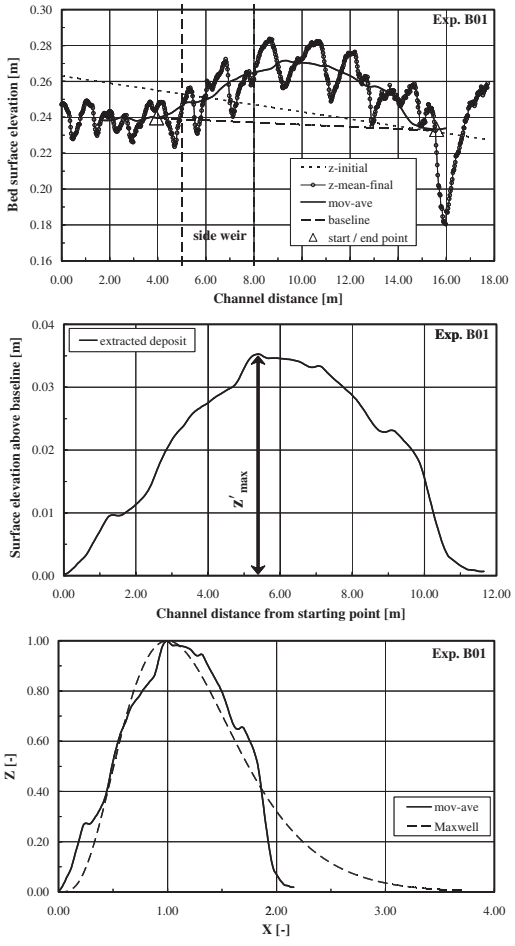


Figure 8. Top: Initial mobile bed, cross sectional averaged final bed, moving average corresponding to the cross sectional averaged final bed, starting and ending points of the aggraded reach and baseline connecting the two local minima defining the aggraded reach. Middle: Extracted deposit. Bottom: Normalised moving average and corresponding Maxwellian distribution function.

aggraded reach is located slightly lower than the corresponding initial bed). These phenomena are likely to be attributed to the fact that sediment supply is estimated and/or to the length of the testing facility. An error estimation reveals that the shape of the aggraded reach (moving average) and consequently the shape factor n are not significantly influenced by this vertical offset. However, the present analysis is conducted including possible vertical offset. For the establishment of design criteria to predict the diverted discharge which are based on the model of the aggraded reach, this vertical shift has to be taken into account, since a lower or higher starting/ending point of the deposit will affect the spilled discharge. As mentioned before, the overall shape of the deposit is rightly assumed and does not change significantly due to the vertical shift.

Due to the above reasons, the requested starting and endpoints are found by searching a local minimum of the moving average in the respective region (instead of taking the corresponding initial bed). For the starting point, the requested value is found where a clear and distinct aggradation compared to the upstream part of the moving average is evident. This location is characterised by a significant change of slope. For the ending point, the same procedure is applied.

Once these two local minima are identified, they are linked with a linear function being the tangent in each point. This tangent represents a reference level or baseline to obtain the difference between the values of the moving average and the baseline. By this procedure the aggraded channel reach is extracted and dissociated from the channel and the original data set, respectively.

In Figure 8 (top), the initial mobile bed, the cross sectional averaged bed, the moving average corresponding to the cross sectional averaged bed, and the starting and ending points of the aggraded reach as well as the connecting tangent (baseline or reference level) are represented. Figure 8 (middle) shows the extracted deposit.

In a further step, the maximum elevation z_{max} and the corresponding position x_{max} of the moving average are determined for and from the extracted deposit. Since the net aggradation maximum in the channel (initial bed level as reference level) differs from the maximum elevation of the extracted deposit (baseline as reference level), the corresponding x_{max}- and z_{max}-values in Equation 2 have to be substituted by x'_{max} and z'_{max}. Thereafter, the Maxwell distribution function is applied to these values (Fig. 8, bottom). The shape factor n is found by a trial-and-error procedure. The prediction accuracy or the optimal n-value, respectively, to describe the moving average is obtained using the least squares method (LSM). The least squares error analysis (Π) is performed for the vertical difference according to Equation 4:

$$\Pi = \sum_{i=1}^{n} \left[\left(Z_{mov-ave} \right)_i - \left(Z_{Maxwell} \right)_i \right]^2 = \min \qquad (4)$$

3.4 *Results for deposition shape*

According to the previous paragraphs, the shape factor n has been determined for the present data set (Table 1). Most values for n are located in a rather narrow range going from $n = 3.00$ to 5.40 (Fig. 9). The mean value for these experiments is $n = 4.27$.

Despite this close correlation, three values exceed this range. For experiment B04 a value of 1.30 is

Copyright © 2006 Taylor & Francis Group plc, London, UK

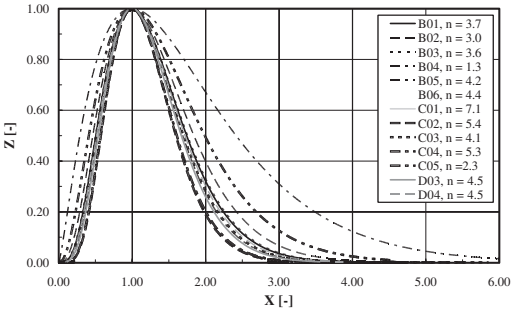


Figure 9. Shape factor n for the entire experimental data set (test series according to Table 1).

obtained, for C01 $n = 7.10$ and for C05 a value of $n = 2.30$ is determined. Referring to Figure 9, the shape factor for C01 and C05 are still in the range of the totality of the experiments. A reasonable physical explanation appears to be difficult to give. For experiment B04, owing the most considerable deviation, a possible explanation is the combination of a comparatively low discharge with a rather mild slope. These experimental conditions seem to emphasize the formation of a well pronounced and extended deposit.

4 MODEL DEVELOPMENT AND PROPOSED METHOD

As mentioned in paragraph 3.2, the shape factor n, the maximum bed elevation z_{max} (z'_{max}) and the position x_{max} (x'_{max}) of z_{max} (z'_{max}) are the main characteristic parameters to describe the aggraded reach (extracted deposit). In the following paragraphs each of these parameters will be assessed in order to develop a relationship able to describe the respective parameter.

In a first step, a description of the extracted deposit as shown in Figure 8 (middle) is developed. The objective of this analysis is to obtain an expression for n, z'_{max} and x'_{max}.

The second step is dedicated to the transfer of the extracted deposit to the channel. For this purpose, the maximum elevation z_{max} and its position x_{max} in the channel have to be known. The anchor point where the extracted deposit is integrated in the channel (origin coordinates of the deposit) refers to the side weir position in the channel and its crest height w_D, since these two values normally are fixed and their coordinates are known a priori.

A reflection of the problem of mutual interaction of lateral overflow and bed morphology leads to the conclusion that four components have to be taken into account:

– geometry of the channel
– geometry of the weir
– hydraulic parameters (flow)
– sediment transport (bed-load).

As mentioned above, the two dimensional or even three dimensional flow pattern tend to deposit bed-load material in the downstream weir alignment. The intensity of this effect certainly depends on the ratio between the flow discharge at the entrance and exit section of the channel reach bounded by the weir. Since the lateral outflow and consequently the flow discharge at the exit section are not known a priori, this ratio cannot directly be used finding suitable relationships. On the contrary, it is rather the very purpose of this study to determine the diverted outflow, hence knowing the exit discharge. Nevertheless, as will be shown in the following paragraph, a ratio of exit and entrance values will be used. This ratio refers to the bed-load transport intensity, thus indirectly dealing with exit and entrance flow discharges.

4.1 *Shape factor* n *for the extracted deposit*

The development of a relation determining n is based on the idea that the four components mentioned in the previous paragraph will be of importance.

Concerning sediment transport, the different sediment transport capacity upstream and upstream of the side weir is taken into account.

From the different empirical bed-load formulae the one proposed by Schoklitsch in 1934 is used (Graf, 1971):

$$q_{sb} = \frac{2.5}{s} S_e^{3/2} \left(q - q_{cr}\right) \tag{5}$$

where q_{sb} is the volumetric solid discharge per unit width, s the relative density ($s = \rho_s/\rho$), S_e the energy slope, q the liquid discharge per unit width and q_{cr} the critical discharge for incipient motion. It has to be noted that any other appropriate formula, e.g. the one of Smart & Jäggi (1983) could be used.

The critical liquid discharge q_{cr}, usually expressed by τ_{cr}, is given with the use of the Manning-Strickler formula such as:

$$q_{cr} = 0.26(s-1)^{5/3} \frac{d^{3/2}}{S_e^{7/6}} \tag{6}$$

where d is the grain size diameter (usually d_{50}).

The intensity of the solid discharge as bed-load can then be expressed in dimensionless form as:

$$\Phi \equiv q_{sb*} = \frac{q_{sb}}{\sqrt{(s-1)gd^3}} \tag{7}$$

Φ usually is referred to as Einstein – factor. Using Equation 7 upstream and downstream of the side weir,

Copyright © 2006 Taylor & Francis Group plc, London, UK

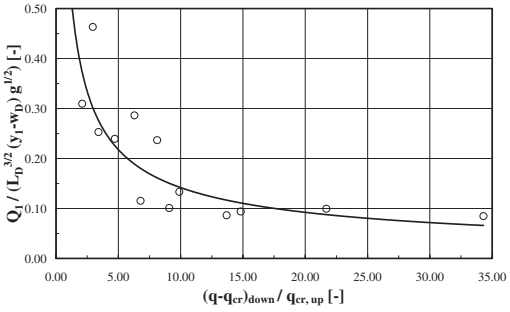


Figure 10. Relation between geometric side weir parameters, flow variables and incipient motion criteria yielding Eq. 8.

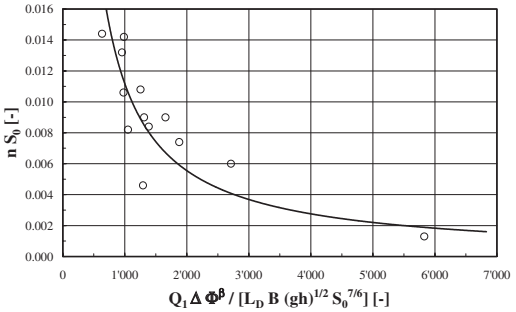


Figure 11. Relationship for the shape factor n (Eq. 9).

the ratio $\Delta\Phi = \Phi_{upstream}/\Phi_{downstream}$ of intensity of bed-load can be determined.

For the upstream part of the channel all variables occurring in Equation 7 are known or can be calculated. The Φ-values for the channel stretch downstream of the side weir are not known a priori, since the effect of the mobile bed on the diverted discharge and consequently the remaining discharge in the channel is not yet quantified.

Based on the present data set, a relation for $(q - q_{cr})_{downstream}/q_{cr,upstream}$ is developed. Since $q_{cr,upstream}$ can be calculated using Equation 6, the unknown term $(q - q_{cr})_{downstream}$ can be calculated. Knowing this term, Equation 5 yields q_{sb} and subsequently Φ for the downstream channel reach is known by applying Equation 7.

The proposed relation shown in Figure 10 reads:

$$\frac{Q_1}{L_D^{3/2}\left(y_1 - w_D\right)\sqrt{g}} = 0.59\left(\frac{\left(q - q_{cr}\right)_{down}}{q_{cr,up}}\right)^{-0.62} \quad (8)$$

The R^2-value is 0.73. To develop Equation 8, the measured water surface slope has been used instead of S_e. For a first approximation the initial bottom slope S_0 can be used but better results were obtained with the water surface slope which differs slightly from the initial bottom slope.

Finally, from Figure 11 the following relation to determine the shape factor n is obtained ($R^2 = 0.78$):

$$n\,S_0 = 11.85\left(\frac{Q_1\,\Delta\Phi^{\beta}}{\left(y_1 - w_D\right)^{3/2} B\sqrt{g}\,S_0^{7/6}}\,\frac{y_1 - w_D}{L_D}\right)^{-1.0} \quad (9)$$

where B is the channel width and β a correlation factor being 0.175.

It has to be noted that the Froude number influences bed form pattern. It is a well-known phenomenon that bed forms generated at low velocities are washed out at high velocities. Especially for test series C high Froude numbers close to unity have been observed (transition regime, washed-out dunes). The corresponding bed surface has been comparatively smooth with a roughness almost equal to grain roughness. For this reason, the Froude number is incorporated in Equation 9, expressed as $Q_1/[(y_1 - w_D)^{3/2}\ B\ g^{1/2}]$. The difference of this Froude number in comparison with the traditional Froude number is that it refers to the upstream side weir head instead of water depth. Thus, besides hydraulic parameters and channel geometry, a third component of the four components to be taken into account, namely the weir geometry, expressed in terms of w_D, could be incorporated.

Furthermore, the exponent 7/6 of the bottom slope is a well known value occurring in incipient motion criteria (e.g. Eq. 6).

4.2 *Maximum elevation z'_{max} of the extracted deposit*

A first attempt to find a relationship for $z'_{\max}$ has been a combination of $z'_{\max}$ and $y_{1,cr}$ on the one hand and q_{sb} and q_{cr} on the other. An approach of this kind has been used by Requena et al. (2005) to determine the vertical bed elevation shift at the beginning of a local river widening. The analysis using data from the present study did not yield any satisfactory relation.

Due to this reason, the functional relationship presented in Figure 12 has been developed in order to obtain the maximum elevation $z'_{\max}$ of the extracted aggraded channel reach. The ratio $(q - q_{cr})_{down}/q_{cr,up}$ on the x-axis can be obtained by the help of Equation 8.

It can be noted that the shape of the presented curve is similar to the shape of the Shields-curve.

4.3 *Position x_{max} of the extracted deposit*

Since by definition, $X = x/x_{max} = 1.00$ (or $X = x/x'_{max} = 1.00$ for the extracted deposit), one of the three

Copyright © 2006 Taylor & Francis Group plc, London, UK

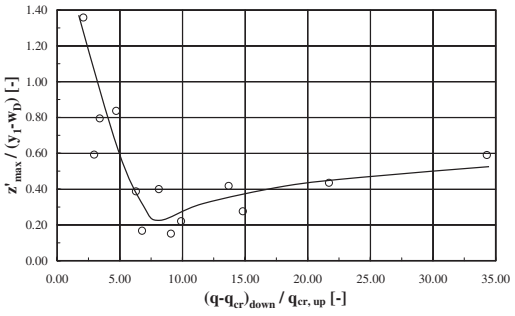


Figure 12. Relationship to determine z'_{max} for the extracted deposit.

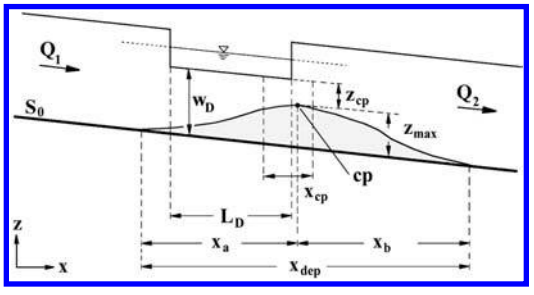


Figure 13. Definition sketch illustrating the position of the coupling point *cp* as well as its coordinates z_{cp} and x_{cp}.

unknown variables is known or can be constructed, respectively. For modelling purposes, beginning at $X = 1.00$, arbitrarily increments for $X < 1.00$ until $X = 0.00$ have to be chosen. For $X > 1.00$, discrete increments until a certain X-value depending on the underlying problem have to be chosen. For the present data set, $X = 4.00$ to 6.00 appears to be an appropriate range (cf. Fig. 9).

4.4 *Vertical reference point* z_{cp} *for coupling extracted deposit with channel geometry*

Once the shape of the extracted deposit is known, it has to be transferred to the channel. The reference point *cp* (*cp* meaning coupling point) is defined by the maximum bed elevation z_{max} and its position x_{max} in the channel (cf. Fig. 13). It is this point where the peak of the extracted deposit and the peak of the aggraded channel reach coincide.

A rather simple relationship for the vertical coordinate z_{cp} of the coupling point *cp* is obtained by using the sill height w_D as a reference. The resulting relation is given by Equation 10:

$$\frac{w_D - z_{cp}}{w_D} = 1/4 \quad \text{or} \quad z_{cp} = 0.75\, w_D \tag{10}$$

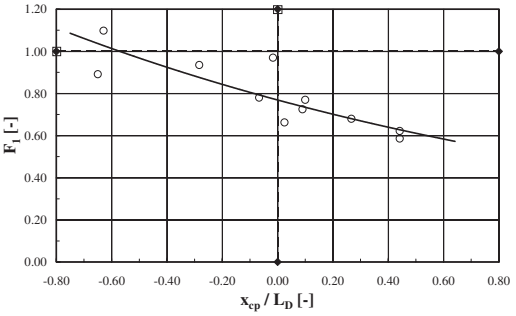


Figure 14. Influence of approach Froude number F_1 on the horizontal coordinate x_{cp} of the coupling point *cp*.

The advantage of the top crest as an anchor point is that the weir height can generally be assumed to be a fixed and known elevation given by the design procedure.

4.5 *Horizontal reference point* x_{cp} *for coupling extracted deposit with channel geometry*

For the horizontal coordinate of the coupling point, the downstream weir corner is used as a reference.

Values for the ratio x_{cp}/L_D obtained by the experiments are in the following range:

$$-0.65 < \frac{x_{cp}}{L_D} < 0.44 \tag{11}$$

Since the location of the maximum deposition constitutes a kind of control section, an improvement of Equation 11 can be achieved considering the approach-Froude number F_1. In Figure 14, it becomes evident that close to $F_1 = 1.0$ the negative range given in Equation 11 ($-0.65 \div 0.00$) serves as a reference whereas for lower Froude numbers ($0.50 < F_1 < 0.80$) the positive range should be applied ($0.00 \div 0.44$). By the use of Equation 12 extracted from Figure 14 an estimation of the respective ranges is possible:

$$F_1 = 0.77\, e^{-0.46\frac{x_{cp}}{L_D}} \tag{12}$$

At this point it has to be mentioned that the range of F_1 is rather narrow and comparatively high values are observed for some experiments (mainly test series C). This is not astonishing since the background of the present study is the use of side weirs in flood protection engineering. Nevertheless, it has to be kept in mind that for Froude numbers close to 1.00 both the flow and sediment transport regime might change. With respect to sediment transport, for the present

Copyright © 2006 Taylor & Francis Group plc, London, UK

data set, especially for test series C, the transition regime is observed. This means, dunes from the lower regime change to washed-out dunes for the transition regime and a comparatively smooth bed surface is achieved.

Moreover, the distance x_b between the end of the aggraded reach and the position x_{cp} of the maximum bed elevation z_{max} appears to follow Equation 13:

$$\frac{x_b}{L_D} = 2.024 \quad \text{for test series } B \tag{13a}$$

$$\frac{x_b}{L_D} = 1.042 \quad \text{for test series } C \text{ and } D \tag{13b}$$

The total deposition length x_{dep} can then be described by the following range:

$$0.5 < \frac{x_b}{x_{dep}} < 0.6 \tag{14}$$

meaning the position of the maximum bed elevation is located approximately in the center (50%) or slightly upstream of the center (60%) of the total deposition length. This behaviour is also represented in Figure 9, showing that the extracted aggraded reach is skewed to the left.

4.6 *Synopsis of model development and proposed method*

The aggraded reach can mainly be parameterized by its maximum elevation, the location of the maximum elevation and its shape.

The shape n is obtained by the help of Equation 9. Equations 5–8 are necessary to obtain the bed-load intensity ratio $\Delta\Phi$ in Equation 9.

The maximum elevation z'_{max} is provided using Figure 12 and Equation 8.

The position x'_{max} is designed using the definition $X = x/x_{\text{max}} = 1.00$ or $X = x/x'_{\text{max}} = 1.00$, respectively, of the Maxwell-type distribution function. In the upstream direction, distinct increments from 1.00 to 0.00 are constructed, in the downstream direction distinct increments from 1.00 to a requested value, e.g. 4.00 to 6.00, are build.

Once the aforementioned parameters are determined, the modeled deposit has to be transferred to the channel. For this reason, the horizontal and a vertical coordinates (x_{cp}, z_{cp}) of the coupling point cp are needed. The vertical coordinate is provided by Equation 10, the horizontal one by Equation 11 and Figure 14.

Knowing the position of x_{cp} (Eq. 11 and Fig. 14), the downstream length x_b of the aggraded reach is obtained by Equation 13. Using Equation 14, the total deposition length x_{dep} can be estimated.

5 DISCUSSION

The experimentally observed increased spilled discharge over a side weir due to morphological bed changes depends on the aggraded channel reach, form induced roughness and local energy losses created by the 3-dimensionality of the deposit(s).

The aggraded channel reach or the shape of the local deposit, respectively, appears to be satisfactorily modelled by a Maxwellian distribution function. The main parameters to describe the sedimentary deposit are the maximum elevation, the position of the maximum elevation and the shape. Based on these variables, four parameters are assumed to be of major influence: channel geometry, side weir geometry, flow parameters and bed-load transport. Relationships, taking into account a combination of these four parameters have been developed to describe the aggraded channel reach. An important parameter within these relationships is the ratio of flow discharge at the entrance and exit section of the channel reach bounded by the weir. Since the main objective of this study is to predict the diverted flow discharge taking into account the interaction with the mobile bed, this ratio cannot directly be implemented because neither the diverted discharge nor the discharge at the exit section are known a priori. Nevertheless, a ratio of entrance and exit flow discharges is indirectly incorporated by introducing entrance and exit bed-load intensities.

Since the Froude number plays an important role regarding flow and sediment transport regime it is implemented using the side weir head instead of flow depth.

Since the presented model results from an ongoing research project, the generality and application ranges of the present study, as for all experimental studies, are limited to the experimental conditions. Some parameters occurring in the model have no or no sufficient variation. For example, the grain diameter and the channel width have been constant throughout the test series and the weir height only changes slightly. With regard to the movable bed properties, fine material has been used. The choice of this material has been inspired by the Rhone river upstream of Lake Geneva in Switzerland. This reach is characterized by a bottom slope of $S_0 \approx 0.1\%$ and a gravel bed ($d_{50} = 15$ mm to $d_{50} = 35$ mm). In flood seasons, the slightly armoured bed surface is destroyed and rather fine material resulting among other sources from glacier abrasion is present. Thus, despite a certain lack of generality, similar effects as being observed in the present flume study might be expected in nature.

Copyright © 2006 Taylor & Francis Group plc, London, UK

The disadvantages of the present model mentioned above will be improved incorporating other flume and field data as well as numerical simulation techniques.

The superposition of form roughness constitutes a next step of the ongoing research project. While introducing form induced roughness using bed form geometry, the aggraded channel reach which has already been modelled has to be taken into account. Moreover, traditional approaches to determine bed form geometry and corresponding roughness (e.g. Van Rijn, 1984) do not seem to be appropriate in the side overflow influenced channel reach (Rosier et al., 2005).

Since the deposit is not homogeneously distributed over the entire cross section but varies in lateralwise direction, local energy losses created by contraction and expansion phenomena might have to be taken into account using a 2D morphological model, e. g. introducing the Bordat-Carnot formula. This implies a clear distinction of the local deposit close to the weir from the general aggradation of the channel reach and bed form patterns which is not that obvious because these morphological effects are superimposed. Thus, the intention of the present study is to present a rather simple 1D morphological model before increasing the complexity using a 2D model.

6 CONCLUDING REMARKS

In the present study the interaction of a side overflow with a mobile bed in a channel has been investigated experimentally.

Due to the lateral loss of water the sediment transport capacity is significantly reduced within a rather short channel reach resulting in sediment deposition. As a consequence, an elevated mean bed level and the formation of a local sedimentary deposit in the reach of the lateral side weir are observed. This leads to backwater effects and local energy losses.

For the prediction of side over flow discharge and modelling purposes, the extent and the shape of the aggraded channel reach have to be known.

The aggraded reach can be fairly well described using a Maxwell-type distribution function. The characteristic parameters are expressed in terms of geometric, flow and bed-load transport variables.

The transfer of the modelled deposit to the channel is achieved by a coupling point referring to the downstream weir coordinate and sill height.

By the help of the developed semi-empirical model, numerical simulations for steady flow conditions dedicated to the estimation of spilled discharge taking into account side weir induced morphological bed changes are possible.

ACKNOWLEDGEMENT

The authors would like to express their gratitude to the *CTI* (Swiss Innovation Promotion Agency) and the *FOWG* (Swiss Federal Office for Water and Geology) for their sustained funding.

NOTATION

The following symbols are used in this paper:

B = channel width
cp = coupling point to incorporate deposit in the channel
g = acceleration due to gravity
L_D = length of weir crest
n = shape parameter (Maxwell)
n_D = number of weirs
q = unit discharge
q_{cr} = critical unit discharge for incipient motion
q_{sb} = solid unit discharge
Q_1 = approach discharge
S_0 = bottom slope
S_e = energy slope
t = duration of experiment
w_D = sill height
x = distance along channel axis
x_{max} = location of maximum bed elevation (Maxwell)
x_{cp} = reference point in channel to incorporate deposit
x_{dep} = deposition length in channel
x_a = upstream deposition length until maximum
x_b = downstream deposition length from maximum
X = peak parameter of Maxwell distribution
y = lateralwise position in channel width
y_1 = water level at upstream weir corner
Z = peak parameter of Maxwell distribution
z = bed elevation
z_{max} = maximum bed elevation (Maxwell)
z_{cp} = reference point in channel to incorporate deposit
β = correlation factor in Eq. 9
ω = variation of longitudinal mean bed elevation
ω_{mean} = mean variation of longitudinal mean bed elevation
ω^* = window length of moving average
Φ = dimensionless solid discharge intensity.

REFERENCES

Borghei, S.M., Jalili, M.R. & Ghodsian, M. 1999. Discharge coefficient for sharp-crested side weir in subcritical

Copyright © 2006 Taylor & Francis Group plc, London, UK

flow. *Journal of Hydraulic Engineering, ASCE* 125 (10): 1051–1056.
Coleman, S.E. & Melville, B.W. 1994. Bed form development. *Journal of Hydraulic Engineering, ASCE*, 120 (4): 544–560.
Graf, W. 1971. *Hydraulics of sediment transport*. McGraw-Hill Company, Inc. London.
Hager, W.H. 1987. Lateral outflow over side weirs. *Journal of Hydraulic Engineering, ASCE* 113 (4): 491–504.
Metflow 2000. UVP Monitor Model UVP-XW User's guide. Metflow SA, Lausanne, Switzerland.
Nadesamoorthy, T. & Thomson, A. 1972. Discussion of 'Spatially varied flow over side weirs'. *Journal of the Hydraulics Division, ASCE* 98 (HY12): 2234–2235.
Requena, P., Bezzola, G. R. & Minor, H.-E. 2005. Aufweitungen in erodierenden Flüssen. *Wasser Energie Luft* 97 (7/8): 183–189.
Ranga Raju, K.G., Prasad, B. & Gupta, S.K. 1979. Side weir in rectangular channel. *Journal of the Hydraulics Division, ASCE* 105 (HY5): 547–554.
Rosier, B., Boillat, J.-L. & Schleiss, A.J. 2004. Mapping of bed morphology for lateral overflow using digital photogrammetry. *Proceedings*, 2nd International Conference on Scour and Erosion (ICSE), Singapore, 14–17 November.
Rosier, B., Boillat, J.-L. & Schleiss, A.J. 2005. Influence of side overflow induced local sedimentary deposit on bed form related roughness and intensity of diverted discharge. *Proceedings*, XXXI IAHR Congress, Seoul, 11–16 September.
Singh, R., Manivannan, D. & Satyanarayana, T. 1994. Discharge coefficient of rectangular side weirs. *Journal of Irrigation and Drainage Engineering, ASCE* 120 (4): 814–819.
Smart, G.M. & Jäggi, M.N.R. 1983. Sedimenttransport in steilen Gerinnen. In Vischer, D. (ed.), *Mitteilungen der Versuchsanstalt für Wasserbau, Hydrologie und Glaziologie (VAW)* 64. Zürich: Eidgenössische Technische Hochschule Zürich (ETHZ).
Subramanya, K. & Awasthy, S.C. 1972. Spatially varied flow over side weirs. *Journal of the Hydraulics Division, ASCE* 98 (HY1): 1–10.
Van Rijn, L.C. 1984. Sediment transport, Part III: Bed forms and alluvial roughness, *Journal of Hydraulic Engineering, ASCE*, 110 (12): 1733–1754.

Copyright © 2006 Taylor & Francis Group plc, London, UK

Morphology, flow and sediment transport over a natural 3D dune field: Rio Paraná, Argentina

D.R. Parsons & J.L. Best
Earth and Biosphere Institute, School of Earth and Environment, University of Leeds, Leeds, UK

S.N. Lane & R.J. Hardy
Department of Geography, University of Durham, Durham, UK

R. Kostaschuk & D. Shugar
Department of Geography, University of Guelph, Ontario, Canada

O. Orfeo
Centro de Ecologica Aplicada del Littoral (CECOAL), Corrientes, Argentina

ABSTRACT: The morphology, flow and process mechanics of river dunes has attracted much interest over many years. However, many of these studies have concentrated on investigating two-dimensional (2D) bed features and their associated flow structures and bed stress distributions. This morphological simplification imposes inherent limitations on our interpretation and understanding of dune form and flow dynamics, as natural dunes are invariably three-dimensional (3D) with an associated fully 3D flow structure. For example, studies over 2D forms neglect the significant effect that lateral flow and secondary circulation may have on the flow structure and thus dune morphology. This paper details a field investigation of the interactions between the 3D morphology, 3D turbulent flow structure and suspended sediment movement over large alluvial sand dunes in the Rio Paraná, NE Argentina. Fixed point and moving vessel surveys enabled the links between three-dimensionality, large-scale turbulence and sediment suspension over the dunes to be investigated.

1 INTRODUCTION

Dunes are ubiquitous forms in river channels, occurring within a wide range of bed sediment sizes. The presence of dunes on the bed significantly influences both the nature of the mean and turbulent flow structure, and consequently exerts a strong control on the entrainment, transport and deposition of bed sediment. As a result of their importance, the morphology, flow and mechanics of river dunes have attracted much interest over many years (e.g. McLean and Smith 1986, Yalin 1992, Nelson 1993, McLean et al. 1994, Bennett and Best 1995, Best 1996, Amsler and García 1997, Shimizu et al. 1999, Kostaschuk 2000, Best and Kostaschuk 2002, Carling et al. 2000, Yue et al. 2003)

This interest in dune flow and form dynamics has enabled elucidation of the main characteristics of flow associated with dunes, which are: (a) accelerating flow over the dune stoss side, (b) flow separation or deceleration (Best and Kostaschuk 2002) from the dune crest in the lee side, (c) flow reattachment at 4 to 6 dune heights downstream, (d) a shear layer between the separated flow zone and streamwise flow above, which expands as it extends downstream, and (e) an internal boundary layer that grows from reattachment beneath the wake along the stoss slope of the next dune downstream. Most of the studies that have contributed to describing these key flow features over dunes have however concentrated on simplified two-dimensional (2D) bedforms, with constant heights and straight crestlines transverse to the flow. Given that natural bedforms are invariably three-dimensional (3D) (e.g. Allen 1982, Baas 1994) this morphological simplification has imposed inherent limitations on our interpretation and understanding of dune form and flow dynamics.

Natural dunes often have variation in crestline planform curvature, crestline height, and crestline continuity (Allen 1982, Dalrymple and Rhodes 1995, Roden 1998), with phase differences between successive crests often producing variability in dune wavelength and steepness (Gabel 1993). This three-dimensionality has significant implications for understanding the flow structure over dunes. For example, simplified 2D

Copyright © 2006 Taylor & Francis Group plc, London, UK

forms do not possess lateral flows and secondary circulation present in more three dimensional forms, which will have major impacts on the lee side flow structure, bed shear stress and overall dune dynamics. This complexity of bedform morphology in alluvial environments has been known for many years (e.g. Sorby 1859, Neill 1965, Allen 1968) and the considerable complications that the three-dimensionality of form can introduce into the flow structure over bedforms highlighted (e.g. Allen 1968). However, only recently have the full 3D effects of dune form been investigated in detail in the laboratory (Maddux et al. 2003a,b, Venditti 2003). Maddux et al. (2003a,b) investigated dunes in which the planform crestline was straight (i.e. orthogonal to the mean flow at all positions), but where the dune height varied in the cross-stream direction in the form of a full cosine wave. Successive crestlines were 180 degrees out of phase, creating three-dimensional forms where the crest height maxima was followed immediately downstream by a crest height minima. Maddux et al. (2003a) found that these spanwise variations in form significantly altered the flow compared to that found over 2D dunes with a similar crest height. Maximum streamwise velocity was found to be highest over the crestline nodes, rather than the maxima in crestline height, and a significant amount of momentum flux over the dune was transformed into secondary currents induced by topographic forcing due to the three dimensionality in dune height (Maddux et al. 2003a).

Venditti (2003) also performed laboratory investigations into the effects of dune three-dimensionality on flow structure in which dune planform curvature was altered, but crest height and the three-dimensional volume of the dunes were maintained. Results indicate that a convex downstream planform crestline (a lobe) possesses lower average velocities for a given discharge than straight-crested 2D dunes. However, lobes were found to produce a well-defined lee side separation zone, with an intense downstream wake structure and an enhanced level of turbulence with more vigorous mixing in the separation cell than observed over 2D straight-crested dunes. In contrast, dunes with a crestline that is concave downstream (a saddle) were found to have higher average flow velocities, weakly defined separation cells, and wakes that were not a significant component of the flow field (Venditti 2003). Venditti (2003) argues that lower mean velocities associated with the lobe were caused by higher turbulence intensities in the lee, as a result of flow divergence, whereas in the case of the saddle, convergence of flow in the lee of the dune results in lower turbulence intensities but higher average flow velocities.

The experiments of Maddux et al. (2003a,b) and Venditti (2003) demonstrate that even a simple three-dimensionality in dune form can significantly influence the average flow velocity and flow distribution, secondary currents and lateral flows, and the size and intensity of the separation zone, turbulence and downstream wake. There is thus a significant gap in the understanding of turbulent flow over fully 3D dunes and that there is a pressing need for studies and measurements over natural three-dimensional field dunes. This paper presents a first step towards this goal and details a study of a field of 3D dunes in the Rio Paraná, NE Argentina. A large (0.35 km wide, 1.2 km long) area of dunes was surveyed using a Multibeam Echo Sounder (MBES), providing high-resolution 3D detail of the river bed. Simultaneous with the MBES survey, 3D flow information was obtained with an acoustic Doppler current profiler (aDcp), including at-a-point velocity measurements over key areas of the channel bed. The present paper presents details of the methodology and results using this integrated approach that has enabled investigation of the interactions between the 3D morphology and 3D turbulent flow structure of large alluvial sand dunes. The turbulent flow structures over different sections of dunes with distinct 3D morphologies are also highlighted, and used to discuss the implications for understanding dune flow structure and dune dynamics.

2 FIELD SITE AND FIELD METHODS

The study area is a field of dunes in the Rio Paraná, 16 km north of the city of Corrientes, NE Argentina (Fig. 1). The Paraná River basin occupies 2,600,000 km^2, with a mean annual discharge of the Rio Paraná of 17,000 m^3 s^{-1} (Orfeo and Steveax 2002). At the field site, the Rio Paraná is approximately 2.5 km wide and 5–12 meters deep and, at the time of surveying in May 2004, the discharge of the full river section was about 11,000 m^3 s^{-1}. Measurements

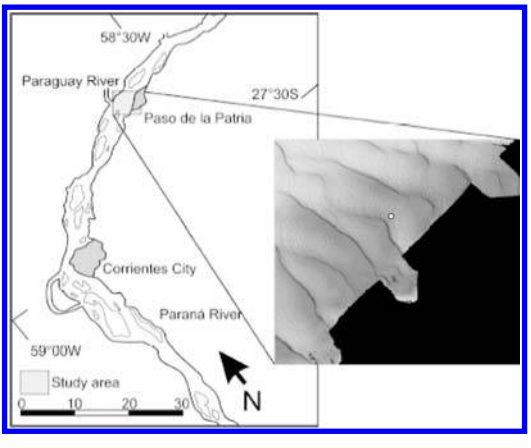


Figure 1. Field site location and inset (multibeam image of river bed). White dot indicates location of moored vessel measurements.

Copyright © 2006 Taylor & Francis Group plc, London, UK

of the 3D bathymetry and 3D flow structure were made from a small vessel simultaneously using a Reson™ SeaBat® 8101 Multi-Beam Echo Sounder (MBES) and an RDInstruments™ RioGrande® 600 kHz acoustic Doppler current profiler (aDcp). Both instruments were located together spatially and temporally using a Leica™ differential global positioning system (DGPS) in real time kinematic (RTK) mode, which produced an accuracy in relative position of +/−0.02 m and +/−0.03 m in the horizontal and vertical positions respectively, with the boat velocity being approximately 1 m s^{-1} during measurements.

The Reson SeaBat 8101 MBES is a 240 kHz system, which measures the relative water depth across a wide swath perpendicular to the track of the survey vessel. A transmit projector array on the sonar head transmits pulses of acoustic energy into the water column, with reflections from the water column and bed being 'heard' on a semicircular receive array. The SeaBat 8101 has 101 beams with a total across-track subtended angle of 210 degrees, permitting the MBES to measure a swath width ∼7.4 times the water depth. A combined motion and gyro sensor (a TSS® Meridian Attitude & Heading Reference System (MAHRS)) was used to provide full 3D motion and orientation data for the MBES processing, and the DGPS was set to output a pulse per second, which is used to remove all latency from the MBES processing. The MBES provides information on the river bed morphology at a centimetric resolution and millimetric precision over scales from ripples superimposed on dunes to the entire river reach, and provides an unparalleled methodology by which to examine the form of alluvial roughness.

Simultaneous with the MBES survey, the aDcp was used to quantify the 3D flow structure over the swath of dunes. The aDcp has a 4 beam (transducer) system, each with an orthogonal angle of 20 degrees in the vertical (RD Instruments 2001), and emits acoustic pulses of energy that are backscattered by particles in the water column. The Doppler shift principle is used to convert the change in frequency into weighted averages of components of flow velocity within each depth range bin. The aDcp was set to pulse (or 'ping') at 5 Hz, although measurements were then averaged over 12 pulses to increase the signal:noise ratio, and yielded instantaneous 3D velocity profiles at ∼0.54 Hz. Since all velocities measured by the aDcp are relative to the aDcp, and hence the boat velocity, these measured aDcp velocities must be corrected for this motion by removing the DGPS-derived boat velocity, thereby producing measurements of the flow velocity (cf. Yorke and Oberg 2002). Flow velocities were finally converted from beam coordinates into an Earth referenced coordinate system, using the simultaneous measurements made by the aDcp's 'on-board' attitude and gyro sensor. Since the boat velocity was ∼1 m s^{-1}, each profile was averaged over an area of diameter ∼1.5 m at the first sampling bin nearest the water surface. An inherent limitation of the aDcp is that since each beam is oriented at 20 degrees to the vertical, the measurements are being made, and averaged across, different volumes of fluid in the vertical profile. This limitation increases with depth of measurement, such that static measurements in 10 m of water produce readings at the bed that are averaged over an area of 9.7 m in diameter.

MBES and aDcp measurements were made along a total of 14 parallel streamwise transects, each approximately 25 m apart, and six spanwise cross-sections approximately 200 m apart. For analysis of the large scale turbulent structures associated with the dunes, aDcp measurements were then taken at two fixed (moored points) as guided by the MBES survey. This included a fixed point positioned close to a dune crest and a point over the dune lee.

3 RESULTS

3.1 *Bed morphology*

Figure 2 shows the quantified bathymetry of the full field of dunes surveyed by the MBES. Flow depth increases to the SSW corner of the survey area, with a corresponding increase in dune size, and is related to the presence of a large mid-channel bar upstream of the survey area. Overall, the dunes have a relatively complex 3D pattern throughout the surveyed area (Fig. 2), with the dunes being ∼1.2 to 2.5 m high and possessing a range of wavelengths from 45–85 m, yielding a range in the dune form index (or aspect ratio; height/wavelength) of ∼0.021–0.029.

A streamwise profile through the field of dunes (Fig. 3, see location on Fig. 2) shows that the vast majority of the dunes are highly asymmetric, with

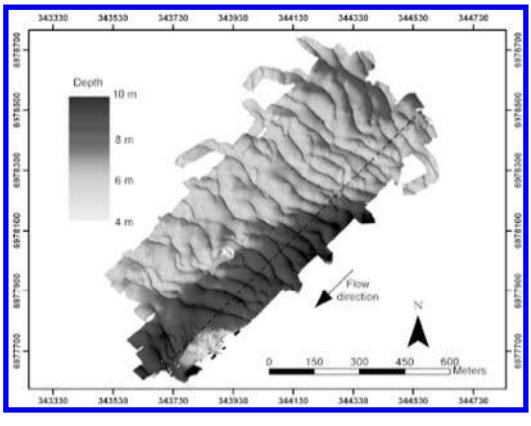


Figure 2. Bathymetric contour map of the dune field obtained using multibeam sonar.

Copyright © 2006 Taylor & Francis Group plc, London, UK

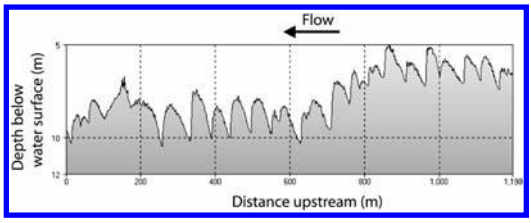


Figure 3. Profile of bed morphology, obtained with MBES, along the streamwise transect indicated in Fig. 2. Note the superimposed bedforms on the larger dunes and the crest-brink separation as shown by the gentle rounded nature of the surface close at the crest followed by a sharper break of slope into the lee.

lee side slope angles typically around ∼8.5 to ∼22 degrees. Dune stoss slope angles are much shallower, typically around ∼1.5 to 2.5 degrees.

The dunes have clearly identifiable crestlines in planform (Fig. 2), many of which are laterally continuous throughout the ∼200 m width of the survey area. However, there are several discontinuous crestlines in-between the more continuous crestlines, frequently resulting in bifurcation of individual crestlines (Fig. 2). Most crestline planform profiles also have zones of pronounced curvature, which produces saddles (where the planform crestline is concave downstream) and lobes (where the planform crestline is convex downstream) along individual crestlines. Venditti (2003) suggests that such distortion is related to maintaining the 3D bed, which exerts a significant control on sediment transport over individual dunes and thus downstream changes in bedform morphology. Indeed one would expect the variations in dune height, and shear stress profiles, produced by planform curvature of the crestlines to produce preferential sediment pathways along a particular dune, with a subsequent influence on the dune dynamics immediately downstream. The control of sediment transport directions by crestline curvature is likely to be important within the study reach, and further influenced by the locations of crestline bifurcations and crestline junctions (Fig. 2).

Numerous variations in the crest heights are present within the dune field in the study reach, even along laterally continuous crestlines (Fig. 2). Moreover, the lee side troughs of many of the dunes also have a large variability in their scour depth, with such variability being up to ∼1.5 m along an individual crest, which may be greater than the variation in the crest height between dunes. The variability in scour depth appears to be correlated to areas of planform crestline curvature, with saddle-shaped crests generally having greater, but more localized, areas of scour in their lee compared with straighter crested dunes (Fig. 2). Conversely, lobe-shaped crestlines appear to possess more laterally extensive but shallower lee side scour zones.

The stoss side slopes of the dunes in the reach are commonly convex up (Fig. 3). Most dunes also appear to have a distinct crest-brink parting (i.e. the highest point of the crest and the brinkline of any steeper slipface are not coincident), as indicated by the gentle rounded dips at the crest followed by a sharper break of slope into the lee (Fig. 3). This separation between the crest and the brink is known to have significant implications for shear and turbulence production in the lee side (Best and Kostaschuk 2002), with an influence on sediment movement over the dune crest into the lee side. Despite the variability in lee side angle across the field of dunes, most of the lee slope angles (∼>10 degrees) may be expected to produce a separation zone in the dune lee (e.g. Ogink 1988, van Rijn 1993, Wilbers 2002), with low-angle dunes also possessing intermittent flow separation (Best and Kostaschuk 2002). The presence of lee side flow separation is a significant feature of the dune dynamics, exerting significant controls on turbulence production and sediment transport (e.g. McLean et al. 1994, Bennett and Best 1995).

The different aspects of dune three-dimensionality revealed by this MBES survey therefore appear interrelated and may be expected to influence the dune flow dynamics (e.g. Venditti 2003). Planform crestline curvature seems related to variations in crestline height and patterns of leeside scour depth. Moreover, the linkages between crestlines in terms of crestline discontinuities, bifurcations and junctions also appear related to the influence of the upstream dune three-dimensionality, and in particular dune height and variations in lee side scour.

3.2 *Flow structure*

The flow structure obtained with the aDcp over three dunes identified from the MBES survey are shown in Figures 4, 5 and 6. The dunes selected for more detailed analysis possess: a straight crest, a lobe-shaped crest, and a saddle-shaped crest, and were formed within similar flow depths with relatively uniform local crestal heights (2.1–2.3 m). Importantly, the high-resolution bed morphology obtained from the MBES is used to place the individual dunes and their associated flow fields into their full three-dimensional morphological context.

The straight crested dune (Fig. 4) shows many features present over 2D fixed dunes (e.g. McLean et al. 1994, Bennett and Best 1995), including acceleration of streamwise flow along the stoss side of the dune, particularly at the crest, associated with a zone of positive vertical velocity slightly removed from the bed. This is followed by a significant deceleration of flow and a zone of high negative vertical velocity in the dune lee, with a separation zone present in the lee side as indicated by the ∼100 degree change in flow direction

Copyright © 2006 Taylor & Francis Group plc, London, UK

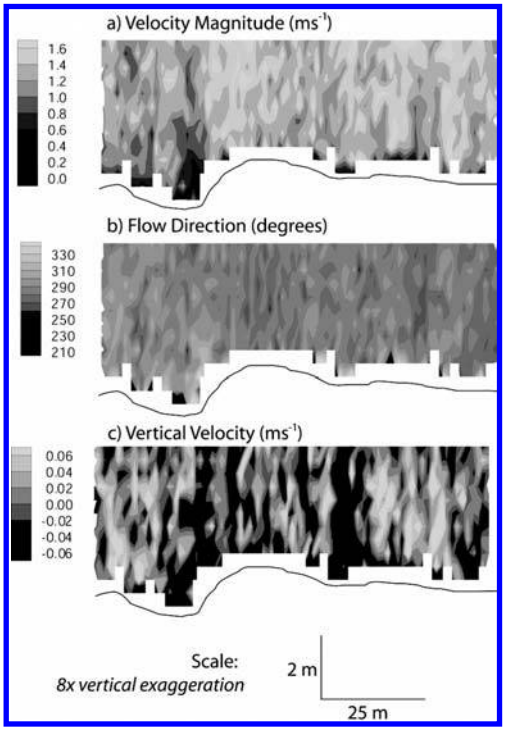


Figure 4. Flow velocity magnitude, direction and vertical velocity over a straight-crested dune. Flow is from right to left.

though the leeside scour (Fig. 4b). This flow separation is associated with a leeside angle of 18 degrees.

Over the saddle-shaped crestline (Fig. 5), a similar pattern of higher streamwise velocity over the stoss side and lower streamwise velocity in the dune lee is apparent, although the deceleration of velocity in the lee is not as marked as over the straight-crested dune. There is also a clear pattern of enhanced vertical velocity over the dune, with a zone of strong upwelling along the stoss side approaching the dune crest, and a stronger zone of downwelling throughout the region of lee side scour. The magnitude of the vertical velocity is also enhanced over the saddle-shaped crestline compared to the straight-crested dune, particularly in the region of downwelling in the dune lee. However, despite this clear pattern in vertical velocity, no flow separation zone is detected in the dune lee, probably due to the spatial sampling limitations of the aDcp. As the angle of the lee side slope over this saddle (14.5 degrees) would suggest that a permanent separation zone may be present, the non-detection of flow separation by the aDcp suggests that flow separation is probably spatially less extensive than associated with the straight-crested dune.

In the case of the lobe-shaped crestline (Fig. 6), the general flow pattern is once again similar to the other

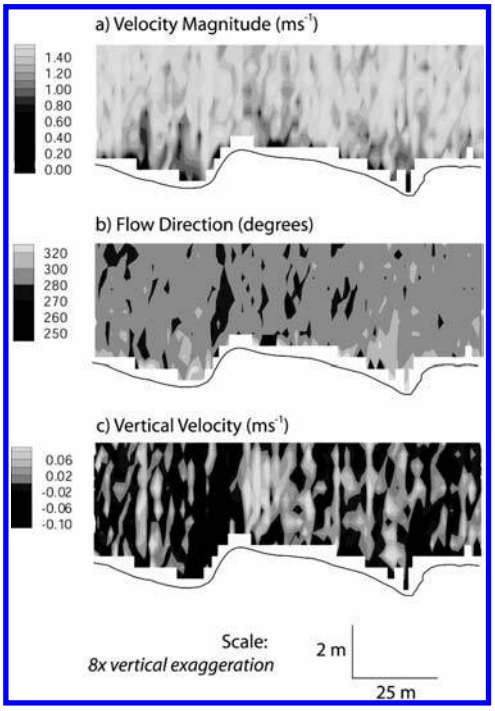


Figure 5. Flow velocity magnitude, direction and vertical velocity over a saddle-crested dune. Flow is from right to left.

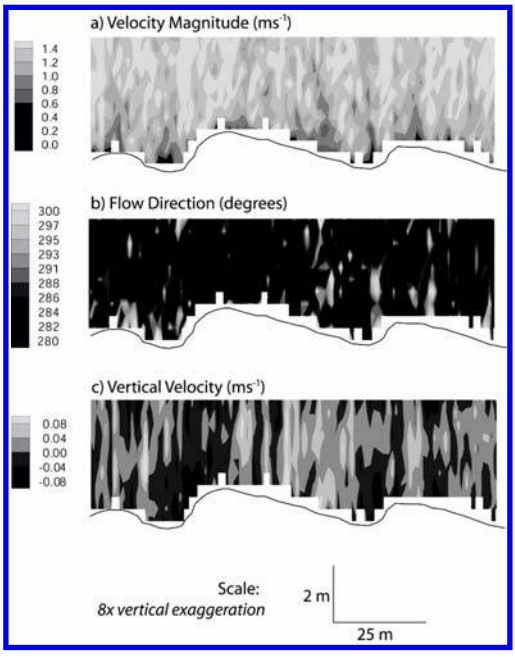


Figure 6. Flow velocity magnitude, direction and vertical velocity over a lobe-crested dune. Flow is from right to left.

Copyright © 2006 Taylor & Francis Group plc, London, UK

two cases, although the velocity over the whole dune is slightly lower (1.2 ms^{-1}). A small zone of decelerated flow is again prevalent in the lee side, with the vertical velocity again being enhanced over the dune form, and being greater than the straight-crested dune but less pronounced than in the saddle-shaped crest. Despite the high negative vertical velocity in the lee side, there is no measured flow reversal, with only a ~20 degrees deviation in flow direction detected in lee side. Again, since the lee side angle of the dune (14 degrees) would suggest the likelihood of permanent flow separation, this suggests that the separation zone is again smaller than over the straight-crested dune.

These results from a field study of mean flow over 3D dunes, and the recent physical modeling studies of Maddux et al. (2003a,b) and Venditti (2003), have several important implications for sediment entrainment, deposition, sediment transport rates, dune migration and thus the overall stability of a sand bed. The smaller separation zones and lower velocity gradients associated with the leeside of 3D dunes may be associated with a smaller level of large-scale turbulence, and thus amount of sediment entrained into suspension (e.g. Jackson 1976, Kostaschuk and Church 1993) than their 2D counterparts. Moreover, as form drag can be reduced by ~52% over a 3D irregular dune pattern (Venditti, 2003) and turbulence intensities are generally less over 3D dunes compared with 2D dunes (Maddux et al. 2003a), the spatially-averaged bed shear stress is likely to be less over the whole dune: sediment transport rates may thus be expected to be lower over a 3D dune than over a 2D dune profile. The effects of differential dune height, wavelength and form index associated with dune three-dimensionality, which will affect the presence, location and permanence of flow separation, and their influence on flow structure and sediment entrainment may thus be expected to be important in affecting flow resistance over dune-covered beds. More research in this area is vital to better understand dune dynamics.

3.3 *Large-scale turbulence analysis*

The acoustic backscatter signal from the aDcp was used as a proxy for suspended sediment concentration (see Shugar 2005). The backscatter from each of the four instrument beams was averaged for of the bins in the vertical. Time series from a location close to the bed (about 2 m from the bed) at both the dune crest and dune trough were used for comparisons (see Fig. 1 for location).

Wavelet analysis was used to compare the time series. The wavelet transform was designed to analyze time series containing nonstationary power over many different frequency scales (see Daubechies 1990). The wavelet transform used herein is the continuous version, where the transform is calculated for all scales

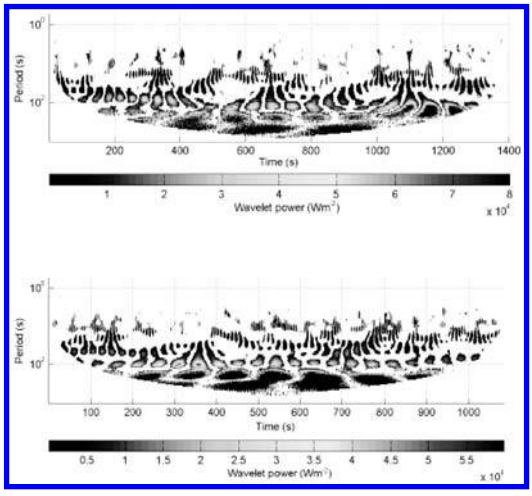


Figure 7. Wavelet power spectrums of calibrated suspended sediment concentration at (a) the dune crest and (b) at the dune trough. Both time series are taken 2 meters above the channel bed.

and positions in time. Wavelet analysis offers several advantages over more traditional spectral analyses based on the Fourier transform. The Fourier transform decomposes a signal into a series of sine and cosine waves, and expresses the signal in terms of the frequency (x) and power (y) of its constituent waves, without reference to when the frequencies occur. Furthermore, strong inhomogeneities in a turbulent series mean that the physical meaning of a Fourier decomposition is lost. Wavelet transforms however allow one to unfold a signal into both space and scale using analyzing functions called wavelets, which are localized in space (Farge 1992). A time series is decomposed into a set of scaled and translated versions of wavelet functions, with the scale of the wavelet varying with frequency. Thus, where a Fourier transform in the frequency domain yields a power value for each frequency and is inherently nonlocal, wavelet analysis produces power values for a set of locations in time and for a range of frequencies, the latter related to the scales of the wavelet function considered. Wavelet analysis is therefore useful in analyzing time series that contain nonstationary power at various frequencies and expresses a time series in three-dimensional space: time (x), scale/frequency (y) and power (z).

Figure 7 shows wavelet transforms for suspended sediment concentrations at 1 meter above (a) the crest surface and (b) trough locations over the dune. Wavelet analysis identifies coherent flow structures at a range of frequencies from 1 to 1×10^{-3} Hz, with structures having periods of ~100 seconds dominating the time

Copyright © 2006 Taylor & Francis Group plc, London, UK

series at both the crest and the trough, but with significantly lower wavelet power for the trough time series. Periodicities of flow structures with high suspended sediment content of 0.01 Hz are common, with both records exhibiting these larger, lower frequency structures. As these regions of enhanced suspended load correlate well with streamwise flow deceleration over both crest and trough, these events are interpreted as fluid ejections, which have a streamwise velocity lower than the average and are responsible for increased suspension of sediment. These results suggest that these larger scale structures (~100 s) move over the crest and are then transmitted through the lee side scour, with the lower wavelet power indicative of less coherence as the flow structure moves through the lee side.

4 CONCLUSIONS

Detailed measurements of bed morphology and three-dimensional flow structure over a field of sand dunes in the Rio Paraná, Argentina, have enabled an initial field testing of recent laboratory findings concerning 3D dune morphology and flow dynamics.

Dune morphology is complex with considerable variations in dune height, wavelength, scour depth and crestline curvature. For instance, dune three-dimensionality may induce larger changes in dune height than the variation present between different dunes. Variability in crestline direction and curvature along with crestline continuity are also present. Crestline discontinuities, bifurcations and junctions appear related to the influence of upstream dune three-dimensionality.

Three-dimensionality in dune morphology is also shown to significantly influence the flow structure. Both lobe and saddle shaped dune crestlines produce smaller regions of lee side flow separation, with higher vertical velocities when compared with a straight crested dune. These findings suggest that if the flow structure over 3D dunes is associated with smaller levels of large-scale turbulence, this may also result in less suspension of bed sediment, and thus sediment transport over the dune field may be reduced.

This field study also highlights that further research is clearly required into the interacting effects of dune curvature and dune height on flow structure, from a combination of laboratory and theoretical work aligned with targeted field investigations. An advance in understanding is also required on the influence of natural 3D dune geometry on macroturbulent flow structures and their spatial variability. Furthermore, detailed information is needed as to how dune migration rates and sediment transport are linked to the morphology of natural 3D dunes, which can then be linked though to an increased understanding of the temporal changes in 3D dune flow structure.

ACKNOWLEDGEMENTS

This research was enabled through award of grants NER/A/S/2001/00445 and NER/B/S/2003/00243 from the UK Natural Environment Research Council for which we are extremely grateful. We would like to gratefully acknowledge the outstanding and full support of RESON (www.reson.com), and John Fraser in particular. Additionally, we also extend thanks to the staff of CECOAL-CONICET (Corrientes, Argentina), and in particular Lolo Roberto and Luis Bonnetti, for their field support. Mark Franklin, Pam Montgomery, & Mat Roberts.

REFERENCES

Allen, J.R.L. 1968. *Current Ripples: their relation to patterns of water and sediment motion*. North Holland Publishing Company, Amsterdam. 433 pp.

Allen, J.R.L. 1982. *Sedimentary Structures: Their Character and Physical Basis*, Elsevier, Amsterdam.

Amsler, M.L. and M.H. Garcia, 1997. Sand dune geometry of large rivers during floods, Discussion. *Journal of Hydraulic Engineering, 123*, pp. 582–584.

Baas, J.H. 1994. A flume study on the development and equilibrium morphology of current ripples in very fine sand, *Sedimentology*, *41*, 185–209.

Bennett, S.J., and J.L. Best 1995. Mean flow and turbulence structure over fixed, two-dimensional dunes: implications for sediment transport and bedform stability, *Sedimentology*, *42*, 491–513.

Best, J.L. 1996. The fluid dynamics of small-scale alluvial bedforms, in *Advances in Fluvial Dynamics and Stratigraphy*, edited by P.A. Carling and M.R. Dawson, pp. 67–125. John Wiley and Sons, Chichester.

Best, J.L. and R.A. Kostaschuk 2002. An experimental study of turbulent flow over a low-angle dune, *Journal of Geophysical Research*, *107*, 3135, 1–18. doi:10.1029/2000JC000294, 2002.

Carling, P.A., E. Gölz, H.G. Orr and A. Radecki-Pawlik 2000. The morphodynamics of fluvial sand dunes in the River Rhine near Mainz, Germany, Part I: sedimentology and morphology, *Sedimentology*, *47*, pp. 227–252.

Dalrymple, R.W. and R.N. Rhodes 1995. *Estuarine dunes and bars*. In: Developments in sedimentology, 53, G.M.E. Perillo (Ed.) Elsevier Science.

Daubechies, I. 1992. Ten lectures on wavelets. Society for Industrial and Applied Mathematics, Philedelphia, PA., 357 pp.

Farge, M. 1992. Wavelet transforms and their application to turbulence. Annual Review of Fluid Mechanics 24:395:457.

Gabel, S.L. 1993. Geometry and kinematics of dunes during steady and unsteady flows in the Calamus River, Nebraska, USA, *Sedimentology 40*, pp. 237–269.

Jackson, R.G. 1976. Sedimentological and fluid-dynamic implications of turbulent bursting phenomena in geophysical flows, *Journal of Fluid Mechanics 77*, 531–560.

Kostaschuk R.A. and M.A. Church 1993. Macroturbulance generated by dunes: Faser River, Canada, *Sediment Geol.*, *85*, 25–37.

Copyright © 2006 Taylor & Francis Group plc, London, UK

Kostaschuk, R.A. 2000. A field study of turbulence and sediment dynamics over subaqueous dunes with flow separation, *Sedimentology 47*, 519–531.

Maddux, T.B., J.M. Nelson and S.R. McLean 2003a. Turbulent flow over three-dimensional dunes: 1. Free surface and flow response, *J. Geophysical Research 108*, F1, doi:10.1029/2003/JF000017.

Maddux, T.B., S.R. McLean and J.M. Nelson 2003b. Turbulent flow over three-dimensional dunes: 2. Fluid and bed stresses, *Journal of Geophysical Research 108*, F1, doi:10.1029/2003/JF000018.

McLean, S.R., and J.D. Smith 1986. A model for flow over two-dimensional bedforms: implication for sediment transport. *Journal of Geophysical Research*, *99*, pp. 12729–12747.

McLean, S.R., J.M. Nelson and S.R. Wolfe 1994. Turbulence structure over two-dimensional bedforms: Implications for sediment transport, *Journal of Geophysical Research*, *99*, 12729–12747.

Neill, C.R. 1965. Bedforms in the lower Red Deer River, Alberta. *Journal of Hydrology*, *7*, pp. 58–85.

Nelson, J.M., S.R. McLean and S.R. Wolfe 1993. Mean flow and Turbulence over two-dimensional bedforms, *Water Resources Research*, *29*, 3935–3953.

Ogink, H.J.M. 1988. *Hydraulic roughness of bedforms*. Delft Hydraulics Report M2017.

Orfeo, O. and J. Steveax 2002. Hydraulic and morphologic characteristics of middle and upper reaches of the Paraná River Argentina and Brazil, *Geomorphology 44*, 309–322.

Roden J.E. 1998. The Sedimentology and dynamics of mega-dunes, Jamuna River, Bangladesh, Unpublished PhD thesis, Department of Earth Sciences and School of Geography, University of Leeds, Leeds, United Kingdom, 310 pp.

Shimizu Y., M.W. Schmeeckle, K. Hoshi and K. Tateya 1999. Numerical simulation of turbulence over two-dimensional dunes, In: *River, Coastal and Estuarine Morphodynamics*, Proceedings International Association for Hydraulic Research Symposium, Genova, pp. 251–260.

Shugar, D. 2005. The evolution of coherent flow structures over dunes, Paraná River, Argentina. MSc Thesis, University of Guelph, Canada.

Sorby, H.C. 1859. On the structures produced by the currents present during deposition of stratified rocks. *The geologist 2*, 137–147.

van Rijn 1993. Principles of Sediment Transport in Rivers, *Estuaries and Coastal Seas*, Aqua, Amsterdam.

Venditti, J.G. 2003. Initiation and development of sand dunes in river channels, Unpubl. Ph.D. thesis, Department of Geography, University of British Columbia, 291 pp.

Wilbers, A.W.E 2004. *The development and hydraulic roughness of subaqueous dunes*, Ph.D. thesis, Faculty of Geosciences, Utrecht University, Netherlands Geographical Studies 323, 224 pp.

Yalin, M.S. 1992. *River Mechanics*, Pergamon Press, New York.

Yue, W., C-L. Lin and V.C. Patel 2003. Numerical investigations of turbulent free surface flows using level set method and large eddy simulation, *IIHR Technical Report 435*, 170 pp.

Copyright © 2006 Taylor & Francis Group plc, London, UK

Flow resistance associated to a schematic step-pool pattern

F. Canovaro & L. Solari
Department of Civil Engineering, University of Firenze, Italy

ABSTRACT: Flow resistance developed by macro-roughness represented by pebbles positioned on a granular layer according to a regularly spaced stripe pattern on steep bed slopes is here investigated. Flume experiments under various geometrical and hydraulic conditions are carried out and interpreted by means of a theoretical model. Results indicate that when the macro-roughness stripes are spaced according to some optimal wavelength, flow resistance is maximum. A statistical analysis of a large number of step-pool geometry data suggests that this spacing corresponds to one of the statistically most frequent wavelength observed in natural step-pool sequences.

1 INTRODUCTION

Step-pool are characteristic bedforms that widely take place in steep mountain streams, occurring when gradients ranges between 3% and 30%, even if not fully developed step-pool sequences have been observed for slopes down to 1% (Montgomery & Buffington, 1997; Lenzi, 2001). Step-pool pattern provides a fundamental role in mountain stream hydraulics, developing the major portion of flow resistance (Abrahams et al., 1995). This flow resistance is essentially due to a loss of kinetic energy, dissipated by roller eddies that occur when water flows over a step rise and plunges into the pool below, creating a tumbling flow (Peterson and Mohanty, 1960). As a result much of the energy which might be otherwise available for sediment erosion is lost, providing a bed stabilization (Ashida et al., 1976). Following this idea some authors (e.g. Davies & Sutherland, 1980; Whittaker & Jaeggi, 1982; Abrahams et al., 1995) have suggested that step-pool streams evolve toward a maximum flow resistance condition in the way to achieve a maximum bed stabilization. In particular Abrahams et al. (1995) suggests that maximum flow resistance occurs when $1 < H/L/S < 2$, where H is the step height, L the step-pool wavelength and S the average bed channel slope. Later field investigations (Wohl et al., 1997; Chartrand & Whiting, 2000; Zimmermann & Church, 2001) have somewhat extended the validity of Abrahams et al. (1995) results suggesting that, where average channel slope is below 5–7%, H/L/S is greater than 2. Notwithstanding several field and laboratory studies have been carried out about step-pool geometry (Whittaker & Jaeggi, 1982; D'Agostino & Lenzi, 1998; Chin, 1999; Chartrand & Whiting, 2000; Lenzi, 2001; Zimmermann & Church, 2001; Gomi et al., 2003; Curran & Wilcock, 2005), very few data (Lee & Ferguson, 2002; Aberle & Smart, 2003; Curran & Wilcock, 2005) are available about the behaviour of hydraulic quantities and so very little is known about the flow resistance developed by step-pool streams. This lack of hydraulic data is due to the difficulties of survey low-frequency high-magnitude formative discharges, especially when step-pool sequences occur in rugged, mountainous and often inaccessible terrain (Chin, 1999).

In the present work we investigate, by means of a theoretical analysis and a laboratory activity, flow resistance when macro-roughness elements are positioned according to a regularly spaced stripe pattern on a layer of relatively fine material, representing a step-pool-like bed arrangement. Experiments are carried out changing size of macro-roughness elements, spacing of the macro-roughness stripes, flow discharge and slope of the flume. Experimental results are interpreted by means of a theoretical model in order to investigate the behavior of flow resistance as a function of hydraulic variables and geometric properties of macro-roughness stripes. Results show that flow resistance reaches a maximum when the spacing between macro-roughness stripes is about 10 times the average macro-roughness height. A statistical analysis based on various field observations of step-pool geometry underlines that this spacing appears to be one of the most frequent occurring in step-pool bed morphology sequences, suggesting that natural mountains stream bed-forms evolve toward a bed configuration maximizing flow resistance.

Copyright © 2006 Taylor & Francis Group plc, London, UK

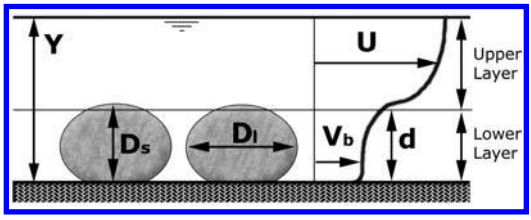


Figure 1. Sketch of a free surface flow over a bed with macro-roughness elements and notations.

2 THEORETICAL BACKGROUND

Flow resistance is herein evaluated by means of a theoretical model developed by Canovaro et al. (in prep.). According to this model, dimensionless Chezy coefficient C is calculated from the average longitudinal velocity profile in the case of steady flow and spatially averaged uniform conditions.

In order to obtain the longitudinal velocity profile, the flow region is assumed to be composed by two layers (Figure 1). A bottom layer, laying on the bed and containing the major part of the macro-roughness elements, in which the flow is dominated by the loss of momentum due to the drag around the obstacles. In such layer of thickness d the flow velocity V_b is relatively low, and approximately constant over the depth. An upper layer, extending up to the free surface, of height $Y-d$; in this layer, characterized by a mean flow velocity U, the flow velocity is relatively high and the major part of flow discharge occurs.

According to the double-layer approach herein adopted, the mean flow velocity profile is characterized by four variables: Y, U, d and V_b. Such quantities allow to estimate flow resistance in the case of macro-roughness flow conditions.

Taking into account a control volume of unit bed area extending from the bed to the water free surface, the two governing equations, continuity and momentum balance, read as follows:

$$q = (Y-d)U + d\psi V_b, \tag{1}$$

$$F_g = F_d + F_s, \tag{2}$$

where q is the flow discharge per unit width, F_g the streamwise water mass weight, F_d the macro-roughness-induced drag force, F_s the surface-induced friction, and ψ a reduction coefficient, being $\psi < 1$, for the bottom layer flow velocity V_b, taking into account the effective flow area among the macro-roughness elements. Therefore ψV_b denotes the mean (apparent) flow velocity in the lower layer. It is worth to notice that the ψ coefficient depends on the effective bed arrangement. For a regularly spaced stripe arrangement of the macro-roughness, the reduction factor is estimated as follows:

$$\psi = 1 - D_m D_l N_u \tag{3}$$

where D_m and D_l are the median axis diameter and the long axis diameter of macro-roughness elements respectively and N_u is the number macro-roughness elements arranged on an unit bed area along the channel.

The streamwise water mass weight component per unit bed area involved in equation (2) is expressed as follows:

$$F_g = \rho g Y S \left(1 - \frac{2 D_s \Gamma}{3Y}\right), \tag{4}$$

where S is the channel slope, Γ is the spatial density (defined as the ratio between the number of macro-roughness elements arranged in an unit bed area, and the maximum number that is possible to arrange in the same area: $\Gamma = N_u / N_{\max}$) and D_s is the short axis diameter of the macro-roughness elements. In eq. (4) the term into brackets acts as a reduction factor in order to exclude from calculations the control-volume fraction occupied by macro-roughness elements. This latter volume is calculated resembling macro-roughness elements to ellipsoids and estimating $N_{\max}$ as the ratio between the unit bed area and the area projection of ellipsoid to the bed.

The drag force per unit bed area can be written as follows:

$$F_d = \frac{1}{2} \rho C_D N_u A_f' V_b^2, \tag{5}$$

where ρ is the water density, C_D the drag coefficient and A_f' the area perpendicular to the flow interested by V_b for a single macro-roughness element, defined as follows:

$$A_f' = \begin{cases} \frac{\pi}{4} D_m d & \text{if} \quad d < D_s \\ \frac{\pi}{4} D_m D_s & \text{if} \quad d \geq D_s \end{cases}. \tag{6}$$

Note that in equation (5) the effective lower layer velocity V_b is employed instead of the apparent velocity ψV_b, being a more appropriate characteristic velocity for evaluating the macro-roughness element drag. Notwithstanding that drag coefficient should reasonably be a function of stripe spacing, due to the lack of information about step-pool stream hydraulics the drag coefficient C_D is assumed constant to 1.5 as suggested by other authors (Robertson et al., 1974; Bathurst, 1996).

Finally, the surface friction per unit bed area takes the following expression:

$$F_s = \rho U^2 \left[\frac{(1-\Gamma)}{C_G^2} + \frac{\Gamma}{C_P^2} \right], \tag{7}$$

being C_G and C_P the Chezy coefficients of a channel bed without macro-roughness elements ($\Gamma = 0$), and

Copyright © 2006 Taylor & Francis Group plc, London, UK

completely covered by macro-scale roughness ($\Gamma = 1$), respectively.

In the present study Y and U are obtained through an experimental activity, while d and V_b are unknowns to be determined by solving the governing equation system composed by the equations (1) and (2).

The mean flow velocity profile is then estimated as follows:

$$\overline{U} = \frac{(Y-d)U^2 + d(\psi V_b)^2}{q}. \quad (8)$$

The dimensionless Chezy coefficient is finally evaluated with the following:

$$C = \frac{\overline{U}}{\sqrt{F_g/\rho}}. \quad (9)$$

3 LABORATORY EXPERIMENTS

The experiments are carried out in a 10 m long, 36.5 cm wide and 50 cm deep glass-walled recirculating tilting flume. The measuring reach is 4 meter long with a bed covered by a layer of granular uniform material having a medium size of 7 mm. In order to dissipate flow disturbances, before the beginning of the measuring reach a transition reach composed by little quarry rubbles is positioned (figure 2). Three different sets of pebbles are used as macro-roughness elements, characterized by different medium axis values according to the Wentworth sedimentological scale Φ, as presented in table 1.

Macro-roughness elements are positioned according to a regularly spaced stripe pattern along the experimental reach. Each stripe is made by pebbles, placed over the granular layer with the long axis D_l in the flow direction and the short axis D_s perpendicular to the bottom of the flume.

For each set of pebbles the "wave length" L, i.e. the spacing between two following stripes, is varied from 6 to 160 cm. Experiments have been carried out for various flow discharges and channel slopes. No bed load occurred during the experiments.

For each run both total water depth Y and mean flow velocity U are measured; several time-averaged values of these quantities are taken during each run along the measuring reach. Water surface elevation is measured by means of a set of 40 piezometers placed below the granular layer; by averaging these 40 values one space-time averaged water depth value is obtained for each run.

Flow velocity is taken in 33 points according to a regular distribution along one wavelength across the middle stripe (figure 3), by means of a micro-propeller meter. As for the water surface elevation measurements, one space-time averaged velocity value is obtained for each run. Each value is the result of a 400 velocity time-averaging readings, corresponding to a measurement time of 10 seconds.

The experimental activity is composed by 147 runs divided into 17 experiments, each experiment is characterized by either different stripe height, bed slope or flow discharge. A summary of the performed experiments is reported in table 2.

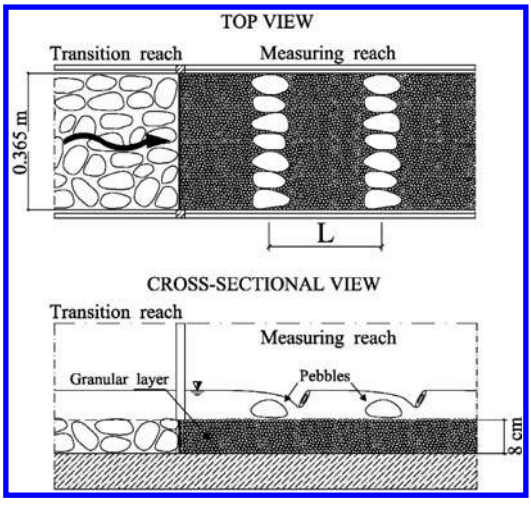


Figure 2. Sketch of the experimental set-up.

Table 1. Mean geometrical properties of the pebbles employed.

Set of pebbles	Φ [–]	D_s [cm]	D_m [cm]	D_l [cm]
1	−5.25	2.6	3.8	5.5
2	−5.75	4.3	5.4	8.0
3	−6.25	5.3	7.6	9.8

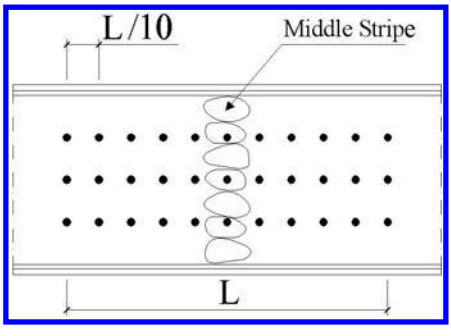


Figure 3. Sketch of the points of velocity measurement.

Copyright © 2006 Taylor & Francis Group plc, London, UK

Table 2. Summary of performed experiments.

Experimental series	Φ [–]	S [–]	q [l/s/m]	L [m]
I	−5.25	0.025	20.0	0.06–0.6
II	−5.75	0.010	20.0	0.08–0.8
III	−5.75	0.010	38.4	0.08–0.8
IV	−5.75	0.025	38.4	0.08–0.8
V	−6.25	0.025	38.4	0.10–0.8
VI	−5.75	0.025	13.0	0.08–1.6
VII	−5.75	0.025	20.0	0.08–1.6
VIII	−5.75	0.030	13.0	0.08–1.6
IX	−5.75	0.030	20.0	0.08–1.6
X	−5.75	0.030	22.6	0.08–1.6
XI	−5.75	0.040	14.3	0.08–1.6
XII	−5.75	0.040	17.4	0.08–1.6
XIII	−5.75	0.040	20.0	0.08–1.6
XIV	−5.75	0.040	22.6	0.08–1.6
XV	−5.75	0.060	17.4	0.08–1.6
XVI	−5.75	0.060	20.0	0.08–1.6
XVII	−5.75	0.060	22.6	0.08–1.6

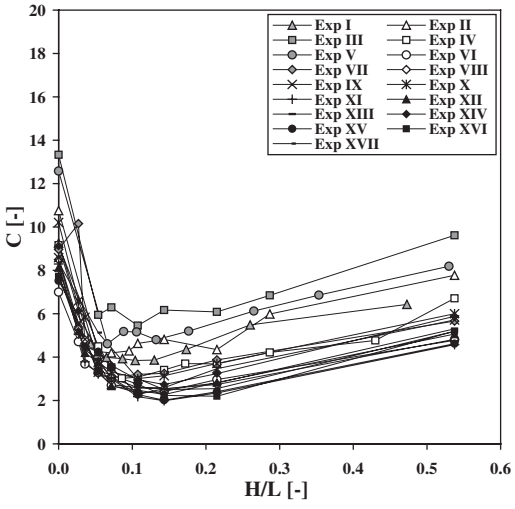


Figure 4. Chezy coefficient (C) as a function of ratio stripe height (H) to stripe wavelength (L).

4 EXPERIMENTAL RESULTS

Results obtained during the experimental activity described in the previous section are here presented.

In figures 4 and 5 dimensionless Chezy coefficient (C) and ratio of drag shear stress (τ_d), defined as the drag force F_d per unit bed area, to total shear stress (τ_g), defined as the total force F_g per unit bed area, are presented as functions of the ratio of stripe height (H) taken equal to D_s to macro-roughness stripe wavelength (L). Both plots show a non monotonic behaviour of the investigated quantities for all the experimental

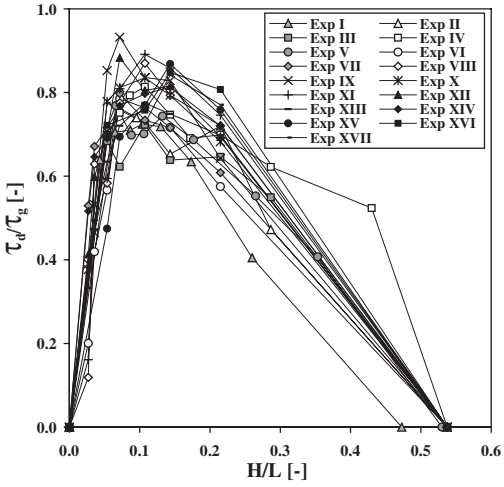


Figure 5. Ratio of drag shear stress (τ_d) to total shear stress (τ_g) as a function of the ratio stripe height (H) to stripe wavelength (L).

series. In particular it is apparent the existence of an "optimal" dimensionless spacing value (H/L), ranging around 0.15, maximising both flow resistance and ratio drag shear stress to total shear stress.

When maximum flow resistance conditions are attained C is about 2–3 times smaller than in the case of no macro-roughness presence ($H/L = 0$) but note that C is also smaller than in the case when the spacing between stripes is minimum ($L = D_l$).

When flow resistance is maximum, drag shear stress is about 80% of total shear stress, suggesting that in this condition stripes develop a fundamental role in energy dissipation while surface resistance plays an almost negligible role.

Notwithstanding the presence of some scattering in the data points, it seems that flow discharge, flume slope and stripe height do not significantly affect the value of the observed "optimal" dimensionless spacing H/L. On the other hand, for a given H/L, flow resistance seems to increase with stripe height and bed slope while it decreases with the flow discharge (compare figure 4 with table 2).

The presence of an "optimal" H/L value maximizing flow resistance has been also observed in other investigations (e.g. Johnson & Le-Roux, 1946; Wohl & Ikeda, 1998) devoted to study the influence on flow resistance C and on equivalent roughness size K_s of macro-roughness positioned according to a regularly spaced stripes pattern, under various geometric and flow conditions. In figures 6 and 7 two comparisons respectively with Wohl & Ikeda (1998) and Johnson & Le-Roux (1946) experiments in the case of macro-roughness composed by transverse rectangular ribs are presented. The comparisons show a fairly good

Copyright © 2006 Taylor & Francis Group plc, London, UK

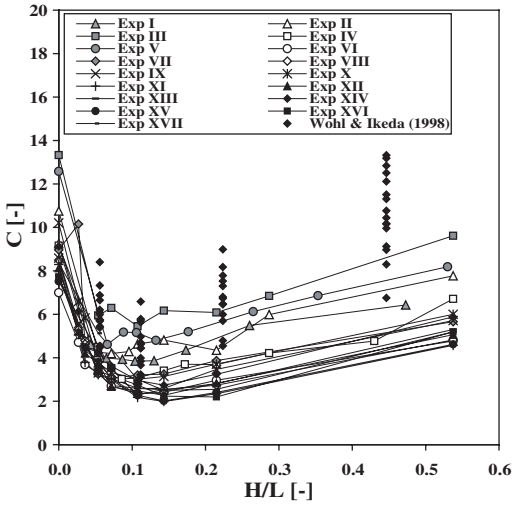


Figure 6. Comparison with Wohl & Ikeda (1998) experiments.

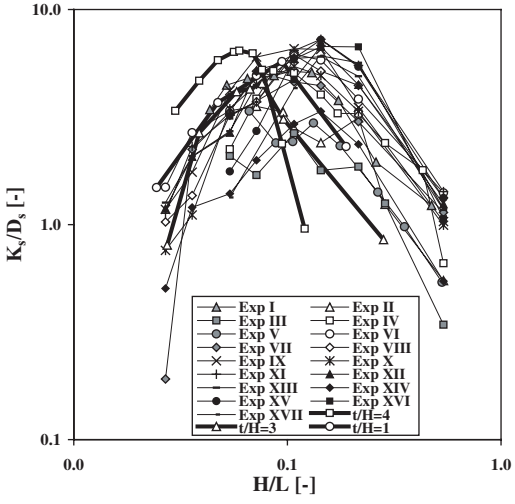


Figure 7. Comparison with Johnson & Le-Roux (1946) experiments (solid lines); for the present experiments t/H is around 2, being t equal to D_l and H equal to D_s.

agreement; in particular the presence of an "optimal" spacing value maximizing flow resistance is revealed in both cases when H/L is around 0.15 as found in the present study. These findings suggest that the present experiments are representative of a common behaviour in the dissipative mechanism associated to regularly spaced stripes.

The presence of a maximum in flow resistance was also found for macro-roughness spatial arrangements different from the one employed in the present study. Rouse (1965) indicates, in the case of a regular pattern of macro-roughness disposition, that the maximum flow resistance is achieved when macro- roughness spatial density (the sum of all basal areas of the macro-roughness elements arranged in an unitary bed area) is ranging between 0.15–0.20. As pointed out by Morris (1971) for flow in closed conduits, the presence of a maximum in flow resistance may be explained in terms of a different behaviour of flow motion in relation to the spacing value (or to the spatial density) of macro-roughness stripes. For high spacing values, when macro-roughness stripes are "isolated", motion might be regarded as a "non wake interfering"-like, while for low spacing values, the vortex generation and dissipation associated to a stripe is no complete before the flow meets the next stripe.

5 CONCLUDING REMARKS

The present investigation shows that maximum flow resistance in the case of macro-roughness positioned according to regularly spaced stripes occurs when the spacing between the stripes is about 10 times the stripe height. In this condition flow resistance consists almost entirely in form resistance, the latter is associated to the plunging of flow downstream each stripe and the formation of roller eddies developing in the pool between two successive stripes.

This mechanism can be commonly observed in natural step-pool sequences (Abrahams et al., 1995; Chin, 1998; Chartrand & Whiting, 2000) unless for high flow discharges when the step-pool shape is hidden. Even if the present regular spaced stripe pattern is only a rough schematization of a natural morphology, in the light of the above findings it seems reasonable to consider some general analogies between flow resistance developed by natural step-pool sequences and the laboratory results herein presented.

In figure 8 a statistical frequency distribution of natural step-pool gradient (H/L) based on 177 field and laboratory data about step-pool geometry, obtained from various authors (Whittaker & Jaeggi, 1982; Abrahams et al., 1995; D'Agostino & Lenzi, 1998; Chin, 1999; Chartrand & Whiting, 2000; Lenzi, 2001; Zimmermann & Church, 2001; Gomi et al., 2003; Curran & Wilcock, 2005) is presented.

It appears that the range of most common spacing values observed in step-pool sequences is very close to the "optimal" spacing value that maximizes flow resistance in the present flume experiments. This finding seems to suggest that natural step-pool sequences evolve toward a bed configuration maximizing flow resistance, in order to achieve a bed stabilization (Abrahams et al., 1995), since much of the energy which might otherwise be available for sediment erosion is lost (Ashida et al., 1976).

The latter results suggest to consider as representative of real step-pool sequences only the presentflume

Copyright © 2006 Taylor & Francis Group plc, London, UK

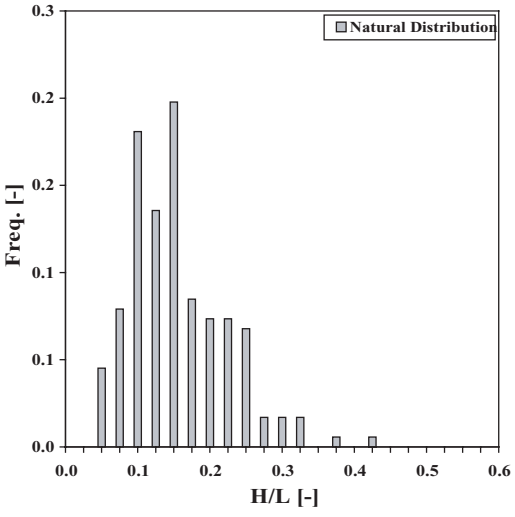


Figure 8. Statistical distribution of the ratio of step height H to step spacing L observed in natural step-pool beds.

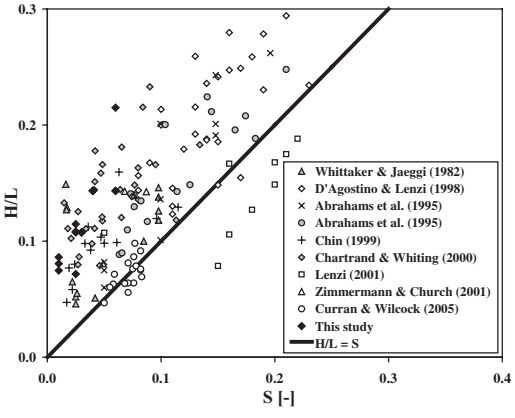


Figure 9. Flume and field measurements of step spacing L, step height H and channel slope S. The line represents $H/L = S$.

data whose macro-roughness geometry maximizes flow resistance.

In figure 9 a comparison between geometric characteristics of employed flume pattern and natural step-pool sequences, showing the local step-pool gradient H/L as a function of channel slope S, confirms the hypothesis of considering employed pattern as a laboratory model for step-pool sequences. From the plot it appears that the present flume ($S - H/L$) pairs fall in the same range of real step-pool sequence observed geometry. In figure 9 the line for $H/L = S$ is also reported, a somewhat different behavior is associated to the data reported by Lenzi (2001) as in general step-pool patterns are characterized by $H/L > S$.

Notwithstanding the present results refers to a rough representation of step-pool morphologies, the latter findings seem to suggest the present model may be extended to provide an interpretation of flow resistance developed by natural step-pool morphologies. These development are in progress.

ACKNOWLEDGEMENTS

The Authors are grateful to Prof E. Paris, University of Florence (Italy), for his valuable comments and suggestions. The Authors wish also to thank Elena Facchini and Luca Nelli, who have carried out a part of experimental activity herein presented.

The "CERAFRI – CEntre of Research and Advanced education For hydrogeological RIsk prevention" is kindly acknowledged for its assistance.

REFERENCES

Aberle, J. & Smart, G.M. 2003. The influence of roughness structure on flow resistance on steep slopes. *Journal of Hydraulic Research*, *IAHR*, 41 (3): 259–269.

Abrahams, A.D., Li, G. & Atkinson, J.F. 1995. Step-pool stream: Adjustment to maximum flow resistance. *Water Resources Research*, 31 (10): 2593–2602.

Ashida, K., Takahashi, T. & Sawada, T. 1976. Sediment yield and transport on a mountainous small watershed. *Disaster Prevention Research Institute Bulletin*, Kyoto University, 26 (240): 119–144.

Bathurst, J.C. 1996. Field measurement of boulder flow drag. *Journal of Hydraulic Engineering*, 122 (3): 167–169.

Canovaro, F., Paris, E. & Solari, L. Analysis of resistance of flow over macro-scale roughness. *In preparation*.

Chartrand, S.M. & Whiting, P.J. 2000. Alluvial architecture in headwater streams with special emphasis on step-pool topography. *Earth Surface Processes and Landforms*, 25: 583–600.

Chin, A., 1998. On the stability of step-pool mountain streams. *The Journal of Geology*, 106: 59–69.

Chin, A. 1999. The morphologic structure of step-pools in mountain streams. *Geomorphology*, 27 (3–4): 191–204.

Curran, J.C. & Wilcock, P.R. 2005. Characteristic dimensions of the step-pool bed configuration: An experimental study. *Water Resources Research*, 41.

D'Agostino, V. & Lenzi, M.A. 1998. La massimizzazione della resistenza al flusso nei torrenti con morfologia a step-pool. In *XXVI Convegno di Idraulica e Costruzioni Idrauliche*, Catania, ITALY, Sept. 9–12, Vol. 1, 281–293.

Davies, T.R. & Sutherland, A.J. 1980. Resistance to flow past deformable boundaries. *Earth Surface Processes*, 5 175–179.

Gomi, T., Sidle, R.C., Woodsmith, R. & Bryant, M.D. 2003. Characteristics of channel steps and reach morphology in headwater streams, southeast Alaska. *Geomorphology*, 51: 225–242.

Johnson, J.W. & Le-Roux, E.A. 1946. Discussion of Powell R. W. 'Flow in a channel of definite roughness'. *Transactions, ASCE*, 111: 531–566.

Lee, A.J. & Ferguson, R.I. 2002. Velocity and flow resistance in step-pool streams. Geomorphology, 46: 59–71.

Copyright © 2006 Taylor & Francis Group plc, London, UK

Lenzi, M.A. 2001. Step-pool evolution in the Rio Cordon, Northeastern Italy. *Earth Surface Processes and Landforms*, 26: 991–1008.
Montgomery, D.R. & Buffington, J.M., 1997. Channel-reach morphology in mountain drainage basins. *Geological Society of America Bulletin*, 109 (5): 596–611.
Morris, H.M. & Wiggert, J.M. *Applied hydraulics in engineering*. New York: John Wiley & Sons, inc.
Peterson, D.F. & Mohanty, P.K. 1960. Flume studies of flow in steep, rough channels. *Journal of the Hydraulics Division*, ASCE, 86: 55–79.
Rouse, H. 1965. Critical analysis of open channel resistance. *Journal of the Hydraulic Division*, ASCE, 91 (4): 1–25.
Whittaker, J. & Jaeggi, M. 1982. Origin of step pool system in mountain streams. *Journal of the Hydraulics Division*, *ASCE*, 108: 758–773.
Wohl, E.E. & Ikeda, H. 1998. The effect of roughness configuration on velocity profiles in an artificial channel. *Earth Surface Processes and Landforms*, 23: 159–169.
Wohl, E.E., Madsen, S. & MacDonald, L. 1997. Characteristics of log and clast bed-steps in step-pool streams of northwestern Montana, USA. *Geomorphology*, 20: 1–10.
Zimmermann, A. & Church, M. 2001. Channel morphology, gradient profiles and bed stresses during flood in step-pool channel. *Geomorphology*, 40 (3–4): 311–327.

Copyright © 2006 Taylor & Francis Group plc, London, UK

Three-dimensional properties of laboratory sand waves obtained from two-dimensional autocorrelation analysis

H. Friedrich, B.W. Melville, S.E. Coleman & T.M. Clunie
The University of Auckland, New Zealand

V.I. Nikora
University of Aberdeen, Engineering Department, Aberdeen, Scotland, UK

D.G. Goring
National Institute of Water and Atmospheric Research, Christchurch, New Zealand

ABSTRACT: A comprehensive data set of 3-D sand waves developing from a flat bed to equilibrium stage (known as the research program SWAT.nz – Sand Waves and Turbulence New Zealand) was obtained during investigations in a 5-ft-wide flume at The University of Auckland. The recorded sand bed is treated as a continuous field of sand-bed elevations, rather than subdivided into discrete sand waves. Aiming at 3-D interpretation of the random field of sand-bed elevations, 2-D autocorrelation analyses are introduced. It is shown that the 2-D autocorrelation function approach is a useful tool to depict 3-D characteristics of sand waves and their further potential is outlined.

1 INTRODUCTION

Best (2004) gives an up-to-date description of the complexity of the field of underwater bed morphology, and refers to the lack of knowledge of the interaction of 3-D dune shape and the surrounding flow field. He notes that a better understanding of the 3-D behavior of sand forms in uniform flow conditions is needed to provide information for future research aimed at combining the complex morphodynamic and hydraulic features, which are inherent during the development of sand waves.

In order to gain advances in the understanding of 3-D sediment and flow-field interaction, progress must be made in describing 3-D characteristics of subaqueous bed forms.

Allen (1968) provided an earlier classification scheme for the 3-D nature of bed forms. He observed visually the position of the crest line in a plane parallel to the water surface (planimetric view) and distinguished the crest line characteristics as straight, sinuous, caternary, linguoid, cuspate, or lunate.

Ashley (1990) proposes to use the term 'dune' for all large-scale subaqueous bed forms, the wide variety which are subject to effects such as sediment size, water levels, unsteady and reversing flows and channelization. As one of the characteristics to describe the term with more detail, the dunes were distinguished according to their shape into 2-D dunes, which develop at lower flow speeds, and 3-D dunes, which occur at higher speeds.

In contrast to previous technology that did not allow 3-D dune information to be gained very easily, the advances in the last decades now enable us to record and analyze 3-D dune fields.

2-D sand waves can be comfortably analyzed using one transect parallel to the flow, mostly recorded along the centre line of the channel. For 3-D dunes, an analysis technique covering the whole surface area should provide enlightening new information about the pattern.

Even though technological advances have enabled us to record 3-D surfaces, few researchers have previously tried to follow up this extended area of interpretation of submerged sediment waves.

One of the most recent works was by Venditti (2003). He describes features of the planimetric view of sand waves with the help of video analysis. He used the non-dimensional span Λ_{NDS} as a parameter (see Fig. 1) to describe the 3-D characteristics of bed forms.

A critical value of 1.2 for the non-dimensional span is proposed to distinguish between 2-D and 3-D bed forms. His work is based on the pioneering work of Allen (1968) nearly 40 years earlier. The use of

Copyright © 2006 Taylor & Francis Group plc, London, UK

spatial recognition software prevents this method gaining universal status, along with difficulties associated with identifying certain crest lines, which is a very subjective procedure (see Fig. 2).

In the present paper it is proposed to treat a recorded 3-D sand-bed elevation field as a random field rather than discrete sand waves, following Nikora et al. (1997) who used longitudinal and transverse spectra, correlation and structure functions to describe statistical sand wave dynamics.

2 EXPERIMENTAL INVESTIGATION

A 5-MHz Seatek ultrasonic ranging system, comprising 31 transducers (see Fig. 3), was employed for the measurements of the sand bed. The moving probe arrangement, which was traveling up-and-down the flume on a moving carriage and which measured the 3-D elevations of a developing sand bed, was introduced in Friedrich et al. (2005), a methodology paper describing experiments undertaken in a narrow 440-mm-wide flume. This paper utilizes data obtained during experiments in a larger 5-ft-wide flume. Brief explanatory notes illustrating additional to Friedrich et al. (2005) 5-ft-flume methodology are given below.

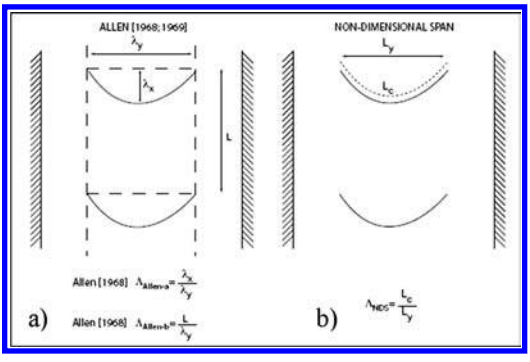


Figure 1. (a) Ratio Λ of λ_x (the stream wise distance that the lobes extend downstream) and λ_y (the cross-stream distance between lobes of a crest line), after Allen (1968), and (b) the non-dimensional span Λ_{NDS} for closing crest lines L_c and L_y, after Venditti (2003).

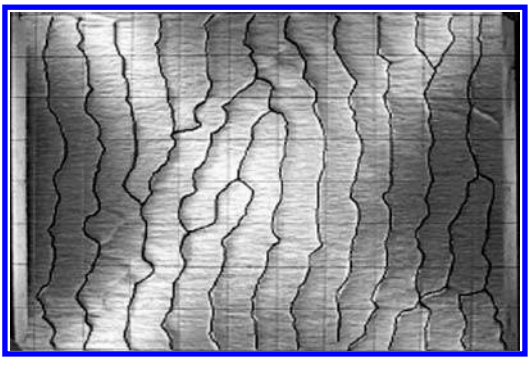


Figure 2. Identification of crest lines in order to determine the non-dimensional span, after Venditti (2003).

The 31 transducers were interrogated sequentially (starting from sensor 1 and finishing with sensor 31), with the same sequence repeated every 0.2-s. The sensors were mounted on a skewed grid (see Fig. 4) to allow for the movement of the carriage in the time interval between readings of the components of the sensor array. This ensured that measurements were obtained on an equivalent rectangular recording grid (Fig. 5). With a carriage velocity = 0.33-m/s, the rectangular recording grid shown in Figure 4 was generated.

Each mobile-bed experiment (flat sand bed to equilibrium bed forms) utilizing moving probes was carried out over several hours. Experimental parameters for these experiments are given in Table 1.

The sequence of operation was as follows. Initially, the moving carriage with submerged sensors traveled downstream for 56-s. Then the carriage was stationary

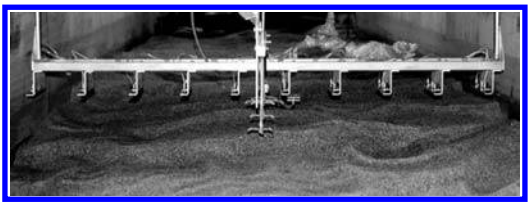


Figure 3. Arrangement of the moving probes across the 5-ft flume. Four Acoustic Doppler Velocimeters (ADVs) are placed in front of the acoustic sensors in the centerline of the flume to measure the flow field at different water depths.

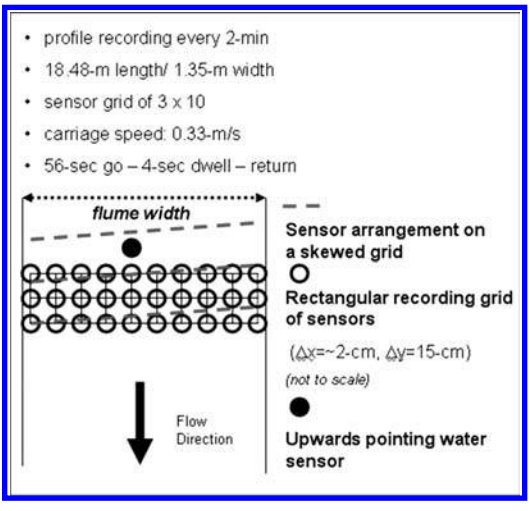


Figure 4. Moving probe arrangement for the 5-ft flume.

Copyright © 2006 Taylor & Francis Group plc, London, UK

for a waiting period of 4-s, which was used to move the sensors up out of the water, in order to reduce the water surface disturbance when traveling upstream. Afterwards, the carriage traveled upstream for 56-s. After a further waiting period of 4-s, and submerging the sensors again, the carriage moved downstream into the second cycle. Each cycle duration was two minutes. The experiment was continued with repeated cycles until appropriate bed-form development had occurred. Recording of the bed profiles occurred only during the downstream-moving portion of each cycle, based on the configuration of the recording grid. The frequency of recording of bed profiles was one profile every two minutes. As one can see from Figure 4, sensor no. 31 was inverted and used to record the water surface elevation, meaning that only 30 sensors were used to record bed elevations. Overall, ten longitudinal profiles with a transverse resolution of 150-mm were recorded over each sweep of a length of 18.48-m.

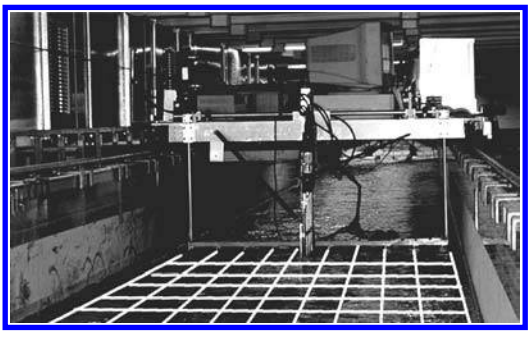


Figure 5. Schematic display of sand bed elevation recording grid in the 5-ft flume. Moving carriage is traveling downstream (recording) and upstream (sensors out of the water) along the flume over a length of 18.48-m.

3 METHODS

3.1 *Data processing*

Firstly, the ten longitudinal profiles recorded for each sweep along the flume were considered individually. Filtering methods were applied to remove faulty signals and to take into account the detection of suspended particles. Afterwards, interpolation procedures were used to fill the gaps in the profiles. The sand-bed elevation surfaces were detrended linearly for every individual snapshot. Then the following autocorrelation procedures were applied with the help of Matlab routines. The sand-bed elevations were considered as a 3-D random field.

3.2 *2-D Autocorrelation functions*

As a simple introduction to correlation functions, one can say: everything is related to everything else, but like things are more related than unlike things. For a vivid description of one case of correlation functions, the spatial auto-correlation function showing the correlation of a variable with itself through space), one can say:

- if there is any systematic pattern in the spatial distribution of a variable, it exhibits spatial autocorrelation;
- nearby or neighboring areas being more alike gives positive spatial autocorrelation;

Table 1. Experimental parameters.

Run Name	d_{50} [mm]	D [m]	T [°C]	S_e [-]	Run Duration [hh:mm:ss]	Equilibrium	U_{avg} [m/s]	Fr [-]	Re ($\times 10^3$)
wsc07b	0.85	0.15	22	0.292	05:50:00	no	0.38	0.313	190
wsc85a	0.85	0.15	18	0.350	04:44:00	yes	0.43	0.354	215
wsc85b					05:34:00	yes			
wsc10a	0.85	0.15	18	0.394	05:02:00	yes	0.48	0.396	241
wsc10b					05:16:00	yes			
wsc115	0.85	0.15	18	0.430	03:58:00	yes	0.57	0.470	286
wsc115					03:56:00	yes			
wdc25a	0.85	0.52	17	0.058	07:02:00	no	0.56	0.248	692
wdc25b					05:34:00	no			
wdc30a	0.85	0.52	17	0.146	05:18:00	yes	0.70	0.310	865
wdc33a	0.85	0.52	17	0.190	06:54:00	yes	0.75	0.332	926
wdc33b					02:26:00	no			
wdc35a	0.85	0.52	17	0.219	06:14:00	yes	0.81	0.359	1000
wdc35b					04:04:00	yes			

Note: Kinematic viscosity $\nu = 0.000001$-m^2/s; Specific gravity s = 2.65; Critical shear velocity u$\cdot_c$ ($d_{50} = 0.85$-mm) = 0.0215 m/s.
d_{50} Median grain size, D Flow Depth, T Water Temperature, S_e Flume Slope, U_{avg} Average Flow Velocity, Fr Froude Number, Re Reynolds Number.

Copyright © 2006 Taylor & Francis Group plc, London, UK

- negative autocorrelation arises for patterns in which neighboring areas are unlike, and
- fully random signals or fields exhibit no spatial autocorrelation.

A full-dimensional correlation function $R(\Delta x, \Delta y, \tau)$ (spatial and temporal) is practically difficult to evaluate. In the past researchers used 1-D autocorrelation functions (spatial and temporal) to determine the wavelength of bed forms and the duration how long it takes for a bed form to move past a stationary object. Often a spatial or temporal longitudinal centerline flume profile of a sand bed has been used for the analysis (Andreotti et al. 2006; Callander 1978; Coleman & Eling 2000).

The normalized spatial 1-D autocorrelation function R at $\Delta x = k\delta x$ between two values of sand-bed elevation z at distances x_i and x_{i+k} along the flume ($i = 1$ to $N-k$, with N equal to the number of points in the data vector z along x) is defined as:

$$R(\Delta x,0,0) = \frac{\sum_{i=1}^{N-k}(z(x_i)-\bar{z})(z(x_{i+k})-\bar{z})}{\sigma^2} \quad (1)$$

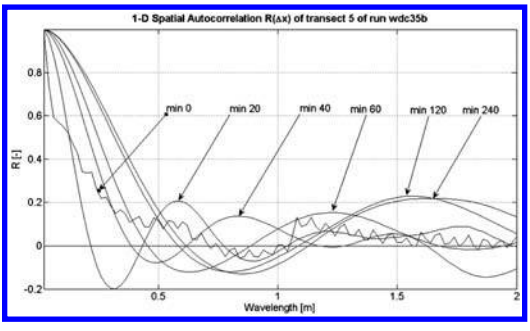


Figure 6. 1-D spatial autocorrelation function for selected times of run wdc35b centreline, developing from flattened sand bed.

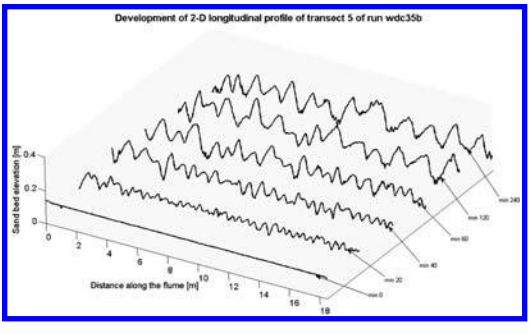


Figure 7. Corresponding centerline longitudinal sand bed profiles for the autocorrelation function of Figure 6.

With $\bar{z}$ being the mean value of the data vector z along the flume, and σ being the standard deviation. The wavelength can be generally obtained by the position of the first peak of the autocorrelation function. 1-D spatial autocorrelation functions (see Figure 6) and the corresponding bed profiles (see Figure 7) are shown below for selected times of run wdc35b.

Having recorded a random field along and across the flume, one can apply the 2-D spatial autocorrelation function defined as:

$$R(\Delta x,\Delta y,0) = \frac{\sum_{i=1}^{N-k}\sum_{j=1}^{M-l}(z(x_i,y_j)-\bar{z})(z(x_{i+k},y_{j+l})-\bar{z})}{\sigma^2} \quad (2)$$

with z being a 2-D data matrix along x and y, and the correlation being done at $\Delta x = k\delta x$ and $\Delta y = l\delta y$ between measurement points (i,j) and $(i+k, j+l)$. As a result, one obtains the 1st Quadrant ($(\Delta x >= 0, \Delta y >= 0)$ autocorrelation function of Figure 8.

Mirroring the information on the x and y axes results in the typical 2-D autocorrelation function, as is shown in Figure 9 for minute 240 of run wdc35b.

The locations of hills and troughs in all directions of the 2-D autocorrelation plot shows the 3-D character of the recorded sand bed.

For the evaluation of 2-D autocorrelation functions, the restricted width of the flume prevents a sufficient number of data points across the flume to see a fully developed autocorrelation function with pronounced fluctuating characteristic in all directions. For the start of sand wave development, starting from a flat sand bed, which is exposed to a uni-directional water flow, the sediment transport's main direction is downstream and therefore the crests of the developing sand waves keep roughly perpendicular to the flume wall (Fig. 10). Once a certain development is reached, either the flume walls or the flow depth act as a restricting factor in further growth of sand waves.

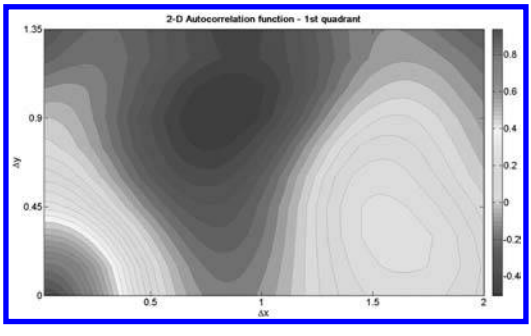


Figure 8. Contour plot of 2-D spatial autocorrelation function for 1st quadrant ($\Delta x >= 0, \Delta y >= 0$) for min 240 of run wdc35b. See colorbar for correlation values. Axes dimensions in m.

Copyright © 2006 Taylor & Francis Group plc, London, UK

As one expects, a random sand-bed field that has crest lines parallel to the flow (see Fig. 10), as happens at the beginning of sand wave development or in flumes with a small width, will reveal a 2-D autocorrelation function as seen in Figure 11.

The 2-D autocorrelation function in itself shows a very 2-dimensional character, as the correlation across the flume is very similar at every transect across the flume. Only minor changes between the transects are displayed in an uneven outline across the autocorrelation function.

As soon as the crest lines start to bend and lose their parallel character, with individual transects across the flume showing more differences compared to each other, the typical peak and trough characteristics of the 2-D autocorrelation function (e.g. Fig. 9), revealing 3-D characteristics of the random field.

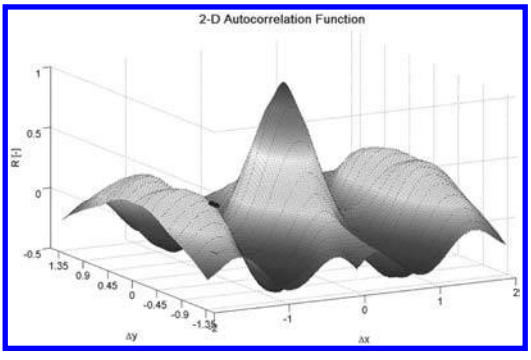


Figure 9. Typical 2-D spatial autocorrelation function displayed for all four quadrants. Minute 240 of run wdc35b is shown. Axes dimensions in m.



Figure 10. Recorded 6.25-m long and 0.175-m wide dune bed. Red indicates crests, and yellow troughs. The crest lines are parallel to each other and perpendicular to the flume wall. These measurements in a small 440-mm wide flume were discussed in Friedrich et al. (2005).

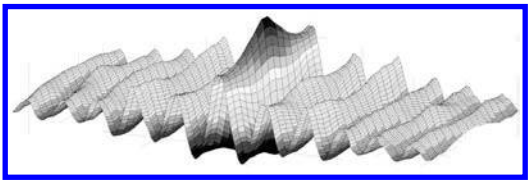


Figure 11. Schematic display of 2-D spatial autocorrelation function for a 2-D dune bed as shown in Figure 10. The autocorrelation function has a very pronounced 2-D character.

In an ideal case, the first peak of the contours along and across the flume could be used to determine the 3-D characteristics of a bed-form field, including the dominant wavelength along the flume and separation between individual bed forms across the flume. As the development of the bed forms across the flume is restricted by the flume walls, the bed forms are not free to spread out in that direction. Therefore one can not use the first peak in all directions to determine 3-D characteristics of bed forms. Nevertheless, by looking at the surface of the 2-D autocorrelation function (see Fig. 9) one can see, that the centre cone shows distinctive features, which relate to 3-D characteristics and changes in the texture of the observed sand bed field.

Based on the assumption that the slopes of the centre cone are constant between the correlation value of 1 and the first negative peak (see Fig. 6), a horizontal cut at any correlation level between roughly 0.7 and 0.2 results in obtaining an ellipse shape along the horizontal cut (see Fig. 12). The main objective for choosing the cut-off value is the closure of the ellipse, which is describing the centre cone. After the cut-off value is determined, ellipses describing bed-form parameters can be calculated, which provide information of the 3-dimensionality of the random field of sand bed elevations as well as information about the direction of the bed-from field.

Taking into account the uniformity of the slope of the cone, the ellipticity of the surface at the contour level will provide measured 3-dimensionality of the bed-form field.

3.3 *Determination of uniformity*

To determine the appropriate contour levels where the ellipse will be closed, contour plots such Figure 13 were visually evaluated.

From Figure 6 one can see that a correlation level of 0.4 ensures information on longitudinal levels even

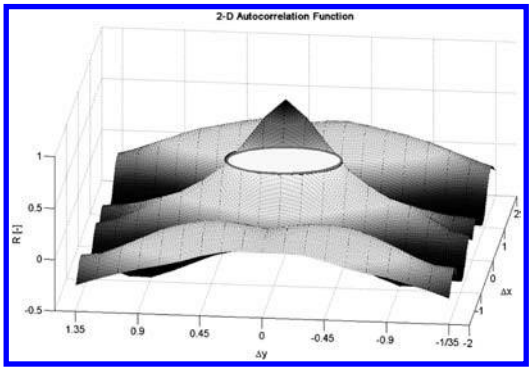


Figure 12. Ellipse shape of the horizontal cut of the centre cone of the 2-D autocorrelation functions (run wdc35b, min 240, correlation level 0.4).

Copyright © 2006 Taylor & Francis Group plc, London, UK

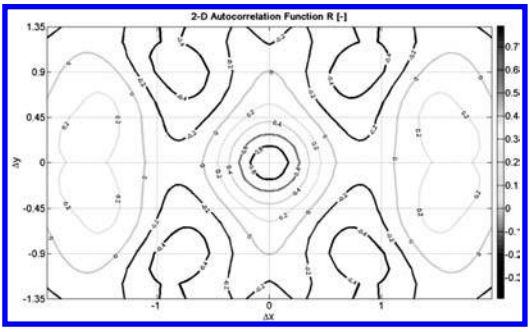


Figure 13. Typical contour plot at a certain time of a recorded sand-wave bed (min 240 of run wdc35b).

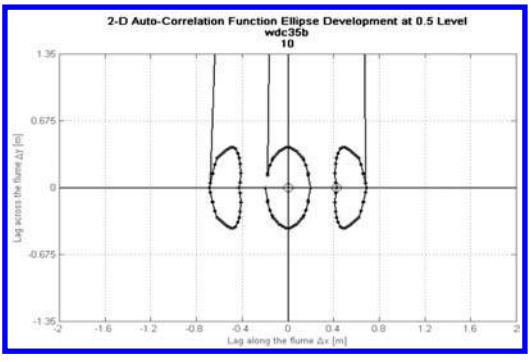


Figure 14. Determination of contours at a correlation level of 0.5. The fluctuating nature of the autocorrelation function causes several contours to display, where only the centre cone is important for the present calculations (run wdc35b, minute 10 of development).

for early times in the development of sand waves. Furthermore, this gains closed ellipses around the centre cone of 2-D autocorrelation functions in all directions. For the early minutes of development from a flat sand bed, there might however be no information about the shape of the centre cone, as the chosen level does not close completely around the centre cone for the 2-D dunes at that time.

Figure 14 shows that contours at the threshold level also exist outside the main centre cone, these contours being caused by the fluctuating nature of the 2-D autocorrelation function. In order to access the ellipticity of the centre cone, a routine was developed in Matlab to delete secondary cut-off contour-level information and yield only the shape of the central contour (see Fig. 15).

Determination of information about the ellipticity of the centre cone at a certain correlation level is done accordingly to Goring et al. (1999). Following their procedure for 2-D structure functions, we determined for the central ellipse (see Fig. 16):

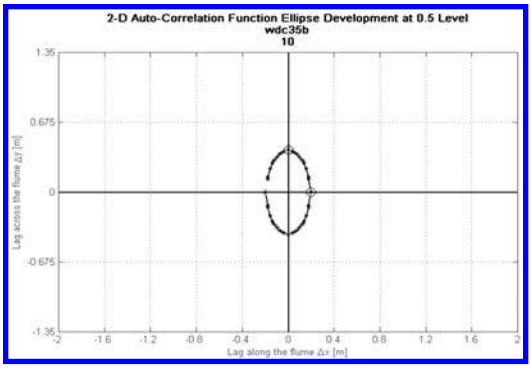


Figure 15. Filtering method applied for multiple correlation peaks as displayed in Figure 14. Afterwards only the outline of the centre cone is left (run wdc35b, minute 10 of development).

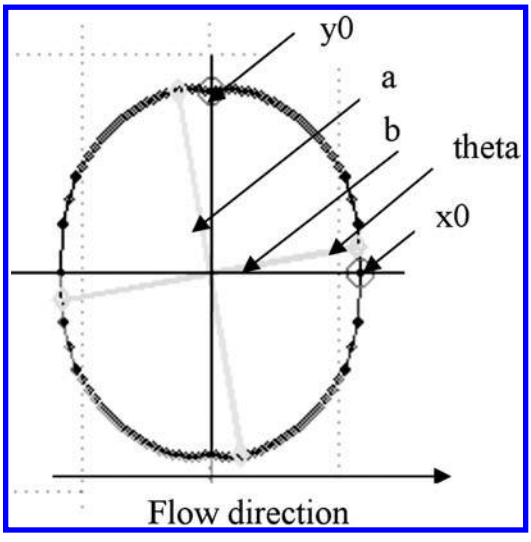


Figure 16. Schematic display of geometrical information describing the shape of the ellipse obtained when cutting through the centre cone of the 2-D autocorrelation function at a certain correlation level.

- *x0*, the longitudinal distance defined by the chosen correlation value.
- *y0*, the transverse distance defined by the chosen correlation value.
- *a*, the major axis of the ellipse at the chosen correlation value.
- *b*, the minor axis of the ellipse at the chosen correlation value.
- *theta*, the angle of rotation of the ellipse describing the cone shape.

3-D properties of the shape of the centre cone of the 2-D autocorrelation functions are principally described by the ratios $x0/y0$ and a/b, as well the

Copyright © 2006 Taylor & Francis Group plc, London, UK

angle of rotation of the ellipse, *theta*. Owing to the constant near-origin slopes of a correlation surface, the ratios and theta should not significantly depend on the threshold correlation levels selected. Indeed test have shown this to be the case.

4 RESULTS AND DISCUSSIONS

4.1 *General interpretation for all runs*

The experimental runs of Table 1, were analyzed using the 2-D autocorrelation function. Sand-bed elevation fields of a length of 18.48-m and a width of 1.35-m exist for every second minute over the run durations (from flat bed conditions) given in Table 1. For each 3-D bed surface recorded, the ellipticity of the centre cone of the 2-D autocorrelation surface was calculated.

Generally, three different cases of ellipticity can be distinguished according to their $x0/y0$ ratio (see Fig. 17):

(a) With a ratio of 1, the shape of the cone is circular and isotropy exists. This stage of isotropy is rarely achieved, as it indicates a uniform spread of the bed forms along as well as across the flume.

(b) A ratio of less than 1 typically occurs early on in development, when neither the flume width nor the water depth restrict sand wave development. This shape indicates the formation of 2-D dunes. They are characterized by crest lines perpendicular to the flow across the whole width of the flume. After a certain stage of development is reached, which is indicated by reaching a minima in the a/b ratio for the ellipse shape, the ellipse is growing again and 3-D dunes develop. With growing sand wave length, the flume walls act as a restricting factor and limit sand wave separation across the flume, keeping the ratio $x0/y0 < 1$. The flow field is constricted by the walls to emphasize uni-directional flow downstream.

(c) A ratio larger than 1 indicates that the flow depth, and not the flume walls, act as the restricting factor of the 3-D development of bed forms. Sand waves are broken up across the flume and a very pronounced 3-D sand bed field can develop.

One also needs to take into account the rotation of the ellipse (see) as well as the values of the size of the ellipse. The rotation *theta* indicates the main average direction of the crest lines, and the values of a and b indicate the relative major and minor magnitudes of the sand wave lengths.

Therefore, with the help of analyzing the elliptical shape of the centre cone of the 2-D autocorrelation function, results can be used to see the transition from 2-D to 3-D dunes. Furthermore, for bed-form development in the later stages, restrictions in the development of bed forms can be easily associated to either the flow depth or the flume walls. Both scenarios will be discussed in the following.

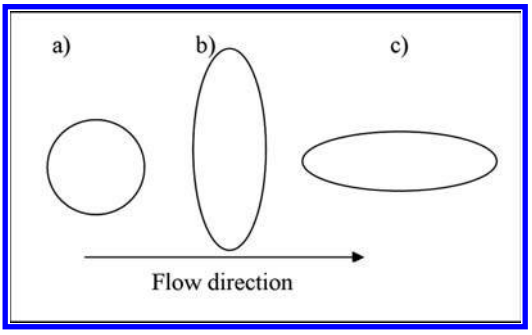


Figure 17. Different cases of ellipticity.

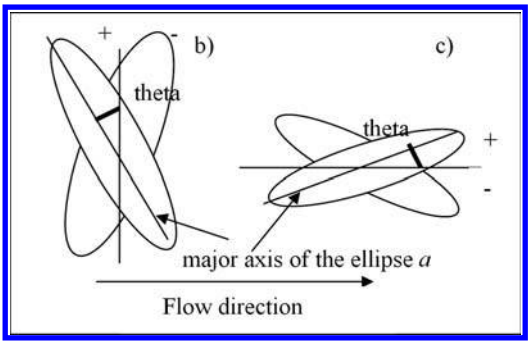


Figure 18. Rotation of the ellipse for cases (b) and (c) from Figure 17 indicates the main direction of the average crest line. Rotation *theta* is relative to the y axis for $x0/y0 < 1$ and the x axis for $x0/y0 > 1$.

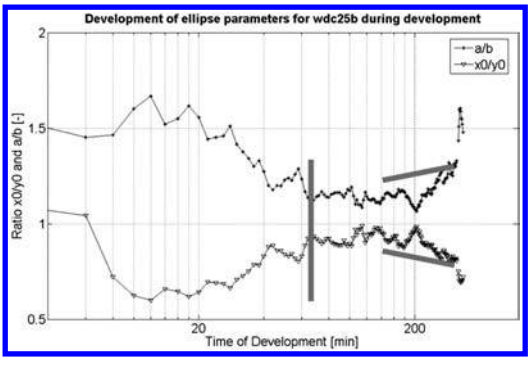


Figure 19. Ellipse ratios for run wdc25b – see level off at minute 60, with fluctuating levels from there on.

4.1.1 *2-D to 3-D dune changes for deep flows*

For the deep flows of Table 1, 2-dimensionality of bed form development in the early stages can be observed. According to Figure 11, 2-dimensionality would result

Copyright © 2006 Taylor & Francis Group plc, London, UK

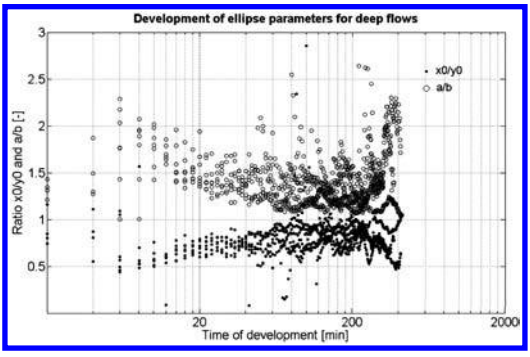


Figure 20. Ratios for the whole development all deep flows.



Figure 21. Typical developed bed forms for the deep flow. The main crest lines are still stretching over most of the flume width, with minor separation across the flume.

in a ratio of less than 1 for $x0/y0$ and a ratio of larger than 1 for a/b. Figure 19 and Figure 20 show the development of both ratios over time for selected runs. Figure 19 shows results for run wdc25b in detail. One can see, that at around minute 60, both ratios, $x0/y0$ and a/b, level off and a stage is reached where the bed forms have the most uniform character along and across the flume. It is proposed that at around that time, the transition from 2-D to 3-D dunes proceeds.

When one has a look at the complete development process for all runs (see Fig. 20), after the leveling-off stage, both ratios continue to fluctuate away from unity and even grow away again for some runs from a uniform distribution. This indicates the bed-surface development of a more 3-dimensional bed surface causing the crest lines to break up at the flume walls with occurrence of local scour. The growth of bed forms along the flume still continues. Figure 21 shows a typical sand bed after development for one of the deep flows.

Figure 22 shows contour plots of the sand-bed elevation of run wdc33a at different stages. At minute 12 of the bed-form development, one can see that the crest lines are still very perpendicular to the flume walls, and no major separation occurs across the flume.

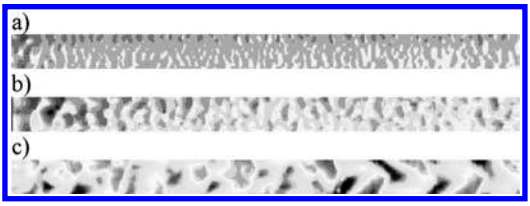


Figure 22. Snapshots (length = 18.48-m, width = 1.35-m) of sand bed elevations at (a) min 12, (b) min 30 and (c) min 230 for run wdc33a.

At minute 30, the crest lines are still mainly orthogonal to the flume walls, but minor separation across the flume starts. The transition from 2-D to 3-D sand waves proceeds. This is the stage where according to Figure 20 the most uniform stage of bed form development along and across the flume appears for the whole development. After this stage, the sand waves continue to grow along the flume, but are restricted in their growth across the flume by the flume walls, which is shown here in the snapshot of minute 230 of development.

4.2 *Differences in bed-form development associated with water depth*

As one can see from Table 1, the sand bed was exposed to two water depths, 0.15-m and 0.52-m. Results of the 2-D autocorrelation functions can be used to show the differences in development for these two different water depths.

For the shallow flow, the water depth acts as the restricting force in the development of the dunes, with the bed surface losing its one-directional character early on in the development stage. The shallow depth and the wide flume causes a more pronounced separation across the flume of bed forms early on.

This is reflected in ellipse shapes with ratios of $x0/y0$ larger than 1. Even for early stages, as soon as the flat sand bed is exposed to the water flow, bed forms separate across the flume, leading to 3-D dune development. For the deep flow, the flume walls act to restrict the development of the dunes, with no major separation of bed forms across the flume taking place and a transition from 2-D to 3-D dunes is the result.

Figure 23 shows ratios $x0/y0$ for all runs over time. As one can see, for the shallow flows the ratio $x0/y0$ essentially never goes to less than 1 over the whole time of development. Minor changes here are caused by having the sand bed exposed to different flow velocities. The rotation *theta* of the ellipse (see Fig. 23) shows either no rotation at all or a skewed fluctuation to a positive rotation. Both ellipse shape properties together indicate that the main average crest line keeps orthogonal to the flow with a slight skewness relative to the main flow direction.

Copyright © 2006 Taylor & Francis Group plc, London, UK

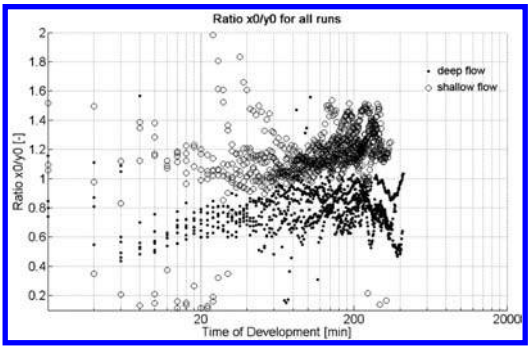


Figure 23. Ratio of *x0/y0* for all runs at correlation value 0.4.

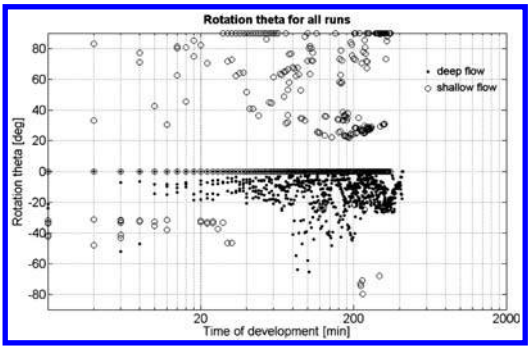


Figure 24. Angles of rotation of ellipse *theta* for all runs at correlation value 0.4.

On the contrary, for the deep flow, the ratio $x0/y0$ approaches unity very fast at the beginning of development, indicating a degree of 2-dimensionality for the early stage. Additionally the degree of rotation is close to 0 at the beginning of development, which indicates 2-D dunes, or 3-D dunes perpendicular to the flow. Theta increases slightly with increasing flow strength. The crest lines at the beginning of bed-form development remain predominantly perpendicular to the flume wall, whereas with the 2-D to 3-D transition, the crest lines begin to skew across the flume.

5 CONCLUSION

In this paper we have presented a new approach to gain 3-D sand-wave characteristics for sand beds developing from flat bed to equilibrium stage. The 2-D autocorrelation function has been applied on random fields of sand-bed elevations, each of a length of 18.48-m and a width of 1.35-m. The contours of the centre cone of the 2-D autocorrelation function become generally elliptical and the shape and degree of rotation varies as the bed develops.

For a shallow flow (ratio of flow depth to flume width less than 0.1), the major axis of the ellipse is oriented with the main direction of the flow field, which indicates 3-D development of the bed forms, from early on in the development stage. For a deeper flow (ratio of flow depth to flume width of 0.35), the major axis of the ellipse is orientated perpendicular to the main direction of the flow field, throughout the bed-form development. This indicates that the flume width is the restricting factor when it comes to the 3-D development of sand waves. As a deeper flow allows the sand waves to grow larger along the flume, this increase in growth potential is not supported across the flume with the flume walls acting to restrict development.

An automatic method to determine 2-D to 3-D dune transition is introduced. This paper's findings are preliminary. From the first tests, as introduced above, we suggest the following:

(a) $x0/y0 < 1$ indicates that the 3-D development of sand waves is wall-influenced; $x0/y0 > 1$ indicates that the 3-D development of the sand waves is flow-depth-influenced;
(b) *theta* tends generally to zero for 2-D wall influenced and 3-D sand waves. Some high *theta* values can be obtained for 3-D flow-depth-influenced runs, when ratio $x0/y0$ drops briefly below 1. For 3-D wall-influenced dunes, *theta* is skewed away from zero.
(c) for the deep flow, once the ratio $(x0/y0)/(a/b) > 0.9$, the 2-D to 3-D dune transition proceeds.

Generally it can be said, that the introduced technique requires more testing on a more varied data set, which is currently done at The University of Auckland, using additional data sets similar to Friedrich et al. (2005).

The application of 2-D autocorrelation functions of sand-bed surfaces requires further analysis, although the present results highlight that insights into 3-D characteristics of sand waves can be readily and objectively gained from this approach.

ACKNOWLEDGEMENT

The research was partly funded by the Marsden Fund (UOA220) administered by the New Zealand Royal Society.

REFERENCES

Allen, J. R. L. (1968). *Current Ripples – Their relation to patterns of water and sediment motion*, North-Holland Publishing Company, Amsterdam.

Andreotti, B., Claudin, P., and Pouliquen, O. (2006). "Aeolian Sand Ripples: Experimental Study of Fully Developed States." *Physical Review Letters*, 96(2), 028001-1-4.

Copyright © 2006 Taylor & Francis Group plc, London, UK

Ashley, G. M. (1990). "Classification of large-scale subaqueous bedforms: a new look at an old problem." *Journal of Sedimentary Petrology*, 60(1), 160–172.

Best, J. (2004). "The dynamics and morphology of river dunes: synthesis and future research directions." *Marine Sandwave and River Dune Dynamics*, Enschede, The Netherlands, pp. I–V.

Callander, R. A. (1978). "River Meandering." *Annu. Rev. Fluid Mech.*, 10, 129–158.

Coleman, and Eling. (2000). "Sand wavelets in laminar open-channel flows." *Journal of Hydraulic Research*, Vol. 38(5).

Friedrich, H., Melville, B. W., Coleman, S. E., Nikora, V. I., and Clunie, T. M. (2005). "Three-Dimensional measurement of laboratory submerged bed forms using moving probes." *Proceedings of XXXI International Association of Hydraulic Engineering and Research Congress*, Seoul, Korea, pp. 396–404.

Goring, D. G., Nikora, V. I., and McEwan, I. K. (1999). "Analysis of the Texture of Gravel-Beds using 2-D Structure Functions." *I.A.H.R. Symposium on River, Coastal and Esturine Morphodynamics*, Genova, Italy, 111–120.

Nikora, V. I., Sukhodolov, A. N. and Rowinski, P. W. (1997). "Statistical sand wave dynamics in one-directional water fows." *Journal of Fluid Mechanics*, Vol. 351, pp. 17–39.

Venditti, J. G. (2003). "The Initiation and Development of Sand Dunes in River Channels," Doctoral Thesis, University of British Columbia, Vancouver.

Copyright © 2006 Taylor & Francis Group plc, London, UK

Spatial development of turbulent open channel flow over bottom with multiple dunes

N.Th. Fourniotis, A.A. Dimas & A.C. Demetracopoulos
Department of Civil Engineering, University of Patras

ABSTRACT: The spatial development of turbulent open channel flow over bottom with five consecutive, identical dunes is studied by numerical solution of the RANS equations utilizing either the $k-\varepsilon$ or the Spalart-Allmaras turbulence models and the VOF free-surface formulation. Results are presented for several dune sizes: (a) constant dune length to channel depth ratio $L/d = 5$ and dune heights $h/d = 0.15, 0.25, 0.35$, and (b) constant ratio $L/h = 20$ and dune heights as in (a). The mean free-surface level decreases, for all cases, in the flow direction over the dunes, while, locally over each dune, the free-surface amplitude increases with increasing dune height and increasing dune length. The spatial distribution of the wall shear stress presents a wave-like behavior and its amplitude increases with increasing dune height and decreasing dune length. Flow separation at each dune crest is followed by a recirculation region and reattachment at a distance $x_R/d \sim (h/d)^{3/2} \cdot (L/h)^{-4/3}$ from the dune crest.

1 INTRODUCTION

The interaction of river flow and sediment transport creates a variety of bed forms such as ripples, dunes, antidunes or other irregular shapes and obstacles. Their presence, in general, causes flow separation and recirculation, which can alter the overall flow resistance and, consequently, can affect sediment transport within the river and erosion of river banks. For dunes, in particular, the flow is characterized by an attached flow on their windward side, separation at their crest and formation of a recirculation eddy in their leeside. The eddy dimensions depend on the dune length L, the dune height h and other flow characteristics, i.e., water depth d, Froude number Fr and Reynolds number Re. The resulting shear stress and pressure distributions on the bed, as well as turbulence in the bulk of the fluid, determine the total flow resistance and the rates of sediment transport.

The turbulent open channel flow over bottom with sand dunes has been studied, under the assumption of a fixed bed without sediment movement, both experimentally and numerically. Experimental data are available by Raudkivi (1963, 1966) for dunes with $L/2 = 12.87$ and 17.23, Van Mierlo & De Ruiter (1988) for dunes with $L/h = 20$, Lyn (1993) for dunes with $L/h = 12.5$, Kadota & Nezu (1999) for dunes with $L/h = 20$, and others. In recent years, numerical studies seek to describe the developing turbulent flow by either a solution of the Reynolds-averaged Navier-Stokes (RANS) equations, along with a turbulence model, or a large-eddy simulation (LES), along with a subgrid scale model. In both cases, significant role plays the free-surface treatment.

Van der Knaap et al. (1990) studied the dune cases, considered experimentally by Van Mierlo & De Ruiter (1988), by solving the RANS equations and employing the $k-\varepsilon$ turbulence model with wall functions. The effect of sand-grain roughness was taken into account with the wall-function approach, while the free surface with the rigid lid approximation. They were able to obtain quite good predictions of the flow features, including mean velocity, separation and reattachment.

Mendoza & Shen (1990) studied the turbulent open channel flow over flat bottom with a single dune by solving the RANS equations and employing the $k-\varepsilon$ model but with an algebraic stress in place of the more common eddy-viscosity assumption. The bottom roughness was considered by the wall-function approach, while the free surface was approximated as a rigid lid. In the streamwise direction, either periodic or inflow/outflow conditions were applied. Their results compared well with the mean velocity, wall shear stress, wall pressure and turbulence data of Raudkivi (1963, 1966).

Yoon & Patel (1996) studied the turbulent open channel flow over a single dune by solving the RANS equations and employing the $k-\omega$ turbulence model without use of wall functions. Periodic conditions were applied in the streamwise direction, while the free surface was treated as a flat plane of symmetry (rigid lid). They considered dunes with $7.14 \leq L/h \leq 12.5$ and found that the total flow resistance increases with decreasing L/h. Their predictions were in general

Copyright © 2006 Taylor & Francis Group plc, London, UK

agreement with the experimental data of Van Mierlo & De Ruiter (1988).

Cheong & Xue (1997) studied the turbulent open channel flow over bottom with three dunes solving the RANS equations and employing a three-layer near-wall $k-\varepsilon$ model. They used a general curvilinear coordinate system, applied periodic conditions in the streamwise direction and treated the free surface as a frictionless, rigid lid, symmetry plane. Their mean velocity, wall shear stress and turbulence results compared well with the data reported by Raudkivi (1963, 1966) and Van Mierlo & De Ruiter (1988).

Yue et al. (2005) studied the turbulent open channel flow over a single dune by a large eddy simulation. Periodic conditions are applied in the streamwise direction, while the free surface motion was simulated using the level set method. They employed two subgrid scale models, namely, the dynamic Smagorinsky model and the dynamic two-parameter model, in order to assess model effects on the free surface flow. They examined the coherent structures induced by the dune and their interactions with the free surface. Their numerical predictions were in good agreement with experimental data.

In the present work, a numerical study of the two-dimensional, fully-turbulent, subcritical, free-surface flow over a bed with five consecutive, identical dunes is conducted. The dune shape defined by Kadota & Nezu (1999) is used, for cases with $14.29 \le L/h \le 33.33$ and $3 \le L/d \le 7$, which are typical values of those observed in river flows (Nezu & Nakagawa 1993). Our aim is to examine the effect of dune dimensions on the flow characteristics. The RANS equations are solved utilizing either the $k-\varepsilon$ or the Spalart-Allmaras (S-A) turbulence models. The free-surface shape is tracked by applying a modified volume of fluid (VOF) method (Hirt & Nichols 1981), while the numerical solution is based on a finite-volume discretization, using the commercial CFD code FLUENT (Fluent 2005). Inflow/outflow conditions are applied in the streamwise direction. The formulation is presented in the next section, the problem description and the computation setup are presented in section 3, while the results are presented in section 4 followed by the conclusions.

2 FORMULATION

For steady-state, incompressible, turbulent open channel flow, the governing equations are the RANS equations. In two-dimensional form, the continuity and momentum equations, respectively, are

$$\frac{\partial U_i}{\partial x_i} = 0 \tag{1}$$

$$U_j \frac{\partial U_i}{\partial x_j} = -\frac{1}{\rho}\frac{\partial P}{\partial x_i} + \frac{1}{\rho}\frac{\partial \tau_{ij}}{\partial x_j} + g_i \tag{2}$$

where $i,j = 1,2$, x_1 is the streamwise coordinate, x_2 is the vertical coordinate, U_i is the time-averaged velocity component in x_i direction, ρ is the density, P is the dynamic pressure, g_i is the gravity force per unit volume and τ_{ij} is the Reynolds stress tensor, which represents the effects of the turbulent fluctuations in the fluid flow, defined as

$$\frac{\tau_{ij}}{\rho} = \nu\left(\frac{\partial U_i}{\partial x_j} + \frac{\partial U_j}{\partial x_i}\right) - \overline{u_i u_j} \tag{3}$$

where ν is the kinematic viscosity and u_i is the fluctuating part of the velocity.

The turbulent Reynolds stresses $-\overline{u_i u_j}$ are calculated using the Boussinesq relationship

$$-\overline{u_i u_j} = \nu_t\left(\frac{\partial U_i}{\partial x_j} + \frac{\partial U_j}{\partial x_i}\right) - \frac{2}{3}k\delta_{ij} \tag{4}$$

where k is the turbulent kinetic energy, δ_{ij} is the Kronecker delta function and ν_t is the eddy viscosity. For closure of the governing equations, a model of the turbulent Reynolds stresses has to be introduced. In the present study, the standard $k-\varepsilon$ two-equation model and the S-A one-equation model are used.

In the $k-\varepsilon$ model (Launder & Spalding 1974), the eddy viscosity of equation (4) is expressed in terms of the turbulent kinetic energy k and the turbulent dissipation rate ε via the Kolmogorov-Prandtl expression

$$\nu_t = C_\mu \frac{k^2}{\varepsilon} \tag{5}$$

where C_μ is a constant. The turbulent kinetic energy k and the turbulent dissipation rate ε are computed by the respective transport equations

$$U_i \frac{\partial k}{\partial x_i} = \frac{\partial}{\partial x_i}\left(\frac{\nu_t}{\sigma_k}\frac{\partial k}{\partial x_i}\right) + P_k - \varepsilon \tag{6}$$

$$U_i \frac{\partial \varepsilon}{\partial x_i} = \frac{\partial}{\partial x_i}\left(\frac{\nu_t}{\sigma_\varepsilon}\frac{\partial \varepsilon}{\partial x_i}\right) + \frac{\varepsilon}{k}\left(C_1 P_k - C_2 \varepsilon\right) \tag{7}$$

where σ_k, σ_ε, C_1, C_2 are empirical constants and P_k is the production term, which is modeled in the standard fashion of the $k-\varepsilon$ model. The usual values of the constants are used: $C_\mu = 0.09$, $C_1 = 1.44$, $C_2 = 1.92$, $\sigma_k = 1.0$, and $\sigma_\varepsilon = 1.3$.

In the S-A model (Spalart & Allmaras 1992), the eddy viscosity is expressed in terms of a modified eddy viscosity $\tilde{\nu}$

$$\nu_t = \tilde{\nu} f_{v1} \tag{8}$$

Copyright © 2006 Taylor & Francis Group plc, London, UK

where $f_{u1} = r^3/(r^3 + C_{u1}^3)$ is a viscous damping function, $r = \tilde{\nu}/\nu$ and $C_{u1} = 7.1$. The modified eddy viscosity is computed by the transport equation

$$\rho\frac{D\tilde{\nu}}{Dt} = G_\nu - Y_\nu + \frac{1}{\sigma_{\tilde{\nu}}}\left[\frac{\partial}{\partial x_j}\left((\mu+\rho\tilde{\nu})\frac{\partial\tilde{\nu}}{\partial x_j}\right) + C_{b2}\rho\left(\frac{\partial\tilde{\nu}}{\partial x_j}\right)^2\right] \quad (9)$$

where $\sigma_{\tilde{\nu}} = 2/3$ and $C_{b2} = 0.622$ are empirical constants, while G_ν and Y_ν are the production and dissipation terms, respectively, which are modeled in the standard fashion of the S-A model.

A modified VOF method (Hirt & Nichols 1981) was employed for computing the free-surface elevation. The VOF formulation relies on the assumption that two or more fluids are immiscible. In open channel flow, a new field variable F is introduced, which is the water volume fraction. The governing equations for the water flow, under the free surface, and the air flow, above the free surface, are expressed in a single form as given by (1) and (2), but the physical properties that appear in (1) and (2) are defined by the volume-fraction-weighted average of the physical properties of air and water as follows

$$\rho = F\rho_{water} + (1-F)\rho_{air} \quad (10)$$

$$\mu = F\mu_{water} + (1-F)\mu_{air}. \quad (11)$$

According to the law of mass conservation of air and water, the volume fraction of the water satisfies the equation

$$\frac{\partial F}{\partial t} + U_i\frac{\partial F}{\partial x_i} = 0 \quad (12)$$

For the numerical implementation of VOF by a finite volume method, the water volume fraction F is defined in each computational cell as follows

$$F = \frac{\delta V_{water}}{\delta V_{cell}} \quad (13)$$

where δV_{cell} is the volume of the computational cell and δV_{water} is the fraction of the volume of the cell filled with water. Therefore, we have $F = 1$, $F = 0$ or $0 < F < 1$ when the cell is full of water, is full of air or contains a free surface, respectively.

3 PROBLEM DEFINITION AND COMPUTATION SETUP

In the present study, we consider the turbulent open channel flow over a train of five consecutive, identical dunes. Far from the dunes, where the channel bottom is flat, we have normal depth $d = 1$ m,

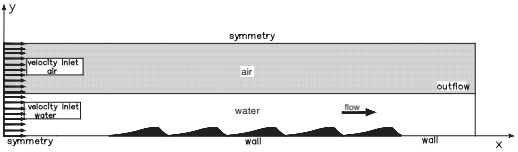


Figure 1. Computational domain of open channel flow with a train of five consecutive, identical dunes on the bottom.

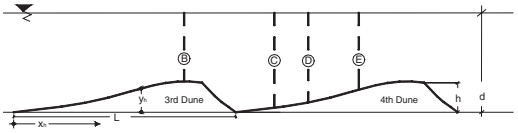


Figure 2. Dune shape parameter definitions and profile cross-sectional locations in the region of the 3rd and 4th dunes.

subcritical Froude number $Fr = 0.3$ and Manning coefficient $n = 0.02$. We consider water temperature 20°C where density is $\rho = 998.2\,\mathrm{Kg/m^3}$ and kinematic viscosity is $\nu = 1.005 \times 10^{-6}\,\mathrm{m^2/s}$. One-dimensional analysis of the flow gives channel slope $S = 0.35316 \times 10^{-3}$, mean velocity $U = 0.94$ m/s, Reynolds number $Re = 4dU/\nu = 3.74 \times 10^6$, which corresponds to fully turbulent flow, bulk friction velocity $U_* = (gdS)^{1/2} = 0.059$ m/s and wall roughness height $K_S/d = 0.018$, which corresponds to fully rough flow since $K_S^+ = U_* K_S/\nu = 1054$.

The numerical solution of the equations described in the previous section is based on a finite-volume discretization, using the commercial CFD code FLUENT (version 6.2.16). A sketch of the computational domain for the open channel flow over a train of five consecutive, identical dunes is shown in Figure 1. The VOF implementation requires the use of a multiphase flow domain with water and air. Initially, the water layer has uniform depth d, which is equal to the normal depth of the corresponding open channel flow over flat bottom. The thickness of the air layer is set to $4d$ so that the upper boundary of the computational domain does not affect the development of the water-air interface. In the present study, all lengths are presented normalized by d.

The five dunes along the bottom are located far from the inflow and outflow boundaries, so that the flow becomes fully developed before the first dune and fully developed again before the outflow boundary. In the present study, the total length of the computational domain is $200d$ and the first dune starts at $x/d = 90$ where $x = 0$ corresponds to the inflow plane and $y = 0$ to the flat bottom. The notation $x = x_1, y = x_2$ and $U = U_1$ is adopted in the rest of this paper.

The dune shape adopted in the present study is shown in Figure 2, and corresponds to the function (Kadota & Nezu 1999)

Copyright © 2006 Taylor & Francis Group plc, London, UK

Table 1. Dune sizes and corresponding number of cells.

Dune case	h/d	L/d	Number of cells
1	0.15	3	169,010
2	0.15	5	199,515
3	0.25	5	200,220
4	0.35	5	105,030
5	0.35	7	200,080

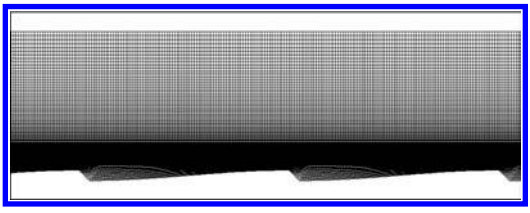


Figure 3. Mesh detail in the region between dunes for case 4.

$$\frac{y_h}{h}=\frac{1}{2}\left[1+\sin\left(\left(2X+\frac{1}{2}\right)\pi\right)\right] \tag{14}$$

where y_h is the dune profile height, h is the maximum dune height at the dune crest, $X=20x'/38$ for $-0.95<x'\le 0.0$, $X=10x'-9$ for $0\le x'\le 0.05$, $x'=x_h/L$ is the normalized local streamwise coordinate and L is the dune length. The five combinations considered, in the present study, are given in table 1.

The computational mesh is non-uniform along the two directions. Along the x direction, the grid size is $\Delta x/d=0.2$ for $0\le x/d\le 15$, it decreases linearly from $\Delta x/d=0.2$ to $\Delta x/d=0.1$ between $x/d=15$ and $x/d=90$, where the dunes start, and it increases linearly from $\Delta x/d=0.1$ to $\Delta x/d=0.2$ between the last dune and the outflow plane. Over the dunes, the grid size is $\Delta x/d=0.1$ upstream and $\Delta x/d=0.05$ downstream of the crest. In the y direction, the grid size on the wall is $\Delta y/d=0.04$, which is about twice the wall roughness height, and decreases gradually to $\Delta y/d=0.01$ at $y/d=1$. Then, the grid size increases gradually to $\Delta y/d=0.1$ at $y/d=5$ resulting in a coarser mesh in the air layer. The total number of cells for each case is given in table 1. The mesh for case 4 is shown in Figure 3.

FLUENT solves the governing equations sequentially using the control volume method. The governing equations are integrated over each control volume to construct discretized algebraic equations for the dependent variables. These discretized equations are linearized using an implicit method. As the governing equations are nonlinear and coupled, iterations are needed to achieve a converged solution. A donor-acceptor scheme is used to prevent numerical diffusion of F, the water volume fraction, and, thus, preserve a sharp interface. Schemes of the higher available level of accuracy are employed for the other variables with certain under-relaxation factors for promoting convergence. The discretization schemes are: PRESTO for pressure, QUICK for momentum, turbulent kinetic energy k and turbulent dissipation rate ε, and modified HRIC for the VOF implementation. The PISO scheme is utilized for the velocity-pressure coupling. For stable convergence, we use low under relaxation factors: 0.1 for pressure, momentum, turbulent kinetic energy, turbulent dissipation rate and volume fraction and 1.0 for density, body forces and turbulent viscosity. The continuity equation and transport equations of velocities, turbulence quantities and water volume fraction are solved in the steady-state mode until equilibrium conditions are achieved. A value of 10^{-7} is employed as convergence criterion for the sum of each normalized residual over the whole fluid domain for all the governing fluid flow equations, including the mass residuals.

There are four types of boundary conditions that are applied in this open channel flow problem; one for each of the four boundaries of the computational domain, namely, inflow plane, outflow plane, wall and air-layer boundary.

At the inflow plane, a uniform streamwise velocity distribution is prescribed for the water layer equal in magnitude to the mean velocity $U=0.94$ m/s obtained from the one-dimensional analysis. Uniform velocity distribution with the same magnitude is prescribed for the air layer as well. It has been observed that if no air is allowed to enter through the upstream boundary, or if the airflow rate is too small, then large recirculation regions of air may occur above the water. This reversal of air flow in the upstream direction of the channel causes computational instabilities (Ma et al. 2002).

The turbulent kinetic energy k and the turbulent dissipation rate ε at the inflow plane are specified, respectively, by the equations (e.g. Versteeg & Malalasekera 1995)

$$k=(IU)^2 \tag{15}$$

and

$$\varepsilon=C_\mu^{3/4}\frac{k^{3/2}}{0.1d} \tag{16}$$

where I is the turbulence intensity. In this paper, a value of three percent, $I=0.03$, is assumed for both the water and the air layer.

At the outflow plane, an overall mass balance correction and zero diffusion flux (zero normal gradients) for all flow variables are implemented. The water level at the outlet is not prescribed and is allowed

Copyright © 2006 Taylor & Francis Group plc, London, UK

to be predicted numerically according to the outflow boundary condition.

On the wall, the boundary condition is the no-slip condition, which is realized by a standard wall-function approach where the viscous sub-layer is not resolved. The wall-function, for the fully turbulent region outside the viscous sub-layer, is expressed as

$$\frac{U_P}{U_*} = \frac{1}{\kappa}\ln\left(Ey_P^+\right) - \Delta B \tag{17}$$

where U_P is the tangential velocity at the wall-adjacent cell, $U_* = (\tau_w/\rho)^{1/2}$ is the friction velocity, τ_w is the wall stress, $y_P^+ = U_* y_P/\nu$ is the node coordinate of the wall-adjacent cell in wall-coordinates, $\kappa = 0.41$ is the von Karman constant, $E = 9.793$ is an empirical constant and ΔB is a roughness parameter. In the fully rough regime ($K_S^+ > 90$), considered in the present study,

$$\Delta B = \frac{1}{\kappa}\ln\left(1 + C_S K_S^+\right) \tag{18}$$

where $C_S = 0.5$ is an empirical roughness constant (Fluent 2005).

For the wall treatment of turbulence quantities (Fluent 2005), the k transport equation (6) is solved at the wall-adjacent cells subject to the boundary condition

$$\frac{\partial k}{\partial n} = 0 \tag{19}$$

on the wall where n is the wall-normal direction, while ε is not computed by the solution of the transport equation (7) at the wall- adjacent cells but directly from

$$\varepsilon_P = \frac{C_\mu^{3/4} k_P^{3/2}}{\kappa y_P}. \tag{20}$$

At the upper boundary of the computational domain, above the air layer, symmetry boundary condition is applied. Symmetry condition is also prescribed at the channel bottom for $0 \le x/d \le 15$ to avoid a sudden transition from the uniform velocity profile at the inflow plane to the boundary layer development.

Initially, the computation assigns on all cells, both in the water and the air layers, velocity, turbulent kinetic energy and dissipation rate values equal to their counterparts at the inflow plane.

4 RESULTS AND DISCUSSION

First, the corresponding turbulent open channel flow with a flat bottom is considered for code validation, and to serve as a basis of comparison for the cases with dunes on the bottom. The wall stress distribution, for both turbulence models, is shown in Figure 4. The wall stress magnitude agrees with the one-dimensional prediction $\tau_w = \rho g d S = 3.46$ Pa after $x/d \approx 40$ where transition ends. The velocity profile at $x/d = 50$ and $x/d = 100$ is shown in Figure 5. In both locations, the results agree with the logarithmic law of a fully-developed, turbulent open channel flow. The turbulent viscosity ($\mu_t = \rho \nu_t$) profile is shown in Figure 6. The results follow the parabolic profile (Nezu & Nakagawa 1993) close to the bottom but deviate substantially from it close to the free surface due to the use of isotropic turbulence models ($k - \varepsilon$ and S-A) that over-predict the magnitude of vertical velocity fluctuations and, hence, the turbulent viscosity.

The turbulent open channel flow over the train of dunes is characterized by the modification of the free-surface level, the separation of the flow at the dune crest and the reattachment at the windward side of the next dune. Typical streamlines, for case 4, are shown in Figure 7.

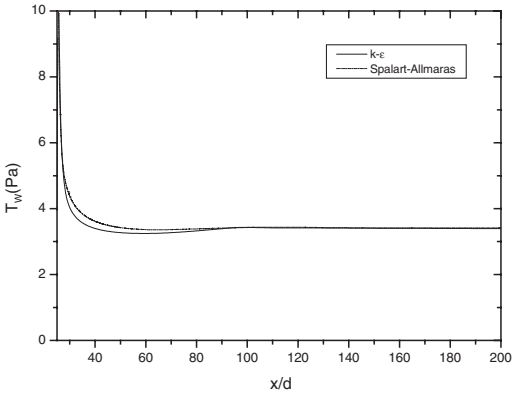


Figure 4. Wall stress distribution of turbulent flow in open channel with flat bottom.

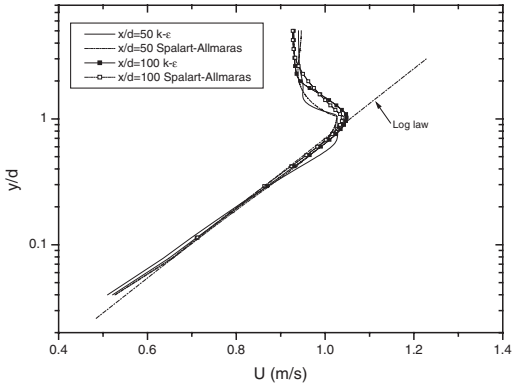


Figure 5. Streamwise velocity profile of turbulent flow in open channel with flat bottom.

Copyright © 2006 Taylor & Francis Group plc, London, UK

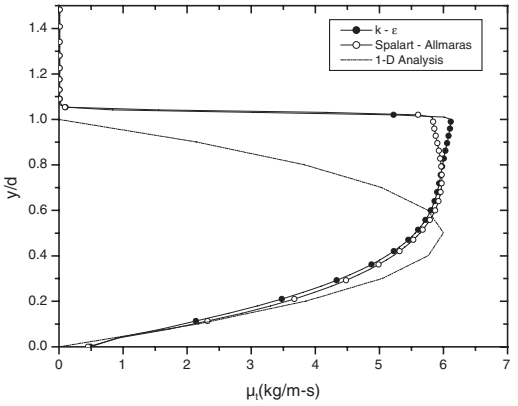


Figure 6. Turbulent viscosity profile at $x/d = 100$ in open channel with flat bottom.

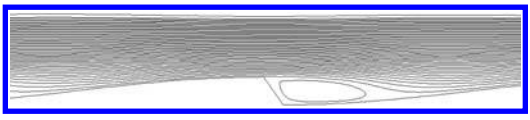


Figure 7. Streamlines in the region downstream of the 3rd dune for case 4.

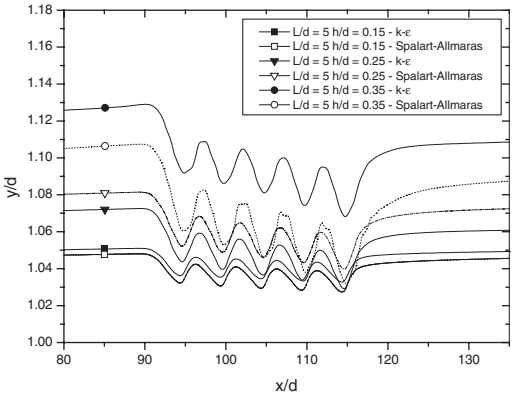


Figure 8. Free-surface elevation in the region over the dunes for cases 2, 3 and 4. The dune train is at $90 \leq x/d \leq 115$.

The free-surface profile, for each of the five dune configurations, is shown in Figures 8–9. In Figure 8, the free-surface profiles, for $L/d = 5$, are shown for all three h/d values. The mean free-surface level decreases, for all cases, in the flow direction over the dunes, while, locally over each dune, the amplitude of the free-surface elevation increases with increasing dune height. In Figure 9, the free-surface profiles, for $L/h = 20$, are shown for all three h/d values. Again, the mean free-surface level decreases, for all cases, in the flow direction over the dunes, while, locally over each dune, the amplitude of the free-surface elevation

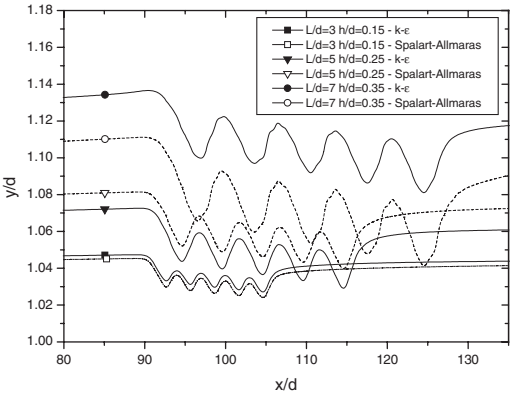


Figure 9. Free-surface elevation in the region over the dunes for cases 1, 3 and 5. The dune train starts at $x/d = 90$.

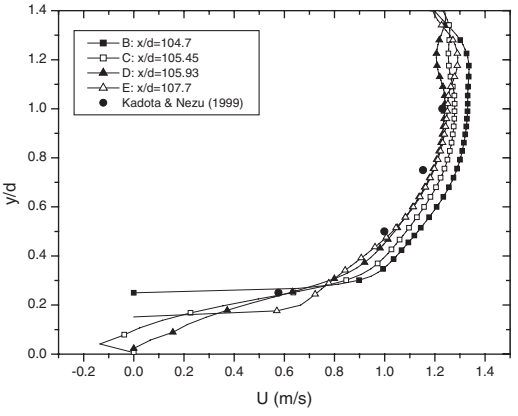


Figure 10. Streamwise velocity profile at cross-sections B, C, D and E for case 3 using the $k - \varepsilon$ model.

increases with increasing dune length. There is a small difference (less than 2%) in the mean free-surface level between the predictions of the two turbulence models.

The velocity profiles are presented at cross sections between the third and the fourth dune according to the sketch of Figure 2. Typical velocity distributions, for case 3, are shown in Figures 10–11. The flow accelerates (cross section B) over the windward side of the dune, separates at the dune crest, forms a recirculation region (cross section C) in the leeside of the dune, reattaches (cross section D) at a distance x_R from the dune crest and accelerates (cross section E) again. Kadota & Nezu (1999) considered experimentally the same dune with our case 3 but for $Fr = 0.29$ and $Re = 1.75 \times 10^4$. Their experimental data, for the velocity profile at reattachment (cross section D) where $U(y/d = 1) = 1.23$ m/s, are also shown in Figures 10–11. The agreement with the predictions of both turbulence models is very good. The velocity

Copyright © 2006 Taylor & Francis Group plc, London, UK

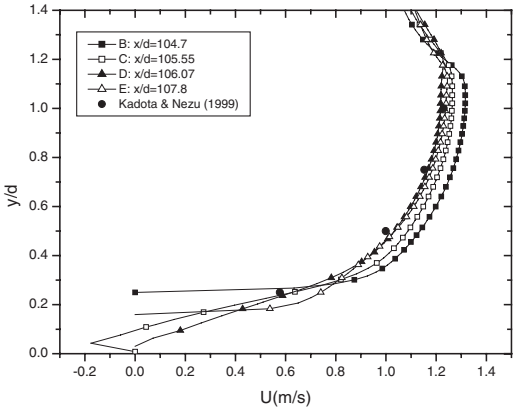


Figure 11. Streamwise velocity profile at cross-sections B, C, D and E for case 3 using the S-A model.

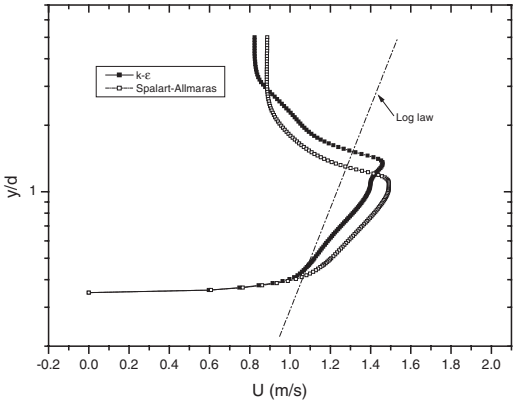


Figure 12. Streamwise velocity profile at the crest of the 3rd dune for case 5.

at the crest of the third dune, for case 5, is shown in Figure 12 and compared to the logarithmic law. The resulting velocity presents a steeper profile than the logarithmic law and is similar to the velocity profile observed in flat bottom boundary layer under favorable pressure gradient. The S-A model predicts a steeper profile than the $k-\varepsilon$ model.

The wall shear stress distribution, for each of the fine dune configurations, is shown in Figures 13–15. In Figure 13, the wall stress profiles, for $L/d=5$, are shown for all three h/d values. The profiles present a wave-like behavior that deviates substantially from the corresponding flat bottom case, while the amplitude increases with increasing dune height. In Figures 14–15, the wall stress profiles, for $L/h=20$, are shown for the lower and the higher h/d values. Again, the profiles present a wave-like behavior that deviates substantially from the corresponding flat bottom case, while the amplitude increases with decreasing dune length. The

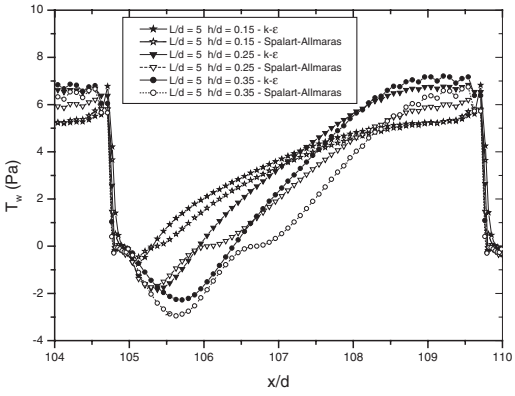


Figure 13. Wall stress distribution in the region downstream of the 3rd dune for cases 2, 3 and 4.

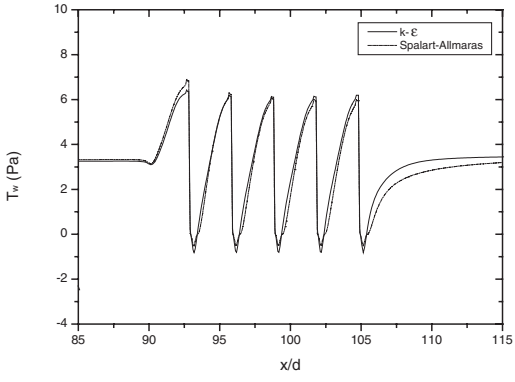


Figure 14. Wall stress distribution in the region over the dunes for case 1.

reattachment point is defined as the location on the windward side of the dune where the wall shear stress is zero.

The horizontal distance of the reattachment point from the dune crest is called reattachment length x_R. The S-A model predicts a longer reattachment length and lower wall shear stress on the windward side of the dunes than the $k-\varepsilon$ model. It should be noted here that the same grid was used for both models without tailor-refinement to any of the two models. The value of x_R obtained by the S-A model is always larger than the $k-\varepsilon$ one by as much as 25%. The predictions $x_R/h=4.72$ of the $k-\varepsilon$ model and $x_R/h=5.28$ of the S-A model, for case 3, compare with the value $x_R/h=5$ measured by Van Mierlo & De Ruiter (1988) for $Fr=0.23$ and $Re=4\times10^5$ and the value $x_R/h=4.05$ measured by Kadota & Nezu (1999) for $Fr=0.29$ and $Re=1.75\times10^4$. Based on the five configurations considered in the present study, the reattachment length x_R is found to correlate with

Copyright © 2006 Taylor & Francis Group plc, London, UK

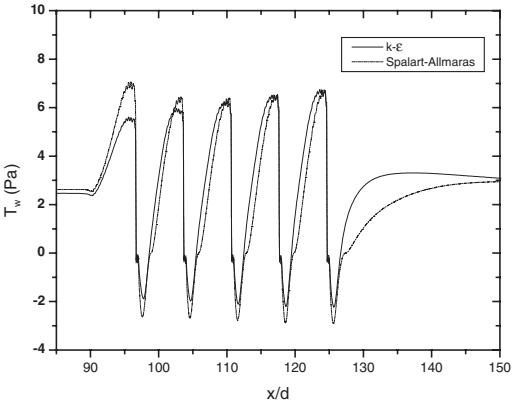


Figure 15. Wall stress distribution in the region over the dunes for case 5.

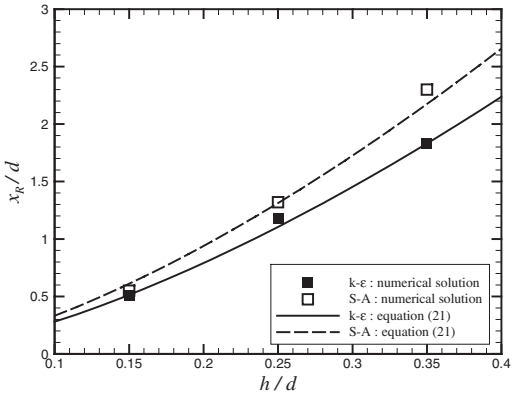


Figure 16. The correlation of the reattachment length to dune height and water depth for $L/h = 20$.

the channel depth d, the dune height h and the dune length L according to the following expression

$$\frac{x_R}{d} = a\left(\frac{h}{d}\right)^{\frac{3}{2}} \cdot \left(\frac{L}{h}\right)^{-\frac{4}{3}} \qquad (21)$$

where $a = 480$ for the $k - \varepsilon$ model and $a = 570$ for the S-A model. A comparison of the numerical results with (21) is shown in Figures 16–17.

5 CONCLUSIONS

The turbulent open channel flow over bottom with a train of five consecutive, identical dunes was studied by the numerical solution of the RANS equations using the $k - \varepsilon$ and Spalart-Allmaras turbulence models and the VOF free-surface treatment.

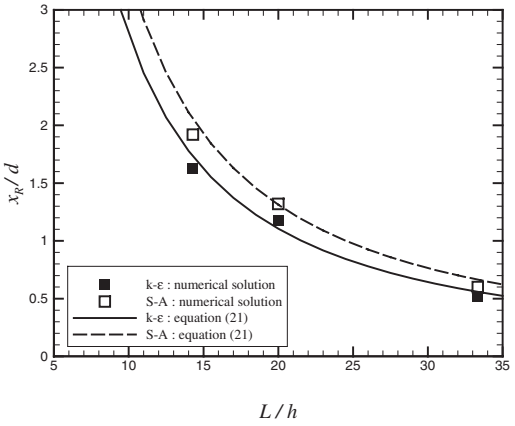


Figure 17. The correlation of the reattachment length to dune length and dune height for $L/d = 5$.

Our aim was to identify the effect of the dune dimensions on the flow characteristics. It was found that over the dunes, the mean free-surface level decreases, for all cases, in the flow direction, while, locally over each dune, the amplitude of the free-surface elevation increases with increasing dune height and increasing dune length. The spatial distribution of the wall shear stress presents a wave-like behavior and its amplitude increases with increasing dune height and decreasing dune length. The flow separation at each dune crest is followed by a recirculation region and reattachment at a distance $x_R/d \sim (h/d)^{3/2} \cdot (L/h)^{-4/3}$ from the dune crest.

The turbulence results are reasonable from about the half-depth point to the bottom and inaccurate from the half-depth point to the free surface. A modification to the synergy between the turbulence models and VOF is required to represent the reduced vertical velocity fluctuations that exist in turbulent flow close to a free-surface.

ACKNOWLEDGEMENTS

The financial support by the European Union and the Hellenic Ministry of National Education and Religious Affairs under program "Pythagoras II" is greatly appreciated.

REFERENCES

Cheong, H.F. & Xue, H. 1997. Turbulence model for water flow over two-dimensional bed forms. *J. Hydraul. Eng.* 123(5): 402–409.

Fluent, Inc. 2005. FLUENT 6.2 User's Guide. Lebanon, NH: Fluent Inc.

Copyright © 2006 Taylor & Francis Group plc, London, UK

Hirt, C.W. & Nichols, B.D. 1981. Volume of fluid (VOF) method for the dynamics of free boundaries. *J. Comput. Phys.* 39: 201–222.

Kadota, A. & Nezu, I. 1999. Three-dimensional structure of space-time correlation on coherent vortices generated behind dune crest. *J. Hydraul. Res.* 37(1): 59–80.

Van der Knaap, F.C.M., Van Mierlo, M.C.L.M. & Officier, M.J. 1990. Measurements and computations of the turbulent flow field above fixed bed-forms. Pub. 437. Delft: Delft Hydraulics.

Launder, B.E. & Spalding, D.B. 1974. The numerical computation of turbulent flow. *Comput. Methods Appl. Mech. Eng.* 3: 269–289.

Lyn, D.A. 1993. Turbulence measurements in open-channel flows over artificial bed forms. *J. Hydraul. Eng.* 119(3): 306–326.

Ma, L., Ashworth, P.J., Best, J.L., Elliot, L., Ingham, D.B. & Whitcombe L.J. 2002. Computational fluid dynamics and the physical modelling of an upland urban river. *Geomorphology* 44: 375–391.

Mendoza, C. & Shen, H.W. 1990. Investigation of turbulent flow over dunes. *J. Hydraul. Eng.* 116(4): 459–477.

Van Mierlo, M.C.L.M. & De Ruiter, J.C.C. 1988. Turbulence measurements above artificial dunes. TOW A55, Q789. Delft: Delft Hydraulics.

Nezu, I. & Nakagawa H. 1993. Turbulence in open-channel flows. IAHR Monograph. Rotterdam: Balkema.

Raudkivi, A.J. 1963. Study of sediment ripple formation. *J. Hydraul. Div.* 89(6): 15–33.

Raudkivi, A.J. 1966. Bed forms in alluvial channels. *J. Fluid Mech.* 26: 507–514.

Spalart, P.R. & Allmaras, S.R. 1992. A one-equation turbulence model for aerodynamic flows. AIAA Pap. 92–439. Reston, VA: American Institute of Aeronautics and Astronautics.

Versteeg, H.K. & Malalasekera, W. 1995. An introduction to computational fluid dynamics. The finite volume method. Edinburgh: Longman.

Yoon, J.Y. & Patel, V.C. 1996. Numerical model of turbulent flow over sand dune. *J. Hydraul. Eng.* 122(1): 10–18.

Yue, W., Lin, C.L. & Patel, V.C. 2005. Large eddy simulation of turbulent open-channel flow with free surface simulated by level set method. *Phys. Fluids* 17(2): 1–12.

Copyright © 2006 Taylor & Francis Group plc, London, UK

Bed forms and transport characteristics of a partly cohesive sediment

R. Banasiak & R. Verhoeven
Hydraulics Laboratory, Department of Civil Engineering, Ghent University, Belgium

ABSTRACT: In a laboratory study an artificial partly cohesive sediment made from mineral components was tested along with a noncohesive reference sediment. The experimental approach included the registration and analysis of bed form development, flow resistance, shear stress, total load transport (bed and suspended load) in a range of the Froude number up to 0.8. The paper highlights the essential differences between the mobility of noncohesive and partly cohesive sediment beds. In contrast to sand with typical bed configurations (ripples, dunes and washed-out dunes), the cohesive-like bed under erosion became covered with isolated ripples or with a rippled granular moving layer covering an intact substrate. The dimensions of bed forms for cohesive material were up to ten times smaller than in the case of sand. Consequently, significantly lower flow resistance was recorded for partly cohesive sediment. Although for both types of sediment the active sediment layer is composed of granular material only, the bed load transport rates as a function of effective shear stress were significantly smaller for the partly cohesive bed. On the other hand, no significant differences between studied sediments were found for the suspended load function.

1 INTRODUCTION

The dynamic response of a sediment bed to flow action depends not only upon the dominant grain size of the deposit but also on other fractions appearing even in small quantities. In particular, fine, cohesive particles of clay and silt have the potential to affect significantly the mobility of a sediment mixture. Sediments containing predominantly granular material and a certain amount of cohesive (in)organic fraction are termed to as semi- or partly cohesive sediments, and have been pointed out only over a decade ago in respect of sediments occurring in sewer pipelines (Crabtree, 1989). The partly cohesive sediment was described as a sediment that has a greater resistance to erosion than it would be anticipated from a purely granular one of similar grain size. According to Mitchener & Torfs (1996) the addition of a cohesive fraction to a sand bed influences both the critical shear stress and the mode of erosion. They reported about a limit content for the cohesive fraction that changes the erosion resistance from that of pure sand and which is related to the type of cohesive binder and to the size of the granular fraction. For instance, for kaolinite added to sand ($d_{50} = 230\,\mu m$) this limit is about 3% of clay. For Laponite clay added to sand (Alvarez-Hermandez, 1990), the transition between cohesionless and cohesive erosion behaviour occurred at between 5% and 15% clay content. Alvarez-Hermandez (1990) has also reported that once partly cohesive sediment is mobilized to motion, it behaves as a noncohesive sediment with a bed covered with bed forms.

Bed forms occurring during the erosion of sand with an addition of a cohesive fraction were also observed by other investigators during low flow conditions with deposited sediment bed in conduits (Skipworth, 1996, Tait et al. 1998, De Sutter, 2000, Banasiak et al. 2005). However, no verifiable data on the bedforms have been provided and rather little is known about the bed form dimensions and bed resistance in case of cohesion affected sediments. Most of the researchers focused instead on establishing critical shear stresses as a function of grain size composition and physical properties and on producing sediment transport functions or erosion formulas depending, however not distinctly, on the mode of erosion.

This study aims therefore to bring more recognition about sediment transport in transition between cohesive and noncohesive sediments. It focuses on the assessment of the bed surface response, the evaluation of the bed friction and shearing characteristics as a base for formulation of sediment transport formulas.

2 EXPERIMENTAL METHOD

2.1 *Experimental flume*

Experiments were conducted in a tilting 11 m long recirculating flume with a semi-circular cross-section

Copyright © 2006 Taylor & Francis Group plc, London, UK

and diameter of 0.39 m. The flume has a discharge maximum capacity of 40 l/s, and flows with water depths up to 0.15 m and velocities up to approximately 1 m/s can be realised. The flume internal surface was covered with an abrasive paper to imitate the hydraulic roughness of concrete pipes. The roughness coefficient k_w of the flume wall was determined experimentally to be 0.3 mm. The bed slope of the tilting flume was fixed at 0.002.

The flume was divided into three reaches. The upstream reach provided a 3 m length of the channel for the flow, bed forms, surface waves and sediment transport to stabilize. The second reach, the tested sediment section, was 4.2 m long. The downstream reach served as an outrun section to minimize the effect of the backwater in the testing zone.

The discharge was controlled by the adjustment of a computer controlled butterfly valve and measured by an electromagnetic discharge meter. Two hydrostatic pressure transducers measured the upstream and downstream water level at both ends of the tested sediment bed section. A slot type bed load trap was located at the end of the sediment bed section. It had a load cell which records the accumulated weight of trapped sediment. Material that entered this trap is considered as the bed load whilst the sediment remaining in the flow is regarded as suspended load. The latter was measured using a set-up pumping samples from five points over the vertical. Suspended sand transport rates are estimated by integrating products of velocity and concentration values. The velocities were measured by a 3D acoustic Doppler velocitymeter (ADV).

2.2 *Test performance*

Tests were conducted using sand and a mixture of sand and an artificial inorganic cohesive binder. The sand had a mean grain size of 0.19 mm and a standard deviation $\sigma = 1.4$. The cohesive-like mixture was made of the same sand with addition of kaolinite clay ($d_{50} = 6\,\mu$m) in a proportion of 6% by weight (of the dry mixture).

The sand and the wet prepared sediment mixture were placed in the pipe invert and leveled to obtain a sediment bed with a thickness of approximately 4 cm alone the pipe centreline. During the erosion tests the discharge was gradually increased up to its maximum and maintained constant sufficiently long to obtain uniform flow and steady sediment transport, for which the sediment transport controlling parameters were determined. The restriction for the test duration was imposed by the scouring at the beginning of the erodible section (no sediment feeding was provided). After each run, the deposit surface was measured using a laser distometer, and the bed was again prepared for a next test.

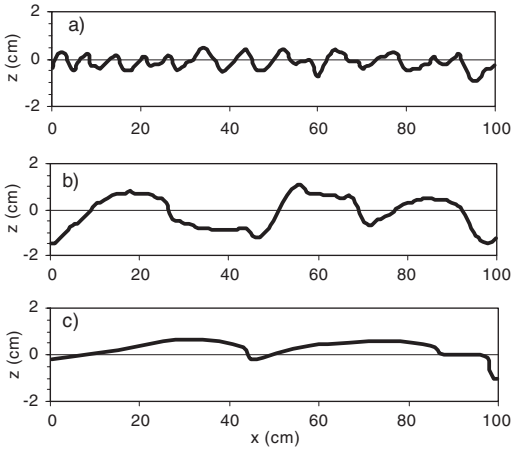


Figure 1. Bed forms for sand a) $U = 0.34$ m/s – ripples, b) $U = 0.61$ m/s – dunes and c) $U = 0.72$ m/s – washed-out dunes (U – mean cross-section flow velocity).

3 RESULTS

3.1 *Bed forms*

The bed forms development for sand are illustrated in Figure 1. As typical for noncohesive fine sand, at lower flow regime the bed formed into ripples with a gradual growth in size. After reaching a flow rate of $Q \approx 20$ l/s (Froude number Fr between 0.5 and 0.7) the bed formed into dunes, that can be seen in Figure 1b. Further increase of the flow strength and Froude number ($Fr > 0.7$) resulted in an increasing dune length together with a decrease of the form height, which means that the transition regime was reached; the bed flattened due to washing out (Fig. 1c).

Figure 2 presents the topography of the bed recorded after the tests with the partly cohesive sediment. It is visible that the bed formation consisted of low-relief features in the order of a few millimeters in height. These separated ripples on top of the substrate created a quite uniform pattern along the channel and moved individually downstream during the lower flow regime. For maximum flow rate the granular sediment layer covered the underlying substrate, and the ripple crests were flattened.

The average bed form sizes for both sediment types are depicted in Figures 3a,b. This comparison clearly indicates the effect of the cohesive strength on the bed formation; bed forms are nearly ten times smaller in the case of the mixture than those for pure sand. For a sand and clay mixture the ripple height varies little with flow rate. Also the bed form lengths are significantly reduced and no dunes are detected over the partly cohesive sediment bed; the ripples undergo directly the washing out at the transition regime and the bed smoothens.

Copyright © 2006 Taylor & Francis Group plc, London, UK

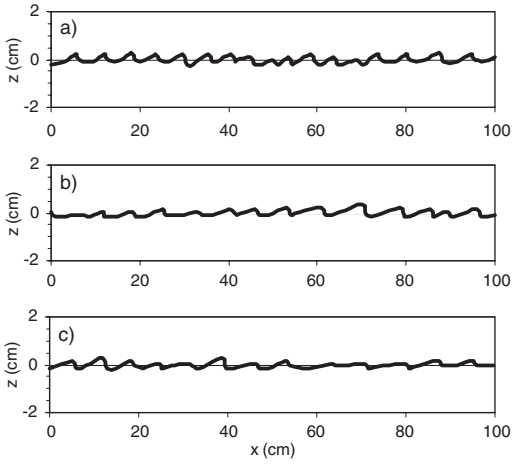


Figure 2. Bed forms for partly cohesive sediment bed: a) $U = 0.48$ m/s, b) $U = 0.63$ m/s, and c) $U = 0.73$ m/s.

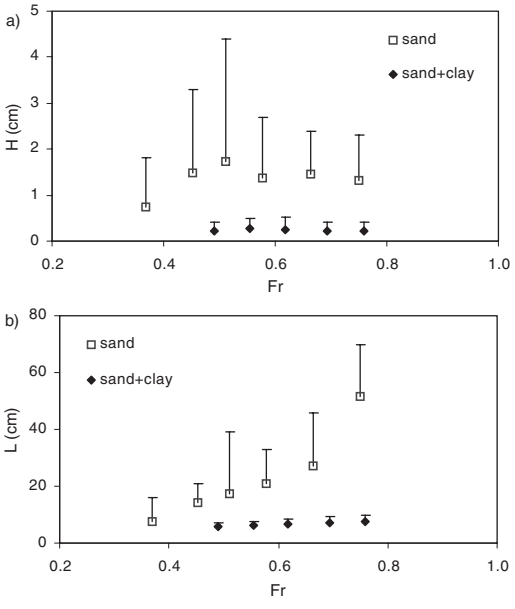


Figure 3. Bed form height a) and length b) (vertical bars indicate the maximum values).

3.2 *Bed roughness and shear stress*

Following the bed form size development, it can be expected that the bed form friction for cohesion affected sediment will change in respect of noncohesive sediment. In Figure 4 the equivalent sand roughness, k_s, normalized by the mean particle diameter of sand d_{50} is used and related to the Froude number Fr to show the variance of the bed resistance with flow

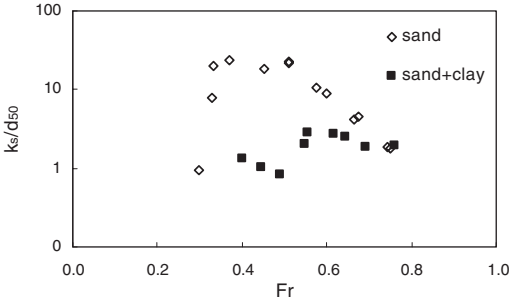


Figure 4. Bed friction against Froude number.

rate. The differences are again striking. The friction for sand bed increases up to a limit value $k_s/d_{50} = 23$ during appearance of dunes, and then diminishes as the dunes are washed out. For a cohesion affected bed the roughness height ratio is about 1 for a flat bed, which extends over a wider flow range due to increased critical shear stress (no motion), and increases to 2.9 as a maximum value once the bed forms develop under the shear stress exceeding the critical value.

When coping with a bed forms covered bed it is expedient to account for the part of the friction related to the presence of the bed forms. Here, the friction will be translated into the shearing on the bed. In a linear superposition of the resistance it is that the shear stress felt at the bed, called the skin friction shear stress, τ_b', is not equal to the spatially-averaged total bed shear stress, τ_b. The difference between the skin friction shear and the total shear is the form drag τ_b''

$$\tau_b = \tau_b' + \tau_b'' \tag{1}$$

This is the well know concept introduced by Einstein (1950). The reference plane-bed shear stress and bed form shear stress is calculated from

$$\frac{n'}{R_b^{1/6}}\sqrt{g} = \frac{\sqrt{\tau_b'/\rho}}{U} \tag{2}$$

$$\frac{n''}{R_b^{1/6}}\sqrt{g} = \frac{\sqrt{\tau_b''/\rho}}{U} \tag{3}$$

where g is the gravity constant, ρ – water specific density, U – the cross-section average flow velocity, and R_b – the hydraulic radius determined according to a side-wall elimination of Kleijwegt (1992).

The calculated total bed shear stress and the grain shear stress is shown in Figure 5. It is visible that whereas for sand the bed forms account for up to a half of the total shear stress, for partly cohesive sediment τ_b does not deviate so much from τ_b'; the form drag is then relatively small.

Copyright © 2006 Taylor & Francis Group plc, London, UK

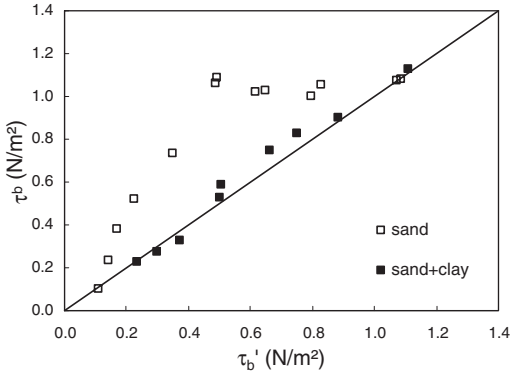


Figure 5. Bed and grain shear stress.

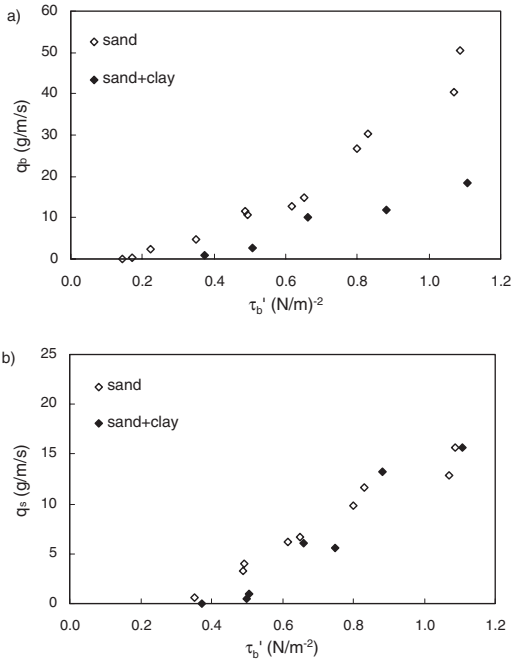


Figure 6. Bed a) and suspended b) load transport.

3.3 *Transport rates*

It is also interesting to have a look on the sediment transport intensities both for bed and suspended load. Figures 6a,b present sediment transport rates against the grain shear stress as this part of shear stress is deemed responsible for sediment transport. For the bed load data there is a clear influence of the cohesion on the sediment transport, both in respect to the beginning of motion and the transport intensity at a given shear rate.

For the suspended load (suspended sand) these differences are less pronounced. They appear mainly for lower flow rates; while the sand sheet layer develops over the cohesive substrate, the particles enter into suspension at nearly the same rate as in the case of a sand bed.

4 DISCUSSION

It is remarkable that the presence of a relatively small amount of cohesive binder has a big potential to modify the overall erosion behaviour of a sediment bed. In the current study, due to the addition of 6% of kaolinite clay the critical shear stress raised from $0.12\,N/m^2$ for pure sand to about $0.33\,N/m^2$. This resulted in a drastic change in the active layer thickness, bed topography along with friction factor and sediment transport rates. For a partly cohesive mixture the disturbance depth increased only slightly with flow intensity. This is important to recognize, since under the equilibrium sediment transport there is a little or no deepening erosion as it can be anticipated for cohesive sediment. In this sense the partly cohesive sediment behaves like a noncohesive one. The moving, continues or discountinues granular layer, depending on the flow regime, 'protects' the underlying cohesive layer against the erosion. The role of isolated small bed forms on the shearing over the bed is still to be clarified. The development of the active bed load layer and presence of bed forms over a cohesive bed type will certainly depend on the degree of cohesion. It will be conditioned by the rate of disintegration of grains from the bed and the transport capacity of the flow. Once the flow is able to carry the separated particles at a rate larger than the erosion rate, the moving granular layer will be vanishingly small and susceptible to suspension. On the other hand, once the cohesive strength is low, the fine particles will be easily washed out; the coarser particles will move as noncohesive sediment layer.

Because of the change in the mode of transport, it is reasonable that the bed load transport differs significantly between the two types of sediment, despite of the fact that the bed load consists of the same granular material. Apart of increased critical shear stress, the primary reducing factor for bed load transport is the reduction of active bed load layer thickness due to the cohesion in the substrate. Remarkably, no big difference is recorded regarding the suspended load except for the situation with ripples/early dunes for sand as for this flow conditions the cohesive bed was rather weakly developed.

An important issue in this study is the assessment of the friction factor during the sediment motion. Although the rise of this friction factor is not as big as for noncohesive sediment, it can be 3 times of that for a flat bed for the present bed. Consequently, there

Copyright © 2006 Taylor & Francis Group plc, London, UK

is need to account this rise due the presence of bed forms in the calculations of the effective shear stress relating the sediment transport. For certain flow conditions neglecting this can result in a 15% error in the shear stress, with as a consequence of about 50% error in the bed material transport prediction.

5 PARTLY COHESIVE SEDIMENT – THE DEFINITION

Based on the current observations and reported in literature, a definition for partly cohesive sediments is tempted. The characteristic feature for the sediment in transition between noncohesive and cohesive sediment is that it produces a granular top layer over an unremoulded substrate. On the one hand, this layer approaches in thickness and continuity the active bed load layer for noncohesive sediments, and on the other hand diminishes with increasing cohesion strength. If the cohesive fraction content of a mixture exceeds the upper transition value, the erosion rates can be modeled using the existing equations for cohesive sediments. For cohesive fraction content below the lower transition value, the mixture behaves as a noncohesive sediment and sand transport theories can be applied to predict the sediment transport rates. However, for transition sediments neither of these approaches seems to be correct. A modified non-cohesive prediction tool is needed and combined with an erosion describing formula. The knowledge of the shear stress distribution within this granular layer is desirable as well. On a longer time scale the erosion/transport mode will depend much on (non)equilibrium conditions for sediment transport.

6 CONCLUSIONS

The sediment mixture composition strongly influences the erosion behaviour of partly cohesive sediments. Addition of just a few percent of cohesive material can increase the critical shear stress of the sediment mixture and change its behaviour from noncohesive to cohesive-like. The conducted experiments demonstrated that sediments in general do not follow a strict distinction between noncohesive and cohesive types. There is a gradual change in the mode of sediment erosion/transport, bed forms development and friction characteristics. Obviously, more experiments are needed to relate the erosion behaviour to clay characteristics and to the characteristics of natural mixtures (muds).

REFERENCES

Alvarez-Hermandez, E.M. 1990. The influence of cohesion on sediment movement in channels of circular cross-section. *PhD. Thesis*. University of Newcastle upon Tyne, 263 p.

Banasiak, R., Verhoeven, R., De Sutter, R., & Tait, S. 2005. The erosion behaviour of biologically active sewer sediment deposits: Observations from a laboratory study. *Water Research* 39, 5221–5231.

Crabtree, R.W. 1989. Sediments in sewers. *Journal of the Institute of Water and Environmental Management* 3, 569–578.

De Sutter, R. (2000). Erosion and transport of cohesive sediment mixtures in unsteady flow. *Ph.D. Thesis*, Ghent University, 283 p.

Einstein, H.A. 1950. The bed-load function for sediment transportation in open channel flows. *Technical Bulletin* No. 1026, U.S. Dept. of Agr., Washington, D.C.

Kleijwegt, R.A. 1992. Sediment transport in circular sewers with non-cohesive deposits. *PhD. Thesis*, TU Delft.

Mitchener, H., & Torfs, H. 1996. Erosion of mud/sand mixtures. *Coastal Engineering* 29, 1–25.

Skipworth, P.J. 1996. The erosion and transport of cohesive-like sediment beds in sewers. *Ph.D. Thesis* University of Sheffield.

Tait, S.J., Rushforth, P.J., & Saul, A.J. 1998. A laboratory study of the erosion and transport of cohesive-like sediment mixtures in sewers. *Water Science and Technology* 37 (1), 163–170.

Copyright © 2006 Taylor & Francis Group plc, London, UK

Bed morphology and flow resistance in steep open channels with varying widths

R.B. Weichert[1], G.R. Bezzola[2] & H.E. Minor[1]
[1] *Laboratory of Hydraulics, Hydrology and Glaciology (VAW), Zürich, Switzerland*
[2] *Federal Office for the Environment FOEN, Switzerland*

ABSTRACT: Steep open channels are often characterised by bed forms in different scales. In the meso-scale, the typical bed features are usually described as successions of steps and pools. Depending on the channel width, the step-pool morphology can be superposed by macro-scale bed forms as e.g. bar structures. In steep headwater streams bed roughness is large relatively to flow depth. Consequently, flow field and flow resistance are significantly influenced by the bed morphology. In order to study the flow resistance in steep open channels, flume experiments were carried out at the Laboratory of Hydraulics, Hydrology and Glaciology (VAW) of the Swiss Federal Institute of Technology (ETH) in Zurich, Switzerland. The results show that for experiments where bar structures occurred, a significant influence of the macro-scale bed features on flow resistance could be ascertained. A new approach is proposed to compute flow resistance in steep-open channels with macro- and meso-scale bed features.

1 INTRODUCTION

The roughness scale, expressed by the ratio of flow depth to roughness height, h/d, controls the extent bed morphology affects flow field and energy dissipation. Usually, three different roughness scales are distinguished: small-scale, intermediate-scale and largescale. The flow in steep open channels is usually characterized by large-scale roughness, i.e. flow depths are in the same order of magnitude as the bed roughness heights. For these conditions, the local relation between the size of a bed element d and the flow depth h largely influences the turbulent flow field and therefore, the energy losses in the vicinity of the roughness elements. In addition, the roughness structure, such as the relative position of one boulder to another, leads to superpositioning of vortices resulting in a very complex and irregular flow field (Buffin-Belanger and Roy, 1998; Lawless and Robert, 2001) with spatially and temporally high variations in flow velocities, flow depths, air entrainment, water-surface slopes and energy gradients. Following this, the flow in steep boulder-bed channels resembles more a jet and wake type rather than a shear flow type (Bray, 1987).

2 BED MORPHOLOGY

Longitudinal stream profiles in mountainous regions usually do not exhibit a smoothly varying slope but reaches of alternately steeper and flatter slopes associated with shallower and deeper flow sections respectively (Leopold et al., 1964). Several authors recognised that these successions of steep- and gentle-gradient segments are found in a wide range of geomorphologic scales. Within the present paper, two different geomorphologic scales will be considered more in detail.

2.1 *Meso-scale: Steps and pools*

In the meso-scale, the accumulation of the largest bed elements results in organised bedforms, that are often situated approximately transverse to the direction of flow. Successive groups of boulders forming such transverse structures are separated by pools (see Figure 1), so these river segments are often called step-pool-systems (Zimmermann and Church, 2001; Mac-Farlane and Wohl, 2003).

In flows with small-scale roughness that are characterised by a flat and stable bed, the effective bed roughness is well described by a characteristic grain size of the bed material. In steep open channels with large-scale roughness, the roughness geometry determines the flow field, and vice versa. For these channels, the concept of a representative grain size fails, as a single linear dimension basing on a particle size is insufficient to describe the complex roughness geometry (Bathurst, 1978; Aberle, 2000). Alternatively, the standard deviation of the bed elevations, s, has been used as a parameter to describe the bed

Copyright © 2006 Taylor & Francis Group plc, London, UK



Figure 1. Bedforms in steep open channels can be observed in different scales. Left: Steps and pools, right: Riffles and pools.

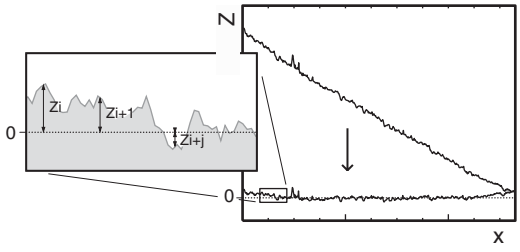


Figure 2. The standard deviation of the roughness heights is determined from a slope-detrended longitudinal profile.

roughness in rough channels (Furbish, 1987; Aberle, 2000; Aberle and Smart, 2003). From the residuals of slope-detrended longitudinal profiles (see Figure 2), the standard deviation of the bed elevations can be calculated as

$$s = \sqrt{\frac{1}{n_m - 1}\sum_{i=1}^{n_m}(z_i - z_m)^2}, \qquad (1)$$

where n_m denotes the number of measuring points, z_i is the elevation of point i, and z_m denotes the mean of the bed elevation level.

2.2 *Macro-scale: Riffles and pools*

In the macro-scale, successions of steeper and flatter sections are denoted as riffle-pool sequences and are often associated with bar features. In straight channels, these bar features are usually located alternately at the channel banks and have mainly been observed and described for gravel-bed streams (Leopold et al., 1964; Richards, 1976; Thompson, 2001). In general, the bed slopes of the riffle sections are steeper than the reach-averaged value and are charaterised by small flow depths and high flow velocities, whereas the pools are gently sloping sections with large flow depths and low flow velocities (see Figure 1).

As width is often constricted in steep open channels, riffles and pools in connection with alternate bars tend to be absent from or poorly developed in boulder-bed streams. Even for cases where sufficient width is available, a variable course often inhibits a rhythmic development of bar features. Nevertheless, bar features as well as meandering tendencies have also been described for boulder-bed channels (Leopold et al., 1964; Wohl et al., 1993).

3 FLOW RESISTANCE

For uniform flow conditions, the water-surface slope, friction slope, and energy gradient are parallel to the streambed and the cross-sectional area, hydraulic radius and flow depth remain relatively constant throughout the stream reach. In contrast to this, the flow in mountain torrents is highly nonuniform with zones of separation, acceleration and deceleration around the roughness elements. Following this, uniform flow conditions in steep open channels are not present at a local scale. However, considering a spatial average of the hydraulic parameters, the flow is usually assumed as quasi-uniform (Bathurst, 1978).

3.1 *Model of composite roughness*

For stable-bed channels, flow resistance can be considered to arise from skin friction and form resistance. Whereas skin friction can be described by the concept of bed shear stress, form resistance is better expressed by the sum of the hydrodynamic forces acting on the individual bed features. Nevertheless, form resistance is often expressed by a shear stress as well, so that the total bed shear stress, τ (or equivalently channel gradient, S) can be subdivided into a component assigned to skin friction, and a component that is attributed to the bed irregularities (Einstein and Barbarossa, 1952; Yalin, 1977).

Copyright © 2006 Taylor & Francis Group plc, London, UK

For losses due to isolated roughness elements, Einstein & Banks (1950) proved for a certain range of roughness concentrations that the total flow resistance could be expressed by the sum of resistances offered by the individual roughness elements, corresponding to the isolated roughness flow as defined by Morris (1959). However, in flows with large scale roughness, wake interferences are the standard case as bedforms exist in different orders of magnitude. These bedforms interfere with each other in such a complex way that the application of a linear superposition of roughness components does not reproduce the existent physical conditions. However, due to the lack of alternatives, this concept is also applied to steep open channels (Egashira and Ashida, 1991; Curran and Wohl, 2003).

3.2 *Meso-scale: Steps and pools*

The energy dissipating mechanisms in step-pool streams predominantly correspond to form resistance which includes form drag, wake interference, and free surface distortion. A fundamental understanding of flow resistance in step-pool channels requires the knowledge of the temporal and spatial variations of the energy dissipating mechanisms. Following this, the model of composite roughness basing on linear superposition of resistance components should not be considered to have a fundamental physical background, as it does not represent the variable conditions found in steep open channels.

A variety of flow resistance equations have been proposed that consider conditions typical for steep open channels. Most of these approaches in steep rough channels contain a characteristic grain size (Rickenmann, 1990; Vogel, 2003) to describe the bed roughness geometry which has been found to be unsuitable for the complex geometries of mountain torrents (Aberle and Smart, 2003; Weichert, 2006).

For step-pool channels, Aberle and Smart (2003) introduced the standard deviation of the roughness heights as characteristic roughness parameter (see Equation 1) and verified its validity by the analysis of experimental data. From this set of data the following flow resistance equation has been proposed, where U denotes the average velocity, U_* is the bed shear velocity, h expresses the average flow depth, and s the standard deviation of the roughness heights, as defined in Equation 1

$$\frac{U}{U_*} = 0.91\frac{h}{s}. \tag{2}$$

Aberle and Smart's considerations are based on experiments with small $W_f - d_{max}$-ratios (see Table 2), where W_f denotes the flume width and d_{max} is the maximum grain size. Hence, it can be assumed that macro-scale bed features were mainly absent.

3.3 *Macro-scale: Riffles and pools*

In case of gravel-bed rivers with macro-scale bed features, some attempts have been made to evaluate the flow resistance with the specific objective to identify the portion of total flow resistance that is directly attributed to the riffle-pool sequences (Parker and Peterson, 1980; Prestegaard, 1983; Hey, 1988). At low flow stages, bedforms in the macroscale become exposed and contribute substantially to the total flow resistance whereas at flood stages, they usually are submerged and contribute little to the total resistance. According to Parker and Peterson (1980), the mechanisms that contribute to the extra resistance include expansion losses in the lee of the bar fronts, antidune and standing wave formation when the flow is near critical or supercritical and dropstructure losses in the riffles when the flow is so shallow that they act as controls.

Both, Parker and Peterson (1980) and Prestegaard (1983) applied the concept of composite roughness where the energy slope is divided into a grain and a bar influenced component, S_{gr} and S_{fo}, respectively. Correspondingly, flow resistance is divided into its components as well, and the bar resistance component, expressed by a Chézy-coefficient c_{fo} is calculated by the difference between the total, measured flow resistance c and a grain resistance component c_{gr} calculated from the Keulegan-Equation

$$\frac{U}{U_*} = 2.5ln\frac{h}{k_s} + 6.0. \tag{3}$$

Parker and Peterson (1980) used field data to account for the influence of the bar features with

$$c_{fo} = 2.33 \cdot 10^{-6}\left(\frac{RS_{gr}}{s-1}\right)^{-1.744}. \tag{4}$$

Parker and Peterson (1980) proposed the hydraulic roughness parameter in Equation (3) to be $k_s = 2d_{90}$. This choice largely influences the derivation of Equation (4). Prestegaard (1983) used $k_s = d_{84}$. According to Hey (1988), this leads to a significant underestimation of the grain friction slope and an overestimation of the bar friction slope. Robert 1997 criticised that the approach of Parker and Peterson (1980) does not directly take into account the morphology of pools and riffles, as e.g. size and spacing of the bed features.

4 FLUME EXPERIMENTS

The purpose of the experiments described herein was to study the bed morphology, flow resistance and stability in steep open channels that exhibit steps and pools. The experiments were carried out in a rectangular flume of 13.40 m length and 0.60 m depth (see

Copyright © 2006 Taylor & Francis Group plc, London, UK

Figure 3). The width of the channel could be adjusted, so that different widths (0.15 m, 0.30 m, 0.60 m) were considered in the experiments. The sidewalls of the flume were made of glass and steel. The influence of the channel boundary was tested with a sidewall correction. However, due to the extreme bed roughness and relatively high ratios of channel width to flow depth the resistance was little affected by the sidewalls. As a consequence, for the evaluation of the present data set, no differentiation was made between the flow depth, h, and the hydraulic radius of the bed section, R.

A widely-graded sediment mixture was used that roughly corresponded to the Steinibach-torrent, Canton of Obwalden in the Swiss Alps with a scale of 1 : 20 (Table 1). This mixture in connection with the examined flume slopes of 5%, 9%, 13% guaranteed that a step-pool morphology developed.

The ratio of flume width to maximum grain size, W_f/d_{max}, is an important parameter with respect to the development of bed features in different scales. Within the present study, the W_f/d_{max}-ratio was varied between 3.3 and 13.2. A comparison with other step-pool flume studies (see Table 2) reveals that most of the previous investigations focussed on smaller W_f/d_{max}-ratios.

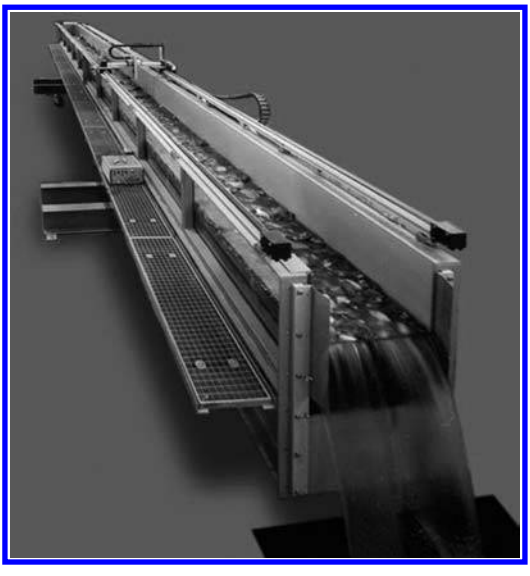


Figure 3. Flume used for the experiments.

Table 1. Grain size distribution applied in the flume experiments.

d_{16}	2 mm
d_{50}	6 mm
d_{65}	10 mm
d_{84}	19 mm
d_{90}	26 mm
d_{max}	45 mm
d_m	10 mm

After an experimental run, the channel bed was scanned by a laser displacement sensor in a predetermined regular, dense grid with sample intervals of $\Delta x = 0.02$ m in the main flow direction, and $\Delta y = 0.01$ m in the lateral direction. Compared to the maximum grain size, this is equivalent to $0.44\, d_{max}$ in the x-direction, and $0.22\, d_{max}$ in the y-direction. Depending on flume width, between 12 and 54 longitudinal profiles were recorded. The laser measurements were carried out at dry and wet bed conditions, respectively. At a dry bed, the laser data was used to obtain a detailed map of the bed topography. At a wet bed condition, the laser data was used to distinguish between wet and dry channel bed sections. Most of the experimental results were based on the analysis of longitudinal profiles obtained from the laser measurements. The discrimination between wet and dry sections allowed to adapt the analysis of the longitudinal profiles to the stream course. In this respect, an automated algorithm was developed and was applied to the digital elevation data. If no bar structures were present, the longitudinal profiles were taken in the lengthwise direction of the flume, parallel to the flume side walls. If bar features were present, the longitudinal profiles were defined by following the channel alignment (see Figure 4).

In addition to the laser sensor, an ultrasonic probe was installed at the positioning system in order to detect the free water surface. For a calm water surface, the probes gave a digital distance reading with a resolution of ± 0.5 mm. However, for the small relative submergences considered in the present study, a heavily disturbed, unsteady water surface existed. The measuring signal had a conical extension with an angle of propagation of 10 degree on each side of the 13 mm wide probe. The shortest distance within the considerable large detection area in a specific time interval was recorded. Following this, the ultrasonic devices were not considered to deliver highly accurate values of the local flow depth. However, preliminary tests revealed that averaging of the local values over a length of 8 cm $\equiv 1.8\, d_{max}$ was sufficient to remove the influence of the unsteady free surface.

Table 2. Ratios of flume width to maximum grain size for different step-pool flume studies.

Author	W_f/d_{max}
Whittaker & Jaeggi (1982)	2.6
Grant & Mizuyama (1991)	7.8–8.3
Rosport (1997)	3.1–6.3
Lee (1998)	4.7
Crowe (2002)	2.3–3.3
this study	3.3–13.2

Copyright © 2006 Taylor & Francis Group plc, London, UK

Detailed information about the experimental procedure and the measuring apparatus can be obtained from Weichert (2006).

5 ANALYSIS

5.1 *Bed morphology*

According to Leopold and Wolman (1957) river channels possess three characteristic fluvial morphologies: straight, meandering and braided. Bar structures alternately located on both banks may be a fundamental prerequisite for meandering or braiding, hence, they can be considered as a transition bed form from a straight channel to meandering or braiding. Several authors (Anderson et al., 1975; Jaeggi, 1983; da Silva, 1991) presented delimitation criteria for the different channel forms depending on the main parameters which are channel width, W, flow depth, h, channel gradient, S, and a characteristic grain size diameter, d. The delimitation diagrams proposed by several authors are mostly limited to observations of channel patterns at relatively small slopes compared to step-pool channels. As width, slope and discharge were varied within the flume experiments, the delineation criteria can be compared for steep open channels with slopes ranging up to 13%. Table 3 lists the observed morphologies for the different experimental runs. In Figure 5, the experimental data is compared with the delimitation criteria of da Silva (1991) and the modifications

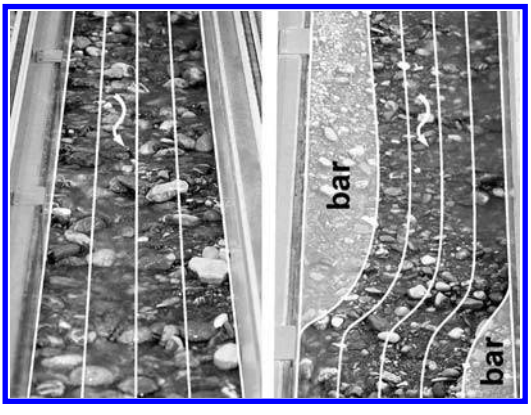


Figure 4. Evaluation of the longitudinal profiles depending whether bar features were present or not.

Table 3. Macro-scale structures observed in the flume experiments. Run denotations in brackets correspond to Figure 5. S denotes the flume slope, W_f the flume width, Q the discharge. The morphologies are abbreviated by *s*: straight, *db*: diagonal bars, and *b*: braided.

S [%]	W_f [cm]	**Q** [l/s]	**Morphology**
5	30	8	s (a_1)
5	30	10	s (a_2)
5	30	12	s (a_3)
5	30	13	s (a_4)
5	30	15	s (a_5)
9	30	5	s (b_1)
9	30	6	s (b_2)
9	30	7	s (b_3)
9	30	8	s (b_4)
13	30	2	db (c_1)
13	30	3	s/db (c_2)
13	30	5	s (c_3)
13	30	6	s (c_4)
5	60	10	db (d_1)
5	60	14	db (d_2)
5	60	18	db (d_3)
9	60	2	b (e_1)
9	60	6	db (e_2)
9	60	8	db (e_3)
13	60	2	db/b (f_1)
13	60	3	db (f_2)
13	60	4	db (f_3)
13	60	5	db (f_4)
13	60	6	db (f_5)
13	60	7	db (f_6)

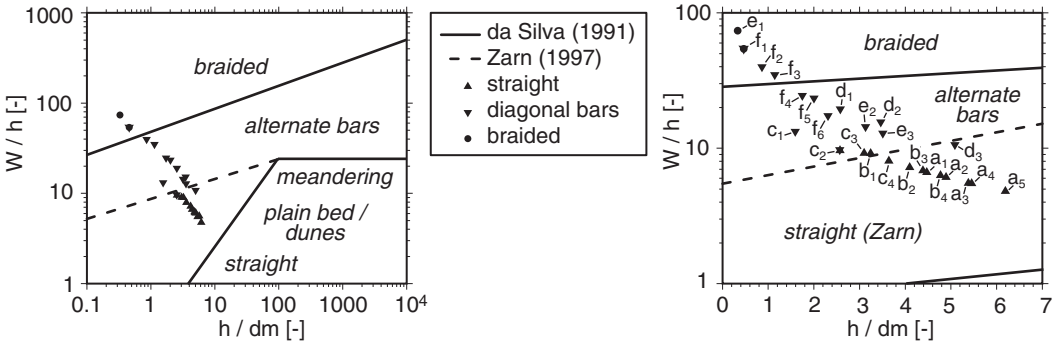


Figure 5. Delimitation diagram proposed by da Silva (1991) with the modifications of Zarn (1997) compared with the flume observations in a log-log-scale (left) and in a semi-logarithmic scale (right). Points are denoted according to Table 3.

Copyright © 2006 Taylor & Francis Group plc, London, UK

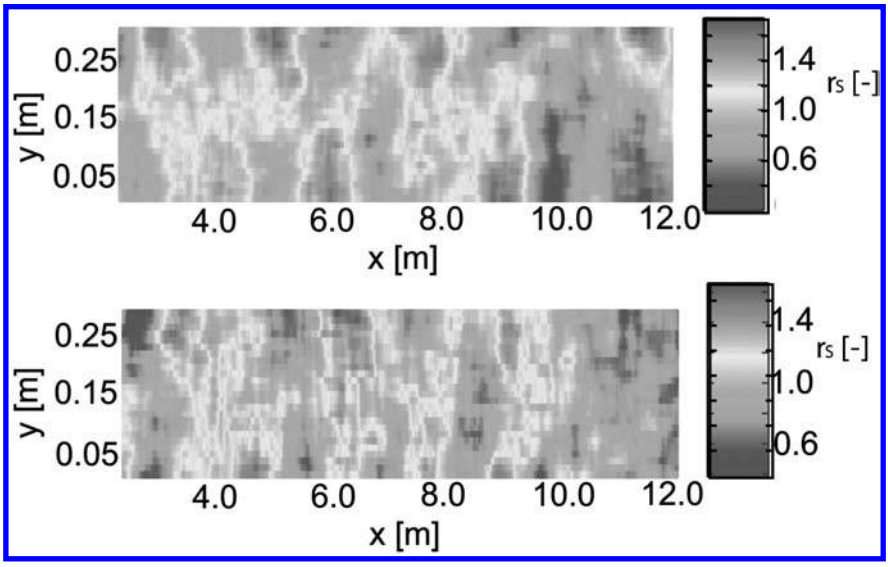


Figure 6. Ratio of the local slope to the average slope over the whole flume, $r_S = S/S_{reach}$ for the experiments with a flume slope of 9%, a flume width of 30 cm and a discharge of 5 l/s (above). The picture below represents a flume slope of 9%, a flume width of 30 cm and a discharge of 8 l/s.

proposed by Zarn (1997). It should be emphasised that in nature, the transitions from one bedform to another occur gradually rather than abruptly, as it is suggested from the diagram. Figure 5 in combination with Table 3 demonstrate that the predicted bedforms from the diagram are mostly consistent with the experimental data when the modifications by Zarn (1997) are taken into account. This result suggests an analogy for the formation processes of the macro-scale bed features in flat and steep channels.

In the present study, the classification of the morphologies is based on the visual impression of the planform morphology. In case of diagonal bars, this corresponds to a horizontal variation of the stream course. In addition to this horizontal oscillation, a vertical variation of the channel bed existed. In the following, the interconnection between the horizontal and the vertical variation of the bed is considered in more detail.

Figure 6 illustrates two contour plots, where the ratio, r_S, of the local slope to the reach-averaged slope (average over the whole flume length) is shown for every measuring point in the flume. The local slope was determined over a section length of 1 m. The upper part of the figure corresponds to the experiment with a flume slope of 9%, a flume width of 30 cm and a discharge of 5 l/s, whereas the figure below represents the experiment with a flume slope of 9%, a flume width of 30 cm and a discharge of 8 l/s. As listed in Table 3, bar structures were absent for both runs.

In contrast to the visual impression of the bed morphology, the slopes for the run with $Q = 5$ l/s clearly indicate alternately located bed features at the sidewalls. These features are associated with gradients steeper than the average ($r_S > 1$) and gradients smaller than the average slope in the reach-scale ($r_S < 1$). As a consequence, they are denoted as riffles and pools. The wavelengths, λ (defined in Figure 7) are approximately 3–5 flume widths, which are similar values as observed for gravel bed rivers. For the flume experiments in the present study, the discharge is increased in small increments starting from a plane bed. Hence, for small discharges, diagonal bar structures tend to form at every flume width investigated. As a consequence, the generation of the horizontal and the vertical structures are closely associated with each other. As already noted by Parker and Peterson (1980), riffles and pools are nothing more than juxtapoints of successive diagonal bar structures. With increasing discharge, the bar structures vanish, whereas the riffle-pool features prevail. However, at large discharges, these macro-scale bed features rearrange in the way, that the oppositely at the side walls located riffle-structures tend to join with each other. This results in transversely oriented macro-scale bed features (see Figure 6).

Although the described macro-scale bed features resemble riffle-pool sequences in gravel-bed rivers, they differ with respect to their appearance in the meso-scale. In gravel-bed rivers, the riffle sections usually exhibit meso-scale bedforms, whereas the pools are mainly free of bedforms. On the contrary, in boulder-bed streams meso-scale bedforms could be observed independently on the location (compare Figure 7).

Copyright © 2006 Taylor & Francis Group plc, London, UK

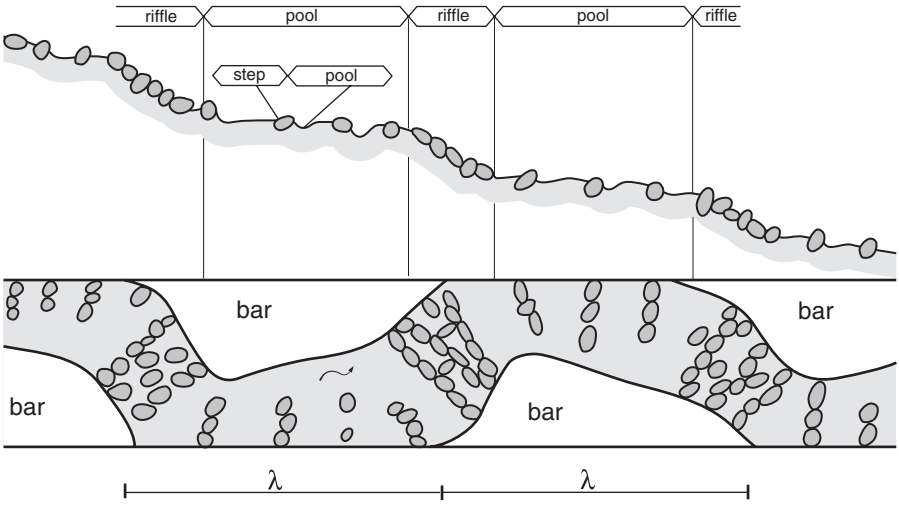


Figure 7. Macro-scale bed features as observed in the flume experiments.

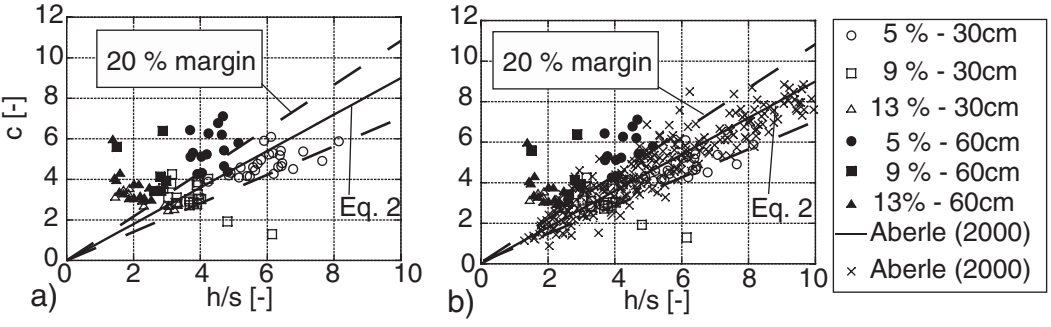


Figure 8. Comparison between the flow resistance equation of Aberle and Smart (2003) and the present data – (a) without the original data of Aberle and (b) with the original data of Aberle. The flow resistance, expressed by the Chézy-coefficient c, is illustrated depending on the relative submergence h/s. Herein, s denotes the standard deviation of the roughness heights.

However, in accordance to gravel-bed rivers, more of the coarse material could be found on the riffles than in the pools. Whereas the riffles exhibited meso-scale structures that correspond to boulder-glide sections or large steps, in the pools smaller step structures developed.

5.2 *Flow resistance*

In the following, the present data set is evaluated with respect to the flow resistance. The inadequacy of flow resistance equations that contain a characteristic grain size to describe the conditions of step-pool channels is discussed in Aberle (2000) or Weichert (2006). The present paper mainly focusses on a comparison between the flume data of this study and Equation 2 in order to evaluate the influence of the macro-scale bed features on the flow resistance.

Flow resistance can be expressed by the Chézy-coefficient, which is defined as

$$c = \frac{U}{\sqrt{ghS}} = \frac{q}{\sqrt{gh^3S}}. \quad (5)$$

For the following considerations, the bed area was divided into 5 sections, each with a length of 2.12 m, as the Chézy-coefficient is based on the assumption of quasi-uniform flow conditions which require an temporal and spatial averaging of the local parameters (flow depth, h, and channel gradient, S). The specific discharges were obtained by dividing the discharge Q by the channel width W (see Figure 10).

In Figure 8 the Chézy-values of the present data set are compared with Equation 2 proposed by (Aberle and Smart, 2003). For flume widths of 30 cm, the measured values fit relatively well with Equation 2. In contrast,

Copyright © 2006 Taylor & Francis Group plc, London, UK

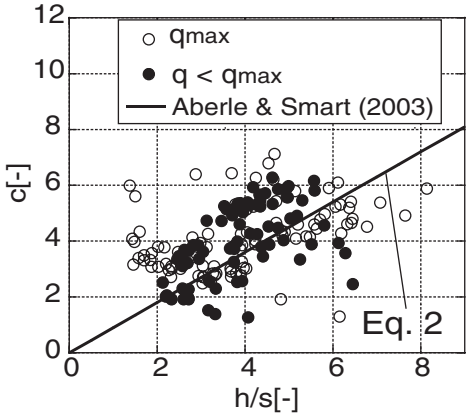


Figure 9. The influence of flow stage on the flow resistance.

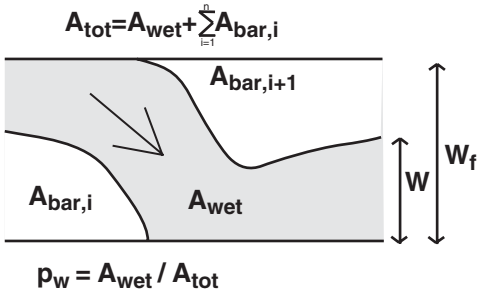


Figure 10. Definition sketch for p_w (see Equation 6).

the runs with a flume width of $W_f = 60$ cm deviate significantly from Aberle's approach. This behaviour indicates an influence of the macro-scale bar features on the flow resistance.

No difference could be established between the data of experiments at bedforming discharges or at smaller discharges (see Figure 9).

The influence of the macro-scale bar features on the flow resistance is analysed in Figure 11, where the ratio of the total, measured flow resistance, c, and the flow resistance of the meso-scale structures, c_{meso}, is shown. In this respect, c_{meso} is calculated with Equation (2) proposed by Aberle and Smart (2003). In order to account for the observed difference in flow resistance whether bar features were absent or not, the portion of the wetted area, A_{wet}, on the whole area of the channel bed, A_{tot}, is taken as a parameter to describe the pronouncement of the bed features in the macro-scale (see Figure 10). This means, the larger p_w, the smaller the influence of macro-scale bed features.

$$p_w = \frac{A_{wet}}{A_{tot}}. \tag{6}$$

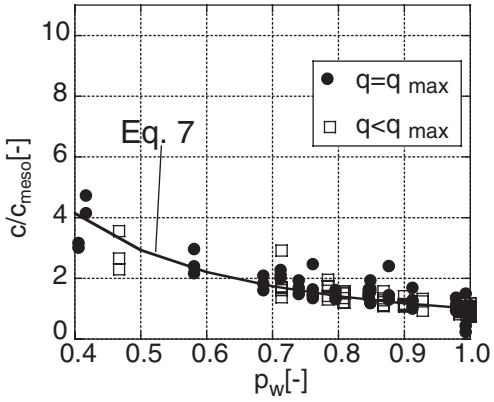


Figure 11. The influence of macro-scale bed features on the flow resistance.

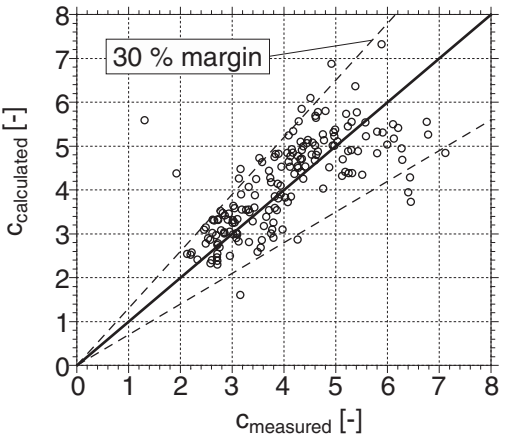


Figure 12. Comparison between measured Chézy-coefficients and those calculated with Equation 8.

In general, Figure 11 shows that the ratio c/c_{meso} decreases with increasing value of $p_w = A_{wet}/A_{tot}$. The best fit ($r^2 = 0.84$) of the data in Figure 11 is

$$\frac{c}{c_{meso}} = p_w^{-1.58} \tag{7}$$

for $p_w \geq 0.4$.

Expressing c_{meso} by Equation (2), the data of the present study is best described with

$$c = 0.91 \cdot p_w^{-1.58} \cdot \frac{h}{s}. \tag{8}$$

With this equation, the effects of the different geomorphologic scales are separatively but not additively taken into account. Whereas the standard deviation of

Copyright © 2006 Taylor & Francis Group plc, London, UK

the roughness heights, s, focusses on the mesoscale structures, the parameter, p_w accounts for the macroscale bed features. In Figure 12, the comparison between the measured and the calculated Chézy-coefficients demonstrate the adequacy of Equation 8 (compared to the errors of other flow resistance equations – see Weichert 2006) to consider the flow resistance in steep open channels.

In general, the results shown in Figure 11 are not evoked by a resistance-diminishing effect of the bar features. On the contrary, they demonstrate the effect of the bar features on the development of the mesoscale roughness structure. As a conclusion, the introduction of p_w in Equation 8 points out the necessity for an adequate description of the roughness structure when different geomorphologic scales are present.

Although the previous considerations showed the adequacy of the parameter p_w to explain the processes within the flume, a fundamental aspect concerns its applicability under field conditions. The parameter p_w is defined by the wetted channel bed area, A_{wet}, divided by the whole area of the channel bed, A_{tot} (see Figure 10). Whereas A_{wet} can be measured under field conditions, the question remains how to determine A_{tot}. Here, it is proposed to assess A_{tot} by considering the bankfull width of the channel. As the determination of the bankfull width is not a straight-forward issue in steep open channels, p_w can only be determined as an approximation.

6 CONCLUSIONS

Steep open channels are characterised by coarse, structured armour layers that are often denoted as step-pool systems. Additionally, the ratio of flume width to maximum grain size plays a significant role, as it determines the number of boulders required for a total blocking of the channel. For larger flume widths, the occurrence of macro-scale bed features could be observed, which influence all relevant processes. Following this, the description of the roughness structure depending on the existent geomorphologic scales is an important aspect regarding the assessment of all important processes. In this connection, the present study shows the suitability of the standard deviation of the roughness heights to describe the roughness geometry in the meso-scale.

The considered ratios of flume width to maximum grain size allowed for an assessment of the macroscale bed features. These structures are characterised by both a horizontal as well as a vertical variation of the channel bed. The horizontal, quasi-meandering tendency is evoked by bar features located alternately at the channel sides. These features could be identified with delimitation criteria as e.g. the one proposed by da Silva (1991), if the modificatons of Zarn (1997) are taken into account.

In addition to the horizontal oscillation, vertical variations express successions of steep and gentle gradient sections, i.e. riffle and pool sections. An important result of the present study concerns the observation that these features possibly occur although the horizontal oscillations are not apparent, i.e. for relatively small flume widths.

The macro-scale bed features significantly influence the flow resistance. For the conditions without macro-scale bed features, the flow resistance data of the present study can be predicted by the equation proposed by Aberle and Smart (2003). In contrast, the deviations increase when pronounced macro-scale bed features are present. Experiments with wellpronounced bar features had smaller values of the flow resistance. This effect can be attributed to differences in the meso-scale structure, that occur depending whether bar features are present or not. The effect of the macro-scale bar features can be taken into account with Equation 8 which is an extension of the approach proposed by Aberle and Smart.

REFERENCES

Aberle, J. (2000). Untersuchung der Rauheitsstruktur zur Bestimmung des Fließwiderstandes in Gebirgsbächen unter Klarwasserabfluss. *Mitteilungen des Instituts für Wasserwirtschaft und Kulturtechnik. Universität Karlsruhe (TH). Heft 207*.

Aberle, J. and Smart, G. M. (2003). The influence of roughness structure on flow resistance on steep slopes. *Journal of Hydraulic Research*, 41(3):259–269.

Anderson, A. G., Parker, G., and Wood, A. (1975). The flow and stability characteristics of alluvial channels. *Project Report 161, St. Anthony Falls Hydraulic Laboratory, Minneapolis, Minnesota*.

Bathurst, J. C. (1978). Flow resistance of large-scale roughness. *Journal of the Hydraulics Division-ASCE*, 104(12):1587–1603.

Bray, D. I. (1987). Estimating average velocity in cobble-bed channels. In Ragan, R. M., editor, *Proc. of the 1987 National Conference on Hydraulic Engineering*, Williamsburg, Virginia. American Society of Civil Engineers.

Buffin-Belanger, T. and Roy, A. G. (1998). Effects of a pebble cluster on the turbulent structure of a depth-limited flow in a gravel-bed river. *Geomorphology*, 25(3-4):249–267.

Crowe, J. (2002). *An experimental study of the step-pool bed form*. PhD thesis, The Johns Hopkins University.

Curran, J. H. and Wohl, E. E. (2003). Large woody debris and flow resistance in step-pool channels, Cascade Range, Washington. *Geomorphology*, 51(1-3):141–157.

da Silva, A. M. A. F. (1991). *Alternate bars and related alluvial processes*. PhD thesis, Queent's University, Kingston Ontario, Canada.

Egashira, S. and Ashida, K. (1991). Flow resistance and sediment transportation in streams with step-pool bed morphology. In Armanini, A. and Di Silvio, G., editors,

Copyright © 2006 Taylor & Francis Group plc, London, UK

Fluvial hydraulics of mountain regions, Lecture notes in earth sciences, pages 45–58. Springer-Verlag, Berlin.

Einstein, H. A. and Banks, R. (1950). Fluid resistance of composite roughness. *Trans. Amer. Geophys. Union*, 31(4): 603–610.

Einstein, H. A. and Barbarossa, N. L. (1952). River channel roughness. *Transactions of the American Society of Civil Engineers*, 117:1121–1132.

Furbish, D. J. (1987). Conditions for geometric similarity of coarse stream-bed roughness. *Mathematical Geology*, 19(4):291–307.

Grant, G. E. and Mizuyama, T. (1991). Origin of step-pool sequences in high gradient streams: a flume experiment. In *Proc. Japan-USA workshop on snow avalanche, landslide and debris flow prediction and control*, pages 523–532, Tsubuka, Japan. Japan Science and Technology Agency, National Research Institute for Earth Science and Disaster Prevention.

Hey, R. D. (1988). Bar form resistance in gravel-bed rivers. *Journal of Hydraulic Engineering ASCE*, 114(12): 1498–1508.

Jaeggi, M. N. R. (1983). Alternierende Kiesbänke. *Mitteilungen der Versuchsanstalt für Wasserbau, Hydrologie und Glaziologie (VAW). ETH Zürich. Nr. 62*.

Lawless, M. and Robert, A. (2001). Three-dimensional flow structure around small-scale bedforms in a simulated gravel-bed environment. *Earth Surface Processes and Landforms*, 26(5):507–522.

Lee, A. (1998). *The hydraulics of steep streams*. Phd-thesis, Sheffield University.

Leopold, L. B. and Wolman, M. G. (1957). River channel patterns: braided, meandering and straight. *U.S. Geological Survey Professional Paper, GPO, Washington. Vol. 282-B*.

Leopold, L. B., Wolman, M. G. and Miller, J. P. (1964). *Fluvial processes in geomorphology*. W.H. Freeman, San Francisco, California.

MacFarlane, W. A. and Wohl, E. (2003). Influence of step composition on step geometry and flow resistance in step-pool streams of the Washington Cascades. *Water Resources Research*, 39(2):art. no. 1037.

Morris, H. (1959). Design methods for flow in rough channels. *Proc. ASCE, Journal of the Hydraulic Division*, 85 (HY7):43–62.

Parker, G. and Peterson, A. W. (1980). Bar resistance of gravel-bed streams. *Journal of the Hydraulics Division-Asce*, 106(10):1559–1573.

Prestegaard, K. L. (1983). Bar resistance in gravel bed streams at bankfull stage. *Water Resources Research*, 19(2): 472–476.

Richards, K. S. (1976). Morphology of riffle-pool sequences. *Earth Surface Processes and Landforms*, 1(1):71–88.

Rickenmann, D. (1990). Bedload transport capacity of slurry flows at steep slopes. *Mitteilungen der Versuchsanstalt für Wasserbau, Hydrologie und Glaziologie (VAW). ETH Zürich. Nr. 103*.

Robert, A. (1997). Characteristics of velocity profiles along riffle-pool sequences and estimates of bed shear stress. *Geomorphology*, 19(1-2):89–98.

Thompson, D. M. (2001). Random controls on semi-rhythmic spacing of pools and riffles in constriction-dominated rivers. *Earth Surface Processes and Landforms*, 26(11):1195–1212.

Vogel, S. (2003). *Ansätze zur Bemessung rauer Rampen in aufgelöster Bauweise*. PhD thesis, Institut für Wasserwesen, Universität der Bundeswehr München.

Weichert, R. (2006). Bed morphology and stability in steep open channels. *Mitteilungen der Versuchsanstalt für Wasserbau, Hydrologie und Glaziologie (VAW). ETH Zürich. Nr. 192*.

Whittaker, J. G. and Jaeggi, M. N. R. (1982). Origin of step-pool systems in mountain streams. *Journal of the Hydraulics Division-ASCE*, 108(6):758–773.

Wohl, E. E., Vincent, K. R., and Merritts, D. J. (1993). Pool and riffle characteristics in relation to channel gradient. *Geomorphology*, 6(2):99–110.

Yalin, M. (1977). *Mechanics of sediment transport*, volume 2nd edition. Pergamon press, Oxford.

Zarn, B. (1997). Einfluss der Flussbettbreite auf die Wechselwirkung zwischen Abfluss, Morphologie und Geschiebetransortkapazität. *Versuchsanstalt für Wasserbau, Hydrologie und Glaziologie (VAW). ETH Zürich. Mitt. Nr. 74*.

Zimmermann, A. and Church, M. (2001). Channel morphology, gradient profiles and bed stresses during flood in a step-pool channel. *Geomorphology*, 40(3-4):311–327.

Copyright © 2006 Taylor & Francis Group plc, London, UK

A vertical two-dimensional morphodynamic model for bedform simulation

S. Giri & Y. Shimizu
Hokkaido University, Sapporo, Japan

ABSTRACT: A vertical two-dimensional morphodynamic model with non-hydrostatic, unsteady free surface flow is proposed herein. Model simulates flow and turbulence structures induced by sand waves under free surface flow condition. Furthermore, model can reproduce physically the formation and migration process of sand waves from an initially flat bed condition. A moving boundary coordinate system is employed. A state-of-the-art turbulence closure is used, known as nonlinear k-ε model with an allowance for anisotropy of Reynolds stresses in region with flow separation. A high order Godunov scheme referred to as Cubic Interpolated Pseudo-particle (CIP) numerical technique is employed to compute advection phase of Navier-Stokes equations. An Eulerian stochastic formulation of sediment exchange process as pick up and deposition function that explicitly considers the local flow variability during morphodynamic computation is incorporated to compute non-equilibrium sediment transport. The model prediction capability is verified against laboratory observations on dune evolution. In addition, prediction of dune geometry by numerical model is compared with results obtained by using some empirical relations.

1 INTRODUCTION

The microscale sand waves, particularly dunes, in alluvial streams are usually formed in lower flow regime under rough turbulent condition. Several investigations have been carried out so far that have made invaluable contributions to improve understanding on morphodynamic features of bedforms as well as flow and turbulence characteristics induced by sand waves. The complex hydraulic and morphodynamic aspects associated with bedform evolution have an important bearing on problems; however still remain poorly understood despite numerous efforts that have been made since long.

Understanding flow and turbulence induced by sand waves is of importance to explicate their formation mechanism and further development. Number of physical studies in this regard was made in the past (Bennet & Best, 1995; Nelson et al., 1993; Best et al.,1997). For instance, Nelson et al. (1993) conducted flow and turbulence measurement over two-dimensional fixed dunes, in which effects on bedform instability and finite amplitude stability along with the coupling of mean flow and turbulence were examined. Schmeeckle et al. (1999) conducted laboratory visualization of turbulence and suspended sediment transport over two-dimensional dune. Furthermore, some notable numerical studies were also carried out (Mclean & Smith, 1986; Mendoza-Cabrales, 1987). Shimizu et al. (2001) performed a three-dimensional direct numerical simulation of flow and turbulence over two-dimensional fixed dunes. The numerical model was able to reproduce the coherent structure induced by dune crest adequately. Most observations yielded strong correlation between coherent turbulence structure induced by flow separation, bed resistance and sediment transport mechanism. The flow field and bed configuration are found to be interdependent having direct and converse effect on each other that creates difficulties in appropriate physical interpretation and quantitative determination of the said problem. Numerous approaches were developed in order to quantify sand wave induced morphology of alluvial channels. Most early investigations were conducted using theoretical, semi-empirical and empirical approaches (Engelund, 1970; Engelund & Fredsoe, 1982). Among them, theoretical studies are largely based on linear stability theory which is, in effect, not appropriate approach for the determination of natural phenomena having finite amplitude features (Nelson et al.,1993). Scant attention has been given in regard to numerical modeling of sand waves morphodynamics (Fredsoe & Tjerry, 2001; Tjerry & Fredsoe, in print). Nakayama and Shimizu (2001) carried out a numerical study on suspended sediment transport over sand waves. They compared the computation result of time averaged concentration of suspended sediment with Rouse distribution curve as well as laboratory

Copyright © 2006 Taylor & Francis Group plc, London, UK

measurements. One of the significant studies was made by Onda & Hosoda (2004), in which a depth-integrated flow model was proposed with an allowance for vertical acceleration. They described bottom shear stress based on potential flow analysis considering acceleration-deceleration effect near the bed. In order to compute water surface profile, a numerical technique was used to simulate undular bore and flow over dunes with an attempt to eliminate the deficiency of hydrostatic pressure assumption by introducing a reduction factor to the vertical acceleration terms. Furthermore, they used sediment pick up and deposition function (Nakagawa & Tsujimoto, 1980) to simulate sand dune formation. Finally, they analyzed temporal variation of sand wave spectrum as well as dune geometry using their numerical results. However, this flow model cannot reproduce separation behind dune crest and, thereby, its effect on flow field and sediment transport. Recently, a comprehensive review has been conducted by Best (2005) where principal feature of mean flow and turbulence over dunes has been summarized as well as prospective areas for future research have been pointed out.

Present research has been prompted by the need to develop a more complete and reliable computational model to simulate flow and morphodynamic features of sand waves in a physically based manner. There is no doubt that earlier proposed three-dimensional model (Shimizu et al., 2001) is more complete approach for computation of flow and turbulence over bedforms. However, coupling this flow model with a morphodynamic module may inhibit it from being applied efficiently because of rather high computational effort. Consequently, aforesaid three-dimensional hydrodynamic model is simplified to be a vertical two-dimensional model and enhanced by imposing non-hydrostatic, free surface flow condition and coupled with a morphodynamic module. The model is verified against laboratory measurement of bedform geometry and visualization of dune migration process. Likewise, prediction of geometric characteristics of bedforms is validated with some relations for bedform geometry proposed by van Rijn (1983b) and Julien & Klaassen (1995).

2 HYDRODYNAMIC MODEL

2.1 *Conservation equations*

The governing equations for vertical two-dimensional flow in cartesian coordinate system reads as:

$$\frac{\partial u}{\partial x}+\frac{\partial v}{\partial y}=0 \tag{1}$$

$$\frac{\partial u}{\partial t}+u\frac{\partial u}{\partial x}+v\frac{\partial u}{\partial y}=-\frac{1}{\rho}\frac{\partial p}{\partial x}+\frac{\partial}{\partial x}\left(-\overline{u'u'}\right)+\frac{\partial}{\partial y}\left(-\overline{u'v'}\right) \tag{2}$$

$$\frac{\partial v}{\partial t}+u\frac{\partial v}{\partial x}+v\frac{\partial v}{\partial y}=-\frac{1}{\rho}\frac{\partial p}{\partial y}+\frac{\partial}{\partial x}\left(-\overline{u'v'}\right)+\frac{\partial}{\partial y}\left(-\overline{v'v'}\right)-g \tag{3}$$

where x and y = coordinates in horizontal and vertical direction respectively; u and v = components of velocity in horizontal and vertical direction respectively, $-\overline{u'u'}$, $-\overline{u'v'}$ and $-\overline{v'v'}$ = Reynolds stress tensors, ρ = fluid density, g = gravitational acceleration, p = pressure.

Equations (1)–(3) are transformed from x, y, t cartesian coordinate system to a moving boundary fitted ξ, η and τ coordinate system (Shimizu & Itakura, 1994).

Pressure term in momentum equations can be computed considering non-hydrostatic component as follows:

$$p=p_0+p'=g\int_y^H \rho\,dz+p'=\rho g(H-y)+p' \tag{4}$$

Eq. (4) can be rewritten as:

$$p=\rho g(H-y)+p' \tag{5}$$

in which, p' = non-hydrostatic component of pressure, H = the elevation of free surface. Calculation is performed substituting pressure term (p) by Equation (5) in momentum equations, consequently, computing the non-hydrostatic component.

2.2 *Free surface oscillation*

Computation of time-dependent water surface change is of importance for the realistic reproduction of free surface flow over migrating bedforms. Basically, majority of morphodynamic numerical models developed earlier have assumed the rigid lid water surface condition to achieve numerically stable solution. In present study, the kinematic condition is imposed along the free surface to compute temporal water surface elevation. The kinematic condition, which constraints fluid particles to remain on the water surface at any time following the local flow velocity, is expressed as follows:

$$\frac{\partial H}{\partial t}+u\frac{\partial H}{\partial x}=v \tag{6}$$

$$H=y_b+h \tag{7}$$

where y_b = bed elevation and h = local flow depth.

2.3 *Turbulence model*

In conventional k-ε model, turbulence stress tensors are evaluated using linear relationship. In order to reproduce turbulence characteristics more accurately in shear flow with separation zone, a nonlinear term is

Copyright © 2006 Taylor & Francis Group plc, London, UK

added to the standard k-ε model as follows (Kimura & Hosoda, 2003):

$$-\overline{u_i'u_j'} = \nu_t S_{ij} - \frac{2}{3}k\delta_{ij} - \frac{k}{\varepsilon}\nu_t \sum_{\beta=1}^{3} C_\beta \left(S_{\beta ij} - \frac{1}{3} S_{\beta\alpha\alpha}\delta_{ij} \right) \tag{8}$$

$$\nu_t = C_\mu \frac{k^2}{\varepsilon} \tag{9}$$

where ν_t = eddy viscosity coefficient, δ_{ij} = Kronecker delta, k = turbulent kinetic energy, ε = dissipation rate of k. The detailed description and formulation of strain tensors S_{ij}, $S_{\beta ij}$, $S_{\beta\alpha\alpha}$, as well as coefficient C_β can be found elsewhere (Kimura & Hosoda, 2003).

k-ε equations can be expressed as follows:

$$\frac{\partial k}{\partial t} + u\frac{\partial k}{\partial x} + v\frac{\partial k}{\partial y} = \frac{\partial}{\partial x}\left(\frac{\nu_t}{\sigma_k}\frac{\partial k}{\partial x} \right) + \frac{\partial}{\partial y}\left(\frac{\nu_t}{\sigma_k}\frac{\partial k}{\partial y} \right) + P_h - \varepsilon \tag{10}$$

$$\frac{\partial \varepsilon}{\partial t} + u\frac{\partial \varepsilon}{\partial x} + v\frac{\partial \varepsilon}{\partial y} = \frac{\partial}{\partial x}\left(\frac{\nu_t}{\sigma_\varepsilon}\frac{\partial \varepsilon}{\partial x} \right) + \frac{\partial}{\partial y}\left(\frac{\nu_t}{\sigma_\varepsilon}\frac{\partial \varepsilon}{\partial y} \right) + C_{1\varepsilon}\frac{\varepsilon}{\kappa}P_h - C_{2\varepsilon}\frac{\varepsilon^2}{k} \tag{11}$$

$$P_h = -\overline{u_i'u_j'}\frac{\partial u_i}{\partial x_j} \tag{12}$$

where σ_k, σ_ε, $C_{1\varepsilon}$ and $C_{2\varepsilon}$ are standard model constants.

Boundary conditions are no slip at the bed and free flow at the surface. Following expression for near-bed region is adopted:

$$\frac{u_p}{u_*} = \frac{1}{\kappa}\ln\frac{y_p}{y_0} \tag{13}$$

where u_p = velocity at near-bed grid point, u_* = bed shear velocity, κ = Karman constant, y_p = distance from bed to nearest grid, $y_0 = k_s/30$, k_s = roughness height (=2.5d), d = sediment diameter.

Periodic boundary condition is employed in streamwise direction. Turbulent energy and its dissipation in near-bed region are evaluated as proposed by Kimura & Hosoda (2003):

$$\frac{k}{u_*^2} = \frac{1}{\sqrt{C_\mu}} \tag{14}$$

$$\varepsilon = \frac{u_*^3}{ky} \tag{15}$$

In order to account for the diminution of turbulence length scale at the free surface layer, they proposed a damping function to the eddy viscosity:

$$f_s = 1 - \exp\left(-B\frac{(h-y)\varepsilon_s}{k_s^{3/2}} \right) \tag{16}$$

where $B = 10$.

The dissipation rate of turbulent energy at the surface layer is evaluated using following equation (Sugiyama et al., 1995)

$$\varepsilon_s = \frac{C_{\mu 0}^{3/4} k_s^{3/2}}{0.4\Delta y_s} \tag{17}$$

where Δy_s = distance from water surface to first grid and coefficient $C_{\mu 0} = 0.09$

$$\frac{\partial k}{\partial y} = 0 \tag{18}$$

2.4 *Numerical method*

The transformed equations are numerically solved by splitting them into non-advection and pure advection phase. The non-advection phase is computed using central difference method. The pressure field is resolved using SOR method. The advection phase is calculated using a high-order Godunov scheme known as CIP method (Yabe et al.,1990). In this scheme, at very small time increment, the change in time of velocity components at a point in space can be split into the time evolution of the inhomogeneous terms and the time evolution at a point due to the advection of the field. A brief description of CIP numerical scheme to solve advection terms in generalized coordinate system can be found elsewhere (Shimizu, 2004).

3 SEDIMENT TRANSPORT MODEL

Some earlier investigations (Schmeeckle et al., 2003; Sumer et al.,2003) have revealed that spatially or/and temporally averaged sediment transport models are inadequate to describe the extremely inconsistent nature of sediment particle motion particularly in the region with high near-bed turbulence. In effect, a direct computation of sediment particle motion, viz. Discrete Element Model (DEM), which responds to the local and temporally variable flow field, is physically more complete approach. However, coupling this approach with an advanced hydrodynamic model, at present, seems to be rather sophisticated in view of computational complexity and expenses, in particular, for solving comparatively big scale problem.

Copyright © 2006 Taylor & Francis Group plc, London, UK

Computationally efficient and relatively comprehensive approach is believed to be the modeling of pick up and deposition of sediment particles in terms of a stochastic formulation. Consequently, an Eulerian stochastic formulation of sediment transport proposed by Nakagawa & Tsujimoto (1980) is incorporated in our numerical code. This method yielded one of the best predictions of pick up function for fine sediment grain as described by van Rijn (1983a). Moreover, this approach was effectively used and validated in earlier investigations (Onda & Hosoda, 2004).

The dimensionless pick up rate is expressed as follows (Nakagawa & Tsujimoto, 1980):

$$p_s\sqrt{d/(\rho_s/\rho-1)g} = 0.03\tau_*(1-0.035/\tau_*)^3 \qquad (19)$$

where p_s = sediment pick up rate, ρ and ρ_s = fluid and sediment density respectively and τ_* = dimensionless local bed shear stress.

The sediment deposition rate reads as:

$$p_d = p_s f_s(s) \qquad (20)$$

where p_d = sediment deposition rate and $f_s(s)$ = distribution function of step length.

Distribution function of step length is found to be exponential as follows (Nakagawa & Tsujimoto):

$$f_s(s) = \frac{1}{\Lambda}\exp\left(-\frac{s}{\Lambda}\right) \qquad (21)$$

where Λ = the mean step length and s = the distance of sediment motion from pick up point.

The mean step length can be calculated as $\Lambda = \alpha d$, in which α is an empirical constant and proposed to be 100.

In order to consider the instability of bedforms in upper flow regime, a module to compute suspended sediment transport is also incorporated in proposed numerical model. Considering suspended sediment transport, the bed deformation rate can be computed using following sediment continuity equation:

$$\frac{\partial y_b}{\partial t} + \frac{1}{1-\lambda}\left[\frac{A_3}{A_2}(p_d - p_s)d + (q_{sui} - w_f c_b)\right] = 0 \qquad (22)$$

where y_b = bed elevation, λ = porosity of sediment particle, A_2 and A_3 = shape coefficients of sand grain with two- and three-dimensional geometrical properties, q_{sui} = upward suspended sediment flux per unit area, w_f = falling velocity and c_b = reference concentration of suspended sediment.

In case of equilibrium suspended sediment transport, the third term in Equation (22) vanishes.

q_{sui} is calculated using equation proposed by Itakura & Kishi (1980):

$$q_{sui} = K\left(\alpha_*\frac{\rho_s-\rho}{\rho_s}\frac{gd}{u_*}\Omega - w_f\right) \qquad (23)$$

in which,

$$\Omega = \frac{\tau_*}{B_*}\frac{\int_a^\infty \xi\frac{1}{\sqrt{\pi}}\exp(-\xi^2)d\xi}{\int_a^\infty \frac{1}{\sqrt{\pi}}\exp(-\xi^2)d\xi} + \frac{B_*\eta_0}{\tau_*} - 1 \qquad (24)$$

$$a = \frac{B_*}{\tau_*} - \frac{1}{\eta_0} \qquad (25)$$

where B_*, η_0, α_* and K are constants, the values of which are adopted as: $B_* = 0.143$, $\eta_0 = 0.5$, $\alpha_* = 0.14$ and $K = 0.008$.

The falling velocity is calculated using well-known Rubey's formula:

$$w_f = \sqrt{\frac{2}{3}Sgd + \frac{36\nu^2}{d^2}} - \frac{6\nu}{d} \qquad (26)$$

where S = relative density of sediment in water, namely 1.65, ν = kinematic viscosity of water.

4 MODEL VALIDATION

4.1 *Physical experiment*

An experimental investigation on sand dune formation and migration process was carried out under the department of hydraulic research of Hokkaido University. Experiments were performed in laboratory flume of CERI of Hokkaido. The total length of the flume was 30 m, width was 10 cm and height was 30 cm having 1/500 slope, regulated by automatic control system. The middle part of flume (10 m) was covered with 5 cm thick sediment layer with 0.28 mm median diameter, which was trapped by using sediment stoppers at the part of upstream and downstream having length of 10 m each. The sand feeding was done manually by filling up the space between movable bed and sand stopper in the upstream boundary, which formed because of transported sand. The migration process of sand dunes was visualized using high resolution video camera. Quantitative evaluation of bedform geometry was made at the end of each experiment. The experimental condition is listed in Table 1. In addition, experiments by Venditti et al (2005) were also used to verify model.

Copyright © 2006 Taylor & Francis Group plc, London, UK

4.2 *Simulation results*

4.2.1 *Flow and vorticity visualization*

Visualization of the flow and vorticity simulation over fixed dunes reveals the existence of flow separation behind dune crest (**Fig. 1**) which seems to be realistic as observed in most physical investigations. For the sake of comparison, same simulation was made using standard k-ε model. In this case, the instantaneous motion of vorticity behind dune crest as well as recirculation can not be reproduced well (**Fig. 1**). This evinces the reliability of nonlinear turbulence model for such a region with flow separation. More detail analysis on flow and turbulence was made by authors elsewhere (Giri & Shimizu, accepted).

4.2.2 *Bedform simulation-effect of grid resolution*

An attempt has been made to simulate sand wave formation and migration from a nearly flat sand bed for all experimental cases. It was found that grid resolution near the bed has significant impact on dune evolution. The dune geometry seems to be poorly predicted by numerical model in case when vertical grid is distributed uniformly. On the other hand, when same number of grid was exponentially stretched in vertical direction, the result appears to be changed dramatically. In this case, grid is dense near bed (**Fig. 2**). For the sake of comparison, simulation result of dune geometry for a typical case (Run A-5) with uniform grid and stretched grid spacing for a selected time increment is depicted in **Figure 3**. Moreover, simulation of temporal bedform evolution shows that model with non-uniform grid can reproduce rather realistically one of the important physical processes during dune evolution observed in natural rivers, namely amalgamation. A typical example of bedform evolution from a flat bed condition can be seen in **Figure 4**. It can be noticed in visualization of bedform migration that small size dunes migrate faster at first and become slower as bedform geometry increases.

Table 1. Experimental condition.

Run	Time (min)	Discharge ($cm^3/s \times 10^3$)	Flow depth (cm)	Froude number
A-1	250	2.0	7.0	0.34
A-2	105	4.0	9.9	0.41
A-3	90	6.0	12.1	0.46
A-4	75	8.0	15.2	0.43
A-5	60	10.0	16.7	0.47

4.2.3 *Prediction of dune characteristics*

Proposed morphodynamic model can reproduce dune geometry in physically based manner that appears to be realistic and close to physical observation. Some quantitative comparison between simulated and visualized dune geometry is depicted in **Figure 5**. In effect, the geometric characteristics of dunes for these experimental cases look similar since hydraulic and sediment conditions are related to the limited range. Nonetheless, prediction of such a phenomenon by

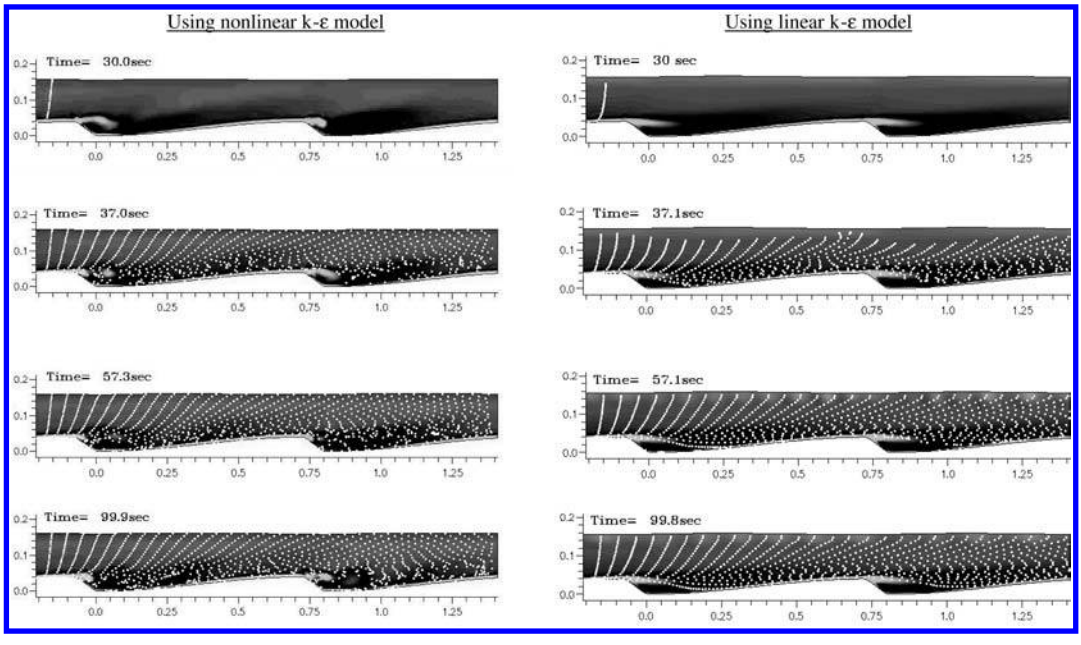


Figure 1. Instantaneous flow particle and vorticity simulation- performance of linear and nonlinear k-ε models.

Copyright © 2006 Taylor & Francis Group plc, London, UK

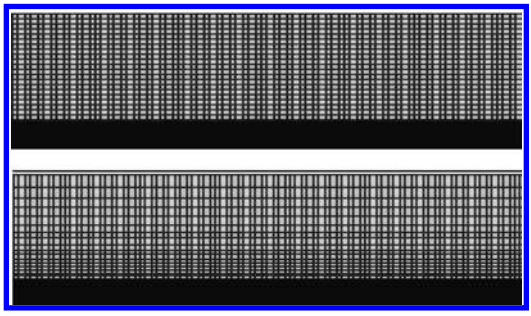


Figure 2. Grid generation- uniform & non-uniform.

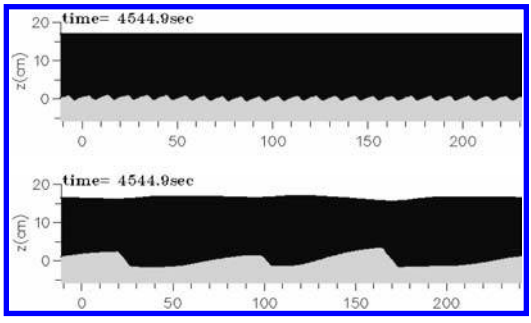


Figure 3. Typical example of instantaneous bedform evolution for uniform (upper) & non-uniform (lower) grid in vertical direction.

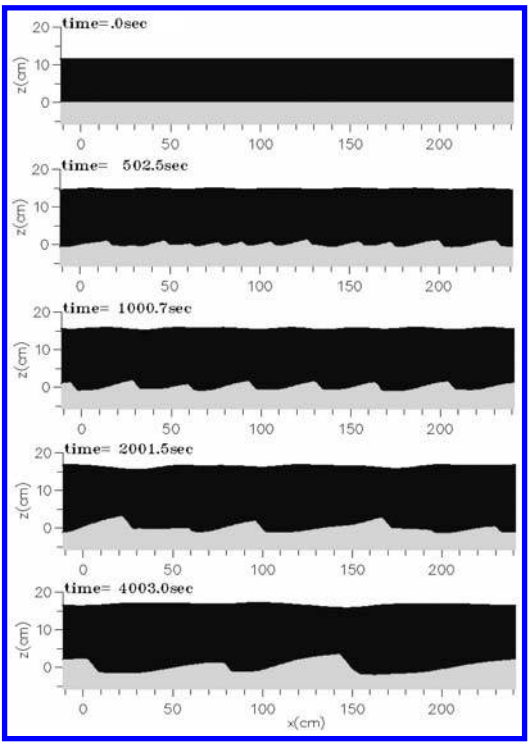


Figure 4. Typical example of bedform evolution simulated by numerical model (run A-5).

numerical model seems to be rather promising. Likewise, numerical simulation of dune migration reveals identical qualitative characteristic as in laboratory observation. Computed results show some quantitative inconsistency for prediction of bedform migration speed. However, these comparisons are subjected to further study. Simulated dune migration process is compared with the experimental visualization of Run A-2 for the qualitative assessment of model performance (see visualization).

For further validation of model prediction capabilities, empirical approach proposed by van Rijn (1983b) and Julien & Klaassen (1995) is used, which is based on large range of laboratory and field observations on dune geometry. Julien & Klaassen (1995) collected wide range of data on sand dune geometry of large rivers and revised the van Rijn's approach to predict dune geometry. We have used both relations proposed by van Rijn (1983b) and Julien & Klaassen (1995) to predict dune characteristics and compared them with numerical results as depicted in **Figures 6–7**. We have used van Rijn's method herein to predict dune length only (**Fig. 7**). Prediction of geometric characteristics of dunes by numerical model with compare to calculated results seems in trend. The discrepancy is likely to be due to the approaches used in empirical relationships as well as effect of sidewall in authors' experiment. Venditti et al. (2005) reported in their work that their experimental results are well predicted.

Model simulation on bed form migration showed some discrepancies, particularly for authors' experiments. From the simulation result, it can be identified that bed form celerity is higher in the beginning and decreases with the growth of bed form geometry. Most laboratory and field observations revealed similar feature of bed form celerity. For instance, Venditti et al.(2005) observed in their experiments decrement of migration rate with respect to the temporal development of bed form. They measured migration rates in initial as well as equilibrium stages of bed form development (Table 3 in Venditti et al., 2005). They reported that for their experiments A and B, migration rate showed a decrease from ~1.5 to 0.2 mm/s during 6000 seconds. It is also found from our computation that there is a decrease in migration rates from 1.0 to 0.3 mm/s for these experiments, which is almost of the same order. Computation result of dune migration also showed agreement with their experiments except for the case with low flow stages (**Fig. 9**). The discrepancies that were observed particularly in

Copyright © 2006 Taylor & Francis Group plc, London, UK

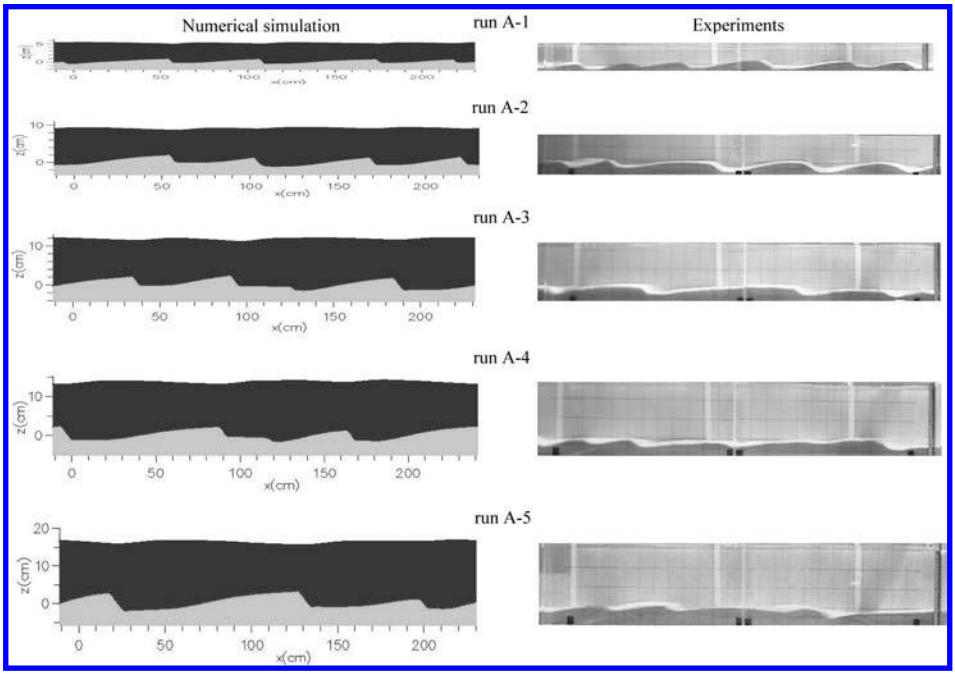


Figure 5. Comparison between numerical simulation and laboratory visualization of bedform feature.

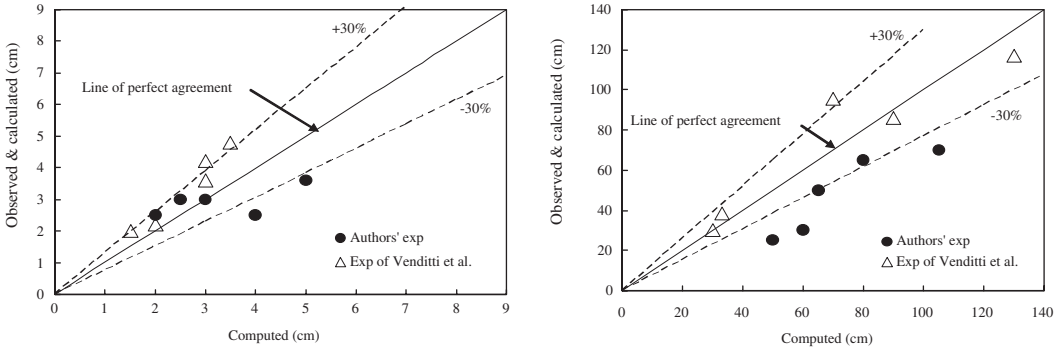


Figure 6. Quantitative comparison between geometric characteristic of bedforms predicted by numerical model and laboratory observation-bedform height (left) and bedform length (right).

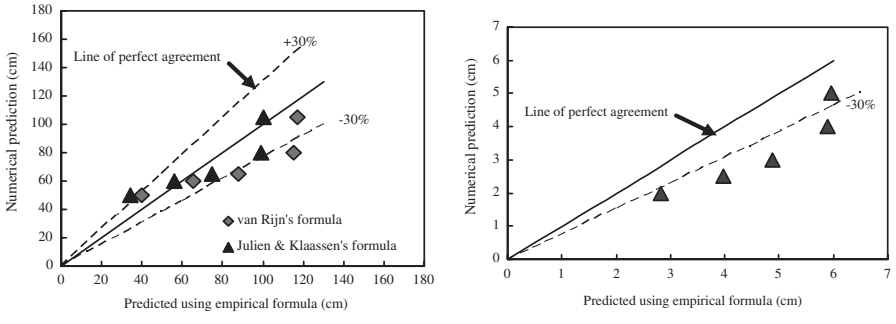


Figure 7. Quantitative comparison between geometric characteristic of bedforms predicted by numerical model and empirical formulae-bedform length (left) and bedform height using Julien & Klaassen's formula (right).

Copyright © 2006 Taylor & Francis Group plc, London, UK

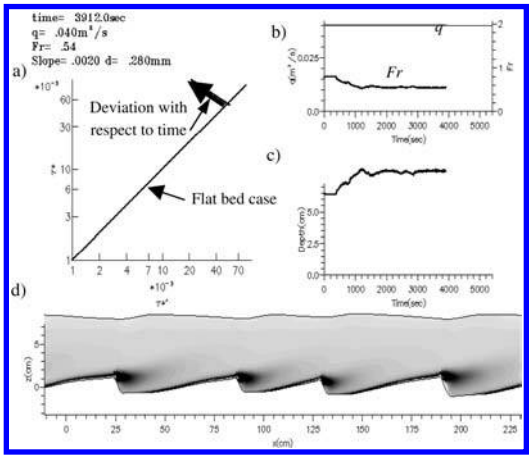


Figure 8. Numerical simulation of physical characteristics of bedforms: a) relation between total shear stress (τ^*) and grain shear stress ($\tau^{*\prime}$) b) discharge and Froude number variation c) flow depth variation d) instantaneous feature of bedforms.

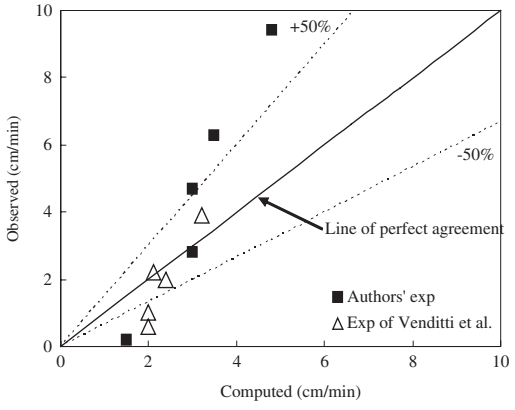


Figure 9. Numerical simulation of bedform migration in later stage (quasi-equilibrium stage).

authors' experiments can be attributed to the side wall effect.

Overall, numerical simulation of dune evolution showed fairly identical trend for characteristic of bed forms (dunes) as observed in laboratory. It can be inferred that the range of prediction capability of proposed computational model is acceptable considering sophisticated nature of the problem.

4.2.4 *Temporal change of flow resistance and flow depth simulation*

It is well-known that flow resistance is associated with skin friction of sediment particle and form drag exerted by bedforms. In case of flat bed, effective shear stress is equal to the grain shear stress. Whereas, in presence

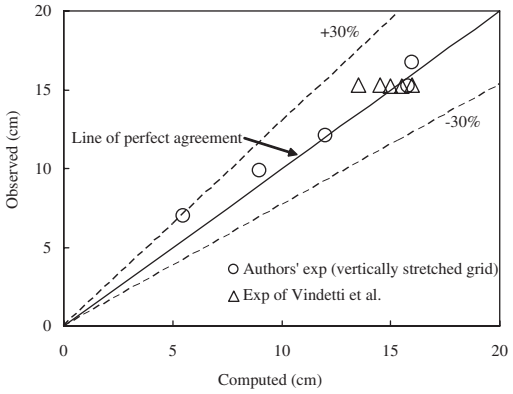


Figure 10. Comparison between observed and computed flow depth after bedform development.

of bedforms, contribution of form drag becomes significant and effective shear stress starts to increase. This phenomenon can be simulated using proposed model and thereby can be assessed deviation of bed shear stress according as bedform growth. **Figure 8** represent an instantaneous feature of total shear stress deviation (**Fig. 8a**). In the same figure, variation of Froude number (**Fig. 8b**) and depth variation **(Fig. 8c**) associated with temporal bedform growth can be assessed. In **Figure 8d** instantaneous bedform associated with given time event (3912 seconds) is depicted. Using this model, all aforementioned features can be visualized for each time step according as bedform evolution. Furthermore, quantitative comparison between observed and computed average flow depth for all experimental cases is depicted in **Figure 10**. It can be seen that model shows quite good prediction of bedform-induced flow depth. Model capability to simulate bedform-induced flow depth for given discharge could be useful in river engineering practice.

5 GENERAL CONCLUSION

A vertical two-dimensional hydrodynamic and morphologic model has been developed that can simulate flow, turbulence and morphodynamic features induced by sand waves, particularly dunes. The hydrodynamic model with a nonlinear k-ε turbulence closure has been found to be adequate to reproduce flow and turbulence characteristics as well as vorticity field in separation region behind the bedform crest. Likewise, the simulation result of water surface oscillation due to the form drag exerted by migrating bedforms seems to be realistic. The sediment transport modeling approach, namely modeling the exchange of sediment particles as pick up and deposition rate, shows fairly good performance. The proposed approach is believed to be

Copyright © 2006 Taylor & Francis Group plc, London, UK

more appropriate for non-equilibrium sediment transport with bedforms than generally used morphologic modeling approach. Additionally, module to compute suspended sediment flux could also be relevant to consider the bedform instability during upper flow regime, though still remains to be verified.

An attempt has been made here to develop a reliable and physically based modeling approach which was able to embody known concepts to characterize bedform evolution mechanism from a flat bed condition. Model can predict all physical characteristics of bedforms particularly dunes, namely height, length, shape, form drag as well as migration physically. In general, computation results seem to be realistic and promising, which demonstrate scope and usability of numerical simulation technique that could be a supplementary tool to comprehend a sophisticated river engineering phenomenon. Proposed model is not validated for upper flow regime. Moreover, effort is being made in order to incorporate in existing model the unsteady condition for flow rate and simulate hysteresis of bedform evolution.

ACKNOWLEDGEMENTS

This study was supported by Japan Society of Promotion of Science fellowship grant (Grant-in-aid 17-05093). We gratefully acknowledge Kazutake Asahi who carried out experiments as a part of his graduate study.

REFERENCES

Bennet, J.S. and Best, J.L. 1995. Mean flow and turbulence structure of fixed, two-dimensional bedforms; implication for sediment transport and bedform stability, *Sedimentology*, Vol.42, pp.491–513.

Best, J. 2005. The fluid dynamics of river dunes: A review and some future research directions, *Journal of Geophysical Research*, Vol.110, pp.1–21.

Best, J., Bennet, J.S., Bridge, J. and Leeder, M. 1997. Turbulence modulation and particle velocities over flat sand bed at low transport rate, *J. Hydraul. Eng.*, ASCE, 123 (12), 1118–1129.

Engelund, F. 1970. Instability of erodible beds, *J. Fluid Mech*., Vol.42, pp.225–244.

Engelund, F. and Fredsoe, J. 1982. Sediment ripples and dunes, *Ann. Rev. Fluid Mech.*, Vol.14, pp.13–37.

Fredsoe, J. and Tjerry, S. 2001. Morphological computation of dunes, *Proc. Int. Conf. Riv. Coast. Morph. Dyn*., Obihiro, Japan, pp.225–231.

Giri, S. and Shimizu, Y. Numerical computation of sand dune migration with free surface flow, *Water Resources Research* (accepted).

Itakura, T. and Kishi, T. 1980. Open channel flow with suspended sediments, *Proc. of ASCE*, 106 (8), 1325–1343.

Julien, P.Y. and Klaassen, G.J. 1995. Sand-dune geometry of large rivers during floods, *J. Hydraul. Eng.*, ASCE, 121(9), 657–663.

Kimura, I. and Hosoda, T. 2003. A nonlinear k-e model with realizability for prediction of flows around bluff bodies, *Int. J. Num. Meth. Fluids*, Vol.42, pp.813–837.

McLean, S.R. and Smith, J.D. 1986. A model for flow over two-dimensional bedforms, *J. Hydraulic Div. Am. Soc. Civ. Eng*., 112(4), 300–317.

Mendoza-Cabrales, C. 1987. Refined modeling of shallow, turbulent flow over dunes, PhD dissertation, *Colo. State Univ., Fort Collins*.

Nakagawa, H. and Tsujimoto, T. 1980. Sand bed instability due to bed-load motion, *J. Hyd.Div., ASCE*, 106, pp. 2029–2051.

Nakayama S. and Shimizu, Y. 2001. Numerical calculation of suspended sediment over sand waves, *Proc. Int. Conf. Riv. Coast. Morph. Dyn*., Obihiro, Japan, pp.217–224.

Nelson, J.M., McLean, S.R. and Wolfe, S.R. 1993. Mean flow and turbulence over two-dimensional bedforms, *Water Resour. Res*., Vol.29 (12), pp.3935–3953.

Onda, S. and Hosoda, T. 2005. Numerical simulation on development process of micro scale sand waves and flow resistance, *J. Hydrosc. Hydr. Eng*, pp.13–26.

Schmeeckle, M.W. and Nelson, J. M. 2003. Direct numerical solution of bedload transport using local, dynamic boundary condition, *Sedimentology*, Vol.50, pp. 279–301.

Schmeeckle, M.W., Shimizu, Y., Hoshi, K. and Tateya, K. 1999. Turbulent structures and suspended sediment over two-dimensional dunes, *Proc. Int. Conf. Riv. Coast. Morph. Dyn., Genova,* pp.261–270.

Shimizu Y. 2004. A method for simultaneous computation of bed and bank deformation of a river, *Proc. Int. Conf. Fluv. Hydraul*., Louvain, Belgium, 793–801.

Shimizu, Y., Schmeeckle, M.W. and Nelson, J.M. 2001. Direct numerical simulation of turbulence over two-dimensional dunes using CIP methods, *J. Hydrosci. Hydr. Eng.*, Vol. 19 (2), pp.85–92.

Shimizu, Y. and Itakura, T. 1991. Calculation of flow and bed deformation with a general non-orthogonal coordinate system, *Proc. XXIV IAHR Cong*., Madrid, Spain, 241–248.

Sugiyama, H., Akiyama, M. and Matsubara, T. 1995. Numerical simulation of compound open channel flow on turbulence with Reynolds stress model, J. Coast. Envir. Eng., 515/II (31), 55–65 (in Japanese).

Sumer, B.M., Chua, L.H.C., Cheng, N.S. and Fredsøe, J. (2003), Influence of turbulence on bed load sediment transport, *J.Hydraul. Eng.*, ASCE, 129(8), 585–596.

Tjerry, S. and Fredsøe, J. 2005. Calculation of dune morphology, *Earth Surf. Processes Landforms* (in print).

Van Rijn, L.C. 1984a. Sediment pick-up funtion, *J. Hydraul. Eng*., ASCE, 110 (10), 1494–1502.

Van Rijn, L.C. 1984b. Sediment transport, Part III: Bedforms and alluvial roughness, *J. Hydraul. Eng.*, ASCE, 110 (12), 1733–1753.

Venditti, J.G., Church, M. and Bennett, S.J. (2005), Morphodynamics of small-scale superimposed sand waves over migrating dune bed forms, Water Resour. Res., 41, doi:10.1029/2004WR003461.

Yabe, T., Ishikawa, T., Kadota, Y. and Ikeda, F. 1990. A multidimensional cubic-interpolated pseudoparticle (CIP) method without time splitting technique for hyperbolic equations, *PSJ*, Vol.59, pp.2301–2304.

Copyright © 2006 Taylor & Francis Group plc, London, UK

Experimental study on steady flow in a channel with macro-roughness at the side walls

T. Meile, J.-L. Boillat, J. Dubois & A.J. Schleiss
Ecole Polytechnique Fédérale de Lausanne (EPFL), Laboratory of Hydraulic Constructions (LCH)
EPFL-ENAC-ICARE-LCH, Bâtiment GC, Lausanne, Switzerland

ABSTRACT: Water levels of rivers are influenced by the material and the form of bed and banks, which are producing skin friction and form drag. Morphological measures on banks can have an influence on the flow, especially when the flow depth becomes significant comparing to the river width. 36 configurations of the side walls producing a macro-roughness have been tested in a laboratory flume. The test configurations were formed by rectangular, local widenings with varying geometrical proprieties (widening length, widening lateral depth and distance between widenings). The analysis of the water level measurements was based on backwater curve calculations. It was possible to quantify equivalent sand roughness of the side walls including the effect of macro-roughness, effective flow widths at the enlarged sections and friction factors of the composite sections. Results reveal that macro-roughness produces rising characteristics for the relationship between friction factor and Reynolds numbers.

1 INTRODUCTION

Water levels of rivers are influenced by the roughness of the bed and the roughness of the banks. For low relative flow depths the roughness of the banks is of secondary importance. This is generally the case for wide rivers at low and moderate discharge. With increasing relative flow depths, which can be found in side-channels or streams, the influence of bank roughness becomes more significant. This leads to composite channel resistances. Different equations issuing from various researches for composite channel resistance exist. They are based on numerous assumptions summarized in Yen (2002).

In addition to the effect of bed and bank, the total resistance in a channel is depending on both, grain roughness and form roughness, for example generated by the bed forms of alluvial channels as described by several authors (Einstein & Barbarossa 1952; Graf 1984; Van Rijn 1993).

For the flow in rough conduits, Morris (1955) and Morris & Wiggert (1972) applied a concept based on skin friction, caused by the roughness of the material, and form drag. A first friction factor for smooth-turbulences corresponding to walls without macro-scale roughness and a second friction factor caused by roughness elements are considered. The importance of the second friction factor depends on size, form and spacing of the roughness elements.

More recent studies on macro-rough flow deal with flow resistance of mountain streams respectively flow over macro-scale roughness. First attempts to quantify the flow resistance in function of relative submergence, and parameters related to the geometry and density of macro-rough elements were made by Bathurst et al. (1981). Canovaro et al. (2004) relate Chezy coefficients to pebble concentrations and arrangements. A minimum of Chezy coefficients corresponds to a spatial density of pebbles of 0.1.

Recently, numerical simulations have been established for artificially roughened beds. Macro-roughness was introduced by rectangular cavities (Leonardi et al. 2003; Stoesser et al. 2004). Depending on the ratio cavity width to roughness height, they have simulated the three roughness types according to Morris (1955). The maximum total flow resistance is observed for the mentioned ratio equal to about 7 and the resistance is mainly due to the form drag of the macro-roughness elements.

The present article aims to provide information for a better understanding of the effect of macro-roughness at the side walls on steady flow in channels.

2 EXPERIMENTS

2.1 *Setup*

The experiments have been realized in a channel of the Laboratory of Hydraulic Constructions at EPFL.

The channel has a useful length of $L_{tot} = 38.25$ m and a mean slope of 1.15‰. The base width is

Copyright © 2006 Taylor & Francis Group plc, London, UK

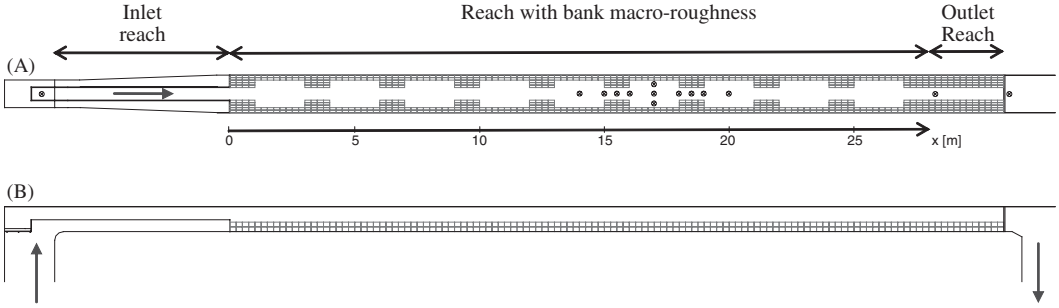


Figure 1. (A) Plan view of the laboratory channel divided in three reaches: Inlet-reach, reach with macro-roughness, outlet-reach. ⊗ level measurements with ultrasonic-probes. (B) Longitudinal section of the flume.

$B = 0.485$ m. The channel is divided in an inlet reach ($L_{in} = 7.35$ m), a reach with macro-roughness at the side walls ($L_{MR} = 26.9$ m) and an outlet reach ($L_{out} = 4$ m). The exact length of L_{MR} and L_{out} depends on the configuration of macro-roughness. The sum of both is constant.

The sidewalls of the reach with macro-roughness and the outlet reach are formed by limestone bricks (Fig. 2). The equivalent sand roughness of the limestone bricks has been determined by means of backwater curve computations in a rectangular, prismatic configuration ($k_{sw} = 0.021$ mm). The equivalent sand roughness of the bottom, also found by backwater curve computation is $k_{s0} = 0.001$ mm.

An outlet control section is placed at the end of the outlet reach. The geometry of this section is optimized in order to simulate a long channel at normal depth (Carlier 1998). The channel slope is small enough to guarantee subcritical flow at every position of the channel for the range of tested discharges.

The plan view and the longitudinal section of the laboratory channel are shown on Figure 1.

Water levels have been measured at different points along the channel axis as well as in the left and right widening of section $x = 17.0$ m. A velocity profile was measured in the axis of the channel at $x = 17.0$ m using the Ultrasonic Doppler Shift effect (Takeda 1985). Finally, at the same section the pressure on the bottom has been measured.

The channel has a fixed bed without sediment transport.

2.2 *Test configurations*

A prismatic reference configuration with constant width $B = 0.485$ m is compared to 36 geometrically different test configurations, formed by symmetric widenings (Fig. 2). The widenings, considered as a macro-roughness at the side walls, have been obtained by a modular system of limestone bricks. The bottom level is the same for the main channel and for widenings.

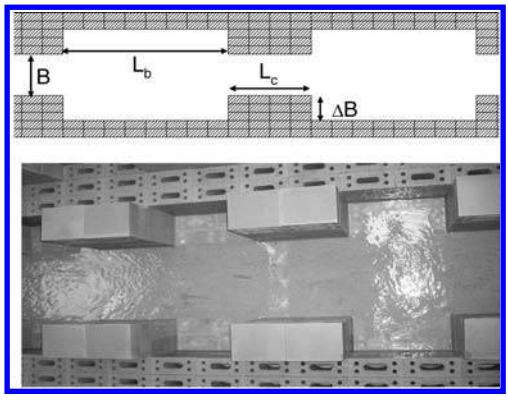


Figure 2. Definition of the geometrical parameters of the test configurations (above) and example of widenings (macro-roughness) built using the modular system of limestone bricks.

The geometrical parameters are defined on Figure 2 and the 36 different test geometries are summarized in Table 1. The base width $B = 0.485$ m remains constant during all the tests. L_b is the length of the widening. L_c is the distance between two widenings, ΔB is the depth (or lateral extent) of the widening.

A linear widening density can be defined as the ratio $D_L = L_b/(L_c + L_b)$ and a surface widening ratio as $D_S = \Delta B \cdot L_b/(B \cdot (L_c + L_b))$.

Generally, 12 different discharges within a range of about 5 l/s to max. 140 l/s have been studied. This range led to Froude numbers between 0.37 and 0.64 and to Reynolds numbers between 6,800 and 110,000 at the section $x = 17.0$ m.

3 RESULTS

3.1 *Flow behavior*

Different flow behaviors can be observed in the channel (Fig. 3). By increasing the discharge, flow depths,

Copyright © 2006 Taylor & Francis Group plc, London, UK

Table 1. Configurations and their geometrical properties.

Configuration	L_b [m]	L_c [m]	ΔB [m]	D_L [-]	D_S [-]
111	0.5	0.5	0.1	0.500	0.100
112	0.5	0.5	0.2	0.500	0.200
113	0.5	0.5	0.3	0.500	0.300
114	0.5	0.5	0.4	0.500	0.400
121	0.5	1.0	0.1	0.333	0.067
122	0.5	1.0	0.2	0.333	0.133
123	0.5	1.0	0.3	0.333	0.200
124	0.5	1.0	0.4	0.333	0.267
141	0.5	2.0	0.1	0.200	0.040
142	0.5	2.0	0.2	0.200	0.080
143	0.5	2.0	0.3	0.200	0.120
144	0.5	2.0	0.4	0.200	0.160
211	1.0	0.5	0.1	0.667	0.133
212	1.0	0.5	0.2	0.667	0.267
213	1.0	0.5	0.3	0.667	0.400
214	1.0	0.5	0.4	0.667	0.533
221	1.0	1.0	0.1	0.500	0.100
222	1.0	1.0	0.2	0.500	0.200
223	1.0	1.0	0.3	0.500	0.300
224	1.0	1.0	0.4	0.500	0.400
241	1.0	2.0	0.1	0.333	0.067
242	1.0	2.0	0.2	0.333	0.133
243	1.0	2.0	0.3	0.333	0.200
244	1.0	2.0	0.4	0.333	0.267
411	2.0	0.5	0.1	0.800	0.160
412	2.0	0.5	0.2	0.800	0.320
413	2.0	0.5	0.3	0.800	0.480
414	2.0	0.5	0.4	0.800	0.640
421	2.0	1.0	0.1	0.667	0.133
422	2.0	1.0	0.2	0.667	0.267
423	2.0	1.0	0.3	0.667	0.400
424	2.0	1.0	0.4	0.667	0.533
441	2.0	2.0	0.1	0.500	0.100
442	2.0	2.0	0.2	0.500	0.200
443	2.0	2.0	0.3	0.500	0.300
444	2.0	2.0	0.4	0.500	0.400

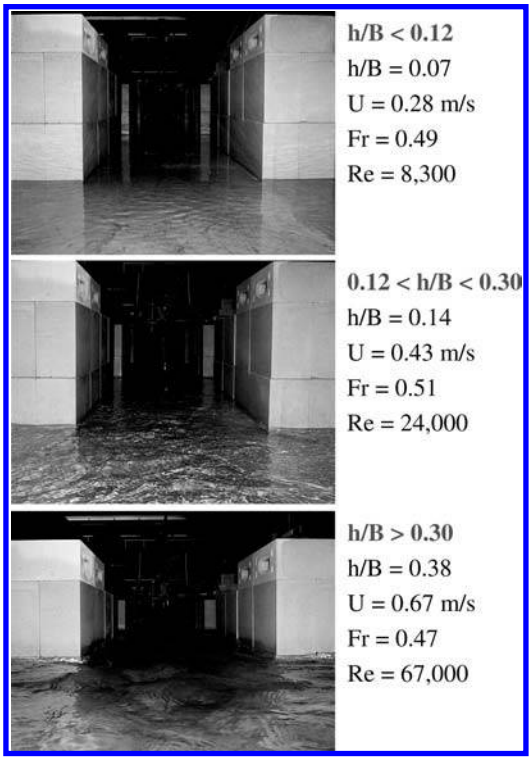


Figure 3. Flow conditions for three different discharges for the geometrical configuration 223 ($L_b = 1$ m, $L_c = 1$ m, $\Delta B = 0.3$ m). Flow direction is in direction of the view.

mean velocities and Reynolds numbers become more important in a given channel section. Instead, Froude numbers remain more or less constant.

For relative flow depths of $h/B < 0.12$ and Reynolds numbers $Re < \sim$15,000, the water surface is smooth, flat with possible small surface waves. For relative flow depths h/B > 0.3 and Reynolds numbers $Re > \sim$50,000, the water surface gets uneven and wavy.

Observations with tracer show that the flow pattern in the widenings corresponds to the ones of emerged groin fields when flow depths and velocities remain low. As pointed out by several researches, the ratio of $\Delta B/L_b$ affects dead zones and eddies. Yossef & Vriend (2004) show a flow pattern composed by a primary, secondary and a dynamic eddy. The experiments of Weitbrecht & Jirka (2001) put in evidence that the presence of these three eddies is depending on $\Delta B/L_b$. Dye tests reveal that the region between the widening and the main channel is dynamic. The dynamic eddy at the upstream part of the widening is frequently taken by the current and migrates downstream. It does then either directly disappears in the main stream or it merges with the primary eddy.

For higher flow depths and thus higher velocities, flow structures can not be detected applying dye tests. The flow acts like an expanding jet arriving in an enlargement. If the ratio $\Delta B/L_b$ is small, reattachment of the flow seems possible. If the depth of the widening is important compared to its length, the jet directly hits the contraction of the section at the end of the widening.

Finally, in some cases, significant water surface oscillations between two opposite widenings can be observed. This has already been detected in other researches (Ohmoto et al. 2005). The phenomenon is in particular present for small and medium relative flow depths. For high relative flow depths, the flow arrives with a higher velocity in the widening and it becomes therefore stable enough to avoid the interaction between the widening on the left and right channel side wall. If transverse surface oscillations

Copyright © 2006 Taylor & Francis Group plc, London, UK

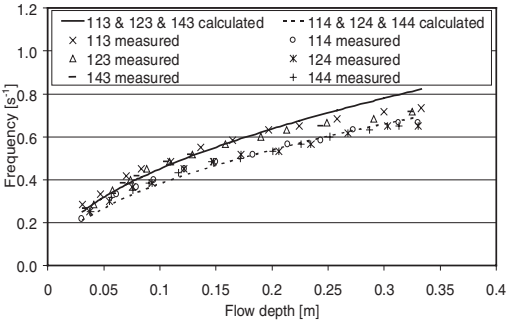


Figure 4. Calculated (from flow depths) and observed frequencies of the transverse oscillations in the widenings.

arise, the observed main period, found by spectrum analysis, corresponds to the natural period of a seiche in a rectangular basin:

$$T = \frac{2 \cdot L}{n\sqrt{gh}} \tag{1}$$

where T = period; $L = B + 2\Delta B$ = width of the basin; n = number of nodes; g = gravity constant and h = flow depth.

If the ratio $L_b/(B + 2\Delta B)$ is smaller than about 0.5 to 1, the oscillations are present for most of the discharges and their period is in good agreement with the theory of a rectangular basins (first mode, $n = 1$).

The observed frequencies are lower than the calculated ones for higher flow depths (Fig. 4). This can be explained by the coexistence of transverse and longitudinal seiches, which leads to an increase of the period according to the generalized Merian's formula (Wüest & Farmer 1998).

3.2 *Roughness quantification*

Several phenomena are responsible for the additional head loss along the channel. The major source of friction is the generation, spreading, and subsequent dissipation of vortices from the wake and separation zones following the roughness elements. According to Morris (1972), a depression, like the tested widenings, can also be considered as a roughness element. A second, minor source of energy loss is the momentum exchange caused by turbulent exchange and geometrical transfer at the interface between the widenings and the main channel (Bousmar & Zech 1999). Transverse oscillations (see Chapter 3.1) may enhance this flow exchange.

Two different calculation methods have been considered for the analysis of the water level measurements. Both are based on a water level computation from downstream upwards. Starting point is the known water level in the outlet-reach. The first method (Chapter 3.2.1) considers that the widenings produce an additional linear headloss. The computation method is a 1D prismatic approach for a non prismatic channel and should be seen as an inverse roughness modeling. The calibration of a factor related to the roughness allows fitting calculated on measured water levels. The second method (Chapter 3.2.2) considers the single head losses along the channel produced by the sudden expansions and contractions of the flow. Calculations are done based on the specific energy $H_s = h + U^2/(2g)$. A theoretically effective flow width is then used to fit calculated on measured water levels.

3.2.1 *Governing equations: Method 1*

The energy equation is used for the backwater curve computation. The standard step method leads to:

$$\left(h_{i+1} + z_{i+1} + \frac{U_{i+1}^2}{2g}\right) - \left(h_i + z_i + \frac{U_i^2}{2g}\right) = \overline{S_{fm}}(x_{i+1} - x_i) \tag{2}$$

where S_f = friction slope; h = flow depth; x = channel section; z = bottom level; U = mean velocity related to the base width B; B = base width. The subscript $_m$ indicates that the friction slope is composed of a wall friction (subscript $_w$) including effect of the macro-roughness and a bottom friction (subscript $_0$).

The friction slope is calculated by the Darcy-Weisbach formula:

$$\overline{S_{fm}} = \overline{f_m}\frac{\overline{U}^2}{8g\overline{R_h}} \tag{3}$$

where R_h = hydraulic radius; f = friction coefficient.

The channel has been considered as a composite section. If the hypothesis is made that the Einstein (1934) approach for a composite section is applicable, it can be written as follows:

$$\frac{R_{h0}}{f_0} = \frac{R_{hw}}{f_w} = \frac{R_{hm}}{f_m} = \frac{U^2}{8gS_{fm}} \tag{4}$$

where R_{h0} = hydraulic radius referred to the bottom; R_{hw} = hydraulic radius referred to the wall; R_{hm} = hydraulic radius referred to the composite section.

The friction coefficient of the composite section f_m is calculated according to Hersberger (2003) as:

$$f_m = \frac{Bf_0 + 2hf_w}{B + 2h} \tag{5}$$

where f_0 = bottom friction coefficient; f_w = wall friction coefficient including the effect of macro-roughness of the widenings.

Copyright © 2006 Taylor & Francis Group plc, London, UK

After all, the bottom and wall friction coefficients can be determined with the following logarithmic Colebrook-White laws:

$$\frac{1}{\sqrt{f_0}} = -K_1 \log\left(\frac{k_{s0}}{K_2 R_{h0}} + \frac{K_3}{4Re_0\sqrt{f_0}}\right) \quad (6)$$

$$\frac{1}{\sqrt{f_w}} = -K_1 \log\left(\frac{k_{sw}}{K_2 R_{hw}} + \frac{K_3}{4Re_w\sqrt{f_w}}\right) \quad (7)$$

where Re_0 = Reynolds number related to the bottom; Re_w = Reynolds number related to the wall; k_{s0} = equivalent bottom sand roughness; k_{sw} = equivalent wall sand roughness including the effect of macro-roughness of widenings. $K_1 = 2.03$, $K_2 = 10.95$ and $K_3 = 1.70$ are the constants used by Rouse (1946).

The hydraulic radius R_{h0}, R_{hw}, and the Reynolds numbers Re_0 and Re_w are calculated with the following formulas:

$$R_{h0} = \frac{R_{hm}}{f_m} f_0 \quad (8)$$

$$Re_0 = \frac{U R_{h0}}{\nu} \quad (9)$$

$$R_{hw} = \frac{R_{hm}}{f_m} f_w \quad (10)$$

$$Re_w = \frac{U R_{hw}}{\nu} \quad (11)$$

The equivalent sand roughness of the wall k_{sw} which includes the effect of macro-roughness of the widenings can be used to fit the calculated water levels with the observed ones and a dataset of k_{sw}-values can be obtained. The k_{sw}-values can be either determined globally for all discharges of one geometrical configuration or individually for every discharge of the geometrical configuration.

The friction coefficients of the composite section f_m can be extracted from equation (5) as second information obtained from the backwater curve computation. The f_m-values must be considered as more global information's than the k_{sw}-values. Moreover, they are practically not depending on the hypothesis made by formulas (4) to (11) and nearly constant for a given discharge and a given geometrical configuration. The equivalent sand roughness of the wall k_{sw} and the friction coefficients f_m present two different sets of values related to the macro-roughness configurations.

3.2.2 *Governing equations: Method 2*

Backwater curves can also be computed by considering the single head losses produced by the sudden expansions and contractions of the flow due to the widenings. Calculations are based on the specific energy $H_s = h + U^2/(2g)$ (Fig. 5). The skin friction is thus assumed to be compensated by the bottom slope of the channel.

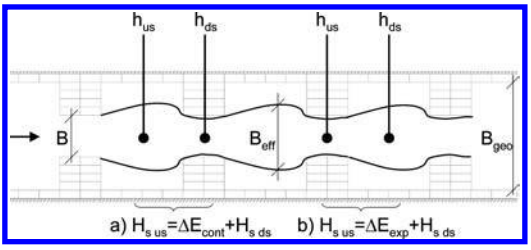


Figure 5. Scheme of backwater curve calculations for sudden contractions (a) and expansions (b).

The single head loss for an abrupt expansion ΔE_{exp} is given by (Henderson, 1966) The subscript $_{us}$ refers to the upstream section (width B) and the subscript $_{ds}$ to the enlarged section (width B_{eff}):

$$H_{s\,us} = H_{s\,ds} + \Delta E_{exp} \quad (12)$$

with:

$$\Delta E_{exp} = \frac{\left(Q/B h_{us}\right)^2}{2g}\left[\left(1 - \frac{B}{B_{eff}}\right)^2 + \frac{2 Fr_{us}^{\,2} B^3 \left(B_{eff} - B\right)}{B_{eff}^{\,4}}\right] \quad (13)$$

where H_s = specific energy; ΔE_{exp} = single headloss for the expansion; Q = discharge; B_{eff} = effective flow width at the enlarged section; Fr_{us} = Froude number at the upstream section.

The upstream flow depth h_{us} is calculated knowing the flow depth h_{ds} at the enlarged section by iterating the following formula:

$$h_{us} = h_{ds} + \frac{\left(Q/B_{eff}\, h_{ds}\right)^2}{2g} + \frac{\left(Q/B h_{us}\right)^2}{2g}\left(A - 1\right) \quad (14)$$

with:

$$A = \left(1 - \frac{B}{B_{eff}}\right)^2 + \frac{2 Fr_{us}^{\,2} B^3 \left(B_{eff} - B\right)}{B_{eff}^{\,4}} \quad (15)$$

The single head loss for the abrupt contraction ΔE_{cont} is calculated as proposed in Sinniger & Hager (1989). The downstream section (subscript $_{ds}$) has now the width B and the upsteam section (subscript $_{us}$) is enlarged:

$$H_{s\,us} = H_{s\,ds} + \Delta E_{cont} \quad (16)$$

Copyright © 2006 Taylor & Francis Group plc, London, UK

with ΔE_{cont}:

$$\Delta E_{cont} = \xi \frac{\left(Q / B h_{ds}\right)^2}{2g} \quad (17)$$

with ξ given by Matthew (1975):

$$\xi = \left(1 - B/B_{eff}\right)^{2-(\alpha/11)} \sin^2\left(\alpha/2\right) \quad (18)$$

where α = contraction angle (in the present case 90°).

Finally, the flow depth in the enlarged, upstream section is calculated by iterating the following formula:

$$h_{us} = (\xi + 1)\frac{\left(Q / B h_{ds}\right)^2}{2g} + h_{ds} - \frac{\left(Q / B_{eff} h_{us}\right)^2}{2g} \quad (19)$$

The backwater curve can be calculated moving from downstream to upstream. B_{eff} is unknown and used to fit the calculated water levels with the observed ones. Therefore it is possible to get an effective width used by the flow at the enlarged sections for every geometrical configuration. The B_{eff}-values are forming the third set of values related to the macro-roughness configurations.

Some results of the three data sets, k_{sw}, f_m and B_{eff}, are presented in the following chapters.

3.2.3 *Equivalent wall sand roughness values*

The equivalent sand roughness values of the wall k_{sw} including the effect of macro-roughness of the widenings are summarized in Table 2. The given values are global values for each geometrical configuration, which, by definition, are independent of the discharge. They allow the best fit between the calculated water-surface and the water level measurements. Δh_{ksw} is the mean absolute error resulting from measured and calculated water depths. Water depths are varying between 0.04 m and 0.3 m. The relative errors remain therefore quite small.

Nevertheless, the use of a global equivalent sand roughness value for the side walls generally leads to an overestimation of the calculated flow depths for lower discharges and an underestimation of the flow depths for higher discharges. For the analysis done by method 1 it can thus be concluded that the k_{sw} values are not only dependent on the geometrical characteristics of the widenings but also on the characteristics of the flow. This can be shown in Figure 6 where the k_{sw}-values have been determined individually for every tested discharge. For the geometrical configurations 221 to 224, it clearly appears that the found equivalent sand roughness increases in the range of Re_w-numbers between 50,000 and 120,000. For higher Re_w-numbers the k_{sw}-values become again constant. The dependence of k_{sw}-values on the Reynolds numbers is not as obvious for all tested configurations as it is in Figure 6. Nevertheless it exists in most of the cases.

Table 2. Equivalent sand roughness of the wall k_{sw} (including the effect of the macro-roughness of the widenings) and effective flow width B_{eff}.

Configuration	k_{sw} [mm]	Δh_{ksw} [mm]	B_{eff} [m]	Δh_{Beff} [mm]
111	74	5.3	0.579	5.1
112	41	4.3	0.551	3.8
113	49	2.8	0.557	2.7
114	139	2.8	0.631	3.2
121	48	2.5	0.593	2.3
122	37	2.8	0.577	2.6
123	47	2.2	0.591	2.8
124	117	3.1	0.679	3.5
141	14	2.2	0.587	**2.2**
142	12	**1.3**	0.662	3.6
143	21	**1.4**	0.681	4.2
144	61	3.9	0.699	6.0
211	97	7.0	0.656	6.9
212	133	8.3	0.701	7.7
213	148	7.8	0.719	7.3
214	98	7.3	0.658	6.7
221	58	4.6	0.650	4.1
222	70	3.9	0.669	3.4
223	79	4.6	0.685	4.1
224	60	4.4	0.653	3.9
241	42	3.2	0.702	2.4
242	60	4.4	0.753	3.6
243	69	2.9	0.778	**2.3**
244	50	5.3	0.727	4.4
411	76	5.5	0.724	5.5
412	139	6.2	0.861	5.9
413	147	7.0	0.879	6.6
414	151	5.9	0.889	5.5
421	11	6.0	0.591	5.1
422	52	**8.9**	0.732	**7.9**
423	63	**9.0**	0.762	**7.9**
424	65	8.1	0.817	4.8
441	23	2.8	0.700	**2.3**
442	70	3.7	0.898	3.0
443	84	4.7	0.961	3.9
444	82	3.3	0.953	2.5

The bigger the mean absolute error Δh_{ksw}, the more dependent is k_{sw} on the Re_w-number. Therefore the computation with a global k_{sw}-value leads to increasing errors for these cases.

It is difficult to relate the global k_{sw} values directly to the geometry of the widenings. Detected trends are increasing k_{sw}-values with increasing widening depths ΔB, increasing widening lengths L_b and decreasing distance between the widenings L_c. The increase of the geometric parameter ΔB is more important than the one of L_b for the increase of k_{sw}.

Copyright © 2006 Taylor & Francis Group plc, London, UK

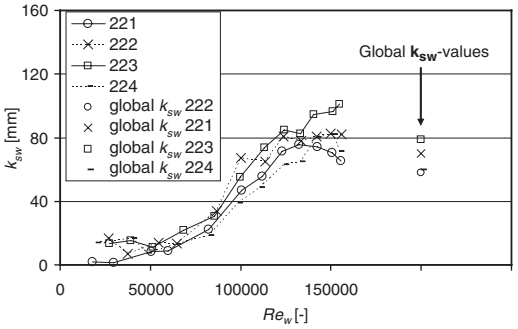


Figure 6. Equivalent sand roughness values of the wall k_{sw}-for 4 of the 36 tested geometrical configurations. Increasing Reynolds numbers indicate increasing discharge.

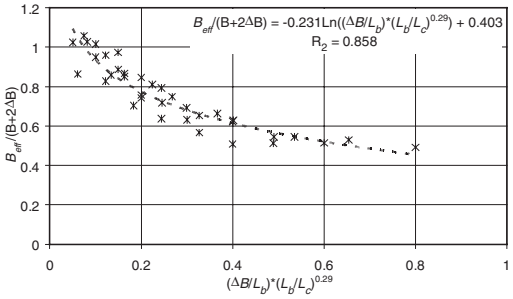


Figure 7. Ratio of effective to geometrical width B_{eff}/B_{geo} as a function of $\Delta B/L_b$ and L_b/L_c.

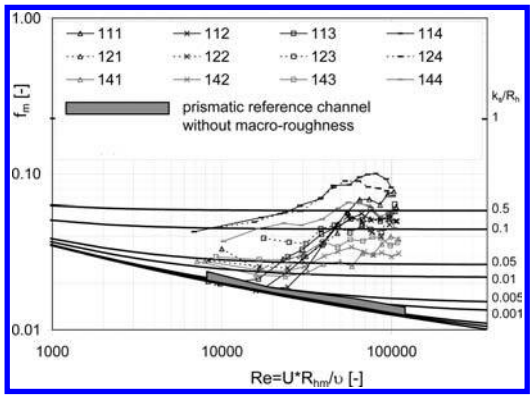


Figure 8. Friction coefficients of the composite section f_m for geometric configurations 111 to 144 (see Table 1). Widening length $L_b = B$.

3.2.4 *Flow width B_{eff} at the enlarged sections*

The values of the theoretically effective flow widths at the enlarged sections B_{eff} are given for all geometrical configurations in Table 2. Δh_{Beff} is the mean absolute error between measured and calculated backwater curves for the approach based on the single headlosses. The mean absolute errors Δh_{Beff} are similar to the Δh_{ksw}-values corresponding to the first approach. As already noticed in Chapter 3.2.2, the backwater curve is difficult to predict with a global B_{eff}-value for geometrical configurations showing high mean absolute errors (Table 2).

The effective flow widths B_{eff} can be compared to the geometric width of the widening $B_{geo} = B + 2\Delta B$. It is interesting to note that for relatively long but not too wide widenings (configurations: 411, 412, 421, 441, 442, 211, 221, 241), the geometrical width and the determined effective flow width are very close. This indicates reattachment of the flow. For ratios $\Delta B/B = 0.6$ and 0.8, the effective flow widths always remain smaller than the geometric widths.

If B_{eff} would be related to the geometry of the widenings, it can be done by taking account the ratios $\Delta B/L_b$ and L_b/L_c (Fig. 7). The ratio $\Delta B/L_b$ is more important to explain B_{eff} than L_b/L_c. Values of B_{eff}/B_{geo} fairly higher than 1.0 indicate that taking into account skin friction and single headlosses only is not sufficient to explain completely the rising of water levels in presence of macro-roughness.

3.2.5 *Friction coefficients f_m of the composite section*

The friction coefficients of the composite section f_m are presented on Figures 8–10. They have been extracted individually for each discharge from formula (5) for every geometrical configuration. The f_m-values of the prismatic reference configuration without macro-roughness are also presented on Figures 8–10.

The following points can be observed:

1 Comparing to the prismatic reference channel, macro-roughness leads to significantly increased f_m-values.
2 Macro-roughness leads to rising characteristics of the f_m-Re curves, especially for Reynolds numbers greater than 25,000 to 30,000.
3 For short widenings ($L_b = B$; Fig. 8), no further increase of f_m-values seems to be produced for Reynolds numbers greater than about 60,000. For long widenings (Figs 9–10), the increase of f_m-values is still present but reduced for Reynolds numbers greater than about 70,000.
4 According to Morris (1972), three types of flow behaviour can be observed in the channel with macro-roughness at the side walls: A) Smooth and semi-smooth (isolated roughness) flow for Reynolds numbers lower than 25,000. B) Wake interference (also called hyperturbulent) flow for Reynolds numbers greater than 25,000 to 30,000. C) Quasi-smooth flow for geometries with short

Copyright © 2006 Taylor & Francis Group plc, London, UK

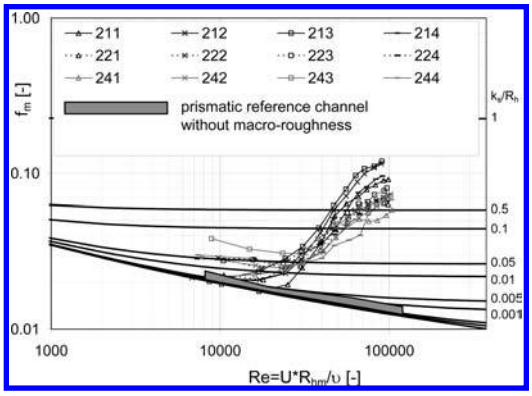


Figure 9. Friction coefficients of the composite section f_m for geometric configurations 211 to 244 (see Table 1). Widening length $L_b = 2B$.

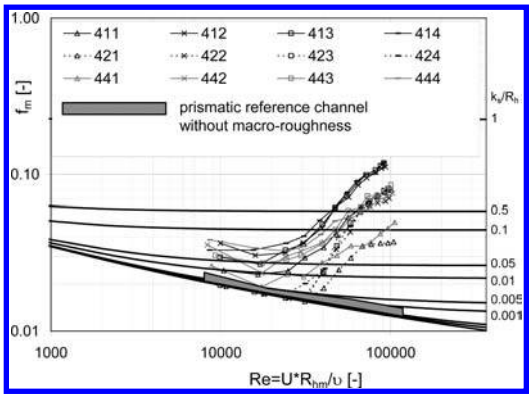


Figure 10. Friction coefficients of the composite section f_m for geometric configurations 411 to 444 (see Table 1). Widening length $L_b = 4B$.

widenings (Fig. 8) and Reynolds numbers greater than 60,000 to 70,000.

5 Differences in f_m-values between the different geometrical configurations exist although they are not as important as the difference between the prismatic reference and the configurations with macro-roughness (rectangular widenings).

Further investigations are necessary in order to quantify in detail the effect of the different geometric parameters of the rectangular widening on the flow resistance.

4 CONCLUDING REMARKS

The experiments performed in this study show the influence of macro-roughness at the side walls on steady flow in a laboratory channel. The macro-roughness (or form-roughness) was given by regular rectangular widenings on both channel side walls. 36 geometrical configurations have been tested for several discharges. The analysis of the flow and the results of backwater curve calculations with two different methods reveal that:

– The flow pattern in rectangular widenings corresponds with the ones of emerged groin-fields if the relative flow depth h/B remains lower than about 0.12 and the Reynolds number is lower than 15,000.
– The influence of the macro-roughness increases with the relative flow depth according to the theory of composite channels.
– For increasing discharges and therefore increasing velocities and Reynolds numbers, the influence of the macro-roughness at the channel side walls becomes important. The values of the friction coefficients of the composite section f_m are clearly higher than for a prismatic reference configuration. The f_m-Re curves show rising characteristics for Reynolds numbers from about 25,000 to 65,000 depending on the geometrical configuration. All of the three flow types given by the roughness concept of Morris (1955 & 1972) can be observed in the channel with macro roughness: A) smooth or isolated roughness flow for low Reynolds numbers; B) wake interference flow for intermediate Reynolds numbers; C) quasi smooth flow for some configurations at high Reynolds numbers.
– The difference of roughness between a prismatic reference configuration and the tested geometrical configurations is significantly higher than the difference of roughness between the different configurations with macro-roughness.
– The determined theoretically equivalent sand roughness of the wall k_{sw} including the macro-roughness of the different geometrical configurations is not independent of the hydraulic characteristics of the flow. Using global k_{sw}-values generally leads to an overestimation of the calculated flow depths for lower discharges and an underestimation of the flow depths for higher discharges.
– A second approach, comparing the effective flow width at the enlarged section to the geometric width of the widening, indicates that the reattachment of the flow probably produces for ratios $\Delta B/L_b$ smaller than 0.1.

In the ongoing research the detailed relationship between the different geometrical characteristics of the tested widenings and the flow resistance is identified.

ACKNOWLEDGEMENTS

This research is part of the interdisciplinary project "RHONE-THUR – sustainable use of rivers" founded

Copyright © 2006 Taylor & Francis Group plc, London, UK

and financed by the Swiss Federal Office for Water and Geology (FOWG).

NOTATIONS

The following symbols are used in this paper:

- A: section area
- B: channel base width
- B_{eff}: effective flow width at enlarged section
- B_{geo}: geometric width of the widening
- D_L: $D_L = L_b/(L_c + L_b)$; linear widening density
- D_S: $\Delta B^* L_b/(B^*(L_c + L_b))$; surface widening ratio
- f: friction coefficient
- Fr: Froude number related to B
- g: 9.81 m/s^2, gravity constant
- h: flow depth
- H_s: specific energy
- $K_{1,2,3}$: constants for logarithmic law
- k_s: equivalent sand roughness
- L: width of the basin for calculation of transverse oscillations
- L_b: widening length
- L_c: distance between widenings
- L_{in}: length of the inlet reach
- L_{MR}: length of the reach with macro-roughness
- L_{out}: length of the outlet reach
- L_{tot}: total channel length
- n: number of nodes of seiches
- Q: discharge
- Re: $Re = UR_h/\nu$; Reynolds number related to B
- R_h: hydraulic radius
- S_0: bottom slope
- S_f: friction slope
- T: period of transverse oscillations
- U: mean flow velocity related to B
- x: channel section
- z: bottom level
- α: contraction angle
- ξ: single head loss coefficient
- ΔB: widening depth (the lateral extent)
- ΔE_{cont}: single headloss for the contraction
- ΔE_{exp}: single headloss for the expansion
- Δh_{Beff}: mean absolute error between measured and calculated water depths (approach 2)
- Δh_{ksw}: mean absolute error between measured and calculated water depths (approach 1)

The following subscripts are systematically used in this paper:

- 0: concerning the bottom
- w: concerning the wall (with or without the effect of macro-roughness)
- m: concerning the composite section
- us: concerning the upstream section
- ds: concerning the downstream section
- i: positive integer designating the section

REFERENCES

Bathurst, J.C., Simons, D.B., Li, R.-M. 1981. Resistance Equation for Large-Scale Roughness. *Journal of the Hydraulics Division* Vol. 107: 1593–1613.

Bousmar, D., Zech, Y. 1999. Momentum transfer for practical flow computation in compound channels. *Journal of Hydraulic Engineering* Vol. 125: 696–706.

Canovaro, F., Paris, E., Solari, L. 2004. *Influence of macro-roughness arrangement on flow resistance.* In: Proc. of River Flow 2004. London: Taylor & Francis Group.

Carlier, M. 1998. *Hydraulique générale et appliquée*. Paris: Eyrolles.

Einstein, H.A. 1934. Der Hydraulische oder Profilradius. *Schweizerische Bauzeitung* Vol. 103: 89–91.

Einstein, H.A., Barbarossa. N.L. 1952. River Channel Roughness. *Transactions. American Society of Civil Engineers* Vol. 117: 1121–1146.

Graf, W.H. 1984. *Hydraulics of Sediment Transport*. New York: McGraw-Hill.

Henderson, F.M. 1966. *Open channel flow*. New York: MacMilan.

Hersberger, D. 2003. *Wall roughness effects on flow and scouring in curved channels with gravel bed*. Communication 14, Ed. by A.J. Schleiss. Lausanne: LCH-EPFL.

Leonardi, S., Orlandi, P., Smalley, R.J., Djenidi, L., Antonia, R.A. 2003. Direct numerical simulations of turbulent channel flow with transverse square bars on one wall. Journal of Fluid Mechanics Vol. 491: 229–238.

Matthew, G.D. 1975. Simple approximate treatment of certain incompressible duct flow problems involving separation. *Journal of Mechanical Sciences* Vol. 17: 57–64.

Morris, H.M. 1955. Flow in rough conduits. *Transactions. American Society of Civil Engineers* Vol. 120: 373–410.

Morris, H.M., Wiggert, J.M. 1972. *Applied hydraulics in engineering*. New York: The Ronald Press Company.

Ohmoto, T., Hirakawa. R., Watanabe, K. 2005. *Interaction between water surface oscillations and large eddies in an open channel with spur dikes.* In: Proc. XXXI IAHR Congress, Ed. by B.-H. Jun et al.. Seoul: Korea Water Resources Association.

Rouse, H. 1946. *Elementary Mechanics of Fluids*. New York: Wiley.

Sinniger, R.O., Hager, W.H. 1998. *Constructions hydrauliques, écoulements stationnaires.* Lausanne: Presses polytechniques romandes.

Stoesser, T., Rodi, W., Jirka, G.H. 2004. *Large-eddy simulation of flow over rough channel beds.* In: Proc. of River Flow 2004. London: Taylor & Francis Group.

Takeda, Y. 1985. Velocity profile measurement by ultrasound Doppler shift method, *Fluid Control and Measurement*. Ed. by M. Harada. Tokyo: Pergamon Press.

Van Rijn, L.C. 1984. Sediment transport, Part III: Bed forms and alluvial roughness. *Journal of Hydraulic Engineering* Vol. 110: 1733–1754.

Weitbrecht, V., Jirka, G.H. 2001. *Flow patterns and exchange processes in dead zones of rivers*. In: Proc. XXIX IAHR

Copyright © 2006 Taylor & Francis Group plc, London, UK

Congress. Ed. by Guiven et al.. Beijing: Tsinghua University Press.
Wüest, A., Farmer, D.M. 1998. *Seiches.* In: McGraw-Hill Encyclopedia of Science&Technology, 9th Edition. New York: McGraw-Hill.
Yen, B.C. 2002. Open Channel Flow Resistance. *Journal of hydraulic engineering* Vol. 128: 20–39.
Yossef, F.M., Vriend, H.J. 2004. *Mobile-bed experiments on the exchange of sediments between main channel and groyne fields*. In: Proc. of River Flow 2004. London: Taylor & Francis Group.

Copyright © 2006 Taylor & Francis Group plc, London, UK

Weakly nonlinear analysis on interaction of alternate bars and double-row bars

Y. Watanabe
Civil Engineering Research Institute for Cold Region, Sapporo, Japan

K. Hasegawa
Foundation of River and Watershed Environment Management, Sapporo, Japan

ABSTRACT: This research incorporates mode interference into the weakly nonlinear analysis of sandbar growth, to improve explanation of the mode reduction process in sandbar formation. The study attempts to clarify the degree of the interference. Introduction of linear amplication into the nonlinear analysis model made it possible to examine alternate bars and double-row bars on the same order. The analysis used hydraulic conditions with large width/depth ratio in which double-row bars form. Although it did not accurately reproduce the quantitative results of the experiments, this analysis was able to explain the qualitative characteristics of the reduction process, in which sandbars of both modes cannot simultaneously occur.

1 INTRODUCTION

Toward improving flood control, studies have been conducted on the behavior of bar formation on the riverbed, because once such sand waves form, they start to cause local scouring and make the river channel meander, promoting riverbank erosion. Conventionally, the initial growth rate during sandbar development is used to classify the mesoscale riverbed configuration. Theoretical studies on bar formation have been conducted several researchers. Colombini et al. (1987), Schielen et al. (1993) and Izumi & Pornprommin (2002) conducted weakly non-linear stability analysis on bar developments in straight channel. They clarified the bar formation process. However, these analysis were not considered the interaction of two modes (alternate bars and double-row bars). Various hydraulic tests (Fujita 1989, Fujita et al. 1992) and numerical simulations (Takebayashi et al. 2001, Teramoto & Tsujimoto 2005) have reported that under the condition in which sandbars of higher mode form during the initial period, mode reduction occurs over time. This means that there may be a situation in which the sandbar mode differs from the mode predicted by the initial growth rate for that riverbed configuration. In fact, there are river sections with hydraulic conditions under which double-row bars are expected to form but where mode reduction is occurring or has occurred. This difference between the theoretical, initially predicted mode and the reduced mode that occurs over time must be addressed in planning flood control revetments and river conservation, since these are greatly influenced by riverbed microtopography.

Watanabe & Kuwamura (2004) experimented sandbar formations by setting several hydraulic conditions under which either alternate bars or double-row bars formed. They applied the weakly nonlinear analysis in describing sandbar development which was established by Colombini et al. (1987) and tried to explain the mode reduction process of double-row bars (Watanabe & Kuwamura 2005). In that experiment, alternate bars and double-row bars were examined separately, and analysis was simplified by neglecting any interference between the two modes. The experiment resulted in the conclusion that reduction from double-row bar mode to alternate bar mode could be explained even from experiments in which the two types of bars were examined separately.

This present study incorporates the interference between modes into nonlinear analysis to clarify the mutual influence of the modes in the mode reduction process.

2 GROWTH RATE EXPANSION METHOD CONSIDERING MODE INTERFERENCE

2.1 *Basic equations and dimensionless forms*

Basic equations and dimensionless forms are set in the same form as Colombini et al. (1987). Equations 1, 2, 3 and 4, respectively, are two steady two-dimensional

Copyright © 2006 Taylor & Francis Group plc, London, UK

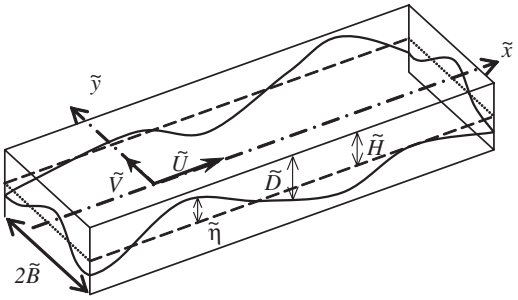


Figure 1. Definitions of coordinate system of the flow model.

shallow-water flow equations where the diffusion terms are omitted, the continuity equation, and the continuity equation of bedload, for a straight channel (width: $2\tilde{B}$) under the coordinate system shown in Figure 1.

$$\tilde{U}\frac{\partial \tilde{U}}{\partial \tilde{x}} + \tilde{V}\frac{\partial \tilde{U}}{\partial \tilde{y}} + \tilde{g}\frac{\partial \tilde{H}}{\partial \tilde{x}} + \frac{\tilde{\tau}_x}{\tilde{\rho}\tilde{D}} = 0 \quad (1)$$

$$\tilde{U}\frac{\partial \tilde{V}}{\partial \tilde{x}} + \tilde{V}\frac{\partial \tilde{V}}{\partial \tilde{y}} + \tilde{g}\frac{\partial \tilde{H}}{\partial \tilde{y}} + \frac{\tilde{\tau}_y}{\tilde{\rho}\tilde{D}} = 0 \quad (2)$$

$$\frac{\partial\left(\tilde{U}\tilde{D}\right)}{\partial \tilde{x}} + \frac{\partial\left(\tilde{V}\tilde{D}\right)}{\partial \tilde{y}} = 0 \quad (3)$$

$$\frac{\partial \tilde{\eta}}{\partial \tilde{t}} + \frac{1}{1-p}\left(\frac{\partial \widetilde{Q_{bx}}}{\partial \tilde{x}} + \frac{\partial \widetilde{Q_{by}}}{\partial \tilde{y}}\right) = 0 \quad (4)$$

where $\tilde{t}$ = time; $\tilde{x}$ = longitudinal coordinate; $\tilde{y}$ = transverse coordinate; $\tilde{U}$ = flow velocity in the $\tilde{x}$ coordinate direction; $\tilde{V}$ = flow velocity in the $\tilde{y}$ coordinate direction; $\tilde{H}$ = water level; $\tilde{D}$ = water depth; $\tilde{\eta}$ = riverbed elevation ($=\tilde{H}-\tilde{D}$); $\tilde{\tau}_x$ = shear stress in the $\tilde{x}$ coordinate direction; $\tilde{\tau}_y$ shear stress in the $\tilde{y}$ coordinate direction; $\widetilde{Q_{bx}}$ = bedload transport rate in the $\tilde{x}$ coordinate direction; $\widetilde{Q_{by}}$ = bedload transport rate in the $\tilde{y}$ coordinate direction; $\tilde{\rho}$ = density of water; $\tilde{g}$ = acceleration of gravity; and p = porosity of bed. Parameters capped with have dimensions.

Equations 1, 2, 3 and 4 are made dimensionless using the parameters of uniform flow on a flat riverbed:

$$(U,V) = (\tilde{U},\tilde{V})/\widetilde{U_0};\ D = \tilde{D}/\widetilde{D_0};\ H = \tilde{H}/(F_0{}^2\widetilde{D_0});\ (Q_{bx},Q_{by}) = (\widetilde{Q_{bx}},\widetilde{Q_{by}})/(\delta\tilde{g}\tilde{d}_s{}^3)^{1/2};\ (\tau_x,\tau_y) = (\tilde{\tau}_x,\tilde{\tau}_y)/(\tilde{\rho}\widetilde{U_0}{}^2);\ (x,y) = (\tilde{x},\tilde{y})/\tilde{B};\ t = \tilde{t}/(\tilde{B}/\widetilde{U_0});\ \text{and } F_0 = \widetilde{U_0}/(\tilde{g}\widetilde{D_0})^{1/2}\ .$$

Here, the suffix 0 indicates a value for uniform flow. $\tilde{d}_s$ = the grain size of the riverbed material; and δ = the submerged specific gravity of the riverbed material. The resultant equations are as follows:

$$U\frac{\partial U}{\partial x} + V\frac{\partial U}{\partial y} + \frac{\partial H}{\partial x} + \beta\frac{\tau_x}{D} = 0 \quad (5)$$

$$U\frac{\partial V}{\partial x} + V\frac{\partial V}{\partial y} + \frac{\partial H}{\partial y} + \beta\frac{\tau_y}{D} = 0 \quad (6)$$

$$\frac{\partial (UD)}{\partial x} + \frac{\partial (VD)}{\partial y} = 0 \quad (7)$$

$$\frac{\partial \eta}{\partial t} + Q_0\left(\frac{\partial Q_{bx}}{\partial x} + \frac{\partial Q_{by}}{\partial y}\right) = 0 \quad (8)$$

where $Q_0 = (\delta d_s{}^3)^{1/2}/[F_0(1=p)]$.

2.2 *Conventional perturbation method (Colombini et al. 1987)*

When alternate bars and double-row bars are considered separately, (U,V,H,D) in these equations are substituted by their expansions whose perturbation parameters are $\varepsilon^{1/2}$, as shown by Equations 9, 10, 11, 12 and 13.

$$(U,V,H,D) = (1,0,H_0,1) + \varepsilon^{1/2}(U_1,V_1,H_1,D_1) + \varepsilon^{2/2}(U_2,V_2,H_2,D_2) + \varepsilon^{3/2}(U_3,V_3,H_3,D_3) \quad (9)$$

$$(U_1,V_1,H_1,D_1) = \begin{cases} A_{(T)}(S_1u_{111},C_1v_{111},S_1h_{111},S_1d_{111})E_1 + c.c. & ;\text{mode} = 1 \\ A_{(T)}(C_2u_{121},S_2v_{121},C_2h_{121},C_2d_{121})E_1 + c.c. & ;\text{mode} = 2 \end{cases} \quad (10)$$

$$(U_2,V_2,H_2,D_2) = \begin{cases} A_{(T)}{}^2E_2[(C_2u_{222},S_2v_{222},C_2h_{222},C_2d_{222}) + (u_{202},v_{202},h_{202},d_{202})] + c.c. \\ +A_{(T)}\overline{A}_{(T)}[(C_2u_{220},S_2v_{220},C_2h_{220},C_2d_{220}) + (u_{200},v_{200},h_{200},d_{200})] \\ +(0,0,H_{200},0) \quad ;\text{mode} = 1 \\ A_{(T)}{}^2E_2[(S_4u_{242},C_4v_{242},S_4h_{242},S_4d_{242}) + (u_{202},v_{202},h_{202},d_{202})] + c.c. \\ +A_{(T)}\overline{A}_{(T)}[(S_4u_{240},C_4v_{240},S_4h_{240},S_4d_{240}) + (u_{200},v_{200},h_{200},d_{200})] \\ +(0,0,H_{200},0) \quad ;\text{mode} = 2 \end{cases} \quad (11)$$

Copyright © 2006 Taylor & Francis Group plc, London, UK

$$(U_3, V_3, H_3, D_3) =$$

$$\begin{cases} A_{(T)}{}^2\overline{A}_{(T)}\,(S_1u_{311}, C_1v_{311}, S_1h_{311}, S_1d_{311})\,E_1 \\ \qquad +c.c. + h.h. \qquad ;\mathrm{mode} = 1 \\ A_{(T)}{}^2\overline{A}_{(T)}\,(C_2u_{321}, S_2v_{321}, C_2h_{321}, C_2d_{321})\,E_1 \\ \qquad +c.c. + h.h. \qquad ;\mathrm{mode} = 2 \end{cases} \tag{12}$$

$$(S_m, C_m, E_m) =$$

$$\left(\sin\left(\frac{1}{2}\pi my\right), \cos\left(\frac{1}{2}\pi my\right), \exp\left[mi\left(\lambda x - \omega t\right)\right]\right) \tag{13}$$

where, $c.c.$ = the complex conjugate of the immediately preceding term; $h.h.$ = a term of high order; m = the mode number of bar formation; and $A_{(T)}$ = the amplitude of small perturbation at time T. T is a time scale introduced to express the variation of small perturbation. Its relation to the time scale of flow, t, is given by Equation 14. $\overline{A}_{(T)}$ is the complex conjugate of $A_{(T)}$.

$$T = \varepsilon t \tag{14}$$

The time scale necessary for expressing development of sandbars is much greater than that for changes of water flow. On the order of $\varepsilon^{3/2}$, a modified Landau-Stuart equation shown as Equation 15 is obtained for alternate bars and double-row bars.

$$\frac{dA_{(T)}}{dT} + \alpha_1 A_{(T)} + \alpha_2 A_{(T)}{}^2\overline{A}_{(T)} = 0 \tag{15}$$

Equation 16 is the solution of Equation 15:

$$|A| = \sqrt{\frac{-\mathrm{Re}\,(\alpha_1)}{\mathrm{Re}\,(\alpha_2) - a_0\mathrm{Re}\,(\alpha_1)\exp\left[-2\mathrm{Re}\,(\alpha_1)\,T\right]}} \tag{16}$$

where, $|A|_0$ = assumed to be the initial value of small perturbation; and a_0 = expressed by Equation 17.

$$a_0 = \frac{1}{|A|_0{}^2} + \frac{\mathrm{Re}\,(\alpha_2)}{\mathrm{Re}\,(\alpha_1)} \tag{17}$$

When the growth rate expansion method is applied to nonlinear analysis of sandbar development, the perturbation parameter, $\varepsilon^{1/2}$, is the square route of the ratio ε obtained by dividing the difference between β_c (the minimum river width/depth ratio for which the initial perturbation is neutral, i.e., whose initial growth rate Ω_0 is 0 in linear stability analysis) and β (the river width/depth ratio under the test conditions) by β_c, as shown by Equation 18:

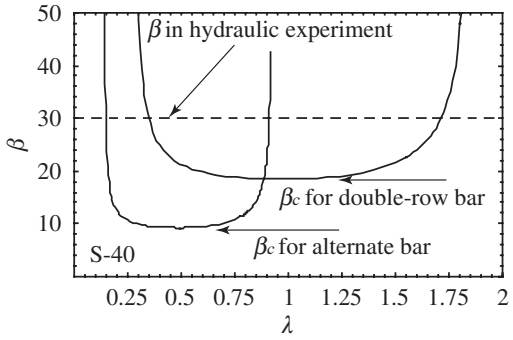


Figure 2. Neutral curves of initial growth rates calculated by the linear stability analysis.

$$\beta = \beta_c\,(1 + \varepsilon) \tag{18}$$

For application of nonlinear analysis, the river width/depth ratio β needs to be close to β_c. The wavenumber of sandbar λ is given by Equation 19. For the sake of analysis, however, here we assume that $\lambda_1 = 0$, because it does not greatly affect the analysis result.

$$\lambda = \lambda_c + \varepsilon\lambda_1 \tag{19}$$

2.3 *Mode interference method*

The growth rate expansion method was used to consider the development process of alternate bars and double-row bars on the same order. As shown in Figure 2, the critical river width/depth ratio β_c, or the minimum river width/depth ratio when the initial growth rate Ω_0 of the sandbar is 0, differ between alternate bar and doublerow bar. In the growth rate expansion method, which describes sandbar development in a channel whose width/depth ratio is close to the critical width/depth ratio, it is theoretically impossible to simultaneously examine the growth of sandbars in channels that have different critical river width/depth ratios. In addressing the mode change from double-row bar to alternate bar, one must consider the interference between the two modes. Thus, the alternate bar and the double-row bar need to be considered under conditions in which there is the same order of perturbation. Toward solving this problem, some preconditions are set as follows.

When perturbation expansion is applied to more than one type of sandbar under the condition of the same order of perturbation, a uniform perturbation parameter is required. The region in which alternate bars and double-row bars can be considered is the region that is conventionally classified as the region

Copyright © 2006 Taylor & Francis Group plc, London, UK

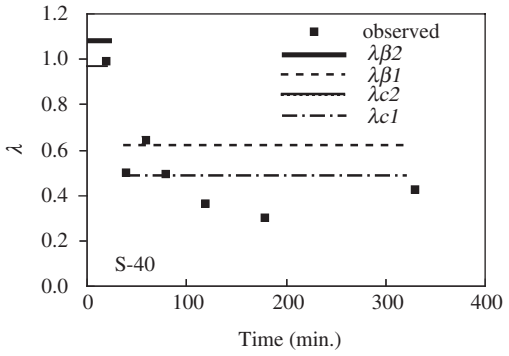


Figure 3. Changes in wavenumber of bars in hydraulic tests.

for double-row bars. Therefore, analysis is applied to a case in which the critical river width/depth ratio, or the minimum river width/depth ratio, is β_c when the initial growth rate of a double-row bar Ω_0 is 0, and a uniform perturbation parameter is used. In this case, the critical river width/depth ratio differs from that for an alternate bar, and the alternate bar has an initial growth rate that exceeds 0.

Figure 3 shows the changes in wavenumber of sand bars obtained in a previous hydraulic test on the process of reduction from double-row bar mode to alternate bar mode. The figure also contains the wavenumber λ_c at β_c obtained by linear stability analysis and the wavenumber λ_β at β obtained in the experiments. The suffix refers to the mode number. In Figure 3, the wavenumber for the alternate bar mode becomes roughly half that for the double-row bar mode as the mode reduction progresses. Thus the wavenumber for the alternate bar mode will be considered to have the fixed value of half that for the double-row bar mode.

When the above conditions are applied, it is impossible to satisfy equations on the first order for both the alternate bars and the double-row bars. Thus, the amplitude of the double-row bar continues to be $B_{(T)}$, a function of T, but for the alternate bar $W_{(t)}$, a function of t is used in addition to $A_{(T)}$, a function of T, because the alternate bar mode has an initial growth rate that exceeds 0. This is equivalent also to changing the time scale of development in the mode 1 and the mode 2.

Accordingly, Equations 20, 21 and 22 replace Equations 9, 10, 11 and 12.

$$
\begin{aligned}
&(U_1, V_1, H_1, D_1) = \\
&\quad A_{(T)} W_{(t)} \left(S_1 u_{111}, C_1 v_{111}, S_1 h_{111}, S_1 d_{111}\right) E_1 + c.c. \\
&\quad + B_{(T)} \left(C_2 u_{122}, S_2 v_{122}, C_2 h_{122}, C_2 d_{122}\right) E_2 + c.c.
\end{aligned} \tag{20}
$$

$$
\begin{aligned}
&(U_2, V_2, H_2, D_2) = \\
&{A_{(T)}}^2 {W_{(t)}}^2 E_2 \left[\left(C_2 u_{222}, S_2 v_{222}, C_2 h_{222}, C_2 d_{222}\right)\right. \\
&\qquad \left. + \left(u_{202}, v_{202}, h_{202}, d_{202}\right)\right] + c.c. \\
&+ A_{(T)} \overline{A}_{(T)} W_{(t)} \overline{W}_{(t)} \left[\left(C_2 u_{220}, S_2 v_{220}, C_2 h_{220}, C_2 d_{220}\right)\right. \\
&\qquad \left. + \left(u_{200a}, v_{200a}, h_{200a}, d_{200a}\right)\right] \\
&+ {B_{(T)}}^2 E_4 \left[\left(C_4 u_{244}, S_4 v_{244}, C_4 h_{244}, C_4 d_{244}\right)\right. \\
&\qquad \left. + \left(u_{204}, v_{204}, h_{204}, d_{204}\right)\right] + c.c. \\
&+ B_{(T)} \overline{B}_{(T)} \left[\left(C_4 u_{240}, S_4 v_{240}, C_4 h_{240}, C_4 d_{240}\right)\right. \\
&\qquad \left. + \left(u_{200b}, v_{200b}, h_{200b}, d_{200b}\right)\right] \\
&+ \overline{A}_{(T)} B_{(T)} \overline{W}_{(t)} E_1 \left[\left(S_1 u_{211}, C_1 v_{211}, S_1 h_{211}, S_1 d_{211}\right)\right. \\
&\qquad \left. + \left(S_3 u_{231}, C_3 v_{231}, S_3 h_{231}, S_3 d_{231}\right)\right] + c.c. \\
&+ A_{(T)} B_{(T)} W_{(t)} E_3 \left[\left(S_1 u_{213}, C_1 v_{213}, S_1 h_{213}, S_1 d_{213}\right)\right. \\
&\qquad \left. + \left(S_3 u_{233}, C_3 v_{233}, S_3 h_{233}, S_3 d_{233}\right)\right] + c.c. \\
&+ \left(0, 0, H_{200}, 0\right)
\end{aligned} \tag{21}
$$

$$
\begin{aligned}
&(U_3, V_3, H_3, D_3) = \\
&\quad \left({A_{(T)}}^2 \overline{A}_{(T)} {W_{(t)}}^2 \overline{W}_{(t)} + A_{(T)} B_{(T)} \overline{B}_{(T)} W_{(t)}\right) E_1 \\
&\qquad \left(S_1 u_{311}, C_1 v_{311}, S_1 h_{311}, S_1 d_{311}\right) + c.c. \\
&\quad + \left({B_{(T)}}^2 \overline{B}_{(T)} + B_{(T)} A_{(T)} \overline{A}_{(T)} W_{(t)} \overline{W}_{(t)}\right) E_2 \\
&\qquad \left(C_2 u_{322}, S_2 v_{322}, C_2 h_{322}, C_2 d_{322}\right) + c.c. \\
&\quad + h.h.
\end{aligned} \tag{22}
$$

where, the leftmost number of the three-digit suffix in Equations 21 and 22 is the order, the middle number is the wavenumber of small perturbation in the transverse direction, and the rightmost number is the wavenumber of small perturbation in the longitudinal direction. By substituting them into Equations 5, 6, 7 and 8, Equations 23 and 24 are obtained on the order of $\varepsilon^{1/2}$ (the first order):

$$
\begin{bmatrix}
p_{111,11} & p_{111,12} & p_{111,13} & p_{111,14} \\
p_{111,21} & p_{111,22} & p_{111,23} & p_{111,24} \\
p_{111,31} & p_{111,32} & p_{111,33} & p_{111,34} \\
p_{111,41} & p_{111,42} & p_{111,43} & p_{111,44}
\end{bmatrix}
\begin{bmatrix}
u_{111} \\ v_{111} \\ h_{111} \\ d_{111}
\end{bmatrix} = 0 \tag{23}
$$

Copyright © 2006 Taylor & Francis Group plc, London, UK

$$\begin{bmatrix} p_{122,11} & p_{122,12} & p_{122,13} & p_{122,14} \\ p_{122,21} & p_{122,22} & p_{122,23} & p_{122,24} \\ p_{122,31} & p_{122,32} & p_{122,33} & p_{122,34} \\ p_{122,41} & p_{122,42} & p_{122,43} & p_{122,44} \end{bmatrix} \begin{bmatrix} u_{122} \\ v_{122} \\ h_{122} \\ d_{122} \end{bmatrix} = 0 \quad (24)$$

For Equations 23 and 24 to have solutions, Determinants 25 and 26 are derived:

$$\begin{vmatrix} p_{111,11} & p_{111,12} & p_{111,13} & p_{111,14} \\ p_{111,21} & p_{111,22} & p_{111,23} & p_{111,24} \\ p_{111,31} & p_{111,32} & p_{111,33} & p_{111,34} \\ p_{111,41} & p_{111,42} & p_{111,43} & p_{111,44} \end{vmatrix} = f_{111(W_{(t)},\beta_c,\lambda_c,\omega;\theta_0,d_s)} = 0 \quad (25)$$

$$\begin{vmatrix} p_{122,11} & p_{122,12} & p_{122,13} & p_{122,14} \\ p_{122,21} & p_{122,22} & p_{122,23} & p_{122,24} \\ p_{122,31} & p_{122,32} & p_{122,33} & p_{122,34} \\ p_{122,41} & p_{122,42} & p_{122,43} & p_{122,44} \end{vmatrix} = f_{122(\beta_c,\lambda_c,\omega;\theta_0,d_s)} = 0 \quad (26)$$

By adding the condition that β_c, λ_c and ω be real numbers in Equation 26, the values of β_c, λ_c and ω are determined for given values of θ and d_s. By substituting them into Equation 25, $W_{(t)}$ is obtained. That is, $W_{(t)}$ will be determined by linear analysis. When $d_{111} = 1$ and $d_{122} = 1$ in Equations 23 and 24, amplitudes on the first order, namely u_{111}, v_{111}, h_{111}, u_{122}, v_{122} and h_{122} are calculated for each wave.

Regarding the order $\varepsilon^{2/2}$ (the second order), equations in the same form as Equations 23 and 24 are obtained for the components of waves having transverse and longitudinal wavenumbers of (1, 1), (1, 3), (2, 2), (3, 1), (3, 3), (4, 4), (2, 0), (4, 0), (0, 2), (0, 4) and (0, 0) respectively.

$$\begin{bmatrix} p_{2ij,11} & p_{2ij,12} & p_{2ij,13} & p_{2ij,14} \\ p_{2ij,21} & p_{2ij,22} & p_{2ij,23} & p_{2ij,24} \\ p_{2ij,31} & p_{2ij,32} & p_{2ij,33} & p_{2ij,34} \\ p_{2ij,41} & p_{2ij,42} & p_{2ij,43} & p_{2ij,44} \end{bmatrix} \begin{bmatrix} u_{2ij} \\ v_{2ij} \\ h_{2ij} \\ d_{2ij} \end{bmatrix} = q_{2ij} \quad (27)$$

where, i and j are the transverse and longitudinal wavenumbers of small perturbation. These equations, however, are nonhomogenous, which means that the right-hand side of each equation exceeds zero. Thus, amplitudes on the second order can be obtained for u_{211} and other values of the second order by using the values obtained on the first order.

The same order can be applied to the waves of (1, 1) and (2, 2), which represent an alternate bar and a double-row bar, respectively. So, when the perturbation parameter for nonlinear analysis is ε, it is theoretically possible to determine $A_{(T)}$ and $B_{(T)}$, which represent bar formation processes on the second order, and Equations 28 and 29 are obtained. However, each equation diverges over time when they are used for calculation under the conditions of hydraulic tests described below. Therefore, nonlinear analysis was redone with a perturbation parameter of $\varepsilon^{1/2}$:

$$\frac{dA_{(T)}}{dT} + \alpha_1 A_{(T)} + \alpha_2 B_{(T)} \overline{A}_{(T)} = 0 \quad (28)$$

$$\frac{dB_{(T)}}{dT} + \alpha_4 B_{(T)} + \alpha_5 {A_{(T)}}^2 = 0 \quad (29)$$

When waves having the transverse and longitudinal numbers of (1, 1) and (2, 2) are subjected to the above on the order of $\varepsilon^{3/2}$ (the third order), then Equations 30 and 31 are obtained.

$$\frac{dA_{(T)}}{dT} + \alpha_1 A_{(T)} + \alpha_2 {A_{(T)}}^2 \overline{A}_{(T)} + \alpha_3 A_{(T)} B_{(T)} \overline{B}_{(T)} = 0 \quad (30)$$

$$\frac{dB_{(T)}}{dT} + \alpha_4 B_{(T)} + \alpha_5 {B_{(T)}}^2 \overline{B}_{(T)} + \alpha_6 B_{(T)} A_{(T)} \overline{A}_{(T)} = 0 \quad (31)$$

If these equations are solved simultaneously, the values $A_{(T)}$ and $B_{(T)}$ are obtained. Analytical solutions, however, are impossible, and thus numerical calculation is used. $W_{(t)}$ are included in the coefficients α_1 to α_6. It is shown that the fourth term on the left side of Equations 30 and 31 represents interference and that these equations have the same form as Equation 15 when the fourth term is omitted.

3 COMPARISON BETWEEN NONLINEAR ANALYSIS RESULTS AND HYDRAULIC TEST RESULTS

3.1 *Outline of hydraulic test*

To examine the results of nonlinear analysis in which mode interference is considered, those results are compared with the results of hydraulic tests (Watanabe & Kuwamura 2005) in which there was mode reduction from double-row bars to alternate bars. The experiments were conducted in a flume with a length of 50 m and a width of 0.9 m. The flume was filled with 0.76 mm silica sand, and a bed with a slope

Copyright © 2006 Taylor & Francis Group plc, London, UK

of 1/80 was formed for all experiments. In each experiment, bar height and bar wavelength were measured continuously until the bars were fully developed.

The items of hydraulic tests are shown in Table 1. In test S-30, the double-row bars that formed in the early stages of water flow transformed into alternate bars. In test S-40, although double-row bars formed in the very early stages of water flow, they soon transformed into alternate bars. For test S-50, alternate bars immediately formed in the early stages of water flow.

3.2 *Comparison result*

The bedload and the coefficient of riverbed resistance used for analysis are represented by Equations 32 and 33 below, which are respectively the equations of Meyer-Peter & Müller, and of Engelund & Hansen.

$$\phi = (\theta - \theta_{cr})^{3/2} \tag{32}$$

$$C_f = \frac{1}{\left[6 + 2.5 \ln\left(\frac{D}{2.5 d_s}\right)^2\right]} \tag{33}$$

where, $\phi =$ the dimensionless bedload transport rate for a unit width; $C_f =$ the drag coefficient of riverbed; $d_s = \tilde{d}_s / \tilde{D}_0$ (dimensionless grain size); $\theta =$ the dimensionless shear stress; and $\theta_{cr} =$ the dimensionless critical shear stress. Both equations reproduce the test results accurately and thus can be used for analysis without problems (Watanabe & Kuwamura 2005).

In Figure 4, the observed amplitudes $\acute{a}11$ and α_{22} are compared with the calculated amplitudes $|A_{(T)}W_{(t)}(F_0^2 h_{111} - d_{111})|$ and $|B_{(T)}(F_0^2 h_{122} - d_{122})|$. The amplitude α_{11} is for the wave that has the wavenumber of 1 in the transverse and longitudinal directions, and α_{22} is the amplitude of the wave that has the wavenumber of 2 in the transverse and longitudinal directions. The observed amplitude was obtained by wavenumber analysis applied to the riverbed configuration identified in the hydraulic tests. $|A_{(T)}W_{(t)}(F_0^2 h_{111} - d_{111})|$ is the calculated amplitude of the wave that has a wavenumber of 1 and $|B_{(T)}(F_0^2 h_{122} - d_{122})|$ is the calculated amplitude of the wave that has the wavenumber of 2 (the third digit of the three-digit suffix) in the transverse and longitudinal directions. The calculated wavenumber was obtained by weakly nonlinear analysis on the first order. It is shown that the calculated values are larger than the experimental values. However, as the river width/depth ratio increases, the amplitude tends to become smaller, and the general tendency of transition from double-row bars to alternate bars is represented well. Particularly well represented is the attenuation with time in the components of double-row bars, whose wavenumber is 2. In solving Equations 30 and 31, the values shown in Table 1 were used as the initial values for $A_{(T)}$ and $B_{(T)}$, for the sake of calculation stability. In analysis on the second order, waves having the longitudinal and transverse wavenumber of 1 and 2, expressed as $|\overline{A}_{(T)}W_{(t)}B_{(T)}\ (F_0^2 h_{211} - d_{211})|$ for wave number 1 and $|A_{(T)}^2 W_{(t)}^2\ (F_0^2 h_{222} - d_{222})|$ for wave number 2, appear. These waves are taken into consideration, and the calculated heights of sandbars are compared with the hydraulic test results in Figure 5. It is shown that solutions oscillate over time as the perturbation parameter $\varepsilon^{1/2}$ grows. This may suggest, as Pornprommin et al. (2004) propose, that the irregularity of the amplitude increases when the river width/depth ratio becomes large. But the time change in the value of $|W_{(t)}|$ for S-40 shown in Figure 6 suggests that $|W_{(t)}|$ tends to diverge over time. It is possible that this irregularity results from the method used in this study. In other words, although the method is originally formulated for phenomena that take place near the growth rate of 0, the linear growth rate $W_{(t)}$ was applied in this

Table 1. Hydraulic conditions of experiments and initial conditions of analysis.

Run	β	d_s	θ	$A_{(0)}$	$B_{(0)}$	β_c	$\varepsilon^{1/2}$
S-30	37.5	0.063	0.12	0.0065	0.0010	17.5	1.07
S-40	30.0	0.051	0.15	0.0020	0.0010	18.5	0.79
S-50	25.0	0.042	0.18	0.0010	0.0010	19.2	0.55

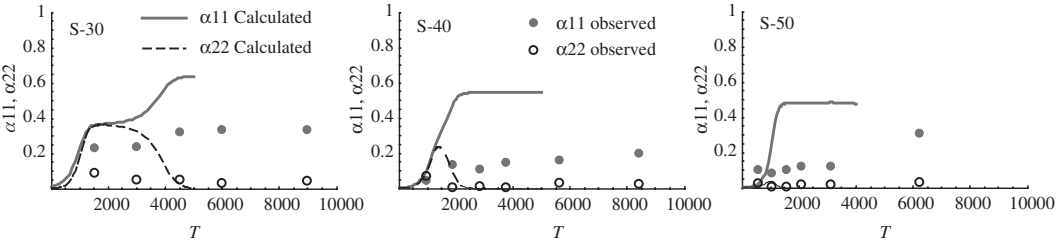


Figure 4. Experimental values and calculated solutions on the first order: temporal changes in the components of alternate bars and double-row bars.

Copyright © 2006 Taylor & Francis Group plc, London, UK

study. At the same time, the irregularity might arise as a result of applying the method to a region having a relatively large growth rate. It is also shown that each wave expressed in the equation does not diverge but instead maintains a steady value, despite $W_{(t)}$ having a relatively large value. The irregularity found in this study needs to be addressed. While the above irregularity remains to be solved, comparison between the results of Figure 4 and Figure 5 shows that the analysis results conform to test results (Watanabe 2004). Even when the amplitude $|A_{(T)}W_{(t)}\,(F_0^2 h_{111} - d_{111})|$ of a wave having a wavenumber of 1 on the fist order increases and the amplitude $|B_{(T)}\,(F_0^2 h_{122} - d_{122})|$ of the wave having the wavenumber of 2 on the first order decreases, the amplitude $|A_{(T)}^2 W_{(t)}^2\,(F_0^2 h_{222} - d_{222})|$ of the wave having the wavenumber 2 on the second order grows and the characteristics of the double-row bar are maintained.

4 DISCUSSION OF THE MODE REDUCTION PROCESS

The characteristics of transition from double-row bars to alternate bars are reproduced satisfactorily by this weakly nonlinear analysis. The mode interference working in the process of mode reduction from double-row bars to alternate bars is examined on the basis of the results of this analysis as follows.

The results of hydraulic test S-40 are used, because in S-40 the mode reduction from double-row bars to alternate bars is clearly shown and the perturbation parameter $\varepsilon^{1/2}$ is the smallest. Figure 7(a) shows the temporal changes in $|A_{(T)}W_{(t)}|$, $|B_{(T)}|$, $|A_{(T)}W_{(t)}B_{(T)}|$ and $|A_{(T)}^2 W_{(t)}^2|$ when the initial values of $A_{(T)}$ and $B_{(T)}$ are set at 0.002 and 0.001, respectively. This means that $A(T)$ exceeds $B_{(T)}$ in the early stages of development process. While $|B_{(T)}|$ grows in the early stages of water flow just as $|A_{(T)}W_{(t)}|$ does, it begins to attenuate when $|A_{(T)}W_{(t)}|$ grows to some level. This agrees well with the results of the hydraulic tests.

Figure 7(b) shows the results when the initial value is set at 0.001 for both $A_{(T)}$ and $B_{(T)}$. In this case, the results of analysis differ from the hydraulic test results: $|A_{(T)}W_{(t)}|$ attenuates, but $|B_{(T)}|$ keeps on growing.

Thus, the results shown in Figure 7(a) and (b) indicate that different initial values result in different tendencies. It is shown in the same figures that on the first order only one mode can grow. This can also be interpreted to mean that interference between the modes is almost unilateral and that one mode cannot grow when the other mode is predominant. Regarding this difference that results from different initial values, further study is needed.

5 CONCLUSIONS

In this study, weakly nonlinear analysis, which can represent mode interference, was conducted to understand phenomena in reduction of mode from double-row bars to alternate bars. Although there are some problems in terms of quantitative evaluations, the characteristics of the mode reduction process are qualitatively reproduced. It is shown that when the two modes are on the same order, they cannot grow simultaneously. The study indicates that disagreement between the calculated values and the experimental values seem to be influenced by the divergence of $W_{(t)}$, the linear growth rate introduced into analysis in this study, and also

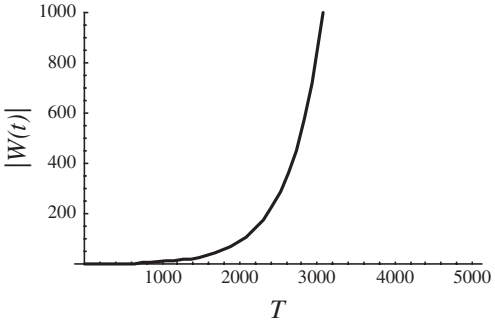


Figure 6. Temporal change of linear growth rate $|W_{(t)}|$ for S-40.

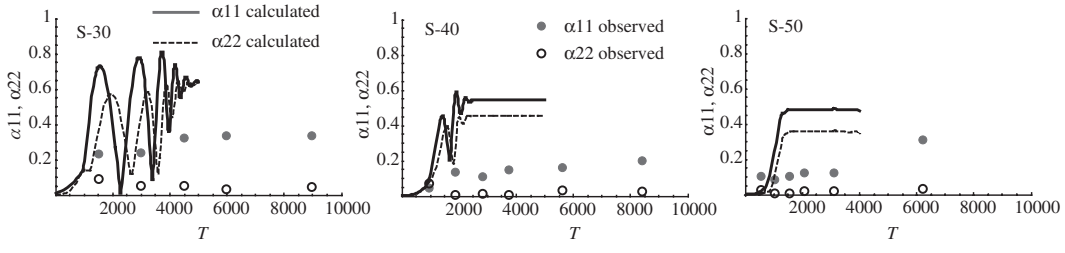


Figure 5. Experimental values and calculated solutions (on the first order and the second order): temporal changes in the components of alternate bars and double-row bars.

Copyright © 2006 Taylor & Francis Group plc, London, UK

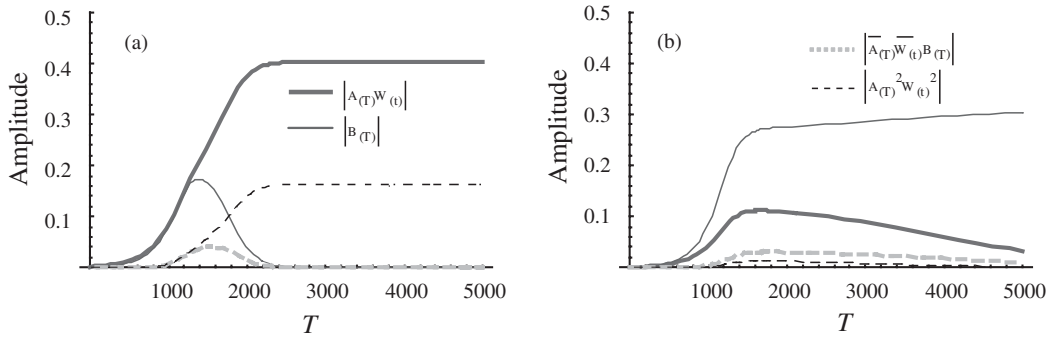


Figure 7. Difference in temporal changes in amplitude by different initial values.

by the difference in the initial values. This should be examined in future studies.

ACKNOWLEDGEMENTS

We would like to thank the Hokkaido Regional Development Bureau of the Ministry of Land, Infrastructure and Transport, for commissioning CERI with this work; the Foundation of River and Watershed Environment Management, for a grant; and the Japan Society for the Promotion of Science, for research aid (Basic research (B) (1) 16360242).

REFERENCES

Colombini, M., Seminara, G. & Tubino, M. 1987. Finite amplitude alternate bars. *Journal of Fluid Mechanics* 181: 213–232.

Fujita, Y., Nagata, N. & Muramoto, Y. 1992. Formation process of braided stream. *Annual Journal of Hydraulic Engineering of JSCE* 36: 23–28 (in Japanese with English abstract).

Fujita, Y. 1989. Bar and channel formation in braided streams. In S. Ikeda & G. Parker (eds), *River meandering; Water Resource Monograph* 2: 417–462.

Izumi, N. & Pornprommin, A. 2002. Weakly nonlinear analysis of bars with the use of the amplitude expansion method. *Journal of hydraulic, coastal and environmental engineering of JSCE* 712 II-60: 73–86 (in Japanese with English abstract).

Schielen, R., Doelman, A. & de Swart, H. E. 1993. On the nonlinear dynamics of free bars in straight channels. *Journal of Fluid Mechanics* 252: 325–356.

Pornprommin, A., Izumi, N. & Tsujimoto, T. 2004. Weakly Nonlinear Analysis of Multimodal Fluvial Bars. *Annual Journal of Hydraulic Engineering of JSCE* 48: 1009–1014.

Takebayashi, H., Egashira, S. & Okabe, T. 2001. Stream formation process between confining banks of straight wide channels. *2nd Proc. RCEM of IAHR*: 575–584.

Teramoto, A. & Tsujimoto, T. 2005. Effects of size heterogeneity of bed materials on mechanism to determine bar mode. *Proceedings of the 4th IAHR Symposium on River, Coastal and Estuarine Morphodynamics*: 433–444.

Watanabe, Y. & Kuwamura, T. 2005. Mode-decrease process of double-row bars. *Proceedings of the 4th IAHR Symposium on River, Coastal and Estuarine Morphodynamics*: 445–453.

Watanabe, Y. & Kuwamura, T. 2004. Experimental study on mode reduction process of double-row bars. *Annual Journal of Hydraulic Engineering of JSCE* 48: 997–1002 (in Japanese with English abstract).

Copyright © 2006 Taylor & Francis Group plc, London, UK

Three-dimensional numerical modeling of flows over a natural dune field

R.J. Hardy
Department of Geography, University of Durham, Durham, UK

D.R. Parsons & J.L. Best
Earth and Biosphere Institute, School of Earth and Environment, University of Leeds, Leeds, UK

S.N. Lane
Department of Geography, University of Durham, Durham, UK

R. Kostaschuk
Department of Geography, University of Guelph, Ontario, Canada

O. Orfeo
Centro de Ecologica Aplicada del Littoral (CECOAL), Corrientes, Argentina

ABSTRACT: Our ability to numerically predict the interaction between complex topography and three dimensional flow at large scales (∼1 km) has yet to be fully developed. This is the result of our inability to design numerically stable meshes for complex topographies at these spatial resolutions. This paper deals with the numerical simulation of flow over a natural dune field located in the Rio Paraná, NE Argentina. The methodology is based upon the development and application of a new five term porosity algorithm that modifies the mass conservation equation within a regular Cartesian mesh. Bathymetric measurements were made in the field using a multibeam echo sounder which provided an unparalleled topographic dataset to test this new numerical modeling approach. Measurements of flow were made using an acoustic Doppler current profiler and are used as inlet boundary conditions and validation data. The results demonstrate simple flow acceleration due to topographic forcing over the dune stoss and expansion and deceleration over the dune lee.

1 INTRODUCTION

Dunes are one of the most common depositional bed forms in river channels, forming in a range of sediment sizes from silt and sand through to gravel (Dinehart, 1992; Best, 1996; Carling, 1999; Kleinhans, 2001, 2002; Carling et al. 2005). Their presence significantly influences both the nature of the mean and turbulent flow and consequently exerts a strong control of the entrainment, transport and deposition of sediment (Parsons et al. 2005, Best, 2005). In recent years progress has been made in our knowledge of dune dynamics due to the significant advances in our ability to monitor flow and dune morphology both in the laboratory and field (Best, 2005). Previous research has determined the main flow characteristics associated with dunes dynamics, which are; (1) accelerating flow over the dune stoss side; (2) flow separation or deceleration (Nelson et al. 1993; McLean et al. 1994; Best & Kostachuck, 2002) from the dune crest in the lee side; (2) flow reattachment at 4 to 6 dune heights downstream (Engel, 1981); (4) a shear layer between the separated flow and stream wise flow above which expands as it extends downstream and; (5) an internal boundary layer that grows from reattachment beneath the wake along the stoss slope of the next dune downstream. However, virtually all process understanding has been deduced from work that has dealt with morphologies that are essentially regular and two-dimensional, a situation that is rare in natural river channels. Records of bed morphology from natural channels show the frequent occurrence of dunes of different scales (Allen & Collinson, 1974; Allen, 1978; Rubin & McCulloch, 1980; Harbor, 1998; ten Brinke et al. 1999; Wilbers & ten Brinke, 2003; Wilbers, 2004; Parsons et al. 2005) possibly as a response to both non-uniform and unsteady flow, hysteresis effects within a flood hydrograph, or the developing internal boundary layer on the stoss side of large dunes. Although, the effect of three dimensional

Copyright © 2006 Taylor & Francis Group plc, London, UK

dune morphology on flow structures generation has been recognized for a long time (e.g. Allen, 1968), it has only recently been fully explored. Maddux et al. (2003a,b) report that the friction coefficients for 3D dunes are 50% greater compared to their 2D dunes which has the direct effect of reducing turbulence. However, the observed sinuous crest lines imply the presence of secondary circulation, which are responsible for a large percentage of the momentum flux over the dune (Maddux et al. 2003a, b). These form-induced stresses are secondary circulation and augment the low Reynolds stresses present over the 3D dunes (Maddux et al. 2003 a,b). Recent summaries on the dynamics and role of dunes (ASCE Task Force, 2002; Bridge, 2003; Best, 2005) highlighted that in order to gain a more complete understanding of the dynamics of river dunes, a fuller appreciation is needed of the complex links between turbulence, natural bed morphology and sediment transport.

One approach that has yet to be fully explored to gain an insight into the interaction between dune dynamics and morphology is through the application of numerical models. The application of Computational Fluid Dynamics (CFD) schemes have the potential, but are yet to be fully developed because of; i) our inability to collect high resolution topographic data that is required as a boundary condition for a CFD scheme and; ii) the inclusion of this topography into a CFD scheme. Recent application of multibeam echo sounding permits full quantification of river bed topography at centimeter resolution over km reach lengths. This has been applied by Parsons et al. (2005) to a natural sand bed river where three-dimensional dunes where identified over scales from superimposed bed forms ($\sim$<0.20 m high) to larger dune forms ($\sim$2 m high). This provides an unparalleled topographic dataset to test this new numerical modeling approach within a Computational Fluid Dynamics scheme. In this paper we outline a new methodology that incorporates complex topography into a CFD scheme over a river length of approximately 1 km. This allows the interaction between form and flow to be studied numerically over a naturally occurring dune field.

2 NUMERICAL METHODOLOGY

The incorporation of complex topographies within a CFD scheme has been problematic to date as the representation of the large scale topographic features has required the application of boundary fitted co-ordinates (BFC's), which involve mesh deformation in the Cartesian space (if not in the computational space). Mesh deformation may change the magnitude of numerical diffusion in the model and lead to uncertainties as to whether observed changes in process representation are due to topographic effects or grid adjustment effects. Therefore, there have been several new approaches to include complex topography into numerical schemes.

The methodology presented here is a mass flux scaling algorithm based upon a porosity approach within a regular Cartesian mesh. This approach has previously been developed and validated for high resolution applications (Lane et al. 2003; Lane et al. 2004; Hardy et al. 2005) for the inclusion of complex topography (individual gravel particles) in high resolution (spatial resolutions of 0.002 meters) CFD applications. Here a methodology is extended to consider greater spatial scales so that the approach can be used to study geomorphological problems over spatial scales of hundreds of meters. The original method was based upon a numerical porosity treatment, similar to that of Olsen and Stokseth (1995), which used a structured grid but specifies cell porosities to block out bottom topography (P = 1 for cells that are all water, P = 0 for cells that are all bed and 0 < P < 1 for partly blocked cells) with appropriate drag terms introduced into the momentum equations. The fundamental difference from the original methodology is that instead of using a single term volume approach the approach is modified to a five term porosity algorithm which includes the four vertical faces of the cell and a cell volume. This is achieved by a porosity value representing a blockage in each cell being introduced into the equations by modifying the effective cell face area. This subsequently reduces the amount of flux which can pass through each cell. Assuming the steady state case, this is represented by,

$$\begin{aligned} a &= \min\left((\rho uA),0\right) - \frac{A\Gamma}{\Delta} && \text{for upwind} \\ a &= \rho uA\frac{\delta}{\Delta} - \frac{A\Gamma}{\Delta} && \text{for linear,} \end{aligned} \qquad (1)$$

where δ = distance between the relevant face and the cell centre; Δ = distance between the cell centre and the next adjacent node in the direction normal to the face. As the area of the face appears in both terms in these expressions, the modification of face area can be considered as a multiplier of a. Therefore, for the transient case, where a includes an extra term of the form $V\rho/\Delta t$, the multiplier applies only to those terms containing A. This is represented schematically for a simple two-dimensional case in Figure 1 and simplified for diagrammatical purposes with face areas replaced by edge lengths.

In this application a Cartesian mesh is used so that the grid is rectangular, therefore A_e and A_w are replaced by Δy and A_n and A_s are replaced by Δx. The bed topography cuts through the cell in question, reducing the flux through the east (e) face to 30% and west (w) face to 60% and completely blocking the south (s) face (0%). The north (n) face is not affected

Copyright © 2006 Taylor & Francis Group plc, London, UK

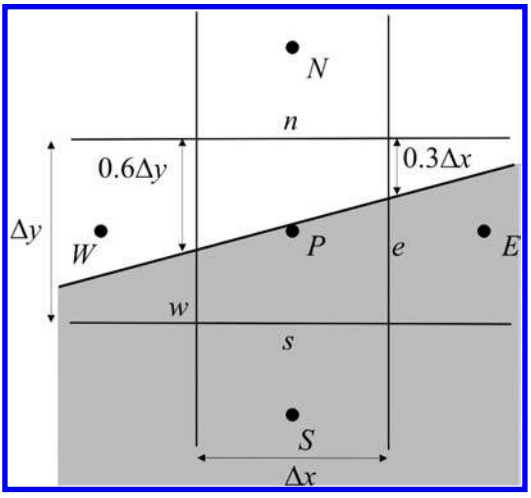


Figure 1. A schematic diagram illustrating the porosity method in two dimensions.

(100%). Therefore, the two-dimensional finite volume equation becomes:

$$a_P\varphi_P + 0.3a_E\varphi_E + 0.6a_W\varphi_W + a_N\varphi_N + 0.0a_S\varphi_S = Q_P. \quad (2)$$

The value of a_P is modified through the continuity condition:

$$a_P + 0.3a_E + 0.6a_W + a_N = 0, \quad (3)$$

For this method to work the digital elevation model which contains the topographic data must be on the same resolution as the computational grid. A computational sequence is then applied to every (i,j) location of cells to calculate the blockage term. Initially the cells which contains the interface between the bed and water is found using the mean of the four elevations at each of the cell corners and all cells below this height are assigned a volume porosity of zero, allowing no flux though the cell and effectively blocking it completely. The most complex calculations occur for the cells where the bed-water interface is located. Initially porosity values are calculated for the two vertical faces on the downstream and left sides of the cell which is based on the elevations at the cell corners. This porosity is calculated by taking the mean of the two elevations and subtracting the elevation of the base of the cell;

$$\mathrm{FP} = 1 \quad \frac{1}{\Delta z} \quad \frac{z_e + z_w}{2} \quad z_{\mathrm{cell}} \ , \quad (4)$$

where Δz is the vertical extent of the cell, z_e and z_w are the elevations of the bed at the edges of the face in question and z_{cell} is the elevation of the cell base. The elevations here are given with respect to the lower extent of the computational domain. If one or more of the bed elevations is above the elevation of the top of the cell then the bed will 'cut through' the top of the cell and a porosity is applied to restrict the flux through the top of the cell. Here linear interpolation between adjacent elevations is used to find where the bed and water interface is located along the cell edge(s). The porosity value for the face is then found by calculating the area of the triangular or trapezoidal part(s) of the face which is blocked as a proportion of the cell face area. The assumption introduced here is that the change in bed elevation between adjacent data points is linear.

The model described above still requires uses a of wall functions to model the laminar sub-layer as the method described above can only include a finite amount of information in the model. Specifically, any variation in the bed at a scale smaller than that of the computational cell cannot be represented directly. The 'roughness height' in these wall functions should therefore be set to represent the effect of the grains smaller than the grid cells on the flow itself. The wall functions used in this research are the non-equilibrium form proposed by Launder and Spalding (1974):

$$\frac{u\sqrt{k}}{u_*^2} = \frac{1}{0.25c'_\mu\kappa}\ln\left(0.25c'_\mu\frac{\sqrt{k}}{u_*}\frac{z}{z_0}\right), \quad (5)$$

where u = velocity parallel to the wall; z = distance from the wall, z_0 = roughness height; k = turbulent energy per unit mass; c'_μ = empirically derived coefficient equal to 0.09 (Lauder and Spalding, 1974); κ = von Karman constant (=0.4); ρ = fluid density; u_* = shear velocity ($u_* = \sqrt{\tau_b/\rho}$, where τ_b = the bed shear stress and ρ = density of water).

3 FIELD SITE AND DATA COLLECTION

The study area is a 0.25 km wide, 1.8 km long area of dunes in the Rio Paraná, just upstream of the confluence of the Rio Paraguay, NE Argentina. At the dune field, the Rio Paraná is 2.5 km wide and 5-12 meters deep and at the time of survey the discharge of the full river section was 11 000 $\mathrm{m^3 s^{-1}}$. Measurements of the 3D bathymetry and 3D flow have previously been discussed by Parsons et al. (2005). MBES and aDcp measurements were made along a total of 14 parallel stream wise transects, each approximately 25 m apart, and six span wise cross-sections approximately 200 m apart. The Digital Elevation model (represented in the numerical scheme through the porosity approach) used here is shown Figure 2.

Copyright © 2006 Taylor & Francis Group plc, London, UK

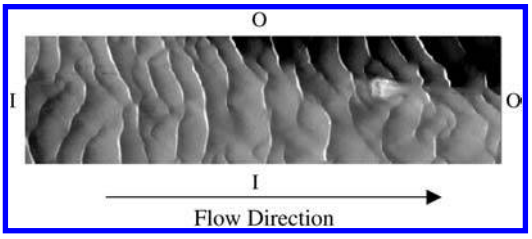


Figure 2. The digital elevation model represented in the porosity algorithm. I marks inlets, O outlets.

4 NUMERICAL SCHEME

The numerical scheme solves the full three-dimensional Navier-Stokes equations discretised using a finite-volume method. The interpolation scheme used is hybrid-upwind, where upwind differences are used in high convection areas (Peclet number >2) and central differences are used where diffusion dominates (Peclet number <2). Although this scheme can suffer from numerical diffusion, it is very stable. The pressure and momentum equations are coupled by applying SIMPLEST, a variation on the SIMPLE algorithm of Patankar and Spalding (1972). This convergence can proceed either smoothly or with damped oscillations to the final solution. To achieve relaxation either: (i) realistic maximum and minimum values may be imposed on the solution; or (ii) relaxation may be used to limit the amount of change allowed in any variable at a given iteration. Weak linear relaxation was used for the pressure correction, while weak false time step relaxation was used for the other variables. The convergence criterion was set such that the residuals of mass and momentum flux were reduced to 0.1% of the inlet flux.

Figure 2 shows the field site which the flow was modeled across. Two inlets, at the upstream end and on the south boundary, and two outlets where specified as the general flow conditions where across the domain. Inlet conditions were taken from aDcp data collected in the field which provided flow results for the u-, v- and w-component of flow. The aDcp data was collected from a moving boat along transects and therefore the flow fields are continuous in both time and space. In order to remove the highly complex nature of flow observed in this data, which may have caused instability, the inlet flow velocity was smoothed with a 3×3 box function. At the free surface, the method applied by Bradbrook et al. (2000) has been adopted, which uses a symmetry plane at the surface across which all normal resolutes are set to zero. The bed was represented by the porosity algorithm while no-slip conditions were specified at the walls. The standard RNG theory k-ε turbulence model is not modified at the sidewalls or the bed and the equilibrium wall function is used.

The computational domain was regular in the x,y directions, with a grid resolution of 2 m. In the z direction the grid resolution was increased 0.25 m. To allow inclusion of topography data using the porosity treatment, the maximum extent of the domain was set at 11 m. Thus, the computational grid was sized at $484 \times 139 \times 44$ (2 960 144 grid cells).

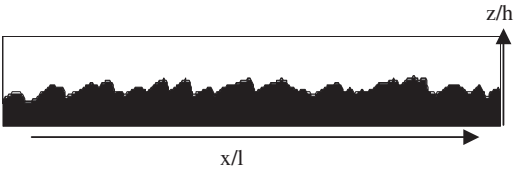


Figure 3. The dune morphology down the midline of the domain. The vertical axis has been increased by a factor of 2.

5 RESULTS

5.1 *Dune morphology*

Using the MBES, bed forms were identified over scales from superimposed bed forms ($\sim<0.20$ m high) to larger dune forms ($\sim$2 m high), providing an unparalleled topographic dataset to test this new numerical modeling approach at a large scale. Figure 2 shows the complete topography of the domain which includes a series of dune profiles down the reach. Previous analysis of this topography has calculated that dune height ranges between 1.2 to 2.5 m high and possess a range of wavelengths from 45 to 85 m (Parsons et al. 2005). This yields a range in the dune form index (or aspect ratio; height/wavelength) of 0.021 to 0.029 (Parsons et al. 2005).

In addition to this there are two main features which can be identified in the domain which will influence the flow field. The first of these is a bedrock protrusion, labeled A on Figure 2, located at 0.8 x/l down the reach. This protrudes approximately 2 meters above the surrounding bed and appears to affect the bed forms, identified in the crest line of the dunes, downstream. Secondly, there is a cross stream gradient with deeper flow located in the top right of the domain. The effect of the cross domain gradient is observed in the orientation of the crest lines which appear normal to the gradient.

The general downstream profile is observed in Figure 3 which represents the dune topography down the midline of the channel represented through the porosity algorithm. Classical low angle dunes are observed that with the majority of forms being highly asymmetric, with leeside slope angles typically around 8.5 to 18°, but with lee slopes up to 22° in individual dunes (Parsons et al. 2005). Dune stoss slope angles are much shallower, typically around 1.5° to 2.5° (Parsons et al. 2005). There is, therefore, considerable topography to determine complex flow structures.

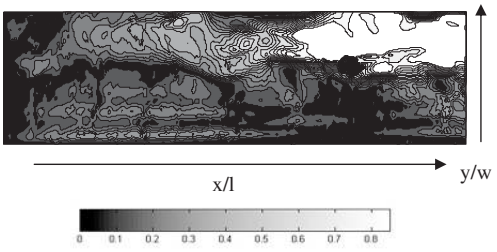
Copyright © 2006 Taylor & Francis Group plc, London, UK



(a) The velocity magnitude for height 0.4 z/h



(b) The velocity magnitude for height 0.5 z/h



(c) The velocity magnitude for height 0.6 z/h

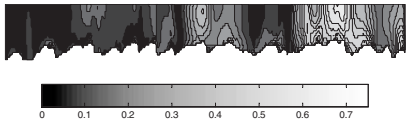
Figure 4. Plan form plots for the velocity magnitude at three successive height. Flow is from left to right.

5.2 *The predicted flow fields*

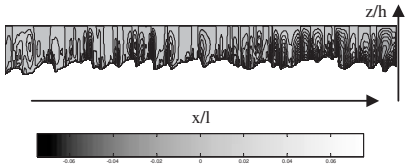
In most of the analysis the velocity magnitude is used to visualize the results. This is the resolved component on the *u*-, *v*- and *w*- component of velocity. The area which is white within the graph is the region that is topography and has been blocked out of the numerical mesh with the porosity algorithm.

5.2.1 *Plan form analysis*

Figure 4 shows three velocity magnitude plots at 0.41, 0.5, 0.6 z/h above the bed where the flow direction is from left to right. Figure 4a demonstrates the prediction at a height of 0.4 z/h. There are two distinct characteristics that can be observed. The first is the effect of the deepening flow in the top right hand of the domain where faster flow is predicted ($>0.4\,\mathrm{ms}^{-1}$). The second characteristic that can be observed is the low flow ($<0.1\,\mathrm{ms}^{-1}$) located in the lee of each of the dunes. Towards the deeper part of the domain flow the flow in the lee of the dunes is steered towards the deeper water. The influence of this topographic hollow can be seen to be dominant through the flow depth. In Figure 4b only a few dune crests can be seen with a complex pattern of skimming flow being observed.



(a) The velocity magnitude down the midline



(b) The w-component of velocity down the midline

Figure 5. Velocity contour maps down the midline of the domain. The vertical axis have been increased by a factor of 2.

This can be detected in the bottom of the images where two separate bands of faster flow ($\sim 0.3\,\mathrm{ms}^{-1}$) compared to the surrounding flow ($\sim 0.1\,\mathrm{ms}^{-1}$) can be detected forming over the dune crests. This pattern is more dominant higher in the flow, (Fig. 4c). The most dominant pattern that is observed throughout the domain is the effect of the deeper flow. The topographic forcing caused by the deeper flow generates a strong process gradient that the effect of the bedrock protrusion (Fig. 2, Region A) is not clearly detectable. It would be possible to speculate that with a protrusion of this magnitude a junction vortex system would be expected to form, however this can not be detected in the velocity contours.

5.2.2 *Midline predictions*

Figure 5 shows the predicted values for the velocity magnitude (Fig. 5a) and the vertical (*w*-) component (Fig. 5b) down the midline of the domain. The velocity magnitude shows complex flow patterns with regions of both high and low flow. Classical flow separation can not be identified, which has previously been identified over 2D dunes, due to the influence of the three dimensional morphology. As previously identified in Figure 4, the effect of the deeper flow can be observed at 0.7 x/l downstream where high flow starts to move across.

A more classical flow structures over dunes can be observed when the *w*-component is studied independently, Figure 5b. This includes flow separation and reattachment with most of the generated flow structures influencing the whole flow depth. However, the complex nature of these structures increase at 0.7 x/l where the lateral process gradient determined by the movement of flow in to the deeper water influence the flow structure. This confirms the previous observations of Allen (1968).

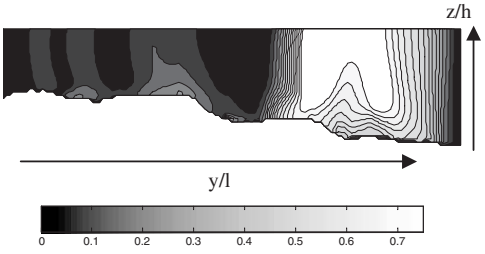
Copyright © 2006 Taylor & Francis Group plc, London, UK



(a) The velocity magnitude at 0.2 x/1



(b) The velocity magnititude at 0.4 x/1



(c) The velocity magnitude at 0.6 x/1

Figure 6. A series of velocity contour plots for y/w plots downstream.

5.2.3 *Cross stream plots*

Figure 6 shows a series of velocity magnitude plots for y/w at 0.2, 0.4 and 0.62 x/l downstream. The first cross section (Fig. 6a) shows the predicted velocity magnitude which is influenced by the local morphological form. A shear layer is starting to develop at approximately 0.55 y/w with very low flow ($<0.1\,\mathrm{ms}^{-1}$) contained within two higher cores of fluid. The core on the right of the image ($\sim$0.7 y/w) becomes more dominant further downstream with the effect of the deeper flow. The opposite is true for the flow on the left as the core of the fluid looses structure with more regions of alternate high and low flow forming. These appear in streaky structures which have previously been identified in Figure 4c.

6 DISCUSSION

This paper has presented a new methodology for the inclusion of complex topography into a Cartesian mesh. The methodology now enables the prediction of flow structures with the application of a three dimensional Computational Fluid Dynamics scheme over scales of 1 km. The present limitation of this methodology is that it is dependent on the quality and resolution of the topographic boundary condition. If high resolution topography does not exist the methodology is not applicable. The results from qualitative validation are encouraging and full validation of the numerical scheme is presently been undertaken with comparison against the aDcp data collected at various transects throughout the domain.

The results have demonstrated that the larger scale topography significantly influence the flow structure. Even though high resolution topographic form, such as dune height, wavelength, scour depth and crest line curvature the main are included the main flow structures are formed by the cross stream gradient located in the top right of the domain. Such enhanced topographic steering of the flow may have a significant influence on the distribution of shear stresses and sediment transport rates over the dune crests.

ACKNOWLEDGEMENTS

The field work was funded on NERC grant NER/A/S/2001/00445. RJH was funded on NERC fellowship NER/J/S/2002/00663. The authors would also like to thank Mr Richard Hunt for his help on the development of the methodology.

REFERENCES

Allen, J.R.L. 1968. *Current Ripples: Their Relation to Patterns of Water and Sediment Motion*. Elsevier, New York.

Allen, J.R.L. 1978. Polymodal dune assemblages: An interpretation in terms of dune creation-destruction in periodic flows. *Sediment. Geol*. 20: 17–28.

Allen, J.R.L. & Collinson, J. D. 1974. The superimposition and classification of dunes formed by unidirectional aqueous flows. *Sediment. Geol*. 12: 169–174.

ASCE Task Force 2002. Flow and transport over dunes. *J. Hydraul. Eng*. 127: 726–728.

Best, J.L. 1996. The fluid dynamics of small-scale alluvial bedforms. In: *Advances in Fluvial Dynamics and Stratigraphy*, edited by P. A. Carling & M. R. Dawson, pp. 67–125, John Wiley, Hoboken, N. J.

Best, J.L. 2005. The fluid dynamics of river dunes: A review and some future research directions. *J. Geophys. Res*.: JF000218.

Best, J.L. & Kostaschuk, R.A. 2002. An experimental study of turbulent flow over a low-angle dune. *J. Geophys. Res*.: 107(C9), 3135, JC000294.

Bradbrook, K.F., Lane, S.N. & Richards, K.S. 2000. Numerical simulation of three-dimensional, time-averaged flow structure at river channel confluences. *Water Resour. Res*. 36: 2731–2746.

Bridge, J.S. 2003. *Rivers and Floodplains: Forms, Processes and Sedimentary record*. Oxford: Blackwell.

Carling, P.A. 1999. Subaqueous gravel dunes. *J. Sediment. Res*. 69: 534–545.

Carling, P.A., Richardson, K. & Ikeda, H. 2005. A flume experiment on the development of subaqueous fine-gravel dunes from a lower-stage plane bed. *J. Geophys. Res*. 110: F04S05.

Copyright © 2006 Taylor & Francis Group plc, London, UK

Dinehart, R.L. 1992. Evolution of coarse gravel bed forms – field measurements at flood stage. *Water Resour. Res*. 28: 2667–2689.

Engel, P. & Lau, Y.L. 1980. Computation of bed load using bathymetric data. *J. Hydr. Eng. ASCE* 106: 380–639.

Hardy, R.J., Lane, S.N., Lawless, M.R., Best. J.L., Elliot, L. & Ingham. D.B. 2005. Development and testing of numerical code for treatment of complex river channel topography in three-dimensional CFD models with structured grids, *J. Hydr. Res*. 43: 468–480.

Harbor, D.J. 1998. Dynamics of bed forms in the lower Mississippi River. *J. Sediment. Res*. 68: 750–762.

Kleinhans, M.G. 2001. The key role of fluvial dunes in transport and deposition of sand-gravel mixtures, a preliminary note. *Sediment. Geol*.,143: 7–13.

Kleinhans, M.G. 2002. *Sorting out sand and gravel: Sedimenttransport and deposition in sand-gravel bed rivers.* Neth. Geogr.Stud. 293, 317 pp., Fac. of Geogr. Sci., Utrecht Univ., Utrecht, Netherlands.

Lane, S.N., Hardy, R.J. Elliot, L. & Ingham, D.B. 2003. High resolution numerical modelling of three dimensional flows over complex river bed topography. *Hydrol. Proc*. 16: 2261–2272.

Lane, S.N., Hardy, R.J. Elliot, L. & Ingham, D.B. 2004. Numerical modelling of flow processes over gravelly-surfaces using structured grids and a numerical porosity treatment. *Water Resour. Res*.: W01302, WR001934.

Launder, B.E. & Spalding, D.B. 1974. The numerical computation of turbulent flows. *Comput. Methods in Applied Mechanics and Engineering* 3: 269–89.

Maddux, T.B., Nelson, J.M. & McLean, S.L. 2003a. Turbulent flow over three-dimensional dunes: 1. Free surface and flow response. *J. Geophys. Res*. 108(F1): 6009.

Maddux, T. B., McLean, S.R. &. Nelson, J.M. 2003b. Turbulent flow over three-dimensional dunes: 2. Fluid and bed stresses. *J. Geophys. Res. 108(F1)*: 6010, JF000018.

McLean, S.R., Nelson, J.M. & Wolfe, S.R. 1994. Turbulence structure over two-dimensional bedforms: Implications for sediment transport. *J. Geophys. Res*. 99: 729–747.

Nelson, J.M., McLean, S.R. & Wolfe, S.R. 1993. Mean flow and turbulence fields over two-dimensional bed forms. *Water Resour. Res*. 29: 3935–3953.

Olsen, N.R.B. & Stockseth, S. 1995, Three-dimensional numerical modelling of water flow in a river with large-bedform roughness. *J. of Hydr. Res*. 33: 571–581.

Patankar, S.V. & Spalding, D.B. 1972. A calculation procedure for heat, mass and momentum transport in three-dimensional parabolic flows. *Int. J. of Heat and Mass Trans*. 15: 1782.

Parsons, D.R., Best, J.L., Orfeo, O., Hardy, R.J., Kostaschuk, R. & Lane, S.N. 2005. Morphology and flow fields of three-dimensional dunes, Rio Parana, Argentina: Results from simultaneous multibeam echo sounding and acoustic Doppler current profiling. *J. Geophys. Res*. 110: F04S03.

Rubin, D.M. & McCulloch D.S. 1980. Single and superimposed bedforms: A synthesis of San Francisco Bay and flume observations. *Sediment. Geol*. 26: 207–231.

ten Brinke, W.B.M., Wilbers, A.W.E. & Wesseling, C. 1999. Dune growth, decay and migration rates during a large-magnitude flood at a sand and mixed sand-gravel bed in the Dutch Rhine river system. In *Fluvial Sedimentology VI*, Edited by N. D. Smith and J. Rogers, Spec. Publ. Int. Assoc. Sedimentol., 28, 15–32.

Wilbers, A. 2004. *The development and hydraulic roughness of subaqueous dunes,* Neth. Geogr. Stud. 323, 224 pp., Fac. of Geosci., Utrecht Univ., Utrecht, Netherlands.

Copyright © 2006 Taylor & Francis Group plc, London, UK

B.3. Large scale river morphology and morphodynamics

Copyright © 2006 Taylor & Francis Group plc, London, UK

Effect of vegetation growth and unsteady characteristics of water supply on formative condition of mesoscale channel configuration

H. Takebayashi, M. Teraoka & T. Okabe
University of Tokushima, Tokushima, Japan

S. Egashira
Ritsumeikan University, Shiga, Japan

ABSTRACT: Braided streams and alternate bars under unsteady water and sediment supply conditions were reproduced via flume tests and numerical analysis, and the effects of the unsteady characteristics of water and sediment supply on the geometric characteristics of streams and bars are discussed. The results show that sediment deposits in smaller channels at higher locations during floods and bed at riffles is eroded during low flows. These phenomena force water to flow into larger streams. As a result, the bed elevation in streams decreases. Furthermore, the presence of vegetation enhances sediment deposition at higher bed elevation regions and contributes to a decrease in the number of streams. These results also indicate that the unsteady condition of water and sediment supply and vegetation growth in rivers are absolutely essential for formation of single thread meandering channels.

1 INTRODUCTION

Formative hydraulic conditions for mesoscale bed configurations have been studied by many researchers. A wide range of methods has been used, which include linear bed instability analyses (e.g. Fredsøe 1976, Parker 1976, Kuroki & Kishi 1982) and dimensional analyses based on field data (e.g. Muramoto & Fujita 1978). Results of those studies showed that the width-depth ratio plays an important role in determining formative hydraulic conditions for mesoscale bed configurations. As the width-depth ratio increases, the bed configuration changes in the order of No bar, Alternate bars, and Multiple row bars. Although the applicability of these studies to hydraulic conditions for generation of bed configurations and to conditions for cases in which dry bed regions like islands are not generated in the channel is clear, the applicability to the fully developed bed geometry in dynamic equilibrium state and to conditions that dry bed regions are generated in the channel remains unclear. Furthermore, with natural rivers, water and sediment supply conditions are unsteady while vegetation grows. Therefore, applicability of the previous studies to natural rivers is also unclear.

Using a mesoscale bed configuration regime criterion based on the bed instability analysis, it is assumed that the generation hydraulic condition of alternate bars are equivalent to those of a meandering stream, and that the generation hydraulic condition of a multiple row bars are equivalent to those of braided streams. It is then considered that, in the case in which alternate bars are considered for an initial bed configuration in a straight channel with erodible banks, banks are eroded alternately by alternate flows on the alternate bars, thereby forming a meandering stream (Kinoshita 1961). However, bed instability analysis that is used as the basis of mesoscale bed configuration regime criterion treats a straight channel with rigid banks only. It is not the analysis for meandering streams or braided streams. Furthermore, water and sediment supply conditions are intended for a steady state in which the entire bed is covered by water. Such a condition, which allows formation of a stream with dry bed regions within the analysis domain, is not discussed.

According to the mesoscale bed configuration regime criterion based on data from natural rivers and flume experiments, braided streams which are formed near the generation hydraulic conditions of alternate bars are hard to be discriminated from alternate bars (Egashira and Takebayashi 1999). Therefore, the possibility that these are regarded as the same cannot be denied.

The present study examines the bed and channel configurations composed of non-cohesive materials. The effect of vegetation growth and unsteady characteristics of water supply on a mechanism for determining beds and stream geometry are discussed based on

Copyright © 2006 Taylor & Francis Group plc, London, UK

Table 1. Hydraulic conditions.

		Hydrograph	Vegetation	Width (m)	Water discharge (m^3/s)	Non-dimensional shear stress	Width-depth ratio
Case 1	Exp. & Analysis	Steady	No	1.5	0.00250	0.039	239
Case 2	Exp. & Analysis	Unsteady	No	1.5	0.00125, 0.00375	0.026, 0.050	363, 188
Case 3	Analysis	Steady	Yes	1.5	0.00250	0.039	239
Case 4	Analysis	Unsteady	Yes	1.5	0.00125, 0.00375	0.026, 0.050	363, 188
Case 5	Analysis	Unsteady	Yes	1.0	0.00125, 0.00375	0.033, 0.064	190, 98
Case 6	Analysis	Steady	Yes	0.55	0.00250	0.072	48
Case 7	Analysis	Steady	Yes	0.8	0.00133	0.039	128
Case 8	Analysis	Steady	Yes	0.26	0.00043	0.039	42
Case 9	Analysis	Unsteady	No	0.55	0.00125, 0.00375	0.047, 0.091	73, 38
Case 10	Analysis	Unsteady	Yes	0.55	0.00125, 0.00375	0.047, 0.091	73, 38

results of flume experiments and of two dimensional bed deformation analysis. In addition, it is revealed that formative hydraulic conditions of meandering streams are appeared under the larger width-depth ratio conditions.

2 METHOD OF FLUME EXPERIMENTS AND NUMERICAL ANALYSIS

2.1 *Method of flume experiments*

The channel used in the experiments is a straight rectangular one in 7.5 m length. The bed slope is 1/100 and the initial bed geometry is made flat. The bed materials are nearly uniform sediments with average particle diameter of 1 mm. Table 1 shows hydraulic conditions used in the experiments and the numerical analyses. Figure 1 shows these conditions on the mesoscale bed configuration regime criterion (Kuroki and Kishi 1982). Experiments are carried out for Case 1 and Case 2 to investigate the effects of the unsteady characteristics of water and sediment supply on geometry of braided streams. The sole difference between these two conditions is a method of supplying water and sediments. Under the unsteady conditions (Case 2), the water discharge has been changed every 30 min between 1.25 l/s and 3.75 l/s. The water supply cycle is enough short not to change bed configuration completely in a cycle. Consequently, the bed configuration differs from the bed configurations corresponding to each water discharge. Sediment is supplied so that the initial bed elevation at the upstream end might not be lowered. According to Fig. 1, hydraulic conditions in Case 1 and Case 2 (both large and small water discharges) are all within the formative regime of multiple row bars (modified to the formative regime of braided streams (Takebayashi et al. 2001)). Although a non-dimensional shear stress at a small water discharge is less than the non-dimensional critical shear stress, sediment moves if a bed configuration is generated and flows are concentrated in channels.

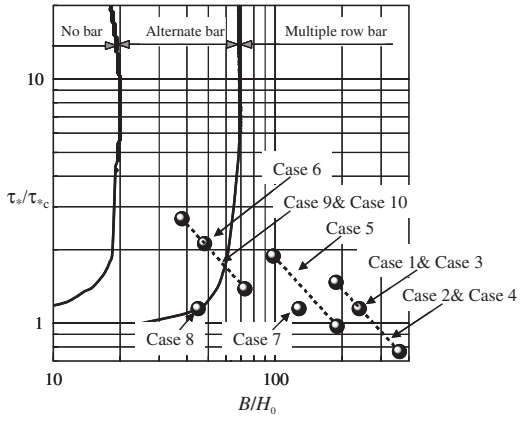


Figure 1. Hydraulic conditions of flume experiments and numerical analysis on the mesoscale bed configuration regime criterion (Kuroki & Kishi 1982), (x and y axes indicate the width-depth ratio and the shear stress normalized by critical shear stress, respectively, critical shear stress is 0.034).

Photographs are taken every hour; measurements of the bed geometry are taken 6 hr later, when no change was noticed in channel configurations.

2.2 *Method of numerical analysis*

Computation of surface flow is performed by the use of the governing equation for the horizontal two-dimensional flow averaged with depth. The conservation of mass, i.e., inflow and outflow of mass by seepage flow, is taken into consideration as shown in the following equation (Takebayashi & Egashira, 2003).

$$\Lambda\frac{\partial z}{\partial t}+\frac{\partial}{\partial x}(uh)+\frac{\partial}{\partial y}(vh)+\frac{\partial}{\partial x}(u_g h_g)+\frac{\partial}{\partial y}(v_g h_g)=0 \quad (1)$$

Copyright © 2006 Taylor & Francis Group plc, London, UK

where, t is the time and x and y are the coordinates along the longitudinal and the transverse directions, respectively. Surface flow depth is represented as h, and the seepage flow depth is h_g. u and v represent depth-averaged flow velocity along the longitudinal and the transverse directions, respectively. Depth-averaged seepage flow velocities along the longitudinal and the transverse directions are shown as u_g and v_g, respectively. z is the water surface level. Λ is a porosity parameter related to the relative elevation of bed surface and water surface, wherein $\Lambda = 1$ as $z > z_b$, and $\Lambda = \lambda$ as $z < z_b$, where z_b is the bed level and λ is the porosity of the bed material. Seepage flow is assumed to be a horizontal two dimensional saturated flow. Momentum equations of the surface water are as follows:

$$\frac{\partial}{\partial t}(hu)+\frac{\partial}{\partial x}(huu)+\frac{\partial}{\partial y}(huv) = -gh\frac{\partial}{\partial x}(h+z_b)-\frac{\tau_x}{\rho}+\frac{\partial}{\partial x}(h\sigma_{xx})+\frac{\partial}{\partial y}(h\tau_{yx})-\frac{F_{vx}}{\rho} \quad (2)$$

$$\frac{\partial}{\partial t}(hv)+\frac{\partial}{\partial x}(huv)+\frac{\partial}{\partial y}(hvv) = -gh\frac{\partial}{\partial y}(h+z_b)-\frac{\tau_y}{\rho}+\frac{\partial}{\partial x}(h\tau_{xy})+\frac{\partial}{\partial y}(h\sigma_{yy})-\frac{F_{vy}}{\rho} \quad (3)$$

where g is the gravity and ρ is the water density. The conservation of momentum, i.e., inflow and outflow of momentum by seepage flow, is not considered because their values are very small. τ_x and τ_y are the shear stresses along the longitudinal and the transverse directions, respectively, as follows:

$$\tau_x = \tau_b \frac{u_b}{\sqrt{u_b^2+v_b^2}} \quad (4)$$

$$\tau_y = \tau_b \frac{v_b}{\sqrt{u_b^2+v_b^2}} \quad (5)$$

$$\frac{\tau_b}{\rho} = u_*^2, \quad u_*^2 = \frac{u^2+v^2}{\left(6+2.5\ln\frac{h}{k_s}\right)^2} \quad (6)$$

where u_* is the friction velocity and k_s is the roughness height. u_b and v_b represent velocity near the bed surface along the longitudinal and the transverse directions, respectively. Velocities near the bed are evaluated using the curvature radius of the streamlines as follows:

$$u_b = u_{bs}\cos\alpha_s - v_{bs}\sin\alpha_s \quad (7)$$

$$v_b = u_{bs}\sin\alpha_s + v_{bs}\cos\alpha_s \quad (8)$$

$$u_{bs} = 8.5u_* \quad (9)$$

$$v_{bs} = -N_*\frac{h}{r}u_{bs} \quad (10)$$

where $\alpha_s = \arctan(v/u)$, N_* is 7.0 (Engelund, 1974) and r is the curvature radius of the stream lines obtained by the depth integrated velocity field as follows (Shimizu & Itakura, 1991):

$$\frac{1}{r} = \frac{1}{\left(u^2+v^2\right)^{3/2}}\left\{u\left(u\frac{\partial v}{\partial x}-v\frac{\partial u}{\partial x}\right)+v\left(u\frac{\partial v}{\partial y}-v\frac{\partial u}{\partial y}\right)\right\} \quad (11)$$

σ_{xx}, σ_{yy}, τ_{xy} and τ_{yx} are turbulence stresses as follows:

$$\sigma_{xx} = 2\nu\frac{\partial u}{\partial x}-\frac{2}{3}k_t \quad (12)$$

$$\sigma_{yy} = 2\nu\frac{\partial v}{\partial y}-\frac{2}{3}k_t \quad (13)$$

$$\tau_{xy} = \tau_{yx} = \nu\left(\frac{\partial v}{\partial x}+\frac{\partial u}{\partial y}\right) \quad (14)$$

$$\nu = \frac{\kappa}{6}u_*h \quad (15)$$

$$k_t = 2.07u_*^2 \quad (16)$$

where ν is the coefficient of kinematic eddy viscosity, κ is the Karman constant, and k_t is the depth averaged turbulence kinetic energy (Nezu & Nakagawa, 1993). F_{vx} and F_{vy} are the drag forces due to the vegetation along the longitudinal and the transverse directions, respectively, as follows (Shimizu & Tsujimoto, 1995):

$$F_{vx} = F_v\frac{u}{\sqrt{u^2+v^2}} \quad (17)$$

$$F_{vy} = F_v\frac{v}{\sqrt{u^2+v^2}} \quad (18)$$

$$\frac{F_v}{\rho} = \frac{1}{2}C_{dv}\lambda_v\left(u^2+v^2\right)h \quad (19)$$

where C_{dv} (=1.0) is the coefficient of form drag and λ_v is the vegetation density. Figure 2 describes the vegetation model. The vegetation density is determined so that it is increased linearly from 0 to $\lambda_{v\max}$ as follows (Takebayashi & Egashira, 2003):

$$\lambda_v = \lambda_{v\max}\left(t_d/T_f\right) \quad (20)$$

Copyright © 2006 Taylor & Francis Group plc, London, UK

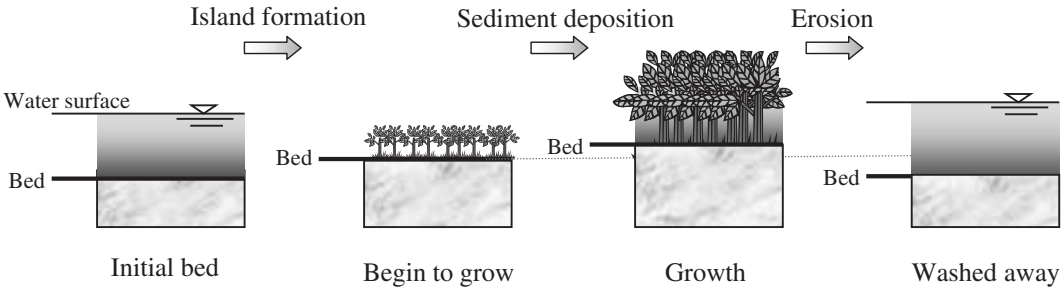


Figure 2. Vegetation model.

where $\lambda_{v\max}$ is the maximum vegetation density and should be estimated according to the kind of vegetation, t_d is the accumulated dry bed time and T_f is the time wherein the relevant region is filled with vegetation. Bed degradation is assumed to cause vegetation extinction; the vegetation is washed out when the bed level decreases lower than that at the vegetation invasion, so that the density is set to 0. Momentum equations of seepage flow are as follows:

$$u_g = -k_{gx}\frac{\partial z}{\partial x} \tag{21}$$

$$v_g = -k_{gy}\frac{\partial z}{\partial y} \tag{22}$$

where k_{gx} and k_{gy} are the coefficients of permeability along the longitudinal and the transverse directions respectively. When the water depth of surface flow becomes less than the mean diameter of the bed material, the surface flow is computed only in consideration of the pressure term and bed shear stress term in the momentum equation of surface flow (Nagata, 1999).

The temporal change in bed elevation is evaluated by use of the following equation.

$$\frac{\partial z_b}{\partial t} + \frac{1}{1-\lambda}\left(\frac{\partial q_{bx}}{\partial x} + \frac{\partial q_{by}}{\partial y}\right) = 0 \tag{23}$$

q_{bx} and q_{by} are sediment transport rates along the longitudinal and the transverse directions, respectively, as follows (Ashida & Michiue, 1972, Liu, 1991, Kovacs & Parker, 1994):

$$q_{bx} = q_b \cos\beta \tag{24}$$

$$q_{by} = q_b \sin\beta \tag{25}$$

$$q_b = 17\frac{\rho u_{*e}^3}{(\rho_s - \rho)g}\left(1 - \sqrt{K_c}\frac{u_{*c}}{u_*}\right)\left(1 - K_c\frac{u_{*c}^2}{u_*^2}\right) \tag{26}$$

Here ρ_s is the sediment density and u_{*e} is the effective shear velocity as follows:

$$u_{*e}^2 = \frac{u^2 + v^2}{\left(6 + 2.5\ln\dfrac{h}{d_m(1+2\tau_*)}\right)^2} \tag{27}$$

where d_m is the mean diameter of the bed material and u_{*c} is the non-dimensional critical friction velocity. u_{*c} is evaluated by using the Iwagaki's formula (Iwagaki, 1956) which is formulated for uniform bed material.

K_c is a correction factor due to the influence of bed inclination on sediment motion:

$$K_c = 1 + \frac{\left[\left(\dfrac{\rho}{\rho_s - \rho} + 1\right)\cos\alpha\tan\theta_x + \sin\alpha\tan\theta_y\right]}{\mu_s} \tag{28}$$

$$\theta_x = \arctan\left(\partial z_b/\partial x\right) \tag{29}$$

$$\theta_y = \arctan\left(\partial z_b/\partial y\right) \tag{30}$$

The angle of deviation of the near bed flow from the longitudinal direction is as follows:

$$\alpha = \arctan\left(v_b/u_b\right) \tag{31}$$

The coefficient of static friction is μ_s. The deviation angle of the bed load to the depth averaged flow direction (β), which depends on the flow near the bed and the inclination of the bed, is calculated by the following relations

$$\tan\beta = \frac{\sin\alpha - \Pi\Theta_y\left(\dfrac{u_{*c}^2}{u_*^2}\right)\tan\theta_y}{\cos\alpha - \Pi\Theta_x\left(\dfrac{u_{*c}^2}{u_*^2}\right)\tan\theta_x} \tag{32}$$

$$\Pi = K_{id} + 1/\mu_s \tag{33}$$

Copyright © 2006 Taylor & Francis Group plc, London, UK

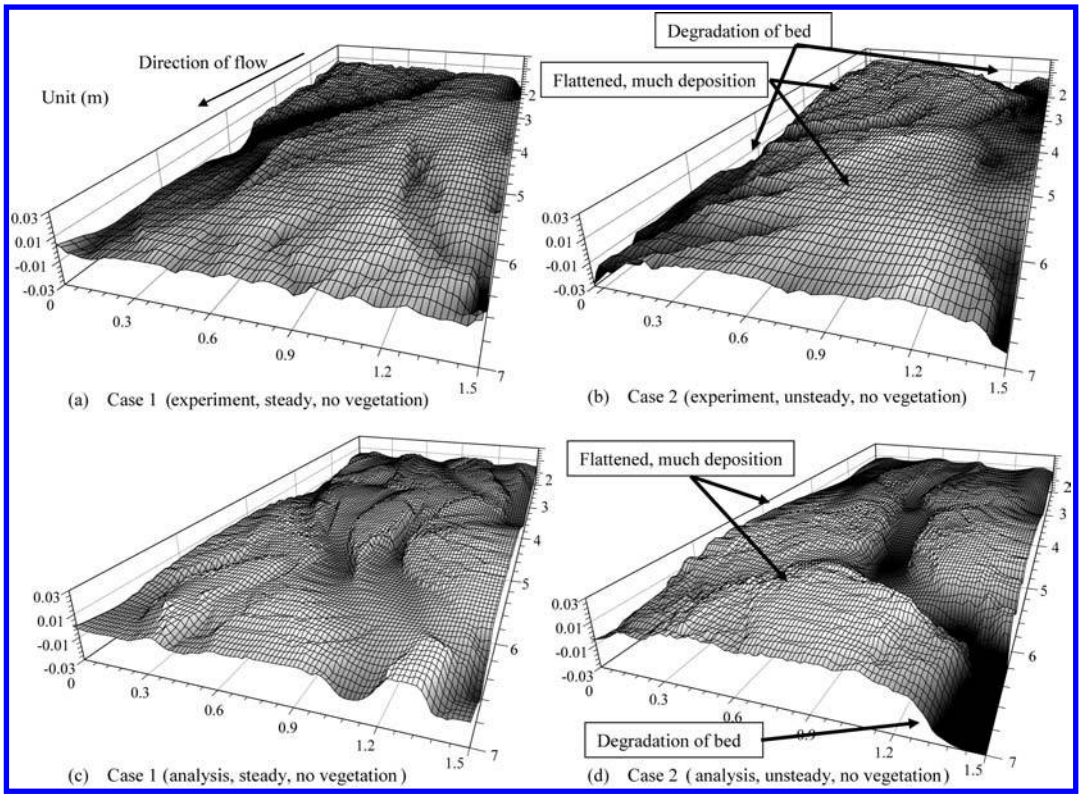


Figure 3. Bed geometry (flume experiment and numerical analysis in Case 1 and Case 2).

$$\Theta_x = \Theta_y + \frac{\rho}{\rho_s - \rho}\cos^2\theta_x \tag{34}$$

$$\Theta_y = \frac{1}{1+\tan^2\theta_x + \tan^2\theta_y} \tag{35}$$

where K_{ld} (=0.85) is the ratio of the lift force to the drag force. The local bed slope is adjusted to be smaller than the angle of repose (Michiue et al 1995).

Hydraulic conditions used in the analysis are also shown in Table 1 and Fig. 1. The bed slope is 1/100. The bed materials are treated as uniform sediment with a particle diameter of 1 mm. Case 1 and Case 2 have the same conditions used in flume experiments. Vegetation growth is taken into account in Case 3 and Case 4. The flow hydraulic conditions of Case 3 and Case 4 are identical to those of Case 1 and Case 2. Water discharge under Case 5 is the same as that under Case 4, but the width is different. Water discharge under Case 6 is the same as that under Case 3, but the width is different; it is in the formative regime of alternate bars that are approximately in the formative region of multiple row bars. In Case 7 and Case 8, the width is changed with same unit width water discharge conditions as those used in Case 3. In Case 9 and Case 10, Case 6 is converted to unsteady conditions that are used as the formative hydraulic conditions of alternate bars at a large water discharge and as the formative hydraulic condition of multiple row bars at a small water discharge. Vegetation growth is not considered in Case 9.

3 EFFECTS OF UNSTEADY CHARACTERISTICS OF WATER SUPPLY ON BED AND CHANNEL CONFIGURATION

Figure 3 shows bed geometries obtained through flume experiments and numerical analysis under steady water and sediment supply conditions (Case 1) and unsteady water and sediment supply conditions (Case 2), where vegetation growth is ignored. These hydraulic conditions are in the formative regime of multiple row bars. Although some parts of the bed geometries by flume experiments are not reproduced well by numerical analyses, the bed elevation of dry bed regions during low flow is higher and flattened under unsteady water and sediment supply conditions in both flume experiments and numerical analyses. In addition, the bed elevation in the stream is lowered

Copyright © 2006 Taylor & Francis Group plc, London, UK

further in unsteady conditions than in steady conditions. This lowering is due to the fact that, at a large water discharge, sediment is transported to and deposited on bars, thereby choking smaller scale streams. At a small water discharge, flows are concentrated to larger scale streams with the deepest bed, thereby developing streams further.

Numerical analyses clearly revealed that the streams are fewer in unsteady conditions than they are in steady conditions. However, bed geometries obtained by flume experiments did not confirm that fact. This matter should be judged using a steady water supply on the rigid bed obtained by unsteady conditions.

Figure 4 shows bed geometries obtained through numerical analyses under steady water and sediment supply conditions where vegetation growth is neglected (Case 6), unsteady water and sediment supply conditions where vegetation growth is neglected (Case 9), and unsteady water and sediment supply conditions where vegetation growth is taken into account (Case 10). These hydraulic conditions are in the formative regime of alternate bars. The wavelength of bars in unsteady water and sediment supply conditions is longer than that in steady conditions as reported by the previous study (Watanabe et al. 2001). Furthermore, it is noticed that in unsteady conditions, the water surface slope becomes steeper from a riffle towards a pool during low flow, and the riffles are eroded and its bed elevation is lowered. Case 10 will be discussed in section 4.

4 EFFECTS OF VEGETATION GROWTH ON BED AND CHANNEL CONFIGURATIONS

Figure 5 shows bed geometries obtained by numerical analysis under steady water and sediment supply conditions (Case 3) and unsteady water and sediment supply conditions (Case 4). These hydraulic conditions are in the formative regime of multiple row bars. A comparison of Case 1 and Case 2 is made with the

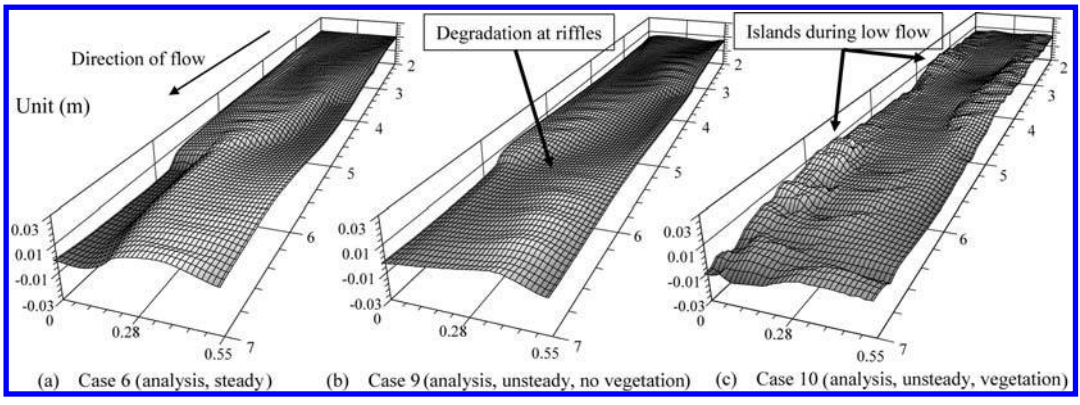


Figure 4. Bed geometry (numerical analysis in Case 6, Case 9 and Case 10).

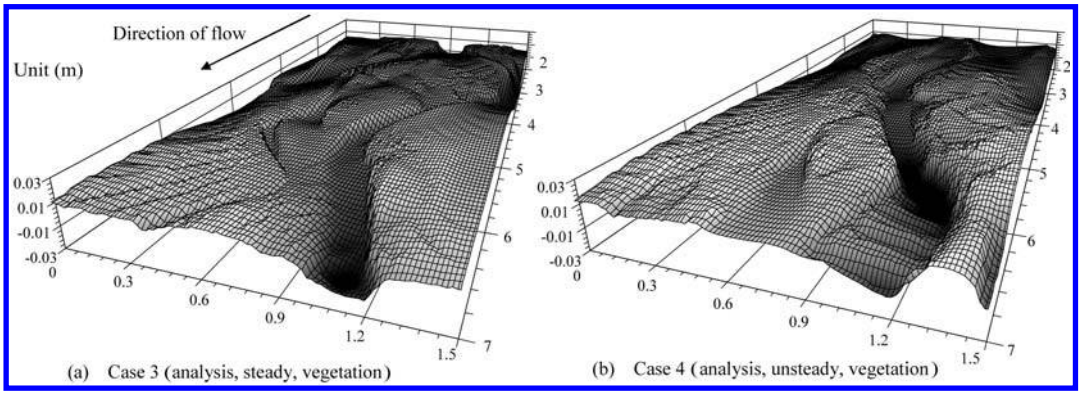


Figure 5. Bed geometry (numerical analysis in Case 3 and Case 4).

Copyright © 2006 Taylor & Francis Group plc, London, UK

same conditions, but ignoring the vegetation growth. If the vegetation growth is considered, the sediment deposition at the area of higher bed elevation is accelerated. Furthermore, the bed elevation in the stream is lowered in both steady and unsteady conditions. Simultaneously, the number of streams decreases. In the unsteady condition (Case 4), it is noted that one meandering stream with smaller anabranches is formed. This result shows that the formative region of a meandering stream appears with greater width-depth ratio in the field with rigid banks, if both vegetation growth and unsteady characteristics of water and sediment supply are considered. The definition of width is very important here. Under formative hydraulic conditions of alternate bars, no dry bed region is formed with steady water and sediment supply conditions. Hence, the width of a flow is equal to the width of analysis domain. On the other hand, under formative hydraulic conditions of multiple row bars, the stream width is not the same as the width of analysis domain, because a dry bed region is formed even under steady water and sediment supply conditions. Hence, the width of the analysis domain becomes braiding width or flood plain width. With previous linear bed instability analysis, the treatment of the dry bed regions within the analysis domain is difficult. For this reason, formative mechanism of bars with dry bed regions has not been studied well. As a result it is considered that the concept that "formative hydraulic conditions of alternate bars are equivalent to formative hydraulic conditions of meandering streams" has been confirmed.

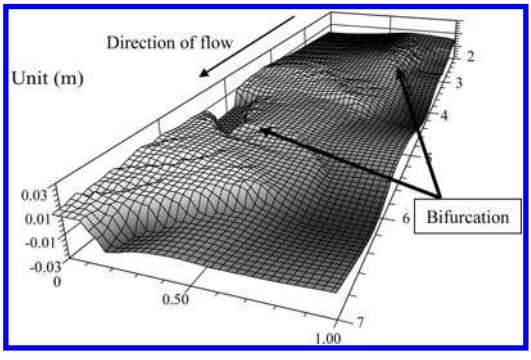


Figure 6. Bed geometry (numerical analysis in Case 5).

Figure 6 shows bed geometries obtained through numerical analysis of Case 5 using a smaller width-depth ratio, in which unsteady water and sediment supply conditions, where effects of vegetation growth are considered. This condition is in the formative region of multiple row bars. Compared with Case 4 shown in Fig. 5, in Case 5, despite a smaller width-depth ratio, the main stream is bifurcated and the number of streams with largest stream scale is greater than that of Case 4. These differences contradict the previous findings derived from linear bed instability analysis. It is considered that vegetation growth produces these differences. Figure 7 shows a horizontal distribution of the degree of vegetation growth obtained from Case 4 and Case 5. The degree of vegetation growth 0 is for no vegetation and 1 is for perfect growth. Figure 7 shows that, compared with Case 4, the vegetated area is narrowed with regard to the total area of the analysis domain in Case 5

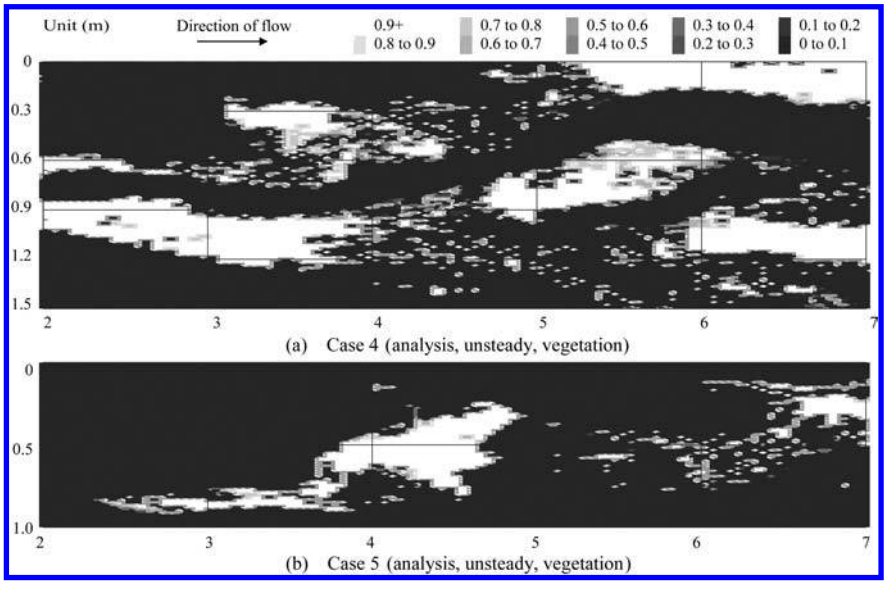


Figure 7. Vegetation growth rate (numerical analysis in Case 4 and Case 5, 0: no vegetation, 1: perfect growth).

Copyright © 2006 Taylor & Francis Group plc, London, UK

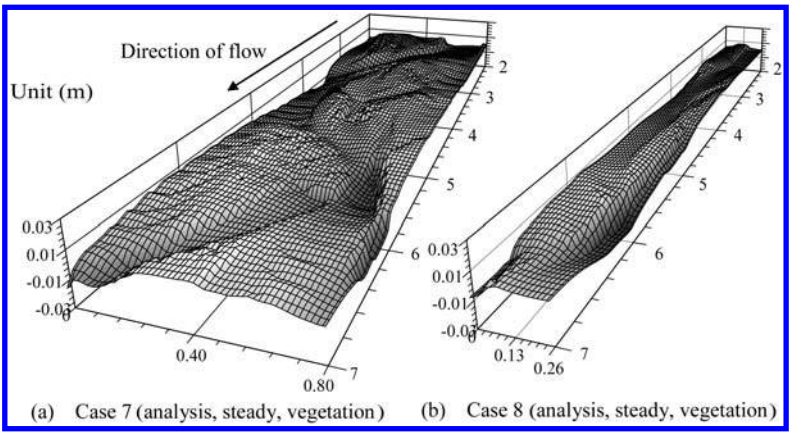


Figure 8. Bed geometry (numerical analysis in Case 7 and Case 8).

with a smaller width depth ratio. This is due to the high shear stress by narrowing the analysis width. Disturbances to bars by flowing water are increased and vegetation growth is suppressed. It is considered that suppression of vegetation growth enhanced stream deformation and accelerated generation of stream bifurcations.

Figure 8 shows bed geometries obtained through numerical analysis of Case 7 and Case 8 with a smaller width-depth ratio under steady water and sediment supply conditions, in which effects of vegetation growth are considered and the non-dimensional shear stress is the same as that of Case 3. Comparison of Case 3 and Case 7 shows that, despite a greater width-depth ratio, the number of main streams in Case 3 is only 1–2, which is nearly equal to that of Case 7. The same description used for Case 4 and Case 5 are also applicable here. Bifurcation of streams is suppressed by the vegetation growth, even with increased width-depth ratio and where the number of streams is not increased significantly. Furthermore, the bed geometry in Case 8 shows a formation of nearly one stream flowing from bank to bank alternately. In other words, under the formative condition for braided streams the number of streams is determined by a balance between instability of the bed surface and resistance characteristics of vegetation. Under the condition in which resistance characteristics of the vegetation are low, the number of streams increases as the width-depth ratio becomes greater, thereby forming braided streams. With greater resistance characteristics of vegetation, the number of streams reaches a maximum value at a certain level of width-depth ratio: the meandering stream is formed with a greater width-depth ratio.

Figure 4 shows bed geometries obtained through numerical analysis of Case 10 under unsteady water and sediment supply conditions in which effects of the vegetation growth are considered. The hydraulic conditions are in the formative region of alternate bars. Although bars are formed alternately along with the right and left banks, it is noticed that by considering the unsteady characteristics of water and sediment supply, and vegetation growth, a channel configuration is formed that has entirely different geometric characteristics from those of well-known alternate bars. These differences are from the fact that the riffles are eroded during low flow. In addition, vegetation grows on areas where the bed elevation is higher during low flow, sediment is deposited only on the vegetated area resulting in increased bed elevation further, and flows are concentrated to the main stream with lower bed elevation. Concentration of flows to lower bed elevation areas because of vegetation growth is similar to such a field in which the dry bed regions are formed. It is therefore considered that under formative hydraulic conditions of alternate bars close to formative hydraulic conditions of multiple row bars and phenomena in natural rivers tend to be shifted to a greater width-depth ratio side.

The vegetation effect to reduce sediment transport rate is expected to cohesive materials in the flood plain. Therefore, it is expected that a meandering stream is formed, if cohesive material exists, even if vegetation does not grow (Ashida & Sawai 1977).

5 CONCLUSIONS

Based on results of flume experiments and of two dimensional bed deformation analysis in which beds are composed of non-cohesive materials, effects of the unsteady characteristics of water and sediment supply and of vegetation growth on the formative mechanisms of meso-scale channel configuration were

Copyright © 2006 Taylor & Francis Group plc, London, UK

investigated. Results obtained through this study are summarized as follows:

(1) Both flume experiments and numerical analysis showed that, compared with steady conditions, the bed elevation on dry bed regions at low water flow is elevated and flattened under formative hydraulic conditions of multiple row bars and unsteady conditions. In addition, compared with steady conditions, the bed elevation in the stream is lowered under unsteady conditions. These phenomena are due to the fact that sediment is brought to and deposited at such areas where the bed elevation is high during high flow, thereby smaller scale streams are choked. In addition, flows are concentrated to a larger scale stream where the bed elevation is low, thereby developing the stream further.
(2) In the formative region of alternate bars, compared with steady hydraulic conditions, the wavelength of bars is lengthened under unsteady conditions. Furthermore, under unsteady conditions, the water surface slope becomes steeper from a riffle toward a pool during low flow, thereby bed elevation becomes lowered at riffles.
(3) Under both steady and unsteady conditions, if the vegetation growth is taken into account, deposition of sediment on a higher bed elevation area is accelerated and the bed elevation in the stream is lowered. In addition, under unsteady conditions, number of streams is reduced and nearly one meandering channel is formed with the large width-depth ratio. This suggests that in a field with rigid banks, the formative region of meandering streams appears in the condition with larger width-depth ratio if vegetation grows and water and sediment supply condition are unsteady.
(4) Because of the fact that opportunities for bifurcation of streams are suppressed by vegetation growth even if the width-depth ratio is increased, the number of streams does not increase remarkably. This fact suggests that under formative hydraulic conditions of braided streams, the number of streams is determined by the balance between the instability of bed surface and the resistance of vegetation. The number of streams increases as the width depth ratio increases with small vegetation resistance. On the other hand, with large vegetation resistance, the number of streams reaches a maximum value, resulting in a meandering stream in a large width-depth ratio region.
(5) Even if mean hydraulic conditions are in the formative region of alternate bars, a channel configuration is formed that has entirely different geometric characteristics from those of well-known alternate bars because of the vegetation growth during low flow under unsteady conditions. It is therefore considered that under formative hydraulic conditions of alternate bars close to formative hydraulic conditions of multiple row bars, phenomena in natural rivers tend to be shifted to a larger width-depth ratio side.

ACKNOWLEDGEMENTS

Mr. Sugai, formerly of the Graduate School of University of Tokushima, assisted flume experiments performed in this study. This work is funded by Grant-in-Aid for Scientific Research (B) (Representative: Yasuyuki Shimizu) and Grant-in-Aid for Scientific Research for young researchers (B) (Representative: H. Takebayashi).

REFERENCES

Ashida, K. and Michiue, M., 1972, Study on hydraulic resistance and bed-load transport rate in alluvial streams, *Proc. of JSCE*, No. 206, pp. 59–69.

Ashida, K. and Sawai, K., 1977, A study on the stream formation process on a bare slope (3) – Three dimensional channel form-, *DPRI Annual*, No. 20, B-2.

Egashira, S. and Takebayashi, H., 1999, Self-formed low water channel in straight channel, *Proc. IAHR Symposium on River, Coastal and Estuarine Morphodynamics*, pp. 509–518.

Engelund, F., 1974, Flow and bed topography in channel bends. *Jour. of Hy. Div*. ASCE, Vol. 100, No. HY11.

Fredsøe, J.: Meandering and braiding of rivers, *J. Fluids Mech.*, vol.84, part4, pp. 609–624, 1978.

Iwagaki, Y., 1956, Hydrodynamic study on critical shear stress. *Proc. of JSCE*, No. 41, pp. 1–21.

Kinoshita R., 1961, Field survey on channel deformation of the Ishikari River, Body text and Reference data, Resource Bureau, Science and Technology Agency, No. 36.

Kuroki, M. and Kishi, T., 1982, Study on regime criteria of river morphology, *Annual Journal of Hy. Eng*. JSCE, Vol. 26, pp. 51–56.

Kovacs, A. and Parker, G., 1994, A new vectorial bedload formulation and its application to the time evolution of straight river channels. *J. Fluid Mech*. Vol. 267, pp. 153–183.

Liu, B. Y., 1991, Study on Sediment Transport and Bed Evolution in Compound Channels. *Thesis presented to Kyoto University*.

Michiue, M., Fujita, M. and Kusakabe, S., 1995, Formation of Meandering Streams in Mountain River Beds. *Annual Journal of Hy. Eng*. JSCE, Vol. 39, pp. 613–618.

Muramoto, Y. and Fujita, Y., 1978, The classification of meso-scale river bed configuration and the criterion of its formation, *Annual Journal of Hy. Eng.* JSCE, Vol. 22, pp. 275–282.

Nagata, N., 1999, Numerical analysis of the 2-dimensional unsteady flow using a generalized coordinate system, The lecture collection on the computer use in hydraulic engineering, *the Japan Society of Civil Engineers*, pp. 51–76.

Nezu, I. and Nakagawa, H., 1993, H. Turbulence in open channel flows, *IAHR Monograph*, Balkema, Rotterdam, The Netherlands, pp. 53–56.

Copyright © 2006 Taylor & Francis Group plc, London, UK

Parker, G., 1976, On the cause and characteristic of meandering and braiding in rivers, *J. Fluids Mech*., vol.76, part3, pp. 457–480.
Shimizu, Y. and Itakura, T., 1991, Calculation of flow and bed deformation with a general non-orthogonal coordinate system, *Proc. of XXIV IAHR Congress*, Madrid, Spain, C-2, pp. 41–48.
Shimizu, Y. and Tsujimoto, T., 1995, Numerical Calculation on Depth-averaged Flow in a Straight Stream with Vegetation Zone, *Annual Journal of Hy. Eng.* JSCE, Vol. 39, pp. 513–518.
Takebayashi, H., Egashira, S. and Okabe, T., 2001, Stream formation process between confining banks of straight wide channels. *Proc. 2nd IAHR Symposium on River, Coastal and Estuarine Morphodynamics*, pp. 575–584.
Takebayashi, H. and Egashira, S., 2003, Numerical analysis of braided streams formed on beds with non-uniform sediment, *Annual Journal of Hy. Eng*. JSCE, Vol. 47, pp. 631–636.
Watanabe, Y., M. Tubino, G. Zolezzi and Hoshi K., 2001, Behavior of Alternate bars under unsteady flow conditions. *Proc. 2nd IAHR Symposium on River, Coastal and Estuarine Morphodynamics*, pp. 575–584.

Copyright © 2006 Taylor & Francis Group plc, London, UK

Location of hills and deeps in meandering streams: An experimental study

A.M. Ferreira da Silva
Associate Professor, Department of Civil Engineering, Queen's University, Kingston, Ontario, Canada

T. El-Tahawy
Assistant Professor, Department of Civil Engineering, Helwan University, Cairo, Egypt

ABSTRACT: The effect of geometric and flow related parameters on the location in flow plan of the laterally adjacent erosion "deeps" and deposition "hills" of meandering streams is investigated. The centerlines of the regular meandering streams follow sine-generated curves; the banks are rigid; the flow is turbulent and sub-critical. A series of experimental runs carried out in a channel having a deflection angle $\theta_0 = 70°$ is presented. The results of these runs are analysed together with those from runs reported in previous works by other authors. It is found that the location of deeps and hills is strongly dependent on θ_0 (i.e. on the stream sinuosity), and to a smaller extent also dependent on the ratio of the meander wavelength to flow width and possibly the flow friction factor. For the same remaining conditions, the location of hills and deeps continuously moves upstream from the crossovers to the apexes as θ_0 increases from small to large.

1 INTRODUCTION

1.1 *General*

This paper concerns the nature of the deformed bed in regular meandering streams. The centerlines of the streams follow sine-generated curves (see Section 2, paragraph (i)); the banks are assumed to be rigid. The work is restricted to turbulent, sub-critical and "wide" streams, "wide" stream being defined for the present purposes as a stream having a width-to-depth ratio $B/h_{av} > \approx 10$. The elements of bed topography under consideration are those brought into being by the curvature of the stream. Elements due to other reasons, namely bed forms (ripples, dunes, bars, etc.) are not considered here. The paper is an extension of previous experimental studies by Losiyevskii (reported by Makaveyev 1975), Hooke (1974), Hasegawa (1983), Whiting & Dietrich (1993a,b), and Termini (1996), who investigated the nature of the developed (or equilibrium) bed topography in laboratory sine-generated streams having movable beds. Table 1 presents a summary of the hydraulic conditions used by these authors. Here θ_0 = deflection angle, Λ_M = meander wavelength (see the definition sketch in Figure 1, where the geometry-related notation is introduced), Q = flow rate, D = average grain size, B = flow width, h_{av} = channel-averaged flow depth, S_c = bed slope along the channel centerline, $(c_f)_{av}$ = dimensionless (Chézy) flow friction factor, Re = flow Reynolds number, Fr = Froude number, and Re_* = roughness Reynolds number (see also the List of Symbols). The quantity λ is introduced in Sub-Section 1.2. All runs were carried out starting from a flat movable bed at $t = 0$, the bed subsequently being allowed to deform until the equilibrium state (or the equilibrium bed topography) was achieved. From Table 1, it should be clear that in most of the experiments carried out to date, the channels used had mainly small or large values of θ_0.

As is well known, the bed in meandering streams deforms so as to acquire laterally adjacent erosion "deeps" and deposition "hills". In the case of the periodic (along x) sine-generated streams, each deep+hill complex forms a large-scale erosion-deposition zone having the length $L/2$. The largest erosion-deposition occurs somewhere in the midst of the erosion-deposition zone. From experiment (the laboratory experiments in Table 1 as well as field measurements), it is known that the location in flow plan of hills and deeps is not "standard", i.e. it is not the same or approximately the same for every meandering stream. Indeed, consider Figures 2 and 3, showing the bed in actual streams, and observe that in Figures 2a and 3a, where θ_0 is "small", the deeps and hills are centered approximately around the crossover-sections O, while in Figures 2b and 3b, where θ_0 is "large", they are centered around the apex-sections a.

On the basis of their own experimental observations, as well as those of other authors, Whiting & Dietrich (1993b) indicated that the location of the

Copyright © 2006 Taylor & Francis Group plc, London, UK

Table 1. Review of previous bed topography experiments in sine-generated channels.

Author	Run	θ_0 (deg)	Λ_M/B	Q (l/s)	D (mm)	B (m)	h_{av} (cm)	S_c	B/h_{av}	$(c_f)_{av}$	Re	Fr	Re_*	λ
Losiyevskii	–	20	≈6.0	(*)	(*)	(*)	(*)	(*)						0.23
Whiting & Dietrich 1993a	OM20W8. 1040	20	8.0	1.04	0.67	0.25	1.45	0.0064	17.2	12.4	4160	0.76	40.4	0.26
Hasegawa 1983	ME-3	20	10.6	0.54	0.43	0.22	0.93	0.00625	23.7	12.8	2455	0.87	20.5	0.25
	ME-3	20	10.6	0.59	0.43	0.22	1.37	0.00625	16.1	13.7	2682	0.53	24.9	0.25
	ME-1	30	6.8	0.75	0.43	0.30	0.89	0.01410	33.7	13.4	2500	0.95	30.2	0.23
	ME-2	30	6.8	1.87	0.43	0.30	2.60	0.00333	11.6	15.3	6233	0.48	25.0	0.24
Hooke 1974	10	55	10.3	10.0	0.30	1.00	5.20	0.00213	19.2	18.0	10000	0.27	19.8	0.05
	20	55	10.3	20.0	0.30	1.00	7.30	0.00207	13.7	18.8	20000	0.32	23.1	0.05
	35	55	10.3	35.0	0.30	1.00	9.50	0.00221	10.5	19.3	35000	0.38	27.2	0.06
	50	55	10.3	50.5	0.30	1.00	12.80	0.00223	7.8	20.0	50500	0.35	31.8	0.06
Termini 1996	–	110	2π	6.5	0.65	0.50	3.0	0.00370	16.7	14.2	13000	0.80	42.9	0.07 0.07 0.06
Whiting & Dietrich 1993b	100-3	100	8.0	1.18	0.62	0.25	1.66	0.0040	15.1	13.1	4648	0.70	31.6	0.06

(*) not reported

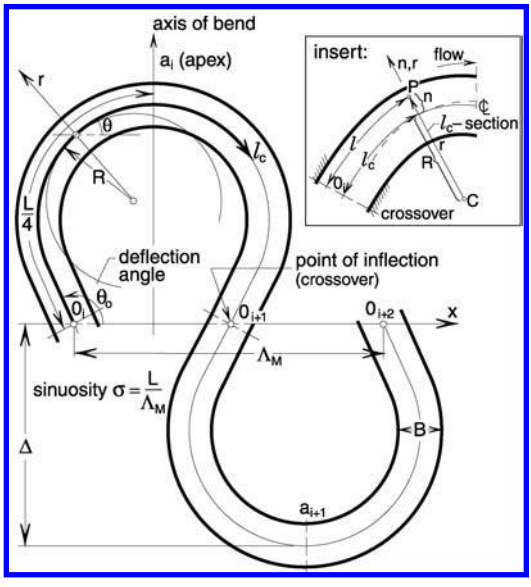


Figure 1. Definition sketch.

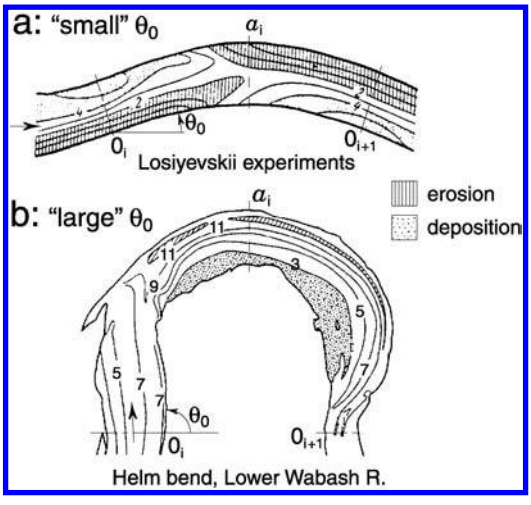


Figure 2. Examples of measured bed topography. a) Laboratory measurements carried out by Losiyevskii and reported by Makaveyev (1975); b) Measurements carried out by Jackson (1975).

erosion-deposition zones varies depending on the plan shape of the stream, i.e. depending on the values of the initial deflection angle θ_0 and Λ_M/B. According to these authors, "the larger the bend angle (i.e. θ_0) and the narrower the channel with respect to the cartesian wavelength, the further upstream is the pool" (Whiting & Dietrich 1993b, p. 3610). Using dimensional analysis, Yalin & da Silva (2001) have shown that, in addition to θ_0 and Λ_M/B, the location of the erosion-deposition zones may be expected to vary also depending on flow-related parameters, namely the channel-averaged values of the flow width-to-depth ratio B/h_{av} and the dimensionless (Chézy) flow friction $(c_f)_{av}$ (which reflects the influence of the granular skin roughness as well as of the grain size Reynolds number). However, no attempt has been made to date to determine how exactly does the location of

Copyright © 2006 Taylor & Francis Group plc, London, UK

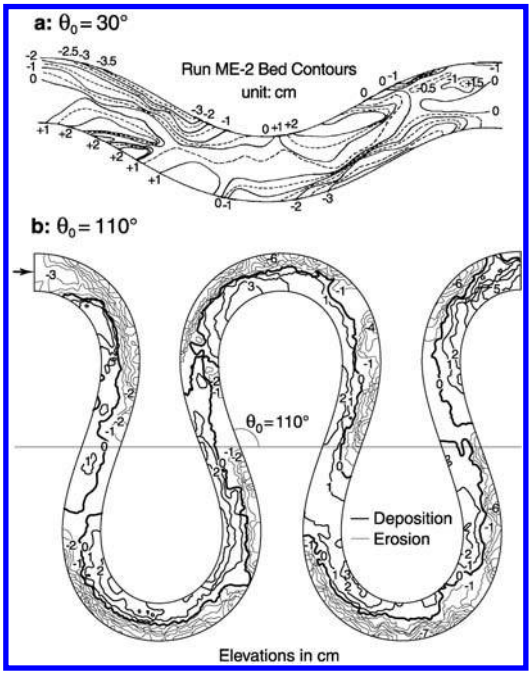


Figure 3. Examples of measured bed topography. a) Measured by Hasegawa (1983) in a 30°-channel (Run ME-2); b) Measured by Termini (1996) in a 110°-channel.

erosion-deposition zones depend on the geometric and flow-related parameters. This paper is the authors' contribution to this end.

1.2 *Aims of the paper and approach*

In order to define a quantity to characterize the type of distribution in flow plan of the $L/2$-long erosion-deposition zones, consider any meander loop between two consecutive crossovers (O_i and O_{i+1}, or O_{i+1} and O_{i+2}, etc. – see Figures 1 and 2). Within such a meander loop, locate the $L/2$-long erosion-deposition zone where deposition (D) occurs at the inner bank and erosion (E) at the outer bank. As can be inferred from Figure 4 (showing a schematic representation of the erosion-deposition zones in channels having "small" and "large" θ_0), the aforementioned $L/2$-long erosion-deposition zone may be only partially located in the meander loop (O_i and O_{i+1}, say) as in Figure 4a ($\theta_0 \rightarrow 0$), or fully located within it as in Figure 4b ("large" θ_0). Let $\tilde{l}_c$ be the distance from the apex a (a_i if the meander loop under consideration is $O_i\,O_{i+1}$; a_{i+1} if the meander loop under consideration is $O_{i+1}O_{i+2}$; etc.) to the mid-section of the aforementioned erosion-deposition zone, as shown in Figure 4a. Clearly, the location in flow plan of the erosion-deposition zones occurring in any given sine-generated stream can be

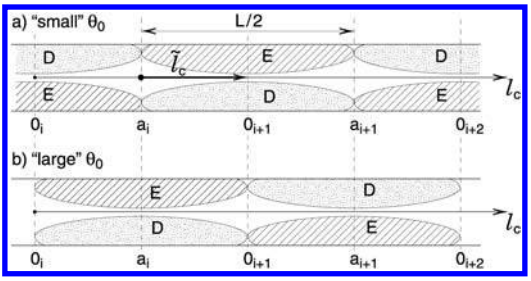


Figure 4. Schematical representation showing the location of L/2-long erosion-deposition (E-D) zones in sine-generated streams (streams "straightened" for the sake of simplicity); definition of $\tilde{l}_c$.

fully characterized by $\tilde{l}_c$ – or, equivalently, by its dimensionless counterpart $\lambda = \tilde{l}_c/L$. In other words, each different distribution in plan of the erosion-deposition zones is associated with its "own" value of λ. (For example, for the distribution in Figure 4a, $\lambda \approx 0.25$; for that in Figure 4b, $\lambda \approx 0$.) Following Whiting & Dietrich (1993b) and Yalin & da Silva (2001), in this paper $\lambda = \tilde{l}_c/L$ is treated as the following function of four dimensionless variables:

$$\lambda = \varphi_\lambda\left(\theta_0, \frac{\Lambda_M}{B}, \frac{B}{h_{av}}, (c_f)_{av}\right). \qquad (1)$$

The present paper has the following two aims:

1. to present the results of a series of experiments carried out by the authors in order to reveal the bed topography in a sine-generated channel having an intermediate value of θ_0. This value of θ_0 is selected so as to extend the range of θ_0-values investigated by previous authors; and
2. to investigate the form of the functional relationship (2), and thereby gain some insight into how the location of erosion-deposition zones depends on the relevant geometric and flow-related parameters. For this purpose, the λ-values resulting from the present measurements are analysed together with all the available data from previous works.

Throughout the paper, the position of a point P in the flow plan will be specified by the channel-fitted coordinates l_c and n (see insert in Figure 1) or by their dimensionless counterparts $\xi_c = l_c/L$ and $\eta = n/B$.

2 PERTINENT ASPECTS OF THE PLAN AND BED GEOMETRY IN SINE-GENERATED STREAMS

Before proceeding to the description of the experimental runs and their results, the following pertinent

Copyright © 2006 Taylor & Francis Group plc, London, UK

aspects of the geometry of sine-generated streams and their deformed beds – invoked throughout this paper – should be mentioned:

(i) The centerlines of sine-generated streams are given by the following equation (due to Leopold & Langbein 1966, Langbein & Leopold 1966)

$$\theta = \theta_0 \cos\left(2\pi \frac{l_c}{L}\right). \tag{2}$$

Eq. (2) appears to have become generally accepted as best representing the path of the channel centerline of natural regular meandering streams. Owing to this reason, current laboratory and numerical research on the mechanics of alluvial meandering flows and related processes is often carried out by idealizing the stream centerline as a sine-generated curve (see Smith & McLean 1984, Chang 1988, Nelson & Smith 1989, Shimizu 1991, Lyness et al. 2001, Jia & Wang 1999, Termini 2004, etc.).

(ii) The sinuosity $\sigma = L/\Lambda_M$ of sine-generated streams is uniquely determined by θ_0 as

$$\sigma = \frac{1}{J_0(\theta_0)} \tag{3}$$

(see Yalin 1992, Yalin & da Silva 2001). Here $J_0(\theta_0)$ is the Bessel function of first order and zero-th kind of θ_0. Fig. 5 shows how the computed sinuosity σ $(= L/\Lambda_M)$ of sine-generated channels corresponding to various θ_0 compares with its values measured in large Russian lowland rivers.

Note that the maximum possible value of θ_0 is $\approx 138^\circ = 2.41$ *rad*. This corresponds to $J_0(\theta_0) = 0$ and $L, \sigma \rightarrow \infty$. However, in practice, this can never occur, for when θ_0 reaches the value $\approx 126^\circ = 2.20$ rad ($\sigma \approx 8.5$), the meander loops come into contact with each other and the meandering pattern is destroyed.

(iii) It has since long been established that the meander wavelength Λ_M is proportional to the flow width B. Yalin (1992), Yalin & da Silva (2001) have shown that the relation

$$\Lambda_M \approx 2\pi B \tag{4}$$

best characterizes the average behaviour of natural streams. However, as pointed out by these authors, "the random element in natural meandering streams is rather strong; hence the coefficient of B in (3) may, in some cases, deviate substantially from $\approx 2\pi$, which is to be considered as the average value only" (Yalin & da Silva 2001, p. 103). This explains why Λ_M/B is included in the set of variables in Eq. (3) and also why different authors carried out their experiments in channels where this quantity differed somewhat from $\approx 2\pi$ (see Table 1).

(iv) Sine-generated streams consist of a sequence of anti-symmetrically identical loops conveying anti-symmetrically identical flows. Thus the sediment transport rates entering and leaving a meander loop are equal. But this means that the bed deforms with the passage of time around an unchanging average bed surface, which is the same as the flat initial bed at time $t = 0$ (+ and – areas at any section are the same for any t, as shown in Figure 6 (see e.g. Levi 1957, Ikeda & Nishimura 1986, Yalin & da Silva 2001)). In other words, the channel-averaged flow depth h_{av}, and thus B/h_{av}, can be regarded as constant throughout the process of bed deformation (and $h_{av} \approx h_0$).

In the following, the difference between the bed surface elevation at equilibrium, $(z_b)_T$, and the elevation of the initial bed surface, $(z_b)_0$, will be termed $(\Delta z_b)_T$ (see Fig. 6):

$$(\Delta z_b)_T = (z_b)_T - (z_b)_0. \tag{5}$$

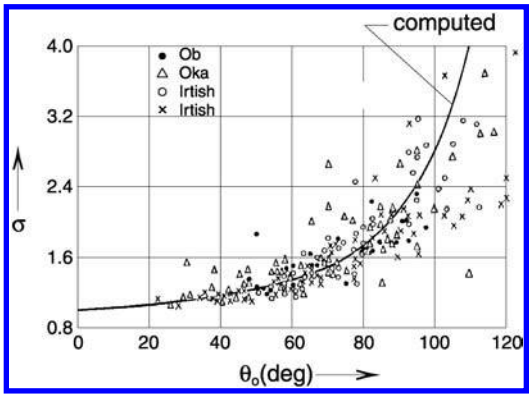


Figure 5. Plot of computed and measured sinuosity σ versus θ_0 (after Kondratiev et al. 1982).

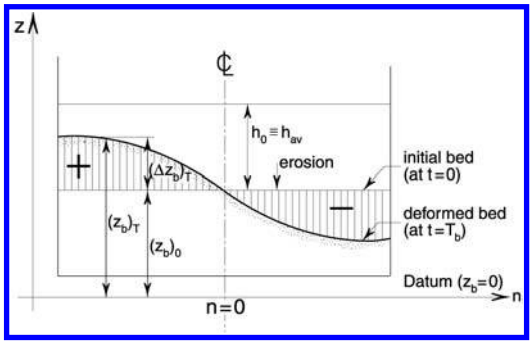


Figure 6. Bed deformation and related notation.

Copyright © 2006 Taylor & Francis Group plc, London, UK

3 EXPERIMENTAL SETUP AND RUNS

The present runs were carried out in a sine-generated meandering channel having $\theta_0 = 70°$ (which corresponds to a sinuosity $\sigma = 1.52$ (Eq. (3)). The flow width B was 0.80 m. The meander wavelength Λ_M and B were related by the proportionality (3). The channel had the total extent, L_T, of two meander lengths ($L_T = 2L = 15.2\,m$), its first and last sections coinciding with apex-sections (see Figure 7). The upstream-end of the meandering channel was connected to a 2 m-long straight approach channel. The vertical channel walls were made of 5 mm-thick plywood sheets, painted with an Epoxy paint; the channel bed consisted of a well-sorted silica sand having an average grain size (D_{50}) of 0.65 mm. The granular skin roughness $k_s \approx 2D_{50}$ (Kamphuis 1974) was 1.3 mm. The specific density of the sand was 2.65.

In total six runs were carried out. In each run, the flow rate Q was constant (steady flow). All runs started from a bed having zero radial slope and a specified longitudinal slope S_c (flat initial bed at $t = 0$). A tailgate was used to set the water elevation at the downstream-end of the channel so that the free surface slope was identical to the longitudinal bed slope S_c ("uniform" flow conditions). No sediment was fed to the channel throughout the duration of the runs. At the end of each run, the water was drained from the channel very slowly in order to ensure that the resulting deformed bed was not disturbed. The bed topography was measured only after the channel was completely drained.

The channel-averaged flow depth h_{av} was identified with the (identical) flow depth h_0 at the centreline of the four consecutive crossovers 1_1, 1_2, 1_3 and 1_4 – see Section 2, paragraph (iv). The flow depth h_0 at each crossover was obtained as the difference between the free surface elevation measured immediately after the "uniform" flow conditions were established and the elevation of the surface of the flat initial bed $(z_b)_0$. Measurements of the elevation of the deformed bed surface $(z_b)_T$ (see Figure 6) were carried out in three consecutive loops Λ_1, Λ_2, Λ_3, and in each loop in sixteen equally spaced cross-sections 1_i to 16_i ($i = 1$ to 3) as shown in Figure 7. The distance between two adjacent measurement cross-sections along the channel centerline was $\delta l_c = 23.8\,cm$ (or $\delta\xi_c = 0.03125$, where $\delta\xi_c = \delta l_c/L$). In each cross-section, the bed surface was measured at twenty-two equally spaced points (from $n = -36.75\,cm$ to $n = 36.75\,cm$). The bed surface elevation measurements were carried out by using as reference level (datum) a horizontal plane located 30 cm below the top of the channel walls.

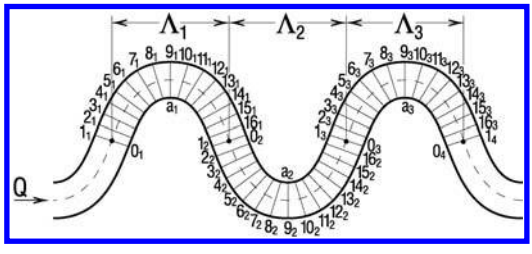


Figure 7. Experimental sine-generated channel and cross-sections for measurement of bed surface elevation.

A complete description of the experimental installation and the measurement techniques is given elsewhere (see El-Tahawy 2004).

The hydraulic conditions in each run are summarized in Table 2. Table 3 shows the values of the pertinent dimensionless variables for each run. Following Grishanin (1979), Kondratiev et al. (1982), Nelson & Smith (1989), etc., the values of the channel-averaged friction factor $(c_f)_{av}$ of gradually convergent (in both longitudinal sections and plan) meandering flows are invariably identified with those of the corresponding uniform flows. In accordance with this, $(c_f)_{av}$ was calculated from the following well-known equation (of uniform flows):

$$(c_f)_{av} = \frac{1}{\kappa}\ln\left(0.368\frac{h_{av}}{k_s}\right) + B_s, \qquad (6)$$

where κ = von Karman constant, k_s = granular roughness of the bed surface, and $B_s = \varphi(\mathrm{Re}_*)$ = roughness function (determined in this paper with the aid of Eq. (1.10) in Yalin & da Silva 2001). The values of

Table 2. Summary of experimental conditions in present runs ($\theta_0 = 70°$, $B = 0.80\,m$, $\Lambda_M = 2\pi B$, and $D = 0.65\,mm$).

Run	Q (l/s)	h_{av} (cm)	S_c	u_{av} (m/s)
1	11.0	7.5	1/450	0.18
2	13.4	7.3	1/290	0.23
3	10.5	6.0	1/420	0.22
4	9.80	5.0	1/250	0.25
5	7.60	4.4	1/250	0.22
6	6.50	3.5	1/250	0.23

Table 3. Values of pertinent dimensionless variables in present runs.

Run	B/h_{av}	$(c_f)_{av}$	Re	Fr	Re_*
1	10.7	16.4	13750	0.21	53
2	11.0	16.3	16750	0.27	65
3	13.3	15.9	13125	0.29	49
4	16.0	15.4	12263	0.36	58
5	18.2	15.1	9475	0.33	54
6	22.9	14.6	8125	0.39	48

Copyright © 2006 Taylor & Francis Group plc, London, UK

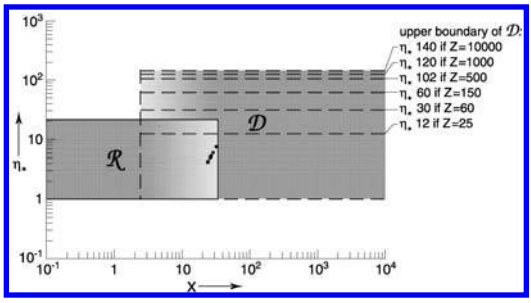


Figure 8. Existence regions of ripples (R) and dunes (D) in the $(\eta_*; X)$-plan of Yalin & da Silva (2001); dots mark the present runs.

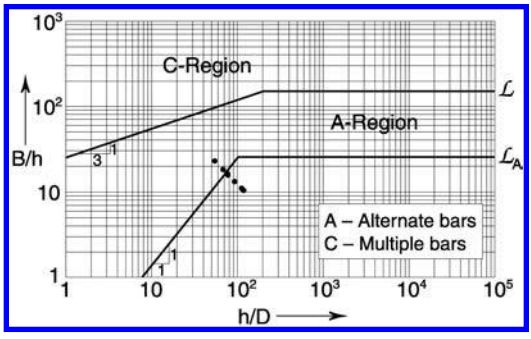


Figure 9. Existence regions of alternate bars (A) and multiple bars (M) in the $(B/h; h/D)$-plan of da Silva (1991); dots mark the present runs.

$(c_f)_{av}$ were similar in all runs, their average value being 15.6, while the values of B/h_{av} were increased from 10.7 in Run 1 to 22.9 in Run 6. Therefore, in the present series of runs, the values of $(c_f)_{av}$ can be regarded as fixed ($(c_f)_{av} \approx const = 15.6$), B/h_{av} being the only parameter in the functional relationship (2) that was varied.

The conditions in the experimental runs were selected so as to eliminate the possibility of occurrence of bed forms (ripples, dunes, alternate bars), or at least to ensure that eventual bed forms were small enough so as not to obscure the bed features under investigation. Consider Figure 8, showing the $(\eta_*; X)$-plan defining, according to Yalin & da Silva (2001), the existence regions of ripples (R) and dunes (D). Consider also Figure 9, showing the $(B/h;\ h/D)$-plan defining, according to da Silva 1991 (see also Yalin & da Silva 2001), the existence regions of alternate bars and multiple bars. The present runs are plotted as black dots in both of these Figures. Note from Figure 8 that the runs are located very near the vertical line implying the upper X-boundary of the region of ripples superimposed on dunes – where ripples are virtually non-existent. Four of the runs (namely runs 1 to 4) are located outside the alternate bar region in the $(B/h; h/D)$ in Figure 9. Runs 5 and 6 are within the A-region, but relatively near its lower boundary (especially Run 5), where alternate bars are the least prominent. During the runs, only small dunes were occasionally observed in some parts of the bed – which is consistent with the plots in Figures 8 and 9. The dune length varied from approximately 15 to 30 *cm*, the dune height typically being less than 1 to 1.5 *cm*.

4 EXPERIMENTAL RESULTS AND OBSERVATIONS

As examples, the bed topography maps at the end of Runs 1, 3 and 5 are shown in Figure 10a, b and c, respectively. These maps were produced from the measured $(\Delta z_b)_T$-values (see Figure 6 and note that $(\Delta z_b)_T > 0$ implies deposition, and $(\Delta z_b)_T < 0$ implies erosion).

The deformation of the bed was observed to progress very rapidly at the early stages of a run, and then to gradually slow down with the passage of time. The bed deformed by developing bars and pools, which over time grew in their prominence (magnitude), their location in flow plan remaining essentially the same.

As should be clear from Figure 10a to c, the deposition bars were always asymmetric. That is, the maximum deposition was not at, or near, the centre (mid-section) of the bar, but rather at a location further upstream, somewhere in the first half of the bar. As a bar grew in prominence, it deflected more and more the flow towards the pool at the opposite bank, which continued to deepen. The bars grew in their height until they became nearly exposed. At the later stages of a run, the flow was being strongly deflected by the bars towards the deeps.

Runs 1, 2 and 3 were stopped at times 75, 45 and 60 minutes, respectively, when the bottom of the channel became exposed at the locations of most intense erosion. Since the bed changes over time had already slowed down considerably, the measured deformed beds in these runs can be regarded as being near, although not exactly, at equilibrium. Runs 4, 5 and 6 were stopped at times 170, 180 and 120 minutes, respectively, some time after bed changes became no longer noticeable. Therefore, the measured deformed beds in these runs can be regarded as being in equilibrium.

From Figures 10a to c, it should be clear that in the present 70° -channel, the beginnings of the erosion-deposition zones do not coincide with the apexes a_i as in the case of small sinuosity (see Figures 2a and 3a), and also not with the crossovers O_i as in the case of large sinuosity (see Figures 2b and 3b). Rather, their beginnings occur somewhere in between the crossovers O_i and apexes a_i. In order to determine the exact location (i.e. the beginnings and ends) of

Copyright © 2006 Taylor & Francis Group plc, London, UK

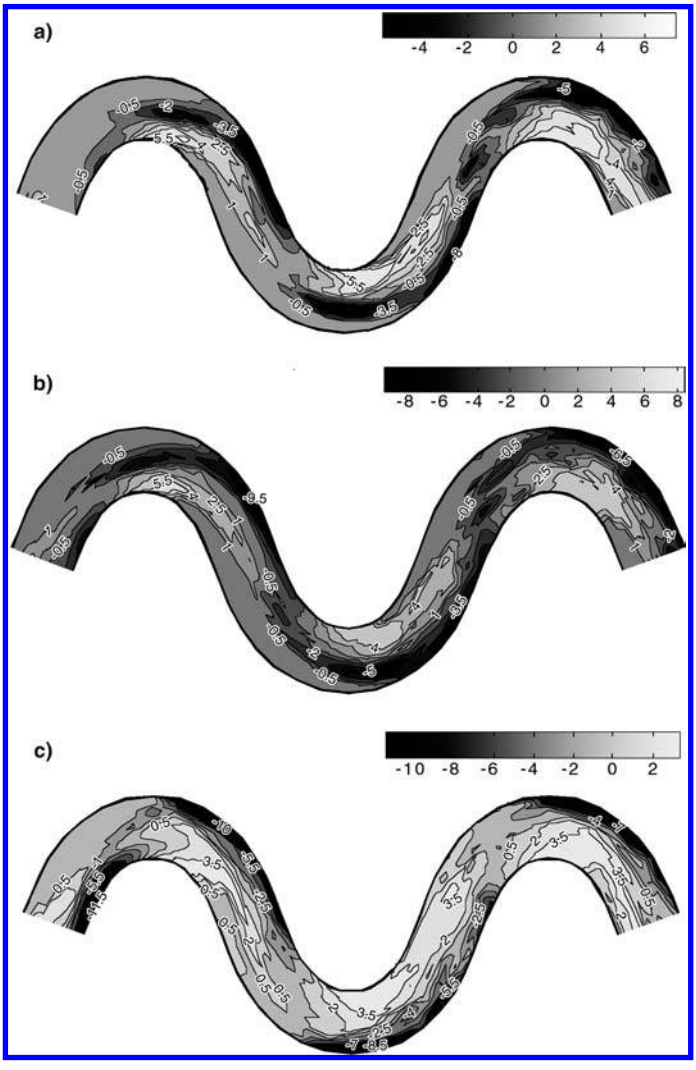


Figure 10. Bed elevation contour maps (contours based on $(\Delta z_b)_T$-values; units are cm; flow from left to right.) (a) Run 1; (b) Run 3; (c) Run 5.

the deformed beds and, consequently, the values of λ, plots of E_V and D_V versus ξ_c $(=l_{c/L})$ were produced for each run. Here E_V is the volume of space between any two consecutive measurement cross-sections which became void of sand over the duration of the run (i.e. from $t=0$ to $t=T_b$), and D_V the volume of space which became filled with sand over the same period of time. Clearly, no erosion or deposition occurs at the cross-sections coinciding with the beginning (i.e. upstream-end) and end (downstream-end) of each erosion-deposition zone, and therefore at these cross-sections $E_V;D_V \rightarrow 0$. The $E_V;D_V$-plot corresponding to Run 5 is shown, as example, in Figure 11. In this Figure, the cross-sections where $E_V;D_V \rightarrow 0$, corresponding to the beginnings (and ends) of each erosion-deposition zone, are marked by the vertical dashed lines labelled "Beginning of nth E-D zone" (with $n=1$, 2, 3).

The dimensionless length of the first erosion-deposition zone was systematically less than the expected (theoretical) value of 0.50 (its average value for the six runs being 0.43). On the other hand, the downstream end of the third erosion-deposition zone was invariably located after the last measurement cross-section. Considering this, the values of λ were determined for the second erosion-deposition zone (where λ is to be measured from the apex-section a_2 (i.e. 5_2 – see Figure 7). The resulting values are $\lambda=0.125$, 0.120, 0.100, 0.135, 0.135 and 0.145 for Runs 1 to 6, respectively.

Copyright © 2006 Taylor & Francis Group plc, London, UK

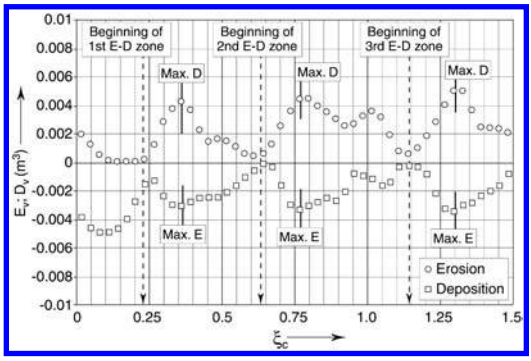


Figure 11. Plot of E_V (eroded volume) and D_V (deposited volume) versus ξ_c: Run 5.

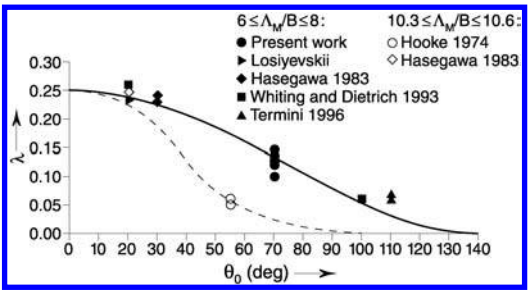


Figure 12. Plot of λ versus θ_0.

The location in flow plan of the $L/2$-long erosion-deposition zones was remarkably similar in all runs, irrespective of their values of B/h_{av}. Indeed, for all runs the topographic maps and the E_V;D_V-plots show a $L/2$-long erosion-deposition zone starting approximately at cross-section 5_2 and another approximately at cross-section 5_3, with $\lambda \approx const = 0.125$.

5 EFFECT OF PLAN SHAPE AND FLOW RELATED PARAMETERS

Using the topographic maps produced by Losiyevskii, Whiting & Dietrich (1993a,b), Hasegawa (1983), Hooke (1974) and Termini (1996), values of λ were estimated also for each of the runs in Table 1. The resulting values of λ are shown in the last column in this Table. (The three values shown for the run by Termini 1996 correspond to measurements in three consecutive meander loops).

The width-to-depth ratio was varied in the series of runs by Hasegawa (1983), Hooke (1974) and the present runs. For the range of B/h_{av}-values investigated by these authors, B/h_{av} had no significant effect on the values of λ (and thus on the location of the erosion-deposition zones). The parameter B/h_{av} thus will be disregarded in the discussion below.

No single author has substantially varied $(c_f)_{av}$ for constant θ_0, Λ_M/B and B/h_{av}. Therefore no definite conclusions can be drawn from the experiments carried out to date on the effect of $(c_f)_{av}$.

It is clear that the values of λ are strongly dependent on θ_0. A plot of the measured values of λ versus θ_0 is shown in Figure 12. The "black" data-points correspond to runs where $6 \leq \Lambda_M/B \leq 8$ and $12.4 \leq (c_f)_{av} \leq 16.4$. The solid line in this Figure represents the trend followed by these data-points. This line thus gives the variation of λ for specified values of Λ_M/B, $(c_f)_{av}$ and B/h_{av}, namely $\Lambda_M/B = const \approx 7$, $(c_f)_{av} = const \approx 14.5$ and $\approx 10 \leq B/h_{av} \leq \approx 30$. Here the values 7 and 14.5 are the average-values of the ranges of Λ_M/B- and $(c_f)_{av}$-values of the aforementioned data.

The "white" circles in Figure 12, which correspond to the runs by Hooke (1974), plot substantially below the aforementioned solid line. In these runs, the values of Λ_M/B and $(c_f)_{av}$ were 10.3 and ≈19, respectively. Given these data, it appears reasonable to expect the variation of λ for these values of Λ_M/B and $(c_f)_{av}$ (i.e. $\Lambda_M/B = 10.3$, $(c_f)_{av} = 19$ and $\approx 10 \leq B/h_{av} \leq \approx 30$) to be approximately as indicated by the dashed line in Figure 12. The deviation between the solid and dashed lines can be due entirely to differences in the values of Λ_M/B, or partially to differences in the Λ_M/B-values and partially to differences in the $(c_f)_{av}$-values. This is a point which can be clarified only through further research in the future. In spite of this, the results of the present analysis suggest that there is a trend for the location of the erosion-deposition zones to move further upstream for larger values of Λ_M/B (other conditions remaining the same) – as apparently first suggested by Whiting & Dietrich (1993b).

6 CONCLUDING REMARKS

From the analysis in this paper, it follows that:

1. The location of the erosion-deposition zones is strongly dependent on θ_0 (i.e. on stream sinuosity). For the same remaining conditions, the location of the erosion-deposition zones which are centered around the crossovers O_{i+1} for small θ_0, continuously moves upstream so that for large θ_0 they are centered around the apexes a_i.
2. Accordingly, for specified values of Λ_M/B, B/h_{av} and $(c_f)_{av}$ the quantity λ reflecting the distribution in flow plan of the erosion-deposition zones plots as an inverted S-curve (see Figure 12).
3. The present analysis suggests that the location in flow plan of erosion-deposition zones is affected also by Λ_M/B and possibly by $(c_f)_{av}$. For a specified θ_0, the larger Λ_M/B (and perhaps also $(c_f)_{av}$), the

Copyright © 2006 Taylor & Francis Group plc, London, UK

further upstream will the erosion-deposition zones be located.

4. Within the range of B/h_{av}-values of the data used in this work (namely $\approx 10 \leq B/h_{av} \leq \approx 30$), B/h_{av} did not play any detectable role in determining the location of the erosion-deposition zones.

ACKNOWLEDGEMENT

This research was supported by the Natural Sciences and Engineering Research Council of Canada (NSERC) through a Discovery Grant provided to the first author.

REFERENCES

Chang, H.H. 1988. *Fluvial processes in river engineering*. John Wiley and Sons Inc., New York.

da Silva, A.M.F. 1991. *Alternate bars and related alluvial processes.* M.Sc. Thesis, Queens' University, Kingston, Canada.

El-Tahawy, T. 2004. *Patterns of flow and bed deformation in meandering streams: an experimental study*. Ph.D. Thesis, Queens' University, Kingston, Canada.

Grishanin, K.V. 1979. *Dynamics of alluvial streams*. (In Russian) Gidrometeoizdat, Leningrad.

Hasegawa, K. 1983. *Hydraulic research on planimetric forms, bed topographies and flow in alluvial rivers*. Ph.D. Thesis (in Japanese), Hokkaido University, Sapporo, Japan.

Hooke, R.L. 1974. *Distribution of sediment transport and shear stress in a meander bend*. Rept. 30, Uppsala Univ. Naturgeografiska Inst., 58.

Ikeda, S. & Nishimura, T. 1986. Flow and bed profile in meandering sand-silt rivers. *J. Hydraul. Eng. 112(7): 562–579*.

Jackson, R.J. 1975. Velocity-bed-form-texture patterns of meander bends in the lower Wabash River of Illinois and Indiana. *Geol. Soc. Am. Bull. 86(11): 1511–1522*.

Jia, Y. & Wang S.S.Y. 1999. Numerical model for channel flow and morphological change studies. *J. Hydraul. Eng. 125(9): 924–933*.

Kamphuis, J.W. 1974. Determination of sand roughness for fixed beds. *J. Hydraul. Res. 12(2): 193–203*.

Kondratiev, N., Popov, I., Snishchenko, B. 1982. *Foundations of hydromorphological theory of fluvial processes*. (In Russian) Gidrometeoizdat, Leningrad.

Langbein, W.B. & Leopold, L.B. 1966. "River meanders – theory of minimum variance". *U.S. Geol. Survey Prof. Paper 422-H: 1–15*.

Levi, I.I. 1957. *Dynamics of alluvial streams*. (In Russian) State Energy Publishing, Leningrad.

Lyness, J.F., Myers, W.R.C., Cassels, J.B.C. & O'Sullivan, J.J. 2001. The influence of planform on flow resistance in mobile bed compound channels. *J. Water & Maritime Eng., Proc. Instn. Civ. Engrs. 148(1): 5–14*.

Leopold, L.B., Langbein, W.B. 1966. River meanders. *Sci. Am., 214(6): 60–70*.

Makaveyvev, N.I. 1975. *River bed and erosion in its basin*. Press of the Academy of Sciences of the USSR, Moscow.

Nelson, J. M. & Smith, J. D. 1989. Evolution and stability of erodible channel beds. in S. Ikeda & G. Parker (eds.), *River Meandering; American Geophysical Union, Water Resources Monograph, 12: 321–378.*

Shimizu, Y. 1991. *A study on prediction of flows and bed deformation in alluvial streams*. (In Japanese) Civ. Eng. Res. Inst., Hokkaido Development Bureau, Sapporo, Japan.

Smith, J.D. & McLean, S.R. 1984. A model for flow in meandering streams. *Water Resour. Res. 20(9): 1301–1315*.

Termini, D. 2004. Flow in meandering bends. *Proc. 2nd Int. Conf. on Fluvial Hydraulics, River Flow 2004*, A. A. Balkema, The Netherlands: 109–117.

Termini, D. 1996. *Evolution of a meandering channel with an initial flat bed. Theoretical and experimental study of the channel bed and the initial kinematic characteristics of flow*. (In Italian) Ph.D. Thesis, Dept. Hydraulic Engineering and Environmental Applications, University of Palermo, Italy.

Whiting, P.J. & Dietrich, W.E. 1993a. Experimental constraints on bar migration through bends: implications for meander wavelength selection. *Water Resour. Res. 29(11): 1091–1102*.

Whiting, P.J. & Dietrich, W.E. 1993b. Experimental studies of bed topography and flow patterns in large-amplitude meanders. 1. Observations. *Water Resour. Res. 29(11): 3605–3614*.

Yalin, M.S. & da Silva, A.M.F. 2001. *Fluvial Processes*. IAHR Monograph, IAHR, Delft, The Netherlands.

Yalin, M.S. 1992. *River Mechanics*. Pergamon Press, Oxford.

LIST OF SYMBOLS

B	flow width
$(c_f)_{av}$	dimensionless (Chézy) friction factor
D_V	volume of space between any two consecutive measurement cross-sections that became filled with sand over the total duration of a run
D_{50}	representative grain size
E_V	volume of space between any two consecutive measurement cross-sections that became void of sand over the total duration of a run
Fr	Froude number ($= u_{av}/\sqrt{gh_{av}}$)
g	acceleration due to gravity
h_{av}	channel-averaged flow depth
h_0	flow depth at time $t = 0$, over the flat initial bed
$J_0(\theta_0)$	Bessel function of first kind and zero-th order (of θ_0)
k_s	granular roughness of bed surface ($k_s \approx 2D_{50}$)
l	longitudinal coordinate; $l = 0$ at the crossover O_i (see Figure 1)
L	meander length (measured along l_c)
l_c	longitudinal coordinate along the centreline of a meandering flow; $l_c = 0$ at the crossover O_i (see Figure 1)

Copyright © 2006 Taylor & Francis Group plc, London, UK

$\tilde{l}_c$ distance measured along the channel centreline from the apex-section a to the mid-section of a $L/2$-long erosion-deposition as shown in Figure 3a

n radial coordinate of a meandering flow; $n = 0$ at the flow centreline (see insert in Figure 1)

Q flow rate

r radial coordinate of a meandering flow; $r = 0$ at the centre of channel curvature (see Figure 1)

R local radius of curvature

Re flow Reynolds number ($= u_{av}\, h_{av}/\nu$)

Re_* roughness Reynolds number ($= v_*\, k_s/\nu$)

S_c bed slope along the centreline of a meandering flow

t time

T_b duration of development of the deformed bed of a meandering stream

u_{av} channel-averaged flow velocity

v_* shear velocity ($= \tau_0/\rho = \sqrt{g h_{av} S_c}$)

X grain size Reynolds number ($= v_*\, D/\nu$)

z_b bed elevation measured with regard to an arbitrary reference datum (see Figure 6)

γ_s specific weight of grains in fluid

Δz_b local difference between the elevations of the deformed bed surface and the initial flat bed surface ($\Delta z_b = z_b - (z_b)_0$)

η dimensionless counterparts of n ($\eta = n/B$)

η_* relative flow intensity ($\eta_* = Y/Y_{cr}$, where Y is the mobility number (Shields parameter) and Y_{cr} is the value of Y at the stage of initiation of sediment transport

θ, θ_0 deflection angle of a meandering flow at any l_c and at $l_c = 0$, respectively (see Figure 1)

λ dimensionless counterpart of $\tilde{l}_c$ ($\lambda = \tilde{l}_c/L$)

Λ_M meander wavelength

ν fluid kinematic viscosity

ξ_c dimensionless counterpart of l_c ($\xi_c = l_c/L$)

ρ fluid density

σ sinuosity of a meandering flow ($\sigma = L/\Lambda_M$)

τ_0 bed shear stress

Subscripts:

av marks the channel-averaged value of a quantity

T marks the value of a quantity at time $t = T_b$

0 marks the value of a quantity at time $t = 0$

Copyright © 2006 Taylor & Francis Group plc, London, UK

B.3. Large scale river morphology and morphodynamics (continued)

Copyright © 2006 Taylor & Francis Group plc, London, UK

On the bed deformation in meandering streams

A.M. Ferreira da Silva
Associate Professor, Department of Civil Engineering, Queen's University, Kingston, Ontario, Canada

M.S. Yalin
Emeritus Professor, Department of Civil Engineering, Queen's University, Kingston, Ontario, Canada

ABSTRACT: The bed deformation in meandering streams is explained in the light of the sediment transport continuity equation and the convective behaviour of the vertically-averaged flow: the width-to-depth ratio is "large", the meandering channel is sine-generated. The plan shape of the channel and flow rate are assumed to remain constant during the bed formation process. It is shown that each erosion-deposition zone of the *developed* (or equilibrium) *bed* at time $t = T$ is brought into being by a corresponding convergence-divergence zone of the vertically-averaged *initial flow* over the flat (movable) bed at time $t = 0$. A series of experimental runs involving the systematic variation of the channel's deflection angle θ_0 is used to establish how the location of the convergence-divergence zones of the vertically-averaged initial flow varies with θ_0. The implications regarding the variation with stream sinuosity of the location in flow plan of erosion-deposition zones are discussed.

1 INTRODUCTION; FUNDAMENTALS

(i) This paper concerns the bed development in meandering streams. Following Leopold & Langbein (1966) (see also Langbein & Leopold 1966), the centerlines of the streams (in plan view) are idealized as sine-generated functions, where

$$\theta = \theta_0 \cos\left(2\pi \frac{l_c}{L}\right), \tag{1}$$

the different plan shapes being due to the different values of the deflection angle θ_0 only (see the schematic Figure 1, where a meandering stream having a "large" θ_0 is used to introduce the geometry-related notation). As shown by Yalin (1992), the deflection angle θ_0 and the stream sinuosity $\sigma (= L/\Lambda_M)$ of sine-generated channels are uniquely interrelated:

$$\sigma = \frac{1}{J_0(\theta_0)} \quad \left(= \frac{L}{\Lambda_M}\right). \tag{2}$$

here $J_0(\theta_0)$ is the Bessel function of the first kind and zero-th order (of θ_0).

(ii) In accordance with the majority of current publications on the topic, the present study rests on the following assumptions:

1. The stream is imbedded in a cohesionless alluvium which is homogeneous and isotropic;
2. The B/h_{av}-ratio of the stream is "large" (larger than ≈ 20, say, as in most of the large natural streams);
3. The flow is rough turbulent.

The implications of assumption 2 are of particular significance, and they are outlined below.

Assumption 2 gives the possibility to replace the study of an actual 3D-stream by that of its *vertically-averaged* 2D counterpart, where the location of a point in the flow plan can be specified by the "channel-fitted" polar coordinates $(l_c; r)$ or $(l_c; n)$ (Figure 2). This approach, which seems to have been first introduced in Smith & McLean (1984), Nelson & Smith (1989a), Struiksma et al. (1985), Shimizu & Itakura (1989) (see also Shimizu 1991), is adopted in the present text.

Assumption 2 also implies that the bank-friction is negligible. Considering this, one can express the Chézy resistance formula in the following manner

$$u_{av} = c_{av}\sqrt{g S_c h_{av}}\,. \tag{3}$$

here the dimensionless resistance factor c_{av} is related to the original (dimensional) Chézy's C_{av} by $c_{av} = C_{av}/\sqrt{g}$. [In order to save the space, the Symbols are not always defined where they appear, and the reader is invited to consult the "List of Symbols" at the end of the text.] It should be noted that since the energy losses due to the channel curvature are insignificant in

Copyright © 2006 Taylor & Francis Group plc, London, UK

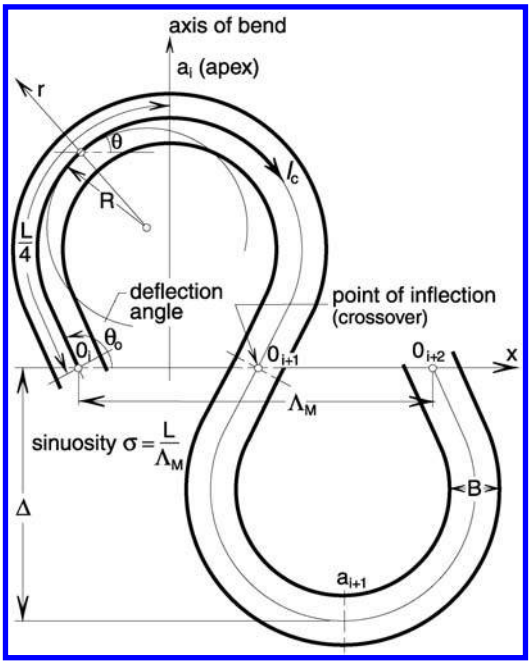


Figure 1. Definition sketch.

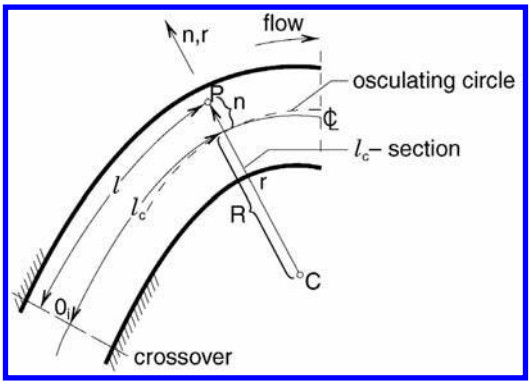


Figure 2. Channel-fitted polar coordinates.

comparison to the bed-friction losses (Leopold et al. 1960, Rozovskii 1957, Chang 1983; see also James 1994), the value of the resistance factor c_{av} does not differ appreciably from the value of the friction factor $(c_f)_{av}$: i.e. $c_{av} \approx (c_f)_{av}$.

Finally, assumption 2 conveys that the role of the cross-circulation (Γ) is negligible with regard to the present study. Indeed the relation

$$\left(\frac{\bar{v}'_\Gamma}{\bar{u}}\right)^2 = \alpha c_{av}^2[\theta_0 J_0(\theta_0)]\sin\left(2\pi\frac{l_c}{L}\right)\cdot\frac{h_{av}}{B} \qquad (4)$$

(derived in Yalin & da Silva 2001, pp. 136 to 140) indicates that $\bar{v}'_\Gamma/\bar{u} \to 0$ when $B/h_{av} \to \infty$, and thus

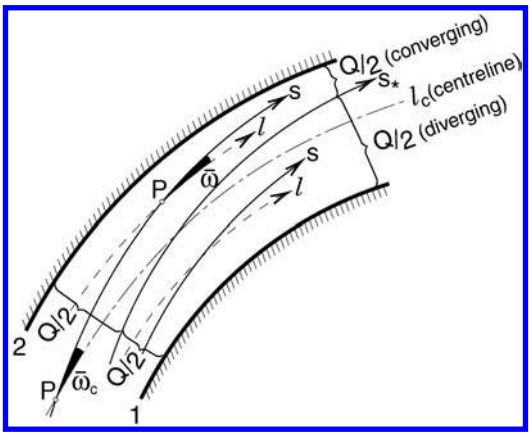


Figure 3. Laterally adjacent convergence-divergence flow zones in a meandering flow.

that Γ ($\sim \bar{v}'_\Gamma$) can be ignored when B/h_{av} is "large". The irrelevance of Γ with regard to the formation of wide natural streams has been independently pointed out in the past by many eminent field-research engineers (such as Leliavskii 1959, Matthes 1948, 1941, Kondratiev et al. 1982, Velikanov 1955 and Makaveyev 1975). [More on the topic in Chapter 5 of Yalin & da Silva 2001; see also Hooke 1974 and Hooke 1980.]

2 CONVECTIVE FLOW AND SEDIMENT TRANSPORT

(i) Consider the flow in a wide meandering channel at the beginning of experiment (at the time $t = 0$): the channel bed is *flat* (it is the graded surface of a mobile bed). The vertically-averaged streamlines s of this (initial) flow are not parallel: in some parts of the flow-plan they converge, in some others they diverge from each other (Figure 3). Let s_* be the streamline separating two (laterally adjacent (inner and outer)) zones, each conveying half the flow rate ($Q/2$). It can be demonstrated, on the basis of longitudinal periodicity of meandering flow (see Yalin & da Silva 2001), that s_* is at the same time the line which separates the laterally adjacent zones of converging and diverging flows. e.g. in Figure 3, s_* separates the converging (convectively accelerating) flow-zone on the side of the Bank 2, from the diverging (convectively decelerating) flow-zone on the side of the Bank 1.

In sine-generated streams, the pattern formed by the streamlines in plan view varies periodically along l_c: the flow characteristics in the cross-sections separated by the length L are identical, those in the cross-sections separated by $L/2$, are antisymmetrically identical.

Copyright © 2006 Taylor & Francis Group plc, London, UK

(ii) Since the local sediment transport rate q_s is an increasing function of the (local) vertically-averaged flow velocity $\overline{U}$, the convective variation of $\overline{U}$ in a flow zone must inevitably cause the corresponding convective variation of q_s in that zone; i.e. it must cause the scalar $\nabla \mathbf{q}_s$ to acquire a non-zero value. But $\nabla \mathbf{q}_s \neq 0$ must, in turn, induce the displacement of the bed surface in vertical direction (z) – as required by the sediment transport continuity equation

$$W = (1-p)\frac{\partial z_b}{\partial t} = -\nabla \mathbf{q}_s , \tag{5}$$

where W is the vertical displacement velocity of the bed surface. This equation indicates that if $\nabla \mathbf{q}_s > 0$, then $W < 0$ (erosion), and if $\nabla \mathbf{q}_s < 0$, then $W > 0$ (deposition). Only in the locations where the flow is parallel, and thus $\nabla \mathbf{q}_s = 0$, the elevation z_b of the bed surface can remain unchanged ($W = 0$).

Let T be the duration of bed development. Integrating (5) over $0 < t < T$, we obtain

$$(z_b)_T \sim -\int_0^T \nabla \mathbf{q}_s dt \tag{6}$$

i.e.

$$(z_b)_T \sim -(\nabla \mathbf{q}_s)_m T = W_m T . \tag{7}$$

This relation conveys that the (total) displacement $(z_b)_T$ of the bed surface at a location of flow plan is an increasing function of $-(\nabla \mathbf{q}_s)_m = W_m$, i.e. of the intensity of convective behaviour of flow at that location. At this stage it may also be mentioned that for the same remaining conditions, the plan-geometry of the streamlines s and thus of the converging-diverging flow zones varies depending on the plan shape of the meandering stream, i.e. with the value of the deflection angle θ_0.

3 BED DEVELOPMENT

The deformed bed of a meandering stream consists of a longitudinal sequence of laterally adjacent "deeps" and "hills" (see Figure 4a, where, as example, an intermediate value of θ_0 is used). Each (deep) + (hill) complex can be viewed as one erosion-deposition zone (in short [ED]). From the preceding section it should be clear that each [ED] is brought into being by a (corresponding) convergence-divergence zone (in short by [CD]) of the initial flow. Hence the length of each [ED] must be the same as that of each [CD], viz $L/2$. The channel cross-sections separating the successive [CD]'s (and [ED]'s) are identifiable by the fact that the streamlines s at those sections must be parallel to each other, i.e. we must have at those sections, $\overline{\omega} = 0$ (see Figure 3). Moreover, the deeps and

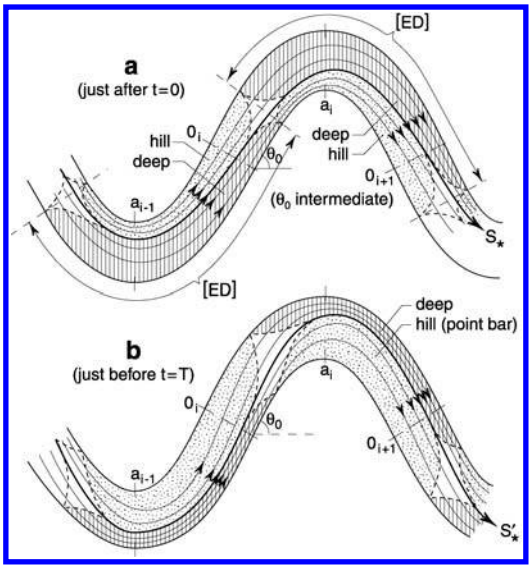


Figure 4. Schematical representation of convergence-divergence zones [CD]'s and corresponding erosion-deposition zones [ED]'s.

hills forming an [ED] of infinitesimal amplitude, just after $t = 0$, must be expected to be separated from each other by the same streamline s_* which separates the convergence-divergence zones of the initial flow (Figure 4a). The meandering streams under study are periodic along x, and therefore the consecutive [ED]'s are anti-symmetrically identical.

Both hills and deeps are rather flat (non-prominent) at any t ($\in[0; T]$). Their longitudinal and radial steepnesses can be expressed as

$$S_l \approx \delta/(L/2) < 2h/L \tag{8a}$$

and

$$S_r \approx \delta/(B/2) < 2h/B , \tag{8b}$$

respectively. Here $\delta(=\delta_H$ or $\delta_D)$ implies the height of hills and the depth of deeps (at a time t), respectively. Since δ_H and δ_D are comparable, we can write roughly

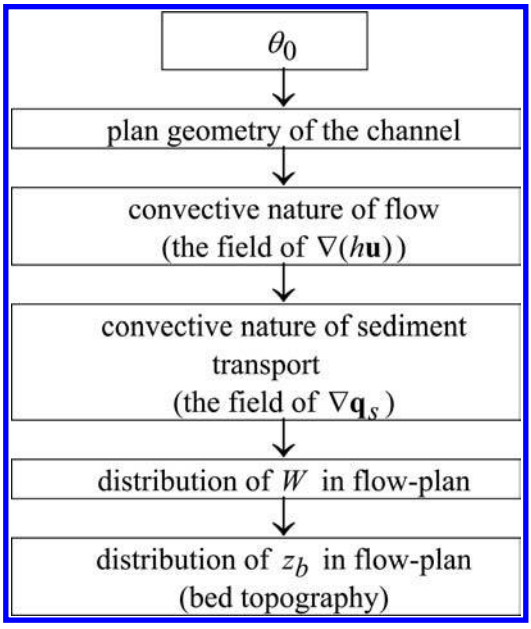
$$S_l / S_r \approx \frac{B}{L} . \tag{9}$$

The process of bed deformation is solely due to the transfer of bed material from the area of deeps to the area of hills (as effected by the convective flows over these areas). These locally transferred transport rates, which occur only during $0 < t < T$, are superimposed on the (always present) "transit" transport rate. In wide natural meandering streams, the material eroded from a deep (and/or banks) is deposited predominantly on the next hill (bank) on the *same* side of the flow: "only

Copyright © 2006 Taylor & Francis Group plc, London, UK

a small portion of eroded material crosses the channel" (Leliavskii 1959, Matthes 1941, 1948, Kondratiev et al. 1982, Velikanov 1955, Makaveyev 1975).

The cause-effect sequence embodied in the present approach can be summarized as follows:



From laboratory measurements of sine-generated meandering flows having a flat bed (see Whiting & Dietrich 1993a,b, da Silva 1995, Termini 1996) it follows that:

If θ_0 is "small" (Figure 5a), then a [CD] extends between the apex-sections a_i and a_{i+1} (where $\overline{\omega} = 0$), the most intense convergence/divergence ($\overline{\omega}_{\max}$) being at the crossover-section O_{i+1};

If θ_0 is "large" (Figure 5b), then the analogous [CD] extends between the crossover-sections O_i and O_{i+1} (where $\overline{\omega} = 0$), the most intense convergence/divergence ($\overline{\omega}_{\max}$) being at the apex-section a_i.

Hence the deepest erosions and highest depositions must be expected to occur around the crossovers O_i if θ_0 is "small", and around the apex-sections a_i if θ_0 is "large". The examples of actual streams shown in Figure 6 appear to validate these expectations.

The following two assertions can be made on the basis of the aforementioned:

1. Every different plan geometry of a meandering stream (i.e. every different θ_0) possesses "its own" type of convective flow and thus its own distribution of [CD]'s in the flow plan. (There is no "standard" pattern of streamlines of a meandering flow).
2. The locations (in plan view) of [ED]'s of a deformed bed are approximately in coincidence with the locations of [CD]'s of the initial flow past the flat bed. ([ED]'s are the "imprints" of [CD]'s).

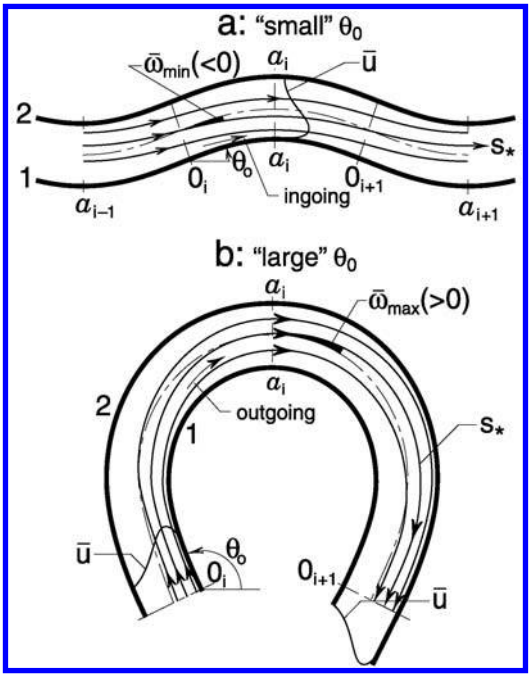


Figure 5. Convergence-divergence zones of initial flow in channels having "small" and "large" θ_0.

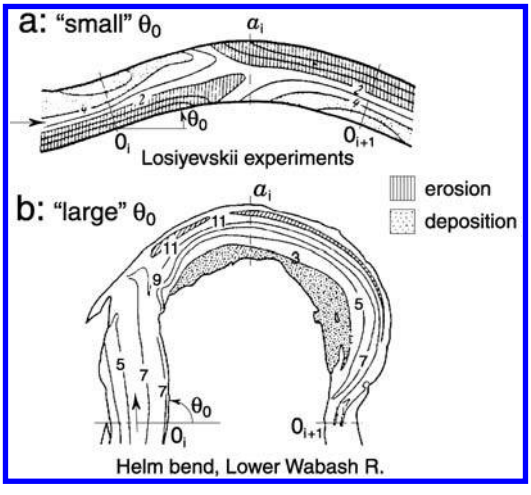


Figure 6. Bed topography in actual streams. a) Measurements reported by Makaveyev 1975; b) Measurements carried out by Jackson 1975.

The second assertion may not sound readily acceptable: "perhaps [ED]'s are moving (migrating) in longitudinal direction l_c during T, their locations at $t = T$ thus becoming different from those at $t = 0$ (i.e. from the locations of the initial [CD]'s)". With regard to this point, it should be mentioned that the displacement of

Copyright © 2006 Taylor & Francis Group plc, London, UK

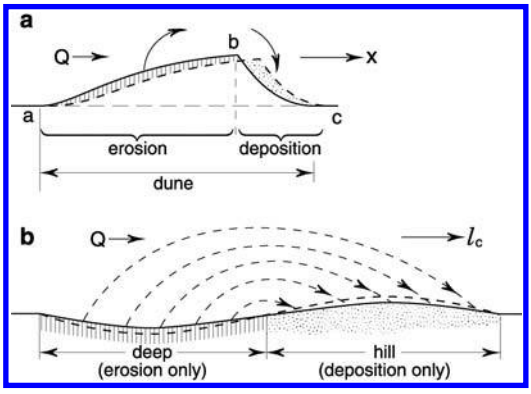


Figure 7. Migrating versus non-migrating "bed forms".

a bed feature can take place only if while one part of the feature is eroded, its remaining part is deposited. e.g. the ripples and dunes are moving (migrating) because while their upstream part $\overline{ab}$ is eroded, their (remaining) downstream part $\overline{bc}$ is deposited (Figure 7a). This is not the case of deeps and hills under study. Indeed, not a part, but the whole surface of a deep is subjected only to erosion, while that of a hill, only to deposition (by definition of these features). Hence, the deeps and hills can grow and deform, but they cannot move in longitudinal direction (Figure 7b).

The hills impede and thus repel the flow. By contrast, the deeps "invite" it. Hence the continual growth of the amplitude of hills and deeps during T causes a progressive "shift" of the flow from hills to deeps ("topographic steering" (Nelson & Smith 1989a,b)). In the process the flow velocity over the hills decreases, that over the deeps increases: hills themselves widen, deeps become narrower. As a result, the initial s_*-line approaches more and more to the bank on the side of the deep (s'_* in Figure 4b). The bed formation process stops (at $t = T$) when

$$W = (1-p)\frac{\partial z_b}{\partial t} = -\nabla \mathbf{q}_s = 0 \qquad (10)$$

is reached.

As mentioned earlier, in previous works the location of [CD]'s has been established experimentally only for the cases of "small" and "large" θ_0. From the considerations in this paper, it follows that if θ_0 is "intermediate", then the [CD]'s must necessarily be located in an intermediate position between that of "small" and "large" θ_0. However, it is not known at the present how exactly does the location of [CD's] in a meander loop vary as a function of θ_0. The following Section, where a series of flow measurements involving the systematic variation of θ_0 is used to establish the location of [CD]'s in streams of varying θ_0, is the authors' contribution to this topic.

4 LABORATORY INVESTIGATION ON LOCATION OF [CD]'S; VARIATION WITH θ_0

4.1 *Description of experimental setup and runs*

The measurements reported below were carried out in five sine-generated channels having $\theta_0 = 30°$, 50°, 70°, 90°, and 110°.

In all channels, the flow cross-section was rectangular, the flow width being $B = 0.40\,m$. In agreement with the conditions present in natural alluvial streams, and following Yalin 1992, Yalin & da Silva 2001, the flow width B and the meander wavelength Λ_M were related as $\Lambda_M \approx 2\pi B$. For the present flow width, this gives $\Lambda_M = 2.51\,m$. Each channel had the total extent of two meander lengths, viz $2L$, with the entrance- and exit-sections being in coincidence with apex-sections. The upstream-end of each channel was connected to a $0.8\,m$-long straight approach-channel; the downstream-end to a $0.6\,m$-long straight exit-channel leading to a return channel. The channel walls were made of Plexiglas; the channel beds were formed by sand having $D_{50} = 2.2\,mm$. The bed surface was scraped so as to have along the channel centerline the desired slope S_c; the bed slope in radial direction was zero. The grains of the uppermost layers were then immobilized by spraying the bed surface with a (50%) diluted varnish. The flow rate Q was kept constant throughout the duration of each run (steady flow). The free surface slope was adjusted by means of a tailgate until the flow depth h at the centerline of the four consecutive crossover-sections (sections 1_1, 1_2, 1_3, and 1_4 in Figure 8 later on) became identical.

The pertinent parameters characterizing the plan geometry and hydraulic conditions in each channel are summarized in Table 1. Here $h_{av} =$ channel-averaged flow depth, $S_c =$ bed slope along the channel centerline, $u_{av} =$ channel-averaged flow velocity ($=Q/(Bh_{av})$). Table 1 also displays the values of the following channel-averaged quantities: $v_* =$ shear velocity, $c_{av} =$ dimensionless (Chézy) resistance factor, $B/h_{av} =$ width-to-depth ratio, $Re =$ flow Reynolds number, $Fr =$ Froude number, and $Re_* =$ roughness Reynolds number. The values of Fr and Re_* in Table 1, which fall in the ranges $0.271 < Fr < 0.363$ and $71 < Re_* < 78$, indicate that the flow was subcritical and rough turbulent in all experimental runs. The values of B/h_{av} and c_{av} were similar in all runs: $B/h_{av} \approx 13$; $c_{av} \approx 10$.

The effective (or measurement) region in each channel consisted of three consecutive meander loops Λ_1, Λ_2, and Λ_3, as shown in Figure 8. In each loop $\Lambda_i (i = 1, 2, 3)$, the values of $\overline{u}$, h and $\overline{\omega}$ were measured in eight equally spaced sections 1_i, 2_i, …., 8_i. In each of these "l_c-sections", $\overline{u}$ and h were measured, with the aid of a traversing mechanism, at several points along the cross-section; $\overline{\omega}$ was measured only at the centreline (i.e. only $\overline{\omega}_c$ was measured). For complete

Copyright © 2006 Taylor & Francis Group plc, London, UK

details on equipment and measurement techniques, see da Silva 1995 and Tape 2001.

The value of η_* at each l_c-section was calculated from the measured values of $\overline{u}$ and h (at that l_c-section).

4.2 *Experimental results*

(i) The distribution of the convergence-divergence flow zones in flow plan can be revealed with the aid of the "$\overline{\omega}_c$-curve", which indicates how the deviation angle $\overline{\omega}_c$ (at the channel centerline) varies along ξ_c. On the other hand, these zones can be revealed also by means of the streamline s_*, i.e. by means of the function $\eta_* = \varphi_{\eta_*}(\xi_c)$, where $\eta_* = n_*/B$ is the (positive or negative) lateral dimensionless deviation of s_* from the centerline ξ_c. In the following, the plan distribution of convergence-divergence zones of the experimental meandering flows will be revealed by determining both, their η_*- and $\overline{\omega}_c$-curves.

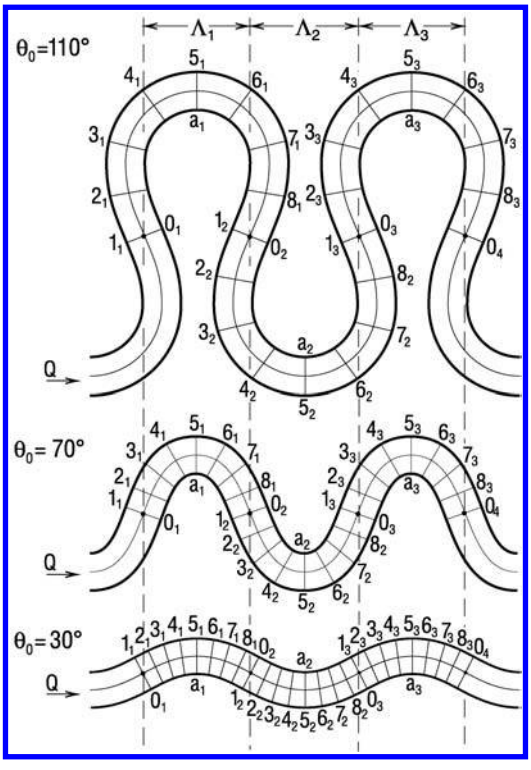


Figure 8. Schematical representation of the experimental channels having $\theta_0 = 30°$, 70° and 110°.

Before proceeding to the presentation and discussion of the results of the measurements, it may be useful to consider first the relation between the η_*- and $\overline{\omega}_c$-curves. For this purpose, consider the behaviour of the streamline s_* and of $\overline{\omega}$ for the cases of "small" and "large" θ_0 (see Figures 5a and b). Clearly, at the cross-sections (l_c-sections or ξ_c-sections) where $\eta_* = n_*/B = 0$, then $\overline{\omega}_c$ is either max or min, while at the sections where η_* is max or min, then $\overline{\omega}_c = 0$. It follows that, for any given θ_0, the curves representing the variation of the normalized $\overline{\omega}_c/(\overline{\omega}_c)_{\max}$ and $\eta_*/(\eta_*)_{\max}$ along ξ_c must be expected to be two (likely similar) sinusoidal curves separated from each other by the horizontal distance $\Delta\xi_c = 1/4$, the $\overline{\omega}_c/(\overline{\omega}_c)_{\max}$-curve always lying to the left of the $\eta_*(\eta_*)_{\max}$-curve.

(ii) Figures 9a to e show the plots of the (normalized) measured $\overline{\omega}_c$-data versus ξ_c and η_*-data versus ξ_c^* ($= \xi_c - 1/4$) for the channels having $\theta_0 = 30°$, 50°, 70°, 90° and 110°, respectively. The values of $\eta_*/(\eta_*)_{\max}$ are plotted versus ξ_c^*, rather than versus ξ_c, so that the $\overline{\omega}_c$- and η_*-point patterns overlap (see paragraph (i) above).

The solid line in each of Figure 9a to e is the best visual "sine-like" fit to the point-pattern formed by both, the plot of measured $\overline{\omega}_c/(\overline{\omega}_c)_{\max}$ versus ξ_c and $\eta_*/(\eta_*)_{\max}$ versusξ_c^*. (The utilization of one single "sine-like" curve to fit the two data sets in each of Figure 9a to e is justified on the basis of paragraph (i).)

(iii) For the sake of clarity, in this paragraph we will focus exclusively on the $\overline{\omega}_c/(\overline{\omega}_c)_{\max}$-curves. However, a discussion similar to the one below could equally well be carried out on the basis of the $\eta_*/(\eta_*)_{\max}$-curves.

The solid lines in Figures 9 represent, for the present experimental conditions, the distribution of $\overline{\omega}_c/(\overline{\omega}_c)_{\max}$ along three consecutive [CD]'s. The

Table 1. Summary of experimental conditions.

Channel	σ	Q (l/s)	h_{av} (cm)	S_c	u_{av} (m/s)	v_* (m/s)	c_{av}	B/h_{av}	Re	Fr	Re$_*$
30°-channel*	1.07	2.10	3.20	1/1000	0.164	0.0177	9.3	12.5	5250	0.293	78
50°-channel**	1.22	2.53	3.14	1/1000	0.201	0.0178	11.3	12.7	6325	0.363	78
70°-channel**	1.51	1.84	3.08	1/1000	0.149	0.0174	8.6	13.0	4600	0.271	78
90°-channel**	2.12	2.21	3.05	1/1000	0.181	0.0173	10.5	13.1	5525	0.331	76
110°-channel*	3.70	2.01	3.00	1/1120	0.167	0.0162	10.3	13.3	5025	0.309	71

(*) da Silva 1995; (**) da Silva et al. 2001

Copyright © 2006 Taylor & Francis Group plc, London, UK

occurrence of $\overline{\omega}_c = 0$ and thus $\overline{\omega}_c/(\overline{\omega}_c)_{\max} = 0$ signify simultaneously the end of one [CD], and the beginning of a new one. More specifically, a transition from $\overline{\omega} < 0$ to $\overline{\omega} > 0$, say, indicates a transition from a $L/2$-long *convergence-divergence* zone to a $L/2$-long *divergence-convergence* zone. In these figures, ξ_{c0} is the value of ξ_c where the first transition from $\overline{\omega} < 0$ to $\overline{\omega} > 0$ occurs.

Consider first Figure 9a, which corresponds to $\theta_0 = 30°$. In this Figure, $\overline{\omega}_c$ maintains its (positive or negative) sign throughout [CD]'s whose upstream- and downstream-ends are slightly upstream of two consecutive apex-sections (a_i and a_{i+1}, say). In particular, $\overline{\omega} > 0$ nearly between a_1 and a_2. In Figure 9e, which corresponds to $\theta_0 = 110°$, $\overline{\omega}_c$ maintains its (positive or negative) sign throughout flow regions of the length $L/2$ whose upstream- and downstream-ends are slightly downstream of two consecutive crossover-sections (O_i andO_{i+1}, say). In particular, $\overline{\omega} > 0$ nearly between O_1 and O_2. In Figures 9b to d, which correspond to $\theta_0 = 50°$, 70° and 90°, respectively, $\overline{\omega}_c$ maintains its sign in $L/2$-long flow regions situated somewhere between those for $\theta_0 = 30°$ and $\theta_0 = 110°$, with the $\overline{\omega}_c$-curves clearly shifting more and more to the left as θ_0 increases (note from Figures 9a to e how ξ_{c0} decreases as θ_0 increases).

The gradual shifting-to-the-left of the $\overline{\omega}_c$-curves observed in Figures 9a to e is summarized in the conceptual Figure 10. It is postulated that the upstream- and downstream-ends of the decelerated region at the inner bank 1 (defined as shown in Figure 3) coincide *exactly* with the apex-sections a_i and a_{i+1} in the limit $\theta_0 \to 0$ ($\sigma \to 1$); and that the upstream- and downstream-ends of the decelerated region (at the bank 1) coincide *exactly* with the crossover-sections O_i and O_{i+1} when $\theta_0 \to 138°$ ($\sigma \to \infty$). Thus, in Figure 10, the curves C_0 and C_{138} are the limiting curves corresponding to $\theta_0 = 0$ and $\theta_0 = 138°$. [It should be noticed that the maximum possible value of θ_0 is $\theta_0 \approx 138° = 2.41$ rad, which corresponds to $J_0(\theta_0) = 0$ and $L, \sigma \to \infty$ (see Eq. (2)). However, in practice, this can never occur, for when θ_0 reaches the value $\approx 126° = 2.20$ rad ($\sigma \approx 8.5$), the meander loops come into contact with each other and the meandering pattern is destroyed.]

(iv) Consider now two consecutive meander loops $O_iO_{i+1}O_{i+2}$ (where O_i is a crossover-section as shown in Fig. 1), and let L be the [CD] within these two loops where $\overline{\omega}$ is positive, say (and thus

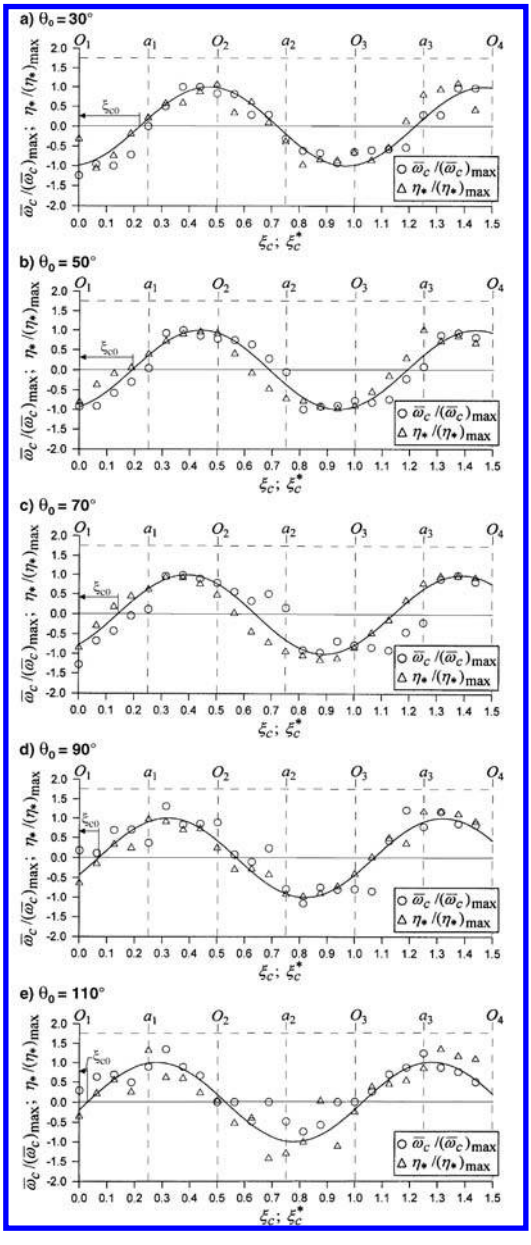


Figure 9. Plots of measured $\overline{\omega}_c/(\overline{\omega}_c)_{\max}$ versus ξ_c and $\eta_*/(\eta_*)_{\max}$ versus ξ_c^* ($= \xi_c - 1/4$).

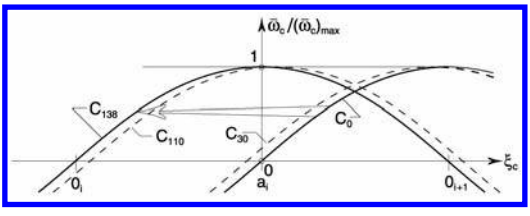


Figure 10. $\overline{\omega}_c/(\overline{\omega}_c)_{\max}$-curves corresponding to different values of θ_0 (e.g. C_0 corresponds to $\theta_0 = 0$, etc.).

Copyright © 2006 Taylor & Francis Group plc, London, UK

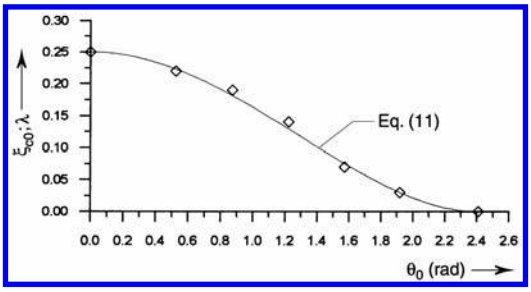


Figure 11. Plot of $(\xi_c)_0$ and λ versus θ_0.

where the flow diverges from bank 1 and converges to bank 2 (banks 1 and 2 being as defined in Figure 2)). It should be clear that the gradual shifting-to-the-left of the $\overline{\omega}_c$-curves described above implies that the location of L in the flow plan gradually shifts upstream as θ_0 increases. Observe that ξ_{c0} is but the (normalized by L) longitudinal coordinate of the ξ_c-section coinciding with the upstream-end of L. From Figures 9 and 10, it follows that ξ_{c0} gradually decreases from 0.25 to 0 as θ_0 increases from 0° to 138°. [It should be noted that from the knowledge of ξ_{c0} alone, it is possible to infer the distribution in plan of flow convergence-divergence zones of flow throughout the entire flow domain (the entire length of the channel). For the aforementioned [CD] where $\overline{\omega} > 0$ (region L) is preceded and followed by [CD]'s where $\overline{\omega} < 0$, which in turn are preceded and followed by [CD]'s where $\overline{\omega} > 0$, etc.).]

(v) The $(\xi_c)_0$-values supplied by the diagrams in Figures 10a to e are plotted versus θ_0 in Figure 11. Since in the limits $\theta_0 \to 0$ and $\theta_0 \to 138°$, the value of $(\xi_c)_0$ is expected to approach 0.25 and 0, respectively, these values of $(\xi_c)_0$ are also included in Fig. 11.

The resulting point-pattern is well approximated by the fourth degree polynomial

$$(\xi_c)_0 = 0.0033\theta_0^4 + 0.0198\theta_0^3 - 0.1100\theta_0^2 + 0.25 \ , \qquad (11)$$

where θ_0 is in radians.

Using dimensional analysis, Yalin & da Silva 2001, pp. 134 to 136, have shown that the convective nature of meandering flows must be expected to depend on θ_0, B/h_{av} and c_{av}. This implies that $(\xi_c)_0$ – and thus the distribution of [CD]'s in flow plan – is a function of three variables: $(\xi_c)_0 = \varphi(\theta_0, B/h_{av}, c_{av})$. The solid line in Figure 11 represents the variation of $(\xi_c)_0$ with θ_0 for specified B/h_{av} and c_{av} (namely $c_{av} \approx 10$ and $B/h_{av} \approx 13$ of the present experiments). Future research involving the systematic variation of B/h_{av} and c_{av} for specified values of θ_0, and directed towards the determination of the function $(\xi_c)_0 = \varphi(\theta_0, B/h_{av}, c_{av})$ would be worthwhile. In particular, it would be relevant to establish the extent to which variations in B/h_{av} and c_{av} lead to deviations form the solid line in Fig. 11.

(vi) Within a meander loop $O_i a_i O_{i+1}$, let λ be the dimensionless coordinate, measured with regard to the apex-section a_i, of the ξ_c-section where maximum erosion-deposition must be expected to occur (erosion at the outer bank, deposition at the inner bank). Since the [CD]'s of the vertically-averaged initial flow are approximately in coincidence with the [ED]'s of the developed bed, the graph of $(\xi_c)_0$ versus θ_0 is, at the same time, the graph of λ versus θ_0 (which explains why in Fig. 11, both $(\xi_c)_0$ and λ are used as ordinate). But this means that, for the same remaining conditions, the location of "deeps" and "hills" continuously moves upstream from the crossover O_{i+1} to the apex a_i as θ_0 increases from "small" to "large". The study on the location of erosion-deposition zones in da Silva and El-Tahawy 2006 (paper in these Proceedings) confirms that this is indeed the case.

5 CONCLUDING REMARKS

The approximate coincidence between the location of the convergence-divergence zones of the initial flow (over the flat (moveable) bed surface at $t = 0$) and the location of the erosion-deposition zones of the developed (equilibrium) bed (at $t = T$) is explained on the basis of the sediment transport continuity equation. It is concluded that the "information" needed for a flow to (subsequently) generate its deformed bed surface at $t = T$ is already locked in the convective structure of the (vertically-averaged) meandering flow at its initial stage at $t = 0$ (when the bed is still flat).

It follows that the nature of bed topography can be inferred from the structure of the initial flow. In particular, the "property" ξ_{c0} of the initial-flow can be used as a (rough) estimate of the dimensionless coordinate λ, measured with regard to the apex-section a_i, of the ξ_c-section where maximum erosion-deposition must be expected to occur (erosion at the outer bank, deposition at the inner bank).

ACKNOWLEDGMENTS

This research was supported by the Natural Sciences and Engineering Research Council of Canada (NSERC) through a Discovery Grant provided to the first author. The authors thank William D. Tape, M.Sc. candidate, who carried out some of the measurements used in this paper, and Tarek El-Tahawy, Ph.D. candidate, who contributed to the data reduction.

Copyright © 2006 Taylor & Francis Group plc, London, UK

REFERENCES

Chang, H.H. 1983. Energy expenditure in curved open channels. *J. Hydr. Engrg.*109(7).

da Silva, A.M.F., Yalin, M.S., El-Tahawy, T., Tape, W.D. 2001. Patterns of flow in meandering channels of varying sinuosity. *Proc. XXIX IAHR Congress, Beijing, Sept. 17–21*: 251–257.

da Silva, A.M.F. 1995. *Turbulent flow in sine-generated meandering channels.* Ph.D. Thesis, Dept. of Civil Engrg., Queen's Univ., Kingston, Canada.

Hooke, R.L. 1980. Shear-stress distribution in stable channel bends. *Discussion, J. Hydr. Div., ASCE, 106(7)*.

Hooke, R.L. 1974. Distribution of sediment transport and shear stress in a meander bend. *Rept. 30, Uppsala Univ. Naturgeografiska Inst., 58*.

Jackson, R.J. 1975. Velocity-bed-form-texture patterns of meander bends in the lower Wabash River of Illinois and Indiana. *Geol. Soc. Am. Bull.*, Vol. 86, Nov.

James, C.S. 1994. Evaluation of methods for predicting bend loss in meandering channels. *J. Hydr. Engrg. 120(2)*.

Kondratiev, N., Popov, I., Snishchenko, B. 1982. *Foundations of hydromorphological theory of fluvial processes*. (In Russian) Gidrometeoizdat, Leningrad.

Langbein, W.B., Leopold, L.B. 1966. River meanders – theory of minimum variance. *U.S. Geol. Survey Prof. Paper 422-H*.

Leliavskii, S. 1959. *An introduction to fluvial hydraulics*. Constable and Company.

Leopold, L.B., Langbein, W.B. 1966. River meanders. *Sci. Am. 214*.

Leopold, L.B., Bagnold, R.A., Wolman, M.G., Brush, L.M. Jr. 1960. Flow resistance in sinuous or irregular channels. *U.S. Geol. Survey Prof. Paper 282-D*.

Makaveyvev, N.I. 1975. *River bed and erosion in its basin*. Press of the Academy of Sciences of the USSR, Moscow.

Matthes, G.H. 1948. Mississippi River cutoffs. *Trans. ASCE, 113*.

Matthes, G.H. 1941. Basic aspects of stream meanders. *Amer. Geophys. Union*.

Nelson, J. M., Smith, J. D. 1989a. Evolution and stability of erodible channel beds. in S. Ikeda & G. Parker (eds.), *River Meandering*; *American Geophysical Union, Water Resources Monograph, 12*: 321–378.

Nelson, J. M., Smith, J. D. 1989b. Flow in meandering channels with natural topography. in S. Ikeda & G. Parker (eds.), *River Meandering*; *American Geophysical Union, Water Resources Monograph, 12*: 69–102.

Rozovskii, J.L. 1957. Flow of water in bends of open channels. *The Academy of Sciences of the Ukrainian SSR, 1957, Translated from Russian by the Israel Program for Scientific Translations, Jerusalem, 1962*.

Shimizu, Y., Itakura, T. 1989. Calculation of bed variation in alluvial channels. *J. Hydr. Engrg. 116(3)*.

Shimizu, Y. 1991. *A study on prediction of flows and bed deformation in alluvial streams*. (In Japanese) Civil Engrg. Research Inst., Hokkaido Development Bureau, Sapporo, Japan.

Smith, J.D., McLean, S.R. 1984. A model for flow in meandering streams. *Water Resources Research 20(9)*.

Struiksma, N., Olesen, K.W., Flokstra, C. De Vriend, H.J. 1985. Bed deformation in curved alluvial channels. *J. Hydr. Res. 23(1)*.

Tape, W. 2001. *Experimental investigation of flow patterns in meandering channels of moderate sinuosity*. M.A.Sc. Thesis, University of Windsor, Windsor, Canada.

Termini, D. 1996. *Evolution of a meandering channel with an initial flat bed. Theoretical and experimental study of the channel bed and the initial kinematic characteristics of flow*. (In Italian) Ph.D. Thesis, Dept. Hydraulic Engineering and Environmental Applications, University of Palermo, Italy.

Velikanov, M.A. 1955. *Dynamics of alluvial streams. Vol. II. Sediment and bed flow.* State Publishing House for Theoretical and Technical Literature, Moscow.

Whiting, P.J., Dietrich, W.E. 1993a. Experimental studies of bed topography and flow patterns in large-amplitude meanders. 1. Observations. *Water Resour. Res. 29(11)*.

Whiting, P.J., Dietrich, W.E. 1993b. Experimental studies of bed topography and flow patterns in large-amplitude meanders. 2. Mechanisms. *Water Resour. Res. 29(11)*.

Yalin, M.S., da Silva, A.M.F. 2001. *Fluvial Processes*. IAHR Monograph, IAHR, Delft, The Netherlands.

Yalin, M.S. 1992. *River Mechanics*. Pergamon Press, Oxford.

LIST OF SYMBOLS

B	flow width
c_{av}	dimensionless Chézy resistance factor ($c_{av} = u_{av}/v_*$)
C_{av}	original (dimensional) Chézy resistance factor ($C_{av} = c_{av}/\sqrt{g}$)
D_{50}	representative grain size
Fr	Froude number ($= u_{av}/\sqrt{gh_{av}}$)
g	acceleration due to gravity
h	flow depth
h_{av}	channel-averaged flow depth
$J_0(\theta_0)$	Bessel function of first kind and zero-th order (of θ_0)
k_s	granular roughness of bed surface ($k_s \approx 2D_{50}$)
L	meander length (measured along l_c)
l_c; n	longitudinal and radial coordinates of a meandering flow, respectively; $l_c = 0$ at the crossover O_i (see Figure 2)
p	porosity of bed material
Q	flow rate
q_s	specific volumetric sediment transport rate
R	curvature radius of the centerline of a meandering flow
Re	flow Reynolds number ($= u_{av}\, h_{av}/\nu$)
Re_*	roughness Reynolds number ($= v_* k_s/\nu$)
S_c	bed slope along the centreline of a meandering flow
t	time
T	development duration of the bed of a meandering stream
$\overline{u}$; $\overline{v}$	scalar projections of the vertically-averaged local flow velocity

Copyright © 2006 Taylor & Francis Group plc, London, UK

	vector in longitudinal and radial directions, respectively
U	magnitude of the flow velocity vector
u_{av}	channel-averaged flow velocity
v_*	shear velocity ($=\tau_0/\rho=\sqrt{gh_{av}S_c}$)
$\overline{v}'_\Gamma$	average radial velocity of the cross-circulatory flow directed towards inner bank
W	local displacement velocity of the meandering bed surface (in the vertical direction)
z_b	bed surface elevation
Γ	cross-circulation
η_*	value of η defining the position of the stream-line s_* at any l_c-section
θ	deflection angle of a meandering flow at any l_c (see Figure 1)
θ_0	deflection angle of a meandering flow at $l_c=0$ (see Figure 1)
Λ_M	meander wavelength
ξ_c, η	dimensionless counterparts of l_c and n, respectively ($\xi_c=l_c/L$ and $\eta=n/B$)
$(\xi_c)_0$	dimensionless longitudinal coordinate, measured with respect to the crossover O_i, of the upstream-end of a $L/2$-long convergence-divergence * flow zone where $\overline{\omega}>0$
ξ_c^*	longitudinal coordinate related to ξ_c by $\xi_c^*=\xi_c-1/4$
σ	sinuosity of a meandering flow ($\sigma=L/\Lambda_M$)
$\overline{\omega}$	deviation angle (angle between the vertically-averaged streamline s and the coordinate line l of a meandering flow) ($\overline{\omega}=\tan\ \overline{v}/\overline{u}\approx\overline{v}/\overline{u}$)
$\overline{\omega}_c$	value of $\overline{\omega}$at the centerline of a meandering flow

Subscripts:

max, min	mark the maximum and minimum values of a quantity, respectively
m	marks the value of a quantity averaged over the time interval T

Copyright © 2006 Taylor & Francis Group plc, London, UK

Gravitational effects on river morphodynamics

Simona Francalanci & Luca Solari
University of Florence, Department of Civil Engineering, Florence

Gianluca Vignoli
CISMA srl c/o BIC Suedtirol, Bolzano

ABSTRACT: In the present work an experimental study devoted to investigate the effects of transversal slopes on the bedload sediment transport and on the morphodynamic evolution of a mobile bed was carried out. The general aim of such investigation is the experimental observation of the evolution of a laterally tilted bed from the initial configuration to the final one, laterally flat, under conditions of uniform flow. The bottom topography was measured at the beginning and during the experiments for different time lengths; complementary data regarding the applied shear stresses and the particle velocity are inferred from a previous experimental activity on bedload transport over an non-erodible bed. The experimental results about the evolution of the bed were interpreted theoretically by solving numerically the 3-D governing morphodynamic problem employing the non linear theoretical model for bedload transport over sloping beds proposed by Parker, Seminara and Solari (2003). The experimental observations are compared to the results obtained from the numerical model in terms of the evolution of the bed topography, applied shear stress and sediment transport rate in longitudinal and transversal directions. In the present contribution, both experimental and numerical results are presented and discussed.

1 INTRODUCTION

The evaluation of the bedload transport on an arbitrarily sloping bed is one of the crucial aspects in any morphodynamic model that considers the evolution of the bed: when the bed is tilted in both longitudinal and transversal direction the gravity plays an important role on particle dynamics and on bedload transport (Sekine and Parker 1992; Kovacs and Parker 1994; Nino and Garcia 1994a; Nino and Garcia 1994b; Talmon et al. 1995).

This problem has been recently tackled by Parker et al. (2003) through a non-linear theoretical model which provides a vectorial description of the bedload transport on arbitrarily sloping beds at low Shields stress. The results of this model were verified by Francalanci & Solari (2005) by means of an experimental activity devoted to study the sediment motion over a plane, non-erodible, artificially roughened bed tilted longitudinally and laterally. The latter experimental observations on the non-erodible bed showed a good agreement with the theoretical model, and an interpolated equation for bedload transport was then derived by Francalanci & Solari (2006) to employ Parker et al. (2003) model, which may increase the computational costs of the morphodynamic modeling.

In the present work an experimental study devoted to investigate the effects of transversal slopes on sediment transport dynamics and on the morphodynamic evolution of a mobile bed is presented. The experimental observation of the evolution of a laterally tilted bed from the initial configuration to the final one, laterally flat, under conditions of uniform flow, was monitored and measured.

The whole experimental activity here presented was based on experiments on both non-erodible and mobile sloping bed in longitudinal and transversal direction: the experiments on the non-erodible bed revealed the bed shear stress, the particle velocity and the bedload transport rate, while the experiments with mobile bed revealed the gravitational effects on the bed evolution.

The evolution of the bed was monitored and interpreted theoretically by solving numerically the three-dimensional morphodynamic problem with the help of the sediment transport relationship inferred both from the non-linear model of Parker et al. (2003) and from the linear model of Ikeda (1982). The experimental observations are compared to the results obtained from the numerical model in terms of the evolution of bed topography, applied shear stress at the bed and sediment transport rate in longitudinal and transversal directions. This comparison suggests that the evaluation of the transversal component of the bedload transport is crucial to describe the morphodynamic evolution of the bed.

Copyright © 2006 Taylor & Francis Group plc, London, UK

2 EXPERIMENTAL SET-UP

2.1 *Experimental apparatus*

The evolution of the mobile bed was investigated in a free surface laboratory flume. The experiments were carried out in a tilting, recirculating flume, 10 m long, 0.365 m wide and 0.45 m deep, equipped for clear water flows up to 28 l/s and slope adjustment up to 5°. In order to obtain higher bed inclinations, a 2 m long 0.23 m wide plane was built inside the flume with inclination adjustable up to 15°. Due to entrance effects the length of the measuring reach was about 1 m. Water flow was supplied at one end of the flume from a centrifugal pump and the water discharge was monitored by an electromagnetic flow-meter. The sediment particles were fed at a constant discharge by means of a sediment feeder.

2.2 *Sediment material*

The employed particles satisfied the following requirements in all the range of investigated bed slopes: mobility at low Shields stress; ratio of water depth to particle size sufficiently high to allow particle saltation, even in the case of high bed slope; relatively high friction angle. The selected material was represented by steel particles with a density of 7850 kg/m^3, shaped like disks with almost uniform size of 3 mm of maximum diameter and of 0.6 mm thickness. The use of steel particles with a higher density, compared to the common fluvial sediments, allowed one to perform sediment transport experiments on a free surface laboratory flume with high local inclinations of the bed and sufficiently high water depth. The not spherical shape allowed particles disposition according to a given transversal inclination, for performing the mobile bed experiments.

2.3 *Mobile bed set-up*

The mobile bed was disposed according to a given longitudinal α and transversal φ inclination. The cross-section was constant and the flow was uniform. Two zones of fixed bed were located upstream and downstream of the mobile bed which was 5 m long. A sketch of the experimental set-up is shown in Figure 1. Along the mobile bed the bed elevation was measured in different cross-sections. The measuring cross-sections were located at a distance of 50 cm at the beginning of the mobile bed and of 25 cm closer to the end, where the equilibrium configuration was reached, as shown in Figure 2.

For each cross-section, the bed elevation was measured using a pointgage in 7 verticals, spaced about 3 cm.

3 EXPERIMENTAL PROCEDURE

At the beginning of each experiment, the mobile bed was arranged according to the given longitudinal and transversal inclination and the initial configuration of the bed elevation was measured.

After the preparation, the experiments were performed according to the following procedure. First the flow discharge was adjusted to the assigned value: during this transient period the bed was not allowed to evolve. Then the experiment was started and the evolution of the bottom topography was observed, using a video recorder. Different experiments with different time length were performed in order to measure the bed elevation at the end of each run, in dried condition. The transient period at the end of the run was such that it did not influence the bed configuration. The bottom topography was measured at the beginning and at the end of the experiments for different time lengths; additional data regarding the applied shear stresses and the particle velocity are inferred from the previous experimental activity of bedload transport on non erodible bed.

4 MOBILE BED EXPERIMENTS

The initial experimental conditions for the performed runs are reported in Tab. 1, in particular the longitudinal inclination of the bed is from 1.72° to 10° while the transversal inclination is 5° and 10°. In order to relate the initial conditions of the mobile bed with the complete set of measurements collected during the non-erodible bed experiments, the initial conditions for the present experiments were selected among the whole set of configurations for which the experiments on the non-erodible bed were performed. In this way the quantities bed shear stress, flow velocity profile, particle velocity and bedload transport rate were known at the beginning of each experiment. The experiments Run 2b and Run 4 were performed with a shorter mobile bed reach, 1.5 m instead of 5 m.

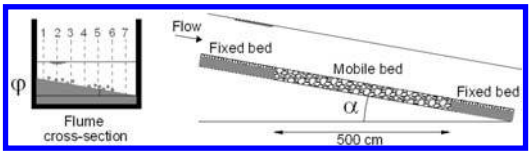


Figure 1. Sketch of the set-up for the mobile bed experiments.

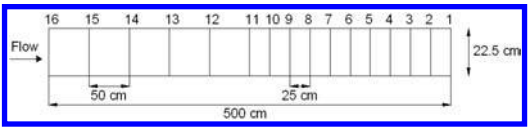


Figure 2. Plan view of the mobile bed, the numbers specify measuring cross-section locations.

Copyright © 2006 Taylor & Francis Group plc, London, UK

Moreover, the all cross-sections needed to be invaded by the flow as phenomena such as bank collapse were not addressed in this study.

To underline the equilibrium configuration that the cross-section is able to reach, the bottom evolution of Run 2a is shown here (Fig. 3). After 30" an erosion phenomenon can be observed at the beginning of the mobile bed due to the transition from fixed to mobile bed, and the laterally tilted bed started to evolve from the initial configuration. After 60" the mobile bed is close to the equilibrium configuration, which can be observed for the bottom profile measured after 210": the erosion phenomenon at the beginning of the mobile bed is increased due to the difficulties on maintaining the sediment feeding in equilibrium with the bedload transport capacity, while at the end of the mobile bed the equilibrium cross-section laterally flat can be observed.

The Run 1 was performed with a relative low longitudinal inclination. The initial bottom topography showed a transversal inclination. The topography of the bed was measured for 4 different time lengths. The beginning of the mobile bed was affected by a local

Table 1. Initial experimental conditions for the mobile bed experiments.

Run Code	α [°]	φ [°]	Q_w $[l/s]$	Time [″]
Run 1	1.72	10	15.4	180–270–360–540
Run 2a	5	5	5.98	30–60–210
Run 2b	5	5	7.5	30–180
Run 3	5	10	7.02	30–60–150–210
Run 4	10	5	4.5	20–40–72

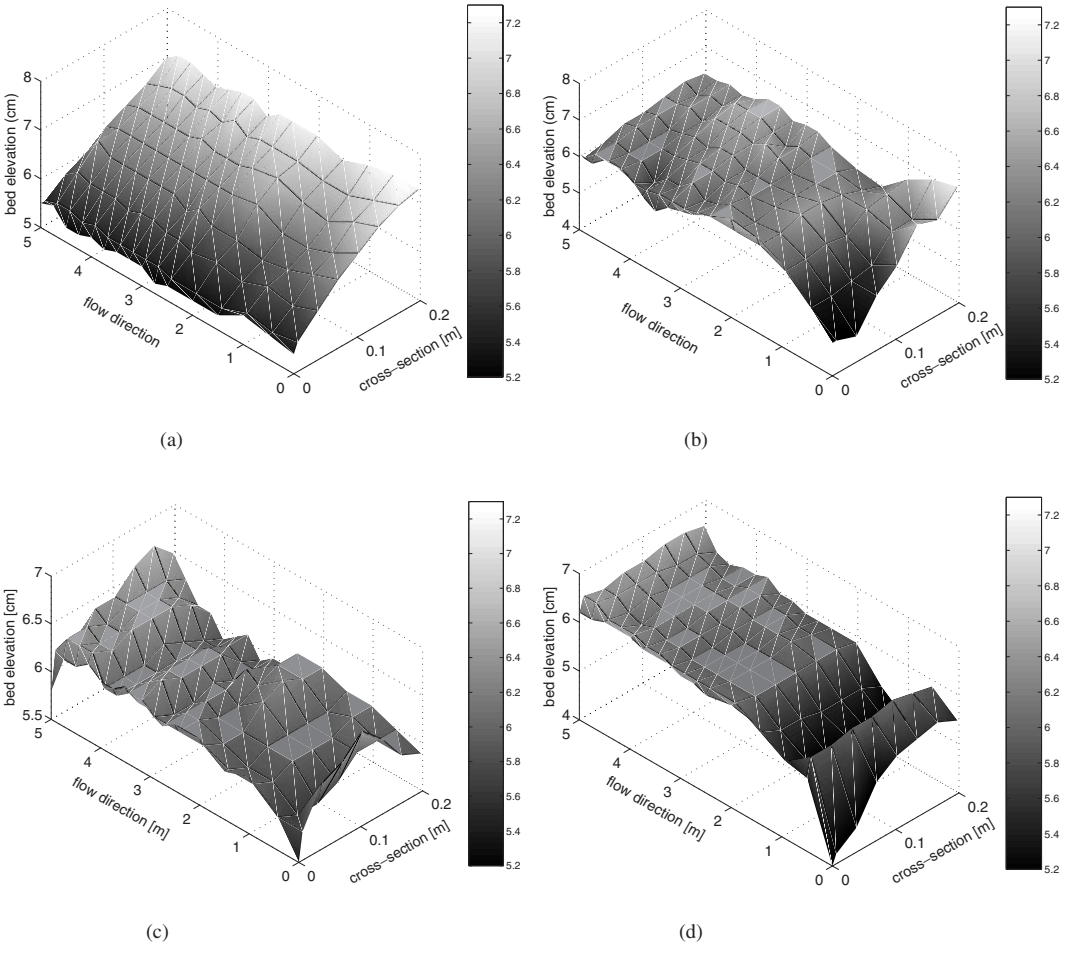


Figure 3. Configuration of the bed elevation for experimental Run 2a. (a) Initial contiguration; (b) Contiguration after 30"; (c) Contiguration after 60"; (d) Contiguration after 210".

Copyright © 2006 Taylor & Francis Group plc, London, UK

erosion phenomenon, but the equilibrium mobile bed was achieved at the end of the reach. The measured cross-sections are averaged at the end of the measuring reach. The mobile bed reached the transversal equilibrium configuration after about 540", as shown in Figure 4(a).

The Run 2 was performed with two different flow discharges. The experimental results of the Run 2a are reported in Figure 4(b). The Run 2b showed a faster evolution of the mobile bed because the intensity of the bedload transport was increased along the cross-section (Fig. 4(c)).

The Run 3 was performed with a higher transversal inclination than Run 2: the mobile bed reached the equilibrium configuration and then a slow average erosion phenomenon is observed in the equilibrium cross-section, due to the changing of the bedload discharge according to the flow (Fig. 4(d)).

The Run 4 was performed with a high longitudinal inclination ($\alpha = 10°$), and the mobile bed reach was 1.5 m long. In this experiment the time evolution of the observed phenomenon was rapidly changing and hence the bottom topography was difficult to control and monitorate. The final profiles along the cross-section are shown in Figure 4(e).

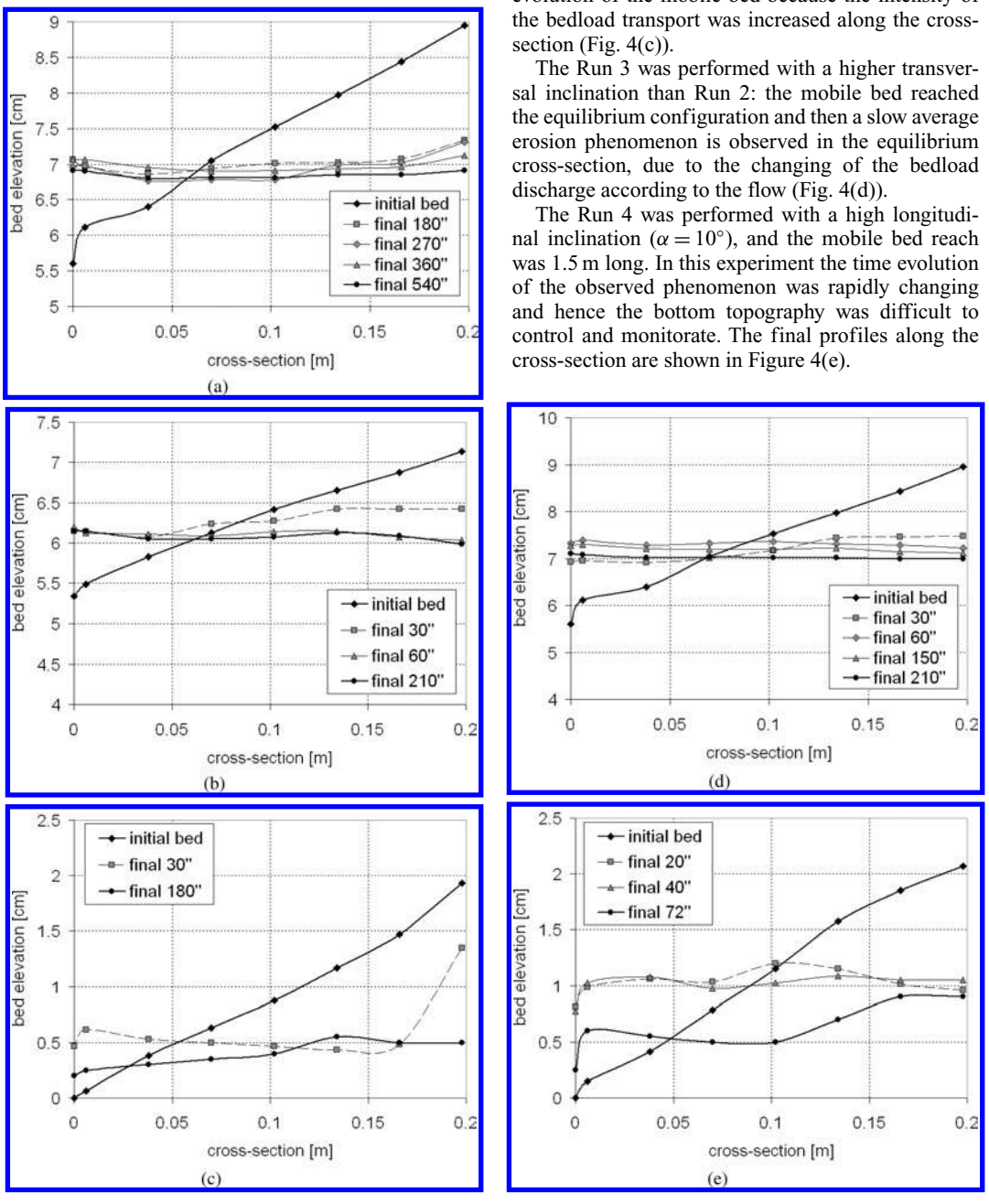


Figure 4. Evolution of the bed elevation within the cross-section for the experimental runs. (a) Run 1; (b) Run 2a; (c) Run 2b; (d) Run 3; (e) Run 4.

Copyright © 2006 Taylor & Francis Group plc, London, UK

5 EVOLUTION OF A LATERALLY TILTED MOBILE BED

The evolution of the bed was monitored and interpreted theoretically by solving the three-dimensional morphodynamic problem with the help of the sediment transport relationship proposed by Francalanci & Solari (2006), derived by the theoretical model of Parker et al. (2003) and verified by means of the experimental observations on a non-erodible sloping bed. The experimental observations on the mobile bed are here compared to the results obtained from the numerical model that employs the verified theoretical model, in terms of the evolution of bed topography, applied shear stress and sediment transport rate in longitudinal and transversal directions.

5.1 *3D numerical model*

The numerical model adopted in the present analysis is the one proposed by Vignoli (2004) suitable modified in order to employ Parker et al. (2003) non linear model. The model is here briefly summarized. The model considers a straight channel with vertical banks, characterized by cohesionless bed and constant width $2B^*$.

The dimensional variables are made dimensionless adopting suitable scales: the channel half width B^* to scale the planimetric coordinates; a reference flow depth H_o^* to scale the vertical coordinate z^*, the local free surface elevation h^*, bed elevation η^* and flow depth H^*, a reference flow velocity U_o^* to scale the velocity components. Furthermore a characteristic time scale $T_o^* = B^*/U_o^*$ is introduced. The reference values U_o^* and H_o^* can be readily defined in the river case as the depth averaged velocity and depth of the uniform flow, for given discharge, bed slope and sediment size. In dimensionless form such reference state is completely determined once the following dimensionless parameters are given:

$$\beta = \frac{B^*}{H_o^*} \tag{1}$$

$$D_s = \frac{D^*}{H_o^*} \tag{2}$$

$$\tau_{*o} = \frac{(U_o^*)^2 C_{fo}}{(s_g - 1)\, g D^*} \tag{3}$$

$$R_p = \frac{\sqrt{(s_g - 1)\, g D^{*3}}}{\nu} \tag{4}$$

where D^* is sediment diameter, s_g is the specific density of sediment, ν is the kinematic viscosity of water, and C_{fo} is the friction coefficient of the reference uniform flow.

In dimensionless form, and keeping only significant turbulent flux, the Reynolds equations along the longitudinal and transversal direction, the flow continuity equation and the sediment continuity equation read:

$$\frac{\partial U}{\partial t} + U\frac{\partial U}{\partial x} + V\frac{\partial U}{\partial y} + \beta W\frac{\partial U}{\partial z} - \\ -\gamma\frac{\partial}{\partial z}\left(\nu_T\frac{\partial U}{\partial z}\right) + \frac{1}{F_o^2}\frac{\partial h}{\partial x} + \frac{i_F}{F_o^2} = 0 \tag{5}$$

$$\frac{\partial V}{\partial t} + U\frac{\partial V}{\partial x} + V\frac{\partial V}{\partial y} + \beta W\frac{\partial V}{\partial z} - \\ -\gamma\frac{\partial}{\partial z}\left(\nu_T\frac{\partial V}{\partial z}\right) + \frac{1}{F_o^2}\frac{\partial h}{\partial y} = 0 \tag{6}$$

$$\frac{\partial U}{\partial x} + \frac{\partial V}{\partial y} + \beta\frac{\partial W}{\partial z} = 0 \tag{7}$$

$$(1 - \lambda_p)\frac{\partial \eta}{\partial t} + Q_o\left(\frac{\partial Q_{bx}}{\partial x} + \frac{\partial Q_{by}}{\partial y}\right) = 0 \tag{8}$$

where (U, V, W) denote the three-dimensional velocity field and F_o is the Froude number of the reference flow.

The model yields the following boundary conditions for the flow field: the dynamic condition is satisfied imposing the vanishing stress at the free surface, which yields the zero vertical derivatives of longitudinal and transversal flow velocity; the kinematic conditions at the bed and at the free surface are automatically satisfied provided zero values of the vertical velocity and imposing no slip at the bottom, which yields zero velocity at the bed.

Closure assumption for the eddy viscosity ν_T is introduced assuming that the slowing varying character of the flow field both in space and in time leads to a sequence of equilibrium states. The eddy viscosity is evaluated using an algebraic approach, namely involving the local values of the shear velocity and of the flow depth; for the vertical distribution of the eddy viscosity we adopt the formulation given by Dean (1974).

A closure for the bedload transport need to be introduced. In the original implementation of the model, bedload transport $\mathbf{Q}_b$ is quantified in terms of the local and instantaneous value of the Shields stress, the intensity of bedload transport is evaluated using Parker (1990) formula. The gravitational effects on bedload transport are taken into account through a simplified semi-empirical approach which is formally justified only for small values of local bed slopes (Ikeda 1982;

Copyright © 2006 Taylor & Francis Group plc, London, UK

Kovacs and Parker 1994):

$$Q_{bx} = \frac{|\mathbf{Q}_b|}{|\boldsymbol{\tau}|}\left[\tau_x cos\left(\psi\right) - \tau_y sin\left(\psi\right)\right] \quad (9)$$

$$Q_{by} = \frac{|\mathbf{Q}_b|}{|\boldsymbol{\tau}|}\left[\tau_x sin\left(\psi\right) + \tau_y cos\left(\psi\right)\right] \quad (10)$$

$$tan\left(\psi\right) = -\frac{r}{\beta\sqrt{\tau_*}}\frac{\partial\eta}{\partial n} \quad (11)$$

where s is directed as the local bed shear vector, while n is orthogonal to the above direction, and ψ is the deviation angle of the bedload transport vector from the applied bed shear stress. Finally bedload intensity $|\mathbf{Q}_b|$ is assumed to be a function of $(\tau_* - \tau_{*c})$, with

$$\tau_{*c} = \left(\tau_{*co} + \frac{r_1}{\beta}\frac{\partial\eta}{\partial s}\right)\sqrt{1 - \frac{\left(\partial\eta/\partial n\right)^2}{tan^2\left(\phi\right)}} \quad (12)$$

According to experimental observations the empirical constants r and r_1 fall in the range (0.3–0.6) and (0.1–0.2), respectively. The bedload transport equation has been modified according to the bedload transport equations on arbitrarily sloping bed proposed by Francalanci and Solari (2006), to employ Parker et al. (2003) formulation.

The proposed equation has a simple polynomial expression of the bedload transport rate as a function of the applied Shields stress:

$$|Q_b| = A_q\left(\alpha,\varphi\right)\cdot\left(\frac{\tau_*}{\tau_{*co}}\right)^2 + B_q\left(\alpha,\varphi\right)\cdot\left(\frac{\tau_*}{\tau_{*co}}\right) + \\ + C_q\left(\alpha,\varphi\right) \quad (13)$$

while the direction of the bedload transport with respect to the direction of the applied bed shear stress is evaluated with the following expression:

$$\psi = A_\psi\left(\alpha,\varphi\right)\cdot\left(\frac{\tau_*}{\tau_{*co}}\right)^{B_\psi(\alpha,\varphi)} \quad (14)$$

where A_q, B_q, C_q, A_ψ and B_ψ are polynomial functions of α and φ.

The model follows the numerical semi-implicit procedure proposed by Casulli and Cattani (1994), according to which the non-linear terms appearing in the momentum equations are discretized using a Lagrangian approach, while the pressure term and the viscous term are solved implicitly; the approach has been modified to account for the no slip condition at the bed. In the present model a suitable logarithmic vertical coordinate is introduced such that the grid density decreases from the bed to the free surface: the logarithmic vertical coordinate minimizes the numerical truncation errors and achieves a better accuracy with the same number of grid points.

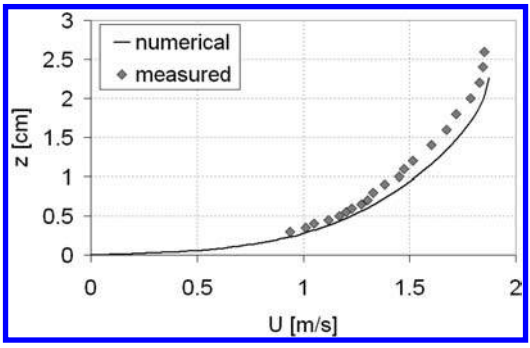


Figure 5. Fitting of the simulated flow velocity profile with the measured one, taken at a distance of 5 cm from the wall, Run 2a.

The solutions for the flow field are obtained using finite-differences technique. The solution for the bed elevation is evaluated from Exner's equation, solved with a decoupling algorithm between the hydrodynamics and the morphodynamics. The spatial mesh adopted in the numerical solution is a staggered grid and consists of rectangular boxes. The resulting numerical scheme seems sufficiently accurate and efficient to represent adequately the flow on fluvial system and their role in the development of bed topography.

5.2 *Comparison of experimental and numerical results*

The measurements of the mobile bed profiles are here compared to the results of the three-dimensional numerical model.

The numerical model simulated the experimental conditions in the flume, reproducing the measured quantities, such as the bed shear stress and the bedload transport intensity. The roughness coefficient was set such that the velocity flow profiles measured in the experimental activity on the non-erodible fixed bed were fitted to the profiles numerically simulated at the beginning of the run. The measured flow velocity profile compared to the numerically estimated ones is shown in Figure 5, in the experimental conditions of Run 2a; a similar fit was obtained for the other experimental conditions.

The measured profiles of the bed elevation are compared to the numerically computed ones, for different time length of the experiments, for Run 2a in Figure 6. The time evolution of the phenomenon is well reproduced, as well as the final equilibrium configuration in the cross-section. The numerical model is able to reproduce the equilibrium bedload transport, which is changing during the experiment; vice versa during the experimental Run the fed bedload discharge was adjusted to the changing stresses along the cross-section: this induced a net erosion phenomenon of the

Copyright © 2006 Taylor & Francis Group plc, London, UK

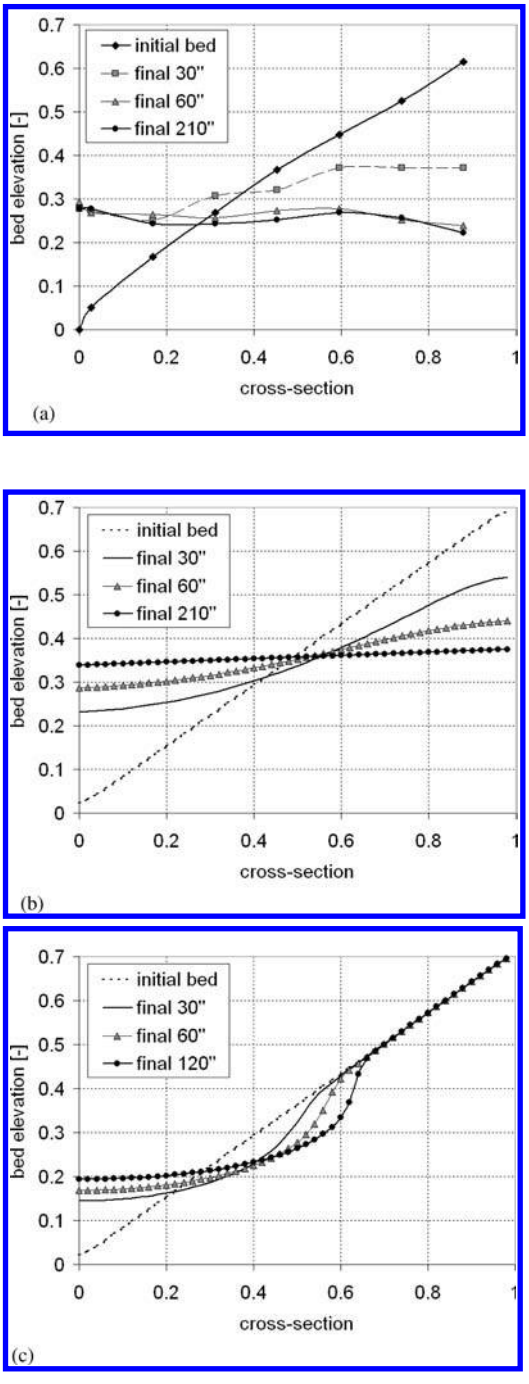


Figure 6. Comparison between the measured dimensionless bed elevation profiles and the numerically computed ones (Run 2a). (a) Measured bed profiles; (b) Numerical bed profiles employing the non-linear bed load transport of Parker et al. (2003). (c) Numerical bed profiles employing a linear bedload transport of Ikeda (1982).

average elevation within the cross-section. However, this phenomenon did not affect the transversal evolution of the bottom topography which reached a flat configuration.

The numerical results obtained employing Parker et al. (2003) formulation are compared with the results obtained employing Ikeda (1982) formulation: the comparison of the bed profiles reveals a different time and spatial evolution of the phenomenon, due to the under-estimation of the transversal bedload transport and of the bedload intensity estimated with the Ikeda (1982) formulation. In particular, the under-estimation of the lateral bedload transport with the linear formulation did not allow the bed to evolve in the upper part of the cross-section, while the flattening process is limited to a narrow region of the cross-section.

6 CONCLUSIONS

In the present work the experimental observations of the evolution of a mobile bed from the initial arbitrarily sloping configuration to the final laterally flat equilibrium configuration are presented and discussed.

The measured bed profiles are compared with the results obtained from a three-dimensional numerical model employing both the linear (Ikeda 1982) and the nonlinear formulation (Parker et al. 2003) to evaluate the bedload transport over an arbitrarily sloping bed. Results suggest that the linear formulation lead to a great underestimation of the lateral bedload transport which prevents the model to adequately describe the evolution of the bed whereas in the case of the non linear formulation the time and spatial morphodynamic evolution of the bed is well reproduced.

ACKNOWLEDGEMENTS

The authors are grateful to Prof E. Paris, University of Florence (Italy), for his valuable comments and suggestions. CERAFRI is acknowledged for sustaining the publication of this work.

REFERENCES

Casulli, V. and E. Cattani (1994). Stability, accuracy and efficiency of a semi-implicit method for three dimensional shallow flow. *Computers and Mathematics with Applications 27*(1), 99–112.

Dean, R. B. (1974). *Aero Rep.,* volume 74–11, *Imperial College, London*.

Francalanci, S. and L. Solari (2005). Gravitational effects on bedload transport at low Shields stress: experimental observations. *Water Res. Research.*, submitted.

Francalanci, S. and L. Solari (2006). Bedload transport equation on arbitrarily sloping beds. *J. Hydraul. Eng.*, submitted.

Copyright © 2006 Taylor & Francis Group plc, London, UK

Ikeda, S. (1982). Incipient motion of sand particles on side slopes. *J. Hydr. Div. 108(1)*, 95–114.
Kovacs, A. and G. Parker (1994). A new vectorial bedload formulation and its application to the time evolution of straight river channel. *J. Fluid Mech. 267*, 153–183.
Nino, Y. and M. Garcia (1994a). Gravel saltation, 1. Experiments. *Water Resour. Res. 30(6)*, 1907–1914.
Nino, Y. and M. Garcia (1994b). Gravel saltation, 2. Modeling. *Water Resour. Res. 30(6)*, 1915–1924.
Parker, G. (1990). Surface-based bedload transport relation for gravel rivers. *J. Hydr. Res. 20(4)*, 417–436.
Parker, G., G. Seminara, and L. Solari (2003). Bedload at low shields stress on arbitrarily sloping beds: alternative entrainment formulation. *Water Resour. Res. 39(7)*, 1183, doi:10.1029/2001WR001253.
Sekine, M. and G. Parker (1992). Bedload transport on transverse slopes. *J. Hydraul. Eng. 118(4)*, 513–535.
Talmon, A. M., M. C. L. M. Van Mierlo, and N. Struiskma (1995). Laboratory measurements of the direction of sediment transport on transverse alluvial-bed slopes. *J. Hydraul. Res. 33*, 495–517.
Vignoli, G. (2004). Modelling the morphodynamics of tidal channels. *Ph.D. Thesis in Environmental Engineering University of Trento*.

Copyright © 2006 Taylor & Francis Group plc, London, UK

Entropy and river meander planform

A.J. Teuling[a], S.J. van Andel[a*], P.A. Troch[a**] & A.J.F. Hoitink[a,b]
[a]*Hydrology and Quantitative Water Management Group, Wageningen University*
[b]*Institute for Marine and Atmospheric Research Utrecht / IMAU, Utrecht University*
[a*]*Now at the Department of Hydroinformatics and Knowledge Management, UNESCO-IHE Institute for Water Education*
[a**]*Now at the Department of Hydrology and Water Resources, University of Arizona*

ABSTRACT: Equilibrium meander bends shift downstream with a constant speed while maintaining a coherent form. Based on a dynamical description of flow in alluvial river bends and a kinematic description of continuous bank erosion, Parker et al. (1983) derived a class of equilibrium meander planform shapes known as Kinoshita curves. These equilibria were found to be unstable, which has lead to the common idealized view that meanders alternately elongate by gradual bend erosion and shorten due to cut-off, and do not reach a true equilibrium. It is herein argued that the extremely slow rate of change of near-equilibrium meanders in conjunction with neglected aspects such as time variation of the threshold of sediment motion can be the reason why most undisturbed meanders found in nature are in fact near-equilibrium. It is therefore worthwhile to further examine and describe equilibrium meanders, which is the subject of the present study. Starting from the hypothesis that for equilibrium meanders the variance of entropy production is minimized, most probable planform parameter values are derived that determine how fattening and skewing (parameterized by c_f and c_s, respectively) of an equilibrium meander depend on sinuosity. Sinuosity, in turn, is mainly externally controlled. It is shown how the hypothesis ofminimumvariance of entropy production practically boils down to the assumption ofminimization of channel morphology change rates, revealing the mechanistic interpretation of the theory. The validity of our hypothesis is elucidated by a comparison with twenty four meander reaches of various geographical locations, and by the fact that for arbitrary sinuosities a unique minimum for the variance of entropy production in the (c_f, c_s)-plane exists.

1 INTRODUCTION

Present-day understanding of the mechanistic evolution of river meanders is captured by idealized models derived from the shallow water equations and the continuity equation of sediment. These meander bend models go back to the work of Ikeda et al. (1981), who delineated a bend equation by coupling the flow theory of Engelund (1974) for river bends to a kinematic treatment of bank erosion. Subsequent progress was due to Johannesson and Parker (1989), who added the effect of convective transport of primary flow momentum by the secondary flow, as formulated by Kalkwijk and De Vriend (1980). Zolezzi and Seminara (2001) further increased the level of detail of modelling the flow in their meander bend model, by extending the flow decomposition proposed by Kalkwijk and De Vriend (1980) with the aim to preserve the memory of the centrifugally induced secondary flow. Recently, Camporeale et al. (2005) performed long-term simulations with the three models mentioned above, for various river parameter configurations. They showed that each of the three models predict the same long-term statistics for geometrical planform parameters, indicating that the bend model by Ikeda et al. (1981) already contains all the necessary ingredients to describe the long-term dynamics.

In the research line described above, the existence of an equilibrium in which a meander shifts downstream with a constant speed while maintaining a coherent form was shown to exist for the model by Ikeda et al. (1981) (Parker et al. 1983), albeit an unstable equilibrium (Parker and Andrews 1986). Seminara et al. (2001) found that there are no equilibrium solutions to the model equations by Zolezzi and Seminara (2001). River meanders are hence considered to evolve towards a dynamical state, characterized by alternating phases of elongation induced by the local bend erosion and sporadic shortening caused by cutoff events. This gives an idealized view of alluvial river behavior on a millennial timescale, suggesting that neglected aspects such as discharge variation and associated variation

Copyright © 2006 Taylor & Francis Group plc, London, UK

of the threshold of sediment motion are irrelevant to the long-term behavior. Herein it is argued that it is worthwhile to elaborate on the equilibria described by Parker et al. (1983), despite their instability. Parker and Andrews (1986) showed that the rate of change of meanders near their equilibrium is markedly low, as the corresponding characteristic timescales are an order of magnitude longer than the timescales of meanders with the same parameter settings at a non-equilibrium stage. Meander bends of longer as well as smaller bend angle amplitude can evolve more than an order of magnitude faster. Considering this and the fact that slowly evolving rivers are prone to consolidate, which further retards or even halts their natural evolution by the increased threshold of incipient sediment motion, it is not surprising that many river meanders found in nature are nearequilibrium.

The equilibrium solutions admitted by the bend equation formulated by Ikeda et al. (1981) were termed Kinoshita curves, defined by:

$$\Theta(s) = \Theta_0 \cos\phi - \Theta_0^3(c_f \cos 3\phi + c_s \sin 3\phi) \qquad (1)$$

where Θ denotes the bend angle between the tangent to the curve and the downvalley x-axis, $\phi = 2\pi s/L$ with s the coordinate along the curve and L the meander length measured along the curve, and Θ_0 is the bend angle amplitude (see Fig. 1). The coefficients c_f and c_s respectively determine fattening and skewing of the equilibrium meander. The infinitesimal distances along the curve ds and in the downvalley direction dx relate as in $dx = \cos\Theta ds$. The sinuosity k, defined as the ratio of distance along the curve and downvalley distance averaged over a single wave length, proceeds from Eq. 1:

$$k = \overline{(1/\cos\Theta)} \qquad (2)$$

where the overbar denotes averaging over a wave length. Parker et al. (1983) found that for equilibrium meanders the bend angle amplitude Θ_0 is imposed by sinuosity according to:

$$k = 1 + \frac{1}{4}\Theta_0 \qquad (3)$$

Hence, for a given sinuosity, which is in turn largely controlled by valley slope (Schumm et al. 1972; Nakagawa and Scott 1984), near equilibrium meanders are parameterized by two unknown coefficients c_f and c_s.

The theory by Parker et al. (1983) indicates that c_f and c_s relate to scour, expressing the role of secondary currents, and to the Froude number, but no means was presented to evaluate their value for an arbitrarily sinuosity. The present paper shows that starting from the hypothesis that in equilibrium meanders the variance of entropy production is minimized, most probable values of c_f and c_s can be found for a given sinuosity.

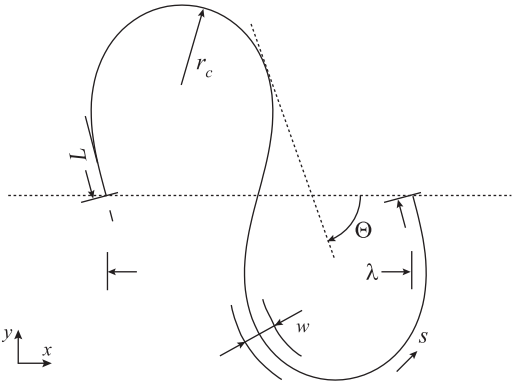


Figure 1. Sine-generated curve and definition of planform parameters.

For a specified value of k a unique minimum for the variance of entropy production is shown to exist in the (c_f, c_s)-plane. Both the existence of this unique minimum and comparison with meander reaches of various geographical locations support the hypothesis presented herein, which is based on the second law of thermodynamics (cf. Prigogine and Stengers 1985).

Section 2 explains how minimum variance of entropy production can be quantified from the velocity gradients in a flow model and gives a mechanistic interpretation of the theory based on thermodynamics. Section 3 describes the flow model used in this paper, which was developed by Odgaard (1986a), and it explains the way in which the state of minimum variance of entropy production is found for a given sinuosity. In Section 4 results are presented, showing how fattening and skewing of near-equilibrium meanders in which the variance of entropy production is minimized depend on sinuosity, and on three additional model parameters. In Section 5 the results are discussed.

2 ENTROPY PRODUCTION IN A MEANDERING RIVER

In an near-isothermal system such as a river, entropy production is caused by irreversible friction losses within the fluid. For incompressible fluids, the entropy production per unit volume and unit time (σ), reads (Yang 1992):

$$T\sigma = -(\tau : \nabla \mathbf{v}) \qquad (4)$$

in which T is the absolute temperature, τ is the stress tensor and $\mathbf{v}$ is the velocity vector. Eq. 4 can be obtained by combining the first law of thermodynamics with the equation of motion for an isothermal system and incompressible fluid. It is assumed that the stress tensor for turbulent flow in a river can be written

Copyright © 2006 Taylor & Francis Group plc, London, UK

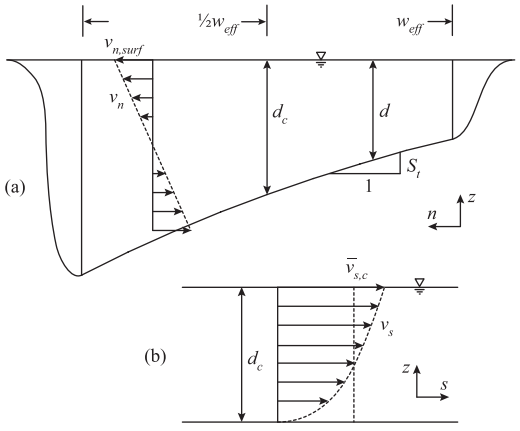


Figure 2. Longitudinal and transverse vertical velocity profiles, transverse depth distribution and definition of model parameters. Vertical scale is exaggerated.

in terms of a rate of strain tensor and a kinematic eddy viscosity, ϵ. This implies that the influences of turbulent flow on themeander planformis neglected (Smith and McLean 1984; Odgaard 1986a). The stress tensor may then be written as:

$$\tau_{ij} = -2\rho\epsilon\psi_{ij} \tag{5}$$

in which ρ the density of the fluid and ψ_{ij} the rate of strain tensor. The rate of strain tensor is given by:

$$\psi_{ij} = \frac{1}{2}(\nabla v_{ij} + \nabla_{ji}) \tag{6}$$

in which i and j represent the directions s, n and z. The components of the rate of strain tensor proceed from Eq. 4. The velocity gradient tensor will be expressed in a right-handed, orthogonal, curvilinear coordinate system with a downstream s-axis, a cross-stream n-axis and a vertical z-axis. The physical (Cartesian) space and the computational space resulting from the transformation of Cartesian into curvilinear coordinates are illustrated in Fig. 2. In curvilinear coordinates, the velocity gradient tensor is given by:

$$\nabla v_{ij} = \begin{bmatrix} N\frac{\partial v_s}{\partial s} - \frac{v_n}{r_c - n} & \frac{v_s}{r_c - n} + N\frac{\partial v_s}{\partial s} & \frac{v_s}{r_c - n} + N\frac{\partial v_z}{\partial s} \\ \frac{\partial v_s}{\partial n} & \frac{\partial v_n}{\partial n} & \frac{\partial v_z}{\partial n} \\ \frac{\partial v_s}{\partial z} & \frac{\partial v_n}{\partial z} & \frac{\partial v_z}{\partial z} \end{bmatrix} \tag{7}$$

in which r_c is the radius of curvature of the river centerline and $N = 1/(1 - n/r_c)$. As the situation of a moderately meandering, shallow river with steady, subcritical flow is considered, several components can be neglected. Under the assumption of incompressible fluid, the contribution of the normal stresses can be neglected. Moderate meandering justifies omission of terms depending on $\partial v_s/\partial n$ and $\partial v_n/\partial s$. Finally, in a shallow river flow near the banks is small and relatively unimportant, so when bankflow is neglected, the gradients of vertical velocity $\partial v_z/\partial s$ and $\partial v_z/\partial n$ can also be neglected. The effective width of a river, w_e is introduced as the part of the river not influenced by bankflow (see Fig. 2). After these simplifications, calculation of the tensor product (Eq. 4) results in an expression for only dependent on the vertical gradients of the longitudinal and transverse velocity. Because the main interest is in the distribution of the entropy production along the river, this expression is integrated over a cross section of the river. This yields:

$$\sigma_{cs} = \frac{\rho}{T}\int_{-\frac{1}{2}w_e}^{\frac{1}{2}w_e}\int_0^d \epsilon\left(\left(\frac{\partial v_s}{\partial z}\right)^2 + \left(\frac{\partial v_n}{\partial z}\right)^2\right) dz dn \tag{8}$$

in which σ_{cs} is the entropy production for a cross-section of a river, w_e is the effective river width and d is the local depth. To determine σ_{cs} the distribution of the longitudinal and transverse velocities in a meander bend have to be known.With the assumption of steady flow it is implied that the meander planform is determined by one unique discharge (see e.g. Chang (1979), Chang (1984), Ikeda et al. (1981), Parker et al. (1983), Odgaard (1986a), Odgaard (1986b)).

The product of temperature (T) and entropy production per unit volume (σ) is equal to the energy dissipation rate per unit volume (E). Minimizing the variance of entropy production is hence equivalent to minimizing the variance of energy dissipation. Energy dissipation, in turn, bears a direct relation with the capacity of a local flow volume to carry sediment in suspension, and hence sediment transport (Yang 1991; Yang 2005). As a consequence of conservation ofmass (Exner equation), morphological changes are driven by gradients in depth-mean total sediment transport. In our analysis, the hypothesis of minimum variance of entropy production thus boils down to the assumption that the most likely equilibrium river meanders are the ones in which the (steady state) channel morphological change rates are minimal, which reveals the mechanistic interpretation of the entropybased hypothesis.

3 FLOW MODEL

The meander flow model developed by Odgaard (1986a) is used here for its compatibility with the

Copyright © 2006 Taylor & Francis Group plc, London, UK

assumptions made in the former section. The constraints in the model are (1) the effective river width is constant; (2) the centerline radius of curvature is large compared to width; (3) the width to depth ratio is large; (4) transverse velocity components are small compared to longitudinal ones; (5) turbulence is isotropic. The meander flow model is slightly modified for a dimensionless treatment. The dimensions present in the problem are length, time, mass and temperature. Since the entropy production in Eq. 8 will be written times temperature and per unit mass, only characteristic scales for length and time have to be de- fined. For both quantities a suitable reference value is present in the model. Both effective width and centerline depth are assumed constant in the model, as well as the averaged centerline longitudinal velocity. Therefore all lengths are normalized with respect to width and all velocities are normalized with respect to the averaged centerline longitudinal velocity $\overline{v}_{s,c}$. The dimensionless downstream direction and transverse velocity s̃ and transverse velocity are taken as:

$$\tilde{s} = \frac{s}{w_e} \tag{9}$$

$$\tilde{v}_n = \frac{v_n}{\overline{v}_{s,c}} \tag{10}$$

in which the tilde denotes a dimensionless variable. Because the bed topography and the longitudinal velocity profile are dependent of the actual velocity and friction coefficient, a fully dimensionless treatment is not possible. However the scale-dependent parameters are found to have only small effect on the results.

The analytical relationships for velocity profiles in Odgaard's model allow to solve the first integral of Eq. 8. This results in an expression independent on vertical changes in velocity. The general power law is used to describe the vertical distribution of the longitudinal velocity (Odgaard 1986a):

$$\frac{\tilde{v}_s}{\overline{\tilde{v}}_s} = \frac{m+1}{m}\left(\frac{\tilde{z}}{\tilde{d}}\right)^{\frac{1}{m}} \tag{11}$$

in which the dimensionless velocity-profile exponent m is a linear function of the Chézy coefficient. The vertical transverse velocity profile is assumed to be linear. Since we only use the differentiated form of the velocity profiles in Eq. 11, this relation can be described in its simplest form (Odgaard 1986a):

$$\frac{\tilde{v}_n}{\tilde{v}_{n,surf}} = 2\left(\frac{\tilde{z}}{\tilde{d}} - \frac{1}{2}\right) \tag{12}$$

in which $\tilde{v}_{n,surf}$ is the transverse surface velocity. Again the interaction with the riverbed is not accounted for. Therefore the violation of the no-slip condition on the riverbed is legitimate. Examples of the velocity profiles described by Eqs. 11 and 12 are given in Fig. 2. With Eqs. 12 and 2 and the assumption of a parabolic profile of the eddy viscosity ϵ it is possible to solve the first integral of (10). Normalizing by the temperature, density, effective width and averaged centerline longitudinal velocity, integrating and rearranging of terms yields:

$$\begin{aligned}\tilde{\sigma}_{cs} &= \frac{T\sigma_{cs}w_e}{\rho\overline{v}_{s,c}^3} \\ &= \kappa^2 \int_{-\frac{1}{2}}^{\frac{1}{2}} \left(\frac{(m+1)^2}{4m^3+2m^4}\tilde{\overline{v}}_s^{\,3} + \frac{4\tilde{v}_s\tilde{v}_{n,surf}^2}{6m} \right) d\tilde{n}\end{aligned} \tag{13}$$

The entropy production is now only dependent of the transverse surface velocity and the averaged centerline longitudinal velocity. A complicated determination of the three-dimensional velocity field is thus avoided.

The central equation of the meander flow model describes the longitudinal or streamwise variation of the centerline transverse bedslope $S_{t,c}$. This equation is derived from a combination of the equation of motion for the transverse velocity component, a parabolic eddy viscosity profile, a parabolic velocity profile, the mass balance at the centerline to compensate for mass-shift and a simple linear relationship between the transverse bedslope and the transverse velocity at the bottom. At the centerline of the river this yields (Odgaard 1986a):

$$\frac{d^2D_{t,c}}{d\tilde{s}^2} + c_1\frac{dS_{t,c}}{d\tilde{s}} + c_2S_{t,c} = \frac{c_3}{\tilde{r}_c} \tag{14}$$

in which c_1, c_2 and c_3 are functions depending on sediment characteristics and cross section geometry. In Eq. 14, only the centerline radius of curvature $\tilde{r}_c$ is a function of $\tilde{s}$. From the centerline transverse bedslope, the local transverse depth distribution can be calculated from the simple relationship (Odgaard 1986a):

$$\frac{S_t}{S_{t,c}} = \frac{\tilde{d}}{\tilde{d}_c}\frac{\tilde{r}_c}{\tilde{r}} \tag{15}$$

in which $\tilde{d}_c$ is the (constant) centerline depth and $\tilde{r}$ is the local radius of curvature. The convex transverse depth distribution described by Eq. 15 is illustrated in Fig. 2. The depth distribution is needed to calculate the longitudinal velocity distribution. From the equation of motion in longitudinal direction, written in terms of the average longitudinal velocity and with the use of the parabolic eddy viscosity profile, it follows

Copyright © 2006 Taylor & Francis Group plc, London, UK

that the change in average longitudinal velocity along a path of constant distance from the centerline can be approximately written as (Odgaard 1986a):

$$\frac{d(\tilde{\bar{v}}_s)^2}{d\tilde{s}} + c_4 \frac{\tilde{d}_c}{\tilde{\bar{d}}} (\tilde{\bar{v}}_s)^2 = c_4 \frac{\tilde{r}_c}{\tilde{\bar{r}}} \tag{16}$$

in which the function c_4 is again depending on sediment characteristics and cross section geometry. Finally it is assumed that the local transverse bedslope is proportional to the transverse bottom velocity. Since it follows from Eq. 12 that the transverse surface velocity has the same absolute value (but different sign) as the transverse bottom velocity, the transverse surface velocity can be written in terms of the centerline transverse bedslope as (Odgaard 1986a):

$$\tilde{v}_{n,surf} = c_5 S_{T,c} \frac{\tilde{\bar{d}}}{\tilde{d}_c} \frac{\tilde{r}_c}{\tilde{\bar{r}}} \tag{17}$$

in which the function c_5 depends on sediment and flow characteristics and cross section geometry. We now define ξ as the dimensionless variance of cross-sectional entropy production along arbitrary meander bends:

$$\xi = \frac{1}{p-1} \sum_{i=1}^{p} \left(\tilde{\sigma}_{cs,i} - \tilde{\bar{\sigma}}_{cs} \right)^2 \tag{18}$$

in which p is the discrete number of cross-sections. As a necessary boundary condition it is imposed that a change in shape of the meander bend does not lead to a change in the meander length and wavelength. From Eq. 1, the longitudinal variation in the centerline radius of curvature can be determined as in:

$$\frac{1}{\tilde{r}_c} = \frac{d\Theta}{d\tilde{s}} \tag{19}$$

The values of c_f and c_s are taken between -0.1 and 0.1, with intervals of 0.01. Higher or lower values result in physically unlikely curves. For a constant sinuosity, the curves that minimize entropy production are thus determined out of 441 possible curves. Since the meander flow model is dimensionless, the number of parameters that influences the result is strongly reduced. The spatial dimensions are all expressed with respect to the effective width, so only three spatial ratios remain to be chosen: the ratios of wavelength, meander length and centerline depth to effective width. The ratio of effective width to centreline depth shows considerable variations in natural rivers. A reference value of 10 is chosen, and the influence of this variable is investigated. To close the geometry problem (Hey 1976), we assume the wavelength to equal eleven times the width, following Davy and Davies (1979). In terms of effective width and in dimensionless notation:

$$\tilde{\lambda} = \frac{\lambda}{w_e} = 13.2 \tag{20}$$

Regarding sinuosity, a maximum value of 5 is considered. Above this value cut-offs are likely to occur. The depth/width ratio also shows considerable variations in natural rivers. A reference value of 0.1 is chosen, but the influence of this variable is also studied. According to Odgaard (1986a) bankflow influences the flow pattern to a distance of approximately one time the depth. With a depth/width ratio of 0.1, neglecting bankflow thus leads to a ratio of the wavelength to effective width of 13.2.

Besides the geometrical parameters mentioned above also two parameters related to flow and sediment characteristics are dependent on scale. Although the velocity profile exponent and the particle Froude number are both dimensionless, their value cannot be determined because the velocity profile exponent is a function of the scale dependent Chézy coefficient and the particle Froude number is a function of the actual velocity and sediment size. The values of the velocity profile exponent and the particle Froude number are taken as 2.8 and 6.78 (respectively), the average values of the two river sites tested in Odgaard (1986b). On both parameters a sensitivity test is performed.

4 RESULTS

The variance of the entropy production per cross section for different Kinoshita curves with a constant sinuosity clearly shows one unique minimum. This is shown in Fig. 3, where ξ is plotted in the (c_f, c_s)-plane.

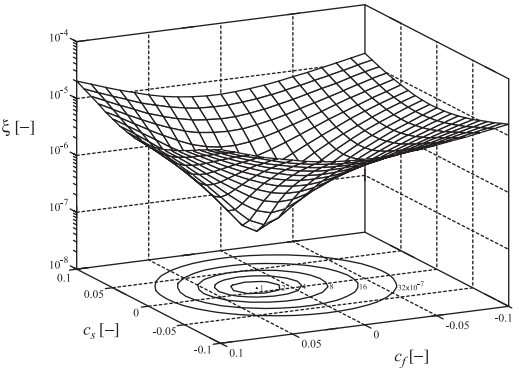


Figure 3. Variance of the entropy production per cross-section (vertical axis) versus fattening and skewing parameters for the Kinoshita curve ($k = 3$).

Copyright © 2006 Taylor & Francis Group plc, London, UK

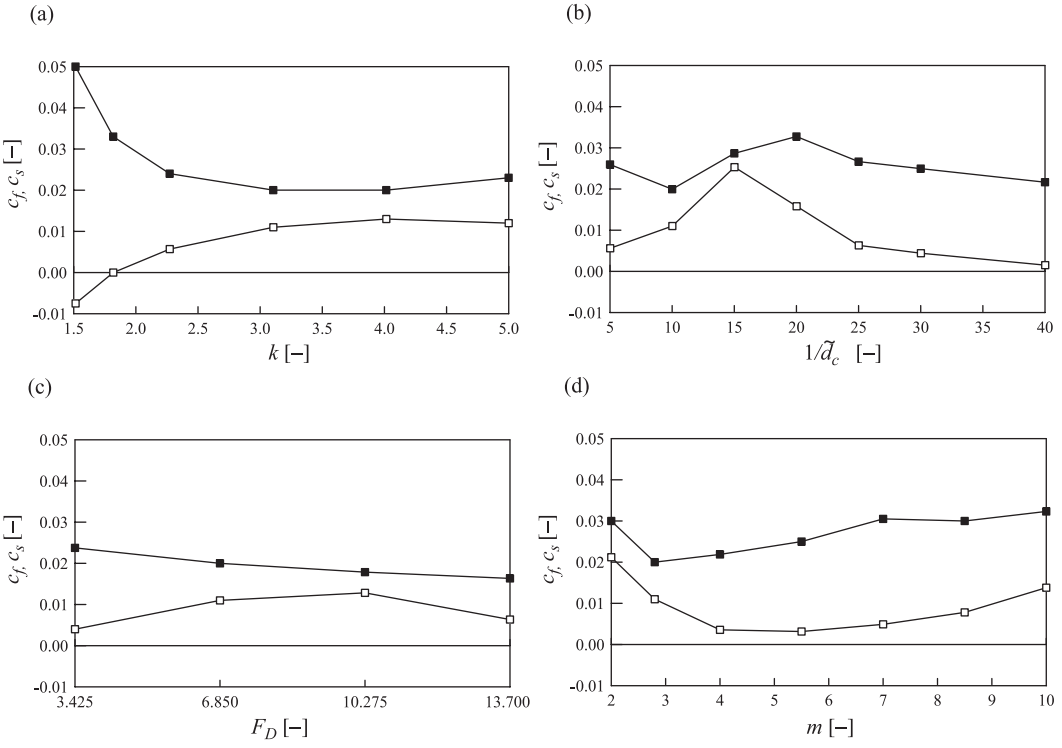


Figure 4. Effect of model parameters on the values of fattening (dotted line) and skewing (solid line). (a) Sinuosity, (b) Ratio of effective width to centerline depth, (c) Particle Froude number, (d) velocity profile exponent.

The location of the minimum clearly differs from the first order sine-generated curve (located at $c_f = 0$ and $c_s = 0$), which would result if the entropy production would be a simple linear function of the curvature. Linear interpolation shows that the minimum is located at $c_f = 0.020$ and $c_s = 0.011$. This leads to a fattening and upvalley skewing in comparison with the first order sine-generated curve.

The results depend on two geometrical parameters and two flow parameters, as discussed earlier. The effect of the sinuosity and the depth/width ratio on the result is shown in Fig. 4a and b. The upvalley skew in meanders is the most pronounced at higher sinuosities. At a sinuosity of 1.8, the model predicts a symmetric meander as the most probable one, while at an even lower sinuosity the most probable meander shows a slight downvalley skew. The influence of the sinuosity on the most probable meander planform is illustrated in Fig. 5. The depth of the river also influences the most probable combination of fattening and skewing parameters. From Fig. 4b it can be seen that theres a maximum upvalley skew at a centerline depth of 1/15 times the effective width. The effect of the particle Froude number and the velocity profile exponent on the result is shown in Fig. 4c and d. The particle Froude number shows to have only little effect on the result. Skewing is more pronounced at low and high values of the velocity profile exponent, while at median values skewing is less pronounced.

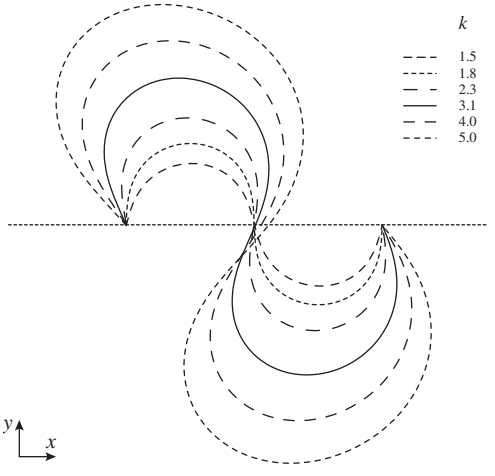


Figure 5. The most probable meander planform for different sinuosities. Direction of flow is from left to right.

Copyright © 2006 Taylor & Francis Group plc, London, UK

We selected regular meanders and confronted these meanders with our optimalized equilibrium curves. Only few examples of undisturbed meanders have been documented, as many meandering rivers are found in remote areas or have been straightened in the past century. Consequently, we also selected meanders from satellite images and old maps. Fig. 6 compares these meanders with one complete wavelength of our optimized equilibrium curves. No quantitative comparison was made for several reasons. First natural meanders are not necessarily in equilibrium. The starting point of the curve and the location and direction of the downvalley axis is a subjective matter. This is also true for scale and sinuosity of the curve to be fitted, as a good comparison can only be made between curves of the same sinuosity. However as can be seen in Fig. 6, a visual comparison is based on shape rather than on sinuosity. Furthermore the exact centreline of the river depends on unknown depth distribution and stage. Because of this lack of data, average parameter values as discussed in the previous section were used for the curves in Fig. 6.

The old and distinct meanders of the Mississippi River near Greenville (Fig. 6a) are perhaps the most cited in literature. They have been used to illustrate earlier theories on meander planform (Langbein and Leopold 1966; Parker et al. 1983) or just to illustrate the typical meander planform (Chitale 1973; Jefferson 1902; Chitale 1973; Davies and Tinker). Where the first order sine generated curve gave a reasonable agreement (Langbein and Leopold 1966) with the Mississippi meanders, the equilibrium curve for which the variance of entropy production is minimized matches almost exactly. A large aerial photograph of the incised San Juan River (Fig. 6b) was used by Leopold and Langbein (1966) to introduce their Theory of minimum variance. Langbein and Leopold (1966) concluded that during incision, irregularities apparently tend to be averaged out and only the regular form is preserved. This is confirmed by the good agreement with our optimized equilibrium curve. Examples of smaller scale used by (Langbein and Leopold 1966) are Baldwin Creek (Fig. 6j) and the Popo Agie River (Fig. 6r), which was by far the most symmetrical and uniform meander reach they had ever seen. Again the curves obtained here show good agreement.

Some of the most extensive meandering systems are found in tectonically stable Precambrian shield areas like the Amazon basin and the Congo basin. Satellite images available from the Global Rain Forest Mapping Project allowed easy analysis of larger rivers. Meandering rivers in these areas often show remarkable regularity in their planform. Nice examples of 'approximately free and unforced meandering' rivers (Stø lum 1998) are the Juruá River (Figs. 6c,g,u,x) and Jutai River (Figs. 6f,i,k) in Brazil. Even the large meanders in the Solimões River (Fig. 6w) show a regular pattern. One of the finest examples of regular meanders was found along the reaches of the Maringa River in Congo (Fig. 6m). Satellite images where also used to identify regular reaches along the freely meandering Kahayan River in Kalimantan (Figs. 6e,q) and Salonga River in Congo (Fig. 6t). The regular meanders found in these areas can be assumed close to an equilibrium in which variance of entropy production is minimized.

In, or close to The Netherlands we found three examples of regular meandering rivers of different scale. The River Rhine (Figs. 6l,d,o) and the River Meuse (Fig. 6h) once were freely meandering rivers, but many meandering reaches have been straightened in the past century. Abandoned meanders and old maps however show that before the straightening these too were rivers close to equilibrium. The Geul Brook (Fig. 6s) is generally considered as one of the finest examples of a meandering brook in The Netherlands, as it remained largely untouched by human influence (Overmars et al. 1996). Other examples of regularly meandering rivers were found in the literature, such as the River Myittha in Myanmar. The Muddy Creek was used by Odgaard (1986b) as a validation site for the meander flow model (see previous section).

A first glance of Fig. 6 already reveals a large geometric similarity in meander planforms, which seems to be independent of geographical location or scale. The scale of the meanders in Fig. 6 ranges over four orders of magnitude, from 1 m (Fig. 6p) to 10 km (Fig. 6w). At large sinuosities (3–4) the same upvalley skewing is apparent for rivers of four different continents. At mediate sinuosities (2–3) most meanders are symmetric. At lower sinuosities (1.5–2) some meanders show a slight downvalley skew. This behaviour is in correspondence with our theoretical findings (Fig. 4). A good overall correspondence is found between equilibrium meanders in which variance of entropy production is minimized and meanders with the same sinuosity encountered in nature.

5 DISCUSSION

The use of thermodynamic principles in fluvial geomorphology is not new. The concept that landscapes or landscape elements evolve towards a state of maximum probability was already used by Davis in the end of the 19th century (Davis 1899). Leopold and Langbein (1966) introduced the use of entropy in fluvial geomorphology. Thermodynamic principles were also applied byWoldenberg (1966), Scheidegger (1967) and Yang (1971). Recently, similar concepts have provided new insights in the structure and development of drainage networks and hydraulic geometry (Kapoor 1990; Ijjász-Vásquez 1993; Rodríguez-Iturbe and Rinaldo 1997; Molnár and Ramírez 1998; Huang and Nanson 2000).

Copyright © 2006 Taylor & Francis Group plc, London, UK

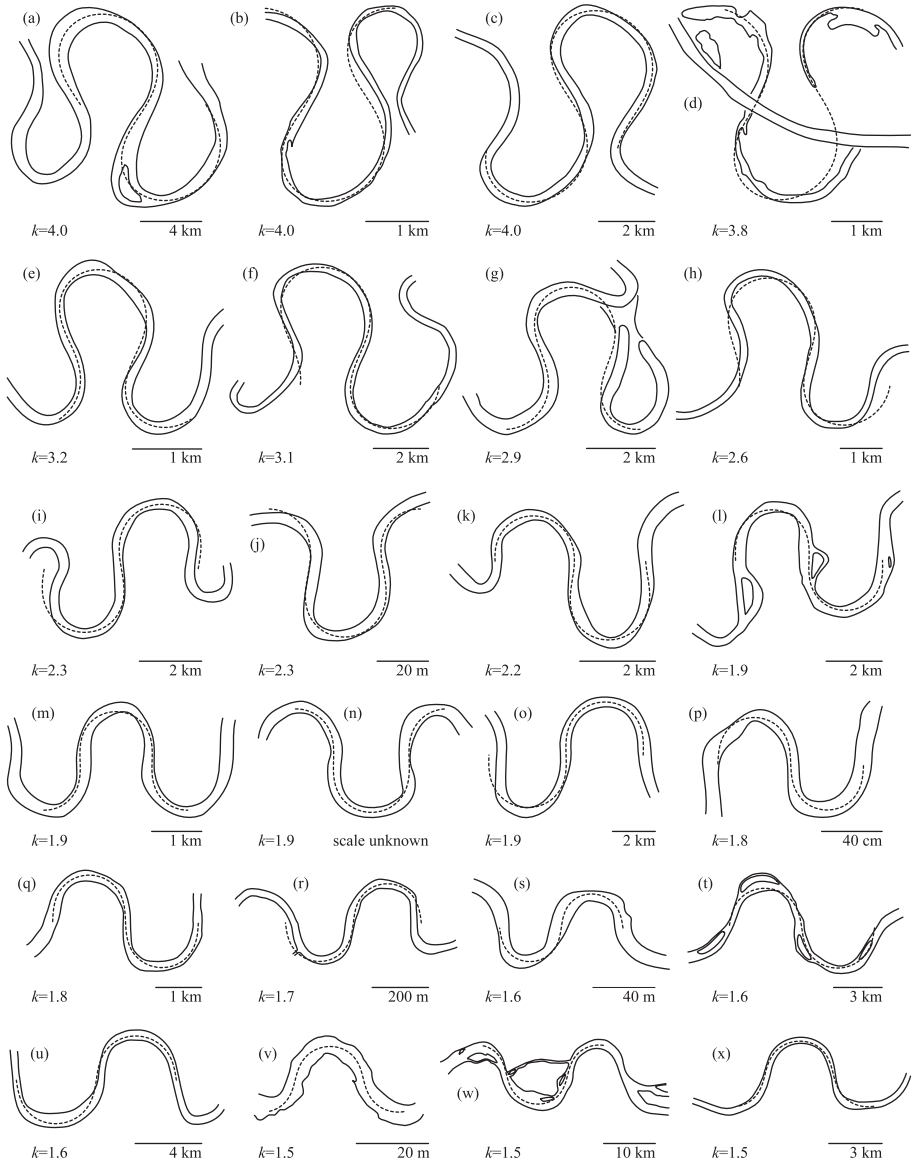


Figure 6. Regular meander bends of different scale and sinuosity compared with the optimized equilibrium curves, in order of decreasing sinuosity. (a) Mississippi River near Greenville, Miss., U.S.* (b) Incised San Juan River at The Loop, Utah, U.S. (c) Juru River, southern central Amazon basin, Brazil. (d) Straightened River Rhine with old meanders, 43 Ketsch, Germany. (e) Kahayan River near Palangkaraya, central Kalimantan, Indonesia. (f) Jutai River, southern central Amazon basin, Brazil. (g) Juru River with oxbow lake. (h) River Meuse near Grave, The Netherlands*. (i) Jutai River. (j) Baldwin Creek near Lander,Wyo., U.S. (k) Jutai River. (l) River Rhine near Speyer, Germany*. (m) Maringa River near Bususulu, Congo. (n) River Myittha, Burma. (o) River Rhine near Düsseldorf, Germany. (p) Laboratory meander. (q) Kahayan River. (r) Popo Agie River near Hudson, Wyo., U.S. (s) Geul Brook near Partij, The Netherlands. (t) Salonga River near Ingende, Congo. (u) Juru River. (v) Muddy Creek, Wyo., U.S. (w) Solimões (Amazone) River, Amazon basin, Brazil. (x) Juruá River. In all cases flow is from left to right. *Situation before artificial cut-off. River planforms have been reproduced from: (a),(b),(j),(r): Langbein and Leopold (1966); (c),(f),(g),(i),(k),(m),(t),(u),(w),(x): Synthetic aperture radar (SAR) images from Global Rainforest Mapping Project (http://southport.jpl.nasa.gov/amazon and project cd-roms); (d),(o): Internationale Kommission zum Schutze des Rheins gegen Verunreinigung, 1998; (e),(q): ESA-images provided by Sarvision (www.sarvision.nl), (h):Maas (2000), (l):Mangelsdorf et al. (1990), (n): Knighton (1990), (p): Schumm et al. (2000), (s): Overmars et al. (1996), (v): Odgaard (1986b).

Copyright © 2006 Taylor & Francis Group plc, London, UK

At the same time the use of extremal hypotheses related entropy in fluvial hydraulics has often been a subject to debate, and can even be considered controversial (Griffiths 1984; Lamberti 1992;Mosselman 2000). For this reason the mechanistic interpretation of the hypothesis of minimal variance of entropy production was included in Section 2, showing that minimization of entropy production of water is largely equivalent to minimization of channel morphology change rates, leading to a near-uniform dissipation of kinetic energy. It is acknowledged that the correct application of the second law of thermodynamics to an open dissipative system as a river meander is not straightforward, yet the law itself is not under dispute and equally fundamental as Newton's second law that provides the basis for the equations of motion.

A contestable assumption made in this paper is that entropy production of water only is to be minimized, whereas suspended sediment particles also produces entropy. Especially since bankfull discharge conditions are considered normative for meander formation, the focus on entropy production by water only may not be justified, as the sediment discharge may be significant in mass and energy. Furthermore, the constraints implied by the flow model leave room for improvement, as the level of detail of the flow description is limited. Despite these remarks, the existence of unique minimum of the variance of entropy production for arbitrary sinuosities and the favorable comparison with a variety of field situations strongly suggest a basic validity of the theory presented.

REFERENCES

Camporeale, C., P. Perona, A. Porporato, and L. Ridolfi (2005). On the long-term behavior of meandering rivers. *Water Resour. Res. 41*(12).

Chang, H. H. (1979). Minimum stream power and river channel patterns. *J. Hydrol. 41*, 303–327.

Chang, H. H. (1984). Analysis of river meanders. *J. of Hydraulic Eng. 110*(1), 37–50.

Chitale, S. V. (1973). Theories and relationships of river channel patterns. *J. Hydrol. 19*, 285–308.

Davies, T. R. H. and C. C. Tinker. Fundamental characteristics of stream meanders. *Geol. Soc. America Bull. 95*, 505–512.

Davis, W. M. (1899). The geographical cycle. *Geographical Journal XIV*.

Davy, B. W. and T. R. H. Davies (1979). Entropy concepts in fluvial geomorphology: a reevaluation. *Water Resour. Res. 15*(1), 103–106.

Engelund, F. (1974). Flow and bed topography in channel bends. *J. Hydraul. Div. 100*, 1631–1648.

Griffiths, G. A. (1984). Extremal hypotheses for river regime: an illusion of progress. *Water Resour. Res. 21*(1), 113–118.

Hey, R. D. (1976). Geometry of river meanders. *Nature 262*, 482–484.

Huang, H. Q. and G. C. Nanson (2000). Hydraulic geometry and maximum flow efficiency as products of the principle of least action. *Earth Surf. Proc. and Landf. 25*, 1–16.

Ijjász-Vásquez (1993). Are river basins optimal channel networks? *Adv. Water Resour. 16*, 69–79.

Ikeda, S., G. Parker, and K. Sawai (1981). Bend theory of river meanders. Part 1. Linear development. *J. Fluid Mech. 112*, 363–377.

Jefferson, M. S. W. (1902). The limiting width of meander belts. *National. Geogr. Mag., Oct.*, 373–384.

Johannesson, H. and G. Parker (1989). Linear theory of river meanders. In H. Ikeda and G. Parker (Eds.), *River Meandering, Water Resour. Monogr.*, Volume 12, pp. 181–214. Washington D.C.: AGU.

Kalkwijk, J. P. T. and H. J. De Vriend (1980). Computation of the flow in shallow river bends. *J. Hydraul. Res. 18*(4), 327–342.

Kapoor, V. (1990). Spatial uniformity of power and the altitudinal geometry of river networks. *Water Resour. Res. 26*(10), 2303–2310.

Knighton, D. (1990). *Fluvial forms and processes: A new perspective*. Wiley, New York.

Lamberti, A. (1992). Dynamic and variational approaches to the river regime relation. In V. P. Singh and M. Fiorentino (Eds.), *Entropy and energy dissipation in water resources*. Dordrecht: Kluwer.

Langbein, W. B. and L. B. Leopold (1966). River meanders – theory of minimum variance. *U.S. Geol. Surv. Prof. Pap. 422-H*.

Leopold, L. B. and W. B. Langbein (1966). River meanders. *Sci. Am. 214*, 60–70.

Maas, G. J. (2000). Historical geomorphology of the River Maas and distributaries: Oude Maas, Merwede-Hollandse Biesbosch, Afgedamde Maas en Maaskant. (Historische geomorfologie Maas en benedenrivieren: Oude Maas, Merwede-Hollandse Biesbosch, Afgedamde Maas en Maaskant.). Technical report, Alterra, Wageningen.

Mangelsdorf, J., K. Scheurmann, and F. H. Weiss (1990). *River morphology: a guide for geoscientists and engineers*. Springer, Berlin.

Molnár, P. and J. A. Ramírez (1998). Energy dissipation theories and optimal channel characteristics of river networks. *Water Resour. Res. 37*(7), 1809–1818.

Mosselman, E. (2000). River width adjustment I: Processes and mechanisms – Discussion. *J. of Hydraulic Eng. 126*(2), 159–160.

Nakagawa, T. and J. C. Scott (1984). Stream meanders on a smooth hydrophobic surface. *J. of Fluid Mech. 149*, 89–99.

Odgaard, A. J. (1986a). Meander flow model. I: Development. *J. of Hydraulic Eng. 112*(12), 1117–1136.

Odgaard, A. J. (1986b). Meander flow model. II: Applications. *J. of Hydraulic Eng. 112*(12), 1137–1150.

Overmars, W., W. Helmer, G. Litjens, W. Felder, T. Garritsen, H. Hilligers, and A. Klink (1996). Development of the Beneden-Geul valley. (Beekdalontwikkeling Beneden-Geul. *Stroming, Laag Keppel*.

Parker, G. and E. D. Andrews (1986). On the time development of meander bends. *J. of Fluid Mech. 162*, 139–156.

Parker, G., P. Diplas, and J. Akiyama (1983). Meander bends of high amplitude. *J. Hydraul. Div. ASCE 109*, 1323–1337.

Copyright © 2006 Taylor & Francis Group plc, London, UK

Prigogine, I. and I. Stengers (1985). *Order out of chaos: Mans new dialogue with nature*. Fontana.

Rodríguez-Iturbe, I. and A. Rinaldo (1997). *Fractal River Basins: Chance and Self-organization*. Cambridge Univ. Press.

Scheidegger, A. E. (1967). A thermodynamic analogy for meander systems. *Water Resour. Res. 3*(4), 1041–1046.

Schumm, S. A., J. F. Dumont, and J. M. Holbrook (2000). *Active tectonics and alluvial rivers*. Cambridge Univ. Press.

Schumm, S. A., H. R. Khan, B. R. Winkeley, and L. G. Robbins (1972). Variability of river patterns. *Nature Phys. Sci. 237*, 75–76.

Seminara, G., G. Zolezzi, M. Tubino, and D. Zardi (2001). Downstream and upstream influence in river meandering. Part 2. Planimetric development. *J. of Fluid Mech. 438*, 213–230.

Smith, J. D. and S. R. McLean (1984). A model for flow in meandering streams. *Water Resour. Res. 20*(9), 1301–1315.

Stø lum, H. H. (1998). Planform geometry and dynamics of meandering rivers. *Geol. Soc. America Bull. 110*, 1485–1498.

Woldenberg, M. J. (1966). Horton's laws justified in terms of allometric growth and steady state in open systems. *Geol. Soc. America Bull. 77*, 431–434.

Yang, C. T. (1971). On river meanders. *J. Hydrol. 13*, 231–253.

Yang, C. T. (1991). Energy-dissipation rate and sediment transport. *J. of Hydraulic Res. 29*(4), 457–474.

Yang, C. T. (1992). Force, energy, entropy and energy dissipation rate. In V. P. Singh and M. Fiorentino (Eds.), *Entropy and energy dissipation in water resources*. Dordrecht: Kluwer.

Yang, S. Q. (2005). Formula for sediment transport in rivers, estuaries and coastal waters. *J. of Hydraulic Eng. 131*(11), 968–979.

Zolezzi, G. and G. Seminara (2001). Downstream and upstream influence in river meandering. Part 1. General theory and application to overdeepening. *J. Fluid Mech. 438*, 183–211.

Copyright © 2006 Taylor & Francis Group plc, London, UK

Downstream stable channel configuration: Preliminary analysis

Beatrice Mengoni & Enio Paris
CERAFRI (CEntre of Research and Advanced education For hydrogeological RIsk prevention), Retignano (LU), Italy
DIC (Department of Civil Engineering, University of Florence), Florence, Italy

ABSTRACT: A new analytical method for determinating stable channel configuration of self formed river is presented. The method is based on a downstream approach and includes spatial variability along the river reach of quantities related to hydrological and sedimentological river basin characteristics. It combines one-dimensional steady water and sediment continuity equations, friction factor and sediment transport laws together with given analytical expressions of river basin input quantities along the river reach. A differential equation is obtained and solved to calculate the downstream equilibrium geometric and hydraulic variables.

1 INTRODUCTION

Since the beginning of the previous century the determination of the equilibrium configuration of a river has fascinated many Authors that have developed both empirical methods (e.g. Blench 1957, Simon and Albertson 1963), extremal hypothesis method (e.g. Chang 1979, White et al. 1982), mechanistic method (e.g. Parker 1978, Diplas and Vigilar 1992, Kovacs and Parker 1994), and experimental methods (e.g. Ikeda 1981, Diplas 1990).

All the above cited methods, have been developed following an approach at station, where the entire spatial variability of quantities related to river basin characteristics is not considered but instead averaged and represented by a single value of water discharge and sediment load. This assumption is associated with a channel forming discharge concept: where a single theoretical discharge and sediment load if maintained indefinitely, would produce the same channel geometry as the one modelled by the entire-long term discharge cycle.

Nowadays the determination of the equilibrium configuration following a downstream direction approach seems, instead, not to have been investigated in similar details. For this reason, in the present work the stable configuration of self formed river has been studied developing a new method in downstream direction, based on an extensive basin scale approach. The method combines one-dimensional steady water and sediment continuity equations, friction factor and sediment transport laws together with given analytical expressions of river basin input quantities such as longitudinal bed profile, sediment size, water and sediment discharges distributions along the river reach. A differential equation is obtained and solved to calculate the downstream geometric and hydraulic variables.

A first example of application procedure is presented mainly to show potential applicability of the method that looks very promising especially to predict downstream stable configuration and to help to provide a rational interpretation of relationships of the regime theory that still need further clarifications.

2 FORMULATION OF THE MODEL

The form of a fluvial system results from the complex interaction between variables superimposed by the river basin (independent) and variables that the system is able to modify and adjust (dependent). The independent variables are essentially related to the hydrological, physiographic and sedimentological river basin characteristics and usually include water discharge (Q), sediment load (Q_s) and the sediment size distribution (D_s) whereas the dependent variables are generally related to the geometry and planimetric-altimetric configuration of the river such as cross section shape (water depth H and surface width W) and longitudinal profile (slope i). It is know how by adjusting the dependent variables the system tries to reach a quasi-steady state configuration, indicated as equilibrium (or stable) configuration.

In order to reproduce the spatial variability along the stream length of both dependent and independent variables, the present method is developed assuming a

Copyright © 2006 Taylor & Francis Group plc, London, UK

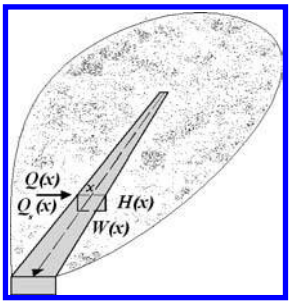


Figure 1. Simplified river system: the river is assumed rectilinear with rectangular cross section and the hydraulic variables are function of downstream coordinate x.

1D approach along river length. In particular the distributions along the river reach of water discharge Q, sediment load Q_s and sediment size D_s are considered as input variables. Because vertical variations of bed level profile usually occur on a time scale that is much greater than the variations of other variables, by considering an appropriate time scale (e.g. graded time scale, Schumm and Lichty 1965), the bed level profile can also be considered as an independent variable.

The method intends to obtain the river system configuration that is able to carry in each cross section along the river axis the superimposed values of water discharge and sediment load without generating any erosion or deposition and hence variations in bed level profile.

Time-averaged steady flow conditions, with reference to dominant discharge, along the entire river axis, are considered; as consequence all variables are function only of their position along the river axis x (in the following x-coordinate dependence is omitted, e.g. $Q(x)=Q$; $Q_s(x)=Q_s$; $D_s(x)=D_s$; $i(x)=i$; $H(x)=H$; $W(x)=W$).

The mechanical processes through which the river achieves the stable configuration are not reproduced. Only the equilibrium relationships between independent and dependent variables are modelled by employing the basic laws of flow motion and sediment transport.

Assuming the simplified conditions of rectangular cross section shape composed by homogeneous and non cohesive bed and banks material, the method has been developed combining the *1D steady flow equation* (Eq. 1) with the 1D flow and sediment continuity equation at equilibrium condition (Eq. 2 and Eq. 3):

$$\frac{d}{dx}\left(H+\frac{U^2}{2g}\right)=i-j \tag{1}$$

$$\frac{dQ}{dx}=q \tag{2}$$

$$\frac{dQ_s}{dx}=q_s \tag{3}$$

(where U = flow velocity; j = energy gradient loss; q = downstream unit length inflow water discharge; q_s = downstream unit length inflow sediment discharge).

Among the several relations available in literature, the following general power function formulation has been chosen as flow resistance formula:

$$C=K_c\left(\frac{H}{D_s}\right)^{\alpha} \tag{4}$$

(where K_c and α are dimensionless constants), together with the following general expression of *sediment transport formula*:

$$Q_s=K_{q_s}(\vartheta-\vartheta_{cr})^n W\sqrt{g(s-1)D_s^3} \tag{5}$$

(where K_{q_s} and n are dimensionless constants).

Under the assumption of wide rectangular cross section shape, velocity U, energy gradient loss j and dimensionless shear stress ϑ assume the following expressions:

$$U=\frac{Q}{WH} \tag{6}$$

$$j=\frac{U^2}{gC^2H}=\frac{1}{g}\frac{Q^2}{W^2H^3C^2} \tag{7}$$

$$\vartheta=\frac{U_*^2}{g(s-1)D_s}=\frac{1}{g(s-1)D_s}\cdot\frac{Q^2}{W^2C^2H^2} \tag{8}$$

which substituted in Eq. 1 lead to the well know *1D backwater equation*:

$$\frac{dH}{dx}=\frac{-\frac{1}{g}\frac{Q^2}{W^2H^2}\left(\frac{1}{Q}\frac{dQ}{dx}-\frac{1}{W}\frac{dW}{dx}\right)-\frac{dZ_b}{dx}-\frac{1}{g}\frac{Q^2}{W^2H^3}}{\left(1-\frac{Q^2}{gW^2H^3}\right)} \tag{9}$$

and substituted in Eq. 5, under the assumption of fully developed sediment transport conditions ($\vartheta >> \vartheta_{cr}$), lead to the following:

$$Q_s=\frac{K_{q_s}}{[g(s-1)]^{n-\frac{1}{2}}}\cdot\frac{Q^{2n}D_s^{\frac{3}{2}-n}}{C^{2n}H^{2n}W^{2n-1}} \tag{10}$$

Substituting flow resistance formula (Eq. 4) in Eq. 10 the following expression is obtained:

$$Q_s=\frac{K_{q_s}}{[g(s-1)]^{n-\frac{1}{2}}K_c^{2n}}\cdot\frac{Q^{2n}D_s^{2n\alpha+\frac{3}{2}-n}}{H^{2n(\alpha+1)}W^{2n-1}} \tag{11}$$

Copyright © 2006 Taylor & Francis Group plc, London, UK

Assuming the classic flow resistance formula exponent $\alpha = 1/6$ (Strickler 1923), Eq. 11 becomes:

$$Q_s = \frac{K_{q_s}}{[g(s-1)]^{n-\frac{1}{2}} K_c^{2n}} \cdot \frac{Q^{2n} D_s^{\frac{9-4n}{6}}}{H^{\frac{7}{3}n} W^{2n-1}} \tag{12}$$

For sediment transport exponent $n = 3/2$ (e.g Meyer-Peter and Muller 1948, Shields 1936, Ashida and Michiue 1971), the sediment transport capacity is function of the sediment size D_s only only through the flow resistance formula (see Eq. 10). This is due the assumed simplifying hypothesis of wide rectangular cross section shape and fully developed sediment transport conditions.

Subsequently width W is obtained by Eq. 10, Eq. 11 and Eq. 12 as follow:

$$W = \frac{K_{q_s}^{\frac{1}{2n-1}}}{\sqrt{g(s-1)}} \cdot \left(\frac{Q^{2n} D_s^{\frac{3}{2}-n}}{Q_s H^{2n} C^{2n}} \right)^{\frac{1}{2n-1}} \tag{13}$$

$$W = \frac{K_{q_s}^{\frac{1}{2n-1}}}{\sqrt{g(s-1)} K_c^{\frac{2n}{2n-1}}} \cdot \left(\frac{Q^{2n} D_s^{\frac{3}{2}-n+2n\alpha}}{Q_s H^{2n(\alpha+1)}} \right)^{\frac{1}{2n-1}} \tag{14}$$

$$W = \frac{K_{q_s}^{\frac{1}{2n-1}}}{\sqrt{g(s-1)} K_c^{\frac{2n}{2n-1}}} \cdot \left(\frac{Q^{2n} D_s^{\frac{9-4n}{6}}}{Q_s H^{\frac{7}{3}n}} \right)^{\frac{1}{2n-1}} \tag{15}$$

Let us notice how adopting an *approach at a station* width W and water depth H are inversely proportional to each other (Eq. 13, 14, 15) and thus characterized by opposite behavior with respect to input variables (under the admissible condition of $n > 1/2$). This disagrees with the behaviour showed by *classical* regime formula, according to which the hydraulic variables are characterize by the same proportionality against input variables (e.g. Blench 1957, Bray 1982). As consequence, in order to obtain the same proportionality, it seems necessary to include the downstream variation of the input variables.

Starting from Equation (15) the derivative of width W is obtained (Eq. 16) and subsequently included in Equation (9).

$$\frac{1}{W}\frac{dW}{dx} = \frac{2n}{2n-1} \cdot \frac{1}{Q}\frac{dQ}{dx} - \frac{1}{2n-1} \cdot \frac{1}{Q_s}\frac{dQ_s}{dx} + \frac{9-4n}{6(2n-1)} \cdot \frac{1}{D_s}\frac{dD_s}{dx} - \frac{7n}{3(2n-1)} \cdot \frac{1}{H}\frac{dH}{dx} \tag{16}$$

Expressing everything as function of water depth H, the following 1st order, variable coefficient, ordinary differential equation is achieved:

$$\frac{dH}{dx} = \frac{F_2 H^{\frac{2(n+3)}{3(2n-1)}} + F_3 H^{\frac{10-6n}{3(2n-1)}} + i}{1 + F_1 H^{\frac{9-4n}{3(2n-1)}}} \tag{17}$$

where F_1, F_2, F_3 are the variable coefficients of the differential equation, defined as:

$$\begin{cases} F_1 = \frac{n+3}{3(2n-1)} A_s \left(\frac{Q_s}{Q}\right)^{\frac{2}{2n-1}} \frac{1}{D_s^{\frac{9-4n}{3(2n-1)}}} \\ F_2 = \frac{A_s}{2n-1} \left(\frac{Q_s}{Q}\right)^{\frac{2}{2n-1}} \frac{1}{D_s^{\frac{9-4n}{3(2n-1)}}} \cdot \left(\frac{1}{Q}\frac{dQ}{dx} - \frac{1}{Q_s}\frac{dQ_s}{dx} + \frac{9-4n}{6}\frac{1}{D_s}\frac{dD_s}{dx} \right) \\ F_3 = -\frac{A_s}{K_c^2} \left(\frac{Q_s}{Q}\right)^{\frac{2}{2n-1}} \frac{1}{D_s^{\frac{10-6n}{3(2n-1)}}}. \end{cases} \tag{18}$$

and where A_s is a constant defined as:

$$A_s = (s-1) \left(\frac{K_c^{2n}}{K_{q_s}} \right)^{\frac{2}{2n-1}} \tag{19}$$

It is know that when the Froude number ($Fr = U/\sqrt{gH}$) is equal to 1, a critical flow condition occurs since the denominator of Eq. 9 tends to 0.

It is interesting to observe that the denominator of Equation (17) is always positive and thus no critical flow condition is found along the entire river length. Analytical investigations confirm that the validity of this result is not affected by both employed values of sediment transport exponent n and flow resistance formula exponent α.

This result could be explained noticing that natural system usually tries to smooth local discontinuities reaching a configuration where critical flow condition does not occur.

The hydraulic variables obtained by means of Equation 17 are then employed to calculate exponents E_H and E_W (see Equation 20). The obtained exponents are then investigated in order to find rational interpretation of classical *Regime formula* exponents.

$$H = K_H Q^{E_H} \tag{20}$$

$$W = K_W Q^{E_W} \tag{21}$$

3 BOUNDARY CONDITION ANALYSIS

In order to solve the 1st order variable coefficients ordinary differential equation (17) a boundary condition is needed. Uniform flow condition at boundary cross section is assumed by imposing equality between channel slope i and energy gradient loss j (Eq. 6) that gives the following:

$$H = \left[\left(\frac{i}{s-1} \right) \left(\frac{K_{q_s}}{K_c} \frac{Q}{Q_s} \right)^{\frac{2}{2n-1}} \right]^{\frac{2n-1}{2\alpha-2n+3}} D_s \tag{22}$$

Copyright © 2006 Taylor & Francis Group plc, London, UK

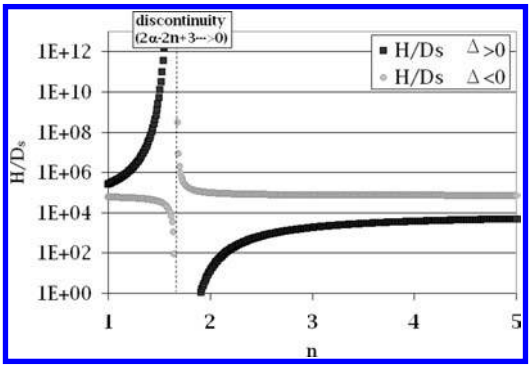


Figure 2. Dual behavior of H/D_s against n (input quantities: $Q = 10\,m^3/s$; $Q_s = 10^{-4}\,m^3/s$; $\alpha = 1/6$ (for $\Delta > 0$, $i = 1.2 * 10^{-5}$; for $\Delta < 0$, $i = 2.3 * 10^{-6}$).

Analytical investigations of Eq. 22 show how water depth H (and thus all related hydraulic variables) are strongly influenced by chosen value of both input variables Q, Q_s, D_s, i and exponents n and α.

In particular it can be analytically demonstrated that H behavior against n and α depends on the sign assumed by the following quantity:

$$\Delta = \left[\left(\frac{i}{s-1}\right)\left(\frac{K_{q_s}}{K_c}\frac{Q}{Q_s}\right)^{\frac{1}{\alpha+1}} - 1\right] \tag{23}$$

An example of H function against n, considering both positive and negative Δ cases, is presented in Figure 2. The plot shows how H function is characterized by dual behavior depending on Δ sign.

Furthermore let us also notice the existence of a specific combination of exponents α and n for which a discontinuity characterized by duality of H depending on quantity Δ, occurs in Equation (22) as:

$$\lim_{(2\alpha-2n+3)\to 0^+} H = \begin{cases} 0 & \text{if } \Delta > 0 \\ +\infty & \text{if } \Delta < 0 \end{cases}$$

$$\lim_{(2\alpha-2n+3)\to 0^-} H = \begin{cases} +\infty & \text{if } \Delta > 0 \\ 0 & \text{if } \Delta < 0 \end{cases}$$

Taking advantage of Equation (22), the expression of uniform flow Froude number is obtained (Eq. 24) and then employed to investigate physical explanation of H discontinuity. In particular as the quantity $(2\alpha - 2n + 3) \to 0$ a passage between supercritical and subcritical flow is detected: according to above introduced limits if the flow is subcritical H tends to 0 whereas if the flow is supercritical H tends to infinite.

$$Fr = \frac{U}{\sqrt{gH}} = C\sqrt{i} = K_c\left(\frac{H}{D_s}\right)^{\alpha}\sqrt{i}$$

$$= K_c\sqrt{i}\left[\left(\frac{i}{s-1}\right)\left(\frac{K_{q_s}}{K_c}\frac{Q}{Q_s}\right)^{\frac{2}{2n-1}}\right]^{\frac{2\alpha(2n-1)}{2\alpha-2n+3}} \tag{24}$$

The present analysis underlines how approaching to the limiting value of $(2\alpha - 2n + 3) \to 0$, the solution can be strongly affected by employed exponents α and n. The sign of quantity $(2\alpha - 2n + 3)$ influences both quantitatively and qualitatively the solution.

As example let us assume the classical case of $\alpha = 1/6$ (Strickler 1923). The limiting value of n that determine the sign of quantity $(2\alpha - 2n + 3)$ can be easily calculated as follow:

$$n = \tfrac{3}{2} + \alpha = \tfrac{5}{3}$$

In this case the proportionality of dependent variables against independent is the opposite employing sediment transport formula with exponent $n < 5/3$ (e.g. Meyer and Peter 1948, Shields 1938) or formula with exponent $n > 5/3$ (e.g. Engelund and Hansen 1967, Brown 1950). Hence also the exponents E_H and E_W are influenced by the employed value of sediment transport formula exponent n.

These considerations developed for uniform flow condition *at a station* can be extended also to 1D steady flow condition *in downstream direction*. Therefore awareness about the choice of exponents α and n is then recommended.

4 APPLICATION OF THE METHOD

In the present section a first example of application procedure is presented mainly to introduce potential applicability of the method such as rational derivation of exponents of river regime equations.

The method is applied to a real case study: a reach of the Italian river Ombrone-Grossetano (Grosseto-central Italy). In the recent decades no consistent artificial modifications have been performed on the Ombrone-Grossetano river, as consequences the river is almost in natural conditions. Moreover since there are not very pronounced erosion or deposit processes, the river can be assumed to be approximately in equilibrium conditions.

4.1 *Model set up*

The case study reach, approximatively 56.4 Km long, is located between the head of the river and the confluence with the Trasubbie river.

Copyright © 2006 Taylor & Francis Group plc, London, UK

The distributions of input variables along the river axis are calculated employing simple power functions, which are obtained directly from regression equations of Ombrone-Grossetano river field data (Paris 1991; Paris and Billi, 1996).

In particular the water discharge distribution Q (return period = 2 years), is calculated from:

$$Q = 16.133 \cdot x^{0.3841} \tag{25}$$

The total sediment discharge distribution Q_s, which increases in downstream direction, is calculated from:

$$Q_s = 4 \cdot 10^{-5} \cdot x^{0.4241} \tag{26}$$

The fining sediment size distribution D_s is calculated from:

$$D_s = -10^{-6} \cdot x + 0.1244 \tag{27}$$

The downstream decreasing bed slope i is calculated by employing the following:

$$i = -10^{-8} \cdot x + 0.0015 \tag{28}$$

Downstream relationships between independent and dependent variable are investigated by means of two cases:

- *Case 1*: all input functions (Q, Q_s, D_s) except bed slope i, are variable in downstream direction;
- *Case 2*: all input functions (Q, Q_s, D_s, i) are variable in downstream direction;

The value of dimensionless input quantities (at initial and final cross sections) employed in the application test are summarized in Table 1.

Strickler (1923) flow resistance formula and Brown (1950) sediment transport formula are employed to perform the calculations ($\alpha = 1/6$, $K_c = 21.1/\sqrt{g}$, $K_{q_s} = 100$, $n = 3$).

The non linear differential equation (Eq. 17) is solved, assuming the uniform flow at boundary condition introduced in Equation (22) and numerically integrated employing a *predictor corrector* method. Integration is performed according to flow characteristics which are verified by means of Fr number introduced in Equation (24).

4.2 *Results*

In Figures 3 and 4 dimensionless water depth H/H_{in} and dimensionless width W/W_{in} , obtained by means of Equations (15) and (17), are shown against corresponding dimensionless water discharge Q/Q_{in}. Let us obverse how the inclusion of whole variability of all input variable looks necessary in order to guarantee an increasing behavior in downstream direction of both H and W.

Table 1. Dimensionless input quantities for application case (Ombrone-Grossetano river: Paris 1991, Paris and Billi 1996).

$\frac{x_{fin}}{x_{in}}$	$\frac{Q_{fin}}{Q_{in}}$	$\frac{Q_{sfin}}{Q_{sin}}$	$\frac{D_{sfin}}{Q_{sin}}$
8.79	2.30	2.50	0.52

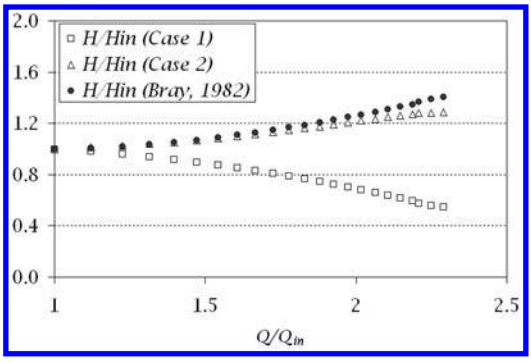


Figure 3. Dimensionless water depth H/H_{in} against dimensionless water discharge Q/Q_{in} (Bray 1982 formula; Case 1: Q, Q_s, D_s variable and i constant; Case 2: Q, Q_s, D_s, i variable).

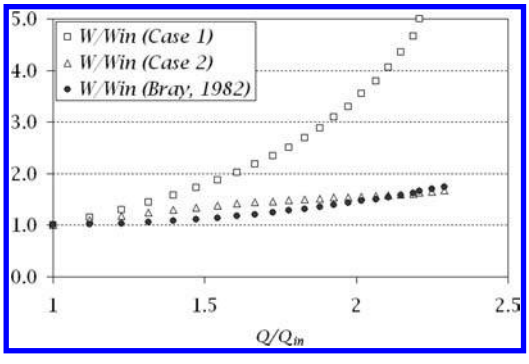


Figure 4. Dimensionless width W/W_{in} against dimensionless water discharge Q/Q_{in} (Bray 1982 formula; Case 1: Q, Q_s, D_s variable and i constant; Case 2: Q, Q_s, D_s, i variable).

In order to compare the results with classical *Regime equations exponents* the obtained hydraulic variables are subsequently interpolated by means of power functions previously introduced (Eq. 20): a comparison between obtained exponents and Blench (1957) and Bray (1982) formula is shown in Table 2. Case 1, where slope variability is not included, induces downstream decreasing water depth H (Fig. 3) and consequently negative E_H exponent, whereas Case 2 is

Copyright © 2006 Taylor & Francis Group plc, London, UK

Table 2. Application case: comparison of power function exponents with Regime formula of Bray (1982) and Blench (1957).

	Bray	Blench	Case 1	Case 2
E_H	0.33	0.33	−0.79	0.36
E_W	0.50	0.50	2.17	0.55

characterized by complete analogy behavior predicted by regime formula.

These considerations underline the importance of including the whole entire spatial variability of river basin input quantities which can be achieved only employing an approach in downstream direction.

5 CONCLUSIONS

A new analytical method based on a '*downstream*' approach for determination of equilibrium configuration of self formed channel has been presented.

The approach includes the spatial variability along the river reach of the quantities related to hydrological, morphological and sedimentological river basin characteristics, assuming as input variables water discharge, sediment size and sediment load distributions together with longitudinal bed slope along the river axis.

The stable configuration is obtained under the hypothesis of steady flow condition and no change in the bed level. To this aim 1D steady flow equation, 1D sediment continuity equation has been combined with two general expression of flow resistance formula and sediment transport formula obtaining a 1st order variable coefficients ordinary differential equation. The obtained differential equation points out that at the equilibrium configuration no critical flow condition occurs along the entire river length: the result is found valid for every combination of sediment transport and flow resistance formula exponents α and n. Further inspections on the possible physical justification of such phenomena are recommended.

It has been pointed out also how adopting an *approach at a station* width W and water depth H are inversely proportional to each other (Eq. 13, 14, 15) and thus characterized by opposite behavior with respect to input variables: this result suggests that in order to obtain *classical* hydraulic variables regime exponents (e.g. Blench 1957, Bray 1982) it is necessary to include downstream variation of the input variables.

Furthermore, analytical investigation has pointed out how hydraulic variables are both quantitatively and qualitatively strongly influenced by the chosen value of exponents n and α, in particular when the quantity $(2\alpha - 2n + 3)$ is approaching to zero.

A preliminary application test (Ombrone-Grossetano river, Italy) has been carried out, mainly to show the application procedure of the present method. The results show the importance of including the whole entire spatial variability of river basin input quantities and thus the appropriate characteristics of the proposed downstream method, that looks promising, especially to find rational explanation to *Regime formula* exponents.

ACKNOWLEDGEMENTS

The authors wish to thank Alberto Pistolesi (University of Florence, Italy) and Dr. Bruno Volzone (Department of Mathematics and Applications 'R. Caccioppoli', University of Naples, Italy) for the precious help concerning the analytical developments of the present method.

SYMBOLS

C : flow resistance coefficient;
D_s : sediment size;
D_{sin} : initial cross section sediment size;
D_{sfin} : final cross section sediment size;
E_H : depth regime power function exponent;
E_W : width regime power function exponent;
H : water depth;
i : longitudinal bed slope;
j : energy gradient loss;
K_C : flow resistance formula constant;
K_{Qs} : sediment transport formula constant;
n : sediment transport formula exponent;
Q : water discharge;
Q_{in} : initial cross section water discharge;
Q_{fin} : final cross section water discharge;
Q_s : sediment load;
Q_{sin} : initial cross section sediment discharge;
Q_{sfin} : final cross section sediment discharge;
R : hydraulic radius;
U : velocity;
U^* : shear velocity;
W : surface width;
x : downstream coordinate along river axis;
x_{in} : initial cross section downstream coordinate;
x_{fin} : final cross section downstream coordinate;
α : flow resistance formula exponent;
ϑ : dimensionless shear stress;
ϑ_{cr} : critical dimensionless shear stress;
g : acceleration due to the gravity;
s : specific gravity.

REFERENCES

Blench, T. (1957). Regime behaviour of canal and river. *Butterworths scientific publication 17.*

Copyright © 2006 Taylor & Francis Group plc, London, UK

Brown, C. (1950). *Sediment transportation*. New York, USA: H. Rouse (Eds), John Wiley.

Chang, H. H. (1979). Minimum stream power and river channel pattern. *Journal of Hydraulic Division 105*(6), 303–327.

Diplas, P. (1990). Characteristics of self formed straight channels, *Journal of Hydraulic Engineering 116*(5), 707–728.

Diplas, P. and G. G. Vigilar (1992). Hydraulic geometry of threshold channels. *Journal of Hydraulic Engineering 118*(4), 597–614.

Ikeda, S. (1981). Self formed straight channels in sandy bends. *Journal of Hydraulic Division 108*(1), 389–406.

Kovacs, A. and G. Parker (1994). A new vectorial bedload formulation and its application to the time evolution of straight river channel. *Journal of Fluid Mechanics 267*. 153–183.

Paris, E. (1991). Studi preliminari per il piano di bacino del fiume Ombrone. Dinamica fluviale ed aspetti progettuali. Regione Toscana.

Paris, E. and P. Billi (1996). Progetto dell'impianto di monitoraggio delle portate liquide e solide nel bacino del fiume Ombrone. Regione Toscana, Ufficio del Genio Civile di Grosseto.

Parker, G. (1978b). Self-formed straight rivers with equilibrium banks and mobile bed. Part 2: The gravel river. *Journal of Fluid Mechanics 89*(1), 127–146.

Schumm, S. and R. Lichty (1965). Time, space and causality in geomorphology. *American Journal of Science 263*, 110–119.

Simons, D. B. and M. Albertson (1963). Uniform water conveyance channels in alluvial material. *Trans. ASCE 128*(1), 65–167.

Strickler, A. (1923). Beitrage zur frage der geschwinddigkeitsformel und der rauhigkszahlen fur strome, kanale und geschlossene leitungen. *mitt. des Arm. fur Wasserwirtschaft 16*.

White, W., R. Bettess, and E. Paris (1982). Analytical approach to river regime. *Journal of Hydraulic Division 108*(10), 1179–1193.

Copyright © 2006 Taylor & Francis Group plc, London, UK

Two-layer approach for transcritical flow on mobile bed: Nickpoint migration

C. Savary, M. Bellal & Y. Zech
Dept. of Civil and Environmental Engineering, Université catholique de Louvain, Louvain-la-Neuve, Belgium

ABSTRACT: The transcritical flow presented in the paper consists in a transition from a mild to a steep bed slope, with a change in the flow regime from subcritical to supercritical at the transition (nickpoint). Experiments were carried out in the UCL sediment flume with uniform non-cohesive sediment under various hydraulic and geometric conditions. A two-layer model is proposed, able to cope with intense transport and severe transients. The Chezy-like friction coefficients of the model are calibrated on uniform flows conditions. Then the way to handle the boundary conditions is exposed, with a comparison between the common (Saint-Venant-Exner) and the two-layer approaches. The numerical and experimental results are successfully compared (bed and water levels) and the numerical evolution of the solid transport with time and space is analysed. Finally, evolution in time of the boundary conditions is presented.

1 INTRODUCTION

Transcritical flows over mobile bed are challenging to model due to the rapid variation in space and time of the solid transport and to the specific treatment required for boundary conditions. The experiment carried out by Bellal (Bellal et al. 2004) illustrates the morphological changes due to a transition from a mild to a steep bed slope. A change is observed in the flow regime from subcritical to supercritical at the transition (nickpoint). Such a transition generates a critical section moving upwards with regressive erosion. The nickpoint is associated with an important increase in bed shear stress and transport rate.

The common Saint-Venant-Exner approach (Rahuel 1988, Correia 1990, Correia et al. 1991) may fail in reproducing such sudden variation of transport due to the discontinuities in regime. A two-layer approach (Capart, 2000) is proposed, where the bed-load transport layer is explicitly considered. Moreover, it offers more possibilities to deal with boundary conditions including those associated to morphodynamics, above all if transcritical flow is expected. The solid discharge depends on the shear stresses applied at each layer interface. These shear stresses are linked to Chezy-like friction coefficients, which are calibrated in uniform flows conditions using the Meyer-Peter-Müller and Manning formulae. Then the way to handle the boundary conditions is exposed, with a comparison between the common (Saint-Venant – Exner) and the two-layer approaches. Afterwards, the water and bed profiles computed with the two-layer model are compared with measurements. The evolution of the solid transport with time and space and the displacement of the control section are analysed numerically. Finally, the change in time of the boundary conditions and the occurrence of a mixed control section are presented.

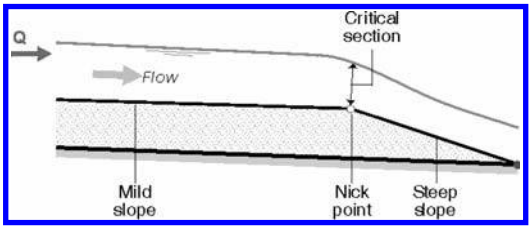


Figure 1. Initial condition.

2 EXPERIMENT

A control section over a changing erodible slope has been experimented by Bellal et al. (2004). The experiment represents the transition from a subcritical flow (water profile M_2) to a supercritical one (water profile S_2), transition from a mild slope to a steep slope (Fig. 1). A nickpoint is defined as the point of abrupt change in the longitudinal bottom profile of the channel. The control section is located at the nickpoint, the time-evolution is represented on Figure 2. The nickpoint and the control section propagates upwards, there is an erosion wave. The toe of the steep slope is non

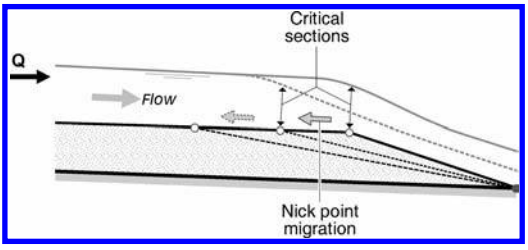


Figure 2. Nickpoint migration.

Table 1. Experimental data.

Test #	Q (l/s)	S_0^{up}(%)	S_0^{dwn} (%)
Run 1	4.90	0.4	2.02
Run 2	6.15	0.47	2.03
Run 3	7.33	0.45	2.00
Run 4	5.01	0.42	3.02
Run 5	6.18	0.44	5.03

erodible, it corresponds to the downstream end of the channel. The level of the toe of the steep slope thus remains the same during the regressive erosion.

In initial conditions, the nickpoint is pre-formed, it is located at 1 m (Table 1, run 1–3) or 1.1 m (Table 1, run 4–5) from the downstream end of the flume. The sediment bed is saturated with a small liquid discharge. Afterwards, the liquid discharge is progressively increased up to the experimental value. No sediment supply is furnished upstream.

At the end of the experiment, the control section and the nickpoint vanish as a supercritical flow takes place. As there is no sediment supply, no equilibrium state is reached.

Several experiments were performed within the following ranges of initial parameters reported in Table 1.

The experiment modelled below is run 1 (Table 1), the liquid discharge is 4.9 l/s, there is no sediment supply upstream. The upstream slope is 0.004 and the downstream slope is 0.02, these values respectively correspond to a mild and a steep slope.

3 NUMERICAL MODEL

To simulate such transient fluvial flows, a two-layer model developed by Capart (2000) and improved by Capart & Young (2002) in which boundary conditions treatment is introduced, is proposed. In this paper a one-dimensional model is used. Assuming the shallow-water hydrostatic pressure distribution, the flow is divided in two layers constituted of incompressible fluid. The main variables are the thickness of the water layer h_w and of the transport layer h_s, the

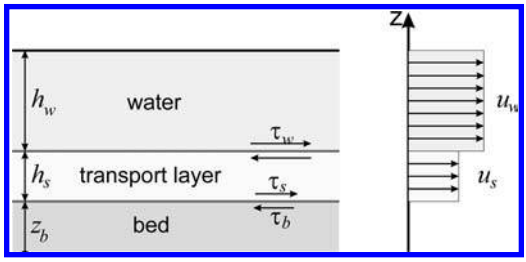


Figure 3. Two-layer model.

velocity in each layer u_w and u_s, respectively, and the level of the interface between the transport layer and the bed z_b (Fig. 3).

The transport layer and the fixed bed are constituted of a water-sediment mixture with a sediment concentration C, assumed as constant in time and in space. The volumetric density of this transport layer is $\rho_s' = (1-C)\rho_w + C\rho_s$ where ρ_w and ρ_s are the water and the grain density, respectively. In fact sediment mobilisation often requires a decrease of concentration (Spinewine, 2005) but, by seek of simplicity, this is not taken into account in the model here presented. The velocity in the transport layer u_s is allowed to be distinct from the velocity in the water layer u_w, but both are assumed to be uniform in their layer. As only the bed load is modelled, there is no mass and momentum exchange between the transport layer and the water. The only possible mass exchange occurs between the bed and the transport layer. The five-equation system proposed by Capart & Young (2002) results from mass (Equations 1–2) and momentum (Equations 4–5) conservation in each layer and from the definition of the erosion rate e_b(3).

$$\frac{\partial h_w}{\partial t} + \frac{\partial h_w u_w}{\partial x} = 0 \tag{1}$$

$$\frac{\partial h_s}{\partial t} + \frac{\partial h_s u_s}{\partial x} = e_b \tag{2}$$

$$\frac{\partial z_b}{\partial t} = -e_b \tag{3}$$

$$\frac{\partial h_w u_w}{\partial t} + \frac{\partial\left(h_w u_w^2 + \frac{1}{2} g h_w^2\right)}{\partial x} + g h_w \frac{\partial\left(z_b + h_s\right)}{\partial x} = -\frac{\tau_w}{\rho_w} \tag{4}$$

$$\frac{\partial h_s u_s}{\partial t} + \frac{\partial\left(h_s u_s^2 + \frac{1}{2} g h_s^2\right)}{\partial x} + g h_s \frac{\partial\left(z_b + \frac{\rho_w}{\rho_s'} h_s\right)}{\partial x} = \frac{\tau_w}{\rho_s'} - \frac{\tau_b}{\rho_s'} \tag{5}$$

where the erosion rate e_b depends on the shear stresses τ_s and τ_b:

$$e_b = \frac{\tau_s - \tau_b}{\rho_s' u_s} \tag{6}$$

The shear stress between the water and the transport layer τ_w and the shear stress applied on the fixed bed τ_s are assumed to follow a Chézy-like friction law:

$$\tau_w = \rho_w C_{f,w} |u_w - u_s| (u_w - u_s) \quad (7)$$

$$\tau_s = \rho'_s C_{f,s} |u_s| u_s \quad (8)$$

where $C_{f,w}$ and $C_{f,s}$ are water and sediment friction coefficients. The resistance shear stress to the flow, exerted by the fixed bed, is expressed by a Mohr–Coulomb relation.

$$\tau_b = \tau_{crit} + tg\,\varphi(\rho'_s - \rho_w) g h_s \quad (9)$$

where τ_{crit} is the threshold value of τ_s allowing erosion and φ is the angle of repose of the soil. This two-layer numerical scheme is documented in more details in Chen et al. (in press), where it is applied to flows involving water and mud layers.

A finite-volume approach is adopted to discretise the system. The system is solved in two steps (Capart & Young, 2002), the first solving the hyperbolic part of the system and the second the source terms. The hyperbolic part of the system is integrated using the Godunov scheme developed by Harten et al. (1983). This method allows to solve the conservative part of the system, it was extended by Fraccarollo et al. (2003) to take into account the non conservative products (pressure on the sloping interface) as additional terms (called lateralised terms) of the fluxes.

4 CALIBRATION

The friction coefficients are calibrated on base of uniform flow conditions. In uniform steady flow conditions, Equations (1–5) simplify since the partial derivatives $\partial/\partial t = 0$ and $\partial/\partial x = 0$, except $\partial z_b/\partial x = -S_0$. The solid transport is in equilibrium, which means that neither erosion nor deposition occurs; thus $\tau_s = \tau_b$.

The calibration consists in finding the friction coefficients corresponding to a flow described by five parameters, for given slope and water discharge, the uniform depth is calculated with the Manning formula and the solid discharge and the critical shear stress are evaluated with the Meyer-Peter-Müller formula. The calibration conditions depend on the flow characteristics. In the present application, the solid transport takes place mainly in the supercritical part of the flow, downstream the nickpoint. It was thus chosen to calibrate the friction coefficients using the parameters (q_w, h_w, q_s, S_0 and τ_{crit}) of a flow corresponding to a Froude number:

$$\mathbf{Fr}_w = \frac{u_w}{\sqrt{g h_w}} = 1.2 \quad (10)$$

which is a good average of the observed Froude number. If the calibrated friction coefficients are acceptable, the computed solid discharge should be close to Meyer-Peter-Müller predictions (Fig. 4) and the Manning coefficient should be close to the measurements (Fig. 5).

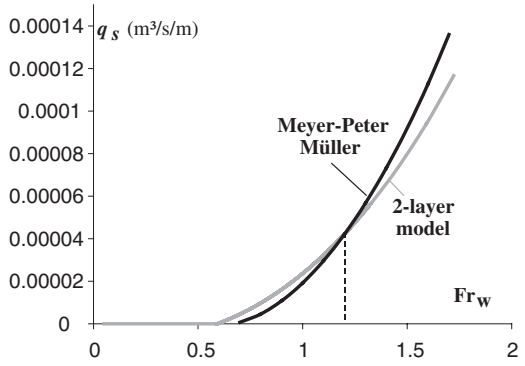


Figure 4. Evolution of solid discharge q_s with Froude number $\mathbf{Fr_w}$: comparison between two-layer model and Meyer-Peter-Müller formula (run 1 (Table 1), $C_{fw} = 0.02$, $C_{fs} = 0.128$).

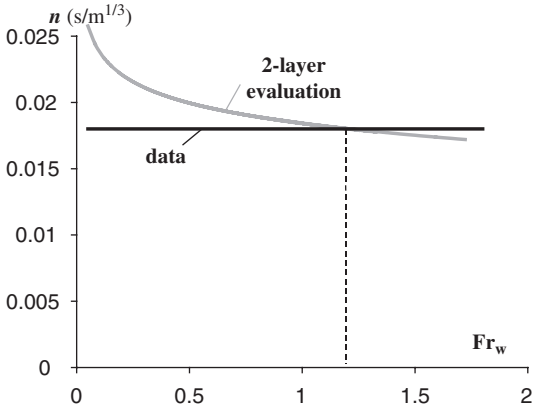


Figure 5. Evolution of roughness Manning coefficient n with Froude number $\mathbf{Fr_w}$: comparison between two-layer model and datas (run 1 (Table 1), $C_{fw} = 0.02$, $C_{fs} = 0.128$).

The solid discharge q_s is overestimated for Froude numbers lower than the calibration value ($\mathbf{Fr_w} = 1.2$) and underestimated for higher Froude numbers. In the range of $\mathbf{Fr_w} = 1 \ldots 1.4$, where the most important solid transport is noticed during the experiment, the estimations of the two-layer model and the Meyer-Peter-Müller formula are close. The Manning coefficient (labeled as data) is an estimation of the average experimental Manning coefficient. The main difference between this constant coefficient and the one deduced from the two-layer model is due to the difference between Manning formulation, used for calibration, and Chezy form, used to express the shear stresses.

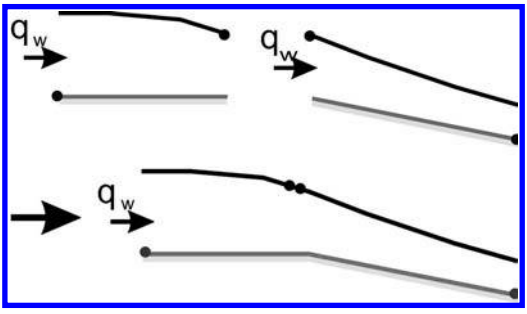


Figure 6. Classical boundary conditions in the case of the nickpoint migration transcritical case.

5 BOUNDARY CONDITION

First, the way the boundary conditions are treated with a classical model based on the Saint-Venant-Exner equations is exposed. Then the characteristic method (Abbot 1979) is applied to the two-layer model which is used here to model the nickpoint migration.

5.1 *Classical approach*

The main unknowns of the Saint-Venant-Exner equations are the water depth h_w, the water discharge q_w and the bed level z_b. Contrarily to the two-layer model, the transport layer is not explicitly considered in this approach. The boundary conditions have to be expressed as functions of the main unknowns h_w, q_w and z_b. As the solid discharge is calculated with a closure relation and is not one of the unknowns, it can not be imposed as a boundary condition. The Saint-Venant-Exner system of equations (Cunge et al. 1980) have three eigenvalues, for each Froude number, two of them are positive and one is negative (Vreugdenhil & de Vries 1967). It is usually stated that in supercritical flows, the two upstream conditions (linked to the positive eigenvalues) concern the hydrodynamic variable (h_w and q_w) and the downstream one (linked to the negative eigenvalues) concerns the sediments (z_b). By the same way, in subcritical flow, conditions on hydrodynamic have to be imposed upstream (q_w) and downstream (h_w), the second upstream condition concerns the sediments (z_b).

The flow is divided into two parts (Fig. 6), the reach located upstream the nickpoint (subcritical) and the one located downstream (supercritical). In each reach two conditions have to be imposed upstream and one downstream. As the two parts are joined, the bed level z_b should be imposed upstream and downstream and the water discharge q_w should be imposed upstream.

Of course, in the experiment, the bed level at the upstream reach can not be constant as there is no sediment supply. The boundary condition on the bed level is not adapted to this case, it would have been better to be allowed to impose the solid discharge instead of the bed level.

5.2 *Two-layer model*

Boundary conditions have to be expressed as functions of the main unknowns (h_w, h_s, z_b, q_w, q_s) of the five-equation system (1–5). In opposition with the previous classical approach, it is possible to express boundary conditions on the solid discharge q_s. Neglecting the source terms, the five-equation system (1–5) can be written

$$\frac{\partial \mathbf{U}}{\partial t}+\frac{\partial \mathbf{F(U)}}{\partial x}+\mathbf{H(U)}\frac{\partial \mathbf{U}}{\partial x}=\frac{\partial \mathbf{U}}{\partial t}+\frac{\partial \mathbf{F(U)}}{\partial \mathbf{U}}\frac{\partial \mathbf{U}}{\partial x}+\mathbf{H(U)}\frac{\partial \mathbf{U}}{\partial x}$$

$$=\frac{\partial \mathbf{U}}{\partial t}+\mathbf{A(U)}\frac{\partial \mathbf{U}}{\partial x}+\mathbf{H(U)}\frac{\partial \mathbf{U}}{\partial x}=\frac{\partial \mathbf{U}}{\partial t}+\mathbf{A'(U)}\frac{\partial \mathbf{U}}{\partial x}=0 \quad (11)$$

where $\mathbf{A(U)}$ is the Jacobian matrix and $\mathbf{A'(U)}=\mathbf{A(U)}+\mathbf{H(U)}$ a kind of pseudo-Jacobian matrix.

The five-equation system has five eigenvalues, one of them is equal to zero. To analyse the sign of the other four eigenvalues, the characteristic polynomial (12) and the product (13) of the non-zero roots λ_i, $i=1\ldots4$ are written ($\mathbf{I}$ is the identity matrix):

$$\left|\mathbf{A'}-\lambda\mathbf{I}\right|=0 \Rightarrow \lambda\left(a\lambda^4+b\lambda^3+c\lambda^2+d\lambda+e\right)=0 \quad (12)$$

$$\prod_{i=1}^{4}\lambda_i=\frac{e}{a}=c_s^2c_w^2\left(1-\frac{\rho_w}{\rho_s'}\right)+u_s^2u_w^2-\left(c_w^2u_s^2+c_s^2u_w^2\right) \quad (13)$$

with $c_w=(gh_w)^{1/2}$ and $c_s=(gh_s)^{1/2}$, respectively the celerity in the water and the transport layer. The sign of the non-zero eigenvalue product (13), and thus of the characteristics, changes when

$$\mathbf{Z_{sw}}=\frac{c_s^2c_w^2\left(1-\frac{\rho_w}{\rho_s'}\right)+u_s^2u_w^2}{c_w^2u_s^2+c_s^2u_w^2}=\frac{\left(1-\frac{\rho_w}{\rho_s'}\right)+\mathrm{Fr}_s^2\mathrm{Fr}_w^2}{\mathrm{Fr}_s^2+\mathrm{Fr}_w^2}=1 \quad (14)$$

where $\mathbf{Fr_s}=u_s/c_s$ is the sediment Froude number. The non-dimensional number $\mathbf{Z_{sw}}$ is a kind of two-layer Froude number describing the interference between water and sediment wave celerities. According to Equations (13–14), if $\mathbf{Z_{sw}}>1$, the number of negative characteristics is even (0 or 2 negative characteristics) while if $\mathbf{Z_{sw}}<1$, this number is odd (1 negative characteristic). If the transport layer vanishes ($h_s\rightarrow 0$), $\mathbf{Z_{sw}}$ becomes equivalent to the square of the water Froude number $\mathbf{Fr_w}$. If the water layer disappears ($h_w\rightarrow 0$), $\mathbf{Z_{sw}}$ becomes equivalent to the square of the sediment Froude number $\mathbf{Fr_s}$. If $\mathbf{Z_{sw}}=1$ there is a kind of control section, which corresponds to a relation between the depths (h_w and h_s) and the discharges (q_w and q_s) in each layer.

The non-dimensional number $\mathbf{Z_{sw}}$ (Fig. 7) is calculated for a range of water Froude numbers with the friction coefficients calibrated above.

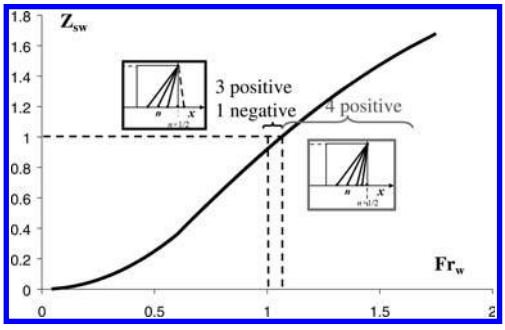


Figure 7. Evolution of the number Z_{sw} computed with the water Froude number Fr_w (run 1 (Table 1), $C_{fw} = 0.02$, $C_{fs} = 0.128$).

Three areas have to be distinguished:

Subcritical flow

– $\mathbf{Fr_w} < 1$: ($\mathbf{Z_{sw}} < 1$) three positive eigenvalues and one negative imply three upstream boundary conditions (e.g.: q_w, q_s, h_s) and one downstream (e.g.: h_w or control section)

Supercritical flow

– $1 < \mathbf{Fr_w} < 1.07$: ($\mathbf{Z_{sw}} < 1$) three positive eigenvalues and one negative imply three upstream boundary conditions (e.g.: q_w, q_s, h_s) and one downstream (e.g.: h_w or control section)

– $\mathbf{Fr_w} > 1.07$: ($\mathbf{Z_{sw}} > 1$) four positive eigenvalues imply four upstream boundary conditions (e.g.: q_w, q_s, h_w, h_s)

Till the control section vanishes, the flow at the upstream boundary remains subcritical and three upstream boundary conditions have to be imposed. The flow at the downstream boundary is always supercritical during the experiment, the number of downstream boundary conditions will depend on the Froude number. Till the Froude number is higher than 1.07, there is a total transmission without any downstream boundary condition. If the Froude number decreases below 1.07, the downstream end may influence the flow and a boundary condition has to be imposed (Fig. 8).

The eigenvalues are ranked from the highest to the lowest. The unknowns at the upstream interface ($h_{w,1/2}$, $h_{s,1/2}$, $z_{b,1/2}$, $q_{w,1/2}$, $q_{s,1/2}$) are obtained by the solution of the system composed of the three boundary conditions

$$q_{w,1/2} = q_{w,up} \tag{15}$$

$$q_{s,1/2} = q_{s,up} = 0 \tag{16}$$

$$h_{s,1/2} = 0 \tag{17}$$

one compatibility relation linked to the vertical (18) characteristic (eigenvalue equal to zero λ_4).

$$\left(z_{b,1/2}^{t+dt} - z_{b,1/2}^{t}\right)_{\lambda_4} = 0 \tag{18}$$

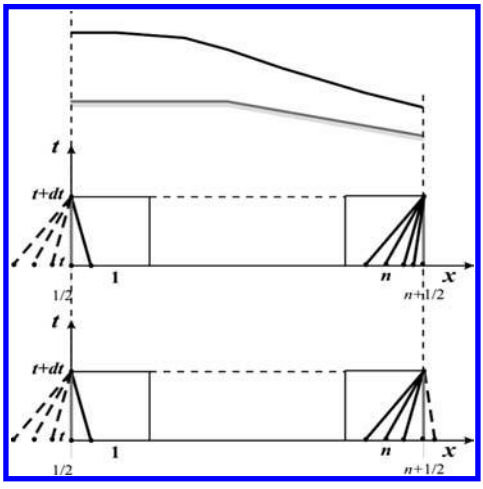


Figure 8. Two-layer boundary conditions in the case of the nickpoint migration transcritical case.

and another compatibility relation linked to the negative characteristic (negative eigenvalue λ_5) (Savary & Zech, submitted).

In the case of 4 positive eigenvalues downstream, the unknowns at the downstream interface ($h_{w,n+1/2}$, $h_{s,n+1/2}$, $z_{b,n+1/2}$, $q_{w,n+1/2}$, $q_{s,n+1/2}$) are obtained by the resolution of the system composed of the five compatibility relations which can be simplified to express a total transmission.

$$h_{w,n+1/2} = h_{w,n} \qquad h_{s,n+1/2} = h_{s,n} \qquad q_{w,n+1/2} = q_{w,n}$$

$$q_{s,n+1/2} = q_{s,n} \qquad z_{b,n+1/2}^{t+dt} = z_{b,n+1/2}^{t} \tag{19}$$

In the case one of the eigenvalue is negative downstream, even if the flow is supercritical, a boundary condition has to be imposed at the downstream end, this case will be exposed below.

6 COMPARISONS

The experimental and numerical initial conditions are plotted on Figure 9. The numerical initial bed level is compound of two constant slopes, contrarily to the experimental one, which is more irregular, due to difficulty to realise a perfect slope in a flume. Some differences between the numerical results and the experimental data are due to this initial dicrepancy. The non erodible bed (bottom of the flume) is set to level 0.11 m.

Figure 10 illustrates the evolution with time of water and bed levels. The regressive erosion induces the slope upstream the nickpoint increases as the slope downstream decreases till the two slopes become identical in order that the nickpoint and the control section

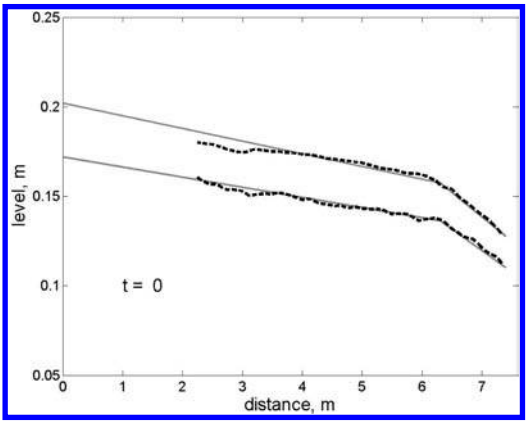


Figure 9. Comparison between experimental (.....) and numerical (—) levels: initial conditions.

vanish. The bed level at the downstream end remains the same during all the computation, the downstream slope decreases taking this fixed point as tilting point. There is no sediment supply upstream, the flow thus erodes a part of the bed at the upstream part to constitute a transport layer. The erosion in the upstream end stops when the shear stress applied to the bed decreases below the critical treshold. The erosion area enlarges downwards with time. In the downstream part, the computed bed level is a little higher than the experimental one. As exposed in the calibration section (Fig. 4), for high Froude numbers, the computed solid discharge is a little lower than the one estimated by Meyer-Peter-Müller inducing a lower erosion. Moreover, when the Froude number is lower than 1.2 (mainly upstream the nickpoint), the solid discharge is overestimated in comparison with Meyer-Peter-Müller predictions. An overestimated solid discharge coming from the upstream reach induces an overestimated deposition in the downstream reach. As the bed and water levels are not measured there, no comparison near the upstream boundary is possible.

The evolution of the solid discharge along the flume with time is plotted in Figure 11. In initial conditions, there is no transport layer, thus the solid discharge is equal to zero everywhere. The evolution with time allows to identify three areas.

– First, the upstream part of the flow (distance $<\sim$1.8 m) corresponds to the creation of the transport layer. The slope and the solid discharge decrease with time in this area. At the upstream end, as it is imposed like a boundary condition, the solid discharge is zero. Once the shear stress applied to the bed decreases below a threshold value, no solid transport occurs. The area without any solid discharge enlarges with time, the solid discharge inquiring some space to increase.
– The second area (1.8 $<\sim$ distance $<\sim$ 6 m) is the part of the flow located between the nickpoint and the upstream area. At the beginning of the experiment, a water profile M_2 develops from the critical depth at the nickpoint. As the length is important enough and till the slope is quite regular, it reaches the uniform depth upstream. For the two or three first computation times, there is an area ($\sim$=2 m or 2.5 m) where the flow is close to uniform and the solid discharge is close to equilibrium. The solid discharge increases approaching the nickpoint. The solid discharge also increases with time inducing a rise of slope in this area.
– The last zone is the part of the flow, downstream the nickpoint, where the flow is supercritical. At the beginning of the experiment, the solid discharge increases sharply in this area. Due to the regressive erosion, the solid discharge and the bed slope decrease with time in this part of the flow.

At the end of the experiment/computation, the nickpoint vanishes and the different areas become less distinguishable.

The transport layer depth h_s is set to zero at the upstream interface, however the flow generates a transport layer in the first cell. Even if the solid discharge is equal to zero, the proximity of the threshold leads to a small fictitious transport layer depth but with a velocity equal to zero (Fig. 12).

The water Froude number (Fig. 13) and the solid discharge (Fig. 11) are closely linked, the three areas described above appear in both figures. In the upstream area, the flow becomes more and more subcritical with time, the slope and so the Froude number decrease. In the middle area the slope and the Froude number increase with time. Downstream the nickpoint, the regressive erosion makes the slope and the Froude number decrease. During all the experiment, the flow remains transcritical, the movement of the control section is depicted in Figure 14, the control section propagates first upwards and then downwards in a space interval smaller than 1 m (during the experiment). When the non-dimensional number $\mathbf{Z_{sw}}$ becomes lower than 1 (589 s and 851 s) (Fig. 15), the downstream end influences the flow and the nickpoint stops propagating upwards to move downwards. The intuition, mentioned before, that the nickpoint propagates upwards is thus only partly confirmed by the numerical results. Unfortunately the profiles are not smooth enough to observe the displacement of the control section experimentally. If the computational time was longer, the nickpoint would reach the downstream end and the flow would become subcritical all along the flume.

For the two last computation times (589 s and 851 s), the non-dimensional number $\mathbf{Z_{sw}}$ (Fig. 15) is lower than 1 at the downstream end ($\mathbf{Fr_w} < 1.07$). It implies,

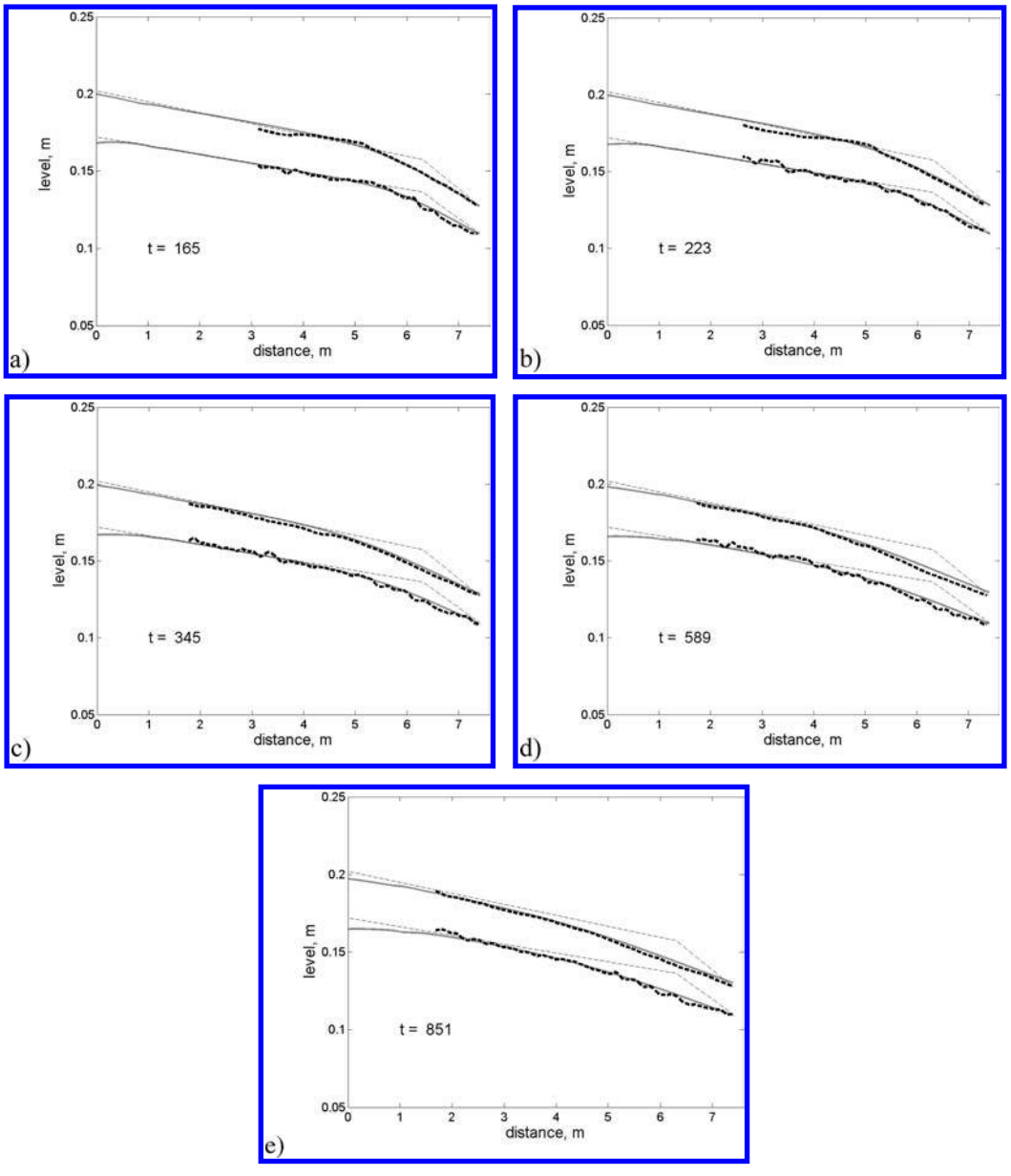


Figure 10. a–e. Comparison between experimental (…..) and numerical (—) levels: time evolution (108 s–851 s) (initial conditions (- - - -)).

as illustrated in Figure 7, one boundary condition has to be imposed at the downstream end. Looking at the experiment, the choice of which condition to impose is not obvious. A parallelism is made with a pure hydrodynamic example (Fig. 16). A supercritical water profile S_2 develops on a steep slope flume, if the slope decreases under the critical slope, the flow becomes subcritical, the water profile becomes M_2. The location of the control section changes from the upstream to the downstream end. If the slope decreases again, the downstream condition remains a critical section $\mathbf{Fr_w} = 1$ (corresponding to a eigenvalue equal to zero). In the case of a two-layer flow, when the slope decreases, the non-dimensional number $\mathbf{Z_{sw}}$ decreases till it reaches 1 at the downstream end. Then, the influence on the flow moves from the upstream to the

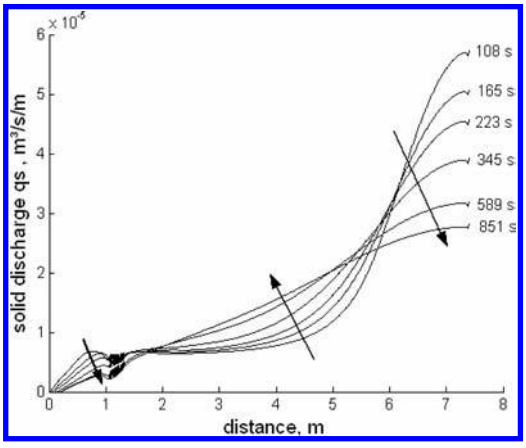


Figure 11. Variation of the computed solid discharge q_s along the flume with time.

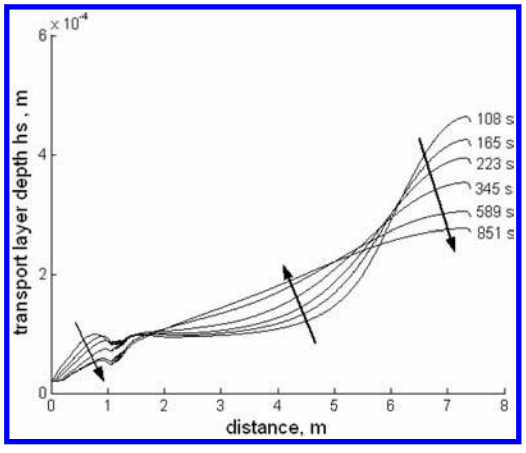


Figure 12. Variation of the computed transport layer depth h_s along the flume with time.

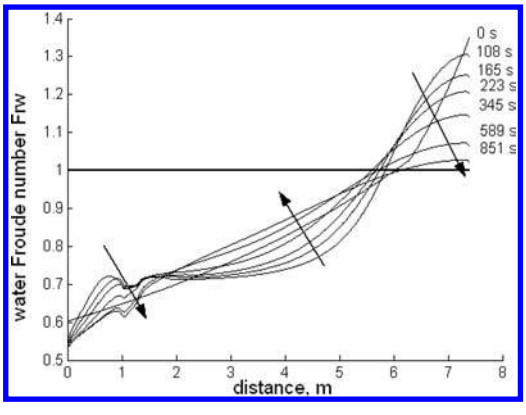


Figure 13. Variation of the computed Froude number $\mathbf{Fr_w}$ along the flume with time.

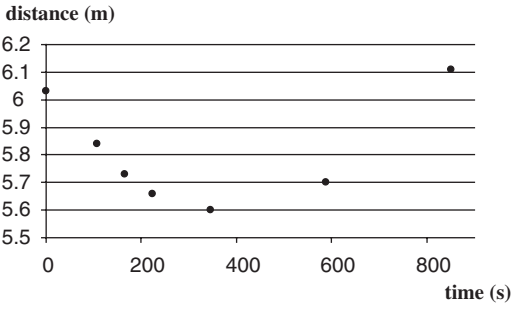


Figure 14. Position of the control section along the flume with time.

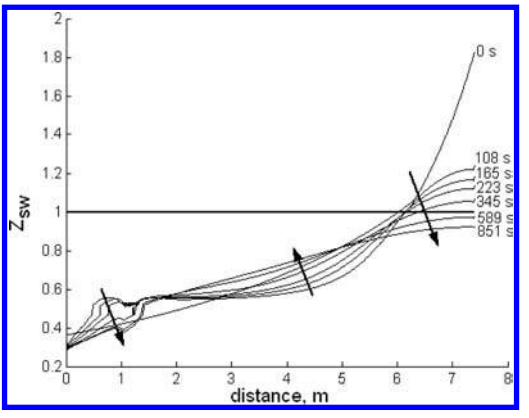


Figure 15. Variation of the computed non-dimensional number $\mathbf{Z_{sw}}$ along the flume with time.

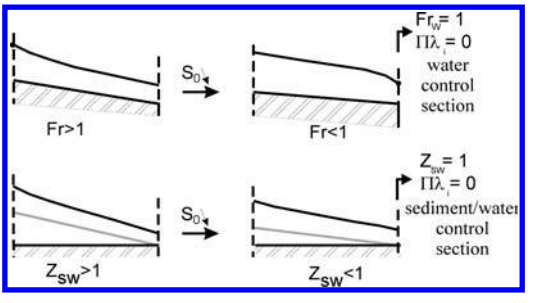


Figure 16. Comparison between hydrodynamic case, control section.

downstream end. If the slope decreases again, there is a kind of mixed control section at the downstream end, the non-dimensional number $\mathbf{Z_{sw}}$ remains equal to 1 (corresponding to a eigenvalue equal to zero).

In this case, one of the compatibility relation has to be replaced by a mixed control section condition. $\mathbf{Z_{sw}}$ is fixed to 1, implying one of the eigenvalue is equal to zero.

7 CONCLUSIONS

The case of a transcritical flow over a changing bed slope was discussed. A two-layer model was proposed as an alternative to common models based on Saint-Venant-Exner equations. After a short description of the experimental conditions and the two-layer model proposed (Capart & Young, 2002), the friction coefficients appearing in the model were calibrated using Manning and Meyer-Peter-Müller formulations. Then, the way to treat the boundary conditions was exposed for both, classical and two-layer, models. Concerning boundary conditions, the two-layer approach revealed to be more flexible and closer to real conditions. A good agreement was observed between the two-layer model and the experiment the boundary conditions treatment revealed a mixed water-sediment control section downstream. It would be interesting to test and compare various boundary conditions to observe their influences on the results.

ACKNOWLEDGEMENTS

The authors would like to thank H. Capart for his advices about using the eigenstructure to handle the boundary conditions and for the access to his two-layer software. The authors are thankful to the laboratory staff for his help during the measurement campaign.

REFERENCES

Abbot, M.B. 1979. Computational hydraulics. Elements of the theory of free-surface flows. Pitman, London.

Bellal M., Iervolino M. & Zech Y. (2004). Nickpoint migration process: experimental and numerical approaches. Proceedings 12th conference on "sediment and sedimentation particles", Prague (Czech Republic), 20–24 September 2004.

Capart H. (2000). Dam-break induced geomorphic flows and the transition from solid- to fluid-like behaviour across evolving interfaces. PhD thesis, Université catholique de Louvain, Louvain-la-Neuve, Belgium.

Capart H. & Young D.L. (2002). Two-layer shallow water computations of torrential geomorphic flows. Proceedings of River Flow 2002, Louvain-la-Neuve, Belgium, September 2002, 1003–1012.

Chen, S.-C., Peng, S.-H., & Capart, H. Two-layer shallow water computation of mud flow intrusions into quiescent water. *Journal of Hydraulic Research* (in press).

Correia L.R.P. (1990). Numerical modelling of unsteady sediment transport, PhD thesis, Ecole Polytechnique Fédérale de Lausanne, Lausanne, Switzerland.

Correia L.R.P., Krishnappan B.G. & Graf W.H. (1991). Laboratory verification of a coupled unsteady flow model. Proceedings of XXIV IAHR Congress, Madrid, Spain, 1991, A471–A480.

Cunge J.A., Holly F.M. & Verwey A. (1980). Practical aspects of computational river hydraulics. Pitman Advanced Publishing Program, London.

Fraccarollo L., Capart H. & Zech Y. (2003). A Godunov method for the computation of erosional shallow water transient. Int. Journal of Numerical Methods in Fluids, 41, 951–976.

Harten A., Lax P.D. & van Leer B.(1983). On upstream differencing and Godunov-type schemes for hyperbolic conservation laws. SIAM Review, 25, 35–61.

Rahuel, J.L. (1988). Modélisation de l'évolution du lit des rivières alluvionnaires à granulométrie étendue (in French), Institut National Polytechnique de Grenoble, Grenoble, France.

Savary, C. & Zech, Y. Boundary conditions in a two-layer geomorphical model. Application to a hydraulic jump over a mobile bed. *Journal of hydraulic research* (submitted)

Spinewine B. 2005. Two-layer flow behaviour and the effects of granular dilatancy in dam-break induced sheet flow. PhD thesis, Université catholique de Louvain, Louvain-la-Neuve, Belgium.

Veugdenhil C.B. & de Vries M. (1967). Computation of non-steady bed-load transport by a pseudo viscosity method, Delft Hydr. Lab. Publ. No 45, Delft, The Netherlands.

On the effect of the bed morphology on the river confluence hydrodynamics

D. Đorđević & M. Jovanović
Faculty of Civil Engineering, University of Belgrade, Belgrade, Serbia & Montenegro

ABSTRACT: A river confluence is known for the strong three-dimensional flow effects. The confluence hydrodynamics is significantly influenced by the river bed morphology. Two morphological features are typical for river confluences: a discordance of the two river bed elevations at the entrance to the confluence and presence of a scour hole in the post-confluence channel. The objective of this paper is to examine the influence of these morphological features on the flow structure by using a three-dimensional numerical model. The confluence of the Sava and Danube Rivers (in the city of Belgrade) offers excellent possibilities for this investigation, as both bed elevation discordance and scour hole are present. The results of numerical simulations for this case are compared to the results obtained for the three hypothetical bed configurations of the same confluence: a) concordant bed elevations and the scour hole, b) concordant bed elevations and no scour hole, and c) discordant bed elevations and no scour hole. An attempt is made to generalise the results of numerical simulations. Results are discussed in terms of the secondary flow pattern and the distribution of the turbulent kinetic energy.

1 INTRODUCTION

A river confluence has always been a challenging subject for river hydrodynamics and morphodynamics investigations due to complex flow phenomena and processes occurring in both the confluence and the post-confluence channel. The complexity of the phenomena and processes arises from the strong three-dimensional flow effects resulting from the interaction of the incoming flows and the interaction thereof with the river bed. In the last decade, new methods and tools for investigation of complex flows were developed and/or the existing methods and tools were improved, offering opportunities to shed more light on the processes characteristic for a river confluence. The majority of investigations were, however, concerned with the laboratory models of confluences (Best & Reid 1984, Biron et al. 1996b, 2004, Bradbrook et al. 2000, 2001, Huang et al. 2002). There are only a few field investigations, mostly on the small rivers (Biron et al. 1996b, Bradbrook et al. 2000, Rhoads & Sukhodolov 2001).

Unlike a river confluence, a laboratory model of a confluence assumes a simplified plan-form and cross-section geometry of the main river, tributary and post-confluence channels. Hence, not all relevant factors necessary for complete understanding of the confluence hydrodynamics can be encountered for with a laboratory model of a confluence. Field investigations have shown, for instance, that transition between the shallower tributary bed and the main river bed at the entrance to the confluence of alluvial rivers is not as vertical as considered in the laboratory models of confluences (Rhoads & Sukhodolov 2001, Jovanović et al. 2005). Also, no significant increase in the width of the post-confluence channel was observed. Confluences are observed to have a form of the scour hole, too (Rhoads & Sukhodolov 2001), the position and size of which are influenced by the plan-form of the confluence, geological composition of the river bed and the upstream hydrologic regimes of the confluent streams.

The confluence of the Sava and Danube Rivers in the city of Belgrade is a typical example of an asymmetrical confluence with the shallower channel of the Danube river, no significant increase in the post-confluence channel width, and presence of the scour hole. With such a complex plan-form and bed morphology it was interesting to investigate how different river bed configurations may influence the confluence hydrodynamics. Therefore numerical simulation results of the three-dimensional flow at the confluence with the observed bed topography were compared to the results for three hypothetic river bed morphologies: a) concordant beds and the scour hole, b) discordant beds and no scour hole and c) concordant beds and no scour hole. Simulations were performed for various combinations of the upstream hydrologic regimes of the confluent streams.

2 PROBLEM DESCRIPTION

The confluence of the Danube and Sava Rivers in the city of Belgrade is depicted in Figure 1. The

Copyright © 2006 Taylor & Francis Group plc, London, UK

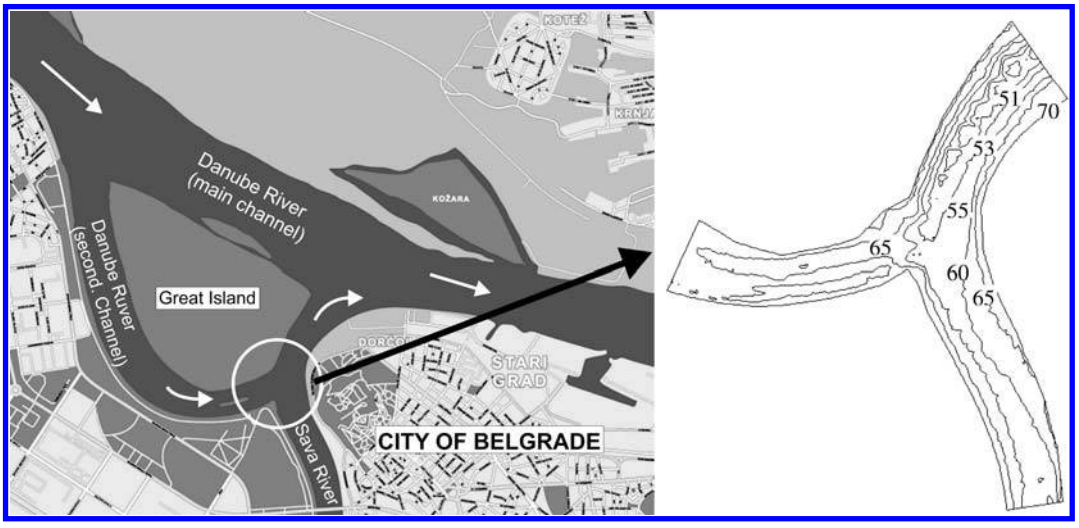


Figure 1. Site location (left) and bed elevation contours (right).

characteristic shape of the network is caused by the presence of the Great Island which divides the Danube River into the so called "Main channel" with the wider, almost straight channel, and a narrower secondary channel. The later one forms a bend in its downstream reach. Upstream from the confluence the channel of the Sava River is almost straight, while downstream from the confluence it forms a bend of radius R = 700 m.

The subject of the present study is a portion of the confluence encircled in Figure 1. It includes the Sava River (the main river in this case), and the branch of the Danube River (the tributary in this case). The junction angle at the confluence is 78°. Surveys of the river network bathymetry indicate that the bottom of the tributary channel is approximately 10 m above the bottom of the main river at the entrance to the confluence, and that there is a bar along the right bank of the main river immediately upstream from the confluence. In addition, scour hole is formed in the central part of the post-confluence channel with the deepest region of approximately 10 m in the vicinity of the cross-section D (Figs. 1 and 2). The widths of all three channels are almost the same varying in the range between 275 m and 290 m (Tab. 1).

Bathymetries for the other three river bed configurations (Tab. 2) were defined either by lowering the bottom of the tributary channel to match the bed level of the main river channel (case 3), or by "filling" the scour hole in the post-confluence channel (cases 2 and 4) to the level of 54 m.

The effect of the bed morphology on the confluence hydrodynamics can be analysed by covering a range of possible hydrological conditions at the confluence. A set of considered discharge combinations

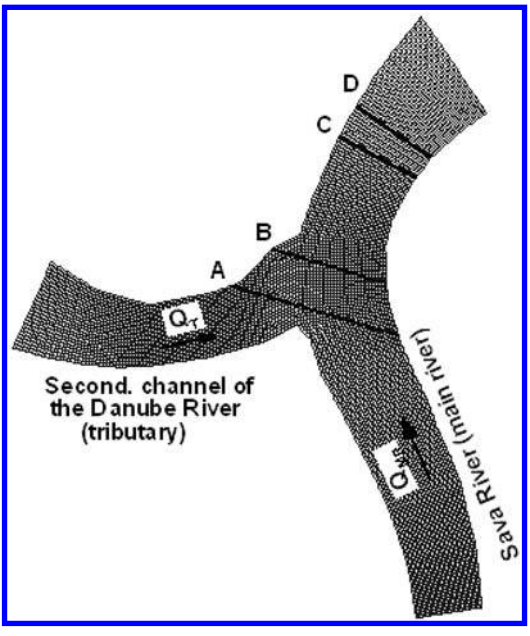


Figure 2. Computational mesh and position of the analysed cross-sections.

is given in Table 3. For the sake of simplicity, non-deformable bed was assumed for all considered river bed configurations.

A momentum-flux ratio ($M_R = \rho V_{MR} Q_{MR} / \rho V_T Q_T$) differs for different river bed configurations. The two values of M_R correspond to each D_R value, since two combinations of the bed morphology at the entrance to the confluence (concordant and discordant beds) were

Copyright © 2006 Taylor & Francis Group plc, London, UK

Table 1. Summary of the confluence site characteristics.

River	Bank full width (m)	Junction angle (°)	Backstep height (m)
Sava River (Main river)	≈290		
Second.chan. of the Danub River (Tributary)	275	78	10
Sava River (postconfl. ch.)	≈290		

Table 2. Analysed configurations of the bed morphology.

Case no.	Description
1	Discordant beds and scour hole (surveyed bathym)
2	Concordant beds and scour hole
3	Discordant beds and no scour hole
4	Concordant beds and no scour hole

supposed (Tab. 4). The M_R values for concordant and discordant beds differ by 13% at most. This should be kept in mind during the results discussion, since the discharge-ratio value was chosen as a common parameter for the comparison of the results.

3 NUMERICAL MODELLING

The three-dimensional numerical model (SSIIM2) used for the modelling is described elsewhere (Olsen 2000, 2002, 2004). The model solves the three-dimensional Reynolds averaged Navier-Stokes equations, with the standard k-ε turbulence-model closure. As this model assumes isotropic eddy viscosity, it should to be calibrated when considering strongly anisotropic flows, such as those occurring in river confluences (Bradbook et al. 2000). Since the field measurements of the flow field at the confluence of the Sava and Danube Rivers are still under way, no calibration is possible yet. Therefore, the original values of the k-ε model constants (C_μ, $C_{\varepsilon 1}$, $C_{\varepsilon 2}$, σ_k, and σ_ε) were used. For this reason, numerical simulation results obtained for the four considered bed configurations can only be used for the qualitative comparative analyses. As will be shown later, these comparative analyses provide a ground for some general conclusions.

The SSIIM2 model solves the governing equations using the finite-volume method on a three-dimensional non-orthogonal unstructured grid. This type of grid allows for flow simulation in dendritic channel networks with complex bathymetry, characteristic for river confluences. The model uses

Table 3. Analysed combinations of the upstream hydrologic regimes of the confluent streams.

	Sava river	Danube river		
p^* %	Q_{MR} m^3/s	Q_{total} m^3/s	Q_T m^3/s	$D_R = Q_{MR}/Q_T$ –
0.56	600	5700	1130	0.53
6.59	400	2500	385	1.04
4.53	800	2800	455	1.76
2.60	1300	3500	615	2.11
2.59	1555	2480	395	3.94
0.66	2500	2800	400	6.25

* Probability of occurrence of discharge combination is denoted by p (Jovanović et al. 2005).

SIMPLE method for the pressure term modelling and the second-order upwind scheme for discretisation of the convective terms. A wall law is used along solid boundaries.

In the present study, steady flow conditions were assumed. Symmetric boundary conditions were used for all variables at the surface and the outflow boundary. The water surface was fixed, which can be justified by the fact that the confluence of the Sava and Danube Rivers is under the strong influence of the Iron Gate Dam backwaters and the water level may be considered nearly horizontal. At the inflow boundaries constant fluxes were specified. To ensure mass continuity, a constant flux was prescribed at the outflow boundary.

Computational domain included channels of the main river and the tributary in the length of 1 km each and 1 km of the post-confluence channel. The length of 1 km along each confluent stream ensured no influence of the upstream boundary condition on the flow pattern in the confluence. The non-orthogonal unstructured grid consisted of two non-orthogonal structured grids – one along the main river and the post-confluence channel (block1) and the other along the tributary (block 2). After detailed grid sensitivity analysis, a grid with the following dimensions was used for all considered river bed configurations: $201 \times 31 \times 11$ for block 1 and $91 \times 26 \times 11$ for block 2 (Fig. 2).

Bed material in the tributary is finer than bed material in the main river ($d_{50,T} = 2$ mm, $d_{50,MR} = 8$ mm). Therefore, non-uniform roughness was used. The roughness was defined according to the given grain sizes.

4 RESULTS AND DISCUSSION

The effect of the bed morphology on the confluence hydrodynamics is analysed by observing the forms of *secondary circulation* and the change in the *turbulent kinetic energy* distribution at chosen cross-sections at

Copyright © 2006 Taylor & Francis Group plc, London, UK

Table 4. Momentum-flux ratios (M_R) for the four analysed geometries.

		CASE							
		1		2		3		4	
D_R –	V_{MR} m/s	V_T m/s	M_R –	V_T m/s	M_R –	V_T m/s	M_R –	V_T m/s	M_R –
0.53	0.21	0.46	0.24	0.42	0.26	0.46	0.24	0.42	0.26
1.04	0.17	0.19	0.93	0.17	1.04	0.19	0.93	0.17	1.04
1.76	0.32	0.22	2.56	0.19	2.96	0.22	2.56	0.19	2.96
2.11	0.49	0.27	3.84	0.24	4.32	0.27	3.84	0.24	4.32
3.94	0.61	0.18	13.34	0.16	15.01	0.18	13.34	0.16	15.01
6.25	0.91	0.17	33.46	0.15	37.92	0.17	33.46	0.15	37.92

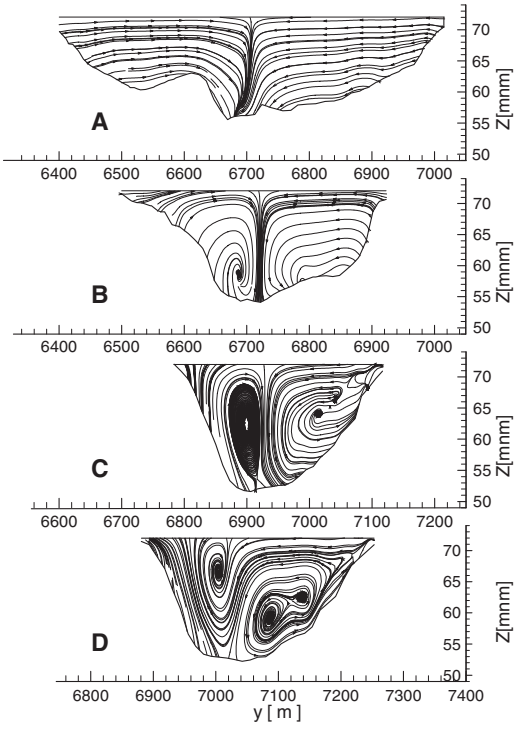


Figure 3. Streamlines at chosen locations showing secondary circulation in the cross-section (case 1 – discordant beds and a scour hole – surveyed bathymetry) for $D_R = 2.11$.

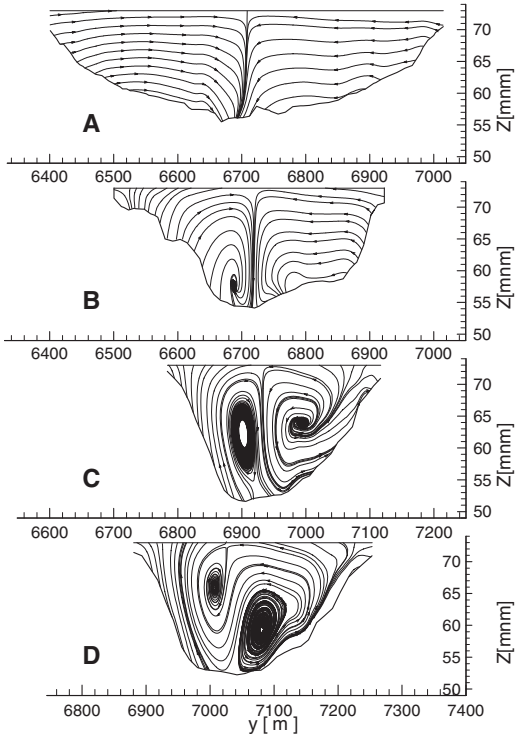


Figure 4. Streamlines at chosen locations showing secondary circulation in the cross-section (case 2 – concordant beds and a scour hole) for $D_R = 2.11$.

the confluence and in the post-confluence channel. Secondary circulation shall be discussed, first.

Depending on the D_R (M_R) value, magnitudes of the cross-stream velocity vectors in the post-confluence channel may be an order or two orders of magnitude lower than the intensities of the main stream velocity vectors. Therefore, cross-section surface streamlines were used to illustrate secondary circulation for all the considered D_R (M_R) values.

Four cross-sections were chosen, two of which are situated at the very confluence, and the other two in the scour hole (Fig. 2). All cross-sections are viewed in the downstream direction and perpendicular to the cross-section.

Development of the secondary circulation through the confluence and the post-confluence channel is presented on Figures 3–6, for the case when two secondary circulation counter-rotating vortices are formed in the

Copyright © 2006 Taylor & Francis Group plc, London, UK

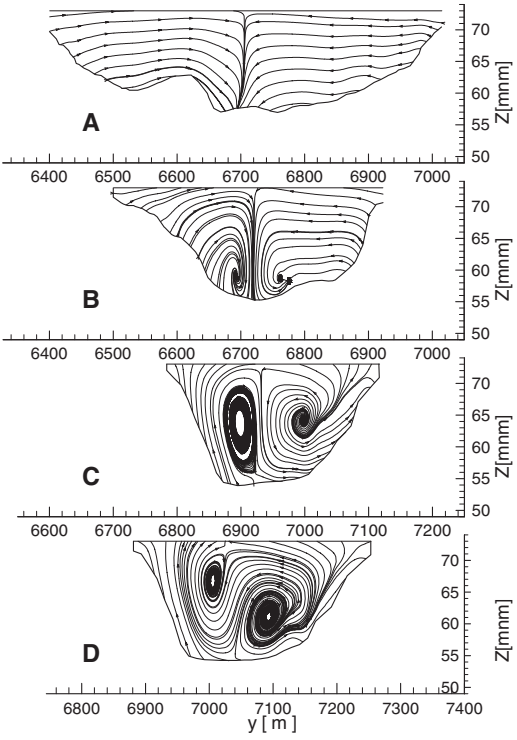


Figure 5. Streamlines at chosen locations showing secondary circulation in the cross-section (case 3 – discordant beds and no scour hole) for $D_R = 2.11$.

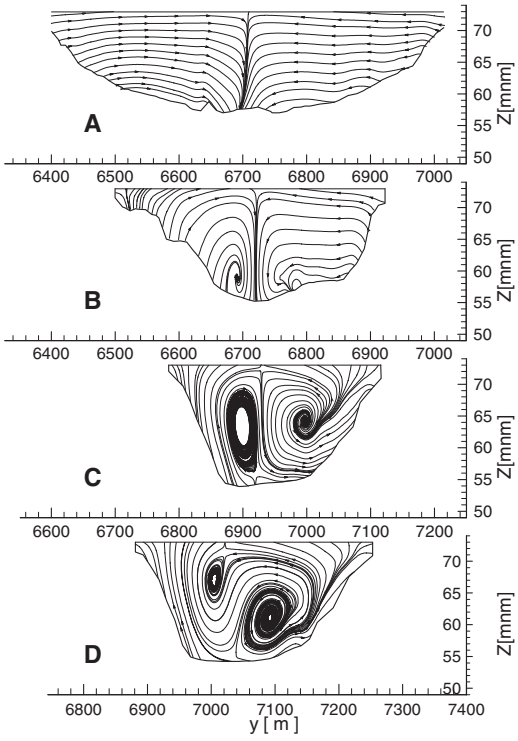


Figure 6. Streamlines at chosen locations showing secondary circulation in the cross-section (case 4 – concordant beds and no scour hole) for $D_R = 2.11$.

post-confluence channel ($D_R = 2.11$). At the cross-section closest to the confluence apex (cross-section A), cross-stream velocity vectors from the confluent streams converge to each other, as was observed in all investigated confluences (Biron et al. 1996b, Bradbrook et al. 2000, Rhoads & Sukhodolov 2001). In the cases 1 and 3 (discordant bed cases – Figs. 3 and 5) deflection of the streamlines from the vertical towards the sloping backstep at the mixing interface is a result of topographic steering at the back-step. Similar circulation pattern characterises the cross-section B.

However, flow patterns at the cross-sections C and D differ from case to case. Generally, two counter-rotating vortices are formed for all cases at both cross-sections. In the cases 3 and 4 (Figs. 5 and 6), no difference between the secondary flow patterns at C can be noticed for the considered D_R value. The same holds for the cross-section D, which leads to a conclusion that in the absence of the scour hole, the bed discordance at the entrance to the confluence does not influence the secondary circulation far downstream in the post-confluence channel.

In the cases with a scour hole (Figs. 3 and 4) the bed discordance (Fig. 3) weakens the right vortex at the section C and strengthens the left one, which now occupies more vertical space in the cross-section. At the cross-section D, a single right vortex, which rotates close to the bottom in the central part of the section, is lifted from the bottom, moved towards the right bank and its core is split into two smaller ones. The left vortex is moved towards the water surface. All these differences indicate that for a specific D_R value, the flow pattern in the scour hole is strongly governed by the momentum-flux ratio at the confluence (Tab. 4). In the cases 3 and 4 (Figs. 5 and 6) the right vortex is less elongated in the vertical direction as the dynamic pressure at the bottom is greater in the absence of the scour hole. The size of the left vortex decreases between the sections C and D due to better realignment of the dominant-flow streamlines (flow in the main stream direction).

Changes in the secondary circulation with respect to the change in the discharge-ratio value D_R are shown only for the cross-sections C and D (Figs. 7 and 8). As was observed for $D_R = 2.11$, in the absence of the scour hole (cases 3 and 4 – Figs. 7 and 8), change in the M_R value due to the discordance at the confluence does not influence the flow pattern in the post-confluence channel for neither of analysed combinations of the

Copyright © 2006 Taylor & Francis Group plc, London, UK

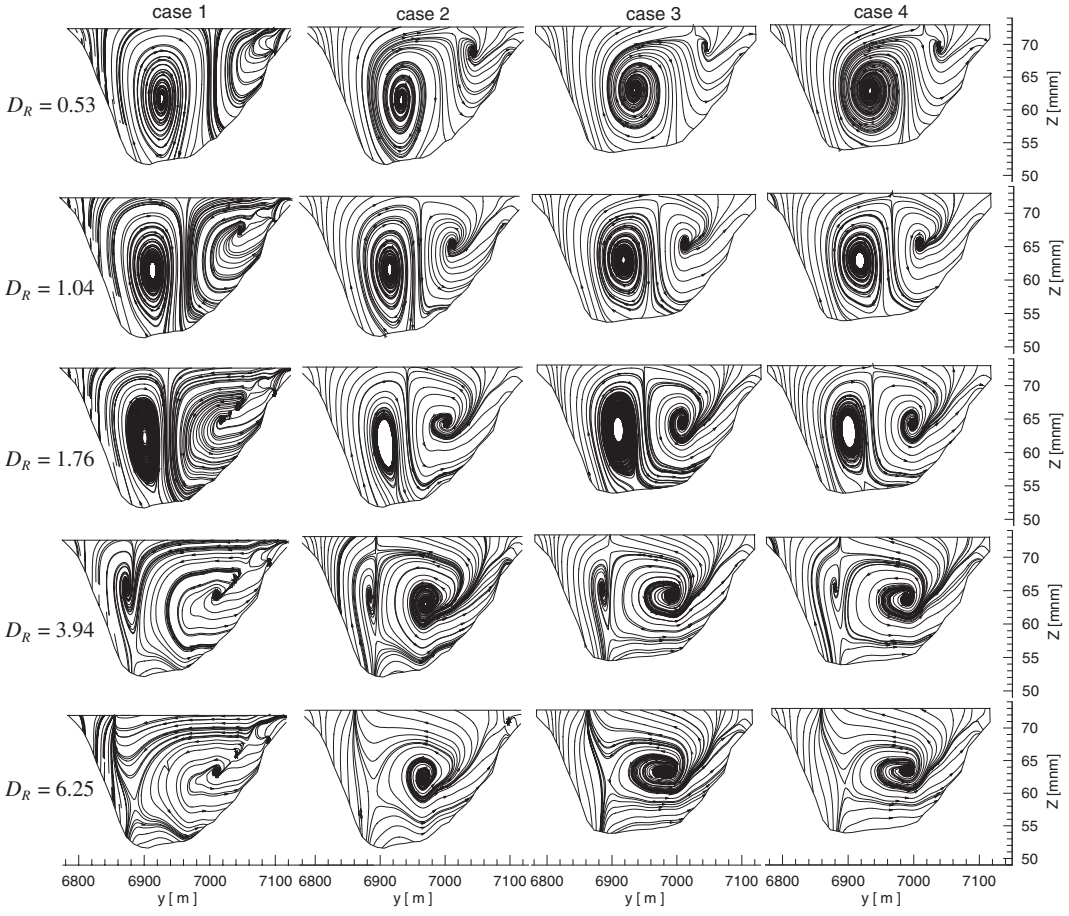


Figure 7. Streamlines showing change in the secondary circulation at the cross-section C with respect to change in the discharge-ratio value (D_R) for the four analysed river bed configurations.

hydrologic regimes of the confluent streams. However, this is not true when the scour hole is formed downstream from the confluence (cases 1 and 2).

Generally, the cases 2, 3 and 4 are characterised by the same type of secondary circulation. The only difference is in the dimensions and shape of the vortices. When there is a scour hole (cases 1 and 2), the vortices are more elongated in the vertical direction as a consequence of the topographic steering and resulting lower dynamic pressure. In contrast to the other three cases, in the case 1, decrease in the momentum-flux ratio value at the confluence due to the bed discordance, results in complete or almost complete diminishing of the vortex core on the right side of the channel at the cross-section C (Fig. 7). At the cross-section D, changes in flow patterns due to decrease in M_R depend on the D_R value (Fig. 8). For $D_R < 1.0$ the right vortex is isolated from the rest of the flow in the cross-section; for $D_R \approx 1.0$ the right vortex is larger than the one pertaining to the case 2. For the D_R values 1.76 and 2.11, the core of the vortex is split into two smaller ones, while for the higher D_R values ($D_R \geq 3.94$) the right vortex is moved to the centre of the cross-section and consists of one big and one very small core.

Changes in the D_R value influence the flow pattern at the cross-section C in the following (Fig. 7). For $D_R < 1.0$ a single large dominating clockwise vortex forms in the centre of the channel due to fast realignment of the streamlines that describe the dominant flow. This fast realignment of the streamlines results from the fact that the M_R value is still less than unity, which is in accordance with similar investigations (Bradbrook et al. 2000) (Tab. 4). For $1.0 < D_R < 2.5$ dominant-flow streamlines are not completely aligned by the cross-section C, and two counter-rotating vortices are formed. The stronger one to the left is formed above the deepest part of the cross-section. With further increase in D_R, the main river

Copyright © 2006 Taylor & Francis Group plc, London, UK

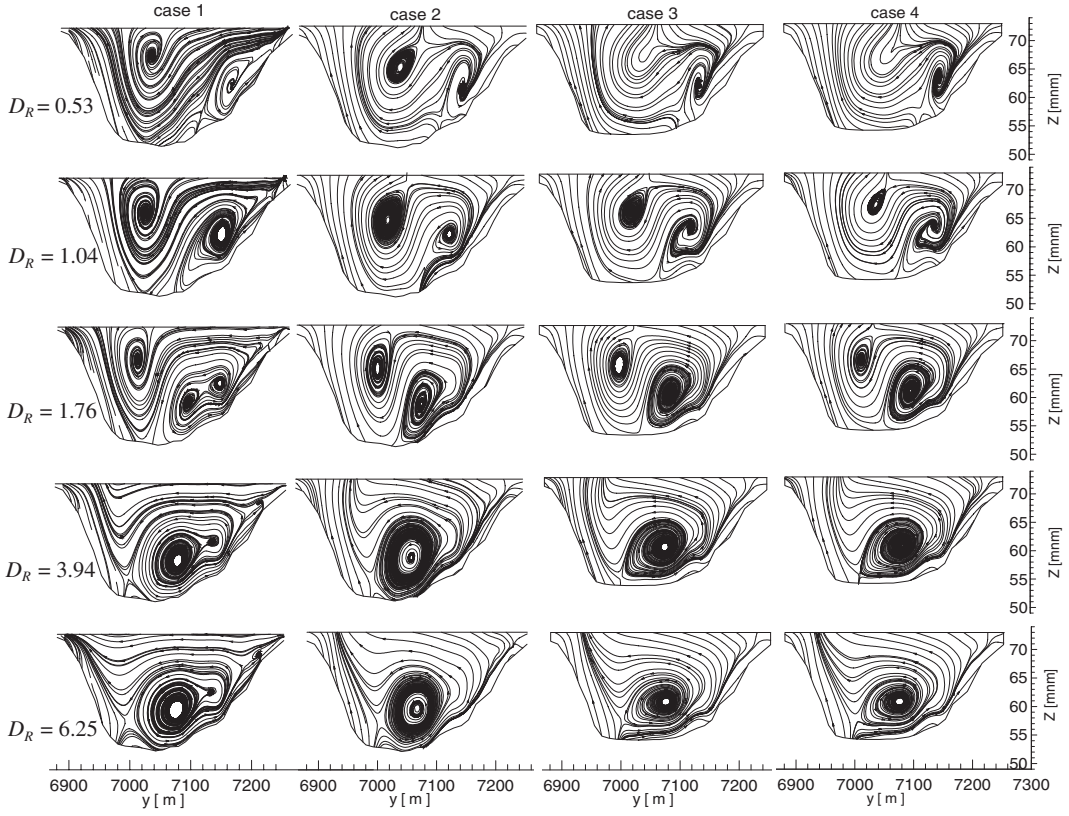


Figure 8. Streamlines showing change in secondary circulation in the cross-section D with respect to change in the discharge-ratio value (D_R) for four analysed river bed configurations.

dominates ($M_R > 10$). The strength of the left vortex gradually diminishes, but there is still a clear dividing line which moves towards the left bank.

In contrast to the cross-section C, at the cross-section D, which is depicted in Figure 8, alignment of the dominant-flow streamlines is better and dimensions of the vortices are either decreased ($D_R < 1.0$), or "redistributed" between the vortices ($1.0 < D_R < 1.76$), including additional splitting of the right vortex core into two smaller ones. For $D_R \geq 3.94$ the same can be claimed as for the cross-section C, but there is an evident increase in the dimensions of the vortex. This could be explained by additional widening of the channel and entering the deepest zone of the scour hole.

The presented secondary flow patterns are the time-averaged flow structures. In addition to the time-averaged structures, confluences are observed to have periodical flow structures, too (Bradbrook et al. 2000, Kapor 1997). These structures cannot be dealt with the numerical models of a time-averaged flow. However, distribution of the turbulent kinetic energy k, obtained by such models, may indicate where periodical flow structures may be expected to form. As Bradbrook et al. (2000) claim, the stagnation zone where the two converging flows meet, may be the source of these structures. The stagnation zone is characterised by a strong shear between the flows, formation of the shear layer which allows momentum exchange, and high values of the turbulent kinetic energy. Therefore, it was decided to investigate how the river bed morphology influences intensity and distribution of the turbulent kinetic energy at the confluence cross-section A.

Change in the k distribution at this cross-section is presented in Figure 9 in a form of contour lines for all considered D_R values. It can be noticed that the greatest values of the turbulent kinetic energy are attained in the case 1 when the scour hole is present and the beds are discordant. In the cases 2 and 4 distributions of k are almost identical for all D_R values. The only notable difference is for $D_R < 1.0$, which probably results from minimal differences in the cross-section slicing process. There is also quite a resemblance between the case 3 and the cases 2 and 4, for $D_R \geq 2.11$. Close observation reveals that similarities between the cases 1 and 3 exist in the form of contour lines in the

Copyright © 2006 Taylor & Francis Group plc, London, UK

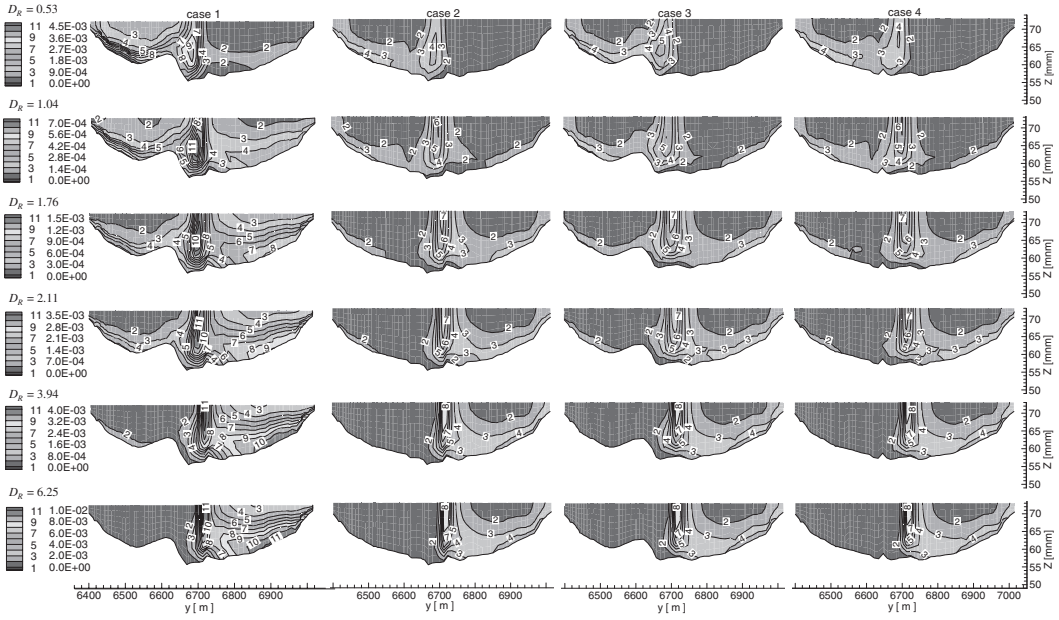


Figure 9. Contour lines showing change in the turbulent kinetic energy distribution at the cross-section A with respect to change in the discharge-ratio value (D_R) for the four analysed river bed configurations. The left bank belongs to the tributary whereas the right bank belongs to the main river.

stagnation zone. However, there is a difference in the k intensities. This proves the importance of a combined effect of the topographic steering and the changes in the upstream hydrologic regimes of the confluent streams on the confluence hydrodynamics.

There is no significant transfer of the turbulent kinetic energy from the tributary into the main river for $D_R < 1.0$. Contributions of the main river and the tributary are, as expected, almost equal when $D_R \approx 1$. For the D_R values ranging between 1.0 and 2.11 some of the turbulent kinetic energy is transferred from the main river to the tributary, whereas for the higher D_R values there is no transfer of k to the tributary.

Finally, the effects of the bed discordance and the scour hole on the distribution of the turbulent kinetic energy in the post-confluence channel were analysed for the cross-section C (Fig. 10). Results for $D_R < 1.76$ show resemblance between the cases 1 and 3 and between the cases 2 and 4. This means that in the range of D_R values less than, say 1.8, the bed discordance at the entrance to the confluence plays a key role in the distribution of the turbulent kinetic energy in the post-confluence channel. Again, the absence of the scour hole in the case 3, results in the lower k intensities when compared to the case 1. Transition area in which the influence of the bed discordance still cannot be neglected, but the effect of the scour hole (topographic steering) is yet not strong enough to overcome the influence of bed discordance, is characteristic for $2.11 < D_R < 3.94$. For the higher D_R values, distribution of k in the absence of scour hole is not influenced by the bed discordance (cases 3 and 4). When the scour hole is present, k distribution depends on the bed discordance – intensities of k are lower for the concordant bed case (case 2).

5 CONCLUSIONS

The aim of this paper was to analyse effects of the bed morphology on the confluence hydrodynamics by modifying the original bathymetry of the field confluence. Therefore, numerical simulations of the three-dimensional time-averaged flows for different combinations of the upstream hydrologic regimes of the confluent streams and four possible river bed configurations were performed. Changes in the bathymetry violate equilibrium between the flow and the bed, which can lead to the bed deformation. However, the paper only aims at investigating the effect of different bed morphologies on the flow process. Therefore, non-deformable bed was assumed. The influence on the secondary flow circulation in the post-confluence channel and distribution of the turbulent kinetic energy in the confluence, and the post-confluence channel were analysed. Comparison of the results led to the following conclusions.

(1) A change in the M_R value due to the bed discordance at the entrance to the confluence is 13% at most for all considered D_R values. The difference

Copyright © 2006 Taylor & Francis Group plc, London, UK

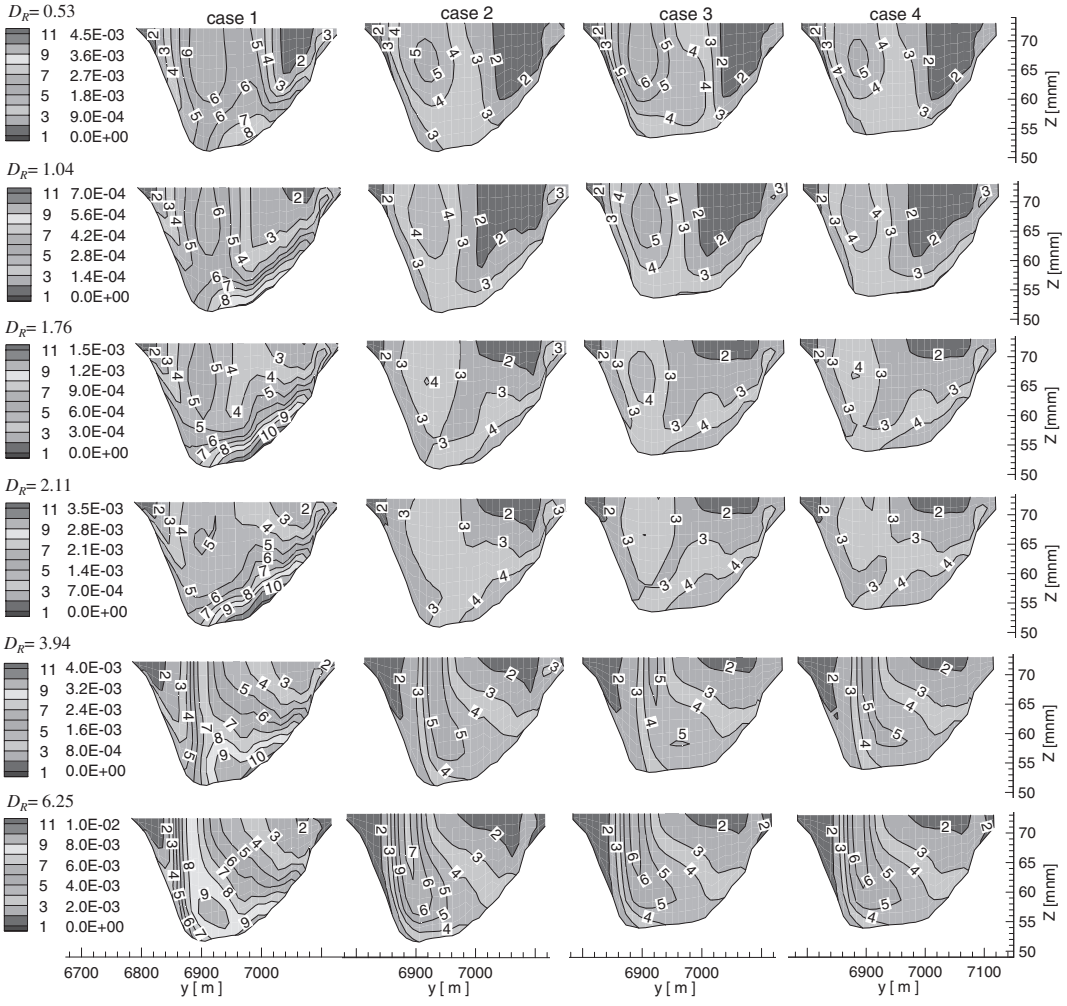


Figure 10. Contour lines showing change in the turbulent kinetic energy distribution at the cross-section C with respect to change in the discharge-ratio value (D_R) for the four analysed river bed configurations.

for the majority of combinations is less than 10%, which justifies the use of the discharge ratio (D_R) as a common parameter for the comparison.

(2) In the absence of the scour hole, the bed discordance at the entrance to the confluence has no influence on the secondary circulation in the post-confluence channel for any combination of the upstream hydrologic regimes of the confluent streams. In this case it means that the secondary flow patterns are only governed by the confluence plan-form and the discharge-ratio value and some topographic steering due to presence of other bed forms.

(3) When the scour hole is formed in the post-confluence channel, the secondary flow circulation is influenced by the presence of the bed discordance at the confluence and the D_R value. For a D_R value, a secondary flow pattern is strongly governed by the simultaneous action of the confluence plan-form and topographic steering at the confluence and in the post-confluence channel.

(4) Decreasing the D_R value below 1.0 and increasing above 4.0, causes, for the considered plan-form of the confluence, a significant increase in the k value in the stagnation zone at the confluence which may be an indicator for the development of some periodic flow structures.

(5) Generally, the highest values of k are observed for the case with the bed discordance and the scour hole in the post-confluence channel, which

Copyright © 2006 Taylor & Francis Group plc, London, UK

suggests that the intensity of k and its distribution at the confluence is influenced by the overall topography of the confluence and the post-confluence channel and, of course by the D_R value.

(6) As for the post-confluence channel, the influence of the bed discordance on the distribution of k depends on the D_R value. For D_R values less than approximately 1.8 the distribution of k is strongly governed by the bed discordance at the confluence, while topographic steering due to presence of the scour hole has no influence on the k distribution. In the range of D_R values between 1.8 and 4.0 the distribution of k is influenced by both, the bed discordance and the presence of the scour hole. For $D_R > 4.0$, the bed discordance has no effect on the k distribution when there is no scour hole, whereas in the presence of the scour hole, the bed discordance influence is significant.

ACKNOWLEDGEMENT

The authors wish to thank Professor N.R. Olsen from the Norwegian University of Science and Technology of Trondheim for providing them with the SSIIM2 model.

REFERENCES

Best, J.L. & Reid, I. 1984. Separation zone at open-channel junctions, *Journal of Hydraulic Engineering*, 110(11): 1588–1594.

Biron, P., Best, J.L. & Roy, A.G. 1996b. Effects of bed discordance on flow dynamics at open-channel confluences. *Journal of Hydraulic Engineering*, 122(12): 676–682.

Biron, P.M., Ramamurthy, A.S. & Han, S. 2004. Three-dimensional numerical modeling of mixing at river confluences. *Journal of Hydraulic Engineering*, 130(3): 243–253.

Boreli, M., Bruk, S. 1963. *The Danube and Sava Rivers in Belgrade – Hydraulic Problems and Investigations*. Belgrade: Institute of Water Resources "Jaroslav Černi". (in Serbian)

Bradbook, K.F., Lane, S.N. & Richards, K.S. 2000. Numerical simulation of the three-dimensional, time-averaged flow structure at river channel confluences. *Water Resources Research*, 36(9): 2731–2746.

Bradbook, K.F., Lane, S.N., Richards, K.S., Biron, P.M. & Roys, A.G. 2001. Role of bed discordance at asymmetrical river confluences. *Journal of Hydraulic Engineering*, 127(5): 351–368.

Jovanović, M., Đorđević, D., Kapor, R., Prodanović, D. 2005. *Hydraulic analysis of the Sava and Danube Rivers in Belgrade*. Belgrade: Institute of Hydraulic Engineering – Faculty of Civil Engineering. (in Serbian)

Huang, J., Weber, L.J. & Lai, Y.G. 2002. Three-dimensional numerical study of flows in open-channel junctions, *Journal of Hydraulic Engineering*, 128(3): 268–280.

Kapor, R. 1997. *Mathematical model of flow in shallow flow domains with space averaged basic equations*, PhD thesis, Belgrade: University of Belgrade. (in Serbian)

Olsen, N.R. 2000. *CFD Algorithms for Hydraulic Engineering*. Trondheim: The Norwegian University of Science and Technology.

Olsen, N.R. 2002. *Hydroinformatics, Fluvial Hydraulics and Limnology*. Trondheim: The Norwegian University of Science and Technology.

Olsen, N.R. 2004. *A three-dimensional numerical model for simulation of sediment movements in water intakes with multi-block option – User's Manual*, Trondheim: The Norwegian University of Science and Technology.

Rhoads, B.L. & Sukhodolov, A.N. 2001. Field investigation of the three-dimensional flow structure at stream confluences: 1. Thermal mixing and time-averaged velocities. *Water Resources Research*, 37(9): 2393–2410.

Copyright © 2006 Taylor & Francis Group plc, London, UK

The overdeepening theory in river morphodynamics: Two decades of shifting interpretations

Erik Mosselman
Delft University of Technology & WL/Delft Hydraulics, Delft, The Netherlands

Marco Tubino & Guido Zolezzi
Dipartimento di Ingegneria Civile e Ambientale, University of Trento, Italy

ABSTRACT: Theoretical analysis of mathematical equations is complementary to numerical solution as it offers additional insights into the fundamental behaviour of the corresponding physical system. An example is the theory of overdeepening in river morphodynamics. This theory explains why outer-bend pools can be locally deeper than the equilibrium outer-bend water depth in infinitely long river bends. Its essence lies in the superimposition of a steady alternate bar pattern on a streamwise uniform river bed topography. The same steady alternate bar pattern arises in a straight channel in response to a local permanent geometrical disturbance. Basically, the overdeepening theory describes river bed topography by a double-periodic function with an amplitude decaying exponentially along the river. This function yields two problems of interpretation. First, certain parameter combinations produce a growing rather than a decaying amplitude. Which phenomena are related to this situation? Originally, the growing amplitudes were explained as an indication of incipient braiding, but this interpretation was soon discarded because growing bed deformations in a linear theory may still reach a finite amplitude by nonlinear effects. The second problem of interpretation was whether the double-periodic function holds upstream or downstream of the local disturbance, or both. Originally it was assumed to hold only downstream, because of the very short adaptation length of the upstream flow accelerating towards a local constriction. Later upstream influence was revealed to occur as well, albeit with initially differing opinions on the corresponding parameter ranges. We review the history of the shifting interpretations of the overdeepening theory. In this way we seek to demonstrate that mathematical analyses of physical systems do not produce straightforward answers or predictions, but inherently require interpretations based on experimental evidence and a thorough understanding of the underlying physical processes.

1 INTRODUCTION

Theoretical analyses of mathematical equations are complementary to numerical solutions, as they offer additional insights into the fundamental behaviour of the corresponding physical system. Designing numerical models requires theoretical analyses to determine the appropriate numerical scheme and the type and location of the boundary conditions to be imposed. Theoretical analyses also help the optimization of calibration strategies for numerical models, as they reveal which parameters are responsible for different aspects of the solution. They help the interpretation of results from numerical models as well, because numerical solutions may exhibit spurious wiggles, phase lags or attenuation that in this way can be distinguished from real physical phenomena. Furthermore, analytical solutions provide exact solutions for certain idealized cases that may serve as validation cases for numerical models. Finally, analytical solutions can be used as rapid assessment models or rules of thumb.

However, the interpretation of results from mathematical analyses of physical systems is not always straightforward. Often a thorough understanding of the physical processes, rooted in observational or experimental evidence, is required to arrive at a correct interpretation. We seek to demonstrate this on the basis of the overdeepening theory in river morphodynamics (Struiksma et al, 1985), which has undergone several shifting interpretations in the past two decades. Part of the shifts resulted from debates between the two research groups that Parker & Johanneson (1989) have called the "Delft School" and the "Genova School". Here we review the history of the shifting interpretations. To that end, we review the theory only briefly. Seminara (1998) presents a more thorough overview of mathematical analyses in river morphodynamics. We use the dimensional notations of the Delft School

Copyright © 2006 Taylor & Francis Group plc, London, UK

because they are closer to the notations that are familiar to river engineers. From a mathematical point of view, the nondimensional notations of the Genova School might have been preferable.

2 STRUIKSMA'S THEORY

Struiksma et al (1985) derived a linear model from the basic depth-averaged equations for water flow and sediment transport. They found that this model could be simplified to a second-order system for parameter ranges that are representative for the branches of the Rhine delta in the Netherlands. For clarity, we review their analysis by *a priori* assuming the validity of these simplifications.

The simplified linear equation for conservation of streamwise flow momentum retains only a convective term and a friction term, because pressure gradient perturbations are neglected and because the flow is assumed to be quasi-steady. The assumption of quasi-steadiness is valid as long as morphological changes operate on a much slower time scale than adaptations of water flow to changing conditions (De Vries, 1965). The resulting linear equation reads

$$u_0 \frac{\partial u}{\partial x} + \frac{g u_0^2}{h_0 C^2}\left(\frac{2u}{u_0} - \frac{h}{h_0}\right) = 0 \tag{1}$$

where u denotes the perturbation of streamwise flow velocity with respect to the reach-averaged (zero-order) streamwise flow velocity, u_0. Similarly, h denotes the flow depth perturbation with respect to the reach-averaged (zero-order) flow depth, h_0. Furthermore, x is the streamwise co-ordinate, g the acceleration due to gravity and C the Chézy coefficient for hydraulic roughness. Equation (1) can be interpreted as a relaxation equation for u with a source term depending on h and a characteristic length scale, λ_w, given by $\lambda_w = h_0 C^2/2g$. Substitution yields

$$\frac{\lambda_w}{u_0}\frac{\partial u}{\partial x} + \frac{u}{u_0} - \frac{h}{2h_0} = 0 \tag{2}$$

A rigid-lid assumption is applied to the sediment balance, which means that water level perturbations are neglected. This implies that all bed level perturbations are equal, though with opposite sign, to perturbations in flow depth. The linear sediment balance reads

$$\frac{\partial h}{\partial t} = \frac{b q_{s0}}{u_0}\frac{\partial u}{\partial x} + q_{s0}\frac{\partial}{\partial y}\left(\frac{v}{u_0} + \frac{1}{f_s}\frac{\partial h}{\partial y}\right) = 0 \tag{3}$$

where t denotes time, y is the cross-stream co-ordinate, q_{s0} is the reach-averaged (zero-order) volumetric sediment transport rate per unit width, b is the degree of nonlinearity in $q_{s0}(u)$ defined by $b = (u_0/q_{s0})\mathrm{d}q_s/\mathrm{d}u$, v is the perturbation of cross-stream flow velocity and f_s is a function weighing the effect of gravity pull along transverse bed slopes on the direction of sediment transport. The first term in the right-hand side of equation (3) represents streamwise gradients in streamwise sediment transport, the second term cross-stream gradients in cross-stream sediment transport. The effect of helical flow has been neglected. Always $b > 3$ (e.g. Mosselman, 2005).

Generally, the equations (2) and (3) can have periodic solutions in both x and y direction, i.e. they allow solutions in the form of double-periodic functions $\exp(ikx + ik_B y)$, where k is the streamwise wave number and k_B is the cross-stream wave number. The wave numbers of periodic solutions in streamwise direction have a continuum of possible values, but the wave numbers of solutions in cross-stream direction can only assume integer multiples of half the river width due to the boundary conditions at the banks: $k_B = m\pi/B$ with $m \in \{1, 2, ..\}$. Here B denotes river width. The lowest mode ($m = 1$) is the most unstable. This implies

$$\frac{\partial^2 h}{\partial y^2} = -k_B^2 h \tag{4}$$

This can be substituted in the last term of equation (3). Furthermore, the cross-stream flow velocity can be eliminated by using the quasi-steady linear continuity equation for water flow ($v_0 = 0$):

$$h_0\frac{\partial u}{\partial x} + u_0\frac{\partial h}{\partial x} + h_0\frac{\partial v}{\partial y} = 0 \tag{5}$$

The substitutions (4) and (5) transform equation (3) into

$$\frac{h_0}{q_{s0}}\frac{\partial h}{\partial t} = \frac{h_0(b-1)}{u_0}\frac{\partial u}{\partial x} - \frac{\partial h}{\partial x} - \frac{k_B^2 h_0}{f_s}h \tag{6}$$

where h and u now refer to perturbations along a bank (Figure 1). The steady-state version of this equation ($\partial h/\partial t = 0$) can be interpreted as a relaxation equation

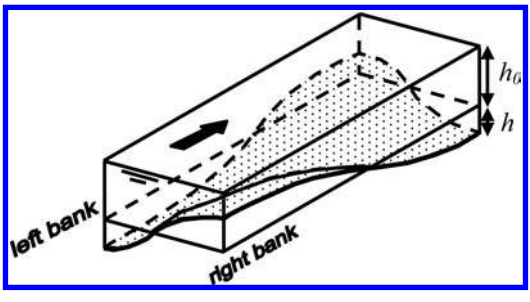


Figure 1. Near-bank flow depth perturbation, h, with respect to reach-averaged flow depth, h_0, as an indicator of cross-sectional bar-pool deformation.

Copyright © 2006 Taylor & Francis Group plc, London, UK

for h with a source term depending on $\partial u/\partial x$ and a characteristic length scale, λ_s, given by $\lambda_s = f_s/k_B^2 h_0$.

Solutions of the form $u = U \exp\{ikx - i\omega t\}$ and $h = H \exp(ikx - i\omega t)$ (+ complex conjugates) are substituted into equations (2) and (6). Here U and H are complex amplitudes, k is the complex streamwise wave number and ω is the complex frequency. All complex quantities consist of a real and an imaginary part. Thus the complex amplitudes consist of the real amplitudes and the phases. The complex wave number consists of the real wave number, $Re(k) = 2\pi/L_P$, where L_P denotes streamwise wave length, and the damping coefficient, $Im(k) = 1/L_D$, where L_D denotes damping length. The real frequency, $Re(\omega)$, can be used to calculate the propagation speed, c, of bars through $c = Re(\omega)/k$. The imaginary part, $Im(\omega)$, describes the growth or attenuation of the amplitude in time. These substitutions result in a system with the following characteristic equation:

$$\begin{vmatrix} ik\lambda_w + 1 & -\frac{1}{2} \\ (b-1)k & \frac{h_0}{q_{s0}}\omega - k + \frac{i}{\lambda_s} \end{vmatrix} = 0 \qquad (7)$$

For the steady state of non-propagating and non-developing bars ($\omega = 0$), equations (2) and (6) can be combined into the following single second-order equation:

$$\frac{\partial^2 h}{\partial x^2} + 2\,\mathrm{Im}(k)\frac{\partial h}{\partial x} + \left(\mathrm{Re}^2(k) + \mathrm{Im}^2(k)\right)h = 0 \qquad (8)$$

with

$$\mathrm{Re}(k) = \frac{2\pi}{L_P} = \frac{\sqrt{(b+1)\frac{\lambda_w}{\lambda_s} - \left(\frac{\lambda_w}{\lambda_s}\right)^2 - \left(\frac{b-3}{2}\right)^2}}{2\lambda_w} \qquad (9)$$

and

$$\mathrm{Im}(k) = \frac{1}{L_D} = \frac{\frac{\lambda_w}{\lambda_s} - \frac{b-3}{2}}{2\lambda_w} \qquad (10)$$

The ratio of λ_s to λ_w arises as a key parameter for this second-order system. Struiksma called it the "*interaction parameter*", because it stems from the interaction of two first-order relaxation equations with length scales λ_s and λ_w. It is defined by

$$\frac{\lambda_s}{\lambda_w} = \frac{2gf_s}{C^2\left(k_B h_0\right)^2} = 2\pi^2 f_s \frac{g}{C^2}\left(\frac{B}{h_0}\right)^2 \qquad (11)$$

The dominant contribution to this parameter is the width-to-depth ratio, B/h_0. Its role is therefore similar to the role of the Genova School's key parameter, β, defined as $\beta = B/2h_0$.

The second-order equation (8) makes the morphodynamic system analogous to a mass-spring-damper system (Figure 2). The latter is described by the same equation, but with derivatives to time instead of space.

The decaying oscillation of a mass-spring-damper system after an initial excitation finds its analogy in a steady pattern of spatially decaying alternate bars downstream of a local permanent geometrical disturbance (Figure 3). Examples of such disturbances are spur dikes, abrupt variations of river width or discontinuities in channel curvature. The steady bars downstream of a local permanent disturbance represent a free response to the upstream disturbance and yet they are forced to remain at the same location. They thus form an intermediate class of "*spatial bars*" between truly *free bars*, that spontaneously develop and migrate, and truly *forced bars*, that can be produced by a channel curvature distribution along the river. Struiksma et al (1985) found that the bed topography in the Waal branch of the Rhine delta in the Netherlands could be understood as a superimposition of forced bars and pools (axisymmetric bend profiles) and spatial bars and pools. The spatial bars and pools appeared as an overshoot that made outer-bend pools locally deeper than the equilibrium outer-bend water

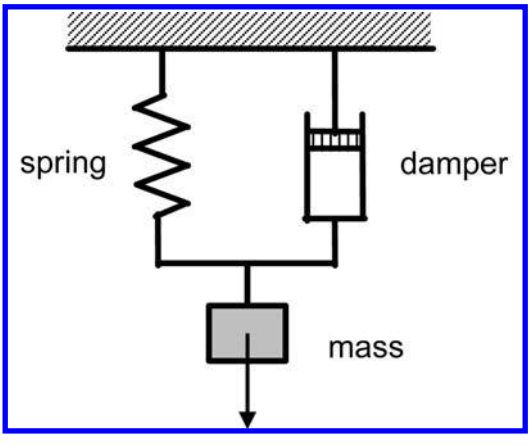


Figure 2. Mass-spring-damper system as an analogy for Struiksma's second-order model for river morphodynamics.

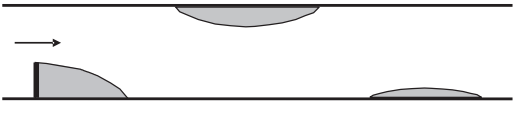


Figure 3. Underdamped bars: spatially decaying alternate bars downstream of a local permanent geometrical disturbance.

Copyright © 2006 Taylor & Francis Group plc, London, UK

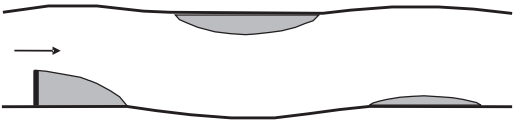


Figure 4. Incipient meandering induced by underdamped spatial bars.

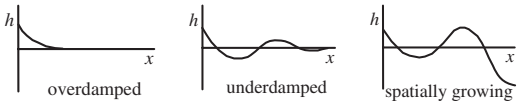


Figure 5. Near-bank flow depth perturbation for three solution regimes of equation (8).

depth in infinitely long river bends of constant curvature. Parker & Johanneson (1989) introduced the term "*overdeepening*" for this overshoot. They also showed that the independent analyses of Blondeaux & Seminara (1985) and Struiksma et al (1985) have many elements in common.

The Genova and Delft Schools proposed more or less simultaneously that spatial bars rather than migrating alternate bars could explain for many rivers why straight channels with erodible banks tend to develop into meandering water courses (Figure 4). A review by Rhoads & Welford (1991) confirmed this, with the noteworthy implication that helical flow, unlike previous widespread belief, is not a necessary ingredient to explain river meandering.

3 INTERPRETATION OF SPATIALLY GROWING BARS

The analogy with mass-spring-damper systems has proven to be useful. Blondeaux & Seminara (1985), for instance, identified the existence of *resonance* for vanishing values of the damping coefficient. However, the analogy also poses questions. In mass-spring-damper systems, the damping coefficient cannot be negative, but the damping coefficient in equation (10) does allow negative values. The solutions of equation (8) can thus fall in a *subresonant* regime for relatively narrow rivers ($\lambda_s/\lambda_w < 2/(b-3)$) or a *superresonant* regime for relatively wide rivers ($\lambda_s/\lambda_w > 2/(b-3)$). The superresonant regime corresponds to bars that grow spatially downstream in the sense that they are higher as the distance to the local permanent disturbance upstream is longer. The question is which phenomena are related to this regime. Struiksma & Klaassen (1988) attempted to answer this question by realizing that solutions of equation (8) actually have three regimes: overdamped bars, underdamped bars and spatially growing bars (Figure 5).

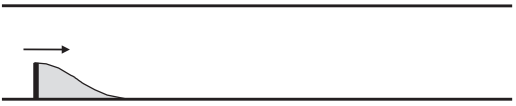


Figure 6. Overdamped bars.

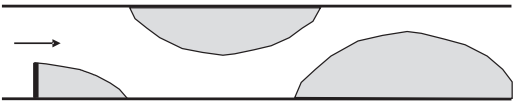


Figure 7. Spatially growing bars.

The corresponding ranges for the interaction parameter are:

$$\begin{aligned} &\frac{\lambda_s}{\lambda_w} \le \frac{2}{b+1+2\sqrt{2b-2}} \quad : \text{ overdamped} \\ &\frac{2}{b+1+2\sqrt{2b-2}} < \frac{\lambda_s}{\lambda_w} \le \frac{2}{b-3} \quad : \text{ underdamped} \\ &\frac{\lambda_s}{\lambda_w} > \frac{2}{b-3} \quad : \text{ spatially growing} \end{aligned} \tag{12}$$

The solution has no periodic components if the system is overdamped (Figure 6). It does have periodic components, leading to overdeepening, if the system is underdamped (Figure 3). The overdamped and underdamped regimes correspond to the subresonant regime, whereas the spatially growing regime corresponds to the superresonant regime (Figure 7).

Struiksma & Klaassen (1988) linked the overdamped regime to straight rivers, the underdamped regime to meandering rivers and the spatially growing or superresonant regime to braiding, in analogy to the classical three river channel patterns of Leopold & Wolman (1957). They took this as the basis for a discriminator between meandering and braiding. The Genova School pointed at the fallacy of this, because a linear prediction of exponential growth does not necessarily imply that the bars will actually reach the water level, as nonlinear effects may prevent growth beyond a finite amplitude. A better way to assess the transition from meandering to braiding is an analysis of the stability of higher modes in transverse direction, such as the pattern for $m = 2$ ($k_B = 2\pi/B$) in Figure 8. This was subsequently accepted by the Delft School (e.g. Mosselman, 1992). A weakly nonlinear analysis by Seminara & Tubino (1992) confirmed that bars in superresonant channels do not grow beyond a finite amplitude.

Copyright © 2006 Taylor & Francis Group plc, London, UK

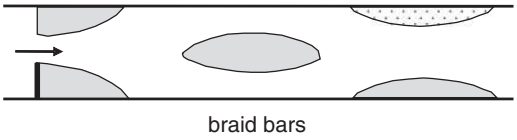


Figure 8. Braiding.

4 DIRECTION OF INFLUENCE

4.1 *Problem statement*

The concepts for overdamped, underdamped and spatially growing regimes in the previous sections are all based on the implicit assumption that the influence of a local geometrical disturbance extends in downstream direction alone. This is definitely true in the analogous mass-spring-damper system, where the influence of a perturbation at a certain moment can only have an effect forward in time, not backward. The spatial direction of influence for the morphodynamic system, however, is not that obvious. A solution decaying in downstream direction equally satisfies a growing solution in upstream direction and *vice versa*. It is not immediately clear whether a certain solution applies to the river upstream of the perturbation, downstream of the perturbation, or both.

4.2 *Struiksma's arguments for downstream influence*

Struiksma thought of the second-order system expressed by equation (8) as a combination of two first-order relaxation equations, i.e. equation (2) and the steady-state part of equation (6). The very concept of relaxation to an unperturbed flow and bed topography implies for these equations that the direction of influence must be downstream. Hence it was not expected that the combined system could produce an influence upstream of the local disturbance. An additional argument was that equation (2) represents a friction-dominated redistribution of the flow, whereas the flow upstream of the disturbance was assumed to be accelerating over a short distance only, without dissipation and characterized by equations from potential theory. The possibility of a larger zone of upstream influence due to morphological feedback was not taken into consideration. Accordingly, Struiksma & Crosato (1989) did not carry out any measurements upstream of the local disturbance in their laboratory experiment to verify the overdeepening theory.

4.3 *Discovery of upstream influence*

Zolezzi & Seminara (2001) discovered the possible existence of upstream influence when revisiting the linear theories of river meanders with the initial aim of deriving an exact solution of the flow field and the bed topography in arbitrarily curved channels. A main concern was the appropriate location of the boundary conditions to be imposed in the longitudinal domain. This led to the question whether the presence of curvature discontinuities could be felt in the upstream direction under suitable conditions. A physical explanation was sought in the migration of free bars, as free bars in subresonant channels migrate invariably downstream and free bars in superresonant channels might migrate upstream, at least in a linear context. The interpretation of the direction of influence thus became closely related to the interpretation of spatially growing spatial bars.

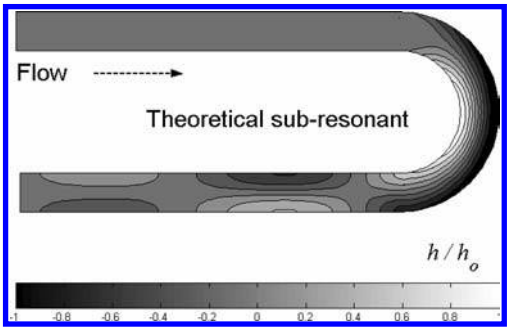


Figure 9. Theoretical bed topography in curved flume under subresonant conditions.

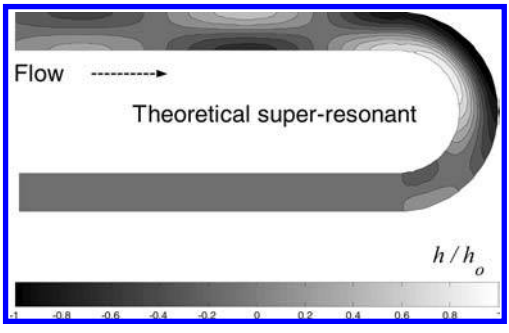


Figure 10. Theoretical bed topography in curved flume under superresonant conditions.

Figures 9 and 10 show Zolezzi & Seminara's (2001) theoretical predictions of overdeepening under sub- and superresonant conditions, the hydraulic and granulometric conditions of the subresonant case (Figure 9) being those of experiment T2 by Struiksma et al (1985). The straight-curved-straight channel sequence is characterized by two discontinuities in channel curvature. Both discontinuities trigger overdeepening, downstream in Figure 9, upstream in Figure 10.

4.4 *Analysis of characteristics*

The Delft School accepted the possibility of upstream influence in general, for instance through backwater

Copyright © 2006 Taylor & Francis Group plc, London, UK

effects, but Mosselman questioned the explanation by the Genova School that upstream influence for spatial bars is related to the migration direction of free bars, as well as the apparent implication that downstream influence would disappear under superresonant conditions. He argued that, formally, the direction of influence should be determined by means of an analysis of characteristics. Such an analysis assesses how infinitesimal perturbations propagate through a mathematical system, thus revealing the direction in which information is transmitted. Conceptually, the infinitesimally small size of the perturbations in a characteristics analysis refers not only to the amplitude of the perturbations, as in a linear analysis, but to their length as well. Hence an analysis of characteristics for spatial bars can be derived roughly from the linear analysis by rewriting equation (7) as

$$\begin{vmatrix} i\lambda_w + \frac{1}{k} & -\frac{1}{2k} \\ (b-1) & \frac{h_0}{q_{s0}}\frac{\omega}{k} - 1 + \frac{i}{k\lambda_s} \end{vmatrix} = 0 \qquad (13)$$

and subsequently taking the limit as $k \to \infty$. The result reads

$$\begin{vmatrix} i\lambda_w & 0 \\ (b-1) & \frac{h_0}{q_{s0}}\frac{\omega}{k} - 1 \end{vmatrix} = 0 \qquad (14)$$

The solution of this simplified equation is that the celerity of infinitesimally small perturbations is equal to

$$c = \frac{\omega}{k} = \frac{q_{s0}}{h_0} \qquad (15)$$

in downstream direction.

Mosselman hinted that a more complete analysis of characteristics might reveal that upstream influence is actually related to supercritical flow, in analogy to the upstream influence for infinitesimal bed perturbations in the 1D analysis of characteristics by De Vries (1959).

4.5 *Latest findings*

The actual occurrence of upstream overdeepening has been verified in laboratory flumes by Zolezzi et al (2005). Figures 11 and 12 show the patterns of spatial bars under subresonant and superresonant conditions respectively. In the subresonant case (Figure 11), overdeepening takes place both within the bend and in the downstream straight reach, whereas the upstream reach is characterized by an almost complete absence

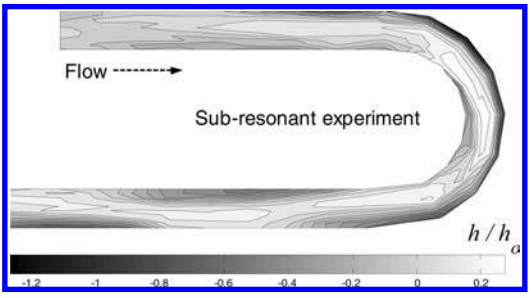


Figure 11. Observed bed topography in curved flume under subresonant conditions.

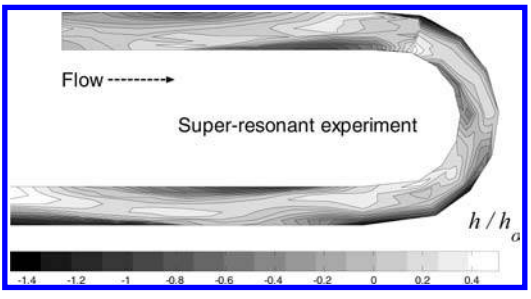


Figure 12. Observed bed topography in curved flume under superresonant conditions.

of steady bed deformations. This complies with Struiksma's original ideas on downstream influence.

Upstream overdeepening is observed under superresonant conditions (Figure 12), both in the upstream straight reach and in the bend, triggered by the two curvature discontinuities. This confirms the theoretical findings of Zolezzi & Seminara (2001). The observed wave length of the perturbations is closely reproduced by the linear theories. The most evident difference between the theoretical predictions and experimental observations, however, is that downstream overdeepening is also found to occur in the superresonant regime. This complies with Mosselman's argument that downstream influence does not necessarily disappear if free bars migrate upstream.

The experimental test of upstream influence by Zolezzi et al (2005) has also revealed how difficult it is to reproduce superresonant conditions in laboratory channels, since this requires to combine high channel width-to-depth ratios with values of the Shields stress high enough for sediment transport to occur at almost every location in the flume. The flume width is often limited by the requirement of reproducing the relatively long overdeepening wave (about 15–20 channel widths long), which implies the necessity to reduce the average water depth in order to meet superresonance. The resulting small water depth reduces sediment mobility. These difficulties explain

Copyright © 2006 Taylor & Francis Group plc, London, UK

why upstream influence had never been observed before and needed a specifically focused experimental activity.

The concept of upstream influence calls for a sound reproduction by 2D and quasi 3D numerical models that are increasingly employed for river engineering and management purposes. Despite some first attempts (Ferriani, 2003; Federici & Solari, 2004), satisfactory results are still to be achieved.

Finally, evidence of upstream influence in a broader sense is suggested by both experimental observations (Tubino & Bertoldi, 2006) and numerical simulations (Kleinhans et al, 2006) of the dynamics of channel bifurcations, which may imply unforeseen consequences also for the dynamics of braided streams.

5 CONCLUSIONS

The shifting interpretations of the overdeepening theory in river morphodynamics demonstrate that mathematical analyses of physical systems do not always produce straightforward answers or predictions, but inherently require interpretations based on experimental evidence and a thorough understanding of the underlying physical processes.

Upstream influence has been demonstrated to occur under superresonant conditions, but superresonant conditions do not imply that downstream influence disappears. The main challenge is now to obtain a sound reproduction of superresonant phenomena in 2D and quasi 3D numerical modelling.

REFERENCES

Blondeaux, P. & Seminara, G. 1985. A unified bar-bend theory of river meanders. *J. Fluid Mech.* 157: 449–470.

De Vries, M. 1959. *Transients in bedload-transport*. Report R3, Delft Hydraulics Laboratory.

De Vries, M. 1965. Considerations about non-steady bedload transport in open channels. *Proc. 11th Congress IAHR*, Leningrad (also Delft Hydr. Lab. Publ. No.36).

Federici, B. & Solari, L. 2004. Preliminary numerical simulations of upstream and downstream overdeepening. *Proc. 29th Italian Hydraulics and Hydraulic Structures National Meeting*, Trento, September, 445–452.

Ferriani, C. 2003. *Alvei meandriformi: un confronto fra soluzioni analitiche, modelli numerici e osservazioni sperimentali*. Master thesis, University of Trento, 210pp.

Kleinhans, M., Jagers, B., Mosselman, E. & Sloff, K. 2006. Effect of upstream meanders on bifurcation stability and sediment division in 1D, 2D and 3D models. *Proc. River Flow 2006*, Lisbon, September.

Leopold, L.B. & Wolman, M.G. 1957. River channel patterns: braided, meandering and straight. *Professional Paper* 282B: 39–85, U.S. Geol. Survey.

Mosselman, E. 1992. Mathematical modelling of morphological processes in rivers with erodible cohesive banks. *Communications on Hydr. and Geotech. Engrg.* 92-3, Delft Univ. of Technol., ISSN 0169–6548.

Mosselman, E. 2005. Basic equations for sediment transport in CFD for fluvial morphodynamics. In P.D. Bates, S.N. Lane & R.I. Ferguson (eds), *Computational Fluid Dynamics; Applications in environmental hydraulics*, Wiley, 71–89.

Parker, G. & Johanneson, H. 1989. Observations on several recent theories of resonance and overdeepening in meandering channels. In S. Ikeda & G. Parker (eds), *River meandering*, AGU, Water Resources Monograph 12: 379–415.

Rhoads, B.L. & Welford, M.R. 1991. Initiation of river meandering. *Progress in Phys. Geogr.*, 15(2):127–156.

Seminara, G. & Tubino, M. 1992. Weakly nonlinear theory of regular meanders. *J. Fluid Mech.*, 244: 257–288.

Seminara, G. 1998. Stability and morphodynamics. *Meccanica* 33: 59–99.

Struiksma, N., Olesen, K.W., Flokstra, C. & De Vriend, H.J. 1985. Bed deformation in curved alluvial channels. *J. Hydr. Res.* 23(1): 57–79.

Struiksma, N. & Klaassen, G.J. 1988. On the threshold between meandering and braiding. *Proc. Int. Conf. River Regime*, 1988, Wallingford.

Struiksma, N. & Crosato, A. 1989. Analysis of a 2-D bed topography model for rivers. In S. Ikeda & G. Parker (eds), *River meandering*, AGU, Water Resources Monograph 12: 153–180.

Tubino, M. & Bertoldi, W. 2006. Bifurcations in gravel bed streams. *Proc. Gravel Bed Rivers VI; From process understanding to river restoration*, in press.

Zolezzi, G. & Seminara, G. 2001. Downstream and upstream influence in river meandering; Part 1, General theory and application to overdeepening. *J. Fluid Mech.*, 438: 183–211.

Zolezzi, G., Guala, M., Termini, D., Seminara, G. 2005. Experimental observations of upstream overdeepening. *J. Fluid Mech.*, 531: 191–219.

Copyright © 2006 Taylor & Francis Group plc, London, UK

Prevalent morphodynamic regime and short-term dynamics of meandering rivers

Guido Zolezzi, Rossella Luchi & David Marchiori
Department of Civil and Environmental Engineering, University of Trento, Italy

ABSTRACT: The role of factors such as flow discharge, valley slope, and sediment size on meander morphodynamics has been often reported referring to individual cases but lacks generality. Moreover recent observations of upstream and downstream influence in river morphodynamics still wait for close comparisons with observed features in the field. We seek to provide a unified description of how variations in relevant natural and anthropogenic controls affect the morphology of meandering rivers. We focus on the short-term planimetric evolution of a "Kinoshita curve" before cutoff, of most interest for management purposes. The examined gravel bed meandering river reaches are mainly super-resonant with dominant upstream influence at this time scale. A relatively narrow threshold range seems to distinguish between sub- and super-resonant rivers. Predicted properties of regular meander loops satisfactorily agree with field observations, supporting the use of the present model to support restoration projects involving re-meandering of channelized streams.

1 INTRODUCTION

Rapid changes undergone by our society in the last decades are reflected also in the evolution of classical approaches to river management, which progressively shifts towards philosophies of river and floodplain restoration that aim to keep the river and its surroundings fit for multiple functions, such as navigation, risk mitigation, ecosystem productivity and recreational use. The implementation of restoration measures and of those associated with traditional river engineering often implies changes in river morphology at different spatial and temporal scales. These interventions must be accompanied with an improved understanding of and ability to model the river response to both anthropogenic and natural factors (De Vriend 2002).

In the case of single thread, meandering rivers, the morphological response to variations in different types of environmental controls has been widely documented since decades (e.g. Hickin 1977, Hooke 1995, Amsler and Ramonell 2002 among others). A considerable advance in process understanding in the last two decades has led to the generation of physically based simulation models that can predict the planimetric evolution of the channel axis at much different time and spatial scales, including those significant for river management purposes (for a recent review see Seminara 2006).

A major point is that related to morphodynamic influence (Zolezzi and Seminara 2001), including its implications for the planimetric evolution of river meanders (Seminara et al. 2001). Theoretical and experimental (Zolezzi et al. 2005) analysis indicate that two well distinct regimes characterize meander dynamics, whereby the effect of geometrical disturbances, related to both anthropogenic and natural causes, can dominantly be felt in the downstream (upstream) direction essentially depending on the width to depth ratio of the channel falling below (above) a threshold value. Such value coincides with the resonant value of Blondeaux and Seminara (1985), and the morphodynamics in both regimes (therefore called suband super-resonant respectively) strongly affects the planimetric evolution at different time scales (Lanzoni et al. 2006).

Despite the large amount of available field observations and the considerable theoretical improvements, however, at least two major issues still need to be clarified.

First, a quantitative field evidence of the correspondence between sub- and super-resonant regimes with dominant downstream and upstream influence has never been reported so far. Which morphodynamic regime characterizes real rivers? Can a prevalent regime be detected? Can any clear distinction be made based, for example, on the prevalent mechanism of sediment transport or on other geomorphic controls, such as the valley slope?

Second, despite the great detail of planimetric evolution models, only qualitative comparisons with observed natural features has been reported at present. Are state-of-the-art evolution models able to reproduce

the well known field observations concerned with meander migration rate (Nanson and Hickin 1983) and sinuosity (e.g. Bridge 2003)? Assessing model performance in closer comparison with field data is now necessary to make a step forward and it is the main goal of the present work.

We have employed a model already developed in previous works (Seminara et al. 2001) in order to attempt a first answer to the above questions. The formulation of the mathematical problem of meander morphodynamics is synthetically recalled in §2 and the solution procedure is summarized in §3. §4 is devoted to illustrate the field data set and the procedure developed to adapt dimensional data to the dimensionless input parameters required by the model. Results are widely discussed in §5 and 6, while §7 shows a quantitative comparison with field observations. A summary of the open issues for future work finally concludes the paper in §8.

2 OVERVIEW OF THE PROBLEM FORMULATION

A meander evolves planimetrically on a much larger time scale (years or tenth of years) compared to that typical of the altimetric evolution of its bed topography, which is usually rearranged within a single flood event, and therefore evolves over periods of hours or days. The driving mechanism of meandering planform change is commonly assumed to be the excess near bank longitudinal velocity (e.g. Hasegawa 1989), determined by the interaction between the flow and the bed topography field.

A mathematical model of meander morphodynamics commonly consists of a planimetric evolution equation (Seminara et al. 2001) whose time integration assumes that the flow and bed topography instantaneously adapt to planform changes. We follow this approach and refer the analysis to a constant width meandering channel with constant cross-sectional width that flows along a floodplain lying on the (x^*, y^*) plane whose longitudinal slope S_v is assumed to be constant over the time scale of meander evolution (Figure 1).

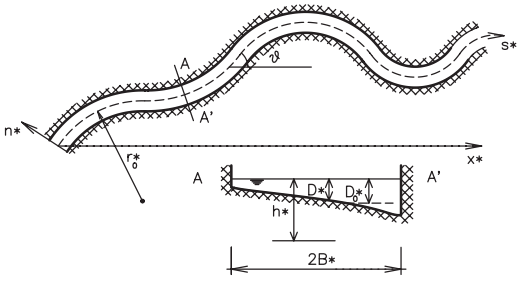


Figure 1. Sketch of a meandering channel and notations.

Several models have been proposed by far to study the flow field and bottom topography in meandering streams: for our purpose it is appropriate to employ steady, depth averaged models (e.g. Seminara and Tubino 1989) able to retain three dimensional information associated with bottom stresses and momentum redistribution due to secondary flows with vanishing depth average that develop in curved channels due to centrifugal effects and longitudinal variations of streamlines curvature. Several models have been proposed that incorporate these characteristics: based on recent comparative studies (Camporeale et al. 2005, Lanzoni et al. 2006) we choose to employ the $2.5D$ model proposed by Zolezzi and Seminara (2001) which reads:

$$UU_{,s}+VU_{,n}+H_{,s}+\beta\frac{\tau_s}{D} = \nu_o f_{11}\,, \tag{1}$$

$$UV_{,s}+VV_{,n}+H_{,n}+\beta\frac{\tau_n}{D} = \nu_o g_{11}\,, \tag{2}$$

$$(DU)_{,s}+(DV)_{,n} = \nu_o m_{11}\,, \tag{3}$$

$$q_{s,s}+q_{n,n} = \nu_o n_{11}\,, \tag{4}$$

where:

$$(\tau_s,\tau_n') = C_f(U,V)|\mathbf{U}|;\ \ \tau_n = \tau_n' + \tau_H; \tag{5}$$

with boundary conditions imposing vanishing water and sediment flux at lateral walls. The dimensionless differential system $(1,\ldots,4)$ is referred to the curvilinear orthogonal coordinates (s,n) with s measured along the channel axis and n orthogonal to s lying in the (x,y) plane. Flow and geometric variables have been made dimensionless with respect to an ideal condition referring to the same discharge Q^* flowing uniformly with an average velocity U_o^* in a straight channel characterized by the same longitudinal slope S, width $2B^*$ and mean sediment diameter d_{50}^*, the star denoting dimensional variables. In $(1,\ldots,4)$ (τ_s,τ_n) and (q_s,q_n) represent the bottom stress and the bedload discharge vector respectively; the $3D$ effect associated with secondary flows are retained in the τ_H component of the lateral bottom stress. The dimensionless flow field $\mathbf{U}=(U,V)$, the free surface elevation and water depth (H,D) and the planimetric coordinates (s,n) have been obtained from the corresponding dimensional quantities through a classical scaling procedure (Zolezzi and Seminara 2001). The relevant dimensionless parameters of the analysis read:

$$\nu_o=\frac{B^*}{R_o^*},\quad \beta=\frac{B^*}{D_o^*},\quad d_s=\frac{d_{50}^*}{D_o^*},\quad \tau_*=\frac{S}{\Delta d_s}.$$

In the above expression ν_o is the curvature ratio, β denotes the width ratio, d_s the relative roughness and

τ_* the shields stress. The friction factor is computed through classical logarithmic formulas and the sediment rate is assumed to be dominantly carried as bedload, which has been computed through the formula of Parker (1990) for gravel bed rivers in the plane bed case and through the expression of Engelund and Hansen (1967) in the case of sandy channels with dune covered bed.

The forcing terms $(f_{11}, \ldots, n_{11})$ are related to channel curvature $C(s) = -(1/v_o)d\vartheta/ds$ and redistribution coefficients related to the interaction between the main and secondary flows. $\vartheta(s,t)$ denotes the angle that the local tangent to the channel centerline forms with the x direction.

The planimetric evolution of the channel is described by the following integro-differential equation (Seminara et al. 2001):

$$\vartheta_{,t} - \vartheta_{,s} \int_0^s \zeta \vartheta_{,s} ds = \zeta_{,s}. \tag{6}$$

In (6) $\zeta(s)$ represents the erosion rate in the n direction at a given cross section s and its longitudinal distribution is assumed to adapt almost instantaneously to changes in meander planform. It is widely recognized that the appropriate measure of flow perturbations determining channel shift is the excess near bank longitudinal velocity u related to the transverse rate of meander migration by the following linear relationship (e.g. Ikeda et al. 1981):

$$\zeta = E\left[u|_{n=1} - u|_{n=-1}\right], \tag{7}$$

with E erodibility coefficient depending on the bank properties.

3 QUASI-ANALYTICAL SOLUTION

We will herein only recall the most relevant assumptions and steps of the solution procedure, for whose details the interested reader is referred to Zolezzi and Seminara (2001) and to Seminara et al. (2001). The observation that v_o is typically a small parameter allows to linearize the governing differential system through the following perturbation expansion:

$$(U, V, D, H) = (U_o, 0, D_o, H_o) + \nu_o(u, v, d, h) \tag{8}$$

where $(U_o, 0, D_o, H_o)$ refer to uniform flow conditions. The solution for the flow – bed topography field is obtained on substituting (8) into (1, . . . , 4) and then performing a Fourier expansion of the linear perturbations (u, v, d, h) in the transverse direction. The governing system is then transformed into the following fourth order ordinary differential problems for the amplitude of the m^{th} Fourier harmonic of the near bank excess longitudinal velocity u_m (m = 0, 1, 2, . . .):

$$\mathcal{L}^{(IV)} u_m = -A_m \sum_{j=o}^{6} \varrho_{j+1} \frac{d^{(j)}\mathcal{C}}{ds^{(j)}} \tag{9}$$

with

$$\mathcal{L}^{(IV)} = \left(\sum_{i=o} \sigma_i \frac{d^{(i)}}{ds^i} \right) \tag{10}$$

The recurrence of regular meandering patterns in natural rivers (Figure 2) (Kinoshita 1961, Langbein and Leopold 1964) suggests to look for periodic solutions of the above system, corresponding to a theoretically indefinite sequence of identical and periodic meander loops with wavenumber $\lambda = 2\pi/(L^*/B^*)$ and L^* intrinsic meander wavelength. Under these conditions channel curvature is described by the classical "Kinoshita curve":

$$\mathcal{C}(s) = \mathcal{C}_o \left[cos(\lambda s) + \mathcal{C}_F cos(3\lambda s) - \mathcal{C}_S sin(3\lambda s) \right] \tag{11}$$

where (C_F, C_S) are used to quantify the "fattening" and "skewing" properties of individual meander loops. The periodic solution of the system corresponding to the periodic curvature distribution (11) then takes the form:

$$\begin{aligned} u_m &= \sum_{k=1}^{3} u_{mk}(t) \exp(i\lambda_k s + c.c.)]; \\ u_{mk}(t) &= \vartheta_k(t) A_m \frac{\sum_{j=1}^{7} \varrho_j (i\lambda_k)^j}{\sum_{j=0}^{4} \sigma_j (i\lambda_k)^j}, \end{aligned} \tag{12}$$

with $\lambda_k = k\lambda$. The periodic solution of (9) displays the typical features of linear damped oscillators: namely resonance occurs when the meander wavenumber



Figure 2. Classical regular forms of natural meanders: Red River, Manitoba, Canada.

and width ratio coincide with the values (λ_R, β_R) that depend on (τ_*, d_s) such that β_R increases with the Shields parameter and decreases for higher relative channel roughnesses. Zolezzi and Seminara (2001) have shown that the condition $\beta = \beta_R$ discriminates between two markedly different morphodynamic regimes (Zolezzi et al. 2005), characterized by dominant upstream (downstream) morphodynamic influence when the width ratio exceeds (lowers) the resonant value.

Under the above assumptions the planimetric evolution equation reduces to the following ordinary differential system for the first and the third harmonic of the inflection angle ϑ and for meander wavenumber λ:

$$\begin{aligned} \frac{d\vartheta_1}{dt} &= \mathcal{F}_1(u_{m1}, u_{m3}, \vartheta_1, \vartheta_3, c.c.) \\ \frac{d\vartheta_3}{dt} &= \mathcal{F}_3(u_{m1}, u_{m3}, \vartheta_1, \vartheta_3, c.c.) \end{aligned} \tag{13}$$

$$\frac{d\lambda}{dt} = \lambda^2 \left[i(3\bar{\zeta}_3 \vartheta_3 \bar{\vartheta}_3 + \bar{\zeta}_1 \vartheta_1 \bar{\vartheta}_1) + c.c. \right] \tag{14}$$

where an overbar denotes the conjugate of a complex number and $\mathcal{F}_1, \mathcal{F}_3$, are complex algebraic expressions reported in Seminara et al. (2001).

4 THE INPUT DATA SET

We seek to compare model-based predictions of meander properties with field observations and to detect how these features are affected by changes in relevant geomorphic controls such as the valley slope and the flow discharge. To these aims suitable data sets have been employed to provide field based input for the simulation model described in the previous sections. Model-based prediction of meander properties is commonly pursued on the basis of non dimensional input data; dimensional analysis applied to river morphodynamics indicates that an appropriate input data set is provided by specifying reach-averaged values of the width ratio, of the Shields parameter and of the relative roughness (β, τ_*, d_s) together with the bank erosion coefficient E. Most theoretical investigations of meander behavior focus on the dependence of meander dynamics on a single dimensionless parameter, while the other are kept fixed; for instance this allows to isolate the role of the channel aspect ratio β (and of τ_* and of d_s). Typical results also refer to given parameter configurations and describe how meander properties vary with time.

In the present work we want to isolate the effect of different geomorphic controls such as the river discharge or the valley slope: therefore we have calculated the dimensionless input data sets from directly

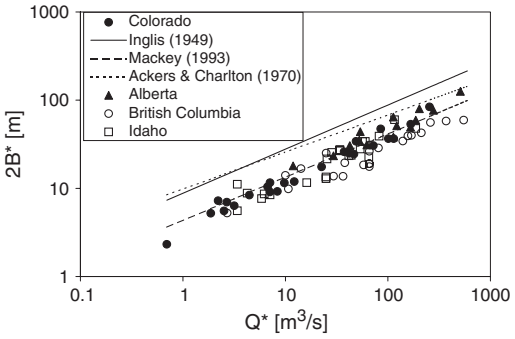


Figure 3. Comparison between different bankfull width estimations and field data relative to single thread, meandering gravel bed rivers.

measurable quantities (Q^*, S, d_{50}^*) by letting one of them to vary while keeping the others fixed. A major requirement is that the input data must reflect hydraulic conditions actually observed in natural rivers.

In order to quantitatively check the consistency of the input data with actual river conditions we have referred to the data set relative to single-thread rivers reported in Gary Parker's e-book (Parker 2004). The data set includes reach averaged characteristics of gravel and sand bed rivers, namely bankfull discharge (Q^*), channel width $(2B^*)$, longitudinal slope (S) and representative sediment size (d_{50}^*). In the present work we have mainly focussed on gravel bed rivers for essentially two reasons. First, the simulation model described in §2 assumes sediment transport to occur mainly as bedload; moreover, the number of data concerning sand bed rivers is relatively too small (<10) for the purpose of describing typical ranges of Q^*, S, d_{50}^* and their correlation properties.

Figure 3 shows the relationship between flow discharge and bankfull river width for the considered gravel bed river reaches. We have compared the field data with empirical relationships proposed by several authors (Inglis 1949, Carlston 1965, Ackers and Charlton 1970, Dury 1976, Mackey and Bridge 1993) for gravel bed, meandering rivers: only the best performing predictors have been reported. Figure 3 suggests that the formula of Mackey and Bridge (1993) most adequately reproduces observed channel widths and reads:

$$B^* = 2.165 Q^{*0.49}. \tag{15}$$

Equation (15) has therefore been used to calculate variations in (β, τ_*, d_s) values corresponding to variations in bankfull discharge with constant values of valley slope and sediment size. Examination of the field data has also suggested that the mean sediment diameter d_{50}^* should be chosen in the range $20 \div 170$ mm with valley slopes not to exceed 0.03. The upper S limit is

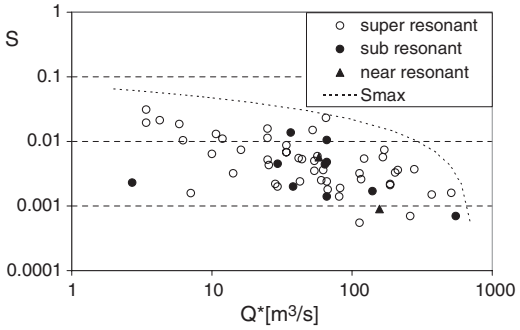


Figure 4. Sub- and super-resonant regimes in gravel bed rivers with different bankfull discharges and longitudinal slopes. The dotted line defines the upper S limit imposed in the input data set for a given flow discharge.

actually bounded by the value of flow discharge, and it has been calculated through an envelope curve based on the given data. Such curve is reported in Figure 4 and can be obtained through the following expression:

$$S_{max} = 2\left[-0.0055 \ln(Q) + 0.0363\right]. \qquad (16)$$

The input dimensionless parameters (β, τ_*, d_s) have been computed for any given combination of (Q^*, S, d_{50}^*) and B^* (from equation (15)) through the same closure relationships employed to evaluate flow resistance indicated in §2 and 3. A further check on the input data has been performed in order to ensure that sediment transport dominantly occur as bedload. We have referred to the classical marginal condition $(W_s^*/u_*^* = 1)$ for the occurrence of suspended load, where W_s^* represents the particle fall velocity, evaluated through the recently proposed expression of Jimenez and Madsen (2003), and u_*^* is the friction velocity. The minimum calculated value of the longitudinal slope corresponding to incipient suspended load is in fairly good agreement with the limit empirically defined by expression (16).

5 PREVALENT SUPER-RESONANT REGIME OF SINGLE THREAD, GRAVEL BED RIVERS

We have calculated the resonant conditions for approximately 60 gravel bed river reaches reported in the reference data set. Sub-resonant (super-resonant) reaches correspond to $\beta < \beta_R$ ($\beta > \beta_R$), while we have referred to near-resonant river reaches when the absolute value of the difference $(\beta - \beta_R)$ is lower than 10% β_R. Results are reported in Figure 5, where each point refer to a given reach: open circles (○) denote super-resonant river reaches, closed circles (●) refer to sub-resonant reaches while near-resonant reaches are represented by black triangles. Several interesting observations arise.

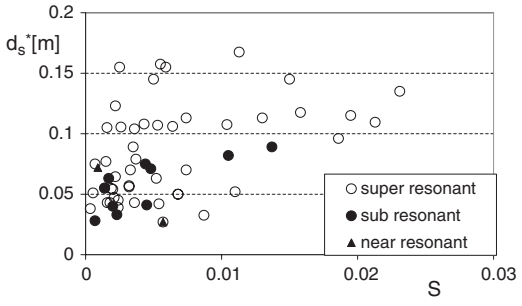


Figure 5. Sub- and super-resonant regimes in gravel bed rivers with different sediment sizes and longitudinal slopes.

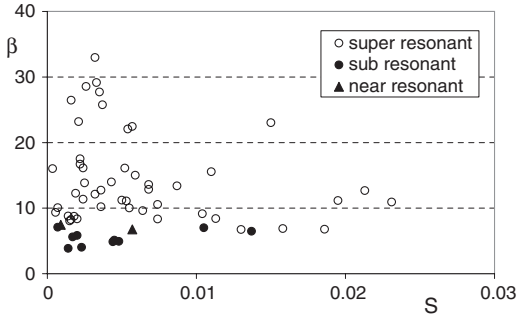


Figure 6. Bankfull width ratios and longitudinal slopes of the examined gravel bed river reaches.

First, it appears that most (~75%) gravel bed river reaches fall under super-resonant conditions. Indeed most sub-resonant rivers seem to occur only for relatively mild longitudinal bed slopes ($S < 0.005$) except for two cases. Sub-resonant conditions are not met also for mean sediment size d_{50}^* exceeding 9 cm. The observations are somewhat confirmed by the typical values of bankfull discharge in sub-resonant channels, which almost invariably exceed 30 $m^3 s^{-1}$ (Figure 4); indeed reaches with high slopes and large sediments are usually found in the upper part of river basins where bankfull discharges tend to keep relatively small. We have plotted the values of β and of β_R for the examined river reaches in Figures 6 and 7 respectively. The picture arising from Figure 6 is somewhat surprising: a sharp threshold appear to separate river reaches falling in the two regimes. Indeed every sub-resonant reach displays values of the width ratio that do not exceed 7; in addition no super-resonant river reach can be found for $\beta < 6.5$. The existence of such thin range of the width ratio separating sub- and super-resonant regime is not obvious at all, since resonant values for the examined reaches cover a much wider interval, with values of β_R for sub-resonant rivers falling between 6 and 10. If confirmed, however, the above observation might provide a simple

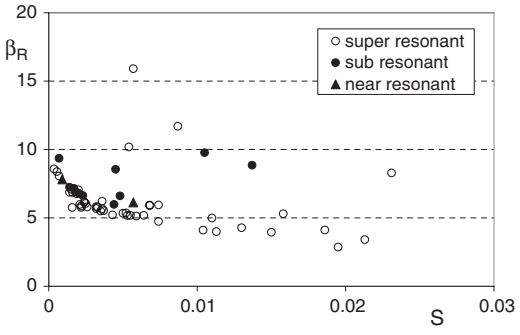


Figure 7. Resonant values of the width ratio as function of the longitudinal slope for the examined gravel bed river reaches.

width-ratio-based criterion for an expedite assessment of the morphodynamic regime of a river reach. It is worth noticing that, especially for low river slopes, a close relationship appears between β_R and S. This can be understood through a careful investigation of the effects that contribute to resonance conditions, which are mainly related to the nonlinearities in the closure relationships employed to evaluate the bedload transport. The choice of Parker (1990) formula implies that at low values of the Shields parameter the quantity $\phi_T = (\tau_{*o}/\phi_o)(\partial\phi/\partial\tau_*)$ keeps constant, thus determining a close relationship between S and d_s which gives rise to the observed biunique correspondence between β_R and S at low slopes. All the above observations seem to support the idea that sub-resonance could be an exception for gravel bed rivers, mostly characterized by relatively large values of their bankfull width ratio normally exceeding the resonant value β_R that keeps generally quite low (below 10) due to the effect of the large relative roughness typical of gravel bed streams. Sub-resonance might be more frequent in sand-bed streams, but this has not been investigated in detail in the present paper. The only supporting argument in this direction might be provided by the observed occurrence of sub-resonant gravel bed rivers in correspondence of relatively small sediment size and mild bottom slopes.

6 SHORT TERM MEANDER DYNAMICS IN GRAVEL BED RIVERS

We have examined the role of variations in bankfull discharge and of the alluvial valley slope on the planimetric evolution of gravel bed meandering rivers, performing simulations in the super-resonant regime which has been identified as the most typical for gravel bed rivers. Simulations started from a slightly perturbed straight channel whose wavelength corresponded to the maximum linearly unstable meander

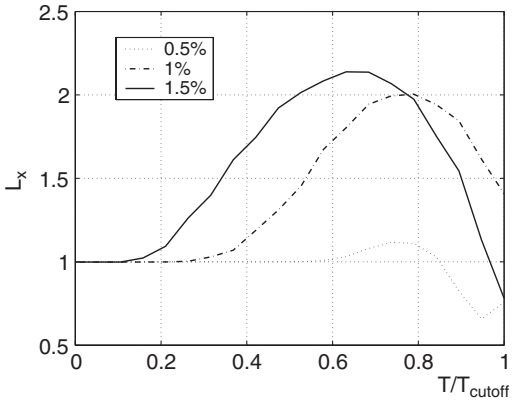


Figure 8. Time evolution of the cartesian meander wavelength L_x for different values of the valley slope, expressed in %.

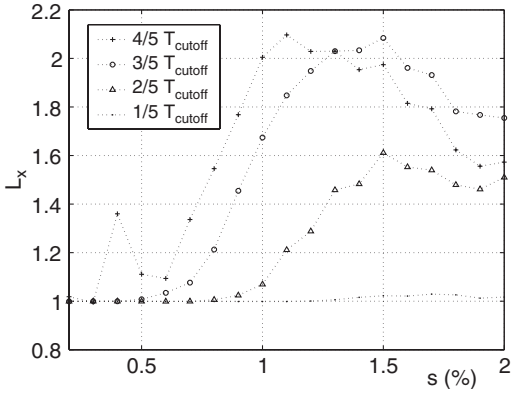


Figure 9. Variation of the cartesian meander wavelength L_x with the valley slope.

wavenumber (e.g. Ikeda et al. 1981, Blondeaux and Seminara 1985). We have investigated the evolution of channel planform until the first cutoff event, concentrating our attention to the short term dynamics of major interest for engineering applications.

We have focussed on the time evolution of meander wavelength and sinuosity as well as on the characteristics of channel planform, described through the fattening and skewing coefficients $(\mathcal{C}_F, \mathcal{C}_S)$ of the Kinoshita curve (11).

The time evolution of the cartesian dimensionless wavelength L_x, scaled with its initial value, is reported in Figure 8: it invariably appears that in the short time span the cartesian wavelength evolves up to a maximum and then decreases before cutoff; a similar tendency also appears when examining the dependence of L_x from the valley slope (Figure 9) at different

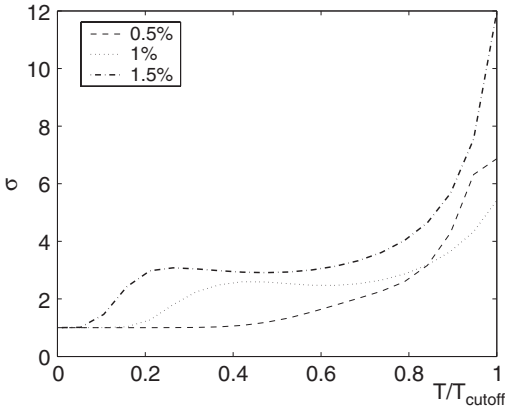


Figure 10. Time evolution of meander sinuosity for different valley slopes.

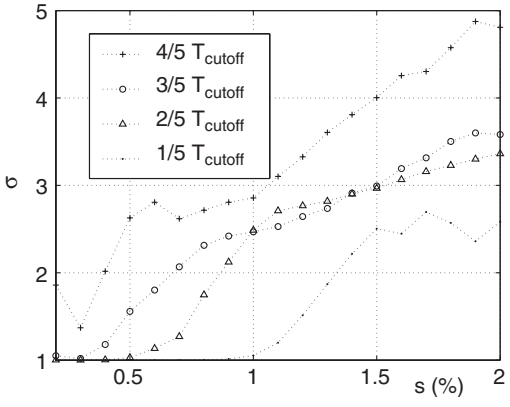


Figure 11. Variation of meander sinuosity with valley slope, at different stages of meander evolution.

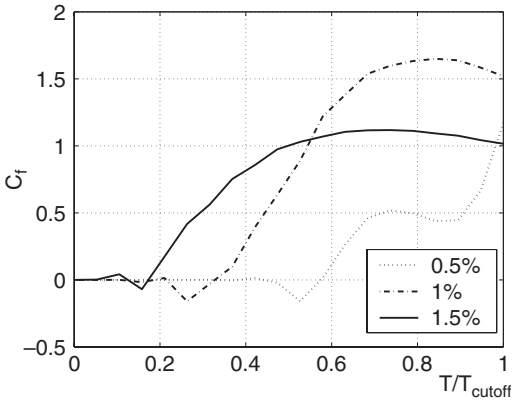


Figure 12. Temporal evolution of the fattening coefficient C_F for different values of the valley slope S.

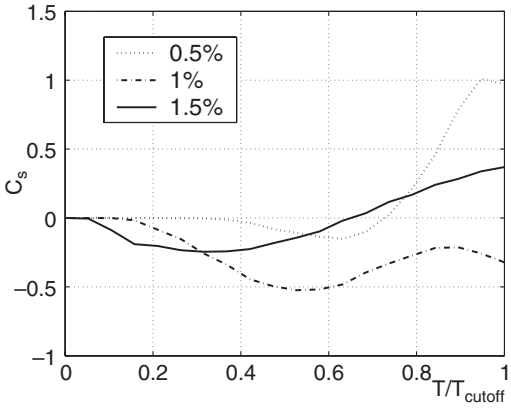


Figure 13. Temporal evolution of the skewing coefficient C_S for different values of the valley slope S.

evolution stages, measured by their relative distance to the occurrence of the first neck cutoff.

Such behavior is reflected in the evolution of channel sinuosity $\sigma = L/L_x$: Figure 10 indeed indicates that the temporal evolution of meander sinuosity is characterized by three distinct stages: an initial growth is followed by a substantially constant region which finally ends up increasing towards cutoff. Indeed the intrinsic wavelength invariably increases until the occurrence of the first neck cutoff (e.g. Seminara et al. 2001), while the presence of a maximum in the evolution of L_x accounts for the nearly constant value of the sinuosity observed in middle stages of meander growth. The highest sinuosities occur only at later stages when L_x is decreasing (Figure 8).

Figure 11 shows that meander sinuosity invariably increases with valley slope. This result confirms similar experimental tendencies reported by various authors (e.g. Bridge 2003) that indicate similar $(\sigma - S)$ relationships for meandering rivers; sinuosity is experimentally observed to sharply decrease for higher slopes which correspond to the shift to the braided morphology.

The planform evolution of a Kinoshita curve (11) can be described in terms of the fattening ($\mathcal{C}_F$) and skewing ($\mathcal{C}_S$) coefficients that can be obtained from the complex Fourier harmonics (ϑ_1, ϑ_3, solution of 13, 14). Figure 12 indicates that fattening is almost invariably positive during meander evolution, except for very short time intervals in the intermediate stages. Fattening of meander loops develops in a relatively short time compared to that needed for the first neck cutoff to occur; once reached a maximum, $\mathcal{C}_F$ keeps almost constant or slightly decreases until the neck cutoff, whose occurrence seems mainly related to the progressive skewing of meander shape, whose indicator, $\mathcal{C}_S$ displays more distributed variations along the whole evolution period. This is shown in Figure 13,

indicating also a more pronounced tendency towards oscillations of the values and the sign of $\mathcal{C}_S$: a persistence in the sign of $\mathcal{C}_S$ cannot be detected, which implies a possible temporal shift from upstream to downstream skewed meander loops (and viceversa) under super-resonant conditions.

Finally note that the dependence of meander properties from flow discharge has not revealed any clear tendency and related results have not been reported here for the sake of brevity.

7 MEANDER MIGRATION IN THE BEATTON RIVER, CANADA

We have performed a comparison of model predictions with the field data related to a widely studied meandering river, the Beatton River in British Columbia, Canada (Hickin and Nanson 1975). The analyzed river reach is approximately 50 km long and has a mean sediment size $d_{50}^{*} = 2.5$ mm, longitudinal slope $S = 0.0003$, formative discharge ranging between 60 and 200 $m^3 s^{-1}$ and bankfull width in the range $20 \div 30$ m. A series of field observations carried out in the late '70s and in the early '80s (Hickin and Nanson 1975, Hickin 1977, Nanson 1979, Nanson and Hickin 1983) have focussed on the migration properties of several meander loops along the freely evolving river reach. It appears that the migration speed of meanders, measured along the n direction, peaks when the curvature ratio ν approximates $0.15 \div 0.20$. Despite several qualitative features of such behavior have been already reproduced (Seminara et al. 2001), a close comparison with meander model predictions is still absent.

We have pursued such comparison for the meander bends analyzed by Nanson and Hickin (1983) employing different values of the flow discharge falling in the formative range and evaluating sediment transport with the formula of Engelund and Hansen (1967) in order to account for the possible coexistence of both bedload and suspended load, the Shields parameter ranging between 0.12 and 0.2.

Model predictions show good qualitative and quantitative agreement with field observations. The reach under investigation falls in the sub-resonant regime. Indeed within the given discharge range, β falls between 11 and 10 while β_R keeps always greater than 13; this picture is independent from the choice of the sediment transport formula. This finding is consistent with the typical shape displayed by the bends reported by Nanson and Hickin (1983), consisting of mature, upstream skewed bends, and with the observed tendency of meander loops to migrate downstream (Nanson 1979). Figure 14 shows the measured migration speed (in channel widths per year) for the investigated meander bends together with the computed maximum values displayed by the same bends over time. It appears that the model correctly predicts the value of the curvature ratio corresponding to peak migration rates.

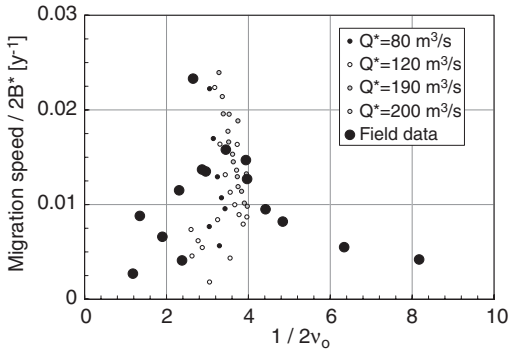


Figure 14. Computed and measured migration speed of several meander loops along the Beatton River.

8 CONCLUSIONS

A first assessment of the ability of a simulation model for river meanders to reproduce field observations has been performed and yielded fairly satisfactory results. Moreover the implications of the morphodynamic influence regimes (sub- and super-resonant, see Zolezzi and Seminara 2001) have been extensively examined in the case of gravel bed rivers for the first time. The present analysis has been carried out under some simplifying assumptions which allowed to focus on the most relevant processes for meander dynamics in the short time span, preceding the first neck cutoff. Results indicate previously undetected features of meander evolution and open promising perspectives for future work. A few interesting issues are summarized. The classical planform of mature meander loops, whose upstream skewness typically allows to detect the flow direction in meandering rivers by simply looking at an aerial picture, seems to occur quite seldom among gravel bed rivers; this might imply that such shape be typical of sand bed rivers, an assessment that requires a suitable morphodynamic model of river meanders able to account for the effect of suspended load. The fact that very few rivers display near-resonant conditions might indicate a tendency for river evolution to keep far from resonance conditions. Moreover the existence of a very narrow threshold between the width ratios of sub- and super-resonant rivers may also suggest that the evaluation of regime properties of gravel bed rivers could be affected by their morphodynamic regime.

Improvements of the present work shall incorporate a wider and more detailed field data set, especially for

sand bed rivers; moreover the present findings need to be verified with more complete numerical models accounting for arbitrary distribution of channel curvature.

ACKNOWLEDGMENTS

This work has been developed within the CUDAM Research Center and of the projects "La risposta morfodinamica di sistemi fluviali a variazioni di parametri ambientali – COFIN 2003", co-funded by the Italian Government (MIUR) and the University of Trento and of the "RIMOF" project financed by the Fondazione CaRi Verona, Vicenza, Belluno e Ancona.

REFERENCES

Ackers and Charlton (1970). Dimensional analysis of alluvial channels with special reference to meander length. *Journal of Hydraulic Research 8*, 287–314.

Amsler, M. and G. Ramonell (2002). Parana river adjustments to dominant discharge changes. Volume Proc. of Riverflow 2002 conference. Balkema.

Blondeaux, P. and G. Seminara (1985). A unified bar-bend theory of river meanders. *Journal of Fluid Mechanics 112*, 363–377.

Bridge, J. (2003). *Rivers and Floodplains. Forms, processes and sedimentary records*. Blackwell.

Camporeale, C., P. Perona, A. Porporato, and L. Ridolfi (2005). On the long term behavior of meandering rivers. *Water Resources Research 41*, W12403, doi:10.1029/2004WR003333.

Carlston (1965). The relation of free meander geometry to stream discharge and its geomorphic implications. *American Journal of Science 263*, 864–885.

De Vriend, H. (2002). Model based morphological prediction: from art to science. In *Proceedings of RiverFlow 2002*, pp. 3–12. Lovain la Neuve (Belgium).

Dury, G. (1976). Discharge prediction, present and former from channel dimension. *Journal of Hydrology 30*, 219–245.

Engelund, F. and E. Hansen (1967). *A monograph on sediment transport in alluvial streams.*, Volume 33. Danish Technical Press, Copenhagen.

Hasegawa, K. (1989). Studies on qualitative and quantitative prediction of meander channel shift. S. Ikeda & G. Parker (Eds.), River Meandering, Washington DC, Water Res. Monograph **12**, Amer. Geoph. Union.

Hickin, E. (1977). *The analysis river planform responses to changes in discharge.* (K. J. Gregory ed.), Volume River Channel Changes, pp. 249–263. Wiley.

Hickin, E. and G. Nanson (1975). The character of channel migration the beatton river. northeast british columbia, canada. *Geological Society of America Bullettin 86*.

Hooke, A. (1995). Processes of channel planform changes on meandering channels in the uk. Volume Changing river channels. John Wiley.

Ikeda, S., G. Parker, and K. Sawai (1981). Bend theory of river meanders. part 1 – linear development. *Journal of Fluid Mechanics 112*, 363–377.

Inglis (1949). The behaviour and control of rivers and canals (with the aid of models). Technical report, Central water power, irrigation, and navigation research station pub. 13-1, Poona, India.

Jimenez, J. and O. Madsen (2003). A simple formula to estimate settling velocity of natural sediments. *Journal of Waterway, Port, Coastal and Ocean Engineering*, 70–78.

Kinoshita, R. (1961). Investigation of channel deformation in ishikari river. Technical report, Bureau Of Resources, Dept. Science and Technology, Japan. in Japanese.

Langbein, W. B. and L. B. Leopold (1964). Quasi equilibrium states in channel morphology. *Amer. J. of Science. 262*.

Lanzoni, S., A. Siviglia, and G. Seminara (2006). Long waves in erodible channels and morphodynamic influence. *Water Resources Research*. accepted.

Mackey, P. and J. Bridge (1993). Three dimensional modelling of alluvial architecture. In *Fifth Int Conference of fluvial sedimentology*. Brisbane, (Australia).

Nanson, G. (1979). A regional trend to meander migration. *The Journal of Geology 88*, 100–108.

Nanson, G. and E. Hickin (1983). Channel migration and incision on the beatton river. *Journal of Hydraulic Engineering 109*, 327–337.

Parker, G. (1990). Surface-based bedload transport relation for gravel rivers. *Journal of Hydraulic Research 28*, 417–436.

Parker, G. (2004). *1D Sediment Transport Morphodynamics with applications to Rivers And Turbidity Currents*. available at http://www.ce.umn.edu/ parker.

Seminara, G. (2006). Meanders. *Journal of fluid mechanics*. paper invited for the 50th Anniversary issue.

Seminara, G. and M. Tubino (1989). *Alternate bars and meandering: Free, forced and mixed interactions*, pp. 267–320. in River Meandering, S. Ikeda and G. Parker (Eds.), Water Resources Monographies, 12.

Seminara, G., G. Zolezzi, M. Tubino, and D. Zardi (2001). Downstream and upstream influence in river meandering. PART 2. planimetric development. *Journal of Fluid Mechanics 438*, 213–230.

Zolezzi, G., M. Guala, D. Termini, and G. Seminara (2005). Experimental observation of upstream overdeepening. *Journal of Fluid Mechanics 531*, 191–219.

Zolezzi, G. and G. Seminara (2001). Downstream and upstream influence in river meandering. PART 1. general theory and application of overdeepening. *Journal of Fluid Mechanics 438*, 183–211.

Migration of a dredging pit in the Rhone River

J.-L. Boillat
Ecole polytechnique Fédérale de Lausanne (EPFL), Laboratory of Hydraulic Constructions, Switzerland

J. Dubois
HydroCosmos, Numerical Engineering Company, Vernayaz, Switzerland

N. Nilipour
STUCKY Ltd, Renens, Switzerland

ABSTRACT: Extraction of sediments in a riverbed is currently operated to regulate its profile equilibrium. The excavation pit is submitted to a migration process characterized by successive convection and diffusion phases. This phenomenon has been investigated in a case study of gravel exploitation on the Rhone River in Switzerland. A first approach was conducted on a physical model in order to quantify the impact of the main geometrical parameters of the pit, particularly its length, width and depth. The experimental results have then been used for the development and calibration of a numerical model simulating transient flow on a non-cohesive mobile bed. Numerical simulations allowed proceeding to a sensitivity analysis of the pit migration related to its depth, length and width as well as to the riverbed material gradation. The results highlight the erosion processes which develop upstream and downstream of the excavation zone.

1 INTRODUCTION

Disruption of sediment transport in rivers caused by sand and gravel pits modify the bed geometry and can endanger the stability of the banks and structures, e.g. bridges. Sediment transport is affected by a sudden change in the riverbed geometry and consequently erosion is anticipated downstream of the pit. Therefore, geomorphic and also environmental effects of material extraction are one of the main concerns in river training projects (Kondolf, 1994).

The 3rd correction enterprise of the Rhone River is a project at national scale, which deals with all kind of hydraulic activities and structures in the Swiss part of the river, upstream of Lake Geneva. Sand and gravel extraction is carried out at particular locations along the river, among which the Rarogne Region.

The evolution of the bed geometry due to this mine pit was examined. A 1:45 scale physical model with mobile bed was submitted to experimental tests in order to investigate the pit migration and the downstream erosion resulting from the dredging activity. The main goal was to define the depth and extend of the erosion in the affected zone in order to establish the criteria for the dredge operator.

Although research was carried out in the past based on laboratory tests and numerical modeling (Lee & Song, 1993, Bianco et al., 1997 and Gill, 1993), due to the complexity of this phenomenon, scale hydraulic modeling is necessary for each particular case in order to obtain appropriate results. For a first approximation, Lee & Song (1993) proposed formulas derived from experimental results as a general solution to this problem. This set of formulas was obtained for a rectangular mining pit with uniform sediments over the whole river width and in a limited range of Froude numbers (0.40–0.47).

Its application is limited to cases presenting no lateral contraction and only within the range of the original study. Referring to these investigations, two different stages can be distinguished in the mining pit migration process, the convection and the diffusion phases (Fig. 1). The transition occurs when the lowest point of the pit coincides with the downstream extremity of the pit.

2 PHYSICAL MODELING

2.1 *Model boundaries and characteristics*

The simulated river reach extends to some 800 m (Fig. 2), which was modeled at a geometrical scale 1/45 giving the length and width of the model as 16 m to 2.4 m, respectively.

In order to find out the impact of the dredging pit during different flood events, a series of tests was carried out for three discharges listed in Table 1.

The hydraulic model constructed for this study is schematically shown in Figure 3. In order to meet the similarity laws in case of mobile bed modeling, the grain diameter has been chosen considering the riverbed roughness and type of the bed form. The total roughness coefficient can be computed taking into account the grain size roughness and the bed form. Based on the empirical formulas and charts determining the bed form (Larras, 1972, Yalin & Ferreira, 2001) the Rhone River is characterized by a regime of dunes and bars. Considering the total roughness, uniform graded fine sand of 0.2 mm diameter was adopted as bed sediment.

Sediment feeding was evenly done at the upstream limit of the model during tests. The sediment discharge has been computed for each case based on the empirical relations of Smart & Jaeggi (Jaeggi, 1994) and Schoklitsch (Graf & Altinakar, 1998). Average values issued from the mentioned methods were applied as sediment discharge (Table 2).

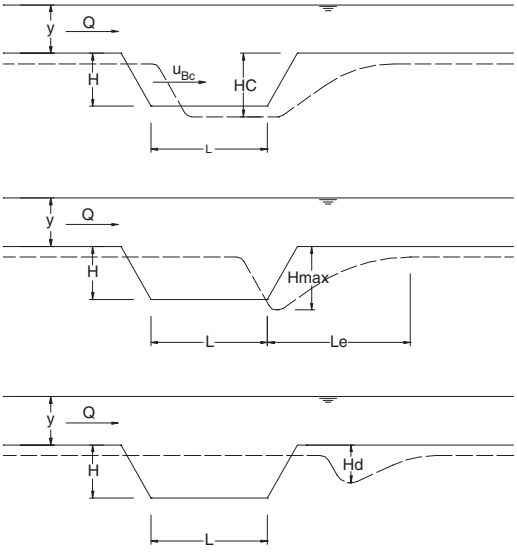


Figure 1. Migration of a rectangular mining pit composed of uniform sediments according to Lee & Song (1993).

2.2 *Instrumentation*

Four UVP (Ultrasonic Velocity Profiler) transducers were mounted on a mobile measurement platform moving along the model length (Fig. 4).

A series of 2 MHz transducers were adopted for the test taking into account the following three parameters:

- Measurement distance range.
- Maximum estimated velocity range.
- Required accuracy in terms of width of the measurement channel and velocity resolution.

Velocity profile measurements were conducted every 25 cm close to the pit and every 50 cm in the other parts.

In each measurement station, 100 profiles were measured by each of the four probes, having one second delay to activate the next probe. One full measurement set over the model was performed at an interval of half an hour. Additional detailed information about

Table 1. Discharge values used in the study.

Return period (yr)	10	50	100
Discharge in prototype (m^3/s)	580	740	820
Discharge in model (l/s)	42.7	54.5	60.4



Figure 2. Limits of the hydraulic model and available cross sections of the Rhone River used in this study.

the transducers and measurement interpretation can be found in Nilipour et al. (2004) and Hersberger (2002).

2.3 *Tested configurations*

The analysis of systematically repeated bathymetric measurements, performed at different periods of the mine operation during the last 14 years, reveals important variations of the riverbed configuration between cross sections BWW57 and BWW58 (Fig. 2).

Furthermore, temporary material deposits causing a contraction of the river could be observed periodically on the operation site (Fig. 2). Based on this information, three different configurations of the dredging pit geometry were considered:

– Big dredging pit, 2 m long, 10 cm deep.
– Big dredging pit with contraction, 2 m long, 10 cm deep.
– Small dredging pit, 1 m long, 10 cm deep.

The river contraction has a maximum being half of the width at the beginning of the pit and reaches until zero at the end of the pit. In all cases, the pit extent occupies the total available width of the river bed, as presented in Figure 5.

2.4 *Experimental results*

As expected Yalin & Ferreira (2001), bed forms developed with a predominant influence of multiple bars caused by horizontal turbulence (Fig. 6). Inside the mining pit, dune formation can be observed due to the water depth increase (Fig. 6).

The temporal migration of the mining pit and the velocity field inside the excavation were measured for the three steady state flow conditions given in Table 1. An example of results is presented on Figures 7 and 8 for configuration (a) of the mining pit (Fig. 5) and a flow discharge corresponding to a 50 years return period. Values are given at model scale with the following characteristics:

– The longitudinal distance grows in flow direction starting from the upstream end of the model;
– The longitudinal profile of the mining pit is given at three different instants in order to illustrate the progression of the upstream front and the downstream erosion of the pit;

Table 2. Sediment feeding discharge.

Water discharge (l/s)	Solid discharge (l/s.m)
42.7	0.0060
54.5	0.0075
60.4	0.0100

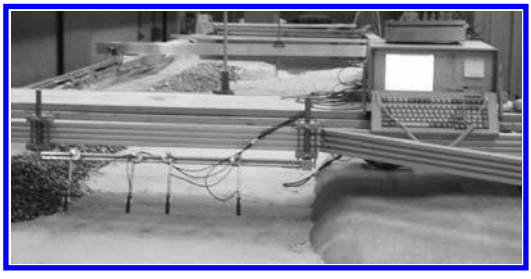


Figure 4. UVP transducers mounted on the measurement mobile frame.

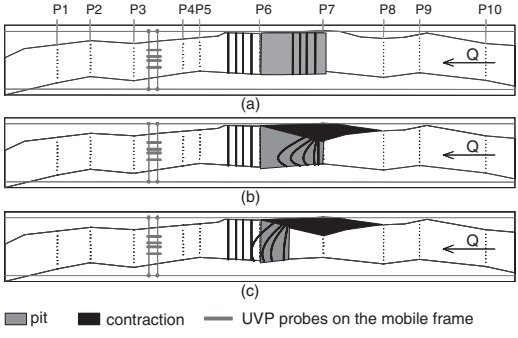


Figure 5. Plan view of the modeled reach of the Rhone River with pit front movement and downstream erosion; (a) big dredging pit; (b) big dredging pit with contraction; (c) small dredging pit with contraction.

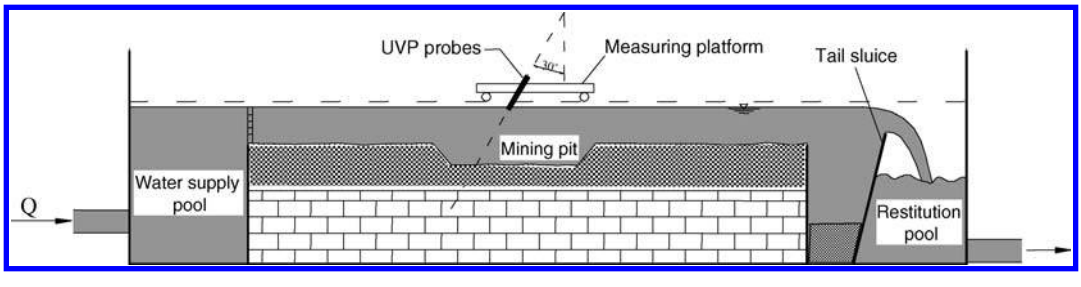


Figure 3. Schematic profile of the hydraulic model.

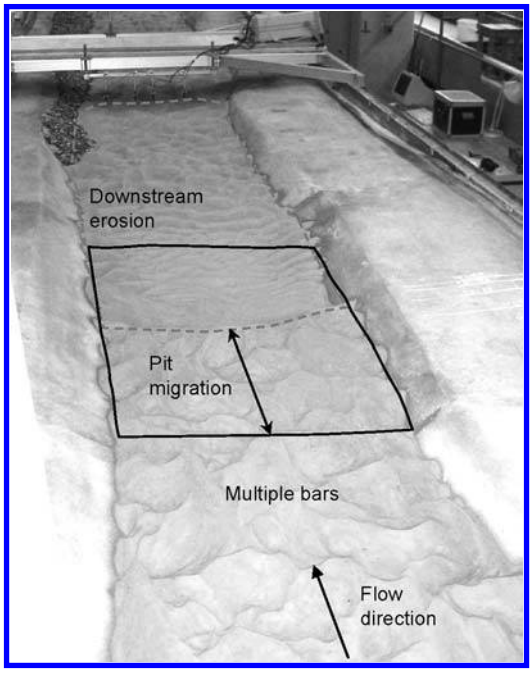


Figure 6. Migration of a rectangular mining pit with formation of bed forms on the mobile bed.

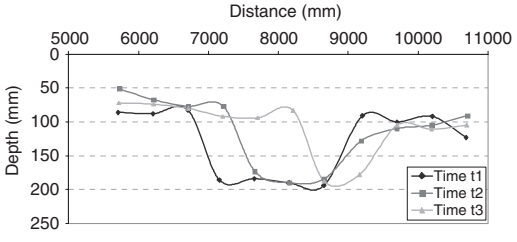


Figure 7. Migration of the big dredging pit for a 50 years return period discharge.

– Velocity profiles are given on five vertical axis uniformly distributed along the initial configuration of the pit at time t_1;
– Mean velocity and standard deviation are given on 128 vertically distributed points;

The observed migration process, illustrated by Figure 7, corresponds fairly well to the stages described in Figure 1, however with some particularities:

– The pit fills from upstream and the downstream erosion is clearly observed but without any deepening of the initial bottom;
– The multiple bars bed forms which develop on the river bed upstream of the mining pit have a significant influence on the upstream flow boundary condition; during filling up, a dune regime develop over the pit (Fig. 6);
– The velocity profiles clearly show the influence of the pit, particularly in the deepened section where a dead zone exists.

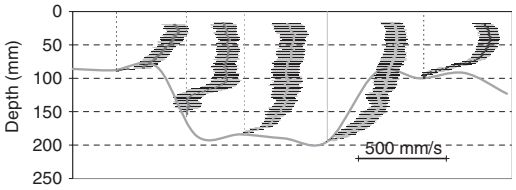


Figure 8. Velocity profiles measured by UVP probes in different sections at time t_1.

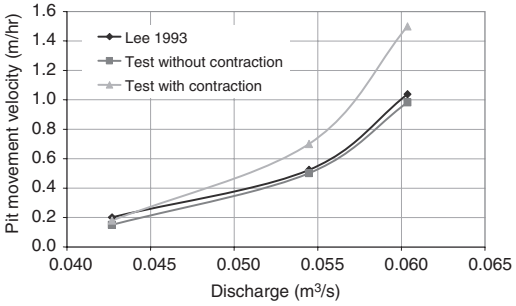


Figure 9. Comparison of the pit movement velocity for different discharges.

2.5 *Summary*

The advancing velocity of pit movement of the big dredging pit was determined for each discharge tested (Fig. 9). Measurements carried out with configuration 1, i.e. without contraction, are compared with the calculated values using the theory of Lee (1993). The movement of the big dredging pit with contraction is faster, particularly for the high discharges. This can be explained by having a smaller excavated volume as well as head losses due to sudden deepening at the beginning of the dredging pit.

The zone submitted to erosion downstream of the pit is not significantly influenced by the discharge (Fig. 10). Its extent is only 25% greater for Q_{100} compared with that of Q_{10}. The effect of the contraction leads to a reduction in the range of 7 to 8% of the erosion extent.

During saturating and filling of the model, it was observed that the bed is deepened at the upstream front of the pit. This phenomenon is particularly perceptible with the contracted configuration where the additional hole reaches 1.5 m at prototype scale for Q_{100}.

It should be mentioned that the results of the experimental model study are used as a first approximation

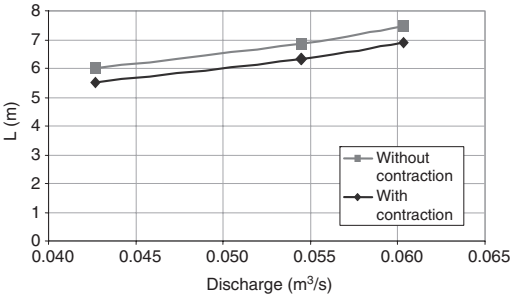


Figure 10. Comparison of the extent of downstream erosion for different discharges.

of the pit migration phenomenon. In order to examine in detail this phenomenon and to show the influence of the different main parameters, the experimental results were used to calibrate a numerical model with mobile bed for transient calculation. This model allows performing a sensitivity analysis on the main parameters, particularly the size of the pit and the gradation of the bed material.

The tests on the model reveal a multiple bars bed regime, which influences the filling of the pit. In fact, the length of the dunes is reduced above the pit with an increased steepness.

It is also interesting to see that the velocity of the pit movement was higher at the beginning of the test, when the initial bed has not yet reached its dune regime.

These different impacts of the bed forms as well as initial condition during the temporal evolution are not modeled in the numerical tool, where a flat bed is considered.

3 NUMERICAL MODELING

3.1 *Mathematical equations*

For the purpose of the project, a new computational model has been developed inside the Excel programming environment. This numerical tool performs the coupled hydrodynamic simulation of 1D flow behavior and bed load transport. The main theoretical aspects of numerical modeling are presented below.

The basic continuity and momentum equations are expressed in the form

$$\frac{\partial A}{\partial t}+\frac{\partial Q}{\partial x}=S \tag{1}$$

$$\frac{\partial Q}{\partial t}+\frac{\partial}{\partial x}\left(\frac{Q^2}{A}+gI_1\right)=gA\left(\frac{\partial z}{\partial x}-J_f\right)+gI_2 \tag{2}$$

$$(1-p)\frac{\partial z}{\partial t}+\frac{\partial q_s}{\partial x}=0 \tag{3}$$

Where A is the wetted surface, Q the discharge, S a source term, J_0 the bed slope, z the bottom elevation of the cross section, I_1 the term of pressure in the wetted cross section, I_2 the term of pressure taking into account the non prismatic geometry of the reach and q_s the bed load unit discharge. The two terms of pressure are computed using the following relations:

$$I_1=\int_0^h (h-\eta)\,b(\eta)\,d\eta \tag{4}$$

$$I_2=\int_0^h (h-\eta)\left.\frac{\partial b}{\partial x}\right|_{h=\eta} d\eta=\frac{\partial I_1}{\partial x}+A\frac{\partial h}{\partial x} \tag{5}$$

An additional semi-empirical closure relation is necessary for coupling the bed load discharge and the hydraulic parameters. In the present case, the equation of Smart and Jaeggi (Jaeggi, 1984) has been implemented:

$$Q_s=\alpha\frac{B_z}{B}2.5QJ_f^{0.6}\left(J_f-\frac{d_m}{12.1h}\right) \tag{6}$$

Where α is a calibration parameter, B_z and B are widths as defined in the schematic cross section of Figure 11, d_m is the mean diameter of the sediments and h the water depth.

Finally, the friction head loss is computed according to the equation of Manning-Strickler:

$$J_f=\frac{Q^2}{K^2A^2R_h^{4/3}} \tag{7}$$

Where K is the Strickler coefficient and R_h the hydraulic radius of the cross section.

3.2 *Cross section geometry*

The coupled 1-D simulation between hydrodynamics and sediment transport has to be able to consider the cross sectional variations induced by deposition and erosion processes. When conceiving the model, the hypotheses related to 1-D modeling have to be kept in mind, in particular that only one value describes the flow or the geometry in any point along the river axis.

By definition, if hydraulics is modeled at 1-D, the same approach has to be applied for the bed load transport. Consequently, the mobile bed elevation must be defined by one single value, considering a horizontal movable bed in the cross sections as described by equations (2) and (3).

Regarding the general morphology of the Rhone River, the trapezoidal cross section presented in Figure 11 was adopted for the study.

Where B_0 is the reference width of the bed at reference elevation z_0, B_z the bed width at elevation z, B the

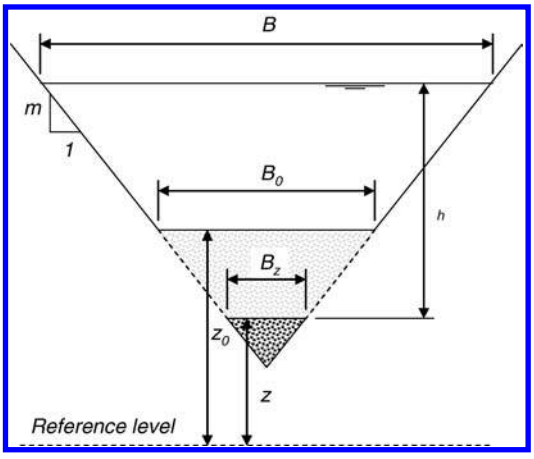


Figure 11. Geometrical model of the cross section.

width at the free water surface and m the inverse slope of the riverbanks. The knowledge of B_0 at elevation z_0 and the inclination m of the riverbanks is sufficient for the definition of the cross section.

3.3 *Numerical solution*

Equations (1) and (2) describe the conservative form of the 1-D St-Venant equations and Equation (3) the sediment continuity, also known as "equation of Exner". In matrix form, this system can be written like:

$$\frac{\partial \mathbf{u}}{\partial t} + \frac{\partial \mathbf{f}}{\partial x} = \mathbf{s} \tag{8}$$

with:

$$\mathbf{u} = \begin{bmatrix} A \\ Q \\ z \end{bmatrix} \tag{9}$$

$$\mathbf{f} = \begin{bmatrix} Q \\ \frac{Q^2}{A} + gI_1 \\ \frac{q_s}{1-p} \end{bmatrix} \tag{10}$$

$$\mathbf{s} = \begin{bmatrix} S \\ gA\left(\frac{\partial z}{\partial x} - J_f\right) + gI_2 \\ 0 \end{bmatrix} \tag{11}$$

Where the vector **u** represents the primary variables (unknown), the vector **f** represents the fluxes (mass, momentum and sediments) and the vector **s** contains the source terms (likewise mass, momentum and sediments).

Equation (8) being hyperbolic, the propagation of perturbations from the primary variables follows characteristic lines. In order to take into account this propagation along characteristic directions in the numerical scheme, the spatial derivates are discretized in a decentralized manner. However, as the characteristic velocities don't have the same sign at subcritical flow conditions, the moving off center of all derivates in the same way is not acceptable. It is necessary to separate the flux judiciously and to move it partially off center in both upstream and downstream directions. This type of scheme is physically based and allows avoiding the appearance of oscillation characteristics of centered schemes.

Two families of methods propose adequate taking off center ways:

- Flux difference splitting: this type of method (Roe, Osher, HLL…) integers directly the notions of wave celerity for the weigthening of the spatial derivates.
- Flux vector splitting: this technique of fractioning fluxes consists in separating the fluxes vector in two parts and taking off center each in a different way. For the present study, the original algorithms of fractioning fluxes developed by Prof. Michel Pirotton at the University of Liège, Belgium, (http://www.hach.ulg.ac.be/), has been used.

3.4 *Model calibration*

When using a numerical model, the first step is devoted to calibration. For hydraulics, the single calibration parameter is the Strickler coefficient in each cross section. The well-documented flood occurred in October 2000 could be used for calibration but no other event was available for validation. According to this procedure, a rather good result was obtained with only two values of the Strickler coefficient: 35 $m^{1/3}/s$ between cross sections P10 and P7, and 24 $m^{1/3}/s$ between P7 and the downstream end of the model (Fig. 2).

The reach located upstream of the mining pit is calibrated with a very classical value for the Rhone river. Nevertheless, the morphological changes due to the pit induce an additional head loss, which has repercussions on the reduction of the Strickler coefficient in this sector. The sediment transport calibration in the present study could be achieved with reference to the experimental results issued from the physical model. This operation refers to the parameter α of Equation (6), which allows weighting the bed load discharge computed from the Smart and Jaeggi equation.

According to the experimental tests, the coefficient α needs to be nearly 3 in order to reproduce all

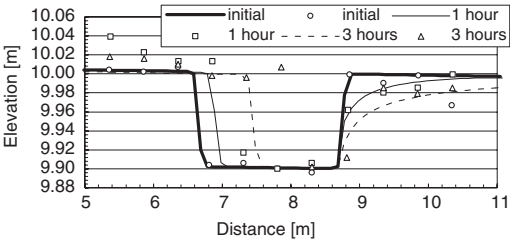


Figure 12. Sediment transport calibration of the numerical model by comparison with measured points of the physical model.

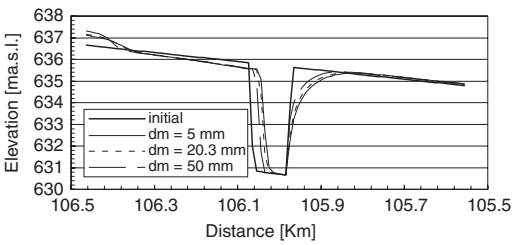


Figure 13. Influence of mean grain size.

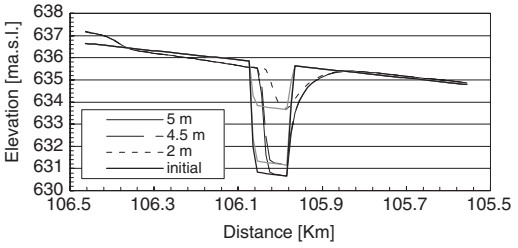


Figure 14. Influence of pit depth after 20 hours.

observed phenomena as good as possible (Fig. 12). Some comments are useful at this point:

- The mean slope of the Rhone River is about 2‰ in this reach, which corresponds to the lower application limit of the equation of Smart and Jaeggi.
- Due to the progressive modification of the initial equilibrium state in the upstream part of the model the progression velocity of the front of the pit was not constant.
- A dune regime developed on the movable bed of the physical model. These bed forms which cannot be reproduced numerically have a significant influence on the energy slope and consequently on the bed load transport.

3.5 *Sensitivity analysis*

Different scenarios were then simulated with the numerical model. The sensitivity analysis refers to the following parameters:

- Flow discharge.
- Grain size distribution.
- Depth of the pit.
- Width of the pit.
- Length of the pit.

Finally, the historical event of October 2000 was simulated in order to examine the behavior of the dredged pit during a high flood.

3.5.1 *Influence of flow discharge*

Three characteristic values of the flow discharge corresponding to high return periods, $Q_{10} = 580\,m^3/s$, $Q_{50} = 740\,m^3/s$ and $Q_{100} = 820\,m^3/s$, have been simulated.

For this range of flow discharge, no significant differences can be mentioned. The flood duration, considered as 20 hours in all cases, reveals as main factor for the filling rate.

3.5.2 *Influence of grain size*

Three different mean grain sizes were used for simulation. The first considered of $d_m = 20.3$ mm, which corresponds to the mean diameter of the extracted sediments, the two other are $d_m = 5$ mm and $d_m = 50$ mm. The profiles obtained after 20 hours for a constant discharge of $740\,m^3/s$ are presented in Figure 13.

It can be observed that the grain size doesn't have a great influence on the pit migration. However, this effect is more noticeable than the previous one related to the discharge.

3.5.3 *Influence of the depth of the pit*

Three different depths of the pit have been investigated, being 5 m, 4.5 m and 2 m. The discharge was kept constant at $740\,m^3/s$ during 20 hours and the mean grain size was 20.3 mm. The computational results are presented in Figure 14.

The influence of the initial depth of the pit is well marked. The sediment transport capacity in the upstream reach is identical in all cases, but the storage capacity of the pit differs. For a 2 m depth it can be observed that the transition phase is ended after 20 hours and the diffusion phase will start at this time.

In order to define the influence of the pit migration on the maximal erosion of the riverbed, the simulation duration was extended up to 10 days. Although maintaining a flow discharge over such a long time is not reasonable in reality, the results give a long-term idea of the pit migration. The envelope curves of the maximal erosion depth are presented in Figure 15.

3.5.4 *Influence of pit width*

Two different widths of the pit were considered in a same manner than in the physical model. The widths are $B = 40$ m and $B = 26.6$ m. The simulation results obtained after 20 hours with a flow discharge of

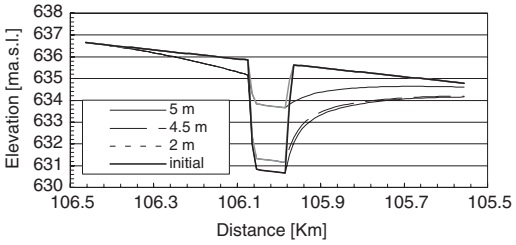


Figure 15. Envelope curves of the maximal erosion for three initial depths of the pit.

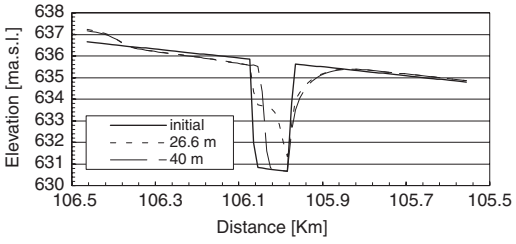


Figure 16. Influence of the pit width after 20 hours.

740 m^3/s and a mean grain size of $d_m = 20.3$ mm are presented in Figure 16.

As expected, the front moves more rapidly in the contracted pit. For the flow discharge of 740 m^3/s, the filling process reaches the downstream end of the pit after 20 hours. The form of the front is different in this particular case with an intermediate landing about two meters below the river bed.

As shown in the previous case, simulations over a long time were performed for both widths of the pit. The envelope curves of the maximal erosion depth (Fig. 17) show that a contraction of the cross section reduces the influence on the downstream erosion. This effect is noticeable for the depth as well for the distance. Thus the diffusion phase of the pit can be significantly damped.

3.5.5 *Influence of pit length*

Simulations with two different lengths of the big dredging pit (Fig. 5), $L = 100$ m and $L = 50$ m, were accomplished. The simulation results obtained after 20 hours with a flow discharge of 740 m^3/s and a mean grain size of $d_m = 20.3$ mm are presented in Figure 18. The envelope curves of the maximal erosion depth resulting from simulations over a long time are given in Figure 19.

The influence of pit length of the on erosion is similar to that related to width. A short pit will have less impact on the downstream erosion than a longer one.

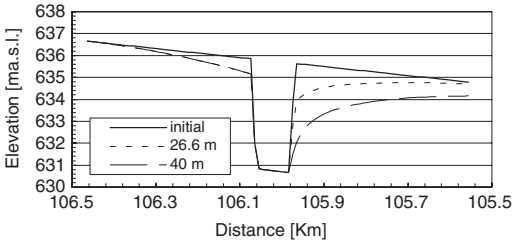


Figure 17. Envelope curves of the maximal erosion depth for two different widths of the pit.

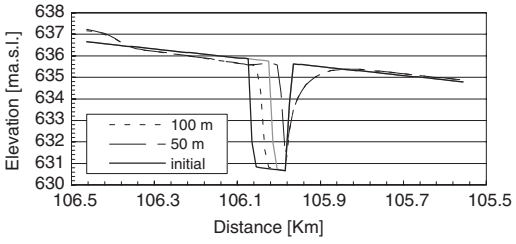


Figure 18. Influence of the length of the big dredging pit after 20 hours.

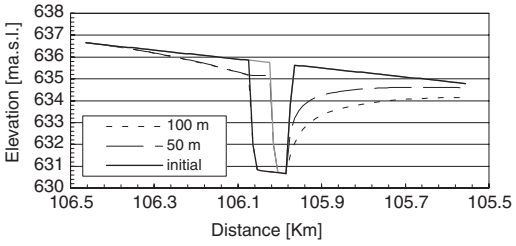


Figure 19. Envelope curves of the maximal erosion depth for two different lengths of the big dredging pit.

3.5.6 *Simulation of the 2000 flood event*

Finally, in order to illustrate the dynamic behavior of the pit during a real flood event, the hydrograph measured on the Rhone River in October 2000 has been simulated (Fig. 20). The return period of the peak discharge is estimated to be approximately 100 years. The initial configuration of the pit has a length of 100 m, a depth of 5 m and two different widths, 26.6 m and 40 m. The mean grain size of the sediments is 20.3 mm.

The temporal evolution of the profile with the broad cross section is presented in Figure 21, respectively with the reduced cross section in Figure 22.

With the broad cross section, the filling process nearly reaches the downstream limit of the pit at the end of the flood. Concerning sediment management, it is interesting to note that this important flood event was not able to completely fill the dredged pit.

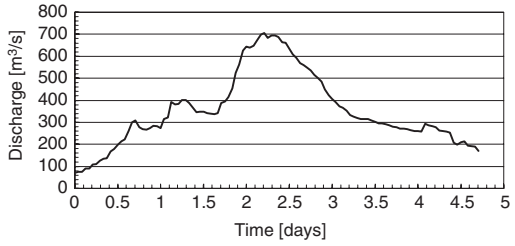


Figure 20. Hydrograph of the 2000 flood event.

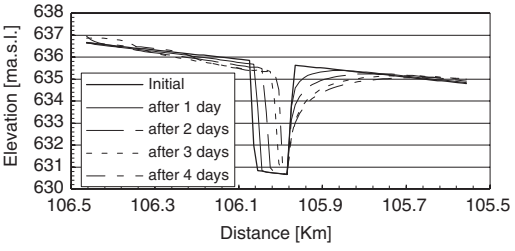


Figure 21. Temporal evolution of the profile during the 2000 flood event with the broad cross section.

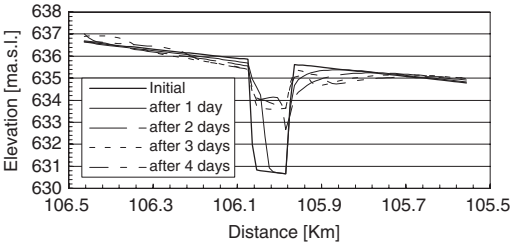


Figure 22. Temporal evolution of the profile during the 2000 flood event with the contracted cross section.

In the case of a pit with contracted cross section, the convection progress takes about 2 days before the beginning of the diffusion phase. It is worthy to note that the reduction of the cross section results in a local dredging effect at the downstream end of the pit.

4 CONCLUSIONS

Extraction of sand and gravel from a river causes a disruption of bed load supply in the downstream part of a mining pit. As a consequence, erosion occurs at that place and the dredged pit itself is submitted to a diffusion process following the filling process. Different parameters influence the evolution and extent of erosion in the affected zone. Among the most important, the depth, the width and the length of the pit, the sediment size and the discharge could be analyzed using a combination of experimental and numerical approaches.

The presented models were developed for application to the particular case of the mining pit of Rarogne on the Rhone River in Switzerland. Nevertheless, the obtained results can be used in a general way for similar situations.

The main goal was to define the depth and extent of erosion in the affected zone in order to establish criteria for the mine operator.

The experimental results obtained for different configurations of the dredged pit were used for the development and calibration of a 1D numerical model for non-steady flow simulation on mobile bed. This model was then used for a sensitivity analysis of the main parameters mentioned above, whose main results can be summarized as follows:

- The discharge doesn't significantly influence the erosion profile in the upstream as well as in downstream part of the dredged zone;
- The uncertainty related to the sediment size only has a weak influence on the downstream erosion and no perceptible effect upstream of the pit;
- The initial depth of the pit has a significant impact on the downstream erosion depth; this influence is proportional to the initial depth; however, no difference can be observed on the erosion upstream;
- The width of the pit has a direct influence on its filling velocity which is obviously related to the available volume; however, a width reduction has a significant effect on the downstream erosion; this effect is reduced the more the pit is narrow;
- The length of the pit exerts a significant influence on the erosion depth in the downstream reach. This influence increases with the length of the pit;
- The numerical simulation of the flood of October 2000 highlights the temporal evolution of the filling process during a real event; it is noticeable that a dredged pit with 100 m length and 4.5 m depth over the total width of the Rhone River could not be completely filled during the four days of the flood event; obviously, the pit with a reduced width fills more rapidly.

The experimental and numerical results confirm that the erosion which develops upstream and mainly downstream of a dredged pit has a negative effect on the stability of the riverbanks and the civil works built in the riverbed. This influence increases with the length and the depth of the pit. However, a pit of a reduced width diminishes the erosion depth downstream.

The results obtained in the case study of Rarogne help to quantify the impact of different configurations of the mining pit on the riverbed. The analysis of these results will be useful for defining an exploitation strategy according to the hydrological regime of the river.

However, it has to be mentioned that the experimental and numerical results are overestimated to a certain extent due to the fact that uniform grain size distribution used for the study impeaches the formation of a protective armoring layer in the eroded zones. This fact places the designer on the safe side.

REFERENCES

Bianco, G., Cargnelutti, M., Gadin A.C. 1997. Study of local phenomena in natural rivers: comparison among experimental results in a flume with mobile bed and numerical simulations with a MIKE 11 – ST model. 2nd DHI Users Conference, June 9–11, 1997.

Gill, M.A. 1993. Hydrodynamics of mining pits in erodible bed under steady flow. *Journal of Hydraulic Engineering*, Vol. 120, N° 11.

Graf, W.H., Altinakar, M.S. 1998. *Fluvial Hydraulics: Flow and Transport Processes in Channels of Simple Geometry*. John Wiley and Sons, England, ISBN 0-471-97714-4.

Jaeggi, M. 1984. Der Geschiebetransport in Flüssen nach der VAW-Formel 1983. *Schweizer Ingenieur und Architekt*, Heft 47, Zürich.

Hersberger, D.S. 2002. Measurement of 3D flow field in a 90° bend with ultrasonic Doppler velocity profiler. *Proc. Of the 3rd International Symposium on Ultrasonic Doppler Methods for Fluid Mechanics and Fluid Engineering*, p. 59–66, Lausanne, Switzerland, Sept. 2002.

Kondolf, G.M. 1994. Geomorphic and environmental effects of instream gravel mining. *Landscape and Urban Planing*, Vol. 28,225–243.

Larras, J. 1972. *Hydraulique et granulats*. Collections du centre de recherches et d'essais de Chatou, N° 15, Eyrolles, Paris.

Lee, H-Y., Song, M-H. 1993. Migration of rectangular mining pit composed of uniform sediments. *Journal of Hydraulic Engineering*, Vol. 119 (1): 64–80.

Nilipour, N., De Cesare, G., Boillat, J-L. 2004. Application of UVP transducers to measure bed geometry and velocity profiles in a hydraulic scale model with gravel pit. *4th International Symposium on Ultrasonic Doppler Method for Fluid Mechanics and Fluid Engineering*, Sapporo, Japan, 6–8.

Yalin, M.S., Ferreira da Silva, A.M. 2001. *Fluvial Processes Monograph*. International Association of Hydraulic Engineering and Research, Delft, The Netherlands, ISBN 90-805649-2-3.

Bed levelling investigations on transverse sloped beds

Jens-Uwe Wiesemann, Peter Mewis & Ulrich Zanke
Institute of Hydraulic and Water Resources Engineering, Darmstadt University of Technology, Darmstadt, Germany

ABSTRACT: An experimental investigation on the sediment transport process on transverse sloped beds is presented. Experiments were conducted in a 60 m long laboratory tilting flume which is 1 m wide and 0.5 m deep. During the experiments bed levels have been measured at several positions of the cross section with a non-touch method. Longitudinal bed profiles were continuously measured from the chosen positions of the cross section to observe the bed levelling process. Based on the experimental data an accurate characterization of the bed morphology and the prevailing bed forms is given. With respect to the prevailing bed forms the experiments were conducted under different hydraulic and sedimentologic conditions to develop ripples and dunes. The presented work illustrates some new experimental results for the description of the transverse transport process. The transverse transport is an important process in morphologic evolutions. The knowledge of this component of the general, total sediment transport and the development of a useful approach are essential for testing as well as improving and applying numerical models.

1 INTRODUCTION

The sediment transport in transverse direction to the main flow is a very important factor in numerical computations with morphodynamic models. The transport direction differs from the direction of main flow affected by an inclined bed. Following the gravity force the sediment particle moves downwards the bed slope. The quantitative knowledge of this effect is relevant for simulations of scouring and river morphology with numerical models. This transverse transport process is a phenomenon which is not sufficiently investigated and described yet. The inclined bed affects the beginning of sediment transport and also the general transport process over a wide range of hydraulic and sedimentologic parameters. The still existing lack of exact experimental data describing the sediment transport in downslope direction transverse to the main flow field makes some further investigations necessary to develop and to verify approaches which are suitable for numerical investigations.

The transverse directed downslope transport is a very important factor for the appearance and development of bed forms and scours, particularly in river bends. The interaction between downslope transport and secondary flow is described in literature (e.g. Zimmermann & Kennedy (1978). This interaction reaches an equilibrium condition at the final developed scour. The relevance for the implementation of a downslope transport approach in a morphodynamic numeric model is shown e.g. in Mewis (2002) or Rüther & Olsen (2005) among others.

In the present study experiments on sediment transport on a transverse sloped bed were conducted. Different grain materials were used and the experiments were carried out with various hydraulic and morphodynamic conditions, like bed shear stress and given bed forms. The results are compared with those reported in the technical literature. For analyzing the downslope transport and the sediment transport direction a similar arrangement like that used by Talmon et al. (1995) was applied (Wiesemann et al. (2004)).

2 TASK COMPLEX

2.1 *Workflows and conditions*

The investigation, conducted in a 60 m long tilting flume, include experiments with prevailing bed-load transport and experiments with a noticeable fraction of suspended load. The laboratory tilting flume is 1 m wide and 0.5 m deep. Figure 1 shows the sediment characteristics and the prevailing conditions and parameters are given in table 1.

The mobile bed was preformed previous to every experiment. The profile of the bed can be described with a cosine function (Talmon et al. (1995), Wiesemann et al. (2004)). An important advantage of this geometry is the conservation of the bed's shape throughout the experiment. Only the amplitude

Copyright © 2006 Taylor & Francis Group plc, London, UK

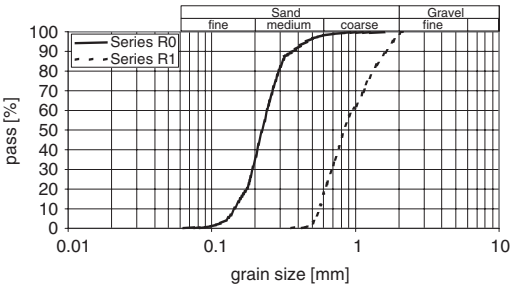


Figure 1. Sediment characteristics of experimental series R0 and R1.

Table 1. Conditions and parameters.

Experiment	d_m [mm]	h [m]	U [m/s]	Θ [–]
Series R0	0.25	0.3	0.22–0.64	0.11–0.57
Series R1	0.96	0.3	0.48–0.77	0.12–0.53

decreases with time according to equation (3). This provides an improved accuracy in the measurements of the decaying amplitude, especially if bed forms occur.

The bed levels at different positions in the cross section, the water levels and the total sediment transport rate were measured. The location of the bed level measurements was chosen in accordance with the requirements of the bed morphology. In this investigation it is necessary to conclude from five bed profile values on the cross sectional shape of the flume bed. For data acquisition five Laser-Distance-Sensors (LDS) were used to detect the bed levels and two Ultrasonic-Distance-Sensors (UDS) were used to detect the water levels. Figure 2 shows the positioning of the Laser-Distance-Sensors. The sensors were positioned at the transversal coordinates 0.96 m, 0.79 m, 0.5 m, 0.21 m and 0.06 m with placing the origin at the right side of the flume (see fig. 3).

In figures 3 and 4 a typical process of transverse located bed levels is given. The sediment transport rates were measured by gathering the material at the end of the flume and for the experiments with prevailing dunes by analysing the movement of bed forms. The experimental setup and the used devices enables a high resolved simulation of the movable flume bed. The experiment was controlled by adjusting the tilt of the flume, adjusting the flow discharge and positioning the sliding panel at the outlet of the flume.

Some disturbances caused by the inflow and the outflow conditions affect the evolution of the bed morphology. By locating the measurement section in a sufficiently long distance from the boundaries these interferences could be regarded as negligible. Every run includes several measurements of longitudinal bed

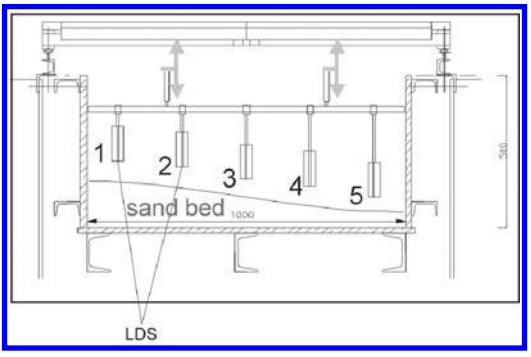


Figure 2. Cross sectional view of measuring carriage with mounted LDS.

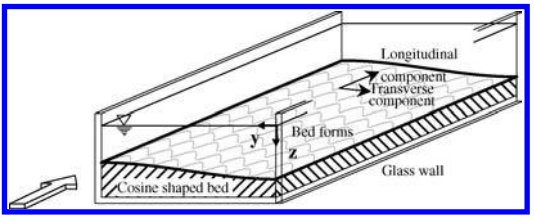


Figure 3. Extract of experimental setup with prevailing bed forms.

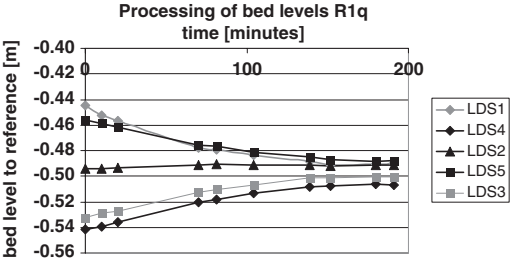


Figure 4. Depicted bed levels over time (example run r1q). The decay of the bed level difference is visable.

profiles of 30 m length, which were measured by moving the devices on a measuring carriage with mean flow velocity to minimize the disturbances to the flow conditions. Each run is short because the main goal was the bed levelling. No feeding of sediment at the inflow was necessary.

During an experiment bed forms evolved from the initially plain bed. The evolution of bed forms continues until the geometry of bed forms is fully developed or reaches an quasi-equilibrium-condition.

2.2 *Direction of sediment transport on a transverse sloped bed*

Based on the work of van Bendegom (1963) the force balance of transport in longitudinal and transverse

Copyright © 2006 Taylor & Francis Group plc, London, UK

direction specifies the actual sediment transport direction. The balance of forces on a grain which moves on a transverse sloped bed includes the fluid drag force and the gravity force. Gravity force affect the movement of the sediments. The inclined bed turns the resulting force in downslope direction (see also Mewis (2002), Wiesemann et al. (2004).

Regarding the experimental setup in this investigation the longitudinal transport rate is as necessary as the transverse component of transport in order to get some information about the transport direction. Because of the nonlinearity of this process a separated analysis of longitudinal and transverse transport is not suitable. Measured data of downslope transport leads to reliable results if the longitudinal transport is known, because the longitudinal transport rate includes information about the hydraulic and sedimentologic conditions.

Figure 3 shows an extract of the used experimental setup. A transversely to the main flow direction inclined bed with prevailing bed forms is in accordance with a cosine function inserted in the straight flume. A separation in a longitudinal and a transverse component of the sediment transport is defined by observing the transport direction.

3 DOWNSLOPE TRANSPORT APPROACHES

3.1 *Basis of approaches*

A general approach to describing the sediment transport direction was presented by van Bendegom (1963) based on the longitudinal coordinate of the flume. This formulation can be simplified for the case where no general longitudinal direction of the channel or flume exists and the longitudinal slope is negligible. This leads to the following formula:

$$\frac{q_y}{q_x} = \tan(\alpha) = -\frac{1}{f(\Theta)}\frac{\partial z_r}{\partial y} \tag{1}$$

with α = angle between sediment transport direction and longitudinal direction, $f(\Theta)$ = weight-function to be determined, Θ = Shields parameter, y = longitudinal direction or main flow direction, x = direction orthogonal to longitudinal direction or main flow direction, q_y = sediment transport in transverse direction, q_x = sediment transport in longitudinal direction, z_r = depth under reference level.

3.2 *Overview of downslope transport approaches*

In table 2 an overview over some downslope transport approaches is given. The approaches consist of formulations which include the Shields parameter and the critical shear stress. The variation in the approaches is the different exponent of the Shields arguments and a deviating factor. The general formulation for the downslope transport $f(\Theta)$ has to be determined with regard to equation 4. The analysis of this investigations based on the general formulation

$$f(\Theta) = \mathrm{a}\,\Theta^{\mathrm{m}}. \tag{2}$$

Table 2. Downslope transport (from Mewis (2002) and Sekine & Parker (1992) respectively).

Author/ Source	$f(\Theta)$	m (exponent of Θ)
Engelund 1974	$\mu_d \approx \frac{1}{1{,}73}$	0
Engelund 1981	$\mu_d = \tan\varphi = 1{,}6\sqrt{\Theta}$	0,5
Hasegawa 1981	$\sqrt{\mu_d \mu_s}\sqrt{\frac{\Theta}{\Theta_c}}$	0,5
Ikeda 1982	$\frac{\lambda\mu_d}{1+\alpha\mu_d}\sqrt{\frac{\Theta}{\Theta_c}}$	0,5
Parker 1984 Struiksma et al. 1985	$f_s\Theta; f_s = (1\ldots2)$	1,0
Sekine and Parker 1992	$\frac{1}{0{,}75}\left(\frac{\Theta}{\Theta_c}\right)^{0{,}25}$	0,25
Talmon et al. 1995	$1{,}7\sqrt{\Theta}$	0,5
Wiesemann, Mewis, Zanke 2004	$1{,}0\sqrt{\Theta}$	0,5

4 BED LEVELLING EXPERIMENTS IN THE LABORATORY

4.1 *Experimental procedure and analysis*

The determination of experimental series with the experimental arrangement, described in Wiesemann et al. (2004), yields bed level data which gives information about the transverse transport. The initial bed slope inside the flume, which was preformed at the initial state of $t = 0$, decays with time. This decay was checked by measuring longitudinal bed profiles with laser distance sensors (non-touch method) and compared with the results of the mathematical formulation:

$$h(y) = \hat{h} + a_i \cdot e^{-t/T}\cos\left(\pi\frac{y}{B}\right) \tag{3}$$

$$T = \left((1-p)\left(\frac{B}{\pi}\right)^2\frac{f(\Theta)}{q_s}\right) \tag{4}$$

where B = width of the flume, h = water depth, a_i = amplitude of bed slope, $\hat{h}$ = *mean water depth;*

Copyright © 2006 Taylor & Francis Group plc, London, UK

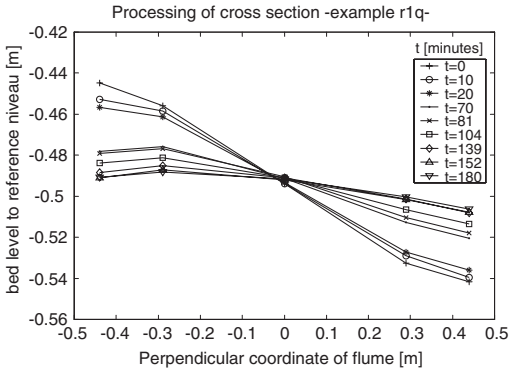


Figure 5. View of cross section with representation of different bed slopes decreasing with time.

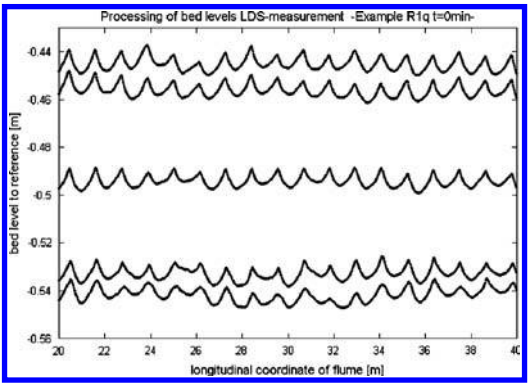


Figure 6. Depiction of longitudinal bed profiles of run r1q at the initial state (t = 0 min). Filtered profiles to smooth the original data for illustration.

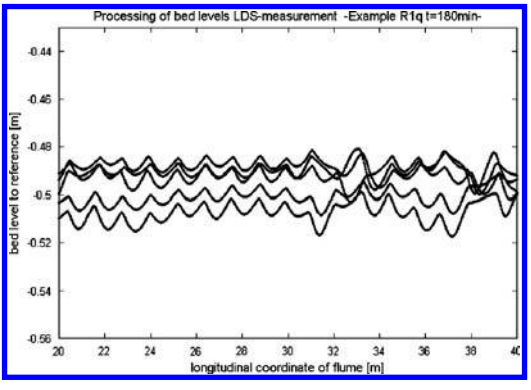


Figure 7. Depiction of longitudinal bed profiles of run r1q at the point of time t = 180 min. Filtered profiles to smooth the original data for illustration.

p = porosity of bed material, q_s = longitudinal transport rate and $f(\Theta)$ = function for the transverse transport.

Based on this comparison the general formulation for downslope transport (eq. 2) could be modified and adapted to the measured data. To analyze the data the measured total sediment transport rate was used.

In the following depictions the decay of the initial bed level differences is visible. As a representative example for a typical run of the series R1 the bed level process of run R1q is given in figures 4 and 5. The localisation of the LDS is described in section 2.1 and in figure 3. The progression of the bed levels is illustrated by plotting the asymptotic merging of the bed levels (fig. 4), the rotation of the inclined bed about the center of the flume (fig. 5) and the merging of the measured longitudinal bed profiles in the analyzed measurement section (fig. 6 and fig. 7).

The longitudinal bed profiles at two different time steps are given in figures 6 and 7. The transversal located LDS-measurements yield the bed level at five points in the cross section. The transverse slope is given with the bed level difference of the bed profiles. With comparison of figures 6 and 7 the merging of the bed profiles is visible which indicates the decay of the transverse bed slope. The bed profiles proceed quasi-parallel.

Above the longitudinal bed profiles of run R1q are given. The decay of the initial bed slope (amplitude of inserted cosine function) is clearly observed.

The measured longitudinal bed profiles in figures 6 and 7 were smoothed due to a better illustrating. The vertical oscillation is here only about 2 cm whereas the real dune heights were bigger. The tilting of the flume is not included in this depictions.

In figure 5 the pivot is placed in the center of the flume, so there was no general erosion in the measurement section. By monitoring the water levels and the flume inclination the normal flow condition could be checked or achieved, which leads to a quasi equilibrium state of transport in the measuring section. The normal flow conditions avoid the occurrence of a net erosion. That means that the average bed level in the cross section is constant during the experiments and no general raise or descent of the flume bed appears.

In the presented experimental series a sand feeding at the beginning of the sand bed was not necessary. Additionally a faulty sand feeding at the inlet leads to an incorrect assessment, particularly in experiments in shorter flumes.

In figures 8, 9 and 10 the decay of the initial amplitude of a run of the experimental series R0 is visible. The initial smooth bed changes into a ripple bed. In the depicted three time steps the decay of the transverse bed inclination and the evolving bed forms are observable.

The experimental series R1 with the coarse sand is depicted in figures 11, 12 and 13. Comparable with the bed evolution of the runs of the experimental series

Copyright © 2006 Taylor & Francis Group plc, London, UK

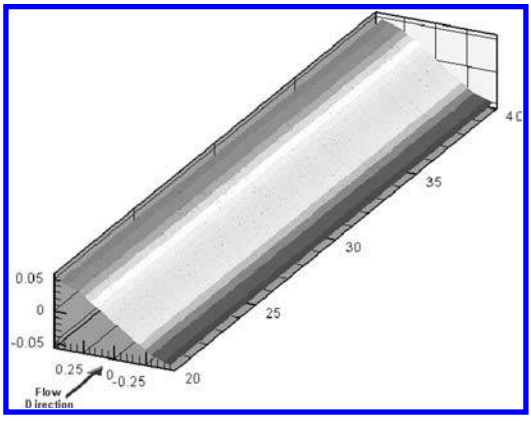


Figure 8. Depiction of initial smooth bed of the experimental series with fine sand ($d_m = 0.25$ mm).

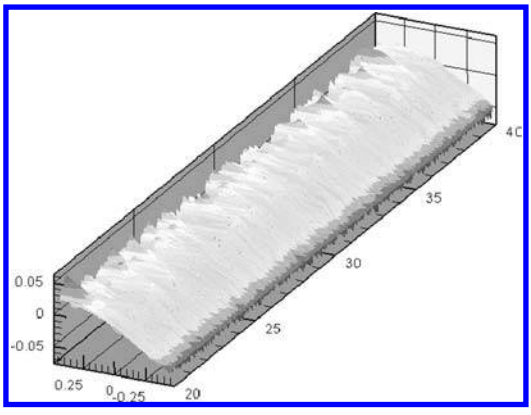


Figure 9. Depiction of the bed of the experimental series with fine sand ($d_m = 0.25$ mm) after running time t = 41 min.

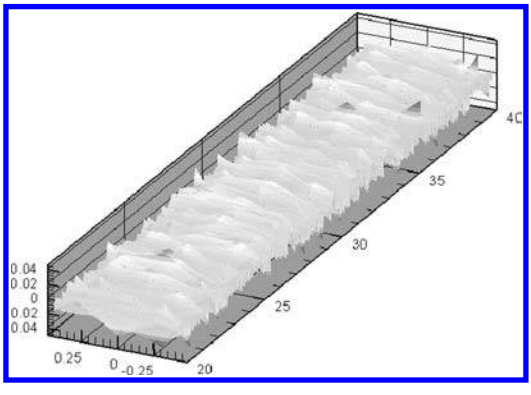


Figure 10. Depiction of the bed of the experimental series with fine sand ($d_m = 0.25$ mm) after running time t = 302 min.

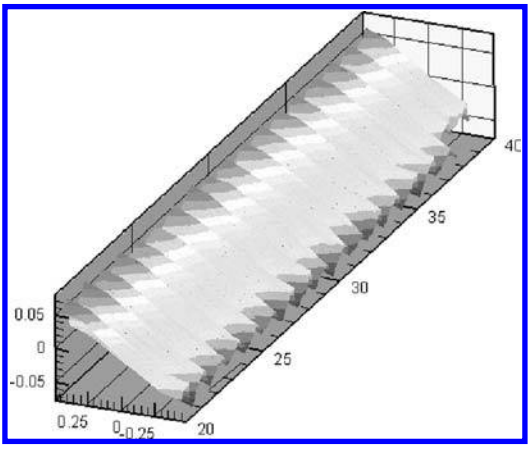


Figure 11. Depiction of initial dune bed of the experimental series with coarse sand ($d_m = 0.96$ mm).

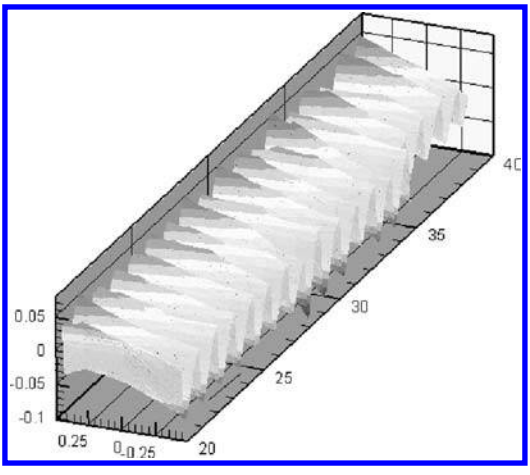


Figure 12. Depiction of the dune bed of the experimental series with coarse sand ($d_m = 0.96$ mm) after running time t = 70 min.

R0 the decay of the initial transverse sloped bed is visible. At the initial state of the bed in this exemplary run the dunes already exist. These bed forms were preformed in order to accelerate their evolution. It is observable that the preformed bed forms are stable over the running of the experiment. The profile of the dunes remains similar, only the height of the dunes increases, while the transverse bed slope decreases.

4.2 *Experimental results*

Figure 14 shows the measured data of the experimental series R0 and literature data. Plotted is Θ versus $1/f(\Theta)$. The Shields parameter for this measurement series is in the range from 0.1 to 0.6. A good correlation is observed.

Copyright © 2006 Taylor & Francis Group plc, London, UK

With increasing Shields parameters there were two experiments observed which yield different values for the existing downslope transport approach. Remarkably dunes were present at this two runs whereas in all other runs a three dimensional ripple bed evolved.

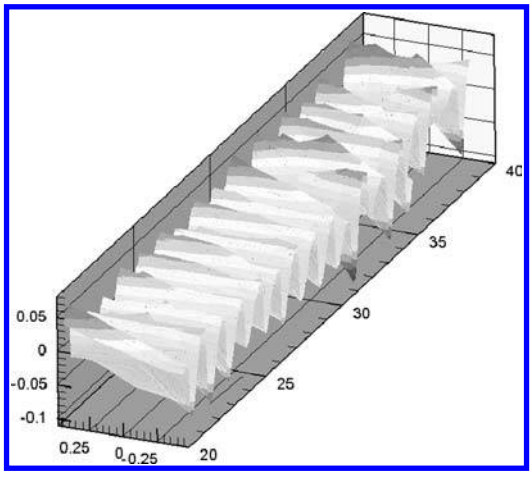


Figure 13. Depiction of the dune bed of the experimental series with coarse sand ($d_m = 0.96$ mm) after running time $t = 180$ min.

The quite good correlation for a three dimensional ripple bed is no longer existing for a condition where dunes evolved from the bed. This leads to the conclusion that the bed forms have an important effect on the transverse transport.

In the region with small shear stresses, where some two dimensional ripple formations were observable, one measurement deviates from the line of best fit too. This has to be investigated in further experiments to confirm this first impression.

An adaption of the general downslope transport approach (eq. 2) in the region of Shields parameters from 0.16 to 0.5 according to the measurement data leads to the following downslope transport approach (Wiesemann et al. (2004)):

$$f(\Theta) = 1.0\,\Theta^{\frac{1}{2}}. \tag{5}$$

In the experimental series R1 with coarse sand ($d_m = 0.96$ mm) dunes were present at the bed.

In figure 15 particularly the deviating gradient of the fit is remarkable, which leads to a differing exponent in the downslope transport approach.

The aforementioned adaption to measurements leads for this experimental series with a 960 µm sand

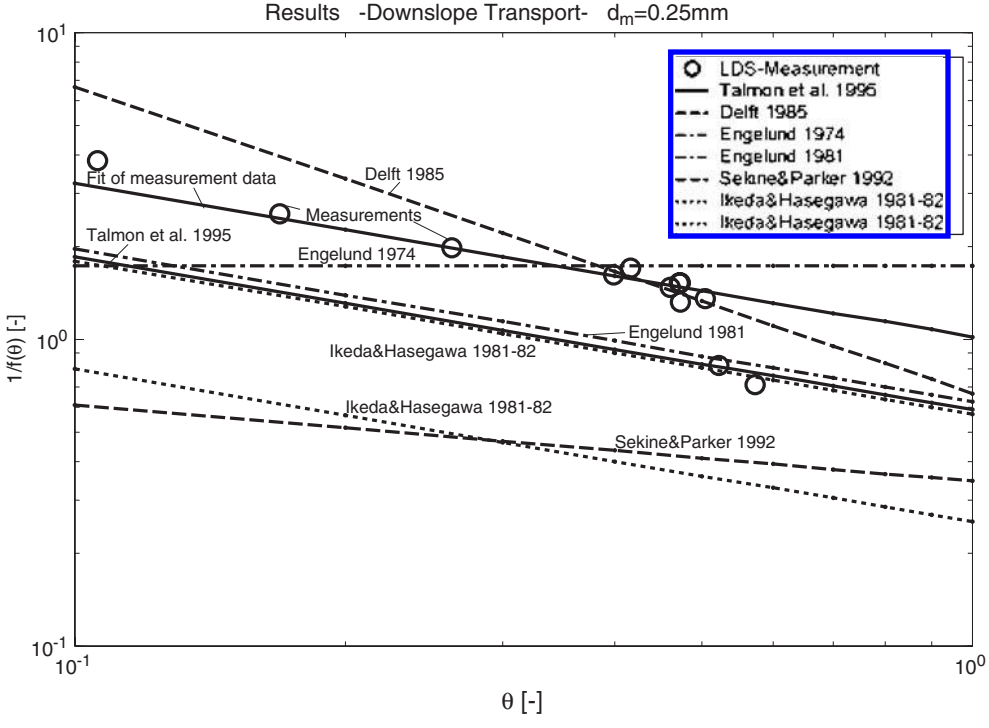


Figure 14. Comparison of results and existing approaches depending on Θ. Fine sand (0,25 mm).

Copyright © 2006 Taylor & Francis Group plc, London, UK

to the following downslope transport approach:

$$f(\Theta) \approx 0.9 \quad . \tag{6}$$

This tendency of the downslope transport function was already proposed by Engelund (1974) however there was a different magnitude of $f(\Theta)$ given. Engelund revised his first proposal in 1981 and found a similar tendency as Talmon et al., Ikeda and Hasegawa.

An interpretation of the deviating formulation of this experimental series cannot be given at the moment. A verification of these new results and the arising approach for the downslope transport (eq. 6) is aspired in following investigations.

5 DISCUSSION AND CONCLUSIONS

The results given in fig. 14 as well as in eq. 5 yield an exponent of ½ in the downslope transport approach. So the exponents proposed already by Engelund, Ikeda and Hasegawa and Talmon et al. could be verified. In contrast to the other formulations a different factor in the function $f(\Theta)$ was obtained. The factor a is 1, as given in equation 5. This relationship is valid for a bed with ripples.

Additionally to that conclusion a difference in the factor a was observed for different bed form conditions. It seems to be necessary to consider the bed forms, because results of some more recent experiments with dunes lead to other values of parameter a. The experiments of the first experimental series lead to a separation of results depending on the bed forms. For a nearly 2D-ripple bed the results are different from a 3D-ripple bed and for a condition with prevailing dunes the results differ and are closer to the results from Talmon et al. (1995). This first estimation was partly verified with the second experimental series. The investigation with a 960 μm sand yields a different order of magnitude of the downslope transport.

An important new output of these experimental series is the different exponent in the downslope transport approach. This differing tendency of the transverse transport approach has to be investigated in further experimental series. In addition the transport on a smooth bed should be investigated for a better understanding of the downslope transport.

There is not enough experimental data about the influence of the suspended load on the transverse transport present yet. A more specific investigation could be helpful in order to understand the role of the suspended load. This should be considered in future investiga-

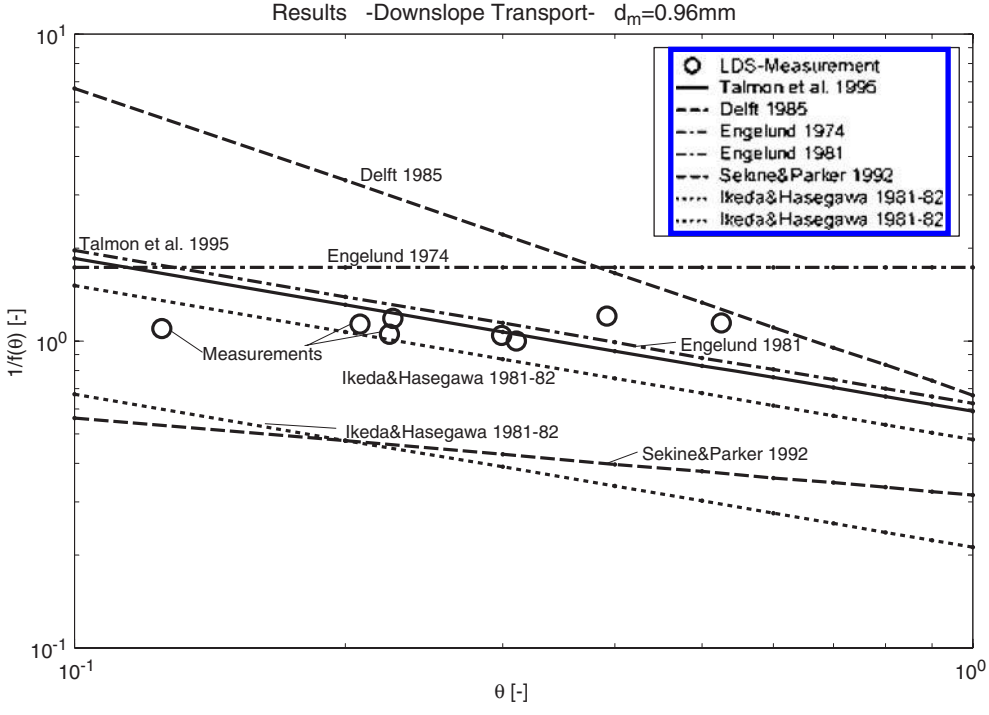


Figure 15. Comparison of results and existing approaches depending on Θ. Coarse sand (0,96 mm).

Copyright © 2006 Taylor & Francis Group plc, London, UK

tions. A new proposal to investigate fine sand with a recent part of suspended load is formulated.

Furthermore there are no experiments available about the investigation of bed material with a different density. Important results with regard to the influence of the density were expected from experiments with a synthetic material bed. The gravity force component, which drives the downslope transport, is smaller than that in the available experiments. Simultaneously the less weight leads to an increasing longitudinal transport rate. Resulting from this inspection a more general formulation for the transverse directed downslope transport can be expected. If necessary the form factors for such an intention should be adapted. Normally the form of synthetic material is different from the natural sand material one.

REFERENCES

Bendegom, L. van, 1963. Eenige beschouwingen over riviermorphologie en rivierverbetering, De Ingenieur, 1947, Vol. 59, No. 4, pp. B1-B11, in Dutch, English translation: "Some considerations on river morphology and river improvement", Nat. Res. Council of Canada, Tech. Transl. 1054.

Engelund, F., 1974. Flow and bed topography in channel bends, Journal of the Hydraulics Division, ASCE, 100(HY11), Proc. Paper 10963, 1631–1648.

Engelund, F., 1981. The motion of sediment on an inclined bed, Prog. Rep. Inst. Hydrodyn. and Hydraulic Engrg., Tech. Univ. Denmark, No. 53, pp. 15–20.

Hasegawa, K., 1981. Bank-erosion discharge based on a non-equilibrium theory, Trans. Japan Soc. Civ. Engrg., 316, 37–52 (in Japanese).

Ikeda, S., 1982. Lateral bed load transport on side slopes, Journal of Hydraulic Division, ASCE, 108(11), 1369–1373.

Mewis, P., 2002. Morphodynamisch-numerische Modellierung von Flußkurven, Dissertation, Mitteilungen des Institutes für Wasserbau, Heft 126, TU Darmstadt.

Parker, G., 1984. Discussion of lateral bed load transport on side slopes, Journal of Hydraulic Engineering, ASCE, 110(2), 197–199.

Rüther, N., Olsen N.R.B., 2005, Three Dimensional Modeling of Sediment Transport in a Narrow 90° Channel Bend, Journal of Hydraulic Engineering, Vol. 131, No. 10, 917–920.

Sekine, M., Parker G., 1992. Bed load transport on a transverse slope, Journal of Hydr. Engrg., ASCE, Vol. 108, No.4, 513–535.

Struiksma, N., Olesen, K.W., Flokstra C., de Vriend, H.J., 1985. Bed deformation in curved alluvial channels, Journal of Hydraulic Research, 23(1), 57–79.

Talmon, van Mierlo, Struiksma, 1995. Laboratory measurements of the direction of sediment transport on transverse alluvial-bed slopes, Journal of Hydraulic Research, Vol. 33, No. 4.

Wiesemann, J.-U., Mewis P., Zanke U., 2004. Laboratory measurements of sediment Transport on transverse sloped beds, Second International Conference on Scour and Erosion, Singapore, Proceedings, Volume 2, 252–259.

Zanke, Ulrich C.E., 1999: Zur Physik von strömungsgetriebenem Sediment (Geschiebetrieb), Mitteilungen des Instituts für Wasserbau und Wasserwirtschaft, Technische Universität Darmstadt, Heft 106.

Zanke, U., 2002. Sedimenttransport auf geneigter Sohle (Hangabtrieb), Wasserbauliche Mitteilungen der Technischen Universität Dresden, Heft 23, S. 96–105.

Zimmermann, C., Kennedy J.F., 1978. Transverse bed slopes in curved alluvial streams, Journal of Hydraulic Engineering ASCE 104, No. HY 1.

Copyright © 2006 Taylor & Francis Group plc, London, UK

Effective use of non-erodible layers for improving navigability

C.J. Sloff & E. Mosselman
WL/Delft Hydraulics & Delft University of Technology, Delft, The Netherlands

J. Sieben
Ministry of Transport, Public Works and Water Management, Institute of Inland Water Management and Water Treatment, Arnhem, The Netherlands

ABSTRACT: By constructing a non-erodible layer in the pool of a river bend, the distribution of flow and sediment discharge can be modified such that the shallow inner bend will degrade to a certain extent. This results in a larger width for navigation. The approach has been successfully applied in two river bends in the Waal River in the Netherlands. We analyzed the governing processes to estimate the effectiveness of these non-erodible layers. We also applied a 2-D morphological model to laboratory experiments and to the Waal River with a special sub-model for simulating the effect of non-erodible layers. The results have been compared with measurements of bed development, water motion and bed form propagation. A conceptual analytical approach verifies the answers from the more advanced 2D model. From the analysis of field data and model approaches it is concluded that in most conditions the non-erodible layer can be used effectively to reduce the bed level in the inner bend. However, in certain situations such as narrow rivers like the IJssel River in the Netherlands, the flow re-distribution in the cross-section is such that the net degradation of the point bar does not occur.

1 INTRODUCTION

The shallow point bar developing in meander bends often leads to unfavorable conditions for navigability. The available width is reduced, and safety is threatened (chance to run aground, danger of collision). With the busy navigation on the lower Rhine River in the Netherlands and Germany this issue has become quite an important problem for the river managers. To provide a safe and fast fairway for cargo traffic between the port of Rotterdam and the German hinterland a long term investment has been made to deal with the bottlenecks that are caused by shallow point bars and other types of shoals. In the Dutch part of the Rhine River, particularly the Waal River part, two types of measures have been taken or planned:

(a) Durable measures (low maintenance) by using structures in the river bed (non-erodible layers, bendway weirs, bottom vanes) or changing the river alignment (groynes, bend cut-off).
(b) Dredging strategies that aim at removing the shoals without disrupting the sediment balance (i.e. with dumping near the dredge location)

Although various types of measures have been applied in the Dutch and German rivers with varying degrees of success, the application of non-erodible layers in the Waal River has been found to be quite successful in permanently lowering the point bar, and increasing the available navigation width. The effect is induced by filling the pool of a meander bend and covering it with a non-erodible rip-rap, as shown in Figure 1. A redistribution of flow then causes an increase of flow velocity on the point bar, forcing an erosion of the inner bend.

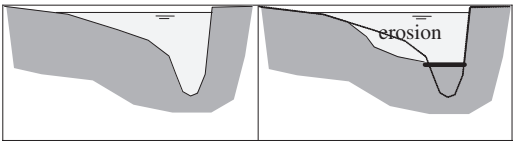


Figure 1. Lowering of the point bar by applying a non-erodible layer in the outer bend.

In the Netherlands erodible layers have been applied in two bends of the Waal River, at St. Andries and at Nijmegen (see Figure 2).

The non-erodible layer at Nijmegen:

- was constructed between 1986–1988 in the sharp river bend at Nijmegen, between chainage km 883.18 and km 885.1.
- has a depth below the low flow reference OLR of 3.50 m, a length of about 2 km, and a width of about 150 m.

Copyright © 2006 Taylor & Francis Group plc, London, UK



Figure 2. Locations of non-erodible layers in the Waal River at St. Andries and Nijmegen.

The non-erodible layer at St. Andries:

- was constructed between 1997 and 1999, in the sharp river bend at Sint Andries, between chainage km 925 and 928.
- has a depth below the low flow reference OLR of 3.50 m, a length of about 3.1 km, and a width of 140 m.

For the design and evaluation of these measures several modelling approaches have been applied in the past, ranging from laboratory scale models to physically based mathematical models. These studies have led to the development of a computational modelling approach, which has been implemented in one-dimensional (1D) and two-dimensional (2D) computational models. In this paper the modelling approach, following Struiksma (1999), is presented and discussed. Also the results are shown of the evaluation of the computational approach by a comparison with recent high-resolution multi-beam data.

The success of this measure depends on a sufficient increase of flow velocities in the inner bend to induce erosion. However, the layer also increases the amount of sediment transport through the inner bend (as the helical flow sweeps all sediment from the non-erodible layer). This decreases the effectiveness of the measure. An analysis of model applications in this paper shows that the increased sediment transport makes that this measure will not be effective in the IJssel River (one of the Rhine branches).

2 MODELLING THE EFFECT OF NON-ERODIBLE LAYERS IN BENDS

2.1 *General*

The non-erodible layer in an outer bend reduces its depth. This causes an increase of discharge and flow velocity in the inner bend. This effect is enhanced when the non-erodible layer is rougher than the alluvial bed, which is often true when riprap is used.

At the upper edge of the non-erodible layer sediment is supplied (by the river) over the full width of the river bed and the layer. This sediment is transported downstream over the non-erodible layer, but it is gradually swept towards the inner bend by helical flow effects. As no sediment is added from the non-erodible layer, theoretically after some distance the layer is 'swept clean', and all sediment is moving through the inner bend.

In the final equilibrium situation all sediment supplied from upstream is transported (after some distance) through the inner bend. Compared to the original situation without non-erodible layer this means a substantial increase of transport through the inner bend.

The main characteristic of the relation between sediment transport and flow velocity can be expressed by a power law, in which the transport rate is a function of flow velocity:

$$s = m \cdot u^n \tag{1}$$

where m is a coefficient (depends on roughness, grain size, etc.); n is the power of the transport formula (always larger than 3, in practice 4 to 5); s is the sediment-transport capacity per unit of width; and u is the local flow velocity.

On basis of this general sediment-transport relation for the transport capacity three possible morphological equilibrium conditions can be defined:

Equilibrium 1	Equilibrium 2	Equilibrium 3
Supply = Transport capacity	Supply < Transport capacity	Supply > Transport capacity
Bed level inner bend remains unchanged	Erosion in inner bend (until supply = capacity)	Sedimentation in inner bend (until supply = capacity)

Erosion is therefore only expected if the redistributed flow velocities will increase the transport capacity more than the increase in sediment supply through the inner bend. The probability of occurrence of this equilibrium increases when the power n in equation (1) is high, which is typical for conditions with bed-load transport at low shear stresses. For example, and increase of flow velocity of 10% will lead to an increase of transport capacity of 50% for $n = 4$, and an increase of almost 100% if $n = 7$.

Side effect of the increased sediment transport rate through the inner bend is a local increase of amplitude of migrating bed forms (dunes), and of bar patterns which are forced by the alignment (by groynes). These effects have been observed in laboratory experiments and recent field observations. The amplified bed forms will oppose the actual gain of navigation depth.

Furthermore, the lack of transport over the non-erodible layer causes a scour hole in the river bed just downstream of this layer. This effect is clearly visible downstream of the non-erodible layers at St. Andries and at Nijmegen (see Figure 3).

Copyright © 2006 Taylor & Francis Group plc, London, UK

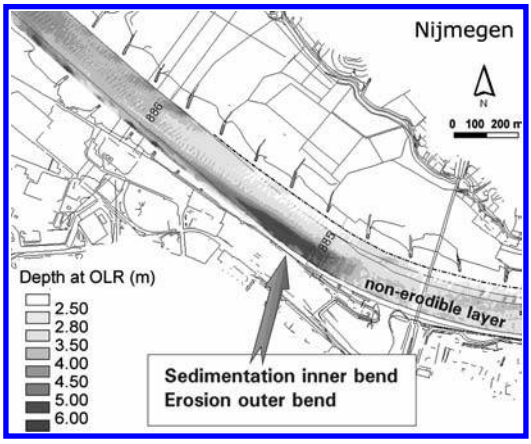


Figure 3. Measured water depth (multi-beam sounding) at lower edge of non-erodible layer at Nijmegen (flow is from East to West).

2.2 *Modelling concept*

The model concept for non-erodible layers has been defined in the early 1980s, and is based on a correction of bed-load transport capacity. The model concept was subsequently implemented in the numerical models SOBEK and Delft3D. The theoretical backgrounds and experimental verification of this approach have been presented in a conference paper of Struiksma (1999).

Usually bed load is modeled with a simple predictor in which sediment transport is a function of the local transport capacity of the flow. However, when transported over a non-erodible layer, no sediment can be supplied from the bed when the capacity increases. The sediment transport thus becomes supply-limited rather than capacity-limited. At first glance, this might seem to necessitate an entirely different computational approach in which volumes of sediment supplied at the boundaries are followed as they travel over the non-erodible layer. However, the model concept of Struiksma (1999) retains the relation with local transport capacity. This model concept accounts for the transport limitations on non-erodible layers through a reduction of the transport layer thickness on the bed.

In this concept the volumetric sediment transport per unit width (according to a customary transport predictor), s_f, is modified with a correction factor, ψ, to obtain the actual sediment transport per unit width, s, over the non-erodible layer (including pores):

$$s = \psi\left(\frac{\delta}{\delta_a(h)}\right) s_f(u) \tag{2}$$

in which δ is the thickness of alluvium on the non-erodible bed, δ_a is the maximum thickness of alluvium at which the non-erodible layer affects the sediment transport, h is the local water depth and u is the local depth-averaged flow velocity. The bed is non-alluvial ($\psi < 1$) if $\delta/\delta_a < 1$ and alluvial ($\psi = 1$) if $\delta/\delta_a \geq 1$ (Fig. 4). The correction factor, ψ, accounts for the reduction of the transport capacity due to a thinner transport layer and hindered bed-form development. Basically, the information on the reduction is carried by the sediment layer thickness, δ. Local increases in s_f are counteracted by decreases in δ and ψ in such a way that the resulting erosion cannot reach below the surface of the non-erodible layer. This limits the supply of sediment from the bed. The supply of sediment from upstream is limited by the occurrence of similar reductions upstream. The maximum alluvium thickness for influence of the non-erodible layer, δ_a, corresponds to the thickness of the transport layer on an alluvial bed. It can be taken equal to half the bed-form height and is therefore primarily a function of the local water depth.

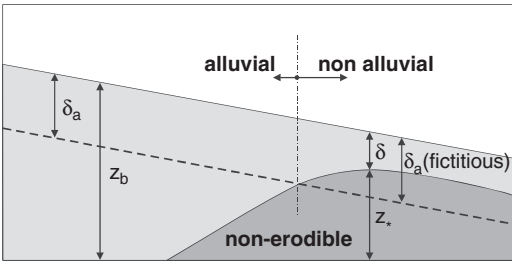


Figure 4. Definition sketch (Struiksma, 1999).

Indicating the level of the top of the non-erodible layer with z_*, the alluvium thickness satisfies $\delta = z_b - z_*$, where z_b represents the bed level which is equal to the level of the top of the layer of alluvium. Using this relation, equation (2) is substituted into the one-dimensional sediment balance

$$\frac{\partial z_b}{\partial t} + \frac{\partial s}{\partial x} = 0 \tag{3}$$

where t denotes time and x denotes the streamwise co-ordinate. This yields

$$\frac{\partial z_b}{\partial t} + \psi \frac{\mathrm{d}s_f}{\mathrm{d}u}\frac{\partial u}{\partial x} + \frac{s_f}{\delta_a}\frac{\mathrm{d}\psi}{\mathrm{d}(\delta/\delta_a)}\left(\frac{\partial z_b}{\partial x} - \frac{\delta}{\delta_a}\frac{\mathrm{d}\delta_a}{\mathrm{d}h}\frac{\partial h}{\partial x}\right) = \frac{s_f}{\partial_a}\frac{\mathrm{d}\psi}{\mathrm{d}(\delta/\delta_a)}\frac{\partial z_*}{\partial x} \tag{4}$$

which shows that the correction factor, ψ, modifies the free morphodynamic behaviour and that the level of the non-erodible layer, z_*, acts as an external forcing of the system.

The dependence of the correction factor, ψ, on the relative alluvium thickness, δ/δ_a, is represented by an assumed function which increases monotonously from

Copyright © 2006 Taylor & Francis Group plc, London, UK

zero to unity for $0 \leq \delta/\delta_a < 1$ with a smooth transition to the constant value of $\psi = 1$ for $\delta/\delta_a \geq 1$. In the one-dimensional numerical model SOBEK, this function reads

$$\psi = \sin\left(\frac{\pi}{2}\frac{\delta}{\delta_a}\right) \quad \text{for} \quad \frac{\delta}{\delta_a} < 1 \tag{5}$$

In the two- and three-dimensional modelling system Delft3D, the function reads

$$\psi = \frac{\delta}{\delta_a}\left(2 - \frac{\delta}{\delta_a}\right) \quad \text{for} \quad \frac{\delta}{\delta_a} < 1 \tag{6}$$

On basis of a characteristic analysis of the governing equations Struiksma (1999) concluded that a non-erodible layer significantly increases the celerities of bed perturbations. This implies that the numerical stability of computations requires smaller time steps.

The concept presented above has been implemented in Delft3D modelling software, which is a tool that can be used to compute morphology in 2D-mode (depth-averaged flow and sediment transport) and 3D-mode (fully 3D hydrodynamics and 3D sediment transport processes). The algorithm is applied in the bed-level update module, and satisfies the principles of conservation of mass. A comparable algorithm for non-erodible layers can be found in Hanson & Militello (2005), but they approach the reduction of the transport capacity in a physically different way than Struiksma.

In practice most river-morphology applications are run in 2D, for which the 3D helical flow in bends has to be approached using a parameterization. In 2D mode, the Delft3D system the flow is calculated according to De Vriend (1981). The bed slope effect on sediment transport is calculated according to Koch & Flokstra (1981), see also Talmon et al. (1995).

$$\tan(\alpha_s) = \frac{\sin(\alpha_f) + \frac{1}{f(\theta)}\cdot\frac{\partial z_b}{\partial y}}{\cos(\alpha_f) + \frac{1}{f(\theta)}\cdot\frac{\partial z_b}{\partial x}} \tag{7}$$

In this equation α_f and α_s are the angle of bed-shear stress (flow) and bed-load transport respectively, and θ is the Shields parameter (defined as $u^2/[C^2 \Delta D]$ with Δ is the relative density of sediment equal to about 1.65). The function $f(\theta)$ determines the effect of bed-slope, and can be approximated by the following relation:

$$f(\theta) = A_{shld} \cdot \theta^{1/2} \tag{8}$$

In which A_{shld} is a coefficient, which is found to be in the order of 0.85 in natural rivers, and 1.7 in laboratory experiments. The parameterized effect of spiral flow is used to adapt the flow angle α_f in eq. (7).



Figure 5. Photograph of curved flume experiment in 1987.

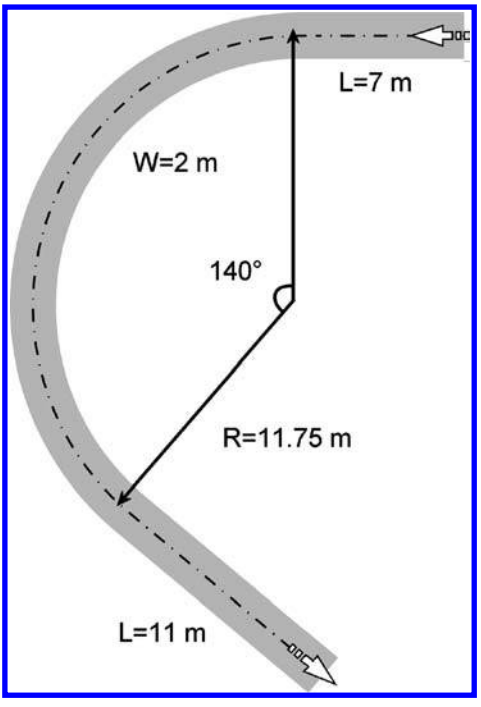


Figure 6. Dimensions of curved flume.

2.3 *Experimental verification of the modelling concept*

In 1987 experiments have been carried out in a curved flume at WL | Delft Hydraulics to verify the presented theoretical model. Figure 5 shows a photograph of the model looking in downstream direction. The actual dimensions of the flume are presented in Figure 6. The flume was equipped with a sand recirculation system. The sediment in these experiments has a median grain size D_{50} of 780 μm.

Copyright © 2006 Taylor & Francis Group plc, London, UK

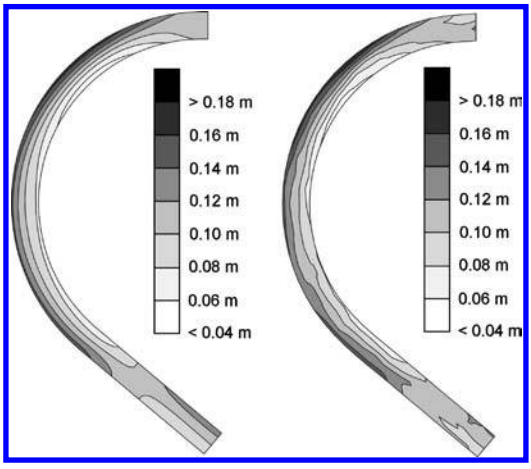


Figure 7. Water depth simulated with Delft3D (left) and in the laboratory flume (right) for reference simulation T2.

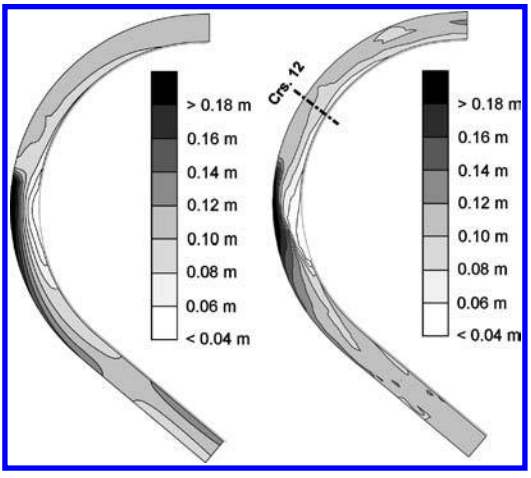


Figure 8. Water depth simulated with Delft3D (left) and in the laboratory flume (right) for non-erodible layer experiment.

Several types of experiments have been carried out, among which the experiment T2 (reference situation without measures) and experiment T3 with non-erodible layer. The non-erodible layer in T3 was placed in the upper part of the curved section over a length of 15 m, and was composed of sediment with coarse sediment having a grain size $D_{50} = 13.4$ mm. Some other characteristics of the experiments are listed in the table below:

Discharge	0.09 m^3/s
Chézy roughness value	27.66 $m^{1/2}/s$
Slope	$2.46 \cdot 10^{-3}$ m/m
Average depth	0.106 m
Average velocity	0.425 m/s
Average sediment transport	60 to 70 l/hr
Dune height	0.03 m
Duration of experiment	6 days
Transport formula	Engelund & Hansen (1967)

For the analysis only the final equilibrium situation has been considered. Simulations with Delft3D have been carried out for both the reference experiment T2, and the fixed-layer experiment T3.

Figure 7 shows the computed bed levels for the calibration simulation of the reference experiment T2. For calibration a coefficient $A_{shld} = 2.1$ combined with a reduction factor of 0.5 for spiral flow intensity has been chosen to obtain the best reproduction of transverse slopes, wavelength of point bar, and overshoot (effect of overshoot causes two peaks on the point bar). A comparison of the two plots in Figure 7 shows an excellent agreement.

In Figures 8 and 9 the results are plotted for experiment T3 with the non-erodible layer. In the Delft3D simulation the maximum alluvium thickness for influence of the non-erodible layer, δ_a, is set to 0.02 m

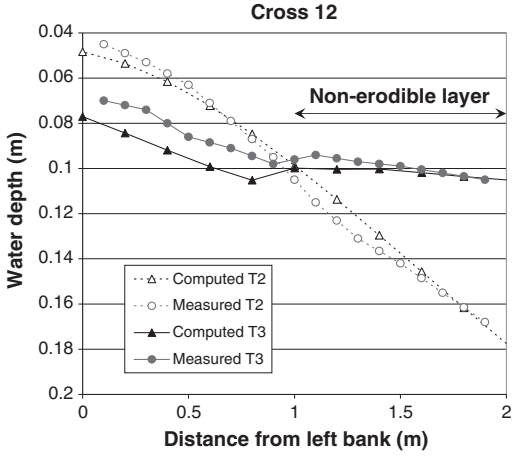


Figure 9. Water depth in cross-section 12 (indicated in Figure 8), in computational model and laboratory experiment, and with and without non-erodible layer.

(based on the observed bed-form height in experiment T2). Other parameters are maintained from run T2, hence no change in roughness has been used for the non-erodible layer and inner bend (so no further calibration has been applied).

The results show that the effect of the non-erodible layer is reproduced quite well, although the increase of depth in the inner bend is slightly overestimated in the computations. Note that this might be influenced by applying a transverse variation in roughness.

Furthermore it has been found that just downstream of the non-erodible layer a quite strong bed-tilting is triggered. In both the experiment and in the computational model a scour hole develops just downstream

Copyright © 2006 Taylor & Francis Group plc, London, UK

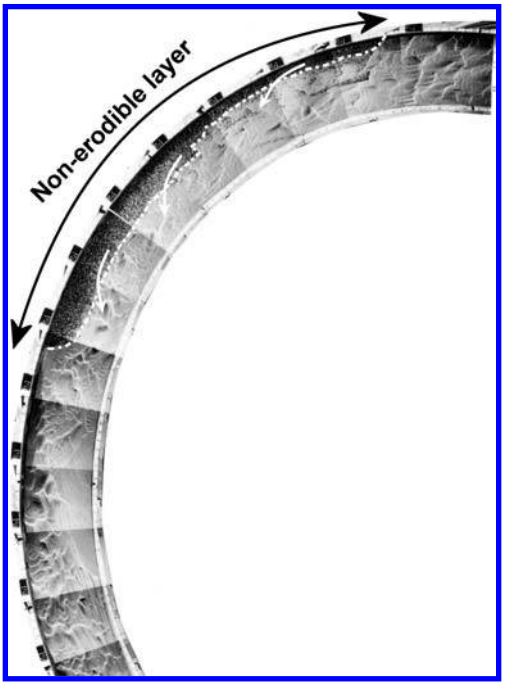


Figure 10. Photograph of bed in flume with non-erodible layer exposed (indicated by dashed line) showing how sediment is swept towards the inner bend (arrows).

of the non-erodible layer (in the outer bend), whereas a strong deposition occurs on the opposite side of the river (in the inner bend), see Figure 8. The responses in both models are quite similar with respect to maximum scour depth and bar height, but the width of the scour hole appears to be slightly narrower in the laboratory experiment.

In both the computation and the experiment it has been found that the non-erodible layer is swept clean from the sediment after some distance. In Figure 10 the area of the non-erodible layer that is uncovered is indicated by a dashed line. Arrows indicate the sweeping process that is induced by the spiral flow effect.

Only at the upstream part some barchan shaped dunes travel over the non-erodible layer, after which they migrate gradually towards the inner bend. In a more or less similar way small patches of sediment supplied from upstream travel in a similar way over the non-erodible layer in the computational model. These patches of sediment are the mechanism in which bed-load is transport over the non-erodible layer, but it is not a physically correct representation of the dunes mentioned above (dimensions and propagation of these patches do not correspond to bed forms).

It should further be noted that the dune heights in the model cannot be scaled up to prototype conditions, because then they are too high. The dunes may therefore overestimate the roughness in the experiment when compared to the prototype.

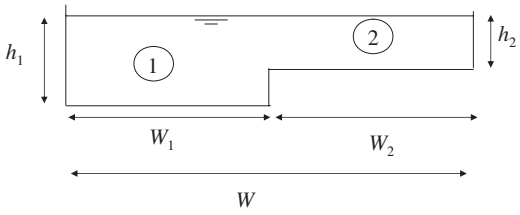


Figure 11. Schematization of a cross section into two sections.

2.4 *Analytical approach*

Based on the modelling concept presented before, it is possible to derive a simple analytical approach for simplified conditions. Consider the cross-section to be represented by two sections: a deep section "1" (outer bend) and a shallow section "2" (inner bend) as shown in Figure 11.

In the following we assume that the time-average morphology of the cross-section can be determined from conditions at a characteristic mean discharge (e.g. the discharge that produces the same yearly transport rate as the full hydrograph). Assuming an axi-symmetric cross-section in a bend, the depth of the sections can be written as:

$$\begin{aligned} h_1 &= h_{avg} + \frac{1}{2}(W - W_1) I_n \\ h_2 &= h_{avg} - \frac{1}{2} W_1 I_n \end{aligned} \tag{9}$$

in which h_{avg} = average depth, and I_n is the average transverse slope in an axisymmetric bend profile. The slope I_n is computed from:

$$I_n = \frac{2\varepsilon}{\kappa^2}\left(1 - \frac{\sqrt{g}}{\kappa C}\right) \cdot \mathrm{f}(\theta) \cdot \frac{h_{avg}}{R} \tag{10}$$

in which f(θ) is the transverse slope function expressed by equation (8), R is the radius of curvature (at the axis), κ is the Von Karman coefficient (~0,4), and ε is a spiral flow coefficient. It is assumed that the surface slope for both sections are identical, i.e. assuming a weak curvature, hence using the Chézy formula for the sections it is found that:

$$\frac{u_1^2}{C_1^2 R_1} = \frac{u_2^2}{C_2^2 R_2} \quad with \quad R_1 = \frac{h_1 W_1}{h_1 + W_1}; R_2 = \frac{h_2 W_2}{h_2 + W_2} \tag{11}$$

where R_1 and R_2 are hydraulic radii of the sections. We can assume roughly that $R_1 \approx \xi_{R1} \cdot h_1$ and $R_2 \approx \xi_{R2} \cdot h_2$

Copyright © 2006 Taylor & Francis Group plc, London, UK

with $\xi_{R1,2} \approx 0{,}9$ if $W_1 = W_2$. Furthermore it is assumed that sediment transport can be expressed by a power law, as in equation (1). A power function $s = au^n/C^k D^l$ (with a is a factor, D is grain size, and k,l,n are powers) is applied. Furthermore we assume that the reference situation (situation without non-erodible layer) is denoted by variables having a subscript 0, and in the situation with non-erodible layer with subscript n.

$$\left\{\frac{u_{10}}{u_{20}}\right\}^n \left\{\frac{C_{20}}{C_{10}}\right\}^k = \left(\frac{\xi_{R10}}{\xi_{R20}}\right)^{n/2} \left(\frac{h_{10}}{h_{20}}\right)^{n/2} \left(\frac{C_{10}}{C_{20}}\right)^{n-k} \tag{12}$$

Considering the part of the bend where all sediment is transported through the inner bend, and assume that this transport rate is equal to the total rate of the reference situation, then we find that ($S_{2n} = S_0$):

$$\frac{u_{2n}^n}{C_{2n}^k} = \frac{u_{20}^n}{C_{20}^k}\left(\frac{W_{10}}{W_{20}}\left\{\frac{\xi_{R10}}{\xi_{R20}}\right\}^{n/2}\left\{\frac{h_{10}}{h_{20}}\right\}^{n/2}\left\{\frac{C_{10}}{C_{20}}\right\}^{n-k}+1\right) \tag{13}$$

Approximating that the alluvial roughness is constant in the sections $C_{2n} = C_{10} = C_{20}$ it is found that:

$$\frac{u_{2n}}{u_{20}} = \left(\frac{W_{10}}{W_{20}}\left\{\frac{\xi_{R10}}{\xi_{R20}}\right\}^{n/2}\left\{\frac{h_{10}}{h_{20}}\right\}^{n/2}+1\right)^{1/n} \tag{14}$$

and with $B_1 = B_2$, using equations (9) and (12) it can be derived that:

$$\frac{u_{2n}}{u_{20}} = \left(1+\left\{\frac{h_{avg}+\frac{1}{4}W\cdot I_{n0}}{h_{avg}-\frac{1}{4}W\cdot I_{n0}}\right\}^{n/2}\right)^{1/n} \tag{15}$$

in which u_{2n}, and u_{20} are the velocities in the inner bend in the situation with and without non-erodible layer respectively. Note that u_{2n} in this formula is highly influenced by the power n of the transport formula.

To determine the depth of the inner bend h_{2n} after construction of the non-erodible layer, equations (13), (11) and a continuity equation ($u_{2n}h_{2n}W_2 + u_{1n}h_{1n}W_1 = Q_{total}$) are used. Assume that roughnesses are known, and depth h_{1n} is given (because the elevation of the non-erodible layer is known).

$$h_{2n}\left(h_{2n}^2u_{2n}^2W_2^2 - 2h_{2n}u_{2n}W_2Q_{totaal} + Q_{totaal}^2\right) = h_{1n}^3W_1^2u_{2n}^2\left(\frac{C_{1n}}{C_{2n}}\right)^2\frac{\xi_{R1n}}{\xi_{R2n}} \tag{16}$$

Solution of this 3rd order polynomial gives for the depth at the inner bend:

$$h_{2n} = \frac{2}{3}\left(\frac{Q_{totaal}}{u_{2n}W_2}\right)\left\{\cos\left[\frac{1}{3}\text{asin}\left(1-\frac{27}{2}\Pi\right)-\frac{\pi}{2}\right]+1\right\} \tag{17}$$

Table 1. Effect of non-erodible layer ($h_{20} - h_{2n}$) determined from field observations and 2D model simulation, Nijmegen km 884.

	h_{10}	h_{20}	h_{1n}	h_{2n}	ξ_{R10}/ξ_{R20} (−)	$h_{20} - h_{2n}$
2D Model	6.91 m (B_1 = 80 m)	2.80 m (B_2 = 170 m)	4.97 m	4.24 m	0.83	−1.44 m
Prototype	6.52 m (B_1 = 80 m)	2.87 m (B_2 = 74 m)	5.06 m	4.12 m	0.82	−1.26 m

Table 2. Effect of non-erodible layer ($h_{20} - h_{2n}$) determined from analytical model, Nijmegen (using $B_1 = 80$ m, $B_2 = 170$ m).

C_{1n} ($m^{1/2}/s$)	h_{10} (m)	h_{20} (m)	h_{1n} (m)	n	u_{20} (m/s)	u_{2n} (m/s)	h_{2n} (m)	ξ_{R10}/ξ_{R20}	$h_{20} - h_{2n}$ (m)
45	7.9	2.9	4.2	4	1.08	1.53	4.2	0.93	−1,3

in which

$$\Pi = \frac{u_{2n}^3W_2W_1^2h_{1n}^3}{Q_{totaal}^3}\left\{\frac{\xi_{R1n}}{\xi_{R2n}}\right\}\left\{\frac{C_{1n}}{C_{2n}}\right\}^2 \tag{18}$$

We have applied the relations above to the existing non-erodible layers in the Waal River, as well as to a non-existing non-erodible layer in the IJssel River (the Rhine River branch that flows to the North in the Netherlands).

The analysis for the non-erodible layer at Nijmegen is based on data from the prototype and data from Delft3D simulations for this reach, as summarized (and translated to the schematized cross-section of Figure 11) in table 1. From the last column can be read that the water depth in the inner bend has increased between 1.2 and 1.5 m. Note that the effective width (uncovered) of the non-erodible layer is only 80 m in this cross section.

In table 2 the result from the calculation using the analytical model is presented. The values for the reference depths are obtained from the axisymmetric solution, equation 10, with a mean grain size of 1 mm, a characteristic discharge of 1600 m^3/s, a h_{avg} of 4.5 m, an ε of 1.45, and a radius of curvature of 750 m. The increase of depth at the inner bend is 1.3 m, which is in close agreement with the results from table 1.

Using the analytical relationships it can be analysed how certain parameters in this model influence the efficacy of the non-erodible layer. For instance in Figure 12 is shown how with an increasing value of the power n the lowering effect at Nijmegen is decreasing.

Copyright © 2006 Taylor & Francis Group plc, London, UK

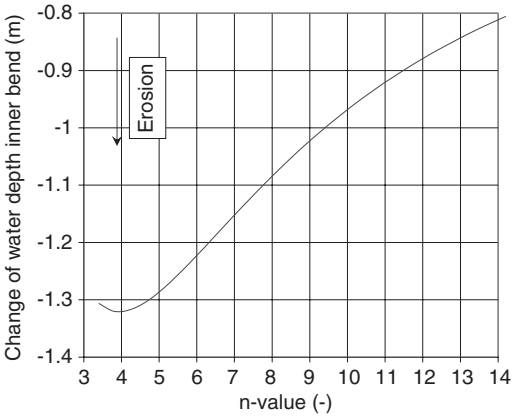


Figure 12. Influence of power n in transport formula on effect of non-erodible layer in Nijmegen (analytical approach).

Table 3. Effect of non-erodible layer ($h_{20} - h_{2n}$) determined from analytical model, St. Andries.

h_{10} (m)	h_{20} (m)	C_{1n}, C_{2n} ($m^{1/2}/s$)	h_{1n} (m)	n	u_{20} (m/s)	u_{2n} (m/s)	h_{2n} (m)	$h_{20} - h_{2n}$ (m)
6.5 ($B_1 =$ 120)	4.8 m ($B_2 =$ 140)	35, 50	5.85	5	1	1.23	5.72	−0.9

For the non-erodible layer in St. Andries a similar result has been obtained. In table 3 the result from the calculation using the analytical model is presented. The increase of depth at the inner bend is 0.9 m, which is also in close agreement with the observations and the 2D model computations.

In relation with improvement of navigability of the IJssel River, the possibility of applying non-erodible layers in some sharp bends has been considered. Simulations with Delft3D modelling system revealed unexpectedly that the effect of the non-erodible layers appeared to be opposite: the inner bend showed some aggradation instead of erosion, see Figure 13. Clearly the increase of transport rate through the inner bend cannot be compensated by an increase of velocity.

The deposition can also be predicted from the analytical model as shown in table 4. However, the analytical model appears to underestimate the effect in most cases.

The reason of this unexpected sedimentation of the inner bend is the relatively narrow main channel of the IJssel River, with protected banks. In comparison to the much wider Waal River, the fixed sloping bank sections in the IJssel River cover a rather large part of the cross-section as shown in Figure 14. Analysis of the transverse distribution of flow velocities shows

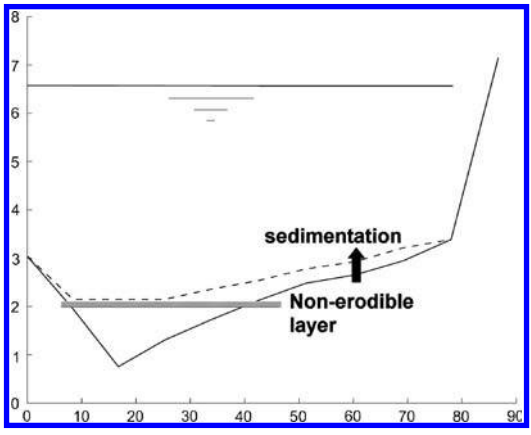


Figure 13. Cross-section with computed bed level in IJssel River with and without non-erodible layer.

Table 4. Effect of non-erodible layer ($h_{20} - h_{2n}$) determined from analytical model, Nijmegen.

W_{1n} (m)	C_{1n} ($m^{1/2}/s$)	h_{1n} (m)	n	u_{20} (m/s)	u_{2n} (m/s)	h_{2n} (m)	$h_{20} - h_{2n}$ (m)
20	39	4.52	4.1	0.69	0.84	2.88	+0.25

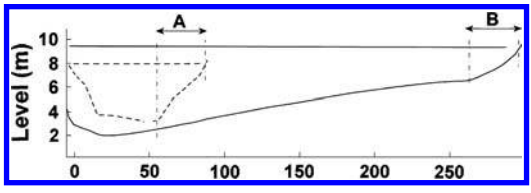


Figure 14. Cross-section of main channel in Waal River with bank section B (drawn line) and IJssel with bank section A (dashed line).

that after the pool is filled with a non-erodible layer, the increase of velocities in the remaining cross-section is absorbed by the bank sections, and the increase on the alluvial part of the inner bend is limited.

3 SIMULATIONS AND OBSERVATIONS IN PROTOTYPE

In the past years multi-beam soundings have become available for the river bed of the Waal River. The resolution of these soundings (as shown in Figure 3) is sufficiently high to analyze the bed forms and indirectly assess the bed-load transport rate from bed-form migration. After all, bed-load transport and bed forms are coupled phenomena in this river. In the statistical analysis the observed bed-forms can be considered as the standard deviation of bed-level variations

Copyright © 2006 Taylor & Francis Group plc, London, UK

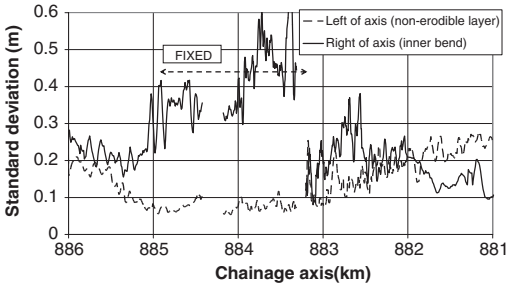


Figure 15. Standard deviation of bed-levels on the non-erodible layer at Nijmegen at two longitudinal sections.

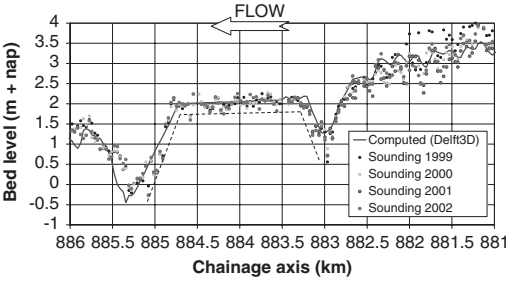


Figure 16. Measured and computed bed level at a grid line left of the river axis. Dashed line indicates expected position of non-erodible layer.

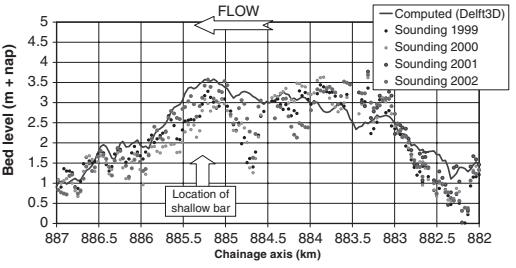


Figure 17. Measured and computed bed level at a grid line right of the river axis.

around the spatially averaged bed level (averaged on 500×20 m cells). The standard deviation scales with the bed form height. Figure 15 shows how the standard deviation varies along two longitudinal sections at Nijmegen, at the non-erodible layer and through the inner bend respectively.

The standard deviation disappears rapidly on the non-erodible layer (it reduces to 0.06 m, which is the inaccuracy of the sounding). On the other hand it increases significantly in the inner bend. This behaviour proves that all bed-load transport is passing through the inner bend such that the non-erodible layer is practically clear of sediment. It should be noted that the scour and deposition pattern forced by the groynes in the inner bend has also been amplified by the increase of transport.

Also recently developed 2D morphological models (used to ongoing Rhine flood-protection and navigation studies) have profited from analysis of the high-resolution multi-beam soundings.

For instance the resulting bed-levels computed with Delft3D for the river bed at Nijmegen are shown in Figure 16 (section at outer bend, non-erodible layer) and Figure 17 (section at inner bend). The simulations have been carried out with a 2D flow and uniform sediment approach (i.e. sediment of one size fraction). It has been concluded that the present level of the non-erodible layer was lower than the design level, which is probably due to consolidation after placement. The exact position can only be guessed.

Furthermore, it was found in the simulations that the scour depth downstream of the layer, and in response the associated bar in the inner bend, was overestimated. This could be fixed by locally increasing the sediment grain size of the bed in the scour hole. This can be justified from an armouring of the river bed in the scour hole that is expected for the relatively graded sediment in this reach (although also parts of the rip rap have shown up in the scour hole). Indeed, both in the much more uniform sediment bed at the river bend of St. Andries, and in the scale model with uniform sediment, the computed scour depth matches better. Note that sediment-sorting effects might also explain differences in length of the scour holes at Nijmegen and St. Andries. For instance Mosselman et al. (2004) show how lateral sorting effects increase the length scales, which explains the longer scour hole at Nijmegen.

4 DISCUSSION

Application of non-erodible layers in outer bends have proven to be quite effective in lowering the inner bend in two sharp bends of the Waal River. However, the experiences from these cases and simulations for the IJssel River have resulted in a few points of caution:

- As at the lower end of the non-erodible layer a scour hole and deposition occurs, it is necessary to extend the layer in such a way that the deposition will not lead to a new bottleneck for navigation.
- In relatively narrow rivers, in which bank-sections form a large part of the cross-section the effect of non-erodible layers may be reversed because the increase of transport rate through the inner bend cannot be compensated by an increase of velocity (increases of velocity are absorbed by the bank sections). The inner bend will then aggrade instead of erode.

Copyright © 2006 Taylor & Francis Group plc, London, UK

- Non-erodible layers are made of coarse material, and therefore they have a higher hydraulic roughness (v.d. Zwaard, 1974).

The model concept presented in this paper properly describes the observed physical processes. Strictly speaking, the model concept holds only for bed load. Transport predictors based on local conditions alone, however, are also utilized for the total load when the characteristic adaptation lengths of the suspended part of the transport are small compared to the meshes of the computational grid. This can be justified for the present model concept as well. A different approach is required, however, for suspended sediment transport with significantly long adaptation lengths. Such cases require the solution of a convection-diffusion equation with a proper source term for the exchange of sediment with the bed load layer. The formulation of this exchange above non-erodible layers is a topic for further research.

The bed of the Rhine River shows a gradual degradation as a consequence of river-training, sediment mining and reduced sediment inflow in the past and present. At locations with non-erodible layers this erosion will be amplified, as the erosion is restricted to the inner bend. The outer bend is fixed by the non-erodible layer, but this layer is usually restricted in width. The accelerated erosion does not only lead to a much higher erosion depth that can reach far below the non-erodible layer level, but also appears to increase the degradation rate upstream. Furthermore, as the surrounding river reaches are lowering, the non-erodible layer can become an obstruction for navigation by itself.

5 CONCLUSIONS

Non-erodible layers in outer bends can be effectively used to lower the inner bend, such that navigability in river bends can be improved. By the non-erodible layer both transport rate and flow velocity in the remaining alluvial part in the inner bend are increased. A net lowering of the bed is achieved provided that increased flow velocity mostly contributes to the shear stress in the inner bend, and is not absorbed by wide bank sections (e.g. in narrow rivers like the IJssel river).

The mathematical approach presented in this paper for modelling bed-load transport over non-erodible layers has been successfully applied to simulate laboratory experiments and for the non-erodible layers at Nijmegen and St. Andries in the Waal River. The observed processes by which through helical flow effects the sediment is swept from the non-erodible layer towards the inner bend is simulated correctly, and such that the final lowering of the inner bend is well reproduced. Also the development of a scour hole downstream of the non-erodible layer is simulated with the 2D (Delft3D) morphological model. A simplified analytical approach can be derived that can be used to analyze the effect of different parameters on the effect of the non-erodible layer.

The simulations and prototype observations show that it is necessary to extend the non-erodible layer past the bend, such that the sedimentation facing the downstream scour hole does not result in a navigation problem. Furthermore it is found that general degradation of the river bed can be amplified in the inner bend next to a non-erodible layer, and that this might increase degradation upstream.

REFERENCES

De Vriend, H. 1981. Steady flow in shallow channel bends. Comm. on Hydr. Engrg, Dept. of Civil Engrg, Delft University of Technology, Report 81-3.

Engelund, F. & Hansen, E. 1967. A monograph on sediment transport in alluvial streams. Kobenhavn, Denmark: Teknisk Forlag.

Hanson, H. & Militello, A. 2005. Representation of nonerodible (hard) bottom in Two-Dimensional morphology change models. US Army Corps of Engineers Publication, ERDC/CHL CHETN-IV-63.

Koch, F. & Flokstra, C. 1981. Bed level computations for curved alluvial channels. Proc. of the XIX Congress of the Int. Ass. for Hydr. Res., New Delhi, India 2, 357.

Mosselman, E., Sieben, A., Sloff C.J., & Wolters, A. 1999. Effect of spatial grain size variations on two-dimensional river bed morphology. Proc. IAHR symposium on River, Coastal and Estuarine Morphodynamics (RCEM), Genova, Sept. 1999, p. 499–507.

Struiksma, N. 1999. Mathematical modelling of bedload transport over non-erodible layers. Proc. IAHR symposium on River, Coastal and Estuarine Morphodynamics (RCEM), Genova, Sept. 1999, p. 89–98.

Talmon, A.C., Struiksma, N. & Van Mierlo, M.C.L.M. 1995. Laboratory measurements of the direction of sediment transport on transverse alluvial-bed slopes. *J. Hydraul. Res.* 33, 495–518.

Zwaard, J.J. van der 1974. Roughness aspects of sand transport over a fixed bed. XVth IAHR Congress, Istanbul, September 2–7, 1973. Delft Hydraulics Laboratory Publication, 118.

Copyright © 2006 Taylor & Francis Group plc, London, UK

Morphodynamic modeling of sand bar evolution under unsteady flow

K. Kobayashi, Y. Shimizu & S. Giri
Hokkaido University, Sapporo, Japan

Y. Watanabe
Civil Engineering Research Institute of Hokkaido, Sapporo, Japan

ABSTRACT: This paper presents investigations on sand bar formation and evolution process in consequence of unsteady flow. Firstly, experiments have been carried out to investigate the sand bar response to the unsteady flow under laboratory condition. Observations have revealed some notable outcomes, which indicate the effect of unsteady flow condition on sand bar development mechanism. Sand bar evolution in unsteady flow appears to be altered in comparison with sand bar formation under steady flow condition. Furthermore, a two-dimensional morphodynamic model has been developed to reproduce sand bar evolution under unsteady flow condition. Proposed model solves depth-averaged flow equations with a simplest turbulence closure in a generalized coordinate system. A Cubic Interpolated Pseudo-particle (CIP) numerical technique is employed to solve advection phase of momentum equations. Likewise, model solves two-dimensional sediment continuity equation for bedload sediment transport considering the effect of secondary current. Computation has been performed for variety of boundary conditions in upstream and downstream end to evaluate their effect on ultimate results. Results of numerical computation have been verified against laboratory observations. Numerical simulation of aforesaid phenomenon using proposed model has been found to be reasonably consistent.

1 INTRODUCTION

Morphodynamic behavior of meso-scale bedforms like sand bar in alluvial rivers is of importance from practical engineering point of view. Several investigations were conducted in the past that have provided essential insight into the channel evolution mechanism induced by sand bars. Amongst the pioneer works, Leopold and Wolman (1957) and Kinoshita (1961) are noticeable. They made significant studies that enabled some key features of alternate bar to be identified. Some noticeable laboratory observations were performed by Fujita and Muramoto (1985), Lazoni (1999). Kinoshita and Miwa (1974) investigated the bar migration in straight and curved channel. Shimizu and Itakura (1989) were able to replicate this phenomenon using a morphologic numerical model. Some researchers performed theoretical analysis on bar formation (Parker, 1976; Fredsoe, 1978; Kuroki and Kishi, 1984; Columbini et al., 1987; Garcia and Nino, 1993; Tubino et al., 1999). Some recent works on weakly nonlinear analysis have appended some supplementary knowledge as well (Izumi et al., 2002; Watanabe & Kawamura, 2005).

Most of these studies explored features of alternate bars under steady discharge condition. Consideration of sand bar evolution under unsteady discharge, for instance during flood event, is of importance. Moreover, behavior of downstream morphology induced by several control structures is also subjected to the consideration of unsteady flow. The significance of unsteady discharge on channel evolution was figured out by Tubino (1991). He conducted a weakly nonlinear analysis to formulate a model to investigate the development of the amplitude of alternate bars in unsteady flow. Recently, some notable laboratory observations were made by Watanabe et al. (2001). They found significant distinction between bar characteristics developed under steady and unsteady discharge conditions. They concluded that hysteresis effect of flow condition must be taken into account to analyze sand bar evolution under unsteady discharge. Additionally, they conducted a linear stability analysis to formulate development of bar amplitude under unsteady flow.

In this research, we performed some laboratory investigations on sand bar evolution under unsteady discharge in addition to those performed by Watanabe et al. In effect, it is rather difficult to conduct this kind of physical study for range of hydraulic conditions. Consequently, we propose herein a numerical model that can be used to reproduce sand bar formation

Copyright © 2006 Taylor & Francis Group plc, London, UK

under unsteady discharge. To authors' knowledge, no numerical work has been done so far that can simulate bar formation under unsteady discharge (except for the work conducted by our group of researchers, e.g. Yokoyama et al., 2004).

2 MODEL DEVELOPMENT

2.1 *Hydrodynamic equations*

The two-dimensional, unsteady, incompressible flow has been calculated using the following continuity and momentum equations in a generalized coordinate system (Shimizu & Itakura, 1991).

$$\frac{\partial}{\partial t}\left(\frac{h}{J}\right)+\frac{\partial}{\partial \xi}\left(\frac{hu^{\xi}}{J}\right)+\frac{\partial}{\partial y}\left(\frac{hu^{\eta}}{J}\right)=0 \tag{1}$$

$$\frac{\partial u^{\xi}}{\partial t}+u^{\xi}\frac{\partial u^{\xi}}{\partial \xi}+u^{\eta}\frac{\partial u^{\xi}}{\partial \eta}+\alpha_1 u^{\xi}u^{\xi}+\alpha_2 u^{\xi}u^{\eta}+\alpha_3 u^{\eta}u^{\eta}$$
$$=-g\left[\left(\xi_x{}^2+\xi_y{}^2\right)\frac{\partial H}{\partial \xi}+\left(\xi_x\eta_x+\xi_y\eta_y\right)\frac{\partial H}{\partial \eta}\right]$$
$$-\frac{C_b u^{\xi}}{J}\sqrt{\left(\eta_y u^{\xi}-\xi_y u^{\eta}\right)^2+\left(-\eta_x u^{\xi}+\xi_x u^{\eta}\right)^2}+D^{\xi} \tag{2}$$

$$\frac{\partial u^{\eta}}{\partial t}+u^{\xi}\frac{\partial u^{\eta}}{\partial \xi}+u^{\eta}\frac{\partial u^{\eta}}{\partial \eta}+\alpha_4 u^{\xi}u^{\xi}+\alpha_5 u^{\xi}u^{\eta}+\alpha_6 u^{\eta}u^{\eta}$$
$$=-g\left[\left(\eta_x\xi_x+\eta_y\xi_y\right)\frac{\partial H}{\partial \xi}+\left(\xi_x{}^2+\xi_y{}^2\right)\frac{\partial H}{\partial \eta}\right]$$
$$-\frac{C_b u^{\eta}}{J}\sqrt{\left(\eta_y u^{\xi}-\xi_y u^{\eta}\right)^2+\left(-\eta_x u^{\xi}+\xi_x u^{\eta}\right)^2}+D^{\eta} \tag{3}$$

in which, x, y are orthogonal coordinate axis, t is time, ξ, η is plane coordinate axis in generalized coordinate, h is water depth, H is water level, u^{ξ}, u^{η} is contravariant tensor in ξ or η direction, J is Jacobian determinant in coordinate transformation, C_b is bed friction coefficients. Other coefficients and diffusion terms are as follows:

$$\alpha_1=\xi_x\frac{\partial^2 x}{\partial \xi^2}+\xi_y\frac{\partial^2 y}{\partial \xi^2} \tag{4}$$

$$\alpha_2=2\left(\xi_x\frac{\partial^2 x}{\partial \xi\partial \eta}+\xi_y\frac{\partial^2 y}{\partial \xi\partial \eta}\right) \tag{5}$$

$$\alpha_3=\xi_x\frac{\partial^2 x}{\partial \eta^2}+\xi_y\frac{\partial^2 y}{\partial \eta^2} \tag{6}$$

$$\alpha_4=\eta_x\frac{\partial^2 x}{\partial \xi^2}+\eta_y\frac{\partial^2 y}{\partial \xi^2} \tag{7}$$

$$\alpha_5=2\left(\eta_x\frac{\partial^2 x}{\partial \xi\partial \eta}+\eta_y\frac{\partial^2 y}{\partial \xi\partial \eta}\right) \tag{8}$$

$$\alpha_6=\eta_x\frac{\partial^2 x}{\partial \eta^2}+\eta_y\frac{\partial^2 y}{\partial \eta^2} \tag{9}$$

$$D^{\xi}=\frac{\partial}{\partial \xi}\left[\frac{\tau_{\xi\xi}}{\rho}\right]+\frac{\partial}{\partial \eta}\left[\frac{\tau_{\eta\xi}}{\rho}\right] \tag{10}$$

$$D^{\eta}=\frac{\partial}{\partial \xi}\left[\frac{\tau_{\xi\eta}}{\rho}\right]+\frac{\partial}{\partial \eta}\left[\frac{\tau_{\eta\eta}}{\rho}\right] \tag{11}$$

in which, τ_{ab} is component of a shear force along b-axis (the plane normal to a-axis), ρ is density of water.

Bottom friction was determined as follows:

$$C_b=\frac{gn^2}{h^{1/3}},\quad n=\frac{d^{1/6}}{6.8\sqrt{g}} \tag{12}$$

A simple zero equation model was used as turbulence closure.

2.2 *Sediment transport model*

The continuity equation of two-dimensional bedload transport in a general coordinate system reads as:

$$\frac{\partial}{\partial t}\left(\frac{Z}{J}\right)+\frac{1}{1-\lambda}\left[\frac{\partial}{\partial \xi}\left(\frac{q^{\xi}}{J}\right)+\frac{\partial}{\partial \eta}\left(\frac{q^{\eta}}{J}\right)\right]=0 \tag{13}$$

where Z is bed elevation, λ is porosity of the bed material, q^{ξ} and q^{η} are contravarient components of the bedload transport rate per unit width in the ξ and η directions. The sediment transport of q^{ξ} and q^{η} in two-dimensional general coordinate (ξ,η), depend on the velocity vector specifically near the bed, therefore:

$$q^{\xi}=q_b\left[\frac{u_b^{\xi}}{V_b}-\gamma\left(\frac{\partial Z}{\partial \xi}+\cos\theta\frac{\partial Z}{\partial \eta}\right)\right] \tag{14}$$

$$q^{\eta}=q_b\left[\frac{u_b^{\eta}}{V_b}-\gamma\left(\frac{\partial Z}{\partial \eta}+\cos\theta\frac{\partial Z}{\partial \xi}\right)\right] \tag{15}$$

in which,

$$\gamma=\sqrt{\frac{\tau_{*c}}{\mu_s\mu_k\tau_*}} \tag{16}$$

where u_b^{ξ} and u_b^{η} are flow velocities near the bed in the ξ and η directions, V_b is resultant velocity near the bed, q_b is bedload sediment transport rate, θ is intersection angle between ξ and η axes, γ is a correction coefficient to account for the bed slope, μ_s is static coefficient of Coulomb friction (=1.0), μ_k is dynamic coefficient of Coulomb friction (=0.45). The

Copyright © 2006 Taylor & Francis Group plc, London, UK

sediment transport rate was calculated based on the Ashida and Michiue's formula.

$$\frac{q_b}{\sqrt{s_g g d^3}} = 17\,\tau_*^{3/2}\left(1-\frac{\tau_{*c}}{\tau_*}\right)\left(1-\frac{u_{*c}}{u_*}\right) \tag{17}$$

in which,

$$\tau_* = \frac{hI}{s_g d} = \frac{C_f V^2}{s_g g d} = \frac{n^2 V^2}{s_g d h^{1/3}} \tag{18}$$

$$V = \sqrt{u^2 + v^2} \tag{19}$$

where s_g is specific weight of grain in fluid, d is grain diameter, τ_* is non-dimensional shear stress, τ_{*c} is critical non-dimensional shear stress obtained by Iwagaki's formula, u_* is bed shear velocity.

2.3 *Flow velocities near the bed*

The streamwise velocity component near the bed can be defined as:

$$u_b^s = \beta V \tag{20}$$

Assuming that the parabolic distribution of the flow over depth, β can be defined as:

$$\beta = 3(1-\sigma)(3-\sigma), \quad \sigma = \frac{3}{\phi\kappa+1} \tag{21}$$

where ϕ is velocity factor $(=V/u_*)$, κ is von Karman constant $(=0.4)$.

Secondary flow is generated by the variation of centrifugal force caused by streamline curvature. The effect of secondary flow on near-bed transverse velocity can be estimated as follows:

$$u_b^n = u_b^s N_* \frac{h}{r_s} \tag{22}$$

where r_s is radius of curvature of the streamline and N_* is coefficient that takes into account the strength of secondary flow $(=7.0)$. The radius of streamline curvature is determined by:

$$\frac{1}{r_s} = \frac{1}{V^3}\left[\begin{array}{l} u^2\left(\xi_x\frac{\partial v}{\partial \xi}+\eta_x\frac{\partial v}{\partial \eta}\right)+uv\left(\xi_y\frac{\partial v}{\partial \xi}+\eta_y\frac{\partial v}{\partial \eta}\right) \\ -uv\left(\xi_x\frac{\partial u}{\partial \xi}+\eta_x\frac{\partial u}{\partial \eta}\right)-v^2\left(\xi_y\frac{\partial u}{\partial \xi}+\eta_y\frac{\partial u}{\partial \eta}\right) \end{array}\right] \tag{23}$$

In the Eq. (14) and (15), u_b^ξ and u_b^η are given by:

$$u_b^\xi = \frac{1}{\xi_r}\left\{\begin{array}{l} (\cos\theta_s\xi_x + \sin\theta_s\xi_y)u_b^s \\ +(-\sin\theta_s\xi_x + \cos\theta_s\xi_y)u_b^n \end{array}\right\} \tag{24}$$

$$u_b^\eta = \frac{1}{\eta_r}\left\{\begin{array}{l} (\cos\theta_s\eta_x + \sin\theta_s\eta_y)u_b^s \\ +(-\sin\theta_s\eta_x + \cos\theta_s\eta_y)u_b^n \end{array}\right\} \tag{25}$$

where θ_s is the angle between x- and s-axis. With compare to u_b^s, u_b^n is small by an order thus can be neglected, then the resultant near-bed velocity V_b reads as

$$V_b = \sqrt{u_b^{s\,2} + u_b^{n\,2}} \approx u_b^s \tag{26}$$

In the Eq. (14) and (15), the longitudinal and transverse channel bed slopes are determined by following equations:

$$\frac{\partial Z}{\partial s} = \frac{\partial Z}{\partial \xi}\left(\xi_x\frac{\partial x}{\partial s}+\xi_y\frac{\partial y}{\partial s}\right)+\frac{\partial Z}{\partial \eta}\left(\eta_x\frac{\partial x}{\partial s}+\eta_y\frac{\partial y}{\partial s}\right) \tag{27}$$

$$\frac{\partial Z}{\partial n} = \frac{\partial Z}{\partial \xi}\left(\xi_x\frac{\partial x}{\partial n}+\xi_y\frac{\partial y}{\partial n}\right)+\frac{\partial Z}{\partial \eta}\left(\eta_x\frac{\partial x}{\partial n}+\eta_y\frac{\partial y}{\partial n}\right) \tag{28}$$

in which,

$$\begin{array}{l} \frac{\partial x}{\partial s} = \frac{u}{V} = \cos\theta_s, \quad \frac{\partial y}{\partial s} = \frac{v}{V} = \sin\theta_s \\ \frac{\partial x}{\partial n} = -\frac{v}{V} = -\sin\theta_s, \quad \frac{\partial y}{\partial n} = \frac{u}{V} = \cos\theta_s \end{array} \tag{29}$$

2.4 *Calculation condition*

Numerical computation was performed for two experimental cases (U30 and U50).

A periodic boundary condition can be applied with a random field of initial bed perturbation. On the other hand, a non-periodic boundary condition can be imposed with some perturbation added to the flow at the upstream end.

The periodic boundary condition might be suitable in case of dynamic equilibrium bed evolution. However, this condition may not work well when temporal change of the wavelength takes place. In this case, non-periodic boundary condition is desirable. The shortcoming of this boundary condition is that it requires long calculation domain, which affects the calculation time.

We performed computation using both boundary conditions for the sake of comparability. In case of non-periodic boundary condition,, a non-periodic perturbation of all but ±5% was added to upstream flow. Likewise, a random field of bed perturbation was also added for both conditions.

Total calculated domain was 80 m long. However, we presented here calculation result for 15 m long domain in the middle.

Copyright © 2006 Taylor & Francis Group plc, London, UK

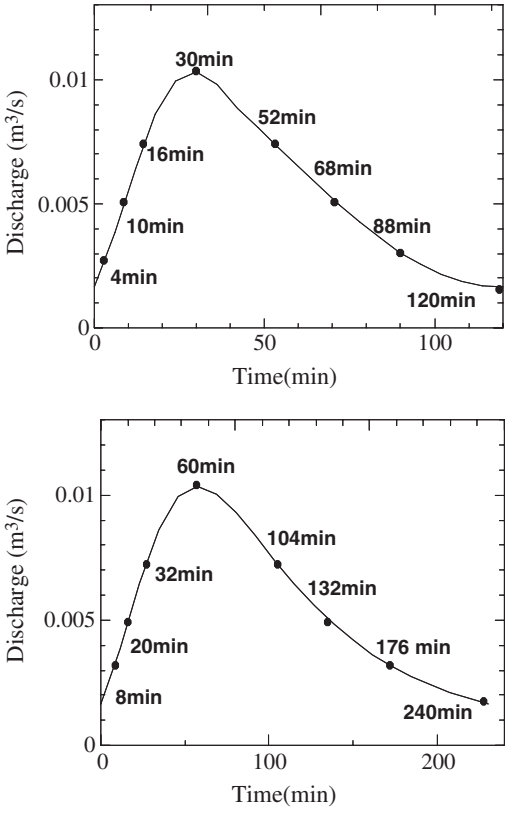


Figure 1. Stage hydrograph for flume experiment case U-50 (upper) and U-30 (lower).

3 MODEL VALIDATION

3.1 *Experiment*

Experiment was conducted in a laboratory fume of CERI. The width of flume was 0.9 m and the length of the flume was 50 m. The diameter was 0.76 mm. The slope of flume was 1/80. At the downstream end, the weir of the same height as water depth was set. Two typical experimental cases are reported herein (U30 and U50). Figure 1 shows the hydrograph in the flume experiment for both of the cases. The peak discharge is 10.3(l/s) for both cases. The experiment was performed for 2 hours for U50 and 4 hours for U30. One case with steady discharge has also been incorporated in this study.

3.2 *Result and discussion*

3.2.1 *Sand bar characteristics*

Calculation result of bed topography was compared with experimental data which is depicted in Figure 2. Moreover, computed temporal evolution of sand bar characteristics (height and wave length) was compared with observation. Calculation was performed for non-periodic boundary condition. Comparing the calculation result with the experimental one, we found that sand bar formation in numerical computation is slower than in observed case. For this particular case, results are not identical until 30 min of calculation. However, after 30 minutes the bed topography reproduced by numerical model appears to be in good agreement with observed quantities (Fig. 2).

With regard to the temporal evolution of bar height, from depicted result (Fig. 3) it can be seen that computed result match well with experimental one. It was revealed that the peak of hydrograph does not coincide with the maximum bar height. The bar height evolution shows some lag with respect to discharge variation. The maximum bar height was observed in falling stage. This can be attributed to the hystereris effect of the flow. Interestingly, numerical model was able to reproduce this phenomenon rather realistically.

With the increment of time, the shape of alternate bar was found to be somewhat irregular. In Figure 3, a quantitative comparison of wavelength growth is depicted. In this case, the variation of wavelength is not so clear. Nonetheless, it can be seen that the maximum wavelentgh is deflected from the point of maximum discharge. The model overestimated the wave length, though within the satisfactory range. The wavelength was apperaed to be increased with time.

3.2.2 *Computation with periodic boundary condition*

For the sake of comparison, we performed calculation for these cases using periodic boundary condition. We revealed that the sand bar wavelength in this case significantly alters due to the decrease of wavenumber in latter stage of calculation. We attempted to increase the length of calculation domain. However, no noteworthy difference was found. Some comparison between computed results using periodic and non-periodic boundary conditions can be seen in Figure 4. From this figure, one can see that the predicted wave length is somewhat similar in initial stage of calculation. However, it became all but twice bigger in case of periodic boundary condition after 80 minutes and 120 minutes of calculation for U30 and U50 respectively. This leads to the conclusion that the periodic boundary condition is not appropriate for sand bar growth simulation under unsteady flow.

3.2.3 *Comparison between computational results for steady and unsteady flow conditions*

An attempt was made to evaluate the distinction between physical characteristics as well as bar evolution under steady and unsteady flow conditions. We performed calculation for steady flow case for each particular discharge that we used for unsteady simulation.

Copyright © 2006 Taylor & Francis Group plc, London, UK

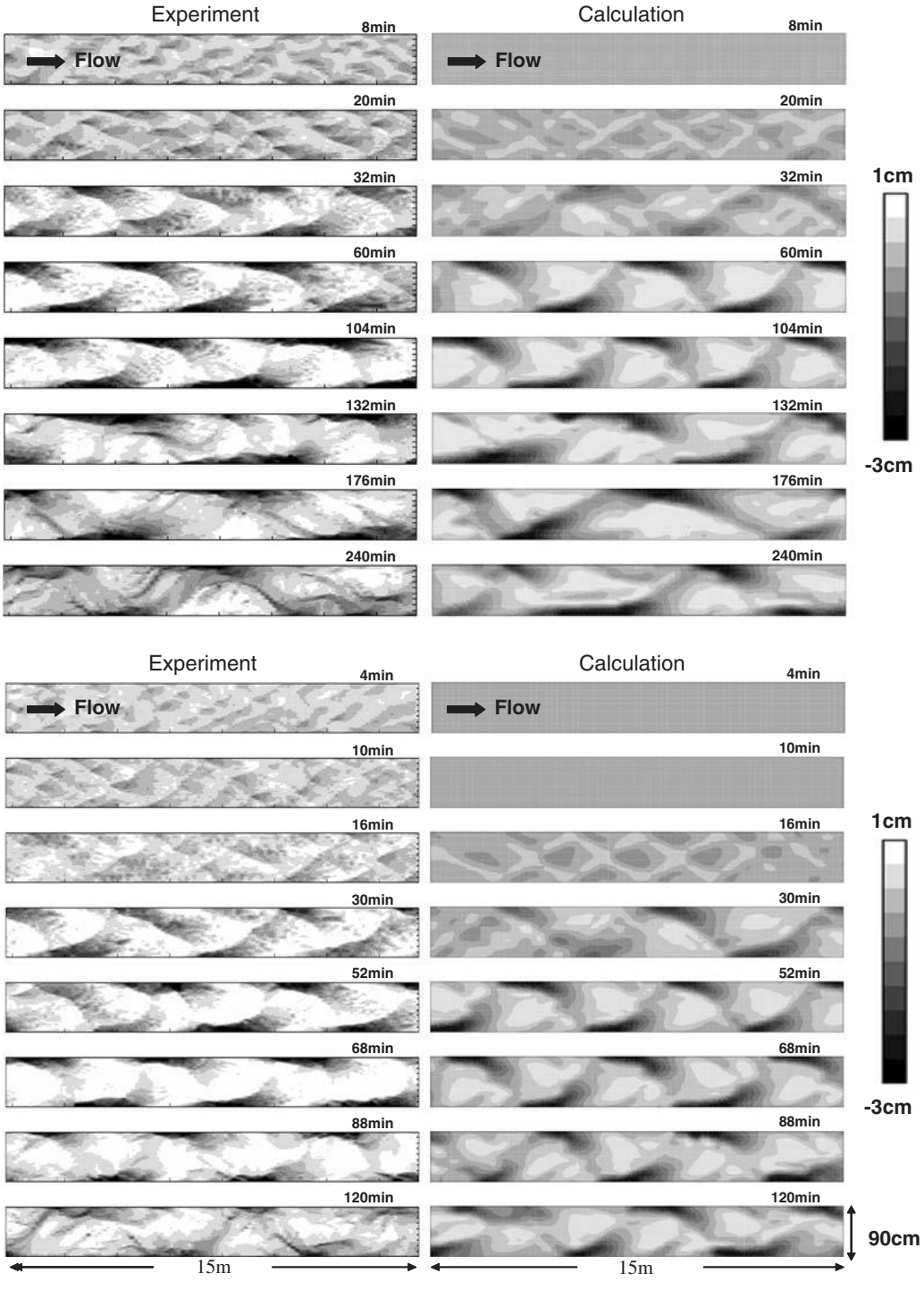


Figure 2. Comparison between numerical simulation and experiment for case U-30 (upper) and U-50 (lower).

Copyright © 2006 Taylor & Francis Group plc, London, UK

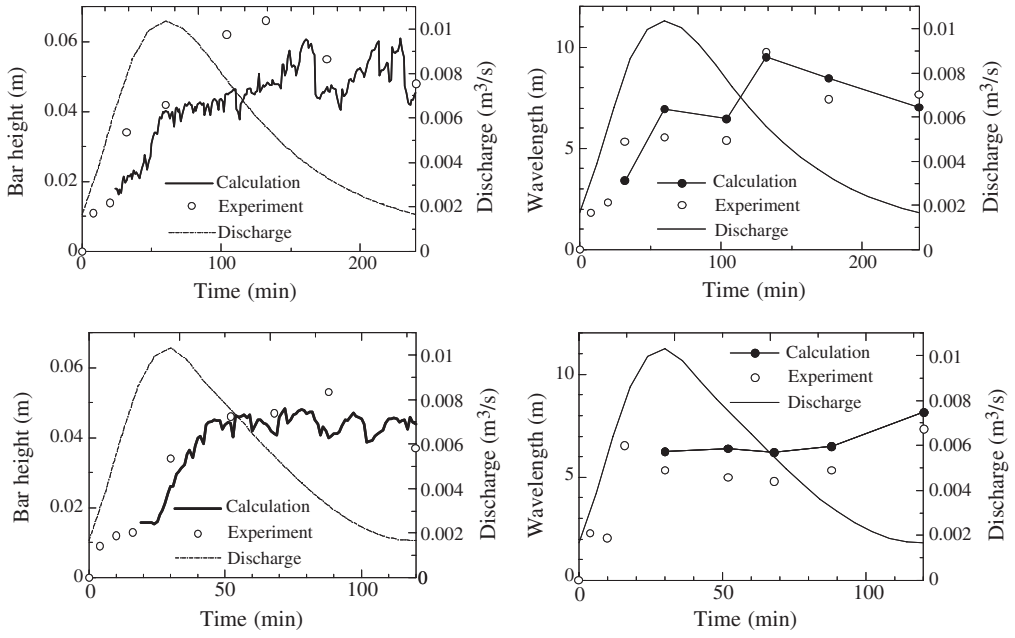


Figure 3. Comparison between computed and observed time evolution of sand bar characteristics for case U-30 (upper) and U-50 (lower).

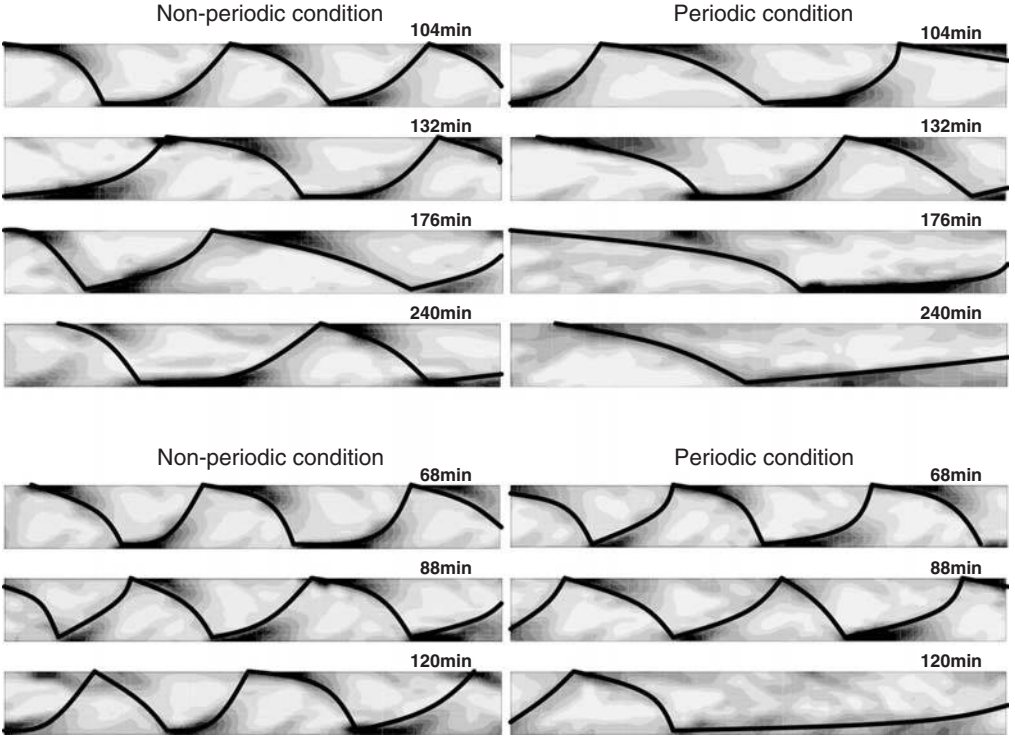


Figure 4. Comparison between computation results with periodic and non-periodic boundary conditions for case U-30 (upper) and U50 (lower).

Copyright © 2006 Taylor & Francis Group plc, London, UK

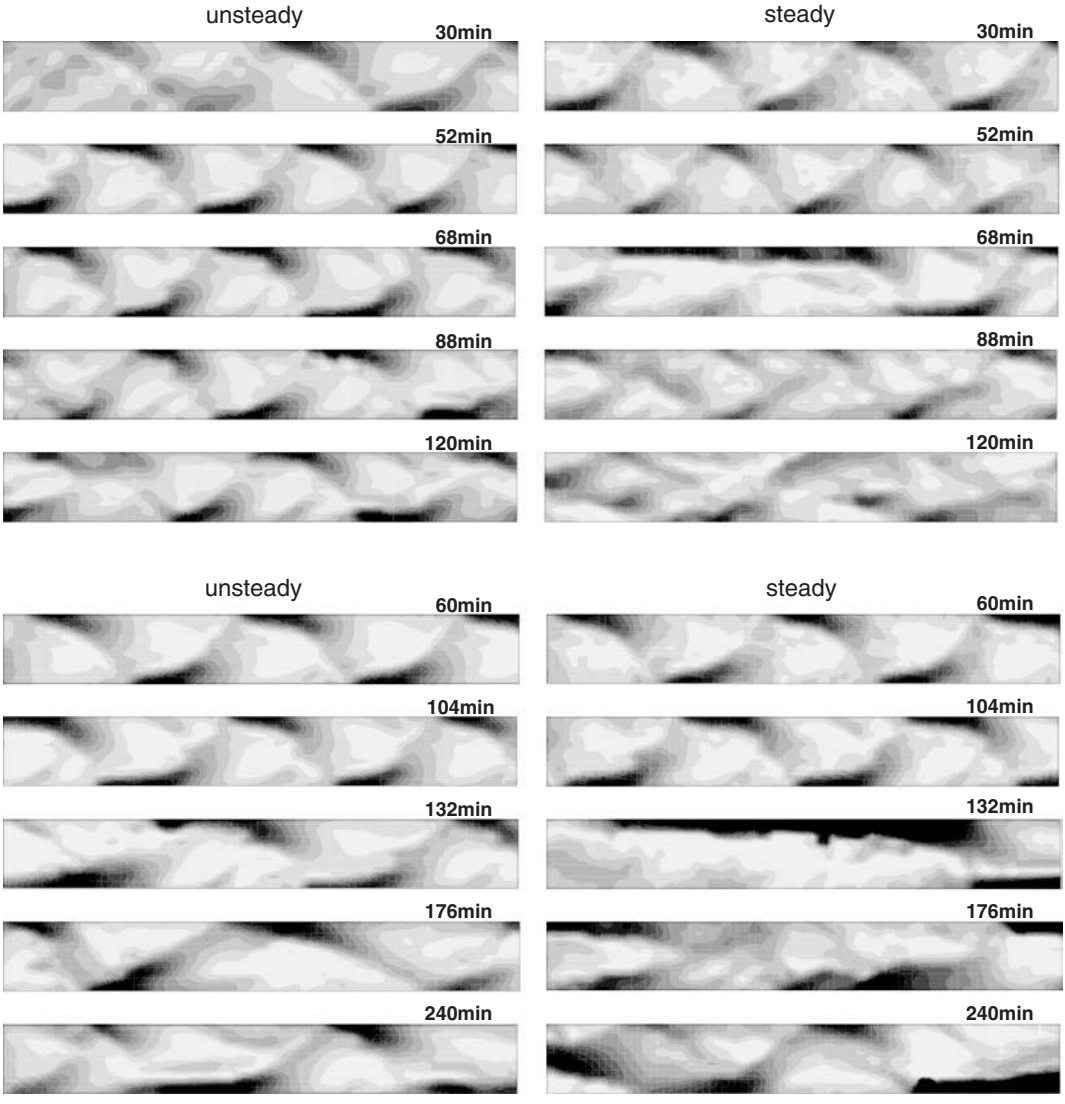


Figure 5. Comparison between computed results of sand bar evolution for steady and unsteady cases (U-30 upper figures and U-50 lower figures).

A qualitative comparison between computed results under these conditions has been depicted in Figure 5. It can be seen that feature of sand bar evolution is different for these two cases. The sand bar evolution appears to possess clear trend in case of unsteady flow. Likewise, quantitative comparison between sand bar characteristics for both cases depicted in Figure 6. From this figure, it can be seen that bar heigth increased with time and then became constant in latter stage for the case of unsteady condition. While, it is unclear (practically constant) for steady case. With regard to wavelength, the trend doesnot seem to be so clear. Most notable result is that the wavelength is similar in the region with maximum discharge for both cases but differs significantly in falling stage. For the sake of verification, comparison between calculation and experiment for one of the steady cases was also made that is depicted in Figure 7.

Overall, for each stage of discharge, the sand bar characteristics were found to be altered depending on the flow condition. Moreover, it can be noticed that for similar discharge in rising and falling stages, bar evolution shows distinctive characteristics. This evidence

Copyright © 2006 Taylor & Francis Group plc, London, UK

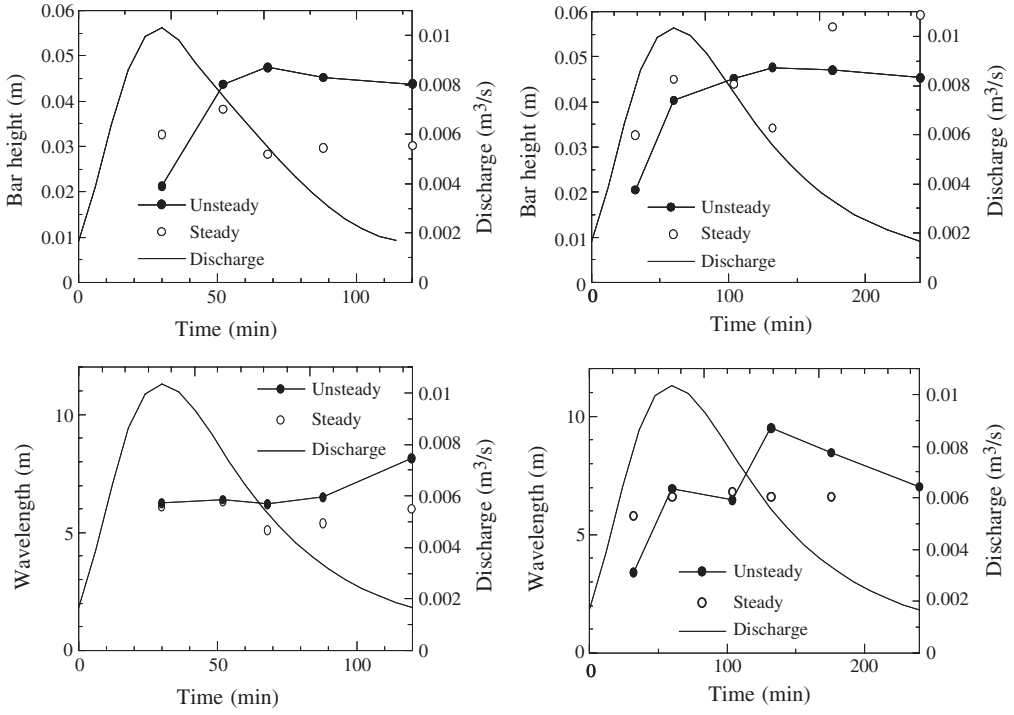


Figure 6. Comparison between computed results of sand bar characteristics for steady and unsteady cases (U-30 upper figures and U-50 lower figures).

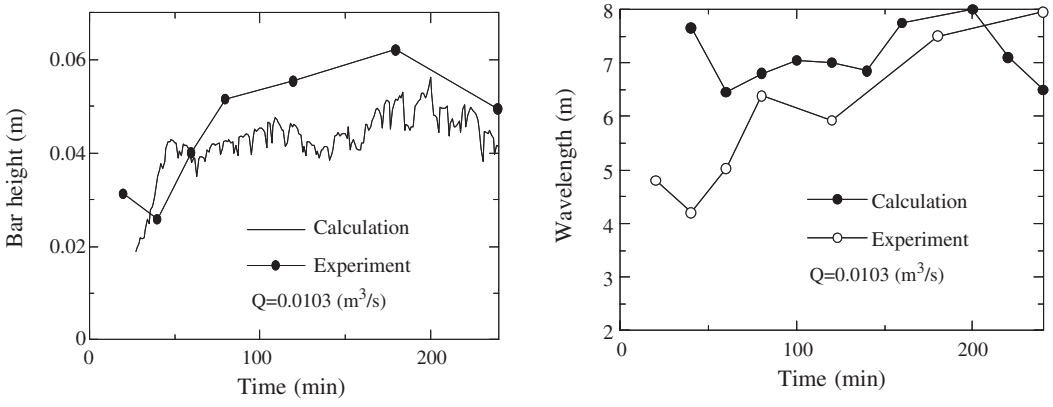


Figure 7. Comparison between computed and observed time evolution of sand bar characteristics for steady case.

points out towards the histeresis effect induced by unsteady flow condition.

4 CONCLUSION

A state-of-the-art morphodynamic model was developed that can simulate meso-scale bedforms under unsteady flow condition in physically based manner. Model was able to capture most physical characteristics of sand bar.

It is evident that the behavior of sand bar under unsteady flow condition is different in comparison with steady flow condition. Consideration of hysteresis characteristics of sand bar evolution under unsteady flow condition appears to be essential. The hysteresis

Copyright © 2006 Taylor & Francis Group plc, London, UK

effect of unsteady flow was replicated realistically by proposed numerical model. Furthermore, periodic boundary condition was found to be inappropriate for the computation under the conditions similar to the ones presented in this work. It can be inferred that the model performance is fairly satisfactory taking into account the complicated nature of the phenomenon.

REFERENCES

Colombini, M., Seminara, G. and Tubino, M. 1987. Finite-amplitude alternate bars, *J. Fluid Mech*., 181, 213–232.

Fujita, Y. and Muramoto, Y. 1982. Experimental study on stream channel processes in alluvial rivers. *Bull. Disas. Prev. Res. Inst.*, Kyoto Univ., 35 (314), 55–86.

Garcia, M. and Nino, Y. Dynamics of sediment bars in straight and meandering channels: experiments on the resonance phenomenon. *J. Hydraul. Res*., 31(6), 739–761.

Izumu, N. and Pornprommin, A. 2005. Weakly nonlinear analysis of bars with the use of the amplitude expansion method, *J. Hydraul. Coast. And Env. Engrg*., 712/II-60, JSCE, 73–86.

Kinoshita, R. 1961. Investigation of channel deformation in Ishikari River. *Report of Bureau of Resources, Department of Science and Technology*, Japan (in Japanese).

Kinoshita, R. and Miwa, H. River channel formation which prevents downstream translation of transverse bars, *Shinsabo*, 94, 12–17 (in Japanese).

Kuroki, M. and Kishi, T. 1984. Regime criteria on bars and braids in alluvial straight channels, Proc. JSCE, 342, 87–96.

Lazoni, S. 2000. Experiments on bar formation in a straight flume 1 Uniform sediment, *Water Res.*, 36(4), 1109–1118.

Leopold, L.B. and Wolman, M.G. 1957. River channel patterns: Braided, meandering and straight, *U.S. Geol. Surv. Prof. Pap.*, 282-B.

Parker, G. 1976. On the cause and characteristic scale of meandering and braiding in rivers, *J. Fluid Mech*., Vol. 76, 457–480.

Shimizu, Y. 2004. A method for simultaneous computation of bed and bank deformation of a river, *Proc. Int. Conf. Fluv. Hydraul*., Louvain, Belgium, 793–801.

Shimizu, Y. and Itakura, T. 1989. Calculation of bed variation in alluvial channels, *J. Hydraul. Engrg*, ASCE, 115(3), 367–384.

Tubino, M. 1991. Growth of alternate bars in unsteady flow, *Water Res. Res*., 27(1), 37–52.

Watanabe, Y. and Kawamura, K. 2005. Mode-decrease process of double-row bars, *Proc. Int. Conf. Riv. Coast. Morph. Dyn*., Illinois, USA, 445–453.

Watanabe,Y., Sato, K., Hoshi, K. and Oyama, F. 2004. Experimental study in bar formation under unsteady flow condition, *River Flow*, Napoli, Italy, 277–286.

Yokoyama, H., Watanabe, Y. and Shmizu, Y.2004. Numerical simulation of sand bars using 2-D shallow water equation under unsteady flow, *River Flow*, Napoli, Italy, 297–303.

Copyright © 2006 Taylor & Francis Group plc, London, UK

Experimental investigation of flow expansions over fans

L. Sittoni, C. Paola & J. Fedele
National Center for Earth-surface Dynamics, University of Minnesota, Minneapolis,
St. Anthony Falls Laboratory, University of Minnesota, Minneapolis,
Department of Civil Engineering, University of Minnesota, Minneapolis

M. Tubino
Department of Civil and Environmental Engineering, University of Trento, Trento, Italy

ABSTRACT: We present experimental evidence on the occurrence of large angles of flow expansion with no flow separation over depositional fans. The evolution of a number of self-formed experimental fans was analyzed using overhead images and detailed topographic surveys taken from a run of the Experimental EarthScape basin at St Anthony Falls Laboratory. Instability phenomena produce narrow, upstream migrating channels coupled to lobes with large opening angles and sheet flow over them. Most of deposition appears to occur relatively rapidly during the initial perturbed expansion phase. Our analysis confirms that steady conditions can develop over large angles of expansion (half angle over 20 degrees). The steady condition is maintained with the help of a downstream-decreasing transverse bed curvature (with a normalized average value of 0.1). The bed curvature transfers flow momentum toward the banks, preventing flow separation and maintaining the high divergence angle. The bed curvature thus appears sufficient to explain the common occurrence of unchannelized, simple fans with opening angles, and hence rates of bedload divergence, much larger than would be predicted from jet theory. Furthermore, at equilibrium conditions, the deposit displays a conical shape, well described by a linear relation. We have also analyzed fan development. An initial channel perturbation causes an upstream migrating scour, which leads to an abrupt downstream increase in width and a consequent heart-shaped deposit. In this phase, flow shows the largest divergence angles values (half angle up to 50 degrees) in the upstream fan part. The fan then reaches a final cone-shape, developing an unchannelized low depth-width ratio flow.

1 INTRODUCTION

The evolution of flow expansions is important because represents a primary mechanism of deposition in many fluvial and submarine environments. Water flow, expanding, decreases its momentum and therefore its transport capacity, allowing large deposition and fans self-formation. Understanding this mechanism can aid to understand the general evolution of the larger depositional system, with practical applications in the land management and, with the support of stratigraphic investigations, in the estimation of the volume of subsurface reservoirs.

Different alluvional architectures, like channels, bifurcations, junctions and fans, forming on the surface of a depositional system directly influence the stratigraphic structure, affecting the entrapment of subsurface fluids, as oil and water.

In this work we analyzed fluvial fans that were observed to form over the surface of the eXperimental EarthScape basin (XES). This experimental feature, located at the St. Anthony Falls Laboratory (University of Minnesota), is designed to study the evolution of a fluvial depositional system under conditions of net deposition produced by steady basement subsidence and base level variation. This feature allows also further stratigraphic elaborations of the fluvial deposit. This basin presents some peculiar experimental parameters to take into account in this analysis, including the absence of vegetation, non-cohesive material, high water discharge, high slope. These parameters are related to a high activity depositional environment which leads to an easier formation of different alluvional architectures and, in particular of fluvial fans. We believe that at least some aspects of fan mechanics are sufficiently general to allow a future extension to submarine cases as well.

Several instability phenomena over the surface of the XES produce upstream perturbation waves along channels causing a significant water flow widening

and the development of large angles of expansion which leads to the formation of fan deposits. Subjected to further deposition, deposits can be recognized in stratigraphic analysis through the presence of laterally extensive depositionally based strata with convex tops.

Theory states that flow expansions over flat beds with half angles over 5–6° develop flow separation. From a preliminary analysis of the images taken during this experiment, expansion angles seem to show values significantly larger than this threshold. Water is also observed to cover the whole fan deposit with an unchannelized, low depth-width ratio flow with no occurrence of separation. The leading hypothesis investigated in this work is that the presence of a transverse curvature of the bed of the deposit transfers flow momentum toward the banks, suppressing separation and maintaining the high divergence angle. In this case the flow expansion would be dominated by the bed topography, opening up the possibility of finding consistent geometric relations, e.g. between local deposit curvature and deposit length, that can be used for subsurface prediction.

In this paper, a data analysis of experimental fans is presented. We emphasize measurement of flow expansion angles and detailed description of the deposit topography. We then study fan development from the instability phenomena occurring along a channel, through the formation of a concave-shaped deposit, to the cone-shaped equilibrium condition. Deposition seems to decrease with the development of the fans, which appear to reach an asymptotic sediment bypass condition during the equilibrium stage in which liquid and solid discharge remain constant down the fan. This is an unexpected situation for a diverging body, in particular if, as observed in the present case, the fans originate as self-formed depositional phenomena.

Further work on this problem will include analytical and numerical investigations of unchannelized flow over a cone-shaped body under conditions of complete fluid and solid bypass.

2 EXPERIMENTAL DESIGN

Data analyzed here come from the XES basin run XES02-1, performed at the St. Anthony Fall Laboratory. The XES basin develops strata under clearly defined variations in sediment discharge, rates and geometries of subsidence, and absolute base-level change. XES02-1 is designed to investigate the effect of slow, rapid, and superimposed base level cycles on shoreline migration and stratigraphic response, under conditions of passive margin type subsidence. The XES02-1 run had a basin area 5.72 m long and 2.98 m wide, one quarter of the entire basin.

A more detailed description of the XES facility is available at http:// www.geo.umn.edu/orgs/seds/ and it has been reported in Paola (2000), Heller et al. (2001), Paola et al. (2001), Sheets et al. (2003), and Kim et al. (in press). Sediment and water were mixed and fed from a single point source. The sediment feed rate was 0.0182 m^3/hr, the water discharge was 1.5 m^3/hr, and their rates were kept constant throughout the experiment. The sediment mixture comprised 63% quartz sand (110 μm), 27% coal sand (bimodal: 460 and 190 μm), and 10% kaolinite. The coal has a specific gravity of 1.3, whereas quartz has a specific gravity of 2.65, so the coal grains are substantially more mobile than the quartz grains and serve as a proxy for fine-grained clastics. Subsidence rate increases linearly downstream in the basin so as to produce simple linear-hinge type subsidence.

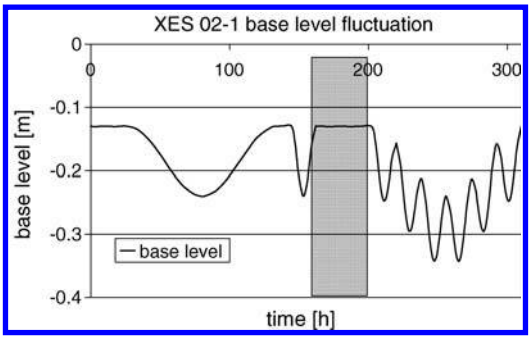


Figure 1. Base level fluctuation. The equilibrium period analyzed in this work is highlighted in the box.

Absolute base-level changes (i.e., absolute change of water surface level in the downstream "ocean" part of the basin) during the XES 02-1 experiment included sinusoidal base-level cycles with two time scales. The first slow base level cycle lasted 108 hours, beginning at runtime hour 26. It was followed by a rapid base level cycle lasting 18 hours beginning at runtime hour 144. Base level was stable before the first slow cycle and between the slow and rapid base level cycles. The second part of the experiment comprised six rapid cycles superimposed on one slow cycle beginning at runtime hour 202 (Fig. 1). All data analyzed in this work come from the equilibrium period between stages one and two (162–202 hours runtime). During this 40 hr equilibrium period base level was constant. The analysis was performed during the equilibrium period to exclude any effect of variable base-level on fan development.

3 PLAN-VIEW ANGLES OF EXPANSION AND BED TOPOGRAPHY INVESTIGATION

Consistently with what stated in the introduction, the first step of this work is to investigate large angles of expansion without flow separation, i.e. involving

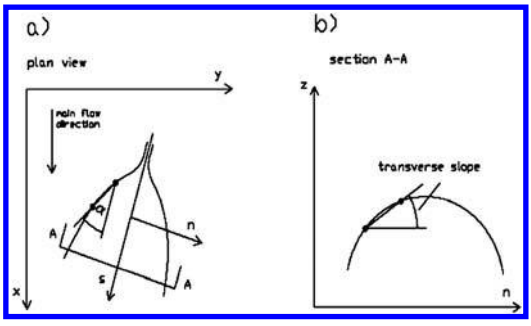


Figure 2. Sketch of the reference frames and notation.

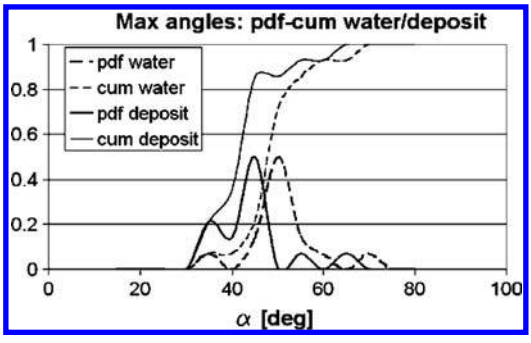


Figure 3. Maximum plan-view angles of expansion: pdf and cumulate curve for water and deposit. x-axis: plan-view angles in degrees; y-axis: dimensionless pdf-cumulate.

half-angles larger than 5–6 degrees. We analyzed fans during their development through a series of time intervals.

Plan-view angles were computed as the local first derivative of the plane shape border with respect to the longitudinal direction. This procedure is performed both for water and deposit expansion. A sketch of the coordinate systems utilized in this work is shown in Figure 2.

The maximum plan-view angles found for each fan are plotted in Figure 3. It was common for the flow to have a somewhat different geometry than the fan surface, so the solid line indicates the deposit, and the dashed line the water expansion. The plotted values represent the maximum angle along the whole longitudinal extension when considering all time intervals. The plot in Figure 3 clearly shows the presence of large angles of expansion with average values of 45 degrees for the deposit and 50 degrees for the water (values refer to half angles).

Overhead images taken during the experiment suggest the presence of a transverse curvature of the deposit that could support the high divergence angles. Topography data for the whole basin, taken every four

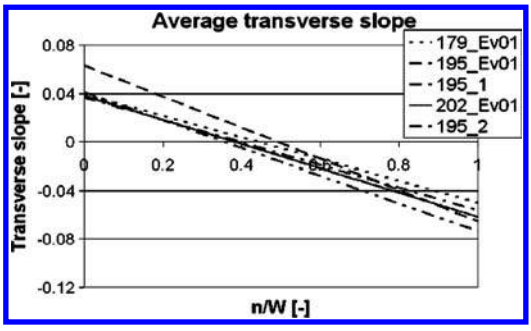


Figure 4. Average width normalized transverse slope. x-axis: transverse coordinate normalized by the local transverse width (n/W); y-axis: average transverse slope.

hours through a high resolution grid, were analyzed for this purpose. Five fans are available for investigation, with consistent and interesting results. A qualitative analysis of the fan bed shape shows a central upstream feeder channel that slowly disappears further downstream, leaving space for a regular concave curved bed. Transverse slope and curvature are then calculated from the topography grid along the direction perpendicular to the midline.

Transverse curvature is always present in all the analyzed fans as shown in Figure 4, where the average transverse slope of the downstream third of each fan is plotted with respect to the local fan width normalized by the transverse direction. The transverse slope decreases from positive to negative values, suggesting a negative curvature (slope of the slope), which, for a varieties of fans, averages around 0.1, when normalized by the local width.

Furthermore, the transverse slope at the deposit boundaries often reaches values of 0.04 with peaks of 0.06. Those values are of the same order of magnitude as the longitudinal slope over the deposit and, from simple further calculations, of the average longitudinal slope of the whole experimental basin. Thus lateral gravitational forces are comparable to downstream ones, and the curvature could transfer enough flow momentum toward the banks to prevent flow separation and maintain the high divergence angle. The bed curvature thus appears to play an important role in the physics of the phenomenon, sufficient to explain the common occurrence of unchannelized simple fans with opening angles, and hence rates of bedload divergence, much larger than would be predicted from jet theory (Hoyal et al. 2003, Van Wagoner et al. 2003).

Local transverse curvature values are summarized in Figure 5, where they are plotted against the length normalized longitudinal direction over the fan (s/L). The absolute value of the curvature clearly shows a consistent decreasing pattern in the downstream direction.

4 FAN DEVELOPMENT ANALYSIS

From observation of fans during their experimental evolution, we find that: the process starts with a perturbation of the bed; a scour then forms and migrates upstream, changing the pre-existent substrate. Once an "equilibrium" is reached and the bed is conveniently modified, migration stops. Downstream of an inertial-dominated region, water flows following the deposit topography with an unchannelized low depth-width ratio motion field. Furthermore, young fans appear to show a concave shape, while old fans a cone shape. A qualitative fan evolution is shown in Figure 6 through a series of images representing successive temporal steps.

A quantitative description of the plan-view border evolution is given in Figures 7, 8 where the border is plotted with respect to the midline. Data in Figure 8 are normalized by the length of the deposit (x-axis) and by its final width (y-axis). Here it is clearly possible to observe the translation from the concave to the conic shape even if any scale information is lost.

A further parameter investigated in fan evolution analysis is the fan length-final width (aspect) ratio. This parameter is generally observed to decrease in time and, in particular, during equilibrium phase, the aspect ratio drops below 4. In these conditions, fans seem to tend to reach an asymptotic equilibrium shape characterized by a status of sediment bypassing, in which liquid and solid discharge remain constant.

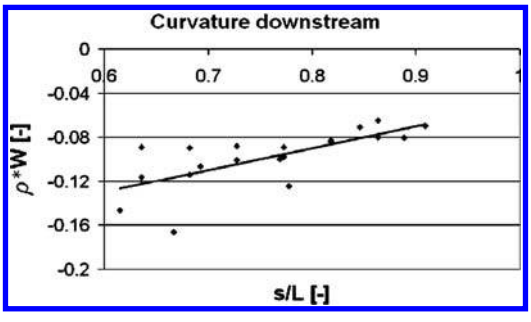


Figure 5. Downstream tendency of the local transverse curvature. x-axis: longitudinal coordinate normalized by the deposit length, y-axis: dimensionless local transverse curvature.

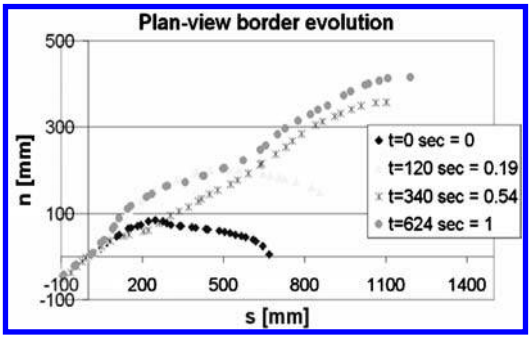


Figure 7. Plan-view border evolution. x-axis: longitudinal direction over the fan (s); y-axis: transverse direction (n).

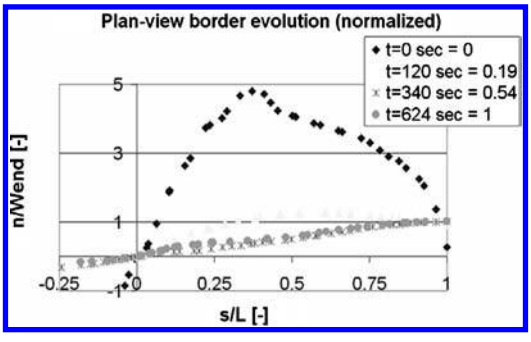


Figure 8. Plan-view border evolution (normalized). x-axis: longitudinal direction over the fan normalized by the fan length (s/L); y-axis: transverse direction normalized by the fan final width ($n/Wend$). The translation from a concave to a conic shape is clear proceeding with time.

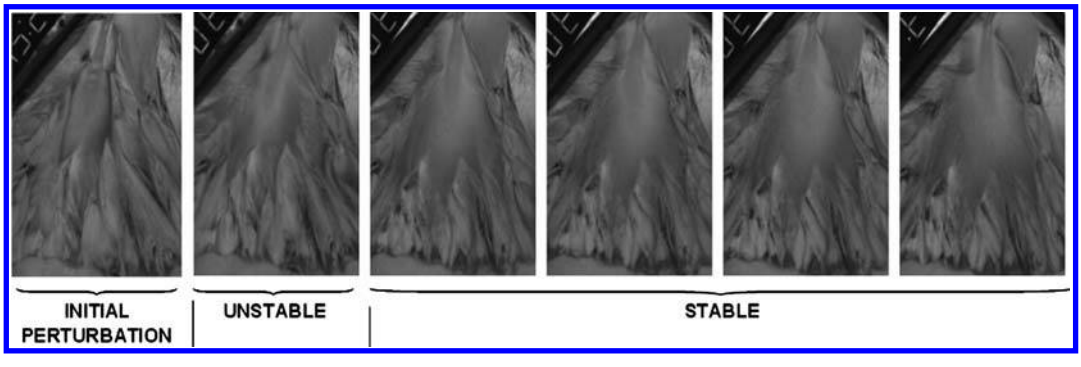


Figure 6. Fan evolution. From left to right: bed initial perturbation and concave shape, unstable phase, stable phase when the fan reaches a conic shape with uniform unchannelized low depth-width ratio flow over the downstream area of the deposit.

All of the deposit plan-view shapes of the fans that reached this stadium are then collected and fitted with a linear relation (1), as shown in the plot in Figure 9:

$$n/L = 0.365\, s/L \; ; \qquad R^2 = 0.92 \qquad (1)$$

where s represents the streamwise direction and n is perpendicular to s; both coordinates are normalized by the deposit length. Plan-view deposit border follows a linear relation which, in association with a transverse curvature, suggests a conical deposit equilibrium shape.

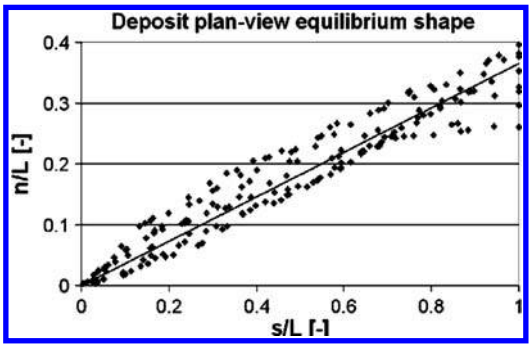


Figure 9. Deposit plan-view shape at equilibrium conditions. x-axis: longitudinal coordinate normalized by the deposit length; y-axis: transverse coordinate also normalized by the deposit length.

Finally, Figure 10 shows a potential application of the results of this work to estimate the shape and hence the volume of a subsurface fluids reservoir when only few data are available, which represents the main goal of this project. For example, knowing the transverse curvature and the deposit width, e.g. from a stratigraphic section, (Fig. 10, top left) it is possible to calculate the dimensionless transverse curvature. Knowing the downstream tendency of the transverse curvature (Fig. 10, top right) one can determinate the corresponding dimensionless longitudinal coordinate. At this point, the plan-view equilibrium shape chart (Fig. 10, bottom right) gives the dimensionless width. From the dimensional width it is hence possible to determinate the surface and hence the volume of the subsurface deposit (Fig. 10, bottom left).

Further analysis in this sense represents the direction of future work. It would be interesting to understand how a self-formed depositional structure evolves tending to become a bypassing body, and, in particular, what is the deposit equilibrium shape and how an unchannelized low depth-width ratio flow field could be maintained over it. In the near future numerical simulations and stability analysis are planned in this direction. The main idea is of investigating the

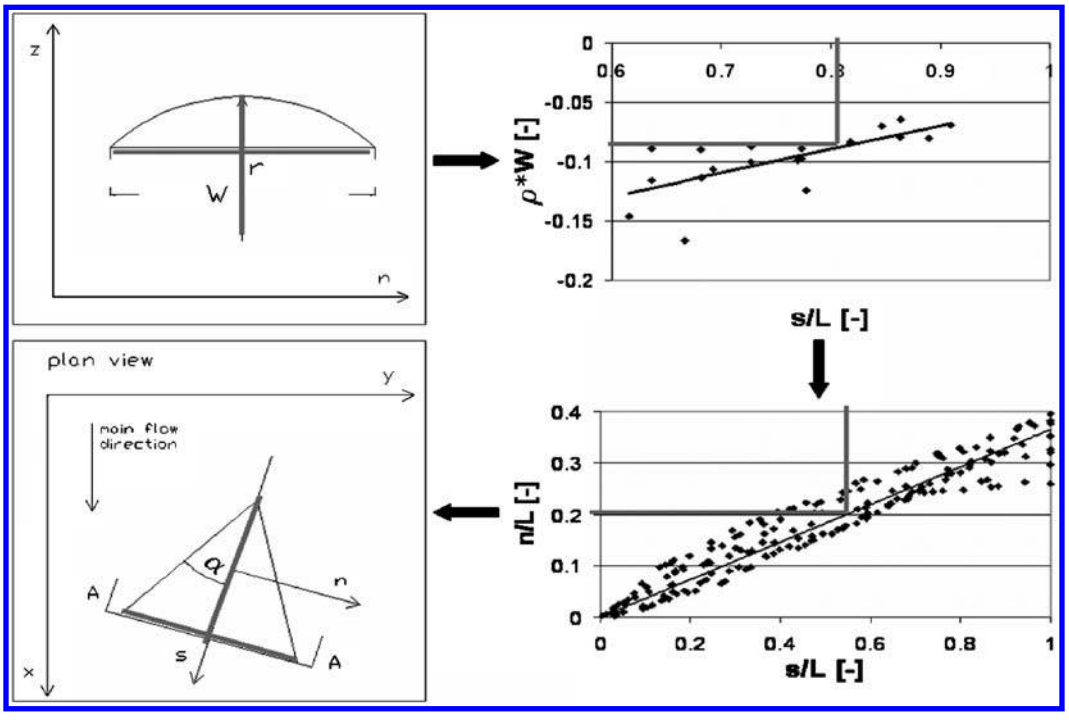


Figure 10. Subsurface deposit geometry determination.

influence of the variation of the deposit transverse curvature on the motion field, under the conditions of conserved liquid and solid discharge. We believe that this procedure can aid to verify if there is an equilibrium shape of the deposit, what this would be, and if the topography of the deposit is the single leading parameter in the occurrence of large angles of expansion and the consequent unchannelized, low depth-width ratio flow over the deposit.

5 CONCLUSIONS

This work shows evidence of the occurrence of large flow expansion angles over fans. Maximum values are found to range between 40–50 degrees half-angle. This phenomenon is made possible by a consistent deposit transverse curvature of around 0.1 when normalized by the fan width. Plan-view expansion angles seem to be independent of the curvature. Fan development analysis shows that an initial channel perturbation causes an upstream migrating scour, which leads to an abrupt downstream increase in width and a consequent concave-shaped deposit. The fan then reaches a final cone-shape, where the aspect ratio maintains approximately constant in the range of 2–4. The consistency of the depositional shapes opens up the possibility of using local shape measures to estimate downdip sandbody extent.

ACKNOWLEDGMENT

This work is supported by the National Center for Earth-surface Dynamics (NCED), a Science and Technology Center funded by the Office of Integrative Activities of the National Science Foundation (under agreement Number EAR- 0120914) and by the Industrial Oil Consortium. We also thank the XES staff for running the experiment and for providing all the useful data and Chris Paola's research group at the SAFL (St. Anthony Falls Laboratory) for the appreciated advice.

REFERENCES

Heller, P. L., Paola, C., and Hwang, I-G. 2001. Geomorphology and sequence stratigraphy due to slow and rapid base-level changes in an experimental subsiding basin (XES 96-1). *American Association of Petroleum Geologists Bulletin* 85(5): 817–838.

Hoyal, D.C.J.D., Van Wagoner, J.C., Adair, N. L., Deffenbaugh, M., Li, D., Sun, T., Huh, C., and Giffin, D. E., 2003. Sedimentation from Jets: A depositional model for clastic deposits of all scales and environments. *Search and Discovery* Article #40081.

Kim, W., Paola, C., Voller, V.R., and Swenson, J.B. in press. Experimental measurement of the relative importance of controls on shoreline migration. *Journal of Sedimentary Research.*

Paola, C. 2000. Quantitative models of sedimentary basin filling. *Sedimentology* 47(1): 121–178.

Paola, C., Mullin, J., Ellis, C., Mohrig, D. C., Swenson, J., Parker, G., Hickson, T., Heller, P. L., Pratson, L., Syvitski, J., Sheets, B., and Strong, N. 2001. Experimental stratigraphy. *GSA Today* 11: 4–9.

Sheets, B. A., Hickson, T. A., and Paola, C. 2002. Assembling the stratigraphic record: depositional patterns and timescales in an experimental alluvional basin. *Basin Research* 14(3): 287–301.

Van Wagoner, J.C., Hoyal, D. C. J. D., N. L., Adair, T., Sun, R. T., Beaubouef, M., Deffenbaugh, P. A., Dunn, C., Huh, D., Li, 2003. Energy Dissipation and the Fundamental Shape of Siliciclastic Sedimentary Bodies. *AAPG Annual Convention, Salt Lake City, Utah*.

Investigation on the dominant discharge in DEZ River and the effect of DEZ Dam on it

M. Ali Pourhasan
Power & Water Institute of Technology, Tehran, Iran

Hamid R. Sadeghi
Amir Kabir University of Technology, Tehran, Iran

Parisa S. Mirja'fari
K.N.T University of Technology, Tehran, Iran

Samira Fartoos
Tarbiat Moddares University, Tehran, Iran

ABSTRACT: Dominant discharge is the one of most important parameters in rivers, the determination of which is of common difficulty in river engineering. This parameter depends on many subjects like the river nature, sediment supply & transport, plan and cross-section of the river and other morphologic and physiographic Specifications of river and its basin. Human affairs, made for exploiting the river, are a leading issue affecting the dominant discharge. DEZ is one of the greatest Iranian rivers with annual flow of 8400 MCM and average discharge of 258 m^3/sec. In this article we are going to determine the dominant discharge in four hydrometric station, that one of them located upstream of DEZ Dam. So with comparing and analysis of results in different stations we can obtain the effect of dam on dominant discharge.

1 INTRODUCTION

Rivers are one of the most important components of the nature, knowing which requires deep insight into their behaviors. For almost all of the projects related to river flow engineering and hydraulic structures, defining the design dominant discharge is of great importance. What we are going to explain in this paper is a brief about the defining of the dominant discharge and then, as a case study, paying attention to DEZ River in Iran and defining the so called factor in its different stations.

1.1 *DEZ River in brief*

Located on the western plains of Iran, DEZ River is one of the longest and most important Iranian rivers. Dez originate from Zagros Mountains and Oshtorankooh heights, and its mean annual flow is 8400 MCM and its annual discharge exceeds 258 m^3/s at Harmaleh station (in the flat plain of Khuzestan). A great dam (DEZ Dam) is located, in the north of Dezfoul, before the river reaches to the plain and there is also an old diversion dam (Dezful Dam) on the downstream of the great dam.

Finally DEZ River contributes the great Karun River at the place of Gheer ancient weir, 40 km far from the north of Ahwaz City then flows towards Persian Gulf. The length of this river is about 510 km from the upstream of DEZ Dam to its contribution with Karun River. Refer to Figure 1 the Dez watershed reaches 22755 km^2 including the cities of Boroojerd, Dorood, Azna, Aligoodarz, Andimeshk and Dezful (Al-e- Yasin, 2000).

2 THE STUDIED HYDROMETRIC STATIONS

There are several hydrometric stations on DEZ River four of which have been studied in this research. The so-called stations include Tale-Zang, Dezful, Harmaleh and Bamdej.

The locations of these four stations are seen in Figure 2 and their specifications are presented in Table1. As seen in the figure, Tale-Zang is the only station located on the upstream and the other ones are on the downstream of DEZ Dam. Among the three Dezful station is located just after the Dezful diversion dam.

Also presented in Table 2 are the hydrometric data acquisition periods of the studied stations. As easily

Copyright © 2006 Taylor & Francis Group plc, London, UK

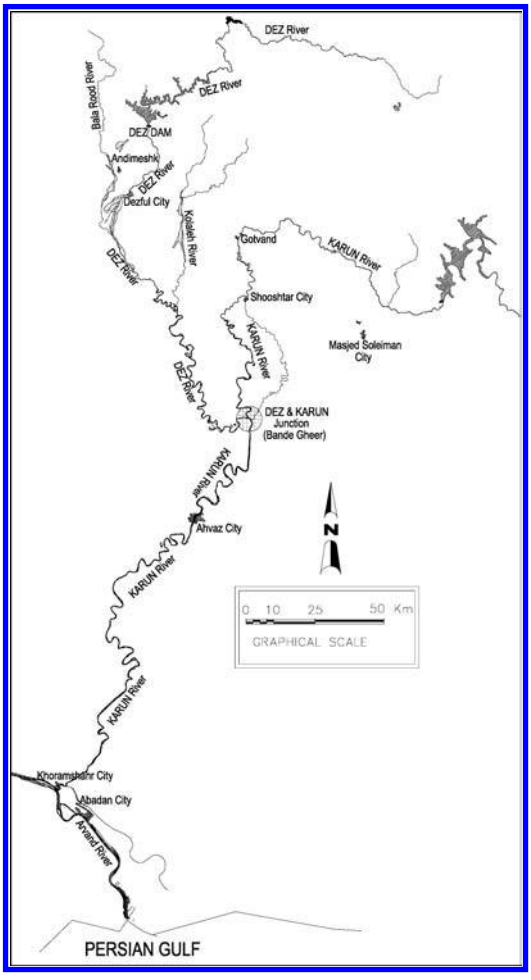


Figure 1. DEZ & KARUN Rivers in the west of Iran.

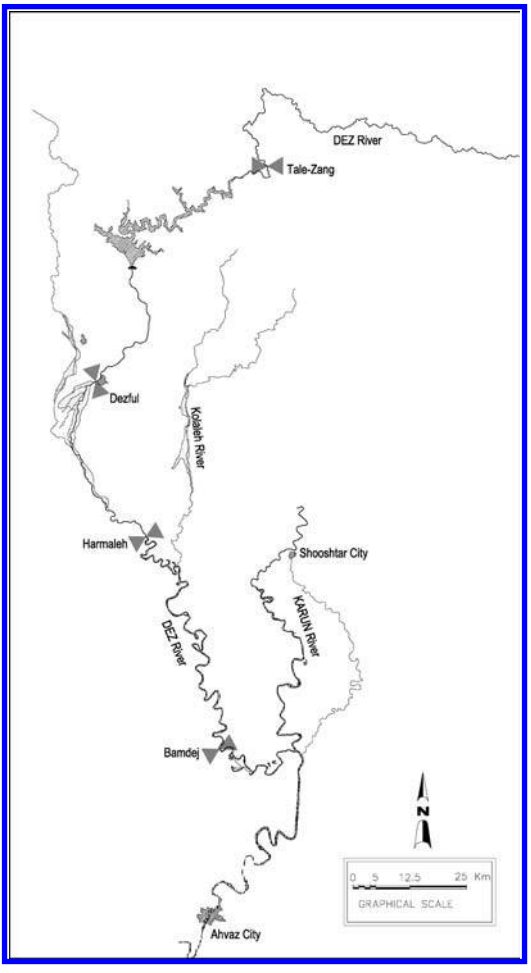


Figure 2. The location of studied hydrometric stations.

seen, we find longer records for Tale-Zang station which is located on the upstream of DEZ Dam. Other records belong to after 1962 which was the end of DEZ Dam construction date.

3 THE DOMINANT DISCHARGE AND HOW TO FIND IT

The rivers dimension and geometry are influenced by different floods, but the only floods that can affect the river physiologic specifications are the ones that exceed the threshold discharge. The main question is that when does the river reach to a dynamic equilibrium. By the means of physical models, Inglis (1941) concluded that rivers can reach the dynamic equilibrium in a specific range of floods and this specific flood range can not only vary from one river to another one, but also in different reaches of a single river. He also found in 1949, following a series of laboratory researches on incohesive bed, that the amount of dominant discharge is about 80% of Bank-full discharge.

Continuing his research, Inglis mentioned the importance of width, depth, longitudinal slope and bed and bank material grain size and related these parameters to flow and sediment discharge. In fact the dominant discharge is a flow that can cause the river equilibrium like a natural flood (Tabatabai & Jaydari, 2002)

Dominant discharge is one of the following three parameters and can be chosen through investigating the physical and morphological specifications of the river:

1. Mean Annual Flood Discharge (MAF)
2. Bank-full Discharge (BF)
3. Effective Discharge

Copyright © 2006 Taylor & Francis Group plc, London, UK

Table 1. The specifications of the studied hydrometric stations.

Station	Location coordinate		Distance from U/S Station	Distance from DEZ Dam	Elevation	Drainage area	Average flow
	Lat	Lon	km	km	m.a.s.l	km^2	m^3/sec
TaleZang	48° 46′	32° 49′	–	62 (U/S)	480	16213	270
Dezful	48° 24′	32° 24′	66	33 (D/S)	150	17813	259
Harmaleh	48° 33′	31° 57′	43	76 (D/S)	38	21800	258
Bamdej	48° 41′	31° 41′	50	136 (D/S)	20	22321	245

Table 2. Hydrometric and sediment data acquisition period of the studied stations.

Station	Hydrometry measured fata	Sediment measured data
Tale-Zang	1955–2004	1970–2004
Dezful	1950–2004	1970–2004
Harmaleh	1992–2004	1962–2004
Bamdej	1962–2004	1968–2004

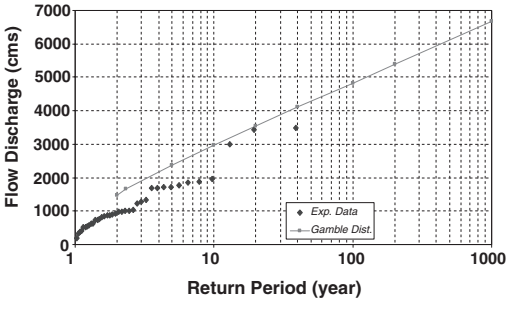


Figure 3. Hydrologic frequency analysis results of annual max series in Harmaleh station.

3.1 *Mean Annual Flood Discharge (MAF)*

The MAF discharge can be obtained by means of hydrologic frequency analysis (HFA) of annual max series (AMS). If the Gamble distribution is the dominant distribution of AMS and we know that the mean value of this distribution is when it's reduced value (y) is 0.5772, then the return period of MAF discharge will be 2.33 years. Obviously if we consider the dominant distribution to be normal or log-normal then the return period will become half year. In our research we found the Gamble distribution to be dominant. Figure 3 shows the HFA of annual Seri in the Harmaleh station. The amounts of MAF discharge of the four stations are presented in Table 4.

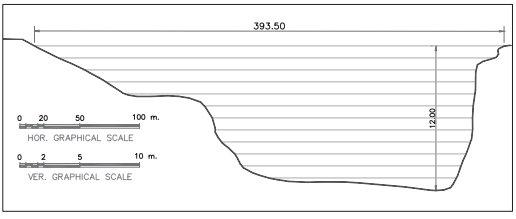


Figure 4. The section of DEZ River in Harmaleh station.

3.2 *The bank-full discharge*

The bank-full discharge is the maximum capacity of the river main channel and any discharge that exceeds this amount will enter the flood plain. It should be mentioned that in many cases, the boundary between the main channel and the flood plain can not be clearly distinguished.

The studies show that the meanders wave length is related to the bank-full discharge. The experimental regime equations also show that the river width has more correlation with instant flow than mean daily discharge (Tabatabai & Hey, 1998). Further more, many researchers have used the bank-full discharge for obtaining the experimental regime equations (Ackers & Charlton, 1970). Regarding these reasons we can imagine the bank-full discharge as one of the candidates for the dominant discharge. For finding the boundary between main channel and the flood plain, we have used the Wolman (1955) method in which we analyze the width to depth ratio versus depth diagram. The minimum point of this diagram shows the depth corresponding to the maximum channel capacity. Having obtained this point and by the usage of flow rating curve of the station, we can determine the bank-full discharge (Osterkamp & Hedman, 1982). Shown in Figures 4 and 5 are the section of DEZ River at Harmaleh station and the determining of the depth corresponding to the bank-full discharge. Using the Wolman method, the bank-full discharge of the four studied stations are determined and the results are shown in Table 4.

Copyright © 2006 Taylor & Francis Group plc, London, UK

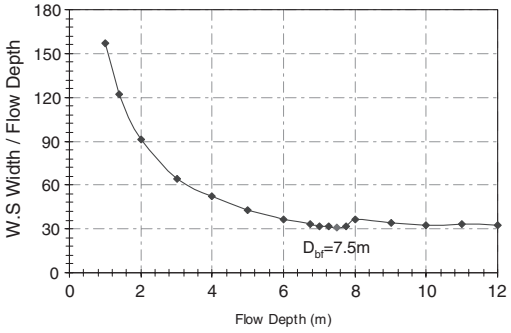


Figure 5. Determining of the depth corresponding to the bank-full discharge (Wolman method).

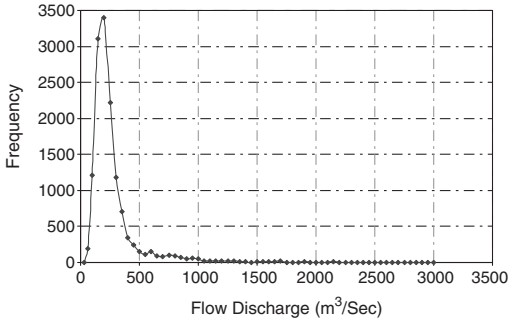


Figure 6. Daily discharge histogram of Harmaleh station.

3.3 *The effective discharge*

The effective discharge is the amount of flow that can supply the maximum rate of sediment during the data acquisition period. For finding the effective discharge we must obtain the daily discharge histogram. In Figure 6 the daily discharge histogram of Harmaleh station is shown.

Then by the means of sediment measured data, the sediment rating curve equation is determined. These equations are generally in the form of:

$$Q_s = a.Q_w^b \quad (1)$$

In this equation Q_s and Q_w are the suspended sediment discharge (ton/day) and the flow discharge (m^3/sec) respectively. Also a and b are constant coefficients. Shown in Figure 7 is the suspended sediment rating curve of Tale-Zang station. The suspended sediment rating curves of the four stations are presented in Table 3.

By using this equation, the sediment supply power of each discharge histogram class can be calculated.

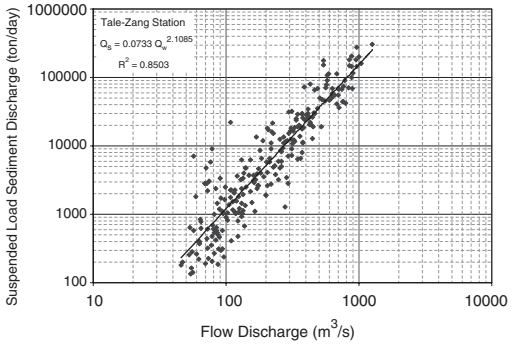


Figure 7. Tale-Zang station suspended sediment rating curve.

Table 3. Suspended sediment rating curve equations of studied stations.

Station name	Sediment rating-curve equation
Tale-Zang	$Q_s = 0.0733\ Q_w^{2.1085}$
Dezful	$Q_s = 1.089\ Q_w^{0.5738}$
Harmaleh	$Q_s = 0.9975\ Q_w^{1.5363}$
Bamdej	$Q_s = 0.2189\ Q_w^{1.8424}$

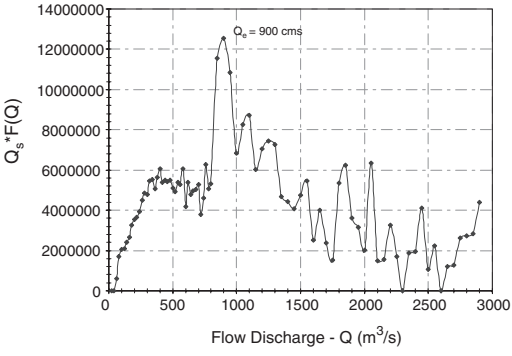


Figure 8. The total suspended sediment histogram and the effective discharge for Tale-Zang station.

By multiplying the frequency of each discharge histogram class in its corresponding sediment discharge ($F(Q)^*Q_s$) and drawing the results versus the discharge histogram classes, the total suspended sediment histogram will be obtained. The discharge corresponding to the maximum of recent histogram will be the effective discharge.

Figure 8 shows the total sediment discharge histogram of Tale-Zang station. Also shown in Table 4 are the results of effective discharge calculations.

Copyright © 2006 Taylor & Francis Group plc, London, UK

Table 4. Summary of the results.

Station	Mean annual flood discharge m^3/sec	Bank-full discharge m^3/sec	Effective discharge m^3/Sec	Comparison
Tale-Zang	2444	2720	900	$Q_e < Q_{MAF} < Q_{BF}$
Dezful	1575	1670	250	$Q_e < Q_{MAF} < Q_{BF}$
Harmaleh	1650	1640	220	$Q_e < Q_{bF} < Q_{MAF}$
Bamdej	1363	1320	200	$Q_e < Q_{bF} < Q_{MAF}$

4 DETERMINING THE DOMINANT DISCHARGE AND DEZ DAM EFFECTS

4.1 *Decision making on the dominant discharge*

A brief of the results are shown in table 4. As seen in this table, the amount of the effective discharge is much less than annual and the bank-full discharge in all four stations. The number of DEZ River floods shows that this river has reached a dynamic equilibrium under the effect of these floods. The little difference between the mean annual flood and the bank-full discharge also admits this idea.

Figure 9 is used for clarify the DEZ River dominant discharge in different stations. In this figure the sediment supply to total sediment discharge ratio for each daily discharge histogram classes is drawn due to the calculations of effective discharge. The vertical axis is cumulative and is shown in percents. This figure shows that the sediment supply to total sediment discharge ratio for Tale-Zang, Harmaleh and Bamdej is a little fraction of total suspended sediment supply for low classes (less than 250 m^3/sec – approximately effective discharge). At Dezful station which is located close to DEZ Dam, more than 80% of the sediment is supplied in less than 350 m^3/sec, while in Tale-Zang, Harmaleh and Bamdej; the same amount of sediments is supply with 1550, 1300 and 1050 m^3/sec of discharge respectively. So it can be concluded that in only a short distance from its down stream, the DEZ Dam has stabilized and the river is influenced by low level flows (close to effective discharge). In the downstream stations (Harmaleh and Bamdej) the river geometry is still highly affected by long return period floods. It can be said as a result that in the Dezful station, the effective discharge should be considered to be dominant but in the other stations, the dominant discharge is mean annual flood or the bank-full discharge.

4.2 *The effect of DEZ Dam on the river sediment supply mechanism*

As seen in figure 9, DEZ Dam has only reduced the dominant discharge in a short reach of its downstream and the rest of downstream; the geometry of the river is affected by the dam spilled flow (artificial floods) or the flows of other branches which pour in the river after the dam in the south of Dezful and Andimeshk. The important branches that pour in are Balaroud and kalaleh River and are shown in figure 1. The dominant discharge in the upstream of the DEZ Dam is almost four times than in the downstream and it's a proof to the dam's great influence on the river dominant discharge.

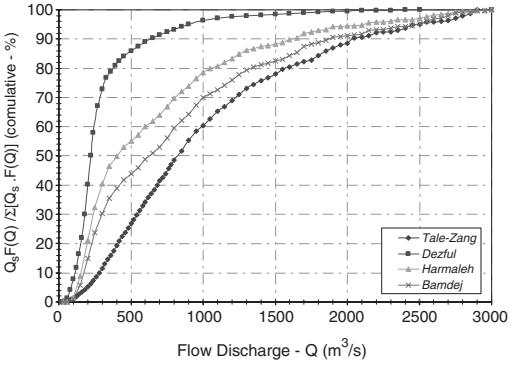


Figure 9. The sediment supply to total sediment discharge ratio for each daily discharge histogram classes.

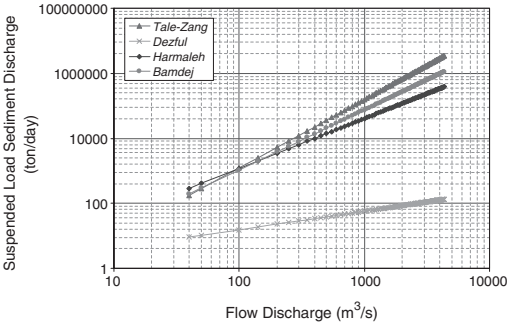


Figure 10. The effect of DEZ Dam on the sediment supply mechanism.

Copyright © 2006 Taylor & Francis Group plc, London, UK

Other point to be mentioned is the great influence of DEZ Dam on sediment trapping and supplying in the downstream reaches. A comparison is done between the sediment rating curve diagram of the stations and the results are shown in Figure 10. By comparing Tale-Zang and Dezful stations it can be said that more than 95 percent of the sediment is settled in DEZ Dam reservoir and astonishingly the same amount of sediment is supply along the rive until Bamdej station and this shows the high erosion potential of DEZ River in the downstream reach of dam.

REFERENCES

Al-e- Yasin, Ahmad, 2000. *Application of River Engineering in KARUN and DEZ River*, Publication No. 1379–33, Tehran – Iran. Ministry of Energy, IRCOLD.

Inglis, C. C., 1941. *Meandering and Their Bearing on River Training.* Institution of Civil Engineering, Maritime & Waterways, Paper No 7.

Inglis, C. C., 1949. *The Behavior and control of Rivers and Canals.* Central Waterpower Irrigation and Navigation Research Station, Poona Research Publication, India. No. 13, pp. 79–91.

Wolman, M. G., 1955. *The natural channel of Brandywine Creek, Pennsylvania.* USGS professional paper No. 271, pp. 56–65.

Tabatabai, M. R. M. & Jaydari, Sh., 2002. *Investigation on the dominant discharge; Case study: Kashkan River.* Proceeding of 6th International conference on River Engineering, Ahwaz, Iran, pp 275–284.

Tabatabai, M. R. M. & Hey, R., 1998. *A Review on Dominant Channel Formatting Discharge in Regime Rivers.* Proceeding of 3rd International Conference on Coasts, Ports and Marine Structures, Vol. 1, pp 185–206.

Ackers, P. & Charlton, F. G., 1970. *Meander geometry arising form varying flows.* Journal of Hydrology, 11, pp 230–252.

Osterkamp, W. R. & R., Hedman, E. R., 1982. *perennial stream flow characteristics related to channel geometry and sediment Missouri River Basin.* United State Geological survey, professional Paper No.1242.37.

Copyright © 2006 Taylor & Francis Group plc, London, UK

Large-scale turbulence and river morphology

M.S. Yalin
Department of Civil Engineering, Queen's University, Kingston, Ontario, Canada

ABSTRACT: The paper shows, on a theoretical as well as experimental basis, that dunes are the products of the vertical turbulent bursts, while all the periodic in the flow-direction bars, are the "imprints" of horizontal bursts. The paper also demonstrates, on the basis of congruence of plan-configurations and wavelengths, that the initiation of meandering and braiding is also due to the large-scale horizontal turbulence. One-row horizontal bursts originate meandering, multiple-row bursts, braiding.

1 INTRODUCTION; FUNDAMENTALS

i) Following Hussain (1983), the term "coherent structure" (CS) is used in this paper to designate the largest conglomeration of turbulent eddies which has a prevailing sense of rotation, the term burst, to designate the evolution of a CS during its life-span T. The bursts can be vertical (V) or horizontal (H). The CS's of the former rotate in the $(x;z)$-planes, those of the latter, in the $(x;y)$-planes (Figure 1).

A burst-forming CS originates (rolls-up) at a point O_i near the flow boundary – if V, near the bed; if H, near the bank. A rolled-up (at O_i) CS moves away from the flow boundary while it is transported by the flow downstream: in the process it is continually enlarging. The conceptual Figure 2a shows (in a stationary frame) a V-burst cycle of an open-channel flow; the cine-record in Figure 2b shows (in a convective frame) an instantaneous view of two consecutive CS's. The analogous is valid, *mutatis mutandi*, for an H-burst.

The present paper intends to demonstrate that the size and plan-configuration of the large-scale (periodic along x) alluvial forms generated by a flow, are in coincidence with those of the bursts of that flow – which would justify the longstanding view of many eminent researchers that the large-scale alluvial forms are due to the large-scale turbulence.

It is assumed throughout this text that the "experiment" commences, at $t = 0$, in a trapezoidal wide initial channel ($B/h > \approx 15$, say): the channel bed and banks are flat, the initial turbulent flow is uniform.

ii) Some pertinent conditions, which follow from recent research on turbulence, are summarized (in a highly idealized manner) below.

If O_i and O_{i+1} are the "birth-places" of two consecutive bursts of a burst-sequence (Figure 2a), then the distance $\overline{O_i O_{i+1}} = \lambda_V$ or λ_H is the burst-length, the life-span of a burst being $T_V = \lambda_V/u_m$ or $T_H = \lambda_H/u_m$ (for CS's are transported by the flow with the velocity

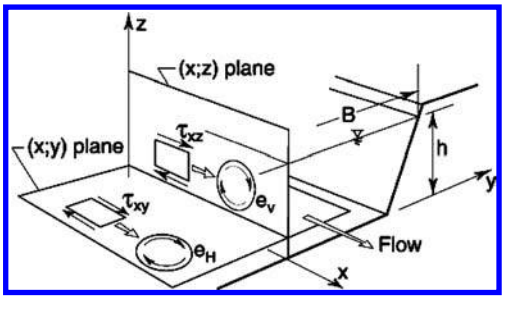


Figure 1. Vertical and horizontal planes of rotation of CS's.

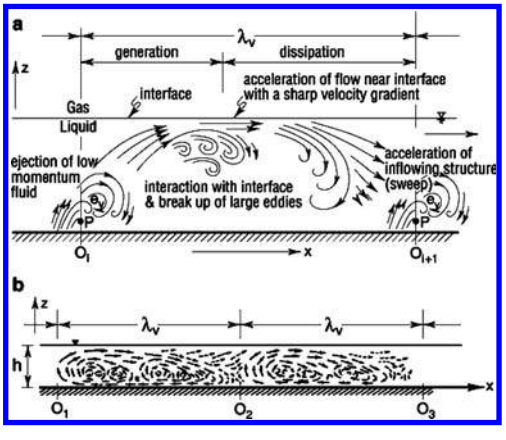


Figure 2. a) Conceptual representation of a V-burst cycle (after Rashidi & Banerjee 1988); b) Cine-record showing instantaneous view of two consecutive CS's (from Klaven 1966).

Copyright © 2006 Taylor & Francis Group plc, London, UK

$\approx u_m$). Let O_0 be the origin of the first burst of a burst-sequence. If O_0 is fixed (e.g. if O_0 is the location of the "local discontinuity" δ in the sense of Yalin (1992)), then the rest of O_i's must also be considered as fixed, for each of them is distant from O_0 by a integer number of the constant lengths λ_V and λ_H. But this means that the straight time-average initial flow is subjected to a perpetual action of bursts "fired" from the (ideally speaking) same location O_i. This action must inevitably render the flow to acquire a sequence of periodic (along x and t) non-uniformities, which, in turn, must cause, by virtue of the transport continuity equation, the emergence of the periodic (along x) bed- and/or bank-forms (j). These initial forms must grow with the passage of time (by coalescence) until they acquire their developed length Λ_j that is the same as the burst length:

$$\Lambda_j = \lambda_V \text{ or } \lambda_H . \tag{1}$$

iii) The burst lengths λ_V and λ_H are found to be independent of the inner variables $v_* k_s/\nu$ and k_s/h: they scale, respectively, with the outer variables h and B (see e.g. Nezu & Nakagawa 1993, Gad-el-Hak & Hussain 1986, Cantwell 1981). Indeed, as can be noted e.g. from Figures 3a and 3b, the data-points of λ_V/h cluster at the level $\approx$6, irrespective of what the value of $\mathrm{Re} = u_m h/\nu$ ($=c(h/k_s)(v_* k_s/\nu)$) might be. Thus

$$\frac{\lambda_V}{h} \approx 6 . \tag{2}$$

Similarly, the oscillograms recorded by Yokosi (1967) in Uji River (Japan), and those obtained by Dementiev (1962) in Syr-Darya River (former U.S.S.R.) indicate that the dimensionless λ_H, viz λ_H/B, can also be expressed as

$$\frac{\lambda_H}{B} \approx 6 . \tag{3}$$

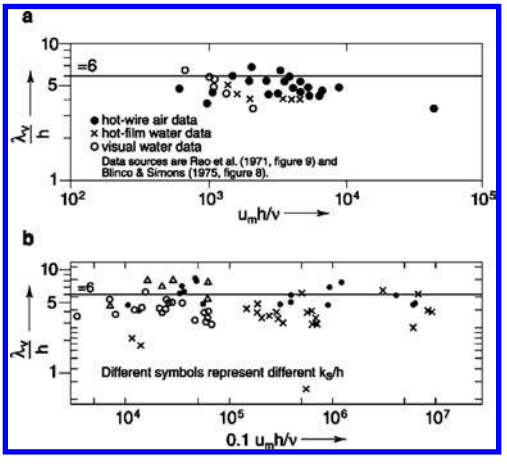


Figure 3. Plots of λ_V/h versus Reynolds number (after Jackson 1976).

However, as will be presently clarified, the relation (3) is valid only if the aspect ratio (B/h) of the flow does not exceed a certain upper limit.

2 DUNES AS BED-FORMS DUE TO V-TURBULENCE

i) If the uniform initial flow can be treated as two-dimensional, then the length Λ_d of the developed dunes produced by this flow can be expressed (Yalin 1992, 1977, Yalin & da Silva 2001) as

$$\frac{\Lambda_d}{h} = 6 \cdot \phi_d(X, Z). \tag{4}$$

From the experimental family of curves implying (4) (Figure 7.28 in Yalin 1977 or Figure 2.8 in Yalin & da Silva 2001), it is clear that if the initial flow is rough turbulent, i.e. if $v_* k_s/\nu \approx 2X > \approx 70$, then $\phi_d(X, Z) \to \approx 1$ and (4) becomes

$$\frac{\Lambda_d}{h} = 6 , \tag{5}$$

as to justify the validity of (1) and (2). The multiplier $\approx$6 in (4) and (5) was determined on a purely experimental basis. It is only recently that it has been demonstrated theoretically, by D. Zhou and C. Mendoza (2005), that $\approx$6 is, in fact, the rounded-up value of 2π. This gave the author the impetus to produce the following (more direct and precise) explanation for $\Lambda_d/h \approx 2\pi$.

ii) Figures 4 and 5 show the classical neutral stability curves which are due to W. Tollmien (1929) and S.F. Shen (1954), respectively. These curves indicate how the range of the wave numbers $\alpha\delta^* = 2\pi\delta^*/\lambda$,

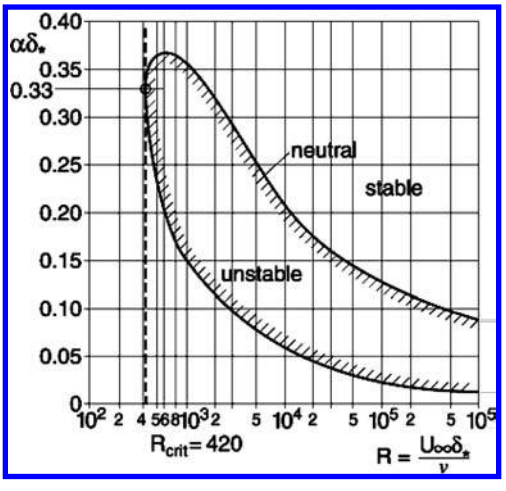


Figure 4. Neutral stability curve (after Tollmien 1929).

Copyright © 2006 Taylor & Francis Group plc, London, UK

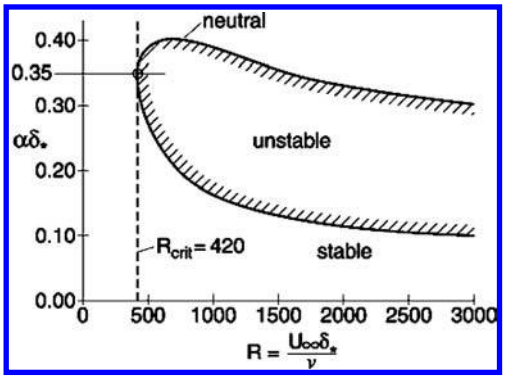


Figure 5. Neutral stability curve (after Shen 1954).

which are capable of converting a laminar boundary layer flow into a turbulent one, varies with the Reynolds number $R = U_\infty \delta^*/\nu$. No analogous curves were computed so far, to the author's knowledge, for open-channel flows. Hence, there is no alternative but to use the above mentioned curves by interpreting δ $(=3\delta^*)$ as h, U_∞ as u_m, and $R = U_\infty \delta^*/\nu$ as Re/3.

Observe from Figures 4 and 5 that only when $R = R_{cr} = 420$ $\mathrm{Re}_{cr} = 1260$) do the ranges of $\alpha\delta^*$, and thus of λ, become reduced into the single values $(\alpha\delta^*)_{cr}$ and λ_{cr}, say. Identifying the disturbance wavelength λ_{cr} at R_{cr} with the burst length at R_{cr} – or, to that matter, with the length (λ_V) of bursts at any Re (for λ_V is practically the same for any Re (Figures 3a and b)) we can write

$$\lambda_{cr} = \lambda_V \,. \tag{6}$$

Now, for $R_{cr} = 420$ (and $\lambda = \lambda_V$) the curve in Figure 4 gives

$$\alpha\delta^* = 2\pi \frac{h}{3\lambda_V} = 0.33 \tag{7a}$$

and thus

$$\frac{\lambda_V}{h} = 2\pi \cdot 1.01 \approx 6.346 \,, \tag{7b}$$

while the curve in Figure 5 gives

$$\alpha\delta^* = 2\pi \frac{h}{3\lambda_V} = 0.35 \tag{8a}$$

and thus

$$\frac{\lambda_V}{h} = 2\pi \cdot 0.95 \approx 5.969 \,, \tag{8b}$$

which indicate that ≈ 6 must indeed be the rounded-up value of 2π.

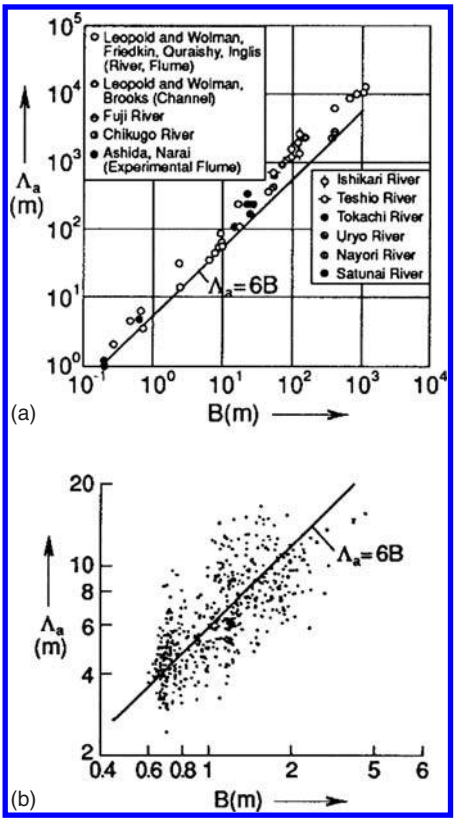


Figure 6. Plots of alternate bar length versus flow width a) from JSCE (1973); b) from Hayashi (1971).

3 BARS AS BED FORMS DUE TO H-TURBULENCE

i) The coherent structures forming the H-bursts of a wide open-channel flow have the shape of the horizontally positioned disks. These "disks" extend (along z) throughout the flow thickness h and they are *rubbing the bed*, with their lower-faces. Hence they are capable of producing "their" bed forms. Since $h \ll B$, the variation of their characteristics along z is negligible, and therefore they are usually referred to as two-dimensional coherent structures (2DCS) (Jirka & Uijttewaal 2004).

It will be assumed throughout the present Section that only the bed is mobile (the banks are "rigid").

ii) From a very large number of field and laboratory measurements (carried out mostly by the Japanese researchers) it follows that the length Λ_a of alternate bars (or of one-row bars) can be expressed as $\Lambda_a \approx 6B$ (Figure 6). Combining this expression with (3), we obtain

$$\Lambda_a \approx \lambda_H \approx 6B \,, \tag{9}$$

Copyright © 2006 Taylor & Francis Group plc, London, UK

which strongly suggests that alternate bars are the "imprints" of the H-bursts "fired" alternatively from the burst-points O_i and O'_i (Figure 7).

Consider the $(B/h;h/D)$-plan in Figure 8, from which the existence-regions of various alluvial forms caused by the H-turbulence can be observed. Note that with some few exceptions (due to experimental scatter), the alternate bar points A remain *below* the line $\mathcal{L}$. This is to be expected, for the disk-like 2DCS's of the H-bursts are rubbing the bed, and therefore their rotational kinetic energy is continually undermined by the bed friction:

1. If B/h is smaller than the ordinates $(B/h)_{1,2}$ of the line $\mathcal{L}$, then 2DCS's "are able" to grow indeed up to the size B, i.e. as to reach the opposite bank, and we have *one-row* horizontal bursts and thus *one-row* bars – each of the length $\approx 6B$ (Figure 7).
2. If, however, $B/h > (B/h)_{1,2}$, then 2DCS's emitted from one bank will not be able to grow as to reach the opposite bank (for they will be destroyed before that by friction). In this case the 2DCS's issued from both banks meet each other in the midst of the stream, and we have *2-row horizontal bursts* and thus *2-row bars*: the width of each row is $B/2$, the length of each bar being $\Lambda_2 \approx 6B/2 = 3B$ (Figure 9a).
3. Similarly, if $B/h > (B/h)_{2,3} > (B/h)_{1,2}$, where $(B/h)_{2,3}$ are the ordinates of the (so far unknown) line separating the zones of the 2- and 3-row bars, then the bursts issued from each bank will not be able to meet each other in the midst of the stream and we will have *3-row horizontal bursts* and thus *3-row bars*: the width of each row is $B/3$, the length of each bar being $\Lambda_3 \approx 6B/3 = 2B$ (Figure 9b).

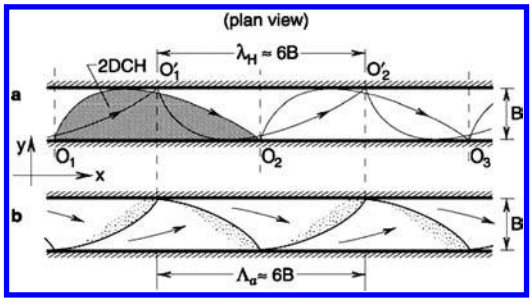


Figure 7. Occurrence of alternate bars as the "imprints" of H-bursts.

iii) Extrapolating the aforementioned, one may erroneously conclude that every open-channel flow, no matter how wide, can have an appropriate number n of burst-rows and thus n-row bars on its mobile bed: the width of each row is B/n, the length of each bar is $\approx(6B)/n$. This is not so, for if the stream is *very wide* it does not manifest itself as a "correlated totality" across its width B: the flow at the left bank "does not know" what the flow at its right bank is doing. Under

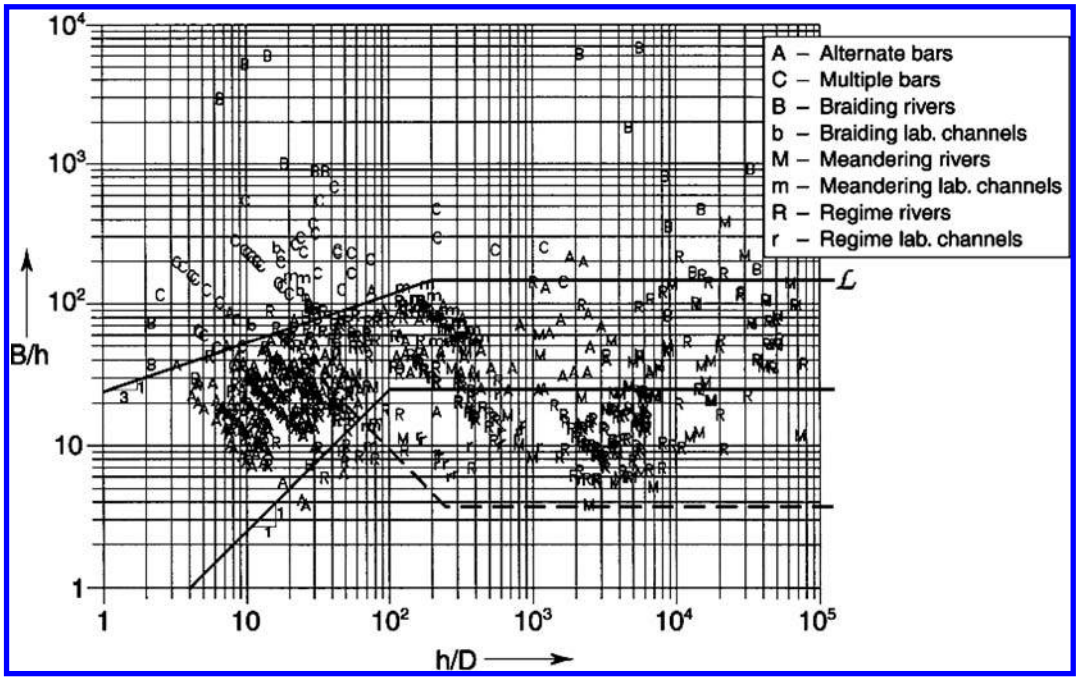


Figure 8. $(B/h;h/D)$-plan (from Yalin & da Silva 2001); existence regions of alluvial forms due to H-turbulence.

Copyright © 2006 Taylor & Francis Group plc, London, UK

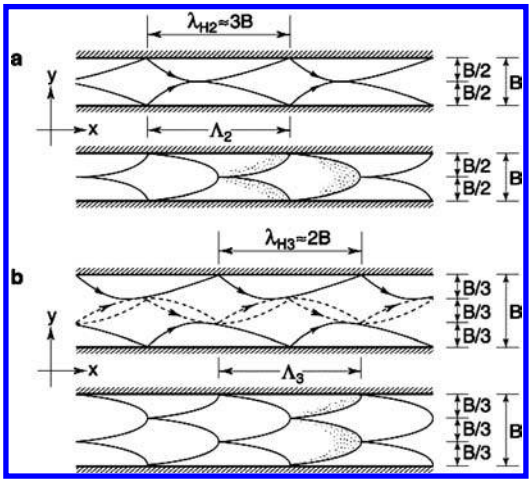


Figure 9. Multiple-row horizontal bursts and related bed forms. a) 2-row; b) 3-row.

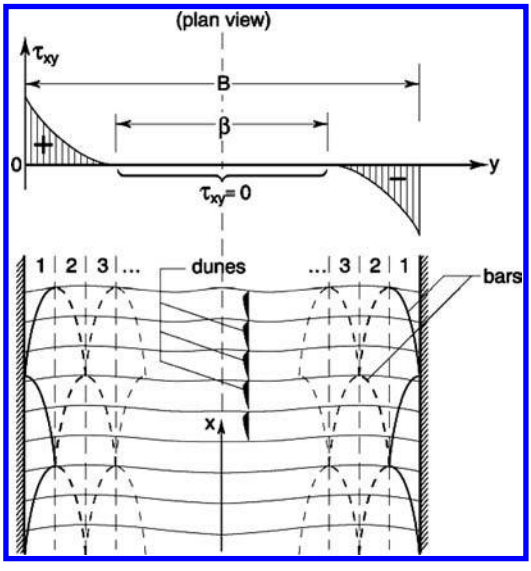


Figure 10. Conditions in very wide streams.

idealized conditions, such streams have $\tau_{xy} \equiv 0$, at any level z, throughout their central regions β (Figure 10). Moreover, it is only the "first" burst-rows adjacent to the banks which consist of the *factual* bursts issued by the banks (Figure 10): the remaining 2DCS-rows are *induced* rows. The farther from the bank, the weaker is the "induction-capacity", and the less prominent are the bar-rows. In reality only two or three rows of bars can be observed along the banks of a very wide stream. In the midst (β) of such streams only the vertical turbulence, and thus only dunes and ripples are present.

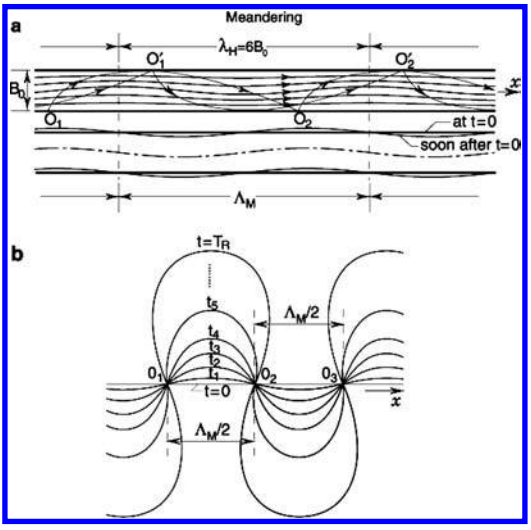


Figure 11. Initiation and subsequent development of meanders.

4 MEANDERING AND BRAIDING AS PLAN-FORMS DUE TO H-TURBULENCE

It will be assumed in this Section that both bed and banks are deformable.

i) Note from Figure 8 that the line $\mathcal{L}$ implying the upper limit for the formation of alternate bars (points A) can also be taken as the upper limit for the formation of meanders (points M and m). Indeed, with few exceptions, the points A, M and m are situated below the line $\mathcal{L}$. This is not surprising, for both alternate bars and meanders are caused by the same agent, viz one-row H-bursts. These bursts, as has already been mentioned, cause the flow to acquire the periodic (along x and t) non-uniformities, which in turn, deform correspondingly the bed and banks. Figure 11a shows the initiation of the periodic (curve-like) deformation of banks. The amplitude of the so initiated meandering grows in the flow plan so that (under ideal conditions) the meander wave length $\Lambda_M \approx \overline{O_i O_{i+2}}$ remains constant (Figure 11b).

But if Λ_a and Λ_M are thus the bed- and bank-"imprints" of the same $\lambda_H \approx 6B$, then we must have

$$\Lambda_M = \Lambda_a = \lambda_H \approx 6B\,, \tag{10}$$

which is the augmented (9). The plot in Figure 12 justifies the validity of $\Lambda_M \approx 6B$.

ii) From Figure 8 one also infers that the bulk of multiple bar points C and the points B and b of the braiding streams remain above the line $\mathcal{L}$ – which can thus be taken as their lower limit. Consider e.g. the 2-row bars generated by the two-row H-bursts in Figure 13. The bars cause the time-average flow to diverge

Copyright © 2006 Taylor & Francis Group plc, London, UK

and converge with the longitudinal period $\Lambda_2 \approx 3B$. Since the banks are erodible, B progressively increases (as in A-A), while h decreases. Consequently, the central bars emerge as "islands" and the single-channel stream turns into a braiding stream.

5 CONCLUDING REMARKS

1) Although the initiation of meandering and braiding is due to the large-scale horizontal turbulence (and so are their wavelengths and geometric nature), the subsequent growth of the "amplitude" (in lateral direction y) of these plan-forms is due to the regime-trend (see Yalin & da Silva 2001). Each stream, "if it is left alone", tends to increase its entropy (Second Law of Thermodynamics) and consequently it tends to reduce its flow velocity u_m (its kinetic energy). In the case of meandering, the reduction of u_m is achieved by the increment of flow length, i.e. by the reduction of S; in the case of braiding by the increment of the number n of branches.

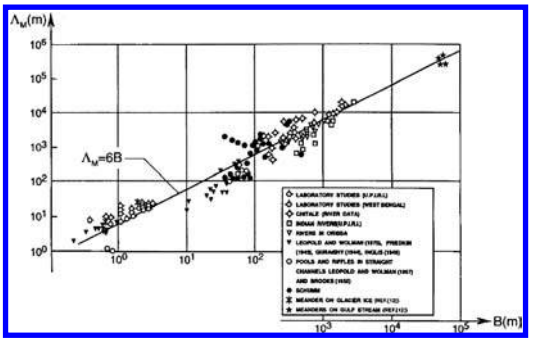


Figure 12. Plot of meander wavelength versus flow width (after Garde & Raju 1977).

The purpose of this remark is to remind the future researchers that the aforementioned growth of the amplitude is due to the Second Law, and it cannot be explained by turbulence.

2) No reference to ripples has been made in this paper. And although they may also be due to the turbulence, they are certainly not due to the turbulent bursts, for, unlike $\lambda_V \approx 2\pi h$, their length $\Lambda_r = D \cdot \varphi_r(v_* D/\nu)$ scales with the inner variables.

A special research directed towards the clarification of the origin of ripples would certainly be very desirable.

REFERENCES

Cantwell, B.J. 1981. Organised motion in turbulent flow. *Ann. Rev. Fluid Mech, Vol. 13*.

Dementiev, M.A. 1962. *Investigation of flow velocity fluctuations and their influences on the flow rate of mountainous rivers*. (In Russian) Tech. Report of the State Hydro-Geological Inst. (GGI), Vol. 98.

Gad-el-Hak, M., Hussain, A.K.M.F. 1986. Coherent structures in a turbulent boundary layer. *Phys. Fluids, Vol. 29, July*.

Garde, R.J., Raju, K.G.R. 1977. *Mechanics of sediment transportation and alluvial stream problems*. Wiley Eastern, New Dehli.

Hayashi, T. 1971. Study of the cause of meanders. *Trans. JSCE, Vol. 2, Part 2.*

Hussain, A.K.M.F. 1983. Coherent structures – reality and myth. *Phys. Fluids, Vol. 26, Oct.*

Jackson, R.G. 1976. Sedimentological and fluid-dynamics implications of the turbulence bursting phenomenon in geophysical flows. *J. Fluid Mech., Vol. 77*.

Jirka, G.H., Uijttewaal, W.S.J. 2004 (eds). *Shallow Flows: Selected Papers of the Int. Symposium on Shallow Flows, 16–18 June 2003, Delft, The Netherlands*. A.A. Balkema, The Netherlands.

JSCE Task Committee on the Bed Configuration and Hydraulic Resistance of Alluvial Streams 1973. The

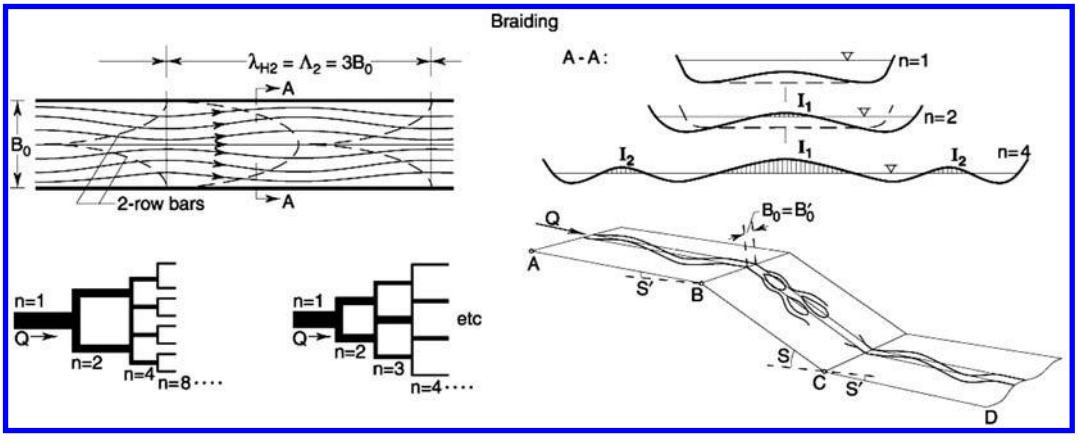


Figure 13. Initiation and subsequent development of braiding.

Copyright © 2006 Taylor & Francis Group plc, London, UK

bed configuration and roughness of alluvial streams. *(In Japanese) Proc. JSCE, No. 210, Feb.*
Klaven, A.B. 1966. *Investigation of structure of turbulent streams*. Tech. Report of the State Hydro-Geological Inst. (GGI), Vol. 136.
Nezu, I., Nakagawa, H. 1993. *Turbulence in open-channel flows*. IAHR Monograph, A.A. Balkema, Rotterdam, The Netherlands.
Rashidi, M., Banerjee, S. 1988. Turbulence structure in free-surface channel flows. *Phys. Fluids, Vol. 31, Sept*.
Shen, S.F. 1954. Calculated amplified oscillations in plane Poiseuille and Blasius flows. *JAS 21*.
Tollmien, W. 1929. *Über die Enrstehung der Turbulenz. 1. Mitteilung. Nachr*. Ges. Wiss. Göttingen, Math. Phys. Klasse; Engl. Transl. in NACA TM 609.
Yalin, M.S., da Silva, A.M.F. 2001. *Fluvial Processes*. IAHR Monograph, IAHR, Delft, The Netherlands.
Yalin, M.S. 1992. *River Mechanics*. Pergamon Press, Oxford.
Yalin, M.S. 1977. *Mechanics of sediment transport*. Pergamon Press, Oxford.
Yokosi, S. 1967. *The structure of river turbulence*. Bull. Disaster Prevention Res. Inst., Kyoto Univ., Vol. 17, Part 2, No. 121, Oct.
Zhou, D., Mendoza, C. 2005. Growth model for sand wavelets. *J. Hydraulic Engrg., 131(10)*.

LIST OF SYMBOLS

B	flow width
c	dimensionless (Chézy) friction factor ($=u_m/v_*$)
D	typical grain size
g	acceleration due to gravity
h	flow depth
k_s	granular skin roughness
R	Reynolds number of boundary layer flow ($=U_\infty \delta^*/\nu$)
Re	Reynolds number of open-channel flow ($=u_m h/\nu$)
Re_*	roughness Reynolds number ($=v_* k_s/\nu$)
t	time
T_V, T_H	duration of vertical and horizontal bursts, respectively
u_m	average velocity of open-channel flow
U_∞	maximum velocity of boundary-layer flow (at $z \geq \delta$)
v_*	shear velocity
x	direction of flow
y	direction laterally perpendicular to x
z	direction vertically perpendicular to x
α	wave-number ($=2\pi/\lambda$)
δ	boundary layer thickness
δ^*	displacement thickness ($=\delta/3$)
$\phi_d(X, Z)$	function of the grain size Reynolds number $X = v_* D/\nu$ and the relative flow depth $Z = h/D$
λ	disturbance length of boundary layer flow
λ_V, λ_H	length of vertical and horizontal bursts, respectively
Λ_j	length of the alluvial form j
ν	fluid kinematic viscosity.

Subscripts:
V marks a quantity related to vertical turbulence
H marks a quantity related to horizontal turbulence

Copyright © 2006 Taylor & Francis Group plc, London, UK

Analysis of water and sediment flows over an alternate bar in a gravel bed river

M. Jodeau & A. Paquier
Cemagref, Hydrology and Hydraulics Research Unit, 3 bis quai Chauveau, Lyon Cedex, FRANCE

ABSTRACT: Bars are present in most gravel bed rivers and exert a strong influence on flow and sediment processes. We focused on topographic changes of an alternate bar in a gravel bed river with high suspended sediment concentration. This phenomenon was studied on the river Arc (French Alps). The area of interest was approximately 600-meter long and quite straight with a gravel bar along the left side of the channel. Bar bed material was gravel and, due to high suspended sediment concentration in this river, fine sediments were found on the bed surface and included in the bed.

To understand how water and sediment flows organized around this alternate bar, a series of measurements was performed in the proximity of the gravel bar during a flushing operation from upstream dams. Topographic surveys helps to identify deposition and erosion areas. During the operation that was equivalent to a one year period return flood, suspended sediment concentration, flow depth and water velocity were monitored. Field measurements were compared with two-dimensional hydrodynamic modeling which permitted to identify zones and times of high/low velocities.

1 INTRODUCTION

Many studies emphasize the effect of bars in river flows. Gravel bars develop in natural rivers and in straight embanked channels with sufficient width to depth ratio (Schielen et al. 1993). In order to control the development of vegetation in the active channel of the river, managers have to deal with bars that constitute one of the areas in which fine sediment deposits are located. Gravel bars represent important instream habitat features at the aquatic terrestrial interface. Besides the establishment of vegetation depends on the evolution of the water level (amount of time the bar is flooded or dry) and if the bar gravels are subject to movement or not. In this case the river is the main factor determining vegetation development (Edwards et al. 1999) but the composition of the river bed is part of the factors determining the establishment of plants (Langlade and Décamp 1995).

Fine and coarse sediment interaction over alternate bars had been studied in laboratory flume (Diplas 1994), which shows an effect of the bed topography: fine sediments were deposited first and removed last from the downstream side of the bar and from the pool area. Experiments also highlighted bed movement is required to remove fine sediments from the subpavement.

1.1 *Objectives*

The objective of this work is to provide a relevant description of water and sediments flows in a reach with alternate bars using in situ measurements. The final purpose is to predict the temporal evolution of the bar in function of water flow, and to specify if vegetation may remain and develop on the bar.

In a first step, we focused on a single reach where there is a sequence of four alternate bars. We performed field surveys during a flushing operation and topographic campaigns. Next we compared field measurements to results from a two-dimensional hydrodynamic modeling. Finally, we expect to be able to extrapolate the results to estimate where and to what extent fine sediments will deposit along a river reach with alternate bars.

2 SITE DESCRIPTION

The field work was conducted on a reach of the Arc river. The total catchment area of the Arc River is 1957 km^2 located in the French Alps. It is a mountain stream which undergoes two different types of hydrological regimes which produce floods, one from west, which is oceanic perturbation, generates small

Copyright © 2006 Taylor & Francis Group plc, London, UK

floods, the other one is from south from Italy and generates the biggest floods. Otherwise the hydrological regime is nival, natural discharge is higher during snow melt. The ten year return period flood is approximately 300 m^3/s.

The river bed is made of gravel, the slope of the bed along the river varies from 1 to 6%. The flow is regulated by several dams and restitutions of clear water along the river, all for hydroelectricity. Only 5% of the river Arc remains with its natural flow and morphology. Tributaries throw lots of fine sediments in the river, the main ones are Arvan and Glandon streams which supply black Lias schists predominantly. Because of dams, the solid flow is stopped in reservoirs. The substantive part of fine sediment discharge occurs during snow-melt (May to July), but most of sediments trapped in the reservoir during the year are flushed downstream when the reservoirs are drained. The three reservoirs on the middle part of the river are flushed every year, otherwise they would be full of fine sediments. Flushing flows are completed as counterpart to mechanical dam cleaning.

The study area was selected because it offers a succession of alternate bars which are reachable and wadable. In the following this place will be named site A. The study site is a 600 m long reach located 33 km upstream of the confluence with the Isére River, and downstream from the city of Saint Jean-de-Maurienne; its altitude is 450 m. Figure 1 shows the location of the reach of investigation. It is a very straight reach with 1 m boulder embankments, the width between dikes is approximately 50 m (Figure 2). The water discharge of this reach is controlled by upstream dams, the discharge is almost constant around 5–15 m^3/s and varies with the upstream water releases. It is the downstream part of a series of alternate gravel bars, we focused on the last downstream bar. This bar is located 200 m upstream from a bridge. The mean slope of this reach is near 0.6%. The bed is made of gravel (mean diameter 10 cm) and fine sediments (sand and silt).

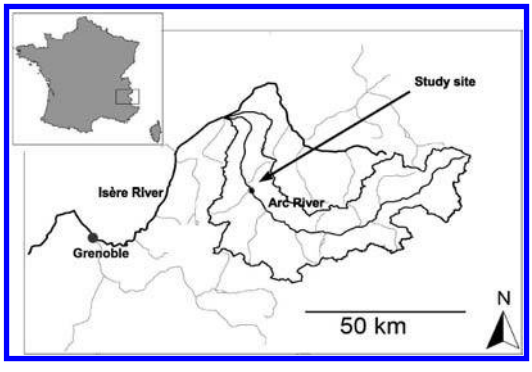


Figure 1. Location of the study reach.

This series of alternate bars fits with the existence criteria established by M. Jaeggi (Jaeggi 1984). This criteria defined the minimum slope for bar formation:

$$S_c = exp(1.07 Z_B^{0.15} + M) * 1/(12.9 Z_B) \quad (1)$$

In which $Z_B = B/d_m$, S is the slope, B the channel width, d_m mean grain size of the bed material and M a factor increasing from 0.34 to 0.7 with increasing sediment gradation.

In this case $B \approx 60$ m, $d_m \approx 0.1$ m which lead to S_c from 0.29% to 0.42% depending on M. In this part of the river Arc, the mean slope is near 0.6% which is higher than the limit for bar-forming range.

Since year 2000, no major flood has occurred and as it is complicated to anticipate floods on the Arc River we focused on the major hydraulic event on the Arc River, that's to say the dam release performed by EDF (Électricité De France) during the beginning of the summer. The last dam release occurred on June, 16th 2005. Three reservoirs were flushed. Table 1 gives the relevant features of these reservoirs. The flushing event began with a warning release, i.e. a clear water release of 10 m^3 from the flap gates, then discharge was increased gradually to reach the maximum discharge in 6 hours, the peak discharge was maintained during 2 hours and eventually the water discharge was decreased gradually. Figure 6 gives the theoretical hydrograph followed by engineers at the dams. Maximum peak discharge was equivalent to a one year period return flood.



Figure 2. Downstream view of the study reach, water flows from the back to the front of the photograph.

Table 1. Reservoirs on the Arc River flushed on 06-16-2005.

Reservoir	Live storage (m^3)	Distance upstream the study from area (km)
Freney	165 000	36.5
Pont des Chèvres	1 200 000	30.25
St Martin la Porte	125 000	18.55

Copyright © 2006 Taylor & Francis Group plc, London, UK

The dam release was significant on two accounts: first it produced an artificial flood, and the water flow from the reservoir had a very high fine sediment concentration.

3 FIELD MEASUREMENTS

In order to evaluate the different flow parameters, we performed very simple measurements. The field work was divided into three phases: topographic data were first collected the day before the event; hydrometric measurements were performed during the flushing flow; after the flushing day a series of topographic data and field observations were made.

3.1 *Morphologic surveys*

Concrete reinforcing bars of 12 mm diameter were used to observe erosion/sedimentation patterns at ten specific places on the alternate bar. The day before and the day after the event, brief topographic surveys were performed in order to identify more precisely erosion/sedimentation areas. Figure 3 is the topographic map after the flushing flow.

3.2 *Flow measurements*

Very basic measurements were performed. The water level was followed on a staff gauge located on the central bridge pier 200 m downstream, meanwhile it was measured and recorded with the help of a pressure transducer (DIVER, Van Essen, The Netherlands) near the right bank in the middle of the reach.

An assessment of surface flow velocities was obtain following floating objects (logs, plastic bottles…). Two series of measurements were performed at 10:00 and 12:00. We assessed the mean surface velocities (v_{surf}), $v_{surf}^{10:00} = 3.7 \pm 0.3$ m/s and $v_{surf}^{12:00} = 4.8 \pm 0.5$ m/s.

3.3 *Sediment and grain size measurements*

Samples of water were taken with a bucket from the bridge. It gave an assessment of fine sediment concentration in the middle of the channel and in the surface of the flow. Suspended sediment concentrations were measured in the laboratory using vacuum filtration on 0.45 µm filters and drying. The graphic on Figure 4 gives the evolution of suspended sediment concentration (ssc) during the flushing event. Note that the concentration reaches 15 g/l, that's why we could not use our turbidimeter on the field, samples needed a dilution. We had also accessed to the measurements made by IRAP (consulting engineer) for EDF downstream every dam.

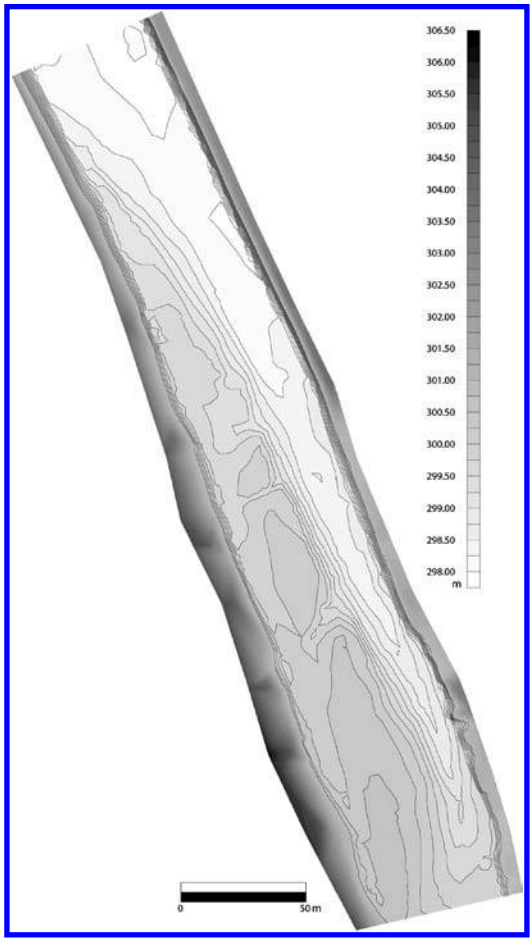


Figure 3. Topography of the study reach as determined by field survey and regular grid interpolation, water flows from the bottom to the top of the picture.

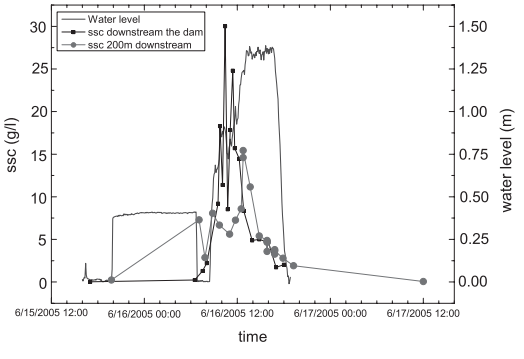


Figure 4. Suspended sediment concentration (ssc) measured just downstream from site A (disks), ssc measured 18 km upstream from site A, downstream the last dam (small squares) and water level measured by the DIVER.

Copyright © 2006 Taylor & Francis Group plc, London, UK

Turbidity was measured in the lab after dilution, turbidity is linked with ssc but the relation is not straightforward.

We made a grain size analysis on three samples to gain insight on the features of suspended sediments. The bulk of fine sediments had a diameter smaller than 50 μm and the composition was quite constant along the flushing event.

4 MODELING TOOLS

4.1 *Model*

Water Flow in the reach was modeled with the two-dimensional model Rubar20. The code Rubar20 used a finite volume scheme that is explicit, Godunov-type and second order accurate (Paquier 1995). It solves the 2-dimensional shallow water equations which are written below:

$$\frac{\partial h}{\partial t} + \frac{\partial hu}{\partial x} + \frac{\partial hv}{\partial y} = 0 \tag{2}$$

$$\frac{\partial hu}{\partial t} + \frac{\partial (hu^2 + gh^2/2)}{\partial x} + \frac{\partial huv}{\partial y} = - gh\frac{\partial Z}{\partial x} - g\frac{u\sqrt{u^2+v^2}}{K_s^2 h^{1/3}} + K\left(\frac{\partial}{\partial x}\left(h\frac{\partial u}{\partial x}\right) + \frac{\partial}{\partial y}\left(h\frac{\partial u}{\partial y}\right)\right) \tag{3}$$

$$\frac{\partial hv}{\partial t} + \frac{\partial huv}{\partial x} + \frac{\partial (hv^2 + gh^2/2)}{\partial y} = - gh\frac{\partial Z}{\partial y} - g\frac{v\sqrt{u^2+v^2}}{K_s^2 h^{1/3}} + K\left(\frac{\partial}{\partial x}\left(h\frac{\partial v}{\partial x}\right) + \frac{\partial}{\partial y}\left(h\frac{\partial v}{\partial y}\right)\right) \tag{4}$$

In which u and v are velocities along respectively x and y axis, h water depth, Z bottom level, g gravity acceleration, K_s Manning Strickler coefficient, K the viscosity coefficient.

4.2 *Mesh, topography and friction coefficient*

The mesh may be constituted of quadrangles or triangles which have 0 or 1 common edge. To build the mesh we used linear interpolation in the stream direction and finer cells where the topography was complex. The reach is approximately 600 m long and 50 m wide, the mesh (named *final mesh*, Figure 5) has 1124 cells, in average the dimensions of cells are 5 m × 5 m, with smaller cells where topography had to be more precise.

The Manning Strickler coefficient of each cell, K_s, came from a survey of the surface grain size composition of the bed. At each topographic point we assessed the main grain size class, then measurements were converted in Manning Strickler coefficients using the formula (from Modeleur, INRS-ete):

$$K_s = \begin{cases} 19.6 & \text{if } d_{50} > 0.7 \text{ m} \\ 34.9(log(\frac{1}{d_{50}}))^{0.31} + 0.0017 & \text{else} \end{cases}$$

where d_{50} is the weighted average of diameters of each of the p grain size class: $d_{50} = \sum_{i=1}^{p} w_i d_i$, and d_i is estimated owing to the bound diameters of grain size class i: $d_i = \sqrt{b_i b_{i+1}}$.

Then K_s was linearly interpolated on a regular mesh made of triangles of 2 m side and interpolated again on the final mesh.

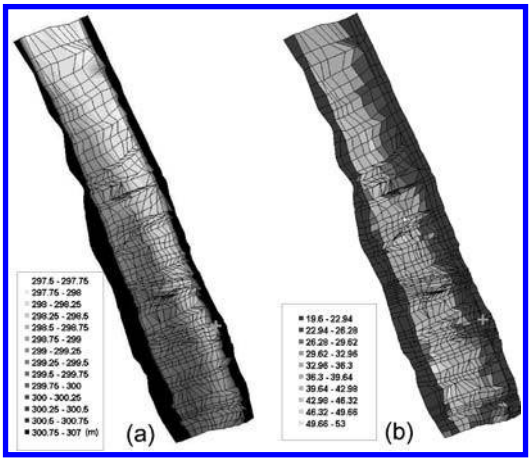


Figure 5. Mesh used for the numerical simulation (*final mesh*). (a) Topography and (b) Friction coefficient map. The cross mark locates the DIVER.

4.3 *Boundary conditions*

One-dimensional model Rubar3 was used to convey the hydrograph from the downstream dam to the reach of interest 18 km downstream. This model has been developed by Cemagref, it solves one-dimensional St Venant equations (Paquier 1995). Cross sections are based on previous topographic campaigns (2000–2001) and the model was calibrated and validated on two major floods (September 1993 and October 2000). Figure 6 shows the hydrographs at the dam, at the upstream boundary of the reach and the simplified hydrograph used as upstream boundary condition.

Water levels at upstream and downstream limits were fitted according to water level measurements made in the middle of the reach (near the right bank, DIVER measurements) and at the bridge. Water level at the downstream boundary has a limited impact on the flow features upstream.

Some simulations were also run at permanent discharges fitting with some times of the hydrograph.

Copyright © 2006 Taylor & Francis Group plc, London, UK

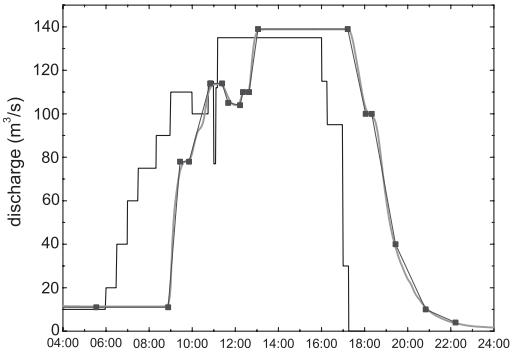


Figure 6. Hydrograph at the dam (black thin line). Hydrograph convey by 1D dimensional model to the upstream boundary of the reach (bold gray line) and the simplified hydrograph used as upstream boundary condition (line and squares).

5 RESULTS

5.1 *Sediment transport, erosion and deposit patterns*

The topography of the bar changed during the flushing flow. Our visual observations showed a widening of the main channel, i.e. where flow concentrates along the right bank, deposition of small gravels ($d_{50} \approx 1$ cm) on the upper left part of the bar, and several cross-bar channels appeared due to high erosion processes. Owing to the fixed marks (concrete reinforcing bars) erosion was observed near the left dike (up to 40 cm of gravel erosion) and downstream the bar. At a particular point in the middle of the bar we noted 20 cm of gravel deposit. We tried to use our topographic survey to specify these few observations. Topographic data of the bar before and after the flushing event were interpolated on the same grid. Unfortunately our topographic survey did not contain enough points to enable an accurate comparison between both states. Nevertheless it confirms fixed marks measurements.

We were also interested in the evolution of the suspended sediment concentration (Figure 4). The ssc evolution at site A is almost similar to ssc evolution downstream the nearest dam. Shape of both graphs are comparable except for a time lag of 2:20 between peak concentrations and higher values of ssc at site A in the rising phase of the flushing event. The time lag is close to the time lag of the maximum peak discharge estimated by the 1D simulation. In addition, at site A, the peak of ssc was reached approximatively at the same time as the maximum discharge. It means that at this point of the river there was no time lag between ssc peak and discharge peak.

According to common sens, the ssc peak (15.43 g/l) 18 km downstream from the dam at site A was lower than the ssc peak (30.02 g/l) at the dam. There may be some deposits in between, but suspended sediment concentrations remained high compared with the concentration before the event (less than 1 g/l).

Higher values of ssc in the rising phase of the flushing event may be due to some contribution from the Arvan tributary. This stream is a significant source of fine sediments. The first high values of ssc may be due to re-erosion of previous deposits in elevated parts of the river channel as well.

Before the flushing event fine sediments were mainly found along the left bank where water flow was stiller, on the bar tail and in the wake of vegetation. Our observations following the event showed a quasi-uniform deposit of fine sediment on the whole surface of the bar, some large (several cm) and localized deposits along the right side of the bank at the boundary with the flow, no deposit along the left bank, large deposits in the wake of vegetation and in the wake of prominent gravels and deposits on the bar tail. These observations fit with the typology of fine sediment deposits developed in (Wood and Armitage 1999). They classified deposits into five classes:

- Marginal deposits associated with reduced flow velocities at the channel margin (most stable and permanent deposits).
- Depression deposits where topography created a small hollow(relatively unstable).
- Macrophyte deposits associated with the presence of plants.
- Obstruction deposits in the lee of larger substrate clasts or debris and extensive deposits located downstream of macrophyte beds
- Fine surficial laminae deposits associated with baseflow conditions.

5.2 *Simulation Results*

We compared the results from the 2D calculation with the measurements from the DIVER (Figure 7). A spatial and a time lag can be observed. The time lag may come from the routing of hydrograph by the one-dimensional model; the friction coefficient for the 1D model will be adjusted to take into account this time lag. There are three possible reasons to explain the spatial lag between hydrographs. First, the discharge hydrograph, and particularly the peak discharge, could have been underestimated because the rating curve at the gates of the dam was not calibrated when there is a transition between subcritical and supercritical flows. That would explain an under-evaluation of the peak discharge value. Second the friction bed coefficient (K_s) in the main channel can be too low although it was fitted with grain size of bed sediments; to test this hypothesis further calculations will be done with higher Manning Strickler coefficient for the part of the bed where the flow concentrates (near the right bank). Third there may be some minor errors due to

Copyright © 2006 Taylor & Francis Group plc, London, UK

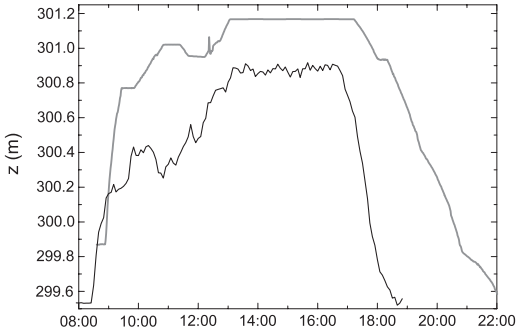


Figure 7. Water level measurements from the DIVER (thin black line) and water level from 2D simulation in cell 324, topographic location of the DIVER (bold gray line).

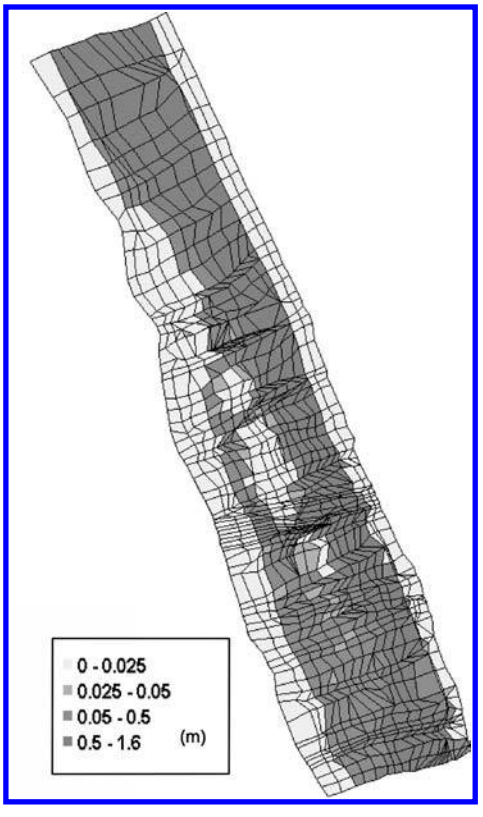


Figure 8. Water depth at 9:02 ($Q \approx 19 m^3/s$), water pattern fits with observations.

interpolation of the topography leading to reduced widths of the channel, which consequently leads to an over-evaluation of the water level.

Moreover the 2D calculation well reproduced water patterns observed during the flushing event. Figure 8 is the water depth at 9:02, it highlights the effect of

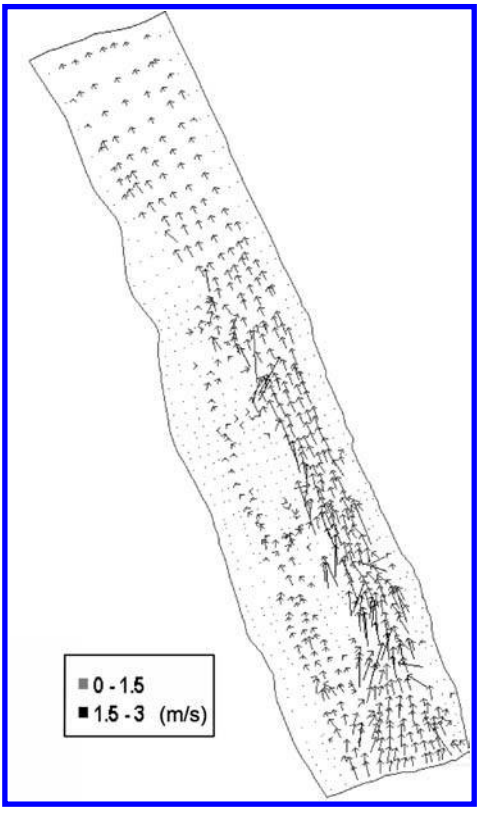


Figure 9. Velocity field at 8:59, during the rising phase, $Q \approx 19 m^3/s$.

cross-bar channels linking the upper left side of the bar with the main channel.

Velocity fields from the two-dimensional simulation were analyzed. At peak discharge, velocities in the river are lower than 6 m/s, but the mean velocity is approximately 3 m/s (Figure 10); maximum simulated water depth at this time is 2.5 m, all the channel is underwater. It fits with the observations: at 12:00 we estimated the mean surface velocities around 4.8 m/s (paragraph 3.2). It must be kept in mind that these velocities represented an assessment of the mean surface velocity of floating objects; they may be characteristic of water surface velocity in the main channel, but it is quite difficult to extrapolate from these values the mean velocity of the flow. These high velocities and high depths involve high shear stress, which explains why we observed gravel movement (see previous paragraph 5.1 for gravel erosion/deposition patterns). During the falling phase of the flushing event (Figure 9), we observed low velocities on the left side of the bar; it explains that the grain size of gravels we found in this part of the study area was lower.

Copyright © 2006 Taylor & Francis Group plc, London, UK

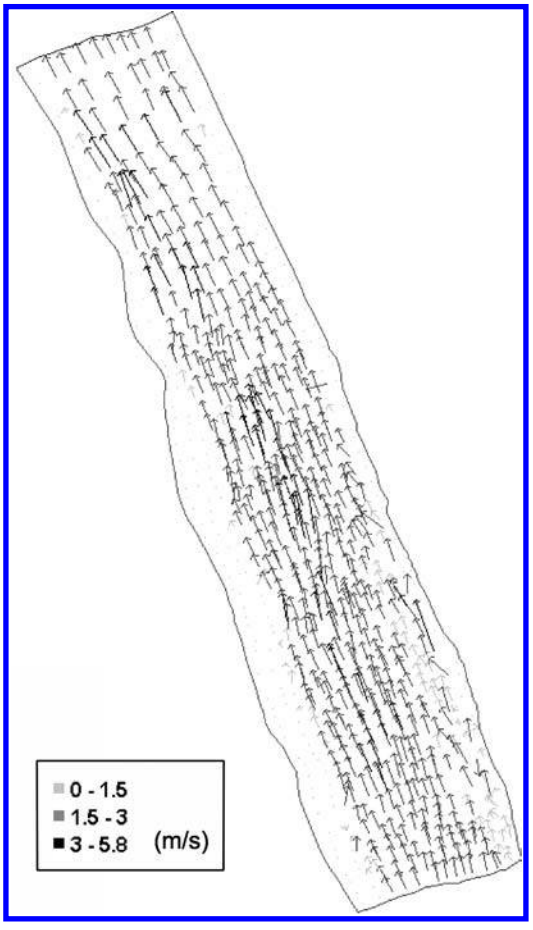


Figure 10. Velocity field at 13:54, at the peak discharge, $Q \approx = 139\,m^3/s$. Note that, for the sake of clarity, velocity field is not scaled the same way as previous figure.

6 CONCLUSION

This paper is essentially based on in situ measurements, visual observations made during a flushing event and comparisons with 2D simulation. Our field measurements provided evidence that the gravel bar we focused on underwent topographic and grain size change. Analysis of the topographic measurements revealed gravel erosion and deposition patterns along the bar. Along the right bank, there was erosion while deposition occurred along the left margin of the bar. More precisely, deposition patches of fine sediments were observed at several places along the bar. This first field campaign rise our awareness on the point that it requires more accurate measurements. Our field survey will be improved to quantify additional parameters, several discharges will be measured from the bridge, topographic surveys will contain more points.

Two-dimensional hydrodynamic modeling permits to reproduce the flushing event in the studied reach. We identify times and zones of high/low velocities. Results from the two-dimensional calculations seem to match with observations of gravel and fine sediment erosion and deposition areas. To improve our understanding of sediment processes, we consider using 2D hydrodynamical modeling with sediment transport modeling.

This presentation is one step toward a more comprehensive study of the phenomena that occur in the vicinity of an alternate bar during flows with high fine sediment concentration. In rivers, bars constitute a place where fine sediments could be stocked, consequently they may be an important component of the river suspended sediment budget. The intent of this study will be to project our observations and conclusions at the bar scale to the whole river.

ACKNOWLEDGMENTS

Authors would like to thank to EDF GEH Maurienne for providing the discharge data and flushing event reports, Cemagref technicians (G. Dramais and F. Thollet) for the field work and J. Lelouvetel for having set up the one-dimensional model of the Arc River.

REFERENCES

Diplas, P. (1994). Modelling of fine and coarse sediment interaction over alternate bars. *Journal of Hydrology 159*, 335–351.

Edwards, P., Kollmann, J., Gurnell, A., Petts, G., Tockner, K. and Ward, J. (1999). A conceptual model of vegetation dynamics on gravel bars of a large alpine river. *Wetlands Ecology and Management 7*, 141–153.

Jaeggi, M. (1984). Formation and effects of alternate bars. *Journal of Hydraulic Engineering 110*, 142–156.

Langlade, L.-R. and Décamp, O. (1995). Accumulation de limon et colonisation végétale d'un banc de galets. *Comptes rendus de lÁcadémie des Sciences Paris, Science de la vie 318*, 1073–1082.

Paquier, A. (1995). Modélisation et simulation de la propagation de lónde de rupture de barrage. Ph. D. thesis, Université Jean Monnet, St Etienne, France.

Schielen, R., Doelman, A. and De Swart, H. (1993). On the nonlinear dynamics of free bars in straight channels. *Journal of Fluid Mechanics 252*, 325–356.

Wood, P. and Armitage, P. (1999). Sediment deposition in a small lowland stream – management implications. *rrrm* 15, 199–210.

Copyright © 2006 Taylor & Francis Group plc, London, UK

ECOMSED – Three dimensional modeling in rivers

M.A. Mekonnen & B. Dargahi
KTH, Royal Institute of Technology, Stockholm, Sweden

ABSTRACT: The 3-D hydrodynamic and sediment transport model ECOMSED was adapted to simulate flow and sediment transport in rivers. A bed load transport model was included in the code. Improvements in treatment of river roughness parameterization, bed form effects, and automatic update of flow depth due to bed evolution were also made. The model was applied to 1-km long reach of the River Klarälven, located in the county of Värmland, Sweden. The model successfully predicted the general flow patterns and sediment transport characteristics of the river reach.

1 INTRODUCTION

Recent research works on 3-D river flow modelling include: Weerakoon and Tamai (1989), Olsen and Stokseth (1995), Weiming *et al*. (1997), Sinha *et al*. (1998), Lane *et al*. (1999), Bradbrook *et al*. (2000), and Chau and Jiang (2001). Olsen and Stokseth (1995) carried out a 3-D simulation of an 80-m long reach of the river Sokna in Norway. The model successfully simulated the flow features and its results were in good agreement with observed data. Sinha *et al*. (1998) did a comprehensive numerical study of the flow through a 4-km reach of the Columbia River. They succeeded in modelling rapidly varying bed topography and the presence of multiple islands. The results agreed well with experiments and field measurements. In a recent study, Bradbrook *et al*. (2000) used Large Eddy Simulation (LES) to model the flow in a natural river channel confluence. The model simulated periodic flow features in river confluences and agreed well with experimental data.

Some recent applications on use of 3-D sediment transport models are those by Gessler *et al.* (1999), Holly and Spasojevic (1999), Fang (2000), Rodi (2000), Weiming *et al*. (2000), Nicholas (2001), and Dargahi (2004). Gessler *et al*. (1999) applied the U.S. Army Corps Engineering code CH3D-SED to the Deep Draft Navigation project on the lower Mississippi River. The code predicted the sediment deposition in the river with an accuracy of less than 13% in comparison with the observations. Holly and Spasojevic (1999) applied and verified the CH3D-SED code to study water and sediment diversion at the Old River Control complex on the lower Mississippi river. Dargahi (2004) predicted secondary flows and the general flow and sediment transport patterns in a river that agreed well with field measurements. A brief review of the major developments in 3-D modeling and the limitations is given by Lane *et al*. (2002).

In this study ECOMSED, 3-D hydrodynamic and sediment transport model by Blumberg and Mellor (1987), was improved and adapted for modeling flow and sediment transport in rivers. The model was originally developed for large water bodies such as lakes and oceans. ECOMSED solves the RANS equations along with a second order turbulence model. A bed load transport model was included in the code. Improvements were also made in the treatment of river roughness parameterization, bed form effects, and automatic update of flow depth due to bed evolution. The improved model was applied to 1-km long reach of the River Klarälven, located in the county of Värmland, Sweden. The water surface and the flow division in the channels were made to agree with field data by specifying a spatially variable bed roughness depending on the local grain size distribution of the river reach and the local flow. The erosion and deposition patterns agreed with observed trends in the river reach.

2 MODIFICATIONS AND IMPROVEMENTS

2.1 *Roughness parameterization*

ECOMSED uses the logarithmic law of the wall as the bottom velocity boundary condition. The bed roughness for the whole computational domain is represented by a constant roughness parameter z_0, distance from the bed where the velocity assumes a zero value. However, in rivers bed roughness varies both spatially and temporally. Model calibration and model

Copyright © 2006 Taylor & Francis Group plc, London, UK

validation of a river reach was found difficult with a constant z_0 value. The specification of the parameter z_0 was modified in the ECOMSED code to vary spatially depending on the local bed roughness and local flow condition. The local bottom roughness is represented by the local equivalent sand roughness (k_s) that is composed of grain and bed form roughness. The grain roughness was taken as αD_{90} where D_{90} is particle diameter for 90% finer of bed material; and the coefficient α was varied between the recommended values of 3 to 5 during calibration of the water surface profile. Field studies showed that the bed of the river reach is composed of three dimensional ripples. The equivalent sand roughness due to ripples was calculated according to Grant and Madsen (1982)

$$k_s = 27.7\frac{\Delta^2}{\lambda} \quad (1)$$

In which Δ is bed form height; and λ is bed form length.

2.2 *Shear stress partitioning*

The other modification made was shear stress partitioning to extract the effective part of the stress that contributes to sediment transport. The effective shear velocity (u'_*) for the lower flow regime (ripples and dunes) was calculated by using the flow resistance relationship by Engelund and Hansen (Yang 1996).

$$u_*' = \left(0.06g(s-1)D_{50} + 0.4\frac{u_*^4}{g(s-1)D_{50}}\right)^{0.5} \quad (2)$$

In which D_{50} is particle diameter for 50% finer of bed material; g is the gravitational acceleration; and s is specific density. The transport stage parameter, T which is used for the computation of suspended and bed loads was calculated using the effective shear velocity (van Rijn 1984a and van Rijn 1984b)

$$T = \left(u_*' / u_{*cr}\right)^2 - 1 \quad (3)$$

In which u_{*cr} is the critical bed shear velocity which was calculated using the Shields curve for initiation of motion. The critical shear velocity was also corrected for the bottom and side slopes according to Chien (1999).

2.3 *Bed load transport and bed evolution*

ECOMSED considers only suspended sediment transport as the contribution of bed load movement in large water bodies such as lakes and oceans is insignificant. However, the bed load contribution can be considerable in the case of rivers. Thus a realistic modeling of sediment transport would require the implementation of the bed load transport. This was done by including the bed load in the sediment mass-balance equation for the bed evolution.

$$(1-p)\frac{\partial z_b}{\partial t} + E - D + \frac{\partial \alpha_{b\xi_1} q_b}{\partial \xi_1} + \frac{\partial \alpha_{b\xi_2} q_b}{\partial \xi_2} = 0 \quad (4)$$

In which E – D is the sediment flux at the water sediment interface which is calculated using the van Rijn (1984a) procedure; q_b is the actual bed load transport; p is the porosity of the bed material; $\alpha_{b\xi 1}$ and $\alpha_{b\xi 2}$ are the direction cosines in the orthogonal curvilinear coordinates ξ_1 and ξ_2, respectively. Rodi's (2000) formulation was used for the bed deformation.

$$(1-p)\frac{\partial z_b}{\partial t} = \frac{1}{L_s}(q_b - q_{b*}) \quad (5)$$

In which $q_b{}^*$ is the equilibrium bed load transport; and L_s is the non-equilibrium adaptation length for bed load transport. According to van Rijn (1984a)

$$q_{b*} = 0.053[(s-1)g]^{0.5} D_{50}^{1.5} \frac{T^{2.1}}{D_*^{0.3}} \quad (6)$$

$$L_s = 3D_{50}D_*^{0.6}T^{0.9} \quad (7)$$

$$D_* = \left[\frac{(s-1)g}{\upsilon^2}\right]^{1/3} D_{50} \quad (8)$$

In which D_* is the dimensionless grain size; and υ is the fluid dynamic viscosity. First order upwind scheme discretization of the equation produced by the combination of equations (4) and (5) resulted in a tri-diagonal matrix which was solved using the modified strongly implicit procedure of Stone (1968). The bed evolution was evaluated using the leap-frog method using equation (5).

3 MODEL APPLICATION

The improved model was applied to the River Klarälven. The River Klarälven enters Sweden in the north of the county of Värmland. Its course in Värmland is south down to the river mouth on lake Vänern at the city of Karlstad where it bifurcates into an east and west channels. A one kilometre long reach of the river was modelled that extends 0.5 km upstream of the bifurcation (Figure 1). To insure uniform inlet boundary conditions, the upper limit of the reach was placed in a straight river section. The river topography was measured in April 2004 at 11312 points through the

Copyright © 2006 Taylor & Francis Group plc, London, UK

river reach. The mean measurement resolution range was 2 m–6 m.

The flow discharges at the inlet and the two outlets defined by east and west channels were measured. Point velocity measurements were also taken at the inlet at 10 m spanwise intervals and at 0.5 m intervals in the vertical direction (all field measurements were taken by the local authorities of the Karlstad city municipality). The wake law was used both to determine the bed shear velocities and to specify the velocity profiles. The observed water levels at the outlet of the east and west channels were specified. Equilibrium bed load and zero suspended sediment concentration were used at the inlet boundary as sediment load data was not available.

3.1 *Grid generation*

The numerical model was built using the interpolated bottom topography (Figure 1). The horizontal orthogonal curvilinear grid was generated by CCHE2D mesh generator using the Poisson scheme with smoothness and orthogonality of 91 and 95%, respectively. The average grid spacing in the computational domain was about 6.0 m. The grid spacing around the bifurcation and around the bends was made finer with an average spacing of 2.0 m.

3.2 *Model calibration*

The model was calibrated for a discharge of 285 m^3/s using the measured water surface profiles and discharge division between the two river channels. The percentage of the discharge into west and east channels were 42% and 58%, respectively. Model calibration was done for a grid number of $126 \times 48 \times 9$ by spatially varying the roughness to satisfy both the water division and the water surface profile. The normalized error in the computed flow division was 0.8% (West channel) and 0.6% (east channel) while the normalized error in the water surface varied from 0.14% to 3%.

3.3 *Grid independence*

A grid dependency study was carried out to minimize numerical errors due to coarse discretization. In the horizontal direction the number of grids was constrained by the available resolution of the bottom topography. The deviation of results from the corresponding observed values is summarized in Table 1 for different number of layers. The normalized errors for a resolution of $126 \times 48 \times 9$ were found to be acceptable.

Table 1. The change in the normalized errors as the number of vertical layers is increased.

Number of layers	Normalized error in water surface [%]	Normalized error in flow [%]		Normalized error in bed shear stress
		West	East	
5	0.20–5.0	0.60	0.40	
7	0.17–4.0	0.66	0.48	>= 10%
9	0.23–5.0	0.58	0.42	>= 3%

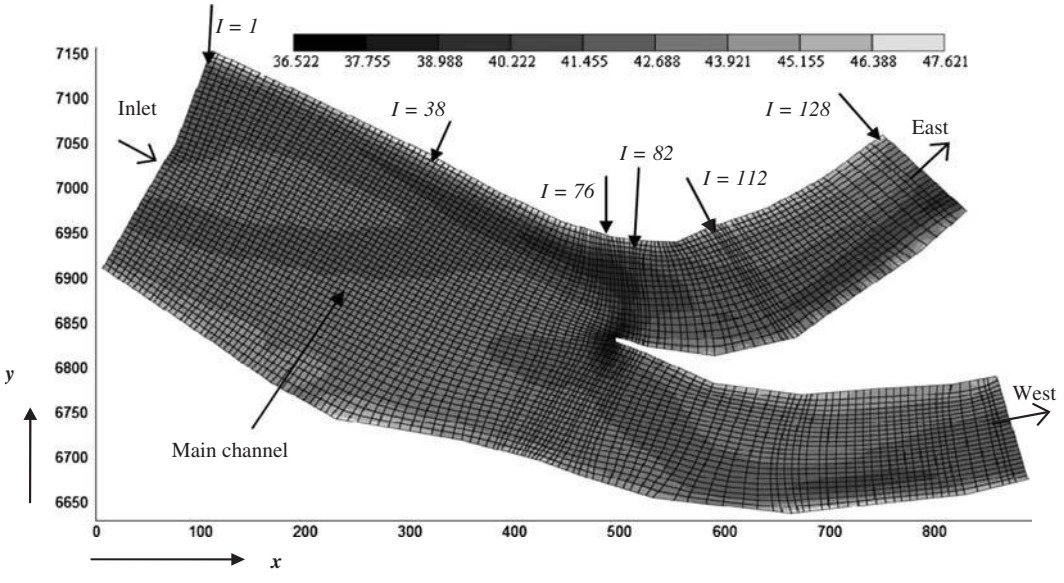


Figure 1. Model boundary, river bed elevation and horizontal orthogonal curvilinear grids (x, y and legend in meters).

Copyright © 2006 Taylor & Francis Group plc, London, UK

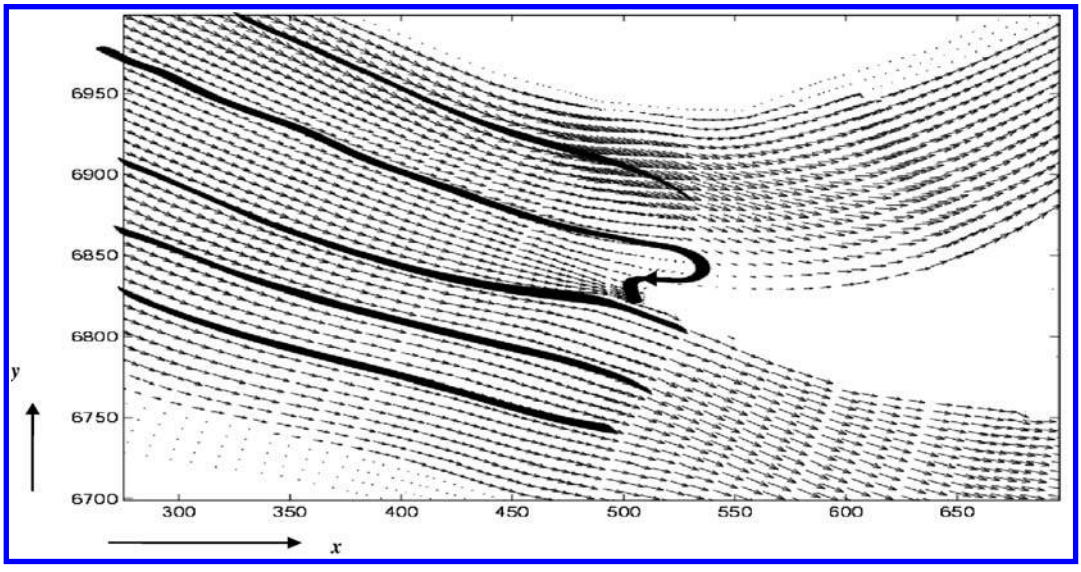


Figure 2. Simulated velocity vectors and observed tracer path lines (solid lines) used for model validation (x, y in meters).

3.4 *Validation*

A comprehensive validation of the model would require extensive field data on water surface profiles, velocity profiles, secondary flow structures and flow circulation regions. For this study limited data were available at two different discharge values of 285 m^3/s and 136 m^3/s. The model was validated with the field data for 136 m^3/s by using the roughness distribution obtained during the calibration analysis. In comparison with field data, the normalized error in the observed water surface profile varied from 0.11% to 1.33%. The normalized error in the flow division was 2.44% for the west channel and 1.56% for the east channel. Regarding the flow field, stream lines and the local flow circulation region upstream of the river bifurcation agreed with the field observations (Figure 2).

4 RESULTS AND DISCUSSION

Flow field: The flow field in the river was successfully simulated by the improved model that included the water surface profiles, velocities, secondary flows, and bed shear stresses. Figure 3 shows the contour lines of the water surface profiles. In the bifurcation region the local increase in water surface elevation is shown. The model also predicted the transverse water-surface slope at the river bend in agreement with the physics of the helicoidal secondary flows. A general flow diversion from the main channel to the east channel was detected that explains the larger portion of the total flow entering the east channel.

Secondary flows: The general patterns of the secondary flows in the vertical planes are given in Figures 4(a-d) where the velocity vectors, velocity contours and the interpolated secondary flows are shown. The spiral motions (helical cells) are shown by circles with rotation direction indicated by arrow. The number of cells increases as the river bifurcation region is approached. In comparison with the other regions of the flow, the bifurcation sections had a greater spatial variation implying an increase in secondary flow cells. The general patterns agree with Dargahi's (2004) finding, although he reports a higher number of cells especially in the river bends. The difference between the present results and his results can be explained partly by a higher grid resolution, and partly by his use of different turbulence model.

Sediment transport: Data for discharge hydrographs were not available and the sediment transport simulation was made for an observed steady flow of 285 m^3/s. The bed shear stresses were computed both as total and as effective stresses. Figures 5 and 6 show the two cases, respectively. The distributions of shear stresses are similar for both cases although the magnitudes of total shear stresses are about four times higher than the effective shear stresses. As the bed shear stress is the primary agent for sediment transport, the difference in magnitude is important. The results emphasize the need of shear stress partitioning for realistic sediment transport computations. In comparison with west channel, the shear stresses are higher in the east channel as well as in the deep region of upstream channel. The lower shear stress regions correspond to the area with little sediment transport activities.

Copyright © 2006 Taylor & Francis Group plc, London, UK

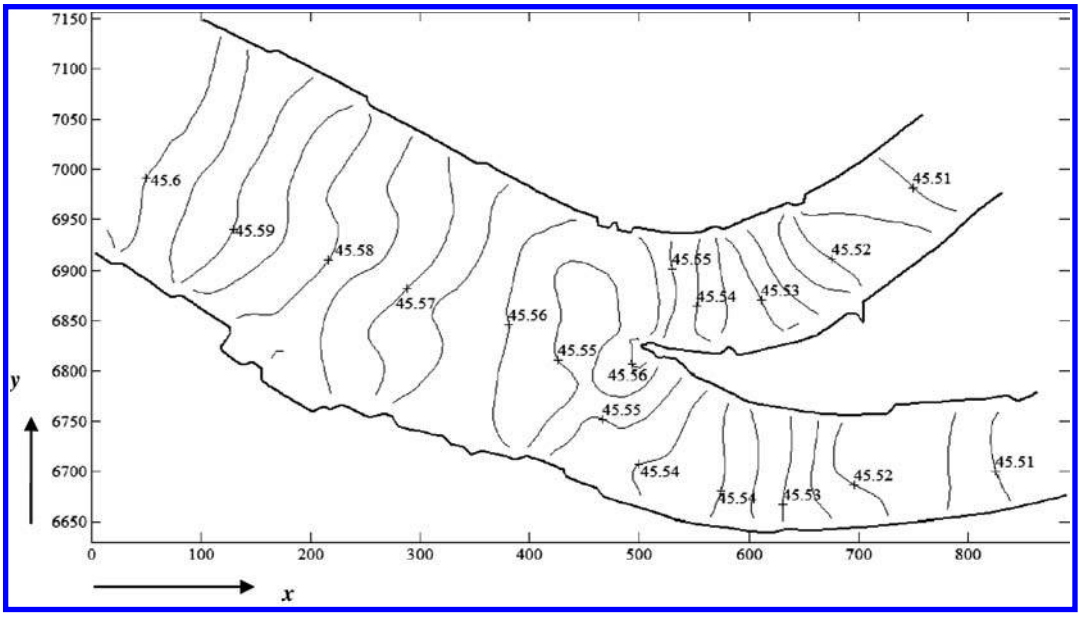


Figure 3. Simulated water surface profile showing a local increase at the bifurcation due to stagnation, and super elevations at the bends (all units in meters).

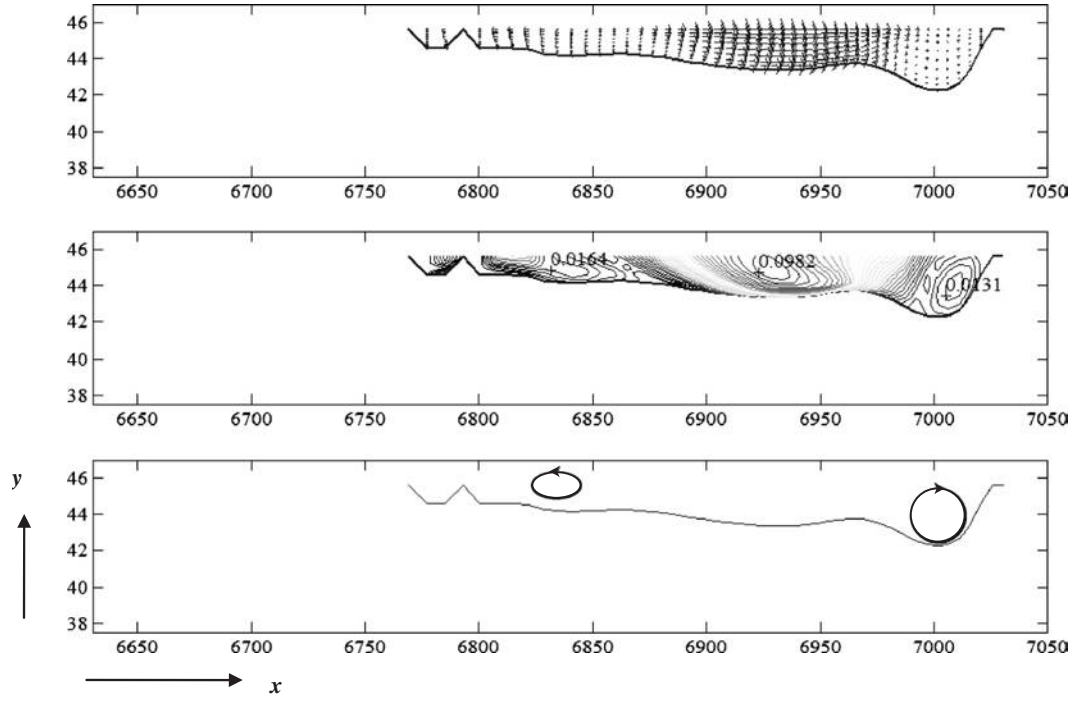


Figure 4a. Velocity vectors, velocity contours (m/s) and interpolated vortices in a vertical plane at section 38 (x, y in meters).

Copyright © 2006 Taylor & Francis Group plc, London, UK

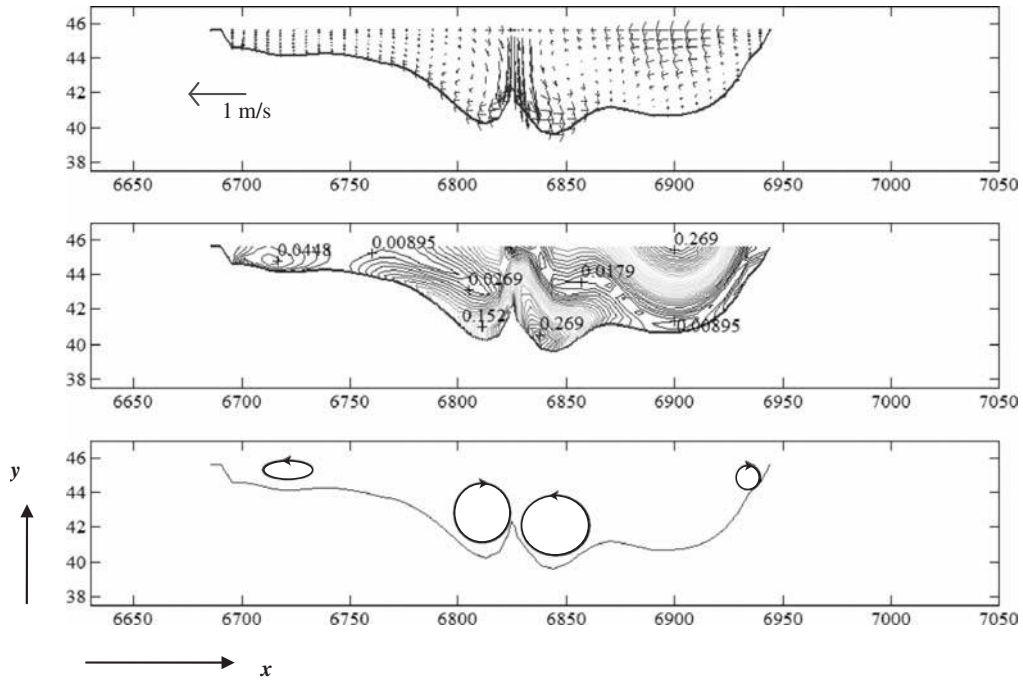


Figure 4b. Velocity vectors, velocity contours (m/s) and interpolated vortices in a vertical plane at section 76 (x, y in meters).

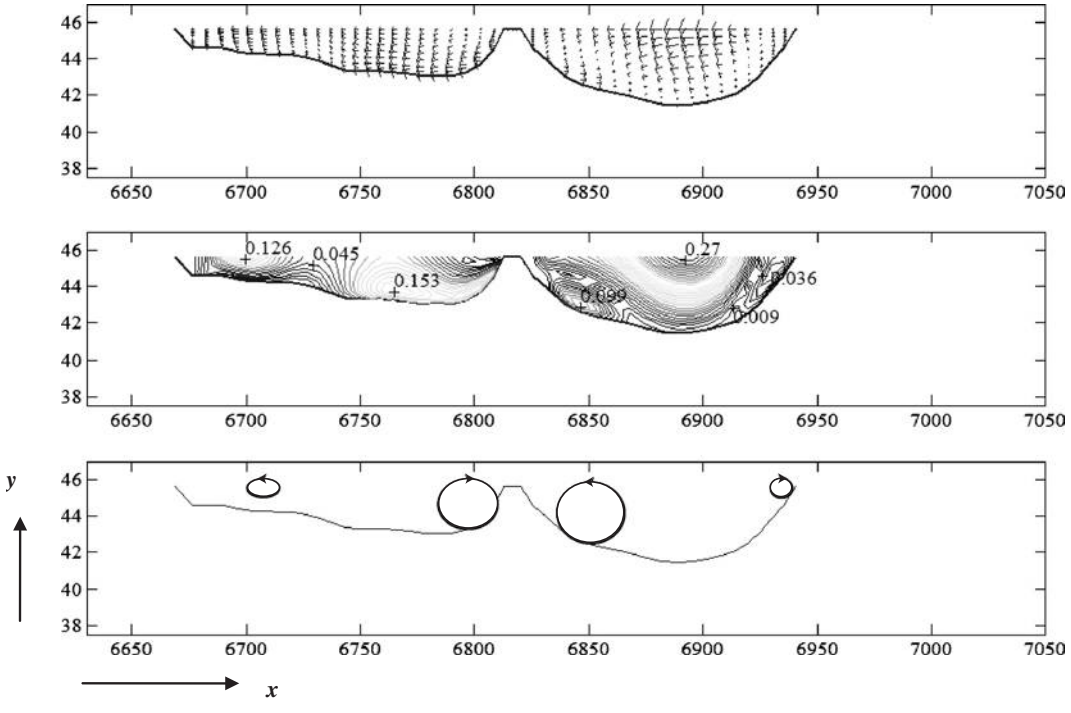


Figure 4c. Velocity vectors, velocity contours (m/s) and interpolated vortices in a vertical plane at section 82 (x, y in meters).

Copyright © 2006 Taylor & Francis Group plc, London, UK

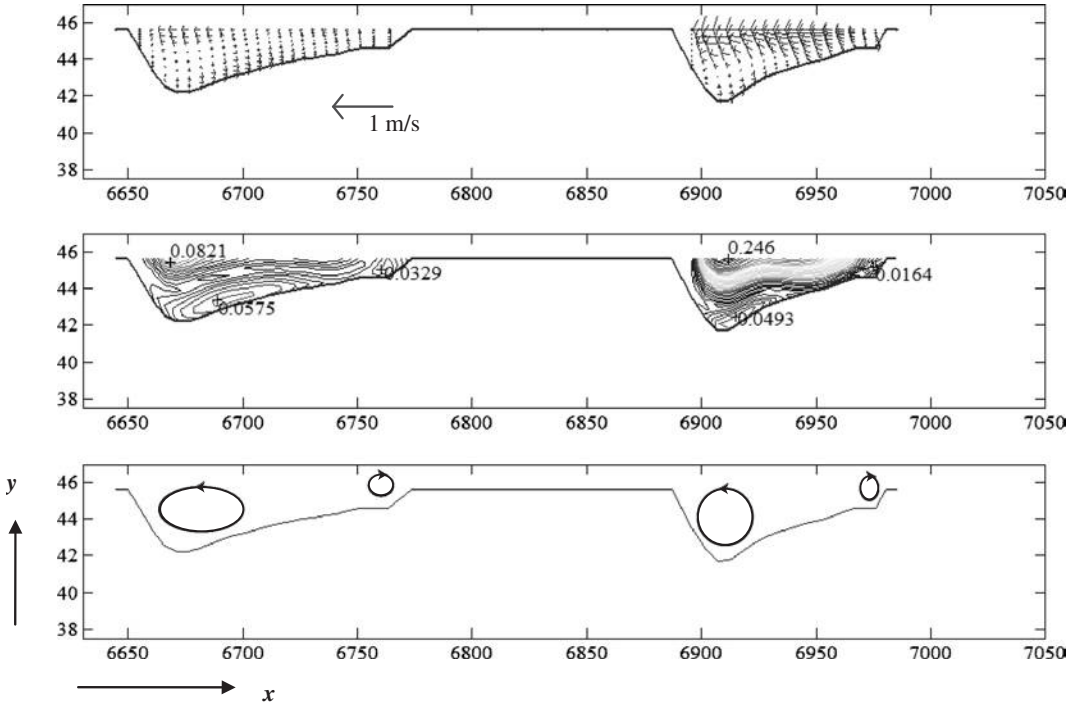


Figure 4d. Velocity vectors, velocity contours (m/s) and interpolated vortices in a vertical plane at section 112 (x, y in meters).

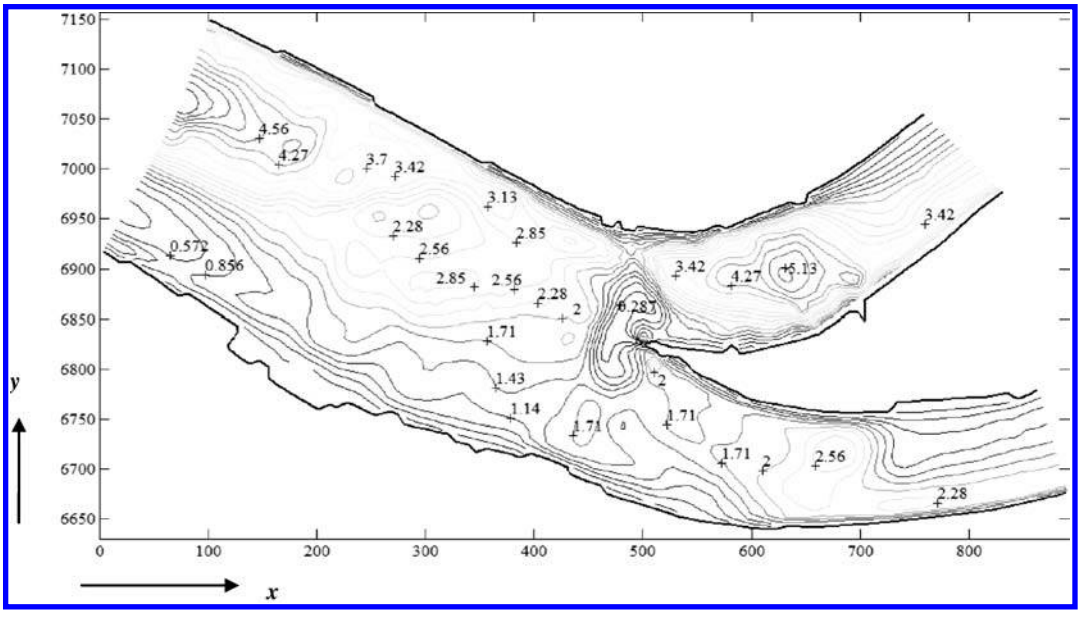


Figure 5. Total shear stress distribution in Pascal (x, y in meters).

Copyright © 2006 Taylor & Francis Group plc, London, UK

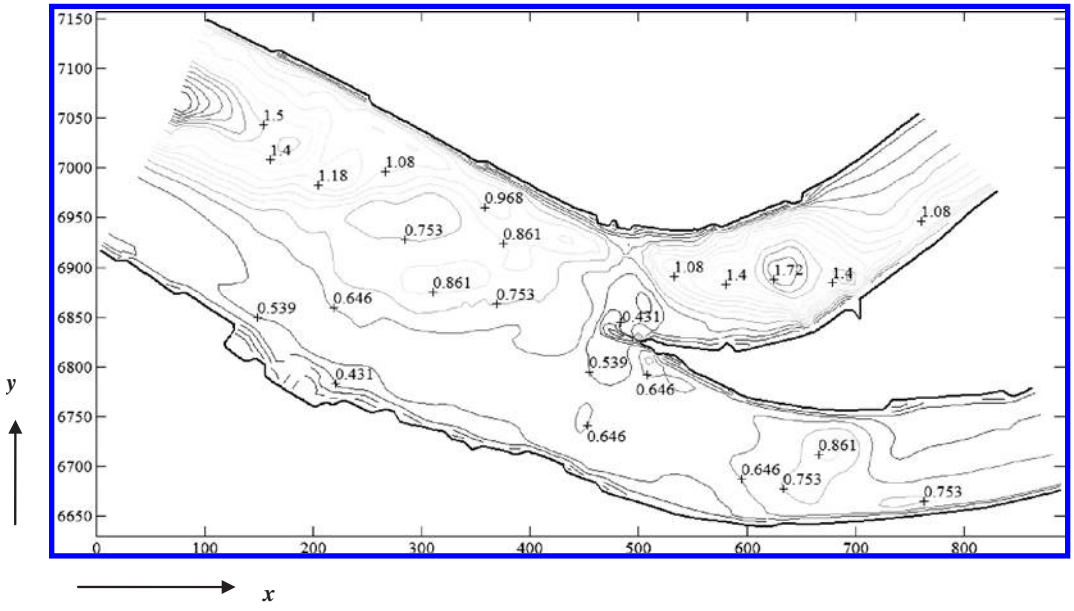


Figure 6. Effective shear stress distribution in Pascal (x, y in meters).

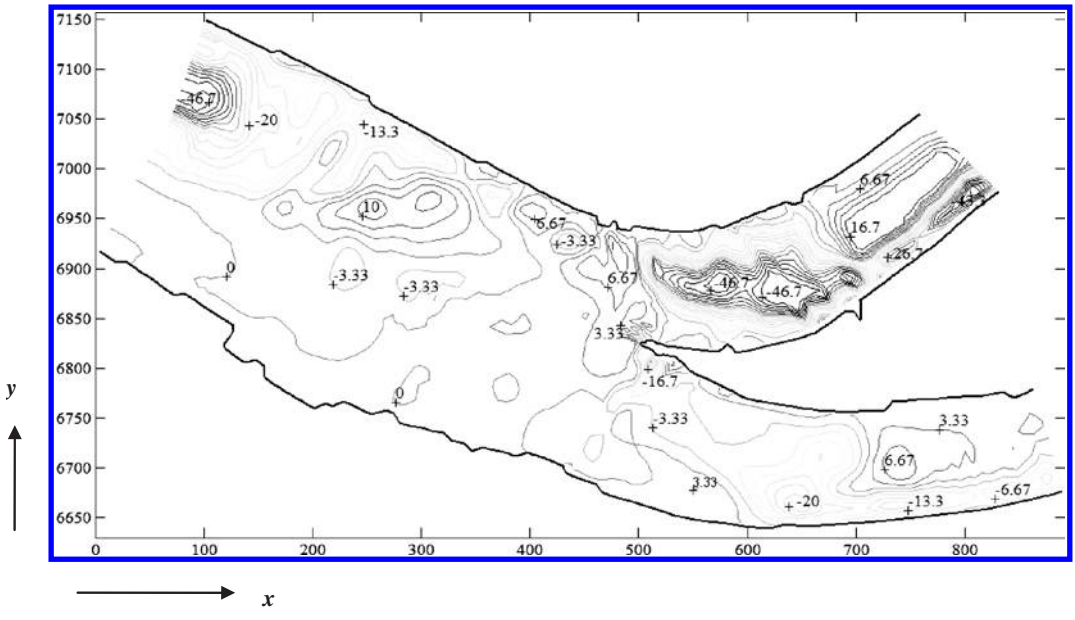


Figure 7. Predicted bed level changes in mm after 2 hours, -ve sign indicates erosion (x, y in meters).

The sediment transport simulation was run for 2 hours which was enough to reach a 'quasi' steady state solution. The general pattern of bed changes after 2-hours is shown in Figure 7. The figure shows the contour lines expressed in the units of millimeter (erosion in negative sign). The main features are the tendency for formation of a new sandbank at the entrance to the east channel and the division of the main channel into two regions of erosion and deposition. The model predicted the classical erosion patterns observed in the river bends. The maximum erosion depth was 46.7 mm, which occurred in the east channel

Copyright © 2006 Taylor & Francis Group plc, London, UK

near the concave curve. A similar trend was found in the west channel bend although the maximum erosion was 20 mm.

5 CONCLUSION

The study led to a number of improvements that should increase the applicability of ECOMSED model to rivers. These are

- Treatment of river roughness parameterization.
- Bed shear stress partitioning.
- Addition of bed load transport model.
- Automatic update of bed evolution.

The improved model successfully predicted the general flow patterns and sediment transport characteristics of the river reach. The adapted model is shown to be a useful tool for determining alluvial-channel response to changes in flow and bed sediment conditions. The model can also be a potential alternative to the expensive CFD commercial codes that have two main disadvantages: commercial codes are not primarily developed for rivers, and they give only a "black box" approach that hampers detailed adjustment of the code.

REFERENCES

Blumberg, A.F. & Mellor, G.L. (1987). A Description of a Three-Dimensional Coastal Ocean Circulation Model. In Three-Dimensional Coastal Ocean Models, Heaps, N. (edited). Coastal and Estuarine Sciences, American Geophysics Union, Washington D.C., 4, 1–16.

Bradbrook, K.F., Lane, S.N., Richards, K.S. & Roy, A.G. (2000). Large eddy simulation of periodic flow characteristics at river channel confluences. *Journal of Hydraulic Research*, 38, 207–215.

Chau, K.W. & Jiang, Y.W. (2001). 3D numerical model in orthogonal curvilinear and sigma coordinate system for Pearl River estuary. *Journal of Hydraulic Engineering*, ASCE, 127(1), 73–82.

Chien, N. & Wan, Z. (1999). Mechanics of sediment transport. ASCE Press, 913 p.

Dargahi, B. (2004). Three-dimensional flow modeling and sediment transport in the River Klarälven. Earth Surface Processes and Landforms, 29, 821–852.

Fang, H.W. (2000). Three dimensional calculations of flow and Bedload transport in the Elbe River. Report no. 763, Institute fur Hydromechanik an der Universitat Karsrulhe.

Gessler, D., Hall B., Spasojevic, M., Holly, F., Pourtaheri, H. & Raphelt, N. (1999). Application of 3D mobile bed, hydrodynamics model. *Journal of Hydraulic Engineering*, ASCE, 125, 737–749.

Grant, W.D. & Madsen, O.S. (1982). Movable bed roughness in unsteady oscillatory flow. *Journal of Geophysics Research*, 87, C1, 469–481.

Holly, M. & Spasojevic, M. (1999). Three dimensional mobile bed modeling of the Old River complex, Mississippi River. 27th IAHR Biennial Congress, Graz, Austria, E2, 369–374.

Lane, S.N., Bradbrook, K.F., Richards, K.S., Biron, P.A. & Roy, A.G. (1999). The application of computational fluid dynamics to natural river channels: three-dimensional versus two-dimensional approaches. *Journal of Geomorphology*, 29, 1–20.

Lane, S.N., Hardy, R.J., Elliott, L. & Ingham D.B. (2002). High-resolution numerical modeling of three-dimensional flows over complex river bed topography. Hydrological Processes, 16, 2261–2272.

Nicholas, A.P. (2001). Computational fluid dynamics modeling of boundary roughness in gravel-bed rivers: an investigation of the effects of random variability in bed elevation. Surface Processes and Landforms, 26, 345–362.

Olsen, N.R.B. & Stokseth, S. (1995). Three dimensional numerical modeling of water flow in a river with large bed roughness. *Journal of Hydraulic Research*, 33, 571–581.

Rodi, W. (2000). Numerical Calculations of Flow and Sediment Transport in Rivers. In Stochastic Hydraulics, Wang, ZY, Hu SX (eds). Balkema, Roterdam. pp 15–30.

Sinha, S.K., Sotiropoulos, F. & Odgaard, A.J. (1998). Three-dimensional numerical model for flow through natural rivers. *Journal of Hydraulic Engineering*, ASCE, 124(1), 13–24.

Stone, H.L. (1968). Iterative solution of implicit approximations of multidimensional partial differential equations. SIAM Journal of Numerical Analysis, 5, 530–558.

Van Rijn, L.C. (1984a). Sediment transport, part I: Bed load transport. *Journal of Hydraulic Engineering*, ASCE, 110, 1431–1456.

Van Rijn, L.C. (1984b). Sediment transport, part II: Suspended load transport. *Journal of Hydraulic Engineering*, ASCE, 110, 1613–1641.

Weerakoon, S.B. & Tamai, N. (1989), Three-dimensional calculation of flow in river confluences using boundary-fitted coordinates. *Journal of Hydro science and Hydraulic Engineering,* 7, 51–62.

Weiming, W., Rodi, W. & Webka T. (2000). 3D numerical modeling of flow and sediment transport in open channels. *Journal of Hydraulic Engineering,* ASCE, 126(1), 4–15.

Weiming, W., Rodi, W. & Wenka, T. (1997). Three dimensional calculation of river flow. Proceedings of the 27th IAHR Congress, San Francisco, CA, 779–784.

Yang, C.T. (1996). Sediment transport: theory and practice. McGraw-Hill Companies, Inc., 393 p.

Copyright © 2006 Taylor & Francis Group plc, London, UK

3D modeling of transient bed deformation in a sine-generated laboratory channel with two different width to depth ratios

N. Rüther & N.R.B. Olsen
Department of Hydraulic and Environmental Engineering, Norwegian University of Science and Technology in Trondheim, Norway

ABSTRACT: A three dimensional numerical model is presented to calculate the sediment transport rate and the corresponding transient bed changes in sine-generated meandering laboratory channels. Transient flow pattern as well as bed movements in simple bended laboratory channels have been successfully modeled with 2D and 3D numerical models before. However, when it comes to the successive formation of meander bends, the spatial propagation of the helical flow and its effect on the bed deformation is not fully understood yet. It is strongly depending on the deflection angle Θ of the meander bend and the width to depth ratio of the channel. In addition to this geometric characteristic, bed forms were prevailing in the experiments. The present study showed how a three dimensional numerical model is able to calculate the flow field and the sediment transport in a sine-generated laboratory channel with two consecutive meander bends and occurring bed forms.

1 INTRODUCTION

Water flow and sediment transport in meandering river is of high interest in the field of river engineering. The major local erosion in river bends under steady or unsteady flow conditions is causing huge problems to the riverine structures. Prediction of the time-dependent bed changes and the lateral bed load transport with the corresponding lateral migration with the help of computer programs is becoming more and more popular. The major problem herein is the fact that the flow field in river bends is highly three-dimensional. The flow is dominated by transverse secondary currents. The sediments are eroded by the accelerated flow at the outer part of the bend and transported by the secondary currents to the inner part. Here they tend to deposit due to the reduced velocity and shear stress, forming a so called point bar. This effect is highly depending on the geometry of the channel, e.g. deflection angle of the bends or number of consecutive bends, and also on the width to depth ratio of the channel. With the increasing computer power over the last 15 years, it is now possible to carry out fully 3D computations for such cases. Demuren & Rodi (1986) used a three dimensional model where the turbulence was predicted by the k-ε model, to calculate the flow and the transport of a neutral tracer in a meandering channel. Recently, Wilson et al (2003) computed the fully developed three dimensional velocity distributions in a meandering channel over a fixed natural bed and showed good agreement with measurements. Ruether & Olsen (2005) computed the bed changes over time in a sharply bended 90° channel with special respect to steep transversal slopes. Wu et al (2000) computed the flow in a 180° bend including suspended and bed load transport. Zeng et al (2005) computed the bed changes in a 180° bend, too. All of the results showed good agreement with measured data. Bed forms did not occur in any of the previous studies.

The present study focused on the simulation of the bed changes in a laboratory channel with sine-generated consequent bends, deflection angle $\Theta = 70°$, and prevailing bed roughness caused of bed forms, like dunes and ripples.

2 SEDIMENT TRANSPORT IN MEANDERING CHANNELS; EXPERIMENTAL DATA

The laboratory data used in the present study were taken from da Silva & Tarek (2006). Movable bed experiments were carried out in a sine generated channel. The 0.8 m wide flume was filled with sand of the size of $D_{50} = 0.65$ mm of about 0.2 m and steady, uniform flow was established. The sediments were relatively well sorted with a ratio of D_{60} to D_{10} of 1.89. There was not sediment feed at the inflow. The measured data for two experimental runs were then compared to the numerical simulation. The two different experiments were denoted Run 1 und Run 5 where the bed changes were measured after 60 min and 170 min for Run 1 and 5, respectively.

Copyright © 2006 Taylor & Francis Group plc, London, UK

Table 1. Hydraulic conditions of the experiments.

	Exp-1	Exp-5		Exp1	Exp-5
Q [m^3/s]	0.011	0.0076	u^* [m/s]	0.04	0.042
B [m]	0.8	0.8	B/h_{av} [−]	10.67	18.18
h_{av} [m]	0.075	0.044	Re^* [−]	53	54
S [−]	1/450	1/250	Re [−]	13750	9475
u_{av} [m/s]	0.18	0.22	T [min]	60	170

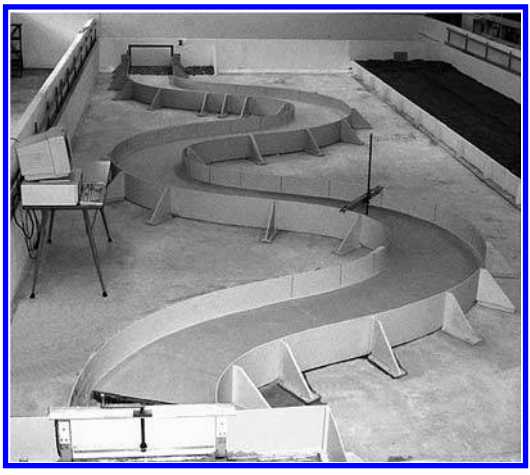


Figure 1. Experimental set up (da Silva & Tarek, 2006).

As it can be seen from table 1, the most significant difference of the two experiments is the width to depth ration of 10.67 and 18.18, respectively. For both experiments, the hydraulic conditions are listed in table 1. Figure 1 shows the experimental setup. The flow is top to bottom. (In the then following Figures the flow is from left to right). In order to establish uniformity, a tailgate at the downstream end of the channel was slightly adjusted. The water level was then controlled at the centerline in three cross sections of the geometry. The bed changes were observed to develop in the early beginning of each run.

According to the different hydraulic setups, two different bed patterns were observed. The bed deformation in Run 1, depicted in Figure 3 can be described in the following way: The locations of the deepest erosion were determined to be in the two cross over parts of the flume. Point bars developed at the inner side of each of the apex, growing with the increasing downstream coordinate. The magnitude of the bed changes over time was in the range of −0.12 m and +0.4 m. In addition one can see that the location of the maximum erosion and deposition in each of the bends were not located in the same cross section.

The bed deformation in Run 5 is depicted in Figure 5. The areas of maximum erosion are located at the outside end of each of the bends with a maximum

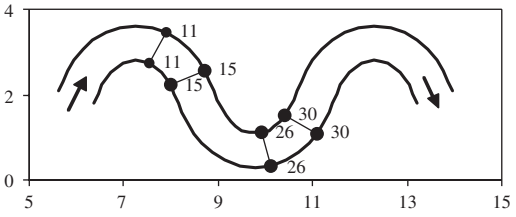


Figure 2. Location of the compared cross section.

bed change of −0.12 m. Similar to Run 1, the characteristic point bars developed and grow with the downstream, increasing coordinate. Where as the scour in the most downstream cross section was with −0.08 m less deep than the scours further upstream. In opposite to Run 1, the location of the maximum erosion and deposition were found to be in the same cross section, just slightly downstream of the apex.

Figure 2 shows the location of the cross section being compared. Cross section 11 and 15 are located right after the first bend and cross section 26 and 30 right after the second bend.

3 NUMERICAL SIMULATION OF TRANSIENT BED DEFORMATION

3.1 *Numerical model*

The flow field for the three-dimensional geometry is determined by solving the continuity equation and the Reynolds averaged Navier-Stokes equations:

$$\frac{\partial U_i}{\partial x_i} = 0 \tag{1}$$

$$\frac{\partial U_i}{\partial t} + U_j \frac{\partial U_j}{\partial x_i} = \frac{1}{\rho}\frac{\partial}{\partial x_i}\left(-P\delta_{ij} - \rho\overline{u_i u_j}\right) \tag{2}$$

U is the velocity averaged over the time t, x is the spatial geometrical scale, ρ is the water density, P is the pressure, δ is the Kronecker delta and u is the velocity fluctuation over time during one time step Δt. The control volume method was used as discretization method (Olsen 2004). The Reynolds stress term was modeled by the k-ε turbulence model. The model computed the turbulent stresses $\overline{u_i u_j}$, using the eddy viscosity relation:

$$-\overline{u_i u_j} = \nu_t\left(\frac{\partial U_i}{\partial x_j} + \frac{\partial U_j}{\partial x_i}\right) - \frac{2}{3}k\,\delta_{ij} \text{ with } \nu_t = \frac{c_\mu \cdot k^2}{\varepsilon}, \tag{3}$$

where the turbulent kinetic energy k and its dissipation rate ε determining the eddy viscosity ν_t were obtained from the following equations:

$$\frac{Dk}{Dt} = \frac{\partial k}{\partial t} + U_j\frac{\partial k}{\partial x_j} = \frac{\partial}{\partial x_j}\left[\left(\nu + \frac{\nu_t}{\sigma_k}\right)\frac{\partial k}{\partial x_j}\right] + P_k - \varepsilon \tag{4}$$

Copyright © 2006 Taylor & Francis Group plc, London, UK

$$\frac{D\varepsilon}{Dt}=\frac{\partial\varepsilon}{\partial t}+U_j\frac{\partial\varepsilon}{\partial x_j}=\frac{\partial}{\partial x_j}\left[\left(\nu+\frac{\nu_t}{\sigma_\varepsilon}\right)\frac{\partial\varepsilon}{\partial x_j}\right]+C_{\varepsilon 1}\frac{\varepsilon}{k}P_k-C_{\varepsilon 2}\frac{\varepsilon^2}{k} \quad (5)$$

The production of turbulent kinetic energy P_k was defined as:

$$P_k=\nu_t\frac{\partial U_i}{\partial x_j}\left(\frac{\partial U_j}{\partial x_i}+\frac{\partial U_i}{\partial x_j}\right) \quad (6)$$

An implicit method was used for transient terms and the pressure field was computed with the *SIMPLE* method (Patankar, 1980). The Rhie and Chow interpolation (Rhie and Chow, 1983) was applied to compute the velocities and the fluxes at the cell surfaces. Zero gradient boundary conditions were used for all variables at the outflow boundary. The upstream velocities were defined by a Dirichlet boundary condition. Wall law functions for rough boundary introduced by Schlichting (1979) were used for the side walls and the bed. In the default configuration the model computes the bed roughness as a function of the grain size distribution on the river bed. This worked well in cases where the roughness is dominated by influence of the grain form. In cases where fine bed material prevailed and bed roughness is affected by bed forms such as dunes and ripples, this approach was not giving appropriate results. Instead, reasonable results were obtained by using the following approach. First the bed form height was calculated with an equation developed by v. Rijn (1984c). The value was depending mainly on the water depth y, the characteristic sediment grain d_{50} and the prevailing shear stress τ.

$$\frac{\Delta}{y}=0.11\cdot\left(\frac{d_{50}}{y}\right)^{0.3}\cdot\left(1-e^{-0.5\left(\frac{\tau-\tau_{c,s}}{\tau_{c,s}}\right)}\right)\cdot\left(25-\left(\frac{\tau-\tau_{c,s}}{\tau_{c,s}}\right)\right) \quad (7)$$

where Δ is the bed form height and $\tau_{c,s}$ the critical shear stress for each fraction. Then the bed form height is converted into bed roughness ks with the following equation.

$$ks=3.0\cdot d_{90}+1.1\cdot\Delta\cdot\left(1.0-e^{\left(\frac{-25\cdot\Delta}{7.3\cdot y}\right)}\right) \quad (8)$$

The bed forms calculated with Eq. 7 were not assumed to be equally distributed over the cross section. That fact resulted in a varying roughness in the plan form. A non-hydrostatic pressure approach was implemented, so the water surface elevation was determined from the computed pressure field, resulting in an authentic computation of lateral slope of the water surface in the bends.

Similar to the upstream boundary condition of the velocities, the boundary conditions for the inflowing sediment transport was specified with a Dirichlet boundary condition and zero gradients for the water surface, the outlet, and the sides. In the present study no sediment inflow was used; neither in the experiments nor in the numerical simulation. The boundary conditions at the bed are given by the sediment transport relations for bed load. In the default configuration of the model, fractional sediment transport was computed by the bed load transport formulas of v. Rijn (1984a) applied individually for each fraction.

$$\frac{q_{b,s}}{d_s^{1.5}\cdot\sqrt{\frac{(\rho_S-\rho_W)\cdot g}{\rho_S}}}=\zeta\cdot\frac{\left(\frac{\tau-\tau_{c,s}}{\tau_{c,s}}\right)^{1.5}}{d_s^{\,2}\left(\frac{\rho_S/(\rho_W-1)\cdot g}{\nu^2}\right)^{0.1}} \quad (9)$$

where $\zeta=0.053$ is used as the default value in the original equation.

The computational domain was subdivided into three layers, a water layer near the river bed, with a mixture of water and sediments, an upper sediment layer were the bed load is calculated, denoted active layer and a lower sediment layer, denoted inactive layer. When fractional transport was computed, sorting mechanisms were considered to happen in the active layer. The height of the active layer was kept constant, equally to the size of the largest grain in the sediment mixture. The height of the inactive layer is set to a large value in order to supply the active layer with the sufficient amount of sediments. The grain size distributions in the two bed layers were obtained by considering sediment continuity for each fraction.

Finally the bed changes were computed from sediment continuity in the bed cell, as the difference between the inflowing and out flowing sediment fluxes. The defect was converted into a vertical bed elevation by dividing it by the submerged density of the sediments, 1320 kg/m^3, to find the volume of the deposits for each time step. This volume was then transformed into bed level changes for the grid. Both the sedimentation and the erosion processes were modeled using the same approach.

For the simulation of the laboratory experiments described in chapter 2, the geometry needed to be discretized. A three-dimensional structured, non-orthogonal, vertically adaptive and curvilinear grid with a non-staggered variable placement was generated. 173 hexahedral cells in the stream wise, 16 cells in the lateral and 5 cells in the vertical direction were used. A time step of 5 seconds was chosen. After each time step, the water and the bed surface were updated.

For discretization of the initial sediment distribution the continuous bed sediment sieve curve was decomposed into five size fractions. Starting with the smaller fraction, the sediment mixture contains of 10% with a size of 0.3 mm. 20% of 0.45 mm, 20% of 0.58 mm, 20% of 0.7, 20% of 0.82 and 10% of 1 mm.

Copyright © 2006 Taylor & Francis Group plc, London, UK

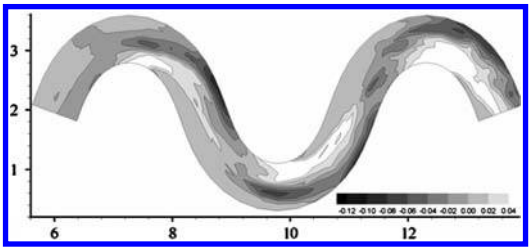


Figure 3. Measured bed changes in Run 1.

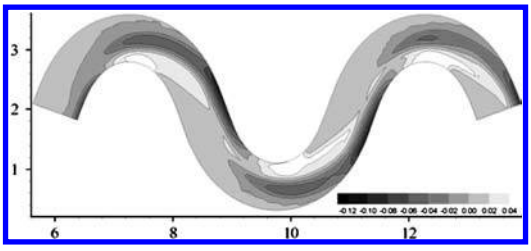


Figure 4. Calculated bed changes in Run 1.

3.2 *Results and discussion*

3.2.1 *Simulation results of Run 1*

Since the hydraulic performance of the present model was tested intensively in meandering channels (Wilson et al., 2003), the present study was focusing on the performance of predicting bed deformation only.

Two different laboratory setups were simulated. The hydraulic conditions of each experiment are described in chapter 2. The results are presented herein. Comparing the plan view of Run 1, depicted in Figure 3 for the experiments and in Figure 4 for the simulation, one can see the overall agreement with the measured data. The first two bends are characterized by a typical point bar at the apex, accompanied by a small scour in the center of the channel. The maximum scour was located further downstream, almost at the cross over, on the outside of the channel. Looking at simulated bed changes in the first two bends, one can see that the bed deformation was predicted well. The location of the maximum scours and bar positions matched. However there was some disagreement in the pattern of the last bend. In the experiment, the scour was located far more at the outside of the bend as in the previous two bends. This characteristic was not found in the results of the numerical run. So far there is no physical explanation for this longitudinal asymmetric bed development (da Silva, 2006).

The bed pattern observed in the plan view can also be shown in a longitudinal view. Figure 9 and Figure 12 show the left and the right side, respectively. One can see that the position of the maxima match well, but the absolute magnitude of the scours is slightly overestimated.

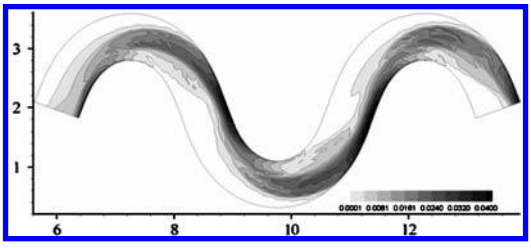


Figure 5. Calculated bed form height in Run 1.

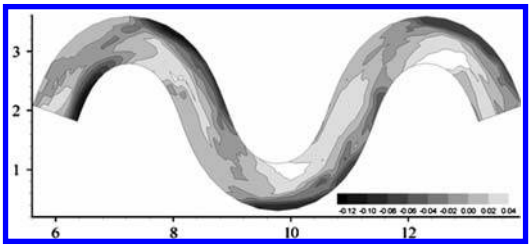


Figure 6. Measured bed changes in Run 5.

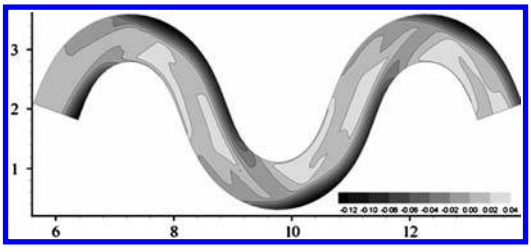


Figure 7. Calculated bed changes in Run 5.

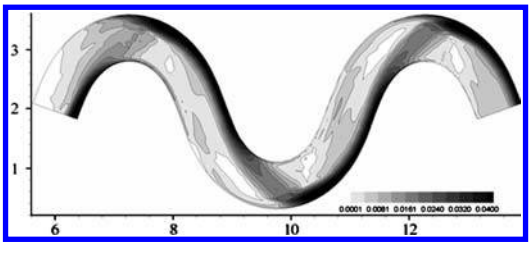


Figure 8. Calculated bed form height in Run 5.

The Figures 10, 11, 13 & 14 show the comparison of the data to the numerical results in the cross sections. Four cross sections are depicted. The locations of the cross section are shown in Figure 2. These cross sections were chosen since they were located where the maximum erosion was found in the experiments. One can see that especially in cross section 15 & 30 the calculated bed changes matched the measurements very well. In the Figures 10 & 11, one can see that the simulated scour locations were shifted towards the left channel side. The calculated bed form height is

Copyright © 2006 Taylor & Francis Group plc, London, UK

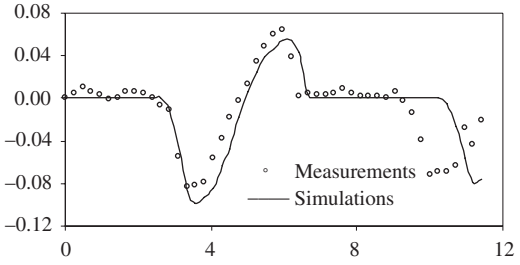


Figure 9. Run 1; Longitudinal view, left channel side.

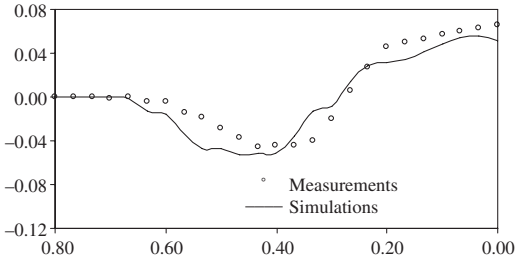


Figure 10. Run 1; Crossectional view, #11.

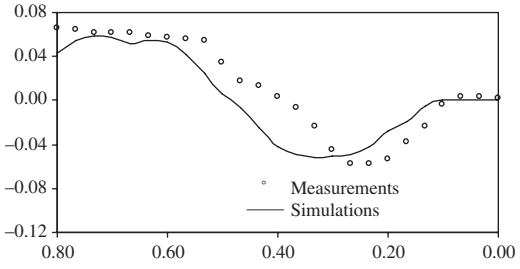


Figure 11. Run 1; Crossectional view, #26.

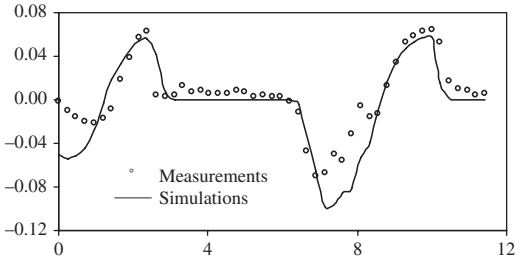


Figure 12. Run 1; Longitudinal view, right channel side.

illustrated in Figure 5. The bed form heights are not equally distributed over the width. The height varied from 0.1 mm to more than 4 cm. The highest values are simulated to be around the places where the maximum erosion occurred.

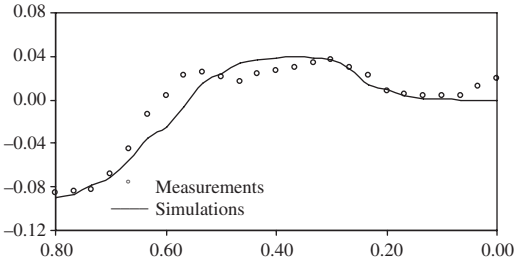


Figure 13. Run 1; Crossectional view, #15.

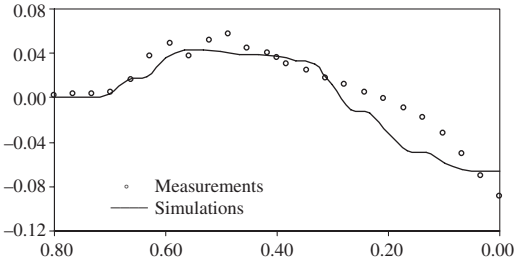


Figure 14. Run 1; Crossectional view, #30.

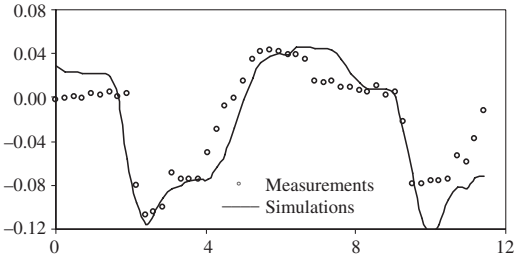


Figure 15. Run 5; Longitudinal view, left channel side.

3.2.2 *Simulation results of Run 5*

The plan views of the bed changes from the experimental and from the numerical model are depicted in the figures 5 and 6, respectively. As well as for the results in Run 1 one can see that the overall pattern matched. The magnitude of the bed changes also matched. However, the scouring in the longitudinal direction was over estimated. The scour spread too far downstream.

Figure 13 shows that the scour in the last bend is not as deep as the previous two bends. This characteristic is not reproduced by the numerical results. Otherwise one can see that the positions of the maxima are calculated to be at the same locations as in the physical model. From Figures 14, 15, 17 & 18 it is observed that the computed bed elevations at cross section 26 match particularly well with the measured data. Figure 14 & 17 show that the deposition pattern is slightly overestimated, but still being in reasonably good agreement

Copyright © 2006 Taylor & Francis Group plc, London, UK

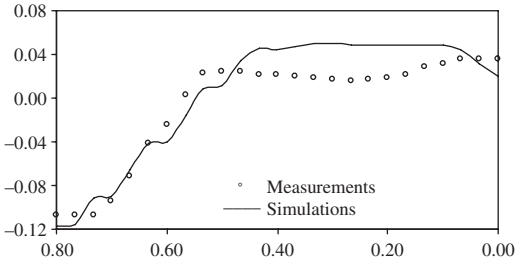


Figure 16. Run 5; Crossectional view, #11.

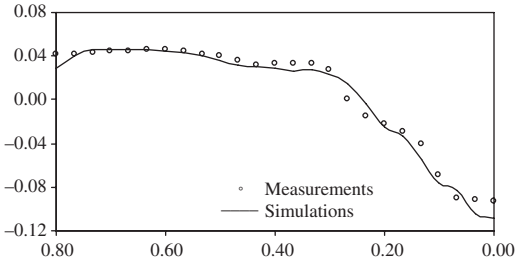


Figure 17. Run 5; Crossectional view, #26.

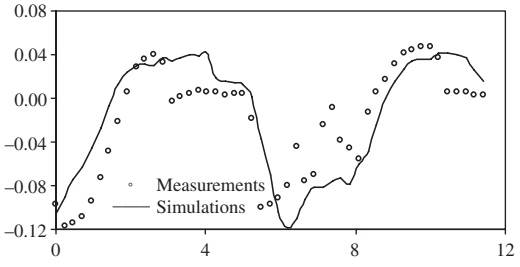


Figure 18. Run 5; Longitudinal view, right channel side.

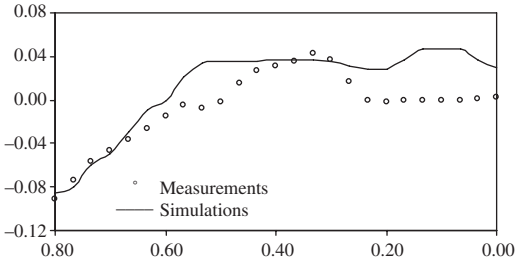


Figure 19. Run 5; Crossectional view, #15.

with the measured data. The distribution of the calculated bed form height in run 5 is depicted in Figure 8. Similar to Run 1, the bed form heights range between 0.1 mm and 4 cm. In areas with strong erosion, values of the more than 4 cm have been observed.

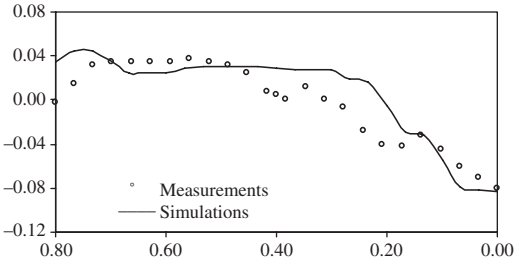


Figure 20. Run 5; Crossectional view, #30.

For Run 5, in the sediment transport capacity formula, the default value of $\zeta = 0.053$ was changed to $\zeta = 0.009$. This means that the sediment transport capacity had to be reduced to get reasonable results. One possible explanation could be the fact that the calculated bed forms are highly over predicted and consequently the bed load capacity, too. This is because the bed shear stress increases with increasing bed roughness. Sediment transport formulas and bed form predictors have uncertainties due to their empirical origin. Their prediction quality is strongly depending on the data the formulae were calibrated on. Since the roughness induced by bed forms and sediment transport are interacting, it would have been possible to modify the bed form predictor instead of modifying the ζ-coefficient in the transport capacity formula. However, more investigations about bed form development and their occurrence in meandering channels have to be done before any speculation about the physical process behind this phenomenon can be defined and adopted by a numerical model.

4 CONCLUSION AND RECOMMENDATIONS

The transient bed changes of a meandering laboratory channel with two different width to depth ratios have been successfully modeled. The calculated bed changes are in good agreement with the measurements for both cases. The numerical model was enhanced with a roughness approach taking into account the presence of bed forms. The results were very sensitive to the formulas for bed form height and bed roughness. The roughness approach seemed to be strongly connected to the development stage of a bed form and therefore to the sediment transport capacity. In the opinion of the authors there is more research needed for the universal implementation of a roughness approach taking bed form roughness into account. Furthermore, a wider range of the width to depth ratio should be tested in order to validate the present results. It seems that the width to depth ratio has a larger influence on the bed pattern in meandering channels as it is believed in literature today. To make any reliable

Copyright © 2006 Taylor & Francis Group plc, London, UK

conclusion, the model should be tested on data from experiments with different deflection angles Θ, too.

ACKNOWLEDGEMENT

The authors would like to thank Dr. A.M. da Silva who was so kind to distribute the data used in this study and giving fruitful advices for a successful modeling of the data. In addition, the first author likes to thank the Norwegian Research Council for their support through the BeMatA Program.

REFERENCES

Demuren, A.O., Rodi, W. 1986. Calculation of flow and pollutant dispersion in meandering channels, *Journal of Fluid mechanics*, 172, 63–92.

Olsen, N.R. B 2004. *Hydroinformatics, fluvial hydraulics and limnology*, Department of Hydraulic and Environmental Engineering, The Norwegian University of Science and Technology, http://folk.ntnu.no/nilsol/tvm4155/flures5.pdf.

Patankar, S., 1980. *Numerical Heat Transfer and Fluid Flow*. Taylor and Francis Publishers.

Rhie, C. and Chow, W., 1983. Numerical study of the turbulent flow past an airfoil with trailing edge separation, *AIAA* Journal, 21 (11).

Rijn, L.C. van, 1984a. Sediment Transport, Part I: Bed Load Transport, *J. Hydraulic Engineering*, 110 (11), pp. 1431–1457.

Rijn, L.C. van, 1984b. Sediment Transport, Part II: Suspended Load Transport, *J. Hydraulic Engineering*, 110 (11), pp. 1613–1641.

Rijn, L.C. van, 1984c. Sediment Transport, Part III: Bed forms and alluvial roughness, *J. Hydraulic Engineering*, 110 (12), pp. 1733–1754.

Ruether, N. and Olsen, N.R.B., 2005. Three dimensional modeling of sediment transport in a narrow 90° channel bend, *J. Hydraulic Engineering*, 131 (10), pp. 917–920.

Schlichting, H., 1979. *Boundary layer theory*, McGraw-Hill Book Company, New York.

Silva, A.M.F. da, 2006. Personal communication.

Silva, A.M.F. da, El-Tahawy, T. 2006. Location of hills and deeps in meandering streams: an experimental study. *Proc. 3rd Int. Conference on Fluvial Hydraulics, River Flow 2006*, A.A. Balkema, Netherlands.

Wilson C.A.M.E., Boxall, J.B., Gymer, I., Olsen, N.R.B. 2003. Validation of a three-dimensional numerical code in the simulation of a pseudo-netrual meandering stream, *J. Hydraulic Engineering*, 129 (10), pp. 758–768.

Wu, W., Rodi, W. and Wenka, T., 2000. 3d numerical modelling of flow and sediment transport in open channels, Journal of Hydraulic Engineering, 126 (1), pp. 4–15.

Zeng, J., Constantinescu, G. and Weber, L. 2005. A fully 3D non-hydrostatic model for prediction of flow, sediment transport and bed morphology in open channels, *Proc., 31st IAHR Congress*, Seoul, Korea.

SYMBOLS

a	index for alternate bars
B [m]	width
c_μ [−]	coefficient
$C_{\varepsilon 1,2}$ [−]	coefficient
δ [−]	Kronecker delta
Δ [m]	bed form height
δ_t	time step
d	index for dunes
D	characteristic grain size diameter
ε	dissipated energy
h_{av} [m]	average water depth
i [−]	index for the
k	kinetic energy
k_s [m]	equivalent roughness
Λ [m]	bed form length
P [pa]	pressure
Pk	production term for kin.energy
q_b [kg/sec]	sediment transport load
Q [m3/sec]	water discharge
Θ [−]	deflection angle
r	index for ripples
Re [−]	Reynolds number
Re^* [−]	particle Reynolds number
ρ_s [kg/m^3]	density of water
ρ_w [kg/m^3]	density of sediments
S [−]	slope
s [−]	index for individual grain sizes
T [min]	time
τ [N/m^2]	shear stress
τ_c [N/m^2]	critical shear stress
u_{av} [m/s]	average velocity
u^* [m/s]	shear velocity
x [m]	longitudinal coordinate
ζ [−]	coefficient

Copyright © 2006 Taylor & Francis Group plc, London, UK

Morphology and flow structures in a large confluence-diffluence: Rio Paraná, Argentina

O. Orfeo
Centro de Ecologica Aplicada del Littoral (CECOAL), Corrientes, Argentina.

D.R. Parsons & J.L. Best
Earth and Biosphere Institute, School of Earth and Environment, University of Leeds, Leeds, UK.

S.N. Lane & R.J. Hardy
Department of Geography, University of Durham, Durham, UK.

R. Kostaschuk
Department of Geography, University of Guelph, Ontario, Canada.

R.N. Szupiany & M.L. Amsler
Consejo Nacional de Investigaciones Científicas y Técnicas (CONICET), Argentina
Facultad de Ingeniería y Ciencias Hídricas, UNL, Argentina.

ABSTRACT: Confluence-diffluence units are key elements within many river systems and present a complex and linked pattern of flow and sediment transport between these two nodes. Past work has seen much progress in our modelling of river confluences, and increasing attention is being paid to bifurcations and the important role of bifurcation asymmetry. However, most of these studies have been conducted in laboratory flumes or within small rivers (depths less than 3 m and widths <100 m). This paper presents a study of the bed morphology and 3D flow within a very large confluence-diffluence unit in the Rio Paraná, Argentina. The paper details the central scour within the reach and reveals that the flow within the confluence-diffluence is dominated largely by the bed roughness, and that the coherent secondary flow cells, that have been identified in smaller channels and assumed to be present within large rivers, are generally absent in this reach.

1 INTRODUCTION

The splitting and joining of channels is a fundamental and common process in many types of multi-channel rivers. Indeed this so called 'confluence-diffluence' unit is a key element within many fluvial networks and they are fundamental forms within braided, anastomosed, and distributary systems such as alluvial fans and river deltas (Slingerland & Smith, 2004). Such sites present a complex and linked pattern of flow and sediment transport though individual channel reaches. Indeed, channel confluence-diffluence units give rise to channel patterns themselves, and within meandering systems diffluences lie at the heart of the process of channel avulsion (e.g. Garcia & Nino, 1993).

The past 25 years has witnessed substantial efforts to understand flow processes, mixing, sediment transport and the influence of channel geometry at confluences (e.g. Ashmore et al. 1992, Best 1987, 1988, Best & Reid 1984, Best & Roy 1991, Biron et al. 1993, 1996, Bradbrook et al., 1998, 2000, 2001, Lane et al. 2000, Mosley 1976, Rhoads & Kenworthy 1998, Rhoads & Sukhodolov 2001). This focus has reflected the importance of river channel junctions as key components of both dendritic drainage networks and braided river systems, including their associated importance for sediment transport and channel change (Mosley 1976, Best 1987, 1988, Ashmore et al. 1992). There has been recent recognition that in the braiding process, the formation and control exerted by diffluences in governing the downstream partitioning of flow could be as, if not more important, than upstream confluence zones (e.g. Pittaluga et al. 2001, Frederici & Paola 2003). Indeed, all braided fluvial systems contain the fundamental confluence-diffluence unit (e.g. Southard et al. 1984, Davoren & Mosley 1986, Nicholas & Smith 1999) and despite extensive research into confluences, there is a far

Copyright © 2006 Taylor & Francis Group plc, London, UK

poorer understanding of flow and sediment dynamics within the confluence-diffluence unit as a whole, including the areas upstream and downstream of confluences. Crucially, very little is known about the transition from confluence to diffluence, and particularly the flow characteristics that are inherited at, and downstream of, these sites (e.g. Richardson & Thorne 2001). Additionally, the nature of the diffluence will also control the character of flow in the downstream distributaries, and therefore will play a critical role in the movement of sediment through the confluence-diffluence unit as a whole, governing the development and maintenance of mid-channel bars, which are central to the unit itself.

Perhaps most importantly, the vast majority of the past work outlined above on both confluences and diffluences has been conducted in laboratory flumes, within small rivers (depths less than 3 m and widths <100 m), and in a range of models based on boundary conditions of these scales. There is therefore little knowledge of how the processes observed at these smaller sites scale to larger rivers. This is a fundamental gap in the current understanding of continental scale river systems. This paper therefore has two main aims. It presents a study of the bed morphology and related 3D flow structure within a very large confluence-diffluence unit in the Rio Paraná, Argentina, and compares the features of mean flow identified with studies from smaller river channel units.

2 FIELD SITE AND FIELD METHODS

The study area is a confluence diffluence unit in the Rio Paraná, downstream of the major Paraguay River confluence and 16 km north of the city of Corrientes, NE Argentina (Figs 1 and 2). The Paraná River is the sixth largest in the world by water discharge and the mean annual discharge of the Rio Paraná is circa 17,000 m^3/s (Orfeo & Stevaux 2002). Its basin occupies some 2,600,000 km^2, mostly within Southern Brazil and Argentina. At the field site, the mean width of Rio Paraná is about 2.5 km and its mean depth at a section varies from 5–12 meters. At the time of surveying in May 2004, the discharge of the full river section was $\sim$12,000 m^3/s^{-1}.

The field methodology employed involved digital, dual frequency single beam echo-sounder surveys of the bed from a small survey vessel along 36 cross-stream traverses approximately perpendicular to the true channel banks. These bed surveys were accompanied by simultaneous acoustic Doppler current profiling (aDcp) surveys using an RDInstruments^{TM} RioGrande® 600 kHz unit. This aDcp has a 4 beam (transducer) system, each with an orthogonal angle of 20 degrees in the vertical, and emits acoustic pulses of energy that are backscattered by particles in the water column. The backscattered signal was set to split into 98 equally spaced 0.5 m bins in the vertical, and the Doppler shift principle used to convert the change in frequency into weighted averages of components of flow velocity within each depth range bin. The aDcp was set to pulse (or 'ping') at 5 Hz, although measurements were then averaged over 36 pulses to increase the signal: noise ratio, and yield 3D velocity profiles averaged over $\sim$ 0.2 Hz. The aDcp was used to trace the pattern of velocity magnitude, vertical velocity and flow direction within the confluence-diffluence unit. Both the bed echo sounder surveys and aDcp survey were located using a Real-Time Kinematic (RTK) Digital Global Positioning System



Figure 1. Overview of the confluence-diffluence field site 20 KM North of Corrientes City, Rio Paraná, Argentina. Copyright CECOAL-CONICET, Argentina.



Figure 2. Arial view of the confluence-diffluence (looking upstream) unit investigated. Note the high concentration of the Paraguay River mixing rapidly into the Paraná.

Copyright © 2006 Taylor & Francis Group plc, London, UK

(dGPS) that allowed accurate differential positioning of the survey lines. This method produced an accuracy in relative position (dGPS base station to rover) of +/− 0.02 m and +/− 0.03 m in the horizontal and vertical positions respectively.

Since all flow velocities measured by the aDcp are relative to the aDcp, and hence the boat velocity (approximately 1 m/s^{-1}), the measured aDcp velocities must be corrected for this boat motion by removing the dGPS-derived boat velocity, thereby producing measurements of the flow velocity (cf. Yorke and Oberg, 2002). Averaging the aDcp profiles over ~ 0.2 Hz therefore produced velocity profiles that were averaged over approximately 5 meters of channel width. The derived flow velocities were finally converted from beam co-ordinates into an Earth referenced co-ordinate system, using the simultaneous measurements made by the aDcp's 'on-board' attitude and gyro sensor. The boat velocity and track position along the survey lines were monitored online and were held as constant as possible during surveying.

3 RESULTS AND DISCUSSION

3.1 *Bed morphology*

River bed surveys show that the maximum depth at the confluence, and through the nodal area of maximum flow constriction, is up to 22 m (Fig. 3), with a scour of up to 12 m compared to upstream bed levels.

There is a pronounced bed discordance at the confluence with the true right, smaller, tributary being up to 6 meters shallower than the deeper true left. This forms a discordant confluence with a mouth bar extending from the smaller tributary and dipping steeply into the central scour. The deeper channel thalweg crosses the main channel downstream of the confluence and is found to extend further into the larger diffluent (true right) channel, which is on the opposite side of the reach to the upstream confluence.

3.2 *Flow structure*

At the flow stage investigated (12,000 m^3/s), the true left channel is dominant in its discharge contribution at the confluence (Figs 4 and 5), with a discharge ratio (minor/major confluent channels) of 0.15. As the flows combine through the confluence there is a slight overall acceleration of flow produced by the reduced cross-sectional area of the downstream nodal constriction. As the deeper channel thalweg crosses the main channel downstream of the confluence, most of the flow discharge is routed into the true right diffluent channel, which is at the opposite side of the channel to the dominant channel at the upstream confluence. The diffluence discharge ratio is approximately 0.6 (true left/true right), showing a more equal division of flow than the two confluent channels upstream.

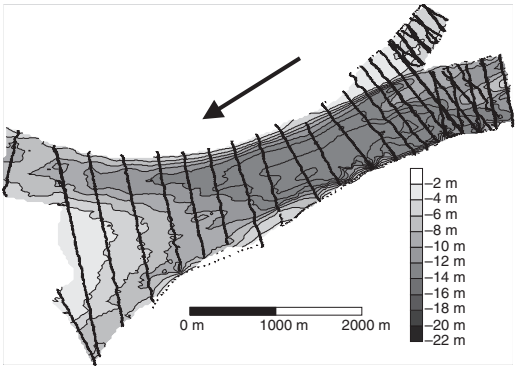


Figure 3. Bed morphology of the confluence-diffluence unit. Black lines show the survey lines. Black arrow shows flow direction.

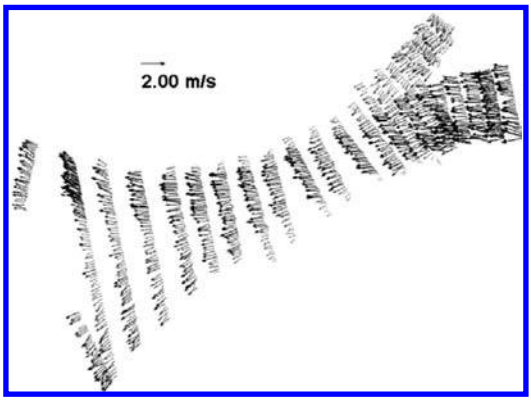


Figure 4. Planform view of the depth averaged flow velocity vectors through the confluence-diffluence unit.

Interestingly, the aDcp surveys show the progressive division of flow upstream of the diffluence. Figure 6 shows the horizontal directions of the flow vectors along each of the surveyed transects. This indicates that the division of the flow begins close to where the central scour begins to shallow, well before the mid-channel bar downstream. As this division of flow begins well before the actual diffluence, the control of the central scour position and orientation would seem to both link and govern the confluence-diffluence unit, with particular regard to the downstream division of flow. Given this finding, linkage to how sediment is routed though these scour holes would provide greater insight into the processes of flow division at diffluences more generally.

3.3 *Secondary circulation*

Secondary flows along each cross-sectional transect were calculated using the Rozovskii (1957) method.

Copyright © 2006 Taylor & Francis Group plc, London, UK

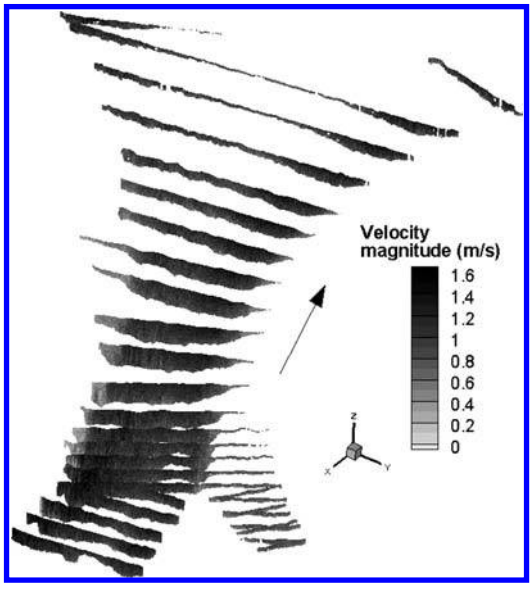


Figure 5. Perspective view of transect contoured velocity magnitude through the confluence diffluence unit.

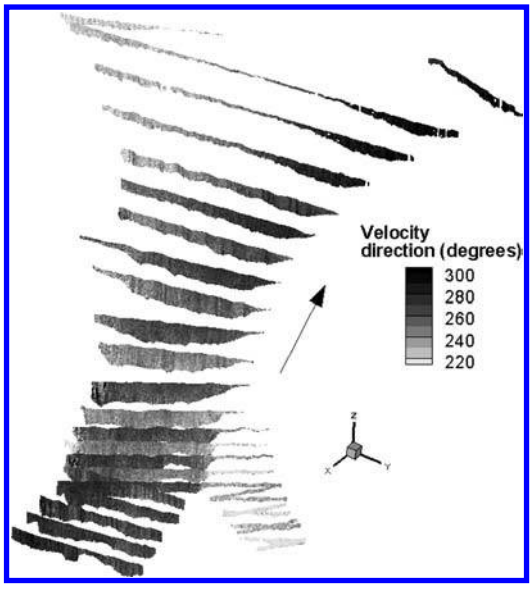


Figure 6. Perspective view of transect contoured velocity vector horizontal direction through the confluence-diffluence unit.

This involves integrating the velocity profile through the depth to obtain a depth averaged vector. The differences from this depth averaged velocity for all measurement within the profile are then computed to provide an indication of secondary motions in the plane perpendicular to the average velocity direction in the profile.

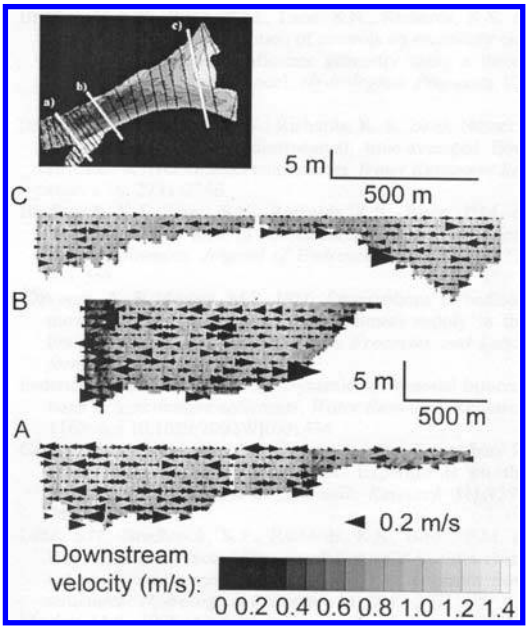


Figure 7. Secondary flow velocity vectors derived using the Rosovskii method for three sections through the confluence-diffluence. Section *a* is close to the confluence, *b* is through centre of the scour and *c* is in the true left side channel at the diffluence.

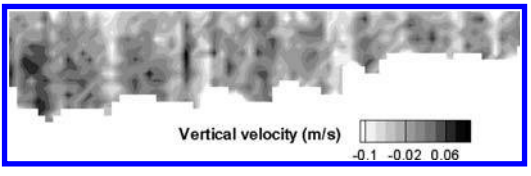


Figure 8. Vertical flow velocities for subset section c. Positive vertical velocities denote flow towards the bed. Note the profile of the bed indicating the presence and locations of dune bedforms.

Figure 7 shows the secondary flow at three sections through the confluence-diffluence unit. Section *a* is close to the confluence zone but shows no real pattern of secondary flow structure. There is some semblance of a definable pattern in section *b*, which is within the central scour, with flow generally moving towards the right bank at the bed and towards the left at the surface. However, no back-to-back cells are apparent as have been found in previous studies at smaller channel confluences (e.g. Rhoads & Kenworthy 1998). At section *c*, which shows flow in the left portion of the diffluence, again no channel scale pattern of secondary flow is present (Fig. 7).

Figure 8 shows the vertical velocities in the left channel at the diffluence (see Fig. 7 for location) and

Copyright © 2006 Taylor & Francis Group plc, London, UK

indicates a strong correlation of upwelling zones with dune bedforms. It therefore seems likely that the presence of any major coherent channel scale secondary flows is curtailed by the function of form roughness in large rivers, where the width: depth ratios are often very high.

4 CONCLUSIONS

The findings presented within this paper indicate that caution must be applied in assuming that processes observed in small channels scale linearly with channel size. The results show a large central scour between a discordant confluence and a downstream diffluence. This scour, its position and orientation in particular, seems to play a crucial role in governing flow division at the downstream diffluence.

The flow field is dominated by the convergence and divergence through this nodal area and at this flow level and discharge ratio no coherent, channel scale, secondary flow cells seem to exist at the confluence. Although there is hint of one full width cell over the central scour, there is no evidence of coherent secondary cells as flow shallows at bifurcation. It is therefore concluded in this wide, shallow river reach, flow mixing and secondary flow is almost completely dominated by bed form roughness, which prevents any coherence existing and that the coherent secondary flow cells that have been identified in smaller channels and assumed to be present within large rivers, are generally absent.

There is, however, the obvious need to repeat these measurements at different flow levels and at different discharge ratio values.

ACKNOWLEDGEMENTS

This research was enabled through award of grants NER/A/S/2001/00445 and NER/B/S/2003/00243 from the UK Natural Environment Research Council for which we are extremely grateful. We would like to gratefully acknowledge the outstanding and full support of Reson Offshore Ltd. (www.reson.com), and John Fraser in particular. We also acknowledge an award a Discovery Grant from the Natural Sciences and Research Council of Canada. Additionally, we also extend thanks to the staff of CECOAL-CONICET (Corrientes, Argentina), and in particular Lolo Roberto and Luis Bonnetti, for their field support. Mark Franklin, Pam Montgomery, Mat Roberts, and Dan Shugar are thanked for their assistance in the field. JLB would like to acknowledge the Leverhulme Trust for award of a Research Fellowship, which facilitated completion of this paper, and Marcelo García and the Ven Te Chow Hydrosystems Laboratory, University of Illinois at Urbana-Champaign, for hosting his stay.

REFERENCES

Ashmore, P.E., Ferguson, R.I., Prestegaard, K.L., Ashworth, P.J. & Paola, C. 1992. Secondary Flow in Anabranch Confluences of a Braided, Gravel- Bed Stream. *Earth Surface Processes and Landforms* 17: 299–311.

Best, J.L. & Roy, A.G. 1991. Mixing layer distortion at a confluence of unequal depth. *Nature* 350, 411–3.

Best, J.L. & Reid, I. 1984. Separation Zone at Open-Channel Junctions. *Journal of Hydraulic Eng*. 110: 1588–94.

Best, J.L. 1987. In Etheridge, F.G. et al., *Spec. Pub Soc Econ Palaeonto. Mineral* 39: 27–35.

Best, J.L. 1988. Sediment transport and bed morphology at river channel confluences. *Sedimentology* 35, 481–498.

Biron, P., Roy, A.G. & Best, J.L. 1996. Turbulent flow structure at concordant and discordant open-channel confluences. *Experiments in Fluids* 21: 437–446.

Biron, P., Roy, A.G., Best, J.L. & Boyer, C.J. 1993. Bed Morphology and Sedimentology At the Confluence of Unequal Depth Channels. *Geomorphology* 8: 115–129.

Bradbrook, K.F., Biron, P.M., Lane, S.N., Richards, K.S. & Roy, A.G. 1998. Investigation of controls on secondary circulation in a simple confluence geometry using a three-dimensional numerical model. *Hydrological Processes* 12: 1371–1396.

Bradbrook, K.F., Lane, S.N.; Richards, K.S. 2000. Numerical simulation of three-dimensional, time-averaged flow structure at river channel confluences, *Water Resources Research* 36: 2731–2746

Bradbrook, K.F., Lane, S.N., Richards, K.S., Biron, P.M. & Roy, A.G. 2001. Role of bed discordance at asymmetrical river confluences. *Journal of Hydraulic Engineering* 127: 351–368.

Davoren, A. & Mosley, M.P. 1986. Observations of bedload movement, bar development and sediment supply in the braided Ohau River. *Earth Surface Processes and Landforms* 11: 643–52.

Federici, B., & Paola C. 2003. Dynamics of channel bifurcations in noncohesive sediments, *Water Resources Research* 1162: doi:10.1029/2002WR001434.

Garcıa, M., & Nino, Y. 1993. Dynamics of sediment bars in straight and meandering channels: Experiments on the resonance phenomenon. *J. Hydraulic Research* 31: 739–761.

Lane, S.N., Bradbrook, K.F., Richards, K.S., Biron, P.M. & Roy, A.G. 2000. Secondary circulation cells in river channel confluences: measurement artefacts or coherent flow structures? *Hydrological Processes* 14: 2047–2071.

Mosley, M.P., 1976. An experimental study of channel confluences„*J Geol* 84: 535–62.

Nicholas A.P., & G.H. Sambrook Smith 1999. Numerical simulation of three-dimensional flow hydraulics in a braided channel. *Hydrological Processes* 13: 913–929

Orfeo, O. & Stevaux, J. 2002. Hydraulic and morphologic characteristics of middle and upper reaches of the Paraná River (Argentina and Brazil). *Geomorphology* 44: 309–322.

Pittaluga MB, Federici B, Repetto R, Paola C, Seminara G, Tubino M. 2001. The morphodynamics of braiding rivers: experimental and theoretical results on unit processes.

Copyright © 2006 Taylor & Francis Group plc, London, UK

In Mosley MP, (ed.), *Gravel-Bed Rivers V*, New Zealand Hydrological Society, Wellington, NZ: 143–180.
Rhoads, B.L. & Kenworthy, S.T. 1998. Time-averaged flow structure in the central region of a stream confluence. *Earth Surface Processes and Landforms* 23: 171–191.
Rhoads, B.L. & Sukhodolov, A.N. 2001. Field investigation of three-dimensional flow structure at stream confluences: 1. Thermal mixing and time-averaged velocities. *Water Resources Research* 37: 2393–2410.
Richardson, W.R. & Thorne, C.R. 2001. Multiple thread flow and channel bifurcation in a braided river: Brahmaputra-Jamuna River, Bangladesh. *Geomorphology* 38: 185–196.
Rozovskii, I.L. 1957. *Flow of water in bends of open channels*, Academy of Sciences of the Ukrainian SSR, Kiev (translated from Russian by the Israel Program for Scientific Translations, Jerusalem, (1961), 233 pp.
Slingerland, R. & Smith N.D. 2004. River avulsions and their deposits, *Annual Review of Earth and Planetary Sciences* 32: 257–285.
Southard, J.B., Smith, N.D., & Kuhnle, R.A. 1984. Chutes and lobes: newly identified elements of braiding in shallow gravelly streams, In Koster,EH; Steel,RJ (eds): S*edimentology of Gravels and Conglomerates, Canadian Society of Petroleum Geologists Memoir*, 51–59.
Yorke, T.H., & Oberg, K.A. 2002. Measuring river velocity and discharge with acoustic Doppler profiler. *Flow Measurement and Instrumentation* 13: 191–195.

Copyright © 2006 Taylor & Francis Group plc, London, UK

Unsteadiness effects on the morphological behaviour of gravel-bed river bifurcations

S. Miori
University of Trento, Trento, Italy

R. Repetto
University of L'Aquila, L'Aquila, Italy

M. Tubino
University of Trento, Trento, Italy

ABSTRACT: In recent works (Bolla Pittaluga et al. 2003a, Miori et al. 2005) the equilibrium configurations of a simple channel division and their stability have been investigated within the context of a one dimensional approach. Physically based relationships for sediment distribution have been employed by the authors at the channel division point, which allow to model the effect of transverse bed slope at the bifurcation on bed load transport. Both works are based on the assumption of steady forcing conditions. Recent experimental observations on gravel-bed channel divisions (Bertoldi et al. 2005) have shown that bar migration along the upstream channel induce time fluctuations in water and sediment feeding of the downstream branches, which significantly affect the morphological behaviour of the system. In the first part of this paper we extend the model proposed by Bolla Pittaluga et al. 2003a to account for such an effect. In the second part of the paper we also investigate the effect of water discharge fluctuations, which are invariably observed in gravel-bed streams in mountain regions, on the time evolution of a channel bifurcation. Results show that both sources of unsteadiness lead to significantly different and richer scenarios of the possible solutions of the system with respect to the steady case conditions.

1 INTRODUCTION

Gravel-bed braided rivers are highly complex natural systems. Such a complexity arises from the coexistence of many morphological structures with different spatial dimensions which evolve on different time scales, interacting in a strongly nonlinear way with each other. Braided river networks are originated and maintained by the tendency of a stream flowing over a non-cohesive sediment bed to bifurcate, generating a channel division. Much research effort has been devoted to study the conditions leading to the generation of a bifurcation, both through experimental approaches (see for instance the classical work by Ashmore (1991) and the more recent study by Bertoldi & Tubino (2005)) and theoretical analyses (Repetto et al. (2002), Slingerland & Smith (1998), Hall (2005)).

Many researches have also studied already formed river bifurcations, trying to characterise their morphological behaviour, the understanding of which is a fundamental step to predict the evolution of the entire network. Experimental observations by Federici & Paola (2003), Bertoldi & Tubino (2005) and field observations by Zolezzi et al. (2005) have brought very informative insight on the characteristics of river bifurcations in gravel-bed rivers. Among the observations reported by the authors we recall here that gravel-bed channel bifurcations are highly unstable systems, particularly at low values of the Shields parameter, and often tend to close one of the two branches. Moreover, even when the two branches keep open over time, the configuration of the bifurcation is typically strongly asymmetrical with one of the tributaries carrying most of the water and sediment discharges. Observations also suggest that the transverse exchange of sediments just upstream of the bifurcation, due to locally significant values of transverse gradient of bottom elevation, plays a key role on the morphological evolution of the system.

Bolla Pittaluga et al. (2003a), Miori et al. (2005) and (2006) have proposed models based on a one dimensional description of the flow, which, in spite of their simplicity, successfully reproduce the aforementioned features. Their models are essentially based on the use of physically based nodal point conditions at the bifurcation, which allow to reproduce the effect

Copyright © 2006 Taylor & Francis Group plc, London, UK

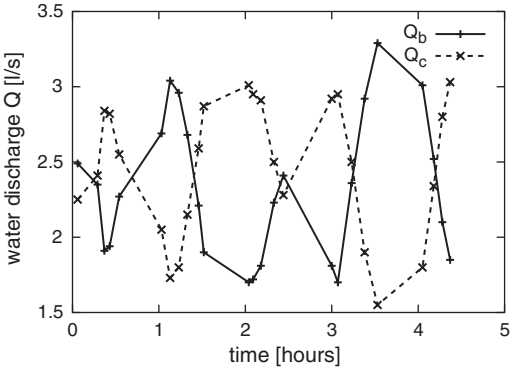


Figure 1. Water discharges measured in the two branches of a bifurcation versus time, in the presence of alternate bars migrating along the upstream channel (from Bolla Pittaluga et al. 2003a).

of transverse bed slope at the bifurcation on bed load transport.

The above models assume steady forcing conditions, however, such conditions are never met in natural braided networks. Unsteadiness may arise, among other effects, from water discharge fluctuations, migration of large scale bedforms along the channels, continuous rearrangements of the network, backwater effects due to changes in downstream boundary conditions of each channel. Experiments performed by Bertoldi et al. (2005) on bifurcations with fixed banks and movable bed have shown that if alternating bars form in the upstream channel their migration towards the bifurcation may induce time fluctuations of water and sediment distribution into the two downstream branches, thus strongly affecting the morphological behaviour of the system. The authors also observed that the complete abandonment of one of the two bifurcating channels, i.e. the obliteration of a bifurcation, is almost invariably associated with the highly non-symmetrical distribution of water and sediment supply into the downstream branches due to the migration of a bar towards the bifurcation. The importance of bars migration in the upstream channel was also recognised by Bolla et al. (2003a) who performed experiments in a straight flume whose downstream part of was divided into two parts of equal width, through a longitudinal panel, thus simulating a simple bifurcation. This is shown in figure 1, from Bolla Pittaluga et al.'s (2003a) paper, in which the measured water discharges into the downstream branches are shown to fluctuate periodically due to bars migration in the upstream channel.

Water discharge fluctuations may also play an important role in governing the morphology of natural river bifurcations, however, to our knowledge no experimental or theoretical studies focused on the role of discharge unsteadiness on bifurcation development yet exist.

With the present paper we extend the model proposed by Bolla Pittaluga et al. (2003a) to account for various unsteadiness forcing effects on bifurcations morphological behaviour. The main aim of the work is to provide some informations on the time evolution of bifurcations in natural environments. Results should not be regarded as quantitatively significant but bear, in our opinion, a conceptual value. Obviously, they will have to be corroborated by field or laboratory observations not yet available. Theoretical results may also help to set up proper experiments to understand the dynamics of river bifurcations, an endeavour which is presently being carried out.

In the first part of the paper we introduce in the model the effect of migration of alternating bars along the upstream channel. This is done in a very simple way by letting the transverse distribution of sediment discharge in the upstream channel fluctuate with time. Even with such a simple forcing, the adopted nodal point conditions reproduce a very sensible behaviour of the bifurcation, leading to the generation of an inlet step, i.e. a difference between bed levels at the mouths of the downstream branches, which fluctuates in time and affects in a complex way the behaviour of the system. Results obtained are in qualitative good agreement with experimental observations by Bertoldi et al. (2005). The model shows that the effectiveness of alternating bars in governing the behaviour of the bifurcation essentially depends on the ratio between the characteristic time scale of bars migration and the intrinsic time scale of evolution of the bifurcation. If such a ratio is small, bar migration does not strongly modify the morphological behaviour of the bifurcation while it becomes of major importance as this ratio is progressively increased. The model also predicts that migration of large and slow enough alternate bars may lead to the complete abandonment of one of the two branches; this was never observed by Bolla Pittaluga et al. (2003a).

In the second part of the paper we account for water discharge variations in time. We consider a simple hydrograph consisting of sinusoidal water discharge fluctuations superimposed to a steady flow. This hydrograph roughly models the feeding of a proglacial braided river in which formative conditions are mainly due to snow melt and water discharge variations are almost periodical, being strictly related to daily temperature variations. A very good example of this kind of hydrograph is found in the Sunwapta river (Jasper National Park, Alberta, Canada) during the ice melting season, as reported by Chew & Ashmore (2001). The model shows how such an unsteady forcing leads to time dependent equilibrium configurations of a bifurcation which may be either symmetrical, with both branches being fed with the

Copyright © 2006 Taylor & Francis Group plc, London, UK

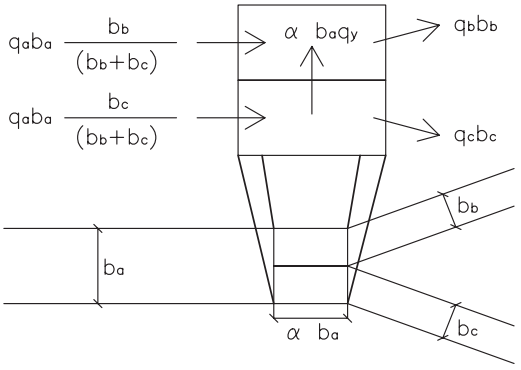


Figure 2. Sketch of the nodal point conditions proposed Bolla Pittaluga et al. (2003a).

same water and sediment discharges, or strongly non symmetrical.

2 FORMULATION OF THE PROBLEM

In the present paper we model morphological behaviour of a gravel-bed river bifurcation with fixed banks through a one dimensional approach. To this end we employ the nodal point conditions originally proposed by Bolla Pittaluga et al. (2003a), whose essential aspects are briefly recalled below; the reader is referred to Bolla Pittaluga's (2003a) and (2003b) papers for a fully detailed description of the model. Let us denote with the subscript letter a the upstream channel of the bifurcation and with b and c the downstream branches, respectively. The nodal point conditions are based on the following ideas. The most downstream part channel a is thought of as being divided into two longitudinal cells of length αb_a, with α an order one parameter and b_a the width of the upstream channel (see figure 2). The authors assume that at an upstream distance of αb_a from the bifurcation the flow in the upstream channel is not affected by the presence of the bifurcation. The nodal point conditions are obtained applying the Exner equation to both such cells and are written by the authors as

$$\frac{1}{2}(1-p)\left(1+\frac{b_a}{b_b+b_c}\right)\frac{\mathrm{d}\eta_i}{\mathrm{d}t} + \frac{q_i - q_a\left(\frac{b_a}{b_b+b_c}\right)}{\alpha b_a} \mp \frac{q_y}{b_i} = 0 \qquad (i=b,c). \tag{1a,b}$$

In the above equations p is sediment porosity, η_i is bed elevation, q_i is the sediment discharge per unit width in channel i, t is time and q_y represents the transverse exchange of sediments per unit width between the two cells. The latter term is evaluated in analogy to the two dimensional case: both the transverse flow velocity effect and the gravitational effect due to the transverse bed slope, which is responsible for the deviation of particle trajectories from flow direction, are accounted for. All the above terms are evaluated through gross relationships involving channels widths b_i, water depths D_i, bed elevations η_i and water discharges Q_i of each branch i. Such relationship are not reported here for the sake of brevity.

Equations (1a,b) are coupled with a water discharge balance and water level constancy relationships at the nodal point to obtain the five nodal point conditions required for the problem to be well posed.

To evaluate the time evolution of a bifurcation system we employ a "local approach" following Miori et al. (2005) and (2006). In fact, we couple the five nodal point conditions with rate-discharge relationships (in the form of uniform flow equations) for the two downstream branches b and c and prescribe a value of the ratio S_b/S_c between the slopes of the two branches, under the assumption that such a ratio is likely to be controlled by the mechanism of generation of the bifurcation and by the topographical characteristics of the network rather than by the evolution of the bifurcation itself. We thus solve 8 equations for the unknowns Q_b, Q_c, D_b, D_c, η_b, η_c, S_b and S_c. Notice that the time scale of system evolution is set by the nodal point conditions (1a,b); this justifies the use of the adjective "local" for this approach. Physically this means that we are neglecting the influence exerted on the bifurcation morphology by downstream conditions. Miori et al. (2006) stress the importance of adopting such an approach to correctly model the time scale of evolution of the bifurcation.

3 THE CASE OF STEADY FORCING CONDITIONS

Before proceeding it is worth while to briefly recall the main results obtained by Bolla Pittaluga et al. (2003a) in the case of a simple channel bifurcation, with downstream branches of equal width, subject to steady forcing conditions (as discussed by the authors, the assumption of $b_b = b_c$ is not essential for the validity of the results discussed below and will be adopted in the rest of the present paper). Bolla Pittaluga et al. (2003a) identify the equilibrium configurations of the system and analyse their stability. For given values of channel slope S_a and width ratio $\beta_a = b_a/(2D_a)$ in the upstream channel their model predicts the existence of a unique equilibrium solution for large enough values of the Shields parameter ϑ_a in the upstream channel. This solution is symmetrical, i.e. both branches are fed with the same water discharge. In this case the solution is stable. As the value of the Shields parameter is decreased two further solutions appear, one

Copyright © 2006 Taylor & Francis Group plc, London, UK

reciprocal to the other, according to which the configuration of the bifurcation is strongly unbalanced and one of the two channels is fed with a much larger discharge than the other. When three solutions exist the unbalanced ones are stable and the symmetrical one is, on the other hand, unstable. In figure 3 the curve in the plane (β_a, ϑ_a) separating the regions where one and three equilibrium solutions exist is plotted for different values of the upstream channel slope S_a.

In figures 4a,b two examples of time behaviour of a bifurcation are shown in terms of the ratio $r_Q = Q_b/Q_c$ between water discharges into the downstream branches. Each line in the two plots refers to a different initial state of the system. Moreover, in the figures T denotes a dimensionless time, scaled with the morphological time scale of the system as

$$T = \frac{t}{D_a b_a / q_a}. \qquad (2)$$

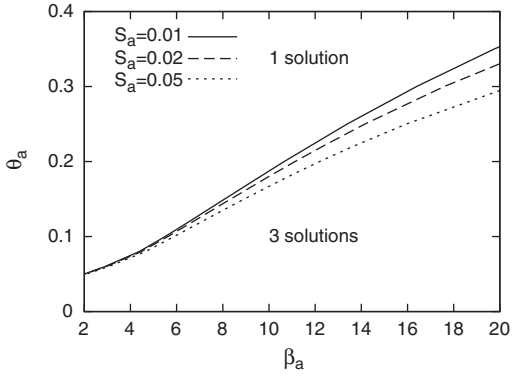


Figure 3. Curves in the plane (β_a, ϑ_a) separating the regions where the model predicts the existence of one or three equilibrium solutions. Each curve corresponds to a different value of the upstream channel slope S_a.

In the case of figure 4a the symmetrical solution is stable and the ratio r_Q tends to 1, whatever the initial condition. On the other hand in figure 4b the situation is represented in which three solutions exist. As in this case the symmetrical solution is unstable the bifurcation evolves towards either one of the unbalanced equilibrium configurations, depending on the initial value of r_Q.

4 THE EFFECT OF BARS MIGRATION ALONG THE UPSTREAM CHANNEL

Bolla Pittaluga et al. (2003a) assume that at an upstream distance αb_a from the bifurcation point, i.e. at the inlet of the two longitudinal cells depicted in figure 2, flow characteristics and bed topography are not affected by the presence of the bifurcation. Consequently, the authors impose that sediment discharge is uniformly distributed in the transverse direction at the entrance of the two cells. This implies that each cell is fed by a fraction of the total sediment discharge which is proportional to its upstream width (see labels in figure 2). This is obviously not true if alternating bars are migrating along the upstream channel: in this case one should expect the transverse distribution of sediment discharge to periodically vary in time as bars approach the bifurcation. In the light of the scheme of the nodal point conditions proposed by Bolla Pittaluga et al. (2003a) this implies that the longitudinal cells of figure 2 are alternatively fed with an excess or a defect of sediment discharge, with respect to the average value.

In the following we use the above observations to include the effect of migrating bars in the model. If we assume that the two downstream branches have equal width and assume that transverse time variations of sediment discharge are purely sinusoidal we can write

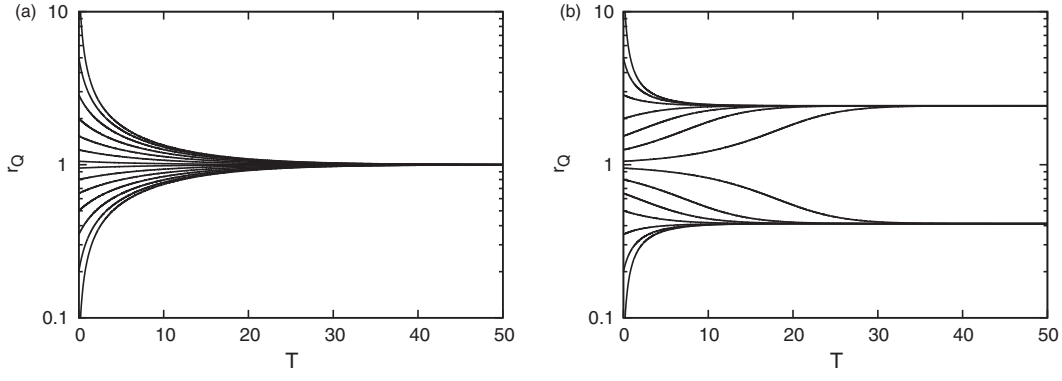


Figure 4. Time evolution of the ratio $r_Q = Q_b/Q_c$ between water discharges into the two branches starting from different initial conditions, in the case of steady forcing. (a) The symmetrical solution is stable ($\vartheta_a = 0.2$, $\beta_a = 10$, $S_a = 0.01$); (b) the symmetrical solution is unstable and the unbalanced solutions are stable ($\vartheta_a = 0.175$, $\beta_a = 10$, $S_a = 0.01$).

Copyright © 2006 Taylor & Francis Group plc, London, UK

the sediment discharge Q_s^{in} feeding the each of the two cells as

$$Q_{s\,b}^{in} = \frac{1}{2} b_a \left[q_a + A \sin(\omega_b t) \right], \tag{3a}$$

$$Q_{s\,c}^{in} = \frac{1}{2} b_a \left[q_a - A \sin(\omega_b t) \right], \tag{3b}$$

where A is the amplitude of sediment discharge variations due the presence of alternate bars and ω_b is the frequency of bar migration. The above relationships can be easily extended to the case of channels with different widths simply by assuming a sensible transverse distribution of sediment discharge. This endeavour, however, does not add any conceptual novelty to the present analysis and is not pursued in the following. Notice that, according to the philosophy of the nodal point conditions adopted, the sediment discharges feeding the two cells is assumed independent of the state of evolution of the bifurcation since the length of such cells (equal to αb_a, with α of order 1) is defined as the upstream distance from the bifurcation at which flow conditions and bed topography are not affected by the presence of the bifurcation.

Figure 5a shows the time behaviour of the bifurcation subject to the above time dependent forcing conditions in terms of the parameter $\Delta = (\eta_c - \eta_b)/D_a$, which represents the dimensionless height of the bed inlet step between the two downstream branches. As in the case of figures 4a,b, and in all the following figures, each line refers to a different initial condition of the system. It appears that, due to the time-dependent non-uniform transverse distribution of sediment discharge imposed upstream of the bifurcation, the nodal point conditions generate perturbations of the bed elevations at the inlets of the downstream branches which suitably model the presence of alternating bars close to the bifurcation.

Once established that the use of equations (3a,b) to describe the sediment feeding of the two cells provides a simple way to suitably include the effect of bar migration in the model let us now turn to a more substantial matter: how do migrating bars influence the morphological behaviour of a bifurcation?

In our model the characteristics of migrating bars are fixed by prescribing the values of the parameters ω_b and A. Let us first investigate the role of bars celerity. We may define a characteristic time scale of bar

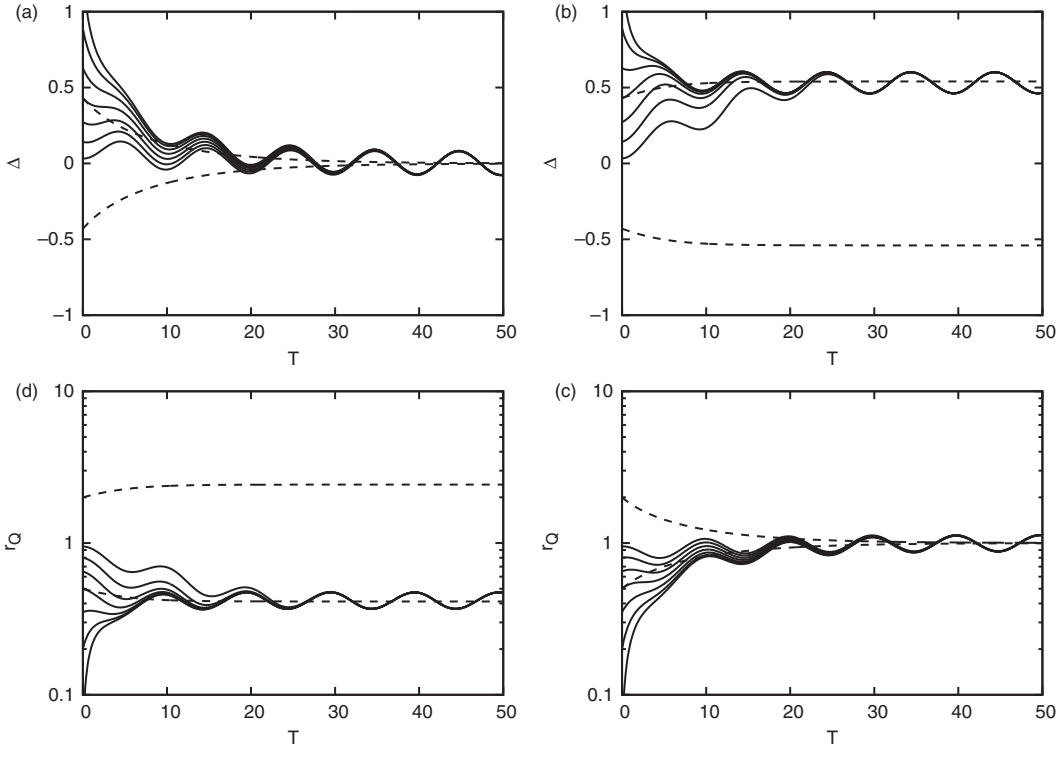


Figure 5. Time evolution of $\Delta = (\eta_c - \eta_b)/D_a$ (a,b) and $r_Q = Q_b/Q_c$ (c,d) starting from different initial conditions in the presence of alternate bars migrating along the upstream channel (continuous lines) and in the case of steady forcing conditions (dotted lines). $T_b/T^* \sim 10$, $\beta_a = 10$, $S_a = 0.01$, (a) and (c) $\vartheta_a = 0.2$, (b) and (d) $\vartheta_a = 0.175$.

Copyright © 2006 Taylor & Francis Group plc, London, UK

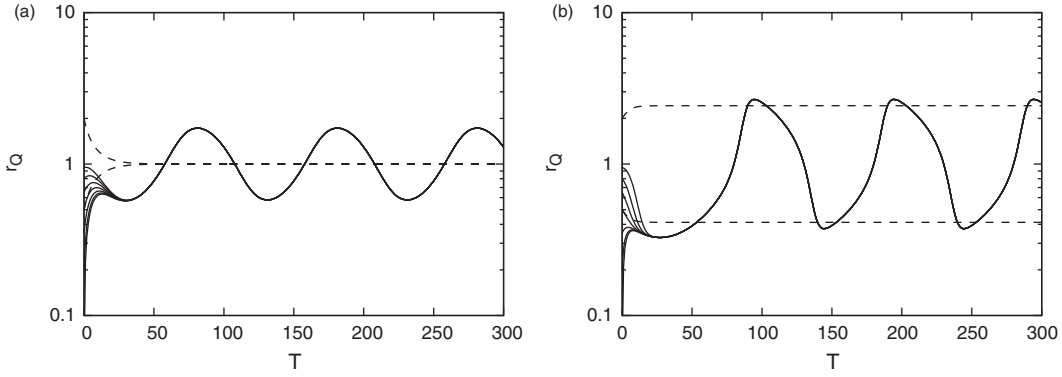


Figure 6. Time evolution of $r_Q = Q_b/Q_c$ starting from different initial conditions, in the presence of alternate bars migrating along the upstream channel (continuous lines) and in the case of steady forcing conditions (dotted lines). $T_b/T^* \sim 100$, $\beta_a = 10$, $S_a = 0.01$, (a) $\vartheta_a = 0.2$, (b) $\vartheta_a = 0.175$.

migration as $t_b = 2\pi/\omega_b$, that can be made dimensionless as $T_b = \frac{t_b}{D_a b_a/q_a}$. The other (dimensionless) time scale which plays a role in the problem is the intrinsic time scale of evolution of the bifurcation, say T^*. Such a time scale is set by the nodal point conditions and can be readily obtained fitting the asymptotic behaviour of any variable characterising the state of the bifurcation, say f (for instance r_Q in figures 4a,b), towards the stable equilibrium configuration f_{eq} with an exponential function of the kind $f_{eq} - C\exp(-T/T^*)$. Considering the upstream flow conditions of figure 4b, it is found that T^* is of order 10. It is reasonable to expect the effect of bar migration on the dynamics of the system to depend on the ratio T_b/T^*.

Figures 5a–d are obtained using a low value of such a parameter ($T_b/T^* \sim 1$), i.e. they represent the effect of fairly rapidly migrating bars (the value of A is also small). In figures 5a,c the parameters adopted are the same as in figure 4a, i.e. in the absence of alternate bars the model predicts that the symmetrical solution is stable (in all the following figures the time evolution of the system in the case of steady forcing conditions is plotted with dotted lines). It appears that, in this case, whatever the initial conditions of the system, the bifurcation evolves towards a time dependent solution which oscillates about the symmetrical configuration. Similarly, figures 5b,d depict the case of a bifurcation in which the symmetrical equilibrium configuration is unstable in the case of steady forcing conditions (figure 5d can be directly compared to figure 4b). Again it appears that the system evolves towards a periodic solution in which each variable oscillates about the the value it assumed in the case of steady forcing conditions. In other words, if alternate bars are fairly small and fast, it is still possible for the system to evolve towards either the symmetrical configuration or towards unbalanced solutions, depending on the dimensionless parameters which characterise the flow in the upstream channel (namely ϑ_a, β_a and S_a). Obviously, when the effect of migrating bars is included such solutions are not steady but periodic in time.

The scenario of the possible solutions is dramatically modified if the ratio T_b/T^* is progressively increased, leaving unchanged the amplitude A, i.e. if alternate bars migration is slowed down. This is shown in figures 6a,b which are obtained for the same values of ϑ_a, β_a and S_a adopted in the previous figures and for $T_b/T^* \sim 10$. In this case the effect of bars completely dominates the behaviour of the system. Indeed, in both cases, the system oscillates about the symmetrical configuration, alternatively feeding preferentially one of the two branches, no matter if, in the case of steady forcing conditions, the symmetrical solution is stable or not. Notice that a gross calculation relative to the case of a gravel bed mountain river, based on a linear stability analysis for bar formation (Colombini et al. (1987)), suggests that T_b/T^* attains a value of order 1. However, preliminary experimental observation conducted in the Hydraulic Laboratory of the University of Trento have also shown that, when migrating bars approach a bifurcation, they tend to significantly slow down their migration speed. Thus the model suggests that, if alternate bars are present in the upstream branch, they may crucially affect the behaviour of the system.

Finally, if we keep fixed such the ratio T_b/T^* and increase A, i.e. simulate the migration bars with a larger amplitude, the scenario is further modified, as shown if figures 7a,b. In this case the system rapidly evolves towards the complete abandonment of one of the two branches. This is in good agreement with the observations of Bertoldi et al. (2005) according to which the closure of one of the two branches is almost invariably associated with the presence, close to the bifurcation, of a strong transverse

Copyright © 2006 Taylor & Francis Group plc, London, UK

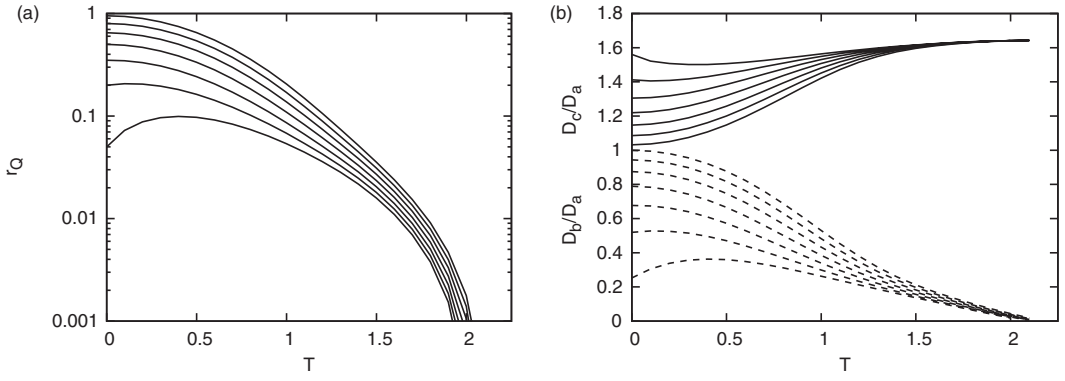


Figure 7. Time evolution of $r_Q = Q_b/Q_c$ (a) and of the dimensionless water depths $D_i/D_a (i = b, c)$ starting from different initial conditions, in the presence of alternate bars migrating along the upstream channel. $T_b/T^* \sim 100$, large amplitude bar, $\vartheta_a = 0.175$, $\beta_a = 10$, $S_a = 0.01$.

bed deformation induced by the presence of a slowly migrating alternate bar.

5 WATER DISCHARGE FLUCTUATIONS

In the present section we consider the effect of discharge variations on the morphological behaviour of a bifurcation. In particular, we focus our attention on the following simple hydrograph

$$Q(t) = Q_0 \left[1 + A_Q \sin(\omega_Q t)\right], \tag{4}$$

consisting of periodic discharge fluctuations of relative amplitude A_Q superimposed to a constant discharge Q_0. Equation (4) roughly models the feeding of a proglacial braided river in which formative conditions are mainly due to snow melt and water discharge variations are almost periodical, being strictly related to daily temperature variations.

The inclusion of discharge fluctuations into the model is straightforward. As in the case of alternate bars, there are two parameters that characterise the unsteady part of the hydrograph: the relative amplitude A_Q and the frequency ω_Q. Following the discussion developed in the previous section, we define the characteristic time scale of discharge variations as $T_Q = 2\pi/\omega_Q$ and compare it with the intrinsic time scale of evolution of the bifurcation T^*.

In figures 8a–d we report, for two different sets of the governing parameters ϑ_a, β_a and S_a (computed using the average discharge Q_0), the time evolution of the ratio r_Q between the discharges into the downstream branches. Results obtained with a constant discharge equal to Q_0 are reported with dotted lines. In each plot the time evolution of water discharge is also shown (right axis scale) to make results more easily readable.

In the case of figures 8a,b, if the discharge is kept constant and equal to Q_0, the system evolves towards the symmetrical solution while in the case of figures 8c,d such a solution is unstable and the bifurcation eventually develops to an unbalanced solution. When the discharge varies in time the situation is more complicated. Indeed, as recalled in section 3, the symmetrical equilibrium configuration, which is stable at large values of the Shields parameter (i.e. for large discharges), may become unstable as ϑ_a decreases (i.e. when the discharge falls). This seems to suggest that the stability properties of the symmetrical solution may vary during a single hydrograph, with consequences on the morphological behaviour of the bifurcation which are difficult to predict by simple means. Moreover, the time evolution of the system is, obviously, faster for large values of the water discharge as the sediment transport is larger in such conditions and, consequently, the bifurcation is morphologically more active.

Let us consider figures 8a,b first, which are obtained setting $A_Q = 0.25$ and $T_Q/T^* \sim 15$ and 60, respectively. The ratio T_Q/T^* does not seem to play an important role in this case: in both situations the bifurcation evolves towards the symmetrical solution. Notice, however, that such a solution is not steady because, even if the ratio $r_Q = Q_b/Q_c$ tends to unity, water discharges in each branch are time dependent. For the chosen values of the parameters, the symmetrical solution is, presumably, not stable for all values of the water discharge reached during the hydrograph, as it seems to be suggested by the time oscillations that r_Q displays in figure 8a. It is so, however, for most part of the hydrograph and, since the time evolution of the system is much slower for low values of the water discharge, the system is unable to leave the symmetrical configuration once it has reached it. Such

Copyright © 2006 Taylor & Francis Group plc, London, UK

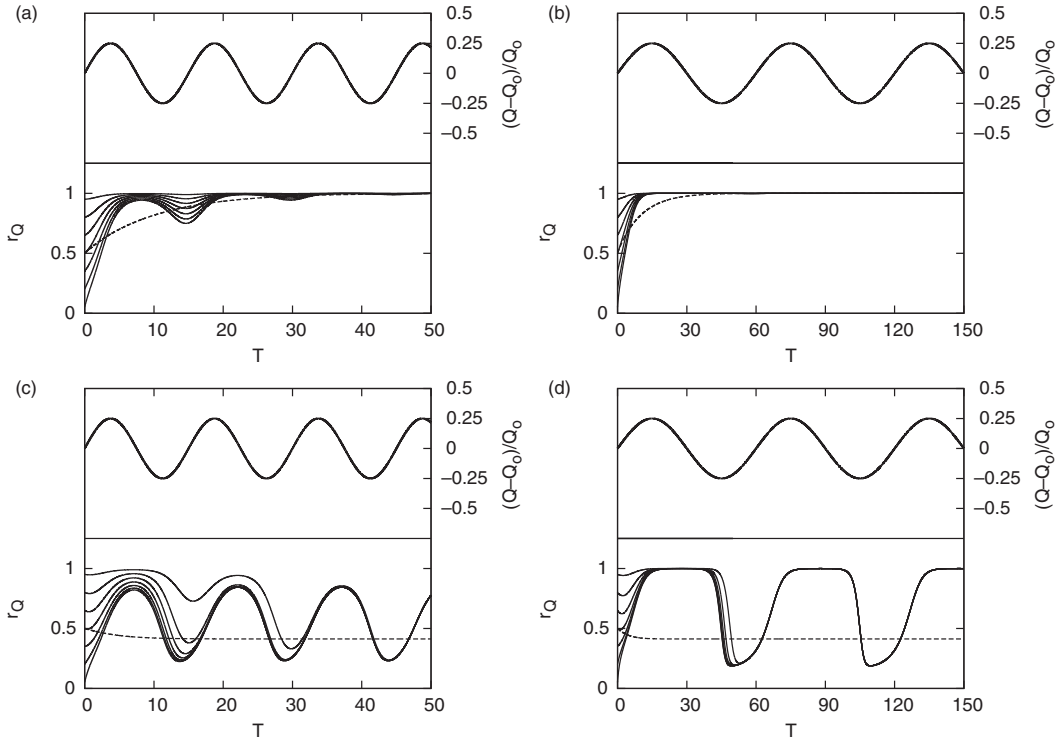


Figure 8. Time evolution of $r_Q = Q_b/Q_c$ starting from different initial conditions, in the case of water discharge fluctuations (continuous lines) and in the case of steady forcing conditions (dotted lines). In each plot the value of the water discharge is also plotted (right axis scale). $A_Q = 0.25$, $\beta_a = 10$, $S_a = 0.01$; (a) $T_Q/T^* \sim 15$, $\vartheta_a = 0.2$; (b) $T_Q/T^* \sim 60$, $\vartheta_a = 0.2$; (c) $T_Q/T^* \sim 15$, $\vartheta_a = 0.175$; (d) $T_Q/T^* \sim 60$, $\vartheta_a = 0.175$.

a solution is thus approximatively maintained during the entire cycle.

In figures 8c,d the counterpart situation is shown, in which, for $Q = Q_0$, the symmetrical solution is unstable and the two unbalanced solutions are stable. Again figure 8c is obtained for $T_Q/T^* \sim 15$ and figure 8d for $T_Q/T^* \sim 60$; in both cases $A_Q = 0.25$. It appears that, during each cycle of the hydrograph, the bifurcation configuration oscillates about some unbalanced state. In the case of slow water discharge fluctuations, however, the system reaches and maintain for a certain time the symmetrical configuration, which is the only state of the bifurcation to represent a stable solution of the system for more values of the discharge during the hydrograph.

6 CONCLUSIONS

In the present paper we have extended the model proposed by Bolla Pittaluga et al. (2003a) to account for the effect of unsteady forcing conditions. In particular we have considered both bar migration along the upstream channel and water discharge fluctuations. Both sources of unsteadiness are very likely to affect the morphological behaviour of bifurcations in gravel-bed braided rivers.

The effect of bar migration has been included into the model through a simple approach which is based on the assumption that the sediment discharge in the upstream channel has a time dependent transverse distribution. The effectiveness of the presence of bars on the dynamics of the bifurcation is found to depend on the ratio between the characteristic time scale of bar migration and the intrinsic time scale of evolution of the bifurcation, which is set by the nodal point conditions. If such a ratio is large enough the presence of bars dominates the morphological behaviour of the system, no matter what such a behaviour would be in the absence of bars. The model also shows that the migration through the bifurcation of large amplitude bars may induce the complete closure of one of the two branches.

Water discharge variations have also been considered in the paper, assuming a simple hydrograph consisting of sinusoidal fluctuation superimposed to a

Copyright © 2006 Taylor & Francis Group plc, London, UK

steady condition. The model shows that the dynamics of the system in this case is much more complicated and richer with respect to the case of steady forcing conditions.

ACKNOWLEDGEMENTS

This work has been developed within the framework of the "Centro di Eccellenza Universitario per la Difesa Idrogeologica dell'Ambiente Montano-CUDAM", of the project "La risposta morfodinamica di sistemi fluviali a variazioni di parametri ambientali COFIN 2003" co-funded by the Italian Ministry of University and Scientific Research and the University of Trento and of the project "Rischio idrogeologico e morfodinamica fluviale RIMOF" co-funded by Fondazione Cassa di Risparmio di Verona, Vicenza, Belluno e Ancona and the University of Trento.

REFERENCES

Ashmore, P. E. (1991). How do gravel-bed rivers braid? *Canadian Journal of Earth Sciences 28*: 326–341.

Bertoldi, W., A. Pasetto, L. Zanoni, and M. Tubino (2005). Experimental observations in channel bifurcations evolving to an equilibrium state. In G. Paker and M. Garcia (Eds.), *Proceedings of "RCEM 2005"*, Volume 1, Urbana-Champaign, Illinois, USA: 409–419.

Bertoldi, W. and M. Tubino (2005). Bed and bank evolution of bifurcating channels. *Water Resour. Res. 41*.

Bolla Pittaluga, M., R. Repetto, and M. Tubino (2003a). Channel bifurcation in braided rivers: equilibrium configurations and stability. *Water Resour. Res. 39*(3): 1046–1059.

Bolla Pittaluga, M., R. Repetto, and M. Tubino (2003b). Correction to "Channel bifurcation in braided rivers: equilibrium configurations and stability". *Water Resour. Res. 39*(11): 1323.

Chew, L. C. and P. E. Ashmore (2001). Channel adjustment and a test of rational regime theory in a proglacial braided stream. *Geomorphology 37*: 43–63.

Colombini, M., G. Seminara, and M. Tubino (1987). Finite-amplitude alternate bars. *J. Fluid Mech. 181*: 213–232.

Federici, B. and C. Paola (2003). Dynamics of bifurcations in noncohesive sediments. *Water Resour. Res. 39, No. 6* (1162): 3–15.

Hall, P. (2005). On the non-parallel instability of sediment-carrying channels of slowly varying width. *J. Fluid Mech. 529*: 1–32.

Miori, S., R. Repetto, and M. Tubino (2005). Morphological evolution of bifurcations in gravel-bed rivers with erodible banks. In G. Paker and M. Garcia (Eds.), *Proceedings of "RCEM 2005"*, Urbana-Champaign, Illinois, USA: 421–430.

Miori, S., R. Repetto, and M. Tubino (2006). A one-dimensional model of bifurcations in gravel-bed channels with erodible banks. *Sumbitted for the publication in Water Resour. Res.*

Repetto, R., M. Tubino, and C. Paola (2002). Planimetric instability of channels with variable width. *J. Fluid Mech. 457*: 79–109.

Slingerland, R. and N. D. Smith (1998). Necessary conditions for a meandering-river avulsion. *Geology 26*: 435–438.

Zolezzi, G., W. Bertoldi, and M. Tubino (2005). Morphological analysis and prediction of river bifurcations. In *Braided River 2003* (Blackwell, UK. ed.).

Copyright © 2006 Taylor & Francis Group plc, London, UK

Sediment dynamics in anabranched channels of the Loire River: The study case of Ingrandes (France)

S. Rodrigues & J.N. Gautier
Equipe Pluridisciplinaire Plan Loire Grandeur Nature, Agence de l'Eau Loire-Bretagne, Orléans, France

J.J. Peters
Bruxelles, Belgique

ABSTRACT: Engineering works were carried out on the Loire River (France) in order to stop the incision of its main channel at the site of Ingrandes characterized by a bifurcation. Topo-bathymetric data collected during and between floods on two channels of the site (main and secondary channel) evidenced an impact of the works on the sediment budgets of the main channel while their impact on the secondary channel seems low. For this secondary channel, the first results show that the morphological evolution of the secondary channel is governed by the growth and migration of large sandwaves. The first results presented here suggest that the dynamic behaviour of bars and dunes is strongly influenced by the morphological configuration and by variation in bedload pulses and discharge. A displacement of the thalweg of the anabranch is also highlighted and linked to the migration of large sandwaves. Scour chains show that reworking of the sediments previously deposited can be significant and can precede sediment deposition. Data presented here constitute the first step of the study and will be completed in order to analyse the behaviour of the anabranched channels system in the Loire.

1 INTRODUCTION

The rapid intensification of the incision of river beds over the last 200 years (Arnaud-Fasseta, 2003) was noted on several European (Petts et al., 1989) and French rivers (Peiry, 1987, Bornette et al. 1996, Bravard et al. 1997, Piégay et al. 2000). The largest river of France, the Loire River, was subjected to this phenomenon. Particularly, a severe deepening of its main channel (with maximum values ranging from 2 to 5 m) was recorded on the reach between Angers and Nantes. This incision is one of the consequences of human activities. Dyke raising since the Middle Ages and construction of oblique groynes during the 19th and 20th century have substantially reduced the width of the river, and thus, have contributed to its incision. Moreover, recolonisation of the upper basin by vegetation, constructions of dams, and intense sediment extraction between 1950 and 1995 (Dambre & Malaval 1993, Belleudy 2000) have reduced the quantity of sediments delivered to the river and thus, accentuated the incision process. Concurrently, a rapid colonization of the shallow secondary channels by woody vegetation and a significant sediment aggradation (Rodrigues et al. 2006) of these areas have caused a reduction of the flow conveyance capacity (increasing the flooding risk). The incision of the main channel contributed to weaken the foundations of bridges and dykes, to dry up the water wells and to decrease the habitat diversity.

In order to stop the incision on the downstream reaches of the river, different kinds of operations have been considered. Particularly, two artificial sills were constructed in the site of Ingrandes where the river bed is asymmetrical and divided into two channels (a deep main channel and a shallow secondary channel). The sills were inserted in the main channel during summers 2002 and 2003 in order to increase the water level during low flows and activate consequently the flow in the secondary channel. An environmental survey was carried out before, during, and after, the construction of the sills in order to monitor the evolution of the stream bed in this area and to improve the knowledge concerning flow and sediment transport processes in the Loire (Peters, 2002).

The paper presents the preliminary results of the study performed on the secondary channel. It aims to understand the sedimentological mechanisms that govern the morphological evolution of the secondary channel and to provide new elements intended for a better management of the river bed. From data and observations collected during and after floods, we will try to explain the morphological response of the bifurcation to flood events of different magnitudes, as well as to the river works done on the main channel.

Copyright © 2006 Taylor & Francis Group plc, London, UK

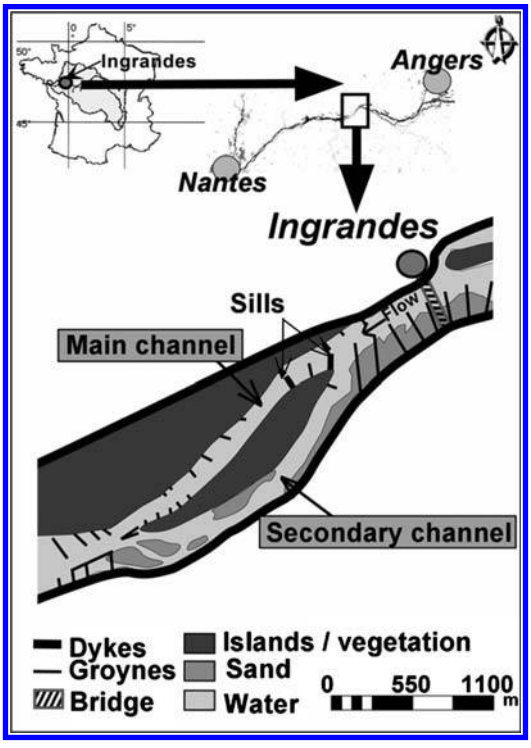


Figure 1. Location of the study site of Ingrandes.

2 STUDY AREA

2.1 *Location and morphological configuration*

The study site of Ingrandes is located approximately 30 km downstream of Angers. In this area the bedrock consists in Devonian and Carbonifereous rocks. At Ingrandes, the presence of resistant conglomerates on the right bank strongly deflects the river course. In this area, the river bed is restricted between dykes and groynes (Fig. 1). Their presence reinforces the asymmetrical configuration of the bed by deflecting the flow towards the deep main channel during low water levels. Close to the village of Ingrandes, the stream bed is characterized by an inflexion and by an average slope of *ca* 0.00025 m/m. The bedload of the river consists in a mixture of sands and gravels. At the gauging station of Montjean (located 6 km more upstream), the discharge is 850 m^3s^{-1} in average and approximately 3200 m^3s^{-1} for the 1-in 2-year flood.

At the upstream part of the study site, the river bed restricted between dykes is 570 m wide and most of the flow is drained by the main channel located on the right bank. Groynes along the left bank determine a higher sandy flat zone that is flooded only during high water levels. Further downstream, the bed divides into two anabranches separated by a vegetated island. The northern branch (main channel) is narrower and deeper than the secondary channel located on the left bank. This can be explained by the effect of the groynes. The secondary channel is 3070 m long and its average width is 300 m. Relics of groynes present in the upstream and downstream parts of this channel affects its morphology: *e.g*. the pool located at the entrance of this branch (on the right bank) is due to the presence of an ancient groyne. A second pool is present in the median part of the channel (left bank). The angle of the downstream connection between the main and the secondary channel is approximately 45°; in this area there is a significant slope discontinuity between the two channels.

2.2 *Works performed for raising the water level at the bifurcation to change the flow distribution*

During summers 2002 and 2003, two artificial sills were constructed in the main channel in order to increase the water level during low flows. These sills are located downstream of the bifurcation (where ancient groynes were present) in order to enhance the inflow into the disconnected secondary channel, mainly during low flows. The sills are connected to the banks of the main channel and are oriented upstream; they are indented in their middle part. The structure consists in boulders (for the foundations) covered with geotextile fenders filled of sand and gravels.

2.3 *Influence of sills on flow distribution and morphological evolution*

As expected, the presence of the sills has induced a raising of the water surface of 0.5 m at Ingrandes during low flows. Concurrently, the duration of inundation of the secondary channel has increased as well as the discharges, restoring the flow balance between the two channels. For a total discharge ranging between 700 and 1200 m^3s^{-1}, discharges recorded in the main channel after the works are 100 m^3s^{-1} lower than those measured before the construction of the sills. Concerning the morphology, the presence of the sills has contributed to a deep scouring just downstream of each sill. Another unwanted effect was the destabilization of the sills close to the banks as a result of the collapse of the bank of the island located between the two channels.

3 METHODS

In order to explain changes of the stream bed morphology, topo-bathymetric surveys were done on the whole reach since 1999. In both main and secondary channels, surveys consisted in bathymetric measurements done using a single-beam echosounder (ATLAS DESO 22). Transverse transect sounding lines were

Copyright © 2006 Taylor & Francis Group plc, London, UK

spaced of 45 m. Longitudinal tracks (almost parallel to the river banks) were also carried out in order to analyse the evolution of the bedforms during flood events (Peters, 1971, Peters, 1978, Ten Brinke et al. 1999, Wilbers & Ten Brinke, 2003). During the bathymetric measurements, the positioning of the vessel was ensured by a differential global positioning system (DGPS Trimble 4700). When the secondary channel was dry, additional topographic measurements were performed in order to detail the morphological evolution of this branch of the river. These measurements were also done using the DGPS.

Digital elevation models (DEMs) were calculated for each topo-bathymetric survey using the TIN (triangular irregular networks) method of Arcgis 9. Afterwards, the TINs were converted into grids and the DEMs were compared in order to obtain sediment budgets for both channels. Comparison between DEMs allowed the mapping of the areas of sediment erosion and deposition between two subsequent surveys.

Scour and fill processes occurring in the secondary channel between two dry periods were assessed using scour chains (Hassan, 1990, Laronne et al. 1994, Hassan et al. 1999). Metal-linked chains were inserted vertically, anchored into the stream bed, and located using a differential global positioning system. After the inundation of the secondary channel, scour chains were relocated and the depth to which movements of bed material occurred was determined by measuring the length of the chain above the elbow (giving the maximum scour depth) and the distance between the elbow and the post flood bed (giving the subsequent sediment deposition).

4 RESULTS

4.1 *Sediment budgets and longitudinal profile*

4.1.1 *Sediment balance between the channels since 1999*

It should be noted that the figures given below do not account for the errors and uncertainties on the bathymetric maps. The balance obtained by comparing measured levels represents an average change in bottom elevation of a few centimetres over the entire area of each channels.

The volumes of sediment eroded and deposited between subsequent surveys are presented in Figure 2. Except for survey 3 (topographic survey of the secondary channel only), all the surveys mentioned here are bathymetric ones. Hence, survey 3 is absent of the comparison done for the main channel (Fig. 2a). The survey 7 is a combination of the two kinds of survey (bathymetry for the main channel and topography for the secondary channel). The comparisons done between surveys 1 and 7 (Fig. 2a) show that the volumes of sediment scoured and filled are higher on the main channel than on the secondary channel (Fig. 2a). The negative sediment budget computed between surveys 5 and 6 for the main channel is strongly linked to the development of the pools located close to the sills: for this same period the secondary channel was subject to sedimentation. Except between surveys 6 and 7, the sediment budgets calculated on the main channel for this period are negative and the volumes of scoured material are at a constant level (*ca.* $-300000\,m^3$). Globally, the main channel is subject to sediment erosion.

In the secondary channel, the scoured volumes are variable according to the period considered and are smaller than on the main channel. The maximum value of scoured volumes ($242350\,m^3$) was recorded between surveys 1 and 2. Low values of scoured or deposited volumes calculated between the surveys 2 and 3 are explained by the low discharges recorded during this period (Fig. 2a). Volumes calculated between surveys 3–4 and between surveys 4–5 are not relevant because some data are lacking for the survey 4 (upstream part of the anabranch, see Figure 4). On the basis of the other set of sediment budgets (1–2, 2–3, 5–6, 6–7), it seems that the secondary channel is quite stable. However, the comparison of survey 7 with a topographic survey done in 2002 (not mentioned in Fig. 2) have shown that the secondary channel was subjected to a scouring of $230000\,m^3$ between 2002 and 2005 (the inundated areas were excluded of this calculation).

In order to analyse sedimentation processes during a single flood event, five bathymetric campaigns were performed on the study reach during the flood of April/May 2001. Scoured and deposited volumes computed for different phases of the flood event (Fig. 2b) show similar trends in both main and secondary channel. Nevertheless, in both cases the volumes are higher in the main channel than in the anabranch.

During the rising limb of the hydrograph (between surveys a and c), the morphological response of the channels was different between surveys a and b than between b and c (Fig. 2b). Between a and b (falling level of the previous hydrograph and beginning of the rising of the studied flood), sediment deposition was the dominant process while scouring prevailed in both channels between campaigns b and c ($-33000\,m^3$ for the main channel and $-19000\,m^3$ for the side channel). During the falling limb of the hydrograph, the sediment budgets were positive between surveys c and d and near equilibrium between d and e. For this time lapse, volumes of sediments deposited in the main channel are two times those deposited in the secondary channel.

4.1.2 *Evolution of the longitudinal profile*

Longitudinal bathymetric profiles were compared in order to determine the influence of the sills on the

Copyright © 2006 Taylor & Francis Group plc, London, UK

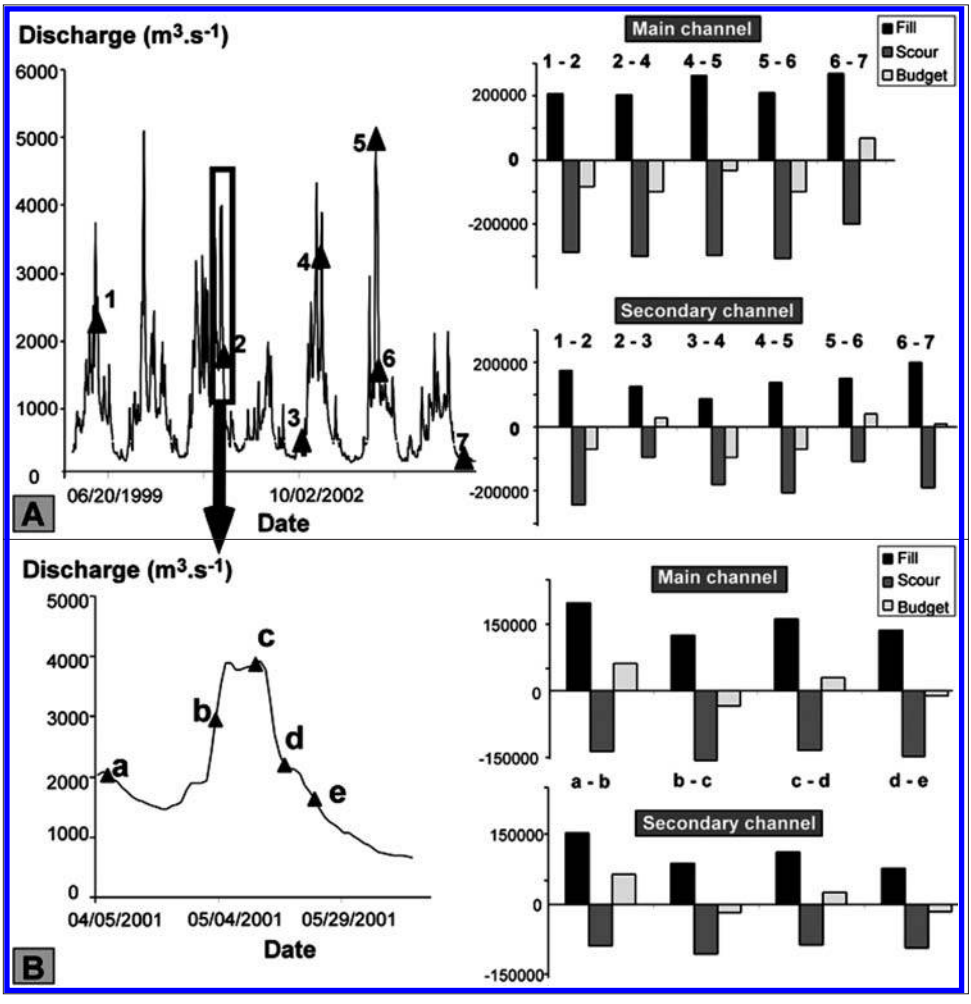


Figure 2. (a) discharge at the gauging station of Montjean (6 km upstream) and sediment budgets computed from digital elevation models (DEM) constructed for the main channel (area located between the upstream sill and the downstream end of the island) and for the secondary channel. Triangles correspond to topographic or bathymetric surveys. Data are lacking for survey 4 (see Fig. 5). (b) sediment budgets calculated for both main and secondary channel during the flood of May 2001; triangles correspond to bathymetric surveys.

sediment dynamics of both main and secondary channels (Fig. 3a, c). In the main channel, an incision – corresponding to the development of scour holes – was noted close to the sills (Fig. 3a, distance 1160 m). This phenomenon is explained by the acceleration of flow, by the chute of the water level and by the presence of significant turbulences. Figure 3a also show the presence of large bedforms in the reach located between the bridge of Ingrandes and the sills (see Fig. 3b for detail).

In the secondary channel (Fig. 3c), the profiles suggest the migration of large sandwaves (distance 1500 m to 2200 m) with superimposed small dunes. Measurements done during the flood of April/May 2001 (Fig. 3b, d) have shown that dunes present in the main channel are characterized by an average height of 2 m while most of the dunes present in the anabranch have a lower height values.

As shown by Figure 3, dunes were less developed in the secondary channel during the rising limb of the hydrograph whereas they were always present in the main channel. The profiles presented in Figure 3 also show that the characteristics of dunes are different according to the stage of the flood, namely rising and falling limbs of the hydrograph. The average height of dunes recorded during survey 2e was lower than during survey 2d.

Copyright © 2006 Taylor & Francis Group plc, London, UK

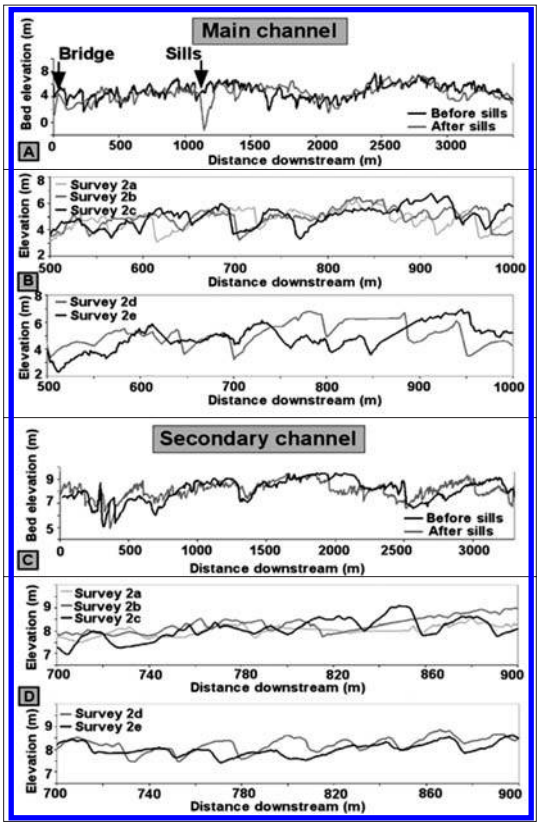


Figure 3. Longitudinal bathymetric profiles measured in the channels of the site of Ingrandes. For discharges, see Figure 2a.

4.2 *Sedimentary behaviour of the secondary channel*

4.2.1 *Morphological evolution of the channel*

The analysis of the DEMs highlighted the presence of relatively stable morphological units such as riffles, pools and a chute. Although these units do not migrate downstream, their morphological evolution is clearly dependent of the migration of 2D sandwaves (Allen, 1984, Ashley, 1990, Miall, 1996), which can partially fill the topographical depressions. The larger of these sandwaves are characterized by a height of 1.5 m, by a wavelength of roughly 500 m, and by an average migration rate of 5 m/day (according to their location in the channel). The slope breaks reported on Figure 4a correspond to lee sides of these bedforms. It seems that large sandwaves growth and extent is linked with the morphological configuration of the secondary channel (*e.g.* migration of sandwave D2 is dependent of the presence of the chute channel). In the downstream part of the channel, sandwaves D5 and D6 amalgamated between March 1999 and April 2001. This coalescence may be due to, in one hand, the confluence with the main channel and on the other hand, to the presence of oblique groynes at the downstream end of the anabranch (see Fig. 1).

The migration of the large sandwaves during flood events influences the variation in position of the thalweg of the secondary channel (Fig. 4b).

The movement of the thalweg is particularly perceptible in the downstream end of the secondary channel (Fig. 4b).

Longitudinal bathymetric profiles measured in order to track dune migration have shown the presence of small dunes (average height of *ca.* 0.35 m) located on the stoss side of the aforementioned sandwaves. The height and length parameters of the small dunes are variable according to the discharge (Fig. 4c). This phenomenon is an evidence of bedload pulses and indicates that large dunes can be reworked during low water levels (Ten Brinke et al. 1999, Carling et al. 2000, Wilbers & Ten Brinke, 2003). This may illustrate changes in hydrodynamics and/or sediment supply during floods. Further investigations will be carried out on this topic in order to understand the sandwaves migration in the secondary channel and to compare these bedforms with those located in the main channel. The maps presented in Figure 4 indicate that sandwaves migration in the anabranch was quite similar before and after the construction of the sills. This observation must be verified with data from the continued monitoring.

4.2.2 *Scour/fill processes*

In order to account for the morphological evolution of the channel bed, topographic differential maps were constructed for this branch of the river (Fig. 5). The comparisons of the DEMs have shown that substantial sediment reworking, linked with sandwaves migration, has occurred between two successive surveys.

The distribution pattern of areas of sediment erosion or deposition is variable according to the period considered: most of the comparisons presented in Figure 5 show that areas of scour and fill are not fixed but tend to migrate downstream. For example, most of the areas scoured between 1997 and 1999 are different from those observed between 1999 and 2001. Moreover, except for comparisons done on a monthly basis (April–May 2001 or January–February 2004), areas of sediment deposition or erosion are clearly separated. Between surveys 1 and 2a (March 1999–April 2001), the migration of sandwave D2 contributed to the filling of pool P2 and the bedform created by the coalescence of sandwaves D5 and D6 was subjected to erosion. The filling of the pool P2 continued until survey 3 (October 2002). Between May 2001 and October 2002 (2e–3), a significant scour of the sandwaves D5 and D6 occurred in spite of a reduced hydraulic activity. During this period, the sandwaves D2 and D3 extended

Copyright © 2006 Taylor & Francis Group plc, London, UK

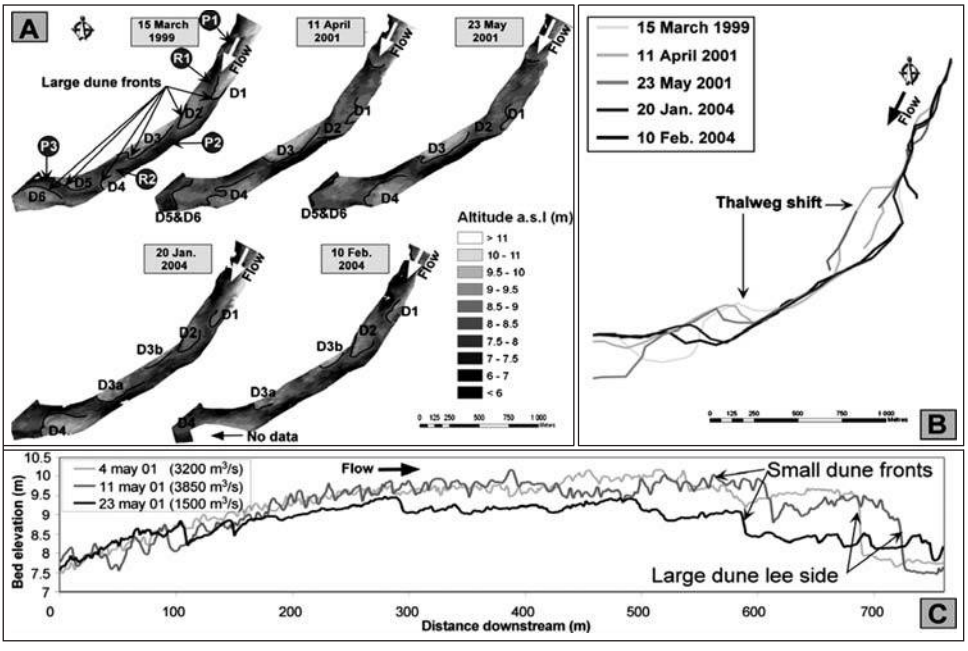


Figure 4. (a) Lee sides of large sandwaves reported on digital elevation models of the secondary channel. P1 to P3 are pools, R1 and R2 are riffles. (b) Thalweg shift in the secondary channel between 15 March 1999 and 10 February 2004. (c) longitudinal bathymetric profile of sandwave D3 for three flow conditions.

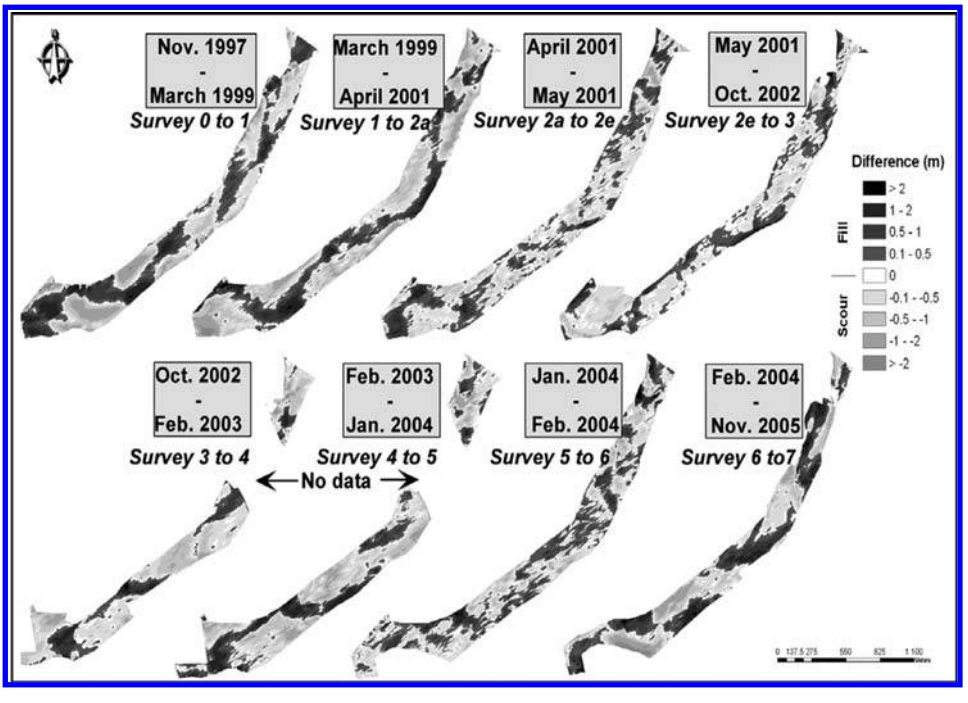


Figure 5. Morphological evolution of the secondary channel between November 1997 and November 2005.

Copyright © 2006 Taylor & Francis Group plc, London, UK

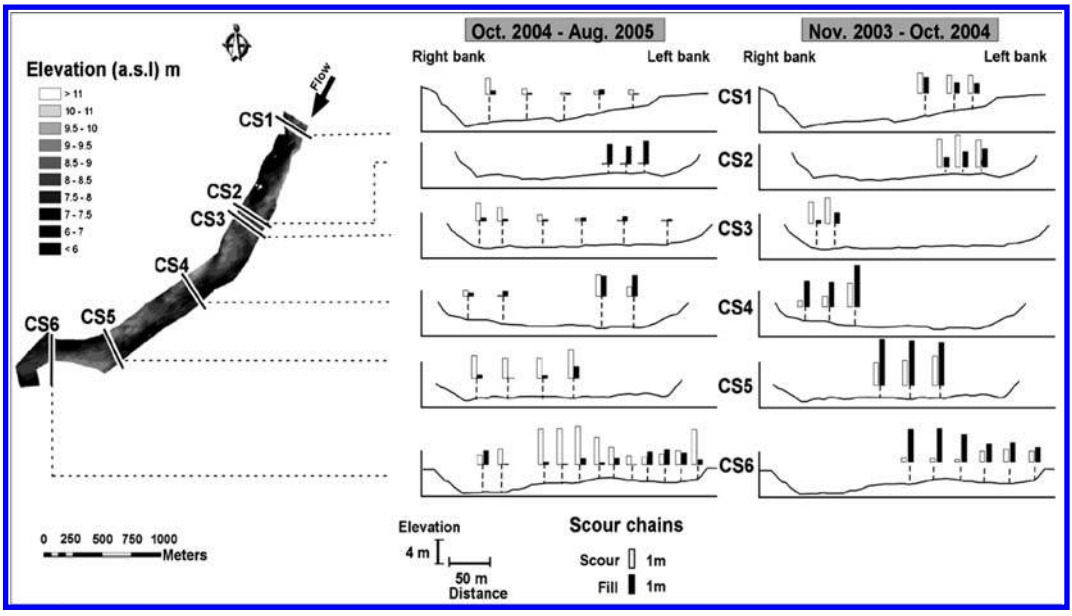


Figure 6. Scour and fill processes in the secondary channel determined from scour chains inserted between November 2003 and August 2005.

laterally. Comparisons done between surveys 3–4 and between surveys 4–5 evidence the migration of large sandwaves in the downstream part of the channel: the old thalweg being buried by one of these bedforms.

Scour chains inserted in the bed of the anabranch (when this channel was dry) completed the topo-bathymetric data (Fig. 6). Two sets of scour chains data acquired according to six cross sections are compared in Figure 6 for the periods November 2003–October 2004 and October 2004–August 2005. Between November 2003 and October 2004, the Loire River experienced a high magnitude flood (peak discharge of 4700 $m^3 s^{-1}$ at Montjean gauging station), while hydrology was reduced between October 2004 and November 2005 (maximum discharge of 2000 $m^3 s^{-1}$). On cross section 1, the thickness of scoured sediments was reduced between October 2004 and August 2005; the values of scour recorded by the chains decrease from the right bank to the left bank. On the left bank of cross section 2, erosion was dominant between November 2003 and October 2004 while sediment deposition occurred between October 2004 and August 2005. During this latter period, significant sediment deposition occurred. This phenomenon evidences the migration of a large sandwave in this area: the migration front of this bedform stopped between cross sections 2 and 3. Downstream of this lee side, on cross section 3, erosion was reduced (except on the right bank). On cross section 6, the morphological changes measured by the scour chains are significant. Thickness of sediment deposited in this area between November 2003 and October 2004 have reached 1.4 m in the central part of the section while scour depths were low: this highlight the deposition of a large sandwave. The significant scour noted on this section between October 2004 and August 2005 may be linked to the shifting of the thalweg in this area.

Except for the lee side of the large sandwaves, scour and fill processes observed in the secondary channel show that sedimentation is not univocal because scour often occurs before sedimentation.

5 CONCLUSION

This paper presents the first results obtained from the survey of the Loire River's bed at the site of Ingrandes where two artificial sills were built. The data from sediment budgets calculated using the DEMs seem to indicate higher reworking in the main channel than in the secondary channel (even if this latter has a larger area than the main branch). In the main channel, the sediment budgets are strongly influenced by the development of scour holes produced by the sills. However, their expected effect on the morphological evolution of the secondary channel seems to be quite limited: no significant changes were noted on the sediment budgets computed for this channel.

The topo-bathymetric survey in the secondary branch allowed observing morphological units (pools/riffles) and large sandwaves. Nucleation and migration of the latter, which are strongly linked to

Copyright © 2006 Taylor & Francis Group plc, London, UK

the morphological configuration, induce a shift of the thalweg and the temporary significant sediment accumulation at the downstream end of the channel, before the confluence. The formation of this bar seems to be linked to the presence of groynes located at the downstream end of the channel. This bar appears to be easily altered, even during low flows.

As the data presented here constitute one part of the measurements done on the site of Ingrandes, further investigations will be done in order to detail the results presented here. Particularly, the evolution of the bedform configuration of the main channel will be analysed and compared to the secondary channel. For example, the variation of the height and length parameters of dunes and sandwaves according to the discharge (Ten Brinke et al. 1999, Carling et al. 2000) will be detailed. Such an analysis, as well as numerical simulations (De Linares, pers. comm.), will support the definition a model of evolution for the bifurcating and asymmetrical reach of the river at the site of Ingrandes.

From the results presented here, the environmental survey performed on the site of Ingrandes will be refined in the future.

ACKNOWLEDGEMENTS

Research presented here was developed under the governmental masterplan *Plan Loire grandeur nature*. The authors wish to thank the *Agence de l'eau Loire-Bretagne* for financial support. The *GIP Estuaire* (S. Aumenier) and *VNF/SMN* are acknowledged for the bathymetric data. *ADESVV* (P. Jugé) provided valuable field assistance for the scour chains. The authors are grateful to P. Belleudy (*Université de Grenoble*) and M. De Linares (*SOGREAH*) for their fruitful collaboration. An anonymous referee is thanked for his review of the paper.

REFERENCES

Allen, J.R.L. 1984. *Sedimentary structures: their character and physical basis.* Amsterdam: Elsevier.

Arnaud-Fasseta, G. 2003. River channel changes in the Rhone Delta (France) since the end of the Little Ice Age: geomorphological adjustment to hydroclimatic change and natural resource management. *Catena* 51: 141–172.

Ashley, G.M. 1990. Classification of large-scale subaqueous bedforms: a new look at an old problem. *Journal of Sedimentary Petrology* 60: 160–172.

Belleudy, P. 2000. Restoring flow capacity in the Loire river bed. *Hydrological processes* 14: 2331–2344.

Bornette, G., Amoros, C. & Rostan, J.C. 1996. River incision and vegetation dynamics in cutt-off channels. *Aquatic Sciences* 58: 31–51.

Bravard, J.P., Amoros, C., Pautou, G., Bornette, G., Bournaud, M., Creuzé des Châtelliers, M., Gibert, J., Peiry, J.L., Perrin, J.F. & Tachet, H. 1997. River incision in south-east France: morphological phenomena and ecological effects. *Regulated Rivers: Research & Management* 13: 75–90.

Carling, P.A., Gölz, E., Orr, H.G. & Radecki-Pawlik, A. 2000. The morphodynamics of fluvial sand dunes in the River Rhine, near Mainz, Germany. I. Sedimentology and morphology. *Sedimentology* 47: 227–252.

Dambre, J.L. & Malaval, P. 1993. Evaluation des conditions de poursuite de la politique de limitation des extractions de matériaux dans le Lit de la Loire du Bec d'Allier à Nantes. Mission d'inspection des services de la navigation – Mission d'inspection spécialisée de l'environnement. Paris.

Hassan, M.A. 1990. Scour, fill, and burial depth of coarse material in gravel bed streams. *Earth Surface Processes and Landforms* 15: 341–356.

Hassan, M.A., Schick, A.P. & Shaw, P.A. 1999. The transport of gravel in an ephemeral sandbed river. *Earth Surface Processes and Landforms* 24: 623–640.

Laronne, J.B., Outhet, D.N., Carling, P.A. & Mc Cabe, T.J. 1994. Scour chain employement in gravel bed rivers. *Catena* 22: 299–306.

Miall, A.D. 1996. *The geology of fluvial deposits: sedimentary facies, basin analysis, and petroleum geology.* Berlin: Springer.

Peiry, J.L. 1987. Channel degradation in the middle Arve River, France. *Regulated Rivers: Research & Management* 1: 183–188.

Peters, J.J. 1970. La dynamique de la sédimentation de la région divagante du bief maritime du fleuve Congo, Primé par l'Académie Royale des Sciences d'Outre-Mer, Publié par le Laboratoire de Recherches Hydrauliques, Ministére des Travaux Publics, Rapport "Mateba 7": 1–120; 109 figs

Peters, J.J. 1978. Discharge and sand transport in the braided zone of the Zaire estuary, Netherlands Journal of Sea Research, 12: 273–292

Peters, J.J. 2002. Appui ponctuel à la restauration de la ligne d'eau en basse Loire par expertise des mesures bathymétriques réalisées au printemps 2001 et adaptation du protocole de suivi à Le Fresne-sur-Loire/Ingrandes. Bruxelles.

Petts, G., Moller, H. & Roux, A.L. (Eds) 1989. *Historical change of large alluvial rivers, Western Europe.* Chichester: John Wiley and Sons.

Piégay, H., Bornette, G., Citterio, A., Hérouin, E., Moulin, B. & Statiotis, C. 2000. Channel instability as a control on silting dynamics and vegetation patterns within perifluvial aquatic zones. *Hydrological processes* 14: 3011–3029.

Rodrigues, S., Bréhéret, J.G., Macaire, J.J., Moatar, F., Nistoran, D. & Jugé, P. In press. Flow and sediment dynamics in the vegetated secondary channels of an anabranching river: the Loire River (France). *Sedimentary Geology,* 186: 89–109.

Ten Brinke, W.B.M., Wilbers, A.W.E. & Wesseling, C. 1999. Dune growth, decay and migration rates during a large-magnitude flood at a sand and mixed sand-gravel bed in the Dutch Rhine river system. *Spec. Publs int. Ass. Sediment.* 28: 15–32.

Wilbers, A.W.E. & Ten Brinke, W.B.M. 2003. The response of subaqueous dunes to floods in sand and gravel bed reaches of the Dutch Rhine. *Sedimentology* 50: 1013–1034.

Copyright © 2006 Taylor & Francis Group plc, London, UK

Man-induced morphological processes in Warta river (Poland), and their impact on the evolution of hydrological conditions

T. Dysarz, J. Wicher-Dysarz & B. Przedwojski
Department of Hydraulic Engineering, Agricultural University of Poznan, Poland

ABSTRACT: In the paper the overview of morphological processes occurring in the selected Warta river reach is given. The processes were induced by the performance of the Jeziorsko dam, which was built in 1986. The main purpose of the presented research is the assessment of these processes impact on the hydrologic conditions in the river system. The historical data and hydrodynamic simulation model are used for the assessment of the hydrologic changes. The data consists of field measurements of the river morphology and hydrologic data from the selected river gages. The hydrodynamic model was used to reconstruct the flow conditions in particular states of the river system evolution. The statistical analysis of the obtained results enabled the assessment of the hydrologic characteristics transformation in the selected Warta river reach. The results are presented as relative and cumulative curves related to the estimated stages of the river system. The presented analyses shows significant changes of the hydrologic regime in the considered area.

1 INTRODUCTION

Our main interest is an impact of the anthropogenic changes on the evolution of hydrologic regime. The presented studies focus on Jeziorsko dam built in the Warta river, Poland, and intensive water management in the reservoir. These actions changed the velocity patterns in the Warta river and induced several sediment transport related processes. The transported material was deposited in inlet part of the reservoir and taken from the reach downstream of the dam. In the presented study we focus on the upper part of the reservoir. The sediment accumulation in the river channel induced one more process affecting hydrologic regime. Due to the increase of floodplain inundation frequency, the luxuriant vegetation start to grow there. These two processes, sediment accumulation and vegetation growth, cause additional increase of floodplain inundation. The processes induced by the dam built and performance seems to be self-driven cycle causing irreversible alterations of hydrologic regime.

The problems studied here are intensively investigated during last decades. The main reason for such interest is their importance for the water management, regional economy and people safety. Example linking hydrological regime and riparian vegetation dynamics was given by Keeland et al. (1997). The Authors linked the annual average depth in the river floodplains and tree diameter. Other example is paper written by Surtevant (1998) who analyzed the riparian wetland vegetation dynamics related to the flow changes and sediment accumulation. The relations between hydrologic regime and riparian vegetation were studied by Stromberg (2001). Similar research done by Nilsson and Svedmark (2002) resulted in formulation of basic principles and consequences of water regime changes.

The changes of the hydrologic regime may be induced by many different factors, anthropogenic as well as natural. However, one of the most important anthropogenic impacts on the hydrologic regime is damming of the river as it is well shown in Petts and Gurnell (2005). The studies on the hydrologic changes and degradation of ecosystems located along the river reaches below the dams were presented by several researches. The examples may be found in Maingi and Marsh (2002), Magilligan and Nislow (2005), Marston et al. (2005) and many others. The dam impact on the upstream condition is also intensively investigated. Interesting examples were given by Mumba and Thompson (2005) and Pinter and Heine (2005). In the first paper the changes in the floodplains located along the Kafue river (Zambia) reach between two dams, Itezhi-tezhi (upstream) and Kafue Gorge (downstream) are analyzed. The Authors proved that dams totally changed the hydrological and ecological conditions in the region due to the almost permanent inundation. Such conditions were imposed by parallel influences of releases from upper dam and high water levels in the lower reservoir. In the second paper, the flood magnitude changes are analyzed in relation to dam, river engineering and climate change impacts.

Copyright © 2006 Taylor & Francis Group plc, London, UK

The methodology used for assessment of hydrologic regime changes ranges from simple approach as equal discharge studies (Pinter and Heine 2005) to complex analysis including discharges and water table frequency (e.g. King et al. 1998, Maingi and Marsh 2002, Magilligan and Nislow 2005, Wellmeyer et al. 2005). This also quite common to simulate the behavior of the water system by means of mathematical model (e.g. Kite 2001, Maingi and Marsh 2002). In each case the methodology applied should match the specific features of the system, processes occurring there as well as data availability.

The main goal of the our paper is to present the hydrological regime evolution in the selected study area. The changes of the hydrologic conditions are caused by three factors. The primary cause is annual scheme of water management in the reservoir. Two next elements are the direct effect of this anthropogenic impact. These are sediment accumulation in the river and vegetation growth. The field measurement data and hydrodynamic simulation model are used for the purpose of our studies. The choice of the methodology is determined by the data availability, the geometrical characteristics of the system and the goal of the research. The final results are presented as relative and cumulative frequency functions related to the particular stages of river evolution.

The paper is divided into six sections. In the first section brief introduction to the investigated problem is given. In the second and third sections the study area and processes occurring there are described. Then the basic elements of the applied methodology are presented. The obtained results are presented and discussed in the fifth section. Finally, last section includes summary and conclusions.

2 CHOSEN STUDY SITE

Jeziorsko reservoir was built in 1986 in central part of Poland. It is located in the Warta river, between the Sieradz (upstream) and Uniejów (downstream) gauge stations. The reservoir inlet with Warta river reach are shown in the attached photo map (fig. 1). The Jeziorsko reservoir is relatively new object. First time it was filled up to the admissible maximum water level (121,50 m a.s.l.) in 1991. The hydropower plant was put into operation in 1995. The schematic view of the reservoir is presented in fig. 2. The main dam is located in the old river stream. The lateral and backwater dams prevent from inundation of adjacent areas. Pichna river is lateral inflow, where Teleszyna is lateral outflow of the reservoir. The total admissible minimum and maximum water levels in the reservoir are 116 m a.s.l. and 121.5 m a.s.l., respectively. The inundation areas related to these levels are shown in the fig. 2.

The Warta catchment area in the inlet of the reservoir is 8450 km^2. The average discharge in the nearest

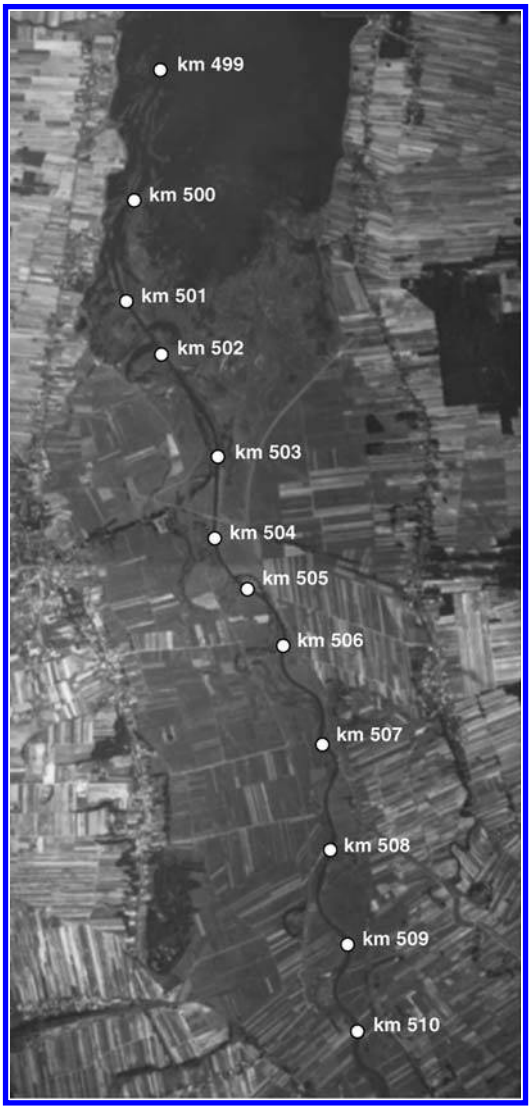


Figure 1. Photo-map of Jeziorsko reservoir inlet part and Warta river.

Sieradz gauge station is about 45 m^3/s, but the discharges variability ranges from 10 m^3/s to 397.5 m^3/s. The wet season during the year is January–May. The lowest discharges are observed during the summer and autumn time, from September to December.

The Jeziorsko reservoir is multipurpose reservoir performing in the annual working scheme (fig. 3). The main purpose of its performance is the flood protection in wet seasons. The reservoir is also the source of water for the big cities in Great-Poland province: Poznan, Kolo, Srem and Konin. The water stored is also used for irrigation purposes and to preserve biological

Copyright © 2006 Taylor & Francis Group plc, London, UK

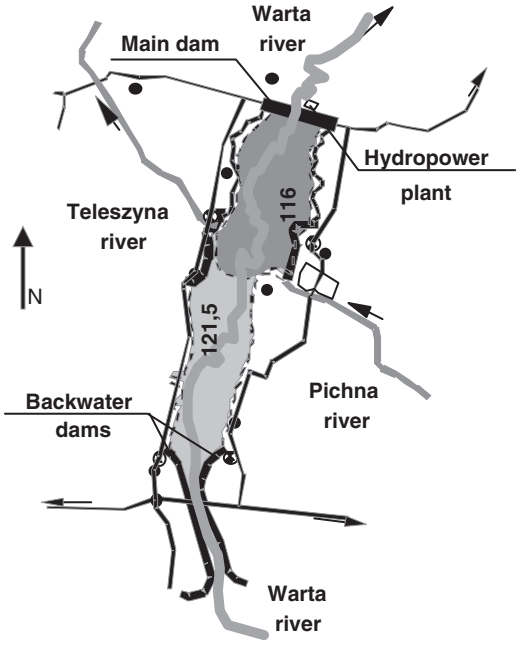


Figure 2. Schematic view of the Jeziorsko reservoir and its main elements.

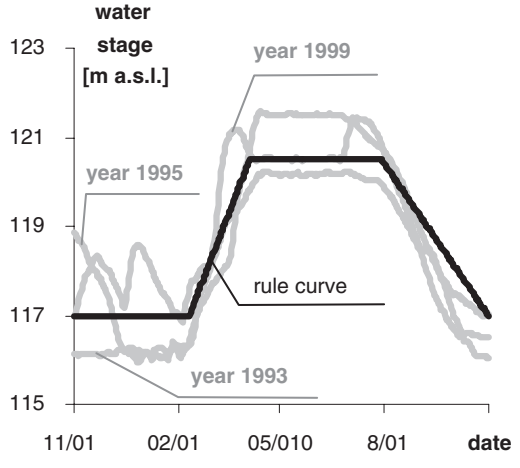


Figure 3. Typical scheme of reservoir performance during a year.

life below the dam. The Pątnów-Konin and Adamów power plants used the water from the reservoir for cooling. Other goal of the Jeziorsko performance is production of hydro-power, though, this is not significant due to the small difference between upper and lower water levels in the dam (about 10 m). The reservoir is also used for recreation and inland fishery.

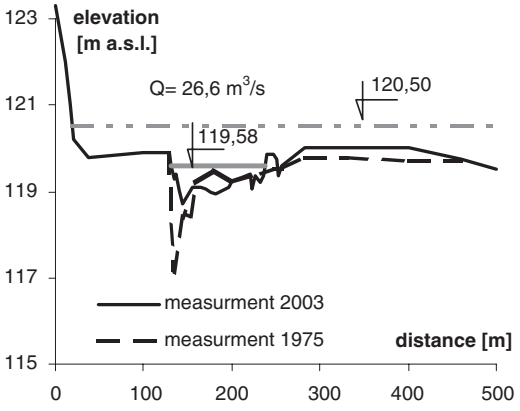


Figure 4. The changes of single cross-section of the Warta river in Km 500 + 510 during period of reservoir performance.



Figure 5. The vegetation growth in the inlet part of the Jeziorsko reservoir.

3 ELEMENTS OF THE INVESTIGATION

Since the very beginning of the reservoir performance the changes of the Warta river bed and floodplains are observed in the inlet part of the Jeziorsko. Due to decrease of flow velocities there the capacity of sediment transport is lower and material is deposited. The most important processes occur in the river reach below the bridge in Warta town, between Km 503 and Km 500 (see fig. 1). The example of the cross-section changes caused by the sediment is shown in fig. 4. This is the cross-section located at Km 500 + 510. It is clearly visible that accumulation of the sediment during the period of reservoir performance totally transformed the river channel causing additional increase of water levels.

The annual scheme of reservoir performance foster the vegetation growth in this area (fig. 5). It enabled

Copyright © 2006 Taylor & Francis Group plc, London, UK

to establish a nature reserve for birds in the upper part of the reservoir in 1998. Since this time the important reservoir performance purpose is conservation of water conditions sufficient for biological life in this area. Due to the existence of the nature reserve and Environmental Protection Ministry act from 1998 the river engineering actions are not allowed in the reservoir. The purpose of this regulation was the protection of birds habitats and biological life in the upper part of the considered object.

The regulation causes also some problems. (Wicher 2004, Wicher-Dysarz and Przedwojski 2005). The water levels in the backwater part are gradually increasing. Long-term results of these processes may cause degradation of the river in the inlet part of the reservoir as well as the reservoir capacity decreasing. Second risk is related to destruction of flood protecting and backwater dikes by overtopping. The losses occurring in such case are difficult to overestimate but the probability of this danger seems to increase.

However, the Ministry act enabled the presented research in some sense. In other conditions the authorities responsible for the reservoir effective and save use should take steps preventing from these processes. Now, it is possible to observe the hydrologic regime evolution in the pure form. The only influences are reservoir performance, sediment accumulation and vegetation growth. Hence, the chosen study area properly fits the research purposes.

4 BASIC METHODOLOGY

The methodology applied for the assessment consists of three main elements. These are: (1) field measurements and data collection, (2) hydrodynamic model simulations and (3) statistical analysis of the results. The listed elements are discussed below.

4.1 *Field measurements and data collection*

The set of available data consists of (a) system geometry, (b) discharges and water stages in the system, (c) state of the vegetation cover.

The channel and floodplain elevations are observed for long period of time in the area under consideration. The most basic set of data consists of the river regulation design prepared in 1975 (Matan 1975). The regulated river seemed to be stable and was not subject to any changes until the reservoir started to perform in 1991. Hence, this set of data may be considered as the original terrain and river bottom without any significant influence of the analyzed processes. The another sets of applied data consists of measurements done in 1997 and in 2004. After a few years of reservoirs performance the Warta river changes were checked and assessed by the team from Department of Hydraulic Engineering, Agricultural University of Poznan (DHE AUP) (Wicher 2004, Wicher-Dysarz and Przedwojski 2005). Hence, the system geometry data consists of three sets of river bottom and floodplain measurements in 37 cross-sections covering the river reach from Sieradz gauge station (Km 520 + 850) to Jeziorsko dam (Km 486 + 500). These data were enabled to describe three stages of the river bottom and floodplain evolution.

Other data used in our analyses are discharges and water stages observed in Sieradz gauge station and water levels measured at the Jeziorsko dam headwater. The set of data from Sieradz gauge station consists of daily measurements done in periods 1963–1970, 1973–1983, 1993–1995 and 1997–2001. These are 27 years of hydrological data. Some of the data were measured and published by Institute of Meteorology and Water Management (IMWM) (1963–1970, 1973–1983). Others were collected by Regional Board for Water Management (RBWM) in Poznan. The later data are made available under the circumstances of cooperation between RBWM and DHE AUP. The data collected from Sieradz gauge station are used to describe the not-affected hydrologic condition in the inlet of the analyzed river reach. The water stages at Jeziorsko headwater were observed during the period of reservoir performance, from 1992 to 2001. This set of data was collected by RWMB which takes care about the reservoir. The data were used to design the average scenario of reservoir performance during the year (see fig. 3).

The impact of vegetation on the roughness coefficients was assessed on the basis of measurements including plants localization and vegetation cover density. The stalk thickness was estimated in the same way. The necessary measurements were done by DHE AUP team in years 2004–05.

4.2 *Hydrodynamic model simulations*

For the simulation of river flow in the study site the HEC-RAS package including hydrodynamic flow model is used. The basis of this methodology is well known set of St. Venant equations approximated numerically. The basic principles and procedures were described in the past by many researchers. Examples may be found in Ligget and Cunge (1975), Abbott (1979) and Cunge et al. (1980). This methodology was developed by Barkau (1982) in order to simulate the flow in meandering river with broad floodplains. Finally, the complete description of the approaches and methods applied in the HEC-RAS package was presented by Brunner (2002).

The main basis of the model is the set of two balance equations. The set of equations is written separately for the main channel and for the floodplains. Typically this procedure provides three sets of equations,

Copyright © 2006 Taylor & Francis Group plc, London, UK

for left and right floodplain and main channel. The floodplain equations are averaged and then added to main channel equations. The summing of equations reduces the source terms describing the exchange of mass and momentum between subsections. Two additional assumptions are necessary: (1) the distribution of discharge in subsections is the same as the distribution of conveyance, (2) water surface elevation is the same in each subsection.

The methodology applied in HEC-RAS package is one of the most developed physically-based models describing 1D free surface flow. The complexity of the complex natural geometries is properly included in 1D model equations. HEC-RAS package was tested and successfully applied in many cases (e.g. Maingi and Marsh 2002). Hence, the model may be applied to solve the described problem. The close relation of the model structure to the physical conservation laws enables proper validation of simulation results done on the basis of accurate field measurement data.

The HEC-RAS model was prepared in such a way, that the system geometry correspond to four stages of river bottom evolution. First analyzed state of the system is the primary bottom described in Matan (1975). This geometry was considered as pre-dam conditions. The second geometry was prepared on the basis of measurements done in 1997 (Wicher 2004). This stage of the system correspond to the system state a few years after the beginning of reservoir performance. The roughness in the particular cross-sections is the same as in the 1975. It does not describe the slight changes of vegetation cover in this period. Hence, the impact of pure sediment deposition may be assessed. The third and fourth geometry of the system was prepared on the basis of measurements done in 2004 and corresponds to current conditions. However, the third scheme does not reflex to the roughness changes due to the vegetation growth. This element is included in the fourth system geometry. Hence, the current state of the system may be assessed in two ways: with and without vegetation growth.

The riparian vegetation impact on the flow conditions may be modeled as the changes of Manning roughness coefficients. However, these coefficients depends on the vegetation characteristics as well as water depth. Klopstra et al. (1997) presented the formula describing velocity changes in the channel with non-submerged vegetation in steady flow conditions.

$$u = \sqrt{\frac{2gi_0}{C_w md}} \tag{1}$$

where g is acceleration of gravity and i_0 is bottom slope. The parameters C_w, m and d describe the characteristics of riparian vegetation. C_w is the coefficient reflecting seasonal changes of leaves cover. Its values were taken as $C_w = 1.05$ for winter period and $C_w = 1.40$ for summer (Armanini et al. 2005). m is

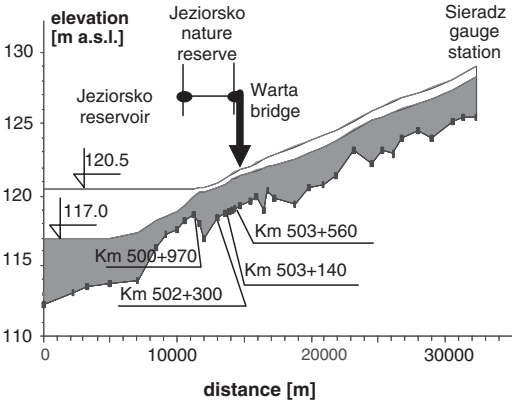


Figure 6. Water profile in the investigated Warta river reach taken from HEC-RAS postprocessor.

average number of plants in one square meter and d is average diameter of bushes stalks.

Following this concept and applying the Manning equation for the wide channel, the formula for the roughness coefficient may be derived

$$n = h^{\frac{2}{3}} \sqrt{C_w \frac{md}{2g}} \tag{2}$$

where n is Manning roughness coefficient, h – the depth.

The presented approach was used to describe the changes of roughness in the floodplain. Parameters m and d were determined on the basis of measurements done in 2004 and 2005.

In the fig. 6 the water profile copied from the HEC-RAS post-processor in shown. The maximum and minimum water stages during the simulations are presented. The area under consideration, Jeziorsko nature reserve is also denoted. In the fig. 6 there are marked the cross-sections for which the results are presented in part five of the paper. The study area is located below the bridge in Warta town which is also marked in fig. 6.

Hydro-morphological stages of the system evolution are presented as five potential river states:

(1) initial bottom reflecting pre-dam conditions (1975) with free outflow in the outlet;
(2) initial bottom reflecting pre-dam conditions (1975) with outflow corresponding to the average annual scheme of reservoir performance (see fig. 3);
(3) bottom measured in 1997, but with the initial roughness and outflow as above;
(4) bottom measured in 2004, but with the initial roughness and outflow as above;
(5) bottom measured in 2004 with roughness reflecting current state of vegetation and its seasonal variation, outflow corresponding to the average annual scheme of reservoir performance.

Copyright © 2006 Taylor & Francis Group plc, London, UK

4.3 *Statistical analysis of the results*

The collected flow data from the Sieradz gauge station are treated as potential scenarios of inputs for the simulation of flow throughout the river. 27 simulations for each of five stages of the hydro-morphological conditions in the river are performed. The computational time step is chosen as 15 minutes to preserve stability of computations. Despite of this only the results produced for each day at 7 a.m. are analyzed. This approach correspond to the procedures of river stages observations in Poland, what should preserve the data homogeneity requirements in any comparative studies.

The obtained results were processed by means of frequency analysis. The basic relative and cumulative frequency curves for the cross-sections in the considered area were prepared. The definitions of relative and cumulative frequencies are adopted from Chow et. al. (1988). The relative frequency $f_s(H)$ of water stages is as follow

$$f_s(H_i) = \frac{n_i}{N} \tag{3}$$

where N is the total number of analyzed results and n_i is the number of such results that

$$H_i - \Delta H < H \le H_i \tag{4}$$

The length ΔH is selected for each analyzed cross-section in such a way that the total interval of water stages variability is divided into 50 sub-intervals. The relative frequency function is linked with the probability density function $f(H)$ according to the formula

$$f(H) = \lim_{\substack{N\to\infty \\ \Delta H\to 0}} \frac{f_s(H)}{\Delta H} \tag{5}$$

The cumulative frequency function $F_s(H)$ is defined as follows

$$F_s(H_i) = \sum_{j=1}^{i} f_s(H_j) = \sum_{j=1}^{i} \frac{n_j}{N} \tag{6}$$

The cumulative frequency function is approximation of probability distribution function $F(H)$ according to the following relationship

$$F(H) = \lim_{\substack{N\to\infty \\ \Delta H\to 0}} F_s(H) \tag{7}$$

For the more clear illustration the probability density curve is fitted to each set of results obtained in each analyzed cross-section. The Pearson type III probability density function is chosen for that purpose. The applied probability density function is defined as follows

$$f(x) = \frac{\alpha^{\lambda}}{\Gamma(\lambda)}(x-\varepsilon)^{\lambda-1}\exp\left[-\alpha(x-\varepsilon)\right] \tag{8}$$

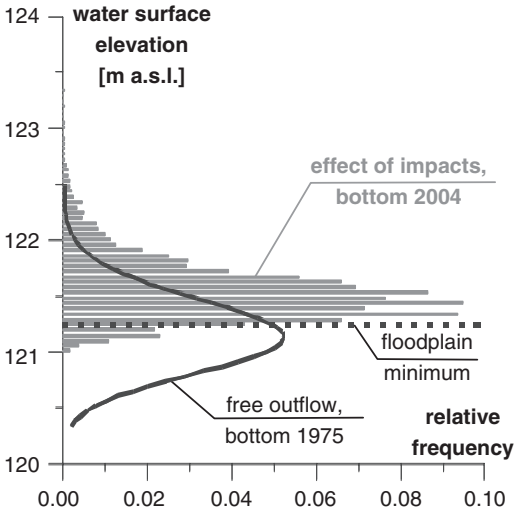


Figure 7. The relative frequency function corresponding to the initial and current state of the hydrological regime in cross section located at Km 503 + 560.

where α, λ and ε are the parameters linked with the sample statistics according to the formulae

$$\lambda = \left(\frac{2}{C_s}\right)^2 \qquad \alpha = \frac{2}{sC_s} \qquad \varepsilon = x_a - \frac{2s}{C_s} \tag{9}$$

In the above equations x_a is the sample data average, s is standard deviation and C_s is the coefficient of skewness. The method of moments is used to fit the distribution to the obtained results.

5 RESULTS

The described analyses are done for the all cross-sections in the river reach between the bridge in Warta town (fig. 6) and the Jeziorsko reservoir. These are sections located at Km 503 + 560, 503 + 380, 503 + 140, 502 + 800, 502 + 300, 501 + 270, 500 + 970, 500 + 510 and 499 + 890. The examples of obtained results are shown in figs 7–15. In the figures presenting relative frequency functions (figs 7, 9, 11, 13) the estimated initial stage is compared with the estimated current hydrologic conditions. The initial stage is represented by Pearson type III probability density function fitted to the results of simulation. In these figures the minimum floodplain elevations are denoted as dashed line. The figs 8, 10, 12 and 14 shows the gradual changes of cumulative frequency functions related to analyzed stages of the hydro-morphological conditions in the river.

Presented results shows two common trends in cross-sections located between Km 503 and 501. The most frequent stages become higher and their relative

Copyright © 2006 Taylor & Francis Group plc, London, UK

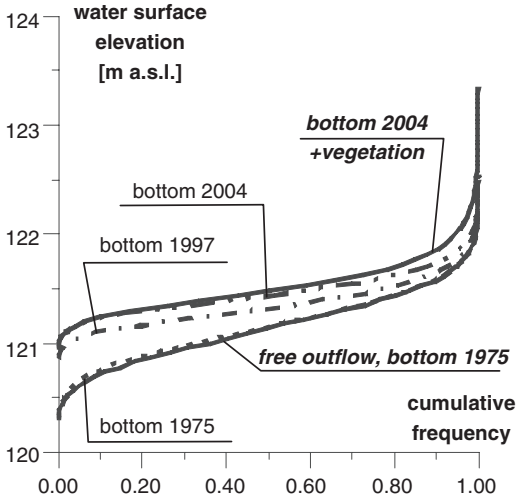


Figure 8. The cumulative frequency function corresponding to the analyzed states of the hydrological regime in cross section located at Km 503 + 560.

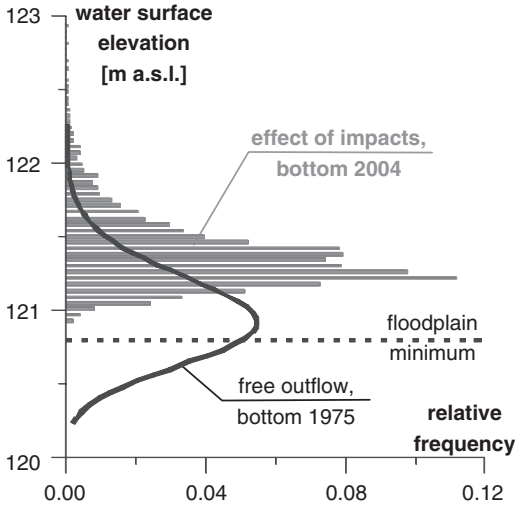


Figure 9. The relative frequency function corresponding to the initial and current state of the hydrological regime in cross section located at Km 503 + 140.

frequency is greater. This means greater frequency of floodplain inundation, what favors the riparian vegetation growth. The same trend is visible in fig. 15, when the most frequent stages and the maximum frequency are presented. More complex changes of hydrological regime may be observed in the cross-sections located near the reservoir, as section in Km 500 + 970 (fig. 13 and 14). The influence of the downstream water stages imposed in the reservoir is clearly visible in fig. 13.

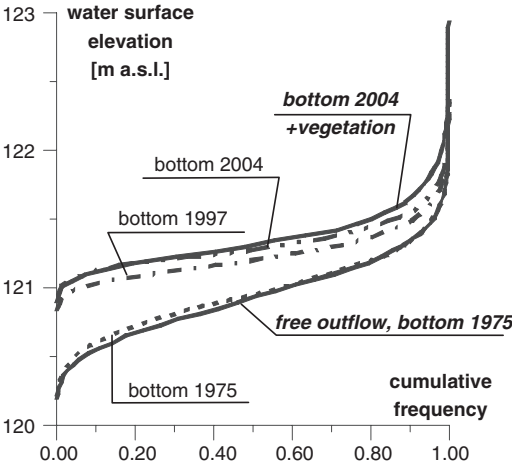


Figure 10. The cumulative frequency function corresponding to the analyzed states of the hydrological regime in cross section located at Km 503 + 140.

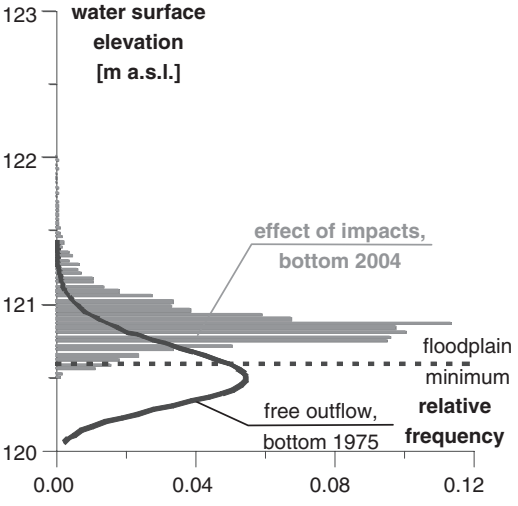


Figure 11. The relative frequency function corresponding to the initial and current state of the hydrological regime in cross section located at Km 502 + 300.

In addition one may notice the shift of lower water stages probably caused by the higher flow resistance upstream.

6 SUMMARY

In the paper the impact of several anthropogenic factor on the evolution of hydrologic regime is presented. The area chosen for investigations is the Warta river in the inlet part of the Jeziorsko reservoir. The

Copyright © 2006 Taylor & Francis Group plc, London, UK

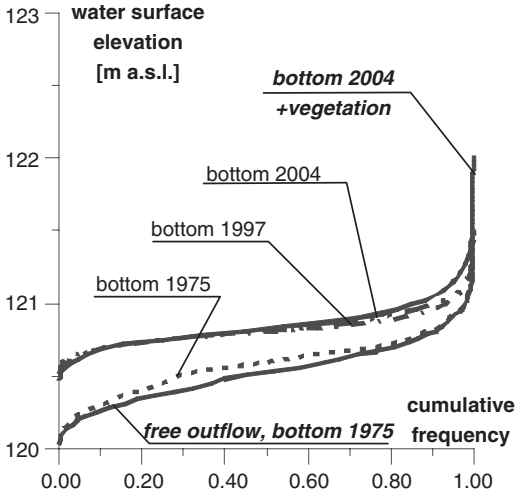


Figure 12. The cumulative frequency function corresponding to the analyzed states of the hydrological regime in cross section located at Km 502 + 300.

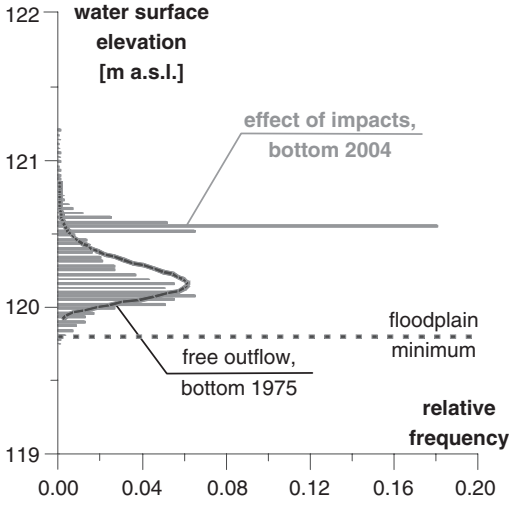


Figure 13. The relative frequency function corresponding to the initial and current state of the hydrological regime in cross section located at Km 500 + 970.

hydro-morphological processes occurring there enable the studies presented in the paper. Our main focus is the effect of aggregated influences on the hydrologic regime changes induced by man-made activity namely the Jeziorsko dam built and performance. The processes analyzed consist of reservoir management and related sediment accumulation with vegetation growth.

For our studies the hydrodynamic flow model is used. Such kind of model supplied with high-accuracy

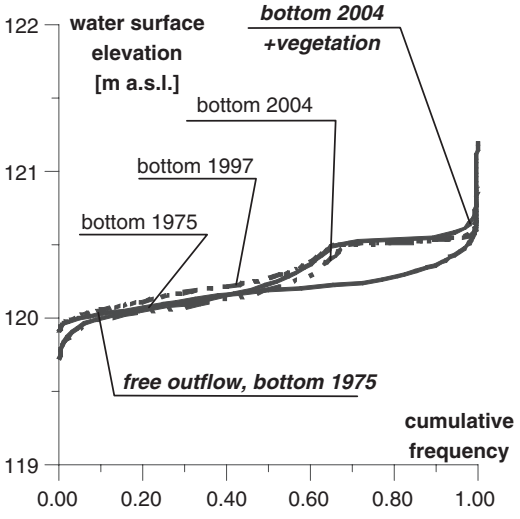


Figure 14. The cumulative frequency function corresponding to the analyzed states of the hydrological regime in cross section located at Km 500 + 970.

field measurement data preserves the appropriateness of simulations. The potential hydrologic conditions in the system were determined on the basis of simulations. The main basis for the computations are as follows: (a) 27 yearly scenarios of inflows to the system observed in the Sieradz gauge station, (b) five stages of the river channel determined on the basis of past and current measurements. Each inflows scenario was tested with each estimated stage of river channel, what gives the total number of simulations equal to 135. The obtained results were processed with the help of statistical analysis preserving the data homogeneity requirements. The relative and cumulative frequency functions related to each river channel state were elaborated in the 9 cross-sections in the analyzed area.

The obtained results shows significant changes of the hydrologic regime along the considered river reach. The impact of reservoir performance may be noticed by comparison of the pre-dam conditions (year 1975, free outflow) and the conditions imposed by reservoir (year 1975, reservoir). This elements are presented in figs 8, 10, 12, 14 and fig. 15. The impact of sediment accumulation after a few years of reservoir performance and now is visible if results obtained for the year 1997 (reservoir) and 2004 (reservoir) are compared. These results are also presented in figs 8, 10, 12, 14 and fig. 15. The total effect of all processes including vegetation growth (year 2004, reservoir + vegetation) is presented in fig. 7–15.

The obtained results shows that potential hydrologic regime in the analyzed area is significantly changed.

Copyright © 2006 Taylor & Francis Group plc, London, UK

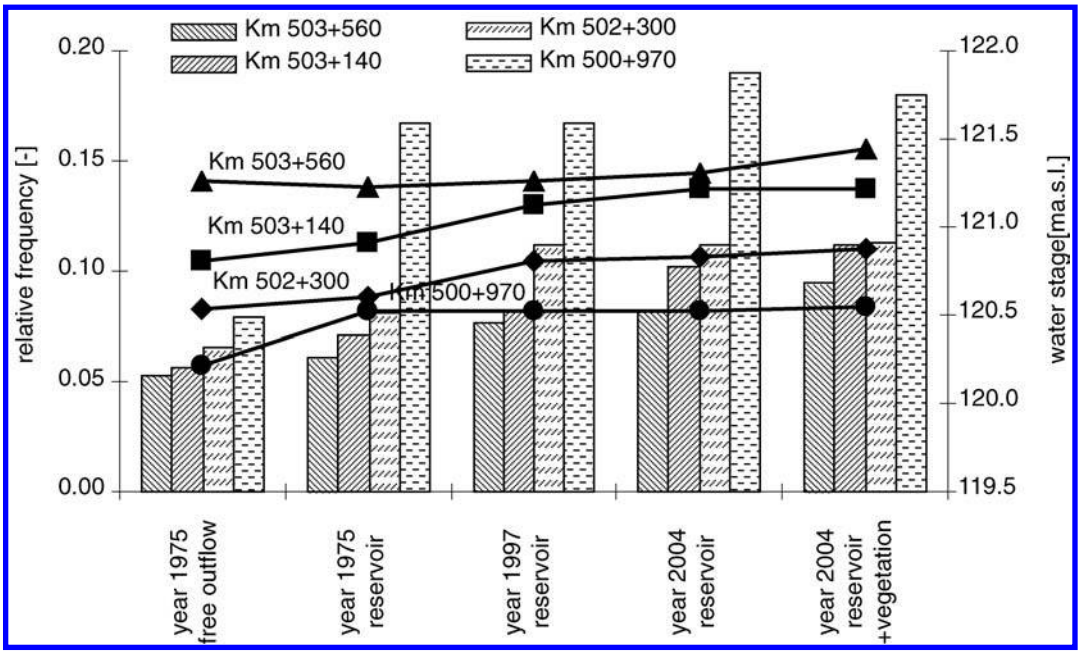


Figure 15. The most frequent water stages and related relative frequency in the selected cross-sections.

The impact of each single process as well as the cumulated impact of all processes have one common trend. The higher water stages become more frequent and their frequency is greater. This is well visible in fig. 15 and figs 7, 9, 11 and 13. The changes are crucial even in the cross-section located in the longest distance from reservoir (Km 503 + 560). The areas located along river reach were not flooded frequently there (fig. 7). Now, the inundation is almost permanent.

Man-made action as dam built induced gradual changes in the natural in environment. This self-driven cycle imposes permanent and probably irreversible change of hydrologic regime. The advantage is luxuriant vegetation growth. However, the changes causes also the increase of risk related to floods occurring in this area every year. Further increase of water stages may cause the dike break by overtopping. The presented results shows that the probability of such an event dramatically increases.

ACKNOWLEDGEMENT

This work was supported by Polish Committee for Scientific Research under grant 'Analysis of morphodynamic and vegetation impacts on the hydraulic conditions in backwater part of lowland reservoirs', project no. 2 P06S 034 30.

REFERENCES

Abbott M.B., 1979. Computational Hydraulics, Elements of the Theory of Free Surface Flows. London: Pitman

Armanini A., Righeti M. & Grisenti P., 2005. Direct measurement of vegetation resistance in prototype scale. Journal of Hydraulic Engineering, 43 (5): 481–487

Barkau R.L., 1982. Simulation of the July 1981 flood along Salt River, Report for CE695BV, Special Problems in Hydraulics. Fort Collins, CO.: Department of Civil Engineering, Colorado State University

Brunner G.W., 2002. HEC-RAS, River Analysis System hydraulic reference manual, computer program documentation. Davis, CA.: US Army Corps of Engineers, Hydrologic Engineering Center

Chow V.T., Maidment D.R. & Mays L.W. 1988. Applied Hydrology. McGraw-Hill International Editions, Civil Engineering Series, McGraw-Hill Book Company

Cunge J.A., Holly F.M.Jr & Vervej A. 1980. Practical aspects of computational river hydraulics, Pitman Advanced Publishing Program

Keeland B.D., Conner W.H. & Sharitz R.R., 1997. A comparison of wetland tree growth response to hydrologic regime in Louisiana and South Carolina. Forest Ecology and Management, 90: 237–250

King S.L., Allen J.A. & McCoy J.W., 1998. Long-term effects of a lock and dam and greentree reservoir management on a bottomland hardwood forest. Forest Ecology and Management, 112: 213–226

Kite G., 2001. Modelling the Mekong: hydrological simulation for environmental impact studies. Journal of Hydrology, 253: 1–13

Copyright © 2006 Taylor & Francis Group plc, London, UK

Klopstra D., Barneveld H.J., Noortwijk J.M. von & Velzen E.H. von, 1997. Analytical model for hydraulic roughness of submerged vegetation. The 27th Congress of the International Association for Hydraulic Research, Proceedings of Theme A, Managing Water: Coping with Scarcity and Abundance, San Francisco, California

Liggett M.B. & Cunge J.A. 1975. Numerical methods of solution of the unsteady flow equations, in Mahmood and Yevjevich (1975)

Magilligan F.J. & Nislow K.H., 2005. Changes in hydrologic regime by dams. Geomorphology, 71: 61–78

Mahmood K. & Yevjevich V. (eds.) 1975. Unsteady flow in open channels. Fort Collins, Colorado: Water Resources Publications,

Maingi J.K. & Marsh S.E., 2002. Quantifying hydrologic impacts following dam construction along the Tana River. Kenya. Journal of Arid Environments, 50: 53–79

Marston R.A., Mills J.D., Wrazien D.R., Bassett B. & Splinter D.K., 2005. Effects of Jackson Lake Dam on the Snake River and its floodplain, Grand Teton National Park, Wyoming, USA. Geomorphology, 71: 79–98

Matan J., 1975. Jeziorsko reservoir in the Warta river, Hydro-engineering and land improvements structures in the reservoir backwater. Poznan: Hydroprojekt (in polish)

Mumba M. & Thompson J.R., 2005. Hydrological and ecological impacts of dams on the Kafue Flats floodplain system, southern Zambia. Physics and Chemistry of the Earth, 30: 442–447

Nilsson C. & Svedmark M., 2002. Basic principles and ecological consequences of changing water regimes: riparian plant communities. Environmental Management, 30 (4): 468–480

Petts G.E. & Gurnell A.M., 2005. Dams and geomorphology: research progress and future directions. Geomorphology, 71: 27–47

Pinter N. & Heine R.A., 2005. Hydrodynamic and morphodynamic response to river engineering documented by fixed-discharge analysis, Lower Missouri River, USA. Journal of Hydrology, 302: 70–91

Stromberg J.C., 2001. Restoration of riparian vegetation in the south-western United States: importance of flow regimes and fluvial dynamism. Journal of Arid Environments, 49: 17–34

Surtevant B.R., 1998. A model of wetland vegetation dynamics in simulated beaver impoundments, Ecological Modeling, 112: 195–225

Wellmeyer J.L., Slattery M.C. & Phillips J.D., 2005. Quantifying downstream impacts of impoundment on flow regime and channel planform, lower Trinity River, Texas. Geomorphology, 69: 1–13

Wicher J., 2004. Sediment accumulation in lowland reservoirs. Ph.D. thesis in the Agricultural University of Poznan (in polish)

Wicher-Dysarz J., Przedwojski B., 2005. Modeling of sediment accumulation in the inlet part of Jeziorsko reservoir, Annual Reviews of Agricultural University of Poznan, 26: 483–493

Copyright © 2006 Taylor & Francis Group plc, London, UK

Morphological description of river bifurcations in gravel-bed braided networks

Walter Bertoldi, Stefano Miori, Martino Salvaro, Luca Zanoni & Marco Tubino
Department of Civil and Environmental Engineering, University of Trento, Italy

ABSTRACT: In this work we provide a detailed description of the morphology of Y-shaped bifurcations in gravel-bed braided networks, focussing the attention on their planimetric configuration and on sediment transport processes within different branches. We discuss the results of a series of experimental runs performed in a wide laboratory flume, with a movable bed. The experiments have been designed in order to trace the evolution of a braided network subject to constant liquid and solid discharges. Sequences of time lapsed images have been acquired, through which the width and the orientation of single branches have been measured. The bifurcations have been classified depending on the occurrence of bed load transport in the branches. On the average only 20% of the bifurcations displayed three morphologically active channels (type AAA), while one of the distributaries was not active in 50% of the monitored bifurcations (type AAN). In the latter case, the asymmetrical behaviour of the node is also reflected by the unequal width of downstream branches and by their orientation with respect to the incoming flux. Moreover, the relative distribution of AAA and AAN bifurcations within the entire network was found to evolve toward an asymptotic state, depending upon the stream power of the total flow. A relationship of the active braiding intensity (defined as the number of active branches for each cross section) and the total braiding intensity can be inferred by the abov analysis.

1 INTRODUCTION

Bifurcation is one of the main recurring elements of a braided stream (Figure 1). Recently various investigations have been focussed on this unit process, analyzing both its occurrence (Ashworth 1996; Richardson and Thorne 2001; Bertoldi and Tubino 2005) and the equilibrium configurations and stability (see Bolla Pittaluga et al. 2001; Tubbino and Bertoldi 2006).

According to the theoretical analysis of Bolla Pittaluga et al. (2003) a Y-shaped bifurcation is likely to assume an asymmetrical configuration, characterized by uneven water discharge and sediment rate distributions within the downstream branches, as well as by a different bed elevation at the node. The theory has been recently improved by Miori et al. (2006) including the effect of channel width adjustment. Analyzing the stability of the above configuration it comes out that the unbalance is enhanced at low values of the bed shear stress and for relatively high values of the aspect ratio of the upstream channel.

The above results have been confirmed by various experimental studies (Federici and Paola 2003; Hirose et al. 2003). Bertoldi et al. (2005) have shown that the timescale of a bifurcation evolving to an equilibrium state is typically much smaller than the morphological timescale which characterizes the long term adaptation of the channel bed to boundary conditions. This result



Figure 1. Bifurcations in a braided river (Sunwapta River, Canada).

suggests that node dynamics is mainly affected by local effects. Moreover asymmetry of the configuration is fostered by the migration of alternate bars in the upstream tributary, an effect which was not included in the theoretical analysis of Bolla Pittaluga et al. (2003).

The uneven discharge partition at the node has been also widely documented by field observations (see for example Ferguson et al. 1992 and Zolezzi et al. 2006). In particular they suggest that node dynamics can affect strongly the sediment transport rate in

Copyright © 2006 Taylor & Francis Group plc, London, UK

downstream distributaries and that the asymmetry is more pronounced for values of the discharge lower than those corresponding to formative conditions.

The above analyses mainly refer to single bifurcation units. On the other hand, it is interesting to explore the dynamics of nodes embedded in a braided network. The aim of this work is to provide a detailed description on the spatial distribution of bifurcations and on their influence on the planimetric evolution of the system. A series of experimental runs has been performed in a wide flume, with a well-sorted sand bed, reproducing a braided stream. We have monitored in detail the morphology of Y-shaped bifurcations forming in the flume, focussing the attention on their planimetric shape and on sediment transport processes. Moreover, we have tried to establish a relationship between the degree of asymmetry of the nodes and their planimetric configuration.

Through the analysis of planimetric data that can be more easily measured in such dynamic system, we have obtained qualitative and quantitative information on discharge distribution and sediment transport. In particular we have found that the number of active bifurcations can be related to the active braided index, as defined by Ashmore (2001).

In the following we describe the experimental setup and the measurements techniques; we then introduce a classification of the bifurcations based on the sediment transport occurrence within the branches joining at the nodes. Finally, we performed a statistical analysis of measured values of the channel width and alignment with respect to the upstream flow and to the mean valley slope.

2 LABORATORY FLUME AND EXPERIMENTAL PROCEDURE

The experiments have been carried out in the Hydraulic Laboratory of the University of Trento in a large concrete flume, 25 m long and 3.14 m wide, called "π-flume". The flume was filled with well-sorted quartz sand characterized by a mean diameter d_s of 0.63 mm, forming a 24 m long and 2.90 m wide floodplain.

The water was recirculated by a submerged pump controlled by a software that managed an inverter and an electromagnetic flow-meter. The sediment was not recycled, but the sand was supplied by a dry-sand feeder at the upstream end of the channel by a rotating screw that could be also automatically controlled.

The slope of the sand bed could be modified levelling the sediment with a wood panel supported by a carriage and mounted on a specific rail system.

During each run the sediment transport rate and the planimetric and altimetric configurations of the network have been monitored. In particular, the bed elevation has been surveyed by a laser profiler with grid spacing equal to 10 cm in the longitudinal direction and 1 cm in the transverse direction. A third carriage supported a digital reflex camera located 4 m above the sand floodplain that has been used to acquire vertical images of the flume. The camera has been kept at fixed positions in order to take frequent time-lapse images of the same reach. In this way the evolutionary process of various bifurcations within the network has been followed, with time interval equal to 1 minute. A further set of data has been collected moving the camera along the rails, in order to obtain mosaic images of the whole channel at specific times.

Further details on the experimental setup can be found in Bertoldi et al. (2006).

In each run the braided pattern has been set starting from an initial straight channel cut into the sand floodplain levelled at a prescribed initial slope. We have performed 13 experiments, keeping the same average slope S and varying the water discharge Q (which has been kept constant during each run). The experimental conditions are summarized in Table 1, where Q_s^{IN} is the sediment discharge supplied at the upstream end,

Table 1. Experimental conditions.

Run	Flow discharge Q [l/s]	Sediment supply Q_s^{IN} [Kg/min]	Slope S	Stream power Ω [W/m]	Width b_0 [m]	Depth D_0 [m]	Duration [hours]
P1	0.70	0.0529	0.013	0.089	0.140	0.0120	14.5
P2	0.50	0.0250	0.013	0.064	0.125	0.0100	37.5
P3	0.50	0.0275	0.013	0.064	0.125	0.0100	30.0
P4	0.50	0.0275	0.013	0.064	0.125	0.0100	110.7
P5	0.70	0.0604	0.013	0.089	0.140	0.0120	79.5
P6	0.70	0.0604	0.013	0.089	0.140	0.0120	30.0
P7	1.00	0.0858	0.013	0.128	0.148	0.0135	42.0
P8	1.00	0.0985	0.013	0.128	0.148	0.0135	30.0
P9	0.80	0.0932	0.013	0.102	0.148	0.0120	90.0
P10	0.50	0.0362	0.013	0.064	0.125	0.0100	59.0
P11	0.50	0.0362	0.013	0.064	0.125	0.0100	30.0
P12	1.50	0.1395	0.013	0.191	0.165	0.0165	18.0
P13	0.60	0.0403	0.013	0.077	0.120	0.0114	58.0

Copyright © 2006 Taylor & Francis Group plc, London, UK

$\Omega = \gamma QS$ is the stream power, where γ is the specific weight of water, and b_0 and D_0 denote the width and the flow depth of the initial straight channel, respectively. The latter values have been selected in order to ensure bank-full conditions, with initial values of the width to depth ratio ranging between 10–12.5.

According to the linear criterion for alternate bars occurrence (Colombini et al. 1987), the above range corresponds to stable plane bed. Hence, in each experiment a similar inception process has been observed, with an initial channel widening followed by the formation of migrating bars and by the consequent establishment of bifurcation points due to chute cut-off processes (Ashmore 1991; Bertoldi and Tubino 2005). Afterwards, a braided pattern started to develop. After few hours a sort of dynamical equilibrium condition was reached, in which the average values of the bulk properties of the network (braiding index, number of bifurcations, outgoing sediment discharge, ...) were no longer observed to change appreciably in time. The total duration of experimental runs varied between 30 and 110 hours, depending upon the speed of morphological processes occurring within the network.

In each run the bifurcation units have been monitored in detail. In particular, both the overall pattern of bifurcation points (number, density, distribution, ...) and the morphological characteristics of individual Y-shaped bifurcations (width of branches, alignment, angle, ...) have been measured. In the former case, subsequent surveys have been carried out with a time step greater than the timescale of bifurcation evolution (see also Bertoldi et al. 2006), in order to keep the data uncorrelated.

Moreover, some diffluence units have been monitored in time, starting from their occurrence, until sediment transport ceased in one of the downstream branches. In the present work bifurcations have been characterized in terms of sediment transport activity. Hence, qualitative direct observations have been continuously repeated during each run in order to detect the occurrence of sediment transport in each branch.

3 BIFURCATIONS CLASSIFICATION

As mentioned before, in this chapter we propos a classification of bifurcations based on bed load activity in their constitutive branches. Data discussed herein mostly refer to the conditions of quasi dynamic equilibrium, which has been reached after few hours of experimental run. Incidentally we notice that such condition was typically characterized by values of the mean ratio between the active channels and the total number of channels ranging between 0.35 and 0.5.

Taking into account the most commonly observed configuration, namely a single Y-shaped bifurcation composed by an upstream channel and two downstream distributaries, four different configurations have been observed (see Figure 2). We denote by 'A' the active channels and by 'N' the non active channels, in terms of sediment transport. Consequently we call AAA the bifurcations composed by three active streams, AAN those with one inactive downstream branch and NNN the bifurcations with no transport both in the incoming channel and in the downstream branches. The fourth configuration (ANN) has been rarely observed to occur within the network, since it has been found to be strongly unstable and to invariably evolve into one of the former three classes.

The NNN bifurcations represent diffluence units that have been abandoned by the main stream, because of a change in the water distribution at an upstream node; therefore at the time of the survey they were not involved in the actual dynamics of the network. On the contrary, the first two classes of bifurcations

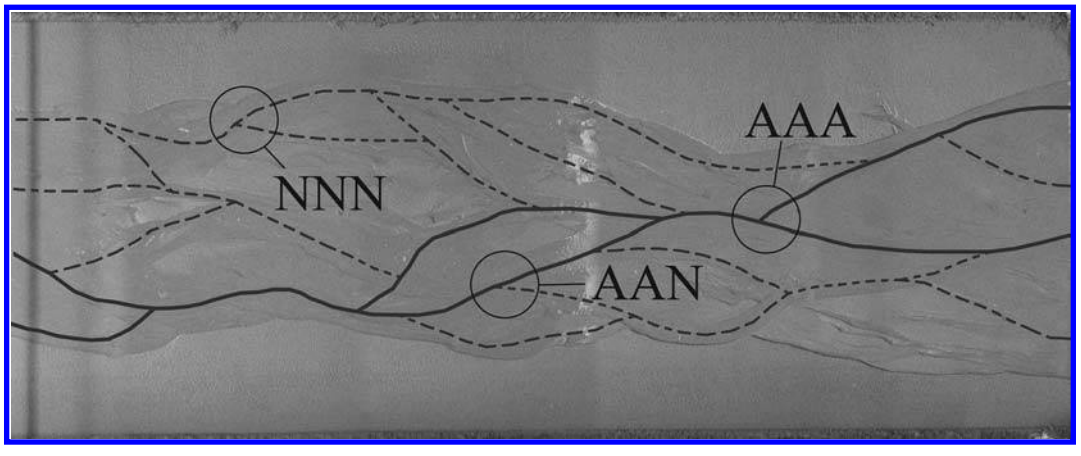


Figure 2. Example of a planimetric configuration in which the active branches and the bifurcations are highlighted.

Copyright © 2006 Taylor & Francis Group plc, London, UK

essentially represent the active part of the network at the time of the survey.

The relative distribution among the above classes of bifurcations observed in run P8 at different time steps is plotted in Figure 3. The first two measures refer to the initial developing stage, when the network is still under construction. In the further steps the network seems to have reached a quasi equilibrium state, though the occurrence of fluctuations testifies the strongly dynamical character of such state. When the above equilibrium is reached, nearly fifty percent of the bifurcations belongs to the class AAN: this finding agrees with previous experimental and theoretical observations on single Y-shaped bifurcations (Bertoldi et al. 2005; Miori et al. 2006), according to which unbalanced equilibrium configurations are more likely to occur, in which one of the downstream distributaries carries a larger part of the water and almost all the sediments. Figure 3 also shows that the network development from one single straight channel toward a dynamic equilibrium is always accompanied by a decreasing percentage of fully active nodes (AAA) and consequently by an increasing number of fully non active bifurcations (NNN).

A similar behaviour has been detected in all the experimental runs, as shown in Figure 4. The Figure suggests that in the early stage of the experiments the percentage of the four classes varies significantly, as the total number of branches in the network increases. At larger values of the braiding index the fraction of active channels decreases; consequently some AAA bifurcations turn to the AAN and NNN typology. After few hours the network reaches an equilibrium configuration in which the relative percentage of bifurcations keeps almost constant.

Moreover Figure 5 shows that the percentages of the three main classes change as a function of the total stream power. In particular, the relative percentage of AAA and NNN bifurcations strongly depends on the stream power, while the frequency of occurrence of AAN keeps almost constant with a value approximately equal to 0.5. The higher sediment mobility is therefore linked to a higher number of AAA units compared to the NNN class.

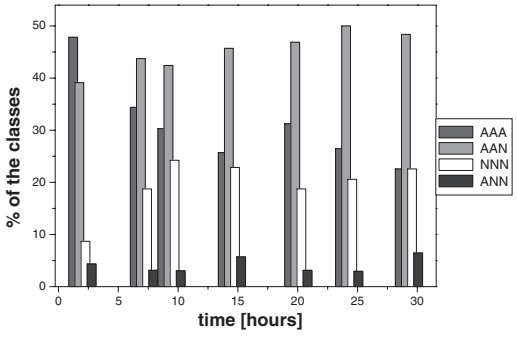


Figure 3. Temporal evolution of distribution of observed bifurcations (run P8).

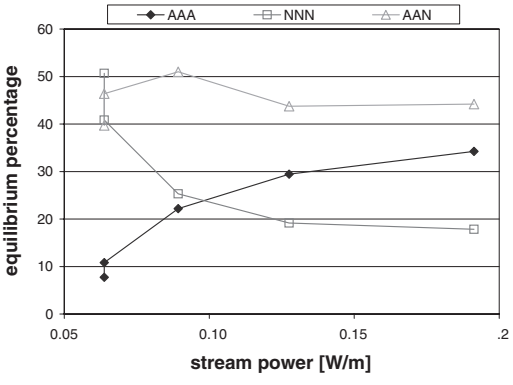


Figure 5. Equilibrium value of the percentage of classes AAA, AAN and NNN as a function of the stream power.

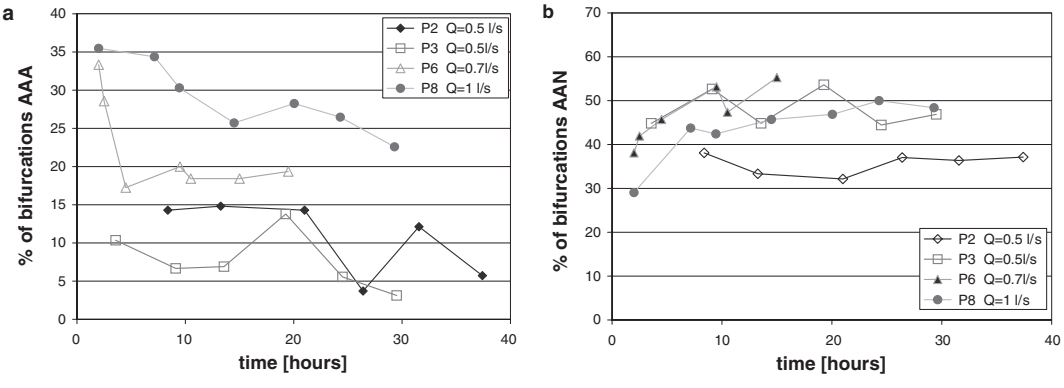


Figure 4. Percentage of AAA (a) and AAN (b) bifurcations as a function of time.

Copyright © 2006 Taylor & Francis Group plc, London, UK

The above distinction in classes based on the sediment load activity suggests an alternative approach to define the "degree" of activity of the network. At first we have measured for each experimental run the value of the braiding index as it is commonly computed (Ashmore 2001), both considering the total number of branches (TBI) and the active fraction (ABI). Figure 6 shows that the ratio between the above parameters reached a well defined value in our experiments, that was found to depend on the stream power. Similar values have been also reported by Egozi and Ashmore (2005). This ratio can be also evaluated considering that active downstream branches are present only in the AAA and in the AAN cases; furthermore only one of the two branches are active in the AAN bifurcations. Hence, we propose the following equation that relates the "degree" of activity of the network (ABI/TBI) to the relative number of bifurcation classes:

$$\frac{ABI}{TBI} = \%AAA + \frac{1}{2}\,\%AAN\,. \qquad (1)$$

Such relationship provides a suitable estimate of the above ratio, taking from direct measurements; it also reflects the increasing degree of activity of the network for increasing values of the stream power. Therefore, Equation (1) can be a useful tool in order to link the information on the number of active channels and the probability of occurrence of fully active bifurcations. It is worth noticing that the morphologic evolution of the AAA nodes is one of the peculiar mechanisms of braiding dynamics, which is responsible for the fluctuations of water and sediment distribution within the network.

4 PLANIMETRIC CONFIGURATION OF BIFURCATIONS

The large number of digital images acquired in the experiments has allowed us to measure in detail and to describe some of the relevant parameters characterizing the planimetric configuration of a bifurcation. The geometrical pattern of individual nodes has been then related to the degree of asymmetry, taking into account both the discharge and the sediment transport distribution.

First of all we have analyzed the number of bifurcations occurring in the network, measuring their spatial density, defined as the total number of bifurcations per unit area. We have found that this parameter does not show a large variability and does not display a specific dependence on the total stream power. As reported in Figure 7, during each run the number of bifurcations increased in the first stage, when the network was evolving from a single straight channel. After this phase, the bifurcation density kept almost constant, reaching a sort of asymptotic value, which was nearly equal in all the runs.

We have then explored the possibility of linking the degree of activity of a bifurcation, namely its typology as defined in the preceding section, with its geometrical properties. In fact, in a braided network laboratory model water discharge measurements in the single branches are quite difficult, as the flow depths are generally very shallow and bed and banks evolution is quite sensible to the disturbances caused by the intrusion of instrumental devices.

Present experimental observations show that the difference between the widths of the downstream distributaries is a suitable parameter which embodies the degree of asymmetry of the diffluence units. We have then introduced a width asymmetry parameter as the ratio between the width difference and the total width:

$$\delta_b = \frac{(b_{rigth} - b_{left})}{(b_{rigth} + b_{left})}\,, \qquad (2)$$

where b_{rigth} and b_{left} are defined in Figure 10. Measured values of δ_b for some AAA and AAN bifurcations are reported in Figure 8. We can observe that fully

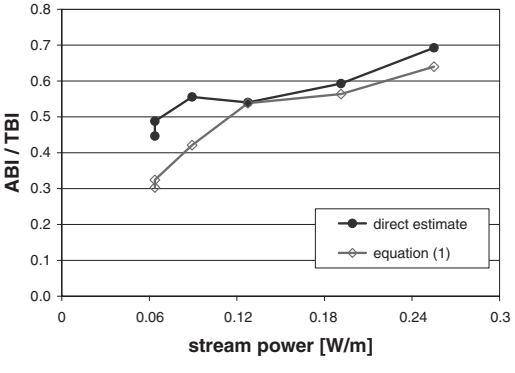


Figure 6. The ratio between the active and the total braiding index as directly measured and evaluated through equation 1 as a function of the total stream power.

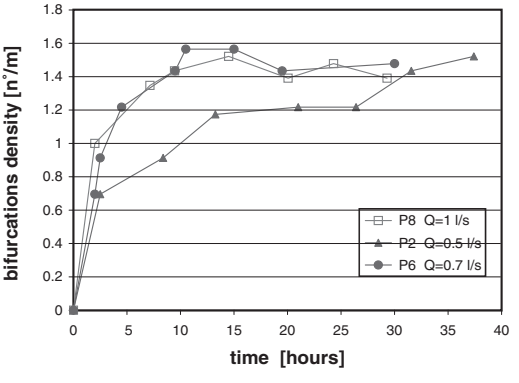


Figure 7. Spatial density of bifurcations as a function of time, for each experimental run.

Copyright © 2006 Taylor & Francis Group plc, London, UK

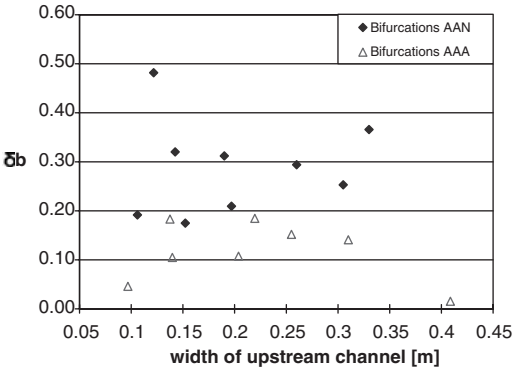


Figure 8. Width asymmetry of the AAA and the AAN bifurcations, as a function of the width of the upstream channel.

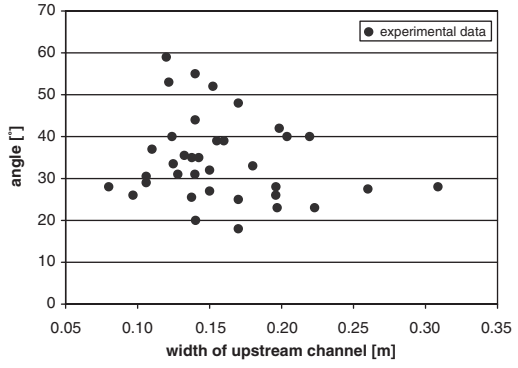


Figure 9. Angles between the downstream branches.

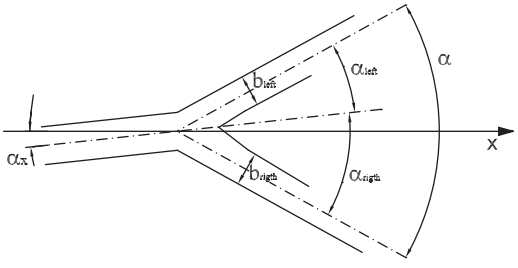


Figure 10. Sketch of the measured angles in a Y-shaped bifurcation.

active nodes show a more balanced pattern, characterized by relatively smaller values of δ_b (note that $\delta_b = 0$ represents a symmetrical configuration). On the contrary, in the AAN bifurcations the downstream branches display fairly different widths, such as δ_b can even reach a value equal to 0.5. Moreover, in this case the width asymmetry exhibits a fairly large variability

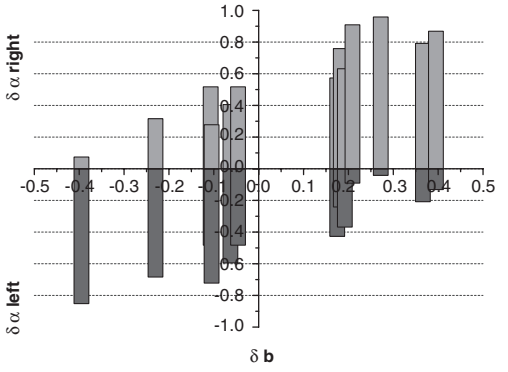


Figure 11. Angle asymmetry as a function of the width asymmetry of the downstream branches.

as the unbalanced character of the AAN class is able to determine a wide range of discharge distributions.

Another relevant parameter is the angle between the downstream branches, defined as the angle formed by the axes of the distributaries. We have found that its value may range from 20 to 55 degrees, with an average value of 35 degrees. These figures are in good agreement with those documented in previous field and laboratory observations (Federici abd Paola 2003; Bertoldi and Tubino 2005).

As a further index of the planimetric asymmetry of the node configuration, we have measured the deviation of the downstream branches with respect to the direction of the incoming flow. Figure 10 summarizes the notation adopted herein: α is the total angle between the distributaries, α_{rigth} and α_{left} are the deviations from the upstream channel direction and α_x is the angle between the longitudinal axis and the upstream branch axis.

We have defined the angle asymmetry as the ratio between the deviation of one branch and the total angle, as reported in the following Equation:

$$\delta\alpha_{rigth} = \frac{\alpha_{rigth}}{(\alpha_{rigth} + \alpha_{left})}, \qquad \delta\alpha_{left} = \frac{\alpha_{left}}{(\alpha_{rigth} + \alpha_{left})}. \tag{3}$$

Present experimental findings show that an asymmetric bifurcation, which is characterized by a large value of the width asymmetry δ_b, generally displays a larger difference in the deviations of the downstream branches. Such relationship suggests that the planimetric configuration of the node is strongly affected by the discharge distribution. In particular AAA bifurcations typically exhibit an almost symmetrical geometry, while in the AAN case the main downstream branch is likely to be oriented as the incoming flow. In this case, the smaller downstream channel behaves as a

Copyright © 2006 Taylor & Francis Group plc, London, UK

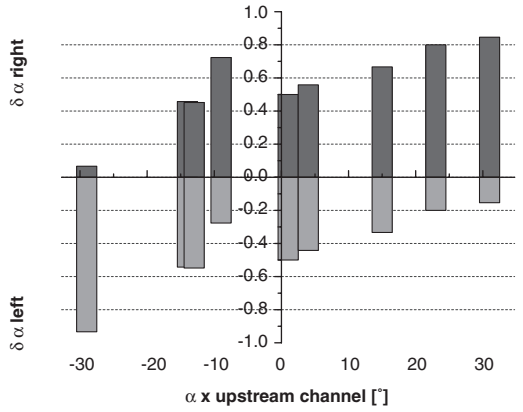


Figure 12. Angle asymmetry as a function of the orientation of the upstream branch, for the AAA bifurcations.

lateral avulsion, draining only a little fraction of the total discharge.

Finally, we analyzed the relationship between the deviation of the distributaries and the orientation of the upstream branch. We have observed that the AAA bifurcations keep more symmetrical when the α_x attains low values. Some examples are given in Figure 12. We may notice that when the upstream channel largely deviates from the main longitudinal direction, one of the downstream branches is almost aligned with the incoming flow, while the second branch generally takes the steeper direction. In this case, the further controlling parameter is the position of the bifurcation inside the network, since we have observed that nodes close to the lateral bank of the floodplain generally display higher values of α_x.

5 CONCLUSIONS

The paper reports on a series of systematic measurements on single bifurcations in a braided network, focussing the attention mainly on the occurrence of sediment transport in the branches and on their planimetric configuration. A classification has been proposed, based on the activity (in terms of bed load transport) of the channels forming the Y-shaped units. Four possible classes have been identified:

- the AAA bifurcations, with all the branches active;
- the AAN, characterized by a strong asymmetry of the water distribution, that implies the inactivity of one of the downstream branches. This class has been found to be the most frequent, nearly corresponding to the 50% of observed bifurcations;
- the NNN type, that represents abandoned bifurcations, that were not involved in the network evolution at the time of the survey;
- the ANN type, a rare and highly unstable configuration, that rapidly evolves into the AAN or the NNN class.

The relative percentage of these classes has been found to provide a suitable parameter in order to define the degree of activity of the network, that is quantified by the ratio between the number of active branches and the total number of wet branches per cross section.

The asymmetry of the planimetric configuration of bifurcations has been described in terms of the width asymmetry of the downstream branches and of the deviations of the axes of branches with respect to the orientation of the incoming flow and to the direction of the main longitudinal direction.

Present experimental results may open the path to the establishment of suitable rules which can be used in order to accurately describe the bifurcation process in a braided stream. In particular they may allow to predict the discharge asymmetry from the planimetric configuration or, in a complementary way, to infer the orientation of the branches joining at the node, when the flow partition is known.

ACKNOWLEDGMENTS

This work has been developed within the framework of the 'Centro di Eccellenza Universitario per la Difesa Idrogeologica dell'Ambiente Montano – CUDAM' and of the project 'La risposta morfodinamica di sistemi fluviali a variazioni di parametri ambientali – COFIN 2003', co-funded by the Italian Ministry of University and Scientific Research (MIUR) and the University of Trento and of the project 'Rischio Idraulico e Morfodinamica Fluviale' financed by the Fondazione Cassa di Risparmio di Verona, Vicenza, Belluno e Ancona. The authors gratefully acknowledge the fundamental support of Federica Castaman and the staff of the Hydraulic Laboratory of the University of Trento who helped in the execution of the experimental runs.

REFERENCES

Ashmore, P. (1991). How do gravel-bed rivers braid? *Canadian Journal of Earth Sciences 28*, 326–341.

Ashmore, P. (2001). *Braiding phenomena: statics and kinetics*, pp. 95–121. in Gravel-bed Rivers V, Mosley M.P. (eds), New Zealand Hydrological Society, Wellington.

Ashworth, P. (1996). Mid-channel bar growth and its relationship to local flow strength and direction. *Earth Surface Processes and Landforms 21*, 103–123.

Bertoldi, W., T. Amplatz, S. Miori, L. Zanoni, and M. Tubino (2006). Bedload fluctuations and channel processes in a braided network laboratory model. In *Proceedings of RiverFlow 2006, Lisboa, Portugal, 6–8 September*. submitted.

Bertoldi, W., A. Pasetto, L. Zanoni, and M. Tubino (2005). Experimental observations on channel bifurcations

Copyright © 2006 Taylor & Francis Group plc, London, UK

evolving to an equilibrium state. In *Proceedings of RCEM2005 Conference, Urbana, Illinois, USA, 4–7 October*, pp. 409–419.

Bertoldi, W. and M. Tubino (2005). Bed and bank evolution of bifurcating channels. *Water Resources Research 41*, W07001, doi:10.1029/2004WR003333.

Bolla Pittaluga, M., B. Federici, R. Repetto, C. Paola, G. Seminara, and M. Tubino (2001). *The morphodynamics of braiding rivers: experimental and theoretical results on unit processes*, pp. 143–181. in Gravel-bed Rivers V, Mosley M.P. (eds), New Zealand Hydrological Society, Wellington.

Bolla Pittaluga, M., R. Repetto, and M. Tubino (2003). Channel bifurcation in braided rivers: equilibrium configurations and stability. *Water Resources Research 39 (3)*, 1046, doi:10.1029/2001WR001112.

Colombini, M., G. Seminara, and M. Tubino (1987). Finite-amplitude alternate bars. *Journal of Fluid Mechanics 181*, 213–232.

Egozi, R. and P. Ashmore (2005). Spatial and temporal variations of braiding intensity at different channel forming discharges using physical models. In *Poster presented at the Gravel-bed Rivers VI, Lienz, Austria, 5–9 September*.

Federici, P. and C. Paola (2003). Dynamics of bifurcations in noncohesive sediments. *Water Resources Research 39 (6)*, 1162, doi:10.1029/2002WR001434.

Ferguson, R., P. Ashmore, P. Ashworth, C. Paola, and K. Prestegaard (1992). Measurements in a braided river chute and lobe. 1. flow pattern, sediment transport and channel change. *Water Resources Research 28 (7)*, 1877–1886.

Hirose, K., K. Hasegawa, and H. Meguro (2003). Experiments and analysis on mainstream alternation in a bifurcated channel in mountain rivers. In *Proceedings 3 International Conference on River, Costal and Estuarine Morphodynamics, 1–5 September, Barcelona (Spain)*, pp. 571–583.

Miori, S., R. Repetto, and M. Tubino (2006). A one-dimensional model of bifurcations in gravel-bed channels with erodible banks. *Water Resources Research submitted*.

Richardson, W. and C. Thorne (2001). Multiple thread flow and channel bifurcation in a braided river: Brahmaputra-Jamuna River, Bangladesh. *Geomorphology 38*, 185–196.

Tubino, M. and W. Bertoldi (2006). *Bifurcations in gravel-bed streams*. in Gravel Bed Rivers 6. (in publication).

Zolezzi, G., W. Bertoldi, and M. Tubino (2006). *Morphological analysis and prediction of channel bifurcations*. in Braided Rivers: Process, Deposits, Ecology and Management G.H. Sambrook-Smith, J.L. Best, C.S. Bristow and G.E. Petts (Eds.), Special Publication 36 IAS, Blackwell.

Copyright © 2006 Taylor & Francis Group plc, London, UK

Study on river change and sediment transportation of Tan Chau reach in lower Mekong river

X.L. Luu & S. Egashira
Ritsumeikan University, Kusatsu, Shiga, Japan

H. Takebayashi
University of Tokushima, Tokushima, Japan

ABSTRACT: This study presents field data of topography change, bed material, water surface elevation and hydrograph at Tan Chau reach in Vietnam to understand mechanism of the river change. The results of field survey show that bank shifting tends to occur toward anti-clock wise and sand bars migrate downstream, resulting in a much larger bar, which is influenced by co-presence of non-cohesive and cohesive sediment and artificial works. In addition, bed material loads are originated by bank erosion. A two dimensional numerical model is proposed to simulate flow pattern and associated river change. In this model, erosion rate formula for cohesive material and formula for estimating the thickness of sediment transport layer as a function of bed shear stress are introduced into the standard layer model which was firstly proposed by Hirano (1971). The proposed model can estimate the sediment transport rate on the bed composed of non-cohesive and cohesive material and predict the topography change of study reach.

1 INTRODUCTION

The Mekong River is ranked twelfth in length and sixth in mean annual discharge, globally. It drains the area of 795,500 km^2 from Himalayas, through Southwestern of China, Laos, Thailand, Cambodia and Vietnam. The Mekong Delta which is located in Vietnam plays an important role in society and economic development, supporting 16 million inhabitants and contributing to over 27% of national GDP. Therefore, river change and associated bank erosion cause serious socio-economic problems.

The study reach is about 18 km long, a part of the Mekong River, which is located at Tan Chau near the national border with Cambodia and 190 km away from coast as shown in Fig. 1. Left bank of the reach in Thuong Phuoc has received strongest and fastest erosion which takes place frequently not only in flood season but also in dry season. Annual averaged erosion rate is estimated at about 30–50 m/year. Such bank erosion causes damages of more than 100 houses a year. The bank erosion at northwest side of Tan Chau City is estimated at about 6 m per year, which is not so large comparing to other places. However, Tan Chau is populated densely and urbanized much more than others. Therefore, damages due to the bank erosion are serious. As above circumstances, it is emphasized that bank protections and preferable counter measures should be conducted.

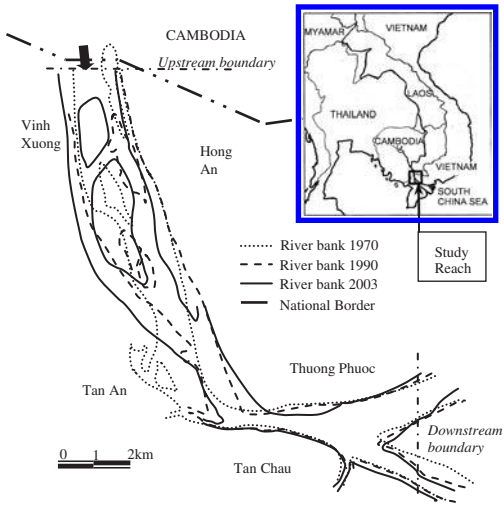


Figure 1. Bank lines measured in 1970, 1990 and 2003.

In 2001, Southern Institute of Water Resource Research – River Training Center conducted a research

Copyright © 2006 Taylor & Francis Group plc, London, UK

about erosion problems at several places. But unfortunately, no reasonable methods have been proposed except temporary bank protections.

Present study described circumstances of bank erosion and associated problems based on field data focusing on Tan Chau reach, 18 km long, and proposed a numerical method to treat such river changes. In the numerical method, new formulas treating with sediment exchange layer as well as with channel erosion rate for sediment composed of non-cohesive and cohesive material, are introduced into the two dimensional numerical models which were proposed by Nagata et al(2000) and Liu(1991).

2 CHARACTERISTICS OF STUDY REACH

Data of hydrograph and water surface elevation were provided by Mekong River Commission. Figure 2 shows water discharge at Neak Luong gauge station, located at about 80 km upstream from Tan Chau reach. The maximum discharge is 31799 m^3/s in September and minimum one is 3050 m^3/s in April, respectively. Flood duration is about 7 months in which water level is rising during 3 to 4 months and lowering during 3 months. Therefore, flow velocity in flood season at some river reach exceeds the specific critical velocity for long time. The specific critical velocity that is a criterion causing active erosion are shown for bed and bank regions in Table 1 (Le, 1997).

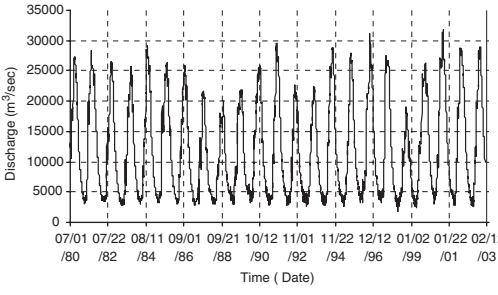


Figure 2. Water discharge of the Mekong River at Neak Luong gauge station (about 80 km upstream from Tan Chau reach).

Table 1. Cross-sectional average flow velocity and specific critical velocity for threshold of active erosion.

Velocity (m/s)	Tan Chau (Mekong)	Long Xuyen (Bassac)
Flow velocity	2.7	1.86
Specific critical velocity of bed erosion	0.5	0.43
Specific critical velocity of bank erosion	0.58	0.78

On the other hand, the Mekong Delta was formed in the duration from Old-Tertiary Period of Cenozoic (ten million years ago) to Pleistocene when the Himalaya Mountains appeared. Thereafter, in the Quaternary Period, Indochina region was affected by sea expanding and 80% of the present Mekong Delta was submerged (Pham et al., 1991). Since then, the Mekong Delta may have been influenced by seasonal and daily changes of hydrological quantities as well as by associated sediment transportation.

3 FIELD SURVEY

Field survey were performed in 2003 and 2005 to measure topography of river and to collect bank and bed material. Cross sections of river reach were measured by Echo Sounder system attaching with GPS, as shown in Figure 4. Specially bed sediment was collected by diver along a deepest line at every 1 km spacing.

3.1 *Size of bed and bank materials*

Figures 5, 6 and 7 show the size distribution curves at left bank, right bank and river bed, respectively. As

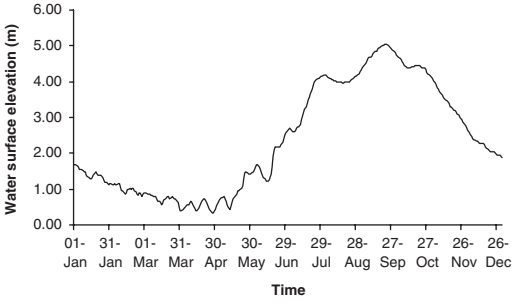


Figure 3. Water surface elevation at Tan Chau gauge station in 2000.



Figure 4. Echo Sounder and GPS system.

Copyright © 2006 Taylor & Francis Group plc, London, UK

shown in these figures, the bank's sediment is composed of wide range of particle size from clay to fine sands, and the medium size is almost smaller than 0.1 mm. Whereas the bed sediment is much coarser than the bank's one, and the medium size ranges 0.15 mm to 0.3 mm. These differences can be seen clearly in Figure 8 in which distributions of mean diameter measured along study reach. Such differences in sediment size between banks and river bed suggests that fine sediment included in side banks , i.e. finer than 0.1 mm in diameter, is released once into flow, and thus transported far as wash load and that the sediment coarser than 0.1 mm deposits onto bed and is transported as bed loads and suspended loads. In addition, bank materials was investigated by core sampling as shown in Figure 9. It suggests that sediment at side banks are effected much by erosion, deposition and channel shifting. Coarse sediment included in side banks, which can be seen partly in Figures 5 and 6, are may deposited by flow recently.

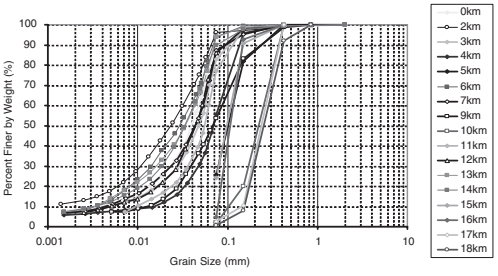


Figure 5. Grain size distribution of left bank material (surveyed on February in 2005).

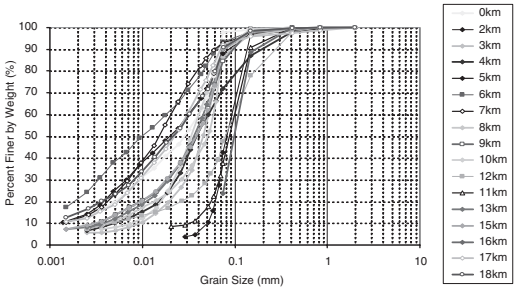


Figure 6. Grain size distribution of right bank material(surveyed on February in 2005).

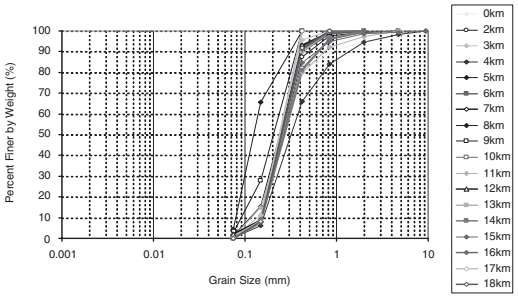


Figure 7. Grain size distribution of bed material (surveyed on February in 2005).

3.2 *Channel deformation*

Figure 1 shows shore lines of study reach. The lines in 1970 and 1990 are obtained by maps which are provided by National Institute of Survey in Vietnam. The line in 2003 is obtained by our measurement. According to Figure 1, two representative characteristics can be distinguished on channel shifting as follows. The bank lines in upstream reach with large islands (submerged bars during flood season) have been shifting to west. Furthermore, the curved reach near Tan Chau City shows a dramatic change that is caused by curved flow. The left bank at the upstream and the downstream of the curvature shift to east and north, respectively. In fact, a stationary point was formed between Tan Chau and Thuong Phuoc. The downstream migration of islands, the rapid development of sand bar at Tan An and the narrow channel at Tan Chau significantly influence to flow pattern as well as direction of hydrodynamic force. These factors may be main reasons of river changes. On the other hand, the right bank at the

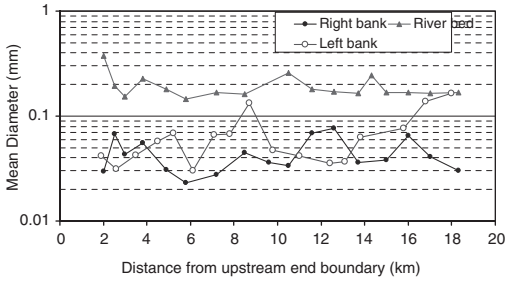


Figure 8. Longitudinal distribution of mean diameter of the materials.

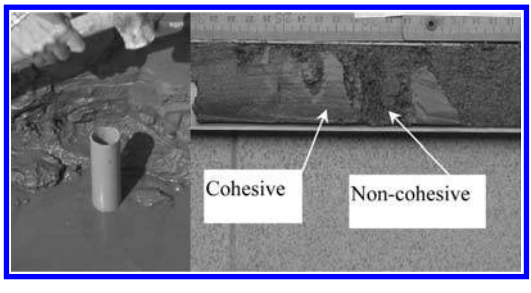


Figure 9. A core sample at river bank. In the deposited layers cohesive and non-cohesive sediment is formed alternatively.

Copyright © 2006 Taylor & Francis Group plc, London, UK

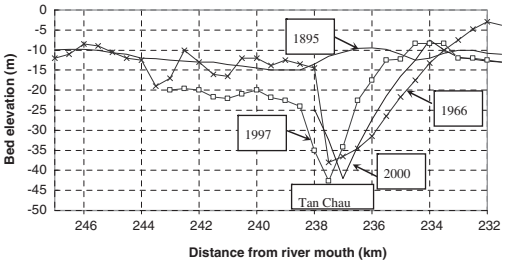


Figure 10. Longitudinal profile of deepest channel bed.

Tan Chau City is consolidated by urbanizing performance, and protected by bank protection works which was constructed from 2000. Hence, the bank erosion along Tan Chau City is almost invisible.

In addition, river bed is expected to be scoured deeply along the right bank at Tan Chau because of curved flow as well as of narrow reach, and its deepest position tends to move to downstream which can be seen in Figure 1 and 10.

4 NUMERICAL CALCULATION

4.1 *Governing equations*

Depth integrated two dimensional form of mass and momentum conservation equations for flow, in addition to these, mass conservation equations of sediment for bed layer as well as for flowing water and sediment transport equations are employed.

Referring to the results on bed and bank material shown in Figures 5, 6, 7, 8 and 9, sediment is transported as bed loads and suspended loads including wash loads. In addition, cohesive sediment exists alternately with non-cohesive sediment, and plays an important role on sediment transport and associated river change. In order to treat such problems, several new relations are introduced into the layer model firstly proposed by Hirano (1971) and bed elevation equation. Specially, in this method, bed surface is clearly defined as the boundary between bed load layer and stationary layer, which is shown in Figure 11. Thickness of bed load layer changes with bed shear stress; i.e. Egashira & Ashida 1992. In addition, as show in chapter 3, some treatments of cohesive material are needed for evaluating sediment transportation and river change.

In Figure 11, bed layer model including bed load layer is shown, in which some parts of bed layer are composed of cohesive sediment.

Supposing that the first layer is composed of non-cohesive material, mass conservation equation of sediment for bed layer (sediment continuity equation/equation for bed elevation) can be given as

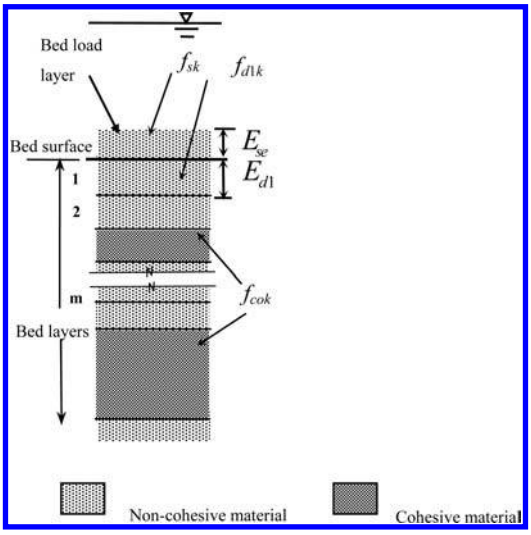


Figure 11. Schematization of sediment exchange process between bed load layer and layers under bed surface.

follows, introducing a new term into a well known formula in order to evaluate the mass change of sediment due to change of thickness of bed load layer.

$$\left(1-\lambda\right)\frac{\partial}{\partial t}\left(\frac{z_b}{J}\right)+\overline{c_s}\frac{\partial}{\partial t}\left(\frac{E_s}{J}\right)+\sum_{k=1}^{n}\left[\frac{\partial}{\partial \xi}\left(\frac{q_{b\xi k}}{J}\right)+\frac{\partial}{\partial \eta}\left(\frac{q_{b\eta k}}{J}\right)+\frac{1}{J}w_k\left(c_{bek}-c_{bk}\right)\right]=0 \quad (1)$$

$$,\left(E_{sd}\geq E_{se}\right)$$

Otherwise, if first layer is composed of cohesive material, and if bed layer is thinner than the equilibrium thickness E_{se}, Equation (1) will be:

$$\frac{\partial}{\partial t}\left(\frac{z_b}{J}\right)+\frac{V_e}{J}=0, \quad \left(E_{sd}\leq E_{se}\right) \quad (2)$$

Continuum equation of each grain size for bed load layer is written as follows.

$$\overline{c_s}\frac{\partial}{\partial t}\left(\frac{f_{sk}E_s}{J}\right)+\left(1-\lambda\right)F_{sk}\frac{\partial}{\partial t}\left(\frac{z_b}{J}\right)+\left\{\frac{\partial}{\partial \xi}\left(\frac{q_{b\xi k}}{J}\right)+\frac{\partial}{\partial \eta}\left(\frac{q_{b\eta k}}{J}\right)\right\}+\frac{1}{J}w_k\left(c_{bek}-c_{bk}\right)=0 \quad (3)$$

in which:

$$F_{sk}=f_{d1k},\ \left(\partial z_b/\partial t\leq 0, E_{sd}\geq E_{se}\right);$$

$$F_{sk}=f_{cok},\ \left(\partial z_b/\partial t\leq 0, E_{sd}\leq E_{se}\right);$$

$$F_{sk}=f_{sk},\ \left(\partial z_b/\partial t\geq 0\right)$$

Copyright © 2006 Taylor & Francis Group plc, London, UK

Continuum equation of each grain size for first is evaluated as follows.

$$E_{d1}\frac{\partial}{\partial t}\left(\frac{f_{d1k}}{J}\right)+\left(f_{d1k}-F_{dk}\right)\frac{\partial}{\partial t}\left(\frac{E_{d1}}{J}\right)=0 \tag{4}$$

in which:

$$F_{dk}=f_{d1k},\quad (\partial z_b/\partial t\le 0);$$

$$F_{dk}=f_{sk},\quad (\partial z_b/\partial t\ge 0)$$

In these equations J = Jacobian; λ = porosity; $q_{b\xi k}$ and $q_{b\eta k}$ = sediment transport rate for size class k in ξ and η directions, respectively; f_{sk} = fraction of size class k in the bed load layer; f_{cok} = sediment fraction of size class k in the cohesive sediment layer; E_{dm} and f_{dmk} = thickness and fraction of size class k in the *m-th* bed layer composed of non-cohesive sediment, respectively (m = 1,2..); $\bar{c}_s$ = sediment concentration of bed load layer ((1-λ)/2 is used as $\bar{c}_s$ for simplicity); V_e = erosion rate of cohesive sediment; E_s = bed load layer thickness; E_{sd} = thickness of non-cohesive sediment over cohesive sediment; E_{se} = thickness of equilibrium or saturated bed load layer estimated by the following equation (Egashira et al.,1992).

$$\frac{E_{se}}{d_m}=\frac{1}{\bar{c}_s\cos\theta\left(\tan\phi-\tan\theta\right)}\tau_{*m} \tag{5}$$

in which d_m = the mean sediment size of bed load; θ = local bed slope; ϕ = the angle of repose; τ_{*m} = non-dimensional bed shear stress specified by d_m. Relations among E_s, E_{se} and E_{sd} are as follows.

$$\begin{aligned} &E_s=E_{se},\quad (E_{sd}\ge E_{se});\\ &E_s=E_{sd},\quad (E_{sd}\le E_{se}) \end{aligned} \tag{6}$$

Sediment transport rates of size class k of non-cohesive material are estimated by following equations.

$$q_{b\xi k}=\xi_x q_{bxk}+\xi_y q_{byk} \tag{7}$$

$$q_{b\eta k}=\eta_x q_{bxk}+\eta_y q_{byk} \tag{8}$$

Herein bed load rate q_{bk} for size class-k is defined as $q_{bk}=\sqrt{q_{bxk}^2+q_{byk}^2}$ and is estimated by the following relation (Liu, 1991; Kovacs and Parker, 1994).

$$q_{bk}=17\frac{\rho u_{*e}^3}{(\rho_s-\rho)g}\left(1-\sqrt{K_c}\frac{u_{*ck}}{u_*}\right)\left(1-K_c\frac{u_{*ck}^2}{u_*^2}\right)f_{sk}r_s \tag{9}$$

In Eq. (9), ρ = water density; ρ_s = sediment density; u_{*e} = effective shear velocity; u_* = shear velocity; u_{*ck} = critical shear velocity of size class k;

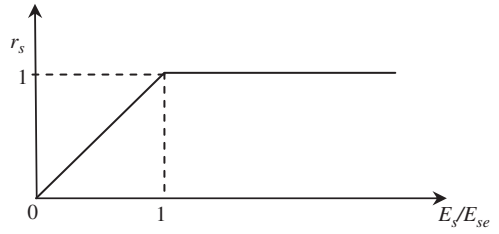


Figure 12. Relation between r_s and E_s/E_{se}.

K_c = correction factor related to bed inclination (Liu, 1991; Kovacs and Parker, 1994). r_s is introduced to describe the unsaturated bed load rate and is a function of relative depth E_s/E_{se} as shown in Figure 12.

The deviation angle β_k of mean path of size class k to the x direction, which depends on the flow near bed and inclination of bed, is calculated by following formulas (Liu, 1991; Kovacs and Parker, 1994).

$$\tan\beta_k=\frac{\sin\alpha-\Pi\Theta_y\left(\frac{u_{*ck}^2}{u_*^2}\right)\tan\theta_y}{\cos\alpha-\Pi\Theta_x\left(\frac{u_{*ck}^2}{u_*^2}\right)\tan\theta_x} \tag{10}$$

$$\Pi=K_{ld}+1/\mu_s \tag{11}$$

$$\Theta_y=\frac{1}{1+\tan^2\theta_x+\tan^2\theta_y} \tag{12}$$

$$\Theta_x=\Theta_y+\frac{\rho}{\rho_s-\rho}\cos^2\theta_x \tag{13}$$

where K_{ld} = the ratio of the lift force to drag force; θ_x and θ_y = the bed inclinations in x and y direction, respectively; α = angle of deviation of flow near bed from x direction; μ_s = coefficient of static friction.

The above mentioned sediment transport rate of size class k in x and y directions are $q_{bxk}=q_{bk}\cos\beta_k$ and $q_{bxk}=q_{bk}\sin\beta_k$, respectively.

The erosion rate of cohesive sediment, V_e, is estimated in terms of Sekine et al.'s formula (Sekine et al., 2003).

$$V_e=\alpha R_{wc}^{2.5}u_*^3(1-r_s) \tag{14}$$

in which α is the empirical coefficient and R_{wc} is the water content ratio of cohesive sediment.

Velocities near the bed are evaluated using curvature radius of streamlines:

$$u_b=8.5u_*,\ v_b=-N_*(h/r)u_b \tag{15}$$

in which N_* = 7.0 (Engelund, 1974); r = the curvature radius of stream lines obtained by depth integrated velocity field.

Copyright © 2006 Taylor & Francis Group plc, London, UK

Settling velocity of suspended sediment of size class-k, w_k, is estimated in terms of Rubey's formula (Rubey, 1933) and quasi-equilibrium suspended concentration, c_{bek}, for size class-k at reference level is evaluated as follows (Lane et al.,1941).

$$c_{bek} = 5.55 f_{sk} \left\{ \frac{1}{2} \frac{u_*}{w_k} \exp\left[-\left(\frac{w_k}{u_*} \right)^2 \right] \right\}^{1.61} r_s \quad \text{[ppm]} \quad (16)$$

in which r_s is the same as the factor in equation (9). It is considered that equilibrium sediment concentration is formed at reference level when bed load layer is saturated, whereas it decreases with the decrease of relative thickness r_s, as shown in Figure 12, because sediment can not be supplied fully through bed load layer for suspension. Therefore, the sediment concentration determined by equation (16) is called "quasi-equilibrium"; c_{bk} = suspended sediment concentration of size class k at reference level. When the vertical distribution of suspended sediment concentration is supposed to be the exponential distribution, the relationship between c_{bk} and the depth-averaged value; c_k is expressed as follows.

$$c_k = \frac{c_{bk}}{w_k h / D_h} \left(1 - e^{-w_k h / D_h} \right) \quad (17)$$

Suspended sediment transport is evaluated using the following continuum equation.

$$\begin{aligned} &\frac{1}{J}\frac{\partial}{\partial t}(c_k h) + \frac{\partial}{\partial \xi}\left(\frac{c_k}{J} Q^{\xi} \right) + \frac{\partial}{\partial \eta}\left(\frac{c_k}{J} Q^{\eta} \right) = \frac{1}{J} w_k (c_{bek} - c_{bk}) \\ &+ \frac{\partial}{\partial \xi} h \left(\frac{D_x \xi_x^2 + D_y \xi_y^2}{J} \frac{\partial c_k}{\partial \xi} + \frac{D_x \xi_x \eta_x + D_y \xi_y \eta_y}{J} \frac{\partial c_k}{\partial \eta} \right) \\ &+ \frac{\partial}{\partial \eta} h \left(\frac{D_x \xi_x \eta_x + D_y \xi_y \eta_y}{J} \frac{\partial c_k}{\partial \xi} + \frac{D_x \eta_x^2 + D_y \eta_y^2}{J} \frac{\partial c_k}{\partial \eta} \right) \end{aligned} \quad (18)$$

in which h is water depth, ξ_t, η_t, ξ_x, η_x, ξ_y, η_y are metrics, D_x and D_y are the dispersion coefficient in x and y directions, respectively ($D_x = D_y = D_h$ as a diffusion coefficient for simplicity).

Bank erosion with non-cohesive material is evaluated using the model of Nagase et al.(1996). This is based on the stability condition by angle of repose of material. In case of cohesive material, equation (2) is applied for this method.

4.2 *Numerical method and computational conditions*

Numerical computations were conducted for two cases. Sediment transport of Case 1 is only bed load. Nevertheless, bed load and suspended load were considered in Case 2. TVD MacCormack numerical scheme is used only for advection terms of momentum conservation equations. Staggered grid system is used and shown in Figure 13, where U, V, Q^{ξ} and Q^{η} are ξ and η components of velocity vectors and discharge fluxes, respectively. In the equations associated with sediment, the first order up-wind scheme is employed for the terms of first-order spatial derivatives, and the central difference approximation is used for the terms of second-order spatial derivatives.

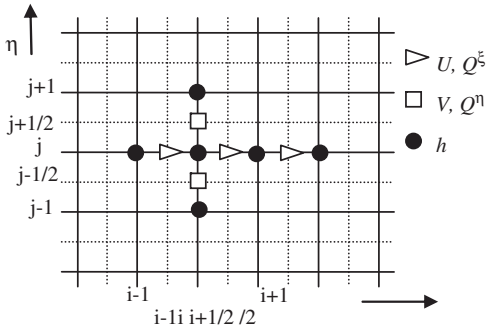


Figure 13. Defined location of variables.

Computational conditions which are employed in this study are summarized as follows. Computation domain, which is shown in Figure 1, is 18 km long. The initial bed geometry is specified based on the data obtained from the field survey in 2003. Flood plain is assumed to be expanded laterally about one kilometer from the both banks and its elevation is assumed to be equal to the bank elevation. The data of the year 2000 in hydrograph which is shown in Figure 2 and water surface elevation which is shown in Figure 3 are used for upstream and downstream boundary condition, respectively. The value of f_{sk} and c_k at the upstream boundary are estimated by use of collected bed material distribution and equilibrium hydraulic conditions. It is supposed that side bank, which is steeper than the angle of repose of non-cohesive sediment, is composed of cohesive sediment. Furthermore, bed is assumed to be covered one meter deep by non-cohesive sediment.

5 RESULTS AND DISCUSSION

The computational domain and its grid system are shown in Figure 14. Figure 15 shows computed results on flow patterns of depth mean. Figures 16 and 17 show contour lines of topography changes and cross-sectional shapes as well as its bed load transport rate in ξ and η direction in flood season (September), respectively. The results shown in Figure 15 suggest that the flow pattern is influenced very much as a whole by initial condition such as a presence of large sand bar and by the narrow channel shape at downstream of

Copyright © 2006 Taylor & Francis Group plc, London, UK

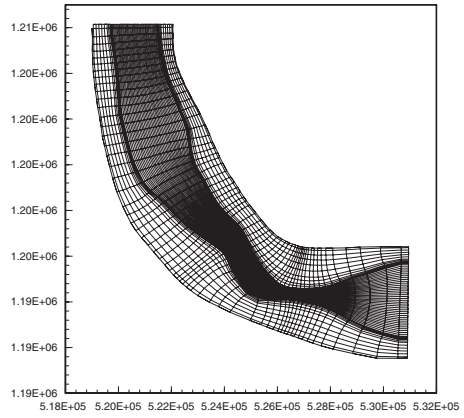


Figure 14. Computational domain and grid system.

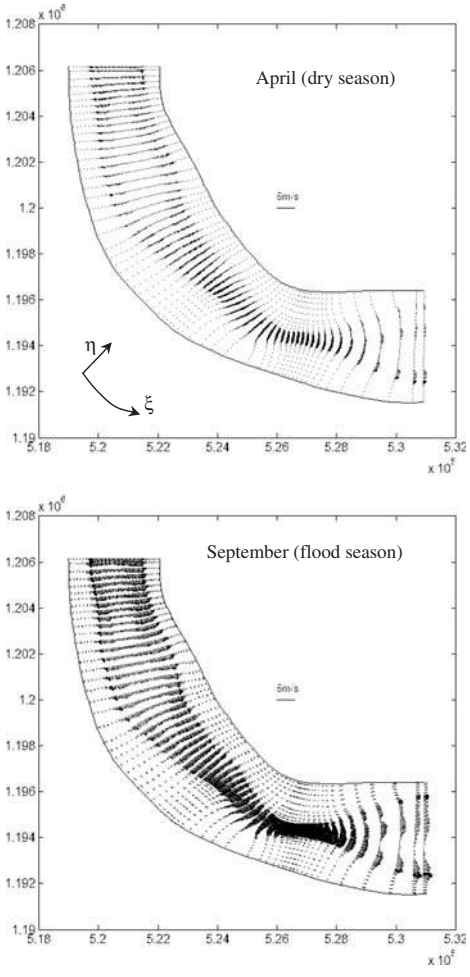


Figure 15. Computed velocity profile in April and September, respectively.

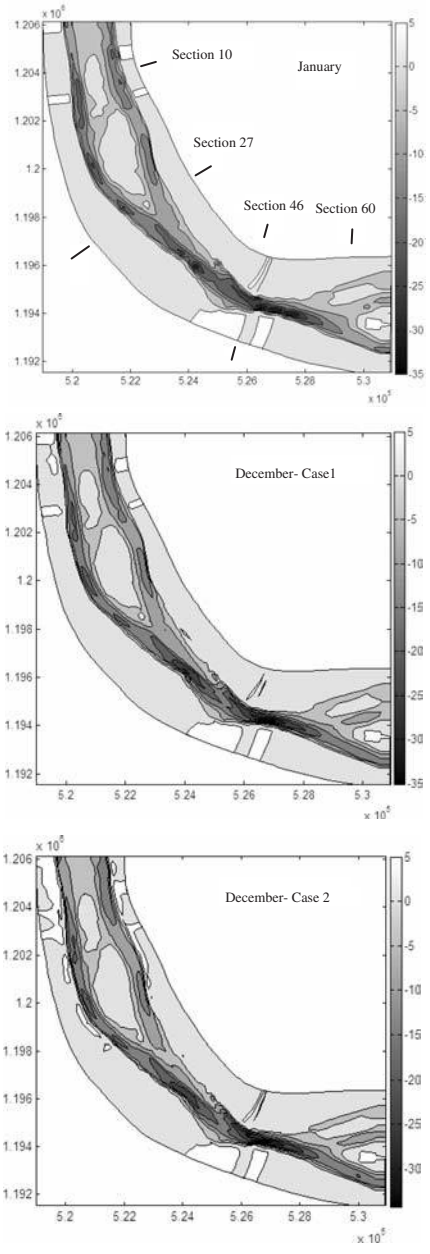


Figure 16. Contour lines of bed elevation in January and December.

section 46. In addition, stream currents were strengthened along the right bank from section 27 and change to left bank before going to right bank again at section 46. Such complex change of flow pattern will cause a channel shift toward anti-clock wise, and also will be affected by the caused channel change.

Copyright © 2006 Taylor & Francis Group plc, London, UK

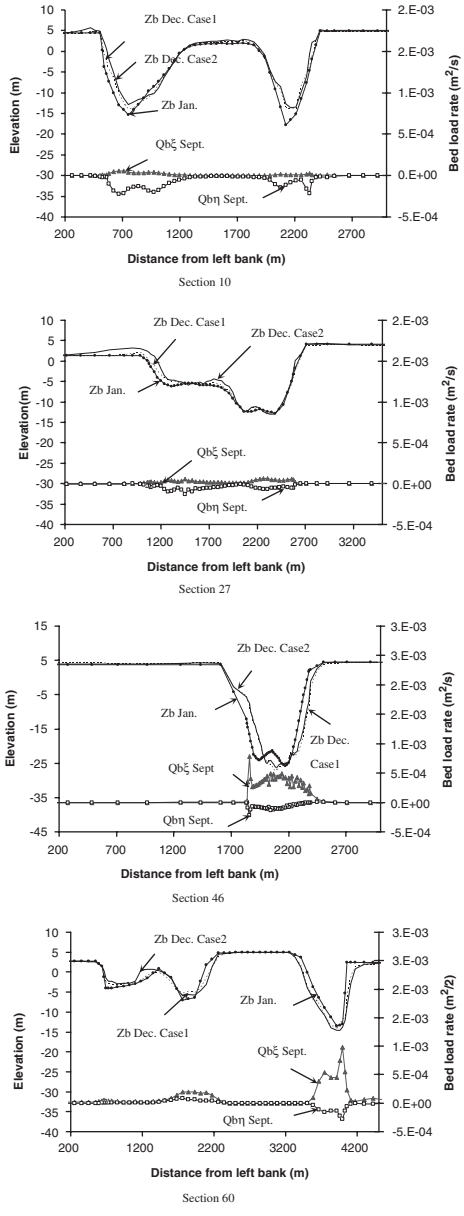


Figure 17. Channel deformation and bed load transported rate of section 10, 27, 46 and 60, respectively.

The Figures 16 and 17 show computed results on topography changes. The influence of suspended load can be easily seen in different results between Case1 and Case2 in Fig 16. This suggests that suspended load deposited much on flood plain where roughness coefficient is high, or deposited at downstream part of sand bar. These cause sand bar develop and migrate to downstream, i.e. development of large sand bar at upstream and sand bar at downstream which located along the left river bank as partly shown in section 60 of Fig 17. In addition, left bank from section 10 to section 27 tend to deposit. This phenomenon agrees with the real situation. However, right bank side at upstream part is not predicted well. This may be caused by upstream boundary conditions, i.e. equilibrium concentration of suspended sediment. The numerical results in section 46 show that right bank is much eroded whereas sediment deposits along left bank. On the other hand, in actual situation, right bank side is covered by protection works, therefore the data which shown in Fig 1 seems to be different with computed results.

As shown in the results of Figure 15, 16 and 17, the computed channel changes correspond qualitatively with the tendency described in Figure 1. However, because of lack of topography data in 1970, 1990, authors must use the topography data of 2005 to predict the river change as the initial condition. Therefore, there is no exact data to verify the results of computation. In addition, actual conditions such as more exactable initial channel shape, sediment characteristics of material which is located under bed surface associated with channel erosion, and artificial works should be introduced into computational conditions.

6 CONCLUSIONS

Channel change in part of Mekong River was investigated using field data and the numerical method to develop a tool treating channel shifting in which the presence of cohesive sediment plays important roles in sediment transport phenomena. Results and further problems are summarized as follows.

Data analysis suggests that bed material can be produced due to bank erosions. River sediment is composed by cohesive and non-cohesive materials. Data of bed and bank material are provided to study the river change which is probably influenced by the co-presence of non- and cohesive sediments.

Bank erosion and associated channel shifting have been controlled by moving of large bar, channel plane form and several artificial performances in addition to the sediment characteristics and hydrological data variations.

A 2-D numerical analysis describing bed deformation and bank shifting was proposed by introducing erosion rate formula for cohesive material and formula for estimating the thickness of bed load layer, and it was used to predict channel morphological process. The simulated results can explain a tendency of the channel shifting, and emphasize that the presence of fine sediment as well as cohesive material influences the channel change.

Copyright © 2006 Taylor & Francis Group plc, London, UK

Further studies are desired for: study of historical formation process on Mekong Delta to evaluate present sediment phenomena, further refinement of numerical model and long time computations of various hydrological conditions to test validity of present model, etc..

REFERENCES

Le, S., Nguyen, A. N., Le, N. B. & Le, M. H. 2001. *Study on predictive shoreline erosion of Mekong River.* Ho Chi Minh City: River Training Center – Southern Institute of Water Resource Research.

Pham, T. H., Nguyen, N. H. & Le, V. L. 1991. On the Paleography of 129 the periods of development of Quaternary deposits in Nam Bo Plain. *Geological – Geographical Association of Ho Chi Minh City*

Nagata, N., Hosoda, T. & Muramoto, Y. 2000. Numerical Analysis of River Channel Processes with Bank. *Journal of Hydraulic Engineering ASCE* 126(4):243–252.

Liu, B.Y., 1991. Study on Sediment Transport and Bed Evolution in Compound Channels. *Thesis presented to Kyoto University.*

Le, N.B., 1997. Study on prediction of erosion and disaster mitigation in Mekong River. (in Vietnamese)

Egashira, S. & Ashida, K. 1992. Unified view of the mechanics of debris flow and bed-load, *Advances in Micromechanics of Granular Materials*, (Edited by H.H.Shen et al.) Elsevier: 391–400.

Engelund, F. 1974. Flow and bed topography in channel bends. *Journal of Hydraulic Division, ASCE*, 100(HY11):1631–1648.

Hirano, M., 1971. River-bed degradation with armoring. *Proc. of JSCE* 195:55–65.

Kovacs, A. & Parker, G. 1994. A new vectorial bed load formulation and its application to the time evolution of straight river channels. *Journal of Fluid Mechanic*, 267:153–183.

Lane, E. W. & Kalinske, A. A. 1941.Engineering calculation of suspended sediment. *Transaction A.G.U.* 22: 603–607.

Rubey, W. W. 1933. Settling velocities of gravel, sand and silt particles. *American Journal of Science* 25:325–338.

Sekine, M., Nishimori, K., Fujio, K. & Katagiri, Y. 2003. On erosion process of cohesive sediment and erosion rate formula. *Annual Journal of Hydraulic Engineering. JSCE* 47:541–546.

Nagase, K., Michiue, M. & Hinokidani O. 1996. Simulation of bed elevation around contraction in mountainous river. *Annual Journal Hydraulic Engineering. JSCE* 40: 887–892.

Copyright © 2006 Taylor & Francis Group plc, London, UK

Morphodynamics of mountain rivers following repeated sediment release from reservoirs

Giacomo Fasolato, Paolo Ronco, & Matteo Tregnaghi
Hydraulic, Maritime, Environmental and Geotechical Engineering Department, University of Padova, Italy

ABSTRACT: In the paper an appropriate morphodynamic model has been developed and applied to simulate flushing operations repeatedly performed from an alpine reservoir in the last decade and to optimize flushing operations in the future. The morphodynamic model is based on a relatively simple hydrodynamic component, while much attention is devoted to the non-uniform distribution of sediment grainsize ranging over four or five order-of-magnitudes (from boulders to silt) which is typical of alpine rivers.

The experimental conditions of the selected river reach are especially favourable to investigate flushing effects, as the release operations from the reservoir can reasonably be controlled, together with their morphological consequences downstream. The chronological sequences of strong deposition and subsequent erosionphases have been simulated with the model. An improvement of the sediment management criteria may be investigated with the same model.

1 INTRODUCTION

1.1 *Impacts of dams on the river morphology*

In numerous catchments throughout the world human intervention has altered natural river dynamics. Among others, dams and reservoirs constructed in the last century for hydroelectric power generation, flood attenuation, storage for irrigation, navigation, etc., are causing substantial changes to the flow and sediment regimes, with significant impacts on the river morphology, upstream and downstream of the dam. A more evident alteration of the river system caused by dams is the trapping of solids conveyed by the river, which in turn causes the reduction of sediment load in the reach downstream (Morris & Fan, 1997). Moreover, reservoirs significantly reduce flood peaks and flood durations, and consequently lower the sediment transport capacity. As years go, natural consequences of these changes are, upstream, the progressive reduction of the reservoir water storage capacity and river overaggradation; downstream, the change of the natural morphological features, general bottom erosion and many other negative consequences with serious economic, sociological and environmental implications (Basson & Rooseboom, 1997).

1.2 *Strategies to control and mitigate negative impacts*

Several procedures and techniques for preventing, reducing or mitigating reservoir sedimentation and its negative consequences have been devised and experimented as described in scientific and technical literature. One of the more efficient and economic intervention is probably the regular releases of sediments from the reservoir to the river (either by flushing or by mechanical means) especially if sufficient water discharge is allowed to convey the sediments along the fluvial system (Di Silvio & Scagnetto, 2001).

Releasing large quantities of sediments concentrated in time and space, on the other hand, may bring about complications. Obviously, release procedures have to be carefully planned, tested and preventively simulated to guarantee full control and safety of the operation.

The purpose of this work is to describe and reproduce with simplified morphodynamic model (Di Silvio & Peviani, 1989) the consequences of sediment management at basin scale and eventually advise for a possible future improvements. The model is intended to reproduce the flushing operations from an alpine reservoirs repeatedly performed in the last decade and their effects along the river. The results are compared with some measurements and data field collected in the last year by the authors and by the reservoirs manager Enel/GEM (Generation Energy Management).

2 THE PIAVE RIVER

2.1 *An example of substantial human impacts*

The Piave River rises in the Eastern Alps at an elevation of 2,037 m a.s.l. and its mouth, in the Adriatic Sea, is

Copyright © 2006 Taylor & Francis Group plc, London, UK

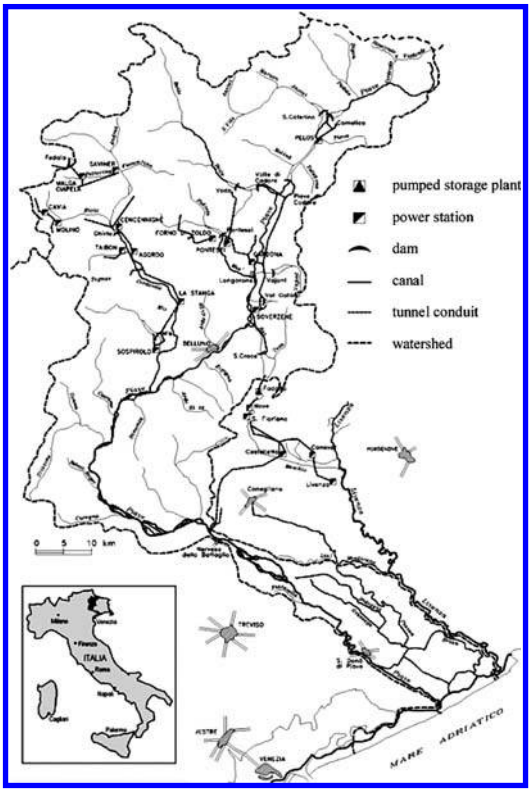


Figure 1. Water resource development in the Piave River Basin (Eastern Alps, Italy).

located about 30 km northeast of Venice. It has a length of 222 km and its watershed has an area of 3,899 km^2 (Figure 1).

During the last 70 years many hydraulic constructions were built for 24 hydroelectric power plants (managed by many different members) with more than 50 dams and 200 km of pipes and channels for irrigation that carry flow and divert water along its course (Enel, 1993).

The present regime of water regulation and diversion has altered both the flow duration and the volume of annual runoff, with consequent reduction of sediment transport capacity. Although it is not possible evaluating with precision the sediment delivery, several dams, along the river and its tributaries, trap sediment yield from an area corresponding to more than 50 per cent of the drainage basin (Surian, 1999, Surian, 2003). Reductions in sediment supply is also due to intense gravel mining. Since 1960s, in fact, in the Piave river and its tributaries a huge volume of sediment was excavated, which was estimated to be in the order of 10^6 m^3 per year (D'Alpaos & Dal Prà, 1996), but no records are available to validate those quantities.

Finally, stream bank protection structures, like groynes and levees, have canalized the river in a single, fixed channel, and reduced in many places bank erosion and consequent sediment load (Surian, 2000).

2.2 *Recent morphodynamic evolution of the river*

As for the evaluation of human impact on the recent dynamics of the Piave River, the research carried out by Surian (1999) is worthy of comment. Historical evolution has been documented using maps, aerial photographs and field data. Morphological features that were examined included channel width, planform configuration, braiding index, bed elevation and grain-size variation. The results indicate that as consequence of decreases in water flow and sediment supply, the river channel has undergone in its main reach a general narrowing to 35 per cent of its initial width. Besides, the planform pattern in several reaches has changed from braided to wandering, with corresponding deepening of the bed and a degradation rate of 20 to 70 mm/per year during this century. As expected, the highest rates were found immediately downstream of the main barrages.

Also the bed material shows a clear evolution. As expected, a general increase of grain size is evident downstream of the structures and describes, very likely, the evolution towards an armored bed (Surian, 2000).

2.3 *Research programs for sediment management*

Many studies are presently being carried on about sediment management of Piave's dams and its consequences, by several agencies and local administrations. The present work, is in part sponsored by the Watershed Agency "Autorità di Bacino dell'Alto Adriatico" in collaboration with the Italian Ministry of Research and University "MIUR" as a part of a national project on reservoir sedimentation (PRIN 2004). ALPRESERV, an European Project dealing with the same problems in many Alpine watersheds, is also involved in the Piave River investigations.

3 MODEL DESCRIPTION

3.1 *Simplified morphological model*

In this work, a simplified morphological model has been selected to reproduce both the quick chronological sequences of strong deposition (hours) due to flushing activities (and probably due also to largest flood) from the reservoir and subsequent slow erosion-phases (months) with moderate flow and relatively small flow (the so-called "vital minimum discharge"). In fact, the same model should be able to describe short time-scale events (e.g. overaggradation phenomena

Copyright © 2006 Taylor & Francis Group plc, London, UK

due to catastrophic floods or flushing operations on dams) as well as long time-scale general aggradation or degradation of the river bottom. In particular, the long term model may be obtained by averaging the unsteady equations over a period of time long enough to eliminate the fluctuations of the hydrological cycle.

Mountain rivers, like Piave, are characterized by geometric irregularities and by frequent alternations of subcritical and supercritical water flow. As the model is intended for a relative coarse space-resolution (about few hundreds meters), the average energy gradient for a sufficiently long reach can be assimilated to the average gradient of the bottom. Therefore the hypothesis of locally quasi-uniform flow (Marin & Di Silvio, 1996) can be generally made. The validity limits of the hypothesis of local uniform flow has been thoroughly analyzed in a recent work (Madeo, 2002) for mountain river.

The hypothesis assumed by the simplified model are described below. A known numerical code (Di Silvio & Peviani, 1989) was used for computation, with some modifications during different simulations.

3.2 *Theoretical assumptions*

The following assumptions have been made to derive the differential equations that describe the physical phenomena:

(I) The celerity of flood waves in mountain rivers is much higher than the celerity of the bottom changes. This leads to assume instantaneous adaptation in time of the water discharge in each branch of the network (a quasi-steady flow condition are assumed).

(II) It is assumed that the motion equation for each sediment fraction, both as bedload and in suspension, is completely governed by the average local parameters, such as discharge, bottom slope, channel width, grain size, etc. (it means, instantaneous adaptation of the vertical sediment concentration in the water stream).

(III) The flow pattern in a mountain river is a sequence of subcritical and supercritical regime, passing through subsequent critical conditions and hydraulic jumps, with a Froude number near to one. The local energy losses at the weak hydraulic jumps as well as the variation of kinetic energy are negligible comparing with the friction losses of the flow itself. This leads to assume that the average flow regime is quite well represented by a quasi-uniform flow, even for relatively short waves of sediment input.

3.3 *Water flow*

Water discharge along the hydrographic network is supposed to be a known function of space and time,

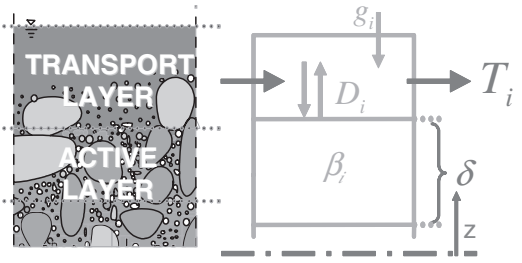


Figure 2. Definition sketch for the sediment balance in the transport- and in the active-layer.

assuming a kinematic wave propagation downstream. Each reach (50–500 m long) is schematized as a rectangular channel with uniform flow condition; width, slope and hydraulic roughness are given.

Water depth is calculated with following Gauckler-Strickler equation (Equation 1):

$$Q = K_s A R^{2/3} S_f^{1/2} \tag{1}$$

where the Strickler coefficient K_s, calculated with Equation 2, may change in time and space.

$$K_s = 26/d_{90}^{1/6} \tag{2}$$

3.4 *Sediment transport*

Modelling erosion and deposition processes in mountain rivers (sediment grainsizes vary over several orders of magnitude from boulders to silt) requires in principles a careful reproduction of a number of phenomena related to the non uniformity of a sediment mixture.

In the present work a simple model based on the "active layer" concept has been selected . The model considers two layers (Armanini and Di Silvio, 1988): the transport layer, containing the particles transported in suspension and as bedload, and the active (or mixing) layer (Hirano, 1971) containing the particles that are not in movement, but are liable to vertical movements to and from the upper transport layer (Figure 2).

The balance in the transport layer between transport T_i and net deposition D_i, is written as Equation 3, where B is the active channel width (m) (different from B_s stream width) and g_i is lateral specific solid discharge (m^2/s).

$$BD_i + \frac{\partial T_i}{\partial x} = g_i \tag{3}$$

Equation 4 expresses the balance in the active layer and it leads to the computation of bedcomposition

Copyright © 2006 Taylor & Francis Group plc, London, UK

changes. In this equation β_i^* is the composition of the undisturbed material below the mixing layer if $D_i < 0$ (erosion), while β_i^* is the mixing layer material composition if $D_i > 0$ (deposition).

$$\frac{\partial(\delta\beta_i)}{\partial t} = D_i - \beta_i^* \cdot \frac{\partial z}{\partial t} \tag{4}$$

Bottom level change is expressed by Equation 5 and the mixing layer thickness is assumed to be twice the representative diameters of the coarsest particles d_{90}, as expressed by Equation 6.

$$\frac{\partial z}{\partial t} = \sum_{i=1}^{4} D_i - \frac{\partial \delta}{\partial t} \tag{5}$$

$$\delta = 2d_{90} \tag{6}$$

The transport equation (Equation 7) for each fraction includes an exposure-correction coefficient ζ_i which accounts for the "hiding and exposure" effect for the non-uniform material:

$$T_i = \alpha \frac{Q^m I^n}{B_s{}^p d_i^q} \beta_i \zeta_i \tag{7}$$

where Q is the water discharge, B_s is the stream width (different from active channel width B, Equation 3), $\zeta_i = (d_i/d_m)^s$ and d_m *is* the mean diameter. The coefficient α and the exponents m, n, p, q and s were empirically evaluated from data in other Alpine rivers (Di Silvio, 1991). In the present formulation of the model the stream width has been evaluated as a function of Q where $B_s = K_p Q^{0,5}$ ($K_p = 3,5$ is assumed as a constant).

3.5 *Numerical solution*

The set of equations is solved numerically using a finite difference approximation. A predictor-corrector method is chosen for the numerical solution of the sediment equations. The predictor step is carried out with a FTBS (Forward Time Backward Space) scheme while the Four-point scheme of Preismann is used for the corrector step (Peviani, 2002).

4 STUDY REACH IN UPPER PIAVE

4.1 *Description of the case study*

An appropriate 8 km reach of the Piave river was selected for a first application and development of the model. It is located in upper area of the Piave basin (Figure 3), between Pieve di Cadore artificial lake (reservoir capacity of $64.3 \cdot 10^6$ m^3) and Santa Caterina dam (reservoir capacity of $6.7 \cdot 10^6$ m^3) and Comelico dam (reservoir capacity of $1.4 \cdot 10^6$ m^3).

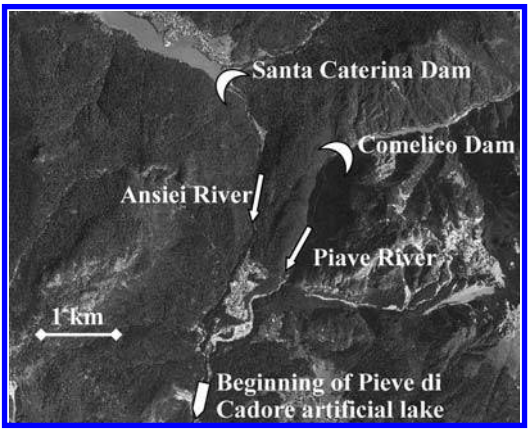


Figure 3. Location of the study site in the upper course of Piave river.

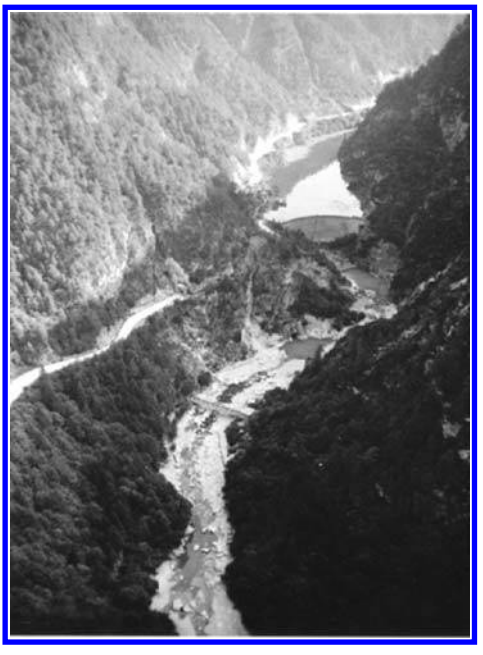


Figure 4. Comelico reservoir and Piave river downstream.

This choice was in part suggested because the boundary conditions are known and, in part, artificially controlled (water and sediment discharge is controlled by reservoirs manager). All the released sediments, moreover, are intercepted by the Pieve di Cadore artificial lake, at the end downstream. It's also a relatively limited area (few hundreds km^2) and easy to be reached for measurements and sampling.

One of the two reservoirs upstream (Comelico, Figure 4) is quite small compared to the catchment area of 372 km^2 and requires frequent removal of sediments

Copyright © 2006 Taylor & Francis Group plc, London, UK

Table 1. Flushing operations from Comelico reservoir during the last 12 years.

Year	Period	Sediment removed mc	Mean water discharge mc/s
1994	23/5–27/5	90,000	13.7
1995	15/5–19/5	80,000	9.9
1996	25/5–31/5	70,000	9.4
1997	26/5–30/5	70,000	7.3
2000	22/5–01/6	120,000	8.6
2002	22/5–31/5	80,000	12.7
2004	24/5–06/6	80,000	11.9

Data was furnished by Enel/GEM (Generation Energy Management).

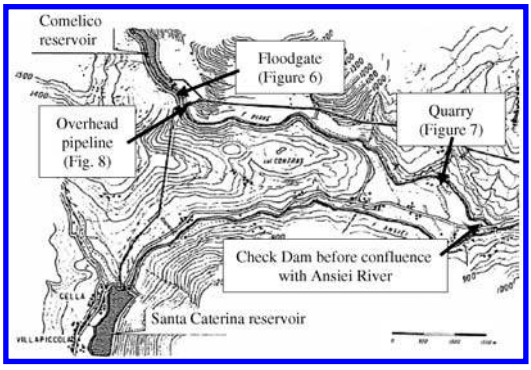


Figure 5. Piave reach between the Comelico Dam and the confluence with Ansiei River.



Figure 6. Floodgate section after flood event registered between 03 and 13 October 2005 (photo taken on 24 November 2005). Thick layer of stratified deposition, created by short period (mainly flushing period but probably also some flood periods) was partially eroded by subsequent long period of water discharged (during low and moderate flow).

by flushing. The water discharge released from the dam is usually on the order-of-magnitude of 1–2 m^3/s, except during the moderate and large floods (during largest flood it can peak also 100–200 m^3/s).

The other reservoir upstream (Santa Caterina) intercepts a tributary of Piave (Ansiei river); it is bigger than Comelico but with a smaller watershed and it is not concerned by flushing operations. The released water discharge, except during moderate flow and large flood, is almost always limited to the "minimum vital flow" prescribed by environmental regulations.

During the autumn of 2005 some samplings have been made by authors in both water courses to characterize the respective granulometry of the bed. As expected, the reach of the tributary Ansiei (where virtually flows only clear water) presents an armoured bed with definitely coarse material. The Piave reach below the Comelico dam, by contrast, presents a more complex pattern, with layers of different material caused by the chronological sequence of strong deposition and subsequent slow erosionphases.

4.2 *Water discharged and flushing operations*

Alternate operations of flushing and flood have continued probably for 70 years (the Comelico dam was built in 1931), but only in the last decades have been quantitatively recorded. The available data covers the period from 1994 to present date. By analysing the water discharges released from Comelico dam (from 1994 to 2005), it was possible to identify three distinct regimes: (i) flushing periods reported on Table 1, (ii) very long minimum flow periods and (iii) moderate flow (from April to June, every year) and flood periods (with a mean of two flood events per year). From autumn 2003, however, the water flow management of Comelico dam has changed because of a new Italian regulations, prescribe a "vital minimum discharge" to be released downstream.

In this paper, particular attention is given to the last flushing operation (May 2004), to the subsequent low flow period and to the last remarkable flood event (October 2005).

By a photographic survey, a qualitative evaluation of morphology can be made along the upper reach of Piave River (Figure 5). The distinctive feature of this riverbed is a thick layer of stratified deposition (created during short flushing period and probably also some flood periods), partially eroded by the subsequent low, moderate water flow and largest flood periods.

Following the flushing operations, in the upper end of the reach (near the flood gate, about 200 m the river downstream, Figures 6, 8a and 8b), bed elevation increased more than 4 m, but this variation rapidly lessened with distance from dam. In the proximity to "quarry zone", located about 3.5–4.0 km downstream, bed deposition is limited to the order of 50 cm (Figure 7).

Copyright © 2006 Taylor & Francis Group plc, London, UK

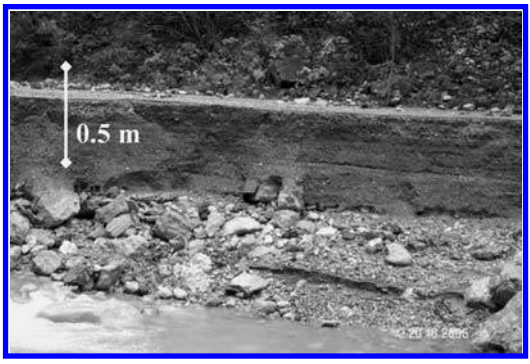


Figure 7. "Quarry zone" section after flood event registered between 03 and 13 October 2005 (photo taken on 20 October 2005). The deposition layer appear less thick at the "Quarry zone".



Figure 8. Cross-section evolution at the "overhead pipeline" respectively before (photo a, taken on 27 July 2005) and after (photo b, taken on 04 November 2005) the flood event registered between 03 and 13 October 2005.

Also granulometry of bed material presents a clear distinction between the sediments transported and the coarser bottom material left after the moderate flow and large flood periods (Figures 6 and 7). Sediment size swings about one or two order-of-magnitude along cross-section. Bed material size was measured

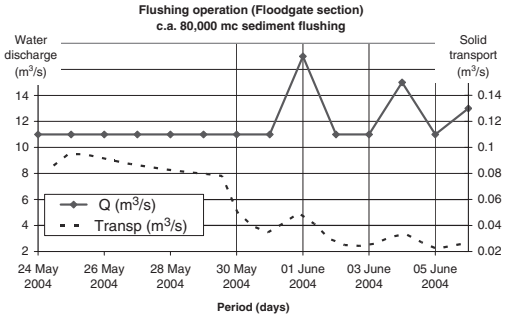


Figure 9. Boundary condition of flushing operation on May 2004 (model simulations at "Floodgate" cross-section).

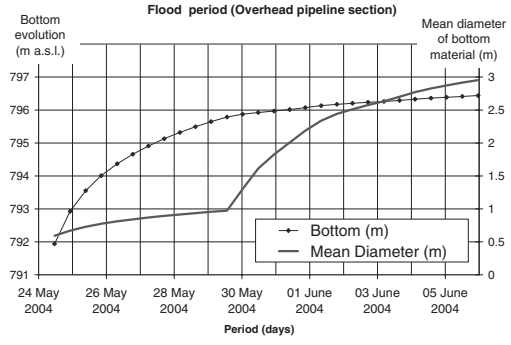


Figure 10. Flushing operation on May 2004 (model simulations at "Overhead pipeline" cross-section).

in different sections using the grid-by-number method (Surian, 2000) but a more deep sampling will start from spring 2006.

5 PRELIMINARY MODEL SIMULATIONS

5.1 *Flushing operations (May 2004)*

A first series of model simulations has been made to reproduce the last flushing operation (May 2004) and consequent evolution of bed elevation and grainsize.

Flushing simulation was performed by considering a given amount of sediments inside the reservoir, to be eroded and released though the floodgate by a mean daily water discharge (Figure 9). Problems rise because the daily water discharge (recorded only once a day) present peaks (during few hours) that, also if they are of the daily water order-ofmagnitude, affect significantly results.

In Figure 10 are reported bottom increase and bed material changes. While the bottom elevation increase seems to be correct, bed material size growth is probably more affected by the initial condition within the

Copyright © 2006 Taylor & Francis Group plc, London, UK

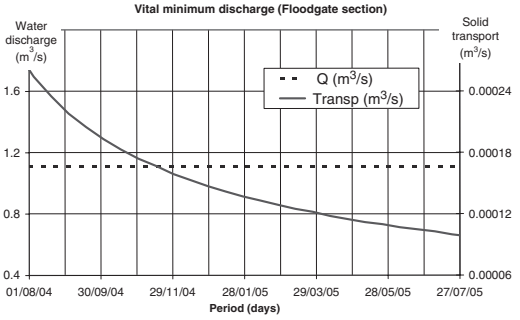


Figure 11. Boundary conditions of "Vital minimum discharge" during period 2004–2005 (model simulations at "Floodgate" cross-section).

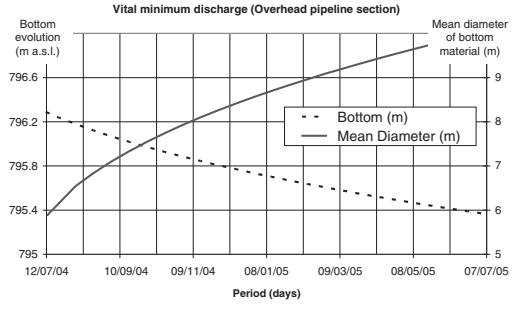


Figure 12. Bottom and mean diameter trend with "Vital minimum discharge" during 2004–2005 (a one year model simulations is reported at "Overhead pipeline" cross-section).

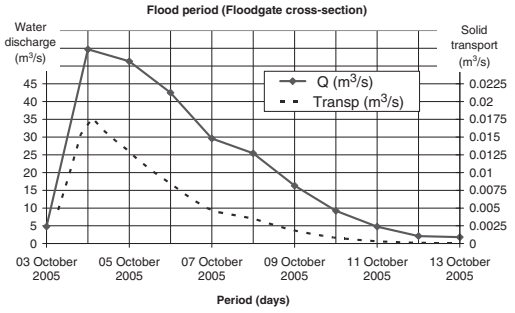


Figure 13. Boundary conditions of flood event (October 2005) (model simulations at "Floodgate" cross-section).

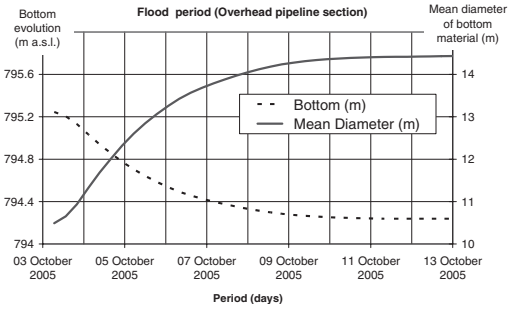


Figure 14. Decrease of bottom elevation and increase of mean diameter following during flood period (October 2005) (model simulations at "Overhead pipeline" cross-section).

reservoir and by the assumed operations of the water and sediment release.

5.2 *Minimum vital flow (from May 2004 to October 2005)*

For the simulation of "Minimum vital discharge" (Figure 11), boundary conditions prescribed at the "floodgate" cross-section show how solid transport discharge decreases during one year. The corresponding bottom erosion and increase of bottom material size is given in Figure 12.

The results show that the bed elevation decreases about 1 m, while the mean diameter size increases more than 1.5 times (Figure 12).

5.3 *Flood event (October 2005)*

An analogous evolution was obtained by modeling the subsequent flood event of October 2005. Again the flood period was reproduced with the available values of discharge recorded once every 24 hours (Figure 13). Also in this case, bottom evolution and gravel size seem to show a realistic trend in different cross sections. For instance, at the "overhead pipeline" cross-section, photographs shot before (Figure 8a) and after (Figure 8b) flood event of 2005 show a general bottom erosion of some meters and a much corser material, that the model correctly reproduces.

On the other hand, comparing the erosion due to 11 days of flood events (with peak discharge bigger than 55 m^3/s) with erosion due to "vital minimum discharge" (order-of-magnitude of 1–2 m^3/s for a period of about 16 months), the order-of-magnitude of change provided by the model appears to be the same (Figure 14). This result seems to indicate an undervalued effect of flood erosion, as indicated from photos of Figure 8.

The final longitudinal profile of the bottom (analyzing globally the three phases) seems to give a realistic trend in several sections analyzed. For instance (Figure 15), the results give a significant overaggradation of the bottom along the Quarry Zone, also during the flood event (this trend can explain the reason of the choice to install in that place a Quarry Zone). Moreover, these modes give a realistic trend of the bottom material size changes along the reach.

Copyright © 2006 Taylor & Francis Group plc, London, UK

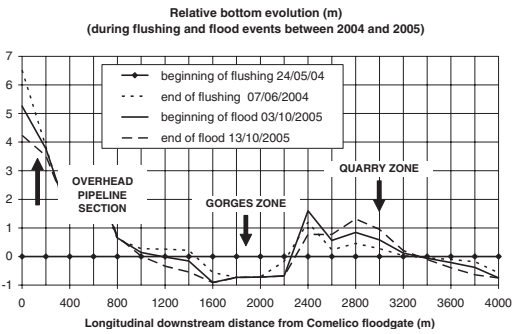


Figure 15. Time and space evolution of relative bottom variation from beginning flushing period until end of flood (initial value of bottom elevation is void).

6 CONCLUSIONS

A preliminary application of a morphological model to a short river-reach downstream a dam has been carried on during the flushing operations (14 days), and the following periods of low flow (483 days) and flood flow (11 days).

Boundary condition presently available are not very detailed (only daily water flows). This probably affects the quantitative results of the model. From the qualitative point of view, however, the deposition/erosion processes in terms of bottom elevation and bottom grainsize composition along the river reach are correctly reproduced, both at the short and the long time scales.

More detailed data regarding the boundary conditions (hourly water discharge, transport composition, modes of flushing operations etc.) will soon be available. These data, together with new measurements along the river reach (bed elevation and grain compositions) will allow a better assessment of the model performance. Improvements of the model (especially as for a the planimetric dynamics of the river width is concerned) will also be carried out, as soon as the experimental data will be available.

ACKNOWLEDGEMENTS

This research has been carried on in the framework of research projects (PRIN 2004) by MIUR (Ministry of Research and University) and Autorità di Bacino Alto Adriatico (River Authority of Northern Adriatic Sea).

A particular acknowledgement to Enel/GEM (Generation Energy Management) for precious collaboration and information (a special thank to Tartaglia ing. Paolo and Spinato ing. Massimiliano of the UBI, Hydroelectric Business Unit, of Vittorio Veneto (TV), and Peviani ing. Maximo of CESI, Bergamo).

REFERENCES

Armanini, A. & Di Silvio, G. 1988. A one-dimensional model for the transport of a sediment mixture in non equilibrium flow conditions. *Journal of Hydraulic Res.,* Vol.26, no.3.

Basson,G.R. & Rooseboom A. 1997. Dealing with reservoir sedimentation. *Water Resources Commission report no. TT91/97. Pretori*. xxxxiii+395 pp.

D'Alpaos, L. & Dal Prà, A. 1996. Studio per la definizione dei vincoli e degli aspetti critici sia idraulici che naturalistici, riguardanti le escavazioni potenziali dell'alveo del Fiume Piave. *Studi finalizzati alla redazione del Piano di Bacino del Fiume Piave,* Autorità di Bacino, 91 pp.

Di Silvio, G. & Peviani, M.A. 1989. Modelling Short- and Long-term evolution of mountain rivers: an application to the torrente Mallero (Italy). Published at *International Workshop on fluvial hydraulics of mountains regions.* Trent, Italy.

Di Silvio, G. 1991. Sediment exchange among layers. *Int. Workshop on Grain Sorting in Rivers, Monte Verità, Ascona (Switzerland) Oct. 21–25, 1991.* ETH Zürich Mitteilingen Vaw 117, pp. 163–192.

Di Silvio, G. & Scagnetto, M. 2001. Controlling reservoir sedimentation by sluicing in the presence of sorted grain sizes. *8th Int. Symposium on River Sedimentation, Cairo (Egypt), 3–5 November 2001.*

ENEL. 1993. Gli impianti idroelettrici tra il Piave e il Brenta. *Grafiche De Bastioni*. Vittorio Veneto, 101 pp.

Hirano, M. 1971. River bed degradation with armouring. *Trans. of JSCE.* 3(2).

Madeo, E. 2002. Influenza delle condizioni al contorno sul comportamento morfodinamico di un corso d'acqua . una soluzione analitica. *Degree thesis University of Padua.*

Marin, A. & Di Silvio, G. 1996. Analysis and evaluation of various simplifying hypothesis in morphological one-dimensional models. *Commission of the European Communities, Directorate General XII for Science, Research and Development, Research and Technical Development Programme in the Field of Environment*. FRIMAR Project, Technical Report n. 1, 1996, pp. 28.

Morris G.L. & Fan J. 1997. *Reservoir Sedimentation Handbook.* McGraw Hill.

Peviani, M.A. 2002. Sviluppo di un modello numerico idraulico- morfologico per fiumi a forte pendenza ed analisi dell'evoluzione degli alvei nei tratti pedemontani. *Doctoral thesis University of Perugia.*

Surian, N. 1999. Channel changes due to river regulation: the case of the piave River, Italy. *Earth Srf. Process. Landforms, 24*. 1135–1151.

Surian, N. 2000. Sediment size in gravel-bed river (Piave River, Italy): longitudinal, vertical and temporal variability. *In: Lenzi M. (ed.), Dynamics of water and sediments in mountain basins. Quaderni di idronomia Montana, 20.* 131–143.

Surian, N. 2003. Impatto antropico sulla dinamica recente del fiume Piave (Alpi Orientali). *Estratto da: Biancotti A & Motta A., "Risposta dei processi geomorfologici delle variazioni ambientali", MIUR*. Glauco Brigati, Genova, 425–440.

Copyright © 2006 Taylor & Francis Group plc, London, UK

Analysis of sediment transport during floods in a large river

J.S. Rocha & J.N. Fernandes
Portuguese National Laboratory for Civil Engineering (LNEC), Lisbon, Portugal

ABSTRACT: The River Tagus is the largest alluvial river bed in Portugal. Studies developed since 1970 give a relatively good opportunity to know the sediment transport behaviour. Three hydrometric gauge stations provided more than four hundred cross sections, surveyed during the velocity measurements for discharge-water level curve determination.

The collected data are highly relevant for calibrating the numerical modelling of hydromorphologic changes, sediment transport and degradation/aggradation phenomena in the river bed.

It is known that the erosion of River Tagus bed during an average flood can reach three meters in a short time. With the restoration of average flow, the river bed will recover its original values during following months.

The paper proposes a simple theoretical interpretation of the sediment transport mechanism of a large alluvial river during the floods, using the data collected in the work to obtain the depth-discharge curves in the gauging stations.

1 INTRODUCTION

The river regime in a movable bed controls in a very complex way its morphology. The river discharge variation implies correspondent bed variations, with significant differences in the behaviour of river bed in low flow and high flow situations.

It is well known that the phenomenon of sediment transport is strongly non-linear. This characteristic made it very hard to determine the right theoretical formulation to be used in a robust way in every case study. The corollary is the long list of available equations to quantify the sediment transport or to quantify the bed movements.

The major part of equations used in professional activity was deduced in experimental facilities, taking into account one of the major theoretical rationales developed during the last century. This may present a scale factor because each experimental facility is a reduced model of the natural system. When the case study is a large river the scale effects may be more significant.

However, the large river case study presents the advantage to be more easily monitored, taking into consideration that all phenomena have longer time periods, making the monitoring work more suitable to the human activities. In large rivers the variations of the main parameters of sediment phenomena are of the order of days or weeks, which may be recorded easily on a large time scale. On the contrary, in small rivers, these variations occur during short time periods, such as hours or minutes, which can only be recorded in automatic devices, not always enough robust to resist the floods.

In the River Tagus, there are enough recorded data to be used in the analysis of sediment transport, and correspondent bed movements.

This paper briefly describes the data collected in River Tagus, from which a case study during a flood was chosen. It also describes the theoretical analysis applied to the numerical simulation of the observed behaviour of bed movements imposed by the flood propagation, the comparison with available methods, as well as the conclusions.

2 THE COLLECTED DATA

The River Tagus basin is one of the largest in the Iberic Peninsula. It cuts longitudinally the Peninsula with a dominant East-West orientation. It covers an area of 80,629 km^2, 69% being in Spain and 31% in Portugal.

The main source is in Albarracin Mountain, at about 1,600 m altitude, falling fast to a 600 m altitude in the confluence of the first tributary, the Guadiela.

The slope is mild in the plain of Castilla-a-Nova, passing in the towns of Toledo (441 m), Talavera de la Reina (392 m) and Alcântara (98 m) in Spain. The 827 km length in Spain is followed by a reach of 43 km at the border of Spain with Portugal and 230 km in Portugal.

Before entering Portugal a large reservoir is formed by Alcântara dam, with maximum water level at 220 m and a volume of 3,333 10^6 m^3.

Copyright © 2006 Taylor & Francis Group plc, London, UK

Table 1. Number of cross sections surveyed in the River Tagus gauging stations.

Station name	Total number	Maximum per year
Tramagal	174	23
Almourol	172	23
Ómnias	109	21

After Cedillo dam, in the border, the River Tagus enters a strong rock reach, with a minimum width in Vila Velha de Ródão (61 m altitude). Afterwards it reaches a movable river bed with rocky banks, passing the urban settlements of Abrantes (21 m), Constância (17 m), Tancos (14.3 m), and finally, in the last 100 km, it enters a large alluvial valley, where it passes urban settlements of Chamusca (9.5 m), Santarém (3 m) and Valada (2.7 m), where the 70 km estuary begins, and finally reaching the Atlantic Ocean downstream the city of Lisbon.

The construction of dams to control the river discharges changed the river regime after 1943, being stabilized after 1983. Presently, there are higher low flow discharges and lower high flow discharges than the natural regime. The annual discharge module is about 360 m^3/s, but it may vary between about 1000 m^3/s in wet years and 90 m^3/s in dry years.

Since 1970 three gauging stations were installed along the alluvial plain. The stations are as follows:

1. Tramagal (100 km from the downstream reference, Vila Franca de Xira),
2. Almourol (85 km),
3. Ómnias (45 km).

The 2 year return flood discharge is approximately 2,300 m^3/s and the maximum observed flood was about 15,000 m^3/s, considered as a 100 year return period flood discharge.

In order to determine the depth-discharge curves the river beds were surveyed when velocity measurements were done. Consequently, relatively long series of data are available to be used in different sediment transport studies, on a large alluvial river.

The available date may be divided in the following three types:

– Instantaneous discharges during the river bed survey,
– Daily discharges in the Water National Information System (SNIRH, www.inag.pt),
– Hydrometric water level in the automatic network in the SNIRH.

The collected data are longer than the analysed ones. It is expectable that, in the future, it will be possible to analyse the older data.

The analysed data are presented in the Table 1.

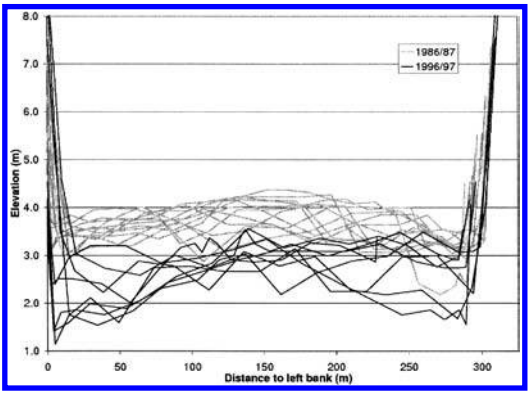


Figure 1. Cross sections at Ómnias station at 1986/87 and 1996/97 hydrological years.

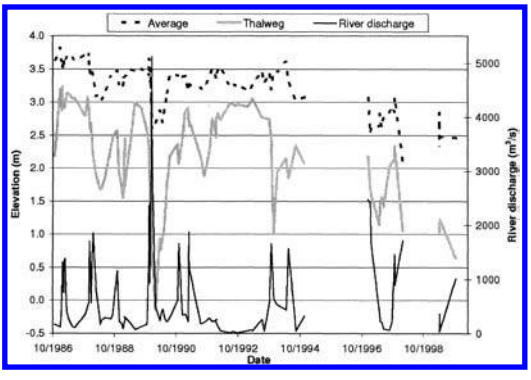


Figure 2. Changes in the river bed elevation at Ómnias station between 1986 and 1998.

In the first two stations, the analysed data were collected between the hydrological years 1990/1991 and 2004/2005, i.e., a total of 15 years. In the Ómnias station, the analysed data were collected between the hydrological years 1986/1987 and 1998/199, i.e., a total of 12 years.

Of note is the fact that the hydrological year in Portugal begins on 1 October and ends on 30 September.

Figure 1 shows a sample of the surveyed cross sections at one of the three gauging stations, Ómnias. The sample shows the natural variation in the cross section along two hydrological years, 1986/87 being in a higher position when compared with 1996/97. In general, the upper and lower position may vary within a 2 m range.

Beside the yearly variations it was also possible to observe a trend to a mild degradation in two of the three stations.

Figure 2 shows the behaviour of the river bed at Ómnias station during 12 years.

Copyright © 2006 Taylor & Francis Group plc, London, UK

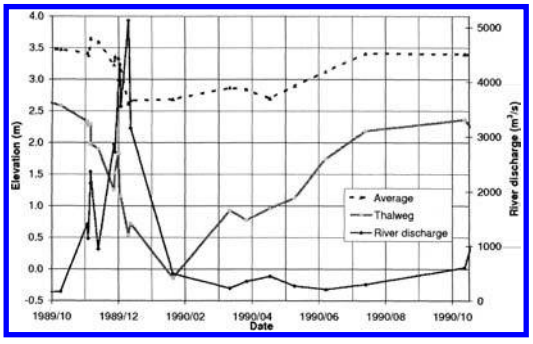


Figure 3. Changes in the river bed elevation at Ómnias station and river discharge during and after flood.

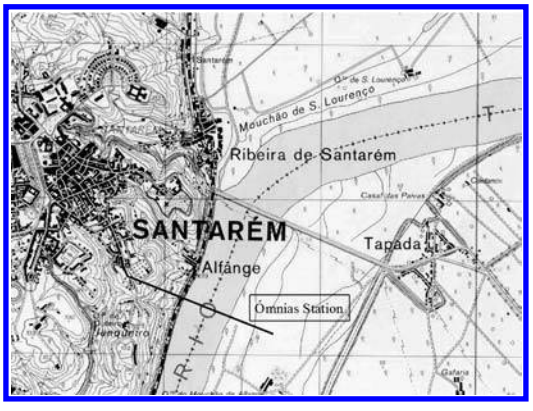


Figure 4. Ómnias gauge station and upstream reach.

3 THE CASE STUDY

Among the hundreds of surveys done in the three gauging stations, one flood event was chosen to analyse in detail the dynamics of the river bed morphology. The time period in which the bed variation related to flood wave was evident begins on 18 December 1989 and ends on 5 February 1990. Figure 3 shows the flood and river bed variations in the chosen time period.

The average river discharge in the period was 1,900 m^3/s. The river bed lowered 1.97 m during the flood passage. Afterwards, since 5 February 1990 until 28 July 1990, the average river discharge being 320 m^3/s, the river bed recovered its initial position going up to a total of 2.33 m, during five months.

This sample of natural river bed behaviour was considered a good case study to analyse in detail the relations between the flood wave and bed variations. There is a simple flood wave with a 5,200 m^3/s peak discharge and discharge decay to a minimum 200 m^3/s. The minimum talweg level occurred during the decay of flow at 1,200 m^3/s discharge.

It is important to note that the Ómnias gauge station is situated in a cross section with width smaller than the upstream reach, Figure 4. The decrease in width is about 30% when comparing with the largest width situated in a bend upstream the bridge.

In Figure 1 it is possible to observe that the cross section is approximately symmetric.

4 THE THEORETICAL ANALYSIS

The analysis of river bed variations in alluvial rivers is concentrated in the prediction of natural scour during floods. It is commonly admitted that during flood water surface rises and river bed decreases.

It is true the scour during floods is more important for practical point of view, in design of structures founded in river beds. The scour is more dangerous to the stability of structures compared with sedimentation.

Also in major situations the structures are built in the encroached cross sections, decreasing the length of river passage, and consequently the construction costs. Consequently, the number of case studies situated in the less than average river width is larger than other cases.

In a strict theoretical reasoning, the hypothesis that, when flood discharge increases the river bed lowers, is not universal.

It is well known the equations to compute the sediment transport in rivers are to be used to estimate the capacity of sediment transport, and they have been deduced in steady conditions. The real sediment transport is one of the two following situations:

- Capacity of sediment transport if the feeding sediment is equal or larger then capacity;
- Feeding sediment if the capacity of sediment transport is larger then feeding.

It is also current to analyse only the behaviour of river bed in the cross section, taken into consideration the equilibrium between actual mean velocity and the competent velocity for the inception of sediment transport. In this analysis the cross sectional area increases which diminishes the flow velocity and then the sediment transport capacity until the erosion process is stopped (Raudkivi, 1990 and Henderson, 1986). In general, the theory admits only the erosion.

It is difficult to find in the nature enough data to confirm different behaviour because the gauging stations are preferable situated in small width cross sections. In laboratory most of experimental tests are done in prismatic flumes with constant width.

Luckily in River Tagus, there is a site upstream all three gauging stations, where data collected can support a more general vision of the river bed behaviour during floods, when there is a substantial increase of river discharge followed by decay.

Copyright © 2006 Taylor & Francis Group plc, London, UK

In that site was done a study, using a mobile river bed model, and two surveys were collected, in a cross section of an enlarged river width compared to a much more smaller width upstream,. In Figure 5 it is presented the plan view of the two surveys done in different dates, upstream to cross section of Figure 6 on low flow conditions, and left to the cross section few months after a flood event (Cardoso, 1991). It was found there was a sedimentation process caused by flood, followed by a recover to the low flow conditions some time afterwards.

The process was reproduced on the mobile river bed model, in tests using unsteady flow conditions.

The Figure 6 shows better the two situations, before and after the flood event. Actually, in this case, the survey is not just after the flood, but some time afterwards. Consequently, the survey after flood shows a transition situation, with a well-defined recovering of talweg, but maintaining sedimentation on the remaining part of cross section.

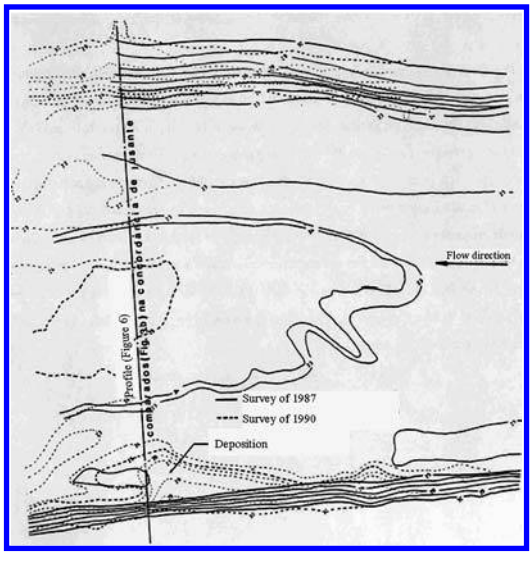


Figure 5. Plan view of the sedimentation after a flood event, in river Tagus.

The river bed variations, scour or sedimentation, shall be explained by the unbalance in sediment transport upstream and downstream, and not by the equilibrium in a cross-section. The experimental tests are mostly done in equilibrium conditions, giving formulations that are good estimators of the sediment transport in mobile river beds. However, an equilibrium condition hardly can be a good way to estimate a process dominated by a non-equilibrium process such as the river bed variation during and after flood wave propagation.

Consequently, a general method is proposed to compute in a simple way the river bed variations. The river bed variation may be computed by the general expression, the sediment continuity equation applied to two cross equations, in general one larger than other

$$\Delta z = (Q_{su} - Q_{sl})\, \Delta t / B_l \qquad (1)$$

where Δz is the river bed variation in a unitary length river reach and in the time period of analysis Δt, and is a function of the difference of sediment discharge, Q_{su}, upstream, and Q_{sl}, local, in a cross section width B_l.

The equations like (1) are very sensitive because the difference is usually a quantity of one or two orders less than the quantity of each sediment discharge value. However, the equation (1) gives directly the type of river bed variation, scour or sedimentation.

The unbalance in sediment transport is considered directly in the computation with mathematical models, such as HEC-6, MOBED, HEC2SR, or similar. However, the application of these models requires heavy work. The analysis presented has only the scope of a quick estimation of river bed variation in a particular site.

The large amount of data available in River Tagus may be used to verify the possibility to use equation (1) to estimate the river bed variation.

Also, it will be convenient to use experimental facilities to confirm the possibility of a general use of equation (1).

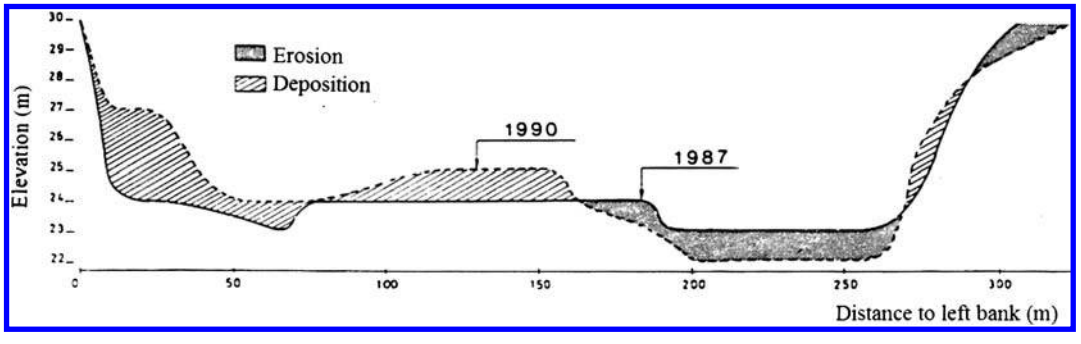


Figure 6. Cross section view comparing before and after a flood event, in river Tagus.

Copyright © 2006 Taylor & Francis Group plc, London, UK

5 THE NUMERICAL ANALISYS

The case study of River Tagus can indicate the order of magnitude of the differences in the sediment transport capacity.

From the data presented in Figure 2 and using a set of the available sediment transport equations, like Meyer-Peter and Muller, Van Rijn, Einstein-Brown, Ackers and White, it is possible to present the Figure 7.

In this Figure it was changed the river discharge, presented in Figure 2, to sediment discharge.

The variations in the river bed are known in enough instants to have a relatively well defined evolution of the river bed. Examples of three positions of the cross section in Ómnias are presented in Figure 8.

Knowing the Δz and Δt, and the B_l, it is possible to obtain the evolutions of the volumes of erosion or sedimentation, that is, the unbalanced sediment discharge, Δq_s, equivalent to $(Q_{su} - Q_{sl})/B_l$. As Q_{sl}, or q_{sl} are also known, the difference can also be compared with the sediment transport in the analysed cross section.

Table 2 presents some computations according to equation (1). It is easy to noticed that the rows on the lower part of the Table are mostly negatives, as expected, because there is erosion in the first phase of the flood wave, and on the upper part of Table 2 the positive values are in accordance with the sedimentation process of recovering the initial position.

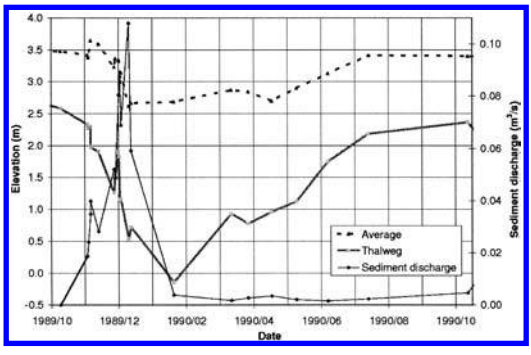


Figure 7. Changes in the river bed elevation at Ómnias station and sediment discharge during and after flood.

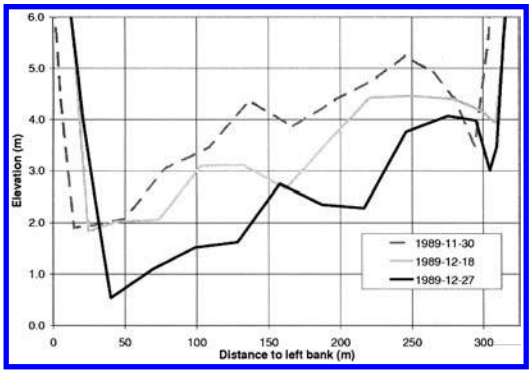


Figure 8. Cross sections in Ómnias station during the flood.

During rise stage of flood, the sediment discharge in the local is higher than the incoming one, consequently, the bed lowers. During the recovering phase, when the river and sediment discharges are lower the trend is for a higher incoming sediment than local capacity. In both cases, the unbalanced values are, in general, one order of magnitude less than the sediment discharge. Table 2 also shows that the values are not always like the described behaviour, and that they correspond to transition phases.

There are not enough data in the sections upstream the Ómnias gauging station to confirm totally the data presented in Table 2. In the future, surveys will be prepared surveys before, during and afterwards a significant flood event, in order to verify equation (1).

6 COMPARISON WITH AVAILABLE METHODS

Most of available analytical approaches for predicting scour during floods (disregarding the possibility of sedimentation) are based on the hypothesis of equilibrium between the actual mean flow velocity and the competent velocity for the inception of sediment transport, corresponding to the time in which scour is stopped (Williman 1970, Neill 1973, Neill 1987, Harris 1988). During floods and after floods, it is common to observe velocities much higher than the inception of sediment transport. The end of scour is not equivalent to the end of sediment transport.

Additionally, there is another fundamental hypothesis of the methods applied to a unique cross section, the equality between the mean velocity and the equilibrium velocity necessary for maintaining a generalized sediment transport over the bed, with a sustained material supply from upstream that compensates the eroded sediment (Maza Alvarez & Echavarria Alfaro 1973). The issue is that the erosion (or sedimentation) is originated by a non-compensation of sediment transport.

Other available methods are also based on regime-type formulas. Those formulas represent, to some extent, a statistical approach to natural alluvial bed configuration, and by consequence, they have an intrinsic guaranty to obtain plausible results in the application on the case studies (Melville & Coleman 2000).

The application of two of the available methods to analysed the present case study gives the values presented in Table 3.

In the River Tagus case study there is the same order of magnitude of estimated and observed scour,

Copyright © 2006 Taylor & Francis Group plc, London, UK

Table 2. Computation of the unbalanced sediment discharge knowing the river bed variations.

Date	River discharge (m^3/s)	Deposition area (m^2)	Eroded area (m^2)	Δq_s (m^2/s)	q_{s1} (m^2/s)
1990-11-09	1663.7	–	−6.75	−5.21E-06	4.25E-05
1990-10-25	607.6	–	−3.44	−4.47E-07	1.51E-05
1990-07-28	302.8	89.26	–	2.87E-05	7.55E-06
1990-06-22	209.3	–	–	–	5.22E-06
1990-06-22	209.3	70.10	–	2.90E-05	5.22E-06
1990-05-25	271.7	62.12	–	3.27E-05	6.77E-06
1990-05-03	450.5	–	−44.25	−2.44E-05	1.12E-05
1990-04-12	355.9	–	−9.19	−7.09E-06	8.87E-06
1990-03-28	231.1	57.39	–	1.30E-05	5.76E-06
1990-02-05	498.1	6.07	–	1.85E-06	1.24E-05
1989-12-29	3153.7	15.09	–	8.73E-05	1.91E-04
1989-12-27	5124.7	–	163.13	−2.70E-04	3.48E-04
1989-12-20	3552.5	46.94	–	5.43E-04	2.22E-04
1989-12-19	4319.4	–	−106.66	−1.23E-03	2.82E-04
1989-12-18	4032.2	–	−8.02	−3.09E-05	2.60E-04
1989-12-15	2720.2	40.67	–	4.71E-04	1.57E-04
1989-12-14	2862.3	–	−110.04	−9.10E-05	1.68E-04
1989-11-30	942.1	–	−18.95	−3.13E-05	9.10E-05
1989-11-23	2358.4	2.43	–	–	1.29E-04
1989-11-23	2151.8	80.35	–	4.65E-04	1.12E-04
1989-11-21	1139.4	–	−12.06	−1.40E-04	7.78E-05
1989-11-20	1400.5	–	−17.83	−8.60E-06	6.02E-05
1989-10-27	164.3	–	−5.94	−1.09E-06	1.44E-08

Table 3. Application of two methods to estimate erosion during floods and comparison with observation.

Methodology	Date	z_e (m)	z_o (m)
Lacey (1930)	1989-12-27	4.05	2.68
Blench (1969)		3.16	
Lacey (1930)	1998-01-28	3.33	3.09
Blench (1969)		4.14	

where: z_e (m) – estimated mean scoured profile elevation; z_o (m) – observed mean scoured profile elevation.

the maximum deviation being about 50%. This is an admissible value for deviations in river hydraulic estimations.

7 CONCLUSIONS

For professional practice, in the first phases of viability studies, in small size projects, before performing computations with a numerical model, where the data collection to build a model can be quite cumbersome, both simple equations and fast estimations of river bed variations during flood passage, may be used. The quantity of data to apply simple equations is much less than that for numerical models.

Most available procedures to estimate river bed variation during floods consider the erosion. There are some cases in which sedimentation might even occur.

Equation (1) deals automatically with the erosion or sedimentation case.

The main difference of the proposed procedure, compared with available procedures, is to consider at least two cross sections to obtain a better estimation of river bed variations.

The case of the quantification of the average river bed was presented, but it can be adapted to other type of analysis, for instance, for the talweg variation.

The simple computation can use also directly the outputs of the fixed bed numerical models like HEC-RAS.

ACKNOWLEDGEMENTS

The data from River Tagus were kindly provided by the Comissão de Coordenação e Desenvolvimento Regional de Lisboa e Vale do Tejo.

REFERENCES

Cardoso, A.H. 1991. Modelo físico do rio Tejo na zona da tomada de água e da rejeição da central termoeléctrica do Pego. 1° Relatório, LNEC, Lisbon, Portugal.

Harris, J.D. 1957. Hydraulic design of bridges. Chapter I, *MTC Drainage Manual*, Drainage and Hydrology Section, Ontario Ministry of Transportation, Downsview, Ontario, Canada.

Copyright © 2006 Taylor & Francis Group plc, London, UK

Henderson, F.M. 1966. *Open channel flow*. MacMillan Publishing Co. Inc., New York, U.S.A.
Leopold, L.B., Wolman, M.G., and Miller, J.P. 1964. *Fluvial Processes in Geomorphology*. W.H. Freeman, San Francisco, California; U.S.A.
Maza Alvarez, J.A. & Echavarria Alfaro, F.J. 1973. *Contribution to the study of general scour*. Proc. International Symposium of River Mechanics, I.A.H.R., Bangkok, Thailand, 795–803.
Melville, B. W. & Coleman, S. E. 2000. *Bridge scour*. Water Resources Publications, Colorado; U.S.A.
Neill, C.R. 1973 (Ed). *Guide to bridge hydraulics*. Roads and Transportation Association of Canada, University of Toronto Press, Toronto, Canada.
Neill, C.R. 1987. B*ridge hydraulics – An updated report*. Roads and Transportation Association of Canada, University of Toronto Press, Toronto, Canada.
Raudkivi, A.J. 1990. *Loose boundary hydraulics*. Pergamon Press, 3rd edition.
Williman, E.B. 1970. Scour prediction. In *Design procedures*, Dossier No. 23, Water and Soil Division, Ministry of Works and Development, Wellington, New Zealand (unpublished).

Copyright © 2006 Taylor & Francis Group plc, London, UK

The case of the Zambezi River in Mozambique: Some investigations on solid transport phenomena downstream Cahora Bassa Dam

Paolo Ronco, Giacomo Fasolato & Giampaolo Di Silvio
Hydraulic, Maritime, Environmental and Geotechnical Engineering Department, University of Padua, Italy

ABSTRACT: The Zambezi River is the fourth largest river in Africa (after Congo, Nile and Niger) and it is the largest river flowing into the Indian Ocean. The Lower Zambezi in Mozambique is strongly influenced by the presence of two very large reservoirs (Kariba Dam and Cahora Bassa Dam) that have modified the natural seasonal flows, as well as the sediment balance and morphology of the river. In particular, the downstream of the Cahora Bassa Reservoir non negligible effects are taking place, such as local scour, bank collapse and shore-line progressive erosion, together with economic and ecologic consequences on shrimp production and biodiversity alteration. In order to assess and possibly mitigate those effects, a quantitative and qualitative analysis of the erosion/sedimentation/sediment transport phenomena along the Zambezi seems to be urgently needed. The main constraint is represented by the scanty and unreliable data available: the Mozambican hydrometric monitoring network is very scarce and no long-historical and systematic measures of flow, sediment transport and reservoir sedimentation are available. The objective of the present study is trying to integrate the disposable data with a simplified model of sediment transport applied to the reach downstream of Cahora Bassa Dam.

1 THE ZAMBEZI RIVER BASIN: AN OVERVIEW

1.1 *Characteristics of the River basin*

The catchment area of the Zambezi River basin is 1,385,300 km^2, and is the fourth largest in Africa after the Congo, the Nile and the Niger. Of this area, about 12% (137,000 km^2) lies within Mozambique. The Zambezi River is approximately 2500 km long. The Basin drains from altitudes around 1600 m in northern Zambia and eastern Angola. The upper catchment lies on a vast plateau, the river being contained within a well-defined channel except for two major flood plains known as the Barotse and Chobe swamps. Its descent from this central plateau commences at Victoria Falls (1078 Km from sources) where its altitude drops from 978 to 870 m a.s.l. In its natural state the mid course of the river from Victoria Falls to Lupata consisted of narrow rapids and falls in mountainous areas and pen plains, with fall of 800 m overall. The major reservoirs at Kariba and Cahora Bassa have modified this section of river to a considerable extent. The river crosses the border into Mozambique near the township of Zumbo at an altitude of 330 m above datum and flows into Cahora Bassa reservoir (1630 Km from sources). At the dam site the gorge in very steep sided with a depth of about 600 meters. From the dam, with an altitude of 220 m a.s.l., the river continues in this gorge for a further 60 km before entering the pen plains. The course of the river is only slightly meandering to Lupata flowing in a well defined channel between 800 and 1000 m wide. After passing a gorge at Lupata at 95 m above datum, the river enter the major flood plain. The final 380 km to the Indian Ocean are characterized by a course of 1–4 km wide with heavily braided with ill-defined banks. The delta can be considered to start at Mopeia, 150 km from the Ocean and tidal influence is evident over the last 80 m (SCC Brokonsult, 2001). Major cities within the Zambezi River basin include Lusaka and Harare, the capitals of Zambia and Zimbabwe, respectively. The river basin is depicted in Figure 1. Table 1 provides a summary of the basin area within the numerous nations that share the river basin (SMEC, 2004).

1.2 *The climate*

The climate of the Zambezi Basin is typically subtropical. The year can be divided in four season:

1. hot season from late August or early September to the beginning of the main rains in October or November;
2. rainy season from October/November to March/April;

Copyright © 2006 Taylor & Francis Group plc, London, UK

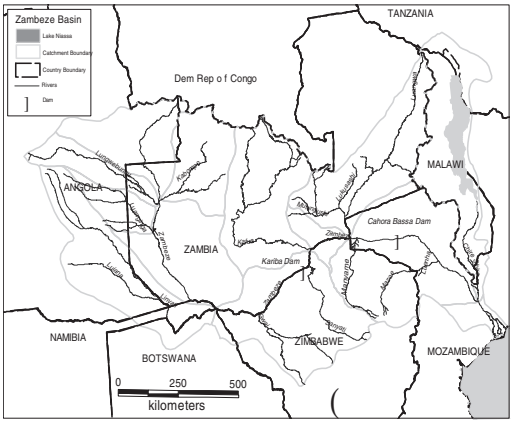


Figure 1. The Zambezi River basin (SMEC, 2004).

Table 1. Zambezi River basin area within nations.

Nation	Area (km^2)	Percentage (%)
Angola	254,600	18.4
Zambia	576,900	41.6
Dem. Rep. of Congo	1100	0.1
Namibia	17,200	1.2
Botswana	1900	1.4
Zimbabwe	215,500	15.6
Tanzania	27,200	2.0
Malawi	110,400	8.0
Mozambique	137,000	12.2
Total:	1,385,300	

Southern African Regional Development Corporation. website: www.sardc.net/imercsa

3. post rainy season in April and May;
4. cool season from June to early August.

Annual rainfall varies from approximately 1500 mm in the northern part of the catchment to approximately 850 mm in the southern part with the lowest rainfall in the order of 600 to 700 mm occurring in the central Zambezi Valley. Maximum rainfall months are December and January with peak discharges at Victoria Falls occurring between the beginning of March and the end of May. The winter rainfall usually account for about 3% of the annual total. With warm sunny conditions prevailing for much of the time in the Zambezi Basin (in the lowest areas of the Zambezi Valley temperatures can exceed 35°C) insulation is high causing mean annual potential evaporation to be high throughout the area. Class A pan evaporation is typically of the order of 1800 to 2200 mm per annum, with a significant seasonal variation from approximately 200 mm per month between October and March to around 125 mm per month in June and July.(Lahmeyer et al., 2001).

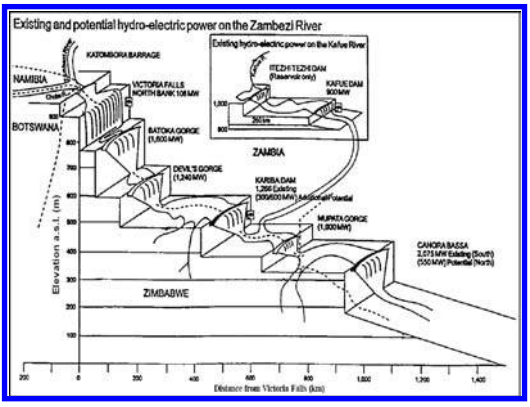


Figure 2. Schematic diagram of reservoirs and potential hydro power production of the Zambezi Basin (after Chounguiça, 1997).

1.3 *Major structures*

Completed in 1959 and situated at Kariba Gorge between Zambia and Zimbabwe (that obtain most of the electricity), the Kariba Dam consists of a double curvature concrete arch dam with a maximum height of about 130 m and a crest length of about 600 m. Six floodgates permit a discharge of 9500 m^3/s. The reservoir has a storage capacity of 180 km^3 and although the live storage is much less, it is the second largest in Africa and one of the largest of the world. Several other impoundment were established within the Zambezi River catchment in Zimbabwe between which are McIlwaine (reservoir capacity 38.8 km^3) and Ngesi (reservoir capacity 26 km^3). For hydroelectric power purpose, in 1972 a dam was built on the Kafue River and a second dam was built upstream, near Itesitesi. With all the construction executed (see Figure 2) in Zambezi River, when entering the territory of Mozambique it can be considered as a regulated river that lost its natural pattern of flow variations in time and in quantity. (Suschka & Napica 1990).

2 THE LOWER ZAMBEZI

2.1 *The Cahora Bassa Dam and Reservoir*

Commissioned in the 1959 by the Portuguese Government in Mozambique for promoting the economic development of the Lower Zambezi Valley through the exploitation of the hydropower potential of the river, the Cahora Bassa (witch means "the work is finish" in Sena idiom and stems from workers who ferries goods and people the nearly 600 Km to Cahora Bassa rapids from the Indian Ocean (Davies et al. 2000)) Dam is one of the most important river impoundment

Copyright © 2006 Taylor & Francis Group plc, London, UK



Figure 3. Cahora Bassa Dam and Reservoir (HCB, 2002).

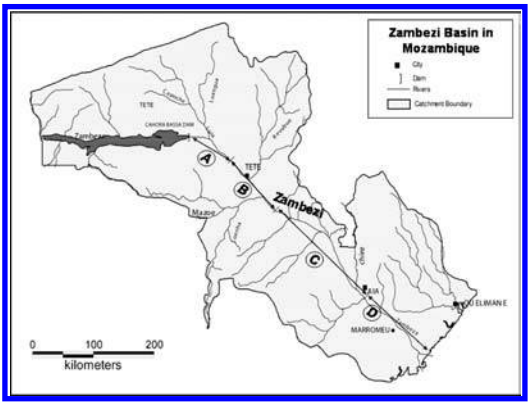


Figure 4. The Zambezi River basin in Mozambique, with the four macro-scale river zones. A: gorges zone; B: transitional zone; C: braided zone; D: distributary zone.

in the Austral Africa. With a maximum height of 164 m, a crest length of 303 m, a total discharge capacity of 13,939 m^3/s through five turbines (2260 m^3/s) and eight sluice gates, it has a power installed of 2075 MW that is mostly sell to South Africa Republic (80%) and Zimbabwe (15%) (HCB, 2004). The 270 Km long and 30 km width reservoir commenced to fill on 5 December 1974 and completed in approximately six months. The created lake has a reference level of 326 m a.s.l. and a surface area of 2660 km^2; the western extremely of the reservoir reaches the junction of the Mozambique, Zambia and Zimbabwe frontiers (see Figure 4).

2.2 *The lower Zambezi Valley*

The Lower Zambezi could be described as a complex physical system with four macro-scale river zones (Davies et al. 2000), comprising narrow gorges, a transitional zone , braided reaches, and a coastal distributary zone (Figure 4.) The complexity is due to the regional geomorphology producing a series of distinct valley-floor-trough, river-floodplain associations. In the uplifted mountainous areas below Cahora Bassa the channel is confined in a narrow wide valley with relatively high gradients. Boulder and bedrock outcrops and high stream energies dominate the instream environment of the gorge zone. Downstream of this zone the valley-floor-trough broadens to several kilometres. With further increases in the width of the valley-floor-trough and a decrease in river channels energies, large floodplains are constructed and a braided sand-river bed dominates. With progressive reduction in bed gradients, the braided give way to a typically coastal distributary channel network where floodplain widths can reach several hundred kilometres (Davies et al. 2000). In Table 2 a summary of the morphological characteristics of the four macro-scale river zones.

Table 2. Morphological parameters (average on the space) of the four macro-scale river zones.

Zone	Area [km^2]	Length [km]	Slope	Width [m]
A	38,587	62	$9.26 \cdot 10^{-4}$	191
B	63,132	158	$5 \cdot 10^{-4}$	1090
C	191,159*	225	$1.83 \cdot 10^{-4}$	1301
D	16,273	155	$1.05 \cdot 10^{-4}$	1021

* 78,215 km^2 after Lake Niassa.

There are many tributaries joining the Zambezi in Mozambique. The largest is the Chire, the catchment of witch is mainly in Tanzania and Malawi, and includes the massive Lake Niassa. Others on the left or northern bank include the Luia River and the Revubue River, and on the right or southern bank are the Luenha River which drains from the north-eastern Zimbabwe (SMEC, 2004).

Average annual rainfall in Mozambique part of the basin varies less than 600 mm around Tete, to over 1400 mm along the northern border with Malawi. In Mozambique most of the basin area is very sparse populated, however the population along the river is significant. The provincial capital of Tete is on the south bank of the Zambezi. Many thousands also live in or rely on the lands of Inhamgoma triangle along the Chire River to east of Mutarara. The delta is very sparsely populated and access is difficult. A large commercial sugar cane operation is located in Marromeu in the upper delta (SMEC, 2004).

2.3 *Principals effects of the Cahora Bassa Impoundment*

2.3.1 *Siltation of the Reservoir*

No quantitative estimate of the rate of sediment accumulation was published in the numerous reports which

Copyright © 2006 Taylor & Francis Group plc, London, UK

formed the basis for the design of the project (Bolton, 1984) and after, during the operational period of the reservoir, no monitoring silt accumulation programme has been developed. This aspects seems to be important in the light of two factor. The first is that 15% of the Cahora Bassa's water comes from the undammed River Luangwa, witch is know to carry a high silt load (the turbidity was measured in 36 ppm at the confluence with Zambezi, close to the CB Reservoir (Hayashi, 2005)), and a further 25% comes from other undammed rivers mainly off the Zimbabwean plateau (Bolton, 1978) The second factor is the relative small "dead" capacity of Cahora Bassa Reservoir: 13 km^3 (HCB, 2004). Due to the lack of systematic quantitative studies of sediment transport rates, bathymetry measurement and monitoring sampling programme, is very hard to evaluate this phenomena. Making assumption on the sediment yield of the basin, the trapping capacity of the upstream Kariba Reservoir and the sediment concentration of the tributaries in Cahora Bassa, Bolton (1984) estimate the total rate of sediment input to Lake Cahora Bassa in the range 20 to 200 $\times$ 10^6 m^3/year.

2.3.2 *Changes in flow pattern*

It is not in the objectives of the present study to produce an extensive quantitative evaluation of the modifications in the flow pattern after the construction of Cahora Bassa Dam. In any case, it is unquestionable fact that the damming of the Cahora Bassa Gorge has considerably changed the hydrological cycle of high and low flow. As evidence data collected at Tete measuring station E320 135 Km downstream of the dam from 1951 to 2004, the presence of the hydropower impoundment regulates the pattern of the monthly runoff in augmenting the minimum value and strongly decreasing the maximum value. As consequence the monthly runoff variation has a much lower amplitude and the discharges are more distributed all along the year changing the normal seasonal flow pattern (the rainfall season starts from January till March) (Figure 5 and Table 3).

2.3.3 *Morphological changes*

Very little information and measurement is available on sediment transport and river bed characteristics, but some considerations are possible. Both Suschka & Napica (1990) Davies et al. (2000) try to evaluate the morphological changes of the Lower Zambezi river after the conclusion of Cahora Bassa Dam but without getting at the same outcome. In fact, since Suschka & Napica in 1990 (ten years after the conclusion of the dam) affirm that "no evident changes in river bed configuration through aggradation or degradation have been measured and a much larger period will be necessary to find noticeable effects", Davies et al. in 2000 emphasize "the dramatic changes in the morphology

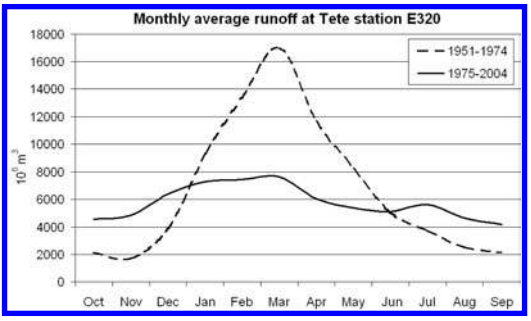


Figure 5. Monthly average runoff at Tete measuring station E320.

Table 3. Variation of monthly average runoff before (1951–74) and after (1975–2004) the construction of Cahora Bassa Dam.

	1951–1974	1975–2004
Minimum monthly average runoff [10^6 m^3]	1737	4180
Maximum monthly average runoff [10^6 m^3]	17,013	7651
Difference [10^6 m^3]	15,275	3471
Mean value [10^6 m^3]	6735	5772
Variance	$3 \cdot 10^7$	10^6
January–March runoff [% of the total annual runoff]	49	32

Data derived from DNA – National Directorate of Water – Maputo, Mozambique.

of the river floodplain system". In his opinion, the constancy of flow imposed by Cahora Bassa Dam (..) has transformed a flood-pulse driven river ecosystem, floodplain and coastal zone, into a series of confined channels. In fact, both the reduction of the sediment load, caused by the trapping of the reservoir, and the flow curtailment produce the removal of the sediment stores in the gorge zone (erosion), the incision of main flow channel with the stabilization of braid and bars in the transitional zone, the dominance of a single main channel that incises and conveys the majority of flow in the braided zone, and the reduction of the Zambezi Delta wetland mangrove swamp area and increase the salt-water intrusion (Chenje, 2000). Unfortunately, at the moment no quantitative evaluations of the morphological changes on the Lower Zambezi due to the impact of the Cahora Bassa Dam and no accurate explications of the sediment dynamics all along the waterflow has been done; some others impacts are still to be discovered and evaluated in the next future. On the basis of the foregoing considerations, a quantitative approach to these phenomena seems to be absolutely necessary.

Copyright © 2006 Taylor & Francis Group plc, London, UK

3 MORPHOLOGICAL MODELS

Conventional morphological models, even if just one-dimensional, are too cumbersome for very long simulations (years, decades, centuries) at basin scale, especially if the river watershed is very large as in the case of the Zambezi River. Acceptable simplifications can be introduced in the one-dimensional equations that describe the waterflow (De St.Venant equations) along the hydrographic network. By contrast, the sediment movement at the erosion/deposition process, should accurately be described by considering a non-uniform material. At the basin scale, in fact, the sediment grainsize may vary over various orders of magnitude (from fine silt to boulders), while the transport in a given cross section presents a quite extended composition (including the so-called "washload", coming in suspension from distant slopes of the watershed). The simple model (Di Silvio & Peviani, 1989) applied in this paper to the Zambezi River is based on the "local uniform-flow" hypothesis. The model includes a module for the evolution of the bottom composition and allows for the change of the river's active width with the water flow in presence of braiding. The model is described more in detail in a paper presented in this meeting (see *Morphodynamics of mountain river following repeated sediment release from reservoirs*. Fasolato et al., 2006) witch reports an application to the Upper Piave River in Italy.

It is to be stressed that the local-uniform flow hypothesis is definitely correct when the slope of the river is relatively high (as in the case of the Upper Piave River). When the river slope is rather small (as in the case of the Lower Zambezi River), the hypothesis is still acceptable for sufficiently large space-steps and time-steps.

A thorough analysis of the validity limits of the model is giving in Madeo (2002). As far as the Zambezi River is concerned, the selected space-step ($\Delta x = 60$ Km) and time-step ($\Delta t = 1$ year) guarantee that the average values of bottom elevation and bottom composition are correctly reproduced. This means, of course, that a number of oscillations with different frequency can be expected within each space- and time-step. In other words, the local uniform-flow hypothesis allows for a general description of the river morphology over the entire length of the river (about 600 km) and over the considered period (several decades), but does not give any information of the morphological changes within each reach and within each year.

4 MODEL APPLICATION

The morphological model based on the local uniform-flow hypothesis has been applied to the Zambezi River between the Cahora Bassa Dam and the Indian Ocean, to investigate the long-term morphological evolution in the present condition (*with dam*) and by assuming that the dam was not built (*without dam*). The initial conditions, in principle, should be given in both cases as the river's morphological and sedimentological configuration of 1974 (closure of the Cahora Bassa Dam). For the model simulation, in fact, the initial grainsize distribution has been selected as the one measured by the Portuguese administration in 1964 (Brigada de Engenharia Hidráulica). As for the initial topography of the Zambezi, by contrast, it has been chosen the actual one (see Figure 6: LANDSAT 7, 2002/08/03), as no precise information is available for the topography in 1974. It is believed, however, that for sake of comparison (with dam and without dam) it is enough that the initial conditions would be the same.

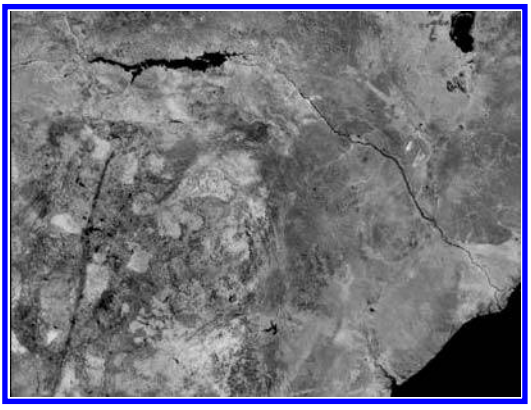


Figure 6. Satellite image of the Zambezi River basin in Mozambique (LANDSAT 7, 2002/08/03).

4.1 *Data processing*

The main constraint for a reliable and realistic hydrological and morphological description of the river, is represented by the scanty and unreliable data available on this matter. In fact, due to a 17 years long civil war and to poor socio-economical conditions, the hydrometric monitoring network of the Mozambican part of the basin is very scarce and, apart from very few specific cases, no long-historical and systematic measures of flow, sediment transport and reservoir sedimentation measurements are available. The Zambezi River Basin is furthermore extended in eight different countries and no single authority has a complete database for all the catchment.

4.1.1 *Hydrological data*

From the data catalogue provided by DNA (National Directorate of Water in Maputo), that list several gauging station all along the Zambezi Basin, only one station is still operating and could provide historical

Copyright © 2006 Taylor & Francis Group plc, London, UK

reliable discharge data. Tete gauging station E320, located next to the only bridge on the entire Lower Zambezi some 135 Km downstream the dam, after the confluence of Luia River and just before the one with Revubue River, provide daily average discharge data from 1951. Cahora Bassa monthly average inflow data, from 1907 to 1997, were provided by HCB (Hidroeléctrica de Cahora Bassa, the owner of the Cahora Bassa Impoundment) and Ara Zambeze (the Lower Zambezi Mozambican Authority) provide dam's daily discharge data from 1999. For the scope of this study, namely the preliminary application of the morphological model at one-year time-step, only an *equivalent* year's average value of the river discharge for the computation of the solid transport is required. In fact, the solid transport Q_s[m^3/s], is computed as:

$$Q_s = M \cdot Q^m \tag{1}$$

where M is a global term that resume the morphological characteristics of the river (see Fasolato et al. 2006) The *equivalent* year's average water discharge Q_{eq} is therefore the value of the water discharge that annually (T) produce the same sediment transport yield V_s, computed by the model, and is calculated as:

$$Q_{eq} = \left(\frac{Q_s}{M}\right)^{1/m} = \left(\frac{V_s}{M \cdot T}\right)^{1/m} \tag{2}$$

where the V_s is:

$$V_s = \int_T Q_s = M \cdot \frac{1}{m} \cdot Q_0^{m-1} \cdot V \tag{3}$$

with Q_0 maximum annual peak discharge and V total annual runoff.

The combination of Eq. 2 and Eq. 3 gives the *equivalent* year's average water discharge as:

$$Q_{eq} = \left(\frac{Q_0^{m-1} \cdot Q_{med}}{m}\right)^{1/m} \tag{4}$$

where Q_{med} is the annual average water discharge. For the application of the morphological model in the configuration *with no dam*, Cahora Bassa Reservoir Inflow data has been used, while in the *with dam* configuration, discharge data from the dam has been used for the computation of the Q_{eq}.

As regard the main tributaries of Zambezi (namely: Luia, Revubue, Luenha and Chire) downstream of the dam, no water discharge measurement are available, but only 10- to 1000-years maximum floods values derived from statistical analysis by some studies and reports (SMEC, 2004; Lahmeyer et al., 2001; SCC Brokonsult, 2001; and Denconsult, 1998). Only the

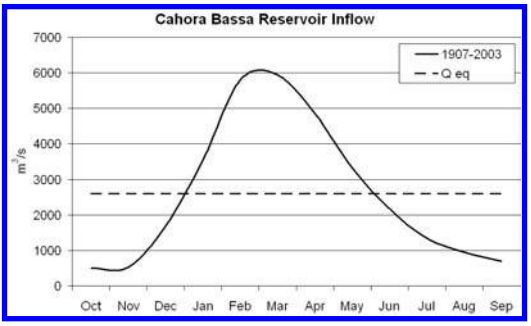


Figure 7. The comparison between the monthly average inflow and the respective Q_{eq} in Cahora Bassa Reservoir from 1907 to 2003. (data from HCB, 2005).

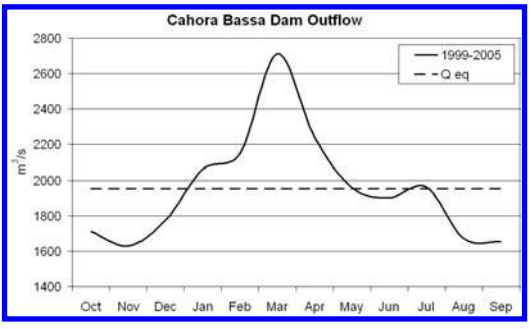


Figure 8. The comparison between the monthly average outflow and the respective Q_{eq}, from Cahora Bassa Dam from 1999 to 2005. (data from Ara Zambeze, 2005).

water discharge from Luia River can be estimated by the difference between the outflow of the Cahora Bassa Dam and the measured flow in Tete E320 (with a certain percentage reduction due to the presence of other minor tributaries between CB and Tete). In this way, using the Q_{eq} values both for Cahora Bassa outflow and for the discharge in Tete, a Q_{eq} value for the Luia River is derived. The ratio between this value and the estimated 10-years maximum flood (estimated by Lahmeyer Int et al., 2001) for the same river, has been applied also to the others three tributaries, obtaining the respective Q_{eq} values.

4.1.2 *Morphological data*

As already anticipate, the grainsize composition of the bottom of the Zambezi and its tributaries, has been extrapolated from the measurement done in the '60 ies by the Hydraulic Engineering Brigade of the Portuguese administration, before the construction of the dam. The samples have been taken from Zumbo (close the Zambian-Zimbabwean border) to the Ocean, about every 15 km, including a large part of the delta coastal profile and the final stretch of the tributaries. As the morphological model requires, the grainsize

Copyright © 2006 Taylor & Francis Group plc, London, UK

Table 4. Q_{eq} values for Zambezi River and main tributaries downstream Cahora Bassa.

River	Q_{eq} [m^3/s]
Zambezi – *without dam* configuration	2607
Zambezi – *with dam* configuration	1969
Luia	452
Revubue	306
Luenha	531
Chire	546

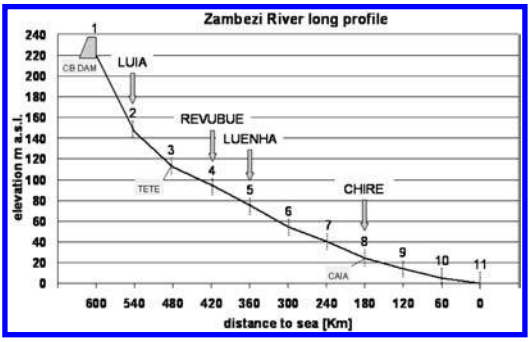


Figure 9. Lower Zambezi simplified configuration for model application.

extension has been splitted in four classes, each one represented by the medium diameter.

The river basin geometrical configuration (width and slopes of the main channels) has been derived from the LANDASAT 7 images, Hydro1K Africa Database (2000) provided by the USGS and "corrected" with the original cartography provided by the local authorities (Cenacarta, 2006).

As far as solid transport is concerned, the two different configurations considered (*with dam* and *without dam*) substantially differed because of the upstream boundary conditions of the model. In fact, the *with dam*-configuration means no solid transport downstream of the dam (hypolimnetic water), while the *with no dam*-configuration considers that an average initial value of 20×10^6 m^3/year of sediment runoff (estimated by Bolton, 1984, as the inflow sediment volume to the reservoir) provides to the sediment transport dynamic downstream of the dam.

4.2 *River's schematization*

With the selected space-step ($\Delta x = 60$ Km), the Lower Zambezi has been divided in 11 cross-sections (see Figure 9) that correspond at the grid calculation of the model. Each cross-sections has been characterized by a series of morphological parameter calculated in the downstream stretch (Table 5). The model's schematization imposed also that tributaries have to be introduced in a specific cross section.

5 PRELIMINARY MODEL SIMULATIONS

A first series of model simulations has been made for a period of 30 years, corresponding to the age of the dam impoundment, to investigate the long-term morphological evolution of the river through the variance of specific indicators, such as the bottom elevation, the total solid transport (bed load plus suspended sediment transport) and the grainsize composition medium diameter in the four macro-scale river zones (section 1: gorge zone; section 3: transitional zone; section 8: braided zone; section 10: coastal distributary zone).

Table 5. Morphological parameters of the selected cross-sections, including tributaries.

Section	Active width [m]	Stream width [m]	slope	Grainsize bottom composition 4 classes β_1	β_2	β_3	β_4
1	154	154	$1.23 \cdot 10^{-3}$	0.05	0.68	0.27	0.01
2[a]	544	544	$5.71 \cdot 10^{-4}$	0.01	0.10	0.79	0.10
3	544	544	$2.89 \cdot 10^{-4}$	0.01	0.36	0.61	0.03
4[b]	1207	1952	$3.22 \cdot 10^{-4}$	0.01	0.83	0.15	0.01
5[c]	857	982	$3.47 \cdot 10^{-4}$	0.02	0.48	0.48	0.03
6	1602	3467	$2.37 \cdot 10^{-4}$	0.01	0.52	0.43	0.04
7	1364	3224	$2.65 \cdot 10^{-4}$	0.23	0.75	0.01	0.01
8[d]	1327	2397	$1.73 \cdot 10^{-4}$	0.19	0.38	0.42	0.01
9	963	2155	$1.49 \cdot 10^{-4}$	0.10	0.78	0.12	0.01
10	825	1506	$8.40 \cdot 10^{-4}$	0.14	0.71	0.14	0.01
11	1147	1812	0.00	0.14	0.71	0.14	0.01
[a] Luia	55	55	$2.03 \cdot 10^{-3}$	0.01	0.63	0.45	0.01
[b]Revubue	208	208	$2.20 \cdot 10^{-3}$	0.01	0.62	0.36	0.01
[c]Luenha	212	212	$1.77 \cdot 10^{-3}$	0.01	0.83	0.15	0.01
[d]Chire	197	197	$2.27 \cdot 10^{-4}$	0.19	0.38	0.42	0.01

From the results obtained with the simulations, it seems that:

(1) Before the construction of the dam, the river appears to be aggrading everywhere downstream the Cahora Bassa Dam (13 cm/year at the transitional zone), especially in the vicinity of the major sediment input (say downstream the tributary Luia, which seems to be the most important source of sediment in the lower reach of the Zambezi). The aggradation seems practically to ends in correspondence of the braided zone, where it is virtually imperceptible (see Figure 11a at section n°8 and Figure 13a at section n°10). The model, however, indicates that, over the centuries, the upgrading profile tends to propagating slowly downstream.

Copyright © 2006 Taylor & Francis Group plc, London, UK

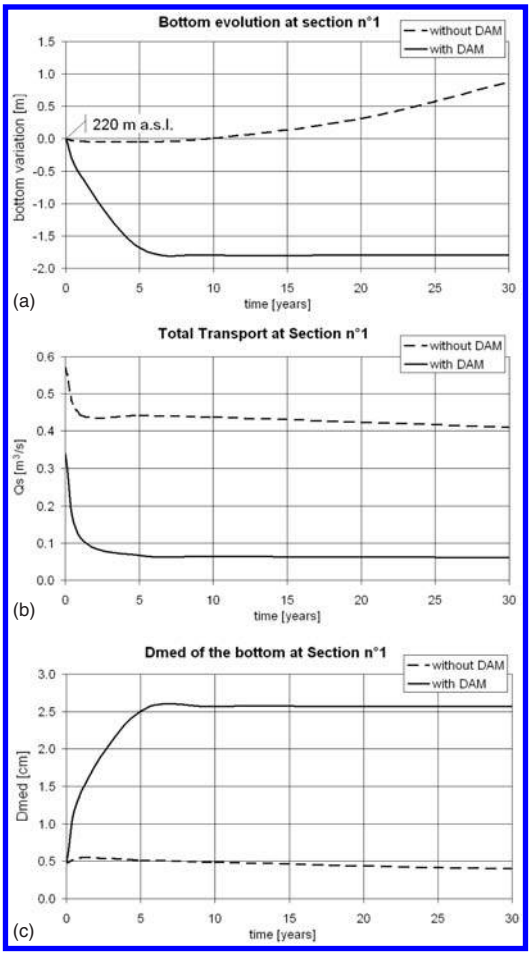


Figure 10(a-c). Bottom evolution, total solid transport and grainsize composition medium diameter in the gorge zone, downstream of cross-section n°1 (Cahora Bassa Dam site).

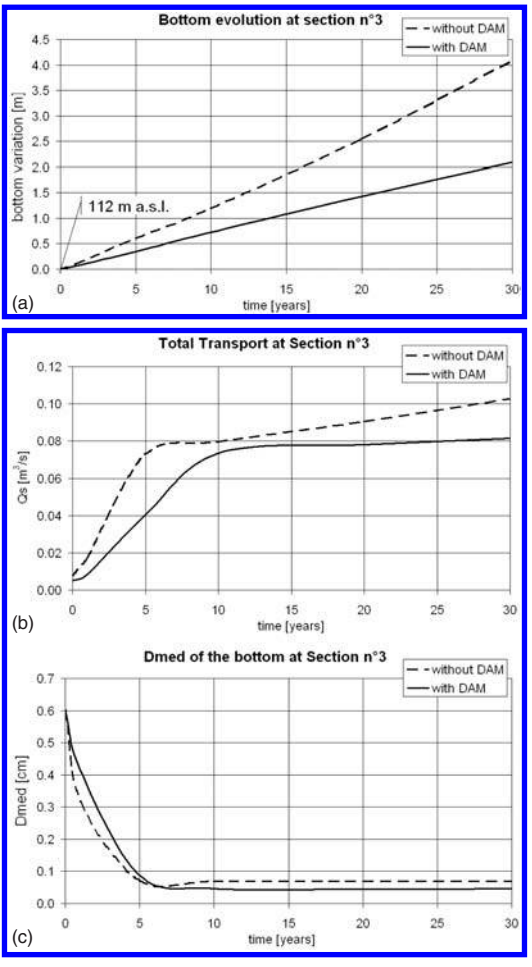


Figure 11(a-c). Bottom evolution, total solid transport and grainsize composition medium diameter in the transitional zone, downstream of cross-section n°3 (city of Tete).

Together with aggradation, the model indicates a corresponding fining of the bottom composition.

(2) The presence of the dam causes, in the first gorge zone, a strong bed erosion, yet limited by the presence of a stony bottom. The model also indicates a consequent thickening of the grainsize bottom composition (armouring), as well as a decrease on solid transport.

6 CONCLUSIONS

A simplified long-term morphodynamic model has been applied to the 600 km lower reach of the Zambezi River, between the Cahora Bassa Dam and the Indian Ocean.

This preliminary application of the model indicates that the present Zambezi River is not in equilibrium but it is slowly aggrading, especially in its upper part closer to the sediment sources.

The presence of the dam since 1974 has given place to a strongly reduction to the sediment input to the river reach and to a less variable waterflow during the year. As a consequence, the "natural" aggradation process has been slowed down, but it is still going on. The aggradation process is limited, at the present, to the upper part of the river, but it is possibly bound to affect the lower part.

It is to be stressed, however, that the conclusions above are definitely provisional. Many more tests, in fact, are necessary (sensitivity analysis) to confirm the results of the model and to check the long-term

Copyright © 2006 Taylor & Francis Group plc, London, UK

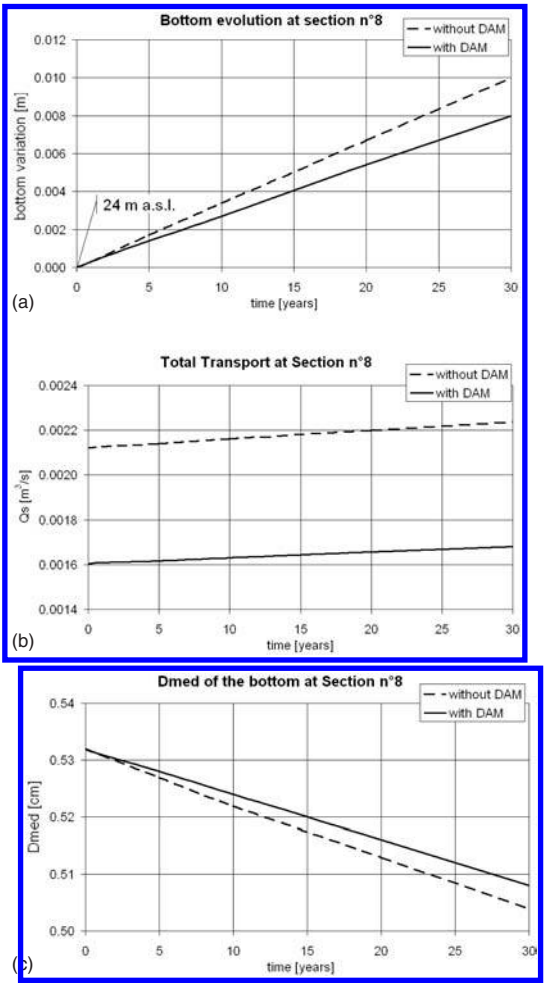


Figure 12(a-c). Bottom evolution, total solid transport and grainsize composition medium diameter in the braided zone, downstream of cross-section n°8 (city of Caia and confluence with Chire River).

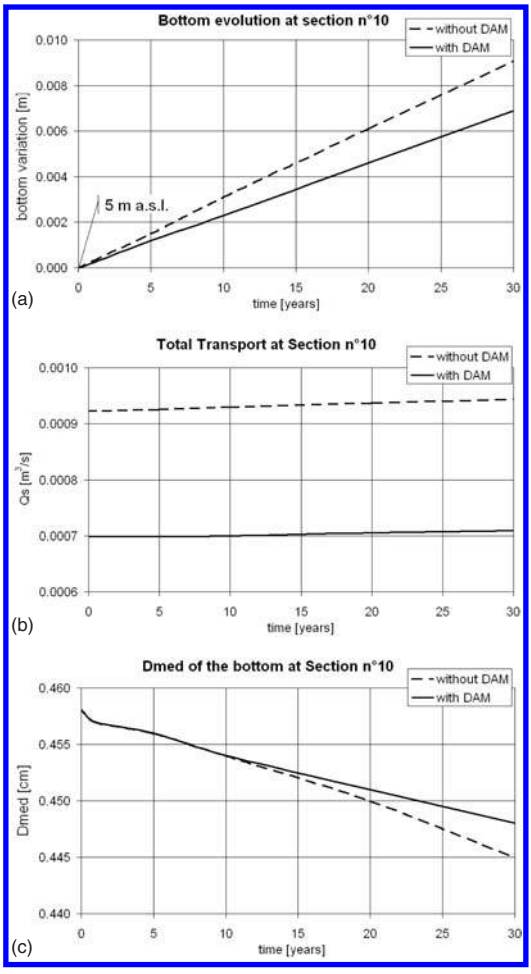


Figure 13(a-c). Bottom evolution, total solid transport and grainsize composition medium diameter in the coastal distributary zone, downstream of cross-section n°10.

tendency of the Zambezi and its delta. Moreover, the present version of the model will be modified to check the limits of the simplified hypothesis of locally uniform flow. Another aspect to be checked is the effect of a more refined grainsize distribution of the material.

AKNOWLEDGEMENTS

This research has been carried on with the support of the International Hydrological Programme (IHP) of UNESCO (a special thank to Prof. Stevan Bruk) thought the Maputo UNESCO Local Office. A particular acknowledgement to the Mozambican River Authorities DNA and Ara Zambeze as well as to HCB for its precious support in the data collection in Mozambique.

REFERENCES

Bolton, P. 1984. Sediment deposition in major reservoir in the Zambezi basin. *Proceeding of the Harare Symposium: Challenges in Africa Hydrology and Water Resources*, 1984. IAHR Publ.n° 144.

Bolton, P. 1978. The Control of Water Resources in the Zambezi Basin and its Implications for Mozambique. *Occasional Paper on Appropriate Technology*. School of Engineering Science, University of Edinburgh, Scotland.

Brigada de Engenharia Hidraulica, Missão de Fomento e Povoamento do Zambeze, 1964. Vale do Zambeze: elementos de estudo, sedimentologia e reconheçimento de

Copyright © 2006 Taylor & Francis Group plc, London, UK

fundações. *Plano geral de fomento e occupação. Anexos*. Lourenço Marques (Maputo). Moçambique.

Chenje, M. (ed.), State of the Environment Zambezi Basin 2000, SADC/IUCN/ZRA/SARDC, Maseru/Lusaka/Harare, 2000. pag. 63.

Davies, R.D., Beilfuss, R.D. & Thoms, M.C. 2000. Cahora Bassa Retrospective, 1974–1997: effects of flow regulation on the Lower Zambezi River. *Limnology in the developing word*, Stuggart. Vol.27, pp 1–9.

Denconsult, 1998. Final Report – Introductory Volume. *Sector Studies under ZACPLAN*. Zambezi River Authority/SADC/Ministry of Foreign Affairs/Danida, Ref.No.104.SADC.31

Di Silvio, G. & Peviani, M.A. 1989. Modelling Short- and Long-Term evolution of mountain rivers: an application to the torrent Mallero (Italy). Published at*: International Workshop on fluvial hydraulics of mountains regions*. Trent, Italy.

Earth Resources Observation & Science (EROS), 2000. HYDRO1K Africa. *Elevation Derivative Database*. U.S. Geological Survey, Sioux Falls. U.S.A. http://edc.usgs.gov/products/elevation/gtopo30/hydro/

Fasolato, G., Ronco, P. & Tregnaghi, M. 2006. Morphodynamics of mountains rivers following repeated sediment release from reservoirs. *International Conference on Fluvial Hydraulics, Riverflow 2006*. Lisbon, Sept. 6–8 2006.

Hayashi, H., Clifford, M. & Banda, D. 2005. Cause of Turbidity in Luangwa River – Case of Dry Season. *Proceeding of the XXXI IAHR Congress, Seoul, Korea, Sept.11–16, 2005*. pp 5335–5340.

Hidroeléctrica de Cahora Bassa, 2004. Technical reports on Cahora Bassa Project. Songo. Mozambique.

Lahmeyer Int, EDF, Knight Piesold, 2001. Final Report on Meteorolgy, Hydrology and Sediment Transport. *Mepanda Uncua and Cahora Bassa North Project.* Republica de Moçambique, Maputo.doc.n° 021

Madeo, E. 2002. Influenza delle condizioni al contornosul comportamento morfodinamico di un corso d'acqua, una soluzione analitica. *Degree Thesis at the University of Padua*, Italy.

SCC Brokonsult (Scandiaconsult), 2001. Final Report: Three Crossing Schemes. *Consulting Services for Zambeze River Crossing at Caia in Mozambique*. Ministerio das Obras Publica e Habitaçao, Republica de Moçambique. Maputo, Cap.5.

SMEC, 2004. Final Report – Zambeze River Basin *Mozambique Flood Risk Analysis Project*, Maputo. Cap.2.

Suschka, J. & Napica, P. 1990. Ten years after the conclusion of Cabora Bassa Dam. *Direção Nacional das Aguas,* Maputo , Republica de Moçambique.

Copyright © 2006 Taylor & Francis Group plc, London, UK

Effect of upstream meanders on bifurcation stability and sediment division in 1D, 2D and 3D models

Maarten Kleinhans
Universiteit Utrecht, Fac. Geosciences, Dept. Physical Geography, Utrecht, The Netherlands

Bert Jagers
WL | Delft Hydraulics, Delft, The Netherlands

Erik Mosselman & Kees Sloff
WL | Delft Hydraulics, and Delft Univ. of Technology, Fac. Civil Eng. and Geosc., Delft, The Netherlands

ABSTRACT: At river bifurcations, water and sediment are divided over two branches. The dynamics of the division determine the long-term evolution of the downstream branches, which can be studied by 1D models. For such models, a relation describing the sediment division is necessary, but this is poorly understood. We study the division of sediment and the morphodynamics on a time scale of decades by idealised 2D and 3D modelling of bifurcations with upstream meanders and dominantly bed load transport. Initially, migrating alternating bars in the models caused damped quasi-periodic fluctuations in bed levels, water and sediment division until the bars are near equilibrium. Varying the radius of upstream meanders and the slope of one of the downstream channels led to subtle changes in the sediment transport direction and the location of bars and pools. This caused large differences in which branch becomes dominant and in the rate of change in discharge asymmetry. The effects of wider downstream branches or of an overall narrower or wider river are dramatic, again demonstrating the importance of bars. The resulting division of sediment, on the other hand, is similar to the division of flow discharge in all runs after the initial fluctuations have damped out and until the discharge division becomes very asymmetrical. We conclude that bifurcations are extremely sensitive to local conditions affecting the secondary currents and the sediment transport direction, and to the downstream boundary conditions. Although most combinations of parameters lead to the development of an asymmetrical discharge division, some combinations lead to a quasi-stable symmetrical division. Finally we discuss the limitations of the models and the applicability to natural meandering rivers.

1 INTRODUCTION

Bifurcations distribute water, sediment and, indirectly, flooding risks over the downstream river branches. Over a much longer time, fluvial plains and river deltas are built up by avulsing and (temporarily) bifurcating rivers. In order to understand these phenomena, the local water and sediment transport division must be understood. Such understanding can be obtained by combining observations and geological reconstructions with models. However, 2D and 3D models are computationally too expensive for such long-term morphological predictions. A 1D model has to be extended with a 'nodal point relation' for dividing the sediment at the bifurcation, which is not well understood.

The objectives are to understand the causes of bifurcation (in)stability in meandering rivers and to predict the division of sediment to aid future 1D modelling. Accurate measurements of bed level evolution and sediment transport rates at meandering river bifurcations are rare for single events and non-existent for periods long enough to cover significant changes in morphology and discharge division. We therefore focus on systematic idealised modelling with 2D and 3D models to study the effect of specific factors such as the radius of a meander bend upstream of the bifurcation, and the slope of the downstream branches. The input parameters of the model are loosely based on the river Rhine in the Netherlands, which had more than 80 bifurcations in the past 8000 years, some of which were destabilised within a few decades after their creation, whereas some others were stable for many centuries (Stouthamer and Berendsen, 2000).

First we compare two state-of-the-art relations for sediment division that are used in 1D models, and

Copyright © 2006 Taylor & Francis Group plc, London, UK

whether these result in stable or unstable bifurcations. Next we describe the 2D and 3D model setup. After presenting the main results, a number of extra tests are presented to assess the effect of various channel widths and other parameters. Finally, the shortcomings of the models are discussed as well as the applicability of the results to real meandering rivers, and general conclusions are drawn.

2 RESULTS OF A 1D MODEL

A 1D model of a river with a bifurcation consists of three branches connected by a node. At the node, discharge and sediment supply from the upstream branch (1) is divided over the two downstream branches (2,3). The division of flow discharge Q_1 into Q_2, Q_3 at the nodal point follows from mass conservation, the condition that the water levels in the three branches are equal at the nodal point and the other specifications. The depth-width-integrated sediment transport S_1 is divided as S_2, S_3 according to the nodal point relation, in this case by Wang et al. (1995) or Bolla Pittaluga et al. (2002). The Bolla Pittaluga et al. relation divides the sediment based on the bed level differences of the downstream channels, assuming that the influence of this difference extends to the area upstream of the bifurcation and ignoring meander bend effects from upstream. The Wang et al. relation is empirical:

$$\frac{S_2}{S_3} = \left(\frac{Q_2}{Q_3}\right)^k \left(\frac{W_2}{W_3}\right)^{1-k} \quad (1)$$

where $k =$ an empirical power. Wang et al. found from a nonlinear stability (phase-plane) analysis that bifurcations are stable for $k > n/3$ and unstable for $k < n/3$, where $n =$ effective power on flow velocity to calculate the sediment transport. For Engelund and Hansen (1967) $n = 5$; for Meyer-Peter and Mueller (1948) $n > 3$ depending on the ratio of actual to critical shear stress.

An intuitive understanding of the Wang et al. model is offered as follows. Suppose the discharge of a branch decreases. The effect of a large k would be a much larger decrease of the sediment input than the decrease of the sediment transport capacity. Consequently, the bed of the closing branch is scoured to some extent, which increases the flow discharge capacity of this channel. So a large k stabilises the bifurcation.

Each branch has a length of 6 km with a step size of 150 m. The model is run for 50 years with a time step of 0.05 year. The flow in the 1D model is based on the Bélanger equation (backwater curve) and the Manning-Strickler roughness predictor. The specified model parameters are upstream discharge ($Q = 2500\,\mathrm{m^3/s}$), width ($W_1 = 532$ m, $W_2 = W_3 = W_1/2$), Nikuradse roughness length ($k_s =$ 0.19 m), calibrated so that the water depth is about equal to that in the 2D model, initial bed and water surface slope ($i_1 = i_2 = 1 \times 10^{-4}$ m/m, $i_3 = 1.1 i_1$) and downstream water levels of the two downstream channels which were chosen such that the flow is uniform initially. The morphology is computed from an initial bed, a sediment transport predictor (Meyer-Peter and Mueller (1948) or Engelund and Hansen (1967)) and the Exner sediment conservation law. The grain size is specified as $D_{50} = 2$ mm.

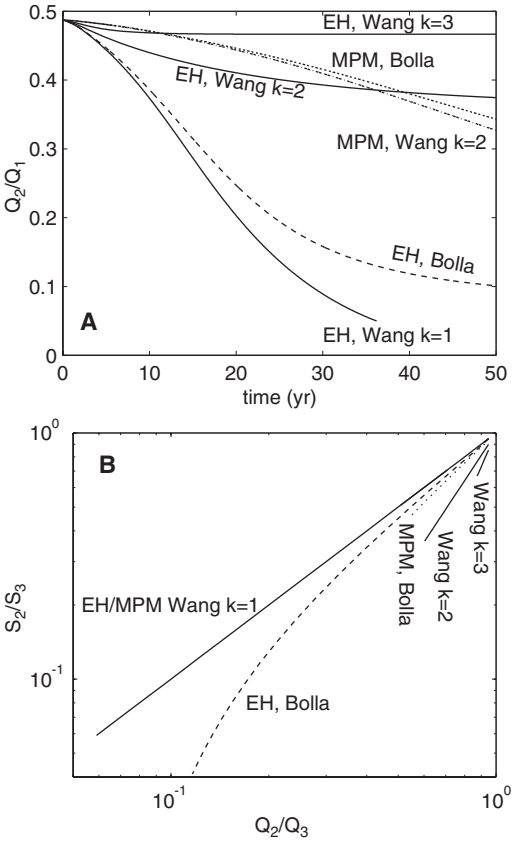


Figure 1. Results of 1D model. A. Time-series of discharge for the less steep branch. B. Sediment and discharge division over the downstream branches.

The 1D model predicts a decrease of discharge through the downstream branch with the smallest slope as expected (Fig. 1). Using the Bolla Pittaluga et al. nodal point relation, the discharge division always becomes very asymmetrical, or, in other words, a dominance of one of the channels. The rate of closure depends on the sediment transport rate, which in the present setting is larger using Engelund and Hansen (1967) than for Meyer-Peter and Mueller (1948). For the Wang et al. nodal point relation the bifurcation

Copyright © 2006 Taylor & Francis Group plc, London, UK

is increasingly asymmetrical for $k = 1$ but stable for $k = 2, 3$. The sediment division by the Bolla Pittaluga et al. relation is initially similar to that of Wang et al. with $k \approx 1$ and gradually changes to $k \approx 2$ for increasing asymmetry.

For both the 1D and 2D/3D model cases we study the range of model conditions from initial plane bed and symmetrical discharge division to (nearly) fully developed bar morphology with highly asymmetrical discharge divisions. For numerical reasons and due to model simplifications it is not possible yet to draw conclusions on the final branch closure process if a branch closes fully at all but this will be addressed in the discussion and in ongoing studies.

3 SETUP OF THE 2DH AND 3D MODELS

The Delft3D-FLOW morphodynamic model system was used (version 3.50.05.00BJ03). The parameters for the 2D and 3D models were very similar to that of the 1D model. The flow and morphology are calculated according to Lesser et al. (2004). The roughness formulation is Darcy-Weissbach with $k_s = 0.15$ m. The initial bed was plane and had a slope of $i = 1 \times 10^{-4}$ m/m, except where the slope of one downstream channel was deliberately increased. The downstream water levels were equal (for cases with $i_2 = i_3$) and chosen such that the flow was uniform initially (± 2 cm). The sediment transport predictor, unless mentioned, is Engelund and Hansen (1967). The bed slope effect on sediment transport is calculated according to Talmon et al. (1995) (see also Struiksma et al., 1985; Lesser et al., 2004). The spiral flow is schematised in the 2D model according to Struiksma et al. (1985), Lesser et al. (2004). The time step of the flow was 30 seconds to ensure numerical stability, and an initial period without morphological updating was allowed to stabilise the flow. Assuming that the flow is not appreciably affected by erosion and sedimentation during a time step, the morphological change in each time step can be multiplied by a large factor to predict the morphological evolution. The chosen factor was 100 which gave no significant differences with larger and much smaller factors.

The grids were curvilinear, and were automatically generated to ensure repeatability. The grids were orthogonalised as much as possible in an automated procedure. The average length of the grid cells was 150 m as in the 1D model. The width of the cells was 28 m for the standard models, 35 m for the wider, and 21 m and 16 m for narrower models. For the 3D models the flow was divided vertically in 10 layers of equal thickness, which was adapted to water depth changes (Lesser et al., 2004).

To split one channel into two, one row of cells had to disappear downstream of the bifurcation for numerical reasons. To ensure that $W_2 + W_3 \geq W_1$, the width of the cells downstream of the bifurcation was increased. The transition to this increased width was done gradually in the five cells upstream of the bifurcation. All three branches had the same lengths and consisted of 40 cells each.

The grids were generated with varying upstream bend radii, where the bend was 17 cells long downstream of a straight stretch. Downstream of the bifurcation a constant bend radius of $R = 20\,W$ was specified.

Avulsions commonly take place because of a slope advantage of the new flow direction over the old channel. To test the effect of an increased slope in one downstream branch, this slope increase was specified in the initial bed levels and the downstream water levels were again adjusted to ensure initial uniform flow.

New downstream branches often are less wide than the old branches, and usually $W_2 + W_3 \geq W_1$. Also, there is an effect of width-depth ratio on the bar dynamics. Three effects of width were tested: an equal increase or decrease of the width of all branches, an equal increase of the width of the downstream branches, and a change in the width ratio of the downstream branches. These were specified as factors on the cell width.

4 RESULTS

4.1 *Bar dynamics*

The 3D model initially predicted a rather complex morphological evolution (Fig. 2). In the first few model years alternating bars developed from the plane bed and migrate downstream. After some time, a fixed bar developed in the inner bend upstream of the bifurcation. Meanwhile, a bar and pool migrated side-to-side into the bifurcated branches and become fixed in position as well. Since more water is discharged into the channel with the pool than into the channel with the bar, the balance of the bifurcation was tipped and one channel became dominant. The rate of bar development and migration depended on the bend radius: the sharpest bends had the fastest development of a fixed bar. Bolla Pittaluga et al. (2002) assumed that the influence of bed level difference of the downstream channels extends to the area upstream of the bifurcation, which is confirmed here (Fig. 2, lowest panel).

4.2 *Effect of bend radius*

The 2D and 3D models always predict a development to a stable, highly asymmetrical discharge division. As expected, the outer-bend branch becomes dominant when the downstream conditions in the two branches are equal (Fig. 3A).

Since the effective secondary flow intensity in the 3D model is slightly smaller than in the 2D model, the bars and pools are slightly less pronounced in the 3D

Copyright © 2006 Taylor & Francis Group plc, London, UK

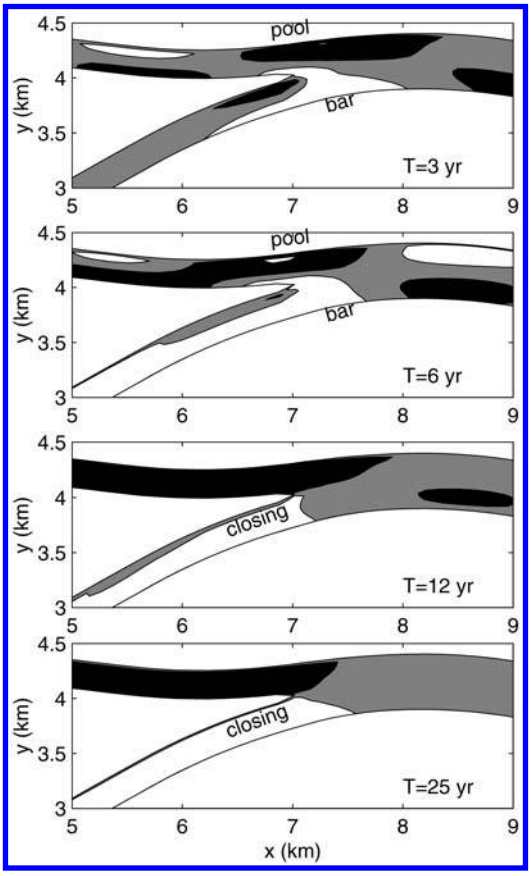


Figure 2. Classified bed levels at 3, 6, 12 and 25 years minus the initial bed level, illustrating the bar and pool evolution. At $T = 25$ years, the bed elevation difference between the downstream branches becomes so large that the inner-bend bar in the upstream bar is no longer visible due to the larger color interval spacing for larger T.

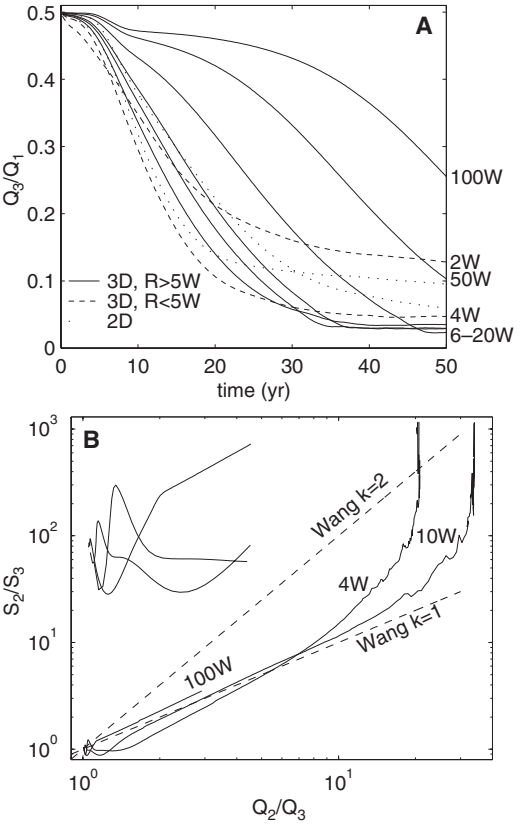


Figure 3. Results of 3D model. A. Time-series of discharge for the inner-bend branch. Labels indicate the bend radius as a multiple of the channel width. B. Sediment and discharge division over the downstream branches compared to the Wang et al. model. Initial quasi-periodic behaviour is magnified in upper left corner.

model and consequently migrate slightly faster. Unexpectedly, the present 2D runs for gentle bends predict dominant *inner*-bend branches although the results are similar to the 3D models for sharper bends ($R > 10W$) (Fig. 3A). This unexpected result might be caused by differences in the submodels for bed-slope and spiral flow effects. In addition, an older version of Delft3D (also in 2DH mode) with which much experience and good results were obtained in the past predicts dominant outer-bend branches. The 2D model results for sharp bends will therefore be interpreted with care and the gentle bends will not be used. Preliminary runs with the latest 2D version demonstrated that this numerical problem has already been solved and that the conclusions in this paper are still valid.

Intriguingly, a plot of S_2/S_3 against Q_2/Q_3 shows a considerable nearly-linear range with $k \approx 1$ (Fig. 3B). This means that the division of sediment transport is fairly similar to that of the flow. Initially the flow and sediment division fluctuates in a damped, quasi-periodic manner. This is caused by the development and migration of the bars from an initially plane bed. Once the bars are nearly in equilibrium and the balance is tipped, the flow and sediment are increasingly discharged into one branch.

In the final stages ($Q_2/Q_3 > 10$) the decline in sediment transport starts to outweigh the decrease in discharge, thereby apparently increasing k from a value below to a value above the stability threshold. The discharge in the closing branch then stabilises at a small but non-zero value in all cases.

4.3 *Effect of asymmetric downstream slopes*

The effect of the upstream bend on the choice which branch becomes dominant can be counteracted

Copyright © 2006 Taylor & Francis Group plc, London, UK

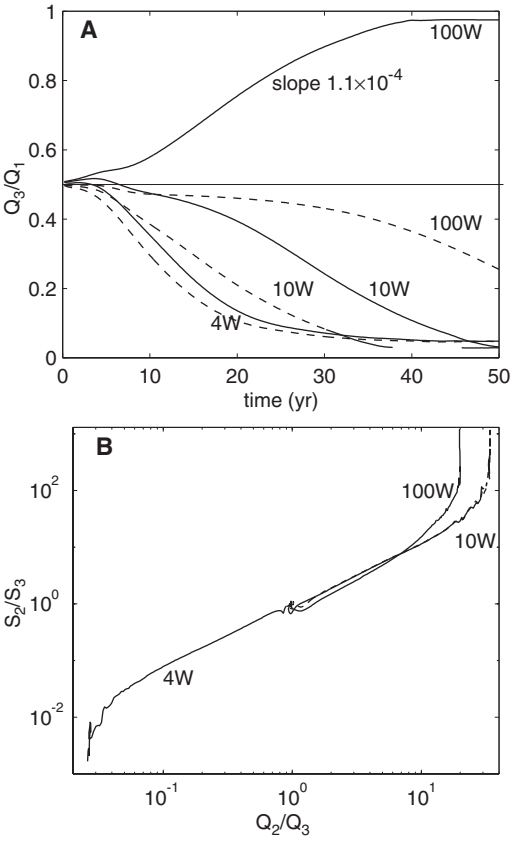


Figure 4. A. Effect of increased slope of the inner-bend branch (–) compared to cases with equal slopes (– –). Time-series of discharge for the inner-bend branch. B. Sediment and discharge division over the downstream branches with asymmetric slopes. The case with $R = 10\,W$ and equal slopes (:) lies on top of the asymmetric case.

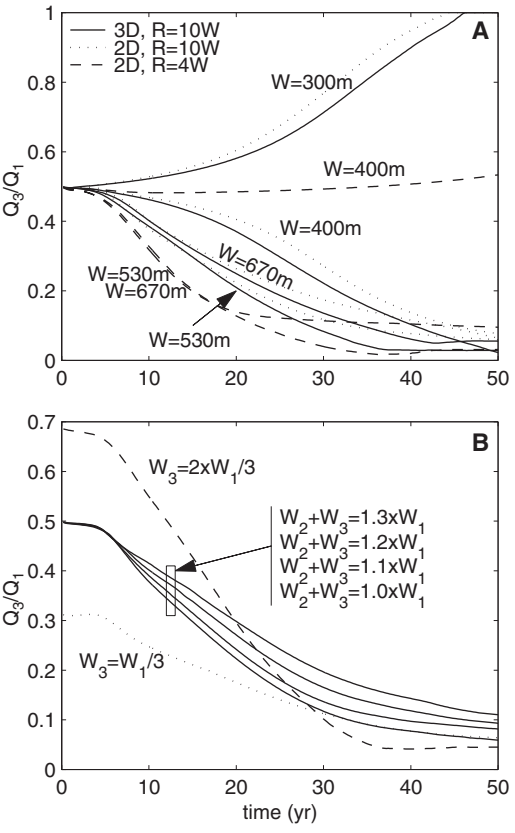


Figure 5. Time-series of discharge for the inner-bend branch. A. Effect of changing the overall channel width. Results with sharper bends are shown for the 2D model. B. Effect of changing the channel width ($W_2 + W_3$, W_2/W_3) downstream of the bifurcation.

by increasing the slope of the inner-bend branch (Fig. 4A). For a slope increase of 30% the inner-bend branch always dominates. For a slope increase of only 10% ($i_3 = 1.1 \times 10^{-4}$ as in the 1D model) the inner-bend branch dominates for gentle bends whereas the outer-bend branch dominates for sharper bends. The nodal point relation remains similar to that in other runs (Fig. 4B). In other words, a larger slope (0–20%) in one branch can be counteracted by upstream meander bend flow depending on the position of the steeper branch along the meander. Thus, there exist combinations of bend radius and downstream slopes for which the bifurcation remains quasi-balanced for a longer time. Such meander effects are not yet included in the existing nodal point relations for 1D models.

4.4 *Effect of different channel widths*

The effect of an equal increase or decrease of the width of all branches is dramatic (Fig. 5A). For narrower channels, all with $R = 10\,W$, the main flow switches from the inner-bend branch to the outer-bend branch in 3D runs. The 2D runs give very similar results. Additional 2D runs show that a sharp bend ($R = 4\,W$) switches the flow for even less narrow channels. This indicates that there also exist combinations of bend radius and channel width for which the bifurcations are quasi-stable, e.g. for $R = 4\,W$ and $W \approx 400$ m.

An equal increase of the width of the downstream branches only, on the other hand, has only a limited effect on the bifurcation stability (Fig. 5B). The closure of the inner-bend branch is slower for increasing downstream widths.

The effect of a change in the width ratio of the downstream branches is limited (Fig. 5B). If either the inner-bend or outer-bend branch is made narrower,

Copyright © 2006 Taylor & Francis Group plc, London, UK

the discharge division eventually approaches that of the symmetrical case. Clearly, an increase of the width of the closing channel does not increase the duration to attain the highly asymmetrical division.

Again, all the runs wherein the widths were varied gave similar nodal point relations with $k \approx 1$ as the other runs.

4.5 *Sensitivity analysis with the 2D model*

The effect of the length of the upstream bend was assessed by increasing this length to 5250 m; almost the whole upstream model domain. The bar pattern changed and the phase of increasing asymmetry took more time. The nodal point relation remained unaffected.

Additional runs with the Van Rijn (1984a,b) sediment transport predictor also gave very similar results for the nodal point relation. In the 2D runs with gentle bends only the outer-bend branches became dominant, contrary to the similar 2D runs with the Engelund and Hansen (1967) predictor. In all these model runs the nodal point relation remained unaffected.

Some model runs in which the downstream water level was varied with discharge ('QH-relation') showed that the outer-bend branch became dominant more slowly compared to runs with a constant downstream boundary, but with the same dependence on upstream bend radius. Runs with a constant Chézy roughness value rather than a constant Nikuradse roughness length gave similar results. In all these model runs the nodal point relation remained – again – unaffected, although the effect of these parameters must be investigated in more detail.

5 DISCUSSION

5.1 *Limitations of the modelling*

Which branch closes off is dramatically sensitive to the model setup. Different setups cause subtle differences in the sediment transport vector field, which decide which branch closes and the rate of closure. Small errors in the numerical scheme, in bed slope effects and in sediment transport predictors therefore have large effects on the outcome at bifurcations, even if the effects on the morphology in single channels are not that sensitive.

Some runs with the 2D model indicate that the results are sensitive to small perturbations of the grid at the bifurcation in cases where both downstream channels tend to be equally dominant initially (for certain combinations of bend radii and downstream slopes). Therefore, they are probably also sensitive to the precise schematisation of the bifurcation. In a curvilinear grid the bifurcation has to be a bluff, whereas in reality it is often a sharp-pointed bar. Further work is planned with a different type of bifurcation with a thin wall in the middle of a simple bend. It is perhaps better to model bifurcations with an unstructured grid, but this option is not yet available in Delft3D.

The models suggest that the bifurcations stabilise in a highly asymmetrical condition. However, the final closure process of one of the branches cannot be understood from the present model runs and has to be studied in more detail. It is possible that several assumptions and numerical aspects affect the value of k in the highly asymmetrical stages. Notably, we assume a constant roughness length and constant downstream water levels, and convert cells to permanently dry cells for water depths <0.1 m.

5.2 *Implications*

The value of $k \approx 1$ for the nearly-linear range in the nodal point relation of Wang et al. is a robust outcome of all given model setups. It means that the division of sediment is close to that of the flow discharge. The implication is that bifurcations are always unstable, or become highly asymmetrical, in partial agreement with Wang et al. (1995). For rivers with parameters similar to the modelled ones, the time scale of reaching the highly asymmetrical condition is of the order of decades to perhaps a few hundreds of years. This is a surprising result, because a number of bifurcations in similar rivers (Red River, Volga) are known to be stable in a more symmetrical condition on much longer time scales of observation, although other bifurcations, such as the historical Rhine bifurcation, were notoriously unstable. In addition, some data sets suggest larger values of k.

Preliminary results of runs with much longer downstream branches suggest that the location of the downstream constant water level (or, the distance from the bifurcation to the lake or sea) is important. For branch lengths approaching the backwater length (which can be estimated as $h/3i$), the discharge distribution becomes asymmetrical much more slowly. Moreover, they stabilise at more symmetrical discharge distributions when they are located at a long distance from the downstream boundary, or have a downstream water depending on the discharge (QH-relation). This is also reflected in the sediment division which follows $k \approx 2$. Runs with tidal water level fluctuations on the other hand de-stabilise more rapidly.

The initial quasi-periodic fluctuations damp out when the bars are nearly in equilibrium with the flow. These bars developed from the initially plane bed in the model. Given a natural river bed that is contingent on earlier conditions, such an initial effect does probably not occur in reality, so that the sediment is divided according to $k \approx 1$ immediately. The initial delay due to the fluctuations is therefore also unlikely to occur in reality.

Copyright © 2006 Taylor & Francis Group plc, London, UK

The duration of the increasing asymmetry phase calculated in the models is probably an underestimate for natural rivers. During an avulsion, a new channel is created. The closure of the old branch commonly happens through sedimentation near the channel entrance rather than narrowing of the channel by sedimentation on the banks. The old channel downstream of the temporary bifurcation may narrow somewhat during the diversion of discharge, but is probably still nearly as wide as the channel upstream of the bifurcation. The models with a larger downstream width show that the closure is slower. Given the right combination of overall width, bend radius and downstream slope asymmetry, the closure may take up to a few centuries based on the present runs, especially for large distances between the bifurcation and the downstream constant water level.

The present model study focussed on dominant bed-load transport conditions. If the suspended bed sediment transport were dominant, then the division of sediment transport would be even closer to that of the discharge because it is less affected by near-bed secondary flow patterns and local bed slopes. According to the analysis of Wang et al. this implies that bifurcations with higher sediment mobilities are even more unstable than low-mobility bifurcations. Preliminary runs with $D_{50} = 0.5$ mm and the Van Rijn (1984b) transport model indeed show that the outer-bend branch becomes dominant even faster. This is highly relevant for many meandering rivers and opposed to the finding of Bolla Pittaluga et al. (2002) that bifurcations are stable for Shields parameters above 0.15.

5.3 *Future directions*

The reality is more complex than the model in some, perhaps crucial, points:

- The discharge is highly variable, affecting the bar development at the bifurcation. The timing of a large discharge peak may tip the balance in the opposite direction.
- In natural rivers, the banks are erodible depending on the bank sediment composition, vegetation, etc. Meander migration changes the boundary conditions at the bifurcation, and the opening downstream branch may widen through bank erosion. Changes in downstream channel width due to deposition also affect the rate of changing asymmetry. Moreover, the bifurcation may migrate downstream with the eroding bends. This may lead to an increase of the angle between the dominant and the subordinate branch, increasing the rate of changing asymmetry.
- The closure of river branches in nature is affected by changing hydraulic roughness and downstream water levels, as well as by large wood deposited after floods, pioneering vegetation and, further downstream, peat development.
- The bed sediment may be sorted in the bend, leading to preferred feeding of coarse sediment to one branch and fine sediment to the other. Moreover, bed surface armouring may stabilise bars.

Since the work of Wang et al. (1995) the common wisdom is that bifurcation stability can be explained from a stability threshold for parameters of the nodal point relation. The present study suggests, however, that bifurcations may develop to become very asymmetrical, which can be interpreted as closure, while persistent bifurcations are related to quasi-equilibria that result from a proper combination of upstream bend radius, channel widths or downstream slopes. Model runs will be done in the future with schematised discharge waves, changing grids, initial bars, other roughness formulations, downstream water levels that depend on discharge and erodible banks to assess their effects on the nodal point relation. Moreover, historical maps and the soil auger archive of the Rhine delta at Utrecht University will be studied (see, e.g., Stouthamer and Berendsen, 2000), as well as satellite images of the Ganges-Brahmaputra delta (see, e.g., Klaassen and Van Zanten, 1989) to test various hypotheses based on the model outcomes.

6 CONCLUSIONS

Based on more than 100 idealised 2D and 3D morphodynamic models we conclude that bifurcations always attain a highly asymmetrical division of discharge and sediment, except for a few specific combinations of parameters that give quasi-stable symmetrical divisions for a much longer period. The division of sediment at the bifurcations is similar to the division of flow discharge during the phase of increasing asymmetry in all models. This is the case for both bed-load and suspended-load transport-dominated conditions.

The models were loosely based on the River Rhine in the Netherlands, and became stably asymmetrical in periods of the order of a decade to perhaps a few centuries for special quasi-balanced cases. The rate of change of symmetry and the choice which branch becomes dominant is extremely sensitive to a number of competitive factors:

1. a slope advantage of one downstream branch increases the discharge through this channel,
2. a bend upstream of the bifurcation can counteract downstream slope advantages of 0–20% for decreasing bend radii,
3. the width of all channels strongly determines the bar pattern and dynamics, which may cause the flow to switch to the other downstream branch compared to cases with other widths,
4. the results are sensitive to the submodels for bed slope effects and sediment transport.

Copyright © 2006 Taylor & Francis Group plc, London, UK

The subordinate branch was never entirely closed in the model runs, but this is perhaps an effect of model assumptions and numerical aspects. The closure process has to be studied further.

ACKNOWLEDGEMENTS

MGK is supported by the Netherlands Earth and Life sciences Foundation (ALW) with financial aid from the Netherlands Organisation for Scientific Research (grant ALW-VENI-863.04.016). Mohamed Yossef is thanked for discussion.

REFERENCES

Bolla Pittaluga, M., R. Repetto, and M. Tubino (2002). Channel bifurcation in braided rivers: equilibrium configurations and stability. *Water Resources Research 39*, 1046.

Engelund, F. and E. Hansen (1967). *A monograph on sediment transport in alluvial streams*. Kobenhavn, Denmark: Teknisk Forlag.

Klaassen, G. J. and B. H. J. Van Zanten (1989). On cutoff ratios of curved channels. In *Proc. 23rd Congress of the IAHR*, Ottawa, Canada. IAHR.

Lesser, G. R., J. A. Roelvink, J. A. T. M. van Kester, and G. Stelling (2004). Development and validation of a three-dimensional morphological model. *Journal of Coastal Engineering 51*, 883–915.

Meyer-Peter, E. and R. Mueller (1948). Formulas for bed-load transport. In *Proceedings 2nd meeting*, Stockholm, Sweden, pp. 39–64. Int. Ass. for Hydraulic Structures Res.

Stouthamer, E. and H. J. A. Berendsen (2000). Factors Controlling the Holocene Avulsion History of the Rhine-Meuse Delta (The Netherlands). *J. of Sedimentary Research 70*(5), 1051–1064.

Struiksma, N., K. Olesen, C. Flokstra, and H. D. Vriend (1985). Bed deformation in curved alluvial channels. *J. of Hydraulic Research 23*(1), 57–79.

Talmon, A. M., N. Struiksma, and M. C. L. M. van Mierlo (1995). Laboratory measurements of the direction of sediment transport on transverse alluvial-bed slopes. *J. of Hydraulic Research 33*(4), 495–517.

Van Rijn, L. (1984a). Sediment transport, part I: bed load transport. *J. of Hydraulic Engineering 110*(10), 1431–1456.

Van Rijn, L. (1984b). Sediment transport, part II: suspended load transport. *J. of Hydraulic Engineering 110*(11), 1613–1641.

Wang, Z., R. Fokkink, M. D. Vries, and A. Langerak (1995). Stability of river bifurcations in 1d morphodynamic models. *J. of Hydraulic Research 33*(6), 739–750.

Copyright © 2006 Taylor & Francis Group plc, London, UK

Bed load management at the River Lech – A physical model

U. Stephan & K. Wibmer
Institute for Hydraulic Engineering and Calibration of Hydrometrical Current-Meters, Vienna, Austria

ABSTRACT: The Tyrolean river Lech is one of the last near-natural Alpine riverine ecosystems of Austria. The flood event in August 2005 led to large flooding in the Reutte area caused by the extreme discharge and a river bed aggradation due to the high bed load from the upstream catchment. The reason for the latter is mainly a reduced bed slope of the Lech resulting in a halved bed load transport capacity despite a canalised river reach upstream of Reutte. A sustainable solution both ecologically and hydraulically satisfying was developed using a physical model test. The physically modelled river was divided into two channels approaching to the natural, braided river morphology. One channel worked as a bed load entrapment only for high discharges. The second channel forwarded the bed load according to the sediment transport capacity of the downstream river reach and remains untouched by the dredging.

1 INTRODUCTION

The Tyrolean Lech Valley with the river Lech and its tributaries is one of the last near-natural Alpine riverine ecosystems of Austria and because of its size and character one of the most important for whole Central Europe. The valley is mostly untouched by flood protection measures which was the reason for defining the whole Tyrolean Lech Valley as a Natura 2000 reserve (Birds Directive 1979, Habitats Directive 1992). This resulted in a particular protection of the whole area. Usually, a Natura 2000 reserve entails a limited anthropogenic utilisation within the concerned area due to the fact that any ecological deterioration is prohibited. Any technical engagement must always be seen in this context and is permitted only in cases of jeopardy of life. Thus, each river training measure has to consider this specific situation.

The flood event in August 2005 in Western Austria led to large flooding in the Reutte area caused, on the one hand, obviously by the extreme discharge with a return period of at least 200 years, and on the other hand, by a river bed aggradation due to the high bed load from the upstream catchment. The reason for the latter is mainly a reduced bed slope of the Lech resulting in a halved bed load transport capacity despite a canalised river reach upstream of Reutte. In the past years, this aggradation tendency regularly entailed large, ecologically disputed bed load dredgings. Since each bed load dredging also means unfavourable effects on the river ecosystem, notably in an ecologically valuable area, a sustainable solution both ecologically and hydraulically satisfying was needed.

2 BASIC CONCEPT

The bed load transport capacity in the Reutte area and downstream of it amounts to 50,000 m^3/y, while it reaches the double amount in the upstream area. Thus, to achieve a morphological dynamic equilibrium in the downstream river reach an amount of about 50,000 m^3/y on the average could be dredged. To achieve a solution which, on the one hand, minimises human influences on the river ecosystem and does not interrupt the flow continuum, and, on the other hand, also approaches to the natural, braided river morphology, the river is planned to be divided into two channels (Hanisch et al. 2005). One channel works as a bed load entrapment only for high discharges. The second channel, forwarding the bed load according to the sediment transport capacity of the downstream river reach, works like a bypass to the deposition zone and remains untouched by the dredging. Hence, the concept achieves both the morphological dynamic equilibrium of the downstream river reach and reduced human influences on the river ecosystem. The bed load entrapment was planned to be situated upstream of the endangered aggradation area (Fig. 1).

On the upstream and downstream end, the bed load entrapment is bordered by two ramps. The second channel – the diversion channel – starts upstream of the upper ramp and meets the river Lech again downstream of the second ramp (Fig. 2). Thus, the length of the diversion channel arises to almost 1000 m. The upper ramp situated at km 183.397 provides a stable head water level for the inflow into the diversion channel. The lower ramp situated at km 182.775, bordering the bed load entrapment at the downstream end,

Copyright © 2006 Taylor & Francis Group plc, London, UK

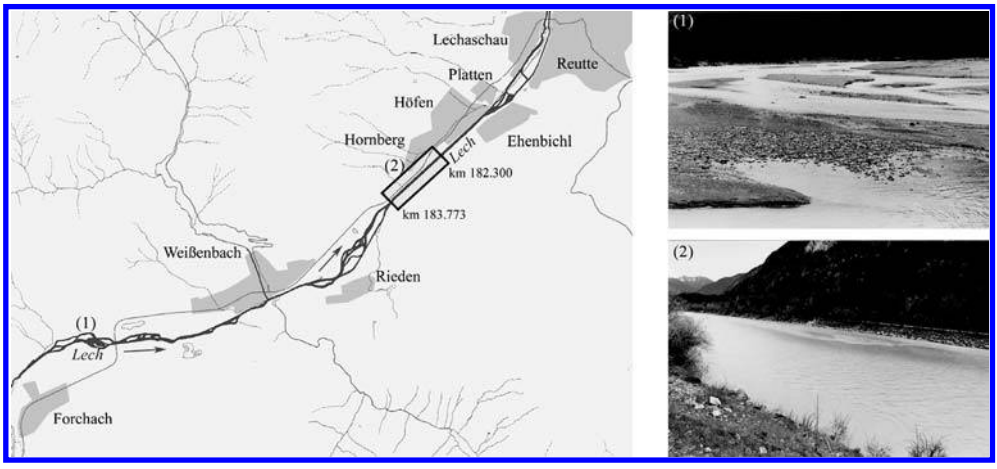


Figure 1. Tyrolean Lech Valley with the river Lech: (1) a natural river stretch upstream of Weißenbach and (2) the constricted river stretch at the location of the planned bed load entrapment.

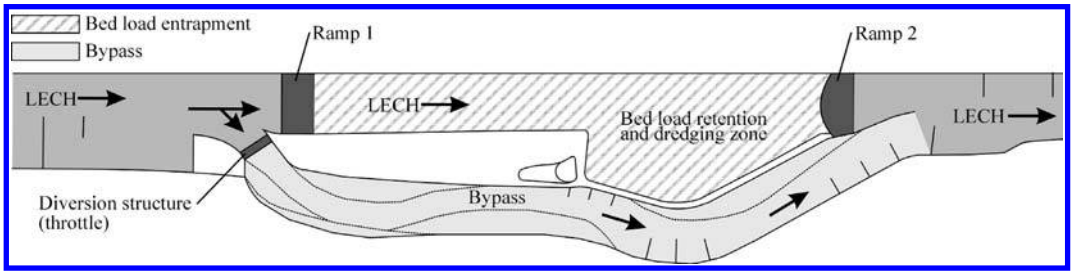


Figure 2. Scheme of the physical model.

reduces the flow velocity inside the entrapment area which leads to a controlled bed load deposition. The river bed widening between the two ramps additionally reduces the flow velocity and the bed shear stress and, thus, increases the retention area.

The inflow into the diversion channel is limited by a discharge throttle (Fig. 2). Discharges lower and equal to the mean flow are forwarded solely to the diversion channel. Discharges higher than the mean flow corresponding to high bed load also flow through the bed load entrapment. Since the bed load entrapment runs dry during low water periods the dredging can be limited to these periods causing only little unfavourable effects on the river ecosystem. These periods mainly occur during the winter, when the whole discharge flows through the diversion channel.

The whole design of the bed load entrapment is based on an optimal discharge and bed load distribution between the two channels. This discharge and bed load distribution mainly depends on the crest height of the upper ramp, on the dimensions of the discharge throttle as well as the position of groynes to direct the flow of water and sediment. Since all these influencing variables were expected to cause highly complex interactions, it was decided to highlight the problem by conducting a physical model test. The model, amongst others, focused on possible control elements such as the discharge throttle or dikes and groynes to influence the discharge and bed load distribution and transport depending on the geomorphologic boundary conditions.

3 PHYSICAL MODEL

The modelled river section had a length of 1573 m and a width of 220 m in nature. According to the available space of the laboratory flume with a length of 25 m and a width of 3 m, the scale factor of the physical model was fixed at 1:80 applying the Froude's law.

The physical model was built with a movable river bed. This scale factor does not allow quantitative but qualitative assessments of morphological results, since the morphological transport processes in nature do

Copyright © 2006 Taylor & Francis Group plc, London, UK

Table 1. Characteristic grain sizes in the physical model compared to the nature sizes.

	Physical model [mm]	Nature [mm]
d_m	52	35
d_{90}	75	95



Figure 3. Development of alternate bars in the physical model at the bed-forming discharge.

not exactly correspond to transport processes in the physical model. The reasons are as follows:

– The sieve curve of the bed material could not be reproduced entirely since grain sizes lower than 0.2 mm might agglutinate.
– Bed forms such as dunes, ripples or bars in the physical model differ from natural ones for high scale factors.

To transfer morphological assessments from the physical model to nature it is important to physically reproduce the grain sizes especially between the mean diameter d_m and the d_{90} (Tab. 1). The grain size was scaled down geometrically. In this case, the model sieve curve sufficiently agreed with the natural sieve curve to derive qualitative assessments of the observed morphological processes (Fig. 4).

Model tests investigating the morphological behaviour of the current situation of the river Lech provided a basis for the comparison of current and planned situation. The characteristic morphological behaviour was derived from steady state experiments for different discharges and compared to natural bed forms. Air photographs from the canalised river reach of the Lech show alternate bars with a mean distance of 260 m. In the physical model, similar bars with a mean distance of 225 m could be observed (Fig. 3) which serves as an example for the qualitative agreement of the

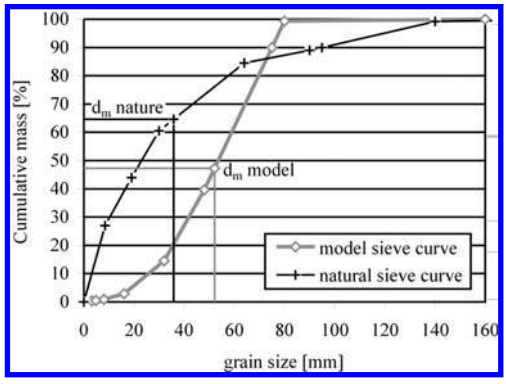


Figure 4. Natural and model sieve curve (both full-scale data).

Table 2. Characteristic discharges.

	Nature [m^3/s]	Physical model [l/s]
MQ	45	0.8
BBQ	147	2.6
HQ1	245	4.3
HQ10	439	7.7
HQ30	570	10.0
HQ100	762	13.3

morphological behaviour in the physical model and in nature. Since bed load transport mainly occurs in terms of alternate bars for the present hydraulic and morphological boundary conditions, an analogous bed load distribution between main and bypass channel can be assumed for both physical model and nature.

In the physical model, the river-adjacent areas were made from concrete and the river bed was a mobile sand bed. The roughness of both the river banks and the river-adjacent areas was simulated by stones of a mean weight of approximately 1000 to 2000 kg per stone which means a stone size of d = 11–14 mm in the physical model (Figs 3, 6). The discharge throttle consisted of a slit PVC-plate which could easily be changed in case of unfavourable results. Thus, different slot sizes could be tested.

The bed load entrapment was optimised within more than 20 experiments varying the crest height of the ramps and ramp heights, the size and height of the slot of the discharge throttle as well as position and layout of different measures to direct the flow and the bed load upstream of the diversion structure.

4 BOUNDARY CONDITIONS

The gauge in Lechaschau was used to define the representative discharges (Tab. 2) for the concerned river reach. The duration curve was calculated from the discharge hydrograph 1996–2001 which serves as a basis

Copyright © 2006 Taylor & Francis Group plc, London, UK

for defining the bed forming discharge BBQ by superposing the duration curve and the sediment transport capacity depending on the discharge (Fig. 5).

The experiments were conducted either as steady state or unsteady state experiments with bed load input into the model inflow. The amount of bed load was calculated according to Meyer-Peter & Müller (1949) using a mean diameter of $d_m = 52$ mm according to the sieve curve of the material used in the physical model (Fig. 4).

5 PROPOSED SYSTEM

The main components of the optimised system (Fig. 6) which yielded the best results concerning the most favourable dividing of flow and bed load between the

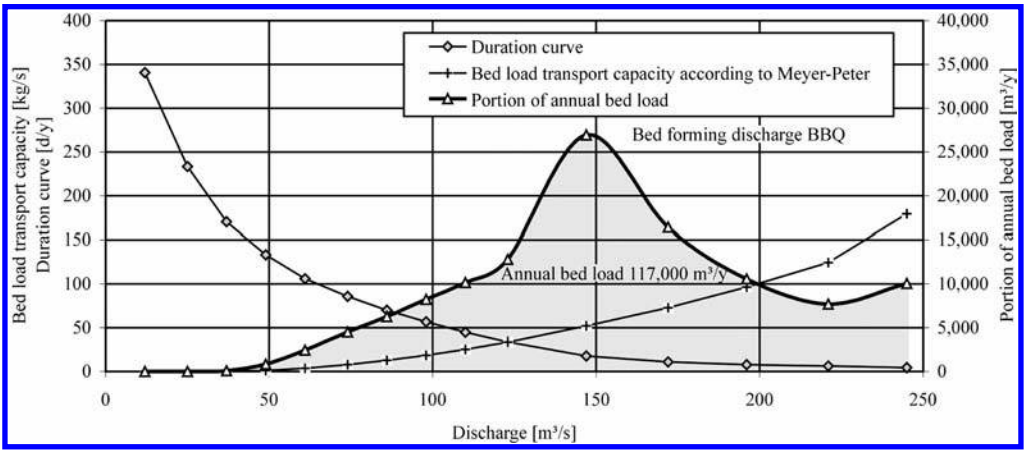


Figure 5. Calculation of bed-forming discharge.

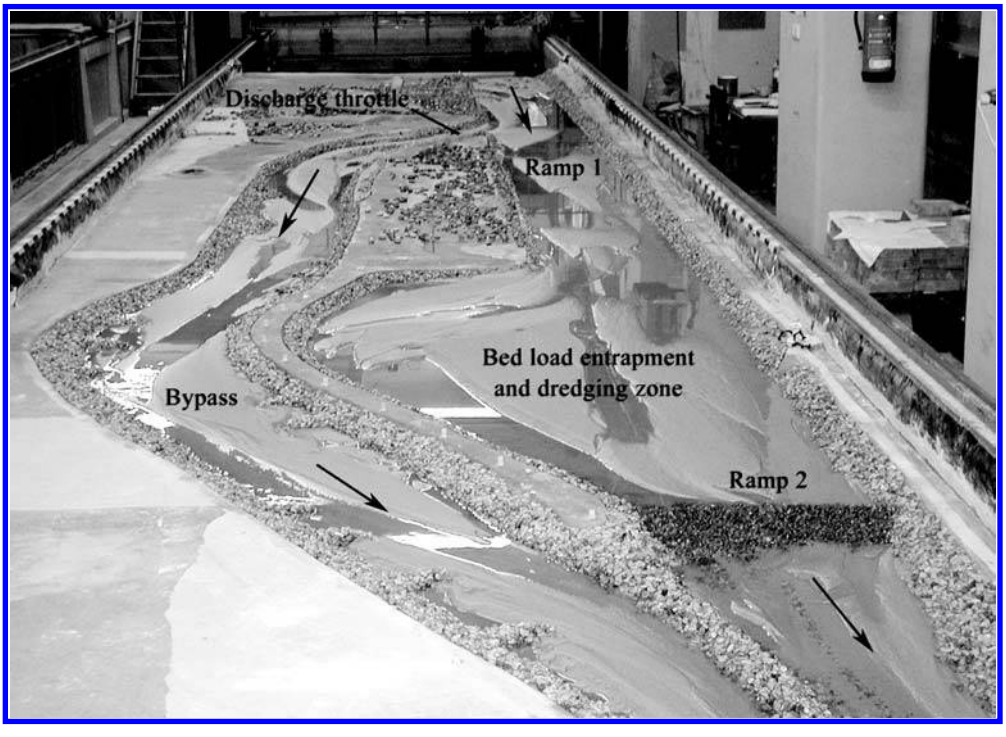


Figure 6. Physical model of the bed load entrapment including the bypass and the dredging zone.

Copyright © 2006 Taylor & Francis Group plc, London, UK

main channel, i.e. the bed load entrapment, and the bypass can be described as follows. The proposed catalogue of measures provided a dynamic equilibrium (Jäggi 1992, Stephan et al. 2003) in the bypass channel, the upstream as well as the downstream river reach and an appropriate bed load supply of the bed load entrapment.

5.1 *Ramps*

The bed load entrapment was situated in the main channel between two ramps. Since the bypass channel started upstream of the upper ramp the crest height of this ramp served as a decisive factor for dividing flow and bed load between the main and the bypass channel. The best results were gained for a crest height being 1.8 m higher than the bed level of the current river bed. Due to the local situation an appropriate flood protection could be guaranteed despite the raised bed level. The crest of the lower ramp had the same height as the base of the upper ramp. The ramp height of the upper ramp was 3.0 m and of the lower ramp 3.4 m. Both ramps had a width of 55 m and a ramp slope of 1:8. Since the upper ramp is expected to be mostly covered with bed load material this ramp was planned as a plane ramp. The lower ramp at the downstream end of the bed load entrapment was planned as a synclinal ramp according to Schauberger (1973). Stone sizes as well as length and size of the bed protection downstream of the ramps were calculated according to Platzer (2000). The stone size of both ramps was fixed to $l_m = 1.5$ m as a mean stone length which means a mean stone weight of approximately 1500 kg.

5.2 *Bed load entrapment (BLE)*

The river section between the two ramps, which served as a bed load entrapment, had a total length of 600 m (Fig. 2). The river width of the upper half of the section being 55 m remained unchanged. The width of the other half of the section was widened up to 130 m which resulted in a reduced flow velocity and, thus, in a favoured bed load deposition within this area. No additional measures to direct flow and bed load between the ramps such as groynes were needed.

5.3 *Discharge throttle*

The slot size of the discharge throttle as shown in Figure 7 was fixed to 15.0 × 1.5 m. To direct flows lower or equal to the mean flow into the bypass channel the bottom line of the throttle had to be 1.7 m below the crest height of the upper ramp. For high discharges the water flowed not only through but also over the discharge throttle. Thus, the river bed had to be protected by a riprap section in front of and behind the throttle to avoid scouring.

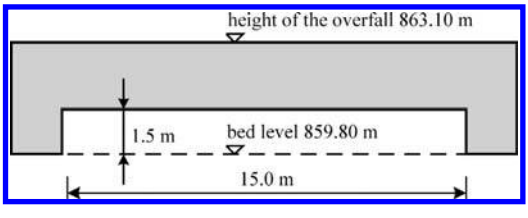


Figure 7. Discharge throttle.

5.4 *Bypass*

The bypass channel showed a slightly curved course with a width ranging from 30 m to 40 m. Alternately situated fields of groynes reduced the channel width by 50% to approximately 15 m for discharges equal and lower than the mean discharge which resulted in the formation of an additional narrower, secondary channel inside the bypass (Fig. 8). It was important to keep the throttle free from deposited bed load material and free flow through the throttle had to be available for every discharge especially for low discharges. Thus, no aggradations should occur in the bypass channel. Best results were obtained for a channel width of 15 m and a bed slope of 0.3%. At discharges larger than 50 m^3/s the groynes were overflowed and, thus, the whole bypass width was available for higher flows decreasing also the sediment transport capacity.

River training structures as well as alternate fields of groynes supported a morphological diversity which strongly enhances also an ecological diversity.

5.5 *Upstream river reach*

Due to the crest height of 861.5 m of the upper ramp, the bed level of the upstream river section was increased by an amount of 1.8 m. This measure was needed to direct low discharges into the bypass, but had also be combined with measures to regulate the bed load input into the bypass channel. Experiments without control measures such as groynes entailed high bed load transport into the bypass resulting in bed load



Figure 8. Bypass channel (view in downstream direction).

Copyright © 2006 Taylor & Francis Group plc, London, UK

Table 3. Test programme for the optimised solution.

Experiment		Maximum discharge [m^3/s]	Bed load input [m^3]	Bed load output [m^3]	Deposited material [m^3]	Deposition in the bed load entrapment [%]
Run 1	HQ1, steady and unsteady state	245	32,873	10,982	21,890	66.6
Run 2	HQ1, unsteady state	215	4099	1946	2153	52.5
Run 3	snowmelt, BBQ, steady state	147	21,806	10,330	11,476	52.6
Run 4	HQ30, unsteady state	570	46,202	13,453	32,750	70.9
Run 5	100 m^3/s, steady state	100	3279	112	3167	96.6
Run 6	HQ100, unsteady state	762	50,728	10,355	40,373	79.6
Run 7	BBQ-MQ, unsteady state, falling limb of the hydrograph	147	2209	0	2209	100.0
Run 8	HQ1, unsteady state	245	5952	2522	3430	57.6
Sum			167,148	49,700	117,448	70.3

deposition close to the discharge throttle and in the bypass. Groynes on the left hand side of the main channel had the same effect on the bed load input into the bypass causing an unfavourable aggradation. The best results were gained by placing two groynes 198 m and 243 m, respectively, upstream of the discharge throttle on the right hand side of the main channel. Thus, especially for high discharges the major part of the bed load material was forwarded into the bed load entrapment avoiding depositions close to the throttle. The groynes being 15 m long were situated right angled to the river bank and were overflowed at a discharge with a return period of one year. In case of changes of the bed load supply from the upstream catchment, design and location of the groynes can easily be adapted to the actual situation. This means a great advantage in meeting changed boundary conditions.

5.6 *Downstream river reach*

The river section downstream of the confluence of bypass and main channel turned out to be endangered by aggradation due to the sudden river widening which, for some cases, proceeded in upstream direction. Hence, to avoid unfavourable bed load depositions behind the confluence the river width had to be reduced locally which was realised by a spur dike and by a single groyne on the right hand side of the river directing the bed load coming through the bypass into the main channel (Fig. 2). Alternately situated fields of groynes in the main channel additionally reduced the river width and, thus, increased the shear stress. They also supported an increased structural variety of the currently canalised river reach since the slightly curved course of the river entailed sequences of bends and fords in longitudinal direction. These measures resulted in a mean bed level 0.3 m lower than the current bed level which still lays within acceptable limits.

6 RESULTS

The optimised solution was investigated by means of a detailed test programme (Tab. 3) with different scenarios and representative flood events from the discharge hydrograph 1996–2001. By comparing bed level measurements of the bypass and the main channel before and after each experiment, bed level changes could be summarised to a cumulative volume describing bed load transport through bypass and main channel, respectively. Table 3 shows eight steady and unsteady state experiments with varying discharges. Five experiments simulating characteristic or extreme scenarios are described more in detail to highlight tendencies of erosion and/or aggradation in bypass and main channel.

The upper chart of the following figures shows the hydrograph of the experimental run (a) and the lower chart presents the deposited area as well as the cumulative volume for both the main (BLE) and the bypass channel (b). All data are converted into full-scale data.

6.1 *Run 1*

The hydrograph of Run 1 consisted of four small flood events approximately corresponding to a discharge with a return period of one year, to the bed-forming discharge and the mean discharge, respectively (Fig. 9). The duration of the first three events was calculated from the duration curve, the fourth curve corresponded to a real flood event of September 2000.

As it can be seen from the deposition curve of the main channel, i.e. the bed load entrapment, adding up the bed level changes of all four flood events, the bed load material was mainly deposited in the widened river section upstream of ramp 2. The bed load material was partly transported to but not over ramp 2.

Copyright © 2006 Taylor & Francis Group plc, London, UK

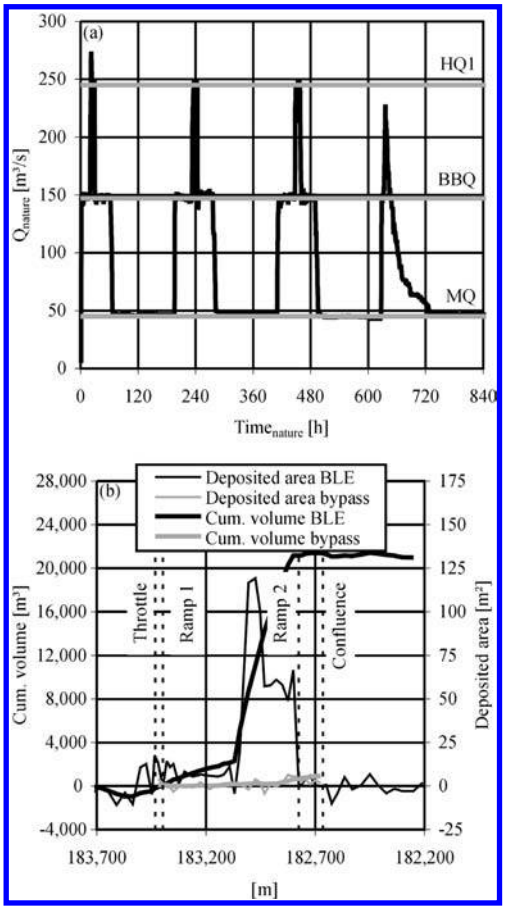


Figure 9. Run 1 – hydrograph (a), deposited area and cumulative volume (b).

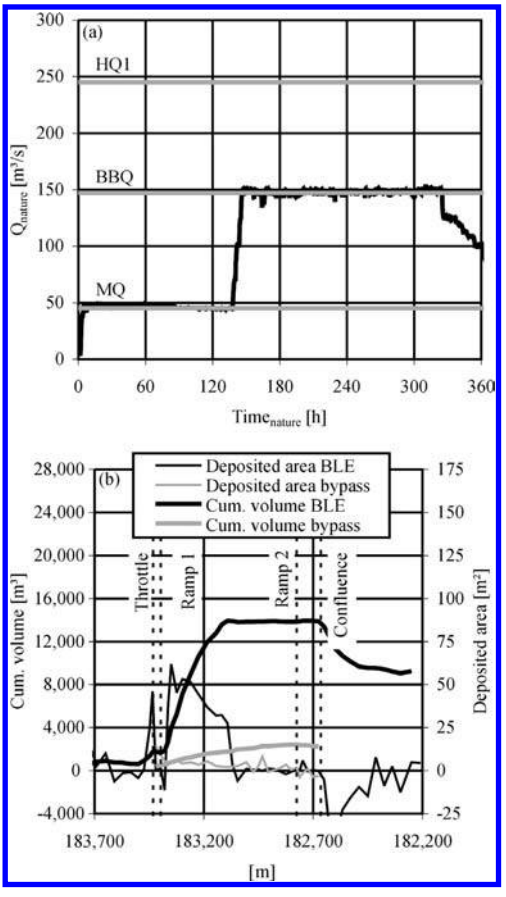


Figure 10. Run 3 – hydrograph (a), deposited area and cumulative volume (b).

Behind the confluence of bypass and main channel neither aggradation nor erosion could be observed which points out a dynamic equilibrium of the downstream river reach. Upstream of ramp 1 the curve reveals a slight tendency of erosion.

The bypass bed levels showed only minor aggradations upstream of the confluence which resulted from alternate fields of groynes. As mentioned above, the groynes reduced the width of the bypass to 15 m for discharges lower than 50 m^3/s and, thus, increased the transport capacity which, finally, resulted in the development of an additional narrower, secondary channel inside the bypass. This secondary, slightly deeper channel enabled discharging of low flows through the bypass whereby the bed load entrapment ran dry. The bed load material deposited near the confluence in the bypass channel was removed again by higher discharges. Thus, the results demonstrate continuous bed load transport into the downstream river reach.

6.2 *Run 3*

The hydrograph of the river Lech in Figure 10 simulated a rather typical scenario during spring time – the snowmelt. Usually, the low flow period during the winter time passes into a long period of higher discharges typically in the range of the bed-forming discharge. For this case, approximately half of the discharge flowed through each of the channels.

Depositions could be observed in front of the discharge throttle and behind the upper ramp 1. The latter seems to be astonishing since the deposition in the main channel did not appear in the widened part of the bed load entrapment but in the narrow part with higher transport capacity. This indicates that the transport capacity related to the remaining discharge in the main channel was too low for the high amount of bed load forwarded over ramp 1 even in the narrow part of the bed load entrapment.

Copyright © 2006 Taylor & Francis Group plc, London, UK

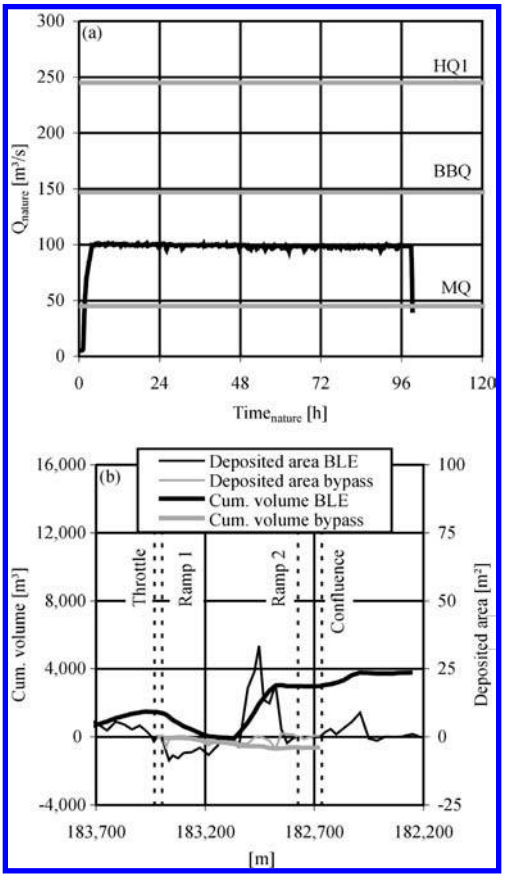


Figure 11. Run 5 – hydrograph (a), deposited area and cumulative volume (b).

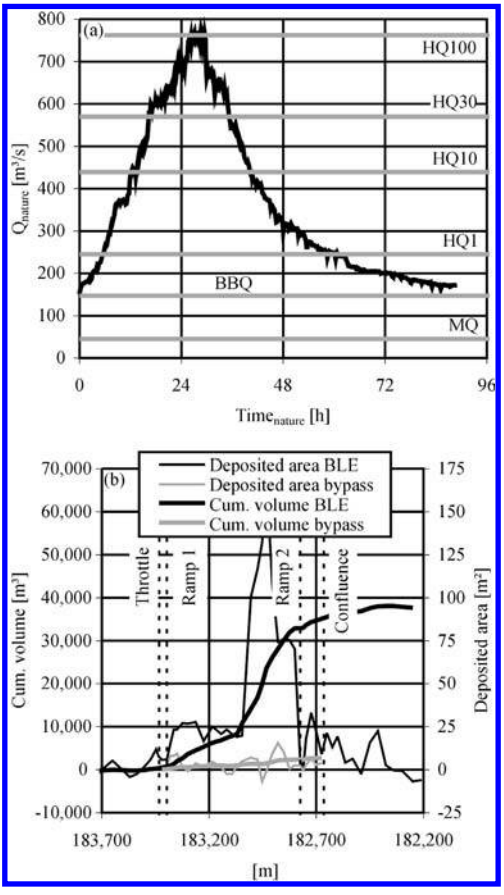


Figure 12. Run 6 – hydrograph (a), deposited area and cumulative volume (b).

Depositions also appeared in the bypass channel, but can be explained by the comparatively high discharge at the end of the experiment. The discharge was not low enough to enable the formation of the additional secondary channel which would accelerate the re-mobilisation of deposited material.

The downstream river reach showed an erosion tendency which resulted from aggradation in both the bypass and the main channel which can be explained by the lack of sediment transport from upstream.

6.3 *Run 5*

To investigate a wide range of different discharges one of the experiments was conducted with a steady state discharge of 100 m^3/s being between the mean and the bed-forming discharge.

Figure 11 exhibits that depositions appeared in both the upstream and the downstream river reach despite a comparatively low discharge. During the experiment, no bed load material was transported over ramp 2 and, thus, depositions occurred in the widened section of the bed load entrapment. The depositions in the downstream river reach resulted from bed load transport through the bypass which indicated minor erosions proving the functional ability to forward the bed load into the downstream river reach especially for low discharges.

6.4 *Run 6*

Figure 12 shows the simulation of a 100 years flood event beginning and ending with the bed-forming discharge.

The river reach upstream of the upper ramp 1 exhibited neither aggradation nor erosion but remained almost unchanged. As also shown in Figure 9, the bed load material was mainly deposited in the widened river section upstream of ramp 2. But aggradation also appeared between ramp 1 and the widened river

Copyright © 2006 Taylor & Francis Group plc, London, UK

section and, to some extent, also in the river reach downstream of ramp 2. This can be explained by the high amount of bed load material mobilised by the high discharge which was also transported over ramp 2. Added up to the bed load material coming from the bypass channel, the total amount of bed load exceeded the transport capacity of the downstream river reach and, thus, caused depositions behind the confluence of main and bypass channel.

The bypass channel also showed a slight tendency of aggradation. This can easily be traced back to the experiment ending with a discharge not lower than the bed-forming discharge. Again, the discharge was not low enough to enable the formation of the additional secondary channel which would enhance the re-mobilisation of deposited material caused by a higher discharge.

6.5 *Run 7*

To investigate the function of the bypass channel during the falling limb of a hydrograph, Run 7 continued Run 6 simulating the falling limb of a flood event beginning with the bed-forming and finishing with the mean discharge (Fig. 13). This scenario led to depositions behind ramp 2 and behind the confluence of bypass and main channel, but not in the bedload entrapment or in the bypass. The bypass even showed an erosion tendency which proofed the re-mobilisation of deposited bed load material after a flood event due to the development of a secondary channel with a higher transport capacity.

6.6 *Summary*

Figure 14, finally, summarizes the bed level changes of all experiments done (see also Tab. 3). The graph demonstrates major depositions of bed load material in the bed load entrapment, especially in the widened section upstream of ramp 2. Only minor depositions can be observed in the bypass channel. But a re-mobilization of this material is to be expected for low flow periods. Both, the upstream and the downstream river reach remain unchanged which is important especially for the downstream river reach. The capacity of the bed load entrapment proved to match very well with the reduced transport capacity of the downstream river reach.

The percentage of deposited material in the bed load entrapment related to all investigated discharges is shown in Figure 15. The linear regression exhibits that the sediment retention in the bed load entrapment increased with higher discharges. For an average year the deposited material amounted to approximately 55% of the total bed load. For extreme flood events even 75% of the total bed load were entrapped in the dredging zone.

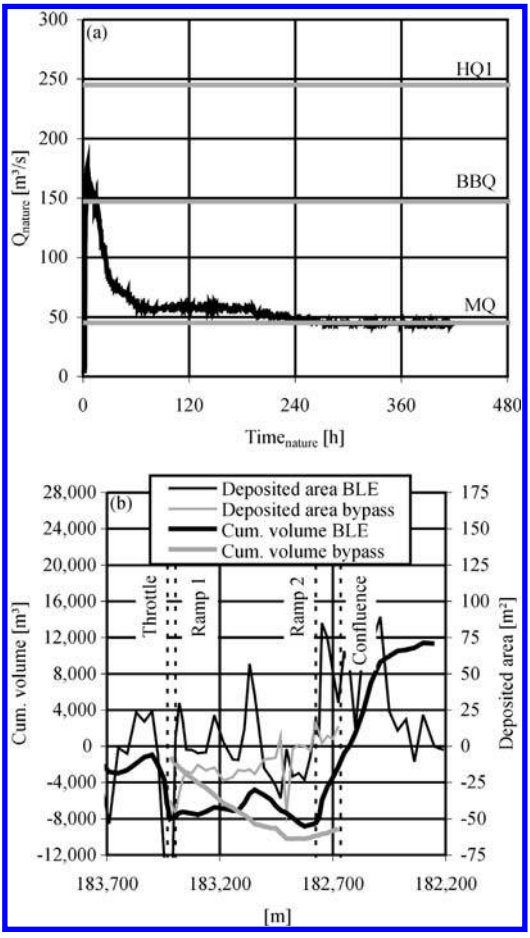


Figure 13. Run 7 – hydrograph (a), deposited area and cumulative volume (b).

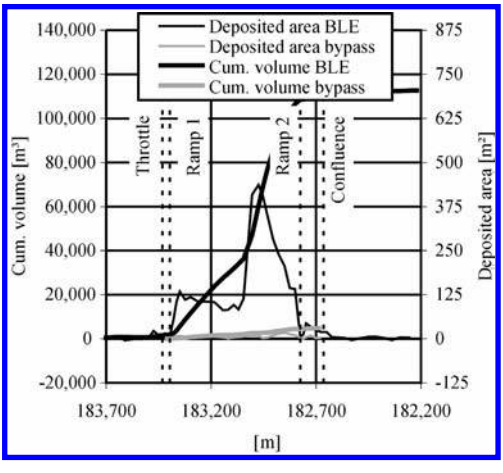


Figure 14. Summarizing Run 1–8 – Deposited area and cumulative volume.

Copyright © 2006 Taylor & Francis Group plc, London, UK

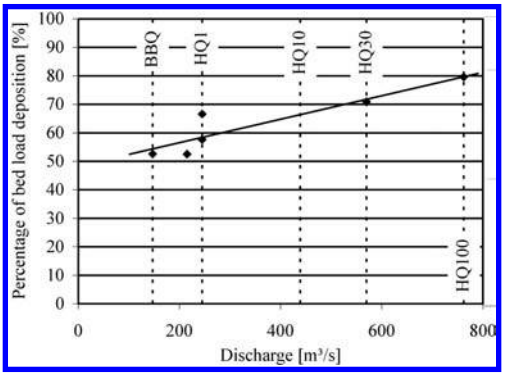


Figure 15. Percentage of bed load retention related to the discharge.

7 CONCLUSIONS

The Tyrolean river Lech is one of the last near-natural Alpine riverine ecosystems of Austria. The valley is mostly untouched by flood protection measures which was the reason for defining the whole Tyrolean Lech Valley as a Natura 2000 reserve. Thus, each river training measure has to consider this special situation. In the Reutte area, a reduced bed slope of the Lech resulting in a halved bed load transport capacity despite a canalised river reach often causes unfavourable aggradations increasing the danger of flooding. A sustainable solution both ecologically and hydraulically satisfying was developed using a physical model test. The physically modelled river was divided into two channels approaching to the natural, braided river morphology. One channel – the main channel – worked as a bed load entrapment only for high discharges and ran dry for discharges lower than the mean discharge. This channel section was bordered by two ramps at the upstream and downstream end. The width of half of the section was enlarged to concentrate the depositions within this channel section by reducing the sediment transport capacity. The second channel – the bypass – forwarded the bed load according to the transport capacity of the downstream river reach. The model results indicated that the deposited material amounted to approximately 55% of the total bed load for an average year. This means that 45% of the total bed load material satisfied the transport capacity of the downstream river reach since the model results adding up all experiments exhibited bed levels being in a morphological dynamic equilibrium. However, the experimental runs provided valuable findings concerning the interplay of deposition and erosion of bed material in both the main and the bypass channel varying with discharge.

The physical model "Lech – Bed Load Entrapment Hornberg-Ehenbichl" was essential for assessing the interaction of the different components and for testing the reliability of the complex site layout in the most efficient way. The model furthermore proved its value in optimizing the design and evaluation of operation and maintenance guidelines. However, stochastic factors like discharge regime or saturation level of the sediment transport capacity affect bed load transport and deposition processes.

Hence the permit planning is complemented by a complex river bed stability and bed load monitoring program, the results of which will be presented in the near future.

REFERENCES

Birds Directive 1979. Council directive 79/409/EEC on the conservation of wild birds. The Council of the European Communities.

Habitats Directive 1992. Council Directive 92/43/EEC on the Conservation of natural habitats and of wild fauna and flora. The Council of the European Communities.

Hanisch, P., Kremser, M. & Wibmer, K. 2005. Lech – Bed Load Entrapment Hornberg-Ehenbichl – A Physical Model. *9th International Symposium on Water Management and Hydraulic Engineering*. Ottenstein/Austria. September 4th–7th 2005.

Jäggi, M. 1992. Sedimenthaushalt und Stabilität von Flussbauten. *Mitteilung der Versuchsanstalt für Wasserbau, Hydrologie und Glaziologie*. Nr. 119. ETH Zürich.

Meyer-Peter, E. & Müller, R. 1949. Formel zur Berechnung des Geschiebetriebs. *Schweizerische Bauzeitung*. 67(3). 29–32.

Platzer, G. 2000. Dimensionierung muldenförmiger Blocksteinrampen. Teil 1: Bemessungsgrundlagen; Teil 2: Anwendung der Grundlagen. *Schriftenreihe des BAW*. Band 9.

Schauberger, W. 1973. Die räumliche Krümmung von Gefällsstufen und Sturzbettendschwellen. *Österreichische Wasserwirtschaft.* 25(5/6). 120–124.

Stephan, U., Hengl, M. & Schaipp, B. 2003. River restoration considering geomorphological boundary conditions. *Proceedings of the 30th IAHR Congress*. Thessaloniki. Theme C. Inland Waters: Research, Engineering and Management. Vol. II, 457–464.

Copyright © 2006 Taylor & Francis Group plc, London, UK

B.4. Debris and hyperconcentrated flows

Copyright © 2006 Taylor & Francis Group plc, London, UK

Intermittency of rheological regimes in uniform liquid-granular flows

A. Armanini, M. Larcher, L. Fraccarollo
CUDAM – Dipartimento di Ingegneria Civile e Ambientale – Università degli Studi di Trento,Trento, Italy

ABSTRACT: To investigate the vertical structure of free-surface liquid-granular flows, it is of particular interest to materialize steady flow conditions. In this contribution, we present a detailed analysis of the rheological stratification of the flow, focusing on the mechanisms governing the transition from the frictional to the collisional regime, on the stress transmission inside the flow and on particles kinematics. In particular, it is observed that in opportune conditions high-concentration flows show locally a typical intermittency of the flow regime, switching alternatively from frictional to collisional. In the experiments a mixture of water and perfectly spherical, identical particles, with a diameter equal to 6 mm and with a density of 2210 kg/m^3, was introduced steadily in the upstream part of the flume and filmed through the sidewall of the channel utilizing a high-speed CCD camera. The reconstruction of detailed particle kinematics and of the effect of the intermittence of the flow regime was obtained utilizing imaging techniques based on the Voronoï polygons.

1 INTRODUCTION

Steady granular flows have been widely studied in literature. Most investigations treat cases where air plays the role of interstitial fluid, while just a few ones consider granular flows in water.

The rheology of granular flows was originally tackled by Bagnold (1954), who analyzed the behavior of a gravity-free dispersion of large solid spheres in a Newtonian fluid under shear. Bagnold distinguished two flow regimes on the base of a non-dimensional parameter, subsequently called the *Bagnold number*, representing the ratio between stresses due to inertia and stresses due to viscosity. Bagnold called *macroviscous* the linear regime characterized by small Bagnold numbers, where the shear stresses behave like in a Newtonian fluid with a corrected viscosity, and *grain-inertia* the one, characterized by large Bagnold numbers, where the stresses were independent of the fluid viscosity but dependent on the square of the shear rate and on the square of the granular-phase concentration.

Recent findings leaded to a better understanding of particle interactions. In particular, a granular material subjected to deformation can determine different types of interactions among grains and, therefore, generate stresses by different mechanisms. Individual particles may interact with the others in form of clusters, generating a network of contact forces through sustained rolling or sliding contacts, or by nearly instantaneous collisions, during which momentum is exchanged and energy is dissipated because of inelasticity and friction. The relative importance of these mechanisms may be used as the characteristic defining the various flow regimes (Savage 1984).

The velocity of each particle may be decomposed into the sum of a mean velocity and of a random component, taking into account the relative motion of the particle compared with the mean value. The concept of *granular temperature* can be introduced to refer to the mean square value of the instantaneous deviation from the mean velocity. The granular temperature plays a fundamental role in generating pressures and governing the internal transport rates of mass, momentum and energy.

The physical similarity between rapid granular flows and dense gases has led to a great deal of work on applying kinetic theories to granular materials, pursuing the idea of deriving a set of continuum equations (typically mass, momentum and energy conservation) entirely from microscopic models of individual particle interactions. All models are based on the assumption that particles interact by instantaneous collisions, implying that only binary or two-particle collisions need to be considered. Particles are usually modeled in a simple way, ignoring surface friction or any other particle interactions tangential to the contact-point, and considering a constant coefficient of restitution to represent the energy dissipated by the impact normal to the point of contact between the particles. Furthermore, molecular chaos is generally assumed, implying that the random velocities of particles are independently distributed.

Coherently to the considerations reported above, two different rheological regimes are observed in

Copyright © 2006 Taylor & Francis Group plc, London, UK

granular flows: a *collisional regime* and a *frictional regime*. The collisional regime is typical of rapid granular flows, and particles interact by means of quasi-instantaneous contacts. This regime was studied widely by many authors, among the others Jenkins & Hanes (1998), and Armanini et al. (2005) showed it to be in strict analogy with the grain-inertia regime identified by Bagnold. The frictional regime, on the contrary, is typical of slow, dense flows of cohesionless granular materials, where the grains move with sustained contacts (Savage 1998).

2 THEORETICAL FRAMEWORK

2.1 *Liquid-granular flows in equilibrium*

In opportune experimental conditions liquid granular flows can take place in equilibrium conditions, in the sense that a moving layer flows over a static loose bed of water-saturated grains. In this case the bottom does not represent an interface where vertical profiles of physical quantities, such as velocity and concentration, change abruptly or present cusps. Therefore velocity, concentration and granular temperature are all continuously varying throughout the flow depth from the top free-surface down to the bottom. This condition importantly influences flow dynamics, which are remarkably different from those that develop over a fixed bed (Larcher 2004, Armanini et al. 2005).

Armanini et al. (2005) showed the experimental evidence of the existence, over the depth of flows in equilibrium, of different rheological mechanisms. In fact, near to the erodeable bed, the frictional (or quasi-static) regime prevails, while near to the free surface any mechanism, including also frictional, pure collisional and turbulent ones, could be present. The distribution of the rheological characterization over the flow depth is responsible of the global flow condition. The flowing layer adjusts its own depth through erosion or accretion of the static deposit. It should be noted that this deposit forms spontaneously.

2.2 *Kinetic theories*

To relate the collisional particle pressure σ_p and shear stress τ_p to the local granular temperature, the following relations, originally derived from kinetic theories in the context of dry granular flows, can be applied to liquid-granular systems:

$$\sigma_p = c\rho_p\left(1+r\frac{\rho_w}{\rho_p}\right)(1+4cg_o)T \tag{1}$$

$$\tau_p = -\frac{8D(1+r\rho_w/\rho_p)\rho_p c^2 g_0 T^{1/2}}{5\pi^{1/2}}\left(1+\frac{\pi}{12}\left(1+\frac{5}{8cg_0}\right)^2\right)\frac{du}{dy} \tag{2}$$

where:

$$g_0(c) = \frac{(2-c)}{2(1-c)^3} \tag{3}$$

describes the variation of the rate of collisions between particles with particles-concentration c (Carnahan & Starling 1969), and where

$$r = \frac{1+2c}{2(1-c)} \tag{4}$$

is the added mass coefficient that takes into account that the motion of a submerged particle is accompanied by the conjugate motion of a portion of fluid (Armanini et al. 2005). In the equations reported above ρ_p and ρ_w represent the density of the granular material and of the interstitial fluid respectively, D represents the diameter of particles and du/dy the shear rate.

2.3 *Uniform granular channel flow*

If the granular phase is completely saturated by water, the external normal stress σ_e and tangential stress τ_e can be written as:

$$\sigma_e = \int_y^h \rho_w g\Delta c\cos\alpha\, dy \tag{5}$$

$$\tau_e = \int_y^h \rho_w g(1+\Delta c)\sin\alpha\, dy \tag{6}$$

Where c is granular concentration by volume, y is the coordinate normal to the bed, h is the free surface level, ρ_p and ρ_w are the densities of the particles and water, $\Delta = (\rho_p - \rho_w)/\rho_w$ is the relative immerse density of the solid phase, g is the acceleration of gravity, and α is the slope angle of the flow.

In uniform flow condition the external stresses are balanced by internal one. While in the direction normal to the flow the external stresses, given by eq. (5), are balanced by the internal stresses due to particle interaction, (eq. 1), the tangential projection of the entire burden of the flow (water + grains) (eq. 6) is charged over the solid phase only (eq. 2), so assuming that the shear stress in the liquid phase is negligibly small.

Armanini et al. (2005) describe the presence of a stratification of rheological mechanisms inside the flow, with the frictional regime located in the slower regions and the collisional layers where velocity and shear rate are larger. This picture of the flow domain was innovative respect to observations keeping collisional and frictional mechanisms in distinct kinds of experiments. However this was not sufficient to satisfy force balances inside the flow domain. In our experiments we recently observed that not only a stratification of rheological mechanisms is possible, but that in certain positions of the flow domain collisional

Copyright © 2006 Taylor & Francis Group plc, London, UK

and frictional regime can coexist, in the sense that they alternate in time. This alternation of different regimes is similar to what happens in the border of a turbulent boundary layer where the alternation between turbulent flow and external potential flow is identified as the phenomenon of *intermittency* (Hinze 1975).

2.4 *Intermittency and coexistence of collisional and frictional regime*

In the case of granular flow the observation was possible accounting time-evolution of the vertical velocity of particles. In fact in the frictional regime particles roll in relatively ordered layers, one on top of the other, and vertical velocity changes in time according to regular sequences, characterized by some peaks at regular intervals. The observation of vertical velocity history denotes that sometimes vertical velocity can exceed these peak values typical of the frictional regime, denoting that the rheological mechanism has switched to collisional conditions. Coherent blocks of particles have been observed also in numerical simulations of dry particles (Drake 1990), in particular Goldhirsch (2003) stressed the emergence of high-density clusters in granular gasses, as a product of external forces. In the present case the large zones of coherent blocks of sliding particles are doubtless due to the action of gravity.

Referring to each particle, it is possible to define an intermittency factor Ω, representing the ratio between the sum of time intervals t_i^{coll} characterized by an instantaneous vertical velocity exceeding the peak value typical of the frictional regime and total time of observation t^{tot}.

$$\Omega = \frac{\sum_i t_i^{coll}}{t^{tot}} \tag{7}$$

All details necessary to define the threshold value of vertical velocity necessary for the definition of the intermittency function are given in section 4.1.

3 EXPERIMENTAL METHODS

3.1 *Experimental setup*

Experiments were carried out in the special laboratory flume developed at the University of Trento for the study of steady uniform liquid-granular flows (Figure 1). The apparatus is composed of two main components: the first is a glass-walled open channel; the second is an external conveyer belt, connected to the channel by chute guides, which recirculates upslope both water and sediment. The channel can be tilted by a telescopic piston served by a hydraulic power station at angles going from 0 to 22 degrees. It has a length of 6 m and a width of 40 cm, narrowed down to 10 cm for the present study by placement of a glass partition. The opaque channel floor is artificially roughened by glued particles. Imaging measurements are made at a distance of about 2 m upstream of the channel outlet, by filming the flow through the sidewalls. To view the basal flow condition at the centre of the cross-section and check if the flow is in equilibrium with the underlying sediment bed, a small port-hole was also pierced through the channel floor. The external conveyer system has a length of 8.40 m, and is equipped with a 50 cm wide U-shaped flexible belt that can be operated at speeds of up to 5 m/s. The belt is aligned to the flume and tilted slightly more, in order to allow the material to be collected from and returned to the flume. A hopper is placed at the end of the flume, to collect water and solid material. This system permits steady flows up to a volume discharge equal to about 20 l/s, without posing limitations to the sediment concentration of the mixture.

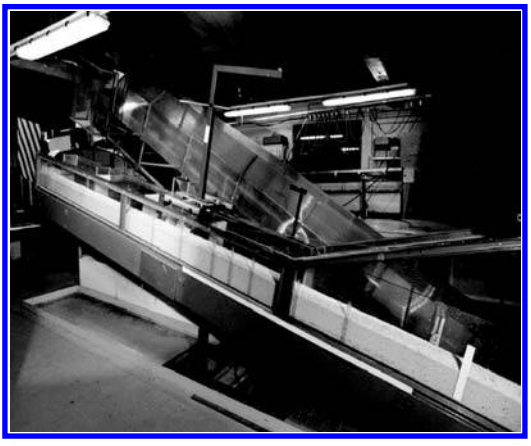


Figure 1. Experimental setup used for the experiments.

During an experimental run, the set-up forms a closed loop, in which a fixed volume of water and granular material circulates. Provided it is sufficiently high, the speed of the conveyer belt does not noticeably influence the flow inside the channel. For the present experiments, fast belt speeds of 5 m/s were adopted. The throughput is then controlled solely by the flow slope, and by the volumes of water and sediment inside the system. When these parameters are kept constant (and aside from certain regimes which exhibit a pulsating behavior that are not object of the present analysis), the recirculating flow settles to a steady state within a matter of minutes. Camera and lighting adjustments can then be made, and video footage acquired. Uniform flow conditions are established in the central reach of the flume, where all measurements can be taken. At the end of a run, the channel outflow is diverted to a trap during a short timed interval

Copyright © 2006 Taylor & Francis Group plc, London, UK

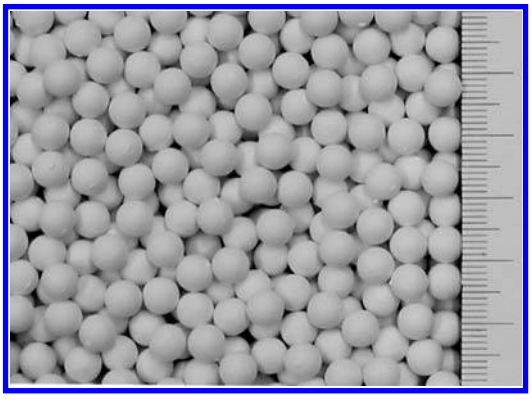


Figure 2. Granular material utilized in the experiments.

(about 10 s), in order to independently measure the water and granular discharges.

3.2 *Characterization of the granular material*

Perfectly identical spherical plastic particles were selected as granular material for the present tests, as shown in Figure 2. They consist in a master composed by barium sulphate and titanium dioxide dispersed on polystyrene.

The particles have a diameter $D = 6.0$ mm and a specific gravity $s = \rho_p/\rho_w = 2.21$. The material is slightly lighter than natural sediment materials ($s \approx 2.65$), hence more readily entrained by water, facilitating observation. Each particle has a volume of 113.04 mm^3 and a weight of 0.25 g. The perfectly white color of the grains contrasts well with darker surrounding fluid, and is ideal for the automated imaging measurements presented in the next section.

3.3 *Imaging methods*

Liquid-granular flows are imaged through the transparent flume sidewall using a gray-scale high-speed digital camera. At the chosen video rate of 500 frames per second, the digital images have a resolution of 1280×1024 pixels. To prevent motion-induced blur, the camera shutter is set at 1/2000 s or 1/4000 s, depending on lighting conditions.

To capture the motions and arrangements of visible particles, imaging methods based on the Voronoï polygons developed specifically for granular flows by Capart et al. (2002) were applied.

To highlight particles on images, the digital frames are first convoluted with a Laplacian-of-Gaussian filter with a width set equal to the pixel diameter of the grains. Particles positions are then obtained by pinpointing local brightness maxima to sub-pixel accuracy. Tracking of the particles on successive frames is performed using a pattern-based matching principle: Voronoï diagrams are constructed on the sets of particle positions identified on separate frames; particles on one frame and the next are then paired based on the goodness-of-match between the shapes of their Voronoï cells and particle trajectories are reconstructed; velocities and are finally derived from the corresponding displacements using the straightforward approximation.

The 2D images are also used to estimate the 3D volumetric granular concentration c (also called solid fraction) near the wall. The point density of visible particles per unit image surface is a poor indicator of 3D concentration, due to the prevalence of occlusion effects. Instead, characteristics of the local particle arrangement can be exploited using the Voronoï diagram built on the particle centers. As the solid fraction rises, excluded volume effects tend to organize a dispersion of identical particles into an increasingly ordered assembly. A measure of this ordering is furnished by the *roundness* of the Voronoï polygons. However the estimation of granular concentration on the base of the analysis of a single 2D image for each instant of time, as it was carried out in the runs presented in the present paper, is still affected by some errors. In fact close to the free surface, where concentration is low and particles in the background may be wrongly recognized by the imaging technique as being near the sidewall, granular concentration can be overestimated. To avoid this kind of error and improve the quality of concentration estimation, future experiments will be carried out filming the flow domain from two different view-points, and applying the concentration estimation based on the stereoscopic Voronoï technique developed by Spinewine et al. (2003).

The typical data set for a single experimental run includes on the order of 100000 velocity vectors and Voronoï cell roundness measurements. This is one order of magnitude higher than the 10000 measurements identified by Louge & Jenkins (1997) as the minimum size needed to obtain statistically meaningful vertical profiles of granular temperature. Such large sample sizes are similar to those generated by computer simulations, and the same statistical techniques are needed to extract useful information. These include methods to characterize velocity correlations in time and space, as well as basic tools to derive average vertical profiles which we sketch in the next paragraphs.

4 EXPERIMENTAL RESULTS

4.1 *Determination of the intermittency*

In order to define the intermittency, it is necessary to determine a threshold value for the velocity fluctuation below which the regime is to be considered purely frictional and above which the regime is collisional.

Copyright © 2006 Taylor & Francis Group plc, London, UK

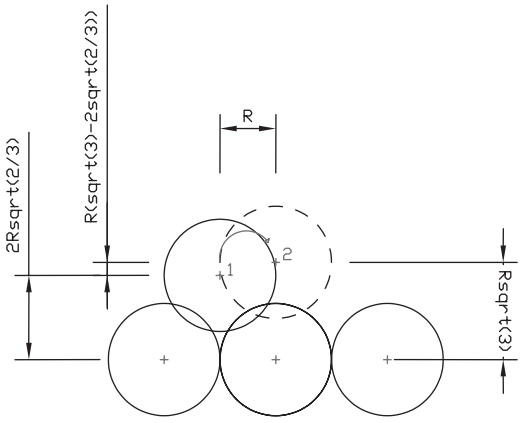


Figure 3. Sketch of the displacement of the center of a spherical particle rolling over an array of spheres of the same diameter.

A precise definition of such a value is very difficult, but a rough estimation of such threshold can be obtained considering a spherical particle rolling over a surface composed by spheres of the same diameter, along a line connecting the more depressed points.

In this case the vertical component of the fluctuating velocity is:

$$u'_y = \left(\sqrt{2} - \frac{4}{3}\right) D \frac{\partial u_x}{\partial y} \cong 0.081 D \frac{\partial u_x}{\partial y} \qquad (8)$$

The threshold value given by eq. (8) could be used to calculate the intermittency: the part of the signal where the fluctuation of velocity is lower than the value given by eq. (8) is considered to belong to the frictional regime, while on the contrary the part of the signal where the fluctuation of velocity is higher that the value given by eq. (8) is considered collisional. In this way it is possible to determine the intermittency function elaborating the signals according to eq. (7). The different functions (T, c, σ_p, τ_p) corresponding to the collisional regime have been calculated as mean values averaged only during the collisional times.

The value given by eq. (8) appeared to be too small to predict correctly the results. This is due to the fact that the particles are not perfectly ordered as it is shown in Figure 3. For example if the center of the particle is constrained to roll remaining in a vertical plane, as it reasonably occurs near the lateral wall of the flume, the coefficient in eq. (8) becomes $(\sqrt{3} - 3/2) \approx 0.232$.

A reasonable agreement between external stresses (equations 5 and 6) and the internal one (equations 1 and 2) calculated on the base of kinetic theories is obtained assuming the following threshold value for the fluctuating component of the velocity:

$$u'_y = 0.8 D \frac{\partial u_x}{\partial y} \qquad (9)$$

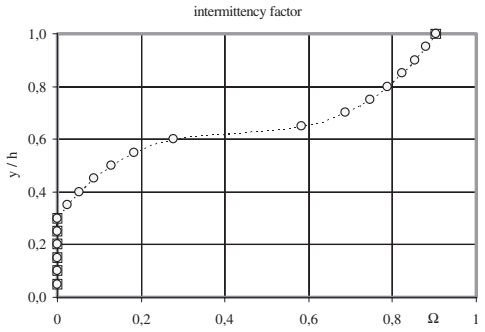


Figure 4. Profile of the intermittency function.

Equation (9) cannot be used when the collisional regime is fully developed, that is when $St = (1/18)\,\rho_p T^{1/2} D/\mu > 5 \div 10$, where St is the Stokes number (Larcher 2004; Armanini et al 2005).

In the next figure the profile of the intermittency function obtained in such a way is reported:

Figure 4 shows that the flow is dominated by the frictional regime in the lower part of the flow, while toward the free surface the collisional regime tends to prevail.

4.2 *Normal and tangential stresses*

As stated in paragraph 2.3, in uniform channel flow conditions external and internal stresses perfectly balance all along the depth. However due to the presence of the collisional regime just part of the flow is susceptible to be described by the kinetic theory: this portion is balanced by the external stresses reduced by the intermittency function:

$$c\rho_p \left(1 + r\frac{\rho_w}{\rho_p}\right)(1 + 4cg_o)T = \Omega \int_0^h \rho_w g \Delta c \cos\alpha \, dy + \sigma_o \qquad (10)$$

In eq. (10) a normal stress σ_o has been added on the free surface, because, otherwise, one should expect that the granular temperature vanishes on the free surface. However it is easy to argue that the free surface acts as a reflective surface for the temperature when the particle concentration in the layer near to the free surface is sufficiently high (*mature debris flow* regime according to Armanini et al. 2005). In this situation the particles reaching the free surface tend, due to inertia, to emerge. When the emersion starts, in fact, a new force appears (due to the reduction in the buoyancy force), which progressively pushes the particle in the downward direction. This effect, hydrodynamic resistance apart, gives to the free surface a reflective behavior.

Copyright © 2006 Taylor & Francis Group plc, London, UK

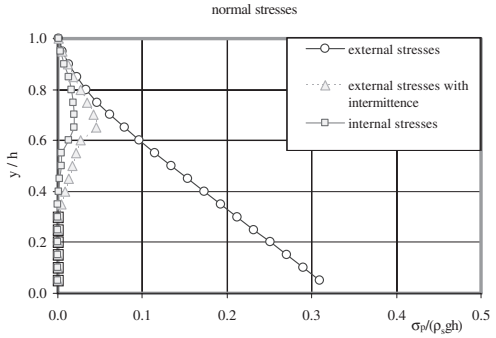


Figure 5. Distribution of normal stresses: internal, external and external reduced according to the collisional intermittency. The stresses are rendered dimensionless respect to $\rho_p gh$.

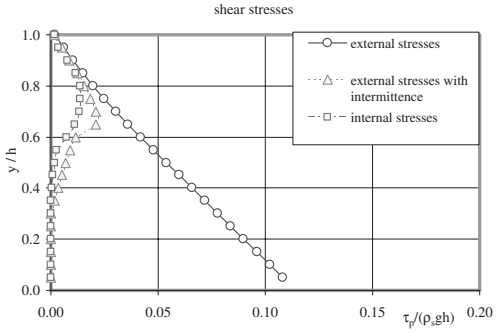


Figure 6. Distribution of tangential stresses: internal, external and external reduced according to the collisional intermittency. The stresses are rendered dimensionless respect to $\rho_p gh$.

In the next figure the distribution of external and internal normal stresses is reported, together with the external stresses reduced according to the intermittency.

From the figure it is first possible to appreciate the unbalance between the external stresses and the internal one, calculated according to the kinetic theory.

The distribution of the external stresses, reduced according to the collisional intermittency, is definitely in better agreement with the kinetic interparticles stress.

The same procedure has been repeated for the shear stresses.

Finally the distribution of particles concentration, granular temperature and particles longitudinal velocity has been calculated. The distributions are reported respectively in the next figures.

It is to be noted that the concentration tends to become smaller and smaller in the vicinity of the free

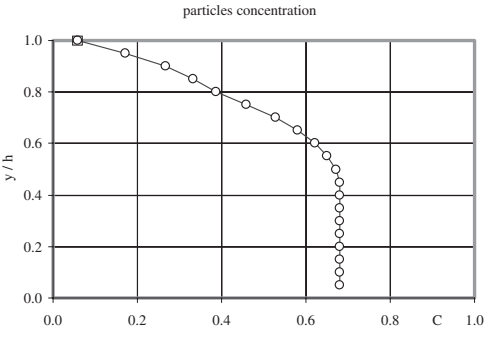


Figure 7. Distribution of the particles concentration.

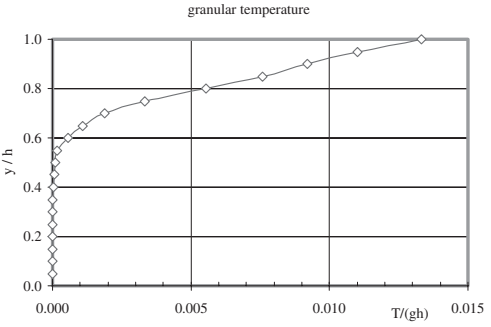


Figure 8. Distribution of the granular temperature dimensionless respect to gh.

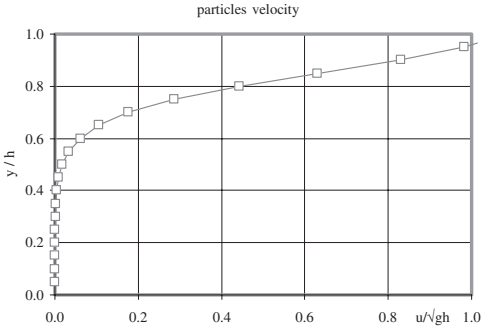


Figure 9. Distribution of the particles longitudinal velocity dimensionless respect to $\sqrt{gh}$.

surface, but apparently it remains finite on the surface (*mature debris flow* regime according to Armanini et al. 2005). However the precision of the measure of this parameter is relatively not high and the method here adopted is not precise especially in this position due to the reflective properties of the free surface.

Copyright © 2006 Taylor & Francis Group plc, London, UK

Future experiments will overcome the limits in concentration estimation thanks to the application of a stereoscopic imaging technique. In the tests with a smaller depth averaged concentration the concentration profile tends to zero at the free surface (*immature debris flow* regime according to Armanini et al. 2005).

On the contrary the granular temperature increases when approaching the free surface.

5 CONCLUSION

The experimental analysis of uniform liquid-granular channel flows in equilibrium gave evidence of the alternate presence of the frictional and of the collisional regime.

The problem was approached introducing an intermittency function based on geometric assumptions, able to take into account the alternation of the two rheological regimes.

The experimental analysis showed that the intermittency parameter, if appropriately calibrated, explains dynamics of granular particles as defined by kinetic theories.

Future developments of the investigation will benefit by a more accurate estimation of granular concentration thanks to the application of a stereoscopic imaging technique.

ACKNOWLEDGMENT

This research has been done thanks to the initial financial support of the center of excellence CUDAM (COFINLAB 2001) and within the activities promoted by the European Projects IMPACT (contract EVG1-CT-2001-00037) and IRASMOS (Specific Targeted Research Project No. 018412). The experimental analysis is part of the master thesis of Mrs. Anna Dalfollo and Mrs. Martina Piccoli, with them the authors are indebt for their help.

REFERENCES

Armanini, A., Capart, H., Fraccarollo, L. & Larcher M. 2005. Rheological stratification in experimental free-surface flows of granular–liquid mixtures. *J. Fluid Mech.* 532: 269–319.

Bagnold, R.A. 1954. Experiments on a gravity-free dispersion of large solid spheres in a Newtonian fluid under shear. *Proc. Roy. Soc. London A* 225: 49–63.

Capart, H., Young, D.L. & Zech, Y. 2002. Voronoï imaging methods for the measurement of granular flows. *Exp Fluids* 32: 121–135.

Carnahan, N.F. & Starling, K. 1969. Equations of state for non-attracting rigid spheres. *J. Chem. Phys*. 51: 635–636.

Dalfollo, A. & Piccoli, M. 2005. Analisi di laboratorio di moti granulari in acqua. *Master thesis in environmental engineering*, University of Trento.

Drake, T.G. 1990. Structural features in granular flows. *J. of Geophys. Res.* 19(3), 8681–8696.

Goldhirsch, I. 2003. Rapid granular flows. Annu. Rev. Fluid Mech. 35: 267–293.

Hinze, J.O. 1975. Turbulence. *McGraw-Hill series in mechanical engineering*. New York: McGraw-Hill.

Jenkins, J.T. & Hanes, D.M. 1998. Collisional sheet-flow of sediment driven by a turbulent fluid. *J. Fluid Mech*. 370: 29–52.

Larcher, M. (2004) Vertical structure of high concentration liquid-granular flows. *Monographs of the School of Doctoral Studies in Environmental Engineering*, Trento, vol. 2, 151. *http://www.ing.unitn.it/dica/eng/monographs/index.php*

Louge, M.Y. & Jenkins J.T. 1997. Microgravity segregation in binary mixtures of inelastic spheres driven by velocity fluctuation gradients. In Chang, C.S., Misra, A., Liang, R.Y. & Babic, M. (eds) *Mechanics of deformation and flow of particulate materials*, ASCE, 370–379.

Savage, S.B. 1984. The Mechanics of Rapid Granular Flows. *Advances in Applied Mechanics*, 24: 289–366.

Savage, S.B. 1998. Analyses of slow high-concentration flows of granular materials. *J. Fluid Mech*. 377: 1–26.

Spinewine B, Capart H, Larcher M & Zech Y 2003. Three-dimensional Voronoï imaging methods for the measurement of near-wall particulate flows. *Exp. Fluids* 34: 227–241.

Takahashi, T. 1991. Debris flow. *IAHR Monograph*. Rotterdam: Balkema.

Copyright © 2006 Taylor & Francis Group plc, London, UK

Morphological modelling of hyperconcentrated floods in the Yellow River

D.S. van Maren[a], J.C. Winterwerp[a], B.S. Wu[b] & J.J. Zhou[b]
[a]*Delft University of Technology, Faculty of Civil Engineering and Geosciences, The Netherlands and WL | delft hydraulics, MH Delft, The Netherlands*
[b]*Tsinghua University, Faculty of Hydraulic Engineering, Beijng, China*

ABSTRACT: A large amount of the total sediment load in the Chinese Yellow River is transported during hyperconcentrated floods. These floods are characterized by very high suspended sediment concentrations and rapid morphological changes with alternating sedimentation and erosion in the main channel, and persistent sedimentation on the floodplain. However, the physical mechanisms driving these hyperconcentrated foods are still poorly understood. Numerical modelling experiments of these floods reveal that sedimentation is largely caused by a collapse of the turbulence structure by sediment-induced density gradients, whereas erosion prevails when this sediment is largely held in suspension due to hindered settling. Observed patterns of erosion and sedimentation during these floods can be well reproduced using a numerical model in which sediment-induced density effects and hindered settling are included. Based on these results a refined definition of hyperconcentrated flow is proposed.

1 INTRODUCTION

The rivers that originate from the Chinese Loess Plateau carry huge amounts of suspended sediment, especially during hyperconcentrated floods when sediment concentrations exceed 100's kg m^{-3}. A large part of the sediment load carried by these rivers is deposited in their downstream reaches. As a result, the bed level of the downstream reaches of these rivers rises rapidly, and because they are confined by training works the height of river bed exceeds the surrounding land. The best known example is the Yellow River, where the river bed is up to 10 m higher than the adjacent areas. Most of this sediment is deposited during hyperconcentrated floods. However, some stages of these floods are characterized by severe erosion instead of deposition. When these floods are well understood and controlled (through water and sediment releasing reservoirs), siltation may be significantly reduced. The Sanmenxia reservoir, operational since 1961, has shown that water and sediment discharge can indeed be regulated to such an extent that it significantly affects downstream channel morphology. Recently, a new reservoir was completed 100 km downstream of the Sanmenxia reservoir to manage siltation and flooding in the lower Yellow River. However, prediction of the effect of different water- and sediment release strategies from this reservoir is limited because no sediment transport model exists today which can accurately simulate hyperconcentrated floods. Therefore a research project was initiated within the Programme of Scientific Alliances between China and the Netherlands, which aims to predictively model sediment transport and morphology in the Lower Yellow River. The purpose of the research presented in this paper is to analyze the morphologic behaviour of hyperconcentrated floods in the Yellow River using numerical model experiments.

2 HYPERCONCENTRATED FLOW

The high concentrations typical for the Yellow River influence both fluid and sediment dynamics significantly. Therefore a brief summary of sediment-fluid interactions is given first (see Winterwerp and van Kesteren (2004) for more details), followed by an overview of hyperconcentrated floods in the Yellow River.

2.1 *Sediment-fluid interactions in highly concentrated flow*

Even moderate concentrations of several g/l increase the density of the water-sediment mixture to such an extent that turbulence can be significantly damped by

Copyright © 2006 Taylor & Francis Group plc, London, UK

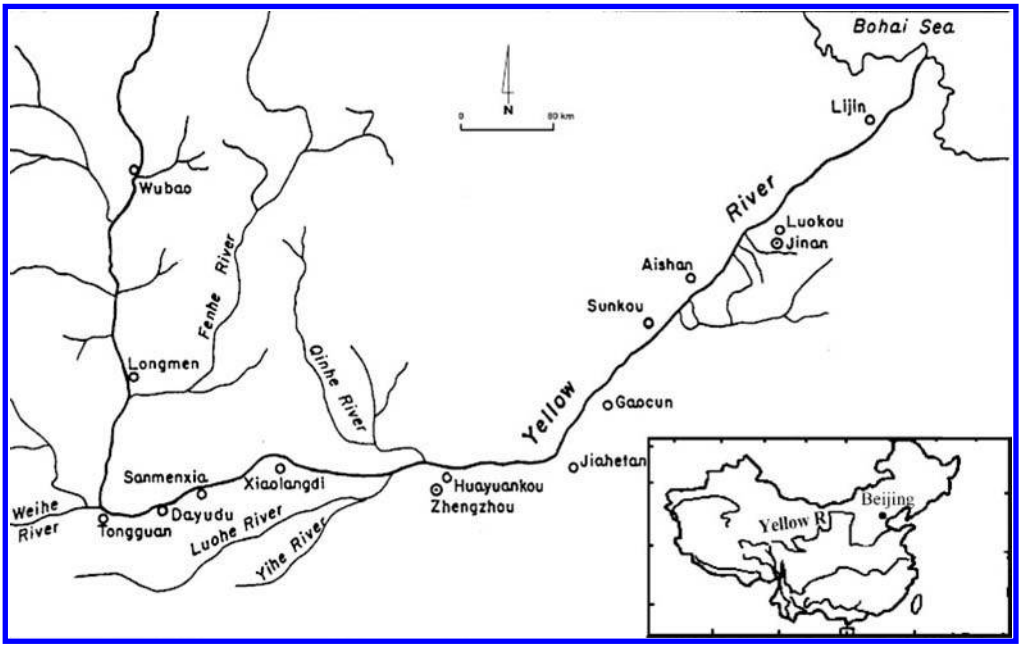


Figure 1. Middle and lower reaches of the Yellow River, China.

the vertical density gradients (Winterwerp 2001). This has two major consequences. The first is a reduced capacity of the flow to keep particles in suspension which, in turn, further increases the vertical density gradients. When the flow is close to saturation, this positive feedback mechanism results in a total collapse of the turbulence and concentration vertical. Secondly, suppression of turbulence leads to a decreasing vertical velocity gradient near-bottom. The velocity profile consequently changes from an almost logarithmic into a more linear profile.

In addition to these turbulence related effects, high sediment concentrations also (1) increase the fluid viscosity and introduce yield strength, (2) decrease the sediment settling velocity and erosion rate (hindered settling and hindered erosion, resp.), and (3) introduce soil mechanical effects such as liquefaction and undrained erosion.

2.2 *Hyperconcentrated floods in the Yellow River*

The Yellow River (Fig. 1) has a length of 5400 km and a basin area of 795,000 km^2. From 1940 to 1969, the average discharge Q in the lower Yellow River was 1630 m^3 s^{-1} transporting 1560 million ton annually. Although most of the water drained by the Yellow River originates in its upper reaches, 90% of the total sediment load is supplied by the highly erodible loess plateau. After flowing through the Sanmenxia gorge the river enters the flat North China Plain where massive amounts of sediment are deposited.

Hyperconcentrated floods are generated on the Loess Plateau by intense rainstorms of short duration (with peaks of 1400 mm in 9 hours; August 1977) which generally occur from half July to half August. For simplicity, floods are called hyperconcentrated here when the sediment concentration C exceeds a critical value around 200–300 kg m^{-3}. The grain size of loess varies between 15 μm in the south to 50 μm in the north, and contains 10–20% clay particles (Wan and Wang 1994). These sediments are easily eroded from the steep slopes resulting in extremely high concentrations, in the order of hundreds of kgm^{-3}. About 40 hyperconcentrated floods occurred between 1960 and 1992 at Longmen station (see Fig. 1), with an average duration of 8–12 days (Zhao et al. 1995). Approximately 1/3 to 1/4 of the annual sediment load of the Yellow River is transported during these hyperconcentrated floods (Wan and Wang 1994). Large floods may transport up to 900 million ton of sediment, which is close to the average annual sediment load.

During normal discharge conditions sedimentation occurs mainly in the river channel, but sedimentation during hyperconcentrated floods is more complicated. According to Li and Zhang (1994), sedimentation during a hyperconcentrated flood can be divided into three stages (see also Fig. 2):

1. The first stage of hyperconcentrated floods between Sanmenxia and Huayuankou is characterized by massive deposition up to several m in the main channel, especially in areas where the river channel

Copyright © 2006 Taylor & Francis Group plc, London, UK

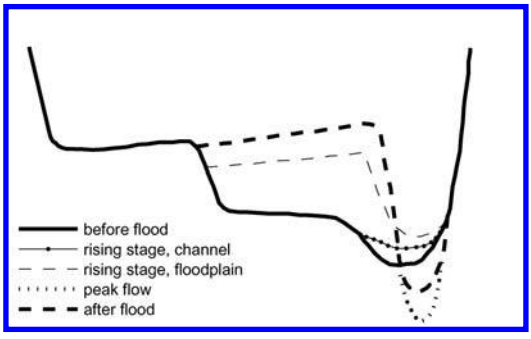


Figure 2. Schematized cross-sectional development during a hyperconcentrated flood.

is shallow and wide. Therefore the discharge capacity decreases, which results in (1) overflowing flood plains, and (2) a very rapid rise of water levels.

2. After the floodplain is flooded, most sediment is deposited on the floodplain, while channel deposition changes into erosion. The main channel erodes, narrows, and becomes more sinusoidal. Consequently, the flow velocity and discharge capacity increase, which in turn results in further channel erosion: the discharge capacity of a channel may double during the passage of a hyperconcentrated flood. Due to this increase in discharge capacity, the water level drops rapidly.
3. The longitudinal water level gradient decreases at the waning stage of the flood, flow velocities decrease, and sediment can no longer be held in suspension. This results in cataclysmic settling from suspension, and rapid deposition. The previously scoured channel is partly filled again, but scouring during stage 2 is larger than sedimentation during stage 3 resulting in net channel erosion during a hyperconcentrated flood.

2.3 *Observations*

Observations of hyperconcentrated floods are logistically complicated because of the high velocities and sediment concentrations. It is very difficult to take samples at these velocities, and most electronic devices are disturbed by the high concentrations. As a result, there is very few data available with a high spatial (both vertically and cross-sectionally) and temporal resolution. The most extensive data collection campaigns in the Yellow River have been carried out in the late 1950's and early 1960's, in order to asses the impact of an upstream dam which was completed in 1961. An example of measured flow velocity, sediment concentration, and grain size D_{50} during a highly concentrated flood in 1959 is shown in Fig. 3. This data shows that at flow velocities over 3 m/s, at a water

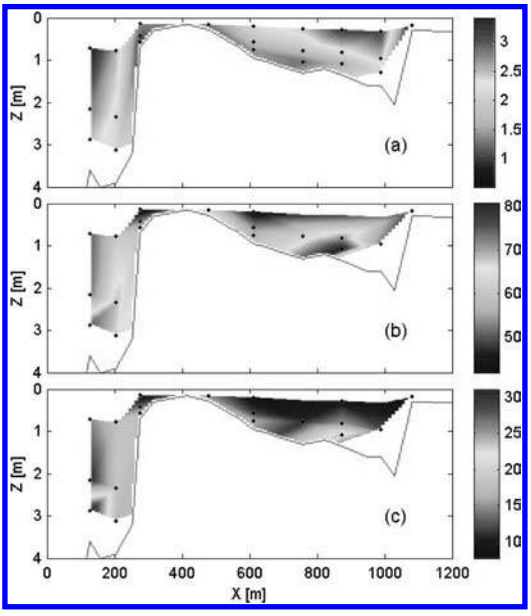


Figure 3. Flow velocity (a) sediment concentration (b, in kg/m^3) and D_{50} (c, in μm) measured at Laitongzai hydrological station (close to Huayuankou) on 15 August 1959.

depth of 1.5 to 3 m, the vertical concentration gradient is still very large. Considering the small grain size (10–25 μm), one would expect a better mixed sediment concentration profile. This is a strong indication that sediment-induced density effects play an important role, which will be analyzed in more detail using a numerical model.

3 MODELLING

3.1 *Model description*

In this study we use the state-of-the-art 'sediment online' version of the Delft3D model to simulate planform morphology development. Delft3D solves the unsteady shallow water equations in 2 or 3 dimensions under the hydrostatic pressure assumption and computes sediment transport and morphological update simultaneously with the flow; see Lesser et al. (2004) for a description and validation. This model simulates the most relevant sediment-fluid interactions described in section 2.1 such as hindered settling and sediment-induced density effects (Winterwerp and van Kessel 2003). This model has been applied previously to reproduce the effect of high sediment concentrations on channel patterns of sediment-laden rivers (van Maren et al. 2005).

Hindered settling is modelled as $w_s = w_0(1-\phi)^5$ (where w_0 is the particle fall velocity in clear water and

Copyright © 2006 Taylor & Francis Group plc, London, UK

w_s the fall velocity reduced by the volumetric sediment concentration ϕ which is given by $\phi = C/C_g$). The gelling concentration C_g is estimated to be 900 kg m^{-3} (see van Maren et al. (2005) for more details). The vertical sediment fluxes are determined by the uplift of sediment by turbulence, and by the downward motion of sediment through the sediment fall velocity w_s. Turbulence is approximately proportional to the cubed depth-averaged velocity. However, sediment-induced density gradients dampen this bed-generated turbulence, leading to a decreasing capacity of the flow to keep sediment in suspension. The turbulent energy k and the turbulent energy dissipation ϵ determine the vertical eddy viscosity ν through $\nu = c_\mu k^2/\epsilon$ (c_μ is a constant equal to 0.09). This eddy viscosity influences the vertical concentration gradients through the eddy diffusivity Γ by $\Gamma = \nu/\sigma_t$, where σ_t is the turbulent Prandtl-Schmidt number. A common assumption is that σ_t equals 0.7. However, Cellino and Graf (1999) observed in laboratory experiments that this value may be valid for clear water flows, but not to flows near sediment saturation when σ_t should be closer to 2 (note that these authors use the β factor common in sand transport studies). Recent numerical experiments by Winterwerp (ress) revealed that sediment-laden flow seems to be described more accurately using $\sigma_t = 2$. A higher Prandtl-Schmidt number reduces the sediment diffusivity Γ ($\Gamma = \nu/\sigma_t$), thereby increasing the vertical concentration gradient and therefore also the sediment-induced density gradients. In order to estimate the effect of σ_t, model runs are done with both 0.7 and 2.0.

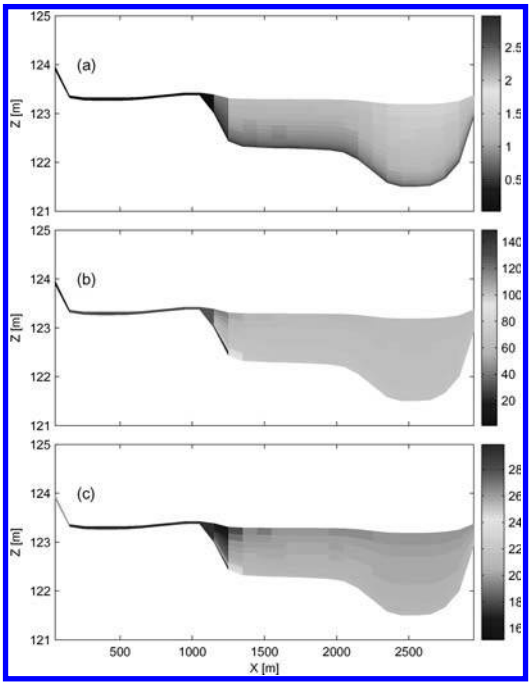


Figure 4. Computed flow velocity (a), sediment concentration (b, in kg/m^3) and D_{50} (c, in μm) during flow conditions similar to those in Fig. 3, using $\sigma_t = 0.7$, 10 km downstream the upper boundary.

3.2 *Model application*

A fundamental problem for modelling hyperconcentrated floods in the Yellow River is the absence of high resolution bathymetric and hydrodynamic data. Even during the extensive measurement campaigns in the late 1950's and early 1960's, there is very little hydrodynamic data required for calibration (such as flow velocity and concentration profiles) available shortly after bathymetric observations. And hydrodynamic data measured several months (or even weeks) after bed level measurements is not suitable for calibration because of the rapid morphologic changes in the Yellow River. As an alternative, we simulate the behaviour of a hyperconcentrated flood using an idealized river stretch. This idealized geometry is used for numerical experiments which should reproduce sediment erosion and deposition patterns similar to those observed in the Yellow River (Fig. 2).

Based on the initial profile in Fig. 2, an artificial river 3 km wide and 40 km long with a constant river cross-section is constructed. The bed level gradient decreases in the downstream direction, and is identical to that near Huayuankou. A time-varying river discharge and sediment concentration per fraction is prescribed at the upstream boundary, with 5 sediment fractions in total (5, 17.5, 37.5, 75, and 150 μm). The discharge and sediment concentration is derived from timeseries measured near Huayuankou in August 1959. The grain size distribution, however, is measured irregularly and therefore a single grain size distribution measured during the flood is used. The river bed is erodible, with an unlimited amount of sediment composed of the same 5 sediment fractions prescribed at the upstream boundary.

Three-dimensional transport of suspended sediment is calculated by solving the three-dimensional advection-diffusion equation for suspended sediment. Exchange of sediment between the bed and the water column is different for the 5 sediment fraction: for the coarse fraction (75 and 150 μm) this is computed with the standard van Rijn formulations (van Rijn 2000) whereas the Partheniades-Krone formulations (Partheniades 1965) are used for the fine sediment fractions (5, 17.5 and 37.5 μm). Critical shear stresses for both erosion and deposition are set to 1 Nm^{-2}, and the erosion rate is set to $5 \cdot 10^{-4}$ kg m^{-2} s^{-1}. The dry bulk density of fresh deposits is estimated at 700 kg m^{-3}.

Copyright © 2006 Taylor & Francis Group plc, London, UK

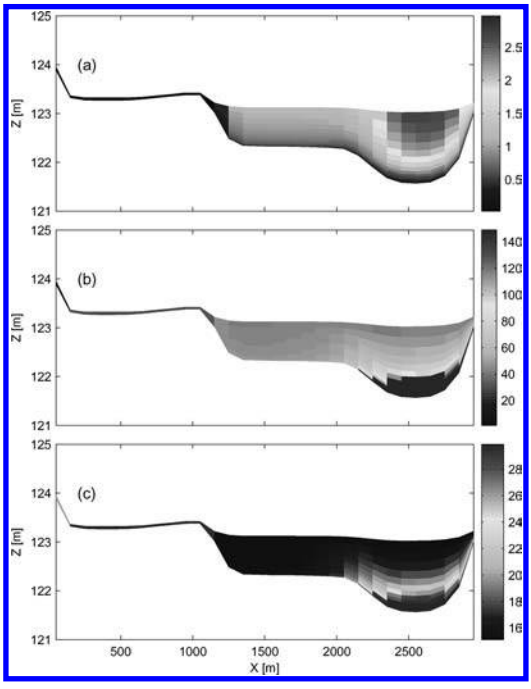


Figure 5. Computed flow velocity (a), sediment concentration (b, in kg/m^3) and D_{50} (c, in μm) during flow conditions similar to those in Fig. 3, using $\sigma_t = 2.0$, 10 km downstream the upper boundary.

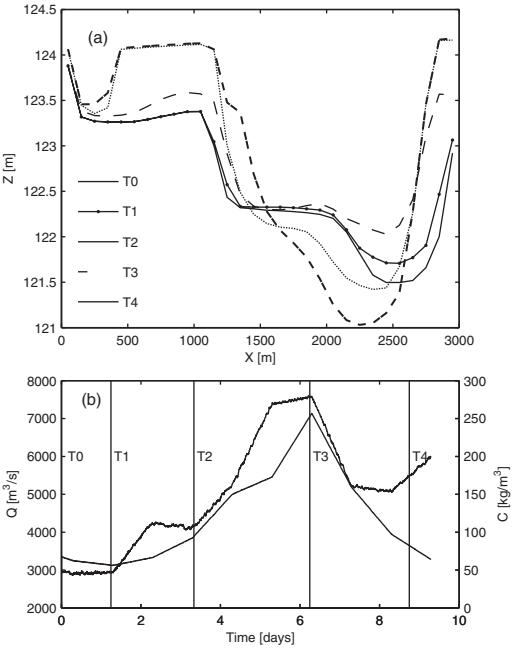


Figure 6. Computed cross-sectional bed level changes using $\sigma_t = 2.0$ and a grain size distribution typical for hyperconcentrated floods, 10 km downstream the upper boundary (a), with prescribed discharge Q (dashed line) and sediment concentration C (solid line) in (b).

3.3 *Model results*

An essential model setting required to simulate the morphodynamic behaviour of the Yellow River seems to be the turbulent Prandtl-Schmidt number σ_t. Using the default setting of 0.7, the sediment concentration profile remains almost vertically uniform (Fig. 4b). In contrast, using $\sigma_t = 2.0$ introduces large vertical gradient in the sediment concentration (Fig. 5b). These model results can be compared qualitatively with the observations in Fig. 3, as the discharge is almost the same. The measured vertical sediment distribution (both concentration C and the grain size D_{50}) is very similar to the computed sediment distribution using a high Prandtl-Schmidt number. Additionally, both measured (Fig. 3) and computed flow velocities using $\sigma_t = 2.0$ (Fig. 5a) have surface flow velocities close to 3 m/s whereas those in the model simulations using $\sigma_t = 0.7$ (Fig. 4a) are only 1.5 m/s. Additionally, sediment deposition rates are unrealistically low using $\sigma_t = 0.7$, while sedimentation rates in the Yellow River are high. We do not have sufficient information to determine the exact value of σ_t, but physical experiments by Cellino and Graf (1999) strongly indicate that σ_t should be closer to 2.0 for flows near saturation. Both Nielsen and Teakle (2004), using mixing length theory, and Nezu and Azuma (2004), using experimental results, conclude that σ_t increases in fine sediment flows with respect to clear water flow but decrease in coarse-grained flow. But although more research is required to determine the exact value (or relationship), $\sigma_t = 2.0$ seems more appropriate than $\sigma_t = 0.7$ for modelling high concentration flows in the Yellow River, and will therefore be used for further analysis.

Large vertical gradients in sediment concentration, such as those in Fig. 5b, damp turbulence and therewith the capacity of the flow to keep sediment in suspension, resulting in further settling (section 2.1). The result is a collapsing turbulence profile, and the effect on the sediment concentration depends on the settling velocity of the sediment in suspension. The sediment concentration profiles of coarse sediment fractions ($D_{50} >= 37.5$ μm) respond rapidly and settle from suspension, whereas the finer grain sizes respond more slowly. The water masses where the turbulence profile has collapsed are advected in the downstream direction, where the turbulence profile re-establishes due to a lower (especially coarse-grained) sediment load. The result is an oscillating sediment concentration, velocity and water level. Such an oscillating water level is occasionally observed in the Yellow River where it is known as clogging (Wan and Wang 1994).

Copyright © 2006 Taylor & Francis Group plc, London, UK

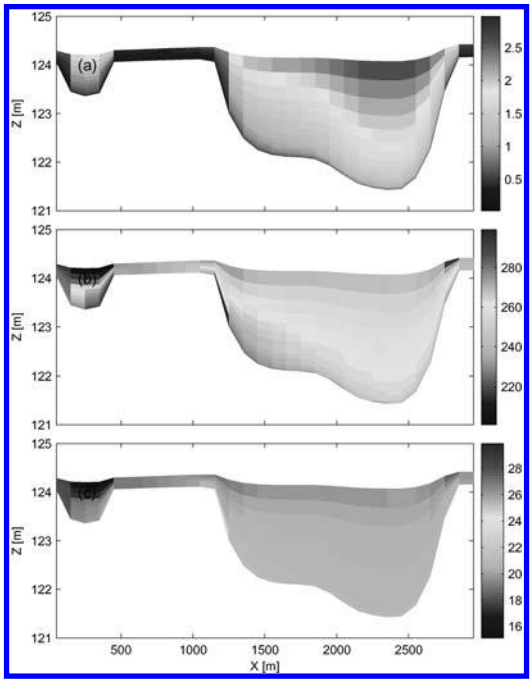


Figure 7. Computed flow velocity (a), sediment concentration (b, in kg/m^3) and D_{50} (c, in μm) during flow conditions T3 in Fig. 6, using $\sigma_t = 2.0$, 10 km downstream the upper boundary.

High near-bed sediment concentrations such as in 5b will probably result in rapid deposition. These conditions coincide with the first phase (T1) in Fig. 6, which do indeed show deposition in the channel. Deposition increases with increasing sediment concentration, which extend onto the floodplain when these are flooded (T2). During the following stage, sedimentation rates are high on the floodplain (nearly one meter in two days), while simultaneously the main channel is eroded. This erosion of the main channel is probably caused by increasing hindered settling with increasing sediment concentration: the sediment concentration profile is more uniform (Fig. 7) and therefore the turbulence does not collapse, thereby preventing the high near-bed sediment concentrations that lead to sediment deposition.

4 DISCUSSION

4.1 *Hyperconcentrated flood simulations*

The most characteristic morphodynamic properties of hyperconcentrated floods in the Yellow River, being channel sedimentation followed by floodplain sedimentation coinciding with channel erosion, are well reproduced. Computed velocity and concentration distributions and morphodynamic behaviour during hyperconcentrated floods show qualitative agreement with observations. During the first stage, collapse of the turbulence profile leads to rapid sedimentation in the main channel. As a result of the increasing river discharge, but also due to the reduced discharge capacity in the main channel, the flood plains are overflown. Sediment deposition rates on these flood plains are high due to the low flow velocities. With increasing upstream discharge and sediment concentration, the fall velocity decreases due to hindered settling effects. Less turbulent energy is therefore required to keep sediment in suspension, and therefore the sediment concentration profile in the main channel is re-established. The result is a deepening of the main channel, in agreement with observations. During the final stage of the flood, it is often observed that the main channel is partly refilled again. This is not reproduced by our model in which the river bed remained stable, even though the discharge conditions during the rising stage (when deposition occurred) and the falling stage of the flood are comparable (e.g. day 4 and day 8 in Fig. 6). To further quantify the exact mechanisms responsible for the transitions described above, and to understand the different morphological response during the rising stage and the falling stage of the flood, we use the stratified flow analogy introduced by Winterwerp (2001) and extended into the hyperconcentrated regime in Winterwerp et al. (2003).

The Ri_f number describes the ratio of potential energy required to keep sediment in suspension to the kinetic energy available to mix sediment, and can be written as:

$$Ri_f = \frac{g\overline{w'\rho'_m}}{\rho_m \overline{u'w'}\partial u/\partial z} \quad (1)$$

where $\overline{w'\rho'_m}$ is the fluctuating part of the vertical velocity w and the density of the water-sediment mixture ρ_m, averaged over the turbulent time scale, $\overline{u'w'}$ is the fluctuating part of w and the horizontal velocity u, averaged over the turbulent time scale, and $\partial u/\partial z$ is the horizontal velocity shear. $\overline{w'\rho'_m}$ can be replaced by $\frac{\rho_s - \rho_w}{\rho_s}\overline{w'c'}$ (with c being the sediment concentration, ρ_s the sediment density, and ρ_w the density of water). Assuming that

(1) the turbulent fluxes are related to the mean velocity gradient (the Boussinesq assumption; $\overline{u'w'} = \nu\frac{\partial u}{\partial z}$),
(2) the velocity profile is logarithmic ($\frac{\partial u}{\partial z} = \frac{u_*}{\kappa z}$ and the viscosity ν is $\nu = \kappa u_* z(1 - \frac{z}{h})$, where κ is the Von Karman constant),
(3) local equilibrium between settling and mixing ($\overline{w'c'} = -w_s C$), and
(4) hindered settling can be simplified as $w_s = w_0(1-\phi)^5$, eq. 1 can be simplified into

Copyright © 2006 Taylor & Francis Group plc, London, UK

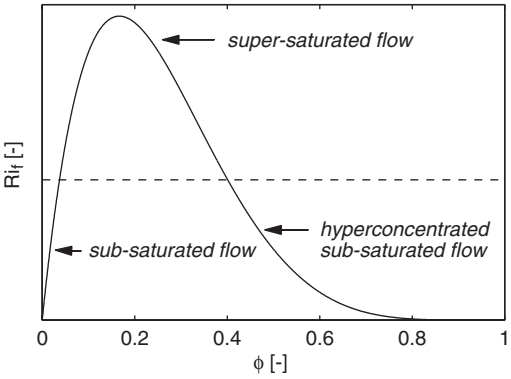


Figure 8. Relation between Ri_f and the volumetric sediment concentration ϕ (solid line); the critical Ri_f is denoted with a dashed line.

$$Ri_f = \alpha \frac{\rho_s - \rho_w}{\rho_m \rho_s} \frac{ghw_0 C\kappa}{u_*^3}(1-\phi)^5 \qquad (2)$$

where α is a coefficient. This expression is valid for sub-saturated conditions, which provides a good starting point to address the problem. For a constant velocity and water depth, Ri_f initially increases with sediment concentration (Fig. 8) At a certain concentration, the turbulent production is damped out by the sediment-induced density gradient. For cohesive sediments, this results in a catastrophic collapse of the turbulence and concentration vertical (Winterwerp 2001), and the sub-saturated flow becomes super-saturated. When the concentration increases further to the point that sediment is held in suspension by hindered settling, a vertical concentration profile is re-established; the supersaturated flow becomes hyperconcentrated sub-saturated (Winterwerp et al. 2003).

Examining Eq. 2, the transition from supersaturated to (hyperconcentrated) sub-saturated flow depends not only on the sediment concentration C, but also on a number of other parameters such as the grain size D_{50} (determining the value of w_0), flow velocity, water depth and gelling concentration C_g. With a decrease in water depth and an increase in flow velocity, the flow becomes hyperconcentrated at lower volumetric sediment concentration ϕ. Similarly, the higher D_{50}, the higher w_0 and therefore Ri_f, and as a result the flow becomes hyperconcentrated at lower ϕ when D_{50} decreases. In addition, the value of ϕ depends not only on the sediment concentration C but also on the gelling concentration C_g (the concentration at which a space-filling network forms). The value for C_g varies between several 10's of kgm^{-3} in cohesive sediment to approximately 1500 kgm^{-3} in sand ($C_g = (1-n)\rho_s$, with the porosity n being approximately 0.45). Therefore ϕ depends on both the sediment concentration, and the amount of cohesive sediment. Based on these considerations, hyperconcentrated flow is therefore a highly concentrated flow where hindered settling effects become so important that sediment can be held in suspension at very low turbulence rates, and occur at a sediment concentration value that exceeds a critical sediment concentration scaling with $1/u^3$, h, D_{50}, and C_g.

The mechanisms described above allow a more physical interpretation of the model results. Sedimentation turned into erosion during the rising stage of the flood because of increasing sediment concentration and flow velocity. The extensive morphologic changes significantly narrowed the main channel, thereby increasing the flow velocities. As a result sedimentation as occurring during the rising stage of the flood, does not occur during the falling stage.

4.2 *Classification of hyperconcentrated flow*

Flows with high sediment concentrations are usually classified according to (1) the triggering mechanism, (2) the sediment concentration, and (3) the rheological and kinematical behaviour (Bradley and McCutcheon 1987). Classifications using the triggering mechanism is mainly limited to lahars, mud flows, debris flows, landslides, debris slides and other type of mass movements. These type of flows occur on steep slopes as a result of excessive rainfall or volcanic eruptions, and are therefore not relevant for channel flow.

Authors that classify sediment-laden flow by sediment concentration usually discern normal flow, hyperconcentrated flow, and mass movements (debris flow, mud flow, and landslides); see e.g. Bradley and McCutcheon (1987) and Costa (1988). Within these classification schemes, the transition between hyperconcentrated flow and higher-concentration flows varies widely. However, since we are concerned with channel flow, our main interest lies in the transition from normal flow to hyperconcentrated flow. Within the commonly applied classification schemes this transition is around $\phi = 0.2$ (Costa (1988) and Bradley and McCutcheon (1987)). Though this classification scheme seems better than the triggering mechanism, it still seems insufficient. Therefore the kinematic behaviour (Newtonian or non-Newtonian flow) has been used, in addition to concentration, as a qualitative measure to distinguish different flow types. The primary mechanism affecting particle support (turbulence, viscosity and buoyancy) may also be important to distinguish different flow types but have only been used very qualitatively. This explains why there is no general consensus on the transitions between normal flow and hyperconcentrated flow. A reason for this may be that here does not seem to be a clear definition of

Copyright © 2006 Taylor & Francis Group plc, London, UK

hyperconcentrated flow. Some authors have defined a hyperconcentrated flow, being:

- 'A highly sediment-laden flow in which the presence of fine sediments materially affects fluid properties and bed material transport compared with the flow without any appreciable quantity of fine sediments' (Julien 1989).
- 'A more or less uniform flow with a high suspended fine-material concentration and a viscosity larger than that of water: coarse sediment may be transported as bed load' (Rickenman 1992).

A description of hyperconcentrated flow without giving a strict definition is more common, some of which can be summarized as:

- A fluid with a logarithmic velocity distribution and a turbulent structure to suspend sediments, a concentration ϕ larger than 0.4, and a certain amount of fine silt and clay (Brush 1989).
- A two-phase turbulent flow that has a sediment concentration C over 300–400 $\mathrm{kgm^{-3}}$, with sediment finer than 0.01 mm being part of the liquid phase, and coarser sediment being the solid phase (Xu 1999).
- A two-phase flow where small-scale turbulence is almost non-existent. When the sediment load is partly cohesive and the sediment concentration high then the fluid is a Bingham fluid, whereas the fluid is non-Newtonian when sediment concentrations are too low or there is no cohesive sediment fraction. The flow can be turbulent, with a logarithmic velocity profile, and laminar, with a uniform velocity profile (Chien and Wan 1998).
- A pseudo-one phase flow of which the fluid properties are considerably affected by sediment carried by the flow. The flow becomes hyperconcentrated at a concentration around 200 $\mathrm{kg\,m^{-3}}$ ($\phi = 0.08$), although this transition is additionally regulated by grain size composition and mineral content (Wan and Wang 1994).

The transition from normal flow to hyperconcentrated flow is associated with a transition from deposition to scouring (Xu 2004). Several attempts have been made to relate the beginning of bed scour (and thus hyperconcentrated flow) to discharge Q or sediment concentration C. Between Aishan and Lijin, for instance, scouring begins when $Q > 1800\,\mathrm{m^3\,s^{-1}}$ whereas sediment is deposited when $Q < 1800\,\mathrm{m^3\,s^{-1}}$ (Wang and Liang 2000). The transition occurs during higher discharges according to Qi (1997): $Q = 3000\,\mathrm{m^3\,s^{-1}}$ in the meandering reach (corresponding to a flow velocity u of 1.9 $\mathrm{ms^{-1}}$) and $Q = 4000\,\mathrm{m^3\,s^{-1}}$ in the braided reach; there is no relation with sediment concentration C. Alternatively, the transition between deposition and erosion in hyperconcentrated floods depends on C and not on Q according to Xu (2004), the concentration C at which the flow becomes hyperconcentrated varies between 200 $\mathrm{kg\,m^{-3}}$ in fine-grained rivers (the Yellow River at Tonguan) and 600 $\mathrm{kg\,m^{-3}}$ in coarser tributaries. If we analyze Eq. 2, however, it is obvious that there cannot be a single discharge, velocity, or sediment concentration at which hyperconcentration, and thereby bed scour, is to be expected.

It can therefore be concluded that there is no clear and widely accepted definition of hyperconcentrated flow. However, numerical modelling experiments using the same basic fluid mechanical theory common for stratified flow produces morphological results in close agreement with observed morphodynamics. We therefore propose that the sub-saturated hyperconcentrated regime (Fig. 8), as defined by the flux Richardson number, can be used to quantify the transition from normal flow to hyperconcentrated flow. This then allows the formulation of a more quantitatively founded definition of hyperconcentrated flow. Hyperconcentrated flow may be defined as a sediment-laden flow in which the vertically homogeneous concentration profile is strongly affected by hindered settling and can be maintained at low turbulence rates, when the sediment concentration exceeds a critical sediment concentration which increases with the water depth, the grain size and gelling concentration and decreases with the cubed flow velocity. Although hyperconcentration therefore preferentially develops in shallow, high-velocity flows carrying fine (partly cohesive) sediments, it may also occur at higher sediment concentrations in deeper channels without a cohesive sediment fraction. When the sediment load is partly cohesive, then the fluid may be non-Newtonian, characterized by increased viscosity, yield strength, and laminar or plug flow. We then have to introduce a second non-dimensional parameter, the effective Reynolds number. This is subject of our further research.

5 CONCLUSIONS

Hyperconcentrated floods, such as those in the Yellow River, are hydrodynamically complex and characterized by rapid morphologic changes. Because of their complex nature, they are still poorly understood. A numerical model based on the standard Delft3D flow model reproduces these complex hydrodynamics and morphodynamics satisfactory. The most important mechanisms are collapse of the turbulence structure due to sediment-induced density gradients leading to deposition, and re-establishment of this profile due to hindered settling, leading to erosion of the bed.

Hyperconcentrated flows have a large spread in grain size, water depth, flow velocity, concentration, and gelling concentration, and may be Newtonian as well as non-Newtonian, turbulent as well as laminar,

Copyright © 2006 Taylor & Francis Group plc, London, UK

two-phase as well as one-phase, and may contain cohesive sediment, but can also be non-cohesive. But despite these differences, they have in common that sediment can be kept in suspension at low turbulence rates due to hindered settling hindered settling. This can be quantified with Ri_f number, and we propose to distinguish hyperconcentrated flow from non-hyperconcentrated flow through Ri_f.

ACKNOWLEDGEMENTS

This work is part of the project 'Predictive Morphological Modelling of the Lower Yellow River', financed by the Dutch Royal Academy of Sciences (KNAW) and the Chinese Ministry of Science and Technology within the framework of the Programme of Scientific Alliances between China and the Netherlands.

REFERENCES

Bradley, J. B. and S. C. McCutcheon (1987). Influence of large suspended-sediment concentrations in rivers. In C. R. Thorne, J. C. Bathurst, and R. D. Hey (Eds.), *Sediment transport in grave-bed rivers*, pp. 645–674. Wiley, Chichester.

Brush, L. M. (1989). Wash load, autosuspensions and hyperconcentrations. *In: L. M. Brush, M. G. Wolman and B. W. Huang, Taming the Yellow River: silt and floods, Kluwer Academic Publishers, Dordrecht*, 31–44.

Cellino, M. and W. H. Graf (1999). Sediment-laden flow in open-channels under noncapacity and capacity conditions. *Journal of Hydraulic Engineering 125*(5), 456–562.

Chien, N. and Z. H. Wan (1998). *Mechanics of sediment transport*. ASCE press, Reston, Virginia, 913 p.

Costa, J. E. (1988). Rheologic, Geomorphic, and sedimentologic differentiation of water floods, hyperconcentrated flows, and debris flows. In V. R. Baker, R. C. Koche, and P. C. Patton (Eds.), *Flood Geomorphology*, pp. 113–122. Wiley, New York.

Julien, P. Y. (1989). Laboratory analysis of hyperconcentrations. In S. S. Y. Wang (Ed.), *Proc. of the Intern. Symp. on sediment transport modelling, New Orleans, Louisiana*, pp. 681–686. ASCE, New York.

Lesser, G. R., J. A. Roelvink, J. A. T. M. van Kester, and G. S. Stelling (2004). Development and validation of a three-dimensional morphological model. *Coastal Engineering 51*, 883–915.

Li, Y. and X. Zhang (1994). On some abnormal phenomena during hyperconcentrated floods in the lower Yellow River. *International Journal of Sediment Research 9*(2), 30–38.

Nezu, I. and R. Azuma (2004). Turbulence characteristics and interaction between particles and fluid in particle-laden open channel flows. *Journal of Hydraulic Engineering 130*(10), 988–1001.

Nielsen, P. and I. A. L. Teakle (2004). Turbulent diffusion of momentum and suspended particles: A finite-mixing-length theory. *Physics of fluids 16*(7), 2342–2348.

Partheniades, E. (1965). Erosion and deposition of cohesive soils. *Journal of the Hydraulic Division, ASCE 91*(HY1), 105–139.

Qi, P. (1997). Effect of perennial sediment regulation in Xiaolangdi reservoir on reduction of deposition in the lower Yellow River. *International Journal of Sediment Research 12*(2), 58–67.

Rickenman, D. (1992). Hyperconcentrated flow and sediment transport at steep slopes. *Journal of Hydraulic Engineering 117*(11), 1419–1439.

van Maren, D. S., J. C. Winterwerp, H. J. de Vriend, Z. B. Wang, Z.-Y. Wang, J. J. Zhou and B. Wu (2005). Sediment-induced density effects on channel patterns of silt-laden rivers. *Proc. of the 2nd Int. Yellow River Forum on River Basin Management, Zhengzhou, China*.

van Rijn, L. C. (2000). General view on sand transport by currents and waves: data analysis and engineering modelling for uniform and graded sand (TRANSPOR 2000 and CROSMOR 2000 models). Technical Report Z2899.20, Delft Hydraulics.

Wan, Z. and Z. Wang (1994). *Hyperconcentrated flow*. IAHR monograph series, Balkema, Rotterdam, The Netherlands, 230 pp.

Wang, Z. Y. and Z. Y. Liang (2000). Dynamic characteristics of the Yellow River mouth. *Earth Surface Processes and Landforms 25*, 765–782.

Winterwerp, J. C. (2001). Stratification effects by cohesive and non-cohesive sediment. *Journal of Geophysical Research 106*(C10), 22.559–22.574.

Winterwerp, J. C. (in press). *Stratification effects by fine suspended sediment at low, medium and very high concentrations*. *Journal of Geophysical Research*.

Winterwerp, J. C., H. J. de Vriend and Z. B. Wang (2003). Fluid-sediment interactions in silt-laden flow. *Proc. of the 1st Int. Yellow River Forum on River Basin Management, Zhengzhou, China Vol. II*, 351–362.

Winterwerp, J. C. and T. van Kessel (2003). Siltation by sediment-induced density currents. *Ocean Dynamics 53*, 186–196.

Winterwerp, J. C. and W. G. M. van Kesteren (2004). Introduction to the physics of cohesive sediment in the marine environment. *Developments in Sedimentology 56, Elsevier, Amsterdam, the Netherlands, 466 p*.

Xu, J. (1999). Erosion caused by hyperconcentrated flow on the loess plateau of China. *Catena 36*, 1–19.

Xu, J. (2004). Double thresholds in scour-fill processes and some implications in channel adjustment. *Geomorphology 57*, 321–330.

Zhao, Y., X. Pan and Z. Fan (1995). Water and sediment inflow of hyperconcentrated floods and the associated channel aggradation in the Yellow River. *International Journal of Sediment Research 10*(1), 69–82.

Copyright © 2006 Taylor & Francis Group plc, London, UK

Fluctuations in surface granular flow via a PIV-edge detection technique

D. Berzi, L. La Rosa, S. Malavasi & A. Radice
Politecnico di Milano, Department of I.I.A.R., Milano, Italy

ABSTRACT: Some preliminary results of laboratory experiments concerning uniform dry granular flow are presented. Experimental set-up is composed of a rotating drum partially filled with homogeneous granular material. Literature studies showed that two distinctive flow regions develop: an active superficial layer and a plug flow. In this work, the fluctuating behaviour of the slope of the free surface and of the position of the inversion point, localized near the interface between the active layer and the plug flow, is investigated. The time evolution of these quantities is provided by image processing (an edge detection procedure and a Particle Image Velocimetry technique). The analysis of the Probability Density Function of the depth h where the flow changes its direction has allowed for assessing the validity also in the quasi-2D rotating drum configuration of the theories by Jop et al. (2005) and by Berzi & Larcan (2006) on the dense granular flow of cohesionless material. The fluctuating values of h, probably due to the existence of clusters in the flow field, are indeed limited when the theoretical value of the depth of the active layer is close to the mean temporal value of h.

1 INTRODUCTION

Many works in the last years focused on the uniform dry granular flow of cohesionless particles, by making use of both numerical and physical experiments (Pouliquen 1999, Ancey 2001, GDR MiDi 2004). The analysis of such flows is a basic step towards a deeper understanding of the dynamics of the grains and is needed in order to define constitutive models for the normal and the shear stresses relative to the disperse phase of a solid-liquid mixture (e.g., debris flow). Focusing on uniform dry granular flow allows clearly to simplify the problem because it is possible to disregard all the phenomena affecting the dynamics of the granular medium (convective and local accelerations, electrostatic and cohesive effects, influence of the continuous phase on the motion of the grains) except for the particles interaction and, in some cases, the gravity.

Among all the possible experimental configurations which allow to obtain the uniform flow condition, the heap flow and the flow in a partially filled rotating drum have the distinctive feature that a granular flowing layer develops over a mobile bed of the same grains (GDR MiDi 2004). At the bed both the shear rate and the velocity vanish. Thus, no particular boundary condition is needed for taking into account the possibility of slip velocity at the walls like in the case of flow over fixed bed (Jenkins & Richman, 1986).

Previous works (Boateng & Barr 1997, Orpe & Khakhar 2001, Jain et al. 2004) have shown that when a drum partially filled with granular material rotates at constant angular velocity, the flow field can be divided into two basic regions (figure 1). In the upper part of the granular medium there is a semi-lunar active layer where the solid volume fraction is less than the static value and the grains behave like a fluid. In the lower part of the granular medium, instead, there is a plug flow region where the grains move rigidly with the tumbler along circular trajectories. The interface between these two regions is located where the velocity, evaluated in a frame of reference rotating solidly with the apparatus, vanishes. If the frame of reference is not taken rotating solidly with the apparatus, instead, an inversion of the flow can be localized in the proximity of the interface between the active layer and the plug flow and can provide useful information about the fluctuating behaviour of the flow field near to the mobile bed.

The aforementioned literature works showed that there is a diametric cross-section of the flow, perpendicular to the free surface of the granular medium, where the particle trajectories in the active layer are sensibly rectilinear, like in a uniform flow. While the dependence of some time-averaged quantities (i.e., velocity, solid volume fraction, temperature) relative to this section on the experimental control parameters has been discussed in other works (Boateng & Barr 1997, Orpe & Khakhar 2001, GDR MiDi 2004), the time evolution of these variables has received much less attention.

Copyright © 2006 Taylor & Francis Group plc, London, UK

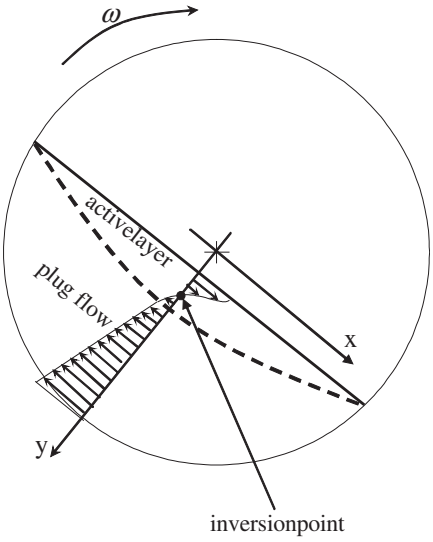


Figure 1. Sketch of the geometry in the rotating drum configuration.

The goal of this paper is to investigate the temporal variations of the position along the y-axis of figure 1 of the free surface and of the inversion point, obtained through two image analysis techniques.

The paper is organized as following. In §2 the experimental set-up is introduced and in §3 a description of the image processing techniques is given. In §4 the experimental results are shown and a possible interpretation is provided on the basis of the theoretical solution of a slow and dense uniform granular flow between smooth sidewalls (Jop et al. 2005, Berzi & Larcan 2006). Finally, some conclusions are given in §5.

2 EXPERIMENTAL SET-UP

The experimental set-up (figure 2) consists of a cylinder (inner diameter $D = 1$ m and axial length $W = 250$ mm), which is mounted on a pair of friction rollers and rotates around its axis at a constant angular velocity ω in the range $3 \div 14$ rpm. One of the endplates of the cylinder is made of a 10 mm thick glass to allow for optical measurements, while the other one is made of steel.

The drum is partially filled with a homogenous cohesionless granular material composed of extruded plastic grains of density $\rho_s = 1164\,\mathrm{kg/m^3}$, median diameter $d_{50} = 2.5$ mm and static friction angle $\phi = 27.6°$. The friction angle between the plastic beads and the glass wall and between the plastic beads and the steel wall has approximately the same value ($\delta = 26°$).

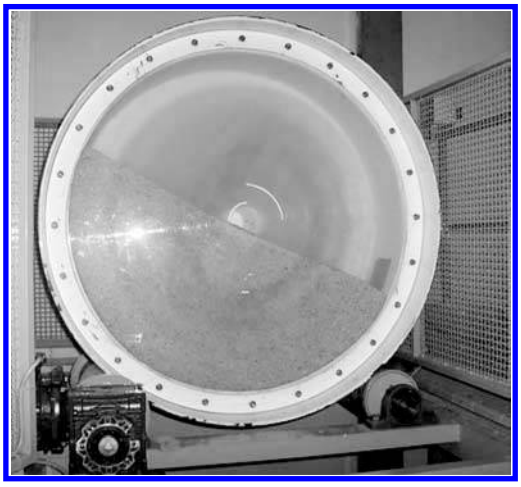


Figure 2. Experimental set-up. Thick rectangle highlights the zone filmed by the CCD.

The results of two experiments, in the following called experiment A and B, characterized by an angular velocity ω respectively equal to 4 rpm and 8 rpm, are presented. Both the experiments have been carried out with the 48% of the volume of the drum filled with the granular material.

A progressive CCD scan-camera was used to record the two-dimensional motion of granular material, with the resulting images stored digitally on processor boards within the camera. The glass wall of the tumbler was illuminated by an halogen lamp to give uniform illumination. In this arrangement monochromatic images with a resolution of 763×576 pixel are grabbed at a frame-rate of 50 Hz for a time interval of 20 s. The shutter time of the video-camera was 1/10000 s. The camera optics zoomed in correspondence with the mid-section of the active layer, where the flow can be considered nearly uniform, to capture a region of about 15×10 cm (figure 2).

3 IMAGE PROCESSING

3.1 *Edge detection*

The free surface of the granular material in the rotating drum was individuated automatically by applying an edge detection procedure to each acquired image. An adequate contrast between the dark background and the light particles was set-up by painting black the rear endplate of the drum.

Typically, edge detection algorithms search for edges in an image as the locations where the intensity gradient is larger than a certain threshold.

Here, the edge detection method proposed by Canny (1986) and implemented in MatLab® is used. As many

Copyright © 2006 Taylor & Francis Group plc, London, UK

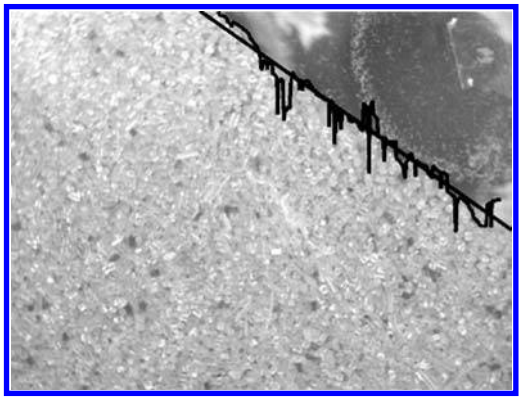


Figure 3. Free surface as evaluated via the edge detection technique. Both edge points and linear interpolation are presented.

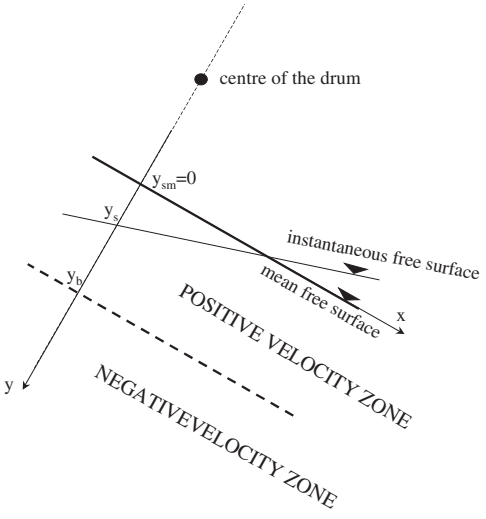


Figure 4. Sketch of the geometry adopted to measure the position of the instantaneous free surface.

other edge detection algorithms, just one calculation parameter has to be set by the operator, i.e. the threshold value of intensity gradient over which a pixel should be considered part of an edge. Given the contrast between the sediments and the black background, the threshold value was set equal to 0.185.

After individuating the edge points in an image, the free surface was determined by linear interpolation. An example of the instantaneous free surface is presented in figure 3.

The x-axis of the fixed frame of reference is taken along the mean free surface, calculated from the sample of the instantaneous ones (figure 4). The y-axis is taken as the orthogonal axis passing for the centre

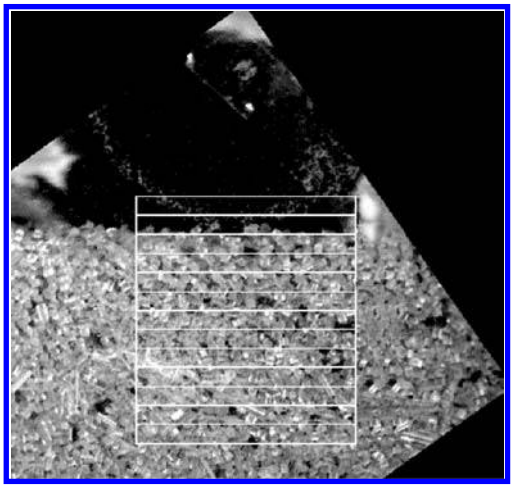


Figure 5. Measuring grid for PIV, experiment A.

of the drum. The coordinate y_{sm} of the average free surface is by definition zero.

In this configuration, the position y_s of the instantaneous free surface was determined as the intersection between the equation of the instantaneous approximately planar free surface and the aforementioned y-axis (see figure 4 for more details).

3.2 *Particle Image Velocimetry*

Velocities in the granular medium were measured by means of a PIV algorithm, derived from that successfully used by Radice et al. (2004) for measurement of sediment velocity in local scour.

An instantaneous velocity field was calculated from two consecutive frames of a movie, namely $F1$ and $F2$. First, the images were rotated in order to make the free surface horizontal; the rotation angle was determined as the mean slope measured by the edge detection technique described above. After contrast enhancing the images were divided into cells of inspection, whose dimensions were 7 cm in the flow direction and 1.8 cm in the orthogonal one. A 30% overlap was used along the y-axis. The upper limit of the measuring grid was located at $y = -0.6$ cm. Figure 5 shows an example of the measuring grid.

On the basis of the expected maximum velocities a limit on the longitudinal and transversal velocities is fixed, before the calculation, respectively equal to 80 cm/s and to 27 cm/s. Then, maximum pixel displacements between two consecutive frames were calculated by knowing the sampling frequency of the CCD and the pixel/cm correspondence C. All the possible pixel displacements within the imposed limits were considered; for each displacement (dx, dy) an interrogation and a target window could be

Copyright © 2006 Taylor & Francis Group plc, London, UK

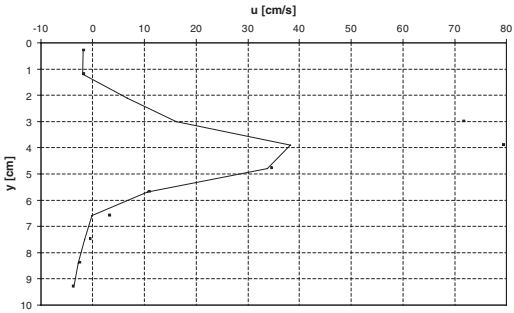


Figure 6. Typical results of PIV measurements. (■, instantaneous velocity profile; —, average velocity profile). Profiles for experiment A are presented.

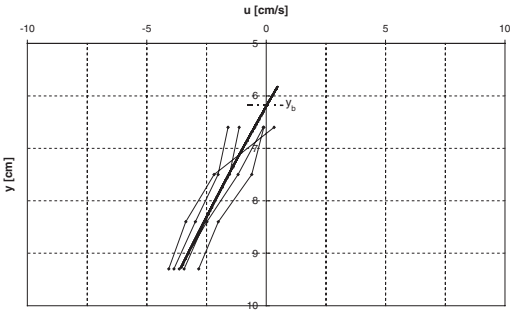


Figure 7. Example of inversion point determination (—, instantaneous velocity profiles; __, parabolic interpolation of the average profile in the plug flow layer). Profiles for experiment A are presented.

fitted within the inspection cell. The most probable movement (dx_m, dy_m) maximizes the parameter:

$$S = \frac{p_x\, p_y}{\sum_{i=1}^{p_x}\sum_{j=1}^{p_y}\left|F_1(i,j) - F_2(i+dx, j+dy)\right|} \quad (1)$$

where p_x and p_y are the pixel dimensions along x and y of the interrogation and target windows, respectively. The velocity components along the x and y directions could then be computed as $u = dx_m/(dt \cdot C)$ and $v = dy_m/(dt \cdot C)$, dt being the inverse of the frame frequency.

Reliability of computed vectors was evaluated by calculating the ratio between the maximum and the average values of S. Vectors were eliminated if this ratio was less than 1.1.

Figure 6 presents the result of a single measurement of the velocity profile in the active layer. Granular velocity in the bottom plug flow is well measured; on the contrary, measurement quality decades as the active layer is considered, probably due to bad reflecting properties of our sediments. In the proximity of the free surface measured velocity is negative, that is physically unsound. Also the time average velocity profile is presented in figure 6.

3.3 *Inversion point determination*

Presented results on velocity measurement showed that was possible to measure velocity in the reverse plug flow, even if velocity determination was still unsatisfactory as the free surface was approached. The negative velocity values in the bottom layer have been used to determine the position of the inversion point, i.e. the coordinate y_b with zero velocity depicted in figure 4.

First, five consecutive instantaneous velocity profiles were averaged; next, a parabolic equation was fitted to the average velocity profile near to the plug flow zone to determine the inversion point. Figure 7 presents the example of one calculation: the five instantaneous velocity profiles are shown in grey, while the parabolic interpolation of the velocity profile is in black; the latter allows determining the value of $y_b = 6.2$ cm.

Repetition of the described procedure for all the instantaneous velocity profiles leaded to the final time series of the inversion point.

4 EXPERIMENTAL RESULTS AND DISCUSSION

Figure 8 shows an example of the time evolution of the surface slope θ concerning both experiment A ($\omega = 4$ rpm) and B ($\omega = 8$ rpm). First of all, it can be noticed that the mean surface slope increases when ω increases, as already found in other works concerning the rotating drum configuration (Boateng & Barr 1997, Orpe & Khakhar 2001, Jain et al. 2004). Averages over a window of 5 data and of 20 data have been performed in order to highlight the presence of two main instabilities in the flow and are depicted in figure 8. It can be seen that there is a low frequency instability affecting both the experiments characterized by a period of about 3 s and by an amplitude of about $2 \div 3°$. The higher frequency instability is instead characterized by a period of about 0.2 s for both the experiments and by an amplitude of about 2° for experiment A and of about 4° for experiment B. Hence, an increase in the angular velocity causes also an increase in the fluctuation amplitude of the surface slope.

Figure 9 shows the time evolution of y_b and y_s for the performed experiments. The mean position of the free surface is taken as reference ($y_{sm} = 0$) for both the experiments (see §3). The mean position y_{bm} of the inversion point increases when ω increases. This result

Copyright © 2006 Taylor & Francis Group plc, London, UK

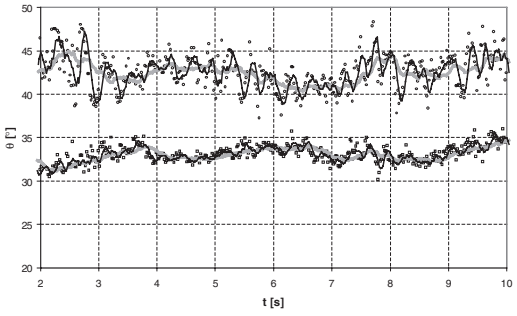


Figure 8. Time evolution of the surface slope θ (□, data from experiment A; ○, data from experiment B; black solid line, average over a window of 5 data; grey solid line, average over a window of 20 data).

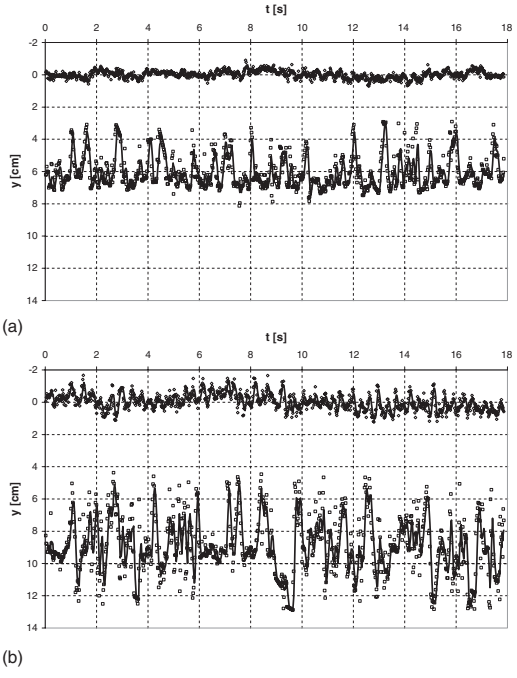


Figure 9. Time evolution of the free surface and of the inversion point (◇, y_s; □, y_b; solid line, average over a window of 5 data) for: (a) experiment A; (b) experiment B.

agrees with the findings of previous works related to the interface between the active layer and the plug flow (Boateng & Barr 1997, Orpe & Khakhar 2001, Jain et al. 2004). Moreover, figure 9 shows that the fluctuations of y_b are stronger than those of y_s. An explanation of this finding can be found if one assumes that the fluctuations of y_s and y_b are connected to the phenomenon of clustering (Bonamy et al. 2002, Goldhirsch 2003) which characterizes the granular flow. In this frame, the fluctuations of y_s and y_b reveal

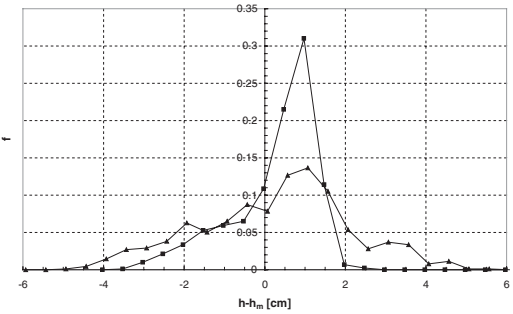


Figure 10. Probability density function of the variable $h - h_m$ (■, experiment A; ▲, experiment B).

the motion of the clusters in the direction of the flow and their amplitude is related to the cluster size.

Experiments performed in a rotating drum by Bonamy et al. (2002) and a recent theoretical analysis by Berzi & Larcan (unpubl.), based on the dimensional theory of Ertas & Halsey (2002), showed that the clusters are multi-scaled in the granular surface flow between sidewalls with their size increasing with the distance from the free surface. The characteristics of the fluctuations of y_b with respect to those of y_s are in agreement with these theories.

Figure 9 shows a further distinctive feature of the behaviour of y_b. For $\omega = 4$ rpm (figure 9a) the fluctuating displacements of y_b seem not symmetrically distributed around the mean value y_{bm} but the low values appear more frequent, as opposed to the case of $\omega = 8$ rpm (figure 9b), where instead y_b values much greater and much smaller than y_{bm} are approximately equally probable. Provided that the displacements of y_b are much greater than the displacements of y_s, the former are representative of the fluctuations of the depth $h = y_b - y_s$ where the flow changes its direction. Figure 10 shows the probability density function (PDF) of the variable $h - h_m$, with h_m the mean temporal value of h. Indeed, it can be noticed that the PDF relative to experiment A is less symmetric than that of experiment B.

Jop et al. (2005) and Berzi & Larcan (2006), even if through different constitutive models for the shear stress, showed that the uniform dense flow of cohesionless solid grains at the surface of a heap between smooth sidewalls is characterized by the following relationship between the depth h_{den} of the flowing layer and the free surface slope θ:

$$\frac{h_{den}}{W} = \frac{\tan\theta - \tan\phi}{\tan\delta} \qquad (2)$$

Here W is the gap between the sidewalls and δ is the friction angle between the grains and the sidewalls.

The non-dimensional mean depth h_m/W against the mean surface slope θ_m for the experiments A and

Copyright © 2006 Taylor & Francis Group plc, London, UK

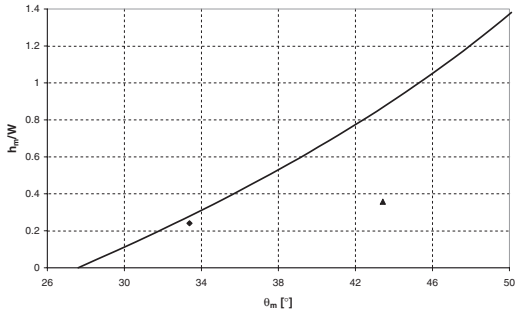


Figure 11. Non-dimensional mean position of the inversion point against the mean surface slope (♦, experiment A; ▲, experiment B; __, equation 2).

B is depicted in figure 11. The curve of equation (2), into which the value $W = 25$ cm and $\delta = 26°$ of our experimental set-up have been substituted, is also shown.

It can be seen in figure 11 that the point related to experiment A is very near to the theoretical curve of equation (2), as opposed to the case of experiment B. If the analysis performed by Jop et al. (2005) and by Berzi & Larcan (2006) on a different flow configuration (heap flow) applied also to the here considered quasi-2D flow in a rotating tumbler, it can be expected that the fluctuations of the depth h could be affected by the presence of this theoretical boundary, i.e., the dimension of the layer in which the granular material can be treated as a fluid.

Figure 12a shows the time evolution of the depth h for the experiment A together with the corresponding value of h_{den}. It can be noticed that the fluctuations of h are indeed limited by h_{den}, originating the asymmetry in the probability density function of h highlighted in figure 10. Hence, this result is a clue of the validity of the theory of Jop et al. (2005) and of Berzi and Larcan (2006) also in the quasi-2D flow in a rotating drum, although more experiments are needed to provide a clear evidence on this argument.

If the mean value of h is instead much lower than h_{den} (experiment B), the fluctuations of the depth h do not suffice at reaching the theoretical limit of equation (2) (Figure 12b). Hence, there is no constraint on the h values and its probability density function is more symmetric (figure 10).

5 CONCLUDING REMARKS

In this paper, the fluctuating displacements of the free surface and of the position where the flow changes its direction concerning the uniform dry granular flow which develops in a rotating drum are investigated. The experimental data have been collected by means

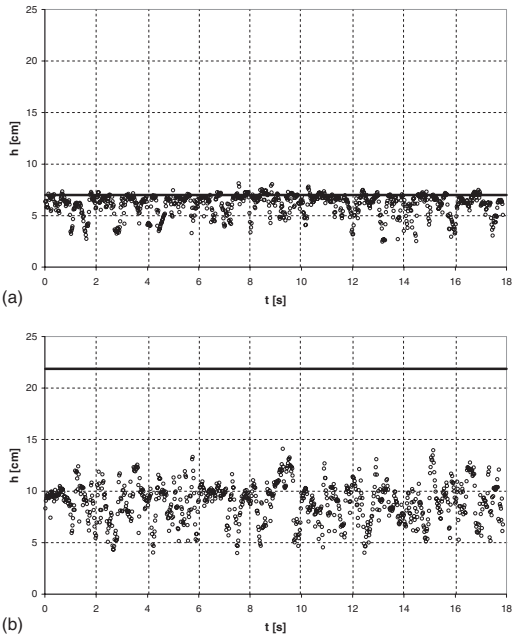


Figure 12. Time evolution of the depth h (○, experimental data; —, theoretical value of h_{den}) for: (a) experiment A; (b) experiment B.

of image processing techniques (edge detection and Particle Image Velocimetry) which allowed to obtain the time series of the variables.

The major conclusions of this work are the following:

(1) it has been possible to measure the fluctuating displacements of the free surface and the grain velocities in the proximity of the interface between the active layer and the plug flow zone which allowed to measure also the fluctuating displacements of the inversion point;
(2) the fluctuations strength is an increasing function of the angular velocity of the rotating drum;
(3) the amplitude of the fluctuations of the free surface is smaller than that of the inversion point. If one assumes that these fluctuations are due to the presence of clusters in the flow field, this result is in agreement with the size distribution of the clusters along the transversal direction observed in the experiments of Bonamy et al. (2002) and with the theoretical analysis of Berzi & Larcan (unpubl.).
(4) The Probability Density Function of the depth h where the flow changes its direction is strongly asymmetric for the experiment A characterized by an angular velocity $\omega = 4$ rpm, as opposed to the case of experiment B ($\omega = 8$ rpm). This asymmetry has been showed to be related to

Copyright © 2006 Taylor & Francis Group plc, London, UK

the constraint on the fluctuations of h posed by the theoretical value of the depth of the flowing layer in dense regime suggested and verified by Jop et al. (2005) and by Berzi & Larcan (2006) in the case of the dry granular flow of cohesionless grains at the surface of a heap between smooth sidewalls. Hence, although a richer experimental campaign is required, the theory by Jop et al. (2005) and by Berzi & Larcan (2006) and in particular the crucial role of the sidewalls in governing the dynamics of the granular flow, seem to apply also to the quasi-2D rotating drum configuration, where the flow cannot be considered quasi-homogeneous even at the centre of the drum (Renouf et al. 2005).

REFERENCES

Ancey, C. 2001. Dry granular flows down an inclined channel: experimental investigations on the frictional-collisional regime. *Phys. Rev.* E, 65, 011304.

Berzi, D. & Larcan, E. 2006. Frictional surface flow of a dry granular medium. *Proc. of the int. conf. Riverflow 2006*.

Berzi, D. & Larcan, E. Sidewalls effect on clustering and jamming of granular matter. *Unpublished*.

Boateng, A.A. & Barr, P.V. 1997. Granular flow behaviour in the transverse plane of a partially filled rotating cylinder. *J. Fluid Mech.*, 330: 233–249.

Bonamy, D., Daviaud, F., Laurent, L., Bonetti, M. & Bouchaud, J.P. 2002. Multiscale clustering in granular surface flows. *Phys. Rev. Lett.*, 89 (3), 034301.

Canny, J. 1986. A computational approach to edge detection. *IEEE Transactions on Pattern Analysis and Machine Intelligence*, PAMI-8(6): 679–698.

Ertas, D. & Halsey, T.C. 2002. Granular gravitational collapse and chute flow. *Europhys. Lett.*, 60 (6): 931–937.

GDR MiDi 2004. On dense granular flows. *Eur. Phys. J.* E, 14: 341–365.

Goldhirsch, I. 2003. Rapid granular flows. *Ann. Rev. Fluid Mech.*, 35: 267–293.

Jain, N., Ottino, J.M. & Lueptow, R.M. 2004. Effect of interstitial fluid on a granular flowing layer. *J. Fluid Mech.,* 508: 23–44.

Jenkins, J.T. & Richman, M.W. 1986. Boundary conditions for plane flows of smooth, nearly elastic, circular disks. *J. Fluid Mech.,* 171: 53–69.

Jop, P., Forterre, Y. & Pouliquen, O. 2005. Crucial role of sidewalls in granular surface flows: consequences for the rheology. *J. Fluid Mech.*, 541: 167–192.

Orpe, A.V. & Khakhar, D.V. 2001. Scaling relations for granular flow in quasi-two-dimensional rotating cylinders. *Phys. Rev.* E, 64, 1302.

Pouliquen, O. 1999. Scaling laws in granular flows down rough inclined planes. *Phys. Fluids*, 11 (3): 542–548.

Radice, A., Malavasi, S. & Ballio, F. 2004. PIV analysis of sediment kinematics in an abutment scour hole. *ICSE 2004, II Int. Conf. on Scour and Erosion, Singapore*, 2: 359–366.

Renouf, M., Bonamy, D., Dubois, F. & Alart, P. 2005. Numerical simulation of two-dimensional steady granular flows in rotating drum: on surface flow rheology. *Phys. Fluids*, 17, 103303.

Copyright © 2006 Taylor & Francis Group plc, London, UK

Numerical simulations of the covering a house by a debris flow

E. Harada
Dept. of Civil Engineering, Toyota National College of Technology, 2-1 Eisei-cho, Toyota, Aichi, Japan

T. Hosoda
Dept. of Urban Management, Kyoto Univ.,Yoshida Honmachi, Sakyo-ku, Kyoto, Japan

H. Gotoh
Dept. of Urban and Environmental Engrg., Kyoto Univ., Yoshida Honmachi, Sakyo-ku, Kyoto, Japan

ABSTRACT: Areas devastated by debris flows are frequently reported. Rapid rescue operations, for which the accurate prediction of buried regions are necessary, are required to reduce the number of casualties. In the present study, numerical simulations of the process of covering a house by a debris flow have been performed using a solid-liquid, two-phase flow model. A granular material model, based on the Distinct Element Method is used for the solid phase. The house is made of several pillars, which are connected by passively moving solids, and an elastic collapse model is applied to the joints between the pillars.

1 INTRODUCTION

Instability of the ground due to the heavy rain by typhoon causes landslide or debris flow. Image of the rescue of life from collapsed and buried house due to the landslide and debris flow are often televised. The fundamental mechanism of the landslide or debris flow has been studied from now, and some prediction becomes possible. As a recent example, Moriwaki et al. (2004) studied the failure process in a full-scale landslide experiment. Satofuka, Y. (2004) carried out the numerical simulation for debris flow for the fields. By the way, although the many studies have been made on the mechanism of debris flows or landslide and the deposition process of debris flow or landslide, study that interaction between houses and debris flow or landslide would be indispensable for the reduction of the damage from debris flow or landslide. Furthermore, the accurate judgment of the position of the buried house is necessary for the rapid rescue of the life, so to estimate the position of the buried house due to the debris flow or landslide would be also important. For these reasons, the numerical simulation for covering process of houses by debris flow or landslide have been performed in the present study.

The modeling of the debris flow, the collapse model of the house, interaction model between house and debris flow are necessary to simulate the process of the buried house due to the debris flow. Debris flow is in the condition that water is fully mixed with sand and the stone particles. Hence, the evaluation of the interaction between stone particles (solid-solid phase) and between stones and water (solid-liquid phase) are required for the modeling of the debris flow in the numerical simulation. From such reasons, solid-liquid two-phase flow model, in which motion of solid phase was tracked by using the granular material model based on the Distinct Element Method (DEM) proposed by Cundall, P.A. & Strack, O.D.L. (1979), which can evaluate the motion of each stone particle with interelement collision, was applied and the interaction between stones and water was evaluated by using drag force. The house was formed by connecting several pillars, which was composed of several elements. Each pillars acts as the rigid body by the passively moving solid proposed by Koshizuka et al. (1988) and the joint between pillars obey the simplified elastic collapse model referring to Hakuno, M. & Meguro, K. (1991) and Kawai, T. & Toi, Y. (1977).

2 SIMULATION MODEL

2.1 *Movable bed simulator*

To describe the unsteady process of the debris flow due to the landslide from the occurrence to the end, the discrete model is convenient. In the present study, dynamic motion of the sliding mass and collapsing house composed of the circular elements are evaluated by the one of the discrete model, or the Movable Bed Simulator proposed by the Gotoh, H. and Sakai, T. (1997), which is based on the Distinct Element Method

Copyright © 2006 Taylor & Francis Group plc, London, UK

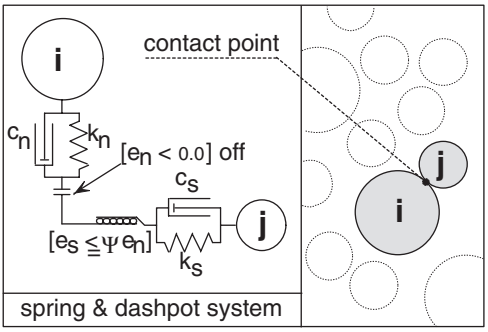


Figure 1. Spring and dashpot system between contacting particles.

proposed by Cundall, P.A. and Strack, O.D.L. (1979). The motion of each circular element in the two dimensional plane is defined by the following translational and rotational equations:

$$m\frac{d\boldsymbol{u}_p}{dt} = -V_p\nabla P + m\boldsymbol{g} + \boldsymbol{F}_P + \boldsymbol{F}_D \tag{1}$$

$$I\frac{d\omega_p}{dt} = \boldsymbol{T}_P \tag{2}$$

$$\boldsymbol{F}_D = C_D\frac{\pi d^2}{4}\cdot\frac{\alpha_l}{2}\rho|\boldsymbol{u}_r|\boldsymbol{u}_r \;;\; \boldsymbol{u}_r = \boldsymbol{u}_f - \boldsymbol{u}_p \tag{3}$$

where ρ = density of fluid; m = mass of the element; d = diameter of the element; $\boldsymbol{u}_f$ = velocity vector of the fluid; $\boldsymbol{u}_p$ = velocity vector of the element; t = time; P = pressure of water; $\boldsymbol{F}_p$ = inter-element force vector; $\boldsymbol{F}_D$ = drag force vector; α_l^p = share of the fluid in the calculated grid; ω_p = angular velocity of the element; $\boldsymbol{T}_p$ = torque acting on the element; $\boldsymbol{g}$ = gravity force vector; C_D = drag coefficient; and V_p = the volume of the element. The judgment of the contact condition is carried out at every calculated time step, and if the element is in the contacting condition, the inter-element force is evaluated by the Voigt system, or the spring and dashpot system shown in Figure 1, which is introduced in both of the tangential and normal direction. In the present simulation, elements are in non-cohesive condition. So the joint, which has no resistance to the tensile force, is assumed in the normal direction. While in the tangential direction, the frictional force works (coefficient of frictional resistance $\psi = 0.577$). To describe these characteristics of inter-element, the joint, which slips at the limit of the shear stress, is assumed in the tangential direction. The detailed model of interaction between elements is mentioned in the paper(Gotoh, H. & Sakai, T. (1997)). The tuning parameters (spring constants in normal and tangential directions (k_n, k_s) and damping constants (c_n, c_s)) used for the debris flow due to the landslide are determined in consideration of the numerical stability by referring the optimization procedure proposed by Gotoh, H. et al. (2001). The tuning parameters are as follows: $k_n = 256.8$ kN/s; $k_s = 98.8$ N/s; $c_n = 0.231$ kNs/m; $c_s = 0.143$ Ns/m. The share of element concentration and the drag force vector in each calculated cell are evaluated from the position of all particles calculated by the governing equations (1) and (2), and these values are used in the solid-liquid coupling.

2.2 *Rigid model*

House is expressed by connecting pillars, which moves as rigid body, with special joint. The pillar is formed with several elements by connecting rigidly. The passively moving solid model proposed by Koshizuka, S. et al. (1998) is applied to the forming of the pillar. At first, the same calculation procedure is applied to both of the element composed of debris flow and house with no distinction, in other words, the conjunction among individual solid elements is not considered in this stage. As a result of this calculation, the components of house deforms, hence the components of house are corrected in the following way.

The translational and rotational velocity vectors $\boldsymbol{T}_k$ and $\boldsymbol{R}_k$ of house is calculated as follows:

$$\boldsymbol{T}_k = \frac{1}{N_k}\sum_{i=1}^{N_k}\boldsymbol{u}_{ki} \tag{4}$$

$$\boldsymbol{R}_k = \frac{1}{I_k}\sum_{i=1}^{N_k}\boldsymbol{u}_{ki}\times\left(\boldsymbol{r}_{ki} - \boldsymbol{r}_{gk}\right) \tag{5}$$

where N_k = number of component of the k-th pillar; $\boldsymbol{r}_{gk}$ = gravity center of the k-th pillar; I_k = momentum of inertia of the k-th pillar; and $\boldsymbol{r}_i$ = position vector of the i-th component. The gravity center and the momentum inertia are given by

$$\boldsymbol{r}_{gk} = \frac{1}{N_K}\sum_{i=1}^{N_k}\boldsymbol{r}_{ki} \tag{6}$$

$$I_k = \sum_{i=1}^{N_k}\left|\boldsymbol{r}_{ki} - \boldsymbol{r}_{gk}\right|^2 \tag{7}$$

Then, the velocity vectors of components of pillar are replaced by

$$\boldsymbol{u}_{ki} = \boldsymbol{T}_k + \left(\boldsymbol{r}_{ki} - \boldsymbol{r}_{gk}\right)\times\boldsymbol{R}_k \tag{8}$$

to satisfy the motion as a rigid body. By applying the above mentioned velocity-vector correction procedure to only components of the pillar, the motion of the pillar as a rigid body can be tracked(refer to Figure 2).

Copyright © 2006 Taylor & Francis Group plc, London, UK

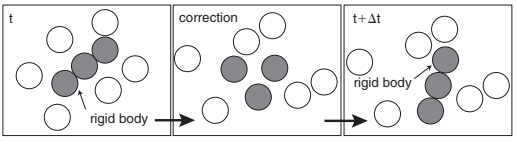


Figure 2. Correction procedure to elements composed of rigid body.

2.3 *Collapse model*

The special joint is applied between pillars. The special joint, which express the elastic failure, is as follows:

$$\left.\begin{aligned} f_n(t) &= e_n(t) \\ f_s(t) &= e_s(t) \end{aligned}\right\} \quad when \quad |f_s(t)| \le f_{limit} \tag{9}$$

where $f_n(t)$, $f_s(t)$ = inter-element force by the spring in the normal and tangential direction respectively. The joint has resistance to the frictional force in the tangential direction till the limitation (f_{limit}), which is parameter for fracture criterion. And after collapse of the house, the interaction between pillar-pillar follows the joint above mentioned 2.1. And also the model parameters applied between pillars are different from using in the 2.1, because the dynamic motion is different between debris flow and pillar. Hence, only the spring constants are used referring to the Kawai, T. and Toi, Y (1977) here. In addition, the similar concept of the collapse model is presented for example Hakuno, M. and Meguro, K. (1991).

2.4 *Model of liquid phase*

The continuity and momentum equations to the local averaged flow in incompressible fluid are described as follows:

$$\frac{\partial u}{\partial t} + \nabla \cdot \alpha_f \boldsymbol{u}_f = 0 \tag{10}$$

$$\begin{aligned} &\frac{\partial \rho \alpha_l u_f}{\partial t} + \nabla \cdot \left(\rho \alpha_l u_f u_f\right) = \\ &-\alpha_l \nabla P + \rho \alpha_l \boldsymbol{g} \\ &+ \nabla \cdot \alpha_l \left(\tau_l + \tau_{Re}\right) - \sum F_D / V \end{aligned} \tag{11}$$

$$\tau_l + \tau_{Re} = \left(\mu + \mu_t\right)\left[\nabla u_f + \left(\nabla u_f\right)^T\right] \tag{12}$$

where V = unit volume of calculation cell in liquid phase; τ_l = stress tensor; τ_{Re} = stress tensor due to turbulent flow; μ = coefficient of viscosity; and μ_t = kinematic eddy viscosity. And the subscript T means the transposed. And the kinematic eddy viscosity was evaluated by the standard k-ε turbulent model in the singlephase flow simply due to the difficulty of the characteristics of the turbulent structure in the sediment laden. The detailed information of the modeling of the liquid phase is in the Harada, E. et al. (2004). And the governing equations are discretized by the finite volume method, or FVM, on the staggered grid, and also upwind difference scheme is applied in the advection term.

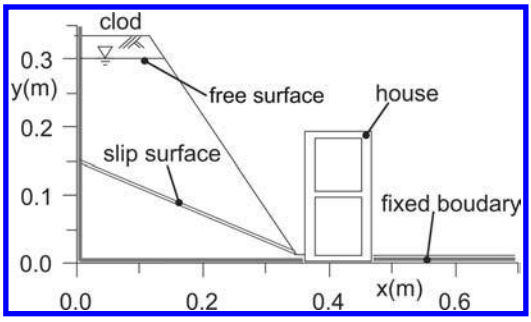


Figure 3. Initial condition and calculated domain as model case.

3 COLLAPSE PROCESS OF HOUSE

3.1 *Calculated condition*

Figure 3 shows the initial condition of the calculation condition. The clod on the slope and the house is formed by using 4721 particles, diameter of which is 0.005 m, 2.65 in specific density. The collapse process of the house located at $x = 3.8$ m due to the landslide of the left side of the clod by the liquefaction over the slip surface is assumed and tracked. The landslide breaks out along with the start of the calculation due to the removing of the sand elements at the bottom of the clod. This operation means the trigger of the landslide due to the liquefaction over the slip surface. And the fully saturated clod is assumed, the Lagrangian mass less marker particles are arranged in the clod shown in Figure 3.

The house is formed by connecting with 7 individual pillars shown in Figure 4. The special joint is applied between same sign elements. The elements of component of the house are made of concrete and wood and so on actually. But in the present simulation, they aren't handled strictly, and the specific density of the element is as same as the clod.

3.2 *Simulation results*

The snapshots of the present simulation are shown in Figure 5. The debris flow due to the landslide starts by the trigger from the time $t = 0.0$ s. Around the time $t = 0.05$ s, the tip of the debris flow reaches to the front of the first floor of the house. The debris flow is

Copyright © 2006 Taylor & Francis Group plc, London, UK

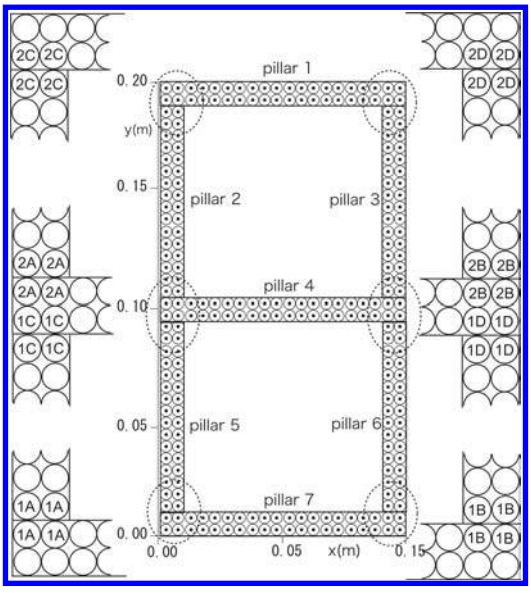


Figure 4. Outline of house composed of 7 pillars and joints between pillars.

blocked by pillar 5 and the separation between water and sand is confirmed. And the water passes through the house, although the increase of the water level due to the resistance of the pillar is shown. The water is actually supposed to be blocked by the pillars, too. However, in this simulation model, the evaluation of the interface between liquid phase and solid phase is imperfect. In other words, the interface between liquid phase and solid phase is estimated by the share of each phase on each calculated cell. Hence, handling of interface between solid phase and liquid phase is obscurity, and the strict evaluation of the interface is impossible. An examination about handling of the interface between different phases is necessary for the strict evaluation. And the slight inclination of the house is confirmed around the same time. The deflection of the house at the part of the first floor keeps increasing around the time $t = 0.35$ s. The significant inclination of the pillars of the first floor is shown, the collapse of the house of the first floor is confirmed from the time $t = 0.45$ s to the time $t = 0.55$ s. While, the slight inclination of the second floor is also confirmed from the time $t = 0.45$ s. After that, around the time $t = 0.65$ s, the conspicuous inclination at the second floor is shown, finally the collapse of the whole of the house is confirmed at the time $t = 0.85$ s.

The path line of the gravity center of the house elements is shown in the Figure 6. The x-axis and the $y$axis indicates the gravity center in the y-direction and the x-direction respectively. The scale of the deflection of the first floor is smaller the that of the second floor, because the the pillar 7 is located as the fundamental part of the house between the fixed boundary elements. And the decrease of the xgc in the first floor is confirmed because of the resistance force at the joints between the first floor and the second floor. It can be confirmed from the snapshot at the time $t = 0.85$ s shown in the Figure 5 as well.

Figure 7 shows the time series of the gravity center of all the components of the house elements in the y direction [upper] and in the x direction [lower] respectively. Around the time $t = 0.25$ s, the significant decrease of the gravity center in the y direction of the first floor is confirmed, which indicates the deflection of the first floor due to the collision of the debris flow. After that, that keeps decreasing by the increasing of the loading of the debris flow till the time $t = 0.46$ s. The decreasing process of the gravity center of the second floor in the y direction along with the decreasing of the gravity center of the first floor is confirmed around the same time, too. Then, although the gravity center of the first floor in the y direction shows calmness, it is confirmed that the gravity center of the second floor in the y direction keeps decreasing due to the pressure of the debris flow. And around the time $t = 0.8$ s, both of the gravity center in both of the x direction and the y direction remain constants, the convergence of the collapse of the house is confirmed. While, these tendencies are also shown in the gravity center of the x direction. In other words, increase of the gravity center in the x direction both of the first floor and the second floor, which indicates the inclination of the pillars, or deflection of the house, due to the increasing of the loading by the debris flow. And after the time $t = 0.46$ s, the stagnation of the gravity center with slight fluctuation of the first floor and the increasing of the gravity center of the second floor are also shown as well as the time series of the gravity center in the y direction.

4 CONCLUSIONS

In the present study, numerical simulation of the collapse process of the house due to the debris flow induced by the land slide has been performed by using the solid-liquid two phase flow model. In the solid model, to track the direct motion of the debris flow and the house, the granular material model(Gotoh, H. & Sakai, T., 1997) based on the Distinct Element Method (Cundall, P.A. & Struck, O.D.L., 1979) was applied. And also, the motion of the house as a rigid body was modeled by introducing the Passively moving solid model (Koshizuka, S. et al., 1998) and the motion of the collapse of the house was modeled by the special joint model, which resists against the tensile force and the shear force till the limitation of the force in the tangential direction.

Copyright © 2006 Taylor & Francis Group plc, London, UK

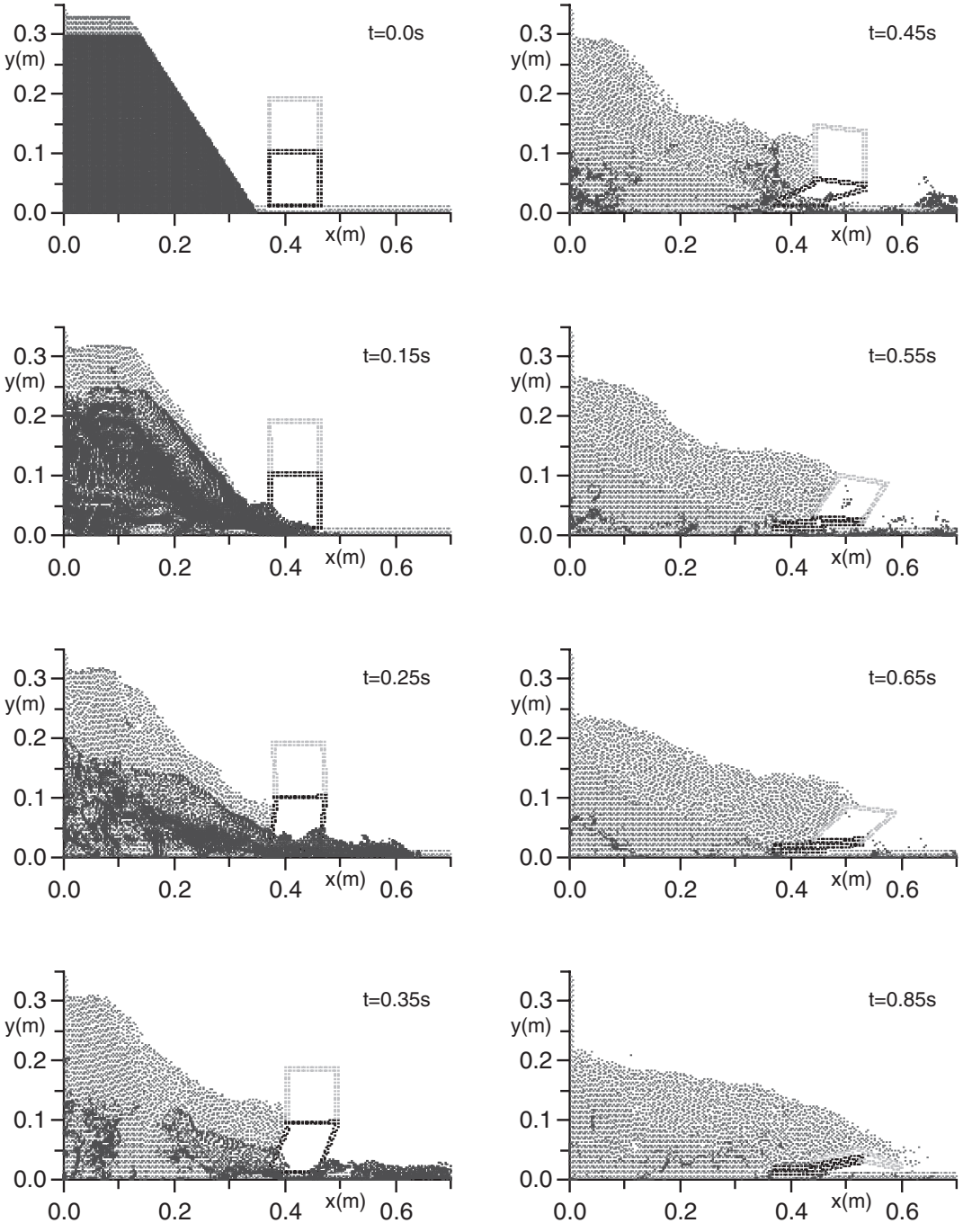


Figure 5. Snapshots of the collapse process of the house due to the debris flow induced by the landslide under the condition of the fully saturated.

Copyright © 2006 Taylor & Francis Group plc, London, UK

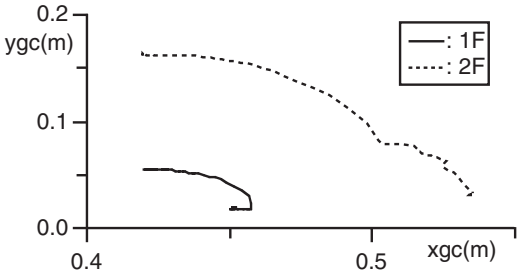


Figure 6. Path line of the gravity center in the *x*-direction and *y*-direction.

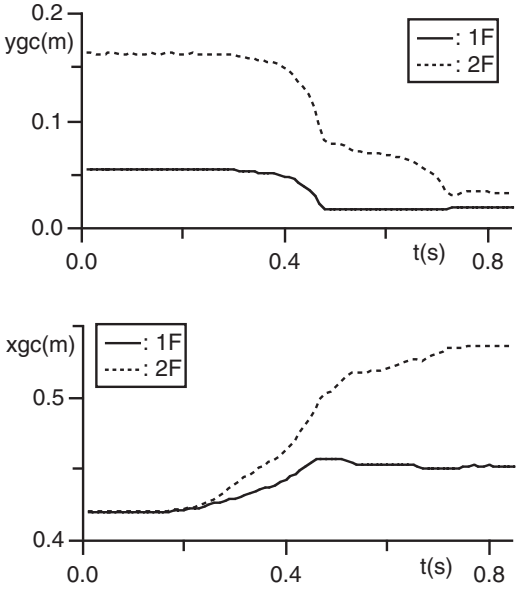


Figure 7. Time series of the gravity center in the *y*-direction [upper] and in the *x*-direction [lower].

Although the simulation of the collapse process of the house due to the debris flow has been performed, the evaluation of the interface between solid phase and liquid phase is imperfect, so the permeation of the water into the pillars was confirmed. In the near future, the investigation of the interface between different phases would be examined. Furthermore, the prompt separation between the clod (solid phase) and the water (liquid phase) is shown in the present simulation. Hence, the development of the liquid phase model in consideration with the surface tension would be necessary for the increase of the accuracy of the simulation model.

ACKNOWLEDGEMENT

This research was supported in part by a grant from Grants-in-Aid for Young Scientists (B) of Ministry of Education, Culture, Sports, Science and Technology of Japan.

REFERENCES

Cundall, P.A. & Strack, O.D.L. 1979. Discrete Numerical Model for Granular Assenblies. *Geotechnique*, Vol.29: 47–65.

Gotoh, H. & Sakai, T. 1997. Numerical Simulation of Sheetflow as Granular Material. *Jour. of Waterway, Port, Coastal and Ocean Engrg., ASCE*, Vol.123, No.6: 329–336.

Gotoh, H. et al. 2001. Optimization of Parameters in DEM-Based Numerical Movable Bed Simulator. *Jour. of Hydraulic, Coastal and Environmental Engrg., JSCE*, No.691/II-57: 159–164.

Hakukno, M. & Meguro, K. 1991. Collapse Process Simulation of Concrete Frame and Stone Masonry Structure by The Extended Distinct Element Method. *Proc. of the 1st International Conference on Seismology and Earthquake Engineering, Tehran, Islamic Republic of Iran*, 859–868.

Harada, E. et al. 2004. Destruction process of rubble mound weir by using Euler-Lagrange coupling model. *Jour. of Hydraulic, Coastal and Environmental Engrg., JSCE*, No.775/II-69: 45–54.

Kawai, T. & Toi, Y. 1977. A new element in discrete analysis of plain strain problems. *Jour. of 'Seisan Kenkyu', Institute of Industrial Science University of Tokyo*, 29–4, 204–207.

Koshizuka, S. et al. 1998. Numerical analysis of breaking waves using the moving particle semi-implicit method. *Int. Jour. Numer. Mech Fluids*, Vol.26, 751–769.

Moriwaki, H. et al. 2004. Failure processes in a full-scale landslide experiment using a rainfall simulator. *Landslides*, 1, 277–288.

Satofuka, Y. 2004. Numerica simulation of the debris flow at the ATSUMARI river. Minamata city, 2003, *Annual Jour. of Hydraulic Engineering, JSCE*, Vol.48(2), 925–930.

Copyright © 2006 Taylor & Francis Group plc, London, UK

Frictional surface flow of a dry granular medium

D. Berzi & E. Larcan
Politecnico di Milano, Department of I.I.A.R., Milano, Italy

ABSTRACT: We focus on the frictional surface flow of dry cohesionless granular material between sidewalls. We use the theoretical model we developed in Berzi & Larcan (unpubl.) for dense granular flow according to which the granular medium is treated as a viscoplastic fluid with a viscosity depending on the normal stress. The model formally includes the influence of the walls in the way suggested by Jop et al. (2005). Our model, as opposed to the empirical two-parameters model of Jop et al.(2005), has the key advantages that (1) there is only one parameter that must be set on the basis of experimental evidences and (2) it is intimately correlated to the type of solid material. We compare the flow properties obtained through the application of the model by Berzi & Larcan (unpubl.) against results of experiments performed by Jop et al. (2005), who analyzed the flow of glass beads on a heap. Although the regime is likely to become collisional near to the free surface (GDR Midi 2004), we obtain a notable agreement between the measurements and what predicted by our theory.

1 INTRODUCTION

The understanding of the dynamics of dry cohesionless granular material in fluid-like condition is a fundamental component for a lot of engineering processes, ranging from industrial to civil applications. Most of the works concerning this topic are devoted to the analysis of the collisional regime, i.e., the regime in which the collisions between the particles are almost instantaneous and the granular medium can be treated as a dense inelastic gas (Jenkins & Savage 1983, Lun et al. 1984, Lun 1991, Goldhirsch 2003).

The frictional regime, sometimes called frictional-collisional (Ancey & Evesque 2000) or dense (GDR MiDi 2004), which is characterized by (a) long-lived interparticle contacts and (b) a major role played by friction in governing the dynamics of the grains, has received much less attention in the literature. This is mainly due to the failure of the kinetic assumptions that makes a mathematical derivation of the closures (shear and normal stress expression, thermal diffusivity) in the balance equations extremely difficult (Zhang & Rauenzahn 1997, Zhang & Rauenzahn 2000). Thus, to our knowledge the study of frictional granular flow has been mainly performed on an empirical basis (Pouliquen & Forterre 2002, GDR MiDi 2004).

In a recent work, Berzi & Larcan (unpubl.) tested an expression for the shear stress in frictional regime in the case of the planar dry flow of cohesionless homogeneous granular material between parallel plates. This expression is characterized by only one fit parameter and is obtained through dimensional analysis, by fully taking into account the main characteristics of the frictional behaviour highlighted in recent theoretical and numerical investigations (Zhang & Rauenzahn 2000, Armanini et al. 2005, Zhang 2005). Here, we test the capability of the aforementioned model of reproducing the properties of a surface granular flow between smooth sidewalls. Experimental runs performed in such a configuration by Jop et al. (2005) are used as a term of comparisons.

2 THEORY

Recent numerical and experimental investigations concerning dense granular flow (GDR MiDi 2004) have shown that the shear stress τ and the normal stress σ are related through a friction law:

$$\left|\frac{\tau}{\sigma}\right| = \mu(I) \tag{1}$$

where the friction coefficient μ only depends on the parameter I, that is the ratio between the time scale given by the confining pressure ($d/\sqrt{\beta_d \sigma/\rho_s}$ with d particle diameter, ρ_s density of the grains and β_d solid volume fraction) and the time scale given by the strain rate ($\dot{\gamma}^{-1}$, $\dot{\gamma}$ being the shear rate). Jop et al. (2005) derived the expression of the friction coefficient in equation (1), as:

$$\mu(I) = \mu_s + \frac{\mu_2 - \mu_s}{I_0/I + 1} \tag{2}$$

Copyright © 2006 Taylor & Francis Group plc, London, UK

on the basis of experimental measurements of the basal friction coefficient performed by Pouliquen & Forterre (2002) under an inclined plane flow configuration. In equation (2) $\mu_s = \tan\phi$, ϕ being the static friction angle of the granular medium, while μ_2 and I_0 are fitting parameters. Jop *et al.* (2005) used the local rheology of equation (1) to write the momentum balance for a granular layer flowing on a heap (figure 1) of width W.

They assumed that a semi-infinite granular medium is sandwiched between two vertical smooth plates (sidewalls) and that the flow is uniform along the x-direction with velocity $u(z)$, at an angle θ with horizontal (figure 2). The force balance for the slice of material of length dx, thickness z and width W can be written as:

$$\rho_s \beta_d z dx W g \sin\theta - \rho_s \beta_d z dx W g \cos\theta \mu(I(z)) + \\ -2\rho_s \beta_d dx g \cos\theta \int_0^z \mu_w z' dz' = 0 \quad (3)$$

where β_d is assumed constant over z, and g is gravity.

The first term on the left hand side of equation (3) is the effect of gravitational forces; the second term is the friction force exerted by the bed in accordance with the rheology of equation (1); the last term is a supplementary resistance force which is due to the friction with the sidewalls. Here we assume that a pure solid friction force develops at the sidewalls. This implies that the wall friction coefficient, μ_w, is constant and equal to $\tan\delta$, with δ the (measured) friction angle between the grains and the wall. In equation (3) there is the further assumption of considering the normal stress in the granular medium as isotropic. This is shown to be reasonable by numerical experiments (Gutfraind & Pouliquen 1996). Jop et al. (2005) used equations (1)–(3) and obtained the velocity profile and the variations of the inclination of the surface velocity and of the thickness with the flow rate. They presented comparisons with experiments related to the flow of glass beads on a heap.

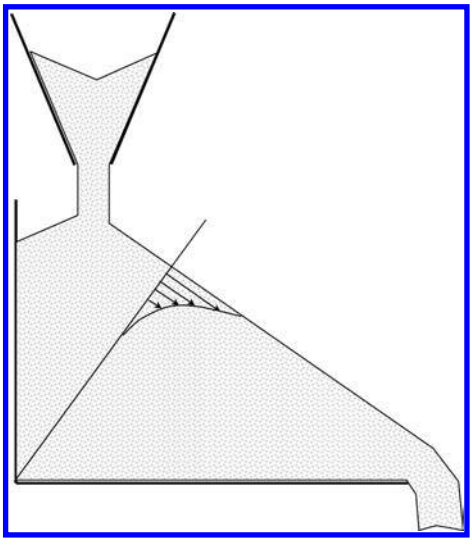


Figure 1. Granular flow on a heap.

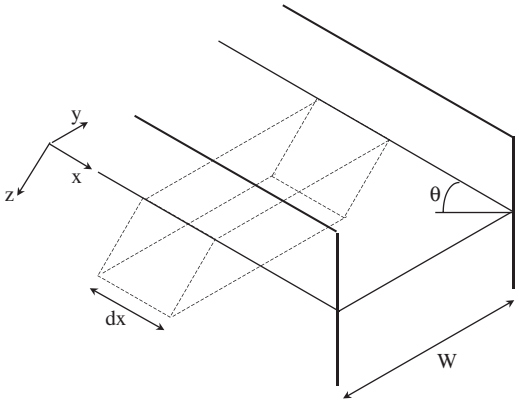


Figure 2. Sketch of the geometry in the force balance of equation (3).

Here, we choose to adopt a constitutive model for the shear stress of a dry granular flow in frictional regime derived by Berzi & Larcan (unpubl.) and successfully tested for reproducing the planar dry flow of cohesionless homogeneous granular material between parallel plates. In the following, the physical arguments behind the constitutive model of Berzi & Larcan (unpubl.) are reported.

Firstly, Zhang & Rauenzahn (2000) showed that in a dense granular flow the shear stress is characterized by an asymptotic finite value when the strain rate goes to zero. However, in order to explain the development of shear zone in the flow domain, also a dependence on the strain rate has to be taken into account. The more simple way for making the shear stress compatible with these statements is to express it as the sum of two components, according to the following expression:

$$\tau = \sigma \tan\phi + \mu_g \dot{\gamma} \quad (4)$$

where the first term on the right hand side of equation (4) is a Coulomb type yield component and μ_g is a granular viscosity coefficient. The last term on the right hand side of equation (4) can be treated in the frame of the kinetic theories (Jenkins & Savage 1983, Lun et al. 1984, Lun 1991) if one assumes that is related to the so called 'weak' population (clusters which are surrounded by network of grains in close contact and mainly experience collisions), as defined by Ancey and

Copyright © 2006 Taylor & Francis Group plc, London, UK

Evesque (2000). Hence the granular viscosity, μ_g, can be expressed as (see, e.g., Lun 1991):

$$\mu_g = \rho_s d T^{\frac{1}{2}} f_1(e, \beta, \beta_d) \tag{5}$$

Here, f_1 is a coefficient, whose expression can be found in the paper of Lun (1991), function of the solid volume fraction β_d, of the restitution coefficient, e, and of the roughness coefficient, β, while T is the granular temperature, defined as one-third the mean squared value of the velocity fluctuations.

Dimensional analysis shows that the constitutive relation for the normal stress has the following general non-dimensional expression:

$$\Im\left(\frac{\sigma}{\rho_s T}, \beta_d, e, \beta\right) = 0 \tag{6}$$

By rendering explicit β_d from equation (6) and substituting into equation (5), one obtains:

$$\mu_g = \rho_s d T^{\frac{1}{2}} f_2\left(e, \beta, \frac{\sigma}{\rho_s T}\right) = \rho_s d T^{\frac{1}{2}} f_3(e, \beta) f_4\left(\frac{\sigma}{\rho_s T}\right) \tag{7}$$

Here, f_2 is a coefficient depending on $\sigma/\rho_s T$, e and β and it is assumed that it can be expressed as a coefficient f_3, which depends on e and β, times a coefficient f_4, which instead depends only on $\sigma/\rho_s T$. In a dense flow the high solid volume fraction causes probably a saturation of the collision rate. Hence, a linear dependence of the shear stress on the strain rate is to be expected (Zhang & Rauenzahn 1997). The μ_g coefficient must be therefore independent on granular temperature and the coefficient f_4 must have the following expression:

$$f_4 = \kappa\left(\frac{\sigma}{\rho_s T}\right)^{\frac{1}{2}} \tag{8}$$

where κ is a dimensionless constant. Using equation (8) into equation (7) leads to:

$$\mu_g = \chi \sigma^{0.5} \tag{9}$$

Here, $\chi = \kappa \rho_s^{0.5} d f_3$ is a coefficient depending only on the grain properties. Finally, the shear stress of equation (4) can be expressed as:

$$\tau = \sigma \tan\phi + \chi\sqrt{\sigma}\dot{\gamma} \tag{10}$$

The coefficient χ appearing in equation (10) is the only parameter of the model. The local rheology of equation (10) is compatible with the analysis of GDR MiDi (2004), provided that a simple manipulation leads to:

$$\frac{\tau}{\sigma} = \tan\phi + \frac{\sqrt{\beta_d}\chi}{\sqrt{\rho_s d}} \frac{\dot{\gamma} d}{\sqrt{\beta_d \sigma/\rho_s}} = \\ = \tan\phi + \frac{\sqrt{\beta_d}\chi}{\sqrt{\rho_s d}} I = \mu(I) \tag{11}$$

Thus, even adopting the constitutive model of equation (10), the friction coefficient μ related to a certain granular material (characterized by a well defined diameter, static friction angle and volume fraction) depends only on the parameter I.

Then, we can use equation (11) and equation (3) to derive the expression of velocity profile of the grains. Equation (3) can be written as:

$$\tan\theta - \tan\phi - \frac{\sqrt{\beta_d}\chi}{\sqrt{\rho_s d}} I - \tan\delta \frac{z}{W} = 0 \tag{12}$$

If we set $I = 0$ in equation (12), we obtain the depth h of the flowing layer over the heap, i.e., the position of the transition between the fluid-like and the solid-like behaviour of the particulate system, where the shear rate vanishes:

$$h = \frac{\tan\theta - \tan\phi}{\tan\delta} W \tag{13}$$

Equation (13) is the same relationship obtained by Jop et al. (2005) and reveals that the depth of the flowing layer is controlled by the sidewalls. Indeed, under the assumption of indefinite planar surface flow ($W \to \infty$), which is mathematically equivalent to considering a negligible effect of the sidewalls ($\tan\delta \to 0$), $h \to \infty$, so that no granular static layer under a granular flowing layer can be observed.

Substitution of the expression of the parameter I and $\dot{\gamma} = du/dz$ into equation (12) leads to:

$$\frac{du^*}{dz^*} = -C_1\left(C_2 z^{*\frac{1}{2}} - C_3 z^{*\frac{3}{2}}\right) \tag{14}$$

where the expressions of the coefficients C_1, C_2 and C_3 are the following:

$$C_1 = \frac{d\sqrt{\rho_s \cos\theta}}{\chi} \\ C_2 = \tan\theta - \tan\phi \\ C_3 = \frac{\tan\delta}{W^*} \tag{15}$$

Here, we have introduced the non-dimensional variables $u^* = u/\sqrt{gd}$, $z^* = z/d$ and $W^* = W/d$.

Copyright © 2006 Taylor & Francis Group plc, London, UK

Integrating equation (14) with the boundary condition $u^* = 0$ for $z^* = h^* = h/d$ leads to:

$$u^* = \frac{2}{3} C_1 C_2 \left(h^{*\frac{3}{2}} - z^{*\frac{3}{2}} \right) - \frac{2}{5} C_1 C_3 \left(h^{*\frac{5}{2}} - z^{*\frac{5}{2}} \right) \qquad (16)$$

Then, integrating equation (16) from the bottom of the flowing layer ($z^* = h^*$) to the free surface leads to:

$$\frac{V^*}{W^{*\frac{3}{2}}} = \frac{4}{35} C_1 C_2 \left(\frac{h^*}{W^*} \right)^{\frac{3}{2}} \qquad (17)$$

where V^* is the non-dimensional mean velocity of the flowing layer. Equation (17) can be written in terms of the non-dimensional flow rate per width unit, $Q^* = V^* h^*$, as:

$$\frac{Q^*}{W^{*\frac{5}{2}}} = \frac{4}{35} C_1 C_2 \left(\frac{h^*}{W^*} \right)^{\frac{5}{2}} \qquad (18)$$

Equations (17)–(18) show the correct scaling for the flow properties already found by Jop et al. (2005).

Equations (13) and (18) show that, once the flow rate is fixed, both the depth of the flowing layer and the inclination of the free surface can be determined. It must be underlined that only one parameter needs to be set, i.e., the coefficient χ relative to the homogeneous granular material used, as opposed to the rheology adopted by Jop et al. (2005) in which there are two fitting parameters. The measurement of the inclination, θ, and of the depth, h^*, for one value of the flow rate Q^* are sufficient to determine the value of the coefficient χ for the granular material used in the experiments. All additional runs, when performed with the same grains, can, therefore, be used for assessing the validity of the equation (11).

3 COMPARISON WITH EXPERIMENTS

Jop *et al.* (2005) performed several tests concerning the surface flow of glass beads (diameter $d = 0.53$ mm, density $\rho_s = 2450$ kg/m^3, static friction angle $\phi = 20.9°$ and $\beta_d = 0.6$) on a heap adjusting the gap W between the smooth lateral glass walls (friction angle $\delta = 10.4°$) from 1 cm up to 30 cm. They were able to set the flow rate and to measure inclination, surface velocity and depth of the flowing layer.

These experimental results can be used as a term of comparison against our theoretical predictions, once the value of the coefficient χ for the glass beads is determined. By substituting equation (13) into equation (18) we obtain a relationship between the non-dimensional flow rate and the inclination of the free surface. Hence, introducing a couple of experimental values of $Q^*/W^{*5/2}$ and $\tan\theta$ in this relation allows for obtaining the coefficient χ. We used the measured values of $Q^*/W^{*5/2} = 0.000384$ and $\tan\theta = 0.443$ and obtained $\chi = 0.03$ (kg/m)$^{1/2}$. We then used this value and solved equations (13)–(18) for different non-dimensional flow rates. The dependence of $\tan\theta$ on the non-dimensional flow rate is depicted in figure 3, together with the experiments performed by Jop et al. (2005) and the results of their model; the arrow indicates the experimental point used for setting the coefficient χ.

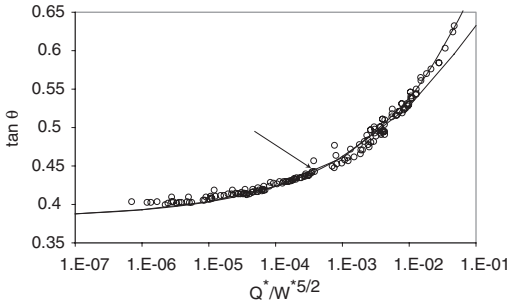


Figure 3. Inclination angle against non-dimensional flow rate (—, present theory; - - -, Jop et al. theory; ○, experiments by Jop et al.).

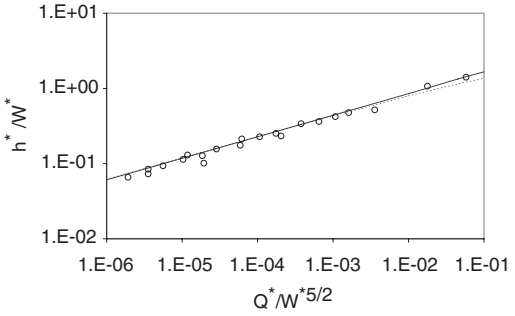


Figure 4. Non-dimensional flow depth against non-dimensional flow rate (—, present theory; - - -, Jop et al. theory; ○, experiments by Jop et al.).

It can be noticed that there is an excellent agreement between the present theory and the experiments, even at the highest values of $Q^*/W^{*5}/2$, where the model proposed by Jop et al. (2005) underestimates the inclination angle.

Figure 4 shows the dependence of the non-dimensional depth of the flowing layer on the non-dimensional flow rate. Once again, the agreement between theory and experiments is excellent. The curve depicted in figure 4 represents the flow rule of

Copyright © 2006 Taylor & Francis Group plc, London, UK

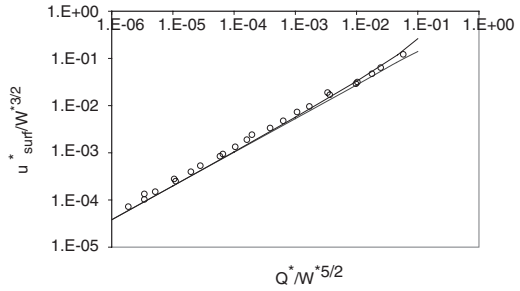


Figure 5. Non-dimensional surface velocity against non-dimensional flow rate (—, present theory; - - -, Jop et al. theory; ○, experiments by Jop et al.).

the granular medium. Thus, it could be used in conjunction with depth-integrated models, such as those based on the Saint Venant equations, to simulate granular avalanche. However, it must be underlined that our model is related to the case of frictional regime, i.e. when most of the flow field is governed by the long-lived interparticle contacts. On the other hand, in a real-scale phenomenon the collisions between the grains could play the major role in governing the dynamics of the granular avalanche.

The agreement between theoretical and experimental results shown in figures 3 and 4 suggests that the flow regime of the granular flows examined was globally frictional. Nevertheless, it is likely that a thin collisional layer develops near to the free surface. The existence of this layer could explain the slight underestimation of the surface velocity $u^*_{surf}/W^{*3/2}$ provided by the curve in figure 5. The theoretical values are obtained by setting $z^* = 0$ in equation (16).

4 CONCLUDING REMARKS

We focused on the frictional surface flow between sidewalls of a dry granular medium over a static layer composed of the same particles of the flux. We tested a constitutive model for the shear stress recently proposed and successfully used in the case of a planar dry granular flow between parallel plates by Berzi & Larcan (unpubl.). This constitutive model allowed to obtain the mathematical relationships between the flow properties and the flow rate and to compare them with the experiments performed by Jop et al. (2005) with glass beads. The notable agreement between theory and experiments confirms the validity of the theoretical model of Berzi & Larcan.

The constitutive models introduced by Berzi & Larcan (unpubl.) and by Jop et al. (2005) suggest that the shear stress is the sum of a rate-independent and a rate-dependent factor. While expressions for the former coincide, the latter factor is different for the two models. The agreement of the present theory with experiments is excellent also at the highest values of the flow rate, i.e., when the rate-dependent part of the shear stress becomes important. Therefore, the constitutive model of Berzi & Larcan (unpubl.) shows a superior capability of predicting the granular flow behaviour under frictional regime and has the additional key advantage of being characterized by only one fitting parameter, which is a function of the type of grains, as opposed to the two-parameters constitutive model of Jop et al. (2005).

REFERENCES

Armanini, A., Capart, H., Fraccarollo, L. & Larcher, M. 2005. Rheological stratification in experimental free-surface flows of granular-liquid mixtures. *J. Fluid Mech.*, 532: 269–319.

Ancey, C. & Evesque, P. 2000. Frictional-collisional regime for granular suspension flows down an inclined channel. *Phys. Rev. E,* 62 (6): 8349–8360.

Berzi, D. & Larcan E. Slow and dense uniform granular flow. *Unpublished*.

GDR MiDi 2004. On dense granular flows. *Eur. Phys. J.* E, 14: 341–365.

Goldhirsch, I. 2003. Rapid granular flows. *Ann. Rev. Fluid Mech.*, 35: 267–293.

Gutfraind, R. & Pouliquen, O. 1996. Study of the origin of shear zones in quasi-static vertical chute flows using discrete element simulations. *Mech. Mater.*, 24: 273–285.

Jenkins, J.T. & Savage, S.B. 1983. A theory for the rapid flow of identical, smooth, nearly elastic particles. *J. Fluid Mech.*, 130: 187–202.

Jop, P., Forterre, Y. & Pouliquen, O. 2005. Crucial role of sidewalls in granular surface flows: consequences for the rheology. *J. Fluid Mech.*, 541: 167–192.

Lun, C.K.K., Savage, S.B., Jeffrey, D.J. & Chepurniy, N. 1984. Kinetic theories for granular flow: inelastic particles in Couette flow and slightly inelastic particles in a general flowfield. *J. Fluid Mech.*, 140: 223–256.

Lun, C.K.K. 1991. Kinetic theory for granular flow of dense, slightly inelastic, slightly rough spheres. *J. Fluid Mech.*, 233: 539–559.

Pouliquen, O. & Forterre, Y. 2002. Friction law for dense granular flows : application to the motion of a mass down a rough inclined plane. *J. Fluid Mech.*, 453: 133–151.

Zhang, D.Z. & Rauenzahn, R.M. 1997. A viscoelastic model for dense granular flows. *J. Rheol.*, 41(6): 1275–1298.

Zhang, D.Z. & Rauenzahn, R.M. 2000. Stress relaxation in dense and slow granular flows. *J. Rheol.*, 44(5): 1019–1041.

Zhang, D.Z. 2005. Evolution of enduring contacts and stress relaxation in a dense granular medium. *Phys. Rev.* E, 71, 041303.

Copyright © 2006 Taylor & Francis Group plc, London, UK

Experiments on the impact process of dry and saturated mixtures against obstacles of various shapes

P. Ghilardi & M. Pagliardi
Dipartimento di Ingegneria Idraulica e Ambientale, Università di Pavia, Pavia, Italy

B. Zanuttigh
DISTART Idraulica, Università di Bologna, Bologna, Italy

ABSTRACT: The purposes of this work are to experimentally analyze the impact of dry and saturated granular flows on obstacles of various shapes and to compare the maximum forces measured in the experiments with the ones predictable with analytical formulae available in the literature.

Effects of interstitial fluid, mixture composition, obstacle size, shape and orientation were examined. Experimental results do not show a particular relevance of grain size composition, whereas obstacle orientation and height clearly affect the maximum force value.

Measurements of the impact process against high dams show that saturated mixtures, like clear water, form vertical jets with instantaneous overshoots one order of magnitude greater than the force corresponding to the hydrostatic front pressure. Immediately after the impulse, measured forces exerted by both dry and saturated mixtures are very similar, accounting for the different mixture densities, and are well approximated by analytical literature equations.

1 INTRODUCTION

Avalanches and debris flows exert enormous impact forces on obstacles in their path, such as bridge piles, defensive walls and buildings. The estimation of these forces is necessary for planning defensive structures (Okuda et al. 1980); researchers developed different automatic devices to measure the debris impact, some of which record only the maximum impact as a pressure mark (Okuda et al. 1980). The Mechanics Institute of the Chinese Academy of Sciences built a specifically designed piezo-electrical sensor: from the more than 70 impact force graphs collected by Zhang (Zhang, 1993) since 1982, fluid dynamic pressures were found as high as 5×10^3 kN/m^2 and impulse forces of individual boulders as great as 3×10^3 kN. Large-scale model tests of flexible barriers by (DeNatale et al. 1997 and 1999) showed that forces in the anchor cables exceeded the loaded cell capacity of 45 kN.

As field monitoring and measurements in mountain areas are generally quite difficult and expensive due to the particular environment and the nature of debris events, experiments are needed to improve the knowledge of debris forces and thus the design of defence works. Until now, physical modeling has been focused on mixture impacts against dams with height equal or higher than flow depth, which are, according to Hungr et al. (1998), the most common case in the field: forces on wall were analyzed by Armanini and Scotton (1993) for water-PolyVinil Chloride (PVC) and anionic-resin mixtures, by Scotton and Deganutti (1997) for granular-water steady surges, by Daido (1993) for sandy mud flows, by Di Paolo et al. (2005) for saturated marble mixtures.

Experiments on granular avalanches motion have been carried out, both for dense and dry snow avalanches, by Naaim-Bouvet et al.(2003), who measured the front velocity variation due to the dam, the dynamic pressures downstream the obstacle and the dependence of run-out shortening on obstacle height.

Objectives of this work are to experimentally analyse debris surge impacts against different type of structures (check-dams, filter-dams, flow-breakers, "houses") in order to find a correct analytical evaluation of impact forces.

The paper is composed of three main parts. The first describes tests carried out with dry and saturated granular mixtures and presents their results: effects on flow energy reduction, deposit extent and shape are investigated accounting for structure's dimensions, shape and orientation with respect to the flow direction.

The second part shows a comparison between some available empirical formulaewhich can be applied to

Copyright © 2006 Taylor & Francis Group plc, London, UK

estimate forces and pressures on the check-dams used in our experiments.

The third part discusses some limitations in the experimental representation of the impact process based on field experience and points out relevant aspects for structural design.

2 EXPERIMENTAL DESIGN

2.1 *Set-up*

Two series of experiments have been carried out, the first, using dry granular mixtures, at the DISTART laboratory (Bologna) while the others, using the same mixtures but in saturated conditions, at the Pavia laboratory.

This section describes first the equipment, which consisted of two chutes, with a reservoir fixed upstream and obstacles fixed downstream. Then, tested materials and measurement devices are presented. Finally, scale effects are discussed.

The DISTART chute is 0.10 m wide and 2.25 m long and is kept at a constant slope of 39° with respect to the horizontal while the Pavia chute is 0.10 m wide and 4.80 m long with a constant slope of 18.5°. The chutes lengths are more than enough to allow the reach of a fully developed flow regime.

The chute bottoms are roughened with 0.3 mm rough sandpaper that was found to properly work under two important aspects, avoiding the material to slide on the bottom as a solid body and avoiding as much as possible the entrapment of finer particles inside the bottom roughness. The different roughness of the bottom and the sides seems to reduce the effects due to chute width and friction at the walls. Chutes sides are transparent to allow optical measurements and video observations.

At the upstream end of the chutes a reservoir with a gate, inclined as the chute, is fixed; a wheel system guarantees a quick opening of the gate and all the material is let rapidly flowing down the chute.

A lever system (the same for both the chutes) is hinged at the downstream end of the chute, see scheme in Figure 1; the obstacle is fixed on the lever system bottom and the impact is transmitted by the upper part of the lever system to the force transducer by means of a screw whose lock has been previously calibrated.

The obstacles are classified into four categories: "houses", flow-breakers, check dams and filter-dams (Figure 2). Houses and flow-breakers are prismatic blocks of square section that differ only for the width; they are positioned in the outlet centre in two ways: perpendicular to the flow (90°, obstacle face orthogonal to the flow) and turned 45° with respect to flow direction. Check dams are prismatic blocks with rectangular section that has the same chute width. Filter dams consist of two teeth with a slope and straight (i.e., perpendicular to the bottom) face and are positioned in two ways: with the straight teeth part facing upstream or downstream the stream.

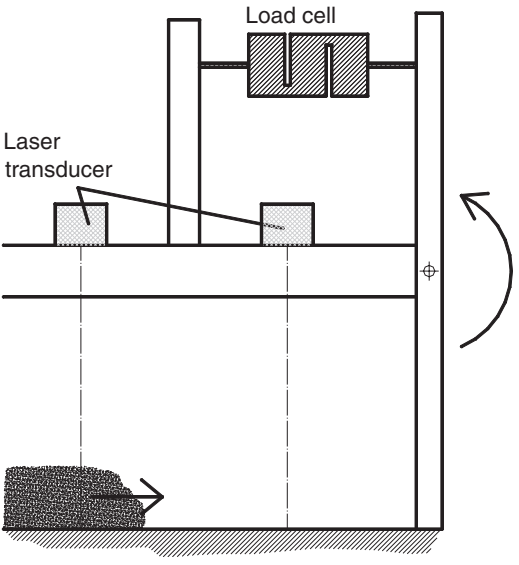


Figure 1. Scheme of measuring system placed at the end of chute.

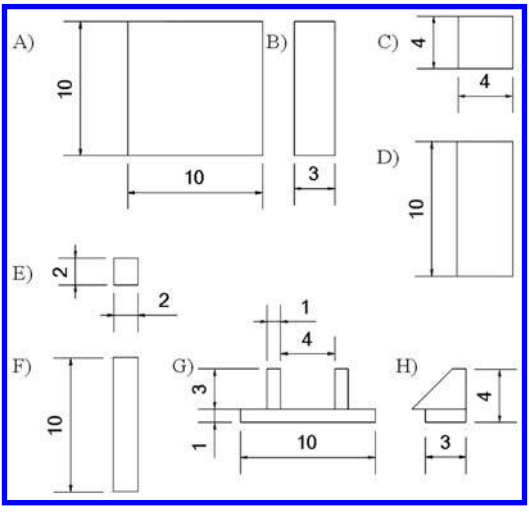


Figure 2. A) frontal and B) side views of the 10 cm high check-dam; D) frontal and C) upper views of the house; F) frontal and E) upper views of the flow-breaker; G) frontal and H) side view of the filter dam. All schemes are quoted in cm.

2.2 *Granular mixtures*

Experiments were carried out using two sandy mixtures having the same lithological compositions but

Copyright © 2006 Taylor & Francis Group plc, London, UK

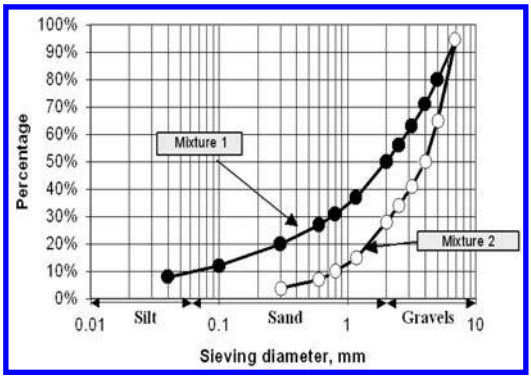


Figure 3. Grain-size curves for the two mixtures adopted in the experiments.

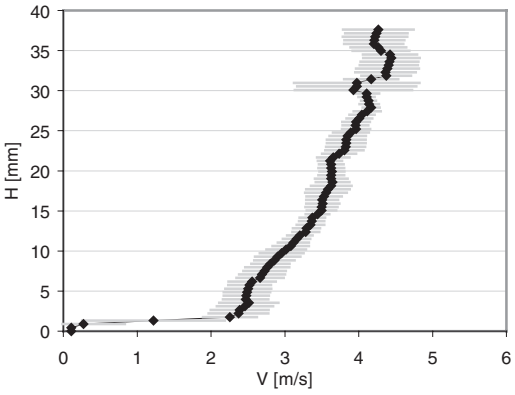


Figure 4. An example of velocity profile obtained with cross-correlation of consecutive frames, recorded with a high speed digital camera. The point refers to a average of 8 consecutive measurements (0.066 s), grey lines represent the standard deviation.

different grain-size assortment; both mixtures were used dry and saturated.

The mixtures were prepared to represent two typical conditions that frequently occur in the field (Berti et al. 1999). In particular, the first mixture (*mixture 1*) is characterized by widely ranging grain size and its distribution curve was derived following the method by Füller for the perfect distribution curve of the fractions used in the preparation of concrete (Burlamacchi 1994); in fact, in several papers debris are recognised to qualitatively flow "as fresh concrete"; this was pointed out, among the others, by Davies (1985) and Iverson (1997). The second mixture (*mixture 2*) was chosen to be less dispersed (pore not filled in with fine fraction) and biased towards the coarser fraction.

For specific practical reasons, the range of grain sizes used in the laboratory is limited to less than two orders of magnitude: 0.2–8 mm. In fact too fine particles would have produced powders very difficult to be controlled and not much significant for results as they can be retained by chute bottom roughness. On the opposite, too big particles would have got stuck among the teeth of filter dams and could have affected the results.

The properties of the two mixtures were measured without any compaction or vibration and produced similar results: the bulk density in air ρ_b is 1530 kg·m^{-3} for *mixture 1* and 1580 kg·m^{-3} for *mixture 2*; internal friction angle ϕ is 31° for mixture 1 and 33° for mixture 2; porosity is around 0.35 for *mixture 1* and 0.36 for *mixture 2*. Concerning the experiments in saturated conditions a volumetric concentration of 40% in reservoir were used, in agreement with some field data (Iverson, 1997). The granular material in the reservoir was placed behind the gate with a angle equal to internal friction angle and then saturated till the required concentration.

At the end of the tests, some fine material was lost but the amount was always less than few percent and thus not relevant to the outcome of the tests.

2.3 *Measurements*

The force impacting on the obstacles was measured with a load cell fixed with the oscillating lever system to the chute outlet (Fig. 1) with a 118N scale. The acquisition frequency is 25 Hz for the DISTART experiments and 250 Hz for the ones in Pavia. The inertia of the measurement system was found not to be relevant for the measured processes; however, the measure cannot represent the rapidly varying transitory in greater details, i.e., the impulsive force at the impact (Di Paolo et al., 2005).

Two laser level transducers were used to measure flow depth at a frequency of 250 Hz: one was placed at about 0.15 m from the chute outlet, and the other 0.20 m from the first. Front velocity was derived by the front travel time between these two transducers.

Video recordings at the chute side were performed to provide a qualitative description of the flow impacting on the obstacle, with a particular attention to the development of dead zones in presence of houses or flow breakers, to particle saltation in case of filter dams and to the back-waves generating inside the chute in case of sufficiently high check-dams. In the experiments with dry mixtures a standard digital camera was used whereas in the ones with saturated mixtures a high speed digital camera, capable of 240 frames per second with a half VGA resolution, was adopted (Biancardi and Ghilardi, 2003). This camera allowed to automatically measure velocity profiles by means of cross correlation of consecutive frames (Barbolini et al., 2005). The front velocities were in agreement with the ones measured wit laser transducer. In Figure 4 there is an example of a measured velocity profile.

Copyright © 2006 Taylor & Francis Group plc, London, UK

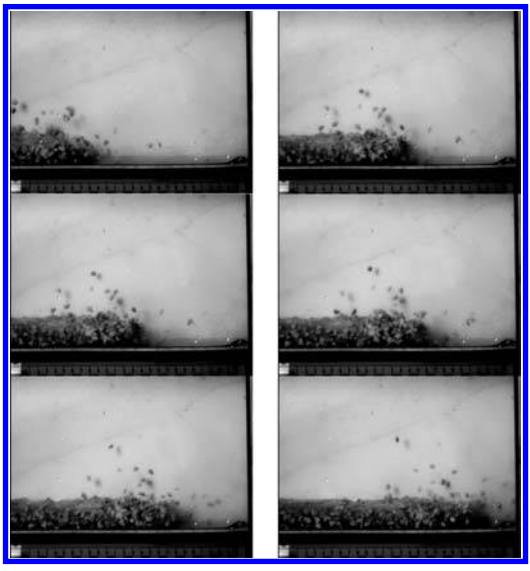


Figure 5. Sequence of images taken with high speed camera of the flow before the impact.

2.4 *Tests*

Several testes were performed, keeping constant for each case (saturated and dry mixtures) channel length, slope and mixture volume whereas mixture composition, obstacle shape and orientation with respect to the flow direction were varied. For each mixture, a preliminary test without any obstacle was carried out in order to evaluate the effects of obstacles on flow and deposition and compare the results with those of the unperturbed case. Tested conditions are summarized in Tab. 1.

At the beginning of each test, the retention gate of the reservoir was instantaneously pulled up, generating at the downstream end of the chute a flow of less than 3 cm peak depth and 3 m/s peak velocity (see results in Tab. 1).

When the front impacts on the obstacle, it produces a force that is transferred by the lever system to the force transducer; the force on the obstacle increases abruptly until a maximum value is achieved, and then decreases with increasing time as flow depth and velocity quickly drop (Figs. 6–7).

All tests were performed more than once in order to check if tested conditions were repeatable and to provide data for possible statistical analysis.

3 RESULTS

The forces on the obstacles develop in time in a way that strictly dependends on the obstacle type: in particular, check-dams retain a certain quantity of material

Table 1. Measured data for experiments carried out. Mx = mixture type (d = dry, s = saturated); Rot = rotation angle respect flow direction, Y_f = front height; U_f = front velocity.

					Flow	
Mx	Obstacle	Rot.	Density ρ, (kg/m^3)	Force F_{max}, (N)	Y_f, (m)	U_f, (m/s)
1d	Check-dam, 1 cm	90°	1530	3.726	0.021	3.2
1d	Check-dam, 6 cm	90°	1530	5.521	0.020	3.2
1d	Check-dam, 10 cm	90°	1530	12.23	0.024	2.9
1d	Filter-dam, slope downstream	90°	1530	4.952	0.023	2.9
1d	Filter-dam, slope upstream	90°	1530	0.716	0.022	3.3
1d	House	90°	1530	3.628	0.023	2.9
1d	House	45°	1530	3.766	0.021	2.9
1d	Flow-breaker	90°	1530	2.618	0.024	2.9
1d	Flow-breaker	45°	1530	2.589	0.023	2.9
1d	No obstacle		1530		0.020	2.9
2d	Check-dam, 1 cm	90°	1580	3.481	0.024	3.3
2d	Check-dam, 6 cm	90°	1580	7.306	0.025	3.3
2d	Check-dam, 10 cm	90°	1580	12.46	0.024	3.1
2d	Filter-dam, slope downstream	90°	1580	5.854	0.028	3.1
2d	Filter-dam, slope upstream	90°	1580	1.043	0.025	3.4
2d	House	90°	1580	4.687	0.025	3.2
2d	House	45°	1580	6.364	0.025	3.2
2d	Flow-breaker	90°	1580	4.148	0.024	3.2
2d	Flow-breaker	45°	1580	3.589	0.025	3.3
2d	No obstacle	–	1580		0.025	3.1
1s	Check-dam, 3 cm	–	1675	10.15	0.024	2.0
1s	Check-dam, 6 cm	–	1675	27.07	0.022	2.6
1s	Check-dam, 9 cm	–	1675	32.13	0.023	2.3
1s	House	90°	1675	7.444	0.022	2.6
1s	House	45°	1675	6.041	0.017	2.7
1s	Filter-dam, slope upstream	90°	1675	4.854	0.023	2.3
1s	Filter-dam, slope upstream	90°	1675	3.030	0.016	2.3
1s	No obstacle	–	1675	-	0.025	2.2
2s	Check-dam, 3 cm	–	1872	8.669	0.023	1.9

Continued

Copyright © 2006 Taylor & Francis Group plc, London, UK

Table 1. *Continued*

Mx	Obstacle	Rot.	Density ρ, (kg/m^3)	Force F_{max}, (N)	Flow Y_f, (m)	Flow U_f, (m/s)
2s	Check-dam, 6 cm	–	1872	23.98	0.026	1.9
2s	Check-dam, 9 cm	–	1872	29.27	0.027	2.2
2s	House	90°	1872	6.561	0.026	2.2
2s	House	45°	1872	3.138	0.019	2.2
2s	Filter-dam, slope downstream	90°	1872	7.159	0.027	2.5
2s	Filter-dam, slope upstream	90°	1872	2.942	0.028	2.3
2s	No obstacle	–	1872	–	0.020	2.0

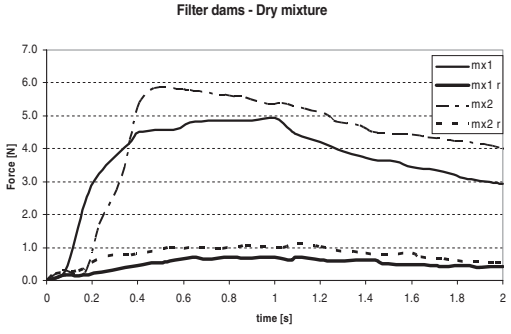


Figure 6. Force versus time for filter dams with dry granular flows, mx1 indicate *mixture 1*, mx2 *mixture 2*. The letter "r" indicate the teeth rotated in the flow direction.

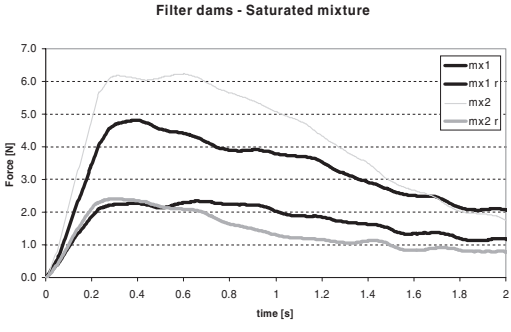


Figure 7. Force versus time for filter dams with saturated granular flows, mx1 indicate *mixture 1*, mx2 *mixture 2*. The letter "r" indicate the teeth torated in the flow direction.

upstream the dam that pushes permanently on the dam itself producing a constant force on the obstacle at the event end, whereas the other obstacles cause only a temporary storage of material that is eventually mobilised at the event tail and therefore no permanent force acts on the obstacle.

3.1 *Mixture saturation*

The presence of water is significant only in the case of wide obstacles with respect to channel section, check-dams and filter dams. Inside a saturated mass, neutral over-pressures are present and persist during the impact process (Iverson 1997; Major et al. 1999); they develop at the impact into vertical accelerations due to the incompressible interstitial fluid. The formation of vertical jets at walls occurs also in case of clear water (Partenscky, 1988; Rams-den 1996), whereas does not show up in case of a dry granular flow, that reflects more or less as a single back-wave. This behaviour is probably due to the compressibility of the dry porous media and thus to its capacity of compressing at the impact and dilating during shearing. Both in water and in saturated mixtures initial overshoots lasting less than 0.1 s were recorded, with peak values one order of magnitude higher than the force corresponding to the hydrostatic front pressure.

3.2 *Obstacle height*

When the whole channel width is crossed by a dam, dam height and slope (if it has) are critical parameters. The higher the dam, the greater the force and the shorter the downstream deposit.

Flow impact on check-dams produces in general a very abrupt arise of the force to the maximum value F_{max} that is strictly related to the ratio of dam height to flow depth. The lowest dam used in the experiments has an height which is less than the peak depth, and it is able to retain only a small amount of material: the force F_{fin} still acting on the dam when the flow stops is very low.

The medium dam and the highest dam, which are more than two times higher than the peak depth, produce an almost complete reflection of the flow inside the chute and a deposit upstream of the obstacle. The force peak values are similar in both cases.

The values of F_{fin} are not negligible and can be compared to those of the soil forces on retaining walls, which can be estimated in the range:

$$F_{fin} = \frac{1}{2}\rho_b g b y_{ob}^2 \frac{1-\sin\varphi}{1+\sin\varphi} \div \frac{1}{2}\rho_b g b y_{ob}^2 \frac{1+\sin\varphi}{1-\sin\varphi} \qquad (1)$$

where y_{ob} is the depth of the material at rest on the obstacle, g is the acceleration due to gravity and b is the chute/dam width. The two expressions in (1) represent, respectively, an active thrust, due to the elastic motion of the soil towards the walls, and a passive thrust, due to the elastic motion of the walls towards the soil. It has to be noted that (1) gives only the range of values for F_{fin}

Copyright © 2006 Taylor & Francis Group plc, London, UK

as it cannot be a priori predicted if the last soil motion will be towards or away from the side walls. In the case of saturated mixture this force slowly decreases because of the water drainage after the stop.

3.3 *Obstacle orientation*

The force exerted on houses and filter dams depends, both in cases of saturated and dry mixtures, on the obstacle orientation. In the first case, the obstacle acts like a spring-board for the coarser particles and the average flow is only decelerated but not retained behind the dam, which generates the lowest value of F_{max} (Tab. 1). In the second case, the flow is decelerated by the dam teeth but continues flowing until the spacing between teeth is partially filled up and then material is retained upstream. In this case, the measured force is larger and is comparable to that exerted on the medium check-dam. In particular, for the filter dams the ratio between F_{max} measured with teeth slope upstream and downstream is about two in the case of saturated mixture and up to five for dry material.

For obstacles such as houses and flow-breakers, a relevant effect on maximum force and deposit extension is the orientation of the obstacle with respect to flow direction. Houses and flow-breakers rotated at 45° are subjected to much greater force, because of the larger surface on which the flow impacts; these obstacles cause wider deposits than all the others because their shape forces the material to divide and flow towards the sides of the deposition plane. The edges of such rotated obstacles appear to be subject to such great forces that may in real cases produce structural damages due to engraving and fatigue effects.

For houses, the rotation from 90° to 45° does not significantly affect the value of impact force except for a small increase due to the wider side of the obstacle exposed to the flow.

3.4 *Mixture composition*

Maximum forces are mainly affected by obstacles design and orientation, but also mixture composition plays an important role since mixtures composed of higher fractions of coarser particles produce higher forces due to greater density and friction angle.

4 EXISTING DESIGN FORMULAE

Formulae for estimation of design debris flow forces per unit width are available only for flows against walls with width equal to channel width and height equal or higher than flow depth. In this case, two 'families' of formulae can be found in the literature.

The first is proper of slow flows and enlightens the pressure term. In the work by Armanini and Scotton (1993), the impact force (per unit width) of water-PVC mixtures F is approximated by:

$$F \approx 9\rho_m g \frac{y_n^2}{2} \tag{2}$$

where y_n can be assumed equal to the obstacle height. Similarly, the recommendations by some European torrent control authorities for designing structures in mountain torrents suggest (1973):

$$F = (7 \div 11)\rho_m g \frac{y_f^2}{2} \tag{3}$$

with y_f defined as the "maximum surge depth".

A similar expression was obtained by Scotton and Deganutti (1997) for the range of pressure increase at a wall with respect to the front hydrostatic pressure:

$$\Delta p = (2.5 \div 7.5)\rho_m g y_f \tag{4}$$

The second type of formulae is proper of rapid flows and enlightens the momentum of the incoming flow. Italian guidelines for mudflows (Commissario di Governo per l'Emergenza Idrogeologica nella regione Campania, 2001) propose to assume the total force as the sum of dynamic pressure and static pressure acting on the obstacle surface:

$$F = \rho_m u_f^2 \cos^2\theta\, y_f + \frac{1}{2}\rho_m g y_f^2 \tag{5}$$

An expression for mud forces against a wall is also given by Daido (1993):

$$F = (5 \div 12)\rho_m y_n u_n^2 \tag{6}$$

where u is the mean flow velocity, or the surge pressure given by Armanini and Scotton (1993):

$$\Delta p = \rho_m u_f (u_f + a) = \alpha_p \rho_m u_f^2 \tag{7}$$

where a is the celerity of the reflected wave and α_p is an impact coefficient that varies from 2.0 for slow and stony debris to 0.7 for rapid and muddy debris.

Equations (2), (3) and (6) propose different coefficients and different parameters, in particular y_n or y_f. In case of multiple surge events, without other specifications, y_f shall be assumed equal to the maximum depth value which can be up to three times y_n and thus the coefficient in (3) results (7 ÷ 11) times greater than the coefficient in (2). It appears thus very dangerous to extend equations like (2), (3) and (6) without taking care of the special conditions for which they were derived and also of the values they adopt (front or

Copyright © 2006 Taylor & Francis Group plc, London, UK

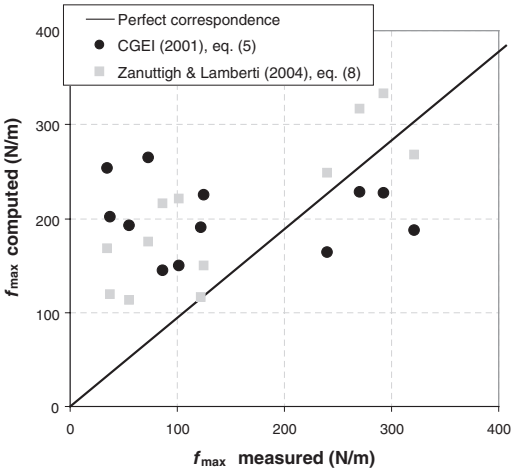


Figure 8. Comparison among measured forces and maximum forces computed with equations (5) and (8).

average or surge depth, front or average or maximum velocity).

Another approach is proposed by Zanuttigh and Lamberti (2006) under the hypothesis of a vertical wall against which a total reflection occurs. It consists of applying the momentum balance to the control volume including the upstream moving hydraulic jump that forms after the impact.

$$F = C_s \frac{(1+\sqrt{2}Fr_f)^2}{2} \rho_m g y_f^2 \qquad (8)$$

where C_s is a safety factor to account for non represented processes in the experiments, as boulders and vertical accelerations at the impact. The values for C_s suggested for calculating F are equal to 1.0 for stony debris and to 1.5 for muddy debris (Zanuttigh and Lamberti, 2006).

4.1 *Comparison with existing formulas*

We tested the capability of some existing formulaeto predict the force values recorded in our laboratories. Since presented formulae do not consider the obstacle shape, in particular the orientation of the obstacles with respect to the flow direction, the data set used for this comparison is made up only of check dam experiments.

Relation proposed by Armanini and Scotton (1993) and Scotton and Deganutti (1997) does not consider the dependence of force from velocity. Calculated forces result higher than those measured in our tests and the behavior of the forces is not well fit.

The Daido (1993) formula overestimates several times the measured forces, probably because the coefficient that multiply dynamic pressure, assumed by the author equal to 5 to 15, is too high and it is more appropriate to calculate impulsive forces due to pore pressure and boulders impact; however, these were not measured by our experimental set-up (Di Paolo et al. 2005).

A good agreement with experimental data is generally given by Italian guidelines (5); however, for the highest values of velocity they underestimate the measured force value. A better result is given from equation (8) with $C_s = 0.3$ for dry granular material and $C_s = 1$ for saturated material (Zanuttigh and Lamberti, 2006). That formula has a good agreement with experimental data, and underestimates measured forces in only one case (Figure 8).

5 CONCLUSIONS

The impact of dry and saturated granular flows on obstacles of various shapes has been experimentally analysed.

The impact process of granular flows on obstacles can be approximated by the impact of an inviscid fluid flow and equation (8) was found to be a good approximation to evaluate debris design force on structures.

Experiments show that the orientation of defence structures with respect to flow direction is strongly relevant on the recorded impact force values, but it is not considered in the existing design formulae.

Dynamic forces in nature are composed by an average and a fluctuant component. Solicitations due to the impacts of single boulders on obstacles and thus the fluctuant force components were not identified in this set of experiments but can be very important in determining fatigue over structures and can be regarded as an aim for a further work to improve the analytical prediction of forces acting on structures during real field events.

REFERENCES

Arattano, M., Deganutti, A. M. & Marchi, L. 1997. Debris flow monitoring activities in an instrumented watershed on the Italian Alps, *Proc. 1st ASCE Int. Conf. on Debris-Flow Hazards Mitigation: Mechanics, Prediction & Assessment*, San Francisco, California, ed. By Chen-lung Chen, 506–515.

Armanini, A. & Scotton, P. 1993. On the dynamic impact of a debris flow on structures, *Proc. of XXV IAHR Congress*, Tokyo, Tech. Sess. B, III; 203–210.

Barbolini, M., Biancardi, A., Natale L. & Pagliardi M. 2005. A low cost system for the estimation of concentration and velocity profiles in rapid dry granular flows. *Cold Regions Science and Technology*, volume 43, iusse 1–2 pag 49,61.

Copyright © 2006 Taylor & Francis Group plc, London, UK

Biancardi, A. & Ghilardi, P. 2003. A Low-cost System for High-speed Video Acquisition, Proc. *3rd IASTED International Conference on Visualization, Imaging and Image Processing, 2003*.

Berti, M., Genevois, R., Simoni, A. & Tecca, P. R. 1999 "Field observations of a debris flow event in the Dolomites", *Geomorphology*, 29, 265–174.

Burlamacchi, L. 1994 "Understanding concrete", in Italian: original title: "Capire il calcestruzzo", Ulrico Hoepli, Milan.

Commissario di Governo per l'Emergenza Idrogeologica nella regione Campania. 2001. *ORDINANZA N. 1991. "Normativa tecnica per la ricostruzione degli edifici privati, ad uso abitativo, danneggiati dalle colate di fango del 5 e 6 maggio 1998, nei comuni di Sarno, Siano, Bracigliano, Quindici e San Felice a Cancello."*

Cross, R. H. 1967. Tsunami surge forces. *Journal of the Waterways and Harbors Division*, ASCE, 93(4), 201–231.

Daido, A. 1993. "Impact force of mud debris flows on structures", *Proc. of XXV IAHR Congress*, Tokyo, Tech. Sess. B, III; 211–218.

Davies, T. R. H. 1985. The investigation of avalanche processes by laboratory experiments; exploratory tests, *Proc. Int. Symp. on Erosion, Debris Flow & Disaster Prevention*, Tsukuba, Japan, 215–218.

Davies, T. R. H. 1997. Large & small debris flows – occurrence & behaviour. *Recent Developments on Debris Flows A.Armanini & M.Michiue Eds, Lecture Notes in Earth Sciences*, 64, Springer-Verlag, 27–42.

Davies, T. R. H. 1997. Using hydroscience & hydrotechnical engineering to reduce debris flow hazard, *Proc. 1st ASCE Int. Conf. on Debris-Flow Hazards Mitigation: Mechanics, Prediction & Assessment,* San Francisco, California, ed. By Chen-lung Chen, 787–796.

DeNatale, J.S., Fiegel, G.L., Iverson, R.M., Major, J.J., LaHusen, R.G., Duffy, J.D. & Fisher, G. D. 1997. Response of flexible wire rope barriers to debris flow loading. *Proc. 1st ASCE Int. Conf. on Debris-Flow Hazards Mitigation: Mechanics, Prediction & Assessment,* San Francisco, California, ed. By Chen-lung Chen, 616–625.

DeNatale, J.S., Iverson, R.M., Major, J.J., LaHusen, R.G., Fiegel, G.L. & Duffy, J.D. 1999. Experimental testing of flexible barriers for containment of debris flows, *U. S. G. S. Open-File Report 99–205, 38, pp.*

Di Paolo, A., Ghilardi, P., Pagliardi, M. & B. Zanuttigh, 2005. "Valutazione sperimentale e analisi della forza d'impatto e delle pressioni esercitate da miscugli granulari saturi contro strutture" (Experimental evaluation and analysis of the impact force and pressures exerted by saturated mixtures against structures), in italian, *Proceedings of "La Mitigazione del rischio da colate di fango a Sarno e negli altri comuni colpiti dagli eventi del Maggio 1998"*, Commissariato di Governo per l'Emergenza Idrogeologica in Campania, Naples.

Hungr, O., Morgan, G. C. & Kellerhals, R. 1984. Quantitative analysis of debris torrent hazard for design of remedial measures, *Can. Geotech. J.*, 21, 663–667.

Iverson, R. 1997. The physics of debris flows. *Rev. of Geophysics*, 35 3, 245–296

Lichtenhan, C. 1973. Die Berechnung von sperren in beton und eisenbeton. *Kolloquium on torrent dams ODC 384.3,* Mitteilungen der forstlichen bundes versuchsanstalt, Wien.

Major, J.J & Iverson, R. 1999. Debris-flow deposition: effects of pore-fluid pressure & friction concentrated at flow margins", *Geological Society of America Bullettin*, 111, n.10, 1424–1434.

Okuda S., Suwa H., Okunishi K., Yokoyama K. & Nakano M. 1980. Observations on the motion of a debris flow & its geomorphological effects. *Z. Geomorph. N.*F., Suppl. Bd. 35, 142–163.

Partenscky, H.W. 1988. Dynamic forces due to breaking waves at vertical coastal structures. *Proc. 21st Coastal Eng. Conf. June 1988.*

Ramsden, J.D. 1996. Forces on a vertical wall due to long waves, bores, and dry-bed surges. *J. of Wat., Port, Coastal and Ocean Eng.ng, May/June, 134–141*.

Scotton, P. & Deganutti, A. M. 1997. Phreatic line & dynamic impact in laboratory debris flow experiments. *Proc. 1st ASCE Int. Conf. on Debris-Flow Hazards Mitigation: Mechanics, Prediction & Assessment,* San Francisco, California, ed. By Chen-lung Chen, 777–786.

Zanuttigh, B. and Lamberti, A. (2006). Experimental analysis of the impact of dry avalanches on structures and implication for debris flows. *in press, J. of Hydr. Res.*

Zhang, S. 1993. A comprehensive approach to the observation & prevention of debris flows in China, *Natural Hazard*s, 7, 1–23.

Copyright © 2006 Taylor & Francis Group plc, London, UK

Limiting conditions for the existence of permanent periodic roll waves in stony debris flows

S. Longo
Department of Civil Engineering, University of Parma, Parma, Italy

ABSTRACT: This paper is about the free surface instabilities of granular flows, usually called roll waves. A shallow layer of dilatant (shear thickening) fluid is considered to study finite amplitude permanent roll waves down a slope, simplified by Karman's momentum integral approach. The existence of conditions of a periodic discontinuous solution is derived, as smooth profiles with depth increasing monotonically between periodic shocks. Energy dissipation in the body of the stream and in the discontinuity are analysed and discussed. Two conditions are derived. The first is related to the physically acceptable shape of the smooth profiles, and the second is related to positive energy loss across the shock. A minimum-length roll wave (MLRW) is defined as the periodic permanent roll waves with zero energy dissipation in the shock. Some properties of the MLRW are compared with the available results.

1 INTRODUCTION

Free-surface instabilities of flows down inclined channels have been widely observed in Newtonian and non-Newtonian fluids. Natural gravity flows as debris flows are recorded in many areas and are a constant reminder of the need for prediction and control. In most cases, the flow of mud and debris is far from uniform and stationary. It manifests a succession of waves which, given enough space, develop into long waves. This behaviour is common to water and many non-Newtonian fluids. Roll waves can develop in laminar or turbulent flows and are essentially controlled by the Froude number. Several authors in many areas have reported observations of roll waves in mud flows. The widespread formation of free-surface instabilities, independent of the rheological properties of the fluid, is due to the effects of inertia: if the flow field could adjust its characteristics instantaneously, it would respond to a variation of the current depth reducing the local mean velocity, and the wave would simply be a kinematic wave. In real situations, the response is delayed, and an increased current depth enhances a positive mass flux, leading to the growth of the perturbation (Smith 1990; Forterre & Pouliquen 2003). In addition, the presumed structure of the wall boundary layer favours the growth of the perturbations: the adverse gradient pressure acts to destabilise the boundary layer, reducing the wall friction and accelerating the wave crest (Longo 2004). Dressler (1949) also emphasised the need for a friction reduction in the flow direction, from smaller to larger water depths, in order to obtain roll waves. Although the rheological properties of the fluid do not control the instability mechanism, all the characteristics of the development of the wave depend on those properties.

The first study of the phenomenon was based on linear-stability analysis of the basic equations written in the long-wave approximation and applied to the laminar current. In turbulent flow in rectangular channels, assuming a Chézy resistance law with a constant coefficient, Jeffreys (1925), Stoker (1957), and Liggett (1975) found a critical Froude number of 2.

Dressler (1949) developed the finite-amplitude wave theory. In his paper, Dressler described discontinuous periodic solutions obtained joining Bresse profiles with shocks. Dressler's theory, originally developed for fully turbulent flows, was extended to laminar flows for Newtonian fluids by Ishihara et al. (1954) and to power-law fluids by Ng & Mei (1994), who essentially focussed on pseudoplastic fluids (mud). Prasad et al. (2000) applied Dressler's theory to flowing dry grains at moderate-low void concentration (the inter-particles fluid is air). In their analysis, which was based on experiments, the authors assumed that a large increase in the volumetric solid fraction takes place near the front of the wave. They approximate the depth-averaged dispersed flow of the grain in a manner similar to those of shallow fluid flow. Forterre & Pouliquen (2003) carried out experiments on long-surface-wave instability in granular material flows in dense regimes, using a linear-stability analysis to predict many features of the waves.

Copyright © 2006 Taylor & Francis Group plc, London, UK

Most of the results available refer to the limit condition for the existence of roll waves, but no one can infer the determination of roll-wave parameters (wavelength, wave height, celerity) for a given system. There are some experimental indications from Ponce & Maisner (1993), who, using Brock's data (1967), found that the observed periodic roll waves match the maximum growth rate (in linear-stability analysis). Referring to frequency, Kapitza (1948) suggested that all waves are expected to be unstable, and the least unstable are selected by the system. He also suggested that the observed waves have the maximum absolute rate of energy dissipation. A different criterion is developed by Ng & Mei (1994), who infer that the observed roll wave has the lowest amplitude corresponding to no energy loss across the shock.

In this paper, Dressler's theory is extended to granular flows in dense regimes. The friction law for dry, granular materials flowing in a dense regime is a subject for research; our assumptions are a simplification. Some recent results on this topic suggest that a generalised basal-friction law (Pouliquen 1999) can quantitatively predict rather well the long-wave instability of dry, granular material (Forterre & Pouliquen 2003). In the present analysis, it is assumed that grains behave like a power-law fluid, with a fluid index (the exponent of the shear rate in the constitutive equation) of $n = 2$ (dilatant fluid). Dilatant fluids in which $n = 2$ were experimentally described and modelled by Bagnold (1954) for granular mixture at a relatively high shear rate. They also correspond to dry, granular material at large grain-volume concentrations and moderate shear rates. We will assume this value for the fluid index, but we need to mention that Chen & Ling (1996, 1998) and Hunt et al. (2002) revisited Bagnold's data and concluded that the value of the fluid index is ~ 1.5. It is assumed that the fluid is homogeneous and that no segregation occurs.

The roll waves herein described are periodic, discontinuous solutions with a discontinuity (shock) connecting a smooth profile in a shallow-flow approximation. The waves are permanent and move downstream with a celerity higher than the maximum fluid velocity. It is assumed that they are permanent and stable.

The next section is devoted to deriving the basic equations applying Karman's momentum-integral method. In §3, we describe the 'special solution', and in §4 we obtain a first admissibility condition for roll waves in a dilatant fluid. In §5, the discontinuity between two subsequent waves is analysed under some restrictive hypotheses. Section 6 is devoted to energy balance in the discontinuity, with the derivation of a second admissibility condition. In §7 and in §8, the Minimum Length Roll Waves is discussed and the limiting discharge condition is interpreted, using the two admissibility conditions, with comparison between experiments and theory. The energy balance in the unstable stream is treated in §9, and discussion and conclusions are given in §10 and §11.

2 BALANCE AND CONSERVATION EQUATIONS

Let us consider a 2D laminar flow of a fluid down a plane of inclination θ. The coordinate system has the x-axis along the bed and the y-axis normal to it. For long waves, we can assume that variations in the flow occur on lengths larger than the thickness. Applying Karman's momentum integral method to mass conservation and linear-momentum balance, we obtain the following set of equations:

$$\begin{cases} y_{,t} + (uy)_{,x} = 0 \\ u_{,t} + \beta u u_{,x} - (\beta - 1)\dfrac{u}{A}\dfrac{dA}{dy} y_{,t} + \\ rg\cos\theta\, y_{,x} + u^2 \beta_{,x} = g\sin\theta - \dfrac{\tau_b}{\rho R} \end{cases} \tag{1}$$

where u is the depth average velocity of flow function of the longitudinal coordinate x at time t, A is the cross-sectional area of flow, y is the depth of the flow, β is the momentum flux factor (equal to 5/4 for a dilatant fluid in laminar condition in a very wide rectangular section and with $n = 2$), and r is the ratio of the normal stress in the x-direction to the normal stress in the y-direction. g is the acceleration of gravity, τ_b is the average boundary shear stress, ρ is the bulk mass density, R is the hydraulic radius of the flow. The first equation is the mass conservation; the second equation is the momentum-balance equation.

For non-uniform flow, r could depend on the divergence of the flow (Gray et al. 1999) but many numerical simulations have shown that this ratio is equal to ~ 1 for dense granular flows (Ertas et al. 2001).

Introducing a moving reference having celerity c, and assuming that in the moving reference the chosen state variables U and Y are functions of $\xi = x - ct$ only, the two equations (1) for a wide channel ($R \approx Y$) become:

$$\begin{cases} (UY)_{,\xi} - cY_{,\xi} = 0 \\ -cU_{,\xi} + \beta U U_{,\xi} + c(\beta - 1)\dfrac{U}{Y} Y_{,\xi} + \\ rg\cos\theta\, Y_{,\xi} = g\sin\theta - \dfrac{\tau_b}{\rho Y} \end{cases} \tag{2}$$

where the spatial variation of the momentum flux correction term has been dropped, even though this term should always be retained in order to satisfy the principle of frame indifference (Chen 1992).

Copyright © 2006 Taylor & Francis Group plc, London, UK

Rearranging the two equations and integrating results:

$$U = \frac{(cY - K)}{Y} \tag{3}$$

where K is the constant discharge per unit width in the moving frame. It was defined as 'overrun' by Chow (1959) and 'progressive discharge' by Dressler (1949). The discharge in the fixed frame varies with space and time.

For dilatant power-law fluid with $n = 2$, the bottom shear stress in a wide channel is

$$\tau_b = \rho a \frac{U^2}{Y^2} \tag{4}$$

and the energy slope is $j = aU^2/gY^3$, where a is a parameter (depending on the density, size, concentration of grains, and internal friction for a granular mixture) with the dimension of a square length.

On using expressions 3 and 4 and assuming a length scale for both horizontal and vertical directions $l = c^2/g$, equation 2 can be rearranged and written in non-dimensional form as:

$$Y^*_{,\xi^*} = \sin\theta \frac{\left[Y^{*5} - b\left(Y^* - K^*\right)^2\right]}{Y^{*2}\left[\beta Y^{*2} - Y^{*2} + rY^{*3}\cos\theta - \beta K^{*2}\right]} \tag{5}$$

where $b = \frac{a}{\sin\theta}\frac{g^2}{c^4}$, K^* is the non dimensional constant discharge per unit width in the moving frame, ξ^* is the non dimensional abscissa in the moving frame and $Y^*_{...} = Y_{...}g/c^2$.

3 THE 'SPECIAL SOLUTION'

Owing to the kind of functions obtained integrating equation 5 (logarithm, hyperbolic function, polynomials), no periodic solution is forecast for the wave profile. A possible solution is a discontinuous periodic solution, piecing together continuous profiles with shocks. Such a solution was suggested by Dressler (1949) for Newtonian fluid. Dressler named it the 'special solution', and we will follow the same definition. As for a Newtonian fluid, the solution has to admit a region with supercritical mean velocity and a second region with sub-critical mean velocity (in the moving reference). The two regions are separated by a critical section with mean velocity equal to the critical velocity. The flow depth in the critical section is Y_c.

There is experimental evidence that a roll-waves profile in a Newtonian fluid has a finite steepness in the critical section. We assume that this holds true also for roll waves in a granular flow and it is possible to demonstrate that no solution with an inflection point is possible.

As a consequence, the possible periodic solution requires that the critical depth also be a root of the numerator in equation 5 in order to have a finite steepness. The pole in $Y = Y_c$ must be erased. The result is that both numerator and denominator vanish in Y_c.

The apparent discharge is also constrained. Using mass conservation and equation 3 results in:

$$K^{*2} = \frac{Y_c^{*2}(\beta - 1) + rY_c^{*3}\cos\theta}{\beta} \tag{6}$$

Substituting equation 6 in the wave profile (equation 5) and considering that both numerator and denominator vanish in the critical section, results in:

$$Y^*_{,\xi^*} = \sin\theta \left[\frac{Y^{*4} + Y_c^* Y^{*3} + Y_c^{*2} Y^{*2} + \left(Y_c^{*3} - b\right)Y^* + \frac{bY_c^*}{\beta}\left[(\beta - 1) + Y_c^* r\cos\theta\right]}{Y^{*2}\left[(\beta - 1)\left(Y^* + Y_c^*\right) + r\cos\theta\left(Y^{*2} + Y_c^* Y^* + Y_c^{*2}\right)\right]}\right] \times \frac{1}{} \tag{7}$$

4 LIMITING CONDITION FOR A POSITIVE STEEPNESS OF THE PROFILE

In order to construct roll waves from the previous profile, it is necessary that $dY^*/d\xi^*|_{Y^*c} > 0$. The denominator in equation 7 is always positive. In the critical section, we simply have to make the numerator positive also. This condition is satisfied if (Longo 2003):

$$b < b_{crit} = \frac{25}{4}\left(\frac{25 - 16\beta}{25r\cos\theta}\right)^3 \tag{8}$$

The inequality 8 can also be expressed as:

$$c > c_{crit} = \left(\frac{ag^2 r^3}{\tan\theta\left(1 + \tan^2\theta\right)}\frac{4}{25}\left(\frac{25}{25 - 16\beta}\right)^3\right)^{1/4} \tag{9}$$

In this form, our findings indicate that, for a given bottom inclination and a given rheological parameter of the dilatant fluid, only waves with celerity higher than the critical celerity can propagate. Roll waves can exist only if the condition $c > U$ is satisfied. As a consequence, equation 9 can be extended in the form $c > c_{crit} > U$, and using the resistance law, the discharge per unit width q has an upper limit given by the following inequality:

$$\left(\frac{gq^3\sin\theta}{a}\right)^{1/5} < \left(\frac{ag^2 r^3}{\tan\theta\left(1 + \tan^2\theta\right)}\frac{4}{25}\left(\frac{25}{25 - 16\beta}\right)^3\right)^{1/4} \tag{10}$$

Copyright © 2006 Taylor & Francis Group plc, London, UK

Equation (10) can be solved in terms of the stream depth for the stable flow with the following result:

$$Y^* < Y^*_{crit} \equiv \left(\frac{4}{25}\right)^{1/6} \sqrt{br\cos\theta\left(\frac{25}{25-16\beta}\right)} \qquad (11)$$

This condition is not necessary, because the condition $c > U > c_{crit}$ also satisfies Whitham's criterion (Whitham 1974) ($c > U$) and inequality (9). However, inequalities 9, 10, and 11, if not satisfied, can prevent the appearance of roll waves or can dump already developed roll waves, depending on the status of the flow. For instance, a well-established pattern of permanent periodic roll waves can be destroyed by increasing the flow discharge, but can appear again downstream, where the celerity of the free-surface perturbations increases over the mean flow velocity. Typically, wave celerity increases with the distance from the inlet of the channel, and we can expect that for sufficiently long channels, the section of first appearance of the permanent roll waves is moved downstream. Obviously, if the permanent roll waves already developed are much faster than the critical value reported in equation 9, they continue to exist also in the presence of an increased discharge with $U > c_{crit}$, given that the condition $c > U$ is satisfied.

This behaviour is consistent with some experimental results (Forterre & Pouliquen 2003; hereafter FP), who described the long-surface-wave instability in dense granular flows of sand and glass beads and, for the former, visually observed that waves develop in the domain between the no-flow state (sediments at rest) and a stable flow at higher discharge. In their description, summarised in a qualitative diagram, if the thickness of the layer at a fixed inclination is increased, then the waves form further and further downstream and eventually disappear. In the present analysis, a finite-amplitude analysis of the roll waves can predict a limiting condition for the existence of permanent periodic roll waves. Later, we shall verify that a second limit on the existence of roll waves is related to the energy balance in the shock. Both limits shall be discussed in §8.

5 SHOCK CONDITION

The shock condition is obtained from the mass-conservation and momentum-balance equations for a control volume across the shock:

$$\begin{cases} c\left[Y\right]_f^b = \left[UY\right]_f^b \\ c\left[UY\right]_f^b = \left[\beta U^2 Y + \frac{1}{2} g Y^2 r\cos\theta\right]_f^b \end{cases} \qquad (12)$$

where the square brackets are the operator $[<.>]_f^b = <.>|_b - <.>|_f$ and b and f stand for the two control sections, back and front.

The weight of the roller and bottom friction have been neglected. In extended form, the details are reported in Longo (2003).

Neglecting the trivial solution $Y_b = Y_f$ (no shock), equation 12 can be solved, obtaining the relation between back and front stream depth. The minimum wavelength $\lambda^* \to 0$ corresponds to $Y \to Y_c$. The maximum wavelength $\lambda^* \to \infty$ corresponds to the maximum depth in front of the shock (and the maximum wave height). The height of the shock is given by $H^* = Y_b^* - Y_f^*$ and it tends to asymptotic values slightly dependent on bottom inclination and strongly influenced by the value of β. The wave steepness also tends to asymptotic values, with faster adjustment towards the limit for larger bottom inclination.

6 ENERGY DISSIPATION IN THE SHOCK

The rate of change of mechanical energy across the jump is equal to the following

$$\begin{aligned} \Delta P^* = &-\frac{1}{2}\left(1-\frac{K^*}{Y_b^*}\right)^2 Y_b^*\left(\alpha_b - \alpha_b\frac{K^*}{Y_b^*} - \beta_b\right) + \\ &\frac{1}{2}\left(1-\frac{K^*}{Y_f^*}\right)^2 Y_f^*\left(\alpha_f - \alpha_f\frac{K^*}{Y_f^*} - \beta_f\right) - \\ &\cos\theta\left[\frac{Y_b^{*2}}{2}\left(r-\frac{K^*}{Y_b^*}(1+r)\right) - \frac{Y_f^{*2}}{2}\left(r-\frac{K^*}{Y_f^*}(1+r)\right)\right] \end{aligned} \qquad (13)$$

Substituting the expression for discharge in the moving frame and dividing by the discharge per unit width in the moving frame, for $\alpha = \beta = 1$ and for $r = 1$, equation 13 has the classical expression:

$$\Delta E_j^* = -\cos\theta\frac{\left(Y_b^* - Y_f^*\right)^3}{4Y_b^* Y_f^*} \qquad (14)$$

Having neglected the thermal energy contribution, a necessary condition for a physically based shock is $\Delta E_j^* < 0$, that is, the shock dissipates mechanical energy. The (mechanical) energy dissipation condition in the shock limits the admissible values of Y_f^* and Y_b^*. Some results are shown in Figure 1. The physically admissible area is the region $Y_f^* < Y_b^*$, also contoured by a curve $f_{crit}(Y_f^*, Y_b^*) = 0$ in which $\Delta E_j^* > 0$. Note that if $\alpha = \beta = 1$ and $r = 1$, the critical curve has equation $Y_f^* = Y_b^*$, and the finitude amplitude shocks always dissipate energy, whereas for different values of the flux factors and of the parameter r, finite amplitude shock without energy dissipation is possible.

A sensitivity analysis indicates that increasing the bottom inclination moves the critical curve towards higher values of front/back stream depth. A reduction of the ratio r enlarges the closed-hatched area, corresponding to energy production in the jump (physically

Copyright © 2006 Taylor & Francis Group plc, London, UK

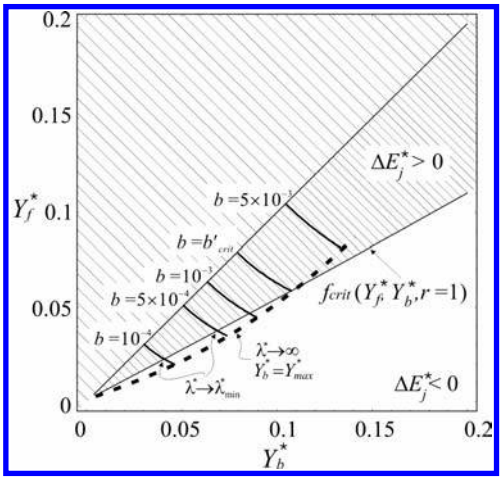


Figure 1. Energy and momentum balance in the jump. The hatched area is unacceptable, because $Y_f^* > Y_b^*$. The closed-hatched area corresponds to energy production in the jump, physically impossible. The thick curves satisfy the momentum balance across the shock, for different values of the parameter b. The dashed-tick curve represents the maximum layer thickness, in front of the shock, for different values of the parameter b, and corresponds to an infinite wavelength. $\beta = 1.25$, $\alpha = 1.705$, $\theta = 30°$, $r = 1$, $b'_{crit} = 0.00216$.

impossible). A reduction in the two factors α and β moves the critical curve towards modest values of the front/back stream depth.

The limitation due to energy dissipation condition in the shock corresponds to a limitation in wave height $(Y_f^* - Y_b^*)$ and is equivalent to imposing a minimum wavelength, since wavelength increases with the wave height.

A double-band structure is observed for $r \to 1$ (not shown), with finite amplitude shock heights corresponding to zero energy dissipation confined to two separated wave-number bands. The intermediate wave band corresponds to a stable state (no shock) and fixes a cut-off frequency. More correctly, the shock acts as a band-rejection filter.

A second limitation on the maximum value of the parameter b is obtained by observing the energy balance in the hydraulic jump and the function $Y_b(Y_f)$, describing the possible back-front heights compatible with the mass and momentum balance for a control volume across the shock. The curves are reported for different values of the parameter b in Figure 1. The starting point of the thick curves corresponds to $Y_b^* \equiv Y_f^* \equiv Y_c^*$ and to $\lambda^* \to 0$. The end point corresponds to $Y_b^* \equiv Y_{max}^*$, $\lambda^* \to \infty$.

A critical value of the parameter b exists which corresponds with a maximum flow depth in front of the shock coincident with the zero energy dissipation in the jump. The critical value b'_{crit} is obtained numerically solving a strongly non-linear system of equations representing energy dissipation and momentum balance in the shock, with the further condition that the wavelength tends to infinity.

For $b < b'_{crit}$, only wavelengths greater than λ_{min} are allowed. The critical value of the parameter b fixed by the existence condition of the wave profile (see §4) is generally larger than b'_{crit}.

The condition $b < b'_{crit}$ is equivalent to

$$c > c'_{crit} = \left(\frac{ag^2}{b'_{crit}\sin\theta}\right)^{1/4} \tag{15}$$

which in non-dimensional form reads

$$Y^* < Y^*_{crit} \equiv \left(\frac{b^3}{b'_{crit}}\right)^{1/6} \tag{16}$$

Similar results were obtained by Ng & Mei (1994) for mud flows. On using the dissipation energy criterion in the shock, they obtained a minimum discharge in the moving frame (equivalent to a maximum discharge in the fixed frame), a minimum celerity of the roll waves and a maximum wave number (corresponding to a minimum wavelength). As for the limit described in §4, this is not a necessary condition for roll waves, because the condition $c > U > c'_{crit}$ also satisfies the Whitham criterion. In §8, there is a discussion of the limiting discharge as computed using the limits 9 and 15.

7 THE MINIMUM-LENGTH ROLL WAVE (MLRW)

The requirement of a minimum energy dissipation in the shock is met by the waves with a wavelength equal to λ_{min}. Herein, these waves are called MLRW. The computation of the relevant characteristics of the MLRW is carried out as follows:

(i) for given b ($<b'_{crit}$), θ, α, β, r, evaluate $\lambda^*_{\min}$, Y_b^* and Y_f^*;

(ii) evaluate Y_c^* and K^* and solve for the average depth and the average discharge in the fixed frame

(iii) on using the velocity law

$$\frac{U}{\sqrt{gY}} = Y\sqrt{\frac{\sin\theta}{a}} \tag{17}$$

as obtained from equations 2 and 4, evaluate the normal velocity Y_n^* and the Froude number as

$$Y_n^* = b^{1/5}\langle q^*\rangle^{2/5}, \quad F = \frac{Y_n^*}{\sqrt{b\cos\theta}} \tag{18}$$

$\langle q^*\rangle$ is the non dimensional average discharge in the fixed frame. The non-dimensional wave celerity is obtained as

$$\frac{c}{U_n} = \sqrt{\frac{b}{Y_n^{*3}}} \tag{19}$$

Copyright © 2006 Taylor & Francis Group plc, London, UK

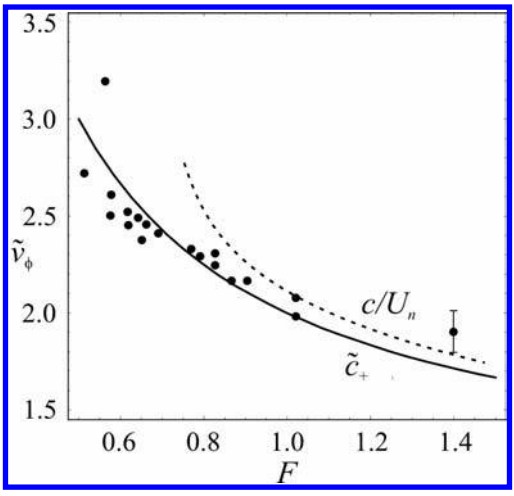


Figure 2. Phase velocity as a function of the Froude number. • experiments by FP; solid line, velocity of the gravity waves as computed by FP (linear model), $\tilde{c}_+ = 1 + 1/\mathrm{F}$; dashed line, MLRW celerity, present model. $\beta = 1.03$, $\alpha = 1.02$, $r = 1$.

In Figure 2, the experimental phase velocity of granular roll waves as a function of the Froude number as reported in FP is compared with the MLRW celerity as obtained in the present model. For $F < 1$, the MLRW systematically has a celerity in excess of the experiments and the linear-model prediction. For $F > 1$, the experiments are few and no firm conclusion can be drawn.

A sensitivity analysis was carried out in order to discover the possible causes of the discrepancy between experiments and the results of the present model. As expected, reducing the two flux factors towards unity improve the overall results, with the MLRW celerity collapsing with the linear model prediction. In fact, for $\alpha \to 1$ and $\beta \to 1$, the MLRW shock height tends to become rather small and the non-linearity is weak.

8 LIMITING DISCHARGE

In FP's experiments (2003), it was observed that granular flows of sand 0.8 mm in diameter down an inclined rough plane develop in roll waves as long as the thickness layer is close to the threshold of the flow. But when one increases the thickness of the layer at a fixed inclination, increasing the discharge, the roll waves disappear and the flow recovers its stability. For granular waves of glass beads 0.5 mm in diameter, the flow is stable and then becomes unstable at a larger flow rate. For sand flows, there must be a mechanism to recover stability, e.g., a drainage of energy which prevents roll waves from growing and which is related to the characteristics of rapid flows. In the present model, two possible mechanisms are detected. The first is related to the physical evidence of a positive steepness of the roll waves in the critical section. The second is related to the energy balance in the shock. Both mechanisms limit the value of the parameter b; these limits can be converted into a limiting thickness of the (normal) flow, even though they do not represent a necessary condition for the existence of roll waves.

8.1 *Results for sand*

In their analysis, FP adopt an experimental velocity law for sand flows expressed as

$$\frac{U}{\sqrt{gY}} = -0.77 + 0.65\frac{Y}{Y_{stop}(\theta)} \tag{20}$$

The function Y_{stop} represents the thickness of the deposit left by a steady uniform flow at the inclination θ. For sand, this function is expressed as

$$Y_{stop}(\theta) = 2.03d\left(\frac{\tan\delta_2 - \tan\delta_1}{\tan\theta - \tan\delta_2} - 1\right) \tag{21}$$

with $d = 0.8$ mm, $\delta_1 = 27.0°$, $\delta_2 = 43.4°$. δ_1 and δ_2 are two parameters of the material.

In the present model, the assumed velocity law is reported in equation 17.

With a different velocity law having been used, a comparison between the present model and the experimental results by FP requires the computation of the equivalent value of the parameter a. It is also realistic to assume a is not constant but is a function of the flow conditions. The equivalent value of a can be evaluated in two ways: (i) imposing an equal velocity computed using equation 17 and equation 20; (ii) imposing the equality only of the quadratic contribution (i.e., equalising the velocity law in equation 17 with the second contribution in equation 20).

In both cases, the equivalence is imposed in the limit stability points (Y_{lim}, θ) reported in Table 1, as obtained from the qualitative diagram sketched by FP.

In keeping with the analysis of Bagnold (1954) and Takahashi (1991), the computed parameter a decreases for decreasing void concentration of the sediments, which is expected for fast flows at increased values of θ. The second criterion for evaluating the equivalent value of the parameter a gives results (last column in Table 1) in fairly good agreement with the experiments (see Figure 3).

These results have been obtained assuming fixed values for the two factors $\alpha = 1.03$ and $\beta = 1.02$. Measurements of velocity profiles in a granular flow on an erodible bottom (Longo & Lamberti 2001) reveal that α and β can assume values much larger than unity, but it is expected that nearly uniform velocity profiles can develop for fast flows down an inclined plane. It is also expected that bottom stress in unsteady flow differs considerably from the corresponding value in

Copyright © 2006 Taylor & Francis Group plc, London, UK

Table 1. Limiting conditions for the existence of roll waves in granular sand flows. The values for b'_{crit} refer to the turbulent profile ($\beta = 1.02, \alpha = 1.03$), with $r = 1$. Y_{lim}, experimental values by FP (2003); b_{crit}, Y_{crit}, computed values using equations 4.9 and 4.13; b'_{crit}, computed value for the limiting condition discussed in §7; $a_{(1)}$, $Y'_{crit-comp1}$, computed values using criterion (1); $a_{(2)}$, $Y'_{crit-comp2}$, computed values using criterion (2).

θ °	Y_{lim} (mm)	(b_{crit})	Y_{crit} (mm)	b'_{crit}	$a_{(1)}$ $\times 10^{-5}$ (m^2)	$Y'_{crit-comp1}$ (mm)	$a_{(2)}$ $\times 10^{-6}$ (m^2)	$Y'_{crit-comp2}$ (mm)
33	6.5	0.4434	6.1	0.1505	11.0	19.4	15.0	7.3
34	5.5	0.4590	4.7	0.1561	5.2	13.2	9.4	5.6
35	4.7	0.4759	3.7	0.1619	2.6	9.1	5.9	4.4
36	4	0.4940	2.8	0.1680	1.4	6.6	3.7	3.4
37	3	0.5135	2.2	0.1745	0.9	5.3	2.3	2.6

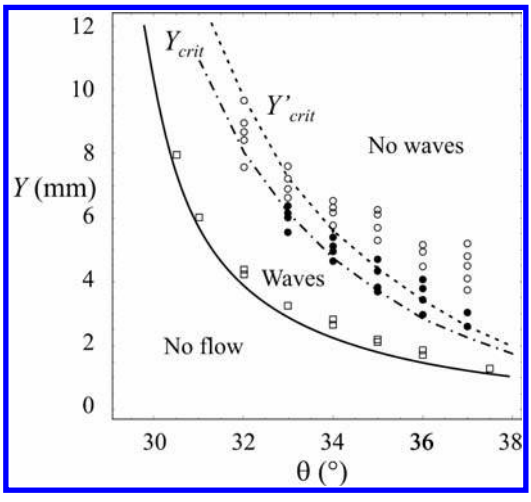


Figure 3. Stability diagram, as sketched by FP (2003) for sand flows, and computed upper limit of existence of roll waves. •, Waves; ○, no waves; □, flow threshold; dashed line, present model, results due to b'_{crit}; dash-dot line, present model, results due to b_{crit}.

steady flow, with a consequent spatial variation of both flux factors. The lack of experimental data to evaluate α and β suggests that it would be better to consider these two factors calibration parameters (see also FP (2003) on this point).

If we express the Froude number corresponding to the limit in equation 11 (first critical Froude number), we obtain

$$F_{crit} = \frac{U_{crit}}{\sqrt{gY_{crit}\cos\theta}} \equiv Y_{crit}\sqrt{\frac{\tan\theta}{a}} \equiv \frac{1}{\left(b_{crit}\right)^{1/6}\sqrt{\cos\theta}} \equiv \frac{1}{\left(\frac{25}{4}\right)^{1/6}\sqrt{\frac{25-16\beta}{25r}}} \qquad (22)$$

The first critical Froude number $F_{crit} = F_{crit}(\beta, r)$ is independent of the bottom inclination and the rheological parameters of the granular medium. For $r = 1$ and $\beta = 1.02$ assume the value $F_{crit} = 1.25$.

If we express the Froude number corresponding to the limit in equation 16 (the second critical Froude number), we obtain

$$F'_{crit} = \frac{U'_{crit}}{\sqrt{gY'_{crit}\cos\theta}} \equiv Y'_{crit}\sqrt{\frac{\tan\theta}{a}} \equiv \frac{1}{\left(b'_{crit}\right)^{1/6}\sqrt{\cos\theta}} \qquad (23)$$

The computed value of F'_{crit} does not depend on the criterion used to evaluate the equivalent a; using the computed values of b'_{crit}, it does not depend on bottom inclination and is constant for given values of α, β and r, i.e., $F'_{crit} = F'_{crit}(\alpha, \beta, r)$ and $b'_{crit} \propto (\cos\theta)^{-3}$. For $\alpha = 1.03$, $\beta = 1.02$ (turbulent flow) and $r = 1$, results $F'_{crit} = 1.496 \pm 0.001$; for $\alpha = 1.704$, $\beta = 1.25$ (laminar flow) and $r = 1$, results $F'_{crit} = 2.99 \pm 0.01$, while for $r = 0.9$ in laminar flow results $F'_{crit} = 3.04 \pm 0.01$.

8.2 *Results for glass beads*

The approach used for sand (§8.1) can also be applied to glass beads, the second material used in the granular flows analysed by FP. In the experiments of the writers, flows of glass beads did not experience natural roll waves; it was necessary to impose a disturbance at the entrance of the flow. The forced instability is convective, and a region of linear instability is present. The experimental velocity law for flows of glass beads is expressed as

$$\frac{U}{\sqrt{gY}} = 0.136\frac{Y}{Y_{stop}(\theta)} \qquad (24)$$

As for sand flows, the function Y_{stop} represents the thickness of the deposit left by a steady uniform flow at the inclination θ, and is expressed as

$$Y_{stop}(\theta) = 1.65d\left(\frac{\tan\delta_2 - \tan\delta_1}{\tan\theta - \tan\delta_2} - 1\right) \qquad (25)$$

with $d = 0.5$ mm, $\delta_1 = 20.9°$, $\delta_2 = 32.76°$.

In order to compare the results of the present model with the experiments, for glass beads we can assume, without further hypothesis, that

$$a = \sin\theta\left[\frac{Y_{stop}(\theta)}{0.136}\right]^2 \qquad (26)$$

The two critical Froude numbers are independent of the specific granular material flowing. The stability diagram for glass beads is reported in Figure 4.

The dot-dashed and the dashed curves in Figure 4 correspond to $F_{crit} = 1.25$ and to $F'_{crit} = 1.496 \pm 0.001$.

Copyright © 2006 Taylor & Francis Group plc, London, UK

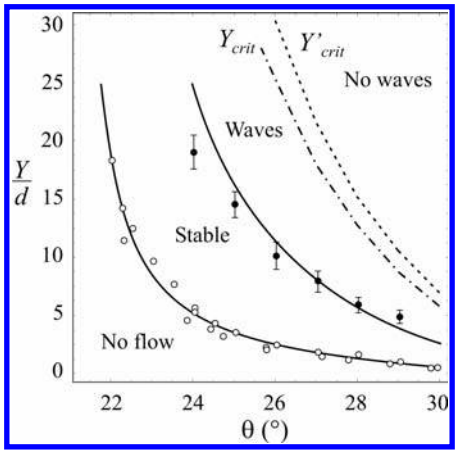


Figure 4. Stability diagram, as sketched by FP (2003) for glass beads ($d = 0.5$ mm), and computed upper limit of existence of roll waves. ○, Flow threshold; ●, waves; continuous line, theoretical predictions by FP; dashed line, present model, results due to b'_{crit}; dash-dot line, present model, results for b_{crit}.

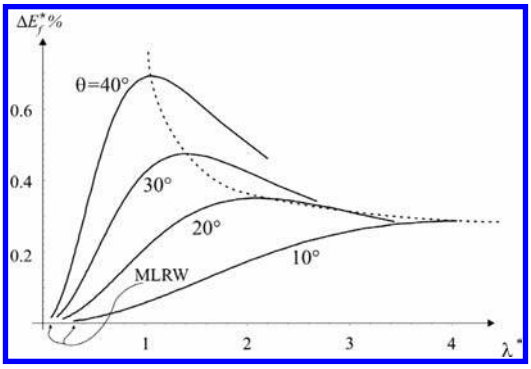


Figure 5. Extra dissipation due to friction. $\beta = 1.25$, $b = 0.01$, $r = 1$.

Unfortunately, the measurements by FP could not be extended to Froude numbers higher than ~1.4 for the maximum bottom inclination ($\theta = 29°$ for glass beads) due to the limited length of the channel, and to Froude numbers higher than ~0.85 for the minimum bottom inclination ($\theta = 24°$ for glass beads) due to the limited discharge rate of the feeding silo. Apparently, observing the published data, a single test is available beyond the first threshold but below the second threshold, and it indicates an unstable flow, whereas a stable flow is expected. No firm conclusions can be drawn about the experimental verification of the present model for flows of glass beads.

9 ENERGY DISSIPATION IN THE UNSTABLE STREAM

The mean energy dissipated for friction in a wavelength is computed in non-dimensional form as

$$\Delta E_f^* = -b \sin\theta \int_{Y_f^*}^{Y_b^*} \frac{U^{*2}}{Y^{*3}} \frac{1}{Y_{crit}^*} dY^* \qquad (27)$$

A stream in steady, uniform motion obviously results in $\Delta E_f^* + \lambda^* \sin\theta = 0$ for any value of the wavelength λ^*. In the presence of roll waves, including the energy dissipated in the jump, the energy balance over a wavelength results in

$$\Delta E^* = \Delta E_f^* + \Delta E_j^* + \lambda^* \sin\theta \qquad (28)$$

Assuming a friction law in non-uniform, unsteady motion equal to the friction law in steady, uniform motion, the energy budget is generally a negative function. That is, the system dissipates more energy than the energy gained from gravity.

The results of numerical integration are shown in Figure 5. In the vertical, the percentage of extra energy dissipation with respect to the stable uniform stream is reported. The starting point corresponds to the MLRW, and all the curves have a maximum value decreasing for lower bottom inclination. The jump enhances dissipation, and the stream in unstable motion dissipates more than the equivalent stream in stable, steady, uniform motion (*equivalent* means having the same average discharge with identical channel characteristics). All the computations have neglected the finite size of the moving shock, the contribution of the weight of the grains in the shock, and the curvature of the trajectories. It has been demonstrated that for roll waves in water streams, inclusion of the weight of the fluid in the jump in linear momentum balance across the shock tends to reduce the ratio Y_b^*/Y_f^* (Brock 1967) and favours smaller wavelengths. Surface tension contrasts the growth of instabilities and rounds the wave crest (Hwang et al. 1994) and the energy balance is very sensitive to small variations in the parameters. Also, the assumption of a different friction law gives different results. In a dry, granular stream, surface tension is not present, but all the other mentioned factors are present. According to Kapitza (1948) and Ng & Mei (1994), the observed roll wave has the smallest mean energy averaged over the wavelength. Such a roll wave clearly meets the condition of finite amplitude shock with zero dissipation across it and has back/front depth on the critical curve, but still dissipates more energy than the energy gained. Dressler's hypothesis (that a roll wave with a minimum of dissipated energy could be present and hence could be the stable solution) unfortunately, is not borne out, at least for granular flows. Unless a different friction law is included, to manage

Copyright © 2006 Taylor & Francis Group plc, London, UK

the boundary layer structure in the presence of adverse gradient pressure, the energy budget is negative. Also, computing the energy budget of the MLRW for varying b (and hence for varying wave celerity c at a given bottom inclination θ) results in a monotonic function, with extra dissipation increasing with decreasing b. This result is not of much help in determining the stable permanent roll wave.

10 DISCUSSION

One of the most striking aspects of granular roll waves is the stabilising effect of an increased discharge. Roll waves appear at the onset of motion and eventually disappear, increasing the discharge or bottom inclination. It seems that the present model gives an answer to the phenomenon, even though more experiments are necessary to better quantify the effects and to extend the validity of the approach to other granular media. Some doubts still remain about the stability of the permanent periodic roll waves. We need to mention that reports on experiments on roll waves in water (Brock 1967) make a substantial difference between natural and periodic roll waves. The former spontaneously appear in a channel as a result of amplification of natural (non-imposed) disturbances and are generally not periodic; the latter are periodic and are usually obtained by forcing the inlet with a paddle and by adjusting the amplitude and period of the paddle motion. This result indicates that roll waves (in water) are not necessarily periodic, and if periodic roll waves are stable, they need a minimum length of the channel to become permanent. This minimum length of the channel is of the order of thousands wavelengths and imposes severe restrictions on its feasibility in the laboratory. If the results for roll waves in water hold true also for granular roll waves, a typical length scale for the channel should be of the order of $\sim$200 m (the typical distance between surges, as observed by FP, is $\sim$20 cm). We can infer that roll waves in a 2 m long channel are presumably not 'mature', in the sense that they have not acquired stable characteristics (if any). It is also difficult to verify that they are strictly periodic.

The hypothesis that the measured granular roll waves are not mature can also explain the apparent overestimation of the wave celerity by the theoretical MLRW model and the good fitting of the linear model by FP. In fact, typical results on natural roll waves in water indicate that the average wave celerity increases downstream, presumably reaching a maximum when a stable, permanent shape is obtained. If it holds true also for granular roll waves, the experimental points in a downstream section of the channel should move up in the diagram reported in Figure 2.

On the basis of the results obtained in §9, two main indications arise. The first is that the resistance law adopted cannot be fully correct in the unsteady motion analysed and the boundary layer structure should be included in order to explain a reduced friction and dissipation; the second is that we can infer that permanent roll waves, as described in the present analysis, cannot completely fill the flow system. They have to coexist with other waves which dissipate less than the energy gained from gravity, leaving the excess for satisfying the energy balance. Otherwise, all the experimentally observed roll waves are unstable (Kapitza 1948), and would disappear if enough space were given (not necessarily recovering a uniform stream). Experimental investigations of roll waves in granular flows may be of considerable help to further analysis. The new experiments should be designed also with the aim of increasing the height of the roll wave and the general vertical scale of the flow, in order to eliminate some concerns that naturally arise modelling with a continuum model a phenomenon where the flow depth is on the order of 10 grain diameters.

In general, we can add that it may be questionable to use an empirical model for rheology (as we did in the present analysis), because, especially for granular flows, the experiments reveal many special characteristics. We have also to add that most, if not all, the stability analysis on roll waves are based on empirical friction laws that, strictly speaking, nothing have to do with constitutive equations, because they do not respect one or more than one of the general rules for constitutive equations. Nevertheless the agreement of theory with the experiments is often surprising.

It is also a subject of discussion that the MLRW herein described and obtained using energy criteria, can be found in real system. We share the idea that a combination of criteria based on energy consideration and linearized instability can be a reasonable approach for studying roll waves in their general form, including irregular, non periodic trains (see Ng & Mei 1994). In the Newtonian limit the properties of the minimum roll waves (shortest wavelength and lowest amplitude without energy loss in the shock) appear to be consistent with the experimental data (Ng & Mei 1994).

11 CONCLUSIONS

The proposed solution for finite amplitude roll waves in a dilatant fluid shares many similarities with the solution proposed by Dressler (1949) for a Newtonian fluid and by Ng & Mei (1994) for mud. The solution is expressed as a discontinuous function obtained by connecting two continuous profiles with a shock. The continuous profiles are obtained in the shallow equations approximation.

In order to construct the profile between two shocks, it is necessary that the steepness of the wave be

Copyright © 2006 Taylor & Francis Group plc, London, UK

finite and positive in the section where critical condition is reached. It results in the inequality $b < b_{crit}$, b being a non-dimensional group based on rheological characteristics of the fluid, wave celerity, and bottom inclination. The inequality can be converted into a limiting minimum wave celerity for given rheological parameters and bottom inclination and in a maximum (mean) flow rate in the fixed frame. It can also be converted into a maximum stream depth or a maximum Froude number, which fixes an upper threshold to the permanent periodic wave existence observed in some experiments on sand flows. This critical threshold is expressed as $F_{crit} = F_{crit}(\beta, r)$.

The energy-balance analysis in the shock reveals that, assuming uniform flux factors (energy and momentum), in the back and in the front of the shock, finite amplitude shocks without (mechanical) energy dissipation are allowed within a single band of wavelength. If different factors are assumed, namely increasing the value of factors from the back (minimum depth) to the front (maximum depth), a double band of wavelength with finite amplitude shocks without energy loss is allowed. These limiting conditions are highly sensitive to r, the ratio of the normal stress in the horizontal direction to the normal stress in the vertical direction. The physical consideration of a non-positive (mechanical) energy balance in the shock requires that a second inequality ($b < b'_{crit}$) be satisfied. This inequality, expressed in a similar fashion by Ng & Mei (1994) for mud flows, leads to the evaluation of a second threshold expressed as $F'_{crit} = F'_{crit}(\alpha, \beta, r)$.

The comparison with experimental results reported by FP (2003) reveals that the prediction of a limiting curve for the existence of permanent periodic roll waves in the plane (Y, θ) is rather good for sand flows. For flows of glass beads, the set-up of the experiments did not allow flows at a Froude number higher than the computed thresholds, and the comparison is not possible. We need to mention that the experimental results are qualitative in respect to stability limit.

The computed wave celerity of the MLRW is in excess respect to the linear model prediction and to the experiments; a correction of the shock dynamics introducing the weight of the roller increases the discrepancies between experiments and the present model. Perhaps a longer channel could lead to measurements with improvement in the overlap of the theoretical and the experimental results. Also, a complete description of the roll waves, introducing different back/front correction flux factors could improve the predictive strength of the model.

Integration of the energy dissipation in the stream reveals that the energy budget is a negative function, also in condition of no dissipation in the shock, i.e., the system with permanent waves dissipates more energy than the energy gained from gravity, with a minimum for the MLRW.

ACKNOWLEDGEMENTS

The author acknowledges support for this work from FIL 2004 and FIL 2005 of the University of Parma.

REFERENCES

Bagnold, R.A. 1954. Experiments on a gravity-free dispersion of large solid spheres in a Newtonian fluid under shear. *Proc. R. Soc.Lond.* A 225: 49–63.

Brock, R. R. 1967. Development of roll waves in open channels. W. M. Keck Laboratory of Hydraulics and Water Resources, California Institute of Technology, Report No. KH-R-16, 226 pp.

Chen, C. L. 1992. Unique laminar-flow stability limit based on shallow-water theory. *J. Hydr. Engrng, ASCE*, 119(7), 816–829.

Chen, C. L. & Ling, C. H. 1996. Granular-flow rheology: role of shear-rate number in transition regime. *Journal of Engineering Mechanics, ASCE* 122 (5): 469–480.

Chen, C. L. & Ling, C. H. 1998. Rheological equations in asymptotic regimes of granular flow. *Journal of Engineering Mechanics, ASCE* 124 (3): 301–310.

Chow, V. T. 1959. *Open Channel Hydraulics*, Mc Graw Hill.

Dressler, R. F. 1949. Mathematical solution of the problem of roll waves in inclined open channels. *Communications on Pure and Applied Mathematics*, vol. 2: 149–194.

Ertas, D., Grest, G. S., Halsey, T. H., Levine, D. & Silbert, E. 2001. Gravity driven dense granular flows. *Europhys. Lett.* 56, 214–220.

Forterre, Y. & Pouliquen, O. 2003. Long-surface-wave instability in dense granular flow. *J. Fluid Mech*., Cambridge, 486, 21–50.

Gray, J. M. N. T., Wieland, J. M. & Hutter, K. 1999. Gravity-driven free surface flow of granular avalanches over complex basal topography. *Proc. R. Soc. Lond*. A 455, 573–600.

Hunt, M. L., Zenit, R., Campbell, C. S. & Brennen, C. E. 2002. Revisiting the 1954 suspension experiments of R. A. Bagnold. *J. Fluid Mech*., Cambridge, England, 452, 1–24.

Hwang, C., Chen, J., Wang, J. & Lin, J. 1994. Linear stability of power-law liquid film flows down an inclined plane. *J. Phys. D: Appl. Phys.* 27: 2297–2301.

Ishihara, T., Iwagaki, Y. & Iwasa, Y. 1954. Theory of the roll wave train in laminar water flow on a steep slope surface. *Trans. JSCE* 19: 46–57 (in Japanese).

Jeffreys, H. J. 1925. The flow of water in an inclined channel of rectangular section. *Philosophical Magazine*, series 6, vol. 49, pp.793–807.

Kapitza, P. L. 1948. Wave flow of thin layers of a viscous fluid. *Zh. Eksp. Teor. Fiz.* 18: 3–28 (also in *Collected Papers of P.L. Kapitza, Vol II*,1938–1964, Pergamon Press 1965, pp.662–709).

Ligget, J. A. 1975. Stability. In *Unsteady flow in Open Channels*, Chapter 6, pp. 259–282, WRP.

Longo, S. 2003. Roll waves on a shallow layer of debris modeled as a dilatant fluid. *(Rickenmann & Chen eds). Proc. of the 3rd Int.DFHM Conf., Davos, Switzerland, September 10–12,* Millpress Science Publishers, Rotterdam, Vol.1, pp. 339–350, 2003, ISBN 90 77017 78 X.

Copyright © 2006 Taylor & Francis Group plc, London, UK

Longo, S. 2004. Effects of gradient pressure on resistance law in roll waves. *(Greco, Carravetta & Della Morte eds), Proc.of River Flow 2004, Int.Conf. IAHR*, Naples, Italy, A.A. Balkema Publishers, London, Vol.2, pp. 885–894, ISBN 90 5809 688 2.

Longo, S. & Lamberti, A. 2002. Granular shear flow mechanics. *Experiments in Fluids*, Springer, 32/3, pp. 313–325.

Ng, C. & Mei, C. C. 1994. Roll waves on a shallow layer of mud modelled as a power-law fluid. *J. Fluid Mech.* 263: 151–183.

Ponce, V. M. & Maisner M. B. 1993. Verification of theory of roll wave formation. *J. of Hydr. Eng.*, ASCE, 119(6): 768–773.

Pouliquen, O. 1999. Scaling laws in granular flows down rough inclined planes. *Phys. Fluids* 11, 542–548.

Prasad, S. N., Pal, D. & Römkens, M. J. M. 2000. Wave formation on a shallow layer of flowing grains. *J. Fluid Mech.* Vol. 413: 89–110.

Smith, M. K. 1990. The mechanism for the long-wave instability in the liquid films, *J. Fluid Mech.* 217: 469–485.

Stoker, J. J. 1957. Mathematical hydraulics, in *Water waves*, Wiley Interscience, pp. 451–509.

Takahashi, T. 1991. *Debris flow*, Monograph Series of IAHR, Balkema, pp. 1–65.

Witham, G.B. 1974. *Linear and nonlinear waves*. Wiley-Interscience Publication, John Wiley and Sons, New York, pp 636 + xvi, ISBN 0 471 35942 4.

Copyright © 2006 Taylor & Francis Group plc, London, UK

Instability and kinematic for sand-water mixture or dry sand flowing past a circular cylinder

S. Longo
Department of Civil Engineering, University of Parma, Parma, Italy

A. Valiani & L. Lanza
Department of Civil Engineering, University of Ferrara, Ferrara, Italy

ABSTRACT: The present analysis refers on experiments with a mixture of grains and water and dry grains around a circular cylinder. The flow is driven by the internal cylinder of a Taylor-Couette cell. Velocity measurements of the mixture at the external surface are carried out using a commercial PIV and a new microPIV. The flow field is quite similar to the flow field generated by a Newtonian fluid around a circular cylinder, with a wake and a re-circulation zone. Near the body, the velocity scale of the wake decays linearly if the asymptotic velocity is high, decays logarithmically for low asymptotic velocity. The transverse length scale increases as x'^n (x' is measured along the axis of symmetry with the origin at the boundary of the body) with $n < 0.5$ (or nearly zero in some flow conditions). For dry grains flow, microPIV reveals strong instabilities, with a fast movement en-block of the grains.

1 INTRODUCTION

The analysis of granular flow in presence of on obstacle is of interest from a theoretical point of view, because allows the study of the complex rheology of the fluid, but also for applications. Many defence structures against debris flow are steel sheeting cylinder piles filled with local materials and capped with concrete. They act dissipating the flow energy, stopping the boulders and favouring water filtration. Other defence structures against snow avalanches have a triangular shape with pyramidal elevation, with a corner in the expected flow direction, and are able to protect the buildings in the wake. There are also many applications in food manufacturing, chemical and pharmacy. Nevertheless experiments and theoretical models are quite few.

Granular flow is often characterized by variations of bulk density. Some experiments by Gray et al., (2003), show that a granular stream impacting an obstacle or being deviated by a wall shows different zones of compression and expansion, with shocks and discontinuities. In these experiments it is very difficult to measure fluid velocity in the body stream. It is possible to use Laser Doppler Anemometry (LDA) (Longo & Lamberti, 2002) and Particle Image Velocimetry (PIV) (Deng & Wang, 2003) for measuring velocities near a transparent wall. Results usually underestimates real velocity due to the wall boundary layer, but fortunately the error is limited due to slip of granular flows at the boundary.

In literature there are several references on Newtonian fluid flows around a circular cylinder (see Zdravkovich 1997), and most of the theory of wings uses conformal mapping of flow round a circular cylinder of infinite extension. In comparison, the studies on non-Newtonian fluid flows are scarce. Sarpkaya et al. (1973) present a detailed analysis on flow of water and polymers additive around a circular cylinder. The most evident effect of the additives is an instability of the separation curve of the stream, due exclusively to the rheology of the fluid.

Nedderman et al. (1980) analyze the gravity driven flow of mustard seeds around a cylinder, adopting a kinematic description based on a stochastic model. Other more detailed analysis refer to the kinematic of complex fluids around bodies (Pilate & Crochet, 1977).

In the present study we report on experiments with a stream of water or air plus sediment at high void concentration around a circular cylinder. In Section 2 there is a description of the experimental set-up, of the measurement technique and of the tests carried out with a mixture of sediments and water.

In Section 3 there is the description of the flow field using the experimental data, with the analysis of the wake, the vorticity field and the divergence of the flow. Section 4 is devoted to the analysis of dry

Copyright © 2006 Taylor & Francis Group plc, London, UK

granular stream (air is the inter-particle fluid), with a short description of a micro-PIV used for the velocity measurements. Conclusions are reported in the last Section.

2 EXPERIMENTAL SET-UP

The flow field is generated in a Taylor-Couette cell (Fig.1), with an internal rotating vertical cylinder in stainless steel $D_{int} = 167$ mm, and an external fixed cylinder in PMMA $D_{ext} = 190$ mm, having a wall thick $s = 5$ mm. The gap between cylinders is equal to $\delta = 11.5$ mm and represents the shear section. The internal cylinder is in motion and, in order to transfer momentum to the granular mixture, its wall is roughed by gluing sand-paper on it. The internal surface of the PMMA cylinder is smooth and allows an almost free-slip of the grains. The rotation of the stainless-steel cylinder is due to a stepper with a resolution of 1000 steps per root, connected to a mechanical gear 1:6 in order to increase the torque. The stepper has a vertical axis, is not fixed and the counter balance torque is obtained using an iron beam, instrumented with strain-gages in order to estimate the torque. In principle the measurement of the torque allows the evaluation of the mean wall stress. Unfortunately, due to mechanical imperfections in the gear system, the S/N ratio is too low, especially in presence of sand-water mixture.

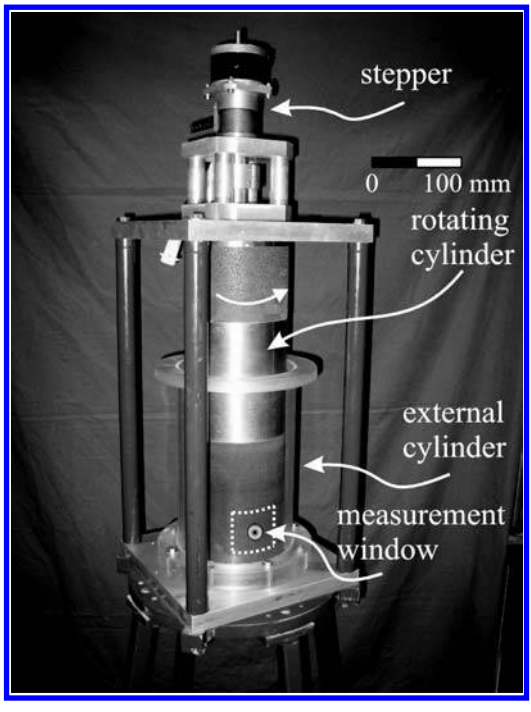


Figure 1. Taylor-Couette cell.

The tests were carried out with a mixture of water and artificial grains used for thermal insulation purposes (Leca is the commercial name), made of clay. The grains where sorted in order to have a diameter in the range $d = 0.25$–0.50 mm. They have an almost spherical shape and a specific weight in water nearly equal to 1.0. Sorting for the specific weight was obtained, eliminating the floating particles. The choice of almost neutrally buoyant particles was forced by the need of reducing at a minimum the normal effective stress increment due to gravity, which would reduce grains mobility.

Measurements were carried out in the Laboratory of Civil Engineering "Paolo Lamberti" of the University of Ferrara, using a commercial TSI PIV with a 2048×2048 pixel video camera, fitted with a 50 mm/f lens. More details on the PIV system are reported in Lanza et al. (2004).

The light source is a laser Ar^+, water cooled and mounted on the same side of the video camera. Usually, the laser has a cylindrical lens for the generation of a light sheet; for the present purposes, the lenses were removed and polarized lens were added to the video camera in order to eliminate reflections. The acquisition frequency of the couple of images is 3.75 Hz, with a time interval between the two images ranging from 600 μs to 1000 μs.

In the tested condition, PIV measures the grain particles velocity. The curvature of the PMMA cylinder and the refraction generate image distortion; an additional distortion is due to the lenses of the video camera. A numerical correction to the acquired data was performed using an algorithm with experimental parameters. The algorithm elaborates the transformation of the pixel position on the CCD of the camera onto metric position in the plane space equivalent to the enrolled cylinder.

The transformation is in terms of quadratic polynomials:

$$\begin{aligned} x_{corr} / x_{meas} &= L_x\left(x_{meas}, y_{meas}\right) \equiv \\ a_1 x_{meas}^2 + b_1 y_{meas}^2 + c_1 x_{meas} + d_1 y_{meas} + e_1 & \\ y_{corr} / y_{meas} &= L_y\left(x_{meas}, y_{meas}\right) \equiv \\ a_2 x_{meas}^2 + b_2 y_{meas}^2 + c_2 x_{meas} + d_2 y_{meas} + e_2 & \end{aligned} \quad (1)$$

used to correct both coordinates. The coefficients of the polynomials are estimated using the maximum likelihood criterion.

Calibration requires the following steps: (1) acquisition with the video camera of a regular grid of 1.0 cm squares, stuck on the external surface of the PMMA cylinder. It is necessary to fix the position of the video camera, in order to keep the same point of view during tests. (2) Estimation of the coordinate (in pixel) of the

Copyright © 2006 Taylor & Francis Group plc, London, UK

knots of the grid, using the acquired image. (3) Minimization of the following residuals, parametric in the coefficient of the interpolating polynomials;

$$\chi_x^2 = \sum \left(L_x(x_i, y_i) - x^*_{i\,real} / x_i \right)^2$$
$$\chi_y^2 = \sum \left(L_y(x_i, y_i) - y^*_{i\,real} / y_i \right)^2 \quad (2)$$

Summation is extended to all knots of the grid. Considering that the grid, for practical purposes, is stuck on the external surface of the PMMA cylinder, (whereas the observed grain particles move near the internal surface), the algorithm does not correct for refraction. This is one of the reasons of the reduced validation rate near the lateral boundaries of the frame, where refraction is more evident.

The correction function could also be evaluated using the criteria of geometrical optics, but it is more complicated and there are not real advantages with respect to the adopted polynomials. The estimated coefficients have an uncertainty of 2% at 95% confidence level. The maximum correction (near the lateral boundaries) is about 20%. Image elaboration was carried out using an interrogation window 32 × 32 pixel (∼8 × 8 d) with 50% overlap. The result is a matrix of vectors in the knots of a square grid, 16 pixel length, corresponding to 1.25 mm (∼4 d).

The output files contain the coordinates (in pixel) of the interrogation window, and the two components of the space vector at time t (first frame) and $t + \mathrm{d}t$ (subsequent frame). Applying the transformation, a matrix containing the velocity vector in the knots of an irregular grid is obtained. For easy use, the matrix is interpolated by a regular grid, with square length equal to 1.3 mm. For each test 100 couples of frame were acquired, correspondent to ∼27 s.

2.1 *The tests*

In a first series f tests, there is a circular cylinder having a diameter $D = 15$ mm and a height of a few millimeters. The cylinder is glued to the internal surface of the PMMA cylinder and has the axis in the radial direction, at ∼50 mm over the bottom of the Taylor-Couette cell. The free surface of water at rest is at ∼150 mm, while grains bottom is at 20 mm below the free surface. At the maximum rotation rate of the internal cylinder, the mixture looks almost homogeneous, with a void concentration reduced to 87% of the void concentration at rest.

The variation in the void concentration is greater near the free surface than near the obstacles. Measurements were carried out imposing a rotation rate ranging from 50 to 200 rpm, corresponding to a peripheral velocity of the internal cylinder from 440 to 1760 mm/s. The undisturbed flow field (without the obstacle), is quite regular, with shear in the radial direction and in the horizontal plane. The mean value of the shear rate in the radial direction and the mean velocity near the external (transparent) wall are shown in Table 1.

It has been verified that the shear in the radial direction is not uniform, with higher values near the driving wall. In most of the flow field, the shear rate is much smaller than the average shear rate. Note that at 200 rpm the measured velocity of the grains near the external cylinder is smaller than the measured velocity at 150 rpm, presumably as a consequence of emerging instabilities in the flow field.

3 DESCRIPTION OF THE FLOW FIELD

The presence of the obstacle modifies the flow patterns, with a low velocity zone upstream, a stagnation or dead zone (sediments at rest) downstream, a boundary layer at the interfaces with the dead zone and the obstacle, a wake, and a re-circulating zone at the beginning of the wake. In Figure 2 the average flow field (100 couples of frames, ∼27 s) is shown. In the

Table 1. Imposed velocity scales.

Imposed rotation rate (rpm)	Lateral velocity of the driving wall (mm/s)	Asymptotic velocity of the flow U_o (mm/s)	Radial shear rate (s^{-1})
50	440	305	11.7
100	880	615	23.0
150	1320	920	34.8
200	**1760**	**760**	**87.0**

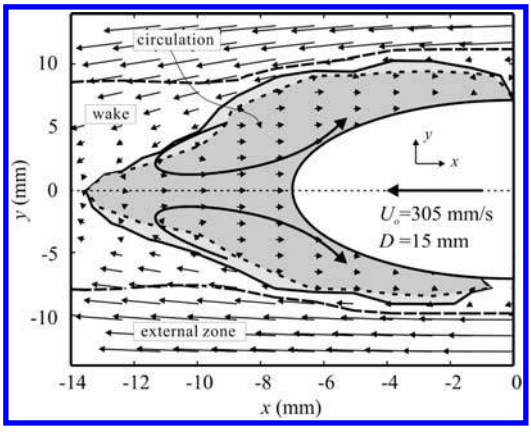


Figure 2. Mean flow past the circular body. Thick line represents the re-circulating zone. The internal dashed line limits the zero velocity, the external dashed line limits the wake boundary. The picture is distorted for an easier visualization.

Copyright © 2006 Taylor & Francis Group plc, London, UK

Table 2. Extension of the re-circulating zone.

Rotation rate (rpm)	Length of the re-circulating zone (measured from the boundary of the cylinder body) x' (mm)
50	6
100	10.7
150	10.3
200	**7.6**

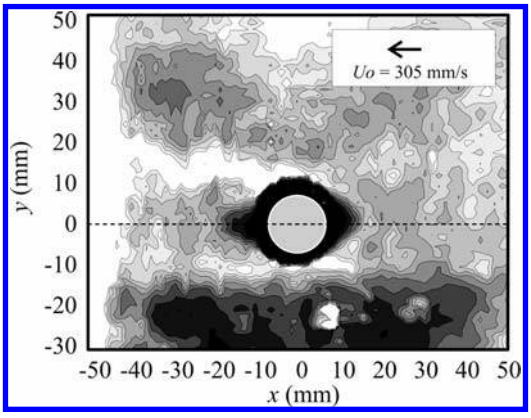


Figure 3. Mean granular temperature. The 'cold' zones are dark.

re-circulating zone (thick line) there are two counter-rotating vortices, while the average velocity is of a few mm-s. The size and the shape of the re-circulating zone are almost not dependent of the asymptotic velocity. In all tests, the length downstream (Tab. 2) is a fraction of the diameter of the obstacle, except for the 200 rpm rotation rate test, presumably characterized by instabilities of the flow. In Figure 3 the mean variance of the grains velocity (defined as 'granular temperature', even though a proportional coefficient is missing in the expression) is shown:

$$T = \overline{\left(U_x - \bar{U}_x\right)^2} + \overline{\left(U_y - \bar{U}_y\right)^2} \qquad (3)$$

The over-bar means time average.

The granular temperature is the trace of the kinetic stress tensor (equivalent to Reynolds' stress tensor); it represents a measure of the grains fluctuations and usually, neglecting mean transport, it is larger in the source areas. The source is essentially due to shear rate. In the present tests, the minimum values of the granular temperature is reached in the dead zones upstream and downstream, near the boundaries of the obstacle, where friction is dominant.

The hot zones define the wake, are due to high shear rate and aid momentum flux from the external zone

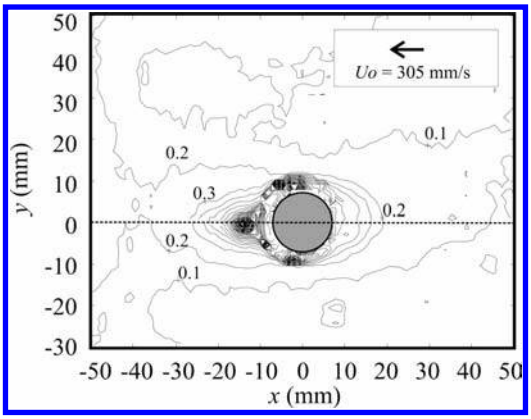


Figure 4. Index of turbulence. Average value on 100 frames (~27 s).

toward the wake, reducing progressively the defect of velocity. The granular temperature distribution is quite similar for all tests, and presents a little asymmetry. The asymmetry is due to the increasing grain volume concentration toward the bottom of the cell, for the combined effects of gravity and for the boundary effects imposed by the rigid wall; in fact, at higher grain volume concentration, collisional and frictional stresses are dominant. The average turbulence index, defined as:

$$\gamma = \left[\frac{\overline{\left(U_x - \bar{U}_x\right)^2} + \overline{\left(U_y - \bar{U}_y\right)^2}}{\bar{U}_x^2 + \bar{U}_y^2}\right]^{1/2} \qquad (4)$$

is shown in Figure 4. The maxima are in the dead zone, where the average velocity is almost zero and fluctuations due to grains in motion and to stick-slip phenomena are dominant.

Note that the data rate of the frames, equal to 3.75 Hz, and the spatial resolution of 8 d, filter most of the high frequency fluctuations related to micro-mechanic collisions, even though the presence of water as inter-particle fluid, favours the dampening of these fluctuations.

3.1 *The wake past the obstacle*

Downstream the obstacle, there is the wake, with a mean velocity lower than the external velocity and a velocity profile almost symmetric and similar to the velocity profile in the wake of a Newtonian fluid.

In Figure 5 the wake is represented as limited by velocity equal to 50% of the axial defect velocity *Us(x)* (with respect to the asymptotic velocity, i.e. the velocity in the external region in the same section). This definition slightly differs from the classical defect

Copyright © 2006 Taylor & Francis Group plc, London, UK

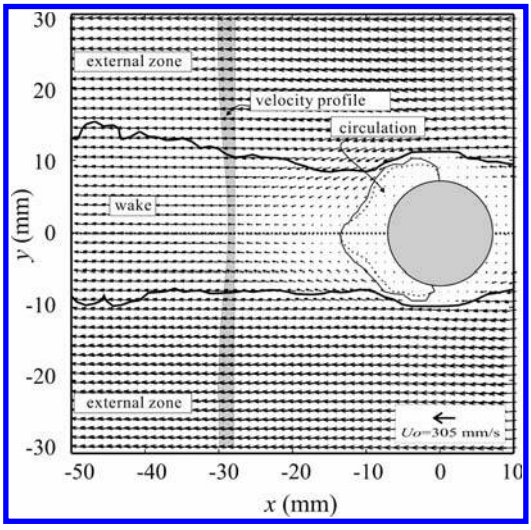


Figure 5. Wake past the obstacle. Average of 100 frames (~27 s).

velocity definition, which refers to the undisturbed velocity. The local width of the wake is often assumed as the geometrical transverse scale, whereas the defect velocity is assumed as transverse velocity scale.

For turbulent wakes of Newtonian fluids in a 2-D flow field at high Reynolds number, the velocity profile becomes self-similar at distance $>80\ D$, with $l \propto x^{1/2}$ and $Us \propto x^{-1/2}$ (Tennekes & Lumley, 1972).

The spatial characteristics of the wake for the present tests is shown in Figure 6. For the test at 50 rpm, the velocity scale has a logarithmic decay, according to the following expression:

$$\frac{U_s}{U_0} = \ln\left[\alpha\left(\frac{x'-D/2}{D}\right)^{\beta}\right] \qquad (5)$$
$$D < x' < 4D$$

with $\alpha = 1.57 \pm 0.8\%$; $\beta = -0.33 \pm 3.2\%$

The parameters were computed using the least squares method, with $R^2 = 0.989$ at a confidence level of 95%.

In all the other tests the velocity scale decays linearly, according to the following expression:

$$\frac{U_s}{U_0} = a - b\left(\frac{x'-D/2}{D}\right) \qquad (6)$$
$$D < x' < 4D$$

The value of the estimated parameters are shown in Table 3.

In Figure 7 the spatial evolution, downstream and upstream, of the transversal length scale is shown.

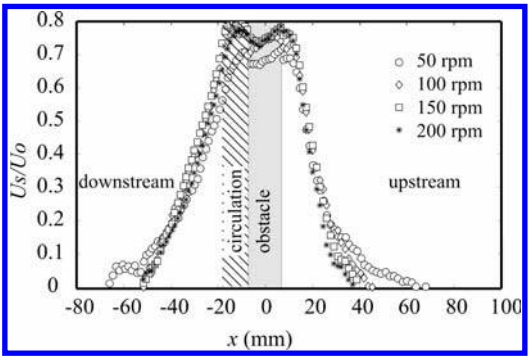


Figure 6. Upstream and downstream variation of the velocity scale *Us*.

Table 3. Parameters of the function in eq.6. The uncertainty is at 95% confidence level.

Test (rpm)	a	b	R^2
100	$0.88 \pm 1.4\%$	$0.31 \pm 4.3\%$	0.988
150	$0.93 \pm 2.8\%$	$0.33 \pm 4.2\%$	0.987
200	$0.81 \pm 4.7\%$	$0.29 \pm 6.4\%$	0.972

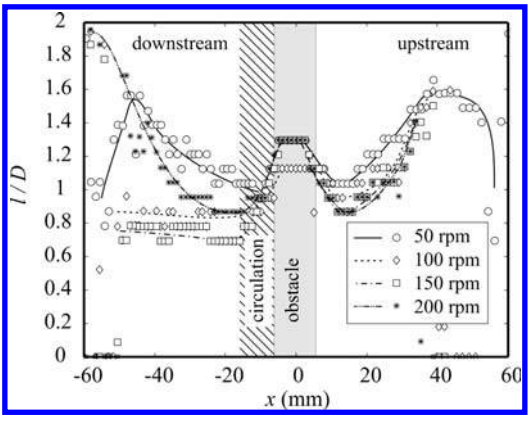


Figure 7. Downstream and upstream transversal length scale.

The data are less coherent than for the velocity scale. For the tests at 100 rpm and 150 rpm the length scale is almost constant or slightly increasing downstream.

The interpolating functions have the following expression:

$$\frac{l}{D} = c\left(\frac{x'-D/2}{D}\right)^{n}, \quad D < x' < 3D \qquad (7)$$

and the least square method estimated parameters are shown in Table 4.

Copyright © 2006 Taylor & Francis Group plc, London, UK

Table 4. Parameters of the interpolating function in eq.7. The uncertainty refers to a 95% confidence level.

Test (rpm)	c	n	R^2
50	$1.13 \pm 4.6\%$	$0.22 \pm 27\%$	0.67
100	$0.76 \pm 4.0\%$	$0.1 \pm 65\%$	0.26
150	$0.72 \pm 2.7\%$	$0.06 \pm 73\%$	0.23
200	$0.91 \pm 5.1\%$	$0.37 \pm 22\%$	0.75

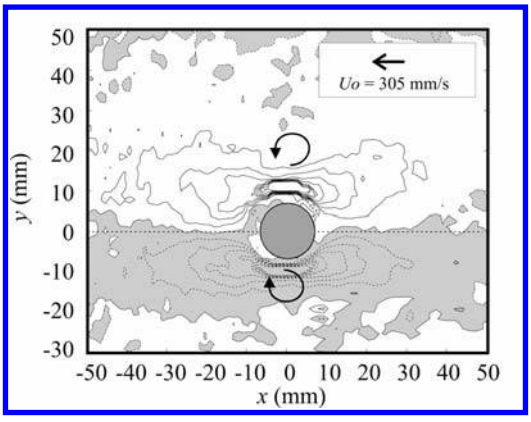


Figure 8. Mean vorticity.

3.2 *Vorticity and divergence*

The average vorticity is shown in Figure 8. Two macro vortices are evident near the upper and lower separation points, two smaller macro vortices appear in the re-circulating zone. Near the bottom and near the free surfaces there are some footprints of local generated vorticity. The variance of vorticity (not shown) is almost uniform, with small values in all the domain. That means that, at least in the analyzed set-up condition, no Von Karman vortices develop.

In Figure 9 the divergence field is shown. In stationary conditions, mass conservation equation for the granular phase can be written as:

$$\mathbf{U} \cdot grad(\ln \rho) = -div\ \mathbf{U} \tag{8}$$

ρ is the bulk density of the grains. Along the symmetry axis the spanwise velocity *Uy* is almost negligible with respect to the streamwise velocity (it should be rigorously zero), and eq. (8) can be integrated to obtain the grain volume concentration:

$$\frac{\rho}{\rho_0} \equiv \frac{C}{C_0} = \exp\left(\int_{x_0}^{x} \frac{-div\ \mathbf{U}}{U_x} dx \right) \tag{9}$$

ρ_0 is the bulk density of the grains in the section x_0; C and C_0 are the corresponding volume concentration of

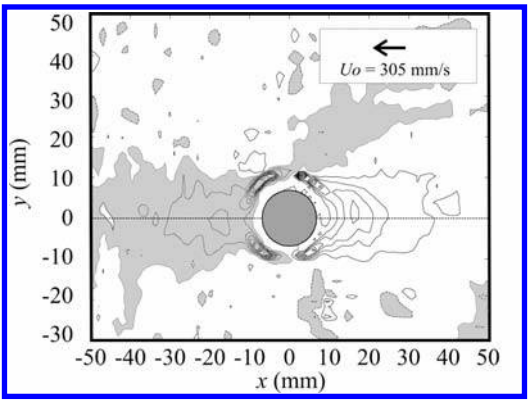


Figure 9. Mean divergence. Dark zones represent positive divergence.

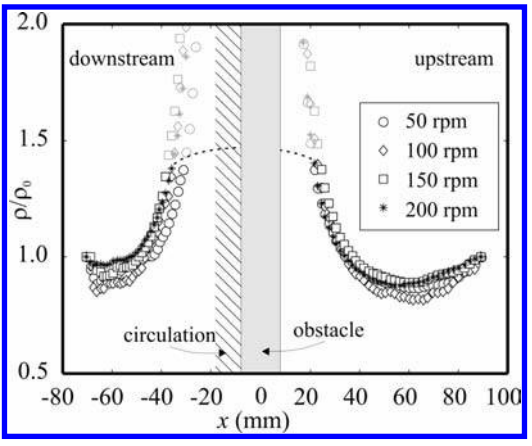


Figure 10. Bulk density variation along the axis of symmetry.

the grains. The results of the integration, carried out separately for the downstream and the upstream areas, are shown in Figure 10.

The uncertainties are high if the velocity is low, i.e. in the zones nearby the dead zones. The results represent only an estimation, because three dimensional effects play an important role, especially in these zones. The indicative limit value of bulk density is shown by the dashed line, but it is affected by a high degree of uncertainty considering that even a small increment in bulk density implies an almost immediate stop of the grains.

4 MEASUREMENTS FOR DRY GRANULAR STREAM

In a second series of tests we analyzed a dry granular stream (air is the inter particle fluid) of almost

Copyright © 2006 Taylor & Francis Group plc, London, UK

spherical particles similar to those used in the first series, $d = 0.25$–0.50 mm. Measurements were carried out using a new instrument able to measure the tangential velocity (two components) of a continuous or discrete surface (Longo, 2004).

The instrument uses PIV technique with an image analysis performed via hardware.

4.1 *Description of the instrument*

The instrument adopts (a) a commercially available opto-electronic chip (Agilent Technologies), (b) a processor by Cypressus, (c) an original interface based on a Microcontroller Microchip PIC. The opto-electronic processor has a micro-CCD which, with a lens, captures the image of the surface, whose velocity has to be measured. A cross-correlation algorithm, applied onto sub-sequent images, allows the estimation of the velocity vector of the patterns contained in the captured images.

The processor by Cypressus codes the output according to a PS/2 protocol. The two processors are available wired and in use on optical mouses, whereas the interface and the software are original. The software, written in Assembly, transforms the binary data from the commercial tool in two analog signals (one for each velocity component), for acquisition by a DAQ board. It is also converted for acquisition through a serial port. It is possible to control the start and the stop of data acquisition. Some tests show that the device can measure the velocity of a continuous surface or of a granular stream apparent surface, with the only limitation that recognizable patterns during motion must exist. The static calibration of the device was carried out measuring the peripheral velocity of a rotating cylinder controlled by a stepper, with an uncertainty equal to 0.6%.

A calibration diagram is shown in Figure 11. The calibration shows an excellent linearity in the range 0–70 mm/s ($R^2 = 0.9986$), a limited STD and an excellent repeatability. According to Agilent, the optical processor can measure up to 300 mm/s (the last generation processors up to 450 mm/s), but a higher velocity also means higher non-linearity and high drop-out rate. The size of the measuring window depends on lenses. With standard lenses in optical mouses it is equal to $2 \times 2\,\text{mm}^2$, with the focal plane at 5 mm from the external surface of the lens and with a focal depth equal to 0.5 mm. The resolution is equal to 2 mm/s and the frequency of acquisition is nearly equal to 200 Hz (the duty cycle lasts for 6 ms) and is limited by software, because the data rate of the optical processor is equal to 1500 frames/s.

It is possible to modify the lens in order to adapt the velocity range and the measuring plane to different needs. We also verified the possibility to use fiber glasses.

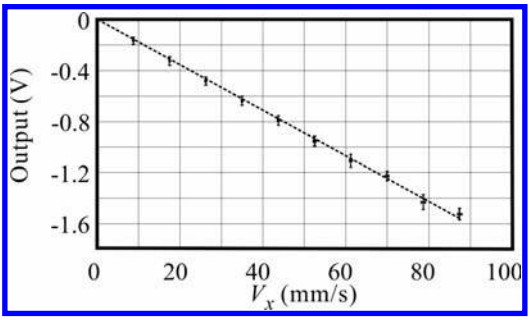


Figure 11. Calibration line of the micro PIV. Single velocity component.

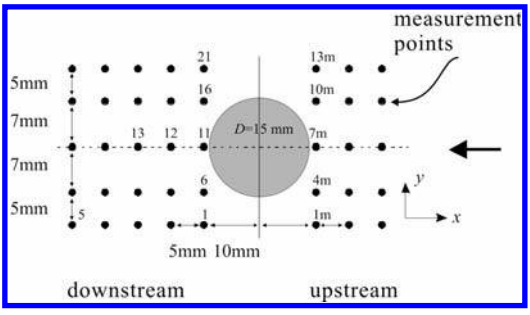


Figure 12. Scheme of the measurement points.

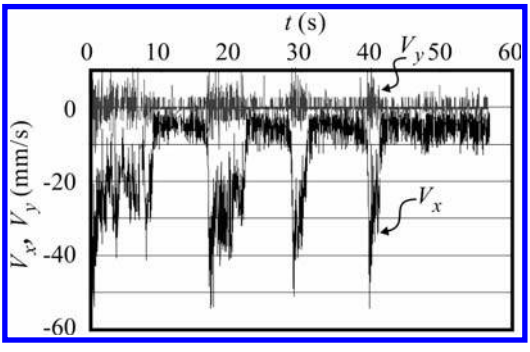


Figure 13. Time series of the two velocity components in point 13. Test at 100 rpm.

4.2 *Application*

The measurements were carried out in a series of points according to the scheme shown in Figure 12, acquiring the velocity signal at 100 Hz for 60 s.

The pattern of velocity field is similar to those obtained using PIV for granular stream in water, even though apparently there is no re-circulation (it could also be the result of a limited resolution of the device). In Figure 13 the two components of the velocity measured along the axis of symmetry, at 20 mm past the axis of the obstacle (point 13, at 12.5 mm past the

Copyright © 2006 Taylor & Francis Group plc, London, UK

boundary of the obstacle) are shown. The rotation rate is equal to 100 rpm and a strong instability is recorded, with stick-slip of the grains at time intervals of few seconds.

The period is of about 10 s. Near the obstacle, the period is the same but the amplitude is smaller. At higher rotation rates the instability disappears.

Upstream the cylinder, the measurements are much more regular and do not show instabilities. Presumably the phenomenon is characterized by large fluctuations of the force exerted by the granular stream on the obstacle. We suppose that the instability is due to the mechanical behavior of the granular stream in static or quasi-static regime. The grains tend to stop for internal friction effects and tend to increase the size of the dead zone. A larger dead zone means a larger force, up to a limiting value, controlled by internal friction. Over this threshold, there is a dilatancy of the grains with a fast and abrupt motion of the grains in the dead zone.

5 CONCLUSIONS

The flow field of a mixture of grains and water round a cylinder is similar to the flow field of a Newtonian fluid.

- Past the obstacle there is a re-circulation zone, a wake zone and an external zone.
- The velocity scale of the wake decays linearly downstream (except for low mean velocity of the stream), the transversal length scale weakly increases. It is still necessary to verify if self-similarity is present, or can be found adopting available rheological models.
- In the range of the present measurements, no Von Karman vortices develop; at high velocity three-dimensional effects, presumably due to flow instabilities, control the flow field.
- Measurements of a dry granular stream were carried out using an innovative PIV and reveal periodic instabilities past the obstacle. The in-stability generates abrupt motion of the grains at rest in the dead zone.

ACKNOWLEDGEMENTS

Sandro Longo was supported by MIUR (Italian Ministry for University and Research) PRIN 2001, project: "Convivere con le frane: effetti su infrastrutture e insediamenti urbani. Strategie di intervento per la mitigazione del rischio". We thanks Roberto Bruni and Nicola Cavallini for contributing to experiments during their Master Thesis at the University of Parma and at the University of Ferrara respectively.

REFERENCES

Deng, R. &. Wang, C. -H. 2003. Particle image velocimetry study on the pattern formation in a vertically vibrated granular bed. *Physics of Fluids*, 15, 3718–3729.

Gray, J. M. N. T., Tai, Y. -C. & Noelle, S. 2003. Shock waves, dead zones and particle-free regions in rapid granular free-surface flows. *Journal of Fluid Mechanics*, 491, 161–181.

Lanza, L., Valiani, A., Bernini, A. & Franchini, M. 2004. Modello fisico della nuova conca di Pontelagoscuro. XXIX *Convegno di Idraulica e Costruzioni Idrauliche, Trento* (in italian).

Longo, S. 2004. Optical instrument for measuring 2-D tangential velocity (patent pending PR2004A000002, 2004).

Longo, S. & Lamberti, A. 2002. Granular shear flow mechanics. *Experiments in Fluids,* 32/3, 313–325, DOI 10.1007/s003480100359.

Nedderman, R. M., Davies, S. T. & Horton, D. J. 1980. The flow of granular materials round obstacles. *Powder Technology*, 25, 215–223.

Pilate, G. & Crochet, M. J. 1977. Plane flow of a second-order fluid past submerged boundaries. *Journal of Non-Newtonian Fluid Mechanics*, 2, 323–341.

Sarpkaya, T., Rainey, P. G. & Kell, R. E. 1973. Flow of diluite polymer solutions about circular cylinders. *Journal of Fluid Mechanics*, 57, 177–208.

Tennekes, H. & Lumley, J. L. 1972. *A first course in turbulence.* The MIT Press, Cambridge, UK EU, ISBN 0 262 20019 8, pp. 300+xiii.

Zdravkovich, M. M. 1997. *Flow around circular cylinders, Vol. 1: Fundamentals*. Oxford University Press, Oxford, UK EU, ISBN 0 19 856396 5, pp 672+xviii.

Copyright © 2006 Taylor & Francis Group plc, London, UK

B.5. Geomorphic dam-break flows and breach formation

Copyright © 2006 Taylor & Francis Group plc, London, UK

A new approach to solving boundary conditions in shallow water equations using a Riemann solver

V.C. Medina Iglesias, A. Bateman Pinzon & D. Velasco Montes
Hydraulic, Maritime and Environmental Engineering Department, Technical University of Catalonia (GITS-UPC), D1 ETSECCPB, Barcelona, Spain

ABSTRACT: In recent years, the finite volume method has been improved by the Godunov method and Riemann solvers, but the method of characteristics (MOC) is generally used to introduce boundary conditions. This paper proposes a new approach to introducing boundary conditions in a way that is consistent with the Riemann problem solution. The same Riemann solver can be used for the entire domain, including the boundaries. This approach allows shocks and waves of any other type to be introduced as boundary conditions in a way that it is compatible with the Riemann problem solution.

1 INTRODUCTION

The use of the finite volume method in shallow water problems has become more widespread. The Godunov method and Riemann solvers have been combined to obtain high-resolution methods capable of solving transcritical regimes. To test the new advances, researchers usually work with typical standard problems such as dam breaks or bottom topography with a bump.

Problems of this type have boundary conditions that make mathematical sense, such as reflecting or non-reflecting boundary conditions. Under these conditions, the values of the dependent variables of the boundaries can be found immediately. Different boundary conditions are found in real computations applied to rivers and channels. In general (subcritical regimes), the boundary conditions are the upstream discharge value and the downstream water level. To apply boundary conditions, two upstream and two downstream dependent variables are needed. Therefore, the values of two free variables (upstream water level and downstream discharge) need to be interpolated.

This task is usually performed using the method of characteristics (MOC), but this involves using two different numerical schemes to solve the problem: a finite volume method inside the domain and the MOC at the boundaries. This solution is subject to the same problem as the MOC – it cannot be used to solve transcritical regimes. Thus, inside the domain we have a method that can deal with transcritical regimes, and at the boundaries we have a method that cannot deal with discontinuities.

This paper proposes a new approach to introducing normal hydraulic boundary conditions in a way that is consistent with a Riemann solver, making it unnecessary to use the MOC for the boundaries. With this method, boundary conditions with shocks and rarefactions can be used. This method determines which boundary conditions imply a well-posed hydraulic problem and which do not.

In a similar work (Bateman, 1993), the transcritical boundary conditions problem was solved using a modified MOC.

2 GODUNOV METHOD AND THE RIEMANN SOLVER IN SHALLOW WATER

The method proposed in this paper can be applied to any hyperbolic problem. To keep the solution scheme consistent, the same method must be used to solve the domain and the boundaries. This method was specially designed to work with a Godunov method (Godunov, 1959). It uses the Riemann problem solution structure, which is described next.

The Riemann problem solution has two different waves, one from the weak form and one from the quasi-linear form. These two forms and their solutions are defined in the next section. The theory introduced in this chapter is discussed in many different publications (LeVeque, 2002), so we describe it only briefly.

Hyperbolic systems usually take the differential form, and we find differentials in the property and the flux.

$$\frac{\partial q(x,t)}{\partial t} + \frac{\partial f(q(x,t))}{\partial x} = 0 \qquad (1)$$

Copyright © 2006 Taylor & Francis Group plc, London, UK

Flux is $f(q(x,t))$, $q(x,t)$ is a state in the state space, x and t are the independent variables, space and time. The rest of this paper deals with shallow water equations, which are systems of two hyperbolic equations that express mass and momentum conservation. There are two conservative dependent variables, depth h(m) and unit discharge hu (m^2/s):

$$q = \begin{pmatrix} h \\ hu \end{pmatrix}$$
$$\begin{cases} \dfrac{\partial h}{\partial t} + \dfrac{\partial hu}{\partial x} = 0 \\ \dfrac{\partial hu}{\partial t} + \dfrac{\partial \left(u^2 h + g \dfrac{h^2}{2} \right)}{\partial x} = 0 \end{cases} \quad (2)$$

Gravity is g, u is the velocity (m/s) defined as hu/h. These equations reproduce the behavior of a rectangular cross section of a channel without friction or slope.

2.1 *Flux computing and discretization*

The relationship between the Godunov method and the Riemann problem is due to the computation of the flux in (1). We have one flux at x_1, upstream of the control volume $[x_1, x_2]$, and the other at x_2, downstream of the control volume. The Godunov method computes these fluxes by solving a Riemann problem. A Riemann problem is a differential problem that has a discontinuity with dependent variable values on either side of it. We can define the average flux between two control volumes at this time as $F^n_{1+1/2}$, and use the self similarity of the hyperbolic equations to compute it.

$$F^n_{i+1/2} = \frac{1}{\Delta t} \int_{t^n}^{t^{n+1}} f\left(q(x_{i+1/2}, t)\right) dt$$
$$F^n_{i+1/2} = f\left(q(x_{i+1/2}, t)\right) \frac{1}{\Delta t} \int_{t^n}^{t^{n+1}} dt \quad (3)$$
$$F^n_{i+1/2} = f\left(q(x_{i+1/2}, t)\right)$$
$$F^n_{i+1/2} = f(q^{\perp}(Q^n_i, Q^n_{i+1}))$$
$$F^n_{i+1/2} = f(q^{\perp}(q_l, q_r))$$

Finally, the Riemann problem solves the hyperbolic equation system between states q_l, q_r, to find the flux solution state $q^{\perp}(q_l, q_r)$. The boundary conditions are an exception because the dependent variables on either side of the Riemann problem are unknown. For example, in the downstream boundary, the right state q_r is known and the left state q_l has one unknown dependent variable (subcritical regime).

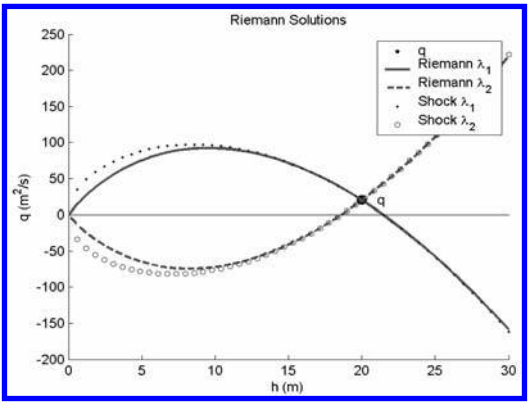


Figure 1. 4 Avaible curves in the state space associated with one state q and solution to a Riemann problem.

2.2 *Riemann solver*

In the SWE Riemann problem there are two families of solution waves, the Rankine Hugoniot waves and the Riemann invariant waves, the first ones are a discontinous waves, namely shocks and the second one are continous waves, namely rarefactions. The solution consists of two states q_l, q_r connected to a third state q_m by waves. Thus, a wave connects q_l, q_m and a wave connects q_m, q_r. Every wave must belong to a family of curves. Each family of solutions has two waves, thus, in every state in the state space, we find four different waves: *Shock* λ_1, *Shock* λ_2, *Riemann* λ_1, *Riemann* λ_1 and *Riemann* λ_2. However, only some parts of these waves are valid. This condition is imposed by entropy (Lax, 1972).

Using the valid solutions from Lax (1972), we constructed a solver by combining the different valid waves to obtain a state q_m, which is connected to a 1-wave in the left state of the Riemann problem q_l and a 2-wave in the right state of the Riemann problem q_r. The valid waves that connect q_l to q_m are:

$$u_m = \begin{cases} u_l + 2\left(\sqrt{gh_l} - \sqrt{gh_m}\right) & h_m < h_l \\ u_l - \left(h_m - h_l\right)\sqrt{\dfrac{g}{2}\left(\dfrac{1}{h_m} + \dfrac{1}{h_l}\right)} & h_m > h_l \end{cases} \quad (4)$$

The valid waves that connect q_r to q_m are:

$$u_m = \begin{cases} u_r - 2\left(\sqrt{gh_r} - \sqrt{gh_m}\right) & h_m < h_r \\ u_r - \left(h_m - h_r\right)\sqrt{\dfrac{g}{2}\left(\dfrac{1}{h_m} + \dfrac{1}{h_r}\right)} & h_m > h_r \end{cases} \quad (5)$$

It's important to note the difference between q_m and $q^{\perp}$, the first one is the Riemann solution and the second

Copyright © 2006 Taylor & Francis Group plc, London, UK

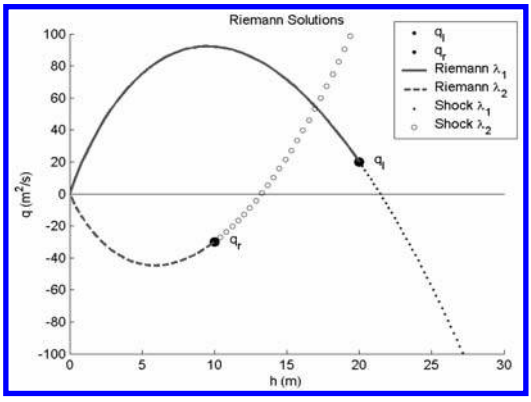


Figure 2. Valid solutions connecting with the two Riemann problem states q_l, q_r.

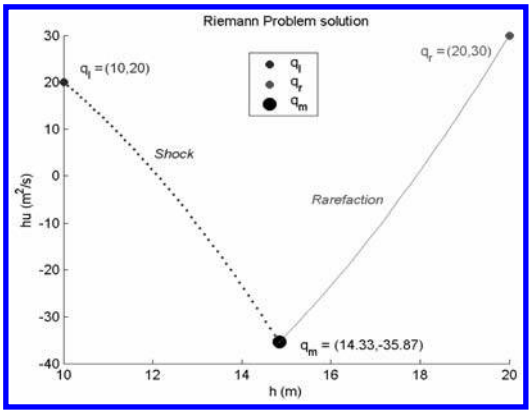


Figure 3. Example of a Riemann problem solution, the left state q_l is connected to the solution state q_m by a *Shock* λ_1 and the solution state is connected to the right state q_r by a *Riemann* λ_2 wave.

one is the flux solution. This difference is essential for the proposed algorithm to solving boundary conditions.

Thus, the algorithm of the Godunov method is:

$$\begin{aligned} &\textit{Dependent Variables} \begin{cases} q_l = Q_i^n \\ q_r = Q_{i+1}^n \end{cases} \\ &\downarrow \\ &q_m = \textit{Riemann Solver}\,(q_l, q_r) \\ &\downarrow \\ &q^{\perp} = q^{\perp}(q_l, q_r, q_m) \\ &\downarrow \\ &F_{i+1/2}^n = f(q^{\perp}) \end{aligned} \tag{6}$$

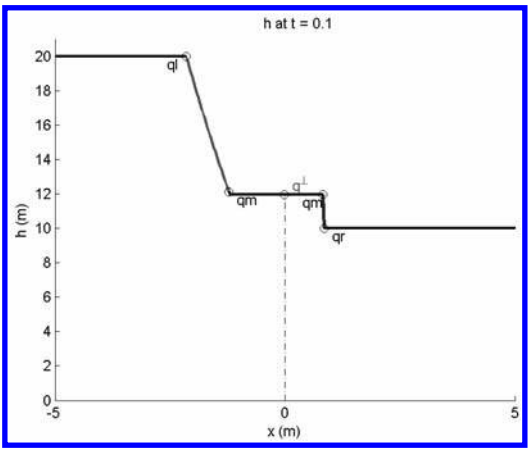


Figure 4. Example of the Riemann problem between q_l, q_r solution q_m and flux computation $q^{\perp}$.

3 BOUNDARY CONDITIONS

With hyperbolic problems, the definition of boundary conditions is not trivial. The number and application points of the conditions determine whether the problem is well posed. The shallow water equation system has two dependent variables and two equations. The system is first-order, so two boundary conditions and an initial state must be imposed. In the domain, there are two different boundaries $x_{1-1/2}, x_{n+1/2}$, and each boundary condition must be imposed on the right boundary.

3.1 *Description of the problem*

In hyperbolic problems, conditions should be imposed on the upwind side, which is defined by the eigenvalues of the hyperbolic system. They can be both positive, both negative, or one negative and one positive. These three cases are the supercritical regime, inverse regime and subcritical regime. In a supercritical regime, the boundary conditions should be defined on the upstream boundary. In an inverse regime, they should be imposed on the downstream boundary. In the subcritical regime, one condition should be imposed on the upstream boundary and the other on the downstream boundary.

As mentioned above, to solve a Riemann problem we need to know the values of the dependent variables on both sides of the Riemann problem. In the supercritical and subcritical regimes, all of the Riemann dependent variables of one boundary are defined and, on the other side, one dependent variable is defined and the other one is unknown. In these regimes, a complete boundary conditions method should test whether the Riemann problem solutions on the boundaries depend on the right dependent variables. On the boundary with

Copyright © 2006 Taylor & Francis Group plc, London, UK

all of the conditions imposed, the solution should be the conditions imposed. On the side without boundary conditions, the Riemann problem solution should not depend on the unknown outside dependent variables. This defines the well-posed problem condition.

The subcritical regime is different. In order to solve the Riemann problem, we have one boundary condition on each side, so the other one must be interpolated. A complete boundary conditions method should find the unknown dependent variable. It should be consistent with the imposed boundary condition and the domain dependent variables. The well-posed problem conditions used for the other regimes should also be applied.

First, the method should test the well-posed condition. Second, the method should interpolate the values of the incomplete dependent variables. These problems have traditionally been solved with the MOC, but this is not consistent with a Godunov method capable of dealing with transcritical regimes.

3.2 *General description of the solution*

This method uses the Riemann problem solution structure to introduce the boundary conditions in the domain. We will use the Riemann solution structure to test whether the boundaries are well posed, and we will use this structure to compute the values of the incomplete boundary conditions (subcritical).

For supercritical and inverse regimes, we need the complete boundary with two imposed conditions (h_{cc}, hu_{cc}) to belong to the supercritical or inverse zone of the state space. We also need the Riemann problem solution state q_m to fulfill another condition, depending on the regime, in order to obtain $q^{\perp} = (h_{cc}, hu_{cc})$.

For subcritical regimes, one dependent variable is imposed on each side of the domain and the other needs to be interpolated. To find this unknown variable, we will impose that it belong to the states connected by valid waves to the inside domain state. Figure 5 shows an example of a subcritical regime with a unit discharge hu_{cc} imposed in the upstream and the other dependent variable h_{cc} interpolated. The state (h_c, hu_{cc}) is connected to the inside state q_r by a *Riemann* λ_2 rarefaction.

$$q_r = Q_1^n \qquad q_l = \begin{pmatrix} h? \\ hu_{cc} \end{pmatrix} \tag{7}$$

Conceptually, this method finds q_m, but for the Godunov method we need $q^{\perp}$. However, as we will see:

In a subcritical regime, boundary conditions are only well posed if $q^{\perp} = q_m$ is fulfilled.

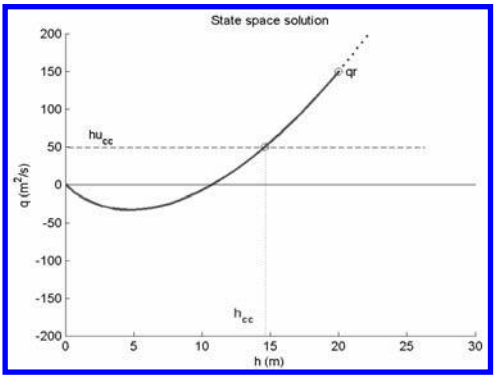


Figure 5. Deduction of the boundary condition h_{cc} from the inside state q_r and the imposed boundary condition hu_{cc}

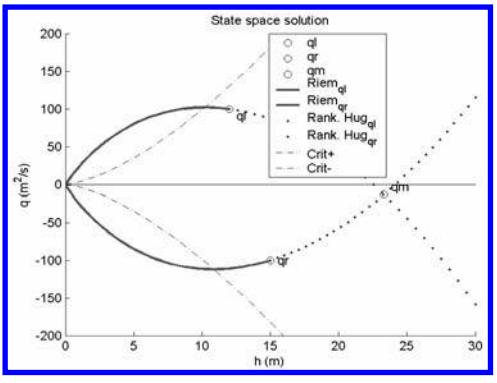


Figure 6. State space figure with the Riemann problem states, the solution state, the waves and the supercritical and inverse zones boundaries.

The demonstration is simple. If we impose a unique boundary condition $(h_{cc} or hu_{cc})$, the resulting flux should depend on the inside state $(q_l or q_r)$ and on the boundary condition itself. The states that depend on the inside state $(q_l or q_r)$ have one degree of freedom, so by imposing the boundary conditions $(h_{cc} or hu_{cc})$, the value of the solution state q_m is defined exactly.

In some cases the solution is undefined, but these cases are not mathematically well posed. The flux solution $q^{\perp}$ should therefore fulfill $q^{\perp} \in [q_m, q_l]$ or $q^{\perp} \in [q_m, q_r]$, depending on the case (downstream or upstream conditions). In some cases, we will find $q^{\perp} = q_m$. However, other cases fulfill $q^{\perp} \in (q_m, q_l]$ or $q^{\perp} \in (q_m, q_r]$, such as transcritical rarefactions. In these cases, the problem is not well posed because $q^{\perp} \neq (h_{cc}, hu_{cc})$, so the boundary condition is not imposed.

3.3 *Figures used to describe the cases*

To illustrate different situations in which this method can be applied, we will use two different figures: one

Copyright © 2006 Taylor & Francis Group plc, London, UK

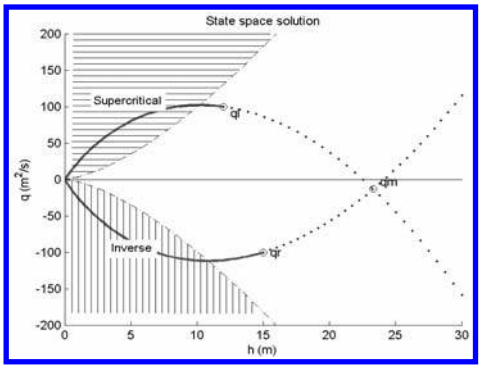


Figure 7. Inverse regime zone and supercritical zone. The remaining zone is for the subcritical regime.

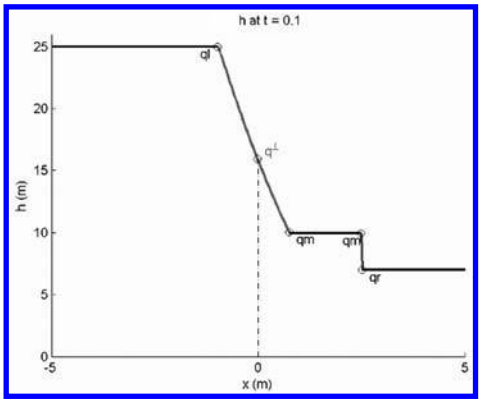


Figure 8. Dependent variable h in the space domain associated with the states $q_l, q_r, q_m, q^{\perp}$. The waves were developed for 0.1 s Possible cases.

with the state space (Figure 7) and another with a dependent variable (h) in the space domain (Figure 8). The latter will reproduce the waves produced in the state space.

The state space graphs will contain the Riemann problem states q_l, q_r, the solution state q_m and the flux state $q^{\perp}$. The valid waves connected to these states will also be drawn. The continuous waves represent the rarefactions; q_l connects to *Riemann* λ_1 and q_r connects to *Riemann* λ_2. The discontinuous lines represent the shocks; q_l connects to *Shock* λ_1 and q_r connects to *Shock* λ_2. We will also find two curves, Crit+ and Crit−, which define the boundaries of the supercritical and inverse regime zones respectively, λ_1, λ_2 are the eigenvalues of the hyperbolic system.

Supercritical regime Crit +

$$\lambda_1 = 0 \Rightarrow u - \sqrt{gh} = 0 \Rightarrow \quad (8)$$

$$u = \sqrt{gh} \Rightarrow \frac{u}{\sqrt{gh}} = 1 = \textit{Froude number}$$

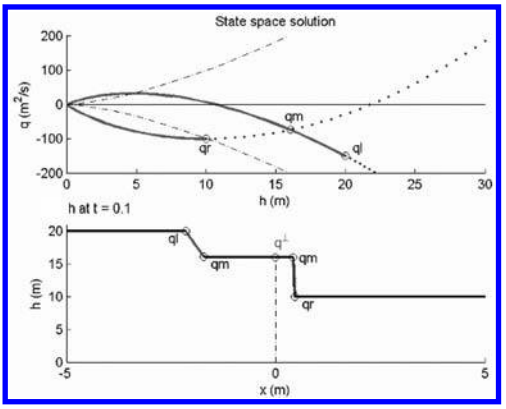


Figure 9. State space and waves.

Inverse regime Crit –

$$\lambda_2 = 0 \Rightarrow u + \sqrt{gh} = 0 \Rightarrow \quad (9)$$

$$u = -\sqrt{gh} \Rightarrow \frac{-u}{\sqrt{gh}} = -1 = \textit{Froude number}$$

3.4 *Possible cases*

This section analyzes various cases and interprets them as boundary conditions. Each case has two interpretations: one as an upstream condition $(q_l, q_m, q^{\perp})$, only one wave connecting q_l, q_m, and the other as a downstream condition $(q_r, q_m, q^{\perp})$, only a wave connecting q_r, q_m. The name of the case depends on q_m.

3.4.1 *Subcritical regime*

In this case, we have $q^{\perp} = q_m$, so the state q_m imposed as a boundary condition for a subcritical regime is valid. If we tried to impose q_l as a supercritical condition on the upstream boundary, it would be wrong because $q^{\perp} \neq q_l$. Likewise, if we tried to impose q_r as an inverse regime boundary condition, it would be wrong because $q^{\perp} \neq q_r$.

In the state space, a *Shock* λ_2 wave connects q_r to q_m and a *Riemann* λ_1 wave connects q_l to q_m.

3.4.2 *Subcritical regime*

In this case, we have $q^{\perp} = q_m$, so the state q_m imposed as a boundary condition for a subcritical regime is valid.

If we tried to impose q_l as a supercritical condition on the upstream boundary, it would be wrong because $q^{\perp} \neq q_l$. Likewise, if we tried to impose q_r as an inverse regime boundary condition, it would be wrong because $q^{\perp} \neq q_r$. In the state space, a *Shock* λ_2 wave connects q_r to q_m and a *Shock* λ_1 wave connects q_l to q_m.

3.4.3 *Subcritical regime*

In this case, we have $q^{\perp} = q_m$, so the state q_m imposed as a boundary condition for a subcritical regime is

Copyright © 2006 Taylor & Francis Group plc, London, UK

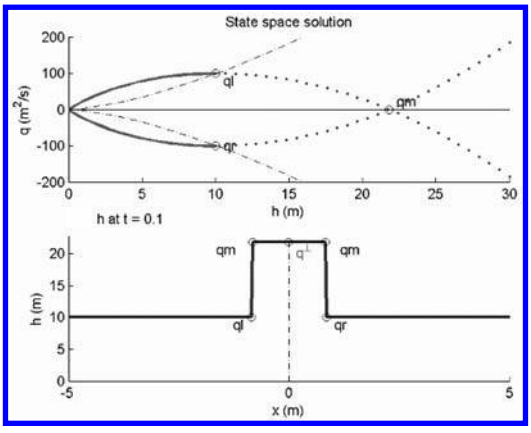


Figure 10. State space and waves.

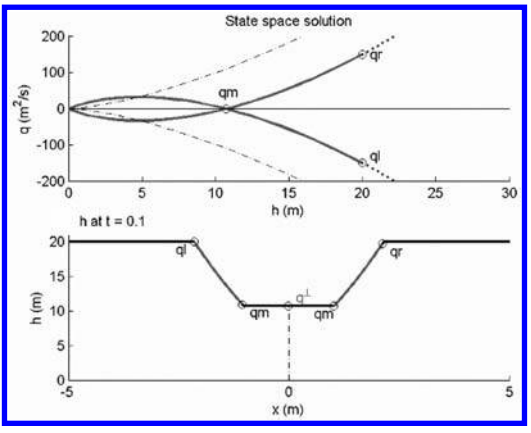


Figure 12. State space and waves.

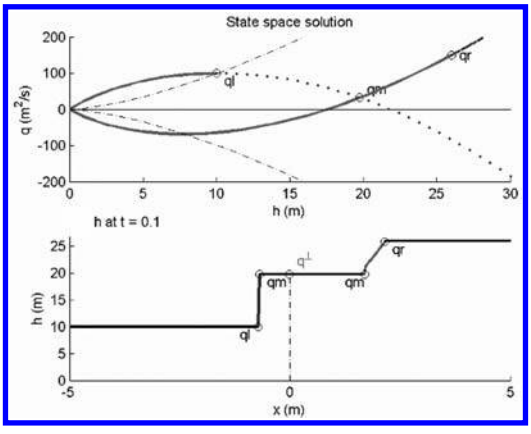


Figure 11. State space and waves.

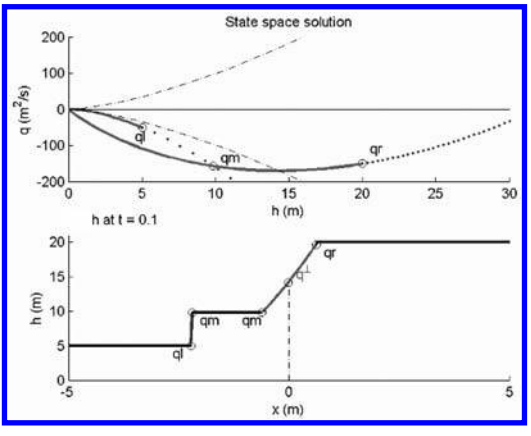


Figure 13. State space and waves.

valid. If we tried to impose q_l as a supercritical condition on the upstream boundary, it would be wrong because$q^{\perp} \neq q_l$. Likewise, if we tried to impose q_r as an inverse regime boundary condition, it would be wrong because $q^{\perp} \neq q_r$.

In the state space, a *Shock* λ_1 wave connects q_r to q_m and a *Riemann* λ_2 wave connects q_l to q_m.

3.4.4 *Subcritical regime*

In this case, we have $q^{\perp} = q_m$, so the state q_m imposed as a boundary condition for a subcritical regime is valid.

If we tried to impose q_l as a supercritical condition on the upstream boundary, it would be wrong because $q^{\perp} \neq q_l$. Likewise, if we tried to impose q_r as an inverse regime boundary condition, it would be wrong because $q^{\perp} \neq q_r$.

In the state space, a *Riemann* λ_1 wave connects q_r to q_m and a *Riemann* λ_2 wave connects q_l to q_m.

3.4.5 *Inverse regime*

As a downstream condition in a subcritical regime (q_r does not exist), q_m would be valid because $q^{\perp} = q_m$. As a downstream inverse regime boundary condition ($q_r = (h_{cc}, hu_{cc})$), q_r would not be valid because $q^{\perp} \neq q_r$.

As an upstream boundary condition (supercritical or subcritical), it would be wrong because $q^{\perp} \neq q_l$ in supercritical ($q_l = (h_{cc}, hu_{cc})$) and $q^{\perp} \neq q_m$ in subcritical.

3.4.6 *Inverse regime*

As a downstream condition in a subcritical regime (q_r does not exist), q_m would be valid because $q^{\perp} = q_m$. As a downstream inverse regime boundary condition ($q_r = (h_{cc}, hu_{cc})$), it would be valid because $q^{\perp} = q_r$.

As an upstream boundary condition (supercritical or subcritical), it would be wrong because $q^{\perp} \neq q_l$ in supercritical ($q_l = (h_{cc}, hu_{cc})$) and $q^{\perp} \neq q_m$ in subcritical.

Copyright © 2006 Taylor & Francis Group plc, London, UK

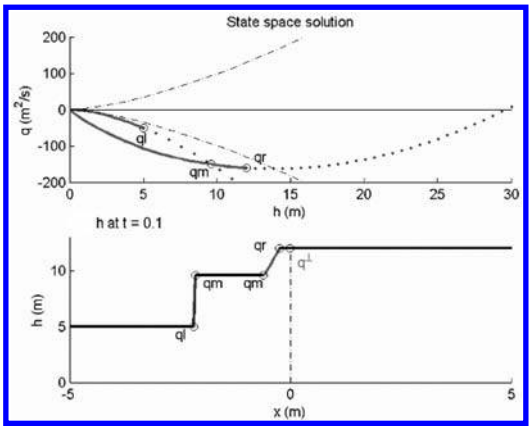


Figure 14. State space and waves.

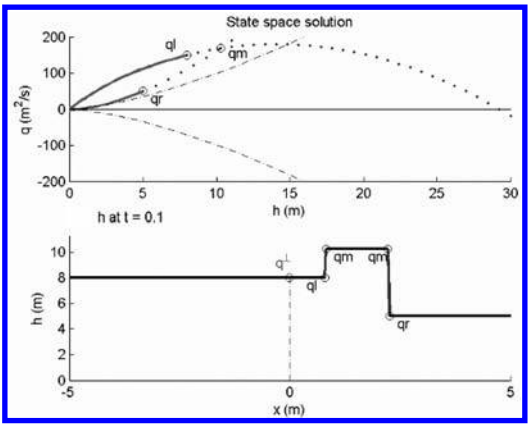


Figure 16. State space and waves.

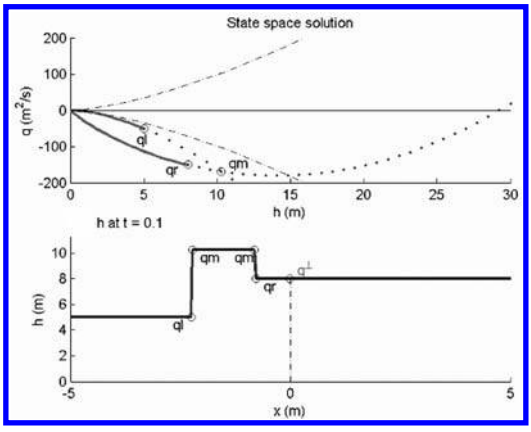


Figure 15. State space and waves.

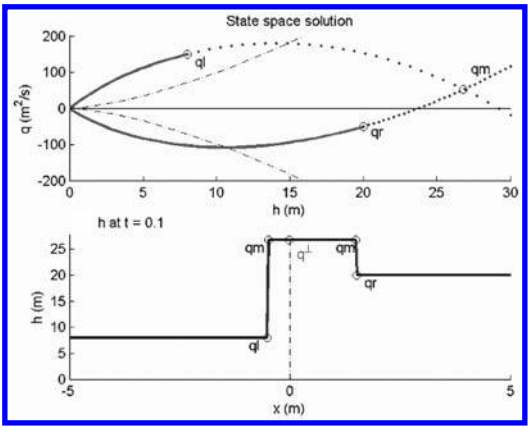


Figure 17. State space and waves.

3.4.7 *Inverse regime*

This case is interpreted like the previous one but has two shocks.

3.4.8 *Supercritical regime*

As an upstream condition in subcritical regime (q_l does not exist), it would be valid because $q^{\perp} = q_m$. As an upstream supercritical regime boundary condition ($q_l = (h_{cc}, hu_{cc})$), it would be valid because $q^{\perp} = q_l$.

As a downstream boundary condition (inverse or subcritical), it would be wrong because $q^{\perp} \neq q_r$ in supercritical ($q_r = (h_{cc}, hu_{cc})$) and $q^{\perp} \neq q_m$ in subcritical.

3.4.9 *Subcritical regime*

This case is important because, if we use $q_l = (h_{cc}, hu_{cc})$ as an upstream supercritical boundary condition, we find that $q^{\perp} \neq q_l$, although q_l is inside the supercritical zone. Thus, it is not a valid upstream supercritical condition.

The condition that must be valid is $s > 0$(Rankine-Hugoniot speed) in this case, the slope of the imaginary line joining q_l and q_m must be positive:

$$\frac{hu_l - hu_m}{h_l - h_m} > 0 \tag{10}$$

A similar condition must be imposed on the inverse regimes. In this case, the slope of the imaginary line joining q_r and q_m must be negative:

$$\frac{hu_r - hu_m}{h_r - h_m} < 0 \tag{11}$$

3.4.10 *Supercritical regime*

This case is the symmetric of 3.4.5, so the interpretation of the boundary conditions is symmetric.

Copyright © 2006 Taylor & Francis Group plc, London, UK

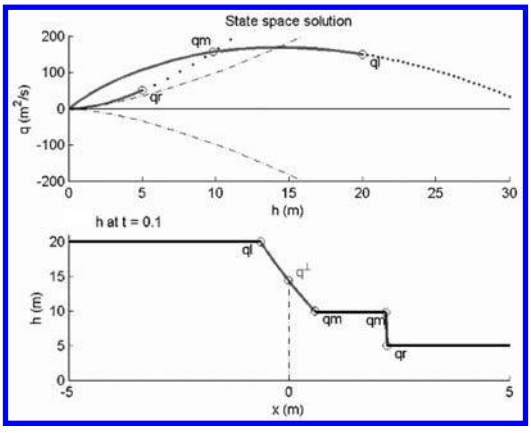


Figure 18. State space and waves.

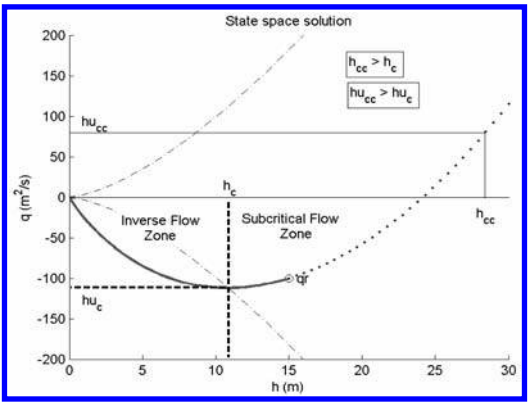


Figure 19. State limit that must be applied to the upstream boundary conditions of subcritical regimes.

3.5 *Solution algorithm*

The type of algorithm depends on the type of boundary condition to be imposed. It does not depend on the regime inside the domain.

3.5.1 *Supercritical regime:*

(a) Check the imposed values of the dependent variables are included in the supercritical regime zone in the state space.
(b) Solve the Riemann problem (q_l, q_r) and find q_m.
(c) Check condition (10) to define $q^{\perp} = q_l$.

3.5.2 *Inverse regime:*

(a) Check the imposed values of the dependent variables are included in the inverse regime zone in the state space.
(b) Solve the Riemann problem (q_l, q_r) and find q_m.
(c) Check condition (11) to define $q^{\perp} = q_t$.

3.5.3 *Subcritical regime:*

To define the subcritical regime algorithm, previous steps must be carried out. In this regime, we impose one boundary condition with a dependent variable (h_{cc} or hu_{cc}) and we interpolate the other dependent variable (hu_{cc} or h_{cc}). To interpolate the unknown dependent variables, we use the waves that connect the known state. In these waves, we find the state that has the imposed boundary condition value (Figure 5). However, the curves are not injective (the shapes are parabolic).

However, there is another limitation. The interpolated state must not be inside the supercritical or inverse regime zones, because if it were it would not be a subcritical condition. Excluding the zones that correspond to supercritical or inverse regimes, the remaining part of the curves is injective. Thus, the mathematical and hydraulic problems are coupled. The limit state is the intersection between the curves and the Crit+ and Crit− curves. This intersection defines the state (h_c, hu_{cc}). For an upstream condition, our boundary condition dependent variables must fulfill:

$$\begin{aligned} h_{cc} &> h_c \\ hu_{cc} &> hu_c \end{aligned} \tag{12}$$

The state is therefore outside of the inverse regime zone.

If we impose a downstream boundary condition, the dependent variables must fulfill:

$$\begin{aligned} h_{cc} &> h_c \\ hu_{cc} &< hu_c \end{aligned} \tag{13}$$

This limitation imposes a maximum for the negative discharges for upstream and downstream boundary conditions. The algorithm is as follows:

(a) Determine the values of h_c and hu_c as interpolation limits.
(b) Considering these limitations, find the unknown dependent variable that corresponds to the known dependent variable imposed as a boundary condition. The result of this step is q_m.
(c) Check that state q_m is not in the supercritical or subcritical zone, because that would indicate a compatible but complete boundary condition (which is only valid for supercritical and inverse regimes).
(d) At this point, we know that $q^{\perp} \in [q_m, q_r]$ or $q^{\perp} \in [q_m, q_l]$. We only need to check that $q_m = q^{\perp}$.

A sufficient condition to fulfill d) is that the inside state (q_l or q_r) is outside of the inverse and supercritical regime zones.

Figure 21 shows an example of this situation. If we impose a subcritical upstream boundary condition (q_m, q_r), q_m fulfills c) but the inside state q_r does not fulfill d). Finally, $q_l \neq q_m$, so it is an invalid upstream boundary condition.

Copyright © 2006 Taylor & Francis Group plc, London, UK

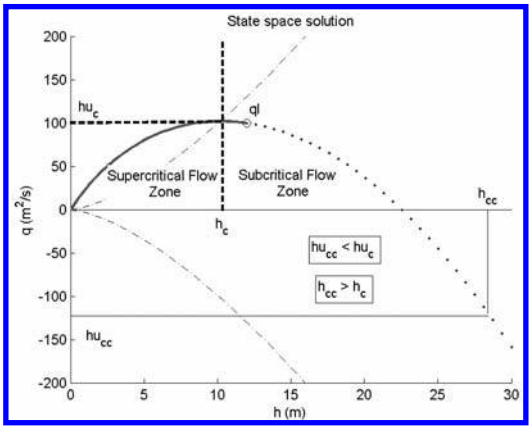


Figure 20. State limit that must be applied to the downstream boundary conditions of subcritical regimes.

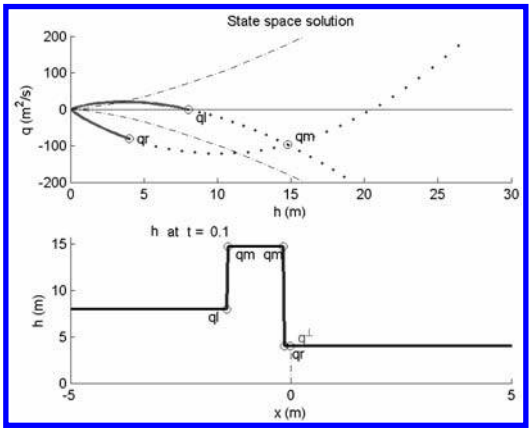


Figure 21. Example of a violation of subcritical boundary conditions.

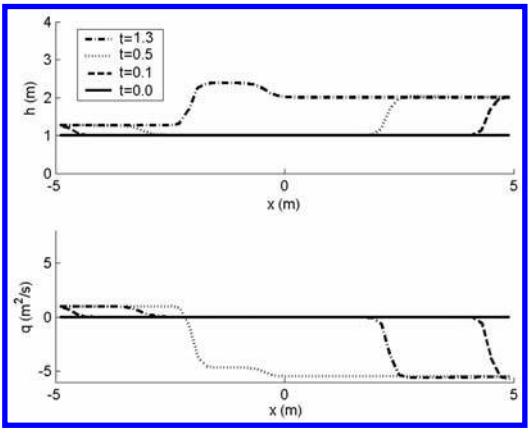


Figure 22. Four states of the channel in the first seconds.

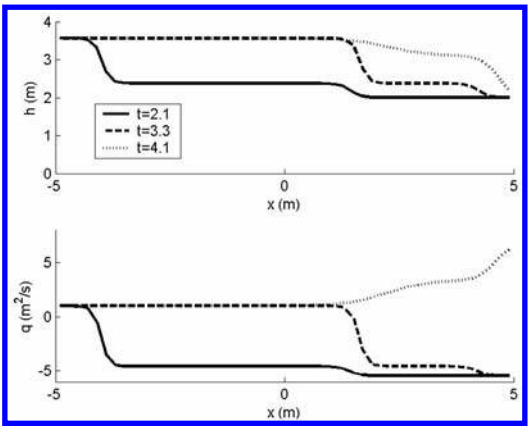


Figure 23. Three states of the channel in the first seconds.

Let us conceptually interpret these limitations. Condition a) imposes that the boundary conditions at least have an influence inside the domain (upwind). Condition c) imposes that the condition may not be complete, because that would imply imposing two values for dependent variables, which is not valid for subcritical regimes.

In hydraulic terms, this condition means that neither the upstream nor downstream discharge may exceed the critical discharge in a channel.

4 RESULTS

This section presents results obtained in a simulation involving a channel 10 meters long and 1 meter wide. The initial conditions are rest, 1 meter depth. The boundary conditions are an upstream discharge of 1 cubic meter per second and a downstream water level of 2 meters.

Figure 22 and Figure 23 show different time results.

When the boundary conditions are imposed, shocks come from the boundaries, and keep unaltered until the wave traveling from the opposite node arrives. Figure 24 shows the changes over time in the depth and discharge in the upstream boundary and in the inside domain node next to the upstream boundary.

Figure 25 shows the changes over time in the state space in the upstream. The boundary curve is always at 1 cubic meter per second because it is imposed, and it changes the depth to adapt to the inside domain situation. The inside node line changes over time until it reaches a steady state, as does the whole channel, in the imposed boundary conditions, discharge 1 m^3/s and depth 2 m. Could happen that the imposed boundary conditions are wrong, in this situation the computation should stop or use spetial condition like critical depth.

Copyright © 2006 Taylor & Francis Group plc, London, UK

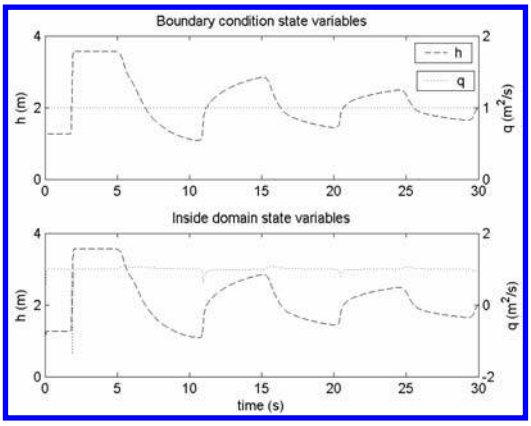


Figure 24. The dependent variables in the upstream boundary and in the inside domain node next to the upstream boundary.

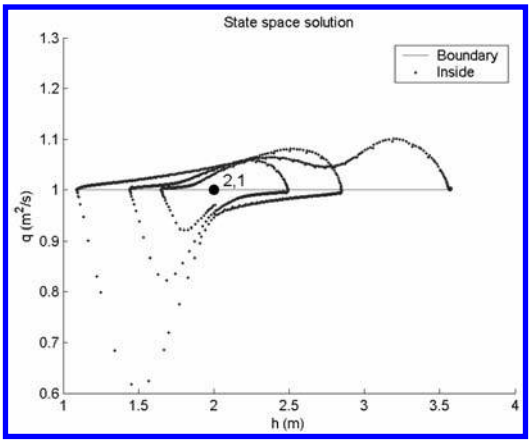


Figure 25. State space variables evolution in the upstream boundary condition and in the inside domain node, both are converging to boundary conditions, $h = 2\,m$, $q = 1\,m^3/s$.

5 CONCLUSIONS

The proposed method combines a filter, which ensures that only well-posed problems are defined, and a method for interpolating the unknown dependent variables in partial boundary conditions (subcritical regimes).

The method is based on the Riemann problem solution and is optimal for the Godunov method.

It allows discontinuities such as boundary conditions to be introduced.

The method can immediately be extended to one-dimensional Euler equations, but more research is required before it can be extended to multidimensional problems.

The method is computed using an exact Riemann solver because is not computationally expensive, so the combination with approximate Riemann solvers should be researched.

ACKNOWLEDGMENTS

This study was carried out as a part of project BTE2002-0375 of the Spanish Ministry of Science and Technology.

REFERENCES

Bateman A. 1993. Formación y propagación de frentes de onda en canales. Estudio teórico numérico y experimental. PhD thesis, UPC.

Godunov S. K. 1959. A difference method for numerical calculation of discontinuous solutions of the equations of hydrodynamics, Mat. Sb., 47, pp. 271–306.

Kruzkov S. N. 1970. First order quasilinear equations in several independent variables, Math. USSR Sb., 10, pp. 217–243.

Lax P. D. 1972. Hyperbolic systems of conservation laws and the mathematical theory of shock waves, SIAM Regional Conference Series in Applied Mathematics 11.

Lax P. D. and Wendroff D. 1960. Systems of conservation laws, Comm. Pure Appl. Maths. (13) pp. 217–237.

LeVeque, R. J. 2002. Finite Volume Methods for Hyperbolic Problems, Cambridge University Press.

Oleinik O. 1957. Discontinuous solutions of nonlinear differential equations, Amer. Math. Soc. Transl. Ser. 2, 26, pp. 95–172.

Stoker, J. J. 1957. Water waves: The mathematical theory with applications, Pure and Applied Mathematics, Vol. IV, Interscience Publishers, Inc., New York, 1957.

Copyright © 2006 Taylor & Francis Group plc, London, UK

The role of quasi-conservative form for morphodynamic modelling in river flow computations

Annunziato Siviglia, Giampiero Nobile & Marco Colombini
DIAM University of Genova

ABSTRACT: Coupling the De Saint-Venant equations with the Exner equation yields to a model for the morphohydrodynamics that can be used to describe flow in rivers the shape of which is determined by the flow itself. Modern numerical models of natural rivers are built upon synchronous solution of the above system, accounting for the strong coupling between water flow, sediment transport, and morphological evolution. Such models are described by a system of hyperbolic equations expressed in primitive (non-conservative) form, thus requiring the use of non-conservative numerical methods for its numerical solution. Methods based on the primitive formulation are known to wrongly compute both the strength and the celerity of shock waves (bores), with consequent loss of mass. Such a problem may affect the numerical solution making it completely useless, in particular for long term morphodynamic simulations. In the present contribution it is shown how a quasiconservative formulation of the governing equations may help to reduce these errors. In particular, numerical solutions are obtained using a quasi-conservative formulation of the well-known MacCormack method. To test the proposed formulation, the model is first applied to idealized benchmark problems. The robustness of the model is then tested routing severe floods through a complex river system and comparing numerical results with the measurements obtained on a physical model of the Vara River in Northern Italy.

1 INTRODUCTION

The relevance of hydro-morphodynamic models (HMM) is essentially based on a simple consideration: water flows in a container which determines the characteristics of the flow but at the same time is amenable of modification by the flow itself. To date, HMM are becoming one of the basic tools for engineering planning, design and assessment. The most widespread class of HMM in literature is the one which uses the De Saint-Venant equations for hydrodynamic flow routing, while bed evolution is described by the Exner equation (Krishnappan 1985; Holly and Rahuel 1990; Cui et al. 1996; Wu et al. 2004).

The majority of the above models are uncoupled (i.e. bed and flow solutions proceed separately) while only few of them solve simultaneously the governing equations. As discussed by Lanzoni et al. (2006), near critical conditions a decoupled approach does predict morphodynamic influence (i.e. propagation of information on bed variations) either upstream or downstream, while only a coupled approach is able to propagate bed information in both directions.

Coupled solutions should then be used for the study of long term evolutions of natural rivers (Cao et al. 2002; Correia et al. 1992; Singh et al. 2004), or, in general, when it is not possible to assume that the flow adapts instantaneously to changes in bed elevation (Colombini and Stocchino 2005).

A second important issue urging for the adoption of a coupled strategy in morphodynamic models is related to the boundary conditions. Lyn (1987) investigated the coupling between flow and sediment dynamics in situations where both the fluid and the sediment discharge are rapidly changing, showing that decoupled models are not capable of satisfying either a general boundary condition or an arbitrary initial condition.

Therefore, adopting a coupled approach for solving the governing equations is a stringent requirement in order to obtain reliable results when flow is close to critical conditions, a situation that characterizes most mountain rivers and, at least locally, is often encountered in natural rivers due to the presence of bridge piers, sudden variations in bed slope or river width.

In all the aforementioned studies, the coupled system is solved without particular focus on the numerical properties of the mathematical formulation adopted for the solution. However, it is well known that a non-conservative (primitive) formulation of the numerical solution leads to a wrong computation of the discontinuities of the solution with consequent loss of

Copyright © 2006 Taylor & Francis Group plc, London, UK

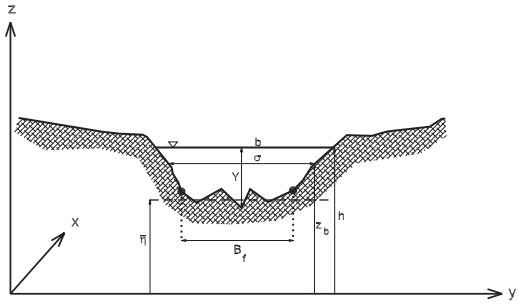


Figure 1. Cross sectional geometry.

mass, thus rendering rapidly meaningless long term morphodynamic simulations.

In his work on the solution of quasilinear hyperbolic system, Lax and Wendroff (1960) proved that conservative numerical methods, if convergent, do converge to correct solutions of the equations. On the contrary, Hou and LeFloch (1994) have shown that non-conservative schemes do not converge to the correct solution if a shock wave is present in the solution, a situation that is often encountered in morphodynamic problems where discontinuities of the solution can appear both in the flow (bores) and on the bed (drop structures, weirs)

To overcome these difficulties a quasi-conservative formulation of the fully coupled De Saint-Venant Exner model, is proposed in the present contribution. An appropriate numerical scheme, based on the well known MacCormack scheme, is also developed to deal with the proposed formulation.

2 PROBLEM FORMULATION

A one dimensional hydro-morphodynamic model which describes the flow over erodible bottom in natural channels is formulated. The riverbed is assumed to be composed of well-graded sediments with the same particle size d_s as those transported by the water flow. The solid transport is characterized by bed-load only, thus ignoring the role of suspension. In such a context, the HMM can be described by a two phase model. The governing equations are obtained imposing mass conservation of the fluid and solid phases and the momentum principle to a dilute suspension of sediment particles flowing in an open channel with a cohesionless bottom. Defining a Cartesian coordinate system (x, y, z) with the x-axis longitudinal, y-axis transversal and the z axis vertical upward (see figure 1), the system of governing equations reads:

Liquid phase continuity equation

$$\frac{\partial A}{\partial t} + \frac{\partial Q}{\partial x} + \lambda_p \frac{\partial B_f \overline{\eta}}{\partial t} = q_l \qquad (1)$$

Solid phase continuity equation

$$(1-\lambda_p)\frac{\partial B_f \overline{\eta}}{\partial t} + \frac{\partial B_f \overline{Q}_s}{\partial x} = q_{sl} \qquad (2)$$

Momentum equation

$$\frac{\partial Q}{\partial t} + \frac{\partial}{\partial x}\left(\beta \frac{Q^2}{A}\right) + gA\frac{\partial h}{\partial x} + gAS_f = \frac{Q}{A} q_l \qquad (3)$$

where A is the cross sectional area, Q and Q_s are the flow rate and the sediment discharge, ql and q_{sl} the liquid and solid discharges per unit length due to lateral inflow/outflow, B_f is the width of the active portion of the bed λ_p is the porosity, η is the bottom elevation, h is the water level, β is the correction coefficient for the momentum, g is the gravitational acceleration and S_f is the friction term. Moreover, in the above equations, an overbar denotes a quantity averaged over the active width B_f.

It is worth noting that the last term on the left hand side of equation (1) accounts for the water that is made available or entrapped through the erosion/ deposition process. The full derivation of equation (1) is given in Lanzoni et al. (2006) (but see also Correia et al. (1992) and Cui et al. (2005)). In the recent literature on the subject of 1-D wave propagation in erodible streams (Cao et al. 2002; Lyn and Altinakar 2002; Cao and Carling 2003) various contributors argued for the significance of the last term which, as clarified by Cui et al. (2005), is likely to be negligible in most natural river and will therefore be ignored in the following.

The above equations can now be written in conservative form. This notion has its roots in the mathematical treatment of the flux and accumulation of physical quantities, e.g., mass, momentum, energy, etc., associated with fluid flow in a control volume. The nature and meaning of conservation-law form have been vastly addressed in the literature (e.g. Cunge et al. (1994), Lai et al. (2002)) and can be traced back to the work of Lax (1957).

Following Cunge et al. (1994), after some algebraic manipulations, the hydrodynamic equations can be rewritten in the following conservative form:

$$\frac{\partial A}{\partial t} + \frac{\partial Q}{\partial x} = q_l \qquad (4)$$

$$\frac{\partial Q}{\partial t} + \frac{\partial}{\partial x}\left(\beta \frac{Q^2}{A} + gI_1\right) = gI_2 + gA(S_0 - S_f) + q_l \frac{Q}{A} \qquad (5)$$

where S_0 is the local bottom slope, I_1 represents a hydrostatic pressure force term

$$I_1 = \int_Y (h - z_b(y))\sigma(x,z)dz \quad , \qquad (6)$$

Copyright © 2006 Taylor & Francis Group plc, London, UK

where Y is the water depth, $zb(y)$ is the bed elevation, with

$$\sigma(x,z,t) = \frac{\partial A(x,t)}{\partial z} \quad , \tag{7}$$

and I_2 accounting for the pressure forces in a volume of constant depth due to longitudinal variations,

$$I_2 = \int_Y (h - z_b(y)) \frac{\partial \sigma(x,z)}{\partial x} dz \, . \tag{8}$$

Assuming that the width of the active portion of the bed does not change in time, thus assuming $B_f = B_f(x)$, the 1-D solid phase continuity equation in conservative form reads:

$$(1-\lambda_p)\frac{\partial \overline{\eta}}{\partial t} + \frac{\partial \overline{Q}_s}{\partial x} = \frac{q_{st}}{B_f} - \frac{\overline{Q}_s}{B_f}\frac{\partial B_f}{\partial x} \tag{9}$$

where the last term on the right hand side is treated as a source term similarly to the term I_2 in the momentum equation.

The unknowns in the governing equations (4), (5), (9), are A, Q, $\bar{\eta}$, S_f, and $\bar{Q}_s$, so that a friction resistance law and a sediment-transport formula are required to evaluate S_f and $\bar{Q}_s$. Both are obtained assuming that, locally and instantaneously, the relationships available for steady and uniform flow conditions still hold.

More precisely, the energy loss per unit length of the channel is expressed through a friction coefficient as:

$$S_f = \frac{Q^2}{g(A^2C^2R)} \, , \tag{10}$$

where C is the global conductivity in the cross section and R is the hydraulic radius. Due to the complexity of natural geometries, the calculation of the quantities (A^2C^2R) has been done integrating over the width b (Engelund 1964):

$$A^2C^2R = \left[\int_b c(y)(h - z_b(y))^{3/2} dy\right]^2 \tag{11}$$

where b is the width of the free surface and $c(y)$ is the local conductivity which is a function of the transversal coordinate y. In order to quantify c the Strickler's formula has been adopted:

$$c(y) = \frac{K_s}{\sqrt{g}}(h - z_b(y))^{(1/6)} \tag{12}$$

with K_s being the dimensional Strickler coefficient dependent on the local bed roughness only.

A similar procedure is followed for the sediment transport, leading to

$$\overline{Q}_s = \frac{\sqrt{(s-1)g d_s^3}}{B_f} \int_{B_f} \Phi(\theta(y), \theta_c) dy \tag{13}$$

where s is the relative density, and the local Shields stress is given by

$$\theta(y) = \frac{S_f(h - z(y))}{(s-1)d_s}. \tag{14}$$

Several formulations are available for the sediment discharge function $\Phi(\theta, \theta_c)$. In the following we have considered the one proposed by Meyer-Peter and Müller (1948), where

$$\Phi = 8(\theta - \theta_c)^{3/2}, \qquad \theta_c = 0.047. \tag{15}$$

and the the relationship proposed by Parker (1990), which reads

$$\Phi = 0.00218\, \theta^{3/2} G(\xi), \quad \xi = \frac{\theta}{\theta_r}, \quad \theta_r = 0.0386, \tag{16}$$

with

$$G = \begin{cases} 5474(1 - 0.853/\xi)^{4.5} & \xi \geq 1.65, \\ \exp\left[14.2(\xi - 1) - 9.28(\xi - 1)^2\right] & 1 \leq \xi 1.65, \\ \xi^{14.2} & \xi < 1. \end{cases} \tag{17}$$

The latter, based on field measurements performed on gravel-bed rivers, is characterized by the absence of critical value of the Shields stress for sediment motion even though very low sediment transport rates are predicted for $\xi < 1$.

3 COUPLED VS. DECOUPLED APPROACHES

The choice of the solution strategy for solving the differential problem given by (4), (5) and (9) relies on the relative order of magnitude of the celerities associated with the characteristic curves of the hyperbolic system. The behavior of such curves is well known (De Vries 1965): far from the criticality ($1-F^2 = O(1)$) the celerity of a bed wave is considerably smaller than that of surface waves. The bed interacts only weakly with the water surface, thus justifying an approach in which the equations that govern the dynamics of the liquid phase are solved separately from those governing the solid phase. Near critical conditions exists a transcritical region, $0.8 < F < 1.2$ (Sieben 1999), in which two of the three celerities have the same order of magnitude; in this region the surface waves strongly interact with bed waves provided $1-F^2 = O(\gamma)$, where $\gamma = (Q_s/Q)$ is the solid to liquid discharge ratio (Lyn and Altinakar 2002).

Based on the above considerations, three different solution strategies can be identified (Kassem and Chaudry 1998) according to the method of solution

Copyright © 2006 Taylor & Francis Group plc, London, UK

employed: *decoupled*, *semicoupled* and *fully-coupled*. In the decoupled (asynchronous) approach, the solution is obtained assuming that the change in one variable during a computational time step is small enough that its effect on the other variables can be ignored. Therefore, the hydrodynamic governing equations (4–5) can be solved separately from the morphodynamic equation (9) and can be expressed in the so called conservative form:

$$\frac{\partial \mathbf{U}}{\partial t} + \frac{\partial \mathbf{F}}{\partial x} = \mathbf{S}\,. \tag{18}$$

where **U** is the vector of unknowns, **F** is the vector of fluxes and **S** is the vector of source terms. They read, for the liquid phase:

$$\mathbf{U} = \begin{bmatrix} A \\ Q \end{bmatrix} \quad , \quad \mathbf{F} = \begin{bmatrix} Q \\ \beta \frac{Q^2}{A} + gI_1 \end{bmatrix} \tag{19}$$

$$\mathbf{S} = \begin{bmatrix} q_l \\ gI_2 + gA(S_0 - S_f) + q_l \frac{Q}{A} \end{bmatrix} \tag{20}$$

while for the solid phase we have:

$$\mathbf{U} = \left[(1-\lambda_p)\overline{\eta}\right], \qquad \mathbf{F} = \left[\overline{Q}_s\right] \tag{21}$$

$$\mathbf{S} = \left[\frac{q_{sl}}{B_f} - \frac{\overline{Q}_s}{B_f}\frac{\partial B_f}{\partial x}\right]. \tag{22}$$

In the semicoupled approach, the solution proceeds through an iterative procedure. At each time step, the flow solution obtained assuming fixed bed is used to predict the changes in the bed level along the channel. Then, the new bed level is used to adjust the flow variables and the previous steps are iterated until convergence is achieved. As well as in the decoupled approach, the governing equations can be written in conservative form.

In the fully coupled (synchronous) approach all the governing equations are solved simultaneously at each time step. In this case, a problem arises in the evaluation of the term S_0, representing the local slope of the bottom,

$$S_0 = -\frac{\partial \overline{\eta}}{\partial x} \quad . \tag{23}$$

This term can be safely treated as a source term when either a decoupled or a semi-coupled approach is adopted since both solution strategies consider the bed as frozen so that, at each time step, this term is function of the instantaneous geometry of the river. On the contrary, in the coupled formulation the term S_0 represents the first derivative of one of the three independent variables of the complete problem and cannot be considered as a source term anymore. How to incorporate the term gAS_0 in the fluxes is still an open issue, so that primitive versions of the complete set of governing equations are usually adopted for the numerical solution (Cao et al. 2002; Correia et al. 1992; Singh et al. 2004):

$$\frac{\partial \mathbf{U}}{\partial t} + \mathbf{J}\frac{\partial \mathbf{U}}{\partial x} = \mathbf{S}\,. \tag{24}$$

where **J** is the Jacobian matrix corresponding to the fluxes **F** given by

$$\mathbf{J} = \frac{\partial \mathbf{F}}{\partial \mathbf{U}}\,. \tag{25}$$

and

$$\mathbf{U} = \begin{bmatrix} A \\ Q \\ (1-\lambda_p)\overline{\eta} \end{bmatrix} \tag{26}$$

$$\mathbf{J} = \begin{pmatrix} 0 & 1 & 0 \\ \frac{gA}{b} - \frac{\beta Q^2}{A^2} & 2\frac{\beta Q}{A} & \frac{gA}{1-\lambda_p} \\ \frac{\partial \overline{Q}_s}{\partial A}|_Q & \frac{\partial \overline{Q}_s}{\partial Q}|_A & 0 \end{pmatrix} \tag{27}$$

$$\mathbf{S} = \begin{bmatrix} q_l \\ q_l\frac{Q}{A} - gAS_f + g\frac{A}{b}\frac{\partial A}{\partial x}|_Y \\ \frac{1}{B_f}\left(q_{sl} - \frac{\partial B_f \overline{Q}_s}{\partial x}|_{Y,Q} + B_f\frac{\partial \overline{Q}_s}{\partial A}|_{x,Q}\frac{\partial A}{\partial x}|_Y\right) \end{bmatrix} \tag{28}$$

4 PRIMITIVE VS. CONSERVATIVE FORMULATIONS

Once the choice of a fully coupled model for the solution of the morphodynamic system of equations is made, a problem remains in terms of *primitive* versus *conservative* formulations. In purely hydrodynamic problems, both the formulations are available.

It is useful in this context to introduce the concept of *primitivity* of the formulation writing the system of governing equation in the generic form:

$$\frac{\partial \mathbf{U}}{\partial t} + \frac{\partial \mathbf{F}}{\partial x} + \mathbf{A}\frac{\partial \mathbf{U}}{\partial x} = \mathbf{S}\,, \tag{29}$$

Setting now **A** to zero produces the conservative form of the equation while setting **F** to zero leads to the primitive form.

Clearly, starting from the conservative form, the primitivity of the equations can be increased moving terms from **F** to **A**, an operation that is always possible while viceversa it can be reduced, when possible, moving terms from **A** to **F**.

Copyright © 2006 Taylor & Francis Group plc, London, UK

The idea behind the *quasi-conservative* formulation presented herein is that the errors related to primitivity can be reduced considerably if all the terms that can be written in a conservative fashion are collected in the fluxes, isolating as much as possible terms that cannot be expressed in conservative form.

The purely hydrodynamic system of equations, which can be written in conservative form, can be of guidance in this procedure leading to the following quasi-conservative formulation of the coupled system

$$\mathbf{U} = \begin{bmatrix} A \\ Q \\ (1-\lambda_p)\overline{\eta} \end{bmatrix} \quad , \quad \mathbf{F} = \begin{bmatrix} Q \\ \beta\frac{Q^2}{A} + gI_1 \\ \overline{Q}_s \end{bmatrix} \tag{30}$$

$$\mathbf{A} = \begin{pmatrix} 0 & 0 & 0 \\ 0 & 0 & \frac{gA}{1-\lambda_p} \\ 0 & 0 & 0 \end{pmatrix} \tag{31}$$

$$\mathbf{S} = \begin{bmatrix} q_l \\ gI_2 - gAS_f + q_l\frac{Q}{A} \\ \frac{q_{sl}}{B_f} - \frac{\overline{Q}_s}{B_f}\frac{\partial B_f}{\partial x} \end{bmatrix} \tag{32}$$

Note that the only non vanishing coefficient of the array $\mathbf{A}$ is the one related to the bottom slope S_0 thus reducing primitivity of the system to the minimum.

5 NUMERICAL SOLUTION: THE MACCORMACK METHOD

In this section primitive and quasi-conservative version of the so called MacCormack method are developed to numerically integrate equations (4), (5) and (9) in their different formulations. This classic scheme, developed in the early 1970's (MacCormack 1971), is still widely used for solving open-channel problems, because of its easy implementation for natural river with variable spatial steps and its ability to capture shock waves with second order accuracy both in time and in space.

The MacCormack method is a predictor-corrector two-steps scheme which proceeds in sequence:

$$\mathbf{U}_i^p = \mathbf{U}_i^n - \frac{\Delta t}{\Delta x}\left[\mathbf{F}_{i+1}^n - \mathbf{F}_i^n\right] + \Delta t\mathbf{S}\left(\mathbf{U}^n, x\right) \tag{33}$$

$$\mathbf{U}_i^c = \mathbf{U}_i^n - \frac{\Delta t}{\Delta x}\left[\mathbf{F}_i^p - \mathbf{F}_{i-1}^p\right] + \Delta t\mathbf{S}\left(\mathbf{U}^p, x\right) \tag{34}$$

where the apexes p and c stand for predictor and corrector, respectively.

In both steps, the source terms are evaluated using the pointwise discretisation, but the source term evaluated in the first step is updated of a time step Δt and used for sources evaluation in the second step. It is worth noting that derivatives which are included in the source terms are discretized at each step with backward or forward differences as well as the flux gradient $\delta\mathbf{F}/\delta x$.

In order to formulate a primitive version of the MacCormack scheme the flux gradient (Toro and Siviglia 2003) can be expressed by:

$$\frac{\partial\mathbf{F}}{\partial x} = \frac{\partial\mathbf{F}}{\partial\mathbf{U}}\left(\frac{\partial\mathbf{U}}{\partial x}\right) = \mathbf{J}\left(\frac{\partial\mathbf{U}}{\partial x}\right) . \tag{35}$$

Using (35) the predictor and corrector steps of the MacCormack scheme can be rewritten in primitive form as follows:

$$\mathbf{U}_i^p = \mathbf{U}_i^n - \frac{\Delta t}{\Delta x}\mathbf{J}_{i+\frac{1}{2}}\left[\mathbf{U}_{i+1}^n - \mathbf{U}_i^n\right] + \Delta t\mathbf{S}\left(\mathbf{U}^n, x\right) \tag{36}$$

$$\mathbf{U}_i^c = \mathbf{U}_i^n - \frac{\Delta t}{\Delta x}\mathbf{J}_{i-\frac{1}{2}}\left[\mathbf{U}_i^p - \mathbf{U}_{i-1}^p\right] + \Delta t\mathbf{S}\left(\mathbf{U}^p, x\right) \tag{37}$$

Different options are available for the coefficient matrix $\mathbf{J}_{i+\frac{1}{2}}$ The most promising results are obtained computing this term as a spatial average, namely:

$$\mathbf{J}_{i+\frac{1}{2}} = 0.5\left(\mathbf{J}_i + \mathbf{J}_{i+1}\right) . \tag{38}$$

The quasi-conservative version of the MacCormack scheme is obtained combining the conservative and primitive formulations presented above so that

$$\begin{aligned} \mathbf{U}_i^p &= \mathbf{U}_i^n - \frac{\Delta t}{\Delta x}\left[\mathbf{F}_{i+1}^n - \mathbf{F}_i^n\right] \\ &- \frac{\Delta t}{\Delta x}\mathbf{J}_{i+\frac{1}{2}}\left[\mathbf{U}_{i+1}^n - \mathbf{U}_i^n\right] + \Delta t\mathbf{S}\left(\mathbf{U}^n, x\right) \end{aligned} \tag{39}$$

$$\begin{aligned} \mathbf{U}_i^c &= \mathbf{U}_i^n - \frac{\Delta t}{\Delta x}\left[\mathbf{F}_i^p - \mathbf{F}_{i-1}^p\right] \\ &- \frac{\Delta t}{\Delta x}\mathbf{J}_{i-\frac{1}{2}}\left[\mathbf{U}_i^p - \mathbf{U}_{i-1}^p\right] + \Delta t\mathbf{S}\left(\mathbf{U}^p, x\right) \end{aligned} \tag{40}$$

Finally, the update of the solution to the new time level $n+1$, in all the three schemes presented above, is evaluated as an average between the predictor and corrector steps:

$$\mathbf{U}_i^{n+1} = 0.5\left(\mathbf{U}_i^p + \mathbf{U}_i^c\right) . \tag{41}$$

Another very important issue to address in the numerical solution is related to the generation of spurious oscillations in the vicinity of strong gradients: according to Godunov's theorem these are unavoidable by linear schemes of accuracy grater than

Copyright © 2006 Taylor & Francis Group plc, London, UK

one. Therefore, another step is introduced in order to furnish the scheme with total variation diminishing (TVD) dissipation capable of making the solution oscillation free while retaining second-order accuracy both in space and time almost everywhere (except at extrema points). Following Garcia-Navarro and Alcrudo (1992), the update step now becomes:

$$\mathbf{U}_i^{n+1} = 0.5\left(\mathbf{U}_i^p + \mathbf{U}_i^c\right) + \frac{\Delta t}{\Delta x}\left(\mathbf{D}_{i+\frac{1}{2}} - \mathbf{D}_{i-\frac{1}{2}}\right) \tag{42}$$

where the TVD flux $\mathbf{D}_{i+\frac{1}{2}}$ is a function of the solution at time level n only.

Finally, the CFL stability condition that governs the choice of time step in the numerical solution, can be written as

$$\Delta t \leq CFL\frac{\Delta x}{\max(\lambda_i)} \tag{43}$$

where CFL is the Courant number (≤ 1), Δx is the grid spacing and λ_i is the local eigenvalue (local celerity).

6 BOUNDARY CONDITIONS

Boundary conditions have to be imposed at the upstream and downstream sections of the domain. Studying the mathematical properties of the governing equations it can be shown that the eigenvalues λ_i are always real and distinct. Moreover, they are always two positive and one negative for both subcritical and supercritical flows. Thus, three of the six unknowns at the boundaries (two upstream and one downstream) can always be prescribed by imposing conditions at the boundaries. Information on the remaining unknowns comes out from the interior of the domain and can be found (Garcia-Navarro and Saviron 1992) using the method of the characteristics. This method requires the solution of the so called characteristic equations, which in this case read:

$$\mathbf{a}_i \cdot \frac{d\mathbf{U}}{dt} = \mathbf{a}_i \cdot \mathbf{S} \qquad i = 1,2,3 \tag{44}$$

where

$$\mathbf{a}_i = \begin{bmatrix} -J_{21}J_{33} + J_{23}J_{31} + J_{21}\lambda_i \\ \lambda_i^2 - J_{33}\lambda_i \\ J_{23}\lambda_i \end{bmatrix} \tag{45}$$

In equations (44), d/dt represents the (total) derivative along the characteristic line

$$\frac{dx}{dt} = \lambda_i \tag{46}$$

where λ_i are the eigenvalues of the matrix $\mathbf{J}$.

7 NUMERICAL RESULTS AND DISCUSSION

In this section we firstly assess the performance of the proposed quasi-conservative method using a model hyperbolic system of equations, namely the timedependent non-linear inviscid shallow water equations, written in conservative, primitive, and quasiconservative form. This model system contains nonlinear wave propagation, with smooth and discontinuous solutions. Moreover, for sufficiently simple initial conditions, such as those for a Riemann problem, these equations possess analytical solutions in the form of rarefaction and shock waves.

With reference to equation (29) the model equations written in primitive form read

$$\mathbf{U} = \begin{bmatrix} Y \\ u \end{bmatrix}, \quad \mathbf{F} = \begin{bmatrix} 0 \\ 0 \end{bmatrix}, \quad \mathbf{A} = \begin{bmatrix} u & Y \\ g & u \end{bmatrix}, \tag{47}$$

while in quasi-conservative form we obtain

$$\mathbf{U} = \begin{bmatrix} Y \\ Yu \end{bmatrix}, \quad \mathbf{F} = \begin{bmatrix} Yu \\ Yu^2 \end{bmatrix}, \quad \mathbf{A} = \begin{bmatrix} 0 & 0 \\ gY & 0 \end{bmatrix}, \tag{48}$$

and in conservative form

$$\mathbf{U} = \begin{bmatrix} Y \\ Yu \end{bmatrix}, \mathbf{F} = \begin{bmatrix} Yu \\ Yu^2 + \frac{1}{2}gY^2 \end{bmatrix}, \mathbf{A} = \begin{bmatrix} 0 & 0 \\ 0 & 0 \end{bmatrix}. \tag{49}$$

Here $Y = Y(x,t)$ is water depth, $u = u(x,t)$ is particle velocity, and g is the gravitational acceleration. Note that the choice of primitive variables is not unique and that $\mathbf{S} = 0$ for all schemes.

The test solves the model equation in the domain $x\epsilon$ [0, 50] with initial conditions

$$\begin{cases} Y(x,0) = Y_L = 1 & \text{if} \quad x \leq 25 \\ Y(x,0) = Y_R = 0.1 & \text{if} \quad x > 25 \\ u(x,0) = 0 & \forall x \in [0,50] \end{cases} \tag{50}$$

which physically represents a typical dam-break problem in inviscid context.

The analytical solution of this problem contains a left-facing smooth rarefaction wave and a right-facing shock wave, which is associated with the nonlinear fields $u \pm \sqrt{gY}$.

In Figures 2–5 the solutions obtained at time $t = 7s$ with the three different (conservative, primitive and quasi-conservative) formulations are compared with the corresponding analytical solutions. All the results have been obtained with a fine mesh (500 cells) in order to have information on the convergence of the numerical method.

Figure 2 suggests that the conservative formulation of the MacCormack scheme using $CFL = 0.95$ converges to the exact solution. There is good resolution of the smooth part of the flow and high resolution of discontinuities even though spurious oscillations

Copyright © 2006 Taylor & Francis Group plc, London, UK

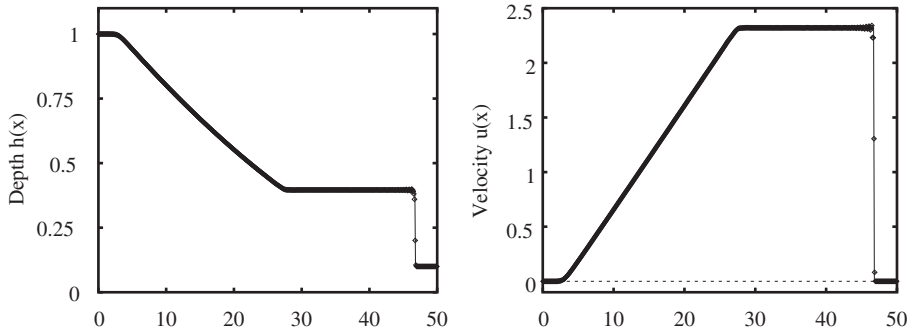


Figure 2. Conservative MacCormack scheme (symbol) and exact solution (line). Results at time $t = 7.0\,s$ for mesh $M = 500$ cells and CFL $= 0.95$.

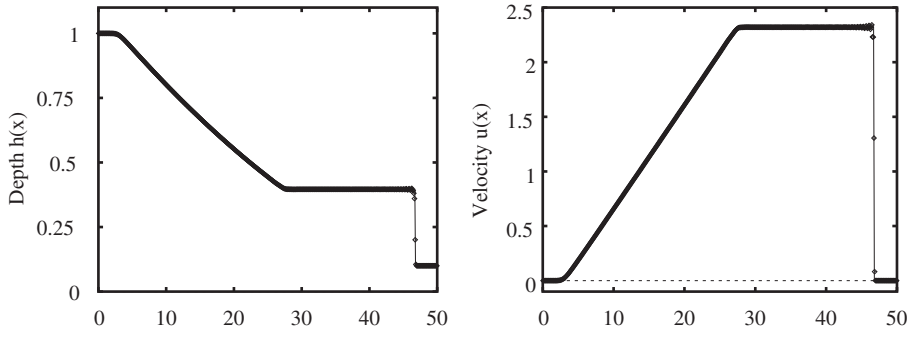


Figure 3. Conservative MacCormack scheme (symbol) and exact solution (line). Results at time $t = 7.0\,s$ for mesh $M = 500$ cells and CFL $= 0.8$.

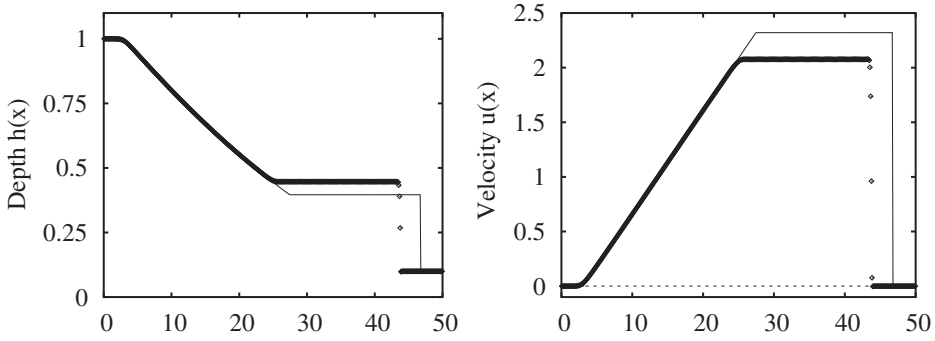


Figure 4. Fully primitive MacCormack scheme (symbol) and exact solution (line). Results at time $t = 7.0\,s$ for mesh $M = 500$ cells and CFL $= 0.8$.

appear in the vicinity of the shock wave. Decreasing *CFL* to 0.8, as shown in Figure 3, makes the oscillations disappear, thus implying that a more stringent stability condition is required by the TVD step. In all the numerical experiments performed, the condition $CFL < 0.85$ was found sufficient to avoid spurious oscillations.

In Figure 4 the results obtained using the fully primitive version of the MacCormack scheme are given. It is clearly shown that both the intensity and the position of the shock are badly predicted, the numerical solution converging to a wrong solution. Note however that the solution is sharply resolved and spurious oscillations are absent in this solution too.

Copyright © 2006 Taylor & Francis Group plc, London, UK

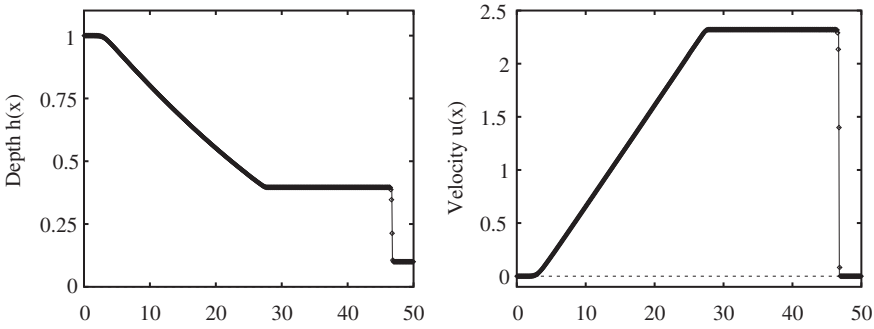


Figure 5. Quasi-conservative MacCormack scheme (symbol) and exact solution (line). Results at time $t = 7.0\,s$ for mesh $M = 500$ cells and CFL $= 0.8$.

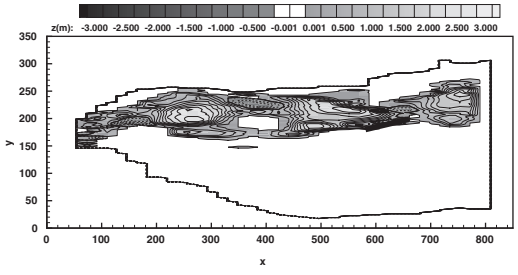


Figure 6. Erosion-deposition contour map at the end of the hydrograph having return period $T = 30$.

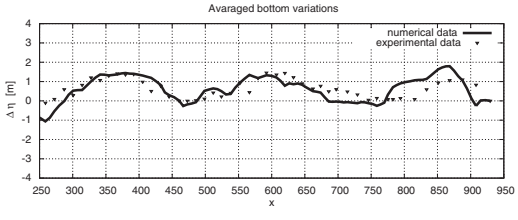


Figure 7. Avaraged bottom variations at the end of the hydrograph having return period $T = 30$.

The above simulations provide an indirect numerical confirmation of the Lax and Wendroff (1960) and Hou and LeFloch (1994) theorems. In fact the conservative numerical method converges to the correct solution of the equations (Lax and Wendroff 1960), while non-conservative (primitive) schemes do not converge to the correct solution if a shock wave is present in the solution (Hou and LeFloch 1994).

The quasi-conservative version of the MacCormack scheme outperforms the fully primitive version of the same scheme. The magnitude of the error related to the primitivity of the mathematical formulation is shown to depend on the relevance of the primitivity itself. Adopting a quasi-conservative formulation, the errors in the computation of the shock speed and strength are sharply reduced to the level that no differences are noticeable comparing Figures 5 and 3.

Once the performances of the proposed model have been numerically tested in a relatively simple configuration, attention has been focused on an application to a natural river. Applications of the present model to the Vara River are part of a more complex river management programme markedly oriented towards the understanding of sediment transport processes. The general aim of the project is to obtain detailed information on some flood defense systems to be constructed along the entire river, with particular emphasis on their interference with the global sediment balance.

At the moment both a physical and a numerical model have been developed In the following some preliminary numerical results are compared with the experimental measurements collected on the physical model.

The Vara River is located in the northern Italy and it drains an area of about 572 Km^2. Reaches morphologically controlled by the massive presence of man-made structures alternates with reaches with either single threaded morphologies with alternate bars or confined meanders. The runoff produced by storm events swiftly exits the watershed, and discharge returns to baseflow levels within 20 h.

In the present study, we focus our attention on a reach of the Vara River which is about 1 Km long and 30 m wide, with an average channel slope of 1% and it is near critical conditions. Along the right side of the main channel, a flood plain is present which is planned to be used as a storage area. At the downstream end of the reach under investigation, a dam with three open gates on the bottom is located to control the flooding of the storage area.

During a flood event, the obstruction created by the dam reduces the velocity of the near critical flow, inducing the formation of an hydraulic jump that in turn increases the water level, progressively flooding the storage area.

Copyright © 2006 Taylor & Francis Group plc, London, UK

The net result in term of peak reduction of the flood is of the order of 20% but, as expected, the dynamics of sediment transport is shown to be strongly affected by the presence of the flood defense system.

The backwater effect induced by the dam implies a decrease of the sediment transport capacity of the flow that ultimately leads to the formation of a significant deposit upstream of the dam. In figure 6 is reported the 2-D erosion-deposition map obtained from the experiments performed on the physical model after one flood having a return period of 30 *years*. The amount of the deposit after just one, even though intense, flood is about 2–3 meters.

The topography shown in the map is obtained scanning the physical model with a laser device and is described, for computational purposes, by a mesh consisting of 140 cross sections. The grain size of the uniform sediment used in the physical model corresponds to an actual diameter d_s of about $9\,cm$. The upstream boundary conditions in both model consists of: i) an hydrograph with a return period of 30 years ($Qmax = 419\,m^3/s$ in the Vara River); ii) equilibrium condition (neither aggradation nor degradation) for the bed. At the downstream end of the reach the rating curve relative to the effect of the dam has been experimentally determined on the physical model.

In order to compare numerical and experimental results, 2D information coming out from the physical model has been transformed in 1D information by means of an averaging procedure over the channel width.

The comparison between numerical and experimental results of the longitudinal distribution of $\bar{\eta}$ after one flood event is given in figure 7 where the difference between the final and initial bed configurations is plotted. Either the intensity or the spatial location of the three regions in which deposition occurs on the physical model are reproduced with a good agreement by the numerical model. No comparisons are made regarding the bed configuration during the flood since it was not possible to stop the simulation on the physical model without altering the bed configuration itself. The numerical simulation shows that deposit just upstream of the dam constantly increases in height during the entire flood, whereas the upstream and middle deposits reach their maximum when the peak of the flood is passing and are slightly eroded during the tail of the hydrograph.

8 CONCLUSIONS

A quasi-conservative formulation of the coupled hydro-morphodynamic model is proposed. New forms of the MacCormack scheme, are also developed and assessed for dealing with the quasi-conservative formulation of the movable-bed model. Comparing numerical results and exact solutions for a test case it is shown that the proposed quasi-conservative formulations outperforms the fully-primitive formulation.

The application of the model to the case of the Vara River, which involves a complex natural geometry and severe flood conditions, reveals its robustness.

A good agreement is found between the numerical results and experimental observations made in laboratory by means of a physical mobile-bed model of the Vara river reach.

Finally, future developments of the present model involve its application to dam break problems over erodible bottom and embankment breaches. Since such phenomena are characterized by rapidly varying flows, the adoption of a quasi-conservative formulation coupled with the quasi-conservative version of the MacCormack numerical scheme proposed in the present contribution, is expected to significantly increase the accuracy of the numerical solutions in these contexts.

ACKNOWLEDGMENTS

The authors wish to acknowledge the financial support offered by the Autorita' di Bacino Interregionale del Fiume Magra.

REFERENCES

Cao, Z. and P. Carling (2003). On evolution of bed material waves in alluvial rivers. *Earth Surface Processes and Landforms 28*(4), 437–441.

Cao, Z., R. Day, and A. Egashira (2002). Coupled and decoupled numerical modeling of flow and morphological evolution in alluvial rivers. *Journal of Hydraulic Engineering, ASCE 128*(3), 306–321.

Colombini, M. and A. Stocchino (2005). Coupling or decoupling bed and flow dynamics: fast and slow sediment waves at high froude numbers. *Physics of Fluids 17*(3).

Correia, L., B. Krishnappan, and W. Graf (1992). Fully coupled unsteady mobile boundary flow model. *Journal of Hydraulic Engineering, ASCE 118*(3), 476–494.

Cui, Y., G. Parker, L. E., J. E. Pizzuto, and A. Dodd (2005). More on the evolution of bed material waves in alluvial rivers. *Earth Surface Processes and Landforms 30*, 107–114.

Cui, Y., G. Parker, and C. Paola (1996). Numerical simulation of aggradation and downstream fining. *Journal of Hydraulic Research 34*(2), 195–204.

Cunge, J. A., F. M. Holly, and A. Verwey (1994). *Practical Aspects of Computational River Hydraulics*. Pitman Publishing Ltd. Reprinted by the University of Iowa.

De Vries, M. (Ed.) (1965). *Considerations about non-steady bed-load transport in open channels*, Number 3.8.1-3.8.8 in Int. Assn. Hydraulic Research. Leningrad.

Engelund, F. (1964). Book of abstracts. Technical Report 6, University of Denmark. Basic Research.

Garcia-Navarro, P. and F. Alcrudo (1992). 1D Open Channel Flow Simulation Using TVD McCormack Scheme. *J. Hydraulic Engineering, ASCE 118*, 1359–1373.

Copyright © 2006 Taylor & Francis Group plc, London, UK

Garcia-Navarro, P. and J. Saviron (1992). McCormack's method for the numerical simulation of one-dimensional discontinuous unsteady open channel flows. *J. Hydraulic Research 30*(1), 95–105.

Holly, F. and J. Rahuel (1990). New numerical/physical framework for mobile bed modelling, part 1: Numerical and physical principles. *Journal of Hydraulic Research 28*(4), 401–416.

Hou, T. and P. LeFloch (1994). Why Non–Conservative Schemes Converge to the Wrong Solutions: Error Analysis. *Math. of Comput. 62*, 497–530.

Kassem, A. and M. Chaudry (1998). Compaison of coupled and semicoupled numerical models for alluvial channels. *Journal of Hydraulic Engineering, ASCE 124*(8), 794–802.

Krishnappan, B. (1985). Modelling of unsteady flows in alluvial streams. *Journal of Hydraulic Engineering 111*(2), 257–266.

Lai, C., R. Baltzer, and R. Schafranek (2002). Conservation-form equations of unsteady open-channel flow. *Journal of Hydraulic Research 40*(5), 567–578.

Lanzoni, S., A. Siviglia, A. Frascati, and G. Seminara (2006). Long waves in erodible channels and morphodynamic influence. *Water Resources Research*. to appear.

Lax, P. and B. Wendroff (1960). Systems of Conservation Laws. *Comm. Pure Appl. Math. 13*, 217–237.

Lax, P. D. (1957). Hyperbolic Systems of Conservation Laws II. *Comm. Pure Appl. Math. X*, 537–566.

Lyn, D. (1987). Unsteady sediment transport modeling. *Journal of Hydraulic Engineering, ASCE 113*(1), 1–15.

Lyn, D. and M. Altinakar (2002). St.venant exner equations for near-critical and transcritical flows. *Journal of Hydraulic Engineering, ASCE 128*(6), 579–587.

MacCormack, R. (1971). Numerical solution of the interaction of a shock wave with a laminar boundary layer. In G. Springer Verlag, Berlin (Ed.), *Proc. 2nd Int. Conf. on Numerical Methods in Fluid Dynamics*, pp. 151–163.

Meyer-Peter, E. and R. Müller (1948). Formulas for bed-load transport. In *Proceedings "2nd Congress International Association for Hydraulic Research"*, Stockholm, Sweden, pp. 39–64.

Parker, G. (1990). Surface-based bedload transport relation for gravel rivers. *J. Hudraul. Res. 28*(4), 417–436.

Sieben, J. (1999). A theoretical analysis of discontinuous flows with mobile bed. *Journal of Hydraulic Research 37*(2), 199–212.

Singh, A., U. Kothyari, and K. Ranga Raju (2004). Rapidly varying transient flows in alluvial rivers. *Journal of Hydraulic Research 42*(5), 473–486.

Toro, E. and A. Siviglia (2003). Price: Primitive centred schemes for hyperbolic system of equations. *International Journal for Numerical Methods in Fluids 42*, 1263–1291.

Wu, W., D. Vieira, and S. Wang (2004). Onedimensional numerical model for nonuniform sediment transport under unsteady flows in channel networks. *Journal of Hydraulic Engineering 130*(9), 914–923.

Copyright © 2006 Taylor & Francis Group plc, London, UK

Front dynamics of a water surge at high Reynolds number: Similarity solutions to the Saint-Venant equations

C. Ancey, S. Cochard, M. Rentschler & S. Wiederseiner
Ecole Polytechnique Fédérale de Lausanne, Ecublens, Lausanne, Switzerland

ABSTRACT: In this paper, we seek similarity solutions to the shallow-water (Saint-Venant) equations for describing the motion of a gravity-driven surge supplied in fluid by a source placed at the inlet of a horizontal plane. Gratton and Vigo have shown that imposing certain conditions on the inflow rate makes it possible to find similarity solutions to the Saint-Venant equations when a Benjamin-like boundary condition is imposed at the front (i.e., non-zero flow depth). When the flow depth is zero at the front, we show that the solution to the Saint-Venant equations is singular: its curve is the limiting curve of the regular solutions. We also show that the front takes the form of an acute wedge, with a straight free boundary, and is separated from the body by a bore. This singular behavior explains why current numerical models fail in computing the front position and velocity when no *ad hoc* downstream boundary conditions are supplemented.

1 INTRODUCTION

There is a growing number of models inspired from shallow-water (Saint-Venant) equations, which are used to describe time-dependent, free-surface flows involving fluids with various rheologies. Essentially, these models are based on a set of hyperbolic partial differential equations that are obtained by integrating the mass and momentum balance equations across the flow depth. Typical examples include density currents (Rottman and Simpson 1983), particle suspensions (Parker et al. 1986), viscoplastic fluids (Huang and Garcìa 1998), dry granular flows (Savage and Hutter 1989), saturated granular fluids (Iverson and Denlinger 2001), etc.

The models cited above have often been used to compute the collapse of a finite volume of fluid or the spread of a surge emanating from a source with a given inflow rate. The common characteristics of these flows is that they have a front exhibiting a significant curvature of the free surface. For an inertia-dominated regime, an *ad hoc* boundary condition must often be imposed at the front by constraining the value of the Froude number in order to take into account the resisting effect of the ambient fluid (Benjamin 1968). This is tantamount to considering the front as a discontinuity (bore) moving at a prescribed velocity. Using phase-plane formalism, Gratton and Vigo (1994) provided evidence that the front controls the dynamics of the body on some specific circumstances. A few analytical results have also been established without imposing this front condition: Ritter (1892) provided an analytical solution to the shallow-water equations for the dam-break problem. In that case, it was shown that the head was an elongating wave presenting an acute angle at the leading edge. Later, Dressler (1952) and Whitham (1954) demonstrated that hydraulic resistance modified the shape and velocity of the front. In addition to providing more rigorous proofs, Hogg and Pritchard (2004) found that taking shearing effects into account substantially alters the mathematical structure of the solution to the dam-break problem, especially in the tip region.

The objective of this paper is to find similarity solutions to the Saint-Venant equations in the context of rapidly varying surges emanating from a source and spreading along a horizontal plane. Similarity solutions were found in an earlier paper by Gratton and Vigo (1994), where these authors considered a Benjamin-like boundary condition at the front, i.e., the Froude number Fr is constant and the flow depth is nonzero. Gratton and Vigo (1994) claimed that the solution associated with the boundary condition $h = 0$ is found by taking the limit $Fr \to \infty$. In this paper, we will show that the proper solution associated with a zero flow depth at the front is a singular curve, which structurally differs from the solutions related to a Benjamin-like boundary condition. Emphasis will be given to the topological structure of the equations in the tip region. It will be shown that the front dynamics is fully controlled by the critical points of the phase plane, implying that the shape and velocity of the tip

Copyright © 2006 Taylor & Francis Group plc, London, UK

region are imposed independently of the far-field conditions. We will show that the solutions found in this paper are in fairly good agreement with the analytical solutions to the Euler equations (Ancey et al. 2006).

2 GOVERNING EQUATIONS

2.1 *Flow-depth averaged equations*

We consider a shallow layer of fluid flowing over a rigid horizontal impermeable plane. The fluid is inviscid and incompressible; its density is denoted by ρ. The ratio $\epsilon = H_*/L_*$ between the typical vertical and horizontal lengthscales, H_* and L_* respectively, is assumed to be small. $U_* = O(\sqrt{gH_*})$ is the velocity scale.

Integrating the local Euler equations over the flow depth provides the shallow-water equations. Since they are classic, the details of their derivation are not reported here (Stoker 1957). The shallow-water equations take the generic dimensionless form

$$\frac{\partial h}{\partial t} + \frac{\partial h\bar{u}}{\partial x} = 0, \tag{1}$$

$$\frac{\partial h\bar{u}}{\partial t} + \frac{\partial h\overline{u^2}}{\partial x} + h\frac{\partial h}{\partial x} = 0, \tag{2}$$

where the bar refers to flow-depth averaged values. The dimensionless velocity, flow-depth, distance, and time were defined as $\bar{u} = \hat{u}/U_*$, $h = \hat{h}/H_*$, $x = \hat{x}/L_*$, and $t = \hat{t}U_*/L_*$, respectively, where the hat refers to dimensional variables. Introducing the Boussinesq coefficient γ makes it possible to relate the mean square velocity to the square of the mean velocity: $\overline{u^2} = \gamma\bar{u}^2$. In so doing and assuming that γ is known, we obtain a closed set of equations for h and $\bar{u}$

$$\frac{\partial h}{\partial t} + \frac{\partial h\bar{u}}{\partial x} = 0, \tag{3}$$

$$\frac{\partial \bar{u}}{\partial t} + (2\gamma - 1)\bar{u}\frac{\partial \bar{u}}{\partial x} + \bar{u}^2\frac{\partial \gamma}{\partial x} = -\frac{\partial h}{\partial x}\left(1 + \frac{\bar{u}^2}{h}(\gamma - 1)\right). \tag{4}$$

When γ is set equal to unity in the momentum balance equation (4), we retrieve the usual form of the shallow-water equations (Stoker 1957). When γ is constant and in excess of unity, the conservation form of Eqs. (3–4) is identical to the equations used by Hogg and Pritchard (2004) to analyse the effect of shear on front structure. In that case, the structure of the governing equations is slightly altered: the convective acceleration term is weighted by the shape factor $2\gamma - 1$, while a Chézy-like term affects the pressure gradient. These modifications are minor and do not disturb the hyperbolic nature of the equations; they may, however, have significant impact on some occasions, e.g. when computing the nose features in the dam-break problem (Hogg and Pritchard 2004). A pervasive assumption is to ascribe the Boussinesq coefficient to unity by advocating that in the high Reynolds number limit, the velocity profile is blunt, which implies that γ must not differ significantly from unity.

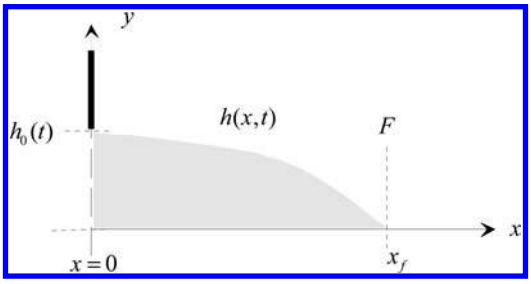


Figure 1. The configuration of the flow.

2.2 *Flow geometry and boundary conditions*

A two-dimensional flow regime is assumed, namely any cross-stream variation is neglected. The depth of the layer is given by $h(x, t)$ (see Figure 1). The flow is generated by a source of fluid: at $t = 0$, the sluice gate at the inlet is raised with a given aperture rate $h_0(t)$. Ahead of the front, there is a dry bed.

At the source $x = 0$, the unleashed volume $\mathcal{V}$ varies with time as follows

$$\mathcal{V} = \int_0^{x_f} h(x, t)dx = At^n, \tag{5}$$

with n a prescribed coefficient; in the forthcoming numerical applications, we will take $n = 5/2$. The boundary condition (5) is equivalent to imposing the flow rate at the inlet: $\bar{u}h = nAt^{n-1}$. To get rid of the initial-value problem, we furthermore assume that the Froude number at the source is imposed: $Fr_0 = \bar{u}/\sqrt{h} = 2a/3$, where a is a constant. The flow depth varies with time: $h = h_0(t) = at^m/d$, where $m = \frac{2}{3}(n - 1)$ ($m = 1$ in the numerical applications here, since $n = 5/2$) and d is a constant. Note that d and a are linked: they both related through the relation $A = \frac{2}{3n}a^{5/2}d^{-3/2}$ (this relation is found by integrating the solution to find the volume).

The other boundary conditions is prescribed at the front. The front position x_f is the point where the flow depth drops to zero: $h(x_f) = 0$; moreover, the front velocity is $\bar{u}(x_f) = \dot{x}_f$.

2.3 *Jump conditions*

The solutions to the system (3–4) may admit discontinuities (shock or hydraulic jump in the hydraulic

Copyright © 2006 Taylor & Francis Group plc, London, UK

literature). The flows either side of these are connected by jump conditions which express conservation of mass and momentum across the moving discontinuity. Denoting the shock speed by σ, these jump conditions associated with conservative form of Eqs. (3–4) are given by (Whitham 1974)

$$[\![h\bar{u}]\!] = \sigma[\![h]\!], \tag{6}$$

$$[\![\gamma h\bar{u}^2 + h^2/2]\!] = \sigma[\![h\bar{u}]\!], \tag{7}$$

where the $[\![\cdot]\!]$ denotes the difference upstream and downstream of the shock.

3 PHASE-PLANE FORMALISM

In order to solve the similarity problem, we will use the 'phase-plane' (or portrait) formalism as earlier authors did for the same kind of problem (Grundy and Rottman 1986; Gratton 1991; Gratton and Vigo 1994). The types and characteristics of the similarity solutions are described in details by Gratton and Vigo in (Gratton and Vigo 1994) when the downstream boundary condition is of the Benjamin type, i.e., at the front, the Froude number is constant and the flow depth is nonzero. Gratton and Vigo claimed that the boundary condition $h(x_f) = 0$ is obtained asymptotically by making the Froude number tend to infinity (Gratton and Vigo 1994), but we will show that in the particular case investigated here, their construction is not possible. Except for this point, the formalism is identical to that used in (Gratton and Vigo 1994) and we will not replicate their results. This notably implies that we will focus on a single particular case $n = 5/2$ in our applications for clarity (the other cases being similar).

Gratton and Vigo (1994) have shown that the governing equations (3–4) admit similarity solutions for a range of conditions at the source $0 \leq n < 4$. This condition on n is needed for the shallowness assumption to be consistent. Following Grundy and Rottman (1986) and Gratton and Vigo (1994), we pose

$$u = \delta\xi t^{\delta-1} V(\xi), \tag{8}$$

$$h = \delta^2 \xi^2 t^{2(\delta-1)} Z(\xi), \tag{9}$$

where ξ is the similarity variable

$$\xi = \frac{x}{t^\delta}, \tag{10}$$

with δ to be determined from the initial conditions (5). The boundary conditions impose

$$Z(\xi_f) = 0 \text{ and } V(\xi_f) = 1, \tag{11}$$

where ξ_f denotes the front position. At the source, we have the asymptotic behaviour

$$Z \propto \frac{a}{d}\frac{1}{\delta^2\xi^2} \text{ and } V \propto \frac{2}{3}\frac{a^{3/2}}{\sqrt{d}}\frac{1}{\delta\xi} \text{ when } \xi \to 0. \tag{12}$$

Since the solution may admit discontinuities, we supplement the following condition derived from Equation (5), which ensures that the mass balance is not violated

$$\int_0^{\xi_P} \xi^2 Z(\xi) d\xi = \delta^{-2}\mathcal{V}, \tag{13}$$

with $\mathcal{V}$ the total volume and ξ_P the front abscissa. When there is not discontinuity, this equation is redundant with Equation (12).

4 SIMILARITY SOLUTIONS

We shall see that ξ is an autonomous variable in the governing equations for Z and V, which means that we can get rid of ξ and directly seek a relation between Z and V by solving a first-order ordinary differential equation in the form

$$\frac{dZ}{dV} = \frac{F(V,Z)}{G(V,Z)}. \tag{14}$$

The behaviour of the solutions to this equation can be qualitatively outlined by working in the $V - Z$ plane and discussing the various possibilities of finding an 'integral' curve passing through a given region.

4.1 *Matrix representation and critical curves*

Substituting the similarity forms into the governing equations (3–4), we obtain two ordinary first-order differential equations for Z and V that can be cast in a matrix form

$$\mathbf{M}(V,Z)\frac{d\mathbf{w}}{d\xi} = \frac{Z}{\delta\xi}\mathbf{S}(V,Z), \tag{15}$$

with $\mathbf{w} = [Z, V]^{\mathrm{T}}$,

$$\mathbf{M} = \begin{bmatrix} V-1 & Z \\ (\gamma-1)V^2 + Z & Z(V(2\gamma-1)-1) \end{bmatrix}, \text{ and} \tag{16}$$

$$\mathbf{S} = \begin{bmatrix} 3V\delta - 2 \\ 2\delta Z + V(V(4\gamma-3)\delta - 1) \end{bmatrix}. \tag{17}$$

The determinant of the matrix $\mathbf{M}$ is

$$\det \mathbf{M} = \delta Z\,(Z - I(V))\,, \tag{18}$$

with $I(V) = 1 + (V-2)V_\gamma$. Along the V-axis ($Z = 0$) and the curve C_I of equation $Z = I(V)$, the solutions

Copyright © 2006 Taylor & Francis Group plc, London, UK

Table 1. Properties of the special curves C_A, C_F, C_I, and C_J.

Label	Equation	Properties
C_A	see Eq. (27)	Exceptional solution to Eq. (14)
C_F	$F=0$	Integral path having horizontal tangent when crossing C_I
C_I	$Z=I(V)$	Critical curve separating sub- and super-critical regimes
C_J	$Z=J(V)$	Integral path having vertical tangent when crossing C_J

$V(\xi)$ and $Z(\xi)$ to Equations (15) are not properly defined because $\det \mathbf{M}=0$: these functions are multivalued except when the crossing occurs close to a critical point. A multivalued behaviour is not physically admissible and this issue is fixed by constructing discontinuous solutions (see Section 5).

When $\det \mathbf{M}$ is nonzero, the system of equations (15) can be inverted to provide

$$\xi\frac{dZ(\xi)}{d\xi}=\frac{F(V,Z)}{\delta\,(Z-I(V))}, \tag{19}$$

$$\xi\frac{dV(\xi)}{d\xi}=\frac{G(V,Z)}{\delta\,(Z-I(V))}, \tag{20}$$

with $F(V,Z)=-Z(2Z\delta+V(-2V\delta\gamma+4\gamma+3\delta-3)-2)$ and $G(U,Z)=Z(2-(V+2)\delta)+V(V(2\gamma+((V-4)\gamma+3)\delta-3)+1)$.

Instead of solving this system of differential equations, we form the ratio of the two equations to arrive at a single ordinary differential equation (14) for $Z'(V)$.

When $\det \mathbf{M}$ is zero, the system may have solutions if the determinant of the cofactor matrix

$$\mathbf{N}=\begin{bmatrix} V-1 & 3V\delta-2 \\ (\gamma-1)V^2+Z & 2\delta Z+V(V(4\gamma-3)\delta-1) \end{bmatrix}, \tag{21}$$

is also zero. In the space (V,Z), the locus of the points for which $\det \mathbf{N}=0$ is a continuous curve C_J of the equation

$$Z=J(V)=\frac{V\,(\gamma\delta V^2+(-4\delta\gamma+2\gamma+3\delta-3)V+1)}{(V+2)\delta-2}, \tag{22}$$

Note that $G(V,Z)=Z-J(V)$, which means that C_J is also the locus of points where the integral curves, solutions to Equation (14) have vertical tangents. Except for the case $\gamma=1$ and $n=1$ ($\delta=1$), the curves C_I and C_J do not coincide, but intersect at two points: A_γ with coordinates $(2/(4\gamma-3),(9-8\gamma)/(4\gamma-3)^2)$ and P_* with coordinates $(1,1-\gamma)$. P_* lies inside the first quadrant only when $\gamma\leq 1$. These points play an important role since their existence means that there may be continuous solutions with discontinuous gradients at points A and P_*. They will be useful thereafter in constructing the solutions (see Section 5). When $\gamma=1$ and $n=1$ corresponding to the dam break problem (Whitham 1974), the curves C_I and C_J coincide, which implies that a piece of this curve is a part of the solution sought.

4.2 *Critical points*

In addition to the curves C_I and C_J, there is another specific curve that plays a role in the phase portrait: the curve C_F is the curve along which F vanishes, i.e., at which the integral path has a horizontal tangent; its equation is given by

$$H=\frac{2+U\,(3-3\delta+2\gamma\,(-2+U\,\delta))}{2\delta}. \tag{23}$$

The properties of these curves are summarized in Table 1.

In the first quadrant of the phase plane $V-Z$, there are three critical points resulting from the crossing of the specific curves C_F and C_J. The first one is the origin point O, which is a node. Point A_γ is also a singularity (node). The third one is referred to as point B_γ and has coordinates $(2/(3\delta),(9-8\gamma)/(9\delta^2))$; it is a saddle.

Figure 2 shows a few trajectories, the specific curves (C_I, C_J, and C_F), the critical points (O, A_γ, B_γ), the intersection point P_* between C_I (solid line) and C_J (dashed line), and the front P. Note that at point A_γ, the three curves C_I, C_J, and C_F meet, which implies significant behaviour changes close to point A_γ. A few trajectories (thin curves with arrows) representing solutions to Equation (14) are also reported and illustrate the behaviour of the solutions close to the critical points; not all the paths are physically meaningful since some cross the critical curve C_I (solid line).

5 FLOW DISCONTINUITIES

5.1 *Rankine-Hugoniot condition*

The crossing of the critical curve C_I at a regular point of intersection is not possible, but is possible at a critical point (A_γ here). When the crossing is not permitted, we consider that a shock occurs, which is ruled by the jump conditions (6–7). If we know the flow variables

Copyright © 2006 Taylor & Francis Group plc, London, UK

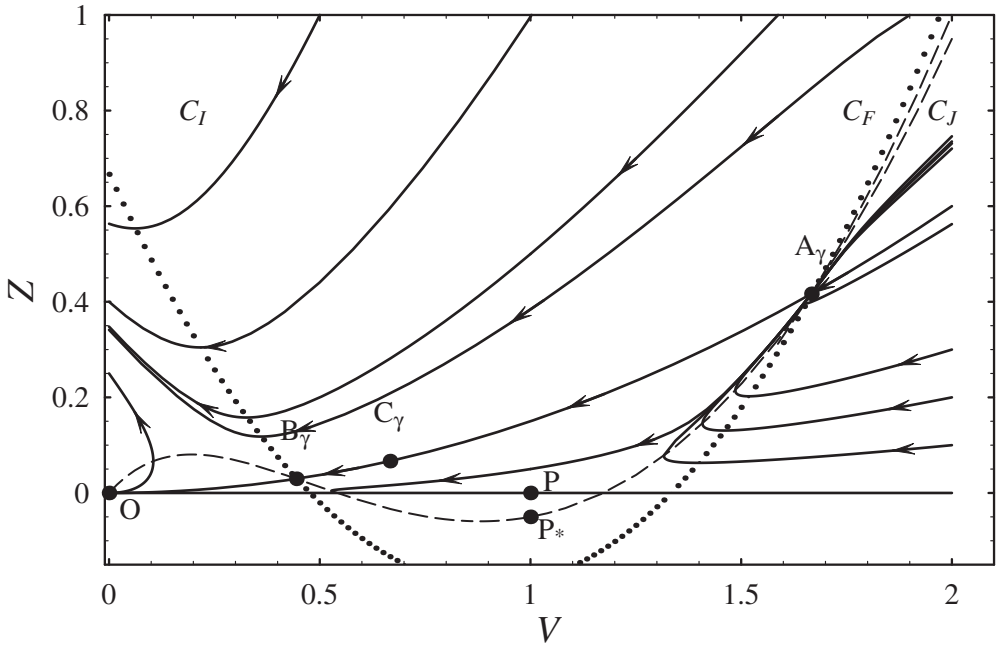


Figure 2. Specific curves C_I (solid line), C_J (dashed line), C_F (dotted line). The thin curves with arrows represent a few trajectories computed numerically. The critical points O, A_γ, B_γ, and C_γ are plotted together with the front (point P). Computations made for $a = 4$, $d = 1$, and $\gamma = 1.05$.

Z_1 and V_1 upstream of the shock, we can solve the shock equations (6–7) to determine the shock velocity σ and a curve referred to as the 'shock curve' $V_2(Z_2|Z_1,\ V_1)$, which is the locus of all the points satisfying the jump conditions (6–7). Solving this system of equations, we derive the shock velocity and the variation in upstream velocity V_2 with upstream flow depth Z_2

$$\sigma = \frac{\gamma}{\chi} V_1 \pm \frac{1}{\chi}\sqrt{\frac{1}{2}\left(\chi(Z_1+Z_2) + 2(\gamma-1)V_1^2\right)\frac{Z_2}{Z_1}}, \tag{24}$$

$$V_2(Z_2|Z_1, V_1) = \frac{V_1}{\chi} \pm \frac{(Z_2 - Z_1)}{\chi}\sqrt{\frac{1}{2}\frac{\chi(Z_1+Z_2) + 2(\gamma-1)V_1^2}{Z_1 Z_2}}, \tag{25}$$

with $\chi = \gamma + (1-\gamma)\frac{Z_2}{Z_1}$. Since there is a quadratic dependence on velocity in Eqs. (6–7), we actually find two shock curves, but a single one is physically admissible by requiring that energy dissipation through the shock be positive. This shock curve is then used to pass from one trajectory to another one that satisfies the boundary conditions downstream. The problem boils down to finding the point (V_1, Z_1) at which the shock occurs. To that end, we use a trial and error procedure: first we select a point (V_1, Z_1) on the integral path emanating from the source S, then we plot the shock curve $V_2(Z_2|Z_1,\ V_1)$, and finally we find the intersection point between the shock curve and the other integral path coming from the front point P. The procedure is iterated until the fluid volume found by numerical integration is consistent by the inflow rate imposed at the plane entrance Equation (13).

5.2 *Weak discontinuities*

It is worth recalling that a particular case of discontinuity includes the functions that are continuous, but whose derivative is not continuous at isolated points. This case is encountered when the curves C_I and C_J coincide (i.e. for $\gamma = 1$ and $n = 1$): when an integral curve crosses the critical curve, we have both $\det \mathbf{M} = 0$ and $\det \mathbf{N} = 0$, which implies that at this point, we can pass from one trajectory to another one and since $\det \mathbf{N} = 0$, the new trajectory is a piece of C_I (Gratton and Vigo 1994).

6 SIMILARITY SOLUTIONS FOR $\gamma > 1$

We first consider the case where the Boussinesq coefficient is prescribed in advance. We are interested in

Copyright © 2006 Taylor & Francis Group plc, London, UK

determining the solutions to Equation (14) evolving in the first quadrant ($V \geq 0$, $Z \geq 0$) and related to $\gamma > 1$ and boundary conditions (11–13).

To simplify presentation, computation and numerical applications were made by taking $n = 5/2$ and $\delta = 3/2$.

6.1 *Special solution*

Note that there is a special analytical solution

$$Z = \frac{1}{4}(9 - 8\gamma)V^2, \tag{26}$$

which is the solution to Equation (14). This curve is a parabola that we call $\mathcal{P}$; the boundary condition (12) implies that the source point S lies at infinity on $\mathcal{P}$. No computation at this stage is needed since the corresponding integral path coincides with the special curve $\mathcal{P}$. As shown in Figure 2, $\mathcal{P}$ crosses the critical curves C_I and the specific curve C_J at point A_γ. Since this point is singular, the crossing is not associated with a hydraulic jump. A bit farther, the parabola once again crosses the curve C_I at point C_γ with coordinates $(2/3, 1 - 9\gamma = 8)$, which is a regular point, implying that the solution should become discontinuous in the neighbourhood of C_γ. The parabola $\mathcal{P}$ does not pass through point $\mathcal{P}$. Since the integral curve crosses the critical curve C_I, discontinuous solutions can be constructed. We then envisage two possibilities.

6.2 *Trajectories in the front neighborhood*

The first possibility occurs that, when reaching point A_γ (for which $\det \mathbf{M} = \det \mathbf{N} = 0$), the integral curves take another path to reach point P. Since A_γ is also a node, all the curves (except for the singular curves) are tangent to a limiting curve C_A, whose equation is given in terms of a Taylor expansion

$$Z = \frac{9 - 8\gamma}{(4\gamma - 3)^2} + \left(V - \frac{2}{4\gamma - 3}\right) \frac{-16\gamma^2 - 4\delta\gamma + 24\gamma + 9\delta - 9}{2(4\gamma - 3)(4\delta\gamma - 4\gamma - 2\delta + 3)} + O(V^2). \tag{27}$$

This equation is obtained by applying L'Hôpital's rule to Equation (14). Note that in numerical applications, we used a power series expansion to order $O(V^6)$ that ensures accuracy to within 10^{-4} in the numerical solution. Except when $\gamma = 1$, this limiting curve does not pass through P. A graphical representation of C_A is given in Figure 3 (dotted line). Since P is a regular point, a single integral curve passes through it: it is

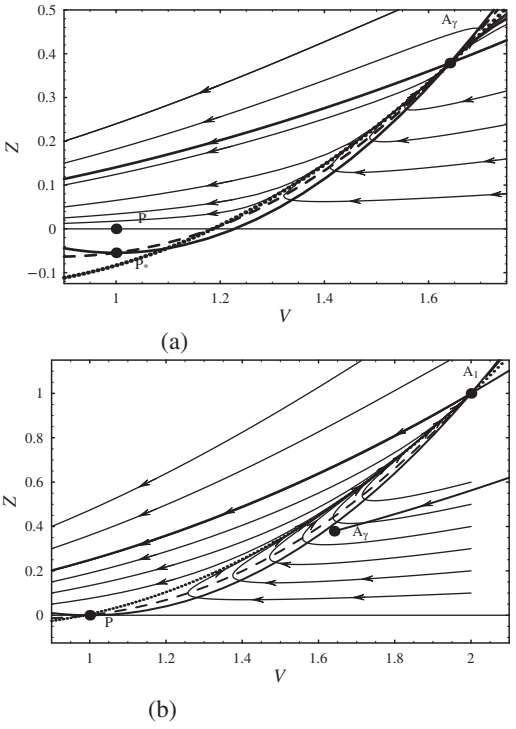


Figure 3. Specific curves C_I (solid line), C_J (dashed line) together with C_A (dotted line). (a) Computations made for $a = 4$, $d = 1$, and $\gamma = 1.05$. (b) Computations made for $\gamma = 1$. The thin curves with arrows represent a few trajectories computed numerically; the arrows indicate increasing ξ. The critical point A_γ (respectively A_1 in subplot b) is plotted together with the front P. The parabola $\mathcal{P}$ is a special trajectory and is plotted in bold; in subplot b, we have also superimposed the parabola $\mathcal{P}$ computed with $\gamma = 1.05$ and ending at A_γ.

the trivial solution $Z = 0$ (the V-axis). The situation is sketched on Figure 3(a): no integral curve except for the trivial solution $Z = 0$ passes through point P representing the front.We conclude that there is no way of joining A_γ and P when $\gamma \neq 1$ by following pieces of integral curves representing regular solutions to Equation (14).

The second possibility occurs when the parabola meets the critical curve C_I at A_γ or C_γ, which would make it possible to use the hydraulic jump conditions (24–25) to find another admissible integral curve. This is not possible because a hydraulic jump cannot form between a dry bed and the current, as mentioned above in solving the Euler equations. Indeed, using the shock conditions (24–25) to relate P to the integral path coming from the source (S) leads to constructing a nonphysical solution since the energy balance equation is violated. Point P can in no way can be located on a shock curve.

Copyright © 2006 Taylor & Francis Group plc, London, UK

6.3 *Construction of the solution within the tip region*

None of these possibilities being effective, we must find another way of constructing the solution. A reasonable assumption is to consider that in the vicinity of the front, the Boussinesq coefficient drops to unity, which ensures that we can find a non-trivial integral path passing through P: the limiting curve C_A, as shown in Figure 3(b) is the only one passing through P except for the trivial solution. We construct the solution as follows. At point A_γ, the flow undergoes a shock: in the phase plane, this implies that there must be a shock curve mapping point A_γ onto another point of the limiting curve C_A that we refer to as point A′. This situation is depicted in Figure 3(b) and Figure 4(a). On Figure 4(a), we have plotted the two shock curves (long-dashed curve) emanating from A_γ using Eqs. (24–25) together with points A_γ and A′; the only physically admissible shock curve is that corresponding to a flow depth increase and a velocity decrease to ensure energy dissipation. Between A′ and P, the integral path follows the limiting curve C_A. We can now compute the solution.

Since the integral path $S \to A_\gamma$ is given by Equation (26), we can analytically compute $V(\xi)$ by integrating Equation (20); we obtain: $\ln \xi^2 = \ln(9V-4) - 3\ln V + e$, where e is a constant of integration. Taking into account the asymptotic behaviour when $\xi \to 0$ given by Equation (12), we deduce

$$\xi_A = \frac{\sqrt{2a^6 - 9a^4 + 27}}{2a^{3/2}\sqrt{3d\delta}}. \tag{28}$$

The path $A' \to P$ must be integrated numerically. For instance, for $a=4$, we find $\xi_A = 1.850$ using the relation just above, $\xi_P - \xi'_A = 1.284$, which leads to $\xi_P = 3.133$. The fluid volume $\mathcal{V}$ is found by numerical integration of $\int_0^{x_p} h(x)dx$ and we find $\mathcal{V} = 8.516t^{5/2}$, which is very close to the exact variation imposed by Equation (13), i.e. $\mathcal{V} = 8.533t^{5/2}$ (relative error of -0.2%). Better agreement can be obtained by considering that the critical transition occurs just upstream of point A_γ; e.g. for $a=4$, the numerical computation (not reported here) showed that the transition occurs at $\xi_A = 1.738$ instead of $\xi_A = 1.850$.

7 SIMILARITY SOLUTION FOR $\gamma = 1$

We are now interested in determining the solution to Equation (14) in the usual case for the Saint-Venant equations, where the Boussinesq coefficient is set equal to unity. The resulting integral path in the phase plane continues to evolve in the first quadrant ($V \geq 0$, $Z \geq 0$) and must satisfy the boundary conditions (11–13). We still take $n = 5/2$ for the computations.

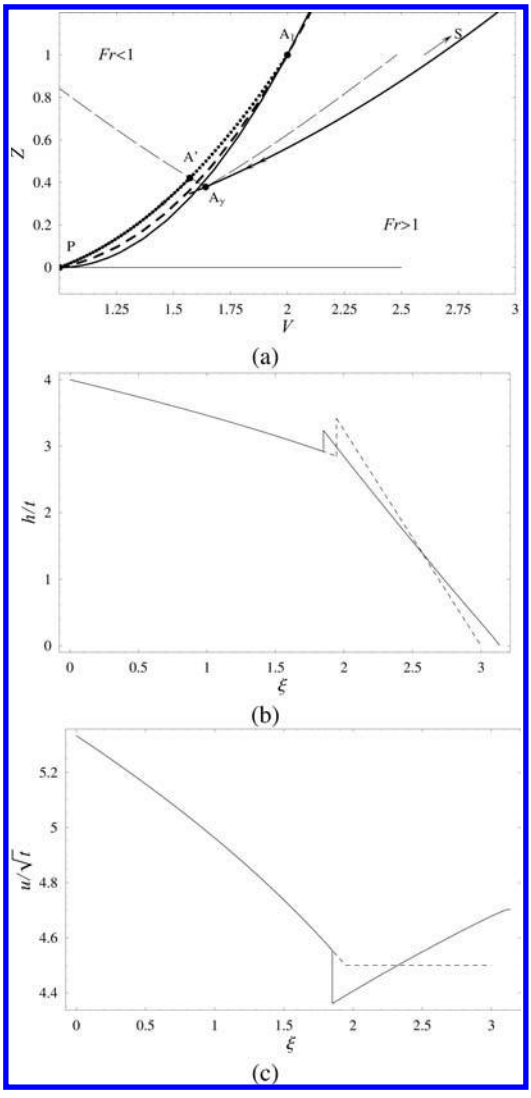


Figure 4. (a) Phase plane in the vicinity of A_γ: the specific curves C_I (solid line), C_J (dashed line), $\mathcal{P}$ (dotted line) are reported. The critical point A_γ is plotted together with the front P. The long dashed lines represent the shock curves emanating from point A_γ. (b) Flow-depth variation with ξ: the solution to the Saint-Venant equations (solid line) is compared with the solution to Euler equations (dashed line). (c) Velocity variation with ξ. All the computations made for $a=4$, $d=1$, and $\gamma = 1.05$.

The general numerical solution of the problem represented by Equation (14) and boundary conditions (11–13) involves computing the solution from the source S to the front P. Given the asymptotic behaviour exhibited by Equation (12), the source is located at infinity on a parabola of equation $Z = (V/\mathcal{F}_0)^2$, where

Copyright © 2006 Taylor & Francis Group plc, London, UK

$\mathcal{F}_0 = \frac{2}{3}a$ denotes the Froude number at the inlet. For numerical purposes, we need to give finite values (V_0, Z_0) to the coordinates of the source point S in the phase plane. Taking large values for the initial value V_0 and posing $Z_0 = (V_0/\mathcal{F}_0)^2$ allows us to reasonably approximate the behaviour close to the source; typically taking $V_0 = 10^4$ is sufficient to obtain solutions accurate to within 10^{-4} close to the inlet. Equation (14) is solved numerically by moving from the source S_0 to the front P. The goal is to find an integral curve reaching point P.

As previously, there is no integral path relating the source point S and the front point P. Moreover, we suspect the occurrence of a jump. Indeed, the topological structure of the phase plane is a bit different compared to the case $\gamma > 1$, since the integral path does not pass through the critical point A1 in the supercritical region and thus crosses the critical curve C_I at a regular point that we refer to as R.

To construct the solution with a discontinuity, we have used the trial and error procedure, as specified in Section 5. As earlier, we note that the only trajectory coming from P is the limiting curve C_A. We then assume that a piece of the path $P \rightarrow A_1$ on this curve is a part of the solution sought; the other part of the solution is a piece of the integral path $S \rightarrow R$. On this latter curve, we guess the position of the point marking the discontinuous transition towards the path $P \rightarrow A_1$; we refer to this point as point E. At regular point E, there is a jump. As a typical example, we have plotted the shock curves (long-dashed line) on Figure 5(a); a single curve crosses the limiting curve emanating from P and we refer to this intersection point as E′.

The path EE′ represents the jump experienced by the surge; the path PE′ is the integral path representing the head while the path ES is the integral curve representing the body. Equations (20) and (14) have been numerically integrated to produce $Z(\xi)$ and $H(\xi)$. For instance, for $a = 4$ and $d = 1$, we found: $\xi_P = 3.077$, $\xi_E = 1.590$ versus $\xi_a = 2.999$ and $\xi_b = 1.945$ for the reference solution given in a companion paper (Ancey et al. 2006), $\xi_P = 3.133$ and $\xi_A = 1.850$ for the Saint-Venant solution related to $\gamma > 1$. The fluid volume $\mathcal{V}$ is found by numerical integration of $\int_0^{xp} \pm h(x)dx$, and we find $\mathcal{V} = 8.533t^{5/2}$, which perfectly matches the fluid volume imposed by Equation (5). It is also worth noting that the solution thus built is sensitive to the numerical estimation of the transition point E: changing the position of the endpoint E by a few percent along the curve SR leads to altering the fluid volume, which shows that there is only one solution for a given set of boundary conditions, at least locally. Similarly to the case $\gamma > 1$, we applied the same shock conditions as used by (Gratton and Vigo 1994) instead of the Rankine-Hugoniot relations (24–25) and again we obtained a solution that differed slightly from the solution given here: indeed, we found $\xi_P = 3.072$, $\xi_A = 1.593$, and $\mathcal{V} = 8.512t^{5/2}$ (i.e. relative deviation of -0.3% with the input volume).

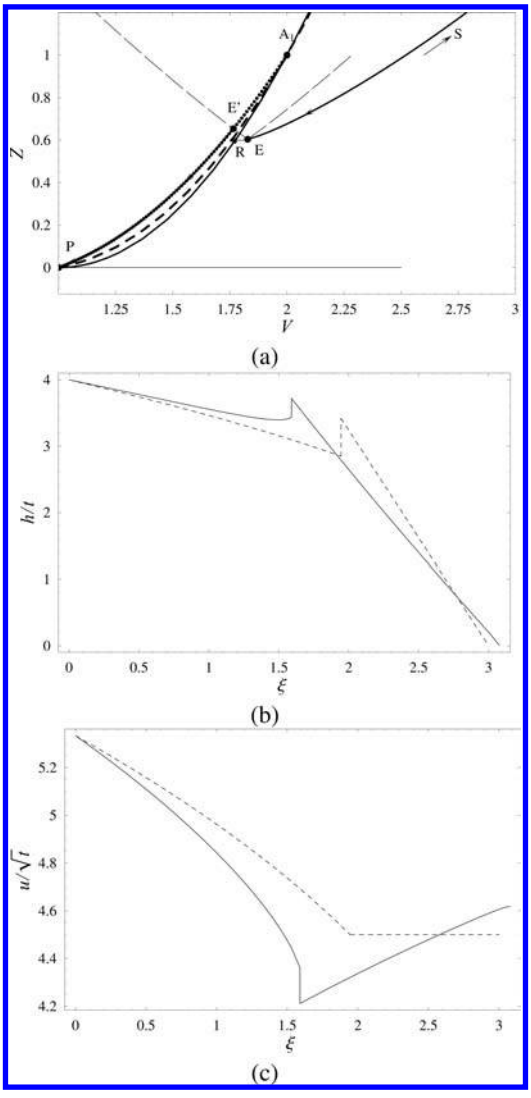


Figure 5. (a) Phase plane in the vicinity of A_1 and construction of the transition point E and its conjugate E'. Same caption as in Figure 4(a). (b) Flow-depth variation with ξ: the solution to the Saint-Venant equations (solid line) is compared with the solution to Euler equations (dashed line). (c) Velocity variation with ξ. All the computations made for $a = 4$, $d = 1$, and $\gamma = 1$.

On Figure 5(b–c), we have reported the flow-depth and velocity variations with the similarity variable ξ (solid lines). We have also reported the reference solution (dashed lines) found in another paper (Ancey et al. 2006). Note the significant difference in the position of the transition point between the solutions, whereas

Copyright © 2006 Taylor & Francis Group plc, London, UK

the front position is properly evaluated to within 5%. In contrast, the departure from the theoretical curve remains moderate since the relative deviation doe not exceed 10% for the velocity and the flow depth.

8 DISCUSSION

A striking feature of our results is that the head of the surge is wedge-shaped with an acute angle. This wedge structure has been observed in experimental realizations of gravity currents in tanks. Different examples drawn from various flow conditions in the laboratory and in nature clearly demonstrate the existence of wedge-like fronts contrasting with the Benjamin assumption. For instance, in the experiments conducted by Simpson (1972), the development of the flow patterns were made visible by using a blend of dense fluid and fine aluminium particles: a stretching vortex occupying the tip region was clearly observed at the leading edge and produced an intense roll-up of fine aluminium particles, which makes it possible to visualize the streamlines and the two vortices; in the upper part of the head, a counter-clockwise rotating vortex occurred. This flow pattern is very close to the one exhibited by the Saint-Venant equations.

In most gravity-current models, the details of the front shape and structure are omitted and the front is replaced by something close to a hydraulic jump and ruled by a Benjamin-like relation according to which the Froude number at the front is a function of the relative submersion of the current and the density ratio between the current and the surrounding fluid. This boundary condition produces currents with a very narrow vertical front, which may appear unrealistic in some circumstances. This is the case of currents with an increasing flow rate, as studied here, where it has been shown that the head occupies one third of the total current length and adopts a wedge shape. The actual shape of the front has drawn little attention so far. In his seminal paper, Benjamin (1968) supplemented the earlier heuristical analysis of von Kármán, demonstrating that a steady front makes an angle of $\pi/3$ with respect to the horizontal: Benjamin provided an approximate analytical solution describing the shape for the lock-exchange problem when the flow depth is half the total depth and again found that the front angle was $\pi/3$. Recently, McElwaine (2005) has extended Benjamin's results by considering steady finite-volume currents down a steep slope, which experience resistance from the surrounding fluid. He also found that the front makes an angle $\pi/3$ with the bottom line. Our result contrasts with the earlier findings: the front angle is not constant, but varies with time. Therefore, there appear to be significant changes in dynamics in the front angle between steady and time-dependent flow conditions. This observation may have a potential impact since until now, most models have used a constant-Froude-number boundary condition even though the flow is not steady.

When compared to analytical solutions to the Euler equations (Ancey et al. 2006), the Saint-Venant equations successfully capture the shape and the dimensions of the front when the Boussinesq coefficient γ is known in advance. In the converse case, when γ is set equal to unity, the front shape is properly predicted, but its dimensions are slightly overestimated. This clearly shows that minute changes in the value of γ markedly affect the solution to the Saint-Venant equations, as shown earlier by Hogg and Pritchard (2004) in the case of a surge induced by a dam break. Surprisingly, whatever the value of γ, the front position is properly evaluated to within 4%. On the whole, despite the potential pitfalls of the problem investigated (strong time dependence, non-hydrostatic pressure, rapid regime transition), we can consider that the Saint-Venant equations provide very satisfactory results, even in the usual case where the Boussinesq coefficient is set equal to unity, since the relative deviation with the solution to the Euler equation usually does not exceed 10%.

9 CONCLUSION

The goal of this paper was to find similarity solutions to the Saint-Venant (shallow-water) equations when the boundary conditions at the front impose a zero flow-depth. The solutions to the Saint-Venant equations were constructed by making use of the phaseplane formalism and seeking similarity forms in a way similar to earlier investigations (Gratton and Vigo 1994).

When the Boussinesq coefficient was in excess of unity, it was not possible to find a physically admissible solution close to the front without providing further information. This conclusion is akin to the observation made by Hogg and Pritchard (2004) in their investigation of drag influence on head shape for the dam-break problem. Instead of using a Benjamin-like condition at the front (imposing a nonzero flow depth), we assumed that the flow-depth averaged velocity was uniform, which implied that the Boussinesq coefficient dropped to unity.

A very important point that did not seem to be noted in the previous investigation was that the only way to construct the solution close to the front was to determine a special curve, referred to as C_A in the phaseplane analysis. Indeed, in the phase plane $V - Z$ (e.g. see Figure 2), the integral path representing the solution must pass through certain points; the front was represented by point P and laid in the neighborhood of a critical point called A, which was a node: all the curves in a given region around A were attracted by A and pass through it tangent to an asymptotic curve

Copyright © 2006 Taylor & Francis Group plc, London, UK

C_A. None of these integral paths passed through A, but the limiting curve C_A did. This curve represented an *exceptional* and local solution to the Saint-Venant equations.

It is worth noticing that this topological structure of the similarity solutions in the front vicinity entails that a specific numerical method must be used to compute accurate solutions to Saint-Venant equations close to the front and explains why the current numerical methods fail to predict the behavior close to the front.

REFERENCES

Ancey, C., S. Cochard, S. Wiederseiner, and M. Rentschler (2006). Existence of similarity solutions for supercritical non-Boussinesq gravity currents. *Physica D*, submitted.

Benjamin, T. (1968). Gravity currents and related phenomena. *J. Fluid Mech. 31*, 209–248.

Dressler, L. (1952). Hydraulic resistance effect upon the dam-break functions. *J. Res. Natl Bur. Stand. 49*(3), 217–225.

Gratton, J. (1991). Similarity and self similarity in fluid dynamics. *Fund. Cosmic Phys. 15*, 1–106.

Gratton, J. and C. Vigo (1994). Self-similar gravity currents with variable inflow revisited: plane currents. *J. Fluid Mech. 258*, 77–104.

Grundy, R. and J. Rottman (1986). Self-similar solutions of the shallow-water equations representing gravity currents with variable inflow. *J. Fluid Mech. 169*, 337–351.

Hogg, A. and D. Pritchard (2004). The effects of hydraulic resistance on dam-break and other shallow inertial flows. *J. Fluid Mech. 501*, 179–212.

Huang, X. and M. Garcìa (1998). A Herschel-Bulkley model for mud flow down a slope. *J. Fluid Mech. 374*, 305–333.

Iverson, R. and R. Denlinger (2001). Flow of variably fluidized granular masses across three-dimensional terrain. 1. Coulomb mixture theory. *J. Geophys. Res. 106*, 537–552.

McElwaine, J. (2005). Rotational flow in gravity current heads. *Philosophical Transactions of the Royal Society of London series A 363*, 1603–1623.

Parker, G., Y. Fukushima, and H. Pantin (1986). Selfaccelerating turbidity currents. *J. Fluid Mech. 171*, 145–181.

Ritter, A. (1892). Die Fortpflanzung der Wasserwellen. *Zeit. Vereines Deutsch. Ing. 36*(33), 947–954.

Rottman, J. and J. Simpson (1983). Gravity currents produced by instantaneous releases of a heavy fluid in a rectangular channel. *J. Fluid Mech. 135*, 95–110.

Savage, S. and K. Hutter (1989). The motion of a finite mass of granular material down a rough incline. *J. Fluid Mech. 199*, 177–215.

Simpson, J. (1972). Effects of a lower boundary on the head of a gravity current. *J. Fluid Mech. 53*, 759–768.

Stoker, J. (1957). *Water Waves*. New York: Interscience Publishers.

Whitham, G. (1954). The effects of hydraulic resistance in the dam-break problem. *Proc. Roy. Soc. London A 227*, 399–407.

Whitham, G. (1974). *Linear and Nonlinear Waves*. New York: John Wiley & Sons. 10

Copyright © 2006 Taylor & Francis Group plc, London, UK

Fully-2D and *quasi*-2D modeling of flooding scenarios due to embankment failure

F. Aureli, P. Mignosa & C. Ziveri
Dipartimento di Ingegneria Civile, dell'Ambiente, del Territorio & Architettura, Parma, Italy

A. Maranzoni
Dipartimento di Ingegneria Civile, Architettura, Territorio e Ambiente, Brescia, Italy

ABSTRACT: The occurrence of river levee breaks due to high return period floods can have catastrophic effects on the environment and human lives. The study of these kinds of problems is of great importance for hydraulic hazard assessment, for the development of civil protection plans and for the organization of corrective and preventative measures to reduce flood damage.

In this context, the paper presents the main results of two case studies concerning two floodable regions located in the middle reach of the Po river (Northern Italy). For the first case, numerical simulations were performed by means of a 2D finite volume MUSCL-Hancock scheme (belonging to the Surface Gradient Methods class) and also by a *quasi*-2D numerical model based on the subdivision of the domain in storage cells linked through weirs.

Even if the flooding dynamics was not correctly described in the first hours after the breaching, the results obtained through the *quasi*-2D approach showed a fairly good agreement with fully-2D ones: flooded areas, maximum water depths and, above all, the discharge flowing through the breach are comparable. The satisfactory results obtained led to the adoption of a hybrid methodology that was applied to the second case study: the discharge flowing through the breach was computed by the *quasi*-2D approach and then adopted as the inflow boundary condition for the fully-2D modeling of the sole area prone to flooding. In this way the flooding dynamics was predicted avoiding the burdensome 2D description of the riverbed; in addition the downstream boundary condition was moved far away from the breach and the computational time significantly reduced.

1 INTRODUCTION

High return period floods are in most cases a severe test for river systems; the levee breaks potentially ensuing from the high stresses induced upon the embankments can have catastrophic effects on the environment, human lives, infrastructures and real estate resting on the flooded areas. Historical information is essential, but sometimes not enough to understand all the potential hazards, as for dam- or levee-breaks that have never occurred before. In these cases the flood hazard evaluation is usually performed with the help of numerical simulations or, only on very rare occasions, by means of physical scale models.

Once a design scenario is identified, the application of a mathematical model can lead to evaluate the main flooding characteristics, such as inundated area, water depths and velocities, arrival times of the wetting front and water stay on the ground (Aureli & Mignosa 2004); nevertheless the mathematical model must allow to take into account the influence of man-made or natural levees (channel embankments, roads, railways, etc.) upon the inundation dynamics. The study of these kinds of problems is of great importance for hydraulic hazard assessment, for the development of civil protection plans and for the organization of corrective and preventative measures to reduce flood damage.

The paper presents the main results of two case studies concerning the floodable regions located in the middle reach of the Po river (Northern Italy) bounded by the river right levee and by the embankments of two couples of consecutive tributaries (Taro-Parma and Parma-Enza). In the Parma-Enza test case fully-2D and *quasi*-2D numerical simulations were compared in terms of flooded areas, flooding dynamics and discharge flowing through the breach.

The satisfactory results obtained led to the adoption of a hybrid methodology applied to the Taro-Parma test case, in which the discharge flowing through the breach was computed by means of a *quasi*-2D

Copyright © 2006 Taylor & Francis Group plc, London, UK

approach and then adopted as the inflow boundary condition for the fully-2D modeling of the sole area prone to flooding.

2 2D NUMERICAL MODEL

The numerical scheme, implemented by the authors themselves, solves the initial and boundary values problem of the 2D shallow water equations in integral form (Toro 2001) by adopting a finite volume approach:

$$\begin{cases} \dfrac{d}{dt}\int_{\Omega}\mathbf{U}\,d\Omega+\int_{C}\mathbf{n}\cdot\mathbf{H}(\mathbf{U})\,dC=\int_{\Omega}\left[\mathbf{S}_0(\mathbf{U})+\mathbf{S}_f(\mathbf{U})\right]d\Omega \\ \text{Initial Condition}: \mathbf{U}(t^0,x,y)=\mathbf{U}_0(x,y),\quad (x,y)\in\Omega \end{cases} \tag{1}$$

In Problem 1 Ω represents the area of the integration cell, C the cell boundary, $\mathbf{n}$ the outward unit vector normal to C, while $\mathbf{H(U)} = [\mathbf{F(U)}, \mathbf{G(U)}]$ is the tensor of fluxes. Moreover:

$$\mathbf{U}(t,x,y)=\begin{pmatrix} h \\ uh \\ vh \end{pmatrix},\quad \mathbf{F}=\begin{pmatrix} uh \\ u^2h+\frac{1}{2}gh^2 \\ uvh \end{pmatrix},$$
$$\mathbf{G}=\begin{pmatrix} vh \\ uvh \\ v^2h+\frac{1}{2}gh^2 \end{pmatrix},\ \mathbf{S}_0=\begin{pmatrix} 0 \\ ghS_{0x} \\ ghS_{0y} \end{pmatrix},\ \mathbf{S}_f=\begin{pmatrix} 0 \\ ghS_{fx} \\ ghS_{fy} \end{pmatrix}. \tag{2}$$

In Equations 1 and 2 the time variable is denoted by t, g is the acceleration due to gravity, h represents the water depth, u and v are the depth averaged velocities in the x and y directions respectively, while S_{0x}, S_{0y}, S_{fx}, and S_{fy} are the bottom and frictional slopes along the same axes. The friction terms are computed according to Manning's equation.

A first order accurate *Godunov splitting* procedure (LeVeque 2002, Toro 2001) of the friction source term replaces Problem 1 by the sequence of the two following de-coupled problems:

$$\left.\begin{aligned} &\frac{d}{dt}\int_{\Omega}\mathbf{U}\,d\Omega+\int_{C}\mathbf{n}\cdot\mathbf{H}\,dC=\int_{\Omega}\mathbf{S}_0\,d\Omega \\ &\text{Initial Condition}: \mathbf{U}=\mathbf{U}(t^n,x,y) \end{aligned}\right\} \xrightarrow{\Delta t^n} \hat{\mathbf{U}}(t^{n+1},x,y), \tag{3}$$

$$\left.\begin{aligned} &\frac{d}{dt}\int_{\Omega}\mathbf{U}\,d\Omega=\int_{\Omega}\mathbf{S}_f\,d\Omega \\ &\text{Initial Condition}: \mathbf{U}=\hat{\mathbf{U}}(t^{n+1},x,y) \end{aligned}\right\} \xrightarrow{\Delta t^n} \mathbf{U}(t^{n+1},x,y) \tag{4}$$

where the superscript n indicates the time level and $\hat{\mathbf{U}}$ is a provisional solution for the vector of the conserved variables $\mathbf{U}$ resulting from the numerical solution of Problem 1 in absence of friction. In (3) and (4) Δt^n represents the current time step and $t^{n+1} = t^n + \Delta t^n$.

The numerical scheme adopted for the discretization of Problem 3 belongs to the *Surface Gradient Methods* class (Zhou et al. 2001) in which the gravitational forcing effect is combined with the propagation algorithm. The scheme is explicit, shock capturing and high resolution. It belongs to the MUSCL-Hancock family and it is second order accurate in space and time (Toro 2001, Hirsch 1990).

For a computational domain divided into Cartesian cells of area $\Delta x \times \Delta y$, the updating conservative *unsplit* algorithm (Toro 2001, Zhou et al. 2001) reads:

$$\hat{\mathbf{U}}_{i,j}^{n+1}=\mathbf{U}_{i,j}^{n}-\frac{\Delta t^n}{\Delta x}\left(\mathbf{f}_{i+\frac{1}{2},j}-\mathbf{f}_{i-\frac{1}{2},j}\right)-\frac{\Delta t^n}{\Delta y}\left(\mathbf{g}_{i,j+\frac{1}{2}}-\mathbf{g}_{i,j-\frac{1}{2}}\right)+ +\Delta t^n\,\overline{\mathbf{S}}_{0_{i,j}}, \tag{5}$$

where the last term represents a suitable local centred estimate (Zhou et al. 2001) of the slope source term, while $\mathbf{f}_{i\pm1/2,\,j}$ and $\mathbf{g}_{i,\,j\pm1/2}$ are the numerical fluxes in the x and y directions respectively (designated by the subscripts i and j). Following Zhou et al. (2001), in order to appropriately predict these numerical fluxes, boundary-extrapolated values (Toro 2001, Hirsch 1990) for the vector of the conserved variables $\mathbf{U}^n = \mathbf{U}(t^n, x, y)$ were achieved, independently in the x and y directions, through a non linear second order accurate reconstruction based on the non conservative vector $\mathbf{Q}^n = \mathbf{Q}(t^n, x, y) = (h + z, uh, vh)^T$ where $z = z(x, y)$ is the bottom surface. In the SGM methodology the water surface, $h + z$, is in fact adopted as the basis for MUSCL data reconstruction at the cell interfaces. Afterwards, in order to achieve second order accuracy in time, a new set of boundary-extrapolated values was obtained through evolution on a half of the current time step Δt^n following the procedure characteristic of MUSCL – Hancock schemes (Toro 2001). Finally the numerical fluxes were computed by the FORCE (*First ORder CEntred*) scheme (Toro 2001, Aureli et al. 2004).

Problem 4 is then solved by a second order implicit trapezoidal method, which allows the numerical code to preserve the explicit structure (Caleffi et al. 2003, Aureli et al. 2004).

The described scheme offers the advantage of accurately predicting the propagation of free surface small perturbations and satisfies the exact C-property (Vázquez-Cendón 1999, Bermúdez & Vázquez, 1994), even on complex topographies. Furthermore, it allows to handle easily (Zhou et al. 2002) unerodible discontinuities in bed topography (embankments, submersible obstacles, etc.). On a flat bed it is absolutely equivalent to a *Depth Gradient Method* (Zhou et al. 2001) and it doesn't entail additional computational costs compared to conventional numerical methods for the homogeneous part of Problem 1. To deal with the evolution in time of wetting and drying fronts, the algorithm was applied at cells in

Copyright © 2006 Taylor & Francis Group plc, London, UK

which $h_{i,j} > \epsilon$ (Toro 2001), where ϵ is a small positive tolerance assumed equal to 10^{-3} m.

From the 2D stability condition $0 < Cr_x + Cr_y \leq 1$ (where $Cr_x$and Cr_y are the Courant numbers in the x and y directions respectively) the following way to compute the time step Δt^n is derived:

$$\Delta t^n = Cr \min\left\{ \frac{\Delta x}{\max\left|u_{i,j} + \sqrt{g h_{i,j}}\right|}, \frac{\Delta y}{\max\left|v_{i,j} + \sqrt{g h_{i,j}}\right|} \right\} \quad (6)$$

where $Cr \leq ½$ (Toro 2001).

The accuracy, robustness and efficiency of the computational code were checked comparing numerical simulations with reference solutions of significant test cases (Maranzoni 2004) with satisfactory results in reproducing steady and rapidly varying flows on complex topographies.

3 *QUASI*–2D APPROACH

The results obtained by means of fully-2D numerical modeling of floodable areas and of part of the adjoining rivers require at first a suitable 2D numerical model and then a significant effort both for data collecting and treatment. Also the numerical elaborations can be demanding from a computational point of view. For these reasons a *quasi*-2D modeling of the system *river-floodable region* was performed in order to verify if comparable results could be obtained with a significantly reduced effort.

The mathematical model adopted is the hydrodynamic module of the software DHI-Mike11 (DHI 2002); the model solves the vertically integrated equations of conservation of mass and momentum under the usual De St. Venant hypotheses.

A model of the river of interest was set up on the basis of cross section surveys; closed flood plains can be described as cells linked to the main channel through broad-crested weirs characterized by the length and elevation of the separation dikes. The topological description of the area prone to flooding can be achieved through the introduction of a number of storage cells, each representing a portion of the domain of interest. Whereas present, elevated roads, railways and minor waterways must be adopted as cell boundaries; sometimes, it is necessary to introduce fictitious borders to limit cell extension (Cunge et al. 1980). Every cell is represented by a computational node and is characterised by a function *water depth-storage volume* derived by the topography of the represented portion of the domain.

Contiguous cells are properly joined by link channels provided with weirs allowing to compute the flow exchange. Each embankment or channel levee is then intended as a broad crested weir between two adjoining cells and its length and width as a function of depth were adopted to define the weir structure.

The structure schematizing the area prone to flooding is linked to the main river at the chainage corresponding to the breach location of the investigated scenario. The link, initially disabled, is activated at the chosen time of breaching to allow the flow exchange across the breach.

4 DESCRIPTION OF THE STUDY AREAS

4.1 *Test case 1: Parma–Enza region*

The first case study concerns a floodable region located in the middle reach of the Po river (Northern Italy), bounded by its right levee and by the embankments of the two tributaries Parma and Enza.

The floodable region and the adjacent Po river reach were described by means of a DTM with a square regular mesh of 50 m, obtained by an interpolation procedure on the available cartographic maps and river cross sections. The dimension of the grid was chosen as a compromise between the estimated computational time and the satisfactory modeling of the region under study. The main constraints were due to the cross extent of the riverbed (somewhere around a few hundred meters), to the assumed breach width (300 m) and to the description of the man-made elements affecting the inundation dynamics (channel embankments, roads, railways, etc.). The modeling of the riverbed is in fact essential to correctly compute the discharge flowing through the breach, especially when the flow is backwatered for the partial filling of the floodable region.

The embankment system of the contouring rivers was considered as a solid and insuperable boundary. This assumption was validated *a posteriori* comparing the maximum computed water stages with the top height of the levees. On the contrary, the interior levees were considered unerodible and potentially overtoppable, since water stages can rise enough to submerge them.

Figure 1 shows a contour map of the whole bathymetry of the considered region, together with the right river embankment of the Po river (in white) and the location of the levee break for the simulated flooding scenario.

In the Po riverbed a Manning's roughness coefficient $n = 0.03\ \mathrm{s \cdot m^{-1/3}}$ was assumed. This value allowed to well reproduce, for a wide range of discharges, the *stage-discharge* relationship observed at a gauged station placed at the downstream boundary of the considered reach. On the contrary, the available documentation on the arrival time of the wetting front in two historical inundations that occurred in 19th and 20th centuries was not enough to calibrate

Copyright © 2006 Taylor & Francis Group plc, London, UK

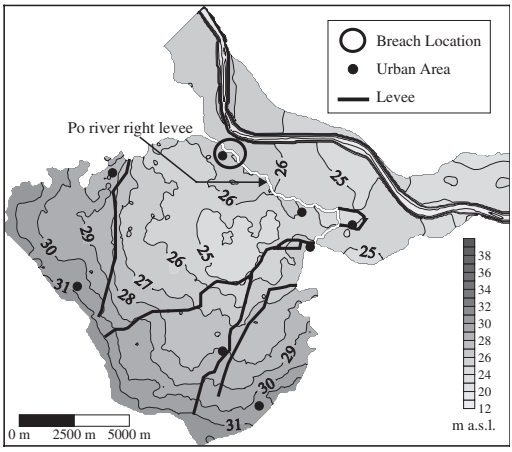


Figure 1. Contour map of the study area for Test case 1.

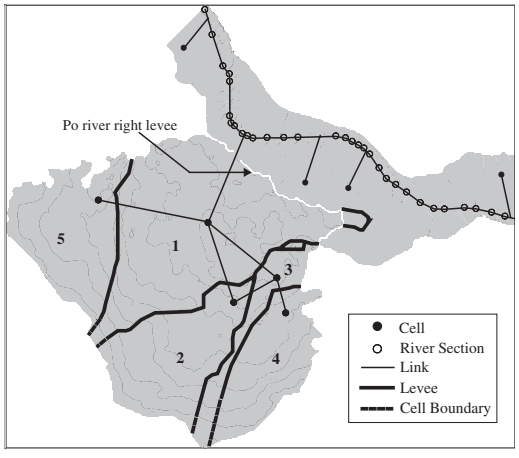


Figure 2. Cell structure describing the study area concerning Test case 1.

a Manning coefficient for the floodable regions. A value of $n = 0.05\,\mathrm{s}\cdot\mathrm{m}^{-1/3}$ was then adopted, based on the results of previous studies on neighbouring areas (Aureli & Mignosa 2004).

For the *quasi*-2D simulation, the floodable domain was divided into five cells bounded by the main interior levees and connected by the net of link channels represented in Figure 2. At this aim fictitious borders were introduced in the south-western region of the domain extending the existing levees.

4.2 *Test case 2: Taro–Parma region*

The second case study considered concerns the floodable region always located in the middle reach of the Po river (Northern Italy) bounded by the river right

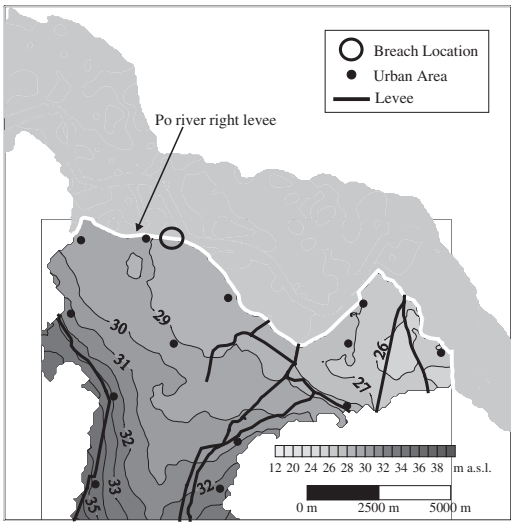


Figure 3. Contour map of the floodable area for Test case 2.

levee and by the embankments of the two tributaries Taro and Parma.

A hybrid approach was adopted for this test case: only the area prone to flooding was described, again by means of a DTM with a square regular mesh of 50 m, obtained by an interpolation procedure on the available terrain data. Particular attention was devoted to the description of the many channel embankments, roads and man-made elements that could affect the inundation dynamics. Once again the interior levees were considered unerodible and potentially overtoppable.

Figure 3 shows a contour map of the bathymetry of the considered floodable region, together with the right river embankment of the Po river (in white) and the location of the levee break for the simulated flooding scenario. As for the previous test case, a value of $n = 0.05\,\mathrm{s}\cdot\mathrm{m}^{-1/3}$ was adopted for the Manning roughness coefficient.

For the *quasi*-2D simulation the floodable domain was divided into thirteen cells bounded by the main interior levees and connected by the net of link channels represented in Figure 4. In order to limit cell extension and at the same time to obtain a better description of flooding evolution, fictitious borders were introduced in the central portion of the floodable region.

5 HYDROLOGICAL INPUT

As a hydrological input, a Synthetic Design Hydrograph of 200 years return period was considered (Maione et al. 2003). The procedure to estimate SDH was based on the statistical analysis of recorded flood waves through the construction of the Flow

Copyright © 2006 Taylor & Francis Group plc, London, UK

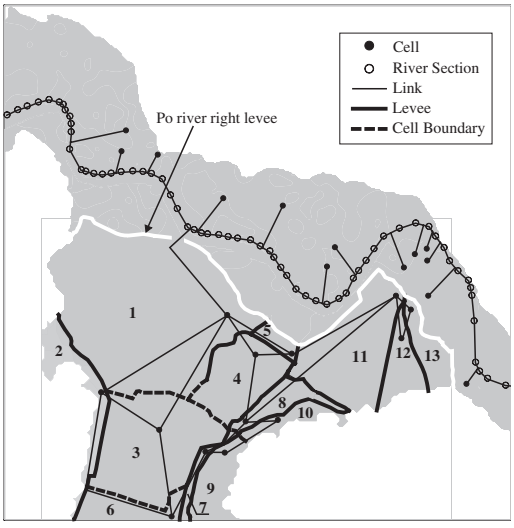


Figure 4. Cell structure describing the study area concerning Test case 2.

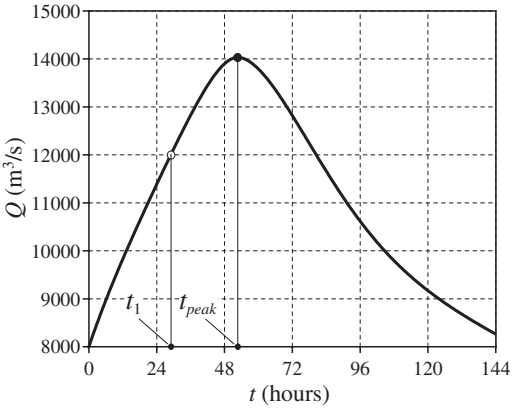


Figure 5. Synthetic Design Hydrograph (SDH) of 200 years return period.

Duration Frequency (FDF) reduction curves and the determination of the peak location (Maione et al. 2000).

Figure 5 shows the adopted SDH together with the chosen time of the levee-break. For both test cases the breach was considered to occur at t_1 on the rising limb of the hydrograph, when the incoming flood wave reached the value of 12000 m^3/s. For this discharge no overtopping occurs in any part of the Po river levee under investigation; however water levels are such to induce high stresses in the earthen embankment, so that erosion or piping phenomena could really develop. A further anticipated time of breaking, albeit more hazardous for the considered area, is impractical and never reported in the historical descriptions.

To point out the more dangerous effects on the flooded areas, the breach was assumed to occur instantaneously: the developing times of the historical breaches were in fact noticeably shorter (order of hours) than the time scale of the floods (order of weeks) in the Po river (Aureli & Mignosa 2004). Hence, to consider the levee-break as instantaneous leads only to a slight overestimation of the water volumes initially flowing through the breach.

6 RESULTS

6.1 *Test case 1: Parma–Enza region*

In the following the results obtained by means of the fully- and *quasi*-2D approaches for the first case study under investigation are presented. A flooding scenario, characterized by a 300 m wide breach (about the mean over 27 historical values, Aureli & Mignosa 2004) occurring in the rising limb of the SDH, was hypothesized; the breach was located in the upstream part of the Po river right levee (Figure 1).

To proceed with the numerical simulations, proper initial and boundary conditions were introduced. The initial conditions in the Po river were obtained by a preliminary simulation with a constant inflow discharge of 8000 m^3/s (the initial value of the SDH) extended in time until steady-state conditions were reached everywhere. Zero water depths and velocities were assumed for all the grid cells in the floodable area outside the riverbed.

At upstream boundary cells (inflow section of the Po river) a time varying discharge derived from the above-mentioned SDH was assigned. The inflow discharge was assumed normal to the boundary string and assigned to each cell proportionally to the 5/3 power of the current water depth.

At solid boundaries representing the river embankments a free-slip (reflective) condition was imposed whereas at the downstream boundary (outflow section of the Po river) a far-field (transmissive) condition was introduced. The assignment of the downstream boundary condition is not straightforward for the scenarios under investigation. The downstream boundary is in fact only a necessary delimitation of the computational domain and it isn't characterized by any particular hydraulic condition; moreover the flooding scenarios are only hypothetical. For these reasons, a constant or time varying water level cannot be applied. At the same time the adoption of a *rating curve* would require a set of assumptions (constant water level across the section, single valued relationship between stage and discharge) that are not easily acceptable in a two dimensional time varying flow. On the basis of several numerical experiments carried out for schematic test cases, the writers found that the transmissive condition imposed at ghost cells provides satisfactory results.

Copyright © 2006 Taylor & Francis Group plc, London, UK

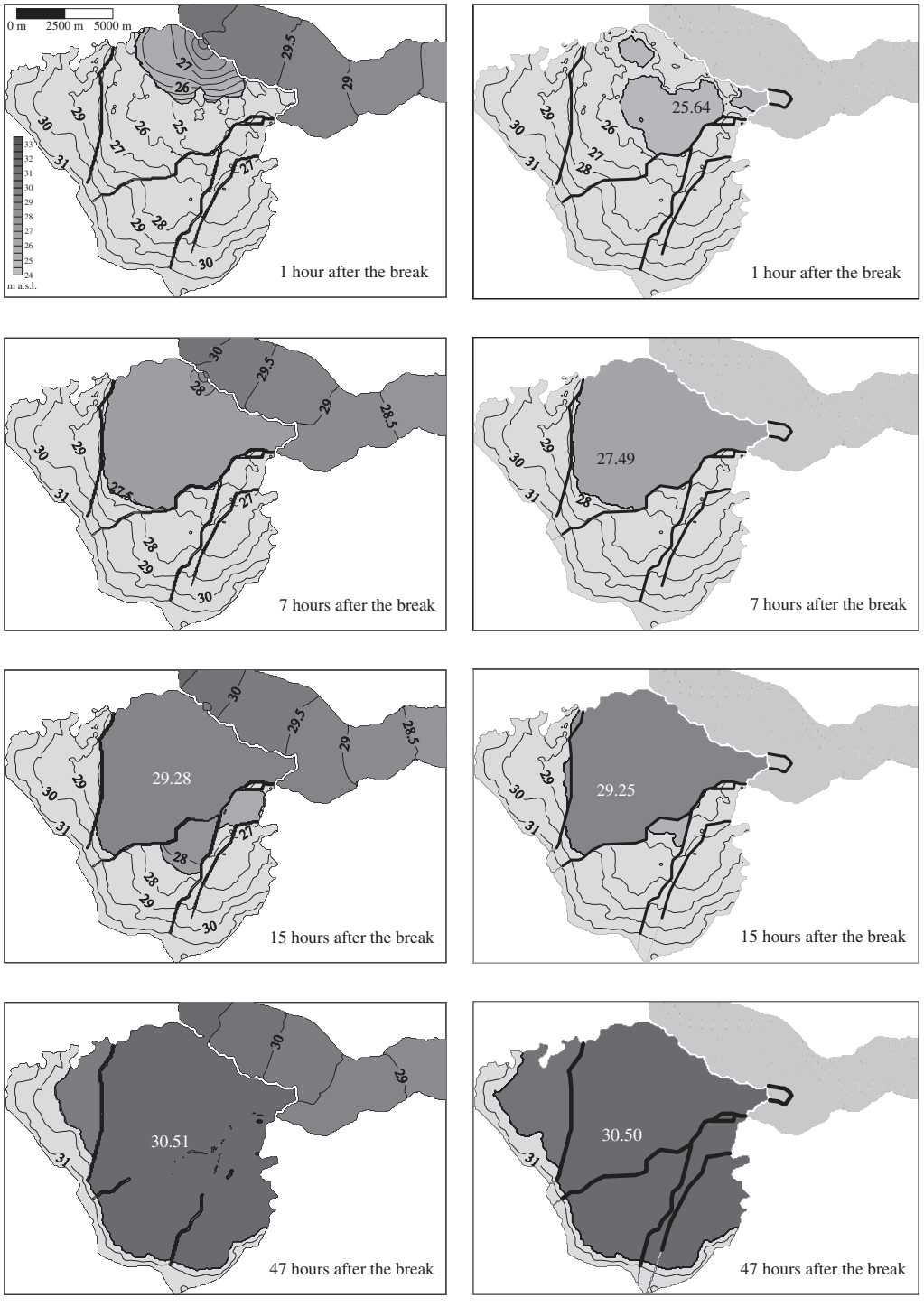


Figure 6. Flooded areas and water stages for Test case 1: fully-2D (left column) and *quasi*-2D model (right column).

Copyright © 2006 Taylor & Francis Group plc, London, UK

Anyway, the computational domain was extended far away downstream the breach site in order to reduce the disturbances potentially induced by the adopted boundary condition.

The simulations were carried on until the maximum water stages were reached in all the flooded areas and the water started to go back into the riverbed across the breach.

Figure 6 (left column) shows water stage contour maps resulting from the 2D numerical modeling at some significant times. About 7 hours after the break, the flood reached the levees contouring the portion of the domain facing the breach. Eight hours later the eastern levee was overtopped and the flooding spread towards the east. The maximum planar extension of the flooding (66 km^2) was reached 47 hours after the levee break with a water stage of about 30.5 m a.s.l., almost constant everywhere in the flooded area.

The same SDH adopted for the fully-2D simulations was then assigned as upstream boundary condition for the *quasi*-2D simulation. At the downstream boundary a *rating curve* was imposed. In order to minimize the influence of this approximated condition, the river reach was extended far away downstream the breach site.

In Figure 6 (right column) the results for the *quasi*-2D approach are presented. Water stages and flooded areas were initially not well predicted through the *quasi*-2D approach: the reservoir behaviour of the cell structure is in fact not capable of reproducing the rapidly varying flow effects that were predominant in the first hours after the breaching. Afterwards, fully-2D and *quasi*-2D flooded areas and maximum water stages are comparable.

Fairly remarkable is the agreement between the discharges flowing through the breach computed by the fully-2D and *quasi*-2D models (Figure 7).

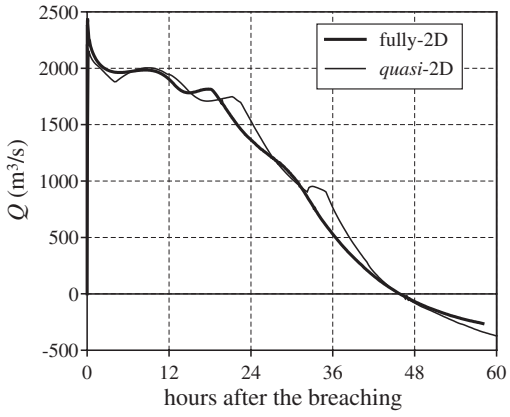


Figure 7. Discharge flowing through the breach for Test case 1: comparison between fully-2D and *quasi*-2D results.

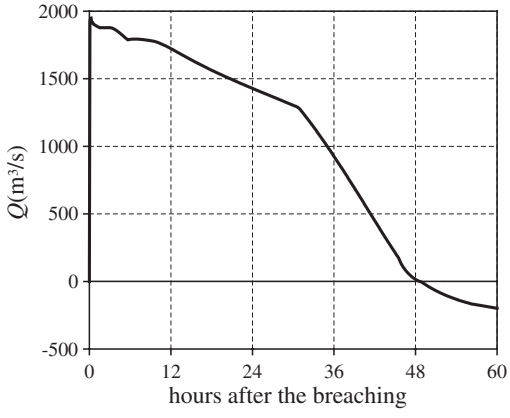


Figure 8. Discharge flowing through the breach for Test case 2.

6.2 *Test case 2: Taro–Parma region*

As previously introduced, for the *quasi*-2D simulation of the Taro-Parma region, the area prone to flooding was described by means of thirteen storage cells (Figure 4) linked to each other through broad-crested weirs characterized by the length and elevation of the separation dikes. Due to the extension of the floodable region investigated and to the absence of natural levees in the central portion of the domain, fictitious boundaries were properly introduced to allow a more realistic description of the flooding. This led to the creation of cells 1, 3, 4 and 6 (Figures 3 and 4). Each cell is represented by a computational node and is characterised by a function *water depth-storage volume* derived by the topography of the represented portion of the domain. This complex structure of cells was linked to the main river stream at the chainage corresponding to the breach location.

Again the link was disabled until t_1 and then activated to allow the flow exchange across the breach.

Taking advantage of the good agreement obtained in the previous test case, the discharge flowing through the breach, computed by means of the *quasi*-2D modeling (Figure 8) was assumed as the inflow boundary condition for the fully-2D simulation of the sole area prone to flooding. This inflow discharge was suitably applied in correspondence to the computational nodes representing the breach location. As for the previous case a 300 m wide breach occurring in the rising limb of the SDH was adopted; the breach was located in the upstream part of the Po river levee (Figure 3). Once again the simulations were carried on until the maximum water stages were reached in all the flooded area and then started to decrease.

Figure 9 shows water stage contour maps resulting from the numerical modeling at 3, 12, 24 and 48 hours

Copyright © 2006 Taylor & Francis Group plc, London, UK

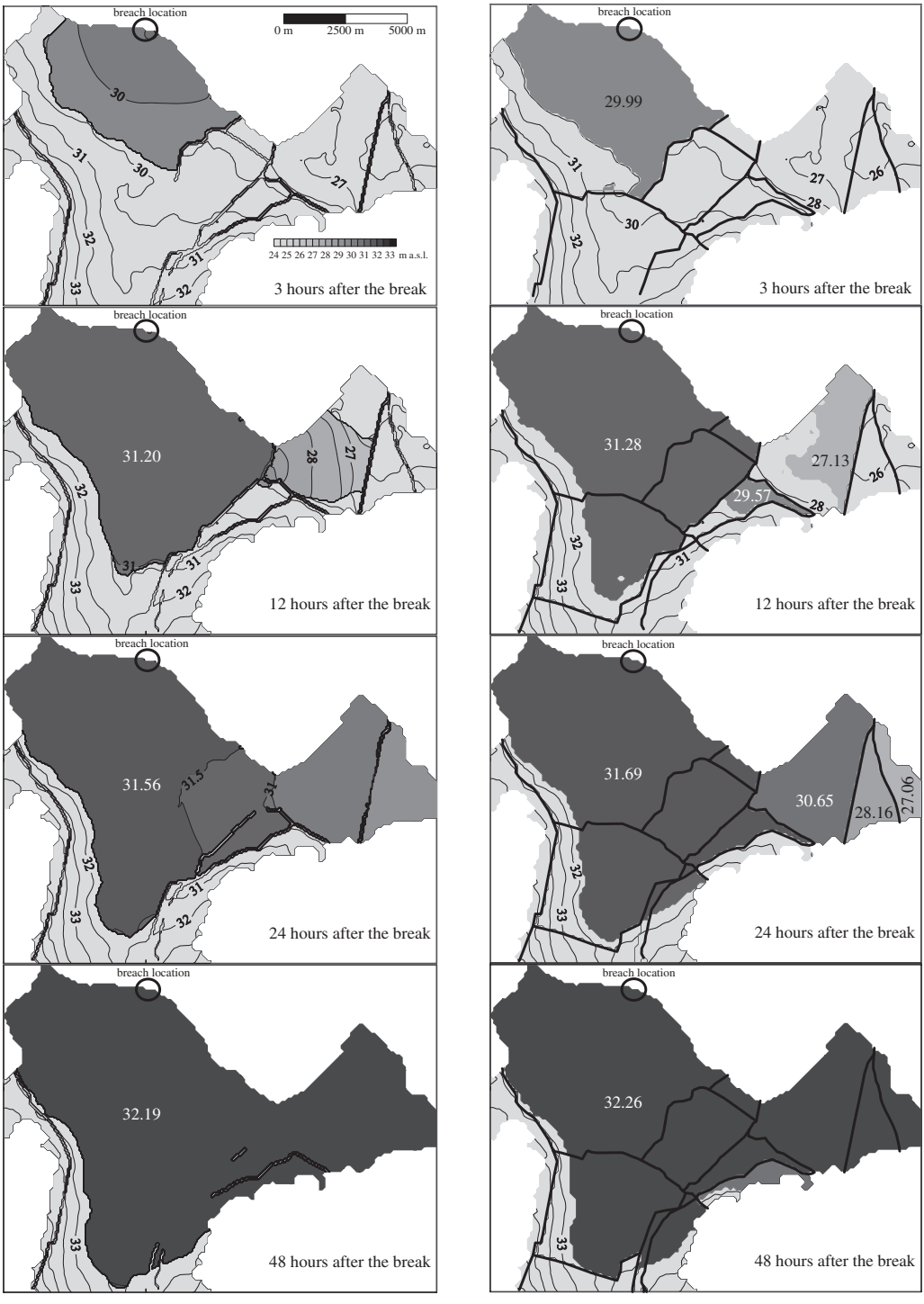


Figure 9. Flooded areas and water stages for Test case 2: fully-2D (left column) and *quasi*-2D model (right column).

Copyright © 2006 Taylor & Francis Group plc, London, UK

after the beginning of the flooding. About 3 hours after the break the flooding spreads on a region of more then 10 km^2 with mean water stages of 30 m above sea level. The agreement between *quasi*- and fully-2D results is satisfactory. Nine hours later the planar extension of the flooding is almost doubled. Water stages are now above 31 m above sea level and the agreement between the results obtained by means of the two approaches is still satisfactory. Anyway the overtopping of some levees in the eastern portion of the domain once again points out the incapability of the cell structure to correctly reproduce the advancing of the wetting front during transients. Twenty four hours after the breaking, water stages in the portion of the domain facing the breach site are above 31.5 m a.s.l. and the flooding has spread towards the east, reaching the Parma river left levee. The agreement between *quasi*- and fully-2D results is very good apart from the extreme eastern portion of the floodable domain in which the *quasi*-2D model underestimates the filling of a small cell.

The maximum planar extension of the flooding (68 km^2) was reached 48 hours after the levee break. The agreement between the computed planar extension of the flooding and water stages is still very good: this result is fairly obvious since in this case the same total volume flowing out of the breach was imposed for both the models and the flow dynamics is very slow. Anyhow, the good results of the first case study, if confirmed by other numerical tests, encourage this kind of hybrid approach.

7 CONCLUDING REMARKS

The results of the first test case showed that the main characteristics of the flooding due to levee breaking in the Po river (Northern Italy) could be described by following a simple *quasi*-2D methodology. This approach combines a 1D description of the main river with a schematization of the floodable region through a proper number of storage cells, each representing a portion of the domain of interest.

Some of the most significant results useful to evaluate hydraulic hazard, such as total flooding extension and maximum water depths, are comparable with those obtained by a more burdensome fully-2D simulation. Another advantage provided by the *quasi*-2D approach is the possibility to easily extend downstream the description of the main river reach, minimizing the influence of the boundary condition that could be assigned far away from the breach site.

However this approach is not able to describe the flooding dynamics, especially in the first hours after the breaching, due to the incapability of the cell structure to correctly reproduce the advancing of the wetting front during rapid transients.

Velocities and arrival times of the wetting front, other two significant parameters that influence the flood hazard, cannot then be evaluated by means of this simple approach.

Taking advantage of the good agreement between the discharge hydrographs flowing through the breach obtained by *quasi*-2D and fully-2D simulations applied to a first test case, a hybrid approach on a second case study was adopted: the discharge flowing through the breach computed by means of the *quasi*-2D methodology was considered as the inflow boundary condition for a fully-2D simulation of the sole area prone to flooding. In this way the computational effort was significantly reduced since: a) the burdensome 2D description of the river can be avoided, b) the number of computing cells is significantly lowered and c) the numerical stability condition – if requested as for explicit schemes – is less restrictive due to the absence of computational nodes of the riverbed where maximum water depths and high velocities take place. At the same time it was possible to evaluate velocities and time arrival of the wetting front in order to evaluate more complete flood hazard maps.

The good results obtained in the first case, if confirmed by other numerical tests, encourage this kind of hybrid (*quasi*-2D + fully-2D) methodology. This approach requires a reduced effort to perform extensive analyses of flooding events, such as those occurred in the past in the Po River valley where the extension of the areas subject to flooding reached several hundreds of square kilometres.

ACKNOWLEDGMENTS

This work was developed within a research agreement between the Civil Engineering Department of Parma University and the Po River Basin Authority. The Authors thank the mentioned Authority for the consent to publish the main results of the study.

REFERENCES

Aureli, F. & Mignosa, P. 2004. Flooding scenarios due to levee breaking in the Po river. *Water Management* 157(WMI): 3–12.

Aureli, F., Maranzoni, A. & Mignosa, P. 2004. Two dimensional modeling of rapidly varying flows by finite volume schemes, In M. Greco, A. Carravetta & R. Della Morte (eds.), *River Flow 2004, Proceedings of the Second International Conference on Fluvial ydraulics*, *Naples, Italy, 23–25 June 2004*. Lisse: Balkema.

Bermúdez, A. & Vázquez, M.E. 1994. Upwind methods for hyperbolic conservation laws with source terms. *Computers & Fluids* 23(8): 1049–1071.

Caleffi, V., Valiani, A. & Zanni, A. 2003. Finite volume method for simulating extreme flood events in natural channels. *Journal of Hydraulic Research* 41(2): 167–177.

Copyright © 2006 Taylor & Francis Group plc, London, UK

Cunge, J.A., Holly, F.M. & Verwey, A. 1980. *Practical Aspects of Computational River Hydraulics*. London: Pitman Publishing Limited.

Danish Hydraulic Institute 2002. *Mike 11 Reference manual*. Hørsholm: DHI.

Hirsch, C. 1988–1990. *Numerical Computation of Internal and External Flows*. Chichester: Wiley & Sons.

LeVeque, R.J. 2002. *Finite Volume Methods for Hyperbolic Problems*. Cambridge: Cambridge University Press.

Maione, U., Mignosa, P. & Tomirotti, M. 2000. Synthetic design hydrographs for river flood management. In Toensmann F., Koch M. (eds.), *Proceedings of the International Symposium on River Flood Defence*, *Kassel, 20–23 September 2000*. Kassel: Herkules Verlag.

Maione, U., Mignosa, P. & Tomirotti, M. 2003. Regional estimation of synthetic design hydrographs. *International Journal of River Basin Management* 1(2): 1–13.

Maranzoni, A. 2004. *Modellazione numerica e fisica di moti bidimensionali a pelo libero*. PhD Thesis: Parma University (in italian).

Toro, E.F. 2001. *Shock-Capturing Methods for Free Surface Shallow Flows*. Chichester: Wiley & Sons.

Vázquez-Cendón, M.E. 1999. Improved treatment of source terms in upwind schemes for the shallow water equations in channels with irregular geometry. *Journal of Computational Physics* 148: 497–526.

Zhou, J.G., Causon, D.M., Mingham, C.G. & Ingram, D.M. 2001. The surface gradient method for the treatment of source terms in the shallow water equations. *Journal of Computational Physics* 168: 1–25.

Zhou, J.G., Causon, D.M., Ingram, D.M. & Mingham, C.G. 2002. Numerical solution of the shallow water equations with discontinuous topography. *International Journal for Numerical Methods in Fluids* 38: 769–788.

Copyright © 2006 Taylor & Francis Group plc, London, UK

Two-dimensional dam-break simulation over movable beds with an unstructured mesh

José A. Vásquez
Northwest Hydraulic Consultants, North Vancouver, Canada

João G.A.B. Leal
University of Beira Interior, Covilha, Portugal

ABSTRACT: This paper reports the application of a two-dimensional (2D) depth-averaged model to dam break flows over alluvial sand beds with an initial bed step. The model applies the Finite Element Method to discretize the computational domain using an unstructured mesh made of triangular elements. Two downstream boundary conditions were tested: zero (dry) and non-zero (wet) initial water depths. The model successfully reproduced the two types of transient waves observed in the experiments: the hydraulic jump produced with wet downstream condition and the surge moving over an initially dry bed. Since the present sediment transport model applied a single layer for sediment transport, comparison and discussion with results of a previous one-dimensional (1D) two-layer model are also provided.

1 INTRODUCTION

1.1 *Dam-breaks and movable beds*

Dam-break flows can lead to highly unsteady flows with fast-moving wave fronts. Traditionally, dam-break phenomenon has been studied under fixed-bed conditions. However, movable beds can affect the celerity of flood waves propagating in rivers after a dam-break. Even more, the wave celerity is influenced by the sediment mobility (Capart & Young 1998, Leal et al. 2002, Fraccarollo & Capart 2002, Cao et al. 2004, Leal et al. 2006). Therefore, dam-break analysis on rivers requires the inclusion of the effects of alluvial bed on the flow hydraulics.

Dams represent an obstacle to the normal sediment transport in a river, inducing sediment deposition upstream from the dam, as well as bed erosion downstream. For an existing dam in an alluvial river, a bed elevation difference will develop between the riverbed elevations upstream and downstream from the dam. During a real dam-break event, it is very likely that a movable bed step will exist at the location of the dam that will impact how the flood wave propagates downstream.

Leal et al. (2002) conducted experimental dam-break research that incorporated the effects of both sediment mobility and bed steps on wave propagation. These experiments provide high-quality data under more realistic conditions than simpler experiments conducted on flat fixed-beds. Leal et al. (2003a,b) successfully simulated these experimental observations using a one-dimensional (1D) numerical model.

In this paper, the two-dimensional (2D) numerical model developed by Vasquez (2005a) is applied to simulate two of the experimental tests of Leal et al. (2002) of dam-breaks over sand beds with an initial bed step. One distinctive feature of the model is the application of an unstructured (irregular) mesh made of triangular Finite Elements. The main objective of the present work is to verify the applicability of such model to dam-break flows over movable beds. Additionally, some qualitative tests of bed changes in a varying width flume, and a dam-break in a sharp 90° bend over a fixed bed, are presented to show the 2D capabilities of the model.

1.2 *Background information*

Vasquez (2005a) developed a 2D river morphology model by extending the existing fixed-bed hydrodynamic model River2D (Steffler & Blackburn 2002). This new movable-bed version is referred as River2D-MORphology. River2D-MOR has been successfully applied to reproduce experiments of bed aggradation and degradation in straight flumes (Vasquez et al. 2005a, Vasquez et al. 2006a), scour and deposition in laboratory bends (Vasquez et al. 2005b) and meandering rivers (Vasquez et al. 2006b), as well as knickpoint migration under transcritical flow conditions (Vasquez et al. 2005c). Preliminary qualitative tests (Vasquez

Copyright © 2006 Taylor & Francis Group plc, London, UK

2005a) suggested that River2D-MOR could be applied to dyke-breach and dam-break analysis. However, until now, it has not been tested quantitatively to verify if the model is indeed suitable for dam-breaks over movable beds.

The main features of River2D-MOR at the moment are (Vasquez 2005a):

- unstructured Finite Element (FE) mesh;
- simulates bedload sediment transport;
- free or forced upstream sediment inflow;
- transcritical flow capabilities;
- secondary flow correction for flow in bends;
- incorporates the effects of transverse bed slope on bedload direction.

Unstructured meshes have the advantage of being more flexible that structured (regular) meshes. Triangular elements allow to easily accommodate practically any planform river geometry with elements that can dramatically change in size to obtained higher resolution around areas of interest. For example, structured meshes based on quadrilateral elements can be problematic in certain channel geometries with sharp angles (Heer & Mosselman 2004), for which triangular elements are perfectly suitable (Vasquez 2005b). River2D-MOR is a decoupled model, that is, sediment equations are solved after the flow equations.

The remaining of the paper is organized as follows. In section 2, information of the hydrodynamic model is briefly introduced; later a qualitative application to dam-break in a channel with a sharp bend is shown to demonstrate the 2D capabilities of the model. In section 3, the bedload model is introduced along with an example application to an alluvial channel with a continuously changing width. In section 4, a description of the experimental tests of dam-break over movable beds is provided. The results of the model are presented in section 5. The discussion of the paper are presented in Section 6. Finally, summary and conclusions are presented in Section 7.

2 HYDRODYNAMIC MODEL

2.1 *River2D*

River2D is a fixed-bed hydrodynamic model that has been developed at the University of Alberta in Canada (it is freely available at www.River2D.ca). River2D is based on the 2D depth-averaged Saint-Venant equations expressed in conservative form; which form a system of three equations representing the conservation of water mass and the two components of the momentum vector. The model is intended for use on natural streams and rivers and has special features for supercritical/subcritical flow transitions, ice covers, and variable wetted area. River2D handles dry beds by changing the surface flow equations to groundwater flow equations in areas where the water depth drops below a minimum value. A continuous free surface with positive (above ground) and negative (below ground) depths is calculated. This procedure allows calculations to carry on without changing or updating the boundary conditions (Steffler and Blackburn 2002).

For the spatial discretization River2D uses a flexible FE unstructured mesh composed of triangular elements. The Finite Element Method used by River2D is based on the Streamline Upwind Petrov-Galerkin (SUPG) weighted residual formulation (numerical details of the model are shown in Ghanem et al. 1995). In this technique, upstream biased test functions are used to ensure solution stability under the full range of flow conditions, including subcritical, supercritical, and transcritical flow. A fully conservative discretization is implemented which ensures that no fluid mass is lost or gained over the modeled domain. This also allows implementation of boundary conditions as natural flow or forced conditions.

The equations solved by the River2D are (Steffler and Blackburn 2002):

The water continuity equation:

$$\frac{\partial h}{\partial t}+\frac{\partial q_x}{\partial x}+\frac{\partial q_y}{\partial y}=0 \tag{1}$$

The vertically averaged momentum equation in the x-direction:

$$\frac{\partial q_x}{\partial t}+\frac{\partial (uq_x)}{\partial x}+\frac{\partial (vq_x)}{\partial y}+\frac{g}{2}\frac{\partial h^2}{\partial x}= gh\left(S_{ox}-S_{fx}\right)+\frac{1}{\rho}\left(\frac{\partial (h\tau_{xx})}{\partial x}+\frac{\partial (h\tau_{xy})}{\partial y}\right) \tag{2}$$

The vertically averaged momentum equation in the y-direction:

$$\frac{\partial q_y}{\partial t}+\frac{\partial (uq_y)}{\partial x}+\frac{\partial (vq_y)}{\partial y}+\frac{g}{2}\frac{\partial h^2}{\partial y}= gh\left(S_{oy}-S_{fy}\right)+\frac{1}{\rho}\left(\frac{\partial (h\tau_{yx})}{\partial x}+\frac{\partial (h\tau_{yy})}{\partial y}\right) \tag{3}$$

where t = time, h = water depth; (u, v) = depth-averaged velocities in the (x, y) directions; $q_x = uh$ = flow discharge in x-direction per unit width; $q_y = vh$ = flow discharge in the y-direction per unit width; (S_{ox}, S_{oy}) = bed slopes in the (x, y) directions; S_{fx} and S_{fy} = corresponding friction slopes; τ_{xx}, τ_{xy}, τ_{yx}, τ_{yy} = components of the horizontal turbulent stress tensor; ρ = water density; and g = gravitation acceleration.

Copyright © 2006 Taylor & Francis Group plc, London, UK

The basic assumptions in equations (1) through (3) are (Steffler and Blackburn 2002):

- The pressure distribution is hydrostatic, which limits the accuracy in areas of steep slopes and rapid changes in bed slopes.
- The horizontal velocities are constant over the depth. Information on secondary flows and circulations is not available.
- Coriolis and wind forces are assumed negligible.

The friction slope terms depend on the bed shear stresses which are assumed to depend on the magnitude and direction of the vertically averaged velocities. For example, in the x direction:

$$S_{fx} = \frac{\tau_{bx}}{\rho g h} = \frac{\sqrt{u^2 + v^2}}{g h C_*^2} u \tag{4}$$

τ_{bx} is the bed shear stress in the x direction and C_* is the dimensionless Chezy coefficient, which is related to the effective roughness height k_s through

$$C_* = 5.75 \log\left(12 \frac{h}{k_s}\right) \quad ; \frac{h}{k_s} \geq \frac{e^2}{12} \tag{5a}$$

$$C_* = 2.5 + \frac{30}{e^2}\left(\frac{h}{k_s}\right) \quad ; \frac{h}{k_s} < \frac{e^2}{12} \tag{5b}$$

$e = 2.7182$; C_* is related to Chezy's C coefficient through

$$C_* = \frac{C}{\sqrt{g}} \tag{6}$$

The depth-averaged turbulent shear stresses are modeled with a Boussinesq type eddy viscosity. For example:

$$\tau_{xy} = \upsilon_t \left(\frac{\partial u}{\partial y} + \frac{\partial v}{\partial x}\right) \tag{7}$$

where υ_t = eddy viscosity coefficient, which is assumed as composed of three components: a constant, a bed shear generated term, and a transverse shear generated term

$$\upsilon_t = \varepsilon_1 + \varepsilon_2 \frac{h\sqrt{u^2 + v^2}}{C_*} + \ldots$$
$$\varepsilon_3^2 h^2 \sqrt{2\frac{\partial u}{\partial x} + \left(\frac{\partial u}{\partial y} + \frac{\partial v}{\partial x}\right)^2 + 2\frac{\partial v}{\partial y}} \tag{8}$$

The default value for ε_1 is 0. This coefficient can used to stabilize the solution for very shallow flows when the second term in equation (8) may not to adequately describe υ_t for the flow. Reasonable values for ε_1 can be calculated by evaluating the second term in equation (8) using average flow conditions (average flow depth and average velocities) for the modeled site. The default value for ε_2 is 0.5. By analogy with transverse dispersion coefficients in rivers, values of 0.2 to 1.0 are reasonable. Since most river turbulence is generated by bed shear, this term is usually the most important. In deeper lake flows, or flows with high transverse velocity outlets gradients, transverse shear may be the dominant turbulence generation mechanism. Strong recirculation regions are important examples. In these cases, the third term, ε_3, becomes important. It is essentially a 2D (horizontal) mixing length model. The mixing length is assumed to be proportional to the depth of flow. A typical value for ε_1 is 0.1, but this may be adjusted by calibration.

In the present application, assuming that turbulence is bed-generated, the default values of the model $\varepsilon_1 = 0$, $\varepsilon_2 = 0.5$ and $\varepsilon_3 = 0$ were adopted. A qualitative application to a dam-break test case is shown below for illustration purposes.

2.2 *Dam-break in channel with 90° bend*

Soares Frazão et al. (2001) and Soares Frazão & Zech. (2002) performed experiments of dam-break through a sharp 90° bend, which consisted of a 2.44 m by 2.39 m upstream reservoir connected to a 0.495 m wide rectangular channel. The upstream channel reach is about 4 m long while the downstream reach, after the bend, is about 3 m long. The downstream end of the channel is open. The sudden raise of the gate between the upstream reservoir and the channel is used to simulate the dam break.

After dam-break, water flows rapidly into the channel and reflects against the bend wall, where a bore forms that travels back in the upstream direction towards the reservoir. Using a 2D Finite Volume model, Aureli et al. (2004) have recently simulated one of the experiments with an initial water level in the reservoir of 0.20 m above the initially dry channel bed. To simulate the free fall at the downstream end an artificial high slope slide was introduced in the numerical model. The same experiment was used for the present qualitative application.

In River2D a constant roughness $k_s = 5$ mm was set throughout the model. Although it is possible to use a downstream boundary condition similar to that used by Aureli et al. (2004), given the illustrative purposes of this test a simple downstream boundary condition with zero depth was assumed. Therefore, the results presented are only qualitative.

Figure 1 shows snapshots of the computed water surface at different times. At $t = 7$ s the reflection in the bend wall becomes evident. Figure 2 shows the

Copyright © 2006 Taylor & Francis Group plc, London, UK

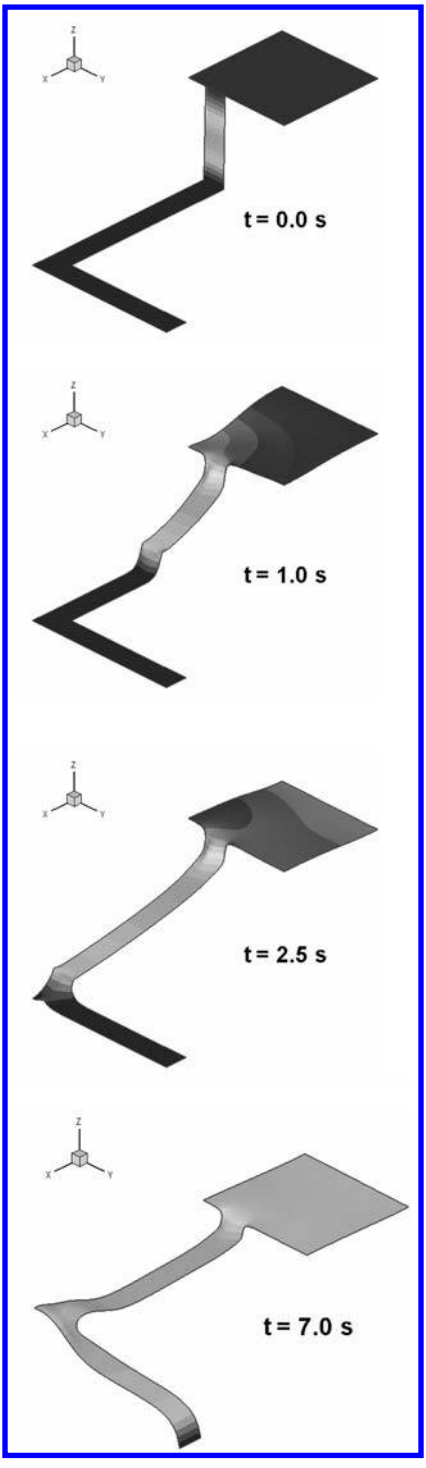


Figure 1. Computed water surfaces for a dam-break in a channel with a 90° sharp bend.

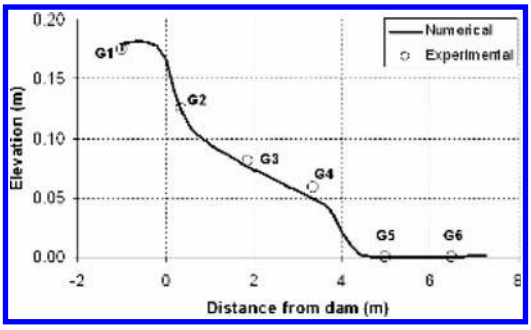


Figure 2. Experimental and numerical results at 2.5 s for dam break through a 90° bend.

comparison between the computed profile and the levels recorded at 6 gauges. Gauge G1 is located at the center of the reservoir, while gauges G2 through G6 at located along the centerline of the channel.

Figure 2 shows that the model produces reasonable results at the beginning of the simulation when the effects of the downstream end are still not important. However, the accuracy of the results deteriorates as time progresses because of the constant downstream water level enforced by the model.

3 BEDLOAD MODEL

River2D was extended by Vasquez (2005a) to incorporate a solver for the bed load sediment continuity (Exner) equation

$$(1-\lambda)\frac{\partial z_b}{\partial t}+\frac{\partial q_{sx}}{\partial x}+\frac{\partial q_{sy}}{\partial y}=0 \tag{9}$$

where z_b = bed elevation; λ = porosity of the bed material (with a default value of 0.4); and (q_{sx}, q_{sy}) = components of the volumetric rate of bedload transport per unit width q_s that depend on the direction α of sediment transport:

$$q_{sx}=q_s\cos\alpha \tag{10a}$$

$$q_{sx}=q_s\sin\alpha \tag{10b}$$

In a straight flume, where the direction of bedload and mean flow coincide, the direction of bedload in equation (10) is simply tan $\alpha = (v/u)$. However, in curved channels the secondary flow produces a deviation between the depth-averaged flow direction and the direction δ of the bed shear stress

$$\delta=\arctan\left(\frac{v}{u}\right)-\arctan\left(A\frac{h}{r_c}\right) \tag{11}$$

The term -arctan(Ah/r_c) is the deviation of the bed shear stress relative to the streamlines, caused by the

Copyright © 2006 Taylor & Francis Group plc, London, UK

secondary flow. A is a parameter of order 10 and r_c is the curvature of the streamlines computed from the flow field as

$$r_c = \frac{(u^2+v^2)^{3/2}}{-uv\frac{\partial u}{\partial x} - v^2\frac{\partial u}{\partial y} + u^2\frac{\partial v}{\partial x} + uv\frac{\partial v}{\partial y}} \quad (12)$$

The direction of bedload is computed taking into account the effects of the bed slopes $\partial z_b/\partial x$ and $\partial z_b/\partial y$ along the x and y coordinates respectively

$$\tan\alpha = \frac{\sin\delta - \frac{1}{f_s\tau^*}\frac{\partial z_b}{\partial y}}{\cos\delta - \frac{1}{f_s\tau^*}\frac{\partial z_b}{\partial x}} \quad (13)$$

τ^* is the dimensionless shear stress or Shield's parameter and f_s is a shape factor of order 1. The applicability of the secondary flow model (equations 11 through 13) has been demonstrated for both curved flumes (Vasquez et al. 2005b) and meandering rivers (Vasquez et al. 2006b).

Equation (9) is discretized using a conventional Galerkin Finite Element Method (GFEM). The time advance is performed using a Runge-Kutta second order scheme. Since GFEM lacks upwinding properties (equivalent to a central difference scheme) it is known to be adequate for diffusive problems, but not for advection-dominated problems (Donea & Huerta 2003, Vasquez 2005a). The model should not be applied to problems where advection is important, such as migrating bedforms or sediment waves. An illustrative application showing the formation of forced bars in a sand-bed channel is presented below.

3.1 *Application to varying width flume*

Tsujimoto (1987) reported experiments of bed level changes in an initially flat alluvial channel with continuous expansions and contractions, produced by changing the channel width $B(x)$ according to a sinusoidal function

$$B(x) = B_o - B_1\sin(2\pi x/L) \quad (14)$$

The only experimental data provided by Tsujimoto (1987) are related to channel plan geometry: $B_o = 0.19$ m, $B_1 = 0.04$ m and $L = 0.40$ m. No more details of the experiment are given such as sediment size, inflow, downstream water level, bed slope, roughness or sediment transport rate, preventing a quantitative comparison with any particular experiment. The measured bed profiles showed very rich bed variability. The transverse concavity of the bed profiles switches from downward across the narrowest section to upward across the widest section. Across the narrow section a central bar develops, while across the wide section two lateral bars are present near the walls. In contrast with free alternate bars in straight channels, which migrate in the downstream direction, the bars formed in the channel with varying width remain fixed in position, similar to the point bars formed in alluvial bends.

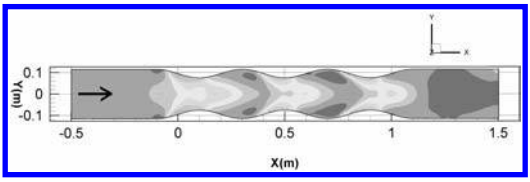


Figure 3. Plan view of computed bed changes in a channel with sinusoidal varying width.

For the numerical simulation, the following values were adopted: discharge 0.0056 m^3/s, depth 0.07 m, bed slope 0.001, roughness $k_s = 0.0014$ m, $A = 2$ and $f_s = 2$. The computational mesh was made of nodes spaced roughly 1 cm apart. Sediment transport was computed using the Engelund-Hansen equation for a 1 mm sand grain. Figure 3 shows the plan view of the computed results after 1000 s using a time step of 1 s. The model correctly predicts the concavity of the bed and the formation of bars. Figure 4 shows the pattern of lateral and central bars computed by the model which agrees, at least qualitatively, with the experimental results.

4 DAM-BREAK OVER MOVABLE BED

Leal et al. (2002) performed dam-break experiments in a rectangular horizontal flume 19.2 m long, 0.5 m wide and 0.7 m high. The dam was simulated by a vertical PVC lift-gate installed at the middle of the flume, which had an opening time between 0.1 and 0.2 s. The wave-front normally took less than 6 s to reach the downstream end of the flume. Three groups of tests were carried out depending on the bed type: fixed-bed, sand-bed and pumice-bed.

Two of the tests performed with an initial bed step of $h_{su} = 0.19$ m over a sand-bed were selected for the numerical simulation. The tests are Ts.25 and Ts.28, their initial conditions are shown in Figure 5 and Table 1. The initial conditions downstream from the dam varied between tests. The bed was dry for Ts.25 ($h_d = 0.0$ m) and wet for test Ts.28 ($h_d = 0.075$ m). The sand had a median grain size $D_{50} = 1.22$ mm, specific gravity $G_s = 2.65$ and settling velocity $w = 9.92$ cm/s.

Leal et al. (2003a) applied the Bagnold sediment transport equation, which can be expressed as a function of the depth-averaged velocity $U = (u^2+v^2)^{1/2}$ as

$$q_s = \frac{\xi\tau_b U}{\rho g(G_s - 1)} \quad (15)$$

Copyright © 2006 Taylor & Francis Group plc, London, UK

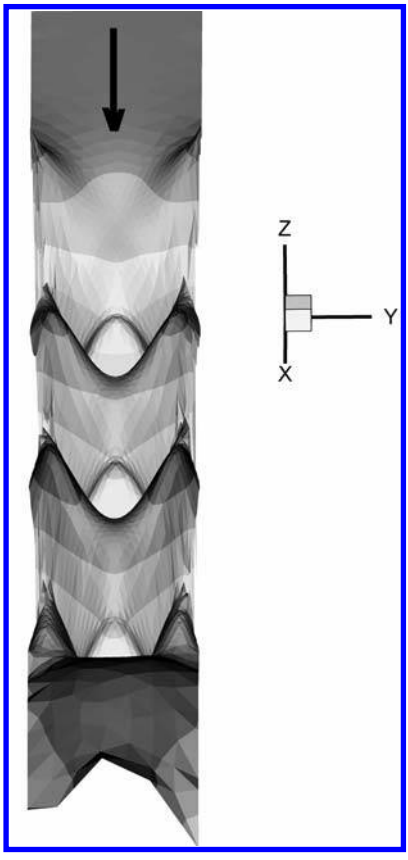


Figure 4. 3D view of computed bed changes in a channel with sinusoidal varying width.

Table 1. Initial conditions of experimental tests.

Test	h_u (m)	h_d (m)	h_{su} (m)	h_{sd} (m)
Ts.25	0.400	0.000	0.190	0.071
Ts.28	0.400	0.075	0.190	0.071

Where ξ is sediment parameter that depends on the sediment transport modes and settling velocity of the sediment and has a value $\xi \approx 0.57$ for the sand used in the experiments. Based on assumptions of sheet (debris) flow and bedload transport under high shear stress, Leal et al. (2003a) transformed (15) into

$$q_s = \frac{8.03\xi\sqrt{g}/C}{(G_s - 1)(C^2 - \xi U^2/h)} U^3 \qquad (16)$$

With a value $C = 31.3\,\mathrm{m}^{1/2}\mathrm{s}$ for the sand-bed experiments.

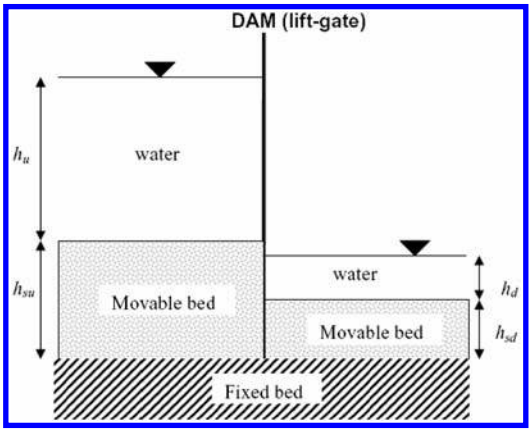


Figure 5. Initial conditions of Leal et al. (2002) experiments of dam-break over movable beds.

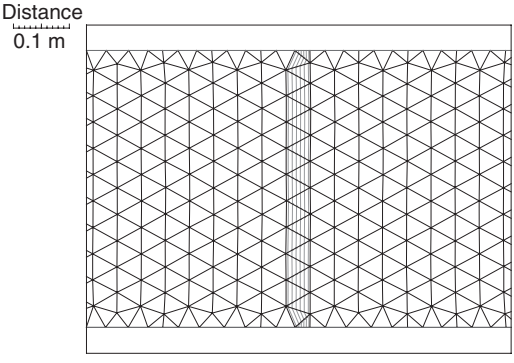


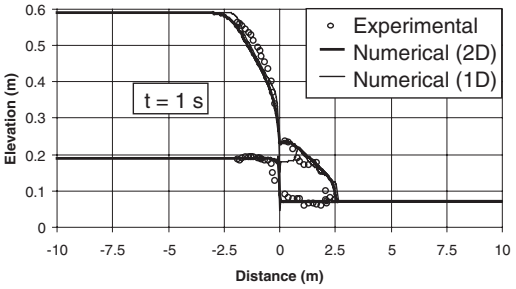
Figure 6. Detail of unstructured mesh near the dam location (dashed lines are bed contours of inclined ramp).

5 RESULTS

Since the vertical bed step at the dam location cannot be reproduced in the model, it was replaced by a steep inclined ramp spanning over a single element. In order to reduce the size of the ramp, the node spacing in the mesh was set to about 5 cm. The computational mesh had roughly 12 nodes in the transverse direction and about 500 nodes in the longitudinal direction, as shown in Figure 6, giving a total of 6076 nodes and 10935 triangular elements. Figure 6 also shows the contour lines of the inclined ramp.

The roughness height adopted was $k_s = 0.0164\,\mathrm{m}$, which gives a Chezy roughness $C = 31.3\,\mathrm{m}^{1/2}\mathrm{s}$ for a water depth $h = 0.075\,\mathrm{m}$. The upstream boundary was set as a no-flow boundary; while the downstream boundary was set to a fixed water level, which changed according to the test simulated. For test Ts.25, the downstream water level was set equal to

Copyright © 2006 Taylor & Francis Group plc, London, UK



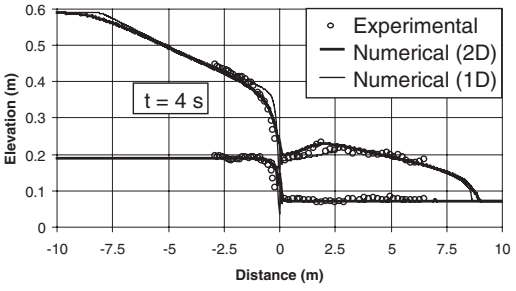
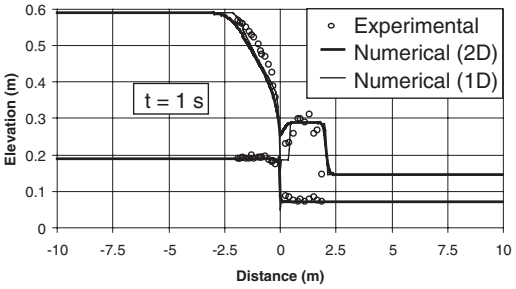


Figure 7. Experimental and numerical results for dam-break experiment Ts.25 at 1and 4 seconds.



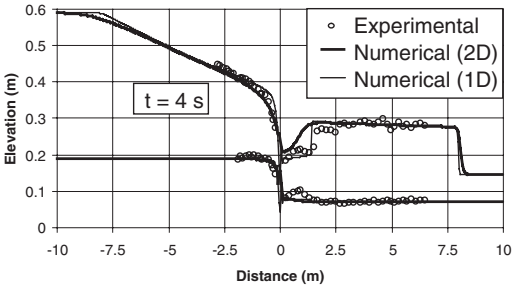


Figure 8. Experimental and numerical results for dam-break experiment Ts.28 at 1and 4 seconds.

the bed elevation, $h_{sd} = 0.071$ m, meaning that all the reach downstream from the dam was initially dry, $h_d = 0.0$ m. For test Ts.28, the downstream water level was set at elevation $h_d + h_{sd} = 0.146$ m. In both cases, the initial water level upstream from the dam was set to elevation $h_u + h_{su} = 0.590$ m.

Similar to the initial bed profile, the initial horizontal water levels upstream and downstream from the dam were connected by an inclined water "ramp" over a single element, to represent the condition immediately after the dam break.

Figure 7 shows the results for test Ts.25, with an initially dry downstream boundary; while Figure 8 shows the results for test Ts.28, with an initial wet downstream boundary. The results for both tests are shown for 1 and 4 seconds after the dam-break. In both Figures are also presented the results of the two-layer 1D model of Leal et al. (2003a).

By looking at the computed water levels upstream from the dam, for both tests the 2D model and the 1D model tend to underpredict the observed levels at 1 s. However, at 4 s, the agreement between the observed and computed water levels upstream from the dam is quite good.

For test Ts.25 (Fig. 7) both models underpredict the bed levels, while the agreement is better for test Ts.28 (Fig. 8). This is in accordance with what was expected, since for the higher initial downstream depth (Ts.28) the sediment transport is less important and the bed changes will be smaller.

6 DISCUSSION

In general, the agreement between measured and computed results is good. Just like the 1D model, the 2D model is able to capture the effects of the downstream water level on the wave fronts, with a weaker hydraulic jump when the bed is initially dry in test Ts.25. At 4 s, the upstream water levels agree very well with the observed data; although at 1 s the agreement is not as good. Probable reasons for the lower prediction accuracy at 1 s could be the assumed initial water profile (not perfectly vertical) and the non-hydrostatic pressure distribution. At the beginning of the experiment, immediately after the dam-break, the water contained upstream rushes down very quickly. The vertical acceleration of the flow is not negligible as assumed in the shallow water equations solved by the depth-averaged model. However, as time progresses, these initial effects tend to vanish (cf. Fraccarollo & Capart 2002) leading to a better agreement with data.

According to Fraccarollo & Capart (2002), the time required for the flow to equilibrate its sediment load is estimated as $20(h_u/g)^{0.5}$. For the experiments presented, this renders a time equal to 4 s. Therefore, for times equal or higher than that value the equilibrium approach assumed in both models is valid and the results show better agreement ($t = 4$ s in Figures 7 and 8).

The 1D model of Leal et al. (2003a,b), when applied to test Ts.25 and Ts.28 generated water surface

Copyright © 2006 Taylor & Francis Group plc, London, UK

profiles with very sharp fronts (wave-front and hydraulic jump), almost square in shape. In contrast, the profiles computed by River2D are smoother with more rounded corners. The 1D model uses a 2nd order MacCormack-TVD scheme that can reproduce better sharp discontinuities.

The discrepancies between the 1D and the 2D numerical results are more pronounced near the dam cross-section. In that section, at 1 s the 1D model imposes small water depths flow due to the initial bed-step, while the 2D model gives higher water depths. Nevertheless, the agreement is still good.

Mention should be made to the fact that the node spacing in both models is equal to 5 cm, therefore the resolution can not explain the differences mentioned before.

The computed bed elevation shows good agreement with the measured data, although some oscillations are visible in the solution, especially on the 1D model. The 2nd order 1D model creates oscillations around discontinuities. The TVD correction minimizes these oscillations. Due to mathematical complexity that correction was not applied to the sediment mass conservation equation, allowing the presence of oscillations in the bed profile. In the 2D model, the oscillations might be the result of applying the conventional Galerkin formulation to solve the sediment continuity equation, which is not suitable for highly convective problems (Donea & Huerta 2003, Katapodes 1984, Vasquez 2005a). Vasquez (2005a) has shown that when migrating bed forms are present in the solution (e.g. free alternate bars, prograding deltas), the bedload model produces spurious oscillations due to its lack of numerical upwinding. The Petrov-Galerkin scheme, which is used by the hydrodynamic model, seems as a good candidate for incorporating upwinding in future versions of the bedload model.

Although the 2D model solves a conventional sediment continuity equation with only one layer of sediment transport, the results are not significantly different to those obtained by the 1D model of Leal et al. (2003a) with a more complex two-layer model. It seems that for the present dam-break application, with relatively heavy bed material ($G_s = 2.65$), the effects of debris flow (sheet flow) are not strong enough to prevent the application of a 1-layer model. A comparative study between 1- and 2-layer models is desirable to gain a better understanding of the real limitations of each approach for dam-break analyses.

7 SUMMARY AND CONCLUSIONS

A 2D river morphology model, originally intended for alluvial meandering rivers, has been tested for dam-break flows over movable sand-beds. The model uses the Finite Element method and unstructured (irregular) meshes made of triangular elements. The model was tested using two experiments with an initial bed step at the dam location, with both dry and wet downstream boundary conditions. The model results were also compared with the results of the 1D model by Leal et al. (2003a). The results show that the 2D model was able to reproduce the observed water levels and the influence of the boundary condition on the wave fronts with reasonable accuracy. Given the other capabilities of the model to simulate bed changes in straight and curved alluvial channels, it seems as a promising tool for practical dam break analysis. However, the model still needs improvements to provide numerical upwinding in the sediment solver for cases of highly convective sediment waves.

REFERENCES

Aureli, F., Maranzoni, A. & Mignosa, P. 2004. Two dimensional modeling of rapidly varying flows by finite volume schemes. In Greco, Carravetta & Bella Morte (ed.) *River Flow 2004*: 837-847. London: Taylor & Francis Group.

Cao, Z., Pender, G., Wallis, S, & Carling, P. 2004. Computational Dam-break hydraulics over erodible sediment bed. *Journal of Hydraulic Engineering* 130(7): 689–703.

Capart H. & Young D.L. 1998. Formation of a jump by the dam-break wave over a granular bed. *Journal of Fluid Mechanics* 372: 165–187.

Donea, J. & Huerta, A. 2003. *Finite Element Methods for Flow Problems.* London: John Wiley & Sons.

Fraccarollo, L. & Capart, H. 2002. Riemann wave description of erosional dam-break flows. *Journal of Fluid Mechanics* 461: 183–228.

Ghanem, A., Steffler, P., Hicks, F. & Katapodis, C. 1995. *Two-dimensional modeling of flow in aquatic habitats.* Water Resources Eng. Report No. 95-S1. University of Alberta.

Heer, A. & Mosselman, E. 2004. Flow structure and bed-load distribution at alluvial diversions. In Carravetta & Della Morte (eds) *River Flow 2004* (2): 801–806. London: Taylor & Francis Group.

Leal, J.G.A.B., Ferreira, R.M.L, Franco, A.B. & Cardoso, A.H. 2002. Dam-break waves on movable beds. In Bousmar & Zech (ed.) *River Flow 2002* (2): 981–990. Rotterdam: Balkema.

Leal, J.G.A.B., Ferreira, R.M.L. & Cardoso, A.H. 2003a. Dam-break waves propagation over a cohesionless erodible bed. *Proc. XXX IAHR Cong.,* Theme C(2): 261–268. Thessaloniki, Greece.

Leal, J.G.A.B., Ferreira, R.M.L., Cardoso, A.H. & Almeida, A.B. 2003b. Comparison between experiments and numerical results on dam-beak waves over dry mobile beds. Proceedings of the 3th IMPACT Workshop, Louvain-la-Neuve, Belgium, http://www.samui.co.uk/impact-project/cd3/de-fault.htm.

Leal, J.G.A.B., Ferreira, R.M.L. & Cardoso, A.H. 2006. Dam-break wave front celerity. *Journal of Hydraulic Engineering* 132(1): 69–76.

Katapodes, N.D. 1984. A dissipative Galerkin scheme for open channel flow. *Journal of Hydraulic Engineering* 110(4): 450–466.

Soares Frazão, S., Spinewine, B. & Zech, Y. 2001. Digital-imaging velocity measurements and numerical modeling

Copyright © 2006 Taylor & Francis Group plc, London, UK

of a dam-break flow through a 90° bend. *Proc. Of XXIX IAHR Congress, Beijing, 16–21 September 2001*. Beijing: Tsinghua University Press.

Soares Frazão, S. & Zech, Y. 2002. Dam-break in channels with 90° bend. *Journal of Hydraulic Engineering* 128(11): 956–968.

Steffler, P.M. & Blackburn, J. 2002. *River2D: Two-dimensional depth averaged model of river hydrodynamics and fish habitat. Introduction to depth averaged modeling and user's manual.* Edmonton: University of Alberta.

Tsujimoto, T. 1987. Non-uniform bed load transport and equilibrium bed profile. *XXII IAHR Congress, Fluvial Hydraulics* (1): 177–182, Lausanne, Switzerland.

Vasquez, J.A. 2005a. Two-dimensional finite element river morphology model. PhD Thesis. University of British Columbia, Vancouver, Canada.

Vasquez, J.A. 2005b. Two-dimensional simulation of flow diversions. *17th Canadian Hydrotechnical Conference, Edmonton, 17–19 August 2005*.

Vasquez, J.A., Millar, R.G. & Steffler, P.M. 2005a. River2D Morphology, Part I: Straight Alluvial Channels. *17th Canadian Hydrotechnical Conference, Edmonton, 17–19 August 2005*.

Vasquez, J.A., Steffler, P.M. & Millar, R.G. 2005b. River2D Morphology, Part II: Curved Alluvial Channels. *17th Canadian Hydrotechnical Conference, Edmonton, 17–19 August 2005*.

Vasquez, J.A., Millar, R.G. & Steffler, P.M. 2005c. Two-dimensional morphological simulation in transcritical flow. In M. Garcia & G. Parker (eds) *4th IAHR Symposium on River, Coastal and Estuarine Morphodynamics*, *Urbana, 4–7 October 2005*. London: Taylor & Francis Group.

Vasquez, J.A., Millar, R.G & Steffler, P.M 2006a. Two-dimensional Finite Element River Morphology Model. *Canadian Journal of Civil Engineering*. Submitted.

Vasquez, J.A., Steffler, P.M & Millar, R.G 2006b. Two-dimensional Morphodynamic Model for Meandering Rivers based on Triangular Finite Elements. *Journal of Hydraulic Engineering*. Submitted.

Copyright © 2006 Taylor & Francis Group plc, London, UK

Numerical simulation of 2D dam break on mobile bed

M. Greco
DIIA "G. Ippolito", University of Napoli "Federico II", Napoli, Italy

M. Iervolino
DIC, Second University of Napoli, Via Roma, Aversa (CE), Italy

A. Leopardi
DiMSAT, University of Cassino, Via Di Biasio, Cassino (FR), Italy

ABSTRACT: A relevant example of unsteady processes with strong interaction between hydrodynamics and solid transport, the propagation of dam-break waves over a mobile bed has been the subject of several recent research works. It has thus gained the role of a benchmark for solid transport models. From a physical point of view, the features of the process lead to the rejection of the hypothesis of immediate adaptation of solid transport to hydrodynamics. From the numerical standpoint, the tracking of water and bed wave fronts requires adequate numerical schemes. In the last few years, extensive work has dealt with the idealized scheme of one dimensional dam break over loose bed. More recently, existing models have been applied to study also the asymmetric wave propagation over the floodplain. In previous works the authors have adopted an original two phase non-equilibrium model to simulate one dimensional dam break over mobile bed. Here the model is extended to a two dimensional depth-averaged framework and then applied to simulate a dam break wave propagation over an alluvial floodplain.

1 INTRODUCTION

Risk protection and public safety have been motivating research about dam failure for a very long time. Among the extremely rich variety of applications, the study of the flow induced by the abrupt failure of a rigid dam has played a major role in the field of hydraulics.

Since the seminal papers by Ritter (1892), Stoker (1948) and Dressler (1952), intense work has been done to bridge the gap between the extremely idealized scheme considered by theoretical analysis and real-scale processes.

From this standpoint, one of the most recent improvements was the inclusion into the analysis of the effect of morphological evolution of the floodplain downstream the dam. In fact, apart from being itself an immediate source of hazard, the dam-break wave may also determine intense erosion of floodplain, which – in turn – substantially modifies the flood propagation.

During dam break wave propagation, entrainment, transport and deposition of solid material occur in a way which can be difficulty represented within the classical framework of alluvial flows (e.g. Graf & Altinakar, 1998).

Applied research about dam break wave propagation over loose bed floodplain is rather recent. Both experimental and theoretical analysis of the process have been started less than one decade ago.

A relevant contribution to the understanding of the process has come from the recent IMPACT EU-funded research project: several research groups from all over the Europe had the opportunity to benchmark their models against well assessed experiments, performed in the most accurate conditions ever adopted.

If we except the qualitative observations of Chen & Simons (1979), the first systematic experiments of dam-break wave on an mobile bed were conduced by Capart & Young (1998) and Ferreira & Leal (1998), both referring to the idealized case of horizontal saturated bed with no water height downstream. The same experimental scheme was further investigated by Spinewine & Zech (2002) and Leal et al. (2003).

Copyright © 2006 Taylor & Francis Group plc, London, UK

By the whole, experiments by the aforementioned authors cover a wide range of sediment properties, from synthetic pebbles slightly heavier than water up to common sand.

Within the IMPACT project (Zech et al., 2005), an additional experimental configuration has been investigated: a one-dimensional dam break with initial bed discontinuity (Spinewine, 2005). The same author also reports some results of experiments about dam break in a channel with sudden expansion.

The complexity of the two-phase flow has gathered an impressive number of theoretical contribution, but still the topic is non completely clarified.

One of the main difficulties involved in the process is the strong coupling between liquid and solid phase during the whole duration. The analysis developed by Fraccarollo & Capart (2002) points out that evolution of liquid and granular flow may – at least in a certain time range of the process – follow comparable timescales. More in detail, the authors recognize the existence of three relevant timescales: the first needed for gravity wave to resemble shallow water condition (i.e.: quasi-hydrostatic pressure), the second for bedload to equilibrate the transport capacity, finally the third for the flow to exhibit diffusive rather than inertial character due to frictional momentum losses. Depending on the relative values of the three timescales, an adequate flow model has to be adopted in order to describe the process both from hydraulics and geomorphic point of view.

This complex behavior motivates the special features of the mathematical models which have been applied to simulate dam break flows over mobile bed.

Among the researchers involved into the IMPACT Project, El Kadi et al. (2003, 2004) used a standard morphological model based upon the Meyer-Peter & Muller (1948) formula with the addition of an explicit spatial lag; Ferreira et al. (2003) adopted some relations derived in the context of sheet flows to calculate the instantaneous solid discharge; the approach used by the Researchers of University of Trento (Fraccarollo et al. 2003) considers constant concentration of sediment between bed and transport layer and equal velocity of the two phases; Spinewine & Zech (2002) applied a refined formulation of the two-layer model proposed by Capart & Young (2002).

The numerical study by Cao et al. (2004) again adopts a non-capacity model for dam-break flow, sediment transport, and morphological evolution.

Finally, dam break over mobile bed has been recently simulated by Iervolino et al. (2005), by means of a two-phase formulation of the dynamical model proposed by Di Cristo et al. (2002) and Leopardi et al. (2003). The same model has been previously applied to simulate also dam erosion due to overtopping (Iervolino et al. 2004), giving promising results.

For what concerns two-dimensional processes, it has to be noted that the equal velocity hypothesis between liquid and solid phase has to be rejected when dealing with intensively scoured topographies. In fact, it may be imagined that even when the two phases move with comparable velocity values, their directions may in many cases be significantly different due to unequal inertia of the two phases. Among the aforementioned models, only the one by Spinewine (2005) does not suffer from this limitation.

In this paper a two-dimensional, depth averaged, two phase model for non-equilibrium solid transport is proposed. The model is applied to the case of a dam break over an erodible bed in a channel with sudden enlargement and its capabilities to re-produce the main features of the process are discussed.

2 THEORETICAL FRAMEWORK

Classical morphodynamical models couple sediment continuity equation (the so-called Exner equation) to hydrodynamic equations. This approach implies the choice of a bed load transport formula. Since this formula is usually an uniform flow formula, the hypothesis of instantaneous adaptation of bed load transport to variations in flow conditions is made (de Vries, 1965).

As a consequence, an accelerating stream causes scouring of the bed, while a decelerating one always causes deposition. This constraint would result in a contradiction with some experimental results, like the earth-dam failure experiment by Benoist (1983, 1989) used as a test-case by many authors (e.g. Leopardi et al. 2003).

During the dam break on a mobile bed the hypothesis of immediate adaptation of solid transport to hydrodynamics has to be rejected. In fact, experimental investigations have shown that the scouring wave evolves with timescales close to that of hydrodynamics.

In the present work a two-dimensional extension of the one-dimensional morphodynamical model proposed by Iervolino et al. (2004) will be used. The model uses the dynamical equation obtained by Di Cristo et al. (2002), which is coupled with a bed evolution equation based on the balance between erosion and deposition, as suggested by Iervolino et al. (2004) following Fraccarollo & Capart (2002).

The hydrodynamics is described using the classical Shallow Water theory equations. In order to explicitly account for the effect of sidewalls, a zero-equation turbulence model is employed.

The water mass conservation equation is

$$\frac{\partial h}{\partial t}+\frac{\partial hU}{\partial x}+\frac{\partial hV}{\partial y}=-\frac{\partial z}{\partial t} \qquad (1)$$

Copyright © 2006 Taylor & Francis Group plc, London, UK

Note the inclusion of the mobile boundary term in equation (1). Little influence on results shown in present work has been found by including this term, but it may have greater role when dealing with higher erosion/deposition rates.

The water momentum conservation equations read:

$$\frac{\partial hU}{\partial t}+\frac{\partial hU^2}{\partial x}+\frac{\partial hUV}{\partial y}+\frac{g}{2}\frac{\partial h^2}{\partial x}+gh\frac{\partial z}{\partial x}= =-ghS_{fx}+\frac{\partial}{\partial x}\left(h\nu_t\frac{\partial U}{\partial x}\right)+\frac{\partial}{\partial y}\left(h\nu_t\frac{\partial U}{\partial y}\right)$$
$$\frac{\partial hV}{\partial t}+\frac{\partial hUV}{\partial x}+\frac{\partial hV^2}{\partial y}+\frac{g}{2}\frac{\partial h^2}{\partial y}+gh\frac{\partial z}{\partial y}= =-ghS_{fy}+\frac{\partial}{\partial x}\left(h\nu_t\frac{\partial V}{\partial x}\right)+\frac{\partial}{\partial y}\left(h\nu_t\frac{\partial V}{\partial y}\right) \quad (2a,b)$$

in which g is gravity, x, y are the space coordinates in an horizontal plane, t is time, $h = h(x,y,t)$ the water depth, $U = U(x,y,t)$ and $V = V(x,y,t)$ are the depth integrated flow velocity in x and y direction, respectively, $z = z(x,y,t)$ is the bottom elevation, and ν_t is the eddy viscosity; Sf is friction slope (estimated with Chezy formula); its components in x and y direction, namely Sf_x and Sf_y results from:

$$Sf_x = Sf\frac{U}{\sqrt{U^2+V^2}},\ Sf_y = Sf\frac{V}{\sqrt{U^2+V^2}} \quad (3a,b)$$

Finally, vectorial friction velocity is defined according to:

$$\mathbf{u}_* = \left(U^*, V^*\right) = =\left(\sqrt{ghSf}\frac{U}{\sqrt{U^2+V^2}}, \sqrt{ghSf}\frac{V}{\sqrt{U^2+V^2}}\right) \quad (4)$$

and eddy viscosity is computed as $\nu_t = \omega|\mathbf{u}_*|h$ (Elder, 1959), where ω is a coefficient. By assuming a logarithmic velocity profile along the vertical direction, the value of 0.066 can be estimated for ω.

Morphological evolution is computed coupling (1) and (2) with the equations describing the sediment mass and momentum conservation. The sediment mass conservation equation is similar to the classical Exner (1925) equation:

$$(1-e)\frac{\partial z}{\partial t}+\frac{\partial C\delta}{\partial t}+\frac{\partial C\delta U_p}{\partial x}+\frac{\partial C\delta V_p}{\partial y}=0 \quad (5)$$

in which $C = C(x, y, t)$ is the sediment concentration in the transport layer, $\delta = \delta(x, y, t)$ the thickness of the transport layer, $U_p = U_p(x, y, t)$ the sediment transport velocity in x direction, $V_p = V_p(x, y, t)$ the sediment transport velocity in y direction and e the–bed porosity.

The equations representing momentum conservation of a mean particle are the 2D extension of the one reported by Iervolino et al. (2004):

$$\frac{\partial U_p}{\partial t}+U_p\frac{\partial U_p}{\partial x}+V_p\frac{\partial U_p}{\partial y}+ \frac{\Delta g tg\varphi}{\Delta+1}\left[\frac{1}{\sqrt{1+\left[\left(\frac{\partial z}{\partial x}\right)^2+\left(\frac{\partial z}{\partial y}\right)^2\right]}}-\frac{1}{tg\varphi}\frac{\partial z}{\partial x}\right]+ -\frac{c_d}{(\Delta+1)c_s d}\left(\beta U^*-U_p\right)\sqrt{\left(\beta U^*-U_p\right)^2+\left(\beta V^*-V_p\right)^2}+ +\frac{\alpha}{c_s d}U_p\sqrt{U_p^2+V_p^2}=0 \quad (6a)$$

$$\frac{\partial V_p}{\partial t}+U_p\frac{\partial V_p}{\partial x}+V_p\frac{\partial V_p}{\partial y}+ \frac{\Delta g tg\varphi}{\Delta+1}\left[\frac{1}{\sqrt{1+\left[\left(\frac{\partial z}{\partial x}\right)^2+\left(\frac{\partial z}{\partial y}\right)^2\right]}}-\frac{1}{tg\varphi}\frac{\partial z}{\partial y}\right]+ -\frac{c_d}{(\Delta+1)c_s d}\left(\beta V^*-V_p\right)\sqrt{\left(\beta U^*-U_p\right)^2+\left(\beta V^*-V_p\right)^2}+ +\frac{\alpha}{c_s d}V_p\sqrt{U_p^2+V_p^2}=0 \quad (6b)$$

in which Δ is the dimensionless ratio $(\rho_s-\rho)/\rho$, with water density ρ and solid phase density ρ_s; α is the Bagnold coefficient (Bagnold, 1954), β the ratio between fluid velocity in the transport layer and shear velocity, φ the sediment friction angle and c_d the drag coefficient; finally c_s is the shape coefficient of the particles, i.e. the ratio between the volume and the cross section area coefficients. In the present computations, it has been evaluated assuming spherical particles.

The first term in equation (5) represents the erosion deposition rate e_b. Closure of the model requires an

Copyright © 2006 Taylor & Francis Group plc, London, UK

independent relation for it. In present work the one proposed by Fraccarollo & Capart (2002) is used:

$$(1-e)\frac{\partial z}{\partial t} = -e_b$$

$$e_b = \pm\frac{|\tau_s - \tau_b|}{\rho_s |U_p|} = \quad (7)$$

$$= \frac{1}{\sqrt{U_p^2 + V_p^2}} \left(\frac{\alpha}{c_s}\left(U_p^2 + V_p^2\right) + \frac{1}{\sqrt{1+\left[\left(\frac{\partial z}{\partial x}\right)^2 + \left(\frac{\partial z}{\partial y}\right)^2\right]}} g \frac{\Delta}{\Delta+1} C\delta \cdot tg\varphi \right)$$

in which $|\tau_s - \tau_b|$ represents the stress excess at the bottom, producing erosion (if greater than zero) or the deposition (otherwise).

Deposition velocity during an unsteady process is assumed to be bounded by sediment fall velocity in still clear-water, w_s. So, if the term obtained by equation (7) is smaller than $-w_s$ it is assumed equal to $-w_s$. Despite the unsteadiness of the process simulated in the present work, this limiter has been found to have little or none influence on the results; it may have greater significance under different flow conditions.

The model is then composed by seven partial derivative equations with the unknown functions: h, U, V, z, $C\delta$, U_p, V_p. Numerical integration is performed using a finite volume formulation on a structured, non staggered grid. The technique is described in detail in Leopardi (2001) and it is based on a parabolic interpolation at the interfaces among adjacent cells and predictor-corrector explicit time stepping. The method has high accuracy both in space and time, along with fairly good shock capturing capabilities. An *ad hoc* treatment for no flow cells (outblock) is used in order to manage complex geometries.

In order to avoid unphysical results, two further limiters are introduce in the implementation of the model. The first is a slope limiter that bounds the bed slope source term in equations (2a,b) to a maximum value of 0.1. When dealing with relatively mild slopes – as in the present case – this limiter has been verified to act only in the sense of improving model stability, while having no perceivable influence on the solution.

The second limiter is designed in order to avoid that the numerical flux of solid phase flowing out of a cell may be greater than the available mass in it.

3 NUMERICAL SIMULATIONS

3.1 *Fixed-bed simulations*

As a preliminary test, the adequacy of the model to reproduce wave propagation over a floodplain with a sudden expansion has been verified by simulating the experiments described by Soares Frazão et al. (2003). The flow domain is sketched in figure 1: it consists of a narrow fixed bed channel (width b, length l) followed by an idealized floodplain generated by the sudden increase of the width on one side (width B, length L-l). Experiments cover both steady and unsteady conditions of flow, the latter obtained producing a dam-break wave. During the evolution of the two processes, wide regions of recirculation as well as steep fronts (shock waves) occur, thus requiring adequate numerical models to be reproduced.

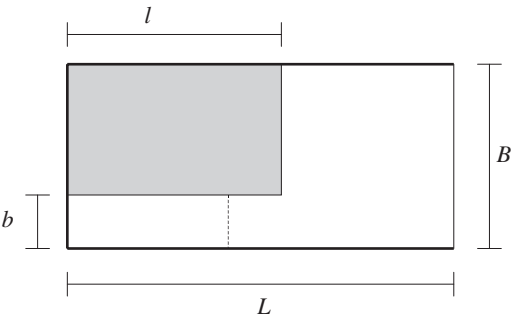


Figure 1. Sketch of the flow domain for dam break with sudden enlargement.

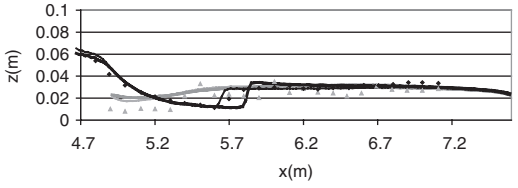


Figure 2. Water profiles along channel sidewalls. Thick lines: without turbulence model. Thin line: with turbulence model.

Simulated tests present $l = 4.82$ m, $L = 7.60$ m, $b = 0.12$, $B = 0.495$ m. Computational grid is made of square cells with $\Delta x = \Delta y = 0.02$ cm, which have been verified to satisfy grid independence.

Non dimensional Chezy coefficient has been calibrated against experimental results, and the classical value of 0.066 has been used for the ω coefficient of the Elder's law.

Results, with reference to steady flow conditions, are summarised by figures 2 and 3. In the first one simulated water profiles along the two sidewalls are compared with corresponding measured ones: black symbols and line are used for the continuous sidewall, gray for the discontinuous. Thick lines correspond to simulation without turbulence model, and thin line to computation performed taking into account sidewall effects. In figure 3, flow trajectories are compared to the one obtained by Frazão et al. (2003) by means of a PIV technique.

Copyright © 2006 Taylor & Francis Group plc, London, UK

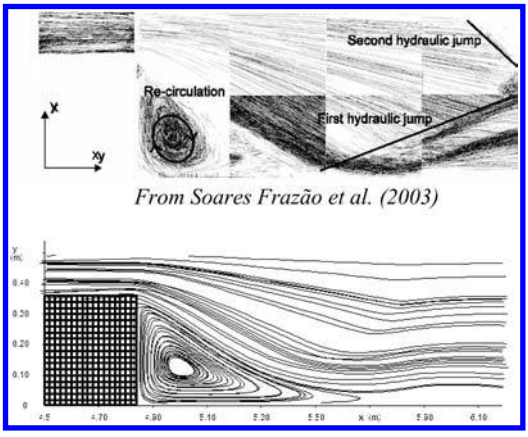


Figure 3. Measured and computed flow trajectories.

A general agreement can be inferred from both figures: water depths are well reproduced, even if with some minor accuracy near the jump (which is sharper in the computation than in the experiments) and in the proximity of the re-circulation zone.

As far as dam-break test is concerned, the unsteady process is triggered by the sudden removal of a dam located at abscissa 4 m with initial depth of 0.2 cm upstream and dry bed downstream. Comparison with experimental and numerical results of Soares Frazão et al. (2003) shows again overall agreement, thus confirming the capabilities of the numerical model to deal with such kind of complex flow.

As an example the instantaneous field of velocity vectors 2.75 s after dam removal is shown in figure 4 and compared with measured velocity magnitude.

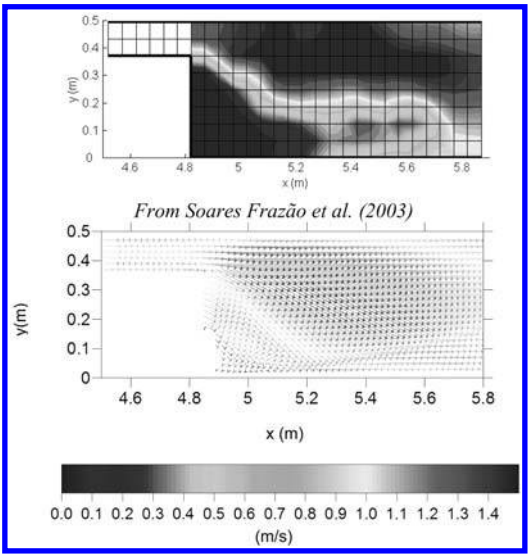


Figure 4. Measured and computed velocity magnitude. t = 2.75 s after dam removal.

3.2 *Mobile-bed simulations*

The scheme considered for two dimensional dam break over mobile bed is the one recently discussed by Spinewine (2005). It is geometrically analogous to the fixed bed case, but with $b = 0.25$ m, $B = 0.50$ m, $L = 6$ m and $l = 4$ m. At $t = 0$, water is stored in the first 3 m of the narrow channel, with saturated granular bed downstream. Experimental installation is designed to guarantee little influence of gate opening on the process.

A computational grid with $\Delta x = 0.05$ m and $\Delta y = 0.025$ m has been used. In order to better reproduce the roughness of the granular bed, Griffiths'law has been adopted to compute the Chezy non dimensional factor

$$C_h = 2.15 + 2.43 \ln\left(\frac{h}{d}\right) \tag{8}$$

whose application range is for h/d between 1 and 200 (Griffiths, 1981).

Sediment parameters have been set to the experimental values, reported by the Author, while β and α have been given the values, respectively, of C_h and 0.114. Results have shown little sensitivity respect to the values two parameters, which have been varied within the same range already used in analogous simulations (Iervolino et al. 2005).

Two computations are shown and discussed in what follows, differing for the inclusion of the turbulence terms by the zero-equation model with $\omega = 0.066$, in order account for sidewall influence hydrodynamics and bed evolution.

For both cases (Figures 5 and 6), gray level maps with simulated bed deformation are shown for t = 1,2,3,5 s after dam removal. The iso-contour relative to initial bed level is superposed as a solid line.

3D-plot for free surface elevation are also reported for same time sequence. Constant-level contours with 1 cm increment are traced on the wireframes to better represent the free surface shape (Figure 7).

Finally, the time evolution of sediment mass discharged out of the domain is reported in figure 8. Again, thick line is used for computations without turbulence, thin one otherwise. Dashed line represents the final measured value of 2.05 kg.

3.3 *Discussion of results*

Experimental observations of Spinewine (2005) are, in the writers' knowledge, the only published data concerning two dimensional dam break wave over mobile bed. This generalised lack of experimental data, even if partially justified by the complex

Copyright © 2006 Taylor & Francis Group plc, London, UK

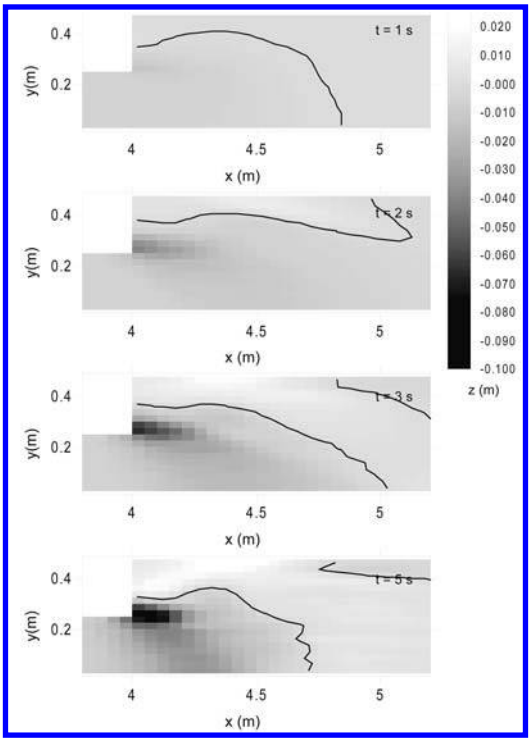


Figure 5. Bed evolution without turbulence model (t = 1,2,3,5 s). The iso-contour relative to initial bed level is superposed as a solid line.

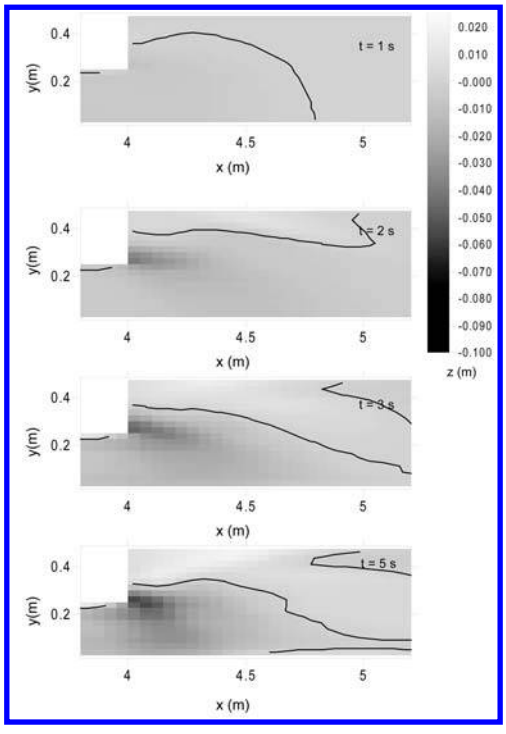


Figure 6. Bed evolution with turbulence model (t = 1, 2, 3, 5 s).The iso-contour relative to initial bed level is superposed as a solid line.

experimental conditions and the strong unsteadiness of the process, should be addressed in the near future, in order to gain insight and provide a fundamental aid to mathematical modelling.

Despite little more than a qualitative comparison can be made with available experiments, present simulation reproduce favourably the overall features of the process:

- Independently on the inclusion of turbulent diffusive terms, the maximum scour depth is located just downstream the inner corner of the floodplain enlargement.
- Its value appears instead to be significantly influenced by the presence of turbulent diffusivity. Maximum scour at $t = 5$ s is, in fact, close to 0.1 m for the former simulation and about 0.06 m for the latter.
- The formation of an oblique hydraulic jump causes a partial re-deposition of the eroded material, up to the appearance of a bar in the floodplain, which is elongated in the longitudinal direction close to the left wall.
- When turbulence is included in the simulation, a second deposition zone can be observed close to the right wall, which spreads in the transversal direction for a length of few centimetres. It is generated by deposition in the low-velocity zones near the wall. So, accounting for the wall effect has a more pronounced positive influence on the reproduction of the process than in the fixed bed case. Due to the depth-to-width ratio of the present laboratory case, this effect can be appreciated also on the free surface configuration, which shows progressively increasing differences between the two simulations.

The total mass discharged from the model in the whole process is 2.56 kg for the simulation without turbulence and 1.97 kg when turbulence is included. Both values are reasonably close to the measured one of 2.05 kg.

Moreover, the comparison of present results with the computations presented by Spinewine (2005), based on a two layer description of the flow of water and sediment, shows that main difference consists in the more pronounced effect of wave reflection against right sidewall.

4 CONCLUSIONS

Dam break on mobile bed is a challenging test for numerical models. Since the scouring wave evolves

Copyright © 2006 Taylor & Francis Group plc, London, UK

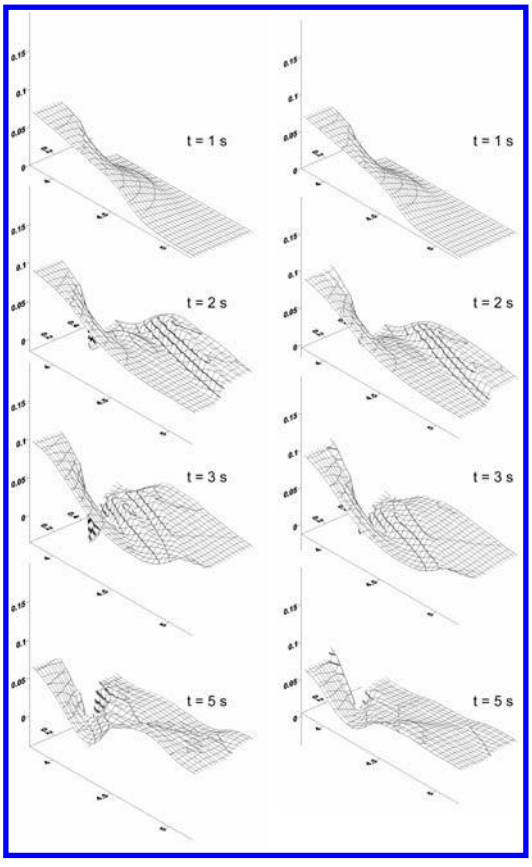


Figure 7. 3D view of computed free-surface at different times. Left: without turbulence model; right: with turbulence model.

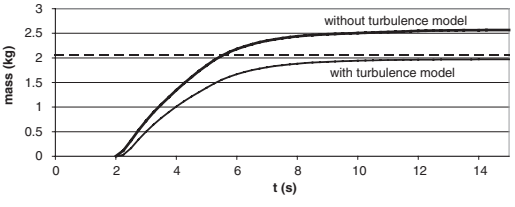


Figure 8. Time evolution of sediment mass discharged out from the experimental plant.

with timescales close to that of hydrodynamics, the hypothesis of immediate adaptation of solid transport to hydrodynamics has to be rejected.

In the present work physical experiments of dam break on mobile bed have been simulated using an original two-phases non-equilibrium model. Moreover, the effect of the inclusion of the sidewall on the results has been investigated. Results show the appearance of a deposition zone close to the sidewalls which is otherwise absent, which in turn contributes to modify the shape of free surface. This suggests that such an effect should be taken into account in some applications, depending on the depth-to-width ratio. Moreover, the estimation of maximum scour depth is sensibly affected by the transversal turbulent diffusivity, and its inclusion leads to predict lower depth.

Model predictions are compared with the experimental documentation of the process, even if little more than a qualitative assessment can be done, and with the computations made with a state-of-the-art model. Both comparisons gave encouraging results.

It has to be stressed that the lack of data about two dimensional dam break over mobile bed claims for future experimental research, a fundamental tool to gain further insight and improve mathematical modelling of the process.

ACKNOWLEDGMENTS

Part of the financial support for this research was funded by the Italian Government under the national grant PRIN 2005 “La dinamica delle inondazioni in ambienti a topografia accidentata”.

REFERENCES

Bagnold, R.A. (1954) *Experiments on a gravity-free dispersion of large solid spheres in a Newtonian fluid under shear.* Proc. Roy. Soc, vol. 225, pp. 49–63.

Benoist, G. (1983) *Calcul de l’érosion d’une digue par surverse.* EDF Internal Report HE 43/83–31.

Benoist, G. (1989) *Les études d’ondes de submersion des grands barrages d’EDF.* La Houille Blanche, n. 1.

Cao, Z., Pender, G., Wallis, S. & Carling, P. (2004) *Computational dam-break hydraulics over erodible sediment bed.* Journal of Hydraulic Engineering, ASCE, Vol. 130, n. 7, pp. 689–703.

Capart, H. & Young, D. L. (1998) *Formation of a jump by the dam-break wave over a granular bed.* J. Fluid Mech. 372, 165–187.

Chen, H.Y & Simons, D.B. (1979) *Geomorphic Study of Upper Mississippi River.* Journal of the Waterway Port Coastal and Ocean Division, ASCE, Vol. 105, No. 3, August 1979, pp. 313–328.

de Vries, M. (1965) *Consideration about Non-Steady Bed-Load-Transport in open Channels.* 11th IAHR Congress, Leningrad, vol. III, paper n. 3.8, 1965.

Di Cristo, C., Leopardi, A. & Greco, M. (2002) – *A bed load transport model for non-uniform flows.* Proceedings of International Conference “River Flow 2002”, Louvain-la-Neuve (Belgio), 3–6 September 2002, Balkema.

Dressler, R.F. (1952) *Hydraulic resistance effect upon the dam break functions.* Journal of Research of the International Bureau of Standards, Vol.49, n. 3.

Elder J.W. (1959) *The dispersion of marked fluid in turbulent shear flow.* J. Fluid Mechanics, Vol. 5.

Copyright © 2006 Taylor & Francis Group plc, London, UK

El Kadi Abderrezzak, K. & Paquier, A. (2003) *IMPACT project: Dam-break waves over movable beds.* In EC Contract EVG1-CT-2001-00037 IMPACT Investigation of Extreme Flood Processes and Uncertainty, Proceedings 3rd Project Workshop, Louvain-la-Neuve, Belgium 6–7, November 2003 (CD-ROM).

El Kadi Abderrezzak, K. & Paquier, A. (2004) *Computations of dam-break waves over a movable bed: Influence of initial bed discontinuity and bed material.* In EC Contract EVG1-CT-2001-00037 IMPACT Investigation of Extreme Flood Processes and Uncertainty, Proceedings 4th Project Workshop, Zaragoza, Spain 3–5, November 2004 (CD-ROM).

Exner, F.M. (1925) *Uber die Wechselwirkung zwischen Wasser und Geschiebe in Flussen, Sitzber.* Akad. Wiss Wien, Part IIa, Bd. 134 (in German).

Ferreira, R.M.L. & Leal, J.G.A.L. (1998) *1-D Mathematical Modelling of the Instantaneous-Dam-Break Flood Wave Over Mobile Bed: Application of TVD and Flux-Splitting Schemes*. CADAM meeting, Munich.

Ferreira R., Leal J., Cardoso A.H. & Almeida A.B. (2003) *Sediment Transport by Dam-Break Flows. A Conceptual Framework Drawn from the Theories for Rapid Granular Flows.* In EC Contract EVG1-CT-2001-00037 IMPACT Investigation of Extreme Flood Processes and Uncertainty, Proceedings 3rd Project Workshop, Louvain-la-Neuve, Belgium 6–7 November 2003 (CD-ROM).

Fraccarollo, L. & Capart, H. (2002) *Riemann wave description of erosional dam-break flows.* Journal of Fluid Mechanics, vol. 461, pp. 183–228.

Fraccarollo, L., Capart, H. & Zech, Y. (2003) *A Godunov method for the computation of erosional shallow water transients*. International Journal for Numerical Methods in Fluids, 41, pp. 951–976.

Graf, W.H. (1998) *Fluvial Hydraulics: Flow and Transport Processes in Channels of Simple Geometry.* John Wiley & Sons.

Griffiths, G. A. (1981) *Flow resistance in coarse gravel bed rivers*. Journal of Hydraulic Division, ASCE, Vol. 107 No. HY7, 899–916.

Iervolino, M., Greco, M. & Oliveri, E. (2004) *Modelli di trasporto solido nella simulazione della rimozione di un rilevato in materiali sciolti.* Proceedings of Idr@Trento: XXIX National Conference of Hydraulics and Hydraulic Structures (in Italian).

Iervolino, M., Greco, M. & Leopardi, A. (2005) *Numerical simulation of dam break on erodible bed.* Proceedings of the XXXI IAHR Congress, Seoul, pp. 2477–2486.

Leal, J., Ferreira, R.M.L., Cardoso, A.H. & Almeida, A.B. (2003) *Comparison between Numerical and Experimental Results on Dam-Break Waves over Dry Mobile Beds*. Proc., 3rd IMPACT Project Workshop CD-ROM, Catholic Univ. of Louvain, Louvain-la-Neuve, Belgium.

Leopardi, A. (2001) Modelli Bidimensionali di Corpi Idrici Naturali. PhD Thesis. University of Napoli "Federico II". (in Italian).

Leopardi, A., Oliveri, E. & Greco, M. (2003) *Numerical simulation of gradual earth-dam failure.* Proceedings of 2nd International Conference "New Trends in Water and Environmental Engineering for Safety and Life", Capri, 24–28 June 2002. L'Acqua, vol. 4, pp. 37–43.

Meyer-Peter, E. & Muller, R. (1948) *Formulas for Bed-Load-Transport.* 2nd IAHR Congress, Stockolm, 1948.

Ritter, A. (1892) *Die Fortplanzung der Wasserwellen.* Zeitschrift des Vereines Deutscher Ingeniere, 36(33).

Soares Frazão S., Lories D., Taminiau S. & Zech Y. (2003) *Dam-break flow in a channel with a sudden enlargement*. Proceedings of XXX IAHR Congress, August 23–30, 2003, Thessaloniki, Greece, pp. 221–228.

Spinewine, B. & Zech, Y. (2002) *Geomorphic dam-break floods: near-field and far-field perspectives*. In EC Contract EVG1-CT-2001-00037 IMPACT Investigation of Extreme Flood Processes and Uncertainty, Proceedings 1st Project Workshop, Wallingford, UK, 16–17 May 2002 (CD-ROM).

Spinewine B. (2005) *Two-layer shallow water modelling of fast geomorphic flows and experimental validation on idealised laboratory dam-break waves*. Proceedings of XXXI IAHR Congress, September 11–16, 2005, Seoul, Korea, pp. 6477–6488.

Stoker, J.J. (1948) *The formation of breakers and bores*. Institute for Mathematics and Mechanics of New York University.

Zech ,Y., Soares Frazão, S., Spinewine, B. & le Grelle, N. (2004) *Dam-break induced flood modelling and sediment movement.* IMPACT WP4 final scientific report. http://www.samui.co.uk/impact-project/default.htm

Copyright © 2006 Taylor & Francis Group plc, London, UK

One dimensional modeling of dam break flow over erodible sediment bed

P. Costabile & F. Macchione
University of Calabria, LAMPIT (LAboratorio di Modellistica numerica per la Protezione Idraulica del Territorio), Dipartimento di Difesa del Suolo, Rende, Cosenza Italy

ABSTRACT: This paper deals with the simulation of dam break waves over movable beds. The aim of this work is to analyze the suitability of a model proposed in the simulation of debris flow events. It is based on a shallow water approach and the system of equations includes two mass conservation equations (one for the mixture and another for the solid phase) and a single momentum balance equation. A uniform distribution of velocity is also assumed in the cross section. Moreover, the model takes into account a non equilibrium transport of the sediments based on an auxiliary relationship that introduces an erosion/deposition velocity. The governing equations are solved in coupled way by the implementation of an explicit first-order finite volume method. The model has been tested in a number of experimental cases and has achieved fairly good agreements between the simulation and the measurement.

1 INTRODUCTION

Over the last decade the problems related to the definition of flooding areas due to partial or total dam failure have been a topic of increasing interest in the fields of hydraulic engineering. This is a tricky subject because dam break waves may cause catastrophic damage to the valley downstream and loss of life.

Some of the most famous dam break events are the Malpasset (France) dam failure in 1959, Banqiao (China) dam break in 1975 and the catastrophic event of Lake Ha! Ha! (Quebec) in 1998 (Lapointe et al. 1998). Many models were developed in order to simulate this phenomenon: finite differences, finite elements and finite volume techniques for the numerical integration of shallow water equations have been significantly improved. Most of them refer to ideal or real situations in which the bed profile does not change over time. Indeed this is a very reasonable hypothesis for rock channels but it is questionable in rivers in which significant erosions and depositions phenomena occur.

The propagation of a dam break wave in natural valleys is very complex since it may produce significant morphological changes to the bed with a large amount of conveyed material. This intense sediment transport may dramatically modify the dynamic behaviour of the flow and, in turn, may affect the arrival time and the maximum water levels, very important factors in the evaluation of the risk assessment.

The water depth profile of a dam break wave over a movable bed is significantly different from that over a fixed bed. It is well known in the literature that, for the fix bed case, the flow exhibits a continuous, monotic decrease in free surface. This behaviour is not observed in the movable case because the physical evidence shows the formation of a hydraulic jump near the centre of dam break wave due to interaction with the evolution of the bed (Capart & Young 1998).

The analysis of a dam break over an erodible bed also represents a chance to improve theoretical knowledge of some key processes linked to sediments transport in shallow water. It is quite evident that the singularities in the water depth profile (i.e. hydraulic jump, shock waves) produce hydrodynamic situations in which sediment transport is very far from equilibrium conditions; in turn, the bed evolution is one of the mechanisms that can lead to the formation of shock waves.

All this provoke a highly unsteady phenomenon with intense sediment transport moving as a sheet flow and debris flow. These kinds of situations occurs in various conditions of engineering interest as fast flows, flash floods (Lapointe et al. 1998) and debris flow (Takahashi 1991, Iverson 1997). Moreover, from analysis of recent natural or constructed dam failures, it has been shown (Zech & Spinewine 2001) that the volume of transported material may, in some instances, even be as important as the volume of water itself. Regardless of the total transported volume, it should be noted that these geomorphic consequences may significantly increase the entity of a flood wave due to localised effects as happened in the catastrophic event of Pollalie Creek (Gallino & Pierson 1985): a temporary artificial

Copyright © 2006 Taylor & Francis Group plc, London, UK

dam originated by the deposition of the materials transported by the flow collapsed causing a considerable increase of the flood.

Recently, sediment transport in highly transient non-equilibrium conditions has been a topic of increasing interest to hydraulic scientists leading to extensive field, laboratory, theoretical and numerical studies.

Several experimental works have been carried out in order to understand the peculiarities of the phenomenon (Capart & Young 1998, Fraccarollo & Capart 2002, Leal et al. 2003). In the context of the IMPACT project different tests were performed: the first test ("flat bed case") assumes the same level of sediment at both sides of the dam (Spinewine & Zech 2002) while in the second test ("stepped bed case") the level of the upstream sediments is higher than the downstream one (Spinewine & Zech 2003); the latter test was performed with material of different size and density in order to magnify the sediment transport processes.

These experimental works represent the benchmarks cases which can be used to validate the numerical model developed by the various research groups within the project.

Different models have been proposed to deal with this problem, all based on a shallow water approach; a possible main classification can be made as regards the conceptual vertical flow structure: one-layer flow models and two-layer models.

One-layer models consider a sediment-water mixture everywhere, that is the absence of a clear water layer: the models of Capart & Young (1998), Caleffi & Valiani (2002), Cao et al. (2004), belong to this category; non equilibrium conditions are generally taken into account by means of a spatial-lag relationship or through formulas of entrainment and deposition fluxes. Another model based on the one-layer description, used within IMPACT project, was developed by El Kadi & Paquier (2004).

Two-layer models are more complex; they assume that the flow is subdivided into two non-miscible layers separated by an interface: in the lower layer the flow is represented as a solid-liquid mixture while the upper layer is sediment free (clear water layer).

The models of Fraccarollo & Capart (2002) and Fraccarollo et al. (2003) belong to this family; the above authors assume a uniform velocity profile and a sediment concentration equal to that of the static bed. A similar approach was undertaken by Spinewine & Zech (2003) in which the velocities of the flow in the layers are not equal and the sediment concentration is different from that of the static bed. Leal et al. (2003) developed another conceptual model in which the wave propagation is idealized as a two layer transport model, where flow velocities and sediment concentrations are considered uniform; localized erosion/deposition processes are represented by vertical fluxes.

This paper deals with the simulation of dam break waves over movable beds. The main purpose of the present work is not so much to improve theoretical knowledge of the hydrodynamics of this particular phenomenon, but to analyze the ability of the model presented herein to simulate highly unsteady flow with intense sediment transport that cannot be simulated with a classical equilibrium transport model.

With this in mind, the authors prefer to analyze the suitability of a simple model based on shallow water equations and that considers the effects of evolution of the bed on the flow, so that it can represent the propagation of a liquid-granular mixture. The hyperbolic conservation system includes two mass conservation equations (one for the mixture and another for the solid phase) and a single momentum balance equation.

In other words, the vertical flow structure is defined by two interfaces: the water free-surface and the morphodynamic bottom profile; a constant vertical profile for the velocity is also assumed. Moreover, the model takes into account a non equilibrium transport of the sediments based on an auxiliary relationship that introduces an erosion/deposition velocity.

As showed in the next section, the bed evolution law is the main feature that makes the proposed model different from the other one layer models. So one of the main purposes of this work is to analyze the suitability of this particular relationship within a model that is based on a mathematical formulation of governing equations well-known in the literature (i.e. Cao et al. 2004).

The governing equations are solved in a coupled way through the implementation of an explicit first-order finite volume method. In previous works (Costabile et al. 2004, Costabile & Macchione 2004), this model was already applied to test cases presented in Capart & Young (1998) and in Fraccarollo & Capart (2002) with fairly good agreement with experimental results.

Some applications to experimental cases used within IMPACT project are shown in this paper, in order to understand if there are any significant differences between the results obtained with the conceptually simple one-layer model presented herein and those from the more complex two layer models.

2 MATHEMATICAL MODEL

This paper considers a one-layer model based upon a solid-liquid mixture moving in unsteady flow conditions. In recent years many authors have presented the governing equations for the water-sediment mixture both for the morphological evolution in alluvial rivers (Cao et al. 2002) and for highly unsteady flow with intense sediment transport such as dam break wave over erodible bed or debris flow (Capart & Young

Copyright © 2006 Taylor & Francis Group plc, London, UK

1998, Brufau et al. 2000, Caleffi & Valiani 2002, Cao et al. 2004). The complete governing equations can be derived from the Reynolds transport theorem. So, apart from certain simplifications in the momentum balance and from different relationships for the bed evolution, the above mathematical formulation is well-known in the literature and has been applied to the available experimental test-cases of dam – break over movable bed.

In order to describe the dynamic of the mixture a 1D shallow water approach is used, so the governing equations are related to the mixture and solid phase mass balance and to the complete mixture momentum balance along the main stream direction (the same velocity for the solid fraction and the interstitial fluid is assumed); moreover, the model includes a bed evolution law.

The set of four differential equations is:

$$\frac{\partial A}{\partial t}+\frac{\partial Q}{\partial x}=rb \tag{1}$$

$$\frac{\partial Q}{\partial t}+\frac{\partial\left(\frac{Q^2}{A}+g\frac{A^2}{2b}\cos\theta\right)}{\partial x}=gA\left(S_o-S_f\right)+ -\left[\frac{bur}{\rho}\left(\rho^*-\rho\right)+\frac{g}{\rho}\frac{A^2}{2b}\cos\theta\frac{\partial\rho}{\partial x}\right] \tag{2}$$

$$\frac{\partial(cA)}{\partial t}+\frac{\partial(cQ)}{\partial x}=rbc^* \tag{3}$$

$$\frac{\partial z}{\partial t}\cos\theta+r=0 \tag{4}$$

The system of equations (1), (2) and (3) can be expressed in the following form:

$$\frac{\partial\mathbf{U}}{\partial t}+\frac{\partial\mathbf{F}(\mathbf{U})}{\partial x}=\mathbf{G}(\mathbf{U}) \tag{5}$$

$$\mathbf{U}=\begin{bmatrix}A\\Q\\cA\end{bmatrix}\qquad\mathbf{F}(\mathbf{U})=\begin{bmatrix}Q\\\left(\frac{Q^2}{A}+g\frac{A^2}{2b}\cos\theta\right)\\cQ\end{bmatrix} \tag{6,7}$$

$$\mathbf{G}(\mathbf{U})=\begin{bmatrix}rb\\gA(S_0-S_f)-\left[\frac{bur}{\rho}\left(\rho^*-\rho\right)+\frac{g}{\rho}\frac{A^2}{2b}\cos\theta\frac{\partial\rho}{\partial x}\right]\\rbc^*\end{bmatrix} \tag{8}$$

where x = space coordinate; t = time level; $\mathbf{U}$ = conservative variable vector; $\mathbf{F}$ = flux vector; $\mathbf{G}$ = source term vector; A = mixture cross section area; Q = mixture discharge; c = dimensionless sediment volumetric concentration; g = acceleration due to gravity; b = channel width; θ = angle of bed inclination; S_0 = local bed slope; S_f = slope friction term; u = mean velocity in the cross-section; r = bed erosion/deposition velocity; ρ = mixture density; c^*, ρ^* = parameter related to sediment concentration and density in a static bed; z = bed level.

Mixture density can be computed as follows:

$$\rho=\rho_s c+\rho_w\left(1-c\right) \tag{9}$$

where ρ_s is sediment density and ρ_w is water density. Bottom slope S_0 can be evaluate as:

$$S_o=\sin\theta=-\frac{\partial z}{\partial x} \tag{10}$$

In this work the temporal evolution of the bottom profile is described by means of an erosion-deposition velocity; for this, the relationship first proposed by Egashira & Ashida (1987) and later modified by Brufau et al. (2000) is used. The erosion/deposition model considered herein has the following expression:

$$r=K_f u\tan\left(\theta_f-\theta_e\right) \tag{11}$$

where θ_e is the equilibrium angle, θ_f is the energy line angle, K_f is a calibration parameter. The equilibrium angle depends on mixture concentration, on density ratio s, and on static internal friction angle; it can be computed as follows:

$$\theta_e=\arctan\left[\tan\phi\frac{c(s-1)}{c(s-1)+1}\right] \tag{12}$$

The density ratio s can be defined as:

$$s=\frac{\rho_s}{\rho_w}$$

The structure of equation (12) may be derived from a simplified stability analysis of an incoherent saturated mass upon an inclined plane of constant slope. The energy line angle is computed as:

$$\theta_f=\arctan\left(\frac{S_f}{\cos\theta}\right) \tag{13}$$

Slope friction is computed by means of Manning-Strickler formula where coefficient n_m is estimated from the value of sediment diameter d:

$$n_m=\frac{21.1}{d_{50}^{1/6}} \tag{14}$$

Copyright © 2006 Taylor & Francis Group plc, London, UK

So according to equations (4) and (11), a positive value of r means that erosion takes place; clearly this happens when $\theta_f > \theta_e$. Obviously the deposition occurs when $\theta_f \leq \theta_e$.

Finally c^*, ρ^* are defined as:

$$c^* = \begin{cases} \max(c, c_D) & r \leq 0 \\ c_b & r > 0 \end{cases} \tag{15}$$

$$\rho^* = \begin{cases} \rho_D & r \leq 0 \\ \rho_b & r > 0 \end{cases} \tag{16}$$

where c_D, ρ_D = volumetric sediment concentration and density of a static bed just after deposition and c_b, ρ_b = volumetric sediment concentration and density in a static bed.

It should be noted that the bed evolution law considered in this work has been proposed in the context of the mathematical modelling of debris flow (Brufau et al. 2000). It is interesting to observe that the mathematical formulation of the governing equations used in Brufau et al. (2000) is very similar to that of Cao et al. (2004) except for the last two terms on the right-hand side of equation (2) that are considered negligible for debris flow events. This conclusion is commonly accepted for the fluvial sediment transport usually encountered but not under extreme situations, as dam-break flow over an erodible bed, in which the use of complete rather than simplified momentum equation is essential (Cao et al. 2003, Cao et al. 2004).

3 NUMERICAL MODEL

An explicit finite volume method is used for the numerical resolution of system (5) so that the temporal evolution of the solution is computed as follows:

$$\mathbf{U}_j^{n+1} = \mathbf{U}_j^n - \frac{\Delta t}{\Delta x}\left(\mathbf{F}_{j+1/2} - \mathbf{F}_{j-1/2}\right) + \Delta t \mathbf{G}_j^n \tag{17}$$

where Δt is the time step; Δx is the spatial step; j is the spatial node index; n is the time step index; and $\mathbf{F}_{j+1/2}$ is the numerical flux at $x = x_{j+1/2}$.

In the present work HLLC approximate Riemann solver is used for the computation of $\mathbf{F}_{j+1/2}$; HLLC numerical flux can be expressed as follows:

$$\mathbf{F}_{j+1/2}^{HLLC} = \begin{cases} \mathbf{F}_L & \text{if } S_L \geq 0 \\ \mathbf{F}_L^* & \text{if } S_L \leq 0 \leq S^* \\ \mathbf{F}_R^* & \text{if } S^* \leq 0 \leq S_R \\ \mathbf{F}_R & \text{if } S_R \leq 0 \end{cases} \tag{18}$$

where $\mathbf{F}_L$ and $\mathbf{F}_R$ stand for $\mathbf{F}(\mathbf{U}_j^n)$ and $\mathbf{F}(\mathbf{U}_{j+1}^n)$ respectively.

$$\mathbf{F}_L^* = \mathbf{F}_L + S_L\left(\mathbf{U}_L^* - \mathbf{U}_L\right) \qquad \mathbf{F}_R^* = \mathbf{F}_R + S_R\left(\mathbf{U}_R^* - \mathbf{U}_R\right) \tag{19,20}$$

$$S_L = u_L - a_L q_L \qquad S_R = u_R + a_R q_R \tag{21,22}$$

In previous relationships q_K ($K = L, R$) are given by:

$$q_K = \begin{cases} \sqrt{\frac{1}{2}\left[\frac{(h_* + h_K)h_*}{h_K^2}\right]} & \text{if } h_* > h_K \\ 1 & \text{if } h_* \leq h_K \end{cases} \tag{23}$$

$$S^* = \frac{S_L h_R(u_R - S_R) - S_R h_L(u_L - S_L)}{h_R(u_R - S_R) - h_L(u_L - S_L)} \qquad h^* = \frac{1}{g}\left[\frac{1}{2}(a_L + a_R) + \frac{1}{4}(u_L - u_R)\right]^2 \tag{24,25}$$

$$\mathbf{U}_K^* = h_K\left(\frac{S_K - u_K}{S_K - S^*}\right)\begin{bmatrix} 1 \\ S^* \\ C \end{bmatrix} \tag{26}$$

$$a_K = \sqrt{g h_K} \tag{27}$$

One can find further details in Toro (1997), Toro (2001). In this way one achieves first order accuracy.

The problems arising from an incorrect treatment of source terms are well known in the literature. In order to avoid spurious numerical oscillations, for example, Bermudez & Vazquez (1994) presented, for the fixed bed case, an upwind representation of the source terms in order to be consistent with an upwind discretization of numerical flux so that avoiding numerical spurious oscillations.

In this work two algorithms are taken into account. The first uses a pointwise approach; the second is based on a splitting scheme (Toro 2001) which consists in solving, in succession, two initial value problems: one can obtain a predicted solution $\mathbf{U}(p)$ by solving the homogeneous pure advection problem with the initial condition of the full problem; the final solution is given by solving the ordinary differential equation:

$$\frac{\partial \mathbf{U}}{\partial t} = \mathbf{G}(\mathbf{U}) \tag{28}$$

with initial condition $\mathbf{U}(p)$. No significant differences were found in the applications of the two methods.

Copyright © 2006 Taylor & Francis Group plc, London, UK

The bed evolution was computed using the following explicit scheme:

$$z_j^{n+1} = \alpha z_j^n + (1-\alpha)\frac{z_{j+1}^n - z_{j-1}^n}{2} - \frac{r_j^n}{\cos\theta_j^n}\Delta t \qquad (29)$$

where $0 \le \alpha \le 1$. Simulations are performed with a value of α very close to unity (0.99–0.999) in order to minimize numerical diffusion.

4 MODEL VALIDATION

In previous works (Costabile et al. 2004, Costabile & Macchione 2004), this model was already applied to some tests presented in the literature (Capart & Young 1998, Fraccarollo & Capart 2002) with fairly good results. The aforementioned tests both refer to a so called "flat bed case" (Spinewine & Zech 2002) in which the same level of sediment at both sides of the dam was imposed; the density ratios used in the tests were $s = 1.048$ and $s = 1.54$, respectively.

In this work the suitability of the model presented is further analysed through its application to the "stepped bed" test cases (Spinewine & Zech 2003). As mentioned in the introduction, these tests were used as benchmarks to validate the numerical models developed during the IMPACT project by several research groups and so one has the opportunity to compare the results achieved in the present work with those obtained from the more complex models above.

The benchmark test conditions are briefly recalled (for further details see Spinewine & Zech 2003). The experiments were carried out at the laboratory of the Civil and Environmental Engineering Department, Université Catholique de Louvaine (UCL) Belgium. The facility consists in a rectangular flume, 6 m long, 0.25 m wide, 0.7 m high. Same initial conditions were assumed for both tests. An initial discontinuity was provided in the bed profile so that the upstream bed level was initially 0.10 m higher than the downstream level. Total hydraulic head upstream h_0 was equal to 0.35 m. Uniform coarse sand ($s = 2.63$, $d = 0.00182$ m) and light PVC pellets ($s = 1.55$, $d = 0.0036$ m) were used in the experiments. A wide analysis of the numerical prediction of the model developed within IMPACT project can be found in Spinewine & Zech (2004).

In the following sections the results of the model presented in this paper are shown. In both tests a value of $\Delta x = 0.01$ m and for numerical stability a Courant number $C_r = 0.1$ are used; the low value of Courant number is due to significant source terms in the equations (Brufau et al. 2000). Moreover, for the sake of simplicity, it is assumed $c_D = c_b$. The following simulations refer to $K_f = 10$ but a sensitivity analysis to this parameter is also presented. Only the comparison between experimental and numerical results of the model here presented are shown; the numerical results of the other modellers are not shown in this paper in order to avoid a limited readability of the figures. We chose the same scale of the figures used by Spinewine & Zech (2004) to make the comparison with the results obtained within IMPACT project easier.

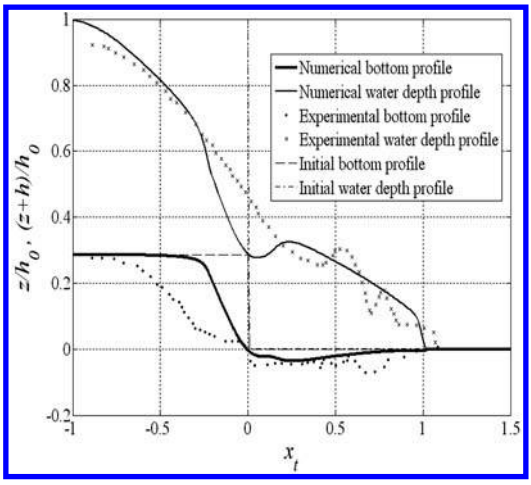


Figure 1. PVC test. Comparison between experimental and numerical results. $t = 0.57$ s.

4.1 *PVC test case*

Figures 1–4 show dimensionless experimental and numerical profiles for different instants of time, where:

$$x_t = \frac{x}{t\sqrt{gh_0}}$$

Figures 1–4 highlight a satisfactory agreement between experimental data and numerical simulations. The model significantly underestimates the bed scour in the early stages of the phenomenon (Fig. 1), but gives good results subsequently (Figs. 3–4). The poor prediction of the bed scour in the early stages was only to be expected. As stated in Spinewine & Zech (2004), strong vertical effects and a plastic mass failure of the soil around the bed step occur just after the initial collapse especially for the PVC test case; it is evident that these processes are not modelled here.

On the other hand all the models failed in this prediction except the UCL models that accounts for the initial mass failure of the bed by means of a liquefaction criterion. Figures 2–3 show that model is able to predict accurately the front wave celerity. In the initial stages, the differences between the experimental

Copyright © 2006 Taylor & Francis Group plc, London, UK

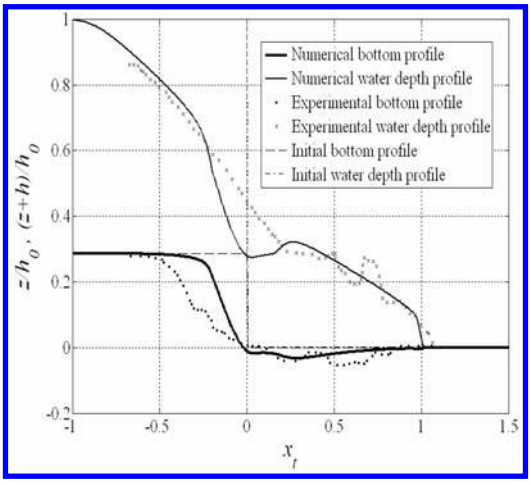


Figure 2. PVC test. Comparison between experimental and numerical results. $t = 0.75$ s.

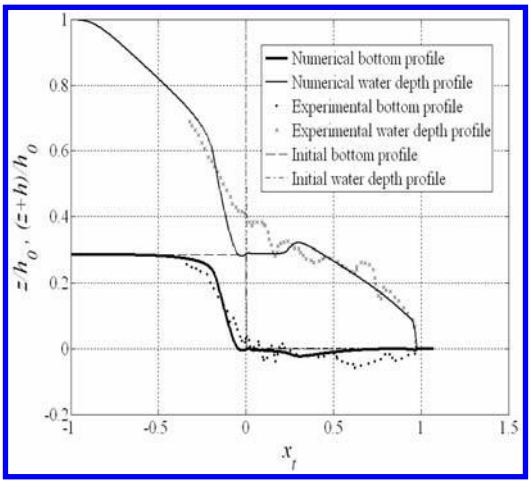


Figure 3. PVC test. Comparison between experimental and numerical results. $t = 1.51$ s.

and numerical water depth profiles are significant but they seem to diminish progressively over time. The re-deposition rate in the first reaches is not reproduced very well as shown in Figure 4; the IMPACT models came up against the same problem (Spinewine & Zech 2004).

The previous considerations are confirmed by the Figure 5 that shows a comparison between numerical and experimental envelopes of maximum water level and minimum bed levels. Despite the clear underestimation in the maximum scour in the early stages, the simulation provides a quite satisfactory result overall.

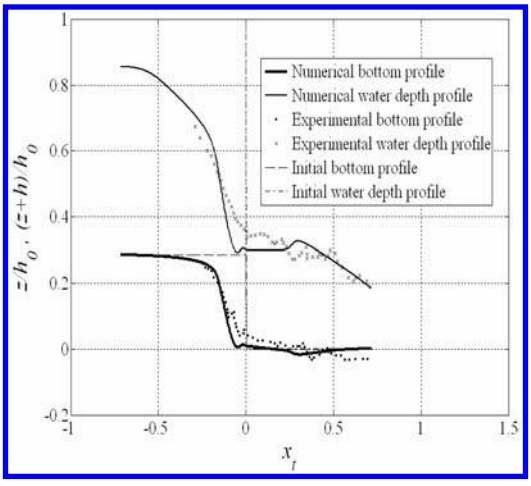


Figure 4. PVC test. Comparison between experimental and numerical results. $t = 2.26$ s.

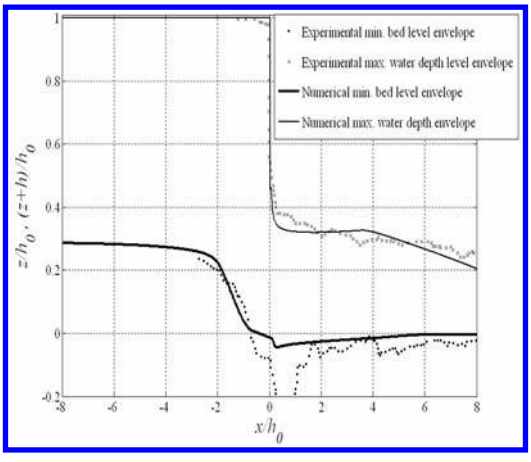


Figure 5. PVC test. Comparison between numerical and experimental envelopes of max. water depth and min. bed level.

4.2 *Sand test case*

Figures 6–9 show dimensionless experimental and numerical profiles for different instants of time. Good results are achieved in the sand case. The computed bed profile shows a good agreement with experimental data even if at the early stages of the process (Fig. 6) the bed scour is underestimated for $x_t > 0.2$. A tendency to slightly overestimate the erosion in the sections just before the initial bed discontinuity may be also noted in Figures 7–9.

Moreover the computed wave has a slower front celerity than the experimental one.

Figure 10 provides a comparison between numerical and experimental envelopes of maximum water

Copyright © 2006 Taylor & Francis Group plc, London, UK

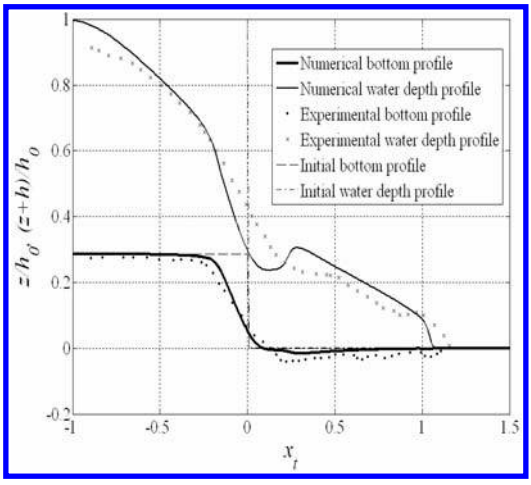


Figure 6. Sand test. Comparison between numerical and experimental results. $t = 0.57$ s.

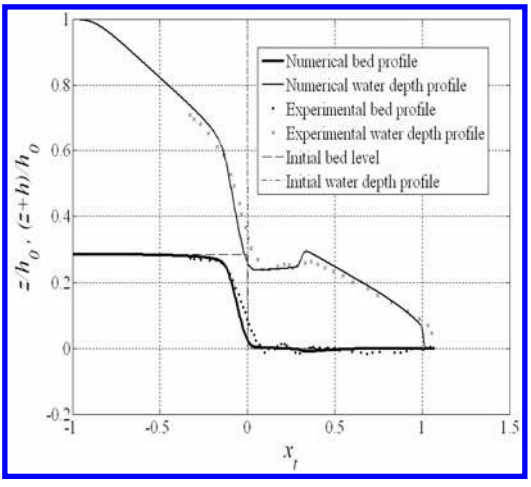


Figure 8. Sand test. Comparison between numerical and experimental results. $t = 1.51$ s.

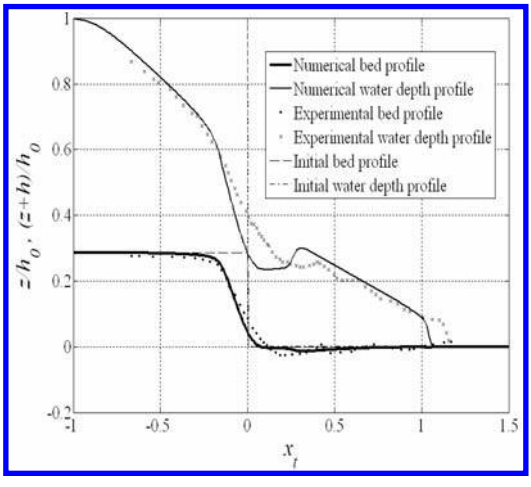


Figure 7. Sand test. Comparison between numerical and experimental results. $t = 0.75$ s.

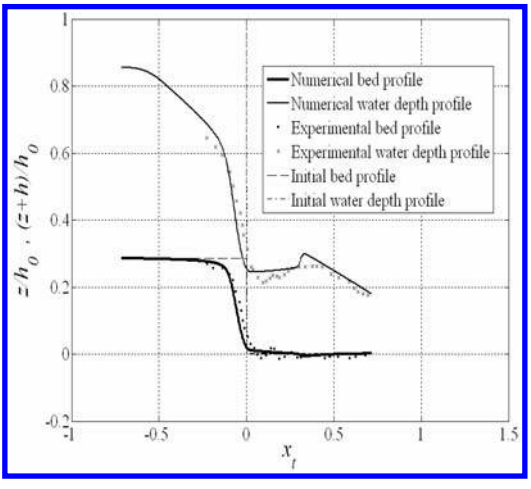


Figure 9. Sand test. Comparison between numerical and experimental results. $t = 2.26$ s.

level and minimum bed level. It confirms the previous considerations on simulated erosion and highlights a slight overestimation on water depth profile.

Nevertheless for the envelope of the minimum bed level the overall result is satisfactory when compared with the predictions of the IMPACT models shown in Spinewine & Zech (2004).

5 SENSITIVITY ANALYSIS

The model has one calibration parameter in the relationship of erosion/deposition velocity. The model sensitivity to above mentioned parameter was performed. In particular, two other values of parameter K_f were taken into account: $K_f = 5$ and $K_f = 20$ that is the half and the double of the reference value.

Figures 11–18 show a zoom near the location of the gate, in order to better analyze the differences among the various simulations.

In Figures 11–14 the sensitivity of the model to K_f for the sand test is shown. It is quite evident that there are no significant differences between the various simulations even at the early stage of the phenomenon; hence one may suggest that parameter K_f does not significantly affect the results for the sand test case in the range of values here examinated.

Copyright © 2006 Taylor & Francis Group plc, London, UK

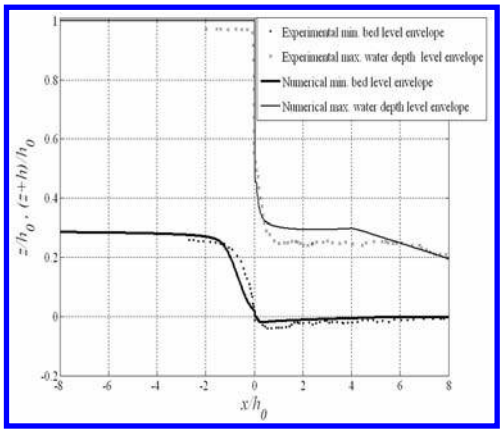


Figure 10. Sand test. Comparison between numerical and experimental envelopes of max. water depth and min. bed level.

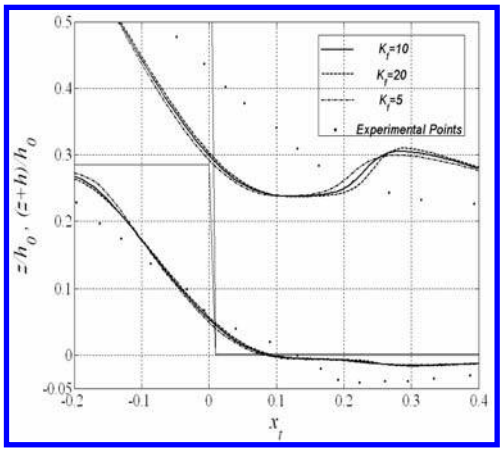


Figure 11. Sand test. Sensitivity to parameter K_f. $t = 0.57$ s.

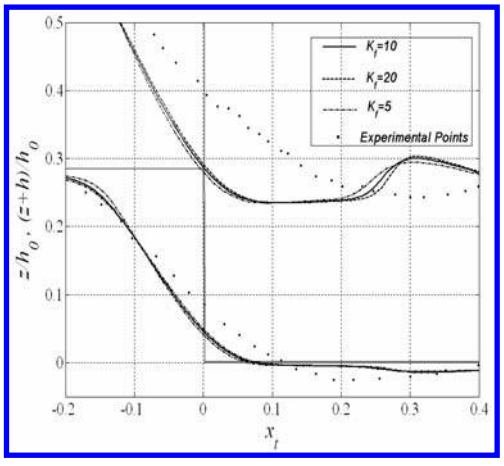


Figure 12. Sand test. Sensitivity to parameter K_f. $t = 0.75$ s.

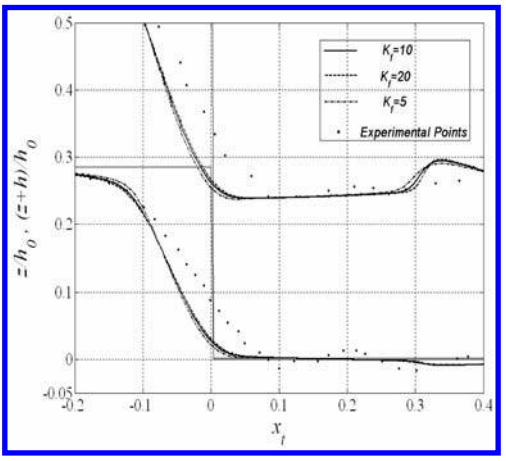


Figure 13. Sand test. Sensitivity to parameter K_f. $t = 1.51$ s.

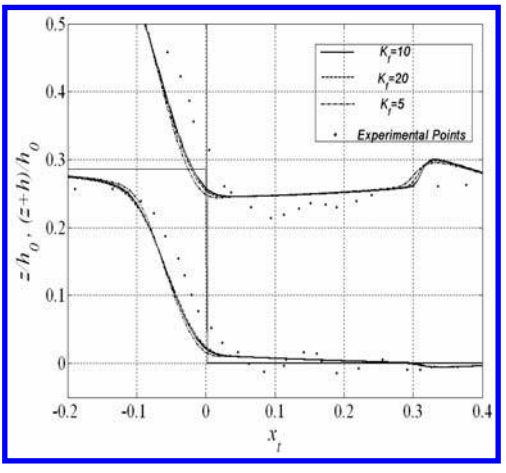


Figure 14. Sand test. Sensitivity to parameter K_f. $t = 2.26$ s.

Different conclusions can be drawn for the PVC test. As shown in Figures 15–18, the solution referring to $K_f = 5$ is different from the reference simulation ($K_f = 10$) while slight discrepancies appear for $K_f = 20$. So it seems that K_f slightly affects the simulation for the PVC test case. In particular, the effect of K_f is more evident in the range of values $0 > x_t > -0.1$ where the erosion/deposition rates are different (Figs. 17–18).

The sensibility analysis highlights that K_f has a little influence on the simulations despite both erosion and deposition rates are proportional to K_f.

Indeed it should be noted that in the early stages of phenomenon the greater K_f the greater both erosion/deposition velocity and local concentration. However in this situation the value of the equilibrium angle θ_e increases (eq. 12) and consequently

Copyright © 2006 Taylor & Francis Group plc, London, UK

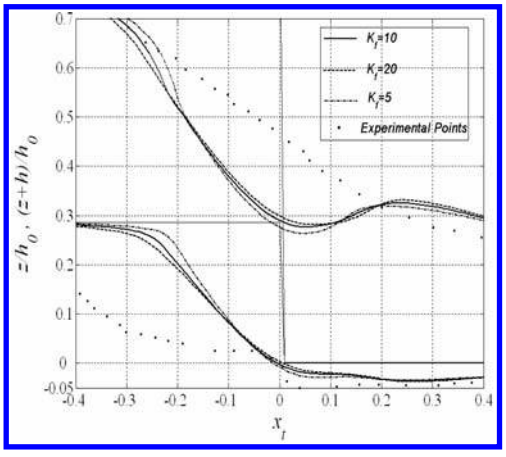


Figure 15. PVC test. Sensitivity to parameter K_f. $t = 0.57$ s.

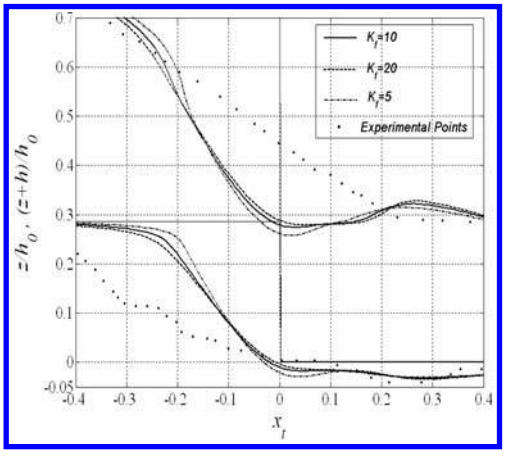


Figure 16. PVC test. Sensitivity to parameter K_f. $t = 0.75$ s.

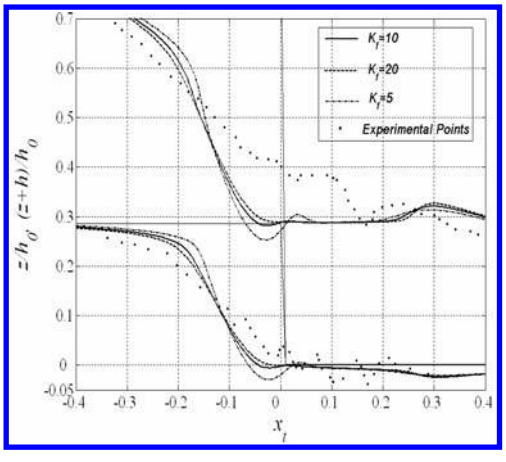


Figure 17. PVC test. Sensitivity to parameter K_f. $t = 1.51$ s.

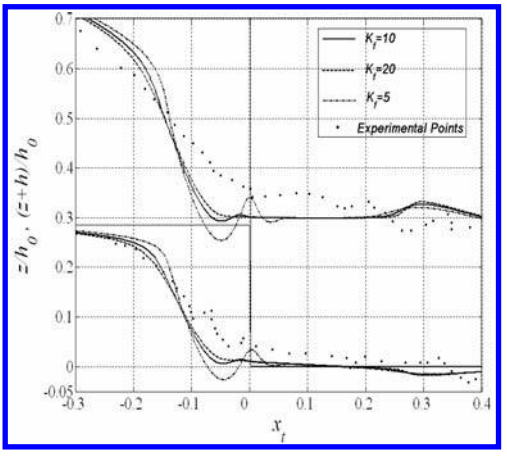


Figure 18. PVC test. Sensitivity to parameter K_f. $t = 2.26$ s.

$\tan(\theta_f - \theta_e)$ diminishes. So the greater K_f the smaller the value of $\tan(\theta_f - \theta_e)$; so this reduction moderates the effects of the increasing values of K_f on the erosion/deposition velocity.

6 CONCLUSIONS

This paper examined the suitability of a one layer model to the computation of dam break waves over movable sediment bed.

The model here presented is based on a shallow water approximation and considers a one layer conceptual idealization of the flow structure; the numerical integration of the governing equations is carried out by means of a first order finite volume method technique.

The simple approach used, both in conceptual and numerical aspects, allowed us to achieve fairly good predictions as regards water depth and bottom profiles. The overall result of the simplified model here presented, especially if compared with those achieved with more complex models within the IMPACT project, seems to highlight a good capability in predicting this phenomenon. In particular the bed evolution law here considered seems to perform well.

The model has just one calibration parameter K_f. A sensitivity analysis was performed to highlight the role of this parameter: it seems that K_f slightly affects the results.

ACKNOWLEDGMENTS

This work was supported in part by the Italian Ministry of Education, University of Research (MIUR) in the PRIN 2005 funding program.

Copyright © 2006 Taylor & Francis Group plc, London, UK

REFERENCES

Bermudez, A. & Vazquez, M.E. 1994. Upwind methods for hyperbolic conservation laws with source terms. *Computer Fluids* 23(8): 1049–1071.

Brufau, P., García-Navarro, P., Ghilardi, P., Natale, L. & Savi, F. 2000. 1D Mathematical modelling of debris flow. *J. Hydraul. Res.* 38(6): 435–446.

Caleffi, V. & Valiani, A. 2002. A mathematical model for dam-break over movable bed. In D. Bousmar & Y. Zech (eds), *River Flow 2002*: 991–1001. Rotterdam: Balkema.

Capart, H. & Young, L. 1998. Formation of a jump by the dam-break wave over a granular bed. *J. Fluid Mech*. 372: 165–187.

Cao, Z., Day, R. & Egashira, S. 2002. Coupled and decoupled numerical modeling of flow and morphological evolution in alluvial river. *J. Hydraul. Eng.* 128(3): 306–321.

Cao, Z., Day, R. & Egashira, S. 2003. Closure of "Coupled and decoupled numerical modeling of flow and morphological evolution in alluvial river". *J. Hydraul. Eng.* 129(3): 743–745.

Cao, Z., Pender, G., Wallis, S. & Carling, P. 2004. Computational dam-break hydraulics over erodible sediment bed. *J. Hydraul. Eng.* 130(7): 689–703.

Costabile, P., Macchione, F. & Rinaldi, L. 2004. Schema monodimensionale per il calcolo dell'erosione di rilevati in materiale sciolto. *Convegno di idraulica e costruzioni idrauliche*, 1: 821–827 (in Italian) Cosenza: Bios.

Costabile, P. & Macchione, F. 2004. Influenza dell'erodibilità dell'alveo sulle piene a rapida evoluzione. In G. Frega (a cura di), *Tecniche di difesa dall'inquinamento*: 119–135 (in Italian), Cosenza: Bios

Egashira, S. & Ashida, K. 1987. Sediment transport in steep slope flume. *Proc. of Roc Japan Joint Seminar on Water Resources.*

El Kadi Abderrezzak, K. & Paquier, A. 2004. Simulation and prediction of river morphology changes using RubarBE. In M. Greco, A. Carravetta & R. Della Morte (eds), *River Flow 2004* 1: 89–98. Rotterdam: Balkema.

Fraccarollo, L. & Capart, H. 2002. Riemann wave description of erosional dam-break flows. *J. Fluid Mech*. 461: 183–228.

Fraccarollo, L. Capart, H. & Zech, Y. 2003. A Godunov method for the computation of erosional shallow water transient. *Int. J. Numer. Meth. Fluids* 41: 951–976.

Gallino, G. & Pierson, T. C. 1985. Pollalie Creek debris flow and subsequent dam break floods of 1980. East Fork Hood River Basin, Oregon. *US Geol. Survey Water Supply, Paper* 2273.

Iverson, R.M. 1997. The physics of debris flow. *Rev. of Geophys*. 35(3): 245–296, American Geophysical Union.

Leal, J.G.A.B., Ferreira, R.M.L. & Cardoso, A.H. 2003. Dam break wave propagation over a cohesionless erodible bed. *Proc. 30th IAHR Congress*, International Association for Hydraulic Research, Delft, 2: 261–268. the Netherlands.

Lapointe, M.F., Secretan, Y., Driscoll, S.N., Bergeron, N. & Lecelerc, M. 1998. Response of the Ha! Ha! River to the flood of July 1996 in the Saguenay Region of Quebec: large scale avulsion in a glaciated valley. *Water Resources Res.* 34: 2383–2392.

Spinewine, B. & Zech, Y. 2002. Dam break waves over movable beds: a "flat bed" test case. *IMPACT, Investigation of Extreme Flood Process and Uncertainty, Proceedings 2nd Project Workshop*, Mo-i-Rana, Norway, 12–13 September 2002.

Spinewine, B. & Zech, Y. 2003. Dam break waves over movable beds: a test case exploring different bed materials and an initial bed discontinuity. *IMPACT, Investigation of Extreme Flood Process and Uncertainty, Proceedings 3rd Project Workshop*, Louvaine-la-Neuve, Belgium, 6–7 November 2003.

Spinewine, B. & Zech, Y. 2004. The stepped dam break test case: results from the IMPACT benchmark. *IMPACT, Investigation of Extreme Flood Process and Uncertainty, Proceedings 4th Project Workshop*, Zaragoza, Spain, 3–5 November 2003.

Takahashi, T. 1991. *Debris Flow*, Balkema, Rotterdam.

Toro, E.F. 1997. *Riemann solvers and numerical methods for fluid dynamics*. Berlin: Springer.

Toro, E.F. 2001. *Shock-capturing methods for free-surface shallow flows.* Wiley & Sons, Ltd.

Zech, Y. & Spinewine, B. 2001. Dam Break induced floods and sediment movement – State of the art and need for research. *http://www.samui.co.uk/impact-project*

Copyright © 2006 Taylor & Francis Group plc, London, UK

Dike erosion – A preliminary outlook

Willi H. Hager & Jens Unger
VAW, ETH Zurich, Zurich, Switzerland

ABSTRACT: Dike breaching along larger rivers result yearly in a great loss of lives and goods. Although this 'classic problem' of hydraulics has threatened people from the old times, few actions have so far been taken by the hydraulics community. The following presents the results of a preliminary study and the future research to be considered by a Swiss National Science Foundation project aiming to understand the essentials of both plane and spatial dike breachings. It is found that this problem may be attacked only as a combined numerical *and* experimental approach, of which this work relates exclusively to the latter aspect. Some experimental findings are described and the results of selected preliminary test observations are discussed to allow for an appreciation of the technical problems involved in such a research project.

1 INTRODUCTION

According to the Thesaurus Dictionary, a *dike* is an embankment of earth and (or) rock built to prevent floods. Dikes are therefore typically used in river engineering. In contrast, a *dam* corresponds to a barrier across a waterway to control the flow or to raise the water level. Whereas the dike is normally made up of loosely placed sediment, a dam often consists of a surface layer and a dam core made up of different material such as clay, rock and possibly also concrete. Dams are normally much higher than dikes but are significantly shorter in length. To withstand the enormous water pressure of up to several hundreds of meters, dams require a much more involved technology than do dikes. Whereas dikes were erected from ancient times, successful dam engineering initiated only in the first decades of the 20th century. The following refers exclusively to dikes as a more or less homogeneous accumulation of natural sediments consisting of sand or gravel. The components silt and sand below 1 mm are not considered here because of their particular mechanical properties involving effects of viscosity, among others (Ivicsics 1979).

A *simple dike* corresponds to a trapezoidal-shaped accumulation of sand or gravel of which the up- and downstream angles are below the angle of natural repose, i.e. some 33° for natural sand. Besides the materials mentioned, no other material such that a core or a surface layer are added to the simple dike. The erosion process of the simple dike is therefore governed exclusively by surface sediment transport. Any surface strengthening such as grass may be considered as an added safety against dike failure by erosion. A simple dike is also resistant against internal erosion such that the failure mode under consideration may be formulated essentially in terms of sediment surface erosion and sediment deposition.

The erosion process of a simple dike may be either plane or spatial. The latter case normally occurs in applications, due to incipient erosion at a location where the dike crest is slightly lower than in the vicinity, resulting for instance from a local settlement of the dike structure. Spatial dike erosion includes the complicated lateral erosion process, of which the fundamentals are currently not completely understood. The following therefore relates mainly to plane dike erosion as a basic erosion process. Once this phenomenon is understood both from the experimental and the numerical points of view, spatial dike erosion is analyzed as a consequence from the processes observed in nature.

Figure 1 shows a historical photograph of a dike breaching having occurred close to the bridge abutment. Upstream from the breach, the dike has resisted against the flood discharge but it failed at this critical location, possibly because of a slight river contraction due to the abutment. The consequence of such a dike failure may be catastrophic because the backland from the dikes is often unprotected and the waters have no blockage and large plains may be inundated within a comparatively short time. Such scenarios have been and are still typical for large floodplains, causing an enormous financial loss and may be accompanied with fatalities. Hydraulics has so far not solved the problem and it is normally impossible to predict the limits of discharge, rainfall and the dike characteristics under which the next failure occurs. This

Copyright © 2006 Taylor & Francis Group plc, London, UK



Figure 1. Flooding of Alpine Rhine Valley upstream of Lake Constance, with bridge failure caused by dike breaching and lateral flow onto flood plain (Minor & Hager 2005).

research project would like to add to this basic feature of dike hydraulics both by an experimental and a computational approach.

2 PRESENT KNOWLEDGE

The erosion of dikes was only considered once the basics of sediment transport were available, despite the damages that occurred with dike breaches for a long time. Therefore, the history of predictive dike hydraulics starts around 1960. An early work on the washout of erodible fuse plugs was conducted by Tinney & Hsu (1961). Using both a laboratory model and small prototype observations allowed defining some characteristics of the side erosion of a dam. Sandover (1969) determined experimentally the discharge coefficients of a dike made up by uniform incohesive sediment during dike erosion. Das (1973) investigated the end scour phenomena downstream of a dike due to dike overtopping without indication of the temporal scour progress. Martins (1981) analyzed the stability of overflow rockfill dams with a model study, thereby concentrating to its downstream face. Note that his dams included an impervious core separating the upstream from the downstream sections. Powledge et al. (1989 a, b) conducted a large study on the overflow erosion of embankments. Part I related to the various protection systems in preventing overflow erosion, whereas Part II accounted for hydraulic observations during dam overtopping and to a number of case stories. Despite this research applies to dams of limited width, it may be considered the most complete study until 1990.

Abt & Johnson (1991) determined the riprap dimensions required for overtopping flow of sloped surfaces. Their result is a diagram in which the riprap diameter is plotted against the unit discharge for various dam surface slopes. Bechteler & Broich (1991) aimed at the mathematical modelling of dike breaching. The sediment transport was described with the standard Meyer-Peter-Müller MPM and the Engelund-Hansen equations. The main purpose of their study was to define the dike outflow hydrograph, resulting in large differences between the computational approaches used. Coleman et al. (2002) considered the overtopping of homogeneous incohesive dikes in a laboratory flume. The breach advance profiles in both the streamwise and the transverse directions were observed using digital potentiometers. Each experiment was repeated several times and stopped at a certain instant to furnish the momentary breach geometry. This approach uses a significant laboratory effort, therefore, and may be applied only to a limited number of experiments. The results of this excellent study include some information on the breach advance geometry, the erosion rate and the breach discharge.

A further study was conducted by Rozov (2003) thereby assuming a rectangular breach geometry. A closed-form solution of the breach width as a function of time may be obtained with a simplified computational approach. Leopardi et al. (2003) presented a computational approach to dike breaching using the shallow-water equations, the Exner equation and the Meyer-Peter-Müller MPM equation for sediment transport. This model was applied to a typical case study resulting in a reasonable overall agreement. Höeg, et al. (2004) conducted a unique series of field experiments in Norway to study the stability of embankment dams constructed of various materials. Up to six meter high dams were investigated in terms of failure characteristics; so far, no final report is available. Cao et al. (2004) presented a computational model to the hydraulics of erodible dikes. Their model was stated to be one of the first so far available; it is based on sediment transport and the morphological evolution of the breach characteristics. The *Landesamt für Umweltschutz* (LfU 2004) proposed means to protect dikes from erosion during overtopping. Finally, an uncertainty analysis of the prediction of the embankment dam breach parameters was conducted by Wahl (2004), thereby involving historical data that may be important for testing novel laboratory observations and predictions using improved computational approaches. A general account on this topic was also presented by Singh (1996).

3 VAW OBSERVATIONS

Figure 2 shows a definition sketch of the experimental set-up for simulating the erosion pattern of a

Copyright © 2006 Taylor & Francis Group plc, London, UK

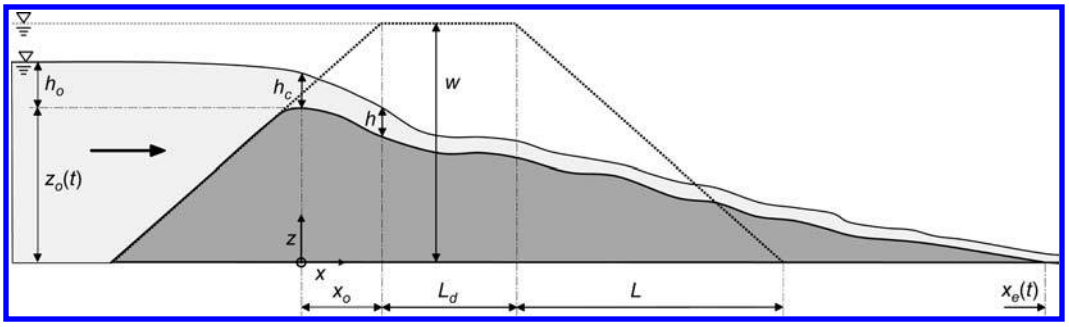


Figure 2. Sectional view of dike for plane erosion tests (Lüthi 2005).

simple dike as used at *Versuchsanstalt für Wasserbau, Hydrologie und Glaziologie* VAW, of ETH Zurich. Following a preliminary test phase, the erosion process of a dike was observed to be almost plane if both the dike width and the sediment size are small. A dike width of only $B = 0.10$ m was adopted for these preliminary tests, therefore. Depending on the sediment size, a meandering flow pattern resulted with only a portion of the dike width eroded for wider dikes consisting of larger sediment sizes. In all tests, a steady discharge scenario was considered.

The main parameters investigated in this project were:

- Critical flow depth $h_c = [Q^2/(gB^2)]^{1/3}$ as discharge load, between discharges $Q = 1$ to 10 l/s,
- Height of dike w, from 0.05 to 0.30 m,
- Slope of dike from 1:2 to 1:5, normally 1:3 both at the up- and downstream dike faces,
- Crest width of original dike $L_d = 0.10$ m, and
- Sediment median size $d_{50} = 1.15$, 2.3 and 5.0 mm for uniform sand, and a sand mixture.

Here h is the local flow depth, z the instantaneous height of dike from the origin and t is time. The origin of the coordinate system $(x;z)$ is located at the bed beneath the instantaneous upstream crest of the dike. The reservoir filling was relatively fast, typically within 1 minute. The dike core was initially dry such that the overflow process started prior to the phreatic surface had reached the dike toe. The approach flow velocity was usually so small that the upstream overflow depth h_u was equal to the overflow energy head. In all tests, no tailwater submergence was applied such that the overflow was free at all times. The deposition pattern was not further investigated in these tests. The data relating to the free surface water profiles were also recorded.

The temporal progress of both the water surface $h(x,t)$ *and* the sediment surface $z(x,t)$ was determined for a total of 40 tests with a CCD camera across the glass wall of the channel. This technique allowed for a simple determination of the two profiles from the test data. Both the free surface and the erosion profiles were further treated to allow for a general insight into the mechanics of plane dike erosion. The following relates to some particular results obtained during this research.

Figure 3 shows the temporal progress of a typical test. Initially, the constant discharge Q was added resulting in dike overtopping at time $t = 0$. Shortly later, at $t = 12$ s, the overflow front reaches the original dike bed elevation; it may be noted that the small overflow discharge at this time results in a step-pool formation down the dike face associated with a retreat of the hydraulic control towards the upstream crest point. At time $t = 7$ s almost half of the dike is eroded with a further retreat of the hydraulic control. A wavy pattern of the erosion surface may be observed without any transition to locally subcritical flow. At time $t = 160$ s, the dike is eroded almost completely leaving an undular erosion surface.

Figure 4 shows the results of two typical runs relative to the temporal progress of the sediment surface $z(x,t)$. Both figures show an important feature that was generally observed: The hydraulic control point separating the reaches of subcritical and supercritical flows moves along the original upstream dike surface. Because both the discharge and the sediment size were small in the tests of figure 4 (a) and large in figure 4 (b), an similar erosion pattern may be observed from the two plots.

It was also stated that the downstream eroded dike face remains almost linear at a certain time during the initial erosion phase, such that two particular points were considered: (1) The hydraulic control point $(x_o;z_o)$, where $x_o(t)$ is approximately known for a certain elevation $z_o(t)$ as previously observed, and (2) the dike end point $(x_e;0)$, where the straight from the hydraulic control point cuts the origin $z = 0$. A simplified analysis of the large data set was therefore conducted using a one-dimensional approach. This research allows to predict the two functions $z_o(t)$ and $x_e(t)$. The details of this analysis are not discussed here. The future application of

Copyright © 2006 Taylor & Francis Group plc, London, UK

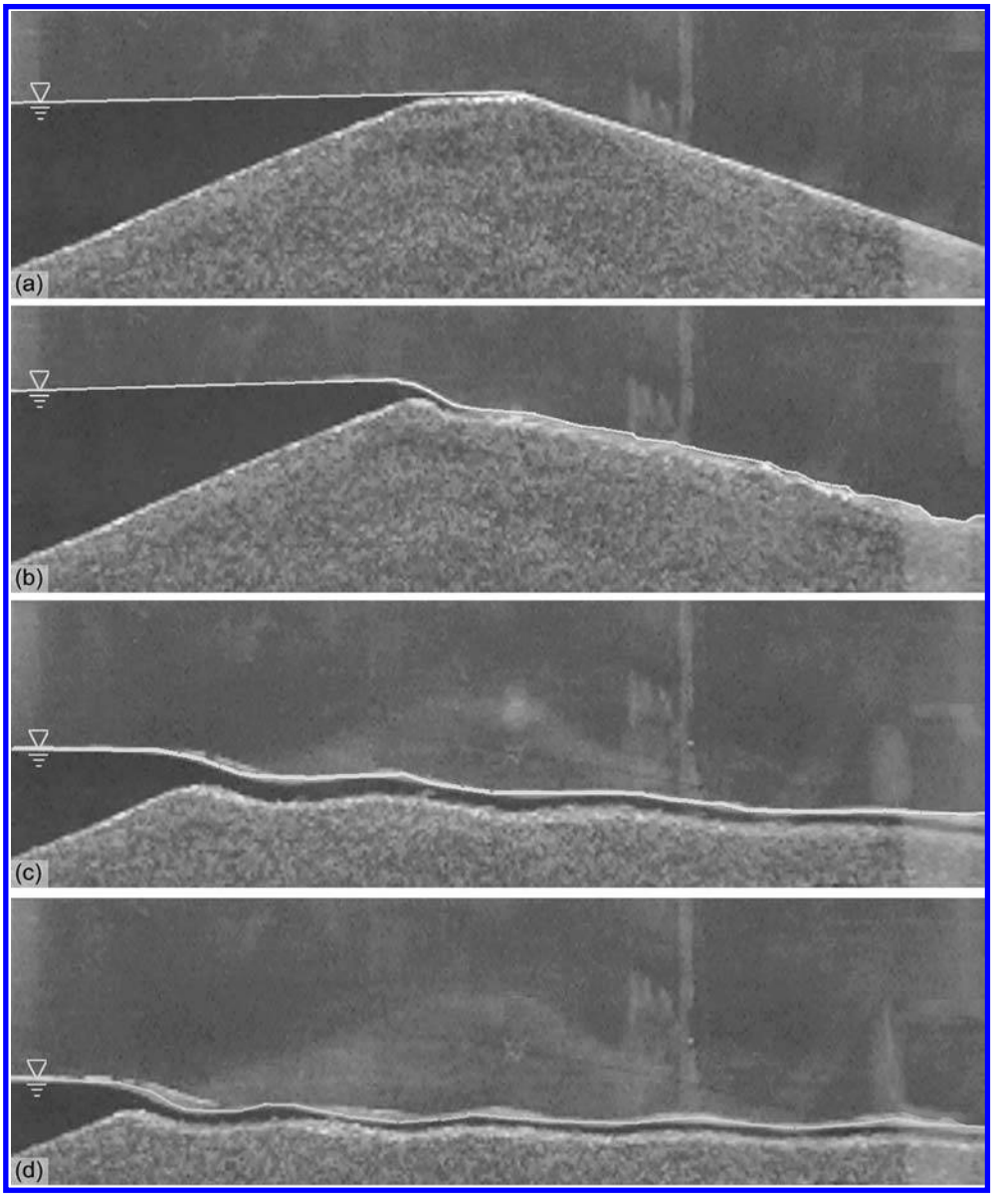


Figure 3. Temporal progress of dike erosion for slope 1:3, $w = 0.20$ m, $d_{50} = 5$ mm at times $t =$ (a) 0, (b) 12 s, (c) 70 s and (d) 160 s.

these results for the present project shall be described below.

4 OUTLOOK

The erosion of dikes modelled both experimentally *and* numerically poses extraordinary problems to both instrumentation and to computational performance. Three items must, therefore, receive a particular attention:

- Transition from subcritical to supercritical flow reaches, and vice versa,
- Changes from wetted to dry, and from dry to wetted surfaces, and
- Erosion and deposition both in the streamwise and in the transverse directions.

Copyright © 2006 Taylor & Francis Group plc, London, UK

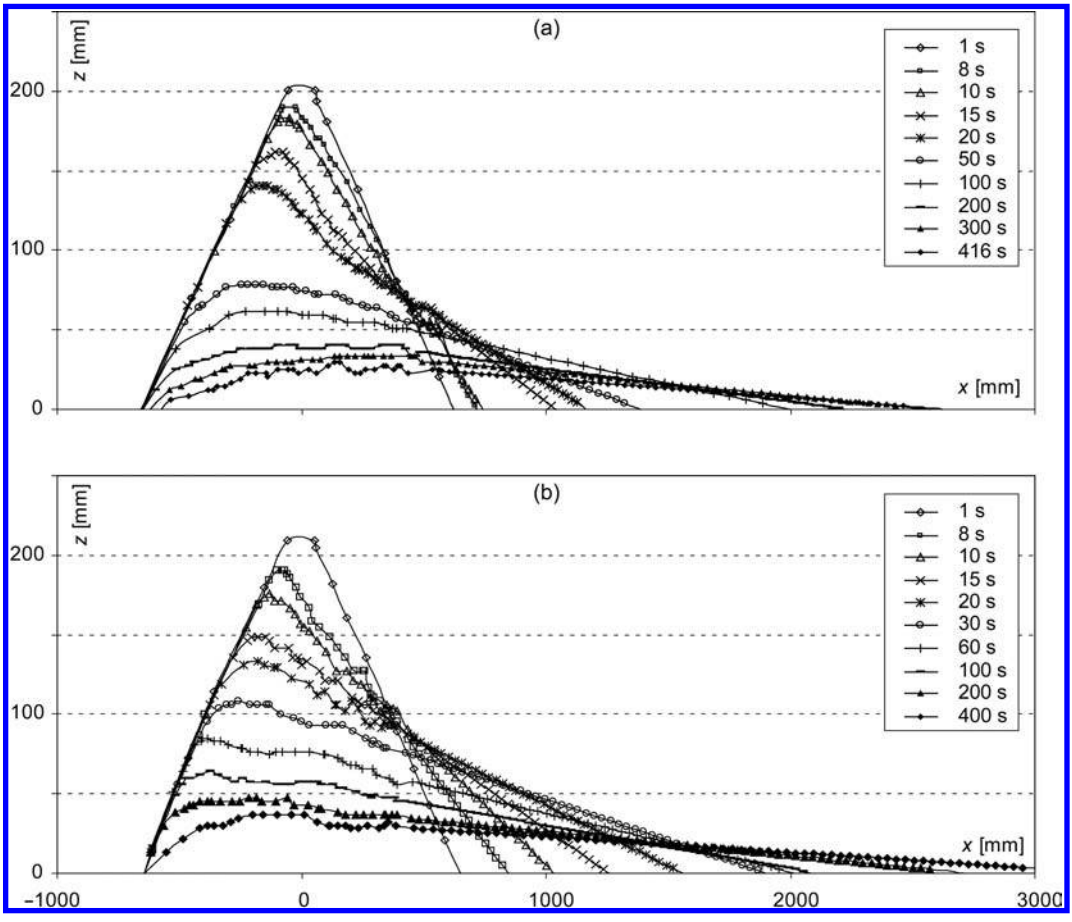


Figure 4. Streamwise erosion progress $z(x,t)$ for (a) $Q = 5$ l/s and $d_{50} = 1.1$ mm, (b) $Q = 11.5$ l/s and $d_{50} = 5.0$ mm (Lüthi 2005).

Item 1 is not only linked to the dike crest zone because of the step-pool pattern of the flow down a dike for a small flow depth and a relatively large sediment size. It was found in the preliminary experimentation that these flows develop particularly during the initial phase for dikes made up of large sediment (Lüthi 2005). Further, this problem also occurs on the downstream flood plain, where the supercritical dike overflow may undergo a change to subcritical flow along with undular or direct hydraulic jumps. Undular jumps are often complex because of local Froude numbers slightly above 1. Handling such flows may ask for the inclusion of the effect of streamline curvature, resulting in complex equations of the Boussinesq type for the free surface.

Item 2 relates to the phase boundaries between the water and the sediment. It applies therefore to the breach region, but also to larger deposition zones in the flood plain. The effect of surface tension is irrelevant in prototype dikes but may be important under laboratory conditions. So far, the existing VAW computational code is able to model these zones relatively well (Faeh 1996, 2000). The results will have to be checked with the hydraulic test data to assess the computational accuracy.

Item 3 is particularly complex because a novel type of sediment transport equation should be developed. The current transport formulae apply essentially for uniform flow conditions in an almost horizontal sediment bed. Dikes have a slope that is of the order 1:5 (V:H) and steeper, such that the slope effect may not be neglected. An even more complex problem involves the side erosion: Currently, no general models are available by which this effect can be accounted for in a thorough approach for incohesive sediment. This latter information is of course essential from the very beginning of a dike breaching because the breach geometry and therefore the breach discharge depend

Copyright © 2006 Taylor & Francis Group plc, London, UK

significantly on it. Model observations allow for a development of the current mathematical formulation, therefore.

It may be clear from the previous discussion that this research is directed to the hydrodynamics of dike breaching. The details of a dike are therefore simplified, resulting in the 'simple dike' model as previously introduced. It was mentioned that a dike made up of incohesive sediment corresponds to the simplest arrangement of which the safety against failure is the smallest for a certain scenario. This 'simple dike' structure retains the basics of the erosion and the deposition problems, relating both to the numerical and the experimental aspects.

5 SPATIAL DIKE BREACHING

Figure 5 shows the temporal advance of a spatial dike breaching, in which the main breaching features may be appreciated. Figure 5 (a) relates to the starting condition, with the upstream water elevation practically at the dike crest level. Note that the dike remained stable at its toe under a slight tailwater submersion. In prototypes, a dry flood plain may be more realistic, a condition that could also be considered in the tests. In Figure 5 (b) the central portion of the dike is overtopped resulting in a central breach geometry which is indicated in the photo with white lines. In the case considered, the dike sediment was relatively small such that there was a smooth overtopping in contrast to conditions involved with larger sediment and a smaller discharge. In Figure 5 (c), the dike is almost eroded to half of the original height: The side erosion progressing along the left dike side is a particular feature. In this test, the right dike side was completely eroded due to the slightly asymmetric dike crest geometry. In prototypes, side erosion is the important mechanism in predicting the temporal advance of the flood plain discharge, dike erosion rate and sediment deposition. The almost final erosion stage is seen from Figure 5 (d), with the remaining left dike abutment. Figure 5 (e) relates to a streamwise look from the glass wall. Note the 'white water' due to suspended silt, preventing any observation of the internal flow patterns because of invisibility.

Figure 6 relates to the end stage of the dike erosion test after the water was almost completely drained from the test section. It is noted from Figures 6 (a) and (b) that the right tailwater portion was eroded during the test, whereas the other side underwent a sediment deposition associated with an undular surface structure at the interface of the two reaches. Figure 6 (c) relates to the remnants of the 'abutment' showing an almost vertical dike flank. This part is complex in the computational approach and needs a particular attention.

6 SIGNIFICANCE OF PROJECT

When initiating the dike breaching project proposed as a general topic of risk mitigation and the assessment of natural hazards, the authors were shocked by the relatively small actions undertaken by the hydraulics community so far. As was evidenced in the state-of-the-art review, a modest amount of works is currently available: What are the reasons for this deficit in knowledge? The authors are of the opinion that the complexity of the overall problem is high, e.g. to investigate a spatial flow field in two-phase flow where erosion and deposition of the granular phase is a key issue. Nevertheless, based on the past achievements in the experimental and the computational analysis of sediment-water flows, this problem can be advanced essentially if adequate instrumentation is available.

The complexity of the dike breaching problem in prototypes stems from the relatively large surface involved allowing exclusively for a refined numerical treatment. However, because a number of processes are currently poorly understood, as previously outlined, additional laboratory observations on particular features are required for an adequate numerical simulation. These relate to the sediment erosion and deposition patterns, and to the side erosion of incohesive granulate. To further these processes from a scientific background, a combined experimental *and* numerical approach to the dike breaching problem is considered essential.

A key issue of the experimental approach is the recording of the flow fields due to a dike breaching. An adequate instrumentation involving e.g. stereo and underwater photography based on advanced videometry to retrace the main features of erosion, and Particle Tracking Velocimetry system to define the velocity fields at any time along the breach surface are required (Godding et al. 2003, Unger 2006). In the computational field, the findings from hydraulic experimentation will have to be implemented thereby advancing several subroutines regarding the sediment transport algorithms. Both the plane *and* a spatial breach development have to be considered because scenarios in the nature may include particularly the latter type of flow. Yet, to advance current knowledge, the simpler plane dike breach has to be understood before the more complex case is considered.

As demonstrated previously, there are currently a number of cases that may result in large damages due to dike overtopping. To predict their essence and to take measures in terms of evacuation and damage reduction, only numerical approaches allow for the proper planning of the major actions that have to be organized prior to an event. These include:

– Evacuation scenarios for the population and protection measures for the infrastructure concerned,

Copyright © 2006 Taylor & Francis Group plc, London, UK

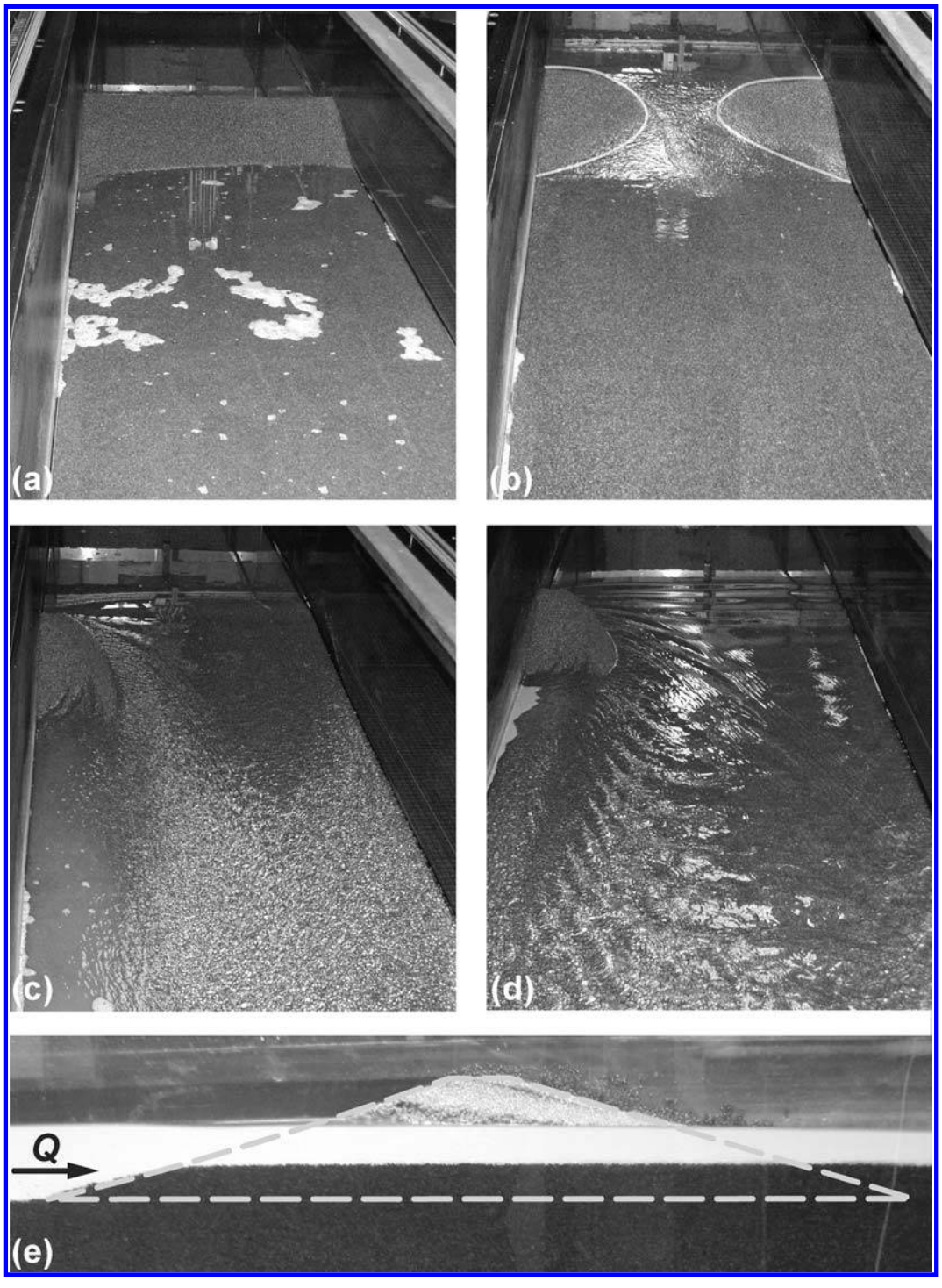


Figure 5. Typical sequences of spatial dike breach, with views from the tailwater (a to d) and from the side (e). Test parameters were $w = 0.15$ m, $Q = 15$ l/s, $d_{50} = 0.0011$ m, dike slope 1:3.

Copyright © 2006 Taylor & Francis Group plc, London, UK

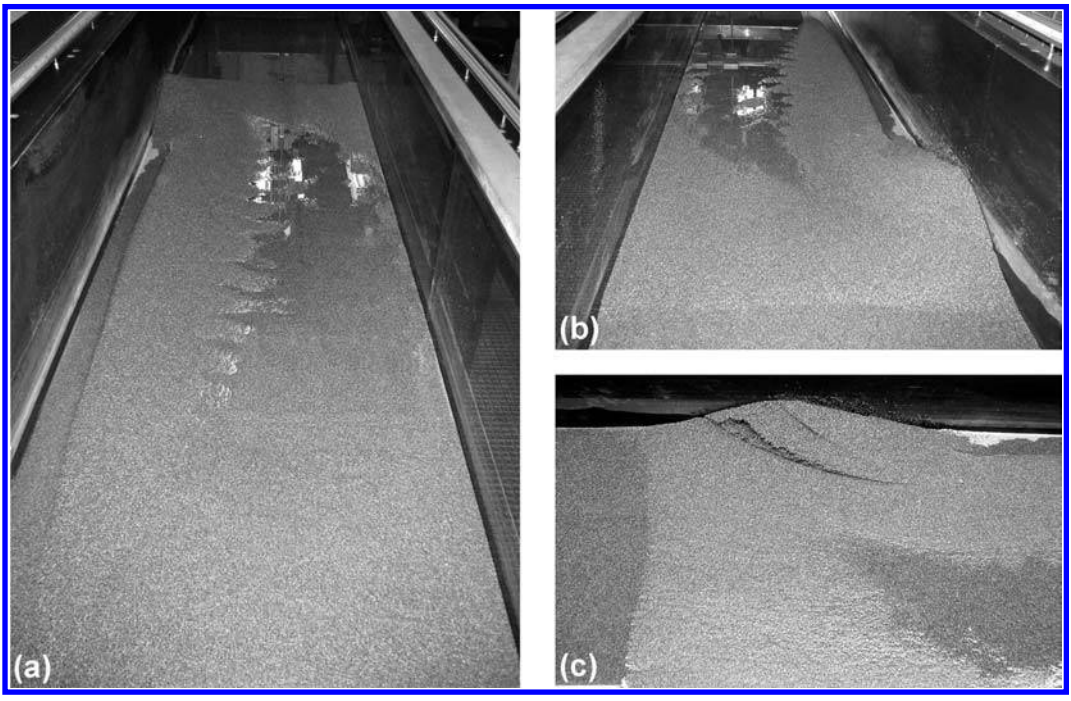


Figure 6. End stage of dike eroded by overtopping (a) from tailwater, (b) from upstream and (c) side view of lateral dike erosion.

– Safety structures to be erected directing the main flood discharge to less critical zones,
– Optimizing tasks to study actions to be undertaken before a dike is about to break, and
– Interactions of hydraulic engineers and the authorities as an important tool in the decision support.

The dike breaching project is considered a great chance to demonstrate the capabilities of modern hydraulic engineers in advancing an exiting hydraulic problem for the safety and the risk reduction from natural hazards.

7 CONCLUSIONS

Dikes are made up mainly of sediment placed along a river to protect the flood plains from inundations. To explore the hydraulics of the dike breaching process, the so-called 'simple dike' was introduced. This structure is made up by an almost homogeneous and practically straight dike subject to erosion exclusively due to overtopping. The experimentation proposed herein points to the definition of the relevant sediment transport equation, to the handling of flow transitions from sub- to supercritical flow, and vice versa, and to the understanding of the wetting and the drying fronts of the dike and the flood plain during the erosion process. These three key issues along with the temporal evolution of the water and the sediment surfaces, and the velocity field both on the dike surface and the tailwater were identified as the parameters of note that have to be known for further predictions. These include flooding maps and the design of flood mitigation structures to effectively protect a certain flood plain from large and unexpected inundations. The major actions to be taken in a future dike breaching project are presented and their relevance for the modern society is described.

REFERENCES

Abt, S.R., Johnson, T.L. (1991). Riprap design for overtopping flow. *Journal of Hydraulic Engineering* 117(8): 959–972.

Bechteler, W., Broich, K. (1991). Effects of dam-break modelling. In D. Ouazar, (ed.), *Computer methods in water resources* II: Computational hydraulics and hydrology: 89–98. Springer: Berlin.

Cao, Z., Pender, G., Wallis, S., Carling, P. (2004). Computational dam-break hydraulics over erodible sediment bed. *Journal of Hydraulic Engineering* 130(7): 689–703.

Coleman, S.E., Andrews, D.P., Webby, M.G. (2002). Overtopping breaching of noncohesive homogeneous embankments. *Journal of Hydraulic Engineering* 128(9): 829–838.

Copyright © 2006 Taylor & Francis Group plc, London, UK

Das, B.P. (1973). Bed scour at end-dump channel constrictions. *Journal of the Hydraulics Division* ASCE 99(HY12): 2273–2291.

Faeh, R. (1996). Erosion-based dambreak simulation. Proc. Second Int. Conf. *Hydroinformatics* '96, Zurich 2: 681–688.

Faeh, R. (2000). Impact of sediment transport on flood risk estimations. *River Flood Defence*, F. Toensmann, M. Koch eds. 1: F-191-F200. Herkules-Verlag: Kassel.

Godding, R., Hentschel, B., Kauppert, K. (2003). Videometrie im wasserbaulichen Versuchswesen. *Wasserwirtschaft* 93(4): 36–40 (in German).

Höeg, K., Lövoll, A., Vaskinn, K.A. (2004). Stability and breaching of embankment dams: Field tests on 6 m high dams. *Hydropower & Dams* 11(1): 88–92.

Ivicsics, L. (1979) *Hydraulic models*. Research Institute Water Resources Development: Budapest.

Leopardi, A., Oliveri, E., Greco, M. (2003). Numerical simulation of gradual earth-dam failure. *L'Acqua* 72(2): 47–54.

LfU (2004). *Überströmbare Dämme und Dammscharten*. Landesanstalt für Umweltschutz Baden-Württemberg: Karlsruhe.

Lüthi, N. (2005). Deicherosion. *Diploma thesis*. VAW, ETH: Zürich (in German).

Martins, R. (1981). Hydraulics of overflow rockfill dams. *LNEC Mémoria* 559. Laboratorio Nacional de Engenharia Civil: Lisboa.

Minor, H.-E., Hager, W.H. eds. (2005). *River engineering in Switzerland*. Stäubli AG: Zürich.

Powledge, G.R., Ralston, D.C., Miller, P., Chen, Y.H., Cloppner, P.E., Temple, D.M. (1989 a). Mechanics of overflow erosion on embankments. I Research activities. *Journal of Hydraulic Engineering* 115(8): 1040–1055.

Powledge, G.R., Ralston, D.C., Miller, P., Chen, Y.H., Cloppner, P.E., Temple, D.M. (1989 b). Mechanics of overflow erosion on embankments. II Hydraulic and design considerations. *Journal of Hydraulic Engineering* 115(8): 1056–1075.

Rozov, A.L. (2003). Modeling of washout of dams. *Journal of Hydraulic Research* 41(5): 565–577.

Sandover, J.A. (1969). Discharge coefficients of constrictions in open channels. *Water Power* 21(7): 256–261.

Singh, V.P. (1996). *Dam breach modeling technology*. Kluwer: Dordrecht.

Tinney, E.R., Hsu, H.Y. (1961). Mechanics of washout of an erodible fuse plug. *Journal of the Hydraulics Division* ASCE 87(3): 1–29.

Unger, J. (2006). *Strömungscharakteristika um kreiszylindrische Brückenpfeiler* – Anwendung von Particle Image Velocimetry in der Kolkhydraulik. *PhD thesis* 16557. ETH: Zürich.

Wahl, T.L. (2004). Uncertainty of predictions of embankment dam breach parameters. *Journal of Hydraulic Engineering* 130(5): 389–397.

Copyright © 2006 Taylor & Francis Group plc, London, UK

Discontinuities in geomorphic dam-break flows

Rui M.L. Ferreira & Sílvia Amaral
Instituto Superior Técnico, Lisbon, Portugal

João G.B. Leal
Universidade da Beira Interior, Covilhã, Portugal

Benoit Spinewine
Université catholique de Louvaine-la-Neuve, Louvaine-la-Neuve, Belgium

ABSTRACT: Geomorphic dam-break flows have been shown to feature discontinuities other than the downstream progressing wavefront. Of particular importance is the jump that forms, for some combinations of initial conditions and bed materials, near the location of the dam. No attempts to characterize this jump were undertaken until recently. In this text, the discontinuities occurring in geomorphic dam-break flows are investigated in the framework of a shallow-flow theory. The main objective is to understand whether they are susceptible to be described by Riemann waves or if they are flow features aroused by momentum sources, namely friction, or by phenomena beyond the shallow-flow theory. For that purpose, experimental results are presented and compared with a theoretical solution of the governing equations given initial discontinuous data. The classification of the discontinuities follows the comparison between the observed and calculated flow features for the same initial conditions. No attempt is made to address the phenomenological aspects of the formation and evolution of the discontinuities. Nevertheless, the observed behavior is discussed in conjunction with the weak solution of the governing equations.

1 INTRODUCTION

Geomorphic dam-break flows arise from the rapid release of stored water into a mobile bed channel and provoke important morphological changes in the downstream valley. Such flows propagate in the form of a bore, a type of wavefront, often laden with sediment, which, given the involved length scales, can be considered a discontinuity. The speed of this discontinuity, along with the maximum water depth associated to the dam-break flow, have been studied at length, as they constitute important elements for downstream risk assessment (Zech et al. 2004).

The wavefront may not be the only discontinuity in geomorphic dam-break flows. A hydraulic jump occurring near the location of the dam was reported in the early mobile-bed experiments of Chen and Simons (1979). More recently, Capart and Young (1998) drew attention to an upstream-progressing jump seen to form at early times at the dam location. For some combinations of initial conditions and bed material, the experimental results of Leal et al. (2002) also exhibit discontinuities forming at the vicinity of the dam and traveling at much smaller velocities than the wavefront. The experiments performed in these works do not provide a coherent body of data, since the shape and the dimensions of the flumes are too distinct to make the results commensurable. On safe grounds, only one observational result can be uttered: on prismatic rectangular mobile-bed channels, geomorphic dam-break flows resulting from the instantaneous removal of a vertical dam exhibit, for some combinations of initial conditions and bed material, a jump that forms near the location of the dam at early times and whose velocity is slower than that of the wave-front. This discontinuity will be henceforth called a *2-jump*.

The characterization of the wavefront benefits from more than one hundred years of theoretical and experimental studies (for the review of early results, *cf.* Stoker 1958, pp. 22–22). Quite on the contrary, the amount of empirical results concerning the 2-jump is virtually limited to the works cited in the preceding paragraph and the theoretical results are almost inexistent (see Ferreira 2005, pp. 303–305, for a review).

In this text, the discontinuities occurring in geomorphic dam-break flows are investigated. Special emphasis is placed on the quantification of the variables that

Copyright © 2006 Taylor & Francis Group plc, London, UK

describe the 2-jump. It should be made clear that the thorough phenomenological characterization of these discontinuities will not be attempted. The main objective is to understand whether they are susceptible to be described by Riemann waves of the weak solution of the homogeneous part of the governing shallow-water equations or if they are flow features whose mathematical description requires a different formal treatment.

Empirical evidence, the experimental results described in Amaral (2004), §5, and Spinewine (2005) is compared with the solution of the governing equations, as presented by Ferreira (2005), pp. 396–430. The classification of the discontinuities follows the comparison between observed and calculated flow features for the same initial conditions. If the solution of the homogeneous shallow-water equations does not seem to describe occurring flow discontinuities, it is concluded that phenomena not included in the inertial and flux terms of the governing one-dimensional equations is responsible for the 2-jump.

The above methodology requires previous acquaintance with the conceptual model for the description of the geomorphic dam-break flows. It also requires some knowledge on the weak solution of the shallowwater equations given the dam-break Riemann problem. Both are addressed in the second section of the text. The third section is dedicated to the presentation of the experimental procedures and results. A comparison between the observed flow profiles and theoretical solution is carried out in the fourth section. The nature of the discontinuities is discussed in the fifth section. Finally, the text is ended by a number of concluding remarks.

2 CONCEPTUAL MODEL AND THEORETICAL SOLUTION

Written in vector notation, the first order, nonhomogeneous, hyperbolic system of conservation laws that describe geomorphic dam-break flows is

$$\partial_t (\mathbf{V}(\mathbf{U})) + \partial_x (\mathbf{F}(\mathbf{U})) = \mathbf{G}(\mathbf{U}) \tag{1}$$

where $\mathbf{V}$: $\mathbb{R} \times]0, +\infty[\rightarrow \mathbb{R}^3$ is the vector of dependent primitive variables, $\mathbf{U}$: $\mathbb{R}^3 \rightarrow \mathbb{R}^3$ is the vector of conservative variables, $\mathbf{F}$: $\mathbb{R}^3 \rightarrow \mathbb{R}^3$ is the flux vector, $\mathbf{G}$: $\mathbb{R}^3 \rightarrow \mathbb{R}^3$ is the vector of the source terms and x and t are the space and time co-ordinates, respectively.

Should the collapse of a dam be idealized as an instantaneous removal of a vertical barrier initially separating two constant states that extend indefinitely on both up- and downstream directions, as seen in figure 1, the mathematical expression of the dambreak problem is a Riemann problem. The conceptual model employed in this study to describe geomorphic dambreak flows is that developed by Ferreira 2005, §3. It

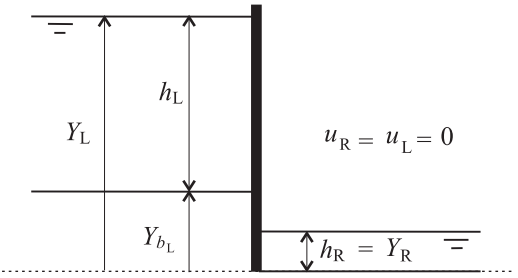


Figure 1. Initial conditions of the dam-break problem. The involved variables are: Y, the water elevation, h the water depth, Y_b the bed elevation and u, the depth-averaged flow velocity. The subscripts L and R stand for the initial left and right states, respectively.

features unsteady flow hydro- and sediment dynamics and channel morphology. In what concerns sediment dynamics, the dense limit approximation of the granular flow theory, rooted in Enskog's kinetic theory of dense gases (Chapman and Cowling 1970, §16), provided the theoretical background for the core of the model.

The one-dimensional conceptual model results from the integration of two-dimensional governing equations in an idealized layered domain. Multiple-layer shallow-water models were introduced by Capart (2000) and further developed by Fraccarollo and Capart (2002) and Spinewine (2005). Ferreira et al. (2003) followed a different approach. They considered that the total shear and normal stresses are continuous across the flow depth and into the bed and that the layers are mathematical idealizations based on the predominant type of stress.

Thus, the conceptual model employed in this study features i) a lowermost layer, the bed, composed of grains with no appreciable vertical or horizontal mean motion, ii) the contact load layer, where collisional stresses are dominant and iii) the suspended sediment layer, where turbulent stresses dominate (details in Ferreira 2005, pp. 229–231).

There is no result guarantying the existence and unicity of the solution to the Cauchy problem represented by governing equations of the conceptual model and any complete set of initial conditions. Furthermore, the theoretical attempts to prove the existence of the a weak solution for the Riemann problem fail because of the source terms, namely friction and non-equilibrium sediment transport. Fraccarollo and Capart (2002) attempted to show that there is a time window where the effects of flow friction are negligible and were local equilibrium is a valid hypothesis for the sediment transport. Although the results of Fraccarollo and Capart (2002) are strictly valid for erosional flows and for a particular conception of a frictional time scale, it will be assumed that

Copyright © 2006 Taylor & Francis Group plc, London, UK

there is indeed a time window for which geomorphic dam-break flows feature equilibrium sediment transport and are marginally affected by the bed shear stress. The conservation equations become homogeneous and are susceptible to be written in the following quasi-conservative form

$$\partial_t (h + Y_b) + \partial_x (hu) = 0 \tag{2}$$

$$\partial_t (a_m hu) + \partial_x \left(a_c u_c^2 h_c + u_s^2 h_s + g\left(\tfrac{1}{2}h_s^2 + \tfrac{1}{2}a_c h_c^2 + h_s h_c\right)\right) + g(a_c h_c + h_s)\,\partial_x (Y_b) = 0 \tag{3}$$

$$\partial_t ((1-p)Y_b + C_c h_c) + \partial_x (Chu) = 0 \tag{4}$$

where h is the water depth, u is the depth averaged flow velocity, Y_b is the bed elevation, h_c, u_c and C_c are, respectively, the thickness, the depthaveraged velocity and the flux-averaged concentration of the contact load layer, h_s and u_s are, respectively, the thickness and the depth-averaged velocity of the suspended sediment layer, $a_m = 1 + (s-1)C$, $a_c = 1 + (s-1)C_c$, s is the specific gravity of the sediments, C is the flow-averaged sediment concentration and g is the acceleration of gravity. The concentration C_s was eliminated since its value is generally much lower than C_c.

Equations (2) to (4) can be solved for the total flow depth, h, the layer-averaged flow velocity, u, and the bed elevation, Y_b. Closure equations for C_c and h_c are derived from the dynamics of the contact load layer (details *in* Ferreira 2005, pp. 277–289). They read

$$C_c = \frac{\theta d_s}{tan(\varphi_b) h_c} \tag{5}$$

$$h_c = m_1 \theta + m_2 \tag{6}$$

The variables and parameters in equations (5) and (6) are θ, the Shields parameter, defined as $\theta = C_f u^2/(g(s-1)d_s)$, d_s the particle diameter, $tan(\varphi_b)$, the ratio of shear to normal stresses near the bed and m_1 and m_2, parameters that should depend on the mechanical properties of the sediment particles, on its diameter and density and on the viscosity of the fluid. Ferreira (2005), pp. 283–285, hypothesized that, for a given fluid, m_1 and m_2 may show little variation with the particle properties and can be considered constants. In this work, it is considered that $m_1 = 6.5$ and $m_2 = 1.5$. The depth-averaged velocity in the contact layer is obtained assuming that $u(y)/u_* \propto (y/h_c)^{\frac{1}{6}}$ where $u_*^2 = C_f u^2$ is the friction velocity. Depth-averaging over the layer thickness, it is obtained

$$u_c = u\left(\frac{h_c}{h}\right)^{\frac{1}{6}} \tag{7}$$

Although equations (2) to (4) express the conservation of fundamental flow quantities and despite being homogeneous equations, Glimm's theorem Glimm (1965) for the existence and unicity of weak solutions of the Riemann problem can not be directly applied. This is so because equations (2) to (4) cannot be written in pure conservative form. Indeed, term $g(a_c h_c + h_s)\partial_x(Y_b)$ represents a source of momentum and is not reducible to a conservative flux.

Ferreira (2005), pp. 361–363, using Glimm's theorem, attempted to prove the existence of weak solutions for the Riemann problem

$$\partial_t (\mathbf{V}(\mathbf{U})) + \partial_x (\mathbf{F}(\mathbf{U})) + \mathsf{A}\partial_x (\mathbf{V}(\mathbf{U})) = \mathbf{G}(\mathbf{U}) \tag{8}$$

$$\mathbf{U}_0 \equiv \mathbf{U}(x, t=0) = \begin{cases} \mathbf{U}_\mathrm{L} & \text{if } x < 0 \\ \mathbf{U}_\mathrm{R} & \text{if } x \geq 0 \end{cases} \tag{9}$$

where equation (8) condenses equations (2) to (4) and where A is a matrix such that $\mathsf{A}_{23} = g(a_c h_c + h_s)$ and $\mathsf{A}_{ij} = 0, (i,j) \neq (2,3)$. Weak solutions were shown to exist but they are not unique. In fact, existence can only be asserted if A is linearized across discontinuities. Thus, the solution depends on the specific linearization carried out. The Rankine-Hugoniot jump conditions derived from the integral form of equation (8) become

$$(\mathbf{U}_\mathrm{d} - \mathbf{U}_\mathrm{u})\, S_j = (\mathbf{F}_\mathrm{d} - \mathbf{F}_\mathrm{u}) + \mathsf{A}^* (\mathbf{U}_\mathrm{d} - \mathbf{U}_\mathrm{u}) \tag{10}$$

where S_j is the velocity of the shock associated to the $\lambda^{(j)}$-characteristic field, A^* is the linearized matrix A and d and the subscripts u stand for "downstream" and "upstream", respectively. A consistent linearization can be obtained by averaging the terms across the discontinuity.

Ferreira (2005), pp. 363–366, showed that the weak solution of system (8) subjected to (9), in which $\mathbf{U}_0$ expresses the geometry seen in Figure 1, admits two types of self-similar solutions, depending on the values of h_L, Y_{b_L} and h_R. If the eigenvalues associated to the eigenvectors of system (8) are such that $\lambda^{(1)} > \lambda^{(2)} > \lambda^{(3)}$, the solution of type A comprises one expansion wave associated to the $\lambda^{(3)}$-characteristic field initial and two shock waves, associated to the $\lambda^{(2)}$- and the $\lambda^{(1)}$-characteristic fields. The wave structure of each of these solutions, represented in the x–t plane, can be seen in Figure 2. The corresponding flow profiles are shown in Figure 3. Solution of type B, first studied by Fraccarollo and Capart (2002) in the wake of Fraccarollo and Armanini (1999), does not admit 2-jumps. On the contrary, in the solution of type A, the shock associated to $\lambda^{(2)}$ is a flow feature that may be associated to the 2-jump.

It is noted that the $\lambda^{(2)}$-shock features a negative jump in the flow depth and a positive, aggradational, jump in the bed elevation. The direction of propagation and the type of morphological impacts featured by the observed jump provide the fundamental criteria to decide whether it is a flow structure describable by a

Copyright © 2006 Taylor & Francis Group plc, London, UK

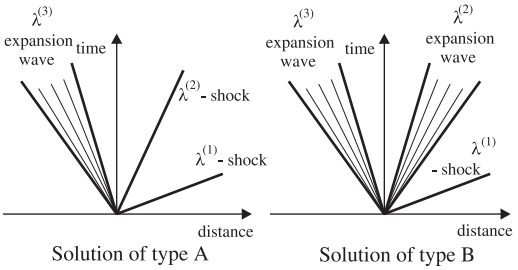


Figure 2. Wave structure of the weak solution of the Riemann problem constituted by system (8) subjected to the initial conditions (9). Left: solution of type A; right: solution of type B.

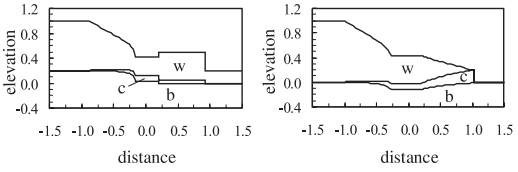


Figure 3. Flow profiles corresponding to the weak solution of the Riemann problem constituted by system (8) subjected to the initial conditions (9). Left: solution of type A; right: solution of type B. The flow regions are: w – clear water/suspended sediment layer; c – contact load layer and b – bed.

Riemann shock or one that requires different conceptualization. Thus, 2-jumps that migrate upstream and that are associated to scour in the bed are clearly not described by the flow and sediment dynamics included in equations (2) to (4).

3 EXPERIMENTAL PROCEDURES AND RESULTS

The experimental work took place in the laboratory of hydraulics of the Department of Civil and Environmental Engineering of the Université catholique de Louvain, Louvain-la-Neuve, Belgium. The experimental tests were performed in 6 m long and 25.1 cm wide horizontal channel. The dam was simulated by a vertical gate, placed at 3 m from the extremities, whose movement is directed downwards (Spinewine 2005, p. 56). A manually activated trigger releases the pressure of 7 bar, generated in a compressor, required to open the gate at a speed of about 5 m s^{-1}. The maximum non-dimensional time necessary to open the gate is $t_0^* = t_0\sqrt{\frac{9.8}{max(h_L)}} = 0.4$ where to is the maximum time necessary to open the gate and $max(h_L)$ is the maximum initial water depth behind the gate.

The experimental texts were recorded in digital video by a CCD camera acquiring 200 fps with the resolution of 512 × 1024. The flow was fully recorded in the downstream reach of the channel. Upstream the gate, only the first 0.8 m were recorded. Since the recording area is about 0.8 m wide per 0.5 m height, each test had to be repeated five times. In order to synchronise the runs, a TTL flash light visible by the camera in each of its positions is triggered by the gate release. It should be mentioned that the repeatability of the tests was found to be highly satisfactory provided that the sameness of the initial conditions was ensured with some zeal. A mote detailed description of the experimental set-up and of the tests, along with additional tests performed for other initial conditions and bed material, may be found in Spinewine (2005).

The sediment particles used in scale laboratory models seldom abide to the global geometric scale. As a result, the mobility of the sediment is generally underestimated. In order to increase sediment mobility, the tests were performed with PVC pellets with $s = 1.56\,\mathrm{kg\,m^{-3}}$. The equivalent diameter of a PVC particle – the diameter of a sphere with the same volume – is 3.9 mm. The dimensions of the particles exhibited little variability.

All tests featured a piecewise horizontal bed. In accordance with figure 1, the datum was set to the level of the downstream bed. It is important to note that the downstream bed was saturated in all tests, even if $h_R = 0$.

The fundamental non-dimensional parameters that describe the initial conditions illustrated in figure 1 must take into account the flow depth downstream the dam and the jump in the bed elevation across the dam. The particular choice of parameters employed in this text are

$$\alpha \equiv \frac{h_R + |min\,(0, Y_{b_L})|}{h_L + max\,(0, Y_{b_L})} \tag{11}$$

and

$$\delta \equiv \frac{Y_{b_L}}{h_L + max\,(0, Y_{b_L})} \tag{12}$$

The length scale implicit in (11) and (12) is

$$L_* = h_L + max\,(0, Y_{b_L})$$

From this length scale, time and velocity scales can be derived. It is obtained $T_* = \sqrt{\frac{L_*}{g}}$ and $U_* = \sqrt{gL_*}$, respectively.

The initial conditions for the nine experimental tests shown here, described with the variables presented in figure 1, are shown in Table 1.

The raw data obtained from the tests is composed of video footages taken in the five locations along the channel. This data was treated to render flow profiles (details in Amaral 2004). In this profiles three surfaces were identified: a) the free surface, b) the boundary between the transport layer and the clear water layer

Copyright © 2006 Taylor & Francis Group plc, London, UK

Table 1. Summary of the initial data for experimental tests.

Name	h_L (m)	Y_{b_L} (m)	h_R (m)	L_* (m)	α (–)	δ (–)
25_-05_00	0.30	−0.05	0.00	0.30	0.167	−0.167
35_-05_00	0.40	−0.05	0.00	0.40	0.125	−0.125
25_00_00	0.25	0.00	0.00	0.25	0.000	0.000
35_00_00	0.35	0.00	0.00	0.35	0.000	0.000
35_05_00	0.30	0.05	0.00	0.35	0.000	0.143
25_05_00	0.20	0.05	0.00	0.25	0.000	0.200
35_10_00	0.25	0.10	0.00	0.35	0.000	0.286
25_05_05	0.20	0.05	0.05	0.25	0.200	0.200
35_10_10	0.25	0.10	0.10	0.35	0.286	0.286

and c) the boundary between the bed and the transport layer. The profile of the water depth was computed as the difference between the the free surface and the bed. From the water depth profiles, it was possible to estimate the location and the strength of the observed discontinuities at each instant.

4 COMPARISON BETWEEN EXPERIMENTAL AND THEORETICAL RESULTS

The observed flow profiles are shown in figure 4 – solution of type B – and 5 – solution of type A. The theoretical profiles, calculated from the weak solution of system (8) given the initial conditions discriminated in table 1, are also shown in these figures, superimposed to the flow profiles.

The values of the friction coefficient employed in the closure equations (5) and (6) are shown in Table 2. They were chosen so to achieve best agreement between the experimental and the theoretical profiles. Sediment concentrations are controlled by the value of $tan(\varphi_b)$. Lacking universally acknowledged estimates for this parameter, it was imposed $tan(\varphi_b) = 0.45$, a value chosen so that the maximum concentration in the contact load layer would be around 0.3 in all tests whose solution is of type B.

Both the experimental profiles and the theoretical solutions are shown in self-similar co-ordinates. It is observed that the thickness of the contact load layer and the minimum bed elevation are correctly estimated in almost all tests. Naturally, phenomena pertaining to soil mechanics, namely slope stability and *en masse* bed movement, could not have been reproduced by the theoretical solution since the governing equations do not incorporate formulations for those phenomena. Hence, the the steep slopes featured by the weak solutions at the end of the expansion wave associated to the $\lambda^{(3)}$– characteristic field in figures 4e, f and g are in clear contrast with the much gentler slopes featured by the observed profiles. This gentle slope was essentially formed at the beginning of the times when the gate was lowered: the sharp bed step could not be maintained by the cohesionless bed material; a fracture surface was formed at the toe of the step with the inclination of the rest angle of the particles; finally the sediment above this fracture surface entered the contact load layer and was eventually deposited further downstream. A simple mechanism accounting for this mass failure was proposed and tested by Spinewine and Zech (2005).

In the tests with a negative bed step (4a and b) the theoretical solution captures the bed profile reasonably well. It is observed that a steep positive slope results from the initial discontinuity. Presumably, it is the flow that provides the extra shear force tomaintain the bed slope larger than the submerged rest slope.

The instability of the initial bed step in the experimental texts shown in figure 5 obeyed same same mechanisms already explained for the tests depicted in figures 4e, f and g. However, because of the presence of a layer of water downstream, the transport capacity is much lower and the flow does not evolve into a debris-flow-like wave front. Hence, the bed material resulting from the initial bed step failure is deposited almost instantaneously at the toe of the step and, as the flow looses memory of the gatemovement, becomes a bed discontinuity progressing downstream along with the jump in water surface. As a result, the bed profile calculated along the expansion wave associated to the $\lambda^{(3)}$-characteristic field is, in these tests, a better description of the observed profile.

The effect of flow resistance is perceived in the observed profiles inasmuch they are not truly selfsimilar. This is particularly true for the flows depicted in figures 4. Furthermore, it is noticed that Froude similarity does not completely determine the flow profiles. If that was the case, parameters α and δ would suffice to determine the profiles. Instead, it is observed in figures 4c and d, whose profiles are both characterized by $\alpha = 0$ and $\delta = 0$, that neither the velocity of the wave front nor the overall shape of the profile is the same for both flows. Ferreira et al. (2006) propose that the shape of the self-similar profile of any flow variable U_i can, under certain simplifying conditions, be determined by

$$\Gamma_i = \Pi_i \left(\alpha, \delta, s, tan(\varphi_b), \frac{d_s}{L_*} \right) \tag{13}$$

In the present case, s and $tan(\varphi_b)$ are constants. Thus, the relative submersion of the particles, d_s/L_*, must be accounted for the differences in the observed profiles. The only way to introduce this effect in the theoretical solution is by varying the friction coefficient. This justifies the values of C_f seen in table 2.

Evidently, all flows exhibit a discontinuous wave front. As for the 2-jumps, their existence and the variables that characterize them were determined in accordance to the principles explained in section 3. It is clear that tests 25_-05_00, 35_-05_00 and 35_00_00

Copyright © 2006 Taylor & Francis Group plc, London, UK

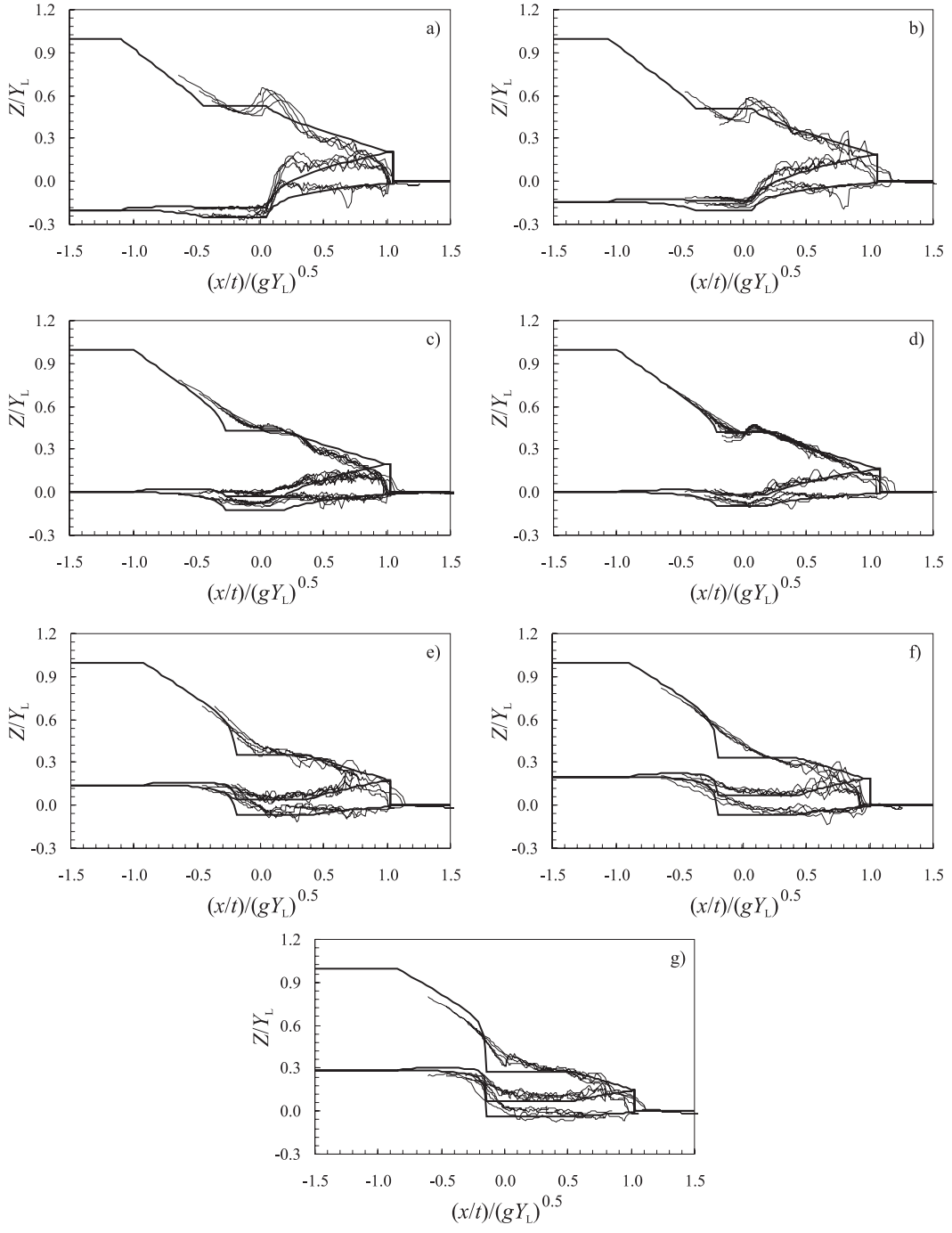


Figure 4. Flow profiles. Solution of type B. Profiles correspond to tests a) 25_-05_00; b) 35_-05_00; c) 25_00_00; d) 35_00_00; e) 35_05_00; f) 25_05_00; g) 35_10_00. Solid thick lines (———) stand for the theoretical solution while solid thin lines (———) stand for the observed profiles.

Copyright © 2006 Taylor & Francis Group plc, London, UK

Table 2. Friction coefficient employed in equations (5) and (6).

Name	α (–)	δ (–)	C_f (–)
25_-05_00	0.167	−0.167	0.017
35_-05_00	0.125	−0.125	0.015
25_00_00	0.000	0.000	0.017
35_00_00	0.000	0.000	0.012
35_05_00	0.000	0.143	0.015
25_05_00	0.000	0.200	0.017
35_10_00	0.000	0.286	0.012
25_05_05	0.200	0.200	0.012
35_10_10	0.286	0.286	0.012

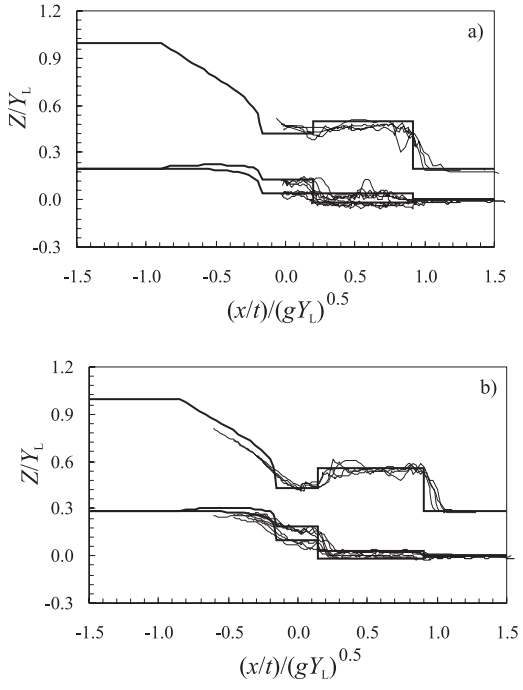


Figure 5. Flow profiles. Solution of type A. Profiles correspond to a) 25_05_05; b) 35_10_10. Solid thick lines (———) stand for the theoretical solution while solid thin lines (——) stand for the observed profiles.

(figure 4a, b and d) develop 2-jumps that progress upstream. Tests 25_05_05 and 35_10_10 (figures 5a and b) develop 2-jumps that move downstream. The properties of these discontinuities will be discussed in the next section.

5 DISCUSSION

In both solutions, the shock associated to the $\lambda^{(1)}$-characteristic field is physically identifiable with the wave-front (see figures 4 and 5). On the contrary, the 2-jump may not always be identifiable by the shock associated to the $\lambda^{(2)}$-characteristic field in the solution of type A. Indeed, it is clear from figures 2 (left) and 5 that this is a downstream progressing shock, while the observed 2-jumps often migrate upstream.

The dynamics and the kinematics of the wave-front are sufficiently well described by the Rankine-Hugoniot jump conditions, equations (10) with $j = 1$. Indeed, the strength of the wavefront, defined as $h_R - h_1$, remains approximately constant throughout the duration of the experimental test (see figure **??**) which enables a meaningful comparison between the weak solutions and the experimental profiles.

The velocity of the wavefront, however, decreases over time, as seen in figure 6, especially for the tests for which $h_R = 0$ (figures 6a to f). This fact prompted Leal et al. (2006) to describe the path of the wavefront in the x_t plane as a 2nd order equation. There is no appreciable decrease in the velocity of the wavefront in the experiments for which $h_R > 0$. This suggests that bottom friction is the main responsible for the delay of the wavefront.

Since bottom friction is not included in the weak solution of 8, in order to delay the velocity of the wavefront in the theoretical solution it is necessary to increase the factors that affect S_1 in 10. Such factors are related to the inertia of the contact load layer and are expressed by its thickness and the sediment concentration. Given that $tan(\varphi_b)$, m_1 and m_2 are constants, a good agreement of the observed and the calculated wavefront velocity requires a good estimate for the friction coefficient C_f.

The influence of d_s/L_* can only be addressed in the theoretical solution with adjustments of the friction factor. Thus, the correct modeling of the velocity of the wavefronts of tests 25_00_00 ($d_s/L_* = 0.0180$) and 35_00_00 ($d_s/L_* = 0.0129$), both characterized by $\alpha = 0$ and $\delta = 0$ can only be attained if the friction factor relative to 25_00_00 is increased. Indeed, as seen in figure 6c, the non-dimensional velocity of the wavefront of the test characterized by $d_s/L_* = 0.0180$ is smaller than that of the test for which $d_s/L_* = 0.0129$. As expected, the friction coefficient is larger for the flow with the smaller relative submersion.

An undesirable consequence of the increase of C_f is the increase of the flow depth in the first constant state (the state upstream the $\lambda^{(2)}$-shock). As seen in figure 7, the theoretical shock strength is consistently overestimated, for the same initial conditions.

Fraccarollo and Capart (2002) noticed that the wavefront propagates as an erosional shock. Since it is associated to the $\lambda^{(1)}$-characteristic field, it is fundamentally a hydrodynamically-driven shock: the bed jump is comparatively small. On the contrary, Ferreira 2005, §5.2.2, showed that the $\lambda^{(2)}$-shock is always an aggradational shock in which morphodynamics is of

Copyright © 2006 Taylor & Francis Group plc, London, UK

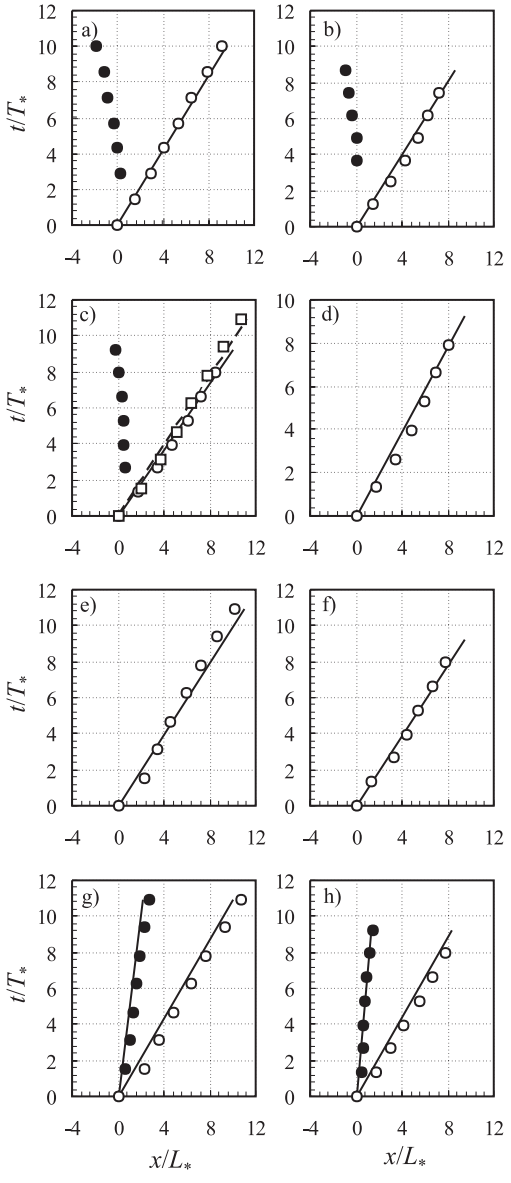


Figure 6. Calculated and measured non-dimensional shock paths. a) $\alpha = 0.167$, $\delta = -0.167$; b) $\alpha = 0.125$, $\delta = -0.125$; c) $\alpha = 0.0$, $\delta = 0.0$ (features tests with $d_s/L_* = 0.0129$ and $d_s/L_* = 0.0180$); d) $\alpha = 0.0$, $\delta = 0.143$; e) $\alpha = 0.0$, $\delta = 0.200$; f) $\alpha = 0.0$, $\delta = 0.286$; g) $\alpha = 0.200$, $\delta = 0.200$; h) $\alpha = 0.286$, $\delta = 0.286$. Solid lines (——) stand for the calculated path of the $\lambda^{(1)}$-and the $\lambda^{(2)}$-shocks; open circles (○) stand for the measured path of wavefront; solid circles (●) stand for the measured path of the 2-jump. In figure c), the convention is maintained for the test with $d_s/L_* = 0.0129$; for the test with $d_s/L_* = 0.0180$, the dashed line (- - - -) stands for the calculated path of the $\lambda^{(1)}$-shock and the open squares (□) stand for the measured path of the wavefront.

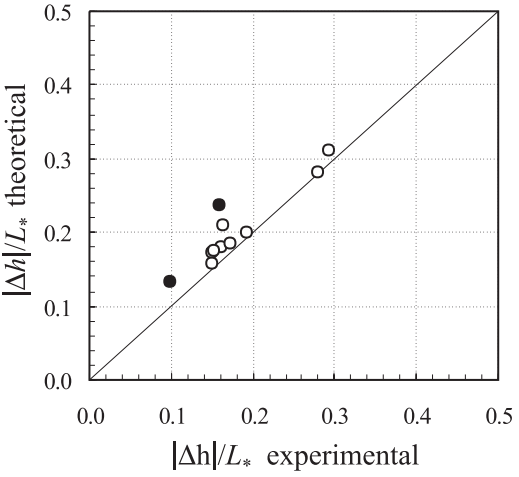


Figure 7. Calculated and measured non-dimensional shock strengths in terms of flow depths. Open circles (○) stand for the wavefront; solid circles (●) stand for the 2-jump.

paramount importance. Since the influence of the variables that describe sediment dynamics is strong in the $\lambda^{(2)}$-characteristic field, the dynamics of the associated shock are fundamentally determined by the solid phase: the $\lambda^{(2)}$-shock progresses with the velocity of propagation of the jump in the bed, much slower than the wavefront.

The experimental work revealed that only the tests depicted in figure 5 featured 2-jumps susceptible to be identified with the $\lambda^{(2)}$-shock. These downstream-progressing discontinuities are driven by the dunelike advancement of a sharp-edged bed wave. The strong coupling between hydrodynamic and morphodynamic variables in the $\lambda^{(2)}$-characteristic field is revealed by the fact that the strength of the shock is of the same magnitude in both types of variables.

Because of the correct coupling between hydrodynamic and morphodynamic variables, the results of the weak solution are a good reproduction of the observed behavior, especially in what concerns the shock velocity (see 6g and h). The shock strength is less well reproduced. As seen in figure 7, the shock strength is overestimated by the theoretical solution. This is mainly due to the fact that the weak solution overestimates the bed elevation in the 2nd constant state.

It is proposed that 2-jumps that occur in geomorphic dam-break flows whose mathematical description is a weak solution of type A are well described by the $\lambda^{(2)}$-shock. Its dynamics traduce the equilibrium of the flux and inertial terms across the shock, being the gravity-related term included in the flux terms, once linearized in accordance with equation 10.

Copyright © 2006 Taylor & Francis Group plc, London, UK

Other types of 2-jump were found in the experimental tests whose profiles are depicted in figures 4. The mathematical description of these tests is a weak solution of type B. Ferreira et al. (2006) determined the locus, in the α–δ plane, of the boundary between solutions of types A and B. When $\alpha = 0$ the solution is necessarily of type B. If $\alpha > 0$ and $\delta < 0$, the solution is also of type B. It follows from the fact that type B solutions exhibit a continuous wave associated to the $\lambda^{(2)}$-characteristic field, that any 2-jump developing from such initial conditions can not be described by the jump conditions (10).

Alcrudo and Benkhaldoun (2001) developed a theoretical solution for the dam-break flow over fixed bed with a discontinuity in the dam location. Their solution features an extra discontinuity, a jump born in the source term that describes the force of gravity. Such discontinuity is impossible in mobile bed problems, as the derivative of the bed elevation, $\partial_x(Y_b)$, ceases to be treated as a source. Thus, the origin of these 2-jumps must be searched in interaction between the bed and the flow in the first instants.

It is observed that these 2-jumps are associated with important scour at the vicinity of the dam. Capart and Young (1998), working with almost neutrally buoyant particles ($s = 1.05$), observed a 2-jump with these properties and whose upstream velocity is comparable to those shown in figures 6a, b and d. They proposed that bottom friction could be a cause of the jump, by slowing down the wavefront.Mathematically, the characteristics in the $\lambda^{(2)}$-characteristic field would fold backwards in the x–t plane until converging into a compressive shock. Capart and Young (1998) backed these model with the early studies of Dressler (1954) on the influence of bottom friction. Numerical experiments carried out for fixed and mobile beds Ferreira et al. (2006) have shown that it is always possible to find continuous solutions even in the presence of very large bottom friction. It is thus unlikely that this 2-jump is mainly originated by the compressing of the $\lambda^{(2)}$-characteristic field under the effect of friction.

Chen and Simons (1979) report an upstream progressing 2-jump in a bed featuring an initial positive bed step. Chen and Simons (1979) believe that the jump is originated by the increased flow velocity over the bed discontinuity, as it would occur in a weir. Although their initial conditions are difficult to interpret, their results may be used to state the case for the influence of two-dimensional effects in the first stages of the flow. A highly accelerated parcel of flow directed downwards would originate an scour hole, not explainable by the shallow water theory. Once formed, this accelerated flow region would progress upstream, a process similar to the knickpoint migration. This would explain the 2-jump observed in test 35_00_00 (figure 4d).

The jumps seen in the tests featuring an initial negative bed step, 25_-05_00 and 35_-05_00 (figures 4a and b) may also owe to two-dimensional flow effects. An accelerated parcel of flow directed upwards would be susceptible to slow down the flow in the vicinity of the bed jump, thus provoking the free surface elevation seen in figures 4a and b. The hydrodynamic response to compatibilize the supercritical and subcritical flow regimes thus created would be forming a jump. It would progress upstream in an antidune-like movement.

6 CONCLUSION

The present study attempted to contribute to the characterization of the discontinuities observed in geomorphic dam-break flows. Special attention was conceded to the often observed 2-jump that forms at early times at the location of the dam.

A comparison between experimental flow profiles and the weak solution of the dam-break Riemann revealed that there is a class of 2-jumps whose mechanics are susceptible to be described by the Rankine-Hugoniot conditions of the shock associated to the $\lambda^{(2)}$-characteristic field. The distinctive traits of these 2-jumps are its positive velocity of propagation and, in what concerns bed morphology, its aggradational nature.

When the weak solution features an expansion wave in the $\lambda^{(2)}$-characteristic field, the causes of the 2-jump must be searched outside the realm of phenomena described by the homogeneous onedimensional governing equations. It is observed that these 2-jumps migrate upstream and are associated to scour holes. Possible explanations comprise: i) frictional effects combined with non-equilibrium sediment transport and; ii) two-dimensional flow effects. More likely, a combination of the preceding effects may be the cause of these 2-jumps. Hence, this flow features certainly call for more effort in their empirical characterization.

ACKNOWLEDGEMENTS

The authors acknowledge the financial support granted by the European Commission to the project IMPACT, under the 5th framework (1998-2002), thematic program for Environment and Sustainable development, officiated by Karen Fabbri.

REFERENCES

Alcrudo, F. and F. Benkhaldoun (2001). Exact solutions to the riemann problem of the shallow water equations with a bottom step. *Computers & Fluids 30*, 643–671.

Copyright © 2006 Taylor & Francis Group plc, London, UK

Amaral, S. R. C. (2004). *Experimental Characterization of 1-D Dam-Break Waves over Cohesionless Sediment Beds*. Final Project for the Graduation in Civil Engineering. Instituto Superior Técnico, Technical University of Lisbon.

Capart, H. (2000). *Dam-break induced geomorphic flows and the transition from solid- to fluid-like behaviour across evolving interfaces.* Ph.D. thesis, Université catholique de Louvain, Louvain-la-Neuve, Belgium.

Capart, H. and D. L. Young (1998). Formation of a jump by the dam-break wave over a granular bed. *J. Fluid Mech. 372*, 165–187.

Chapman, S. and T. G. Cowling (1970). *The Mathematical Theory of Non-Uniform Gases* (3rd ed.). Cambridge, UK: Cambridge University Press.

Chen, Y. H. and D. B. Simons (1979). An experimental study of hydraulic and geomorphic changes in an alluvial channel induced by failure of a dam. *Water Resour. Res. 15*(5), 1183–1188.

Dressler, R. F. (1954). Comparison of theories and experiments for the hydraulic dambreak wave. In *Assemblée General de Rome*, Volume 3, pp. 319–328. Intl. Assoc. of Hydrology.

Ferreira, R. M. L. (2005). *River Morphodynamics and Sediment Transport. Conceptual model and solutions.* Ph.D. thesis, Instituto Superior Técnico, Technical University of Lisbon, Lisboa, Portugal.

Ferreira, R. M. L., J. G. A. B. Leal, A. H. Cardoso, and A. B. de Almeida (2003). Sediment transport by dam-break flows. a conceptual framework drawn from the theories for rapid granular flows. In *Proc. of the 3rd IMPACT Workshop*, Louvain-la-Neuve, Belgium (edited in CD-ROM).

Ferreira, R. M. L., J. G. B. Leal, and A. H. Cardoso (2006). Sensitivity analysis of a riemann solution for the shallow-water equations. *in preparation*.

Fraccarollo, L. and A. Armanini (1999). A semianalytical solution for the dam-break problem over a mobile bed. In *Proc. of 1st IAHR Symposium of River, Coastal and Estuarine Morphodynamics (RCEM)*, Volume 1, pp. 361–369. University of Genova, Genova, Italy.

Fraccarollo, L. and H. Capart (2002). Riemann wave description of erosional dam-break flows. *J. Fluid Mech. 461*, 183–228.

Glimm, J. (1965). Solutions in the large for nonlinear hyperbolic systems of equations. *Comm. Pure Appl. Math. 18*, 697–715.

Leal, J. G. A. B., R. M. L. Ferreira, and A. H. Cardoso (2002). Dam-break waves on movable bed. In D. Bousmar and Y. Zech (Eds.), *RIVER FLOW 2002*, Volume 2, pp. 981–990. Balkema.

Leal, J. G. A. B., R.M. L. Ferreira, and A. H. Cardoso (2006). Dam break wave front celerity. *J. Hydraul. Eng. 132*(1), 69–76.

Spinewine, B. (2005). *Two-layer flow behaviour and the effects of granular dilatancy in dambreak induced sheet-flow*. Ph.D. thesis, Université catholique de Louvain, Louvain-la-Neuve, Belgium.

Spinewine, B. and Y. Zech (2005). Dam-break on a movable bed in presence of an initial bed discontinuity: laboratory experiments and simulations with a multi-layer shallow water model. In *Proc. of XXXI IAHR Congress, Theme D*, Seoul, South Korea, pp. 3434–3445.

Stoker, J. J. (1958). *Water Waves. The Mathematical theory with applications*. Wiley-Interscience Publication (reprinted in 1992).

Zech, Y., S. S. Frazão, B. S. ans Nicholas Le Grelle, A. Armanini, L. Fraccarollo, M. Larcher, R. Fabrizi, M. Giuliani, A. Paquier, K. El Kadi, R. M. L. Ferreira, J. G. A. B. Leal, A. H. Cardoso, and A. B. de Almeida (2004). Sediment movement model development. In *Proc. of Dam Safety 2004, ASDSO National Conference*, Volume 2, Phoenix, USA. Association of State Dam Safety Officials (ed. CD-ROM).

Copyright © 2006 Taylor & Francis Group plc, London, UK

Experimental study of landslide-induced flooding in open channels

Jun Yan, Zhixian Cao & Li Chen
State Key Laboratory of Water Resources and Hydropower Engineering Science, Wuhan University, Wuhan, China

ABSTRACT: There are an increasing number of high dams constructed on valley rivers with steep bank slopes in Southwest China. An appropriate combination of hydroclimatic and geotechnical conditions and reservoir operation may favor the occurrence of large-scales landslides. Large-scale landslides produce landslide dams in rivers, which may block the stream flow and cause inundation upstream, and subsequently fail and lead to devastating flooding downstream. The need for accurate assessment of the potential threat to the society and the safety of hydraulic constructions has been well recognized. However, current understanding of the physical processes of landslide-induced flooding continues to be poor due to the complicated nature of the phenomenon, and inevitably reliable methods and tools for evaluation of possible consequences of river-blocking landslides are still missing. This paper presents an experimental study of landslide-induced flooding in open channels. A flume of 80 m × 1.2 m × 0.8 m is deployed, along with an array of ten automatic water-level probes. Tests are carried out over initially fixed beds. For each of a set of constant incoming clear-water flow discharges, a massive body of loose sediments of a variety of sizes is instantly added to the flow through a sediment-feeder at the middle of the flume, simulating a landslide. Water levels are recorded every half a second at ten cross-sections along the channel. The failure of the landslide body is visually observed. The experiments provide useful data resources for understanding landslide-induced flooding and for testing mathematical river models.

1 INTRODUCTION

High and even unconventionally high dams are being constructed or planned on valley rivers with steep bank slopes in Southwest China. An appropriate combination of hydroclimatic and geotechnical conditions and reservoir operation may trigger the occurrence of large-scale landslides that can induce devastating disasters. When landslides take place, initial waves are first generated, which may threaten the safety of dams and other hydraulic constructions. Subsequently, landslides may block the river channel and form landslide dams. Then inundation upstream of the landslide dams is inevitable. When a landslide dam fails, the devastating floods with large surges or debris flows may lead to catastrophic disasters in the downstream. Landslide dams break down mostly due to the overflowing of water after the landslide dam lakes are fully filled with water.

To date, there have been reports on landslide-induced floods. On June 1, 1786, an earthquake triggered a large landslide that fell into the Dadu River and blocked it. After ten days, the landslide dam failed (Dai *et al*. 2005). In 1967, a landslide blocked the Yalong River, a tributary of the Yangtze River. The height of landslide dam was more than 300 m, and nine days later, the landslide dam failed (Li *et al*. 1986, Chen *et al*. 1992). In Tibet, a super-large landslide occurred along Zhamu Creek and blocked the Yigong River on April 9, 2000. After two months, a catastrophic flood resulted from the landslide dam failure (Shang *et al*. 2003). Large-scale landslide-induced flood events have occurred not only in China, but elsewhere over the world (e.g. Costa & Schuster 1988, Ohmori 1992, Cruden *et al*. 1993, Cruden *et al*. 1997, Bovis & Jakob 2000, Miller & Cruden 2002, Nicoletti & Parise 2002, Abril & Knight 2004). However, existing studies have only reported the occurrences and disasters due to landslide. Current understanding of the physical processes of landslide-induced flooding continues to be poor, and reliable methods for evaluation of possible consequences of river-blocking landslides are still missing. Mathematical modelling and experimental studies for landslide-generated initial waves have been carried out mainly for reservoir and ocean waters (Heinrich 1991, Jiang & Leblond 1992, 1993, Rzadkiewicz *et al*. 1997, Guo *et al*. 2000, Lynett & Liu 2002, Rabinovich *et al*. 2003, Hu *et al*. 2003, Zhou *et al*. 2003, Li *et al*. 2004). Yet, the mathematical models and the experiments are case specific and are not generally applicable to landslide-induced flooding in open channels. Also it is noted that large-scale landslides-induced floods relate to highly unsteady flow, non-equilibrium sediment transport and

Copyright © 2006 Taylor & Francis Group plc, London, UK

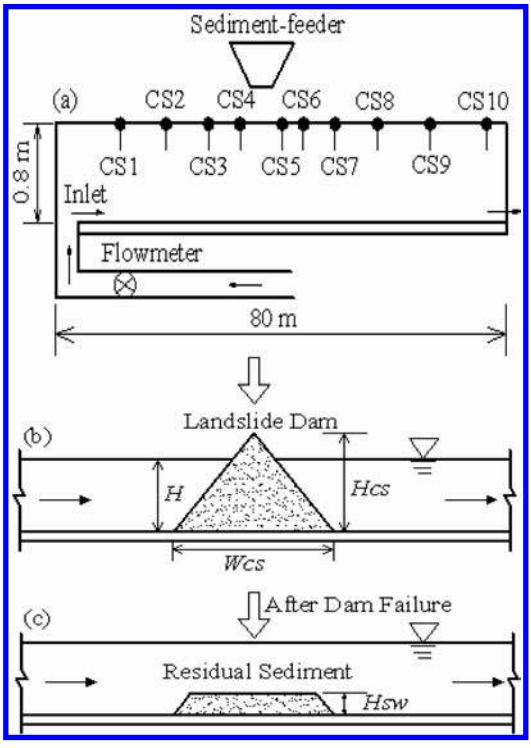


Figure 1. (a) Experimental setup (not scaled); (b) Sketch of landslide dam; and (c) Sketch of residual sediment blocks.

rapid riverbed deformation. Intense interaction exists between flow, sediment, and morphological evolution. To evaluate the flooding induced by landslides, a fully coupled model is normally required.

This paper presents an experimental study of landslide-induced flooding in open channels. Particular attention is paid to the variation of water levels in response to the initial waves, the inundation upstream the landslide dam, and also its failure. The experiments provide useful data resources for understanding landslide-induced flooding and for testing mathematical river models.

2 EXPERIMENTS

2.1 *Experimental setup*

The experimental setup is illustrated in Figure 1a. A flume of 80 m × 1.2 m × 0.8 m, with an array of ten automatic water-level probes, is deployed and a sediment-feeder supplies dry sediments to simulate landslide occurrence. The flume is made of glass with a bottom slope of 1/1000 and the Manning roughness is equal to 0.012. The sediment feeder is located 30 m from the flume inlet. The ten automatic water-level

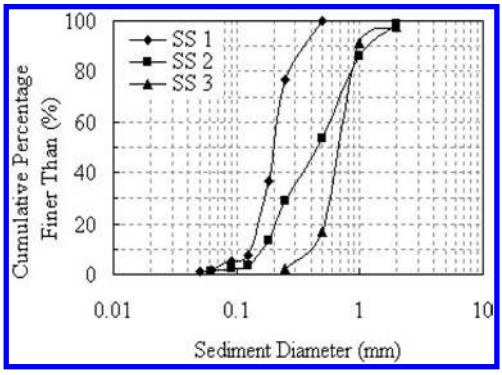


Figure 2. Gradation curve of sediment samples.

Table 1. Flow discharge and landslide volume.

	Q (m^3/s)	V (m^3)		
Case A	0.012	0.135	0.076	0.0375
Case B	0.036	0.218	0.160	0.113

probes are located at the center of the flume, respectively at 15 m, 21 m, 25 m, 28 m, 32 m, 34 m, 37 m, 41 m, 46 m and 60 m from the inlet. The tracking speed of the water level probes is set at 100 mm/s, the corresponding measurement error is within ±0.5 mm, and the sampling frequency is set at 2 Hz. A computer is deployed to process the data transmitted from the water level probes.

2.2 *Experimental procedures*

Experiments are carried out for different landslide volumes, sediment sizes and flow discharges. Three sediment samples are chosen to produce the landslides, and their gradation curves are plotted in Figure 2. The flow discharge (Q) and landslide volume (V) are given in Table 1. Corresponding to a specific discharge, a steady flow is first achieved by regulating the tailgate opening at the outlet of the flume. Then, the sediments uniformly pre-placed in the sediment-feeder are added instantly into the channel to simulate landslide occurrence. The variations of water level at ten cross sections are recorded with the automatic probes.

3 RESULTS AND ANALYSIS

3.1 *Summary of experiments*

In total, 20 cases of experiments are carried out, as summarized in Table 2. In Table 2, *SS* denotes sediment sample; H is water depth at the landslide site; H_u and H_d denote, respectively, the maximum heights of

Copyright © 2006 Taylor & Francis Group plc, London, UK

Table 2. Characteristics of the landslide experiments.

Case	*SS*	Q (m^3/s)	H (cm)	V (m^3)	H_u (cm)	H_d (cm)	H_{cs} (cm)	W_{cs} (cm)	T_b (s)	T_f (s)	H_{sw} (cm)
1	1	0.012	10.05	0.135	3.03	1.65	20.5	76	480.8	88.1	4.5
2			10.27	0.076	2.54	0.71	16.7	61	289.2	87.6	5
3			10.11	0.0375	2.31	0.60	11.7	43	107.7	76.3	6
4		0.036	19.97	0.218	5.99	2.42	30.0	86	133.2	76.5	5.5
5			20.17	0.16	4.18	3.31	26.0	74	77.8	60.6	6
6			20.23	0.113	2.75	0.52	22.3	63	73.6	52.6	11
7	2	0.012	11.32	0.135	3.29	1.46	21.3	79	459.8	120.4	5
8			11.66	0.076	2.46	1.94	15.9	60	189.5	106.6	5.5
9			11.45	0.062	2.47	0.96	14.1	53	119.4	100.1	6
10			11.36	0.05	1.63	0.37	12.6	47	96.6	74.1	6
11			11.32	0.0375	1.26	0.50	11.8	45	92.7	53.6	6.5
12		0.036	20.64	0.218	5.56	1.26	29.4	90	126.1	70.1	6.5
13			20.7	0.16	3.55	0.49	24.4	75	66.4	57.4	8.5
14			20.67	0.113	4.12	0.82	22.2	68	63.2	52.1	12
15	3	0.012	9.8	0.135	2.24	2.29	20.4	74	478	140.6	5
16			9.69	0.076	2.45	0.54	17.4	63	357.3	88.2	5.5
17			9.68	0.0375	2.13	0.37	11.8	42	109.2	88.1	6
18		0.036	20.64	0.218	4.12	0.57	29.3	87	125.3	67.6	9
19			20.67	0.16	4.21	0.64	25.2	75	69.3	64.7	11
20			20.52	0.113	2.98	0.36	22.2	59	60.4	48.1	12

initial waves in the upstream and downstream of landslide dam; H_{cs} and W_{cs} denote the height and bottom length of the landslide dam (Figure 1b); T_b denotes time of river-blockage before dam failure; T_f denotes time of dam failure; and H_{sw} denotes the height of the residual sediment at the landslide site after dam failure (Figure 1c).

3.2 *Analysis*

Typical variation of water levels is illustrated in Figures 3 to 6 for four different landslide volumes of Sediment Sample 2 in two different flow discharges.

3.2.1 *Initial waves*

Initial waves are generated immediately after landslide occurrence, in both the upstream and downstream of the landslide site. The maximum heights of the initial waves are shown in Table 2. The experiments indicate that landslide volume and the initial steady flow depth at the landslide site play important roles in dictating the maximum heights of the initial waves. For a specific case, the maximum heights of the initial waves are higher in the upstream than in the downstream (i.e., $H_u > H_d$), as can be seen in Table 2. Also, comparing Figure 3 with Figure 4, and Figure 5 with Figure 6, one finds that the maximum heights of the initial waves induced by a small landslide are lower than those of a large landslide, as expected. For different cases, the heights of the initial waves for every cross section are illustrated in Figures 7 and 8. It seems difficult to properly explain the complicated nature of the initial waves with currently available knowledge.

When the initial waves propagate to the inlet and the outlet of the flume, the gates prevent them from further progressing. The initial waves are reflected, which propagate towards the location of the landslide dam. For large landslides or large water depths at the landslide site, the reflected waves can overtop the landslide dams and accelerate dam failure through the experimental observation.

3.2.2 *River-blockage and dam failure*

After landslide occurrence in the flume, landslide dams are formed immediately, uniformly covering the entire width of the flume. Subsequently, the channel is blocked and the inundation upstream begins to occur. Water level variations during river-blockage are illustrated in Figures 3 to 6. The rising and falling of water levels, respectively in the upstream and downstream of the landslide dam are demonstrated.

As the upstream water level approaches the height of the landslide dam, overtopping occurs as the water flow gradually erodes the sediment of the top of the dam. In a later time, the landslide dams begin to fail. Water level variations during dam failure are also shown in Figures 3 to 6. For large landslides, surges are generated in the downstream, and for large landslide volumes, hydraulic jumps are also observed in the downstream of the landslide dam. When the water level difference between the upstream and downstream decreases to a certain value, the water flow becomes insufficient to further erode the dam body, and the course of dam failure is completed.

The times of river-blockage and dam failure are summarized in Table 2. Comparing T_b with T_f, the

Copyright © 2006 Taylor & Francis Group plc, London, UK

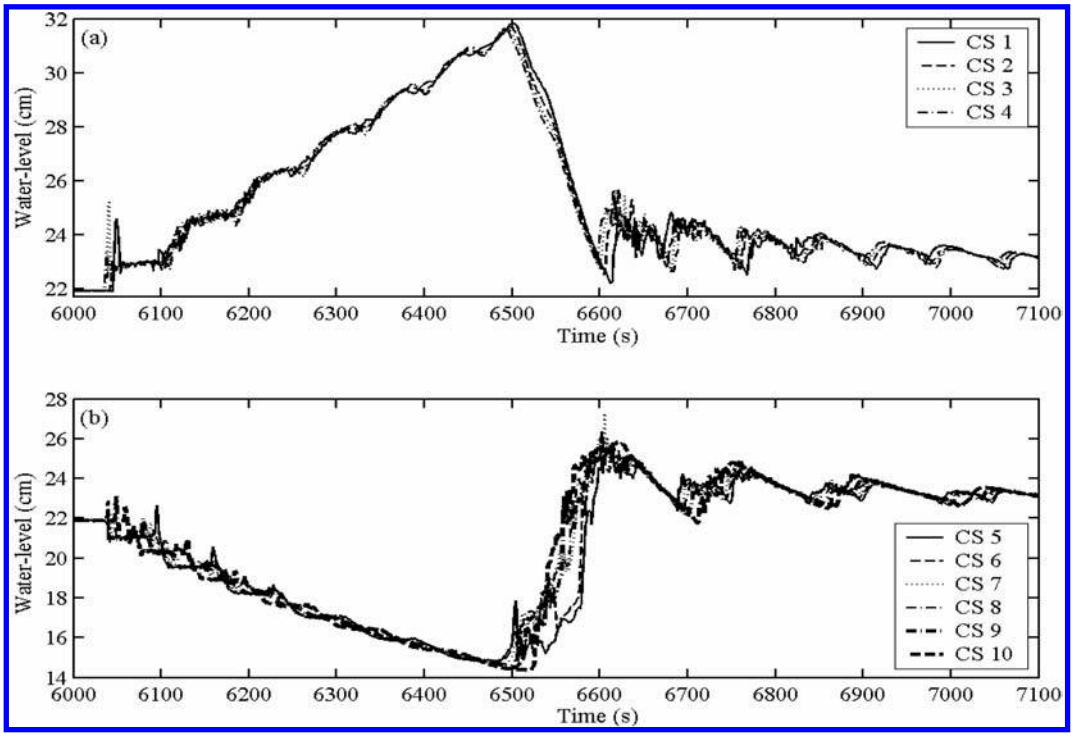


Figure 3. Hydrographs for Case 7: (a) upstream of landslide, and (b) downstream of landslide.

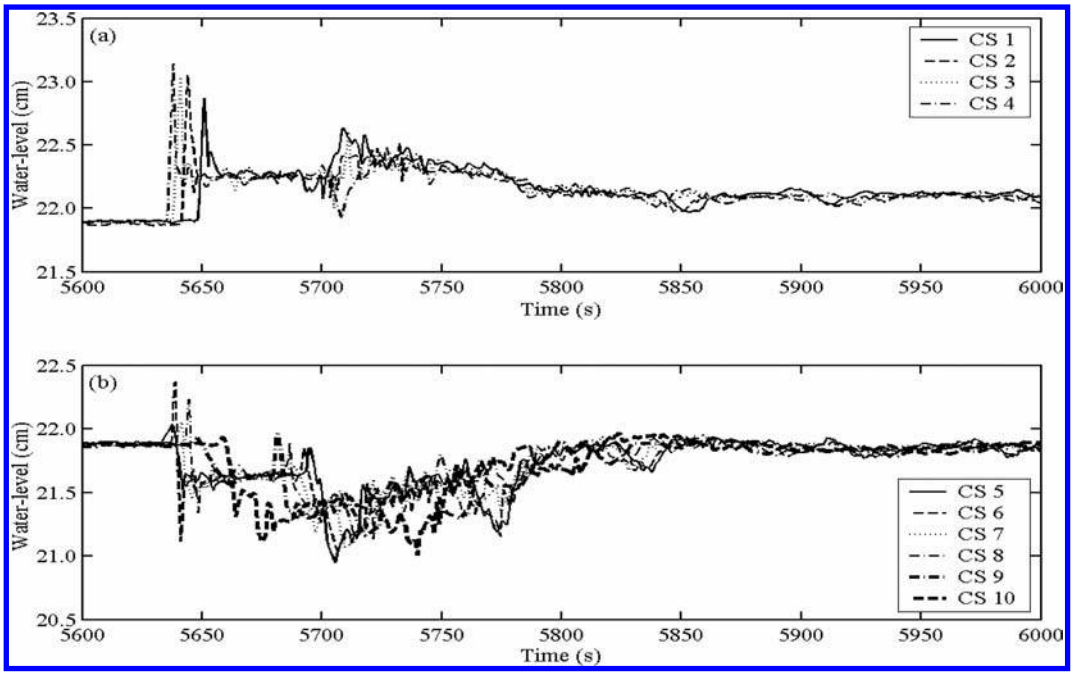


Figure 4. Hydrographs for Case 11: (a) upstream of landslide, and (b) downstream of landslide.

Copyright © 2006 Taylor & Francis Group plc, London, UK

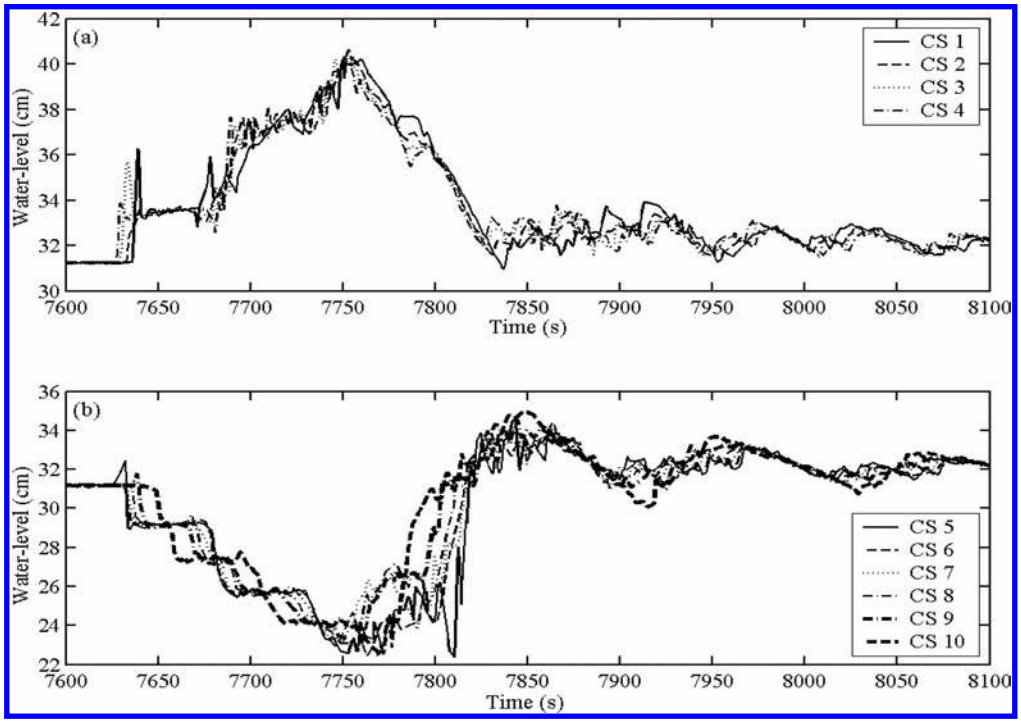


Figure 5. Hydrographs for Case 12: (a) upstream of landslide, and (b) downstream of landslide.

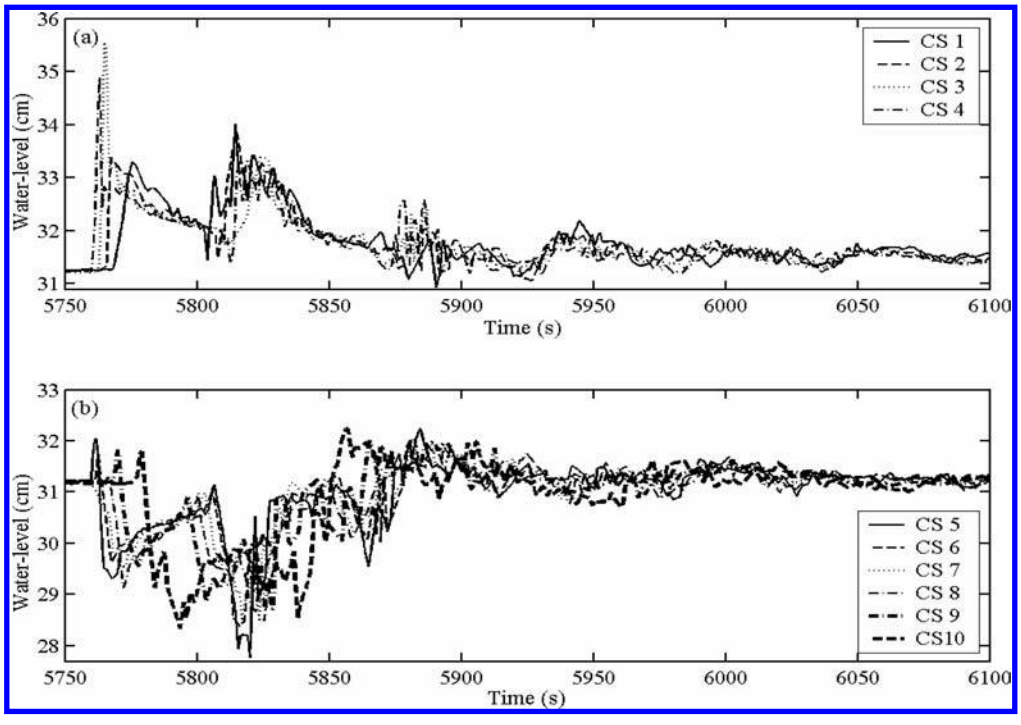


Figure 6. Hydrographs for Case 14: (a) upstream of landslide, and (b) downstream of landslide.

Copyright © 2006 Taylor & Francis Group plc, London, UK

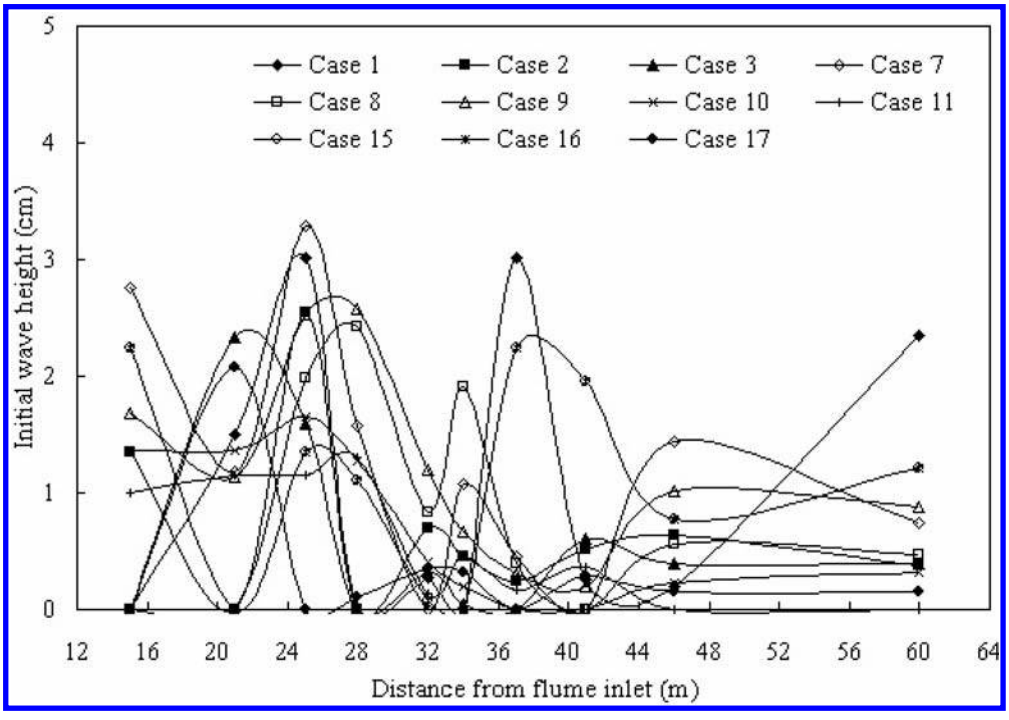


Figure 7. Heights of initial waves at ten cross sections with small inflow discharge.

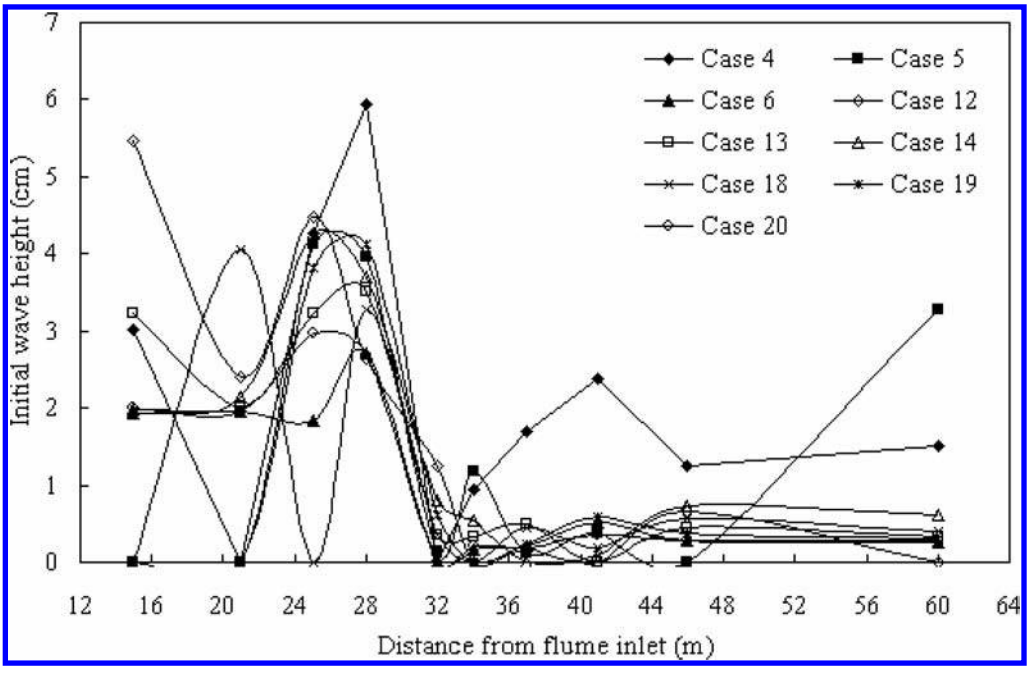


Figure 8. Heights of initial waves at ten cross sections with large inflow discharge.

Copyright © 2006 Taylor & Francis Group plc, London, UK

time of river-blockage is longer than that of the dam failure. Especially, for large landslides, the time difference between them is much more pronounced. According to the volume of landslide, and also H_{cs} and W_{cs}, the underwater repose angle of sediments can be estimated for the three sediment samples. The repose angle normally ranges between 29 degrees and 35 degrees.

3.2.3 *Estimating peak discharge*

There have been empirical relationships for estimating the peak discharge of flood due to dam failure. Chanson (2005) presented a relationship based on the continuity equation and Bernoulli principle. In Chanson's relationship, the total head remains constant throughout the breach. Yet, in the present experiments, there is always inflow from the upstream, which may affect the total head. However, in a quantitative sense, the inflow is unimportant as its quantity is negligible compared to the initial water quantity prior to dam failure. Thus, Chanson's relationship is introduced to evaluate the discharge of the present experiments. The time of dam failure (T_f) are listed in Table 2. Of the total 20 cases of experiments, only Case 4, Case 12, and Case 18 satisfy the applicability conditions of Chanson's (2005) relationship for peak discharge. These three cases assume the same experimental conditions except the different sizes of sediment forming the landslides. The calculated discharge is shown in Figure 9. Apparently, the discharge hydrographs for the three cases show inappreciable differences between each other. Alternatively, the role of sediment size in dictating the breach process is rather weak under the specific conditions.

By revising Costa's (1985) regression relationships, Walder and O'Connor (1997) proposed four predictive methods to estimate the peak discharge of flood due to dam failure, which involve a series of parameters such as dam height and reservoir storage volume.

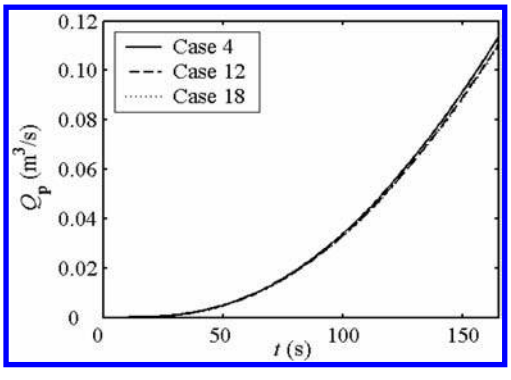


Figure 9. Discharge hydrograph due to Chanson's (2005) relationship.

Figure 10 shows the peak discharges calculated using the four methods due to Walder and O'Connor (1997). Obviously, the four methods deviate from each other significantly, even by an order of magnitude for the same case. This observation characterizes the significant uncertainty of the empirical methods of Walder and O'Connor (1997).

Large-scale landslide-induced floods relate to highly unsteady flow, non-equilibrium sediment transport and rapid riverbed deformation. Dam-break flood flow, sediment and bottom boundary interact with each other strongly. It is difficult to reliably estimate the peak discharges of floods due to landslide dam failure using empirical relationships (e.g., Walder & O'Connor 1997, Chanson 2005). To evaluate the floods more accurately, a fully coupled mathematical modeling methodology will have to be used. Development of such a model is underway by extending the model of Cao *et al*. (2004) to a 2D framework.

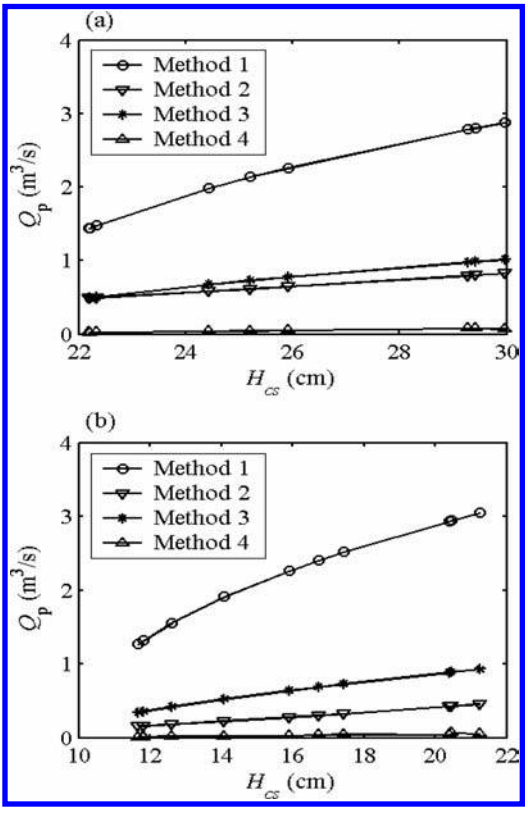


Figure 10. Peak discharge Q_p versus landslide dam height, calculated using the four empirical methods of Walder and O'Connor (1997), under (a) large inflow discharge ($Q = 0.036\,\mathrm{m^3/s}$); and (b) small inflow discharge ($Q = 0.012\,\mathrm{m^3/s}$).

Copyright © 2006 Taylor & Francis Group plc, London, UK

3.2.4 *Sediment transport*

The sediment transport processes differ for different sediment samples and landslide volumes. For Sediment Sample 1 with the finest sediment size (Figure 2), turbidity currents are observed immediately following landslide occurrence at both the upstream and downstream. While propagating upstream and downstream, the turbidity currents gradually die out as the sediments deposit on the bottom of the flume. The maximum distance that the turbidity currents could move is found to increase with the landslide volume.

For large landslides of Sediment Sample 3 of the most coarse sediment size (Figure 2), piping of the landslide dam is observed before dam failure by overtopping. Along with the piping effect, the downstream side slope is eroded gradually and some sediment particles are entrained by seepage flow. However, for small landslides of Sediment Sample 3, piping is not so apparent, and overtopping seems to occur very slowly.

In general, when the upstream water level approaches the top of the landslide dam, overtopping occurs and breaches develop. Then, the breaches are cut deeply by flow and both sides of the breaches collapse gradually. The eroded sediments are carried to the downstream by the energetic dam-break flow, and in this course some particles are seen to deposit on the flume bottom.

It is noted that during the experiments, not all the sediments of the landslide dams can always be eroded and carried away by the flow, depending on the inflow discharge, landslide volume and sediment size. Generally, most sediment particles are eroded during the dam failure, and after that process the steady flow is not competent to carry the residual sediments to the downstream. Alternatively, after dam failure, there are residual sediments that stand at landslide location and form sediment blocks (Figure 1c). The heights of sediment blocks are given in Table 2. For a specific discharge, the residual sediment blocks of small landslides are higher than those of large landslides. The residual sediment blocks can considerably affect the flow, even long after the landslide dam fails. Figure 4 shows such effect for Case 11 of small landslide volume and inflow discharge (Table 2), as the difference in water levels in the upstream and downstream of the landslide site is by far greater than its counterpart before landslide occurs.

4 CONCLUSIONS

A series of flume experiments are carried out to enhance the understanding of flooding due to simulated landslide. The flooding comprises the initial waves generated immediately following the occurrence of landslide, the inundation upstream the landslide dam, and subsequently surge waves in the downstream due to landslide dam failure.

As a landslide slides into the channel, initial waves are generated (Figures 3 to 6). Both landslide volume and initial water depth at the landslide site play important roles in dictating the maximum height of the initial waves. Yet the variation of the maximum height of the initial waves along the channel exhibits a rather complicated picture, which current knowledge seems insufficient to properly explain. This would have to be reserved for future studies by resorting to physically based numerical models.

As a landslide dam blocks the channel, inundation occurs in the upstream as evidenced by the rising of the water levels, irrespective of piping in the landslide dam of coarse sediments. When the upstream water level approaches the top of the landslide dam, overtopping is observed, which cause the landslide dam to fail. For large landslides, hydraulic jumps are observed in the downstream during the process of dam failure.

The sediment transport processes differ for different sediment samples and landslide volumes. For landslides of finer sediments, turbidity currents are observed immediately following the occurrence of a landslide. For large landslides of coarse sediments, piping of the landslide dams is observed before dam fails by overtopping. As the landslide dam fails, the eroded sediments are carried to the downstream and may later deposit on the bed, and the residual sediments may stand at the landslide site.

An attempt is made to estimate the peak discharge of flood due to landslide dam failure as of the present experiments, using the empirical methods by Walder & O'Connor (1997) and Chanson (2005). Significant deviations between the four methods of Walder & O'Connor (1997) are found, and the applicability of Chanson's (2005) relationship is rather limited. This seems to call for the development and application of advanced numerical models.

The data and understanding presented herein are pertinent to landslides of non-cohesive dry sediment on fixed channel bed. The experimental data can be used to test mathematical river models that aim to quantify the phenomenon of landslide induced flooding in open channels.

It is noted that the landslides are simulated in the experiments through the sediment feeder in a very idealized manner. Further studies need to develop a landslide simulator that can better simulate real landslides in nature.

ACKNOWLEDGEMENTS

This work reported is funded by the National Natural Science Foundation of China (under Grant No. 50459001), and also the Open Research Fund of the State Key Laboratory of Water Resources and Hydropower Engineering Science (under Grant No. 2004C013).

Copyright © 2006 Taylor & Francis Group plc, London, UK

REFERENCES

Abril, B. & Knight, D.W. 2004. Stabilizing the Paute River in Ecuador. *Civil Engineering*, Proceedings of Institution of Civil Engineers 156: 32–38.

Bovis, M.J. & Jakob, M. 2000. The July 29, 1998, debris flow and landslide dam at Capricorn Creek, Mount Meager Volcanic Complex, southern Coast mountains, British Columbia. *Canadian Journal of Earth Sciences* 37(10): 1321–1334.

Cao, Z.X., Pender, G., Wallis, S. & Carling, P. 2004. Computational dam-break hydraulics over erodible sediment bed. *Journal of Hydraulic Engineering*, ASCE 130(7): 689–703.

Chanson, H. 2005. The 1786 earthquake-triggered landslide dam and subsequent dam-break flood on the Dadu River, southwestern China. *Journal of hydrology*, Elsevier 71(3–4): 437–440.

Chen, Y.J., Zhou, F. & Xia, Y.C. 1992. Breach of a naturally embanked dam on Yalong River. *Canadian Journal of Civil Engineering* 19(5): 811–818.

Costa, J.E. 1985. Floods from Dam Failures. *USA Geological Survey Open-File Report*: 85–560. Colorado: Denver.

Costa, J.E. & Schuster, R. 1988. The formation and failure of natural dams. *Geological Society of American Bulletin* 100(7): 1054–1068.

Cruden, D.M., Keegan, T.R. & Thomson, S. 1993. The landslide dam on the Saddle River near Rycroft, Alberta. *Canadian Geotechnical Journal* 30(6): 1003–1015.

Cruden, D.M., Lu, Z.Y. & Thomson, S. 1997. The 1939 Montagneuse River landslide, Alberta. *Canadian Geotechnical Journal* 34(5): 799–810.

Dai, F.C., Lee, C.F., Deng, J.H. & Tham, L.G. 2005. The 1786 earthquake-triggered landslide dam and subsequent dam-break flood on the Dadu River, southwestern China. *Journal of Hydrology*, Elsevier 65(3–4): 205–221.

Guo, H.W. 2000. Mathematical Models and Application of Landslides Surge in Reservoirs. *Journal of North China University of Water Conservancy and Electric Power* 21(1): 24–27.

Heinrich, P. 1991. Nonlinear numerical-model of landslide-generated water-waves. *International Journal of Engineering Fluid Mechanics* 4(4): 403–416.

Hu, J. 2003. Landslides Disaster of Reservoir Banks and Analysis of Surge. *Journal of East China Jiaotong University* 20(5): 26–31.

Jiang, L. & Leblond, P.H. 1992. The coupling of a submarine slide and the surface-waves which it generates. *Journal of Geophysical Research-Oceans* 97(C8): 12731–12744.

Jiang, L. & Leblond, P.H. 1993. Numerical modeling of an underwater Bingham Plastic mudslide and the waves which it generates. *Journal of Geophysical Research-Oceans* 98(C6): 10303–10317.

Li, M. 2004. Production of Landslides Surge and Analysis and Calculation of Propagation Waves. *Advances in Water Sciences, Nanjing* 15(1): 45–49.

Li, T., Schuster, R. & Wu, J. 1986. Landslide dams in south-central China. In *Landslide Dams: Processes, Risk and Mitigation*, ed by Robert Schuster, Geotechnical Special Publication No. 3, ASCE: 146–162.

Lynett, P. & Liu, L.F. 2002. A numerical study of submarine-landslide-generated waves and run-up. *Proc. Royal Soc. London, A* 458: 2885–2910.

Miller, B.G.N. & Cruden, D.M. 2002. The Eureka River landslide and dam, Peace River Lowlands, Alberta. *Canadian Geotechnical Journal* 39(4): 863–878.

Nicoletti, P.G. & Parise, M. 2002. Seven landslide dams of old seismic origin in southeastern Sicily (Italy). *Geomorphology* 46(3–4): 203–222.

Ohmori, H. 1992. Dynamics and erosion rate of the river running on a thick deposit supplied by a large landslide. *Zeitschrift fur Geomorphologie* 36(2): 129–140.

Rabinovich, A.B., Thomson, R.E., Bornhold, B.D., Fine, I.V. & Kulikov, E.A. 2003. Numerical modelling of tsunamis generated by hypothetical landslides in the Strait of Georgia, British Columbia. *Pure and Applied Geophysics* 160(7): 1273–1313.

Rzadkiewicz, S.A., Mariotti, C. & Heinrich, P. 1997. Numerical simulation of submarine landslides and their hydraulic effects. *Journal of Waterway, Port, Coastal and Ocean Engineering*, ASCE 123(4): 149–157.

Shang, Y.J., Yang, Z.F., Li, L.H., Liu, D., Liao, Q.L. & Wang, Y.C. 2003. A super-large landslide in Tibet in 2000: background, occurrence, disaster and origin. *Geomorphology*, Elsevier 54(3–4): 225–243.

Walder, J.S. & O'Connor, J.E. 1997. Methods for predicting peak discharge of floods caused by failure of natural and constructed earthen dams. *Water Resources Research* 33(10): 2337–2348.

Zhou, J.H. 2003. Numerical Research of Landslides Surge Hazard at Reservoirs. *Journal of Yangtze River Scientific Research Institute* 20(2): 6–9.

Copyright © 2006 Taylor & Francis Group plc, London, UK

Dam-break propagation over a movable bed in a non-prismatic channel

João G.A.B. Leal
University of Beira Interior, Covilha, Portugal

Pedro Silva
Engidro Estudos de Engenharia, Lisbon, Portugal

Rui M.L. Ferreira
Instituto Superior Técnico, Lisbon, Portugal

ABSTRACT: This paper reports an experimental and numerical study of the 2D dam-break flow propagation. The experiments were carried out in a horizontal flume with a sudden enlargement. The bed was movable (natural sand) up- and downstream of the lift-gate that simulates the dam. The tests were recorded with video cameras. A 2D numerical model by Leal et al. (2005), incorporating two transport layers, was used to simulate the experimental results. The computational domain was discretized with an equally sized square mesh. The numerical results show good agreement with the experimental ones. Some discrepancies were found in the wave-front location. The model successfully reproduced the flow features. Namely the hydraulic jump that result from the reflection of the wave in the enlarged wall. The numerical model reproduces generally well the bed topography observed in the experiments. Nevertheless, some discrepancies can be pointed out. Namely, the numerical scour hole is less pronounced than the experimental one, and is accompanied by a small deposition bar near the non enlarged wall.

1 INTRODUCTION

Dam-break flows are catastrophic events that result from the total or partial failure of a dam. In the last century, some important accidents and failures occurred at, among other places, Vajont, Malpasset, Teton e Machhu II. These accidents have increased society's awareness towards these hazards and have helped devising strategies for risk assessment.

Since Ritter's initial study in 1892, dam-break waves have been studied by many authors. Due to the complexity of the involved phenomena, most of them considered only one-dimensional propagation (1D). Yet, it is clear that dam-break waves have a two-dimensional (2D) behaviour, affecting all flood plain.

The dynamic behaviour of 2D flows features, in general, a decrease of the free-surface level and a diminution of the wave-front celerity relatively to 1D flows. Therefore, the consideration and study of 2D dam-break flows is a necessary evolution of the existing 1D studies.

Two-dimensional dam-break studies are scarce. Dam-break flows in flumes with a sudden enlargement were studied within the framework of CADAM EU project (Frazão et al., 2000).

In the IMPACT EU project efforts were made to upgrade the models developed in CADAM in order to allow the simulation of movable beds. This upgrade is justified by field observations that show the capacity of dam-break flows on changing significantly the bed morphology. A recent example was the dyke failure in Ha! Ha! River (Lapointe et al., 1998), where morphologic impacts included strong erosion of the bottom and margins in convex reaches and generalized deposition at low slope reaches. The interaction between the flow and the bed changes the dynamic behaviour of the flow, inducing intense sediment transport and affecting flow resistance which, generally, provokes the rise of the free-surface and the delay of the wave-front propagation. Furthermore, flow features such as hydraulic jumps or critical flow points can be created or destroyed as the bed morphology evolves (cf. Ferreira et al. 2005). This constitutes a challenge to present-day modelling capabilities. Therefore, accounting for sediment transport emerges as an important step in the evolution of hydrodynamic studies towards a better simulation of flow events.

A conceptual 2D model composed by two transport layers was developed by Leal et al. (2005), based on a 1D conceptual model previously developed by Leal et al. (2003a,b). Those authors compared their

Copyright © 2006 Taylor & Francis Group plc, London, UK

2D numerical results with experiments made with a bed that was movable only in the upstream reach of the flume.

In the present study, new experiments were made with a movable bed in the entire flume, thus allowing for a better evaluation of the morphological capabilities of the numerical model.

The paper is organized as follows. In section 2, a description of the experimental set-up and a characterization of the tests is provided. In section 3.1, a brief review of the conceptual model is presented, highlighting the main hypotheses subjacent to the model. In section 3.2, the most important details of the numerical scheme used are described. The experimental and numerical results are presented and discussed in section 4. The main conclusions of the study are summarized in section 5.

2 EXPERIMENTAL SET-UP

The experimental tests were carried out at the Hydraulics Laboratory of the University catholique de Louvain, in a non-prismatic 6 m long horizontal flume with 0.48 m high rectangular cross sections. The flume is composed of two reaches, the first is 4.0 m long and 0.25 m wide, the second is 2.0 m long and 0.50 m wide (Figure 1 top).

A gate is installed 3.0 m from the upstream end of the flume. The gate is opened downwards, with a opening velocity of approximately 500 cm/s. This allows the simulation of a total and instantaneous dam-break.

The flume walls are transparent permitting flow visualization. For this purpose, two video cameras were used. One was placed laterally (C1), capturing the flow propagation along the enlarged wall, and the other (C2) was placed above the flume, capturing the wave-front location and configuration (Figure 1 bottom).

Each test had to be repeated twice, changing the position of the cameras (R1 to R2, in Figure 1 top), in order film the entire enlarged reach.

Natural uniform sand (mean diameter, $d = 1.82$ mm, and specific gravity, $s = 2.65$) was used as bed material.

The initial conditions (Figure 2) consisted in coincident bed levels up- and downstream ($z_u = z_d = 0.125$ m), i.e., horizontal movable bed, and in dry saturated bed downstream ($h_d = 0$ m). Two initial upstream water levels were tested, $h_u = 0.15$ m and $h_u = 0.25$ m, resulting in two distinct tests (T1 and T2, see Table 1).

The experimental procedure comprised the following steps: i) gate lifting; ii) movable bed smoothing to a height of $z_u = z_d = 0.125$ m, compacting it; iii) turning on the lights and the capturing software; iv) filling the upstream reach with water to a height of $h_u = 0.15$ m or $h_u = 0.25$ m and the downstream reach to saturation of the bed; v) starting the capture.

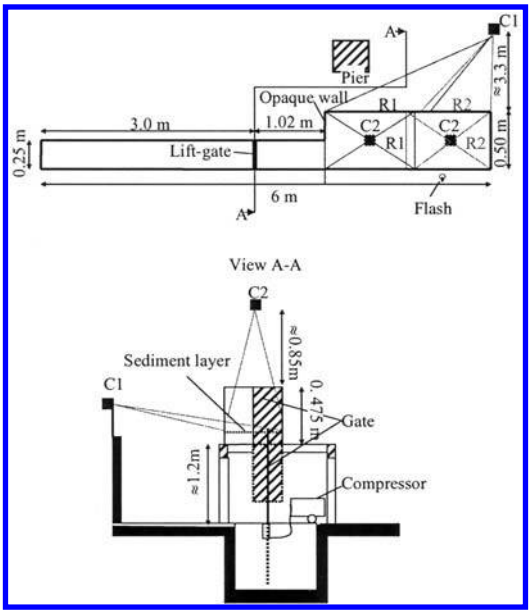


Figure 1. Experimental installations. Top: plan view; bottom: A-A cross-section.

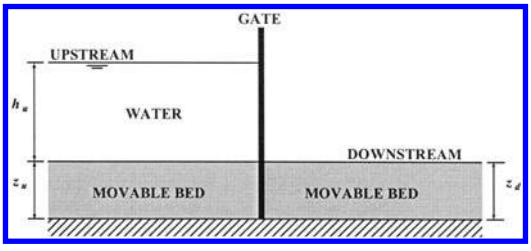


Figure 2. Sketch of initial conditions.

Table 1. Initial conditions of experimental tests.

Test	h_u(m)	h_d(m)	z_u(m)	z_d(m)
T.1	0.25	0.00	0.125	0.125
T.2	0.15	0.00	0.125	0.125

3 MODEL DESCRIPTION

3.1 *Conceptual model*

The model used in the present paper is a 2D generalization of the 1D model with two transport layers of Leal et al. (2003a). The details of the 2D model can be consulted in Leal et al. (2005). The model assumes the existence of two layers, the upper with clean water and the lower with high sediment concentration (sheet-flow). In each layer, velocities and

Copyright © 2006 Taylor & Francis Group plc, London, UK

sediment concentrations are considered to be uniform and the hydrostatic pressure distribution is assumed valid. Mention should be made to the fact that the sheet-flow is modelled as to have smaller velocities than the clear water and as to have smaller sediment concentrations than the immobile bed.

The 2D conservation equations can be written in vector form as (Leal et al. 2005):

$$\frac{\partial \mathbf{U}}{\partial t}+\frac{\partial \mathbf{F}(\mathbf{U})}{\partial x}+\frac{\partial \mathbf{G}(\mathbf{U})}{\partial y}=\mathbf{S} \tag{1}$$

with

$$\mathbf{U}=\begin{bmatrix} z_s \\ \rho u_{(x)} h \\ \rho u_{(y)} h \\ z_e \end{bmatrix}, \tag{2}$$

$$\mathbf{F}(\mathbf{U})=\begin{bmatrix} hu_{(x)} \\ \rho_w u_{w(x)}{}^2 h_w+\rho_c u_{c(x)}{}^2 h_c+\varphi \\ \rho_w u_{w(x)} u_{w(y)} h_w+\rho_c u_{c(x)} u_{c(y)} h_c \\ Chu_{(x)} \end{bmatrix}, \tag{3}$$

$$\mathbf{G}(\mathbf{U})=\begin{bmatrix} hu_{(y)} \\ \rho_w u_{w(x)} u_{w(y)} h_w+\rho_c u_{c(x)} u_{c(y)} h_c \\ \rho_w u_{w(y)}{}^2 h_w+\rho_c u_{c(y)}{}^2 h_c+\varphi \\ Chu_{(y)} \end{bmatrix}, \tag{4}$$

$$\mathbf{S}=\begin{bmatrix} 0 \\ -g(\rho_w h_w+\rho_c h_c)\dfrac{\partial z_b}{\partial x}-\tau_{bc(x)} \\ -g(\rho_w h_w+\rho_c h_c)\dfrac{\partial z_b}{\partial y}-\tau_{bc(y)} \\ 0 \end{bmatrix}, \tag{5}$$

$$\varphi=g\left(\rho_w h_w{}^2+2\rho_w h_w h_c+\rho_c h_c{}^2\right)/2 \tag{6}$$

In the previous equations $z_s=h+z_b$ is the free-surface elevation; $\rho\mathbf{u}\mathbf{h}$ is the density flow rate per unit width; $z_e=(1-p)z_b+C_c h_c$ is an equivalent bed elevation that takes into account the sediment stored in the water column; $p=$ porosity; $g=$ gravitational acceleration (taken equal to 9.8 m/s^2); h, u, C and ρ stand for, respectively, depth, velocity, sediment concentration and density; and τ_{bc} is the bottom shear stress. The subscripts w, c and b represent, respectively, the clear water, the sheet-flow and the immobile bed. The subscripts (x) and (y) stand for, respectively, the components in the longitudinal and in the transversal direction.

The depth-average variables are all considered in terms of the entire flow depth $h=h_w+h_c$, being the depth-average flow velocity, sediment concentration and fluid density given by

$$\mathbf{u}=\left(\mathbf{u}_c h_c+\mathbf{u}_w h_w\right)/h \tag{7}$$

$$C=\left(C_c h_c\sqrt{u_{c(x)}{}^2+u_{c(y)}{}^2}\right)\Big/\left(h\sqrt{u_{(x)}{}^2+u_{(y)}{}^2}\right) \tag{8}$$

$$\rho=\rho_w\left(1+(s-1)C\right) \tag{9}$$

Assuming that the velocity profile for each direction depends only on the flow variables in the direction considered and based on the velocity distribution proposed by Sumer et al. (1996), Leal et al. (2005) obtained the depth-average velocity of the transported sediments in the sheet-flow layer

$$\mathbf{u}_c=\frac{\mathbf{u}}{u}u_c=\frac{10}{7}\beta^{3/4}\sqrt{g(s-1)d\theta}\,\frac{\mathbf{u}}{u} \tag{10}$$

Where the friction velocity and the Shields parameter are, respectively, given by

$$u_*=\sqrt{R}u \tag{11}$$

$$\theta=u_*{}^2\big/\left(g(s-1)d\right) \tag{12}$$

where $R=$ dimensionless friction coefficient that can be quantified on the basis of the sheet-flow experiments of Sumer et al. (1996), by making use of the sediment transport parameter

$$w_*=w\big/\sqrt{g(s-1)d} \tag{13}$$

being $w=$ sediment fall velocity. A value of $R=0.013$ was obtained for sand.

By analysing the sheet-flow data of Sumer et al. (1996) and Pugh & Wilson (1999), Leal et al. (2003b) observed the following linear relation for the sheet-flow height

$$h_c/d=\beta\theta \tag{14}$$

where $\beta=$ constant that depends on the type of sediment, namely on the sediment parameter w_*. The value estimated by Leal et al. (2003b) for the sand is $\beta=7.0$.

Leal et al. (2003a) using Bagnold's sediment transport formula obtain the total volumetric concentration of transported material expressed as

$$C=\frac{8.03\xi\sqrt{gR}}{(s-1)\left(1/R-\xi u^2/h\right)}\frac{u^2}{h} \tag{15}$$

where ξ is a parameter equal to 0.57, for sand.

A Chézy-type friction law can be used if the main dissipation mechanism is born in the granular phase and is proportioned by frequent binary inelastic collisions of the transported grains. In this case the shear stress, τ, is proportional to $(\partial u/\partial z)^2$ (cf.

Copyright © 2006 Taylor & Francis Group plc, London, UK

Bagnold, 1956), being z the elevation, and following Fraccarollo & Capart (2002), the bed shear stress is expressed by

$$\boldsymbol{\tau}_{bc} = \rho_w R \mathbf{u} u \tag{16}$$

3.2 *Numerical model*

The numerical scheme used to solve Equation 1 is a TVD version of MacCormack's scheme. A brief description of the scheme is presented. For a more detailed 1D version, refer to Ferreira & Leal (1998). Two viscosity terms, aroused by the TVD algorithm, are added to the classical MacCormack scheme, thus redefining the update step, which becomes:

$$\mathbf{U}_{i,j}^{n+1} = \mathbf{U}_{i,j\ MacCormack}^{n+1} + \frac{\Delta t}{\Delta x}\left(\mathbf{D}_{i+1/2,j}^{n} - \mathbf{D}_{i-1/2,j}^{n}\right) + \frac{\Delta t}{\Delta y}\left(\mathbf{D}_{i,j+1/2}^{n} - \mathbf{D}_{i,j-1/2}^{n}\right) \tag{17}$$

where vector $\mathbf{D}$ is the TVD correction given by

$$\mathbf{D}_{i+1/2,j}^{n} = \frac{1}{2}\sum_{k=1}^{3}\left[\left(1-\phi\left(\left(r_{i+1/2,j}\right)_k\right)\right)\left(\Psi\left(\tilde{\lambda}_{i+1/2,j}\right)\right)_k \times \left(1-\left|\left(\tilde{C}r_{i+1/2,j}\right)_k\right|\right)\left(\tilde{\alpha}_{i+1/2,j}\right)_k\left(\tilde{\mathbf{e}}_{i+1/2,j}\right)_k\right] \tag{18}$$

Here, ψ is the entropy correction proposed by Harten and Hymen in 1983, $\phi(r)$ is the flux limiter function proposed by Van Leer in 1974 (see Hirsch, 1990), $\tilde{\lambda}$, and $\tilde{\mathbf{e}}$ are, respectively, the Roe's approximate eigenvalues and eigenvectors of the approximate Jacobian matrixes, $\tilde{C}r$ is the approximate Courant number; $\tilde{\alpha}$ represents the projections in the approximated eigenspace of the any jump in the values of $\mathbf{U}$ (cf. Ferreira & Leal, 1998). For the shallow-water equations, Roe's approximations for the depth-averaged flow velocity and the shallow-water propagation speed can be written, respectively, in the x and y directions, as

$$\tilde{\mathbf{u}}_{i+1/2,j} = \frac{\mathbf{u}_{i+1,j}\sqrt{h_{i+1,j}} + \mathbf{u}_{i,j}\sqrt{h_{i,j}}}{\sqrt{h_{i+1,j}} + \sqrt{h_{i,j}}} \qquad \tilde{c}_{i+1/2,j} = \sqrt{g\left(h_{i+1,j} + h_{i,j}\right)/2} \tag{19}$$

$$\tilde{\mathbf{u}}_{i,j+1/2} = \frac{\mathbf{u}_{i,j+1}\sqrt{h_{i,j+1}} + \mathbf{u}_{i,j}\sqrt{h_{i,j}}}{\sqrt{h_{i,j+1}} + \sqrt{h_{i,j}}} \qquad \tilde{c}_{i,j+1/2} = \sqrt{g\left(h_{i,j+1} + h_{i,j}\right)/2} \tag{20}$$

Equation 1 does not allow a simple determination of the approximation vector $\tilde{\mathbf{U}}$. Therefore, and because the use of the TVD algorithm is required for avoiding spurious oscillations in the solution, Leal et al. (2005) proposed the adoption of the following procedure:

- 1st: at time level $n+1$ the dependent variables $\mathbf{U}$ were computed by the classical MacCormack scheme using the information of the previous time level n.
- 2nd: the variables h, $\mathbf{u}$, ρ, C and z_b were determined by applying Newton's method.
- 3rd: the TVD term $\mathbf{D}$ was computed using Roe's approximations (Equations 19 and 20).
- 4th: Jameson's artificial viscosity was applied to z_b (see Hirsch, 1990).
- 5th: the corrected values of variables h, $\mathbf{u}$, ρ, C and z_b were used to determine the final values of $\mathbf{U}$ used in the next time level (return to 1st step).

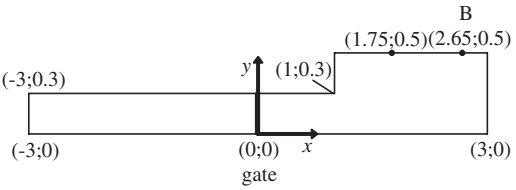


Figure 3. Location of the points where the time evolution was measured.

All physical boundaries were modelled with a free-slip condition, being totally reflective. The downstream end of the flume was modelled with a weir law, where the bed level was computed based on the two previous cells

$$z_{bi_{end},j} = 2z_{bi_{end}-1,j} - z_{bi_{end}-2,j} \tag{21}$$

where i_{end} refers to the computational x coordinate of the flume end section. The spatial domain was discretized using a 0.05 m length size square mesh.

4 RESULTS AND DISCUSSION

The time evolution of the free-surface level, z_s, and the sheet-flow elevation, z_c, were measured at two points (Figure 3). Point A is located in the region where a hydraulic jump occurs, and point B is situated in a region downstream of the hydraulic jump.

In Figures 4 and 5 is presented the time evolution of the free-surface and sheet-flow elevations, measured and computed, at points A and B (Figure 3).

The numerical results are in good agreement with the experimental measurements. The major discrepancies can be identified for the wave-front arrival in the point nearest to the gate (point A). This may be the consequence of a misestimation of the friction coefficient. Indeed, Leal et al. (2005) mentioned that the use of a constant friction coefficient is not sufficient to simulate adequately the wave-front position throughout the entire flood plain.

As for the flow depth, the differences are more evident for the higher upstream initial water depth ($h_u = 0.25$ m). Comparing the experimental results presented in Figures 4 and 5, one can conclude that in

Copyright © 2006 Taylor & Francis Group plc, London, UK

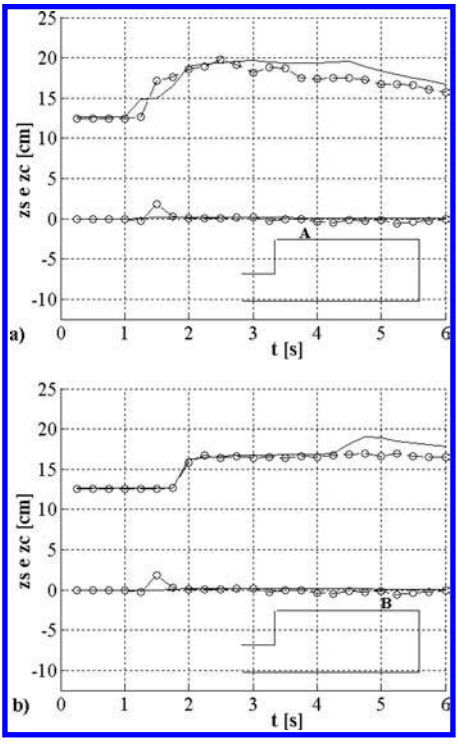


Figure 4. Time evolution of the free-surface and sheet-flow elevations for test T1 ($h_u = 0.25$ m) at: a) point A; b) point B.

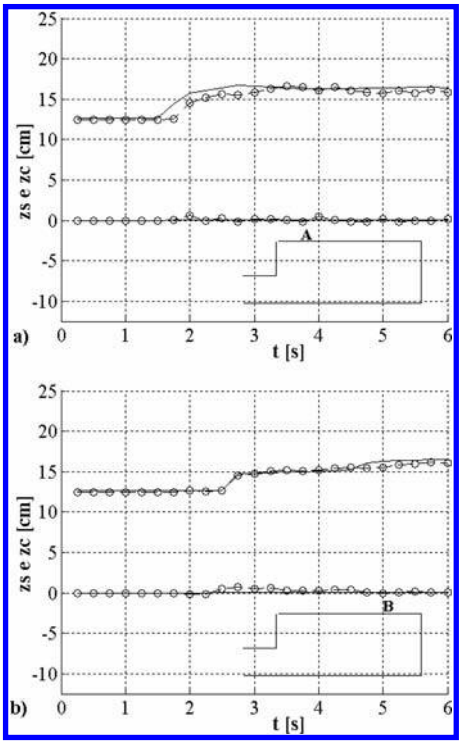


Figure 5. Time evolution of the free-surface and sheet-flow elevations for test T2 ($h_u = 0.15$ m) at: a) point A; b) point B.

the region of the hydraulic jump (point A), where the flow is reflected on the enlarged wall, there is a stronger interaction between the flow and the boundaries in the test for which h_u is larger. As a result, the free-surface is much more irregular in the test depicted in Figure 4.

Reference should be made to the fact that the bed material used, natural sand, does not allow for checking the ability of the model to simulate the sheet-flow layer. For that purpose please refer to Leal et al. (2005), where the model results were compared with lighter bed material tests.

The morphological capabilities of the model can be highlighted by looking at the measured and the computed final bed topography (Figure 6).

The experimental final bed topography (Figure 6a) is composed by a scour hole near the enlargement and a deposition region near the enlarged wall ($y = 0.5$ m). This configuration suggests that the bed material is eroded underneath the accelerated flow caused by the sharp corner of the enlargement located at $(x,y) = (1.0,0.25)$, being deposited in the recirculation zone near the enlarged wall.

The numerical bed topography (Figure 6b) shows the same configuration as the one observed in the experiments. Nevertheless, some discrepancies can be pointed out. Namely, the numerical scour hole is less pronounced than the experimental one, and is accompanied by a small deposition bar near the non enlarged wall. The deposition region near the enlarged wall is reproduced by the model, but shows higher dimensions than the experimental one.

At the downstream end of the measured region, the numerical results present a deposition region in the middle of the flume that was not observed on the experiments. This discrepancy can be caused by the strong interaction between the flow and the boundaries referred previously. As a result, the experimental and numerical wave reflection will, consequently, give raise to different bed topographies.

5 SUMMARY AND CONCLUSIONS

According to the analysis presented above and within the range of tests carried out, the following conclusions can be drawn:

– The numerical free-surface profiles are in good agreement with the experimental measurements. The major discrepancies can be identified for the wave-front location.

Copyright © 2006 Taylor & Francis Group plc, London, UK

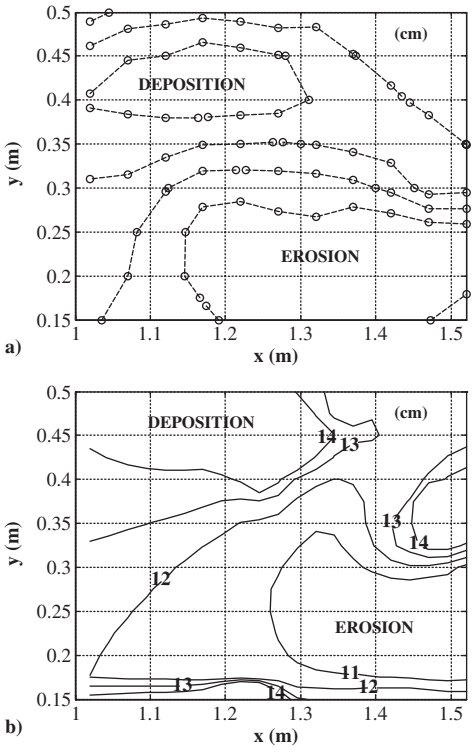


Figure 6. Final bed topography for test T1 ($h_u = 0.25$ m): a) experimental; b) numerical.

- The difference between numerical and experimental flow depths are more evident for the higher upstream initial water depth ($h_u = 0.25$ m). The increase of h_u induces a stronger interaction between the flow and the boundaries, being the free-surface much more irregular.
- The experimental final bed topography is composed by a scour hole near the enlargement and a deposition region near the enlarged wall.
- The numerical model reproduces generally well the bed topography. Nevertheless, the numerical results underestimate the experimental ones. The reason for this underestimation should be investigated in future studies.

ACKNOWLEDGEMENTS

The authors wish to acknowledge Prof. Yves Zech and Dr. Benoit Spinewine for making possible the realization of the experimental study at the University catholique of Louvain (UCL). The contribution of Prof. António Cardoso was also important, allowing the stay of the second author in the UCL. This study was financed by the European Commission through the IMPACT project under the fifth framework programme (1998–2002), Environment and Sustainable Development thematic programme, for which Karen Fabbri was the EC Project Officer.

REFERENCES

Bagnold, R.A. 1955. Some flume experiments on large grains but little denser than the transporting fluid, and their implications. *Proc. Instn. Civ. Engin.*, pt. III, no. 1 (4): 174–205.

Ferreira, R.M.L. & Leal, J.G.A.B. 1998. 1-D Mathematical Modelling of the Instantaneous-Dam-Break Flood Wave Over Mobile Bed: Application of TVD and Flux-Splitting Schemes. *CADAM Concerted Action on Dambreak Modelling meeting*, Munich, Germany.

Ferreira, R.M.L., Leal, J.G.A.B. & Cardoso, A.H. 2005. Mathematical modelling of the morphodynamic aspects of the 1996 flood in the Ha! Ha! River. *Proc. XXXI IARH Cong.*, Theme D: 3434–3445. Seul, South Korea.

Fraccarollo, L. & Capart, H. 2002. Riemann wave description of erosional dam-break flows. *Journal of Fluid Mechanics*, 461: 183–228.

Frazão, S.S., Morris, M. & Zech, Y. 2000. *CADAM Concerted Action on Dambreak Modelling: Objectives, Project Report, Test Cases, Meeting Proceedings*. Univertité catholique de Louvain (edited in CD-rom).

Hirsch, C. 1990. *Numerical computation of internal and external flows: computational methods for inviscid and viscous flows* (2). Wiley-Interscience Publications.

Lapointe, M.F., Secretan, Y., Driscoll, S.N., Bergeron, N. & Leclerc, M. 1998. Response of the Ha! Ha! River to the Flood of July 1996 in the Saguenay Region of Quebec: Large-scale Avulsion in a Glaciated Valley. *Water Resources Research* 34: 2383–2392.

Leal, J.G.A.B., Ferreira, R.M.L, Franco, A.B. & Cardoso, A.H. 2002. Dam-break waves on movable beds. In Bousmar & Zech (ed.) *River Flow 2002* (2): 981–990. Rotterdam: Balkema.

Leal, J.G.A.B., Ferreira, R.M.L. & Cardoso, A.H. 2003a. Dam-break waves propagation over a cohesionless erodible bed. *Proc. XXX IAHR Cong.,* Theme C(2): 261–268. Thessaloniki, Greece.

Leal, J.G.A.B., Ferreira, R.M.L., Cardoso, A.H. & Almeida, A.B. 2003b. Comparison between experiments and numerical results on dam-beak waves over dry mobile beds. Proceedings of the 3th IMPACT Workshop, Louvain-la-Neuve, Belgium, http://www.samui.co.uk/impact-project/cd3/de-fault.htm.

Leal, J.G.A.B., Ferreira, R.M.L. & Cardoso, A.H. 2005. Experimental and numerical results on the 2D propagation of dam-break flows over dry bed. *Proc. XXXI IARH Cong.*, Theme D: 3382-3391. Seul, South Korea.

Leal, J.G.A.B., Ferreira, R.M.L. & Cardoso, A.H. 2006. Dam-break wave front celerity. *Journal of Hydraulic Engineering* 132(1): 69–76.

Pugh, F.J. & Wilson, K.C. 1999. Velocity and Concentration Distributions in Sheet Flow above Plane Beds. *Journal of Hydraulic Engineering* 125(2): 117–125.

Sumer, B.M., A. Kozakiewicz, A., Fredsøe, J. & Deigaard, R. 1996. Velocity and Concentration Profiles in Sheet-Flow Layer of Movable Bed. *Journal of Hydraulic Engineering* 122(10): 549–558.

Copyright © 2006 Taylor & Francis Group plc, London, UK

Levee breach process of a river by overflow erosion

Tetsuro Tsujimoto
Graduate School of Engineering, Nagoya University, Nagoya, Japan

Atsuko Mizoguchi
Dept. of Civil Eng., Meijo University, Nagoya, Japan

Ai Maeda
Graduate School of Engineering, The University of Tokyo, Tokyo, Japan

ABSTRACT: In Japan, most of population and property concentrate to floodplain, and the main facility against flood is continuous flood levee, thus, the river administers have constructed flood levees with arranging flood control dams to suppress the disaster against flood. However, due to heavy rainfalls that exceed the design or equipped facility level, inundation due to breach of flood levee have often caused serious disasters. We are aware that it is necessary to prepare evacuation system against contingency, and in this purpose it is necessary to know how the breach develops as time process. In this paper, we explain how it is important to clarify the evolution process of levee breach, and develop a numerical simulation of the breach process that can evaluate the toughness of levee and floodplain against flood.

1 INTRODUCTION

The flood disasters in Japan are characterized by peculiar climate and geographical conditions and human activities under them. The Japan islands are on the route of Typhoons in July–October, and Bai-u front is active there in June–July, which bring a day or few days heavy rainfall events. The Japan islands are narrow and higher mountains form the backbone, and thus the watersheds are small and rivers are short and steep. These bring rapid runoff process.

On the other hand, the most of human activities (rice paddy fields and urbanization) concentrate on the floodplains of these rivers and they are exposed to risk of inundation during floods.

As the countermeasure against flood disasters, the river administrators have made effort to construct continuous flood levees and flood-control dams. It resulted that the risk of inundation have been reduced from a few years in the basis of the return period to 5–10 years, and the mortality have decreased from the order of 10^3 to that of 10 during this half of the century. This was caused not only by the effect of flood-protection facilities but also by a few decades with mild climate. In these few years, however, heavy rainfalls occurred frequently to cause serious disasters. Heavy rainfalls are particularly concentrated locally and temporally. They might be caused by the global warming and/or by the heat-island phenomena. In addition, the safety level in the master plan has not completed and the increase of the effect in higher safety level might be difficult to be recognized compared with investment. The public works are saturated in these years with lower growth of economy, and have been exposed to opposite opinion from the viewpoint of environment particularly for dam projects. Furthermore, the society has been changed to aged and less communicated neither assisted each other. As a result, peoples are not good at fleeing from inundation.

For examples, in 2000, heavy rainfall attacked Nagoya metropolitan area, and the city perfectly lost the functions and we recognized the fragile structure of urban area against flood. The flood-levee breach brought us particularly serious damage. In 2004, 10 typhoons hitting the Japan islands and heavy rainfalls due to front activities caused levee breaches at many rivers to bring catastrophic disasters, when more than 200 peoples were killed. It was a shock when we considered the recent tendency of decrease of flood damage as mentioned above. We have realized that serious disasters of inundation are brought by breach of flood levee as well as inundations caused by worse drainage.

Against inundations as contingencies when the external force (rainfall or flood discharge) exceeds the present safety level, which are inevitable because of present lower safety level and probabilistic feature of rainfall, residence of the dangerous area would

Copyright © 2006 Taylor & Francis Group plc, London, UK

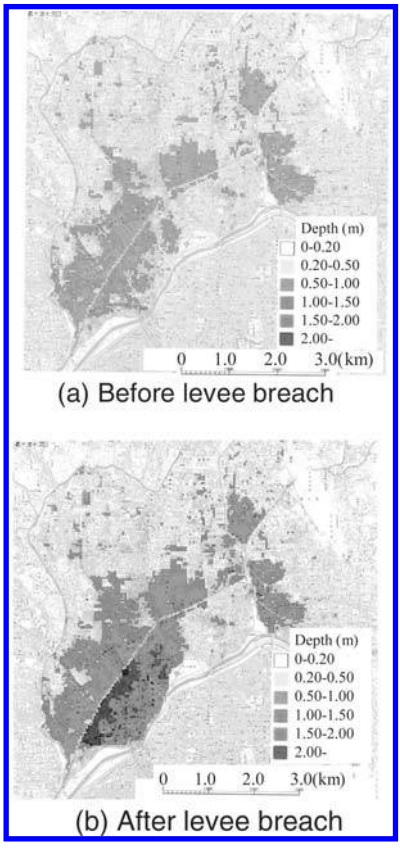


Figure 1. Simulation of inundation in the Shinkawa river basin (Aichi Pref.) on the Tokai heavy rainfall 2000.

flee safely or should be safely evacuated by proper guidance.

Figure 1 shows the example of the results of inundation simulation to reproduce the event of the Tokai heavy rainfall in 2000. Figure 1(a) shows just before levee breach and the wide area is already inundated. When we look at Figure 1(b) showing after the levee breach, we realize how serious what the levee breach brings about. Figure 2 shows another example of the levee breach (Kariyata river in Niigata Pref., 2004), where some houses including a temple were perfectly destroyed and a few peoples were killed.

For safe evacuation, the "hazard map" is prepared by community and distributed to residence, which is a kind of guide map for safe evacuation. The hazard map is made by consulting with a hypothetical map of inundation, that is a map of the inundation depth when the design flood attacks the river with present flood protection facilities. Because the facilities have not completed, there remain several critical points where the water stage exceeds a safety level (a kind of guarantee of the safety of the levee: the level lower free



Figure 2. Levee breach along the Kariyata river in Niigata Pref., 2004.

board below the top of the levee). The inundation flow is calculated often by employing 2D hydraulic model, where the levee breach is assumed at a breach point, and the calculated results of inundation depth for several breaching points are overlaid to obtain the maximum inundation at any points in floodplain. The hazard map is made by consulting such an inundation map, and it might be useful for making evacuation plan at pre-event, for example, designation of refuge and evacuation route, and evacuation-order needed area.

However, a contingency that may happen is quite different from the hazard map. In general, once the breach occurs at one location, the river discharge decreases rapidly which outflows to the floodplain, and the rest of the levee is saved from breach. It is important where the breach occurs, how the breaching evolutes and where becomes seriously dangerous. We have not been familiar yet to the breaching process, and in the manual prepared by the ministry is merely hypothetical based on limited numbers of experiences. Hence, we cannot evaluate the efforts to make the levee and the floodplain tough and to make the inundation propagation retarded. Such efforts are just what are required in order to mitigate the disaster when the external force exceeds the present facility level.

2 LEVEE BREACH

Though the manual recommend a proper mixture of sand (from the river) and clay (from mountain area) as the levee material on design of flood levee, most of levee have been constructed since early days when the riverbed materials have been damped up step by step in its history.

After the survey of the breached levee, the causes of levee breach are categorized into the following three: (1) overtopping of river flow; (2) slope-failure (sliding) and piping by seepage; and (3) bank erosion and/or scouring at the foot of a levee.

Copyright © 2006 Taylor & Francis Group plc, London, UK

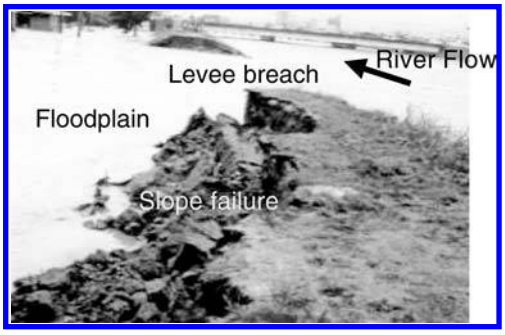


Figure 3. Levee breach in Shinkawa river in 2000 (Aichi Pref.).

In 2004 disasters in Japan, we experienced many levee breaches by overtopping. At the Shinkawa levee breach shown in Figure 3, the overflow eroded the body of the levee and it governed the evolution process of levee breach though the trigger of the breach was slope failure. And, the propagation of inundation was subjected to this evolution process. It determined the water discharge pouring to the floodplain, and it caused the initial rapid and dangerous flow near the levee.

3 MODEL TO DESCRIBE EVOLUTING PROCESS OF LEVEE BREACH

Considering the situations mentioned in Chapter 2, we have conducted to simulate the levee breaching process by applying the 2D horizontal flow model and a model coupling the bed-load transport and morphological change, where the area for simulation includes river, flood levee and floodplain. Previously, the flood in rivers has been treated in longitudinally 1D scheme, the flow over the levee in laterally 1D scheme, and inundation in floodplain in horizontally 2D scheme, separately. Figure 4 shows one of the model fields for simulation, which approximates the levee breaching area of the Sninkawa.

The numerical simulation was conducted in the framework of NHSED2D developed by Nagoya Hydraulic Laboratory (Goto *et al*., 2001). As for the flow, depth-averaged 2D hydraulic model was employed, where the boundary resistance was expressed by the friction factor. Meanwhile, the sediment transport and morphological process were described by Ashida-Michiue bed-load transport formula (1972) and the 2D equation of continuity for sediment transport. The transport fluxes of bed load were distributed to the directional components by considering the direction of bed-load motion subjected to both the bed undulation (gravity effect) and the deflection of bottom flow direction (Nakagawa *et al*., 1986). The difference in flow direction between depth-averaged flow and the near-bed flow were taken into

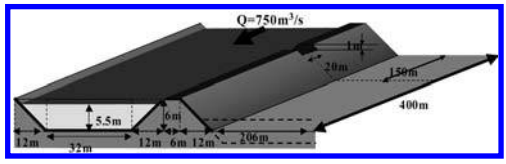


Figure 4. Model area for simulation.

account after Engelund equation (1974) for velocity profile at a river bend. In addition, the collapse was taken into account when the calculated morphology exceeds the angle of repose in the numerical simulation.

The governing equations were discretized by finite volume method, and collocated grid and fractional step method were employed in the numerical simulation. Rhie & Chow (1984) method is employed in interpolating between cells. And, the fractional step method (Ferziger & Peirc, 1997) was applied in time development in calculation.

4 SIMULATED EVOLUTION PROCESS OF LEVEE BREACH

For the first case of the simulation, which is regarded as the reference when we discuss the effect of the site characteristics on levee breach, the followings are set: The bed slope = 1/3690; the levee slope = 1:2; the channel width at the bottom: $B = 32$ m; the levee height = 6 m from the floodplain (the same level as the river bed); friction factor = 0.0167; and size of bed material of river bed, material of levee and floodplain: $d = 0.375$ mm. The discharge Q of the river before the breach is 750 m^3/s that corresponds to the flow depth $h = 5.5$ m, and the overflow starts from a hypothetical notch on the top of the levee (20 m wide and 1 m deep) as a trigger of breach. Though the river discharge has a hydrograph in general, a steady discharge corresponding to the peak is assumed here. These values are roughly set as similar as the flood in the Shinkawa river on the Tokai heavy rainfall in 2000. The domain for calculation is 400 m long in the longitudinal direction, and the floodplain is 400 m × 206 m.

By numerical calculation, the flow behavior around the breach can be described with morphological change (see Figure 5), and we can realized the spatial characteristics of the phenomena as well as the temporal evolution.

From the results of the simulation, it is characterized that the evolution process is divided into the following stages:

(i) the initial stage;
(ii) the second stage when the vertical erosion of bank proceeds dominantly, and the overflow notch is widen towards downstream of the river;

Copyright © 2006 Taylor & Francis Group plc, London, UK

(iii) the third stage when the local scour at the attaching point of the flow along the levee slope to the floodplain becomes remarkable and the width of over flow (breach width) increases dominantly toward downstream of the river. Subsequently, the discharge from the river to the floodplain rapidly increases; and

(iv) the fourth stage when the discharge supplied by the river totally outflows from the breach to the floodplain and the breach width continues to increase even toward upstream of the river.

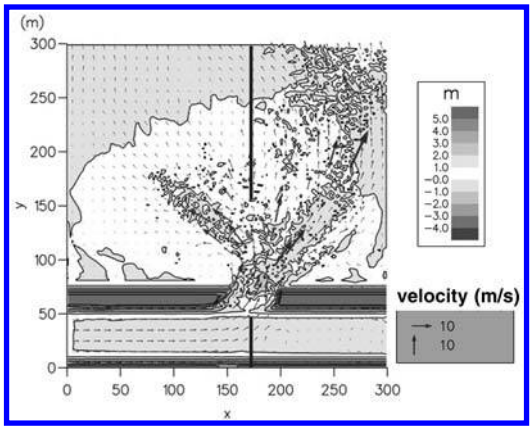


Figure 5. Spatial characteristics of flow and morphological change at levee breach ($t = 55$ min) in case of erodible floodplain.

The initial stage is subjected to the trigger of levee breach (either of overflow, slope failure, piping or bank erosion), of which type may be various, while the fourth stage might be influenced by the hydrograph pattern for each flood. Hence the discussion here should be focused on the second and the third stages mainly.

The above feature coincides the phenomena observed at the real levee breach of the Shinkawa river in 2000.

5 EFFECTS OF FEATURES OF RIVER, LEVEE AND FLOODPLAIN ON LEVEE-BREACHING PROCESS

5.1 *Effects of relative height of levee to floodplain*

In Japan, most of fluvial fan areas have been cultivated as rice paddy field and then often have been urbanized. Resultantly, the river is surrounded by flood levees

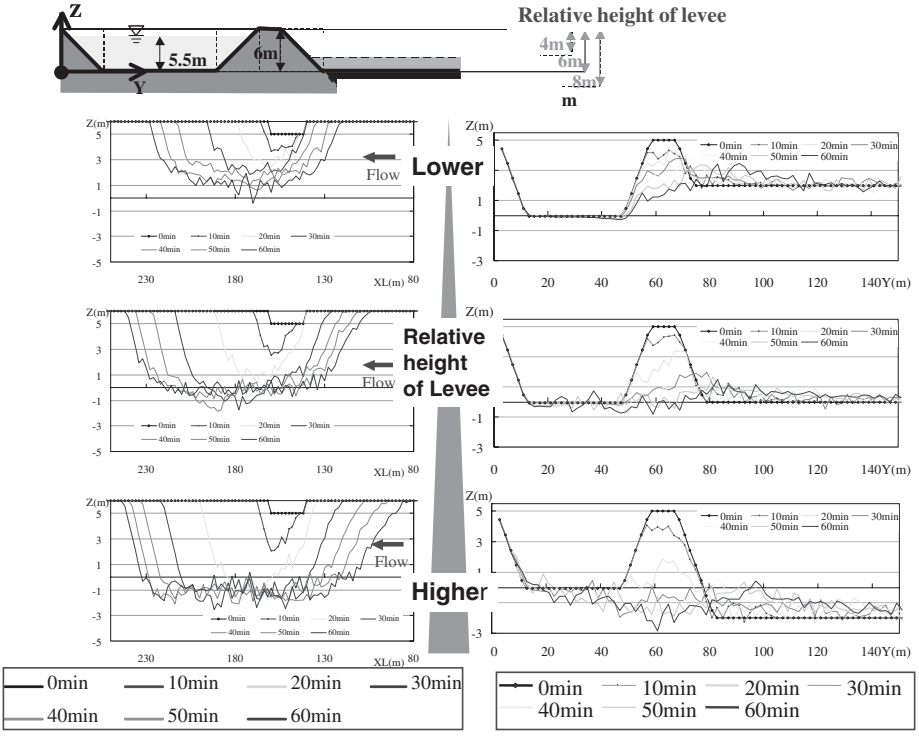


Figure 6. Difference of evolution process of levee reach due to different relative height of levee.

Copyright © 2006 Taylor & Francis Group plc, London, UK

both sides. A rivers in a fluvial fan often flows the highest crest of the fluvial fan, and the river bed is higher than the floodplain. Such a river is often called "Tenjo" river ("Tenjo" means a ceiling in Japanese), which requires higher levees, and it has high risk of disaster on levee breach during flood.

Considering the above, the evolution process are compared with among the levee with different relative height of river bed in order to recognize how high is the risk of a "Tenjo" river. For the time being, the information for the levee breach, that is utilized on preparing a hazard map, is based on the experiences independently the height of levee. When the capacity for flood is the same, a higher-bed river implies a river with higher levee looking at from the floodplain. In this section, the evolution process of levee breach for the three cases are compared each other as shown in Figure 6. In this figure, the breach evolution is expressed as the temporal growth of breaching section (front view) and the temporal loss of levee cross section (side view). Obviously, the breaching section for higher levee is larger, and it results that the large amount of discharge causes serious inundation. In addition, not only the materials but also river-bed materials outflow to the floodplain, and deposition of these debris is another aspect of a disaster.

5.2 *Effect of paved floodplain*

It is interesting that the development of the local scour caused by attacking flow along the levee slope contributes the evolution of the breach and the increase of inundation discharge as already mentioned in Chapter 4. Is the evolution of levee breach possibly suppressed if the area where the overflow along the levee slope attacks is paved? The retardation of breach development of levee must be helpful from the viewpoint of evacuation.

In this section, the evolution process of levee breach is compared between erodible floodplain and paved floodplain.

Figure 7 shows the calculated result of the velocity vector and the morphology after 50 min for paved floodplain that would be compared with Figure 5 (in the same river with the same discharge but with non-paved floodplain). By comparing them each other, it is concluded that the pavement of the floodplain, particularly the place to be attacked by the overflow along the levee slope, considerably retards the evolution process, and subsequently to suppress the rapid increase of discharge of inundation.

5.3 *Effect of river-course shape*

The geometry of river-course, particularly, river bend or meandering, is often paid attention to when we discuss the weak points for levee breach. Some of the

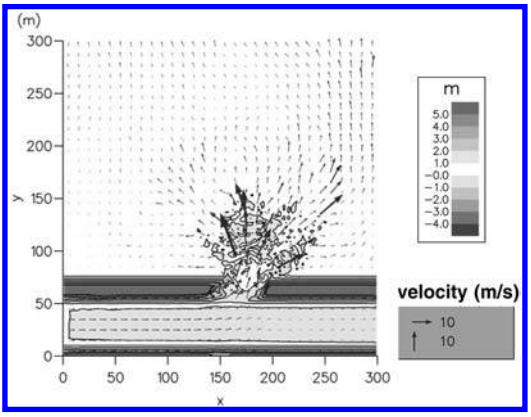


Figure 7. Spatial characteristics of flow and morphological change at levee breach ($t = 55$ min) in case of paved floodplain.



Figure 8. Levee breach at the Ikarashi river, Niigata Pref. in 2004.

historical levee breaches happened in a straight course (for example, at the Shinkawa river in 2000), some at the outer bank (for example, at the Kariyata river), the other at the inner bank (for example, at the Ikarashi river in Niigata Pref., see Figure 8) of river bends. The water stage at the outer bank rises up due to the centrifugal force effect, and if the levee heights are the same in the both sides, the outer has higher risk of overflow. However, some rivers have different height for the each levee historically or with some strategy of flood protection.

When we discuss the risk of levee breach, the hydraulics of flow along a river would be a tool, but once the levee breach starts for example by overtopping, the governing flow is not the flow along the river but the levee-crossing flow. In this sense, 1D model lateral to the river might be employed, and then the evolution process might be same independently of the river-course geometry. However, actual flow is supplied from the river not from a kind of reservoir, and it might affect the evolution process as well as a trigger phenomenon. Hence, 2D-scheme simulation model

Copyright © 2006 Taylor & Francis Group plc, London, UK

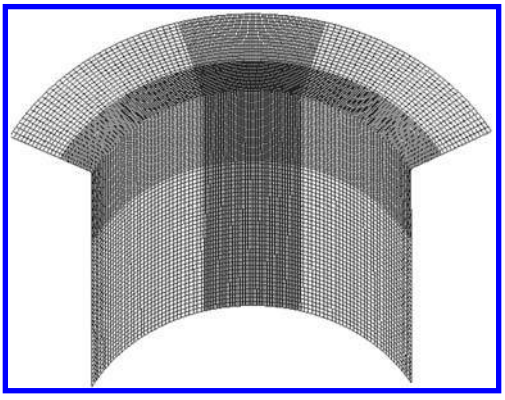


Figure 9. Grids prepared for simulation of levee breach at the inner bank.

has been developed, and it is employed to investigate the difference of evolution process of levee breach due to the river-course geometry.

In this section, river bends of a model river and levees with the same dimension with those investigated in Chapter 4 (bed-slope = 1/3690; size of materials of river bed, levee and floodplain: $d = 0.375$ mm; width of the river at the bottom: $B = 50$ m) are focused on as model courses. The courses with two different values of curvature radius R of river bend (at the centerline) are compared each other respectively for breach at inner and outer bank: (i) $R = 3B$ and (ii) $R = 6B$. The friction factor was adjusted so that the water stage for the given discharge ($Q = 750\ \mathrm{m}^3/\mathrm{s}$) is 0.5 m above the initial notch bottom as a trigger of the levee breach. Figure 9 shows the grids for a model of river course, levee and flood plain when the breach at the inner bank is discussed.

Figure 10 shows the calculated results by the present simulation demonstrated by the temporal development of breach section. Comparing the case of breach at the inner bank with that at the outer bank, the breach section develops almost only toward the downstream of the river for the former case, while it widens both downstream and upstream and it becomes bigger for the latter case. Such characteristics could not be estimated by uni-directional analysis lateral to the river.

As shown in Figure 11, the inundation flow behavior and the subsequent morphological change show some differences between the breach at inner bank and that in the outer bank.

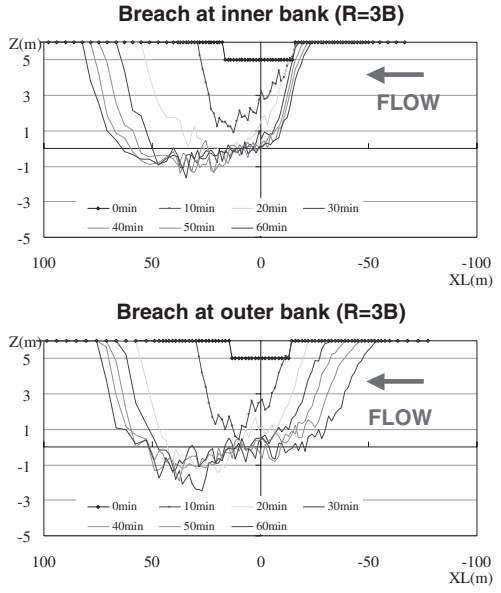


Figure 10. Evolution process of levee breach at river bend. Comparison between inner bank and outer bank.

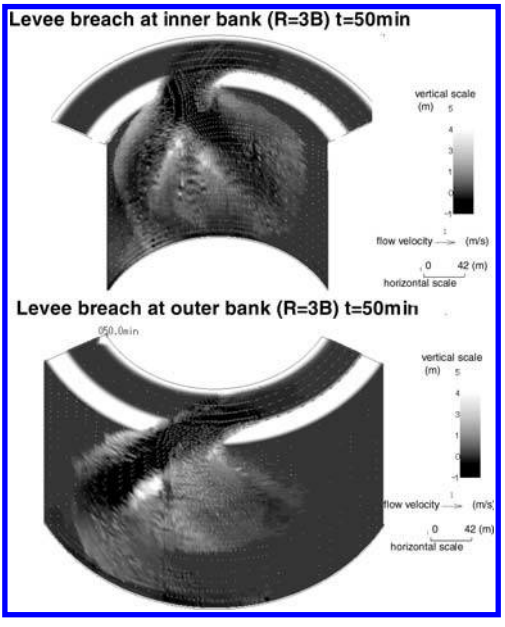


Figure 11. Comparison of flow and morphological change at levee breach between inner-bank case and outer-bank case.

6 DISCUSSION ON ACTUAL LEVEE BREACH EXAMPLES BASED ON SIMULATION

6.1 *Levee breach in Kariyata river in 2004*

The Kariyata river is a tributary of the Shinano River. In July 2004, because of heavy rainfall exceeding 200 mm a day due to an active front, the Kariyata river was suffered levee breaches at several locations. Among them, the levee reach at Nakanoshima district (at the outer bank) brought a serious disaster

Copyright © 2006 Taylor & Francis Group plc, London, UK

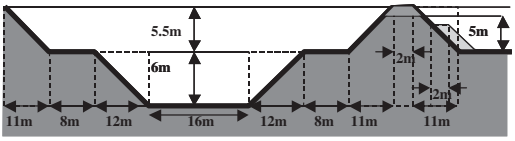


Figure 12. Modeled cross section of river with levee in the levee-breach simulation for the Kariyata river.

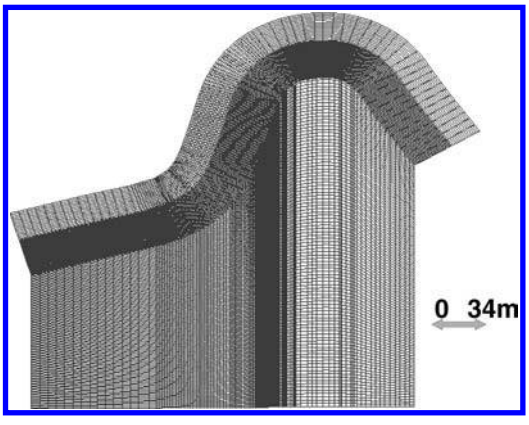


Figure 13. River-course geometry and grids for simulation of levee reach in the Kariyata river.

(see Figure 2). Though the levee height was slightly higher than the other side levee, the overtopping happened at both side. Disadvantage of this side was that the top of the levee was not paved, while the top of the levee was paved in the other side levee. A torrent from the breach destroyed several buildings completely, and rapid rising inundation killed a few peoples. In this chapter, by making use of the simulation developed in this study, it was investigated how the evolution of levee breach caused such a catastrophic situation.

The simulation was conducted under the following condition that roughly approximated the actual event: bed slope = 1/1000; Manning's $n = 0.03$, the size of river-bed, levee and floodplain: $d = 0.375$ mm; and the cross section of the river with the levee is shown in Figure 12. The discharge was set 1850 m^3/s, when the overflow appears 0.5 m deep from the initial notch bottom. The river-course geometry is shown in Figure 13 with the calculation domain and grids.

When the river is managed by a local government, the details of the cross sections of the river with the levees are often unclear. For this site in 2004, various ambiguous information for levee spread, and thus the following three situations were tested: (i) simple cross section; (ii) most of the levee has revetment over the floodplain-side slope except around 50 m segment near the; (iii) there was an additional step slope on the floodplain-side slope.

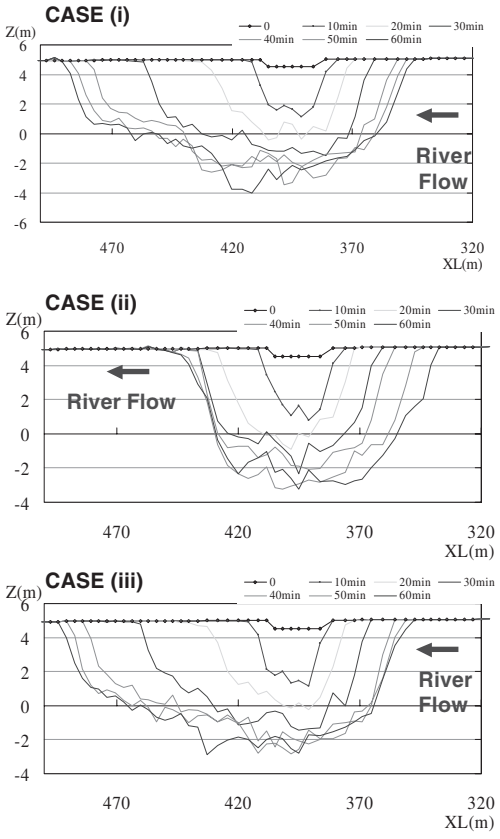


Figure 14. Evolution process of levee breach at Nakanoshima site of the Kariyata river (three scenarios).

In Figure 14, the calculated results were shown as temporal growth of breach section. Independently of the detailed differences (i)–(iii), most of breaching process proceeded within 30 min, and the inundation within such a short time made the disaster extremely serious. Limited opening of the backside revetment suppressed the widening of the breach section, but the flow from the river to the floodplain was limited to this width. And because of the vertical development of the breach, the concentrated intensive flow attacked the locally limited area. The added side step on the backside of the levee retarded the evolution of the levee breach, but its effect was slight.

Figure 15 shows the spatial flow behavior and morphological change in the floodplain for the above three scenarios and the scenario with continuous revetment covering the backside of the levee. As aforementioned, the backside revetment prevents the breach, but if it has an opening, the concentrated flow is intensive and causes severe morphological change though the

Copyright © 2006 Taylor & Francis Group plc, London, UK

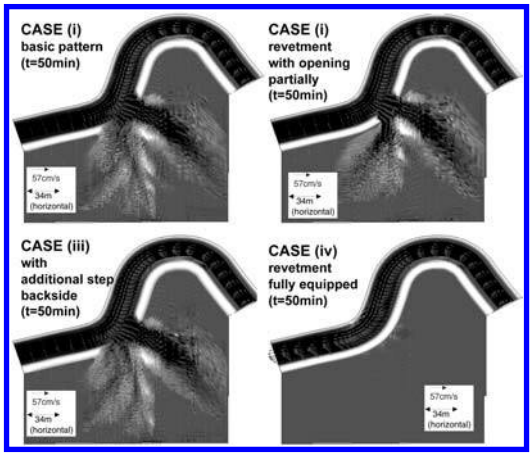


Figure 15. Spatial flow behavior and morphological change at levee breach in the Kariyata river (four scenarios).

evolution of breach section is suppressed in the width of breach.

6.2 *Levee breach in Ikarashi river in 2004*

The Ikarashi river is another tributary of the Shinano River. In July 2004, the heavy rainfall due to active front caused a big flood, and the river flow overtoped the levee several places. At Suwa district, the levee breach occurred at the inner bank (see Figure 8), and the inundation widely propagated down to Sanjo city, where several peoples died because of rapid rising of inundation depth.

Just downstream of the levee breach was utilized as a paddy field, and direct attack of flow due to levee breach never killed persons but rapid propagation of the inundation flow to the residential area caused serious mortality. Deposition of sediment on the paddy field caused the damage for crops. The simulation developed in this study can describe not only the erosion but also deposition, and it can be used for farmland damage estimation.

At the breaching point, the river flow was overtopping, and we estimated that the trigger of levee breach was overflow. Some persons insisted that a piping might have become the trigger of the levee breach and they considered that dispersed gravels remaining in the farmland was a ruin of quick sand. However, such gravels were observed inside the levee as a gravel layer, which were used as levee materials in early days. Thus, we investigated that how the gravels inside the levee were transported on the levee breach to spread in the floodplain.

As seen in Figure 8, the Ikarashi river is meandering and Suwa district faces to the inner bank of the bend. Thus, the river-course geometry adopted as the calculation domain was expressed as similar as Figure 9,

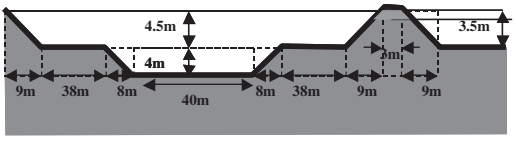


Figure 16. Modeled cross section of river with levee in the levee-breach simulation for the Ikarashi river.

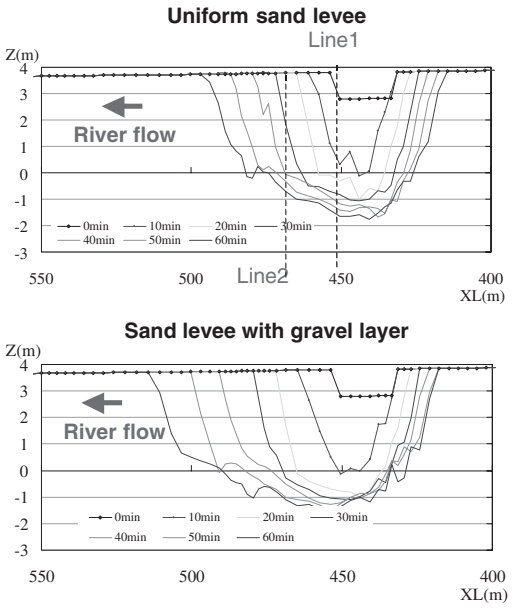


Figure 17. Temporal growth of breach section. Comparison between (i) uniform sand levee and (ii) sand levee with gravel layer (gravel size = 10 cm).

where the bed slope = 1/800, the material size of riverbed, levee and floodplain: $d = 0.375$ mm. Manning's $n = 0.03$, and the cross section of the river was as shown in Figure 16. The discharge was 1580 m^3/s, when the overflow was 0.5 m deep from the initial notch bottom. According to the boring data, the gravel layer was assumed to be 1.0 m thick with the lower boundary 0.5 m above the floodplain level, and the diameter of the gravels was $d_G = 100$ mm.

Figure 17 shows the temporal growth of breach section, where the uniform sand levee and the sand levee with a gravel layer. According to the calculated results, the levee breaching flow can transport gravels as large as 10 cm, and the breach section became larger than the case of uniform sand made levee.

Figure 18 shows the spatial distribution of flow behavior by velocity vector, morphological change by contour lines, and the change of average material size due to dispersion of gravels by grey-scale gradation. The dark zone implies deposition of dispersed gravels

Copyright © 2006 Taylor & Francis Group plc, London, UK



Figure 18. Arrows indicate the flow behavior; contour lines indicate the morphological change; and the dark area in gradation indicate gravels dispersion from the inside of levee.

from the gravel layer inside the levee, and it is recognized that gravels as large as $d_G = 10$ cm inside the sand levee could be transported to the floodplain and form recognizable deposits in the floodplain somehow far from the levee on the occasion of levee breach by flood.

7 CONCLUSION

In this paper, the authors have insisted that the understanding of evolution process of levee breach is important for disaster mitigation on contingency such as evacuation as well as the trigger of levee breach is important for designing and maintenance of the flood levee.

Though the complexities exist on real phenol-mena, 2D depth-averaged flow analysis with model describing morphological change by using the bed-load transport formula and sediment continuity equation have been applied not only to the river course but also levee and floodplain simultaneously, and a simulation model has been developed.

Firstly, the applicability of the model has been verified by discussing the levee breach event in the Shinkawa river (a straight channel) in 2000. Then, the effects of the characteristics of river course have been investigated through the simulation: the effect of the relative height of the river course and the river bend (the difference in levee breach between at the outer bank and at the inner bank). The higher position of a river course with higher levee has higher risk of large breach that causes larger amount of inundation discharge. It suggests higher risk in flood levees in fluvial fan area. At river bend, the water stage at the outer bank is higher, but the breach depends on the overtopping depth. If the overtopping occurs, a levee is possibly breached irrespectively outer or inner bank, and the final breach section has less difference. But, the breach at the inner bank widens only downstream of a river, while the breach at the outer bank widens towards both directions. In addition, it has been clarified that the local scour at the overflow attacks in the floodplain attached to the levee promotes the breach evolution, and the simulation has demonstrated that the paved floodplain delays the evolution of levee breach, which is advantage for proper evacuation.

Furthermore, the present simulations have been roughly applied to the two examples of levee breaches in the Kariyata and the Ikarashi rivers where severe disasters occurred in 2004. For these incidents, several aspects related to the levee breach were disputed, and some of them have been discussed rather objectively by applying the present simulation model: the effect of the condition of revetment cover on the floodplain-side slope of the levee; and the reason why gravels dispersed and spatially distributed in the floodplain near the breaching point. These examples suggest how to use the present model in the survey of the happened disasters with levee breach and in making evacuation strategies.

REFERENCES

Ashida, K. & Michiue, M. 1972. Study on hydraulic resistance and sediment transport formula, *Proc. JSCE*, 206, 55–69 (in Japanese).

Engelund, F. 1974. Flow and bed topography in channel bends, *J. Hydr. Div.,* ASCE, 100(11), 1631–1648.

Ferziger, J. H. & Peirc, M. 1997. *Computational Method for Fluid Dynamics*, Springer, 364p.

Goto, T., Tsujimoto, T. & Kitamura, T. 2001. Advances in *Fluid Modeling & Turbulence Measurements*, edited by Ninokata *et al*., World Scientific, 127–134.

Nakagawa, H., Tsujimoto, T. & Murakami, S. 1986. Non-equilibrium bed load along side bank, *Proc. 3rd Int. Sym. River Sedimentation*, Jackson, Mississippi, USA, 1029–1065.

Rhie, C. M. & Chow, W. L. 1983. A numerical study of the turbulent flow past an isolated airfoil with trailing edge separation, *AIAA J.*, 21, 1525–1532.

Tsujimoto, T., Sumi, T., Teramoto, A. & Maeda, A. 2005. Breaching process of flood levee affected by geometrical properties of riveres, *Advances in River Engineering*, 11, JSCE, 121–126 (in Japanese).

Copyright © 2006 Taylor & Francis Group plc, London, UK

B.6. Sedimentation in reservoirs

Copyright © 2006 Taylor & Francis Group plc, London, UK

A 3-D numerical investigation of the development of density driven finite-channel lock-release currents at high Grashof numbers

Seng Keat Ooi, George Constantinescu & Larry Weber
Civil & Environmental Engineering, IIHR-Hydroscience & Engineering, The University of Iowa, Stanley Hydraulics Laboratory, Iowa City

ABSTRACT: Lock-exchange gravity current flows produced by the instantaneous release of a heavy fluid are investigated using 3D high-resolution Large Eddy Simulation (LES) simulations at Grashof numbers between 9.6×10^8 and 8×10^9. It is found that the finely resolved 3D simulations on meshes containing around 35 million cells correctly predict a constant front velocity over the initial slumping phase and a front speed decrease proportional to $t^{-1/3}$ (the time t is measured from the release) over the inviscid phase, in agreement with theory and experimental observations. It is found that the KH billows do not preserve their structure across the width of the channel and break rapidly into smaller 3D structures. In the near-wall region beneath the upstream part of the current, it is found the intensity of the turbulence is large enough to induce the formation of low and high streamwise velocity streaks, similar to the ones observed in channel flows.

1 INTRODUCTION

Gravity currents form when a heavier fluid propagates into a lighter one (Simpson, 1997). In the case of lock-release gravity currents in channels (see sketch in Figure 1), a lateral wall is present at one of the ends of the channel and the heavier lock fluid occupies initially a finite volume between the lateral wall and the lock gate. When the lock-gate wall is removed a gravity current (GC) will start forming and propagate near the bottom wall. This case is the main focus of the present paper. Also we limit our investigation to compositional currents when the density differences are produced by a difference in a property of the fluid (e.g., temperature, salinity, etc.) and we study only the case when the initial height of the heavier lock fluid is equal to the channel height. Especially because of the possible negative effects on the environment, predicting and understanding the evolution of gravity currents is of considerable interest to both the engineering and geophysical communities (e.g., Simpson, 1997).

For practical applications, accurate prediction of the speed of the current front and the spatio-temporal distribution of the bed shear stress is of great interest. This is because in the case in which these compositional currents propagate over loose beds they can entrain sediment and significantly alter the deposition/entrainment patterns in the region. Also in many applications (e.g., submerged dams) it is important to be able to predict the forces induced by the gravity current on an obstacle situated in the way of the current. Obtaining the bed shear-stress distribution, the pressure distributions on obstacles, the spatio-temporal distribution of the velocity and concentration fields or information on the global energy balance at different stages of the evolution of the GC is quite difficult and very expensive to achieve experimentally. To be able to numerically predict these more complex phenomena in a range of representative flow conditions (high enough Reynolds and Grashof numbers when the flow inside part of the GC is highly turbulent) for practical applications, one has first to validate the method for cases for which experimental data is available and to compare the prediction of some of the global flow features of the current (e.g., speed of propagation) with theory. Our approach is to use highly-resolved fully 3D LES simulations at Grashof numbers around 10^9 and above where highly-resolved Direct Numerical Simulation (DNS) using non-dissipative methods is too expensive computationally.

2 BACKGROUND

For finite-volume lock-exchange GC the flow physics is more complex compared to the classical case of a gravity current that forms in an infinite channel in which the volumes of the heavier and of the lighter fluids are infinite and the current propagates with practically constant speed some short time after the gate release. For finite-volume lock-exchange GC, several phases can be identified in the evolution of the current.

Copyright © 2006 Taylor & Francis Group plc, London, UK

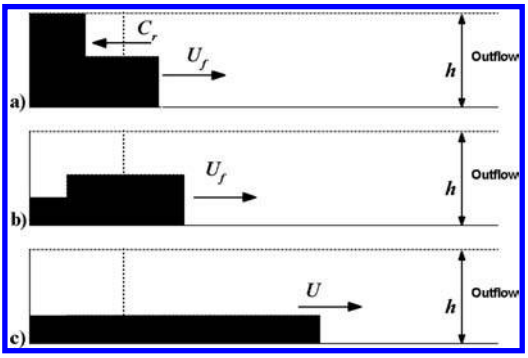


Figure 1. Sketch of lock-exchange flow in a channel limited by an end wall (a) Gravity current immediately after the gate is removed with associated front velocity of denser fluid and bore velocity of lighter fluid; (b) Gravity current in the slumping phase after the bore has been reflected; (c) Gravity current in the self-similar phase after the bore has caught up the front.

Initially, immediately after the gate release, a bore of lighter fluid is observed to form concomitantly with the main GC containing heavier fluid in the lower part of the channel. The speed of propagation of the bore and front of the GC are relatively close to each other initially. Once the bore propagating backwards (Figure 1a) has reflected from the end wall (Figure 1b), a flow of lighter fluid than the one inside the GC starts propagating toward the front of the GC with a velocity (U_{bore}) slightly higher than the front velocity (U_f). The current is in the slumping phase. Rottman and Simpson (1983) have shown that for the case when the initial depth of the lock fluid is close or equal (our case) to the depth of the channel, the bore advancing toward the front has the form of an internal hydraulic jump. During the slumping phase the flow is not self similar. However, the front propagates with practically constant depth and constant velocity (U_f). The ratio between the front velocity and the buoyancy velocity $u_b = (g'h)^{0.5}$ (g' is the reduced gravity and h is the channel depth) is in fact a parameter depending on the ratio between the initial depth of the denser fluid in the lock area and the total depth of the channel.

The inviscid self-similar phase starts once the forward propagating bore has overtaken the front of the GC (Figure 1c). From this moment the front advances with a velocity which decays in time proportional to $t^{-1/3}$. The flow is self-similar (a self-similar solution of the shallow water equations that describes this phase exists) and determined by the balance between the inertial force of the current and the buoyancy force (horizontal density gradient). If the channel is sufficiently long, a third phase, known as the viscous phase, may occur when viscous effects become dominant.

The lock-exchange flow corresponding to a bottom compositional current in a channel with a lateral wall was studied experimentally and analytically by Rottman and Simpson (1983) and by Hacker et al. (1996). Numerous numerical Reynolds Averaged Navier Stokes (RANS) based models and integral models were used by various researchers to predict the main features of compositional currents. A good review is given in Choi and Garcia (2002). The case of the propagation of the lock fluid into a linearly stratified fluid was studied experimentally and numerically by Maxworthy et al. (2002). Their 2-D DNS simulations employed meshes with around 106 grid points for Grashof numbers in the range of 108-4 $\times$ 108 to obtain stable solutions without adding numerical dissipation.

Regarding, 3D simulations using eddy resolving techniques, the first highly-resolved DNS simulations were performed by Hartel et al. (2000a, 2000b) for the case of an infinite-volume lock-exchange compositional GC at a Grashof number (Gr) around 1.2 $\times$ 106 (the corresponding Reynolds number was Re $\sim$ 710). The case of a particle-driven finite-volume lock-exchange GC at Gr = 5 $\times$ 106 was studied using 3D DNS by Necker et al. (2002). These studies were the first to numerically capture the presence of the lobe and cleft instability at the head of the current. Subsequently, the same group (Necker et al., 2005) performed a detailed analysis of the energy budgets, dissipative losses, influence of initial level of turbulence inside the lock fluid and of the mixing between interstitial and ambient fluid for particle-driven GC for the same range of Grashof numbers.

3 DESCRIPTION OF NUMERICAL MODEL AND COMPUTATIONAL TEST CASES

The numerical solver is a finite-volume non-dissipative DNS/LES code (Pierce and Moin, 2001) that solves the conservative form of the Navier-Stokes equations on non-uniform Cartesian meshes. A semi-implicit iterative method that employs a staggered space-time discretization is used to advance the equations in time while ensuring second order accuracy in both space and time. A Poisson equation is solved for the pressure. The algorithm discretely conserves energy which ensures robustness at relatively high Reynolds numbers in the LES regime. All operators are discretized using central discretizations except the convective terms in the scalar transport equations for which the QUICK scheme is used. The code is parallelized using MPI.

In the applications considered in the present study the density variations between the lock fluid and the channel fluid are sufficiently small such that the Boussinesq approximation can be applied to account for buoyancy effects (we assume the fluid density varies linearly with the non-dimensional concentration C). If the terms in the Navier-Stokes and transport

Copyright © 2006 Taylor & Francis Group plc, London, UK

equations for the salinity, temperature, etc., are made dimensionless using the channel depth, h, and the buoyancy velocity, $u_b = (g'h)^{0.5}$, $g' = g(\overline{C}_{max} - \overline{C}_{min})/\overline{C}_{min}$, where g' is the reduced gravitational acceleration, $\overline{C}_{max}$, $\overline{C}_{min}$ are the maximum and minimum concentrations (densities) in the domain, g is the gravitational acceleration, and one defines the non-dimensional concentration $C = (\overline{C} - \overline{C}_{min})/(\overline{C}_{max} - \overline{C}_{min})$, then one can rewrite the governing momentum ($i = 2$, vertical) and concentration transport equations using two dimensionless parameters, the Grashof number, $Gr = (u_b h/\nu)^2$, which is the ratio of the buoyancy forces to the viscous forces in the fluid and the Schmidt number, $Sc = \nu/\kappa$, which is the ratio of the molecular viscosity, ν, to the molecular diffusivity, κ: In the case of LES, due to filtering one has to add the extra sub-grid terms.

$$\frac{\partial u_i}{\partial x_i} = 0 \tag{1}$$

$$\frac{\partial u_i}{\partial t} + \frac{\partial (u_i u_k)}{\partial x_k} = -\frac{\partial p}{\partial x_k} + \frac{\partial}{\partial x_k}\left(\frac{1}{\sqrt{Gr}} + \nu_{SGS}\right)\left(\frac{\partial u_i}{\partial x_k} + \frac{\partial u_k}{\partial x_i}\right) - C\delta_{i2} \tag{2}$$

$$\frac{\partial C}{\partial t} + \frac{\partial (C u_k)}{\partial x_k} = \frac{\partial}{\partial x_k}\left(\left(\frac{1}{\sqrt{Gr}Sc} + \alpha_{SGS}\right)\frac{\partial C}{\partial x_k}\right) \tag{3}$$

where p is the dimensionless pressure. The last term in equation (2) is the non-dimensional gravitational term through which the stratification effects are felt in the momentum equations. This term is active only in the vertical direction ($i = 2$).

As the sub-grid scale (SGS) viscosity and diffusivity in the corresponding terms in equations (2) and (3) are calculated dynamically (Pierce and Moin, 2001) no model constants are needed. All simulations are performed with Sc = 600 (this increases proportionally the equivalent Reynolds number $\sqrt{Gr}Sc$ of the concentration equation compared to the momentum equations) which corresponds to saline diffusion in water.

The lock exchange cases (A, B and C) corresponding to the laboratory experiments carried out by Hacker et al. (1996) are simulated in the present study. In all these cases, the bottom-propagating denser lock fluid extends up to the free surface, initially. The main difference among these three cases in the initial aspect ratio of the denser lock fluid, $R = h/x_o$ (x_o is the initial lock length) which is equal to 0.67, 1.00 and 1.78, respectively. We concentrate most of our analysis on cases B and C, but discuss validation results for all three cases.

The Reynolds numbers defined with the front velocity and the channel half depth ($Re = U_f(h/2)/\nu$) are in the range of 7,000 to 20,000 during the slumping phase (see Table 1), so the flow inside the GC is turbulent, at least in the region behind the front. In agreement with the experimental setup of Hacker et al. (1996), no-slip boundaries were specified on the bottom wall and on the lateral wall, while the top was treated as a slip boundary (zero shear). A convective outflow boundary condition was used at the right extremity of the computational domain. This allows coherent structures to exit the domain in a time accurate way. The size of the grid was $3072 \times 160 \times 72$ in all simulations. The length of the computational domain varied between 8.7 h and 17.4 h. The domain size in the spanwise direction varied between 0.768 h and 1.025 h over which the computational points were distributed uniformly. The typical size of a cell was 0.0045 h in streamwise direction, 0.018 h in the vertical direction and 0.012 h in the spanwise direction. Near the right boundary the streamwise cell size was increased to 0.025 h. Near the end and bottom walls, the cell size in the wall-normal direction decreases to $\Delta n = 0.001$ h. Assuming conservatively $u_\tau/U_f \sim 0.04$ this translates into $\Delta n^+ \sim 1$ wall unit for case B which had the highest Grashof number. The grid spacing in the spanwise direction is close to 10 wall units. The other two cases should be slightly better resolved. The mesh size, especially near the walls in the normal direction, is fine enough for the code to be able to resolve the dynamically important turbulent structures without resorting to wall functions. The flow field for all the simulations was initialized with the fluid at rest, i.e., $u_i = 0$ everywhere. The non-dimensional concentration field was initialized with a constant value of 1 in the lock region and a constant value of 0 in the channel. Additionally, a disturbance was applied on the concentration interface (lock gate region) to accelerate the growth of 3D instabilities and transition to turbulence in the head region of the GC. The simulations were run on 16 or 24 processors of a Xeon PC cluster with Myrinet.

Table 1. Details of the lock-exchange 3D simulations. The Reynolds number $Re = U_f(h/2)/\nu$ and Froude number of the front $Fr = U_f/(g'h)^{0.5}$ correspond to the slumping phase when the front velocity is constant.

Case	Gr	L/h	Aspect ratio, $R = h/x_0$
A	9.6×10^8	18	0.67
B	7.7×10^9	9	1.00
C	2.3×10^9	13.5	1.78

	Experiment		Simulation	
Case	Re	Fr	Re	Fr
A	7,000	0.45 ± 0.01	6,890	0.44
B	19,700	0.45 ± 0.01	19,650	0.45
C	11,000	0.46 ± 0.01	10,875	0.45

Copyright © 2006 Taylor & Francis Group plc, London, UK

4 RESULTS

As observed by Hacker et al. (1996), the dynamics of the GC is strongly dependent on the value of the initial aspect ratio R of the lock fluid. Table 1 summarizes the parameters of the simulations along with the predicted and measured values of the Reynolds and Froude numbers during the slumping phase when the front velocity U_f is practically constant. Figures 2 and 3 visualize the evolution of the GC using spanwise averaged concentration isocontours as predicted by the simulations (cases B and C) along with the corresponding experimental visualizations from Hacker et al. (1996). The position of the reflected bore is denoted x_b in these figures. In case C it is possible to follow the evolution of the GC in the experimental setup until it approaches the self-similar phase. In this case, the higher initial aspect ratio R (shorter lock length) causes the lighter fluid to reflect from the end wall much earlier compared to cases A and B.

It is observed that the flow in the initial moments after the lock release (e.g., compare Figures 2a and 3a corresponding to $t < 2t_0$, $t_0 = h/u_b$) is similar in all three cases, in the sense that a current of denser fluid moving downstream (right) develops at the bottom of the domain. The head region of the GC becomes unstable due to the amplification of the KH instabilities on the interface between the GC and the ambient lighter fluid, and strongly coherent relatively 2D billow structures are forming. The propagation speed of the KH billows is slowly decaying in time. These billows mix the ambient fluid with the heavier GC fluid. This results into a relatively well mixed fluid within their cores. Eventually the KH billows grow in size, become disturbed by the 3D flow instabilities as the flow in the head region becomes turbulent, break into smaller scale structures that eventually diffuse. As a result, the mixing between the ambient fluid and the upper part of the GC is enhanced (Figures 3d to 3j). As most of the coherence of the KH billows is lost, the small scale mixing becomes dominant and the interface region above and behind the head becomes mildly stratified with no sharp density interface present behind the front region.

Looking specifically at the GC evolution for Case B in Figure 2, one can observe that the overall shape and structure of the GC, including the nose region, appear to be reasonably well predicted by the simulation over the whole time interval over which experimental data is available ($t = 6.6t_0$). The simulation was run until about $t = 20t_0$, when the GC started interacted with the exit boundary. Careful inspection of the structure of the nose region as shown by experimental visualizations, particularly the waviness at the top of the head region, suggests that some of the large billows predicted in the simulations are also present in the experiments. The correlation between the crests observed near the current-ambient fluid interface in simulations and experiments is strong especially for the first few eddies behind the front of the GC (e.g., see the first three KH billows in Figure 2c). It is

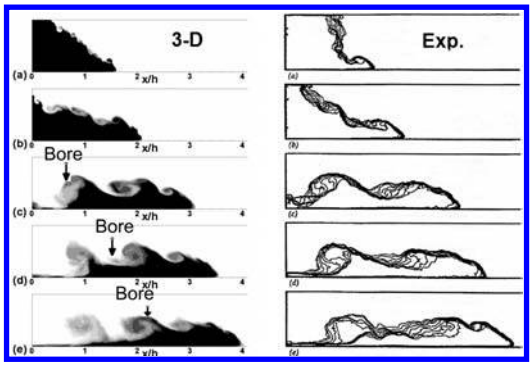


Figure 2. Evolution of gravity current for case B. Concentration (density) contours at subsequent front positions, $l = (x_f - x_0)/x_0$, and non-dimensional simulation times, t/t_0: 3-D spanwise averaged (left); experimental results of Hacker et al. (right). a) $l = 0.60$, $t/t_0 = 1.4$; b) $l = 1.11$, $t/t_0 = 2.4$; c) $l = 2.10$, $t/t_0 = 4.6$; d) $l = 2.56$, $t/t_0 = 5.6$; e) $l = 3.08$, $t/t_0 = 6.6$.

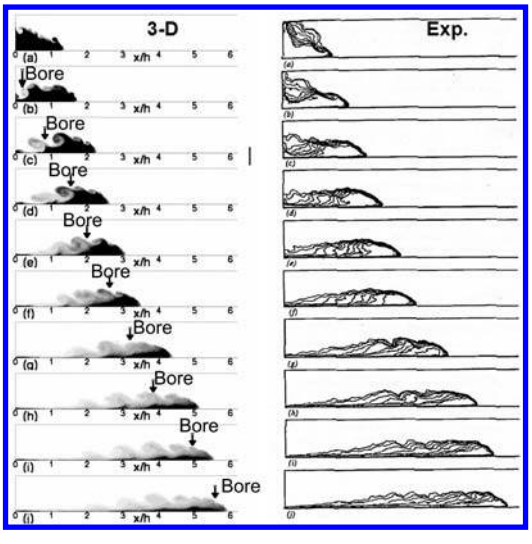


Figure 3. Evolution of gravity current for case C. Concentration (density) contours at subsequent front positions, $l = (x_f - x_0)/x_0$, and non-dimensional simulation times, t/t_0: 3-D spanwise averaged (left); experimental results of Hacker et al. (right). a) $l = 1.33, t/t_0 = 1.7$; b) $l = 2.17, t/t_0 = 2.6$ c) $l = 3.00, t/t_0 = 3.7$; d) $l = 3.73, t/t_0 = 4.6$; e) $l = 4.53$, $t/t_0 = 5.6$; f) $l = 5.27, t/t_0 = 6.6$; g) $l = 6.80, t/t_0 = 8.4$; h) $l = 8.13, t/t_0 = 10.3$; i) $l = 8.93, t/t_0 = 11.4$; j) $l = 9.60$, $t/t_0 = 12.4$.

Copyright © 2006 Taylor & Francis Group plc, London, UK

also interesting to point out that the good agreement observed for the relative position and size of some of the large billows in Figures 2c to 2e is in spite of the fact that in the experiment the gate removal has clearly introduced secondary motions that have altered the symmetry of the GC (compare concentration contours in simulation and experiment in Figure 2a, see also discussion in Hacker et al., 1996).

The simulation results a short time after the gate removal ($t = 1.4t_0$) show that the flow is practically symmetric around $x/h = 1.0$ (the gate position) except for the regions very close to the bottom wall and free surface, where different boundary conditions (no-slip vs. slip) were used. In this respect, numerical simulations have the advantage of allowing 'ideal' initial conditions to be specified. However, by $t = 4.6t_0$ (Figure 2c) the overall shape and length of the head region are quite similar in experiment and simulation. A large billow is present at the rear of the head region ($x/h \sim 1$) in frames c to e. The region of high mixing corresponding to this large eddy at the back of the head region is well predicted by the simulation. If one follows the evolution of this billow one can observe that the passage of the reflected bore is energizing the KH billow. Some of the denser fluid from the rear of the head region is in fact drawn upwards into this structure as the bore is passing (Figures 2c and 2d). The main difference between the simulation and experiment is observed between $x/h = 2$ and $x/h = 3$ in Figures 2d and 2e. While in the simulation a large, relatively coherent, KH billow can be observed around $x/h = 2.2$, in the experiment the mixing in the interface region appears to be stronger and no large scale eddy can be observed.

For case C experimental visualizations are available until $t = 12.4t_0$ close to the end of the slumping phase. Comparison of concentration contours in Figure 3 between experiment and simulation show that the structure of the gravity current is fairly well captured over the entire duration of the slumping phase (Figures 3d to 3j) once the influence of the initial mixing induced by the removal of the gate in the experiment becomes negligible. The KH billows, as visualized by concentration contours, appear to be slightly more coherent in the simulations. However, the main success of the 3D simulation is to predict fairly accurately the mildly stratified region present behind the head region and near the interface between the head and the ambient fluid, as well as the associated break up of the KH billows into smaller 3D eddies that are responsible for the high efficiency of the mixing in these regions. At the Grashof number of this simulation, the turbulence in the head region is strong enough to generate strong instabilities and energetic small scale eddies that can produce the relatively mildly stratified region behind the nose observable in the experiments (Figures 3f to 3j).

The predicted front positions in cases B and C shown in Figures 2 and 3 are close to the ones shown in the experimental visualizations. The corresponding range of Froude numbers ($Fr = U_f/\sqrt{g'h}$) defined with the front velocity U_f varies between 0.44 and 0.45 during the slumping phase for cases A, B and C (see Table 1) which compares reasonably well with the experimental values, $Fr = 0.45/0.46 \pm 0.01$. For the Reynolds number, the values from the simulations in the slumping phase are Re = 6,890, Re = 19,650, and Re = 10,875 which are very close to the experimental values of Re = 7,000, Re = 19,700, and Re = 11,000 for case A, B, and C respectively.

The propagation of the bore in the slumping phase is difficult to infer directly from the concentration contours because the bore propagates into the mixing layer created by the advancing head region of the GC. A more accurate way of determining the bore position is to look at the concentration vs. time variation on a line at a certain distance from the bottom. Such a plot is shown in Figure 4a for case B and in Figure 4b for case C at a relative distance of $y/h = 0.1$ from the

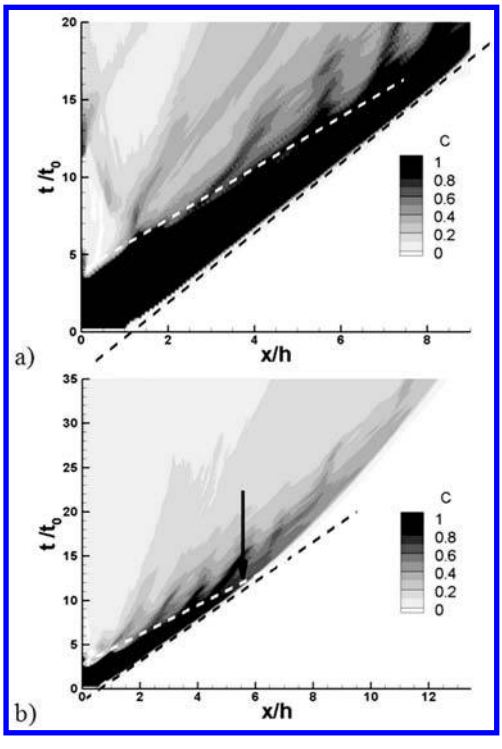


Figure 4. Evolution of concentration (density) with time along the x axis at a distance of $y/h = 0.1$ from the bottom. a) Case B; b) Case C. Dashed black lines correspond to front position, dashed white lines correspond to bore position. Arrow indicates the location where the bore overtakes the front.

Copyright © 2006 Taylor & Francis Group plc, London, UK

Table 2. Comparison of bore and front velocities during slumping phase.

Case	$U_{bore}/(g'h)^{0.5}$	$U_f/(g'h)^{0.5}$	U_{bore}/U_f
A	0.60	0.44	1.36
B	0.61	0.45	1.35
C	0.62	0.45	1.35

bottom. In the frames of Figure 4, one can observe the presence of a dark region in the form of a triangle with a very sharp angle corresponding to the intersection of the trajectories followed by the front and the bore. As these trajectories are close to straight lines, one deduces that the associated front and bore velocities are approximately constant. The slope of the lower dashed line corresponds to the speed of the front while the slope of the top dashed line, which sometimes cuts through the traces induced by the KH billows (observe the dark streaks present above the top dashed line), corresponds to the speed of the reflected bore. One can see that the slope, relative to the time axis, of the top dashed line is slightly higher than the one of the lower dashed line confirming that the bore velocity is higher than the front velocity. Table 2 summarizes the predicted values of the front and bore velocities. For all simulations the ratio of U_{bore}/U_f is between 1.35 and 1.36 which is within the experimental observed range (Rottman and Simpson, 1983).

For case B (Figure 4a) the two dashed lines do not intersect. This proves that the GC is still in the slumping phase at $t = 20t_0$ when the current approaches the right boundary. In contrast to that, incase C (Figure 4b) the intersection of the two trajectories (dashed lines) takes place inside the computational domain at $x/h \sim 5.5, t \sim 12.0t_0$ corresponding to a nondimensional streamwise length of $l \sim 8.9$, ($l = (x_f - x_0)/x_0$, x_f is the front position). The values of l obtained for cases A ($l = 7.4$) and C ($l = 8.9$) are consistent with experiments and theory (Rottman and Simpson, 1983). As the bore overtakes the front in Figure 4b, the border between the ambient fluid and the GC starts curving up. This signifies that the velocity of the front starts decaying in time, as expected to happen once the current transitions to the self-similar inviscid phase. Figure 5 shows the front position as a function of time in log-log scale for cases A, B and C. As expected, during the slumping phase all curves have a practically constant slope equal to 1 which corresponds to a constant front velocity in a log-log plot. As the bore overtakes the front, the GC begins to decelerate and the slope of the trajectory $l = l(t)$ decreases over a relatively short time period corresponding to the transition between the two phases before regaining a fairly constant value of 0.64 very close to the theoretical value of 2/3. This slope corresponds to a decay of the velocity in time proportional to $t^{-1/3}$.

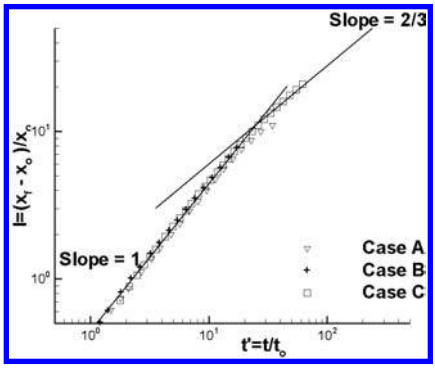


Figure 5. Nondimensional front position l, vs nondimensional time t'. Triangle indicates Case A, cross indicates case B; square indicates case C.

This is especially clear for case C for which the transition starts early at $t \sim 12t_0$ and simulation was run until close to $40t_0$, but less evident for case A where the domain was too short to allow the GC to evolve well into the self-similar phase.

Figure 6 shows the GC interface for case C visualized using a concentration isosurface (C = 0.5) at a time $t \sim 16t_0$ well past the transition into the self-similar phase. In the front part of the advancing head, shifting lobes divided by deep clefts can be observed. The lobe-and-cleft structure of the front region induces strong 3D perturbations of the cores of the KH billows. The width of the largest lobes is of the order of $0.18h$ (see inset in Figure 6 near the front of GC) at this stage of the evolution of the GC. The size of the penetration of the ambient fluid in the clefts is of the same order as the lobe size. Billows formed due to the amplification of the KH instabilities are observed in the shear zone (mixing layer) at the upper part of the head between the front ($x \sim 7.2\,h$) and $x \sim 6.0\,h$. Though these structures are considerably deformed in the spanwise direction, in part due to the presence of the lobes in the front region, the billows appear to span most of or the entire width of the computational domain (h) suggesting that the formation of these structures is a predominantly 2D process. The amplitude of the interface oscillations associated with the presence of these billows is growing between the front region, where they form, and the end of the head region. Downstream of the head region, the energy associated with the small scales is growing substantially, and the coherence of the KH billows is practically lost. This is because downstream of the front region the flow inside the GC head becomes turbulent. The 3D eddies from the near bottom-wall region (see also discussion of Figure 7) get swept into the upper parts of the head where they disturb the mixing layer and KH billows at the interface and force transition to turbulence. Thus, the GC region between x ~ 6 h and x = 2h situated behind the head

Copyright © 2006 Taylor & Francis Group plc, London, UK

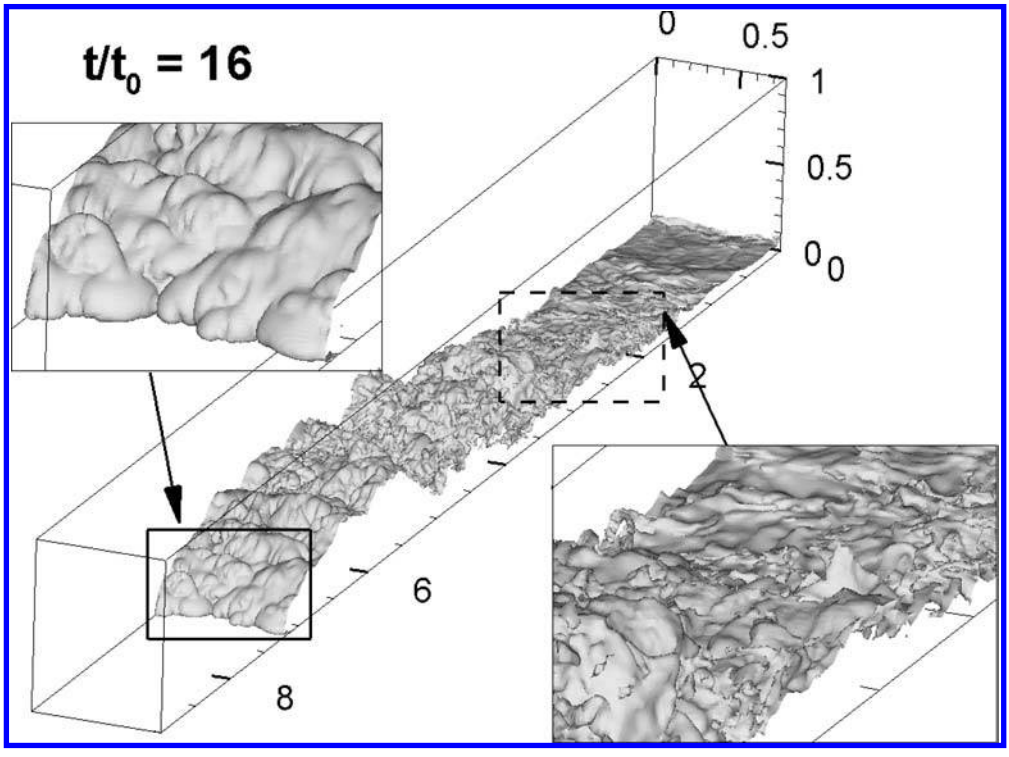


Figure 6. Visualization of gravity current interface for case C (concentration isosurface, $C = 0.5$) at $t/t_0 = 16$ with inset showing details at the front of the current where the lobe-and-cleft instability is captured and at the rear of the current where a the turbulence decay is strong.

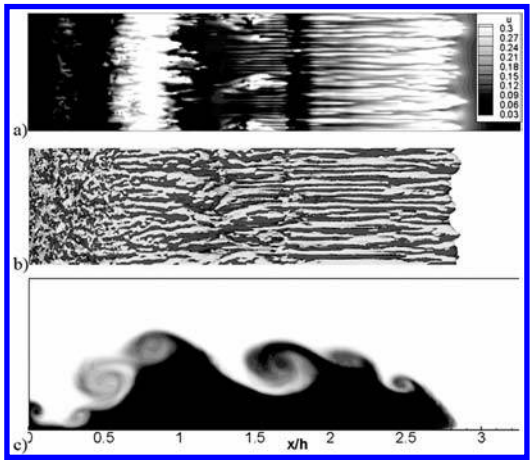


Figure 7. Visualization of the structure of the GC in the near-wall region for case B at $t/t_0 = 5$. (a) Streamwise velocity streaks in a horizontal plane situated at $y^+ \approx 11$ from the bottom wall; (b) Out of plane vorticity at the bottom wall (2 vorticity levels corresponding to $\omega_y = \pm 2u_b/h$ are shown); (c) Cross-sectional profile showing position of the GC using concentration contours.

is populated with small scale energetic eddies that are very effective in enhancing the local mixing. In fact, the flow in this region has most of the characteristics of a turbulent channel flow, including the presence of a broad energetic velocity spectrum with a small inertial range (not shown). This produces the mildly stratified region behind the head of the GC observed in Figures 3f to 3j. The simulation also capture the details of the mixing process in the interface region where wisps of heavier fluid from the downstream part of the head and from the near bed region behind the head are entrained first into the upper parts of the domain by the highly energetic 3D structures that resulted from the breaking of the KH billows before the action of the small scale eddies takes over the mixing process. The wisps are highly three-dimensional as seen in Figure 6. Eventually, these small-scale eddies that loose energy by mixing the lock and ambient fluid dissipate and the flow starts to relaminarize (see second inset in Figure 6). At $t \sim 16t_0$, this corresponds to the region with $x < 2\,h$ where the interface deformations are relatively negligible.

One of the interesting questions which the development of a high Grashof number GC in a channel

Copyright © 2006 Taylor & Francis Group plc, London, UK

raises is whether or not the turbulence content of the near bed region, over the area where the GC is turbulent, resembles the one observed in a constant density turbulent channel flow.

As the Reynolds number defined with the height of the GC in the head region and the front velocity is above 5,000 in all three cases both over the slumping phase and over the initial part of the self-similar phase simulated in the present work, one would expect that high and low speed velocity streaks will form very close to the bed and ejection and sweeps phenomena will be present. As the fluid in this region is in average stably stratified, the intensity of some of these phenomena is expected to be smaller than that observed in an equivalent channel flow. To investigate this, the streamwise velocity contours in a horizontal plane situated at about $y^+ = 11$ from the bottom wall are plotted in Figure 7a along with the out-of-plane vorticity contours on the bottom wall (2 vorticity levels corresponding to $\omega_y = \pm 2u_b/h$ are shown in Figure 7b) for case B at $t/t_0 = 5$. To help investigate the structure of the near-wall flow relative to the position of the head of the GC, the concentration contours in a x-y plane at the same time instant (between frames c and d in Figure 2) are shown in Figure 7c. Clearly, very close to the bottom wall a streaky structure is present in the vorticity contours over the entire length of the head of the GC. These vorticity streaks are clearly associated with the high and low streamwise velocity streaks that develop in the immediate vicinity of the bed as observed from the comparison of the corresponding velocity and vorticity streaks in Figures 7a and 7b. However, the velocity streaks at that position ($y^+ \approx 11$) appear to extend only from the front position ($x = 2.8\,h$) to about $1.3\,h$. Between $x = 2.8\,h$ and the end of the nose region ($x = 0.4\,h$) the streamwise velocity variations appear to be associated mostly with the presence of KH billows at the interface. These billows induce relatively large spanwise bands of low and high streamwise velocity (see discussion of Figure 8). The spanwise low velocity band present at $x \sim 1.7\,h$ is also associated with one of the KH billows. In fact, as shown in Figure 7b, these streaks are present up to the rear of the head region but the additional velocity induced by the billows present in the interface region sometimes masks their presence. Behind the head region the streaks disappear as the local Reynolds number is decaying below values at which turbulent streaks can form or be maintained. The average width of these streaks is about $0.025\,h$ and their average length decays from about $0.8\,h$ in the upstream part of the nose to about $0.5\,h$ in the downstream part of the nose. The streaks appear to be well resolved given the grid density used in the spanwise direction. The presence of these streamwise velocity streaks is associated in channel flows with the legs of the hairpin like vortices that are present over the near-bed region. We suspect a similar phenomenon is

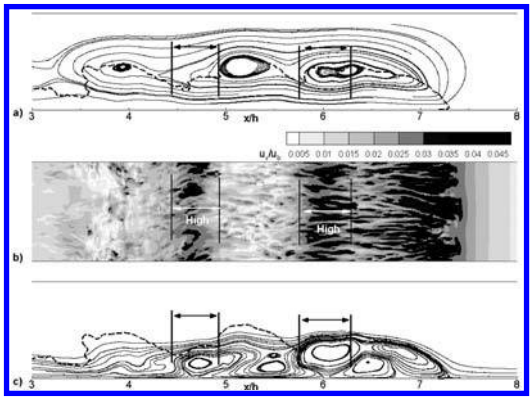


Figure 8. Visualization of GC and bed friction velocity distribution for case C at $t/t_0 = 16$ (a) Instantaneous streamlines in an x-y section. Dashed line corresponds to the GC interface; (b) Instantaneous distribution of bed friction velocity u_τ/u_b; (c) Instantaneous streamlines in the same x-y section in a moving frame of reference translating with the front velocity.

present in the head region where these counter-rotating vortices can displace fluid from the immediate vicinity of the bottom wall toward higher levels, thus promoting mixing. Their presence should also explain the streaky structure of the concentration field observed underneath the head of the GC (not shown). This is especially important in the region close to the front of the nose where the action of these longitudinal vortices can induce further perturbations of the front region that can amplify the instabilities responsible for the formation and growth of the lobes. In fact, one can speculate that some of these counter-rotating vortices can help accelerate the entrainment of some of the lighter ambient fluid overrun by the propagating GC toward higher levels inside the GC.

One of the most important quantities for practical consequences related to the formation and action of compositional GC in rivers and estuaries is the amount of sediment these currents can entrain and carry before the sediment deposits again (e.g., lock structures at dam facilities). To be able to estimate global quantities related to the entrainment (e.g., the scour produced by each passage of such a current), the spatio-temporal distribution of the bed shear stress has to be known, especially in numerical models in which the entrainment is generally function of the difference between the actual bed shear stress and the critical bed shear stress value given by Shields diagram. In this regard, accurate prediction of this quantity is of critical importance for the overall practical use of the model. In this paper, we are going to discuss just one realization corresponding to the distribution of the friction velocity for case C at $t = 16t_0$ well into the self-similar phase. The first obvious feature observed in Figure 8b is the

Copyright © 2006 Taylor & Francis Group plc, London, UK

streaky structure of the zones characterized by high bed shear stress (friction velocity) values in the region beneath the head of the GC. Its position can be inferred from Figure 8a in which the concentration contours and 2D streamlines were represented in an x-y section at the same moment in time. These streaks of high bed shear stress are obviously related to the high velocity of the front and to the presence of high speed velocity streaks in the near bed region beneath the head of the GC as shown in Figure 7.

The other feature is the presence of several spanwise bands of high and respectively low friction velocity values in the downstream part of the GC. Interestingly, the bands of high friction velocity values do not always (in fact animations of the bed shear stress distributions for all the three simulations show that this is the case most of the time) correlate with the presence of a KH billow in the interface region just above it. A good example is the high friction velocity band present at $x \sim 4.7\,h$ which appears to form in between two KH billows (compare Figures 8a and 8b). However, if one draws the same 2D instantaneous streamlines in a frame of reference translating with the front velocity, one can observe that the position of the bands of high bed shear stress correlates quite well with the presence of vortices inside the GC that practically touch the bottom wall. As the friction velocity values inside these spanwise bands are comparable to those observed in the upstream part of the head region, it is clear that the GC will entrain sediment over a relatively large distance behind its front. Whether or not the position and intensity of the bed shear stress inside these bands can be accurately captured by a 2D model needs further investigation.

The streamline patterns (x-y section) drawn in Figure 9 in a coordinate system advancing with the front velocity at two time instances of the evolution of the GC in case C indicate that for gravity currents developing in channels with a lateral wall the foremost point (nose) is not a stagnation point. This is similar to the case of a compositional GC developing into an infinite channel with no end walls at a lower Grashof number studied by Hartel et al. (2000a). The topology of the nose region is similar to the one observed by Hartel et al. (2000a) not only over the slumping phase (see Figure 9a) when the front velocity is constant in both cases and the physics of the GC is similar but also over the inviscid phase (see Figure 9b). The only difference with the patterns observed over the slumping phase is that the flow beneath the nose, but outside the current head, becomes more mixed (Figure 9b). This make us to expect the lobe-and-cleft instability in the case of finite lock volume GC is driven by the same mechanism (unstable stratification region between the nose and the stagnation point) identified by Hartel et al. (2000a) for the case of an infinite lock volume GC. The vertical distance Δy_n between the

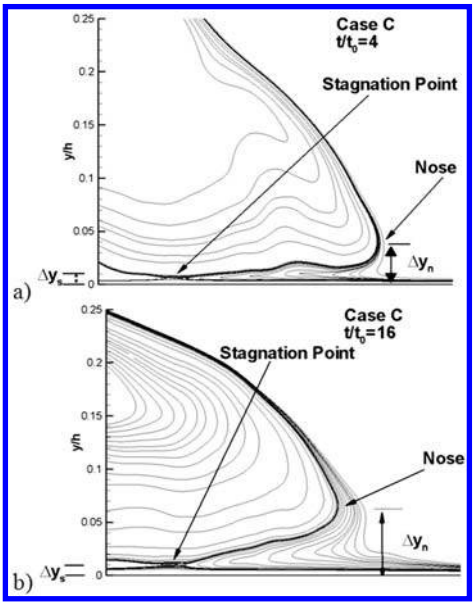


Figure 9. Structure of the head of the gravity current for case C in a moving frame of reference during (a) Slumping phase; (b) Self-similar phase.

nose and the bottom wall appears to increase with time. For instance, $\Delta y_n = 0.039\,h$ at $t = 4t_0$ during the slumping phase and $\Delta y_n = 0.065\,h$ at $t = 16t_0$ during the self-similar phase.

5 CONCLUSIONS

Several high resolution LES simulations of compositional gravity currents at Grashof numbers in the range of 10^8–10^9 ($Re \sim 10^4$, $Sc \sim 600$) were performed. The simulations were carried out using a dynamic model that limited the amount of dissipation introduced into the flow domain and a discrete energy-conserving Navier-Stokes non-dissipative solver than allowed to obtain robust and accurate solutions on meshes that are much coarser than DNS requirements. The present finite-volume lock-exchange simulations allowed the study of the evolution of the current well into the self-similar phase for one of the simulations (case C). Previous 3D highly resolved simulations considered only the case of an infinite channel (no lateral wall) compositional current (Hartel et al., 2000a) where the self-similar phase is not present and the case of a particulate current developing in a finite channel (Necker et al., 2002, 2005) where the physics in the latter stages of evolution of the current is very different from that of a compositional current due to the deposition of the particles. In these previous simulations the values

Copyright © 2006 Taylor & Francis Group plc, London, UK

of the Grashof numbers were around 10^6–10^7 corresponding to Reynolds numbers defined with the front velocity of less than 1,000, about an order of magnitude lower than the ones considered in the present study. This allowed the study of the evolution of the GC and associated instabilities for cases in which the flow in the head region was strongly turbulent.

Three configurations with a different depth over length ratio of the initial lock fluid were considered, corresponding to the cases studied experimentally by Hacker et al. (1996). The results from the 3D LES simulations were found to exhibit the classic characteristics of gravity currents, including the lobe-and-cleft structure at the leading edge of the GC head, the shedding of quasi-2D KH billows from the front region and their subsequent breaking into small scale 3D structures that strongly enhanced the mixing at the interface between the top of the GC and the surrounding fluid. In addition, the simulation results were able to accurately replicate the observed evolution of the nose region, the ratio between the bore and front velocities over the slumping phase, the variation of the front speed over the slumping and self-similar phases and the position of the transition between these two phases. The topology of the flow in the front region was not found to change significantly as the current transitioned between the slumping phase and the self-similar phase and to be similar to the one observed in 3D DNS simulations at lower Reynolds numbers (Hacker et al., 2000) suggesting that the unstable stratification region between the nose and the stagnation point is the main cause for the lobe-and-cleft instability. High and low speed velocity streaks, very similar to the one observed in channel turbulent flows, were identified in the near-bed region beneath the upstream part of the head of the current. As the turbulence started decaying and the flow transitioned back to laminar regime in the region behind the head, the streaky structure was found to disappear. Details of distribution of the bed friction velocity on the bottom wall that controls the entrainment of the sediment in the case in which the compositional current propagates over a loose bed were investigated.

ACKNOWLEDGEMENTS

We would like to thank Prof. S.B. Dalziel for allowing us to use some of his published experimental results for validation of our method.

REFERENCES

Choi, S-U. & Garcia, M.H. 2002. *k-ε* turbulence modeling of density currents developing two dimensionally on a slope. *J. Hydraulic Engineering*. 128(1): 55–63.

Hacker, J., Linden, P.F. & Dalziel, S.B. 1996. Mixing in lock-release gravity currents. *Dynamics of Atmospheres and Oceans* 24: 183–195.

Härtel, C., Meiburg, E. & Necker, F. 2000a. Analysis and direct numerical simulation of the flow at a gravity-current head. Part 1: Flow topology and front speed for slip and no-slip boundaries. *J. Fluid Mech.* 418: 189–212.

Härtel, C., Carlsson, F. & Thunblom, M. 2000b. Analysis and direct numerical simulation of the flow at a gravity-current head. Part 2: The lobe-and-cleft instability. *J. Fluid Mech.* 418: 213–229.

Maxworthy, T., Leilich, E., Simpson, J.E. & Meiburg, E., 2002. The propagation of a gravity current into a linearly stratified fluid. *J. Fluid Mech.* 453: 371–394.

Necker, F., Härtel, C., Kleiser, L. & Meiburg, E. 2002. High-resolution simulations of particle-driven gravity currents. *Int. J. Multiphase Flow* 28: 279–300.

Necker, F., Härtel, C., Kleiser, L. & Meiburg, E. 2005. Mixing and dissipation in particle-drive gravity currents. *J. Fluid Mech.* 545: 339–372.

Pierce, C.D. & Moin, P. 2001. Progress-variable approach for large-eddy simulation of turbulent combustion. *Mech. Eng. Dept. Rep. TF-80.* Stanford University.

Rottman, J.W. & Simpson, J.E. 1983. Gravity currents produced by instantaneous releases of a heavy fluid in a rectangular channel. *J. Fluid Mech.* 135: 95–110.

Simpson, J.E. 1997. *Gravity currents: In the environment and the laboratory. 2nd. Ed.* Cambridge: Cambridge University Press.

Copyright © 2006 Taylor & Francis Group plc, London, UK

Bedload transport in the case of seepage flow

Simona Francalanci[1], Gary Parker[2] & Luca Solari[1]
[1] *University of Florence, Department of Civil Engineering, Florence (Italy)*
[2] *University of Illinois, Department of Civil and Environmental Engineering and Geology, Urbana, Illinois (USA)*

ABSTRACT: The Shields number provides a classical non-dimensionalization expressing the relative mobility of a sediment particle on the bed of a river. It is not commonly recognized, however, that the Shields number implicitly contains the assumption of a hydrostatic pressure distribution in the water immersing the particles. If the concept underlying the Shields number is correct, however, the Shields number should be generalizable to non-hydrostatic pressure distributions. Here such a generalization is attempted for the case of a non-hydrostatic pressure distribution produced by a vertical seepage flow: the effect of both upward and downward seepage flow on bedload transport was investigated (Francalanci, Parker and Paris 2005), suggesting that an appropriately generalized Shields number is needed to capture the effect of a seepage flow on sediment mobility. A theoretical and numerical model is here proposed to account the effect of seepage flow on sediment mobility and bedload transport.

1 INTRODUCTION

The effect of an upward seepage flow on incipient sediment motion has been studied by Cheng and Chiew (1999): they found that the critical shear velocity is reduced in the presence of upward seepage. The same authors studied a turbulent open-channel flow with upward seepage and found out that the bed shear stress also shows a steady reduction with increasing upward seepage velocity (Cheng and Chiew 1998a; Cheng and Chiew 1998b). Also, recently the velocity distribution of turbulent open-channel flow with bed suction was theoretically and experimentally investigated (Chen and Chiew 2004).

In the case of seepage flow, the sediment bed mobility is affected by the vertical distribution of the pressure gradient, which is varying from the hydrostatic distribution, and this deviation creates an increased or decreased buoyant force which can give more or less mobility to the sediment particles. The Shields number itself is affected by the seepage-induced non-hydrostatic pressure distribution.

The effect of vertical seepage flow on bedload transport was recently experimentally investigated (Francalanci 2005; Francalanci, Parker and Paris 2005): the results showed that in the case of upward seepage net scour was observed in the zone of seepage, while the opposite effect was observed in the case of downward seepage.

The main goal of the present contribution is to quantify the effect of seepage flow on bedload transport, underlying the effects which play an important role on the Shields parameter. To this aim, a theoretical and numerical model is developed to solve the morphodynamic evolution of the bed elevation in the case of seepage flow, and to substantiate the generalized Shields formulation, which accounts the effect of the buoyant force on bedload transport due to the seepage flow.

2 EXPERIMENTAL RESULTS

Experiments were carried out in a glass-sided sediment-recirculating, water-feed flume that was 15 m long, 0.61 m wide and 0.4 m deep. A skecth of the experimental set-up is shown in Figure 1. Upward or downward groundwater flow was introduced in a reach between 9 m and 10.1 m downstream of the upstream end of the flume. The seepage flow passed through a seepage box buried underneath the flume bed.

A relatively uniform sediment was chosen for the experiments in order to minimize sorting effects and to avoid the presence of bedforms in flume bed. The sediment in the flume equilibrated to a median size D_{50} and geometric mean size D_g both near 0.84 mm, a size D_{35} near 0.69 mm, a size D_{90} near 1.48 mm and a geometric standard deviation σ_g near 1.62. Hydraulic

Copyright © 2006 Taylor & Francis Group plc, London, UK

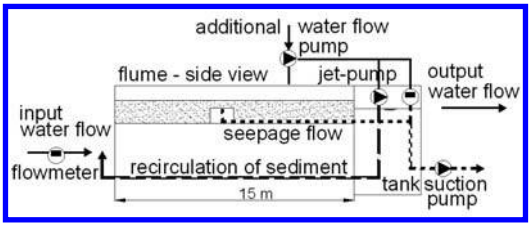


Figure 1. Sketch of the experimental apparatus.

Table 1. Hydraulic conditions for the experiments; Run codes 1 ÷ 3 pertain to runs with upward groundwater flow, and Run codes 4 ÷ 6 pertain to runs with downward groundwater flow.

Run code	Q_w $[l/s]$	$Q_{seepage}$ $[l/m]$
1	20.6	20, 40, 60, 80, 100, 140
2	16	20, 40, 60, 80, 100, 140
3	12	20, 40, 60, 80, 100, 140
4	20.6	30, 60, 90
5	16	30, 60, 90
6	12	30, 60, 90

conductivity K was measured with a D'Arcy tube and found to be near 0.0025 m/s.

Velocity measurements were performed using a micro-propeller with a diameter of 14 mm. A point gage was used to measure water surface elevations and the elevation of the bed. Five bed elevation points were measured for each transverse cross-section; the average of these values was assumed as the crosssectional mean value of the bottom elevation for the purpose of characterizing long profiles. Measurements of sediment transport in the flume were obtained by diverting slurry from the sediment recirculation pipe and measuring the sediment mass collected as a function of time.

The experimental protocol was designed around Table 1. The table encompasses inflow discharges Q_w ranging from 12 to 20.6 liters/sec, upward seepage discharges $Q_{seepage}$ ranging from 20–140 liters/min and downward seepage discharges $Q_{seepage}$ ranging from 30–90 liters/min, for a total of 27 experimental conditions, 18 of which pertained to upward seepage and 9 of which pertained to downward seepage. In principle, each experimental condition corresponded to a set of three experiments, one with no seepage, one with data acquired after 10 minutes of seepage (short-term experiment) and one with data acquired after 2 or 4 hours of seepage (the longer time span corresponding to lower seepage rates).

The experimental set-up and protocol are described in Francalanci (2005), Francalanci et al. (2005), Francalanci et al. (2006), and the results are here briefly summarized in order to discuss the appropriately generalized Shields number able to capture the effect of a seepage flow on sediment mobility. Indeed, the described set-up allowed to measure the scour or fill produced by the seepage flow in a region of the erodible bed.

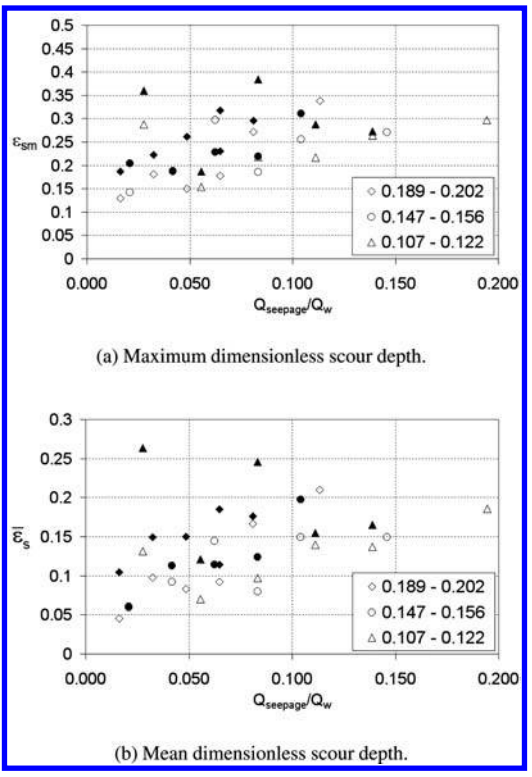


Figure 2. Maximum and mean dimensionless scour depth plotted against discharge ratio $Q_{seepage}/Q_w$ for different range of the average Shields parameter in the case of zero seepage at the equilibrium conditions, for the short-term experiments (white dots – 10 minutes) and for the long-term experiments (black dots – 4 hours, gray dots – 2 hours).

The experiments on the effect of seepage on bed morphodynamics induced to the following observations: the channel has scoured in the zone of upward seepage in the case of both short-term and long-term experiments, the scour in the seepage zone has been accompanied by some bed aggradation in the zone upstream. This latter pattern is dictated by the constraint of sediment recirculation; since the total mass of sediment is conserved, the mass of sediment eroded from the seepage zone must be deposited elsewhere. As a summary of the experimental results, the dimensionless maximum scour depth ϵ_{sm} and the mean scour depth $\overline{\epsilon}_s$ is plotted against the discharge ratio $Q_{seepage}/Q_w$ in Figure 2(a)–2(b). Both the previous quantities were made dimensionless using the mean

Copyright © 2006 Taylor & Francis Group plc, London, UK

flow depth H that prevailed at mobile-bed equilibrium before the onset of seepage. The overall tendency is for both measures of scour to increase with increasing discharge ratio. The experimental results in the case of downward seepage flow showed opposite trend and are not reported here.

3 EFFECT OF SEEPAGE ON SEDIMENT MOBILITY

The experimental results, briefly reported in the section above, clearly indicate that upward seepage induces scour and downward seepage induces deposition. It is of value to provide an overview as to how flow-sediment interaction in the presence of seepage gives rise to scour or deposition. Three effects play important roles: the effect of seepage on the bed shear stress, the direct effect of seepage on the Shields number itself, and the effect of seepage on the critical Shields number for the onset of motion.

Cheng and Chiew (1998a,b) have shown that over a wide range of conditions upward seepage reduces the bed shear stress τ_b in the zone of seepage. The same model implies that downward seepage increases the bed shear stress. The effect can be illustrated in terms of the St. Venant equations for conservation of water and flow momentum in the presence of seepage, which take the forms in the one-dimensional case:

$$\frac{\partial H}{\partial t} + \frac{\partial UH}{\partial x} = v_s \tag{1}$$

$$\frac{\partial UH}{\partial t} + \frac{\partial U^2 H}{\partial x} = -gH\frac{\partial H}{\partial x} + gHS - \frac{\tau_b}{\rho} \tag{2}$$

where x is the streamwise distance, t is time, H is the water depth, U is flow velocity and S is the mean longitudinal slope. The continuity equation (eq. 1) shows the presence of the seepage velocity v_s as boundary velocity at the bottom, which is related to the vertical pressure gradient inside the sand layer by means of the hydraulic conductivity K from the Darcy's law. Reducing the above-two equations for steady flow, Cheng and Chiew (1998a) found that:

$$\tau_{*b} = \rho u_*^2 = \rho g H \cdot sin\alpha - \\ -\rho g H \cdot \frac{dH}{dx}\left(cos\alpha - \frac{\beta U^2}{gH}\right) - 2\beta\rho U v_s \tag{3}$$

In the above relation $u_* =$ shear velocity and $\alpha =$ longitudinal bed slope angle. A deeper analysis of the latter relation, which is discussed in details in Francalanci et al. (2006), proved that the net effect of seepage was always to reduce the bed shear stress relative to the value that would prevail in the absence of seepage.

Two further effects of seepage act to change the mobility of the sediment itself. One of these is the direct effect of the seepage-induced non-hydrostatic pressure gradient on the denominator of the Shields number; the Shields parameter was evaluated with the following generalized expression, which accounts the effect of vertical seepage by means of an additional term on the denominator given by v_s/K:

$$\tau_* = \frac{\tau_b}{\left(\rho_s - \rho\left(1 + \frac{v_s}{K}\right)\right) gD} \tag{4}$$

Hence, when the velocity v_s is positive (upward groundwater flow) the particle is effectively lighter and more movable, and the Shields parameter is increased, while when the velocity is negative (downward groundwater flow) the Shield parameter is decreased.

Hence, there are two combined and opposite effects on the dimensionless Shields parameter in the presence of seepage: the effect of an upward seepage leads to a reduction of the bed shear stress, but also a reduction of the denominator of the Shields parameter due to a non-hydrostatic pressure gradient. The opposite behavior is expected in the case of downward seepage.

The last effect on sediment mobility is associated with a change in the critical Shields number τ_{*cr} in the presence of upward or downward seepage, as elucidated by Cheng and Chiew (1999). The seepage velocity corresponding to the maximum hydraulic gradient is defined as the critical seepage velocity, at which the inception of the quick condition takes place, and is evaluated from Cheng and Chiew (1999) data. The equation derived by Cheng and Chiew (1999):

$$\left(\frac{u_{*c}}{u_{*oc}}\right)^2 = 1 - \left(\frac{v_s}{v_{sc}}\right) \Rightarrow \left(\frac{\tau_*}{\tau_{*oc}}\right) \tag{5}$$

was used to evaluate the ratio between the critical shear velocities, with and without seepage, under the initial condition for sediment transport, as a function of the ratio between the seepage velocity v_s and the critical seepage velocity in the case of quick sand v_{sc}, in the performed experimental conditions. The above relation indicates that upward seepage decreases the threshold Shields number for the onset of sediment motion, as demonstrated by the experiments of Cheng and Chiew (1999). Conversely, downward seepage should increase the threshold Shields number for the onset of motion.

4 THEORETICAL AND NUMERICAL MODEL

The experimental results clearly indicate that upward seepage induces scour and downward seepage induces deposition. A theoretical and numerical model of the morphodynamics of erodible-bed open-channel flow

Copyright © 2006 Taylor & Francis Group plc, London, UK

in the presence of seepage was employed to understand which is the effect on sediment mobility and on the Shields parameter.

The effect of seepage can be modeled numerically using a 1D formulation. Where η denotes bed elevation, the Exner equation of sediment conservation takes the form:

$$(1-\lambda_p)\frac{\partial \eta}{\partial t} = -\frac{\partial q_b}{\partial x} \tag{6}$$

The bedload discharge, q_*, made dimensionless in terms of the Einstein number $\sqrt{(\rho_s-\rho)gD^3/\rho}$, was evaluated with the interpolated relationship from experimental data, measured during the experiments with no seepage:

$$q_* = 0.0201 \cdot \left(\frac{\tau'_*}{\tau_{*cr}}\right)^{2.5266} \tag{7}$$

which agrees well with the Ackers and White (1973) relationship, which was derived in the absence of seepage. Such relation was needed in order to test the Shields number as a characterization of sediment mobility in terms of a sediment transport relation based on the Shields number. The critical Shields number τ_{*cr} takes the above-quoted value of 0.0388, while τ'_* is the reduced Shields number, related to the skinfriction only, and hence to sediment transport.

In a sediment-recirculating flume, the boundary condition on eq. 6 is cyclic; i.e. where $x=0$ denotes the upstream end of the flume and $x=L$ denotes the downstream end,

$$q_b|_{x=L} = q_b|_{x=0} \tag{8}$$

The classical quasi-steady approximation was used in conjunction with the standard shallow water equations in calculating the flow, so that eq. 1 and 2 take the form:

$$\frac{\partial UH}{\partial x} = v_s \tag{9}$$

$$\frac{\partial U^2 H}{\partial x} = -gH\frac{\partial H}{\partial x} + gHS - \frac{\tau_b}{\rho} \tag{10}$$

Bed shear stress τ_b was evaluated from a logarithmic formulation;

$$\tau_b = \rho C_f U^2, C_f^{1/2} = 2.5ln\left(11\frac{H}{k_s}\right) \tag{11}$$

where C_f denotes a bed friction coefficient and k_s denotes a roughness height. The roughness height k_s was compute as $k_s = n_k D_{50}$. The dimensionless parameter n_k was found to vary from flow to flow due to the effect of bedforms. Here the value of n_k was calibrated using experimental data for mobile-bed equilibrium flows in the absence of seepage, and the same value of n_k was applied to a corresponding experiment with seepage.

The system of equations 6–9–10 was solved numerically using a decoupling between flow dynamics and morphodynamics. The latter assumption is reasonable in the case of subcritical flow and in the case of slow changing of bed elevation compared to the flow dynamics. The equations could be solved by integrating upstream from the downstream end of the flume. First, the steady solution of the subcritical backwater profile was evaluated from the flow equation imposing the downstream water depth at the end of the flume. The numerical schemes is explicit, with predictor – corrector steps, and upwinding differencing. The bedload discharge q_b was evaluated, and the input bedload discharge was assumed to be equal to the ones in the downstream cross-section. The wall at the downstream end of the flume, however, imposed a set bed elevation instead. A quasi-equilibrium calculation using the backwater profile evaluated at the previous time step allowed an estimate of the downstream depth that a) led to the satisfaction of sediment conservation and b) specified a downstream boundary condition for a backwater calculation of the flow field which takes into account the constraint of inerodibility of the bed near the overflow wall at the downstream end of the flume. Finally, Exner's equation was solved to estimate the new bed elevation at the following time step.

An abrupt change from a vanishing seepage velocity to a finite seepage velocity at $x=9$ m, and a similar abrupt change to vanishing seepage velocity at $x=10.1$ m tended to result in numerical instability in the model. Spurious oscillations were suppressed in two ways. Firstly, an artificial diffusion term was added to eq. 6, modifying it to

$$(1-\lambda_p)\frac{\partial \eta}{\partial t} = -\frac{\partial q_b}{\partial x} + D_f\frac{\partial^2 \eta}{\partial x^2} \tag{12}$$

Values of D_f in the range $10^{-5}-10^{-4}$m^2/s were found to be adequate for this purpose. Secondly, the abrupt change in seepage velocity at the upstream and downstream ends of the seepage reach was replaced with very short zones over which seepage velocity varied in smoothly according to a sinusoidal function. In addition, the seepage rate was slowly increased at the beginning of each numerical experiment until it attained its asymptotic value. Two input parameters for the model were set as follows: porosity $\lambda_p = 0.3$ and hydraulic conductivity $K = 0.0025$ m/s.

4.1 *Numerical results*

The capability of the numerical model to describe the effect of seepage on sediment mobility is here discussed. As a preliminary result, the numerical model

Copyright © 2006 Taylor & Francis Group plc, London, UK

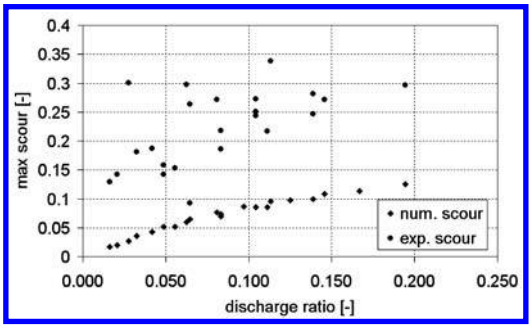


Figure 3. Maximum dimensionless scour in the case of hydrostatic pressure in the sand layer.

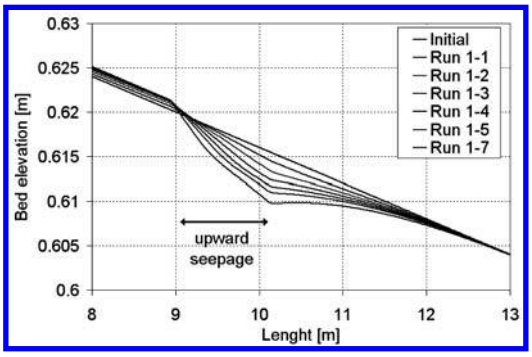


Figure 4. Local bed profiles of scour in the case of hydrostatic pressure. The deeper scour depths are related to the higher seepage flows.

was solved in the case of upward seepage flow at the bed but without considering the effect on the Shields parameter, which was evaluated with the following well-known equation:

$$\tau_* = \frac{\tau_b}{(\rho_s - \rho)gD} \tag{13}$$

In Figure 3 the maximum scour, measured for the short term experiments with increasing upward seepage, is compared with the numerically evaluated scour. The local bed profile at the end of the short term experiments is shown in Figure 4 in the case of hydrostatic pressure distribution in the sand layer, while the evolution of the maximum scour depth in time is shown in Figure 5. The latter results show that this implementation of the model is not able to catch the maximum scour in the area of upward seepage and to reproduce the local bed evolution, in terms of space and time.

Hence, the generalized expression of the Shields parameter (eq. 4) was used in the numerical model to consider the effect of non-hydrostatic pressure and the critical Shields parameter was corrected to take into account the effect of upward seepage (eq. 5). The local

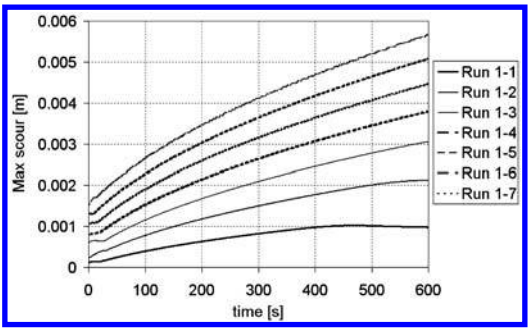


Figure 5. Maximum scour versus time in the case of hydrostatic pressure: the higher scour depths are related to the higher seepage flows.

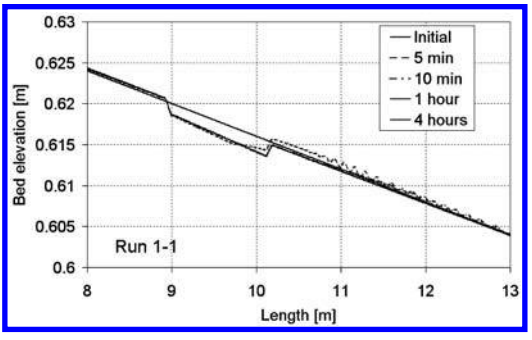


Figure 6. Numerical experiment Run 1-1 ($Q_w = 20.5$ l/m, $Q_{seepage} = 20$ l/m).

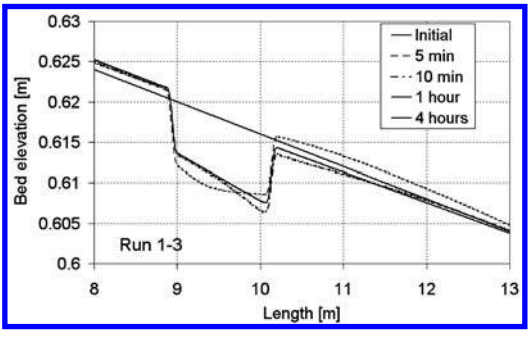


Figure 7. Numerical experiment Run 1-3 ($Q_w = 20.5$ l/m, $Q_{seepage} = 60$ l/m).

bed profile at different times during the experiment is shown in Figures 6 and 7 for two different values of seepage flows, $Q_{seepage} = 20$ l/m, 60 l/m, and the same value of the main flow $Q_w = 20.5$ l/s. As the seepage flow increases, the maximum scour is increased, in well agreement with the experimental evidence. After 5 minutes of groundwater flow the scour is close to the maximum value, while deposition phenomena is

Copyright © 2006 Taylor & Francis Group plc, London, UK

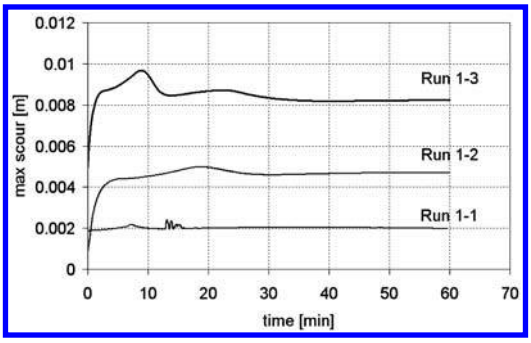


Figure 8. Maximum scour versus time.

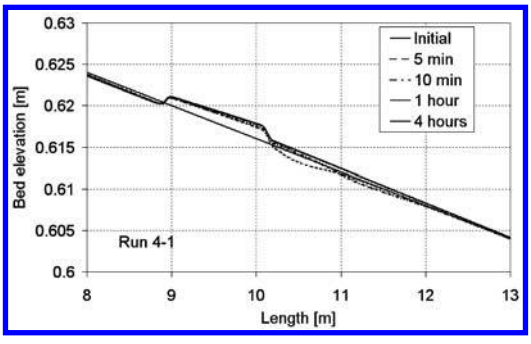


Figure 9. Numerical experiment Run 4-1 ($Qw = 20.5$ l/m, $Q_{seepage} = 30$ l/m).

established downstream and upstream of the seepage area. After 10 minutes the local bed profile is close to the equilibrium configuration, and the bed profile shows deposition upstream and reduced erosion downstream of the seepage area. After 1 hour the bed profile does not change anymore, and it is approximately the same after 4 hours.

The time evolution of the maximum scour depth predicted by the numerical model is plotted in Figure 8 for three different experiments with the same flow Q_w, and increasing seepage flow, $Q_{seepage}$. The maximum scour in time along the flume reaches the maximum value after 10–20 minutes of groundwater flow, after which it stabilizes around a mean value.

The numerical results of a downward seepage experiment are shown in Figure 9. The bed profile shows exactly opposite features of deposit and erosion than in the case of upward seepage flow.

Moreover, it can be observed that the mean slope of the bed in seepage area, numerically computed, is increased in the case of upward seepage flow and decreased in the case of downward seepage flow. The mean slope evaluated from the numerically computed profile is plotted versus the discharge ratio in Figure 10, showing a quasi-linear relationship.

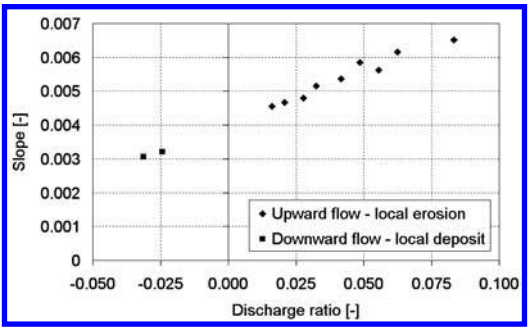


Figure 10. Average local slope, numerically computed, in upward/downward seepage area.

5 COMPARISON OF EXPERIMENTAL AND NUMERICAL RESULTS

The results of the numerical computed profiles are compared to the measured short-term and long term bed profiles. The comparison of the initial measured and numerical bed profiles with the final ones are shown in Figure 11 for Run 1-1. The features of the bed profile which were revealed experimentally are well reproduced by the numerical model. Both the experiments and the numerical model show net scour in the seepage zone, even if the long-term measured scour seems to be under-estimated by the model.

In the case of Run 1-3, Figure 12 shows that the numerical model reasonably captures the observed pattern of seepage-induced scour both in the short and long terms. Also deposit upstream and erosion downstream are shown to be in good agreement. The numerically calculated profiles are smoother than the observed profiles because the numerical model does not capture the individual bedforms.

The comparison of the downward seepage measured profiles with the numerical ones is shown in Figure 13 for Run 4-1. The numerical model somewhat underpredicts the pattern of deposition induced by downward seepage, but the overall patterns of the experiments are clearly reflected in the model results.

Figure 14 allows comparison between predicted and observed mean scour depths/deposition thicknesses. Values are shown for 9 experiments with upward seepage and 2 experiments with downward seepage. The negative scour depths in Figures 14(a) and 14(b) indicate deposition. Figure 14(a) pertains to short-term experiments, and Figure 14(b) pertains to long-term experiments. Dimensionless scour is plotted against the discharge ratio $Q_{seepage}/Q_w$.

Besides some experimental scattering, the agreement is good and the experimental scour is only lightly underestimated: the trends are very similar, and most of the predicted values fall within the scatter of the observed values.

Copyright © 2006 Taylor & Francis Group plc, London, UK

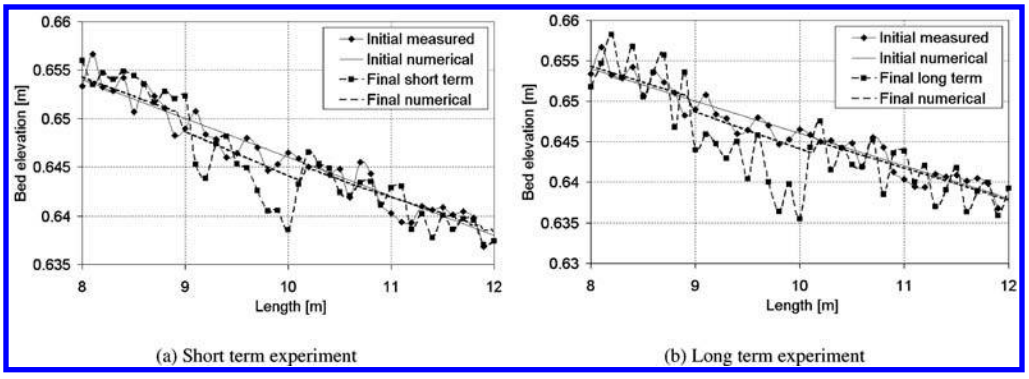


Figure 11. Comparison of experimental and numerical results, Run 1-1 ($Q_w = 20.5$ l/m, $Q_{seepage} = 20$ l/m).

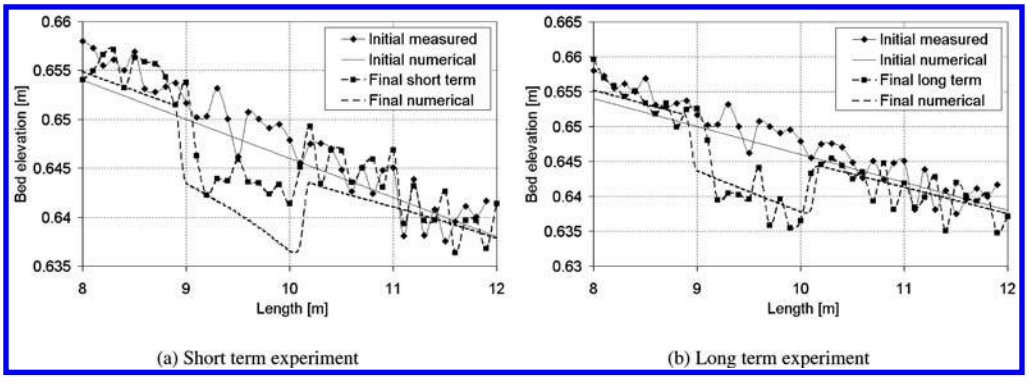


Figure 12. Comparison of experimental and numerical results, Run 1-3 ($Q_w = 20.5$ l/m, $Q_{seepage} = 60$ l/m).

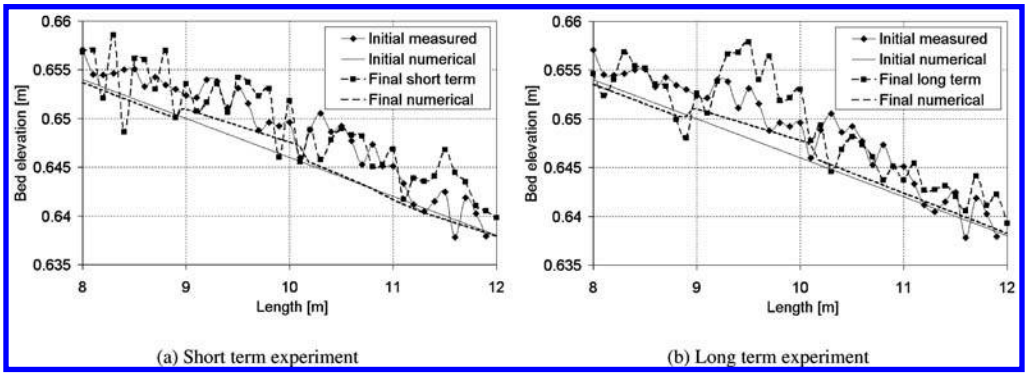


Figure 13. Comparison of experimental and numerical results, Run 4-1 ($Q_w = 20.5$ l/m, $Q_{seepage} = 30$ l/m).

The results of Figure 14 allow for the following tentative conclusion. Incorporation of the effect of seepage so as to a) correct the prediction of the bed shear stress, b) correct the critical Shields number and c) correct the expression for the Shields number itself so as to account for the non-hydrostatic vertical pressure gradient induced by seepage allows the numerical model to capture with reasonable accuracy the effect of seepage on bed morphodynamics. It can similarly be tentatively concluded that the bedload transport equation 7 determined in the absence of seepage effects can be applied to the case where a seepage-induced non-hydrostatic vertical pressure gradient prevails by means of the generalizations 5 and 4.

Copyright © 2006 Taylor & Francis Group plc, London, UK

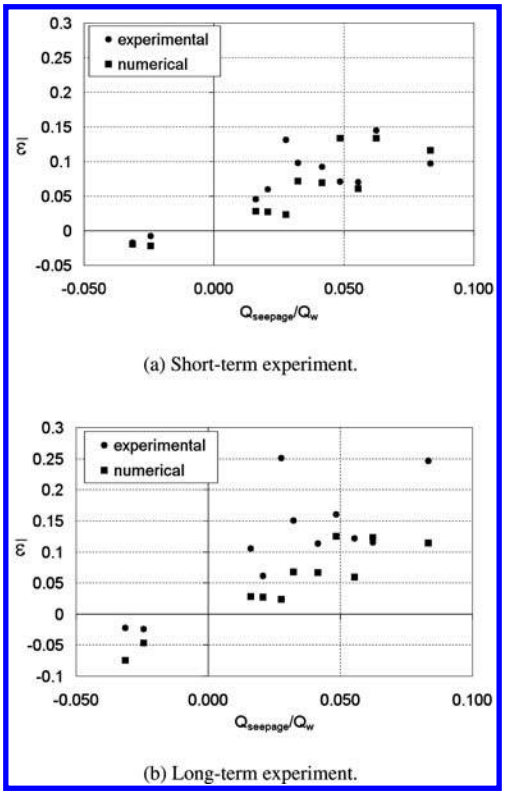


Figure 14. Comparison of experimental and numerical results of the mean scour in the local seepage area. Positive values of mean scour indicate erosion, negative values indicate deposition.

6 CONCLUSIONS

The dimensionless Shields number, or Shields stress, implicitly includes the assumption of a hydrostatic pressure distribution in its denominator. The assumption is reasonable for quasi-steady, quasi-uniform rectilinear sediment transport, but breaks down in the case of sediment transport near an obstacle such as a bridge pier. A generalization of the Shields number is proposed for the case of a near-bed non-hydrostatic pressure gradient in the vertical direction. Such a gradient can be produced by upward or downward groundwater flow.

In the present work the experimental results of the study of sediment transport over a bed with vertical groundwater flow, obtained by Francalanci (2005), are analyzed to estimate the effect of seepage flow on bedload transport. The experimental observations showed a clear effect of seepage on sediment transport: in the case of upward seepage net scour was observed in the zone of seepage; the opposite effect was observed in the case of downward seepage.

A theoretical and numerical model has been implemented to analyze bed morphodynamics in the presence of seepage: the experimentally measured patterns of scour/deposition were predicted reasonably well by the numerical model of morphodynamic evolution that incorporated the following seepage-induced effects: a) modification of the bed shear stress, b) modification of the critical Shields number for the onset of motion and c) modification of the Shields number itself to account for the non-hydrostatic pressure distribution. Comparison of experimental and numerical results show that the sediment transport relation, evaluated in the case of hydrostatic pressure distribution, can be applied to the non-hydrostatic pressure distribution, employing a generalized expression for the Shields parameter, which considers the non-hydrostatic pressure gradient in the sand-layer to drain water, and for the critical conditions of the onset of motion, to estimate the local average scour or deposit depth.

ACKNOWLEDGEMENTS

The authors are grateful to Prof. Enio Paris, University of Florence (Italy), for useful discussions and scientific support on carrying out this work. CERAFRI Research Center is acknowledged for sustaining the publication of this work.

REFERENCES

Ackers, P. and W. White (1973). Sediment transport in open channels: Ackers and White update. *Journal of Hydraulic Engineering 99*(4), 1–37.

Chen, X. and Y. Chiew (2004). Velocity distribution of turbulent open-channel flow with bed suction. *J. Hydraul. Eng. 130*(2), 140–148.

Cheng, N. and Y. Chiew (1998a). Modified logarithmic law for velocity distribution subjected to upward seepage. *J. Hydraul. Eng. 124*(12), 1235–1241.

Cheng, N. and Y. Chiew (1998b). Turbulent openchannel flow with upward seepage. *J. Hydraul. Res. 36*(3), 415–431.

Cheng, N. and Y. Chiew (1999). Incipient sediment motion with upward seepage. *J. Hydraul. Res. 37*(5), 665–681.

Francalanci, S. (2005). Sediment transport processes and local scale effects on river morphodynamic. *Ph.D. Thesis in Hydrodinamic and Environmental Modeling University of Firenze*.

Francalanci S., Parker G. and Paris E. (2005). Effects of Non-hydrostatic Pressure Distribution on Bedload Transport. *River, Coastal and Estuarine Morphodynamics: RCEM 2005. Conference Proceedings, Taylor and Francis Group, London*.

Francalanci S., Parker G. and Solari L. (2006). Effect of seepage-induced non-hydrostatic pressure distribution on bedload transport and bed morphodynamics. *J. Hydraul. Eng. (submitted)*.

Copyright © 2006 Taylor & Francis Group plc, London, UK

Long-term morphological behavior of Verbois reservoir (Geneva)

E. Bollaert & S. André
AquaVision Engineering Ltd., Lausanne, Switzerland

S. Diouf & D. Sidler
SIG, Cellule Environnement Rhône, Geneva, Switzerland

S. Ferretti
DIAE, Geneva, Switzerland

ABSTRACT: This paper presents a study of the long-term morphological behaviour of the Verbois reservoir in Geneva, Switzerland. The reservoir has been constructed on the Rhone River downstream of Geneva in 1942 and has a total length of 12 km. Sedimentation problems appeared immediately after dam construction, with an averaged yearly deposited volume of fine sediments of about 400,000 m^3. To minimize sedimentation, flushing events have been performed on a tri-annual basis. These generate huge environmental impact. To deal with this, a study has been performed of the potential morphological behaviour of the reservoir in the absence of further flushing events for the next 50 years. Analytical and numerical computations have been performed over a total river and reservoir length of about 25 km. These indicate that the reservoir will continue its sedimentation rather quickly during the first 10-15 years after stoppage of flushing, followed by a progressive stabilization of the sedimentation, resulting in a dynamic equilibrium on the long term. This equilibrium corresponds to a main meandering channel with sediments along the inner bends of the former Rhone River.

1 INTRODUCTION

1.1 *Purpose of the study*

This paper presents a study of the long-term morphological behavior of the Verbois reservoir in Geneva, Switzerland. The reservoir has been constructed in 1942 on the Rhône River downstream of Geneva and has a total length of 12 km. Significant sedimentation occurred after dam construction. To minimize sedimentation, flushing events have been performed on a tri-annual basis. These allow maintaining a minimum free volume. However, they also generate huge environmental impact downstream. To deal with this impact, a detailed study has been performed of the potential morphological behavior of the Verbois reservoir in the absence of any further flushing events for the next 50 years.

The main purpose of the study is to generate detailed hydraulic and morphologic characteristics necessary to answer the following questions:

- What are the eventual risks one encounters in case of no further flushing at Verbois Dam?
- What would be the main reasons to maintain flushing events?
- In case of no further flushing, what would be the necessary accompanying measures?

Hence, a detailed study of the hydraulic and morphologic conditions on the long term (=50 years) should allow predicting in a plausible manner all possible effects of stoppage of flushing of the Verbois reservoir. Especially future flood risks and necessary protection at the Junction of Arve and Rhône River in the center of Geneva should be quantified.

This study has been performed within the framework of a more general project aiming at a synergy between the following aspects: juridical framework, hydraulics and sediment transport (morphology), security issues, maintenance and finally sustainable development. For each of these aspects, a study is planified on the following states:

- actual state
- transitional state with/without flushing
- equilibrium state with/without flushing
- end of dam exploitation with/without flushing

The study on hydraulics and sediment transport is the first one to be accomplished yet. Its main results will be used as input to the remaining issues,

Copyright © 2006 Taylor & Francis Group plc, London, UK

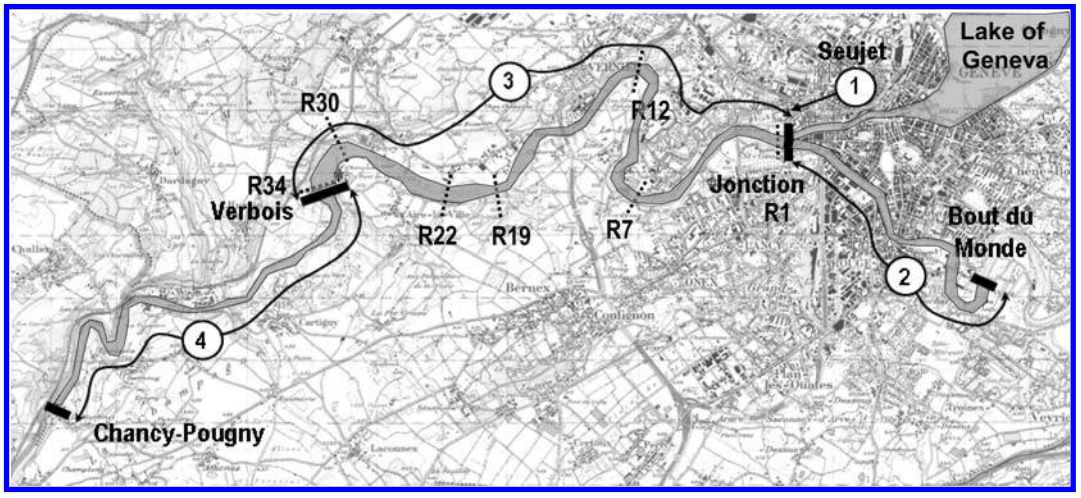


Figure 1. General study area and subdivision into 4 main sections.

followed by a close interaction between all issues and eventually additional hydraulic and sediment transport computations that might reveal necessary.

1.2 *Study area*

The general study area is illustrated in Figure 1 and shows the 4 main river sections that have been studied:

1. Section "Seujet – Jonction": outlet of Lake of Geneva between Seujet and junction with the Arve River (=Jonction)
2. Section "Bout du Monde – Jonction": Arve River upstream of the «Jonction»
3. Section "Jonction – Verbois": Rhône River between junction with Arve and Verbois dam 12 km downstream
4. Section Verbois – Chancy-Pougny: Rhône River between Verbois Dam and Chancy-Pougny Dam 8 km downstream

The present paper specifically deals with section N°3 (Verbois reservoir).

2 DATA COLLECTION

2.1 *Available data*

A huge amount of data has been collected for the 4 main sections of the general study area as illustrated in Figure 1, amongst which:

– cross-sectional profiles and detailed bathymetric surveys before and after flushing events (data available since 1987)
– hydrology of the Arve catchment area and of Seujet power station (Lake of Geneva)
– hydraulic functioning of the main elements of the catchment area (weirs, dams, hydropower stations, etc.)
– sediment concentrations measurements of both fine and coarse material for a large period
– detailed grain size curves along the Arve River and the 12 km long Verbois Reservoir

Table 1. Hydrology of the Mont-Blanc catchment area.

Return period [Years]	Q Arve [m^3/s]	Q Jonction [m^3/s]	Q Chancy-Pougny [m^3/s]
Yearly avg.	79	337	340
1	400	850	850
5	620	1000	1100
10	700	1050	1200
100	950	1250	1500
1000	1200	1450	1900
PMF	1800	2100	2400

2.2 *Hydrology*

The catchment area has a total surface of about 2,000 km^2 and extends towards the Mont-Blanc. Its hydrology is depicted at Table 1.

2.3 *Suspended sediment transport*

Suspended sediment concentration measurements have been made in the Arve River upstream of the Verbois Reservoir since 1890. The measurements made from 1965 to 1989 have been transformed into a general concentration law by Peiry (1989). As shown,

Copyright © 2006 Taylor & Francis Group plc, London, UK

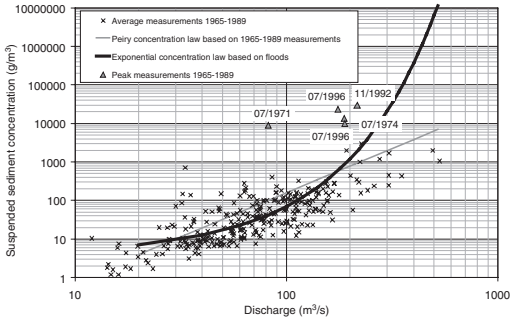


Figure 2. Suspended sediment concentration measurements in the Arve River since 1890 (Peiry, 1989).

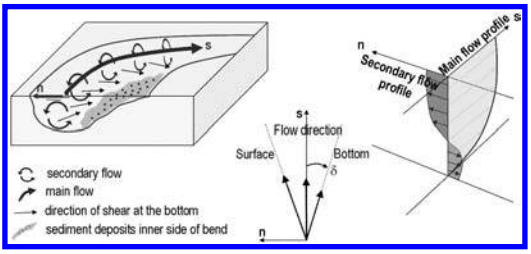


Figure 3. Helical flow pattern along river bend and major influence on sediment deposition.

instantaneous peak measurements during floods may attain concentrations of several tens of g/l. These peak values can be represented by using an exponential concentration law.

Most of the sediments are transported by suspension, with an average yearly transported volume of about 715,000 m^3 (GEOS 2000), from which 355,000 m^3 is trapped in the Verbois reservoir, the remaining being transferred towards downstream (section 4).

Typical grain sizes are between 0.01 and 0.2 mm, corresponding to fine sands and sandy silts. Almost no cohesive material has been detected. During floods, depositing diameters are between 0.2 at the Verbois Dam and 0.7 mm at the Junction.

2.4 *Bed load sediment transport*

Bed load sediment transport in the Arve River has been strongly influenced in the past by major extractions at gravel quarries. About one century ago, the yearly average bed load has been estimated at 150,000 m^3, while systematic and massive extractions in the 20th century have finally led to a lack of material that is actually being estimated at about 10 mio. m^3. The actual yearly average bed load transport is estimated at 60,000 m^3.

2.5 *Morphology of Verbois reservoir*

The actual morphology of the Verbois reservoir is dictated by two major periods:

1. 3-years accumulation period between two consecutive flushing events
2. Flushing event (normal duration about one week)

Sediment volumes evacuated during a typical flushing are between 1.0 and 1.4 mio. m^3 and are mostly situated in the downstream part of the reservoir, i.e. within the last few km upstream of the dam. Flushing events have no substantial influence on the bed morphology at the junction in the center of Geneva. The areas eroded during a flushing event are mostly situated along the inner sides of the Rhône river bends. These are effectively the locations where significant accumulation takes place between two flushing events. Accumulated volumes are between 0.98 and 1.37 mio. m^3, i.e. the efficiency of the current flushing events turns around 89% on the average.

During the past 20–25 years, the total accumulated volume in the reservoir stayed more or less constant, thanks to optimized flushing, but since dam construction in 1942, the reservoir lost already 18% of its total free volume.

3 METHODS OF ANALYSIS

Both analytical and numerical methods have been applied to predict long-term morphological behavior of the Verbois reservoir with or without flushing events. Analytical methods make use of a critical shear stress or flow velocity and have the advantage of ease of application. They allow a global assessment of the problem but do not account for significant physical phenomena such as helical flow patterns in river bends. Numerical methods allow a much more detailed prediction of the morphology, but need a lot of data input and computational time. In the following, the results of both analytical and numerical methods are presented and compared. The applied numerical software is the MIKE-21C curvilinear grid model (Danish Hydraulic Institute, Copenhagen, Denmark), which allows accounting for quasi-3D suspended sediment convection and diffusion as well as helical flow effects on morphology along river bends (see Figure 3).

Helical flow is modeled by using a simplified approach based on De Vriend (1981). The magnitude of the secondary flow (i_s) is assumed proportional to the flow depth (h) and inversely proportional to the radius of curvature of the main stream line (R). This results in a difference between the angle of the bed shear stress δ and the angle of the depth-averaged shear

Copyright © 2006 Taylor & Francis Group plc, London, UK

stress and/or velocity (Figure 3, middle). The former angle is expressed as follows:

$$\tan(\delta) = -\alpha \cdot \frac{2}{\kappa^2} \cdot \left(1 - \frac{\sqrt{g}}{\kappa C}\right) \cdot \frac{h}{R} \qquad (1)$$

where α = calibration constant; κ = Von Karman constant; and C = Chézy number. For the present computations, its value has been set to 1. This means that helical flow effects are of significant importance in the river bends, as has been observed based on bathymetric surveys.

4 LONG TERM RESERVOIR MORPHOLOGY

4.1 *Analytical modeling*

The actual state of the reservoir has been computed for a yearly averaged discharge of 400 m^3/s and for different critical entrainment criteria (Figure 4). The results show that only some tenths of a N/m^2 are needed to erode fine particles in the downstream half of the reservoir, while several N/m^2 are needed in the upstream half. Corresponding critical velocities were computed between 0.20 and 0.60 m/s.

Related stable particle diameters have been computed based on the Shields (1936) criterion and were found between 0.12 and 0.22 mm for 400 m^3/s and between 0.34 and 1.20 mm for 800 m^3/s (~yearly peak discharge at junction upstream).

In a next step, for the same discharge, the reservoir bottom has been artificially heightened from its actual level to about 368 m a.s.l., with steps of about 1 m. This allowed computing the flow velocities and bottom stresses for different future degrees of filling of the reservoir. These were then compared with the critical entrainment criteria explained before at three different cross-sections presented in Figure 1.

As shown in Figure 5, bottom shear stresses computed for 400 m^3/s suddenly increase for reservoir bottom elevations of 363 m a.s.l. or higher. To generate stresses above the critical stresses valid in the upstream part of the dam (see Figure 4), bottom elevations of 362.5 to 364.5 m a.s.l. would be needed. This would more or less correspond to the future new dynamic equilibrium level of the reservoir in the absence of flushing events. In the downstream part of the reservoir, however, critical stress values seem to be attained already with the today's bottom elevation. This, however, is only valid along the main flow, the local flow velocities and shear stresses along the banks being generally much lower and thus allowing sediment deposition and increase of the bottom level. Prediction of an equilibrium bottom level in this downstream part is difficult to define.

Based on critical flow velocities, equilibrium bottom elevations of 363 m a.s.l. have been found in the upstream part of the reservoir and equilibrium conditions are predicted for the downstream part.

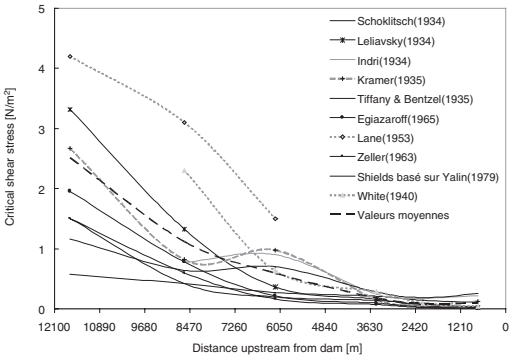


Figure 4. Critical shear stress in Verbois reservoir for an average discharge of 400 m^3/s and different entrainment criteria.

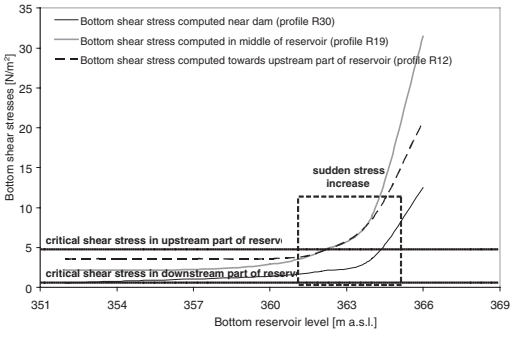


Figure 5. Bottom shear stress in Verbois reservoir for an average discharge of 400 m^3/s and for different fictitious future reservoir bottom elevations.

4.2 *Quasi-3D numerical modeling*

A quasi-3D numerical modeling has been performed accounting for vertically integrated profile functions for both the flow velocities and the suspended sediment concentrations. These have been used to determine helical flow effects along the river bends on local morphology and sediment deposition. The model uses the depth-averaged Navier-Stokes equations together with a convection-diffusion equation for the suspended sediment. Non-equilibrium effects are accounted for by means of a fall velocity factor. Turbulence model is a constant eddy viscosity model. The following parameters have been used during the different model runs:

– sediment transport equation: Van Rijn (1984) or Engelund & Hansen (1967)
– particle diameters (2 or 4 particles)

Copyright © 2006 Taylor & Francis Group plc, London, UK

Table 2. Parametric values of numerical computations.

N° [−]	Expression [−]	Particle diameters [mm]	Time [−]	Comp. accum. [m^3]	Meas. accum. [m^3]
1	Van Rijn	0.002/0.03/	3 yrs	1.5E6	1.2E6
	FV = 0.50	0.15/0.55	48 yrs	6.8E6	–
2	Van Rijn	0.002/0.03/	3 yrs	1.5E6	1.2E6
	FV = 0.05	0.15/0.55	48 yrs	6.4E6	–
3	Van Rijn	0.02 et	3 yrs	3.2E6	1.2E6
	FV = 0.50	0.10	48 yrs	5.7E6	–
4	Van Rijn	0.02 et	3 yrs	1.6E6	1.2E6
	FV = 0.05	0.10	48 yrs	5.9E6	–
5	Van Rijn	0.02 et	3 yrs	4.0E6	1.2E6
	+gravel	0.10	48 yrs	10.2E6	–
6	Eng & Han.	0.02 et	3 yrs	2.9E6	1.2E6
	FV = 0.50	0.06	48 yrs	4.3E6	–

– sediment fall velocity (FV factor)
– sediment concentration (Peiry 1989)

A summary of the most important runs is given at Table 2. Calibration of the model has been performed by comparing the computed morphology with the measured morphology between two consecutive flushing events. Surprisingly, the runs with only 2 particle diameters provided better agreement than the ones with 4 particle diameters. Also, the fall velocity factor (FV) was found to be on the order of 0.05. In other words, non-equilibrium transport effects are of importance, as could be expected based on the fine material that is transported. The Van Rijn expression generated better spatial distribution of sediment deposits than the Engelund & Hansen expression and has been preferred to perform long-term morphologic predictions.

Comparison is made in Figure 6 of the total accumulated volumes per cross-section along the reservoir (profiles R1 at junction to R34 at dam) with and without future flushing events. The total time period is 48 years, with flushing every 3 years. The total reservoir deposition mounts up to 3.2 mio. m^3 with flushing events and 5.7 mio. m^3 without flushing events. Most of the deposits are situated in the last few km upstream of the dam. Very few deposits are observed just downstream of the junction.

Figure 7 shows a summary of the time evolution of the totally deposited volume of sediments in the Verbois reservoir for the different runs of Table 1. The computations performed with only 2 particle diameters show somewhat lower total deposited volumes than the ones with 4 particle diameters. The former computations generally had a much better agreement with bathymetric surveys, the reason for this is not clear.

When maintaining triennial flushing events in the future, reservoir filling will continue, but at a lower rate than without flushing events. Nevertheless, for some runs, the volumetric difference between runs with and without flushing events is not so important.

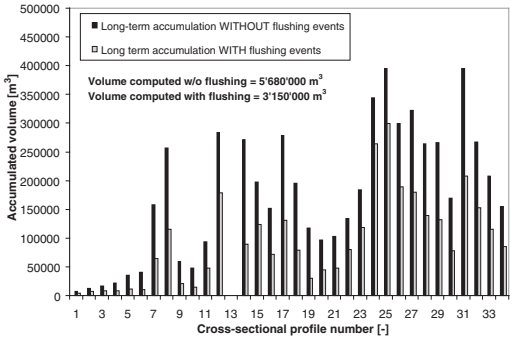


Figure 6. Comparison of total accumulated volumes after 48 years with or without triennial flushing events.

As a first-hand conclusion, it may be stated that, regardless of the future sediment management of the Verbois reservoir, morphology will apparently reach a state of dynamic equilibrium. In case of no further flushing, this equilibrium seems to be reached already after 10-15 years, while in case of further triennial flushing events, much more time would be needed.

Also, as illustrated in Figure 8, the long-term equilibrated morphological state of the reservoir bottom would correspond to a rather small main meandering channel with significant deposits along the inner sides of the actual bends and along the actual enlargements of the river. The deposits are indicated in dark grey and the lower parts of the bathymetry in light grey. Flow is from the right (Junction) to the left (Verbois Dam).

It is pleasant to notice that the equilibrium bottom levels of the main meandering channel have been computed between 361 and 364 m a.s.l., in agreement with preliminary analytical predictions.

Figure 9 compares long term deposits in different cross-sections, with or without flushing events. The computed deposits are also compared with bathymetric measurements made between two consecutive flushing operations in 1997 and 2000. These measurements provide an estimate of the sediment deposits that may occur within a 3-years time period between flushing events. Computed and measured morphologies are generally in reasonable to good agreement. The numerical model is clearly able to simulate erosion along the outer side of bends together with deposition on the corresponding inner side. Also, spatial distribution of deposits along the 12 km long reservoir is correctly simulated by the model. Nevertheless, a detailed quantitative agreement inside each cross-section seems hard to obtain. As could be expected, the long term computations of sediment deposits show significant differences with or without flushing events, particularly in the river bends as well as in the vicinity of the dam.

Copyright © 2006 Taylor & Francis Group plc, London, UK

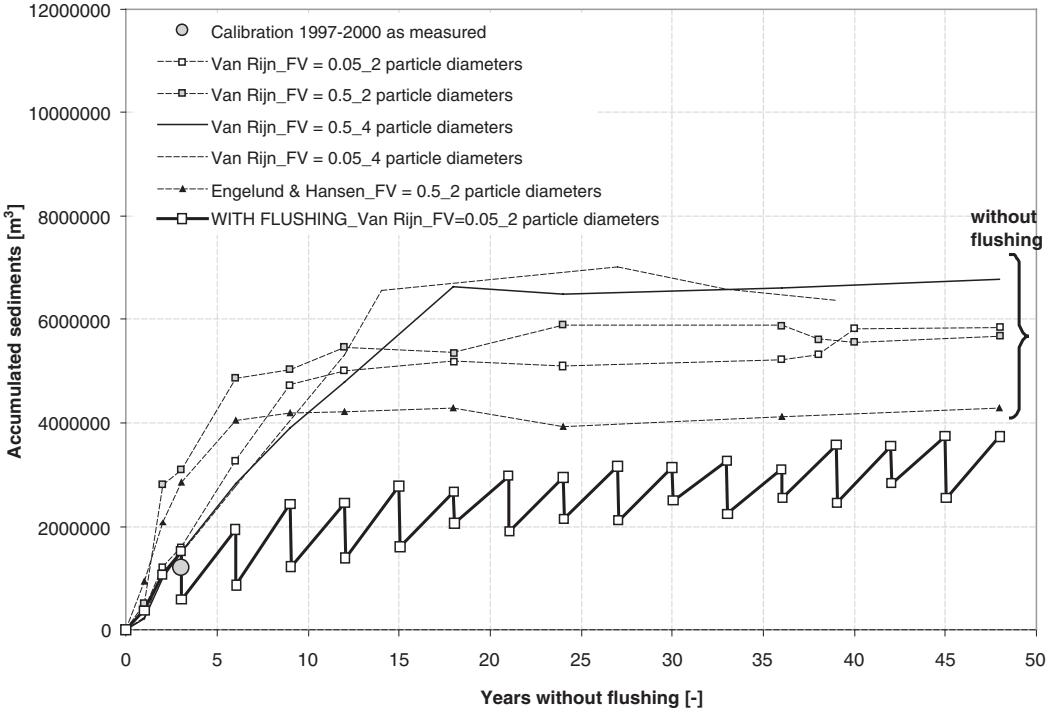


Figure 7. Summary of time evolution of sediment deposits in Verbois reservoir with and without future flushing events.

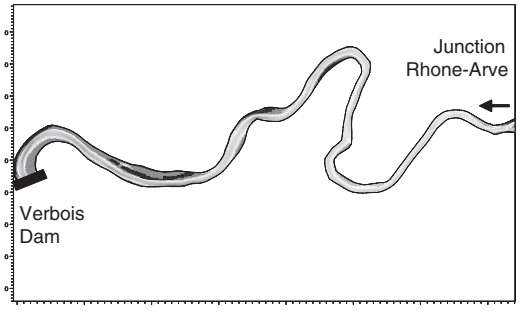


Figure 8. Long-term reservoir morphology without future flushing events (dark grey = deposits; light grey = no deposits).

5 WATER SURFACE LEVELS AT JUNCTION

5.1 *Discharge of 400 m^3/s*

For a discharge of 400 m^3/s, the actual and future water surface lines have been compared in Figure 10 for both cases with and without future flushing events. An increase of about 40 cm of the water surface level at the junction in the center of Geneva can be noticed. In case of maintaining flushing events on a triennial basis, no significant heightening of the water level is computed.

5.2 *Discharge of 800 m^3/s*

For a discharge of 800 m^3/s, the actual and future water surface lines have been compared in Figure 11, for both cases with and without future flushing events. An increase of about 60–100 cm of the water surface level at the junction in the center of Geneva can be noticed.

However, even in case of maintaining flushing events on a triennial basis, an increase of the water level of about 30 cm may reasonably be expected.

6 CONCLUSIONS

The present analytical and numerical computations have shown that, regardless of future sediment management (with or without triennial flushing events) that will be applied to the Verbois reservoir, a state of morphological equilibrium will be reached.

In case of no further flushing events, this state will most probably correspond to a small and meandering main channel together with significant sediment deposits along the banks, mainly along the inner sides of the actual bends. This state of dynamic equilibrium

Copyright © 2006 Taylor & Francis Group plc, London, UK

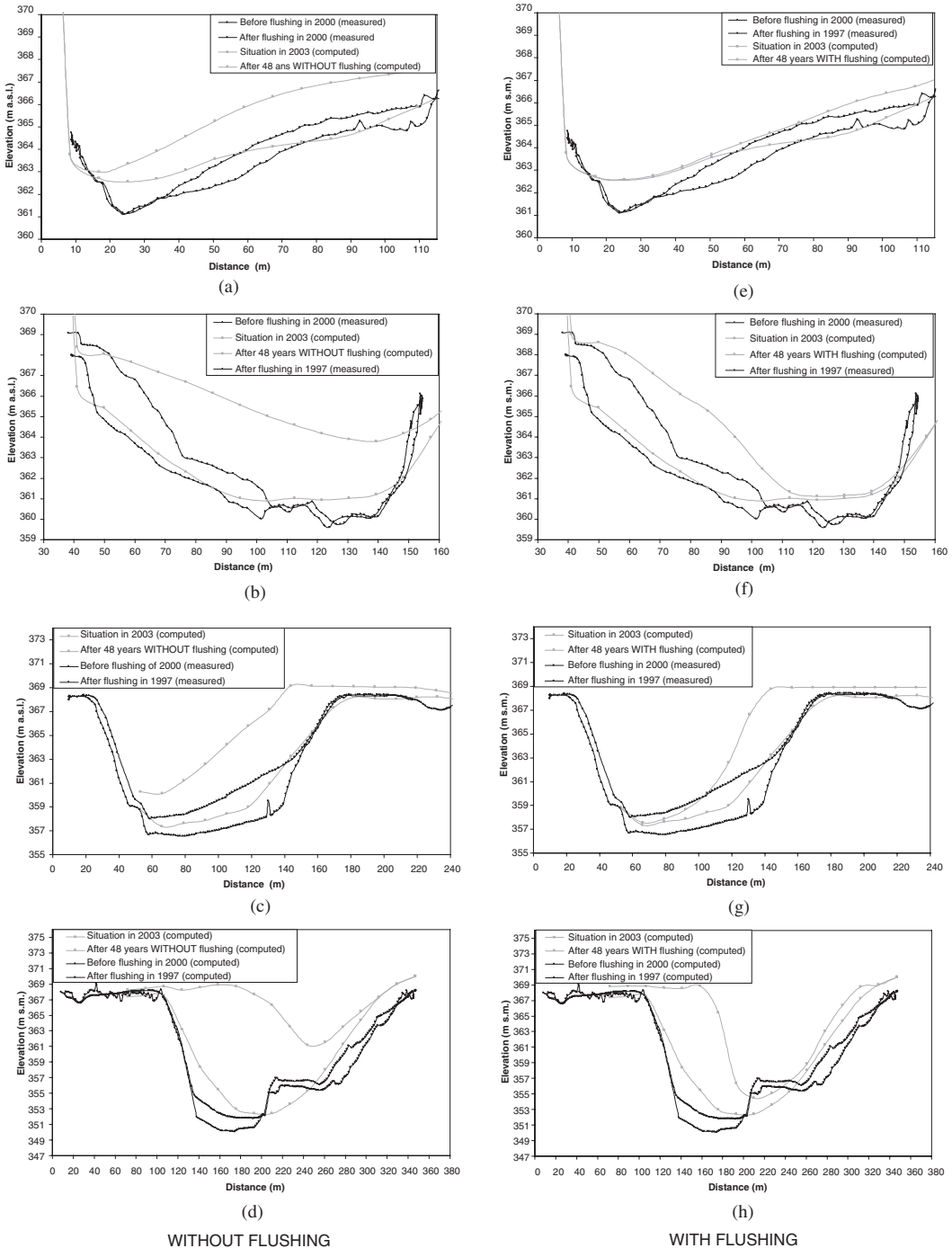


Figure 9. Comparison of sediment deposits computed after 48 years WITHOUT flushing events: a) profile R7; b) profile R12; c) profile R22; d) profile R34. Comparison of sediment deposits computed after 48 years WITH flushing events: e) profile R7; f) profile R12; g) profile R22; h) profile R34.

Copyright © 2006 Taylor & Francis Group plc, London, UK

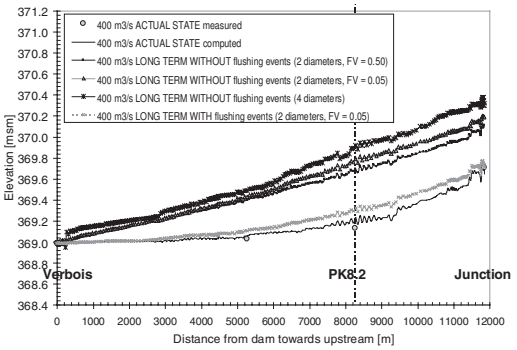


Figure 10. Actual and future water surface lines for 400 m^3/s.

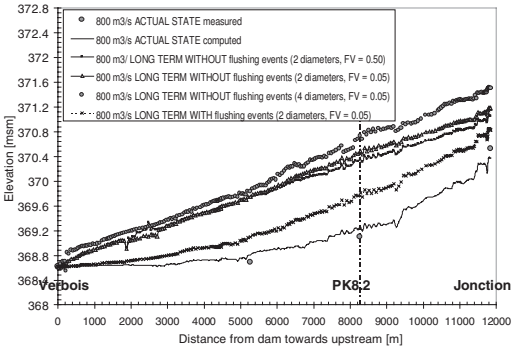


Figure 11. Actual and future water surface lines for 800 m^3/s.

is expected to be reached rather quickly, i.e. within the next 10–15 years.

The future water surface lines at the junction in the center of Geneva will increase regardless of the future sediment management. Nevertheless, in case of no further flushing events, this increase becomes much more important and can reach for example up to 1 m for an annual peak discharge of 800 m^3/s. For extreme floods, increases of about 1.5 m may be expected. These will not only generate flooding in the Junction area in the center of Geneva, but might also create problems for the local sewer system with multiple outlets towards the Arve and Rhône Rivers.

Hence, future sound and plausible sediment management will be necessary in case of no further flushing events. This management could be imagined to be either active, for example by means of new reservoir operating rules during floods to transfer more sediments towards downstream, or rather passive, for example by simply raising the river banks in the center of Geneva.

Subsequent detailed numerical computations will be made of the morphological evolution in the vicinity of the dam to check for potential sediment burying of the bottom outlet gates and the water intakes.

7 RECOMMENDATIONS

The present study only identifies the general concept of long term morphology and points out a few major questions to be answered in case of stoppage of flushing events. It is obvious that numerous other aspects merit to be studied in detail, such as for example:

– Functioning of the intakes to the turbines
– Functioning of the bottom outlets on the long term
– Functioning of specific water intakes on the dam, such as for fish pass
– Functioning of waste water treatment plants along the reservoir
– Functioning of sewer system along reservoir
– Influence of reservoir level drawdown on local bank stability

These aspects are actually being studied to provide answers to the most important hydraulic and morphologic questions and to generate an input to the other main aspects of this project, as for example environmental issues.

REFERENCES

AquaVision Engineering Ltd. 2005. *Barrage de Verbois: Etude hydraulique et morphologique*, Lausanne, Switzerland.

De Vriend. H.J. 1981. *Steady flow in shallow channel bends*. Communication on Hydraulics 81-3, Dept. of Civil. Eng., Delft Univ. of Tech.

Dulal, K. 2005. *Numerical modeling of hydraulics and morphology of the Rhone between Geneva and Chancy-Pougny.* MsC Thesis in Advanced Studies, AquaVision Engineering Ltd, Lausanne.

Engelund & Hansen (1967). A monograph on sediment transport in alluvial streams. Teknisk Forlag, Danish Technological University, Copenhagen, Denmark.

GEOS Ingénieurs conseils S.A. 2000. *Retenue de Verbois – Etude des lignes d'eau du Rhône en cas de suppression des vidanges*- Rapport n° 1092–502.

Peiry, J.L. 1989. *Approche géographique de la dynamique spatio-temporelle des désiments d'un cours d'eau intra-Montagnard : l'exemple de la plaine alluviale de l'Arve* (Hte-Savoie) Thèse présentée à l'université de Jean Moulin, Lyon 3, France.

SIG (2003). *Campagne 2003 Protocole de Vidange, Tome I, Hydraulique*. Genève, Switzerland.

Van Rijn (1984). Part I: Bed load transport. J. Hyd. Eng., 110, October. Part II: Suspended load transport. J. Hyd. Eng., 110. Delft, The Netherlands.

Copyright © 2006 Taylor & Francis Group plc, London, UK

1D Process-based modelling of reservoir sedimentation: A case study for the Barasona reservoir in Spain

G.L. Mamede, A. Bronstert, T. Francke & E.N. Müller
Institute of Geoecology, University of Potsdam, Germany

J.C. de Araujo
Department of Hydraulic and Environmental Engineering, Federal University of Ceara, Brazil

R.J. Batalla
Forestry Institute of Catalonia and University of Lleida, Spain

A. Güntner
GeoForschungsZentrum Potsdam (GFZ), Germany

ABSTRACT: In order to simulate reservoir sedimentation processes and to enhance sediment management strategies, a deterministic, process-based one-dimensional modelling approach has been developed within the framework of an international research consortium. The reservoir sedimentation module simulates the sediment transport along the longitudinal profile of a reservoir. The reservoir is divided into cross sections to elaborate the sediment budget.The sediment transport component is calculated using a non-uniform sediment transport approach based on the concept of sediment carrying capacity. Up to four different sediment-transport equations can be selected for the simulations. The reservoir sedimentation model was applied to the 92.2 Mm^3 Barasona Reservoir, located in in the foothills of the Central Pyrenees (Aragon, Spain). For this study, the reservoir model was parameterised using input parameters derived from an extensive field study within and upstream the Barasona Reservoir. This research presents, tests and discusses the simulation results of the computed sediment deposition and the bed elevation changes of the Barasona reservoir along a longitudinal profile using the different transport equations, a varying number of sediment size classes, and a varying number of cross-sections for the representation of the complex reservoir characteristics.

1 INTRODUCTION

The construction of a dam can significantly affect the balance of sediment inflow and outflow in the impounded reach, resulting in very low flow velocities and efficient sediment trapping. The consequences of reservoir sedimentation can be economically serious. On the one hand, sedimentation leads to quantitative problems, such as storage capacity losses, obstruction of water intakes, sediment deposition in the delta region and streambed aggradation. On the other hand, as a by-product of the human activities upstream of the dam, the fine fraction of the incoming suspended sediments may carry adsorbed pollutants. Its deposition may have disturbing environmental consequences.

In order to simulate bed aggradation and degradation in reservoirs and to enhance sediment management strategies, a deterministic, process-based, one-dimensional modelling approach, named SEMRES Model has been developed within the framework of the SESAM Project, an international cooperation programme between the University of Potsdam (Germany), the GFZ Potsdam (Germany), the University of Lleida (Spain), the Forestry and Technology Center of Catalonia (Spain) and the Federal University of Ceara (Brazil). Overall, the goal of the SESAM Project is to develop an integrated model concept, which enables the simulation of erosion processes at the hillslope and sub-basin scale, the sediment transport processes in rivers and sediment deposition and management in reservoirs.

2 MODEL STRUCTURE

The reservoir sedimentation model is implemented as a module in the WASA model, which was developed at Potsdam during the past five years (Güntner

Copyright © 2006 Taylor & Francis Group plc, London, UK

et al., 2004a; Güntner et al., 2004b). The WASA model is a deterministic, spatially semi-distributed model, which simulates in detail the rainfall-runoff processes for the quantification of water availability and is currently being extended to model sediment transport processes at the hillslope and river scale.

The reservoir sedimentation routine was included into the WASA model to enable the calculation of non-uniform sediment transport along the longitudinal profile of a reservoir and of the reservoir bed changes caused by deposition and erosion processes. Additionally, it is planned to implement routines for the simulation of sediment management scenarios that evaluate the potential reduction of sediment accumulation in reservoirs.

In order to perform the simulation of sediment transport in reservoirs, four processes have to be considered: (1) water balance of the reservoir, (2) reservoir water body hydraulics, (3) sediment transport along the longitudinal profile of the reservoir and (4) reservoir bed elevation changes. The computation of the water balance is based on the continuity equation, which considers all inflows, outflows and changes in storage of the reservoir. For the calculation of the hydraulic properties, the reservoir is divided into two spatial components: the river sub-reach component and the reservoir sub-reach component, as presented in Figure 1. In the river sub-reach, hydraulic calculations are based on the standard step method for a gradually varied flow (Graf & Altinakar, 1998), while in the reservoir sub-reach, a modelling approach adapted from the GSTARS model is used (Yang, 2002). For the calculation of sediment transport within the reservoir, a 1-D equation of non-equilibrium transport of various size groups of sediment particles is used, adapted from Han (1980). Finally, the reservoir bed elevation changes are calculated through the sediment balance in each cross section, considering three conceptual layers above the original bed material. The lowest layer is used for storage where the deposited sediments are compacted and protected against erosion. In the intermediate layer, the sediment can be deposited or re-suspended. In the top layer, a sediment-laden flow occurs.

2.1 *Water balance of the reservoir*

The water-balance module accounts for the interactions between various forms of water going into and out of the reservoir over daily intervals or shorter.

In general, the reservoir water balance can be written as showed in the following equation assuming that the physical properties of the fluid are constant.

$$\Delta V = Q_{in} + Q_{prec} + Q_{gr} - (Q_{evap} + Q_{inf} + Q_{over} + Q_{ws}) \quad (1)$$

where Q_{in} = direct runoff from the tributary rivers; Q_{gr} = groundwater inflow; Q_{prec} = direct rainfall on the reservoir water surface; Q_{ws} = withdrawals for water supply; Q_{sm} = withdrawals for sediment management; Q_{over} = overflow discharges through the spillway; Q_{evap} = direct evaporation from the water surface of the reservoir; and Q_{inf} = groundwater outflow by infiltration. Groundwater inflow and outflow was assumed negligible relative to other inflow and outflow components.

The reservoir water balance computations used in the reservoir module of the WASA Model are summarized within each timestep as follows:

(a) given the initial water volume and the inflow discharge obtained from the river module of the WASA model, determine the overflow discharges in the case that the storage capacity of the reservoir is exceeded by the actual storage volume after inflows.
(b) compute the storage volume reduction of the reservoir by evaporation. Evaporation values are calculated in the climate module of the WASA model.
(c) determine the storage volume increase by rainfall directly into the reservoir. If storage capacity of the reservoir is exceeded by the actual storage volume after precipitation, overflow discharge is updated.
(d) determine the volume of water withdrawn from the reservoir for water supply. The outflow is a fraction of Q_{90}, i.e., the annual runoff from a reservoir, which is provided with a probability of 90% (in 90% of all years). Q_{90} is based on simple hydrological modelling for dryland environments (Güntner, 2004b).
(e) compute the volume of water withdrawn from the reservoir for sediment management proposes as a fraction of the maximum discharge released through the bottom outlets. This fraction is calculated by interpolation between the storage capacity of the reservoir and a minimum reservoir volume, which allows withdrawals through the bottom outlets, given by user.
(f) calculate the actual reservoir level by using a stage-volume curve.

2.2 *Hydraulic calculations in the reservoir*

The determination of hydraulic properties is a prerequisite for sediment transport modelling in general. Here, the reservoir is divided in the river sub-reach component and the reservoir sub-reach component (Fig. 1), taking into account the variation of the reservoir level. Obviously, the length of the river sub-reach becomes longer for lower reservoir levels, whereas length of the reservoir sub-reach decreases.

For the definition of limits between the two spatial components, the normal depth of each cross section is calculated, not taking into account the existence of the reservoir, and then, it is compared to the depth related to water stage of the reservoir at the same cross

Copyright © 2006 Taylor & Francis Group plc, London, UK

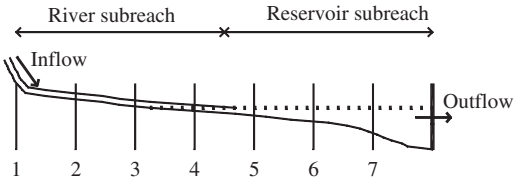


Figure 1. Longitudinal profile of the reservoir (division into river and reservoir sub-reaches).

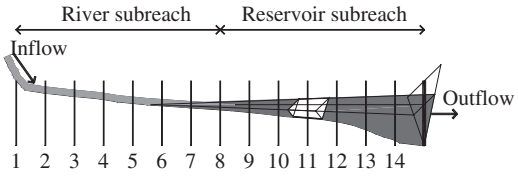


Figure 2. Fraction of the reservoir volume represented by cross section 11.

section. The normal depth is the maximum water depth for a uniform flow, computed by the Manning formula. If the value of normal depth is greater than the depth of the reservoir at the same cross section, it belongs to the river sub-reach.

2.2.1 *Reservoir routing*

The computation of reservoir routing is based on the modelling approach of the GSTARS model (Yang & Simoes, 2002), with some modifications, that will be explained in the following. In the reservoir sub-reach, the water discharge is computed for each cross section from upstream to downstream using a weighting factor, which represents the influence of input discharges and output discharges on that cross section. In the GSTARS model, the weighting factor is the reservoir's surface area represented by each cross section. Here, the weighting factor is calculated from the volume represented by the respective cross section, as showed in Figure 2. The water discharge for each cross section is calculated as follows:

$$Q_j = Q_{in} - (Q_{in} - Q_{out}) \cdot \sum_{k=m}^{j} v_k \qquad (2)$$

where v_k = fraction of reservoir volume represented by that cross section ($v_k = V_k/V_{res}$); V_k = volume represented by cross section k; V_{res} = reservoir volume; m = first cross section belonging to the reservoir sub-reach; Q_{in} = input discharge; and Q_{out} = output discharge. Given the water discharge and water elevation at a cross section, its hydraulic parameters can be calculated.

2.2.2 *River routing*

For the calculation of the hydraulic properties at the river sub-reach, the standard step method for a gradually varied flow (Graf & Altinakar, 1998) was selected. This method will give a water-surface profile for subcritical or supercritical flow regimes, but a constant of integration must be supplied. In the case of subcritical flow, the cross section of control is the first section at the reservoir sub-reach, which has known physical properties. For supercritical flow regime, the water surface profile is computed from known upstream boundary condition. No mixed flow is computed. Calculations must begin at the control section and proceed in the direction in which the control operates, i.e. from the control section to upstream for subcritical flow and to downstream for supercritical flow.

In its general form, the equation of motion was written as

$$\frac{d}{dx}\frac{(Q/A)^2}{2} + \frac{dh}{dx} - S_f = -S_e \qquad (3)$$

where Q = water discharge (m^3/s); A = wetted surface (m^2); h = water depth (m); S_f = slope of the bed (-); and S_e = slope of energy-grade line (-).

The dynamic Equation (3), is rewritten below for the computation of hydraulic properties at the river sub-reach between the current section and the downstream section (Graf & Altinakar, 1998):

$$H_j - H_{j+1} = S_f . L_j + K_{ss} \frac{Q^2}{2g} \left| \frac{1}{A_j^2} + \frac{1}{A_{j+1}^2} \right| \qquad (4)$$

where H = elevation of the energy-grade line; L_j = distance between the current section and the upstream cross section (or downstream cross section if a supercritical profile is being calculated); V = average flow velocity; n = Manning's friction coefficient for the current section; R_h = hydraulic radius of the current section; K_{ss} = head-loss coefficient for a singularity as caused by a change between two consecutive sections or other possible irregularities. For subcritical flow regime, it is internally set to 0.1 for contractions and to 0.3 for expansions. Typical values for gradual transitions in supercritical flow would be around 0.05 for the contraction coefficient and 0.1 for the expansion coefficient (Brunner 2002).

In Equation 4, S_f is the representative friction slope between two sections. It is computed from Manning's equation as follows:

$$S_f = \left(\frac{2Q}{K_1 + K_2} \right)^2 \qquad (5)$$

where K_1 and K_2 = conveyance at the cross section 1 and 2, respectively.

Copyright © 2006 Taylor & Francis Group plc, London, UK

Table 1. Sediment-transport formulae for the calculation of reservoir sedimentation and their limits of applicability.

Formulas	Limits mm
Wu et al. (2000)	0.004 to 100
Ashida & Michiue (1973)	0.001 to 100
Tsinghua University (1985, IRTCES)	0.001 to 100
Ackers & White (1973)	0.040 to 100

2.3 *Reservoir sediment transport*

Most sediment transport models applied in engineering practice are based on an equilibrium sediment-transport approach using the concept of sediment carrying capacity. However, for the case of reservoir sedimentation and scouring process of river channel in the downstream of a reservoir, the sediment carrying capacity is not equal to the actual sediment concentration. Han (1980) proposed the following equation for non-equilibrium sediment transport:

$$\frac{dS}{dx} = \frac{\alpha\omega}{q}(S^* - S) \tag{6}$$

where S = sediment concentration; S* = sediment carrying capacity; ω = settling velocity; and α = coefficient of saturation recovery. Han (1980) recommended 0.25 for reservoir sedimentation and 1 for scouring during flushing of reservoir.

After some rearrangements, the integrated equation from Equation 6 can be expressed as:

$$S_j = S_j^* + (S_{j-1} - S_j^*).e^{-\left(\frac{\alpha.\omega.L}{q}\right)} \tag{7}$$

The sediment carrying capacity S* is computed by four different equations selected from the literature, as presented in Table 1. The criterion to select them was based on the fact that all four equations enable the calculation of both bed load transport and suspended load transport. The sediment transport equations were developed for uniform sediment load. Nevertheless, they are frequently used for non-uniform sediment transport problems.

2.3.1 *Wu et al.*

Wu et al. (2000) developed a fractional formula for bed load transport and a fractional formula for suspended load. The transport rate of the k-th fraction of bed load per unit width ($q_{b,q}$) can be calculated as follows:

$$q_{b,k} = P_k.\phi_{b,k}\sqrt{\left(\frac{\gamma_s}{\gamma} - 1\right).g.d_k^{\,3}} \tag{8}$$

where P_k = percentage of material of size fraction k available in the bed; γ and γ_s = specific weights of fluid and sediment, respectively; g = gravitational acceleration; d_k = diameter of the particles in size class k; and $\phi_{b,k}$ = dimensionless transport parameter for fractional bed load yields. The parameter $\phi_{b,k}$ is computed from

$$\phi_{b,k} = 0.0053.\left[\left(\frac{n'}{n}\right)\frac{\tau_b}{\tau_{c,k}}\right]^{2.2} \tag{9}$$

where $\tau_{c,k}$ = critical shear stress (N/m^2); τ_b = bed shear stress (N/m^2); and n′ = Manning's roughness related to grains (s/m$^{1/3}$).

The suspended load transport rate of the k-th fraction per unit width can be written as:

$$q_{s,k} = P_k.\phi_{s,k}\sqrt{\left(\frac{\gamma_s}{\gamma} - 1\right).g.d_k^{\,3}} \tag{10}$$

where $\phi_{s,k}$ = dimensionless transport parameter for fractional suspended load yields. The parameter $\phi_{s,k}$ is calculated as follow

$$\phi_{s,k} = 0.0000262.\left[\left(\frac{\tau}{\tau_{c,k}} - 1\right)\frac{V}{\omega_k}\right]^{1.74} \tag{11}$$

where τ = bed shear stress on the entire cross section (N/m^2).

The fractional sediment transport capacity for total sediment load (m^3/s) is the sum of the bed load transport rate and the suspended load transport rate.

$$C_k = (q_{b,k} + q_{s,k}).B \tag{12}$$

2.3.2 *Ashida & Michiue*

Ashida & Michiue (1973) proposed a fractional bed load transport equation, as written below:

$$q_{b,k} = 17.P_k.u_e.d_k.\tau_{e,k}\left(1 - \frac{\tau_{c,k}}{\tau_k}\right)\left(1 - \sqrt{\frac{\tau_{c,k}}{\tau_k}}\right) \tag{13}$$

where τ_k = shear stress of the particles in size class k (N/m^2); $\tau_{e,k}$ = effective shear stress (N/m^2); and u_e = effective shear velocity (m/s).

The suspended load transport is adapted from the method of Ashida & Michiue (1970), as proposed by Yang & Simoes (2002) in the GSTARS Model.

$$q_{s,k} = C^*V(e^{-p.a} - e^{-p.h}).\frac{e^{p.a}}{p} \tag{14}$$

where C* = concentration at a reference level (a = 0.05h); p = coefficient computed based on the von Kàrmàn constant.

Copyright © 2006 Taylor & Francis Group plc, London, UK

2.3.3 *Tsinghua university*

The empirical Tsinghua University Method (IRTCES, 1985) was developed to calculate the transport capacity of flushing flows in reservoirs. No distinction was made between bed load and suspended load. The method is based on observations flushing in reservoirs in China, where the predominant practice is annual flushing and so relatively little consolidation occurs between flushing operations. Extrapolation to other reservoirs and conditions should be done with caution.

$$Q_s = \Omega \frac{Q^{1.6} S^{1.2}}{B^{0.6}} \tag{15}$$

where Qs = sediment transport capacity at the current section (tons/s); Q = water discharge (m^3/s); S = bed slope; and Ω is a constant set from the sediment type: 1600 for loess sediments; 650 for other sediments with median size finer than 0.1 mm; 300 for sediments with median size larger than 0.1 mm; and 180 for flushing with a low discharge.

2.3.4 *Ackers & White*

The Ackers & White transport function (1973) is a total load function developed under the assumption that fine sediment transport is best related to the turbulent fluctuations in the water column and coarse sediment transport is best related to the net grain shear with the mean velocity used as the representative variable. The general transport equation for the Ackers & White function for a single grain size class k is represented by:

$$q_{t,k} = P_k . K_k . V . d_k . \left(\frac{V}{u}\right)^{n'_k} . \left(\frac{F_{gr,k}}{Fc_{gr,k} . \xi_k}\right)^{m'k} \tag{16}$$

where $F_{gr,k}$ = sediment mobility number (-); n′, m′, K and Fc_{gr} = dimensionless coefficients. These coefficients depend on the dimensionless particle size d*, calculated as follows:

$$d*_k = d_k \left\{ \frac{\left[\left(\gamma_s / \gamma\right) - 1\right] . g}{\nu^2} \right\}^{1/3} \tag{17}$$

Ackers & White (1973) make a distinction between particles with $1 < d* < 60$ and particles with $d* \geq 60$. Later revisions were made for the K and m′ coefficients (Wallingford, 1990), because there were uncertainties in the original formula in the sediment transport for relatively fine and coarse sediments. Nevertheless, Van der Scheer (2000) showed that the results of the Ackers & White-formula with the modified parameters are slightly worse than the predictions of the original formula. Therefore, the 1973 Ackers & White-formula was included in the reservoir sedimentation model. The parameters of that formula can be found in Table 2.

Table 2. Coefficients of the formula proposed by Ackers and White (1973).

Coefficients	$1 < d* < 60$	$D* \geq 60$
n′	$1 - 0.56.\log(d*)$	0.
m′	$9.66/d* + 1.34$	1.5
log(K)	$-3.53 + 2.86\log(d*) - \log^2(d*)$	0.025
Fc_{gr}	$0.23/(d*^{0.5}) + 0.14$	0.17

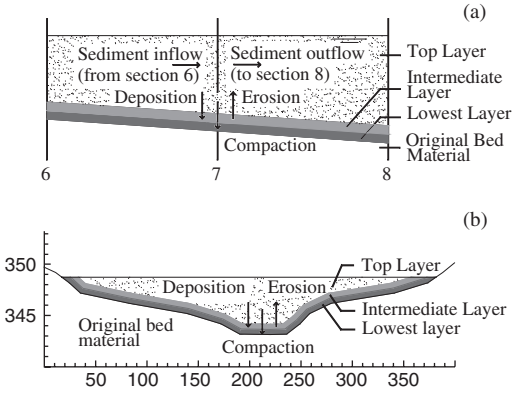


Figure 3. Longitudinal view (a) and cross section (b) with the sediment balance for the three conceptual layers.

2.4 *Reservoir bed elevation changes*

For the calculation of bed elevation changes, each cross section is divided into three conceptual layers above the original bed material as illustrated schematically in Figure 3. The lowest layer is used for storage. There, the sediment is compacted and permanently protected against erosion. In the intermediate layer, the sediment can be deposited or resuspended. In the top layer, the sediment-laden flow occurs.

The time-dependent mobile bed variation can be computed from the following sediment balance equation, as proposed by Han (1980)

$$\frac{\partial(Q.S)}{\partial x} + \frac{\partial M}{\partial t} + \frac{\partial(\rho_d . A_d)}{\partial t} = 0 \tag{18}$$

where Q = water discharge; S = sediment concentration M = the sediment weight in water column with unit length in longitudinal direction; A_d = the total area of deposition; and ρ_d = density of deposited material. If the time span for deposition in a reservoir is not too large, the consolidation of deposits can be neglected and the initial density of deposits is used.

The weight of deposits W can be computed for each grain size k and each cross section j from

$$W_{j,k} = Q_{j-1} . P_{j-1,k} . S_{j-1,k} - Q_j . P_{j,k} . S_{j,k} \tag{19}$$

Copyright © 2006 Taylor & Francis Group plc, London, UK

The amount of incoming sediment at the first cross section of the reservoir is obtained from the river module of the WASA model. Erosion of the bed takes place when the sediment transport capacity at the current cross section exceeds the load incoming into the reach, whereas deposition occurs when the sediment transport capacity is exceeded by sediment inflow. Finally, the amount of sediment transported out of the reach of a cross section is constrained by the sediment transport capacity.

The sediment transport capacity is calculated for each grain size from one of the four available sediment transport formulae presented above, assuming that the entire bed is composed of that size fraction alone. According to the Yang & Simoes (2002), the fractional sediment transport capacity can be written as:

$$C_{j,k} = [r.P_{j,k} - (1-r).P^*_{j,k}].C_{j,k} \quad (20)$$

where: $P^*_{j,k}$ is the percentage of material of size fraction k incoming into the reach represented by the cross section; $P_{j,k}$ is the percentage of material of size fraction k available in the bed; r is a weighting factor that enables the inclusion of incoming sediment into the reach ($0 \leq r \leq 1$); and $C_{j,k}$ is obtained from the sediment transport equations presented above.

The geometry of the cross section is updated whenever deposition or entrainment at the intermediate layer occur. When erosion takes place, sediment transport may be constrained by availability at the intermediate layer. The area of deposited material (A_{dep}) and resuspended material (A_{ero}) are computed by the following equations

$$[A_{dep}]_j = \frac{\sum_{m=1}^{k} [V_{dep}]_{j,m}}{L'_j} \quad (21a)$$

$$[A_{ero}]_j = \frac{\sum_{m=1}^{k} [V_{ero}]_{j,m}}{L'_j} \quad (22b)$$

where L'_j = length of the reach of the subsection, computed from the arithmetic average of the distances L_j and L_{j+1}; V_{dep} = volume of the deposited material; and V_{ero} = volume of the resuspended material.

The area of deposition or entrainment is then used to adjust the bed geometry of the cross section. In the case of deposition, the cross section bed elevation changes using a weighting factor, computed as a ratio between the water depth represented by each point (h) and the maximum water depth at the cross section (h_{max}). For entrainment, a symmetrical distribution of bed thickness at the active layer is assumed adapted from the equilibrium channel width model proposed by Foster & Lane (1983)

$$e / e_{max} = 1 - (1 - 2X_*)^{2.9} \quad (23)$$

where e = bed thickness of the active layer; e_{max} = maximum bed thickness of the active layer, proportional to the geometric mean of the largest size class (the constant of proportionality is user defined); and X_* = a normalized distance along the wetted perimeter starting at the water surface.

3 APPLICATION

3.1 *Study area*

The modelling approach presented above was applied to the 71 Mm^3 Barasona reservoir in the Pre-Pyrenees. The Barasona Reservoir was constructed on the Esera River in Spain in 1932 for irrigation purposes and power generation. In 1972, the crest elevation of the Barasona Dam was increased and the maximum storage capacity reached 92.2 Mm^3. Until the early 1950 the deposited sediments were flushed out yearly through the bottom outlets. After that time, the bottom outlets were not opened every year, resulting in a higher effective sedimentation rate. A bathymetric survey of the reservoir in 1993 indicated that its original storage capacity had been reduced by 24.8 Mm^3. Finally, a complete drawdown of the reservoir was performed after the irrigation season for the three consecutive years 1995–1998 (Valero-Garcés et al., 1999).

The dam controls 1224 km^2 of the Esera catchment (Fig. 4). The climate of the Esera catchment is a typical Mediterranean mountainous type with a mean annual precipitation rate of 600 to 1200 mm and an average potential evaporation rate of 550 to 750 mm. Most floods occur due to the passing of cold fronts in spring and to local thunderstorms in autumn.

The vegetation of the Esera Catchment includes evergreen oaks and pines in the valley bottoms and deciduous oaks in the upper areas.

Erosion processes are very intense in many parts of the basin even under normal precipitation conditions. A significant part of the erosion processes occur on badlands. Badlands are a typical landform of this region within the upper middle part of the catchments, dominated by Mesozoic carbonate rocks and marls. Badlands are heavily dissected barren terrain that is composed of poorly cemented debris and marls lacking any vegetation cover. Badlands are vulnerable to flash flood erosion and produce large amounts of eroded material, that are then transported downstream as suspended sediments in the Esera and Rivers. The large amount of suspended sediments at the outlet of the Esera-Isábena Rivers creates severe sedimentation in the Barasona reservoir.

Copyright © 2006 Taylor & Francis Group plc, London, UK

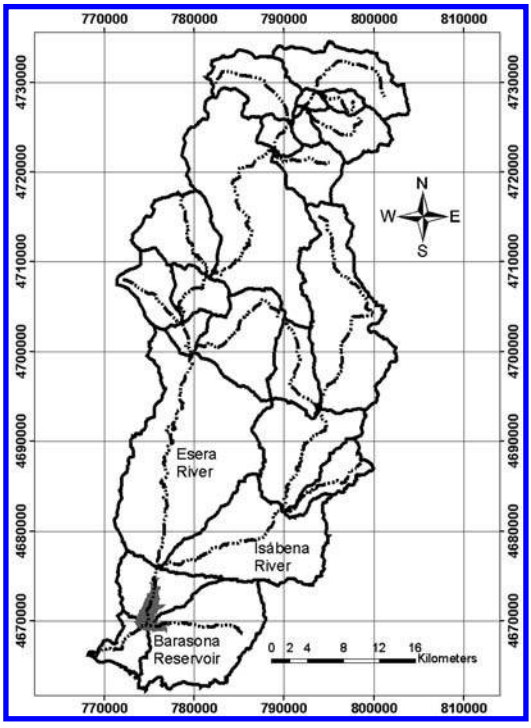


Figure 4. Location of the Barasona Reservoir and the controlled Esera Catchment in Spain (Projection: UTM 30N).

3.2 *Field measurements and parameterisation of the reservoir modelling*

A fieldwork campaign was carried out in autumn 2005 to gain a better understanding of the sedimentation processes of the Barasona Reservoir at the outlet of the Esera Watershed, NE Spain. In particular, field data are required for the parameterisation and validation of the reservoir module of the WASA model. For this purpose, parameters associated with sedimentation processes were collected in and around the reservoir.

Forty-three samples of the deposited material were collected immediately upstream of the Barasona Lake within the inundation area to characterize the deposited material in terms of their physical properties. The results show that the collected material is predominantly silt, with an average percentage of about 70%, as showed in Figure 5, according to the German soil classification.

The collection of water samples at the upstream and downstream sites of a reservoir is very important for the calibration and validation of the simulated reservoir sediment balance. With measured values of suspended sediment concentration at the inlet point, it is possible to obtain a correlation between water input

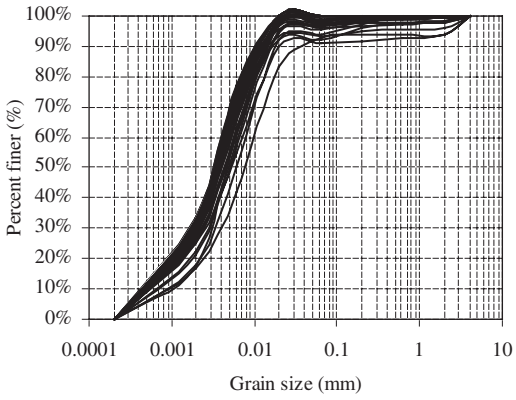


Figure 5. Grain size distribution of the deposited sediment in the Barasona Reservoir, collected during the fieldwork (autumn, 2005).

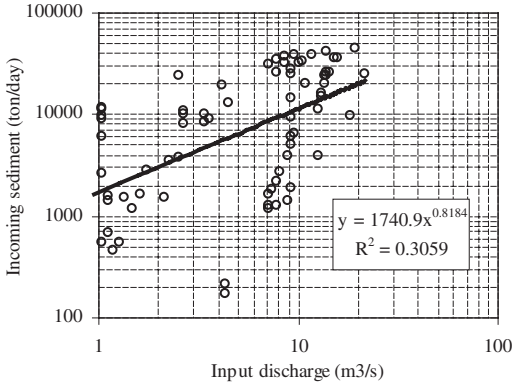


Figure 6. Correlation between incoming sediment and input discharge at the upstream part of the reservoir.

and sediment input into the reservoir, when there is no data available on incoming sediment. From discharge and suspended sediment concentration data obtained during several flood events in the Isabena River a preliminary rating curve was obtained (Fig. 6).

This correlation is used to convert available data of water discharge into the reservoir into suspended sediment input, which in turn is used as a boundary condition for the modelling.

3.3 *Results*

The model simulated 8 years of sediment deposition in the Barasona Reservoir (from 1986 to 1993, when the bathymetric surveys were carried out). The longitudinal profile of the reservoir was initially divided into 51 cross sections. Some results are given here to show the applicability of the reservoir sedimentation model.

Copyright © 2006 Taylor & Francis Group plc, London, UK

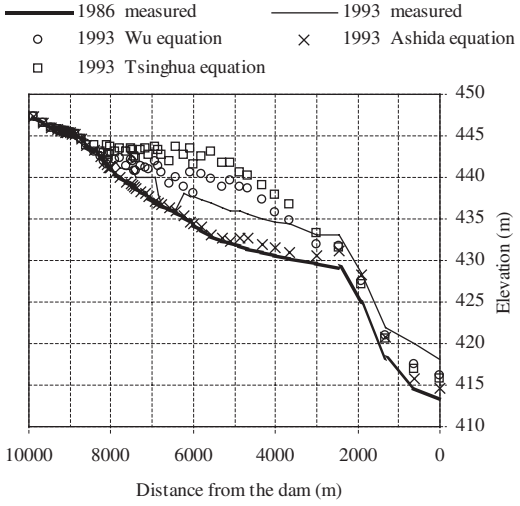


Figure 7. Reservoir bed elevation changes along the longitudinal profile of the Barasona Reservoir, computed by three different sediment transport equations.

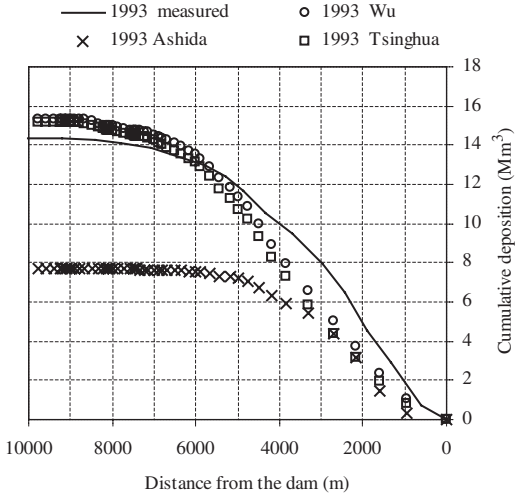


Figure 8. Cumulative sediment deposition along the longitudinal profile of the Barasona Reservoir, computed by three different sediment transport equations.

Figure 7 shows the bed elevation changes along the longitudinal profile of the reservoir for three different sediment transport equations, referring to the lowermost point of each cross section, whereas Figure 8 illustrates the cumulative deposition along the longitudinal profile of the Barasona Reservoir. The results presented in Figures 7 and 8 shows that the Tsinghua University Equation overestimates the sediment deposition at the upstream part of the reservoir,

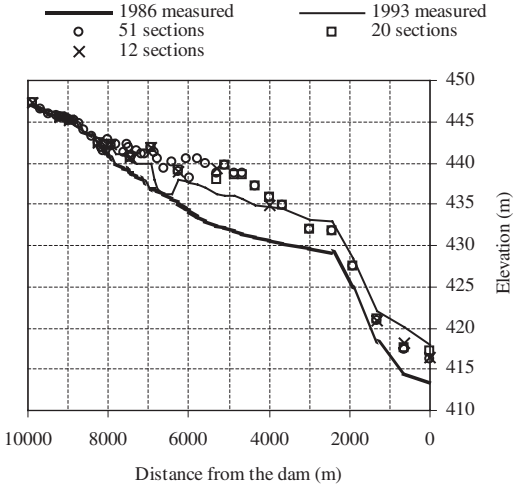


Figure 9. Computed reservoir bed elevation of the Barasona Reservoir using a varying number of cross sections.

whereas the Ashida & Michiue Equation underestimates it in relation to the measured longitudinal profile of the reservoir as derived from the high-resolution bathymetric survey. The Wu equation showed the best results in the simulation of deposition along a longitudinal profile of the Barasona Reservoir. The sediment transport equation proposed by Ackers & White (1973) was not used here because it is not recommended for grain sizes below 0.04 mm.

In order to assess the sensitivity of the model in terms of the number of employed cross sections and number of sediment classes, the Wu equation was selected. The results of the bed elevation change for three different numbers of cross sections (12, 20 and 50 cross sections) are shown in Figure 9. The results shows that the simulation with 51 cross sections can reproduce better the sinuosity of the longitudinal profile.

The sensitivity analysis of reservoir bed elevation changes for a varied number of sediment size classes is presented in Figure 10. The results indicate that a decrease in the number of sediment classes causes an increase of the sediment deposition at the upstream part of the reservoir and a decrease of the sediment deposition at the downstream part of the reservoir.

Results on reservoir bed elevation change along a cross section are presented in Figure 11, exemplarily for the cross sections 25 and 45. The bed elevation change at a cross section is computed as explained in Section 2.4. The results are in good agreement with the topography of the cross sections obtained from the 1993 bathymetric survey, although one-dimensional models have limitations to reproduce bed elevation changes in cross sections with irregular geometry.

Copyright © 2006 Taylor & Francis Group plc, London, UK

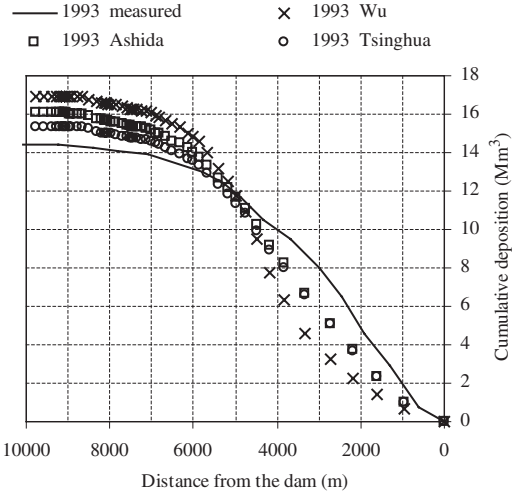


Figure 10. Computed sediment deposition in the Barasona Reservoir using a varying number of sediment classes.

4 CONCLUSIONS AND FURTHER WORK

The paper presented a modelling approach for the simulation of reservoir sedimentation, taking into account non-equilibrium transport processes of non-uniform sediments in reservoirs of dryland environments. Furthermore, related field studies carried out for the model parameterisation, the first model application and preliminary simulation results for sedimentation processes at the Barasona Reservoir in the Pre-Pyrenees of NE Spain were presented and discussed.

A three-layer modelling approach was used to compute separately the sediment transport at the top layer, the sediment exchange between the top layer and intermediate layer caused by deposition and entrainment and the sediment storage at the lowest layer. Overall, the implemented modelling framework for the sediment balance at several cross sections of the Barasona Reservoir enabled a realistic reproduction of non-uniform sediment transport, deposition pattern and bed elevation change along the longitudinal profile of the Barasona Reservoir.

The sediment-transport equation after Wu (2000) yielded the best results in the simulation of bed elevation changes along the longitudinal profile of the Barasona reservoir. Nevertheless, the selection of the appropriate equation depends on the problem at hand.

The reservoir sedimentation model underestimated to some extent the deposition patterns at the downstream part of the Barasona Reservoir in comparison to the measured deposition patterns as were derived from two high-resolution bathymetric surveys of 1986 and 1993. The discrepancy may be explained by

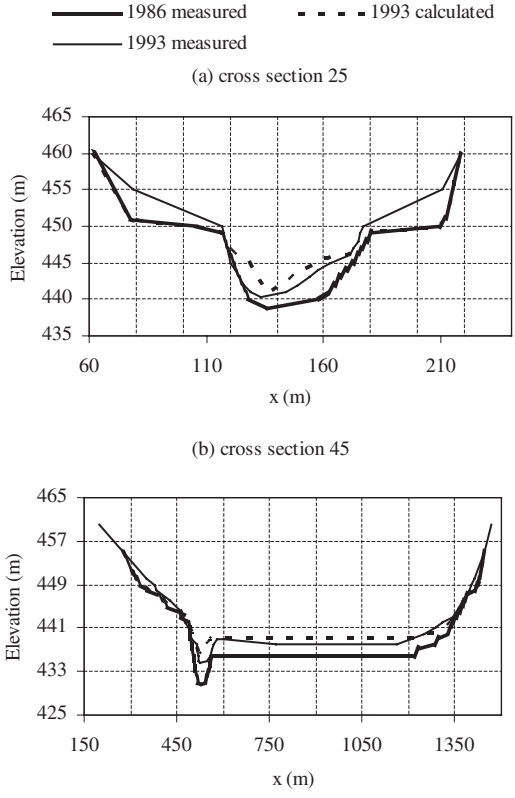


Figure 11. Bed elevation changes at two different cross sections computed from the Wu sediment transport equation: (a) cross section 25 and (b) cross section 51.

the simplified assumption of the correlation between water and sediment input into the reservoir generated from field studies and by the assumption of a constant grain size distribution of the incoming material. A correlation between water and sediment input can either overestimate or underestimate the incoming sediment, while a constant grain size distribution of the incoming material can change strongly the deposition and entrainment along the reservoir. Therefore, the temporal variability of the grain size distribution requires future consideration in the modelling approach. An extensive monitoring program is currently being installed to gain a more in-depth knowledge of the water and sediment fluxes into the reservoir.

Two important physical processes that occur in reservoirs, the turbid density current and cohesive sediment transport were not considered in this study. Currently, an additional module is being developed to assess the influence of the two processes on reservoir sedimentation and thus to enable a more complete description of the involved sedimentation processes.

Copyright © 2006 Taylor & Francis Group plc, London, UK

ACKNOWLEDGEMENTS

This work is funded by the SESAM Project (Deutsche Forschungs-Gemeinschaft) and Brazilian Ministry of Education (CAPES).

REFERENCES

Ashida, K. and Michiue, M. 1973. Studies on bed load transport rate in alluvial streams. *Trans. Japan Society of Civil Engineers*, Vol. 4.

Ashida, K., and Michiue, M. 1970. Study on suspended sediment (1). *Annals DPRI*, No. 13B: 233–242. (in Japanese)

Ackers, P. and White, W.R. 1973. Sediment transport: a new approach and analysis. *Proc. ASCE, Journal of the Hydraulics Division*, Vol. 99, HY11: 2041–2060.

Brunner, G.W. 2002. HEC-RAS, River analysis system hydraulic reference manual. *US Army Corps of Engineers, Hydrologic Engineering Center (HEC)*.

Foster, G.R. and Lane, L.J. 1983. Erosion by concentrated flow in farm fields. *Proceedings, D.B. Simons Symposium on Erosion and Sedimentation*, Colorado State University, Ft. Collins, CO, pp. 9.65–9.82.

Graf, W.H. and Altinakar, M.S. 1998. Fluvial Hydraulics – Flow and transport processes in channels of simple geometry. *John Wiley & Sons LTDA*. ISBN 0-471-97714-4.

Güntner, A. and Bronstert, A. 2004. Representation of landscape variability and lateral redistribution processes for large-scale hydrological modelling in semi-arid areas. *Journal of Hydrology*, 297(1–4), 136–161.

Güntner, A., Krol, M., Araujo, J.C., and Bronstert, A. 2004b. Simple water balance modelling of surface reservoir systems in a large data-scarce semiarid region, Hydrological Sciences Journal 49: 901–918.

Han, Q. and He, M. 1990. A mathematical model for reservoir sedimentation and fluvial processes. *Int. J. of Sediment Res.*, 5(2), IRTCES: 43–84.

IRTCES, 1985. Lecture notes of the training course on reservoir sedimentation. *International Research of Training Center on Erosion and Sedimentation*, Sediment Research Laboratory of Tsinghua University, Beijing, China.

Scheer, P. van der. 2000. Transport Formulae for Graded Sediment – Verification with Flume Data 1999–2000, *M.Sc. thesis, University of Twente*, Enschede.

Valero-Garcés, B.L., Navas, A., Machín, J. and Walling, D. 1999. *Geomorphology*, 28, pp. 23–41.

Wallingford. 1990. Sediment transport: the Ackers & White theory revised. Report SR 237, *HR Wallingford*.

Wu, W., Wang, S.S.Y. and Jia, Y. 2000. Nonuniform sediment transport in alluvial rivers. *Journal of Hydraulic Research*, 38 (6): 427–434.

Yang, T.C. and Simoes, F.J.M. 2002. User's Manual for GSTARS3 (Generalized Sediment Transport model for Alluvial River Simulation version 3.0). *U.S. Department of the Interior, Bureau of Reclamation, Technical Service Center*, Denver, Colorado.

Copyright © 2006 Taylor & Francis Group plc, London, UK

Deposition of fine particles varying with their cohesiveness

G. Hillebrand & F. Nestmann
Institute for Water and River Basin Management, Universität Karlsruhe, Germany

ABSTRACT: Rivers carry enormous amounts of fine particles in suspension compared to the bed load. These particles tend to deposit in regions of low turbulence such as reservoirs, polders or on floodplains. The influence of their respective cohesiveness on the depositional behavior is investigated in a research project. The laboratory study aims to quantify the effect of the cohesive properties of the sediment particles on the deposition process. The cohesiveness is varied by using sediments of different mineralogical composition and by varying the pHvalue of the ambient water.

The experiments are realized in an annular flume with a free water surface, where the flow is driven by the rotation of the inner flume boundary. Two artificial muds of silica and alumina particles and a natural mud taken from a reservoir in the black forest are studied. The results show that the steady state concentrations and the deposition rates differ significantly between the diverse configurations.

1 INTRODUCTION

Rivers carry enormous amounts of fine particles in suspension compared to the bed load. These particles tend to deposit in regions of low turbulence.

The deposition of fine sediments in reservoirs and shipping lanes is of economic interest because its dredging represents a considerable expense. There are also ecological aspects involved as contaminants such as heavy metals or organic pollutants tend to adsorb to fine sediment particles.

Literature on sediment transport mainly focuses on bed load transport. A first theory on sediment transport in suspension is given by Dupuit (1865). A material possessing a density larger than water be still transported in water due to a velocity gradient along the particle causing negative pressure.

In the 1930s, the diffusion theory was established (Schmidt 1925; Rouse 1937), which attributes sediment transport in suspension to a balance of upward movement due to turbulence and downward movement due to the self-weight of the particles.

State-of-the-art approaches on sediment transport often distinguish cohesive and non-cohesive sediments. Especially in the case of cohesive sediments, results of those approaches differ strongly (Schweim et al. 2001) and are therefore unreliable for engineering purposes. The significant discrepancies in the results of diverse formulae indicate that the interaction of flow and cohesive sediment is not completely understood.

Sediment characteristics have a significant influence on the deposition process. This paper addresses the cohesiveness as one aspect of this vital matter.

2 LITERATURE REVIEW

Deposition of fine sediments has been investigated by various authors with varying objectives. Key parameters which were examined are the suspended sediment concentration depending on the bottom shear stress and velocity gradients in the flume, the settling velocity or the deposition rate of particles and flocs respectively, and the characteristics of the flow, the ambient water and the sediment itself influencing the deposition process.

Many of the studies have been carried out in annular flumes. Typically, those annular flumes consist of a circular channel with a rotating lid on the water surface, which drives the flow in the flume. Oftentimes, the channel may be rotated in the opposite direction in order to reduce secondary currents and achieve a relatively uniform distribution of the bottom shear stresses along a virtual flume cross-section.

Typical findings from the experiments on deposition are the following:

- The suspended sediment concentration initially decreases rapidly. Afterwards, the decrease abates and the concentration finally reaches a constant value, frequently termed *equilibrium concentration* C_{eq} (Partheniades et al. 1966; Krishnappan and Engel 1997; Verbeek et al. 1993).
- The ratio of C_{eq} and the initial concentration C_0 is a function of the bottom shear stress τ in the flume. High shear stresses keep larger portions of sediment in suspension (Haralampides et al. 2003; Mehta and Partheniades 1975).

Copyright © 2006 Taylor & Francis Group plc, London, UK

– The ratio C_{eq}/C_0 does not change with variable C_0 (Mehta and Partheniades 1975; Krishnappan and Engel 1997; Verbeek et al. 1993).
– A minimum bottom shear stress exists below which no amount of material can remain in suspension indefinitely (Mehta and Partheniades 1973; Kuijper et al. 1991). On the other hand, there appears to be a critical shear stress above which there is no net deposition (Krone 1993).
– Fine-grained sediment settles in flocculated form. Only flocs with strong interparticle bonds settle through the region of high shear stresses near the bed can deposit to the bed. Weaker flocs are broken up and are brought back into suspension (Krishnappan and Engel 1997).
– The floc size depends on the velocity gradients, but does not directly correlate with the bottom shear stress τ due to two competing processes: The flocculation is improved with increasing τ, as particle collision is enhanced. On the other hand, high shear stresses result in an increased floc break-up, limiting the maximum floc size (Partheniades 1965; Haralampides et al. 2003).
– The strength of interparticle bonds dominates the deposition process rather than the particle weight in case of fine-grained sediment (Partheniades et al. 1966; Krone 1962).
– The flow structure is not significantly influenced by the suspended sediment, nor is the roughness of the flume bed by the deposited sediment (Haralampides et al. 2003).
– For application on field conditions, the shear stresses obtained by laboratory experiments have to be adapted and can not be transferred directly (Krishnappan and Engel 1997; Krone 1993).
– No exchange occurs between suspended and deposited material, i.e. there is no erosion during the experiments (Mehta and Partheniades 1975).

Several authors stress the importance of the particle interaction on the settling and deposition process, for example Partheniades et al. (1966) and Krone (1962). Verbeek et al. (1993) furthermore emphasize that the settling velocity has a large effect on the results of numerical models.

So, the calibration of numerical models relies on the knowledge of upper and lower limits between which the model parameters can vary depending on the particle interaction. The determination of those limits ought to be possible by performing similar deposition experiments using sediments which represent the two supposable extremes in their depositional behavior.

3 MATERIALS AND METHODS

Experiments on deposition behavior of fine particles were carried out in an annular flume using two artificial muds of different cohesiveness and a natural mud for comparison.

3.1 *Annular flume*

Two annular flumes of different diameter are available at the Institute for Water and River Basin Management, Universität Karlsruhe, Germany. They consist of a circular water-filled basin with a rotating cylinder within the basin as shown in Fig. 1. This setup forms a ring-like channel with free water-surface with the flow being driven by a rotation of the inner boundary. By shifting the position of the rotating cylinder within the basin, the channel may be narrowed on one side and expanded on the other side.

The channel width is 0.375 m for both annular flumes, the mean diameters are 1.2 m and 3.6 m, respectively. All presented experiments were carried out in the small annular flume with a flow depth of 0.28 m.

3.1.1 *Bottom shear stresses in annular flume*

The flow in the annular flume is driven by the rotation of the inner boundary. Therefore, the flow velocity is largest at this boundary and decreases gradually towards the outer boundary. The bottom shear stresses accordingly vary across a flume section.

The flow velocities for different rotational speeds of the inner cylinder were measured by a three-dimensional Acoustic-Doppler-Velocimeter. The bottom shear stress is calculated based on the flow measurements by a regression analysis.

The velocity distribution in the main flow direction follows the logarithmic law for turbulent, smooth flow in the lower 20% of the water depth ($y \leq 0.2\,h$) (Nezu and Nakagawa 1993):

$$\frac{u(y)}{u_*} = \frac{1}{\kappa} \ln\left(\frac{y \cdot u_*}{\nu}\right) + C_1 \qquad (1)$$

with the friction velocity u_*, the von Karman constant $\kappa = 0.4$, the kinematic viscosity ν and

$$C_1 = 5.5 \qquad (2)$$

Figure 2 shows the resulting bottom shear stresses along the flume cross-section for different rotational speeds. For the sake of simplification, the shear stresses are normalized by the shear stress $\tau_{b/2}$ at the middle of the flume cross-section. The bottom shear stress is highest at the rotating, inner boundary ($x = 0$) and decreases towards the outer boundary ($x = b = 37.5$).

The bottom shear stresses $\tau_{b/2}$ at the middle of the flume section ($x = b/2$) are shown in Table 1. The values marked by (*) are interpolated between those derived from the measurements.

Copyright © 2006 Taylor & Francis Group plc, London, UK

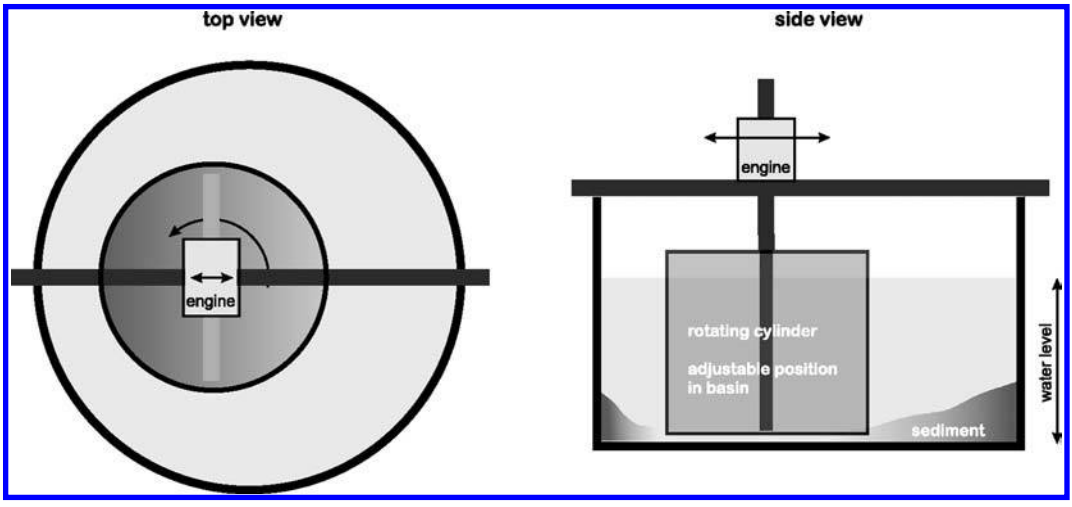


Figure 1. Schematic diagram of annular flume.

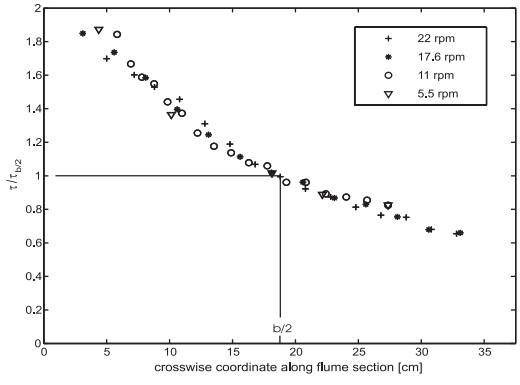


Figure 2. Bottom shear stress in the annular flume for different rotational speeds, normalized by the shear stress at $x = b/2 = 18.75$ cm of the cross-section.

Table 1. Bottom shear stresses $\tau_{b/2}$ at the middle of the flume cross-section ($x = b/2 = 18.75$ cm) for different rotational speeds.

Rotational speed [rpm]	Shear stress $\tau_{x=b/2}$ [N/m^2]
22	0.0412
17.6	0.0265
13.2	0.0151*
11	0.0102
8.8	0.0070*
5.5	0.0032

* Interpolated values.

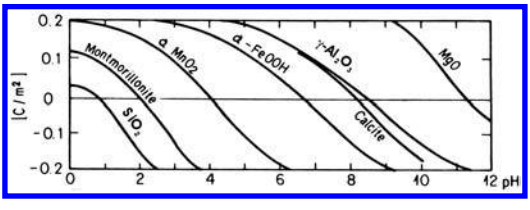


Figure 3. Sediment surface charge depending on pH-value.

3.2 *Investigated sediments*

Silica and alumina powder are used as sediment materials of well-known and unchanging characteristics. Furthermore, the particle surface charge shows a strong dependency on the pH-value (Fig. 3), which implies a significant difference in cohesiveness in deionized water (pH = 7.0).

The term *cohesiveness* in this paper expresses a tendency towards flocculation or aggregation of particles. According to DLVO theory, the interaction of fine particles is characterized by attraction due to van der Waals forces and repulsion due to electrostatic forces. Detailed information on the DLVO theory can be found in literature, for example in Sigg and Stumm (1994).

For high surface charges, the repulsive electrostatic forces dominate the interaction process and the suspension remains stable for a long time. Low surface charges are unable to override the pH-independent van der Waals attraction, so the particles flocculate and the deposition rate increases due to the larger floc size compared to the size of the single particle.

In deionized water, silica has a high negative surface charge, whereas alumina has a surface charge close to zero enhanced by its strong buffer capacity which somewhat alkalinizes the water.

For comparison, a natural mud taken from the reservoir of a pumped-storage power plant is investigated. The sediment from the Wehra reservoir has a mean

Copyright © 2006 Taylor & Francis Group plc, London, UK

particle diameter of $d_{50} = 0.046$ mm and an organic content of about 14%. The d_{50} of both silica and alumina particles is about 0.005 mm.

Silica and alumina are investigated in deionized water. For the Wehra sediment experiments, tap water is used since a transport of original Wehra water was impractical.

3.3 *Experiments on deposition*

Experiments on deposition of silica, alumina and the Wehra sediments in the annular flume are carried out as follows: Prior to inserting the sediment into the annular flume, the sediment is dispersed in deionized water by means of a laboratory stirrer.

The suspension is then gradually inserted into the steady flow in the annular flume at high rotational speeds of the inner cylinder.

The settling process is observed continuously as change in turbidity by a turbidity meter. Additionally, samples are taken from the suspension periodically for the determination of the correlating particle concentrations. Thus, by a correlation function between turbidity and concentration, a continuous monitoring of the decrease in concentration of the suspended particle with time is obtained.

4 RESULTS AND DISCUSSION

4.1 *Equilibrium concentration*

Diffusion theory attributes sediment transport in suspension to a balance of upward movement due to turbulence and downward movement due to the self-weight of the particles. So, for a given flow, i.e. a given turbulence, there is an associated capacity of particles with certain characteristics which may be transported in suspension.

If the particle concentration is higher than this specific capacity, deposition will occur. The deposition will continue until a steady state, the so-called *equilibrium concentration*, is reached, at which point the turbulence just balances the settling process.

Figure 4 shows the deposition of silica particles in deionized water in the annular flume at four different rotational speeds of the inner cylinder. After a duration of about 50 hours, the equilibrium concentration is reached for three experiments.

The final ratios of current to initial concentration range between 0.66 and 0.73. However, the magnitude of the equilibrium concentration does not seem to correlate directly with the flow velocity.

At the lowest tested rotational speed of 8.8 rpm, all particles deposit eventually and no state of equilibrium is reached. The necessary settling time was found to be several hundred hours.

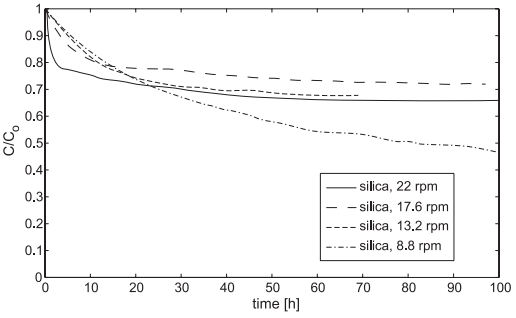


Figure 4. Deposition of silica particles in deionized water for different rotational speeds of the inner cylinder.

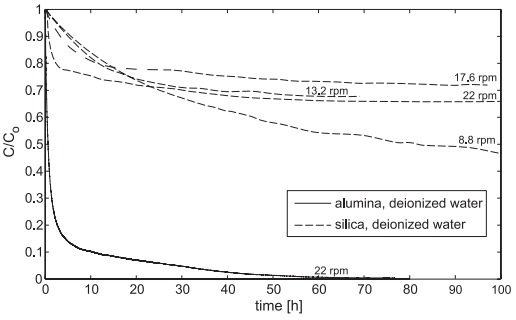


Figure 5. Deposition of particles with different cohesiveness for different rotational speeds of the inner cylinder.

To determine the influence of particle cohesiveness on the equilibrium concentration, a similar experiment was carried out with alumina particles (Fig. 5).

The results clearly indicate the different behavior of the two minerals which is to be attributed to their cohesiveness. Even at the highest rotational speed of the inner cylinder, all alumina particles settle down quickly. After about 50 hours, at which time the equilibrium concentration is reached for the corresponding silica suspension, the alumina concentration has decreased strongly to about $0.02C_0$. After another 25 hours, all alumina particles have deposited.

As aforementioned in Chapter 3.2, the surface charge of alumina in deionized water is very low. Thus, there are no surface forces preventing flocculation. Although the mean diameters of the single particles are equal for both sediments, the change in suspended concentration differs strongly due to the aggregation of the alumina particles and the resulting deposition of flocs rather than single particles.

4.2 *Deposition fluxes*

In addition to the magnitude of the steady state concentration, the change in concentration with time, i.e. the

Copyright © 2006 Taylor & Francis Group plc, London, UK

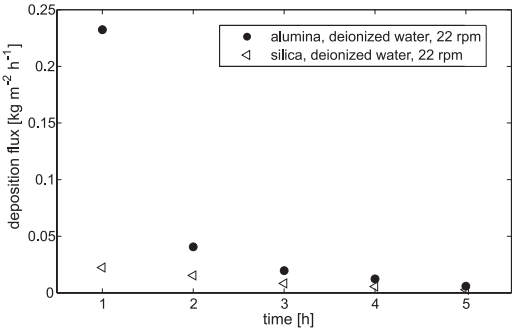


Figure 6. Deposition fluxes for the first 5 hours after start of the experiments.

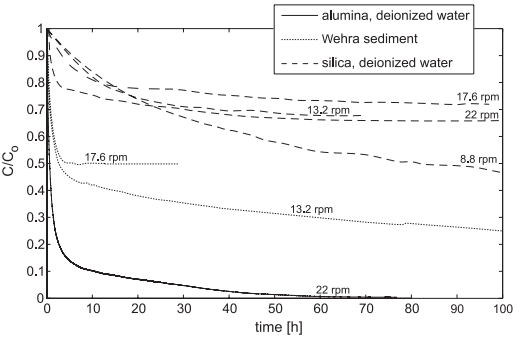


Figure 7. Comparison of depositional behavior for silica, alumina and natural mud.

deposition rate, is a matter of particular interest. The deposition rate is often multiplied by the water depth to get a *deposition flux*.

Exemplarily, the deposition fluxes for alumina and silica suspensions at a rotational speed of 22 rpm are presented in Fig. 6. The initial concentration for both experiments is $C_0 = 2.5\,\mathrm{g/l} = 2.5\,\mathrm{kg/m^3}$. To analyze the concentration time series, a time step of $\Delta t = 1\,\mathrm{h}$ is chosen.

The figure only depicts the deposition flux for the first 5 hours after the start of the experiments, as the deposition rate per hour decreases strongly afterwards.

The deposition flux apparently is a function of the particle concentration in suspension. Nevertheless, the deposition flux of alumina for the first hour is approximately $\Phi_{dep,al} = 0.232\,\mathrm{kg/m^2h}$, which is about ten times the corresponding deposition flux of silica of $\Phi_{dep,si} = 0.022\,\mathrm{kg/m^2h}$.

Analogously to the equilibrium concentration, the only difference between the two experiments evaluated in Fig. 6 is the cohesiveness of the particles used.

At first, when the particle concentration in suspension is still relatively high, the flocculation of the alumina particles immensely enhances the deposition. Afterwards, when the alumina concentration has declined significantly, the deposition rate also decreases, until finally the deposition fluxes for alumina and silica converge.

4.3 *Comparison to natural mud*

Silica and alumina were chosen as sediments which represent the two extremes of cohesiveness in deionized water, silica particles being strongly repulsive and alumina particles aggregating easily.

For comparison, sediment from the Wehra reservoir was used as sediment with "in-between-cohesiveness". Natural muds are a mixture of diverse minerals of different cohesiveness, the clayey fraction for the most part having a negative surface charge at pH 7. The resulting repulsive inter-particle forces are weakened by the natural ionic content of the ambient water and counteracted by the particle-binding effect of organic components.

The data obtained in the deposition experiments with theWehra sediment are added to the afore shown graph (Fig. 7). For a rotational speed of 17.6 rpm, an equilibrium is reached after 10 hours at $0.5\,C_0$. At 13.2 rpm, all sediment particles deposit eventually after several hundred hours.

Evidently, the Wehra sediment shows a depositional behavior which is in between that of silica and alumina concerning the level of the equilibrium concentration and the flow velocities at which an equilibrium (greater than zero) is reached at all.

5 CONCLUSIONS

The two minerals chosen to represent two extremes of cohesiveness in the experiments display a definitely different behavior, although the flume setup and the primary grain sizes were equal.

Alumina particles form aggregates which settle down at high deposition rates. Furthermore, the maximum flow velocity in the small annular flume did not suffice to maintain a steady state suspension.

The silica particles repel each other and therefore stay in suspension for a much longer time. In addition, the equilibrium concentration is reached at a relatively high level for a wide range of flow velocities.

The initial deposition flux of the alumina suspension significantly exceeds that of the silica suspension, even though the experiments were carried out with the same flow velocity and initial concentration, which is supportive of the aforementioned process description.

The investigated natural mud proved to represent a mean cohesiveness in between silica and alumina. Thus, silica and alumina appear to be adequate sediments to define extreme behavior of fine particle suspensions.

Copyright © 2006 Taylor & Francis Group plc, London, UK

The results of those experiment with oppositional materials can serve to test numerical models and to narrow down the range of the values of input parameters to the simulations.

ACKNOWLEDGMENTS

This work was partially supported by the German Research Foundation (DFG), Project No. Ne 614/6-4.

REFERENCES

Dupuit, J. (1865). *Traité théorique et pratique de la conduite et de la distribuition des eaux*. Paris: Dunod.

Haralampides, K., J. A. McCorquodale, and B. G. Krishnappan (2003). Deposition properties of fine sediment. *Journal of Hydraulic Engineering 129*(3), 230–234.

Krishnappan, B. G. and P. Engel (1997). Critical shear stresses for erosion and deposition of fine suspended sediments of the fraser river. In *Cohesive Sediments*. John Wiley & Sons Ltd.

Krone, R. B. (1962). *Flume Studies of the Transport of Sediment in Estuarial Shoaling Processes*. Berkeley: University of California. Final Report prepared for San Francisco District Corps of Engineers.

Krone, R. B. (1993). Sedimentation revisited. In *Coastal and Estuarine Studies 42. Nearshore and Estuarine Cohesive Sediment Transport*. American Geophysical Union.

Kuijper, C., J. M. Cornelisse, and J. C. Winterwerp (1991). *Erosion and Deposition Charactersitics of Natural Muds. Sediments from Loswal Noord*. Delft Hydraulics. Report No. 37.

Mehta, A. J. and E. Partheniades (1973). *Depositional Behaviour of Cohesive Sediments*. Coastal and Oceanographic Engineering Laboratory, University of Florida. Technical Report No. 16.

Mehta, A. J. and E. Partheniades (1975). An investigation of the depositional properties of flocculated fine sediments. *Journal of Hydraulic Research 13*, 361–381.

Nezu, I. and H. Nakagawa (1993). *Turbulence in open channel flows*. Balkema.

Partheniades, E. (1965). Erosion and deposition of cohesive soils. *Journal of the Hydraulic Division 91*(HY1), 105–139.

Partheniades, E., J. F. Kennedy, R. J. Etter, and R. P. Hoyer (1966). *Investigation of the depositional behavior of fine cohesive sediments in an annular rotating channel*. Hydrodynamics Laboratory, MIT. Report No. 96.

Rouse, H. (1937). Modern conceptions of the mechanics of fluid turbulence. *Trans. ASCE 102*, 463–543.

Schmidt, W. (1925). *Der Massenaustausch in freier Luft und verwandte Erscheinungen*. Probleme der Kosmischen Physik. Hamburg: Henri Grand.

Schweim, C., J. V. Prochnow, and J. Köngeter (2001). Combined experimental and numerical investigation of formulae for erosion and deposition of cohesive sediments. *International Journal of Sediment Research 16*(2), 258–267.

Sigg, L. and W. Stumm (1994). *Aquatische Chemie – Eine Einf¨uhrung in die Chemie wässriger Lösungen und natürlicher Gewässer*. Stuttgart: B. G. Teubner.

Verbeek, H., C. Kuijper, J. M. Cornelisse, and J. C. Winterwerp (1993). Deposition of graded natural muds in the netherlands. In *Coastal and Estuarine Studies 42. Nearshore and Estuarine Cohesive Sediment Transport*. American Geophysical Union.

Copyright © 2006 Taylor & Francis Group plc, London, UK

Measurement of flow patterns within an Alpine reservoir

H. Knoblauch, H. Badura & J. Schneider
Institute of Hydraulic Engineering and Water Resources Management, Graz University of Technology

ABSTRACT: Reservoir sedimentation at the Margaritze reservoir, Austria, has already caused problems in the operation of the bottom outlet. At present, the sediments are being transferred within the reservoir to the shallow part. Partly the deposited material is remobilized and conveyed back to the steep part of the water body. In summer 2004 and 2005 measurements were conducted in order to survey the flow patterns. The flow velocities were determined by two Acoustic Doppler Current Profilers. The measurements were taken considering various boundary conditions, such as water level, transfer under progress, amount of inflows and outflows. Different cross sections and singular spots were carefully chosen for receiving the best overview of the reservoirs flow patterns. The results of the measurements demonstrate that the remobilization and transport of the deposited sediment are directly linked to the transfer of sediment to the shallow part of the reservoir.

1 SEDIMENTATION OF THE RESERVOIR

Situated in the heart of the alpine region, Margaritze reservoir is part of the Kaprun Hydro Power Scheme. Its major water inflow area lies at the foot of a glacier. These inflows exhibit average annual sediment concentrations of 40,000 m^3. As a consequence of the increasing sediment deposition in the reservoir, two phenomena can be observed. On the one hand, its storage capacity – and at the same time its benefit for power economy – decreases. On the other hand, sedimentation tends to cause problems in the mechanical equipment parts. In order to keep reservoir facilities in full operation, incoming sediment loads have been removed since the late nineties. By means of a submersible pump a mean daily amount of 3,000 m^3 of water containing glacial silt (average concentration: 1.3 g/l) is dredged from the gorge section and conveyed to the shallow portion of the reservoir, where it is deposited under certain conditions. So far it is unclear why parts of the sediment load which have been moved to the shallower section of the basin are later on remobilized and at an average 10 to 20% of the transferred material gets back to the gorge section of the basin (Figure 1). The slope of the bottom between the shallow and the gorge parts is about 2%.

Moreover, the question remains to be answered, as to whether sediment conveyance back to the gorge portion is probably already happening during ongoing excavation works. Water level fluctuations inside the reservoir as well as hydraulic inflow fluctuations and sediment flows already during dredging works, respectively, may cause a continuous sediment transfer.



Figure 1. Margaritze reservoir.

The 2004 and 2005 measurement campaigns were aimed at explaining all relevant details regarding the reservoir flow situation. In addition to this, a possible change in current conditions during the dredging process is to be investigated.

2 MEASURING APPLIANCES

Apart from two 3-D velocity probes (an ADCP® and an Aquadopp® Profiler), a density current probe as well as a temperature and a conductivity probe were employed for the measurements at Margaritze reservoir in August 2004 and August 2005.

Copyright © 2006 Taylor & Francis Group plc, London, UK

Table 1. Overview of the measuring appliances.

Measuring appliances	Conducted measurements
3D – Aquadopp Profiler®	3D – velocity measurements in transverse profiles and continuous single point meas.
3D – ADCP® Workhorse	3D – Velocity measurement (in profiles and continuous single point meas.)
Temperature and conductivity probe	Temperature and conductivity probes in transverse profiles and single points
Density current probe	Density current probes in transverse profiles and single points
Tracer (sodium chloride) and conductivity probe	Tracer tests

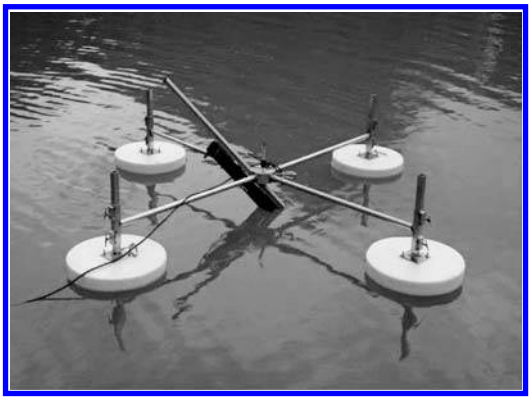


Figure 2. Fixation of the Aquadopp®.

3 THE 3-D ULTRASONIC PROBES

For this project the AQUADOPP® Profiler and the ADCP® Workhorse have been employed measuring velocities by means of Doppler-technology. Unlike single point measurements, these two profilers depict velocities at certain, pre-defined intervals along a depth profile. Compared to single point measurements, its fundamental advantage is its ability to produce a comprehensive recording of the depth profile by way of only a single test. Consequently, a lot of time is being saved. Apart from its high, three-dimensional dissolution, a further advantage of these profilers is the fact that it can be used for extremely low velocities. The employment of the probes required particular adaptations.

The Aquadopp® 3D – velocity probe was fastened to a measuring device, which had been exclusively manufactured for this measuring campaign (Figure 2 and Figure 3). The device comprised four floats and an aluminium framework, to the latter of which the Aquadopp® Profiler had been secured in a 45° angle. This "pontoon" was fastened to a guide rope which was stretched along the profile all across the artificial water basin. In this way, the measuring device was gradually drawn over the cross-section while measurements were conducted at intervals ranging from 4 to 12 meters. While velocity measurements were taking place, also temperature and conductivity measurements were carried out. The respective measuring devices were again fixed to the meter-marked rope and then submerged meter after meter at every single measuring point.

Table 2. Technical data of the ultrasonic probes.

	AQUADOPP®	ADCP®
Acoustic frequency	2000 kHz/3 beams	600 kHz/4 beams
Max. ranges	5 m–12 m	<70 m
Min. cell size	0.1 m	0.25 m
Measuring area	±10 m/s	±3 m/s
Measuring accuracy	1% of the data	0.25% of the data

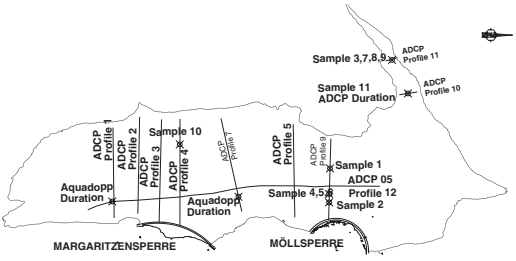


Figure 3. Location of measurements.

The results gained in all theses measurements clearly reflect a connection between the sediment transport at the bottom of the basin and the operation of the submersible pump. During dredging operations, a suspended sediment load accumulated in the bed of the shallow portion of the reservoir, which then flowed at a speed of about 0.1 m/s and a concentration of approx. 1 g/l towards the gorge section.

4 PARAMETERS OF THE MEASURING CAMPAIGNS

4.1 *Overview*

In August 2004 as well as in August 2005 two measuring campaigns were launched to realize the flow pattern situation according to different parameters at the reservoir (inflow, outflow and water level). Great efforts have been taken to ensure that each transverse

Copyright © 2006 Taylor & Francis Group plc, London, UK

profile measurement was performed under approximately the same conditions. That is to say that, as long as a measurement was conducted, there would not be any substantial variation as far as the inflow and outflow conditions, the water level or the dredging system were concerned. Any kind of change in the factors mentioned above was recorded by continuous velocity measurements. As for the arrangement of continuous measurements, altered velocity distributions caused by the dredging system were particularly taken into consideration.

With regards to the results gained in the 2004 and 2005 measurement campaigns, profile measurements may be distinguished from single point measurements (Figure 3). In profiles 1 to 5 velocity ADCP® and AQUADOPP®, turbidity, temperature and conductivity were dealt with whereas in profiles 6 to 11 only turbidity, temperature, conductivity and velocity with the ADCP® probe could be measured because of the considerable water depth. Additionally further 10 single points were largely located in the gorge section, where details concerning temperature, turbidity and conductivity were gathered.

Permanent velocity measurements took place at the marked points in the transverse profiles ("Aquadopp Duration", Figure 3). On average, each profile measurement took two hours depending, however, on both measurement duration and the number of marks on each transverse profile. Measurements on each point took between 150 and 300 sec.

Measurements at Margaritze reservoir can be classified as follows.

4.2 *Transverse profile measurements ("ADCP Profile x" in Figure 3)*

- Velocity transverse profiles (3-dimensional)
- Temperature transverse profiles
- Conductivity transverse profiles
- Density current transverse profiles

4.3 *Single point measurements*

- Continuous velocity measurements (3-D)
- Temperature depth profiles
- Conductivity depth profiles
- Density current depth profiles
- Tracer tests

5 BOUNDARY CONDITIONS

In Figure 4 the rate of inflow respectively outflow of the Margaritze reservoir, the hydrograph of the water level and the working hours of the dredging system are illustrated, exemplary for 2005. The graphs for 2004 show a similar output.

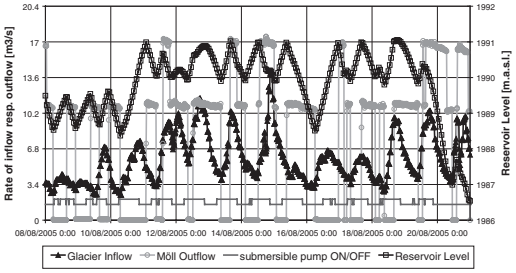


Figure 4. Hydrological situation of the Margaritze reservoir in August 2005.

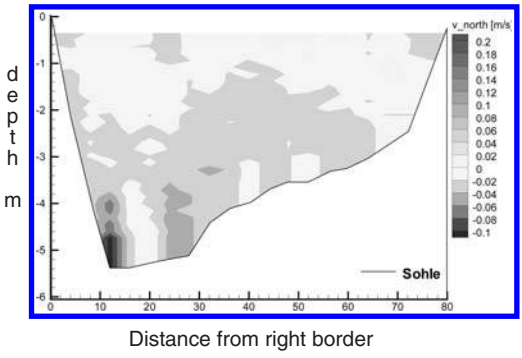


Figure 5. Profile 1, submersible pump OFF, interpolated velocity profile towards the north.

6 RESULTS

6.1 *Profile 1, submersible pump OFF*

When this described measurement of profile 1 (shallow part, Figure 3) was performed, the submersible pump was out of order. The stemming level rose from 1989.0 to 1989.6 masl, which corresponds to a rising speed of 17 cm/h. The velocity profile towards the north (Figure 5) shows mainly negative velocity patterns. Water flows towards the south. This process may be explained by the increase in the hydrograph. This fact principally involves that water has to flow from the northern section of the reservoir to the southern part.

Velocities to the east and vertical are less relevant. However, it can be observed that the flow direction in the upper half of the profile tends to head westwards and downwards whereas it moves rather eastwards and upwards in the lower half of the profile. Suspended sediment concentration comes virtually throughout the whole profile to a standard rate of 0.25 g/l. The temperature profile illustrates a layer structure which is most typical for a lake. Near the bottom of the basin the temperature was 4°C while in higher layers it was up to 8°C.

Copyright © 2006 Taylor & Francis Group plc, London, UK

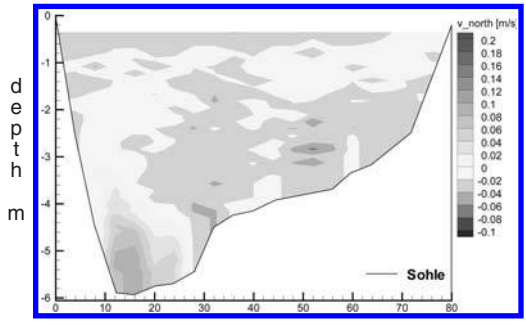


Figure 6. Profile 1, submersible pump ON, interpolated velocity profile towards the north.

6.2 *Profile 1, submersible pump ON*

Unlike the above under 6.1 described measurement of profile 1, the submersible pump was in operation during measurement 2. The pipe ended in the southern section of the reservoir. The stemming level remained virtually constant on 1989.8 masl. The velocity profile towards the north (Figure 6) now distinctly reveals positive velocity patterns in the deep channel. Water flows to the north. Positive velocities came to 10 cm/s. Compared to measurement 1, velocities to the east and upwards changed only to an inconsiderable degree. Suspended sediment concentration, however, increased drastically from 0.25 g/l to 1.3 g/l in exactly those areas of the deep channel in which northwards velocity had remarkably risen.

6.3 *Profile 9, submersible pump ON*

The location of the transverse profile 9 is illustrated in Figure 3. This profile is located at the border between the shallow and the gorge part of the reservoir. The submersible pump was in operation during this measurement. The pipe ended in the southern section of the reservoir. The stemming level remained virtually constant on 1990.0 masl. The velocity profile towards the north (Figure 7) now distinctly reveals positive velocity patterns in the deep channel. Water flows to the north. Positive velocities came to 13 cm/s. Suspended sediment concentration, however, came to 1 g/l in exactly those areas of the deep channel in which northwards velocity had remarkably risen.

7 IMPACT OF THE DREDGING SYSTEM

Judging from the measurements described under 6.1, 6.2 and 6.3, it has become evident, that the operating dredging system has a direct impact on the deep channel sediment transport of profile 1. While

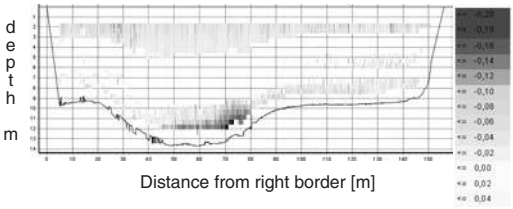


Figure 7. Profile 9, submersible pump ON, interpolated velocity profile towards the south.

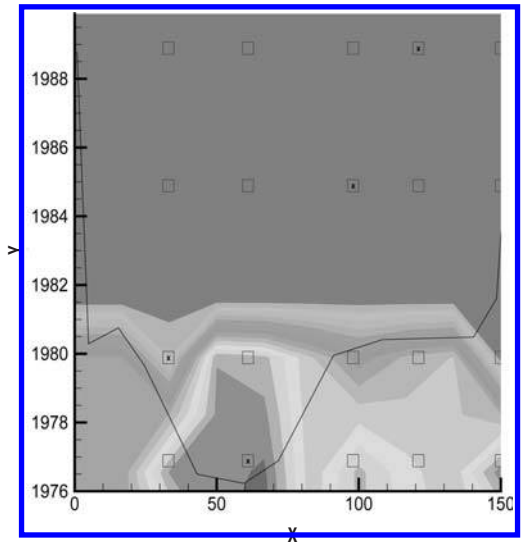


Figure 8. Profile 9, submersible pump ON, interpolated suspended sediment concentration, towards the south.

during the measurements without submersible pump no conspicuous flows or suspended sediment concentrations had been detected, in measurements when the submersible pump was operating exceptionally high velocities towards the north combined with high suspended sediment concentrations (Figure 8) have been found.

8 TRACER TEST RESULTS

During measurement the sediment inflow mark was located in the southern section of the reservoir. Conductivity was measured at a distance of 160 m from the point where the excavator pump pipes had been submerged. The tracer inflow took place at 00:00 o'clock. The measurement was conducted in various water depths at intervals of 30 sec. 40 kg of dissolved sodium chloride were added to the sediment-water-mixture. The result has been illustrated in Figure 9. The x-axis

Copyright © 2006 Taylor & Francis Group plc, London, UK

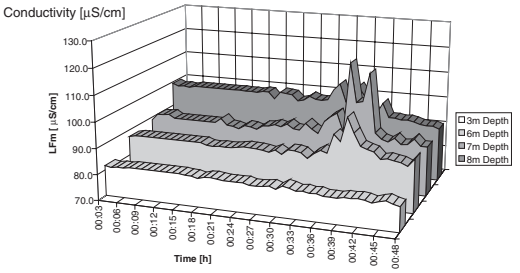


Figure 9. Tracer test results.

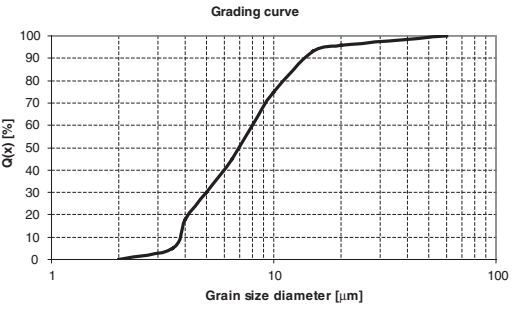


Figure 10. Profile 9, grading curve, water depth 1977 masl.

of the graph shows the measuring duration whereas the z-axis provides data concerning the conductivity in [μ S/cm]. A distinct conductivity increase in t = 6 m, t = 7 m and t = 8 m can be observed with its maximum rate occurring at t = 7 m, whereas in t = 3 m no kind of conductivity increase could be found. Flowing time was 10 cm/s.

The tracer method made it possible to determine the origin of the density current. Similarly, it worked most effectively when it came to detecting the average flowing time. In particular, flowing times accurately correspond with the velocity patterns gained in the Aquadopp® Profiler measurements.

Finally, the density current distribution along the bottom of the basin matches the velocity distribution in the ultrasonic measurements. The results obtained from the conductivity profile draw attention to the fact that inside the deep channel increased conductivity has been recorded. Rates rise from average 100 µS/cm to 115 µS/cm. The extent of increased conductivity corresponds to that of increased suspended sediment concentration

9 GRADING CURVE OF THE SUSPENDED SEDIMENTS

Apart from the long term measurements in 2005 a set of 12 samples were collected to determine the suspended sediment concentration of the supposed density current. The sieve analysis show similar results concerning similar parameters (inflow and outflow to the reservoir, operating hours of the dredging system, water level). The graph in Figure 10 shows the results from profile 9 at a depth of approximately 13 m.

10 MODEL OF STREAM PATTERNS

On account of the results gained in all the measurements dealt with in this study, various models have been designed to provide a detailed description of the various processes going on inside the reservoir. In the following the concept for a model which includes the operation of a submersible pump will be presented in the diagram of Figure 11. The illustration depicts a longitudinal section of the reservoir.

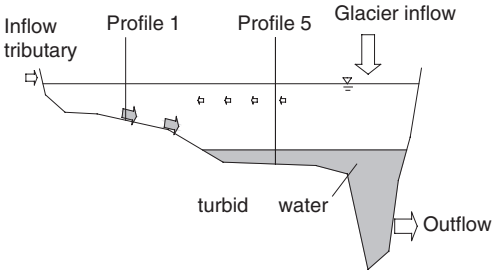


Figure 11. Model of stream patterns, submersible pump ON.

If sediment transfer is performed at constant water level by means of a submersible pump, sediment loads will flow along the bottom of the basin towards the north. This fact has been proven to be accurate by both velocity and density current measurements in profiles 1 to 11.

11 CONCLUSIONS

The substantial glacial silt inflow at Margaritze reservoir results into an average annual sediment deposition of as much as 40,000 m^3. In order to keep the mechanical facilities in full operation, incoming sediment loads are currently transferred by means of a submersible pump from the gorge section to the shallower portion of the basin. It has been unclear, why some of the transferred sediments are remobilized and how they are transported back into the gorge section of the reservoir. Furthermore, it was unknown as to whether the conveyance back to the gorge portion was already happening during the dredging.

Copyright © 2006 Taylor & Francis Group plc, London, UK

The task of the 2004 and 2005 measurement campaigns were to explain all the facts about the reservoir flow situation as well as to investigate possible changes in current conditions due to sediment transfer by dredging. Measurements comprised transverse profile measurements, single point measurements and continuous measurements in single points as well as tracer tests.

The results gained in all theses measurements clearly reflect a connection between the sediment transport at the bottom of the basin and the operation of the submersible pump. During dredging operations, a suspended sediment load accumulated in the bed of the shallow portion of the reservoir, which then flowed at a speed of about 0.1 m/s and a concentration of approx. 1 g/l towards the gorge section.

REFERENCES

Bühler, J.: Trübeströme im Grimselsee; in "Wasser, Energie, Luft", Jahrgang 96, Heft 5/6, Baden, 2004.

De Cesare, G., Schleiss, A., Hermann, F.: Impact of turbidity currents on reservoir sedimentation, Journal of Hydraulic Engineering, January 2001.

Hartmann, S.: Sediment management of alpine reservoirs considering ecological and economical effects, 9th International Symposium on River Sedimentation, 2004, Yichang, China.

Lohrmann, A.: Monitoring Sediment Concentration with Acoustic Backscattering Instruments, Nortek Technical Note No.: 003, October 2001.

Staubli, T., Baumann, S.: Comparative measurements of velocity distributions with acoustic methods, IGHEM 2002, Toronto, Canada.

Copyright © 2006 Taylor & Francis Group plc, London, UK

Reservoir sedimentation: 1D model of turbidity currents and delta deposits

J. González, A. Tamburrino & Y. Niño
Department of Civil Engineering, University of Chile, Santiago, Chile

ABSTRACT: A 1D mathematical-numerical model simulating the flow and sediment deposition in a reservoir is presented. The flow is modeled using Saint-Venant equations discretized with a finite volume numerical scheme capable of dealing with transcritical flows. Evolution of coarse sediment deposits is accounted for by using a choice of four different available bedload relationships. Two of them are based on the surface grain-size distribution and include hiding effects. Modeling of fine sediment transport and deposition is accomplished by the simulation of a turbidity current, for which minor modifications to classical depth-averaged equations allow for a complete representation of the fine sediment fall velocity effect. The numerical scheme used for the flow is adapted and used for turbidity current modeling. The full model is tested in a real reservoir application. Results show that the model is able to reproduce the co-evolution of sediment deposits capturing all the unsteady effects, including the internal hydraulic jump development in the ponded turbidity current and its time evolution in response to variable boundary conditions.

1 INRODUCTION

A dam construction in a natural river breaks the balance between affluent and effluent sediment, and starts its accumulation inside the reservoir. The most important consequence in the long term is the loss of storage capacity. To recover this loss by constructing new dams is not necessarily a feasible choice, so planned management of sediments, supported by modeling tools is required.

Being Chile a mountainous country, most of its rivers have in their upper reach high slopes and an extended grain-size distribution. Most existing reservoirs in the country have been placed in the upper reaches and sediment deposition is a critical aspect of their design and evaluation. It affects directly the projected reservoir life and the mitigation procedures to be considered during operation. Not only the total volume of sediment affluent to the reservoir is a matter of interest, but the sediment deposit distribution is very important when sediment removing measures are developed and executed.

In the presence of high slopes, it is common to find that the river flow regime is nearly transcritical or supercritical. On the other hand, coarse-grain sediment transport and deposition in such flows are complex and nonlinear effects leading to vertical sorting and hiding are everywhere present on the bed. Finally, in most cases, a non-negligible amount of fine suspended sediment is present, thus, in the case of a reservoir, the development of a turbidity current is very probable.

At this time, we do not know of a 1D commercial model that can put all these phenomena together. Most of the existing software have problems to deal with supercritical flow regime, and poorly sorted grain-size distribution and turbidity current development are not considered or must be modeled with additional expensive modules. Here a 1D mathematical-numerical model is presented. The flow is solved numerically using a modified version of the conservative upwind finite volume scheme developed by Ying (2004), which requires no special treatment to capture steep gradients or discontinuities in the solution, being capable of dealing with transcritical and mixed-regime flows typical of Chilean rivers. For bedload computation four relationships are available in the model: the classical relations of Meyer-Peter & Müller (1948) and Ackers & White (1973) which are based on a single representative diameter and the relations of Parker (1990) and Wilcock & Crowe (2003) which are based on bed surface grain-size distribution and apply to poorly sorted sediments and account for hiding effects. In the turbidity current modeling the classical approach for entrainment velocity is modified and fall velocity effect is taken into account, resulting in a continuity equation that captures all the necessary

Copyright © 2006 Taylor & Francis Group plc, London, UK

hydrodynamic effects. A new formulation proposed by Toniolo (2003) is used for the computation of the plunging of the turbidity current.

2 FLOW MODEL

2.1 *Governing equations*

1D unsteady flow in a natural river with irregular cross-sections may be described by Saint-Venant equations. The conservative form of the equations is written as:

$$\frac{\partial \mathbf{U_f}}{\partial t} + \frac{\partial \mathbf{F}(\mathbf{U_f})}{\partial x} = \mathbf{S}(\mathbf{U_f}) \tag{1}$$

Where $\mathbf{U_f}$, $\mathbf{F}(\mathbf{U_f})$ and $\mathbf{S}(\mathbf{U_f})$ are, respectively, the vectors of conserved variables, fluxes and sources, defined as follows:

$$\mathbf{U_f} = \begin{bmatrix} A \\ Q \end{bmatrix}, \quad \mathbf{F}(\mathbf{U_f}) = \begin{bmatrix} Q \\ Q^2/A \end{bmatrix}$$

$$\mathbf{S}(\mathbf{U_f}) = \begin{bmatrix} 0 \\ -gA\dfrac{\partial Z}{\partial x} - g\dfrac{n^2 Q|Q|}{AR_h^{4/3}} \end{bmatrix} \tag{2}$$

where A = cross-sectional area; Q = discharge; g = gravitational acceleration; Z = water level; n = Manning coefficient; and R_h = hydraulic radius. Saint-Venant equations written in the above form have the advantage of using one source term to represent the pressure effect and the bed slope does not appear explicitly.

2.2 *Numerical scheme*

Since reservoir sedimentation simulations are often performed considering an extended period of time, a computationally efficient model is required. It is preferable then, that the numerical scheme be explicit performing the least number of operations per time interval as possible.

The numerical scheme used here was developed by Ying (2004). It consists of an explicit, conservative upwind finite volume scheme, which uses a weighted average for the pressure term, based on local Courant conditions. The scheme is robust and stable when the flow has a unique direction, but it presents some instabilities in the case of reversal flows. In this paper, a minor modification is applied to the flux computation in the case of reversal flows, making the scheme more stable when modeling a reservoir, where high depths and high cross-sectional area values are involved. The local direction of the flow when solving the momentum equation is determined based only on the flow direction at the node. The grid used is cell centered as shown in Figure 1. The grid has N grid points along x.

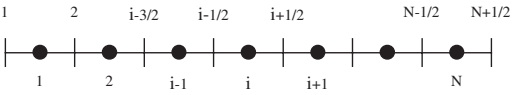


Figure 1. Definition sketch of the grid.

The variables are defined in the nodes and the fluxes are calculated at the interfaces.

Equation 1 integrated over the ith cell, yielding the following discretized equation:

$$\mathbf{U_f}_i^{n+1} = \mathbf{U_f}_i^{n} - \frac{\Delta t}{\Delta x_i}\left(\mathbf{F}_{i+1/2}^n - \mathbf{F}_{i-1/2}^n\right) + \Delta t \mathbf{S}_i \tag{3}$$

where Δx_i is the distance between interfaces surrounding node i and Δt is the time discretization. Superscript n indicates the time step. The flux at the interface is defined as:

$$\mathbf{F}_{i+1/2}^n = \begin{bmatrix} Q_{i+k}^n \\ \left(Q_{i+k}^n\right)^2 / A_{i+k}^n \end{bmatrix} \tag{4}$$

where $k = 0$ if $Q_i^n > 0$ and $Q_{i+1}^n > 0$; and $k = 1$ if $Q_i^n < 0$ and $Q_{i+1}^n < 0$. If reversal flow occurs at the interface, meaning that Q_i and Q_{i+1} have opposite sign, the flux is computed as:

$$\mathbf{F}_{i+1/2}^n = \begin{bmatrix} F_{i+1/2,1}^n \\ F_{i+1/2,2}^n \end{bmatrix} \tag{5}$$

$$F_{i+1/2,1}^n = \frac{Q_i^n + Q_{i+1}^n}{6} - \frac{2}{3} g A_i^n \Delta t \frac{Z_{i+1}^n - Z_i^n}{x_{i+1} - x_i} \tag{6}$$

$$F_{i+1/2,2}^n = \frac{\left(F_{i+1/2,1}^n\right)^2}{A_i^n} \tag{7}$$

This formulation could be interpreted as a correction for the average discharge at the interface, based on water surface gradient information. To evaluate the source term of Equation 3, the local flow direction is defined based on the discharge sign at the node. The source term is then evaluated as:

$$\mathbf{S}_i = \begin{bmatrix} 0 \\ -gA_i^{n+1}\left[w_1\left(\dfrac{\partial Z}{\partial x}\right)_{down} + w_2\left(\dfrac{\partial Z}{\partial x}\right)_{up}\right] - g\dfrac{n^2 Q_i^n |Q_i^n|}{\left(R_{h_i}^n\right)^{4/3} A_i^n} \end{bmatrix} \tag{8}$$

where w_1 and w_2 are weighting factors. The downstream and upstream water surface gradients are defined as:

$$\left(\frac{\partial Z}{\partial x}\right)_{down} = \frac{Z_{i+1-j}^{n+1} - Z_{i-j}^{n+1}}{x_{i+1-j} - x_{i-j}} \tag{9}$$

Copyright © 2006 Taylor & Francis Group plc, London, UK

$$\left(\frac{\partial Z}{\partial x}\right)_{up} = \frac{Z_{i+j}^{n+1} - Z_{i-1+j}^{n+1}}{x_{i+j} - x_{i-1+j}} \quad (10)$$

The weighting factors w_1 and w_2 are evaluated based on numerical local Courant number as follows:

$$w_1 = 1 - c_r^{down}, \quad w_2 = c_r^{up} \quad (11)$$

$$c_r^{down} = \frac{\Delta t}{x_{i+1-j} - x_{i-j}} \frac{V_{i+1-j}^n + V_{i-j}^n}{2} \quad (12)$$

$$c_r^{up} = \frac{\Delta t}{x_{i+j} - x_{i-1+j}} \frac{V_{i+j}^n + V_{i-1+j}^n}{2} \quad (13)$$

$$V_i^n = \left|Q_i^n\right| / A_i^n \quad (14)$$

The subscript j is defined as:

$$j = \begin{cases} 0 & if \quad Q_i^n > 0 \\ 1 & else \end{cases} \quad (15)$$

The scheme is subject to the Courant-Friedrichs-Lewy stability condition, that is:

$$N_{CFL} = \max\left[\frac{\Delta t}{\Delta x_i}\left(\left|V_i\right| + \sqrt{gA_i / l_{wi}}\right)\right] \le 1 \quad (1 \le i \le N) \quad (16)$$

where l_{wi} is the top width of the channel at cell i.

Boundary conditions are treated by introducing two ghost cells to the computational domain. For the reservoir modeling, water surface level is specified at the downstream ghost cell and discharge is determined by a zero order extrapolation from the last interior node. At the upstream ghost cell, discharge is always specified. In the case of subcritical inflow, water surface level is calculated by a linear extrapolation based on values of two adjacent interior cells. If the inflow is supercritical the water level surface is specified at the upstream ghost cell.

3 BEDLOAD TRANSPORT MODEL

3.1 *Governing equations*

Since trapezoidal cross-sections are being used to represent the river and the reservoir, bed evolution must be calculated using an appropriate conservative form of Exner's equation. Conservation of mass over the control volume of Figure 2 states that:

$$\frac{\partial A_s}{\partial t} + \frac{1}{1-\lambda_s}\frac{\partial Qs}{\partial x} = 0 \quad (17)$$

where $A_s =$ deposit cross-sectional area; $Q_s =$ volumetric bedload discharge; and λ_s is porosity of the deposit.

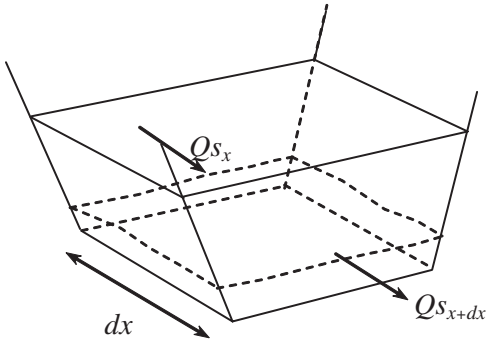


Figure 2. Control volume sketch for sediment mass conservation.



Figure 3. Definition sketch for bedload transport model.

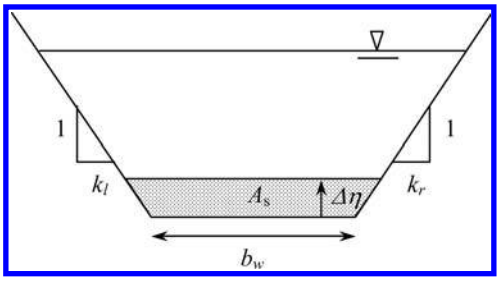


Figure 4. Sketch of cross-section with a sediment deposit.

3.2 *Numerical scheme*

Volumetric bedload discharge is determined from the hydraulic conditions, which are known at the nodes. In order to get a discretized equation for bed evolution, the integration of Equation 17 must be performed with a control volume with interfaces located at cell nodes. The grid used for integrating Equation 17 is shown in Figure 3.

The integration is carried out over the control volume, which involves nodes $i-1$ and i and between instants t and $t+\Delta t$. The increment of deposited sediment cross-sectional area is given by:

$$\overline{A_s}^{n+1} = -\frac{\Delta t}{1-\lambda_s}\frac{Qs_i^n - Qs_{i-1}^n}{x_i - x_{i-1}} \quad (18)$$

where the bar over A_s denotes a spatial mean sediment deposit cross-sectional area between nodes i-1 and i, and it has been considered that the mean volumetric bedload discharge over the time interval can be approximated by its value at the beginning. Figure 4 shows

Copyright © 2006 Taylor & Francis Group plc, London, UK

the relation between the cross-section of the sediment deposit and bed elevation.

$$A_s = k_m \Delta\eta^2 + b_w \Delta\eta \tag{19}$$

$$k_m = \frac{k_l + k_r}{2} \tag{20}$$

The mean cross-sectional area of sediment deposit is defined by averaging the geometric properties of cross-sections at nodes $i-1$ and i.

$$\overline{A_s} = \overline{k_m}\Delta\eta^2 + \overline{b_w}\Delta\eta \tag{21}$$

$$\overline{k_m} = \frac{k_{mi} + k_{mi-1}}{2}, \quad \overline{b_w} = \frac{b_{wi} + b_{wi-1}}{2} \tag{22}$$

Replacing Equation 21 into Equation 18 yields the expression for the bed elevation change at the end of the time interval Δt:

$$\overline{k_m}\Delta\eta_i^2 + \overline{b_w}\Delta\eta_i + \frac{\Delta t}{1-\lambda_s}\frac{Qs_i^n - Qs_{i-1}^n}{x_i - x_{i-1}} = 0 \tag{23}$$

At this point, the volumetric bedload discharge must be calculated in order to get the bed elevation change. For this purpose, four relationships have been implemented in the model and can be selected by the user. These are the relations by: Meyer-Peter & Müller (1948), Ackers & White (1973), Parker (1990), and Wilcock & Crowe (2003). They have been extensively described in literature. The first two relationships are based on incipient motion criteria and are recommended for uniform sediment. Many comments can be found in literature regarding the bedload rates overestimation given by Meyer-Peter & Müller relation (Jäggi 1983, Smart 1984, and Hunziker & Jäggi 2002). The parameters appearing in the Ackers & White formulae were calibrated from flows with Froude numbers less than 0.8 and very few experiments were made using particles larger than 2.5 mm. On the other hand, the relationships proposed by Parker, and Wilcock & Crowe have been developed for gravel mixtures and are based on bed surface grain-size distributions. They include hiding effects and are more appropriate for rivers whose bed exhibits poorly sorted grain-size distributions. The four relations were implemented in the model in order to observe the differences between their results when they are applied to steep mountains rivers.

The boundary condition for inflowing sediment load is treated following the same ideas used for the liquid flow, i.e. the volumetric bedload discharge at upstream ghost cell, is obtained by a linear extrapolation from the interior domain.

4 TURBIDITY CURRENT MODEL

The fine sediment transport is modeled here considering the development of a turbidity current along the reservoir bottom. Since the cross-sections used in the model are not rectangular, cross-section averaged equations of motion were developed. However, these equations contain many unknown shape factors resulting from the similarity hypothesis, which are impossible to estimate, as the required empirical data are not currently available. Because of this, only the classical depth-averaged per unit width equations were used.

When a turbidity current reaches the reservoir dam, an internal hydraulic jump is developed and the flow regime changes from supercritical to subcritical. The supercritical zone of the current has high levels of turbulence which render a diffuse interface between the current and the quiescent water above it, enhancing water entrainment across the interface. In addition, entrainment of sediment into suspension from the bottom is possible. In the subcritical regime the turbulence decays and the interface become sharp and well defined. In this regime, the entrainment of water and sediment from the quiescent water body and the bottom of the reservoir is damped.

Although there is no outflow of the turbidity current, a steady interface in the subcritical zone can be developed. The continuous inflow of water is evacuated through the interface while the inflowing sediment is deposited at the reservoir bottom. Recently, Toniolo (2003) has developed a set of equations that represent adequately both regimes of a ponded turbidity current, by integrating the equations of motion between the bed and the interface of the current. In this paper, an equivalent set of corrected equations is presented, in which suspended sediment fall velocity effect is incorporated in the water entrainment.

4.1 *Fall velocity effect*

The depth-averaged volume continuity equation of a turbidity current is (Parker et al.1986):

$$\frac{\partial h_c}{\partial t} + \frac{\partial U h_c}{\partial x} = w_e \tag{24}$$

where U is the depth-averaged velocity; h_c is the thickness of the boundary layer; and w_e is a water entrainment velocity arising from the nature of boundary layer approximations used through integration. This velocity is commonly related to the depth-averaged velocity, U, through a dimensionless entrainment coefficient, e_w, as follows:

$$w_e = e_w U \tag{25}$$

The entrainment coefficient depends on the Richardson number, Ri:

$$Ri = \frac{RgCh_c}{U^2} \tag{26}$$

where R is the submerged specific gravity of the sediment; and C is the depth-averaged volumetric concentration of suspended sediment.

Copyright © 2006 Taylor & Francis Group plc, London, UK

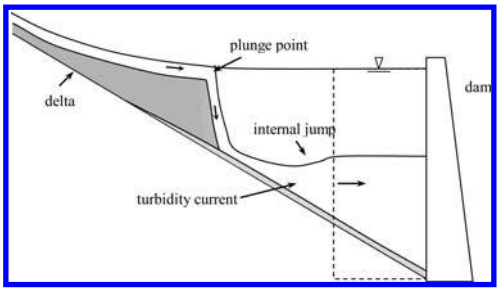


Figure 5. Definition sketch of a reservoir with a ponded turbidity current.

A model for the entrainment coefficient e_w has been proposed by Parker et al. (1986):

$$e_w(Ri) = \frac{0.00154}{0.0204 + Ri} \tag{27}$$

This model states the vanishing of water entrainment with the increase of the Richardson number, representing adequately this phenomenon in the subcritical regime, where Ri becomes large. Replacing Equation 25 into Equation 24, the continuity equation becomes:

$$\frac{\partial h_c}{\partial t} + \frac{\partial U h_c}{\partial x} = e_w U \tag{28}$$

This equation cannot be applied to model a ponded turbidity current. This can be seen when the control volume shown in Figure 5 is considered in the volume conservation analysis. If Equation 28 is integrated in the longitudinal direction along the volume, between positions x_0 and x_m, and considering that in the subcritical regime the water entrainment vanishes, it is found that:

$$\frac{\partial}{\partial t}\int_{xo}^{xm} h_c dx = U h_c\big|_{xo} \tag{29}$$

Since the affluent volume of the turbidity current is positive, Equation 29 states that the turbidity current elevation is rising. This is due to the fact that Equation 28 does not recognize the role played by the sediment fall velocity in the continuity of volume. If the advection would be negligible at the current, fall velocity would make the interface to settle down toward the bed. Water would escape from the solid-water mixture forming the turbidity current while its depth is decreasing at a rate equal to fall velocity, v_s. Thus, entrainment velocity, w_e, would not be null but negative since water is leaving the current. Thus, an alternative representation of entrainment velocity is proposed in this paper:

$$w_e = e_w^* U - v_s \tag{30}$$

where e_w^* is a new dimensionless entrainment coefficient which must tend to zero as the Richardson number increases, just like the original e_w coefficient. Since the model of Parker et al. (1986) for entrainment coefficient has been extensively used for modeling supercritical turbidity currents, it will be used here by introducing the parameter δ such that:

$$w_e = e_w U - \delta v_s \tag{31}$$

The value of δ is equal to unity for the subcritical regime and zero for the supercritical one. Finally, considering that the turbidity current is purely depositional, the equations used to modeling the ponded turbidity current, (volume conservation, suspended sediment mass conservation and momentum conservation respectively) are:

$$\frac{\partial h_c}{\partial t} + \frac{\partial U h_c}{\partial x} = e_w U - \delta v_s \tag{32}$$

$$\frac{\partial C h_c}{\partial t} + \frac{\partial U C h_c}{\partial x} = -v_s C \tag{33}$$

$$\frac{\partial U h_c}{\partial t} + \frac{\partial U^2 h_c}{\partial x} = -\frac{1}{2} Rg \frac{\partial C h_c^2}{\partial x} + RgSCh_c - c_f U^2 \tag{34}$$

where S denotes the bed slope and c_f is a friction coefficient for the turbidity current.

4.2 *Numerical scheme*

In order to use Ying's numerical scheme for solving the turbidity current equations, Equation 34 is rearranged as:

$$\frac{\partial U h_c}{\partial t} + \frac{\partial U^2 h_c}{\partial x} = -\frac{1}{2} Rgh_c^2 \frac{\partial C}{\partial x} - RgCh_c \frac{\partial Z_c}{\partial x} - c_f U^2 \tag{35}$$

where Z_c is the elevation of the current interface. Equations 32, 33 and 35 are written in conservative form as:

$$\frac{\partial \mathbf{U}_{ct}}{\partial t} + \frac{\partial \mathbf{F}_{ct}(\mathbf{U}_{ct})}{\partial x} = \mathbf{S}_{ct}(\mathbf{U}_{ct}) \tag{36}$$

where $\mathbf{U}_{ct}$, $\mathbf{F}_{ct}$ and $\mathbf{S}_{ct}$ are the corresponding variables, fluxes and source terms vectors defined as follows:

$$\mathbf{U}_{ct} = \begin{bmatrix} h_c \\ Ch_c \\ Uh_c \end{bmatrix}, \quad \mathbf{F}_{ct}(\mathbf{U}_{ct}) = \begin{bmatrix} Uh_c \\ UCh_c \\ U^2 h_c \end{bmatrix}$$

Copyright © 2006 Taylor & Francis Group plc, London, UK

$$\mathbf{S}_{ct}(\mathbf{U}_{ct}) = \begin{bmatrix} e_w U - \delta v_s \\ -v_s C \\ -\frac{1}{2} R g h_c^2 \frac{\partial C}{\partial x} - R g C h_c \frac{\partial Z_c}{\partial x} - c_f U^2 \end{bmatrix} \quad (37)$$

The grid used to discretize Equation 36 is the same that was used for the flow (Fig. 1). Following the same procedure used for the flow, yields:

$$\mathbf{U}_{ct\,i}^{\,n+1} = \mathbf{U}_{ct\,i}^{\,n} - \frac{\Delta t}{\Delta x_i}\left(\mathbf{F}_{ct\,i+1/2}^{\,n} - \mathbf{F}_{ct\,i-1/2}^{\,n}\right) + \Delta t \mathbf{S}_{ct\,i} \quad (38)$$

The velocity of the current is taken here to be positive so the fluxes are computed as:

$$\mathbf{F}_{ct\,i+1/2}^{\,n} = \begin{bmatrix} U_i^n h_{c\,i}^n \\ U_i^n C_i^n h_{c\,i}^n \\ \left(U_i^n\right)^2 h_{ci} \end{bmatrix} \quad (39)$$

The source term vector is evaluated as:

$$\mathbf{S}_{ct\,i} = \begin{bmatrix} S_{ct\,i,1} \\ S_{ct\,i,2} \\ S_{ct\,i,3} \end{bmatrix} \quad (40)$$

where:

$$\begin{aligned} S_{ct\,i,1} &= e_{wi}^{\,n} U_i^n - \delta_i^n v_s \\ S_{ct\,i,2} &= -v_s C_i^n \\ S_{ct\,i,3} &= -\frac{1}{2} R g \left(h_c^2\right)_i^{n+1} \sum w_k \left(\frac{\partial C}{\partial x}\right)_k \\ &\quad - R g \left(C h_c\right)_i^{n+1} \sum w_k \left(\frac{\partial Z_c}{\partial x}\right)_k - c_f \left(U_i^n\right)^2 \end{aligned} \quad (41)$$

The dimensionless entrainment coefficient is evaluated from:

$$e_{wi}^{\,n} = \frac{0.00154}{0.0204 + Ri_i^n} \quad (42)$$

$$Ri_i^n = \frac{R g C_i^n h_{c\,i}^n}{U_i^n} \quad (43)$$

$$\delta_i^n = \begin{cases} 0 & if \quad Ri_i^n < 1 \\ 1 & else \end{cases} \quad (44)$$

The weighted sums in the momentum source term are computed from:

$$\begin{aligned} \sum w_k \left(\frac{\partial C}{\partial x}\right)_k &= w_1 \left(\frac{\partial C}{\partial x}\right)_{down} + w_2 \left(\frac{\partial C}{\partial x}\right)_{up} \\ \sum w_k \left(\frac{\partial Z_c}{\partial x}\right)_k &= w_1 \left(\frac{\partial Z_c}{\partial x}\right)_{down} + w_2 \left(\frac{\partial Z_c}{\partial x}\right)_{up} \end{aligned} \quad (45)$$

where the downstream and upstream gradient are defined as:

$$\left(\frac{\partial C}{\partial x}\right)_{down} = \frac{C_{i+1}^{n+1} - C_i^{n+1}}{x_{i+1} - x_i} \quad (46)$$

$$\left(\frac{\partial C}{\partial x}\right)_{up} = \frac{C_i^{n+1} - C_{i-1}^{n+1}}{x_i - x_{i-1}} \quad (47)$$

$$\left(\frac{\partial Z_c}{\partial x}\right)_{down} = \frac{Z_{c\,i+1}^{\,n+1} - Z_{ci}^{\,n+1}}{x_{i+1} - x_i} \quad (48)$$

$$\left(\frac{\partial Z_c}{\partial x}\right)_{up} = \frac{Z_{ci}^{\,n+1} - Z_{c\,i-1}^{\,n+1}}{x_i - x_{i-1}} \quad (49)$$

the weighting factors are computed in the same way they are for the flow, but this time using the turbidity current velocity, i.e:

$$w_1 = 1 - c_{rct}^{down}, \quad w_2 = c_{rct}^{up} \quad (50)$$

$$c_r^{down} = \frac{\Delta t}{x_{i+1} - x_i} \frac{U_{i+1}^n + U_i^n}{2} \quad (51)$$

$$c_r^{up} = \frac{\Delta t}{x_i - x_{i-1}} \frac{U_i^n + U_{i-1}^n}{2} \quad (52)$$

The stability condition now reads:

$$N_{CFLc} = \max\left[\frac{\Delta t}{\Delta x_i}\left(\left|U_i\right| + \sqrt{g h_{ci}}\right)\right] \le 1 \quad (1 \le i \le N) \quad (53)$$

Turbidity current thickness, h_c; depth-averaged velocity, U; and volumetric depth averaged concentration C are obtained from the resulting variables vector $\mathbf{U}_{ct}$ at instant $n+1$.

4.3 *Plunging*

Upstream boundary conditions for the turbidity current are given by the plunging phenomena. To determine the point where the current plunges over the delta, the formulation proposed by Toniolo (2003) is used.

Copyright © 2006 Taylor & Francis Group plc, London, UK

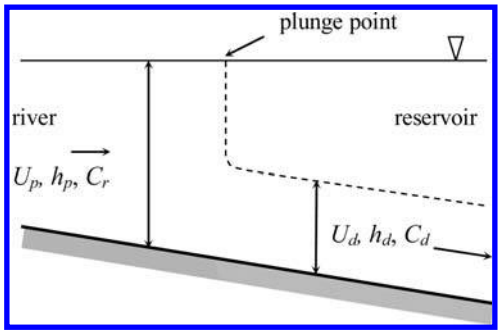


Figure 6. Definition sketch of plunging.

Accordingly to this, the relation between the current depth before and after plunging is determined from:

$$\frac{1}{\gamma_p^2}(1-\varphi)^3 - \frac{1}{\gamma_p^2}\frac{(1-\varphi)^3}{\varphi}(1+\gamma_p)^2 - (1-\varphi)^2 + 1 - \frac{\varphi^2}{1+\gamma_p} = 0 \quad (54)$$

where γ_p denotes the mixing coefficient and ϕ is defined as:

$$\varphi = \frac{h_d}{h_p} \quad (55)$$

Being h_p the depth of the turbidity current just at the plunge point and h_d the depth of the submerged turbidity current just after plunging (Fig. 6). The submerged turbidity current variables, which constitute the upstream boundary conditions for the current, are then obtained as follows: with the value of ϕ determined from Equation 54, and the value of the inflowing suspended sediment concentration at the river, *Cr*, the densimetric Froude number of plunge point, Fr_{dp} is obtained from:

$$Fr_{dp}^2 = \frac{1}{2\gamma_p^2}(1-\varphi)^3 \quad (56)$$

where Fr_{dp}^2 is defined as:

$$Fr_{dp}^2 = \frac{U_p^2}{RC_r g h_p} \quad (57)$$

U_p and h_p are determined from the section of the river where this densimetric Froude number occurs. h_d is obtained using h_p in Equation 55. The densimetric Froude number of the submerged turbidity current is computed from:

$$Fr_{dd}^2 = Fr_{dp}^2 \frac{(1+\gamma_p)^3}{\varphi^3} \quad (58)$$

where Fr_{dd}^2 is given by:

$$Fr_{dd}^2 = \frac{U_d^2}{RC_d g h_d} \quad (59)$$

where C_d is the volumetric concentration of the submerged turbidity current. This is determined from the following relation:

$$C_d = \frac{C_r}{1+\gamma_p} \quad (60)$$

Using Equations 58, 59 and 60, the depth-averaged velocity of the submerged current is obtained.

4.4 *Downstream boundary conditions*

In the suspended sediment mass conservation equation for turbidity current it is considered that particle velocity in the longitudinal direction is equal to flow velocity. Numerical simulations of the turbidity current have shown that a better treatment for downstream boundary condition is reached considering velocity at this location equal to average flow velocity, instead of zero velocity. Simulations have also shown that a downstream zero velocity condition does not allow concentration changes to travel along the turbidity current.

5 MODEL APPLICATION

The three models described in the previous sections were implemented together in a computational code written in Fortran90 language. The resulting software works using text data files as input and output. The input data for the model are: parameters such as number of nodes of the grid, simulation time, Courant numbers for flow and turbidity current, selected bedload relation, Manning coefficient, fall velocity, mixing coefficient and friction coefficient for turbidity current, etc; initial state for the discharge, water surface elevation and bed elevation; boundary conditions for discharge and volumetric concentration of suspended sediment in the river at upstream end, and water surface level at downstream end; grain-size distribution of the bed surface and cross-sectional properties such as basal width and side slopes.

The initial condition for turbidity current is determined internally in the model. In addition, it is considered that if the plunge point occurs before the delta toe, then the turbidity current flows without changing its hydraulic properties until that point. On the other hand, if the plunge point occurs beyond the delta toe, the inflowing suspended sediment concentration remains constant and equal to C_r until the plunge point.

To test the integrated model performance, it was applied using data from a real reservoir project called Puntilla del Viento placed at Aconcagua river in central Chile. Puntilla del Viento is a projected reservoir

Copyright © 2006 Taylor & Francis Group plc, London, UK

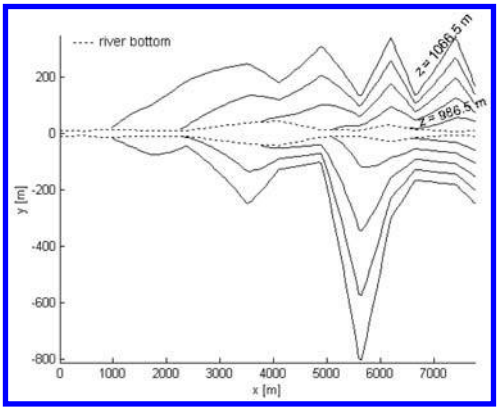


Figure 7. Isolevel curves for Puntilla del Viento reservoir referenced to sea level.

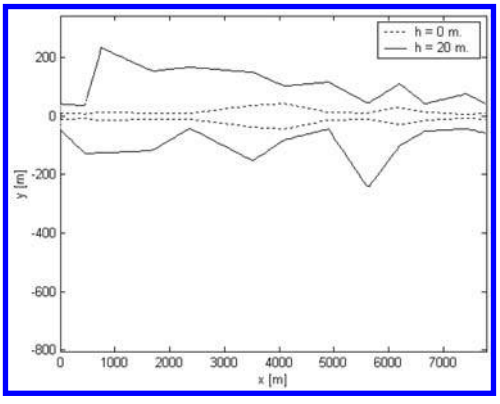


Figure 8. River bottom width and top width at a depth of 20 m.

that would be located at the upper reach of Aconcagua river. The river is born in the Cordillera de Los Andes and crosses the middle valleys of central Chile towards the Pacific Ocean. This example has been selected to test the model because it constitutes a challenge given the topographic configuration and the high slope of the river at the place of the project. The main objective of this application was to test the capabilities of the model when applied to a real engineering problem. The present application did not intend to solve an engineering project, where more reliable and accurate input data would be required. The geometry of the river and reservoir is described in Figures 7 and 8.

The downstream water depth was considered constant and equal to 100 m. The bottom of the reservoir at the dam is located at an elevation of 966.5 m referenced to sea level. The grain-size distribution used in the application was obtained in the lower reach of the Aconcagua River, being the only one available when the model was run (Fig. 9). This has to be kept in mind when analyzing the outcome of the model. The results

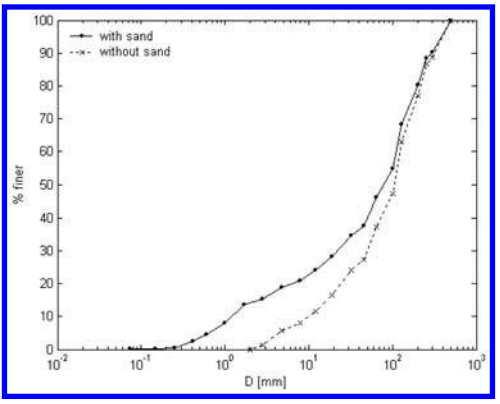


Figure 9. Grain-size distribution used for bed material.

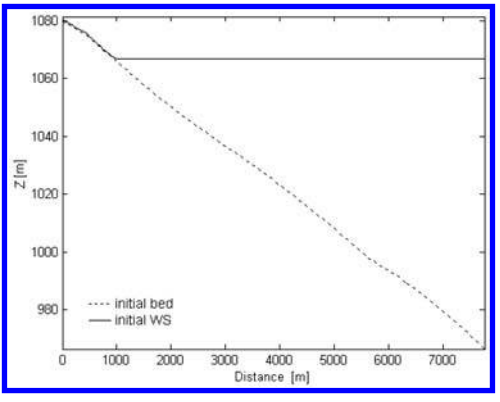


Figure 10. Initial condition for bed and water surface elevation.

obtained after using these data highlight the importance of the adequate representation of bed material. The initial conditions for bed and water surface elevation are shown in Figure 10, and the flow Froude number at that condition is shown in Figure 11. These conditions have been determined with an initial discharge of 22.5 m^3/s and a Manning coefficient of 0.03.

The mixing coefficient for plunging, γ_p, is taken to be equal to 0.6 and the friction coefficient for the turbidity current, c_f, equal to 0.01. Both values have been selected based on previous experimental work (Toniolo 2003, Kostic & Parker 2003a,b). Fall velocity for fine sediment particles was taken equal to 0.001 m/s, and the porosity of the deposit is taken to be 0.3 for both kind of sediments.

The simulation time is one year. The inflowing discharge was obtained from historical data collected between 27/08/91 and 27/08/92. Suspended sediment concentration in the river was related to discharge from samples taken in the river and is given by (Benitez 1997):

$$C_r = 4.741 \cdot 10^{-7} Q^{1.316} \quad (61)$$

Copyright © 2006 Taylor & Francis Group plc, London, UK

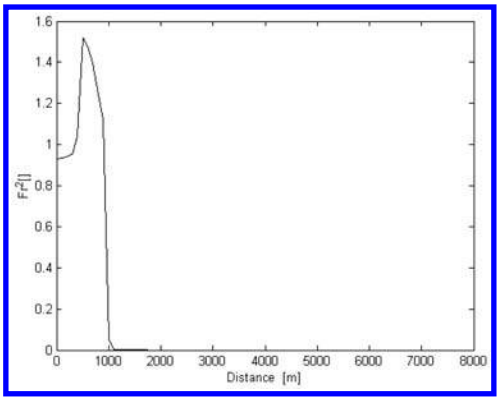


Figure 11. Initial profile of the square of flow Froude number.

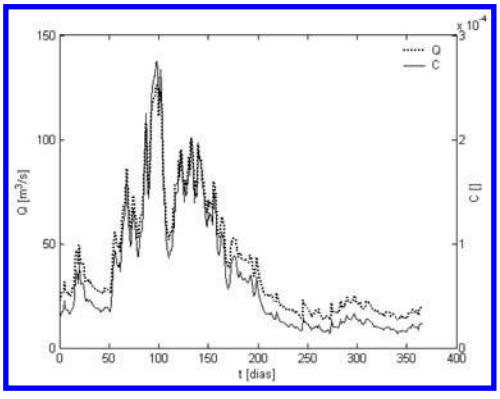


Figure 12. Discharge and suspended sediment concentration statistics used for upstream boundary condition.

where Q is in m^3/s. No attempt was made to discuss the accuracy of this equation. It was used only as an available relationship. It can be seen that according to Equation 61, the resulting concentrations are very small. In spite of that, a turbidity current will be modeled anyway, even when there is a high probability that this becomes dilute. The discharge data and corresponding suspended sediment concentration is presented in Figure 12.

The model was applied using the relations of Meyer-Peter & Müller and Wilcock & Crowe for bedload computation. In order to compare their results, a zoom of the delta deposit with bed profiles at the end of each month is presented in Figures 13 and 14, respectively. The comparison between final bed elevations using each relation is presented in Figures 15 and 16. Figure 16 shows that the turbidity current is strongly diluted. The almost null change in bed elevation of the zone near the dam indicates that turbidity current vanishes before it reaches the dam. However, its effect near the delta toe is still appreciable, rising the bed elevation.

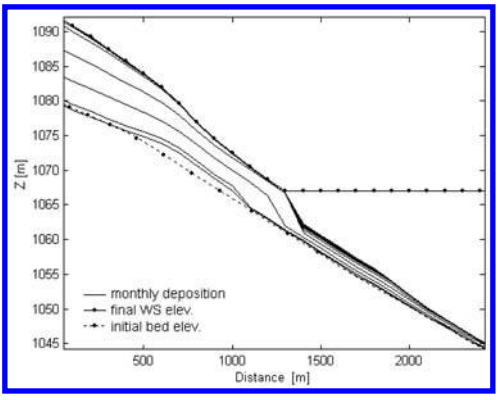


Figure 13. Evolution of sediment deposit obtained using the relation of Meyer-Peter & Müller. Zoom to the delta zone.

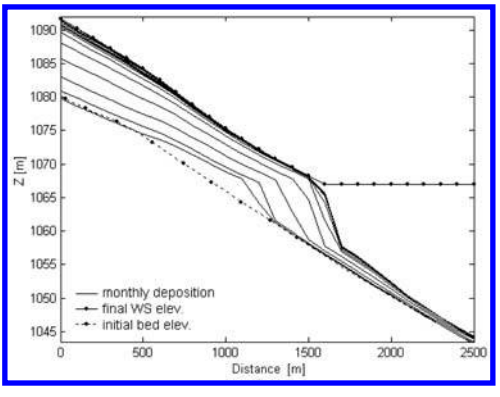


Figure 14. Evolution of sediment deposit obtained using the relation of Wilcock & Crowe. Zoom to the delta zone.

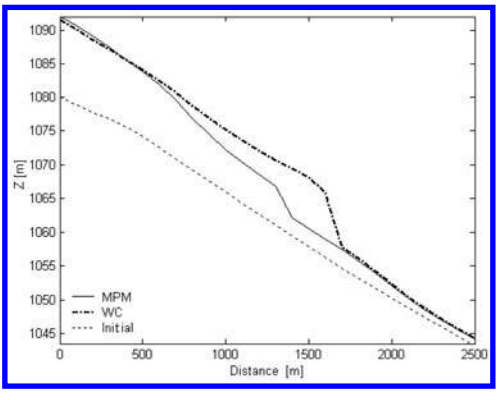


Figure 15. Comparison of the final bed elevations obtained from the application of Meyer-Peter & Müller and Wilcock & Crowe relations. Zoom to the delta zone.

The exaggerated rising of bed elevations at the upstream end obtained from the application of both bedload relations, is a consequence of using a grain-size distribution which is not representative of a steep

Copyright © 2006 Taylor & Francis Group plc, London, UK

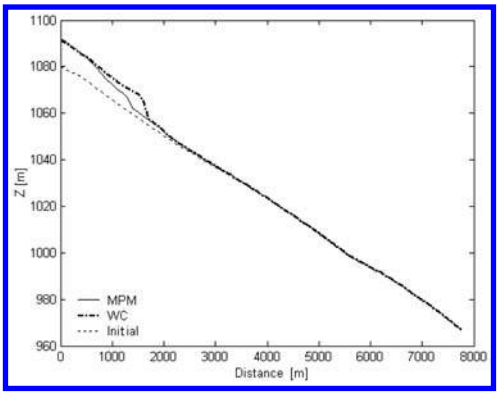


Figure 16. Final bed elevations obtained from the application of Meyer-Peter & Müller and Wilcock & Crowe relations.

slope mountain river. The geometric mean diameter of this distribution is about 39 mm which is a very small value for a river with such a high slope. Generally, the surface bed material at the upper reach of this kind of rivers is characterized by a large amount of boulders and coarse gravel particles.

The sand content of the grain-size distribution can also explain why the deposit determined using the relation of Wilcock & Crowe is larger than that obtained with the relation of Meyer-Peter and Müller. According to the former, during flows capable to mobilize the bed material, the sand content in the grain-size distribution acts to increase the transport of gravels. Furthermore, the relation of Wilcock and Crowe is not based on a critical condition for motion, in contrast to Meyer-Peter & Müller relation which can cease the transport for low flows.

6 CONCLUSIONS

A 1D reservoir sedimentation model that includes coarse and fine sediment transport and deposition has been developed. The model represents natural geometry using trapezoidal cross-sectional areas with variable properties in the longitudinal direction. A new approach to the interfacial entrainment velocity for turbidity currents has been proposed. The resulting equations give a complete representation of the suspended sediment fall velocity hydrodynamic effect. The resulting set of equations represents adequately both regimes of the turbidity current.

A finite volume numerical scheme developed for open-channel flows has been adapted to solve the turbidity current equations.

The model was tested using data from a real engineering project, showing the capability to deal with the characteristics of a steep mountain river, poorly sorted grain-size distribution of bed sediment and to incorporate deposition processes associated to turbidity currents. Future work should be oriented to incorporate in the model the change in time of surface bed grain-size distribution due to deposition. Extension of the model to represent natural cross- sectional geometry is almost direct.

ACKNOWLEDGEMENT

The authors acknowledge the funding provided by the Chilean Fund for Science and Technology, FONDECYT, by means of the grant N°1040494.

REFERENCES

Ackers, P., and White, W. R. 1973. Sediment Transport: New Approach and Análisis. Journal of Hydraulic Division 99(HY11): 2041–2060.

Benítez, A. 1997. Estudio de la Sedimentación Embalse Puntilla del Viento. Departamento de Proyectos, Dirección de Riego, Ministerio de Obras Públicas.

Hunziker, R. P., and Jäggi, M. N. R. 2002. Grain Sorting Processes. Journal of Hydraulic Engineering, ASCE 128(12): 1060–1068.

Kostic, S., and Parker, G. 2003a. Progradational Sand-Mud Deltas in Lakes and Reservoirs. Part 1. Theory and Numerical Modeling. Journal of Hydraulic Research (41)2: 127–140.

Kostic, S., and Parker, G. 2003b. Progradational Sand-Mud Deltas in Lakes and Reservoirs. Part 2. Experiments and Numerical Simulation. Journal of Hydraulic Research.(41)2: 141–152.

Meyer-Peter, E., and Müller, R. 1948. Formulas for Bed-load Transport. Proceedings, 2nd Congress I.A.H.R., Stockholm.

Parker, G. 1990. Surface-based Bedload Transport Relation for Gravel Rivers. Journal of Hydraulic Research (28)4: 417–436.

Parker, G., Fukushima, Y., and Pantin, H. M. 1986. Self-Accelerating Turbidity Currents. Journal of Fluid Mechanics. (171): 145–181.

Smart, G. M. 1984. Sediment Transport Formula for Steep Channels. Journal of Hydraulic Engineering, ASCE (110)3: 267–276.

Toniolo, H. 2003. Debris Flow and Turbidity Current Deposition in the Deep Sea and Reservoirs. Ph.D. Thesis, University of Minnesota 233 p.

Wilcock, P., and Crowe, C. 2003. Surface-based Transport Model for Mixed-Size Sediment. Journal of Hydraulic Engineering, ASCE (129)2: 120–128.

Ying, X., Khan, A. A., and Wang, S. S. 2004. Upwind Conservative Scheme for the Saint-Venant Equations. Journal of Hydraulic Engineering, ASCE (130)10: 967–987.

Copyright © 2006 Taylor & Francis Group plc, London, UK

Jets opposing flow on inclines

J. Bühler
Inst. of Environmental Engineering, ETH, Zurich, Switzerland

Ch. Oehy & A.J. Schleiss
Laboratory of Hydraulic Constructions, EPFL, Lausanne, Switzerland

ABSTRACT: Tracer-based scales for the depth and velocity of gravity currents, and a tentative extension of previous entrainment relations to coflowing ambients are proposed. These scales are consistent with the conventional ones used for open channel flows. They are used here to formulate conservation equations for flows on inclines, which are backed up by water jets directed upstream. The corresponding results for a single layer are compared with experiments carried out for this study.

1 INTRODUCTION

One well-known cause of reservoir siltation are sediment laden inflows which occur in the aftermath of intense rainstorms. After entering a reservoir, such flows tend to plunge to the bottom due to their excess density, and to follow the thalweg as turbidity currents. Most of the sediment is eventually deposited near the dam, and can impede the operation of the bottom outlets. A number of methods have been proposed for slowing down or blocking such turbidity currents along their path, and to let them deposit their load before reaching the dam. They include the installation of permeable screens, obstacles or bubble curtains (Oehy 2003, Oehy & Schleiss 2003, 2005). The concept examined in the present study is to use a number of water jets directed against the oncoming flow.

Water jets can also be used to induce a jump at the tail end of a spillway, or to prevent scour in a river (e.g. Wilson 1977). The corresponding momentum and continuity equations are, therefore, derived for both internal flows and flows in open channels. In contrast to previous studies on single layer flows, the present one is on jets entering obliquely from above, and the results are expressed by a single curve. In two-layer flows oscillations of large amplitude may occur when a jet hits a moving interface (Cotel et al. 1997). As the causes are not well understood yet, experiments for single layer flows were carried out as a first step. A few complementary experiments for turbidity currents were carried out by Oehy (2003), and showed that the sedimentation can be effectively enhanced by counterflowing jets.

In a first section, flow scales for the average depth, velocity and density of gravity currents are proposed, which are based on the density distribution instead of the velocity distribution, and a tentative entrainment relation for gravity currents in a coflowing ambient fluid is outlined. In a second section these flow scales are used to derive the conservation equations for internal and open channel flows backed up by jets. In the third section the result of this analysis is compared with experimental results for single layers, which were obtained in the laboratory of the Institute of Environmental Engineering (formerly IHW) in Zurich. Conclusions of the study are summarized at the end.

2 DEPTH AND VELOCITY SCALES FOR GRAVITY CURRENTS DERIVED FROM THE DENSITY DISTRIBUTION

An important difference between open channel flows and gravity currents on inclines is that the free water surface is much sharper than the upper interface of gravity driven underflows. The surface level of open channel flows is defined by the density jump, as well as by the lack of mixing between the two media, and the pressure distribution is close to hydrostatic in gradually varying flows. Deviations from the average velocity are taken into account by shape constants in the energy and momentum equations, respectively.

A quite different set of flow scales, the maximum velocity and velocity half width, has been used for free shear flows, possibly because early experiments were mainly carried out in wind tunnels on wakes and other nonbouoyant flows without a source of mass. In a related approach, Ellison & Turner (1959) (referred to as E & T) used integrals over the non-Gaussian velocity

Copyright © 2006 Taylor & Francis Group plc, London, UK

distribution in gravity currents to obtain a measure for their average depth H, and their streamwise excess velocity U relative to the ambient. In the frame of reference shown in Figure 1 they related these scales to flux integrals by setting

$$UH = \int (u^* - u_a)\, dy$$

$$U^2 H = \int (u^* - u_a)^2 dy$$

$$(U + u_a)\Delta H = g \int u^* \frac{\rho^* - \rho_a}{\rho_a} dy = B$$

Δ is the scale for the effective gravitational acceleration, B is the buoyancy flux, the star denotes mean local values, and the index a refers to the ambient (i.e. upper) layer.

The density distribution was related to these scales by shape constants S_1 and S_2 according to

$$S_1 \Delta H^2 = 2g \int \frac{\rho^* - \rho_a}{\rho_a}\, y\ dy$$

$$S_2 \Delta H = g \int \frac{\rho^* - \rho_a}{\rho_a}\ dy$$

In the spirit of a well-known approach by Morton, Taylor and Turner (1956) for steady free shear flows and thermals, the entrainment of fluid from the upper layer was specified by an entrainment function E as

$$\frac{d}{dx}\left[H(U + u_a)\right] = EU \qquad (1)$$

For gravity currents, E is a function of the Richardson number $Ri_E = \Delta H \cos\varphi / U^2$, where φ is the slope angle. The authors also carried out experiments on saline gravity currents without coflow ($u_a = 0$), and determined the entrainment function E for different slopes. The shape constants varied in the range from 0.2 to 0.3 for S_1, and 0.6 to 0.9 for S_2. From the velocity and relative excess density distribution they show for a slope of $\varphi = 14°$, it is possible to evaluate S_1 as 0.2 and S_2 as 0.64. An important result for $u_a = 0$ is that the excess velocity U and Ri become constant when the flow reaches an equilibrium state. An analogous transition occurs when free buoyant jets turn into plumes.

Princevac et al. (2005) determined profiles of mean velocity and potential temperature for katabatic winds in an ambient coflow. They used E to specify the excess volume flux according to

$$\frac{d}{dx}(HU) = EU \qquad (2)$$

and found that the entrainment in flows of such geophysical scales is substantially larger than in the earlier laboratory experiments.

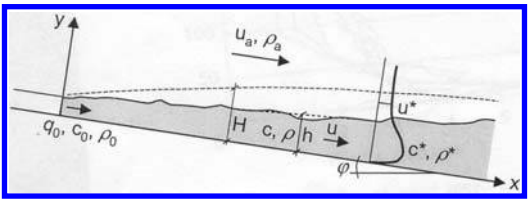


Figure 1. Velocity- and tracer-based flow depths H and h for a gravity current in deep water.

For E = 0 the conservation equations of E & T are consistent with the Bresse equations for open channel flows, except for the definition of the flow scales. Full consistency can be achieved by adopting the same approach for both flows, i.e. by deriving the depth and velocity scales of gravity currents from the density distribution as well. It should be noted that such mass-based flow scales have also been used for thermals, the extent of which was determined in laboratory experiments by adding dye to the flow (Scorer 1997). The momentum of clear ambient fluid, which is carried along with such clouds, is accounted for by an approximate shape factor, called added mass coefficient (Escudier & Maxworthy 1973). By relating the flow scales to the distribution of a dye, they can be used for nonbuoyant shear flows as well. Tracer-based flow scales are also consistent with recent work on entrainment, in which the interface of a jet is defined as the location of the front of a dye, which was added to the injected fluid (Westerweel et al. 2005).

A consistent set of scales for gravity currents containing a passive tracer of high Schmidt number is

$$ch^2 = 2\int c^* y\, dy$$

$$ch = \int c^*\, dy$$

$$cuh = c_0 q_0 \cong \int c^* u^*\, dy$$

Here, c^* is the local volumetric tracer concentration, u^* and u are flow velocities relative to the bed, and q_0 is the discharge from the source of the flow. The last statement implies that the turbulent transport of tracer is included. When the discharge and the concentration at the source are known, the flow scales can thus be determined without measuring velocities (Bühler et al. 1991). The concentration distribution, or at least the integral ch, can often be determined by flow visualization and other techniques, which do not interfere with the flow.

The shape constants are

$$(\gamma u - u_a)h = \int (u^* - u_a)\ dy$$

$$(\beta u^2 - u_a{}^2)h = \int (u^{*2} - u_a{}^2)\ dy$$

Alternatively one may determine a value of β_t, which includes the turbulent momentum flux. u_a is omitted in

Copyright © 2006 Taylor & Francis Group plc, London, UK

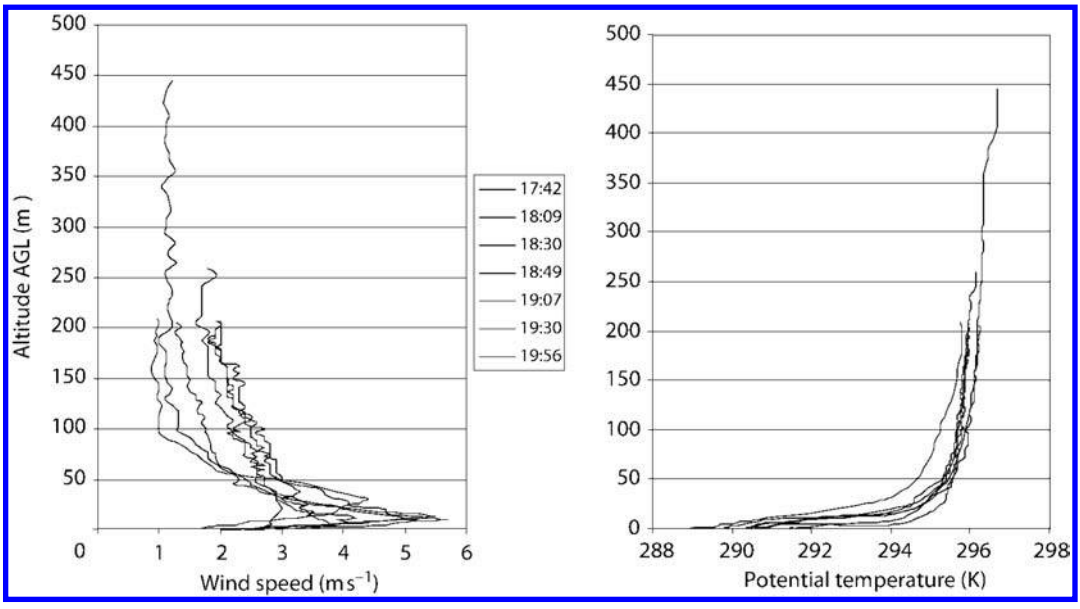


Figure 2. Distribution of wind speed and potential temperature in katabatic winds down a slope (from Princevac et al. 2005).

the case of open channel flows because the dynamics of the atmospheric layer is generally irrelevant, β is called momentum coefficient, and γ is not used as it is equal to one. The simplest equation of state relating the effective gravity g' to c in stratified flows is

$$g' = g\frac{c}{c_0}\frac{\rho_0 - \rho_a}{\rho_0} \tag{3}$$

In open channel flows $c = c^* = c_0$ and $g' = g$. A further advantage of tracer-based flow scales for experiments is that the ambient fluid can be kept uniform, which leads to a well-defined reference for the integrals over the density or tracer distribution, whereas the velocity induced in the ambient fluid by the entrainment can also have a streamwise component. Similar qualitative differences exist between profiles of the wind speed and potential temperature, which were determined by Princevac et al. (2005) in a katabatic downslope wind (Fig. 2). The coflow velocity u_a in the ambient is less well defined than the corresponding reference temperature in the upper layer. It should also be noted that the distributions of the potential temperature, which they obtained at different times, are less contorted and more consistent with each other than the corresponding velocity profiles, which have an inversion point and are strongly influenced by the no-slip condition at the bottom. Similar considerations apply to the velocity and excess density distributions shown by E & T for two distances from the source and a slope of 14°.

Reliable tracer-based width and velocity scales of gravity currents and free shear flows can thus be derived from the readily determinable concentration distribution of a scalar. As a consequence, it seems preferable to tie the more problematic measurements of the fluxes of volume and momentum to the tracer-based scales by means of shape constants instead of pursuing the inverse approach. Special considerations would be required for flows without a source of mass, as well as for two-phase flows like bubble plumes or particle swarms settling in a calm fluid (Bühler & Papantoniou 2001).

The depth-averaged equations of continuity, momentum and tracer conservation can be stated as

$$\frac{d}{dx}(hu) = E'(u - u_a) \tag{4}$$

$$\frac{d}{dx}(\beta h u^2 + \frac{1}{2}g' h^2 \cos\varphi) = u_a \frac{d}{dx}(\gamma h u) + g' h \sin\varphi - c_D u^2 \tag{5}$$

$$\frac{d}{dx}(g' h u) = 0 \tag{6}$$

E' is a function of the bulk Richardson number $Ri'_d = g' h \cos\varphi / (u - u_a)^2$, and c_D is a drag coefficient. By ignoring any variations of φ and the shape constants along x these relations reduce to

$$\frac{dh}{dx} = \frac{E'(1 - \frac{u_a}{u})(2\beta - \frac{1}{2}Ri' - \frac{\gamma}{\beta}\frac{u_a}{u}) - Ri' \tan\varphi + c_D}{(\beta - Ri')} \tag{7}$$

Copyright © 2006 Taylor & Francis Group plc, London, UK

$$\frac{h}{3Ri'}\frac{dRi'}{dx} = \frac{E'(1-\frac{u_a}{u})(\beta+\frac{1}{2}Ri'-\gamma\frac{u_a}{u})-Ri'\tan\varphi+c_D}{(\beta-Ri')} \quad (8)$$

$Ri' = g'h\cos\varphi/u^2$ is the Richardson number related to the long-wave speed on the interface. The flow velocity is related to Ri' by $u = [B\cos\varphi/(Ri')]^{1/3}$. Ri' does not depend on u_a when the upper layer is deep, i.e. the flow is critical when $Ri' = \beta$, as it is for ambients which are at rest, and in open channel flows. To ensure this mutual consistency, the structure of Equation 4 was chosen in accordance with Equation 1. Special considerations would be required for arrested wedges, for which $u = 0$ by definition.

For $u_a = 0$ and $E' = 0$ the above equations reduce to those for open channel flows. For $u_a = 0$ they agree with the ones derived by E & T except for the definitions of the flow scales, which are related to the present ones by

$$g' = \Delta S_2^2/S_1 \qquad u = U/S_2$$
$$h = HS_1/S_2 \qquad E' = ES_1/S_2$$
$$\beta = S_2^3/S_1 \qquad \gamma = S_2^2/S_1$$
$$Ri' = Ri_d' = Ri_E S_2^3$$

The values of β and γ are 1.32 and 2.08, respectively, for the values of S_1 and S_2 obtained for the slope of 14°. Buhler & Schlaepfer (1986) compiled shape coefficients and related quantities for free shear flows, as well as for open channel and ducted flows (see also Chow 1959). The largest value is that of γ for gravity currents quoted above. The other values of β and γ were somewhat larger than one, except for plane plumes and axisymmetric jets, for which they are somewhat smaller. The momentum coefficient β for a gravity current is thus close to the corresponding value in an open channel or duct from which it may emerge. The width of jets and plumes determined from dye visualizations was also found to agree well with h. The depth h and velocity u of gravity currents in calm water can then be estimated on the basis of the information for β and γ provided here, and from the entrainment function E determined from laboratory and field experiments (Princevac et al. 2005).

Some doubts remain about the appropriate form of the entrainment relation for nonzero ambient flows. A further option would be to combine the approaches leading to Equations 1 and 2 by adding a term u_a dh/dx to the right side of Equation 4 for coflows ($u_a > 0$). According to the concept of jet diffusion proposed by Prandtl (1926), this quantity is proportional to $u_a(1-u_a/u)$ in terms of the present notation. His concept is generally used for jets in coflows and for wakes (Wright 1994, Davidson & Wang 2002), but it also works surprisingly well for free shear flows in calm water (Bühler & Papantoniou 2001). The parenthesis $(1-u_a/u)$ modifying E′ in Equations 7 and 8 could then tentatively be replaced by $\{1-(u_a/u)^2\}$, but further work is required to assess this parameterization. In the following sections we shall return to gravity currents in calm water, an approximation which is usually justified for hydropower reservoirs in river valleys.

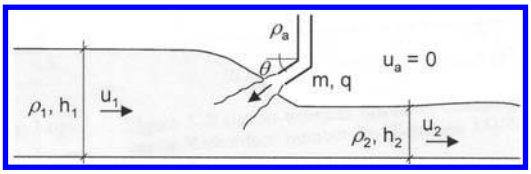


Figure 3. Jets opposing a flow.

3 BACKING UP FLOWS BY OPPOSING JETS

Oehy (2003) explored the possibility of slowing down turbidity currents in reservoirs by means of water jets directed against the flow. He carried out simulations and experiments which showed that this greatly enhances sedimentation and helps to keep bottom outlets from getting clogged. Similar arrangements have been proposed for open channel flows by inducing hydraulic jumps (Wilson 1977). In the following we shall assume that the slope and the sedimentation over the (short) test section can be neglected, that jets emerge from a number of equidistant nozzles arranged in the spanwise direction, and that they are inclined at an angle θ relative to the bed as shown in Figure 3. The jets are associated with a flow rate q, and a momentum flux m per unit width, regardless of the number of nozzles they emerge from. The jets are thus replaced by an equivalent line source (from a slot) for the purpose of the analysis. The upper layer is considered to be at rest ($u_a = 0$). The main difference between internal and free surface flows is that the former ones are diluted by the clear water of density ρ_a injected into them, but not the latter ones.

The conservation equations for the fluxes of volume, momentum and buoyancy are

$$\gamma h_1 u_1 + q = \gamma h_2 u_2 \quad (9)$$

$$\frac{1}{2}g'_1 h_1^2 + \beta u_1^2 h_1 - m\cos\theta = \frac{1}{2}g'_2 h_2^2 + \beta u_2^2 h_2 \quad (10)$$

and for internal flows

$$g'_1 h_1 u_1 = g'_2 h_2 u_2 = B \quad (11)$$

With $q_i = \gamma u_i h_i$ we can wite $q_1 + q = q_2$. For a convenient presentation in graphs we may redefine

Copyright © 2006 Taylor & Francis Group plc, London, UK

$Ri = Ri'/\beta$, such that $Ri = 1$ for critical flow. The flux $u_i^2 h_i$ can be expressed as $(B/\beta Ri_i)^{1/3} q_i/\gamma$, which leaves

$$\frac{1}{Ri_1^{1/3}}\left(1+\frac{1}{2}Ri_1\right) = \frac{q_2}{q_1}\frac{1}{Ri_2^{1/3}}\left(1+\frac{1}{2}Ri_2\right)+\frac{\gamma m\cos\theta}{q_1(\beta^2 B)^{1/3}} \quad (12)$$

For free surface flows $g' = g$, $\gamma = 1$, and $u_i^2 h_i$ can be expressed as $(gq_i/\beta Ri_i)^{1/3} q_i$, such that

$$\frac{1}{Ri_1^{1/3}}\left(1+\frac{1}{2}Ri_1\right) = \left(\frac{q_2}{q_1}\right)^{4/3}\frac{1}{Ri_2^{1/3}}\left(1+\frac{1}{2}Ri_2\right)+\frac{m\cos\theta}{(\beta^2 g q_1^4)^{1/3}} \quad (13)$$

Solutions can be obtained by substituting $Ri_1 = x^3$, and by denoting the RHS of Equation 12 or 13 by r, which leaves $x^3 - 2rx + 2 = 0$. A further substitution of $x = 2(2r/3)^{1/2}\cos\theta$ leads to solutions of the form $\cos(3\theta) = -(3/(2r))^{3/2}$, which can be used to draw the curve in Figure 4 for open channel flows. An analogous procedure can be used for cases where the downstream flow conditions and Ri_2 is known. From Equation 13 we obtain

$$\frac{1}{Ri_2^{1/3}}\left(1+\frac{1}{2}Ri_2\right) = \left(\frac{q_1}{q_2}\right)^{4/3}\frac{1}{Ri_1^{1/3}}\left(1+\frac{1}{2}Ri_1\right)-\frac{m\cos\theta}{(\beta^2 g q_2^4)^{1/3}} \quad (14)$$

This relation is shown in Figure 5.

Both relations can also be expressed in terms of the more generally used Froude Number $F^2 = 1/Ri$. For Equation 13 the result is

$$F_1^{2/3}\left(1+\frac{1}{2F_1^2}\right) = \left(\frac{q_2}{q_1}\right)^{4/3} F_2^{2/3}\left(1+\frac{1}{2F_2^2}\right)+\frac{m\cos\theta}{(\beta^2 g q_1^4)^{1/3}} \quad (15)$$

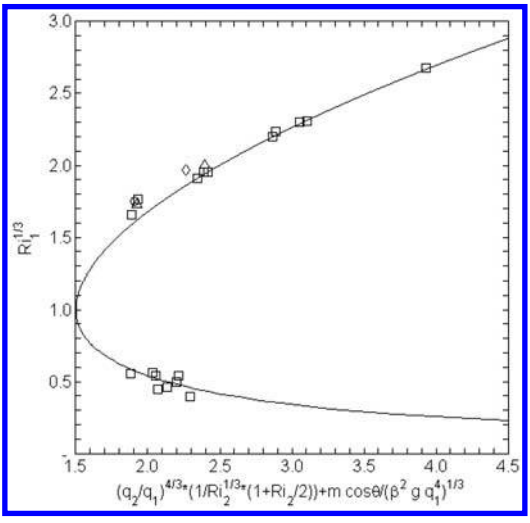


Figure 4. Relation between downstream conditions and upstream Richardson number Ri_1 (Equation 13). Eight 5 mm pipes (squares), four 7.5 mm pipes (circles), eight 10 mm pipes (diamonds), two 10 mm pipes (triangles).

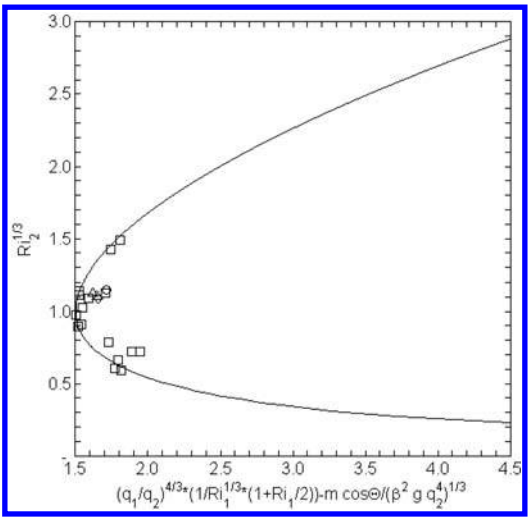


Figure 5. Relation between upstream conditions and downstream Richardson number Ri_2 (Equation 14). Symbols as in Figure 4.

4 EXPERIMENTS

The experiments on flows with a free surface were carried out in a glass-walled flume of 0.4 m width and 0.5 m depth (Fig. 6). A weir, which was located 3 m upstream from the injection pipes, allowed for the establishment of supercritical flows within the test section. The upstream and downstream depths were measured by point gages. In both cross-sections depth measurements made between, and at the spanwise locations of the injection pipes were averaged. The injection angle was $\theta = 15°$. Most of the experiments were performed with eight equidistant discharge pipes, with one-half that distance left free adjacent to the walls. These pipes had an inner diameter of 5 mm. A few other experiments were made with 7.5 and 10 mm pipes as marked in the Figures 4 and 5. For the present purpose β was chosen as 1.07 for both the pipe flow and open channel flow (Chow 1959). The depth h_1 ranged from 0.02 to 0.09 m, u_1 from 0.25 to 1.6 m/s,

Copyright © 2006 Taylor & Francis Group plc, London, UK

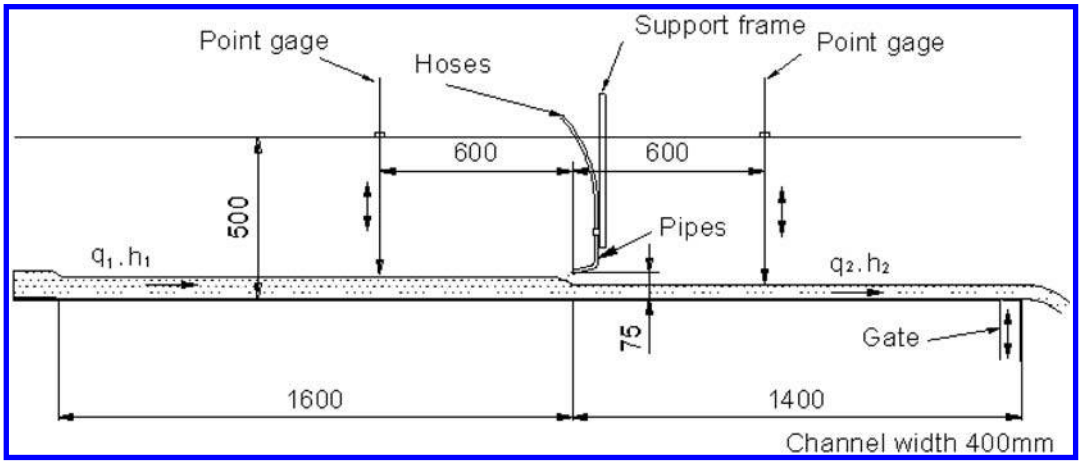


Figure 6. Experimental arrangement for jets opposing an open channel flow (measurements in mm).

and m from 0.9 to $19.6 \cdot 10^{-3}$ m^3/s^2. The agreement with the predictions is quite satisfactory, in particular there is no clear dependence on the number of pipes used within the range of observation.

5 CONCLUSION

Tracer-based depth and velocity scales for gravity currents and free shear flows provide a reliable alternative to scales derived from the velocity distribution. They also provide a good measure for the average flow velocity u and depth h of the layer when the ambient fluid is not at rest. The scales are used determine the depth to which flows on inclines can be backed up by jets directed upstream. Experiments were carried out for single layer flows, and the results agree well with these predictions.

ACKNOWLEDGEMENT

The authors acknowledge the kind support of this study by Wolfgang Kinzelbach and Toni Blunschi.

REFERENCES

Buhler, J. & Schlaepfer, D.B. 1986. New width and other scales for entraining shear flows. *Proc. Int Symp. on Buoyant Flows*, Athens, 37–46.

Bühler, J., Wright, S.J. & Kim, Y. 1991. Gravity currents advancing into a coflowing fluid. *Jour. Hydraulic Res.* 29(2): 243–257.

Bühler, J. & Papantoniou, D.A. 2001. On the motion of suspension thermals and particle swarms. Jour. Hydraulic Res. (39)6: 643–653.

Chow, V.-T. 1959. Open channel hydraulics. Mc Graw Hill

Cotel, A.J., Gjestvang, J.A., Ramkhelawan, N.N. & Breidenthal, R. E. 1997. Laboratory experiments of a jet impinging on a stratified interface. Exp. in Fluids 23: 155–160.

Davidson, M.J. & Wang, H.J. 2002. *J. Hydraulic Engineering*, 128(8): 742–752.

Ellison, T.H. & Turner, J.S. 1959. Turbulent entrainment in stratified flows. *J. Fluid Mech.* 6: 423–448.

Escudier, M.P. & Maxworthy, T. 1973. On the motion of turbulent thermals. J. *Fluid Mech.* 61: 541.

Morton, B.R., Taylor, G.I. & Turner, J.S. 1956. Turbulent gravitational convection from maintained and instantaneous sources. *Proc. Royal Society* A234: 1–23.

Oehy, Ch. 2003. Effects of obstacles and jets on reservoir sedimentation due to turbidity currents. *Faculté ENAC, PhD Thesis Ecole Polytechnique Fédérale de Lausanne, Thèse No. 2684*.

Oehy, Ch. & Schleiss, A. 2003. Beherrschung von Trübeströmen in Stauseen mit Hindernissen, Gitter, Wasserstrahl- und Luftblasenschleier. *Wasser Energie Luft*, 95(5/6): 143–152.

Oehy, Ch.D. & Schleiss, A.J. 2005. Control of Turbidity Currents in Reservoirs by Solid and Permeable Obstacles. Submitted to *J. Hydraulic Engineering*.

Prandtl, L. (1926). Ueber die ausgebildete Turbulenz. *Proc. Int. Congr. of Appl. Mech., Sept. 12–17 Zurich,* 62–74 (see also Schlichting, H., *Boundary layer theory*, McGraw-Hill).

Princevac, M., Fernando, H.J.S. & Whiteman, D. 2005. Turbulent entrainment into natural gravity-driven flows. *J. Fluid Mech.* 533: 259–268.

Scorer, R.S. 1997. Dynamics of metereology and climate: *Wiley – Praxis Series in Atmospheric Physics.*

Westerweel, J., Fukushima, C., Pedersen, J.M. & Hunt, J.C.R. 2005. Mechanics of the turbulent-nonturbulent interface of a jet. *Physical Review Letters* 95 174501: 1–4.

Wilson, E.H. 1977. Stabilization of the hydraulic jump by jets. *Water Power and Dam Construction* 29(3): 40–45.

Wright, S.J. 1994. The effect of ambient turbulence on jet mixing. In: *Recent Research Advances in the Fluid Mechanics of Turbulent Jets and Plumes,* 13–27. NATO ASI Series, Kluwer.

Copyright © 2006 Taylor & Francis Group plc, London, UK

Experimental study of suspended sediment transport and deposition in a rectangular shallow reservoir

S.A. Kantoush, E.F.R. Bollaert, J.-L. Boillat & A.J. Schleiss
Ecole Polytechnique Fédérale de Lausanne (EPFL), Laboratory of Hydraulic Constructions (LCH), Lausanne, Switzerland

W.S.J. Uijttewaal
Faculty of Civil Engineering and geoscience, Delft University of Technology, Delft, Netherlands

ABSTRACT: Large shallow reservoirs of run-of-river power plants on rivers with high suspended sediments are endangered by significant sedimentation. In the framework of a research project, the influence of the geometry of the reservoir on sediment transport and deposition is studied by experimental and theoretical approaches. As a reference case, a rectangular basin geometry was analyzed in detail. The experimental tests have been conducted in a rectangular shallow basin with inner dimensions of 6 m length and 4 m width. Different test procedures were examined. The flow and sediment conditions used during the tests grantee fully developed turbulent flow. Bed level changes, surface, and 3D flow velocities were measured. The results help to understand the mechanism of the flow and the sediment exchange process. In spite of the symmetric setup and only clear water entering; an asymmetric flow pattern developed. But after changing the condition by adding suspended sediment to water in the mixing tank the flow pattern changed and bed forms emerged. They indicate that the flow pattern can easily switch to different directions, depending on the boundary and initial conditions. Moreover, bed forms affect the flow structure. It confirms the important role of boundary conditions in sedimentation and flow field patterns. Furthermore, these first results allow assessing the time evolution of deposition patterns.

1 INTRODUCTION

1.1 *Background*

Shallow flow models play an important role in hydraulic, environmental, river, and coastal engineering. It is thereby important to simulate hydrodynamic phenomena at different length scales that may co-exist in natural flow regimes, e.g. stagnation zones and eddies together with small-scale turbulence. Shallow turbulent flows are common for example in reservoirs, lakes, estuaries and seas. These flows are known to be predominantly two-dimensional, since the limited water depth prevents the development of large-scale three-dimensional structures.

The present study particularly focuses on shallow reservoirs with a prototype depth between 5.0 and 15.0 m and mainly governed by suspended sediments. The modeled bed material has been down scaled to obtain suspended sediment transport over a large part of flow depth. Recent laboratory experiments and numerical simulations for a wide flume (Sloff et al., 2004) showed that channel formation in shallow reservoirs is controlled by the flow pattern. It is highly dependent on the boundary conditions, the initial flow conditions and the geometry. Experimental investigation on the silting process in reservoirs and lakes was carried out systematically by (Mertens, 1985) in a square, shallow basin ($5.00 \times 5.00 \times 0.25$ m) with a horizontal bottom and an approaching channel 0.25 m wide.

The silting-up of reservoirs is a very complex process. Shear flow over a mobile bed induces sediment transport and the generation of bed forms. The interaction between the flow and the bed usually produces different types of regular patterns characterized by a wide range of sizes and shapes (dunes, ripples, anti-dunes, etc.). In turn both, sediment transport and bed forms, influence the flow. The importance of studying the presence and evolution of these regular patterns arises because those bed forms generated by the sediment transport can increase the resistance to flow. In particular, experimental results on the influence of suspended sediment on turbulence are still lacking.

1.2 *Aim of the study*

This study focuses on the sedimentation of shallow reservoirs by suspended sediments and the objective of the experiments is to gain insight into the physical

Copyright © 2006 Taylor & Francis Group plc, London, UK

process behind the sedimentation of shallow reservoirs governed by suspended sediment. Moreover, it is aiming at a better understanding of the mechanism governing the sediment exchange process between the jet entering the reservoir and the associated turbulence structures. Furthermore, we would like to examine different test procedures and find the optimal one to continue with future test configurations. These experiments are part of test series prepared to investigate the ideal reservoir geometry, minimizing the settlement of suspended sediments. The experiment described hereafter is expected to fill in part of our knowledge gap.

2 EXPERIMENTAL SETUP

2.1 *Similarity and dimensions*

Comprehensive information on similitude requirements for movable and fixed bed models can be found in Yalin, 1970 and Kobus, 1980. Scaled physical models are based on similarity theory, which uses a series of dimensionless parameters that fully or at least partially characterize the physics. The choice of a scaling factor $\lambda = L_p/L_m$, or length scale ratio, to be used in the experiments, is determined by the objectives of the research. According to the length of the tested section and the laboratory constraints, the model has been designed with horizontal and vertical scales of $\lambda_l = \lambda_h = 50$ (Kantoush et al., 2005). Application of the above similarity rules is shown in Table 1, with a comparison between the prototype and the model characteristic values.

The experiments were carried out in a specific test facility at the Laboratory of Hydraulic Constructions (LCH) of the Swiss Federal Institute of Technology (EPFL). The dimensions of the model were based on those of the Rhône River and the space available in the laboratory. A schematic view of the experimental setup is shown in Figure 1. The setup consists of an inlet rectangular channel 0.25 m wide and 1.0 m long made of PVC, a rectangular shallow basin with inner dimensions of 6.00 m length and 4.00 m width, an outlet rectangular channel 0.25 m wide and 1.0 m long, a flap gate 0.25 m wide and 0.30 m height at the end of the outlet (to control the water level), a drainage pipe 0.23 m diameter fixed after the flap gate, and stilling basin to collect the sediment and drainage the water in (see Figure 1).

The bottom and the walls of the basin consist of 8 mm thick PVC plates with 0.30 m height on the sides. Adjacent to the experimental reservoir, a mixing tank with a maximum capacity of 200 liters is used to prepare and store the sediment fluid mixture. A sediment supplier tank is mounted above the mixing tank. To control the sediment concentration, a small gate is installed at the down front of the sediment tank. Sediment supplier tank is attached to a vibrator, which has several speeds to increase or decrease the sediment concentrations. The mixing tank is equipped with a propeller type mixer to create a homogenous sediment concentration. After filling the experimental reservoir with water, the water-sediment mixture will flow by gravity into the rectangular basin through a flexible pipe with 0.10 m diameter. To ensure a uniform mixture in the mixing tank and reservoir basin, the density of the sediment mixture and the clear water were controlled before and during the experiments by means of a turbidity meter. On the basin side walls a movable aluminium frame is mounted with 4.0 m length, which carries the measurement instruments can move in three directions. The parameters that were measured during the experimental runs are shown at Table 2.

Table 1. Characteristic values of the prototype and the model (scale 1 : 50).

Item	Prototype	Model
Length, L[m]	300.0	6.0
Width, B[m]	200.0	4.0
Water depth, h[m]	7.6–15.2	0.20
Discharge, Q [m^3/s]	5.0	0.007
Median grain size, d_{50}[mm]	0.037	0.05
Sediment concentration, Cs [g/l]	5.0	3.0
Gradient of section, I [-]	1.0%	0.0%

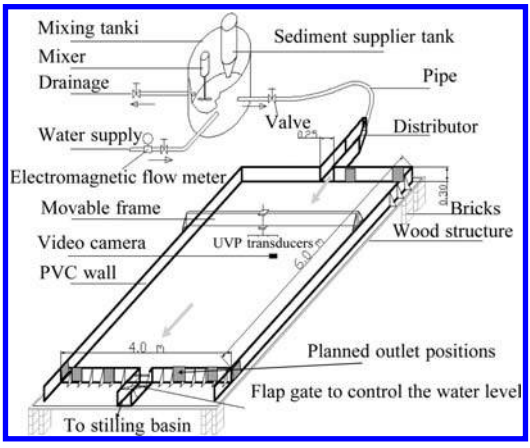


Figure 1. Schematic drawing of the experimental installation.

2.2 *Experimental conditions*

To model suspended sediment currents in the laboratory model, walnut crushed shells with a median grain size $D_{50} = 50\,\mu m$, density 1500 kg/m^3 was used in all tests cases. These are non cohesive, light weight and homogeneous grain material. The sediments are added to the mixing tank during the tests. The hydraulic conditions were chosen to fulfill the sediment transport

Copyright © 2006 Taylor & Francis Group plc, London, UK

Table 2. Model parameters and instrumentation.

Measured parameters	Dimension	Instrument
Water level	[m]	Ultrasonic probe
Sediment thickness	[m]	Echo sounder
Discharge	[m^3/s]	Flow meter
Surface velocity	[m/s]	PIV technique
Sediment concentration	[g/l]	Turbidity meter
Temperature	[C°]	Thermistors

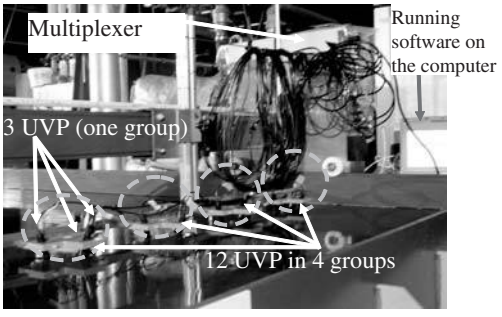


Figure 2. Scheme of UVP installations and data acquisition.

requirements see Table 1. Furthermore, for all test cases, Froude number is small enough and Reynolds number is high enough to ensure subcritical fully developed turbulent flow.

2.3 *Measurements and data acquisition system*

Several parameters were measured during every test; namely: surface velocities, deposited sediment layer thickness, suspended sediment concentration at the outlet, 3D flow velocity, water level and water temperature. Table 2 provides an overview of the measurements and instrumentations used during the tests.

The velocities were measured by means of an Ultrasonic Doppler Velocity Profiler (Metflow SA, UVP-DUO), which allows an instantaneous measurement of the 1D velocity profile over the whole flow depth (Metflow, 2002). The measurement probes were mounted on a support in groups of three, allowing the measurement of the 3D flow field (Figure 2). To cover the whole cross section of the basin, 5 positions were chosen along the cross section; each position has four groups of three probes. All twelve probes were mounted on a frame which moves in the two horizontal directions. The probes were inclined at 20° to the vertical and had an emitting frequency of 2 MHz. The velocity measurements were taken at about 480 measurement points.

The bed level development was measured by means of Miniature echo sounder (UWS) see Table 3. The transmitted ultrasound impulse is reflected at any object serving as a target. This acoustic reflection



Figure 3a. Lab sensor.



Figure 3b. Lab device UWS.

Table 3. Miniature echo sounder UltraLab UWS specifications.

Specification
Lab device ULTRALAB UWS (see Fig. 3b)
Control keys and integrated 4 digit 12 mm LCD-Display
Dimensions: 330/115/260 mm, length/height/depth
Measuring rate: max. 10 Hz
Sensor (see Fig. 3a)
Dimensions: Diameter: 30 mm/
Length: 50 mm
Frequency: 1 MHz
Resolution: 1% of measuring range, max. 1 mm
Accuracy: 1% of measured value at constant circumstances

propagates in space and is received from the ultrasound sensor. In order to measure the effective distance between target and sensor the run-time must be determined which the sound needs from the sensor to the target and back to the sensor again. The measured run-time will be averaged. The distance to the target in meters can be calculated by the run-time and the sound velocity. The UWS was mounted on the movable frame (Figure 4) to scan the whole basin area (6 m * 4 m). The measured cross sections profiles were spaced at 0.05 m and some case 0.025 m was tested, starting from 0.10 m from the model's side wall, and ending at 0.10 m from the other wall, i.e. covering a total model width of 4.0 m with total 77 points. The measured longitudinal profiles were spaced at 0.20 and some case 0.1 was tested, starting from 0.05 m from the upstream sidewall, and ending at 0.10 m from the other downstream wall.

PIV offers a simple method of measurement in areas with complicated geometry and flow conditions. Surface flow measurements with PIV are described for e.g. in (Adrian, 1991). In hydraulic engineering, however, this technique has so far mainly been applied for surface velocity measurements of water and ice flow

Copyright © 2006 Taylor & Francis Group plc, London, UK

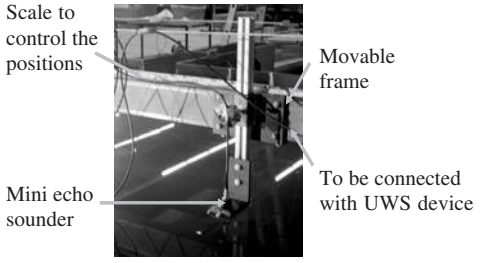


Figure 4. Miniature echo sounder mounted on the frame.

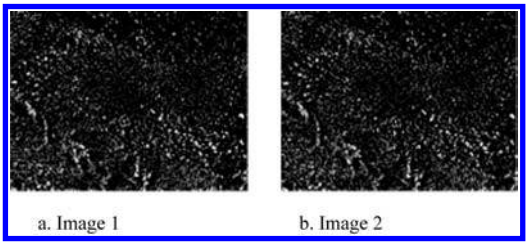


Figure 5. Typical PIV image pair.

in very uniform flow fields as well as in groyne field experiments (Ettema et al., 1997; Fujita et al., 1998; Uijttewaal et al., 2001; Weitbrecht et al., 2002).

The basic principal of PIV is simple: the flow is seeded with plastic particles (with average diameter 3.4 mm and specific weight 960.0 kg/m^3) which are then illuminated and their positions recorded at two successive instant (Figure 5) by video (SMX-155, monochrome, 1.3 megapixel, CMOS camera with USB2.0 interface and frame rate up to 33 FPS). The video of the whole 2D field is then divided into a number of interrogation areas and, in each area, the distance moved by the tracer particles from the time of the first image being recorded to the second is determined. Knowing the distance traveled and the time taken, the velocity of the flow in that area is therefore measured. This is done for every area, giving the 2D map of the instantaneous velocity field at the time of the recording. The camera fixed perpendicular on the basin covering the plane basin area (the whole width 4.0 m and 5.0 from the length, missing 0.5 m from upstream and downstream ends). The displacement of the plastic particle images over the time between the exposure of the first frame and the second analyzed by FlowManager software.

2.4 *Test procedure*

Two different experimental procedures were tested in order to find one approach for all test configurations. For this reason only experimental procedure for carrying out a standard continuously fed suspended sediment experiment will be described. The difference between the two procedures is as follows:

1. Discontinuous feeding: after 1hour of feeding sediment to the water mixture and doing the measurements (UVP, PIV& Pictures); close down-stream flap gate, open water bypass and stop sediment feeding. After suspended sediment deposits, start bed level profile measurements as explained before.
2. Continuous feeding: working the whole duration continuously feeding the mixture and doing the measurements.

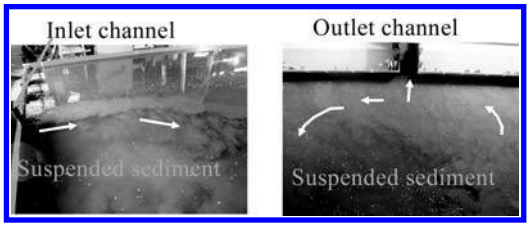


Figure 6. Left: mixture entering; Right: mixture exit.

Prior to each experiment, the mixing tank and the basin were cleaned. The pump was started and the electromagnetic flow meter and a valve were then used to adjust the desired inflow rate. The down-stream flap gate was regulated according to the ultra sound calibration curve to control the water level. Then the basin and mixing tank were filled with clear water. One hour after starting the pump and stabilizing the flow, the PIV measurements were performed for that initial case (only clear water entering the basin). Sediment was added to the sediment supplier tank and the sediment concentration which enters the mixing tank was checked. The mixer guaranteed a homogenous mixture in the tank. Figure 6 shows the homogenous suspended sediment mixture. The left panel shows the sediment entering from the upstream inlet channel to the basin whereas the right one shows the mixture arriving at the outlet in a completely mixed state and a certain concentration flowed from the outlet channel.

UVP probes were mounted to start 3D velocities measurements. The bed profile was measured for specific chosen cross sections every 20 minutes. PIV measurements were repeated during the test every 30 minutes and attention was paid to the transitional case during the test (decided according to the surface velocity observations). All the runs were repeatedly recorded with a digital video camera for selected durations in order to track the changes in flow patterns, and to determine the propagation of the suspended sediment concentration. The experiment was then run until equilibrium conditions were reached, defined as a minimal change in water surface and bed slope over the two consecutive measurements. Equilibrium was usually

Copyright © 2006 Taylor & Francis Group plc, London, UK

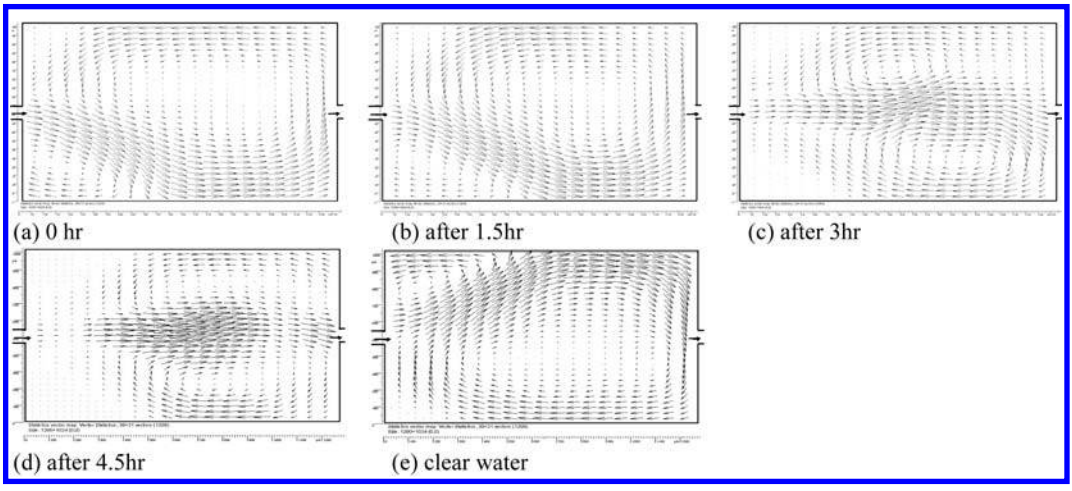


Figure 7. Flow pattern at different run times during test Series 1.

achieved within 4.5 hours after starting the experiments. The flap gate was then closed to permit for the suspended sediment to deposit and then measuring of deposit thickness was started using UWS as explained above. Finally the sediment at the outlet basin was collected, dried and weighted to calculate the trap efficiency coefficient and sediment volumes as well.

2.5 *Test series*

Three different test series have been carried out with the same boundary conditions and initial conditions as explained before but with different test procedure as following:

1. Series 1: The discontinuous feeding procedure has been used.
2. Series 2: Repeated test for Series A, with the purpose to check the reproducibility and the model sensitivity.
3. Series 3: The continuous feeding procedure has been used with the same condition as previous series.

3 RESULTS AND DISCUSSIONS

3.1 *Flow patterns*

Averaged flow fields have been obtained by using Particle Image Velocimetry (PIV) techniques and are depicted in Figures 7 to 9; each figure contains five flow patterns as following:

(a) Flow pattern for the initial state (no sediment neither in the basin nor in the mixing tank)
(b) Flow pattern after 1.5 hour of adding sediment concentration in the mixing tank.
(c) Flow pattern after 3 hours from the start with a constant sediment concentration
(d) Flow pattern after 4.5 hours from the beginning.
(e) Flow pattern using a clear water inflow after completely stopping the sediment supply.

Figures 7(a), 8(a) &9(a) show that the flow enters as a plane jet issuing from the narrow leading channel to the wide basin. After jet issuance, the main flow tends towards the right hand side, generating a large and stable main gyre rotating anticlockwise and two small 'triangular' gyres rotating clockwise in the two upstream corners of the basin. The jet appears to be attracted to one of the side-walls. Its preference for the right side is weak since a stable mirror image of the flow pattern can easily be established by slightly adapting the initial conditions. By following floating particles, it is noticed that in the first meter from the entrance the particle is straightly entering and, in the next two meters, it deflects to the right until it arrives at the stagnation points near the right wall at the middle (3 m from the entrance). The particles that do not leave the basin through the outlet channel circulate with the main gyre to arrive near the separation zone at the farthest left side wall. There, a small gyre has formed at the left corner of the basin with a triangular shape 1.2 m *1.2 m. The circulation pattern sustains itself because the inertia of the main gyre pushes the in-coming jet aside. A bottom that is initially smooth favors this inertia dominated pattern. By comparing the three figures similar gyre patterns are obtained even with different test procedures and different working days.

The water-sediment mixture flows from the narrow inlet channel to the much wider basin. At first, the inflow mixture behaves like a jet that remains quite separated from the clear water in the basin. After some distance, the shear between both bodies of water

Copyright © 2006 Taylor & Francis Group plc, London, UK

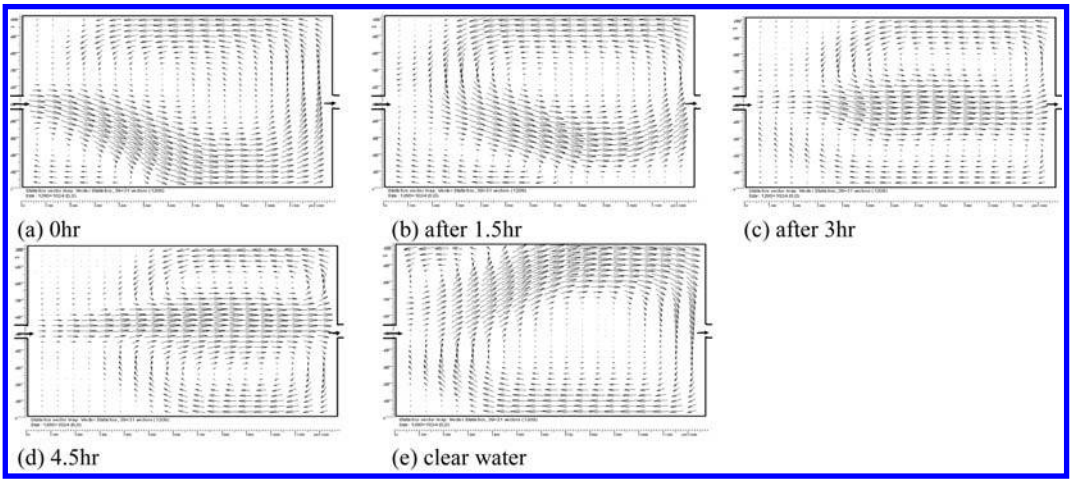


Figure 8. Flow pattern at different run times during test Series 2.

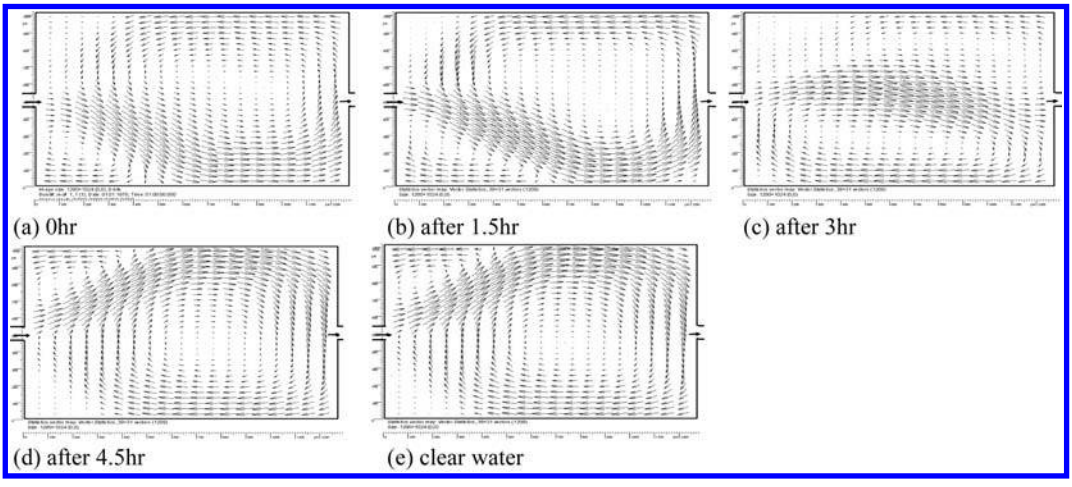


Figure 9. Flow pattern at different run times during test Series 3.

moving at a different speed causes mass and momentum exchange and thus eddies that are peeled off from the core of the jet. This peeling off occurs alternatively on both sides of the jet and generates eddies that increase with longitudinal distance. Furthermore, the jet starts to undulate with a wavelength and amplitude that increase with longitudinal distance. The behavior resembles to a continuously growing instability. This asymmetric and switching flow behavior continues until the downstream end of the reservoir, where the jet is forced to pass through the outlet channel.

During 1.5 hours of adding the sediment the observed flow pattern in Figures 7(b), 8(b) &9(b) did not differ much from what is previously explained for Series (a), except for the increase in size of the right corner gyre and a downstream shifted re-attachment point. Apparently this is due to the suspended sediment entrainment and the associated emergence of bed forms (see Fig. 10). It's clear that the flow structures in the different test series show a similar pattern in these figures.

Figures 7(c), 8(c) &9(c) present the flow patterns after 3 hours of adding sediment for the three test procedures. As a result of ripple formation and suspended sediment concentrations the flow field is completely changed. The gyres in the upstream corners are suppressed if not disappeared and a pattern has emerged that is rather symmetric with respect to the center line. It is also seen that the remaining two gyres interact with the jet which shows some tendency to meander. Since the exchange with the upstream corners of the basin is very small, it is expected that not much deposition

Copyright © 2006 Taylor & Francis Group plc, London, UK

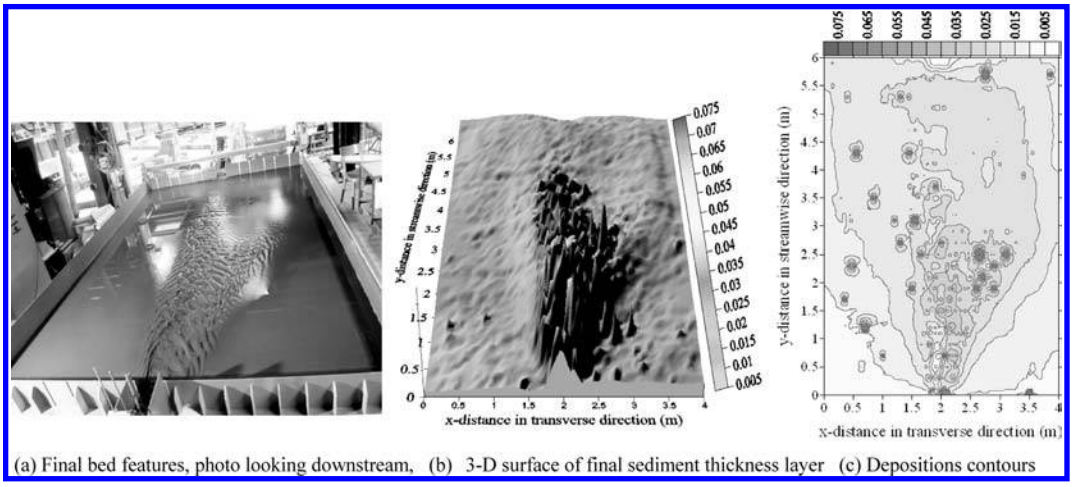


Figure 10. Morphological results after 4.5 hrs of sediment supply for Series 1.

takes place in those areas. Apparently the changes in the bed forms or effective roughness resulting from the sediment deposition are capable of completely changing the overall flow pattern. Through the same mechanism a further development can be expected. By comparing the three figures it can be concluded that similar flow patterns have developed but with small differences regarding the dimensions and strength of the circulation cells. In particular with the continuous feeding experiment (Fig. 9(c)), the asymmetry leading to the subsequent pattern can already be seen.

Figures 7(d), 8(d) &9(d) show the flow patterns that have developed after 4.5 hours of adding sediment for the different test procedures. Figures 7d &8d still show symmetric flow patterns with two gyres coupled to the jet flow. It is noticed that two very weak gyres that might have become laminar or stagnant have hardly any exchange with the main motion. In both figures the same test procedures were used which resulted in virtually identical flow patterns. Figure 9(d) presents the flow pattern of the continuous test procedure after 4.5 hours of adding sediment. It has a flow structure different from those in Figures 7(d) and 8(d). Due to the continuous feeding procedure already during the third hour the right side gyre starts to enlarge in size and develops into the one shown in Figure 9(d). This pattern appears to be rather stable. With the help of bed evolution measurements and final bed deformation pictures, it can be said that during the transition zone from the initial counterclockwise gyre to the final clockwise gyre the roughness of the bed showed strong local variations. It should be mentioned that all the flow patterns shown in the Figures (d) remained during the subsequent 2.5 hours of observation.

Figures 7(e), 8(e) & 9(e) present the flow patterns for the three test procedures After stopping the flow, clear water (without sediment) has been injected into the basin to investigate the further evolution of the bed at different time periods. The flow patterns in Figures 7(e) & 8(e) are similar and equal to the pattern of Figure 9(e). After restarting the flow it chooses the easiest path from the inflow to the outflow gate along the left side wall. The sedimentation from the previous period has apparently become too much of an obstacle to result again in a symmetric flow pattern. It shows at least that the symmetric flow pattern is not a very stable one and that in the long run it would have changed into one of the more stable asymmetric patterns anyhow.

3.2 *Morphological development*

This section presents a comparison of all test series for the time evolution of the bed. Figures 10 to 12 present a detailed comparison of final bed elevation, 3D for sediment thickness layer after 4.5 hour and the contours of deposition patterns. For all the tested scenarios, two typical features were observed. The first was development of sediment deposition with ripples formation concentrated on the right hand side and along the center line later on; the second was concentrated on both right and left sides and very low in the core of the basin. In the following sub sections the results will be described with further details.

Figure 10 presents the final bed elevations after 4.5 hours of testing of series 1. The mixture of water and sediment is advected and diffused throughout the basin following the general flow patterns described above. The footprint of the flow patterns was clearly visible in the morphology as shown in Figure 10(a). The resistance to flow is relatively small for the smooth and plane bed at the start. However, the flow resistance increases as ripples are being formed. The ripples play an important role in the interaction between the boundary layer flow structures and sediment transport.

Copyright © 2006 Taylor & Francis Group plc, London, UK

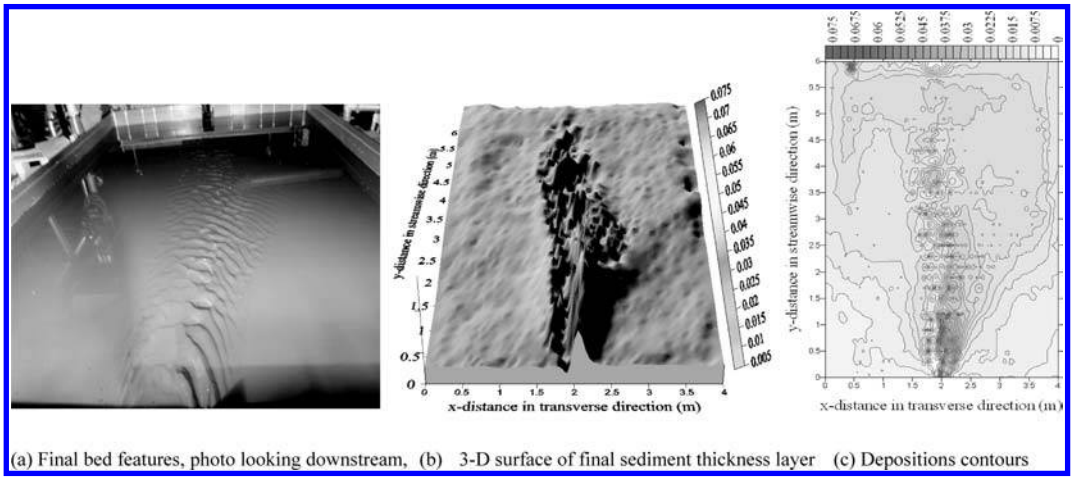


Figure 11. Morphological results after 4.5 hrs of sediment supply for Series 2.

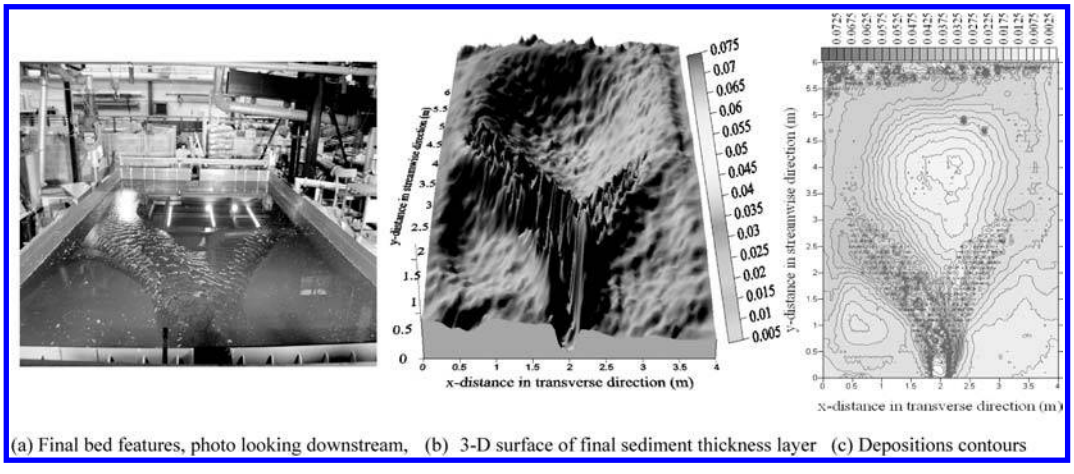


Figure 12. Morphological results after 4.5 hrs of sediment supply for Series 3.

Figure 10(b) shows the processed 3D surface bed elevation for the test series 1 after 4.5 hours. The asymmetric ripple patterns near the right side wall follow the same direction as the flow pattern shown in Figure 7. Ripples characteristics were measured manually before cleaning the basin. Moreover, several reference points were taken manually for calibration comparison with the UWS measurements. It was found that the UWS measures with a high accuracy of ± 1 mm and it's similar for the manual measurements. Nevertheless, some anomalous spikes are observed in Figure 10(b). Figure 10(c) presents the contours for the sediment thickness layer. It can be easily seen that most of the sediment depositions has take place around the centerline and the downstream part. It may be concluded that a stable morphology has been reached after 4.5 hours whereas possibly a longer run would needed to confirm the question of full morphological equilibrium in the basin.

The sediment concentration and sediment depositions are highest along the centerline of the basin and reduce towards the sides as shown in Figures 10 & 11. Figure 11 shows the evolution of the sediment depositions for the test series 2 (repeated test). The figure shows an almost similar sediment deposition pattern as was found for the series 1 presented in Figure 10.

There is a complex relation between flow patterns, sediment exchanges and sediment transport as well. Figure 12 shows the results for the series 3 obtained after 4.5 hours of test run. Figure 12(a) presents a picture of the final bed evolution. It is noticed that the sediment deposition takes place in accordance with the flow patterns of Figures 9(a)–(d). In the beginning it starts to form ripples near the right side wall

Copyright © 2006 Taylor & Francis Group plc, London, UK

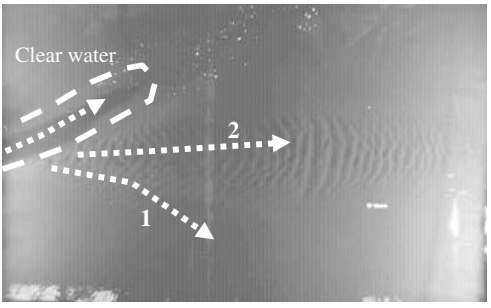


Figure 13. Plan view for the test series 2 with the clear water inflow without sediment.

leaving the area in the upstream corner void, which is associated with action of the small gyre.

From Figure 12(b) it is clearly seen that the deposition at both upstream corners is very small. Most of the sediment deposits right below the main streamlines connected to the inflow channel. After the flow pattern has changed to the clockwise gyre, a symmetric ripple pattern formed near the left side wall, similar to the one at the right side which formed in the beginning. After a certain period of testing, the deposition on the left side gradually increased generating a wider bed elevation underneath the jet centerline with a width of approximately three times the inlet channel. Similarly, in the first few hours of the experiment the elevated bed has reached the right side wall and followed the course of the streamlines down to the outlet channel. It is remarkable that in the downstream part of the basin the bed is elevated on a rather narrow ridge. Figure 12(c) shows the contours for the sediment layer thickness. Here the relatively steep gradients near the inlet channel and the first part of the jet are clearly visible. It is quite likely that on a much larger time scale the relatively quiet zone in the upstream corners and the central part of the main gyre will eventually be filled up with the finest sediment fraction.

The final bed morphology obtained from test series 2 was used as the initial topography for a clear water test. Here, clear water without sediment was introduced into the basin to investigate the further bed evolution under those circumstances. Figure 13 present the final bed deformation after 6 hours of clear water test. The most important change was found in the erosion of the bed near the entrance. No significant change has been observed anymore between the respective bed profiles after that period. Hence, for these flow and sediment conditions, the bed might be considered as stable.

4 CONCLUSIONS

The first results of ongoing research on the influence of the geometry of a shallow reservoir on suspended sediment transport and deposition have been presented. The mechanism of sediment transport and deposition in the basin differs according to the test procedure. In the discontinuous feeding procedure, the gradual changes during the transitional state are missing due to the effect of stopping and restarting the flow. For the continuous feeding procedure, it was easy to reach a stable flow and bed form in the basin after 4.5 hours. Whether this represents a long-term equilibrium morphology will be checked by subsequent tests. It was found that the flow and sediment patterns are quite sensitive to the boundary and initial conditions. Although it is clear that an asymmetric flow pattern is favored, a symmetric pattern can persist for quite a long time. The experiment also shows the mutual interaction between flow and bed forms and the substantial increase in complexity when sediment transport and morphodynamics play a role.

Regarding the continuation of this research project the major goal is to find out which reservoir geometry leads to minimum sediment deposition. This requires experiments of long duration combined with numerical modeling techniques that include the processes as observed in this study.

REFERENCES

Adrian, R.J., 1991. Particle-imaging techniques for experimental fluid mechanics. *Annu. Re. Fluid Mech*. 23, 261–304.

Emttea R., Fujita I., Muste M., & Krufer A., 1997. Particle Image Velocimetry for whole field measurement of ice velocities. *Cold Regions Science and Technology* Vol. 26, 97–112.

Fujita I., Muste M., & Kruger A., 1998, Large scale Particle Image Velocimetry for flow analysis in hydraulic engineering applications, *Journal of hydraulic Research*, Vol. 36, No 3, 397–414.

Kantoush, S.A., Bollaert, E.F.R., Boillat, J.-L., & Schleiss, A.J., 2005. Suspended load transport in shallow reservoirs. *Final Proc. XXXI IAHR Congress*. Korea Water Resources Association, Seoul, South Korea, 1787–1799.

Kobus, H., 1980. Hydraulic Modeling. Pitman, Boston, Mass.

Mertens, W., 1985. Model tests for sedimentation process in reservoirs. In W. Bechteler (cd.). *Proceedings of EUROMECH* 192, Munich, Neubiberg.

Metflow , 2002. UVP Monitor Model *UVP-DUO- Users guide*. July 2002, Metflow SA, Lausanne, Switzerland.

Sloff, C.J., Jagers, H.R.A., & Kitamura, Y., 2004. Study on the channel development in a wide reservoir. *Proc. River Flow, Napoli*, Italy, 811–819.

Uijttewaal, W.S.J. Lehmann, D., Mazijk, & A. van, 2001. Exchange processes between a river and its groyne fields: Model experiments. *J. Hydr. Engrg*.127(11), 928–936.

Weitbrecht, V., Kühn, G., & Jirka, G.H., 2002. Large scale PIV-measurements at the surface of shallow water flows. *Flow Meas. and Instr.* 13, pp 237–245.

Yalin, M.S., 1970. *Theory of Hydraulic Models*. London: Macmillan.

Copyright © 2006 Taylor & Francis Group plc, London, UK

Effects of flushing of two reservoirs in Spain

R. Cobo Rayán
Centro de Estuduios Hidrográficos (CEDEX), Madrid, Spain

C. Mateos Iguacel
E.T.S. Ingenieros de Caminos, Canales y Puertos, Madrid, Spain

ABSTRACT: This paper is a summary of the main results of two flushing operations, one at the Barasona Dam (Huesca, Spain) and the other at the María Cristina Dam (Castellón, Spain). In the Barasona Reservoir the flushing was carried out using the bottom outlets in a short space of time during which a massive discharge of sediment took place. The effects of the full emptying were significant in terms of impacts on various physical and chemical variables, especially oxygen and ammonia. These changes were less intense downstream where the return to their former values was very fast due to the washing effects of natural floods. In María Cristina reservoir the flushing took place in a slower manner over several days without an appreciable quantity of sediment being mobilized.

1 INTRODUCTION

In Spain, the flushing of sediments from reservoirs has taken place since ancient times. In the East of Spain this activity has been especially important (Examples include: Puentes dam. Almansa, Tibi, Elche and Valdeinfierno dams). The procedure followed in the XVIIIth and XIXth Centuries was based on opening the bottom outlets at the same time as the first floods occurred. In this way the water removed part of deposited sediments.

Currently, this practice is less commonplace for environmental concerns and the fact that modern reservoirs are much bigger with a longer expected service life. Nevertheless, reservoir capacity recovery is a necessity that will become more and more important in the future.

In this paper two important recent cases will be discussed. The effects of the flushing operation made in the Barasona Reservoir were closely followed by multidisciplinary studies (Palau, 1988; Avendaño and Cobo, 1988) starting from the "LIVRE" French experience (Cardinal, 1989).

The flushing of María Cristina Reservoir had completely different characteristics: this flushing was accidental so only the end of the flushing operation could be observed.

2 CHARACTERISTICS OF THE RESERVOIRS

Barasona Reservoir which lies in the Esera river, in the Ebro Drainage Basin, came into operation in 1932. From that year until the end of 1993, approximately 18 hm3 of sediment were deposited in it. The height of sediment was 25 m adjoining the dam. Barasona is a gravity dam some 65 m in height and 80 m in crest

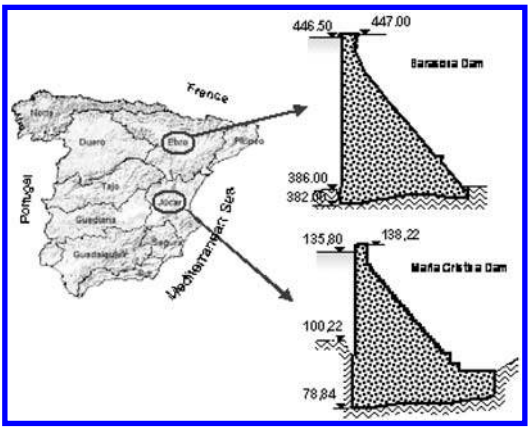


Figure 1. Map showing the location of Barasona and María Cristina Reservoirs.Dam Characteristics.



Figure 2. View of Esera (left) and Rambla de Viuda (right) rivers downstream of the dams.

Copyright © 2006 Taylor & Francis Group plc, London, UK

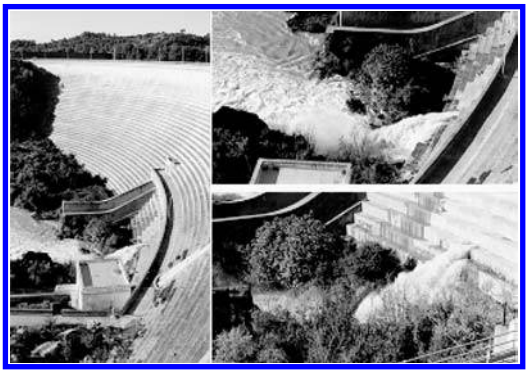


Figure 3. Discharge of water during the flushing of María Cristina Reservoir.

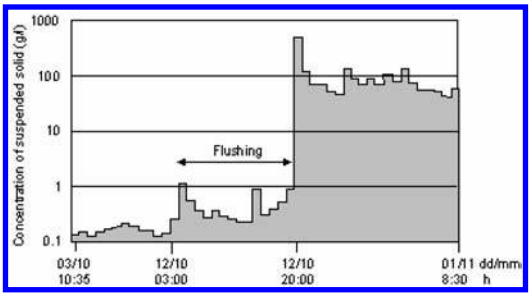


Figure 4. Sediment of María Cristina reservoir after the full emptying.

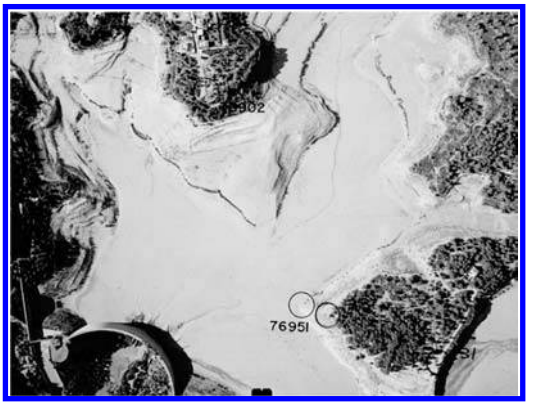


Figure 5. Concentration of suspended solids during the flushing of Barasona Reservoir. The check point is 250 m downstream of the dam in the Esera river.

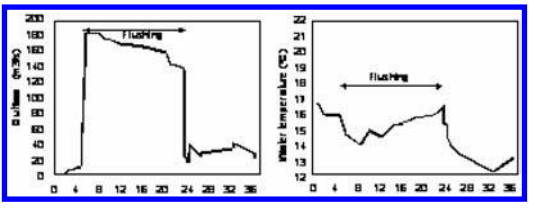


Figure 6. Temporal evolution of outflow and water temperature in the Esera river downstream of the dam.Values of t expressed in hours. (same check point).

length. The reservoir capacity is 92 hm3, and is used for irrigating lands, water supply and hydroelectric power.The bottom outlets are located in two tunnels with three bottom gates for each one.

The Esera river downstream of the dam is 6 km long and its rocky bed lies within a narrow gorge.

The María Cristina reservoir lies on the River Rambla (Gully) de la Viuda in the Júcar Drainage Basin. It came into operation in 1920, and from that year until 2000, 9.6 hm3 of sediment were deposited in it (CEDEX, 1994). The height of sediment was 18 m next to the dam. It is a gravity dam of 59 m height and 318 m crest length. The reservoir has a capacity of 28 hm3. and is used for irrigation.

The Rambla de la Viuda flows through a wide and not very sharp valley.

3 FLUSHING OF MARIA CRISTINA RESERVOIR

The flushing of María Cristina Reservoir took place through an old discharge intake for irrigating land, following the rupture of a concrete plug.

The discharge intake had only a 1 m^2 of cross section, and, therefore, the resulting water flow was small. Full emptying lasted several days during which attempts were made to stop the discharge of water.

When the reservoir was completely empty, it could observe that the sediment had not been mobilized. Downstream of the dam no effects were observed on the river bed nor on the different biological communities.

4 FLUSHING OF BARASONA RESERVOIR

Flushing began on 12th October at 03:00 hours and finished at 20:00 hours. During this time the concentration of solids in suspension were less than 1 g/l. Immediately following the flushing, sediment began to slip through the bottom outlets, with a peak flowrate of 600 g/l.

Later, a fluvial flow began to erode the deposits of sediment giving rise to a concentration ranging from 80 to 100 g/l. The discharge varied from 180 m3/s at the beginning of flushing to 140 m3/s at the end. The fluvial flow dropped to 40 m3/s presenting a series

Copyright © 2006 Taylor & Francis Group plc, London, UK

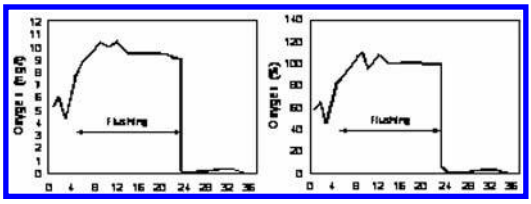


Figure 7. Temporal evolution of dissolved oxygen concentration and saturation in the Esera river downstream the dam (same check point).

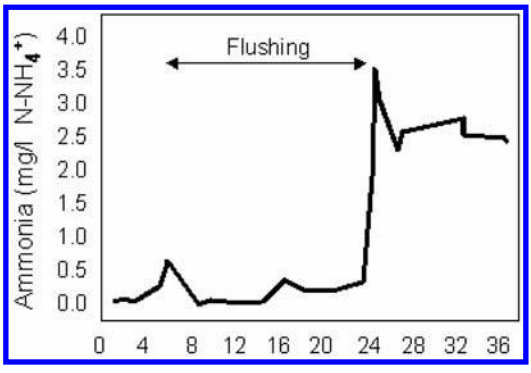


Figure 8. Temporal evolution of ammonia concentration in the Esera river (same check point).



Figure 9. Left: View of the Esera river at the starting of flushing.Right: View in the last phase of flushing. The water flowsover the sediment accumulated in the river bed.



Figure 10. View of the upstream side of dam.OLS: original level of sediment.

of pulses due to the blocking and unblocking of the bottom outlets resulting from the eroded sediment.

The water temperature increased during the flushing, from 14°C (when flushing started) up to 16°C (when the superficial water came out). Following that there was an abrupt fall down to 12°C.

The turbulence taking place during the flushing operation caused oxygen levels to increase up to 10% of saturation. A few minutes after flushing finished the oxygen value went to zero (anoxia). The anoxia condition lasted one day. After that day it started to recover reaching 20% of saturation on the 3rd day and 70% on the 4th day.

The ammonia presented a first peak due to percolation water. After that it decreased during flushing until the moment of the exit of sediment. At that moment a concentration of 3.5 mg/l was reached.

Fish communities upstream of the dam were badly affected by the flushing, due to adults living in the reservoir. In the fisheries downstream the effect was less strong because fisheries were disturbed by the low flow regulation before flushing. (Morillo and García Jalón, 1998).

Aquatic birds showed intense changes in their use of space during the weeks following the flushing. Six months later, a considerable recovery was observed. (Rossel *et al,*1998).

The effect in the riparian vegetation were minimal. There were no significant changes in composition and structure of woody plants communities. (Alcázar and Ferrán, 1998).

After the flushing, upstream of the dam, a great quantity of sediment stored in the river bed was mobilized. This sediment occupied 2 km of channel with some 8 m average height.

5 CONCLUSIONS

The biggest effects, downstream of the dam, took place when the flushing happened quickly and the reservoir is completely empty.

If the flushing is interrupted before all the water is discharged, or flushing is carried out very slowly, the effects are almost null.

Copyright © 2006 Taylor & Francis Group plc, London, UK

REFERENCES

Alcázar, J. and Ferrán, I. 1998 La vegetación de ribera de los ríos Esera y Cinca en el tramo afectado por el vaciado del embalse de Joaquín Costa. *Linmética 14:1–5*

Avendaño, C. and Cobo, R. 1998 Seguimiento de los sólidos en suspensión durante el vaciado del embalse de Joaquín Costa. *Linmética 14:1–5*

CEDEX 1994 Reconocimientos batimétricos de embalses. Embalse de Barasona. *Informe para la Dirección General de Obras Hidráulicas (MOTMA), 27 pg. 4 annexes, 19 map*

Morillo, M. and García de Jalón, D. 1998 Efectos del vaciado del embalse de Barasona en las comunidades fluviales. *Linmética 14:1–5*

Palau Ybars, A. 1988 Estudio limnológico del ecosistema fluvial afectado 'por los vaciados del embalse de Barasona. *Linmética 14:1–5*

Rosell, C. *et al.* 1998 Efectos del vaciado del embalse de Joaquín Costa sobre anfibios, aves y mamíferos vinculados al ambiente de ribera. *Linmética 14:1–5.*

Copyright © 2006 Taylor & Francis Group plc, London, UK

B.7. Local scour and protection

Copyright © 2006 Taylor & Francis Group plc, London, UK

Time evolution of erosion depth and sediment motion for abutment scour in a pressure duct

A. Radice, S. Malavasi & F. Ballio
Politecnico di Milano, Dept. I.I.A.R., Milan, Italy

ABSTRACT: We present the results of abutment clear water scour experiments that were run in a pressurized rectangular duct. Simultaneous measurements of the scour depth and of sediment kinematics were made, in order to support analysis of the measured erosion trends via that of spatial and temporal distribution of sediment fluxes. The latter were measured by image processing from movies of the phenomenon in progress. Measured erosion trends were preliminarily compared to results of standard experiments with a free surface flow, founding that neither the time development of the maximum scour depth nor the scour hole shape were significantly affected by the flow pressurization. Features of sediment kinematics are dependent on the achieved scour levels, in that grain motion is rather regular in time during the first part of the scour process, and becomes more and more variable as a larger scour hole has been scoured. On the other hand, the initial stable sediment motion induces great erosion rates, while successive unsteadiness determines a lower effectiveness of sediment activity. The structure of the sediment pattern is also variable with time, showing an increasing weight of the vortical components of the flow field in determining local scour.

1 INTRODUCTION

Local scour at bridge structures has been extensively studied both experimentally and theoretically over the past fifty years, due to its economical and strategic fallouts.

A typical experimental approach to the phenomenon is the 'black box' analysis, where the dependence of a state variable (typically the maximum scour depth) on a set of bulk control parameters is investigated to tune prediction equations (see for example Coleman et al. 2003).

Experimental and numerical studies of the flow field around the obstacle have been made over the last thirty years in order to clarify the physics of the phenomenon, which cannot be investigated by black box experimentation (examples of such studies for bridge abutments are Kwan & Melville 1994, Barbhuiya & Dey 2003, Ouillon & Dartus 1997, Chrisohoides et al. 2003).

Sediment motion in local scour has not been quantitatively studied, despite some qualitative descriptions can be found in the literature. Analysis of grain kinematics represents the ideal complement to flow field study for a deeper phenomenological description of the process, since grain motion is the immediate consequence of the scouring flow field; furthermore, the composition of sediment fluxes determines the progression of local scour, that makes the analysis of sediment motion an important support to the interpretation of the large scale scour trends.

Eventually, availability of sediment motion data could significantly support calibration of water – sediment interaction equations, to be used in the numerical modelling of the temporal development of local scour. Such modelling has been made in the last years using the typical transport equation for one dimensional bed load on a plane bed (see for example Olsen & Kjellesvig 1998).

In this work we present results of abutment scour experiments where sediment kinematics was measured. The phenomenon in progress was filmed during the experimental tests; next, some image processing techniques recently set by the Authors were applied to the movies. In this way, complete non-intrusiveness of the measure was achieved. The experiments were run in a transparent pressurized rectangular duct, which allowed observing the scour process from the top without the need to locally inhibit the distortion effect of the free surface. Prior to grain motion analysis, similarity between the scour depth trends here obtained and those from earlier experiments with a free surface was verified.

2 EXPERIMENTAL CAMPAIGN

The experimental duct is 5.8 m long, with a rectangular transversal section having width and height equal

Copyright © 2006 Taylor & Francis Group plc, London, UK

to 40 and 16 cm, respectively. The whole duct is made of plexiglass to assure complete transparency of the walls. An upstream and a downstream tank complete the experimental installation; the hydraulic head in the duct is imposed by a Bazin weir posed in the outlet tank. Water entrance in the duct is guided by a streamlined inlet to avoid wake effects in the flow.

The test reach of the duct is deeper than the other parts; it was filled with PVC cylinders having median equivalent diameter $d_{50} = 3.6$ mm, a uniformity coefficient very close to 1 and specific gravity $\Delta = (\rho_s - \rho)/\rho = 0.43$, where ρ_s and ρ are the densities of sediments and water, respectively. In the upstream and downstream reaches, the same bed roughness is obtained by gluing the PVC grains to steel sheets posed onto the duct bottom; as a result, the effective duct height is $h = 15.5$ cm.

The abutment model is located at about 3.4 m from the duct inlet; it is a vertical plate made of transparent PVC, whose dimensions are 10 cm and 1 cm in the transversal and longitudinal directions, respectively.

Water discharge is measured by a magnetic flowmeter posed on the delivery pipe.

Test starting procedure was different from the standard ones for free surface channels. The granular bed was initially levelled, then the duct was filled with water at a very low rate prior to cover closure, to be able to correct any bed perturbation by the incoming flow. Once the water level reached some centimetres, steady conditions were imposed and the duct cover was closed. A two-component resin (DELO AUTOMIX 1895) was used to seal the cover; the use of such a material was preferred to traditional rubber washers, since it allowed a perfect sealing with a vanishing thickness. The resin needed about 24 hours to catalyze; as a result, the test could start only the next day from the duct closure. The water level was incremented until complete filling of the duct. Next, after eliminating the water bubbles accumulated in the upper part, water discharge was gradually increased to the test value; the transition lasted about 30 s.

The scour depth d at the abutment nose (see Fig. 1) was continuously measured by a laser distance sensor (Baumer Electric OADM 20I44/S14C) posed just over the duct ceil. During the test, the scouring process was filmed via a black and white CCD (SONY XC-8500 CE) capable of 50 fps with a resolution of 576×763 pixel. Duration of every movie was equal to 20 s. The digital images were used for two purposes: (i) to measure sediment kinematics by means of proper image processing described in the following; (ii) to measure the scour depth at the lateral wall. The transversal profile of the scour hole on the upstream face of the obstacle can be seen in the images; it is then possible to evaluate scour at the lateral wall by comparison with that at the abutment nose, whose value is known thanks to the laser measures.

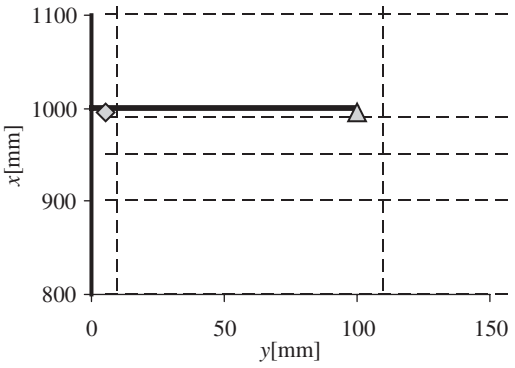


Figure 1. Planimetric definition sketch. Symbols: ▬ duct lateral wall and abutment; ▲ abutment nose measuring point; ♦ lateral wall measuring point; - - - surveyed sections of the scour hole. Flow is from bottom to top.

Profiles of transversal and longitudinal sections of the scour hole were surveyed one or two times during the tests, in order to measure also the scour hole shape. We surveyed transversal sections at $x = 700$, 800, 900, 950, 990 mm (sections upstream of the abutment); transversal sections at $x = 1100$, 1200, 1300, 1400, 1550 mm (downstream of the abutment); longitudinal sections at $y = 10$, 110, 200 mm. Some of the surveyed sections are presented in Figure 1.

We performed four experimental runs with the same water discharge ($Q = 18.5$ l/s), to verify repeatability of the experimental procedure. Water discharge was chosen as that inducing the incipient motion of the bed particles. Following Ballio & Orsi (2001), we defined the threshold conditions as those corresponding to a dimensionless longitudinal solid discharge per unit width equal to $\Phi = q_{sx}/(g \cdot \Delta \cdot d_{50}^3)^{0.5} = 5.7 \cdot 10^{-5}$, where q_{sx} is solid discharge per unit width and g is gravitational acceleration.

3 TEMPORAL AND SPATIAL DEVELOPMENT OF SCOUR DEPTH

Measured scour depth evolution upstream of the abutment is presented in Figure 2 with reference to run 2. Local scour begins at the abutment nose, where the largest scour values were measured during the first part of the process. The plot shows that time evolution of scour depth in this point can be well approximated by two straight lines in the semi-logarithmic plot: the first is steeper than the second, and the change in slope occurs after about 100 s of run. During the first 15–20 s, no scour occurs at the lateral wall; after activation, the scour development in this point can be approximated by a straight line, having a slope almost equal to that of the first line corresponding to the abutment

Copyright © 2006 Taylor & Francis Group plc, London, UK

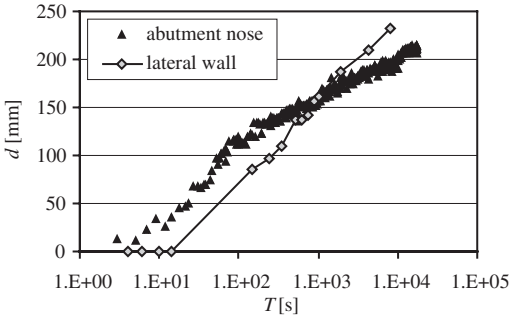


Figure 2. Temporal development of scour depth d upstream of the abutment for run 2. Refer to Fig. 1 for point position.

nose scour trend. After change in slope of the latter, the scour rate at the wall is larger than that at the nose; as a result, after about 900 s of run the scour depths at the nose and at the wall are equal. After this time, maximum scour depth is stably located at the lateral wall. Present result are consistent with earlier ones obtained for free surface experiments (Radice et al. 2002), demonstrating that the flow pressurization does not influence the qualitative features of the erosion process.

Scoured profiles of some transversal and longitudinal sections of the scour hole are presented in Figure 3 for run 2 and time $T = 9000$ s. For such experimental time, maximum scour depth location is stably at the lateral wall. The transversal sections upstream of the abutment have a more or less triangular shape, with a larger slope for the sections closer to the abutment (Fig. 3, a). The transversal sections downstream of the abutment present a sediment plume near the left wall. Sediments are conveyed downstream along two separate channels separated by a sediment ridge (particularly evident for the section at $x = 1400$ mm), whose formation is presumably due the structure of the wake generated by the obstacle. The longitudinal sections present the maximum scour depth in proximity of the abscissa of the abutment; the slope of the scoured profile is larger upstream than downstream, where the sediment are simply conveyed by the flow overpassing the obstacle. Figure 4 presents the three-dimensional reconstruction of the scour hole obtained from the sections of Figure 3, that synthesizes all the observations drawn before. The scour hole shape is consistent with that obtained during experiments with a free surface (Ballio & Orsi 2001); again, the pressurized flow did not affect the scouring process features.

The scour depth evolution at the abutment nose is presented for all the experimental runs in Figure 5. All the experimental curves are qualitatively similar, with some differences in the absolute scour values. For $T < 100$ s, differences are mainly due to the non perfect repeatability in the experimenter recognizing the ideal

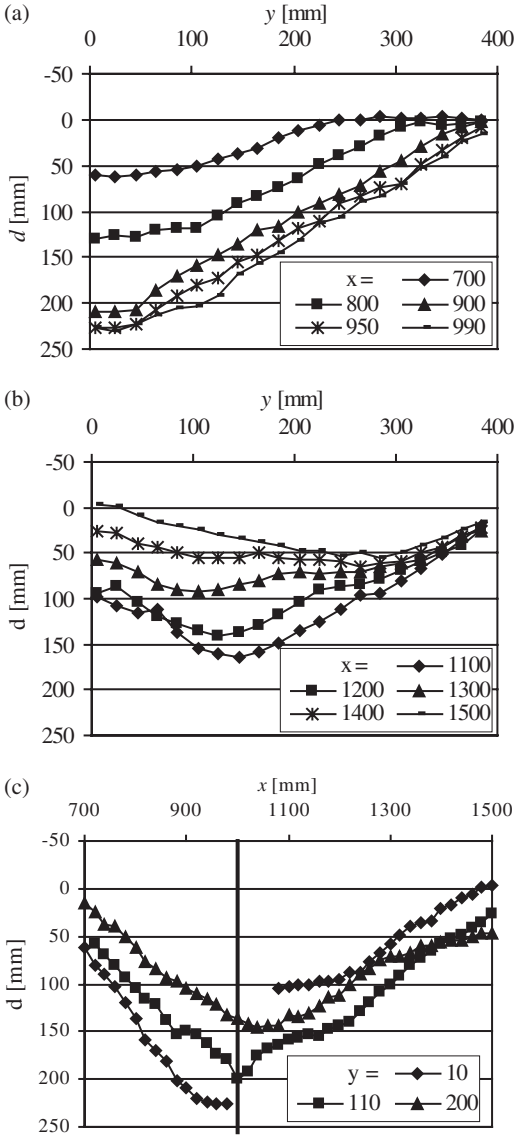


Figure 3. Surveyed section of the scour hole for run 2, time $T = 9000$ s. Transversal sections upstream of the abutment (a); transversal sections downstream of the abutment (b); longitudinal sections (c, position of the abutment indicated). Figure legends show the x position (in mm) of the transversal sections or the y position (in mm) of the longitudinal ones.

starting instant of the process within the transitional phase in which the water discharge is gradually set up to the final value; anyway, after less than two minutes the differences between the four scour trends become negligible, demonstrating that the starting procedure is acceptably repeatable. Then, the scour depth trends

Copyright © 2006 Taylor & Francis Group plc, London, UK

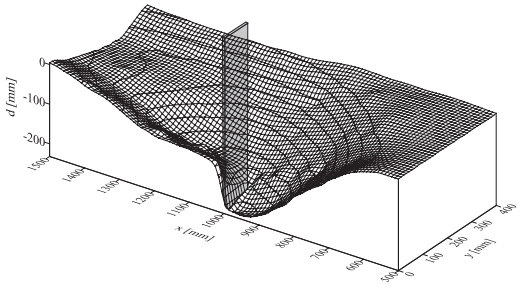


Figure 4. Three-dimensional representation of the scour hole for run 2, $T = 9000$ s.

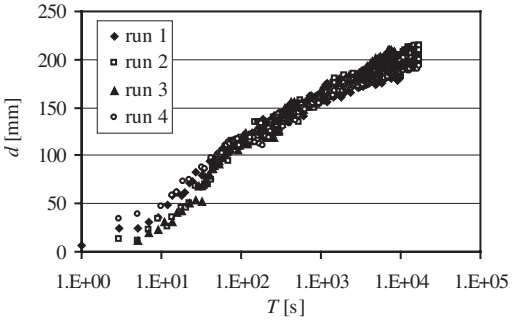


Figure 5. Temporal development of scour depth upstream of the abutment nose for all the experimental runs.

remain very close one to another until time $T = 1000$ s; after this time, the curves relative to the tests remain linear in the semi-logarithmic plot, but present different slopes; this can be due to instabilities either of the scour process for high experimental times or of the experimental installation itself. Anyway, for our test duration the difference between the final scour depth values is smaller than 10%.

4 IMAGE PROCESSING

Sediment motion can be quantified through independent measurement of concentration and velocity of the moving particles. In fact, the vector solid discharge per unit width (hereafter simply called solid discharge) can be calculated as $\boldsymbol{q_s} = C \cdot \boldsymbol{v_s} \cdot d_{50}$, where C is the aerial sediment concentration and $\boldsymbol{v_s}$ is sediment velocity.

Sediment concentration was measured via an image difference technique: consecutive frames in a movie were subtracted to highlight the occurred movements; the difference images were then thresholded and filtered to eliminate the noise and to obtain the definitive image of the displaced particles. After counting the number of displaced particles N, the corresponding concentration could be easily calculated as $C = (N \cdot W_g)/(\Delta x \cdot \Delta y \cdot d_{50})$, where W_g is the volume of a single particle, and Δx and Δy are the dimensions of the measuring cell. Sediment velocity was measured by applying a Particle Image Velocimetry algorithm to a couple of successive difference images. The measuring techniques are more thoroughly described in Malavasi et al. (2004) and in Radice et al. (2004).

Measures of both grain concentration and velocity require definition of spatial and temporal support scales, that have to satisfy opposite requirements. The spatial measuring scale has to be large enough in comparison to grain dimension, to allow for an eulerian continuous representation of movement; on the contrary, it has to be small enough to allow observing the spatial variability of grain motion. The temporal measuring scale has to be large enough to observe non vanishing grain movements between one instant and the next; on the contrary, a too long temporal scale compromises the measures due to dispersion of the grains. In this work, we used spatial measuring cells whose dimension was 2×2 cm^2, while the time sampling interval was the maximum allowed by the CCD, i.e. 0.02 s. Effect of variation of the support scales on the measure are described in Radice (2005).

5 SEDIMENT KINEMATICS

5.1 *Scour activation*

Time evolution of the magnitude of solid discharge is presented in Figure 6 for the start of run 2. Film capturing was started as soon as a non negligible number of moving grains was observed; this is also the condition we chose to identify the start of the process. The presented trends refer to locations in the proximity of the two points were scour depth was measured, i.e. the abutment nose and the lateral wall. Sediments start to move at the abutment nose, where a solid discharge of about 40 mm^2/s was measured since the beginning of the experiment (Fig. 6, a). In the earliest instants, no movement occurred in the proximity of the lateral wall, where the first appreciable motion could be seen after about ten seconds from what we considered the start of the process (Fig. 6, b). Sediment movement a little upstream of the abutment nose (Fig. 6, c) is weak (despite not null) in the first instants, suddenly growing after some seconds.

These observations indicate that at the very beginning of the process, only in the proximity of the obstacle nose the flow field is able to move many grains; given the obvious relation between the scour rate and the spatial distribution of solid discharge:

$$\dot{d} \cdot (1 - p) = \mathrm{div}(\boldsymbol{q}_s) \qquad (1)$$

where p is porosity, precedent observations are in agreement with scour starting at the abutment nose

Copyright © 2006 Taylor & Francis Group plc, London, UK

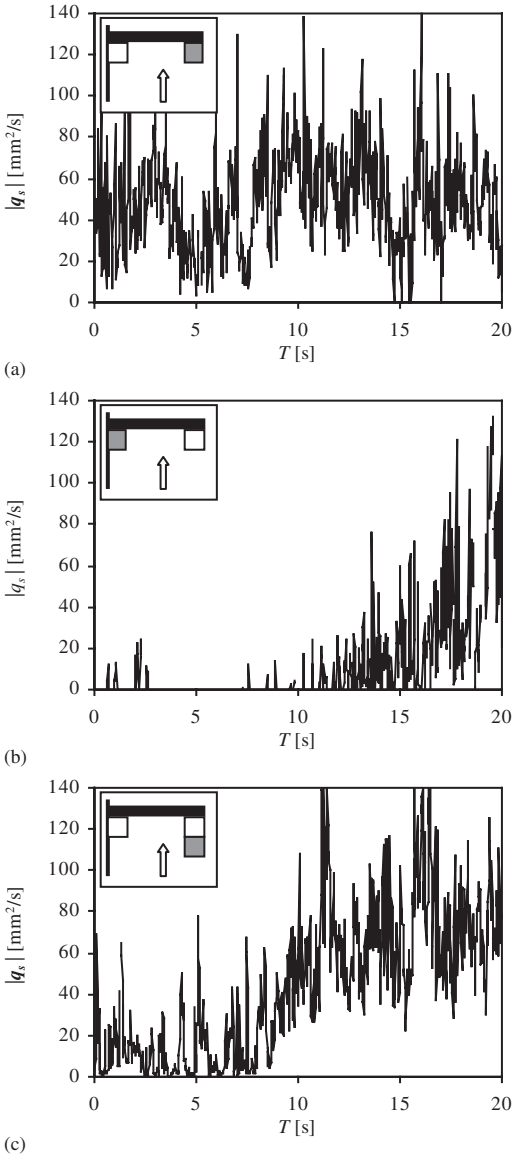


Figure 6. Temporal evolution of measured solid discharge at the start of run 2 upstream of abutment nose (a), in the proximity of the lateral wall (b), and 3 cm upstream of the abutment nose (c). The measuring position is indicated; dimension of measuring cells is $2 \times 2\,cm^2$.

(Fig. 2). From a phenomenological point of view, grain movement at the nose at the test start is very effective, since it is not a simple conveyance of sediments started elsewhere, but a real entrainment of grains from this region, which results in the great erosion rate at the start of the process (Fig. 2). After some moments, grains start to move also elsewhere; it is not clear if first movements are sediment sliding into the developing scour hole or sediment entrainment by the flow field, presumably a combination of both dynamics.

This result is a first index that the phenomenological features of the scouring process evolve during the experiment, since the position where for the developed stages there is the largest scouring activity (the corner region) is completely still in the initial condition of plane bed.

5.2 *Statistical analysis of solid discharge*

Average solid discharge fields around the obstacle are presented in Figure 7 with reference to run 2 and three experimental times, corresponding to the start of the experiment ($T = 0$–20 s), to a time at which scour depths at the nose and at the wall are almost equal ($T = 760$ s), and to the end of the experiment ($T = 17000$ s). The last plot was obtained averaging data from eight consecutive 20 s movies, while each of the former two was derived from a single movie of the same duration; possibility to accumulate movies for the largest experimental time is allowed by the logarithmic evolution of the scour process. The magnitude of average solid discharge was calculated as the composition of the average components along the coordinate axes:

$$q_{s(l)} = \sqrt{\left(\sum_{i=1}^{n} \frac{q_{sx,i}}{n}\right)^2 + \left(\sum_{i=1}^{n} \frac{q_{sy,i}}{n}\right)^2} \qquad (2)$$

where q_{sx} and q_{sy} are the instantaneous components of solid discharge along the coordinate axes and n is the number of measured solid discharge data.

It is evident the decreasing trend of solid discharge all around the abutment, that reflects a general diminishment of the erosive power of the flow field due to the progressively smaller blocking effect of the abutment as the scour hole is eroded.

Maximum solid discharge is located in the proximity of the abutment nose at the beginning of the experiment (Fig. 7, a); it decreases both upstream and towards the lateral wall. This result is the composition of two effects: first, in the nose region all the grains entrained elsewhere by the flow field are conveyed downstream; second, the low average values away from the nose are also determined by the initial stillness before scour activation (see Fig. 6, b and c), since all the zero values were non disregarded in computing the mean.

Streamlines obtained from the average solid discharge vector field are also plotted; for $y > 70$ mm, the sediments seem to be transported by the planimetric deviation of the flow field. Near the wall the streamlines are directed upstream, indicating the action of the principal vortex created by the downflow in front

Copyright © 2006 Taylor & Francis Group plc, London, UK

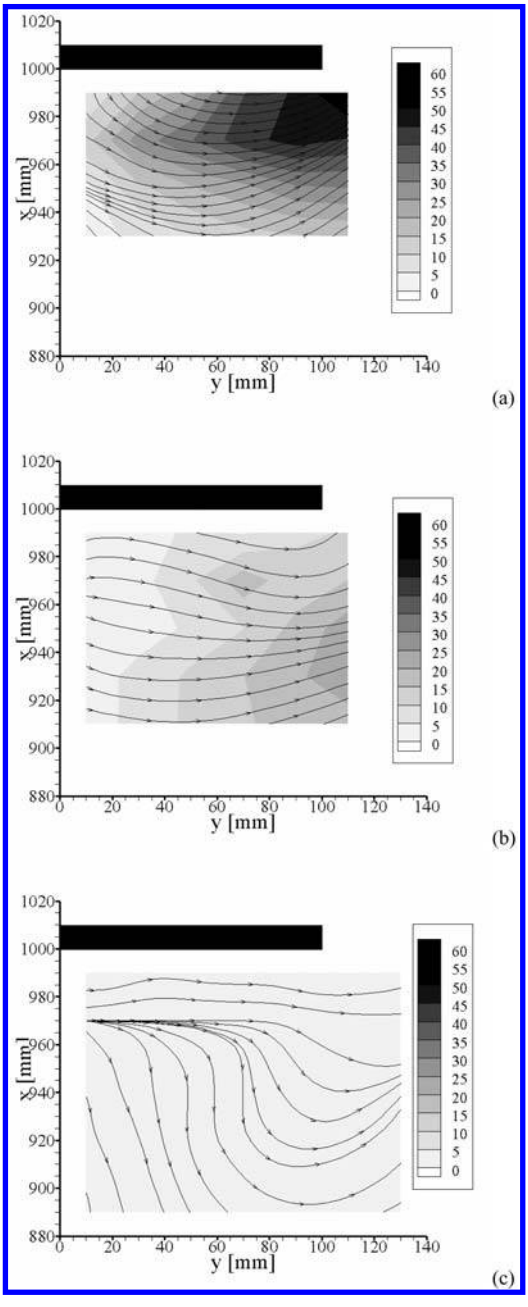


Figure 7. Spatial distribution of average solid discharge $q_{s(1)}$ given by (2) for run 2. Time $T = 10$ s (a), 760 s (b), 17000 s (c). Average streamlines are also indicated.

of the obstacle. In this phase, the vortex appears to be highly stretched by the outer flow field. The solid discharge magnitude increases along all the stream tubes, coherently with the general bed level decreasing.

The average solid discharge field is presented in Figure 7 (b) for an experimental time $T = 760$ s. Again, average solid discharge is minimum at the wall, increasing as the nose region is approached, due to the conveyance of all the sediments. Maximum solid discharge is not close to the abutment nose, but rather a little upstream of it ($x = 930$ mm), due to the presence of appreciable upstream movements also near the abutment nose. The scoured erosion hole determines a smaller concentration of flow at the nose, thus the principal vortex is less stretched than at the beginning of the test. Combination of these effects determines, on average, the existence of a sediment channel about 50–70 mm upstream of the nose.

Observation of the same plot for $T = 17000$ s (Figure 7, c) shows that the magnitude of average solid discharge is rather uniformly distributed in space in comparison to the precedent instants. The sediment pattern resulting from the average streamlines is completely different from what previously seen: upward direction indicates the global action of the principal vortex; all the streamlines come from a small location near the lateral wall ($x = 970$ mm, $y = 0$), showing that this point acts as a sediment source for all the others. This could be a reason for the maximum scour being located at the lateral wall.

Presented results are consistent with those obtained by the Authors in previous works (Malavasi et al. 2004, Radice et al. 2004) dealing with local scour in a free surface channel. Again, there is no substantial distortion imposed to the scour process by the flow pressurization.

Average streamlines are again presented in Figure 8, together with contour lines proportional to average magnitude of solid discharge; in this case, the latter was calculated as the average of the instantaneous magnitudes:

$$q_{s(2)} = \frac{1}{n}\sum_{i=1}^{n}\sqrt{q_{sx,i}^2 + q_{sy,i}^2} \qquad (3)$$

This gives a different information from that given by the magnitude of the average flux $q_{s(1)}$ given by (2): in fact, now we are observing the average intensity of sediment motion regardless of the direction, while the magnitude derived by the average components can be diminished by the presence of opposite direction vectors. The maps in Figure 8 present everywhere larger values than the corresponding ones of Figure 7, indicating that the presence of opposite direction movements is considerable. The increase in the magnitude of solid discharge is most evident in Figure 8 (c), where sensibly higher values are observed upstream of the abutment nose; it can be inferred that in this positions the presence of opposite direction movements is particularly frequent. Direct observation of the phenomenon in progress shows that the opposite events may correspond to grain entrainment by the principal

Copyright © 2006 Taylor & Francis Group plc, London, UK

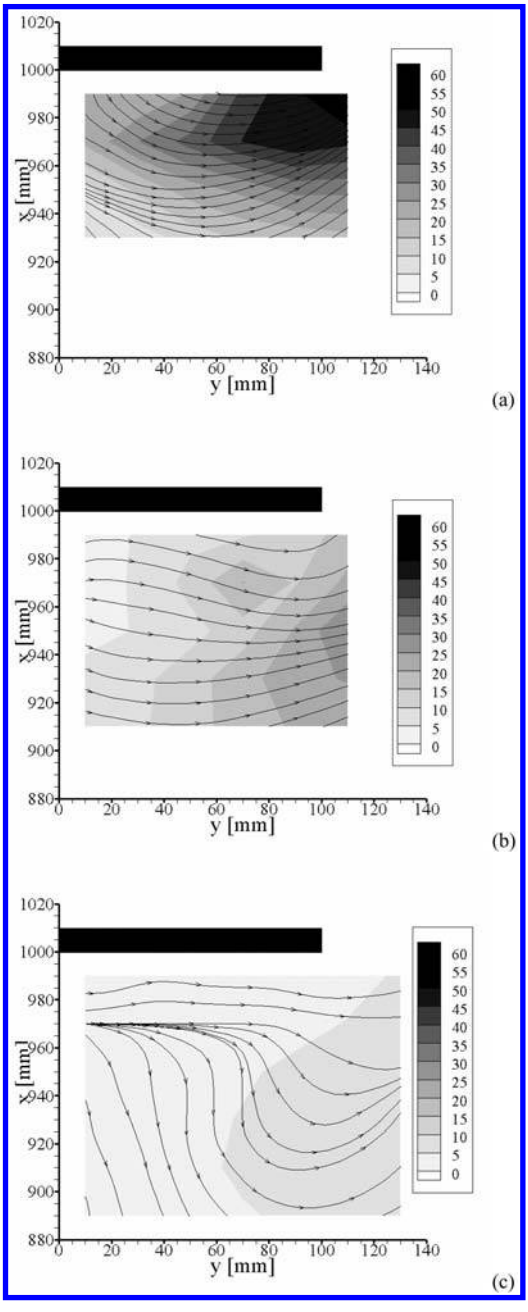


Figure 8. Spatial distribution of average solid discharge $q_{s(2)}$ given by (3) for run 2. Time $T = 10$ s (a), 760 s (b), 17000 s (c). Average streamlines are also indicated.

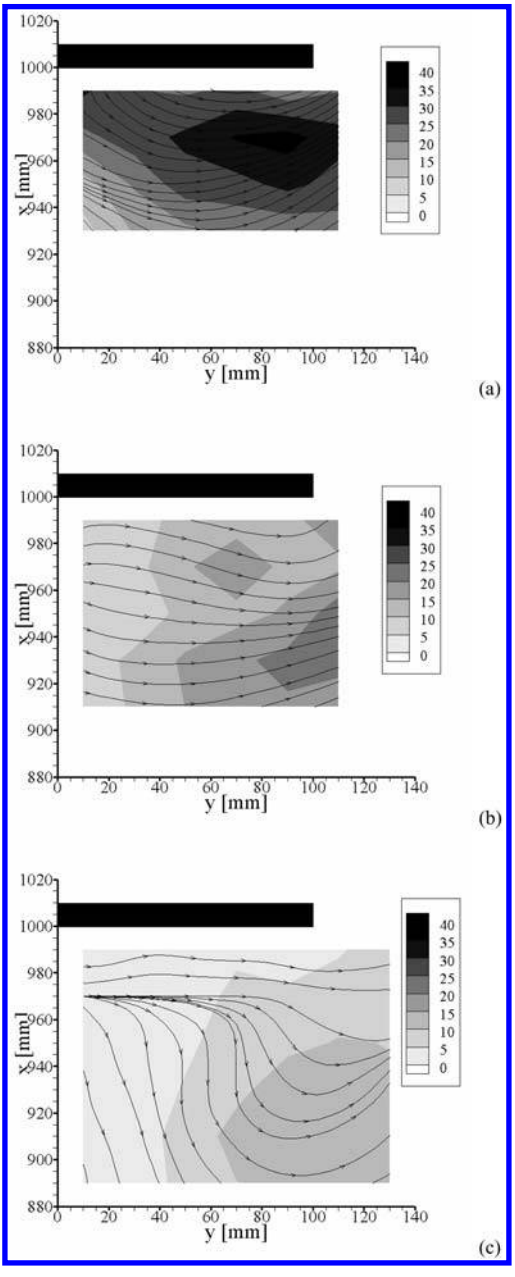


Figure 9. Standard deviation of average solid discharge around the abutment for run 2. Time $T = 10$ s (a), 760 s (b), 17000 s (c). Contour lines are proportional to $\sigma_{|qs|}$ [mm^2/s]. Average streamlines are also indicated.

vortex and to sediment sliding towards the bottom of the scour hole; it is evident that only the first type of movement are induced by the flow field, while the others are substantially related to endogenous instabilities of the scour hole. It is remarkable that if one wants to compare the statistics of grain motion and those of the scouring flow field, he should consider just the movements due to the flow field and not those due to sediment sliding.

Copyright © 2006 Taylor & Francis Group plc, London, UK

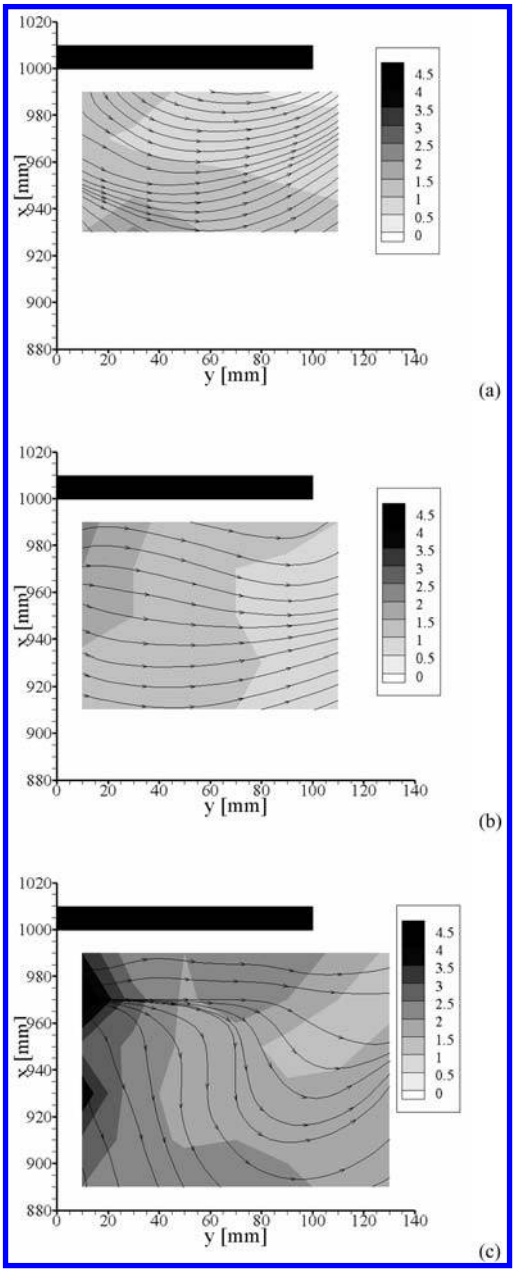


Figure 10. Variation coefficient of average solid discharge around the abutment for test 2. Time $T = 10$ s (a), 760 s (b), 17000 s (c). Contour lines are proportional to $CV_{|qs|}$. Average streamlines are also indicated.

Figure 9 presents spatial distributions of the standard deviation of solid discharge for the previously shown experimental times. Also the standard deviation of solid discharge decreases as scour proceeds. Furthermore, there is a general correspondence between positions of large solid discharge and those of large standard deviation (compare Figs. 8 and 9). The only exception is represented by time $T = 10$ s, where the position of maximum standard deviation is upstream than that of maximum average solid discharge. At the test beginning, grains are initially still, then solid discharge reaches large values after scour activation (Fig. 6, c). The presence of two distinct populations (zero and high values) determines the high standard deviation value.

Figure 10 presents the variation coefficient of the solid discharge (defined as the ratio between the standard deviation and the average value of Fig. 8). In this case, there is a correspondence between the positions of larger sediment activity and those of smaller variation coefficient. The largest values of CV were measured near the lateral wall for time $T = 17000$ s; again, it is possible such values be due to the very high number of zero values in the solid discharge for these locations. Finally, the variation coefficient increases as time proceeds, differently from both the average and the standard deviation, indicating that average values decrease at a higher rate than the standard deviation. As time proceeds, irregularity becomes higher and higher in respect to the sediment activity, indicating a growing role of the unsteady components of sediment motion.

6 CONCLUSIONS

Our works leads to the following major conclusions.

- The pressurized flow does not significantly alter the scour process features, in terms of both the temporal trend of the scour depth and the shape of the erosion hole. In particular, maximum scour is initially at the abutment nose; it successively migrates towards the channel wall.
- Sediment motion is initially mainly due to the planimetric deviation of the flow field; afterwards the action of the three dimensional principal vortex becomes more and more evident thanks to the formation of the scour hole, that reduces the blocking effect of the obstacle.
- Sediment motion analysis can support interpretation of the large scale erosion trends; with reference to the maximum scour displacement, we showed that no motion initially occurs in the corner region, while afterwards all the average sediment streamlines originate from this position.
- Average solid discharge decreases as time proceeds; a similar behaviour was obtained for the standard deviation but not for the variation coefficient, indicating a non similarity in the diminishment of intensity and irregularity of sediment motion.

Copyright © 2006 Taylor & Francis Group plc, London, UK

REFERENCES

Ballio, F. & Orsi, E. 2001. Time evolution of scour around bridge abutments. *Water Engineering Research* 2(4): 243–259.

Barbhuiya, A.K. & Dey, S. 2003. Vortex field in a scour hole around abutments. *Int. Journal of Sediment Research* 18(4): 310–325.

Chrisohoides, A., Sotiropulos, F. & Sturm, T.W. 2003. Coherent structures in flat-bed abutment flow: computational fluid dynamics simulations and experiments. *Journal of Hydraulic Engineering* 129(3): 177–186.

Coleman, S.E., Lauchlan, C.S. & Melville, B.W. 2003. Clear-water scour development at bridge abutments. *Journal of Hydraulic Research* 41(5): 521–531.

Kwan, R.T.F. & Melville, B.W. 1994. Local scour and flow measurements at bridge abutments. *Journal of Hydraulic Research* 32(5): 661–673.

Malavasi, S., Radice, A. & Ballio, F. 2004. Study of sediment motion in a local scour hole through an image processing technique. *River Flow 2004, II Int. Conf. on Fluvial Hydraulics, Naples, Italy*, 1: 535–542.

Olsen, N.R.B. & Kjellesvig, H.M. 1998. Three-dimensional numerical flow modeling for estimation of maximum local scour depth. *Journal of Hydraulic Research* 36(4): 579–590.

Ouillon, S. & Dartus, D. 1997. Three-dimensional computation of flow around groyne. *Journal of Hydraulic Engineering* 123(11): 962–970.

Radice, A. 2005. Cinematica dei sedimenti in un fenomeno erosivo localizzato (Sediment kinematics in a local scour phenomenon). *Ph.D. Thesis, Politecnico di Milano, Milan, Italy* (in italian).

Radice, A., Franzetti, S. & Ballio, F. 2002. Local scour at bridge abutments. *River Flow 2002, I Int. Conf. on Fluvial Hydraulics, Louvain-la-Neuve, Belgium*, 2: 1059–1068.

Radice, A., Malavasi, S. & Ballio, F. 2004. PIV analysis of sediment kinematics in an abutment scour hole. *ICSE 2004, II Int. Conf. on Scour and Erosion, Singapore*, 2: 359–366.

Copyright © 2006 Taylor & Francis Group plc, London, UK

Local scour at elliptical guide banks in plain rivers

B. Gjunsburgs, R.R. Neilands & E. Govsha
Civil Engineering Faculty, Riga Technical University, Riga, Latvia

ABSTRACT: The scour development in floods at abutments (Gjunsburgs & Neilands 2001, 2004, 2005, Gjunsburgs et al. 2004, 2005, 2006) and at elliptical guide banks is studied. The scour hole extents at abutments and guide banks are different. At the upstream head of the elliptical guide banks, a streamline concentration, a local increase in velocity, and the development of a scour hole were observed. The differential equation of equilibrium for the bed sediment movement under clear-water conditions is used, and a method for computing the scour development in floods at elliptical guide banks is elaborated. The method is confirmed by experimental data. The "ERoBo" computer program is elaborated and used in calculations. The scour hole parameters – depth, width, and volume – can be calculated by this method after one, two, or several floods both at the stage of designing the bridge crossings or in the maintenance period.

1 INTRODUCTION

Contraction of river flow by bridge crossings leads to changes in the flow pattern and to a scour at the bridge piers, abutments, and guide banks. The guide banks are constructed on plain rivers on the floodplains. Elliptical guide banks are used to guide the flow and sediments through a bridge opening, to reduce the flow separation at the alignment of the bridge, and to remove the scour hole from the abutment and embankment. The flow pattern and the scour hole dimensions at abutments and elliptical guide banks are different.

The concentration of streamlines, a local increase in velocity, and the development of a scour hole were observed at the upstream head of the elliptical guide banks.

During the past few decades, the equilibrium scour depth at bridge piers, abutments, and spur dikes were studied and fundamental books were published by Breuser & Raudkivi (1991), Hoffmans & Verheij (1997), Melville & Coleman (2000), and May et al. (2002). For determining the scour at the abutments, new approaches were elaborated by Kothyari & Ranga Raju (2001), Armitage & McGahey (2004), Yanmaz & Celebi (2004), Hager et al. (2002), and Gjunsburgs et al. (2001, 2004, 2005, 2006). The flow pattern and the scour process at abutments were studied in detail by Ahmed & Rajaratnam (2000) and Malavasi et al. (2004). However, the development of scour at the head of elliptical guide banks during floods has not yet been studied.

The differential equation of equilibrium for bed sediment movement in clear water is used, and a calculation method for the scour development at the head of elliptical guide banks during floods is elaborated and confirmed by experimental data.

According to the tests and the method suggested, the scour starts when the floodplain is flooded and usually stops at the flood peak. The scour development depends on the flow hydraulics, the river-bed parameters, and the flood duration. At the flood peak, a scour hole is usually formed. Although the scour process can be continued further, it stops, because the flood is time-restricted. The scour time is always less than the flood duration. At the next flood of the same probability, the scour process does not start when the floodplain is flooded, but at a later time step, closer to the flood peak. It happens because of the scour hole developed in the previous flood. The duration of the scour process at the second and forthcoming floods is less than at the previous floods.

The scour-hole parameters at elliptical guide banks can be calculated after one, two, or several floods, either during the maintenance of the bridge or at the design stage. The "ERoBo" computer program was elaborated and used in our calculations.

2 EXPERIMENTAL SETUP

The tests were carried out at the Transport Research Institute (Russia) in a flume 3.5 m wide and 21 m long.

Different forms of guide banks were studied by Latishenko (1960), and he recommended using elliptical guide banks as most acceptable in practice. The dimensions of the upper part of an elliptical guide

Copyright © 2006 Taylor & Francis Group plc, London, UK

bank, namely the turn and the length, were calculated according to the Latishenko (1960) method and were found to be dependent on the flow contraction and the main channel width. The length of the lower part of the guide bank was assumed to be half of the calculated upper part.

The tests were carried out under open flow conditions studying the flow distribution between the channel and the floodplain.

The rigid bed tests were performed for different flow contractions and Froude numbers in order to investigate the velocity and the water level changes in the vicinity of the embankment, along it, and near the modeled elliptical guide bank.

The aim of the sand bed tests was to study the scour process, the changes in the velocity in floods, the effect of different hydraulic parameters, the flow contraction rate, the grain size of the bed material, and the scour development in floods.

The openings of the bridge model were 50, 80, 120, and 200 cm. The flow contraction rate Q/Q_b (where Q is the flow discharge and Q_b is the discharge in the bridge opening under open-flow conditions) varied respectively from 1.56 to 5.69 for floodplain depth of 7 and 13 cm, and the Froude numbers varied from 0.078 to 0.134; the slope of the flume was 0.0012.

The sand bed tests were carried out under clear-water conditions. The sand was placed 1 m up and down the contraction of the flume. The mean grain size was 0.24 and 0.67 mm. The condition that $Fr_R = Fr_f$ was fulfilled, where Fr_R and Fr_f are the Froude numbers for the plain river and for the flume, respectively. The tests in the flume lasted for 7 hours, the length scale was 50 and the time scale was 7. With respect to the real conditions, the test time was equal to 2 days. This was the mean duration of time steps into which the flood hydrograph was divided.

The development of a scour was examined with different flow parameters in time intervals within one 7-h step and within two steps of the hydrograph, 7 hours each.

The tests were carried out with one floodplain model and one side contraction of the flow and with two identical or different floodplain models and two side contractions. The position of the main channel was varied for different tests.

3 METHOD

The differential equation for equilibrium bed sediment movement under clear water conditions at the head of elliptical guide bank has the form

$$\frac{dW}{dt} = Q_s \tag{1}$$

where W = scour hole volume; t = time; and Q_s = sediment discharge out of the scour hole.

In different tests, it was found that the shape of a scour hole is not changing and can be expressed as

$$W = \frac{1}{5}\pi m^2 h_s^3 \tag{2}$$

where m = scour hole steepness; h_s = scour depth.

The left-hand part of Eq. 1 can be written as

$$\frac{dW}{dt} = \frac{3}{5}\pi m^2 h_s^3 \frac{dh_s}{dt} = a h_s^2 \frac{dh_s}{dt} \tag{3}$$

where $a = 3/5\ \pi m^2$.

The sediment discharge was determined by the Levi (1969) formula

$$Q_s = ABV_l^4 \tag{4}$$

where $B = mh_s$ = width of the scour hole; V_l = local velocity at the head of the elliptical guide bank; and A = parameter in the Levi (1969) formula.

The sediment discharge upon development of the scour is given as

$$Q_s = Amh_s V_l^4 = b\frac{h_s}{1+\frac{h_s}{2h_f}} \tag{5}$$

where $b = AmV_l^4$.

Inserting Eqs. 3 and 5, Eq. 1 can be written as

$$ah_s^2 \frac{dh_s}{dt} = b\frac{h_s}{1+\frac{h_s}{2h_f}} \tag{6}$$

Separating and integrating the variables yield

$$t = D_i \int_{x_1}^{x_2} h_s \left(1+\frac{h_s}{2h_f}\right)^4 dh_s \tag{7}$$

An integration with the new variables, $x = 1 + h_s/2h_f$, $h_s = 2h_f(x-1)$, and $1\ dh_s = 2h_f dx$, yields

$$N_i = \frac{t_i}{4D_i h_f^2} + N_{i-1} \tag{8}$$

where $N = 1/6x_i^6 - 1/5x_i^5$; t_i = time interval.

Calculating the value of N_i, we find x_i and the scour depth at the end of time interval:

$$h_s = 2h_f(x-1)k_m k_s k_\alpha \tag{9}$$

where k_m = coefficient depending on the side-wall slope of the guide bank (Yaroslavcev 1956);

Copyright © 2006 Taylor & Francis Group plc, London, UK

k_s = coefficient depending on the guide bank shape; and k_α = coefficient depending on the angle of flow crossing (Richardson & Davis 1995).

Based on the method suggested, the "ERoBo" computer program was elaborated and used in our calculations. The "ERoBo" program allows us to compute and predict scour hole parameters – depth, width, and volume after multiple floods, e.g. after each flood in the course of 50–100 or more years, at the design stage of the bridge crossing lifetime. Considering the flood and river bed parameters, there is no restriction in time for computing the scour at the elliptical guide banks in plain rivers.

To determine the development of scour depth during the flood, the hydrograph was divided into time steps with duration of 1 or 2 days, and each time step was divided into time intervals up to several hours. In the laboratory tests, the time steps were divided into 20 time intervals. For each time step, the following parameters must be determined and entered in the "ERoBo" program: water depth in the floodplain, flow contraction rate, maximum backwater, grain size, thickness of the bed layer with d, and specific weight of the bed material. As a result, we have V_l, V_0, A, D, N_i, N_{i-1}, x, and h_s at the end of time intervals and finally at the end the time step. For the next time step, the flow parameters changed because of the flood and the scour developed during the previous time step. Thus, the depth, width, and volume of the scour hole can be computed after several floods both at the design stage and during the maintenance of bridge crossings.

4 RESULTS

According to the tests at the head of the elliptical guide banks, the concentration of streamlines, a sharp drop in water level, and a rapid increase in velocity were determined.

The local velocity at the head of the guide bank was studied in rigid bed tests, at different contraction rates, and for different flow Froude numbers. The local velocity was found from the formula

$$V_l = \varphi_{el}\sqrt{2g\Delta h} \tag{10}$$

where ϕ_{el} = the velocity coefficient for the elliptical guide banks; g = the gravitational acceleration; and Δh = the maximum backwater determined by the Rotenburg (1969) formula.

According to our tests, the velocity coefficient ϕ_{el} depends on the flow contraction. With increasing flow contraction, ϕ_{el} reduces, while with decreasing flow contraction, it increases. The local velocity and water level changes were measured in tests at the head of the elliptical guide banks. For the known V_l and Δh values, ϕ_{el} was found for each contraction rate of the flow. The coefficient ϕ_{el} as a function of the flow contraction is shown in Figure 1.

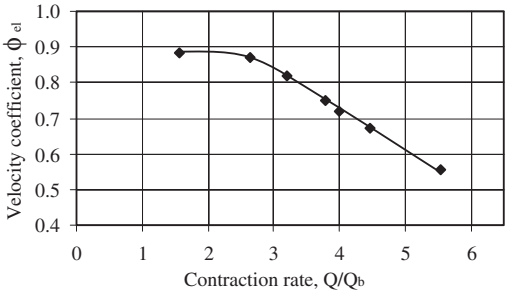


Figure 1. The velocity coefficient ϕ_{el} versus the flow contraction rate for elliptical guide banks (test data for ϕ_{el} with different flow contraction).

Table 1. Comparison between the experimental and calculated data for local velocities at the elliptical guide banks.

Test	Q/Q_b	Δh (cm)	$V_{l.test}$ (cm/s)	$V_{l.calc.}$ (cm/s)	$V_{l.calc}/V_{l.test}$
EL1	5.27	2.220	39.1	36.2	1.080
EL2	5.69	3.620	46.4	46.8	0.991
EL3	5.55	3.950	49.7	52.1	0.954
EL4	3.66	1.189	36.9	35.1	1.051
EL5	3.87	1.795	44.0	45.2	0.973
EL6	3.78	2.350	51.0	53.9	0.946
EL7	2.60	0.557	28.4	26.7	1.064
EL8	2.69	0.993	37.8	37.5	1.008
EL9	2.65	1.280	43.0	51.2	0.840
EL10	1.56	0.380	23.9	22.3	1.072
EL11	1.66	0.455	26.1	23.0	1.135
EL12	1.67	0.530	28.2	30.7	0.919
EL13	4.05	1.420	38.2	32.5	1.177
EL14	3.99	1.800	43.4	37.5	1.157
EL15	4.05	2.700	52.7	49.4	1.067
EL16	3.66	1.189	36.9	35.1	1.051
EL17	3.87	1.795	44.0	45.2	0.973
EL18	3.78	2.350	51.0	53.9	0.946
EL19a	4.46	1.476	36.5	33.0	1.106
EL19b	3.21	0.769	31.4	28.3	1.110
EL20a	4.47	1.795	40.8	40.8	1.000
EL20b	3.24	0.950	34.8	34.4	1.012

A comparison between the experimental and calculated data for local velocities at the elliptical guide banks is presented in Table 1.

Figure 2 shows a scheme of the bed level changes near the elliptical guide bank at the end of test EL9 for $Q/Q_b = 2.65$, $l_b = 120$ cm, $h_f = 7$ cm, and $d = 0.24$ mm. As follows from the test results, near the head of elliptical guide banks, a scour hole is developed. At the lower part of the elliptical guide banks, deposition of the sediments takes place, and the bed level increases.

Copyright © 2006 Taylor & Francis Group plc, London, UK

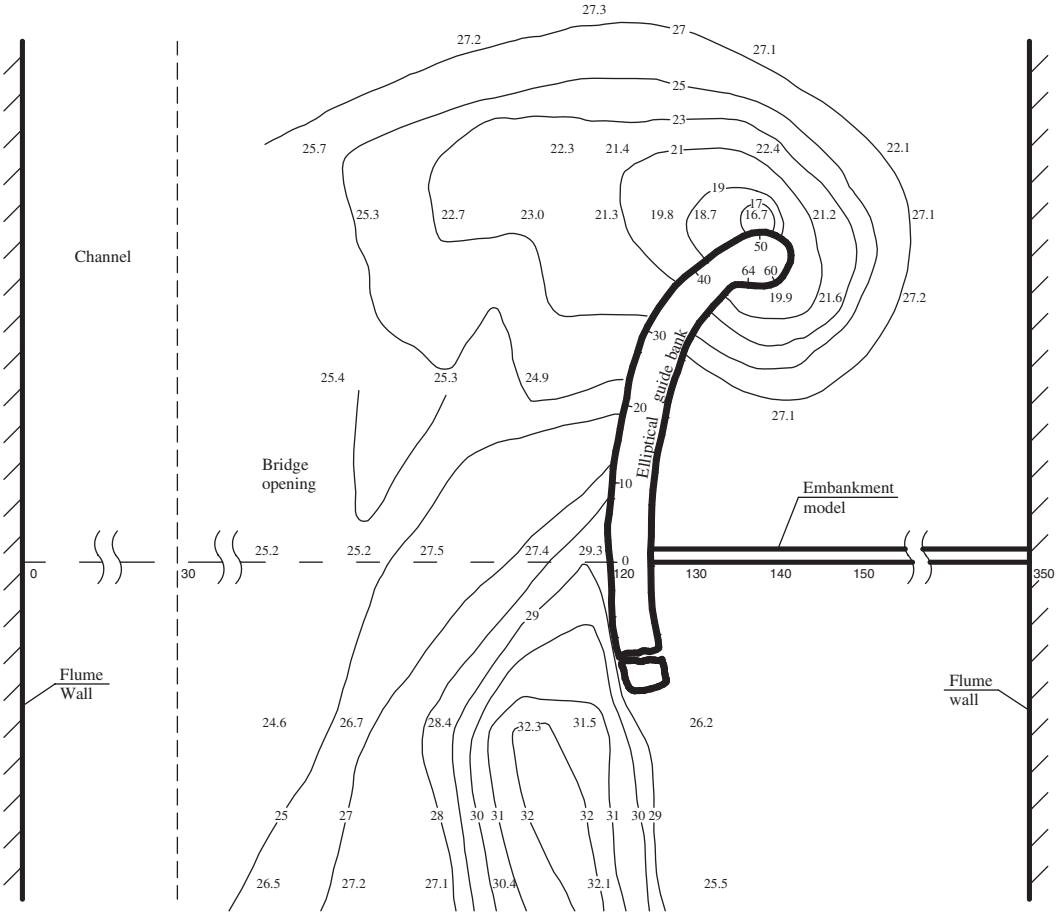


Figure 2. Scour scheme near the elliptical guide bank at the end of test EL9.

The changes in the bed level with time along the guide bank are presented in Figure 3.

Bed levels were measured by an electric pin-pointer along the guide bank length at points 0, 10, 20, 30, 40, 50, 60, and 64, as shown in Figures 2 and 3.

The shape of the scour hole was measured in tests with different Froude numbers, sand bed parameters, and contraction rate of the flow. According to the tests, the shape of the scour hole was not changing, remaining the same.

The volume of the scour hole near the elliptical guide bank can be found by Eq. 2. A comparison between the experimental and calculated volumes of the scour hole is given in Table 2.

In the case of elliptical guide banks, the distribution of velocities and scour in the contraction cross-section of the bridge crossing is more uniform. An example of scour at the contracted cross-section of the modelled bridge crossing with elliptical guide bank

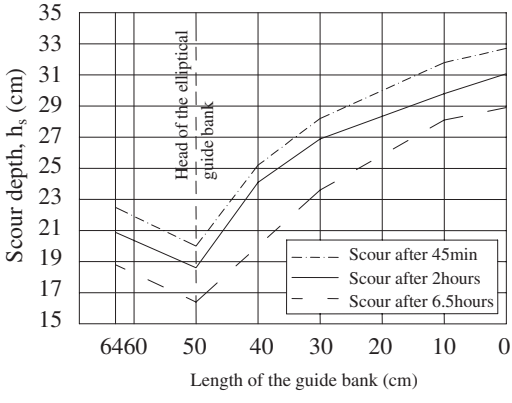


Figure 3. Bed-level profile at the upstream part of the elliptical guide bank.

Copyright © 2006 Taylor & Francis Group plc, London, UK

Table 2. Comparison of the experimental and calculated volumes of scour hole at the elliptical guide banks.

Test	t* h	h_s cm	W_{test} cm^3	W_{calc} cm^3	W_{test}/W_{calc}
EL1	1.500	7.60	715.6	955.0	0.749
EL1	4.333	8.70	1375.0	1360.0	1.011
EL1	7.000	9.40	1526.8	1560.0	0.979
EL2	3.500	10.80	2984.0	3270.0	0.913
EL2	6.000	12.00	3660.0	3296.0	1.110
EL2	7.000	12.40	5851.0	4860.0	1.204
EL3	0.333	9.00	2418.6	2240.0	1.080
EL3	2.000	14.10	7266.5	7420.0	0.979
EL3	0.500	4.30	244.0	272.0	0.897
EL4	2.330	6.00	450.0	415.0	1.084
EL4	3.500	6.60	792.0	700.0	1.131
EL4	0.667	7.30	935.0	1030.0	0.908
EL5	2.000	9.00	1789.0	1910.0	0.937
EL5	6.000	10.60	2406.5	2160.0	1.114
EL5	7.000	11.00	2400.0	2626.0	0.914
EL6	0.333	8.00	1835.0	1889.0	0.971
EL6	1.500	12.60	5305.0	5520.0	0.961
EL6	2.167	13.80	6694.9	6850.0	0.977
EL7	0.917	3.70	86.0	83.9	1.025
EL7	7.000	5.20	236.5	227.0	1.042
EL8	0.083	4.00	120.0	99.5	1.206
EL8	3.333	7.40	562.0	562.0	1.000
EL8	6.500	8.00	680.0	722.0	0.942
EL9	0.500	7.70	801.2	815.0	0.983
EL9	1.500	9.10	1499.0	1555.0	0.964
EL9	7.000	10.70	1992.0	2140.0	0.931

* Time from start of the tests.

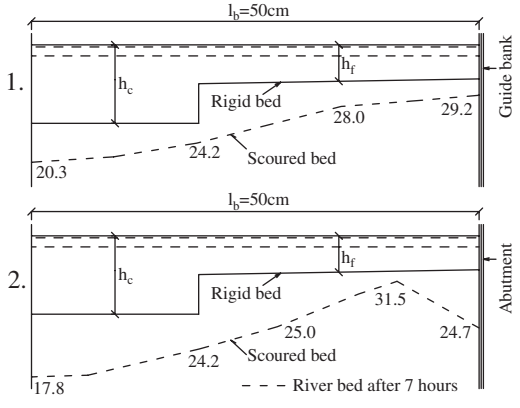


Figure 4. Scour in the contracted cross-section of the bridge-crossing model: with elliptical guide bank (1) and with abutment (2).

and abutment is given in Figure 4. The scour at the elliptical guide bank is smaller in magnitude and more uniform compared with an abutment.

The values of the scour depth development obtained in tests and calculated by the method presented under the steady and unsteady flow conditions are given in Figures 5 and 6. The scour depth development observed and calculated at the head of the elliptical guide banks in tests EL4 and ETL1 is similar – the rapid development at the beginning of the process is gradually reduced with time.

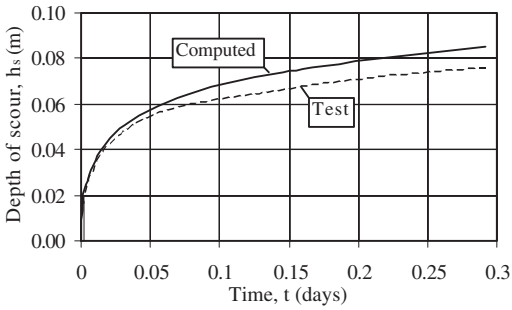


Figure 5. Scour development in time under steady flow conditions at the elliptical guide bank for test EL4.

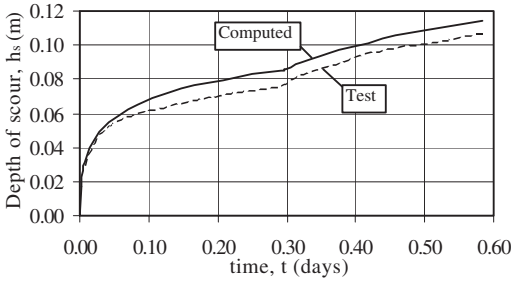


Figure 6. Scour development in time under unsteady flow conditions at the elliptical guide bank for test ETL1.

A comparison of the experimental and calculated scour depth is presented in Table 3.

The development of the scour depth, width, and volume after three floods of the same probability is shown in Figures 7, 8, and 9, respectively. The most rapid development of the scour hole was observed in the first flood. In the following floods, the scour started later and closer to the peak of the flood. The time of scour and the rate of scour hole development in time reduced with every subsequent flood.

5 CONCLUSIONS

The scour development in floods at elliptical guide banks is studied. The differential equation of the equilibrium bed sediment movement under clear-water conditions is used, and a method for computing the scour hole development with time at the head of the elliptical guide bank during floods is elaborated and

Copyright © 2006 Taylor & Francis Group plc, London, UK

Table 3. Comparison between the experimental and calculated scour depth at the elliptical guide banks.

Test no.	l_b cm	Q/Q_b	h_f cm	d mm	t h	$h_{s.test}$ cm	$h_{s.calc}$ cm	$h_{s.test}/h_{s.calc}$
EL1	50	5.27	7	0.24	7	9.40	9.20	1.022
EL2	50	5.69	7	0.24	7	12.20	11.90	1.025
EL3	50	5.55	7	0.24	7	14.30	13.00	1.100
EL4	80	3.66	7	0.24	7	7.60	8.40	0.905
EL5	80	3.87	7	0.24	7	11.00	11.00	1.000
EL6	80	3.78	7	0.24	7	14.00	13.51	1.036
EL7	120	2.60	7	0.24	7	5.20	5.00	1.040
EL8	120	2.69	7	0.24	7	8.30	8.80	0.943
EL9	120	2.65	7	0.24	7	11.50	10.70	1.075
EL10	200	1.56	7	0.24	7	2.40	3.00	0.800
EL11	200	1.66	7	0.24	7	3.70	4.11	0.900
EL12	200	1.67	7	0.24	7	4.70	4.90	0.959
EL13	80	4.05	13	0.67	7	6.40	6.80	0.941
EL14	80	3.99	13	0.67	7	9.10	9.60	0.948
EL15	80	4.05	13	0.67	7	14.00	14.20	0.986
EL16	80	3.66	7	0.67	7	6.10	5.60	1.089
EL17	80	3.87	7	0.67	7	8.40	8.20	1.024
EL18	80	3.78	7	0.67	7	12.20	10.50	1.162
EL19a	80	3.21	7	0.24	7	6.20	6.30	0.984
EL19b	80	4.46	7	0.24	7	6.40	7.30	0.877
EL20a	80	4.47	7	0.24	7	8.70	9.70	0.897
EL20b	80	3.24	7	0.24	7	8.20	7.60	1.079
ETL1	80	3.66	7	0.24				
	80	4.05	13	0.24	14	10.70	11.41	0.938
ETL2	80	3.87	7	0.24				
	80	3.99	13	0.24	14	13.70	14.80	0.926
ETL3	80	3.77	7	0.24				
	80	4.05	13	0.24	14	20.30	18.86	1.076

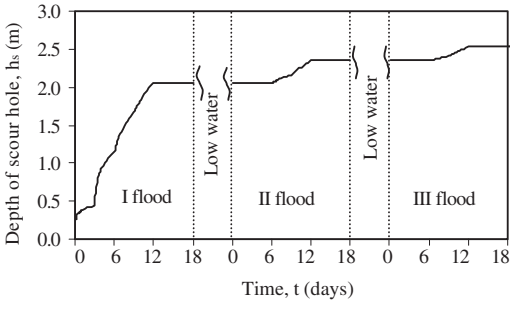


Figure 7. Scour depth development for three floods of the same probability at an elliptical guide bank.

confirmed by experimental data. The "ERoBo" computer program has been worked out and used in our calculations.

The scour at the head of guide banks starts when the floodplain is flooded and usually stops at the flood peak. At the peak of the flood, the scour hole has already been formed. The scour time is always less

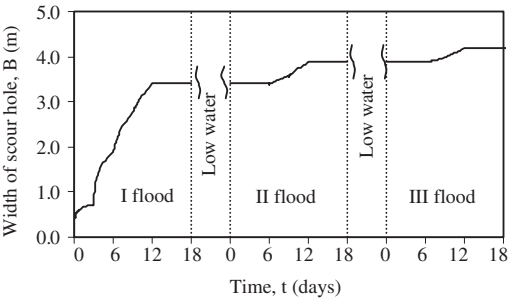


Figure 8. Scour hole width development for three floods of the same probability at an elliptical guide bank.

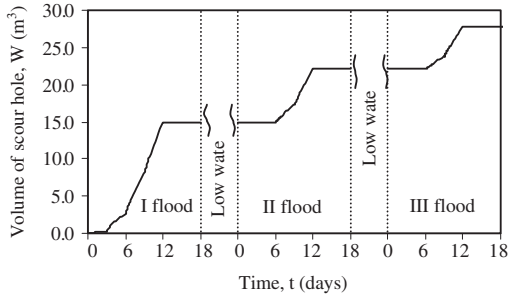


Figure 9. Scour hole volume development for three floods of the same probability at an elliptical guide bank.

than the flood duration, and it reduces with every subsequent flood of the same probability.

According to the method suggested, the depth, the width, and the volume of scour can be computed after several floods either at the stage of design or during the maintenance of the bridge crossing, which gives the possibility of predicting its stability.

REFERENCES

Ahmed, F. & Rajaratnam, N. 2000. Observations on flow around bridge abutment. *Journal of Engineering Mechanics* 126(1): 51–59.

Armitage, N. & McGahey, C. 2004. Scour prediction using the Movability Number criteria for incipient motion. In Greco, Carravetta & Della Morte (eds), *Proc. River Flow 2004, Napoli, Italy, 23–25 June 2004, vol. 1: 511–519*. London: Taylor & Francis Group.

Breuser, H.N.C. & Raudkivi, A.J. 1991. *Scouring*. Rotterdam: A. A. Balkema.

Gjunsburgs, B. & Neilands, R. 2001. Scour development on time at the abutment of the bridge on plain rivers. *Journal Environmental Research, Engineering and Management* 1(15): 8–11. Kaunas: Kaunas University of Technology.

Gjunsburgs, B. & Neilands, R. 2004. Local velocity at bridge abutments on plain rivers. In Greco, Carravetta & Della Morte (eds), *Proc. River Flow 2004, Napoli, Italy, 23–25*

Copyright © 2006 Taylor & Francis Group plc, London, UK

June 2004, vol. 1: 443–448. London: Taylor & Francis Group.

Gjunsburgs, B. & Neilands, R. 2005. Scour development at the abutments during the floods. In Cygas & Froehner (eds), *Proc. 6th Intern. Conf. Environmental Engineering. Environmental Protection. Water Management and Hydraulics, Vilnius, Lithuania, 26–27 May 2005, vol. 1: 362–366.* Vilnius: Technika.

Gjunsburgs, B. & Neilands, R.R. 2006. Scour development and bridge abutment safety during the floods. In Aigner (eds), *Proc. Intern. Conf. Flow Simulation in Hydraulic Engineering, Dresden, Germany, 9–11 March 2006.*

Gjunsburgs, B., Neilands, R. & Kreslins, A. 2005. Abutment scour development during floods. In Schmidt (eds), *Proc. Hydrotechnical Engineering: Cornerstone of a Sustainable Environment; 17th Canadian Hydrotechnical Intern. Symp., Edmonton, Alberta, 17–19 August 2005: 593–601.* Montreal: CSCE/SCGC.

Gjunsburgs, B., Neilands, R. & Neilands, R.R. 2004. Scour development at bridge abutments on plain rivers during the flood: analysis of the method. In Chiew, Lim & Cheng (eds), *Proc. 2nd Intern. Conf. Scour and Erosion, Meritus Mandarin, Singapore, 14–17 November 2004, vol. 1: 199–206.* Singapore: Stallion Press.

Hager, W.H., Unger, J. & Oliveto, G. 2002. Entrainment criterion for bridge piers and abutments. In Bousmar & Zech (eds), *Proc. River Flow 2002, Louvain-La-Neuve, Belgium, 4–6 September 2002, vol. 2: 1053–1058.* Lisse: Swets & Zeitlinger.

Hoffmans, G.J.C.M. & Verheij, H.C. 1997. *Scour Manual*. Rotterdam: A. A. Balkema.

Kothyari, U.C. & Ranga Raju, K.G. 2001. Scour around spur dikes and bridge abutments. *Journal of Hydraulic Engineering* 39(4): 367–374.

Latishenko, A.M. 1960. *Questions of artificially contracted flow*. Moscow: Gostroizdat (in Russian).

Levi, I. I. 1969. *Dynamics of River Flow*. Moscow: Gidrometeoizdat (in Russian).

Malavasi, S., Radice, A. & Ballio, F. 2004. Study of sediment motion in a local scour hole through an image processing technique. In Greco, Carravetta & Della Morte (eds), *Proc. River Flow 2004, Napoli, Italy, 23–25 June 2004: 443–448*. London: Taylor & Francis Group.

May, R., Ackers, J. & Kirby, A. 2002. *Manual on Scour at Bridges and Other Hydraulic Structures*. London: CIRIA.

Melville, B.W. & Coleman, S.E. 2000. *Bridge Scour*. Highlands Ranch, CO: Water Resources Publications.

Richardson, E.V. & Davis, S.R. 3rd ed. 1995. *Evaluating Scour at Bridges*. Hydraulic Engineering Circular, No. 18, Federal Highway Administration, Washington, DC, USA.

Rotenburg, I.S. & Volnov, V.S. 1969. *Project Examples of Bridge Crossing*. Moscow: Vishaja Shkola (in Russian).

Yanmaz, A.M. & Celebi, T. 2004. A reliability model for bridge abutment scour. *Turkish J. Eng. Env. Sci,* 28: 67–83.

Yaroslavcev, I.A. 1956. *Calculation of local scour at bridge piers*. Moscow: Bulletin of TCNIIS N80, Moscow (in Russian).

Copyright © 2006 Taylor & Francis Group plc, London, UK

Local scouring at bridge piers and abutments: Time evolution and equilibrium

C. Grimaldi & R. Gaudio
Università della Calabria, Dipartimento di Difesa del Suolo "V. Marone", Rende (CS), Italy

A.H. Cardoso
Instituto Superior Técnico, Departamento de Engenharia Civil e Arquitectura, Lisboa, Portugal

F. Calomino
Università della Calabria, Dipartimento di Difesa del Suolo "V. Marone", Rende (CS), Italy

ABSTRACT: The problem of assessing the equilibrium scour depth at bridge piers and abutments received great attention in the last two decades. Also the time evolution of scouring was investigated by many authors, and different predictive formulae were proposed in the literature. In this work, laboratory data by different authors are analysed so as to verify the onset of the equilibrium state. The data sets are also used to compare some empirical formulae on the time evolution of the scour depth at piers or abutments. Finally, the minimum test duration for calculating the equilibrium scour depth by extrapolation is investigated by applying the Bertoldi & Jones (1998) formula to the data sets.

1 INTRODUCTION

Local scouring at bridge piers and abutments is a problem of worldwide relevance in Fluvial Hydraulics. In fact, scouring is one of the main causes of damaging or failure of bridges (see e.g. Murillo 1987) and it has attracted significant research efforts.

Several scientific studies have dealt with the prediction of scour depth evolution over time, $d_s(t)$; many more tackle the issue of equilibrium scour depth, d_{se}; both piers and abutments have been studied (see Melville & Coleman 2000).

Empirical formulae proposed in the literature were obtained, mostly, by analysing data acquired in laboratory experiments; predictions of both $d_s(t)$ and d_{se} may differ considerably.

In addition, one important conceptual problem faced by researchers is the definition of the equilibrium condition, with direct implications on the choice of tests duration. Some procedures and criteria to evaluate the threshold duration (in the sense of time needed to reach the equilibrium state) have been suggested in the literature, but there is no universally accepted one.

In this work, the existence of the equilibrium state in experimental data sets generated by several authors will be assessed by adapting a procedure recently suggested by Grimaldi (2005). Then, the same data will be used to evaluate the performance of empirical formulae scrutinised in the literature about the prediction of time evolution as well as the equilibrium scour depth at piers or abutments. Finally, the minimum test duration needed for the prediction of equilibrium scour depth, through extrapolation, on the basis of short non-equilibrium experiments, will be addressed by applying the Bertoldi & Jones (1998) equation to the same data sets.

2 DATA SETS AND ONSET OF EQUILIBRIUM CONDITIONS

Grimaldi (2005) proposed the evaluation of the onset of equilibrium state through three different criteria: the first refers to the test duration, which can be calculated *a priori*; the second takes advantage of the pattern of time evolution of the scour depth; the third one relies on the increment of scour depth in the last 24 hours of a given test.

The test duration can be calculated *a priori*, as suggested, for instance, by Franzetti et al. (1994) or Melville & Chiew (1999) for piers and by Lauchlan et al. (2001) for abutments. The calculated duration can be used as a reference value, t_e, to design new tests or to verify the occurrence of the equilibrium state in past experiments.

Copyright © 2006 Taylor & Francis Group plc, London, UK

Table 1. Characteristic values of the laboratory tests.

Test	h (m)	U (m/s)	U_c (m/s)	d_{50} (mm)	σ_g	b or L (m)	T (h)
CB1	0.031	0.239	0.227	0.84	1.26	0.147	100.5
CB2	0.073	0.262	0.244	0.84	1.26	0.147	142.1
CB3	0.028	0.234	0.220	0.84	1.26	0.270	126.6
CB4	0.078	0.261	0.245	0.84	1.26	0.270	117.5
CB5	0.028	0.237	0.225	0.84	1.26	0.400	104.7
K12	0.050	0.260	0.242	0.80	1.28	0.516	98.9
A1	0.071	0.277	0.294	0.63	1.81	0.180	126.3
A2	0.071	0.251	0.241	0.63	1.81	0.180	94.4
B1b	0.071	0.275	0.289	0.63	1.81	0.400	236.9
B2a	0.072	0.244	0.227	0.63	1.81	0.400	166.6
C1	0.071	0.277	0.294	0.63	1.81	0.500	150.1
C2	0.071	0.251	0.241	0.63	1.81	0.500	94.5
GA0	0.150	0.400	0.400	1.28	1.46	0.075	96.0
GB0	0.250	0.336	0.336	0.63	1.44	0.090	147.9
GC0	0.250	0.336	0.336	0.63	1.44	0.120	146.1

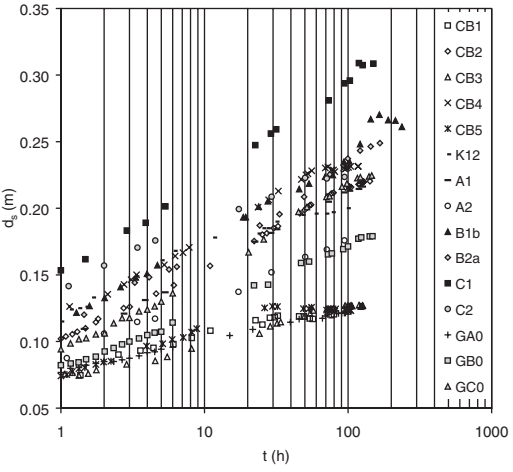


Figure 1. Time evolution of scour depth.

Cardoso & Bettess (1999) assumed that the equilibrium scour depth is reached when an almost horizontal trend is identified in a plot where the scour depth evolution in time is represented in a semi-logarithmic graph. In the present study, this condition will be assumed as mandatory.

If the variation of the scour depth in the last 24 hours of a given test, $\Delta d_{s,24}$, is less than a predefined appropriate threshold value, then the equilibrium state can be assumed as reached for practical purposes. Melville & Chiew (1999) suggested the following threshold value for piers: $\Delta d_{s,24} = 0.05 \cdot b$, where b is the pier width. Grimaldi (2005), having performed laboratory tests on local scouring at a circular pier, noted that the above threshold value did not satisfy the other two equilibrium criteria; therefore, he suggested a more restrictive criterion, namely $\Delta d_{s,24} = 0.05 \cdot b/3$.

In this work, 15 laboratory data sets of $d_s(t)$ were selected in the literature:

- 5 from Cardoso & Bettess (1999) (identified as CB1 to CB5), 1 from Kwan (1988) (K12) and 6 from Santos (1999) (A1, A2, B1b, B2a, C1 and C2) for scouring at vertical-wall abutments;
- 3 from Grimaldi (2005) (GA0, GB0 and GC0) for scouring at a circular pier.

Table 1 reports the characteristic values of these laboratory tests, namely, the water depth, h, the approach flow velocity, U, the critical velocity for the beginning of sediment motion, U_c, the median sediment size, d_{50}, the geometric standard deviation of the grain-size distribution, $\sigma_g = (d_{84}/d_{16})^{0.5}$, the length of the abutment or the pier width, respectively L or b, and the test duration, T. All the tests were performed with sand, for $0.93 \cdot U \le U_c \le 1.06 \cdot U$.

The reference test durations, t_e, were obtained by applying the criteria by Franzetti et al. (1994) for piers and by Lauchlan et al. (2001) for abutments. The former is expressed as: $t_e = 2 \cdot 10^6 \cdot b/U$; the latter as:

$$t_e = 1.1 \cdot 10^6 \frac{L}{U}\left(\frac{h}{L}\right)^{0.75U_c/U}\left(\frac{U}{U_c}\right)^3 \quad (1)$$

Results of these formulations are shown in Table 2. Tests CB4, K12, A2, B2a, C2, GA0, GB0 and GC0 lasted shorter than the calculated time to equilibrium or reference duration, since $T < t_e$. Nevertheless, it is to be noted that the duration of tests GA0 and GB0 is very close to the reference value (the difference $T - t_e$ is equal to 8 h and 1 h, respectively).

The time evolution of the scour depth can be observed in the semi-logarithmic graph of Figure 1. Tests A1, A2 and B2a do not present a clear slope change.

The increment of the scour depth in the last 24 hours of each test was obtained from the records as $\Delta d_{s,24,m}$, and computed according to Grimaldi (2005): $\Delta d_{s,24,c} = 0.05 \cdot b/3$ for piers and, analogously, $\Delta d_{s,24,c} = 0.05 \cdot 2 \cdot L/3$ for abutments, b being equivalent to $2 \cdot L$. Comparison shows that only test A2 does not satisfy the condition $\Delta d_{s,24,m} < \Delta d_{s,24,c}$ (Table 2).

Test A2 does not satisfy any criterion; for this reason it was considered not to have reached equilibrium. Since it was assumed that the criterion of slope change is mandatory, tests A1 and B2a were also considered not at equilibrium. Tests CB4, K12, C2, GA0, GB0 and GC0 were considered equilibrium tests, in spite of the fact that they do not satisfy the test duration criteria by Franzetti et al. (1994) or Lauchlan et al. (2001). All the remaining tests (CB1, CB2, CB3, CB5, B1b, C1) satisfy simultaneously the three criteria and they were equilibrium tests (see Tables 1 and 2).

Copyright © 2006 Taylor & Francis Group plc, London, UK

Table 2. Results of the application of the equilibrium criteria.

Test	t_e (h)	$\Delta d_{s,24,m}$ (m)	$\Delta d_{s,24,c}$ (m)	Slope change	Equilibrium
CB1	72.314	0.0027	0.0049	Yes	Yes
CB2	130.804	0.0024	0.0049	Yes	Yes
CB3	85.899	0.0004	0.0090	Yes	Yes
CB4	158.579	0.0014	0.0090	Yes	Yes
CB5	90.441	0.0003	0.0133	Yes	Yes
K12	148.005	0.0040	0.0172	Yes	Yes
A1	79.603	0.0017	0.0060	No	No
A2	125.917	0.0069	0.0060	No	No
B1b	98.400	−0.0047	0.0133	Yes	Yes
B2a	188.306	0.0025	0.0133	No	No
C1	98.150	0.0012	0.0167	Yes	Yes
C2	167.617	0.0011	0.0167	Yes	Yes
GA0	104.167	0.0010	0.0013	Yes	Yes
GB0	148.810	0.0009	0.0015	Yes	Yes
GC0	198.413	0.0013	0.0020	Yes	Yes

In the next sections, all records will be used to evaluate the time evolution of scour depth; however, the last measurement, $d_s(T)$, of tests A1, A2 and B2a was not retained for the analysis on equilibrium scour since these tests were non-equilibrium tests.

3 EVALUATION OF TIME EVOLUTION AND EQUILIBRIUM SCOUR FORMULAE

Many formulae can be found in the literature for the assessment of the scour depth evolution over time at bridge piers or abutments. In this context, "scour depth" is to be understood as the depth of the deepest point in the scour hole at a given time instant.

Seven formulae were selected for evaluation by comparing their predictions with the experimental data of the tests described in section 2.

The formula of Shen et al. (1966) for piers reads as follows (see Cunha 1975):

$$\frac{d_s(t)}{h} = 2.5 Fr^{2/5} \left(\frac{b}{h}\right)^{3/5} \left(1 - e^{-m \cdot E}\right)^2 \tag{2}$$

$$m = 0.026 e^{2.932h} \tag{3}$$

$$E = \left(\frac{b}{h}\right)^{1/3} Fr^{1/3} \ln \frac{Ut}{h} \tag{4}$$

$$Fr = \frac{U}{\sqrt{gh}} \quad \text{(Froude number of the approach flow)} \tag{5}$$

The contribution of Franzetti et al. (1994) for circular pier scour on granular uniform sand, in the absence of secondary currents and contraction effects, can be written as:

$$\frac{d_s(t)}{b} = f_1(t) f_2\left(\frac{U}{U_c}\right) f_3\left(\frac{h}{b}\right) f_4\left(\frac{b}{d_{50}}\right) \tag{6}$$

$$f_1(t) = 1 - e^{-0.028\left(\frac{Ut}{b}\right)^{1/3}} \tag{7}$$

$$f_2\left(\frac{U}{U_c}\right) = 1 - 10\left(1 - \frac{U}{U_c}\right)^3 \quad for \quad \frac{U}{U_c} \le 1 \tag{8}$$

$$f_3\left(\frac{h}{b}\right) = 1 - e^{-1.3\left(\frac{h}{b}\right)^{1/3}} \quad for \quad \frac{h}{b} \ge 2 \tag{9}$$

$$f_4\left(\frac{b}{d_{50}}\right) = \begin{cases} 3.868\left(\frac{b}{d_{50}}\right)^{1.572} e^{-2.64\left(\frac{b}{d_{50}}\right)^{0.234}} & for\ b/d_{50} \le 50 \\ 2.48 & for\ b/d_{50} > 50 \end{cases} \tag{10}$$

The formula of Melville & Coleman (2000) for piers, valid for uniform sediments is:

$$d_s(t) = K_{hb} K_I K_d K_S K_\theta K_G K_t \tag{11}$$

$$K_{hb} = \begin{cases} 2.4b & for \quad b/h \le 0.7 \\ 2\sqrt{hb} & for \quad 0.7 < b/h < 5.0 \\ 4.5h & for \quad b/h > 5.0 \end{cases} \tag{12}$$

$$K_I = \begin{cases} \frac{U}{U_c} & for \quad \frac{U}{U_c} < 1 \\ 1 & for \quad \frac{U}{U_c} \ge 1 \end{cases} \tag{13}$$

$$K_d = \begin{cases} 0.57 \log\left(2.24 \frac{b}{d_{50}}\right) & for \quad \frac{b}{d_{50}} \le 25 \\ 1 & for \quad \frac{b}{d_{50}} > 25 \end{cases} \tag{14}$$

$$K_S = 1 \quad for\ circular\ pier \tag{15}$$

$$K_G = 1 \quad for\ channel\ with\ rectangular\ cross-section \tag{16}$$

$$K_t = \begin{cases} e^{-0.03\left|\frac{U_c}{U} \ln \frac{t}{t_e}\right|^{1.6}} & for \quad \frac{U}{U_c} \le 1 \\ 1 & for \quad \frac{U}{U_c} > 1 \end{cases} \tag{17}$$

Copyright © 2006 Taylor & Francis Group plc, London, UK

$$t_e(days)=\begin{cases}48.26\dfrac{b}{U}\left(\dfrac{U}{U_c}-0.4\right) & for\ \dfrac{h}{b}>6;\dfrac{U}{U_c}>0.4\\ 30.89\dfrac{b}{U}\left(\dfrac{U}{U_c}-0.4\right)\left(\dfrac{b}{h}\right)^{0.25} & for\ \dfrac{h}{b}\le 6;\dfrac{U}{U_c}>0.4\end{cases} \quad (18)$$

The formula of Oliveto & Hager (2002) applies to piers or abutments (replacing L by b) on rectangular straight channels, clear-water condition, $h/d_{50} > 5$ to 10, $B/b < 20$, d_{50} greater than about 0.8 mm, $F_t < 1.2$ in the approach flow and in the absence of bed-forms. It reads:

$$d_s(t)=0.068Nb^{2/3}h^{1/3}\sigma_g^{-1/2}Fr_d^{1.5}\log T \quad (19)$$

$$N=\begin{cases}1 & for\ pier\\ 1.5 & for\ abutment\end{cases} \quad (20)$$

$$Fr_d=\frac{U}{\sqrt{g\Delta d_{50}}}>Fr_{di}\ \text{(densimetric Froude number)} \quad (21)$$

$$Fr_{di}=\begin{cases}2.33D_*^{-0.25}\left(R/d_{50}\right)^{1/6} & for & D_*\le 10\\ 1.08D_*^{1/12}\left(R/d_{50}\right)^{1/6} & for & 10<D_*<150\\ 1.65\left(R/d_{50}\right)^{1/6} & for & D_*\ge 150\end{cases} \quad (22)$$

$$D_*=\left(g\Delta/\upsilon^2\right)^{1/3}d_{50}\ \text{(non-dimensional grain size)} \quad (23)$$

$$F_t=\begin{cases}\dfrac{U}{2.33D_*^{-0.25}\left(R/d_{50}\right)^{1/6}} & for & D_*\le 10\\ \dfrac{U}{1.08D_*^{1/12}\left(R/d_{50}\right)^{1/6}} & for & 10<D_*<150\\ \dfrac{U}{1.65\left(R/d_{50}\right)^{1/6}} & for & D_*\le 150\end{cases} \quad (24)$$

$$T=\sqrt{g\Delta d_{50}}\,b^{-2/3}h^{-1/3}t \quad (25)$$

In the equations above, $\Delta=(\rho_s-\rho)/\rho$ is the relative submerged density of sediments, ρ_s and ρ being the grain and water density respectively, R is the hydraulic radius and ν is the kinematic water viscosity.

The formula suggested by Cunha (1975) for abutment can be written as follows:

$$\frac{d_s(t)}{h}=189\left(\frac{L}{h}\right)^{0.69}\left(\frac{u_*}{\omega_s}\right)^{3.25}t^{0.16}\quad with\ t\ in\ minutes \quad (26)$$

u_* being the shear velocity and ω_s the fall velocity. These variables can be computed as follows:

$$u_*=\sqrt{gRS}\ \text{(shear velocity)} \quad (27)$$

$$S=\frac{(nU)^2}{R^{4/3}}\ \text{(energy slope; Manning's formula)} \quad (28)$$

$$n=\frac{d_{50}^{1/6}}{21.1}\left(\frac{s}{m^{1/3}}\right)\ with\ d_{50}\ in(m)\ \text{(Strickler's formula)} \quad (29)$$

$$\omega_s=F\sqrt{g\Delta d_{50}}\ \text{(Rubey 1933)} \quad (30)$$

$$F=\sqrt{\frac{2}{3}+\frac{36\nu^2}{g\Delta d_{50}^3}}-\sqrt{\frac{36\nu^2}{g\Delta d_{50}^3}} \quad (31)$$

The formula of Lauchlan et al. (2001) for abutments, on uniform sediments, under clear-water flow conditions, is given by:

$$d_s(t)=K_{hL}K_IK_dK_SK_\theta K_GK_t \quad (32)$$

$$K_{hL}=\begin{cases}2L & for & L/h<1\\ 2\sqrt{hL} & for & 1<L/h<25\\ 10h & for & L/h>25\end{cases} \quad (33)$$

$$K_d=\begin{cases}0.57\log\left(2.24\dfrac{b}{d_{50}}\right) & for & \dfrac{L}{d_{50}}\le 25\\ 1 & for & \dfrac{L}{d_{50}}>25\end{cases} \quad (34)$$

$$K_S=1\quad for\ vertical\ abutment\ walls \quad (35)$$

$$K_G=1\quad for\ channel\ with\ rectangular\ cross-section \quad (36)$$

$$K_t=e^{-0.09\left(\frac{U_c}{U}\right)^{-0.75}\left|ln\frac{t}{t_e}\right|^{1.4}} \quad (37)$$

K_I is evaluated from (13); t_e can be calculated from (1).

The above formulae were applied to the laboratory data (3 sets for piers and 12 for abutments, with a total number of measured scour depths equal to 122 and 353, respectively) in order to assess the scour depth at given time instants.

Figures 2 and 3 show typical comparisons between measured and computed $d_s(t)$, respectively, for circular piers (test GC0) and abutments (test CB5).

As shown in Figure 2, the scour depth for test GC0 was underestimated at all instants by the formula of Shen et al. (1966); on the contrary, it was always overestimated by the formulae of Melville & Coleman (2000) and Oliveto & Hager (2002). These conclusions were verified to be valid for the remaining tests too. The formula of Franzetti et al. (1994) produced very good estimates of $d_s(t)$; in the case of tests GA0 and GB0 the scour depths over time were overestimated of 24% and 11% respectively, whilst in the case of test GC0 predictions followed the measurements up to $t \approx 30$ h and, from there on, they became smaller, leading to a slight underestimation of the equilibrium scour depth, d_{se}.

Copyright © 2006 Taylor & Francis Group plc, London, UK

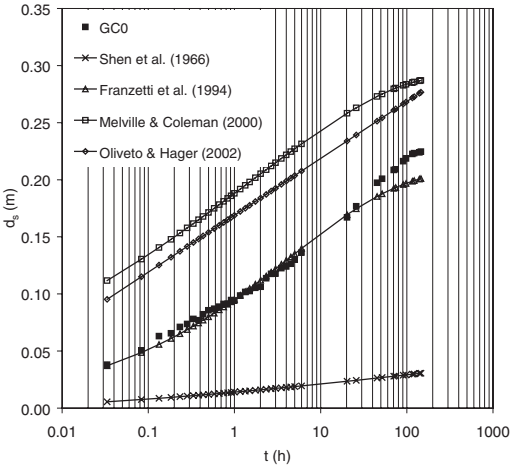


Figure 2. Comparison between computed and measured $d_s(t)$ at a circular pier (test GC0).

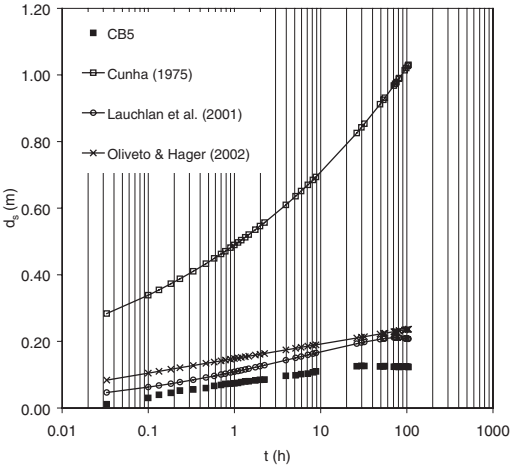


Figure 3. Comparison between computed and measured $d_s(t)$ at a rectangular abutment (test CB5).

Figure 3 shows that, for test CB5, the scour depth is overestimated by the three selected predictors of scour at abutments for all instants. It should be noted that the formula of Cunha (1975) leads to predictions from 5 to 6 times bigger than the observed values. Analogous conclusions can be drawn for tests CB3, CB4, K12, A2, B1b, B2a, C2. The best predictions are given by the Lauchlan et al. formula for tests CB1, CB2, A1 and C1 and by the Oliveto & Hager formula for test CB1. Measures of test CB2 were overestimated for $t < 22$ h and then underestimated by the Oliveto & Hager formula.

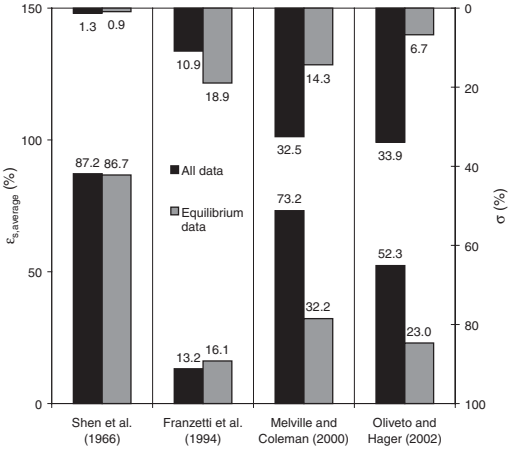


Figure 4. Relative errors and standard deviations of computed vs. measured $d_s(t)$ at circular piers.

The computed values, $d_{s,c}(t)$, were compared with the measured ones, $d_{s,m}(t)$; a percent relative error was calculated as follows for each instant:

$$\varepsilon_s(t)\,(\%) = \frac{\left|d_{s,c}(t) - d_{s,m}(t)\right|}{d_{s,m}(t)} \cdot 100 \qquad (38)$$

This parameter was also calculated for the equilibrium scour depths, i.e. for the particular cases of equilibrium time.

Figure 4 shows the average of ε_s values as well as the corresponding standard deviations, σ, associated with the predictions of each formula for piers. It also shows the same statistics for the equilibrium scour depths (see gray histograms).

Figure 5 replicates Figure 4 for abutments; only 9 equilibrium scour values were considered for abutments since tests A1, A2 and B2a were assumed out of equilibrium, according to section 2.

As it could be anticipated from the discussion of Figures 2 and 3, the best predictions were those given by the formula of Franzetti et al. (1994) for piers and the formula of Lauchlan et al. (2001) for abutments; they lead to average relative errors equal to 13.2% and to 32.2%, respectively; these statistics are quite similar to those associated with the equilibrium scour depth, where the same formulae lead to relative errors equal 16.1% and 32.2%.

The formulae of Melville & Coleman (2000) and Oliveto & Hager (2002) are better predictors of d_{se} than $d_s(t)$. Anyway, with respect to the Oliveto & Hager (2002) formula, it is to be underlined that condition (21) was never verified in the tests considered in the present work: in fact, the densimetric Froude numbers presented percent relative errors $(Fr_{di} - Fr_d)/Fr_d \cdot 100 = 7.3\%$ (tests A1 and C1) to

Copyright © 2006 Taylor & Francis Group plc, London, UK

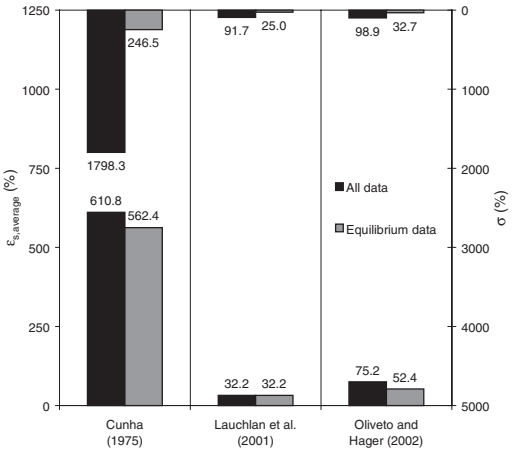


Figure 5. Relative errors and standard deviations of computed vs. measured $d_s(t)$ at abutments.

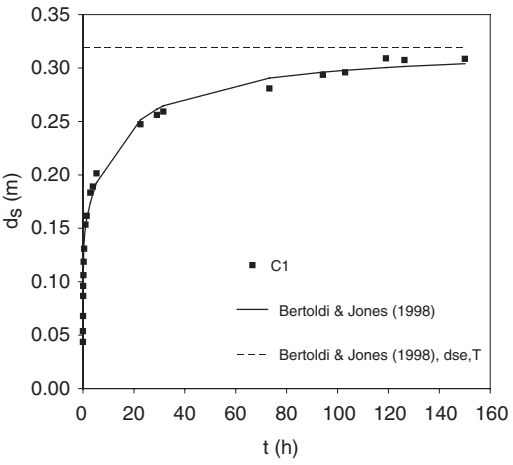


Figure 6. Time evolution of maximum scour depths. Comparison between measured (test C1) and computed (Bertoldi & Jones 1998) values.

30.7% (test CB4); in addition, the condition $B/b < 20$ was not respected either for test GB0 ($B/b = 22.2$).

The formula of Shen et al. (1966) leads to high average relative errors on both $d_s(t)$ and d_{se}, while σ values are the smallest, indicating that ε_s is almost constant at all the examined time instants.

On the contrary, the formula of Cunha (1975) produces very high average relative errors on both $d_s(t)$ and d_{se}, with very high σ values, i.e. the high predictions are equally affected by highly variable errors. In particular, the formula of Cunha (1975) depicts the highest relative errors for $t < 1$ h; in fact, considering only the data for $t > 1$ h, the average relative error reduces from 610.8% to 452.8%, and the standard deviation from 1798.3% to 203.8%. The formula is very sensitive to small variations of the shear velocity and the fall velocity; small errors in the evaluation of these variables may induce high deviations from reality. In addition, as shown in Figure 3, the predictions of $d_s(t)$ keep increasing with time, leading to unrealistic infinity scour depth for infinity time.

4 MINIMUM TEST DURATION

As mentioned before, many studies have been made on the influence of time on local scouring. Just to mention a few more of the most ancient, those of Laursen (1963), Breusers (1965), Rao & Sarma (1967), Sarma (1968) can be listed, together with those of Romita (1953), Shen et al. (1965) or Carstens (1966) for the particular case of bridge piers.

A high number of studies developed between the first and second half of the twentieth century were carried out by performing experiments with very short durations. Test durations of, e.g., Ishihara (1938–42) and Romita (1953) were, respectively, 20 and 30 minutes; equilibrium state was assumed as reached after 120 minutes by Dietz (1972) – see Breusers & Raudkivi (1991) – and Knight (1975); Basak et al. (1975) – see Breusers et al. (1977) – considered equilibrium after 400 minutes.

As shown in section 2 on the analysis of equilibrium, the test duration for equilibrium is of the order of days (Table 1). The increment of scour depth decreases with time, taking values of the order of d_{50} per day at high t values.

It would be interesting to reduce, in practice, the duration of laboratory tests. This would imply the definition of a minimum duration, T_{min}, allowing the determination of d_{se} by extrapolating measurements in the interval $0 < t < T_{min}$ to $t = t_e$. For this purpose, the following Bertoldi & Jones (1998) formula was considered:

$$d_s(t) = a\left(1 - \frac{1}{1+abt}\right) + c\left(1 - \frac{1}{1+cdt}\right) \qquad (39)$$

a, b, c and d being parameters, which can be obtained through regression analysis of $d_s(t)$ values versus t. When $t \to \infty$, Eq. (39) leads to $d_{se} = a + c$. This formulation assumes implicitly that $t_e \to \infty$.

The parameters of the Bertoldi & Jones (1998) formula were assessed for each test with the least squares regression applied to the $d_s(t)$ versus t data, for $0 < t \le t_i$, with t_i in the interval 1 day $\le t_i \le T$. Therefore, for each test, the equilibrium scour depth, $d_{se,i} = a_i + c_i$, was calculated for each t_i, i.e. limiting the data set at time t_i.

For example, Figure 6 shows the comparison among measured and computed $d_s(t)$ for test C1, and the

Copyright © 2006 Taylor & Francis Group plc, London, UK

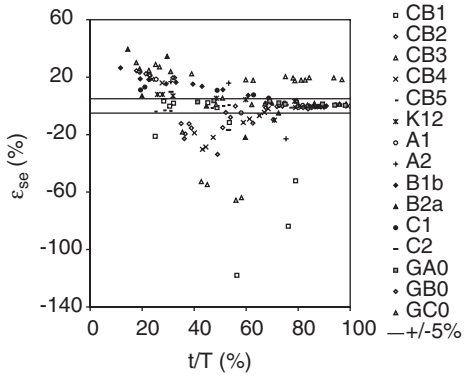


Figure 7. Percent relative errors vs. dimensionless time.

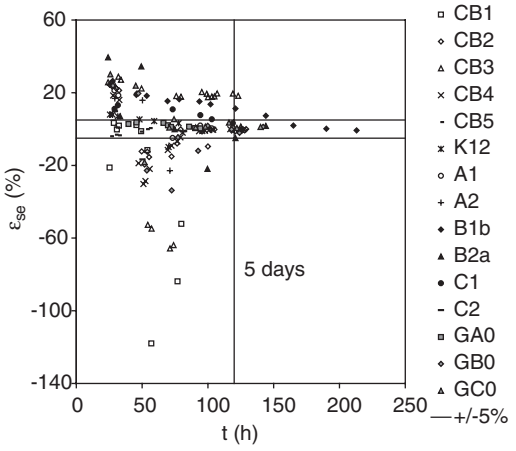


Figure 8. Percent relative errors vs. time.

equilibrium scour depth $d_{se,T} = a_T + c_T$, assessed with the Bertoldi & Jones (1998) formula by using the whole data set.

Assuming that $d_{se,T}$ is the best estimate of d_{se}, i.e. that $d_{se,T} \approx d_{se,\infty}$, the following percent relative error was computed:

$$\varepsilon_{se,i}\,(\%) = \frac{d_{se,T} - d_{se,i}}{d_{se,T}} \cdot 100 \qquad (40)$$

as to evaluate the precision of the d_{se} estimates for all $t_i < T$.

Figure 7 shows the percent relative errors versus dimensionless time, t/T. Each point in the graph represents the couple $(t_i/T, \varepsilon_{se,i})$. The band of ±5% relative error is also shown. The value of t/T after which $\varepsilon_{se,i}$ falls stably in the ±5% band is very different from one test to another. For example, test CB5 reached a maximum scour depth which differs of less than ±5% from $d_{se,T}$ after the 25% of its total duration; on the contrary, the 98% of the total duration of test CB3 was needed to obtain $-5\% < \varepsilon_{se,i} < 5\%$; for tests CB1 and A2, the minimum dimensionless time for estimating $d_{se,T}$ with ±5% relative error is equal to 100%.

Figure 8 shows the percent relative errors versus time. After some oscillations, the relative errors decrease with time. Apparently, within the experimental range covered in this study, test durations shorter than 5 days are not enough to guarantee a correct assessment of d_{se} through the Bertoldi & Jones formula, adjusted to measurements and extrapolated to $t \to \infty$. This conclusion is to be confirmed in future research works, since only 8 tests lasted more than 5 days and only 1 more than 7 days (see Table 1).

The above considerations show that it is not possible to establish the minimum test duration for a correct assessment of the equilibrium maximum scour depth on the basis of the considered data sets and the formula of Bertoldi & Jones (1998).

5 CONCLUSIONS

Fifteen laboratory data sets of scour depth evolution with time at piers and abutments were analysed to verify the onset of the equilibrium state. A multiple criterion was used, for which the test duration is compared with a reference value, the presence of the slope change in the time evolution of the scour depth is verified, and the variation of the scour depth in the last 24 hours of each test is compared with a threshold value. The application of the method to the data sets allowed to verify that three tests could not be considered at equilibrium.

Some formulae were selected in order to perform a comparison between their predictions and the experimental data of the considered laboratory tests. Results showed that the scour depth at piers was always underestimated by the Shen et al. (1966) formula and overestimated by the Melville & Coleman (2000) formula, while the formula of Franzetti et al. (1994) led to the best estimates. The Oliveto & Hager (2002) formula gave overestimations too, but it is to be noted that it was applied in cases in which some of its restrictions were not respected. The scour depth at abutments was generally overestimated by the selected formulae; the Lauchlan et al. (2001) formula gave the best predictions. Similar conclusions can be drawn for the equilibrium depths.

Finally, in order to reduce the duration of laboratory tests, the research of a minimum duration that could allow the calculation of the equilibrium value of scour depth through extrapolation was performed with the formula of Bertoldi & Jones (1998). Results showed that the percent relative error on the assessment of d_{se} presents strong oscillations over time; in some cases, these oscillations remain strong until close to the end of the records. Therefore, it was not possible by this way

Copyright © 2006 Taylor & Francis Group plc, London, UK

to establish the minimum test duration for a correct assessment of the equilibrium maximum scour depth.

REFERENCES

Bertoldi, D.A. & Jones, S.J. 1998. Time to scour experiments as an indirect measure of stream power around bridge piers. *Proc. Int. Water Resources Engrg. Conf.*, Memphis, Tennessee: 264–269.

Breusers, H.N.C. 1965. *Conformity and time scale in two dimensional local scour*. Publication No. 40: Delft Hydraulics Laboratory.

Breusers, H.N.C., Nicollet, G. & Shen, H.W. 1977. Local scour around cylindrical pier. *J. Hydr. Res*., 15(3): 211–252.

Breusers, H.N.C. & Raudkivi, A.J. 1991. Scouring, Hydraulic Structures Design Manual. IAHR. Rotterdam: Balkema.

Cardoso, A.H. & Bettess, R. 1999. Effects of time and channel geometry on scour at bridge abutments. *J. Hydr. Engrg.*, ASCE, 125(4): 388–399.

Carstens, M.R. 1966. Similarity laws for localised scour. *J. Hydr. Div.*, ASCE, 92(3): 13–36.

Cunha, L.V. 1975. Time evolution of local scour. *Proc. 14th IAHR Congress*, Paris, France: 285–299.

Franzetti, S., Malavasi, S. & Piccinin, C. 1994. Sull'erosione alla base delle pile di ponte in acque chiare. *XXIV Convegno di Idraulica e Costruzioni Idrauliche*, Naples, Italy: vol. II T4, 13–24.

Grimaldi, C. 2005. Non-conventional countermeasures against local scouring at bridge piers. Dissertation for Doctorate degree in Hydraulic Engineering for Environment and Territory. Cosenza, Italy: University of Calabria.

Ishihara, T. 1938–1942. An experimental study of scour around bridge piers. Translated from *J. Japan Soc. Civil Engrg*., 24(1) 1938: 23–55; 28(9) 1942: 787–821; 28(11) 1942: 974–1005.

Knight, D.W. 1975. A laboratory study of local scour at bridge piers. *Proc. 16th IAHR Congress*, Sao Paulo, Brazil.

Kwan, T.F. 1988. Study of abutment scour. Rep. N. 328, School of Engrg., Auckland, New Zealand: University of Auckland.

Lauchlan, C.S., Coleman, S.E. & Melville, B.W. 2001. Temporal scour development at bridge abutments. *Proc. 29th IAHR Congress*, Beijing, China: 738–745.

Laursen, E.M. 1963. An analysis of relief bridge scour. *J. Hydr. Div.*, ASCE, 89(3): 93–118.

Melville, B.W. & Chiew, Y.M. 1999. Time scale for local scale at bridge piers. *J. Hydr. Engrg*., ASCE, 125(1): 59–65.

Melville, B.W. & Coleman, S.E. 2000. *Bridge scour.* Highlands Ranch, Colorado, USA: Water Resources Publication, LLC.

Murillo, J.A. 1987. The scourge of scour. *Civil Engineering*, ASCE, 57(7): 66–69.

Oliveto, G. & Hager, W.H. 2002. Temporal evolution of clear-water pier and abutment scour. *J. Hydr. Engrg.*, ASCE, 128(9): 811–820.

Rao, N.S.G. & Sarma, K.V.N. 1967. On limiting scour. *J. Inst. Engrg.*, India, 47(2), CI 6: 1145–1154.

Romita, P.L. 1953. Erosioni d'alveo al piede delle pile di ponte investite obliquamente dalla corrente. *L'Energia Elettrica*, 4: 211–224; 6: 341–349.

Rubey, W. 1933. Settling velocities of gravel, sand and silt particles. *Am. J. of Sci.*, 225(148): 325–338.

Santos, J.P. 1999. Erosões localizadas em encontros de pontes em leitos de rios com secção composta. Dissertation for Master Degree in Hydraulics and Water Resources. Lisbon, Portugal: Technical University of Lisbon, Superior Technical Institute.

Sarma, K.V.N. 1968. Existence of limiting scour depth. *J. Inst. Engrg*., India, 48(1), CI 1: 84–92.

Shen, H.W., Ogawa, Y. & Karaki, S.S. 1965. Time variation of the bed deformation near bridge piers. *Proc. 11th IAHR Congress*, Leningrad, URSS.

Shen, H.W., Schneider, V.R. & Karaki, S.S. 1966. Mechanics of local scour. U.S. Department of Commerce, National Bureau of Standards, Institute for Applied Technology.

Copyright © 2006 Taylor & Francis Group plc, London, UK

Diversity of streambed features caused by open-slot groundsills

Chia-Chun Wu & Yuan-Chiao Lin
National Pingtung University of Science and Technology, Neipu, Pingtung, Taiwan

ABSTRACT: Groundsills and check dams are common practices implemented in mountain streams for grade control. However, both structures not only dissect the channel and create discontinuity in channel flow, but also destroy the diversity of streambed appearances. Therefore, the objective of this research is to experimentally access the feasibility of open-slot groundsills in creating streambed diversity. Groundsills with different numbers of open slots were tested in a laboratory flume. Shannon Diversity Index (SHI) was then used to express the diversity of streambed topographic features at different experiment settings including conventional groundsills as the control setting. Results of this study indicate that conventional groundsill has the lowest SHI value; whereas, groundsill with single slot opening has the highest. Groundsills with two and four open slots possess SHI values in between the preceding extremes. Even though single-slot groundsill produces the highest SHI value that representing the highest bed feature diversity, yet the concentrated scour development creates potential threat to the structure.

1 INTRODUCTION

A groundsill is a man-made structure running perpendicular to the flow. It is a common practice to install a series of groundsills in a channel to serve the purposes of grade control and flow training. However, the installation of groundsills alters both the flow fields and sediment transport in a channel reach, which results in a rather uniform appearance (Fig. 1) as compared to the riffle-pool setting in a natural environment.

Pool is a region of slow moving water with relative deep flow depth. Riffle, on the other hand, is a region of fast moving water with shallow flow depth. Riffle-pool structure not only provides great diversity on streambed bedforms, substrate materials, and local velocity distributions, but also provides shelters and feeding grounds for aquatic habits (Gordon et al. 1992).

Therefore, the objective of this research is to experimentally access the feasibility of open-slot groundsills in creating streambed diversity. The open-slot groundsill in this paper is referred to a conventional groundsill having a slot or few slots cutting on the apron.



Figure 1. Hydraulic environment created by a series of groundsills.

2 LITERATURE REVIEW

Research efforts have concentrated in the aspects of proper spacing interval between groundsills and scour at the toe of a groundsill. For instance, Dietz (1972) proposed an equation that described the equilibrium scour depth based on the velocity differences at the cross section. The equation was written as

$$\frac{y_m}{y_{m,e}} = \frac{\omega(U_0 - U_c)}{U_c} \tag{1}$$

where y_m = maximum scour depth (m); $y_{m,e}$ = equilibrium scour depth (m); U_c = critical velocity (m/s); U_0 = cross-section average velocity (m/s) = Q/A; Q = flow rate (m^3/s); A = cross-section area (m^2); $\omega = 1 + 3\gamma_0$; γ_0 = coefficient of turbulent intensity.

Copyright © 2006 Taylor & Francis Group plc, London, UK

Chang (1994) conducted flume study using three sets of uniform and two sets of non-uniform sands. By assuming streambed friction coefficient was the sum of friction coefficient induced by sand grain and that by groundsill, Chang proposed an equation for estimating the groundsill spacing interval:

$$\frac{L}{L_0} = 10^{9.8}\left(\frac{h}{R}\right)^{-3.46}\left(\frac{\nu}{UR}\right)^{-5.1}\left(\frac{gR}{U^2}\right)^{-3}\left(\frac{\tau_g}{\rho U^2}\right)^{-3.9} \quad (2)$$

where L = groundsill spacing interval (m); L_0 = total length of channel reach that having groundsills installed (m); h = height of the groundsill (m); R = hydraulic radius (m); ν = flow viscosity (m^2/s); U = average flow velocity (m/s); g = acceleration of gravity (m/s^2); τ_g = friction induced by groundsill (N/m^2); ρ = flow density (kg/m^3). However, Equation (2) did not demonstrate the effect of sediment sizes.

Based upon the concept of dynamic equilibrium, results from flume studies, and field survey, Hwang (1995) not only simplified Chang's groundsill spacing equation, but also restored the role that sediment sizes played in the phenomena. The simplified equation read as the following

$$L = 4.67\frac{D_{65}^{0.14}}{H^{0.73}S^{0.45}} \quad (3)$$

where L = groundsill spacing interval (m); D_{65} = representative sediment diameter (m); H = design flow depth (m); S = original channel gradient.

Aderibigde et al. (1998) found the correlation among Froude number, scour depth, and the length of the scour. Other factors that equally important were also identified. They were sediment mean diameter, channel gradient, and especially the variation in approaching flow depth. The reason was because the degree of variation in flow depth that approaching the transverse structure conducted the progression of scour. It was also found that the angle of approaching flow that plunging the channel bed directed the depth of the scour.

Wu (2000) conducted flume studies on the spacing interval for submerged groundsills. The study was carried out from the viewpoint of allowable scour depth under which the submerged groundsill remained durable. The equation was written as

$$L_I = 48.872\frac{h}{\tan^2\phi}\left[\frac{Q}{\sqrt{B\,y_n\left(S_g-1\right)g\,S\,D_{50}{}^3}}\right]^{-0.399} \quad (4)$$

where L_I = submerged groundsill spacing interval (m); h = height of the submerged groundsill (m); ϕ = angle of repose of the sediment that submerged in the flow; Q = designed peak discharge (m^3/s); S_g = specific gravity of the sediment; B = width of the channel between revetments (m); y_n = normal depth (m); g = acceleration of gravity (m/s^2); S = original channel gradient; D_{50} = sediment mean diameter (m).

Under the assumption of independence between groundsill spacing interval and scour development, Gaudio et al. (2000) conducted flume study on the mechanism of scour formation. By further ignoring the effect of turbulence velocity on scour development and assuming the constant sediment density, a simplified relation was obtained as the following

$$\frac{y_s}{H_s} = \phi\left[\frac{a_1}{H_s}, \frac{a_1}{\Delta D}\right] \quad (5)$$

where y_s = maximum scour depth (m); H_s = critical specific energy (m); a_1 = morphological jump (m); a_1/H_s = ratio of energy loss between different forms of hydraulic jump caused by groundsills; $a_1/\Delta D$ = relationship between forms of hydraulic jumps and representative sediment diameter; Δ = specific gravity of the sediment.

Lenzi et al. (2002) extended Gaudio et al. (2000) results to mountain streams, followed by flume studies. Their results indicated that densimetric Froude number calculated from D_{95} produced higher correlation. The resultant equation for the maximum scour depth (y_s) and maximum scour length (l_s); respectively, was written as

$$\frac{y_s}{H_s} = 0.435 + 1.452\left(\frac{a_1}{H_s}\right)^{0.862} + 0.059\left(\frac{a_1}{\Delta D_{95}}\right)^{1.491} \quad (6)$$

$$\frac{l_s}{H_s} = 4.479 + 0.023\left(\frac{a_1}{H_s}\right)^{-1.808} + 2.524\left(\frac{a_1}{\Delta D_{95}}\right)^{1.129} \quad (7)$$

Wu et al. (2002) re-analyzed Wu (2000) data and proposed an equation describing the geometric shape factor of the scour at the toe of the submerged groundsill. The equation was written as

$$\frac{d_{sc}}{L_{sc}} = 2.7046\left[\frac{1}{\left(S_g-1\right)D_{50}\,S\,L_I}\sqrt[3]{\frac{q^4}{g^2}}\right]^{-0.3384} \quad (8)$$

where d_{sc} = maximum scour depth (m); L_{sc} = projected length between the toe of a submerged groundsill and the location where maximum scour occurs (m); q = unit width flow discharge (m^3/m-s); S_g = specific gravity of the sediment; g = acceleration of gravity (m/s^2); S = original channel gradient; D_{50} = sediment mean diameter (m).

Wu et al. (2004) investigated the applicability of open-slot groundsill in the generation of meander in a trained channel through flume studies. Their study suggested that open-slot groundsills encourage the process of selective sediment transport along the thalweg. Scour adjacent to the open-slot was found to be limited to 2~4 times the width of the slot opening. A series of open-slot groundsills was possible to restore

Copyright © 2006 Taylor & Francis Group plc, London, UK

the meander in trained channel except for fine-bed-material channel. They also found that sediment sizes, design discharge, and channel slopes controlled the formation of meander; whereas, groundsill interval controlled the degree-of-freedom of the meandering.

3 EXPERIMENTAL APPARATUS AND MATERIAL

3.1 *Hydraulic flume, open-slot groundsill scaled models, and experiment setup*

The experiment was conducted in a semi-circulated flume located in Steepslope Hydraulics Laboratory at National Pingtung University of Science and Technology. The flume measured 4 m in length, 0.91 m in width, and 0.30 m in depth. A pair of revetments with the face slope of 1:0.3 (V:H) was furnished to imitate the revetments commonly adopted in Taiwan. The bottom width of the experimental channel therefore constrained by left and right revetments was 300 mm.

Groundsill models in the scale of 1:50 were cut from 15 mm-thick waterproof plywood into 300 mm by 315 mm plates. Open slots with constant depth of 15 mm but various lengths were then cut along one edge of the groundsill plates. By taking 150 mm as the total width of the openings ($\sum b$), four slot settings were designed for this study. They were 0, 1, 2, and 4; respectively.

The zero-slot setting represented a conventional groundsill without open slot. One-slot setting represented a single slot with width of 150 mm cut on an edge of a conventional groundsill. The slot was cut in such a manner so that it was centered on the edge of the groundsill. Two-slot setting represented a conventional groundsill with two slots evenly distributed and cut on the edge of the groundsill (Fig. 2). Similarly, four-slot setting represented a conventional groundsill with four slots evenly distributed and cut at the apron of the groundsill.

The process of slot cutting left blocks (white rectangular objects in Fig. 2) at the apron of the groundsill. These blocks created obstruction to the flow. To simplify the discussion, water blockage ratio (W_b) was therefore defined as the ratio between width of the block (T_b) and that of the open slot (b). The scaled open-slot groundsill models and the corresponding dimension as well as parameters were listed in Table 1.

Groundsill models were then installed into the flume and sealed with Silicone along the side and bottom edges of the sill to prevent flow from seepage. Groundsill models were placed 300 mm apart to finally form a train of groundsills. The top rims of groundsill blocks were set 15 mm above the sand-filled channel bed, which made the bottom rims of the open slots set flush with the sand-filled channel bed as shown in Figure 2. For the conventional groundsill, or zero-slot groundsill in this study, the apron of the structure was set 15 mm above sand-filled channel bed. After the seal was set, experiment sand was filled and carefully leveled.



Figure 2. Experiment setup for two-slot groundsills installed.

Table 1. Dimensions and parameters associated with open-slot groundsill models.

Slot setting	Block width (T_b) mm	Slot width (b) mm	Water blockage ratio (T_b/b)
0	300.0	0.0	1.00
1	75.0	150.0	0.50
2	50.0	75.0	0.66
4	30.0	37.5	0.80

Sand originated from river sediment with sizes ranged from 0.063 to 4.75 mm was sieved through U.S. standard sieves of #5, #10, #18, #35, #60, #120, and #230 into 8 size groups. They were then mixed to form three size groups with mean particle diameter (D_{50}) of 0.55, 0.85, and 1.45 mm that imitated 27.5, 42.5, 72.5 mm in prototype; respectively.

Flow was regulated using Omron E5AK-T PID controller and an automatic valve. The steady discharge entering the flume was constantly monitored through Siemens flow meter. Three steady flow rates were selected in this study. They were 0.001, 0.00068, and 0.00043 m^3/s for the models, and 17.67, 12.02, and 7.60 m^3/s for the prototypes, respectively.

The lower limit of the discharge was set at the rate so that not only the minimum level of transport beyond the incipient motion for the coarse sediment would be ensured, but also blocks of groundsills would not be submerged at all times. The upper limit of the flow rate was regulated to ensure the total submergence of the groundsills would occur in all cases. On the other hand, the mid flow rate was set between the two extremes, which could submerge the groundsills at low channel

Copyright © 2006 Taylor & Francis Group plc, London, UK

Table 2. Experiment parameters*.

Flow rate (m^3/s)	Channel slope (%)	Sediment size (mm)	Slot setting
0.00043	2	0.55	0 – conventional
0.00068	4	0.85	1 – one-slot
0.00100	6	1.45	2 – two-slot
			4 – four-slot

*Scale = 1/50.

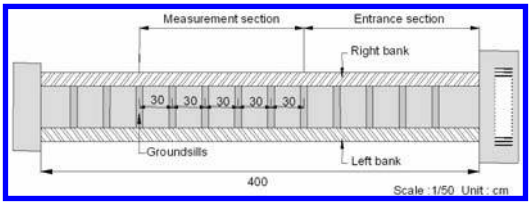


Figure 3. Schematic drawing of the flume and the measurement section.

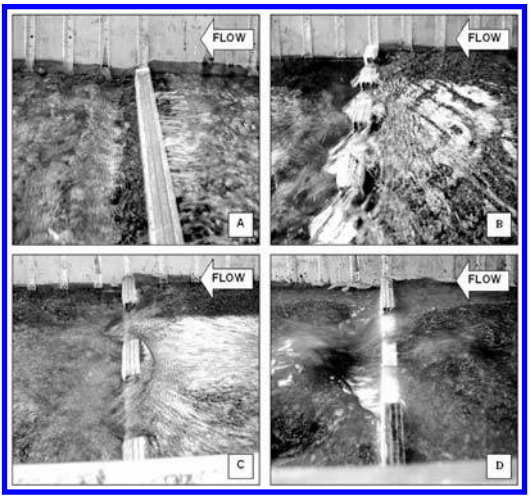


Figure 4. Effect of water blockage created by different slot settings.

gradient. Experiment parameters of this study were listed in Table 2.

3.2 *Flow- and channel-surface profile measurements*

The schematic drawing of the experiment setup was shown in Figure 3, in which measurement section was shown. Measurements conducted in this study included flow- and channel surface measurements. A digital point gauge with the accuracy of 0.1 mm was used for flow- and channel-surface profile measurements. Flow surface profile measurements did not engaged until one hour after the beginning of the experiment, and the measurements were taken as detail as possible to describe the flow surface profile.

Outlet of the flume was first blocked, followed by instant cut off of water supply and slow drain in the flume at the end of each run before the channel bed profile measurements started. Rill meter that often employed in soil erosion research was used with the assistance of a digital camera to capture the images of final channel bed profiles. Digital images were then manually digitized with respect to a reference point on the images to obtain channel bed profiles' elevations. Digital elevation model for each experimental run were finally constructed to data analysis.

4 RESULTS AND DISCUSSIONS

4.1 *Effect of water blockage ratio on flow concentration*

Blocks that created by cutting slots in a conventional groundsill created disturbance to the flow. The disturbance included flow concentration at the slot openings and backwater behind the blocks. Figure 4 demonstrated the effect of different water blockage to the flow that created by different slot settings. All pictures in Figure 4 were taken at the same flow rate, channel gradient, and bed material except the slot setting.

Photo of Figure 4A was taken when flow passed through a conventional groundsill with water blockage ratio of 1.00. Since conventional groundsill ran across the channel with fixed elevation uplift, therefore, the only way that flow could run over the groundsill was by overflowing. The elevation uplift at the cross section of the sill not only created backwater, but also generated elevation drop so that overflowing flow could plunge the streambed at the toe of the sill. The manner how overflowing flow plunged the streambed would be depended upon the flow depth downstream and the energy of the overflowing flow. It could change from plunged flow to pseudo-plunged flow, or into submerged hydraulic jump (Wu et al. 2002, Vischer & Hager 1998).

Photo of Figure 4B was taken when flow passed a four-slot groundsill with water blockage ratio of 0.80. Backwater effect was destroyed and flow became concentrated. Figure 4C was taken at two-slot groundsill with water blockage ratio of 0.66. Figure 4D was taken at one-slot groundsill with water blockage ratio of 0.50 where flow concentration became apparent and limited backwater occurred behind both wings of the groundsill. The effect of water blockage and that of flow concentration was clearly demonstrated as water blockage ratio decreased. Figure 4 also demonstrated how flow changed from uniform distributed plunged flow (Fig. 4A) to block-controlled pseudo-plunged flow (Fig. 4B), to slot-controlled pseudo-plunged flow (Fig. 4C), and to pseudo-submerged hydraulic jump (Fig. 4D).

Copyright © 2006 Taylor & Francis Group plc, London, UK

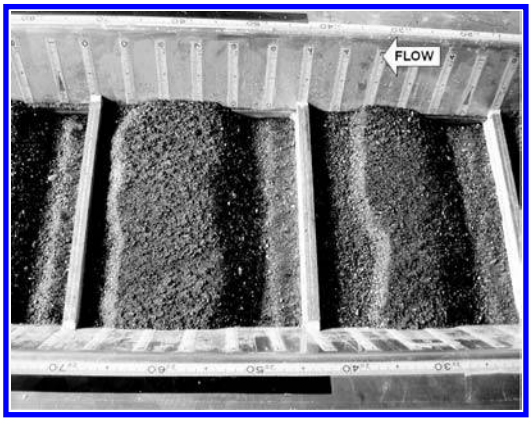


Figure 5. Deposition hump occurred between conventional groundsills.



Figure 6. Diverse streambed features created in one-slot sill setting.

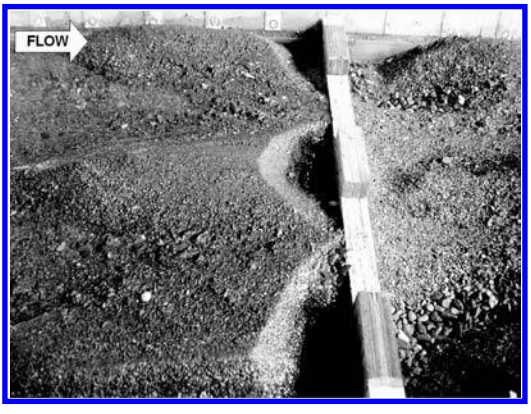


Figure 7. Diverse features caused by two-slot groundsill.

4.2 *Effect of water blockage ratio on streambed topographic feature*

Under the interaction of backwater and plunged flow, various topographic features thus developed at the streambed. For conventional groundsill setting, backwater effect could migrate upstream farther than other slot settings would ever be able to. This pool of relatively slow moving water reduced the flow velocity, which in turns reduced the transport capacity of the incoming flow that carried sediment freshly escaped from the scour hole. At the meantime, backwater also served as cushion at the toe of the sill to confine the scour produced by plunged flow.

The balance in energy between groundsills resulted a unique deposition like the sediment hump shown in Figure 5 near the downstream neighboring sill. This sediment hump was observed throughout the conventional groundsill settings regardless how flow changed from plunged flow at low flow rate, pseudo-plunged flow at mid flow rate, or submerged hydraulic jump at high flow rate (Wu et al. 2002).

Flow concentration reached to the maximum and backwater arrived at the minimum in one-slot groundsill setting as that shown in Figure 4D. The plunged flow dug into the streambed directly in the beginning of the process and gradually turned into submerged flow when scour hole at the toe of the sill become fully developed. Because backwater effect was confined at both wings of the one-slot groundsill, selective sediment transport was observed at the outskirt of the scour hole. Diverse streambed features were therefore cultivated as shown in Figure 6.

As the water blockage ratio increased due to the increase of open slots, flow became less concentrated and plunging effect at the streambed reduced as well. The block(s) that situated in the course of the flow stagnated the flow and caused backwater to occur as well as scour behind the block(s) by circulating flow.

Figure 7 illustrated the scour behind the blocks that sit at the central line of the channel as well as side corners at the wings. As far as the scour at the toe of the sill was concerned, it was caused by pseudo-plunged flow that overflowed the structure. On the other hand, scour behind the blocks and that behind the center block were mainly caused by circulating flow.

The diverse features caused by open-slot groundsills were not only controlled by the water blockage ratio that induced by openings, but also dictated by flow rates, sediment sizes, and channel gradients. Figures 8 and 9 illustrated the effect of flow rates and water blockage ratios imposed on the diversity of streambed features.

4.3 *Diversity of streambed features*

To quantify the channel bed feature changes at different slot settings, digitized channel bed elevation data that measured at the end of each run were used to build a digital elevation model. Elevations at the grid nodes were then categorized into discrete classes

Copyright © 2006 Taylor & Francis Group plc, London, UK

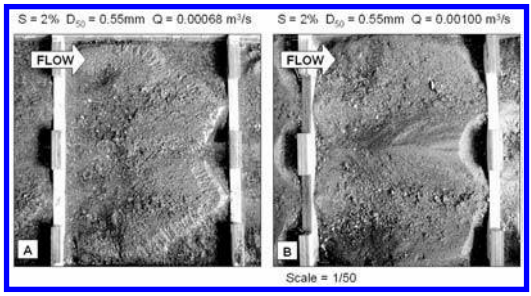


Figure 8. Effect of flow rate induced on the diversity of streambed features in two-slot groundsill setting.

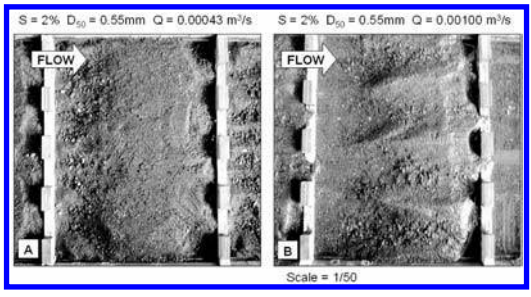


Figure 9. Effect of flow rate induced on the diversity of streambed features in four-slot groundsill setting.

using Sturges classification formula. Sturges formula provided a statistical-sound base that suggested the number of classes should be considered for the data population. The formula was written as

$$K = 1 + 3.3\,(\log n) \tag{9}$$

where K = number of classes, n = number of data points in the population.

Shannon diversity index was used to quantify the streambed elevation, and the formula read as

$$SDI = -\sum_{i=1}^{q}(P_i)\ln(P_i) = -\sum_{i=1}^{q}\left(\frac{m_i}{M}\right)\ln\left(\frac{m_i}{M}\right) \tag{10}$$

where SDI = Shannon diversity index; P_i = elevation richness in the ith elevation class; m_i = number of elevation points in the ith elevation class; M = total number of elevation points in data population; q = number of elevation classes suggested by Sturges formula.

When all nodal points possessed the same elevation, Equation (10) would return zero for SDI value. Table 3 summarized part of the research results obtained for $D_{50} = 0.85$ mm and $Q = 0.001$ m^3/s. Results included original channel slope (S), slot setting, maximum scour depth (d_{sc}); average scour depth ((d_{sc})$_{avg}$), and Shannon diversity index (SDI) for streambed features' elevations. Results from Table 3 were also plotted in Figure 10.

Table 3. Result summary for $D_{50} = 0.85$ mm and $Q = 0.001$ m^3/s runs*.

S (%)	Slot setting	d_{sc} (mm)	(d_{sc})$_{avg}$ (mm)	SDI
2	Conventional	15.0	10.1	0.59
	One-slot	30.1	15.0	1.04
	Two-slot	31.1	19.4	0.95
	Four-slot	21.8	12.9	1.02
4	Conventional	25.8	21.4	1.27
	One-slot	50.1	30.4	1.65
	Two-slot	49.4	29.6	1.55
	Four-slot	35.8	23.6	1.50
6	Conventional	39.0	37.3	1.32
	One-slot	82.2	51.1	2.09
	Two-slot	70.0	40.5	1.82
	Four-slot	49.8	33.6	1.55

*Scale = 1/50.

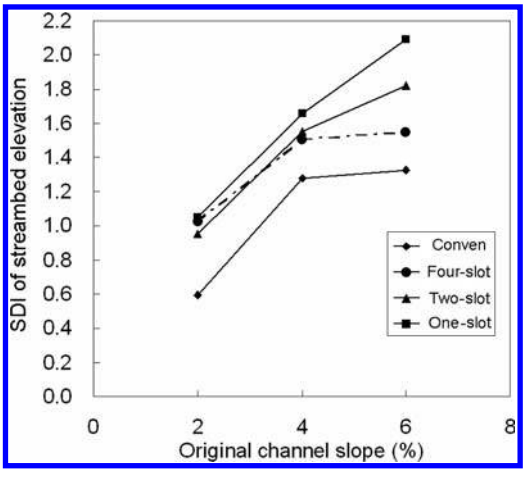


Figure 10. Relation between channel slope and SDI index for $D_{50} = 0.85$ mm and $Q = 0.001$ m^3/s runs.

Few observations could be drawn from Table 3 and Figure 10. One-slot groundsill produced highest SDI for all channel slopes; whereas, conventional groundsill produced the lowest SDI values. The reason was because one-slot groundsill concentrated inflow more effectively that created deeper and longer scour; whereas, conventional groundsill evenly distributed the inflow that equally divide the plunging force across the channel and created shortest and shallow scour.

Regardless the slot setting, all open-slot groundsill had lowest SDI values at 2% slope, and the SDI values increased as channel slope increased. The reason was because channel slope assisted flow to plunge farther and deeper into the channel bed. Hence, deeper and longer scours often occurred at steeper slopes.

Copyright © 2006 Taylor & Francis Group plc, London, UK

Four-slot and conventional groundsills had similar trend in the *SDI* with respect to channel slope. However, *SDI* values at four-slot setting were always higher than that at conventional groundsill setting. In addition, four-slot groundsill generated the shallowest scour among all open-slot settings in this study.

Conventional groundsills produced the shallowest scour as well as the lowest *SDI* values among all groundsill settings. The common deposition hump as that shown in Figure 5 appeared to be the trademark of streambed features carved by flow overflowed the conventional groundsill. Even though the scour depth was the shallowest, conventional groundsill replaced the diversity of the streambed feature with a uniformly distributed scour trench and a regularly shaped hump.

On the other hand, scour trench running in the channel-wise direction resulted from the concentration of flow that enhanced by single slot opening with selective deposition at the outskirt of the trench made one-slot groundsill produced the highest *SDI* values among all groundsill settings. More diverse the streambed elevation appeared, higher the *SDI* values reached. However, the scour caused by one-slot groundsill may cut too deep that eventually put groundsill foundation in risk.

5 CONCLUSION

Results of this study indicate that having open-slot groundsills as grade control practices creates more diverse features on streambed as compared to conventional groundsills. The blocks resting between openings provide obstruction to the incoming flow that create circulating flow behind the blocks and make the streambed packed with patches of pools and sand dune ridges.

One-slot groundsill produces the highest Shannon diversity index values among all groundsill settings; which indicates that diversity in streambed feature's elevations is the richest at one-slot setting. However, deep scour at the toe of the groundsill that caused by the action of flow concentration may put groundsill foundation in risk; especially when the scour undercuts the streambed underneath the sill foundation.

Results from this study seem to suggest the existence of optimum opening setting between two- and four-slot or four-slot to conventional groundsills dependent upon how diverse the streambed features is about to create. Obviously, the interaction between groundsill interval and slot opening settings will make future study in the similar nature interesting and promising in the restoration of streambed diversity.

ACKNOWLEDGEMENT

The support from Council of Agricultural, R.O.C. through Grant #93-AS-2.1.1-FC-S2(10) is gratefully acknowledged. Assistance from graduate student Mr. P.-L. Chen, undergraduates Mr. Q.-Y. Chang, H.-D. Ke, and Y.-S. Chang during experiments are highly appreciated.

REFERENCES

Aberibigbe, J. & Rajaratnam, O. 1998. Effect of sediment gradation on ersion by plane turbulent wall jets. *Journal of Hydraulic Engineering* 124(10): 1034–1042.

Chang, J.-A. 1994. *Study of groundsill spacing interval*. Master thesis, National Chung-Hsing University: 22–31. (in Chinese)

Dietz, J.W. 1972. Ausbildung von langen pfeilern bei Schräganströmung am Beispiel der BAB-Mainbrücke Eddersheim, *Mitteilungsblatt der BAW* 31: 79–94.

Gaudio, R., Marion, A. & Bovolin, V. 2000. Morphological effects of bed sills in degrading rivers. *Journal of Hydraulic Research* 38(2): 89–96.

Hwang, C.-D. 1995. Groundsill spacing interval study based on flume experiments. Master thesis, National Chung-Hsing University: 66–72. (in Chinese)

Lenzi, M.A., Marion, A. & Gaudio, R. 2002. Local scouring in low and high gradient streams at bed sills, *Journal of Hydraulic Research* 40(6): 731–739.

Vischer, D.L. & Hager, W.H. (eds.) 1998. *Dam Hydraulics*. Chapter 5: John Wiley & Sons.

Wu, C.-C. 2000. Studies of spacing interval for submerged groundsills. *FY89 Summary report of research projects, Soil and water conservation/Watershed management division, Council of Agriculture*: 69–98. (in Chinese)

Wu, C.-C., Hou, C.-H., Chen, C.-N. & Shih, C.-Y. 2002. Determination of groundsills interval for stream training. In D. Bousmar & Y. Zech (eds.), *River Flow 2002; Proc. Intern. Conf. on Fluvial Hydraulics, Swets & Zeitlinger, Lisse, The Netherlands, 4–6 September 2002*. Lisse: Balkema: 1109–1115.

Wu, C.-C., Lin, J.-J., Lin, Y.-C. & Yeh, C.-M. 2004. The applicability of open-slot groundsills in trained river to encourage the formation of meandering. In Jessica L. D'Ambrosio (ed.), *Self-sustaining solutions for streams, wetlands, and watersheds; Proc. Intern. Conf., St. Paul, Minnesota, 12–15 September 2004.* St. Joseph: American Society of Agricultural Engineers: 183–190.

Copyright © 2006 Taylor & Francis Group plc, London, UK

Riprap design for spur protection

C. Gisonni
Department of Civil Engineering, Seconda Università di Napoli, Aversa, Italy

W.H. Hager
VAW, ETH-Zurich, Zurich, Switzerland

ABSTRACT: River training techniques are often based on spurs whose main purposes are to prevent bank erosion, besides an enhancement of ecological conditions in the proximity of river shores. Actually, no general design criteria are available, given the large variety of geometrical parameters which characterize a spur set. In addition, the duration and reliability of this river structure are strongly affected by local scour phenomena, whose mechanism is not yet completely understood. A detailed experimental campaign was conducted to investigate the effects of various parameters, namely the spur length, the spur spacing, the spur height, along with the main hydraulic and granulometric parameters on the failure condition for a riprap protection at spur heads. Following a data analysis, design equations were established to predict riprap failure. In particular, different failure modes may occur, according to riprap size and spur displacement.

1 INTRODUCTION

Spurs are considered as one of the oldest river training techniques to protect river banks from erosion and to concentrate flows to the river center; nowadays spurs are widely used because they preserve sustainable ecological conditions along river shores, compared to alternative bank protection techniques. Spurs may be submerged completely under flood conditions and are generally exposed from the water during the low flow season. In the latter case, they behave hydraulically similar to bridge abutments except for certain geometrical parameters.

Research on scour phenomena at spurs has not advanced significantly, compared to bridge scour; one reason is definitely the geometrical complexity of spurs that involves a larger set of design parameters as compared for example to bridge appurtenances (pier or abutment). During the past two decades, a huge set of experimental data was collected, mainly focusing on a description of the scour phenomenon around bridge piers or bridge abutments. In these cases, the scour process may be simply characterized by a limited amount of geometric, hydraulic and granulometric parameters involving:

- the pier diameter (or its geometric shape),
- the approach flow conditions as expressed with the average approach flow velocity V_o and the approach flow depth h_o,
- the fluid viscosity ν, the fluid density ρ and gravitational acceleration g, and
- the sediment properties as expressed with the average sediment size d_{50}, the sediment non-uniformity parameter $\sigma = (d_{84}/d_{16})^{1/2}$ and sediment density ρ_s.

The temporal advance of maximum scour around these elements was described with the densimetric Froude number of the approach flow $F_d = V_o/(g' d_{50})^{1/2}$ (Oliveto & Hager 2002) with the reduced gravitational acceleration defined as $g' = g[(\rho_s - \rho)/\rho]$.

Spurs involve a much more complex geometry as compared with bridge elements. In fact, spur arrangements may be characterized by the following geometrical parameters (Figure 1):

- spur orientation α_s relative to the river axis,
- spur length b as the spur projection perpendicular to river axis,
- spur spacing L_s,
- average spur height $s = (1/2)(s' + s'')$,
- spur permeability,
- and number M of spurs along the streambank.

Based on a literature review, most of the available experimental and theoretical researches refer to single spur, that behaves quite differently from the multiple spur arrangement; it may be stated that no definite design guidelines are presently available, therefore. Melville & Coleman (2000) presented a concise summary on the currently available information of spur hydraulics. The spur spacing ratio was recommended between 3 and 5 (Julien 2002, Kondap & Prayag 1989). Lagasse et al. (1995) provided some additional

Copyright © 2006 Taylor & Francis Group plc, London, UK

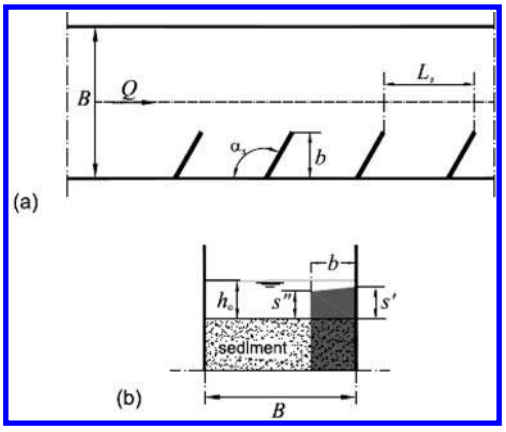


Figure 1. Definition sketch: (a) plan, (b) cross-sectional view.

information, such as the spur length should not be larger than 15% of the river width for impermeable spurs; spurs oriented perpendicular to the river axis are cost-effective because of their maximum projected length; the spur height should not exceed the bank height and a sloping spur towards the river axis was attributed advantageous. In addition these authors advised a riprap protection to the spur head and faces, among other items. The scour depth around a spur was estimated with an equation relating to low weir flow, without including some of the parameters previously mentioned. Lagasse et al. (1995) also stated that no generalized procedure for spur protection can be elaborated because each river reach is site-specific. According to Richardson et al. (1975) few other guidelines are given in the literature, and no definite design criteria are available, but only rules of thumb or special case studies are described.

The present paper reports of laboratory observations conducted at VAW, Swiss Federal Institute of Technology, Zurich, Switzerland. The purposes of the research program was (1) to focus on scour phenomena around spur dikes and corresponding countermeasures, and (2) to define the design criteria for practical applications. No systematic work on riprap protection of spurs has been done so far, even if spurs are used worldwide in river engineering. The knowledge of the failure conditions for spurs has to be considered crucial to the profession because of the costly structures and their effectiveness in terms of streambank protection and river ecology.

2 LABORATORY OBSERVATIONS

2.1 *Hydraulic model and preliminary experiments*

The experimental campaign on spurs was conducted in the VAW scour channel, whose width is $B = 1$ m, as described by Hager et al. (2002).

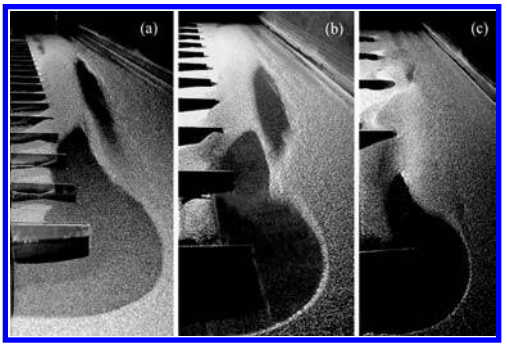


Figure 2. Scour patterns after 20 hours test duration for $F_d = 2.2$: effect of spur spacing for $\lambda = $ (a) 1, (b) 2 and (c) 4. View from upstream.

The experimental program was subdivided into two stages. Preliminary tests were performed to check the influence of different geometrical spur configurations on the scour performance (Gisonni et al. 2005).

Impermeable spurs 0.005 m thick were used. Experiments involved spur lengths of $b = 0.05$, 0.10, 0.15, 0.20, 0.35 and 0.50 m, and spur crest slopes from horizontal to 1:5. The approach flow depth h_o was always larger than 0.05 m to prevent scale effects. The average spur height s varied from 25% to 100% of the approach flow depth h_o, thus covering the range $0 < S \leq 1$ with $S = s/h_o$.

Given that the scour features around a spur head may be considered as a particular case of the scour process around bridge abutment (Oliveto & Hager 2005, Unger & Hager 2006), the hydraulic parameters were not systematically varied because their effect on the temporal scour advance and on the failure mechanism was considered known.

The mobile bed consisted of an almost uniform sand of size $d_{50} = 0.0011$ m ($\sigma = 1.18$); also, the hydraulic effect of the granulometry was not further investigated, because it was considered correctly contained in the failure formula of Unger & Hager (2006). The slope of the sediment bed was adjusted to 0.001 m/m to compensate for frictional effects.

Figure 2 shows upstream views along the spurs perpendicular to the left bank for $\alpha_s = 90°$, of which the relative height was $S = s/h_o = 0.75$. A densimetric Froude number of $F_d = 2.2$ was selected along with a relative spur width $\beta = b/B = 0.20$.

The figure refers to three spur spacings, namely $\lambda = L_s/b = 1$, 2 and 4, after 20 hours of test duration. The photographs were taken after the sediment bed had been drained with a water elevation slightly below the original bed elevation. The photographic light was positioned close to the sediment to increase the contrast between regions of sediment aggradation and scour.

Copyright © 2006 Taylor & Francis Group plc, London, UK

It was evidenced in these preliminary tests that the first spur of a spur arrangement in sand and gravel bed rivers is predominantly scoured. Consequently, a suitable spur protection appears to be essential to limit both the scour depth and the scour extension.

Following extensive experimentation the optimum spur arrangement in a straight river reach was identified for a certain granulometry and by restricting mainly to the clear-water flow regime, resulting in the subsequent recommendations:

1 spur length ratio $\beta = b/B$ up to 0.20;
2 spur spacing $\lambda = L_s/b$ varying between 2 and 4 to preserve a suitable flow recirculation within the spur fields and to guarantee the spur integrity;
3 relative spur height $S = s/h_o$ between 0.25 and 1, thus covering the complete spur overflow conditions up to the 'abutment' configuration;
4 spur alignment α_s equal to 90°, with possible angles between 60° and 120°,
5 spurs staggering, in terms of the average spur height, to reduce the severity of scour process. Accordingly, the crest of the first spur opposed to the flow should be set at a lower elevation as compared to the downstream spurs.

2.2 *Riprap experiments*

Spurs arranged according to the preceding recommendations resulted in an almost uniform distribution of the scour depth along the complete spur set, given that the first two spurs are protected with an adequate riprap to counter excessive scour.

The second part of the experimental program focused on selected ranges of the geometrical spur parameters:

1 spur length ratio $\beta = b/B$ up to 0.50, whereas the spur length b varied from 0 to 0.50 m, with $B = 1.0$ m as the channel width;
2 spur spacing $\lambda = L_s/b$ between 2 and 4;
3 relative spur height $S = s/h_o$ between 0.25 and 1;
4 spur alignment α_s equal to 90°, with selected runs for α_s equal to 60° and 120°;
5 average height of the first spur opposed to the approach flow was always set equal to $0.50s$, with s as the average height of the remaining spurs.

As previously stated, riprap protection was arranged for the first two spurs opposed to the approach flow. An almost uniform riprap was concentrically arranged around these spur heads; the riprap revetment is characterized by the riprap diameter d_R or the relative sediment ratio $\delta = d_R/d_{50}$, and the number of riprap rows n.

A single layer riprap, without any protection such as a filter or synthetic cloth, was carefully placed so that the revetment surface was flush with the surrounding bed sediment (Figure 3); as a consequence there was

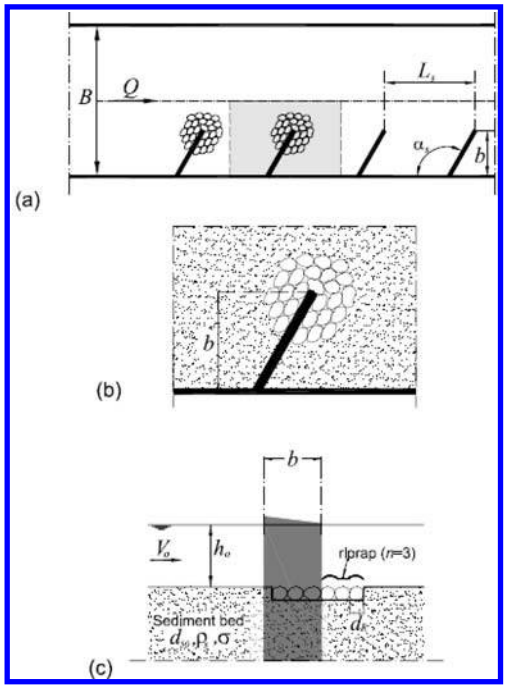


Figure 3. Riprap arrangement, definition sketch: (a) plan, (b) detailed plan view, (c) longitudinal section of one-layer riprap.

no riprap protrusion into the current, that may generate additional turbulence within the flow field.

Different diameters d_R of the riprap elements were considered, namely 5.3, 8.5, 12, 19, 30, and 50 mm; the ratio of riprap to bed sediment diameters δ ranged between 4.8 and 45.5, therefore. The number n of riprap rows concentrically placed around a spur head was 1, 3, 6 and 10. In total, more than one hundred experiments were completed, each running until the riprap failure condition was attained, as described in the following.

2.3 *Failure modes*

By definition, a riprap revetment was considered failed as soon as one of the riprap elements belonging to the inner row was dislodged (Figure 4). Therefore, failure had not yet attained when an outer riprap row was damaged.

Prior to the test beginning, the bed sediment was carefully positioned and the riprap elements were accurately inserted concentrically about the first two spur heads; a slight submergence of the test reach improved the accuracy of these preliminary steps, by reducing the disruption of the flat bed surface. When starting an experiment, the discharge was gradually increased and the sediment entrainment along the test reach was prevented by sufficient submergence. The

Copyright © 2006 Taylor & Francis Group plc, London, UK

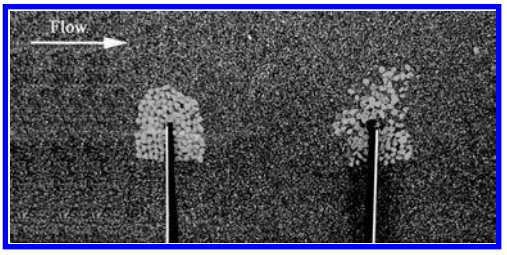


Figure 4. Riprap failure for $\delta = 8.5$, $n = 6$, $\beta = 0.20$, $S = 0.75$, $\alpha_s = 90°$ and $\lambda = 2$.

tailwater level was externally controlled with a flap gate of an accuracy of 0.5 mm; it was thus possible to lower the tailwater until a slight movement of the bed sediment around the riprap was observed. Then the discharge was increased to the test value and the flow depth was kept almost constant through adjustments with the flap gate, such that a certain value of $S = s/h_o$ was finally attained. Both the flow depth and the discharge were slowly varied to suppress inertial effects due to unsteady flow conditions. The failure (subscript f) discharge Q_f and the corresponding approach flow depth h_{of} were noted along with additional information on the failure details, the hydraulic grade line and the overall failure progress.

Figure 4 shows the riprap failure attained at the end of a test characterized by the following parameters: $\delta = 8.5$, $n = 6$, $\beta = 0.20$, $S = 0.75$, $\alpha_s = 90°$ and $\lambda = 2$. Note that the riprap of the first (half-height) spur remained intact whereas few riprap elements at the head of the second spur have slid away; the residual riprap elements in this specific experiment assured some protection against the scour advance around the river structure.

In general, as for the riprap failure at bridge piers, the scour hole close to the spur head increased massively once riprap failure had occurred. This circumstance is clearly shown in Figure 5, referring to a test with $\delta = 12$, $n = 3$, $\beta = 0.20$, $S = 0.75$, $\alpha_s = 90°$ and $\lambda = 2$.

Figure 5(a) shows the riprap arrangement before the experiment was started; Figure 5(b) relates to the end of the run and shows that the riprap at the first (half-height) spur has remained almost intact except for a slight damage along the outer row, whereas riprap failure at the second spur has occurred. The scour pattern and the damages in the vicinity of the structure are also evident from a close illumination of the sediment bed.

When investigating riprap failure at circular bridge piers, Unger & Hager (2006) defined three distinct failures modes, namely:

– *Sliding* a mode occurring once the outer riprap rows are damaged due to the formation of a scour surface between the bed sediment and the riprap; any element from an inner riprap row may possibly fail by sliding into the scour surface.
– *Undermining* as the typical failure mode occurring for a riprap diameter much larger than the bed sediment. In this case, the critical riprap element is not moved horizontally, but sinks into the bed sediment. This condition is less severe than sliding, because a residual protection is guaranteed after failure has occurred.
– *Rolling* as a relatively seldom failure mode, if the sediment ratio δ is close to 1, so that the inner riprap members may roll away by jumping over the outer riprap rows due to the high velocity close to the element perimeter.

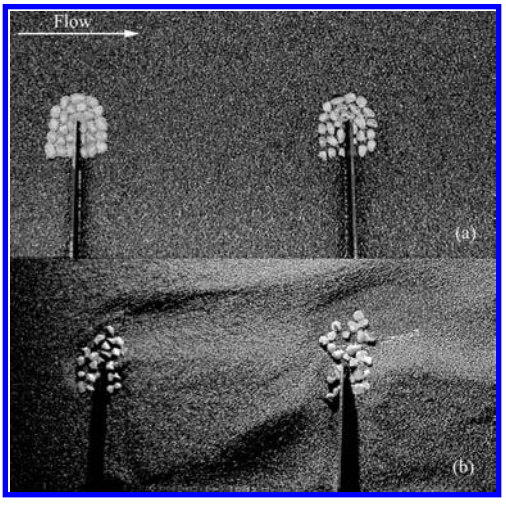


Figure 5. Experimental run for $\delta = 12$, $n = 3$, $\beta = 0.20$, $S = 0.75$, $\alpha_s = 90°$ and $\lambda = 2$; (a) before and (b) after riprap failure.

These failure modes apply to both bridge piers and spurs, except for rolling. In addition, a novel failure mode was observed during the experimental campaign with spurs as described in the following.

Figure 6 shows a typical sequence of sliding riprap failure at the second spur for a test with $\delta = 12$, $n = 3$, $\beta = 0.20$, $S = 0.75$, $\alpha_s = 90°$ and $\lambda = 3$; the riprap at the first half height spur was practically intact at the end of the run. Starting from the original arrangement (Figure 6a), the sliding mechanism was always associated with the displacement of the most peripheral riprap elements; similarly to bridge pier scour, the sediment entrainment normally started at an angle φ roughly equal to 130° measured from the channel axis, creating a scour hole around the riprap zone (Figure 6b). Consequently, outer riprap elements may move towards the river axis from a spur head.

Generally, the scour surface expanded and migrated upstream along the interface between the original bed and the riprap revetment stopping at an angle φ roughly

Copyright © 2006 Taylor & Francis Group plc, London, UK

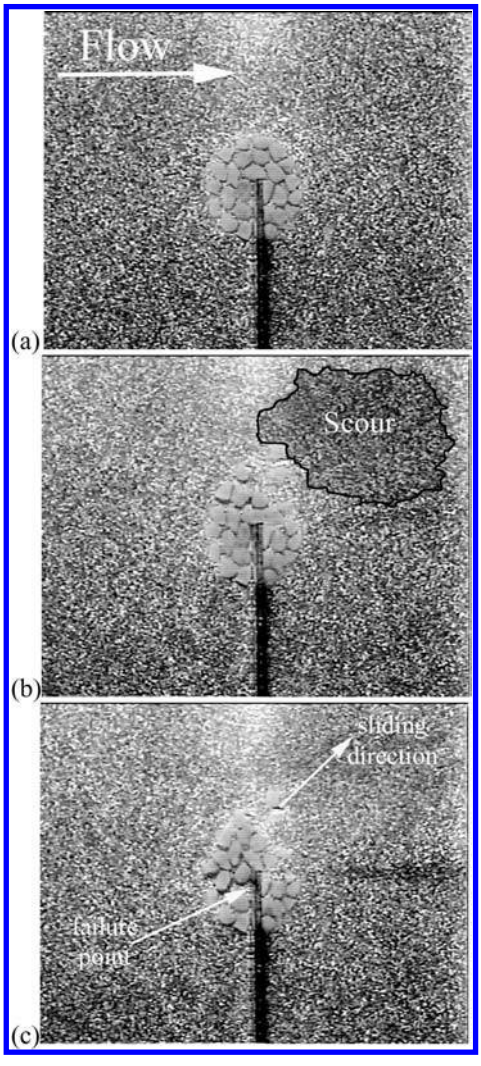


Figure 6. Sliding failure mechanism for $\delta = 12$, $n = 3$, $\beta = 0.20$, $S = 0.75$, $\alpha_s = 90°$ and $\lambda = 3$: plan view of (a) original arrangement, (b) sediment entrainment in the tailwater spur zone, and (c) riprap failure after scour surface has migrated to the spur head zone.

equal to 75°. After the first riprap elements have been entrained, the contiguous stones may slide into the scour surface such that space is available for riprap elements of the next row. The failure process is normally completed when any of the riprap elements along the inner row becomes unstable, as shown in Figure 6c. Note that the upstream riprap zone was never significantly scoured at riprap failure during the sliding mode.

Whereas the sliding failure mode progresses from the riprap periphery towards the spur head, the undermining failure mode attacks directly the key riprap element at the spur head, thereby not seriously attacking the peripheral riprap members.

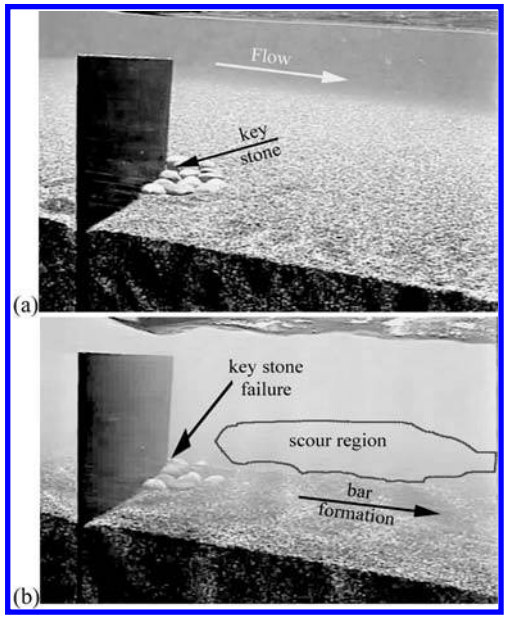


Figure 7. Undermining failure mechanism for $\delta = 19$, $n = 3$, $\beta = 0.20$, $S = 0.75$, $\alpha_s = 90°$ and $\lambda = 3$: side views of (a) original arrangement and (b) riprap failure with typical scour pattern.

Undermining of riprap may hardly be recognized from a top look because the vertical riprap displacement during the failure process cannot be appreciated. This failure mode was considered less severe than sliding because the riprap elements adjacent to the key stone eventually slide into the cavity left by the undermined key element, thus protecting the spur head from a further scour advance. Once undermining has occurred, much less scour activity results in the following stage, until the interface scour has developed so strong that sliding is initiated and the integrity of the riprap protection is lost. The mechanism again is similar to observations conducted by Unger & Hager (2006) on bridge piers.

Figure 7 shows an example of the undermining mechanism at the second spur for a test with $\delta = 19$, $n = 3$, $\beta = 0.20$, $S = 0.75$, $\alpha_s = 90°$ and $\lambda = 3$.

Figure 7a shows the original riprap arrangement, where the proper position of the key element is highlighted. When increasing the discharge, thereby keeping constant the approach flow depth, the sediment entrainment normally starts around the riprap periphery, similarly to the sliding failure mode.

Compared to Figure 6c, Figure 7b shows a larger interface scour with stronger sediment aggradation, forming a bar that eventually migrates downstream of

Copyright © 2006 Taylor & Francis Group plc, London, UK



Figure 8. Final riprap arrangement after 'failure mode 3'.

the spur. In Figure 7b the key element is no more visible because it has sunk below the original bed elevation.

2.4 *Failure mode 3*

Riprap placed around a spur fails either by sliding or by undermining. For selected tests, still another sliding process was observed, defined as failure mode 3. For spurs of extremely small length b and small relative height S, the second spur was subjected with an almost plane jet originating from the overflow of spur 1. This jet impinged onto the second spur and caused downflow, similar to abutments or piers. Instead of generating an interface scour along the riprap periphery towards the channel axis, a downflow scour upstream of the second spur developed eventually so intense that the riprap element located upstream close to the river bank slid into the downflow scour hole.

Figure 8 shows a typical case of failure mode 3, recorded for a test with $\delta = 19$, $n = 3$, $\beta = 0.05$, $S = 0.75$, $\alpha_s = 90°$ and $\lambda = 3$. Note that the diameter of the riprap arrangement at the first spur was not uniform, because the effect of non-homogeneous riprap was verified for selected tests.

This phenomenon was particularly evident for a small spur length for which the relative spur spacing was smaller than $\lambda = 3$. Failure mode 3 occurred also for relatively small spur height S typically below 0.50. The combined spur parameter (βS) was identified as the main controlling parameter.

Experimental data indicated, however, that an additional effect originates from the relative spur length L_s/h_o. Combining the three parameters, the sliding parameter $\Lambda = [(b/B)(s/h_o)(L_s/h_o)]$ was found to describe the geometrical conditions leading to failure mode 3.

Experimental data show that failure modes 1 and 2 arise for $\Lambda > 0.35$, whereas failure mode 3 occurs for $\Lambda \leq 0.35$. Typically, minimum numbers adopted in river engineering practice are $b/B = 0.05$, $s/h_o = 0.50$ and $L_s/h_o = 20$ resulting in a minimum of $\Lambda = 0.50$. Failure mode 3 thus is hardly relevant in applications.

3 INCEPTION EQUATION

Sediment inception is evidently described by the Shields' diagram, indeed a widely used tool in river engineering during last decades. It is well known that the Shields' diagram cannot be used explicitly to evaluate the threshold condition for a uniform sediment to move along the bed. Many equations are currently available to represent the Shields' curve, accounting for different sediment transport regime.

Of particular interest is the fully turbulent regime for which Hager & Del Giudice (2001) found that the inception condition may be described by the following equation:

$$\mathrm{F}_{di} = \sigma^{-1/3} 1.65 (R_h/d_{50})^{1/6} \tag{1}$$

valid for $D_* = (\mathrm{g}'/\nu^2)^{1/3} d_{50}$ larger than 150, being F_{di} the inception densimetric particle Froude number defined as $\mathrm{F}_{di} = V_{oi}/(\mathrm{g}' d_{50})^{1/2}$, V_{oi} the inception velocity, R_h the hydraulic radius, g' the reduced gravitational acceleration, ν fluid viscosity and σ the sediment non-uniformity parameter.

Experimental evidences confirmed that the critical bed shear stress is reduced, e.g. the inception densimetric particle Froude number F_{di}, in the presence of obstacles due to the generation of 'extra turbulence' (Gisonni & Vacca 2005). Consequently the entrainment condition may be expressed through a reduced densimetric particle Froude number $\mathrm{F}_{d\beta}$:

$$\mathrm{F}_{d\beta} = \Phi_\beta F_{di} \tag{2}$$

being Φ_β a disturbance factor, smaller than 1, depending on the obstruction geometry. Hager & Oliveto (2002) found that for bridge hydraulics the disturbance factor may be estimated as:

$$\Phi_\beta = 1 - (2/3)\Sigma\beta^{5/4} \tag{3}$$

with the contraction ratio β equal to D/B where D is the pier diameter or the abutment width, and Σ a shape factor equal to 1 and 5/4 for bridge pier and abutment respectively.

In the present case, both the lateral spur extension as expressed with $\beta = b/B$ and the vertical spur height ratio $S = s/h_o$ are relevant. Given the conceptual approach according to which scour represents a hydrodynamic resistance problem, i.e. the resistance force being equal to a drag coefficient, times the approach flow velocity head times the surface of attack, the governing parameter describing the spur (subscript s) geometry may be identified as $\beta_s = (b/B)(s/h_o) = \beta S$.

The inception densimetric Froude number F_{ds} (subscript s for spurs) depends exclusively on the spur geometry by accounting for the disturbance factor Φ_s

Copyright © 2006 Taylor & Francis Group plc, London, UK

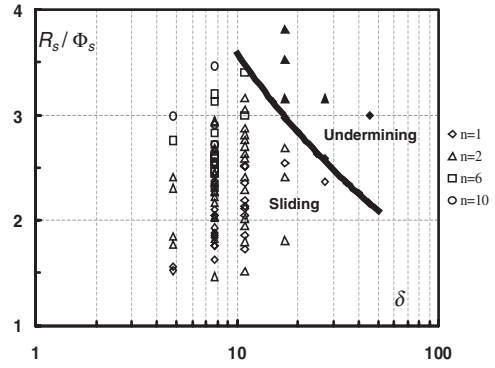


Figure 9. Distinction between Sliding (open symbols) and Undermining (full symbols) failure modes for different riprap row numbers n and relative diameters δ.

computed from equation (3) with Σ equal to 5/4, given that β_s is involved instead of β:

$$F_{ds} = \sigma^{-1/3} 1.65 (R_h/d_{50})^{1/6} \left[1 - (5/6)\beta_s^{5/16}\right], \quad (4)$$

valid for $\beta_s = \beta S$ values between 0.25 and 0.50.

4 PRELIMINARY RIPRAP DESIGN EQUATION

According to the preceding considerations on sediment entrainment at spurs, a similar approach was used to describe the riprap failure condition (subscript R) using the so called spur load factor R_s:

$$R_s = \frac{F_{dR}}{\sigma^{-1/3} 1.65 (R_h/d_{50})^{1/6} \Phi_R} = f(n, \delta, \lambda, \beta, S). \quad (5)$$

Equation (5) shows that the failure densimetric Froude number $F_{dR} = \sigma^{-1/3} V_{oR}/(g' d_{50})^{1/2}$, with V_{oR} as the cross-sectional velocity at riprap failure, depends on the relative riprap diameter δ, the number n of riprap rows, together with the geometrical parameters of spurs arrangement.

The failure disturbance factor Φ_R is similar to Φ_s for sediment inception and may consequently include the effect of β and S. Experiments showed that spur spacing λ has no significant effect on the factor Φ_R; within the experimental range $2 \le \lambda \le 4$, it is thus possible to consider $\Phi_R = \Phi_s = [1 - (5/6)\beta_s^{5/16}]$.

Figure 9 shows the relative hydraulic load factor R_s/Φ_s as a function of the relative riprap diameter δ. As intuitively considered, data referred to the Sliding failure mechanism are located on the lower left of the plot, whereas those with the Undermining failure mechanism are located on the upper right.

It is wise to remark that the Sliding mode is more dangerous than Undermining because riprap elements are 'lost' by Sliding, whilst Undermining reassures a significant residual protection also once failure has occurred. From the experimental data it was possible to locate the threshold line between these two failure modes with:

$$\frac{R_s}{\Phi_s} = 7.7\delta^{-1/3} \quad (6)$$

whose validity is obviously restricted to the experimental range $10 \le \delta \le 50$.

Unger & Hager (2006) expressed the failure condition for a concentric riprap layer of relative size δ with n riprap rows protecting circular piers by concentrating both parameter within the riprap number:

$$N = \delta^{0.20 n^{0.40}} \quad (7)$$

As shown by Gisonni & Hager (2006), the spur load factor R_s may also be considered as a function of the riprap number N, given that the disturbance factor Φ_s is properly assumed, as previously explained. The data may simply be plotted as $R_s(N)$, and the effect of various basic spur features analyzed in a two parameters' plot, as presented in the subsequent paragraphs. Note that equation (5) reduces to the entrainment condition of Hager & Oliveto (2002) for a circular pier or spur without riprap if $\delta = 1$, or $n = 0$, and further reduces to Shields' condition (1) for $\beta_s = 0$, i.e. $\Phi_R = 1$.

As already mentioned, the first spur of half spur height was always less attacked by scour than the second spur. Therefore, the following relates to riprap failure observations at the second spur.

4.1 *Effect of riprap gradation*

The effect of riprap gradation around a spur head was investigated with preliminary tests, in order to check whether a graded riprap assures a better protection compared to uniform riprap with the same average diameter. Three cases were closely considered for otherwise constant conditions, thereby using three riprap rows, namely: (i) uniform riprap, (ii) riprap with the largest element at the spur head and the smallest at the spur periphery, and (iii) inverse set-up with the smallest riprap element at the spur border.

Selected experimental runs were performed with $d_R = 5.3$, 8.5 and 12 mm, for spur length $b = 0.20$ m and various spur heights S. It was found that the hydraulic load factor was not significantly depending on the particular gradation considered; anyhow the performance of case (i) was slightly better than (ii), with case (iii) as the poorer choice. The failure process seemed to be quite abrupt in cases (ii) and (iii) as compared to case (i).

Accordingly, all tests were made with a uniform riprap consisting of diameter d_R and n rows around the spur heads of spurs 1 and 2, to protect the entire

Copyright © 2006 Taylor & Francis Group plc, London, UK

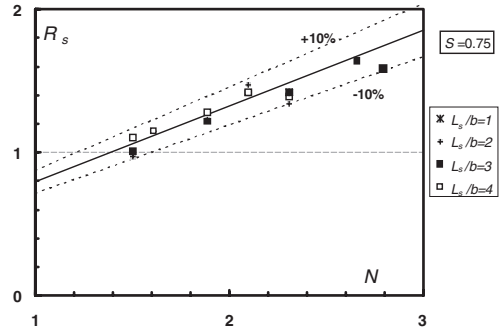


Figure 10. Effects of spur spacing $\lambda = L_s/b$ on the hydraulic load factor R_s as a function of riprap parameter N.

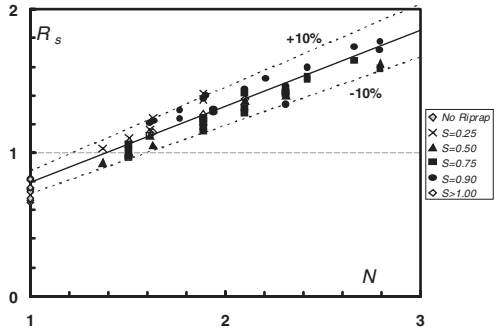


Figure 11. Effects of spur relative height $S = s/h_o$ on the hydraulic load factor R_s as a function of riprap parameter N.

spur set-up. Indeed an important simplification in terms of steering parameters of the phenomenon and, consequently, for design guidelines.

4.2 *Effect of transverse spur slope*

This parameter is hardly mentioned within design guideline, even if 1:10 transverse spur slope is mostly used. Nevertheless a number of experiments were performed with a relative spur height $S = 0.75$, $d_R = 8.5$ mm and $b = 0.20$ m, but different transverse slopes of the spur crest (ranging from horizontal to 1:5). The effect of this parameter was found to be extremely small and the maximum difference in terms of load factor R_s was confined within the $\pm 10\%$ limits. A similar result was obtained for other relative spur heights S, such that the transverse spur slope may be considered insignificant. Based on this conclusion, most part of the experimental set-up is characterized by 1:10 transverse spur slope.

4.3 *Effect of relative spur spacing*

Figure 10 shows the effect of relative spur spacing $\lambda = L_s/b$, for $b = 0.20$ m and $S = 0.75$, using riprap elements between 5.3 and 12 mm, and $1 \leq n \leq 10$.

The effect of the relative spur spacing on the hydraulic load factor was small, for λ between 1 and 4. It was observed, however, that the parameter λ mainly guides the internal flow pattern within the spur fields. Whereas mainly horizontal currents develop for larger λ values, typically above 2, vertical currents appear to form for 'small' relative spur spacing, with the main vortex axis perpendicular to the river bank.

This consideration supports technical recommendations proposing a relative spur spacing between 2 and 4, as mentioned in the introduction.

4.4 *Effect of spur length*

The effect of different spur lengths b was also analyzed, thereby considering riprap with $1 \leq n \leq 10$ and d_R from 8.5 to 19 mm. Many experimental runs were completed with $S = 0.75$ and different spur lengths, namely for $b = 0.10$ m, 0.20 m, 0.35 m and 0.50 m. Overall, the effect of the spur length b, e.g. the relative spur length β, appeared to be correctly contained in disturbance factor Φ_R, leading to maximum deviations of the hydraulic load factor R_s confined within $\pm 10\%$.

4.5 *Effect of spur angle*

The effect of spur angle was experimentally measured within the range $60° \leq \alpha_s \leq 120°$. Spur lengths $b = 0.20$ and 0.35 m were tested, again for a relative spur height $S = 0.75$, along with $d_R = 8.5$ and 12 mm and $1 \leq n \leq 10$. The data for $\alpha_s = 120°$ reveal a somewhat larger hydraulic load factor R_s than those for $\alpha_s = 60°$ and 90°, as was previously found by Oliveto & Hager (2005) for the scour depth at unprotected spurs. The effect of the spur angle α_s is correctly considered once the effective spur length b, e.g. perpendicular to the flow direction, is assumed when computing the disturbance factor Φ_R. Consequently, in straight river reaches as considered in the present research, no particular advantages were noted for spur angles different from $\alpha_s = 90°$.

4.6 *Effect of spur height*

The plot of figure 11 shows the effect of the relative spur height $S = s/h_o$ for $S = 0.25$, 0.50, 0.75, 0.90, and 1.00; hydraulic load factors were measured with spur lengths $b = 0.20$ m, 0.35 m and 0.50 m, riprap arrangements with diameter d_R ranging from 5 to 30 mm and riprap rows $1 \leq n \leq 10$.

It may be noted that the data are generally close to the trend line, even if the data for $S = 0.25$ are relatively high and those for $S = 0.75$ slightly low compared to the trend line, but always within the $\pm 10\%$ limits.

Beside riprap failure, Figure 11 includes also the data for inception at unprotected spurs, e.g. $\delta = N = 1$,

Copyright © 2006 Taylor & Francis Group plc, London, UK

based on selected experimental tests to evaluate sediment entrainment at the first two spurs without riprap placement. For $N = 1$ the hydraulic load factor R_s is observed to be significantly lower than unity and typically of the order 0.75 (±10%), confirming how spur arrangements without a riprap protection (of the first spurs) are not a safe design, as already remarked.

4.7 *Effect of riprap diameter*

The riprap diameter d_R was systematically varied between 5.3 mm and 50 mm and its effect was investigated thereby considering the remaining parameters $0.25 \leq S \leq 1.0$ and b from 0.10 to 0.50 m, along with $1 \leq n \leq 10$ and $2 \leq \lambda \leq 4$. All data demonstrated that the effect of riprap diameter d_R is properly represented by the riprap number N as defined by (7), with a good fitting to the trend line, as shown in Figures 10 and 11.

4.8 *Effect of riprap row number*

Similarly to d_R also the effect of riprap row number n is suitably contained within the riprap number N. For typical sediment size ratio $10 < \delta < 20$ the hydraulic load factor R_s is, respectively, increased by a factor of roughly 1.4 ($n = 3$), 1.7 ($n = 6$), and 2.2 ($n = 10$) as compared to $n = 1$. It is thus evident how an increasing value of n greatly improves the performance of a spur arrangement.

4.9 *Effect of densimetric Froude number*

For the whole set of experimental data the failure densimetric Froude number F_{df} was ranging between 1.4 and 3.4, i.e. from sediment entrainment at unprotected spurs until the transition between clear water and live-bed conditions. Figure 12 shows all the failure data plotted as the ratio of measured $R_{s,meas}$ and computed $R_{s,comp}$ hydraulic load factors versus the failure densimetric particle Froude number F_{df}.

It is evident that all the data, with few exceptions, are confined in the ±10% lines and that the approach is suitably representing the complex phenomenon of riprap failure. Therefore, the design equation for riprap failure can be expressed as:

$$R_s = 0.265(1 + 2N) \qquad \text{for } N_i \leq N \leq 2.8 \qquad (8)$$

with a correlation coefficient r^2 equal to 0.91. Here, N_i is the value of N for sediment entrainment of the order of $F_{di} = 1.5$.

Equation (8) along with figure 12 confirms that the original assumption is correct, according to which the hydraulic load factor correctly expresses the effect of the densimetric Froude number.

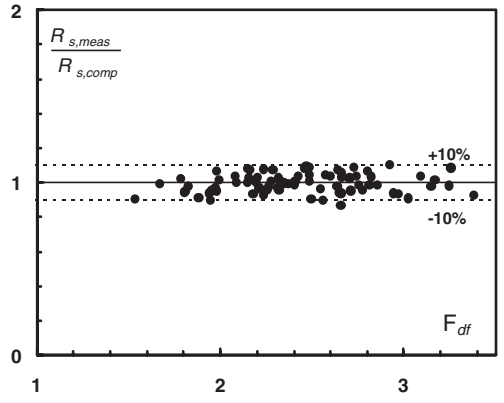


Figure 12. Measured $R_{s,meas}$ and computed $R_{s,comp}$ load factor ratio as a function of the failure densimetric Froude number F_{df}.

5 PRACTICAL ISSUES AND LIMITATIONS

The present research focused on the behavior of spurs arranged along a straight river reach, mainly investigating scour phenomena and the corresponding countermeasures. Given the large set of steering parameters, an experimental campaign was organized to analyze the main features of the spur failure process in the clear-water approach flow regime.

Following to previous experiments on bridge piers (Unger & Hager 2006), an approach based on a generalized Shields' equation was proposed. Experimental runs fall essentially in the rough turbulent regime although the dimensionless grain size is rather in the turbulent transition regime. The riprap failure design equation (8) thus accounts for the effects of hydraulics, granulometry and spur geometry. If both the riprap and the spurs extensions tend to zero, Shields' equation (1) is retained in its basic form.

The following main issues descend from the experiments: Spurs along straight river reaches are optimally arranged when the first spur has half height of all others. In any case the two first spurs must be carefully protected with a suitable riprap revetment to prevent the effects of severe scour action. The experimental set-up considered the simplest riprap configuration arranged in one layer flush with the original bed sediment without any filter. The purpose of this choice was to look for minimum performance in terms of protection, so that any other riprap arrangement is characterized by additional safety against failure. Furthermore, a feasible riprap model was conceived for a systematic experimentation.

Basically two distinct failure mechanisms were identified for riprap placed concentrically around the heads of the two first spurs. These include either Sliding into the interface scour hole that develops along the

Copyright © 2006 Taylor & Francis Group plc, London, UK

riprap periphery, or Undermining at the spur head. A criterion was established to predict the appropriate failure mode, as shown in Figure 9 and expressed with (6).

The average approach flow velocity V_{of} associated with riprap failure was expressed with (8) in which the hydraulic load factor R_s involves the hydraulics of the approach flow and the spur and riprap geometries, as defined with (5). The spur effect as expressed with Φ_s was correlated exclusively with the term βS representing the obstructed cross-sectional area by the spurs both in height and width.

A third riprap failure mechanism was detected for spur arrangements characterized by small length and height, for which an intense scour was noted within the first spur cell close to the river bank. This particular hydrodynamic effect may be described by combining the three governing length parameters to $\Lambda = [(b/B)(s/h_o)(L_s/h_o)]$. It was possible to recognize that failure mode 3 occurs for $\Lambda \leq 0.35$, whereas river applications generally result in a minimum of $\Lambda = 0.50$. Failure mode 3 thus hardly applies in applications, but may be of concern because of its comparatively small hydraulic load factor compared to Sliding and Undermining (Gisonni & Hager 2006).

The impact of the present results is significant in terms of contribution to the river engineering practice; the approach flow hydraulics and the spur arrangement are known for a hydraulic design procedure, and the spur riprap should be sized. However, for an existing spur and riprap arrangement, the existing structure should be checked against failure and the failure hydraulic load should be determined. Such technical issues may be tackled using the results of the present research, thereby also investigating the type of failure mode and the effect of certain parameters on the failure discharge. The proposed approach has inherent limitations due to the complexity of the investigated phenomena and the large number of steering parameters of the spur problem. This is the reason why future research needs to investigate several still open questions such as: (1) spur performance in river bends, (2) the effect of the live-bed regime and (3) the temporal scour advance at spurs once the riprap has failed. Nevertheless the present work may be considered an essential contribution to the study of spur hydraulics, from which the fundamental effects of the basic parameters on the riprap failure emerge, although several simplified conditions were considered.

6 CONCLUSIONS

This experimental study intended to identify the riprap failure conditions for a particular spur arrangement involving a first spur of half height as compared to the remainder, and riprap placed around the first two spurs.

Spur arrangements without a riprap protection at the front spurs are an unsafe design. Physical model tests allowed to evaluate the effects of various parameters on the spur performance and its riprap failure, by using the modified Shields' entrainment approach. The study involved the transverse spur slope, the relative spur height and length, the spur spacing and the effect of riprap diameter and riprap rows placed around a spur head. Finally a number of technical guidelines are proposed according to experimental evidences and the corresponding limitations.

ACKNOWLEDGEMENTS

The first author would like to acknowledge support from VAW during his academic leave to ETH Zurich, Switzerland.

REFERENCES

Gisonni, C., Hager, W.H. & Unger, J. 2005. Spurs in river engineering – A preliminary study. 31 *IAHR Congress*. Seoul, C11-6: 1894–1901.

Gisonni, C. & Hager, W.H. 2006. Spur failure in river engineering. *Journal of Hydraulic Engineering*. Submitted.

Gisonni, C., & Vacca, A. 2005. Discussion to "Influence of turbulence on bed load sediment transport". *Journal of Hydraulic Engineering* 131(1): 72–73.

Hager, W.H. & Del Giudice, G. 2001. Discussion to "Movable bed roughness in alluvial channels". *Journal of Hydraulic Engineering* 127(7): 627–628.

Hager, W.H. & Oliveto, G. 2002. Shields' entrainment criterion in bridge hydraulics. *Journal of Hydraulic Engineering* 128(5): 538–542.

Hager, W.H., Unger, J. & Oliveto, G. 2002. Entrainment criterion for bridge piers and abutments. *River Flow 2002* Louvain-la-Neuve 2: 1053–1058.

Julien, P.Y. 2002. *River mechanics*. Cambridge University Press: Cambridge, UK.

Kondap, D.M. & Prayag, J.D. 1989. On the length and spacing of spurs. Third Intl. Workshop *Alluvial River Problems* University of Roorkee, India: 247–253.

Lagasse, P.F., Schall, J.D., Johnson, F.M., Richardson, E.V. & Chang, F. 1995. Stream stability at highway structures. *Hydraulic Engineering Circular HEC-20*, Report FHWA-IP-90-014. Federal Highway Administration, US Dept. Transportation: Washington DC.

Melville, B.W. & Coleman, S.E. 2000. *Bridge scour*. Water Resources Publications: Highlands Ranch, CO.

Oliveto, G. & Hager, W.H. 2002. Temporal evolution of clear-water pier and abutment scour. *Journal of Hydraulic Engineering* 128(9): 811–820.

Oliveto, G. & Hager, W.H. 2005. Further results to time-dependent local scour at bridge elements. *Journal of Hydraulic Engineering* 131(2): 97–105.

Richardson, E.V., Stevens, M.A. & Simons, D.B. 1975. The design of spurs for river training. 16 *IAHR Congress*, San Paulo B(47): 382–388.

Unger, J. & Hager, W.H. 2006. Riprap failure at circular bridge piers. *Journal of Hydraulic Engineering* 132(4): 354–362.

Copyright © 2006 Taylor & Francis Group plc, London, UK

Numerical simulation of flow and local scour around hydraulic structures

H. Zhang, H. Nakagawa, Y. Muto & Y. Baba
Disaster Prevention Research Institute, Kyoto University, Kyoto, Japan

T. Ishigaki
Dept. of Civil & Environmental Engineering, Kansai University, Osaka, Japan

ABSTRACT: A numerical model is developed to simulate the flow and local scour around hydraulic structures. The model solves the 3D RANS equations for the flow with FVM formulation on an unstructured mesh. Arbitrary polyhedral mesh can be utilized to resolve complex geometries. Local scour due to bedload transport is simulated through the sediment continuity equation and empirical formulae for sediment transport rate. A bed slope factor is derived based on 3D force analyses to account for the local bed effect. Unrealistic bed slope possibly occurring in the computation is avoided by introducing a sediment slide process. The model verification is made by comparing the computed results with some existing experimental data obtained in different laboratory situations. It is shown that both the velocity field and the local scour profiles predicted by the current model are in reasonable agreement with those of the experiments.

1 INTRODUCTION

Researches on the flow and local scour around hydraulic structures (e.g. spur dykes, bridge piers and abutments) have a long history and are of continuous interest in the river engineering. Excessive scour holes have a potential to undermine the structure foundations in a river training project, in particular during flood events. This has resulted in a great number of failures and disasters. With the rapid expanding of the environmental concern, local flows and scour holes have also been found capable of forming satisfactory environment for the flora and fauna in river systems. For instance, Shields et al. (1995) documented significant increases in fish numbers, sizes, species and the area of aquatic habitat after the enlargement of local scour in a river restoration project. In-between the historically built groins along the Yodo River in West Japan, favorable environment for the growth and habitant of a variety of living things have also been observed. These have motivated construction of new groins in this basin (Kinki Regional Development Bureau, MLIT, Japan 2002). Although local scour phenomena are commonly encountered in river engineering practices, related researches are still far from enough and there remain a lot of challenges.

Essentially, local scour is the result of a dynamic feedback process involving the turbulent flow, sediment transport and bed evolution. The flow structure in the vicinity of a local scour hole is usually characterized by several vortex systems of different sizes, which initiate and control the local scour and provide the basic scour mechanism (e.g. Ali & Karim 2002 and Salaheldin et al. 2004). The predominant approaches in the state-of-the-art adopt empirical or semi-empirical formulae based on limited field data and experimental measurements. Despite the large number in amount, these formulae commonly select a number of variables from the approach flow depth, flow intensity, sediment size, the shape, size and alignment of local obstructions, etc. For example, the empirical formula proposed by Melville (1997) and its variants. This kind of methods has achieved a great development with the further understanding of the scour mechanism and more and more calibration data available. However, since these methods involve strong empiricism and introduce many uncertainties, they can provide very limited information and are usually problem-dependent. With the rapid development of both fluid dynamics and computer capabilities, 3D numerical modeling is increasing considered to be a more reliable solution. A well-established numerical model is able to resolve the evolution process of the 3D flow field and the 3D topography of scour holes, which are of significant meaning for engineering use. Previous researches have been carried out by several groups such as Michiue & Hinokidani (1992), Ushijima et al. (1992), Olsen & Melaaen (1993), Fukuoka et al. (1994), Ushijima (1996), Peng et al. (1998), Olsen & Kjellesvig (1998), Watanabe et al. 2001, Yen et al.

Copyright © 2006 Taylor & Francis Group plc, London, UK

(2001), Nagata et al. (2002), Bhuiyan et al. (2004) and Nagata et al. (2005). A brief overview of the recent studies has been reported by Zhang et al. (2005b) and Zhang (2005). It is found that most of the existing researches are based on structured mesh, which is only suitable for relatively simple geometries. However, study domains of engineering interests are generally complicated, especially in the case that the local scour is involved. In view of these arguments, this paper examines the 3D flow and local scour around hydraulic structures with numerical methods based on unstructured mesh. The flow velocity is simulated through solving the RANS (Reynolds-averaged Navier-Stokes) equations with the k-ε model for the turbulence closure. Local scour is assumed to generate due to bed load transport for the time being. The Ashida-Michiue formula (1972) is employed to evaluate the sediment transport rate. The bed evolution is obtained by solving the sediment continuity equation. A bed slope factor is derived to account for the effect of the local bed slope on the sediment transport. In order to guarantee that the local bed slope is not greater than the angle of sediment repose, a sediment slide algorithm is also proposed. Model verifications are performed under two experimental conditions. Both the velocity fields and the local scour profiles predicted by the current model are found to be in reasonable agreement with those of the experiments.

2 MODEL DESCRIPTION

The numerical model consists of a hydrodynamic module, a sediment transport module and a bed deformation module. The modules are linked together in a quasi-steady way on a moving unstructured mesh. The time scale of the bed evolution is assumed to be much larger than that of the flow field. Hence during the calculation of the bed deformation, the flow field and sediment transport conditions are assumed unchanged. These modules are described in the following contexts one after another.

2.1 *Hydrodynamic module*

The unsteady RANS equations written in the Cartesian coordinate system with the convention of Einstein summation are as follows.
Momentum equation:

$$\frac{\partial u_i}{\partial t}+u_j\frac{\partial u_i}{\partial x_j}=f_i-\frac{1}{\rho}\frac{\partial p}{\partial x_i}+\nu\frac{\partial^2 u_i}{\partial x_j\partial x_j}+\frac{1}{\rho}\frac{\partial \tau_{ij}}{\partial x_j} \quad (1)$$

Continuity equation:

$$\frac{\partial u_i}{\partial x_i}=0 \quad (2)$$

where u_i = averaged velocity component; x_i = Cartesian coordinate component; t = time; ρ = density of the fluid; f_i = body force; p = averaged pressure; ν = molecular kinematic viscosity of the fluid; τ_{ij} = Reynolds stress.

Due to the existence of the Reynolds stress terms, Equation 1 and Equation 2 are not a closed system. In the k-ε model, the Reynolds stresses are modeled from the information of the mean flow by introducing a concept of eddy viscosity and constructing two transport equations for the turbulence kinetic energy k and its dissipation rate ε.

In this study, the standard k-ε model is employed. Hence, the Reynolds stresses are estimated from the constitutive equation below.

$$\tau_{ij}=-\rho\overline{u_i'u_j'}=2\rho\nu_t S_{ij}-\frac{2}{3}\rho k\delta_{ij} \quad (3)$$

where u_i' = fluctuating velocity component; ν_t = eddy viscosity; S_{ij} = strain-rate tensor and δ_{ij} = Kronecker delta. The latter three parameters are expressed by

$$\nu_t=C_\mu\frac{k}{\varepsilon}\quad S_{ij}=\frac{1}{2}\left(\frac{\partial u_i}{\partial x_j}+\frac{\partial u_j}{\partial x_i}\right)\quad \delta_{ij}=\begin{cases}1 & if\ \ i=j\\ 0 & if\ \ i\neq j\end{cases} \quad (4)$$

in which C_μ = coefficient, and is usually set to be a constant 0.09. k and ε are solved from their transport equations as follows, respectively.

$$\frac{\partial k}{\partial t}+u_j\frac{\partial k}{\partial x_j}=\frac{\partial}{\partial x_j}\left[\left(\nu+\frac{\nu_t}{\sigma_k}\right)\frac{\partial k}{\partial x_j}\right] \quad (5)$$

$$\frac{\partial \varepsilon}{\partial t}+u_j\frac{\partial \varepsilon}{\partial x_j}=\frac{\partial}{\partial x_j}\left[\left(\nu+\frac{\nu_t}{\sigma_\varepsilon}\right)\frac{\partial \varepsilon}{\partial x_j}\right]+\left(C_{1\varepsilon}G-C_{2\varepsilon}\varepsilon\right)\frac{\varepsilon}{k} \quad (6)$$

in which G = rate of turbulence production, defined as

$$G=-\overline{u_i'u_j'}\frac{\partial u_i}{\partial x_j} \quad (7)$$

and the model constants generally take the universal values as follows.

$$\sigma_k=1.0\quad \sigma_\varepsilon=1.3\quad C_{1\varepsilon}=1.44\quad C_{2\varepsilon}=1.92 \quad (8)$$

2.2 *Sediment transport module*

2.2.1 *Sediment transport rate*

In the absence of suspended sediment, bed variation is due to the movement of bedload. If the shear stress acting on the particle is smaller than a critical value, there is no bed motion. Once the sediment is set in motion, the transport rate of bedload is commonly evaluated

Copyright © 2006 Taylor & Francis Group plc, London, UK

with empirical formulae. In this study, the Ashida-Michiue formula (1972) is employed, which is written as follows.

$$\frac{q_b}{\sqrt{(s-1)gd^3}} = 17\tau_{*e}^{3/2}\left(1-\sqrt{\frac{\tau_{*c}}{\tau_*}}\right)\left(1-\frac{\tau_{*c}}{\tau_*}\right) \quad (9)$$

where q_b = bedload transport rate per unit width; s = specific gravity of sediment; g = gravitational acceleration; d = sediment diameter; τ_{*e}, τ_{*c}, τ_* = dimensionless effective shear stress, critical shear stress and shear stress, respectively. The dimensionless shear stress is connected with the shear stress and the friction velocity via

$$\tau_* = \frac{\tau_b}{(s-1)\rho gd} = \frac{u_*^2}{(s-1)gd} \quad (10)$$

where τ_b = near-bed shear stress and u_* = friction velocity.

In the calculation of bedload transport in a channel with a relatively gentle slope, the critical shear stress can be obtained from the well-accepted Shield's diagram or other popular criteria such as the Iwagaki's relation (1956) and the particle gravity does not affect the sediment motion significantly. However, local bed slope usually becomes very steep in the situation where local scour occurs. According to van Rijn (1993), the bed slope may affect the sediment transport in three ways: (1) the near-bed velocity; (2) the threshold condition, i.e. the condition just sufficient to initiate sediment motion and (3) the transport rate once the sediment is in motion. Since a 3D turbulence model is employed, the first influence has been automatically included in the flow model. The latter two are discussed in the following context.

2.2.2 *Effect of the local bed slope*

The forces acting on a sediment particle resting on a sloping bed under the threshold condition are shown in Figure 1. In this figure, n stands for the normal direction of the local bed plane and α, β & γ are the corresponding direction angles (i.e. $n = \cos\alpha i + \cos\beta j + \cos\gamma k$). The forces include the submerged weight of the particle W and the hydrodynamic force F. The latter one is usually divided into a drag force F_D tangential to the riverbed plane and a lift force F_L normal to the riverbed plane in the analyses of sediment transport.

For reasons of simplicity, the lift force is not taken into account explicitly in the analyses. The effect of the lift force is assumed to be relatively small compared with the submerged particle weight and is accounted for through empirical coefficients in the expression of the drag force. Then it can be assumed that the hydrodynamic force F has a direction almost parallel to the riverbed plane. Hence, the resulted driving force F_r is written as

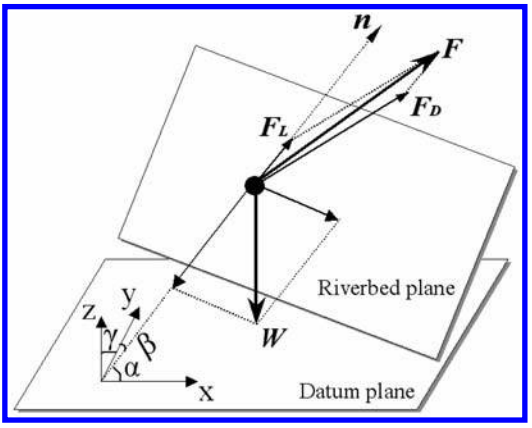


Figure 1. Definition sketch of forces on a sediment particle resting on a sloping bed under threshold condition.

$$\boldsymbol{F}_r = \left(W\cos\gamma\cos\alpha + f_x F\right)\boldsymbol{i} + \left(W\cos\gamma\cos\beta + f_y F\right)\boldsymbol{j} + \left(-W\sin^2\gamma + f_z F\right)\boldsymbol{k} \quad (11)$$

where f_x, f_y & f_z = direction cosines of the hydrodynamic force, i.e.

$$\boldsymbol{F} = F\left(f_x\boldsymbol{i} + f_y\boldsymbol{j} + f_z\boldsymbol{k}\right) \quad (12)$$

The resulted stabilizing force F_s is also easy obtained, which has the form as

$$F_s = W\cos\gamma\tan\varphi \quad (13)$$

where φ = angle of sediment repose.

Under the threshold condition, the resulted driving force equals the stabilizing force, i.e. $F_r = F_s$, one obtains

$$F^2 + 2lWF + \left(\sin^2\gamma - \cos^2\gamma\tan^2\varphi\right)W^2 = 0 \quad (14)$$

in which l is expressed by

$$l = f_x\cos\gamma\cos\alpha + f_y\cos\gamma\cos\beta - f_z\sin^2\gamma \quad (15)$$

The positive solution of Equation 14 is

$$F = \left(\sqrt{l^2 - \sin^2\gamma + \cos^2\gamma\tan^2\varphi} - l\right)W \quad (16)$$

On the other hand, the submerged particle weight W and the hydrodynamic force F including the effect

Copyright © 2006 Taylor & Francis Group plc, London, UK

of both the drag force and lift force are empirically expressed as follows.

$$W = c_1(s-1)\rho g d^3 \quad F = c_2 \tau_b d^2 \tag{17}$$

where c_1 = coefficient related to the shape of the particle; c_2 = coefficient depending on the local Reynolds number. Normalizing Equation 16 with expressions in Equation 17, one has the dimensionless critical shear stress τ_{*c} for a sloping bed as follow

$$\tau_{*c} = \frac{\tau_{bc}}{(s-1)\rho g d} = \frac{c_1}{c_2}\left(\sqrt{l^2 - \sin^2\gamma + \cos^2\gamma\tan^2\varphi} - l\right) \tag{18}$$

where τ_{bc} = critical near-bed shear stress.

In case of a horizontal bed $(\alpha, \beta, \gamma) = (90°, 90°, 0)$, Equation 18 becomes

$$\tau_{*c0} = \frac{c_1}{c_2}\tan\varphi \tag{19}$$

where τ_{*c0} = dimensionless critical shear stress for a horizontal bed. As has been mentioned before, this can be easily obtained from some well-tested criteria such as the Shields' diagram. If one compares Equation 18 with Equation 19, the difference between a sloping bed and a horizontal bed can be expressed by a bed slope factor K

$$K = \frac{\tau_{*c}}{\tau_{*c0}} = \frac{\sqrt{l^2 - \sin^2\gamma + \cos^2\gamma\tan^2\varphi} - l}{\tan\varphi} \tag{20}$$

If there is longitudinal bed slope (denoted as θ_l) only and the longitudinal velocity is predominant, i.e. $(\alpha, \beta, \gamma) = (90° - \theta_l, 90°, \theta_l)$ and $(f_x, f_y, f_z) = (\cos\theta_l, 0, -\sin\theta_l)$, one gets the following bed slope factor

$$K = \cos\theta_l\left(1 - \frac{\tan\theta_l}{\tan\varphi}\right) \tag{21}$$

If there is transverse bed slope (denoted as θ_t) only and still the longitudinal velocity is predominant, i.e. $(\alpha, \beta, \gamma) = (90°, 90° - \theta_t, \theta_t)$ and $(f_x, f_y, f_z) = (1, 0, 0)$, one goes to another bed slope factor

$$K = \cos\theta_t\sqrt{1 - \frac{\tan^2\theta_t}{\tan^2\varphi}} \tag{22}$$

Equation 21 and Equation 22 are commonly used bed slope factors in the literatures (e.g. van Rijn 1993 and Duan et al. 2000). However, these two factors are questionable when they are applied to the sediment transport around hydraulic structures where the magnitudes of the three velocity components are usually comparable. Comparing these two conventional bed slope factors with Equation 20, the new bed slope factor is more general while still maintains the simplicity for programming.

2.2.3 *Sediment slide process*

It is known that there is a critical value for the angle of the local bed slope during the development of the scour hole. This critical angle is generally assumed to be the angle of sediment repose for computational simplicity. In the calculation, the unrealistic steep slope larger than the angle of repose hence should be avoided. In this model, a simple algorithm considering the sediment slide process is introduced here.

A plane-view of the CV (Control volume) surface on the riverbed is shown in Figure 2 (left). At each time step, the program checks the nodes on the riverbed and the corresponding neighbors. If a slope steeper than the angle of repose has been detected connecting node $A(x_A, y_A, z_A)$ and node $B(x_B, y_B, z_B)$, the locations of node A and node B should be adjusted to nodes A' and B' as shown in Figure 2 (right). The change of the elevation is denoted as δz_A and δz_B, respectively. As the bed slope connecting nodes A' and B' equals the angle of repose, one has

$$(z_B - \delta z_B) - (z_A + \delta z_A) = \tan\varphi\sqrt{(x_B - x_A)^2 + (y_B - y_A)^2} \tag{23}$$

On the other hand, sediment conservation should be ensured during the adjustment, i.e.

$$\sum S_{A,neighbor}\delta z_A = \sum S_{B,neighbor}\delta z_B \tag{24}$$

where $S_{A,neighbor}$ = projected area of the mesh surrounding node A (i.e. mesh 1 to mesh 6 shown in Figure 2) and $S_{B,neighbor}$ = projected area of the mesh surrounding node B (i.e. mesh 1, mesh 2 and mesh 7 to mesh10 in Figure 2).

With Equation 23 and Equation 24, the new locations of node A and node B can be obtained. This process is repeated until the bed slopes connecting all the CV nodes and their corresponding neighbors are not more than the angle of sediment repose.

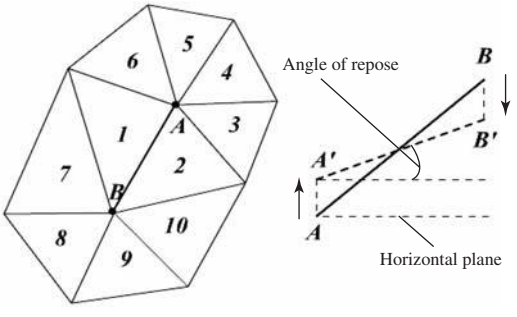


Figure 2. Definition sketch of sand slide process.

Copyright © 2006 Taylor & Francis Group plc, London, UK

2.3 *Bed deformation module*

If the bedload transport rate is known, the bed level is easy to calculate from the mass balance equation in the bedload layer, i.e.

$$\frac{\partial z_b}{\partial t}+\frac{1}{1-\lambda}\left(\frac{\partial q_{bx}}{\partial x}+\frac{\partial q_{by}}{\partial y}\right)=0 \tag{25}$$

where z_b = bed level; λ = sediment porosity; q_{bx}, q_{by} = bedload transport rate in x and y direction, respectively.

2.4 *Boundary conditions*

The boundary conditions include the inlet, the outlet, the impermeable wall, the free surface and the symmetrical plane.

The inlet boundary is usually taken as a Dirichlet boundary. All the quantities are known and prescribed there. At the outlet boundary, zero gradients are assumed along the normal direction. Near the impermeable wall, the flow velocity is assumed to be parallel to the wall. The standard wall function approach is used to link the turbulence domain with the near-wall area. For the time being, the free surface is considered as a rigid lid. As a result, the water level is unchangeable during the computation. In case of flow in a geometrically symmetrical domain, the symmetrical plane boundary is employed to save computer resources and computational time.

2.5 *Numerical scheme & solution procedure*

An FVM (finite volume method) based on a moving unstructured mesh is employed in the model formulation. The governing PDEs (partial differential equations) in the turbulence model are integrated over a number of polyhedral CVs covering the whole study domain in the FVM procedure. The final conservation equations have the following form considering the mesh movement.

$$\frac{\partial}{\partial t}\int_V dV+\int_S\left(u-u_m\right)\cdot ndS=0 \tag{26}$$

$$\frac{\partial}{\partial t}\int_V \phi dV+\int_S \phi\left(u-u_m\right)\cdot ndS=\int_S \Gamma\nabla\phi\cdot ndS+\int_V bdV \tag{27}$$

where V = volume of the CV; S = face of the CV with a unit normal vector n directing outwards; u_m = velocity of the CV face movement; ϕ = general conserved quantity representing either scalars or vector and tensor field components; Γ = diffusion coefficient and b = volumetric source of quantity ϕ.

Equation 26 expresses the mass conservation and Equation 27 stands for the conservation of other quantities such as the momentum. The equation system is mesh-independent and is valid for arbitrary polyhedral CVs. The conserved equations are discretized on a collocated unstructured mesh. For reasons of simplicity and stableness, the power law scheme has been adopted during the spatial discretization for the time being. The surface fluxes are calculated from the Rhie-Chow interpolation (1983) in order to avoid the checkerboard phenomenon. In the temporal integral, the second order implicit Crank-Nicolson scheme is employed. The widely used SIMPLE (semi-implicit method for pressure-linked equations) procedure is included for the coupling of the pressure and the velocity.

The final algebraic equation systems resulted from the discretization process are characterized by sparse and non-symmetrical coefficient matrices. They are solved with a preconditioned GMRES (generalized minimal residual method) incorporated with an ILUTP (incomplete LU factorization with threshold and pivoting) preconditioner proposed by Saad (2003). Before submitted to the solver, the relaxation method proposed by Patankar (1980) is implemented to increase the diagonal dominance of the coefficient matrices.

Based on the shear stress calculated from the turbulence model, the sediment transport rate is evaluated with the Ashida-Michiue formula. The bed deformation at one time step is then computed. If all the local bed slopes are not greater than the angle of sediment repose, a new mesh is generated and the calculation time is forward. This procedure is repeated until the prescribed time is covered or an equilibrium condition is reached.

3 MODEL VERIFICATION

The turbulence model and the proposed unstructured mesh methods have been verified to be capable of predicting some selected flows under fixed bed conditions with reasonable accuracy (Nakagawa et al. 2004 and Zhang 2005a). Hence, this paper examines the model performance under movable bed conditions only.

3.1 *Flow and local scour around a non-submerged cylindrical pier*

One of the most typical problems on local scour in the hydraulic engineering research is the flow passing a circular pier. In this verification case, the experiment carried out by Melville (1975) and Melville & Raudkivi (1977) is tested. The experiment was conducted in a glass-sided flume which was 19 m long, 456 mm wide and 440 mm deep. A cylindrical pier with a diameter of 50.8 mm was used as a bridge pier and installed in a movable bed section. The sediment in the experiment had a specific gravity of 2.65 and d_{50} = 0.385 mm. The experimental setup and the hydraulic conditions are shown in Figure 3 and Table 1, respectively.

Copyright © 2006 Taylor & Francis Group plc, London, UK

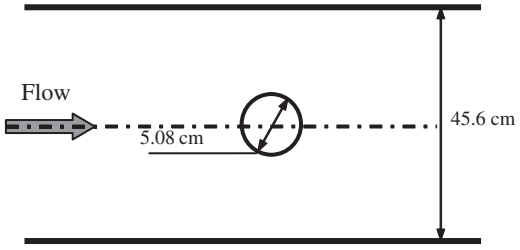


Figure 3. Experimental setup.

Table 1. Hydraulic conditions for the experiment (non-submerged cylindrical pier).

Parameters	Symbols	Values
Flow discharge	Q	17.121 l/s
Water depth	H	15 cm
Mean velocity	u	25.0 cm/s
Sediment diameter	d	0.0385 cm
Critical shear velocity	u_{*c}	1.4 cm/s
Shear velocity ratio	u_*/u_{*c}	0.86
Pier diameter	D	5.08 cm
Reynolds number	$Re.$	37,544
Froude number	$Fr.$	0.21

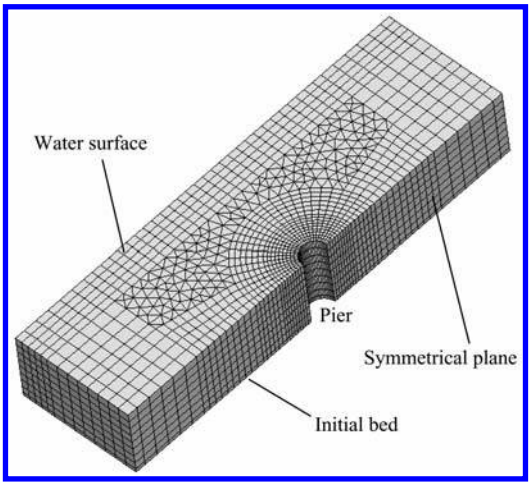


Figure 4. Unstructured mesh system around the pier at initial stage (half domain, not to scale).

Since the study domain is geometrically symmetrical, the calculation is based on half domain only. The mesh system around the pier at the initial stage is shown in Figure 4. It is a combination of both hexahedra and prisms. The inlet boundary is set at around 15D upstream from the pier and the outlet is about 20D downstream from the pier. A logarithmic velocity profile along the vertical direction is assumed at the inlet. The turbulence quantities k and ε are specified

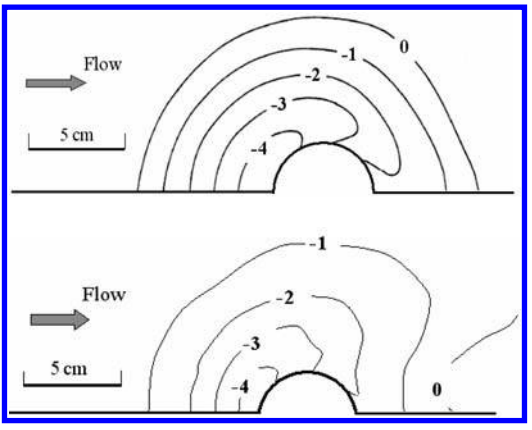


Figure 5. Bed contour after half an hour (Experiment: Top, Melville 1975; Computation: Bottom).

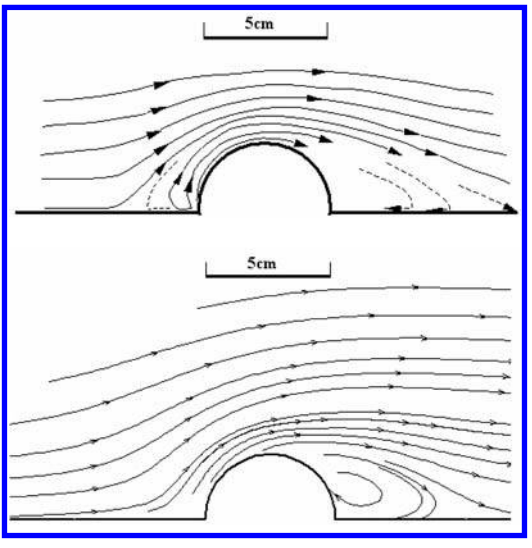


Figure 6. Streamlines at 2 mm from the bed at initial stage (Experiment: Top, Melville & Raudkivi 1977; Computation: Bottom).

corresponding to a turbulence intensity of 8% and taking the viscosity ratio as 10.0.

The bed deformation and corresponding flow field are investigated. The comparisons between the experimental measurements and computational results are shown from Figure 5 to Figure 7.

In Figure 5, the bed deformation around the pier after half an hour is shown. Basically, good agreement between the experimental measurement and computational result can be observed, in particular around the upstream side of the pier. Nevertheless, the computed scour hole appears not so smooth as that of the experiment. The slope is deeper near the pier and becomes

Copyright © 2006 Taylor & Francis Group plc, London, UK

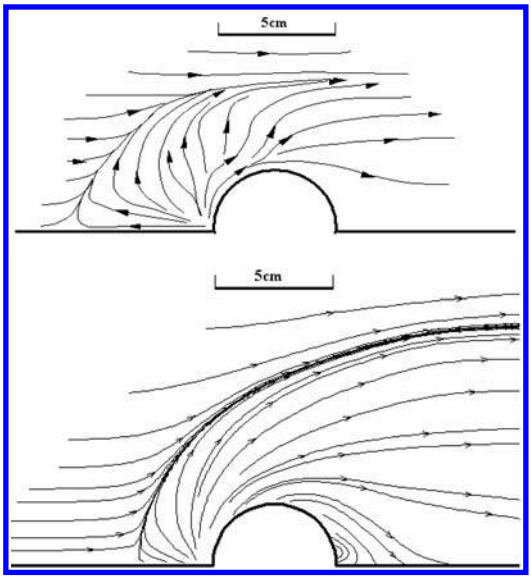


Figure 7. Streamlines at 2 mm from the bed after half an hour (Experiment: Top, Melville & Raudkivi 1977; Computation: Bottom).

milder in the area away from the pier. The zero line is even shifted outside of the plot range and very mild slope forms between line 0 and line −1. It is probably due to the sediment slide algorithm. With the current simple algorithm, the adjustment of the bed slope guarantees that the local bed slope is in the reasonable range. But the general scour geometry turns to be irregular at the same time. Hence a more effective solution is to include the sediment slide process before the bed deformation equation is solved. For instance, Sekine (2004) has considered this process as an additional sediment transport. The sediment slide algorithm is under improvement. In the downstream area, the computed scour hole does not extend as far as that of the experiment. An under-estimated shear stress distribution is responsible for this discrepancy. It will be discussed in the following context regarding the flow field.

The streamlines at 2 mm over the bed around the pier at the initial condition and after half an hour are shown in Figure 6 and Figure 7, respectively. From these two figures, the temporal variation of the flow field can be obtained. When the flow approaches the pier, a separation zone forms in the proximity of the pier. In this zone, the streamlines of the approach flow and some kind of spiraling flow meet together. As a result, a tracer placed upstream near the pier will be directed outward the pier and transported along the separation line after it joins the approach flow. With the development of the local scour and the spiraling flow, the separation zone becomes larger and larger. This phenomenon can be found in both the experiment and the computation. However, the scale of the spiraling flow and the separation area upstream of the pier seem to have been under-estimated by the computation. Figure 7 (Top) and Figure 5 (Top) indicate that the spiraling flow in the experiment almost occupies the whole area of the local scour hole after half an hour. But this kind of flow seems limited in the scour hole area where the bed deformation is more than 2 cm according to Figure 7 (Bottom) and Figure 5 (Bottom). One reason for this difference may be the slope difference between the upper part and the lower part of the scour hole. Moreover, the separation angle has been slightly over-estimated. It leads to a larger area of wake zone behind the pier where the shear stress is very small. In the wake zone, obvious circulating flow has been computed. This confirms the experimental plot (dashed lines) extended from the measured data (Melville & Raudkivi 1975).

3.2 *Flow and local scour around a submerged spur dyke*

Typical spur dykes in the river engineering usually suffer from the over-topping flow during the flood season. In order to understand the flow characteristics and local scour around submerged spur dykes, Ishigaki & Baba (2004) have carried out a series of experiments in the Ujigawa Hydraulics Laboratory, Kyoto University. In this verification, the model is tested under the same hydraulic conditions as one of their experimental cases.

The experimental flume was 10 m long, 1.0 m wide and 0.3 m deep, which was equipped with a discharge control system. A 1.8 m long movable bed was located in the middle part of the flume. It was filled with 0.2 m-thick sediment with a mean diameter of 0.026 cm. The spur dyke was set in the movable bed area and was perpendicular to the side of the flume. The experimental setup and the hydraulic conditions are shown in Figure 8 and Table 2, respectively. The details on the shape and size of the spur dyke are also depicted in Figure 8.

The bed evolution, flow velocity (in the longitudinal and vertical directions) and free surface level were investigated one hour after the experiment started. Before the measurement of the latter two, the bed was converted into a fixed bed with mortar. The measurement devices include a laser level meter, an electromagnetic velocimeter and an ultra-sonic level meter.

In order to diminish the boundary effect of the inlet and outlet, they are set to be far enough from the spur dyke. According to previous experiences and numerical experiments, the inlet is set at about $10H$ from the spur dyke and the outlet is around $20H$ from the spur dyke. A total number of 28,944 polyhedral CVs are employed in the calculation. The unstructured mesh consists of both hexahedra and prisms. The mesh system around the spur dyke is shown in Figure 9.

Copyright © 2006 Taylor & Francis Group plc, London, UK

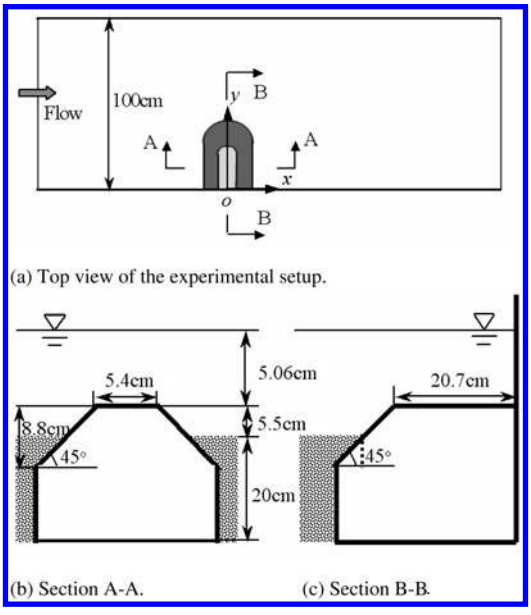


Figure 8. Experimental setup for the submerged spur dyke.

Table 2. Hydraulic conditions for the experiment (submerged spur dyke).

Parameters	Symbols	Values
Flow discharge	Q	21.12 l/s
Water depth	H	10.56 cm
Mean velocity	u	20.0 cm/s
Sediment diameter	d	0.026 cm
Critical shear velocity	u_{*c}	1.523 cm/s
Shear velocity ratio	u_*/u_{*c}	0.78
Spur dyke height	h	5.5 cm
Overtopping ratio	H/h	1.92
Reynolds number	$Re.$	21,120
Froude number	$Fr.$	0.20

Figure 10 shows the comparison of the resulted bed deformation after 1 hour. In Figure 11, the computed streamlines at 2 cm over the initial bed are shown. Figure 12 shows the velocity vector (u, w) 1 cm over the top of the spur dyke.

In both the experiment and the computation, the bed deformation is confined to the proximity of the spur dyke. In general, the scour-deposition pattern shows some simplicity. There are two big obvious scour holes downstream of the spur dyke. In the experiment, the scour hole depths are 2.78 cm and 2.05 cm, respectively. The corresponding results of the computation are 2.33 cm and 2.71 cm, respectively. The occurrence of two big holes can be interpreted as a result of both flow separation and downward overtopping flow. It has been well documented that the flow

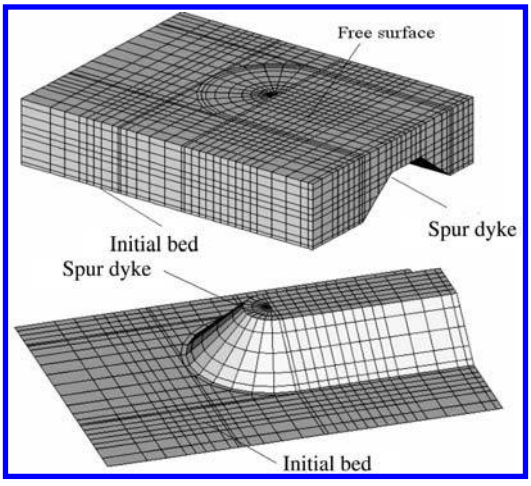


Figure 9. Unstructured mesh system around the spur dyke at initial stage (not to scale).

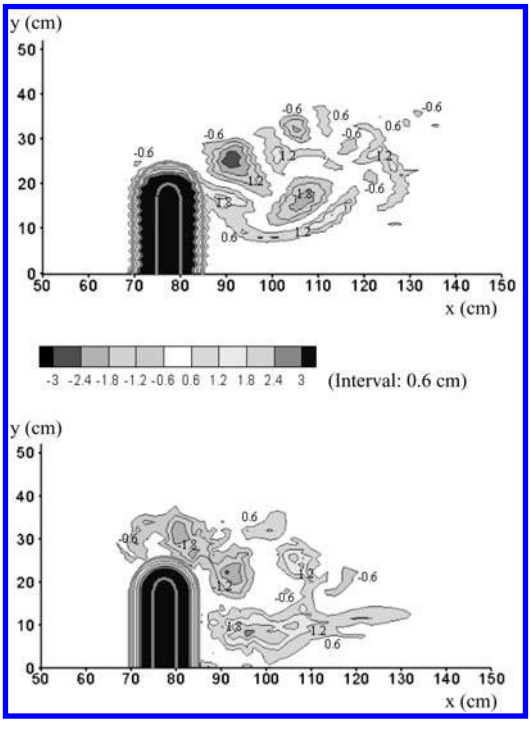


Figure 10. Bed deformation around the spur dyke after 1 hour (Experiment: Top; Computation: Bottom).

will separate when it approaches the head of the spur dyke. A horseshoe vortex forms there. This is the main reason for the scour hole near the head. The computed flow separation can be observed in Figure 11. Due to the overtopping ratio, the flow gets a strong downward

Copyright © 2006 Taylor & Francis Group plc, London, UK

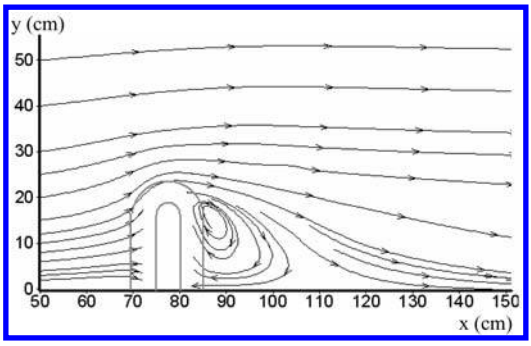


Figure 11. Computed streamlines at 2 cm over the initial bed after 1 hour.

component after it passes the top of the spur dyke. The downward flow intrudes into the wake area behind the spur dyke and leads to sediment erosion there. It also becomes an engine of local scouring. This flow has been observed in a cross-section by a submergible video camera in the experiment (Ishigaki & Baba 2004). However, there is no much evidence that the two big scour holes will maintain their individualities even in the equilibrium condition. Probably, the two scour holes gradually became a bigger one with the development of their scales if the experiment continued till the final equilibrium state.

The predicted local scour holes locate a little different from those of the experiment. The error may come from several sources. The foundation of the spur dyke extends to the movable bed with an angle of 45° (Figure 8c). Hence, the erodible depth in the extent of the spur dyke should be within the foundation limit. However, the foundation under the initial bed has been simplified to be vertical (dashed line in Figure 8c) in the current computation and there is no limit for sediment erosion. This difference will lead to different erosion pattern and velocity field in the extent of the spur dyke. Secondly, the Ashida-Michue formula is used to evaluate the sediment transport rate under equilibrium condition. However, the non-equilibrium transport of sediment load around hydraulic structures has been pointed out by many researchers, e.g. Fukuoka et al. (1994) and Nagata et al. (2005). Finally, the scour process is a dynamic feedback process. A small error in the velocity prediction due to the inherent deficiency of the turbulence model at initial stage will be probably magnified with the development of the local scour. On the other hand, the difference in the scour prediction may become larger with time due to the errors introduced by the flow simulation. This should be also considered as one of the reasons for the discrepancy in the detailed scour geometry as well as the velocity field in Figure 12.

In order to have more detailed information on the overtopping flow, the velocity components (u, w) in

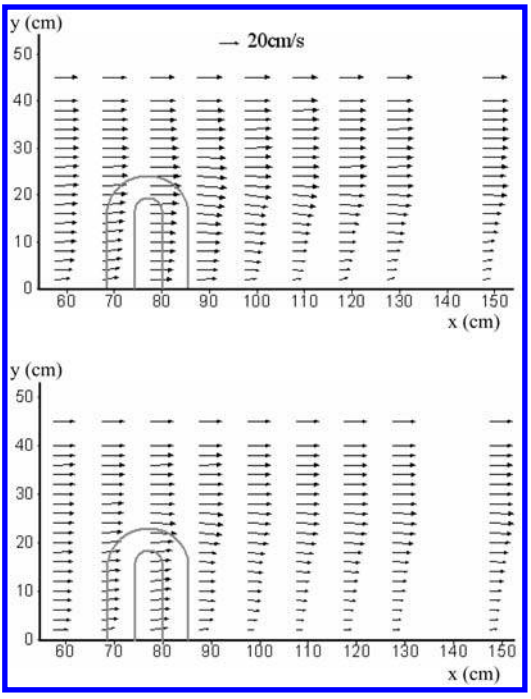


Figure 12. Velocity vectors (u, w) 1 cm over the top of the spur dyke after 1 hour (Experiment: Top; Computation: Bottom).

one layer over the spur dyke are plotted in Figure 12. For clarity, the computed results have been interpolated from the CV centers to the points where the measured data is available. The computational result is very encouraging and in good agreement with that of the experiment. The flow turns upward when it approaches the spur dyke and becomes downward after it leaves the spur dyke. The downward flow propagates for a distance in the wake region behind the spur dyke. As has been mentioned before, this downward flow attacks the riverbed and partially contributes to the development of local scour holes. This kind of flow generally does not appear in non-submerged cases.

Due to the local obstruction, velocity acceleration is observed in the proximity of the spur dyke. The maximum velocity is found to be over the head of the spur dyke where the lowest free surface level has been measured in the experiment.

4 CONCLUSIONS

This study gives a description and some applications of a 3D numerical model, through which the flow structure and the local scour around hydraulic structures can be simulated. The model solves the flow field by using a k-ε turbulence model incorporated with the

Copyright © 2006 Taylor & Francis Group plc, London, UK

wall function approach. In contrast to many existing methods, the current model is based on a moving unstructured mesh. It has significant meaning for engineering practices. Local scour due to bedload transport is simulated by solving the sediment continuity equation with the Ashida-Michiue formula to estimate the sediment transport rate. A bed slope factor is put forward to account for the effect of the local bed slope on the sediment transport. Moreover, a simple sediment slide algorithm is introduced to guarantee that the bed slope is not greater than the angle of sediment repose as well as to ensure that the sediment conservation law is maintained. The model applicability has been confirmed through reasonable predictions of the flow structure and local scour holes in two laboratory experiments.

Nevertheless, this study only constitutes the first step forward in the numerical investigation of the local flow and scour process with unstructured mesh methods. There remains much space for further improvements before it can be used in actual river conditions with sufficient confidence. Firstly, the variation of the free surface is an important phenomenon for flow passing a local obstruction. The rigid-lid assumption adopted in the current model does not allow the resolution of the free surface. It may cause significant error in the velocity and shear stress prediction when the surface variation is not negligible. Secondly, the evaluation of the bedload transport deserves much attention. Existing empirical formulae are generally used for equilibrium sediment transport condition. Since the non-equilibrium transport of sediment load around the hydraulic structures has been reported to be significant (e.g. Michiue & Hinokinadi 1992), the direct use of the existing formulae for equilibrium condition may probably lead to questionable result. Last but not least, the computational time is always an important factor to consider when a 3D model is planned for practical use. Although the authors did not quantitatively evaluate the model efficiency in terms of time consumption per step or per iteration, it has been found that the computational time on a PC (3.2 GHz Intel Pentium 4 CPU and 1G RAM) is at least decades times longer than that of the experiment. Solution methods such as the parallel computing and code optimization should also be paid much attention. These problems will be covered in the future research.

REFERENCES

Ali, K.H.M. & Karim, O. 2002. Simulation of flow around piers, *Journal of Hydraulic Research, IAHR*, 40(2): 161–174.

Ashida, K. & Michiue, M. 1972. Studies on bed load transportation for nonuniform sediment and river bed variation, *Disaster Prevention Research Institute Annuals, Kyoto University*, No. 14B: 259–273 (in Japanese).

Bhuiyan, A.B.M.F., Huque, F. & Saifuddin, A.K.M. 2004. Numerical modeling of flow pattern and bed evolution around spur-type structures, *Proceedings of the 9th International Symposium on River Sedimentation*, Yichang, China, 18–21 October 2004: Tsinghua University Press: 1497–1502.

Duan, J.G., Wang, S.S.Y. & Jia, Y. 2001. The application of the enhanced CCHE2D model to study the alluvial channel migration processes, *Journal of Hydraulic Research, IAHR*, 39(5): 1–12.

Fukuoka, S., Tomita, K., Hotta, T. & Miyagawa, T. 1994. Practical numerical simulation of local scour around a bridge pier, *Journal of Hydraulic, Coastal and Environmental Engineering, JSCE*, No. 497(2–28): 71–79 (in Japanese).

Ishigaki, T. & Baba, Y. 2004. Local scour induced by 3D flow around attracting and deflecting groins, *Proceedings of the 2nd International Conference on Scour and Erosion*, Meritus Mandarin, Singapore, 14–17 November 2004: 301–308.

Iwagaki, Y. 1956. Fundamental study on critical tractive force, *Trans. JSCE*, No. 41: 1–21.

Kinki Regional Development Bureau, MLIT (Ministry of Land, Infrastructure & Transport), Japan. 2002. *Lake Biwa & the Yodo River*.

Melville, B.W. 1975. Local scour at bridge site, *Rep. No.* 117: School of Engineering, the University of Auckland, New Zealand.

Melville, B.W. 1997. Pier and abutment scour: integrated approach, *Journal of Hydraulic Engineering, ASCE*, 123(2): 125–136.

Melville, B.W. & Raudkivi, A.J. 1977. Flow characteristics in local scour at bridge piers. *Journal of Hydraulic Research, IAHR*, 15(4): 373–380.

Michiue, M. & Hinokidani, O. 1992. Calculation of 2-dimensional bed evolution around spur-dike, *Annual Journal of Hydraulic Engineering, JSCE*, No. 36: 61–66 (in Japanese).

Nagata, N., Hosoda, T., Nakato, T. & Muramoto, Y. 2002. 3D numerical simulation of flow and local scour around a cylindrical pier, *Journal of Hydroscience and Hydraulic Engineering*, 20(1): 113–125.

Nagata, N., Hosoda, T., Nakato, T. & Muramoto, Y. 2005. Three-dimensional numerical model for flow and bed deformation around river hydraulic structures, *Journal of Hydraulic Engineering, ASCE*, 131(12): 1074–1087.

Nakagawa, H., Zhang, H., Ishigaki, T. & Muto, Y. 2004. Prediction of 3D flow field with non-linear k-ε model based on unstructured mesh, *Journal of Applied Mechanics, JSCE*, No. 7(2): 1077–1088.

Olsen, N.R.B. & Kjellesvig, H.M. 1998. Three-dimensional numerical flow modeling for estimation of maximum local scour depth, *Journal of Hydraulic Research, IAHR*, 36(4): 579–590.

Olsen, N.R.B. & Melaaen, M.C. 1993. Three-dimensional calculation of scour around cylinders, *Journal of Hydraulic Engineering, ASCE*, 119(9): 1048–1054.

Patankar, S.V. 1980. *Numerical Heat Transfer and Fluid Flow*: McGraw-Hill, New York.

Peng, J., Tamai, N., Kawahara, Y. & Huang, G.W. 1998. Numerical modeling of local scour around spur dykes, *Proceedings of 28th IAHR Congress* (CDs).

Rhie, C.M. & Chow, W.L. 1983. Numerical study of the turbulent flow past an airfoil with trailing edge separation, *Journal of AIAA*, 21: 1525–1532.

Copyright © 2006 Taylor & Francis Group plc, London, UK

Saad, Y. 2003. *Iterative Methods for Sparse Linear System (2nd edition)*: Society for Industrial & Applied Mathematics.

Salaheldin, T.M., Imran, J. & Chaudhry, M.H. 2004. Numerical modeling of three-dimensional flow field around circular piers, *Journal of Hydraulic Engineering, ASCE*, 130(2): 91–100.

Sekine, M. 2004. Numerical simulation of braided stream formation on the basis of slope-collapse model, *Journal of Hydroscience and Hydraulic Engineering, JSCE*, 22(2): 1–10.

Shields, F.D.Jr., Cooper, C.M. & Knight, S.S. 1995. Experiment in stream restoration, *Journal of Hydraulic Engineering, ASCE*, 121(6): 494–502.

Ushijima, S. 1996. Arbitrary Lagrangian-Eulerian numerical prediction for local scour caused by turbulent flows, *Journal of Computational Physics*, 125: 71–82.

Ushijima, S., Shimizu, T., Sasaki, A. & Takizawa, Y. 1992. Prediction method for local scour by warmed cooling-water jets, *Journal of Hydraulic Engineering, ASCE*, 118(8): 1164–1183.

van Rijn, L.C. 1993. Principles of Sediment Transport in Rivers, Estuaries and Coastal Seas: AQUA Publications, the Netherlands.

Watanabe, A., Fukuoka, S., Yasutake, Y. & Kawaguchi, H. 2001. Groin arrangements made of natural willows for reduction bed deformation in a curved channel, *Advances in River Engineering, JSCE*, No. 7: 285–290 (in Japanese).

Yen, C.J., Lai, J.S. & Chang, W.Y. 2001. Modeling of 3D flow and scouring around circular piers, *Pro. Nati. Sci. Counc. ROC(A)*, 25(1): 17–26.

Zhang, H. 2005. *Study on Flow and Bed Evolution in Channels with Spur Dykes*, Doctoral thesis, Kyoto University.

Zhang, H., Nakagawa, H., Ishigaki, T. & Muto, Y. 2005a. A RANS solver using a 3D unstructured FVM procedure, *Annuals of Disas. Prev. Res. Inst., Kyoto University*, No. 48B: 691–707.

Zhang, H., Nakagawa, H., Ishigaki, T., Muto, Y. & Baba, Y. 2005b. Three-dimensional mathematical modeling of local scour, *Journal of Applied Mechanics, JSCE*, No. 8: 803–812.

Copyright © 2006 Taylor & Francis Group plc, London, UK

Dimensional analysis of bridge pier scour and the role of flow intensity

L. Teixeira & G. López
Fluid Mechanics and Environmental Engineering Institute, Universidad de la Republica, Montevideo, Uruguay

G. Simarro, E. Fernandez & M. Ortega-Sánchez
Civil Engineering Department, Universidad de Castilla La Mancha, Ciudad Real, Spain

ABSTRACT: A slightly different dimensional analysis is introduced to analyze the phenomena of local scour around circular bridge piers under clear water flow conditions. Assuming that the local scour process is not affected by the viscosity, in usual laboratory conditions (non cohesive sand below 6 mm and clear water), the flow intensity parameter defined as the ratio of the mean velocity on the critical velocity of the approaching flow is shown not to be a convenient parameter to be used. Therefore, the dimensionless expression considered does not include the flow intensity, but Froude-like numbers. The experimental results for uniform and non cohesive bed material by Melville & Chiew (1999), Ettema (1998) and Mia & Nago (2003) are used to validate the approach. Dimensionless groups such as particle Froude number, the dimensionless flow depth and the dimensionless grain size seem to properly describe the local scour problem.

1 INTRODUCTION

In the last 30 years there has been an intensive research activity in bridge hydraulics and local scour related problems (Melville 1997). Most of the works concentrate on studying the effects over the stability of structures (Melville & Coleman 2000). Other topics of interest are the understanding of the physics of the process and the time evolution of the scour (Oliveto & Hager 2002). A better understanding of the physical mechanisms of the local scour seems to be particularly important in order to find the appropriate dimensionless variables or parameters describing the phenomenon. Although there is a lot of work regarding this topic, there is not a uniform theory of the different parameters involved and their influence on the scouring process.

The flow intensity I (Melville 1997) is a dimensional group defined as the ratio of the approaching velocity (u) on the velocity for the initiation of motion (u_c). The flow intensity has a strong physical meaning, since $I < 1$ indicates clear water condition whereas $I > 1$ indicates live bed. Because of such physical meaning, it has been extensively used. However, there is also an increasingly important number of works which do not consider the flow intensity to describe the process. In this work, emphasis is remarked in the inconvenience of using this parameter.

This paper is structured as follows: in the first section, the flow intensity is shown not to be an adequate parameter to be used in usual laboratory conditions (clear water flow conditions and sediment size below 6 mm) if the local scour problem is supposed not to be affected by the viscosity (common assumption). Instead, a different dimensionless expression is proposed. In the following section, data of 97 experiments published by Melville & Chiew (1999), Ettema (1998) and Mia & Nago (2003) are used to analyze the influence of the different dimensionless groups (two experiments carried out by the authors are also used). Finally, the conclusions are exposed.

2 DIMENSIONAL ANALYSIS

Assuming that contraction effects are negligible (i.e., the cross section is very wide), it is usually considered that the equilibrium local scour depth d_{se} around a circular pier (the analysis is very similar for bridge abutments) depends on the water density ρ, the viscosity ν, the sediment density ρ_s, the sediment size d_{50} (assuming uniform sediment), the approaching flow velocity u, the depth h, the pier diameter d and the gravity g, i.e.

$$d_{se} = f(\rho, \nu, h, u, g, \rho_s, d_{50}, d) \tag{1}$$

A dimensional analysis of the above Expression 1 yields, for instance

$$\frac{d_{se}}{d} = f\left(\frac{h}{d_{50}}, \Delta, \frac{d}{d_{50}}, \frac{g\Delta d_{50}^3}{\nu^2}, \frac{u}{\sqrt{g\Delta d_{50}}}\right), \tag{2}$$

Copyright © 2006 Taylor & Francis Group plc, London, UK

where $\Delta = \rho_s/\rho - 1$ is the relative submerged density. Hereinafter, f stands a generic function.

2.1 *Critical velocity and flow intensity*

Firstly, attention is focused on the introduction of the flow intensity and its dependence on the viscosity. Flow intensity I is defined as the ratio of the approaching mean velocity u on the critical velocity u_c. Because the critical velocity is the mean velocity for the initiation of motion, using Shields analysis and resistance expressions, it can be readily shown that

$$u_c = \sqrt{g\Delta d_{50}\tau_{*c}}\,\phi\left(\frac{h}{d_{50}}, \mathrm{Re}_{*c}\right) \tag{3}$$

where $\tau_{*c} = f(\mathrm{Re}_{*c})$ is the Shields number (the critical dimensionless stress), ϕ stands for the resistance expression and Re_{*c} is the critical Reynolds number of grain

$$\mathrm{Re}_{*c} \equiv \sqrt{\frac{\tau_c}{\rho}}\frac{d_{50}}{\nu} \tag{4}$$

Because $\tau_{*c} = f(\mathrm{Re}_{*c})$ (van Rijn 1984), the above Equation 3 can be also expressed as

$$u_c = \sqrt{g\Delta d_{50}}\,\varphi\left(\frac{h}{d_{50}}, \mathrm{Re}_{*c}\right) \tag{5}$$

or

$$f\left(\frac{u_c}{\sqrt{g\Delta d_{50}}}, \frac{h}{d_{50}}, \mathrm{Re}_{*c}\right) = 0 \tag{6}$$

The dimensionless grain size d_* is defined as

$$d_* = \sqrt[3]{\frac{g\Delta d_{50}^3}{\nu^2}} \quad \left(= \mathrm{Re}_{*c}^2\,\tau_{*c}^{-1}\right) \tag{7}$$

So Shields diagram can alternatively be written as $\tau_{*c} = f(d_*)$ (van Rijn 1984). Moreover, the above Equation 6 can also be written (Simarro et al., in press) as

$$f\left(\frac{u_c}{\sqrt{g\Delta d_{50}}}, \frac{h}{d_{50}}, d_*\right) = 0 \tag{8}$$

showing how the critical velocity u_c depends on the viscosity through d_*. Only if $d_* \geq 150$ viscous effects can be disregarded (Simarro et al., in press) so that

$$f\left(\frac{u_c}{\sqrt{g\Delta d_{50}}}, \frac{h}{d_{50}}\right) = 0 \tag{9}$$

In usual laboratory conditions (clear water, $2\,\mathrm{mm} \geq d_{50}$, $\Delta \approx 1.65$), it is satisfied that $d_* < 150$, so that critical velocity u_c depends on viscosity.

Finally, taking into account Expressions 7 and 8,

$$\frac{g\Delta d_{50}^3}{\nu^2} = f\left(\frac{u_c}{\sqrt{g\Delta d_{50}}}, \frac{h}{d_{50}}\right), \tag{10}$$

so that Equation 2 can also be written as

$$\frac{d_{se}}{d} = f\left(\frac{h}{d_{50}}, \Delta, \frac{d}{d_{50}}, \frac{u_c}{\sqrt{g\Delta d_{50}}}, \frac{u}{\sqrt{g\Delta d_{50}}}\right), \tag{11}$$

or also

$$\frac{d_{se}}{d} = f\left(\frac{h}{d_{50}}, \Delta, \frac{d}{d_{50}}, \frac{u}{u_c}, \frac{u}{\sqrt{g\Delta d_{50}}}\right), \tag{12}$$

which is equivalent (i.e., contains the same information) to the above Equation 2 and introduces the flow intensity parameter.

Alternatively, Equation 12 is also

$$\frac{d_{se}}{d} = f\left(\frac{h}{d_{50}}, \Delta, \frac{d}{d_{50}}, \frac{u}{u_c}, \frac{u_c}{\sqrt{g\Delta d_{50}}}\right), \tag{13}$$

and, again through Equation 8,

$$\frac{d_{se}}{d} = f\left(\frac{h}{d_{50}}, \Delta, \frac{d}{d_{50}}, \frac{u}{u_c}, d_*\right), \tag{14}$$

equivalently.

2.2 *Viscous effects and flow intensity*

Due to the strength of the system of vortex around the pier, it is usually assumed that viscous effects are negligible in the local scour phenomena. This fact is to be used to reduce one of the dimensionless variables in the analysis.

Assuming that the viscous effects are negligible in the local scour phenomena, the viscosity ν is to be deleted from Expression (1). Thus, instead of Equation 2 we get

$$\frac{d_{se}}{d} = f\left(\frac{h}{d_{50}}, \Delta, \frac{d}{d_{50}}, \frac{u}{\sqrt{g\Delta d_{50}}}\right) \tag{15}$$

which has one parameter less in the right hand side, as anticipated.

Although viscous effects are negligible in the local scour process, the approaching flow is affected

Copyright © 2006 Taylor & Francis Group plc, London, UK

by viscous effects in usual laboratory conditions ($d_* < 150$). Therefore, Equation 8 holds (and not Equation 9).

Expression 8, which allowed the introduction of the flow intensity in Equation 2, is not that helpful if we consider Equation 15, since d_* is not present.

Thus, if the flow intensity is to be introduced, Expression 14 can be used, but not the frequently used expression (Melville 1997)

$$\frac{d_{se}}{d} = f\left(\frac{h}{d_{50}}, \Delta, \frac{d}{d_{50}}, \frac{u}{u_c}\right), \tag{16}$$

since d_* in Equation 14 stands for the viscous effects in the approaching flow (not negligible in general).

The problems related to the use of the above Expression 16 can be clearly exposed with a simple counter example. Let us imagine two experiments whose conditions are identical (velocity, water depth, …) except for the viscosity. The second experiment has a viscosity slightly different than the first one. In one hand, assuming that the viscosity does not affect the local scour, the equilibrium scour will be the same in both experiments. However, because critical velocity depends on the viscosity, flow intensities will be different. Thus, two experiments sharing all the dimensionless groups in the right hand side of Expression 16 except for the flow intensity will have the same scour, proving that in such conditions, flow intensity should not be used.

In summary, in usual laboratory experiments ($d_* < 150$ and clear water conditions) and assuming that the viscous effects are negligible in the local scour process, the flow intensity is not a convenient parameter to be used since it does not allow to take advantage of the fact that the viscous effects are negligible to reduce the number of dimensionless groups by one.

3 ANALYSIS OF EXPERIMENTAL DATA

Assuming that the viscous effects are negligible in the scour phenomena, Expression 15 has been proposed. Assuming that $\Delta = 1.65$ is constant, Equation 15 can be reduced to

$$\frac{d_{se}}{d} = f\left(\frac{h}{d}, \frac{d}{d_{50}}, \frac{u}{\sqrt{g d_{50}}}\right) \tag{17}$$

after a simple manipulation (the substitution of h/d_{50} by h/d). If the viscosity is taken into account and $\Delta = 1.65$, from Expression 2 we can get

$$\frac{d_{se}}{d} = f\left(\frac{h}{d}, \frac{d}{d_{50}}, \frac{ud}{\nu}, \frac{u}{\sqrt{g d_{50}}}\right), \tag{18}$$

which reduces to Expression 17 for the inviscid case. Experimental data are used to analyze above expressions. Note that in both Expressions 17 and 18, the particle Froude number $u/(gd_{50})^{0.5}$ can be replaced by the pier Froude number $u/(gd)^{0.5}$.

3.1 *Data from Melville & Chiew (1999) and Mia & Nago (2003)*

Melville & Chiew (1999) presented the results of 84 experiments carried out in different flumes and for cylindrical bridge piers, clear water flow conditions and uniform grain size. The data include the values of d, d_{se}, d_{50}, h, u, t_e (the equilibrium time, that required to reach the equilibrium stage) and flow intensity. The results by Mia & Nago (2003) for 22 experiments and 8 tests presented by Ettema (1998) have been also considered. Finally, two tests carried out by the authors at the University of Castilla La Mancha (López et al., in press) are used. The experiments were carried out at the Hydraulic Engineering Laboratory, University of Castilla – La Mancha (Spain), in a 37 m long and 0.75 m wide rectangular open channel flume with steel bottom and glass sidewalls. The downstream end of the channel is controlled by a tailgate to adjust the flow depth upwards. The channel had a working zone located 27 m downwards from the beginning. This zone is a recess of 3 m long and 0.3 m deep where a 0.09 m diameter cylindrical pier was placed. The whole channel was horizontally covered by a layer of 0.07 m height of sand. The median grain, the standard deviation and the density of the sediment are $d_{50} = 1.65$ mm, $\sigma_g = 1.32$ and $\rho_s = 2650$ kg/m^3, respectively. The scour depth and the water surface were measured using conventional point gauge, and clear-water flow conditions were imposed in all the experiments.

From the whole set of experiments, those corresponding to pier diameter below 4.7 cm were not included in the analysis, so that an overall of 97 tests remained to perform the analysis. The ranges of variation for the dimensional variables were

- $78 \geq d_{50}$ (mm) ≥ 0.26,
- $766 \geq d$ (mm) ≥ 47,
- $600 \geq h$ (mm) ≥ 20,
- $1.21 \geq u$ (m/s) ≥ 0.165.

Expression 18 can be written as,

$$\frac{d_{se}}{d} = f\left(\frac{h}{d}, \frac{d}{d_{50}}, \mathrm{Re}_p, \mathrm{Fr}_s\right) \tag{19}$$

with $\mathrm{Fr}_s = u/(gd_{50})^{0.5}$ the particle Froude number and $\mathrm{Re}_p = ud/\nu$ is the Reynolds number corresponding to the pier. Ranges of variation of the dimensionless variables in the analyzed tests were

- $11.8 \geq h/d \geq 0.07$,
- $901 \geq d/d_{50} \geq 13$,
- $252{,}780 \geq \mathrm{Re}_p \geq 8700$,
- $6.73 \geq \mathrm{Fr}_s \geq 1.70$.

Copyright © 2006 Taylor & Francis Group plc, London, UK

For many of the experiments $d/d_{50} < 100$ so, according to Melville (1997), the influence of d/d_{50} is to be considered. On the other hand, h/d varies in the narrow range $2 < h/d < 4$ and, therefore, its influence will be difficult to assess.

As mentioned above, $\mathrm{Fr}_s = u/(gd_{50})^{0.5}$ can be replaced by $\mathrm{Fr}_p = u/(gd)^{0.5}$ in Expression 19, to get

$$\frac{d_{se}}{d} = f\left(\frac{h}{d}, \frac{d}{d_{50}}, \mathrm{Re}_p, \mathrm{Fr}_p\right) \tag{20}$$

3.2 *The influence of the Reynolds pier number Re_p*

The influence of the pier Reynolds number Re_p shows the weight of the viscosity on the local scour phenomena.

The influence of the Reynolds number can not be established nor neglected from the present experimental data since there is a strong experimental correlation between the Reynolds and Froude numbers (not shown).

In general, it is difficult to isolate the effect of the viscosity in order to measure its relevance. It is usually assumed that viscous effects are negligible but, to the knowledge of the authors, explicit experimental evidences are still required.

It will be assumed, though, that viscous effects are negligible, so that Expressions 19 and 20 read

$$\frac{d_{se}}{d} = f\left(\frac{h}{d}, \frac{d}{d_{50}}, \mathrm{Fr}_s\right) \tag{21}$$

and

$$\frac{d_{se}}{d} = f\left(\frac{h}{d}, \frac{d}{d_{50}}, \mathrm{Fr}_p\right) \tag{22}$$

The above expressions are similar to that by Melville (1997) but introducing a Froude number instead of the flow intensity, for the reasons argued above.

3.3 *Expression for the local scour*

Figure 1 shows the dimensionless scour depth d_{se}/d against the pier Froude number classified in classes by d/d_{50} for a selection of 96 tests.

Figure 1 seems to confirm that d_{se}/d does not depend on the pier Reynolds number, since the correlation is quite good. Moreover, the scour seems not to depend either on h/d for the data analysed (recall the limitations of the data available, for which $2 < h/d < 4$ only).

Therefore, for the available data, Expressions 21 and 22 can be assumed to be of the form

$$\frac{d_{se}}{d} = f\left(\frac{d}{d_{50}}, \mathrm{Fr}_s\right) \tag{23}$$

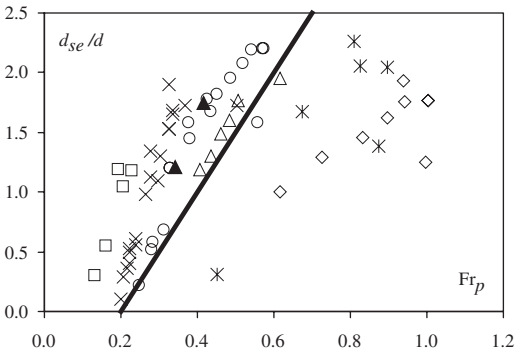


Figure 1. Analysis of $d_{se}/d = f(d/d_{50}, \mathrm{Fr}_p)$ (grouped in classes by d/d_{50}) for $d/d_{50} \approx 19$ (trapezes), $d/d_{50} \approx 27$ (asterisks), $d/d_{50} \approx 47$ (white triangles), $d/d_{50} \approx 53$ (circles), $d/d_{50} \approx 73$ (crosses) and $d/d_{50} \approx 222$ (squares). Black triangles correspond to experiments carried out at University of Castilla – La Mancha, being $d/d_{50} \approx 56$.

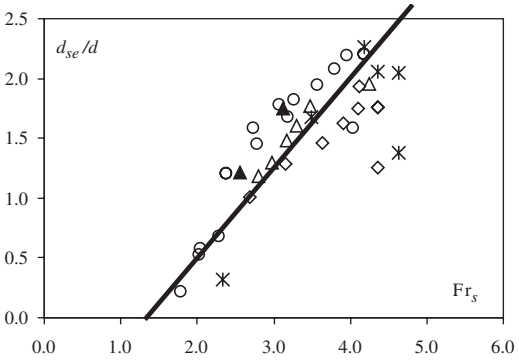


Figure 2. Analysis of $d_{se}/d = f(d/d_{50}, \mathrm{Fr}_s)$ (grouped in classes by d/d_{50}) for $d/d_{50} \approx 19$ (trapezes), $d/d_{50} \approx 27$ (asterisks), $d/d_{50} \approx 47$ (white triangles) and $d/d_{50} \approx 53$ (circles). Black triangles correspond to experiments carried out at University of Castilla – La Mancha, being $d/d_{50} \approx 56$.

and

$$\frac{d_{se}}{d} = f\left(\frac{d}{d_{50}}, \mathrm{Fr}_p\right) \tag{24}$$

Figure 1 shows the trends of the influence on d_{se}/d of both d/d_{50} and Fr_p, for the 62 tests where it was possible to group the results as a function of the parameter d/d_{50}. As it is well known, d_{se}/d increases with the parameter d/d_{50} for small values of d/d_{50} (i.e., $d/d_{50} < 70$). Furthermore, for $d/d_{50} > 70$ the data tend to collapse to

$$\frac{d_{se}}{d} = f\left(\mathrm{Fr}_p\right) \approx 5\mathrm{Fr}_p - 1 \tag{25}$$

Copyright © 2006 Taylor & Francis Group plc, London, UK

Figure 2 shows the results for $d/d_{50} < 70$ against Fr_s for the 37 tests were it was possible to plot the results as a function of d/d_{50}. The scatter that was present in Figure 1 for $d/d_{50} < 70$ is now basically collapsed, and

$$\frac{d_{se}}{d} = f(\mathrm{Fr}_s) \quad (\approx 0.75\mathrm{Fr}_s - 1) \tag{26}$$

works for $d/d_{50} < 70$ (Fig. 2).

4 CONCLUSIONS

Under usual laboratory conditions (small sediment size and clear water flow conditions) and assuming that the viscous effects are negligible in the local scour process, flow intensity is not an adequate parameter to be used.

Instead, assuming $\Delta = 1.65$ constant, an expression of the form

$$\frac{d_{se}}{d} = f\left(\frac{h}{d}, \frac{d}{d_{50}}, \mathrm{Fr}_p \equiv \frac{u}{\sqrt{gd}}\right) \tag{27}$$

or

$$\frac{d_{se}}{d} = f\left(\frac{h}{d}, \frac{d}{d_{50}}, \mathrm{Fr}_s \equiv \frac{u}{\sqrt{gd_{50}}}\right) \tag{28}$$

is proposed, where the Froude numbers play a similar role of that usually assumed by the flow intensity.

The above expressions, which do not include the flow intensity, have shown to be able to explain the trends of the experimental data scrutinized from the literature.

For the experimental data available, the influence of h/d was scarce, in part due to the relatively small range of variation for h/d. The data showed that, for $d/d_{50} < 70$, $d_{se}/d = f(\mathrm{Fr}_s)$ while, for $d/d_{50} \lesssim 70$, $d_{se}/d = f(\mathrm{Fr}_p)$.

ACKNOWLEDGEMENTS

Guillermo López was supported by the visiting professor program from UCLM. The authors would also thank Eduardo Díaz for his able help in preparing the experiments.

REFERENCES

Ettema, R., Melville, B.W. & Barkdoll, B. 1998. Scale Effect in Pier-Scour Experiments. *Journal of Hydraulic Engineering* 124(6): 639–642.

Lopez, G., Teixeira, L., Ortega-Sanchez, M. & Simarro, G. in press. Discussion of "Further Results to Time-Dependent Local Scout at Bridge Elements" by Giuseppe Oliveto and Willi H. Hager. Vol 131, No. 2, pp. 97–105. DOI: 10.1061/(ASCE)0733-9429(2005)131:2(97). *Journal of Hydraulic Engineering*.

Melville, B.W. 1997. Pier and abutment scour: integrated approach. *Journal of Hydraulic Engineering* 123(2): 125–136.

Melville, B.W. & Chiew, Y.M. 1999. Time Scale for local scour at bridge piers. *Journal of Hydraulic Engineering* 125(1): 59–65.

Melville, B.W. & Coleman, S.E. 2000. *Bridge Scour*. Colorado: Water Resources Publications, LLC.

Mia, F. & Nago, H. 2003. Design Method of Time-Dependent Local Scour at Circular Bridge Pier. *Journal of Hydraulic Engineering* 129(6): 420–427.

Oliveto, G. & Hager, W.H. 2002. Temporal evolution of clear-water pier and abutment Scour. *Journal of Hydraulic Engineering* 128(9): 811–820.

Oliveto, G. & Hager, W.H. 2005. Further results to time-dependent local scour at bridge elements. *Journal of Hydraulic Engineering* 131(2): 97–105.

Simarro, G., Teixeira, L. & Cardoso, A. in press. Flow intensity parameter in pier scour abutments. *Journal of Hydraulic Engineering* (in review).

van Rijn, L.C. 1984. *Principles of Sediment Transport in Rivers, Estuaries and Coastal Seas*. Amsterdam: Aqua Publications.

Copyright © 2006 Taylor & Francis Group plc, London, UK

Maximum scour depth around spur dikes

M. Azarderakhsh & H. Norouzi
MSc Student of Tarbiat Modarres University, Tehran, Iran

M. Ghodsian
Professor of Department of Civil Engrg, Tarbiat Modarres University, Tehran, Iran

ABSTRACT: Realistic estimation of scour depth around spur dikes in alluvial rivers is important for safe and economic design of their foundations. Earlier research into the problem has mainly been of an experimental nature, with equations being derived for particular conditions. The available predictive equations for maximum scour depth, are applicable only to a limited range of situations.

There are many empirical equations for estimation of maximum scour depth; however they are derived for a special condition and each equation obtains different values for same case.

It seems necessary to evaluate these equations. We collected different data sets (contain 450 data set) from several researcher's experiments and used them to compare existent equation's ability of accuracy predict. The comparison shows that these equations can't predict scour depth accurately.

Also in this research we re-analysis the scour around a spur dike with dimensional analysis and obtain dimensionless maximum scour depth as a function of dimensionless parameters. Then we derive a new equation from this relation and a wide rang of data set. Finally the previous equations are compared with proposed equation.

1 INTRODUCTION

A spur dike may be defined as a structure extending outward from the bank of a stream for the purpose of deflecting the current away from the bank to protect it from erosion. In addition to bank protection, spur dikes have also been used to enhance aquatic habitat by creating stable pools in unstable streams (Klingeman et al.1984). Fish communities in warm water streams are quite sensitive to the availability of large stable pools (Schlosser 1987).

Spur dikes cause pools to be created and maintained, and have been found, in general, to be more beneficial to aquatic habitat resources than other types of bank protection (Knight and Cooper 1991; Shields et al. 1995a, 2000)(8). The magnitude of the benefit to the habitat in a disturbed stream is related to the scour depth.(Shields et al. 1995b) documented significant increases in fish numbers, size, biomass, and number of species in an incised stream following modification of spur dikes to enlarge scour holes and increase the percentage of pools in the reach. Designers of bank stabilization structures should, where possible, calculate maximum scour depth for determining of foundation elevation. Maximum depth of local scour in the vicinity of a spur dike is difficult to estimate accurately (5).

Although there are many experimental equations for maximum scour depth, they have been derived for a special condition and each equation obtains different values for one case (13).

The majority of previous research in this area has focused on predicting the maximum scour depth in vertical wall abutments and comparatively less studies have been done for prediction the scour depth around wing wall and spill through spur dikes e.g., Liu (1961), Wong (1982), Kwan (1988), Melville (1994, 1997). The effect of alignment of spur dike on the maximum depth of scour for abutments was summarized by (Melville and Coleman 2000). With a few exceptions Kwan 1984; Kandasamy 1985), maximum scour depth increased about 20% as the alignment angle increased from 30 to 150°.

In the present study, an extensive set of data (see tables 1 & 2) were used to evaluate the accuracy of available equations for estimation of maximum depth of scour. The correlation between maximum depth of scour and important parameters such as: angle of spur dike with respect to channel bank, densimetric fraud number; channel contracting relative; uniformity of bed materials and medium diameter of them; relative length of spur dike and type of spur dike were investigated.

Copyright © 2006 Taylor & Francis Group plc, London, UK

Table 1. The range of parameters studied.

Parameter	Range	Unit
Angle of spur dike (α)	45–150	degree
Flow depth (y)	0.26–0.50	m
Velocity (v)	0.09–1.23	m/s
Diameter (d50)	0.26–3.30	mm
Canal width (B)	0.60–2.44	m
Width of spur dike (w)	0.009–2.65	m
Length of spur dike (L)	0.007–1.27	m
Standard deviation of material (δ)	1.13–3.93	–
L/y	0.04–17.4	–
L/B	0.009–0.47	–
Froud number (Fr)	0.062–1.28	–

Table 2. Number of used data.

Type of spur dike	Number of data
Vertical wall	353
Wing wall	62
Spill through	66

2 DATASET

The dataset used in this study consists of experimental data obtained by Tey (1982), Liu (1961), Gill (1972), Garde (1961), Kwan (1984, 1988), Wong (1982), Fathi (1993), Tehrani (1999), Nasrollahi (2001), Razmjoo (2002), Kandasamy (1985), Tison (1962), Counha (1975), Dongol (1994), Ladage (1998). Table (1) shows the range of the datasets that used. Totally 481 data were used. The dataset cover wide range of effective parameters (3), (4), (6), (7), (8), (9), (12).

The number of data for different types of spur dikes is given in table (2). The range of scour depth for each data set is given in table (3). As shown in this table, the scour depth in the collected dataset varies between 0.003 to 0.585 m.

These dataset were used in evaluating the existing scour depth equations. Most of the existing equations were collected and are shown in table (4) and they are collected from several researchers studies (2), (10), (11), (14), (15), (16).

3 EVALUATING THE EXISTING EQUATIONS

To evaluate the available empirical equations, maximum scour depth was calculated from relevant equation. The values of average percentage error E determined by comparing with measured values using:

$$E = \frac{100}{n}\sum_{1}^{n}\frac{ds_c - ds_o}{ds_o} \qquad (1)$$

Table 3. Researchers' data range of scour depth.

Researcher	Scour depth range (m)
Liu(1961)	0.064–0.585
Garde(1961)	0.003–0.18
Tison(1962)	0.068–0.082
Gill(1972)	0.032–0.19
Cunha(1972)	0.039–0.288
Wong(1982)	0.013–0.285
Tey(1984)	0.0785–0.365
Kwan(1984, 1988)	0.085–0.40
Kandasamy(1985)	0.24–0.252
Dongol(1994)	0.11–0.306
Fathi(1993)	0.123–0.23
Ladage(1998)	0.16–0.34
Tehrani(1999)	0.06–0.55
Nasrollahi(2001)	0.06–0.037
Razmjoo(2002)	0.325–0.43

in which *dsc* and *dso* are computed and measured values of scour depth respectively.

The values of E for different equations are shown in table 5. It can be seen from this table that equations of Lacy, Buy Ngok, Das and Ahmad have less errors than other equations and are suitable for predicting scour depth for spill through spur dikes and equations of Zaghloul, Mukhamedov, Neil, Papashvili are suitable for predicting Wing wall spur dikes because of less errors for this type of spur dike as compare with other equations. Moreover equations of Zaghloul, Lim, Neil, Garde, and Dietz are suitable for vertical wall spur dikes. The typical comparisons of computed and measured values of depth of scour for some of equations are shown in Figures 1 to 3.

4 DIMENSIONAL ANALYSIS

A schematic view of spur dike and some of important parameters being effective on scour depth are shown in Figure (4). Before determining the effective dimensionless parameters governing local scour around spur dikes the effective factors should be introduced. These effective parameters can be categorized as (1):

A-Flow condition parameters including: mean flow velocity (u), flow depth (y), fluid density (ρ), kinematic viscosity (υ), gravity acceleration (g).

B-Channel geometry parameter including: channel width (B).

C-Parameters depicting the geometry of spur dike including: length (l), width (w), angle of tip (β), side slope (m) and angle of spur dike with respect to channel bank (α).

D-Bed sediment material parameters including: fall velocity of sediment (ω), mean diameter of bed material (d_{50}), density of bed materials (ρ_s), standard deviation of bed materials (δ) which determined by

Copyright © 2006 Taylor & Francis Group plc, London, UK

Table 4. Researchers' Equation for scour depth.

Researcher	Equation	Researcher	Equation
Inglis	$d_s + y = 2.32 \times \left(q^{2/3} / L \right)^{0.78}$	Das (1976)	$\frac{y + d_s}{y} = 0.56 \times 10^{(0.602n - 0.0294)} \times \left(\frac{y}{d_{50}} \right)^{0.29} \times Fr^{0.85}$
Ahmad	$\frac{y + d_s}{y} = k' \left(\frac{Fr}{1-n} \right)^{2/3}$	Neil (1980)	$d_s + y = 2.1 \approx 2.75 \times \left(\frac{2.59^2}{D^{0.318}} \right)^{0.333}$
Altunine , Buzunov	$\frac{y + d_s}{y} = k_\alpha k_m k_n$	Cunha (1976)	$\frac{d_s}{y} = 189 \left(\frac{L}{y} \right)^{0.69} \times \left(\frac{u_*}{w} \right)^{3.25} + 0.16$
Garde	$\frac{y + d_s}{y} = f_1(cd) \frac{Fr^{f_2(cd)}}{1-n}$	Buy Ngok (1981)	$\frac{y + d_s}{y} = \frac{1.09 \times \exp[-0.075(m-1)]}{(1-n)^{0.3}} * (\alpha/90)^{0.2} \left(\frac{h}{y} \right)^{0.41} f_1(c_d)(Fr)^{f_2(c_d)}$
Lacy	$Y + d_s = 0.47k \left(\frac{Q}{f} \right)^{0.33}$	Zaghloul (1983)	$\frac{d_s}{y} = \frac{2.62}{(180^0 - \alpha)^{0.043}} \times \frac{Fr^{2/3}}{1-n}$
Liu	$\frac{d_s}{y} = K_m \left(\frac{L}{y} \right)^{0.4} Fr^{0.33}$	Richardson et al (1991)	$\frac{d_s}{y} = 1.5 \left(\frac{L}{y} \right)^{0.48}$
Khosla (1963)	$\frac{y + d_s}{y} = \frac{0.9q^{2/3}}{yf^{1/3}}$	Lim et al (1992)	$\frac{d_s + y}{y} = 3.5(Fr)^{0.75} \cdot \left(\frac{d_{50}}{y} \right)^{0.25} \cdot \left(\frac{L}{y} \right)^{0.29}$
Laursen (1963)	$\frac{L}{y} = 2.75 \frac{d_s}{y} \left[\left(\frac{1}{11.5} \frac{d_s}{y} + 1 \right) \right]^{1.7} - 1$	Cardoso et al (1994)	
Maglakelidze(1968)	$\frac{d_s}{y} = 0.56 \left(\frac{\alpha}{90^0} \right)^{1/3} \frac{1 - 0.285m}{1 + 0.09C_b} \times \frac{(U/w)^{0.75}}{0.07 + y/L}$	Clear water	$\frac{d_s}{Y} = 38.3 * (L/Y)^{-0.56} * (Y/d50)^{0.23} \cdot Fr^{2.76}$
Dietz (1969)	$y + d_s = w \frac{q}{u_c}$	Live bed	$\frac{d_s}{Y} = 4.3 (L/Y)^{0.29} * (Y/d50)^{-0.21}$
Mukhamedov (1971)	$\frac{y + d_s}{y} = 15.1 \frac{\sin^{0.25}\alpha \times \cos^{0.5}\beta}{(1-n)\left(\frac{D_{85}}{D_{50}} \right)^{1/6}} \times \frac{Fr^{0.9}}{(1 + 0.09c_v)(1 + 1.08Fr^2)^{0.5}}$	Hoffmans (1995)	$d_s = y\left((1-n)^{-2/3} - 1 \right) + K_B \tanh\left(\frac{y}{L} \right)$
Gill (1972)	$\frac{d_s + y}{y} = 8.375 \times \frac{\left(\frac{D_{50}}{y} \right)^{0.25}}{(1-n)^{0.857}}$	Melville (1997)	$d_s = K_{yl} K_l K_s K_\theta K_G K_d$
Papashvili (1973)	$\frac{d_s}{y} = k_\alpha (1 - 0.285m) \times \frac{\left[\left[1 + k \left(\frac{L}{y} \right)^{1/3} Fr \right] \frac{u}{u_c} - 1 \right]}{\left[1 + 0.154 C_b \left(\frac{D_{50}}{D_{95}} \right)^{1/2} \right]^{1/2}}$	Nasrollahi (2001)	$\frac{d_s}{y} = 103.81 Fr^{1.5} (1-R)^2 \left(\frac{y}{L} \right)^{0.5} \left(\frac{d_{50}}{y} \right)^{0.25}$
		Razmjoo (2002)	$\frac{d_s}{L} = 0.221 \left(1 - R^2 \right)^2 \cdot Fr^{-1.0201}$

$\delta = \sqrt{d84/d16}$ (d84, d16 are the diameter that 84% and 16% of bed materials are less than).

Therefore one can write the following form function for the scour depth:

$$d_s = f(B, L, \rho, \rho_s, d_{50}, u, v, g, w, \beta, \alpha, m, \omega, y, \delta) \quad (2)$$

Using the dimensional analysis, dimensionless parameters for spur dike are obtained generally as:

$$ds/Y = f(L/Y, L/B, U/\sqrt{g.Y}, W/L, \rho/\rho_s, \alpha, \delta, Y/d50, m, \delta) \quad (3)$$

Parameters $y/d50$ and $F = u/\sqrt{g.Y}$ were combined to form the densimetric Froud number $Fd = u/\sqrt{g.d50}$.

The density of bed material is constant, so the relevant parameter ρ/ρ_s is neglected.

The parameter of side slope and width of spur dike can be eliminated with separating the type of spur dike.

Therefore the function form of equation (3) can be written as:

$$ds/y = f(Fd, L/y, L/B, \delta, \alpha, Type) \quad (4)$$

Here the effect of each dimensionless parameter on relative scour depth evaluated using the collected data set.

Effect of relative flow depth L/Y

The effect of this parameter on relative scour depth is shown in Figure (5). It is evident from this Figure that for the same bed material and densimetric Froud number and type of spur dike, the relative scour depth increases with increasing the L/y.

Effect of densimetric Froud number Fd

Another important factor having effect on relative scour depth is the densimetric Froud number. The effect of this factor on relative scour depth is shown on Figure (6). This Figure has been drawn for different L/B and L/y parameters. As shown in this Figure, the relative scour depth increases with increasing the flow intensity or Froud number.

Copyright © 2006 Taylor & Francis Group plc, London, UK

Table 5. Average percentage error for different equations for three types of spur dikes.

Equation owner	Vertical wall	Wing wall	Spill through
Ahmad (1953)	91.9	67.65	61.20
Altunine et al (1953)	148.1	72.9	146.0
Buy Ngok (1981)	95.5	59.7	69.80
Cardoso (1994)	880.0	127.2	382.0
Das (1976)	125.4	79.2	70.30
Dietz (1969)	69.7	59.6	7468
Garde (1961)	75.3	57.7	128.9
Gill (1972)	155.7	74.8	225.5
Inglis (1949)	1689.0	786.1	1260.2
Khosla (1963)	139.9	94.0	314.0
Lacy (1961)	82.97	64.26	69.3
Laursen (1963)	121.2	102.6	302.3
Lim (1992)	49.25	72.25	237.5
Liu (1961)	90.43	74.50	102.9
Maglakelidze (1968)	76.8	163.2	208.8
Hoffmans (1995)	160.4	70.5	95.8
Melville (1997)	115.6	153.5	78.8
Mukhamedov (1971)	95.3	45.11	463.8
Murumov (1970)	189.7	298.3	370.8
Neil (1973, 1980)	70.74	46.6	189.8
Papashvili (1973)	197.3	54.4	79.1
Richardson (1991)	117.46	97.0	291.0
Razmjoo (2002)	155.9	102.3	269.6
Nasrollahi (2000)	492	118.3	530.5
Zaghloul (1983)	72.21	40.1	116.8

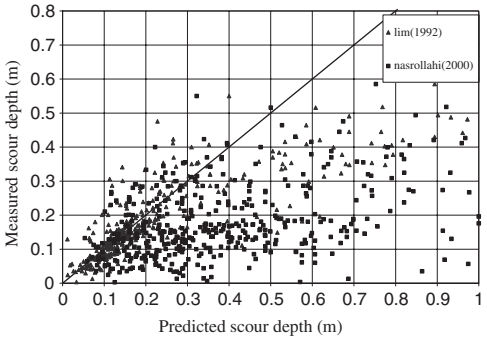


Figure 1. The best and worst equations for prediction of scour depth for vertical wall spur dikes.

Effect of relative length of spur dike L/B

To consider the effect of parameter L/B on relative scour depth the Figure (7) was drawn. All other parameters in this Figure are constant. As shown in this Figure, the L/B directly affects on scouring. It is clear that by increasing L/B the parameter ds/Y will increase.

Any increasing in length of spur dike causes increasing the maximum scour depth because it changes the direction of streamlines in tip of the spur dike and amplifies vortex.

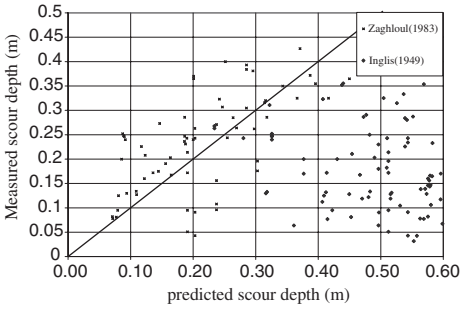


Figure 2. The best and worst equations for prediction of scour depth for Wing wall spur dikes.

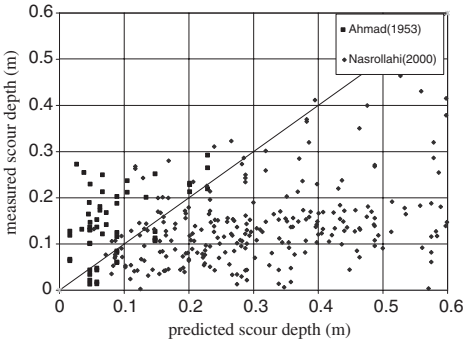


Figure 3. The best and worst equations for prediction of scour depth of spill through spur dikes.

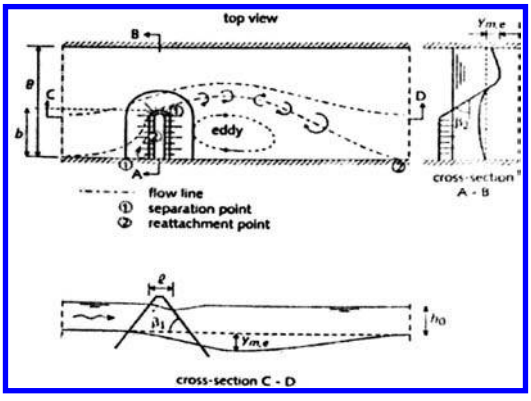


Figure 4. Typical spur dike and some parameters.

Effect of parameters α and δ

The effect of parameters α and δ on scour depth are shown in Figures (8) and (9) respectively. As seen from Figure (8), the relative scour depth increases with increasing the angle of spur dike. When α is less than 90 degree, the scour depth is less because of reducing the intensity of contact between flow and tip of spur dike.

Copyright © 2006 Taylor & Francis Group plc, London, UK

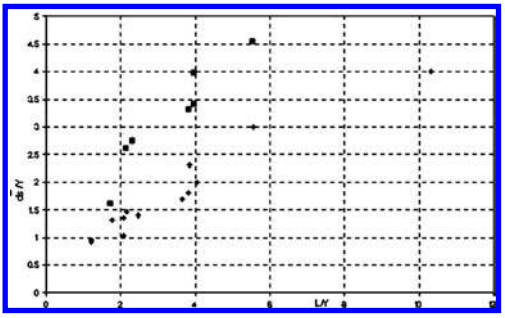


Figure 5. Effect of L/Y on ds/Y.

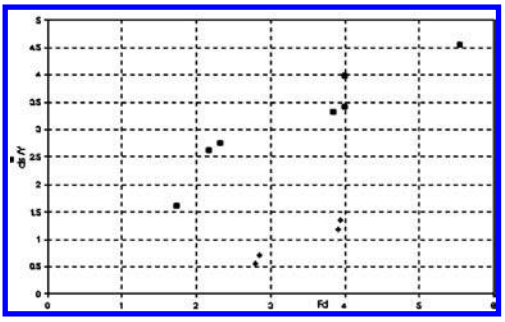


Figure 6. Effect of Fd on ds/Y.

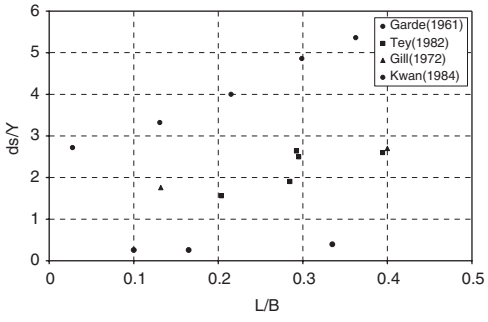


Figure 7. Effect of L/B on ds/Y.

The standard deviation of the bed materials (δ), as seen in Figure (9) affect on relative scour depth. When the ratio of δ increases the scour depth decreases.

Effect of type of spur dike

The effect of type of spur dike on scour depth is shown in Figure (10). As seen in this Figure the relative scour depth around vertical wall spur dike is more than that of the wing wall, and scour depth around wing wall spur dike is more than that of spill trough spur dike. Vertical wall inhibits more effect on flow pattern. It is clear that the scour depth will increase by increasing the intensity of stream flow around spur dike.

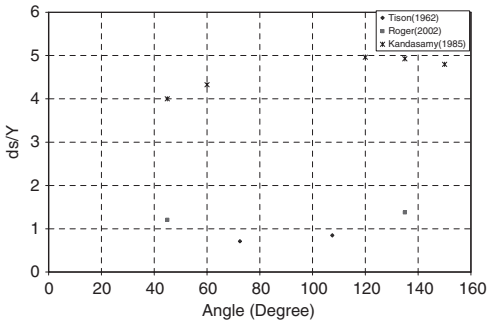


Figure 8. Effect of settlement angle on ds/Y.

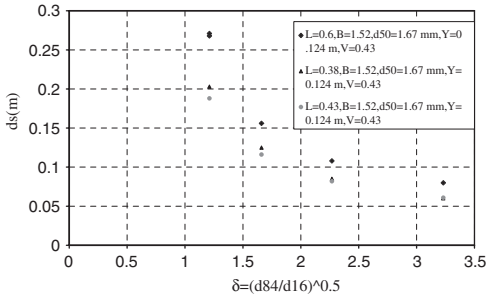


Figure 9. Effect of material homogeneity on ds/Y.

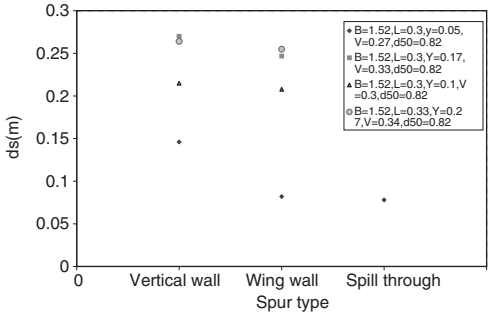


Figure 10. Effect of type pf spur dike on ds/Y.

5 THE PROPOSED EQUATION

The effect of important factors on scour depth around spur dike investigated using the dimensional analysis and data set. We used them to obtain the final function of scour depth. Several analyses were done to reach the final equation with minimum percentage of mean error:

$$ds/y = 0.25 * Fd^{0.614} * (L/y)^{0.3} * (L/B)^{-0.44} * f(\delta) * f(\alpha) * K_T \qquad (5)$$

in this equation, $f(\delta)$ and $f(\alpha)$ are functions of α and δ and are shown in Figures (8) and (9) respectively. The best regression for these functions is the one which has

Copyright © 2006 Taylor & Francis Group plc, London, UK

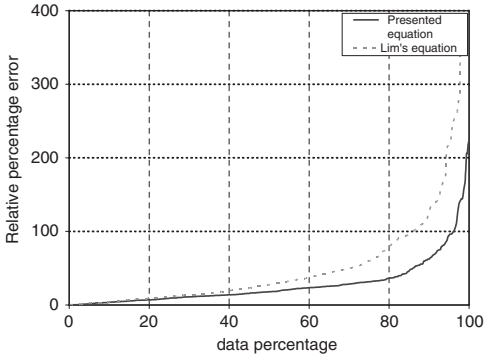


Figure 11. Error frequency of presented equation in comparison between the best earlier equation.

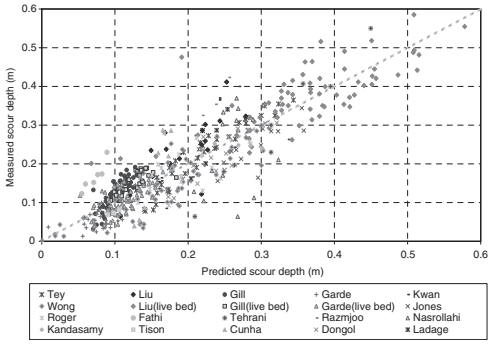


Figure 12. Comparison between predicted scour depth from the presented equation and measured values.

minimum mean error:

$$f(\alpha) = 0.586 + 0.0046 * \alpha \quad (6)$$

$$f(\delta) = 1.45 - 0.34 * \delta \quad (7)$$

the factor of K_t in equation (5) is related to type of spur dike and its value is equal to 1.23 for vertical wall, 1.04 for wing wall and 0.74 for spill through spur dike. This coefficient has been obtained from Figure (10).

The average percentage error of this equation is 29.32% for all the data set. This value is less than error due to other equations. The Figure (11) shows the error frequency for the presented equations. It is clear that 90% of data set have less than 60% error, while 80% of data have at least 36% of mean error and 50% of data have at least 18% of mean error. Also Figure (12) shows presented equation's ability of scour depth prediction.

6 CONCLUSIONS

The recent study was accomplished to evaluate the impression of effective parameters on maximum scour depth around spur dikes and present a new function. In this research, an equation for prediction of maximum scour depth was presented by using the dimensional analysis and the dataset collected from several experiments.

The important results of this study are summarized as:

1. The presented equation can predict the scour depth very well and its prediction error is less than earlier equations.
2. This equation has not the previous equations limitation; it can be used for 3 types of spur dikes considering, change in bed material distribution, angle of spur dike and other factors influencing the scouring.

REFERENCES

Azarderakhsh, M. 2004, "Re-Analysis of maximum scour depth around spur dikes and use of artificial neural networks", MSc thesis, civil engineering department, Tarbiat Modarres university.

Couto, L.T. and Cardoso, A.H., 1999, "Experimental Investigation on Local Scour Around Spill through Spur dikes", International Symposiom East-West, South-North in River Engineering Methods and Philosophies, St. Petersburg, Russia.

Dongol, D.M.S. 1994. Local scour at bridge abutments. Report n. 544, University of Auckland, New Zealand.

Fathi. A. 1993, "scouring around permeable spur dikes", MSc thesis, Civil engineering department, Tarbiat Modarres university.

Hoffmans, G.J.C. and Verheij, H.J. 1997, "Scour Manual", Balkema, Rotterdam.

H. Tehrani, S. 1998, "Scour depth around compound spur dike", MSc thesis, Civil engineering department, Tarbiat Modarres university.

Ladage, F. 1998, "Temporal development of local scour at bridge abutments". Internal report, University of Auckland, Auckland, New Zealand.

Melville, B.W. 1995, "Bridge Abutment Scour in Compound Channels", J. Hydraulic Engineering, Vol. 121, No. 12.

Nasrollahi, A. 2001, "Effect of opening ratio of permeable spur dikes on scour depth" MSc thesis, Civil engineering department, Tarbiat Modarres university.

Palavaccini, M., 1993, "Abutment Scour Data Base", GKY on Web Site.

Przedwajski, B., Blazejewski, P. & Pilaryzk, K.W. 1995, "River Training.

Razmjoo, M. 2003, "The effect of distance between permeable spur dikes on scouring", MSc thesis, Civil engineering department, Tarbiat Modarres university.

Palavaccini, M. 1993, "Abutment Scour Data Base", GKY on Web Site.

Roger, A., Kuhnle, C. and Sheildsjr, D. 2002, "Local Scour Associated with Angled Spur Dikes", J. Hydraulic Engineering, Vol. 128, No. 12.

Yossef, F.M. 2002, "The Effect of Groynes on Rivers", Literature Review, Delft University of Technology.

Copyright © 2006 Taylor & Francis Group plc, London, UK

Modelling the flow and morphology in groyne fields

Mohamed F.M. Yossef
WL | Delft Hydraulics, Delft, the Netherlands, Faculty of Civil Engineering and Geosciences, Delft University of Technology

Rebekka Rupprecht
University of Karlsruhe, Faculty of Civil Engineering and Geosciences, Delft University of Technology

ABSTRACT: Experiments have been conducted in a mobile-bed flume for a straight river with groynes on one side to study the morphological interaction between the groyne fields and the main channel. The flume had a geometrical scale of 1:100 based on typical dimensions of the River Waal. The bed material has been scaled to have bed load as well as suspended sediment transport. In this paper a numerical simulation of an emerged case of the laboratory experiment is presented. The sediment exchange between the main channel and the groyne field are of special interest. The simulation has been carried out using the DELFT3D-FLOW system coupled with Horizontal Large Eddy Simulation (HLES). For the morphological computations, the Online-sediment module was used; it calculates the sediment concentration, the sediment transport, and the bed level changes simultaneously with the flow. The model was calibrated against data from the experiment. The results of the hydrodynamic computations show the typical turbulent structures in emerged groyne fields, which have also been observed in previous experiments and described by several authors. With a sensitivity analysis, the influence of some input parameters on the computed flow field was studied. From this analysis, the effect of some physical parameters was investigated. The results of the morphological computation showed a qualitative accordance with the measured bed levels. In conclusion, we can state that Delft3D computes the morphological pattern in the vicinity of groynes qualitatively well.

1 INTRODUCTION

1.1 *Background*

Groyne fields are a central element in the river Waal and other Dutch branches of the river Rhine. They form a zone of sediment storage. Field measurements by ten Brinke et al. (2001) indicate that they have a significant contribution to the overall sediment balance of the river. Moreover, erosion of the groyne fields may affect the stability of the groynes. Additionally, they provide the sand for the natural formation of wind-blown dunes on the floodplains that are a valuable habitat for riverine flora and fauna.

To understand more the sediment exchange processes between the groyne field and the main channel, mobile-bed experiments have been carried out in the Laboratory of Fluid Mechanics at the Technical University of Delft (Yossef and De Vriend, 2004). In this paper we attempt to model these experiments using Delft3D system. A comparison of the measured and the computed results will be made and the capabilities of the numerical model to simulate the laboratory experiment will be evaluated.

1.2 *Objective*

The objective of the paper is to judge whether the current sediment transport model is capable of simulating the morphological interaction between the main channel and the groyne fields. The results of the morphological computations will be compared to the observations which have been made in the experiment. The results of the hydrodynamic computations need to be compared with the observed flow field as well. Furthermore, a sensitivity analysis will be made for both hydrodynamic and morphodynamic computations in order to study the influence of certain parameters on the result of the computation.

1.3 *Approach*

Numerical simulation has been carried out to model the laboratory experiments. In this paper, we will only present one case of emerged groynes.

The numerical simulations were carried out using the Delft3D system; in which, the flow model is based on the depth averaged shallow water equations. It is not our aim to describe the model equations in this paper;

Copyright © 2006 Taylor & Francis Group plc, London, UK

we will only describe the most relevant functionalities viz. HLES and Online-sediment.

Horizontal eddies are resolved using Horizontal Large Eddy Simulation (HLES), which uses a sub-grid-scale model to calculate the spatially and temporally varying horizontal eddy viscosity (Uittenbogaard and Van Vossen, 2003). With HLES it is possible to simulate the dynamics of the flow near groynes. The morphological simulation was performed, using the "Online-sediment" approach, which computes the sediment concentration, transport, and the bed level changes simultaneously with the flow and which has an immediate feedback to the hydrodynamics (Lesser *et al.*, 2004).

The simulations were done in two steps. Firstly, the hydrodynamic simulation was carried out to calibrate the model so as to reproduce the observed flow pattern. Then, after reaching a satisfactory hydrodynamic result, the morphological computations were performed. The results of the morphological computations are compared with the results of the experiment. The changes of the bed level, such as scour holes near the groyne tips and deposition in the groyne field, are of special interest. The conclusion will contain an evaluation of the model's capabilities to represent the hydrodynamic and morphodynamic situation in the laboratory experiment. Furthermore the model's applicability to other situations will be discussed.

2 LABORATORY EXPERIMENTS

2.1 *Dimensions*

Herein, we briefly present the laboratory experiments; for additional information about the experiments we refer to Yossef and De Vriend (2004). The experiments were carried out in a specially built facility in the Laboratory for Fluid Mechanics of Delft University of Technology. The dimensions of the model were based on those of the River Waal.

The model consisted of a schematised straight river reach, with a geometrically undistorted scale of 1:100 with respect to the Waal River. The working length of the model was 26.85 m, and the width 2 m. In the lateral direction, the model represents half of the river width. The model included nine identical groynes. The first groyne was placed at 4.0 m from the model entrance following three wooden pseudo groynes that were installed to let the inflow of water and sand adjust before reaching the first groyne. The groynes were equally spaced at $S = 2.0$ m, they had a crest length $L = 0.65$ m and a crest height $H_g = 0.25$ m, measured from the concrete bottom. The side slopes were 1 : 3 in all directions. The bed material was chosen such that to ensure both bed load and suspended load transport. As for the flow conditions, both emerged and submerged situations were investigated. Herein, we will consider only one case of emerged groynes.

2.2 *Flow pattern*

During the first few hours of the test, the observed flow pattern did not differ much from what was previously reported by e.g. Uijttewaal et al. (2001) and Yossef & Uijttewaal (2003). When the groynes are not submerged, the flow inside the groyne fields shows an unsteady circulation behaviour as shown in Figure 1 and characterised by a primary circulation cell that forms in the downstream part of the groyne field, a secondary circulation cell driven by the primary one with an opposite rotating direction and much smaller flow velocity, and a dynamic eddy that frequently sheds from the tip of the upstream groyne. This eddy migrates in downstream direction and merges with the primary one, which in return changes in size due to the interaction with the migrating eddy. After this eddy has disappeared, another eddy has room to form. The whole circulation is driven by the main stream via exchange of momentum through the interfacial mixing layer.

Along with the morphological development, the flow pattern changes. With the development of the scour hole, the intensity of the dynamic eddy decreases while stretching in the vertical direction following the newly formed scour hole. After the development of the deposition region, the interaction between the groyne fields and the main channel is hindered and the primary eddy gets slower, which ultimately leads to the disappearance of the secondary circulation cell.

2.3 *Morphological pattern*

In the emerged situation, the footprint of the flow pattern was clearly visible in the morphology. Both the scour hole and the deposition pattern follow the flow pattern, as shown in Figure 2.

The scour hole alignment follows the direction of the dynamic eddy. It is oblique to the flow direction and makes an angle of about 30° with the normal line (the imaginary line that connects the tips of the groynes).

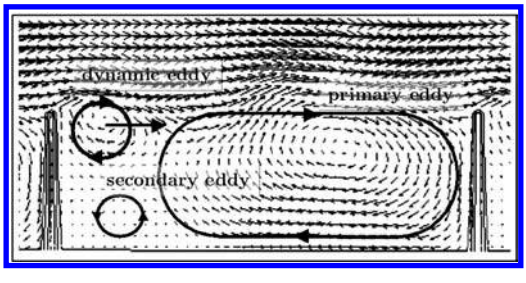


Figure 1. Flow pattern in a groyne field; emerged condition.

Copyright © 2006 Taylor & Francis Group plc, London, UK

In a later stage, the scour causes a feedback to the flow by elongating the dynamic eddy in its direction.

The sediment deposition inside the groyne fields takes place through its downstream part (Figure 2). The sediment is transported from the main channel towards the groyne field following the direction of the primary circulation cell. Along with the drop of the velocity, the sediment settles. The asymmetry of the ripples near the wall deep inside the groyne field is opposite to the main flow direction, but complies with the flow direction inside the groyne fields. This indicates that the effect of the primary circulation cell is extending through the width of the groyne field. The area in the middle of the groyne field, which coincides with the centre of the circulation cell, is free from any bedforms. Figure 3 gives a perspective view of the results of the bed level readings after 40 hours. In this figure we can clearly distinguish the typical erosion deposition pattern of scour hole followed by deposition ridge that is associated with a series of groynes.

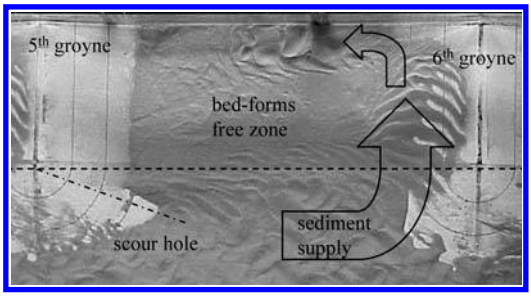


Figure 2. Morphological features for emerged groynes with indication to the sediment transport directions.

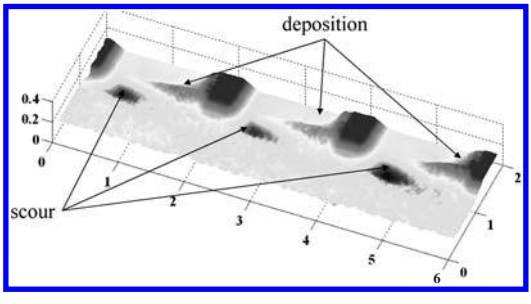


Figure 3. Perspective view of the results of the bed level readings after 40 hours (dimensions indicated on axis in metres).

3 NUMERICAL MODEL

3.1 *Model setup*

The modelled area is meant, as indicated earlier, to represent the laboratory experiments. Figure 4, shows an excerpt from the model grid indicating the test section. As the flume in the model experiment represented a straight river with groynes at a 90°-angle to the main flow, a rectangular grid could be used. Therefore the m and n-axes here correspond to the x and y-axes. When creating the grid attention was paid to guarantee that the crest and base of each groyne are situated at an intersection of grid lines. In order to avoid eroding the groynes, a fixed bed layer was defined at their locations. In order to resolve the high velocity gradient of the mixing layer the grid cells had to be smaller in the area where the dynamic eddy is expected.

The geometry of the flume was simplified by using less number of groynes. Instead of 11 groyne fields, only the three groyne fields of the test section and three adjacent groyne fields were modelled. The grid cell size varied at different locations on the grid with a minimum size of 3.5 cm. The number of grid cells 226×40, the computational time step was guaranteed to satisfy all Courant criteria. The upstream boundary condition was a constant discharge, and the downstream boundary is a constant water level, an overview of the model parameters is given in Table 1.

3.2 *Hydrodynamic results*

When examining the velocity vectors in the groyne field, the computation reproduced the large scale turbulent behaviour with the system of gyres described in Section 2.2. As seen in Figure 5 the presence of a primary gyre that occupies the downstream two thirds of the groyne field is clear. The dynamic eddy, which sheds from the tip of the upstream groyne and move into the groyne field merging with the primary gyre, is visible as well. However, the secondary gyre cannot be identified in the upper left corner; the velocity in that region is nearly zero.

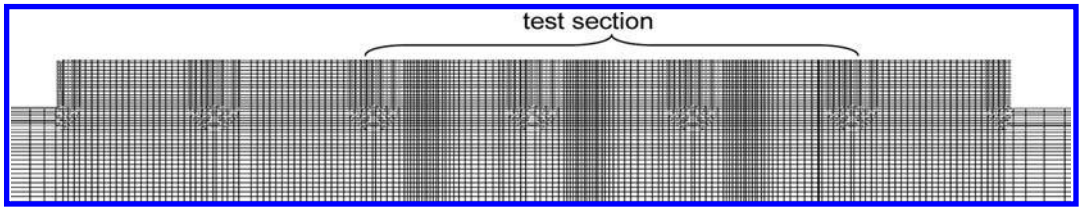


Figure 4. Excerpt from the model grid indicating the test section.

Copyright © 2006 Taylor & Francis Group plc, London, UK

Table 1. An overview of the model parameters.

Time frame	
Computational time step Δt	0.024 s
Total time of simulation	38 (minute)
Start of sediment input after	8 (minute)
Bathymetry updating after	14 (minute)
Real time modelled morphology	40 (hr.)
Initial conditions	
Initial water level H_i	0.245 m
Initial sediment concentration c_i	0.137 kg/m^3
Boundary conditions	
Upstream boundary Q	0.058 m^3/s
Reflection parameter α	10
Sediment concentration c_{US}	equilibrium
Downstream boundary H	0.245 m
Reflection parameter α	12
Sediment concentration c_{DS}	equilibrium
Sediment data	
Sediment density ρ	2650 kg/m^3
Sediment parameter Δ	1.65
Grain size D_{50}	160 (μm)
Sediment mass at bed	in a file (kg/m^2)
Morphological data	
Morphological scale factor	100
Spin-up interval for morph.	14 (minute)
Transport formula	van Rijn
Constants	
Water density ρ_w	1000 kg/m^3
Gravitational acceleration g	9.81 m/s^2
Roughness	
Bed roughness k_s	0.01 m
Slip condition	partial slip condition
Wall roughness	0.0012 m
Parameters concerning HLES	
Relaxation time τ	-1 (minute)
Prandtl-Schmidt number σ_T	0.7
Spatial low-pass filter coeff. f_{lp}	0.3
Number of dimensions n_D(2D/3D)	2
Slope in loglog energy-spectrum α	5/3

Following the picture of the dynamic behaviour of the flow field given in Figure 5, we can identify a periodical behaviour. Using the time series of the velocity components (u, v) at a point near the tip of the groyne, it is possible to obtain the energy density spectrum. The energy spectrum gives the distribution of the turbulent energy over the different frequencies. The energy density spectra presented in Figure 6 shows a clear peak of energy at a frequency of 0.188 *Hz*, i.e. a wave period of 5.3 s; this value is comparable to the same periodicity of the eddy shedding of 5.0 s as observed in the experiment. This indicates that the model is capable of reproducing the dynamic behaviour of the flow near groynes. For additional information about the dynamics of the flow near groynes we refer to Yossef and Uijttewaal, (2003).

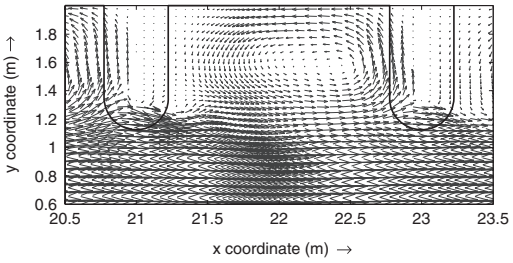


Figure 5. Snapshot of the calculated flow pattern in a groyne field (emerged groynes).

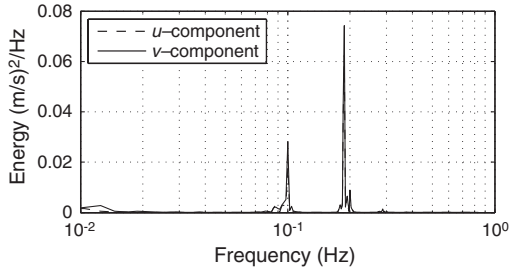


Figure 6. The energy density spectra at a point near the tip of the groyne.

3.3 *Morphodynamic results*

Generally speaking, the numerical simulation reproduced qualitatively well the same erosion and sedimentation pattern as observed in the laboratory experiment. In Figure 7 However, some differences between simulation and experiment are worth reporting.

Firstly, the main channel had a tendency of an over all erosion. The erosion rate in the middle of the main channel in the numerical simulation was larger than that in the experiment. While only little erosion of the bed in the main channel was observed in the experiment, the computed erosion in the main channel reached a maximum of 2.5 cm; note that near the side wall no erosion occurred. In the early stage (during the first 5 hours of morphological simulation) even some deposition was observed in the simulation; this was not observed in the flume experiment.

We must note here that this is attributed to the choice of a partial slip condition that reduces the velocity near the walls of the model. Accordingly, higher velocity is computed in the main channel. If a free slip condition was applied, similar to the glass wall of the experiment, this pattern would not have taken place. However, the partial slip condition and the wall roughness was an important calibration parameter to reproduce the system of eddies as indicated earlier.

Copyright © 2006 Taylor & Francis Group plc, London, UK

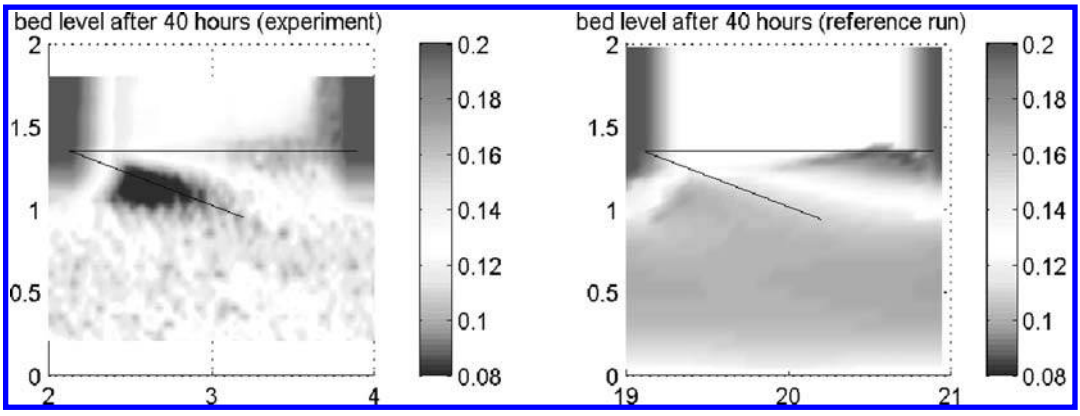


Figure 7. Comparison between the morphological pattern of the simulation and the experiment; bed levels after 40 hours.

Secondly, the scour hole at the groyne tip was less deep compared to the measured scour observed in the experiment, see Figure 7. After 40 hours the maximum computed depth of the scour hole was only 2.5 cm. This is smaller than the measured scour reach up to 6.5 cm. Moreover, the location of the scour hole is not exactly the same as in the experiment. The diagonal lines in Figure 7 indicate the direction of the movement of the dynamic eddy. It can be seen that the measured scour follows the direction of the dynamic eddy whereas in the simulation the scour hole is not located on this line.

Thirdly, the shape and volume of the deposition ridge in the groyne field differs from the measured one. While the deposition ridge in the experiment has a large width and a small height, the simulated deposition ridge has a much larger height and a smaller width (see Figure 7). From this shape it can be deduced that the suspended sediment, which is expected entering the groyne field, immediately settles as soon as the velocity decreases while entering the groyne field.

Finally, with respect to the volume of sand transported, and deposited, into a groyne field. We can observe that most of the computed sediment deposition takes place just across the normal line into the groyne field, approximately at $y = 1.35$ m. Little sediment is transported further into the groyne field. In the experiment the sediment is transported over a longer distance following the direction of the primary circulation cell. However, the total computed volume of deposited sediment in the groyne field amounts to 5.03×10^{-3} m^3, which is around 80% of the measured deposition volume. Even though the total volume of deposition is less than the volume from the experiment, the elevation of the computed deposition ridge is higher than that measured in the experiment.

4 DISCUSSION OF THE RESULTS

4.1 *Hydrodynamics*

When comparing the results of the hydrodynamic simulations with the computed flow pattern, we can confidently say that the numerical model represents the overall flow pattern observed in the experiment (e.g. discharge, water level and velocities) well. The large scale hydrodynamic behaviour was captured as well. Nevertheless, the full shape and distinction of the turbulent eddies and gyres in the groyne field cannot be directly compared with the experiment, since velocities were only measured at few locations in the experiment. The full two dimensional hydrodynamic picture was not recorded in the experiment, as the primary objective of the experiment was to study the morphodynamic behaviour. However, evidence of the presence of a dynamic eddy could be inferred from energy spectra of the velocity signals of the points in the mixing layer. Furthermore, both the primary gyre and an indication of the dynamic eddy were observed utilising dye tests.

In order to calibrate the model, the input parameters (e.g. the slip condition/wall roughness) were set, so that the appearance of the turbulent structures in the groyne field qualitatively matched the appearance of the turbulent structures in literature and in results from previous experiments, where these structures have been measured (e.g. Yossef and Uijttewaal, 2003). This resulted in reproducing the hydrodynamic picture as indicated in Section 2.2. These turbulent flow patterns, which contribute much to the mixing processed between the main channel and the groyne fields, were represented well in the hydrodynamic computation. Nevertheless, the transverse velocity of the water entering the groyne field was slightly under predicted.

Copyright © 2006 Taylor & Francis Group plc, London, UK

The effect of the wall roughness was analysed by comparing a case with free slip condition with a case with a partial slip condition. The case with free slip yielded a large primary gyre and hardly any fluctuations near the groyne tip, instead of a smaller primary gyre and a clear dynamic eddy.

4.2 *Morphodynamics*

The morphodynamic computations gave good results concerning the general erosion/deposition pattern near the groyne tips and in the groyne fields. Even the effect of the side wall in the groyne field (small scour and deposition) is reproduced in the computation. This leads to the conclusion that the morphodynamic pattern is generally well reproduced. However, the model poorly reproduced the sediment transport into the groyne fields (cf. Yossef, and Klaassen, 2002). Furthermore, the depth of the scour hole was underestimated in all simulations.

In all morphodynamic computations that were carried out the scour hole was too shallow compared to the measured scour hole. It appeared from comparison between several simulations that the presence of the dynamic eddy did not influence the depth of the scour hole. In reality this is not true; the presence of the scour hole is strongly attributed to the presence of the dynamic eddy as seen in Figure 2. Apparently the simulated scour hole forms as a result of the narrowing of the flow, instead of the velocity fluctuations near the groyne tip. The under estimation of the scour depth can be explained by lacking important physics in the sediment transport model viz. the effect of horseshoe vortices.

The volume of sediment, which deposited on the upstream side near the groyne tip, was computed to be 80% of the volume computed from the measurements, and could be considered roughly in accordance with the experiment. However, the shape of the deposition ridge did not match with the observations from the experiment. The sediment didn't enter the groyne field before settling, but instead settled in front of the groyne field, as soon as the velocity decreased. This was a major problem with all simulations.

A similar observation was made near the wall of the main channel. At this location the velocity was lower than in the middle of the main channel, which leads to deposition in the early state of the simulation. This has not been observed in the experiment. The differences between the deposition patterns of experiment and simulation lead to the conclusion that the sediment is not kept in suspension long enough. On the other hand a decrease of the grain size or the settling velocity would result in stronger erosion in the main channel, which is not desired either. Apparently the morphological model doesn't include the relevant processes. The area near the groynes and along the normal line exhibits high turbulence intensity as well as high

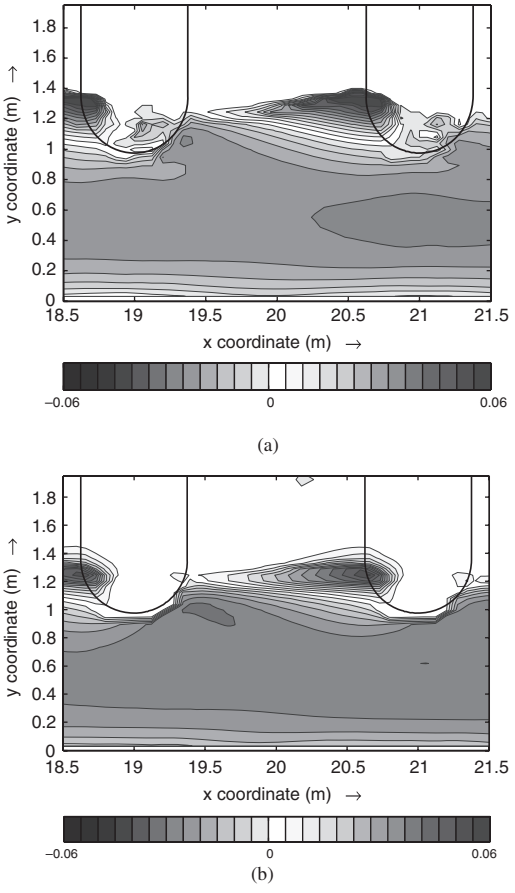


Figure 8. The effect of graded sediment on the morphological pattern; erosion deposition pattern (cm), for (a) single fraction representing D_{50} and (b) three fractions representing D_{10}, D_{50}, and D_{90}.

vorticity. Vortices shed from the tip of the upstream groyne and migrate in the downstream direction following the direction of the primary eddy. These vortices increase the sediment entrainment in their path (as observed from the mobile-bed experiments) causing higher sediment concentrations in the mixing layer that further extends following the path of the primary eddy. The applied/available sediment transport formula, however, ignores the increased turbulence level in the mixing layer, as well as the role of vortical motions that induce additional sediment entrainment in their path.

When using several sediment fractions (graded sediment) the resulting morphological pattern improves (see Figure 8). The depth of the scour hole was enhanced and the deposition ridge extended further into the groyne fields. We can then conclude that the use of graded instead of uniform sediment improves the results.

Copyright © 2006 Taylor & Francis Group plc, London, UK

5 CONCLUSIONS AND RECOMMENDATIONS

From this study we can conclude that it is possible to reproduce morphological pattern associated with groynes in rivers, using a mathematical model that has the capacity to resolve large horizontal eddies. The first requirement to reproduce such a morphological pattern is a correct representation of time-dependent flow field. The flow field compares well to that measured in a laboratory experiment for the case of emerged groynes.

The bed morphology computed, is similar to what has been observed in the laboratory. The large eddies which form at the interface between the main channel and the groyne fields are an important mechanism underling the typical groynes-induced bed pattern.

Further improvements to the model are required in order to improve the results concerning the scour hole and the transport into the groyne fields. Yet, this study has demonstrated the important role that 2D models with HLES can play in improving our predictive capabilities.

The shortcoming of the numerical model in reproducing the morphodynamics of the groyne fields is primarily due to the lack of a transport model that accounts for the increased turbulence level in the mixing layer, as well as the role of vortical motions in picking up sediment and keeping it in suspension for extended distances. With the current performance of the hydrodynamic model, it is time to invest in improving our sediment transport modelling to include vortical motion and increased turbulence level.

On the positive side, it is envisioned that an application to the prototype scale would have better results due to the nature of the problem in hand. For example, the effect of the wall roughness would vanish in the prototype scale; the relative importance of eddiesinduced sediment entrainment would reduce significantly (cf. Ettema and Muste, 2004); and the velocity inside the groyne fields would take a much longer distance to drop below the critical velocity for initiation of motion thus keeping the sediment in suspension for a longer distance.

ACKNOWLEDGEMENTS

This study is carried out within the framework of DIOC Water, theme 1.3 (Intermediate-scale morphological developments in rivers due to human interventions) and Delft Cluster, theme 3 (Coasts and Rivers) under the supervision of Prof. Dr. Huib de Vriend who is deeply thanked for his guidance.

The authors would like to thank the staff members of the Laboratory for Fluid Mechanics of the Delft University of Technology for facilitating the experiment in all its stages, and to thank Ken Thiemann for conducting the experiments.

The authors would also like to thank Messrs. G.J. Klaassen and M. van der Wal, and Drs. E. Mosselman, C.J. Sloff, and W.S.J. Uijttewaal for their constructive comments and discussions during the different stages of the study.

REFERENCES

Ettema, R., and Muste, M. (2004). "Scale Effects in Flume Experiments on Flow around a Spur Dike in Flatbed Channel" Journal of Hydraulic Engineering, 130(7), 635–646.

Lesser, G. R., Roelvink, J. A., Van Kester, J. A. T. M., and Stelling, G. S. (2004). "Development and validation of a three-dimensional morphological model" Coastal Engineering, 51(8–9), 883–915.

Ten Brinke, W. B. M., Bolwidt, L. J., Snippen, E., and van Hal, L. W. J. (2001). "Sedimentbalans Rijntakken 2000" 2001.043, Riza, Arnhem.

Uittenbogaard, R. E., and Van Vossen, B. (2003). "Subgrid-scale model for Quasi-2D turbulence in shallow water" In: Proc. of the Int. Symposium on Shallow Flows, Delft, the Netherlands, 169–176.

Uijttewaal, W. S. J., Lehmann, D., and van Mazijk, A. (2001). "Exchange process between a river and its groyne fields – Model experiments" Journal of Hydraulic Engineering, ASCE, 127(11), pp. 928–936.

Yossef, M. F. M., and Klaassen, G. J. (2002). "Reproduction of groynes-induced river bed morphology using LES in a 2-D morphological model" In: River Flow 2002 – Proc. of the Int. Conf. on Fluvial Hydraulics, Louvain-la-Neuve, Belgium, 1099–1108.

Yossef, M. F. M., and Uijttewaal, W. S. J. (2003). "On the dynamics of the flow near groynes in the context of morphological modelling" In: XXX IAHR Congress, Thessaloniki, Greece, 361–368.

Yossef, M. F. M., and de Vriend, H. J. (2004). "Mobile-bed experiments on the exchange of sediment between main channel and groyne fields" In: River Flow 2004 – Proc. of the 2nd Int. Conf. on Fluvial Hydraulics, Naples, Italy, 127–133.

Copyright © 2006 Taylor & Francis Group plc, London, UK

Experimental study of the scour regimes downstream of an apron for intermediate tailwater depths

P. Espa
Università dell'Insubria, Dept. "Environment-Health-Safety", Varese, Italy

S. Sibilla
Università di Pavia, Dept. of Hydraulic & Environmental Engineering, Pavia, Italy

ABSTRACT: Local scour due to 2-D submerged horizontal jets is a well-known topic of hydraulic research. When the jet is directly injected on the erodible bed and the tailwater depth is either "deep" or "shallow", the equilibrium state characteristics of the scoured bed profile are mainly a function of the densimetric Froude number. If the submergence is between these two extremes, for fixed Froude number, three different scour regimes are possible, depending on the jet mainstream position. This paper integrates previous work by the Authors concerning the experimental description of the three mentioned regimes, in presence of a protection apron. The results of the investigation are also intended as a dataset to validate numerical models able to simulate the interaction between free-surface flows and non-cohesive granular beds.

1 INTRODUCTION

This paper describes the experimental investigation of the local scour of a non-cohesive sand bed, caused by a 2-D horizontal wall-jet issuing from a sluice and developing on a rigid apron.

Figure 1 shows a sketch of the laboratory channel, together with the *x*-*y* reference system and the symbols employed to indicate the main geometrical variables of the problem: l is the apron length, y_H the water level in the upstream tank, y_G the sluice gate opening, y_0 the height of the *vena-contracta* which develops downstream of the sluice, y_T the tailwater depth and y_W the height of the downstream weir. At any time, the maximum depth $h_{S,MAX}$ of the scour hole is located at a distance $x_{S,MAX}$ downstream of the of the apron; the peak of the dune developing downstream of the scour hole is instead located at $x_{D,MAX}$ and $y_{D,MAX}$. Finally, x_0 and x_F are the positions where the scour hole and the ridge end.

Any dimensional feature χ of the flow can be expressed as a function of nine parameters defining the flow and the bed (Ali & Lim, 1986):

$$\chi = \chi\left(u_0, g(\rho_S - \rho), \rho, \nu, y_0, y_T, l, d_G, t\right) \qquad (1)$$

where u_0 is the jet velocity at the contraction-section, ρ_S and ρ are the densities of sediments and water, ν is kinematic viscosity, d_G is a characteristic size of the grains, g is gravity acceleration and t is time. Assuming asymptotic steady-state conditions, the generic non-dimensional feature N_χ can be therefore written in terms of five non-dimensional parameters:

$$N_\chi = N_\chi\left(\frac{u_0}{\sqrt{g\, d_G \frac{(\rho_s - \rho)}{\rho}}}, \frac{u_0 y_0}{\nu}, \frac{y_T}{y_0}, \frac{l}{y_0}, \frac{d_G}{y_0}\right) \qquad (2)$$

where the terms in brackets are the densimetric Froude number F_0, the Reynolds number Re, the relative submergence, the relative length of the apron and the relative roughness, respectively.

Rajaratnam (1981) and Rajaratnam & Mac Dougall (1983) show that, when the protection apron is absent and the tailwater depth is either relatively deep ($y_T/y_0 \geq 10$) or very shallow ($y_T \approx y_0$), the asymptotic-state characteristics of the bed profile are essentially functions of F_0. They consider flows where Re is large enough and d_G/y_0 small enough to neglect their effects and find, in particular, that the maximum scour depth at equilibrium $h_{S,MAX,\infty}$, at a fixed F_0 value, is larger for deeply submerged cases (subscript ∞ refers here to asymptotic equilibrium).

Conditions of intermediate submergence (roughly $1 < y_T/y_0 < 10$) have been experimentally analyzed by Ali & Lim (1986), who show that the asymptotic scour depth at fixed F_0 depends on the tailwater depth.

Copyright © 2006 Taylor & Francis Group plc, London, UK

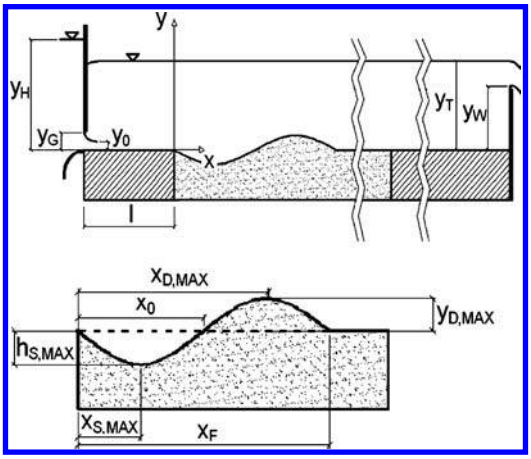


Figure 1. Sketch of the experimental channel with adopted symbols and reference system (x, y axes).

Moreover, they show that, beyond a critical tailwater depth, an increase or decrease in tailwater causes an increase in $h_{S,MAX,\infty}$.

Johnston & Halliwell (1987) propose that the development of the scour hole should be influenced by the different pattern of the jet mainstream, in accordance with their findings on 2-D jets in a rigid bed channel (Johnston & Halliwell, 1986), where, depending on the relative submergence, the jet shifts permanently either towards the bed or towards the free surface; furthermore, for some values of the tailwater depth, both the mentioned configurations may occur. Johnston (1990) confirms the above hypothesis, observing the periodical jet flicking between the free surface and the loose bed for particular values of the flow parameters.

Several works address the localized scour due to submerged 2-D wall jets downstream of protection aprons (Chatterjee & Ghosh, 1980; Nik Hassan & Narayanan, 1985; Chatterjee et al., 1994). Among them, only Espa & Sibilla (2005) report the existence of different patterns of scour hole-jet interaction, when the relative tailwater depth is varied.

2 EXPERIMENTAL SET-UP

The experiments have been performed in a horizontal glass-paneled channel 4.5 m long, 0.102 m wide and 0.44 m deep. A 0.2 m deep bed of non-cohesive sediments is placed between two steel boxes: the length of the upstream one (representing the rigid apron) has been varied during experiments ($l = 0.25$ and 0.5 m), while the downstream one (1.5 m long) has been kept fixed.

Figure 1 shows a sketch of the sharp-edged sluice gate which regulates the water inlet in the channel from an upstream constant-head tank. The reservoir is fed through a 100 mm diameter pipe, equipped with an electromagnetic flow-meter.

The lower and lateral sides of the tank outflow hole are equipped with circumference-arc steel profiles to prevent lateral and upward contraction of the *vena* entering the channel (Fig. 1). Therefore, the *vena contracta* height can be derived by the classical formula $y_0 = c_c y_G$, where c_c is a contraction coefficient. The water level in the channel is controlled downstream by a sharp edged (Bazin-type) weir. The main characteristics of the approximately uniform-sized sand here used are: $d_G = 1.6$ mm; $\rho_S = 2650$ Kg/m^3; porosity $n = 0.45$; angle of repose $\phi = 30°$; mean fall velocity $w_M = 0.13$ m/s.

Images of the bed profiles have been collected by a digital photo-camera. These photos have then been processed to measure the evolution of the bed shape.

A single component back-scattering Laser Doppler probe (TSI – LDP 100) equipped with a 250 mm focal length lens has been used to measure vertical plane profiles of the horizontal velocity component in the mid-channel plane; the 50 mW Laser-diode source generates red light at 694 nm wavelength. The particles dispersed in the water of the laboratory closed-circuit proved to be sufficient to collect a signal of good quality, and no further seeding has been used. The acquired signal has been processed by a completely PC-assisted processor (TSI – IFA 600) using a dedicated software package (TSI – Laservec 1.0). Each LDA measure includes no less than 5000 samples and lasts for at least 40 s (to stabilize the time averaged value of the signal); thus, at high sampling rate, the number of acquired samples exceeds (even by 5 times) the mentioned sample quantity. LDA measures have been carried out 8 hours after the beginning of the tests, assuming that the bed evolution was then slow enough and did not alter significantly the velocity field. These velocity measures may be therefore intended as the equilibrium state ones.

Less time consuming ADV measures have been performed by a system (Signal Processing DOP 1000) equipped with a 4 MHz ultrasound emitter/transducer, seeding the flow by fine clay particles. The pulse repetition frequency (PRF) has been varied between 3.125 and 5.95 kHz, depending on the maximum measurable depth needed; the vertical resolution varied between 1.4 and 2.1 mm. ADV profiles have been obtained by averaging no less than 6000 samples collected for at least 120 s.

3 ANALYZED CASES

The sluice opening y_G, the weir height y_W (and consequently y_T), the apron length l and the flow rate Q have been varied in the course of the investigation. Grain size d_G, sediment density and water viscosity

Copyright © 2006 Taylor & Francis Group plc, London, UK

Table 1. Parameters of the discussed experiments.

No.	Q [l/s]	L [mm]	y_H [mm]	y_G [mm]	y_L [mm]	y_T [mm]	y_W [mm]
1	2	250	136	40	111	120	74
2	2	250	212	40	183	186	140
3	2	250	192	80	186	186	140
4	3	250	176	40	116	134	74
5	3	250	255	40	193	200	140
6	3	250	212	80	198	200	140
7	4	250	224	40	117	145	74
8	4	250	306	40	198	211	140
9	4	250	232	80	207	211	140
10	2	500	139	40	116	120	74
11	2	500	208	40	183	186	140
12	2	500	191	80	186	186	140
13	3	500	182	40	118	134	74
14	3	500	254	40	190	200	140
15	3	500	209	80	195	200	140
16	4	500	223	40	116	145	74
17	4	500	302	40	194	211	140
18	4	500	230	80	204	211	140

Table 2. Parameters of the discussed experiments.

No.	c_c [–]	y_0 [mm]	u_0 [m/s]	Re [–]	F_0 [–]	y_T/y_0 [–]	L/y_0 [–]	
1	0.70	28	0.70	19,600	4.4	4.3	8.9	F
2	0.65	26	0.75	19,600	4.7	7.2	9.6	B
3	0.71	57	0.34	19,600	2.1	3.3	4.4	–
4	0.68	27	1.08	29,400	6.7	4.9	9.2	F
5	0.67	27	1.10	29,400	6.9	7.5	9.4	F
6	0.70	56	0.52	29,400	3.3	3.6	4.5	UB
7	0.68	27	1.45	39,200	9.0	5.4	9.2	F
8	0.67	27	1.46	39,200	9.0	7.8	9.3	F
9	0.70	56	0.70	39,200	4.4	3.8	4.5	F
10	0.73	29	0.67	19,600	4.2	4.1	17.1	S
11	0.70	28	0.70	19,600	4.4	6.6	17.9	UB
12	0.78	63	0.31	19,600	1.9	3.0	8.0	–
13	0.65	26	1.12	29,400	7.0	5.1	19.1	S
14	0.66	26	1.12	29,400	7.0	7.6	19.0	F
15	0.70	56	0.52	29,400	3.3	3.6	8.9	B
16	0.68	27	1.45	39,200	9.0	5.4	18.5	S
17	0.67	27	1.46	39,200	9.0	7.8	18.6	F
18	0.69	55	0.71	39,200	4.4	3.8	9.1	UB

(assumed to be $\nu = 10^{-6}$ m^2/s) have instead been kept fixed in all the experiments.

Each reported test lasts for at least 8 hours. In general, no asymptotic equilibrium has been reached at the end of the tests: as noted by Nik Hassan & Narayanan (1985), asymptotic conditions need a very long time to be reached when the vertical scales of the bed profile (particularly the dune height) are, as in the present case, comparable to the submergence.

The main parameters of the tests are listed in Tables 1 and 2, ordered by run number. The average

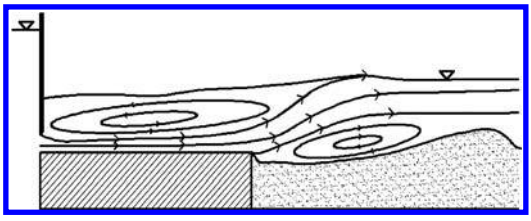


Figure 2. Sketch of the flow pattern for "surface jet" scour regime.

value of the water level just downstream of the sluice, where a submerged hydraulic jump takes place, is indicated by y_L. In tests where the difference $y_T - y_L$ is higher, owing to the free surface oscillations due to the submerged jump, y_T fluctuates and its value is here given as a time-averaged one.

The last column to the right in Table 2 indicates the scour regime which characterizes the test: "surface jet" (S), "bed jet" (B), slightly unstable "bed jet" (UB) and "bed-surface jet" flicking regime (F); the symbol – indicates that no grain motion takes place on the flume bottom. The contraction coefficient c_c (Tab. 2) has been estimated from the measured values of Q and $y_H - y_L$ by assuming energy conservation across the sluice. The values of y_0 and u_0 have been calculated accordingly. Some u_0 values have been checked against available LDA velocity measurements.

The d_G/y_0 ratio ranges from 0.03 to 0.06 in all the reported experiments. Each test is started from rest, the water depth in the tank and in the channel being equal to y_W. When the flow-rate Q is almost impulsively discharged in the tank, the water levels y_H and y_T approach quickly their steady-state values. The influence of the start-up phase on the scour development is therefore negligible.

Bed profile evolution and overall flow pattern in tests 13, 14, 15 are extensively discussed by Espa & Sibilla (2005) and will be recalled in the following.

4 STABLE REGIMES

4.1 *"Surface jet" scour regime*

In tests no. 10, 13 and 16, the jet mainstream directs towards the free-surface just downstream of the apron, as marked by the blowing up on the free-surface which is clearly visible during the experiments (Fig. 3). The flow pattern, deduced from wool-wire visualizations by Espa & Sibilla (2005), is sketched in Figure 2. It is characterized by two counter-rotating vortices: the submerged hydraulic jump and the separation vortex just downstream of the apron.

Regardless of the evolution of the bed (and therefore of the horizontal size of the two vortices, in particular the lower one) the described flow pattern remains the

Copyright © 2006 Taylor & Francis Group plc, London, UK

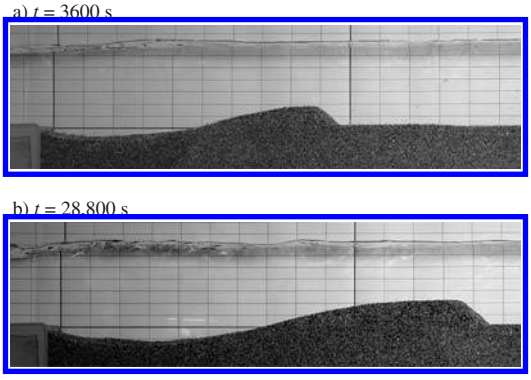


Figure 3. Bed profile after 1 hour (a) and 8 hours (b) for "surface jet" scour regime (run no. 13).

same during the whole run. The resulting "elongated" shape of the bed profile is characterized by relatively small vertical scales ($h_{S,MAX}$ and $y_{D,MAX}$) and relatively large horizontal scales ($x_{S,MAX}$, x_0, $x_{D,MAX}$, x_F). An example is given in Figure 3, where two subsequent images of the bed profile for run no. 13 are given (as in the following photographs, the vertical grid spacing behind the flow is 20 mm and the horizontal one is 50 mm).

The vertical profiles of time-averaged horizontal velocity u, measured by LDA, confirm the described flow pattern. For instance, Figure 4 shows the u profiles collected during run no. 13. Above the wall jet, the detected zone of backflow (Fig. 4a) highlights the presence of the submerged-jump roller, which extends for the whole apron length.

The u profile on the scour hole (Fig. 4b, $x = 150$ mm) displays near the bed a small backflow region, connected to the separation vortex downstream of the apron; the location of the maximum u value near the free surface confirms the behavior of the jet mainstream. Further downstream the velocity profile becomes more regular, almost linear, with maximum close to the free-surface (Fig. 4b, $x = 500$ mm).

4.2 *"Bed jet" scour regime*

In tests no. 2 and 15, the jet mainstream remains attached to the channel bed downstream of the apron and the free-surface appears only slightly perturbed. Runs 6, 11 and 18 show essentially the same behavior, although a displacement of the jet towards the free surface can be noticed for relatively short periods. The flow pattern (inferred from wool-wire flow visualizations by Espa & Sibilla, 2005) is sketched in Figure 5 and is again characterized by two counter-rotating vortices. The submerged jump roller extends now also above the sand bed, further downstream than in previous case. The vortex due to boundary-layer separation from the apron edge is considerably smaller

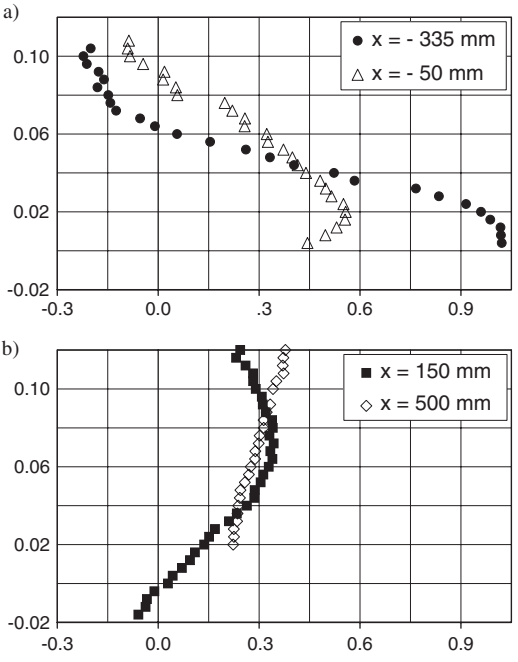


Figure 4. Vertical profiles of u (in m/s) vs y (in m) at different x positions for "surface jet" scour regime (run no. 13). Profiles at $x = -335$ mm and -50 mm (a) are located on the apron; profiles at $x = 150$ mm and 500 mm (b) are located on the scour hole and on the dune, respectively.

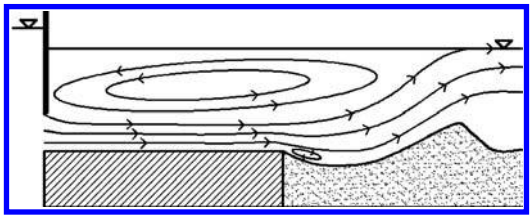


Figure 5. Sketch of the flow pattern for "bed jet" scour regime.

than in previous case; nevertheless, its presence is clearly highlighted by sand motion. When compared to the "surface jet" regime, the bed profile is characterized by larger vertical scales and smaller horizontal scales. Figure 6 displays for instance the bed profile shape at two different times for test no. 15.

The flow pattern has been confirmed even in the "bed jet" regime by measuring vertical profiles of time-averaged horizontal velocity u. Figure 7 shows velocity profiles measured during run no. 15. It must be noted that only ADV measurements could be obtained above the erodible bed, owing to a slight unsteadiness of the flow. However, the comparison between LDA and ADV measurements at $x = -50$ mm (Fig. 7a) shows the reliability of ADV measures.

Copyright © 2006 Taylor & Francis Group plc, London, UK

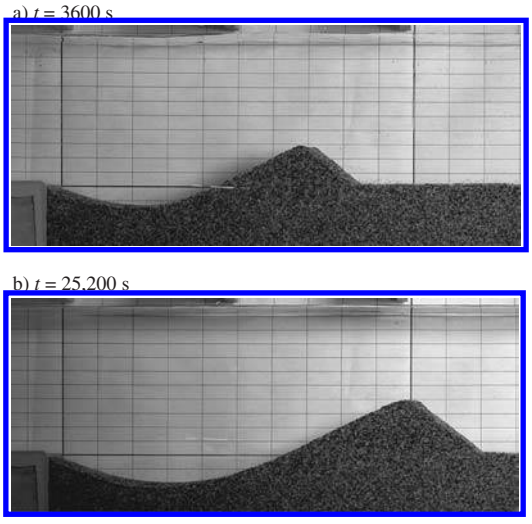


Figure 6. Bed profile after 1 hour (a) and 7 hours (b) for "bed jet" scour regime (run no. 15).

Velocity profiles shown in Figure 7b confirm that downstream of the apron the jet flows along the scour hole. Above the dune crest, the flow shows again an almost linear velocity profile, but its maximum value is now located close to the bed. Moreover, the backflow detected in the velocity profile measured at $x = 130$ mm shows that the submerged jump roller extends above the scour hole.

It should be underlined that in the discussed experiment the relatively small l/y_0 ratio ($\approx$9, Tab. 2) prevents the wall jet from becoming fully-developed at the end of the apron. Actually, the maximum jet velocity at the end of the apron (profile $x = -50$ mm, Fig. 7a) is still almost equal to the one measured just downstream of the sluice (profile $x = -335$ mm) and to the value $u_0 = 0.52$ m/s, which has been computed for run 15 by assuming energy conservation across the sluice (Tab. 2).

This behavior can be compared to the "surface jet" pattern described in Section 4.1. In run no. 13, the maximum velocity of the jet just downstream of the sluice (profile $x = -335$ mm, Fig. 4a) is slightly larger than 1 m/s and it agrees well with the energy-conservation estimate $u_0 = 1.12$ m/s (Tab. 2). When the jet approaches the loose bed (profile $x = -50$ mm, Fig. 4a), its maximum horizontal velocity is lower than 0.60 m/s, i.e. there is an almost 50% velocity decay along the apron. This decay appears to be much larger than the one expected for a simple 2-D wall jet: applying, for instance, a semi-empirical decay law for simple 2-D turbulent wall jets (Rajaratnam, 1976), the maximum velocity reduction at $l/y_0 = 19.1$ (i.e. the present normalized apron length, Tab. 2) should not be larger than 10%. This difference with the plane jet behavior is

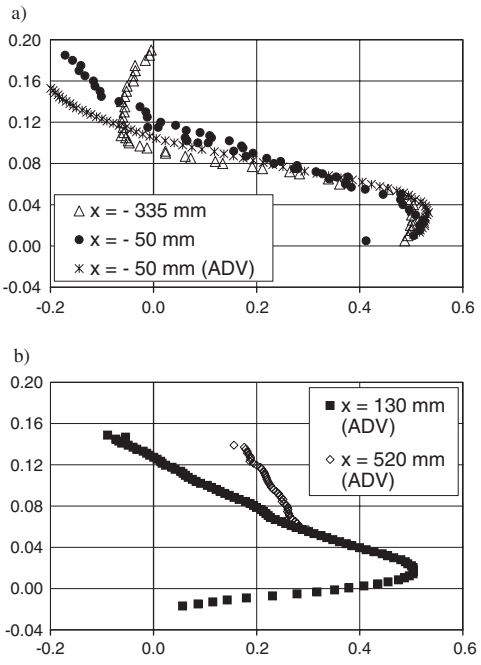


Figure 7. Vertical profiles of u (in m/s) vs y (in m) at different x positions for "bed jet" scour regime (run no. 15). Profiles at $x = -335$ mm and -50 mm (a) are located on the apron; profiles at $x = 130$ mm and 520 mm (down) are located on the scour hole and on the dune, respectively.

the obvious consequence of the reverse flow detected above the jet.

The analysis of these stable regime cases demonstrates that the definition of the proper velocity scale for the scouring jet is not immediate: the classical results concerning plane wall jets cannot be applied when the submergence is not very deep (i.e. when the effect of the submerged jump on the jet development is not negligible).

Most of all, it must be noted that scour profiles are substantially different (Figs. 3 and 6) even when the jet velocities are approximately equal at the end of the apron (as in the mentioned case of runs no. 13 and 15, where the maximum velocity of the jet leaving the apron is about 0.5 m/s). In particular, after comparable elapsed time, the maximum scour $h_{S,MAX}$ in run 15 ("bed jet" scour regime) is about twice as deep than in run 13 ("surface jet" scour regime).

5 "BED-SURFACE JET" SCOUR REGIME

Apart from the two stable regimes discussed in the previous section, an unsteady flow regime is also possible for intermediate tailwater depths. In this case, the jet flicks intermittently between its lower and the upper

Copyright © 2006 Taylor & Francis Group plc, London, UK

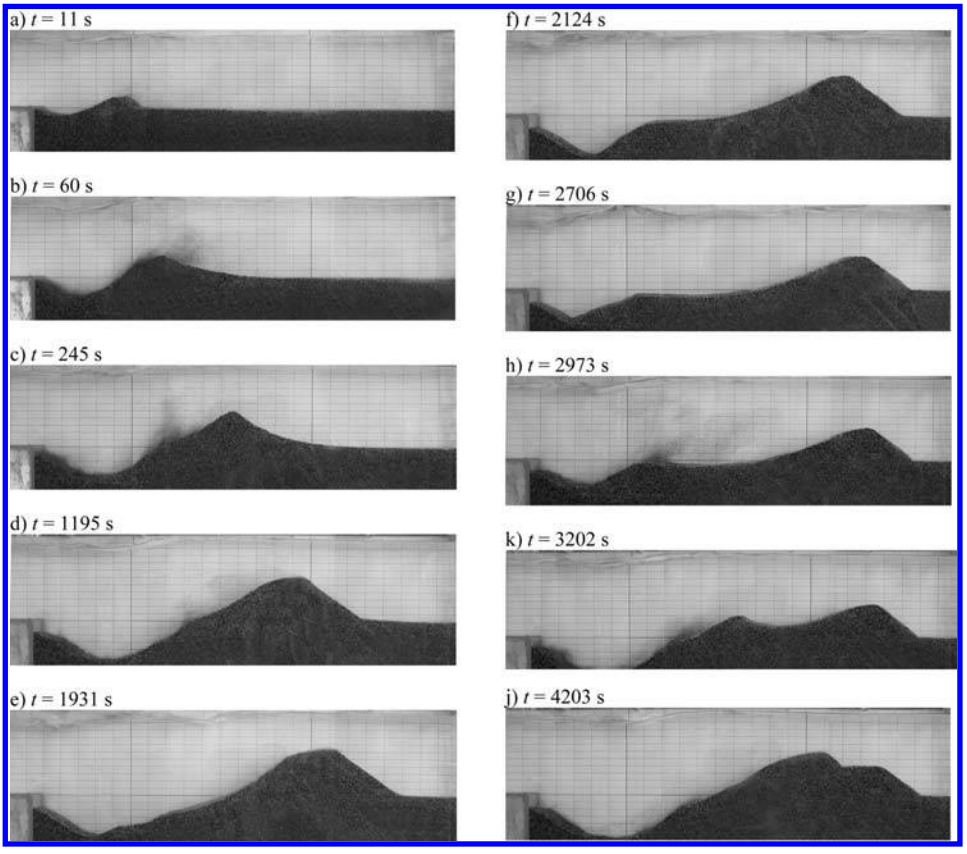


Figure 8. Sequence of run no. 8 showing the first complete cycle and the second "bed jet" phase. First "bed jet" phase is in frames a–d; first "surface jet" phase is in frames e–g; second "bed jet" phase is in frames h–j.

boundaries (the erodible bed and the free-surface, respectively).

At the beginning of each test characterized by this unsteady behavior (runs no. 1, 4, 5, 7, 8, 9, 14 and 17, Tab. 2), the jet remains attached to the bed generating the scour hole and the downstream dune. The strength of the scour process in this phase is evidenced by the frequent bursting of sand grains under the effect of the jet flow (Figs. 8a–d and 9a–b). During this initial phase, the flow pattern is similar to the one described in the "bed jet" regime (Fig. 5).

After a certain time has elapsed, the flow pattern suddenly shifts to the "surface jet" one (Fig. 2): the jet mainstream detaches from the bed and moves towards the free-surface. As a consequence, the upstream side of the dune (whose slope may exceed the repose angle under the effect of the incoming jet) collapses into the scour hole, which is partly filled up and assumes a typical cusp shape (Figs. 8f–g and 9c–d). At the same time, the free-surface hump moves backwards (Figs. 8d–e), marking the displacement of the region of impact between the jet and the free-surface (the submerged jump moves backwards too). The collapsing of the dune is determined not only by the abrupt interruption of the sustaining action of the jet flow, but also by the large recirculation established below the jet mainstream which flows along the free surface (Fig. 2). After maintaining for a certain amount of time the "surface jet" pattern, the jet suddenly shifts again towards the bed and a new cycle starts.

For a given run, the duration of each complete cycle and of each phase within a cycle ("bed jet" or "surface jet" phase) varies without regularity. The average cycle duration Δt together with the percentages of "bed jet" flow $\Delta t_B\%$ and of "surface jet" flow $\Delta t_S\%$ are given in Table 3 for each 8-hours run.

It has been observed that the duration of the "bed jet" phases is on average roughly constant during each test, while the duration of the "surface jet" phases tends to increase slightly with time; furthermore, the longer the jet is attached to the channel bed, the longer the following "surface jet" phase and vice-versa (nevertheless, exceptions to this intuitive rule have been noticed).

Copyright © 2006 Taylor & Francis Group plc, London, UK

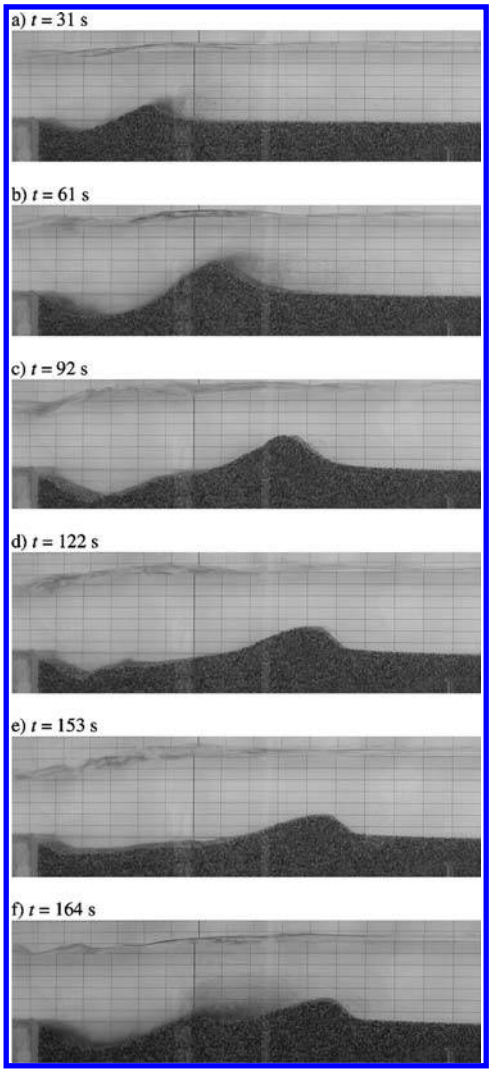


Figure 9. Sequence of run no. 7 showing the first complete cycle and the beginning of the second "bed jet" phase (f). First "bed jet" phase is in frames a-b; first "surface jet" phase is in frames c-e.

Comparisons of tests with approximately equal l/y_0 (as for example runs no. 1, 2, 4, 5, 7, 8, 12, 15, 18) suggest that, for fixed F_0, intermediate y_T/y_0 ratios lead to "bed-surface jet" flows. When the normalized tailwater depth is large, "bed jet" flows are expected while "surface jet" flows develop under low y_T/y_0. Moreover, the higher F_0, the larger the y_T/y_0 interval characterized by the jet flicking. Finally, again for fixed l/y_0 and F_0, the larger the normalized tailwater depth, the longer the average cycle period in "bed-surface jet" flows.

Table 3. Average temporal characteristics of jet cycles (deduced during 8-hours runs) for "bed-surface jet" regime tests.

No.	Δt [s]	Δt_B% [–]	Δt_S% [–]
1	1600	9	91
4	410	8	92
5	12,900	44	56
7	230	8	92
8	3700	47	53
9	4100	21	79
14	900	10	90
17	500	7	93

The jet cyclic behavior gives to the bed profile a less regular shape than that found in steady flow regimes. Two different dunes may be observed during the bed evolution: a main dune, at larger x, and a secondary dune, closer to the scour hole and generated by the "bed jet" flow. The main dune is still present at the end of the "surface jet" phase while the secondary one reaches its maximum height at the end of the "bed jet" phase, but collapses in the scour hole during the following "surface jet" phase. In a given run, the secondary dune at the end of each "bed jet" phase is in general systematically higher (or lower) than the primary one. However, in some cases the maximum height shifts from one dune to the other cycle by cycle. As shown in Figure 10a, after an intense "bed jet" phase, the secondary dune may even completely overlap the primary one.

The description of the time evolution of the bed-profile characteristics is therefore more complex than for stable cases. However, it can be noted that the maximum values of the scour depth $h_{S,MAX}$ and of the secondary dune height are still reached at the end of a "bed jet" phase and that the longer this phase the larger the mentioned geometric scales.

Espa & Sibilla (2005), analyzing run no. 14 and focusing only on cycles characterized by relatively long "bed jet" phases, report that scour hole profiles at the end of these "bed jet" phases are nearly equal; the Authors conclude that for this kind of regime scour depth and (secondary) dune height maximum values seem not to be reached asymptotically.

Analogous considerations can be repeated for other "bed-surface jet" cases, even when the average cycle duration is much larger (run no. 9, Figs. 11 and 12) or when it is shorter and the evolution of the primary dune resembles closely the one observed in the "surface jet" regime (run no. 7, Figs. 13 and 14).

Table 4 reports maximum scour depths $h_{S,MAX}$ measured for "bed-surface jet" regime tests as discussed above. Comparison is made with scour depths computed using the classical formulae by Schoklitsch (Equation 3) and Shalash (Equation 4), reported

Copyright © 2006 Taylor & Francis Group plc, London, UK

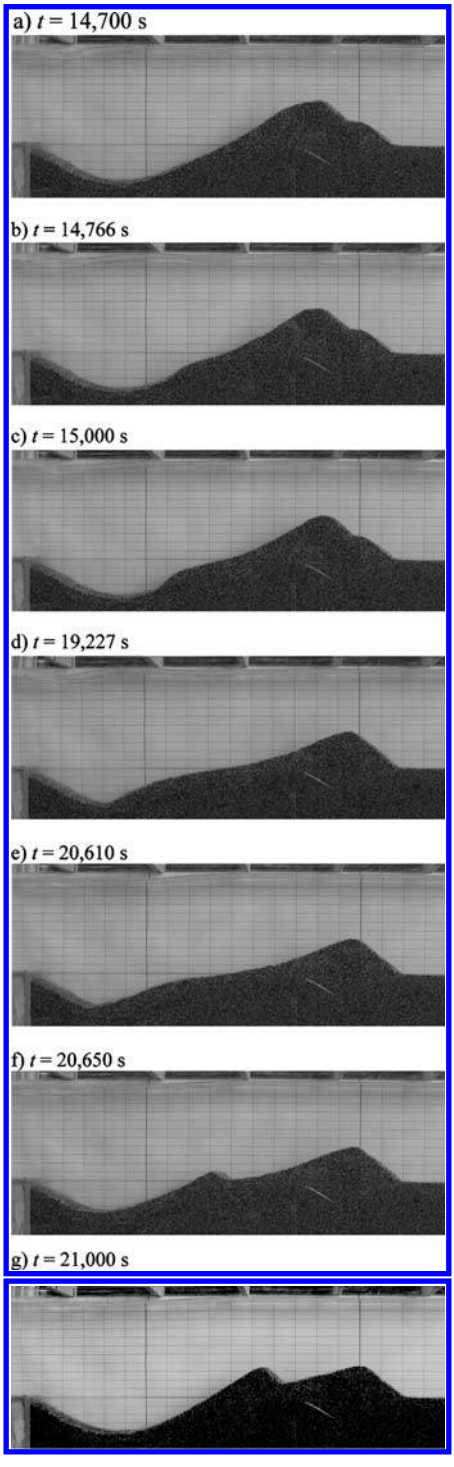


Figure 10. Sequence showing bed profile evolution for run no. 9; photographs a and g concern maximum scour conditions at the end of a "bed jet" phase.

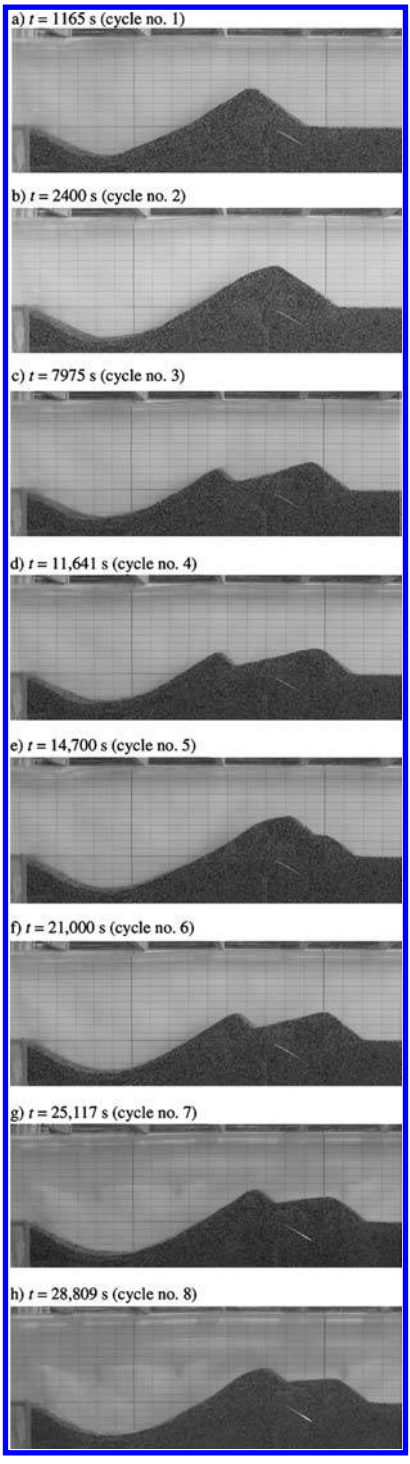


Figure 11. Bed profile at the end of the "bed jet" phase for different cycles of run no. 9.

Copyright © 2006 Taylor & Francis Group plc, London, UK

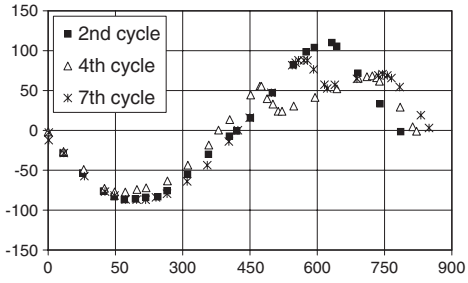


Figure 12. Dimensional bed profiles y vs x (in mm) after the "bed jet" phase for different cycles of run no. 9. Profiles are carried out processing frames b, d, g of Figure 11.

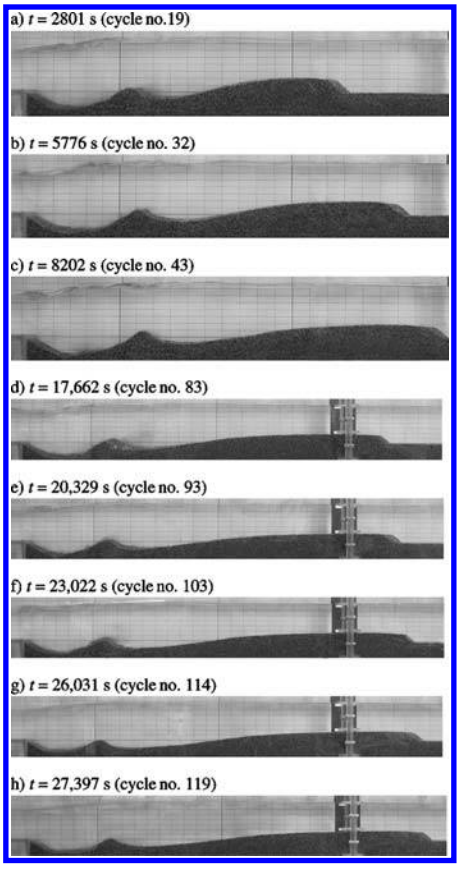


Figure 13. Bed profile at the end of the "bed jet" phase for different cycles of run no. 7 (note that the channel section shot in frames a–c is shorter than the one in frames d–h).

in Breusers & Raudkivi (1991). With the adopted symbols, these formulae are respectively:

$$h_{S,MAX,\infty} = 0.378\, y_H^{0.5}\, q^{0.35} \quad (3)$$

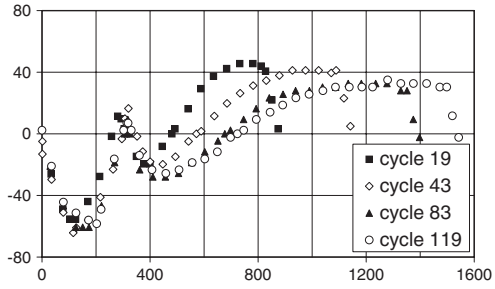


Figure 14. Dimensional bed profiles y vs x (in mm) after the "bed jet" phase for different cycles of run no. 7. Profiles are carried out processing frames a, c, d, h of Figure 13.

Table 4. Maximum scour depths for "bed-surface jet" tests.

No.	$h_{S,MAX}$ measured [mm]	$h_{S,MAX,\infty}$ equation 3 [mm]	$h_{S,MAX,\infty}$ equation 4 [mm]	$l/\Delta y$ [–]
1	38	35	–	15.6
4	54	46	–	6.0
5	113	56	–	4.5
7	65	58	61	3.2
8	131	67	41	2.6
9	91	59	–	11.9
14	45	55	–	9.3
17	45	67	–	5.5

$$h_{S,MAX,\infty} = 9.65\,\Delta y^{0.5}\, q^{0.6}\, d_G^{-0.4}\left(\frac{1.5\,\Delta y}{l}\right)^{0.6} - y_T \quad (4)$$

being $\Delta y = y_H - y_T$ and q the flow rate per unit width; all quantities are expressed in SI units, except d_G which should be in mm.

Equation 3 is based on model tests with short apron length ($l/\Delta y = 1.5$) but it gives acceptable estimates of the magnitude of observed scour depths. Nevertheless, contrary to expectations, the discrepancies between measured and calculated results do not decrease as $l/\Delta y$ approaches 1.5: for example in run no. 8 (whose $l/\Delta y$ ratio is the closest to 1.5 in Tab. 4) the measured scour depth is about twofold than the predicted one. On the other hand, Shalash formula (which explicitly takes into account the apron length) gives negative values (i.e. predicts no scour) for almost all the "bed-surface jet" regime tests of Table 4; moreover, it seems to give better results for smaller $l/\Delta y$ ratios (tests no. 7 and 8), again in disagreement with expectations.

Velocity profiles during both phases of the "bed-surface jet" cycle have been obtained for run no. 14 by averaging several ADV measurements during each phase. The different jet patterns above the scour hole are clearly visible in Figure 15 ($x = 205$ mm): during the "bed jet" phase (Fig. 15a) the velocity peak is closer to the bed and the scour process is consequently more intense; during the "surface jet" phase

Copyright © 2006 Taylor & Francis Group plc, London, UK

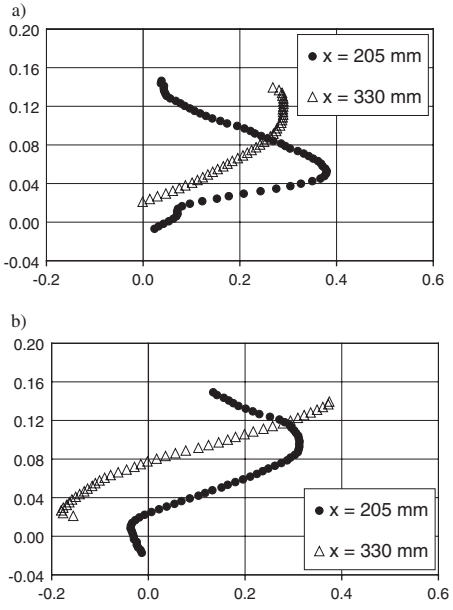


Figure 15. ADV vertical profiles of u (in m/s) vs y (in m) at different x positions, for "bed-surface jet" scour regime (run no. 14). Profile at $x = 205$ mm is located above the scour hole, profile at $x = 330$ mm is located approximately in the position of the secondary dune peak is found after the "bed jet" phase. (a) profiles collected during "bed jet" phase. (b) profiles collected during "surface jet" phase.

(Fig. 15b) the flow shifts towards the free surface and a re-circulation region appears close to the erodible bed. These differences extend downstream ($x = 330$ mm): in the "surface jet" phase (Fig. 15b), a large backflow region is present also above the dune, contributing, as previously observed, to the collapse of the secondary dune into the scour hole.

6 CONCLUSIONS

The scour of a non-cohesive bed downstream of an apron caused by a 2D horizontal jet flowing from a sluice gate has been studied experimentally on a laboratory channel. When the tailwater depth is just a few times the gate opening, but is high enough to guarantee a submerged hydraulic jump downstream of the gate, three distinct scour regimes can arise. In the "surface jet" regime, the jet tends to reach the free surface at the end of the apron and the scour hole and the dune develop mainly horizontally, following an elongated profile with low vertical dimensions. In the "bed jet" regime the jet adheres to the erodible bed and the resulting scour hole and dune are shorter, while their vertical dimensions are larger than in the previous case. An intermediate regime exists in which an unsteady cyclic flow onsets, the jet switching intermittently between the previous flow regimes: the resulting scour hole and dune shapes are also unsteady; in this case the maximum scour depth is not reached asymptotically but at the end of the more intense "bed jet" phases.

At least three non-dimensional parameters (when neglecting the effect of the Reynolds number and the grain size) are needed to predict the flow regime: the densimetric Froude number F_0, the normalized apron length l/y_0 and the normalized tailwater depth y_T/y_0. Comparisons of tests with approximately equal l/y_0 suggest that, for fixed F_0, intermediate y_T/y_0 ratios lead to "bed-surface jet" flows. When the normalized tailwater depth is large, "bed jet" flows are expected while "surface jet" patterns develop under low y_T/y_0. Moreover, the higher F_0, the larger the y_T/y_0 interval characterized by the jet flicking. Finally, again for fixed l/y_0 and F_0, the larger the normalized tailwater depth, the longer the average cycle period in flicking jet flows. Classical formulae by Schoklitsch and Shalash fail to reliably estimate maximum scour depth for "bed-surface jet" regime flows.

LDA and ADV velocity measurements, together with photographs and quantitative bed profiles evaluations, are provided for selected experiments: these data may be useful for the validation of numerical models able to simulate the interaction of free-surface flows with non-cohesive granular beds.

REFERENCES

Ali, K.H.M. & Lim, S.Y. 1986. Local scour caused by submerged jets. *Proc. Inst. Civ. Engnrs – Part 2: Research and Theory* 81: 607–645.

Breusers, H.N.C. & Raudkivi, A.J. 1991. *Scouring*. Rotterdam: A.A. Balkema.

Chatterjee, S.S. & Ghosh, S.N. 1980. Submerged horizontal jet over erodible bed. *J. Hyd. Div.* 106: 1765–1782.

Chatterjee, S.S., Ghosh, S.N. & Chatterjee, M. 1994. Local scour due to submerged horizontal jet. *J. Hyd. Eng.* 120: 973–992.

Espa, P. & Sibilla, S. 2005. *Local Scour Downstream of an Apron for Intermediate Tailwater Depth Conditions.* CD Rom Proceedings of XXXI IAHR Congress, 1602–1613.

Johnston, A.J. 1990. Scourhole developments in shallow tailwater. *J. Hyd. Res.* 28: 341–354.

Johnston, A.J. & Halliwell, A.R. 1986. Jet behaviour in shallow receiving water. *Proc. Inst. Civ. Engnrs – Part 2: Research and Theory* 81: 549–568.

Johnston, A.J. & Halliwell, A.R. 1987: Discussion on paper: Local scour caused by submerged jets (by Ali and Lim). *Proc. Inst. Civ. Engnrs – Part 2: Research and Theory* 83: 875–886.

Nik Hassan, N.M.K. & Narayanan, R. 1985. Local scour downstream of an apron. *J. Hyd. Eng.* 111: 1371–1385.

Rajaratnam, N. 1976. *Turbulent jets*. Amsterdam: Elsevier.

Rajaratnam, N. 1981. Erosion by plane turbulent jets. *J. Hyd. Res.* 19: 339–358.

Rajaratnam, N. & Macdougall, R.K. 1983. Erosion by plane wall jets with minimum tailwater. *J. Hyd. Eng.* 109: 1061–1064.

Copyright © 2006 Taylor & Francis Group plc, London, UK

Scour protection downstream of block ramps

S. Pagliara & M. Palermo
University of Pisa, Department of Civil Engineering Via Gabba, Pisa, Italy

ABSTRACT: Block ramps or rock chutes are structures used in many river restoration projects. Generally, in such structures, a scour that must be controlled is present at the toe of the ramp. Aim of the paper is to analyse the scour that occurs downstream of the ramp and to indicate the protection works needed in order to avoid structural problems. Experimental tests have been carried out at the Hydraulic Lab. of the University of Pisa. Two different channels have been used for a total of about 300 tests. The ramp slope was varied between 1V:4H to 1V:12H while different materials have been used for both the ramp and the downstream base material. The protection has been realized by means of sills with different characteristics (i.e. continuous, permeable, or made by rocks). The advantages of a rock sill protection is evident in the sense of reducing the maximum scour depth.

1 INTRODUCTION

One of the problems in the design of transversal structures in natural rivers is the scour downstream of the toe of the structure. Pagliara & Hager (2004) analysed the scour downstream of a block ramp in absence of any type of protection work. They described the phenomenon and its scour mechanism. In their experiments, the bed and ramp materials were uniform. Two relationships were found both for the relative maximum scour depth Z_{max}, where $Z_{max} = z_{max}/h_1$, and for the relative medium cross-sectional scour depth Z_m, where $Z_m = z_m/h_1$. They found that:

$$Z_{\max} = E\ln(F_{d50}) + F \quad (1)$$

$$Z_{\mathrm{m}} = A\ln(F_{d50}) + B \quad (2)$$

where $A = 2.93i + 1.01$, $B = -0.83i - 0.62$, $E = 6.21i + 0.74$, $F = -2.18i - 0.24$, i is the ramp slope, $F_{d50} = V_1/(g'd_{50})^{1/2}$ the densimetric Froude number, $V_1 = Q/(bh_1)$ with b = channel width, V_1 = the average approach velocity, $g' = [(\rho_s - \rho)/\rho]g$ the reduced gravitational acceleration, ρ_s the sediment density; ρ as the water density, h_1 the approach flow depth at the ramp toe, Q the discharge, g gravitational acceleration, d the sediment size and the number indicates the percentage of the passage across a sediment net; z_{max} is the maximum measured scour depth and z_m the medium cross-sectional scour depth.

Successively, Pagliara (2006) analysed the same phenomenon using a non-uniform material for the downstream channel bed in order to put in evidence the effects of non-uniformity on the scour geometry. He found that:

$$Z_{\max} = Z_m(1 + 1.75F_{d50}^{-1.75}) \quad (3)$$

$$Z_m = 0.58F_{d50}^{1.8}\sigma^{-0.55}i^{0.75} \quad (4)$$

where $\sigma = (d_{84}/d_{16})^{1/2}$ is the geometric standard deviation (sediment non-uniformity parameter).

Aim of this paper is to investigate the effect of different types of protection works on the scour mechanism. Namely, as it was observed that the presence of different protection sills (i.e. continuous, permeable or made by rocks) had a great influence on the geometric scour parameters (length and depth), it seemed necessary to analyse the effects of different protection structure settlements on scour characteristics in order to compare and describe the final configuration. The qualitative description which is given in this paper could be a valid aid to understand the problems connected with the formation of a scour hole at the toe of a transversal structure. Moreover the aim of this paper is to give valuable suggestions for the choice of the protection structure typology and settlement in order to mitigate the scour depth and length in the case of uniform bed material.

2 EXPERIMENTAL SETUP

The experiments were conducted at the Hydraulic Laboratory of the University of Pisa, Pisa – Italy.

Two channels were used for experiments, channel 1-C and channel 1-D. The channel 1-D was rectangular,

Copyright © 2006 Taylor & Francis Group plc, London, UK

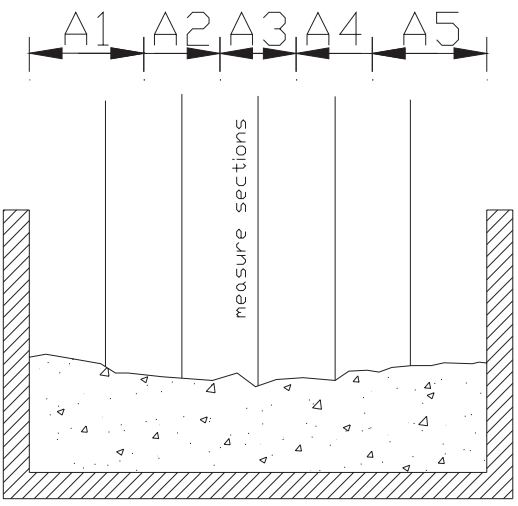


Figure 1. Measurement points in transversal cross-section.



Figure 2. Example of rock-made sill (view from downstream).

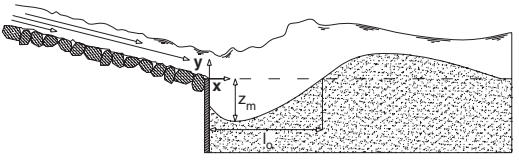


Figure 3. Reference test.

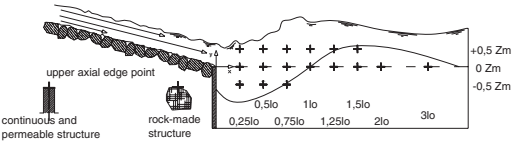


Figure 4. Selected control positions.

0.25 m wide, 3.5 m long and 0.30 m high and the channel 1-C was also rectangular, 0.35 m wide, 6.0 m long and 0.50 m high. Discharges up to 30 l/s were investigated. The ramp in the channels was made by inox steel sheets, on which two uniform granular materials were glued (material 1: $\sigma_1 = 1.17$, $d_{50} = 10.46$ mm; material 2: $\sigma_2 = 1.31$, $d_{50} = 4.00$ mm). The inox steel sheets had the same width of the channels and the length was varied from 0.40 to 1.0 m. The ramp was movable in order to change its slope in a range between 1V:4H and 1V:12H. Two granular uniform materials were put in the channel 1-C and in the channel 1-D, $s_{1\text{-}C} = 1.13$, $d_{50\text{-}C} = 10.60$ mm and $s_{1\text{-}D} = 1.18$, $d_{50\text{-}D} = 6.26$ mm, respectively, and they were graded in order to have an horizontal level downstream of the ramp before starting each experiment. The channelbed was measured both in transversal and in longitudinal direction before the beginning of each test. The distance of the longitudinal points of measurement varied from 5 to 15 cm, while, in the transversal direction, four points of measurement were selected for the narrower channel and five for the other one as shown in Figure 1. The protection works used were of three different types: continuous, permeable and rock-made sills respectively. Figure 2 shows an example of a rock-made sill.

Preliminary tests showed that after about 25 minutes scour progress vanished. For this reason a test duration of 25 minutes was chosen. At the end the measurements of previously selected points were taken after the bed material was completely dried. First of all, experiments were carried out without any type of protection work with the same methodology as mentioned above in order to have the average reference values of depth and length of the scour z_m and l_0, respectively, as shown in Figure 3.

3 DESCRIPTION OF EXPERIMENTAL DATA

Different "control positions" for the insertion of the protection works were fixed. Figure 4 shows the horizontal and vertical "control positions" which were selected for the experiments. The symbol "+" represents the position of the upper axial edge point of the structure, as shown in Figure 4. According to the reference frame, horizontal positions were selected at the distances of $0.25l_0$, $0.5l_0$, $0.75l_0$, $1.0l_0$, $1.25l_0$, $1.5l_0$, $2.0l_0$, and $3.0l_0$ from the toe of the ramp. The choice of the last two points ($2.0l_0$and $3.0l_0$) had the only aim to demonstrate that, if the protection work was put at a great distance from the toe of the ramp and its top was at $0.0z_m$, its effects on the scour process were negligible. Moreover, three vertical positions z_{op} were chosen for the top of the protection work, at $-0.5z_m$, $0.0z_m$ and $+0.5z_m$. A total of seventeen different positions was chosen as shown in Figure 4 with a "+" symbol. For each one of those seventeen different

Copyright © 2006 Taylor & Francis Group plc, London, UK

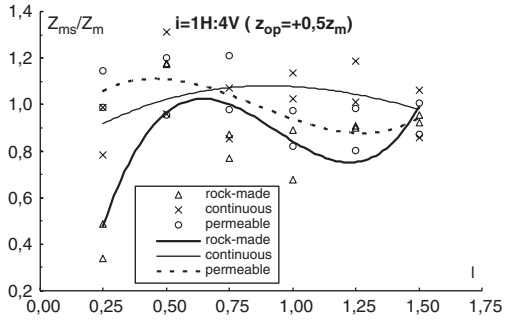


Figure 5a. Relative scour depth for different types of protection works for a ramp slope 1V:4H.

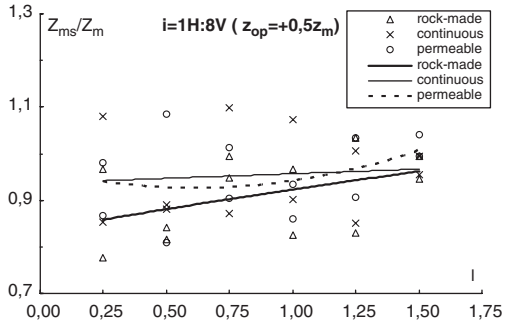


Figure 5b. Relative scour depth for different types of protection works for a ramp slope 1V:8H.

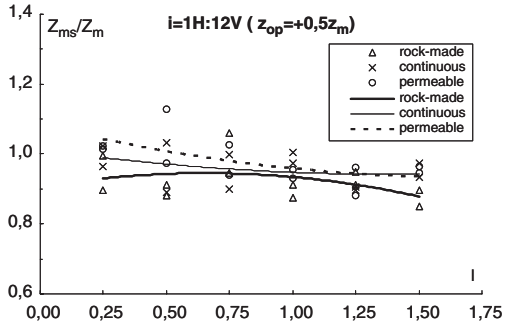


Figure 5c. Relative scour depth for different types of protection works for a ramp slope 1V:12H.

selected positions, many experiments were conducted in order to understand and evaluate the influence of the parameters that affect the phenomenon. For this reason, three different ramp slopes, 1V:4H, 1V:8H and 1V:12H, two discharges and three different protection works were considered. These experimental tests confirmed that an opportune vertical and longitudinal settlement of a rock-made sill can minimize scour length and depth more efficaciously than other tested structures, as shown in Figures 5a, b, c and in

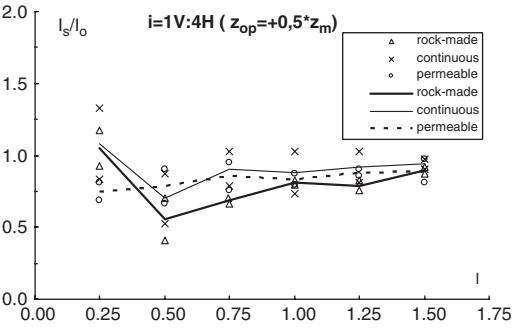


Figure 6a. Relative scour length for different types of protection works for a ramp slope 1V:4H.

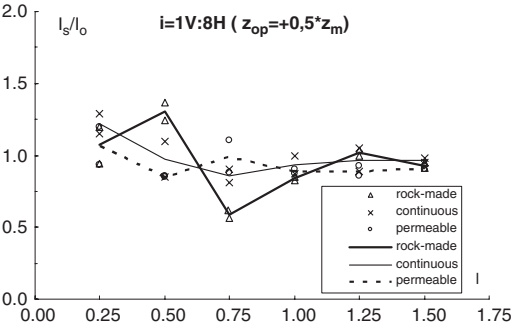


Figure 6b. Relative scour length for different types of protection works for a ramp slope 1V:8H.

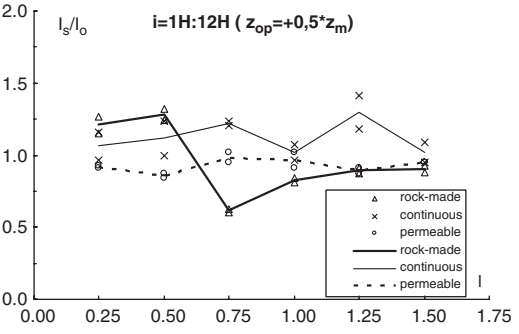


Figure 6c. Relative scour length for different types of protection works for a ramp slope 1V:12H.

Figures 6a, b, c, in which a comparison of the effects of presence of different tested structures (located at $z_{op} = +0.5z_m$) is proposed. In these figures the ratios z_{ms}/z_m and l_s/l_0 are plotted against the dimensionless parameter λ. $\lambda = x_s/l_0$, where x_s is the longitudinal position of the protection work. z_{ms} is the medium cross-sectional scour depth and l_s is the scour length, both in presence of protection works.

Copyright © 2006 Taylor & Francis Group plc, London, UK

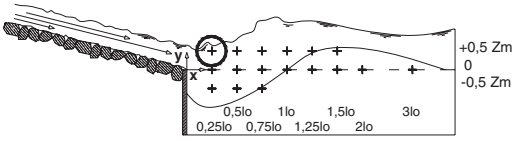


Figure 7. Protection work at $\lambda = 0.25$ and $z_{op} = +0.5z_m$.

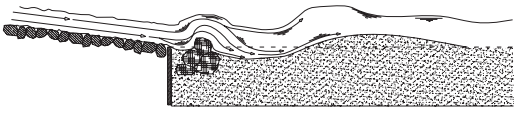


Figure 8. Rs1 scour profile.

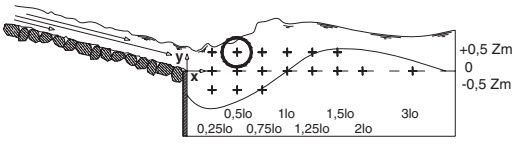


Figure 9. Protection work at $\lambda = 0.50$ and $z_{op} = +0.5z_m$.

Having proved that the rock-made sills performed better than the other structures in order to minimize the scour depth and length, several other experiments were conducted using rock-made sills as protection work. From these experiments four different scour typologies, called Rs1, Rs2, Rs3 and Rs4, were individuated.

Maintaining fixed the top of the protection work, it was possible to show the influence of the other parameters on the scour process. In other words, it was possible to evaluate the influence on the variation of depth, length and the geometrical form of the scour because of the variation of the longitudinal position of the protection work and of the ramp slope. Let us consider now the various typologies of scour that could be possible in the case in which the top of the protection work was set at $z_{op} = +0.5\, z_m$.

If the protection work is located at $\lambda = 0.25$ (Fig. 7), when the ramp slope was 1V:4H, there was a reduction of the scour depth ($z_{ms} < z_m$), and the length was almost the same of the reference prove ($l_0 \approx l_s$). If the ramp slope was 1V:8H or 1V:12H, for both we had $l_s > l_0$, but $z_{ms} < z_m$ and $z_{ms} \approx z_m$, respectively. The energy dissipation was essentially due to the impact of water on the protection work when the ramp slope was 1V:4H, while, in the other two cases, it was essentially due to the erosion downstream of the rock-made sill. In this case, the scour profile was indicated as Rs1, as shown in Figure 8.

If the protection work was put at $\lambda = 0.50$ (Fig. 9), two scour profiles were observed according to the different ramp slopes, Rs 3 and Rs 2 respectively.

When the ramp slope was 1V:4H, the value of the length of the scour was minimum ($l_s = l_{smin} < l_0$) but the depth was maximum ($z_{ms} = z_{msmax} > z_m$), because

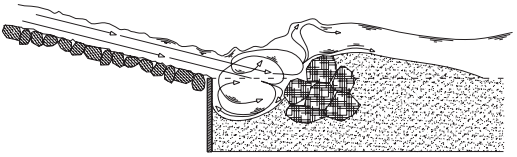


Figure 10. Rs3 scour profile.

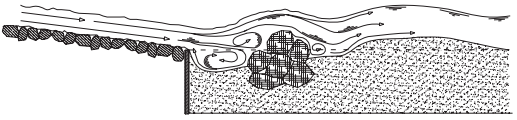


Figure 11. Rs2 scour profile.

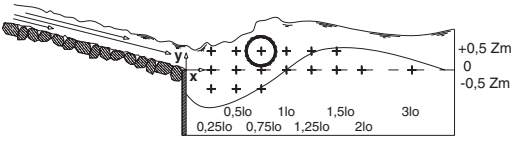


Figure 12. Protection work at $\lambda = 0.75$ and $z_{op} = +0.5z_m$.

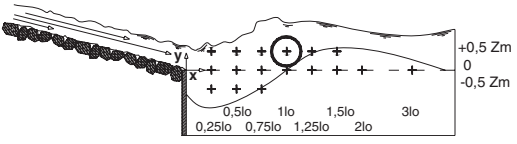


Figure 13. Protection work at $\lambda = 1.0$ and $z_{op} = +0.5z_m$.

of the great dissipation of energy upstream of the protection work. In this case, the scour profile was indicated as Rs 3, as shown in the Figure 10.

If the ramp slope was in the range 1V:12H – 1V:8H, the scour took place both downstream and upstream of the sill, the length of the scour increased, $l_s > l_0$, but there was a decrease in the depth, $z_{ms} < z_m$. In this case, the scour profile was indicated as Rs 2 as shown in the Figure 11.

If the protection work was located at $\lambda = 0.75$ (Fig. 12), the Rs3 scour profile was observed for all the tested ramp slopes.

The experiments showed that there was a scour upstream of the sill where part of the energy of the water was dissipated. For this longitudinal position, the length of the scour decreased, $l_s < l_0$ for all the three slopes, moreover, for ramp slopes 1V:8H and 1V:12H, it reaches its minimum. It was seen that $z_{ms} < z_m$ when the ramp slope was 1V:4H, and it became almost equal to z_m in the other two cases. The scour profile is shown in Figure 10.

If the protection work was located at $\lambda = 1.0$ (Fig. 13), when the ramp slope was 1V:4H, there was a reduction of the depth of the scour ($z_{ms} < z_m$) and of its length ($l_s < l_0$). The same scour profile shown in Figure 10 occurred (Rs3- type), but it was seen that a

Copyright © 2006 Taylor & Francis Group plc, London, UK

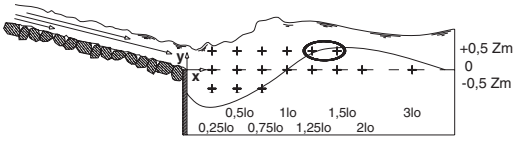


Figure 14. Protection work at $1.25 < \lambda < 1.5$ and $z_{op} = +0.5z_m$.

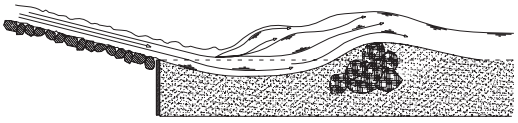


Figure 15. Rs 4 scour profile.

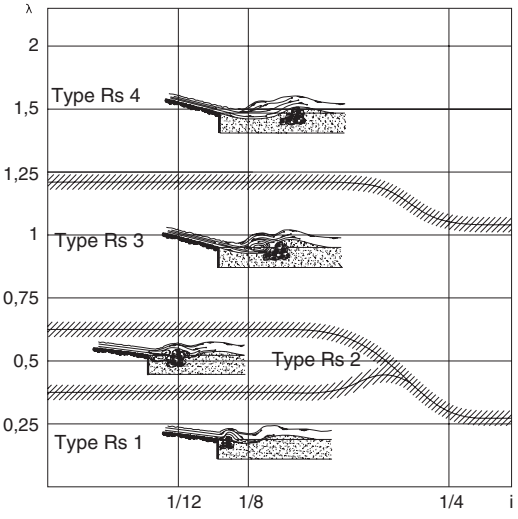


Figure 16. Scour profiles for $z_{op} = +0.5z_m$.

little increase of the longitudinal distance of the protection work caused a variation in the scour profile, which changed from Rs3 to Rs4 type. For ramp slopes 1V:8H and 1V:12H there was a reduction of the depth of the scour ($z_{ms} < z_m$) and of the length ($l_s < l_0$), and a Rs3 profile type occurred.

For the case of protection work located at $1.25 < \lambda < 1.5$ (Fig. 14), it was seen that another scour profile for all the three different ramp slopes occurred and it was called Rs 4 type.

It was observed that Rs4 scour profile (Fig. 15) was quite similar to the Rs3 type. The only difference was that the sill, in this case, was totally submerged by the dune downstream of the scour, while in Rs3 scour profile the sill was partially submerged. A decrease of the value of the scour depth and length, $z_{ms} < z_m$ and $l_s < l_0$, was observed.

Figure 16 shows a synthesis of all the geometric types mentioned above, when $z_{op} = +0.5z_m$.



Figure 17. Rs1 type scour profile.



Figure 18. Rs2 type scour profile.



Figure 19. Rs3 type scour profile.

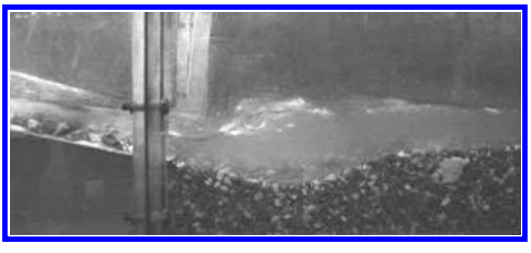


Figure 20. Rs4 type scour profile.

Figures 17–20 show the four scour typologies which were observed in the experiments.

The same methodology, as mentioned above, was followed for the other two positions of the top of the protection work, $z_{op} = 0.0z_m$ and $z_{op} = -0.5z_m$. It was seen that, also in these cases, the quantitative reduction of the scour depth and length due to the presence of a rock-made sill was similar to the examined case ($z_{op} = +0.5z_m$).

Copyright © 2006 Taylor & Francis Group plc, London, UK

4 CONCLUSIONS

The experiments show that opportune settlements of the protection work can reduce the scour depth and the scour length. It was seen that rock-made sills are more efficient than other types in order to reach these results. Particularly, it was seen that, when $z_{op} = +0.5z_m$, if we are interested in the minimization of the scour length two longitudinal positions of the sill have to be chosen: for ramp slope 1V:4H the best position is at $l = 0.5$ while, if the ramp slope is in the range 1V:12H-1V:8H, the best longitudinal position is at $l = 0.75$. Moreover, if we are interested in a reduction of both the scour depth and length, for all different ramp slopes, the longitudinal positions where the sill has to be located are in the range $0.75 < \lambda < 1.5$. The experiments also showed that, if the protection work is located at $l = 0.5$, when $z_{op} = +0.5z_m$ and the ramp slope is 1V:4H, there is an increase of the scour depth and in this position it reaches its maximum.

REFERENCES

Canepa, S. & Hager, W.H. 2003. Effect of jet air content on plunge pool scour. *Journal of Hydraulic Engineering* 129(5): 358–365.

Pagliara, S. 2006. Effect of granulometry on clear water scour downstream of block ramps. ASCE *Journal of Hydraulic Engineering* (submitted).

Pagliara, S. & Hager, 2004. Scour downstream of block ramps. Proc. 2nd Int.nal conference on Scour and Erosion 14-17 nov., Singapore. pp.215–222.

Pagliara, S. & Hager, W.H. & Minor, H.E. 2006. Hydraulics of plane plunge pool scour. *Journal of Hydraulic Engineering*, vol. 132, No.5.

Copyright © 2006 Taylor & Francis Group plc, London, UK

Temporal patterns of the maximum scour depth around a pier

G. Oliveto & A. Di Domenico
DIFA, University of Basilicata, Potenza (Italy)

ABSTRACT: In temporal and spatial development of scour processes around a cylindrical pier, the maximum scour depth does not occur at the same location over the time. It localizes at the pier sides firstly, then it tends to migrate towards the pier leading face at a rate mainly depending on the approach flow densimetric Froude number. Based on experiments carried out at University of Basilicata and experiments previously conducted at VAW-ETH, Zurich, this paper would like to provide mainly a relationship for the switch time T_{sw}, defined as the (dimensionless) time at which the maximum scour depth transfers from the pier sides to the axial pier front. The VAW data were globally processed to identify preventative outcomes. The data collected in the present study were devoted to the capture of T_{sw} and thus were used for a more detailed analysis. Findings, that appear wide-ranging, would provide useful tools for numerical modeling, field diagnostic and for proper analyses of literature data that are frequently based on observations at pier front only.

1 INTRODUCTION

Local scour is an important issue in bridge hydraulics. A great number of studies have been made in this research area, but several aspects are still unexplored or unclear.

With reference to a cylindrical pier it is well known that scour initiates at the sides of the cylinder, at an angle of approximately 70 degrees to the undisturbed flow direction, then advances to the leading face of the pier (Breusers & Raudkivi 1991, Hoffmans & Verheij 1997). Thus, the maximum scour depth at the upstream pier face occurs only at an advanced scour stage (Figure 1).

Moreover, for flow conditions with a densimetric Froude number F_d close to the entrainment condition at pier, this shift of maximum scour could even not occur because of the too small forces involved after the initial scour phase. The densimetric particle Froude number is defined as $F_d = V_o/(g'd_{50})^{1/2}$ with V_o the approach flow velocity and $g' = g(\rho_s - \rho)/\rho$ the modified gravitational acceleration with ρ and ρ_s the fluid and sediment densities, respectively.

According to Hager et al. (2002), one may refer to small, medium or fast scour progress, depending on F_d. Typically, for $F_{d\beta} < F_d < 2$, with $F_{d\beta}$ = densimetric Froude number for the entrainment of scour at pier, scour is weak with a tendency for slightly asymmetric scour on the two pier sides. Typical clear water scour may be expected for $2 < F_d < F_{di}$, with a significant effect of pier diameter on the scour extension. Here, F_{di} is the densimetric Froude number at the inception of sediment transport for the approach (undisturbed) bed. For $F_d > F_{di}$ scour does not really advance after a sufficient time because of an equilibrium between sediment transports into and out of the scour hole (Hoffmans & Verheij 1997).

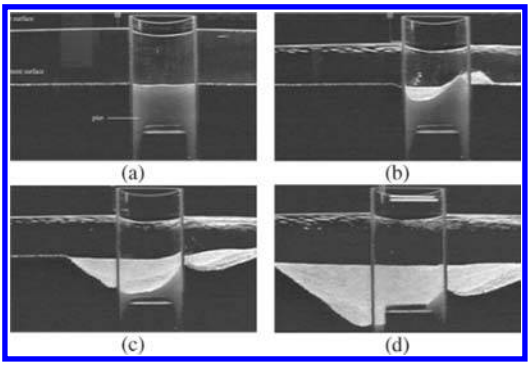


Figure 1. Experiment at VAW-ETH (Hager et al. 2002). Lateral view of scour advance for a half-cylinder. Flow is from left to right. (a) $t = 0$ (run starting); (b) $t = 5$ min; (c) $t = 3$ h; (d) $t = 21$ h with t = time.

Nevertheless, most of the proposed formulas on the scour at a pier are based on the growing of the scour depth axially at the pier front, and thus they could seriously underestimate local scour especially in the starting scour period.

Based on recent outcomes (Oliveto et al. 2005), experimental data previously collected at VAW-ETH (Oliveto & Hager 2002) and new selected tests carried

Copyright © 2006 Taylor & Francis Group plc, London, UK

out at University of Basilicata, this paper would like to set up general equations able to describe the temporal patterns of the maximum local scour around uniformly shaped circular piers.

The results may provide new insights in bridge analysis and design, and for a more intrinsic understanding of local scour processes.

2 EXPERIMENTS AT VAW-ETH

VAW-ETH initiated scour research in 1995 by focusing so-called building scour. The experiments were conducted in a rectangular channel 1.0 m wide and 13 m long with a working section of about 5 m.

Piers of diameters $D = 0.022$, 0.050, 0.064, 0.110, 0.257, 0.400, and 0.500 m were used.

Scour experiments were directed to survey both sediment and water surfaces. These characteristics were determined with conventional gauges. The sediment surface was observed with a shoe gauge, given its similarity with a shoe of 5 mm length to 2 mm width. Sediment surface readings were then much simpler than with a conventional point gauge with an accuracy of about 0.5 sediment diameter.

Sediment readings involved the original bed elevation, the upstream beginning of scour, the transverse extent of scour at the element upstream and downstream sides, the maximum scour depths at these two locations, the location of maximum aggradation downstream of the elements besides particular points for each test. Test readings were made in short intervals close to the beginning, and at longer intervals after the initial scour phase.

Three sediments of almost uniform average size of 0.55, 3.3 and 4.8 mm, and three mixtures, with $d_{50} = 5.3$, 1.2, 3.1 mm, and $\sigma = (d_{84}/d_{16})^{1/2} = 1.43$, 1.80 and 2.15, respectively, were used. The uniform sediment with $d_{50} = 3.3$ mm had a density of $\rho_s = 1.42$ t/m^3 to check for the density effect, whereas the remainder had $\rho_s = 2.65$ t/m^3. More details are given in Oliveto & Hager (2002).

3 NEW EXPERIMENTS

Selected experiments were conducted in a 1.0 m wide and 20 m long rectangular straight channel at the Hydraulic Engineering Laboratory, University of Basilicata, Italy.

The working section was about 10 m. The bed material was a nearly uniform sand with density $\rho_s = 2.65$ t/m^3, grain size $d_{50} = 1.4$ mm and sediment gradation $\sigma = (d_{84}/d_{16})^{1/2} = 1.35$. A pier of diameter $D = 0.12$ m was used. It was located at 5 m from the bed sediment beginning and at 9 m from the channel inlet to have good approach flow conditions and a fully developed turbulent flow at the scour element.

Table 1. Experiments at University of Basilicata: main test conditions and observed scour depths at the end of the run. F_t = threshold Froude number; F_d = densimetric Froude number; t_d = duration test; z = measured scour depth around the pier; subscripts s, f, d = side, front, and downstream, respectively.

Run	F_t –	F_d –	t_d (h)	z_s (cm)	z_f (cm)	z_d (cm)
1	0.73	2.46	1.9	1.10	1.28	0.57
2	0.86	2.84	1.9	1.27	1.47	0.78
3	0.76	2.55	2.2	1.21	1.33	0.70
4	0.82	2.93	1.8	1.37	1.53	0.86
5	0.52	1.82	7.9	0.65	0.71	0.15
6	0.42	1.45	52.5	0.28	0.26	−0.14

All the experiments were run under plane bed conditions, steady flow, and clear-water scour regime. Discharges Q were measured with an orifice plate of ±3% accuracy. Water surface was surveyed with a conventional point gauge, typically ±0.5 to 1 mm, whereas the bed morphology was surveyed with a shoe gauge having 4 mm by 2 mm wide horizontal plate at its base. Sediment readings involved: the scour depth at the pier sides, the scour depth at pier front, and the aggradation height or the scour depth at the rear of the pier. During each run the channel was carefully monitored to capture the time at which the maximum scour depth shifted from the pier sides to the pier front and that one marking the passage from aggradation to scouring phase just downstream of the pier. The main test conditions and the observed scour depths at the end of each run are given in Table 1.

The approach flow depth was controlled by an adjustable sharp-crested weir located at the channel downstream end. Once the bed was accurately leveled the experiment initiated submerging the working section by setting the sharp-crested weir up. This was lowered within 10 to 20 seconds to the pre-selected flow depth and the temporal start of the experiment was set at scour inception.

4 SWITCH TIME RELATIONSHIP

The approach by Oliveto & Hager (2002) for the temporal progress of scour at uniformly shaped piers was assumed as framework for this analysis. The dominant parameter governing scour processes is the densimetric particle Froude number F_d. The reference length, involving the approach flow depth h_o and the pier diameter D, is $z_R = (h_o D^2)^{1/3}$. Accordingly, the time scale is $t_R = z_R/[\sigma^{1/3}(g' d_{50})^{1/2}]$. Finally, the maximum scour depth z at a certain time t is given by

$$Z = z/z_R = 0.068\sigma^{-1/2} F_d^{1.5} \log T \qquad (1)$$

Copyright © 2006 Taylor & Francis Group plc, London, UK

with $T = t/t_R$ the relative time. Equation (1) provides thus the temporal growing of the maximum scour depth around a pier independently of its location.

Figures 2a and 2b provide a set of plots for temporal trend of the scour depth at the pier side (Figure 2a) and at the pier front (Figure 2b), in the domain (ζ, log$T$) with $\zeta = Z\sigma^{0.5}/F_d^{1.5}$. Data refer to the VAW-ETH experiments. Equation (1) is plotted as a full straight line with the ±25% intervals added as dashed lines as in Oliveto & Hager (2002). In the domain (ζ, log$T$), the scour depth at the pier side follows a linear trend almost regularly, growing thus at a constant rate. The temporal scour evolution at the pier front appears clearly different. Scour typically starts at $T = 10^2$ at that location. The growing rate is particularly high for T from 10^2 to 10^4 and then decreases almost in conformity with Equation (1).

According to Oliveto et al. (2005), the switch time T_{sw} can be defined as the dimensionless time T at which the maximum scour depth migrates from the pier sides to the axial pier front.

Thus, referring to the VAW-ETH experimental data, T_{sw} can be approximately determined by the intersection of the temporal trend of the scour depth at the pier front and Equation (1). The plots in Figures 2 reveal that such an intersection typically occurs for T from 10^2 to 10^4. In addition, the plot on the bottom of Figure 2b clearly shows that: for runs with F_t less then 0.5 (data embodied in region A) the above intersection does not occur and thus the maximum scour tends to persist at the pier side; for runs with $0.5 < F_t < 1$ (data embodied in region B) the switch time typically occur in the range 10^2 to 10^4; for runs with $F_t \geq 1$, but still close to 1 (data embodied in region C), T_{sw} tends to zero. Incidentally, F_t is the so called threshold Froude number given by V_o/V_t with V_t the cross sectional flow velocity at which bed sediment inception occurs. It was computed according to relationships suggested by Hager & Oliveto (2002).

Thus, the VAW-ETH data reveal that T_{sw} should be a decreasing function of F_t tending to infinity as F_t tends to 0.5 and to 0 as F_t tends to 1.

To better define this relationship the data collected at University of Basilicata were processed and the plot in Figure 3 resulted.

Thus, in the domain (log T_{sw}, F_t) the experimental data appear to be adequately interpreted by a sigmoidal curve. In particular, for runs with F_t greater than 0.9, but close to 1, as it is usually done in the experimental practice, one can confidently assume that the maximum scour depth is always localized at the pier front.

The above results refer to runs in transitional regime (i.e. dimensionless grain size D_* from 20 to 150 with $D_* = (g'/\nu^2)^{1/3} d_{50}$). In effect, the same results would seem to apply to the runs in viscous regime also, although more experimental data would be needed.

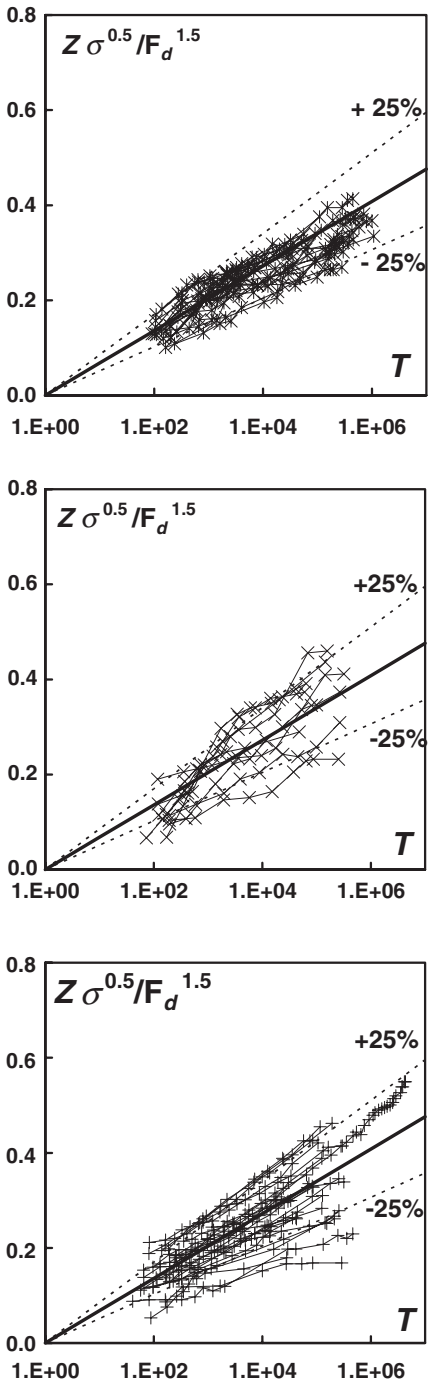
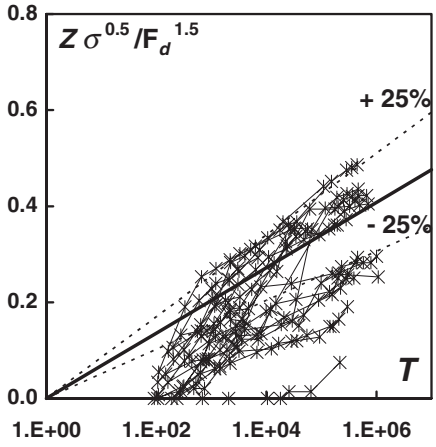
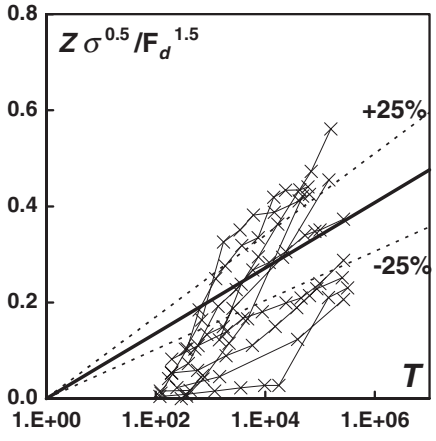


Figure 2a. $\zeta = Z\sigma^{0.5}/F_d^{1.5}$ as a function of the dimensionless time T at the pier side for runs in transitional regime. (∗) $d_{50} = 5.3$ mm; (×) $d_{50} = 4.8$ mm; (+) plastic with $d_{50} = 3.3$ mm.

Copyright © 2006 Taylor & Francis Group plc, London, UK





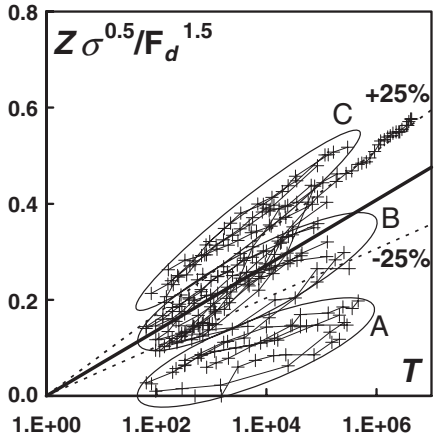


Figure 2b. $\zeta = Z\sigma^{1.5}/F_d^{1.5}$ as a function of the dimensionless time T at the pier front for runs in transitional regime. (∗) $d_{50} = 5.3$ mm; (×) $d_{50} = 4.8$ mm; (+) plastic with $d_{50} = 3.3$ mm.

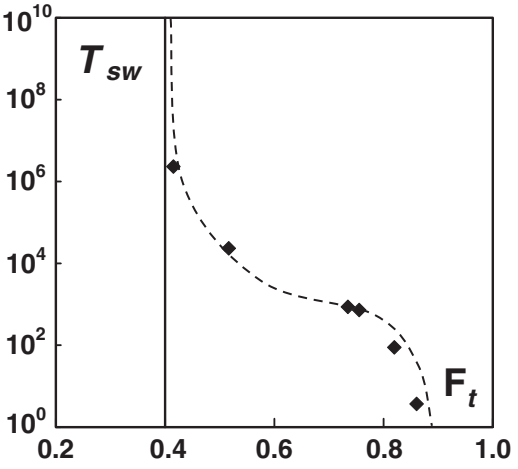


Figure 3. Switch time T_{sw} as a function of the threshold Froude number F_t. (- - - - -) sigmoidal fitting curve by eye.

The plots in Figure 4 represent the data for uniform sand ($d_{50} = 0.55$ mm, $\sigma = 1.37$). Due to viscous effects, Equation (1) should be corrected by a factor of 0.45 (Oliveto et al. 2005). Accordingly, it would seem that for F_t ranging between 0.6 to 0.9, the switch time still would occur in the range 10^2 to 10^4, whereas it would tend to infinity for F_t tending to 0.4.

An analysis on the scour depth at the rear of the pier was also performed for completeness. In particular, a trend similar to that of T_{sw} on F_t was observed for the switch time T'_{sw} marking the transition from the aggradation to the scouring phase. Figure 5 shows this trend which is overall confirmed by the VAW-ETH experimental data. The data collected in the present study confirmed also the appropriateness of the equation (5) given in Oliveto et al. (2005) for the temporal scour evolution at that location, on condition of F_t close to 1 (F_t from 0.8 to 1.0).

5 CONCLUSIONS

Selected experiments on the temporal evolution of clear water pier scour were carried out at the Hydraulic Engineering Laboratory, University of Basilicata, Italy.

The runs were devoted to the capture of the switch time at which the maximum scour depth migrates from the pier side to the pier front.

The experimental results, supported and integrated by some outcomes from several runs performed at VAW-ETH, have revealed that: (i) in the domain (ζ, log$T$) the scour depth grows differently in dependence of the location. At the pier side it exhibits a linear trend growing thus at a constant rate; at the pier front

Copyright © 2006 Taylor & Francis Group plc, London, UK

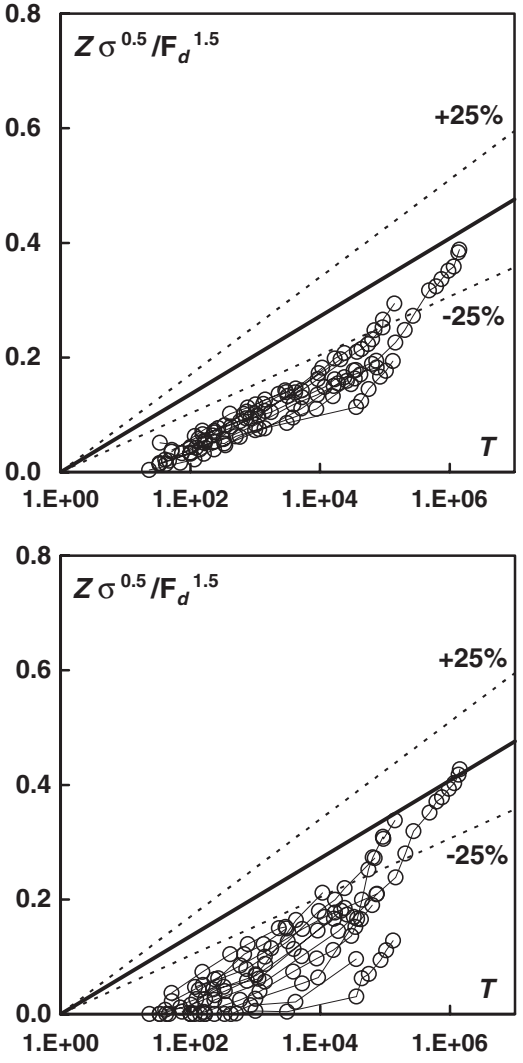


Figure 4. ζ as a function of the dimensionless time T at the pier side (top) and at the pier front (bottom) for runs in viscous regime.

its growing rate is particularly high firstly (for T from 10^2 to 10^4), then decreases by conforming to that of Equation (1); (ii) the switch time T_{sw} is a decreasing function of the threshold Froude number F_t tending to infinity as F_t tends to 0.4 and to 0 as F_t tends to 1. In particular, for runs with F_t close to 1 (F_t from 0.85 to 1.0), as it is usually done in the experimental practice, one can confidently assume that the maximum

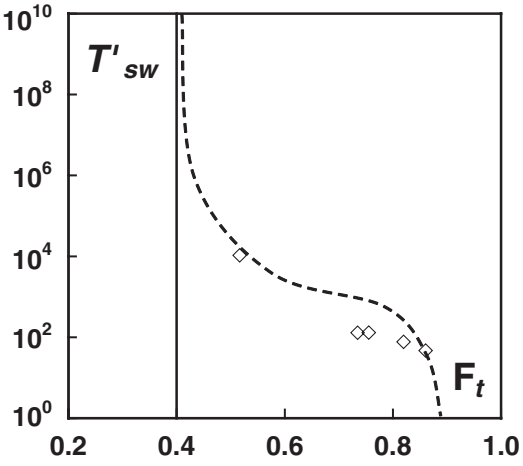


Figure 5. Switch time T'_{sw} at the rear of a cylindrical pier as a function of the threshold Froude number F_t. (- - - - -) sigmoidal fitting curve by eye.

scour depth is always localized at the pier front. These results are overall in agreement with those in Oliveto et al. (2005), but improved because based on runs specifically devoted to the capture of T_{sw}; (iii) a similar trend was observed for the switch time T'_{sw} marking the passage from aggradation to scouring phase downstream of a pier. For F_t close to 1, the temporal trend of the scour depth at this location is suitably interpreted by the equation (5) given in Oliveto et al. (2005).

REFERENCES

Breusers, H.N.C. & Raudkivi, A.J. 1991. *Scouring*. Rotterdam: A.A. Balkema.

Hager, W.H. & Oliveto, G. 2002. Shields' entrainment criterion in bridge hydraulics. *Journal of Hydraulic Engineering, ASCE*, 128(5): 538–542.

Hager, W.H., Unger, J. & Oliveto, G. 2002. *Proc. of First International Conference on Scour of Foundations, College Station, TX, USA, November 2002*, Vol. II: 774–784.

Hoffmans, G.J.C.M. & Verheij, H.J. 1997. *Scour manual*. Rotterdam: A.A. Balkema.

Oliveto, G. & Hager, W.H. 2002. Temporal evolution of clear water pier and abutment scour. *Journal of Hydraulic Engineering, ASCE*, 128(9): 811–820.

Oliveto, G., Hager, W.H. & Di Domenico, A. 2005. Additional results on scour at bridge piers. In J. Byong-Ho Jun, Sang-II Lee, II Won Seo & Gye-Woo Choi (eds), *Proc. of XXXI IAHR Congress, Seoul, Korea, September 2005*, 2005 Korea Water Resources Association: Seoul. Paper D09-2: 2964–2972.

Copyright © 2006 Taylor & Francis Group plc, London, UK

Riverbed scour induced by a long constriction

G. Oliveto, B. Onorati & V. Comuniello
DIFA, University of Basilicata, Potenza (Italy)

ABSTRACT: This study is a part of a more comprehensive research and is focused on the bed scour that would occur when rivers are forced by manmade or natural contractions. To this purpose, some experiments, typically lasted for days, were carried out at University of Basilicata in a straight rectangular channel and under clear water scour regime. The bed material was uniform sand and three contraction models, with opening ratio (i.e. ratio between the widths of the contracted and uncontracted reaches) of 0.9, 0.8, and 0.7, were used. Starting from the monomial form of sediment transport formulas, a new relationship for the quasi-equilibrium scour depth is conjectured based on Froude's similarity and by relating the scour depth to the difference between the actual and the entrainment densimetric Froude numbers in the contracted zone. The proposed approach is validated by the data of the present study, and verified by available literature data.

1 INTRODUCTION

Flow constriction arises from a significant reduction of the width of a watercourse. When the flow is subcritical, the contraction of a river induces an increase in the velocity and in bed shear stresses, which may cause bed scour. Natural constraints as longitudinal bars, confluences and debris accumulations or hydraulic structures as bridge embankments, lateral banks and spur dikes are common examples of stream flow area reductions.

Figure 1 shows an extreme case of a short and abrupt contraction and the related damages caused by the construction of a diversion weir in an alluvial stream.

Most of the published works refers to the long contraction case (i.e. flow can be considered practically uniform in both the approach and restricted reach), which in general occurs when the length L of the constrained reach is one (Komura 1966) to two (Webby 1984) times the width b_1 of the undisturbed approach reach. Recent experimental investigations confirmed that $L/b_1 \geq 1$ is adequate for a contraction to be considered long (Dey & Raikar 2005).



Figure 1. High degree of contraction induced by the building of a diversion weir on the Sauro Creek, southern Italy. The photo on the right shows the flood damages during December 1990.

Straub (1934) was probably the first to introduce a simplified one-dimensional approach for long contractions. His work was based on the DuBoys' transport formula and Manning's equation applied to both the constrained and (unconstrained) approach reach. Afterwards, many equations have been suggested, most of which were derived using Straub's (1934) approach (e.g. Laursen 1960, Komura 1966, Gill 1981, Lim & Cheng 1998). A review of relevant literature is provided by Hager (1998) and Melville & Coleman (2000). Among the more recent papers are those of Briaud et al. (2005) and Dey & Raikar (2005). In particular, this latter work makes available the experimental data for more than 100 runs with uniform sediments under clear-water scour.

Despite the many studies on this topic, there is not a satisfactory concordance of results. Based on long-duration tests, Oliveto et al. (2005) demonstrated the inadequacy of the most common models for the estimation of the quasi-equilibrium scour depth in long contractions. The present paper aims to provide a contribute in this context. In particular, a new straightforward approach is proposed. It is validated by the data collected at University of Basilicata and verified by the data of other investigators.

2 EXPERIMENTAL INSTALLATION AND PROCEDURE

Experiments were conducted in a 1 m wide and 20 m long rectangular straight channel at the Hydraulic

Copyright © 2006 Taylor & Francis Group plc, London, UK

Engineering Laboratory, University of Basilicata, Italy. The working section was about 10 m. The bed material was a nearly uniform sand with density $\rho_s = 2.65$ t/m^3, grain size $d_{50} = 1.7$ mm and sediment gradation $\sigma = (d_{84}/d_{16})^{1/2} = 1.5$. The contracted reach was carried out by two polystyrene elements symmetrically attached to the side glass walls of the channel. This reach was made by three parts. The middle one was straight lined and 1 m long, whereas the entrance and outlet parts had a length of 0.5 m each and were carefully streamlined to minimize energy losses and local scour effects. The upstream end of the contraction model was located at 4 m from the bed sediment beginning and at 8 m from the channel inlet to have good approach flow conditions and a fully developed turbulent flow at the entrance of the contraction. Three contraction ratios $\beta = b_1/b_2$ of 1.11, 1.25, and 1.43 were used; where $b_1 =$ width of the (uncontracted) approach channel and $b_2 =$ width of the uniformly contracted reach. In addition, some experiments were performed with only one polystyrene element mounted at one side of the channel. In such case the constriction ratio was assumed equal to 1.18, by considering the side glass wall without contraction element as the centerline of a channel $2b_1$ wide.

All the experiments were run under plane bed conditions, steady flow, and clear-water scour regime. Discharges Q were measured with an orifice plate of $\pm 3\%$ accuracy. Water surface was surveyed with a conventional point gage, typically ± 0.5 to 1 mm, whereas the bed morphology was surveyed with a so called shoe gage having 4 mm by 2 mm wide horizontal plate at its base. The tests were of long duration, from 1 day up to 15 days, to ensure an adequate accuracy, especially for low degree of contraction, and to get conditions of quasi-equilibrium. Flow depths and bed levels, around and in the contracted zone, were normally recorded each day. The measurements during the test were taken along the channel centerline to minimize the flow disturbance. At the end, more than 500 bed level readings were typically recorded. The main experimental data are given in Oliveto et al. (2005).

The approach flow depth was controlled by an adjustable sharp-crested weir located at the channel downstream end. Once the bed was accurately leveled the experiment initiated submerging the working section by setting the sharp-crested weir up. This was lowered within 10 to 20 seconds to the pre-selected flow depth and the temporal start of the experiment was set at scour inception.

Photographs in Figure 2 refer to the run 18.11.04 with $\beta = 1.43$, discharge $Q = 40$ l/s, and approach flow depth $h_1 = 10.2$ cm. Figure 2a is an upstream view. The nearly streamlined shape of the entrance and outlet of the constriction model can be noted. As for all experiments, the flow was subcritical also in the contracted reach and only small cross waves were

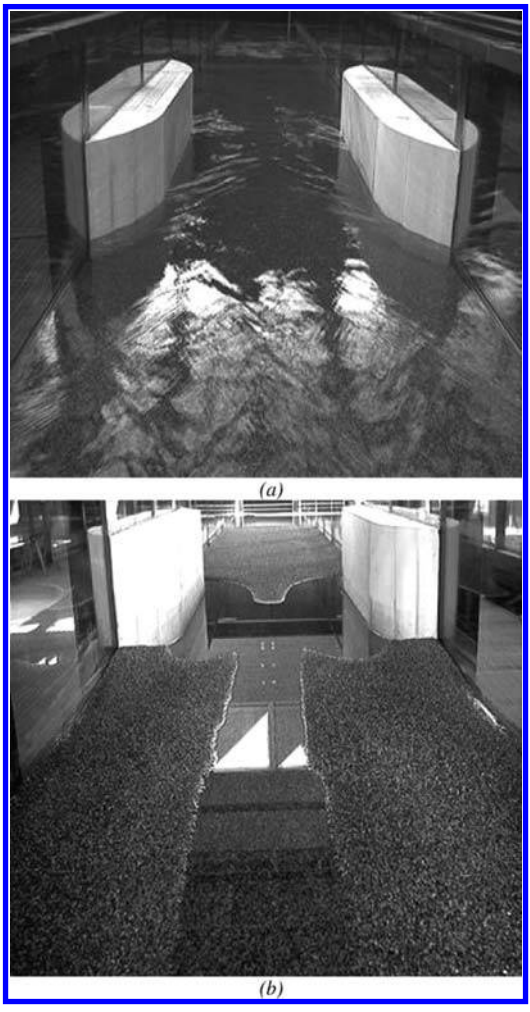


Figure 2. Run 18.11.04: (a) Flow conditions through the contracted reach. (b) Bed morphology at the end after practically water emptying.

observed. Moreover, the constriction reach induced only a small backwater effect so that the approach flow depth h_1 could be confidently measured 2 meters upstream from the model entrance.

Figure 2b is a downstream view at the end of the run and after water emptying. The bed configuration appears to be satisfactorily symmetric. Moreover, it can easily noted as the bed degradation tends to concentrate along the channel centerline and significantly extends downstream of the contracted zone. The deepest contraction scour depth was normally observed downstream of the middle of the model, even outside as for the run considered. There are also evident tracks of local scour in the vicinity and along the constriction elements. In general, local scour was

Copyright © 2006 Taylor & Francis Group plc, London, UK

not completely inhibited, although the elements were streamline shaped. Width constriction effects could be considered independent of local scour ones only when $\beta = 1.11$. Nevertheless, the two scour patterns were always distinguishable.

3 QUASI-EQUILIBRIUM SCOUR EQUATION

Sediment transport formulas for uniform sediment beds are typically given in monomial form as

$$\phi = \frac{q_b}{\sqrt{g' d_s^3}} \propto \theta^n \tag{1}$$

where q_b = volume of bed material in motion per unit width and time; $g' = g(\rho_s - \rho)/\rho$ with g as gravitational acceleration, ρ and ρ_s fluid and sediment densities; d_s = grain size; $\theta = v_*^2/(g' d_s)$ = the Shields' parameter with v_* shear velocity; n = exponent. According to Oliveto et al. (2005), one should expect that q_b and z_e are intimately connected so that Equation 1 could be rearranged as

$$\frac{z_e}{d_s} \propto \theta^n \tag{2}$$

with z_e = quasi-equilibrium scour depth. For nearly uniform sediment beds, Hager & Oliveto (2002) demonstrated that

$$\mathrm{F}_d \propto \left(\frac{R_h}{d_{50}}\right)^{1/6} \theta^{1/2} \tag{3}$$

with R_h = hydraulic radius; d_{50} = particle size for which 50% are finer by weight; F_d = densimetric Froude number. In particular, $\mathrm{F}_d = V/(g' d_{50})^{1/2}$ with V = cross-sectional velocity. Thus, assuming d_{50} as the characteristic grain size, Equations 2 and 3 yield

$$\frac{z_e}{d_{50}} \propto \left(\frac{R_h}{d_{50}}\right)^{-\frac{n}{3}} \mathrm{F}_d^{2n} \tag{4}$$

This latter equation was thus explored by considering the uniformly contracted reach (subscript 2). The densimetric Froude number $(\mathrm{F}_{d,2})_{t=0}$ at time $t = 0$ was considered (i.e. undisturbed bed). In particular, $(\mathrm{F}_{d,2})_{t=0}$ was computed by averaging the observed flow depths h_2 along the centerline. Note that in practical applications, h_2 could be confidently estimated according to Chow (1959). In the present study, the observed values of h_2 were satisfactorily estimated by applying the specific energy equation and by neglecting local energy losses. Equation 4 was validated with the experimental data and its adequacy is demonstrated by the plot in Figure 3.

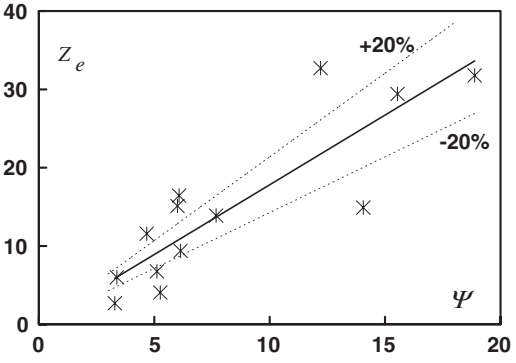


Figure 3. $Z_e = z_e/d_{50}$ as a function of the dimensionless combination $\Psi = \mathrm{F}_{d,2}^4 (R_{h,2}/d_{50})^{-2/3}$. (✳) Experimental data collected at University of Basilicata; (——) Regression line; (· · · · · ·) 20% error bands.

In particular, Equation 4 specializes as

$$\frac{z_e}{d_{50}} = \frac{7}{4}\left(\frac{R_{h,2}}{d_{50}}\right)^{-\frac{2}{3}} \mathrm{F}_{d,2}^4 = \frac{7}{4}\Psi \tag{5}$$

with $r^2 = 0.73$. Despite a certain deviation of the data from the regression line, it is significant that $n = 2$ can be deduced by comparing Equations 4 and 5. This value of n would corroborate the goodness of the above approach. In fact, it is close to the exponent 2.5 of the well known Engenlund-Hansen's sediment transport formula that is particularly indicated for sandy bed as that used in this experimental work. Moreover, from Equation 5, by approximating the hydraulic radius $R_{h,2}$ with h_2 (i.e. wide rivers) and by taking into account the definition of $\mathrm{F}_{d,2}$, one has $z_e \propto V_2^4/(d_{50}^{1/3} h_2^{2/3} g'^2)$. Thus, the cross-sectional velocity V_2 has the most significant effect on the scour process, followed by the effect of the flow depth h_2, whereas the effect of d_{50} is rather small.

More rigorously, Equation 4 should contain the difference between the actual, $\mathrm{F}_{d,2}$, and the entrainment, $\mathrm{F}_{di,2}$, densimetric particle Froude numbers in the contracted zone. $\mathrm{F}_{di,2}$ can be estimated according to the relationships given in Hager & Oliveto (2002). In particular, for transitional regime (i.e. $10 < D_* < 150$), as in the present study, $\mathrm{F}_{di,2}$ is given by

$$\mathrm{F}_{di,2} = 1.08 D_*^{1/12} \left(\frac{R_{h,2}}{d_{50}}\right)^{\frac{1}{6}} \tag{6}$$

where $D_* = (g'/\nu^2)^{1/3} d_{50}$ = dimensionless sediment size with ν = kinematic viscosity. Thus, Equation 4 can be generalized as

$$\frac{z_e}{d_{50}} \propto \left(\frac{R_h}{d_{50}}\right)^p (\mathrm{F}_d - \mathrm{F}_{di})^m \tag{7}$$

Copyright © 2006 Taylor & Francis Group plc, London, UK

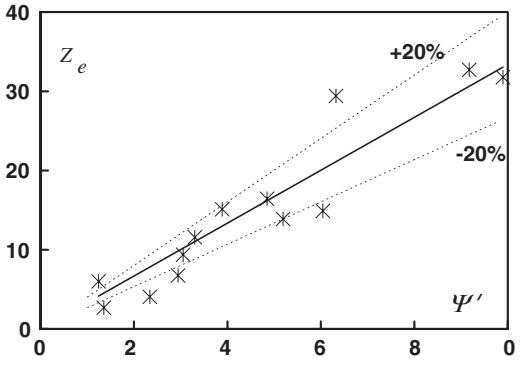


Figure 4. $Z_e = z_e/d_{50}$ as a function of the dimensionless combination $\Psi' = (R_{h,2}/d_{50})^{1/2}(F_{d,2} - F_{di,2})$. (⋇) Experimental data collected at University of Basilicata; (——) Regression line; (· · · · · ·) 20% error bands.

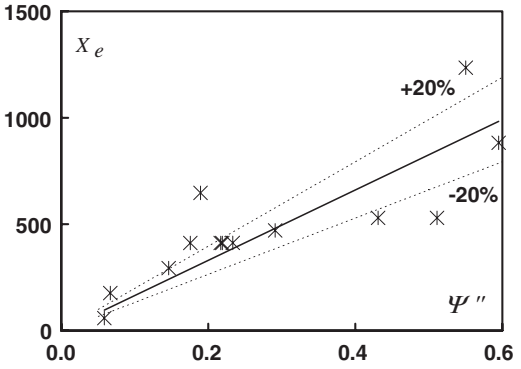


Figure 5. $X_e = x_e/d_{50}$ as a function of the dimensionless combination $\Psi'' = (R_{h,2}/d_{50})^{-1/4}(F_{d,2} - F_{di,2})$. (⋇) Experimental data collected at University of Basilicata; (——) Regression line; (· · · · · ·) 20% error bands.

with the exponent p not necessarily negative because of the dependence of F_{di} on R_h/d_{50}. Equation 7 was thus validated with the experimental data. A more straightforward relationship was found with even a significantly greater value of the coefficient of determination ($r^2 = 0.88$) and a larger amount of data within the 20% error bands. The fitting of the experimental data is shown in Figure 4.

In particular, Equation 7 specializes as

$$\frac{z_e}{d_{50}} = \frac{10}{3}\left(\frac{R_{h,2}}{d_{50}}\right)^{\frac{1}{2}}\left(F_{d,2} - F_{di,2}\right) = \frac{10}{3}\Psi' \qquad (8)$$

With respect to Equation 5, Equation 8 implies a little more uncertainty due to the estimation of F_{di}. But on the other hand, Equation 8 presents the evident advantage of being linear in F_d in contrast with Equation 5 in which F_d is to the power 4.

A similar approach was also applied for the location x_e of the quasi-equilibrium scour depth z_e. Specifically, x_e is the downstream distance from the beginning of the model constriction. The regression analysis revealed the following relationship

$$\frac{x_e}{d_{50}} = \frac{5}{3}10^3\left(\frac{R_{h,2}}{d_{50}}\right)^{-\frac{1}{4}}\left(F_{d,2} - F_{di,2}\right) = \frac{5}{3}10^3\Psi'' \qquad (9)$$

Figure 5 shows the fitting of the experimental data.

In Equation 9, the high value of the coefficient of proportionality is due to the different order of magnitude for x_e and d_{50} values. Although, the fitting was not particularly satisfactory ($r^2 = 0.64$), however the trend is evident. In particular, Equation 9 would imply a dependence of x_e on the flow velocity. This result does not completely match with the findings of Briaud et al. (2005) who found that, in cohesive soils, x_e is only a function of the contraction geometry (i.e. the ratio b_2/b_1 with b_2 as normalizing factor). Moreover, Equation 9 would also imply that x_e increases as d_{50} increases. This latter result, which is not immediately obvious, would need a more robust evidence.

To further validate the above approach, 156 experiments from literature were analyzed (Tab. 2 in Dey & Raikar 2005). Because such data are given in terms of approach flow conditions, Equation 7 was rearranged. In particular, it is reasonable to suppose $(F_{d,2} - F_{di,2}) \propto (b_1/b_2)^f F_{d,1}^m$ and $(R_{h,2}/d_{50}) \propto (R_{h,1}/d_{50})^p$, as corroborated by the experimental data of the present study. Thus, one can write

$$\frac{z_e}{d_{50}} \propto \left(\frac{R_{h,1}}{d_{50}}\right)^p F_{d,1}^m \left(\frac{b_1}{b_2}\right)^f \qquad (10)$$

The regression analysis (Fig. 6) yielded the following relationship

$$\frac{z_e}{d_{50}} = \left(\frac{b_1}{b_2} - 1\right)\left(\frac{R_{h,1}}{d_{50}}\right)^{\frac{3}{4}} F_{d,1} = \Phi \qquad (11)$$

with $r^2 = 0.92$. The computed value of the coefficient of proportionality was 0.93, however for simplicity and conservatively it was approximated to 1.

Equation 11 appears to be satisfactorily straightforward and its adequacy wide ranging. The data analyzed refer in fact to experiments with $d_{50} = 0.81$, 1.70, 1.86, 2.54, 4.10, 5.53, 7.15, 10.25, and 14.25 mm and $\beta = 1.11$, 1.18, 1.25, 1.43, 1.52, 1.54, 1.67, 2.00, 2.50, 3.03, and 4.00.

Copyright © 2006 Taylor & Francis Group plc, London, UK

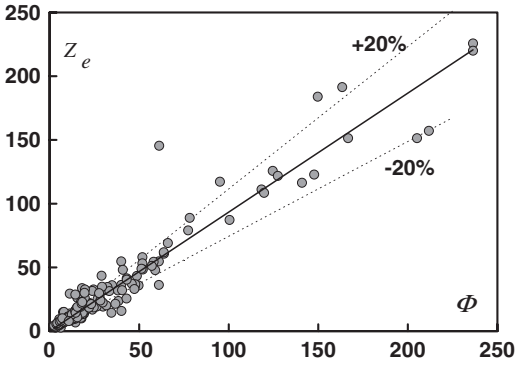


Figure 6. $Z_e = z_e/d_{50}$ as a function of the dimensionless combination $\Phi = (b_1/b_2 - 1)(R_{h,1}/d_{50})^{3/4}F_{d,1}$. (●) Literature data and data collected at University of Basilicata; (——) Regression line; (· · · · ·) 20% error bands.

4 CONCLUSIONS

Selected experiments on the riverbed morphological changes induced by long constrictions were carried out at the Hydraulic Engineering Laboratory, University of Basilicata, Italy.

The runs lasted typically 3 days up to 15 days to obtain quasi-equilibrium conditions and to acquire a suitable measurement accuracy especially at low degree of contraction.

Empirical evidences revealed that (i) the bed degradation tends to concentrate along the channel centerline; (ii) the deepest contraction scour depth localized typically downstream of the middle of the constriction model and even outside; (iii) an equilibrium stage was never observed even for the run of duration 15 days.

Starting from sediment transport formulas, a novel scour equation was conjectured in the light of the densimetric Froude number. (i) The approach was validated by the data collected in the present study. By regression analysis, Equation 8 was found in which the quasi-equilibrium scour depth z_e is linearly related to the difference between the actual and the entrainment densimetric particle Froude number in the contracted zone; (ii) by using the same normalizing factors a new relationship (Eq. 9) was also found for the location x_e of the quasi-equilibrium scour depth z_e; interestingly from Equation 9 would seem that x_e increases as d_{50} increases. This result would need to be corroborated by other assessments; (iii) the novel approach was also rearranged in terms of approach flow conditions. Thus, it was validated by the data from this study and from literature. 156 experiments were analyzed (d_{50} from 0.81 to 14.25 mm and $\beta = b_1/b_2$ from 1.11 to 4.00, with b_1 = width of the approach channel and b_2 = width of the uniformly contracted reach). The regression analysis yielded Equation 11 with a significantly high value of the coefficient of determination ($r^2 = 0.93$). This equation appears to be adequately straightforward and wide ranging; finally, (iv) the dependence from the densimetric Froude number, coming out of Equation 3 suggested by Hager & Oliveto (2002) on the basis of several experiments including also runs with sediment density ρ_s significantly different from 2.65 t/m^3, would confer to the proposed approach more generality than that provided by the (simple) Froude number. This, in a similar way to the recent equation proposed by Oliveto & Hager (2002) for pier and abutment scour. Nevertheless, such a dependence needs to be supported by selected experiments that have been planned to be conducted.

REFERENCES

Briaud, J.L., Chen, H.C., Li, Y., Nurtjahyo, P. & Wang, J. 2005. Scour rate in cohesive soils-erosion function apparatus. Method for contraction scour in fine-grained soils. *Journal of Geotechnical and Geoenvironmental Engineering, ASCE*, 131(10): 1283–1294.

Chow, V.T. 1959. Open channel hydraulics. Singapore: McGraw-Hill Book Company.

Dey, S. & Raikar, R.V. 2005. Scour in long contractions. *Journal of Hydraulic Engineering, ASCE*, 131(12): 1036–1049.

Gill, M.A. 1981. Bed erosion in rectangular long contraction. *Journal of the Hydraulics Division, ASCE*, 107(3): 273–284.

Hager, W.H. 1998. Kontraktionskolk – eine Literaturstudie. *Osterreichische Wasser und Abfallwirtschaft*, 50(5–6): 150–154.

Hager, W.H. & Oliveto, G. 2002. Shields' entrainment criterion in bridge hydraulics. *Journal of Hydraulic Engineering, ASCE*, 128(5): 538–542.

Komura, S. 1966. Equilibrium depth of scour in long constrictions. *Journal of the Hydraulics Division, ASCE*, 92(5): 17–37.

Laursen, E.M. 1960. Scour at bridge crossings. *Journal of the Hydraulics Division, ASCE*, 86(2): 39–54.

Lim, S.Y. & Cheng, N.S. 1998. Scouring in long contractions. *Journal of Hydraulic Engineering, ASCE*, 124(5): 258–261.

Melville, B.W. & Coleman, S.E. 2000. *Bridge scour*. Colorado (USA): Water Resources Publications, LLC.

Oliveto, G. & Hager, W.H. 2002. Temporal evolution of clear water pier and abutment scour. *Journal of Hydraulic Engineering, ASCE*, 128(9): 811–820.

Oliveto, G., Onorati, B. & Comuniello, V. 2005. Scour in long rectangular contractions. In J. Byong-Ho Jun, Sang-Il Lee, Il Won Seo & Gye-Woo Choi (eds), *Proc. of XXXI IAHR Congress, Seoul, Korea, September 2005*, 2005 Korea Water Resources Association: Seoul. Paper D09-6: 3000-3008.

Straub, L.G. 1934. Effect of channel contraction works upon regimen of moveable bed streams. *Trans. American Geophysical Union* Part II: 454–463.

Webby, M.G. 1984. General scour at contraction. *RRU Bulletin 73*, National Roads Board, Bridge Design and Research Seminar, New Zealand: 109–118.

Copyright © 2006 Taylor & Francis Group plc, London, UK

Clear-water scour at bridge piers and abutments

U.C. Kothyari
Department of Civil Engineering, Indian Institute of Technology, Roorkee, India
(Formerly: Visiting Professor, VAW, ETH-Zentrum, Zurich, Switzerland)

W.H. Hager
VAW, ETH-Zentrum, Zurich, Switzerland

G. Oliveto
DIFA, Università della Basilicata, Potenza, Italy

ABSTRACT: Extensive studies on the temporal evolution of scour have been made recently at Versuchsanstalt für Wasserbau, Hydrologie und Glaziologie (VAW), ETH Zürich, Switzerland, and models for scour estimation were presented. The VAW scour model is further investigated in the present study and possibilities for its refinement are identified. It is conceptualized that expression for temporal evolution of scour at bridge elements that is based on Froude's similarity should more logically relate scour depth to the difference between actual densimetric particle Froude number and entrainment densimetric particle Froude number. The analysis of VAW data set on pier and abutment scour validates this concept. Also contrary to the previous assumption of a logarithmic increase in scour depth with time, the characteristics of 'end scour' is noticed to have been exhibited by a few of the VAW scour data on mixtures.

1 INTRODUCTION

In the present age of fast communication, bridges occupy a place of pride in the society as they facilitate rapid movement of material and personnel safely and quickly across the rivers and other drainages. The disruption of traffic due to failure of a bridge therefore results in a disaster. Several bridges failed in the past in many countries and majority of these resulted from the hydraulic conditions and primarily the scour of the foundation material by flow around the bridge elements like piers or abutments.

The process of scour around bridge elements involves the complexities of both the three dimensional flow pattern and the sediment transport. The estimation of the scour characteristics at bridge elements continues to be a major concern for the hydraulic engineers. The underestimation of the scour depth results in a foundation that is exposed to the flow and endangers the structural safety whereas an overestimation of the scour depth results in an uneconomical design.

Figure 1 shows a definition sketch of scour at bridge elements (Oliveto & Hager 2002). Modeling of the temporal scour evolution rather than the equilibrium scour has been emphasized in the more recent literature (Oliveto & Hager 2002, 2005, Chang et al. 2004, Sheppard et al. 2004, Mia & Nago 2003, Kothyari & Ranga Raju 2001, Ahmad & Rajaratnam 2000, Melville & Coleman 2000, Melville & Chiew 1999, Cardoso & Bettess 1999). Kothyari et al. (1992 a, b) were however, among the first investigators who showed that temporal development of scour rather than the equilibrium scour of a peak flood should form the basis of design.

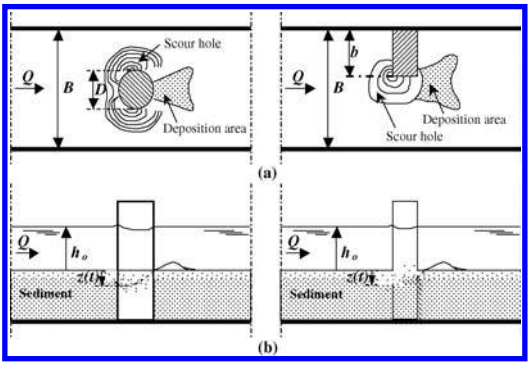


Figure 1. Definition sketch for bridge scour, (a) plan, (b) section for circular pier (left) and abutment (right).

Copyright © 2006 Taylor & Francis Group plc, London, UK

Based on the analysis of a large data set on the temporal evolution of scour collected during long observational periods at Versuchsanstalt für Wasserbau, Hydrologie und Glaziologie (VAW), a logarithmic increase in scour depth with time was noticed by Oliveto & Hager (2002). In the present study however, the features were noticed in the data on scour evolution that are related to the characteristics of the sediment which lead to an 'end scour' condition in steady flows.

From the analogy between hydraulic resistance and scour, Oliveto & Hager (2002, 2005) proposed plausible relationships for the computation of the maximum scour depth z as function of time t. It was observed that the dominant parameter controlling the scour process is the densimetric particle Froude number $\mathsf{F}_d = V_o/(g' d_{50})^{1/2}$; with V_o = velocity of the approach flow; $g' = [(\rho_s - \rho)/\rho]g$ the relative gravitational acceleration; ρ_s sediment density; ρ fluid density; and d_{50} = median grain size. By combining F_d with the parameters for reference length z_R and reference time t_R, the Froude similitude based scour relation was proposed as

$$Z = z/z_R = 0.068 N \sigma^{-1/2} \mathsf{F}_d^{1.5} \log T \quad \text{for } \mathsf{F}_d > \mathsf{F}_{d\beta} \qquad (1)$$

where $\mathsf{F}_{d\beta}$ is the densimetric particle Froude number for the entrainment of scour at the bridge element; the reference length is $z_R = (h_o D^2)^{1/3}$ for the cylindrical pier and $z_R = (h_o b^2)^{1/3}$ for the rectangular abutment with D as the pier diameter, b the abutment width and h_o the approach flow depth. Equation 1 is also applicable to other flow obstructing elements like sloping abutments and submerged spur dikes. The shape factors are $N = 1$ for circular shaped cylindrical pier and $N = 1.25$ for the vertical as well as the sloping abutments, respectively; $\sigma = (d_{84}/d_{16})^{1/2}$ = sediment uniformity parameter; and $T = t/t_R$ = relative time with $t_R = z_R/[\sigma^{1/3}(g' d_{50})^{1/2}]$. Hager & Oliveto (2002) proposed relationships for $\mathsf{F}_{d\beta}$ with regard to bridge pier and rectangular abutments as

$$\mathsf{F}_{d\beta} = \Phi_\beta \mathsf{F}_{di} \qquad (2)$$

where F_{di} is the densimetric particle Froude number for inception (subscript i) of motion in the approach flow and Φ_β represents the ratio between $\mathsf{F}_{d\beta}$ and F_{di}. The following relationships for F_{di} were proposed, based on Shields' diagram:

$$\mathsf{F}_{di} = 2.33 D_*^{-0.25} (R_h/d_{50})^{1/6} \qquad (3)$$

for viscous regime with $D_* \leq 10$,

$$\mathsf{F}_{di} = 1.08 D_*^{1/2} (R_h/d_{50})^{1/6} \qquad (4)$$

for transition regime with $10 < D_* < 150$,

$$\mathsf{F}_{di} = 1.65 (R_h/d_{50})^{1/6} \qquad (5)$$

for rough regime with $D_* \geq 150$, and

$$\Phi_\beta = 1 - (2/3)\Sigma\beta^{\Sigma/4} \qquad (6)$$

where $\beta = D/B$ or b/B for pier and abutment, respectively; with B = channel width, shape effect parameter $\sum = 1$ for piers and $\sum = 5/4$ for abutments.

Oliveto & Hager (2002) considered that $\mathsf{F}_d >> \mathsf{F}_{d\beta}$ for application of Equations 1, 2. However, from a similitude with the sediment transport theory it is logic that a scour equation should contain the term denoting a difference between the actual densimetric Froude number F_d and the entrainment densimetric particle Froude number $\mathsf{F}_{d\beta}$ in presence of an element. The VAW data on pier and abutment scour were therefore, reanalyzed in the present study with this objective. The Equations 1, 2 are not applicable to scour conditions subjected to viscous effects, the VAW data on uniform sand therefore, are excluded from the present work. In addition, the limitations listed by Oliveto & Hager (2002, 2005) for Equation 1 also apply to the present work.

2 CONCEPTUAL APPROACH FOR MODEL OF SCOUR ADVANCE

The sediment transport rate relates strongly to the difference of the total shear stress exerted by the flow and the critical shear stress for the inception of the transport (Meyer-Peter & Müller 1948). Accordingly, it is logic to relate the scour depth to the difference of the actual densimetric particle Froude number and the entrainment densimetric particle Froude number, *i.e.* $Z \approx (\mathsf{F}_d - \mathsf{F}_{d\beta})^\gamma \times f(T)$, where $f(T)$ increases with time and represents the temporal advance function on the right side of Equations 1, 2 and γ is an exponent. Results are obtained concerning the applicability of the proposed concept using all the experimental runs of Oliveto & Hager (2002) on pier and abutment scour. Typical of these results only, however, are illustrated below to avoid overlapping or congested plots and thus to provide a clear representation.

2.1 *VAW Pier Data*

Figures 2a,b depict the variation of $f(Z)$ with log T for piers in uniform sediments (VAW gravel and plastic, respectively) for several experimental runs that corresponded to different values of $(\mathsf{F}_d - \mathsf{F}_{d\beta})$. Here $f(Z) = z/(0.068 N \sigma^{-0.5} z_R)$. Similar plots for sediment mixtures (VAW mix1, mix2 and mix 3, respectively) are shown in Figures 2c-e. The systematical variation in the slope S of the trend lines of $f(Z)$ *versus* (log$T$) relation for different values of $(\mathsf{F}_d - \mathsf{F}_{d\beta})$ as depicted by the runs given in Figure 2 and other such plots,

Copyright © 2006 Taylor & Francis Group plc, London, UK

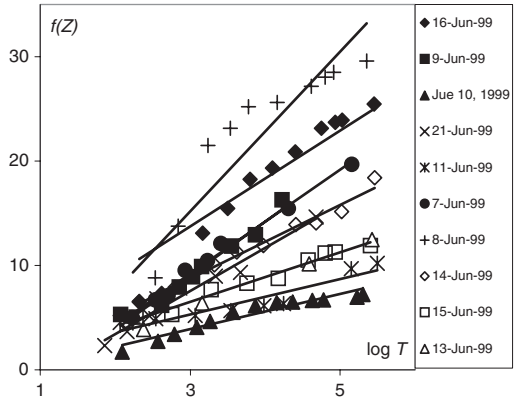


Figure 2a. Variation of $f(Z)$ with log$T$ for VAW data on pier scour (gravel).

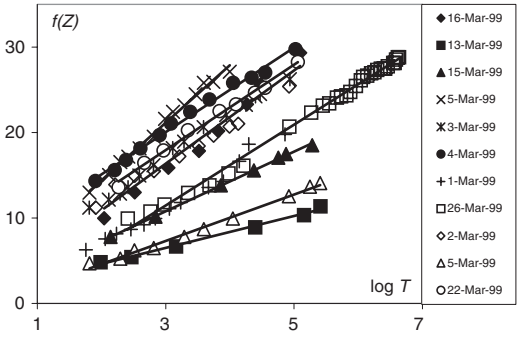


Figure 2b. Variation of $f(Z)$ with log$T$ for VAW data on pier scour (plastic).

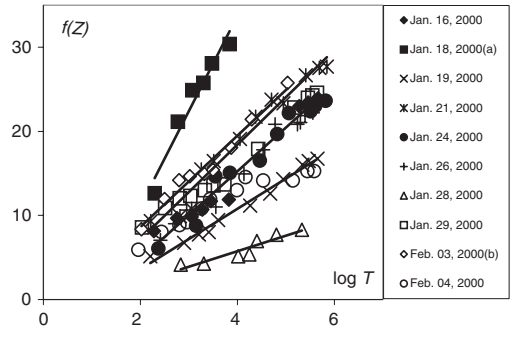


Figure 2c. Variation of $f(Z)$ with log$T$ for VAW data on pier scour (mix1).

not shown here because of space limitations, confirmed the present concept. Value of the coefficient of determination R^2 for the straight line fits to different experimental runs shown in Figure 2 was always more than 0.81 indicating a strong dependence of $f(Z)$

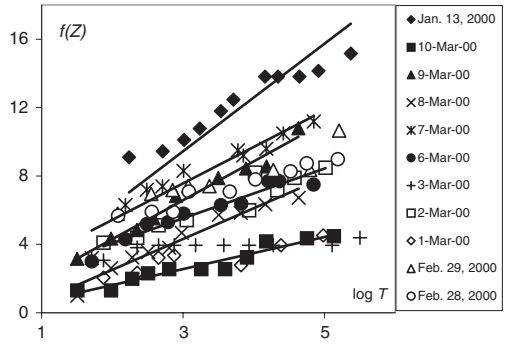


Figure 2d. Variation of $f(Z)$ with log$T$ for VAW data on pier scour (mix2).

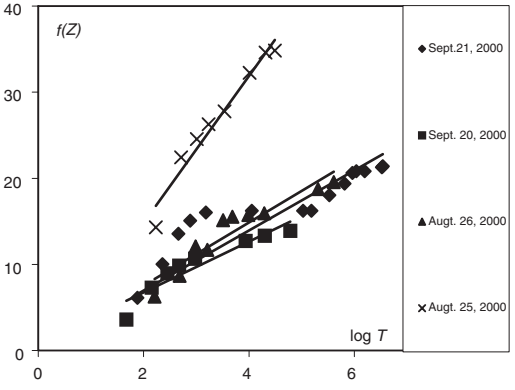


Figure 2e. Variation of $f(Z)$ with log$T$ for VAW data on pier scour (mix3).

on log$T$. The slope S of the $f(Z)$ versus log$T$ relation was determined for the complete VAW data set on pier scour. Results from the analysis on variation in the values of S are presented subsequently.

2.2 *VAW Abutment Data*

Figures 3a,b illustrate the variation of $f(Z)$ with log$T$ for abutments in uniform sediments (*i.e.* VAW gravel and plastic, respectively) and these plots for sediment mixtures (VAW mix1, mix2, and mix3, respectively) are shown in Figures 3c-e. The systematical variation in the values of S with the corresponding values of $(F_d - F_{d\beta})$ for abutment data as depicted for the runs of Figure 3 and other such plots, not shown here, also confirmed the present concept. The R^2 values of straight line fit to different experimental runs shown in Figure 3 was always more than 0.78 indicating a strong dependence of $f(Z)$ on log$T$ for abutment data also. The slope S of the $f(Z)$ versus log$T$ relation was also determined for the complete VAW data set on abutment

Copyright © 2006 Taylor & Francis Group plc, London, UK

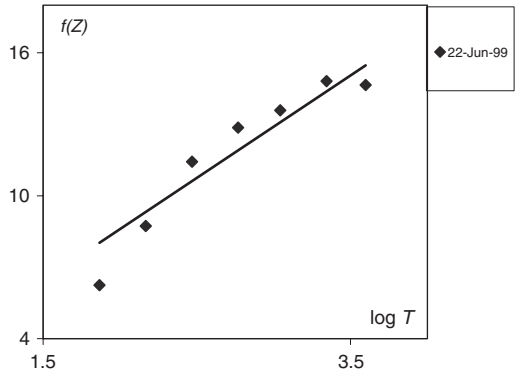


Figure 3a. Variation of $f(Z)$ with log$T$ for VAW data on abutment scour (gravel).

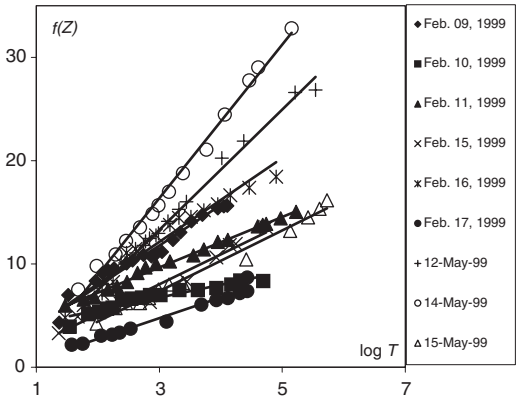


Figure 3b. Variation of $f(Z)$ with log$T$ for VAW data on abutment scour (plastic).

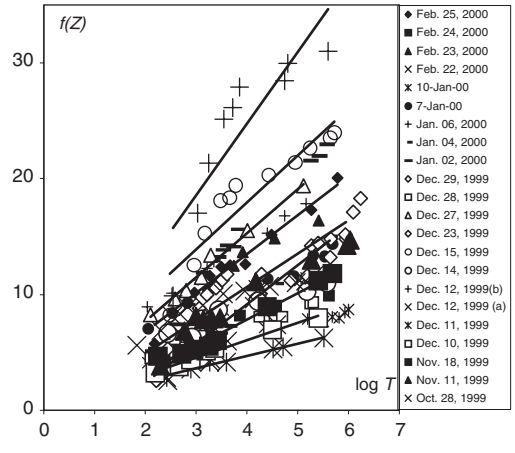


Figure 3c. Variation of $f(Z)$ with log$T$ for VAW data on abutment scour (mix1).

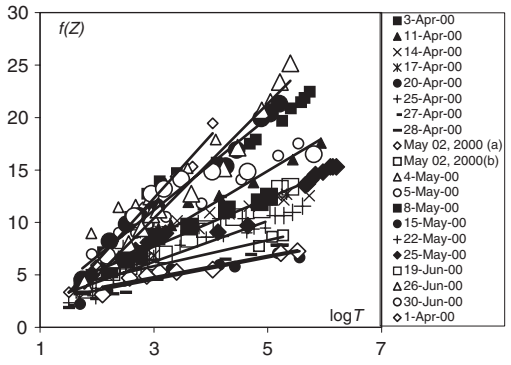


Figure 3d. Variation of $f(Z)$ with log$T$ for VAW data on abutment scour (mix2).

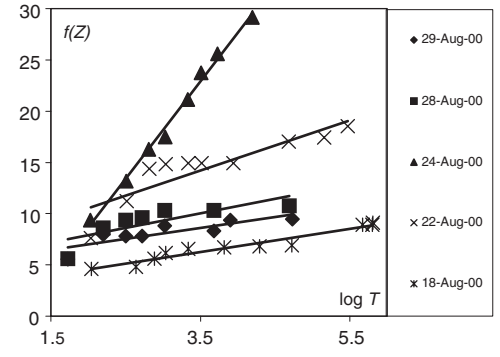


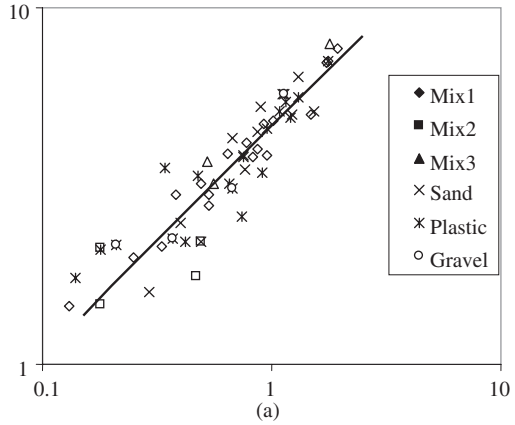
Figure 3e. Variation of $f(Z)$ with log$T$ for VAW data on abutment scour (mix3).

scour and results from the analysis on variation in thus obtained values of S are presented below.

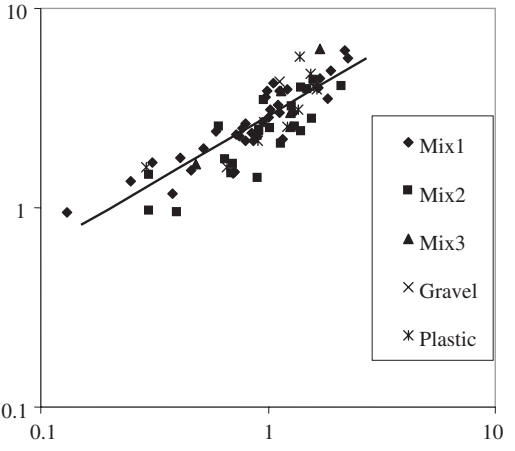
3 TEMPORAL EVOLUTION OF MAXIMUM SCOUR DEPTH

Except for certain conditions (to be described later) the scour process always involves the function $f(T) = \log T$.The variation of S with log$T$ is depicted in Figures 4a,b, respectively, for the pier and the abutment tests suggesting that S is strongly correlated with $(F_d - F_{d\beta})$. Thus from Figure 4 it follows that other conditions remaining the same, the variation of Z is strongly influenced by the variation in $(F_d - F_{d\beta})$. Similar plots between S and corresponding F_d values contained relatively larger scatter than that is seen in Figures 4a,b. Thus, an expression for Z in terms of $(F_d - F_{d\beta})$ should produce a novel relation for scour evolution and giving more realistic estimates of the scour depth than presently available. In contrast to Equation 1 the shape factor N should be unity in such

Copyright © 2006 Taylor & Francis Group plc, London, UK



(a)



(b)

Figure 4. Variation of slope S with ($F_{d-}F_{d\beta}$) for (a) VAW pier data and (b) VAW abutment data.

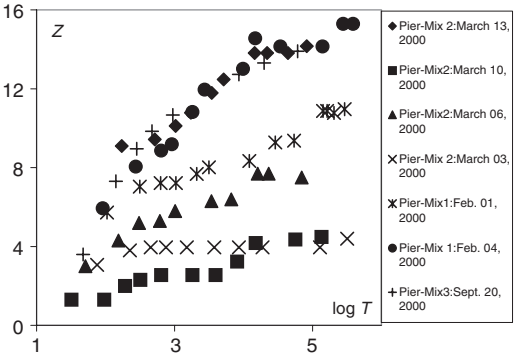


Figure 5. VAW 'End Scour' runs for pier scour.

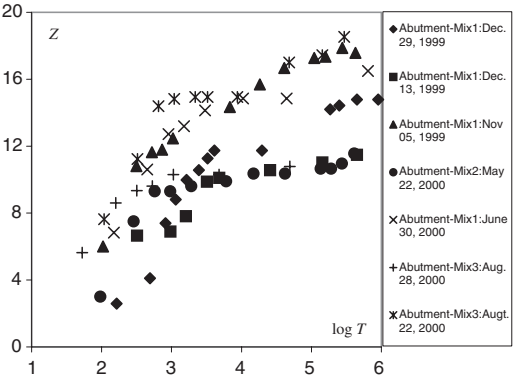


Figure 6. VAW 'End Scour' runs for abutment scour.

novel expression for Z as the relation for $F_{d\beta}$ would account for the shape effects. The accuracy of such a relation for temporal evolution of scour shall be significantly influenced by the method used for the computation of $F_{d\beta}$. Therefore, further investigations are being made by the authors currently for deriving newer relationship for $F_{d\beta}$ and Z that should be applicable to common geometries of the bridge elements.

4 CONDITION FOR END SCOUR

Based on the analysis of a large data set on the temporal evolution of scour collected during long observational periods at VAW, a logarithmic increase in scour depth with time was recommended by Oliveto & Hager (2002). A close scrutiny of the VAW data on scour in sediment mixtures (Figs 5, 6) indicated that Z can become constant beyond certain values of $\log T$ in sediment mixtures. The likelihood of the existence of 'end scour' condition at a bridge element is thus controlled mainly by the bed material characteristics. It is easy to visualize that the logarithmic scour progress would tend to end in sediment mixtures that are likely to form a stable armour layer over the scoured surface due to partial removal of the fines by the flow from the parent bed material around the obstruction. The condition that a stable armour layer develops, or not, and the activity of scour therefore has a definite end, would therefore, be governed by the degree of heterogeneity in the bed material, the flow and the element shape and dimensions, respectively. The criterion for deciding that the 'end scour' condition shall develop in a certain run is also important in design of rip rap protection at bridge elements and therefore needs further investigations.

5 CONCLUSIONS

The VAW studies on temporal evolution of scour of bridge piers and abutments are revisited. Based on

Copyright © 2006 Taylor & Francis Group plc, London, UK

analysis of data on pier and abutment scour it has been proposed that a logical relation for Z based on Froude's similarity should relate scour depth to the difference $(F_d - F_{d\beta})$ rather than F_d only. Contrary to the previous assumption of a logarithmic increase in scour depth with time, a few of the scour data on mixtures are noticed to exhibit the characteristics of 'end scour'. The 'end scour' condition is likely to occur in situations when a stable armour layer can form over the scour hole. The results of present research thus provide basis for developing new expression for scour depth evolution and are important in the design of measures for protection against scour at flow obstructing elements.

ACKNOWLEDGEMENT

The first author wishes to acknowledge the support from ETH Zürich for his academic stay at VAW.

REFERENCES

Ahmad, F. & Rajaratnam, N. 2000. Observations on flow around bridge abutments. *J. Engrg. Mech*. 126(1): 51–59.

Cardoso, A.H. & Bettess, R. 1999. Effects of time and channel geometry on scour at bridge abutments. *J. Hydr. Engng.* 125(4): 388–399.

Chang, W.Y., Lai, J.S. & Yen, C.L. 2004. Evolution of scour depth at circular bridge piers. *J. Hydr. Engng.* 130(9): 905–913.

Hager, W.H. & Oliveto, G. 2002. Shields' entrainment criterion in bridge hydraulics. *J. Hydr. Engng.* 128(5): 538–542.

Kothyari, U.C. & Ranga Raju, K.G. 2001. Scour around spur dikes and bridge abutments. *Journal of Hydraulic Research* 39(4): 367–374.

Kothyari, U.C., Garde, R.J. & Ranga Raju, K.G. 1992a. Temporal variation of scour around cylindrical bridge piers. *J. Hydr. Engng*. 118(8): 1091–1106.

Kothyari, U.C., Garde, R.J. & Ranga Raju, K.G. 1992b. Live bed scour around cylindrical bridge piers. *Journal of Hydraulic Research* 30(5): 701–715.

Melville, B.W. & Coleman, S.E. 2000. *Bridge scour*. Water Resources Publications: Highlands Ranch CO.

Melville, B.W. & Chiew, Y.M. 1999. Time scale for local scour at bridge piers. *J. Hydr. Engng*. 125(1): 59–65.

Meyer-Peter, E. & Müller, R. 1948. Formulas for bed load transport. 2nd *IAHR Congress*, Stockholm, 2, 1–26.

Mia, M.F. & Nago, H. 2003. Design method of time-dependent local scour at circular bridge piers. *J. Hydr. Engng.* 129(6): 420–427.

Oliveto, G. & Hager, W.H. 2002. Temporal evolution of clear-water pier and abutment scour. *J. Hydr. Engng*. 128(9): 811–820.

Oliveto, G. & Hager, W.H. 2005. Further results to time-dependent local scour at bridge elements. *J. Hydr. Engng*. 131(2): 97–105.

Sheppard, D.M., Odeh, M. & Glasser, T. 2004. Large scale clear-water local pier scour experiments. *J. Hydr. Engng.* 130(10): 957–963.

Copyright © 2006 Taylor & Francis Group plc, London, UK

Clear water scour analysis around groynes and bridge abutments

C. Marson, V. Fiorotto & E. Caroni
Dipartimento Ingegneria Civile e Ambientale, Università di Trieste, Italy

L. Da Deppo
Dipartimento Ingegneria Idraulica Marittima Ambientale e Geotecnica, Università di Padova, Italy

ABSTRACT: Groynes are structures built in the rivers to protect the banks from flow erosion and also to divert or guide the flow itself. One of the main problems in the design of these structures is to establish the maximum depth of local scour, which occurs near the groyne's tip, in order to avoid the undermining of its foundation. The local scour is the main cause of damage or collapse in these or analogous structures, like bridge abutments. In the paper, the results of experimental and numerical investigations of 3D turbulent flow around a groyne in presence of local scour are reported. From this analysis a design criterion to predict the local scour via computational fluid dynamics is derived, by comparing the computed shear stress at the scour hole boundary and the particle critical shear stress.

1 INTRODUCTION

Damage to structures due to local scour is a frequently recurring event, particularly affecting structures such as groynes, bridge abutments and piers in alluvial rivers. Thus, some local scour monitoring projects are brought about both in USA and Europe. Research on this topic can lead to significant reductions in damages cost and increase in transport safety. In the last years many experimental studies have been carried out to define the evolution of the scour depth in time and its maximum depth. From the analysis of scour data, several formulations have been proposed to predict scour around these structures (e.g. Dey & Barbhuiya 2005, Kothyari & Ranga Raju 2001, Lim 1997, Melville 1992, Melville 1995, Melville 1997). The proposed formulations are characterized by a different choice in the relevant parameters used, so that the results are hardly comparable, and lead to different evaluations of the maximum scour depth, when applied to practical cases. This evidence emphasizes the necessity to improve the knowledge on the nature and structure of the turbulent flow near groynes, in order to improve the erosion prediction methods.

To this purpose, the 3D turbulent flow around a spur dike in the flat fixed bed case was analyzed experimentally by Rajaratnam & Nwachukwhu (1983b) and Barbhuiya & Dey (2004) and via 3D turbulence numerical models by Tingsanchali & Maheswaram (1990), Mayerle et al. (1995), Ouillon & Dartus (1997), Chrisohoides et al. (2003).

It must be observed that the presence of a scour hole substantially modifies the flow field with respect to the fixed flat bed condition, so that the use of parameters derived from flat bed analysis to predict the maximum scour depth is questionable (Armenio et al. 1998).

Only Kwan & Melville (1994) achieved an experimental analysis of the flow field around a spur dike in presence of a scour hole, using the hydrogen bubble technique, thus defining qualitatively and quantitatively the velocity field. They pointed out a primary vortex (which is analogous to the horseshoe vortex at bridge piers) as the main cause of scour at bridge abutments.

Fiorotto & Cividin (1996), using 3D turbulence models, analyzed the flow field around a groyne in two cases, i.e. in presence and absence of the local scour. They showed a substantial change in the flow field between the case of a non-erodible flat bed and the case of an erodible bed associated with local scour. Experimental runs and numerical simulations confirmed the experimental observations of Kwan & Melville (1994) with reference to the horseshoe vortex but highlighted a change in shape of the downstream recirculation zone that tends to produce also a secondary vortex in form of a frustum of cone with the vertex in the deepest point of the scour. This vortex produces important vertical velocity components (by disequilibrium between the centrifugal forces and pressure gradients inside the hole), which are absent in the case of a flat bed.

The capacity of this vertical velocity component to lift sediments from the deeper zone of the scour is particularly evident during the later phases of the scouring process, when the horseshoe effects on the scour are weakened.

Copyright © 2006 Taylor & Francis Group plc, London, UK

A first objective of the present study is to check the capability of the standard k-ε model to simulate a so complex flow, particularly inside the scour hole. This is done by comparison between the velocity measurements taken using an acoustic 3D Doppler velocimeter in an artificial laboratory flume, in presence of local scour, and the numerical results obtained by the code FLUENT.

Salaheldin et al. (2004), in the case of circular piers, and Fiorotto & Cividin (1996) for an abutment, by comparing the results obtained from the standard k-ε turbulence model with the ones computed using theoretically more accurate closure schemes, showed that the velocity fields have practically the same order of accuracy Salaheldin et al. (2004), comparing the results of the standard k-ε model with experimental data, inferred that it can be used to calculate the flow field around the pier.

A second objective is to highlight, from the numerical results, the most important coherent structures around the groynes that are responsible of the scour and to compute the velocity components close to the alluvial bed and the shear stress at the bottom.

The knowledge of the flow field can bring to an estimate of the equilibrium condition for sand particles on the scour boundary, thus allowing to define a design criterion to predict the maximum scour depth via computational fluid dynamics, which constitutes the third objective of this work.

This task requires to define the limiting stability conditions at the scour bottom. The study of the incipient motion of the sediments along the scour hole boundary is hence required, which must take into account the local slope of the bed. To this purpose, two methods are here used: the first was proposed by Brooks (1963) and modified by Lim (1985); the second, called simple rotation model, is due to Baker (1980). The first method was employed by Ali & Karim (2002) in an analogous study involving numerical simulation around bridge piers and it is based on a correction of the Shields shear stress critical value computed on a flat plane to take into account the local slope of the bed.

The second method presents the condition of incipient motion for particles with diameter d in terms of rotational force balance assuming the flow velocity acting at d/2 above the bed, taking into account the particle packing and geometry effects.

Notwithstanding the complexity of the phenomena, where the intermittent nature of near-bed turbulence, bed packing density etc, play an important role in the initiation of sediment motion (Papanicolau et al. 2002), an engineering criterion to predict the maximum depth of local scour is derived by seeking a bed configuration such that the computed shear stress at the scour hole boundary and the particle critical shear stress are comparable.

2 EXPERIMENTAL AND NUMERICAL METHODS

The laboratory experiment was conducted in a laboratory flume 7 m long and 1 m wide. A perspex rectangular groyne with length 20 cm and thickness 1 cm was placed in the channel, perpendicularly to the flume side wall, at a distance of 3.5 m from the flume inlet. The sand bed material was characterized by a median size d50 = 0.27 mm and geometric standard deviation $\sigma g = 1.3$. A geometric standard deviation less or equal to 1.3 implies that the sediments can be considered as uniform (Breusers & Raudkivi 1991).

The approach flow was set close to the threshold conditions for bed movement, with mean velocity and flow depth in the approach reach equal to v = 0.19 m/s and y = 20 cm respectively. The equilibrium scour hole was obtained with a run test 72 h long, a very larger time as compared to simulations reported in literature. The scour hole depth and the bed elevations were measured with 0.1 mm in accuracy at the nodes of a regular square grid at 2 cm intervals.

The measurement of the instantaneous flow velocity components was performed using a laboratory acoustic Doppler velocimeter (ADV) by Nortek. To avoid noise in measures, the flume bed was fixed by application of a synthetic cement which formed a solid crust, after the scour hole had developed completely.

The sampling volume distance from the probe tip is equal to 10 cm, which reduces the intrusiveness effects of the instrument. The sampling frequency was set to 25 Hz with an uncertainty in the velocity measurements less than 1%. The sampling time was chosen equal to 600 s to satisfy the ergodicity condition, with reference to the velocity mean and variance (Bendant & Piersol 1971). The velocity field was sampled in 1500 points with a total acquisition time of 250 hours. Measurements were taken at nodal points in an ideal regular grid, which is shown in Figure 1. The vertical spacing of nodes was set to 2 cm above the original bed level and 1 cm below into the scour. Therefore the interval among measurement points is reduced near the groyne's tip and into the scour hole where larger gradients in the velocity field are expected (Fig. 1). A set of measures was made at 1.5 m upstream of the groyne in order to define the upstream boundary conditions needed in the numerical simulations.

The accuracy of the data collected by ADV was checked via the WindADV computer program developed by the Bureau of Reclamations, Water Resources Research Laboratory (Wahl 2000) in order to detect anomalies, spikes and ambiguities caused by aliasing of the Doppler signal (e.g. Goring & Nikora, 2002). Moreover all the signals were filtered via the Phase-Space Threshold Despiking algorithm (Wahl 2003, Goring & Nikora 2003) and the difference in variance with the non filtered signal was calculated; the

Copyright © 2006 Taylor & Francis Group plc, London, UK

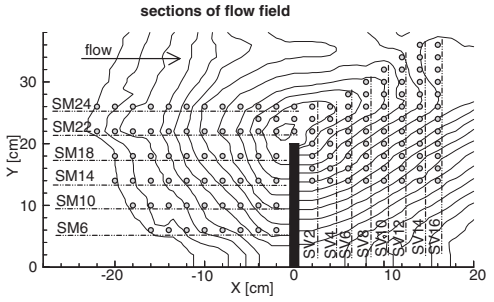


Figure 1. Scour contour lines around a groyne, with the measurement grid. The difference in elevation between the contour lines is equal to 1.0 cm.

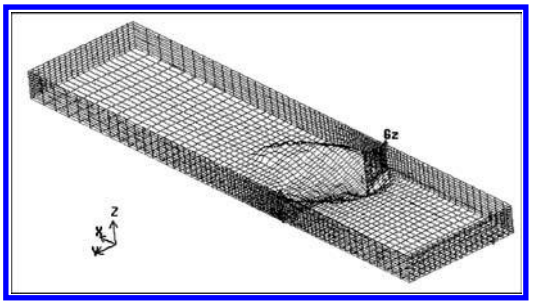


Figure 2. Computational grid.

maximum difference was less than 3% assuring the goodness of the measurements.

The numerical analysis where performed using the FLUENT package which solves the three-dimensional Reynolds-averaged Navier Stokes equations for incompressible flow via the standard k-ε turbulence model.

The computational domain (Fig. 2) was set with a length in the mean flow direction equal to 22.5 L, (L being the transverse length of the groyne) and a width of 1 m, the same of the laboratory flume. The groyne was placed at 7.5 L downstream the inlet boundary and 15 L upstream of the outlet boundary. This distance is larger than the length of the recirculation zone downstream the groyne, estimated in 7 L according to the experimental analysis of Adami (1979). In this context the flow field behavior is independent from the outlet boundary conditions; for this reason they were not imposed. The bed elevations, as measured in the flume at 2 cm regular spaced points, were interpolated to obtain a continuous bed surface needed to build the finite elements mesh. A mesh with 454000 hexahedrical elements refined near the groyne and inside the scour hole, where larger gradients of the velocity and pressure fields are expected, was chosen after several trial runs, with different mesh density, in order to guarantee a grid independent solution.

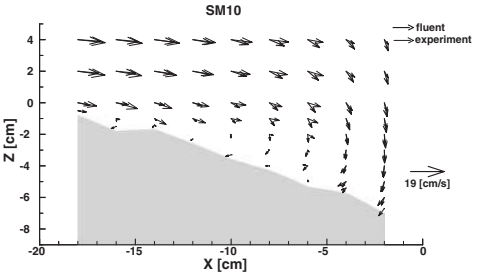


Figure 3. Comparison between numerical and experimental mean velocity components in section m10 (Fig. 1).

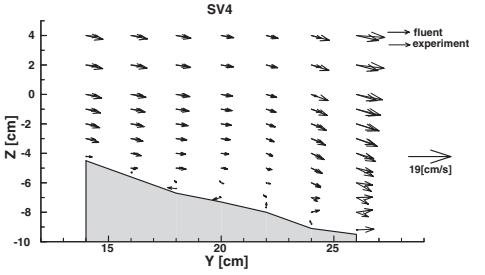


Figure 4. Comparison between numerical and experimental mean velocity components in section v4 (Fig. 1).

The inlet boundary conditions were imposed according to the distribution of velocity and turbulent kinetic energy as measured in the laboratory flume, while along the lateral side wall and groyne wall, in perspex, the smooth wall conditions were imposed. At the bed surface the rough wall conditions were imposed on the bed roughness, which was evaluated using a procedure given by FLUENT. The free surface was modeled via symmetry condition.

3 COMPARISON BETWEEN NUMERICAL RESULTS AND EXPERIMENTAL DATA

Comparisons between measures and numerical results were made along the 14 cross sections indicated in Figure 1, in order to check the goodness of the numerical results. The comparison between experimental measurements and numerical results, in a zone where high gradients in the velocity field are expected, can be affected by difficulties to obtain accurate ADV instantaneous velocity measurements near the bottom, by limits of the closure scheme in turbulence models (Rodi 1993), by approximations in the bed shape and inlet boundary conditions. Nevertheless, the results of the numerical simulations match quite fairly the measurements as put in evidence in Figure 3 and Figure 4.

In the upstream zones (Fig. 3) the presence of a horseshoe vortex is recognized, rotating clockwise

Copyright © 2006 Taylor & Francis Group plc, London, UK

along the axis of the vortex towards the flume centerline, with the groyne on the right bank. This vortex is confined mostly within the scour hole beneath the original bed level in agreement with the experimental evidences of Melville (1992).

Figure 4 shows the mean velocity behavior at cross-sections downstream the groyne, transversal to the mean flow direction. From these graphs, a good agreement between the computational results and measures is pointed out as well. The presence of a vortex system located behind the abutment, inside the recirculation zone transversally to the mean flow direction is observed; near the bottom the flow is directed toward the channel right side wall, congruently with the observed sand grains deposition process. From these measurement points it is very difficult to have an idea of the complex structure of the flow downstream the groyne.

A more evident appraisal of the flow pattern can be derived by plotting the computed pathlines, which is consistent, considering the fair agreement between the experimental measures and the computational results,with reference to the mean flow field. In this framework an analysis in term of mean shear stress on the boundary of scour hole, compared with critical shear stress of the sediment particles, could be useful to define a practical criterion in the design of these structures. This is the goal of the next section.

4 PREDICTION OF SCOUR MAXIMUM DEPTH AND PROFILE

The prediction of incipient motion of the sediment is an important first step for analyzing sediment transport and scour in clear water conditions. The approaches for the practical prediction of the incipient motion are substantially based on two different methods (Marsh et al. 2004): the first method is based on the Shields critical shear stress concept, the second, called simple rotation method, on the equilibrium of moments and forces which drive and resist particle motion.

The critical shear stress concept does not account explicitly for grain stability to predict incipient motion, but it was introduced as a nondimensional framework to analyze experimental evidences. The well-known Shields curve is essentially an empirical result where a threshold limit was drawn within scattered experimental data to separate fixed and moving bed states. The Shields curve is related to channels with a flat bed: to use it in the case of the scour hole, it is necessary to take into account the local slope of the river bed. It is manifest that the critical stress required for moving a grain upslope is larger than that required to move it downslope. This is because in the former case gravity counteracts the impelling stress, whereas in the latter case it acts to enhance it.

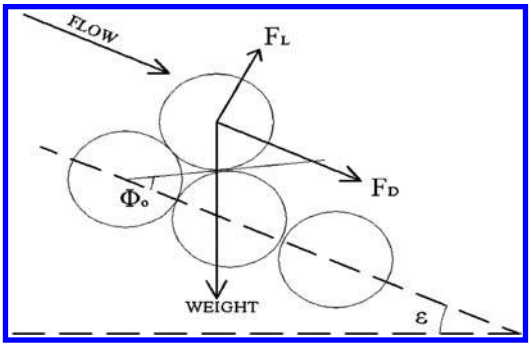


Figure 5. Simple rotation model scheme.

The correction employed by Ali & Karim (2002) to analyze the scour around bridge piers derived by Brooks (1963), is:

$$\frac{\tau_{sc}}{\tau_c} = -A \pm \sqrt{A^2 + B} \tag{1}$$

where: τ_c = critical shear stress on a flat bed according Shields criteria, τ_{sc} = the corrected Shields critical shear stress taken into account the local slope of the river bed, $A = (\sin\phi \cdot \sin\beta)/\tan\vartheta$ and $B = 1 - (\sin^2\phi/\sin^2\vartheta)$ are two parameters where: ϕ = slope angle of bed profile (positive downward slope), β = angle between flow direction and slope direction measured in the plane of the slope while ϑ = static rest angle of sediments.

The second method, based on solving the dynamic equilibrium of a particle, is due to Baker (1980); the incipient motion is presented in terms of the critical velocity V_{c-bed} acting at a height d/2 above the bed, when the particle configuration at the bottom is accounted for via the particle packing angle parameter ϕ_0. With reference to the Figure 5 the formula is given by:

$$V_{c-bed}^2 = \frac{4}{3} \cdot \frac{\sin(\phi_0 - \varepsilon) \cdot (\rho_s - \rho_f) \cdot gd}{\rho_f \cdot (C_L \cdot \sin\phi_0 + C_D \cdot \cos\phi_0)} \tag{2}$$

where: ϕ_0 = particle packing angle, equal to 60°, ε = local bed slope, C_L = uplift coefficient and C_D = drag coefficient equal to 0.3 and 0.6 respectively.

The critical shear stress, according to the simple rotation model, is defined from (2) via the wall function for hydraulically rough conditions with reference to the mean sand diameter at the bottom:

$$\tau_{srm} = \left(\frac{\sqrt{V_{c-bed}^2}}{6.77} \right)^2 \cdot \rho$$

where ρ is the fluid density.

Copyright © 2006 Taylor & Francis Group plc, London, UK

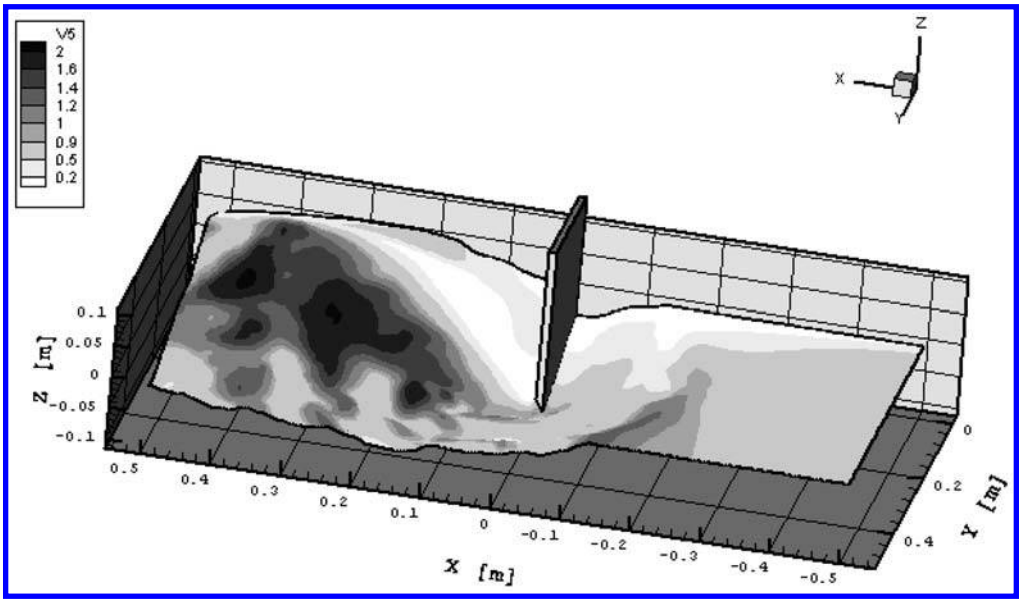


Figure 6. Behavior of the ratio between bottom shear stress and critical shear stress computed by shields criterion.

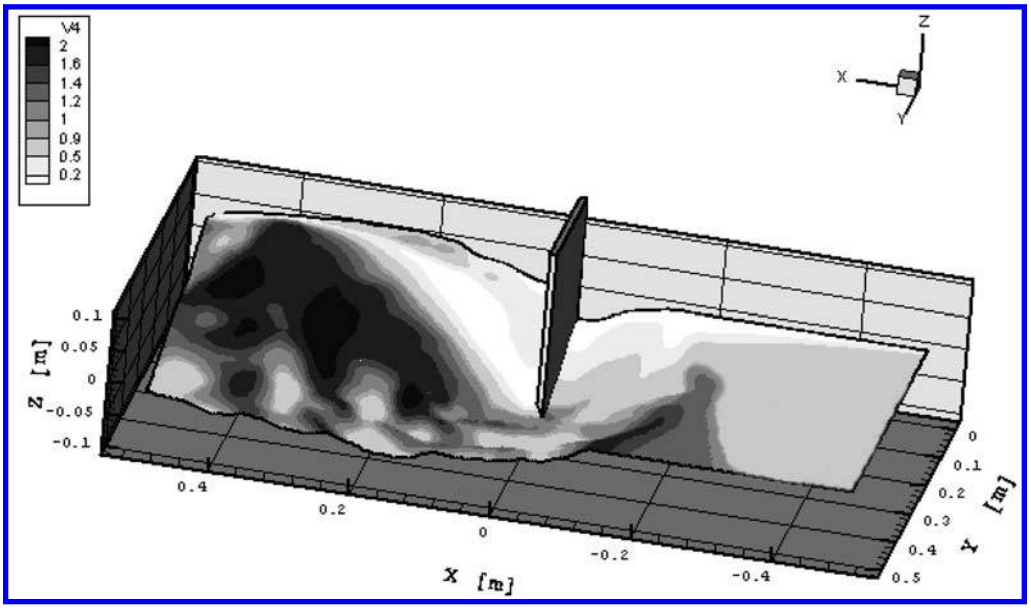


Figure 7. Behavior of the ratio between the bottom shear stress and critical shear stress computed by the simple rotation method.

The following law of the wall, modified for roughness, was used to calculate the bottom shear stress τ (FLUENT 2001):

$$\frac{u_p}{u^*} = \frac{1}{k}\ln\left(E\frac{\rho C_\mu^{1/4} k_p^{1/2} z_p}{\mu}\right) - \Delta B$$

where u_p = mean flow velocity at point p; k = von Karman's constant (k = 0.418); u^* = shear velocity related to the bottom shear stress $\tau = \rho u^{*2}$; ρ is the fluid density; C_μ = constant having a value of 0.09; k_p = turbulent kinetic energy at point p; E = constant having a value of 9.79. The parameter ΔBrepresents

Copyright © 2006 Taylor & Francis Group plc, London, UK

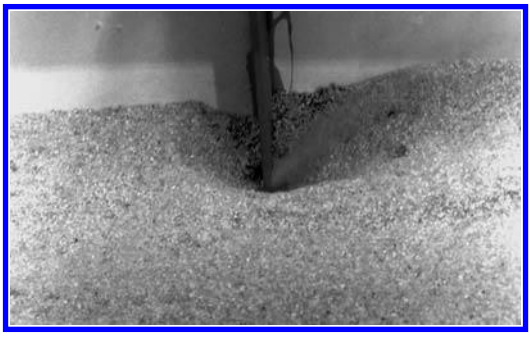


Figure 8. Sediment transport burst plume.



Figure 9. Deposition of painted grains injected into the bottom of the scour.

the roughness function that depends on the nondimensional roughness height $K_s^+ = \rho K_s u^*/\mu$; where K_s is the physical roughness height taken equal to the mean sediment size of the bottom. The formula proposed by Cebeci & Bradshaw (1977) is used by the FLUENT code to compute the ΔB parameter.

By the comparison of the results, as illustrated in the two figures, one can note a good accord between the two solutions, as calculated with the two different approaches in computing the critical shear stress. For practical purposes, either of the two schemes can be used indifferently.

From a theoretical point of view, according to this simplified criterion, a ratio higher than unity indicates instability of the sediment. It is possible to observe a bed shear stress larger than the critical one near the groyne's tip and, downstream, in a zone where the sediments uplift from the scour have been accumulated.

In the upstream zone, where the horseshoe vortex occurs, the bed shear stress is lesser than the critical one. This result seems to prove the experimental evidences that highlight the role of the horseshoe vortex during the initial scour phases as the main responsible of the scouring process while, in later phases, a vertical axis vortex, evidenced in Figure 8 (Fiorotto & Cividin 1996) by a sediment transport burst plume, seems to be the only coherent structure able to uplift and drag particles from the deepest part of the hole.

As further evidence, Figure 9 (Fiorotto & Cividin 1996) shows the zone of deposition of painted grains injected into the bottom of the scour in the final phase of scour hole development, which is incompatible with the action of the horseshoe vortex.

In Figure 10 the computed trajectories of tracer injected in the deeper zone of the scour hole is shown; this trajectory is concordant with the experimental flow visualization of the recirculation behind the groyne (Figs. 11,12 – Fiorotto & Cividin 1996). Particularly, Figure 11 shows a stagnation zone behind the groyne's wall for tracers injected near the groyne's tip. In Figure 12 wool's threads evidence the upward velocity component behind the groyne.

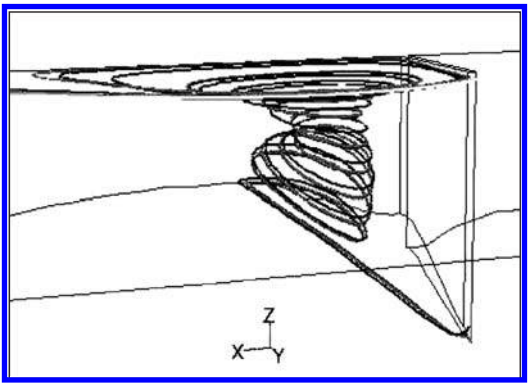


Figure 10. Computed trajectories of tracer.

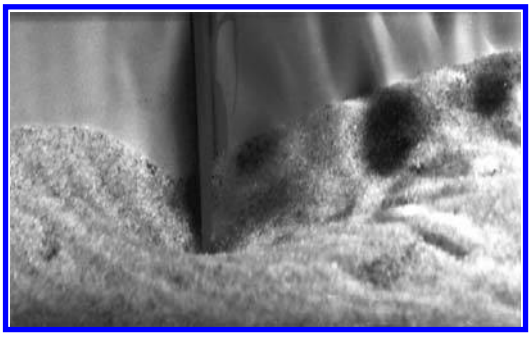


Figure 11. Tracer injected near the groyne's tip.

Both measurements and numerical simulations characterize the recirculation vortex as a frustum of cone with the vertex in the deepestpoint of the scour. The vertical velocity components are generated by disequilibrium between the centrifugal forces and pressure gradients inside the hole. This unbalance can generate a radial flux towards the vortex axis; by continuity, a vertical flux is generated inside the recirculation zone.

Copyright © 2006 Taylor & Francis Group plc, London, UK



Figure 12. Visualization of downstream flow by wool's thread.

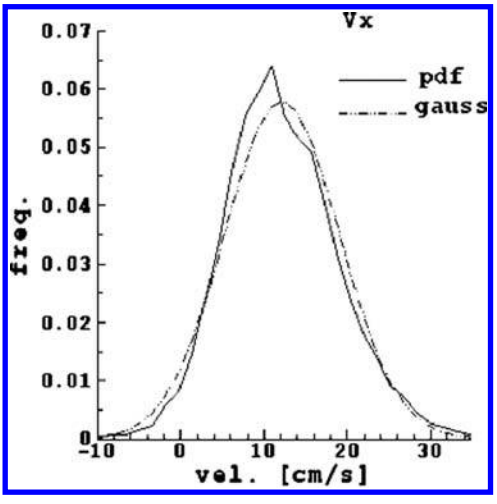


Figure 13. Pdf of vx velocity component.

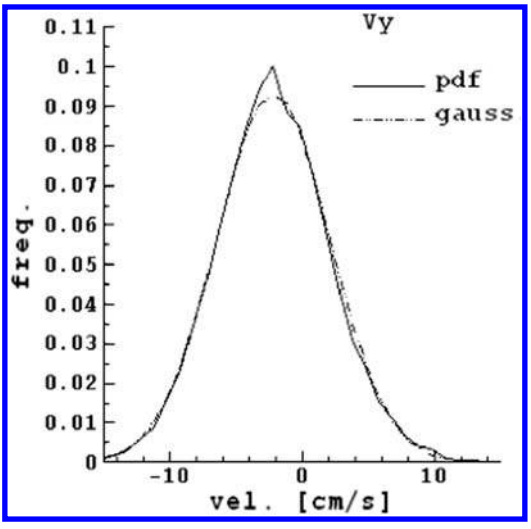


Figure 14. Pdf of vy velocity component.

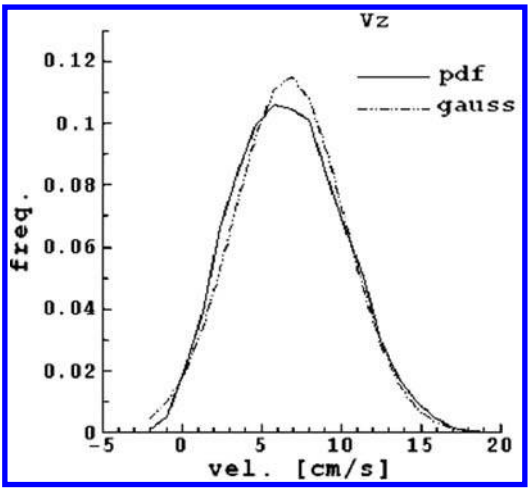


Figure 15. Pdf of vz velocity component.

This flow is able to uplift sand grains from the deepest zone of the scour and deposit them near the channel wall, behind the groyne, in a zone incompatible with the horseshoe vortex trajectory. This fact is particularly evident during the later phases of the scouring process when the horseshoe vortex effects on the scour are weakened, as shown experimentally in Fiorotto (1993).

Detachment of grains from the hole bottom is observed as an intermittent phenomenon, related to the turbulence characteristics of the flow. This vortex structure could prove to be of some importance in determining the maximum scour when very long scouring duration is considered.

In Figures 13–16 the pdfs of the 3D fluctuating velocity components are reported, along the mean flow direction, transversally and in the vertical direction, as measured close to the groyne's tip in the deepest zone of the scour. From the figures one can note the high three-dimensionality of the strong turbulent characteristics of flow, with velocity fluctuations larger than the undisturbed mean velocity. This fact gives reason of the intermittence of the grains detachment in the deeper zone of the scour.

Besides, starting from the deepest zone of the scour, one can note a zone where the shear stress is larger than the critical one, directed bankward behind the groyne. Along this zone the particles, uplifted by the vertical vortex, can travel downstream (Fig. 9).

These numerical results give also a reason of the experimental evidence related to the time evolution and shape of the scour hole as measured by Rajaratnam & Nwachukwu (1983a). Figure 16, showing in the later phases of the scouring, a deepening effect located

Copyright © 2006 Taylor & Francis Group plc, London, UK

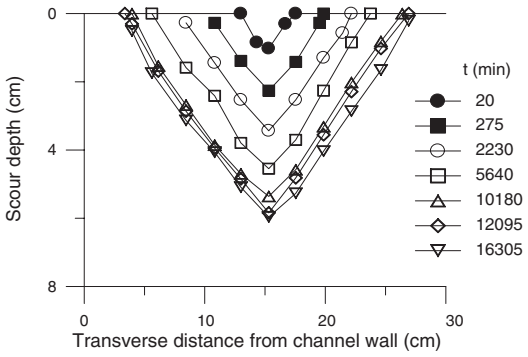


Figure 16. Scour depth versus time along a section transversal to the mean flow direction just upstream of the groyne. Redrawn from Rajaratman and Nwachukwu 1983a.

principally in the deepest zone of the scour hole close to the groyne's tip.

Figures 6,7 suggest a design criterion for defining the maximum depth of scour hole at bridge abutments and groynes in clear water conditions, solving the Reynolds-averaged Navier Stokes equations; this is established by the correspondence between the bed shear stress and the critical shear stress of the sand particles along the scour boundary.

In order to predict the maximum scour depth, further research is needed, aimed to define a realistic shape of the scour, which is required to perform numerical computations. To this purpose, some suggestions are given by Dey & Barbhuiya (2005) that found an average upstream slope of scour hole larger than 10–15% than the rest angle of bed sediments and by Rajaratnam & Nwachukwu (1983a) that detected some similarities in scour profiles by comparison of experimental outcomes in terms of scour hole geometry.

As soon as a sound tool is defined to better predict the scour shape, the stable configuration of the scour hole in clear water conditions could be obtained via an iterative procedure, by varying the scour hole depth and shape properly, until a limit equilibrium condition is reached.

It is obvious that, if this approach is to be applied in real life cases, a suitable safety coefficient in the computation of the maximum scour depth must be used in order to account for the theoretical limits and for the approximations in the sediment incipient motion formulas, in sediment size representation, in the turbulence model, in the approaching flow characterization and in the bed river roughness and shape description.

5 CONCLUSIONS

In this work the k-ε turbulence model was used to predict the main characteristics of the flow field around a groyne. Results, when compared to direct measurements in a laboratory flume, proved satisfactory. Particularly it was possible to highlight the coherent structures mainly responsible of the scour process: the horseshoe vortex located in the upstream zone and a vortex system located behind the abutment, inside the recirculation zone transversally to the mean flow direction, starting from the groyne's tip. These results allow to argue that the primary horseshoe vortex is not the only cause of the scour process. In fact the secondary vortex takes importance in advanced phases of the scouring process and it could be the cause of the deepening effect located principally in the deepest zone of the scour hole close to the groyne's tip observed in these phases (Fig. 16).

Based on k-ε turbulence model, calculation of sediment stability, especially inside the scour hole, highlighted the presence of instable bed particles near the groyne's tip, while in the upstream zone, where the horseshoe vortex is located, the bed particles were stable. This allowed confirming a decreased effect of the primary vortex in the later phases of the scouring process.

In perspective, it is felt that computational fluid dynamics could be applied as a tool to predict maximum scour depth. Once defined a tentative initial scour shape, erosion and aggradation computations could bring to a new scour hole shape up to a stable limit equilibrium condition.

The methodology and the experimental evidences here exposed could help to clear some incongruence in the experimental formulas as pointed out by Richardson (1998) with reference to the I-70 bridge over the Missouri River near Rocheport, where the computed clear water abutment scour using the Lim's formula (Lim 1997) exceeds 100 m while the actual abutment scour at this site is approximately 19 m. In this context, applying the computational fluid dynamics, taking into account the scouring process, could be a suitable alternative to the traditional methods.

REFERENCES

Adami, A. 1979. *Fenomeni localizzati ed erosione negli alvei* (*Local scour and erosion in river bed*). Moderne vedute sulla meccanica dei fenomeni fluviali, Istituto di Idraulica dell'Università di Padova, Bressanone 8–12 ottobre 1979.

Ali, K.H.M. & Karim, O. 2002. Simulation of flow around piers. *J. Hydr. Res.* 40(2).

Armenio, V. et al. 1998. Discussion of 'Equilibrium clear-water scour around an abutment' by Siow-Yong Lim. *J. Hydr. Engrg. ASCE* 124(10).

Baker, C. 1980. Theoretical approach to prediction of local scour around bridge piers. *J. Hydraul. Res.* 18(1).

Barbhuiya, A.K. & Dey, S. 2004. Velocity and turbulence at a wing-wall abutment. *Sādhanā Indian Academy of Sciences* vol. 29(1).

Copyright © 2006 Taylor & Francis Group plc, London, UK

Bendant, J.S. & Piersol, A.G. 1971. *Random data: analysis and measurement procedures*. Wiley-interscience.
Breusers, H.N.C. & Raudkivi, A.J. 1991. *Scouring*. IAHR Hydraulic Structures Design Manual vol. 2.
Brooks, N.H. 1963. Discussion of 'Boundary shear stress in curved trapezoidal channel' by A.T. Ippen and P.A. Drinker. (Proc. Paper 3273). *J. Hydr. Div. ASCE* 88(HY3).
Cebeci, T. & Bradshaw, P. 1977. *Momentum Transfer in Boundary Layers*. New York: Hemisphere Publishing Corporation.
Chrisohoides, A. et al. 2003. Coherent structures in flat-bed abutment flow: computational fluid dynamics simulations and experiments. *J. Hydr. Engrg. ASCE* 129(3).
Dey, S. & Barbhuiya, A.K. 2005. Time variation of scour at abutments. *J. Hydr. Engrg. ASCE* 131(1).
Fiorotto, V. 1993. Discussion of 'Local scour at bridge abutments' by B.W. Melville. *J. Hydr. Engrg. ASCE* 119(8).
Fiorotto, V. & Cividin, R. 1996. Sulle caratteristiche del flusso in corrispondenza di un pennello (On flow characteristics around a groyne, in italian). *L'Acqua* 3/96.
FLUENT 2001. *FLUENT 6.0 User's guide*. December 2001.
Goring, D.G. & Nikora, V.I. 2002. Despiking acoustic doppler velocimeter data. *J. Hydr. Engrg. ASCE* 128(1).
Goring, D.G. & Nikora, V.I. 2003. Closure to 'Despiking acoustic doppler velocimeter data'. *J. Hydr. Engrg. ASCE* 129(6).
Kothyari, U.C. & Ranga Raju, K.G. 2001. Scour around spur dikes and bridge abutments. *J. Hydr. Res.* 39(4).
Kwan, R.T.F. & Melville, B.W. 1994. Local scour and flow measurements at bridge abutments. *J. Hydr. Res.* 32(5).
Lim, S.Y. 1985. *Scour and particle diffusion caused by water jets*. PhD Thesis, University of Liverpool, U.K.
Lim, S.Y. 1997. Equilibrium clear water around an abutment. *J. Hydr. Engrg. ASCE* 237(3).
Marsh, N.A. et al. 2004. Comparison of Methods for predicting incipient motion for sand beds. *J. Hydr. Engrg. ASCE* 130(7).
Mayerle, R. et al. 1995. Verification of a three-dimensional numerical model simulation of the flow in the vicinity of the spur dikes. *J. Hydr. Res.* 33(2).
Melville, B.W. 1992. Local scour at bridge abutments. *J. Hydr. Engrg. ASCE* 118(4).
Melville, B.W. 1995. Bridge abutment scour in compound channels. *J. Hydr. Engrg. ASCE* 121(12).
Melville, B.W. 1997. Pier and bridge scour: integrated approach. *J. Hydr. Engrg. ASCE* 123(2).
Ouillon, S. & Dartus, D. 1997. Three-dimensional computation of flow around groyne. *J. Hydr. Engrg. ASCE* 123(11).
Papanicolau, A.N. et al. 2002. Stochastic incipient motion of spheres under various bed packing conditions. *J. Hydr. Engrg. ASCE* 128(4).
Rajaratnam, N. & Nwachukwhu, B.A. 1983a. Erosion near groyne-like structures. *J. Hydr. Res.* 21(4).
Rajaratnam, N. & Nwachukwhu, B.A. 1983b. Flow near groyne-like structures. *J. Hydr. Engrg. ASCE* 237(4).
Richardson, J.R. 1998. Discussion of 'Equilibrium clear-water scour around an abutment' by S.Y. Lim. *J. Hydr. Engrg. ASCE* 124(10).
Rodi, W. 1993. *Turbulence models and their application in hydraulics – A state of the art Review*. International Association for Hydraulic Research.
Salaheldin, T. et al. 2004. Numerical modeling of three-dimensional flow field around circular piers. *J. Hydr. Engrg. ASCE* 130(2).
Tingsanchali, T. & Maheswaran, S. 1990. 2-D depth averaged flow computation near groyne. *J. Hydr. Engrg. ASCE* 116 (1).
Wahl, T.L. 2000. *WinADV computer program*. Bureau of Reclamation's Water Resources Research Laboratory www.usbr.gov/pmts/hydraulics_lab/twahl/winadv/
Wahl, T. L. 2003. Discussion of 'Despiking acoustic Doppler velocimeter data' by D.G. Goring and V.I. Nikora. *J. Hydr. Engrg. ASCE* 129(6).

Copyright © 2006 Taylor & Francis Group plc, London, UK

Sediment supply effect on local scouring at bed sills in high gradient streams

M. Tregnaghi & A. Marion
Dept. of Hydraulic, Maritime, Environmental and Geotechnical Engineering, University of Padua, Italy

F. Comiti
Dept. of Land and Agroforest Environment, University of Padua, Italy

ABSTRACT: This paper presents the results of an experimental study about the pattern of local scouring generated downstream bed sills commonly used in mountain rivers to limit bed degradation. The effect of sediment supply on the scour depth at the toe of bed sills displaced along a staircase-like sequence is evaluated for the first time. The experiments simulated conditions of steady upstream sediment supply which had the same grain size composition as the deposit placed on the bed of the flume. Results of forty-eight new tests are presented. The geometry of three scour holes developed under conditions of steady flow discharge and steady upstream sediment supply are examined for each test, giving a total of 144 scour holes. Three sediment feed rates were examined. Twelve tests were performed with clear water conditions. The collected data were examined using non-dimensional groups developed by the authors in previous no-feed studies. It is shown that the imposed sediment transport, appearing as a new independent variable, does not require the introduction of new non-dimensional parameters in existing prediction formula calibrated with clear water conditions data. The effects of sediment feed are shown to be incorporated in the existing non-dimensional parameters. The new data set was used to re-calibrate existing scour depth formula. Closer inspection of the data indicates a possible two-stage behaviour, dependent on the range of the ratio between the morphological jump created at a scour hole and the flow specific energy.

1 INTRODUCTION

1.1 *Morphological control structures*

The processes which transport both coarse and fine sediment in high-gradient mountain streams are very effective in defining their morphologic characteristics.

Steep mountain catchments feed a two-phase mixture composed of water and sediment into river channels. River cross-sections are not fixed, and their morphology reflects the pattern of erosion or deposit occurred along the stream. During storm events mountain streams are often subject to channel incision. One method to stabilise them is to use a sequence of transverse grade-control structures.

Traditionally, the principle governing the prevention of channel erosion through bed sills or check-dams is to reduce the mean longitudinal bed slope, S_0, to a lower value S_{eq}, defined as the slope established when dynamic equilibrium between bed scouring and aggradation is achieved.

The equilibrium configuration is reached with reduced delivery of sediment to the downstream reaches of the stream. Excessive sediment release in the steeper reaches can lead to sudden deposition in downstream reaches which may cause flooding of populated areas.

The insertion of sequences of bed sills in a riverbed changes the flow characteristics in proximity of the works themselves, potentially causing the phenomenon of local scouring. The scour develops immediately downstream the bed sills and it arises in addition to the jump produced by the decrease of bed slope.

The overall eroded sediment volume is much less than the volume necessary to erode the whole reach down to the equilibrium slope, but in this way the steps formed downstream of the structure induce the water to plunge over the sill, and, unless the toe of the structure is protected, the plunging jet erodes the bed locally generating a scour hole. Designers must take into account this problem in order to avoid structural failure due to toe scouring, by building foundations with adequate depth. Quantitative predictive formulae of the scour dimensions are therefore required.

Copyright © 2006 Taylor & Francis Group plc, London, UK

1.2 *Local scouring*

Prediction formulae for scour depth, all based on experimental tests on scale models, have been developed by several authors (Rajaratnam 1981, Mason and Arumugam 1985, Whittaker 1987, Chatterjee et al. 1994, D'Agostino 1994, Habib et al. 1994, Marion et al. 1998, Gaudio et al. 2000, Gaudio & Marion 2003, Lenzi et al. 2002, 2003a, b, Marion et al. 2004). These approaches have all been based on the empirical curve fitting of experimental data.

Gaudio et al. (2000) were the first to apply Dimensional Analysis to this problem, in order to define appropriate dimensionless groups before some existing data for gently sloping channels was used to develop empirically fitted relationship. They found predictive formulae for clear-water and long-term scour hole depth. This work was subsequently extended to steep channels by Lenzi et al. (2002) to provide a more generalised relationship:

$$\frac{y_s}{H_s} = 0.44 + 1.45\left(\frac{a_1}{H_s}\right)^{0.86} + 0.06\left(\frac{a_1}{\Delta D_{95}}\right)^{1.49} \quad (1)$$

calibrated in the ranges $0.16 \leq a_1/\Delta D_{95} \leq 1.15$ and $0.22 \leq a_1/H_s \leq 1.87$; where y_s is the maximum scour depth; H_s is the specific critical energy available at each sill; D_{95} is the grain size for which 95% of the sediment by weight is finer; Δ is the sediment relative submerged density; and a_1 is the "morphological jump", i.e. the sill step produced by bed degradation in absence of local scouring.

Marion et al. (2004) found that the dimensionless parameter a_1/H_s is sufficient to describe equilibrium scour depth at high slopes, in the case of non-interfering scours and in uniformly sized sediment. Other parameters were subsequently added to take into account the geometric interference (Comiti et al. 2001, Lenzi et al. 2002), which is the reduction in scouring caused by the closeness of sills, and the effect of sediment composition. The final relationship is:

$$\frac{y_s}{H_s} = 2.7\left(\frac{a_1}{H_s}\right)^{0.43} SI^{-0.19}\left(1 - e^{-0.14\frac{L}{H_s}}\right) \quad (2)$$

which is valid in the range $0.22 < a_1/H_s < 1.87$ and $SI = 1.48 - 5.93$, where L is the sill spacing and SI is a grading parameter called the sorting index (equal to σ_g for log-normal distributions), defined by:

$$SI = \frac{1}{2}\left(\frac{D_{84}}{D_{50}} + \frac{D_{50}}{D_{16}}\right) \quad (3)$$

As recent studies indicate (Lenzi et al. 2003a, b, Marion et al. 2004), normalized maximum scour depth, for long-term and clear-water conditions with non-interfering scours and uniform sediment, can be expressed as function of only one non-dimensional group given by the ratio between the morphological jump:

$$a_1 = (S_0 - S_{eq})L \quad (4)$$

where S_0 and S_{eq} are, respectively, the initial and equilibrium bed slopes and L is the sill spacing, and the specific critical energy available at the sill:

$$H_s = \frac{3}{2}\sqrt[3]{\frac{Q^2}{B^2 g}} \quad (5)$$

where Q is the water discharge, B the channel width and g is gravity. However no local-scouring observations were made in conditions of upstream sediment feed which is common in real mountain rivers.

Experiments aimed to study the influence of upstream sediment transport have been carried out in order to complete the observation of local-scouring mechanisms under all probable conditions.

2 EXPERIMENTS

2.1 *Experimental Set-up*

In these tests a glass sided tilting flume 10 m-long, 0.5 m-wide, 0.5 m-deep was used. The bed of the flume was covered with a 330 mm-deep sediment layer and the gravel was well mixed before starting each test. The sediments used in the tests were graded river gravels, with the following characteristics $d_{30} = 7.3$ mm, $d_{50} = 8.7$ mm, $d_{90} = 13.4$ mm, and uniformity coefficient $C_u = 1.96$. Rectangular wooden plates, 500 mm-wide and 10 mm-thick were used to simulate the presence of morphologic control transverse structures.

During the test bed profile was subject to net degradation under erosive flow action and sediments were transported downstream. At the downstream end of the flume the water flowed over a tail gate into a tank. This was used as a storage basin for the sediment exiting the flume. A schematic diagram for the experimental set-up is shown in Figure 1.

The flow was recirculated: water without sediment passed into a sump and a submerged pump raised the water from the sump to the inlet of the flume. The inlet had a "honeycomb" flow straightener to reduce secondary currents and to create uniform flow in a short reach. The flow discharge was measured using an electromagnetic flow meter, positioned on the inlet pipe; the measurements showed oscillations of flow discharge around a mean of about half litre per second.

Sediment was weighed and placed on a 40 cm-wide and 180 cm-long conveyor belt on the upstream end of the flume. Maximum sediment charge was 60 kg/m, while conveyor velocity ranged between 1.28

Copyright © 2006 Taylor & Francis Group plc, London, UK

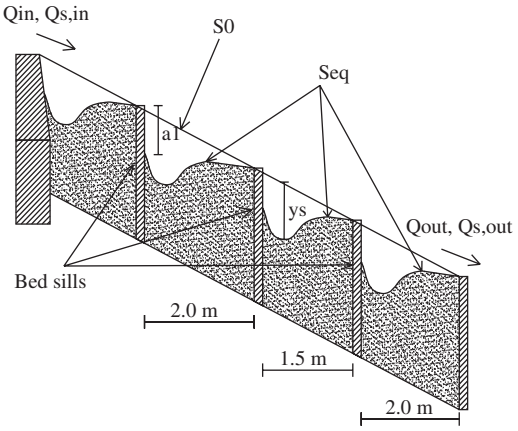


Figure 1. Experimental set-up sketch.

Table 1. Summary of experimental data range.

	S_0	Q	Q_s	L
Parameters	%	l/s	g/s	m
Min	4.2	18.0	0.00	1.5
Intermediate 1	5.0	22.0	10.7	(–)*
Intermediate 2	6.2	(–)*	21.3	(–)*
Max	7.4	26.0	35.5	2.0

* Data not present in these tests.

and 6.23 m/h. This allowed controlling sediment feed rates to be fed into the flume.

Measurements of the water and bed profiles were made with a point gauge mounted on a gantry which was manually moved on rails placed on top of the sidewalls of the flume.

2.2 *New sediment feed tests*

Tests were performed at different initial bed slopes, S_0, between 4.2% and 7.4% with steady flow discharges, Q, between 18 l/s and 26 l/s and with steady input sediment rates, Q_s, between 0.0 g/s and 35.5 g/s (see Table 1).

Before each test series (i.e. tests distinguished by the same initial slope S_0), the flume was tilted to the desired slope. Reaches between sills were filled with gravel and the bed was reconstructed so that sills would be fully inserted into the gravel. At the beginning of each test the sediment was carefully mixed over the whole depth, to avoid preferential sorting and compaction of the gravel at different depths which may have biased scouring measurements.

The pump was started and the water was pumped into the flume with low discharge (4–5 l/s) slowly increasing the flow depth to avoid sediment transport before the designed flow discharge value was attained. Once the whole mass of sediment was saturated, the discharge was raised to the desired value. At the same time, the conveyor belt, previously prepared with an assigned charge of gravel, was turned on. Tests lasted 5 to 6 hours, assuring constant water flow discharge and upstream sediment feed. This duration was found to be long enough to reach final equilibrium conditions, as the scour development always took place within the first two hours. During the last two hours of each test, the three scour holes were measured every ten minutes, recording the maximum scour depth with the respect to the line between the top of sills.

Measurements were made through the glass of the lateral walls and the scour depths of both left and right sides of the flume were recorded. It was necessary to make measurements in this way because observations during preliminary tests showed clearly that there was a temporal oscillation of scour depth around an average value, after the equilibrium configuration has been reached.

This phenomenon was present only during tests with constant sediment transport, it was absent during clear water tests. In addition the input sediment transport caused a lack of two-dimensionality of the scour shape, therefore it was required to hypothesize a linear variation of the depth and to estimate the scour depth as average between the two measured values. A temporal average was used to estimate the equilibrium scour depth.

In the last half an hour of the test, measurements of the water profiles were made at 5 cm intervals along the flume centreline. After the pump is turned off and the flume carefully drained measurements of the bed profiles were made at 5 cm intervals too.

3 RESULTS AND DISCUSSION

The collected data were examined using non-dimensional groups developed by the authors in previous no-feed studies. The most important result of this study is shown in Figure 2. It shows the maximum scour depth normalized to the critical flow energy, y_s/H_s, plotted against the drop ratio a_1/H_s, dividing data in series classified according to the value of the imposed sediment feed.

Trends are roughly estimated as straight lines, which correspond to different values of sediment discharge. These lines appear to collapse along a unique line. This denotes clearly that sediment transport is not influencing the depth of the local scouring in a direct way and suggests that any effect of sediment transport is accounted for in the value of the morphological jump, a_1. The only effect of the introduction of sediment from upstream is to increase the equilibrium bed slope and, as consequence, to reduce the value

Copyright © 2006 Taylor & Francis Group plc, London, UK

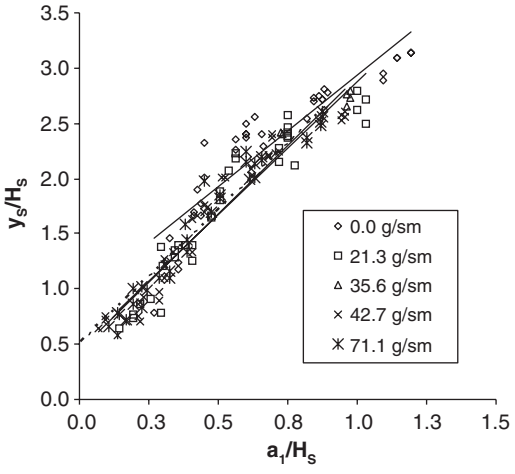


Figure 2. Experimental data divided into series according to upstream sediment feed rate.

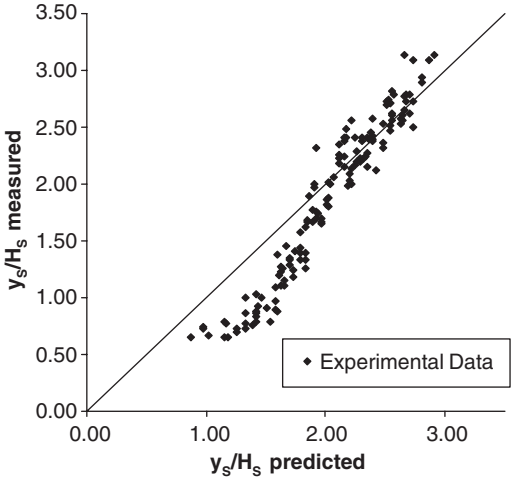


Figure 3. Comparison of measured and predicted maximum scour depths with eq. (2).

of a_1. This experimental evidence justifies the proposed simplification of the problem, since it allows all measurements to be considered in the same way, without distinguishing between clear water and sediment feed conditions. The aim is now to recalibrate the existing scour depth formula using the new scour depth data obtained in both clear water and upstream sediment feed conditions. Figures 3 and 4 show the prediction of the existing formulae of Marion et al. (2004) and Lenzi et al. (2002) with respect to the new experimental measurements. In general the calibrated Equation 2 provides better prediction, even if

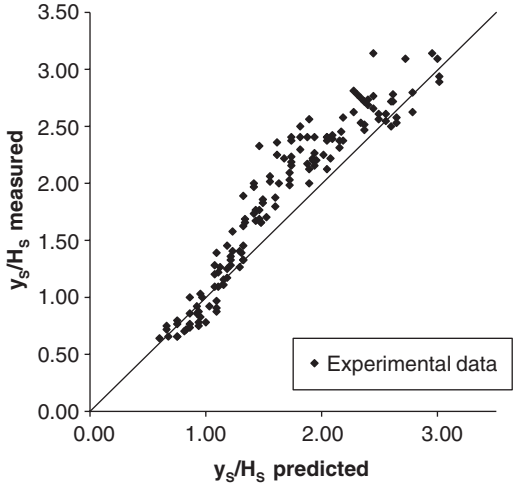


Figure 4. Comparison of measured and predicted maximum scour depths with eq. (1).

it overestimates normalized scour depth for low values of ratio y_s/H_s. Anyway it is noted that validity range of Equation 2 is slightly shifted with the respect to the range in which experimental data fall, which is $0.07 < a_1/H_s < 1.19$. It means that the relationship is more effective for values of the morphological jump, a_1, large with respect to the specific energy of the flow, H_s, which is a common situation for high gradient stream.

Equation 1, obtained by Lenzi et al. (2002) with both high and low bed slopes, slightly underestimates the extent of the measured maximum scour depth over the data interval. It is plausible that the term $a_1/\Delta D_{95}$ can be completely neglected also in the cases of low gradient. This formula shows a better correlation for low values of the ratio y_s/H_s.

Figure 5 contains all data obtained from the current experimental tests, and shows the maximum scour depth normalized to the critical flow energy, y_s/H_s, plotted against the drop ratio, a_1/H_s.

A satisfying correlation over all the full experimental range is attained with a non-linear regression, which gives a curve following a power law similar to Equation 2. The final relationship is:

$$\frac{y_s}{H_s} = 3.0\left(\frac{a_1}{H_s}\right)^{0.6} \tag{6}$$

which is valid for $0.07 < a_1/H_s < 1.19$, with a correlation coefficient $R^2 = 0.93$.

This relation has the same form as the relationship stated in Marion et al. (2004), which is shown in the same graph, and the multiplicative and exponent coefficients are similar (equal respectively to 2.7 and 0.43 in eqn. 2).

Copyright © 2006 Taylor & Francis Group plc, London, UK

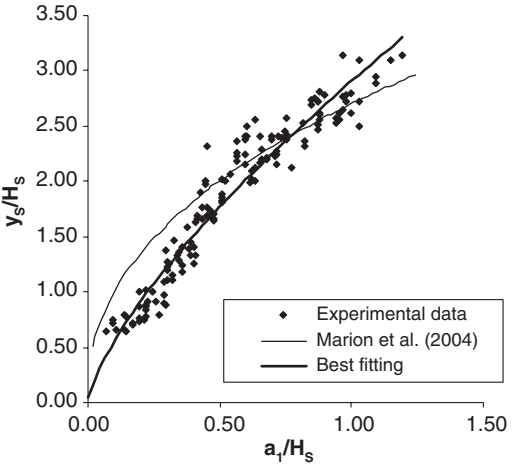


Figure 5. Best-fitting of experimental data; comparison between eq. (2) and eq. (5).

Closer examination seems to show that it is quite difficult to approximate all data with a unique curve. The expression obtained by Marion et al. (2004) is very effective for $a_1/H_s > 0.6$, where non-dimensional maximum scour depth increases approximately with the square root of the normalized morphological jump. Unlike, in the interval $0.0 < a_1/H_s < 0.6$ the trend seems to follow an almost linear law, therefore with an exponent very close to that present in the formula obtained by of Lenzi et al. (2002), equal to 0.86.

This suggests that there may be two types of physical modes of scour hole formation that are not apparent from the initial non-dimensional analysis of the data and that probably depend on the jet inclination and efficiency. Jet inclination plays an important role in entraining sediment particles and sweeping them out of the scour hole, being the more tilted the jet the higher the erosion intensity.

Therefore, with the growth of the morphological jump, maximum scour depth rises not only because of a bigger availability of potential energy (i.e. the morphological jump, a_1), but also because of the more vertical jet. This mechanism becomes weaker in the case of elevated drop heights, because of the pool tailgate depth, so the jet efficiency is not increasing further.

Although jet inclination was not included in the non dimensional analysis it can be stated that it was partially accounted for in the ratio between the morphological jump, a_1, and the critical specific flow energy, H_s.

Furthermore it is noted that, for the lower values of x-axis, more exactly for $a_1/H_s < 0.2$, the non-dimensional ratio between maximum scour depth and specific critical flow energy appears to be attaining a stable value of 0.5 to 0.6 rather than declining steadily towards zero.

4 CONCLUSIONS

Experimental data are presented on local scouring downstream of bed sills placed in high gradient gravel bed streams. The aim was comparing data trends relevant to both clear water and constant sediment feed conditions.

As expected, experiments showed that local scour depth decreased with the increasing of the sediment discharge, once all other factors are fixed. Plotting data normalized accordingly to non-dimensional analysis proposed by previous studies showed that data obtained from clear water tests and sediment feed tests had the same trend. This was justified as sediment discharge, q_s, only implied an increase of the equilibrium bed slope and a consequent decrease of the morphological jump, a_1, which was already accounted for in the analysis. No other effect seems to be produced by the upstream sediment transport rate on the development of the local scouring phenomenon. This allows all data to be analysed using the non-dimensional groups developed with no sediment feed conditions.

Existing non-dimensional relationships to predict scour depth which had originally been developed in experimental tests in clear water conditions were compared with the new data. A good correspondence was observed.

For ratios a_1/H_s greater than 0.6, Equation 2 from Marion et al. (2004), obtained with uniform grain sized sediment, corresponds well with new data. In the range where a_1/H_s is less than 0.6 the relation overestimates normalized scour depth; with regard to this it has been noticed that the interval of validity of the formula is shifted towards the right with the respect to the range, which data fall in. For lower values of the ratio a_1/H_s, Equation 1, obtained by Lenzi et al. (2002) on both high and low gradient streams data, seem to fit better.

In general it can be said that both formulas are valid, if applied on appropriate intervals, but Equation 2 has the great usefulness for evaluating the maximum scour depth, using the only parameter a_1/H_s. Probably this ratio is enough to describe the phenomenon also in the case of low gradient bed slope. A correction of the exponent to the value 0.6 instead of 0.43 improves the prediction performance of this formula for low values of a_1/H_s.

The value $a_1/H_s = 0.6$ describes a point at which the physical mechanisms of erosion that cause the scour depths appear to change and this is reflected in the performance of the two formulae.

REFERENCES

Chatterjee, S.S., Ghosh, S.N. & Chatterjee, M. 1994. Local scour due to submerged horizontal jets. *J. Hydrl. Eng., ASCE* 120(8): 973–992.

Copyright © 2006 Taylor & Francis Group plc, London, UK

Comiti, F., Lenzi, M.A. & Marion, A. 2001. Interference of erosion-control structure in mountain streams, *Proceedings of 3rd Int. Symp. Environmental Hydraulics, ISEH*: Tempe, Arizona (on CD-ROM).

D'Agostino, V. 1994. Indagine sullo scavo a valle di opere trasversali tramite modello a fondo mobile. *L'Energia Elettrica* 71(2), 37–51.

Gaudio, R. & Marion, A. 2003. Time evolution of scouring downstream of bed sills. *J. Hydr. Res., IAHR* 41(3): 271–284.

Gaudio, R., Marion, A. & Bovolin, V. 2000. Morphological effects of bed sills in degrading rivers. *J. Hydr. Res., IAHR* 38(2): 89–96.

Habib, E., Mossa, M. & Petrillo, A. 1994. Scour downstream of hydraulic jump. *Proceeding of Modelling, Testing & Monitoring for Hydro PowerPlants Conference*: Budapest, Hungary, 561–602.

Lenzi, M.A., Marion, A. & Comiti, F. 2003a. Interference processes on scouring at bed sills. *Earth Surf. Process. Landforms* 28(1): 99–110.

Lenzi, M.A., Marion, A. & Comiti, F. 2003b. Local scouring at grade-control structures in alluvional mountain rivers, *Water Resources Research* 39(7): 1176–1188.

Lenzi, M.A., Marion, A., Comiti, F. & Gaudio, R. 2002. Local scouring in low and high gradient streams at bed sills. *J. Hydr. Res., IAHR* 40(6): 731–739.

Mason, P. J. & Arumugam, K. 1985. Free jet scour below dams and flip buckets. *J. Hydr. Eng., ASCE* 111(2): 220–235.

Marion, A., Gaudio, R. & Bovolin, V. 1998. Scour downstream of bed sills, *HR Wallingford Res.* Report TR70, Wallingford, UK.

Marion, A., Lenzi, M.A. & Comiti, F. 2004. Effect of sill spacing and sediment size grading on scouring at grade-control structures. *Earth Surf. Process. Landforms* 29:983–993.

Rajaratnam, N. 1981. Erosion by plane turbulent jets. *J. Hydraul. Div., IAHR* 19(4): 339–358.

Whittaker, J.G. 1987. Sediment transport in step-pool streams. In Thorne C.R., Bathurst J.C, Hey R.D. (ed), *Sediment Transport in Gravel Bed Rivers*, pp. 545–570, Chichester, U.K.: Wiley & Sons.

Copyright © 2006 Taylor & Francis Group plc, London, UK

Riprap protection of vertical-wall bridge abutments

C.M.S. Fael
Universidade da Beira interior, Covilhã, Portugal

C.A.M. Ramos
Laboratório Nacional de Engenharia Civil, Lisboa, Portugal

A.H. Cardoso
Instituto Superior Técnico, Lisboa, Portugal

ABSTRACT: This study addresses the use of riprap as a countermeasure against scouring near vertical-wall bridge abutments under clear water flow conditions. It deals with the diameter of riprap, D_{r50}, the layout of mattresses and their layer thickness, t. It aims to confirm existing criteria and to define appropriate formulations, whenever pertinent. Experiments were performed on a rectangular sand-bed open-channel, by imposing different abutment lengths and by choosing three riprap stone sizes. It became obvious that i) the stone size and mattress extent depend on the ratio between the abutment length and the flow depth and that ii) winnowing can be avoided when the layer acts as a granular filter or the layer thickness exceeds $3D_{r50}$.

1 INTRODUCTION

Scour around bridge abutments is widely recognized as one of the major causes of collapse of bridges. However, due to the complexity of the local scour phenomenon, there is a significant lack of guidelines for the design of countermeasures to mitigate scour. Research efforts are still needed in order to establish sounder guidelines.

Two groups of countermeasures are referred to in the literature. The first group includes armoring countermeasures, where riprap mattresses are the most common; the second group includes flow-altering devices which are not in the scope of this paper.

The riprap matting around abutments is the most widespread countermeasure. It creates a physical barrier intended to resist to the eroding capacity of the flow. However, studies concerning this countermeasure are comparatively rare and the existing guidelines are based on limited evidence. In practice, engineers frequently assume, for instance, that mats should cover the predictable scour area of the unprotected riverbed around the obstacle, ignoring that protection itself is a factor influencing scour. Other key aspects of mattress design are also poorly known or controversial.

Scarcity of information justifies this new investigation effort aiming to confirm existing criteria and to define more appropriate formulations, whenever pertinent. Vertical-wall abutments were chosen for this study since they assumedly induce the most severe conditions concerning design criteria.

The study has adopted an experimental approach. Tests were carried out under clear-water flow conditions, i.e. conditions, in which the mean velocity of the undisturbed approach flow is below or at the threshold velocity for the beginning of motion.

2 LITERATURE REVIEW

Bridge engineers frequently face the need to address the specification of riprap mats for bridge abutments, including the median stone size, layer thickness and mattress plan layout. The correct consideration of these design variables implies the understanding of riprap failure mechanisms.

According to Eve & Melville (2000), the failure mechanisms of riprap are essentially the same for bridge abutments as for piers. For clear water conditions, Parola (1993), Chiew (1995) and Lauchlan (1999) identified three failure mechanisms: shear failure, winnowing failure and edge failure.

Shear failure is clearly linked with the riprap stone size; winnowing depends on the thickness of mats and on the gradation coefficient of the riprap stones; edge failure and plan dimensions of mattresses are also inter-related.

Copyright © 2006 Taylor & Francis Group plc, London, UK

For specifically evaluating the riprap stone size, several authors have suggested empirical formulas. For non-vertical-wall abutments, Simons & Lewis (1971), Croad (1989) and Richardson & Davis (1995) can be quoted. Furthermore, for vertical-wall abutments, the studies of Pagán-Ortiz' (1991), Atayee's et al. (1993), Austroad's (1994) and Richardson & Davis' (1995) studies can be mentioned.

Most of the formulas found in the literature can be arranged as follows:

$$\frac{D_{r50}}{d} = \frac{C}{s_r - 1} F_r^n \quad (1)$$

where D_{r50} = median riprap stone diameter; d = flow depth; s_r = specific gravity of blocks; F_r = flow Froude number; C and n = coefficients.

Regarding thickness, t, of the riprap layer, the Ministry of Works and Development (1979) recommended the value $t = 2D_{r50}$, on top of a suitably graded filter or filter cloth. Later on, Lagasse et al. (1997) improved this criterion recommending that the riprap thickness should be at least $1.5D_{r50}$ or D_{r100}. They also recommended that the riprap thickness should be increased by at least 50% when placed under water, to allow for any uncertainties associated with the placement.

Concerning the layout of riprap mats, Richardson & Davis (1995) and Austroads (1994) recommended the use of riprap around the abutments, down to the expected scour depth. An alternative is to lay an equivalent blanket of riprap, known as a launching apron, on the existing bed.

Based on the studies carried out by Pagán-Ortiz (1991) and Atayee et al. (1993), Richardson et al. (1993) and Richardson & Davis (1995) suggested that, for abutments extending partly into the floodplain, the apron riprap should extend twice the flow depth in flood plain, i.e. $w = 2d_f$ (see Figure 1).

Eve & Melville (2000) have proposed Equation 2,

$$\left(\frac{w}{d}\right) = \left(0.5 - 1.82\frac{D_{r50}}{d}\right)\left(\frac{B}{B-L}\right) \quad (2)$$

which gives the required apron length, w, for a given riprap stone size, as soon as $0.1 < D_{r50}/d < 0.2$. In Equation 2, B = channel width; L = abutment length.

As mentioned before, it is frequently assumed that mats must cover the predictable scour area at the riverbed level of unprotected abutments. Melville & Coleman (2000) suggest $w = \mathrm{H/V} d_{se} \approx 1.5 d_{se}$, where H/V is the horizontal-to-vertical ratio of a spill-through abutment and d_{se} is the equilibrium scour depth of the supposedly unprotected bed.

Below, the mentioned recommendations are evaluated against new laboratory evidence and some alternative guidelines are also presented.

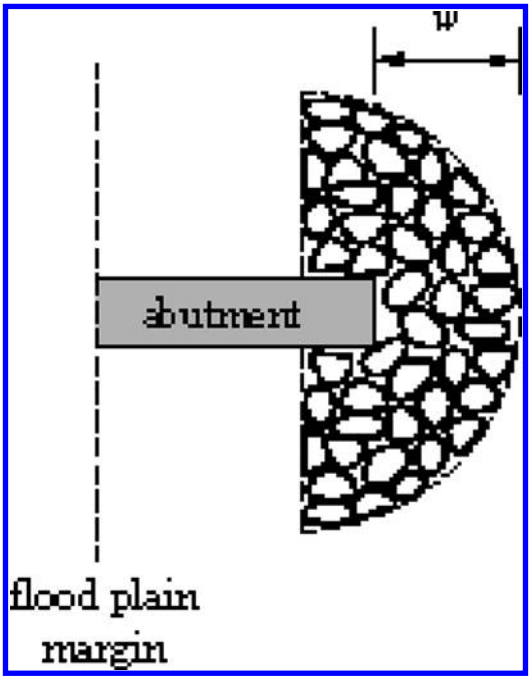


Figure 1. Riprap layout at bridge abutments according to Richardon & Davis (1995).

3 EXPERIMENTS

Experiments were carried out in a 28.0 m long, 4.0 m wide and 1.0 m high concrete flume. The right lateral wall of the flume is made of glass panels, which make it possible to observe the flow in the reach where countermeasures were tested. This reach includes a 3.0 m long, 4.0 m wide and 0.6 m deep recess box, starting at 13.9 m from the flume entrance.

Vertical wall abutments were placed on the bottom of the recess, at its mid cross-section (at 15.4 m from the flume entrance), protruding at right angle from the glass wall. The recess was practically filled with natural quartz sand, of which the median diameter is $D_{50} = 1.28$ mm and the gradation coefficient is $\sigma = 1/2(D_{84.1}/D_{50} + D_{50}/D_{15.9}) = 1.46$ (*cf.* Table 1). Three different types of riprap stones (see Figure 2 and Table 1) were placed around the abutments, on top or embedded in the quartz sand. In Table 1, subscript r, standing for riprap, was not used since the characteristic diameters of sand are also included.

The abutments were simulated by 140 mm wide, vertical wall, parallelepiped perspex boxes. The top of the perspex boxes was kept open, allowing the handling of a video camera to record images of the experiments from inside. Abutment lengths equal to 0.28 m, 0.51 m, 0.72 m, 0.93 m and 1.13 m were used. This way, L/d varied between 2.33 and 9.42.

Copyright © 2006 Taylor & Francis Group plc, London, UK

Table 1. Sand and riprap properties.

Material	$D_{15.9}$ (mm)	D_{50} (mm)	$D_{84.1}$ (mm)	σ (–)	s_r (–)
Sand	0.87	1.28	1.87	1.46	2.65
Riprap #1	2.65	3.59	5.79	1.48	2.65
Riprap #2	5.28	7.48	10.91	1.44	2.65
Riprap #3	13.43	15.69	18.66	1.18	2.65

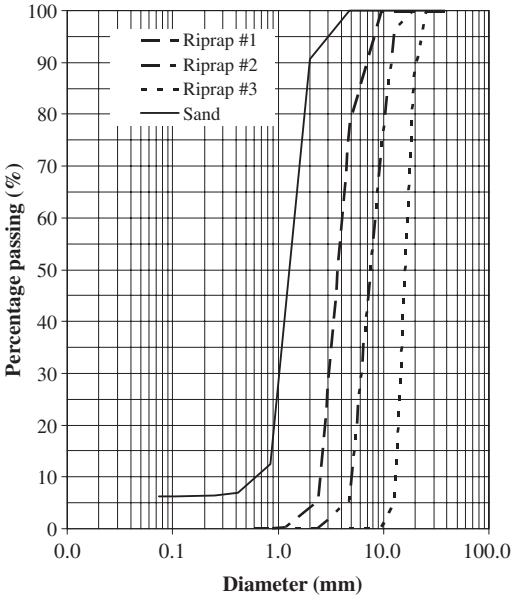


Figure 2. Sand and riprap grading curves.

The study was done for a reasonably high and practically constant flow depth ($d \approx 0.12$ m).

During the experiments, the water is pumped from a reservoir and the discharge can vary continuously from 0.0 m^3/s up to 0.18 m^3/s. Just upstream the flume entrance, a diffuser pipe has been installed to ensure the "uniform" flow distribution along the flume width. At the downstream end of the flume, a hand-operated tailgate makes it possible to regulate the water level. The water falls from the tailgate into the mentioned reservoir, closing the water circuit. The flume is equipped with a moving carriage used to install measuring equipment.

Four sets of experiments were carried out. The first is a set of preliminary tests intended to determine the critical flow velocity, U_c, for the beginning of motion of the quartz sand and the three riprap stone sizes.

The second set of tests aimed at evaluating the critical flow velocity for scour inception, i.e. the approach flow velocity above which scour develops close to the abutment. Fifteen short duration tests were carried out. For each type of riprap, the quartz sand in the recess box was entirely covered with a filter cloth and one upper layer of riprap. The thickness of this layer, levelled with the concrete flume bottom, was $3D_{r50}$. Tests started with a very low flow velocity. Velocity was successively increased while the flow depth was maintained constant by handling the downstream tailgate. The procedure was repeated until the first riprap stones began to move close to the abutment.

The third set of tests was designed so as to further address the thickness of the mattresses. Eight tests were performed without filter cloth, for riprap #2 and riprap #3. Tests were conducted for the two extreme lengths of the abutment, i.e. for $L/d = 2.33$ and $L/d = 9.42$. As for the second set of tests, the sand recess box was covered by a riprap layer levelled with the adjacent concrete flume bottom. Two riprap layer thicknesses, t, were tested per setup, i.e. per combination of L/d and type riprap stones: $t = D_{r50}$ and $t = 2D_{r50}$ or $t = 2D_{r50}$ and $t = 3\ D_{r50}$. Approach flow velocities were kept equal to 90% of the corresponding critical values of scour inception, as defined in the second set of tests. A rule was fixed to the transparent wall of the abutment and scouring was monitored with the video camera placed inside the abutment until equilibrium could be practically guaranteed.

The last set of the experiments was intended to evaluate the minimum plan dimensions of mats. In this case, the recess box was filled with sand. Mattresses, made of riprap #3 and set on filter cloth were embedded in the sand, being leveled with it, around the abutment noses. Tests were accomplished for $L/d = 9.42$, 7.75, 6.00 and 4.25, on filter cloth, for $U \approx U_{cs}$, U_{cs} being the critical approach velocity for the beginning of sand motion. The layer thickness was, in all cases, $t = 2D_{r50} \approx 31$ mm.

4 DISCUSSION

4.1 *Beginning of motion in the approach flow*

The beginning of sediment motion is difficult to identify in the laboratory, because this is not a neat, unambiguous phenomenon. It rather depicts a random character, of which the visual evaluation is somewhat subjective. Therefore, two values of U_c – critical velocity for the beginning of motion – were retained: a lower limit, where motion is about to but still does not exist, and an upper one, corresponding to a very weak sediment motion (incipient motion). Table 2 presents the observed values of U_c, together with the results of Neil (1967) and Garde (1970) equations, as well as the results of Shields diagram.

Apart from the intrinsic value of the measured values of U_c for the subsequent discussion, the following result can be drawn: within the experimental range of

Copyright © 2006 Taylor & Francis Group plc, London, UK

Table 2. Critical velocity for the beginning of motion of sand and tested riprap stones.

Materials	U_c (ms^{-1}) Neil (1967)	Garde (1970)	Shields	Observed Lower	upper
Sand	0.34	0.37	0.48	0.36	
Riprap #1	0.54	0.58	0.82	0.50	0.57
Riprap #2	0.73	0.78	1.11	0.67	0.77
Riprap #3	0.98	1.04	1.38	1.01	1.10

Table 3. Coefficients C and n of Equation (1), according to different authors.

Authors	C (–)	n (–)
Pagán-Ortiz (1991)	1.16	1.62
Atayee et al. (1993)	1.12	1.62
Austroads (1994)	1.03	2.00
Richardson & Davis (1995)	1.02	2.00

this study, Garde (1970) and Neil (1967) equations lead to better predictions than the Shields diagram.

4.2 *Size of riprap stones, D_{r50}*

As for the beginning of motion (see §4.1), the determination of critical flow velocity for scour inception is subjective; it also led to the definition of intervals. The values reported below correspond to the centre of such intervals.

The results of the fifteen tests carried out to evaluate the critical flow velocity for scour inception were used to check the applicability of Equation (1). Values of C and n understandably differ with the bibliographic source. Some authors use the undisturbed approach flow depth, d, and Froude number, F_r whereas others suggest the corresponding values at the contracted cross-section.

Pagán-Ortiz' (1991), Atayee's et al. (1993), Austroads's (1994) and Richardson & Davis's (1995) contributions were chosen for the analysis. Their values of C and n are summarized in Table 3.

Figure 3 compares the fifteen pairs of D_{r50}/d *versus* F_r issued from the experiments with the results obtained via Austroads (1994) equation, where d and F_r are defined for the undisturbed approach flow corresponding to scour inception close to the abutments. The same applies to Figure 4 regarding the Pagán-Ortiz' (1991), Atayee's et al. (1993) and Richardson & Davis' (1995) contribution, but here d and F_r are defined at the contracted cross-section.

From Figures 3 and 4 there can be concluded that none of the equations adequately fits the experimental

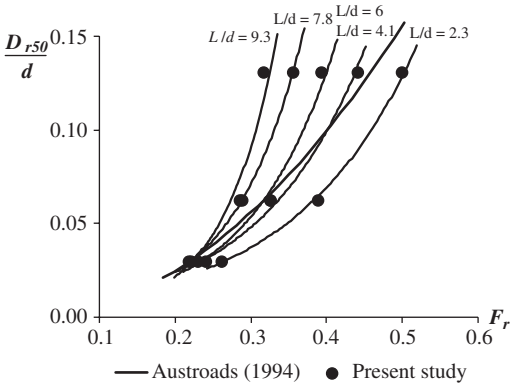


Figure 3. Variation of D_{r50}/d with the Froude number of the approach flow.

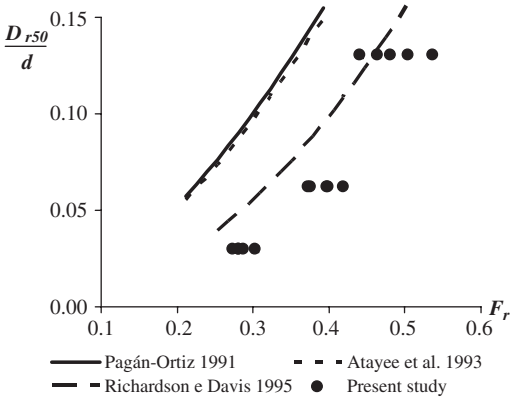


Figure 4. Variation of D_{r50}/d with the Froude number of the contracted cross-section.

data. Nonetheless, Austroads' (1994) and Richardson & Davies' (1995) contributions produce results in the range of the observed values. It is clear that D_{r50} depends both on the Froude number and on L/d. Again, it should be noted that D_{r50} refers to the minimum stone size assumed to resist to scouring in the neighbourhood of the abutment. In this sense, it can be considered as a critical diameter. The inability for the tested equations to predict the critical value of D_{r50} derives from the fact that coefficients C and n might not take into account the effect of L/d.

An alternative approach to access D_{r50} is to define the critical value, I_c, of the approach flow intensity, $I = U/U_c$, below which scour does not show up, for a given value of L/d.

When no obstacle exists in the flow, it is clear that the beginning of motion can be predicted through formulations like those used in §4.1.

It is also consensual that the presence of obstacles increases, in their vicinity, the susceptibility for the

Copyright © 2006 Taylor & Francis Group plc, London, UK

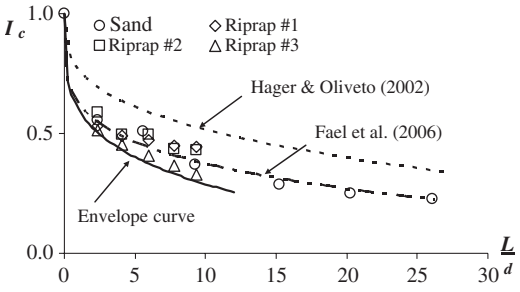


Figure 5. Variation of I_c with L/d for sand and for riprap stones.

motion of particles. In practice, this means that, even for flow intensities less than 1, scour may occur close to obstacles. Some controversy exists on the lower value of I, i.e. I_c, below which no scour exists. Some authors have adopted Chabert & Engeldinger's (1956) result for piers: no scour would occur as long as $I < I_c = 0.5$. Cardoso et al. (2002) corroborated this conclusion for comparatively short abutments ($L/d < 7$). On the contrary, Melville (1992) and Melville (1997) implicitly suggested $I_c = 0$. Hager & Oliveto (2002) have proposed an equation to calculate I_c as a function of the flow contraction, L/B, where B = channel width. According to these authors,

$$I_c = 1 - \frac{5}{6}\left(\frac{L}{B}\right)^{5/16} \quad (3)$$

For wide open channels where scour is not influenced by flow contraction, Fael et al. (2006) suggested one equation that can be rewritten as

$$I_c = 1 - \frac{3}{8}\left(\frac{L}{d}\right)^{2/9} \quad (4)$$

It should be emphasized that Equations 3 and 4 were established for sand bed material. *A priori*, they may or may not directly apply to the design of riprap stones.

Figure 5 compares the results of these equations with the "measured" values of I_c. It is clear that I_c depends on L/d. As L/d increases, there is an increasing susceptibility for scour inception. It seems that Fael et al. (2006) equation performs the best. Still, it should be noted that the observed values of I_c might be smaller than those issued from this equation, particularly for the coarser riprap. For $L/d = 9.42$, I_c may be as low as 0.31. In practice, it is clear that the widespread Hanco (1971) value – $I_c = 0.5$ – leads to unstable riprap stones, as soon as $L/d > 3 \sim 4$.

Figure 5 presents important information towards the design of stones for riprap mattress at abutments. Since the Fael et al. (2006) equation may over predict I_c, a lower envelop curve

$$I_c = 1 - \frac{2}{5}\left(\frac{L}{d}\right)^{1/4} \quad (5)$$

is also included. This equation is suggested for practical engineering applications. Let us assume a 20 m long vertical wall abutment inserted in a 4 m deep flow, of which the approach velocity is 2 ms^{-1}. According to Equation 5, $I_c = 0.39$. This means that the riprap stones around the abutment must be designed as if they were to remain stable for a fictitious flow velocity $U = I_c^{-1} \times 2\,\text{ms}^{-1} = 5.2\,\text{ms}^{-1}$ in the bottom of the approach channel. From Neil (1967) and Garde (1970) equations, the stone size of stable riprap, D_{r50}, would then be about 0.4 m.

Table 4. Scour depth due to winnowing *versus* riprap layer thickness.

Test	L/d (–)	Layer variables: Riprap	N	T (mm)	T (h)	d_{se} (m)
1	9.33	#2	1	7.5	123	0.015
2		#2	2	15.0	97	0.000
3		#3	1	15.7	142	0.046
4		#3	2	31.4	130	0.000
5	2.33	#2	1	7.5	54	0.000
6		#2	2	15.0	30	0.000
7		#3	2	31.4	216	0.056
8		#3	3	47.1	126	0.008

4.3 *Riprap layer thickness, t*

The main objective of this section is to assess the minimum mattress thickness, t, needed to avoid failure due to winnowing of the underlying sediment particles through the voids of the riprap stones. No comment can be made on the thickness, t, of mattresses laying on filter cloth, because no experiments were carried out for this setup.

Since experiments were run for approach flow intensities below I_c of scour inception, shear failure was neither expected nor observed; as the entire recess box was covered with riprap, edge failure was not possible. Thus, only failure due to winnowing was expectable.

Table 4 summarizes the results of the third set of experiments described in §3. In the same table, N = number of equivalent layers, such that $t = ND_{r50}$, T = test duration. The most relevant result for the analysis is the equilibrium scour depth, d_{se}, generated by winnowing, as measured at the end of each experiment.

Copyright © 2006 Taylor & Francis Group plc, London, UK

According to Table 4, scour is practically nonexistent for riprap #2 regardless of the layer thickness. The exception is test 1 ($L/d = 9.23$; $N = 1$), where a 1.5 cm deep scour hole was observed at the end of a 5-days run. The reason for this excellent behavior of riprap #2 is, probably, its acting as a filter. In fact, it fulfils Terzaghi-Vicksburg criterion: $D_{r15} < 5D_{85}$; $5D_{15} < D_{r15} < 20D_{15}$; $D_{r50} < 25D_{50}$. It should be noted that the subscript r applies to riprap while the absence of this subscript is valid for the underlying sand. The existence of scour for test 1 may be explained by the phenomenon of winnowing through the practically unavoidable spaces between the vertical surface of the abutment and the surrounding riprap stones.

Table 4 also shows that, on the contrary, scour is possible for riprap #3. This is compatible with Terzaghi-Vicksburg criterion since the condition $D_{r15} < 5D_{85}$ is not verified. It should be noted that the deepest scour depth was observed at the shorter abutment ($L/d = 2.33$) for $N = 2$. It would certainly be deeper for a hypothetical test carried out for $N = 1$. The occurrence of the deepest scour hole for the shortest abutment is somewhat surprising since the wake vortices at the edge of longer abutments are expectably stronger and should render winnowing stronger too. Since this is not confirmed, further experiments are needed with the simultaneous measurement of the flow field to obtain an insight into the physics of phenomena.

From Table 4, it seems that scouring is negligible in the absence of filters of any kind as soon as $N \geq 3$. However, this result should be confirmed too, since, according to Parker et al. (1998), p. 242, winnowing can act down to depths of about $12D_{r50}$ around cylindrical piers.

4.4 *Mattress plan dimensions*

Experiments on edge failure and minimum mattress plan dimensions were carried out for 31 mm thick layers ($\approx 2D_{r50}$) of riprap #3, laying on filter cloth, so as to avoid winnowing failure. Since the approach flow velocity was approximately equal to the threshold velocity for the beginning of motion of the surrounding sand, shear failure was avoided too.

At the beginning of the fourth set of experiments, it was assumed that a reasonable layout for the mattresses would correspond to the configuration of scour holes previously observed by Fael et al. 2006 at the undisturbed sand-bed level of similar unprotected abutments. For this reason, w (see Figure 6) was predicted as $w = d_{se}/tg\theta$, where d_{se} = calculated equilibrium scour depth for unprotected bed; θ = angle of repose of sand. In this way, w was set equal to 0.75 m for test 1 (see Table 5).

Experience has shown that values of w of this order of magnitude do not lead to mattresses that completely avoid scouring at their edges, particularly downstream. It was also observed that increasing the dimension of mattresses does not lead, necessarily, to completely inhibit scour but, simply, to further deviate the scour hole from the abutment. Besides, riprap stones tend to roll into the scour hole that appears close to the mattress. Thus, a decision was made to reassess edge failure, assuming it to occur only when riprap stones are removed from the immediate vicinity of the abutment toe, by rolling into the scour hole.

For $L = 0.70$ m, tested mattresses evolved from a comparatively large mattress (test 1) to the one that strictly fulfilled the reassessed failure criterion (test 2).

Table 5 summarizes the results of ten experiments. It includes the values of L as well as those of w = characteristic length of the tested mattress; T = test duration; d_{se} = equilibrium depth of the observed scour hole; d_x and d_y = distances of the scour hole deepest point to the upstream vertical edge of the abutment; and α = angle defining the position of the deepest point (see Figure 6). It also indicates the results of edge failure assessment.

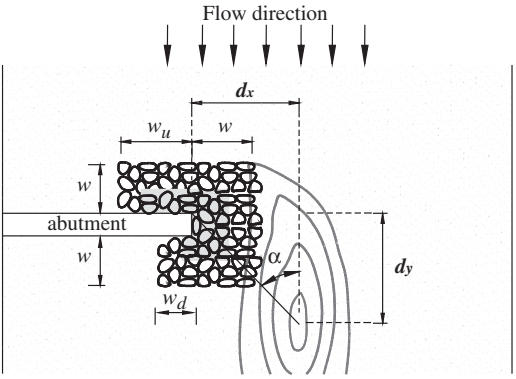


Figure 6. Characteristic dimensions of riprap mattresses; position of the deepest point of scour, defined by d_x, d_y and α.

Table 5. Plan dimensions of tested mattresses and results of the tests on the layout of riprap mattresses.

Text	L (m)	w (m)	T (h)	Failure	d_{se} (m)	d_x (m)	d_y (m)	α (°)
1	0.72	0.75	289.0	No	0.34	0.93	1.45	33
2	0.72	0.15	137.8	Yes	0.33	0.52	0.85	31
3	0.72	0.17	143.9	No	0.34	0.51	0.93	29
4	0.93	0.45	264.0	No	0.21	0.91	0.71	52
5	0.93	0.20	139.0	No	0.35	0.53	0.96	29
6	0.93	0.17	74.0	Yes	0.33	0.51	0.95	28
7	1.13	0.20	137.2	Yes	0.35	0.60	0.95	32
8	1.13	0.23	162.8	No	0.33	0.63	0.84	37
9	0.51	0.13	97.3	Yes	0.30	0.44	0.76	30
10	0.51	0.14	164.3	No	0.30	0.45	0.83	28

Copyright © 2006 Taylor & Francis Group plc, London, UK

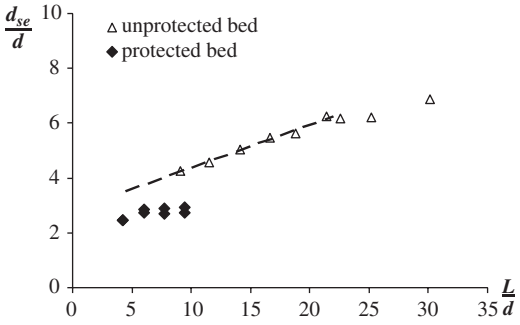


Figure 7. Effect of mattresses on equilibrium scour depth.

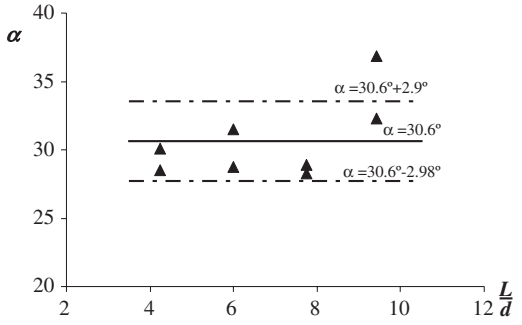


Figure 8. Variation of α with L/d.

It should be noted that the dimensions of the filter cloths used in these tests were set equal to 75% of the dimensions of the riprap layers, according to Melville & Coleman (2000).

Since scour is assumed as inevitable, a decision was made to evaluate the maximum observed scour depth by comparing the values issued from the protected-bed tests with those of similar tests carried out for unprotected bed by Fael et al. (2006). A comparison is presented in Figure 7, in which the dashed line is just intended to produce a comparison framework. In this figure, tests 1 and 4 were not included because they do not correspond to conditions close to the threshold of edge failure.

It seems that the riprap protection reduces the equilibrium depth of the associated scour hole. However, the reduction is not very significant, particularly for short abutments.

For practical engineering applications it may be important to address the position of the deepest point of the scour hole. Consequently, a decision was made to characterize α, d_x and d_y.

Figure 8 presents the variation of α with L/d. As for Figure 7, it does not include the results of tests 1 and 4 but their inclusion would not change the conclusions.

The figure does not make it possible to identify any trend of α with respect to L/d. It seems that $\alpha = 30.6° \pm 2.9°$ (average $\pm$ standard deviation), independently of L/d.

Figure 9 shows the variations of d_x/d and d_y/d with L/d. There is a small increasing trend of both d_x and d_y with L, but, for the reported experimental range, it may be assumed that $d_x \approx 4.5d$ and $d_y \approx 7.5d$ (in coherence with α).

The most important results reported in Table 5 refer to the values of w corresponding to the threshold of edge failure.

From Figure 10, it can be concluded that w increases with L/d. The influence of d/D_{r50} cannot be addressed since it was kept practically constant and equal to $120/15.69 \approx 7.65$, which indicates the need to vary

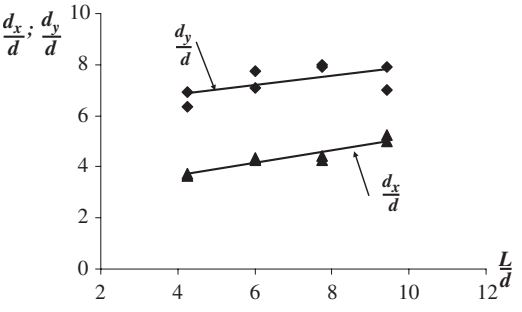


Figure 9. Variation of d_x/d *and* d_y/d with L/d.

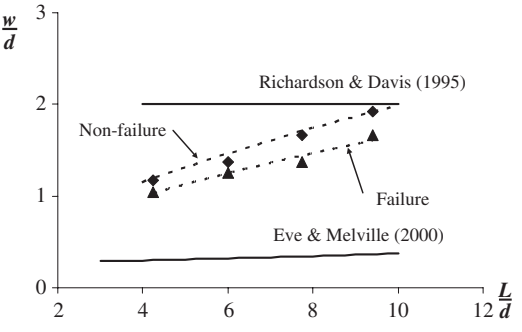


Figure 10. Variation of w/d with L/d.

d/D_{r50} in future research studies. It is also clear that Richardson & Davis's (1995) proposal – see Figure 1 – leads to safe predictions of w, within the experimental range of this study. Again, Figure 10 suggests the need to extend research for values of $L/d > 10$.

Eve & Melville (2000) Equation (2) seems to underestimate w. This may derive from the fact that the work of these authors applies to spill-through abutments, where the strength of the vortex system is presumably weaker than for the vertical-wall. This implies a reduced scour potential in the former and,

Copyright © 2006 Taylor & Francis Group plc, London, UK

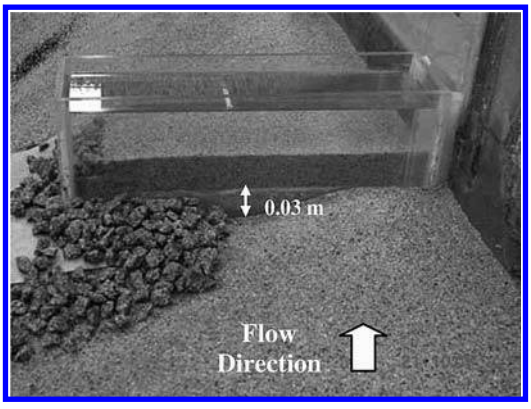


Figure 11. Scour hole immediately upstream of the abutment.

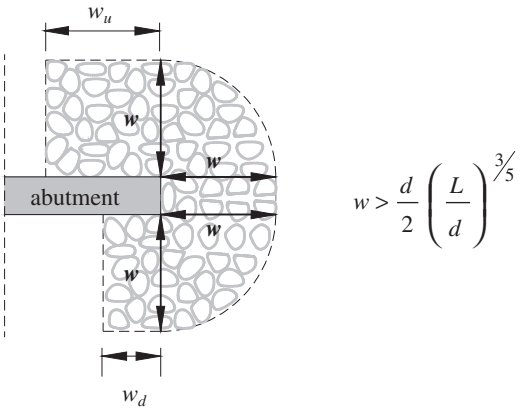


Figure 12. Layout of riprap mattresses for vertical-wall abutments.

therefore, weaker conditions for edge failure and smaller required apron length. Since the values of L/B varied, in this study, between 0.13 and 0.28 – with no visible contraction effect – while Eve & Melville's (2000) ones varied between 0.41 and 0.49, there may be different effects of contraction as a source for the discrepancies depicted in Figure 10.

According to Figure 10, there can also be concluded that edge failure can be avoided as soon as:

$$\frac{w}{d} > \frac{1}{2}\left(\frac{L}{d}\right)^{3/5} \quad (6)$$

under the conditions of $d/D_{r50} \approx 7.5$ and existence of filter cloth underneath riprap stones.

Preliminary experiments were also carried out on the specification of w_u and w_d (see Figure 6). It seems that w_u may be bigger than w itself, particularly for short abutments. This is illustrated in Figure 11 regarding test 10, where scour was observed at the toe of the abutment by the end of the run, although $w_u = 0.19$ m, while $w = 0.14$ m. It seems also clear that w_d can be very small or even null. The criterion $w_d = 3D_{r50}$ was observed to avoid edge failure along the mattress boundary facing the channel wall.

From the experiments reported in this section, it seems that the adequate layout of riprap mattresses for vertical-wall abutments would be as sketched in Figure 12. However, this proposal has to be regarded with caution since it only applies to $d/D_{r50} \approx 7.5$, in the range of L/d values between 4.25 and 9.42. Little evidence was produced on the values of w_u and w_d.

5 CONCLUSIONS

The use of riprap protection of vertical-wall abutments under clear-water flow conditions was addressed in this study. Abutments protruded at right angle from the wall of a rectangular, sand-bed channel. For the experimental range of this study ($4.25 \leq L/d \leq 9.42$), the following conclusions can be drawn:

i) Regarding the design of stable riprap stone sizes, it is clear that characteristic diameters depend on the Froude number as well as on L/d. The influence of L/d is not taken into consideration by several formulations selected in the literature.
ii) The concept of critical flow intensity, I_c, for scour inception applies to the design stone sizes. Equation 5 is suggested, which, leads to increasing stone sizes as L/d increases.
iii) Scour due to winnowing did not develop when the riprap layer acted as a granular filter. Scour seems negligible when, in the absence of filters of any kind, the riprap thickness is such that $N \geq 3$.
iv) For reasonable mattress extensions, scouring at its boundaries seems unavoidable, inducing the rolling of riprap stones into the scour hole.
v) Scour holes develop downstream the abutment; their depth seems to be mitigated as compared with unprotected bed. The deepest scour hole occurs at $d_y \approx 7.5d$ for $\theta \approx 30°$ (see Figure 6).
vi) Assuming edge failure to occur when stones are removed from the toe of the abutment, the lateral extent, w, of mattresses resisting to edge failure increases with L/d, according to Equation 6 for the range of L/d values mentioned above, $d/D_{r50} \approx 7.5$ and riprap layers placed on filter cloth. Richardson & Davis' (1995) proposal seems to predict safe w values.

The study reported in this paper encourages the adoption of the layout presented in Figure 12 but further research is needed so as to extend the conclusions and proposals, for different abutment shapes, to a wider range of L/d values as well as to different

Copyright © 2006 Taylor & Francis Group plc, London, UK

values of d/D_{r50} and D_{r50}/D_{50}, where D_{50} stands for the under laying sand.

ACKNOWLEDGMENTS

The writers wish to acknowledge the financial support of the Portuguese Foundation for Science and technology, through POCI/ECM/59544/2004.

REFERENCES

Atayee, A.T., Pagán-Ortiz, J.E., Jones, J.S. & Kilgore, R.T. 1993. A study of riprap as scour protection for spill-through abutments. *ASCE Hydraulic Conference*, San Francisco, CA.

Austroads, 1994. Waterway design – A guide to the hydraulic design of bridges, culverts and floodways. Austroads, Sydney, Australia: p. 139.

Cardoso, A.H., Santos, J.S. & Roca, M. 2002. Effects of flow intensity, obstacle alignment and cross-section geometry on scour at bridge abutments. *International Journal of Sediment Research* 17(2): 102–113.

Chabert, J. & Engeldinger, P. 1956. Etude des affouillements autour des piles de ponts. *Laboratoire National d'Hydraulique*. Chatou. France.

Chiew, Y.M. 1995. Mechanics of riprap failure at bridge piers. *Journal of Hydraulic Engineering* 121(9): 635–643.

Croad, R.N. 1989. Investigation of the pre-excavation of the abutment scour hole at bridge abutments. *Central Laboratories, Works and Development Services Corporation*. Report n° 89-A9303: 21. New Zealand.

Eve, N.J. & Melvile, B.W. 2000. Riprap protection of bridge abutments under clear water conditions. *Proc. ASCE Joint Conference on Water Resources Engineering and Water Resources Planning and Management*. Minneapolis.

Fael, C.M.S., Simarro, G., Martín-Vide, J.P. & Cardoso, A.H. 2006. Local scour at vertical-wall abutments under clear water flow conditions. *Water Resources Research* (submitted).

Garde, R.J. 1970. Initiation of motion on a hydridynamically rough surface. Critical velocity approach. *JIP* 6(2). India.

Hager W.H. & Oliveto, G. 2002. Shields' entrainment criterion in bridge piers. *Journal of Hydraulic Engineering* 128(5): 538–542.

Hanco, S. 1971 – Sur le calcul des affouillements locaux dans la zone de piles de pont, *XIV Congrés de IAHR*, Communication C36 aux, Paris.

Lagasse, P.F., Byars, M.S., Zevenbergen, L.W. & Clopper, P.E. 1997. Bridge scour and stream instability countermeasures. *Report n° HEC23 (FHWA-HI-030)*. Federal Highway Administration.

Lauchlan, C.S. 1999. Countermeasures for pier scour. *PhD. Thesis*. The University of Auckland. Auckland. New Zealand.

Melville, B.W. 1992. Local scour at Bridge abutments. *Journal of Hydraulic Engineering* 184(4): 615–631.

Melville, B.W. 1997. Pier and abutment scour: integrated approach. *Journal of Hydraulic Engineering* 123(2): 125–136.

Melville, B.W. & Coleman, E. 2002. Bridge scour. *Water Resources Publications*. *LLC*.

Ministry of Works and Development 1979. Code of practice for the design of bridge waterways. *Civil Division Publication CDP 705/C*, *Ministry of Works and Development*: 57. Wellington. New Zealand.

Neil, C.R. 1967. Mean velocity criterion for scour of coarse uniform bed-material. *Proceedings of the XII IAHR Congress*: 46–54. Fort Collins. Colorado.

Parker, G., Toro-Escobar, C., Voigt, R.L., Melville, B.W., Hadfield, A., Lauchlan, C, Chiew, Y.M., Parola, A.C. & Hagerty, D.J. 1998. Countermeasures to protect bridge piers from scour: *User's guide, National Cooperative Highway Research Program, Transportation Research Board, National Research Council*, USA.

Pagán-Ortiz, J.E. 1991. Stability of rock riprap for protection at the toe abutments located at the floodplain. *Federal Highway Administration, Department of Transportation*. *Report n° FHWA-RD-91-057*: 125. Washington.

Parola, A.C. 1993. Stability of Riprap at Bridge Piers. *Journal of Hydraulic Engineering* 119(10): 1080–1093.

Richardson, E.V., Harrison, L.J., Richardson, J.R. & Davis, S.R. 1993. Evaluation scour at bridges. *Hydraulic Engineering Circular n° 18, FHWA-IP-90-017, FHWA*: 105.

Richardson, E.V. & Davis, S.R. 1995. Evaluating scour at bridges. *Hydraulic Engineering Circular n° 18 (HEC-18)*. *Report n° FHWA-IP-90-017*: 204. Federal Highway Administration, U.S. Department of Transportation. Washington.

Simons, D.B. & Lewis, G.L. 1971. Flood protection at bridge crossing. *Wyoming State Highway Department and U.S. Department of Transportation*, *C.S.U. Civil Engineering Report n° FHWA-AZ-89-260*.

Copyright © 2006 Taylor & Francis Group plc, London, UK

Geometrical effects in non-continuous riprap stability

Gustavo A. Mazza de Almeida & Juan P. Martín-Vide
Department of Hydraulic Engineering, Technical University of Catalonia (UPC), Barcelona, Spain

ABSTRACT: An experimental investigation was performed to determine the influence of geometrical characteristics (length and protrusion) on shear failure conditions of non-continuous riprap protections. Incipient motion of particles was used as failure criterion and the reference transport method was used to establish flow conditions for the threshold of motion. Altogether 201 experiments were conducted in a 30-m long, 0.75-m wide tilting flume with a fixed bed. Riprap materials were represented by four groups of uniform crushed rock with a median particle size $D_{50} = 0.85$, 1.25, 1.57 and 1.75 cm and the same shape. Flow conditions ranged from Froude numbers between 0.3 and 1 and relative depths Y/D_{50} between 9.4 and 19.4. In each test riprap transport rates were measured at different time intervals using a sediment trap placed immediately downstream from the test reach so that time dependence could be described well. A statistical method was developed to convert riprap transport rates into a fractional number of entrainments using standard video-imaging techniques. First results reveal that incipient motion conditions are strongly influenced by both protrusion and length of bed protection, indicating that stability significantly increases with increasing protection length and decreases with increasing protrusion.

1 INTRODUCTION

Rock riprap is widely used as a countermeasure against river scouring. As a consequence, during the last decades considerable effort has been devoted to develop new methodologies for determining its size, gradation, layer thickness and filter characteristics (Stevens et al. 1976; Maynord et al. 1987; Escarameia and May 1995; Pilarczyk 1998). Most of these design techniques consider the most general case of a continuous revetment or some very specific protections such as those used for bridge piers. On the other hand there seem to be an increasing tendency of using riprap in other river engineering works. Among these applications we give emphasis to those non-continuous cross sectional protections such as bed sills (fig. 1) or pipeline revetments. This type of protections are commonly built partially buried, allowing for a certain degree of protrusion.

Flow field surrounding these structures is extremely dependent on its particular geometry (length and protrusion) and, consequently, failure conditions may differ strongly from those observed for continuous protections. The purpose of this article is to investigate the influence of geometrical variables on shear failure of non-continuous riprap protections by comparing its critical conditions with those observed for continuous riprap protections.

Incipient motion of particles was used as failure criterion and the reference transport method was used to establish flow conditions for the threshold of motion. Although there are several good studies on incipient motion of gravel bed and continuous riprap protections, some authors (Buffington and Montgomery 1997) have highlighted a considerable scatter in τ_c^* values. This scatter may be explained by differences in experimental conditions and methodologies assumed



Figure 1. Riprap bed sill under construction. Besòs river close to Barcelona (Martín-Vide, 2002).

Copyright © 2006 Taylor & Francis Group plc, London, UK

by each author. To avoid errors related to the comparison of failure conditions of non-continuous protections with those "universal" values found in the bibliography (e.g. Shields entrainment function), a group of experiments were conducted to estimate failure conditions of a continuous riprap bed with the same conditions (flume, rock characteristics, relative depth, etc) and criteria used for the other experiments.

2 EXPERIMENTAL SETUP

An experimental program was conducted in a 30-m long 0.75-m wide glass-sided tilting flume to determine failure conditions of non-continuous riprap protections. Test reach consisted in a 3-m long recess located 9 m upstream from the channel outlet. Water was pumped by a set of three pumps, each of them able to produce a flow up to 90 ls^{-1}. The slope of the flume can be set up to 0.04. An adjustable gate at the downstream end of the flume was used to control flow depth in each experiment. Both the gate and the channel slope were adjusted to ensure uniform flow in the test reach before each run. All tests used the same flow depth $Y = 16.5$ cm. An area with dissipation screens was installed at the channel entrance to prevent large-scale disturbances. Coarse natural gravel was used to roughen the upstream part of the channel, needed to achieve uniform flow.

Flow discharges were measured by a V-shape sharp crested weir installed upstream of the channel. Velocity measurements were conducted using a 3D acoustic Doppler velocimeter (ADV:SonTek). The sampling frequency of the ADV was set 25 Hz and the duration of the measurements at each point was 80 s. A point gauge with precision of 0.1 mm was used for measuring water level. The movements of the ADV and the point gauge in both longitudinal and vertical directions were controlled by a mechanism with an accuracy of 0.01 mm. The particles displaced from the protection were computed by weight and number using a replaceable sediment trap located downstream of the test reach. The trap is 75-cm wide and 5-cm high and is placed on the bottom of the flume.

Riprap materials were represented by four types of uniformly distributed sharped edge particles with quite similar shape factors. Rock characteristics are shown in table 1, where λ is the porosity of the material, γ_s and γ_w are respectively the rock and water specific weight and σ is the rock standard deviation

$$\sigma = \sqrt{\frac{D_{84}}{D_{16}}} \tag{1}$$

Experiments may be divided in two categories: continuous (C) and non-continuous (NC) protections. For continuous bed experiments all the bottom of the 3-m test reach was covered by a layer of rock with thickness $T = 2D_{50}$. To avoid problems related with internal boundary layer development due to the transition from the roughened reach (upstream) to the test reach, the first 1 m of bed was made rigid by gluing the rocks. Furthermore, this transition also prevents the sudden change of bed level at the upstream boundary of the movable bed. Figure 3 shows the schematic diagram of the flume and experimental setup of continuous protection experiments. The 200-cm movable bed was considered large enough to behave the same way as an infinite protection.

Non-continuous tests were prepared dumping rock material inside a slot at the bottom of the channel. The slot have the same width of the flume, a depth (below the flume bottom) $T = 2D_{50}$ and variable length l (figs. 2 and 4). Particles were laid in the slot allowing different values of protrusion p. The level of topmost particles and the bottom level were measured at several points prior to each test using the point gauge, so that protrusion values were computed as the difference between their mean values. The placement was also controlled by the total weight of the rocks in the slot.

Table 1. Rock characteristics.

Rock type	D_{16} (cm)	D_{30} (cm)	D_{50} (cm)	D_{84} (cm)	σ	$\frac{\gamma_s - \gamma_w}{\gamma_w}$	λ
I	0.66	0.74	0.85	1.10	1.29	1.89	0.48
II	1.10	1.15	1.25	1.48	1.16	1.82	0.47
III	1.33	1.42	1.57	1.80	1.16	1.92	0.47
IV	1.60	1.68	1.75	1.93	1.10	1.92	0.47

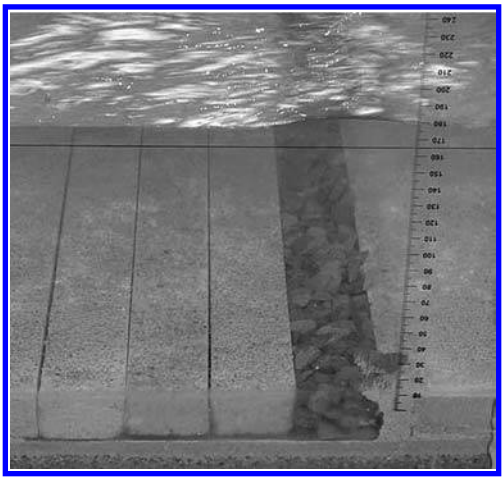


Figure 2. Non-continuous riprap test. Flume at the University of Castilla-la Mancha. Flow is from the left to the right. The shorter bed sill is being tested.

Copyright © 2006 Taylor & Francis Group plc, London, UK

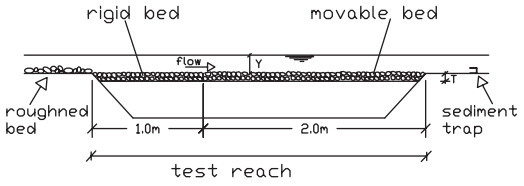


Figure 3. Experimental setup for continuous bed test.

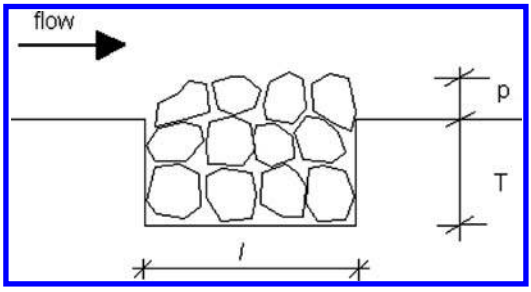


Figure 4. Non-continuous tests setup.

3 EXPERIMENTAL PROGRAM

In C experiments four series of tests were conducted to determine incipient motion conditions of the four rock types presented in table 1 (series 1 to 4 in table 2). Each series consisted in a number of tests with different discharges, providing sufficient information so that the relationship between shear stress and transport rate of riprap particles could be well described.

NC experiments aimed at verifying the influence of protection length and protrusion on incipient motion conditions. In series 5 to 8 the four rock types were tested with a fixed value of relative length $l/D_{50} = 4$ and an initial value of relative protrusion $p/D_{50} = 0.95$. Each of series 6, 9, 10, 11 and 12 had the same characteristics (width, D_{50}, p, Y) but protections with varying lengths. Series 6, 13 and 14 used the same variables (width, D_{50}, l, Y) but two different initial values of protrusion.

As shown in table 2, although in some series the relationship between shear stress and transport rates was established through many tests, most of the series counted with 8 tests.

The first step prior to each test was to adjust both the flume slope and the tailgate position to produce, for a given water discharge, the water depth $Y = 16.5$ cm. The preparation of the bed for continuous experiments consisted in mixing the material so that it represented the condition of dumped riprap. Then it was leveled with a leveling bar. Non-continuous protections preparation consisted in placing the material inside the slot and carefully measuring its protrusion with the point gauge, as mentioned before. After the bed was prepared the channel was slowly filled with water.

Table 2. Experimental program. C:continuous; NC: non-continuous.

Series	Prot. type	N. of tests	l (cm)	D_{50} (cm)	p (cm)	Q ls^{-1}
1	C	14	200	0.85	0	90–120
2	C	41	200	1.25	0	90–132.5
3	C	8	200	1.57	0	95–135
4	C	8	200	1.75	0	124–155
5	NC	45	3.4	0.85	0.81	60–95
6	NC	8	5.0	1.25	1.19	80–132.5
7	NC	8	6.3	1.57	1.49	95–130
8	NC	8	7.0	1.75	1.66	95–130
9	NC	8	10	1.25	1.19	95–130
10	NC	8	20	1.25	1.19	95–130
11	NC	8	35	1.25	1.19	95–130
12	NC	8	50	1.25	1.19	95–130
13	NC	8	5	1.25	0.35	95–130
14	NC	21	5	1.25	0.76	80–130

Obstacles were introduced downstream the test reach to increase the water level and ensure no bed motion. After steady flow conditions had been reached the obstacles were removed, the 16.5-cm water depth was achieved, and time began to be computed. Transport rates of riprap particles were measured by removing the sediment trap and extracting the trapped solid material.

Time dependence of transport rates may introduce important errors in incipient motion determination and must be taken into account. Measurements of transport rates were made at different time intervals. First measurement was taken at $t = 40\,s$ and time intervals gradually increased until $\Delta t = 5\,min$ at $t = 10\,min$. After $t = 10\,min$ all measurements were taken at $\Delta t = 5\,min$ intervals. Almost all experiments had a total duration of 1 hour.

This experimental procedure was repeated for different water discharges in the ranges shown in table 2, changing the flume slope to obtain the same flow depth ($Y = 16.5$ cm).

4 BASIS FOR ANALYSIS

4.1 *Reference transport method*

As mentioned before, reference transport method is used in this paper to estimate critical shear stresses for initiation of motion. The method consists in applying different shear stresses to a bed and measuring the corresponding bed load transport rates. Then, from a fitted relation between shear stress and transport rates, the threshold value of bed shear stress may be determined both by extrapolating to zero transport or by an arbitrary definition of a small but finite constant transport rate (Wilcock 1988; Parker et al. 1982; Fenton and

Copyright © 2006 Taylor & Francis Group plc, London, UK

Abbott 1977; Shvidchenko and Pender 2000). As suggested by Fenton and Abbott (1977), "this procedure is appropriate to a physical situation in which quantities vary randomly in time and space, for by collecting a large number of individual grains removed from the bed over a long period, the statistical population is large enough that the values obtained for transport rates, and subsequently threshold stress, may be considered reliable". Several reference transport parameters have been proposed to represent the level of transport activity. Most of them represent bed mobility in some dimensionless form of unit transport rates (Parker et al. 1982; Einstein 1950). Due to the stochastic nature of both fluctuating forces associated with turbulent flow and particle position distribution the probabilistic approach is certainly the most appropriate.

Shvidchenko and Pender (2000) in their study on the influence of relative depth on incipient motion conditions have linked incipient motion to the probability of sediment entrainment through the intensity of sediment motion:

$$I = \frac{m}{N\Delta t} \tag{2}$$

in which I is the intensity of sediment motion and m is the number of particle displacements observed during the time interval Δt on an area that contains N surface particles. As stated by Einstein (1942) (extracted from Shvidchenko and Pender (2000)) I can obviously be regarded as the probability that a particle be detached from the bed in a given unit time interval.

In this study the intensity of sediment motion (eq. 2) is used as a measurement of bed activity. This approach requires measurements of the number of entrainments per unit bed area instead of the cross section solid discharge measured in the experiments using the sediment trap. Yalin (1972) (extracted from Shvidchenko 2000) proposed the relationship between unit weight solid transport discharge q_s and the number of particle entrainments per unit area:

$$q_s = \frac{m}{A\Delta t} G L_m \tag{3}$$

where G is the mean particle weight, A is the bed area in which m entrainments are observed and L_m may be regarded as a characteristic or "mean" value of particle displacement after dislodgement. This relationship may be considered valid for all those cases in which the maximum particle displacement is smaller than the bed length. In the present study non-continuous riprap protections with small length do not fulfil this condition. In other words, two protections having the same relative number of displacements (e.g. I values) but different lengths will obviously generate different q_s values. As a result, the relationship between I and q_s must be based on particle displacement statistics rather than on its mean values.

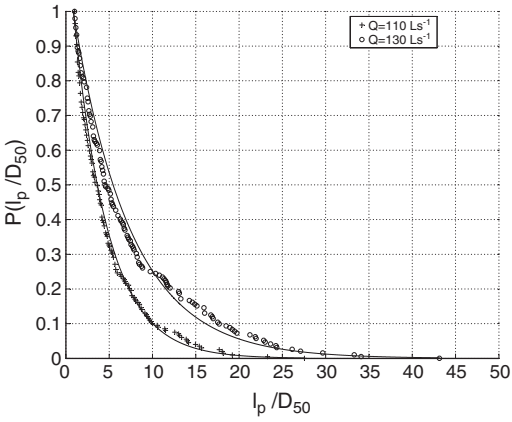


Figure 5. Particle displacement distribution tests using rock type II. Observed data (from video) in dots and eq. 5 in continuous line.

4.2 *Conversion of transport rates into intensity of sediment movement*

In this study particle displacement distribution is estimated by using standard image processing techniques. Nine tests were conducted using rock types II, III and IV (table 1) for flows ranging from $\tau^* = 0.022$ up to $\tau^* = 0.059$, where τ^* is the dimensionless shear stress, defined as

$$\tau^* = \frac{\tau_o}{(\gamma_s - \gamma_w) D_{50}} \tag{4}$$

and τ_o is the mean bed shear stress.

For each test a number of displacements ranging from 100 to 200 was recorded. Only particle displacements with length greater than $1D_{50}$ were considered. Data was fitted using an exponential probability distribution

$$P\left(\frac{l_p}{D_{50}}\right) = e^{-\alpha\left(\frac{l_p}{D_{50}} - 1\right)} \tag{5}$$

where $P(\frac{l_p}{D_{50}})$ is the probability that dimensionless particle displacement $\frac{l_p}{D_{50}}$ be greater than a fixed value, and l_p the absolute value of particle displacement. Figure 5 shows two distributions and the corresponding fitted curves.

Linear regression was then used to estimate a relation between α and τ^*, resulting:

$$P\left(\frac{l_p}{D_{50}}\right) = e^{(3.04\tau^* - 0.29)\left(\frac{l_p}{D_{50}} - 1\right)} \tag{6}$$

The relation between the number of particles collected in the sediment trap N_t and a relative measure of entrainments

Copyright © 2006 Taylor & Francis Group plc, London, UK

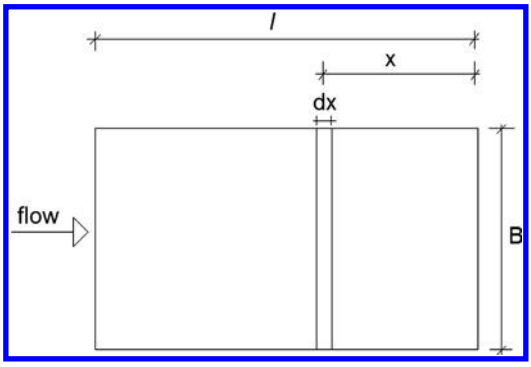


Figure 6. Diagram showing variables used in eq. 8.

$$m' = \frac{m}{A} \tag{7}$$

may now be derived as

$$N_t = Bm'\left(D_{50} + \int_{D_{50}}^{l} P(x)dx\right) \tag{8}$$

where B is the channel width, x is the longitudinal coordinate, starting at the downstream boundary of the protection and l is the total length of the protection (fig. 6). The first term in the right-hand side of equation (8) is due to the assumption that the most downstream particle will always reach the trap after dislodgement. The integral means the fraction of dislodged particles that will leave the protection and then will be collected in the trap. This fraction may be regarded as the probability that the length of the particle motion l_p be greater than its x coordinate.

Substituting (6) into (8) and solving the integral:

$$m' = \frac{N_t}{BD_{50}\left(1 + \frac{e^{(3.04\tau^* - 0.29)\left(\frac{l}{D_{50}} - 1\right)} - 1}{3.04\tau^* - 0.29}\right)} \tag{9}$$

Defining N' as the particle surface density:

$$N' = \frac{N}{A} \tag{10}$$

$$\frac{m}{N} = \frac{m'}{N'} \tag{11}$$

Substituting (11) into (9):

$$\frac{m}{N} = \frac{N_t}{N'BD_{50}\left(1 + \frac{e^{(3.04\tau^* - 0.29)\left(\frac{l}{D_{50}} - 1\right)} - 1}{3.04\tau^* - 0.29}\right)} \tag{12}$$

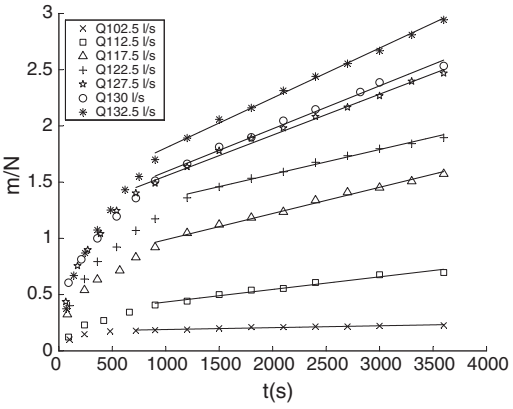


Figure 7. Time evolution of accumulated m/N values. Series 2.

Defining ϕ as

$$\psi = BD_{50}\left(1 + \frac{e^{(3.04\tau^* - 0.29)\left(\frac{l}{D_{50}} - 1\right)} - 1}{3.04\tau^* - 0.29}\right) \tag{13}$$

it results:

$$\frac{m}{N} = \frac{N_t}{\psi N'} \tag{14}$$

The values of N' were determined for each rock types by counting the number of surface particles contained in an area of known dimensions. Equation (14) provides the relation to convert measured N_t into relative number of entrainments in the riprap blanket.

4.3 *Time dependence*

As observed by other investigators (Shvidchenko and Pender 2000; Froehlich and Benson 1996) transport rates in experiments with a bed composed of dumped stones is not a constant but varies with time. The initial stages present a higher transport that asymptotically decreases to a steady value. Figure 7 shows the time evolution for series 2. The transport rates shown in this figure have been already converted to m/N values, where m represents the accumulated number of movements computed since the start of the experiment (since $t = 0$). This is the typical behavior observed in continuous bed experiments and corresponds to the process of reorganization of bed structure toward the more stable condition of "water worked" bed. The steady values of I reached after this reorganization will be used in this study for determining incipient motion. These values correspond to the slopes of the fitted lines in figure 7.

Copyright © 2006 Taylor & Francis Group plc, London, UK

Transport rates in the case of non-continuous riprap protections also present higher values of I at the first stages of the experiments but gradually converges to a zero transport. This phenomenon may be explained by the dependence of transport rates on protrusion values, which vary significantly during the tests. Some authors have observed decreasing values of τ_c^* as particle protrusion increases (Fenton and Abbott 1977; James 1989; Coleman et al. 2003). During non-continuous experiments the erosion process reduces protrusion of the protection gradually increasing its stability. This behavior may be modeled by establishing a relation between the protrusion and the erosion rate. Herein we have assumed the potential relation:

$$\frac{dp}{dt} = -K(p - p_e)^a \tag{15}$$

where K and a are constants and p_e is the equilibrium protrusion, defined as the value of p for $t \to \infty$.

Integrating (15) and rearranging constants the expression describing the time evolution of protrusion may be written as:

$$p = K_2 (at - t + C_2)^{\frac{1}{1-a}} + p_e \tag{16}$$

The eroded thickness may be written as a function of the number of riprap particles dragged by flow:

$$e = \frac{N_t G}{\gamma_s (1 - \lambda) lB} \tag{17}$$

where γ_s is the particle specific weight and λ is the porosity of the material. The product $\gamma_s(1 - \lambda)$ will be called γ_b.

Therefore, protrusion may also be expressed as a function of the eroded thickness $e(t)$:

$$p(t) = p_o - e(t) \tag{18}$$

where p_o is the initial protrusion (at $t = 0$).

Substituting (16) and (17) into (18):

$$N_t = \left[-K_2(at - t + C_2)^{\frac{1}{1-a}} + p_o - p_e\right]\left(\frac{\gamma_b lB}{G}\right) \tag{19}$$

From (19) and (14):

$$\frac{m}{N} = \left[-K_2 (at - t + C_2)^{\frac{1}{1-a}} + p_o - p_e\right]\left(\frac{\gamma_b lB}{\psi G N'}\right) \tag{20}$$

Equation (20) was best fitted for all non-continuous tests (series 5 to 14). Figure 9 shows an example of fitting equation (20) with the experimental data from one of the tests of series 5.

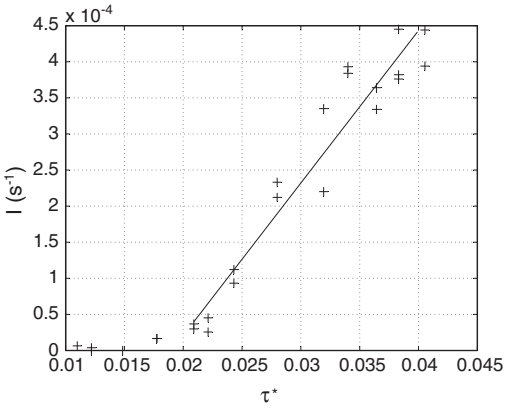


Figure 8. Estimation of critical shear stress. Series 2.

4.4 *Incipient motion estimation*

Following the criterion used by Shvidchenko and Pender (2000) critical shear stresses were determined as the bed shear stresses that produced an intensity of sediment motion $I = 10^{-4} s^{-1}$.

For continuous bed experiments I values were taken as those corresponding to the "water worked" situation by fitting straight lines of accumulated $\frac{m}{N}$ as a function of t once a constant transport rate was reached. Figure 7 shows the temporal evolution of accumulated $\frac{m}{N}$ and the fitted lines.

I values were then plotted against dimensionless bed shear stresses τ^* and a linear relation was fitted.

Bed shear stresses were calculated by

$$\tau = \rho v^* \tag{21}$$

where v^* is the shear velocity estimated for each test by fitting the logarithmic velocity profile

$$\frac{V}{v^*} = \frac{1}{K} ln\left(\frac{y}{y_o}\right) \tag{22}$$

A sensitivity analysis was carried out to determine the influence of datum level, deviations from logarithmic profiles in the outer flow region and the choice of using fitted or fixed values for y_o on shear velocities results. Results showed the best correlations when using data including part of outer flow layer and fitting both v^* and y_o.

Figure 8 shows the results for series 2.

In non-continuous experiments velocity profiles were measured at a point located 8 cm upstream from the protection where velocities may be assumed not disturbed by its presence. As a result, τ values may be considered representative of "mean" bed stresses (τ_o) rather than "local" stresses above the protection (τ_p). Although local stresses are the most suitable for

Copyright © 2006 Taylor & Francis Group plc, London, UK

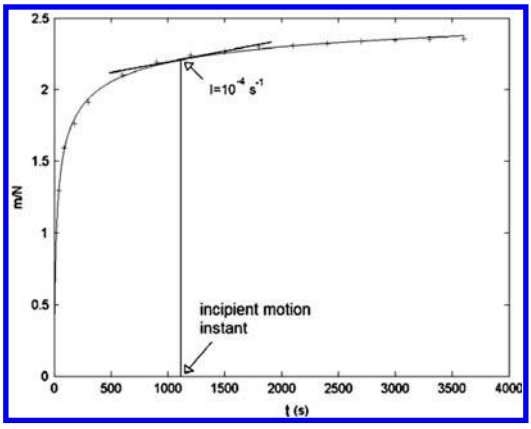


Figure 9. Determination of incipient motion instant. Series 5, $Q = 95\, ls^{-1}$.

describing the transport phenomenon in the protection, τ_o seem to be the most suitable variable for engineering applications.

For non-continuous protections, for a given value of τ_o, the intensity of sediment motion gradually decreases with time as the protection is being eroded. As a result, each value of $I(t)$ may be associated with a specific value of protection protrusion $p(t)$. The time derivative of (20) gives the function $I(t)$ and the time instant corresponding to incipient motion may be found by:

$$\frac{d\left(\frac{m}{N}\right)}{dt} = I(t) = 10^{-4} \tag{23}$$

Figure 9 illustrates the instant corresponding to $I = 10^{-4} s^{-1}$. The protrusion corresponding to the incipient motion (p_c) is finally calculated using (16).

5 RESULTS

Figure 10 illustrates the relation between the critical protrusion p_c, made dimensionless with D_{50}, and τ^* for series 5, 6, 7 and 8. These series have the same value of $l/D_{50} = 4$ and $p_o/D_{50} = 0.95$ but each of them corresponds to one of the four rock types presented in table 1.

Results show that dimensionless shear stresses values for "complete stability" ($p_c = p_o = 0.95 D_{50}$) are about 10% of Shields critical stresses found in the bibliography. For increasing τ^* values there is a linear reduction of critical protrusion values. For $\tau^* \simeq 0.016$ the critical protrusion is $p_c \simeq 0$. In other words the bed sill is "swept" to the general bed level.

The influence of the relative length on incipient motion conditions is shown in figure 11. This figure shows data of series with different relative lengths but

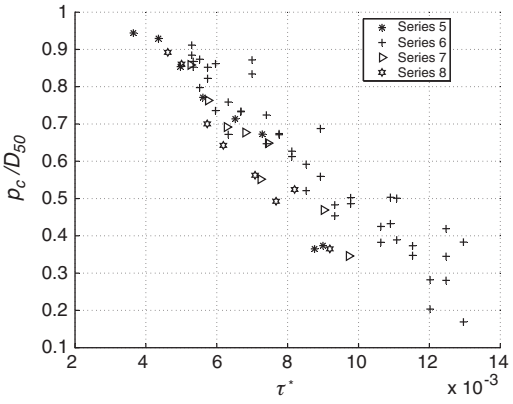


Figure 10. Critical protrusion for series 5, 6, 7 and 8.

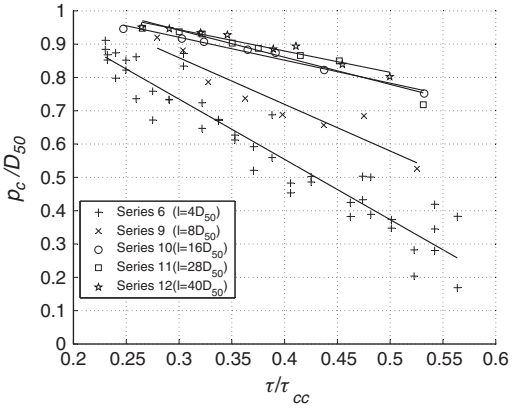


Figure 11. Analysis of the influence of relative length on critical protrusion values.

the same values of both p_o and D_{50}. Values of p_c/D_{50} are plotted against shear stresses, made dimensionless with critical shear stresses found for continuous protection tests (τ_{cc}). Fitted linear relationships corresponding to each series are also plotted. Data from series 6 is used both in figure 10 for protrusion effect and in figure 11 for length effect.

From figure 11 we observe that as the relative length increases, stability is significantly enhanced. For a fixed value of critical relative protrusion, say $p_c/D_{50} = 0.8$, shear stresses for a relative length $l/D_{50} = 16$ is almost twice the corresponding value for $l/D_{50} = 4$. For relative lengths greater than $l/D_{50} = 16$ this variable seems to have no influence on incipient motion conditions. The last observation confirms the intuitive idea that as the protection becomes longer it tends to behave as a continuous protection.

Fitted lines for series 10, 11 and 12 all have approximately the same slope, which is milder than those

Copyright © 2006 Taylor & Francis Group plc, London, UK

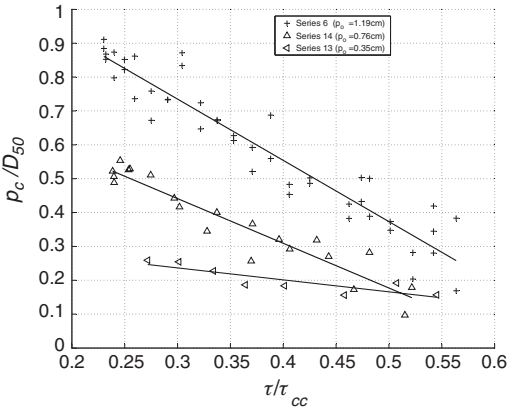


Figure 12. Analysis of the influence of initial values of relative protrusion on incipient motion conditions.

corresponding to series 6 and 9. This demonstrates that critical protrusion of a larger protection is less sensitive to shear stresses. Another feature in figure 11 is the fact that all the fitted lines intersect $p_c = p_o = 0.95D_{50}$ for τ/τ_{cc} around 0.2 (i.e. 20% of critical shear stress for a continuous revetment).

The influence of initial protrusion is analyzed in figure 12. This figure presents three series of experiments with different values of initial protrusion p_o but with the same values of l and D_{50}. Figure 12 demonstrates that designing protections with protrusion values corresponding to the "stable zone" of figure 11 does not ensure that no motion will occur. Even for very low initial protrusions some displacements were recorded. In other words, the equilibrium of a higher bed sill after 1 hour of flow does not imply that a bed sill with this initial height is stable under the same flow. For practical purposes, the idea of a sacrifice thickness to take this into account is recommended.

6 CONCLUSIONS

An experimental investigation on the effect of geometrical variables on shear failure of riprap protections has been presented.

Complete stability (no motion) of a non-continuous riprap protection requires shear stresses values about 10% of Shields critical values usually found in bibliography and approximately 20% of critical values determined in this paper for a continuous riprap bed.

Increasing the length of the protection significantly increases its stability. On the other hand for relative lengths greater than $l = 16D_{50}$ it appears that this variable has no effect on incipient motion conditions.

Although all tests with non-continuous protections reached a stable protrusion for a given shear stress, this value does not assure that no motion will occur. Particle losses were recorded even for initial protrusion values much lower than those corresponding to p_c in tests with higher p_o using the same shear stresses.

REFERENCES

Buffington, J. M. and D. R. Montgomery (1997). A systematic analysis of eight decades of incipient motion studies, with special reference to gravel-bedded rivers. *Water Resources Research 33*, 1993–2029.

Coleman, S. E., B. W. Melville, and L. Gore (2003). Fluvial entrainment of protuding fractured rock. *Journal of Hydraulic Engineering 129*, 872–884.

Einstein, H. A. (1950). The bed-load function for sediment transport in open channel flows. Technical report, U.S. Department of Agriculture, Soil Conservation Service.

Escarameia, M. and R. W. P. May (1995). Stability of riprap and concrete blocks in highly turbulent flows. *Proc. Instn. Civ. Engrs. Wat. Marit. & Energy 112*, 227–237.

Fenton, J. D. and J. E. Abbott (1977). Initial movement of grains on a stream bed: the effect of relative protrusion. *Proc. R. Soc. Lond. 352*, 523–537.

Froehlich, D. C. and C. A. Benson (1996). Sizing dumped rock riprap. *Journal of Hydraulic Engineering 122*, 389–396.

James, C. S. (1989). Prediction of entrainment conditions for nonuniform noncohesive sediments. *Journal of Hydraulic Research 28*, 25–41.

Martín-Vide, J. P. (2002). *River Engineering*. Ed. UPC (in spanish).

Maynord, S. T., J. F. Ruff, and S. R. Abt (1987). Riprap design. *Journal of Hydraulic Engineering 115*, 937–949.

Parker, G., P. C. Klingeman, and D. G. McLean (1982). Bedload and size distribution in paved gravel-bed streams. *Journal of the Hydraulics Division 108*, 544–571.

Pilarczyk, K. W. (1998). *Dikes and Revetments. Design, maintenance and safety assessment.* Balkema.

Shvidchenko, A. B. and G. Pender (2000). Flume study of the effect of relative depth on the incipient motion of coarse uniform sediments. *Water Resources Research 36*, 619–628.

Stevens, M. A., D. B. Simons, and G. L. Lewis (1976). Safety factors for riprap protections. *Journal of the Hydraulic Division 102*, 637–655.

Wilcock, P. R. (1988). Methods for estimating the critical shear stress of individual fractions in mixed-size sediment. *Water Resources Research 24*, 1127–1135.

Copyright © 2006 Taylor & Francis Group plc, London, UK

B.8. Bank erosion and protection

Copyright © 2006 Taylor & Francis Group plc, London, UK

An integrated model for the evolution of channel morphology, including cohesive bank erosion

A.N. Menéndez, P.E. García & J. Rodríguez Ardila
Hydraulics Laboratory, INA (National Institute for Water) & Mathematical Modelling Laboratory (LaMM), School of Engineering, University of Buenos Aires, Argentina

C.E. Laciana & A. Sfriso
Mathematical Modelling Laboratory (LaMM), School of Engineering, University of Buenos Aires, Argentina

ABSTRACT: An integrated hydrodynamic-sedimentologic-morphological model is proposed to deal with the morphological evolution of channel cross-sections in practical situations. While based on a physically sound formulation, efficiency is attained by considering only the relevant physical mechanisms, in view of the geometric scales of the water course, and the time scale of the observer. Its performance is assessed through specific validation tests for the different mechanisms. A numerical experiment is undertaken.

1 INTRODUCTION

Water courses that develop on alluvial material show a changing morphology, determined by the variable water current action. Variations are observed in both the channel depth (bottom evolution) and width (bank evolution). Water acts on the channel boundaries by exerting a shear stress, which depends on the flow velocity. In curved channels, in addition to the longitudinal velocity component, a transversal component also exists, constituting the so called secondary currents.

To numerically simulate these processes, it is necessary to formulate an integrated hydrodynamic-sedimentologic-morphological model. This formulation is conditioned by the geometric scales of the water course, and the time scale of the observer. In this paper, such a model is presented, valid for practical values of those scales.

2 MODEL FORMULATION

2.1 *Hydrodynamic model*

For an open-channel flow problem, we can distinguish locally three 'natural' spatial coordinates: one along the flow direction (longitudinal), a second one in the horizontal plane and across the flow direction (lateral), and a third one in the vertical direction (assuming a mild channel slope). We will consider that, as usual, the characteristic scales are very different in those three spatial directions, allowing for some simplifications. In the first place, it will be assumed that the longitudinal scale of interest (the scale of the observer) is much larger than the transversal dimensions of the cross section, i.e.,

$$L_{ox} \gg \hat{B}, \hat{h} \tag{1}$$

where $\hat{B}$ is a scale for the channel width, $\hat{h}$ a scale for the water depth, and L_{ox} is the longitudinal spatial scale of the observer, which is calculated as (Menéndez 2003) $L_{ox} \equiv \hat{U}\hat{T}$, with $\hat{U}$ being a scale for the longitudinal flow velocity, and $\hat{T}$ the observer time scale. Condition (1) means that the problem can be treated with the 1D approximation (Menéndez 2003), i.e., that the longitudinal variation of the cross-sectional mean flow velocity can be calculated independently of the transversal variation of the flow velocity, using a 1D Longitudinal Model as the well known Saint Venant Equations (Jain 2001).

In the second place, the cross section will be considered as shallow:

$$\hat{B} \gg \hat{h} \tag{2}$$

As a consequence of condition (2), the lateral distribution of flow velocity, if needed, can be determined independently of the vertical distribution.

In the third place, it will be assumed that the lateral spatial scale of the observer L_{oy}, which is calculated as (Menéndez 2003) $L_{oy} \equiv (\hat{\varepsilon_y}\hat{T})^{1/2}$, with $\hat{\varepsilon_y}$ being a scale

Copyright © 2006 Taylor & Francis Group plc, London, UK

for the lateral diffusivity, is at most of the same order of the lateral dimension of the cross section, i.e.,

$$L_{oy} \tilde{<} \hat{B} \tag{3}$$

As a consequence of (3), it is pertinent to calculate the lateral distribution of the longitudinal flow velocity (Menéndez 2003), which may be obtained from a 1D Lateral Model, such as the Lateral Distribution Method (LDM) proposed by Wark et al. (1990):

$$ghI_x - \frac{B_g f}{8} U^2 + h \frac{\partial}{\partial y}\left[\varepsilon_y \frac{\partial U}{\partial y} \right] = 0 \tag{4}$$

where y is the lateral coordinate measured from the right bankline, $h(y)$ the local flow depth, $U(y)$ the vertically averaged local longitudinal flow velocity, I_x the longitudinal flow slope (obtained from the 1D Longitudinal Model), and f the Darcy-Weisbach friction factor; B_g is a geometrical factor and ε_y the lateral eddy viscosity; they are given by

$$B_g = \sqrt{1 + \tan^2\alpha + \tan^2\omega}\,, \quad \varepsilon_y = \chi U_* h \tag{5}$$

where α is the angle of the longitudinal channel slope, ω the angle of the lateral channel slope (Figure 1), χ the dimensionless lateral eddy viscosity coefficient (taken as 0.25), and $U_* = \sqrt{\tau_b}$ the shear velocity, with τ_b being the kinematic bottom shear stress, which is parameterized as

$$\tau_b = \frac{1}{8} f B_g U^2 \tag{6}$$

As boundary conditions for eq. (4), the free-slip condition may be imposed:

$$\left.\frac{dU}{dy}\right|_{\text{bankline}} = 0 \tag{7}$$

which physically means that the wall boundary layers by the banklines are not solved.

For the present applications, the non linear ordinary differential equation (4) is solved numerically. It is discretized using a centered finite difference scheme. The resultant non linear algebraic system is solved by means of the Newton-Raphson method.

As a consequence of curvature, in addition to the longitudinal flow velocity there are transversal components, which constitute the secondary flow. In particular, the lateral velocity component at the bottom, $u_r(y)$, is of relevance for bed load transport. It has been determined from the parametric vertical velocity profile model of Kikkawa et al. (1976), which assumes

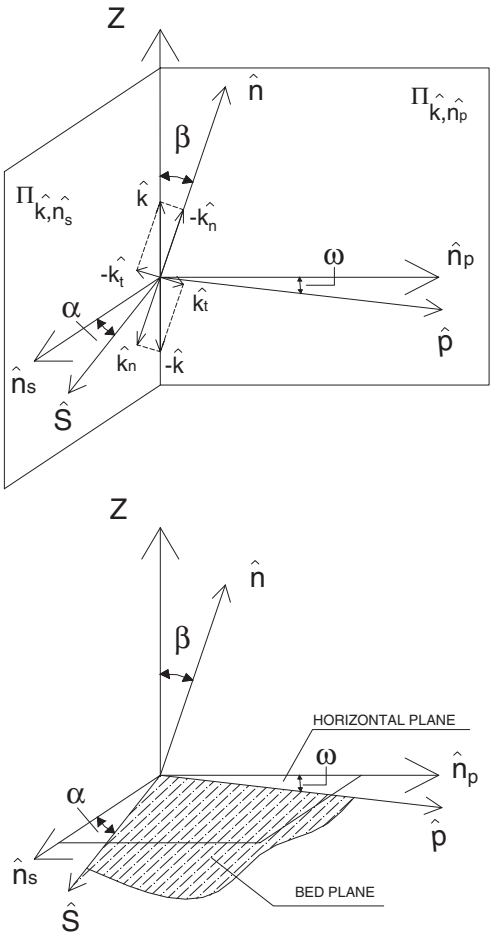


Figure 1. Geometrical parameters.

that the radius of curvature of the channel is much larger than its width. The expression is the following:

$$u_r = \frac{U^2}{\bar{U}} \frac{h}{r} \frac{1}{\kappa} \left(4.167 - 2.640 \frac{1}{\kappa} \frac{\bar{U}_*}{\bar{U}} \right) \tag{8}$$

where $\bar{U}$ and $\bar{U}_*$ are the transversally-averaged longitudinal flow velocity and shear velocity, respectively, $r = r(y)$ the radius of curvature, and κ von Karman constant (≈ 0.4).

At the banklines it must hold the impenetrability condition

$$u_{rb}\big|_{\text{bankline}} = 0 \tag{9}$$

The transition between the parametric model value, given by eq. (8), and the bankline value, eq. (9), is

Copyright © 2006 Taylor & Francis Group plc, London, UK

taken into account by means of a modulating function, or mask, $M(y)$, with the following form:

$$M(y)=\begin{cases}1-\left(\dfrac{\delta-y}{y}\right)^{1/2} & \text{if } 0\le y\le\delta\\ 1 & \text{if } \delta\le y\le B-\delta\\ 1-\left(\dfrac{\delta+y-B}{\delta}\right)^{1/2} & \text{if } B-\delta\le y\le B\end{cases} \tag{10}$$

where B is the channel top width, and δ the bank boundary layer thickness, which is proposed to scale with the near-bank depth h_b, i.e.

$$\frac{\delta}{h_b}=\kappa_b=const. \tag{11}$$

where the value of κ_b is to be determined from experimentation. Hence, the lateral bottom flow velocity component is given by

$$u_{rb}(y)=M(y)u_r(y)\big|_{\text{model}} \tag{12}$$

2.2 *Sediment transport model*

Kovacs & Parker (1994) model, based on force balances, is used. In the first place, the forces acting on a sediment particle are considered: the drag force due to the moving fluid, which is the driving mechanism; the component of the immersed weight of the particle tangential to the plane of the bed, that also constitutes a driving force; and the dynamic Coulomb resistive force, which represents the momentum loss due to collisions. The following equation follows:

$$\left|\vec{u}_\Delta^*\right|\vec{u}_\Delta^*=a\tau_{C0}^*\left(\left|\vec{k}_n\right|\hat{t}_{v_p}-\frac{\vec{k}_t}{\mu_C}\right) \tag{13}$$

where $\vec{u}_\Delta=\vec{u}_b-\vec{v}_p$, with $\vec{u}_b$ and $\vec{v}_p$ being the bottom fluid velocity and the particle velocity, respectively, $a\equiv(\vec{u}_b/U_*)^2$, τ_{C0}^* is the dimensionless shear stress (or Shields parameter) for initiation of motion on a flat bottom, $\hat{t}_{v_p}\equiv\vec{v}_p/|\vec{v}_p|$ the versor in the direction of the particle velocity, μ_C the dynamic Coulomb friction factor, and $\vec{k}_n$ and $\vec{k}_t$ the components of the vertical versor, pointing downwards, along the normal and transversal directions to the bottom, respectively. The fluid velocity can be expressed as

$$u_b=\varepsilon U\,\hat{s}\;+\;u_r\sqrt{1+\cos^2\alpha\tan^2\omega}\;\hat{p}' \tag{14}$$

where $\hat{s}$ is the versor in the longitudinal direction of motion, $\hat{p}'$ the versor on the plane tangent to the bottom and normal to $\hat{s}$, and ε the relation between the longitudinal component of the bottom velocity and the mean transversal velocity U.

To solve eq. (13) for the sediment particle velocity, it is proposed to split it into components, by multiplying it alternatively by versors $\hat{s}$ and $\hat{p}'$, obtaining

$$\begin{aligned}\left|\vec{u}_\Delta^*\right|\left(u_{bs}^*-v_p^*\cos\psi\right)-a\tau_{C0}^*\left(\left|\cos\beta\right|\cos\psi-\frac{\sin\alpha}{\mu_C}\right)=0\\ \left|\vec{u}_\Delta^*\right|\left(u_{bp}^*-v_p^*\sin\psi\right)-a\tau_{C0}^*\left(\left|\cos\beta\right|\sin\psi-\frac{1}{\mu_C}\frac{\sin\omega\cos^2\alpha}{\sqrt{\sin^2\omega\cos^2\alpha+\cos^2\omega}}\right)=0\end{aligned} \tag{15}$$

where

$$\left|\vec{u}_\Delta^*\right|=\left(u_{bs}^{*2}+u_{bp}^{*2}+v_p^{*2}-2u_b^*v_p^*\cos\psi-2u_{bp}^*v_p^*\sin\psi\right)^{1/2}, \tag{16}$$

$v_p=|\vec{v}_p|$, ψ is the angle between the velocity vector and the s direction, and the asterisc indicates dimensionless velocities, with the scale $\sigma\equiv\sqrt{Rgd}$, being R the relative grain density, which diameter is d. System (15) is solved by means of Newton-Raphson method, to obtain the two unknowns v_p^*, and ψ.

The dimensionless vectorial volume bedload sediment transport rate per unit normal width (made dimensionless with the scale $d\sigma$) is calculated as

$$\vec{q}_b^*=\xi^*\vec{v}_p^* \tag{17}$$

where ξ^* is the dimensionless volume of particles participating in bedload transport. To obtain this volume, Kovacs & Parker (1994) perform a momentum balance for the bed layer. The generalization of their formulation to include curvature effects leads to

$$\xi^*=\frac{\tau_b^*-\tau_C^*}{\left(\mu_C\left|\vec{k}_n\right|\hat{t}_{v_p}-\vec{k}_t\right).\hat{s}'} \tag{18}$$

where $\hat{s}'=\cos\alpha_s\,\hat{s}+\sin\alpha_s\,\hat{p}'$,

$$\tau_b^*=\frac{\varepsilon^2U^2}{aRgd\cos\alpha_s} \tag{19}$$

is the bottom shear stress, and τ_C^* is the dimensionless critical shear stress for initiation of motion. This is obtained by specializing (13) for critical conditions. Taking into account curvature effects, and squaring it, we obtain

$$\left(\frac{\tau_{Cs}^*}{\tau_{C0}^*}\right)^2+\frac{2}{\mu_C}\frac{\vec{s}_p.\vec{k}_t}{s_p^2}\frac{\tau_{Cs}^*}{\tau_{C0}^*}+\frac{1}{\mu_C^2}\frac{k_t^2}{s_p^2}-\cos^2\beta=0 \tag{20}$$

where $\vec{s}_p\equiv\sqrt{1+\tan^2\alpha_s}(\hat{s}+\tan\alpha_s\hat{p}')$, which physically meaningful solution is

$$\frac{\tau_{Cs}^*}{\tau_{C0}^*}=-\frac{1}{\mu_C}\frac{\vec{s}_p.\vec{k}_t}{s_p^2}+\sqrt{\cos^2\beta+\frac{1}{\mu_C^2}\left[\left(\frac{\vec{s}_p.\vec{k}_t}{s_p^2}\right)^2-\frac{k_t^2}{s_p^2}\right]} \tag{21}$$

Copyright © 2006 Taylor & Francis Group plc, London, UK

2.3 *Morphologic model*

The channel bottom evolution is calculated through Exner equation, which arises from the sediment mass conservation condition (Raudkivi 1990):

$$\frac{\partial z_0}{\partial t}+\frac{1}{1-\lambda}\left[\frac{1}{r}\frac{\partial}{\partial y}\left(rq_{by}\right)+\frac{\partial q_{bx}}{\partial x}\right]=0 \qquad (22)$$

where z_0 is the bed elevation, t the time coordinates, λ the porosity of the bottom sediment, q_{bx} and q_{by} the total stream-wise (longitudinal) and lateral volumetric sediment load per unit width, respectively, and where no suspended sediment load is considered.

For the present applications, uniform longitudinal conditions are assumed, i.e., $\partial/\partial x = 0$. Hence, eq. (22) was discretized by means of a simple explicit centered finite-difference scheme:

$$\frac{\left[z_0\right]_j^{n+1}-\left[z_0\right]_j^n}{\Delta t}+\frac{\left[r\right]_{j+1/2}^n\left(\left[q_{by}\right]_{j+1}^n-\left[q_{by}\right]_j^n\right)-\left[r\right]_{j-1/2}^n\left(\left[q_{by}\right]_j^n-\left[q_{by}\right]_{j-1}^n\right)}{(1-\lambda)\left[r\right]_j^n\Delta y^2}=0 \qquad (23)$$

where n is the time coordinate index, and j the spatial coordinate index.

Non-cohesive bank erosion is taken into account through the following algorithm, which assumes that the water level is equal to the streambank level (bankfull conditions):

a) After each calculation step, the bank slope at the two border nodes of the calculation domain (in the following, bank-nodes), are determined.
b) If the slope is lower than the critical value, given by the condition $\tan\omega_C = \mu_C$, no action is taken.
c) On the contrary, if the slope is equal or higher than the critical value, a local "slide" process is considered: the bank-node height is lowered so as the slope becomes critical, and a new node (with the streambank level) is added to the calculation domain (towards the exterior of the channel) to represent the new bank location (i.e., it becomes the bank-node for the next time step). To account for mass conservation, the slide volume is next distributed among nodes adjacent to the bank.

If a cohesive stratum exists on top of the non-cohesive bank, the retreat of the latter produces undermining of the former, leading eventually to cantilever type failure. A geotechnical stability analysis is performed which, following Darby & Thorne (1996), includes the effects of positive pore water pressure in the saturated portion, negative pore water pressure in the unsaturated portion, and hydrostatic confining pressure due to the water level in the river, considering a relatively general bank profile geometry. A planar failure type is supposed, common for streambanks destabilized by severe bed degradation (Darby et al. 2000), with the failure plane passing through the top point of the non-cohesive portion of the bank. All possibilities, regarding the relative elevations of water surface, phreatic surface, and tension crack depth are considered, as pointed out by Darby & Thorne (1996), but properly adapted to deal with this specific failure type, as schematized in Figure 2. A search is performed, sweeping the possible fail angle range. Once the safety factor falls below one, the angle corresponding to the minimum cohesion is selected as the fail angle.

The computational treatment of the cohesive stratum is very simple: two nodes (per bank) are used to define it, as shown in Figure 3 as open circles (a third node will be used in the future to indicate the tension crack depth). When a failure is assumed, the bottom node is moved to coincide with the extreme node of the non-cohesive base (black circle), while the top node is located so as to define the failure angle.

The coarse fraction of the failure material is considered to fall at the bank toe, and distribute laterally according to its angle of repose (Figure 4), as proposed by Darby et al. (2002), while the fine fraction is supposed to incorporate to the wash load, and hence ignored. An ad-hoc algorithm was devised to perform the coarse failure material distribution. This material is then treated as non-cohesive material of a mean grain diameter different from that associated to the bottom sediment.

3 VALIDATION

3.1 *Validation strategy*

In order to validate the proposed integrated model, the effects of the main erosion mechanisms are tested separately, comparing the model predictions with existing experimental data and/or previous calculation results. In the first place, a straight channel with non-cohesive banks is considered, so as to check that the methodology can successfully deal with the original problem of Kovaks & Parker (1994). In the second place, a curved, fixed banks channel is taken, where the incorporated secondary flow effects are validated. For both cases, uniform longitudinal conditions are assumed, i.e., $\partial/\partial x = 0$. The time evolution of the channel cross section is analyzed. In the third place, the cohesive stratum failure algorithm is tested. The validation of the procedure for the treatment of the failure material is still under way.

3.2 *Straight channel with non-cohesive banks*

The experiments performed by Ikeda (Kovacs & Parker 1994) are chosen as the first validation test. The channel is straight, prismatic, and symmetric, with a 0.220 m base width, and a longitudinal slope of 0.00215. The initial channel cross section is

Copyright © 2006 Taylor & Francis Group plc, London, UK

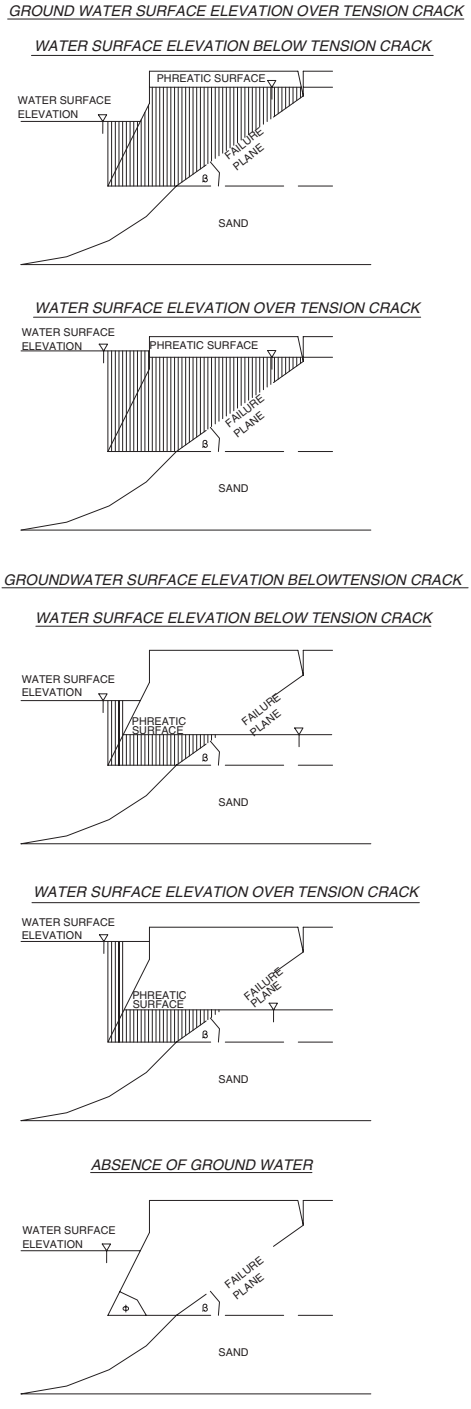


Figure 2. Bank failure cases.

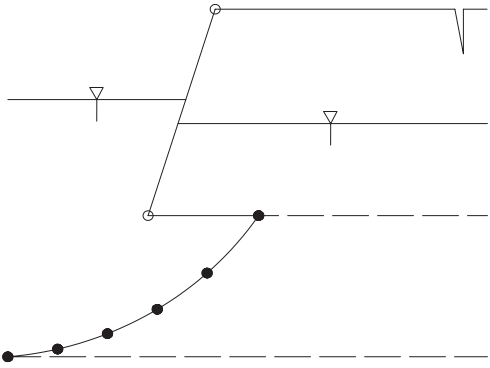


Figure 3. Cohesive-bank nodes (open circles).

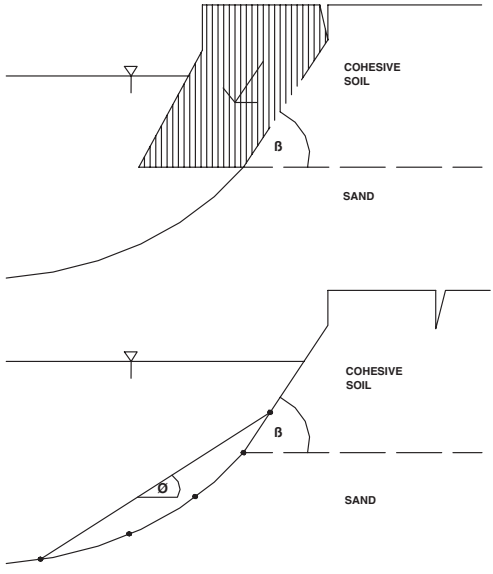


Figure 4. Distribution of failure material.

trapezoidal, with bottom and banks made of sand, with mean diameter $d_{50} = 1.3$ mm. The initial depth was 0.061 m The model parameters were fixed at the values used by Kovacs & Parker (1994). The initial lateral model domain was discretized into 100 intervals, resulting a spatial step $\Delta y = 0.00438$ m. The temporal step was chosen as $\Delta t = 1$ second, which produces a bed elevation change no larger than 1 mm per time step, thus providing enough accuracy to the solution, while preserving numerical stability.

Figure 5 presents the comparison for the (right half-) channel cross section evolution between the present numerical results and the ones obtained by Kovacs & Parker (1994), identified as K&P in the figure. The latter authors used a 2D transversal hydrodynamic model,

Copyright © 2006 Taylor & Francis Group plc, London, UK

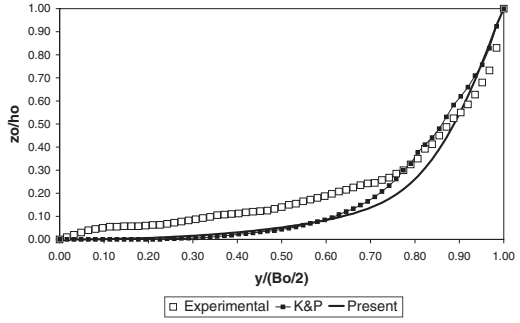


Figure 5. Comparison between K&P and present model results, for the cross section evolution.

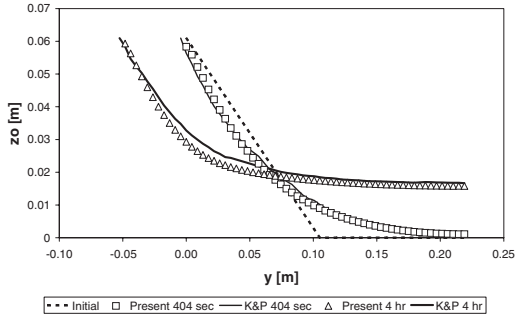


Figure 6. Comparison among K&P, present model results, and experimental results, for the cross section form after 12 hours.

i.e., they did not decouple the vertical and lateral directions of motion, and took into account the vertical velocity component, which lead to a more complex calculation procedure. Additionally, they pushed the validity of their bed load transport model beyond the water surface, to account for sediment delivery from the dry bank. The very satisfactory agreement between the two solutions observed in Figure 5 indicates that the present simpler, but physically sound, approach is good enough to capture all the relevant phenomena.

In Figure 6 the normalized (left half-) channel profile (B_o is the initial bottom width, and h_o the initial centerline depth) according to both models and Ikedas's experimental results, are presented. It is observed that K&P model seems to capture more accurately the bank slope, which could be due to their more elaborated hydrodynamic and bank erosion model. The deviations of the model results from experimental data in the bottom zone are thought to be due to the presence of bottom forms, not included in the present theory.

Similar comparisons are presented in Figure 7 for the time evolution of the top width W and centerline depth h, relative to their initial values (W_o is the

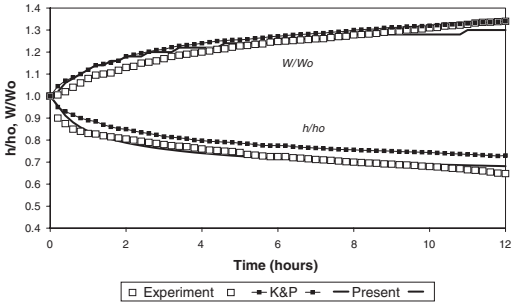


Figure 7. Comparison among K&P, present model results, and experimental results, for the top width and depth evolution.

initial top width). In the case of the top width, it is observed that the present approach, which gives stair-like responses due to the impulsive nature of the bank erosion algorithm, follows the trend of K&P results, with both of them overestimating the experimental rate of increase at the initial stages, but improving the agreement as time flows. Regarding the centerline depth evolution, the present model provides a better overall agreement with experimental results.

3.3 *Curved channel with fixed banks*

The second validation test refers to the experiments performed by Kikkawa et al. (1976). The experimental apparatus was a curved open channel, with vertical rigid walls, bed width $B_o = 1$ m, longitudinal bottom slope $I_x = 0.002$, initial uniform depth $h_o = 0.063$ m, sand bed with $d_{50} = 0.9$ mm, and curvature radius varying from 4 m at the inner bank to 5 m. at the outer one. The flow discharge was 30 l/s.

The channel width was represented with 100 intervals, which gives a spatial step $\Delta y = 0.01$ m. A temporal step $\Delta t = 1$ second was taken, which produces a bed elevation change no larger than 1 mm per time step, keeping the numerical solution accurate enough.

Taking as bank- depth h_b the one corresponding to the node adjacent to the bank-node, the best results were obtained for $\kappa_b = 420$.

Figure 8 shows the comparison between model predictions and experimental data, using Kikkawa et al. (1976) lateral velocity model, which in the following will be called, for simplicity, Kikkawa model. The agreement is considered as satisfactory, in view that the model represents the correct evolution trend and gives the right magnitude of the bottom height change. The most significant qualitative and quantitative departures occur close to the left bank ($y/W_o \approx 1$).

3.4 *Failure of cohesive stratum*

The third validation test consisted in comparing the failure angle of the cohesive stratum as predicted by the

Copyright © 2006 Taylor & Francis Group plc, London, UK

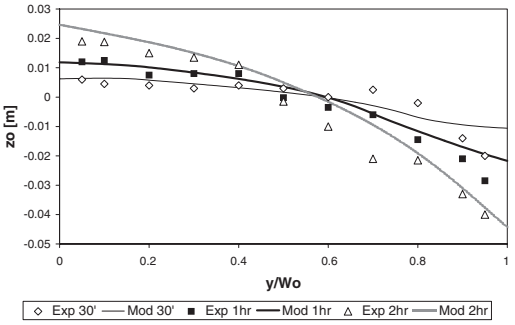


Figure 8. Comparison between experimental data and model results using Kikkawa lateral velocity model.

Table 1. Fail angle for different phreatic and water surface depths.

Experiment	1	2	3	4	5	6
Phr. Surf. depth (m)	1.27	1.27	1.27	3.27	3.27	3.27
Wat. Surf. Depth (m)	4.27	3.27	2.27	5.27	4.27	3.57
Fail angle Darby (°)	59	59	59	59	59	59
Fail angle Present (°)	57	56	55	58	59	58

present model and Darby et al. (2000) model (the computer program was kindly made available to the authors by request), for the particular case of the failure plane passing through the toe of the stratum (the only matching situation between the two models). The stratum height was taken as 5.86 m, with an initially practically vertical bank slope (89°), in order to guarantee unstable conditions, and a tension crack depth of 2 m. The soil parameters were selected as follows: cohesion = 14.9 kN/m^2, friction angle = 29°, and specific weight = 20.9 kN/m^3. For two phreatic surface depths (relative to the streambank level), different water surface depths were used. Table 1 shows the comparisons between the results obtained from both models. It is observed that the fail angles provided by the two models are very similar, so the present formulation is considered as validated, taking into account that some truncation errors occur during the angle searching.

4 NUMERICAL EXPERIMENT

A numerical experiment was performed for an initially very unstable straight channel, with a trapezoidal form 22 m wide, 9 m deep, and 20° bank slopes. The non-cohesive base stratum has $d_{50} = 0.130$ mm and a friction angle of 20°, while the cohesive stratum (at

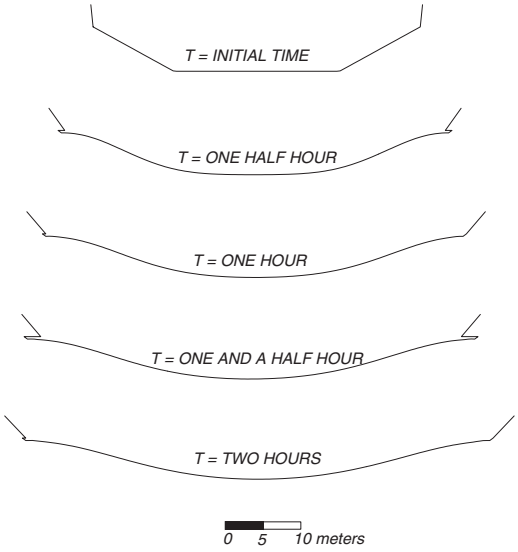


Figure 9. Cross-sectional (undistorted) form for different instants of time.

both banks) is 3 m thick, with cohesion 20 kN/m^2. The spatial step is 0.43 m, while the time step amounts to 1 second.

The channel cross-sectional form evolves very fast during a single day, increasing its width about three times, and reducing its depth to about half the initial value. Figure 9 shows the cross-section form for different instants of time. It is observed how the widening process proceeds through undermining and failure of the cohesive strata, while the non-cohesive base flattens, with its bottom level growing. The failure material is not considered. The small asymmetry observed between the two banks is due to round-off errors, which sometimes trigger bank failure with a difference of one computational time step.

As an illustration, Figure 10 presents a detail of the undermining process, till failure, for the right bank.

5 CONCLUSIONS

The integrated hydrodynamic-sedimentologic-morphological model proposed in the present paper constitutes an efficient tool to deal with the morphological evolution of channel cross-sections in most practical situations, i.e., while based on a physically sound formulation, it preserves simplicity by considering only the relevant physical mechanisms. The treatment of the non-cohesive bank base and the cohesive bank upper stratum has been validated separately, thus expecting

Copyright © 2006 Taylor & Francis Group plc, London, UK

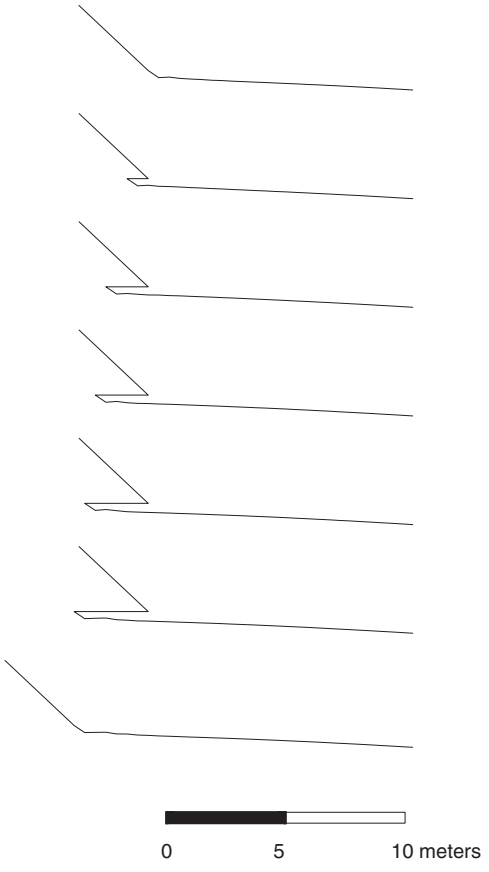


Figure 10. Undermining process for the right bank. Cross section each half hour, since 16.5 hours after start.

that their combined action performs well. Work is still under way to incorporate the failure material.

REFERENCES

Darby, S.E. & Thorne, C.R. 1996. Development and Testing of Riverbank-Stability Analysis, *Jr. of Hydr. Eng.*, **122**, 8, August, 443–454.

Darby, S.E., Gessler, D. & Thorne, C.R. 2000. Computer Program for Stability Analysis of Steep, Cohesive Riverbanks, *Earth Surface Processes and Landforms*, **25**, 175–190.

Darby, S.E., Alabyan, A.M. & Van de Wiel, M.J. 2002. Numerical simulation of bank erosion and channel migration in meandering rivers, *Water Resources Research*, **38**, 9.

Jain, C. 2001. *Open-Channel Flow*. John Wiley and Sons, New York.

Kikkawa, H., Ikeda, S. & Kitagawa, A. 1976. Flow and Bed Topography in Curved Open Channels, *Journal of the Hydraulics Division*, **102**, HY9, September, 1327–1343.

Kovacs, A. & Parker, G. 1994. A new vectorial bedload formulation and its application to the time evolution of straight river channels, *J. Fluid Mech.*, **267**, 153–183.

Raudkivi, A.J. 1990. *Loose Boundary Hydraulics*, 3rd Edition, Pergamon Press, New York.

Menéndez, A.N. 2003. Selection of optima mathematical models for fluvial problems, *Proc. Third IAHR Symposium on River, Coastal and Estuarine Morphodynamics*, *September*, Barcelona, Spain.

Wark, J.B., Samuels, P.G. & Ervine, D.A. 1990. A practical method of estimating velocity and discharge in a compound channel. In W.R. White (ed.), *River Flood Hydraulics*, John Wiley & Sons, Inc., Chichester, UK, 163–172.

Copyright © 2006 Taylor & Francis Group plc, London, UK

Bend scour reduction and flow pattern modification by an outer bank footing

M. Roca & J.P. Martín-Vide
Department of Hydraulic Engineering, Technical University of Catalonia (UPC), Barcelona, Spain

K. Blanckaert
ICARE-ENAC, Ecole Polytechnique Fédérale, Lausanne, Switzerland

ABSTRACT: This paper investigates in an experimental flume the efficiency of scour reduction and bank protection near the outer bank in open-channel bends by means of a horizontal foundation, called footing, protruding into the flow. Comparison of experiments with and without footing under similar hydraulic conditions convincingly demonstrates the efficiency of this bank protection technique: a maximum scour reduction of more than 40% was obtained with an optimal choice of the footing width and elevation. The scour reduction by the footing is attributed to two phenomena: (i) the development of a transversal bed slope is attenuated; (ii) the outward velocity redistribution by the secondary flow is attenuated.

1 INTRODUCTION

Embankments are designed to confine the flood flows. Therefore, bank scour and failure can lead to devastating inundations that endanger property and cause important damage, especially in urbanized areas. The protection of river banks against erosion is essential but very costly.

The interaction between the main downstream flow component, the secondary flow and the bed topography leads to an increased erosive attack on the outer bank in open channel bends. Secondary flow induced by streamline curvature, also called helical flow or spiral flow, is a characteristic feature of flow in open-channel bends (Rozovskii 1957, Engelund 1974, Struiksma et al. 1985, Blanckaert & de Vriend 2004). By advecting momentum, it redistributes the downstream velocity and causes it to increase/decrease in the outer/inner part of the cross-section (Blanckaert & Graf 2004), hence also an increased/decreased erosive capacity of the flow. Moreover, the secondary flow transports sediment from the outer to the inner part of the cross-section and thereby creates the typical bar-pool bed topography in alluvial bends (Whiting & Dietrich 1993, Odgaard 1982, Yalin & Ferreira 2001).

Thus, outer banks in river bends need to have a more resistant scour protection and a deeper foundation than straight river banks. Several techniques are reported in literature to reduce the attack and the scour on the outer bank. Groynes direct the flow towards the center of the channel and promote sedimentation near the bank (Przedwojski et al. 1995). Submerged vanes counteract the secondary flow and reduce bend scour but create obstacles in the river (Odgaard & Mosconi 1987). Macro-roughness elements at vertical outer banks frain the flow velocity adjacent to the bank and reduce bend scour (Hersberger 2002).

This paper considers rigid horizontal footings as a part of vertical outer banks, and aims at optimizing the footing width, b and depth, z_f (Fig. 1). This type of protection is especially relevant in urban environments

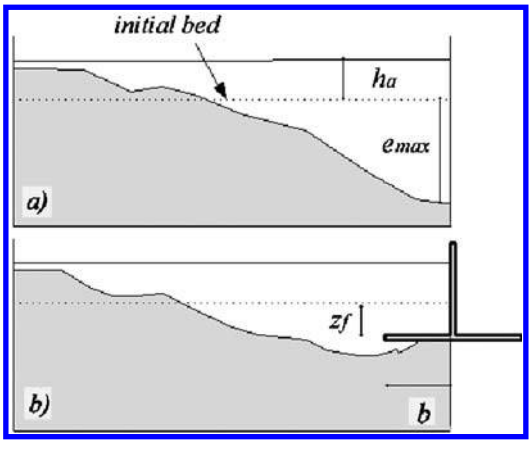


Figure 1. (a) Typical bed topography in a cross section of a river bend; (b) Reduction of bed scour by an optimally designed bank footing.

Copyright © 2006 Taylor & Francis Group plc, London, UK

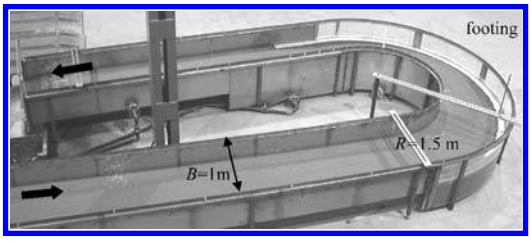


Figure 2. Laboratory flume with the footing on the outer bank (at the University of Castilla-La Mancha).

where vertical banks are imposed by space limitations or preferred by their visual aspect.

Figure 1 illustrates the principles underlying the optimal design of the bank footing. Figure 1a shows the typical bed topography in the cross section of a river bend without outer bank protection. An outer bank foundation below the maximum scour depth, e_{max}, is unconditionally stable, but over conservative. An optimal choice of the footing width and elevation can lead to a reduction of the maximum scour depth (Fig. 1b), and thus a more economical bank protection. Moreover, the flow depth is more homogeneous over the width of the river.

The aim of this paper is to investigate changes of bed topography due to the presence of the bank footing and the mechanisms underlying the protective effect of the outer bank footing, by comparing the patterns of downstream flow, secondary flow, turbulence and bed topography. More details and extended data are reported in Roca (2003) and Roca et al. (in prep.).

2 THE EXPERIMENTS

The experiments were carried out in a single bend laboratory flume of constant width, $B = 1$ m, consisting of a straight 9 m long inflow reach followed by a 186° bend with constant radius of curvature, $R = 1.5$ m, and a straight 5 m long tailwater reach (Fig. 2). The bed was composed of a quasi-uniform natural sand with a mean diameter of $D_{50} = 1.65$ mm and a geometric standard deviation, $(D_{84}/D_{16})^{1/2}$, equal to 1.26.

The A1 reference experiment was carried out without footing. Subsequently, experiments were carried out with different footing configurations (z_f, b) but under similar hydraulic conditions. The footing on the outer bank was made of 1 cm thick PVC plate rigidly fixed to the bank. The footing was installed in the bend reach and extended over a length of $0.75B$ in the straight tailwater reach.

The hydraulic conditions are the same for all the experiments: $Q = 0.042$ m^3/s, $h_a = 0.098$ m and $U_f = 0.39$ m/s. A horizontal flat bed and a free fall tailwater are the initial conditions in all experiments. For a constant discharge, the bed topography will deform due to bend effects, but ultimately reach equilibrium allowing the univocal definition of the maximum scour depth, e_{max}, in the river bend. All experiments were continued until the equilibrium scour depth was attained.

Water discharge was measured by a thin-plate V-notch weir upstream of the flume.

Bed and water surface elevations were measured with point gauges installed on a carriage on top of the flume walls, which were accurately levelled to be used as a datum. Additional staff gauges were used at the outer bank to track the bed and water surface. Bed elevation under the footing was measured after carefully removing the PVC plate.

Velocities were measured in detail in tests A1 and B4 with an acoustic Doppler velocimeter (ADV) developed by Nortek. Data of the 3D flow structure was collected at several verticals (located every 10 cm across the channel width) of different cross-sections (each 10° or 20° from $\theta = 20°$ to 100°). Vertical distance between points from the same profile was about 1 to 3 cm, depending on the local water depth. The sampling rate was 25 Hz and 4500 data were collected for each point.

The adopted ADV configuration does not allow measuring inside a flow region of 5 cm near the water surface. The computation of depth-averaged velocities requires extrapolations inside this region. The increased uncertainty in the depth-averaged velocities due to these extrapolations does not alter the conclusion of this research.

3 BED TOPOGRAPHY

The influence of the footing design on bend scour is investigated by varying the footing's vertical depth, z_f, and width, b. An outer bank foundation below the maximum scour depth without bank protection, $e_{max,A1}$, is unconditionally stable but over conservative. Vertical depths tested range between the position of the initial flat bed ($z_f/e_{max,A1} = 0$) and the ultimate maximum scour depth without bank protection ($z_f/e_{max,A1} = 1$). Increasing its width should improve the effectiveness of the footing, but also its construction cost. Footing widths investigated were of the order of the approach flow depth, h_a. The footing configurations investigated are summarized in Table 1.

The bed topography in the experiments with outer bank footing is characterized by the same main features as in the experiment without, as illustrated in Figure 3. A typical bar-pool topography with two scour holes develops around the bend due to the same physical mechanisms and the transversal bed slope shows an oscillating behavior.

However, these main features are affected by the outer-bank footing. The outer bank footing

Copyright © 2006 Taylor & Francis Group plc, London, UK

Table 1. Footing parameters and results of experiments with outer bank footing.

Test	$z_f/e_{max,A1}$	b/h_a	θ_{max}	$V_o/V_{o,A1}$	e_{max}/h_a	SR* %
A1	–	–	80	1.00	2.4	–
B1	0.33	0.7	60	1.00	2.1	13
B2	0.67	0.7	50	1.07	1.9	22
B3	0.17	1.1	50	1.01	2.2	8
B4	0.33	1.1	60	1.09	1.7	28
B5	0.50	1.1	40	1.10	2.1	11
B6	0.67	1.1	60	1.08	2.1	13
B7	0.33	1.5	40	1.04	1.4	42
B8	0.60	1.6	40	1.07	1.9	22

* SR is the scour reduction factor defined as 1-$e_{max}/e_{max,A1}$.

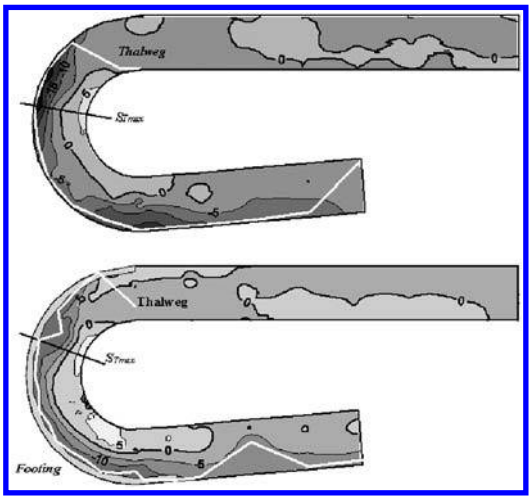


Figure 3. Bed topography in the A1 experiment without footing (upper) and the B4 test with footing (lower). Bed elevations are in cm above the flume averaged initial bed level.

significantly reduces the bend scour. The maximum scour depth in the bend is significantly reduced by up to more than 40% (Table 1). The maximum transversal bed slope is reduced and its oscillation around the bend is attenuated for footings with optimal width and depth parameters, as in tests B4 and B7 (Fig. 4).

The thalweg is not found at the outer bank, but is shifted to the edge of the outer bank footing (Fig. 3). Even though the flow erosive attack on the bed increases in outward direction, the footing protects the underlying bed, even in cases where underscour develops. This protective effect increases from the footing's tip towards the outer bank.

The scour holes are slightly shifted in upstream direction (see θ_{max} in Table 1). This behaviour could tentatively be attributed to a reduction in width of the mobile bed zone. The total eroded volume around the

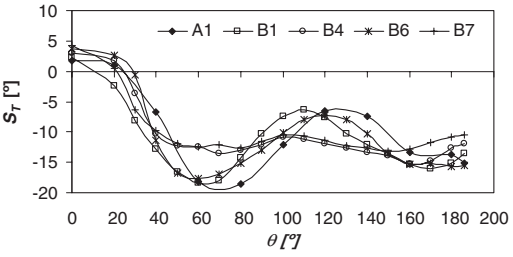


Figure 4. Evolution of transversal bed slope, $S_T(°)$ in four experiments with footing compared with A1 experiment without.

bend, V_o, is slightly increased. This means that the outer bank footing does not minimize the total scour but merely redistributes and uniformizes it around the bend (Table 1).

Wider footings yield a larger reduction in bend scour, as illustrated by experiments B1, B4 and B7. With the footing placed at one third of the maximum scour depth, $z_f/e_{max,A1} = 0.33$, the scour reduction increases from 13% for a footing width of $b/h_a = 0.7$, to 28% for $b/h_a = 1.1$, and reaches a maximum of 42% for $b/h_a = 1.5$.

Experiments B3 to B6 investigate the influence of the footing elevation for a constant footing width of $b/h_a = 1.1$. Elevations of $z_f/e_{max,A1} = 0.17$, 0.33, 0.50 and 0.67 are investigated. The maximum scour reduction in this series of experiments is obtained for $z_f/e_{max,A1} = 0.33$. Placing the footing at a lower level reduces its efficiency, which should vanish for $z_f/e_{max,A1} = 1$.

Obviously, the footing's width and elevation interact. The optimal vertical elevation of the footing will depend on its width.

When the footing is not wide enough or is placed at a higher level scour can develop below it, which can endanger the footing's structural stability.

The following paragraphs compare the distributions of downstream flow, secondary flow and turbulence in the A1 reference experiment without footing and the B4 experiment with successful footing design.

4 DOWNSTREAM FLOW

The depth-averaged downstream velocity, U, and the downstream unit discharge, $q = Uh$, are the main flow parameters, since they determine the sediment transport that shapes the bed topography.

The depth-averaged velocities are computed by adopting linear extrapolations in the flow region near the water surface where no velocity measurements could be carried out. The uncertainty in the depth-averaged values is less than 2% when comparing different possible and reasonable extrapolations.

Copyright © 2006 Taylor & Francis Group plc, London, UK

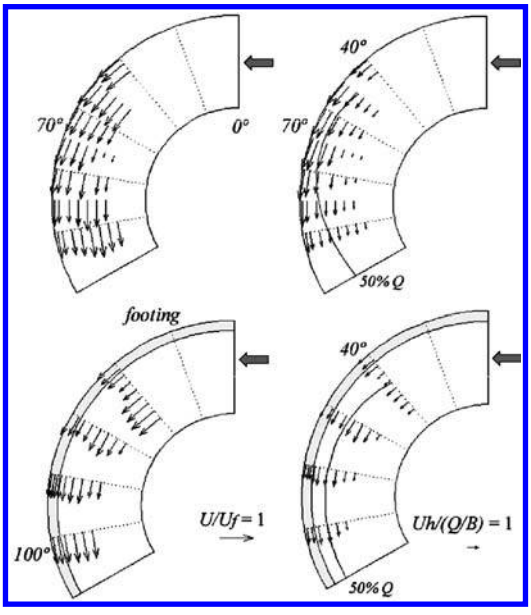


Figure 5. Depth averaged downstream velocity, U (left); Downstream unit discharge, $Uh/(Q/B)$ and streamtubes containing 50% of the discharge (right) in the A1 experiment without footing (top) and the B4 experiment with footing (bottom).

In the A1 experiment without footing, the downstream velocity U is quite uniform from the bend inlet, but at section at 60° and more clearly at 70° the maximum values are found near the outer bank (Fig. 5). Downstream of the section at 80° maximum values are found in the middle of the cross-section.

The pattern of unit discharge, $q = Uh$, is modulated by the water depth. Without footing it is more non-uniform than the velocity pattern, with greater values near the outer bank. It reaches a maximum in the cross-section at 70° where the transversal bed slope is maximum.

The presence of the footing clearly modifies this pattern. In the B4 experiment, the cores of maximum velocity and maximum unit discharge are found nearer the centerline of the flume in all the cross-sections; they do not reach the outer bank as in the experiment without footing. Between the core of highest velocities and the outer bank, the depth-averaged downstream velocity first reaches a minimum value (see $\theta = 40°$) and then again somewhat increases.

The distribution around the bend of the downstream velocity (Fig. 6) clearly deviates from typical straight-flow distributions that monotonously increase from the bed towards the water surface.

In the A1 experiment without footing, the downstream velocity starts increasing near the outer bank and close to the bed in the cross-section at 60°. Further downstream in the bend, in the cross-section at 100°, the maximum velocities are found close to the bed and they decrease towards the water surface. This pattern is explained by the influence of the secondary flow. The high velocities near the bed enhance the erosive attack on the toe of the bank and are an important cause of bank failure.

In the B4 experiment with footing, the 3D flow patterns also illustrate the shifting of core of highest velocities towards the edge of the footing. The core of highest velocities remains further away from the bed than in the A1 experiment. The area of lower velocities that occurs between the core of highest velocities and the outer bank gets weaker along the bend and shifts towards the water surface.

5 SECONDARY FLOW

The redistribution of the downstream velocity may be attributed to advective momentum transport by the cross-stream motion and to the non-uniformity of the bed topography, which is also indirectly caused by the cross-stream motion (Blanckaert & Graf 2004).

Cross- stream motion (v, w) is defined as the projection of the velocity vector in the cross-section. The transversal velocity, v, can be decomposed into a translatory part, V, called cross-flow, and a circulatory part, v^*, called the transversal component of the secondary flow or the 'identifiable downstream vortices' (Bradshaw 1987). Depth-averaged values of $v*$ are zero by definition.

The circulatory part of the cross-stream motion, (v^*, w), can also be represented by the downstream component of the vorticity vector, defined as:

$$\omega_s = \frac{\partial v}{\partial z} - \frac{\partial w}{\partial n} = \frac{\partial v^*}{\partial z} - \frac{\partial w}{\partial n} \qquad (1)$$

which has the advantage of being a scalar quantity.

The patterns of the normalized downstream vorticity, $\omega_s H/U_f$ in the experiments with and without footing are shown in Figure 7. These patterns are obtained by first extrapolating the measured (v,w) patterns by Krigging and subsequently evaluating the derivatives in Equation 1 by means of two-point central finite-differences scheme. Note that the cross-flow, V, does not contribute to ω_s, which is not affected by the extrapolations outside the measuring grid near the water surface.

In the A1 experiment without footing, a vorticity cell develops in the cross-section at 60° over the deepest part of the cross-section. This cell weakens downstream and almost disappears at $\theta = 100°$. This characteristic feature of flow in open-channel bends is often called secondary flow, spiral flow or helical flow, and has been abundantly investigated (Rozovskii 1957, Struiksma et al. 1985, Blanckaert & de Vriend 2004). It appears due to the interaction between the

Copyright © 2006 Taylor & Francis Group plc, London, UK

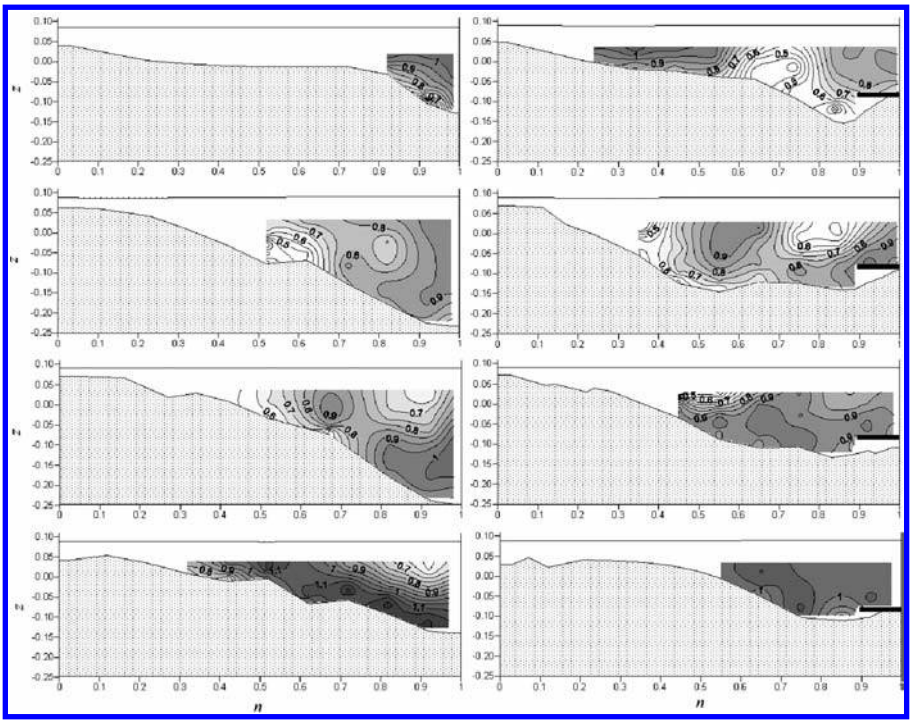


Figure 6. Isolines of normalized downstream velocity u/U_f in cross-sections at 40°, 60°, 80° and 100° in the bend (from top to bottom) in the A1 experiment (left) and the B4 with bank protection (right).

centrifugal force and the pressure gradient induced by the tilting (superelevation) of the water surface.

In B4 experiment with footing, maximum values of vorticity are lower than in the A1 experiment, but the downstream distribution is more uniform. The core of the cells is located close to the edge of the footing near the location of the core of minimum downstream velocity (Fig. 6). It seems to gradually shift towards the outer bank around the bend. A second and stronger cell of downstream vorticity is observed near the centreline in the cross-section at 60° in both experiments.

6 TURBULENCE

Turbulence plays an important role in the formation of the pattern of downstream vorticity cells in open-channel bends (Blanckaert & de Vriend, 2004). In spite of its relevance, little is known about the turbulence characteristics in open-channel bends.

In straight uniform flow, the vertical distribution of the turbulent kinetic energy, $k = 1/2\ (u'^2 + v'^2 + w'^2)$, is well approximated by an exponential profile (Nezu & Nakagawa 1993). The observed patterns in the curved-flow experiments are fundamentally different (Fig. 8).

The profiles do not monotonically decrease from the bed towards the surface, but the core of highest values is found in the middle or even in the upper part of the water column. The distributions of k and of the mean flow kinetic energy, $K/(1/2U_f^2) \approx (u/U_f)^2$ (Fig. 6) exhibit opposite patterns in the water column as well as over the width. The core of minimum k-values nearly coincides with that of maximum u-values, and positive/negative gradients of k correspond to negative/positive gradients of u. Similar behavior has been observed and explained by Blanckaert & de Vriend (2005). The zones of high k are located near the eye of the downstream vorticity cell (Fig. 7). These maximum values in the cross-section are larger than in straight uniform flow, indicating that the turbulent kinetic energy content of the investigated flow is increased by the curvature and/or the bed topography. The turbulent activity seems to decay in the second part of the bend, which resembles the evolution of the strength of the downstream vorticity cells.

7 CONCLUSIONS

One of the most important variables in bank protection design is the depth of foundation.

The present experimental results convincingly show that a well-designed horizontal bank foundation that protrudes into the flow (called footing) can

Copyright © 2006 Taylor & Francis Group plc, London, UK

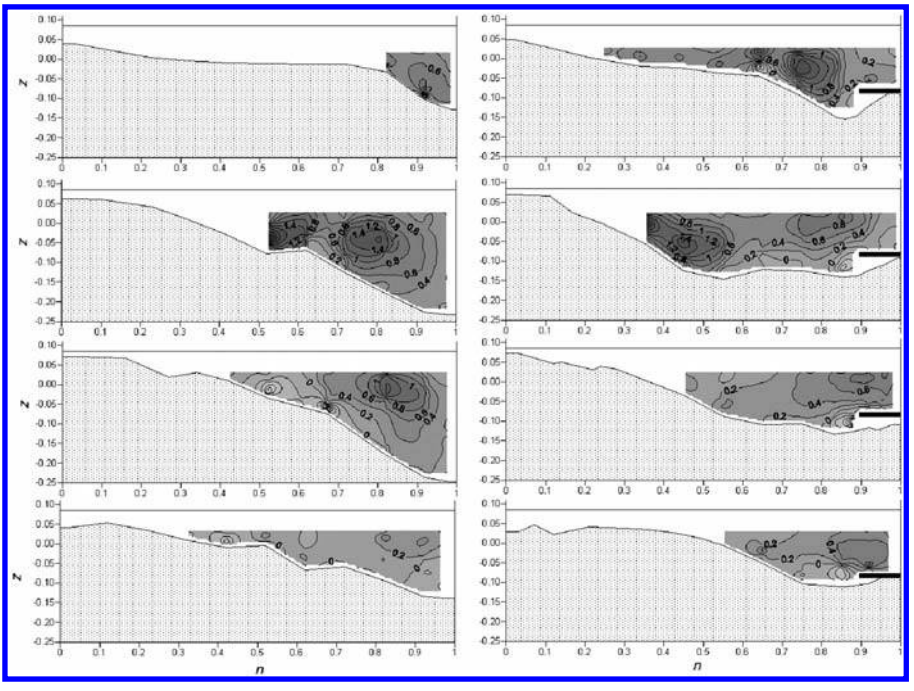


Figure 7. Isolines of dimensionless downstream vorticity $\omega_s H / U_f$ in cross-sections at 40°, 60°, 80° and 100° in the bend (from top to bottom) in the A1 test (left) and B4 test (right).

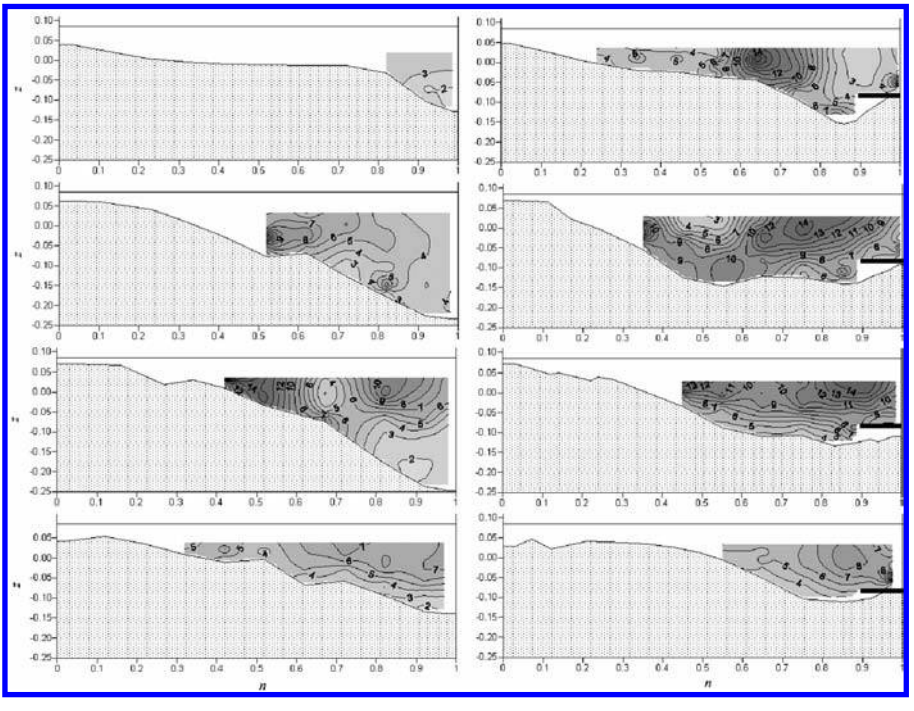


Figure 8. Isolines of dimensionless turbulent kinetic energy $k/(1/2\ u_*^2)$ in cross-sections at 40°, 60°, 80° and 100° in the bend (from top to bottom) in the A1 test (left) and B4 test (right).

Copyright © 2006 Taylor & Francis Group plc, London, UK

significantly reduce bend scour, allowing for reduced construction costs of bank protections.

Widening the footing reduces scour depth and risk of underscour, but increases construction cost. Lowering the footing also limits the risk of underscour, but reduces its protective efficiency. A maximum scour reduction by more than 40% was obtained in the reported experiments with footing parameters of $b/h_a \approx 1.5$ and $z_f/e_{max,A21} \approx 0.33$.

The presence of the outer bank footing modifies the mechanisms of bend scour. It reduces the flow depth in the outer-half of the cross-section; hence, the outward increase of the downstream velocity is also reduced. Vorticity cells are clearly observed from cross-sections at 40° to 100°, but their shape and intensity are modified comparing with the experiment without footing.

The outer bank footing increases the turbulence activity in its neighborhood. This leads to an increase in the erosive capacity of the near bank flow, which is however outweighed by its reduction thanks to the more favorable distribution of the main downstream velocity component.

This paper presents a preliminary study to show the benefits of an optimal footing design on the bend scour reduction. More research is needed before defining generally valid design rules that avoid underscour.

NOTATION

B = flume width [m]
b = width of wall footing [m]
D_{50} = mean diameter of sand bed [m]
e_{max} = maximum erosion [m]
H = averaged water flow depth along the flume [m]
h = local water flow depth [m]
h_a = approach water depth [m]
n = transverse reference axis; 0 at the inner bank and 1 at the outer one
K = mean flow kinetic energy per unit mass [m^2/s]
k = turbulent kinetic energy per unit mass, $1/2(\overline{u'^2} + \overline{v'^2} + \overline{w'^2})$ [m^2/s], where u', v' and w' are the velocity fluctuations
Q = water discharge [m^3/s]
q = downstream unit discharge [m^2/s]
R = radius of curvature [m]
S_T = transversal bed slope, defined as the slope of a straight line giving the same flow area and first moment as the original cross-section [°]
U = depth-averaged downstream velocity [m/s]
U_f = averaged downstream velocity in the flume [m/s]
u = downstream velocity [m/s]
V = depth-averaged transversal velocity [m/s]
V_o = total eroded volume around the bend [m^3]
v = transversal velocity [m/s]
v^* = transversal component of the secondary circulation, $v^* = v - V$ [m/s]
w = vertical velocity [m/s]
z = elevation above the initial flat bed [m]
z_f = vertical position of foundation below initial flat bed [m]
θ = cross-section angle [°]
θ_{max} = cross-section angle where maximum water depth is located [°]
τ_{sz} = turbulent shear stress, $-\rho\overline{u'w'}$ [N/m^2]
ω_s = downstream vorticity [s^{-1}]

subscript $A1$ means values obtained at the A1 test.

REFERENCES

Bradshaw, P. 1987. *Turbulent secondary flows.* Annual Rev. Fluid Mechanics, 53–74.

Blanckaert, K. & de Vriend, H.J. 2004. Secondary flow in sharp open-channel bends. *Journal of Fluid Mechanics*. Vol. 498, 353–380.

Blanckaert, K.& Graf, W. H. 2004. Momentum transport in sharp open-channel bends. *Journal of Hydraulic Engineering.,* ASCE, 130(3), 186–198.

Blanckaert, K. & de Vriend, H.J. 2005. Turbulence characteristics in sharp open-channel bends. *Physics of Fluids*. (in press).

Engelund, F. 1974. Flow and bed topography in channel bends. *Journal of the Hydraulic Division*, ASCE, Vol. 100(11), 1631–1648.

Hersberger, D. 2002. *Wall roughness effects on flow and scouring in curved channels with gravel bed*. PhD-thesis Nr 2632, École Polytechnique Fédérale Lausanne, Switzerland.

Odgaard, A.J. 1982. Bed characteristics in alluvial channel bends. *Journal of the Hydraulics Division*, ASCE, Vol. 108, n°11.

Odgaard, A.J. & Mosconi, C.E. 1987. Streambank protection by submerged vanes. *Journal of Hydraulic Engineering*, ASCE, Vol. 113(4), 520–536.

Przedwojski, B., Blazejewski, R. & Pilarczyk, K.W. 1995. *River training techniques*. Rotterdam: Balkema.

Roca, M. 2003. *Scour in a sharp bend. Effect of the outer bank wall footings*. PhD Thesis. Technical University of Catalonia, UPC, Barcelona (in spanish).

Roca, M., Martín-Vide, J.P., & Blanckaert, K. Reduction of bend scour by an outer bank footing. Footing design and bed topography. (in prep.)

Rozovskii, I.L. 1957. *Flow and water in bends of open channels*. Kiev: Academy of Sciences of the Ukrainian SSr.

Struiksma, N., Olesen, K.W., Flokstra, C., & de Vriend, H.J. 1985. Bed deformation in curved alluvial channels. *Journal of Hydraulic Research*, Vol. 23(1), 57–79.

Whiting, P.J. & Dietrich, W.E. 1993. Experimental studies of bed topography and flow patterns in large amplitude meanders. 1. Observations. *Water Resources Research*, Vol. 29(11), 3605–3614.

Yalin, M.S. & Ferreira da Silva, A.M. 2001. *Fluvial Processes*. IAHR Monograph. Delft: Balkema.

Copyright © 2006 Taylor & Francis Group plc, London, UK

Self widening by lateral erosion in gravel bed rivers

P. Requena, R.B. Weichert & H.-E. Minor
Laboratory of Hydraulics, Hydrology and Glaciology (VAW), ETH Zurich, Zurich, Switzerland

ABSTRACT: River widening is an effective measure to reduce the flood hazard and to improve the ecologic situation by restoration of the original morphologic dynamics. The widened river reach can be achieved due to lateral erosion after removing existing bank protection works. In order to understand the morphological dynamics of the lateral erosion process and to describe and quantify the influence of relevant parameters, as e.g. discharge, bed slope, sediment supply and grain size distribution, physical model investigations are carried out at the VAW. In the present paper, the experimental set-up and the procedure of this study are described. A method for analyzing the spatial and temporal evolution of the lateral erosion is presented and finally, observations and preliminary results from the first experiments are discussed. The developed method allowed the quantification of erosion rates with high precision. First results show that the lateral erosion does not progress continuously, but has a pulsating behavior.

1 INTRODUCTION

River correction works carried out in the 19th century in Switzerland to prevent flooding as well as malaria and to fulfill an increasing land demand for industry and agriculture, resulted in monotonous river landscapes with confined narrow channels. The objective at that time was to increase the sediment transport capacity of the rivers to initiate bed erosion and consequently to increase the discharge capacity of the rivers. However, today excessive bed erosion leads to a number of negative consequences, such as undermining of the river bank foundations, lowering of the groundwater level and reduction of the typical river habitat (fauna and flora). Furthermore, recent flood events have shown the limits of conventional river training. It has been realised that rivers in Switzerland need to be given more space. This can be achieved by re-widening of selected river reaches.

Since 1990, various river reaches in Switzerland have been widened. Today, a meandering, partly braided river with pool-riffle systems and variable velocities has developed in these reaches (Fig. 1). In the widened river reach the riverbed erosion has been stopped and flood protection has also been improved. As a result of the varying river morphology the ecological value has increased and the typical river habitat has reappeared. The experiences of the last 15 years have proved that river widening is an effective river renaturation measure, which at the same time satisfies the requirements of flood protection and ecology.

A number of research projects focusing on river widening were carried out at the VAW. These studies investigated the effect of river widening on bed morphology and sediment transport in gravel bed rivers as well as the morphological dynamic of the widening process (Zarn 1993, 1997, Hunzinger & Zarn 1997, Hunzinger 1998, Marti 2002, Requena et al. 2005). The widening of a river reach can be achieved by excavating the floodplains along the reach in question, or naturally by lateral erosion after the bank protection works have been removed. However, lateral erosion is not allowed to progress unchecked because urban areas and infrastructures are often situated close to the rivers. An area must therefore be defined within which the river is allowed to erode its banks and consequently to develop dynamically (Fig. 2). In this context, an understanding of the lateral erosion process is of considerable interest. The present paper focuses on this process.

2 LITERATURE REVIEW

The lateral erosion process in sand and gravel bed meandering rivers was investigated using field or laboratory data by many authors (e.g. Hooke 1980, Ikeda et al. 1981, Parker 1983, Nanson & Hickin 1986, Odgaard 1987, 1989, Osman & Thorne 1988, Thorne & Osman 1988). Within these studies, the main influencing parameters were identified and investigated. This intensive research focused on meandering

Copyright © 2006 Taylor & Francis Group plc, London, UK

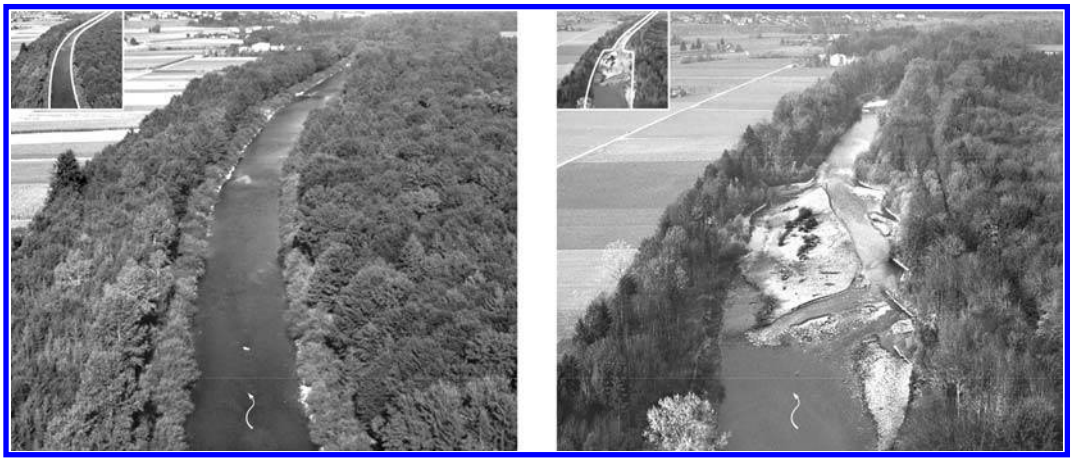


Figure 1. The River Emme in Switzerland before (left) and after (right) the realization of the widening project. A partly braided river with riffle-pool structures has developed producing variable flow velocities. With the varying river morphology, the ecological value has also been improved (Documenta Natura, 1991 and 2004).

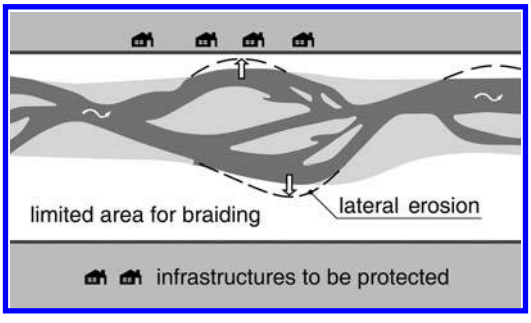


Figure 2. Limited area where the river is allowed to develop.

channels, but few investigations considered so far the lateral erosion process in gravel bed rivers with the tendency to develop braided morphologies. Most of the research works about braided rivers focused on the development of braided structures starting from a straight channel. The main topics of these investigations were the mechanisms of braiding (Ashmore 1982, 1991), the bed load transport and its spatial and temporal fluctuations (e.g. Ashmore 1988, Hoey & Sutherland 1991, Warburton & Davies 1994), the relationship between bed load transport, braiding intensity and channel width (Ashmore 2001) or the sorting process of the bed material in gravel bed streams (Ashworth & Ferguson 1989, Ashworth et al. 1992). Warburton (1996) considered the bank erosion rate by investigating the interrelation between sediment transport, braiding morphology and braided channel width. Schmautz (2004) developed a method to estimate the maximum expected river width during the widening process. In general, the lateral erosion process in gravel bed rivers has not yet been examined in detail and its spatial and temporal evolution have not been quantified.

3 GOAL OF THE PRESENT STUDY

In order to understand the morphological dynamics of the lateral erosion process, physical model investigations have been carried out at the VAW. The aim of this research project is to describe and quantify the influence of the relevant parameters, such as discharge, bed slope, sediment supply, grain size distribution and initial river width, on the lateral erosion process. These results should enable the interrelation between lateral erosion rate, sediment transport, braiding morphology and braiding width to be determined. In the present paper, the experimental setup, the procedure and the methods for data analysis of this study are described. Finally, observations and preliminary results from the first experiments are presented.

4 FLUME EXPERIMENTS

4.1 *Experimental setup*

The experiments presented here were performed in a concrete flume that was 28.5 m long and 3.2 m wide (Fig. 3). The slope of the flume could be varied between 0.8% and 2.2%. Water discharge and the sediment supply were remotely controlled by a computer. Flow rates were measured by an electromagnetic flow meter. Dry sediment was introduced at the head of the flume by a sediment feeder. The sediment output at the downstream end of the flume was collected and continuously weighed. A sediment

Copyright © 2006 Taylor & Francis Group plc, London, UK

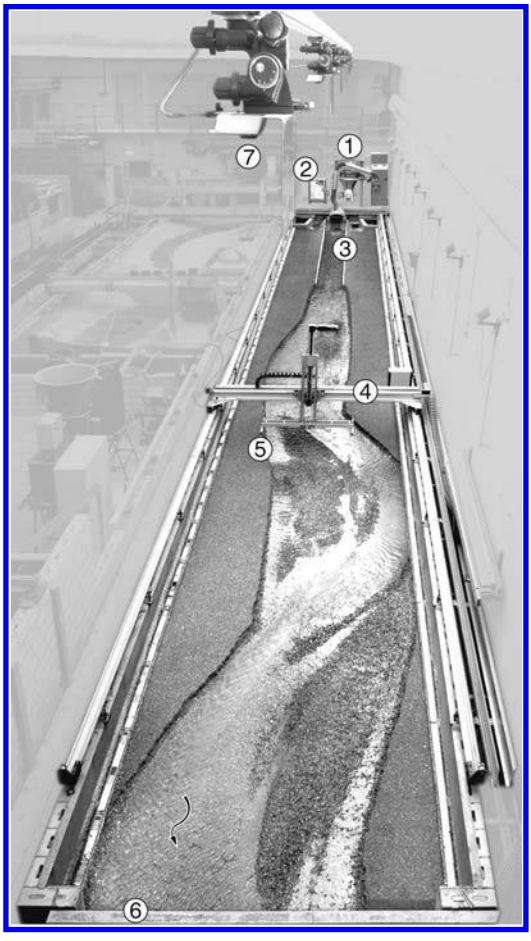


Figure 3. Photo of the laboratory flume: 1) Sediment feeder; 2) Computer unit; 3) Fixed sidewalls; 4) xyz-positioning system; 5) Laser and ultrasonic sensors; 6) Sediment collector; 7) Digital cameras.

mixture, which is typical for Alpine gravel bed rivers, was used in this study. This mixture was widely graded with $D_{50} = 3.2$ mm, $D_{90} = 9.4$ mm and $\sigma = D_{84}/D_{16})^{0.5} = 3.3$. Grain Reynolds numbers obtained for the investigated discharges were higher than 100 and therefore fully turbulent conditions were guaranteed. The topography and the water level were surveyed by laser and ultrasonic sensors installed on a xyz-positioning system, which automatically scanned the bed surface in a predetermined regular, dense grid. Seven digital cameras were installed above the flume (Fig. 3) to monitor the morphological dynamic of the braiding process over the full duration of the experiment (1 photo per min).

Furthermore, the time-lapse photos were used to quantify the lateral erosion process. A method, developed to analyze and quantify the spatial and temporal evolution of the lateral erosion, will be described in detail in Section 5.

4.2 *Experimental procedure*

In the present project several experiments were planed to quantify the influence of discharge, bed slope, sediment supply and initial river width on the lateral erosion rate. With each experiment different combinations of one initial width (to be varied between 40 and 80 cm), one discharge (to be varied between 10 and 40 l/s) and one sediment supply rate (to be varied between 0 and 80 g/s) are investigated. All the chosen discharge values were higher than the critical flow discharge at which, sediment transport begins.

Sediment supply rates were calculated for the given combination of discharge and width according to the bed load transport formula of Hunziker (1995). These values represent the transport capacity for the given hydraulic conditions. In order to investigate the influence of low bed load rates on the lateral erosion process, experiments with the sediment rate matching 50% and 0% of the transport capacity for the specific hydraulic conditions will also be performed.

Until now, three experiments have been conducted. The experiments were interrupted after a certain time to refill the sediment feeder, to empty the sediment basket and to survey the bed topography in a dry state. Each experiment was divided into two phases: the equilibrium phase and the widening phase.

4.2.1 *Equilibrium phase*

In this phase the channel alignment was determined by fixed sidewalls over the whole length and lateral erosion was not yet allowed (Fig. 4a). Starting from a straight, narrow channel an equilibrium state had to be reached for the specific combination of discharge, width and bed load rate. The state of equilibrium was reached by steady-state conditions when the sediment output approximately equaled the sediment input, so that the mean bed slope remained constant during the considered time interval.

The reason for carrying out this phase was to start the widening phase of all the experiments under the same initial conditions, namely with the equilibrium channel bed slope. Furthermore, this procedure guaranteed that before the process of lateral erosion started, the channel bed resembled conditions, which corresponded to existing configurations in nature (e.g. bed material sorting process). The equilibrium bed slope could be predetermined for the given discharge, channel width and bed load rate by means of one of the available sediment transport formulas. By building an initial channel bed slope which approximately matched the expected equilibrium bed slope, the duration of this phase could be reduced considerably. In the experiments, the initially built channel bed slope was

Copyright © 2006 Taylor & Francis Group plc, London, UK

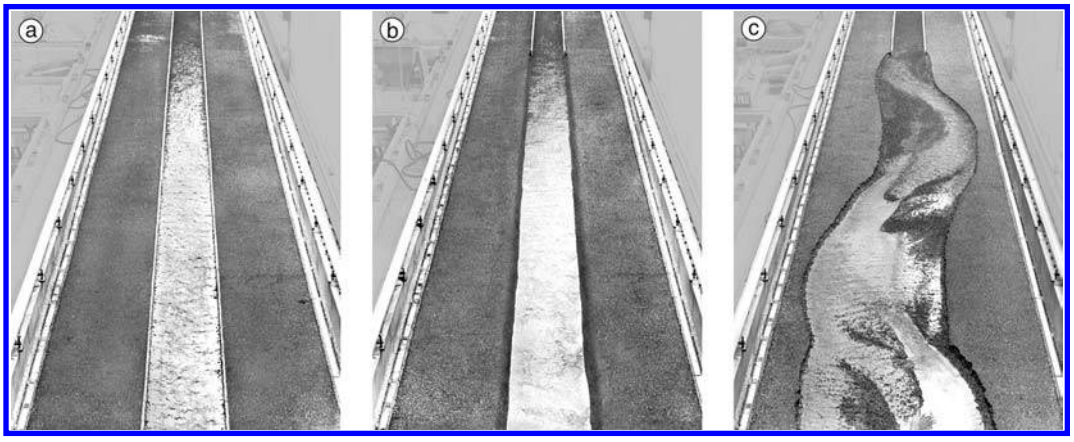


Figure 4. Experimental procedure: a) Equilibrium phase with fixed sidewalls over the whole length. In this phase lateral erosion was not allowed; b) Removed sidewalls at the beginning of the widening phase. At the head of the flume the sidewalls stayed fixed over a 7 m long section; c) Widening phase with lateral erosion.

first determined by the formula of Hunziker (1995), a slightly modified form of the Meyer-Peter & Müller's (1948) formula:

$$\phi = 5(\theta' - 0.05)^{1.5} \quad \text{where} \tag{1}$$

$$\phi = \frac{g_b}{\rho_s}\left[\left(\frac{\rho_s}{\rho} - 1\right) \cdot g D_m^{\,3}\right]^{-0.5} \tag{2}$$

$$\theta' = \frac{v_*^{\,2}}{\left(\frac{\rho_s}{\rho} - 1\right) \cdot g D_m} \tag{3}$$

In the above relations $\phi =$ dimensionless bedload transport rate per unit channel width (Einstein number), $\theta' =$ dimensionless boundary shear stress (Shield number) and $g_b =$ bedload transport rate per unit channel width.

4.2.2 *Widening phase*

For this phase the sidewalls were removed (Fig. 4b). In the three experiments conducted so far, the discharge and the sediment rate was the same as for the first phase (sediment supply matched 100% of the transport capacity). In further experiments the sediment supply will be reduced in the widening phase to 50% or 0% of the transport capacity in order to model states with low or no bed load respectively. During this second phase the channel width began to increase by means of lateral erosion (Fig. 4c) and consequently to develop new dynamic morphologies. This phase finished when the maximal braiding width was attained or until the channel reached the sidewall of the flume.

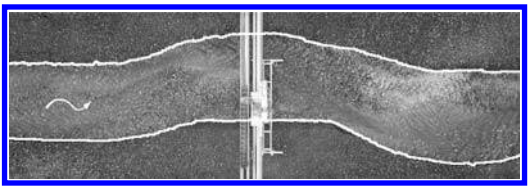


Figure 5. Eroded bank lines, detected from the digital photos. In this figure a 10 m long section of the flume is shown.

5 EVALUATION OF THE LATERAL EROSION

In this project, a method to analyze the spatial and temporal evolution of the lateral erosion was developed. The digital cameras installed above the flume (Fig. 4) automatically took vertical photos at one minute intervals. All the cameras were positioned at the same level and synchronized. Each camera covered a part of the flume and they simultaneously took the photos in the defined time step. Assembling the photos resulted in one picture of the entire flume. Based on an edge detection algorithm, a program was developed to analyze the photos and to identify the position of the laterally eroded banks automatically (Fig. 5). These lines are detected by identifying the different contrast values of the wetted and the dry bed zone respectively. The accuracy of the results was improved by increasing the contrast of the photos before detailed analysis. With this method, the position of the left and right eroded bank is known for any time during the experiment. This allows analysis of the spatial and temporal evolution of the lateral erosion with a high time resolution.

Copyright © 2006 Taylor & Francis Group plc, London, UK

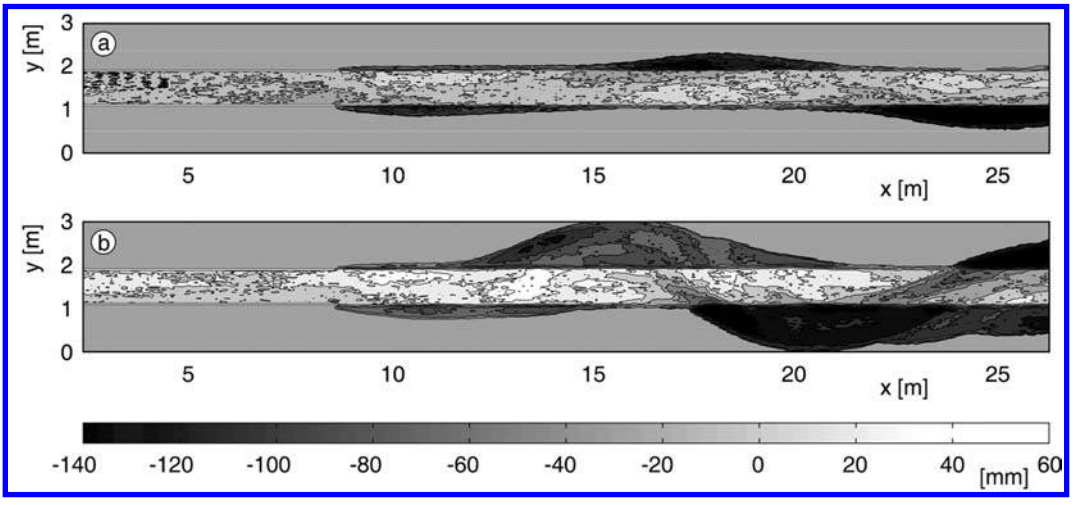


Figure 6. Difference of the bed level elevation heights for two topographies measured in the widening phase, a) after 7 hours and b) after 30 hours, compared to the topography measured at the end of the equilibrium phase. The showed plots correspond to topography measurements of the first experiment (discharge = 25 l/s and sediment rate = 30 g/s).

6 PRELIMINARY RESULTS

As the experimental investigation is in its initial stage, only some observations and preliminary results from the first three experiments are presented in this paper.

6.1 *Equilibrium state*

In the first phase an equilibrium state was reached according to the experimental procedure (see Section 4.2). In the three experiments this state was reached after approximately 30 h. The equilibrium bed slopes at the end of this phase, obtained from the measurements of the bed topography, closely matched the bed slopes calculated using Hunziker's formula (1), as described in Section 4.2.1.

Applying the formula of Meyer-Peter and Müller (1948), the computed bed slope values were approximately 20% lower than the measured ones. In terms of sediment transport, this difference means an overprediction of the bed load rates when this formula is used. This is in line with the specifications that can be found in the literature (e.g. Hunziker & Jäggi 2002, Parker et al. 1982, Wong & Parker 2005).

6.2 *Initiation of channel widening*

The observed mechanism to initiation of channel widening and consequently channel braiding within the three experiments was very similar. After removing the sidewalls, the channel width slightly increased. From the beginning, it was observed that the bed load transport occurred in pulses. Due to the initial width increase sediment material was deposited and after 4 to 6 hours the development of alternating bars could be observed. These bars grew rapidly so that after 7 to 9 hours from the beginning of the experiment a meandering thalweg was established and the flow began to erode the banks on the opposite side of the bars (Fig. 6a). The sinuosity of the meandering channel then increased continuously due to the lateral erosion. The bank erosion migrated in an upstream direction (compare Figs. 6a and 6b). The material from the eroded banks was deposited directly downstream, forming a middle bar. The flow began to bifurcate due to these bars, so that the braiding process started. The maximum braiding width could not be reached in these experiments because the channel first touched the side wall of the flume. The spatial and temporal fluctuations of the bed load transport, observed from the beginning of the experiments, are known to be a typical feature of the braided stream dynamic (Ashmore 2001) and they were observed and investigated by many authors (e.g. Hoey & Sutherland 1991, Warburton & Davies 1994, Ashmore 1988, Cudden & Hoey 2003).

6.3 *Mean bed level*

When designing the widening of a river reach, it is very important to quantify the effects that influence the adaptation of the river bed level upstream and downstream of the widened section. This influence was investigated in detail by Hunzinger & Zarn (1997) and Hunzinger (1998) for rivers which are in a state of equilibrium regarding the sediment transport conditions.

Copyright © 2006 Taylor & Francis Group plc, London, UK

The three experiments evaluated so far were carried out with a bed load rate that matched 100% of the transport capacity (equilibrium state). Within the three experiments, typical effects of river widening were observed. Figure 7 shows a longitudinal profile of the mean bed level in one of the experiments. From this longitudinal profile the bed slope was estimated by linear regression.

As can be seen in Figure 7, the channel bed gradient became steeper in the widened river section.This led to a parallel elevation of the bed level upstream of the widened reach. The observed processes correspond to the investigations by Hunzinger (1998) for rivers that are in a state of equilibrium. However, by some evaluated widening projects in Alpine eroding rivers, which are not in a state of equilibrium, this bed elevation upstream of the widened section was not observed; instead, the river bed was eroded further (Requena et al. 2005). In the present study, the experiments carried out with low bed load rates will allow to quantify the effects of widening on the mean bed level for rivers that are in an eroding state.

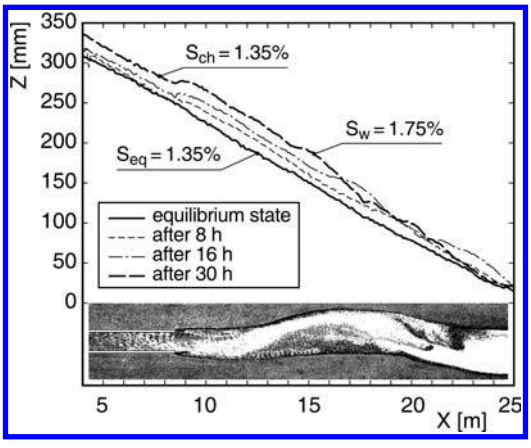


Figure 7. Longitudinal profile of the mean bed level for the first experiment (discharge = 25 l/s and sediment rate = 30 g/s). The bed slopes were estimated by linear regression of the longitudinal section. In the figure S_{eq} = equilibrium bed slope at the beginning of the widening phase, S_{ch} = bed slope after 30 hours for the channel reach and S_w = bed slope after 30 hours for the widened reach.

6.4 *Lateral erosion*

From the analysis of the experiments carried out so far, some qualitative tendencies of the lateral erosion process can be concluded.

6.4.1 *Spatial evolution*

As described in Section 5, a program was developed for analyzing the photos and detecting the positions of the eroded banks. Knowing the position of the left and right eroded banks at an interval of one minute allows a highly precise analysis of the progress of the lateral erosion. Figure 8 shows the result of this analysis for a time interval of 800 minutes. It illustrates the successively detected positions of the eroded banks for a 10 m long section of the flume. It can be seen that the eroded bank line moves upstream, namely against the flow direction. This development was observed in all experiments and contrasts with the downstream meander migration observed in field and laboratory investigations by many authors (e.g. Odgaard 1987, 1989, Nanson & Hickin 1986).

6.4.2 *Temporal evolution*

An important parameter to quantify the widening process is the lateral erosion rate, defined as the velocity

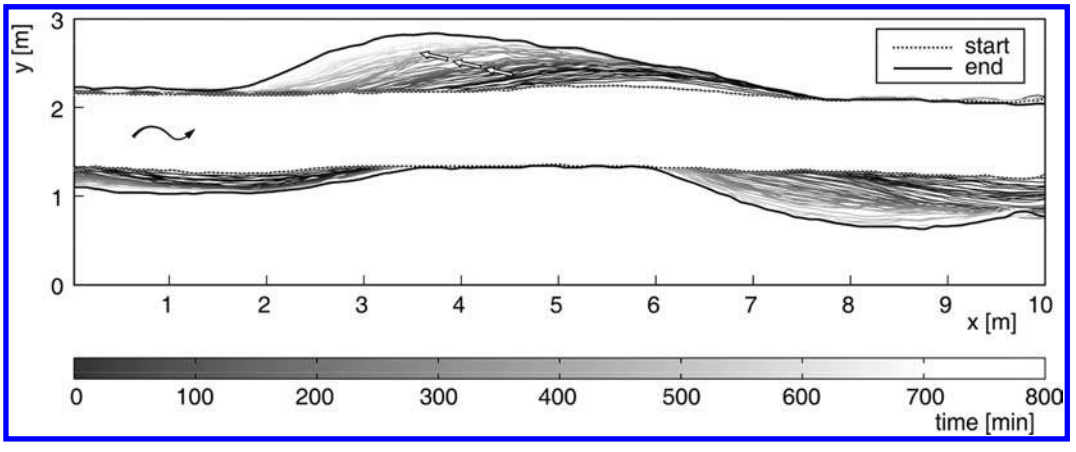


Figure 8. Successively detected positions of the eroded banks for a time interval of 800 minutes. Each line in the figure corresponds to a detected position.

Copyright © 2006 Taylor & Francis Group plc, London, UK

of bank erosion at a considered time increment and measured perpendicular to the initial bank line of the straight channel. The high density of the detected eroded bank lines (Fig. 8) allows the erosion rate to be estimated with precision. Figure 9 shows a 3D plot of the spatial and temporal evolution of the erosion of the left bank for one experiment. The grey shading illustrates the absolute values of the erosion rates estimated for the 800 minutes measured and for a 10 m long section of the flume. In Figure 9, the lightest grey zones correspond to high values of erosion rate.

For this experiment, the maximal value of erosion rate was 0.27 cm/min, occurring after 520 minutes at the position X = 4.2 m (Figure 9). Observing the time-dependent evolution of the high values of erosion rate (lightest grey zones in Figure 9), a pulsating mode of the erosion rate can be found. This confirms the observation that the erosion of the banks does not occur continuously, but has a pulsating behavior. As described in Section 6.2 it was also observed that the bed load transport occurred in a pulsating mode. Following this, the correspondence of these two observations suggests a correlation between the bed load transport and the lateral erosion rate.

Another interesting observation was made by considering only the maximum values of erosion rate of the left bank plotted in Figure 9 for the 800 minutes measured. These maximum values were plotted in Figure 10. The same values for the right bank were added to this figure. Figure 10 illustrates then for the 800 considered minutes the absolute maximum value of erosion rate found at any position of the banks (along the considered 10 m long section). From this plot it can be seen that during the experiment the absolute maximum value of erosion rate did not occur at the same time at both banks. When one of the banks was eroded intensively, the lateral erosion at the other bank was not prominent at any position x [m] of the channel.

Similarly to Figure 9, the pulsing progression of the erosion rate can also be observed in Figure 10.

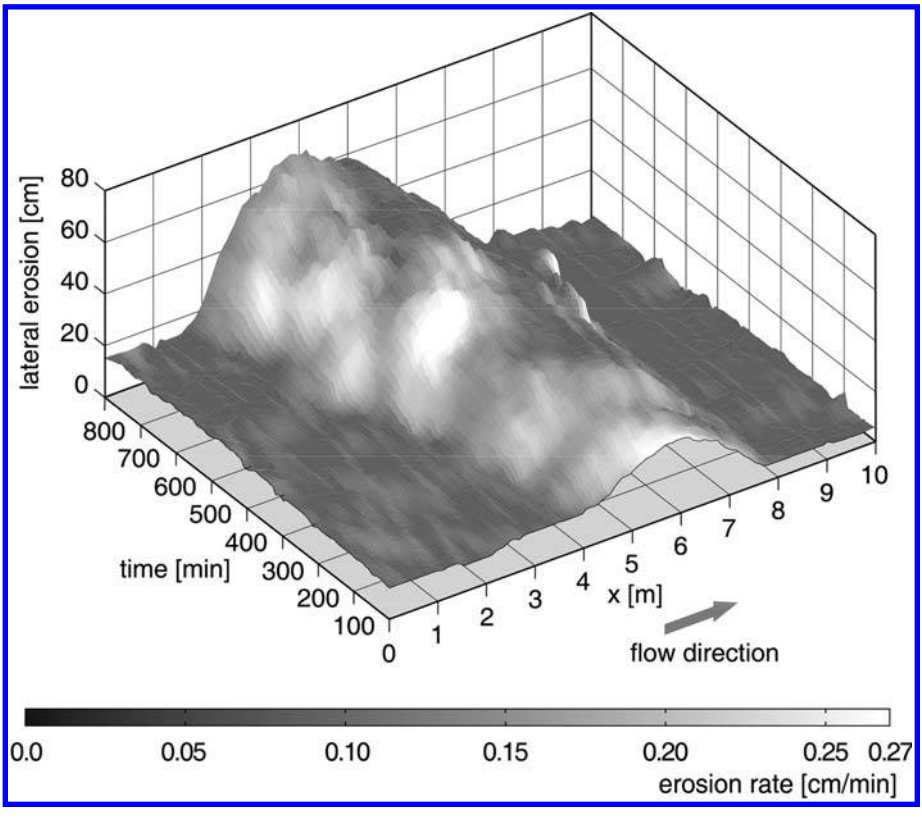


Figure 9. 3D plot of the spatial and temporal evolution of the lateral erosion of the left bank for a time interval of 800 minutes. The grey shading indicates erosion rates deducted from the same data set.

Copyright © 2006 Taylor & Francis Group plc, London, UK

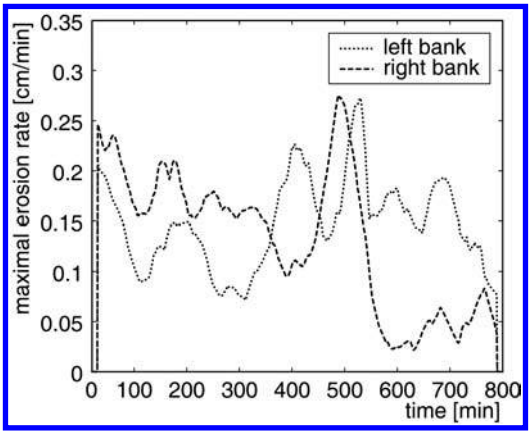


Figure 10. Temporal evolution of the maximal erosion rate for a time interval of 800 minutes for one experiment. Note that the banks within the time are changing their alignment due to lateral erosion and that the location of the maximum erosion rate consequently is changing with the time.

7 CONCLUSIONS

Physical model investigations are carried out in order to describe and quantify the lateral erosion process by channel widening. The observed mechanism for the development from an initially straight channel toward a widened channel with a poorly braided pattern was similar in the three evaluated experiments. In a first step alternating bars developed. These features were responsible for an initial erosion of the bank and the formation of a meandering channel. Thereafter, the eroded material deposited directly downstream, forming a central bar. The flow began to bifurcate due to these bars, so that the braiding process started.

Based on an edge detection algorithm, a program was developed to analyze the lateral erosion process. This program automatically analyzes the digital photos and detects the eroded banks. As the cameras take a photo per minute, the position of the left and right bank lines is known at any time of the experiment (Fig. 8). This allows a detailed analysis of the development of the lateral erosion. Through analysis of the spatial evolution of the lateral erosion it was found that the eroded banks moved upstream, namely against the flow direction.

As could be shown, the erosion rate of the banks can also be estimated with high precision due to the presented method in Section 5. The erosion rate, which is an important parameter to quantify the widening process, is defined as the velocity of bank erosion at a considered time increment and measured perpendicular to the initial bank line. Initial results in the experiments show that the erosion of the banks occurred in pulses. This pulsing behavior of the erosion rate is presumed to be related to the pulsating mode of the bed load transport, which was also observed in the experiments. Furthermore, it could be demonstrated that the location of the maximum erosion rate was changing with the time and the maximum erosion rates did not occur at the same time at both banks.

In addition to the observations and to the topography measurements, the presented method to identify the eroded bank lines constitutes the basis for analyzing the lateral erosion rates. This will allow to describe and to quantify the influence of the investigated parameters (discharge, bed slope, sediment supply and initial river width, on the lateral erosion process. Furthermore these results allow analyzing the interrelation between lateral erosion rates, sediment transport and braiding morphology after widening initiation.

NOTATIONS

D_{16}	particle size for which 16% of the sediment is finer by weight
D_{50}	particle size for which 90% of the sediment is finer by weight
D_{84}	particle size for which 84% of the sediment is finer by weight
D_{90}	particle size for which 90% of the sediment is finer by weight
D_m	mean diameter of the sediment
σ	$=(D_{84}/D_{16})^{0.5}$ sediment non uniformity
ϕ	dimensionless bedload transport rate per unit width (Einstein number)
θ'	dimensionless boundary shear stress (Shield number)
g_b	bed load transport rate per unit channel width
g	acceleration due to gravity
ρ_s	sediment density
ρ	water density
v_*	shear velocity for the bed region.

REFERENCES

Ashmore, P.E. 1982. Laboratory modeling of gravel braided stream morphology. *Earth Surface Processes and Landforms* 7: 201–225.

Ashmore, P.E. 1988. Bed load transport in braided gravel-bed stream models. *Earth Surface Processes and Landforms* 13: 677–695.

Ashmore, P.E. 1991. How do gravel-bed rivers braid? *Canadian Journal of Earth Sciences* 28:326–341.

Ashmore, P.E. 2001. Braiding phenomena: statics and kinetics, In: *Gravel-bed Rivers V* (Ed. M.P. Mosley): 95–120. New Zealand Hydrological Society, Wellington, New Zealand.

Ashworth, P.J., Ferguson, R.I. 1989. Size-selective entrainment of bed load in gravel bed streams. *Water Resources Research* 25(4): 627–634.

Copyright © 2006 Taylor & Francis Group plc, London, UK

Ashworth, P.J., Ferguson, R.I., Powell, M.D. 1992. Bedload transport and sorting in braided channels. *Dynamics of Gravel-Bed Rivers*: 498–513. John Wiley & Sons Ltd.

Cudden J.R., Hoey, T.B. 2003. The causes of bedlaod pulses in a gravel channel: The implications of bedload grain-size distributions. *Earth Surface Processes and Landforms* 28: 1411–1428.

Hoey, T.B., Sutherland, A.J. 1991. Channel morphology and bedload pulses in braided rivers: A laboratory study. *Earth Surface Processes and Landforms* 16: 447–462.

Hooke, J.M. 1980. Magnitude and distribution of rates of river bank erosion. *Earth Surface Processes and Landforms* 5: 143–157.

Hunziker, R. P. 1995. "Fraktionsweiser Geschiebetransport." *VAW Mitteilung No. 138.* ETH Zurich.

Hunziker, R. P., Jäggi, M. N. R. 2002. "Grain sorting processes." *Journal of Hydraulic Engineering* 128(12): 1060–1068.

Hunzinger, L.M., Zarn, B. 1997. Morphological changes at enlargements and constrictions of gravel bed rivers. In *3rd International Conference on River Flood Hydraulics* Stellenbosch: 227–236.

Hunzinger, L.M. 1998. Flussaufweitungen – Morphologie, Geschiebehaushalt und Grundsätze zur Bemessung. *VAW Mitteilung No. 159.* ETH Zurich.

Ikeda, S., Parker, G., Sawai, K. 1981. Bend theory of river meanders. Part I. Linear development. *Journal of Fluid Mechanics* 112: 363–377.

Marti, C. 2002. Morphodynamics of widening in steep rivers. *River Flow 2002* Louvain-la-Neuve 2: 865–873.

Meyer-Peter, E., Müller, R. 1948. Formulas for bed load transport. In *2nd Conference of the International Association for Hydraulic Research* Stockholm: 39–64.

Nanson, G.C., Hickin, E.J. 1986. A statistical analysis of bank erosion and channel migration in western Canada. *Geological Society of America Bulletin* 97: 497–504.

Odgaard, A.J. 1987. Stream bank Erosion along two rivers in Iowa. *Water Resources Research* 23(7): 1225–1236.

Odgaard, A.J. 1989. River-meander model. I: Development. *Journal of Hydraulic Engineering* 115(11): 1433–1449.

Osman, A.M., Thorne, C.R. 1988. Riverbank stability analysis I: Theory. *Journal of Hydraulic Engineering* 114(2): 134–150.

Parker, G. 1983. Theory of meander bend deformation. In *River Meandering* New Orleans: 722–733.

Parker, G., Klingeman, P.C., McLean, D.G. 1982. Bed load and size distribution in paved gravel-bed streams. *Journal of Hydraulics Division, American Society of Civil Engineers*, 108:544–297.

Requena, P., Bezzola, G.R., Minor, H.E. 2005. Aufweitungen in erodierenden Flüssen. *Wasser, Energie und Luft* 97(7/8): 183–189.

Schmautz, M. 2004. Gravel river widening by bank erosion in a straight stretch of river – investigations on a numerical model. *River Flow 2004* Napoli 1: 99–107.

Thorne C.R., Osman, A.M. 1988. Riverbank stability analysis II: Applications. *Journal of Hydraulic Engineering* 114(2): 151–171.

Warburton, J., Davies, T.R.H. 1994. Variability of bed load transport and channel morphology in a braided hydraulic model. *Earth Surface Processes and Landforms* 19: 403–421.

Warburton, J. 1996. Active braid plain width, bed load transport and channel morphology in a model braided river. *Journal of Hydrology* (NZ) 35(2): 259–285.

Wong, M., Parker, G. 2005. The bedload transport relation of Meyer-Peter and Müller over predicts by a factor of two. *Journal of Hydraulic Engineering*, resubmitted December 2005.

Zarn, B. 1993. Stabilising a riverbed by local widening – a case study of the river Emme, Switzerland. In *Sediment Transport Mechanisms in Coastal Environments and rivers* Le Havre, Euromech 310: 388–396.

Zarn, B. 1997. Einfluss der Flussbettbreite auf die Wechselwirkung zwischen Abfluss, Morphologie und Geschiebetransportkapazität. *VAW Mitteilung No. 154*. ETH Zurich.

Copyright © 2006 Taylor & Francis Group plc, London, UK

C. Interdisciplinary approaches for river management

C.1. Innovative field and laboratory instrumentation

Copyright © 2006 Taylor & Francis Group plc, London, UK

DPIV study of the turbulent boundary layer over V-shaped cavities

A. Amador
Escola Superior de Tecnologia do Barreiro/IPS, Barreiro, Portugal

M. Sánchez-Juny & J. Dolz
Universitat Politècnica de Catalunya, Barcelona, Spain

ABSTRACT: In the present work the digital particle image velocimetry technique (DPIV) is used to study the turbulent boundary layer over a surface made up of V-shaped cavities placed transversely to the flow direction. The integral measures of the boundary layer like the displacement and momentum thickness are estimated from the mean velocity field. The wall shear-stress is higher than the corresponding smooth surface values. From the fluctuating velocity field it is observed maximum turbulence levels in the region just above the cavities. Study of coherent turbulent structures suggests the presence of strong outflows of fluid from the cavities as well as inflows into the cavities. It is conjectured that the mass transfer/exchange between cavities and main stream, play an important role in the high levels of turbulent energy observed.

1 INTRODUCTION

The present study on wall turbulence concerns open-channel flows over V-shaped cavities.

The equations of motion indicate that energy is removed from the mean flow and transferred into the turbulent motion by the action of the Reynolds shear stresses. The turbulence energy production and resulting turbulence characteristics depends on the nature of the surface (Djenidi et al, 1999). For turbulent flow over smooth surfaces the periodic bursting process is the predominant mode of turbulence production (Tantirige et al, 1994). Over rough surfaces, coherent structures are more intense than for a smooth wall layer. Antonia (1994) based on measurements over three different types of surfaces (d-type roughness, V-grooves and k-type roughness), indicated that Reynolds stresses are increased relative to smooth wall. It was also mentioned different changes to the turbulence structure as a result of the different types of surface. Experimental studies of side-cavity open channel flows by Nezu and Omnitsuka (2002 a,b), reported that coherent eddies are generated in the roughness element and contribute significantly to momentum and mass transfer between cavity and main channel.

Most experimental studies of turbulent boundary layers over rough surfaces (Perry et al., 1969; Wood and Antonia, 1975; Antonia, 1994; Tantirige et al., 1994; Djenidi et al., 1999; Kameda et al., 2004) employed as measurements tools flow visualizations, hot wire anemometry and laser Doppler velocimetry. Kameda et al. (2004) attributed the few quantitative studies of the roughness sub-layer, to the difficulty of measurement, which is complicated by the presence of reverse flow and intense turbulence. Sousa and Pereira (2002) demonstrated the advantages of using digital particle image velocimetry (DPIV) for identification of large scale vortical structures embedded in the flow.

The aim of the present work is to better understand the effect of V-shaped cavities have on the physical processes responsible for enhancement of turbulence production. The flow over a steeply sloping wall made up of two-dimensional V-shaped cavities placed transversely to the flow direction is measured using a DPIV system. The effects of the rough wall on the mean and fluctuating velocity field are investigated and discussed. The behaviour of the separated free shear layer formed behind the roughness elements is studied and the wall shear stress is determined. An effort is made to identify coherent structures that may contribute to turbulence production.

2 EXPERIMENTAL SET-UP

The experiments were performed in a large-scale water channel assembled at *A Coruna* University. The experimental facility and measurement technique are described in the following.

The free-surface water channel is 0.50 m wide, 2.0 m high and the bottom inclination is 51.3°. The rough wall is composed of transverse V-shaped

Copyright © 2006 Taylor & Francis Group plc, London, UK

cavities. The height of the roughness elements is 0.031 m (k_s) and the width is 0.064 m (L_{cav}), which corresponds to a roughness pitch ratio (p) of 2.1 ($p = L_{cav}/k_s$). The tested unit water discharge (q) was 0.11 m^2/s that corresponds to a Reynolds number ($Re = q/\nu$) of 1.1×10^5. The electromagnetic flowmeter installed in the supply conduit of the model had an accuracy of $\pm 2\%$.

The DPIV system is composed of a double-pulsed Nd-Yag laser, with 400 mJ of energy per pulse, a 1280×1024 pixel resolution, high sensitive peltier cooled, CCD camera. A Nikkor 50 mm 2.8, together with a narrow bandwidth filter that passes the 532 nm light from the Nd-Yag laser, is mounted on the CCD camera. An electronic sequencer synchronizes the camera and laser pulses.

The water was seeded with 70μm ceramic micro spheres. The images cover two steps. Bigger measurement areas imply unacceptable perspective errors (Fig. 1). The camera captured double frame, double exposure particle images. The separation time was adjusted at 200–250μs between two laser pulses in order to give a maximum particle image displacement of eight pixels.

Both image frames are subdivided into small interrogation areas that are partially overlapping. Interrogation areas at identical positions in the images frames are correlated by means of Fast Fourier Transformation. From the two dimensional cross-correlation function, the position of the highest peak representing the mean displacement of the particle images is estimated. In order to obtain high-accuracy estimators of the particle displacements, the correlation peak position is calculated at sub-pixel level by the three point Gaussian interpolation scheme. The accuracy of the resulting DPIV estimators is about 0.1 pixel, which in the present study corresponds to an accuracy regarding the measured velocities of 50–62.5 mm/s.

Zero offsetting is applied in order to optimize the signal and to minimize biasing effects in the PIV estimators (Westerweel et al., 1997). The interrogation of the images initiates with large dimensions of the interrogation areas that are reduced in size after each interrogation. In this way, high dynamic velocity ranges can be combined with a high spatial resolution. In this study adaptive interrogation area sizes have been used from 128×128 pixels to 32×32 pixels, with an overlapping of 50% (i.e. 16 pixels). Some data sets are checked on peak-locking effects by examining the statistics of the DPIV estimators at sub-pixel level. All data are validated on outliers by the median test (Keane and Adrian, 1990; Westerweel, 1994). Detected outliers are substituted by the local mean value of its neighbouring estimators.

The study region comprises seven V-shaped cavities. The distance from the channel crest to their leading edges (X) is respectively of 0.343 m (cavity E35), 0.407 m (cavity E34), 0.471 m (cavity E33), 0.535 m (cavity E32), 0.599 m (cavity E31), 0.663 m (cavity E30) and 0.727 m (cavity E29).

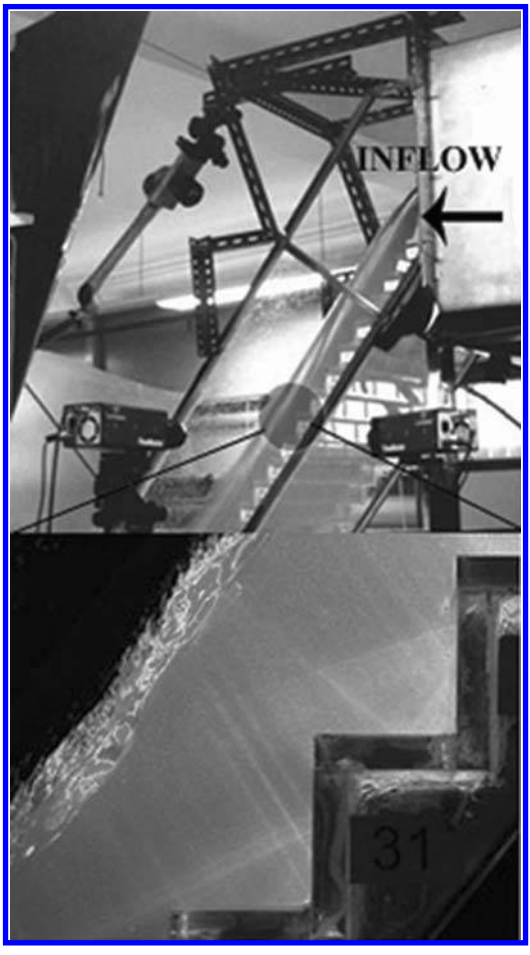


Figure 1. Experimental facility, $q = 0.11$ m^2/s; Image captured by CCD camera for cavities E34 ($X/k_s = 13.04$) and E33 ($X/k_s = 15.09$).

3 MEAN VELOCITY FIELD

The mean velocity field over the seven V-shaped cavities was obtained from 500 instantaneous velocity fields. The velocity vector spacing is 2.0 mm (i.e. 16 pixels) and kriging interpolation was chosen as a gridding method.

From the mean velocity contour map, shown in Figure 2, it can be observed that the flow is accelerating and developing in the downstream direction. The flow over the rough wall consists of a turbulent boundary layer next to the pseudo-bottom (imaginary

Copyright © 2006 Taylor & Francis Group plc, London, UK

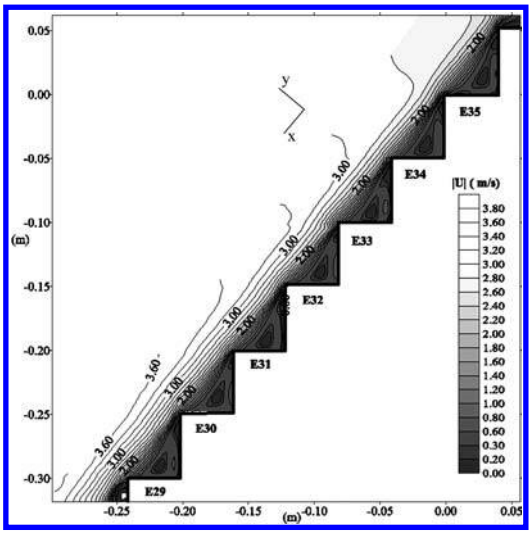


Figure 2. Contour map of mean absolute velocity (*|U|*).

line joining the leading and trailing edges of a cavity) and a frictionless fluid flow region above. Near the free surface the velocity varies from 2.8 to 3.7 m/s, corresponding to the potential flow velocity.

A well defined recirculation zone occupies part of the cavities. The quasi-steady rollers are maintained through the transmission of shear stress from the overlying flow. Considering the reverse flow a solid body rotation, for an equivalent circumference trajectory of 2 cm, the angular velocity and frequency of rotation were estimated to be approximately 40–50 rads^{-1} and 6–8 Hz in the cavities studied.

3.1 *Turbulent boundary layer*

The boundary layer thickness in the study region was evaluated. The boundary layer thickness (δ) is defined as the perpendicular distance from the pseudo-bottom to where the velocity is 99% of its maximum value (U_0).

The boundary thickness was obtained from the forty velocity profiles obtained over cavities E34, E33, E31 and E29 (Fig. 3). This is a difficult quantity to estimate, since it depends on measurements of small velocity differences and of the irregular behaviour of the outer edge of the boundary layer. The development of the boundary layer may be expressed by (U.S. Bureau of Reclamation, 1977):

$$\frac{\delta}{X} = a \cdot \left(\frac{X}{k_s}\right)^b \qquad (1)$$

where X is the streamwise distance from the start of the growth of the boundary layer assumed to be the channel crest; k_s is the roughness height, and "a" and "b" are constants which according with the experimental results are equal to: a=0.112 and $b = 0.309$.

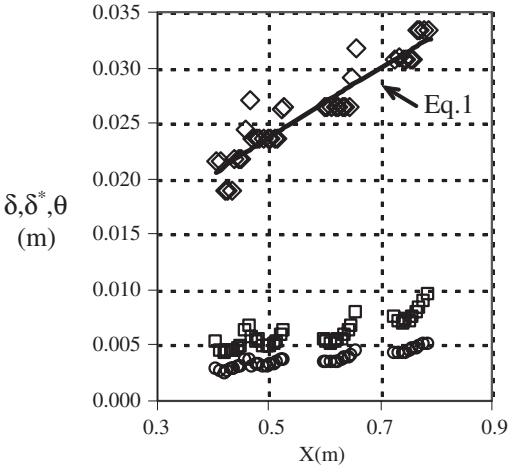


Figure 3. Evolution of the $\delta(\Diamond)$, $\delta^*(\square)$, $\theta(\bigcirc)$.

In Figure 3 is also shown other integral measures of the boundary layer obtained from the velocity profiles, as the displacement thickness (δ_*):

$$\delta^* = \int_0^\delta \left(1 - \frac{U(y)}{U_0}\right) \cdot dy \qquad (2)$$

and the momentum thickness (θ):

$$\theta = \int_0^\delta \frac{U(y)}{U_0}\left(1 - \frac{U(y)}{U_0}\right) \cdot dy \qquad (3)$$

where $U(y)$ is the streamwise mean velocity at y transverse coordinate and U_0 is the freestream velocity.

The use of the von Karman integral momentum equation (Pope, 2000) allows the estimation of the flow resistance coefficient (c_f) in the developing flow region:

$$c_f \equiv \frac{\tau_w}{\frac{1}{2}\rho U_0^2} = 2\frac{d\theta}{dx} + \frac{(4\theta + 2\delta^*)}{U_0}\frac{dU_0}{dx} \qquad (4)$$

where τ_w is the wall shear stress.

It was considered that the momentum thickness (θ) increased linearly in the flow direction (x) in accordance with Djenidi et al. (1999) that studied a similar surface. The data analysis gave a $d\theta/dx = 0.0052$. The term dU_0/dx is deduced from the Bernoulli equation. In Figure 4 is plotted the flow resistance calculations for four V-shaped cavities. The c_f seem to present a linear growth at each half end of the cavity and a global constant mean value of 0.031 for all cavities.

Copyright © 2006 Taylor & Francis Group plc, London, UK

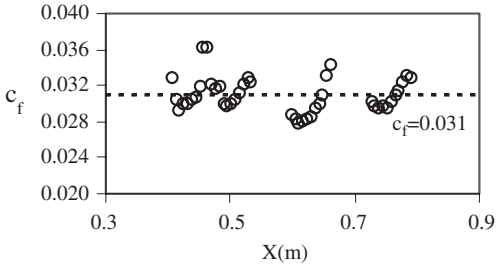


Figure 4. Flow resistance coefficient (c_f) along the study region.

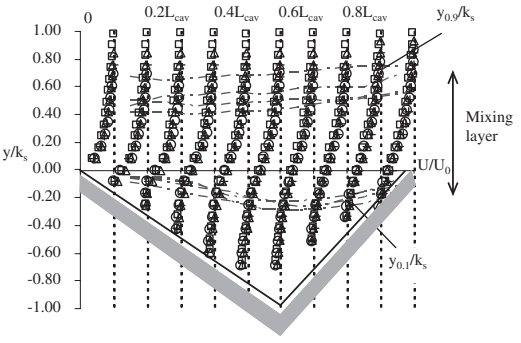


Figure 5. Mean velocity profiles (U/U_0) and variation of y_α along the V-shaped cavities: E29, $X/k_s = 23.29$ (□); E31, $X/k_s = 19.19$ (Δ); E33, $X/k_s = 15.09$ (+); E29, $X/k_s = 13.04$ (◯).

3.2 *Velocity distribution*

The mean velocity distribution can be divided in two zones: above the boundary layer, where the mean velocity can be considered constant and equal to the ideal-fluid flow velocity (U_0) and the boundary layer where the mean velocity gradient is relevant. In Figure 5 mean velocity profiles normal to the pseudo-bottom and taken at different positions along the cavities E34, E33, E31 and E29 are shown. At the cavity edges, the velocity distribution in the boundary layer can be approximated by a power law (Chanson, 2001), with an exponent determined for the four cavities edges equal to 3.0, This is in close agreement with the value of 3.3 obtained by Matos (1999) using a flushed Pitot tube in a similar model. In smooth walls with identical slopes, the value of $N = 6.0$ from the analysis of Cain (1978) and Chanson (1989), is usually suggested for the developing boundary layer upstream of the inception point. comparison shows that the mean velocity profile rises much more steeply from the reference level ($y = 0$) in smooth walls than in rough walls and then is flatter away from the "bottom".

Between the step edges ($0 < x < L_{cav}$), the velocity profiles suggest a local developing mixing layer that forms at the leading edge. Defining the characteristic width (b) of the mixing layer as (Pope, 2000):

$$b(x) = y_{0.9}(x) - y_{0.1}(x) \tag{5}$$

where y_α is the coordinate y where $U = \alpha U_0$.

In Figure 5 it is shown the spreading of the mixing layer by plotting the evolution of $y_{0.9}/k_s$ and $y_{0.1}/k_s$ along the cavities E34, E33, E31 and E29.

It seems that the mixing layer spreads linearly with a maximum of b at $x/L_{cav} = 0.7$. The displacement of $y_{0.1}$ to the interior of the cavity is much more noticeable than the variation of $y_{0.9}$ to the free surface. This is a typical characteristic of a mixing layer that spreads preferentially into the low speed stream (Pope, 2000). The maximum reverse flow velocities found in the recirculation zone are $0.15U_0$ and are located near the cavity boundaries.

3.3 *Mean velocity gradient tensor*

The 2D DPIV data provides two velocity components. This data can be differentiated in two directions and thus some terms of the mean velocity gradient tensor or deformation tensor can be estimated with PIV. Therefore the spanwise vorticity (ω_z) and in-plane shear strain (ε_{xy}) can be determined as follows:

$$\omega_z = \frac{dV}{dx} - \frac{dU}{dy} \tag{6}$$

$$\varepsilon_{xy} = \frac{dU}{dy} + \frac{dV}{dx} \tag{7}$$

The second order central-difference scheme was employed for estimation of the spatial derivatives, this scheme is implemented for data spaced at uniform ΔX, according:

$$\left(\frac{d\phi}{dx}\right)_i = \frac{\phi_{i+1} - \phi_{i-1}}{2\Delta X} \qquad O\left(\Delta X^2\right) \tag{8}$$

The shear strain contour map (Fig. 6) shows maximum levels just behind the upstream corner, where the separation of the shear layer begins. The peaks of shear strain develop in the flow direction, highlighting the pseudo-bottom as the most active zone in terms of shear stress. A gradual decrease of the shear strain is observed towards de free surface, where the flow can be considered irrotational.

Assuming the turbulent-viscosity hypothesis valid, as the production/generation of turbulent kinetic energy (P) is defined by (Pope, 2000):

$$P = -\overline{u'v'} \cdot \varepsilon_{xy} = \nu_t \cdot \varepsilon_{xy} \cdot \varepsilon_{xy} \tag{9}$$

where $\overline{u' \cdot v'}$ is the mean Reynold shear stress and ν_t is the turbulent viscosity.

Copyright © 2006 Taylor & Francis Group plc, London, UK

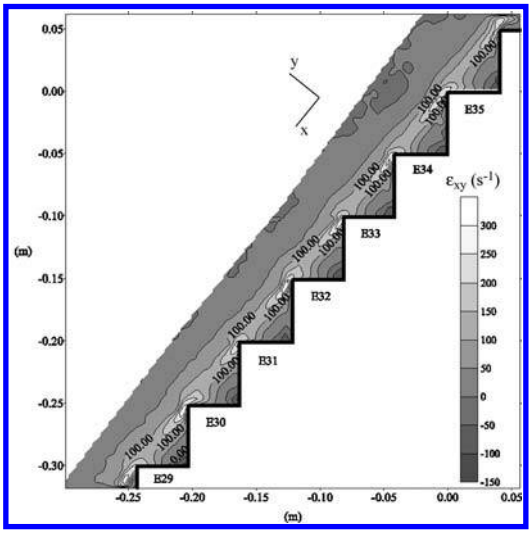


Figure 6. Contour map of mean shear strain (ε_{xy}).

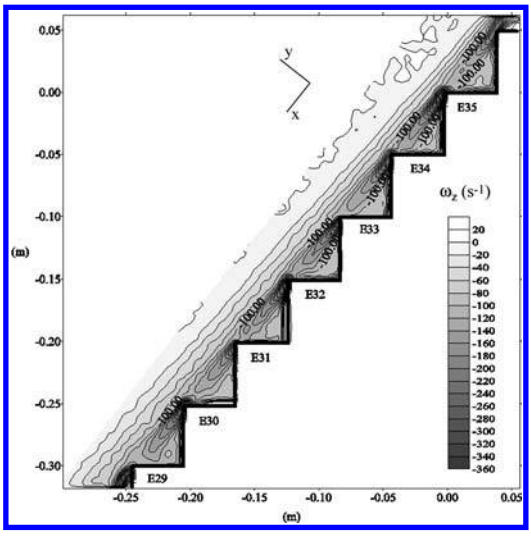


Figure 7. Contour map of mean spanwise vorticity (ω_z).

The production (P) is proportional to the mean shear strain rate. It is possible then to identify the zone just behind the leading edge as a region of formation and growth of large-scale turbulent structures, associated with local pressure reduction in the vicinity of the vortex cores.

The vorticity contour map (Fig. 7) presents a similar pattern with the shear strain map; the negative vorticity is due to counter clockwise rotation. Very high levels of vorticity are generated immediately downstream of the corner and occur over a relatively small characteristic thickness. This is most likely linked to the rapid onset of small-scale vortical structures, which appear immediately downstream the leading corner of the cavity. The dominant vorticity levels extend along the separated shear layer between the leading (upstream) and trailing (downstream) corners. Within the cavity, the flow pattern exhibit a large-scale recirculation flow, the vorticity results from agglomeration of the small scale concentrations.

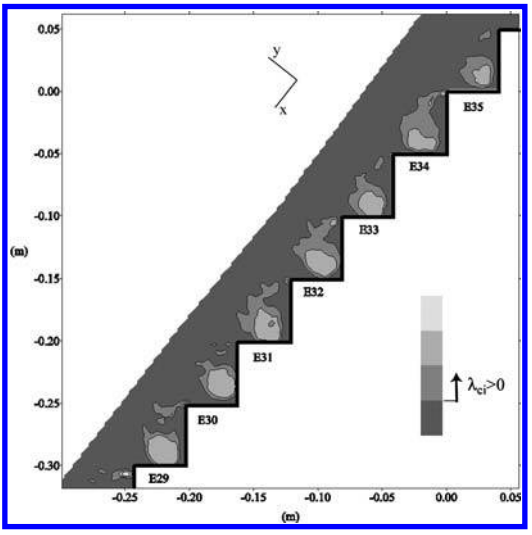


Figure 8. Contour map of swirling strength.

The vorticity level inside the cavity varies between 80 and 100 s^{-1}, which is in close agreement with the angular velocities estimated from the mean velocity field for the large recirculation zone, following the Stokes theorem equation.

The vorticity not only identifies vortex cores but also any shearing motion present in the flow. Adrian et al. (2000) proposed vortex identification based on the swirling strength. This method does not reveal regions which contain significant vorticity but do not have any local swirling motion (i.e. shear layers). It is based on the analysis of the mean, local velocity gradient tensor and its corresponding eigenvalues. The local 2D velocity gradient tensor will either have two real eigenvalues (λ_r) or a pair of complex conjugate eigenvalues ($\lambda_{cr} \pm \lambda_{ci}$). The vortices are identified by plotting iso-regions of $\lambda_{ci} > 0$ (Adrian et al. 2000). Iso-regions of swirling strength are shown in Figure 8. Swirling strength is noted just behind the leading edge and inside the cavity due to the presence of the recirculation vortex. This quantity proved to be more useful than vorticity as a means of identifying eddies.

4 TURBULENCE CHARACTERISTICS

The 500 velocity fields measured allow studying the mean velocity field and the fluctuating velocity field.

Copyright © 2006 Taylor & Francis Group plc, London, UK

The turbulent kinetic energy was chosen to represent the turbulent flow field. As the spanwise velocity component is not available, it is estimated from the other two components. The turbulent kinetic energy (k) is then expressed by (Sousa and Pereira, 2002):

$$k = \frac{3}{4} \cdot \left(\overline{u'^2} + \overline{v'^2} \right) \tag{10}$$

where $u' = u - U$ is the velocity fluctuation in the streamwise direction, $v' = v - V$ the velocity fluctuation in the transverse direction.

Figure 9 confirms that the maximum turbulent kinetic energy is located in the region near the pseudo-bottom. In the shear strain field (Fig. 6) the region of production of turbulent kinetic energy was identified: the mean velocity gradient removes kinetic energy from the mean flow and transfers it to the fluctuating velocity field. Also it can be observed the turbulent kinetic energy levels increasing in the downstream direction with more and more important values appearing in the overlying flow closer to the free surface.

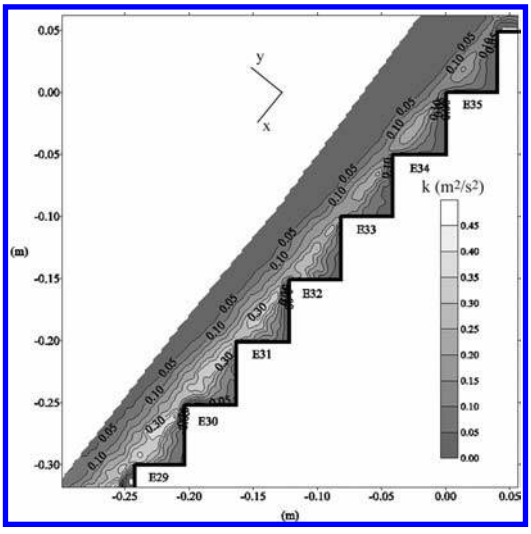


Figure 9. Contour map of turbulent kinetic energy (k).

4.1 *Turbulence intensity distribution*

As for the mean velocity, ten equally spaced turbulence intensity profiles were obtained over the cavities E34, E33, E31 and E29.

The turbulence intensity in the flow direction (T_u) is defined as:

$$T_u(y) = \frac{\sigma_u(y)}{U(y)} \tag{11}$$

where $\sigma_u\,(y)$ is the root mean square of the streamwise component of turbulent velocity and $U(y)$ is the mean streamwise velocity at y coordinate.

A gradual reduction of the turbulence intensity towards the edge of the boundary layer (δ) can be observed in Figure 10. In the transition between the boundary layer and the irrotational flow region were measured turbulence intensity (T_u) levels of 0.04. Near the pseudo-bottom ($y/\delta \approx 0$) the turbulence intensity ranges from 0.40 to 0.65.

The degree of turbulence intensity is much higher than the maximum levels reported for a turbulent boundary layer over a smooth open channel, $T_u = 0.2$ (Nezu y Nakagawa, 1993).

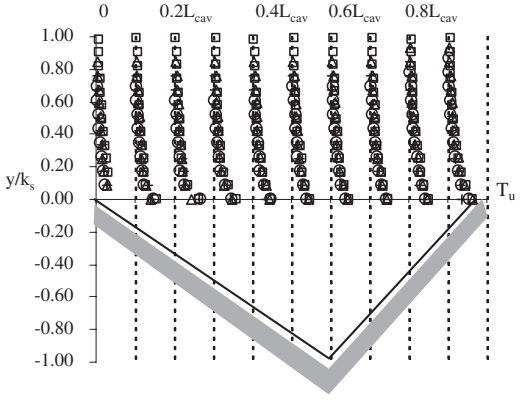


Figure 10. Turbulence intensity (T_u) profiles normal to the pseudo-bottom, along the V-shaped cavities. Symbols as in Figure 5.

4.2 *Quadrant Analysis*

The u'v' quadrant splitting scheme is one of the existent eduction techniques to study turbulent structures (Willmarth and Lu, 1972). This technique is based on the joint distribution of the velocity fluctuations on both longitudinal ($u' = u - U$) and vertical ($v' = v - V$) components. Four quadrants are defined in the $u'v'$ plane (Fig. 11): quadrant I ($u' > 0$ and $v' > 0$); quadrant II ($u' < 0$ and $v' > 0$); quadrant III ($u' < 0$ and $v' < 0$) and quadrant IV ($u' > 0$ and $v' < 0$).

Each quadrant represents an event; quadrant II is associated with "ejection" that can be schematically characterized by an upward movement ($v' > 0$) of a low-speed fluid ($u' < 0$), in quadrant IV are the sweeps that are downward movements ($v' < 0$) of high speed ($u' > 0$) fluid. Events in these regions correspond to the production of turbulent energy (see Equation 8) (Pope, 2000). Quadrants I and III are outward and inward interactions respectively.

Copyright © 2006 Taylor & Francis Group plc, London, UK

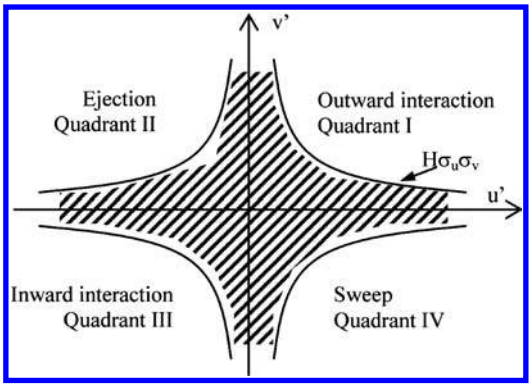


Figure 11. Definition sketch of the $u'v'$ plane (after Nezu and Nakagawa, 1993).

In Figure 11 the cross-hatched zone is bounded by the curves:

$$|u'\cdot v'| = H\cdot\sigma_u\cdot\sigma_v \tag{12}$$

where σ_u and σ_v are the root mean square values of the u and v velocity components. Only the region out of the cross-hatched zone is considered contributing to the events. The threshold values defined by H, allow distinguishing high-magnitude events (H high) and most frequent events (H equal to zero).

The quadrant contributions in each velocity field can be evaluated by the following discriminating function (Cellino and Lemmin, 2004):

$$I_H^i(x,y,n) = \begin{cases} 1, & [u'(x,y,n), v'(x,y,n)] \in Q^i \wedge |u'\cdot v'| > H\cdot\sigma_u\cdot\sigma_v \\ 0, & otherwise \end{cases} \tag{13}$$

The occurrence probability ($f_H^i = x$) of each quadrant (Q^i), over the 500 (N) instantaneous velocity fields can be determined by:

$$f_{H=x}^i = \frac{\sum_{n=1}^{N} I_{H=x}^i(x,y,n)}{N} \tag{14}$$

In this study two threshold values were adopted: $H = 0$, where all events within a quadrant are considered; and $H = 2$ where only the strongest events are considered, the value 2 has been used in other quadrant analysis studies (Bélanger and Roy, 1998).

Figures 12 and 13 shows that the events associated to quadrant II and IV are the most frequent or have the highest probability in the flow field. For $H = 0$ (Fig 12) ejections (Q^2) have the highest probability of occurrence over the region near the pseudo-bottom and inside the cavity, while the sweeps (Q^4) are the most frequent in the upper region of the overlying flow.

For the high-magnitude events, $H = 2$, occurs precisely the inverse. In the zone near the pseudo-bottom

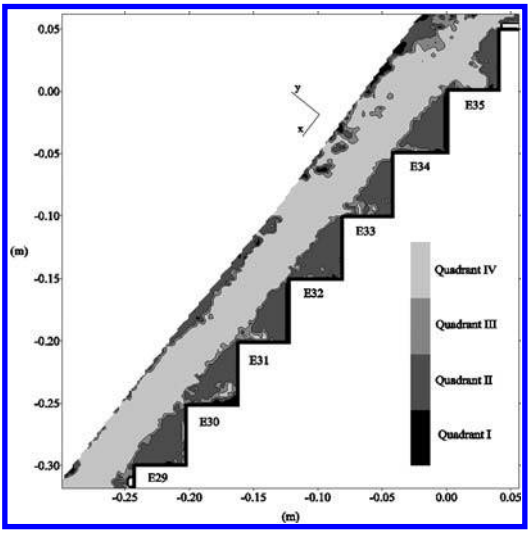


Figure 12. Contour map of the dominant quadrant in terms of occurrence probability for $H = 0$.

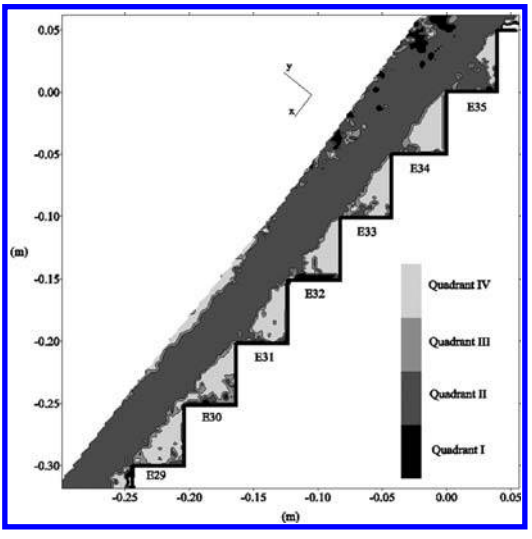


Figure 13. Contour map of the dominant quadrant in terms of occurrence probability for $H = 2$.

and inside the cavity, the highest probabilities of occurrence are for the sweeps and in the upper region of the coherent steam that skims over the cavities the dominant event is the ejection (Fig 13).

The previous considerations seem to corroborate the flow visualizations over transverse square cavities made by Djenidi et al. (1999). The visualizations indicated random occurrence of three types of events: outflows from the cavities into the overlying flow; inflows into the cavities; and, periods where the overlying flow

Copyright © 2006 Taylor & Francis Group plc, London, UK

skims over the cavities with no significant exchange of fluid. The highest occurrence probability of high magnitude ejections in the overlying flow (Fig. 13) corroborates the existence of important outflows from the cavities. Continuity demands that an outflow which occurs at a spanwise location must be balanced, at the same time, by one or more inflows at other spanwise positions into thecavity, and that would explain why sweeps are dominant inside the cavity.

Djenidi et al. (1999) also observed that outflows occur sequentially in the downstream direction: an outflow from one cavity is followed by another in the adjacent downstream cavity.

These sequences of outflows indicate that the initiating mechanism for the outflows may be triggered by the overlying flow rather than have its origin within the cavity (Townes and Sabersky, 1966; Djenidi, 1999). The passage of quasi-streamwise vortices near the pseudo-bottom could pump fluid out of the cavities as these turbulent structures have associated pressure minimum at its core.

The outflows of strong magnitudes from the cavities into the overlying flow could play an important role in the increased turbulent intensities measured over surfaces composed of V-shaped cavities in comparison with smooth surfaces.

5 CONCLUSIONS

The experimental study presented herein investigated the developing turbulent boundary layer over a steeply sloping surface made up of V-shaped cavities. The main conclusions are summarized below:

(1) In the region upstream the inception point of air entrainment the flow is accelerating and the turbulent boundary layer is developing and growing in the downstream direction. The recirculation inside the cavity can be approximated to a solid body rotation. The velocities measured confirm the hypothesis of irrotational flow in the region closer to the free surface;
(2) The boundary layer thickness, δ depends on the distance from the channel crest and roughness height and can be predicted by Equation 1;
(3) The Von Karman integral momentum equation was applied to estimate the flow resistance coefficient (c_f). The mean value obtained was 0.031;
(4) The shear strain (Fig. 6) and vorticity (Fig. 7) contour maps agree in showing maximum levels just behind the leading edges, where the separation of the shear layer begins. These regions can be associated with the formation and growth of large scale turbulent structures which are convected in the downstream direction. The swirling strength proved to be an appropriate quantity to identify existent eddies in the mean velocity field (Fig. 8);
(5) The measured turbulence intensities (T_u) between 0.40 and 0.65 near the pseudo-bottom are much higher than the corresponding smooth surfaces values;
(6) A quadrant analysis was performed to study turbulent structures. It shows that "ejections" are the most frequent events in the region near the pseudo-bottom and "sweeps" dominate the upper region of the skimming flow, Figure 12. When considering only high magnitude events ($H = 2$), the opposite situation occurs. The "sweeps" are dominant near the pseudo-bottom and inside the cavity and the "ejections" are more frequent in the upper region of the overlying flow, Figure 13. This analysis seems to corroborate the flow visualizations of Djenidi et al. (1999). Along the span of the cavities, the outflows alternate with inflows of appreciable magnitude and contribute in producing and maintaining turbulence intensities and Reynolds shear stresses by exchanging momentum between the cavities and overlying layers. The fluid trapped within the cavities functions as a natural reservoir of low-momentum that facilitates the exchange of momentum between cavities and the overlying stream. It is conjectured that these would help maintaining a higher turbulent energy of the flow over a rough wall in comparison with a smooth wall.

ACKNOWLEDGEMENTS

The authors are very grateful to CITEEC (Centro de Innovación Tecnoloxica en Edificación e Enxeneria Civil) and Prof. Jerónimo Puertas from A Coruña University for the financial and technical support given in the experimental work. The first author acknowledges the financial support of the Fundação para a Ciência e Tecnologia (Portugal, Praxis XXI, BD/3056/2000).

REFERENCES

Adrian, R., Christensen, K. and Liu, Z. 2000. Analysis and interpretation of instantaneous turbulent velocity fields. *Experiments in Fluids* 29: 275–290.

Antonia, R. 1994. *The effects of different types of surface conditions on a turbulent boundary layer In Proc. First Int. Conf. On Flow Interaction*. Ed. N.W.M.Ko & B.H.Lee: 64–79.

Belanger, T. and Roy, A. 1998. Effects of a pebble cluster on the turbulent structure of a depth-limited flow in a gravel-bed river. *Geomorphology* 25: 249–267.

Cain, P. 1978. *Measurements within self-aerated flow on a large spillway*. *Phd Thesis* Univ. of Canterbury, New Zealand.

Cellino, M. and Lemmin, U. 2004. Influence of coherent flow structures on the dynamics of suspended sediment transport in open-channel flow. *J.Hydraul. Eng.* 130 (11): 1077–1088.

Copyright © 2006 Taylor & Francis Group plc, London, UK

Chanson, H. 1989. Flow downstream of an aerator. Aerator spacing. *J. Hydraul. Research* 27 (4):.519–536.

Chanson, H. 2001. *The hydraulics of stepped chutes and spillways*. Lisse: Swets & Zeitlinger.

Djenidi, L., Elavarasan, R. and Antonia, R. 1999. The turbulent boundary layer over transverse square cavities. *J. Fluid Mechanics* 395: 271–294.

Kameda, T., Mochizuki, S. and Osaka, H. 2004. *LDA measurement in roughness sub-layer beneath turbulent boundary layer developed over two-dimensional square rough surface, in Proc. int. symp. on applic. of laser tech. to fluid mech.*, Lisbon 11–15 July.

Keane, R. and Adrian, R. 1990. Optimization of particle image velocimeters Part I: Double pulsed systems. *Meas. Science Technology* 1: 1202–1215.

Nezu, I. and Nakagawa 1993. *Turbulence in open-channel flows. IAHR monograph serie.* Rotterdam: Balkema.

Nezu, I. and Onitsuka, K. 2002a. LDA measurements of side-cavity open-channel flows, wando model in rivers. *Advances in fluid modelling, and turbulence measurements*, Ninokata et al., eds, World Scientific, River Edge, N.J.:169–176.

Nezu, I. and Onitsuka, K. 2002b. PIV measurements of side cavity open-channel flows, wando model in rivers. *J. Vis.* 5(1):77-84.

Perry, A., E.Schofield, W.H. and Joubert, P. N. 1969. Rough wall turbulent boundary layer. *J. Fluid Mechanics* 177: 383–413.

Pope, S. 2000. *Turbulent flows*. Cambridge: Cambridge, University Press.

Sousa, J. and Pereira, J. 2002. DPIV study of the effect of a gabble roof on the flow structure around a surface-mounted cubic obstacle. *Experiments in Fluids* 37: 409–418.

Tantirige, S., Iribarne, A. P., Ojha, M. and Trass, O. 1994. The turbulent boundary layer over single V-shaped grooves. *Int. J. Heat Mass Transfer* 37: 2261–2271.

Townes, H. and Sabersky, R. 1966. Experiments on the flow over a rough surface. *Int. J. Heat Mass Transfer* 9: 729–738.

Westerweel, J. 1994. Efficient detection of spurious vectors in particle image velocimetry. *Experiments in Fluids* 16: 236–247.

Westerweel, J., Dabiri, D. and Gharib, M. 1997. The effect of a discrete window offset on the accuracy of the cross-correlation analysis of digital piv recordings. *Experiments in Fluids* 23: 20–28.

Willmarth, W. and Lu, S. 1972. Structure of the Reynolds stress near the wall. *J. Fluid Mechanics* 55: 65–92.

Wood, D. and Antonia, R. 1975. Measurements in a turbulent boundary layer over a d-type surface roughness. *J. Appl. Mechanics* 42:591–597.

U.S. Bureau of Reclamation 1977. *Hydraulic Design Criteria-Sheet 111-18 to 111-18/5*. U.S.Corps of Engineers.

Copyright © 2006 Taylor & Francis Group plc, London, UK

Time variation of three-dimensional scour geometry

Oscar Link & Ulrich Zanke
Institut für Wasserbau und Wasserwirtschaft, Technische Universität Darmstadt, Germany

ABSTRACT: An experimental investigation on time variation of three-dimensional scour geometry at a circular pier in sand is presented. Experiments were conducted in a relative large laboratory flume that has length, width and depth of 26, 2 and 1 m respectively. During experiments high-resolution scour geometry measurements has been carried out applying a non-intrusive measurement method in which a laser distance sensor placed inside the plexiglas pier is used. Radial and vertical position of the sensor was controlled by precision step-motors. Data were aquired with a frequency of 70 Hz. Whole topography was measured within two minutes. From the experimental results an accurate characterization of scour-hole geometry is presented, quantitatively defining the different scour phases, namely initial, development, stabilisation and equilibrium phase. The data are useful for testing results of numerical simulations.

1 INTRODUCTION

Pier scour is a topic of continuous interest in civil engineering. State-of-the-Art reviews have been given by Breusers et al. (1977), Hoffmans & Verheij (1999) and Melville & Coleman (2000). Mostly, past experimental investigations focused on measurement of time-dependent and equilibrium scour depth at the pier nose.

Regarding geometry of scour-hole, slopes of symmetry axis of a scour-hole has been studied by Dargahi (1987). Equilibrium scour-hole geometry has been presented by Melville (1975), Olsen & Melaeen (1993) and Yanmaz & Altinbilek (1991). Link & Zanke (2004) presented an experimental curve relating scour-hole volume with scour depth at the pier front. Nevertheless, a systematic study on time-dependent scour-geometry remains undetected. The possible reason is partly attributed to the difficulties araising in the necessary measurement technique, which should include a non-intrusive sensor that rapidly moves to get the scour hole geometry especially during scour initial phase. Information on time-dependent scour-hole geometry is crucial for validation of three-dimensional numerical models. Scour hole geometry has been assumed as a frust of an inverted cone in simulations by Richardson & Pachang (1998).

In this article we present an experimental setup for the non-intrusive high-resolution measurement of the complete scour-hole in time. The measuring system was used to investigate the time-dependent characteristics of scour-hole geometry in a well graded sand at a single cylindrical pier.

The results describe scour mechanism quantitatively well, allowing definition of threshold values for the scour phases: initial, development, stabilisation and equilibrium phase, first proposed by Zanke (1978a,b) for two-dimensional scour and generalised for the three-dimensional case by Hoffmans & Verheij (1997).

The structure of the paper is organized as follows: In the second part we present the experimental setup and measurement technique. In the third part we present laboratory measurements. In the fourth part threshold values for the scour phases are defined.

2 EXPERIMENTAL SETUP AND MEASURING TECHNIQUE

2.1 *Experimental facilities*

Experiments were conducted in a rectangular flume with glass side-walls, 26 m long, 2 m wide and 1 m deep, at the Institute for Hydraulic and Water Resources Engineering, Darmstadt University of Technology, Germany. A 20 cm diameter plexiglas cylindrical pier was mounted in the middle of a working section with movable bed. This is located 16 m downstream of the flume entrance, having a length of 4 m, width of 2 m and depth of 0.5 m. A false bottom made of concrete plates was installed outside the working section in order to avoid filling the whole flume with sand. The plates rested on bricks, 0.5 m over the original flume bottom. The sides of the working section

Copyright © 2006 Taylor & Francis Group plc, London, UK

were coated with absorbing material in order to avoid secondary flows.

2.2 *Sediment material*

The bed material was a mixture of sand with grain sizes ranging between 0.06 and 2.00 mm and having a representative particle diameter $d_{50} = 0.25$ mm. The geometric standard deviation $\sigma_g = (d_{84.1}/d_{15.9})^{0.5}$ of the particle size distribution was 1.37. Figure 1 shows the sieve curve of the employed sediment material.

The critical velocity for the initiation of motion of isolated sediment particles, in the following called critical velocity, u_{cr} was equal to 0.26 m/s. The natural repose angle of sediment particles ϕ was 30°.

The sand was filled in the working section up to 5 cm over the false bottom level having 10 m upstream and 2 m downstream of the pier also covered with a 5 cm thick sediment layer.

2.3 *Measurement method*

The flow discharge, controlled by an inlet valve, was measured using a magnetic inductive sensor attached at the flume inlet. The flow depth, adjusted by a tailgate, was recorded by an acoustic sensor with an accuracy of ±0.5 mm. Initially, the flume was slowly filled with water. The flow discharge was increased and once the predetermined stable flow condition attained the measurement was taken.

A laser distance sensor located in the plexiglas pier (see Fig. 2) was used to measure the scour-hole radius with an accuracy of ±0.4 mm. The sensor was driven by high-precision step-motors in the vertical and radial directions with an accuracy of ±0.1 mm and ±0.5° respectively.

Vertical profiles containing about 20–30 points were taken in 24 different directions around the pier by turning the distance sensor in steps of 15 degrees around its vertical axis. Figure 3 shows a schematic diagram with the pier and measurement directions.

In order to compute maximum scour depth at each profile, vertical steps were adjusted according to the actual radius measured by the laser. In that way, when the sensor approached the scour-hole bottom, the vertical step was continuously reduced to a minimum value of 0.4 mm.

Point-data were aquired with a frequency of 70 Hz allowing a fast measurement of the complete scour-hole. A measurement of the whole scour-hole topography took about 30 seconds at the beginning of the experiments and about 2 minutes at the end of them.

Experiments with different section-average flow velocities, u_∞ have been carried out. Experimental runs were taken until maximum scour depth increased at a rate of about one representative particle diameter d_{50} per hour. Scour was studied under both, clear-water and live-bed conditions.

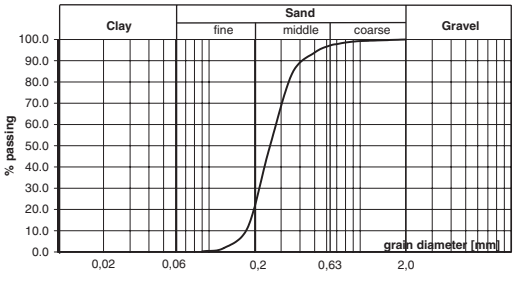


Figure 1. Sieve curve.

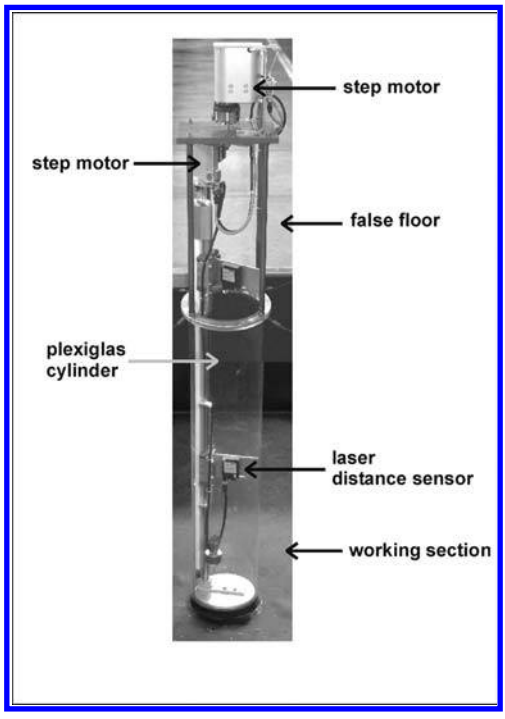


Figure 2. Experimental setup.

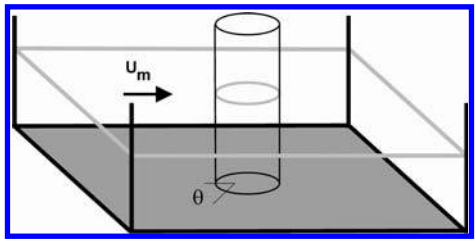


Figure 3. Schematic diagram with pier and measurement directions determined by angle θ.

Copyright © 2006 Taylor & Francis Group plc, London, UK

3 RESULTS

3.1 *Maximum scour depth in azimuthal planes*

Results correspond to a 20 hours duration scour experiment under the clear-water condition, with $u_m = 0.95u_{cr}$. After about 16 hours, the sediment transport rate in the scour hole was considered negligible. For the plots in Figure 7, 120 hours scouring has been analysed.

Dimensionless scour depth is defined as the maximum actual scour depth in a given plane at a certain time normalized by the maximum reached scour depth i.e. maximum scour depth at the front of the pier at the end of the experiment. Dimensionless time is the actual time normalized with the experiment duration.

Figure 4 shows dimensionless scour depth on dimensionless time in azimuthal planes with $\theta = 0°$, $60°$ and $105°$ for the first 20% of the maximum dimensionless time.

As scour initiates at the sides of the pier, at azimuthal planes with $\theta = 65°–75°$, curves present an offset in time within the first 2% of maximum dimensionless time. During this lapse, scour progresses faster downstream than upstream (compare slope of curves corresponding with $\theta = 60°$ and $\theta = 105°$).

At the pier nose ($\theta = 0°$) scour begins after a very short time of about 2% of experiment duration.

As it is well known, about 70–80% of scour develop in the first 10–20% of the maximum dimensionless time. Remarkably, the experimental curves show that the maximum depth of scour-hole is observed at the pier nose first after about 70% of scour has developed.

After about 20% of maximum dimensionless time maximum scour-hole depth is observed at the pier front (between $\theta = -30°$ and $+30°$).

Figure 5 shows dimensionless scour depth (at $\theta = 0°, 30°, 60°, 90°, 120°$ and $150°$) on dimensionless time after maximum scour depth reaches the azimuthal plane $\theta = 0°$. Scour progresses with the same velocity in all planes i.e. curves in Figure 5 are nearly parallel until time reaches about 50–60% of maximum dimensionless time.

After about 60% of maximum dimensionless time, scour progresses slower, with different velocity at the different azimuthal planes, i.e. curves of scour-depth on time change from a parallel to a slightly divergent development.

Figure 6 shows dimensionless scour depth on dimensionless time at azimuthal planes with $\theta = 0°$, $30°$ and $60°$.

3.2 *Scour volume*

Figure 7 show the scour-hole volume on maximum scour depth during 120 hours experimentation. The plotted curve confirms the tendency indicated in Figure 6. When scour reaches about 80% of maximum

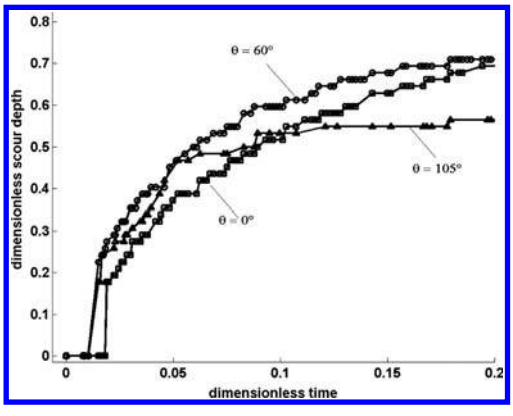


Figure 4. Dimensionless scour depth on dimensionless time in azimuthal planes with $\theta = 0°$, $60°$ and $105°$.

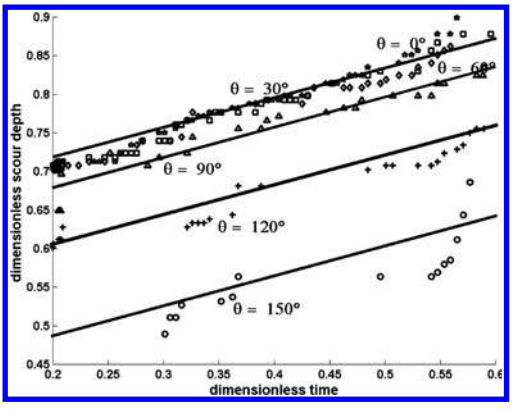


Figure 5. Dimensionless scour depth on dimensionless time in azimuthal planes with $\theta = 0°, 30°, 60°, 90°, 120°$ and $150°$.

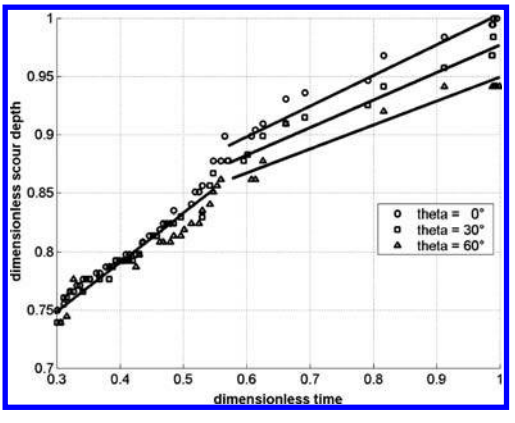


Figure 6. Dimensionless scour depth on dimensionless time in azimuthal planes with $\theta = 0°$ (circles), $30°$ (squares) and $60°$ (triangles).

Copyright © 2006 Taylor & Francis Group plc, London, UK

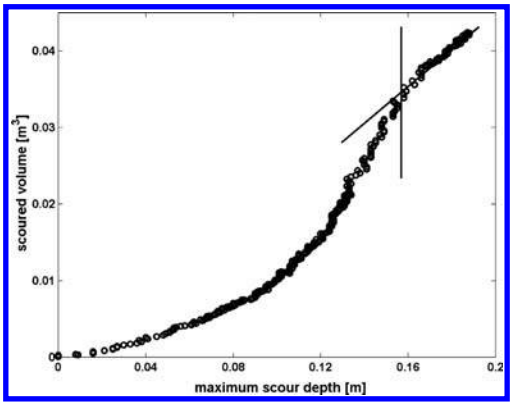


Figure 7. Scour-hole volume on maximum scour depth.

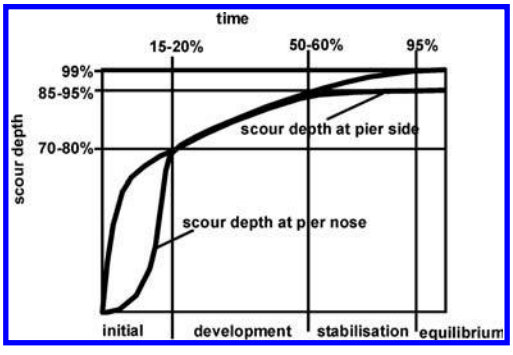


Figure 8. On definition of scour phases: initial, development, stabilisation and equilibrium.

depth, a new inflection point in volume on maximum scour depth is observed. Erosion intensity at the scour-hole decays to a small constant rate which growth nearly linear with maximum scour depth signalising a tendency to stabilisation.

4 DISCUSION

The presented high resolved measurements of scour-hole geometry in space and time suggest a threshold criteria to define scour phases. The presented measurements correspond to clear-water scour experiments with $u_m = 0.95\ u_{cr}$.

Schematically, scour phases can be defined as shown in Figure 8, extending the concepts suggested by Zanke (1978a,b) and adopted by Hoffmanns & Verheij (1997).

During initial phase, a given design scour depth, i.e. 70–80% of equilibrium scour depth is first achieved at the sides of the pier. Bridge scour monitoring should take this characteristic of scour-geometry into account, placing scour measurement devices at the pier sides rather than at the pier nose.

The validity of the proposed threshold values for experiments with lower and higher approach velocities is discussed by Link et al. (2006). Further research with different approaching flow depth and sediment materials is under development to investigate the influence of hydraulic and sedimentologic parameters on scour phases.

5 CONCLUSIONS

An experimental investigation on time variation of three-dimensional scour-hole geometry at a circular pier in sand has been presented.

Time-dependent scour-hole geometry has been measured by a new high-resolution non-intrusive method.

Experimental results provide information for a quantitative definition of the different scour phases, namely initial, development, stabilisation and equilibrium phase.

The presented data can be used in improving bridge scour monitoring and testing results of numerical simulations.

ACKNOWLEDGEMENTS

The first author thanks the financial support of the german academic exchange service DAAD through a PhD scholarship.

This study is part of the research project ZA 93/14-1 “Messung der Kolkentwicklung an Brückenpfeilern in sandigem Boden” (“Measurement of time-dependent scour at bridge piers in non-cohesive sediment”) founded by the German Research Council DFG.

REFERENCES

Breusers, H., Nicollet, G. & Shen, H. 1977. Local scour around cylindrical piers. *Journal of Hydraulic Research*. 15(3): 211–252.

Dargahi, B. 1987. Flow field and local scouring around a cylinder. Bulletin Nr. TRITA-VBI-137. *The Royal Institute of Technology. Stockholm, Sweden*.

Hoffmans, G. & Verheij, H. 1997. *Scour Manual*. Rotterdam: Balkema.

Link, O. & Zanke, U. 2004. On the time-dependent scour-hole volume evolution at a circular pier in uniform coarse sand. In *Proceedings of the Second International Conference on Scour and Erosion. Meritus Mandarin, Singapore*: 207–215.

Link, O., Pfleger, F. & Zanke, U. 2006. Scour at bridge piers: high-resolution measurement in space and time. *submitted for journal publication*.

Melville, B. 1975. Local scour at bridge sites. Rep. No. 117, *School of Engrg, The University of Auckland, New Zealand.*

Copyright © 2006 Taylor & Francis Group plc, London, UK

Melville, B. & Coleman, S. 2000. *Bridge Scour*. Water Resources Publications, Fort Collins, Colorado.

Olsen, N. & Melaaen, M. 1993. 3D calculations of scour around cylinders. *Journal of Hydraulic Engineering*, 119(9): 1048–1054.

Richardson, J. & Panchang, V. 1998. Three-dimensional simulation of scour- inducing flow at bridge piers. *Journal of Hydraulic Engineering*. 124(5): 530–541.

Yanmaz, M. & Altinbilek, D. 1991. Study of time-dependent local scour around bridge piers. *Journal of Hydraulic Engineering*. 117(10): 1247–1268.

Zanke, U. 1978a. Zusammenhänge zwischen Strömung und Sedimenttransport, Teil 1: Berechnung des Sedimenttransportes, -allgemeiner Fall-. *Mitteilungen des Franzius Instituts, TU-Hannover*. Heft 47.

Zanke, U. 1978b. Zusammenhänge zwischen Strömung und Sedimenttransport, Teil 2: Berechnung des Sedimenttransportes hinter befestigten Sohlenstrecken, -Sonderfall zweidimensionaler Kolk-. *Mitteilungen des Franzius Instituts, TU-Hannover*. Heft 48.

Copyright © 2006 Taylor & Francis Group plc, London, UK

Discharge measurement using Large Scale PIV under varied flow conditions – Recent results, accuracy and perspectives

A. Hauet, J.D. Creutin & P. Belleudy
Laboratoire d'Etude des Transferts en Hydrologie et Environnement, Grenoble, France

M. Muste & W. Krajewski
IIHR-Hydroscience & Engineering, The University of Iowa, Iowa City, USA

ABSTRACT: For 10 years now, Large Scale Particle Image Velocimetry (LSPIV), an image-based method, has been increasingly used for non contact rivers survey. LSPIV is a statistical identification of displacement flow from images on natural scale of rivers. This includes measurements of surface velocity distribution and discharges for very different sizes of rivers with sections as small as few meters and as large as hundreds of meters, without and with seeding of the flow, and with different sensing systems. This presentation is a review of a number of experiments, using the LSPIV method, conducted those last 10 years under varied flow conditions, i.e. from low flow to high flow. The authors present results of those experiments and highlight the advantages and weaknesses of the LSPIV measurements. The authors also present recent collaborative work between IIHR-Hydroscience & Engineering, Iowa City, USA and the Laboratoire d'étude des Transferts en Hydrologie et Environnement (LTHE), Grenoble, France. Those include measurements (i) from a mobile LSPIV platform, i.e. a truck-based system and (ii) from a permanent location at the Iowa River, where continuous real-time estimations of the discharge are performed. The authors present results of those experiments and highlight the advantages and weaknesses of the LSPIV measurements in field conditions.

1 INTRODUCTION

In the last decade, image-based methods have been increasingly used for non-contact measurements in rivers. The Large Scale Particle Image Velocimetry (LSPIV) used for this purpose is an extension of the conventional Particle Image Velocimetry and mainly consists in the statistical identification of the displacement of tracers floating at the surface of natural rivers.

The LSPIV measurements involve four steps: (i) recording of images, (ii) geometric transformation and image reconstruction, (iii) processing of the images by the way of statistical correlation to obtain a surface velocity field, and (iv) post-processing and quality check of the obtained velocity field. That measurement conveniently provides surface velocity distribution in straight channels as well as in more complex structures such as recirculation at junction between channels Lecoz (2005) or flow around hydraulic structures Dermisis & Papanicolaou (2005) or Fujita et al. (1998). By adding a fifth step, the free surface velocity associated with river bathymetry and hydraulic hypothesis leads to the discharge estimation.

This study is focused on the discharge estimation with LSPIV. We identify main problems of the actual hydraulic and hydrometry and explain, by the way of a review of selected papers, the contributions but also the limitations of LSPIV in the resolution of those problems. Recent results concerning a Mobile LSPIV unit and a continuous real-time LSPIV station are discussed.

2 LSPIV: AN INTERESTING TOOL FOR SOLVING MAJOR PROBLEMS OF HYDROMETRY

2.1 *Low flows*

Low flow measurements are very important for the study of physical and biological processes in coastal wetlands, marshlands, small channels or streams during drought conditions. Low flow discharges estimates are usually obtained by combining continuous water stage measurements at streamgages with rating curves. However, the uncertainty of the rating curves for low flow can be very important, especially for the small

Copyright © 2006 Taylor & Francis Group plc, London, UK

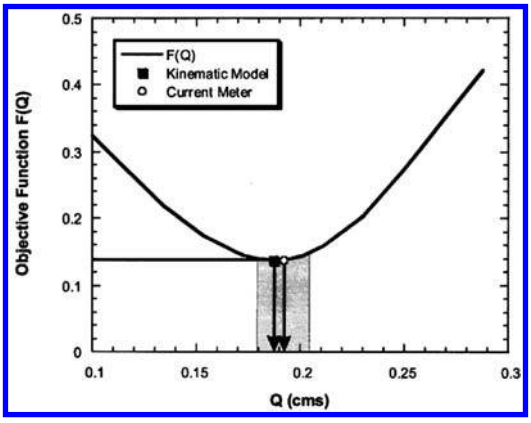


Figure 1. Mean-squared difference F(Q) between the PIV surface velocity estimates and the simulated velocities by the kinematic model as a function of discharge. The final estimate (corresponding to the minimum) is 0.187 cms. The current meter measurement (also shown) is 0.192 cms. The shaded area defines the range within one standard error of the current meter measurement. From Bradley et al. (2002).

streams Pelletier (1988). This has several causes. First of all, direct measurements of low flows with traditional equipment, such as current meter or ADCP, are in limited number, because (i) of the low return period of such events and (ii) of the difficulty of making such measurements with immersed material in very small water depth layer. The narrow channel width and shallow water depth usually make it impractical to follow recommended current meter guideline Buchanan & Somers (1969) regarding the minimum number of vertical profiles for the cross-section, and minimum number of depth velocity measurements at each profile. For ADCP, the blanking distance and the side lobe interference Simpson (2001) make the measurement impossible for shallow water. Furthermore, the modifications in the streamgage cross-section bathymetry, in alluvial channels, during floods have significant impact on low flow ratings.

LSPIV seems to be very well adapted for measurements in low flow conditions. Bradley et al. (2002) proved that, in a 5.7 m wide and 0.2 m deep channel at Clear Creek (Iowa), image velocimetry combined to a kinematic flow analysis allows a very good estimation of the discharge (0.187 $m^3\,s^{-1}$ for LSPIV, 0.192($\pm$6.4%) $m^3\,s^{-1}$ with current meter, see Figure 1).

At the same time, the USGS gage located approximately 15 m downstream of the experimental site, gave an estimate via the rating curve of 0.085 $m^3\,s^{-1}$, that is of the current meter measurement. Bradley et al. (2002) concluded that the large observed difference illustrate the significant errors that can results for low flow estimates based on traditional stage-discharge rating curve. The major limitation concerning LSPIV measurements in field conditions highlighted by the authors is the need for tracers at the free surface during low flow. Bradley et al. (2002) artificially seeded the surface of the river with fallen leaves, which limits the benefit of the "noncontact" aspect of the method.

Meselhe et al. (2004) studied the efficiency of LSPIV for low velocity measurement by the way of laboratory experiment. The velocity tested ranged from 0.013 to 0.044 $m\,s^{-1}$, which correspond to discharges from 0.002 to 0.0038 $m^3\,s^{-1}$ in a 1.524 m wide rectangular channel. By selecting appropriate seeding density and flow field sampling frequency, Meselhe et al. (2004) found that the LSPIV surface velocity have an average error of $\pm$5%, which proves the efficiency of the technique for low velocity measurement.

2.2 *Floods*

Accurate knowledge of the flow during a flood is crucial for hydrologist, fluvial geomorpholmogist, and river ecologist. Current meter and acoustic gauging methods require boat, cable cars or bridges, or wading into the stream in order to measure discharge for the cross-section. This procedure is time consuming and labor intensive. As noted by Creutin et al. (2003), gauging with this traditional equipment is difficult during periods of high flows for at least two reasons: (i) high flow velocities and floating debris endanger the operators and the equipment, and (ii) the river level and discharge can significantly change during the measurement, compromising the quality of the discharge estimate. As a result, 80% of the French rivers are not gauged for discharges with return periods superior greater than 10 years. An alternative is the use of aerial photographs, but they are associated with several deficiencies Fujita et al. (1997). LSPIV is an indirect (i.e. without contact with the water) method which can be applied by any flow condition, from a flood protected area. During floods, velocity measurements can be made from naturally occurring tracers, including foam, boil and ripple structures, and debris.

In an application to the Yodo River (Japan), Fujita et al. (1998) used LSPIV for monitoring a flood plain of a 100 m wide stream. The velocity measured reached 4 $m\,s^{-1}$. The authors observed a good representation of the velocity distribution of the flood plain, and the measurement of the discharge was in very good agreement (within 3%) with an estimation of discharge from a gauging station, where the stagedischarge curve was known, at the same location.

Because of it's fastness, LSIPV measurement seems to be also particularly adapted for the monitoring of flash floods. The imagery technique is ideally suited for making repeated measurement at low cost, so that it allows measuring not only the peak of the flood but all the dynamic of the periods of increasing and decreasing of the flow.

Copyright © 2006 Taylor & Francis Group plc, London, UK

The main problems that come up against the application of LSPIV for floods monitoring are: (i) the very important size of the area of interest to be recorded, which means a low resolution of the images. Flood plains are usually areas of several hectares. The tracers need to be larger than the resolution of one pixel to be followed. (ii) the deficiency of illumination and seeding. Floods happen most of time during rain periods, i.e. with cloudy weather and so poor illumination. Moreover, rain can destroy tracers such as bubbles or foam, or created patterns at the surface of the water that created errors in the PIV surface velocity computation.

2.3 *Rating curve improvement*

Most of time, the stream-flow records do not come from direct measurements of the discharge but are computed from continuous water stage measurements (pneumatic level indicator, float gauge . . .). The water stage is linked with the discharge using a rating curve that is unique for each stream gauging location. As the bed and the banks of a river are not static, the rating curve could change in time. A major task is then establishing and updating the stage-discharge relation. For the USGS Hirsch & Costa (2004), a good updating means direct discharge measurements 8 times a year for each gauging station. As explained in section 2.2, traditional gauging are time consuming and labor intensive. Following the USGS guideline, it needs at least 2 hours and 2 operators to estimate a discharge at a cross-section using current meter. Finally, the budget allowed for the updating of the rating curve is considerable. It represents 12K$ per year per gauging station for the USGS. 50% of this cost is dedicated to the maintenance of the infrastructure and 50% is dedicated to the operators. As a consequence, the majority of the rating curves are based on few measurements, and the uncertainty is high.

Creutin et al. (2003) demonstrate the capability of LSPIV for repeated measurements at the same location. In a time period of only 20 days, 10 LSPIV measurements were realized on the Iowa River, in Iowa City (USA). The experimental area was situated close to a USGS gauging station. Naturally occurred foam was used as tracer of the flow. Discharge for the experiment ranged from 50 to 300 $m^3\,s^{-1}$, which covers a large portion of the existing rating curve. As illustrated in Figure 2, Creutin et al. (2003) showed that the LSPIV measurements were very consistent with the 215 current meter measurements made by the USGS at the same site since 1984.

The authors suggested that image-based approach may be a reliable way to establishing and updating a stage-discharge relationship at a site at very low cost. They identify limitations including the need of recognizable tracer particles or flow patterns to detect motion, problem associated with shadows and reflections on the water surface, as well as the problem of the need for survey information on the channel cross-section.

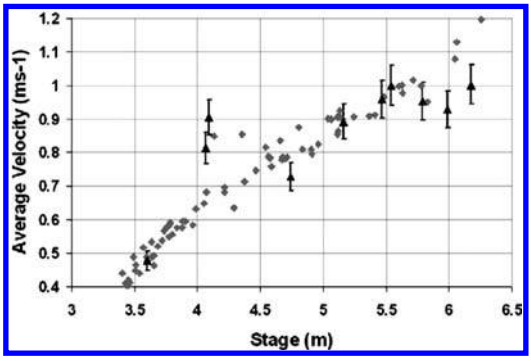


Figure 2. Display of the average velocity of the flow as a function of the river stage for both the USGS gauging (gray squares) and the PIV measurements (black triangles). The error bars on the PIV measurements indicate the sensitivity due to the correction coefficient applied to derive the mean vertical velocity from the surface velocity. From Creutin et al. (2003).

3 IIHR – LTHE COLLABORATIVE WORK

3.1 *Mobile LSPIV for monitoring of ungauged sites*

As Moss (2003) noted, "the problem of estimation of hydrological variables at ungauged sites is perhaps among the oldest challenges for the hydrological practitioner". This problem is especially strong in developing countries, where a decline of measuring networks and poor quality of available data is observed Smakhtin (2004). Some statistical physically based methods have been developed to estimate discharge at ungauged basins, but those formulas are not easy to apply, need a measuring network in the region of the studied basin, and cannot access to very small time step. With traditional equipment, the cross-section of the stream to be gauged needs to be geographically ideally situated, i.e. close to a road, on flat banks.

The Mobile LSPIV (MLSPIV) unit, a truck-based system that essentially comprises an image device (video or camera) set on a telescopic mast (Fig. 3), is in development at IIHR in order to deal with that problem.

In that unit, camera positioning and control and the image processing are conducted remotely from a laptop. The MLSPIV is equipped with a mast, a power generator, uninterrupted power supply (UPS) and two batteries. The light weight aluminium hydraulic operated mast allows setting the camera from 5 m to 14 m above the ground level to accommodate imaging of

Copyright © 2006 Taylor & Francis Group plc, London, UK

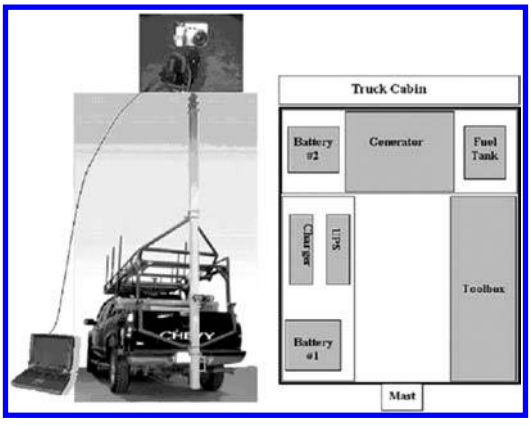


Figure 3. MLSPIV and equipment.

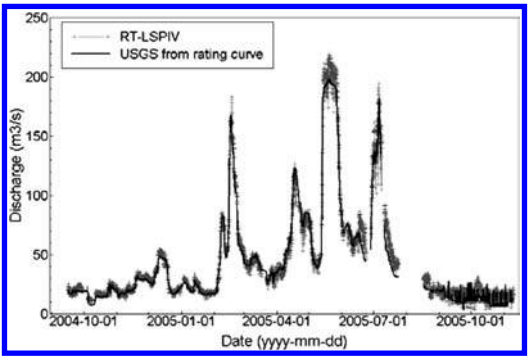


Figure 4. Sample time series of discharge estimates made by USGS, and using the RT-LSPIV.

various stream widths. Three guy lines secure the mast after positioning against wind and accidental oscillations. The assembly for capturing images is composed of a pan-tilt unit, which allows the positioning of the image device with a resolution of 0.0514 degree. The image device is used to record successive images with a pre-selected time delay and resolution. An in-house developed software allows the computation of the surface velocities, and of the discharge (if the bathymetry of a cross-section is known) in "real-time", i.e. with a computational time of around 1 minute.

A case study of the MLSPIV was realized by Kim et al. (2005) at Clear Creek near Coralville (USA). The stream was about 20 m wide and 0.5 m deep at that location. Two measurements of discharges were conducted using digital and video camera, during normal flow condition, and compared to estimations, via a rating curve, of a USGS gauging station located 25 m upstream from the studied cross-section and recorded stage every 30 minutes. The MLSPIV gave good agreements with the USGS estimations, as the error, defined as $100^* (Q_{MLSPIV} - Q_{USGS})/Q_USGS$ was −2.53% for the digital camera, and 4.46% for the video camera.

The MLSPIV has capabilities to measure discharges and free-surface velocity distribution in stream during normal and extreme flow conditions during daylight, and in situations where the interior of the flow is, for one reason or an other (low flows, flows over rock beds and submerged control structures), inaccessible or difficult to reach. At that time, experiments using MLSPIV have only been conducted on small to medium river sizes. The capability of theMLSPIV to estimate discharge, with good accuracy, in very large rivers needs to be assessed with more experiments. The system can not only provide a cost-effective means to measure discharge at ungauged sites, but can improve rating curves at existing gauging sites during extreme flow conditions.

3.2 *Real-Time, continuous LSPIV*

Previous studies of image-based approaches for river discharge estimation (see the previous sections) have demonstrated the accuracy of LSPIV for brief measurements (recordings of 10 minutes or less) and under good to ideal illumination conditions. Hauet et al. (2005) examined the feasibility of a continuous, real-time, image-based, non-contact approach for estimating discharge in rivers, called Real-Time LSPIV (RT-LSPIV). The continuous operation of RTLSPIV throughout the year implies that estimates can be evaluated over a large range of discharge, and under varied natural weather conditions (illumination, wind, rain). Continuous real-time operation also imposes computational requirements for data transmission, computer memory, and processing time.

The experimental site for the prototype system is the same than in the experiment of Creutin et al. (2003) (see section 2.3). A web cam autonomously records an image pair of the river every 2 minutes, and the discharge estimation is computed in real-time. Weather data are recorded at the same time step from a NOAA station. A data base is updated with the new images, discharge estimation, stage measurement and weather data every 2 minutes. The results are posted in real-time at the IIHR website, along with real-time estimates from the USGS (based on rating curves). From the experience over the first 14 months of operation, the authors found that, most of time, the realtime PIV discharge and cross-sectional average velocity estimates were consistent with those based on USGS current meter measurement at this site since 1984, and with other image-based measurement made by Creutin et al. (2003), as demonstrated by the discharge chronology in Figure 4.

Several challenges with the field PIV technique for continuous real-time discharge estimation was identified by the authors. The most significant challenges are illumination of the river surface, seeding conditions,

Copyright © 2006 Taylor & Francis Group plc, London, UK

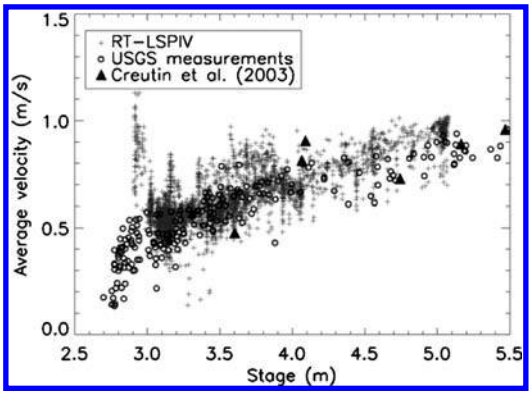


Figure 5. Average flow velocity (discharge divided by the crosssectional area) from USGS measurements, (Creutin et al. 2003), and RT-LSPIV.

wind effect and rainfall effect. Discharge estimates during those conditions are highly variable and have systematic errors. In consequence, as illustrated in Figure 5, the RT-LSPIV measurements are consistent with the USGS measurements, but have more dispersion.

The long-range vision for the Iowa River demonstration site is as a test-bed for research on imagebased discharge measurement techniques. Its location at a USGS gauge site facilitates comparisons with direct measurements. In addition, raw images, USGS data and weather data are archived continuously, which will provide extensive data for retrospective testing, comparison, and validation of image processing and discharge estimation algorithms.

4 CONCLUSIONS

In that study, we present a review of papers dealing with the application of LSPIV, an image-based method, in the discharge monitoring of streams. Recent works, resulting from a collaboration between IIHR-Hydroscience & Engineering, Iowa, USA, and the Laboratoire d'étude des Transferts en Hydrologie et Environnement, Grenoble, France, and new results are presented. The limitations of LSPIV identified in the reviewed papers and in the works in progress include problems of:

- Illumination: general illumination intensity and local illumination nonuniformity (light reflections and shadows)
- Seeding: density, size, brightness and contrast, wind effect
- Recording: image resolution, time between images, sampling time, camera movement during recording
- Geometrical transformation
- PIV processing

Despite all the challenges, there are many aspects of PIV discharge measurement that make it attractive for river monitoring. The capabilities of LSPIV for measurement of extreme events, floods or low flows, and its interest in the establishment and the updating of rating curve at very low cost are exposed in that paper. The equipment used is simple, light-weight, and inexpensive, and can be mounted well above the river surface, protected from floods. Rather than estimating discharge from measured stage using an empirical rating curve, the discharge is estimated from measured surface velocities every few minutes. Whereas a rating curve must be extrapolated beyond the range of direct measurement, in principle, the image-based approach is valid for any river stage (from very low to high flows). Indeed, one can see that PIV measurement could provide a means to construct a rating curve quickly and efficiently. Although individual PIV discharge measurements have greater uncertainty than direct measurements, in a very short time, one can obtain many more PIV discharge measurements, spanning a range wide range of flow conditions, using a continuously operating system.

REFERENCES

Bradley, A., A. Kruger, E. Meselhe, & M. Muste. 2002. Flow measurement in streams using video imagery. *Water Resources Research 38*(12), 1315.

Buchanan, T. J. & W. P. Somers. 1969. *Discharge measurements at gaging stations*, Volume 3.

Creutin, J., M. Muste, A. Bradley, S. Kim, & A. Kruger. 2003. River gauging using piv technique: Proof of concept experiment on the iowa river. *Journal of Hydrology*.

Dermisis, D. & A. Papanicolaou. 2005, May. Determining the 2-d surface velocity field around hydraulic structures with the use of a large scale particle image velocimetry (lspiv) technique. In *World Water and Environmental Resources Congress 2005*, Anchorage, Alaska, USA.

Fujita, I., S. Aya, & T. Deguchi. 1997. Surface velocity measurement of river flow using images of an oblique angle. In *Proceedings XXVIIth IAHR Conference, Theme B*, Volume 1, San Fransisco, CA, pp. 227–232.

Fujita, I., M. Hara, T. Morimoto, & T. Nakashima. 1998, December. Visualization and piv measurement of river surface flow. In *Proceeding of VSJ-SPIE98*.

Fujita, I., M. Muste, & A. Kruger. 1998. Large-scale particle image velocimetry for flow analysis in hydraulic engineering applications. *Journal of Hydraulic Research 36*(3), 397–414.

Hauet, A., A. Kruger, W. Krajewski, A. Bradley, M. Muste, J. Creutin, & M. Wilson. 2005. Real-time estimation of discharges of the iowa river using an image-based method. *submitted to Journal of Hydrologic Engineering*.

Hirsch, M. & J. Costa. 2004, May. U.s. stream flow measurement and data dissemination improve. *EOS, Transactions, American Geophysical Union 85*(21), 197–203.

Kim, Y., M. Muste, A. Kruger, W. Krajewski, A. Bradley, & L. Weber. 2005. Real-time stream monitoring using

Copyright © 2006 Taylor & Francis Group plc, London, UK

mobile large-scale particle image velocimetry. In *XXXI IAHR Congress*, Séoul, Korea.
Lecoz, J. 2005. Junction between an abandonned channel and the river. Personal communication.
Meselhe, E. A., T. Peeva, & M. Muste. 2004. Large scale particle image velocimetry for low velocity and shallow water flows. *Journal of Hydraulic Engineering 9*, 937–940.
Moss, M. E. 2003. Thoughts on the ungaged basin problem. In *Workshop on Prediction of Ungauged Basins*.
Pelletier, P. M. 1988. Uncertainties in the single determination of river discharge: A literature review. *Canadian Journal of Civil Engineering 15*, 834–850.
Simpson, M. 2001. Discharge measurements using a broadband acoustic doppler current profiler. Open-file report 01-1, USGS, Sacramento, California.
Smakhtin, V. U. 2004. Hydrological data provision for ungauged rivers in developing countries: Use of pragmatic methods. In *1st international Conference on Managing Rivers in the 21st Century: Issues & Challenges*.

Copyright © 2006 Taylor & Francis Group plc, London, UK

Discharge measurements in a small ungauged river: Comparison between conventional current-meter and tracer dilution methods

A. Bolognesi, G. Gottardi & M. Maglionico
DISTART – Università di Bologna, Viale Risorgimento 2, Bologna, Italy

ABSTRACT: The majority of small rivers and channels that flow across the Emilia-Romagna region (Northern Italy) are monitored by an extensive network of level meters. Unfortunately a stage-discharge relationship is available only for the main among them. The purpose of this study is to determine the reliability and accuracy of discharge measurements carried out by tracer dilution method. Experimental investigations have been carried out on a small river nearby Bologna (Italy), performing slug injections of a conservative tracer (NaCl) and recording electrical conductivity in a downstream section, while at the same time, conventional current meter measurements have been taken in a section placed between the injection point and the conductivity meters. Data obtained from both the methods have been compared each other, giving also main relevance to the uncertainty analysis. Monte Carlo Simulations were performed to integrate single uncertainties coming from different potential sources of error, either experimental or analytical.

1 INTRODUCTION

The determination of discharge value is certainly one of the most relevant aspects within the study of open channel flows and related processes. Reliable knowledge of flow data is a fundamental issue in many branches such as water quality monitoring, water resource management, as well as hydraulic devices design and control. The most common approach to measure discharge is the so called conventional current-meter method. The method is based on determining the mean streamflow velocity and flow cross sectional area; the product of these variables determines the stream discharge. Applicability of velocity measurements using a current meter appears rather hard in small streams (Hudson & Fraser, 2002), like the steep ones, such as mountain streams or in general the ones where small water depths and velocities, approach the unreliability ranges of the method. These characteristics are common in a large part of the small rivers flowing across the main plain of Northern Italy, most of which passing through urban or densely populated areas. In those streams and channels, whose catchments rarely exceed a few hundred km^2, and where the outlets of waste water treatment plant are often the only source of flow, low water depth conditions almost always occur during dry weather period.

In order to test the reliability of a suitable discharge measuring strategy for those streams, a comparison between traditional current-meter measures and salt dilution method has been carried out in a small river near Bologna, Italy.

The characteristics of the investigated reach, are within the range of applicability for both the methods. Stream width and water depth (further details in the following paragraph) are big enough to take several current meter measures, as well as small enough to justify the use of salt dilution method.

2 THE EXPERIMENTAL SITE

The Navile channel is an ancient artificial channel dug in the 12th century, in which typical features of a small natural river have developed during the years. The Canale Navile has its origin inside the urban area of Bologna city, receiving water from both natural and artificial sources. One of the most relevant among those sources, comes from the waste water treatment plant of Bologna (650000 E.I.), whose outflow gives, in particular during the summer months, a great part of the total conveyed flow. Consequently during dry weather periods, the Navile discharge rarely exceed 2 m^3/s, while during heavy stormwater events reaches up to sensibly higher values.

The reach chosen for the experimental comparison flows across the village of Bentivoglio, almost 15 km north of Bologna. Located in a flat territory, which means negligible bed slope values, the reach is placed downstream a sluice gate, whose opening has been kept constant during the entire measuring campaign, in order to achieve steady state conditions. The aerial photo in Figure 1 shows the Navile channel at Bentivoglio, evidencing with “Section B” the

Copyright © 2006 Taylor & Francis Group plc, London, UK

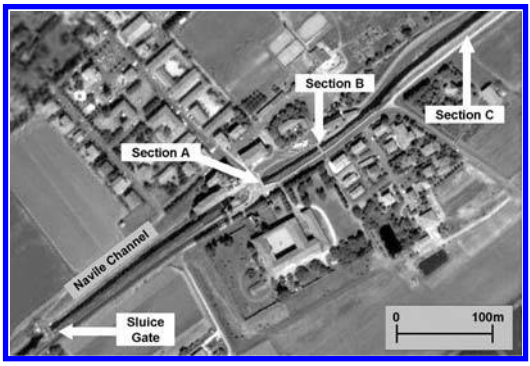


Figure 1. Aerial view of the Navile reach involved in the experimental activity.

bridge where velocity measures have been taken with a current meter, while in "Section A" and "Section C", respectively the salt solution injection point, and the section where conductivity has been measured for the tracer dilution method. Distance between section A and C, which is indeed the investigated reach, is about 300 metres.

The channel path is almost completely straight, its free surface width ranges from 6 to 10 metres and its depth from 0.5 to 1 meter.

In order to improve the measurement conditions, maintenance works have been executed on the river bed and embankments. In fact the effect of unexpected irregularities in such a small channel could deeply affect the final results.

3 THE CURRENT METER METHOD

Streamflow discharge is defined as the volume of water flowing past a fixed point in a fixed unit of time. If the water velocity distribution over a cross section normal to the direction of flow and the area A of that fluid section are known, then the discharge Q is given by:

$$Q = \iint_A \boldsymbol{v} \cdot \boldsymbol{n}\, dA = \iint_A v(x,y)dx\, dy \qquad (1)$$

where: v = velocity vector, n = the unit vector normal to the cross section in the considered point; $v(x,y)$ = the velocity field as a function of width x, and depth y.

In practice, theoretical integral is approximated by the sum:

$$Q = \sum_{i=1}^{m} b_i d_i \overline{v_i} \qquad (2)$$

where: b_i = the width oh the i_{th} vertical sub-section; d_i = the depth of the i_{th} vertical sub-section; m = the number of vertical sub-sections in which the entire cross section is divided.

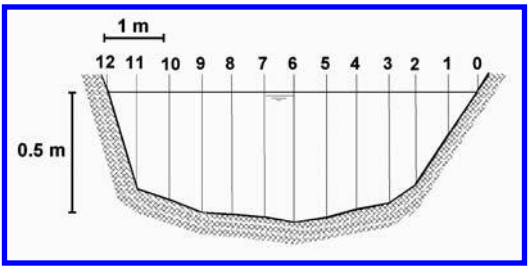


Figure 2. Cross section where current meter measurements have been taken. In evidence the 11 vertical sub-sections.

In order to obtain a mean velocity for the considered cross section, several velocity measures have to be taken at different points.

A current meter is an instrument that measures the velocity of flowing water. Traditional mechanical current meters are based on the principle that the velocity of water is proportional to the angular velocity of the meter's rotating propeller. A relationship exists therefore between stream velocity and the number of spins during a certain lapse of time.

Current meters are classified according to their rotors. Vertical-axis rotors normally operate in lower velocities than horizontal axis meters, while the last ones disturb less flow because of the axial symmetry with the flow direction. Their propeller is therefore less likely to be obstructed by debris or leaves.

Both natural water bodies and artificial channel show the presence of turbulent flow and local eddying. This results in velocity pulsations at a point, which have been proved to be higher for lower velocities (Rantz et al., 1982). Therefore, in order to obtain a better representation of the average velocity at a point, current meter observations should cover a longer period, especially when low velocities are being measured.

3.1 *Experimental activity*

A pedestrian bridge (section B in Figure 1) has been chosen as the gauging section (Figure 2), allowing easy installing and management of the current meter but also satisfying the method requirements. In fact no piers occupy the wetted section and the river bed has no evident irregularities, therefore streamlines flow quite uniform, parallel to each other and normal to the bridge.

Velocity measurements have been taken with a SEBA horizontal axis current meter, having a propeller diameter of 125 mm and weight of 50 kg.

The chosen section, which has a free surface width of 6.25 m and a maximum depth of 0.55 m, has been divided into 11 verticals, almost equally spaced by

Copyright © 2006 Taylor & Francis Group plc, London, UK

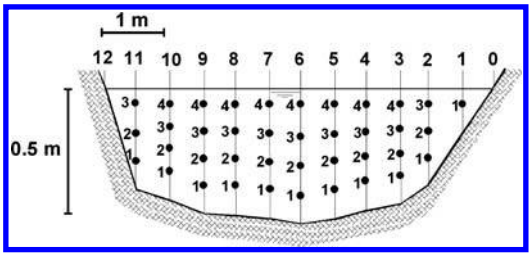


Figure 3. Gauging cross section with all the 39 measuring points.

0.52 m. Along each one of the verticals, up to 4 measuring points have been defined at different depths (Figure 3), for a total amount of 39 points within the section.

For each of those points 6 or 7 readings have been recorded, in order to assess velocity fluctuations due to turbulence and also to avoid accidental bad measures, allowing about 30 seconds for each reading to stabilise. Each point took therefore at least 3 minutes. Even though the regularity of the cross section as well as the stream velocities, probably did not require such a large number of points and so many repeated measures for each point, it has to be pointed out that this somehow redundant procedure has been carried out for research purpose and therefore not accomplishing the traditional cost and time saving procedures, but literally fulfilling the ISO EN 748:2000 requirements.

3.2 *Data processing and results*

Different readings at each measuring points allow a statistical analysis for the mean velocity variable, according to the "Student" small-sample theory.

Considering "N" samples extracted from a quasi-normal population having mean μ, it is possible to obtain:

$$t = \frac{\overline{X} - \mu}{\hat{s}/\sqrt{N}} \tag{3}$$

where: $\overline{X}$ = the sampled mean; $\hat{s}$ = the standard deviation; t = the Student distribution, having N − 1 degrees of freedom.

Starting from observed data, it is then possible to obtain a probability density estimate for each of the 39 measuring points (Figures 4, 5), built through Monte Carlo random sampling from the distribution (3) and then, sampling once again from those probability estimates, it is possible to generate *n* vectors, each one containing 39 velocity values.

Consequently, each vector represent one of the potential velocity fields over the gauging section, which can be now integrated according to different methodologies reported in the ISO EN 748-2000, ISO

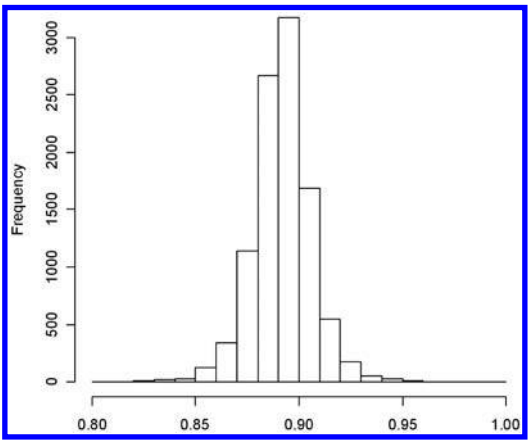


Figure 4. Frequency histogram of the velocity value at point no. 1 on vertical line no. 3, for n = 10000 generations.

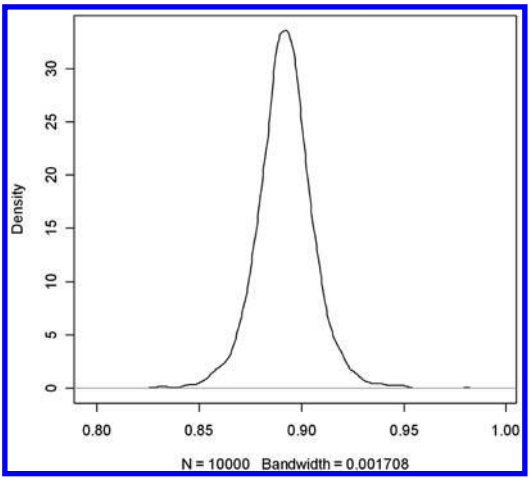


Figure 5. Probability density distribution derived from the frequency histogram of Figure 4.

1088-1985, ISO/TR 7178-1983, in order to obtain N values of discharge (i.e. a mean value and its confidence intervals) for each single integration method (Figure 6).

The computation of the discharge basically consists in the approximation of (1), hence the application of (2). The first common step is to calculate the discharge per unit width, which is based on the construction of the usually parabolic velocity profile along a single vertical (Figure 7) and of its integration over the total depth H:

$$q = \int_0^H v\,dh \tag{4}$$

Copyright © 2006 Taylor & Francis Group plc, London, UK

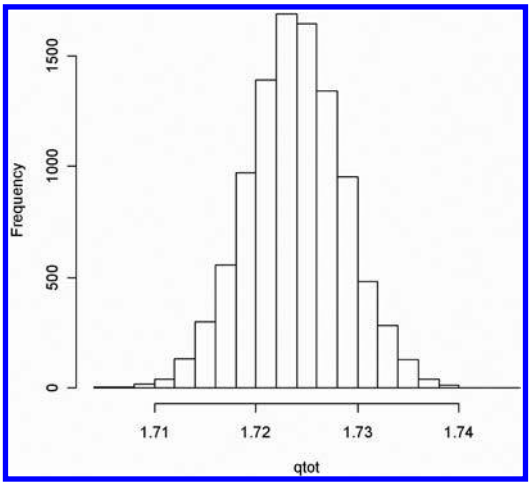


Figure 6. Frequency histogram of the discharge value simulated with n = 10000 generations (Method 1).

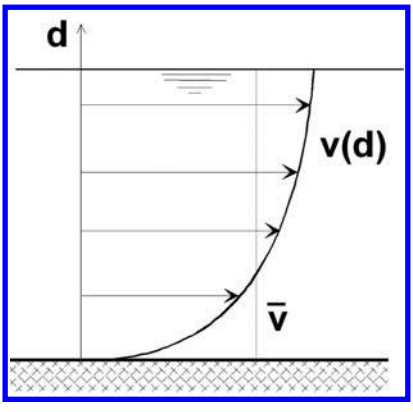


Figure 7. Vertical velocity profile and its mean value $\bar{v}$.

Integral (7) is then approximated by:

$$q = \sum_{i=1}^{n} \frac{(v_i + v_{i+1}) \cdot (d_{i+1} - d_i)}{2} \quad (5)$$

Assuming that bed velocity is null and surface velocity equal to the one measured 6 cm under the free surface.

Total flow is then calculated by integration of unit width discharge over the cross section extent (Figure 8), whose approximated solution, according to (2), is based on the "Mid-section method". From now on this method will be called "Method 1".

$$Q = \sum_{i=1}^{m} q_i \frac{b_i + b_{i+1}}{2} = \sum_{i=1}^{m} \bar{v}_i d_i \frac{b_i + b_{i+1}}{2} \quad (6)$$

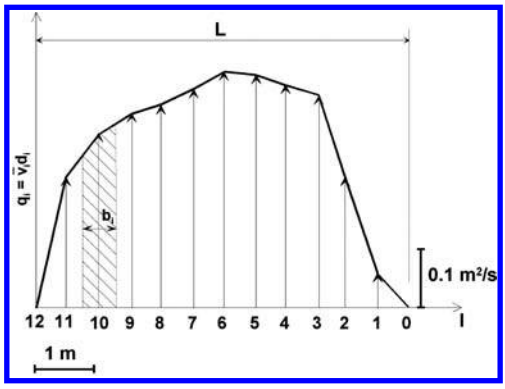


Figure 8. Unit width discharge distribution over the cross section.

As previously mentioned, discharge value has been calculated through other methods, based on different numerical simplification of (1) and on different hypotheses about the vertical velocity profile.

In "Method 2", usually called "Mean-section method" (Young, 1950), the cross-section is regarded as being made up of a number of segment, each bounded by two adjacent verticals.

If $\bar{v}_i$ and $\bar{v}_{i+1}$ are the mean velocities at the i and $i+1$ verticals respectively, if d_i and d_{i+1} are the total depths measured at vertical i and $i+1$ respectively, and if b is the horizontal width between the said verticals, the discharge q of a segment is taken to be:

$$q_{\bar{i}} = \frac{(\bar{v}_i + \bar{v}_{i+1})}{2} \cdot \frac{(d_i + d_{i+1})}{2} \quad (7)$$

This is repeated for each segment and the total discharge is obtained by the sum of single contribution:

$$Q = \sum_{i=1}^{n} q_{\bar{i}} \quad (8)$$

"Method 3" is formally equivalent to "Method 1", except for the assumption made on the vertical velocity profile. In fact bed velocity is not supposed to be null, but equal to the 70% of the value measured at 12 cm above the bed itself. (Figure 9).

This hypothesis, which is not uncommon in such measurement conditions, considerably affects the mean vertical velocity value.

"Method 4" prescribes that once unit width discharges have been obtained by Method 1, total discharge is then computed by the "truncated pyramids" schematization, where the width discharges q_i and q_{i+1} represent the base surfaces and the distance b_i between them is the height. Partial flow referred to the i_{th} segment is then given by the pyramid volume:

$$Q_i = \frac{(q_i + q_{i+1}) + \sqrt{q_i \cdot q_{i+1}}}{3} \cdot b_i \quad (9)$$

Copyright © 2006 Taylor & Francis Group plc, London, UK

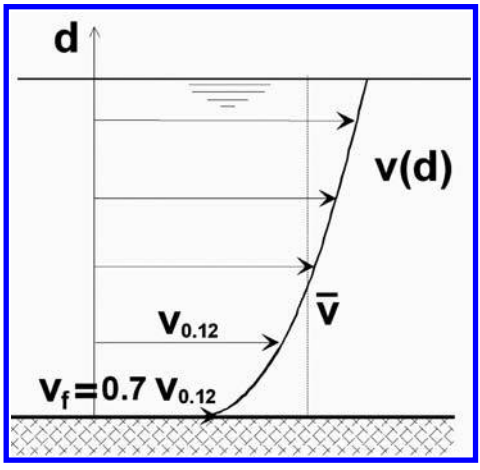


Figure 9. Vertical velocity profile and its mean value $\bar{v}$, assuming that bed velocity $v_f = 0.7v_{0.12}$.

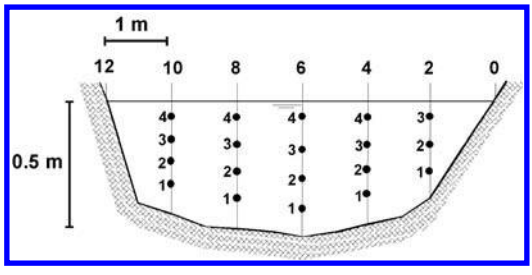


Figure 10. Reduced number of measurement points within the cross section, according to method 5.

and finally total flow comes from:

$$Q = \sum_{i=1}^{n} Q_i \tag{10}$$

"Method 5" considers instead just 6 out of the 11 measured verticals, therefore average spaced by 0.89 m (Figure 10), satisfying therefore the time saving indications, according to which a measure must be a compromise result between accuracy and time availability. In addition to this, it must be noticed that the longer the measurements take, the higher is the probability of discharge variation during the measure.

All the previous introduced methods can be combined in different ways producing therefore a wide range of possible results, here synthesized in Table 1. The same table also presents a sensitivity analysis to the number of random generations produced during Monte Carlo simulations (n = 100, n = 10000), which has been performed for every reported method.

Table 1 and Figure 6 before, clearly show how the variability of the resulting mean discharge values do not depend on the uncertainty of the single velocity values. In fact firstly there is no significant difference between the results obtained after 100 and 10000 generations, secondly the variance of the results distribution appears almost negligible if compared to the mean value (Figure 6).

Table 1. Final results of mean discharge values obtained by Monte Carlo generations, for the different methods applied.

	Discharge Q [m^3/s]	
Method	N = 100	N = 10000
1	1.723959	1.723866
2	1.678593	1.678471
3	1.888714	1.888575
4	1.704999	1.704891
5	1.603540	1.603076
1 + 3 + 5	1.749866	1.749206
2 + 3	1.839684	1.839512
2 + 5	1.463283	1.462853
2 + 3 + 5	1.595128	1.594514
3 + 4	1.854000	1.853837
3 + 4 + 5	1.645516	1.644884
4 + 5	1.509198	1.508755

The lowest value is obtained with Method 5, while the highest belongs to Method 3, not casually the ones having the most simplifying assumptions. Method 2 shows a light underestimation if compared to similar Methods 1 and 4.

In synthesis, the mean value calculated from all the mean discharges reported in Table 1 is $Q = 1.688$, which is almost identical to the median value (less influenced by the outliers) of $Q = 1.691\ m^3/s$. According to this, Method 2 seems to be the closest to the general mean value, ranging within a 95% confidence interval from 1.677 to 1.679 m^3/s, showing therefore once again the non influence of the random generations.

4 THE SALT DILUTION METHOD

The basic principle of salt dilution methods (Moore, 2004), with particular reference to the one involving slug injection (Hudson & Fraser, 2005) is to add a known mass of a conservative non cohesive solute (i.e. sodium chloride) in an upstream river section, which causes a perturbation in the water base conductivity that can be measured in a downstream river section. The main hypothesis of the method are: constant discharge (steady flow), no lateral inflows or outflows within the investigated reach; suspended load only (negligible bed load); minimal pools or backwater areas in general; complete vertical mixing and complete lateral spreading, which indeed occurs only after a certain distance called the complete mixing length (Day, 1977, Fischer et al., 1979).

Copyright © 2006 Taylor & Francis Group plc, London, UK

Conductivity values must be therefore measured at very close intervals (a few seconds) in order to build the so called "breakthrough curve" representing the conductivity pattern over time.

The choice of common table salt (sodium chloride) as a tracer derives from many factors: it is not expensive and easily available, its effects can be rather accurately and almost continuously measured using an electrical conductivity meter and it is non-toxic for the concentrations and permanence times usually detected within the range of applicability of the method (Wood & Dykes, 2002). The procedure aimed to obtain a discharge estimation starts imposing the continuity of mass between the injection and the measuring section (Elder et al., 1990):

$$M = \int Q \cdot C(t) dt \tag{11}$$

where M = the mass of tracer injected; Q = the unknown flow (supposed steady); $C(t)$ = the tracer concentration over time; hence:

$$Q = \frac{M}{\int C(t) dt} = \frac{M}{A} \tag{12}$$

where A = the area under the graph of concentration over time.

Since no direct measurement of tracer concentration is provided, it is anyway proved that an almost linear relation exists between conductivity and concentration value. The concentration can be then calculated as:

$$C(t) = \left(\chi(t) - \chi_o(t)\right) \cdot \alpha \tag{13}$$

where $\chi(t)$ = the conductivity value, $\chi_o(t)$ = the baseline conductivity and α = the coefficient in the almost linear relation between conductivity and concentration.

Therefore, baseline conductivity ("background noise") has to be removed through a regression line that follows the trend of pre-existing conductivity in the river, in order to analyze only the effect produced by the tracer. Then the wave can be transformed from conductivity [μS/cm] into concentration [mg/l] with the linear relation obtained in laboratory in standard conditions during the calibration of the instrument.

Under suitable conditions, discharge measurements made by slug injection can reach up $\pm$5% accuracy (Day, 1976). Different sources of error may arise (ISO 9555: 1994), such as the incomplete dissolving of tracer, the injection solution in fact must be fully mixed across the channel at the section where the conductivity is recorded; the inaccuracy in measuring the mass of tracer injected; the uncertainty in the determination of the relation between conductivity and concentration; the unknown potential amount of tracer lost by adsorption or entrapped in a dead zone.

The slug injection method may also become unreliable when too low velocities are detected which means poor lateral mixing and excessive long salt wave durations.

4.1 *Experimental activity*

The experimental measures has consisted in 3 different injections, separated each other by 30 minutes. For each injection 8000 grams of salt have been diluted in almost 40 liters of water taken directly from the Navile Channel, producing therefore 200 g/l saline solutions in accordance with water temperature and similar experiences found in literature (Oestrem, 1964, Kite, 1993).

The solution has been injected from a bridge (Section A in Figure 1) whose piers induced slight turbulence effects for a few meters downstream, giving therefore a positive contribution to the vertical and also to the transverse mixing of the tracer within the stream.

Great attention has been paid in injecting solution in the center of the channel where the main streamline components flow, since it has been proved that lateral injections require a greater mixing length and increase the probability of tracer losses.

In order to check the achievement of complete transverse mixing, two conductivity meters have been installed in Section C (Figure 1) 300 m downstream the injection point. The first placed in the center of the cross section and the second about one meter from the right bank.

Due to a misfunctioning only 2 of the 3 curves have been recorded by the "lateral" probe (Figure 11), but they have anyway proved a good mixing state, in fact the area under the lateral probe graph is over 96% the one under the central probe graph, which is between the acceptable and optimal values of 95% and 98% (Rutherford, 1994; Kilpatrick & Cobb, 1985). This result was in accordance with the complete mixing length estimates of 200 m (Day, 1977) and 215 m (Fischer et al., 1979).

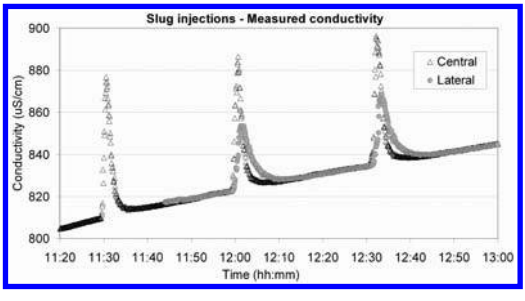


Figure 11. Measured conductivity in section C by 2 differently placed probes.

Copyright © 2006 Taylor & Francis Group plc, London, UK

4.2 *Data processing and results*

Water level upstream of the sluice gate appeared to be almost constant during the whole measuring campaign, but anyway small discharge fluctuation could not be avoided. Therefore it must be noticed that the discharge values presented in the following results are averaged on the 3 injections.

The determination of the discharge and of its uncertainties has required the development of some post processing strategies. The first issue concerns the baseline conductivity removal. In natural free surface waters the baseline pattern is usually quite easy to identify and/or to reproduce, but the decision of where to start and stop cutting as well as which point are to be included in baseline interpolation, leaves too much subjectivity in this sensitive part of the procedure. In addition, the presence of a waste water treatment plant a few kilometers upstream the experimental reach, gives the background noise a further variability (base line growth in figure 11).

In order to avoid this, a new baseline removal strategy has been introduced, which consist in generating a large number of interpolating lines, based every time on different, though acceptable, points. This technique produces therefore not just one, but several breakthrough curves as many as the number of the generated interpolating baselines. Each of those curves will then be used to calculate a range of discharge values with a Monte Carlo simulation.

Another important factor is given by the relation between conductivity and concentration. This relation must be experimentally determined and thus should be different, but known for each single conductivity probe. However, the coefficient α (13) is not a constant, since the conductivity itself certainly depends on stream temperature (for this a compensation is given by the instrument) and its relation with concentration is also affected by the background chemistry (Hongve, 1987), i.e. ion concentration and type. These effects constitute a potential source of error that has been here managed assuming a minimum and a maximum value for the coefficient α ("alfa"), whose mean value is the one experimentally found in laboratory. Laboratory calibration has been carried out with water having a conductivity value similar to the Navile one.

A third source of uncertainty comes from the exact weight of tracer injected. Depending on the amount of salt to be injected or on the precision of the balance adopted, this fundamental data which directly influences the resulting flow (12) has been given a tolerance of $\pm 1.5\%$.

The amount of tracer lost, due to vegetation adsorption or to the presence of dead zones along the investigated reach is the last source of uncertainty considered in this study and probably the most difficult to assess. The channel reach conditions at the time of measurements did not present excessive presence of vegetation within the streamflow, nor evident transient storage zones such as pools, however the effects produce by streambed adsorption or due to density currents can't be determined with enough precision. Possible values of tracer losses ranging from 0% to 15% have been therefore taken into account within the Monte Carlo simulation.

Figure 13 show the results in form of frequency histogram and of cumulated distribution obtained with 10000 generations considering all the previously introduced sources of uncertainty, while figure 14 represents the probability distribution of the resulting discharges as a function of the single source of error. This means, for instance, that the distribution related to the "mass" is the one obtained taking into account only the uncertainty of the mass value and assuming a fixed determined mean value for all the other sources. No appreciable differences has been found between the results obtained after 100 and 10000 generations, neither for the means, nor for the 95% confidence intervals.

Box plots reported in Figure 14 confirm what previously supposed about tracer loss, which is indeed the most impacting source of uncertainty among those

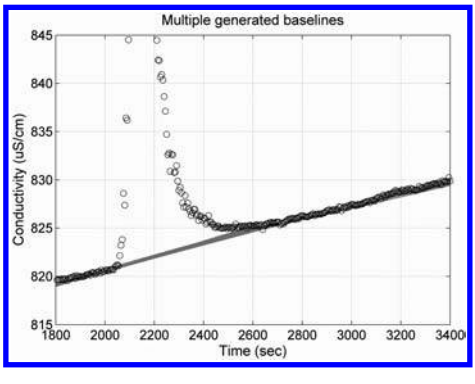


Figure 12. Generation of multiple linear interpolating baselines in order to reproduce the background conductivity value.

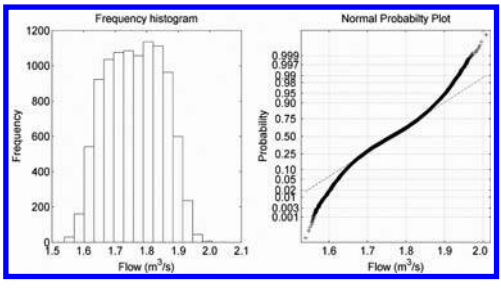


Figure 13. Frequency distribution histogram and cumulated distribution of the 10000 discharge values generated accounting for all error sources.

Copyright © 2006 Taylor & Francis Group plc, London, UK

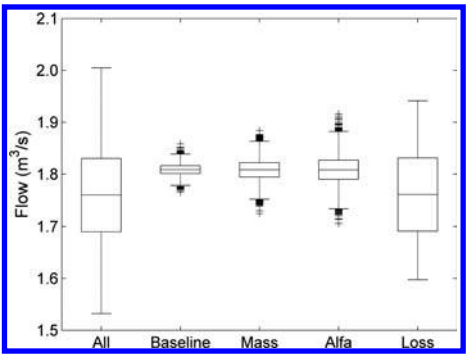


Figure 14. Probability distribution of the 10000 generated discharge values as a function of the single source of error.

considered. Anyway, the mean values range from 1.762 m^3/s to 1.809 m^3/s and the 95% confidence interval for the solution which considers all the sources is set between 1.607 m^3/s and 1.920 m^3/s, leading eventually to a satisfactory ±9% accuracy over the mean value.

5 CONCLUSIONS

In order to test the reliability of a relatively cheap and robust technique for measuring discharge in small streams within the Emilia-Romagna (Northern Italy) plain, the well known salt dilution method, widely adopted for turbulent upland streams, has been experimentally compared to the traditional current meter method.

Various potential sources of error have been considered for both the methods, performing Monte Carlo simulations and hence obtaining an uncertainty estimate for the computed discharge values.

Good agreement has been found between the global average values of each method (1.688 m^3/s and 1.762 m^3/s) and also between the boundary values, ranging approximately from 1.6 m^3/s to 1.9 m^3/s.

Important indications come from the different nature of the results. In fact, while the 5 scenarios simulated with the salt dilution method present similar mean values with different uncertainties, the current meter results show negligible uncertainties for each chosen integration method, but appreciably different mean values.

This implies that the final result obtained with the current meter method is affected by the subjective choice for the integration method. The tracer method instead gives a reliable mean value, whose uncertainty ranges can be reduced improving the accuracy on some experimental facilities and do not depend on an individual choice.

REFERENCES

Day, T.J. 1976. On the precision of salt dilution gauging. Journal of Hydrology 31:293–306.

Day, T.J. 1977. Observed mixing lengths in mountain streams. Journal of Hydrology 35:125–136.

Elder, K., Kattelmann, R. and Ferguson, R. 1990. Refinements in dilution gauging for mountain streams. In Hydrology in Mountainous Regions. I – Hydrological Measurements; the Water Cycle. International Association for Hydrological Science (Proceedings of two Lausanne symposia, August 1990). IAHS Publication No. 193, pp. 247–254.

Fischer H.B., List, E.J., Koh, R.C.Y., Imberger, J. and Brooks, N.H. 1979. Mixing in inland and coastal waters. Academic Press, San Diego.

Hongve, D. 1987. A revised procedure for discharge measurements by means of the salt dilution method. Hydrological Processes 1:267–270.

Hudson, R. and Fraser, J. 2002. Alternative methods of flow rating in small coastal streams. B.C. Ministry of Forests, Vancouver Forest Region. Extension Note EN-014 Hydrology. 11 p.

Hudson, R. and Fraser, J. 2005. The Mass Balance (or Dry Injection) Method. Streamline Watershed Management Bulletin 9(1):6–12.

ISO 9555-3:1994. Measurement of liquid flow in open channels – Tracer dilution methods for the measurement of steady flow – Part 3: Chemical tracers.

ISO EN 748:2000. Measurement of liquid flow in open channels. Velocity-area methods.

ISO 1088:1985. Liquid flow measurement in open channels – Velocity-area methods – Collection and processing of data for determination of errors in measurement.

ISO/TR 7178:1983. Liquid flow measurement in open channels – Velocity-area methods – Investigation of total error.

Kilpatrick, F.A. and Cobb, E.D. 1985. Measurement of discharge using tracers: USGS Techniques of Water-Resources Investigations, Book 3, Chapter A16, 52p.

Kite, G. 1993. Computerized streamflow measurement using slug injection. Hydrological Processes 7:227–233.

Moore, R.D. 2004. Introduction to salt dilution gauging for streamflow measurement: Part 1. Streamline Watershed Management Bulletin 7(4):20–23.

Østrem, G. 1964. A method of measuring water discharge in turbulent streams. Geographical Bulletin 21:21–43.

Rantz, S.E., et al., 1982. Measurement and Computation of Streamflow. USGS Water Supply Paper 2175.

Rutherford, J.C. 1994. River Mixing, John Wiley & Sons, Chichester, England.

Wood, P.J. and Dykes, A.P. 2002. The use of salt dilution gauging techniques: ecological considerations and insights. Water Research 36:3054–3062.

Young, K.B. 1950. A comparative study of mean-section and mid-section methods for computations of discharge measurements. USGS open-file report, 52p.

Copyright © 2006 Taylor & Francis Group plc, London, UK

Recirculating flow assessment from aDcp, LS-PIV and 2Dh modelling

J. Le Coz[1], A. Hauet[2], F. Védie[1], G. Dramais[1], B. Chastan[1] & A. Paquier[1]
[1] *Cemagref, Unité de Recherche Hydrologie-Hydraulique, 3 bis quai Chauveau, Lyon Cedex, France*
[2] *LTHE – Laboratoire d'Etude des Transferts en Hydrologie et Environnement, Grenoble Cedex, France*

ABSTRACT: Downstream connection of abandoned channels during floods is a key process for the assessment of water exchange, sedimentation rate and biodiversity in oxbow-lakes. The flow-induced morphological evolution of the confluence (stability, occlusion, scour…) governs the frequency and the intensity of downstream submersion. Recirculating flow patterns at the junction between a former meander and the Ain river, France, have been investigated for different discharge values through detailed in situ measurements: acoustic Doppler current profiler (aDcp) and image-based velocimetry (LS-PIV). Detailed topographic data have been collected in order to feed a 2Dh hydraulic model representative of the study reach, using the RUBAR20 code. Post-processing tools were developed in order to get the mean velocity patterns from aDcp and LS-PIV data. Then observed velocity fields were compared to RUBAR20 outputs. The simulated distribution of velocity vectors in the natural dead-zone is quite in agreement with field measurements: the main flow pattern is a large plane recirculation in the mouth of the former channel. However the recirculating flow intensity is underestimated.

1 BACKGROUND AND PURPOSE

In its lower part, the Ain river, South-Eastern France, is a gravel-bedded river with gradients ranging from 0.12% to 0.18% and with a multi-annual mean annual discharge of 120 m^3/s (Piégay et al. 2000). During the first half of the twentieth century, the river channel pattern changed from braided to a free-meandering type. Though regulated by dams, the fluvial dynamics was still quite active so that many abandoned channels with very different origins and shapes remain.

The Ain abandoned channels constitute very important natural areas, some of them being protected, monitored and even restored. One of the main concerns lies in fine sediment deposition during the flooding of oxbow-lakes. This silting-up trend leads towards terrestrialization and vegetalization of such water bodies. So it was decided to study the flow properties of the river sediment-laden waters, at the downstream inlet of an abandoned channel. This paper reports how this recirculating flow was investigated through field measurements and numerical modelling. Specific details are given about field deployment and field data post-processing in order to get representative mean velocity fields.

The Port-Galand abandoned channel was previously a meander of the Ain river. This reach was artificially cut-off in 1964 in order to protect the new-built bridge visible on Fig. 1. As can also be seen in this picture, the new river channel largely bended in the opposite direction it previously did. This study site was chosen because its downstream mouth presents several advantages for hydrodynamical investigation: frequent connection to the river flow, easy access by car, overhanging embankment for visual and video observation, wide and slightly vegetalized former channel.

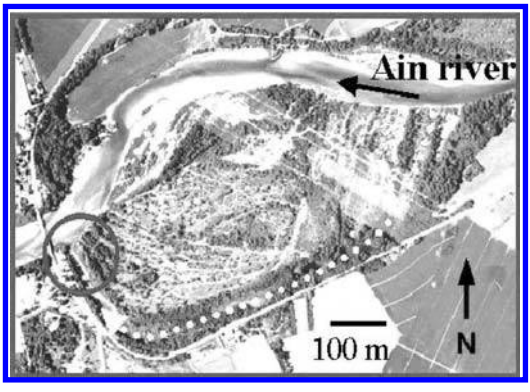


Figure 1. Aerial view of the study site. *Ain river flow (black arrow), Port-Galand former channel (white dot arrow), downstream entrance (circle).*

Upstream submersion of the Port-Galand abandoned channel occurs for discharges greater than 1000 m^3/s, which corresponds to a 2.5 year return period (Roche Campo 2002). In contrast, downstream

Copyright © 2006 Taylor & Francis Group plc, London, UK

Table 1. Hydraulic conditions during campaigns.

Dates	aDcp1 050304	LS-PIV1 050214	LS-PIV2 050408	aDcp2 050425
Time	10:30–12:30	16:00–16:30	15:00–15:30	15:00–16:30
Mean discharge $\bar{Q}$ and discharge variations				
$\bar{Q}$ $[m^3/s]$	200	325	365	650
$var.\ Q$ $[m^3/s/h]$	+1	−6.5	+37	+22.5
$var.\ Q$ $[\%\bar{Q}/h]$	+0.5%	−2%	+10%	+3.5%

hydrological connection is almost continuous (about 300 days per year). Sedimentation rate is estimated to 1.4 cm.yr^{-1} in the oxbow-lakes and to 0.5 cm.yr^{-1} over the downstream alluvial "plug" in the vicinity of the river. From an ecological point of view, the Port-Galand abandoned channel is considered as a healthy ecosystem. Along this reach, the river bed showed a mean degradation rate of 0.8 cm between 1986 and 1999 (Rollet et al. 2005), i.e. almost no bed level evolution.

2 FIELD MEASUREMENT CAMPAIGNS

2.1 *Hydrodynamical conditions*

Field measurement campaigns took place during small floods from February to April. Two aDcp surveys and two LS-PIV surveys were achieved, each of them lasting from 30' to 2 hours (Table 1).

The river discharge is regulated by a series of dams, but flow conditions were not controlled specifically for our experiments. So each of the four surveys met with contrasted river hydraulic conditions (Fig. 2). Discharge time series is most stationary for the 200 m^3/s aDcp1 campaign, slightly changing for LS-PIV1 (end of falling limb) and aDcp2 (end of rising limb) campaigns, significantly rising for the 650 m^3/s LS-PIV2 campaign.

2.2 *aDcp transects*

Acoustic Doppler current profilers (aDcp) have been first used in rivers to estimate the total discharge through a given cross-section (Gordon 1989). Such a device can measure instant velocity components on vertical profiles, from the Doppler shift between emitted ultrasonic signals and echoes backscattered by suspended matters (e.g. Yorke and Oberg (2002), Le Coz et al. (2006)). Similarly, water depth and bottom apparent displacement are computed from dedicated acoustic pulses, which allows mobile measurements and valid discharge computation: most authors report

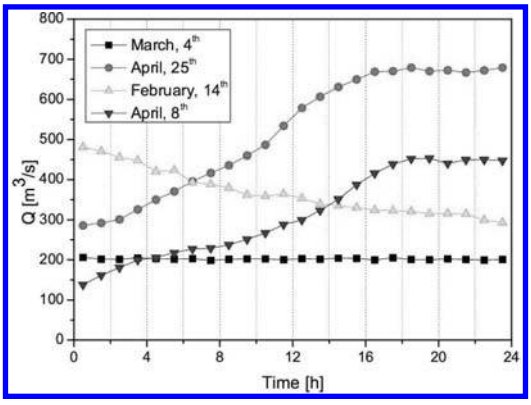


Figure 2. Measured hourly discharge during each campaign day (year 2005). *By courtesy of CNR hydrometric network.*



Figure 3. ADcp deployment during 2005, April 25th flood. *The Ain river is flowing from the top left corner; transects A, B, C are delimited by white tight ropes.*

a total discharge accuracy of about 5% for a few (4–8) transects across the river section. Significant errors may arise when the bottom is actually moving due to sediment transport. Even if aDcp measurement uncertainty has not been properly estimated yet (Muste et al. 2004a), aDcps have been used for velocity field survey (Shields 2005; Muste et al. 2004c), point velocity time series and even turbulence analysis (Barua and Rahman 1998; Muste et al. 2004b).

For the present study, moving-vessel aDcp measurements have been performed in order to get instantaneous and mean velocity data on transects across the area of interest. As the abandoned channel was not wadable, the aDcp was moved by two men in a boat maintained by tight ropes (Fig. 3). We used a Teledyne RDI WorkHorse Rio Grande 1200 kHz aDcp installed on a small buoyant board and equipped with a prism for topographic positioning. All water velocity data were acquired with the RDI default *Broadband* mode 1 and bin size 30 cm. In order to reduce dispersion, aDcp data were 5-ensemble-averaged afterwards as if we had

Copyright © 2006 Taylor & Francis Group plc, London, UK

chosen to get multi-ping ensembles (RDI command WP5). No apparent sign indicated any significant bed motion.

2.3 *Image-based surface velocimetry (LS-PIV)*

A solution to obtain an instantaneous 2D surface velocity field in natural flow is video image analysis, when tracers such as solid particles, bubbles or turbulence-driven patterns are advected by the river flow. The Particle Image Velocimetry (PIV) is a statistical technique which has been extensively used in laboratory fluid experiments for two decades (e.g. Adrian (1991)). The name of Large Scale PIV (LS-PIV) describes the application of the PIV method to natural scale systems with relatively large imaging areas. Readers could refer to Leese et al. (1986) for application to identify cloud motions using satellite images, or Bradley et al. (2002) and Creutin et al. (2003) for applications at different scales of rivers.

A commercially available digital camera (CANON MV 750i) was used to record the experimental area. Two video sequences of 2' (LS-PIV1 campaign) and 5'43 (LS-PIV2 campaign), sampled at a frequency of 1 Hz each (120 and 344 images respectively), were selected. The topography of the experimental site and the size of the area of interest forced the tilt angle of camera view axis to be very small (around 10 degrees). This causes important deformation in the recorded images. In order to conserve a maximum of reliable information, the PIV analysis is performed on images on their raw-state (perspective affected). A classical cross-correlation analysis (see section 4.1) is applied on each pair of successive images for the four videos in order to identify tracer displacements in the image coordinates system, i.e. in pixels per second, without artificially seeding the stream free surface. Vegetable fragments and turbulence-driven patterns acted as flow tracers.

To be usable, this velocity field must be converted into real velocities (in metres per second) in a Cartesian space coordinate system. We use here an implicit geometric transformations method based on Ground Reference Points (GRPs), i.e. points of known coordinates in both image and physical Cartesian coordinate systems, according to:

$$X = \frac{a_1 i + a_2 j + a_3}{a_7 i + a_8 j + 1} \qquad Y = \frac{a_4 i + a_5 j + a_6}{a_7 i + a_8 j + 1} \tag{1}$$

where $[i, j]$ are the coordinates of a point in the image coordinate system (in pixels), $[X, Y]$ are the coordinates of the same point in the field coordinate system (in meters), a_i are the height projective transformation parameters.

The elimination of the Z coordinate assumes a horizontal water surface and requires control points



Figure 4. LS-PIV picture during 2005, April 8th flood. *The left-bank 4 Ground Reference Points installed at the same elevation.*

to be chosen in the same horizontal plane for the determination of transformation parameters. Thus a set of 4 GRPs is sufficient to solve the 8 a_i parameters of Equation 1. Nevertheless, a set of at least 6 GRPs and a least-square method are advised for a better accuracy (Fujita and Komura 1992). In this study, 10 GRPs were placed on the field in order to be distributed as well as possible on the recorded images: 4 GRPs on the left bank (image near-field) and 6 GRPs on the right bank (image far-field). The GRPs used are white $30 \times 30\,\text{cm}^2$ squares with black concentric squares painted inside (Fig. 4).

3 2D-H NUMERICAL MODELLING

3.1 RUBAR20 *code*

RUBAR20 solves two-dimensional shallow water equations in unsteady flow conditions (equations 2, 3, 4 here below) on an irregular grid made of quadrangles and triangles. Numerical resolution is achieved by a finite volume method based on a second order Godunov-type scheme (Paquier 1995). RUBAR20 was developed by the *Cemagref* in order to simulate flooding along rivers either caused by dam failure or due to natural causes. Fudaa0.17 was used as a pre- and post-processing tool for model set-up and result visualization.

$$\begin{aligned} &\frac{\partial h}{\partial t} + \frac{\partial (hu)}{\partial x} + \frac{\partial (hv)}{\partial y} = 0 \\ &\frac{\partial (hu)}{\partial t} + \frac{\partial (hu^2 + gh^2/2)}{\partial x} + \frac{\partial (huv)}{\partial y} = -gh\frac{\partial z_b}{\partial x} \end{aligned} \tag{2}$$

Copyright © 2006 Taylor & Francis Group plc, London, UK

$$-gn^2\frac{u\sqrt{u^2+v^2}}{h^{1/3}}+\nu_{ef}\left[\frac{\partial}{\partial x}\left(h\frac{\partial u}{\partial x}\right)+\frac{\partial}{\partial y}\left(h\frac{\partial u}{\partial y}\right)\right] \quad (3)$$

$$\frac{\partial(hv)}{\partial t}+\frac{\partial(hv^2+gh^2/2)}{\partial y}+\frac{\partial(huv)}{\partial x}=-gh\frac{\partial z_b}{\partial y}$$
$$-gn^2\frac{v\sqrt{u^2+v^2}}{h^{1/3}}+\nu_{ef}\left[\frac{\partial}{\partial x}\left(h\frac{\partial v}{\partial x}\right)+\frac{\partial}{\partial y}\left(h\frac{\partial v}{\partial y}\right)\right] \quad (4)$$

in which h is the water depth, u and v are velocities along x- and y-axis, z_b is the bottom level, n is Manning's roughness coefficient, g is the gravity acceleration, ν_{ef} is the effective kinematic viscosity (set as one single constant value all over the domain).

3.2 *Model set up and calibration*

The computational geometry (Fig. 5) was built up from different sets of topographical data. The river main channel geometry and the abandoned channel geometry were respectively interpolated from 500 m-spaced cross-sections measured in March 2004 and from 50 m-spaced cross-sections measured in 2002. The simulated river reach was chosen long enough to get a well-organized velocity field near the confluence. Both domains were meshed and connected to each other. Quadrangle sizes are quite homogeneous over the whole domain and at the very confluence cells are close to 1 m squares. The mesh was that refined in order to compare flow patterns with field data, but it induced very long computational times (74,929 cells). For the same reason, the local geometry was also refined through extra sets of points measured in the area of interest (confluence and surroundings).

A uniform Strickler coefficient of $30\,m^{1/3}/s$ (Manning's $n=0.33\,s/m^{-1/3}$) was arbitrarily set over the whole domain, except for vegetalized areas where it was set equal to 20 or $10\,m^{1/3}/s$. As run tests with a wide range of ν_{ef} values induced very little change in the velocity field in the area of interest, ν_{ef} was eventually kept equal to zero. A constant $200\,m^3/s$ entering discharge was uniformly distributed on the upstream wetted cells. As a downstream boundary condition, the experimental rating curve $z(Q)$ established near the confluence was imposed at the model outlet. It was later shifted down in order to calibrate water levels in the river and in the cavity: differences between computed and observed water levels eventually don't exceed 10 cm.

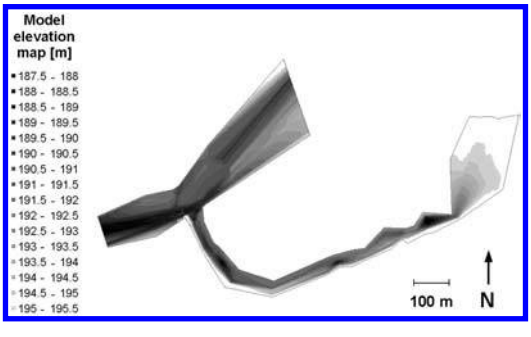


Figure 5. Geometry of the computational domain.

4 FIELD DATA PROCESSING

4.1 *LS-PIV data processing*

In this study, we use a PIV algorithm for large scale applications with low resolution images, developed by Fincham and Spedding (1997). It calculates the correlation between the interrogation area (IA) centered on a point a_{ij} in the first image (image A) and the IA centered at point b_{ij} in the second image (image B) recorded with a time interval of δt seconds (Fig. 6).

The correlation coefficient $R(a_{ij}, b_{ij})$ is a similarity index for the grey-scale intensity of a group of pixels contained in the two compared IAs, expressed as:

$$R_{ab}=\frac{\sum_{\substack{1\le i\le Mi\\1\le j\le Mj}}\left(A_{ij}-\overline{A_{ij}}\right)\left(B_{ij}-\overline{B_{ij}}\right)}{\left[\sum_{\substack{1\le i\le Mi\\1\le j\le Mj}}\left(A_{ij}-\overline{A_{ij}}\right)^2\sum_{\substack{1\le i\le Mi\\1\le j\le Mj}}\left(B_{ij}-\overline{B_{ij}}\right)^2\right]^{1/2}} \quad (5)$$

where Mi and Mj are the sizes of the interrogation areas (in pixels), and A_{ij} and B_{ij} are the distributions of the

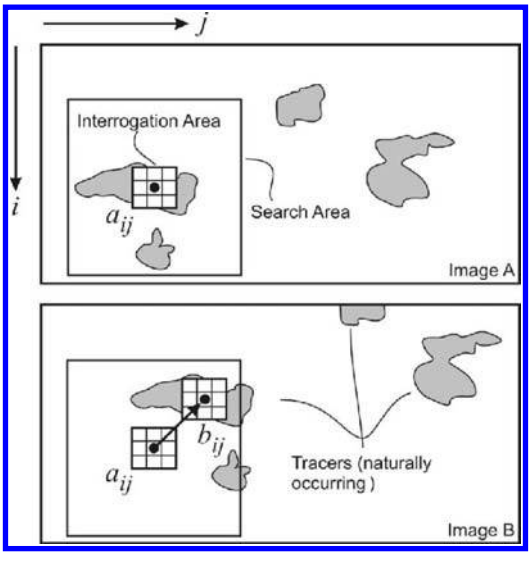


Figure 6. Principle of Particle Image Velocimetry.

Copyright © 2006 Taylor & Francis Group plc, London, UK

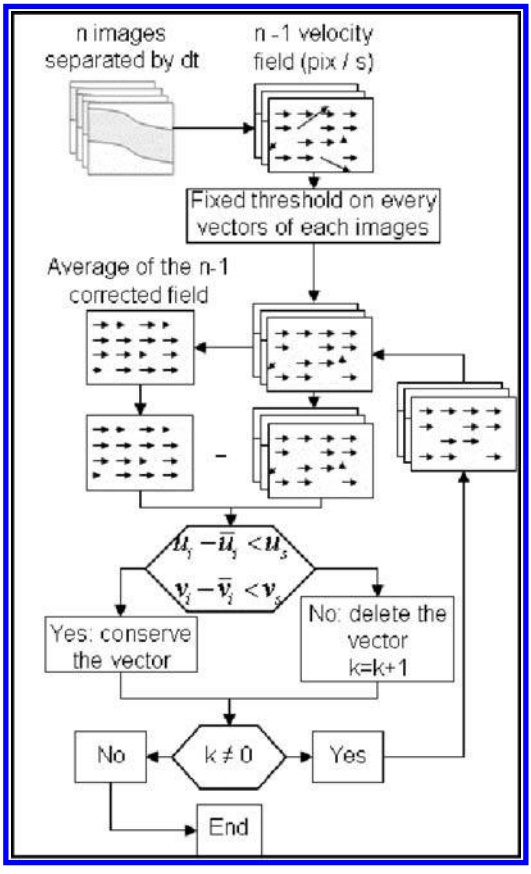


Figure 7. LS-PIV correction algorithm.

grey-level intensities in the two interrogation areas. Correlation coefficients are only computed for points b_{ij} within some search area (SA). The PIV approach assumes that the most probable displacement of the fluid from point a_{ij} during period δt is the one corresponding to the maximum correlation coefficient. Sub-pixel displacement accuracy can be reached using a parabolic fit (Forliti et al. 2000). Velocity vectors are derived from these displacements by dividing them by δt. The process is iteratively conducted for the whole image. Because of the flow recirculating pattern, no specific shapes could be given to the search area.

Due to the slight density of tracers, erroneous vectors are computed. Traditional erroneous vector correction algorithms (developed for river main channel flow, e.g. Fujita et al. (1998)) cannot be used in our experiments because of the flow complexity. Consequently a singular correction procedure has been implemented (Fig. 7): on every computed velocity field, a first filter is applied to remove spurious vectors with u or v components above a fixed threshold. Then, we compute the average of all the corrected displacement fields. Each corrected displacement field is compared with the averaged one. If the difference between a vector and the corresponding averaged vector is greater than a threshold, the vector is removed. Then a new averaged displacement field is computed, and a new comparison begins between the corrected displacement field and the averaged one. The final time-averaged velocity field is used for comparison with the model and aDcp results.

4.2 *aDcp data processing*

For more than 15 years, moving-vessel aDcp data have been routinely collected in rivers for river discharge measurement. But usual commercial aDcp software tools don't offer the required post-processing steps for hydrodynamical studies. Indeed, aDcp velocities post-processed by *WinRiver1.06* or *RiverSurveyor* in order to compute discharges are often difficult to compare with other field measurements or numerical modelling outputs. Consequently home-made routines were developed in *Fortran90* to post-process ASCII data files from Teledyne RDI ADCP™ data with reasonable computational times. The need for such post-processing tools has been recognized by several authors (e.g. Dinehart and Burau (2005)).

First we present the way vertical velocity profiles were finally depth-averaged once the data had been positioned, projected, interpolated, etc. As it is potentially difficult to calibrate theoretical profiles from this recirculating flow, we chose the simplest and most direct computation way:

$$\langle u \rangle = \frac{1}{h} \sum_{i=0}^{N-1} h_i \frac{u_{i+1} + u_i}{2} \qquad (6)$$

with $\langle u \rangle$ the depth-averaged velocity, $h = \sum_{i=0}^{N-1} h_i$ the water depth, h_i and u_i the heights and velocities depicted on Fig. 8 for $1 \leq i \leq N-1$. We assume that the bottom velocity is zero ($u_0 = 0$) and that velocities are constant in the upper flow layer ($u_N = u_{N-1}$).

Before this final depth-averaging step, the main problem stems from the moving-vessel deployment of the aDcp. This method allows to quickly scan large water bodies for depths, velocities and backscatter intensities. As practitioners usually do, we got several successive aDcp transects along more or less irregular vessel tracks, in order to average velocity field fluctuations. So velocity fields from different crossings are not distributed along the same horizontal segment, neither on the same regular grid. An illustration of various post-processing steps of aDcp velocity data is presented on Fig. 9. Depth-averaged post-processed velocities from 5 successive crossings on transect T1 (campaign aDcp1) are shown.

Copyright © 2006 Taylor & Francis Group plc, London, UK

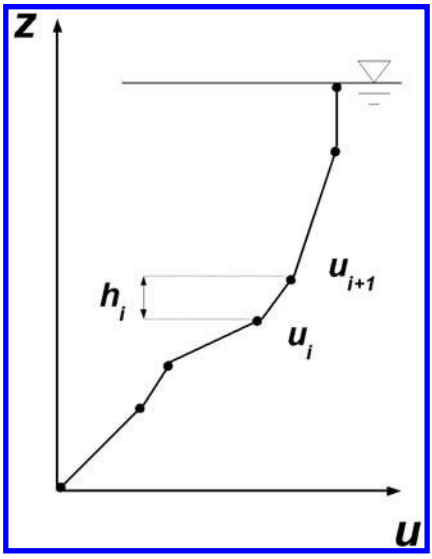


Figure 8. Depth average computation of aDcp velocities. *u stands for each velocity component and z for elevation above the bed.*

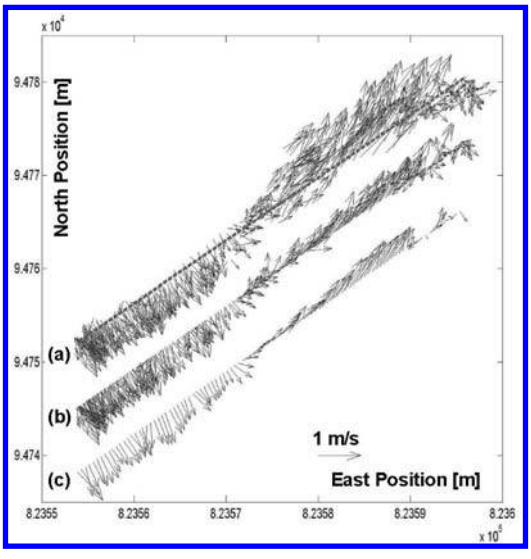


Figure 9. Depth-averaged post-processed aDcp velocities from 5 aDcp crossings of the same transect T1. *(a) repositioned velocities; (b) projected velocities; (c) interpolated velocities; the reference segment (dashed line) is shifted south for (b) and (c).*

First of all, all depth and velocity data had to be positioned in the same topographic reference system. As no GPS device was available to us, we measured the aDcp position by tacheometer at the beginning and the end of each crossing. As no bed motion occurred,

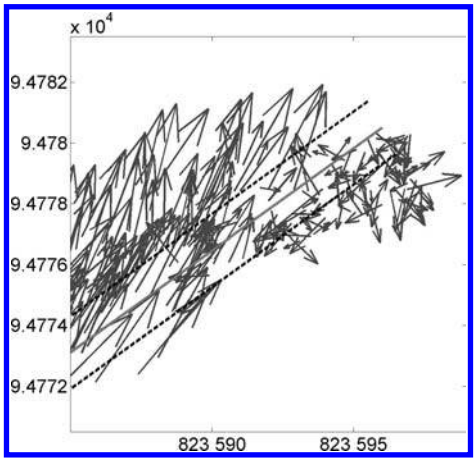


Figure 10. Close-up view of the end of transect T1.

the aDcp bottom-tracking data were used to compute the ship track and the Earth coordinates of the velocity and depth data (a). Then two methods can provide a representative velocity field on a straight user-defined cross-section. First, these referenced data can be projected on this mean cross-section, provided they are close enough to it ((b), >1 m far data are discarded). The referenced data can also be interpolated (c) on a regular vertical grid through inverse distance weighting averaging:

$$\bar{u}(x',z) = \left(\sum_{i=1}^{N_n} \frac{1}{d_i}\right)^{-1} \cdot \sum_{i=1}^{N_n} \frac{u_i}{d_i} \qquad (7)$$

with $\bar{u}$ each of the 3 interpolated velocity components, u_i each the 3 velocity components of the N_n closest neighbouring data, d_i their distances to the interpolation grid node (x', z).

Interpolation parameters – grid density, number of neighbouring data, search volume – must be chosen carefully to fit aDcp data spatial density. For instance, aDcp2 data were interpolated every 0.5 m in x' and 0.3 m in z from the 15 closest neighbouring data searched in a 0.6 m high and 1 m radius cylinder centered on (x', z).

Results are quite identical from different sets of interpolation parameters provided they are realistic. Interpolated velocities appear as an efficient way of representing space- and time-averaged velocity patterns from a dense enough set of moving-vessel aDcp data. However, the zoom on Fig. 9(a) presented on Fig. 10 illustrates the limitations that arise when the velocity field is unstable and data too scarce. At the end of transect T1 indeed, a small fluctuating gyre develops inducing some disorder in the local velocity data. One can easily see that available data for interpolation

Copyright © 2006 Taylor & Francis Group plc, London, UK

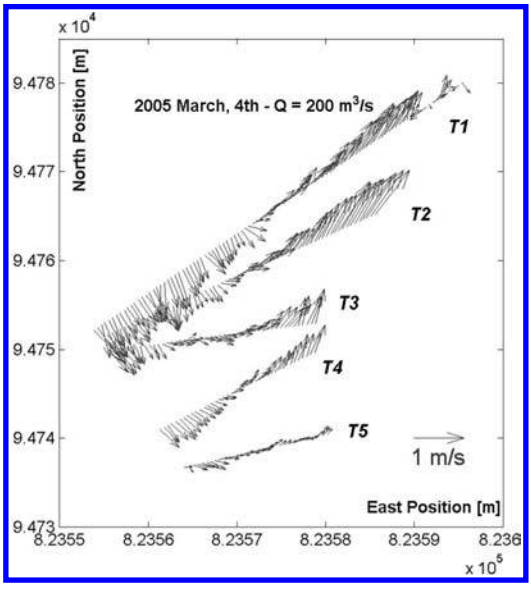


Figure 11. Depth-averaged interpolated transects T1 to T5. *aDcp1 campaign.*

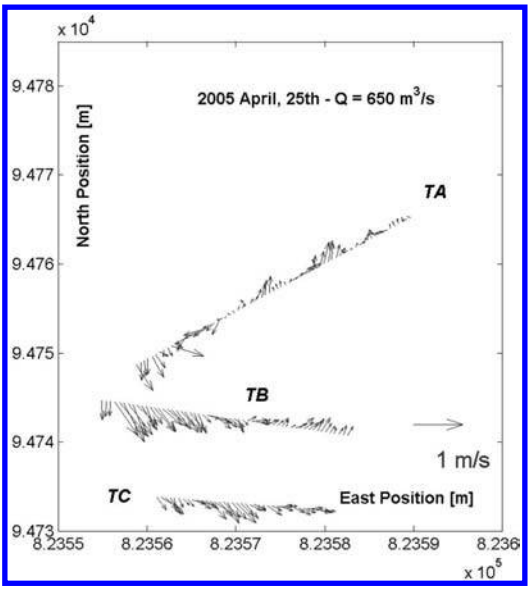


Figure 12. Depth-averaged interpolated transects TA to TC (in accordance with Fig. 3). *aDcp2 campaign.*

(within the dashed lines) were not dense enough for a proper time and space interpolation.

5 COMPARATIVE ASSESSMENT OF MEAN FLOW PATTERNS

5.1 *Observed flow patterns*

Depth-averaged interpolated velocities from aDcp1 and aDcp2 campaigns are presented in Figs. 11 and 12. The first set of data measured during steady state conditions (200 m^3/s) presents a quite "harmonious" recirculating flow pattern: velocity directions and intensities are smoothly inverted from the beginning to the end of each transect.

The velocity inflexion points are located near the centre of each transect. Discharges to the abandoned channel (not presented here) are close to zero across each transect, and there is very little mass transfer to the oxbow-lake through transect T5.

The situation is quite different during the aDcp2 campaign, performed at the end of the several hour rising limb of a 650 m^3/s flood. The mean water level was 1 m higher than previously. The overall recirculating pattern is quite similar but velocities entering the oxbow-lake are much higher than outlets (transects TB and TC). Discharges (not presented here) are close to $-10\ m^3/s$ which means that a part of the river diverted inflow was actively filling in the abandoned channel. The main gyre being weaker than for the previous case, transect TA shows slightly more disordered and much lower velocities than transects T1, T2, T3 and even T4. It should be noted that due to operator safety concerns, no aDcp transect could be acquired as close to the river as transect T1.

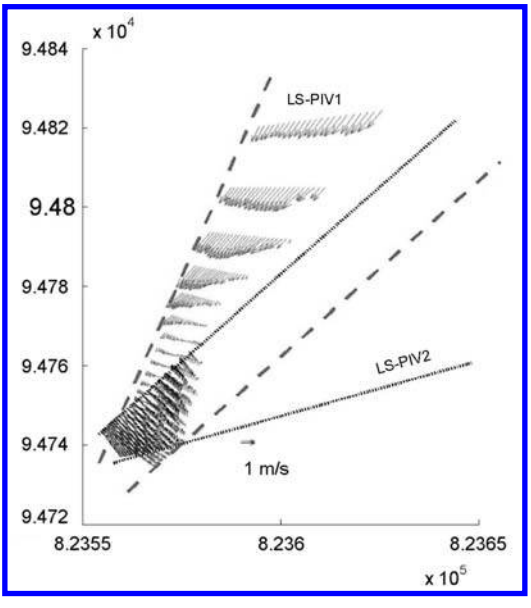


Figure 13. Mean velocity fields from LS-PIV1 (up, with a part of the river flow) and LS-PIV2 campaigns.

Figure 13 gives an overview of mean velocity fields from LS-PIV1 and LS-PIV2 campaigns. Camera view

Copyright © 2006 Taylor & Francis Group plc, London, UK

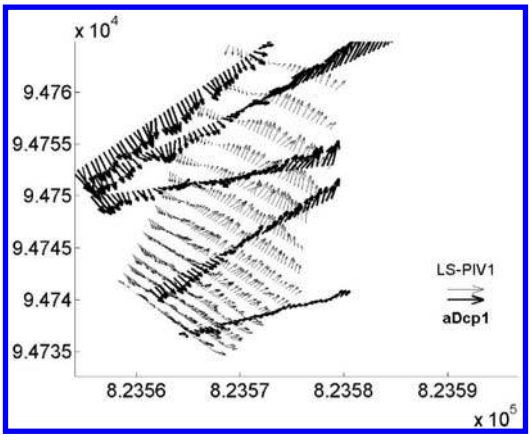


Figure 14. Comparison between aDcp1 and LS-PIV1 data.

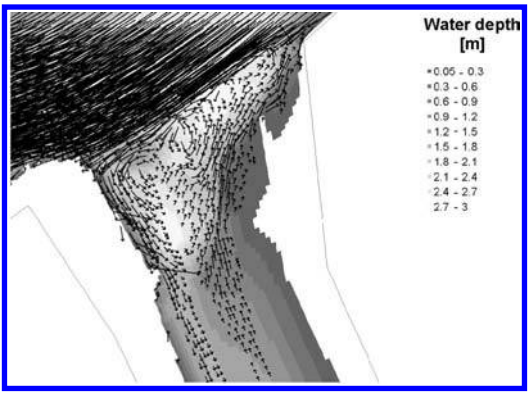


Figure 15. 2Dh modelling output – 200 m^3/s.

angles are indicated (lines) and spurious data out of free-surface areas have been discarded. The LS-PIV1 view angle (close to that of Fig. 3) gives an interesting view on the time-averaged river velocity field coming by the side-cavity. Unfortunately, we couldn't find a view angle allowing us to record the whole area investigated by aDcp. This problem could be solved in next campaigns by using a dedicated 10 m-high observation mast.

The recirculating flow patterns from both LS-PIV campaigns are very similar to each other and agree fairly well with aDcp1 results. For instance, mean velocity fields in the side-cavity from aDcp1 and LS-PIV1 (Fig. 14) are in acceptable agreement. Both sets of data correspond to similar river discharge values and quite stationary conditions. Velocity vector inflexions do occur by the same regions and velocity intensities are reasonably similar, despite the difference of nature between depth-averaged and surface velocities.

5.2 *A first comparison with 2Dh outputs*

As for the comparison of experimental velocity fields, no quantitative assessment of differences between computed and observed velocities has been achieved yet. A first example of a 200 m^3/s steady-state simulation is presented in Fig. 15. Velocities lower than 7 cm/s and water depths lower than 5 cm have been filtered out. The main recirculating pattern is correctly reproduced in the side-cavity, but the small intermittent gyre (Fig. 10) can't be clearly recognized. As observed in situ, highest velocities appear close to the cavity margins, and enter the abandoned channel a little further than suggested by field measurements.

But the main problem is a severe underestimation of velocity intensities: whereas maximum velocities from aDcp1 are close to 0.8–1 m/s, simulated velocities only reach 0.3 m/s for the same event. Velocity intensities in the side-cavity showed little sensitivity to friction or effective viscosity coefficient calibration attempts. As river flow velocities don't seem to be underestimated, there may be a problem in the way momentum transfer from the main flow to the gyre is taken into account in the model. Further analysis and tests are needed to investigate more precisely what is actually occurring.

6 CONCLUSIONS

In order to study the recirculating flow that develops at the downstream mouth of an abandoned meander, aDcp and LS-PIV data were acquired and compared with 2Dh modelling outputs. Beyond positioning in the same reference system, several post-processing steps were necessary to analyse and compare the mean velocity field measurements:

- because of the recirculating pattern of the flow, dedicated corrections had to be applied to the LS-PIV surface velocity field;
- LS-PIV velocities computed each second were averaged on sequences of a few minutes;
- 3D velocity scans from aDcp transects had to be ensemble-averaged, interpolated onto a regular grid, depth-averaged.

In situ measurements suggest some differences in flow patterns according to the river discharge value and evolution. Further field observation and numerical simulation will help for the accurate understanding of flow structure according to river flow conditions. A first comparison between observed and simulated velocity fields is encouraging even if velocity intensities are significantly underestimated.

ADcp and LS-PIV methods appear to give subsidiary results: once post-processed, depth-averaged and surface velocity fields can be successfully compared. Some tools have been developed but some others are still required to make the most of such spatially-distributed instantaneous velocities. Beyond

Copyright © 2006 Taylor & Francis Group plc, London, UK

the side-cavity recirculating flow studied here, aDcp and LS-PIV survey generally appear as promising tools for the analysis of complex flow dynamics in field conditions.

ACKNOWLEDGEMENTS

This work was supported by the *Cemagref* and the LTHE. Funding was provided by Région Rhône-Alpes and Programme National de Recherche en Hydrologie (ACI ECCO PNRH). We are grateful to the Compagnie Nationale du Rhône (CNR) for providing discharge time series and to Mickaël Lagouy and Jean-Pierre Laskowski for technical support.

REFERENCES

Adrian, R. J. (1991). Particle-imaging techniques for experimental fluid mechanics. *Annu. Rev. Fluid Mech. 23*, 261–304.

Barua, D. K. and K. H. Rahman (1998). Some aspects of turbulent flow structure in large alluvial rivers. *Journal of Hydraulic Research 36*(2), 235–252.

Bradley, A. A., A. Kruger, E. A. Meselhe, and M. Muste (2002). Flow measurement in streams using video imagery, *Water Resources Research, 38*(12).

Creutin, J. D., M. Muste, A. A. Bradley, S. C. Kim, and A. Kruger (2003). River gauging using PIV techniques: a proof of concept experiment on the Iowa river. *Journal of Hydrology 277*, 182–194.

Dinehart, R. L. and J. R. Burau (2005). Averaged indicators of secondary flow in repeated acoustic Doppler current profiler crossings of bends. *Water Resources Research 41*(9), 1–18.

Fincham, A. and G. Spedding (1997). Low cost, high resolution DPIV for measurement of turbulent fluid flow. *Experiments in Fluids 23*(6), 449–462.

Forliti, D., P. Strykowski, and K. Debatin (2000). Bias and precision errors of digital particle image velocimetry. *Experiments in Fluids 28*(5), 436–447.

Fujita, I., M. Hara, T. Morimoto, and T. Nakashima (1998). Visualization and PIV measurement of river surface flow. In *Proceeding of VSJ-SPIE98*.

Fujita, I. and S. Komura (1992). On the accuracy of the correlation method. In *Proceedings of the 6th International Symposium on Flow Visualization*, pp. 858–862.

Gordon, R. L. (1989). Acoustic measurement of river discharge. *Journal of Hydraulic Engineering 115*(7), 925–936.

Le Coz, J., B. Chastan, F. Védie, and G. Dramais (2006). Emplois de l'aDcp en rivière: une revue de synthèse, *Submitted to La Houille Blanche*.

Leese, J., C. Novak, and B. Clarke (1986). An automated technique for obtaining cloud motion from geosynchronous satellite data using cross correlation. *Journal of Applied Meteorology 10*, 118–132.

Muste, M., K. Yu, J. A. Gonzalez-Castro, M. Ansar, and R. Startzman (2004a). Methodology for estimating ADCP measurement uncertainty in open-channel flows. In *World water congress 2004: critical transitions in water and environmental resources management*, Salt Lake City, Utah, USA,

Muste, M., K. Yu, T. Pratt, and D. Abraham (2004b). Practical aspects of ADCP data use for quantification of mean river flow characteristics; Part II: fixed-vessel measurements. *Flow Measurement and Instrumentation 15*, 17–28.

Muste, M., K. Yu, M. Spasojevic (2004c) Practical aspects of ADCP data use for quantification of mean river flow characteristics; Part I: moving-vessel measurements. *Flow Measurement and Instrumentation 15*, 1–16.

Paquier, A. (1995). *Modélisation et simulation de la propagation de l'onde de rupture de barrage*. Ph. D. thesis, Université Jean-Monnet.

Piégay, H., G. Bornette, A. Citterio, E. Hérouin, B. Moulin, and C. Statiotis (2000). Channel instability as a control on silting dynamics and vegetation patterns within perifluvial aquatic zones. *Hydrological processes 14*, 3011–3029.

Roche Campo, E. (2002). Modélisation hydraulique en milieux complexes: les bras morts de l'Ain, projet de fin d'études. Technical report, Cemagref.

Rollet, A.-J., H. Piégay, J. Lejot, A. Citterio, and S. Dufour (2005). Programme LIFE Nature – conservation des habitats créés par la dynamique de la rivière d'Ain. Technical report, UMR 5600, CNRS.

Shields, F. D. J. (2005). River habitat quality from river velocities measured using Acoustic Doppler Current Profiler. *Environmental Management 36*(4), 565–575.

Yorke, T. H. and K. A. Oberg (2002). Measuring river velocity and discharge with acoustic Doppler profilers. *Flow Measurement and Instrumentation 13*, 191–195.

Copyright © 2006 Taylor & Francis Group plc, London, UK

Filtering ADV data on highly turbulent free surface flow

L. Cea, L. Pena & J. Puertas
Civil Engineering School, University of A Coruña, Spain

ABSTRACT: In this paper the 3D instantaneous velocity registered with an ADV in a vertical slot fishway is analysed using several filters in order to eliminate the corrupted data from the sample. The filters used include the minimum/maximum threshold, the acceleration threshold, and the phase-space threshold. A new filter based on a cross-correlation threshold is proposed and tested. The influence of the filtering process in the mean velocity, turbulent energy and power spectrum is discussed. The flow in the vertical slot fishway is quite complex. The turbulence intensity and air entrainment vary widely within the flow, which produces data records of different quality depending on the measurement point. The filtering process has a significant influence on the computed statistics of the samples.

1 INTRODUCTION

Acoustic Doppler Velocimeters (ADV) are often used for the measurement of 3D velocity fields in turbulent flows. The ADV is a relatively simple to use device which registers the instantaneous 3D velocity at one spatial point. Although strictly speaking the ADV is an intrusive device, the distance between the control volume and the probe is large enough to avoid considering its effect in the measurements. The instantaneous data registered with an ADV is generally used to compute mean flow statistics such as the 3D mean velocity, the turbulent kinetic energy and the Reynolds stresses. The sampling rate of the ADV (50 Hz) permits also the computation of frequency spectra up to 25 Hz. Nonetheless, care should be taken when computing these flow statistics from the raw velocity data. The main problems which should be addressed are the Doppler noise and the aliasing of the Doppler signal.

The Doppler noise is a source of error which is present when measuring turbulence with any Doppler-based backscatter system (Lohrmann, Cabrera, and Kraus 1994). The relative importance of this error depends on the fluid characteristics as well as on the flow conditions (flow velocity, presence of particles in the flow, air bubbles, ...). The main consequence of the Doppler noise is that the turbulent kinetic energy given by the ADV is larger than the real turbulent kinetic energy of the flow. This energy is mainly introduced in the high frequency range of the horizontal components (meaning by horizontal components those ones perpendicular to the ADV's longitudinal axis). For this reason, the spectrum of the horizontal velocity components is biased high for frequencies above 5 Hz (Lohrmann, Cabrera, and Kraus 1994). Nikora and Goring (Nikora and Goring 1998) also studied the ADV measurements of turbulence under several flow conditions, obtaining the following conclusions: (1) the noise in the two horizontal components (those ones which are perpendicular to the ADV's longitudinal axis) is up to 30 times larger than the noise in the vertical component (which is parallel to the ADV's axis), and that is due to the sensor geometry; (2) there is a great increase of noise in the presence of bubbles (up to 5 times in the experiments by Nikora and Goring). These findings are of great interest, specially those ones regarding the nonisotropic distribution of the noise between the three velocity components, and the increase of noise due to the presence of air bubbles in the flow. If a measurement is made when one of these bubbles is inside the control volume, an erroneous velocity is registered, and a spike is introduced in the record. Considering the high turbulent kinetic energy, and the air entrainment which occurs near the vertical slot in the fishway, it should be expected a high level of noise in that region.

The other source of error is related to the aliasing of the Doppler signal. The ADV measures the phase shift between two acoustic pulses. This shift must lie between $-180°$ and $180°$. Otherwise the velocity is not correctly measured (for the ADV, a phase shift of $270°$ is identical to a phase shift of $-90°$). The aliasing of the signal introduces spurious data in the sample, increasing substantially the variance of the velocity (and therefore the turbulent kinetic energy), and modifying the power spectra, specially in the high frequency range.

Copyright © 2006 Taylor & Francis Group plc, London, UK

In order to compute the correct flow statistics it is necessary to eliminate the corrupted values by filtering the raw data. If we are interested in computing the mean velocity and turbulent kinetic energy, then the filtering process consists only in removing the spikes (despiking process). On the other hand, if we are interested in computing the power spectra, it is convenient to replace the removed data with some kind of artificial data using a fitted polynomial or any other replacement technique (replacement process). The replacement technique is quite arbitrary. A cubic or any other high order polynomial might be a sensible option if the measurements are well correlated. On the other hand, in highly turbulent flows with a time integral scale of the same order as the sampling time step, its simpler to use a linear interpolation between adjacent values.

In this paper the 3D velocity data registered with an ADV in a vertical slot fishway is filtered using several despiking methods, including minimum and maximum thresholding, acceleration thresholding, and phase space thresholding. A new filter based on a cross-correlation threshold is proposed and tested. The influence of the filtering process in the mean velocity, turbulent energy, Reynolds stresses, and power spectrum is discussed.

2 EXPERIMENTAL MEASUREMENTS

The ADV's experimental velocity records were obtained from measurements carried out in a fishway scale model at the CITEEC (Centro de Innovación Tecnolóxica en Edificación e Enxeñería Civil, University of A Coruña, Spain). The experimental model was built in a 12m long channel, with a 1m width square cross section and a bed slope of 10%. The channel was divided into nine active pools. The water discharge was fixed to $125l = s$ at the inlet boundary. At the lower end of the flume, a tailgate causing over- flow was used to fix the water depth in order to obtain a uniform state of the flow in all the pools. The design of the fishway is shown in Figure 1. The location of the data points inside the pool is defined in Figure 2. All the data points are located 25 cm above the bottom of the pool.

The sampling volume of the ADV is a 6 mm length cylinder with a diameter of 4 mm (sample volume of 0:08 cm^3). The control volume is located 5 cm away from the probe in order to reduce flow interference (Figure 3). The maximum sampling rate of the ADV (50 Hz) was used in the experiments. Approximately 50000 samples were obtained at each point, over a total measuring time of 15 minutes.

The upper left corner of the pool (point P1) is a very quiet region. Point P2 is located in the middle of the pool. The velocity here is generally small, and, depending on the flow conditions, it can be the centre

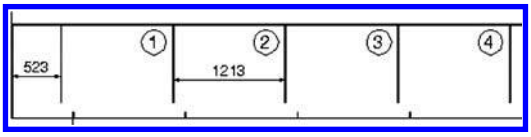


Figure 1. Fishway design.

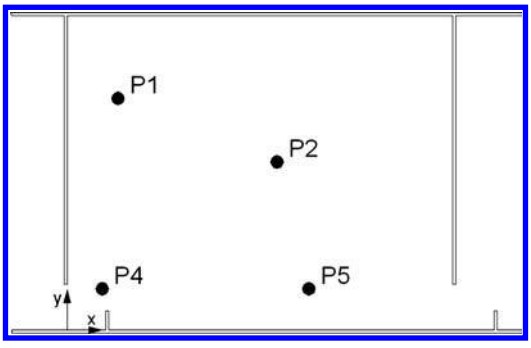


Figure 2. Experimental data points.

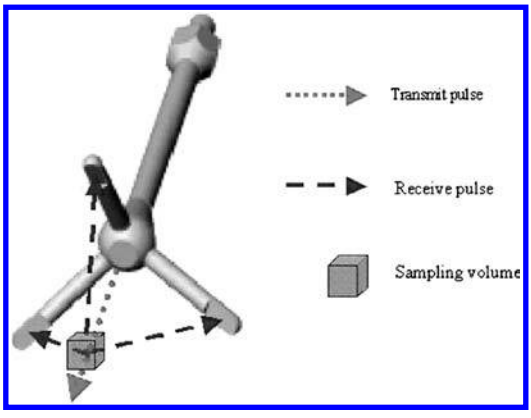


Figure 3. ADV's sampling probe.

point of a large eddy. The highest velocity and turbulent kinetic energy occur near the slot (point P4). The flow is accelerated just before going through the slot and decelerated afterwards, producing a high amount of turbulence. At this point there is also a large entrainment of air in the flow, which generates even more turbulence and produces a large concentration of air bubbles. Some bubbles are convected downstream to point P5, which is located in the main flow stream across the pool.

3 FILTERING METHODS

The filtering of the raw data consists in two processes: first, the spikes must be removed from the data (despiking process); and second, the removed data must be

Copyright © 2006 Taylor & Francis Group plc, London, UK

Table 1. Time integral scales (seconds).

	P1	P2	P4	P5
$T_{int,u}$	0.15	0.32	0.009	0.02
$T_{int,v}$	0.35	0.35	0.015	0.02
$T_{int,w}$	0.38	0.44	0.018	0.005

replaced in order to compute the power spectrum (replacement process). If possible, it is convenient to use the maximum sampling rate of the measuring device (f_{max}) for two reasons: first, because the detection of corrupted data with the acceleration and phasespace methods is more accurate when using high sampling frequencies; second, because the accuracy of the replacement method increases as the time step decreases. This is true when using a fitted polynomial as the replacement method. In addition, the computed spectrum extends up to a frequency of $f_s/2$, where f_s is the sampling frequency, and therefore, it is convenient to use $f_s = f_{max}$ in order to compute the largest range of the power spectra.

Considering that in the fishway the turbulence level is very high, and that the time integral scale (Table 1) is of the same order as the sampling time step, we have used a linear interpolation as the replacement technique. In any case, the replacement technique is always rather arbitrary.

For the despiking process, four different filters have been considered: a maximum/minimum threshold, an acceleration threshold (Nikora and Goring 2000), a phase-space threshold (Goring and Nikora 2002), and a cross-correlation threshold.

3.1 *Minimum/maximum threshold filter*

This is the simplest filter of the four. It establishes a range defined by a minimum threshold and a maximum threshold. All the data lying inside this range are considered to be valid, while the data lying outside that range are considered to be corrupted, and therefore it is removed and replaced. The maximum and minimum thresholds are rather subjective, and must be established after visual inspection of the time series. Different thresholds are needed for each velocity component.

3.2 *Acceleration threshold*

The acceleration threshold filter (Nikora and Goring 2000) computes accelerations as $a_i = (u_i - u_{i-1})/\Delta t$ for each velocity component, and establishes a maximum acceleration a_{max} in order to detect spikes. The maximum acceleration is expressed as $a_{max} = k_g g$, where g is the gravity acceleration, and k_g is a constant. A data point is considered a spike if $a_i > a_{max}$ and $u_i > \bar{u} + k_\sigma \sigma$, or if $a_i < -a_{max}$ and $u_i < \bar{u} - k_\sigma \sigma$, where

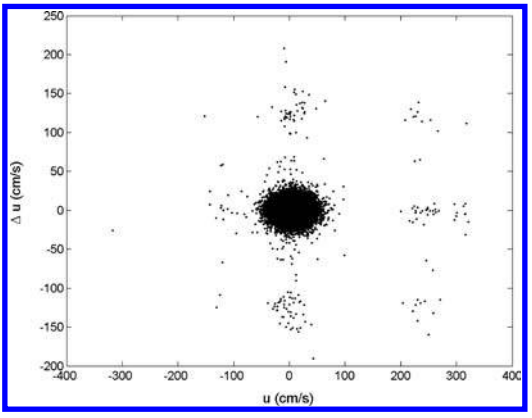


Figure 4. Raw velocity data in the x-direction at point P1 plotted in the phase space $u - \Delta u$.

σ and $\bar{u}$ are the standard deviation and mean velocity of the correspondent spatial component, and k_σ is a constant. The method has therefore two constants which must be fixed: k_g and k_σ. Based on their own experience, Goring and Nikora (Goring and Nikora 2002) suggest the following values: $k_g = 1 - 2$, and $k_\sigma = 1.5$. These values are only based on their experience, after filtering different experimental data, and it has no theoretical background.

3.3 *Phase-space threshold filter*

The phase-space threshold filter (Goring and Nikora 2002) is based on the fact that derivation of a signal enhances its high frequency components. The method plots the variable, its first time derivative and its second time derivative against each other in a three dimensional phase-space. It is assumed that all the valid data cluster inside an ellipsoid, and all the data points lying outside that ellipsoid are considered to be spikes. Figure 4 shows the projection of the raw velocity at point P1 on the space $u - \Delta u$.

Most of the data cluster in an ellipsoid, while some data are clearly out of that ellipsoid. Those points lying apart are considered to be corrupted data. In order to define the three axes of the ellipsoid which defines the valid data, a threshold based on a constant λ is used. Such a threshold was first used by Donoho and Johnstone (Donoho and Johnstone 1994), and it is obtained from a theoretical result which claims that the expected maximum of N independent, normal distributed, random variables, with zero mean and σ standard deviation, is equal to $\lambda\sigma$, with $\lambda = \sqrt{2Ln(N)}$. Nonetheless, it should be remarked that turbulence is not normally distributed and therefore, the theoretical result concerning the *universal* constant λ applies only approximately. A detailed description of the method is presented by Goring and Nikora in (Goring and Nikora 2002).

Copyright © 2006 Taylor & Francis Group plc, London, UK

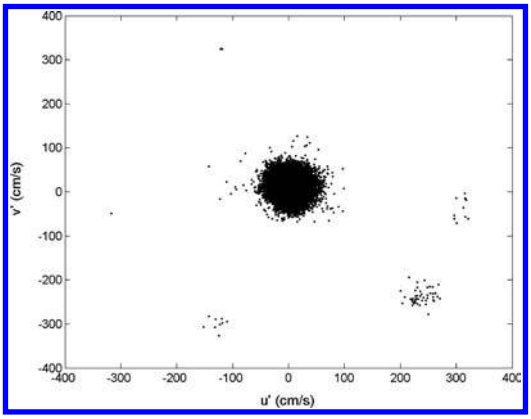


Figure 5. Raw velocity data at point P1 plotted in the correlation space $u' - v'$.

3.4 *Cross-correlation threshold filter*

All the previous methods filter each velocity component independently, and then, if a a spike is identified in one velocity component, the other two velocity components are also filtered. In order to include information of the three velocity components at the same time in the filtering process, and following the idea that valid data should cluster in a cloud of points, we tried a filter based on the representation of the three fluctuation velocities against each other. In a similar way as in the phase-space filter, it is assumed that the good data cluster inside an ellipsoid, the axes being given as a function of the constant λ, as $\lambda\sigma_u$, $\lambda\sigma_v$ and $\lambda\sigma_2$, where σ_u, σ_v and σ_w refer to the standard deviation of the fluctuation velocity in each of the spatial directions. All the data lying outside the ellipsoid are considered to be a spike, and it is removed and replaced. Figure 5 shows the projection of the raw velocity at point P1 on the space $u' - v'$. Again, most of the data cluster together, and the corrupted data, separated from this cluster, can be clearly identified.

3.5 *Comparison and application of the different filters*

The main advantage of the phase-space threshold method is that it requires no parameters, since the constant λ is claimed to be universal. On the other hand, the maximum/minimum and acceleration threshold methods require six and two parameters respectively, which makes the results rather dependent on the specific choice of parameters.

Trying to eliminate the rather subjective choice of parameters of the minimum/maximum and acceleration threshold methods we have used the constant λ in order to define them. In such a way, the maximum and minimum limits for the instantaneous velocity in the sample are defined as $u_{max} = \bar{u} + \lambda\sigma_u$ and $u_{min} = \bar{u} - \lambda\sigma_u$ for each velocity component, where $\bar{u}$ is the mean velocity. In the same way, in the acceleration threshold, the maximum and minimum accelerations are defined as $a_{max} = \lambda\sigma_a$ and $a_{min} = -\lambda\sigma_a$ for each spatial component, where it has been taken into account that the mean acceleration of the sample is zero. From this definition it follows that $k_g = \lambda\sigma_a/g$. The phase-space method can be seen as an extension of the acceleration method, because it considers not only the accelerations, but also the velocity and the derivative of the acceleration.

We have found that the acceleration filter is much more sensitive to the value of k_g than to the value of k_σ, and thus, we have maintained a value of $k_\sigma = 1$ in all the cases. A modification of the value of k_σ will increase or decrease the data which is filtered, but it does not have a great influence on the value of the filtered statistics, neither in the spectra obtained from the filtered data.

The cross-correlation threshold that we have applied in this work uses similar concepts to the phas-espace method, but instead of plotting the velocity and its derivatives, it plots the three components of the instantaneous velocity at a time.

Finally, we would like to notice that the fact of using universal parameters speeds and simplifies the filtering process. However, visual inspection of the data before filtering is also valuable and recommended, and, in some cases it can be used to fix the parameters of a filter in a relatively simple way. To this purpose, we have tried a methodology to fix the constant k_g in the acceleration threshold method, based on the inspection of the results obtained with several values of k_g. Although visual inspection might seem less accurate than using universal constants (it is more subjective, at least), we should remember that the universal constant is obtained after assuming that turbulence is normally distributed, which is not. In any case, visual inspection is always more tedious than a *universal* criterion.

4 RESULTS

The four filters presented in the previous section have been applied to the data records registered in the fishway flow. All of them produce quite similar results for the data registered at points P1 and P2. The number of corrupted data is not too large at these points. The filtering process at point P5 is more complex, because the turbulence level is higher and there are much more air bubbles in the flow, producing a rather large number of spikes. The concentration of air bubbles in the flow at point P4 is so large, and the turbulent kinetic energy is so high, that it is not possible to distinguish between valid and corrupted data. We have not been able to obtain satisfactory results with any of the filters at that point.

Copyright © 2006 Taylor & Francis Group plc, London, UK

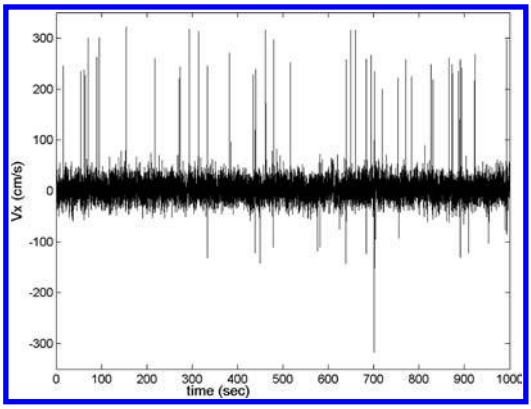


Figure 6. Instantaneous velocity in x-direction at point P1 before filtering.

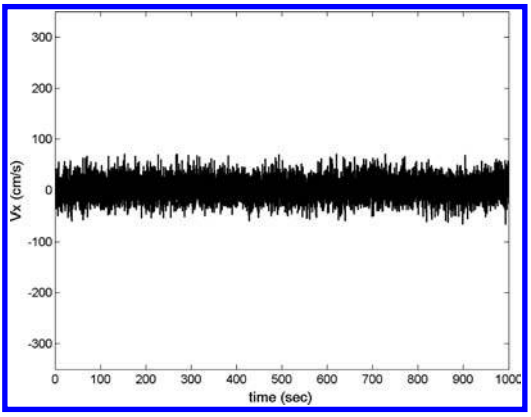


Figure 7. Instantaneous velocity in x-direction at point P1 after filtering.

4.1 *Results at point P1*

The measurement point P1 is located in the upper left corner of the pool. Figure 6 shows the x-component of the instantaneous velocity before filtering. The variance and the mean computed from the raw data for each spatial component are $\sigma_x^2 = 310\,cm^2/s^2$, $\sigma_y^2 = 377\,cm^2/s^2$, $\sigma_z^2 = 98\,cm^2/s^2$, and $\bar{u} = 3\,cm/s$, $\bar{v} = 18\,cm/s$, $\bar{w} = -32\,cm/s$.

In order to filter the data with the minimum/maximum threshold filter, we can establish by visual inspection a range given by $-100\,cm/s$–$100\,cm/s$. Similarly, after inspection of the other velocity components, the ranges of valid data can be established as $-100\,cm/s$–$100\,cm/s$ for the y-component and $-80\,cm/s$–$20\,cm/s$ for the z-component. Applying these minimum/maximum thresholds, 84 spikes are detected, the variance of the filtered data is $\sigma_x^2 = 234\,cm^2/s^2$, $\sigma_y^2 = 296\,cm^2/s^2$, $\sigma_z^2 = 98\,cm^2/s^2$, and the mean is $\bar{u} = 3\,cm/s$, $\bar{v} = 18\,cm/s$, $\bar{w} = -32\,cm/s$. Figure 7 shows the x-velocity component after filtering. It should be noticed that the variance of the x and y-components is reduced approximately 30%, while the variance of the z-component does not change after filtering. This is probably because the corrupted data is mainly caused by the air bubbles in the flow, and these ones only affect the x and y-components of the velocity. It should also be remembered here the finding of Goring and Nikora concerning the non-isotropic distribution of the noise between the 3 velocity components, which is in agreement with our results. The mean velocity computed from the filtered and the raw data are the same, which seems to indicate that the spikes are randomly distributed with zero mean.

If the constant $\lambda = \sqrt{2Ln(N)}$ is used in order to compute the maximum and minimum thresholds, as it was suggested in the previous section, then the number of filtered data is 114, and the variance of the filtered data is $\sigma_x^2 = 231\,cm^2/s^2$, $\sigma_y^2 = 294\,cm^2/s^2$, $\sigma_z^2 = 97\,cm^2/s^2$. The results are very similar to those ones obtained by visual inspection , but the process is much faster and simpler, since no parameter needs to be fixed.

Table 2. Number of spikes and normal Reynolds stresses computed with several filters at point P1.

	N_f	σ_x^2	σ_y^2	σ_z^2
Raw data	–	310	377	98
Max/min visual	84	234	296	98
Max/min λ	114	231	294	97
Accel. $\lambda, k_\sigma = 2$	189	234	299	97
Accel. $\lambda, k_\sigma = 1$	252	235	300	97
Accel. $\lambda, k_\sigma = 0$	300	236	301	97
Accel. $k_g = 1.5, k_\sigma = 1.5$	1562	212	280	96
Phase-space	623	232	295	96
Cross-correlation	169	230	292	97

In this case the acceleration threshold produces quite similar results. Using the constant λ to compute $k_g = \frac{\lambda \sigma_a}{g}$, and taking $k_\sigma = 1$, the number of filtered spikes is 252, and the variance of the filtered data is $\sigma_x^2 = 235\,cm^2/s^2$, $\sigma_y^2 = 300\,cm^2/s^2$, $\sigma_z^2 = 97\,cm^2/s^2$. Note that, when taking $k_g = \frac{\lambda \sigma_{ax}}{g}$ we are using three different values of k_g, one for each velocity component.

Increasing/decreasing the value of k_σ decreases/increases the number of filtered data, but it does not produce significant changes in the variance of the filtered signal (see Table 2). Notice that, even though the number of detected spikes is larger with the acceleration method, the variance is not smaller, even more, it is slightly larger. This is because many of the spikes filtered are in between the valid range defined by the min/max threshold. Those are spikes of small amplitude, with a relatively low energy level. Using

Copyright © 2006 Taylor & Francis Group plc, London, UK

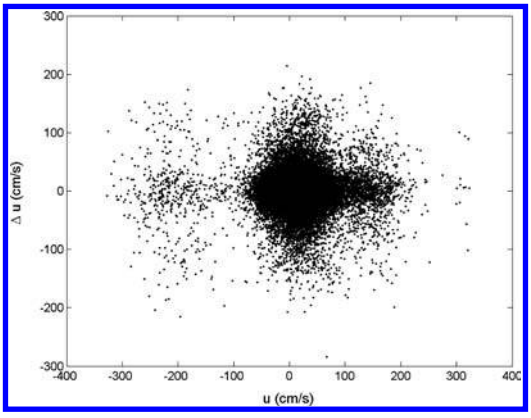


Figure 8. Raw velocity data at point P5 plotted in the phase space $u - \Delta u$.

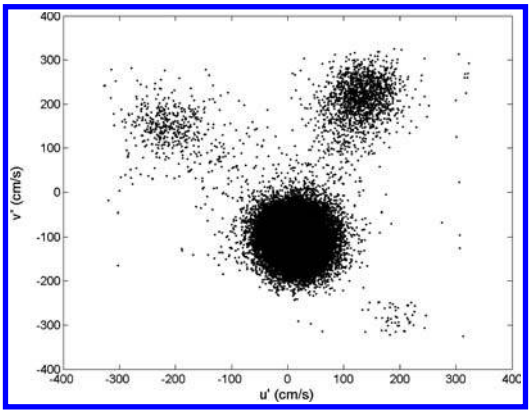


Figure 9. Raw velocity data at point P5 plotted in the correlation space $u' - v'$.

the values $k_g = 1.5$ and $k_\sigma = 1.5$ (Goring and Nikora 2002), the number of spikes increases considerably, and the variance diminishes.

4.2 *Results at point P5*

The flow around the measurement point P5 is much more complex. The turbulent kinetic energy is much higher, and there are many air bubbles present in the flow. This creates more spikes in the data, and at the same time, since the turbulent fluctuations are also higher, it is more difficult to identify the corrupted data. This is clearly shown in Figures 8 and 9, which show the raw velocity data at point P5 plotted in the phase space and correlation space. A main core of data can still be identified, but in this case, it is not so easy to identify the corrupted data lying outside of this core, specially when comparing with the data at point P1 (Figures 4 and 5).

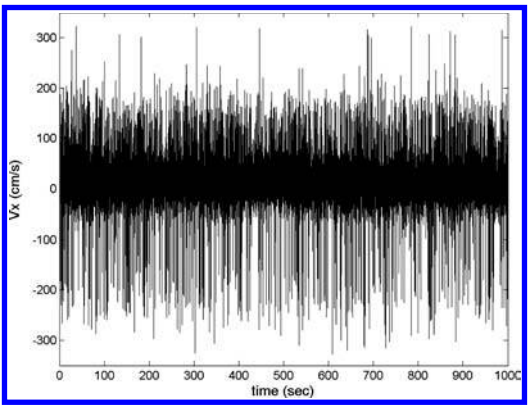


Figure 10. Instantaneous velocity in x-direction at point P5 before filtering.

Figure 10 shows the x-component of the instantaneous velocity before the filtering process. The variance and the mean computed from the raw data for each spatial component are $\sigma_x^2 = 1747\, cm^2/s^2$, $\sigma_y^2 = 4893\, cm^2/s^2$, $\sigma_z^2 = 368\, cm^2/s^2$, and $\bar{u} = 16\, cm/s$, $\bar{v} = -90\, cm/s$, $\bar{w} = -8\, cm/s$. The variance is much larger than the variance at point P1 for two reasons: first, because the turbulence level is higher; and second, because the number of spikes is larger.

In this case it is difficult to establish minimum and maximum velocity thresholds by visual inspection of the data. Therefore, the λ constant must be used in the minimum/maximum threshold filter. With this filter the number of spikes identified is 2141, which means that around a 5% of the data is filtered (at point P1 only 0.2%–0.5% of the data was filtered). The variance of the filtered signal is $\sigma_x^2 = 821\, cm^2/s^2$, $\sigma_y^2 = 1491\, cm^2/s^2$, $\sigma_z^2 = 371\, cm^2/s^2$. The x-component is reduced by a factor 2, the y-component is reduced by a factor 3, and the z-component remains the same. That means very large reductions in the turbulent kinetic energy. As it happened at point P1, there is no variation in the mean velocity, which remains mostly the same ($\bar{u} = 16\, cm/s$, $\bar{v} = -90\, cm/s$, $\bar{w} = -8\, cm/s$). Figure 11 shows the x-component of the instantaneous velocity after filtering with the minimum/maximum threshold.

We have done several tests with the acceleration threshold filter. Using the λ constant to evaluate k_g, we have tried several values of k_σ in order to see the sensitivity of the filter to its value (see Table 3). For values of k_σ different than zero the results are quite similar, which confirms that the sensitivity of the results to k_σ is low. Using the values $k_g = 1.5$, $k_\sigma = 1.5$ (Goring and Nikora 2002), the number of identified spikes increases to 12547, which is about 25% of the total data. This is excessively high, and in any case, if 25% of the data was corrupted the filtered record

Copyright © 2006 Taylor & Francis Group plc, London, UK

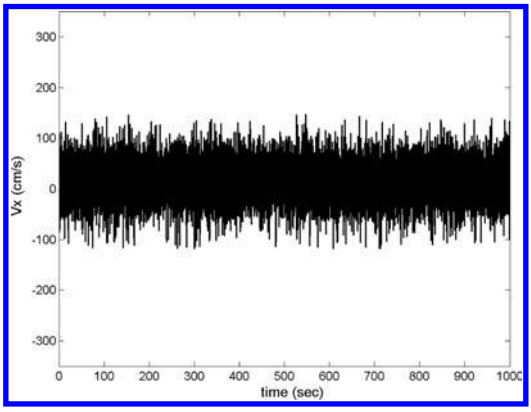


Figure 11. Instantaneous velocity in x-direction at point P5 after filtering.

Table 3. Number of spikes and normal Reynolds stresses computed with several filters at point P5.

	N_f	σ_x^2	σ_y^2	σ_z^2
Raw data	–	1747	4893	368
Max/min visual	–	–	–	–
Max/min λ	2142	821	1491	371
Accel. $\lambda, k_\sigma = 4$	1756	962	2038	371
Accel. $\lambda, k_\sigma = 2$	1871	937	1983	370
Accel. $\lambda, k_\sigma = 1$	2164	977	2115	368
Accel. $\lambda, k_\sigma = 0$	2746	1076	2550	361
Accel. $k_g = 5, k_\sigma = 1$	3244	783	1384	366
Accel. $k_g = 1.5, k_\sigma = 1.5$	12547	487	955	290
Phase-space	3579	864	1646	362
Cross-correlation	2209	789	1422	371

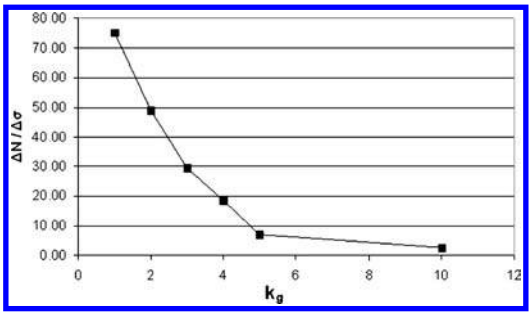


Figure 12. Acceleration filter with different values of k_g. Point P5.

would be very dependent on the replacement algorithm. Figure 12 shows the ratio $\Delta N/\Delta\sigma$ for different values of k_g, where ΔN is de difference in the number of spikes and $\Delta\sigma$ is the difference in the variance between different values of k_g. It can be clearly seen that there is a boost in the ratio for values of k_g smaller

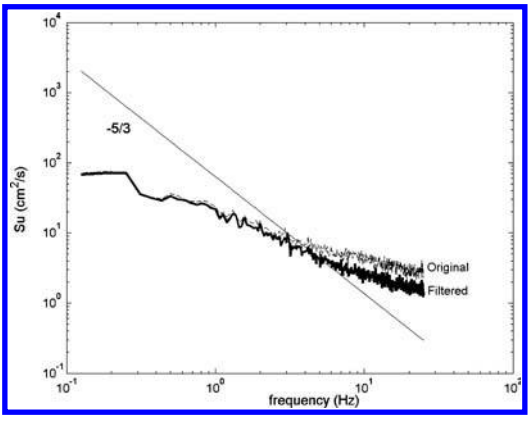


Figure 13. Power spectrum at point P1. Max/min threshold with λ.

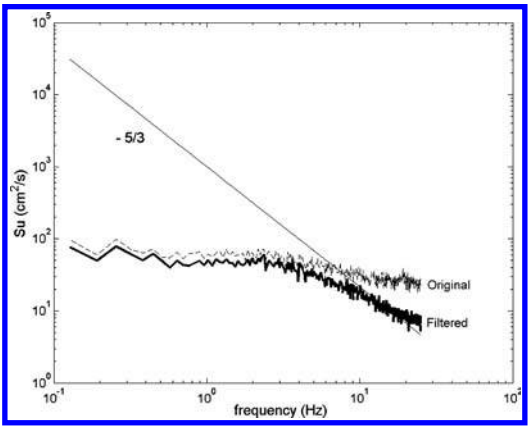


Figure 14. Power spectrum at point P5. Acceleration threshold with λ.

than 5. This sudden change in the slope of the curve might be related to the limit between spikes and valid data, i.e. large values of $\Delta N/\Delta\sigma$ might indicate that too much valid data is being identified as corrupted. Based on this assumption, we can establish an optimum value of $k_g = 5$. Using this value the number of spikes is 3244, slightly larger than the number of spikes obtained using the constant λ. In fact, taking $k_g = \frac{\lambda\sigma_a}{g}$ is in this case equivalent to use the values of the parameter $k_g = 7.8$, 10.5, 4.5 for each velocity component.

The largest number of spikes is given by the phas-espace filter, and the largest reduction in turbulent energy by the cross-correlation filter.

Figures 14 to 17 show the power spectra of the x-velocity component, computed from the original and filtered signals. No matter which filter is used, the main effect of the filtering process is to remove energy

Copyright © 2006 Taylor & Francis Group plc, London, UK

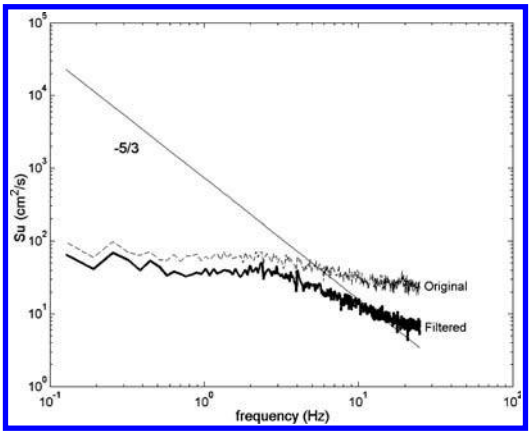


Figure 15. Power spectrum at point P5. Correlation threshold.

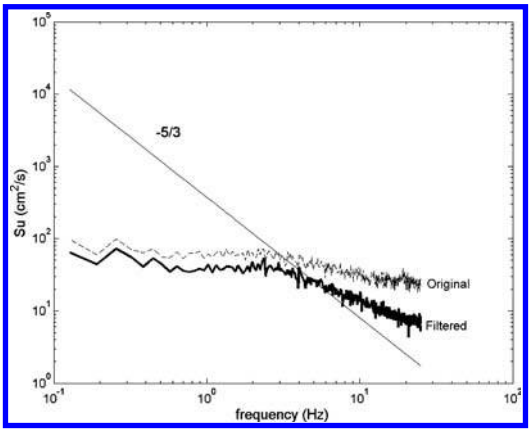


Figure 16. Power spectrum at point P5. Max/min threshold with λ.

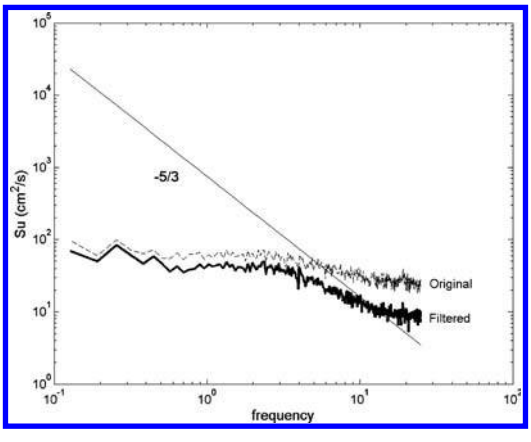


Figure 17. Power spectrum at point P5. Phase-space filter.

Table 4. Number of spikes and normal Reynolds stresses computed at point P1 if measured with a sampling frequency of 10 *Hz*.

	N_f	σ_x^2	σ_y^2	σ_z^2
Raw data	–	315	365	98
Max/min λ	28	227	288	97
Accel. $\lambda, k_\sigma = 2$	27	227	289	97
Accel. $\lambda, k_\sigma = 1$	35	227	289	97
Accel. $\lambda, k_\sigma = 0$	46	230	289	97
Phase-space	168	226	288	95
Cross-correlation	45	225	286	96

from the high frequency range (the spikes are mainly high frequency oscillations with a large amplitude). Some energy is also removed from the low frequency range.

4.3 *Decreasing the sampling frequency*

In order to check the performance of the filters when the sampling frequency is smaller, we have picked up just one measure of each five. In this way we obtain the data which we would have measured if we had sampled at a frequency of 10 *Hz* instead of 50 *Hz*. Table 4 shows the results obtained at the measuring point P1. The difference in the turbulent kinetic energy between the record measured at 50 *Hz* and the record measured at 10 *Hz* is not significant (smaller than 5% in all cases). It should be noticed that the phase-space filter identifies around 3 times more spikes than the other filters, while the variance of the filtered signal is the same for all the filters.

5 CONCLUSIONS

From these results it is difficult to assess which filter works better. When applied to our data in the fishway, none of them can be considered to be clearly superior to the others.

The fact of using the constant λ removes much subjectivity from the choice of the parameters and at the same time it speeds the filtering process. For this reason we recommend to use this approach in order to determine the parameters of any filter.

All of the filters used produce a significant reduction in the variance of the instantaneous velocity, removing in such a way most of the spurious turbulent kinetic energy which is present in the raw data. At the measurement point P5 the turbulent energy can be reduced up to a factor 3. On the other hand, the mean velocity computed from the filtered and the raw data are almost the same, which confirms that the spurious spikes are randomly distributed with zero mean.

Copyright © 2006 Taylor & Francis Group plc, London, UK

REFERENCES

Donoho, D. L. and I. M. Johnstone (1994). Ideal spatial adaptation by wavelet shrinkage. *Biometrika 81*(3), 425–455.

Goring, D. G. and V. I. Nikora (2002). Despiking acoustic doppler velocimeter data. *J. Hydraul. Eng. 128*(1), 117–126.

Lohrmann, A., R. Cabrera and N. C. Kraus (1994). Acoustic doppler velocimeter (ADV) for laboratory use. In *Proc. Symp. on Fundamentals and Advancements on Hydr. Measurements and Experimentation*, pp. 351–365. ASCE.

Nikora, V. I. and D. G. Goring (1998). ADV measurements of turbulence: can we improve their interpretation? *J. Hydraul. Eng. 124*(6), 630–634.

Nikora, V. I. and D. G. Goring (2000). Flow turbulence over fixed and weakly mobile gravel beds. *J. Hydraul. Eng. 126*(9), 679–690.

Copyright © 2006 Taylor & Francis Group plc, London, UK

Accurate measurements of free-surface in the dam-break problem

Steve Cochard & Christophe Ancey
École Polytechnique Fédérale de Lausanne

ABSTRACT: The dam-break problem (i.e. the sudden release of a given volume of fluid along a slope) has attracted much attention from mechanicians and physicists over the last years. Of particular interest are the free-surface profile and the spreading rate. From the experimental viewpoint, impediments to accurate measurements of the free-surface evolution are many because of the significant variations in its curvature and velocity.

In order to accurately measure the free-surface variations (position, flow depth profile, leading edge, surface velocity) of a high-speed surge, a new imaging system has been developed at EPFL. The imaging system consists of a digital camera coupled with a synchronised micro-mirrors projector. The object surface is imaged into a camera and patterns are projected onto the surface under an angle of incidence that differs from the imaging direction. From the deformed pattern recorded by the camera, phase can be extracted and, by using unwrapping algorithms, height can be computed and the free surface is reconstructed. We measure the free surface of the flow to within 0.1 mm over a surface of $1.8 \times 1.1\,\mathrm{m}^2$.

1 INTRODUCTION

Shallow-water equations have been originally designed by saint venant (1871) to compute flood propagation along rivers. Their use was gradually extended to strongly time-dependent flows such as waves induced by a dam break (Ritter 1892). There is currently a growing number of models based on the shallow-water equations, which are used to describe natural flows such as flash floods (Hogg and Pritchard 2004), floods with sediment transport (Pritchard 2005), snow avalanches (Bartelt et al. 1999), debris flows (Iverson 1997; Huang and Garcìa 1997), lava flows (Griffiths 2000), subaqueous avalanches (Parker et al. 1986), etc. In the derivation of these models, a number of assumptions are used, the most important of which are: the long-wave approximation (no significant curvature of the free surface), hydrostatic pressure, blunt velocity profile, and no change in the bulk composition or rheology. Furthermore, in these models, the bottom shear stress is computed using either *ad hoc* expressions (e.g., Chézy friction) or non-Newtonian constitutive equations, with the difficult question of parameter fitting. Given the number of approximations and assumptions needed for obtaining these models, one can be legitimately be suspicious about their reliability and performance.

Essentially, our idea was to test the shallow-flow equations under extreme conditions in a well controlled environment—the laboratory—, where both the initial and boundary conditions are prescribed. Here, 'extreme conditions' mean that we focus our attention on time-dependent flows (surges with a front) mobilizing non-Newtonian fluids, experiencing different stages from release to run-out: acceleration (balance between inertia and pressure gradient), nearly fully developed regime (flow at equilibrium), and deposition (prevalence of dissipation processes). Preliminary experiments are run with viscoplastic materials.

The objective of this paper is to describe the experimental facilities and procedures. Emphasis is given to accurate reconstruction of three-dimensional flow depth profiles. These measurements are particularly difficult to perform, especially when fastness and accuracy are sought. Various techniques have been proposed over the last years (e.g., laser probe, videogrammetry). For our purpose, we have used image-processing techniques based on the projection of patterns (Desmangles 2003). In the following, we will describe the technique adapted to our particular case and provide an example of application.

2 FACILITY AND PROCEDURES

2.1 *Overview*

Figure 1 shows the experimental setup. The typical procedure is the following. A viscoplastic fluid is placed in a reservoir on the top of an inclined plane. The fluid is suddenly released by opening the dam

Copyright © 2006 Taylor & Francis Group plc, London, UK

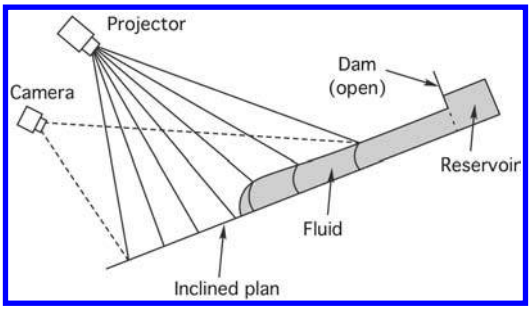


Figure 1. Sketch showing the experimental setup and the measurement system.

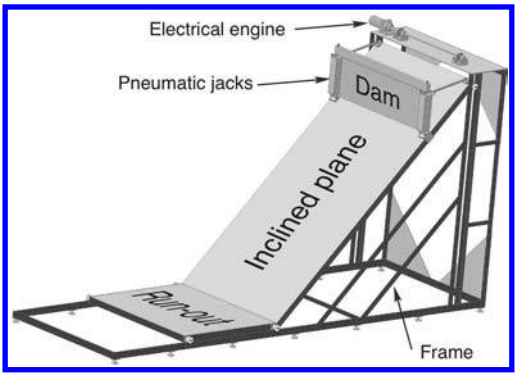


Figure 2. Schematic perspective of the facility.

sluice gate. Using a high-speed digital camera, we then record how a fringe pattern projected on the flow surface is deformed, which makes it possible to measure the flow depth at any place on the surface.

More specifically, our system operates in the following way. A micro-mirror projector projects periodic fringe patterns of incoherent light onto the surface (see Sect. 3.3). We place the digital camera above the flow, but with an offset and a given inclination so that the camerawork angle differs from the projection angle. This camera records how the projected fringes are deformed by the free surface. From the optical point of view, fringe deformation induces a phase offset, which is directly proportional to the flow thickness. Thus, measuring flow depth boils down to measuring phase offset. A phase map is calculated using a 3–4 image algorithm (as described in Sect. 3.4 and 3.4.1). Fast flows require adapting this algorithm and in that case, we use a 1 image algorithm (see Sect. 3.5). Once the phase map obtained, the flow depth can be deduced by unwrapping the phase signal (see Sect. 3.6). This last step requires a calibration procedure, which is described in Sect. 3.7.

2.2 *Experimental facility*

The facility is made up of a metallic frame supporting an inclined plane, horizontal plane (run-out zone), and reservoir (see Fig. 2). This structure is 6 meters long, 1.8 meters wide, and 3.5 meter high. The 4.5 m long aluminium inclined plane can be inclined from 0° to 45° by the means of an electrical engine. Its position is accurately determined using a laser-meter to within 1 mm, which means that the accuracy on slope inclination is of the order of 10^{-2} °. The 6 mm thick aluminium plate is supported by a frame made up of 40×80 mm profiled aluminium beams that ensure rigidity.

A PVC reservoir of varying volume and shape is positioned at the top of the inclined plane behind the dam wall. The maximum capacity of the reservoir is 120 kg. The dam wall is composed of a $1.6 \times 0.8\,\mathrm{m}^2$ ultralight carbon plate. The 35 cm high sluice gate is opened within 0.8 seconds by two pneumatic jacks on each side. Using ultralight dam wall was needed to reduce dam-wall inertia, induced vibration, and jerk. The two jacks are fast rose by injecting 7 mPa pressured air. Two electromagnetic sensors have been located at the tip of each jack to control its position and reset the clock.

The run-out plane has two functions: first, it collects the fluid flowing from the inclined plane, which makes the cleaning operations easier. Second—and this is the most important point—, the flowing material is forced to experience a transition from a flow regime to a deposition (run-out) regime. The 1.5 m long, 1.8 m wide run-out plane is maintained in a horizontal position and is connected to the inclined plane by a sealing plastic band. The projector and the camera are fixed on another frame, which is independent of the main frame.

2.3 *Experimental procedure*

A typical experimental run can be split into 4 phases. First, the fluid is prepared in advance (i.e., one or two days) and stocked in a 60 l drum to ensure sufficient resting time. Our viscoplastic fluid is a stable polymeric gel (Carbopol Ultrez). Polymer chains are vigorously mixed into a sodium-hydroxide/water solution at a given pH. This blend is left at rest for a long time so that all polymer chains have time to unroll and form a dispersion (repulsive interactions between chains). To ensure good light contrast, whitening Titanium Dioxide (TiO_2) is added when mixing Carbopol.

Second, the fluid is gently poured into the reservoir, while the inclined plane is kept in horizontal position. The material is then slowly mixed and its free surface is smoothed out by hand. A viscoplastic fluid does not flow if shear stresses are too low, which means that its free surface stays in the reservoir as it stands after pouring; there is no stress relaxation (viscoelasticity),

Copyright © 2006 Taylor & Francis Group plc, London, UK



Figure 3. View on the sluice gate and the reservoir at the channel inlet.

nor creeping (viscosity), which would cause flattening of the free surface. The upper plane is then inclined at a given value and its position is checked using a laser-meter.

Third, the measurement device is calibrated. Calibration will be explained in detail in section 3.7. Just before starting the test, we collect a fluid sample and test it with a Bohlin CVOR rheometer to characterize its rheological properties.

Four, we lift up the sluice gate and the material starts accelerating and flowing. The surge motion is followed up by the digital camera. When there is no significant motion, we stop to record images. The material is then removed from the flume.

3 MEASUREMENT SYSTEM

3.1 *How to measure the free-surface variation with time?*

The crux of the difficulty in the dam-break experiments lies in the proper measurement of the free surface. We thought of different systems. Three criteria guided our choice. First, we needed a non-invasive system to avoid disturbing the free boundary. Second, our preference was on global methods that are able to capture the flow surface with a single pass in contrast with scanning methods, which are not well suited to providing snapshots. Third, we wished to develop a method consistent with high-speed acquisition rates.

Three global systems were considered:

1. A method, which involves projecting patterns onto the fluid surface. Pattern deformation is recorded by a camera. This method is described in section 3.2.
2. A stereoscopic system, with two cameras scrutinizing the same surface. This method performs well with surfaces of varying color and contrast since colored pixels can be used as reference points and tracked (Kraus and Waldhäusl 97). The height is computed by the taking the difference between two successive images recorded by the two cameras. Since our fluids are monochromatic, this method has been discarded.
3. A system based on the time of fly of emitted photons. Photons are emitted by a source, a number of which are back-scattered by the surface. The time between their emission and their reception provides an estimate of the travelled distance (Niclass et al. 2005). This method performs well only for static objects, but should be a promising technique for our purpose in the forthcoming years.

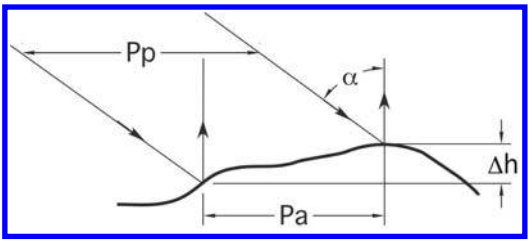


Figure 4. Projection of parallel lines on a surface and the retrieved height.

3.2 *Projecting patterns*

Measuring the shape of an object using the pattern projection can be broken down into three steps:

1. a given pattern is projected onto an object;
2. the object surface is imaged into a camera under an angle of incidence that differs from the imaging direction;
3. the surface height is retrieved from the image.

For the sake of simplicity, two parallel lines are projected onto a surface, as shown in figure 4. The height difference Δh can be then expressed as

$$\Delta h = \frac{\Delta p}{\tan \alpha}, \tag{1}$$

where $\Delta p = p_p - p_a$ is the difference between p_p the projected lines onto the object and p_a the apparent line on the surface viewed by the camera; α is the angle between the projected lines and the camera.

This simple relationship emphasizes two points. First, the closer the projected lines p_p are, the greater the accuracy in Δh is. Second, the closer to 90° the angle α is, the better the accuracy in Δh is.

A problem with projecting lines is that any valuable information between two lines is lost. There is another technical problem related to the camera resolution: for two lines to be distinguished by the camera, there must be a minimum distance of three pixels, which imposes a lower bound on the accuracy of Δh according to equation (1).

Copyright © 2006 Taylor & Francis Group plc, London, UK

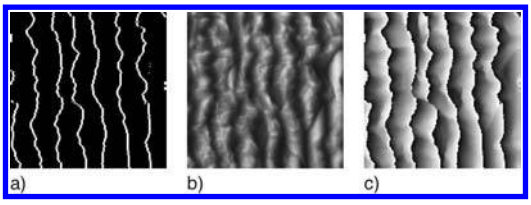


Figure 5. Comparison between: a) projection of lines, b) projection of fringes and c) the resulting phase map.

3.3 *Projecting fringes*

Cosine fringe patterns are projected instead of isolated lines. Information theory would say that we replace a 2 bit system into an 8 bit system, which should improve accuracy and robustness. Moreover, instead of relating height with light intensity, height is linked to fringe phase. The observed intensity at a given point (x,y) can be written as

$$I_k(x,y) = A_k(x,y) + B_k(x,y)\cos\phi_k(x,y), \qquad (2)$$

where A_k and B_k represent the background and the modulation intensities and ϕ_k the phase. The phase varies within the interval $[0, 2\pi[$.

Working with phase instead of intensity has the substantial advantage that alteration in surface reflectivity does not influence the outcome.

The imaging system consists of a digital camera coupled with a synchronized micro-mirror projector working at a maximum rate of 48 Hz. The 1000×1000 px CCD camera and the projector are synchronized by the frame grabber. The actual projection surface is 1.8×1.1 m^2. The main advantage of a micro-mirror projector (MMD) lies in its capacity to instantaneously project a given pattern. As mentioned in section 3, achieving high resolution in time and space requires global acquisition and projection. Compared to a laser interferometer, projecting fringe patterns with a MMD has also the advantage of versatility and safety. Any kind of pattern can be projected at any time and any rate. As an example, we can project images in 8 bit mode at a frequency of 150 Hz. There is, however, a price to pay when using a MMD instead of a laser interferometer: we have to use non-coherent light, which implies lower intensity. Perfect grabbed images would be characterized by intensity consistently with the intensity scale of a 8 bit camera; in other words, image intensity would range from 0 (deep black) to 255 (white). The technique is, however, quite robust since a phase map (see Sect. 3.4) can be can established using a limited range of 30 gray values.

The projector involves micro-mirrors. The light of a led is projected onto a micro-mirror device (MMD) composed of 1024×768 micro-mirrors oscillating between two positions; for one position, light is reflected through the projector lens, while for the other position, light is not reflected. It is a binary system: for a given pixel, light is on or off. A 8 bit grey level is achieved by changing the projection time of each micro-mirror.

At its maximum rate, the camera records an image within 20.7 ms, while the fringes are projected for 20.3 ms. A time lag of 0.1 ms separates two images. Special attention is paid to insuring that the whole projection occurs during the acquisition time and that there is no synchronization delay. This would have no consequence with projection continuously operating with time (as laser interferometry) but, as the MMD is a 2 bit projection system, relative intensity is controlled by the projection duration, which means that projection involves discretized time steps.

Capturing 48 images per second with a 1000×1000 px camera (i.e. 48 Mbytes/s) during time intervals as long as 10 minutes requires a CameraLink connection between the camera and the frame grabber. To store a huge amount of data within short intervals of time, we have implemented 4 hard disks in parallel. All the acquisition program has been developed using LabView.

3.4 *Phase map*

The phase map is only composed of the $\phi_k(x,y)$ term in equation (2). Optic convention is used here, high values (2π) are in white, whereas lower values (0) are in black.

Most algorithms for retrieving phase from an image or a series of images use either phase shifting , Fourier transform (Takeda et al. 1982), or wavelets (Liebling et al. 2004). The two first methods are explained in Sects 3.4.1 and 3.5. The phase map is often called the wrapped phase. During the first seconds of the test, a one-image algorithm is used and, after the flow has slowed down, a 3 or 4 image algorithm is used.

3.4.1 *Phase shifting*

Its principle consists in projecting $N \geq 3$ images of a fringe pattern shifted by $(i-1)2\pi/N$, with $i = 1 \ldots N$ (Desmangles 2003). The phase can be analytically computed from the series of images. An example with a series of $N = 4$ images is given in figure 6, with the following intensities:

$$\begin{cases} I_1(x,y) &= A + B\cos(\phi(x,y)), \\ I_2(x,y) &= A + B\cos(\phi(x,y) + \frac{\pi}{2}), \\ I_3(x,y) &= A + B\cos(\phi(x,y) + \pi), \\ I_4(x,y) &= A + B\cos(\phi(x,y) + \frac{3\pi}{2}), \end{cases}$$

where

$$\phi = f(I_1,I_2,I_3,I_4) = \frac{I_4 - I_2}{I_1 - I_3}. \qquad (3)$$

The phase map resulting from this method is accurate since it results from analytical calculation. A phase

Copyright © 2006 Taylor & Francis Group plc, London, UK

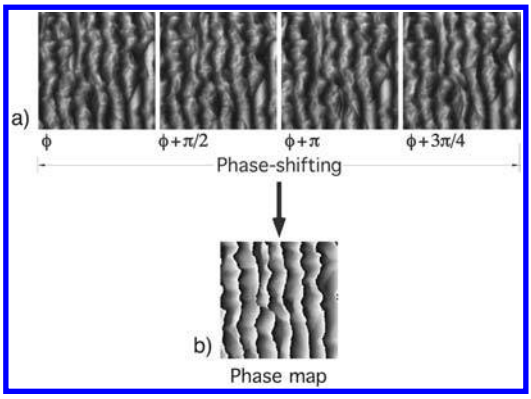


Figure 6. Phase shifting: a) with 4 images and b) the resulting phase map.

map can be extracted with each new image using the $N-1$ preceding ones.

The 3 fringe patterns can be projected at the same time using a red-green-blue (RGB) color coding. An independent phase map can be extracted with each new images. The idea is attractive, but requires a complicated and expensive setting (Jeong and Kim 2002).

The method based on 3 or 4 images is more appropriate when the fluid slows down and the relative motion between the first and the last images is less than a 1 or 2 pixels. This method is not suitable at earlier times, when the fluid is released because the displacement of the fluid between the first and the last images is too large. The resulting phase map is blurred and unusable. During the first instants of the test, the phase map must be computed with just one image; this computation can be done with a FFT algorithm, as explained in section 3.5 or with a wavelet algorithm.

3.5 *Fourier transformation profilometry (FTP)*

Fourier transformation profilometry (FTP) was first introduced by Takeda et al. (1982). The idea is to work in the frequency domain of the recorded images in order to filter and keep only the desired frequencies (Sansoni et al. 1999a).

In this subsection, we shall not explain how FTP works, but just provide some ideas on how we have implemented FTP in our setup. A cosine fringe pattern with 45° inclinations is projected onto the surface of the reference plane during the calibration, as shown in figure [see Fig. 7 (a), see also Sect. 3.7]. Two-dimensional Fourier transform analysis is then carried out on the recorded images, which consists in 5 points: first, the central peak related to frequencies close to zero is removed. Second, the frequency F_ϕ of the cosine fringe projected is located [see Fig. 7 (a)]. Third, the frequency map is filtered to keep only the

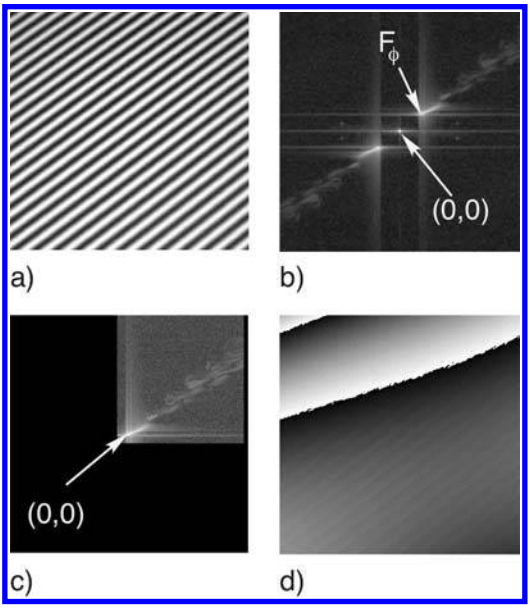


Figure 7. Reference plane: a) projected fringes, b) image in FFT domain with the frequency F_ϕ of the projected fringe, c) image filtered and shifted and d) reference plane phase map.

desired values [see Fig. 7 c)]. Fourth, the frequency map is shifted to position F_{cos} at the center $F=0$ [see Fig. 7 (c)]. Fifth, the angle of the inverse FFT is computed, which provides us with the phase map of the reference plane [see Fig. 7 (e)].

The same procedure is then repeated, during the test, with the recorded images except that the frequency map is shifted by F_ϕ (computed during the calibration). The wrapped phase is then obtained by subtracting the new phase and the phase of the reference plane [see Fig. 8 (f)].

FTP can be improved by removing image modulation so that the central peak of frequencies close to zero in the frequency map (related to the plane) is eliminated. This is achieved during the calibration procedure by shifting $N \geq 3$ fringe patterns by $(i-1)2\pi/N$ with $i=1\ldots N$, as explained in section 3.4.1. The modified image is then

$$I = I_1 - \frac{1}{N}\sum_{n=1}^{N} I_n.$$

FTP performs much better when the frequency of the projected cosine fringe is high and fringes are inclined at 45° in the recorded image because the cosine frequency F_ϕ in the FFT map is further away from the origin 0, filtering and shifting are more accurate.

Su and Chen (2001) discussed the influence of sampling in FTP. They emphasized that the recorded images as well as the discrete Fourier Transform (DFT)

Copyright © 2006 Taylor & Francis Group plc, London, UK

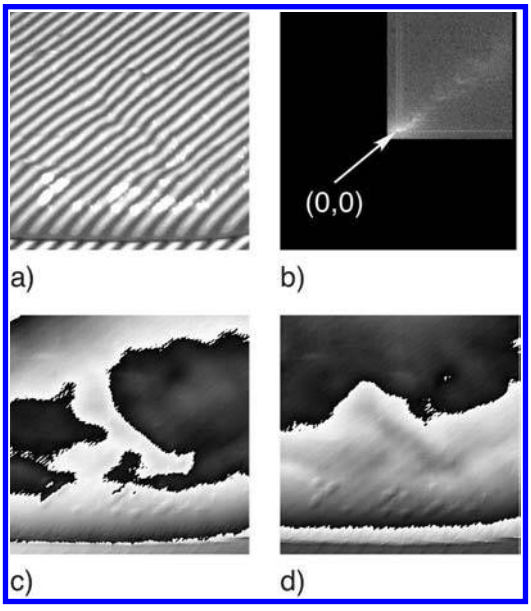


Figure 8. Object: a) projected fringes, b) object image filtered and shifted in Fourier domain c) resulting phase map and d) difference between the object phase map and the reference plane phase map.

are digital, whereas FTP theory is based on continuous Fourier transform. This inconsistency between theory and experience induces errors at high frequencies values. We are working to implement methods for reducing errors arising at high frequencies, even though we are convinced that this is a minor issue in our context (since our flows involve low frequencies most of the time).

FTP efficiency depends a great deal on filtering, i.e. which frequencies are kept or not. A good user can easily pinpoint frequencies that must be removed in order to obtain a more accurate phase map. Making this process automatic is, however, quite difficult.

It is almost impossible to know, in advance, when a phase-shifting algorithm can be used and can replace FTP. To avoid this issue, we project the 45° – inclined fringe with a phase shift of $2(i-1)\pi/N$ with $i = 1 \ldots N$. Both phase-shifting and FTP algorithms can then be used depending on the quality of their respective phase map.

3.6 *Phase unwrapping*

Once we have obtained the phase map, we can compute the height by unwrapping the phase map. The principle of phase unwrapping is fairly easy to understand in one-dimensional problems. Let us consider that we have a phase signal ϕ contained in the interval $[0, 2\pi[$ and we want to unwrap it. Every time the signal jumps

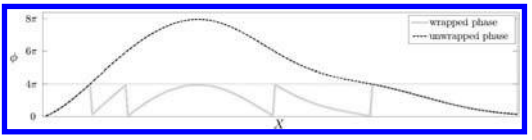


Figure 9. Example of phase unwrapping in 1D.

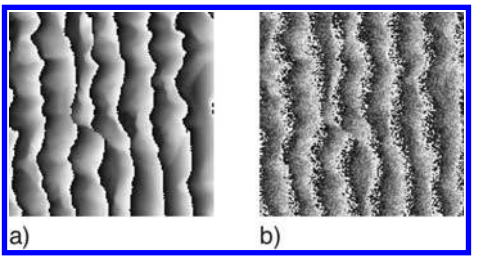


Figure 10. Phase map: a) original b) with noise.

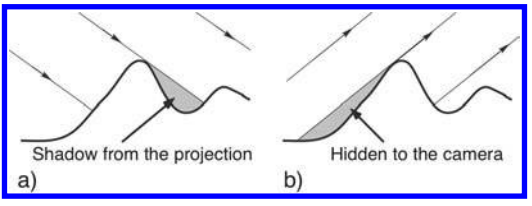


Figure 11. a) Shadow from the projector, b) hidden parts to the camera.

from 0 to 2π, we add or subtract 2π depending on the derivative $\partial_x \phi$, as is illustrated in figure 9.

Without noise and shadow, phase unwrapping would have a unique solution. Any unwrapping algorithm tends to provide a proper approximate solution.

Noise blurs the sharp frontiers of the phase jump between 0 and π, as shown in figure 10.

Shadow regions appear when the projection does not enlighten all the surface or when a part of the surface is hidden to the camera, as sketched in figures 11 and 12. All the information in the shadow or hidden parts is lost. In order to obtain results as good as possible, one should be careful and avoid having shadow or hidden parts, while keeping the angle between the projecting and acquiring beams as close as possible to 90°.

There is not a single solution, but several approximate solutions. Two-dimensional phase unwrapping algorithms aim to find the best approximation.

In their book, Ghiglia and Pritt (1998) reviewed the main different strategies to phase unwrapping. They also provided eight valuable C++ routines illustrating those strategies. There are two different approaches to phase unwrapping: one is based on path-following methods or local methods and the other one is based on minimum-norm methods or global methods. The path-following methods starts at a given point in the phase

Copyright © 2006 Taylor & Francis Group plc, London, UK

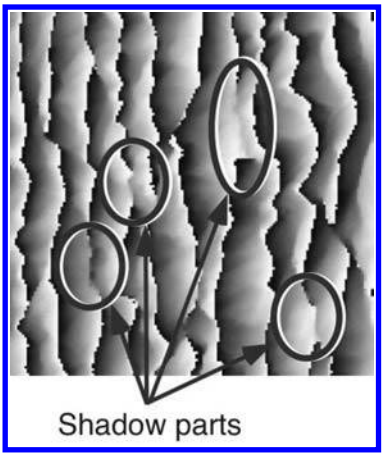


Figure 12. Shadow on an image.

map and computes the neighboring points by following a predefined path. The main difficulty is to choose 'the best path' to avoid shadowed or noisy parts in order to find the best approximation. Minimum-norm methods minimize the integral of the square difference between the gradients of the solution and the path obtained using different strategies. It is recommended to try the algorithm in the following order from the simplest and fastest ones to the more complex but slower ones.

1. Goldstein's branch cut algorithm, *path-following*,
2. Quality-guided algorithm, *path-following*,
3. Unweighted least-squares algorithm, *minimum-norm*,
4. Preconditioned conjugated gradient (PCG) algorithm, *minimum-norm*,
5. Mask-cut algorithm, *path-following*,
6. Multigrid algorithm, *minimum-norm*,
7. Flynn's minimum discontinuity algorithm, *path-following*, ,
8. Minimum L^p-norm algorithm, *minimum-norm*.

Better results are obtained with more complex algorithms. The last two algorithms are the most robust ones. We mainly use Flynn's method because its calculation time is much shorter than the Minimum L^p-norm. For our regular case, Flynn's method takes about 1'30" (Flynn 1997), while the Minimum L^p-norm requires 1 hr. However, using Flynn's algorithm on a 5 min sequence (14400 images) is quite impossible with a personal computer since it would take 15 days. One way for speeding up calculations is to run them on a computer cluster. To do so, we use the *distributed computing toolbox* from Matlab, with a cluster including up to 12 computers. Another way of reducing computation time is to unwrap the difference of the two phase maps (related to the flow

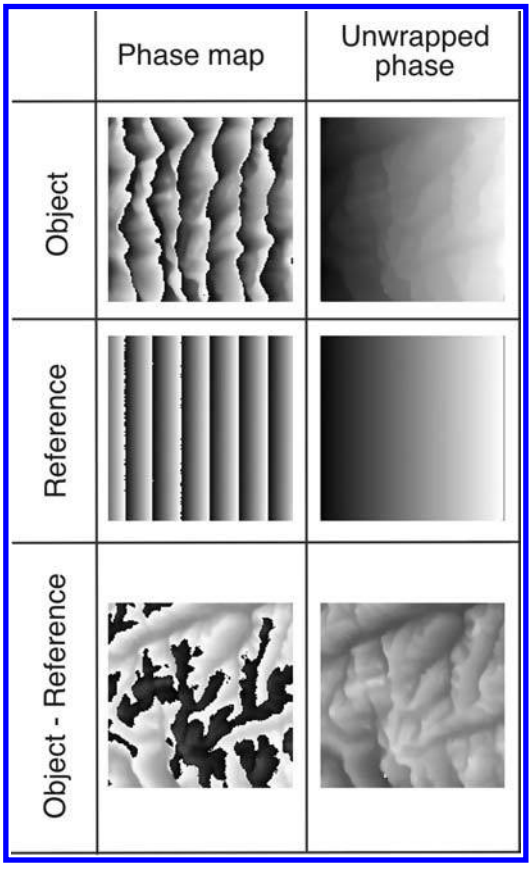


Figure 13. Unwrapping the difference of the object phase map and the reference phase map is equal to the difference of the unwrapped phases.

and the reference plane) instead of computing the difference of the respective unwrapped phase, as shown in figure 13. The resulting map shows less jumps of 2π, which makes the reconstruction of the unwrapped phase easier, faster, and more accurate.

These algorithm have many input parameters, which have not only a large influence on the execution time, but also on the quality of the results. Various techniques have to be tested to evaluate the quality of the results and make them less dependent on the user. Even though we prefer Flynn's algorithm because of its accuracy, the other algorithms ought be tested because occasionally, they might give better results and require lower CPU time.

3.7 *Calibration*

Equation (1) give the height as a function of the angle α and the distance between two line P_p. Behind this equation, there is the following assumption: projection

Copyright © 2006 Taylor & Francis Group plc, London, UK

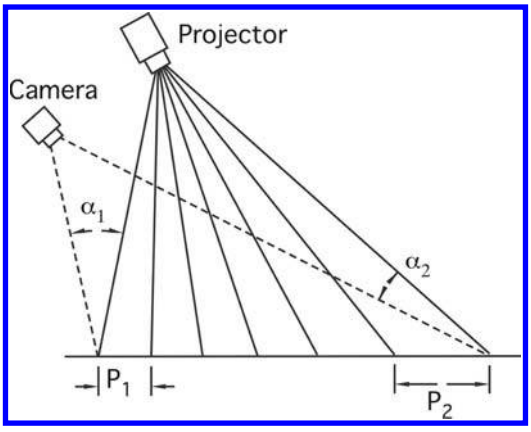


Figure 14. Variation of the angle α in a non-telecentric setup.

and acquisition are telecentric, which is not the case in our setup (Chen and Quan 2005). Figure 14 show how, in a non-telecentric setup, the angle α between the angle of projection and the angle of acquisition varies along the axe X; $\alpha_1 \neq \alpha_2$. The same also holds for the projected lines P_p and the apparent line P_a view by the camera; $P_1 \neq P_2$. A similar figure could be done along the Y-axis. Knowing the relative position of the camera, the projector and the inclined plane as well as the projection angle and the camera angle makes it possible to mathematically modify equation (1) and then have a height factor for each position (Desmangles 2003). This method requires accurately measuring the position of each elements of the setup, it is time-consuming, and does not take into account optical deformation. Instead of this method, we have chosen to use the more practical calibration based on a modified version of the virtual calibration plane method (Xiaoling et al. 2005).

The first step of the calibration is to project sharp patterns, such as squares, on the inclined plane to focus the projector and the camera. To check that the recorded images from the camera properly include the zone studied, the projection should envelop the acquisition zone, but should not be larger so that light power and projection resolution are optimized.

In order to relate the Cartesian coordinates XYZ of the plane with the unwrapped phase in the pixel coordinate ij, we need to calibrate our setup. A calibration plate, with gray circles of 2 cm in diameter and distant of 10 cm, is placed on the inclined plane at $z_0 = 0$. All fringe patterns, which will be used during the test run, are then projected on the calibration plane [see figure 15 (a)]. The module of the reference plane is computed [see figure 15 b)] and the position of the circle centers are found using a least-square approach [see figure 15 (c)]. The wrapped phase is referred as

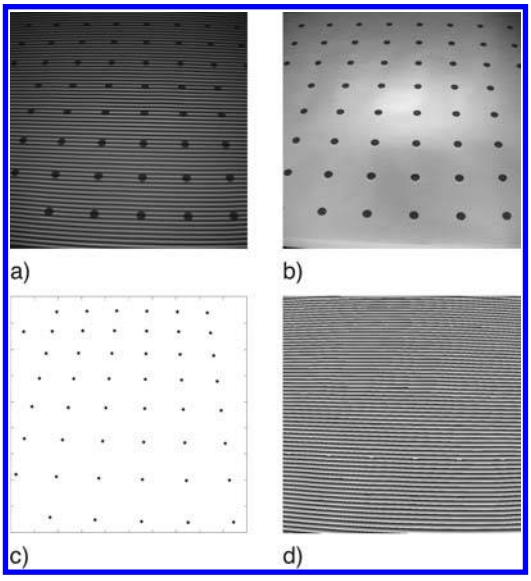


Figure 15. a) Projection of the fringe on the calibration plate, b) module with the calibration circles, c) position of the circle in the camera pixel coordinates and d) phase map of the calibration plane.

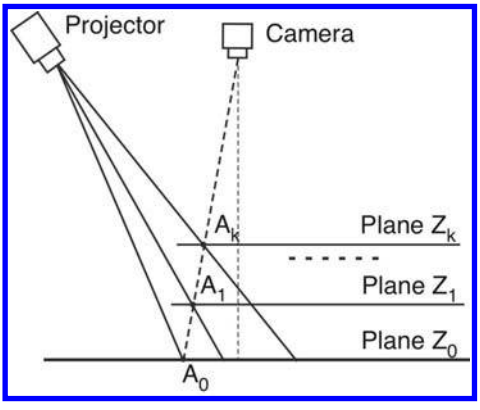


Figure 16. Calibration with virtual planes z_k.

ϕ_{z_0} [see figure 15 (d)]. A relation between the plane XY_{z_0} and the camera coordinates ij is obtained using a piecewise linear interpolation.

All the circles cut by the frame of the image are removed since their center can not be properly calculated (information is partly lost). If they were kept, they would introduce distortion.

The same procedure is repeated k times with the calibration plate placed over the inclined plane at an elevation z_k, with $k = 1, 2, \ldots, K$ (see Fig. 16). A relation between the plane $XY_{z_k} (k = 1, 2, \ldots, K)$ and the camera coordinates ij is obtained using

Copyright © 2006 Taylor & Francis Group plc, London, UK

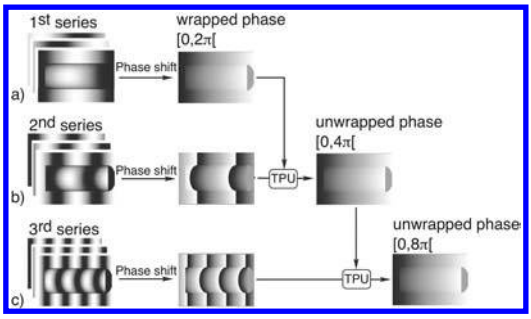


Figure 17. Temporal phase unwrapping: a) a first series of images with a large length wave, so the wrapped phase is set equal to the unwrapped one, is projected, b) the length wave is divided by 2 and a new series is projected, the unwrapped phase is obtained by looking up at the fist unwrapped phase, c) a new series is then projected with a length wave divided again by 2.

a piecewise linear interpolation. The corresponding wrapped phase ϕ_{z_k} is computed and the phase difference $\phi_{z_k} - \phi_{z_0}$ is unwrapped and denoted by ψ_{z_k}. ψ_{z_k} is not unique since $\phi_{z_k} - \phi_{z_0} \in [0, 2\pi[$. z_k is a function of $\varphi_{z_k} = \psi_{z_k} + j\pi$, with $j = 1, 2, \ldots$. A way to find j is explained in section 3.7.1. Once $\varphi_{z_k} = \psi_{z_k} + j\pi$ has been defined, a piecewise-linear-interpolation method is used to achiever Z-axis calibration. The unwrapped phases $\varphi_k (k = 1, 2, \ldots, K)$ at elevation $z_k (k = 1, 2, \ldots, K)$ are considered as reference phases. Based on the reference phases and their elevations z_k, every pixel height (Z-axis coordinate) can be obtained by linearly interpolating φ_k and z_k.

We end up with a calibration matrix M_{ijk}, which relates the value of the unwrapped phase φ_k in the pixel coordinates ij with the elevation z_k in the plane coordinates XY.

Compared with traditional way of calibration, this method reduces the hardware requirement of the system. It also simplifies the process of grabbing and processing data. Better accuracy is achieved by increasing the number of virtual calibrating planes z_k. The standard deviation error, using 5 virtual planes, is of the order of 1%.

3.7.1 *Temporal phase unwrapping*

Temporal phase unwrapping (TPU), presented in detail by Huntley and Saldner (1997), consists of unwrapping a phase with high sensitivity by means of others phases with lower sensitivity. First, a series of phase shifted images (see 3.4.1) is projected with a projected lengthwave L_{p_1} longer or equal to the surface to be measured. The wrapped phase ϕ_1 is then set equal to the unwrapped phase φ_1 [see figure 17 (a)]. Height resolution is low. A second series of phase shifted images is projected onto the surface, but with a lengthwave

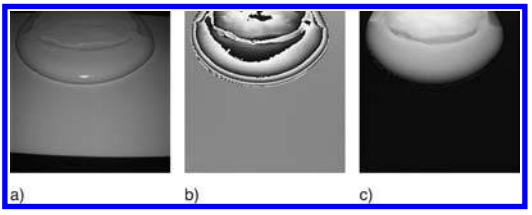


Figure 18. Free surface at $t_2 = 2.4\,s$: a) 1 image used for the FTP algorithm, b) the wrapped phase and c) the height of the free surface.

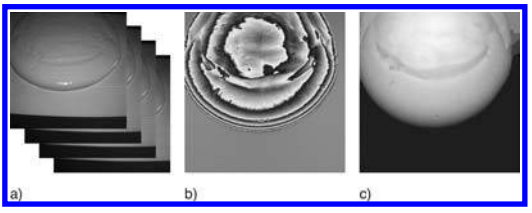


Figure 19. Free surface at $t_2 = 38.5$ s: a) 4 images used for the phase-shift algorithm, b) the wrapped phase and c) the height of the free surface.

$L_{p\frac{1}{2}}$ set to half the size of L_{p_1}. The wrapped phase $\phi_{\frac{1}{2}}$ is unwrapped by looking up at the wrapped phase φ_1 (see Fig. 17b)). This process is repeated n times until the desired $\phi_{\frac{1}{n^2}}$ is reached.

4 EXAMPLE

In this example, a 60 l volume of Carbopol Ultrez 10 at a solid concentration of 0.4% is released. The plane is inclined at 15°.

Figure 18(a) represents the grabbed image of the flow at time $t_1 = 2.4$ seconds. The wrapped phase [see Fig. 18 (b)] is obtained by a FTP. The unwrapped phase was computed using Flynn's algorithm. The final height is obtained using the calibration matrix [see Fig. 18 (c)].

The same test run but at $t_2 = 38.5$ seconds. The flow has slowed down and a 4 image phase-shift algorithm can be used. Figure 19 (a) shows the 4 images used to calculate the wrapped phase [see Fig. 19 (b)]. The wrapped phase is computed using Flynn's method. The height is shown in figure 19 (c).

5 CONCLUSION

New experimental facilities and procedures have been built to accurately measure the three-dimensional flow depth profiles in the dam-break problem. A mass of viscoplastic fluid is suddenly released by opening the dam sluice gate down a 4.5 m long inclined plane.

Copyright © 2006 Taylor & Francis Group plc, London, UK

The three-dimensional flow-depth profiles are measured using a high-speed digital camera, which records how a fringe pattern projected onto the flow surface is deformed. To ensure uniform projection, a micro-mirror projector is used. The projector and the camera are synchronized at 48 Hz.

A cosine fringe pattern is projected onto the surface by the micro-mirror projector. A wrapped phase, from the recorded deformed images, is obtained using a 3–4 images phase shift algorithm or using a single image with Fourier transformation profilometry (FTP). The wrapped phase is then unwrapped using algorithms proposed by Ghiglia and Pritt (1998). The quality of the unwrapping algorithm depends on many parameters, which are user-dependent. Flynn's algorithm (Flynn 1997) tends to give the best time/accuracy ratio.

Height can be related to the unwrapped phase by a calibration matrix. The calibration matrix is obtained by placing a calibration plate at different elevation z_k and relating the pixel coordinates ij with circles on the plane to get the XY coordinates. At the same time, the phase of each z_k plane is recorded.

The 3 images phase-shifting method is used when the distance travelled by the surge is lower than one or two pixels between the first and the last image. Fourier transformation profilometry (FTP) is preferred when the flow is fast because only one image is needed. The drawback of this method is that a 'good' user dependent filtering is needed to remove parasitical frequencies.

Even though we are still improving the procedure to reduce the dependency of the results on the user, we are quite confident of the method expounded in this paper. The characteristics of the flow down the inclined plane (e.g., flow depth profile, front velocity) can be related with its rheogical properties. The precision on the surface height is of the order of 0.1 mm for a surface of $1.8 \times 1.2\,\mathrm{m}^2$.

REFERENCES

Bartelt, P., B. Salm, and U. Gruber (1999). Calculating dense-snow avalanche runout using a Voellmy-fluid model with active/passive longitudinal straining. *J. Glaciol. 45*, 242–254.

Chen, L. and C. Quan (2005). Fringe projection profilometry with nonparallel illumination: a least-squares approach. *Optics Letter 30*(16), 2101–2103.

Desmangles, A.-I. (2003). *Extension of the fringe projection method to large objects for shape and deformation measurement*. Ph. D. thesis, EPFL.

Flynn, T. (1997). Two-dimensional phase unwrapping with minimum weighted discontinuity. *Journal of the Optical Society of America 14*(10), 2692–2701.

Ghiglia, D.C. and M.P. Pritt (1998). *Two-dimensional phase unwrapping: theory, algorithms, and software.* Wiley-Interscience. Wiley, cop.

Griffiths, R. (2000). The dynamics of lava flows. *Annu. Rev. Fluid Mech. 32*, 477–518.

Hogg, A. and D. Pritchard (2004). The effects of hydraulic resistance on dam-break and other shallow inertial flows. *J. Fluid Mech. 501*, 179–212.

Huang, X. and M. garìa (1997). A perturbation solution for Bingham-plastic mudflows. *Journal of Hydraulic Engineering 123*, 986–994.

Huntley, J.M. and H.O. Saldner (1997). Shape measurement by temporal phase unwrapping: comparison of unwrappingalgorithms. *Meas. Sci. Technol. 8*, 989–992.

Iverson, R. (1997). The physics of debris flows. *Rev. Geophys. 35*, 245–296.

Jeong, M.-S. and S.-W. Kim (2002). Color grating projection moire with time-integral fringe capturing for high-speed 3-D imaging, *Opt. Eng 41*(8), 1912–1917.

Kraus, K. and P. Waldhäusl (1997). *Manuel de photogrammérie, principes et procédés fondamentaux*. Hermes.

Liebling, M., T. Blu, and M. Unser (2004). Complexwave retrieval from a single off-axis hologram. *J. Opt. Soc. Am. A 21*(3), 367–377.

Niclass, C., A. rochas, P. Besse, and E. Charbon (2005). Design and characterization of a CMOS 3D image sensor based on single photon avalanche diodes. *Journal of Solid-State Circuits*, 1847–1854.

Parker, G., Y. Fukushima, and H. Pantin (1986). Selfaccelerating turbidity currents. *J. Fluid Mech. 171*, 145–181.

Pritchard, D. (2005). On fine sediment transport by a flood surge. *J. Fluid Mech. 5343*, 239–248.

Ritter, A. (1892). Die Fortpflanzung der Wasserwellen. *Zeit, Vereines Deutsch. Ing. 36*(33), 947–954.

Saint Venant, B. (1871). Théorie du mouvement non permanent des eaux, avec application aux crued des rivières et àl' introduction des marées dansleur lit. *C. R. Acad. Sci. Paris Sér. I 173*, 147–154– 237–240.

Sansoni, G., M. Carocci, and R. Rodella (1999). Three-dimensional vision based on a combination of gray-code and phase-shift light projection: analysis and compensation of the systematic errors. *Appl. Optics 38*, 6565–6573.

Su, X, and W. chen (2001). Fourier transform profilometry: a review. *Optics and Lasers in Engineering 35*, 263–284.

Takeda, M., H. Ina, and S. Kobayashi (1982). Fourier-transform method of fringe-pattern analysis for comuter-based topography and interferometry. *Journal of the Optical Society of America 72*(1), 156–160.

Xiaoling, Z., L., Yuchi, Z. Meirong, N. Xiaobing, and H. Yinguo (2005). Calibration of a fringe projection profilometry system using virtual phase calibrating model planes. *J. Opt. A: Pure Appl. Opt 7*, 192–197.

Copyright © 2006 Taylor & Francis Group plc, London, UK

Study on river-discharge measurements with a bottom-mounted ADCP

Y. Nihei & T. Sakai
Tokyo University of Science, Dept. of Civil Engineering, Chiba, Japan

ABSTRACT: To examine the accuracy of discharge measurements in rivers, continuous measurements of flood flows were conducted with a bottom-mounted ADCP. The observed data indicates that the vertical distribution of the velocity varied considerably in the rising and falling stages of a hydrologic event, in which the unsteadiness parameter α and H.W.L. were relatively larger. It should be noted from the observed data that the averaged coefficients of float were in good agreements with well-known empirical values, while the coefficients of float varied appreciably in each hydrologic event. The accuracy for evaluating river discharge is investigated by using the rating curves with H-Q and V-Q, showing that the rating curves with H-Q and V-Q are appropriate for the evaluation of discharge in the upper and lower reaches of the river, respectively.

1 INTRODUCTION

River discharge is essential for river planning and management. In measuring river discharge, rod-float measurements are widely adopted under flood-flow conditions. Using a rating curve between the observed discharge Q and water elevation H at a cross-section of a river, so called an H-Q curve, the continuous data for river discharge Q can be obtained from the observed water elevation H. Therefore a huge number of gauging stations recording water elevation have been developed.

However, under flood-flow conditions, the discharge in a rising stage tends to be higher than that in a falling stage at a same water elevation, producing a looped rating curve. Further the discharge monitoring with floats may have measuring errors due to various hydraulic phenomenon. From the above viewpoints, it is necessary to evaluate the accuracy and applicability of previous methods for discharge measurements. Moreover it is expected to develop a more accurate technique for measuring river discharge.

For this purpose, the continuous measurements of flood flows were conducted with a bottom-mounted ADCP (Acoustic Doppler Current Profiler) which can record a vertical distribution of velocity. An ADCP has already been used as a standard current meter of physical oceanography and coastal environments (*e.g.*, Pettigrew et al. 1986). The recent ADCP technology can realize to measure the three-dimensional velocity with fine vertical resolution in which the minimum cell size is 1 cm. Then the potential for applying the ADCP into current measurements in shallow-water flow like river flow has been increasing. In the present paper, the field measurements were done in the Oohori River in Japan, an urban small river. The analysis of the observed data was employed to examine the vertical distribution of velocity in rising and falling stages and then evaluate a coefficient of float which is the ratio of depth-averaged velocity to velocity in surface layer. In addition, the accuracy of rating curves with H-Q and V-Q (Huang 2004) is discussed, in which V means a depth-averaged velocity.

2 OUTLINE OF FIELD MEASUREMENTS

The Oohori River chosen as a field site inflows into the western part of Lake Teganuma, one of typical eutrophied lakes in Japan. As shown in Fig. 1, the measuring stations were in lower reach of the Oohori River at Stns.1 and 2 which were located at 1.5 km and 0.9 km upstream from the river mouth, respectively. The backwater from the lake was known to affect time variations

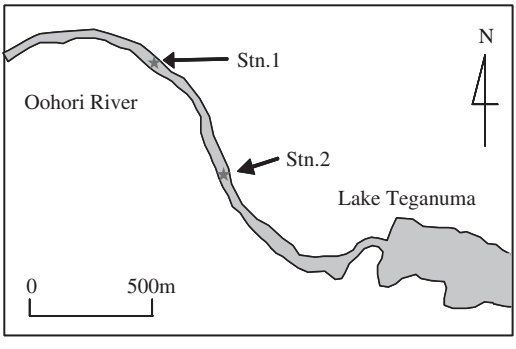
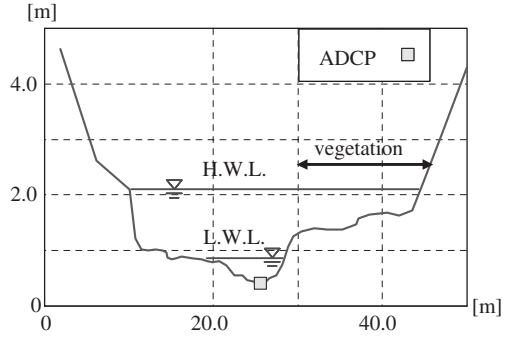
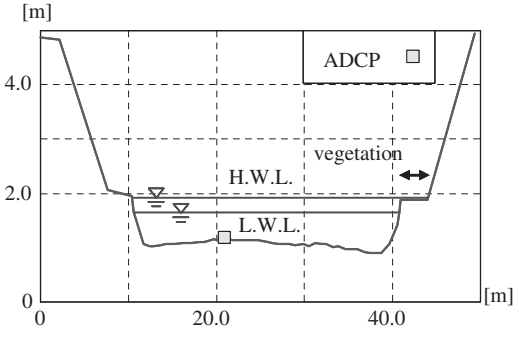


Figure 1. Field site and location of measuring stations.

Copyright © 2006 Taylor & Francis Group plc, London, UK



(a) Stn.1



(b) Stn.2

Figure 2. Cross-sectional view at both the measuring stations.

of the water elevation at both the stations. The influence from the lake appeared more appreciably at Stn.2 than at Stn.1. Figure 2 describes the cross-sectional view at both the stations. The Oohori River is a compound channel and the width of the flood plane with vegetation layer at Stn.1 is much larger than that at Stn.2. The ADCP is bottom-mounted in the center of the main channel.

The instrument used in the present study was a 1200 kHz WorkHorse Sentinel ADCP (RD Instruments, Inc.). The ADCP was installed on the river bed looking upward, to give the vertical profile of velocity, as indicated in Fig. 3. The configuration parameters of the ADCP are summarized in Table 1.

In the configuration, the blank zone, in which no measurements were taken near the head of the ADCP, was 0.14 m. The measurements of water elevation were also conducted with the pressure gauge (Diver, Eijikelkamp Co.).

The ADCP was installed at Stn.1 in 2004 and at Stn.2 in 2005, respectively. From these field measurements, the observed data in five hydrologic events were selected to perform the analysis of observed data. The information for the events are detailed in Table 2, in

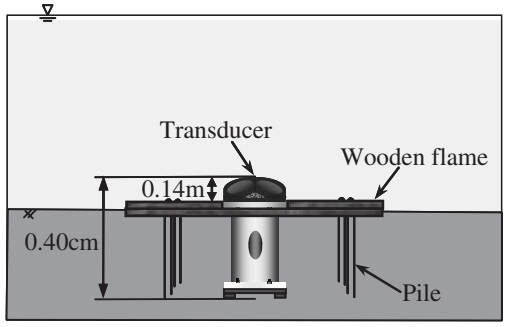


Figure 3. Schematic view of the bottom-mounted ADCP in the field measurements.

Table 1. Configuration of the ADCP used in the field measurements.

Cell size	0.02 m
Cell number	150
Sampling interval	5 minutes
Blank zone	0.14 m

which the unsteadiness parameter α proposed by Nezu et al. (1997) is defined as

$$\alpha = \frac{\Delta h}{T_d}\frac{1}{U_c}, \tag{1}$$

where Δh is the difference of maximum flow depth and the base flow depth, T_d means the time duration of the rising or falling stage in the hydrograph and U_c represents the average of peak flow and base flow depth-averaged velocity. In Table 2, these parameters are displayed in the rising and falling stages of each event. Since two peaks of the hydrograph appeared in the event C, the period of the event is separately denoted as event C-1 and C-2 in Table 2.

3 VERTICAL FLOW STRUCTURE IN FLOOD EVENTS

3.1 *Vertical distribution of streamwise velocity*

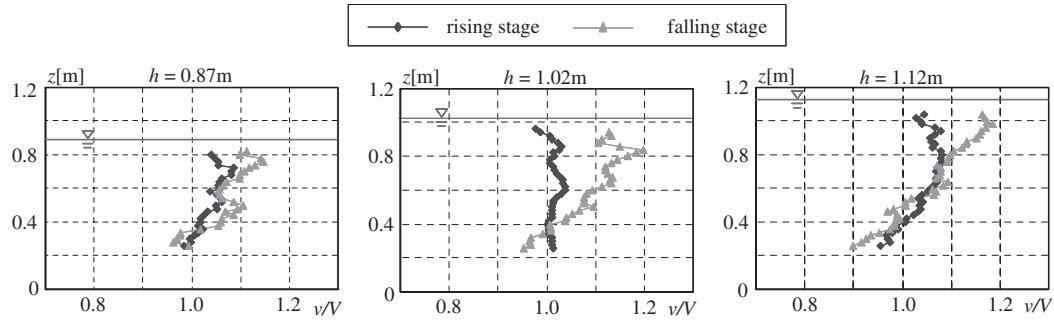
To examine the fundamental vertical flow structure in the rising and falling stages, Fig. 4 indicates the vertical distribution of streamwise velocity in the events A and D. The horizontal axis in the figure means the streamwise velocity v normalized by the depth-averaged velocity V. For evaluating the depth-averaged velocity V, the velocity in the blank zone near the riverbed are estimated with the approximation described as $v = az^b$ (z: the height from the riverbed; a, b: constants).

The observed results in the event A shows that, in shallower water depth ($h = 0.87$ m), the velocity

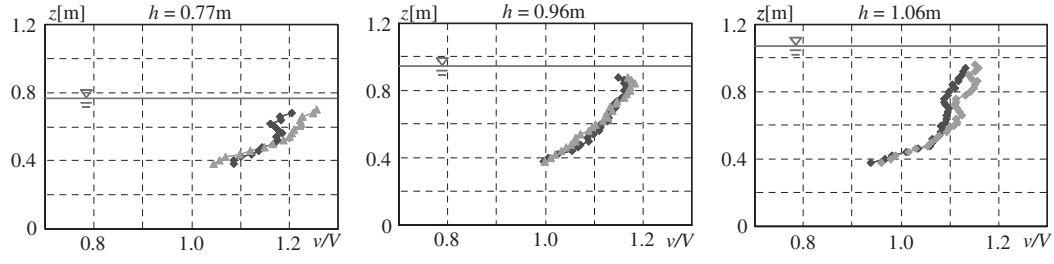
Copyright © 2006 Taylor & Francis Group plc, London, UK

Table 2. Outline of the hydrologic events.

Event	Station	Period		T_d[s]	h[m]	U_c[m/s]	
A	Stn.1	May 20 to 21, 2004	Rising stage	14100	0.938	0.748	8.9×10^{-5}
			Falling stage	37800	0.815	0.612	3.5×10^{-5}
B		June 11 to 12, 2004	Rising stage	7200	0.248	0.497	6.9×10^{-5}
			Falling stage	15600	0.246	0.455	3.5×10^{-5}
C-1		November 12, 2004	Rising stage	6900	0.335	0.552	8.8×10^{-5}
			Falling stage	6300	0.171	0.677	4.0×10^{-5}
C-2		November 12, 2004	Rising stage	13500	0.363	0.697	3.9×10^{-5}
			Falling stage	29100	0.513	0.638	2.8×10^{-5}
D		November 15, 2004	Rising stage	20700	0.681	0.609	5.4×10^{-5}
			Falling stage	20100	0.557	0.682	4.1×10^{-5}
E	Stn.2	July 3 to 4, 2005	Rising stage	10500	0.217	0.446	4.6×10^{-5}
			Falling stage	10500	0.129	0.455	2.7×10^{-5}



(a) Event A (Peak depth = 1.66m)



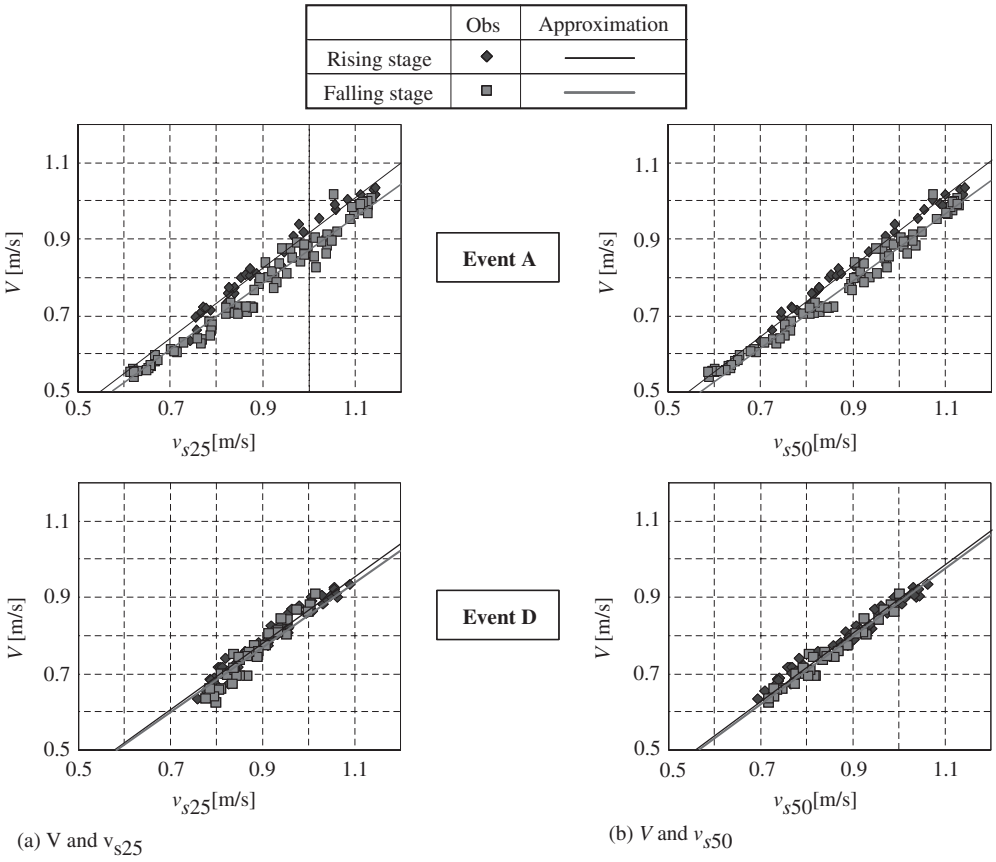
(b) Event D (Peak depth = 1.20m)

Figure 4. Vertical distribution of streamwise velocity in the rising and falling stages (h: water depth).

distributions in the rising and falling stages almost coincided with each other. However, in deeper depth ($h = 1.02$ m and 1.12 m), the velocity in the rising stage tended to be uniform vertically, while the velocity distribution in the falling stage was inclined in the vertical direction. The results in the event A demonstrate that the vertical distribution of the velocity varied considerably in the rising and falling stages of the hydrologic event. On the other hand, the observed results in the event D reveal that the velocity distributions in the rising stage were almost agreements with those in the falling stage at three depth conditions.

The observed results for the vertical flow structure indicate that the appreciable differences of the vertical distribution of the velocity were found only in the event A. It is noted from Table 2 that the unsteadiness parameter α and depth difference Δh in the event A were larger than those in the other events. These parameters may be closely related to the difference of the vertical flow structure in the hydrograph. In near future, hence, it is necessary to collect further ADCP data to clarify the vertical flow structure under various flow conditions. It is also noteworthy that $\alpha = 8.9 \times 10^{-5}$ in the event A may be regarded as a weak unsteadiness

Copyright © 2006 Taylor & Francis Group plc, London, UK



(a) V and v_{s25} (b) V and v_{s50}

Figure 5. Comparison between the depth-averaged velocity V and the surface velocity v_{s25} and v_{s50}.

condition in the laboratory experiments done by Nezu et al. (1997).

3.2 *Coefficient of float*

In discharge measurements with rod floats flowing near water surface, it is necessary to convert measured surface velocity with rod floats into a depth-averaged velocity V. In the evaluation for the river discharge, one needs to use a coefficient of floats which is a ratio of the depth-averaged velocity to the surface velocity. The ADCP can monitor the vertical distribution of velocity. It is therefore possible to confirm the validity of well-known coefficients of float by using the vertical distribution of velocity obtained by the bottom-mounted ADCP. In general float measurements, a surface float and a 0.5 m long rod are adopted in $h < 0.7$ m and $0.7\,\text{m} < h < 1.3$ m, where h is water depth, respectively. The relationship between the depth-averaged velocity and surface velocity in the events A and D are illustrated in Fig. 5. Here two surface velocities v_{s25} and v_{s50} are introduced as the velocity averaged in the surface layer with the thickness of 25 cm and 50 cm, respectively. The surface velocities v_{s25} and v_{s50} corresponds to the velocities measured by surface float and a 0.5 m long rod, respectively. The observed results are separately depicted in the rising and falling stages in the figure.

Table 3. Coefficients of float in each hydrologic event.

Event	Rising stage	Falling stage	Rising stage	Falling stage
A	0.916	0.867	0.925	0.883
B	0.746	0.759	0.779	0.778
C	0.826	0.811	0.876	0.878
D	0.866	0.851	0.900	0.883
E	0.812	0.805	0.902	0.885
Average	0.830		0.874	

The correlations between the depth-averaged velocity V and the surface velocities v_{s25} and v_{s50} in the event A indicate that, under the same surface velocity,

Copyright © 2006 Taylor & Francis Group plc, London, UK

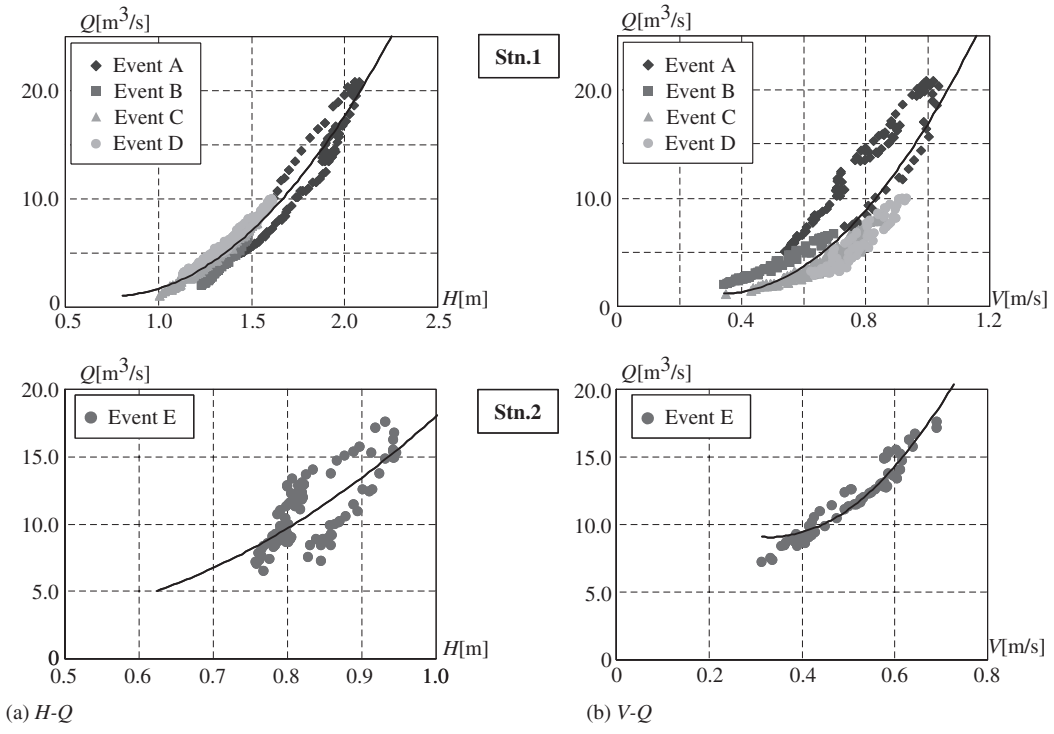


Figure 6. *H-Q* and *V-Q* curves at Stns.1 and 2.

the depth-averaged velocity V in the rising stage was larger than that in the falling stage. These tendencies were found in both the surface velocities. On the other hand, the difference of the depth-averaged velocity in the rising and falling stages was not observed in the event D. The relations between the depth-averaged and surface velocities are almost similar to the vertical flow structure mentioned in the above.

In Fig. 5, linear approximations for the correlations between the depth-averaged and surface velocities are also exhibited. The slopes of the linear approximations correspond to the coefficients of float ($=V/v_{s25}$ or V/v_{s50}). The evaluated coefficients of float in each hydrologic event are summarized in Table 3. In the event A, the difference of the coefficients of float in the rising and falling stages was 0.04–0.05, while, in the other events, the coefficient in the rising stage was comparable to that in the falling stage. The results are also similar to those shown in Figs. 4 & 5.

The averaged coefficients for v_{s25} and v_{s50} were 0.83 and 0.87, respectively, almost corresponding to well-known empirical values for the coefficients of float (=0.85 and 0.88, respectively). In each hydrologic event, however, the coefficients of float for the surface velocities v_{s25} and v_{s50} varied appreciably. The coefficients for v_{s25} and v_{s50} were from 0.75 to 0.92 and from 0.78 to 0.93, respectively.

4 ACCURACY OF DISCHARGE EVALUATION WITH H-Q AND V-Q CURVES

4.1 *Procedure of discharge evaluation*

Accuracy of discharge evaluation with rating curves is examined using the observed data with the ADCP. For this purpose, it is necessary to evaluate river discharge with the depth-averaged velocity obtained by the ADCP mounted at a point in a cross section. To obtain the transverse distribution of velocity in a cross section from the ADCP data, a dynamic interpolation method presented by Nihei & Kimizu (2006) is introduced, in which observed velocities can be spatially interpolated in the cross section with satisfying the fundamental dynamic principle of fluid motion. With the dynamic interpolation method, the time sequence of the discharge can be calculated from the depth-averaged velocity and water elevation.

4.2 *H-Q and V-Q curves*

The correlations of *H-Q* and *V-Q* at Stns.1 and 2 are displayed in Fig. 6. Approximations for the correlations are also depicted in the figures. At Stn.1, both the rating curves of *H-Q* and *V-Q* were looped in the hydrograph. The loop of the *V-Q* curve was larger than that of the *H-Q* curve.

Copyright © 2006 Taylor & Francis Group plc, London, UK

Table 4. Comparison of the observed and evaluated discharge in each hydrologic event.

	Event	[m^3/s]	H-Q	V-Q
A	Total	8.4	101.5	78.8
	Rising stage	9.4	88.9	103.7
	Falling stage	8.0	107.0	67.9
B	Total	3.4	123.6	67.1
	Rising stage	4.5	115.3	75.4
	Falling stage	2.9	129.4	61.3
C	Total	3.8	96.6	123.9
	Rising stage	5.0	93.6	130.4
	Falling stage	3.1	99.3	117.7
D	Total	3.9	88.9	142.6
	Rising stage	4.5	86.1	151.9
	Falling stage	3.2	93.0	129.1
E	Total	12.4	100.0	103.7
	Rising stage	13.8	93.1	104.6
	Falling stage	11.0	107.1	102.8

In contrast, at Stn.2, the H-Q rating curve was looped more largely than the V-Q curve. The influences of the backwater from Lake Teganuma appeared more appreciably for water elevation at Stn.2 than that at Stn.1 due to the difference of the distance from the river mouth. Therefore larger loop of the H-Q curve was found at Stn.2.

4.3 *Results and discussion*

The discharge can be evaluated by using the approximations for H-Q and V-Q as shown in Fig. 6. Table 4 reveals the observed and evaluated discharges averaged during a hydrologic event. In the table, the observed discharge $\overline{Q}_{obs}$ and the ratio of the evaluated discharge $\overline{Q}_{cal}$ to $\overline{Q}_{obs}$ are separately expressed in the rising and falling stages and total period of each event. The results for the total periods of events A, B, C and D at Stn.1 illustrate that the ratio $\overline{Q}_{cal}/\overline{Q}_{obs}$ with the H-Q curve was from 89 to 124%, while $\overline{Q}_{cal}/\overline{Q}_{obs}$ with the V-Q curve was from 67 to 143%. This fact exhibits that the accuracy of the V-Q curve was lower than that of the H-Q curve due to larger loop of the V-Q curve at Stn.1 as mentioned in Fig. 6. Furthermore the accuracy of the H-Q and V-Q curves was lower in the rising stage or falling stage because of the existence of the loop of the rating curves. Then the temporal variations of discharge may not be accurately evaluated with H-Q and V-Q curves.

On the other hand, $\overline{Q}_{cal}/\overline{Q}_{obs}$ in the event E at Stn.2 suggests that the accuracy of the H-Q curve was lower than that of the V-Q curve. It should be noted from the result that at measuring stations with significant backwater influences from lakes like Stn.2, a V-Q curve is more appropriate to accurately evaluate river discharge than an H-Q curve.

5 CONCLUSIONS

The flood-flow measurements were done with the bottom-mounted ADCP. With the observed data, the vertical flow structure and the evaluation of the discharge with the H-Q and V-Q curves are discussed. Main conclusions in the present study are as follows:

(1) In the event A with relatively larger unsteadiness parameter α and stage variation Δh, the vertical flow structure and the coefficient of floats were found to be different appreciably in the rising and falling stages.
(2) The averaged values of the float coefficients for v_{25} and v_{s50} were 0.83 and 0.87, respectively, almost corresponding to the well-known empirical values. In each hydrologic event, however, the coefficients of float varied considerably. The coefficients for the surface velocities v_{s25} and v_{s50} were from 0.75 to 0.92 and from 0.78 to 0.93, respectively.
(3) The H-Q and V-Q curves are appropriate for the evaluation of discharge in the upper and lower reaches of the river, respectively, due to the difference of the backwater effect from the lake.
(4) The temporal variations of discharge may not be accurately evaluated with the H-Q and V-Q curves.

ACKNOWLEDGMENTS

This study was partially supported by Japan Society for the Promotion of Science, Grant-in-Aid for Scientific Research (C) (2) (no.16560453), the River Fund in charge of the FOREM and Academic Frontier Project (2005) of MEXT. The authors would like to express their deep thanks to students in hydraulics laboratory, Department of Civil Eng., Tokyo University of Science, for their help in conducting field observations in the present study.

REFERENCES

Huang, H. 2004. Index-velocity rating development for rapidly changing flows in an irrigation canal using broadband StreamPro ADCP and ChannelMaster H-ADCP, *Proc. of River'04*: 146–154.

Nezu, I., Kadota, A. and Nakagawa, H. 1997. Turbulent structure in unsteady depth-varying open-channel flows, *J. Hydraul. Eng.* 123(9): 752–763.

Nihei, Y. and Kimizu, A. 2006. Evaluation of river velocity and discharge with a new assimilated method, *J. River Basin Management* 4(1): 1–4.

Pettigrew, N. R., Beardsley, R. C. and Irish, J. D. 1986. Field evaluations of bottom-mounted acoustic Doppler profiler and conventional current meter moorings, *IEEE*: 153–162.

Copyright © 2006 Taylor & Francis Group plc, London, UK

Experimental procedure to obtain 2D time-space high-speed water surfaces

A. Bateman, A. Granados, V. Medina & D. Velasco
Hydraulic, Maritime and Environmental Engineering Department,GITS-UPC. Technical University of Catalonia, Spain. D1, c/Gran Capitan s/n, Barcelona, Spain.

M. Nalesso
Fluid Mechanics Institute, Central University of Venezuela

ABSTRACT: Numerical validations always require a major effort involving laboratory measurements. In 2D models, it is unusual to see comparisons between measurements (in space and time) and the numerical results of a model. Measuring a surface involves many problems because collecting sufficient data in space and time is very complex. This paper indicates how to measure a liquid surface by taking 2D measurements (in space and time) of a set of cross-sections of a water surface experiencing a dam-break phenomenon. This work was carried out by a research group (GITS-UPC) at the Hydraulics Laboratory of the Department of Hydraulic, Maritime and Environmental Engineering of the Technical University of Catalonia. The paper details our mathematical framework and experimental methodology, which involves 3 mW laser beams and high- and medium-speed cameras, and compares a numerical surface to an experimental surface. The numerical data were modelled using FLATMODEL, which was developed entirely by the research group.

1 INTRODUCTION

Mathematical sketching is a method that can deal with very complex problems. It is also very clear and introduces the new concept of making hydraulic laboratory measurements using images. This method can recreate 3D representations of high-speed flow surfaces in space and time, using a single photograph for each time step. Cameras have already been used in laboratories to recreate certain physical phenomena, but here an entire surface is recreated at each instant to calibrate a 2D model. Here we present the mathematical methodology used to scan surfaces and its application to a dam-break problem. We developed this technique for characterizing moving surfaces in order to calibrate a 2D Saint-Venant numerical code and evaluate the divergence of the model from reality.

2 POINTS, SPACE AND PLANE CORRESPONDENCE

Figure 1 shows that taking a picture is like projecting one point in space onto a point photograph through a point called the focus (F). This projection is determined by fixing a reference point in space, knowing the position of the camera plane and locating the focus. That is, for each point in space, it is possible

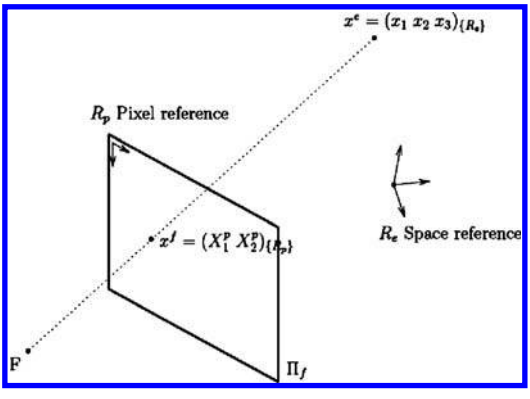


Figure 1. Space and photograph reference.

to determine the corresponding pixel of the photograph by noting where the straight line defined by the point and the focus intersects with the photograph plane. However, it is practically impossible and unnecessary to know all of these parameters directly. Through projective geometry, an application known as camera calibration can project the point from the reference in space to the coordinates in the photograph (real coordinates or pixels) without explicitly needing to know these parameters.

Copyright © 2006 Taylor & Francis Group plc, London, UK

2.1 *From space to the photograph: Direct Linear Transformation (DLT) (Abdel-Aziz, 1971 and Faugeras 1993)*

How can the corresponding point in the photograph be obtained for a given point $x_e = (x_1\ x_2\ x_3)$ in space in any reference R_e (Figure 1)? If we know the equation of the photograph plane $\Pi_f: ax + by + cz + d = 0$, and the coordinates of the focus $F = F1\ F2\ F3$), then the point to be determined in the reference R_e is given by the intersection of the line r: $(x\ y\ z) = F + \lambda(F - x^e)$ with the plane Π_f (Figure 1). However, in addition to being nonlinear in the x_e coordinates, this equation depends on parameters that are impossible to define directly, i.e. the expression in the reference R_e for the photograph plane Π_f and the focus F. We need another way to find the projected point in the photograph.

Imagine that, instead of taking a space R_e as a reference, we take a reference R_c (Figure 2), which we will call the camera reference. The axis z of this reference is perpendicular to the plane Π_f, with origin at the focus F. This reference is located at a distance of 1 from the photograph plane (focal distance). In these conditions, the straight line r has the mathematical expression r: $(x\ y\ z)_{\{Rc\}} = \lambda(x1\ x2\ x3)_{\{Rc\}}$ and the plane is Π_f: $z_{\{Rc\}} = 1$. Therefore, their intersection is $x^j_{\{Rc\}} = \left(\frac{x1}{x3}\ \frac{x2}{x3}\ 1\right)$ Instead of projecting the point $x^e(x_1\ x_2\ x_3)_{\{R_c\}}$, a multiple of it, $\mu x^e = (\mu x_1\ \mu x_2\ \mu x_3)_{\{R_c\}}$, is projected, which is the same as projecting x^e. This is because both points are in the same straight line, $r = \lambda(x1\ x2\ x3)_{\{Rc\}}$, which is perpendicular to the projective plane Π_f. Therefore, the intersection with the plane is the same for both points.

Rather than relating points in the space with points in the plane, the idea is to relate the lines in $\mathbb{R}^3$ that pass through the origin (F) to points of the plane Π_f. Thus, we can relate the direction of the straight line $r = \lambda(x1\ x2\ x3)_{\{Rc\}}$, which is the point $(x1\ x2\ x3)_{\{Rc\}}$ and all of its multiples, with the point $\left(\frac{x1}{x3}\ \frac{x2}{x3}\ 1\right)_{\{R_c\}}$ of the photograph plane.

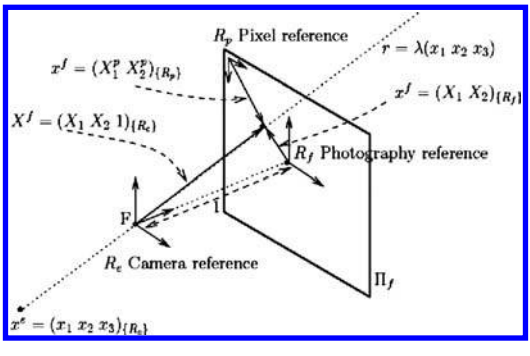


Figure 2. Camera reference.

We must also project straight lines that are parallel to the plane Π_f. To do so, we must construct an abstract mathematical object that defines points of infinity or improper points. This is the vectorial space known as projective plane $\mathbb{P}_2$, which is the same as plane Π_f, except for the improper points that we cannot see but can manipulate algebraically. In $\mathbb{P}_2$, we can use the following homogeneous coordinates: if $(x1\ x2\ x3) \in \mathbb{R}^3$ with $x_3 \neq 0$, the straight line will be represented by the point $\left[1\ \frac{x_1}{x_2}\ 0\right]$. The improper points are then represented by points whose third component is equal to 0 in the homogeneous coordinates.

With the sole aim of grouping all the representative elements of $\mathbb{P}_2$ in one element, it is common to use the generalized coordinates. This consists in eliminating the third coordinate when it is 1 (that is, when the point is not improper). Then, the rest of the coordinates are represented as: $(X_1\ X_2) = \left(\frac{x_1}{x_3}\ \frac{x_2}{x_3}\right)$. Whenever we work with improper points, which implies using a plane that is parallel to the photograph and passes through the focus F, it makes no sense. In such a case, we work with the region of $\mathbb{P}_2$ called D, which corresponds to the photograph paper and does not contain improper points.

We can identify the generalized coordinates $(X_1\ X_2)_{\{R_f\}} \in \mathbb{P}_2$ as the point x_f in real coordinates in the photo reference. This reference is obtained by orthogonally projecting the axes $x - y$ of the camera reference over the plane Π_f (Figure 2). That is, $x_f = (X_1\ X_2)_{\{R_f\}} \in \mathbb{R}_2$.

Now we want to work with a reference R_p (pixel reference) other than R_f, with the origin in the upper-left corner of the photograph (see Figure 2), in which the points of the photograph are expressed in pixels. A new change of reference must therefore be added.

A change of reference in the plane can be written in matrix form as

$$\begin{pmatrix} X_1^p \\ X_2^p \end{pmatrix}_{\{R_p\}} = \begin{pmatrix} r_{11} & r_{12} & t_x \\ r_{21} & r_{22} & t_y \end{pmatrix} \begin{pmatrix} X_1 \\ X_2 \\ 1 \end{pmatrix}_{\{R_f\}} \quad (1)$$

in which the vector $(t_x\ t_x)$ represents the translation of the origin and the matrix $(r_{ij})_{ij}$ represents the basis change due to the rotation of the axis system. Before performing the transformation in $\mathbb{R}_2$, it is a good idea to perform another change of reference in the projective plane. Thus, in homogeneous coordinates, the change takes the form of a linear application, Φ_2, of $\mathbb{P}_2$.

$$\begin{pmatrix} X_1^p \\ X_2^p \\ 1 \end{pmatrix}_{\{R_p\}} = \begin{pmatrix} r_{11} & r_{12} & t_x \\ r_{21} & r_{22} & t_y \\ 0 & 0 & 1 \end{pmatrix} \begin{pmatrix} X_1 \\ X_2 \\ 1 \end{pmatrix}_{\{R_f\}} \quad (2)$$

Copyright © 2006 Taylor & Francis Group plc, London, UK

Hitherto we have seen how to relate points in space with those of the photograph if the former are expressed in some reference denoted by $\{R_c\}$ (camera reference). However, as detailed above, it is impossible to have the points in $\mathbb{R}^3$ in that reference because they depend on the position of the focus and the photograph plane, which cannot be determined directly.

If we have properly selected the points at reference $\{R_e\}$ (Figure 1), and we assume that there exists an application that passes the points from $\{R_e\}$ to $\{R_c\}$, this is a change of reference in $\mathbb{R}^3$ similar to (1) but in $\mathbb{R}^3$ instead of $\mathbb{R}^2$.

$$\begin{pmatrix} x_1^c \\ x_2^c \\ x_3^c \end{pmatrix}_{\{R_c\}} = \begin{pmatrix} r_{11} & r_{12} & r_{13} & t_x \\ r_{21} & r_{22} & r_{23} & t_y \\ r_{31} & r_{32} & r_{33} & t_z \end{pmatrix} \begin{pmatrix} x_1 \\ x_2 \\ x_3 \\ 1 \end{pmatrix}_{\{R_e\}} \tag{3}$$

Like (2), it can change the reference in $\mathbb{R}^3$ into a linear application from $\mathbb{P}_3$ to $\mathbb{P}_3$.

$$\begin{pmatrix} x_1^c \\ x_2^c \\ x_3^c \\ 1 \end{pmatrix}_{\{R_c\}} = \begin{pmatrix} r_{11} & r_{12} & r_{13} & t_x \\ r_{21} & r_{22} & r_{23} & t_y \\ r_{31} & r_{32} & r_{33} & t_z \\ 0 & 0 & 0 & 1 \end{pmatrix} \begin{pmatrix} x_1 \\ x_2 \\ x_3 \\ 1 \end{pmatrix}_{\{R_e\}} \tag{4}$$

By calling this linear application Φ_1, we can define a linear application A from $\mathbb{P}_3$ to $\mathbb{P}_2$.

The composition $\Phi_1 \circ A \circ \Phi_2$ as a linear application M between $\mathbb{P}_3$ and $\mathbb{P}_2$ includes the changes of reference and the projection in a strict sense. Therefore, this method is called Direct Linear Transformation (DLT).

The linear transformation can be written as

$$\begin{bmatrix} n.X_1^p \\ n.X_2^p \\ n \end{bmatrix} = \begin{pmatrix} m_{11} & m_{12} & m_{13} & m_{14} \\ m_{21} & m_{22} & m_{23} & m_{24} \\ m_{31} & m_{32} & m_{33} & m_{34} \end{pmatrix} \begin{bmatrix} x_1^e \\ x_2^e \\ x_3^e \\ 1 \end{bmatrix} \tag{5}$$

in which $M = (m_{ij})_{ij}$.

Why does n appear here? It was omitted in the previous reasoning. In fact, a change of reference in $\mathbb{R}^2$ is assumed to be a basis change in $\mathbb{P}_2$ in homogeneous coordinates. However, changes of this sort are determined by just three points in $\mathbb{R}^3$, except for proportionality factors. The $3x3$ basis-change matrix Φ_2 gives three points of $\mathbb{R}^3$ to determine a basis change in homogeneous coordinates in $\mathbb{P}_2$. However, four points are needed to determine the transformation uniquely. The same occurs in a change of reference in $\mathbb{R}^3$. Five points of $\mathbb{R}^4$ are needed to uniquely determine a basis change in $\mathbb{P}_3$, but only four points are given: the three vectors of the coordinates and the origin. Then, n represents the two proportionality factors of the basis change that are omitted.

Therefore, a projection of a point from $\mathbb{R}^3$ over a plane Π_f is determined by a linear application M of $\mathbb{P}_3$ in $\mathbb{P}_2$, except for a proportionality factor n. That is, the third coordinate of a point in $\mathbb{P}_2$ obtained by applying M is not equal to 1. To obtain $(X_1^p \;\; X_2^p)$, the first two coordinates of the obtained point are divided by the third component when changing from $\mathbb{P}_2$ to $\mathbb{R}^2$.

Finally, the matrix M can be obtained numerically by relating known points in space with points in the photograph. This process is known as camera calibration.

2.2 *From the photograph to space: the inverse process (Hatze, 1988) or (Chen, 1994)*

Once we have obtained the projectivity that connects the points in space with the points in the photograph through the focus, we can use the inverse process to obtain the point we need. However, a given point in the photograph plane is not represented by a single point in space but by a whole line projected through it. We need more information about the position of the point to be determined in space – for example, a plane that it belongs to.

Algebraically, the matrix M is not square, and it makes no sense to evaluate the inverse, at least not without limiting the starting space $\mathbb{P}_3$ to the homogenized points of $\mathbb{R}^3$ located in a certain plane. Then, the dimension of the arriving and starting space equals converting the projectivity in an isomorphism between the projective spaces.

From a practical point of view, it is a good idea to request that the points to be surveyed belong to a certain known plane.

Imagine that we know the projection matrix transformation M and that the point to be determined in $\mathbb{R}^3$, $(x_1 \;\; x_2 \;\; x_3)$, belongs to a known plane defined by the equation $\Pi : ax_1 + bx_2 + cx_3 + d = 0$. In homogeneous coordinates, the point x^f can be written as $x^f = [X_1 \;\; X_2 \;\; 1]$ and the plane can be written as

$$\Pi : ax_1 + bx_2 + cx_3 + dx_4 = 0 \tag{6}$$

The point to be determined is $x^e = [x_1 \;\; x_2 \;\; x_3 \;\; x_4] \in \mathbb{P}^3$ anti-image by M of x^f (in homogeneous coordinates) that fits equation (6). Using points x^f and x^e, the following equation is obtained from (5):

$$\begin{cases} 1 = m_{31}x_1 + m_{32}x_2 + m_{33}x_3 + m_{34}x_4 \\ X_1 = m_{11}x_1 + m_{12}x_2 + m_{13}x_3 + m_{14}x_4 \\ X_2 = m_{21}x_1 + m_{22}x_2 + m_{23}x_3 + m_{24}x_4 \end{cases} \tag{7}$$

Copyright © 2006 Taylor & Francis Group plc, London, UK

In some way, x_4 plays the role of n in equation (5). If $a \neq 0$, we can write:

$$x_1 = -\frac{bx_2 + cx_3 + dx_4}{a} \tag{8}$$

By substituting the value of (8) in (7), the following system is obtained in matrix notation:

$$\begin{bmatrix} X_1 \\ X_2 \\ 1 \end{bmatrix} = \begin{bmatrix} \left(m_{12} - \frac{m_{11}b}{a}\right) + \left(m_{13} - \frac{m_{11}c}{a}\right) + \left(m_{14} - \frac{m_{11}b}{a}\right) \\ \left(m_{22} - \frac{m_{21}b}{a}\right) + \left(m_{23} - \frac{m_{21}b}{a}\right) + \left(m_{24} - \frac{m_{21}b}{a}\right) \\ \left(m_{32} - \frac{m_{31}b}{a}\right) + \left(m_{33} - \frac{m_{31}b}{a}\right) + \left(m_{34} - \frac{m_{31}b}{a}\right) \end{bmatrix} \begin{bmatrix} x_2 \\ x_3 \\ x_4 \end{bmatrix} \tag{9}$$

in which the matrix of (9) is the restriction for Π of M, which is square, and it is possible to find the points x_2, x_3 and x_4 (x_1 is defined by the known plane Π through (8)) . To obtain the point x_e, the homogeneous coordinates (x_1 x_2 x_3 x_4) are divided by x_4 to obtain 1 in the last element or coordinate. That is, it is de-homogenized:

$$\begin{pmatrix} x_1^e & x_2^e & x_3^e \end{pmatrix} = \frac{\left(-\frac{bx_2 + cx_3 + dx_4}{a} \; x_2 \; x_3 \right)}{x_4} \tag{10}$$

To sum up, given a point in the photograph $x^f = [X_1 \; X_2] \in \mathbb{R}^2$, it is homogenized to obtain $x^f = [X_1 \; X_2 \; 1] \in \mathbb{P}^2$.

Then, $x^e = [x_1 \; x_2 \; x_3 \; x_4] \in \mathbb{P}^3$ is calculated using equations (8) and (9). Finally, it is de-homogenized to obtain $x^e = (x_1^e \; x_2^e \; x_3^e) = \left(\frac{x_1}{x_4} \frac{x_2}{x_4} \frac{x_3}{x_4} \right) \in \mathbb{R}^3$.

2.3 *Determining the matrix M or projectivity: Camera calibration*

In the system of equations (5), the unknowns are the parameters of the M matrix m_{ij}. For each point in space (x_1 x_2 x_3) and its correspondents in the photograph (X_1 X_2), two equations (solved for n) can be obtained as follows:

$$\begin{aligned} &m_{31}x_1X_1 + m_{32}x_2X_1 + m_{33}x_3X_1 + m_{34}X_1 \\ &\qquad - m_{11}x_1 - m_{12}x_2 - m_{13}x_3 - m_{14} = 0 \\ &m_{31}x_1X_2 + m_{32}x_2X_2 + m_{33}x_3X_2 + m_{34}X_2 \\ &\qquad - m_{21}x_1 - m_{22}x_2 - m_{23}x_3 - m_{24} = 0 \end{aligned} \tag{11}$$

At first glance, then, it seems that we will need the correspondence of at least six points in space and six points in the photograph, since there are twelve unknowns and each pair of points gives two equations.

Nevertheless, the system defined by (11) is homogeneous, and a trivial solution $m_{ij} = 0$ always exists. In fact, the value of n is undetermined because it has a value of zero, which makes no sense.

If this parameter n does not exist, we can determine the values of m_{ij} simply by giving four points. However, this is not the case. In order to solve the problem, we must therefore add a restriction to the matrix M.

Suppose we have the points in space expressed in the camera reference used above (Figure 2). In these circumstances, the matrix projection M has the following form (Faugeras, 1993), (Olagué, 2001):

$$M_c = \begin{pmatrix} -f & 0 & u_0 & 0 \\ 0 & -f & v_0 & 0 \\ 0 & 0 & 1 & 0 \end{pmatrix} \tag{12}$$

where (u_0 v_0) are the coordinates of the centre of the photograph (focus projection) in the pixel system and f is the focal (Chen, 1994). This matrix corresponds to $M_c = \Phi_2$. To work in the reference $\mathbb{R}^3$, $\{R_e\}$, M can be composed with the basis change Φ_1, that is:

$$M = M_c \cdot \Phi_1 \tag{13}$$

in which

$$\Phi_1 = \begin{pmatrix} r_{11} & r_{12} & r_{13} & t_x \\ r_{21} & r_{22} & r_{23} & t_y \\ r_{31} & r_{32} & r_{33} & t_z \\ 0 & 0 & 0 & 1 \end{pmatrix} = \begin{pmatrix} \mathrm{r}_1 & t_x \\ \mathrm{r}_2 & t_y \\ \mathrm{r}_3 & t_z \\ 0 & 1 \end{pmatrix} \tag{14}$$

is the basis change in $\mathbb{P}_3$ in Equation (4).

This decomposition makes it possible to find a projection matrix M through the intrinsic parameters (M_c) and extrinsic parameters (Φ_1) of the camera.

The submatrix $\Phi_1(r_i)_{(i)}$, in which r_i is a row vector of a composition of rotations, requires that $\|r_3\| = 1$ (Pizarro, 2005). From (13), it follows that

$$\sqrt{m_{31}^2 + m_{32}^2 + m_{33}^2} = 1 \tag{15}$$

With this restriction, there are now eleven unknowns instead of twelve. The new unknown matrix can be written as: (Chen, 1994)

$$L = \begin{pmatrix} \frac{m_{11}}{m_{34}} & \frac{m_{12}}{m_{34}} & \frac{m_{13}}{m_{34}} & \frac{m_{14}}{m_{34}} \\ \frac{m_{21}}{m_{34}} & \frac{m_{22}}{m_{34}} & \frac{m_{23}}{m_{34}} & \frac{m_{24}}{m_{34}} \\ \frac{m_{31}}{m_{34}} & \frac{m_{32}}{m_{34}} & \frac{m_{33}}{m_{34}} & 1 \end{pmatrix} = \begin{pmatrix} L_1 & L_2 & L_3 & L_4 \\ L_5 & L_6 & L_7 & L_8 \\ L_9 & L_{10} & L_{11} & 1 \end{pmatrix} \tag{16}$$

Copyright © 2006 Taylor & Francis Group plc, London, UK

By pairing n points in space $(x_i \;\; y_i \;\; z_i)_i$ with n points in the photograph $(X_i \;\; Y_i)_i$ and applying the change of variables to (11), the new system to be solved is made up of a system with eleven unknowns and $2n$ equations, as:

$$\begin{pmatrix} x_i & y_i & z_i & 1 & 0 & 0 & 0 & 0 & -x_i.X_i & -y_i.X_i & -z_i.X_i \\ 0 & 0 & 0 & 0 & x_i & y_i & z_i & 1 & -x_i.Y_i & -y_i.Y_i & -z_i.Y_i \\ & & & & & \vdots & & & & & \end{pmatrix}$$
$$\begin{pmatrix} L_1 & L_2 & \cdots & L_{10} & L_{11} \end{pmatrix}^T = \begin{pmatrix} X_i & Y_i & \cdots \end{pmatrix}^T \qquad (17)$$

This system is over-determined and can be solved using the least-squares method.

Once the system has been solved, to recover the projective matrix M, it follows that:

$$M = \frac{1}{\sqrt{L_9^2 + L_{10}^2 + L_{11}^2}} \begin{pmatrix} L_1 & \cdots & \cdots & L_4 \\ \vdots & \ddots & \ddots & \vdots \\ L_9 & \cdots & \cdots & L_{12} \end{pmatrix} \qquad (18)$$

thereby undoing the change of variables and imposing the restriction (15).

3 EXPERIMENTAL SET-UP

3.1 *Flume dam break*

We studied the changes over time in water-surface position (height) caused by suddenly opening the gate. The experiment involved high-speed movements in the water surface, which were recorded with two different digital cameras: a high-speed Basler camera and a medium-speed Lumenera camera.

The first experiment was a typical one. A flume filled with water was controlled by a sluice gate and connected directly to a platform, as shown in Figure 3. The platform was initially dry. The gate was removed manually from its original position and water flowed from the flume to the platform. The flume used in the first experiment was 9 m long, 40 cm wide and 60 cm high. It was tilted from 0 to 27°. The flume ended at a platform 4 m long, 2.4 m wide and 60 cm tall. In this experiment, the effective flume length was just 2 m (Figure 3). A fixed volume of water was held between two gates about 2 m apart. This part of the flume was connected to the platform by a manual sluice gate. A 50 cm deep volume of water was held.

Between 5 and 10 parallel laser beams were placed vertically over the platform, generating lines perpendicular to the flume axis in order to obtain cross-sections of the water surface. The water was mixed with milk at a concentration of 2% so that it would reflect the laser beams and make it possible to take photographs. Higher concentrations of milk caused more reflection, and lower concentrations allowed the light to penetrate the mixing fluid to a greater degree. We tried out different mixtures and found that the minimum concentration of milk was about 2% by volume. This allowed us to use as little milk as possible and obtain strips of light that were not too thick, thus preventing them from overlapping.

The Basler camera can capture images at up to 1000 fps with a resolution of 1200×1000 pixels or more, depending on the frame size. The Basler camera used normal Nikon lenses that produce high-quality images without optical aberration. The Lumenera camera had higher luminescence than the Basler because its lens had higher luminescence and also because the Basler's minimum shooting frequency was higher. The Lumenera had a wide-angle lens, which caused significant image deformation, which had to be corrected. A new MATLAB code was produced to correct this aberration.

A series of photographs of the light reflecting from the mixture were taken and processed. The idea was to obtain different cross-sections of the surface using the laser beams, in order to reconstruct the surface at

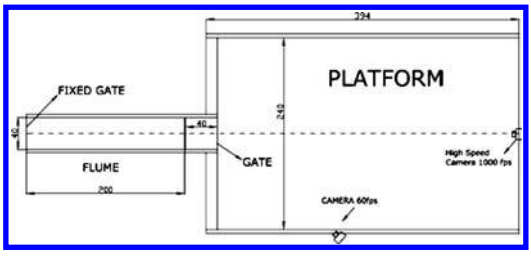


Figure 3. Flume and platform set-up and the positions of cameras, with dimensions in cm.

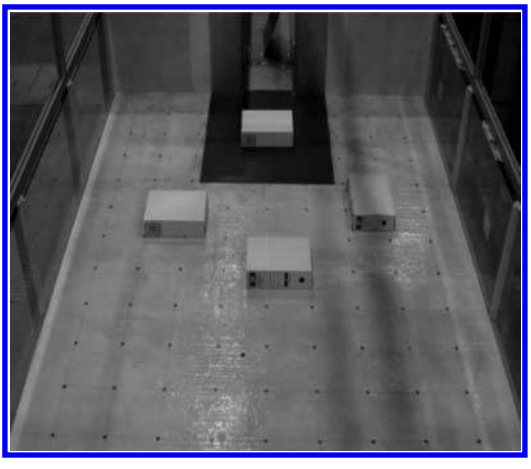


Figure 4. Lasers and general view of the experimental set-up.

Copyright © 2006 Taylor & Francis Group plc, London, UK

each time step. We could not use many lasers because the beams could have overlapped and the numerical process would have failed. A minimum distance was therefore maintained between lasers.

3.2 *Camera position*

The cameras were placed in such a way that the projection of the laser beams in the film did not cross at any time. They needed to be able to perceive water-level fluctuations accurately. In our experiments, the camera angle ranged from 20 to 30°. The camera distance depended on the area being analysed. Neither the distance nor the angle mattered because the camera needed to be calibrated and there were intrinsic values throughout the process.

3.3 *Camera calibration*

Once the aberration had been corrected, the camera needed to be calibrated. As mentioned above, at least six points must be identified in the space of known coordinates and correlated with six points in the photograph in order to determine the M projection matrix. As a calibration object, we used a meshed box located in a known position (Figure 5).

The points in the space used to calibrate the camera were located throughout the volume of study in order to avoid extrapolation problems that would increase the estimation error. We used a set of points taken from different positions of the meshed object in the area of interest.

3.4 *Detection of laser beams*

There are various techniques for finding the pixels that belong to a laser beam in a photo. Depending on the quality of the photograph, the layout of the laser beams, the contrast of the beams, the background of the image and other factors, one technique may be better than another. All techniques require a pre-filtering or post-filtering process. Here we present two different techniques, detection by maximum and morphological image treatment, which we applied to two cameras that observed the same experiment from different positions. Frontal (Basler) and lateral (Lumenera) points of view were used in the subsequent analysis, as shown in Figure 6.

The frontal view had certain advantages over the lateral view. The main advantage lies in the layout of the laser beams in the photograph. It was easy to apply an intuitive technique to detect the maximum of the column of pixels (by colour index), which match up with the laser beams.

The photograph resolution of the Basler camera was higher than that of the Lumenera camera. The area of study occupied the entire frame area and we were

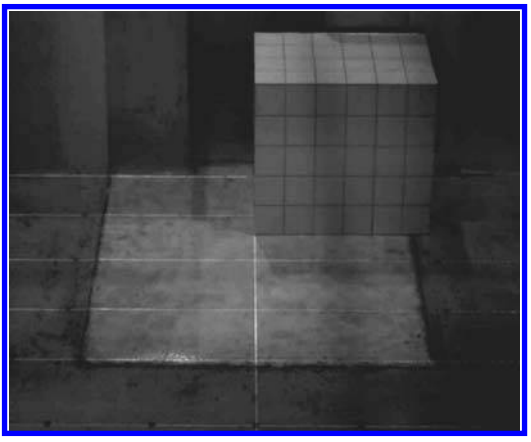


Figure 5. Meshed box used in the calibration procedure.

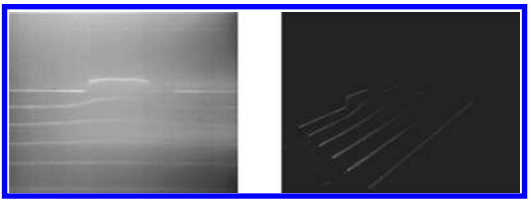


Figure 6. Frontal (left) and lateral (right) views.

able to obtain more information about the process. However, in this specific example, the frontal view presented a difficulty: the image could not describe the high lateral gradients of the flow as well as images from the lateral view did. See Figure 6 to appreciate this problem.

3.5 *Laser-beam detection techniques. Frontal view.*

First, we corrected the photograph by refining it. Because the illumination condition was poor, the Basler took the photographs with an artificial gain that introduced some noise, which appeared as fine vertical highlight lines. Because the analysis is performed by pixel columns, we needed to smooth the image horizontally. The selected filter presents a constant known as lag ($n/2$, where n is the order). Each pixel needed to be moved $n/2$ to the left in order to restore the image. Figure 7 shows the graph of the pixel values of column 500 of the original photograph and the filtered data, which appears very smooth.

Once the image had been filtered, we studied it, for example, by focusing on the pixels of column 460, shown in Figure 8. The maximum intensity (points with a high value) corresponds to the intersection between column 460 and the laser beams. The signal progressively descends from left to right. This implies that the bottom part of the photograph is a

Copyright © 2006 Taylor & Francis Group plc, London, UK

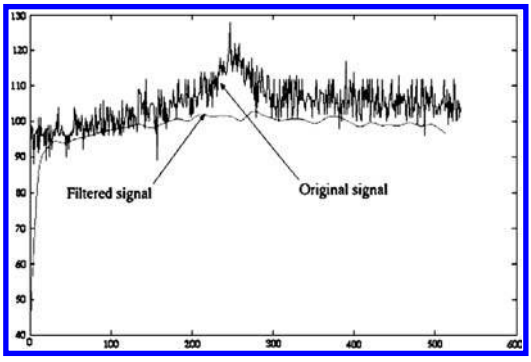


Figure 7. Filtered signal of column 500 of the image matrix.

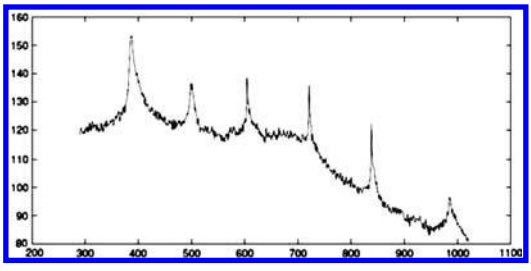


Figure 8. Pixel intensity distribution of column 460. The peaks are the laser beams.

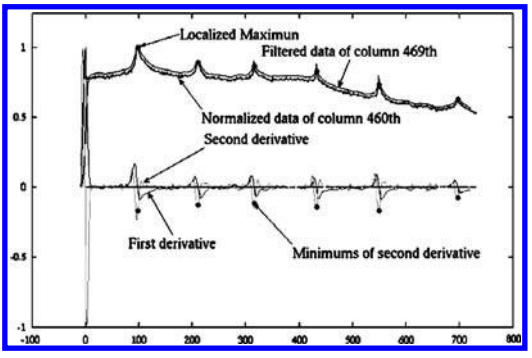


Figure 9. Column 460 filtered, localized and ordered by the lowest second derivative.

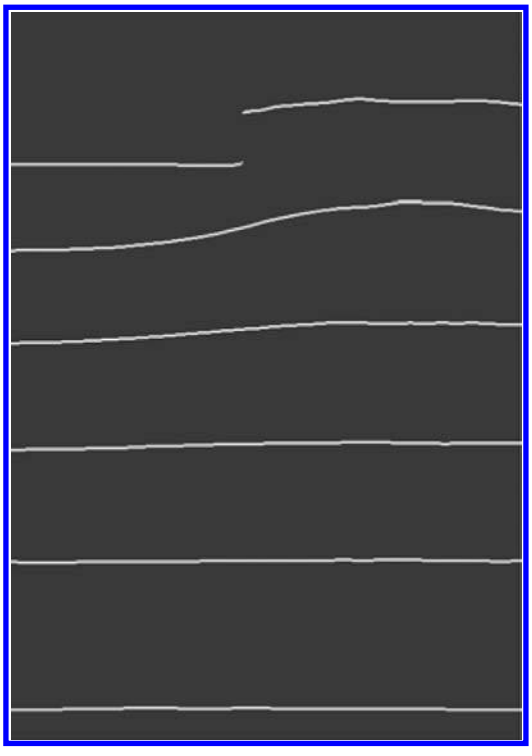


Figure 10. A frontal image taken by the Basler camera that has been treated mathematically.

little darker than the upper part. The six maximum points representing the position of the lasers cannot be obtained because there may be other relative maximums that do not correspond to a laser beam. A more detailed algorithm was applied in order to detect the laser beams. A new FIR filter was also applied to the image in order to smooth the high-frequency noise signal. Figure 9 shows column 460 after being filtered and selected according to the lowest second derivative. Once the column had been filtered, practically the only peaks that remained were those that needed to be determined. A series of different pre-processing steps were carried out on the image before it was in the best condition for the beams and the surface to be surveyed. That is, some pixels not correctly detected in the image needed to be eliminated, some maximums were not real, etc. After this process, Figure 10 was obtained.

3.6 *Laser-beam detection techniques. Lateral view.*

Certain problems appeared in this situation. First, the resolution of the camera was lower (460×640) than that of the Basler, the lens was wide-angle and precision was lost because the density of information in the final image was lower. Second, the laser beams were seen in a tilted view and the detection of the maximum by columns was therefore discarded. A new technique, morphological image treatment, needed to be used in this image view (Serra, 1994).

The first step was to convert the image to a binary image by means of a threshold: 1 was given over a certain pixel threshold value and 0 was given to the rest. The threshold was chosen by reaching a compromise between losing good information and adding extra bad information. This made image treatment difficult, i.e. there were gaps in white areas, overlapping laser

Copyright © 2006 Taylor & Francis Group plc, London, UK

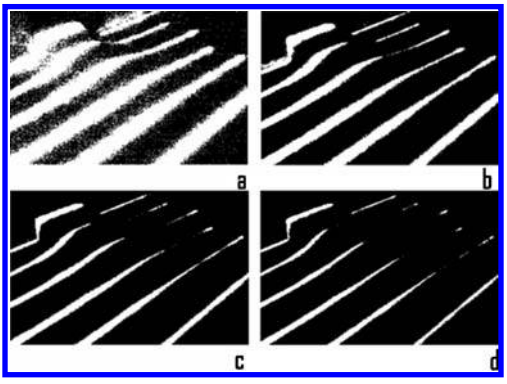


Figure 11. The process of applying different thresholds (a to d) caused a loss of information. The lines appear to be cut.

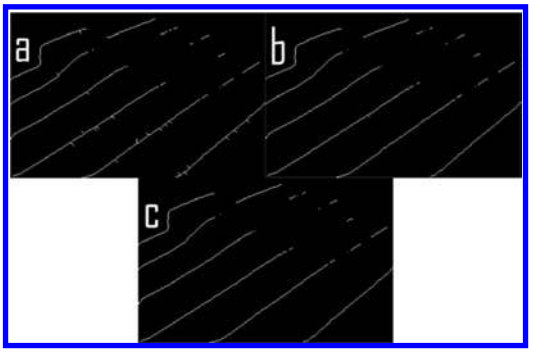


Figure 12. Results for different procedures. Dendrites are attached to the main lines.

beams, etc. Figure 11 shows the results obtained by applying different thresholds in the binary-conversion process.

Once the image had been processed, the skeleton of the image was found. First, however, we made a series of corrections, as in the frontal view. We eliminated some spurious points and groups of points that interfered with the detection of the main laser beams. To do this, we used a MATLAB image function called "*bwmorph*" with options such as "Clean, Fill or Spur". The image was then ready for the skeleton process.

We performed successive "*thinning*", so the lines became thinner and thinner and the border pixels were erased until no change was noticeable. We used MATLAB and the image function with the "*thin inf*" option. Finally, dendrite forms grew indiscriminately from the main laser beams, and we generated a new code to trim the skeleton. Figure 12 shows different skeletons obtained with different procedures.Another procedure that worked well was applying a filter, before applying the threshold, defined by the matrix

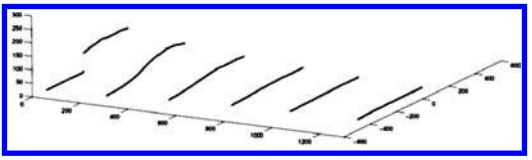


Figure 13. Reconstruction of laser beams from the Lumenera camera.

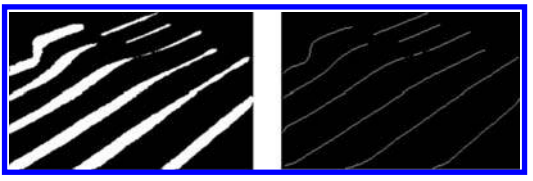


Figure 14. Result obtained by applying the mask given by the matrix of Equation (19).

$$h=\frac{1}{9}\begin{pmatrix}0&0&1&1&1\\0&1&1&1&0\\1&1&1&0&0\end{pmatrix} \tag{19}$$

which simply assigns the mean of the eight neighbours and itself and respects the laser direction. Figure 12 shows that the application of this mean smoothes the line and fills the gaps. The threshold is therefore necessary to obtain the skeleton.

4 RESULTS

We used frontal images taken with the Basler camera (Figure 10). The entire exercise involved 30 fps for 6 seconds.

Calibration: First, a vector x contains the calibration points in $\mathbb{R}^3$ and X represents its correspondents in the photograph. In this example, we added 195 calibration points from three different calibration box positions and some points on the floor in order to obtain the matrix projection

A column vector d was declared to contain the coordinates of the laser planes. The curve i belonging to the plane $x = d(i)$ was obtained.

Laser curve determination: If pixel value matrix A contains the photograph to be treated, the technique of maximum and the filter must be applied to smooth the image and to trim the dendrite forms attached to the main lines. Thus, we obtained a structure that had the proper pixel position and curve order.

Surveying: We then obtained the coordinates in $\mathbb{R}^3$ by applying the inverse transformation M, which converts pixel coordinates into real coordinates. Figure 13 presents the results, which show how the water formed a vertical wall near the exit wall.

Copyright © 2006 Taylor & Francis Group plc, London, UK

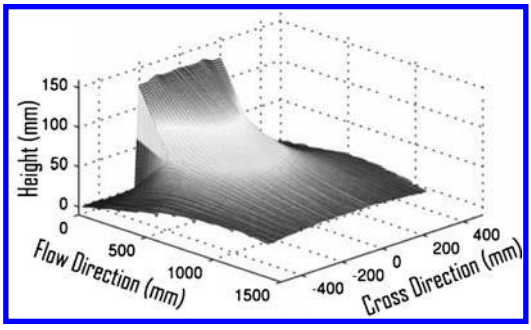


Figure 15. Experimental 3D surface from the Basler camera at 2.45 s.

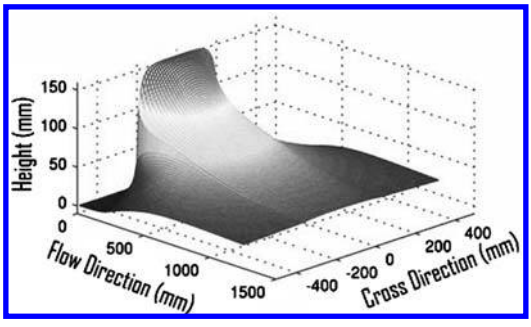


Figure 16. Numerical 3D water surface from FLATMODEL at 2.45 s.

Results from the Basler camera position: Due to the excellent position and high-quality information of the Basler camera, a numerical/experimental comparison is presented here. The mixture of water and milk flowed very quickly across the platform, producing a jet flow that increased in width from 40 to 240 cm. The front of the flow moved very quickly, close to 342 cm/s, which was faster than the theoretical value of 221 cm/s given by the Ritter solution.

Figures 15 and 16 show the experimental and numerical results respectively. The numerical data were taken from FLATModel, which was created by GITS (some aspects are discussed in Medina et al. 2006), and the experimental datea were obtained by interpolating Figure 13. The instant compared is 2.45 seconds after the flow passed the end of the flume. The numerical data has a smoother shape than the experimental data. Also, the flow of water is more vertical in the experimental images than in the numerical results. This is because reality is more complex than the 2D Saint-Venant solution. The vertical zones do not obey the Saint-Venant hypothesis. The shapes and heights appear similar in both representations but are slightly higher in the numerical results. The following comparison between experimental and numerical data refers to fan expansion. Figure 17 shows all data below a

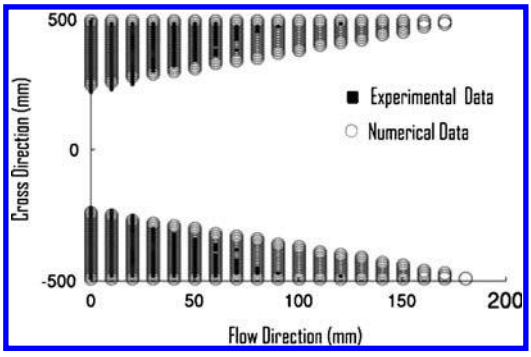


Figure 17. Comparison of the fan in the experimental and numerical data. T = 2450 ms. The data is cut off at a height of 2 mm.

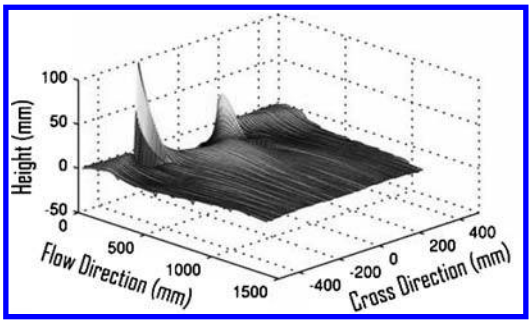


Figure 18. 3D diagram of absolute error. The highest errors are located in the area with high water gradients.

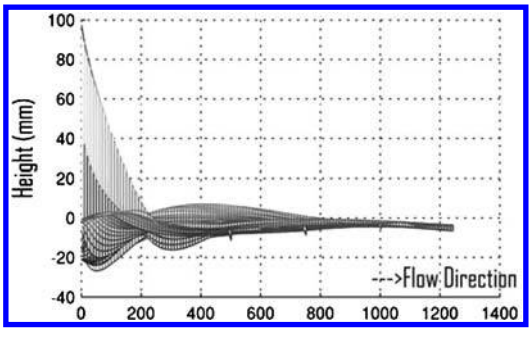


Figure 19. Lateral view of the absolute error surface data.

height of 2 mm. The resulting angles are 36 and 23° for the numerical and experimental data respectively. The experimental fan opens faster than the numerical one.

Figures 18 and 19 show the behaviour of the absolute error, which is calculated as the experimental data minus the numerical data. The numerical and experimental data agree throughout the area of study. The only regions that are very different are those which fail to meet the Saint-Venant conditions. Nevertheless,

Copyright © 2006 Taylor & Francis Group plc, London, UK

the comparison shows that the data that has an absolute error of less than 40% has a mean error of 13.9% throughout the area of study, whereas the data that has an absolute error of 20% has a mean error of 9%.

5 CONCLUSION

This paper presents a procedure that works well in 2D water-surface treatment. The camera must be properly calibrated and geometrical aberrations should be corrected if necessary. The use of Nikon or other high-quality lenses (and other pre-process corrections) clearly makes image processing easier. Milk is essential to obtaining clean, bright laser beams because only opaque liquids work well with laser light. The numerical/experimental comparison shows good agreement. The experimental data shows certain numerical difficulties in the high-gradient zone, where the Saint-Venant hypothesis fails due to the high curvature of the current lines and the non-hydrostatic pressure distribution. The overall absolute error for the surface showed good agreement, with a mean error of around 9% when the threshold is 20%.

ACKNOWLEDGMENT

This study was funded by CICYT under project BTE2002-00375.

REFERENCES

Abdel-Aziz, Y.I. and Karara, H.M. 1971. Direct linear transformation from comparator coordinates into object space coordinates in close-range photogrammetry. Proceedings of the Symposium on Close-Range Photogrammetry (pp. 1–18). Falls Church, VA: American Society of Photogrammetry.

Chen, L., Armstrong, CW. and Raftopoulos, DD. 1994. An investigation on the accuracy of three-dimensional space reconstruction using the direct linear transformation technique. J Biomech.;27(4):493–500.

Faugeras, O. 1993. Three-Dimensional Computer Vision: A Geometric Point of View. MIT Press.

González, Rafael and Woods, Richard (1992). Digital Image Processing. Addison Wesley Publishing Company, Inc.

Hatze, H. 1988 High-precision three-dimensional photogrammetric calibration and object space reconstruction using a modified DLT-approach. J. Biomech.; 21(7):533–8.

Hecht, Eugene 2000. Optics. Addison Wesley.

Kofman, J., Miller, D. L., Knopf, G. K. and Zecevic, A. 1998. Calibration and measurement accuracy of a stereophotogrammetric system using the direct linear transformation. North American Congress on Biomechanics. University of WaterlooWaterloo, Ontario, Canada.

Medina, V., Bateman, A. and Velasco, D. A New Approach to Solve the Boundary Conditions in the Shallow Water Equations Using a Riemann Solver. River Flow 2006, Lisbon, Portugal.

Olague, G. and Ramírez, R. 2001. Artificial Image Generation from Digital Images. American Society of Photogrammetry and Remote Sensing (ASPRS).

Pizarro, Campos and Tozzi 2005. Comparación de técnicas de calibración de cámaras digitales. Rev. Fac. Ing.-Univ. Tarapacá. Vol. 13.

Pribanic, T., Sturm, P. and Cifrek, M. 2005. Proceedings of the 4th International Symposium on Image and Signal Processing and Analysis, 2005. ISPA 2005. ISSN: 1845-5921.

Sánchez Moreno, Francisco 2000. Reconstrucción 3D con iluminación láser: aplicaciones a la fotogrametría industrial. UPM-DISAM r T-2000.31v1.0.

Serra, J. and. Soille, P. eds., 1994: Mathematical Morphology and its Applications to Image Processing, Kluwer Academic Publishers, Dordrecht-Boston-London.

Copyright © 2006 Taylor & Francis Group plc, London, UK

A three-dimensional model of flow dynamics around paired deflectors for fish habitat enhancement

D.M. Carré & S.J. Gaskin
McGill University, Montréal, Quebec, Canada

P.M. Biron
Concordia University, Montréal, Quebec, Canada

ABSTRACT: Schemes to restore fish habitat in rivers often involve installing instream structures such as current deflectors to create and maintain riffle-pool sequences. To improve the success rate of the many restoration schemes that fail or require costly maintenance, we need to develop tools such as numerical modeling to test scenarios prior to the implementation of structures. The objective of this research is to use a three-dimensional numerical model to characterize flow dynamics and sediment transport around paired deflectors used to enhance fish habitat in a natural river. Calibrating and validating such a model requires accurate measurements of these parameters in the natural river. Particle Image Velocimetry (PIV), typically used in laboratory flumes, was used to obtain detailed velocity measurements at the surface. These data serve to validate the 3D model of the study reach. It is hoped that this model will help maximizing deflector efficiency and success rate for future implementation.

1 INTRODUCTION

In many rivers, human impacts have resulted in a deterioration of the riffle-pool sequences, with serious consequences for fish habitat quality (Thompson, 2002a). A large number of restoration projects have thus focused on fish habitat enhancement, particularly on salmon and trout habitats which are of vital economic importance. Stream deflectors are considered the most successful instream-structure methods for restoring or enhancing low-gradient channels for trout (Hunter, 1991; Thompson, 2002b) and are in widespread use in stream restoration projects for salmonids (Brookes *et al.*, 1996; Roni *et al.* 2002). These in-stream structures constrict the channel section, and by consequence increase flow velocity, causing an increase in bed shear stress which should in theory create or maintain a deep pool downstream (Booker *et al.*, 2001). Many deflectors, however, are installed in rivers on a "trial-and-error" basis (Brookes *et al.*, 1996). Recently, some laboratory studies have shed more light on the complex flow dynamics and resultant bed topography around deflectors (Biron *et al.*, 2004). They compared design of deflectors with different angles, heights and lengths and provide useful design recommendation for paired deflectors.

To improve the success rates of restoration projects, however, tools need to be developed to examine different designs *prior* to the implementation of the structures in rivers. Three-dimensional numerical modelling, which has been successfully used over the last 10 years in many natural river studies (Lane *et al.*, 1999; 2002; Nicholas and Smith, 1999; Ferguson *et al.*, 2003), is well suited for this task as the flow field around deflectors is complex and cannot be properly simulated with a depth-averaged model (Biron *et al.*, 2005). Furthermore, the detailed near-bed velocity flow field is needed in order to predict bedload transport patterns around these structures. These models, however, require detailed spatially distributed datasets of three dimensional flow variables to be validated (Ferguson *et al.*, 2003; Lane *et al.*, 2005). With a few exceptions (e.g. Thompson, 2002b), there is very limited, if any, field data available on flow velocity around deflectors in natural rivers.

The objectives of this study are 1) to use a three-dimensional numerical model to simulate the complex flow field around existing deflectors in the Nicolet River (Québec, Canada), and 2) to compare the model output with detailed velocity measurements obtained with Particle Image Velocimetry (PIV). The ultimate goals of this project are to develop numerical modelling tools for river management and guidelines on optimal location of dug pools when installing flow deflectors in rivers.

Copyright © 2006 Taylor & Francis Group plc, London, UK

2 METHODOLOGY

The Nicolet River, near Victoriaville (Québec, Canada), is located within the Nicolet sub-basin that covers an area of 265 km^2. Founded in 1988, the "Corporation de gestion des rivières des Bois-Francs" (CGRBF), has the task since 1993 to restore the physical habitat of the Nicolet River for sport fishing (Brook, Brown and Rainbow trout), mainly using single and paired deflectors. Field data collected in this study include topography surveying, velocity measurement and bedload sediment movement in a 115 m long reach on the Nicolet River which includes a set of paired boulder deflectors oriented upstream at 135° (Figure 1). This reach is characterized by a highly heterogeneous bed with a median diameter (D50) of 90 mm, and a D84 (where 84% of the particles are finer) of 180 mm. It has a bankfull width of around 35 m, and a discharge varying from about 1 m^3/s at low flow up to 16 m^3/s at bankfull.

Bed, bank topography and water surface were measured at several cross-sections using a total station, with a higher density of points where change was the greatest. The flow stage was monitored with a pressure transducer, and a stage-discharge rating curve was established based on local measurements of velocity using a propeller current meter, and data from an Environment Québec gauging station (# 030103) located around 65 km downstream of the field site.

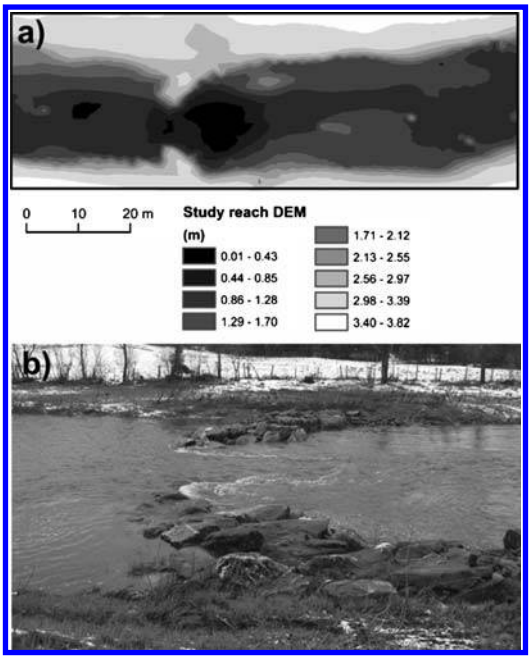


Figure 1. a) Bed topography of the study reach with paired flow deflectors in the Nicolet River. b) Photograph of the black box zone.

Bedload sediment transport movement was assessed using Passive Integrated Transponder (PIT) tags, a method that was recently developed for tracking individual particles in gravel-bed rivers (Lamarre et al. 2005). A total of 110 rocks were collected and sorted into four categories: <64 mm, <90 mm, <125 mm, and <250 mm. They were given three coats of fluorescent orange paint, drilled, and glass tags were implanted and sealed with resin. They were then assigned an ID code in order to follow individual particles using either a Stick Antenna (Texas Instruments), or a Gate Antenna (Texas Instruments), depending on whether rocks were located below the armour layer, or covered with sand and algae. Detailed information on this method is provided in Carré *et al.* (in review).

One of the major difficulties in validating a three-dimensional numerical model is to obtain field velocity data a density comparable to the output of the model. We have therefore decided to use PIV, a method typically used only in laboratory flumes (Grant, 1997; Weitbrecht *et al.*, 2002), but recently adapted to natural rivers (Fujita *et al.*, 1998; Creutin *et al.*, 2003) to obtain a high density of longitudinal and lateral velocity measurements at the water surface. A Panasonic digital camcorder (720 × 480 resolution) was equipped with a polarized lens to avoid reflection. Two docking stations for the camera were built on each bank near the deflectors to raise the camera by 2.5 m. The camera could be adjusted to cover the area around deflectors, in particular in the pool, the riffle, and the recirculation zones. Different methods of flow seeding were tested: foam generation (by mixing water and soap with a powered pump), natural foam, Cheerios™ cereals, and paper confetti. The latter was adopted as it permits a homogeneous tracer distribution, in addition to being inexpensive, easy to use and transport. The seeding density used was between 10 to 30% of the surface flow area (Meselhe *et al.*, 2004).

Mean values for both components of the surface planform velocity were obtained for different video sequences sampled at 30 frames per second. Films were taken from both banks in order to minimise the distortion, as pixel size increases towards the outer bank. The cross-correlation commercial software VIDPIV was used to obtain average longitudinal (Vx) and lateral (Vy) velocities for the centre of the interrogation window, based on 60 second films. Different sizes of interrogation window were tested, and it was found that a window of 32 pixels provided the best results. Further tests were carried out to determine the best sampling interval. It was found that 0.5 s worked well in the recirculation zone where velocities are markedly reduced, but that a faster sampling interval of 0.1 s was more appropriate in the faster zone between

Copyright © 2006 Taylor & Francis Group plc, London, UK

the deflectors in order to avoid "contamination" with the slower moving particles from the recirculation zone. Lastly, masks were used to focus only on one of the recirculation zones, or on the central zone, therefore minimising "contamination" in the area at the edge between the faster flow between the deflectors and the slower flow in the recirculation zones.

One of the problems in using PIV in a natural setting is the distortion created by the angle of the camera, inevitable even if the camera is raised as high as possible on the bank. Here, we have used the method developed by Fujita *et al.*, (1998) and adapted by Bérubé *et al.*, (2004) and Smith *et al.*, (2005) to orthorectify the images based on four control points taken at the water surface with the total station for each video sequence.

Near-surface velocities were also measured with an Acoustic Doppler Velocimeter (ADV) in order to validate the PIV data. The comparison showed good results for the magnitude of the vectors, with a coefficient of correlation of 0.93, with more variation when comparing longitudinal and lateral velocity components separately. This may be related to the difficulties in aligning the ADV exactly in the same reference frame as PIV vectors. A good agreement was also found when comparing our VIDPIV results with those obtained from the algorithm of Bérubé *et al.*, (2004) for the same video sequences (correlation coefficient of 0.91 and 0.90 for Vx and Vy, respectively). The differences were mainly observed at the edge of the recirculation zone, where the lateral gradient of velocity is large and where the size of the interrogation window can markedly affect the results.

The three-dimensional CFD model Phoenics (version 3.6.1, from CHAM) was used to run simulations of the flow field at the Nicolet River. The software uses the finite volume approach to solve the fully three-dimensional form of the Reynolds Averaged Navier-Stokes (RANS) equations in each cell of the modeling domain. The model is described in detail elsewhere (Bradbrook *et al.*, 1998; 2001) and has been used extensively in both laboratory (Bradbrook *et al.*, 2001) and field studies (Ferguson *et al.*, 2003). All simulations were performed using the RNG k-ε turbulence model, previously shown to perform well for simulation of flows in areas affected by high shear (Richardson and Panchang, 1998) such as regions of significant separation and recirculation (Ferguson *et al.*, 2003), as is the case near deflectors. Here, results from a simulation where PIV measurements are available are presented. Discharge was 3.6 m^3/s and the inlet velocity was 0.42 m/s. The water surface representation can be achieved by variable porosity in the surface layer cell (Ouillon and Dartus, 1997; Bradbrook *et al.*, 2001). However, a rigid-lid surface was used here, as tests in a laboratory flume simulation using the same model indicated that activating the porosity algorithm produced no effect on the simulations (Haltigin, 2005)

Designing the numerical mesh is an important and difficult step in a 3D model of a complex river reach. Here, there is the additional complexity of flow deflectors which create a sharp constriction of the flow field (Figure 1). Boundary-fitted coordinates (BFC) are typically used for natural rivers (e.g. Ferguson *et al.*, 2003) to properly represent the changes in bed topography from one cross-section to the next. However, using BFC in this case would have created highly skewed cells around the deflectors, and potentially numerical instability. Instead, following Rodriguez *et al.*, (2004), the detailed bed topography point data, up to a bankfull level, were interpolated to a regular grid of 0.5 × 0.5 m cells using GIS software (ArcGIS 9.1). This grid was then converted into a 3-D solid object using a graphic software (AC3D version 5). Thus, the bed, bank and deflector topography was included into one single object in a Cartesian grid. For near-bed cells that are partially covered by the object, the PARSOL (PARtial SOLid) extension was used in the model, so that the mass continuity equations were modified to reflect that flow is passing through only a fraction of the cells obstructed by the bed, bank or deflector. The key advantages of this method are that 1) different flow conditions can easily be tested using the same object, simply by varying the domain size, 2) the mesh resolution can also be modified easily without changing any other parameter, and 3) the angle between the cells always remain at 90°, thus minimising numerical instabilities.

An alternative method is to use a structured grid with a bed porosity assigned to each cell, based on a detailed DEM (Lane *et al.*, 2004; Hardy *et al.*, 2005). The disadvantage is that a new DEM is required each time the mesh resolution is changed. However, this has been shown to be a very reliable method to accurately represent roughness in a gravel-bed river (Lane *et al.*, 2004; Hardy *et al.*, 2005).Tests are currently under way to compare these two options, as an appropriate representation of the complex bed topography and roughness is critical in these types of simulation (Biron *et al.*, in prep.). Different mesh resolutions were tested here, and it was concluded that a 300 × 75 × 30 m grid (in the X, Y and Z direction, respectively) was sufficient to produce accurate results. However, due to time constraints, it was not possible to run a formal mesh sensitivity test such as the Grid Convergence Index approach (Hardy *et al.*, 2003).

3 RESULTS

Five video sequences (three taken from the right bank, two from the left bank) were used to obtain a dense coverage of two-dimensional velocity measurements

Copyright © 2006 Taylor & Francis Group plc, London, UK

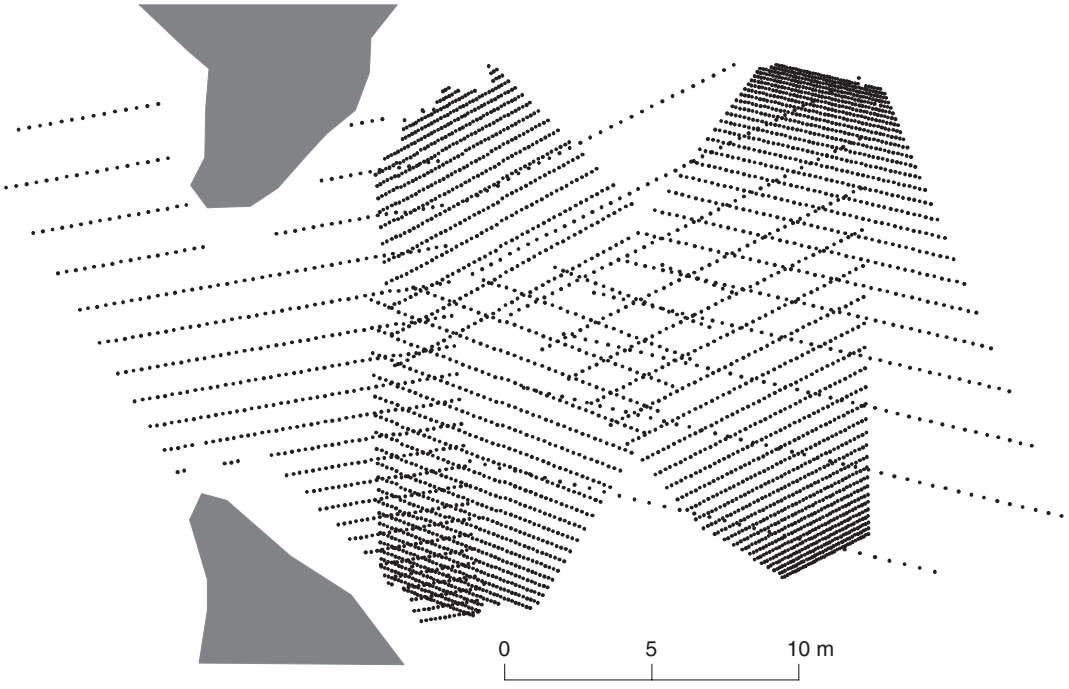


Figure 2. Position of the PIV measurements (black points) obtained from five video sequences (three from the right bank, and two from the left bank). Flow is from left to right, and flow deflectors are shown in grey.

(4310 points in total) near the deflectors (Figure 2). As can be seen on Figure 2, one of the difficulties with PIV taken from the banks is that the pixel size increases from the position of the camera to the outer bank. Hence, the quality of the computed vectors from the cross-correlation analysis decreases with increasing distance from the camera, as the size of the interrogation window increases in real distance (although it is constant in number of pixels). This is particularly problematic where large lateral velocity gradients are present, such as is the case here with two marked circulation zones downstream of the deflectors. In order to compare PIV results with the simulated flow field, we have decided to limit the analysis to the zones where the camera pixel size was sufficiently small to ensure reliable results. Figure 3 shows the velocity vectors obtained from the 3-D simulation, decimated by using one out of four simulated points to improve the readability of the vectors, with the nearest PIV measurements. It can be seen that the overall pattern is consistent, and that the limit of the two recirculation zones is in good agreement between the simulated and observed flow field. This is particularly the case for the recirculation zone near the right bank (looking downstream), but the agreement is less in the left recirculation zone. However, the quantitative agreement (based on all the simulated cells in the zone covered by the PIV) is not as strong as could be expected, with a correlation coefficient for the velocity magnitude of 0.67 between the simulated and PIV vectors. Figure 4 presents the simulated flow field for a larger reach of the Nicolet River, illustrating the marked acceleration between the deflectors, and the markedly reduced velocities both upstream and downstream of the deflectors. The left deflector is slightly longer than the right one, creating an increased deviation on the left side, as well as a larger recirculation zone.

The velocity pattern at the water surface shows a strong deviation of the vectors towards the centre, where the pool is located. This would seem to imply that bed shear stress would be larger in this area. Our observations of bedload transport with PIT tags, however, showed that particles were not moving much in the centre of the channel, but that the bedload movement was occurring on each side of the pool, with more important displacement overall on the left side (looking downstream) (Carré *et al*., in review). When examining the simulation results near the bed (not shown here), a divergence of the flow vectors towards each side of the pool can be seen, which is very different from the pattern observed at the water surface.

Copyright © 2006 Taylor & Francis Group plc, London, UK

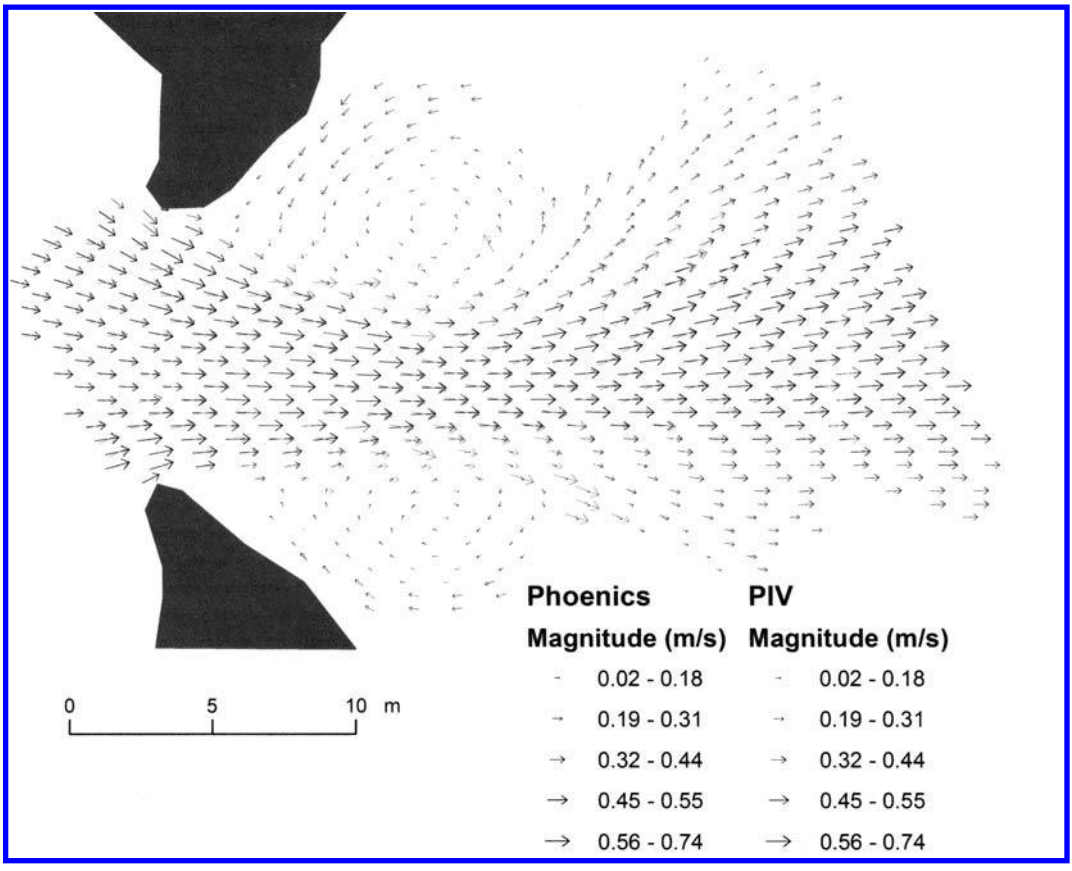


Figure 3. A comparison between velocity vectors at the water surface near the deflectors (in dark grey) resulting from the three-dimensional simulation (in black) and from the PIV analysis (in grey) for points with a dense PIV coverage.

4 DISCUSSION

This is to our knowledge the first attempt to use PIV to validate a three-dimensional model of a natural river. The modeled reach is quite complex due to irregular bed topography (with a deep pool) and the presence of two deflectors generating two large recirculation zones. It is therefore not surprising that the quantitative agreement we have observed between the simulated vectors and those obtained from the PIV analysis is not as high as that obtained in other river modeling studies, where velocity measurements were obtained with an ADV (e.g. Ferguson et al., 2003). Furthermore, the points where the agreement between the model and PIV should be best are those located in the relatively simple flow dynamics zone in the centre of the channel. However, these are the points where the error in PIV will always be highest as it is always located at a large distance from the camera. Thus, the more accurate PIV points were located in areas with very high lateral gradients (the two separation zones), which is problematic when trying to validate the simulated flow field. More work is required to assess how different parameters such as the camera angle, the size of the interrogation window, the use of masks, the type of seeding, etc., affect PIV results. Nevertheless, the high density of velocity measurements obtained with PIV makes it an invaluable tool for validating 3-D models in the future.

5 CONCLUSION

Particle Image Velocimetry results were compared to a three-dimensional numerical simulation of the flow field around flow deflectors to enhance fish habitat in the Nicolet River. The PIV method was successfully tested against ADV measurements, and the agreement between PIV and the model was qualitatively good, particularly in terms of the size of the two recirculation zones downstream from the deflectors. These results are encouraging, and indicate that the 3D modelling

Copyright © 2006 Taylor & Francis Group plc, London, UK

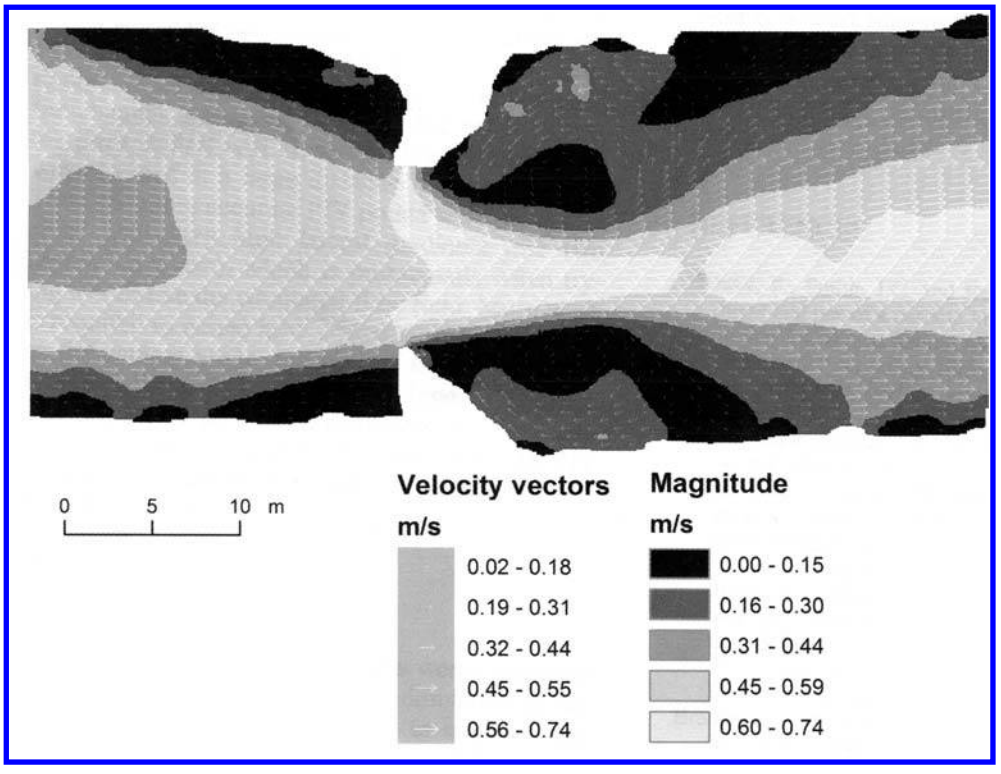


Figure 4. Simulated velocity field at the water surface.

approach to test different river restoration designs prior to their implementation should be pursued. More data at high flow, when water is overtopping deflectors, are required to fully understand the complex flow dynamics around these structures, and the resultant bedload transport. The "object-bed" method used here to design the computational mesh requires less fine-tuning than body-fitted coordinate methods, where problems of skewness or low angles between adjacent cells can be difficult to solve in a complex bed topography problem such as the Nicolet River one. It is therefore faster to test various designs in terms of deflector angle, height and length, and to assess their impact on the flow field and bed shear stress. This will hopefully improve the success rate of future river restoration projects. However, more tests are required to determine whether the object-bed method is adequate to properly represent roughness in gravel-bed rivers with highly heterogeneous bed particles.

ACKNOWLEDGMENTS

This research was funded by NSERC grants (Biron and Gaskin). It has also received the financial support from Project AWARE. We thank Patricia Brelle, Robert Massarelli, Karen Rodrigue-Gervais for field work and PIV analysis assistance. Thanks to the Corporation de Gestion des Rivières des Bois-Francs for permitting us to monitor this field site.

REFERENCES

Bérubé, F., Smith, J.C. and Bergeron, N.E. 2004. Development and use of a particle image velocimetry (PIV) application for aquatic habitat mapping. In: Lastra, D.G.J. and Martinez, P.V. (eds.): Fifth International Symposium on Ecohydraulics, *IAHR Congress Proceedings*, 1223–1226.

Biron, PM., Robson, C., Lapointe, MF, and Gaskin, S. 2004. Deflector designs for fish habitat restoration. *Environmental Management* 33 (1): 25–35.

Biron, P.M., Haltigin, T.W., Hardy, R.J. and Lapointe, M.F. in prep. Assessing different methods for generating a three-dimensional numerical model mesh for a complex stream bed topography. To be submitted to *Journal of Hydraulic Engineering*.

Booker, D.J., Sear, DA. and Payne, AJ. 2001. Modeling three-dimensional flow structures and patterns of boundary shear stress in a natural pool-riffle sequence. *Earth Surface Processes and Landforms* 26 (5): 553–576.

Bradbrook, K.F., Biron, P.M., Lane, S.N., Richards, K.S. and Roy, A.G. 1998. Investigation of controls on secondary

Copyright © 2006 Taylor & Francis Group plc, London, UK

circulation in a simple confluence geometry using a three-dimensional numerical model. *Hydrological Processes* 12: 1371–1396.

Bradbrook, K.F., Lane, S.N., Biron, P.M. and Roy, A.G. 2001. Role of bed discordance at asymmetrical river confluences. *Journal of Hydraulic Engineering*, ASCE, 127(5): 351–368.

Brookes, A., Knight, S. S. and Shields Jr. F. D. 1996. Habitat enhancement, pp. 103–126 *in* A. Brookes and F. D. Shields Jr. [eds.], *River Channel Restoration: Guiding principles for sustainable projects*. John Wiley and sons, New York.

Carré, D.M., Biron, P.M. and Gaskin, S.J. in review. Flow dynamics and bedload sediment transport around paired deflectors for fish habitat enhancement: a field study in the Nicolet River. *Canadian Journal of Civil Engineering*.

Carré, D.M., Biron, P.M. and Gaskin, S.J. 2005. Flow dynamics and sediment transport around paired deflectors for fish habitat enhancement. *Proceedings of the 17th Canadian Hydrotechnical Conference*, Edmonton, Canada.

Creutin, J.D., Muste, M., Bradley, A.A, Kim, S.C., Kruger, A. 2003. River gauging using PIV techniques: a proof of concept experiment on the Iowa River. *Journal of Hydrology*, 277: 182–194.

Ferguson, R.I., Parsons, D.R., Lane, S.N. and Hardy, R.J. 2003. Flow in meander bends with recirculation at the inner bank. *Water Resources Research*, 39(11): 1322–1334.

Fujita, I., Muste, M., Kruger, A. 1998. Large-scale particle image velocimetry for flow analysis in hydraulic engineering applications. Journal of Hydraulic Research, 36, 3: 397–414.

Grant, I, 1997. Particle Image Velocimetry: A review. Proceedings of the institution of mechanical engineers. *Journal of Mechanical Engineering Science* 211 (1): 55–76.

Haltigin, T.W. 2005. Three-dimensional numerical modeling of flow dynamics and investigation of temporal scour hole development around paired stream deflectors in a laboratory flume. *Unpublished MSc thesis*, McGill University, Montreal, 155pp.

Hardy, R.J., Lane, S.N., Ferguson, R.I. and Parsons, D.R. 2003. Assessing the credibility of a series of computational fluid dynamic simulations of open channel flow. *Hydrological Processes*, 17, 1539–1560.

Hardy, R.J., Lane, S.N., Lawless, M.R., Best, J.L., Elliott, L. and Ingham, D.B. 2005 Development and testing of a numerical code for treatment of complex river channel topography in three-dimensional cfd models with structured grids. *Journal of Hydraulic Research*, 43, 5, 468–480.

Hunter, C.J. 1991. *Better Trout Habitat*. Island, Washington, D.C.

Lamarre, H., McVicar, B. and Roy, A.G. 2005. Using passive integrated transponder (PIT) tags to investigate sediment transport in gravel-bed rivers. *Journal of Sedimentary Research*, 75, 4, 736–741.

Lane, SN., Bradbrook, KF., Richards, KS., Biron, PM. and Roy, AG. 1999. The application of computational fluid dynamics to natural river channels: three-dimensional versus two-dimensional approaches. *Geomorphology* 29 (1–2): 1–20.

Lane, S.N., Hardy, R.J., Elliott, L. and Ingham, D.B. 2002. High-resolution numerical modelling of three-dimensional flows over complex river bed topography. *Hydrological Processes*, 16: 2261–2272.

Lane, S.N., Hardy, R.J., Elliott, L. and Ingham, D.B. 2004. Numerical modeling of flow processes over gravelly surfaces using structured grids and a numerical porosity treatment. *Water Resources Research*, 40(1): 1302–1319.

Lane, S.N., Hardy, R.J., Ferguson, R.I. and Parson, D.R. 2005. A framework for model verification and validation of CFD schemes in natural open channel flows. In: Bates, P.D., Lane, S.N. and Ferguson, R.I. (eds.) *Computational Fluid Dynamics: Applications in Environmental Hydraulics*. Wiley, 169–192.

Meselhe, E.A., Peeva, T. and Muste M. 2004.Large scale particle image velocimetry for low velocity and shallow water flows. *Journal of Hydraulic Engineering,* ASCE, 130 (9): 937–940.

Nicholas, A.P. and Smith, GHS. 1999. Numerical simulation of three-dimensional flow hydraulics in a braided channel. *Hydrological Processes* 13 (6): 913–929.

Ouillon, S. and Dartus, D. 1997. Three-dimensional computation of flow around groyne. *Journal of Hydraulic Engineering,* ASCE, 123(11): 962–970.

Richardson, J.E. and Panchang, V.G. 1998. Three-dimensional simulation of scour-inducing flow at bridge piers. *Journal of Hydraulic Engineering, ASCE*, 124(5): 530–540.

Rodriguez, J.F., Bombardelli, F.A., Garcia, M.H., García, M.H., Frothingham, K.M., Rhoads, B.L. et Abad, J.D. 2004. High-resolution numerical simulation of flow through a highly sinuous river reach. *Water Resources Management*, 18: 177–199.

Roni, P., Beechie, T. J., Bilby, R. E., Leonetti, F. E., Pollock, M. M. and Pess, G. R. 2002. A review of stream restoration techniques and a hierarchical strategy for prioritizing restoration in Pacific northwest watersheds. *North American Journal of Fisheries Management*, 22: 1–20.

Smith, J.C., Bérubé, F. and Bergeron, N.E. 2005. A field application of particle image velocimetry (PIV) for the measurement of surface flow velocities in aquatic habitat studies. *Proceedings of the 26th Canadian Symposium on Remote Sensing*, Wolfville, Canada.

Thompson, D. M. 2002a. Long-term effect of instream habitat-improvement structures on channel morphology along the Blackledge and Salmon Rivers, Connecticut, USA. *Environmental Management* 29 (1): 250 65.

Thompson, D. M. 2002b. Channel-bed scour with high versuslow deflectors. *Journal of Hydraulic Engineering*, 128 (6), 640-643.

Weitbrecht, V., Kühn, G., Jirka, G.H. 2002. Large scale PIV-measurements at the surface of shallow water flows. *Flow Measurement and Instrumentation,* 13, 237–245.

Copyright © 2006 Taylor & Francis Group plc, London, UK

C.2 Information technologies and modelling tools for river management

Copyright © 2006 Taylor & Francis Group plc, London, UK

How advances in hydraulic modelling can contribute to solve real problems of flooding: Three examples

A. Paquier
Cemagref, Research Unit Hydrology – Hydraulics, Lyon, France

ABSTRACT: Three cases of flood studies are detailed. The Rivière aux Herbes in Guadeloupe shows an intense sediment transport that increases the water level during flood events. The works along a few hundred metres of the river proved to be dangerous using a 1-D sediment transport model while a simple flow model found lowering of the flood levels. Breaching of the dikes along Ill River is considered in order to define the more risky areas and 2-D modelling is necessary. Along Agly River, a 100-year flood occurred in 1999. This event demonstrated that details representation and model calibration should be improved to simulate more exactly what occurred but modelling met limits because of the lack of observations during the flood. Then, it appears that, by more relevant modelling, the uncertainty of the results could be evaluated and included in the communication process to the users of the potentially flooded areas.

1 INTRODUCTION

For assessing flooding risks, it is necessary to model rare floods that reach areas with specific high stakes. In hilly areas, sediment transport rate can be very high and change the water levels. The use of a model taking into account such a transport is illustrated on the case study of the Rivière aux Herbes (Weeds River). In flat areas when events inundate wide flood plains, 2-D modelling is often required (Paquier & Farissier, 1996). In the Ill flood plain as well as for the Agly River, the dikes and their casual breaching are the main concerns that should be taken into account in flood risk plans. The two cases mainly differ from the recent history: along Agly river, a huge flood occurred in 1999 while such an event has not occurred in the last 100 years along Ill river. The study of these three cases and the applied models are detailed hereafter.

2 FLOODING AND SEDIMENT TRANSPORT ALONG THE RIVIÈRE AUX HERBES

2.1 *Features of the case study*

The Rivière aux Herbes is a torrent of the Island of Guadeloupe in the West Indies. The average slope of the river is more than 5% for most of its length. Along the downstream kilometre, the riverbed has been narrowed because the river crosses the town of Basse Terre. Because of three bridges and a slope reduced to about 1%, flooding is feared along the downstream 200 meters inside the centre of the town.



Figure 1. The works (concrete section) of the Rivière aux Herbes in the town of Basse Terre.

In 1997, calculations showed that the design discharge of 180 m^3/s (corresponding to a 100-year peak flood) could not flow without overtopping of the banks at the second bridge site. In 2001, some works were performed, in particular, the construction of a concrete bed in a 100 m reach (Fig. 1). Sediment transport was not taken into account and the huge amount of boulders deposited in the bed after the first flood (November 2004) clearly showed that a risk of flooding still exists (Fig. 2). To illustrate the effect of these works on the peak water levels during a 100-year flood, it was decided to perform calculations with a model simulating the sediment transport and the change of riverbed during the flood (Paquier, 2005).

Copyright © 2006 Taylor & Francis Group plc, London, UK



Figure 2. The Rivière aux Herbes crossing the town of Basse Terre after the flood event of November 2005.

2.2 *Description of the sediment transport model*

RubarBE is a 1-D model that has been developed by the Hydrology and Hydraulics Research Unit of Cemagref. The model has two components: a component to simulate the flow and a component to characterise the changes in river morphology due to erosion or deposition of sediment. The water routing component relies on De Saint Venant equations for water, solved by a second order Godunov-type explicit scheme (Paquier, 1995). The sediment routing component has the following major features:

1. computation of sediment transport capacity using a suitable *bed load* formula ((Meyer-Peter & Müller, 1948)'s equation in the present study),
2. computation of the actual sediment transport rate Q_s by introducing a space lag equation (the sediment transport capacity and the actual transport rate may differ if geometry is not uniform),
3. numerical solution of the continuity equation for sediment (Exner equation).

At each time step, sediment routing and changes in channel profile are calculated by a finite difference method, coupled with the water surface profile computations (El Kadi & Paquier, 2004).

RubarBE represents sediments by the mean diameter D_{50} and the standard deviation σ. The standard deviation is assessed as the square root of the ratio between d_{84} and d_{16} ($\sqrt{d_{84}/d_{16}}$). It was selected as it appears convenient to describe grain size distribution in a river for which sediments are homogeneous (Shih & Komar, 1990).

The boundary shear distribution τ_j in a cross-section can be calculated by two different methods: either from the uniform equation using water volumetric density ρ, gravity acceleration g, hydraulic radius R and energy slope J ($\tau_j = \rho g R J$, R is computed on the base of the total area and perimeter of the flow) or from the Merged Perpendicular Method (MPM). The first method assumes that the boundary shear stress is constant around the wetted perimeter. The second one is a geometrical method that assumes that the energy gradient is the same in all the sub areas. More precisely, it shares the wetted area in small sub areas using the lines perpendicular to the bottom following a complex procedure described in (Khodashenas & Paquier, 1999). The boundary critical shear distribution τ_{cj} in a cross-section can be calculated in two ways: either from the (Ikeda, 1982) relation that introduced the effect of the local side slope or kept constant as on a horizontal bottom. The mass of sediment eroded or deposited in one cross-section obtained by the computation is distributed along the section. RubarBE incorporates various empirical relationships between deformation and shear stress. In the case of erosion, the deformation ΔZ_j is assumed to be proportional to $(\tau_j - \tau_{cj})^{1.5}$. In the case of sedimentation, deposited sediment in one cross-section can be distributed in four different ways. The selection of the method should usually be based on field observations and on calibration by comparison to field topographic measurements. In the present case study, the deposition was simply set in horizontal layers.

2.3 *Results of the calculations*

In the calculation, the 100-year discharge hydrograph used was a triangular hydrograph that lasts one hour and rises from 1 to 180 m^3/s in half an hour. According to the various sediments covering the bed of the river, the mean diameter of the surface layer ranged from 1 cm (downstream) to 1 m (upstream).

Figure 3 shows that, during such a flood, the deposition or erosion can reach more than one metre and that the works that narrowed part of the river are rather increasing these depths (distance 1920 to 2070). This was in agreement with the observations for a lower flood (Fig. 2). Due to thicker deposits, the calculated water level after the works is higher (Fig. 4). The blockage of boulders there prevents deposits further downstream resulting in lower bed levels after the flood (Fig. 3) and lower peak water levels during the flood (Fig. 4). More precise calibration of the model is necessary to validate these results. However from now, the change in the location of overflows above the banks between the situations with and without works and between the calculations with or without sediment transport means that additional risk has been created by the works and that the calculation with fixed bed cannot provide a relevant estimate of peak water levels.

3 DIKE BREACHING ALONG ILL RIVER

3.1 *Description of case study*

The Ill River, a tributary of Rhine River, crosses the Alsace plain between dikes the crests of which are

Copyright © 2006 Taylor & Francis Group plc, London, UK

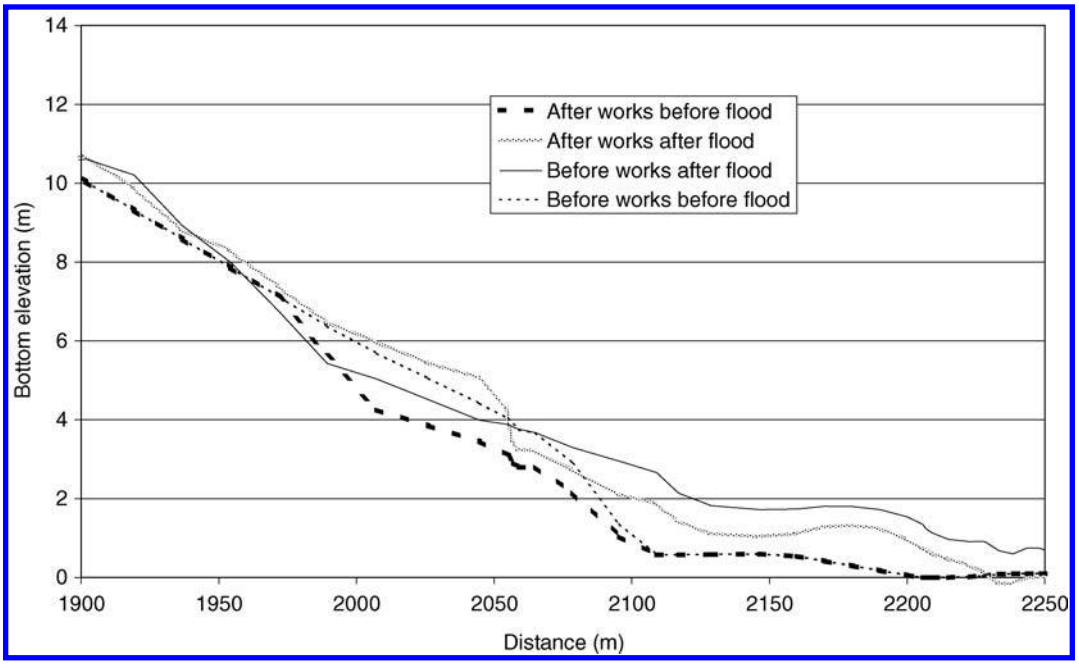


Figure 3. Bottom longitudinal profiles.

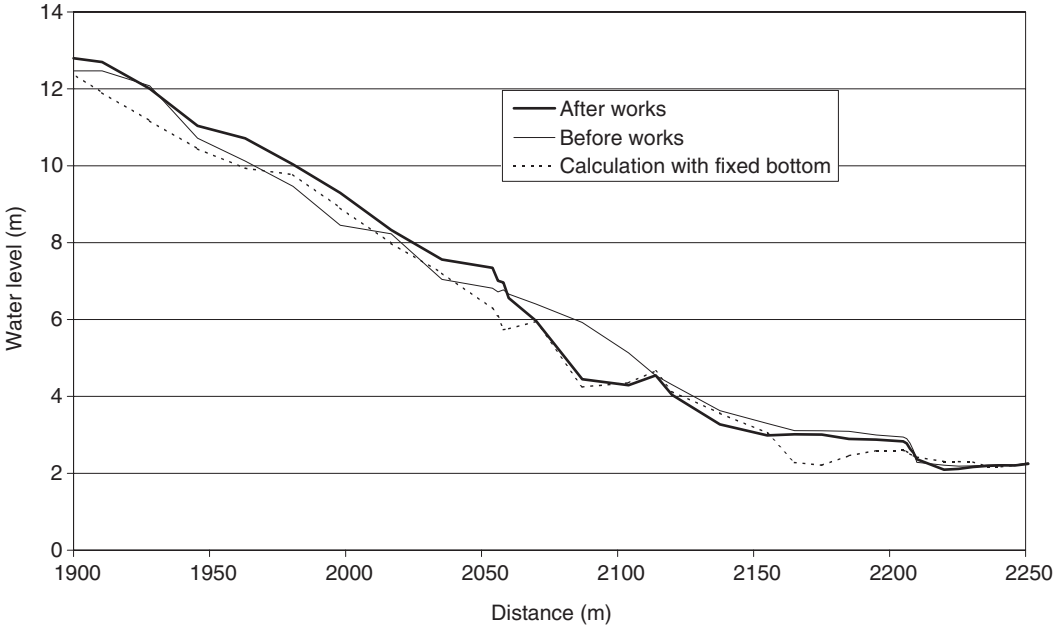


Figure 4. Peak water levels for a 100-year flood.

generally 1 to 2 metres above the mean ground level of the plain. Preparing the plan for flood risks mitigation (PPRI), a hydraulic study using 1-D model concluded that that the dikes are generally high enough for a 100-year flood; the possibility of flowing some discharge in the lower areas and some additional cultivated areas is enough to ensure that the dikes are not overtopped at the location of main villages and towns.

Copyright © 2006 Taylor & Francis Group plc, London, UK



Figure 5. The dikes of Ill River protecting the studied area seen from the river.

The main remaining risk is thus the breaching of these dikes (Fig. 5) because of piping or bank slip.

A first calculation with the hypotheses of instantaneous breaching and 1-D propagation downstream in a direction perpendicular to the dike concluded that there was a high risk in several villages. Thus, it was necessary to perform more detailed hydraulic calculations taking into account the progressive erosion of the embankment and the propagation in all the directions downstream. These two factors could result in less pessimistic results.

A sample calculation was performed in one village, Horbourg-Wihr near the town of Colmar, in order to evaluate the situation there. The model selected was RUBAR 20 that simulates 2-D flow upstream and downstream from the breach and includes the calculation of the breaching process.

3.2 *Description of the model RUBAR 20*

The finite volume scheme used is explicit and second-order accurate. It solves 2-D shallow water equations written as:

$$\frac{\partial h}{\partial t}+\frac{\partial (uh)}{\partial x}+\frac{\partial (vh)}{\partial y}=0 \qquad (1)$$

$$\frac{\partial (hu)}{\partial t}+\frac{\partial (hu^2)}{\partial x}+\frac{\partial (huv)}{\partial y}+gh\frac{\partial h}{\partial x}=\ldots$$
$$\ldots -gh\frac{\partial Z}{\partial x}-g\frac{u\sqrt{u^2+v^2}}{K_s^2 h^{l/3}} \qquad (2)$$

$$\frac{\partial (hv)}{\partial t}+\frac{\partial (huv)}{\partial x}+\frac{\partial (hv^2)}{\partial y}+gh\frac{\partial h}{\partial y}=\ldots$$
$$\ldots -gh\frac{\partial Z}{\partial y}-g\frac{v\sqrt{u^2+v^2}}{K_s^2 h^{l/3}} \qquad (3)$$

in which u and v are velocities along respectively x and y axis, h water depth, Z bottom level, g acceleration due to gravity, K_s Manning Strickler coefficient.

The mesh consists of quadrilaterals or triangles having 0 or 1 (full) common edge. The mixing of these 2 kinds of cells provides various possibilities to adapt to any detail of topography.

The scheme includes 4 steps:

1. computing slope of each one of the 3 variables h (or z water level), hu and hv in every cell on x and y axis by the method of the least squares and applying limitations of slopes.
2. computing values of $W=(h,hu,hv)$ at intermediate state $t_{n+1/2}$ in the middle of the edge m_{ij} of cell i

$$W_{m_{ij}^L}^{n+1/2}=W_{m_{ij}^L}^{n}-0.5\Delta t\ldots$$
$$\ldots\left[f_1'\left(W_i^n\right)W_{xi}^n+f_2'\left(W_i^n\right)W_{yi}^n\right]+0.5\Delta t\,S_i^n \qquad (4)$$

in which f_1 (respectively f_2) are the fluxes on x (respectively y) axis, S the second member, W_{xi}^n the slope of W along x-axis, index L (respectively R) means left (respectively right) side of the edge.

3. solving a 1-D Riemann problems in the direction normal to the edge (equation (5) similar to equations $(1)+(2)+(3)$ on x-axis as these last equations do not vary through a rotation) at $t_{n+1/2}$ in order to estimate the fluxes through edges for the conservative part of the equations. It is possible to use a Roe type linearization which directly gives an estimate of the fluxes

$$\begin{cases}\dfrac{\partial W}{\partial t}+\dfrac{\partial}{\partial x}\left(f_1(W)\right)=0\\ W\left(x,t_{n+1/2}\right)=W_{m_{ij}L}^{n+1/2} & \text{if } x<0\\ W\left(x,t_{n+1/2}\right)=W_{m_{ij}R}^{n+1/2} & \text{if } x>0\end{cases} \qquad (5)$$

4. integrating second member on the surface of the cell in order to add the corresponding contribution and obtaining final value of the 3-D variable W_i^{n+1} by adding second member $S_i^{n+1/2}$ at intermediate time:

$$W_i^{n+1}=W_i^n+\sum_j\frac{\varepsilon_{ij}l_{ij}}{A_i}\Delta t\,f_1\left(W_{m_{ij}}^{n+1/2}\right)+S_i^{n+1/2}\Delta t \qquad (6)$$

in which f_1 represents flux along x axis, summing on j cells which have a common edge with cell M_i (of area A_i) and ε_{ij} equals 1 or -1 according the orientation of edge m_{ij} (length l_{ij}) common to the cells M_i and M_j.

The contribution of the second member includes gravity or slope terms ($-gh\frac{\partial Z}{\partial x}$ or $-gh\frac{\partial Z}{\partial y}$) that are treated as fluxes in such a way as an horizontal water surface remains strictly horizontal, bed friction terms that are more simply assessed at the centre of the

Copyright © 2006 Taylor & Francis Group plc, London, UK

cell. Their computation uses an implicitation in time (Paquier, 1995) in order to avoid numerical instabilities when a rapid change in water depth or velocity occurs.

Dry cells are specifically treated. A cell is considered as dry as long as the water volume entering a cell during one time step provides a water depth below a minimal value (0.1 mm generally). The drying process is the only source of error for the mass conservation; an error more than 0.01% of the total mass generally means instability during computation.

RUBAR 20 may be extended by integration of hydraulic structures where discharge is directly linked with water levels upstream and downstream. One of these structures can represent progressive erosion of an embankment by piping (Paquier et al., 1998). For calculation of flow in this structure, the main hypothesis is that the hydraulic characteristics of water are not modified by the high concentrations of sediment, even during the beginning of the erosion process. During a first step, water starts flowing through a circular pipe and erodes the walls of the pipe so that its diameter is increasing with time. In a second step, when the diameter of the pipe reaches 2/3 of the dam height, the vault of the pipe is assumed to fail; then, water flows in a rectangular channel the width of which is increasing due to erosion of its walls. The embankment is supposed to be of trapezoidal shape and of homogeneous material. Flow characteristics within the pipe are computed from Bernoulli equation with a head loss at the entrance and a linear head loss in the pipe, the sum of which is equalled to the head between the upstream and downstream sides of the embankment.

The initial conditions consist of a small pipe diameter so that the discharge is very low: it may be the median diameter of the material or a little more till 10 cm. The diameter of the pipe increases due to erosion. The volume of material V eroded at each time step Δt is computed from the sediment discharge Qs by $V = Qs * \Delta t$. The sediment discharge is computed from the hydraulic variables by the Meyer Peter Müller's formula. The volume eroded is distributed uniformly over the cross-section, so that the pipe remains circular. The only parameters of the sediment that are taken into account are the density, the diameter and the porosity.

Main result of the computation of the structure is the discharge hydrograph that flows through the breach but the size of the breach can be used as a calibration parameter.

3.3 *Results of the calculations*

The 2-D model (28 226 cells) was applied to 6 kilometres of the river with upstream and downstream boundary conditions defined from 1-D model results. The model was calibrated to obtain, for the 100-year flood calculation without breach, the same levels and flooded areas as the 1-D calculation. Breaches in four different places were successively modelled and, in the central location, three water elevations were supposed in order to estimate the influence of the dike height (Paquier et al., 2005). Several hypothesis on the dike material were also studied because there was uncertainty about the real behaviour of the dike material face to such a 100- year flood; the last extreme flood occurred in the 19th century and the more recent ones that breached the dikes occurred before the dikes were reinforced.

It appears that for a given water depth near the dike, the peak discharge (about 60 m^3/s for the 100- year flood) was mainly related to the final breach width that was set to about 40 metres. In fact, the flood lasts several days and, after the breach formation period, a steady discharge flows through the breach. However, it appears that, with similar discharge, the risk downstream from the breach is very different for different breach locations and depends mainly on local topography that can create local high velocities or local high water depths. However, it appears clearly that the 1-D hypothesis is too pessimistic for water depths and that the instantaneous failure hypothesis creates too high velocities that are not found if the erosion is more progressive.

For practical purpose, the "risky" areas are defined by the values of peak water depth h and peak water velocity v on the basis: $h > 1$ m or $v > 1$ m/s or ($h > 0.5$ m and $v > 0.5$ m/s). The maximum distance from the breach was in the range 60 to 350 metres (example of result with the central breach and instantaneous breaching on figure 6) depending on the case and if a continuous area is considered or not. This rather high range means that the extension of this result to other breach locations and to other villages will be very difficult, which implies that such a detailed calculation should be performed if vulnerability is high in the areas protected by the dikes. If the water elevation in the river is reduced by one metre (the water elevation near the dike goes below one metre), the risky area is limited to the breach area.

4 THE 100-YEAR FLOOD ALONG AGLY RIVER

4.1 *Hydrological context*

The high flood that occurred in the southern part of France near the Spanish Border in November 1999 was one of the highest of the 20th century in the lower reach of Agly River. On November 12 and 13, 1999, the studied area received rainfalls of between 200 and 400 mm within about one day.

The specific configuration of the process in which the higher catchments received less water than the middle and lower catchments, generated relatively

Copyright © 2006 Taylor & Francis Group plc, London, UK

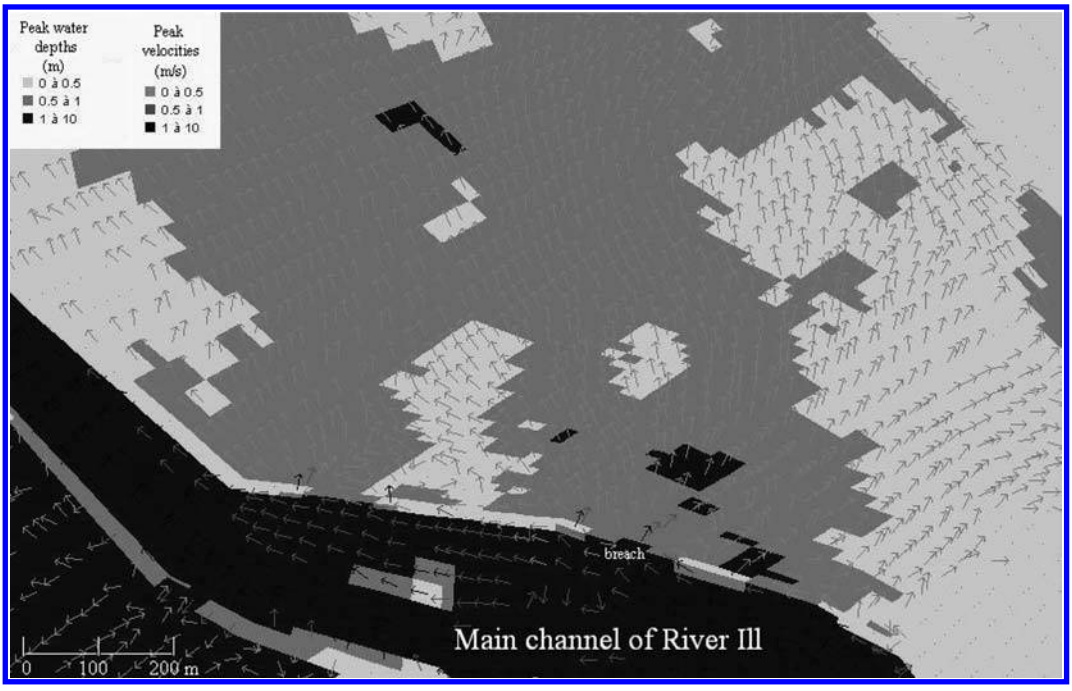


Figure 6. Ill River at Horbourg-Whir – Flooded area downstream the breach for the case of central breaching and instantaneous failure (with peak velocities represented by arrows).

common floods (peak discharge of 180 m^3/s) on the higher catchment of Agly river, which is controlled by a dam, whereas, in Rivesaltes, the main city of this plain, the peak discharge reached about 2000 m^3/s. This discharge was higher than the conveyance of the main channel between the dikes in the lower reach. The dikes and the channel widening carried out in the 1970's were designed for a discharge of 1250 m^3/s and may accommodate a discharge of about 1500 m^3/s without free board.

In November 1999, several overflows occurred along the dikes. These overflows were the cause of the flooding of large areas but only with a few centimetres of water. However, one of these overflows was the origin of a breach that suddenly released a two metre high wave that destroyed a sewage plant in Saint Laurent de la Salanque. This breach, which lowered the water levels in the downstream reach of the main channel, avoided other breaches by reducing or stopping the overflows.

4.2 *Steps of the study*

In 1996, a 2-D model was built in order to simulate the 100-year flood that was supposed to inundate the coastal plain in very limited extent. After completion of the building of a dam in the early 1990's and of dikes along the 13 kilometres downstream reach, the aim was to define the areas that may be considered as safe enough for extension of villages or of commercial areas. The study (BRL Ingénierie et al., 1996) considered the areas directly flooded by the overflows but also those flooded after a breaching of the dikes at some location. From the results of these calculations, some rules were established concerning building in the coastal plain in order not to increase potential damages in the case of a 100-year flood. However, it should be noted that, due to the change in land use (particularly, since 1940), only recent floods may be used for model calibration; thus, only the higher one, the 1992 flood that only inundated a small area, was selected for that purpose.

Immediately after the 1999 flood, the Authorities gathered observations concerning the event and particularly the highest water levels reached during the flood. Topographical campaigns surveyed 43 cross sections of the main channel and the longitudinal profiles of the dikes. In parallel, some urgent works were performed to repair the damage to the dikes (breach and places where either foot erosion or overtopping occurred).

A complementary study (BRL Ingénierie et al., 2001) was carried out in order to get a diagnosis of the state of the dikes and define the short term and long-term works necessary to increase their safety. The definition of some of these works required precise modelling of their effects relative to present situation.

Copyright © 2006 Taylor & Francis Group plc, London, UK

Thus, it appeared necessary to make available a numerical model that would be calibrated from the 1999 flood. This flood was much closer to the 100-year flood (peak discharge: 2295 m^3/s) than the 1992 flood used for calibration of the 1996 model (peak discharge about 1200 m^3/s). To obtain the detailed calibration required, the 1996 model's 2-D grid was refined in order to better represent the main channel of Agly river as well as some places in the right bank near the town of Rivesaltes that was flooded in 1999. The number of cells increased from 8848 to 18568, which means that it was necessary to calibrate the model again.

4.3 *Calibration on the 1999 flood*

Although there was heavy rain over the area, a first simplification was to introduce only one discharge hydrograph at the upstream end of the Agly main channel. This hydrograph was determined from the measurements of water levels at the hydrometric station of Rivesaltes, situated near the RN9 bridge, and their extrapolations after the failure of the device. The peak discharge was estimated at 2000 m^3/s after calibration (comparison with 2-D model results) with a secondary peak at 1900 m^3/s. A sensitivity analysis showed that taking into account the rainfall does not change the general conclusions although it could imply a peak water depth a few centimetres higher in some locations.

Selected Manning coefficients varied from 0.0125 in the river at the crossing of the town of Rivesaltes to 0.14 in the old villages. The Manning values in the flood plain generally do not influence the results too much because of the influence of the embankments and ditches that cross the flood plain. However, it should be stressed that one of the difficulties of the model calibration is the choice of the Manning coefficient values in the Agly main channel because neither the flow discharge between the dikes nor the topography of the main channel during the flood were very certain: no flow measurement occurred at the time of the peak flow and, at the end of the flood, deposits occurred, which reduced the cross section. Thus it was necessary to use lower Manning coefficients to take into account the reduction of cross section between the peak flow and the topographic survey a few weeks after the flood. For some specific areas, other parameters should have been calibrated. Locally, to model some overflows, it was necessary to correct the interpolation of the crest level of the dikes. The sea water level and the Manning coefficient of the outlet to the sea have been modified to obtain the observed water level in the Agly reach downstream of the last bridge: it appeared that a local rise of the sea level, a strong wind or the deposition of sediment significantly raised the water levels there.

More upstream, in Saint Laurent, the modelling of the breach in the dike supposed a very rapid opening (corresponding to the related 2 metres high wave) with the full cross section of the breach as measured (about 40 m wide and 3 m high) and a relatively low Manning coefficient (0.02). The peak discharge through the breach was estimated to be 170 m^3/s; other modelling by a hydraulic structure, either a weir (from the time of the failure) or a specific structure modelling a progressive breaching, provided very similar results.

4.4 *Conclusions on calibration and planning*

It can be stressed that, after such a calibration, the mean difference between observed and calculated maximum water levels in the flood plain was about 10 cm. This difference originates mainly from the Saint Laurent area. The standard deviation was about 40 cm, which seems nearly the minimum possible value if one takes into account the uncertainty in the flood marks and in the topography of the flood plain. The flooded areas are shown on figure 7. To be consistent with observed flooded areas, the limits should be 0 or 20 centimetres water depths depending of the location. Such result is linked with the drainage system status or with local protection structures and no general explanation can be found. After calibration, the water levels remain low in Saint Laurent and slightly too high in Rivesaltes.

In this latter town, a few people discussed because model provided higher water levels than observed in 1999. Although the difference (about 30 cm) remains relatively low and agreed with the general precision of the model, some additional action was necessary. The uncertainty of the model was illustrated by casual events such as blocking of water evacuation structures by trees. However, as financial interests were concerned, simple explanations are not enough. Fortunately, as 100-year flood discharges are slightly higher than the 1999 flood, results of the calculation for the 100-year flood were kept for planning purposes. Moreover, as the model represents quite well the propagation processes, it was pointed out that the main requirement to improve the adequacy of the model was to incorporate additional data such as observations during next flood events.

5 CONCLUSIONS

For the simulation of a flood extending over a large flood plain or coming from a breach or a hydraulic structure in a dike, it is necessary to use 2-D shallow water equations completed by relations such as those of hydraulic structures (weirs, gates…). Such a tool is efficient to represent the main processes met during such events. However, during calibration, it is very difficult to represent all the details of a real event (Agly case). This implies that events selected for planning should be typical events (for instance, of a selected

Copyright © 2006 Taylor & Francis Group plc, London, UK

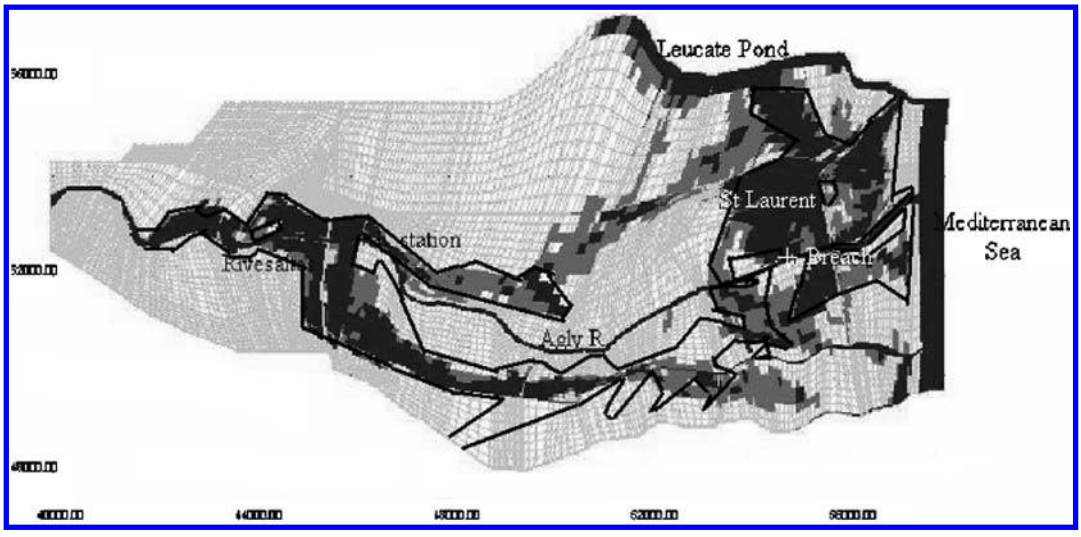


Figure 7. Lower Agly flood plain – Comparison of calculated flooded area (darker area means water depth more than 20 cm) with the limit estimated from observations (black line).

return period for all the durations) and not real ones to avoid discussions on the planning decisions.

When no similar event exists (Ill case), the use of such a 2-D model that reduces the uncertainty linked with the representation of the processes, could ensure that the level of mitigation measures is not too high.

In the context of high sediment discharge during the flood (case of Rivière aux Herbes but, also in a smaller extent, case of Agly river), it is necessary to use a sediment transport model that can take into account the change in bed elevation during the flood. For the Rivière aux Herbes, it is shown that sediment transport can imply a change in the location of the flooded areas and, sometimes, a rise in peak water level, which means an increase of the flood risk.

The calculations cannot provide precise results as often no calibration data are available neither for sediment transport nor for extreme flooding but they can contribute to assess the uncertainty of modelling and thus contribute to the awareness of the concerned people.

REFERENCES

BRL Ingénierie & Cemagref 2001. Etude hydraulique de l'Agly de Rivesaltes à la mer, DDE Pyrénées Orientales, Perpignan, France. 140 p.

BRL Ingénierie & Cemagref 1996. Etude des débordements de l'Agly en aval de Rivesaltes, DDE Pyrénées Orientales, Perpignan, France. 80 p.

El Kadi, K., Paquier, A. & Sardoy, N. 2004. Sediment transport and morphology in the Loire River – Site of Fresne sur Loire. *12th International Conference on Transport & Sedimentation of Solid Particles*, Prague, Czech Republic, 257–265.

Ikeda, S. 1982. Incipient motion of sand particles on side slopes. *Journal of the Hydraulics Division*, 108(HY1), 95–114.

Khodashenas, S. R. & Paquier, A. 1999. A geometrical method for computing the distribution of boundary shear stress across irregular straight open channels. *Journal of Hydraulic Research*, 37(3), 381–388.

Meyer-Peter, E. & Müller, R. 1948. Formulas for bed-load transport. *Report on second meeting of IARH*, Stockholm, Sweden, 39–64.

Paquier, A. 1995. Modélisation et simulation de la propagation de l'onde de rupture de barrage (Modelling and simulating the propagation of dam-break wave). PhD thesis, Université Jean Monnet, Saint Etienne, France.

Paquier, A. & Farissier, P. 1996. Use of a 2-D model for simulating the flooding of a plain, *in* Muller, A., ed., Hydroinformatics' 96, Volume 1: Zurich, Switzerland, Balkema, Rotterdam, 129–136.

Paquier, A., Nogues, P. & Herledan, R. 1998. Model of piping in order to compute dam break wave, *in* Wallingford, H.R., ed., Second CADAM meeting proceedings: Munchen, Germany, European Commission, Science Research Development, Hydrological and hydrogeological risks., Paper 4, 6p.

Paquier, A. 2005. Expertise sur les aménagements prévus sur la Rivière aux Herbes. Cemagref, Lyon, France.

Paquier, A., Lang, M. & Royet, P. 2005. Expertise de l'étude hydraulique préalable au PPR de l'Ill. Cemagref, Lyon, France.

Shih, S.-M. & Komar, P. D. 1990. Hydraulic controls of grain-size distributions of bedload gravels in Oak Creek, Oregon, USA. *Sedimentology*, 37, 367–376.

Copyright © 2006 Taylor & Francis Group plc, London, UK

Solute transfer from soil surface to runoff as a boundary condition in open channel flow modeling

M. Nofuentes
Sustainable Agriculture Institute, Consejo Superior de Investigaciones Científicas, Córdoba, Spain

M.J. Polo
Agricultural Hydrology and Hydraulics Research Group, University of Córdoba, Spain

J.V. Giráldez
Sustainable Agriculture Institute, Consejo Superior de Investigaciones Científicas, Córdoba, Spain,
Agricultural Hydrology and Hydraulics Research Group, University of Córdoba, Spain

L. Mateos
Sustainable Agriculture Institute, Consejo Superior de Investigaciones Científicas, Córdoba, Spain

ABSTRACT: Solute transfer from soil surface to runoff is a complex process where soil characteristics,solute chemical kinetics and surface flow conditions interact. Up until now, it has rarely been included as a boundary condition in open channel flow models. The objective of this study is the characterization of this transfer process in shallow water flows. To this purpose, a series of experiments were carried out in a laboratory flume, 9 m long with a 0.002 slope, over a loam texture soil, where a tracer was located transversally over the surface of an area 0.05 m long, under different inlet flow conditions. The results show the temporal evolution of the tracer transfer to the surface flow, together with the parameterization of the load function obtained and its relation with flow characteristics.

1 INTRODUCTION

Solute transfer from soil surface to runoff constitutes a potential source of pollutants for surface waters and, indirectly, for groundwater as well. This is a complex process where the soil parameters and initial conditions that determine infiltration and runoff generation evolution, and the solute chemical kinetics interact with the surface flow characteristics, especially those related to advective and diffusive-dispersive transport (Ahuja 1990).

Moreover, the nonlinearity exhibited by solute transport in such conditions makes it necessary to obtain a good definition of solute transfer from soil as a boundary condition when modeling surface water flow quality, for both punctual and distributed sources of substances. This fact, which is important in Mediterranean basins, is a widespread phenomenon during the summer period when salt excess, nutrients or pollutants are concentrated in the upper layer of the soil due to the extreme atmospheric evaporative conditions, and where intermittent shallow flows frequently occur after summer storms. Furrow irrigation of crops is another good example.

Two approaches have been proposed to describe this process, depending on the predominant transport process considered: the first approach assumes the existence of a dead water layer in the soil-surface water interface, from which solute transfer to runoff takes place by molecular diffusion (Wallach et al. 1988), whereas the second approach defines a narrow surface layer of soil, called the mixing zone, where rainfall/irrigation water and the soil solution instantaneously mix (Zhang et al. 1997), and it is considered the only source for solute transfer to runoff.

Most previous work so far (Ahuja 1990) has been based upon the second theory, and has focused on solute transfer when runoff generation results from precipitation events, since there is little or no data available nor experimental studies of shallow flows, such as furrow irrigation, or intermittent summer flows in semiarid environments.

This research thus provides a first characterization of solute transfer from soil to runoff for the latter

Copyright © 2006 Taylor & Francis Group plc, London, UK

conditions, where the saturation of the soil top layer (ponding condition) almost instantaneously occurs. This differs from rainfall occurrence, where a ponding condition usually lags behind the initiation of rainfall, enhancing solute transport downwards through the soil profile to groundwater. The following sections describe the experimental work and data analyses carried out. The resultant load function is to be integrated as a boundary condition in a 1D numerical model of surface water-solute flow over a porous bed for application in furrow irrigation.

2 MATERIALS AND METHODS

2.1 *Experimental design and measurements*

In order to establish the effects of surface water flow characteristics on soil solute transfer potential, a set of laboratory assays was carried out in a 9 m long flume channel with a uniform rectangular 0.5 m wide cross section, and a uniform 0.002 longitudinal bed slope, where the top layer of a cropland soil was reproduced. Runoff was generated by the application of a constant water flow rate Q_0 at the flume head during each experimental performance, ranging from 0.54 to 4.72 L s^{-1} between assays, with no water column at any point of the flume as initial conditions (dry condition).

The soil filling consisted of a layer of 2 mm sieved soil, 30 cm deep, from an alluvial bank of the Guadalquivir River Valley in Córdoba (Southern Spain), where previous experimental work on fertigation had been carried out by the authors (Nofuentes et al. 2004). This soil filling was sampled from the three upper sublayers of soil, corresponding to 0–5, 5–18, and 18–30 cm deep divisions, and it was orderly packed in the flume to a bulk density value similar to the original field conditions. The soil layer was placed over a 10 cm deep filtering gravel bank, which had previously proven sufficient to ensure free draining conditions at the bottom of the flume bed.

The soil was classified as a *Typic xerofluvent* (Soil Survey Staff 1999), or *Eutric fluvisol* (FAO 1988), with a loam textural class, low organic matter content (1%), and significant calcic carbonate presence (20%).

A concentrated 5 cm long and 1 cm deep cross fringe of highly soluble non-reactive tracer (KBr) was located at a 4 m distance from the flume head to avoid border effects from the water source point. The tracer fringe was prepared after previous mixing of the upper soil sublayer with an excess quantity of tracer (calculated for each Q_0 interval and run duration from preliminary work) to ensure that the transfer process was not limited by the initial tracer concentration in the soil. Table 1 shows Q_0 values, applied KBr mass, and the initial water content of soil for each run performed.

The evolution of the KBr concentration in the runoff along the channel was estimated from EC measurements made with portable conductivity meters throughout each run at three different stations located at a distance of 3 cm upstream from the fringe, and 3 and 200 cm downstream from the fringe, known as stations 1, 2, and 3, respectively. Previously calibrated KBr-EC curves obtained from laboratory determination in standard solutions were used for the calculation of KBr concentrations. Stations 2 and 3 monitored solute transfer to runoff and loss along the channel by infiltration, along with dispersion effects, respectively, whereas station 1 was used to check the possible solute dispersion upstream of the source.

Advancing time and water depth evolution were measured at nine cross sections along the channel, which included the previously mentioned solute monitoring stations. The outflow at the end of the channel was gauged by volumetric measurements.

Figure 1 shows a schematic description of the experimental design and Figure 2 the experimental flume channel and a fringe detail.

Table 1. Head constant water flow rate applied (Q_0), initial tracer mass in the fringe (M_o), and initial soil water content (θ) for each experimental run.

Run	Q_0 (Ls^{-1})	M_o (kg)	θ ($kgkg^{-1}$)
1	0.54	0.372	0.076
2	1.00	0.672	0.140
3	2.50	0.372	0.150
4	3.22	0.372	0.155
5	4.72	0.372	0.180

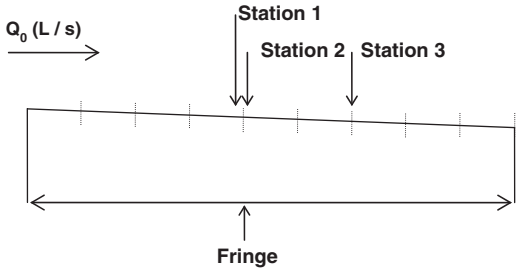


Figure 1. Schematic description of the experimental device along the flume channel. ……Depth and advancing time measuring section locations.

2.2 *Water flow modeling*

Instantaneous water flow rate values and section-averaged velocity were calculated along the channel from a 1-D numerical model following the MacCormack method (Burguette 2003, Maikaka 2004), applied to the cross integrated Saint Venant equations

Copyright © 2006 Taylor & Francis Group plc, London, UK

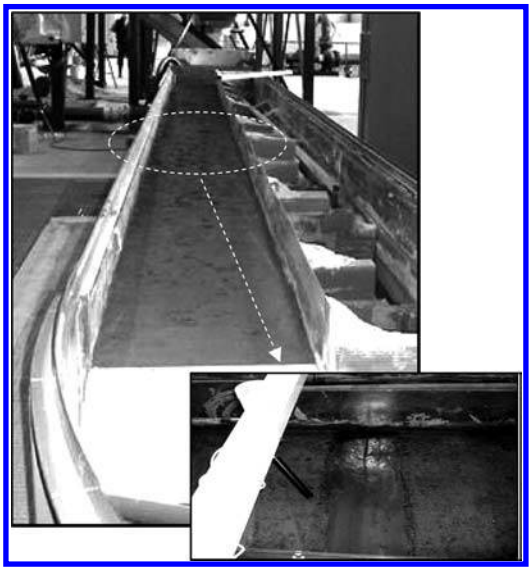


Figure 2. Experimental flume channel and fringe detail with a portable conductivity meter in the first station.

for mass and momentum conservation in surface flow (Equations 1 and 2, respectively),

$$\frac{\partial A}{\partial t}+\frac{\partial Q}{\partial x}+\frac{\partial Z}{\partial t}=0 \tag{1}$$

$$\frac{\partial Q}{\partial t}+\frac{\partial}{\partial x}\left(\frac{Q^2}{A}+gI_1\right)= =gI_2+gA\left(S_0-S_f\right)+D_i \tag{2}$$

where, at a time t and a distance x from the water source, A is the cross sectional area; Q is the instantaneous volumetric water flow rate; Z is the accumulated infiltration volume per unit length; I_1 and I_2 represent the unit hydrostatic pressure force and unitary pressure force due to longitudinal width gradient, respectively; S_0 and S_f are the bed and friction slopes, respectively; g is the acceleration of gravity; and D_i the momentum transfer associated with seepage outflow in the direction of the flow (Playán et al. 1997).

These equations were developed in a one-dimensional approach, using the Manning equation to calculate the friction slope.

The temporal evolution of Z can be estimated from the Kostiakov – Lewis equation, commonly used for water irrigation infiltration modeling (e.g. Walker 1989),

$$Z=k\cdot t_{opp}^{a}+f_0\cdot t_{opp} \tag{3}$$

where t_{opp} is the opportunity time at a distance x from the water source ($t_{opp}=t-t_{ad}$, t_{ad} is the time the water front arrives at a point x, the advancing time); k and a are empirical parameters (see Table 2 for dimensions); and f_0 stands for the stationary value that the unit length infiltration rate tends to reach, provided sufficient time has elapsed.

Table 2. Kostiakov-Lewis equation parameter and Manning coefficient (n) calibration for each run.

Run	f_0 ($m^3m^{-1}s^{-1}$)	k (m^2s^{-a})	a	n (SI units)
1	$0.045\cdot10^{-4}$	0.0025	0.050	0.031
2	$0.131\cdot10^{-4}$	0.0180	0.018	0.020
3	$0.240\cdot10^{-4}$	0.0048	0.050	0.019
4	$0.062\cdot10^{-4}$	0.0075	0.052	0.019
5	$0.072\cdot10^{-4}$	0.0030	0.002	0.020

Table 2 shows the calibrated values for Equation 3 parameters and the Manning coefficient for each run, from the water flow measurements, assuming homogeneous soil behavior.

2.3 *Solute transfer from soil to runoff modeling*

An exponential load function, $W(\zeta)$, is proposed in this study to describe punctual solute transfer from soil to runoff (Chapra 1997),

$$W(\zeta)=W_0\cdot e^{\beta\zeta} \tag{4}$$

where W_0 [MT^{-1}], is the solute mass load at the initial time of the transfer process; $\beta[T^{-1}]$ is a transfer coefficient; and ζ is the time interval elapsed since the beginning of the transfer process. In this study ζ equals the opportunity time, t_{opp}, since solute transfer is initiated once the water front meets the fringe location (i.e. at the advancing time).

Experimental $W(\zeta)$ curves were obtained for each run from the calculated KBr concentration values from station 2 EC measurements, and the instantaneous water flow rate values from the numerical model for $x=4$ m, adjusting W_0 and β values by lineal regression. Dispersion effects at station 2 during the transfer process were regarded as negligible and thus not considered in our calculations.

2.4 *Longitudinal dispersion coefficient*

Non-reactive substance transport in longitudinal systems, such as streams or channels, can be described by the cross section integrated one-dimensional form of the advection-diffusion equation (e.g. Rutherford 1994), which can be written as Equation 5 for non-uniform flows,

$$\frac{\partial(AC)}{\partial t}+\frac{\partial(AvC)}{\partial x}=\frac{\partial}{\partial x}\left(AE\frac{\partial C}{\partial x}\right) \tag{5}$$

where C and v are the averaged values of solute concentration and velocity at a cross-section, for the time

Copyright © 2006 Taylor & Francis Group plc, London, UK

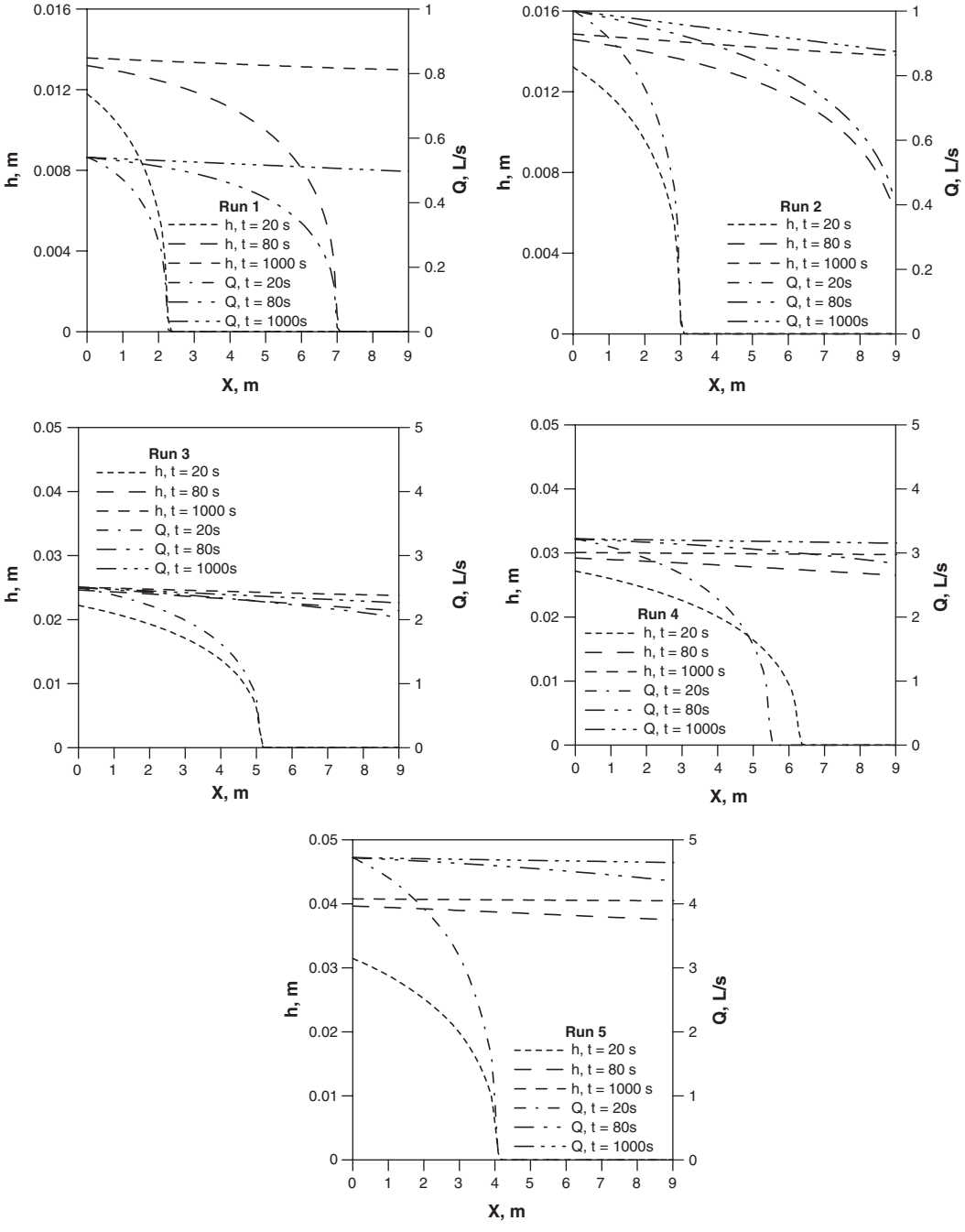


Figure 3. *Q* and *h* evolution along the channel for runs 1 to 5, respectively; x is measured from the water source point at the head of the channel; the tracer fringe is located at x = 4 m (station 2 in fig. 1).

Copyright © 2006 Taylor & Francis Group plc, London, UK

t, and E is the longitudinal dispersion coefficient, which accounts for vertical and cross velocity gradient contribution to the dispersion term.

The relative importance of the advection and dispersion term in Equation 5 can be tested by comparison of the Peclet number along the channel.

To that purpose, the stationary velocity value at the head cross section and the distance between the fringe location and the end of the channel were taken as characteristic velocity and length, respectively (v_0 and L, in Equation 6 after the non-dimensioning of Equation 5.

$$Pe = \frac{v_0 L}{E} \tag{6}$$

The local values of the longitudinal dispersion coefficient were estimated from the expression developed by Fischer et al. (1979) for logarithmic vertical velocity profiles in natural streams,

$$E = 0.011 \frac{v^2 b^2}{h u_*} \tag{7}$$

where b is the channel width, h is the cross section-averaged water depth, and u_* is the shear velocity. All of these variables are expressed in SI units. The shear velocity is given by

$$u_* = \left(\frac{\tau}{\rho}\right)^{1/2} \cong \sqrt{ghS_0} \tag{8}$$

where τ is the shear stress over the channel bed approximated by:

$$\tau = \rho g S_0 h \tag{9}$$

ρ is the water density, and h, the water depth at the section.

3 RESULTS AND DISCUSSION

Q and h evolution along the channel calculated by the numerical model described in section 2.2 for each run performed can be seen in Figure 3. The experimental water depths and advancing time measurements made during each run were used to calibrate the model (see Table 2 for Manning coefficient values).

From the results, it can be seen how soil surface saturation is promptly achieved, with a transient period very close to 20 minutes in all runs.

Figure 4 shows v evolution at station 2, where the tracer fringe was located, along with the Froude and Reynolds numbers.

The temporal evolution of KBr concentration at the three monitoring stations is shown in Figure 5 for each run, versus the opportunity time (t_{ad} = advancing time at station 2 for runs 1 to 5, respectively).

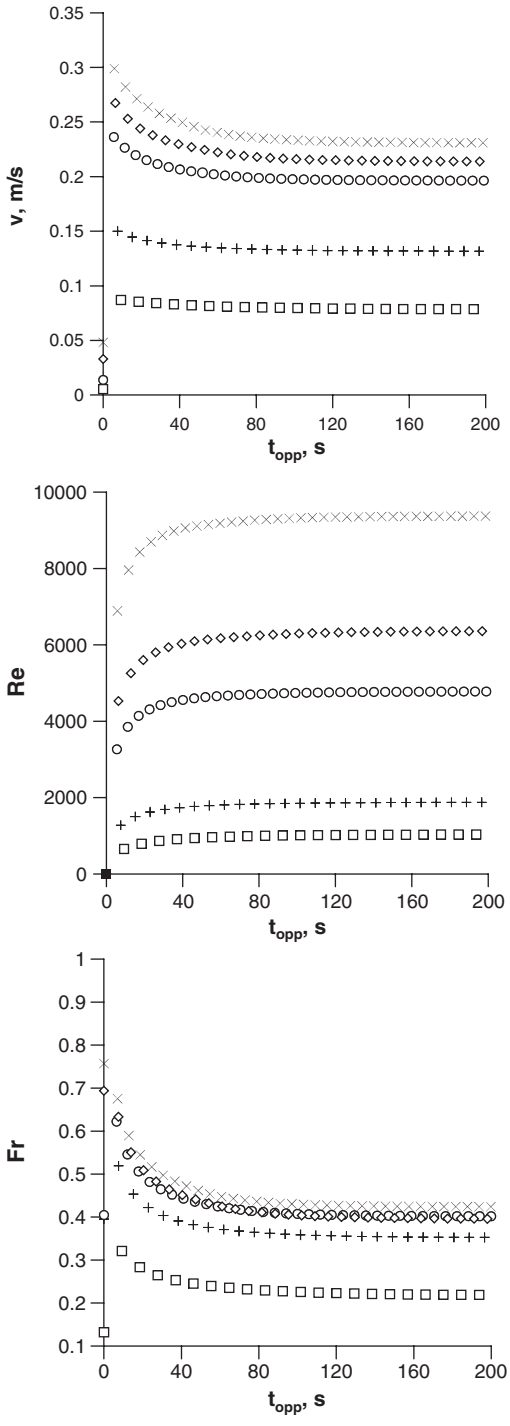


Figure 4. *v, Re*, and *Fr* temporal evolution at station 2 for each run performed; □ run 1, + run 2, ○ run 3, ◇ run 4, × run 5; t_{opp} is opportunity time at station 2.

Copyright © 2006 Taylor & Francis Group plc, London, UK

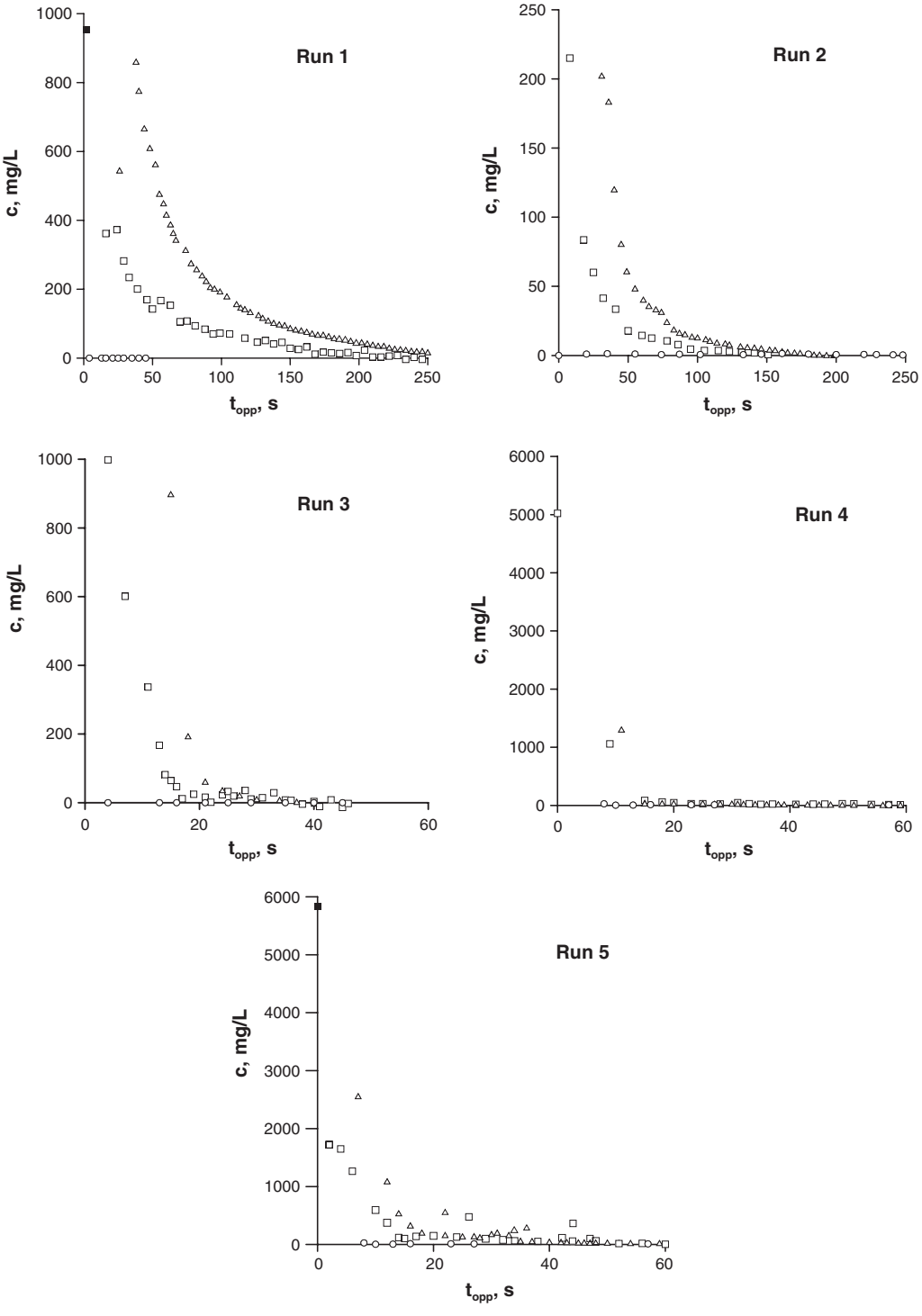


Figure 5. Temporal evolution of tracer concentration at the monitoring stations for each run; ○ station 1 (3 cm upstream of the solute fringe), □ station 2 (over the fringe), △ station 3 (2 m downstream of the fringe), t_{opp} is opportunity time at station 2.

Copyright © 2006 Taylor & Francis Group plc, London, UK

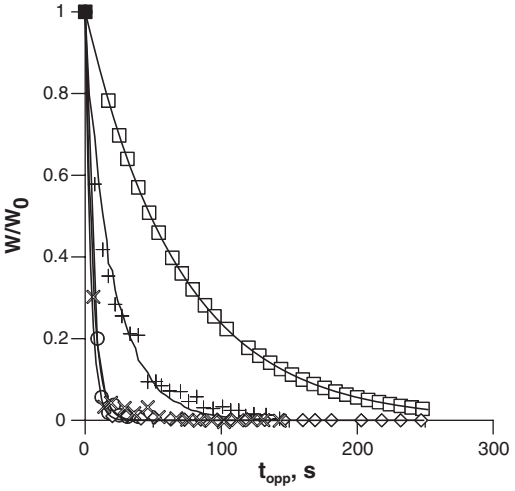


Figure 6. Observed and calculated non-dimensional $W(t_{opp})$ curves at station 2 for each run; □ run 1, + run 2, ○ run 3, ◇ run 4, × run 5; t_{opp} is opportunity time at station 2.

Table 3. W_0, β adjusted values in Equation 4 for each run, and solute mass recovery, at station 2.

Run	W_0 (kg s^{-1})	β(s^{-1})	R^2	$T_{0.99}$(s)	M(kg)
1	$0.077 \cdot 10^{-3}$	0.014	0.95	200	$5.1 \cdot 10^{-3}$
2	$0.123 \cdot 10^{-3}$	0.045	0.98	68	$2.6 \cdot 10^{-3}$
3	$1.237 \cdot 10^{-3}$	0.185	0.95	40	$6.7 \cdot 10^{-3}$
4	$11.56 \cdot 10^{-3}$	0.186	0.94	22	$61.1 \cdot 10^{-3}$
5	$13.58 \cdot 10^{-3}$	0.246	0.99	20	$54.8 \cdot 10^{-3}$

Higher concentrations were reached at station 2 over the fringe. As expected, non-detectable concentrations were found at station 1 in all cases. This result validates the hypothesis of negligible dispersion effects upstream of the solute source for these experimental conditions.

Concentration values are lower at station 3 not only because of the dispersion effects along the reach, but also because of the simultaneous advance of water and solute, as the initial concentrated flow was infiltrated immediately downstream of the fringe position. This effect decreases with time as stationary conditions are approached. The non-dimensional form of the load function points, calculated at station 2 as described in section 2.3, are presented in Figure 6 for each run, along with their respective adjusted curves W/W_0 after Equation 4.

Table 3 shows the calibrated parameter values obtained, and the corresponding correlation coefficient, with the total solute mass transferred to runoff, M, and the response time for a 99% solute mass recovery, $T_{0.99}$.

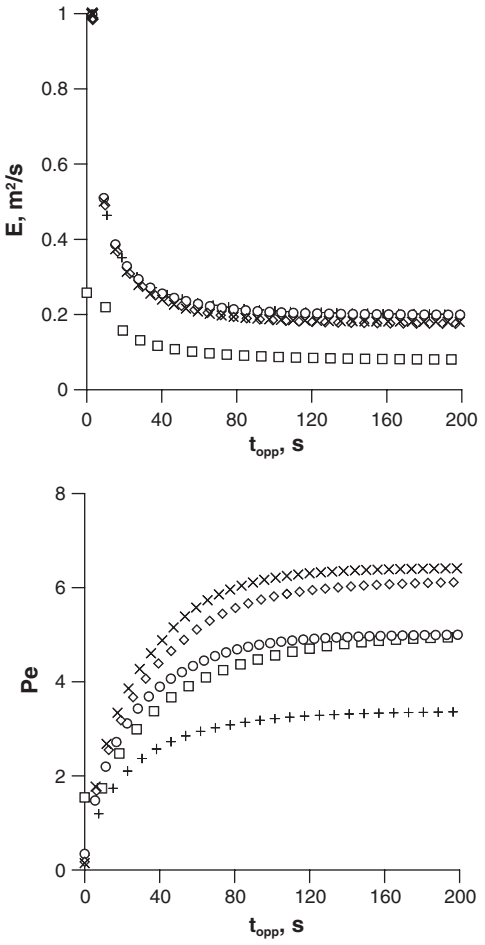


Figure 7. E and Pe evolution at station 2 for each run; □ run 1, + run 2, ○ run 3, ◇ run 4, × run 5; t_{opp} is opportunity time at station 2.

From Table 3 values, it can be seen that both W_0 and β grow with increasing flow rates. In other words, for higher Q values solute transfer rate is initially higher too, but it evolves more quickly, fading in a shorter period. Similar trends were reported by Wallach & Van Genuchten (1990), and Zhang et al. (1997), though with different mass recovery results due to runoff generation from rainfall occurrence dynamics.

Accordingly, the total solute mass transferred from soil to runoff, M, was increased for higher flow rate values, whereas the response time, $T_{0.99}$, decreased.

Finally, the temporal evolution of E and Pe in station 2 for each run, calculated after Equations 7 and 6, respectively, are presented in Figure 7. During each run, the highest E values were found at the transient period for water flow, decreasing with time, with the corresponding inverse trend for Pe. For stationary flow

Copyright © 2006 Taylor & Francis Group plc, London, UK

conditions, runs 2 to 5 can be grouped separately from run 1. The reason can be found in Figure 4, where a different Reynolds regime applies for each group, with marked turbulence in runs 3 to 5, and very low Froude values for run 1. However, differences between E values between groups tend to decrease as stationary conditions are approached, whereas it is the contrary for Pe values.

4 CONCLUSIONS

Solute transfer from soil to runoff from a cross concentrated narrow fringe during transient flow advance conditions can be adequately described by an exponential load function, as shown in this research. The equation parameters W_0 and β have been quantified for different flow conditions, under a non-limited solute supply from soil, showing an intensification and shortening of the transfer process with growing water flow rates. In general, for the flow conditions experimented the process is very quick, with marked dispersive predominance during the transient period, whereas the stationary conditions exhibit a predominantly advective character. This behavior is not expected in slower flows with higher infiltration rates and/or wider sections.

The comparison between trends showed by E and Pe values at the source location underlines the relevance of taking into account the temporal aspects of the solute transfer to water flow when characterizing dispersion in surface waters: application time and duration of solute entry to flows.

The results of this work are being included in a 1-D numerical model for transient flow conditions, with application in fertigation modeling.

ACKNOWLEDGEMENTS

This work was funded by the National Plan of Research and Development of the Spanish Ministery of Education and Science, in the project AGL 03-01958 *Agrochemical and sediment transport in furrow irrigation*. The authors wish to thank the University of Castilla-La Mancha, Spain, for the use of the Hydraulics Laboratory of the Technical School of Civil Engineering for the experimental work. M.J. Polo would like to thank Gloria Gómez for her valuable help.

REFERENCES

Ahuja, L.R. 1990. Modeling soluble chemical transfer to runoff with rainfall impact as a diffusion process. *Soil Sci. Soc. Am. J.* 54: 312–321.

Burguette, J. 2003. Modelos unidimensionales de flujos de superficie libre y transporte en geometrías irregulares: Aplicación al flujo en ríos. Unpublished Ph.D. thesis, University of Zaragoza, Spain.

Chapra, S.C. 1997. Surface Water-Quality Modeling. McGraw-Hill. New York.

FAO. 1988. Soil Map of the World. Revised Legend. World Soil Resources Report. FAO. Roma.

Fischer, H.B., List, E.J., Koh, R.C.Y., Imberger, J. & Brooks, N.H. 1979. Mixing in Inland and Coastal Waters. Academic Press. New York.

Maikaka, M. 2004. Modelos numéricos unidimensionales en riego por superficie. Unpublished Ph.D. thesis, University of Zaragoza, Spain.

Nofuentes, M., Polo, M. J., Giráldez, J. V. & Mateos, L. 2004. Aspectos temporales de la eficiencia del fertirriego por surcos. *Actas XXII Congreso Nacional de Riegos* (Logroño, 15–17 June, 2004), B-12, 10 pp. Logroño, Spain.

Playán , E. & García-Navarro, P. 1997. Radial flow modeling for estimating level-basin irrigation parameters. *J. Irri. Drain. Engng.*123: 229–237.

Rutherford, J. C. 1994. River Mixing. J. Wiley, Chichester.

Soil Survey Staff. 1999. Soil Taxonomy, Agr. Hbk. no. 436, 2nd ed., USDA. Washington.

Walker, W.R. 1989. Guideline for designing and evaluating surface irrigation systems. *Irrigation and Drainage* Paper No. 45. FAO, Roma.

Wallach, R., Jury, W.A. & Spencer, W.F. 1988. Transfer of chemicals from soil solution to surface runoff: A diffusion-based soil model. *Soil Sci. Soc. Am. J.* 52: 612–618.

Wallach, R. & Van Genuchten, M. T. 1990. A physically based model for predicting solute transfer from soil solution to rainfall-induced runoff water. *Water Resour. Res.* 26: 2119–2126.

Zangh, X.C., Norton, D. & Nearing M.A. 1997. Chemical transfer from soil solution to surface runoff. *Water Resour. Res.* 33: 809–815.

Copyright © 2006 Taylor & Francis Group plc, London, UK

Loose-bed models for river structure design: Two example studies on river Po

M. Guerrero & A. Lamberti
DISTART Idraulica, University of Bologna, Italy

ABSTRACT: Objects of the study are the predictable effects on river Po local bed morphology of two structures of national interest: the new railway bridge between Revere and Ostiglia, and the entrance of the new Pontelagoscuro navigation lock. Aiming to adequately represent alluvial bed forms and local scour and deposition effects of the structures, two movable-bed physical models were constructed: one for the bridge in planimetric scale 1:150, vertical 1:120, and one in undistorted scale 1:100 for the lock entrance. The inner harbor physical model results were compared with bi-dimensional hydro-morphological numeric simulations carried out with the mathematical model Mike21C. Physical and numerical models provided results in good agreement and useful for the design of the inner harbor, the first physical model suggested a variant in the designed construction programme and confirmed the construction process and design of bridge piers, including the type and dimension of bed protections.

1 INTRODUCTION

Aiming to adequately represent the alluvial bed forms and local scour-deposition effects of two national projects on river Po, two movable-bed physical models were constructed: one for the railway bridge between Revere and Ostiglia (Bologna-Verona railway), and one for lock entrance of the inner harbor of Pontelagoscuro near Ferrara.

The first physical model had suggested a variant in the designed construction programme and confirmed the construction process and design of bridge piers, including the type and dimension of bed protections.

The inner harbor physical model results were useful in choosing the best lock entrance configuration in order to minimize sand deposition, and were compared with bi-dimensional hydro-morphological numeric simulations carried out with the mathematical model Mike21C by DHI Water and Environment (Danish Hydraulic Institute 1999).

2 PHYSICAL MODEL FOR THE REVERE OSTIGLIA NEW RAILWAY BRIDGE

The river reach between Risvolta di Ostiglia and Isola Boschina, 2100 meters long was modeled (Fig. 1). As can be seen in Figure 1 this branch will be crossed by the new Bologna-Verona railway bridge and is crossed by the existent railway bridge.

A movable-bed model was realized with a planimetric scale of 1:150 and with a vertical one of

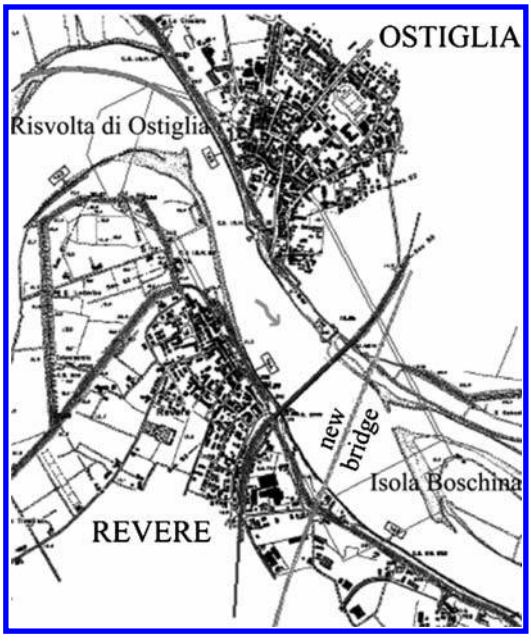


Figure 1. Modeled Po branch for railway bridge.

1:120, the little distortion aided in modeling river bed forms and roughness (Adami 1994, Hughes 1993). The model was realized mirrored compared to prototype because of the conformation of the existent laboratory model tank, and being the Corioli forces negligible in

Copyright © 2006 Taylor & Francis Group plc, London, UK

prototype and in the model. In Figure 1 can be seen contour of model tank mirrored and sketched over the modeled area.

Three prototype flow conditions were simulated: 2200 m^3/s is a medium water condition, 7600 m^3/s is a very unlikely flood during bridge construction period, it's occurrence probability during construction time is 1/200, 13500 m^3/s is the project condition for the new bridge, which has the occurrence probability of 1/200 or a time frequency of 1 year each 200.

2.1 *Principles of similitude and scale effects*

Two kinds of test were carried out; first sediment transport and bed forms process were simulated with a morphological criteria, then on the same model with the adjusted bed forms, surface waves were simulated using Froude velocity scale.

The mean diameter of prototype sand is 0.3×10^{-3} m, which would be scaled to clay by the geometric vertical scale. Fine sand, mean diameter 0.07×10^{-3} m, was used in the model instead of clay, in order to avoid the arising of unrealistic cohesive forces. Not perfectly scaled mean diameter introduces in the model a different densimetric Froude number (Hughes 1993):

$$F_* = \frac{\rho \cdot v_*^2}{\gamma_s \cdot D} \qquad (1)$$

where ρ and γ_s are water density and specific weight of grains in water respectively, which are the same in model and prototype, instead v_* and D, shear velocity and mean grains diameter respectively, are scaled in the model.

Densimetric Froude number is the ratio of shear bed stress to grains weight, and can be seen as a bed-load parameter defining bed form geometric characteristics and formation process (Yalin & Ferreira da Silva 2001). Model flows were increased respect to values scaled with velocity Froude criteria, in order to balance model densimetric Froude number, reduced by not respecting geometric scale for sediment diameter. Consequently Froud velocity scale was increased up to bed sediment transport and bed formation were similar to prototype, but assuring that Froude number model was less than 0.5 as in prototype and the surface waves not affecting sand bottom (Richards 1982). The morphological scale adopted for velocity was 1:5 instead of 1:11 Froude velocity scale. In that way was possible to simulate the prototype bed formation attitude: bed forms height decreasing while flow increasing to yield flat bed at high stages (Yalin & Ferreira da Silva 2001).

Suspended load concentrations measured in the model were compared to prototype data, in order to scale flows duration and decide simulation time length (Hughes 1993).



Figure 2. Detail of configuration C before tests, where pier and pit protections and provisional groin are visible.



Figure 3. Detail of configuration B before tests, where the old bridge is visible upstream the new bridge in construction.

Bed roughness, and suspended load rate, were proportionally greater in the model than in prototype, due to the impossibility to respect perfectly and at the same time: densimetric Froude number, grain size Reynolds number, vertical length to diameter ratio parameter and relative fall speed parameter (Adami 1994, Hughes 1993). These effects must be considered when simulation results are analyzed.

2.2 *Tested configurations*

Four configurations were tested, following the bridge construction program from the start, bridge absent, up to the final whole realization.

The configurations were: A, river in the actual configuration with the existent bridge and without the new bridge; B, first critical construction phase with the provisional groin for the construction of piers near Ostiglia river side realized up to pier 7 and the contemporaneous construction of pier 4, 6 and 7 inside their provisional pits; C, second critical construction phase with the provisional groin resized up to pier 8 and the contemporaneous construction of pier 3, 5 and 8 inside their provisional pits; D, final configuration with the whole bridge realized and without provisional structures. Construction configurations B and C were tested only with flows scaled from 2200 and 7600 m^3/s prototype values, the second being the value with the same occurrence probability during construction time of 13500 m^3/s, the project condition for the new bridge. The other configurations were tested with all three chosen prototype flows, scaled with morphological and Froude criteria.

Copyright © 2006 Taylor & Francis Group plc, London, UK

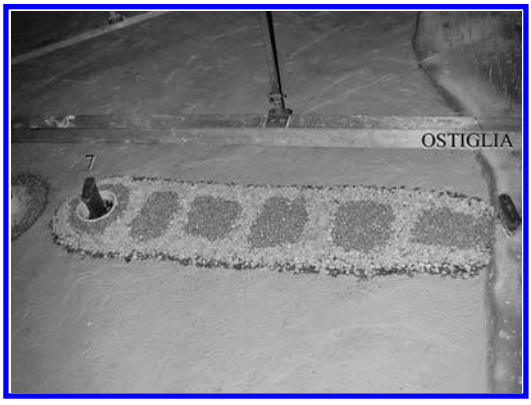


Figure 4. Detail of configuration B before tests, where provisional groin is visible at its maximal extension.

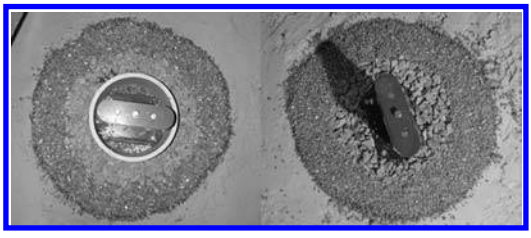


Figure 5. Details of provisional pits and of the final pier protection before tests.

Figures from 2 to 5 show some model details, where pier and pit protections and the provisional groin are visible. These structures were realized with natural granular material scaled with the morphological criteria from the prototype design, assuring the same mobility parameter in the model and in prototype.

At the end of each morphological test, when the equilibrium of the bed was achieved, a short time test was carried out in order to reproduce realistic surface waves with flow scaled with velocity Froude criteria.

2.3 *Simulation results*

The carried out tests gave some evidences about the fluvial processes of the modeled reach, due to bridge realization.

In particular the interesting aspect for the new bridge are: the embankment erosions on the bridge section, bed erosions near pier foundations, the erosions near provisional structures for bridge realization (i.e. pits and groin).

2.3.1 *Embankment erosions*

On the Revere side water flows in contact with the embankment. An important erosion was surveyed on the model at Revere embankment after tests carried out

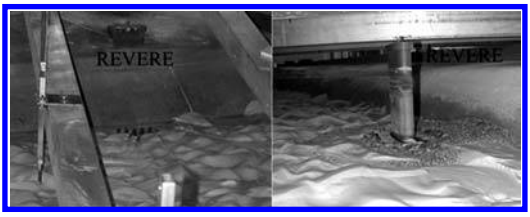


Figure 6. Pier 3: emerging foundation pails (configuration A), and stabilizing effect of pier protection (configuration D).



Figure 7. Pier 6 after tests (configuration D).

on the A configuration (bridge absent). The erosion was maximal for the lowest flow (2200 m^3/s in prototype) when water flows mainly on the Revere side, velocity field was more uniform along all river section for test carried out with greater flows.

The erosion on Revere side for the other three configurations was limited by bed protection of the pear 3 near Revere embankment, which made locally steady river bed. Figure 6 show the river bank erosion after tests carried out on the configuration A e D with the most erosive flow.

During physical simulations Ostiglia embankment was never eroded, in fact it is placed in a river deposition zone and water touches it only during extreme flood (13500 m^3/s in prototype).

2.3.2 *Bridge piers*

River bed protections around piers were steady for all simulated flows, only a little erosion on the protection of central pier number 6 was seen after test carried out on the final configuration with the greatest flow (13500 m^3/s in prototype).

For this reason an heavier protection was suggested with a mean diameter in prototype of $0.6 \div 0.8$ m, instead of the designed $0.3 \div 0.4$ m which was scaled in the model. Also a foundation of pier 6 four meters deeper in prototype would be useful in order to avoid bed protection erosion.

Copyright © 2006 Taylor & Francis Group plc, London, UK

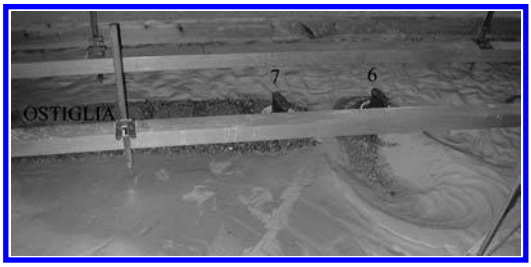


Figure 8. Erosion between provisional groin and pier 6 pit (configuration B), after test with lowest flow.

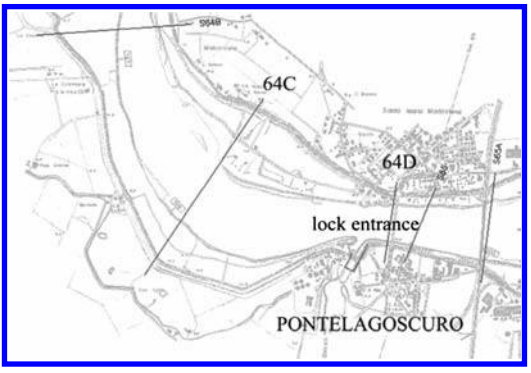


Figure 9. Modeled Po reach for inner port.

2.3.3 *Provisional structures*

B and C configurations simulated critical construction phases, when the provisional groin for the realization of piers near Ostiglia embankment and provisional pits for the realization of central piers obstruct the river.

Both piers pits and groin were steady for flows tested (2200 and 7600 m^3/s in prototype) on the construction configurations, and were not flooded by the lowest flow.

A big erosion was surveyed in the model for the configuration B, when groin length is maximal for the construction of pier 7, and the simultaneously construction of the adjacent pier 6 inside its pit.

This erosion was maximal for the lowest flow because in that case flow is gathered between pit 6 and groin head, greater flows floods pits and groin leading to a spreader flux. As can be seen in Figure 8 part of pit protection collapsed inside the hole between piers 6 and 7. Next test carried out with scaled flow from prototype value of 7600 m^3/s, covered part of the erosion, which at its maximal develop was 15 deep and 100 m wide meters, scaled in prototype.

A different construction bridge program was suggested in order to avoid the simultaneously construction of two adjacent piers which are respectively realized on the head of the provisional groin and inside a pit directly founded in the river bed.

3 PHYSICAL MODEL FOR THE PONTELAGOSCURO LOCK ENTRANCE

Goal of the inner harbour physical model was to choose between two possible lock entrance configurations, comparing the sand deposition and turbulent velocities in front of the entrance and inside the port.

The Po branch 1300 m long between sections 64C and 64D was modeled with a movable bed model at an undistorted geometric scale of 1:100, inside the same model tank where the railway physical model was realized. Figure 9 show the modeled river reach and the position of the inner port on the right river side.

3.1 *Principles of similitude and scale effects*

Tests were carried out with a morphological scale criteria, as for the Revere-Ostiglia physical model, to balance the increased grains weight in the model due to the not geometrically scaled mean diameter of bed sediment. In this way was possible to simulate the prototype bed formation process.

The velocity scale adopted (1:6) doesn't meet the velocity Froude scale (1:10) criteria and is impossible to respect at the same time all the dimensionless involved numbers. But measuring sediment concentration in the model and comparing it to prototype data, experiments time length was adjusted in order to achieve a steady bed configuration. Nevertheless, as for the railway model, due to scale effects, bed roughness and suspended load rate, were proportionally greater in model than in prototype, and these effects must be considered when results are analyzed.

3.2 *Tested configurations*

Two different configurations of the lock entrance were tested: the first with a 80 m long opening to the Po river, and the second one was only 60 m long, with the aim to decrease the sediment deposition in front of and inside the lock entrance.

The simulated flows were four between 1400 and 8000 m^3/s in prototype, starting from the lowest up to 8000 m^3/s, outside this range yearly sediment transport is negligible because of pour flow velocity or very short flow duration.

3.3 *Simulations results*

During all tests, velocities outside and inside the lock entrance were measured with a micro acoustic doppler velocimeter, which gives the three-dimensional velocities in one point with time resolution of 30 Hz. These data were used to compute mean velocities, velocity oscillations, Reynolds stresses and flow turbulence

Copyright © 2006 Taylor & Francis Group plc, London, UK

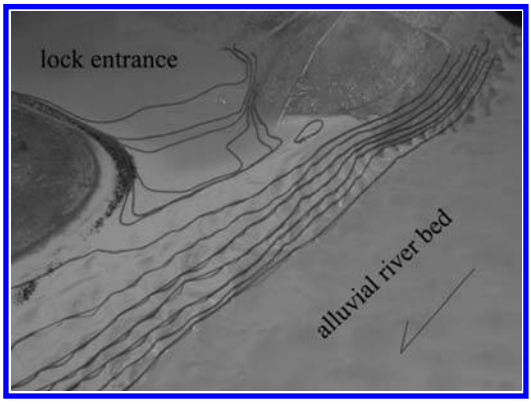


Figure 10. Sand bar at entrance after tests (wide opening).

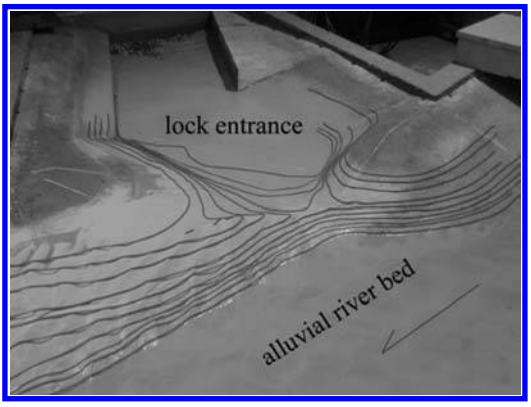


Figure 11. Sand at entrance after tests (narrow opening).

which is the cause of sediment diffusion and sediment transport processes (Jansen & al. 1979, Yalin & Ferreira da Silva 2001).

Bed topography near the lock entrance was surveyed in the model with a detailed digital image acquisition before and after each test in order to compute total deposition or erosion with a computer assisted image processing.

To suggest the best project configuration, bathymetries modifications (i.e. deposition or erosion) and turbulent velocity fields near the lock entrance were compared for the two tested configurations.

3.3.1 *Near lock entrance bathymetry*

A bar developing with flow, wide from the upstream embankment to the downstream one, was observed during tests (Figs. 10, 11).

The bar ridge was surveyed in the model at the end of the greatest flow simulation near the same height for both configurations. This bar was compared to prototype bathymetry, surveyed after a flood event in front of the old existent lock entrance. The bar observed on the prototype was not so high as in the model. This difference between model and prototype is due to the realized flow sequence during tests, which doesn't simulate the natural flood flow hydrograph but an artificial sequence with similar yearly flows grouped together.

Figure 12 shows bathymetries acquired on the model before and at the end of tests for both configurations. Inside the lock entrance a deposition of 33000 m^3 and 31000 m^3, prototype scaled, were computed from the acquired bathymetries, respectively for configuration with the 80 and 60 meters long lock entrance.

3.3.2 *Flow turbulence*

Measures of velocity acquired during tests showed a bi-dimensional velocity field, where the vertical components were negligible.

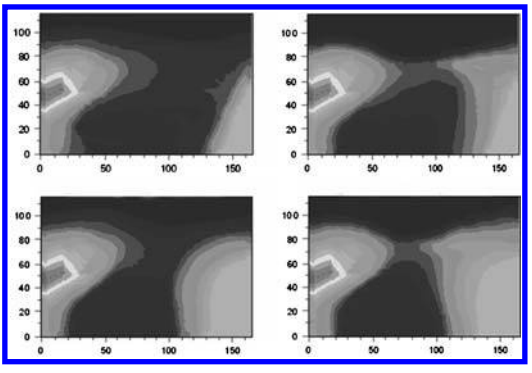


Figure 12. Starting (column 1) and final (column 2) bathymetries acquired on model; row 1 wide opening configuration, row 2 narrow opening configuration.

Reynolds stresses and tensor were computed from velocity data acquired inside and outside the lock entrance. Reynolds tensor eigenvalues and vectors identifies turbulent velocities modules and directions respectively (Jansen & al. 1979).

Figure 13 and 14 show mean velocities and ellipses of turbulent velocities centered on the measurement points. Turbulent ellipses were greater in the first configuration (Fig. 13) with lock entrance opening 80 meters long. The second configuration (Fig. 14) showed a lower turbulence in front of and inside lock entrance, which gave rise to a lower water circulation inside the port going in and out at downstream and upstream embankment respectively.

Lower turbulence of second configuration means lower sediment convection and diffusion near the lock entrance and inside the port, in conclusion decreased lock entrance opening dampens sediment transport processes, assuring a lower dredging frequency in front of and inside the port.

Copyright © 2006 Taylor & Francis Group plc, London, UK

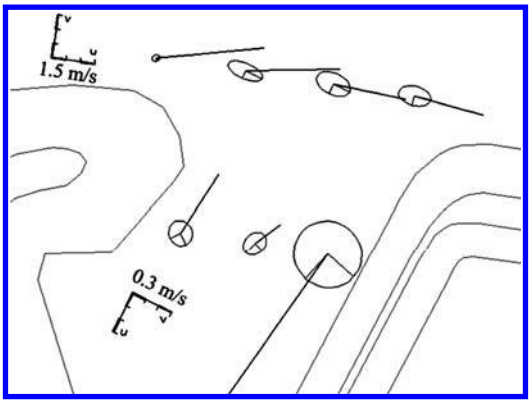


Figure 13. Mean velocities and turbulent velocity ellipses centered on the measurement points (wide opening configuration).

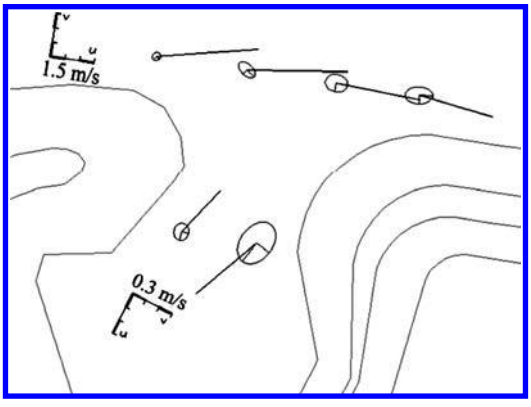


Figure 14. Mean velocities and turbulent velocity ellipses centered on the measurement points (narrow opening configuration).

4 NUMERICAL MODEL FOR THE PONTELAGOSCURO LOCK ENTRANCE

Aiming to test the commercial numeric model Mike21C by Danish Hydraulic Institute, Pontelagoscuro physical model results were compared to numerical simulations carried out with the numerical model on the same river Po branch.

Numerical models has been improved in their capability to simulate river hydrodynamics and morphodynamics. Mike21C is a quasi-three-dimensional numerical model based on a curvilinear grid which can follow river embankments. It simulates river flow hydrodynamics, helical flow, sediment transport, alluvial resistance, bank erosion and plan form changes; with feedback from calculated bed forms and roughness

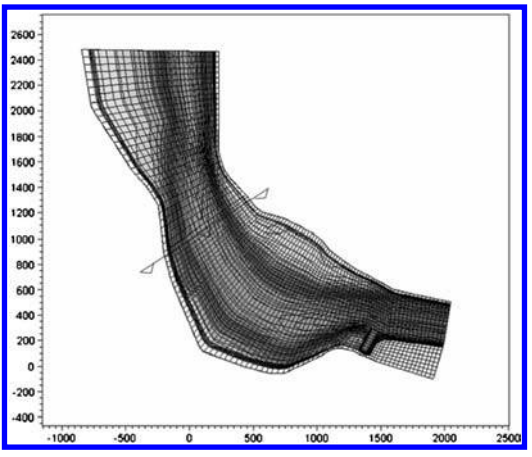


Figure 15. Bathymetry and computational grid.

changes on following hydrodynamic and morphological steps (Danish Hydraulic Institute 1999).

The same flow range used for the physical model was numerical simulated on the largest lock entrance configuration.

In order to investigate the effect of the position of upstream boundary condition, two different computational grid were realized: the first 2200 m long is only a bit upstream extended than the physical modeled reach 1300 m long, the second is 3700 m long and made the upstream boundary condition very far from the lock entrance. In that way was possible to make flows in front of lock entrance more uniform, as was achieved in the physical model with flow guides installed at the model tank intake.

Figure 15 shows the modeled bathymetry with the longest grid, and the upstream limit of the short one.

4.1 *Simulations results*

The longest grid gave results more reliable and similar to physical model results, because the flows trajectory in front of the lock entrance were similar to the velocity field achieved in the physical model.

Figures 16 and 17 compare velocity fields corresponding to 4000 m^3/s and over the physical model area, for the two different computational grids.

Velocity field is more uniform for the longest computational grid (Fig. 16), in fact in that case the main flow (clear gray-white track) in the middle of alluvium bed is more prolonged and uniform along the central fluvial line than for the short grid (Fig. 17). A strong deceleration (dark gray track) is evident in front of the lock entrance, and only for the longest computational grid a clear clockwise water circulation was achieved inside the port as for the physical model, see detail in Figure 18. Also the sediment deposition closing the lock entrance opening was similar to the longitudinal

Copyright © 2006 Taylor & Francis Group plc, London, UK

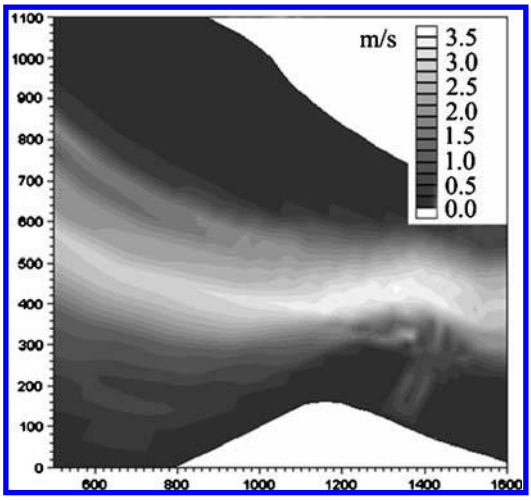


Figure 16. Computed velocity field (long grid).

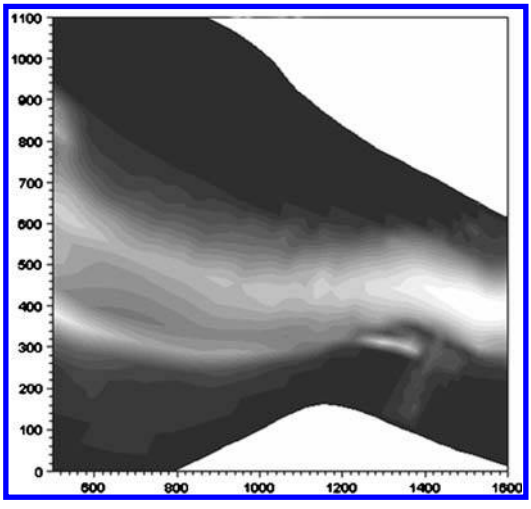


Figure 17. Computed velocity field (short grid).

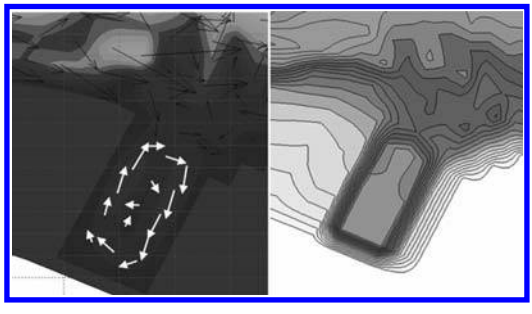


Figure 18. Details of water circulation inside lock entrance and sand deposition in front of entrance opening.

bar observed in the physical model, as can be seen in Figure 18.

5 CONCLUSION

Physical models give detailed and complete results not always available by computational models, especially when local turbulence and sediment processes near structures (piers, groins and embankments) are investigated.

Examples on river Po showed in this paper are emblematic.

Physical simulations gave answer to some questions regarding pier and provisional structures design for the Revere-Ostiglia railway construction. Mean mass diameter for bed protection around pier and construction program (groin length and pits realization time sequence) were suggested by model results.

The Pontelagoscuro physical model was useful for investigate turbulent flow near designed embankments of the new lock entrance, cause of sediment transport processes, local sand deposition and inner port water circulation.

Bi-dimensional numerical model for the Pontelagoscuro new lock entrance was able to extend simulations to a longer Po branch at a very low cost, not comparable to physical model cost. Results regarding the mean bi-dimensional velocity field and bar formation closing to lock entrance are comparable to physical models results, if the upstream condition is correctly represented. Instead local turbulent velocities inside and in front of inner port were not simulated by this kind of numerical models.

In general commercial numerical fluvial model are not able to investigate local turbulent and sediment processes due to interaction between structures and alluvial river bed, because they are designed in order to simulate the main fluvial processes of quite long reach and at a long time scale as river braiding and meandering or bed form developing.

In conclusion both physical and bi-dimensional numerical models are useful in order to investigate structures effects on alluvial river bed: the first testing structures design at a little scale (up to some meters), showing local turbulence and short time sediment transport processes, and the numerical ones investigating project effects at a higher scale, computing modifications on long time fluvial processes as bar formation or bend-meander modifications due to the designed structures.

REFERENCES

Adami, A. 1994. *I Modelli Fisici nell'Idraulica*. Padova: Cleup.

Copyright © 2006 Taylor & Francis Group plc, London, UK

Danish Hydraulic Institute. 1999. *Mike21C Scientific Documentation*. Horsholm: DHI.

Hughes, S.A. 1993. *Physical Models and Laboratory Techniques in Coastal Engineering*. Singapore: World Scientific.

Ph Jansen, P., Bendegom, L., Den Berg, J., Vries, M. & Zanen A. 1979. *Principles of River Engineering (The Non-Tidal Alluvial River)*. London: Pitman Publishing Limited.

Richards, K. 1982. *Rivers (form and process in alluvial channels)*. London: Methuen & Co.

Yalin, M.S. & Ferreira da Silva A.M. 2001. *Fluvial Processes*. Delft: IAHR.

Copyright © 2006 Taylor & Francis Group plc, London, UK

River Energy Auditing Scheme (REAS) for catchment flood management planning

N.P. Wallerstein
University of Nottingham, Nottingham, United Kingdom

P.J. Soar
Jeremy Benn Associates Ltd, Atherstone, United Kingdom

C.R. Thorne
University of Nottingham, Nottingham, United Kingdom

ABSTRACT: An approach is presented that aims to provide a quantitative geomorphological audit of a river system to facilitate channel management and to better inform catchment flood management planning. This is a strand of research currently being undertaken at the University of Nottingham, UK in its role as a member of the Flood Risk Management Research Consortium. The auditing system uses a broad scale method (that is flexible to data availability) to classify reaches as acting predominantly as sediment sources (eroding), pathways (transfer links) or sinks (depositing) over a period of years. This is achieved by estimating the difference in time-integrated specific stream power between consecutive reaches to indicate potential continuity or imbalance in the sediment transfer system. A pilot study has been performed on the Hawkcombe Stream, Somerset, England. Initial results are encouraging and compare favorably with those of a previous geomorphological study that used the well-established Fluvial Audit technique.

1 INTRODUCTION

1.1 *Background*

Until recently, sediment dynamics were rarely taken into account when comparing options for flood defence schemes. However, imbalances in sediment supply and transport capacity may lead to progressive reduction in the standard of protection provided by a scheme (Fig. 1).

For example, channel bed degradation may undermine flood defence assets reducing their condition and increasing the risk of failure under load, while bed aggradation can significantly reduce conveyance and make overtopping more likely. In addition, flood defence infrastructure may impact on the sediment dynamics in a reach with, for example, enlargement of a channel resulting in a tendency for sediment trapping. Sediment dynamics in turn impact on river morpho-dynamics and the diversity and quality of river and floodplain habitats, which are increasingly recognized as key factors in achieving good ecological status, as required under the European Water Framework Directive (WFD) (The European Parliament and the Council of the European Union 2000).

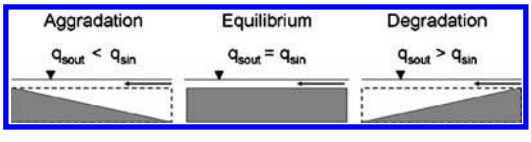


Figure 1. Schematic diagram of sediment fluxes that result in aggradation, equilibrium, and degradation of a reach: where q_{sin} = incoming sediment load; and q_{sout} = outgoing sediment load.

There is, therefore, a need for the planners and designers of flood defence schemes to predict and account for sediment dynamics and their impacts when appraising options for flood risk management. While available models of hydrodynamics, sediment transport and bed level change provide the capability to investigate sediment impacts at the reach scale, they are too data intensive and resource expensive to apply at the catchment scale.

In England and Wales, the Environment Agency is tasked with coordinating flood risk management at the system scale through the development of Catchment Flood Management Plans (CFMPs). Their statement of intent is that measurable modeling outcomes should be risk based and reach national targets for flood control, but also channel habitat diversity as stressed in the Water Framework Directive.

Copyright © 2006 Taylor & Francis Group plc, London, UK

At present in the UK, routine assessments of sediment-related problems within a wider, catchment context are performed using the qualitative Fluvial Audit (Environment Agency 2004, Sear et al. 2003). In this approach, a field and documentary investigation is used to divide the fluvial system into geomorphic reaches designated as: source (degradational); transfer (equilibrium); or sink (aggradational) reaches. The approach involves detailed field reconnaissance of the watercourse (Thorne 1998), performed by an experienced fluvial geomorphologist. While the Fluvial Audit has proven very useful in river conservation and restoration projects, in its present form it does not support quantification of the sediment dynamics required to interface effectively with the engineering components of strategic flood studies and CFMPs. Certainly, Fluvial Audits provide useful insights into catchment sediment dynamics, but the approach requires extended inputs by experienced geomorphologists and is of limited utility for strategic planning due to its somewhat subjective technical approach and qualitative outcome. To address the need for quantitative assessment of sediment dynamics at the catchment scale, a work package of the Flood Risk Management Research Consortium (FRMRC) was commissioned at the University of Nottingham. The intention of the research is to develop a quantitative method capable of validating and building upon the insights gained from qualitative assessments of sediment dynamics, such as the Fluvial Audit. The approach being sought must be credible from a theoretical stand point, while still being practical to apply to rivers with limited data. It was considered necessary therefore to develop a simple, yet robust, tool which fills the gap between empirical, qualitative and complex, sediment transport modelling approaches. Also, to support wide uptake, the method must be adaptable to varying data availability. These success criteria recognise that a balance must be struck between available resources, scientific method and acceptance by end users (Fig. 2).

It should be recognised that scientific complexity is only one of a number of criteria which must be considered in river management. Management technologies will only be taken up if the end user can fund such modelling given the resource constraints of time (many projects have completion times of only a matter of weeks), money (a numerical modeler is an expensive resource), and modelling capability (the results are only as good as their interpretation). Society (individual stake holders in a river and politicians) will also only sanction a scientific approach if it can be cognizised to some degree.

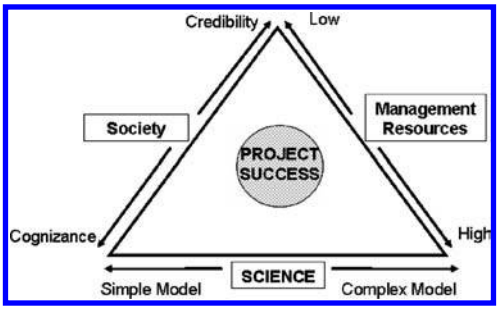


Figure 2. Balancing management resources, the science of predictive models and acceptance by society.

The need to place the new method in the centre of the triangle in Figure 2 dictated the specific objectives of the research, which are outlined in the following sections.

1.2 *Objectives*

Theoretically, system scale sediment dynamics could be quantified using established sediment routing models such as HEC-6 (HEC 1976) and ISIS (ISIS 2006), which predict bed material loads and bed level changes by solving the St. Venent equations for gradually varied unsteady flow, coupled with equations for sediment transport and continuity. However, these models are highly data and time intensive and the considerable input of resources, coupled with long run times, limits their application to studies of reach-scale scour/fill rather than issues related to catchment scale sediment transfers and imbalances. Also fully unsteady flow numerical models suffer from issues associated with convergence, consistency and stability (Versteeg & Malalasekera 1995), the understanding of which, and ability to mitigate these through code adjustment requires finesse and many years of knowledge. Finally, channel boundary adjustment models rely on sediment transport equations that characteristically predict sediment load to within $\pm 50\%$ about 60% of the time (Yang 1996). This makes selecting an appropriate sediment transport equation crucial to producing a successful simulation and there are no universally accepted rules concerning which equation is suitable for a particular river environment.

Counteracting uncertainty is a critical component of all research conducted by the FRMRC and so this capability was a primary objective of the research. The approach adopted here is aimed at a broad representation of a catchment scale potential for channel adjustment, it does not purport to represent local conditions in detail. The development of a numerical model at the whole catchment scale would be very time, labour, and resource intensive, commodities which the EA and its contractors simply do not have free reign to use. Thus in the approach adopted here numerical modelling schemes are replaced by an alternative reliable indicator of the river's potential to perform geomorphological work through expending energy which thus enables the transport of sediment. By invoking this approach the authors are not proposing that more complex models generate a worse representation of a river system,

Copyright © 2006 Taylor & Francis Group plc, London, UK

simply that the approach outlined below is robust and a good first approximation of geomorphological adjustment. Before discussing the approach a criticism of the model must be addressed, that being that it suffers from the same problems as complex numerical models but by not using sediment transport relationships provides less reliable results. This statement may be counteracted by the following observation made by Beven (2002), 'In science where unique local characteristics so affect local observations as to make the application of small-scale physical theory intractable at the larger scale we must look to alternative larger scale descriptions and must recognize that there may be many possible descriptions that provide equally good predictions of the observations'. With this in mind we shall proceed to describe the model invoked here.

The theoretical justification for this approach stems from the concept of specific stream power proposed by Brigadier R. A. Bagnold (Bagnold 1966), in which he defined specific stream power as a measure of the flow's ability to perform work on its boundary. The rate of doing work through sediment transport is defined by Bagnold in terms of the specific stream power multiplied by an efficiency factor. Bagnold's approach has been further developed by several authors to predict sediment movement and geomorphological adjustments in rivers (for example; Langbein 1964, Yang 1971, Chang 1979, Graf 1983, Lawler 1992, Magilligan 1992, Molnar & Ramirez 1998, Knighton 1999). However, the approach developed does not attempt to predict sediment transport or route sediment (or energy) through an event hydrograph. Instead, it calculates the balance or imbalance between the specific stream power available in a reach in a year (that is the annual stream energy in $KJyr^{-1}$) with that in the next reach downstream.

Further objectives were that the River Energy Auditing Scheme (REAS) must be generically applicable, amenable to use by river scientists and engineers with a modest amount of specialised training, applicable within the resources available for typical strategic catchment studies, and capable of producing robust results in situations with very limited data availability - albeit accepting a greater degree of uncertainty. The last and perhaps most important objective is for the REAS output to be readily understood by those responsible for river management and planning at the catchment scale.

With respect to data requirements, there are only five input variables to REAS for each study reach in the river system:

1 Representative bed material particle size (s);
2 Representative flow duration curve;
3 Representative channel cross-section;
4 Representative bed slope, and;
5 Representative roughness values for the channel and floodplain.

The manner in which these variables are employed is discussed in the next section. It must be stressed at this point that REAS is not a sediment routing model, but instead generates indicative, quantitative trends in river energy, and therefore the ability for the flow to perform work through sediment transport, during an average year in which runoff is similar to that associated with the long term flow duration curve. The REAS will only be judged a success if it can be operated by the end user community in the UK, both in the public and private sectors. To this end, in the latter half of the FRMRC project a working version of REAS will be tested by typical end users in the Environment Agency and training workshops will be held for a range of potential stakeholders and interested parties.

1.3 *Study area*

A pilot data-set comprising the variables required to run the model has been collected from the Hawkcombe Stream, in Somerset, England (Fig. 3). This is a steep, upland catchment with a relief of 436m over a length of about 8 km. Base flows are generally less than $1\,m^3\,s^{-1}$, with maximum discharges of up to $10\,m^3s^{-1}$. The channel has a boulder, cobble and gravel bed and is generally armoured. HEC RAS (Brunner 2002) modeling of the Hawkcombe suggests that at high discharges the flow is supercritical in many places, indicating that the stream is a high energy environment. In 2002, a Fluvial Audit of the Hawkcombe was performed (Thorne et al. 2002) and the main stream was divided into 17 reaches (Fig. 3) characterised as sediment sources (degradational), transfers (throughputs), exchanges (dynamic equilibrium), and sinks (aggradational). In 2004, the lower 4.5 km of the Hawkcombe was surveyed in detail. One hundred and twenty seven cross-sections were surveyed, located at major breaks of slope and positions of significant channel geomorphological change and fifty four bed material samples were taken. Bed material was analysed using size-by-number for particles

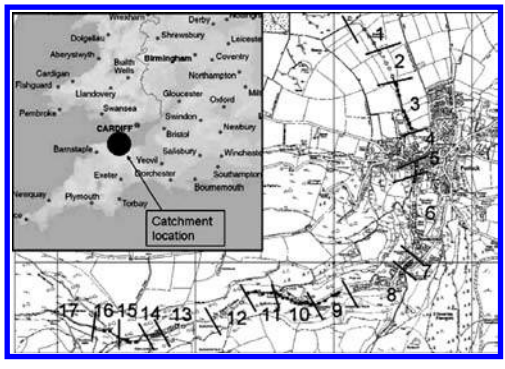


Figure 3. Hawkcombe stream location and geomorphological reaches.

Copyright © 2006 Taylor & Francis Group plc, London, UK

between 1025 mm and 8 mm, sieving and size-by-weight between 8 mm and 0.063 mm, and using a Coulter Counter below 0.063 mm.

The Hawkcombe has several hydraulic structures along it, including bridges, mill weirs, gravel traps, bed sills and bank protection works. It flows through an 83m long culvert, beneath the village of Porlock. This culvert has required maintenance de-silting in the past as sediment deposition has occurred, reducing its capacity to convey floods. In 2005, the floor of the culvert was re-profiled to reduce sediment trapping in a scheme designed by Royal Haskoning Consulting Engineers.

2 APPROACH

2.1 *Calculating available stream power*

Stream power per unit bed area (ω) is expressed in Wm^{-2} and is termed specific stream power. It is defined by:

$$\omega = \frac{\gamma Q S_e}{W} \quad (1)$$

where γ = bulk unit weight of water (Nm^{-3}); Q = discharge ($m^3 s^{-1}$); S_e = energy slope; and W = geomorphologically active channel width (m) for the discharge in question. S_e can usually be approximated by the bed slope (S_o) for channels with moderate to low slopes and this approach will be adopted here. Note that in Bagnold's (1966) version of Equation (1) he used water density (ρ_w: kgm^{-3}) in place of bulk unit weight, γ. The bulk unit weight of water is used in most derivations of specific power. This has often been a source of error in calculations of sediment load using Bagnold's transport functions (Bagnold 1977, 1980) i.e. as Bagnold did not use g (where g = gravitational constant: approx. 9.81 ms^{-2}) and because $\gamma = \rho_w \times g$ results can be out by a factor of 10 (Ferguson 2005).

The geomorphologically active channel width is defined as the area of channel bed and banks beneath the flow top width for a given discharge which is within the bankfull channel cross-section (Richards 1982), i.e. it does not extend onto the left hand and right hand floodplain if flow depth becomes higher than the bankfull elevation.

To calculate an excess specific stream power (ω_e), which is that actually available to perform work on the channel boundary by moving sediment, it is necessary to subtract the critical specific stream power for mobilizing the bed (ω_c) from the available specific stream power:

$$\omega_e = \omega - \omega_c \quad (2)$$

Bagnold (1980) defined critical specific stream power as:

$$\omega_c = 290 D_m^{1.5} \log\left[\frac{(12d)}{D_m}\right] \quad (3)$$

where; D_m = mean grain size in the size distribution representing the bed of the channel (m); and d = flow depth (m).

Ferguson (2005) provides a full derivation of the terms, but essentially, the term $290D_m^{1.5}$ is derived from the Shields equation and the log term is derived from the 'law-of-the-wall' velocity profile (Richards, 1982). The approach is further developed here by replacing an estimate of the critical specific stream power based on a single mean grain size with a formulation that better represents the range of grain sizes present on the bed. This is achieved by multiplying the critical power for the median grainsize in each size class (1024 mm, 724 mm, etc) by its frequency of occurrence, and then summing all values. Thus, for a given depth, excess power ω_e' is equal to:

$$\omega_e' = \sum_{i=1}^{n} \left[P_i (\omega - \omega_{ci})\right] \quad (4)$$

where P_i = proportion (from 0 to 1) of that size class in the whole sample; and ω_{ci} = critical specific stream power for a given grainsize class.

ω_{ci} is calculated using Equation (3) in which D_m is replaced by D_i (m), the median grainsize in each class. The justification for the formulation and use of Equation (4) is that use of a single particle size such as the D_m might not be a suitable parameter alone given a highly variable bed sediment gradation. Thus Equation (4) offers a more integrated approach which is preferable where sediment grainsize distribution data is available. It is recognized that for some applications of this model a full grain size sample may be too time-consuming and costly to collect and a single representative grain size for each reach may be all that is available. An option for using either a single grain size value or a full distribution has therefore been made available in the model.

Note that the recommendation is to use the size distribution of the surface sediment layer on the bed as research has shown that sediment transport equations best fit empirical data when this layer is used (Parker 1990, Wilcock & Crowe 2003).

2.2 *The REAS annual energy budget*

The annual energy budget for a reach must take into account the full range of discharges acting on the channel over a period of years. This is done by integrating ω_e' with a representative flow duration curve, adopting the procedure set out by Biedenharn et al. (2001). This is performed by taking the entire flow record available for the reach in question (15 minute or mean daily values), ranking the values from lowest to highest and producing a cumulative probability curve. The discharges are then split into ranges (usually 25–35 classes) and their frequency determined. If gauged data are not available for the reach in question, or the

Copyright © 2006 Taylor & Francis Group plc, London, UK

discharge record is short, surrogate methods have to be used. These include:

1 Scaling discharge from a gauge elsewhere in catchment. This can be achieved through simply scaling by the ratio of drainage areas;
2 Scaling discharge from a donor catchment with similar hydrological and morphological characteristics, or;
3 Calculation using hydrological modeling packages; for example HEC-1 (HEC 1998).

Integrating for the expected range of discharges yields:

$$\omega_e = \sum_{j=1}^{n}\left[F_j \sum_{i=1}^{n}\left[P_i(\omega - \omega_{ci})\right]\right] \quad (5)$$

where F_j = frequency (from 0 to 1) of each discharge class. Note that discharge, width and depth in Equation (4) are adjusted to the values appropriate for each discharge class.

The difference in excess annual specific stream power between consecutive reaches gives the balance for a reach ($\Delta\omega_e$):

$$\Delta\omega_e = \omega_{e(r=n)} - \omega_{e(r=n+1)} \quad (6)$$

where the subscripts r = reach; and n = reach number from 1 to n_t (where n_t = total number of reaches). Reaches are numbered sequentially from upstream to downstream. Equation (6) is then multiplied by the gravitational constant because Bagnold's formulation of Equations (1) and (3) do not incorporate g. This value is then multiplied by the number of seconds in a year to give a measure of annual excess energy in $KJyr^{-1}$ at a single point in a cross section.

Equation (6) is comparable in essence to a sediment budget calculation (refer to Fig. 1) except that the sediment transport rate has been replaced by a term representing excess specific stream power. Thus, if $\Delta\omega_e$ is greater than zero then the reach has the potential to aggrade (it is likely to be a sediment sink), while if $\Delta\omega_e$ is less than zero then the reach has the potential to degrade (it is likely to be a sediment source).

Initial trials using a prototype version of REAS were conducted using the Hawkcombe dataset. For each of the 17 reaches the most downstream cross-section was used to represent the geometry of that reach. Discharge for each reach was scaled from a donor catchment, the River Horner. An estimated lateral floodplain slope was set as 0.01; floodplain Manning's n was set as 0.07 and the active channel Manning's n set as 0.035. The full bed material sediment grainsize distributions were used. As the REAS output will be used in the context of risk it was felt that differences in excess annual energy in $KJyr^{-1}$ should be expressed in dimensionless form. The output from the Hawkcombe is therefore presented in Figure 4 using a scale between +1 and −1, where values between 0 and +1 indicate increasing potential for sediment storage, values between 0 and −1 indicate increasing potential for sediment scour, and values close to 0 indicate channel stability.

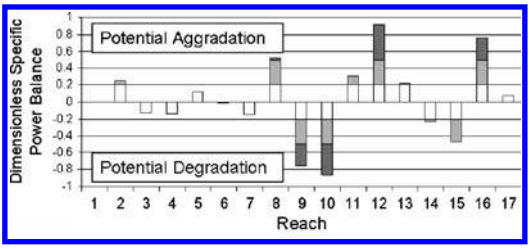


Figure 4. Excess energy budgets for the Hawkcombe stream.

This relative scale has been generated by dividing the differential values measured in $KJyr^{-1}$ by a user defined absolute sensitivity value. Methods to achieve this scaling in a less subjective manner are currently being explored. The grey scaling in Figure 4 represents bands of low, medium and high risk of aggradation or degradation based upon the magnitude of energy imbalance between consecutive reaches.

The distribution of sediment stores and sinks generated here using the REAS compares favorably with those that are based on the Fluvial Audit of the Hawkcombe, although it must be stressed that outputs from this model are preliminary at this stage of the project. Improvement of predictive capabilities is discussed in Section 4.

3 DISCUSSION

3.1 *Solution for flow width and depth*

Because REAS uses a range of discharges a flow depth and channel top width must be defined for each flow. Manning's flow resistance equation is used for this purpose (Chow 1959):

$$Q = \frac{1}{n}\frac{A^{5/3}}{P^{2/3}}S_e^{1/2} \quad (7)$$

where n = Manning's roughness coefficient; A = channel cross-sectional area (m^2); and P = channel wetted perimeter (m).

Values for Manning's n can be obtained from, for example, Barnes (1967) or Chow (1959).

It is acknowledged that in a simple model such as this obtaining the energy gradient may prove to be impossible due to the wide spacing of cross sections which would prevent generation of a gradually varied flow profile. This source of uncertainty will be small in channels with low bedslopes due to the fact that the energy slope will approach that of the bedslope. In higher gradient streams or channels with very variable bedslopes the source of error caused by the approximation of energy slope by using bedslope is

Copyright © 2006 Taylor & Francis Group plc, London, UK

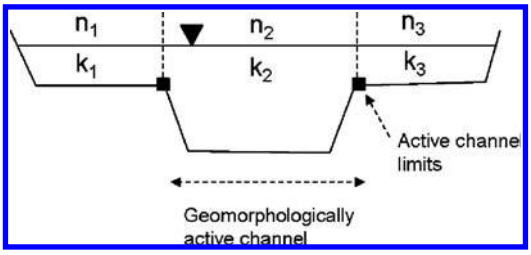


Figure 5. Definition of parameters required to solve Manning's equation. n = Manning's roughness coefficient; and K = conveyance.

acknowledged as potentially a significant source of uncertainty.

To solve Manning's equation a cross-sectional representation of the channel for the reach in question must be defined. This requires a survey of what is considered to be the geomorphologically active channel and, if out of bank flows are thought to be significant, the floodplain as well. It is recognised that field survey data will probably be the most costly input to obtain when using the REAS and the longstream spacing of cross-sections may have to be significant. This will inevitably reduce the resolution of the model in terms of the number of reaches that can be defined. To solve Equation (7) flow depth must be adjusted iteratively to solve for A and P until the value of the right hand side of Equation (7) converges to the value of the left hand side. Iterative techniques available include the Newton-Raphson and secant methods. The normal flow depth for a given discharge is solved by apportioning flow between the main geomorphologically active channel and floodplain areas (left and right) (Fig. 5). If the lateral topography of the floodplain is unknown, the model has the option for the user to assign an estimate of the lateral floodplain slope. This ensures that large flows are not contained within vertical walls either side of the main channel which would otherwise overestimate flow depth. Such a problem can occur in 1-D flow models such as HEC RAS if the floodplain is not extended either side of the channel. A value of n must be prescribed for the channel and floodplains, along with the limits of the geomorphologically active channel (Fig. 5). The term active channel is used here to describe that part of the channel within which the excess stream power acts to perform significant geomorphic work through transporting sediment.

Of significant importance in the calculation of in-channel power is how to account for channel area and wetted perimeter at those discharges that involve overbank flow. It is assumed here that a 'glass wall' extends vertically above the bank markers, thus defining the maximum width and discharge used in Equation (1). Flow depth within the bank markers above the bankfull depth is used but, importantly wetted perimeter is not extended vertically as there is no actual physical boundary. This last assumption grossly simplifies floodplain-channel flow interaction as there will be significant momentum exchange at this location. Methods are available to account for momentum loss (for example; Thorne & Soar 2000, Thorne & Soar 2001), but they are considered to be beyond the scope of this model as it is truly only one dimensional and thus designed to be simple in its representation of flow processes. Indeed many far more complex 1-D flow models such as HEC RAS and HEC 6 do not incorporate any momentum exchange calculations.

To solve Equation (7) for the full channel section it is normal to sum conveyances (K) for each section (Chow 1959):

$$Q = \sum_{i=1}^{n} K_i S_e^{1/2} \tag{8}$$

where K_i = conveyance for panel i. K_i is defined as:

$$K_i = A_i R_i^{2/3} \frac{1}{n_i} \tag{9}$$

where A_i = cross-sectional area for panel i; R = hydraulic radius for panel i; and n_i = Manning's roughness coefficient for panel i.

3.2 *Representing stream power in a variable cross-section*

Flow depth for a given discharge must be defined to solve Equation (3). Two approaches were identified:

1 Based on hydraulic radius, and;
2 Based on panels.

For case 1 Equation (3) becomes:

$$\omega_c = 290 D_i^{1.5} \log\left[\frac{(12 d_h)}{D_i}\right] \tag{10}$$

where d_h = hydraulic depth (m) = A/W.

This seems to be a reasonable and simple assumption on initial inspection but it can be a misleading interpretation in variable cross-sections. Imagine a geomorphologically active channel cross-section (within the in-channel markers) that has an irregular cross-section (Fig. 6). At low flows, when $W = W_1$ an increase in discharge will cause an increase in power (Eq. 1) because the rise in W is proportionally small compared to the rise in Q and critical power. Thus, excess power will increase with stage. Now, however consider the case where flow depth increases to W_2 due to an increase in discharge. It is possible at this stage that the rise in W is disproportionately greater than the numerator in Equation (1), causing excess specific stream power for a given discharge to actually fall or even go to zero, even though the shear stress applied to the bed below W_1 has increased. In reality this cannot

Copyright © 2006 Taylor & Francis Group plc, London, UK

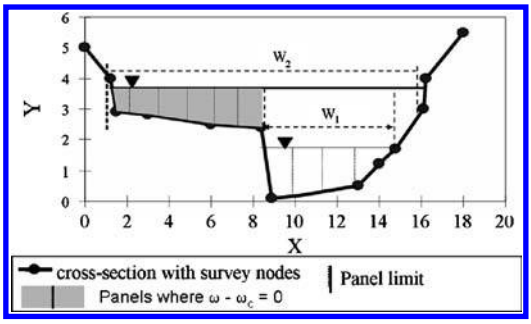


Figure 6. Width variation over a berm within the geomorphologically active channel.

be the case as in the inner low flow channel (W_1) particles will still be mobile, and to a greater degree because Q has increased. Thus, the mathematical definition in Equation (10) does not tally with the process which would actually occur in nature.

However it is considered that a fall in specific stream power for an increase in stage is tenable because excess power is a width averaged variable and must therefore take into account the full channel width, but powers falling to zero cannot be justified. An alternative approach has therefore been investigated and is the preferred option in REAS.

A better approximation of depth can be gained by sub-dividing the active channel cross-section into panels of equal width and with average panel depth d_z. Panels can be generated by interpolating areas between each node generated from the survey of a reach cross-section. For this case the excess specific power equation becomes:

$$\omega_e = \frac{\gamma Q_m S_e}{W} - \frac{290 D_i^{1.5}\left[N_m \log\left[\frac{12}{D_i}\right] + \sum_{z=1}^{n} \log d_z\right]}{N} \quad (11)$$

where Q_m = discharge for those panels where the bed is mobile; N_m = number of panels where the bed is mobile; and N = total number of panels.

The reason for not showing a division of the total power in Equation (11) by N is that the summed division of γQmSe in the total stream power term by the width for each individual panel and then division by the number of panels N, is exactly same as the use the whole width. That is:

$$\frac{\sum_{i=1}^{n}\left[\frac{\gamma Q_{mi} S_e}{dW_i}\right]}{N} = \frac{\gamma Q_m S_e}{W} \quad (12)$$

where dW = individual panel width.

Under this approach, for a given discharge and water surface elevation, the depth for each panel can be determined. Next, a check is made to see if bed particles would be mobile (each size class in the distribution is considered as discussed in Section 2.1) for a given flow depth. It would appear in the first instance that this could be achieved by simply calculating total stream power for a panel and subtracting its corresponding critical power using Equations (1) and (3). However this is actually not possible because of a phenomenon first recognised by Garbrecht & Brown (1991). If discharge is calculated based upon a single panel for an entire cross-section using Manning's equation a given depth and width will be determined. However if a cross-section is panelized and a conveyance is calculated for each, the implicit assumption is made that the channel elements have frictionless walls and no lateral momentum exchange, thus resulting in a lateral velocity gradient. This approach violates the postulate of a single mean velocity across the section for the application of Manning's formula. The result is that a panelized approach will overestimate conveyance, and therefore discharge and consequently flow depth for each panel, as compared with the calculation made using an integrated cross-section. This phenomenon appears to be little known and may result in conveyance over estimation in flow models where the user has the option of dividing the cross-section of a channel into a significant number of panels each with their own roughness coefficient.

An alternative approach has therefore had to be adopted. This has been achieved by simply using a form of the Shields entrainment function (Yang 1996):

$$\theta = \frac{\tau_o}{\gamma(G_s - 1)D_i} \quad (13)$$

where θ = Shields parameter; τ_o = bed shear stress = γRS_o (Nm^{-2}); G_s = specific gravity of the sediment; and R = hydraulic radius (m).

With some rearrangement of Equation (13) we get:

$$R = \frac{\theta(G_s - 1)D_i}{S_o} \quad (14)$$

To distinguish between mobile and immobile panels, Equation (14) is solved using a critical Shields value. Here, a value of 0.04 is used as this was the value used by Bagnold (1980) in his derivation of Equation (3). When Equation (14) is solved using a critical Shields value, R is equal to R_c, the critical hydraulic radius. R_c for a particular panel can then be compared with the actual hydraulic radius computed for the panel. If $R_c > R$ the panel will be immobile at the given flow and given grain size. When all panels are checked in this manner, N_m can be determined. The critical specific power is then calculated using Equation (11). Note that N is the total number of panels including those where $R_c > R$.

Copyright © 2006 Taylor & Francis Group plc, London, UK

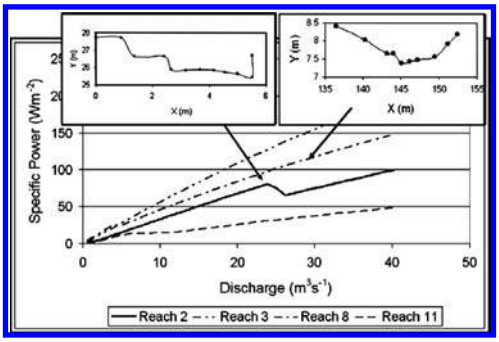


Figure 7. The relationship between channel cross-sectional geometry and specific power – discharge curves.

Once this has been done the total discharge for the mobile panels (Q_m) can be calculated using Manning's equation. Now we can calculate total specific power based upon the mobile panels using the first term on the right hand side of Equation (11).

Using this scheme excess specific stream power can fall if the width suddenly increases, but it should never fall to zero. An example of the functional relationship between discharge and excess power for the Hawkcombe data-set is shown in Figure 7.

It can be seen in this diagram that the cross-section for Reach 2 has a distinct berm and this has an impact on the discharge – power curve where, as the flow initially passes over the berm, the sudden increase in width results in a fall in power. As discharge for this larger width increases again so the upward trend between discharge and power starts again. The trend for Reach 8 is monotonic because the cross-sectional form is reasonably uniform.

3.3 *Relationship between total specific power and excess power*

When Equation (11) is applied to a single or whole range of grain sizes present in the cross-section a relationship is formed between total specific stream power and excess specific stream power. The form of this relationship is shown in Figure 8.

Here the relationship between total and critical power is shown for a nominal discharge of 100 m^3 s^{-1}. Depth for this discharge has been calculated using Manning's equation based upon an idealized, rectangular channel with a slope of 0.0001, a Manning's n coefficient of 0.035 and a channel width of 5 m. The total power which is calculated using the above parameters is indicated by the dashed horizontal line in Figure 8. An example of critical power and excess power values for a sediment size of 0.02 m is shown in the figure.

The relationship that is developed shows that, as grain size increases, critical power also increases thus reducing excess power (ω_e). The functional relationship between the critical power and grain size is formed

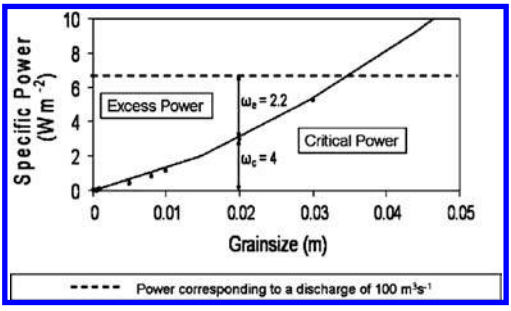


Figure 8. The relationship between critical and excess power over a range of grainsizes.

by a power-based curve. It can be seen that for a limiting value of 0.035 m, excess power falls to zero. The power form of the critical curve is explained by the fact that the term, $290D^{1.5}$ in Equation (3) is a power function. What is also apparent from Equation (3) is that, for the log term, as depth rises so critical depth will also increase relative to grain size. This means that for a greater flow depth the critical curve on Figure 8 should shift upward from, and parallel to, the critical specific power curve for a lower depth. However manipulation of depth values over a wide range shows that the position of the critical power curve varies only fractionally. This can be explained because the log term in Equation (3) is based upon the $\log_{10}$ of d/D and therefore even for a great range of depths the difference in the log term will be almost minimal (this can be illustrated by, for example, the fact the for $d = 2$, $\log_{10} d = 1$ and, for $d = 100$, $\log_{10} d = 2$). This has implications for the academic development of critical power equations as, for example, hiding functions such as that suggested by Ferguson (2005) are, in part, based upon the log term.

4 FUTURE DEVELOPMENTS

The next step in developing the model will be to add the ability to take into account lateral sediment inputs. It is envisaged that bank erosion/accretion might be accounted for using a width (and thus power) scaling factor of severe, moderate, and minor bank adjustment which would be represented by a scaling factor between 0.5 and 1.5. Another element of ongoing research is the introduction of greater robustness in the model if data are limited. Examples of limited data might include poor knowledge of bed material size and a limited number of cross-sections. Overcoming these limitations will require a degree of interpolation of data within the river network.

The type of model presented here lends itself well to fast scenario modelling such as predicting the effects of channel enlargement due to dredging or contraction due to levee construction as in such cases only top width need be changed.

Copyright © 2006 Taylor & Francis Group plc, London, UK

The model is now undergoing sensitivity analysis whereby the full model will be compared with the predictive capability of the following formulations:

1 Simple QS calculation for each reach for a single discharge;
2 QS calculation for each reach integrated over a flow duration record, and;
3 Simple QS/W calculation for each reach.

A second comprehensive data set from the River Wharfe in Yorkshire, UK, is also currently being analysed to further test the model. This data-set has time series cross-sectional surveys that can be used to corroborate the model output.

5 CONCLUSIONS

Accounting for sediment dynamics in river channel networks must become a key component of flood risk management planning. To date the approaches for accounting for sediment in analysis of the fluvial system are generally based either on complex numerical models or qualitative interpretation of the results of stream reconnaissance. Both of these approaches have benefits but also considerable pitfalls in that highly trained modellers and geomorphologists are required to use such tools. Time and financial constraints are also a significant factor. A need for an approach which lies between these two techniques has therefore been identified in the UK as a key resource that will be used to facilitate river flood risk management within the context of meeting statutory requirements for ecological status and goals for habitat preservation and enhancement.

A novel approach, the River Energy Auditing Scheme (REAS), is therefore being developed as part of research performed by the Flood Risk Management Research Consortium (FRMRC). The approach is based on an audit of excess specific stream power in which excess reach-averaged specific stream power is used as a surrogate for sediment transport to give an excess specific stream power budget between consecutive reaches in the channel network. Excess power available to perform work on the channel boundary is defined as total specific stream power minus critical specific stream power, using Bagnold's (1980) formulation of both parameters. Only five input variables are required for the calculations: a flow frequency curve; channel cross-sectional geometry; a bed slope; a roughness coefficient and a representative bed material grainsize or grain size distribution. The approach given here has is mind the fact that geometry data available to the UK Environment Agency and its contractors has widely spaced cross-sections. Also a single representative grainsize can be used to solve Equation (4) if a full distribution is not available.

The approach for generating a flow duration curve has been described along with specific solutions for calculating flow top width and depth using Manning's equation. Interesting properties have been found in the relationship between the variables, showing that excess specific stream power can fall even as discharge rises. The reason for this apparent inconsistency is explained by the manner in which flow depth is derived. This leads to the justification of one particular solution (Eq. 11). The Shields equation is used to predict panel depth because of the phenomenon that calculating discharge using panels rather than using an integrated cross-section will overestimate conveyance and therefore flow depth for a given discharge. The functional form of the relationship between total power and critical power is discussed and indicates the importance of previously unconsidered factors in the derivation of critical power equations.

The test-bed data used for initial exploration of the model structure has been obtained from a comprehensive data-set collected from the Hawkcombe Stream in Somerset, UK. Results are at this stage preliminary and are, therefore, not discussed in-depth here, but in general they have been found to correlate reasonably with the results of a Fluvial Audit. A criticism that has been leveled at this approach is that it is of less utility in terms of predictive capability than more complex numerical models. The reader might bare in mind the following statement made by Overton and Meadows (1976), '…if a highly complex mathematical representation of the system under study is made, the risk of not representing the system will be minimized, but the difficulty of obtaining a meaningful solution will be maximized as much data will be required, and mathematical handling in computer models (e.g. convergence and consistency) and complexity of mathematical processes may even render the problem formulation intractable. Further, the resource constraints of time, manpower and money may be exceeded. Conversely, if a greatly simplified model is selected the risk of not representing the physical system will be maximized, but the difficulty in obtaining a solution will be minimized'. We suggest that the model presented here lies somewhere between the two extremes.

The model is still in the developmental stage and the intention is to add more predictive factors and increase functionality during the coming months.

ACKNOWLEDGEMENTS

This research was performed as part of a multi-disciplinary project programme undertaken by the Flood Risk Management Research Consortium (www.floodrisk.org.uk). The Consortium is funded by the UK Engineering and Physical Sciences Research Council under grant GR/S76304/01, with additional

Copyright © 2006 Taylor & Francis Group plc, London, UK

contributions from the Defra/EA Joint R&D programme on Flood and Coastal Defence, the Scottish Executive, the Rivers Agency (Northern Ireland) and UK Water Industry Research. The authors would like to thank the anonymous reviewer for their valuable input.

REFERENCES

Bagnold, R.A. 1966. *An approach to the sediment transport problem from general physics*. United States Geological Survey Professional Paper 4221.

Bagnold, R.A. 1977. Bed load transport by natural rivers. *Water Resources Research* 13: 303–312.

Bagnold, R.A. 1980. *An empirical correlation of bedload transport rates in flumes and natural rivers*. London: Royal Society of London Proceedings A405: 369–473.

Barnes, H.H. JR. 1967. *Roughness Characteristics of Natural Channels*. U.S. Geological survey water-supply paper 1849 Washington: United states government printing office.

Beven, K. 2002. Towards an alternative blueprint for physically based digitally simulated hydrological response modelling systems. *Hydrological Processes* 16: 1–17.

Biedenharn, D.S., Thorne, C.R., Soar, P.J., Hey, R.D. & Watson, C.C. 2001. Effective discharge calculation guide. *International Journal of Sediment Research* 16(4): 445–459.

Brunner, G.W. 2002. *HEC RAS User's Manual: version 3.1*. California: U.S. Army Corps of Engineers Hydraulic Engineering Centre. CPD-68.

Chang, H.H. 1979. Minimum stream power and river channel pattern. *Journal of Hydrology* 41: 303–327.

Chow, V.T. 1959. *Open-channel hydraulics*. New York: McGraw-Hill.

Environment Agency. 2004. *Catchment Flood Management Plans: Volume i* – Policy Guidance. Bristol: Environment Agency.

Environment Agency. 2005. *Sustainable flood and coastal management; Final draft technical repro. Part 1: Handbook*.: Bristol: Environment Agency.

Ferguson, R.I. 2005. Estimating critical stream power for bedload transport calculations in gravel-bed rivers. *Geomorphology* 70: 33–41.

Garbrecht, J. & Brown, G.O. 1991. Calculation of total conveyance in natural channels. *Journal of Hydraulic Engineering* 117(6): 788–798.

Graf, W.L. 1983. Downstream changes in stream power in the Henry Mountains, Utah. *Annals of the Association of American Geographers* 73(3): 373–387.

HEC, 1976. *HEC-6: Scour and deposition in rivers and reservoirs: Users Manual*. California: Hydrologic Engineering Centre. US Army Corps of Engineers. Computer Program 723-G2-L2470.

HEC, 1998. *Flood Hydrograph Package: User's Manual*. California: California: U.S. Army Corps of Engineers Hydraulic Engineering Centre. CPD-1A.

ISIS, 2006. ISIS Flow / Hydrology. Wallingford: Wallingford Software Ltd. and Halcrow Group Ltd.

Julien, P.Y. 1998. *Erosion and Sedimentation*. Cambridge: Cambridge University Press.

Knighton, D.A. 1998. *Fluvial Forms & Processes: A New Perspective*. London: Arnold.

Knighton, D.A. 1999. Downstream variation in stream power. *Geomorphology* 29: 293–306.

Langbein, W.B. 1964. Geometry of river channels. *Journal of Hydraulic Engineering* 90: 301–312.

Lawler, D.M. 1992. Process dominance in bank erosion systems. In P.A. Carling & G.E. Petts (eds). *Lowland Floodplain Rivers: Geomorphological Perspectives*: 117–143. London: John Wiley & Sons Ltd.

Magilligan, F.J. 1992. Thresholds and spatial variability of flood power during extreme floods. *Geomorphology* 5: 373–390.

Molnar, P. & Ramirez, J.A. 1998. An analysis of energy expenditure in Goodwin Creek. *Water Resources Research* 37 (7): 1819–1829.

Overton, D.C. & Meadows, M.E. 1976. *Stormwater Modelling.* New York: Academic Press.

Parker, G. 1990. Surface-based bedload transport relation for gravel rivers. *Journal of Hydraulic Research*, IAHR 119 (11): 417–436.

Richards, K.S. 1982. *Rivers: Form and Process in alluvial channels*. London: Methuen & Co. Ltd.

Richards, K.S. 1997. Prediction of morphological changes in unstable channels. In C.R. Thorne, R.D. Hey & M.D. Newson (eds), *Applied fluvial geomorphology for river engineering and management*: 268–292. Chichester: John Wiley and Sons.

The European Parliament and the Council of the European Union. 2000. *Directive 2000/60/EC*.

Sear, D.A., Newson, M.D. & Thorne, C.R. 2003. *Guidebook of Applied Fluvial Geomorphology*. Swindon: Defra R&D Technical Report FD1914, Environment Agency R&D Dissemination Centre, WRc. ISBN 0-85521-053-2.

Thorne, C.R. 1998. *Stream Reconnaissance Handbook: Geomorphological Investigation and Analysis of River Channels*. Chichester: John Wiley & Sons Ltd, UK.

Thorne, C.R. & Soar, P.J. 2000. *Analysis of channels with compound channels for channel restoration design. Final report submitted to United States Army*. London: Research Development and Standardisation Group – UK. Contract No. N68171-00-M-5506, Project No. W90C2K-8913-EN01.

Thorne, C.R. & Soar, P.J. 2001. *Performance of channels with compound channels for channel restoration design. Final Report submitted to United States Army*. London: Research Development and Standardisation Group-UK. Contract No. N68171-01-M-5483, Project No. W90C2K-9125-EN01.

Thorne, C.R., Skinner, K.S. & Priestnall, G. 2002. *Geomorphology of the Hawkcombe Stream*: *CD-ROM*. *Submitted to the Environment Agency, Wessex Region*. Nottingham: Nottingham University Consultants Limited.

Versteeg, H.K. & Malalasekera, W. 1995. *An introduction to computational fluid dynamics: The finite volume method.* London: Prentice Hall, an imprint of Pearson Education.

Wilcock, P.R. & Crowe, J.C. 2003. Surface-based transport model for mixed-size sediment. *Journal of Hydraulic Engineering* 129(2): 120–128.

Yang, C.T. 1971. Potential energy and stream morphology. *Water Resources Research* 7(2): 311–322.

Yang, C.T. 1996. *Sediment Transport: Theory and Practice*. London: McGraw-Hill.

Copyright © 2006 Taylor & Francis Group plc, London, UK

Fluid–structure interaction modeling with a coupled 1D–2D free surface flow solver

S. Erpicum, P. Archambeau, B. Dewals, S. Detrembleur & M. Pirotton
Laboratory of Applied Hydrodynamics and Hydraulic Constructions, Civil Engineering Institute, University of Liege, Belgium

ABSTRACT: Wolf software is a set of coupled numerical tools developed for almost ten years for simulating a wide range of free surface flows and transport phenomena. In the scope of new applications in hydraulic structure design and fluid-structure interaction, additional developments have been implemented in the finite volume 2D model to deal with boundaries not aligned along axis or with moving structures. The cut cell based approach, simpler than other classical methods, is based on the division with a sub-grid of the initial Cartesian meshes. While keeping the advantages of regular grids in terms of simplicity, accuracy and storage capacity, it enables to compute instantaneous effects of a structure movement on the fluid or to deal with complex boundaries inclined compared to mesh axis. Several test cases are presented, as well as an application of the enhanced model, coupled with a 1D one, to the computation of the hydrodynamic fields induced by a lock-door movement.

1 INTRODUCTION

Today, hydraulic engineering studies use more and more numerical models to predict or assess flow conditions. Depth-integrated models are very efficient in this field as they represent a good compromise between problem implementation and computation times in comparison with results quality and accuracy. Discretization in two dimensions allows using fine meshes without leading to prohibitive memory requirements, while well-known equations sets and resolution schemes provide a reliable modeling of the most important flow variables for practical engineering applications.

On the other hand, the finite volume method seems to be currently the most suited to solve the hyperbolic partial differential equations system characterizing flow movement (Valiani et al. 2002). As the method is based on the integral form of the conservation equations, the derived numerical scheme is conservative (Hirsch, 1988) and satisfies the shock-capturing property (Toro, 2001).

The application field of such numerical models solving the so-called shallow water equations (SWE) is very broad. Among others, they are used for dam-break (Valiani et al. 2002, Erpicum et al. 2004a) or dam-breaching (Dewals et al. 2002, Froehlich, 2002) simulations, flood inundation mapping even in urban areas (Alcrudo & Mulet, 2005, Archambeau et al. 2004) as well as hydraulic structure design (Erpicum et al. 2004b, Dewals et al. in press) or sedimentation assessment (Dewals et al. 2004).

Generally, grids used for 2D simulation are classified regarding the type of meshes they use. The two main families are the structured and unstructured grids. While unstructured grids allow dealing with complex geometries, they are more computation time consuming than structured ones, even more if the latter are Cartesian. Indeed, to achieve the same global order of precision for the calculation, they need a higher precision of reconstruction of the unknowns (Mouzelard, 2002).

To limit the restriction of the Cartesian grids to fit to complex geometries, methods based on a cut cell approach (Causon et al. 2000) can be used. They can also easily be extended to the simulation of moving bodies (Ingram et al. 2003), and thus reproduce fluid-structure interaction. Such a method is presented in this paper.

Based on a sub grid approach to define complex geometries, the present method is simpler than classical cut cell approaches but is more easily implemented in an existing code. It constitutes thus an appropriate first approach in the domain.

In this paper, the developments realized to simulate fluid-structure interaction by means of mobile boundaries on a fixed Cartesian grid are presented in detail. After its implementation in the free surface flow solver Wolf2D (Erpicum et al. 2004a), the modified SWE model is applied to a bore reflection on

Copyright © 2006 Taylor & Francis Group plc, London, UK

a fixed inclined wall and to the simulation of a moving plate in a channel. Finally the modified 2D model, coupled with the one-dimensional free surface flow solver Wolf1D (Erpicum et al. in prep.), is applied to assess the hydrodynamic effects of a ship lock door movement.

2 EQUATIONS

2.1 *1D approach*

Consider a general 1D conservative law such as:

$$\frac{\partial}{\partial t}s+\frac{\partial}{\partial x}f=S \tag{1}$$

where $s=$ unknown; $f=$ advective term; $S=$ source term; $x=$ space coordinate; and $t=$ time.

Let us solve the equation using a finite volume method with a cell-centered approach (Fig. 1), considering fixed nodes but cell edges moving with velocity $v_{G,x}$ along x-axis. Integration of (1) over a finite volume i lead to:

$$\int_{x_{i-1/2}}^{x_{i+1/2}}\frac{\partial}{\partial t}s\,dx+\int_{x_{i-1/2}}^{x_{i+1/2}}f\,dx=\int_{x_{i-1/2}}^{x_{i+1/2}}S\,dx \tag{2}$$

After Leibnitz theorem application, time derivative integral becomes:

$$\frac{\partial}{\partial t}\int_{x_{i-1/2}}^{x_{i+1/2}}s\,dx-s\big|_{i+1/2}\frac{\partial}{\partial t}x_{i+1/2}+s\big|_{i-1/2}\frac{\partial}{\partial t}x_{i-1/2} \tag{3}$$

and is equal to:

$$\frac{\partial}{\partial t}\bar{s}\Delta x_i-s\big|_{i+1/2}v_{G,x}\big|_{i+1/2}+s\big|_{i-1/2}v_{G,x}\big|_{i-1/2} \tag{4}$$

where $\Delta x_i=$ cell i length; and symbol $\bar{a}$ stands for the mean value of a over the finite volume.

Green-Gauss theorem application to second term of (2) and source term integration lead to, respectively:

$$f\big|_{i+1/2}-f\big|_{i-1/2}\ \text{and}\ \bar{S}\Delta x_i \tag{5}$$

Using expressions (4) and (5), equation (2) becomes:

$$\frac{\partial}{\partial t}\bar{s}+\frac{\partial}{\partial x}\left[\left(f-sv_{G,x}\right)_{i+1/2}-\left(f-sv_{G,x}\right)_{i-1/2}\right]=\bar{S} \tag{6}$$

Grid movement affects advective terms by mean of additional exchanges through cells faces. For example, regarding mass conservation equation for a 1D flow in a rectangular channel, s is the water height h and f is the unit discharge q while S is zero if no mass exchange occurs with outside. Equation (6) writes:

$$\frac{\partial}{\partial t}h+\frac{\partial}{\partial x}\left[\left(q-hv_{G,x}\right)_{i+1/2}-\left(q-hv_{G,x}\right)_{i-1/2}\right]=0 \tag{7}$$

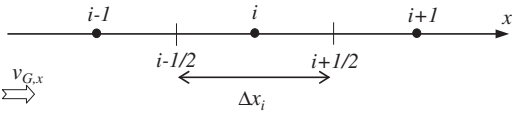


Figure 1. Sketch of 1D grid for cell-centered finite volume method.

It is the classical form of mass conservation equation for a 1D flow except additional mass transfers $hv_{G,i}$ through cells sides.

If the calculation grid is fixed but a boundary moves through the calculation domain with the velocity $v_{G,x}$, the equation is the same with term $v_{G,x,i}$ equals to zero everywhere except at instantaneous boundary location. For a solid boundary, as there is no mass exchange, fluid velocity u is equal to$v_{G,x}$ and corresponding advective flux in (7) is zero.

On the other hand, the cell length is changing along time. This can be taken into account by an occupancy rate parameter θ affecting the cell length.

2.2 *Generalization to shallow water equations*

Shallow water equations (SWE) can be written under a general form such as:

$$\frac{\partial}{\partial t}\mathbf{s}+\frac{\partial}{\partial x}\mathbf{f}+\frac{\partial}{\partial y}\mathbf{g}=\mathbf{S} \tag{8}$$

where $\mathbf{s}=$ unknowns vector; $\mathbf{f}$ and $\mathbf{g}=$ advective terms vector; and $\mathbf{S}=$ source terms vector.

Generalization of previous developments on a moving Cartesian grid provides for the integration over a finite volume of equation (7):

$$\frac{\partial}{\partial t}\bar{\mathbf{s}}\Delta x\Delta y+\oint\left(\mathbf{F}-\mathbf{s}\mathbf{v}_\mathbf{G}\right).\mathbf{n}\,d\Gamma=\bar{\mathbf{S}}\Delta x\Delta y \tag{9}$$

where $\mathbf{F}=[\mathbf{f},\mathbf{g}]$; $\mathbf{v}_G=$ grid velocity vector; $\mathbf{n}=$ normal vector; $\Gamma=$ cell outline; and $\Delta x=\Delta y=$ grid dimensions.

Developments are still the same if the grid is fixed but a boundary moves through the cell with ve locity $\mathbf{v_G}$.

Considering Figure 2, outline integral in (9) can so be expressed as:

$$\sum_{k=1}^{N}\int_{\Gamma^k}\left[\left(\mathbf{f}-\mathbf{s}\mathbf{v}_\mathbf{G}\right)n_x+\left(\mathbf{g}-\mathbf{s}\mathbf{v}_\mathbf{G}\right)n_y\right]d\Gamma^k \tag{10}$$

where $N=$ number of cell sides.

For SWE, without taking into account diffusive effects:

$$\mathbf{s}=\begin{Bmatrix}h\\uh\\vh\end{Bmatrix};\mathbf{S}=\begin{Bmatrix}0\\-gh\dfrac{\partial z_b}{\partial x}+ghJ_x\\-gh\dfrac{\partial z_b}{\partial y}+ghJ_y\end{Bmatrix} \tag{11}$$

Copyright © 2006 Taylor & Francis Group plc, London, UK

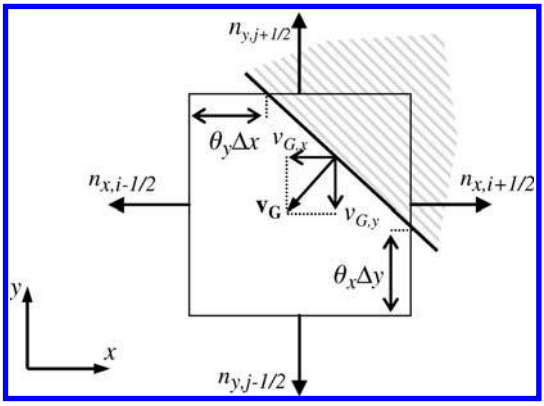


Figure 2. Sketch of the normal vector **n** components on a 2D finite volume and solid boundary moving with velocity $\mathbf{v_G}$.

$$\mathbf{f} = \begin{Bmatrix} uh \\ u^2h + g\dfrac{h^2}{2} \\ uvh \end{Bmatrix}; \mathbf{g} = \begin{Bmatrix} vh \\ uvh \\ v^2h + g\dfrac{h^2}{2} \end{Bmatrix} \quad (12)$$

where u, v = fluid velocity vector components along x and y-axis; g = gravitational acceleration; z_b = bed elevation; and J_x, J_y = friction slope components along x and y-axis, classically expressed by Manning's formula.

Considering sliding condition against boundary:

$$\mathbf{u}.\mathbf{n} = \mathbf{v_G}.\mathbf{n} \quad (13)$$

where $\mathbf{u}$ = fluid velocity vector.

Formulation for SWE, taking into account a solid boundary moving across grid, expresses finally using (11), (12) and (13) in (9) and (10) as:

$$\begin{aligned} &\frac{\partial}{\partial t}(\theta h) + \frac{\partial}{\partial x}(\theta_x uh) + \frac{\partial}{\partial y}(\theta_y vh) = 0 \\ &\frac{\partial}{\partial t}(\theta uh) + \frac{\partial}{\partial x}\left(\theta_x u^2 h + g\frac{h^2}{2}\right) + \frac{\partial}{\partial y}(\theta_y uvh) = \\ &\qquad -gh\theta\left(\frac{\partial}{\partial x} z_b - J_x\right) \quad (14) \\ &\frac{\partial}{\partial t}(\theta vh) + \frac{\partial}{\partial x}(\theta_x uvh) + \frac{\partial}{\partial y}\left(\theta_y v^2 h + g\frac{h^2}{2}\right) = \\ &\qquad -gh\theta\left(\frac{\partial}{\partial y} z_b - J_y\right) \end{aligned}$$

where θ = occupancy rate of the cell by water, i.e. percentage of the cell surface not occupied by solid; θ_x, θ_y = free portion of cell sides (Fig. 2), i.e. part of cell sides where mass and momentum exchanges can occur.

Pressure terms are not affected by a moving solid boundary, but other advective terms involving mass transfers are directly modified as the length of the cell side they can pass trough is reduced. Terms involving mean unknown value over the cell are also modified as the cell area decreases by solid intrusion.

3 NUMERICAL ASPECTS

3.1 *Wolf package*

Wolf software includes a series of interconnected numerical tools for simulating a wide range of free surface flows and transport phenomena, from hydrological runoff and river propagation to extreme erosive flows on realistic mobile topography. It has been entirely developed at the University of Liege for almost ten years and is still continuously enhanced (Pirotton et al. 2003).

In all the solvers, the space discretization of the conservative equations is performed by a finite volume method. Flux treatment is based on an original flux-vector splitting technique developed for Wolf. The hydrodynamic fluxes are split and evaluated partly downstream and partly upstream according to the requirements of a Von Neumann stability analysis (Mouzelard, 2002, Dewals, 2006). Optimal agreement with non-conservative and source terms as well as low computational cost are the main advantages of this original scheme. Constant or linear reconstruction of the variables is used to achieve a global first or second order of precision.

As we are mostly interested in transient flows and flood waves, explicit Runge-Kutta schemes are used for time integration.

Equations (14) have been implemented in Wolf2D, specifically devoted to the resolution of the SWE. It includes an efficient mesh generator and deals with multiblock Cartesian grids (Erpicum et al. 2004a). The algorithm is also designed to deal automatically with any moving boundary between wet and dry cells.

A spatially distributed hydrological solver, WolfHydro, a one-dimensional free surface flow solver, Wolf1D, and an optimization tool based on genetic algorithms technique, WolfAG, complete the Wolf software package (Pirotton et al. 2003).

3.2 *Coupling of models*

As an extension of the multiblock feature of Wolf2D, and thanks to the use of the same discretization and calculation techniques for all the solvers of Wolf software, a coupling between the 1D and the 2D models has been achieved. It allows simulating in a unified way large river reaches (in 1D) with a very fine computation of local areas (in 2D) without leading to prohibitive computation times (Erpicum et al. in prep.)

Copyright © 2006 Taylor & Francis Group plc, London, UK

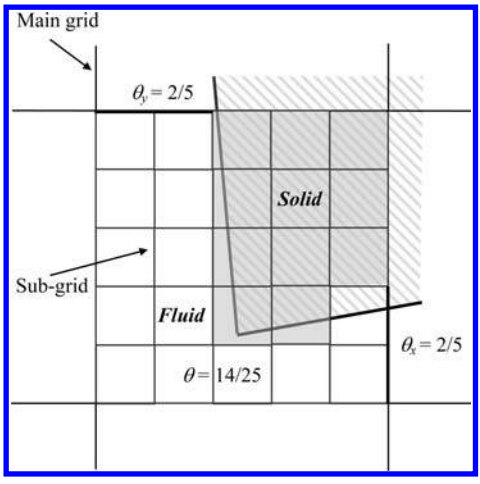


Figure 3. Example of application of the sub-grid to evaluate boundary location and occupancy rate in a mesh – *step* factor = 5.

3.3 *Sub grid approach*

In order to deal with mobile structures or boundaries inclined along mesh axis, a simple approach based on a regular sub-grid has been applied.

To calculate a cell water occupancy rate and the free length of its sides as a function of the solid boundary instantaneous position, the mesh is subdivided by a *step* factor. The position of the sub-grid cells gravity center automatically defines whether they are under water or not (Fig. 3).

The main advantage of this simple technique is that the cell water occupancy rate is never lower than one *step*, and thus calculation stability criterion is easily evaluated. In addition, updating the boundary position and cells occupancy rates is very easy and rapid.

If *step* equals one, boundary discretization is as rough as the initial Cartesian grid. When *step* increases, the representation of inclined boundary becomes better.

To solve the problem of a mesh leaving the calculation domain between to time steps while respecting the mass conservation principle, the following operation is performed. If the cell i leaving the calculation domain in time t:

$$0 < \theta_i^{t-\Delta t} \leq 1 \text{ and } \theta_i^t = 0 \tag{15}$$

Calculation in the entire domain is realized in time t for cells containing water, i.e. without cell i. After time step evaluation, water heights in the four cells adjacent to cell i is increased as a function of their respective occupancy rate:

$$h_l \rightarrow h_l + \frac{\theta_l h_l}{\sum_{k=1}^{4} \theta_k} \theta_l \text{ with } l = 1,\ldots,4 \tag{16}$$

On the contrary, when a cell enters the calculation domain, its hydrodynamic variables are initialized as a function of those of its neighbors containing water. The water height of all the adjacent meshes containing water and of the new mesh is leveled:

$$h_l = \frac{\sum_{k=1}^{M+1} \theta_k}{\sum_{k=1}^{M} \theta_k h_k} \text{ with } l = 1,\ldots,M+1 \tag{17}$$

where M = number of cells adjacent to cell i with θ higher than zero.

For the specific discharges, they are initialized to the mean value of the corresponding variables in the two adjacent cells containing water on the same axis.

3.4 *Stability criterion*

As explicit time integration scheme is used in the solver, the calculation stability criterion remains classically in the form of a Courant-Friedrichs-Lewy number *CFL* maximal value (Hirsch, 1988). For a Runge-Kutta scheme RK*PQ*, where P is the number of sub-steps to calculate one time step and Q is the order of precision of the method, *CFL* condition writes (Dewals, 2006):

$$CFL = \frac{(\|\mathbf{u}\| + c)\Delta t}{\Delta x} \leq \frac{R_0}{2} \tag{18}$$

where c = wave celerity; Δt = time step; R_0 = factor depending on the Runge-Kutta scheme.

In practice, *CFL* number is evaluated for each cell of the calculation domain to identify the local stable time step Δt_i, and the most restrictive one is chosen as the effective calculation time step Δt.

Because of the sub-grid, the effective size of the cells near an inclined boundary can be smaller than Cartesian steps Δx or Δy. A good approximation is the smallest length of the free sides of the cell (Fig. 3), and condition (18) becomes for cells near a mobile boundary:

$$CFL = \frac{(\|\mathbf{u}\| + c)\Delta t}{\min(\theta_y \Delta x, \theta_x \Delta y)} \leq \frac{R_0}{2} \tag{19}$$

4 VALIDATION AND CASE STUDIES

4.1 *Bore reflection*

The example of a bore reflection on an inclined bank in shallow water has first been investigated. A linear incident bore wave moves from right to left and encounters a solid boundary inclined at a fixed angle into the flow

Copyright © 2006 Taylor & Francis Group plc, London, UK

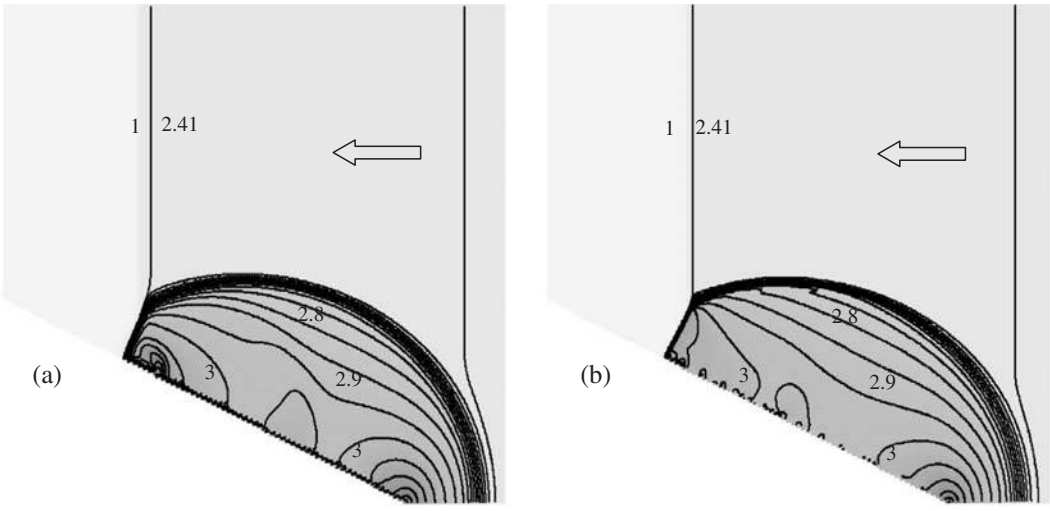


Figure 4. Single Mach reflection of a bore on an inclined solid wall. No sub grid (step = 1 – (a)) and sub grid with step = 5 (b) – Representation of water heights (m).

direction. The bore is therefore reflected (Causon et al. 2000) .

If the incident bore is defined by a Froude number F_s equal to 2.03 and the boundary is inclined of an angle α_w of 27°, a so called single Mach reflection occurs (Causon et al. 2000).

To assess the influence of the developments proposed in this paper, the simulations have been realized with the new model with and without a sub-grid (*step* = 5).

A grid with 200 × 200 meshes 5 cm long has been used. Initial conditions (Causon et al. 2000) were water at rest with a height of 1 m everywhere in front of the bore, and water height of 2.41 m with a specific discharge from right to left of 8.965 m^2/s behind the discontinuity. No roughness effects have been considered.

Results are presented on Figure 4. Even if the two calculations show physically meaningful results, less spurious effects near the inclined boundary are observed with the new model. Reflected shock is also sharper, and so the results are globally better.

4.2 *Moving plate*

Consider a plate moving with constant velocity v_P in a frictionless horizontal rectangular channel containing water initially at rest with height h_0 (Fig. 5). Under the assumption that fluid velocity near the plate is equal to the piston velocity, the analytical solution of the waves propagation in the channel can be calculated, both behind and in front of the plate.

Indeed, from mass and momentum conservation equations applied on both sides of the flow discontinuities, Rankine-Hugoniot shock propagation principle

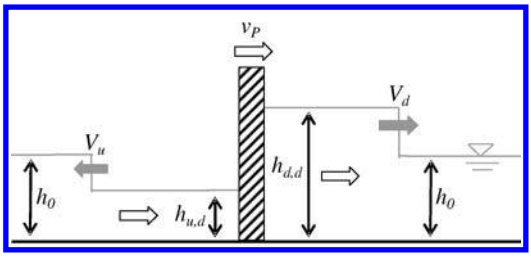


Figure 5. Sketch of shocks propagating around a plate moving with constant velocity v_P in a channel where water is at rest with height h_0.

provides two relations linking the two unknowns: front velocity V and water height of the waveh_d:

$$V = \underbrace{\frac{h_d v_P}{h_d - h_0}}_{mass} = \underbrace{\frac{v_P^2 h_d + \frac{g}{2}\left(h_d^2 - h_0^2\right)}{v_P h_d}}_{momentum} \quad (20)$$

For example, if $h_0 = 1$ m and $v_P = 0.2$ m/s, $h_{d,d} = 1.065$ m and $V_d = 3.28$ m/s downstream of the plate, while $h_{d,u} = 0.937$ m and $V_u = 2.98$ m/s upstream.

The numerical simulation of this test case has been realized.

A channel 1 km long and 1 m wide has been modeled using 1 to 1 m regular meshes. A plate 2 m thick divided it into to reaches 499 m long. No bed slope nor friction effects have been considered. All the simulation limits were assumed to be impermeable.

Hydraulic initial condition was water at rest with height $h_0 = 1$ m everywhere in the reaches.

Copyright © 2006 Taylor & Francis Group plc, London, UK

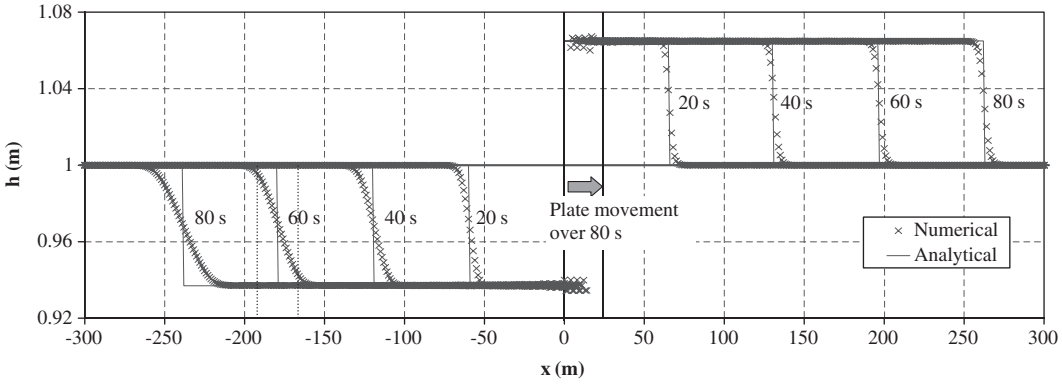


Figure 6. Waves propagation in a rectangular channel induces by the movement with a constant velocity $v_P = 0.2$ m/s of a vertical plate – Comparison between numerical results and analytical solution at times 20, 40, 60 and 80 s. Water level initially at rest at height $h_0 = 1$ m.

At time t = 0 s, the plate instantaneously began to move from left to right with a constant velocity $v_P = 0.2$ m/s. Sub grid 0.01 m ($step = 100$) has been used for plate movement.

Numerical results are illustrated in Figure 6. Water heights and propagation times are in satisfactory agreement with the analytical solution.

The shock propagation in front of the plate is well represented, with a sharp front moving in accordance with the analytical celerity. Behind the plate, the wave is smoother. This is in agreement with the physics of the problem and can be explained by the characteristics theory for shallow flows.

The celerity c of a wave in water with height h is:

$$c = \sqrt{gh} \tag{21}$$

In the channel, water height is $h_0 = 1$ m and thus waves celerity c_0 is 3.13 m/s.

In front of the plate, front velocity V_d is higher than waves celerity c_0 and thus a shock occurs. Beside the plate, front velocity V_u is a bit smaller than waves celerity c_0 and the front is smoothed as information propagates faster in the fluid than the wave.

Considering more precisely the characteristics curves behind the plate (Pirotton, 1994), only two lines exist. The faster one has a celerity $-c_0$, as explained above, and the second one has a celerity equal to:

$$\frac{3}{2}v_P - c_0 = -2.83\ m/s \tag{22}$$

Between the moving plate and this second characteristic, nothing else occurs and water height is constant.

For each time, the wave upstream the plate is bounded between two instantaneous positions defined by these two characteristic lines. For example, for $t = 60$ s, x-abscissa related to the faster characteristic is equal to 187.8 m and those related to the second one is equal to 169.8 (Fig. 6).

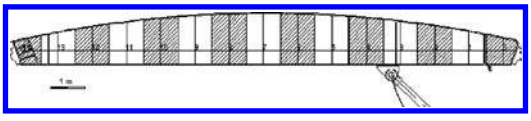


Figure 7. Shape of a downstream gate of the new Lanaye lock.

4.3 *Lock door movement*

In the scope of the studies of a new 225 × 25 × 14 m lock in Lanaye on the river Meuse in Belgium, numerical simulations of the hydrodynamic effects of the downstream mitering gates movements have been realized. Both opening and closure operations have been modeled.

The door is made of two gates, symmetrical regarding lock longitudinal axis and vertically articulated on lock walls. Plane dimensions of a gate are 14.3 m long and 0.9 to 1.5 m wide (Fig. 7). Its height is 17.5 m.

Water height in the lock and the channel, during door movement, is 4.8 m. Water is initially at rest.

By symmetry, only a gate and half a lock have been simulated. Cartesian meshes from 1 × 1 m to 0.2 × 0.2 m have been used. The coarser grid was for lock and downstream channel, while the finer one was for door location.

The lock layout has been modeled in 2D, with the upstream lock wall represented as an impermeable boundary. Downstream, the channel is going to the Meuse river. A suitable boundary condition has to be used to allow waves propagation without introducing spurious numerical reflections. 2D simulations domain has so been completed with a reach modeled in 1D. Thanks to this original approach, wave

Copyright © 2006 Taylor & Francis Group plc, London, UK

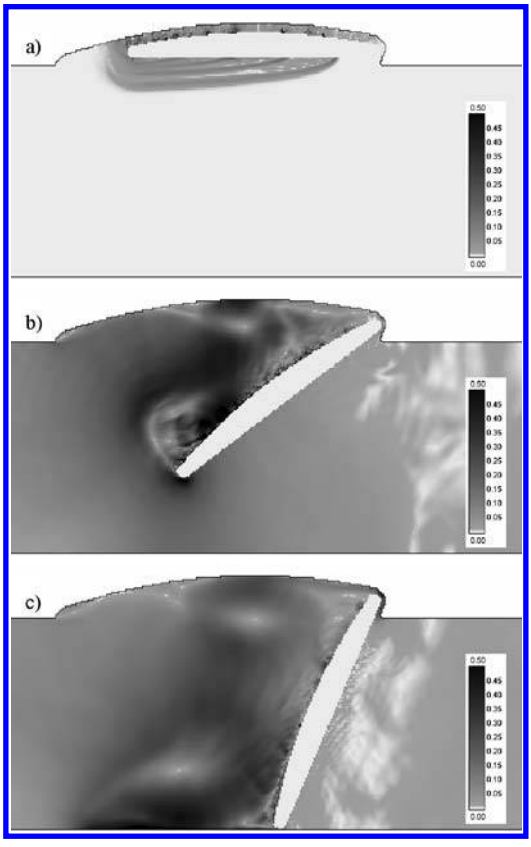


Figure 8. Instantaneous velocity fields (m/s) near the gate during closure operation to time t = 2 s (a), 50 s (b) and 100 s (c).

propagation is very well represented, without any numerical reflection at the boundary between 1- and 2D models (Erpicum et al. in prep).

The area for the 2D simulation is 470 m long and 30 m wide, with 27,000 meshes. The 1D reach is 8 km long with finite volume cells of 1 m.

A sub-grid with *step* equal to 10 has been used. A representation of the door with regular meshes of 0.02×0.02 m is thus performed.

Electromechanical engineering designers have provided the kinetics of the door movement. Time for a gate operation is 105 s. The course angle is 68.1°. Maximal angular velocity is 0.8°/s.

Examples of instantaneous results for the gate closure are shown on Figure 8 in terms of flow velocity fields. The simulations allowed assessing water levels variation along the gate faces, and thus evolution of the hydrostatic resultant along time to be counterbalanced by the door mechanism.

To complete this numerical approach, experiments are currently carried out at the Laboratory of Hydraulic Constructions of the University of Liège.

5 CONCLUSIONS

2D finite volumes free surface flow solvers are of great interest in most fields of hydraulic engineering. Among them, those based on Cartesian grids, such as Wolf2D, are simple, accurate and require less storage capacities than models using unstructured meshes.

Even if Wolf2D multiblock or coupling potentialities allow mesh refinement near interesting areas without increasing dramatically the number of cells and thus computation time, the main problem of structured grids remains their inability to model boundaries inclined compared to Cartesian axis, and thus complex geometries. Fluid-structure interaction modeling has to face the same problem to accurately take into account the movement of a solid on the simulation domain.

A first approach has been developed and presented in this paper to deal with boundaries inclined compared to axis or moving structures on Cartesian grid in Wolf2D. Based on the cut cell approach, the method is simpler than classical ones as it uses a sub-grid of the initial Cartesian meshes to assess structure instantaneous position. It allows keeping the advantages of regular grids in terms of simplicity, accuracy and storage capacity and is weekly restrictive on solver stability criterion.

The model showed its potentialities through several test cases and an application to the computation of the hydrodynamic fields induced by a lock-door movement. In this last case, 2D model has been coupled with a 1D one to extend the simulation domain without increasing too much computation time.

Improvements of the model should be considered to increase the precision of fluxes evaluation near moving boundaries and to refine the representation of inclined ones. For example, more precise calculation of the structure occupation rate in a cell should be realized.

NOTATIONS

c = wave celerity
CFL = Courant-Friedrichs-Lewy number
$\mathbf{F}$ = advective terms vector = [**f**,**g**]
$\mathbf{f}$ = x-component of advective terms vector
f = generic advective term
$\mathbf{g}$ = y-component of advective terms vector
g = gravitational acceleration
h = water height
J_x = friction slope component along x-axis
J_y = friction slope component along y-axis
M = number of calculation adjacent cells
N = number of cell sides
$\mathbf{n}$ = normal vector
n_x = normal vector component along x-axis
n_y = normal vector component along y-axis
q = specific discharge

Copyright © 2006 Taylor & Francis Group plc, London, UK

$\mathbf{s}$ = unknown vector
s = generic unknown
$\mathbf{S}$ = source terms vector
S = source term
t = time
$\mathbf{u}$ = fluid velocity vector
u = average fluid velocity along x-direction
v = average fluid velocity along y-direction
V = front velocity
$\mathbf{v_G}$ = grid velocity vector
$v_{G,x}$ = grid velocity along x-direction
$v_{G,y}$ = grid velocity along y-direction
v_P = plate velocity
x = x Cartesian coordinate
y = y Cartesian coordinate
z_b = bed elevation
Δx, Δy = cell dimensions
Δt = time step
θ = cell occupancy rate parameter
θ_x = x-side occupancy rate parameter
θ_y = y-cell occupancy rate parameter
Γ = cell outline

REFERENCES

Alcrudo, F., Mulet, J. 2005. Urban inundation models based on the shallow water equations. Numerical and practical issues. In Benkhaldoun, Ouazar, Raghay (ed.), *Finite volumes for complex applications, Proc. 4th intern. symp., Marrakech, July 2005*. London, England: ISTE.

Archambeau, P., Dewals, B., Erpicum, S., Detrembleur, S., Pirotton, M. 2004. New trends in flood risk analysis: working with 2D flow models, laser DEM and a GIS environment. In Greco, Carravetta & Della Morte (Ed.), *River Flow 2004, Proc. 2nd intern. conf. on fluvial hydraulics, Napoli, 23–25 June 2004*. Rotterdam, the Netherland: Balkema.

Causon, D., Ingram, D., Mingham, C., Yang, G., Pearson, R. 2000. Calculation of shallow water flows using a Cartesian cut cell approach. *Advances in Water Resources*. Vol. 23: 545–562.

Dewals, B., Archambeau, P., Erpicum, S., Mouzelard, T., Pirotton, M. 2002. Coupled computations of highly erosive flows with WOLF software. In Holz, Kawahara & Wang (ed.), *Proc. 5th inter. conf. on Hydro-Science & -Engineering, Warsaw, 18–21 September 2002*.

Dewals, B., Erpicum, S., Archambeau, P., Detrembleur, S., Fraikin, C., Pirotton, M. 2004. Large scale 2D numerical modelling of reservoirs sedimentation and flushing operations. In Hu & Tan (ed.), *Proc. of the 9th inter. symp. on River Sedimentation, Yichang, 18–21 October 2004*.

Dewals, B., Erpicum, S., Archambeau, P., Detrembleur, S., Pirotton, M. In press. Depth-integrated flow modelling taking into account bottom curvature. *Journal of Hydraulic Engineering*. Accepted for publication.

Dewals, B. 2006. *Une approche unifiée pour la modélisation d'écoulements à surface libre, de leur effet érosif sur une structure et de leur interaction avec divers constituants*. PhD Thesis. Liège, Belgium: University of Liège.

Erpicum, S., Archambeau, P., Dewals, B., Detrembleur, S., Pirotton, M. 2004a. Computation of the Malpasset dam break with a 2D conservative flow solver on a multiblock structured grid. In Liong, Phoon & Babovic (ed.), *Proc. of the 6th inter. conf. on Hydroinformatics, Singapore, 21–24 June 2004*. Singapore: World Scientific Publishing.

Erpicum, S., Dewals, B., Archambeau, P., Detrembleur, S., Fraikin, C., Pirotton, M. 2004b. Global design of hydraulic structures optimized with physically based flow solvers on multiblock structured grids. In Hu & Tan (ed.), *Proc. of the 9th inter. symp. on River Sedimentation, Yichang, 18–21 October 2004*.

Erpicum, S., Archambeau, P., Dewals, B., Detrembleur, S., Pirotton, M. In prep. 1D and 2D solvers coupling for free surface flows modeling. in *Proc. of the 7th inter. conf. on Hydroinformatics, Nice, 4–8 September 2006*.

Froehlich, D. 2002. Project Field Tests 1 & 2: "Blind Simulation by Davef", in *2nd IMPACT Project Workshop, Mo-i-Rana, 12–13 September 2002*.

Hirsch, C. 1988. *Numerical computation of internal and external flows. Vols. I–II*. Chichester, England: Wiley.

Ingram, D., Causon, D., Mingham, C. 2003. Developments in Cartesian cut cell methods. *Mathematics and Computers in Simulation*, Vol. 61: 561–572.

Mouzelard, T. 2002. *Contribution à la modélisation des écoulements quasi tridimensionnels instationnaires à surface libre*. PhD Thesis. Liège, Belgium: University of Liège.

Pirotton, M. 1994. *Modélisation des discontinuités en écoulement instationnaire à surface libre. Du ruissellement hydrologique en fine lame à la propagation d'ondes consécutives aux ruptures de barrages*. PhD Thesis. Liège, Belgium: University of Liège.

Pirotton, M., Lejeune, A., Archambeau, P., Erpicum, S., Dewals, B. 2003. Numerical – experimental interaction in hydrodynamics: an integrated approach for the optimal management of hydraulic structures and hydrographic basins. In Lu, Lamas, Li & Mok (Ed.), *Computational methods in engineering and science*. Rotterdam, the Netherlands: Balkema.

Toro, E. 2001. *Shock-capturing methods for free-surface shallow flows*. Chichester, England: Wiley.

Valiani, A., Caleffi, V., Zanni, A. 2002. Case study: Malpasset dam-break simulation using a two dimensional finite volume method, *Journal of Hydraulic Engineering*, Vol. 128, No. 5: 460–472.

Copyright © 2006 Taylor & Francis Group plc, London, UK

Roughness parameterization for 2D hydrodynamic models from QuickBird spaceborne imagery

S. Rath, B. Gunawan & E. Pasche
Institute for River and Coastal Engineering, Hamburg University of Technology, Germany

A. Frick
LUP Gesellschaft für Landschafts, Landes- & Umweltplanung, Fernerkundung & digitale Verarbeitung von Planungsdaten mbH, Potsdam, Germany

U. Teschke
IMS Ingenieurgesellschaft mbH, Hamburg, Germany

ABSTRACT: Remote sensing contributes high resolution data permitting a-priori parameterization for automation of the model generation process in hydroinformatics. This likewise holds for the representation of the fluvial topography and the roughness parameterization of river systems. The later is considered throughout this paper, focusing on parameterizations based on spaceborne QuickBird imagery, currently providing the highest resolution commercial data source of its kind. An automated method to derive reproducible roughness classes from a panchromatic and multispectral image bundle is presented, suiting to extract land cover with sub-meter pixel resolution via a knowledge-based classification. A scheme to aggregate, parameterize and assess the quality of transformations to hydraulic roughness classes in discrete meshes is presented and illustrated for an alluvial stream in the North German lowlands. The impact of high resolution roughness parameterization is validated for a comparison with a parameterization based on a coarse field survey.

1 INTRODUCTION

Roughness parameterizations together with representations of topographic gradients are essential concerns while building hydronumeric models to solve the shallow water equations. This paper assesses benefits for the physical quality of 2D hydronumeric models from high resolution roughness parameterization via spaceborne imagery.

For this purpose this paper suggests to exploit the panchromatic and multispectral image layers of highest-resolution commercial remote sensing satellites. It focuses on QuickBird imagery and suggests the use of knowledge based classifications to derive land cover classification with 0.61 m resolution. This accuracy of this classification is shown to be highly reliable. It exceeds rough aggregations of field surveys or cadastral coarse data sets. Ultimately it provides an up-to-date definition of the land cover.

Successive aggregation together with a series of transformations converts the pixel-based land cover classes to an adequate set of discrete, hydraulic distinct roughness classes. An automation of this processing stage primarily uses the definition of hydraulic relevant classes being aggregated on pixel level prior to a discrete transformation. Whereas this automation conceptually behaves similar to manual assignments it inherently provides the opportunity to express the quality of the discrete parameterization as metadata, which can be used for mesh adaptations enhancing the roughness representation.

Apart from being far more efficient in the parameterization than initial captures via field surveys, this concept provides a reproducible and highly accurate parameterization for physical based modeling concepts.

2 IMAGE SOURCE

The QuickBird image has been acquired on September 21, 2005. Purchased via Eurimage, European representative of DigitalGlobe™, its acquisition to no-cloud cover conditions and an off-nadir angle of 7° was initialized at 10:39:50. Delivered in WGS84-projection ($\mathrm{Lat/Lon_{NW}} = 54.045°/9.643°$; $\mathrm{Lat/Lon_{SE}} = 53.919°/9.822°$) it covers 64 $\mathrm{km^2}$ and represents 17 km river as buffer along the river and its floodplains at Kellinghusen. The total coverage

Copyright © 2006 Taylor & Francis Group plc, London, UK

denotes the minimum order size. The lateral coverage of about 5 km reflects the minimum requirements of the viewing geometry. The covered reach of River Stör ranges from Wittenbergen up to Willenscharen. It's tributary Bramau in covered to Wrist. Since October 2005 this image is listed in the DigitalGlobe ImageLibrary™.

Achieved as standard imagery the image processing level two of three includes radiometric and geometric corrections for the panchromatic (PAN) and multispectral (MS) image layers. Subsequent pansharpening merges both image layers via wavelet transformations, fusing the lower resolution of the multispectral channels (B, G, R, NIR at 2.4 m) with the higher resolution information of the panchromatic channel (B/W at 0.61 m) to enhance high resolution feature identification via strong edge detection in the image.

3 LAND COVER CLASSIFICATION

Unsupervised pixel classification concepts adequately amend attempts to automate meshing processes in hydroinformatics. The hierarchical scheme accounting for the classification of QuickBird image pixels to land cover classes (LC_{QB}) is illustrated in Figure 1, comprising a set of methods and associated rules.

The pre-structuring-stage of the image classification scheme reduces inter-band correlation via principal component analysis. This image transformation essentially minimizes the redundancy in the multispectral bands, reduces the dimensionality of the original data set and serves to speed-up the subsequent automated classification. Additionally the pre-structuring-stage determines texture measures. The frequency of tonal change on an image, aggregated by units of features that can be smaller than the image pixels (e.g. leaves of trees and their shadows) reflects their individual size, shape, pattern, shadow and tone. Image texture supports separation of features with similar reflectance. Results of the pre-structuring-stage are a series of individual image layers identifying suitable areas for extractions of land cover specific spectral signatures. These characteristic reflection properties over the bands of the image ultimately provide the means to assign each pixel to a specific land cover class in an iterative classification involving three classes of rules throughout the knowledge based modeling-stage: formalized experience of the human interpreter (e.g. 'trees cause shadows'), spectral characteristics derived from large sample sets (e.g. 'clear water has a NDVI below zero') and existing 'old' or 'coarse' land cover data enhancing the classification of pixels with similar spectral signatures (e.g. CORINE land cover classifications).

Rules for the iterative, knowledge-based pixel classification are derived throughout classifications in the

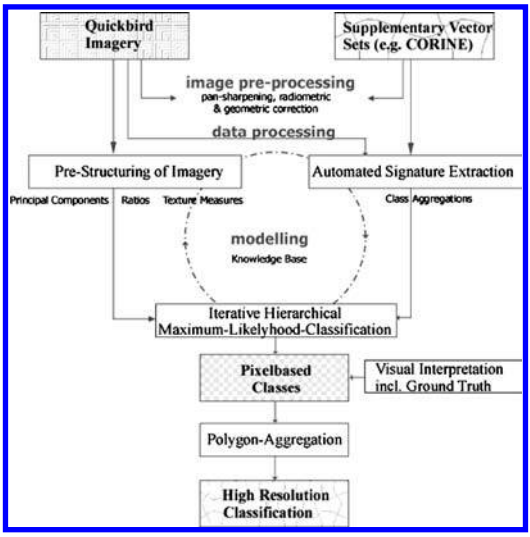


Figure 1. Hierarchical LC_{QB}-classification scheme.

Table 1. Spectral characteristics for knowledge base.

Parameter	'Open sandy soil'	'Tall wet forbs'
Local min. (PAN)		
Texture (PAN)		
Texture (MS)		
NDVI	<0	> +0.5
Ratio NIR/Blue		[+1.5–+3.0]
Ratio Red/Blue		[+0.4–+0.6]
Ratio Green/Blue		
Signal-to-noise		
Diff. (Red-Blue)	>0	< +20
Diff. (Green-Blue)	>0	[−10–−0]
Diff. (NIR-Red)	> −20	
Diff. (Red-Green)	< +20	[−20–−10]
Diff. (NIR-Green)		> +50
Diff. (NIR-Blue)		> +40
StDev. (Red)*	Loc. max.	> +2
Max. (Red)	Open LUT	Open LUT, near water

* For 11 × 11-kernel, ** land use-type.

German Federal State Brandenburg. Their relative formulation permits transferability. Frick et al. (2005) illustrate the performance of this transfer for six distinct project areas, amongst them two urban projects with strong relation to water (Potsdam, Falkensee), two river systems (Odra, Warta) and military training areas (Jüterbog, Falkensee). Table 1 refers essential rules establishing the knowledge base. It refers the parameterization of rules to identify two specific land cover types in the LC_{QB}-classification, the initial processing stage of Figure 2 characterizing the roughness parameterization.

Copyright © 2006 Taylor & Francis Group plc, London, UK

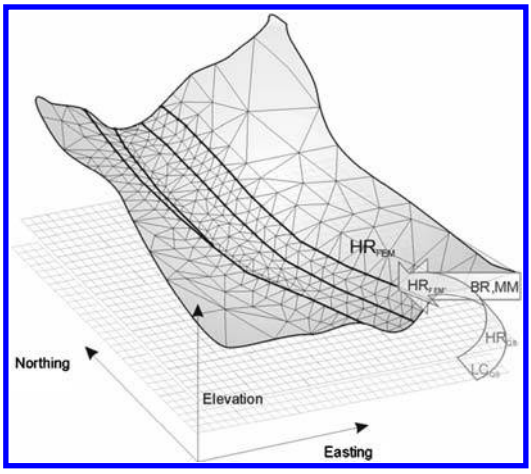


Figure 2. Roughness parameterization scheme.

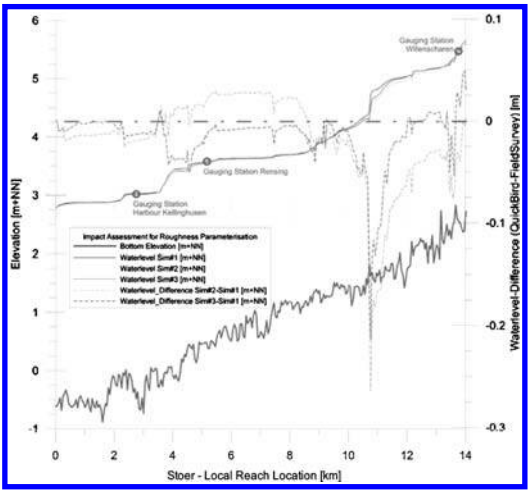


Figure 3. Impact of high resolution roughness parameterization on water level. Reach bottom track.

The aggregation of pixel based land cover classes LC_{QB} to pixel based, hydraulic relevant roughness classes HR_{QB} involves specific aggregation schemes based upon hydraulic consciousness for considered fluvial domain, the considered boundary conditions and the classification potential of the classification scheme. However, for any aggregation this simple key ensures reproducible HR_{QB}-classifications.

Identification of hydraulic roughness classes via this transformation maintain an average user and producer accuracy exceeding 80%, based on a field validation four weeks after image acquisition (Rath, 2006), facing similar challenges throughout identification of relevant features in the fluvial domain as Leckie et al. (2005) in the vicinity of shadows. This aggregated global accuracy slightly exceeds recent publications addressing the roughness parameterization, e.g. van der Sande et al. (2003) using IKONOS imagery. However it can be acknowledged that specific habitat types may be identified higher classification accuracies exceeding 90% while remaining on the land cover level (Frick et al., 2005).

4 ROUGHNESS AGGREGATION

Integral roughness parameterizations for a discrete area, e.g. a finite element E comprising all HR_{QB}-contributions represented within its area are neither computationally adequate nor physically required. Similar to visual analysis, statistical distribution of individual contributions of HR to E are considered. The simplest yet coarsest approximation for roughness class assignments to E is expressed via the dominant HR member in the finite element, subsequently being referred as majority fraction.

$$HR_{E,ideal} = \int_{i=1}^{m} HR\,d\Omega_E \quad , i = \{1,...,m\}^T \tag{1}$$

$$\overline{HR}_E \; ; \; HR\left(\max_i \left(\frac{A_{HR(i)}}{\Omega_E} \right) \right) \quad , i = \{1,...,m\}^T \tag{2}$$

Suitable indicators for the roughness parameterization are the majority fraction (MF), reflecting by the ratio A_{HR}/Ω, as well as the number of competing roughness classes inside a discrete surface element, i.e. $m \in E$, shortly being referred as diversity index (DI). The majority index suits an indicator for the element adequacy for the discrete representation of the hydraulic impact of the land cover. The diversity index reflects the spectral homogeneity in the discrete element and likewise describes the adequacy of the global mesh discretisation for roughness parameterization.

An aggregated composition of ten roughness classes is considered (i.e. sealed, open soil, mewed grassland, high dry grass, tall moist grass, intensive field/meadows, swamps/canebrake, tree, shrubs, water). For these ten classes and the river system being modeled (17 km length, average element size 230 m^2) it has been revealed that the standard-deviation of the diversity for all classes ranges relatively stable in a range of 1.2–1.7, whereas the mean diversity may vary by a magnitude of two. Sealed surfaces and the bathymetry (or the water surface) are relatively homogeneous represented in the considered mesh with an average diversity of about 2.2 (while the MF = 40% indicates DI = 1), whereas an average diversity of

Copyright © 2006 Taylor & Francis Group plc, London, UK

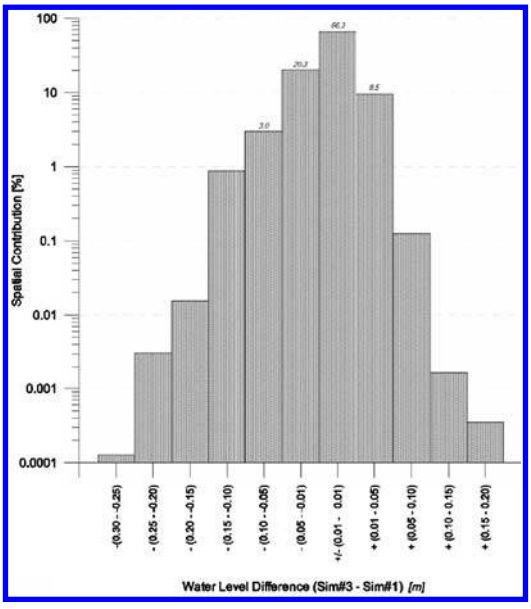


Figure 4. Impact of high resolution roughness parameterization on water level. Spatial contributions.

four is exceeded by the representation of rather heterogeneous land covers, i.e. mowed grassland, tall moist grass, swamps/canebrake (where the MF = 36% indicates DI = 4).

Denoting the lacking opportunity to publish colored prints this paper refers to Rath (2006), revealing the spatial correlation of the pansharpened image, the classifications and the validation of the mesh parameterization.

Prior to proceed with the parameterization of this automated roughness parameterization this chapter refers to Figure 2, to point out that a continuous transformation of HR_{QB}-classes from image space to discrete model space, i.e. HR_{FEM}, requires to acknowledge two additional data sources in hydroinformatics, ensuring continuity in the surface parameterization within the hydraulic context. These classes comprise spatial information on man-made structures (MM) and the parameterization of the bottom roughness (BR). Their implementation can be likewise use the MF-criterion, whereas the elimination of unclassified elements (about 2%) requires supervised assignments overcoming misleading parameterizations particularly in the vicinity of the stream, e.g. shadows due to trees ranging above the river.



Figure 5. B/W-reproduction of colored pansharpened image for LC_{QB}-classification. Flow acceleration/decelerations due to high resolution roughness parameterization (triangles/circles). Maximum differences – 0.50 m/s.

Copyright © 2006 Taylor & Francis Group plc, London, UK

5 HYDRONUMERIC VALIDATION

Apart from providing a fast, efficient and physically accurate parameterization coming along with a quality review, this parameterization provides the means to achieve parameterizations that are by far more physically realistic. This particularly holds for simple roughness models, here comprising the constant eddy viscosity concept to represent the Reynolds stresses, a product of depth-averaging the Navier-Stokes equations. In analogy to modeling viscous shear stresses this concept assumes proportionality for the turbulent shear stresses to the velocity gradients of the average flow. The constant representation of the turbulent viscosity ν_T is a major simplification which particularly reveals its impact when focusing on the resistance of vegetation, being substituted mixing length concepts. However, the constant eddy viscosity concept is widely used and its parameterization frequently exceeds physical based ranges of rarely available measurements by several orders of magnitude (Lippert, 2004), introducing a dampening of the fluid motion.

This effect for constant eddy viscosity models is significantly reduced via the presented high resolution roughness parameterizations. It enables more heterogeneous roughness assignment to individual finite element representation as assignments on the basis of field surveys or rather coarse base data would support. This higher heterogeneity can indeed physically be justified on the basis of the pan-sharpened image. This heterogeneity requires and permits that model calibrations remain with their parameterizations in tighter bounds of physically based measurements. Maintaining comparable parameterization for the bottom roughness on the basis of Nikuradse's equivalent and roughness k_s this paper achieved reductions of ν_T for class aggregations being referred as sealed, field, grass and bathymetry. A reduction factors between three and five could be achieved, leading to a parameterization of the turbulent eddy viscosity exceeding measured magnitudes merely be two. However, apart from enabling to achieve higher adequacy for the physical basis of the model, the higher resolution supporting the roughness parameterization does not reveal a significant spatial on the global water level. For the shallow topography of the considered stream Stör in the North German lowlands Figure 3 reveals that merely regions of higher surface inclination or constraint due to bridge are sensitive towards the resolution roughness parameterization.

The effect of strongly localized water level differences is illustrated in Figure 4, revealing that two third

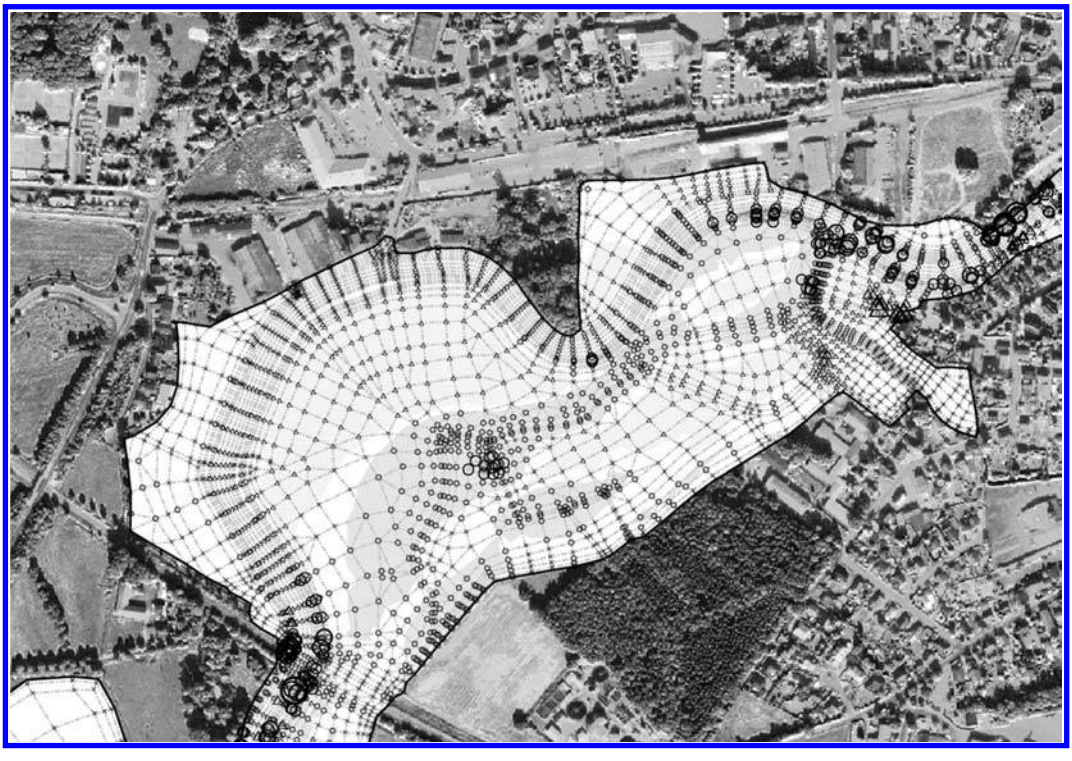


Figure 6. Flood peak breaking out of the meandering river bed. Flow field deceleration on the short-cut of the floodplains.

Copyright © 2006 Taylor & Francis Group plc, London, UK

of the fluvial domain comprises a neglectable range of ±1 cm. The water level and the flow velocity merely differ in 4% of the considered fluvial domain more than ±30 cm.

6 CONCLUSIONS

Within the limitations of grey-scale image reproduction this paper points out that high resolution imagery may contribute to accurate and efficient roughness parameterizations. Their performance in the context of water level computations is similar. Differences to parameterizations from field surveys affect localized areas which in the considered lowlands amount to 4%. However the physical parameterization can be shown to be more accurate, which particularly holds for simple turbulence models. Consequently, high resolution roughness parameterizations might particularly contribute to enhance model predictions for steeper topographic gradients and likewise suit to generate fast model updates in regions where insufficient or aged data bases are available.

REFERENCES

Frick, A., Weyer, G., Kenneweg, H., Kleinschmit, B., 2005. A knowledge-based approach to vegetation monitoring with QuickBird imagery. Proceedings of ISPRS Hanover Workshop 2005, High resolution earth imaging for geospatial information.

Leckie, D.G., Cloney, E., Cara, J., Paradine, D., 2005. Automated mapping of stream features with high resolution multispectral imagery: an example on the capabilities. Photogrammetric Engineering & Remote Sensing, Vol. 71, No. 2, pp. 145–155.

Lippert, K., 2004. Analyse von Turbulenzmechanismen in naturnahen Fließgewässern und ihre mathematische Formulierung für hydrodynamische Modelle. PhD-Thesis, Hamburger Wasserbau-Schriften, Heft 4, ISBN 3-937693-03-3.

Rath, S., 2006. Model Discretisation in 2D Hydroinformatics based on High Resolution Remote Sensing Data and the Feasibility of Automated Model Parameterization. PhD-Thesis, Hamburger Wasserbauschriften, Institute of River & Coastal Engineering, Hamburg University of Technology (in print).

Van der Sande, C.J., de Jong, S.M., de Roo, A.P.J., 2003. A segmentation and classification approach of IKONOS-2 imagery for land cover mapping to assist flood risk and flood damage assessment. International Journal of Applied Earth Observation and Geoinformation, Vol. 4, pp. 217–229.

Copyright © 2006 Taylor & Francis Group plc, London, UK

Multi-attribute decision making and cost-sharing tool for planning urban river rehabilitation schemes

M. Brilly & S. Rusjan
Faculty of Civil Engineering, University of Ljubljana, Slovenia

ABSTRACT: River rehabilitation is a long-term, costly and complex process involving numerous actions. The process of development via a bottom-up approach is described in the paper. The emphasis in the presented methodology is in active involvement of stakeholders and citizens who are driven with their particular interests. The integrity of action-taking is established at a lower level and in a smaller stretch of a river and its relevant corridor. Crucial is the direct involvement of interested parties in the decision making process and actions. The willingness to cooperate and the level of social capital are the key elements. The operation is integrated and driven by a steering committee recognised by the involved parties. The consideration of stakeholder's interests is provided through the application of the Multi-Attribute and Cost-Sharing model developed on the Glinscica stream case study.

1 INTRODUCTION

Urbanisation and river regulations go back to ancient times. They gradually evolved in the 19th century and intensified in the second half of the 20th century with irrigation, water power development and river regulations for urbanisation of inundated land. River regulation and deterioration have a long history lead by economically defined interests and simple decision-making schemes. Today, urban river corridors are loaded with different interests, which are the main obstacles to river restoration, which involves the enlargement of the stream channel and rehabilitation of river banks. That is also the reason why river rehabilitation is costly and time consuming. It is difficult to perform river restoration only by short and intensive action, thus trying to re-establish the entire river watershed. Mostly, river restoration is a set of broad actions different in scale, size, timing etc., which step by step redesign the river and its watershed. The implementation depends on different financial sources and decision-makers driven by different interests, which should all be coordinated in a common task. Such a complex process with numerous actors should include social analysis and tentative actions.

Many guidelines and manuals have been written on river restoration and environmental protection (UNEP, 2004; Fogg and Wells, 1998; EU 2002). Quality ideas for implementation should be adapted to the own specific natural situation and social conditions. Examples of good practice could provide encouragement but they cannot simply be transferred or copied elsewhere without a critical review of actions. Action-taking should be tailored to the local natural and social conditions.

The problem of different, conflicting interests has been frequently translated into the Multi-Attribute Decision Making procedures which try to ensure active and transparent consideration of involved stakeholders and their effective communication with decision makers (Moshkovitch et al., 2002). Therefore, in the concluding section of the paper, a description of the Multi-Attribute Decision Making and Cost-Sharing model developed on the Glinscica case study in the urban area of Ljubljana, Slovenia, is given.

2 STRATEGY OF IMPLEMENTATION

2.1 *Establishing the framework*

Water management policy proceeds from development to management. The importance of environmental sustainability has been recognized overall. The decision making should integrate more interests, calls for a greater decentralization, more participation and greater financial viability. A new paradigm of Integrated Water Resources Management (IWRM) has been developed in the guidelines of WFD and worldwide. The IWRM is complex, requiring an almost idealistic approach (Brilly 2001). Today, there are no economically well-defined interests and simple decision making schemes that would involve few stakeholders. The results should provide an environmental benefit, which is, however, difficult to evaluate financially.

Copyright © 2006 Taylor & Francis Group plc, London, UK

Actions should be organised and driven by a body recognised by all involved parties (UNEP, 2004). Efforts must involve a pro-active participation and contributions of both governmental and non-governmental stakeholders. An NGO or the private sector can act as a partner in action. The form of organisation depends on the local practice, legislation and size of action. Actions should take place at the lowest possible level, then demand-driven approaches can be applied. The lowest level of participation is usually considered by means of providing the access to information and active dissemination of information (HarmoniCOP, 2005). All stakeholders should be involved from the beginning in selecting the appropriate solution and management options. Attention must be given to local demands. Comprehensive analyses of present and future societal demands are required, and strong support and acceptance from the local communities should be secured. With such analyses realistic choices can be made from a wide range of technological, financial and management options. River rehabilitation must include maintenance and care, which is not possible without full co-operation of locals and stakeholders.

In management and decision-making processes transparency should be ensured, establishing trust of the inhabitants. Early, continuous, targeted and transparent communication between all parties is required to establish firm partnerships. Management of problems is related to the interests, knowledge and experience. The idealistic technical approach lies in sophisticated modelling with all necessary data including the assessment of possible risk. The lack of data and knowledge asks for a more simple analysis with good expert estimation, but such a system fails if experts develop a particular interest or if they want to promote particular solutions. Independent facilitators of the decision making process could be beneficial when problems are particularly difficult with opposing interests of stakeholders. A third party also helps to avoid that the competitive authorities dominate in the process.

Regardless of the approach chosen, each river restoration asks for a flexible, tailor-made set-up. Each necessary step can be taken at different points in time, depending on available resources and capabilities. It is thus advisable to apply a well-defined logical framework, consisting of a comprehensive set of logically related tasks:

1. Identification of the need for action
2. Establishing a steering committee
3. Setting boundaries
4. Development of preparation plan
   - Review of information
   - Goals and objectives (new techniques)
   - Identification of needs and opportunities (RBD plan)
   - Identification of financing sources
   - Formulation of management plan
   - Setting objectives
   - Formal adoption.
5. Implementation
   - Operational management: on-site versus off-site
   - Institutional arrangements, such as capacity building, awareness raising, and
   - Public participation
6. Monitoring and evaluation
   - Monitoring
   - Evaluation

The incentive for action may come from several sources: state, town council, NGO, stakeholder or interested groups, and individuals. The administration may initiate the restoration effort as a result of a directive to implement the RBD plan. Citizen groups or groups with special cultural or economic interests (e.g. landowners, sport fishermen) may also initiate a restoration effort. Others might undertake river restoration as part of a broad initiative that is funded from various sources and addresses a diversity of interests and objectives. The local representatives familiar with the situation should be involved from the start.

2.2 *Steering committee*

An important step in the process is the formation of a steering committee. The steering committee includes key stakeholders, interested citizens, public officials, and any other groups or individuals who are interested in or might be affected by the restoration initiative (Fogg and Wells, 1998). Local citizen groups comprise multiple interests that hopefully share a common concern for environmental conservation and interest of local community. Such broad-based participation helps ensure that self-interests of administration do not operate the process from the top down. The steering committee ensures high level participation in the development and implementation of the revitalization action. Interested parties will participate actively in the planning process by discussing issues and contributing to their solution as members of the steering committee. They will share the decision making and objectives. Shared decision-making implies that the interested parties not only participate actively in the planning process, but also become partly responsible for the outcome (EU, 2002).

The steering committee generally takes care of the following:

- Carrying out restoration planning activities.
- Coordination of development of the preparation and implementation plan.
- Identifying public's interest in the restoration effort.
- Making diverse viewpoints and objectives known to decision-makers.

Copyright © 2006 Taylor & Francis Group plc, London, UK

– Ensuring that local values are considered during the restoration process.

It is important to remember that the true role of the steering committee is to advise the decision-maker or sponsor (the agency, organisation, or individuals that support the restoration effort) on the development of the restoration plan and execution of restoration activities. The primary decision-making authority should be in the hands of the stakeholders. The steering committee will provide recommendations and inform the decision-makers of various restoration options and the opinions of the various participants. It is important to note that the decision-maker, as well as the steering committee, may be composed of a collection of interests and organisations. Other relevant sectors should be included, such as urban development and implementation of the RBD plan. Although the steering committee will play an active planning and co-ordinating role, it will not always make the final decisions. It is thus important that all members of the steering committee understand the issues, develop practical recommendations, and achieve consensus (Fogg and Wells, 1998). The identification of the key participants is the most critical issue. The exact number of groups or individuals that will compose the steering committee is difficult to determine and is different from situation to situation. Membership in the steering committee should be free and open. In general, it is important that the group should have representatives of all involved stakeholders, landowners and citizens, who are in touch with the action.

The steering committee activities require a lot of precious voluntary work. The members are in place according to their interests. The steering committee could collect its own funds from donors or own participatory financing action or technical support. There might be cases where a landowner or stakeholder chooses to take on all the responsibilities of the steering committee group in addition to playing the leading or decision-making role. Regardless of the number of individuals involved, it is important for all project participants to note that the usual duration of a project is 2 to 3 years (Fogg and Wells, 1998). There are no guarantees that every project will be a success, and in some cases a project may fail simply due to lack of funds, lack of time or lack of the willingness to act. All participants must be reminded at an early stage to set realistic expectations for the project and for themselves.

2.3 *Preparation plan*

The preparation plan is an essential document for the task force action. It contains major information for possible solutions, including cost, legislative issues and control of possible funding. An interdisciplinary team should carry out the study with the suggested contents. The size of the document differs from a short memorandum to full-sized detailed project documentation, and is situation-specific. Each stream corridor that is targeted for restoration is unique. Each stream targeted for restoration is unique. A project goal of restoring multiple ecological functions might include the channel systems, the active floodplain, and possibly adjacent buffer areas that have the potential to directly and indirectly influence the project. In the urban areas, land uses close to the stream bank are a major obstacle for environmental protection; however, the restoration of the surrounding land is an opportunity for restoration of the nearby river. The restoration stretch of the river should be as wide as possible. The steering committee should optimize the interests of the participants with the available funds. A wide river corridor restoration is possible outside of urban areas, but inside, the development is limited by land use and town development plans. The objective of the past river regulation works was to take the minimum space for the river flow and demand for flood protection produced channelisation of the river with the minimum roughness coefficient. Any restoration work in such a channelized stream will increase the roughness and the water level during floods. The additional space for flood flow inside the river corridor is crucial for possible restoration measures. The problem is how much public land is available in the corridor and how high is the willingness of landowners to support such project.

Identification of funding sources is often the first and most important step toward an effective stream restoration. The funding may be minimal or substantial, and it may come from a variety of sources. Funding may come from EU, country or local sources that have recognised the need for restoration. Funding may come from any entity that has taxing authority. Charities, non-governmental organisations, landowners' associations or any developer that invested in river corridor and voluntary contributions are other funding sources. Regardless of the source of funds, the sponsor will almost certainly influence restoration decisions or act as the leader and decision-maker in the restoration effort. The attributes in the tool for assessing the potential for rehabilitation are weighted taking in account financial sources for action.

3 MULTI-ATTRIBUTE DECISION MAKING AND COST-SHARING MODEL FOR THE GLINSCICA CASE STUDY

Problems of Multi-Attribute Decision Making (MADM) are encountered under various situations where a number of alternatives and actions or candidates need to be chosen based on a set of criteria or attributes (Aouami et al. 2003; Cagno et al., 2001). Advantages of MADM are that it facilitates community-based collaborative

Copyright © 2006 Taylor & Francis Group plc, London, UK

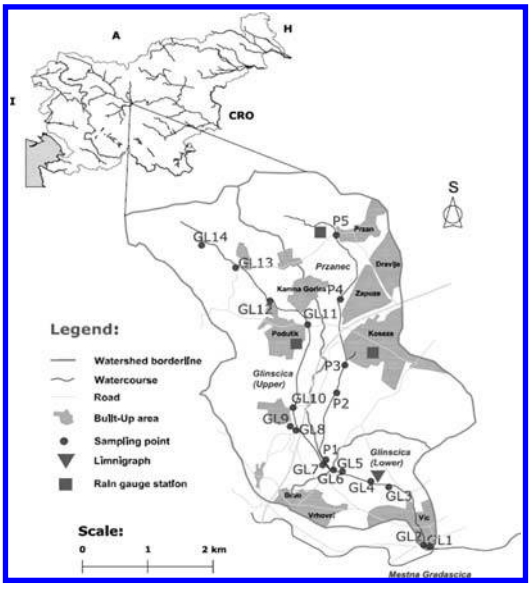


Figure 1. Glinscica stream study area with ecohydrological monitoring system.



Figure 2. Heavily regulated channel of the Glinscica stream.

Table 1. List of the main stakeholders.

Stakeholders	Interests
Biotechnical faculty	– Stream as a natural scientific testing ground – Ecology: Bio-diversity, Composition and abundance of aquatic flora, vertebrate fauna, Channel vegetation, Bank vegetation – Aesthetics: Welcoming area – River- Flood vulnerability – Accessibility: River crossings
Residents of the Municipality of the city of Ljubljana	– Water quality: Colour, Odour – Ecology: Nature of surrounding catchment – Aesthetics: Landscape perception, Natural components – Social importance: Activities on river front (recreation), Accessibility
Fish angling society	– Water quality: Dissolved oxygen, BOD, pH, Pollutants, Temperature – Ecology: Abundance and bio-diversity of fish population, River morphology, Water abundance (pools), Channel and bank vegetation
Municipality of the city of Ljubljana	– Ecology: Planning of the green system of the city, Development of thematic parks – Urban development: University center, Development of traffic infrastructure – Aesthetics: Natural components inside the urban area

decision-making, avoids some of the ethical, theoretical and practical shortcomings of conventional economic approaches, does not require assigning monetary values to ecological services, allows consideration of multiple attributes and is not culturally biased (Prato, 1999).

Comparing the alternatives is the key to decision-making in such cases. Often in planning a river rehabilitation project, we are faced with making a choice among various options – alternatives. If the only consideration is costs, we can use economic principles to guide our selection. Many times, however, the choice involves both strictly quantitative measures (such as costs) and strictly qualitative measures (aesthetical aspects or even political viability). In such cases we must use a process to approximately "quantify" all measures at a similar, numerical scale, so that we can perform mathematical calculations which assist the decision maker to consider preferences and interests of all parties involved (stakeholders).

3.1 *Structure of the model*

The Glinscica stream watershed is positioned in the urban area of the city of Ljubljana, Slovenia. The study site area with the ecohydrological monitoring system is shown in Figure 1.

The Glinscica stream MADM and Cost-Sharing model is based and developed on the database which includes hydrological data, data on water quality, water flora and fauna data of the study site (Brilly et al., 2004). A two-year ecohydrological monitoring established on the Glinscica watershed showed that the ecohydrological degradation of the stream is mainly the consequence of the heavily regulated stream channel (Brilly et. al., 2004), Figure 2. Additionally, main stakeholders were identified together with the range of their interests. These stakeholders were the Biotechnical faculty of the University of Ljubljana as the major owner of the land in the study area, residents of the Municipality of Ljubljana as the users

Copyright © 2006 Taylor & Francis Group plc, London, UK

of the surrounding urban green areas, the fish angling society and the Municipality of the city of Ljubljana. Their interests are listed in Table 1.

When developing the model the problem we tried to solve was not only how to achieve an agreement and cooperation between key stakeholders with their different, potentially contrasting interests. We were trying to develop a tool that would enable decision makers or key stakeholders (organized in the steering committee) the distribution of costs for rehabilitation measures among interested parties.

The model consists of five main parts:

1. *Interface*. The "Interface" spreadsheet enables the analysis of different combinations of relative importance weights assigned to the main objectives and the numerical and graphical comparison of different alternatives (Fig. 1). The combination or the preference of a certain objective expressed by a relative importance factor should be based on the stakeholder agreement.
2. *MADM-WAM*. The "MADM-WAM" spreadsheet is used for rating the impact of a certain alternative on the attribute. An attribute is by definition a measure (criterion) which enables the assessment of the amount of satisfaction of a certain objective.
3. *Alternatives*. Alternatives are combinations of certain elements of a rehabilitation scheme. The selection of the elements of the rehabilitation scheme and the alternatives are made by the decision maker. The elements of the rehabilitation scheme should be expressed by approximate costs for their implementation. The development of different alternatives (combinations of the elements of rehabilitation scheme) should consider possible budget restrictions which are not included into the model.
4. *Stakeholders*. The list of main stakeholders together with their interests is included in the model so that the decision maker has an overall picture of the preferences for a certain state of the water body and also possible conflicting interests.
5. *Cost-Sharing.* The main idea of Cost-Sharing is distribution of costs for realization of selected alternatives among interested stakeholders. The basis for Cost-Sharing derives from performance of each alternative regarding the pre-defined objectives of river rehabilitation and satisfaction of stakeholders' interests.

3.2 *Application of the model*

The steps for the application of the model are as follows:

1. In agreement, stakeholders determine the main objectives that should be considered in choosing the best alternative. These objectives should be reasonably independent. To assure better independence between different main objectives the proper attributes should be assigned. Main objectives in our case study were improvement of river ecology, habitats, flood protection, recreation and urban green space.
2. Determine the relative importance of these objectives to each other. A common approach is to select the least important objective and assign it a value of 1. Then for each of the other objectives, ask the question "*How many times more important is this objective than the least important objective?*" The answer will relate to the value assigned, for example, if the selected objective is twice as important as the least important objective, it would receive a value of 2, or if it were equally important it would have a value of 1. It is necessary to limit the maximum value that is assigned to any objective. A maximum value of 3 or 4 is a good choice (Goicoechea et al., 1982). If the maximum value is too large, it has the numerical effect of reducing the problem to a single objective problem. After a relative importance value is obtained for each objective then a normalized importance "weight" for each attribute is obtained by dividing the individual relative importance value by the summation of all the relative importance values. This produces a set of "importance weights" that sum to one.
3. Use a process similar to Step 2) to assign normalized importance weights to defined attributes in spreadsheet "MADM-WAM".
4. Select the alternatives to consider. Costs for the elements of the rehabilitation scheme are just illustrative. For each alternative, evaluate the performance of that alternative with respect to each objective or its attributes. This performance might be described as a number or it might be a word (such as good or poor). It is advisable that one alternative represents the present condition of the stream or "do nothing scenario". This alternative can be used for comparison with other alternatives and for assessment of the improved conditions which are expected to be achieved by applying the selected alternative.
5. Convert the evaluations of Step 4) to a common numerical score called "rating". A commonly used scale is 1 to 5, where 5 represent the best condition and 1 represents the worst condition. A scale of 5 fits word descriptions such as: Poor(1) Fair(2) OK(3) Good(4) Excellent(5). It is important to make sure that none of the alternatives is completely "dominated" by the others. The results of ranking are summarized in the so called "impact matrix" as shown in spreadsheet "MADM-WAM".
6. The ratings for each alternative are combined into a final score for each alternative. One of the most common MADM methods used for this is the *weighted average method (WAM)*. The score for

Copyright © 2006 Taylor & Francis Group plc, London, UK

an alternative (S_i) is defined as the summation of the products of the normalized weights (W_i) times the rating for each objective ($R_{i,j}$). For example, the overall score for alternative 1 would be computed as:

$$S_1 = \sum_{i=1}^{4} W_i * R_{i,1} \quad (1)$$

where i represents the various criteria. In general then, the score for alternative j is found by:

$$S_j = \sum_{i=1}^{4} W_i * R_{i,j} \quad ; \text{where } j = 1, 2, 3 \quad (2)$$

The alternative with the highest score (maximum value of S_j) is the preferred alternative (Fig 3). It is said to have a "rank" of 1. The second highest score is the second preferred alternative (rank 2) and so forth.

7. The spreadsheet for Cost-Sharing evaluation enables the analysis of the financial aspects of the implementation of the selected alternative. The stakeholders are encouraged to define their involvement (financial contribution, volunteering work) into the project. This involvement depends on the proportion of the satisfaction of their interests. For example, stakeholder No.1 is prepared to contribute 10 % of the expenses for the project if the selected alternative raises the objective of river ecology (as one of the objectives) to a minimum acceptable value of 3 (according to the selected scale of 1 to 5 where 1 means poor and 5 means excellent). In the case when the selected alternative provides even better river ecology, then our stakeholder No. 1 agrees to contribute additional 3% for the realization of the selected alternative. Analyses as the one presented in the example above should be done for each stakeholder. The final result is the proportion of expenses for selected alternatives (or only for the few preferred alternatives) that could be covered by stakeholders' contributions (Table 2).

Alternative No. 1 represented the "do nothing scenario". Alternative No. 2 was oriented towards the improvement of the flood protection and recreation areas near the Glinscica stream channel with widening of the regulated channel, provision of footpaths along the banks but without the removal of the concrete paving from the channel. Alternatives Nos. 3 and 4 were directed towards the improvement of the ecological state of the channel which included removal of the concrete paving from the channel bottom and banks (Fig. 2). Alternative No. 3 considered the introduction of structural elements such as pools and small stone weirs into the channel. Alternative No. 4, which has been assessed as the most expensive one, included the reconstruction of the channel to provide meandering appearance of the stream and prevision of a dry retention area upstream of the studied reach. Alternative No. 5 considered mainly the flood vulnerability issue with widening of the cross section and arrangement of levees along the stream and some limited improvements of the ecohydrological state of the channel, such as selective clearing of riparian vegetation without the removal of the concrete paving. While using the model it was easily noticed how the selection of the preferred alternative depends on the combination of the relative importance weights assigned by stakeholders to each proposed rehabilitation alternative (Fig. 3).

Table 2. The cost sharing evaluation of urban river rehabilitation alternatives.

	Alternatives				
Stakeholders	1	2	3	4	5
Biotechnical faculty	0	5	31	28	18
Residents of the Municipality of Ljubljana	0	10	13	18	3
Angling society	0	0	25	15	0
Municipality of the city of Ljubljana	0	25	15	25	10
SUM	0	40	84	86	31

4 CONCLUSION

In our case study each set of the alternative preference is a result of the combination of relative importance weights assigned to the main objectives of the urban river rehabilitation. The selected key objectives identified by the stakeholder who should be included into the steering committee were river ecology, habitats, flood protection, recreation and urban green space. Thus the resultant objective and attribute weights and rankings of alternatives reflect both the subjective considerations of a decision maker, stakeholders and the objective information of the expert.

The agreement of the stakeholders on the importance of certain objective is the crucial aspect for the application of the model. Otherwise, if the agreement of the stakeholders on the importance of defined objectives is not reached, the selection of the preferred alternative can be easily manipulated (Fig 3). On the other hand, Cost-Sharing provides an insight into the preparedness of stakeholders to realize their interests through their actual involvement in the selected alternative.

Copyright © 2006 Taylor & Francis Group plc, London, UK

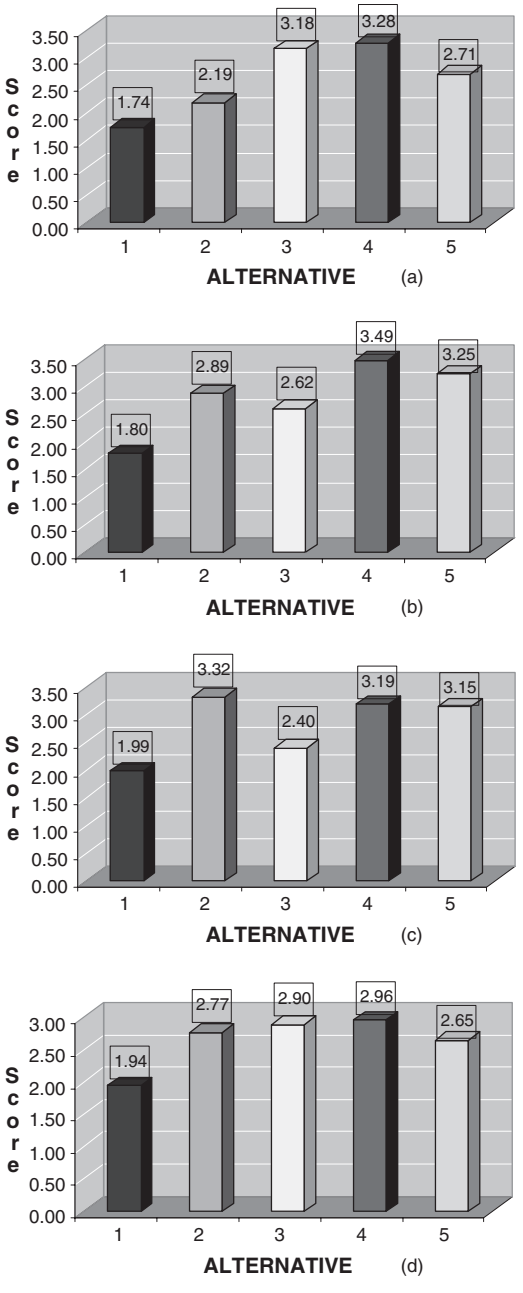


Figure 3. Preference of urban river rehabilitation alternative for relative importance weights assigned by different stakeholders; (Fig 3a: Angling society; Fig 3b: Biotechnical faculty; Fig 3c: Municipality of the city of Ljubljana; Fig. 3d: Residents of the Municipality of Ljubljana).

ACKNOWLEDGEMENT

The research was funded by the 5th EU URBEM project.

REFERENCES

Aouami, T., Chang, S.I, Lee, S.E., (2003). Fuzzy MADM: An outranking method, European Journal of Operational research, 145, 317–328.

Brilly, M., 2001. The integrated approach to flash flood management. In: GRUNTFEST, Eve (eds.), HANDMER, John W. (eds). Coping with flash floods, (NATO science series. 2, Environmental security, v. 77). Boston: Kluwer Academic Publishers, p. 103–113.

Brilly, M., Toman, M.J., Rusjan, S., (2004). The study site monitoring of the Glinščica catchment. v: Tropeano, D. (eds). Progress in surface and subsurface water studies at the plot and small basin scale, ERB2004 – Euromediterranean conference. Torino, str. 79–82.

Cagno, E., Caron, F., Perego, A., (2001). Multi-criteria assessment of the probability of winning in the competitive bidding process, International journal of Project Management, 19, 313–324.

EU 2002, Guidance on public participation in relation to the water framework directive.

Goicoechea, A., Hansen, D., Duckstein, L., (1982). Multi-Objective Decision Analysis with Engineering and Business Applications, John Wiley and Sons, 321 pp.

HarmoniCOP, 2005, Learning together to manage together, Improving participation in water management, University of Osnabruck, Institute of Environmental System Research, 99 pp.

Moshkovitch, H.M., Mechitov, A.I., Olson, D.L., 2002. Decision Aiding, Ordinal judgments in multiattribute decision analysis, European Journal of Operational Research, 137, 625–641.

Fogg, J., Wells, G., 1998. Stream Corridor Restoration, Principles, Processes, and Practices, U.S. Department of Agriculture, U.S. Environmental Protection Agency, Tennessee Valley Authority, Federal Emergency Management Agency, U.S. Department of Commerce, U.S. Department of Housing and Urban Development, U. S. Department on the Interior, 536 pp.

Prato, T., (1999). Multiple attribute decision analysis for ecosystem management, Ecosystem Economics, 30, 207–222.

UNEP, 2004, Guidelines on municipal wastewater management, A practical guide for decision-makers and professionals on how to plan, design, and finance appropriate and environmentally sound municipal wastewater discharge systems, UNEP/GPA, UNEP/IETC and UNESCO-IHE. UNEP/GPA Co-ordination Office, The Hague, The Netherlands, 2004.

Copyright © 2006 Taylor & Francis Group plc, London, UK

The influence of errors in Digital Terrain Models on flood flow routes

S. Néelz & G. Pender
School of the Built Environment, Heriot-Watt University, Edinburgh, UK

ABSTRACT: The modelling of flood inundation patterns on rural and urban river floodplains is making increasing use of high-resolution and high-accuracy Digital Elevation Models (DEMs) based on LiDAR (airborne laser scanning) data. LiDAR measurements are reported to be subject to root mean square errors of 0.15 m vertically and 0.50 m horizontally. The aim of the paper is to investigate the implications of these uncertainties in terms of the reliability of model results, concentrating on the modelling of overland flood flow using a 2D fully hydrodynamic model. A flood event caused by overflow from a river is simulated using three different DEMs: a benchmark error-free DEM, and 2 "altered" DEMs with added LiDAR errors of different magnitudes. These altered DEMs are a less accurate representation of reality, and also have an artificial roughness that is typical of LiDAR-based DEMs used in practice. The main conclusions are that: (1) this artificial roughness can significantly slow down the flow in the simulation, resulting in an incorrect representation of the flow dynamics, and (2) the LiDAR errors can have a significant impact on the routes taken by the flow, and on modelled water levels and velocities.

1 INTRODUCTION

Since 1994, the modelling of flood inundation patterns and flow routes on rural and urban river floodplains has made increasing use of high-resolution and high-accuracy Digital Terrain Models (DTMs) based on LiDAR (Light Detection And Ranging or airborne laser scanning) data. LiDAR is a modern technology in the field of remote sensing that can rapidly generate high-density, high-accuracy, geo-referenced digital elevation data. LiDAR measurements are claimed to be subject to errors smaller than 0.15 m vertically and 0.50 m horizontally (Root Mean Square Errors). This is increasingly recognised as one of few technologies (with for example photogrammetry) that can provide topographic data with suitable accuracy and resolution for applications in river and floodplain flow modelling.

Despite their great future potential, the availability of LiDAR-based bathymetric DTMs for rivers is scarce and very few studies on the subject have been published to date. Such data are at present very rarely used by engineers and consultants. Most river flow models (at least at catchment scale) still rely on cross-sections surveyed using ground-based techniques.

LiDAR-based DEMs and DTMs of the floodplains are used in different ways depending on the type of hydraulic model used. In 1D models they allow the extension of channel cross-sections onto the floodplains. In quasi-2D (storage cell) models, they are used to calculate storage (volume vs. water level) curves. In 2D models they provide cell or node elevations (Bates & De Roo 2000, Cobby et al 2003). In addition, they may provide the geometry of any spill cross-section in storage cell models and combined 1D/2D models. In all these models, water depths are calculated by subtracting DEM/DTM elevations from the computed water levels.

The suitability of LiDAR for such applications has been extensively investigated (Gomes Pereira and Wicherson 1999, Marks & Bates 2000), but the effects of any errors and uncertainties in LiDAR digital elevation data on hydraulic model results have been scarcely studied to date.

2 BACKGROUND

2.1 *LiDAR and LiDAR-based Digital Elevation Models*

LiDAR is based on the combination of three different data collection tools: a laser scanner mounted on an aircraft; a Global Positioning System (GPS) providing the laser sensor position; and a Inertial Navigation System (INS) or Inertial Measurement Unit (IMU) providing the orientation of the aircraft (yaw, pitch and roll). Light pulses directed towards the ground are provided by the laser at a specific frequency (up to 100 kHz in state-of-the-art systems). The sensor oscillates at a frequency and within a scan angle that can

Copyright © 2006 Taylor & Francis Group plc, London, UK

be set to provide the required swath width and data density (these also depend on the flight height). Each laser pulse (a decimeter-wide beam) is reflected by the ground or by objects above the ground. In some modern systems multiple returns from the same laser pulse can be recorded (for example high vegetation, low vegetation, and ground). Each laser return provides a measured distance, which is then combined with the simultaneous INS and GPS measurements to provide a georeferenced "raw" LiDAR data point. Typical swath widths are between 0.25 h and 1.5 h, where h is the flight height (h is typically between a few hundred meters and 1000 m), and a typical raw data density is of a few points per square meter (but data collection at a much higher resolution is feasible and is becoming less onerous). It should be noted that most LiDAR systems to date do not penetrate water, so that LiDAR data are presently available mainly for floodplains. However, some modern systems do provide river and coastal bathymetric data.

Raw LiDAR data are normally turned (often by the companies by which they are collected) into Digital Elevation Models (DEMs), or "raster" grids, where elevation data are presented on a georeferenced square regular grid. Such grids have a cell size of 1 m at best (in most UK studies), so that each cell elevation is based on many raw data point elevations averaged in some way. Triangular Irregular Networks (TINs) are less common, largely because many data processing techniques have been designed for raster grids. Data processing techniques include such tasks as feature extraction, filtering, and segmentation. For applications such as flood modelling, it is often necessary to perform a segmentation process, i.e. to separate the DEM into areas such as bare earth, vegetation, buildings, etc. These features may be extracted, resulting in a DTM (Digital Terrain Model), which contains only ground elevations (Mason et al 2003, Sithole & Vosselman 2004).

2.2 *LiDAR accuracy*

Accuracy of LiDAR data is neither thoroughly understood nor well documented. Many surveyors and data providers quote accuracy figures such as 0.15 m Root Mean Square Error (RMSE) vertically, or h/1000 horizontally (the flight height is usually below 1000 m), which are meant to refer to the raw LiDAR data. However, errors are subject to considerable variability, depending on system characteristics, observation angle, type of land cover, slope of the terrain, etc. (Ahokas et al 2003, Gomes Pereira & Wicherson 1999, Hodgson & Bresnahan 2004, North Carolina Floodplain Mapping Program 2006). In addition, the figures reported refer to bulk statistics and do not reflect any spatial distribution. It is indeed the case that most sets of LiDAR data examined at a local scale would exhibit a significant systematic or smoothly varying component (Ahokas et al 2003). Such systematic errors would result for example from difficulties in the functioning of the GPS (the positioning data are collected by the GPS at a relatively low frequency of between 1 and 10 Hz).

In addition to the errors affecting the raw LiDAR data, additional errors are introduced during the data processing stage. These are mainly due to the difficulties in automatically segmenting the DEM between vegetation and bare earth, or between buildings and bare earth. DTMs are often of poor quality in densely vegetated areas and in urban areas large buildings are easily mistaken for small scale land forms. In addition, features that critically affect flow routes, such as thin embankments, may be erroneously removed by filtering algorithms.

3 EXPERIMENTAL SETUP

This study considers the 2D modelling of a hypothetical flood event affecting a $\sim$0.5 km^2 area in Greenfield, a suburb of Glasgow, UK (see map in Figure 1). Simulations were carried out using three different DEMs: a benchmark high-resolution DEM (DEM1) and two DEMs (DEM2 and DEM3) based on DEM1, but with LiDAR errors of different magnitudes added according to a process described in section 3.2. Results were compared in terms of flow routes, maximum velocities and depths, and inundation timing.

3.1 *Study site*

The study site is a $\sim$0.5 km^2 area (Fig. 1), consisting of a combination of small apartment blocks and semi-detached houses, some of which are set within small fenced gardens. It also comprises some open park land covered mainly with short grass with some thick low vegetation in places. The modelled flood is assumed to originate from the entrance of a culvert carrying a local stream (the Camlachie Burn), and it is supposed



Figure 1. Map of the study area. Darker areas indicate higher ground. The origin of the flood is indicated by an arrow. (© Crown Copyright Ordnance Survey. An EDINA Digimap/JISC supplied service.)

Copyright © 2006 Taylor & Francis Group plc, London, UK

to be caused by this culvert reaching capacity. This is a simplification of a real flood that occurred in this location in July 2002. From the culvert entrance at altitude ~31 m, most of the excess water flows down a ~1.5% terrain slope until in reaches a low-lying area at altitude ~24 m in the south-western quarter of the study area.

3.2 *Building the Digital Elevation Models*

It is emphasised that although DEM1 is the outcome of an attempt by the authors to build an enhanced high-accuracy DEM of Greenfield based on an available 1 m (grid resolution) LiDAR, the issue of whether or not DEM1 is a more accurate representation of the real site than the original LiDAR DTM is irrelevant to the present study. Its strength lies instead in the fact that the relationships between DEM1, DEM2 and DEM3 are well known.

DEM1 is based on the combination of a 1 m LiDAR DTM provided by Infoterra and OS Mastermap® data (high accuracy topographic information, mostly in the form of polygons, representing all landscape features such as roads, pavements, buildings, etc.) provided by Ordnance Survey, the national mapping agency of Great Britain. The work was carried out using a Geographic Information System (GIS) software and some ad hoc programming. The Mastermap® data were used to identify the different land-cover categories, and a different treatment was applied to each of these categories. For the reason stated in the previous paragraph, the details of the procedure followed to build DEM1 are not relevant to this study. The main characteristics of DEM1 are that it is of very high-resolution (a 0.1 m grid), with all surfaces exhibiting a smoothness that reflects reality. The camber of the roads is represented as well as 10 cm high kerbs. Buildings are also included, but the DEM is vegetation-free. A 3D sample of DEM1 is shown in Figure 2.

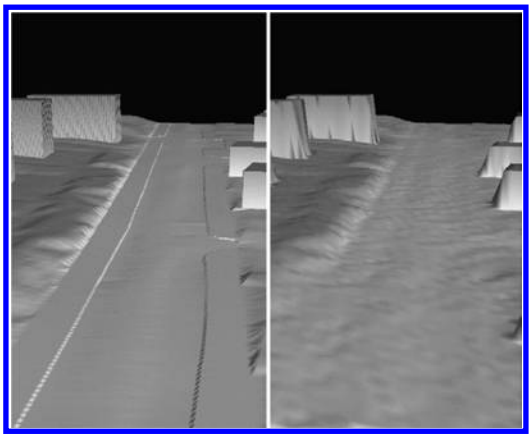


Figure 2. Sample of DEM1 (left) and the corresponding view in DEM3.

DEM2 and DEM3 were built according to a procedure similar to the way in which LiDAR DEMs are normally produced. Points at a density of 5 points per m^2 (meant to represent raw laser hits) were first projected onto the surface of DEM1. Then vertical and horizontal errors were applied to these points. These errors were applied randomly but in such a way that the vertical errors and the horizontal errors were distributed according to normal distributions with zero mean and specified standard deviations. The values of these standard deviations, σ_V and σ_H (respectively vertically and horizontally) were chosen to reflect typical LiDAR accuracy characteristics (RMSE values of 0.15 m horizontally and 0.50 m vertically). However, as mentioned in Section 2.2, these RMSE values include a component that at the scale of the present study can be identified as systematic or quasi-systematic (for example a general tilt of the terrain). Such systematic and quasi-systematic errors are beyond the scope of this paper. They can be partly suppressed in theory by DEM calibration (for example using evidence from a limited number of high-accuracy GPS point measurements), and whenever they remain they have very specific implications in terms of flood modelling results which are not studied here. For these reasons the values of σ_V and σ_H were chosen smaller than the reported RMSE values, as follows:

Finally, DEM2 and DEM3 were formed by gridding the raw LiDAR elevation modified as explained above onto 2 m grids (with each cell elevation calculated as the average value of all point elevations contained in the cell). A remarkable feature of DEM2 and DEM3 is that they possess the characteristic roughness and irregularities of most LiDAR-based DEMs used in the industry, unlike DEM1 (see Figure 2).

It should also be noted that since DEM1, DEM2 and DEM3 do not include any vegetation, the study focusses on LiDAR errors on bare surfaces. LiDAR errors in vegetated areas and filtering errors are beyond the scope of this paper.

3.3 *TUFLOW model*

TUFLOW is a computational engine that provides dynamically linked 2D and 1D solutions of the free-surface flow equations to simulate river flow and flood propagation. TUFLOW's 2D solution is based

Table 1. Vertical and horizontal error standard deviations used in building DEM2 and DEM3.

	σ_V	σ_H
DEM2	0.05 m	0.15 m
DEM3	0.10 m	0.30 m

Copyright © 2006 Taylor & Francis Group plc, London, UK



Figure 3. TUFLOW model of Greenfield. Locations of the upstream boundary condition and of 10 output points (velocity and free surface elevation) and 4 output lines (flow discharge). (© Crown Copyright Ordnance Survey. An EDINA Digimap / JISC supplied service.)

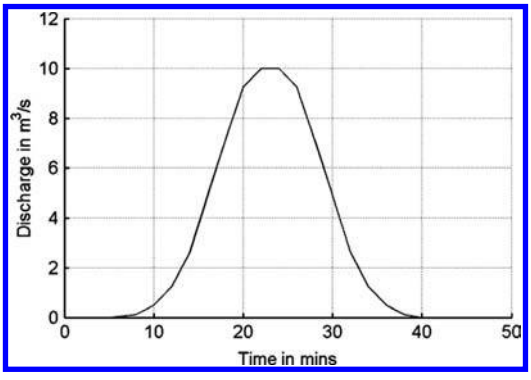


Figure 4. Upstream boundary condition.

on the Stelling finite difference, alternating direction implicit (ADI) scheme that solves the full 2D St-Venant equations (Stelling 1984) on a regular square mesh.

Only the 2D solver was used in this study, with a flow vs. time upstream boundary condition at the location indicated in Figure 3. A water level vs. time downstream boundary condition was used at a location outside Figure 3, several hundred meters away from the left-hand edge of the figure. The grid size used was 2 m. Grid cell elevations were directly taken from the underlying DEMs throughout the domain, including the buildings. Results were output either as flood depth maps at specific times, or as time series at locations indicated in Figure 3. Free surface elevation and velocity time series were output at point locations 1 to 10. Flow time series through lines 1 to 4 were also recorded.

3.4 *Simulations*

The upstream boundary condition was as shown in Figure 4 in all simulations. The downstream boundary condition was simply in the form of a constant water level set beneath the ground surface. Appropriate sensitivity checks were made to ensure that none of the results in the area of interest depended on the downstream boundary condition.

Table 2. Manning's *n* combinations used in simulations.

	1	2	3	4	5	6
Roads	0.008	0.009	0.010	0.011	0.012	0.013
Land	0.015	0.020	0.025	0.030	0.035	0.040
	7	8	9	10	11	12
Roads	0.014	0.015	0.016	0.017	0.018	0.019
Land	0.045	0.050	0.055	0.060	0.065	0.070
	13					
Roads	0.020					
Land	0.075					

Three initial simulations where carried out using respectively DEM1, DEM2 and DEM3. In these, Manning's n was set to 0.015 for any paved surface (roads, pavement and footpaths) and to 0.05 for all other areas (this is combination 8 in Table 2 below). These values are in line with standard values for floodplain roughness coefficients (see for example Chow 1998), but they were adjusted in an attempt to take into account obstacles such as hedges, fences and bushes.

An additional 12 simulations based on DEM2 and the Manning's n values listed in Table 2 were made, for the reasons detailed in section 4.4.

Sensitivity checks were made to ensure that the reported results were not dependent on the choice of time step. Also the maximum mass error was kept below 5% in all simulations. This implied the use of time steps of either 0.25 s or 0.5 s.

4 RESULTS

4.1 *Routes taken by the flow*

The LiDAR errors had a limited effect on the extent of inundation: a visual comparison of inundation extent maps could not reveal any significant differences. However, a significant impact on the flow distribution between the different routes was observed at least with the DEM based on the larger errors, DEM3. This was assessed by monitoring the discharges flowing through 4 lines indicated on Figure 3. These discharges are referred to as Q1 through to Q4, for which time series are shown in Figures 5 and 6. The results show that the LiDAR errors changed the peak values of these discharges by 11% at most in the case of DEM2 compared to DEM1 (Fig. 5a). In the case of DEM3, the proportion of the flow flowing southwards through a park (Q1) instead of flowing westwards along a street (Eskbank Street – Q2) increased from ~28% to ~44% because of the LiDAR errors (this is in terms of the peak discharge). The corresponding total volume of water (area under the Q curve) flowing through the

Copyright © 2006 Taylor & Francis Group plc, London, UK

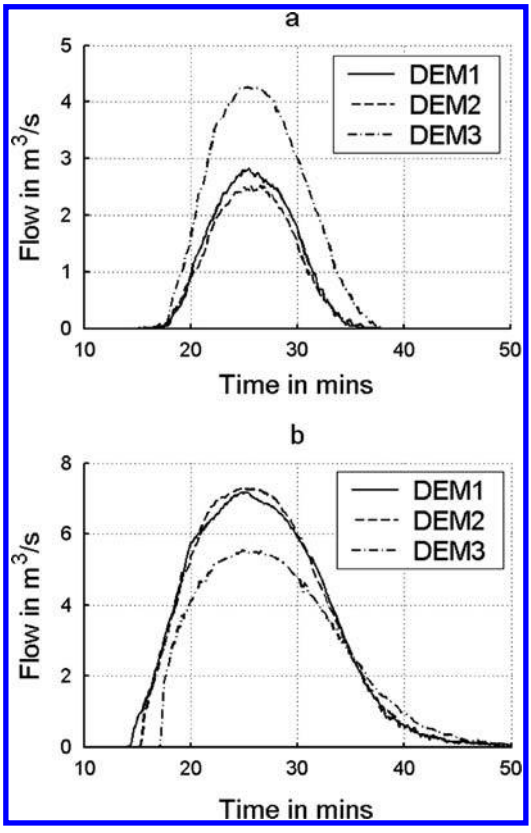


Figure 5. Results from initial simulations with DEM1, DEM2 and DEM3. Time series of discharges Q1 (a) and Q2 (b).

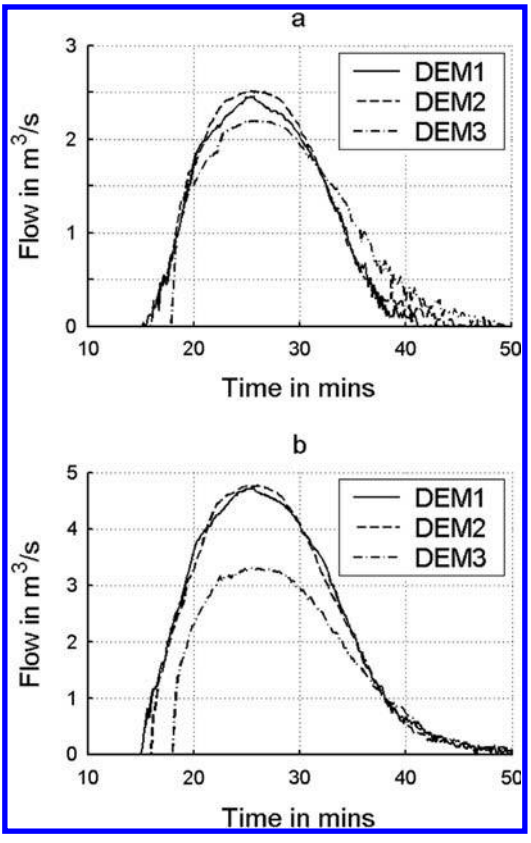


Figure 6. Results from initial simulations with DEM1, DEM2 and DEM3. Time series of discharges Q3 (a) and Q4 (b).

park increased by 1215 m^3, from 1616 m^3 to 2831 m^3, or from 19% to 34% out of a total of ~8300 m^3. Similarly, the proportion of water flowing down into a perpendicular street (Cockenzie Street) through line 3 (Q3) instead of westwards along Eskbank Street through line 4 (Q4) increased from 31% to 39% (out of the total flowing through either 3 or 4).

Such differences are explained by the fact that fine features such as kerbs and narrow land forms are not adequately represented in DEMs with errors as large as in DEM3. These features may play a significant role in channelling overland flow particularly for shallow flood depths, and their correct representation is critical to the accuracy of the results. It should also be noted that the choice of too coarse a model grid resolution would have similar implications even though this is outside the scope of this study (all the simulations reported used the same 2 m grid).

The magnitude of the differences reported above is such that cases where this would result in large differences in terms of final or maximum inundation extent and water levels are possible. However, the study did not highlight any major effect on the flow routes in the case of the DEM with the smaller errors, DEM2. More research results from the remote sensing community are needed to clarify whether (non systematic) errors in LiDAR DEMs can be as large as the errors involved in building DEM3.

4.2 *Maximum water levels*

The topography of this particular study area meant that most of the flood finished its course in the same "pond" located in the lower part of the catchment (southwest quarter of Figure 3). Therefore no significant difference in terms of the final water level was observed in this location (Fig. 8a). However the flow progressed in different ways along the catchment slopes as indicated in the previous section, so that for example differences of up to 10 cm were observed for example at location 1 (see Figure 7a). This lies in the path of the flow going through line 1 for which large flow rate differences are reported above. Such differences were observed in the

Copyright © 2006 Taylor & Francis Group plc, London, UK

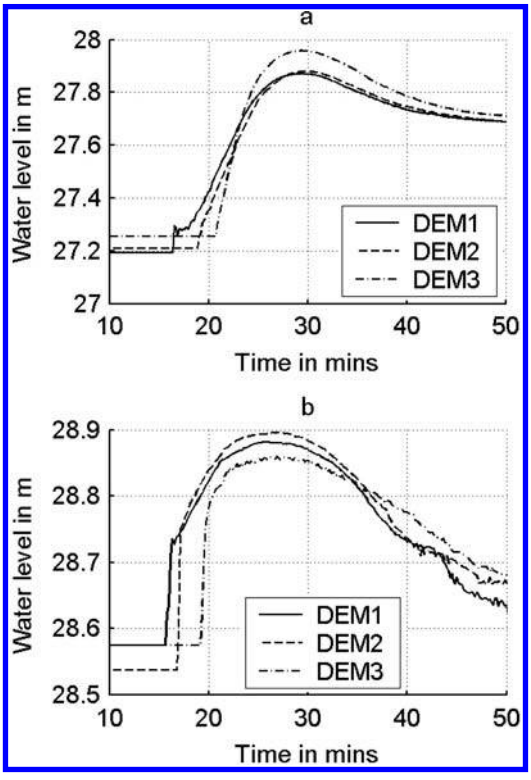


Figure 7. Free surface elevation vs. time at locations 1 (a) and 2 (b).

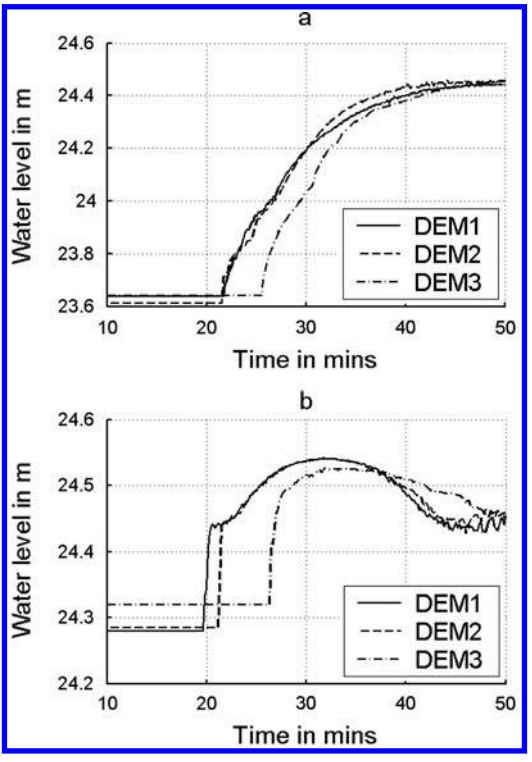


Figure 8. Free surface elevation vs. time at locations 3 (a) and 4 (b).

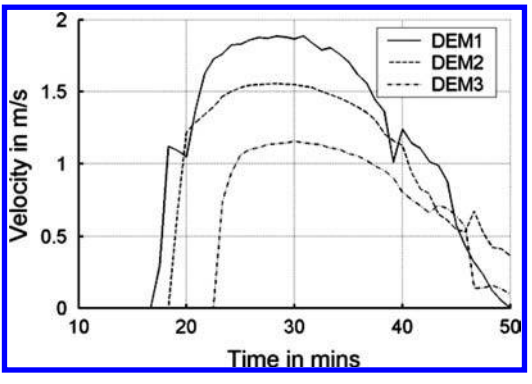


Figure 9. Velocity vs. time at location 10.

case of DEM3 but again much less so for DEM2. It is emphasised that even though the ground elevations at the output points varied from one DEM to the other by a few cms, this does not explain the differences in observed water levels. This was verified by analysing the shape of the water surface which was smooth and did not reflect in any way the cell-to-cell differences in ground elevations.

4.3 *Maximum velocities*

The effects of LiDAR errors in terms of modelled flow velocities were difficult to assess because they resulted from complex interactions between several factors. On the one hand, there were effects in terms of the flow discharge going down the different routes (section 4.1), and this affected the velocities. For example, the flow going through line 1 (Fig. 5a) was much larger with DEM3, which should have led to higher velocities as well. On the other hand, it was also observed (see next section) that the progression of the flow was slower with the DEMs containing LiDAR errors. Velocities were generally found lower with DEM2 and DEM3, particularly so with DEM3. A representative example is location 10 where the modelled velocity was as shown in Figure 9. The figure shows that the peak velocity at this location was lower by ~39% with DEM3 compared to with DEM1. This is partly attributed to the lower flow going along Eskbank Street through line 4, see section 4.1. Figure 9 also shows that the modelled velocity was lower (by ~19%), even with DEM2. The effects of the choice of DEM in terms of flow propagation speed are shown more extensively in the next section.

Copyright © 2006 Taylor & Francis Group plc, London, UK

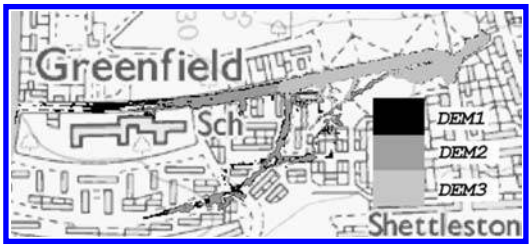


Figure 10. Snapshot of inundation extent at time t = 18 mins, for DEM1, DEM2 and DEM3. (© Crown Copyright Ordnance Survey. An EDINA Digimap/JISC supplied service.)

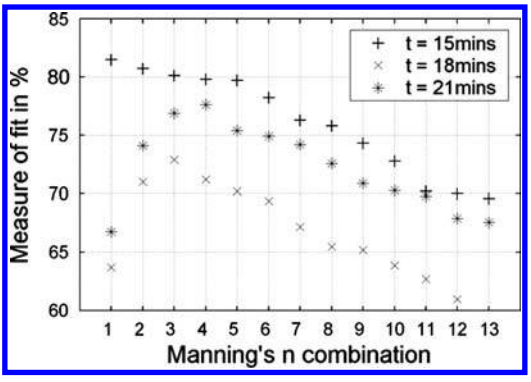


Figure 11. Goodness of fit between results based on DEM2 and 13 sets of alternative roughness values, and results based on DEM1.

The effects in LiDAR errors in terms of velocities can be of concern if an estimation of flood flow velocities is required.

4.4 *Progression of the flow*

In the simulations using the DEMs with errors and the original roughness values, the flow propagation speed was found lower than in the simulation using DEM1. This is illustrated by Figures 7 and 8 that show that the flow reached gauges 1 to 4 at a later time than in the benchmark simulation. The time lag was up to ∼2 minutes with DEM2 (although close to zero at gauge 3), and up to ∼10 minutes with DEM3. This is also illustrated by Figure 10, which shows snapshots of inundation extent at time t = 18 mins using the different DEMs.

Such effects can be explained by the additional head losses involved in the modelling of the flow between adjacent computational cells featuring larger elevation differences. For example, the flow along a smooth downhill road is incorrectly modelled as a succession of downhill and uphill segments. The effects in terms of inundation timing may be of concern particularly for larger areas, for example in real-time flood forecasting applications where end-users of flood forecasting systems (such as local authorities) may need an estimation of the time taken for the flood to reach particular locations. More importantly, discrepancies in terms of timing or velocities reflect the fact that the flow dynamics are not adequately modelled. This can impact on flood depths and flow routes in various ways.

As mentioned earlier, a set of simulations using DEM2 and alternative values of Manning's n were carried out, in an attempt to calibrate out the discrepancies between the results using DEM1 and DEM2. The purpose of this was to identify the values of n that result in a case of equifinality as defined in, for example, Aronica et al 1998. This was not done using DEM3, because as detailed in section 4.1, the results using DEM 3 showed differences in terms of the flow distribution between different flow routes which clearly could not be calibrated out simply by adjusting the roughness parameters.

The calibration exercise was made using the Manning's n combinations listed in Table 2. The agreement between the results using the DEM1 and the results using DEM2 and these roughness parameters was calculated using a measure of fit F defined as $F = Num(A)/(Num(A) + Num(B))$, where A is the set of wet cells predicted to be inundated in both simulations, B is the set of cells predicted to be inundated in either simulation but not both, and Num() represents the number of cells within each of these sets. This was calculated at times t = 15 mins, t = 18 mins, and t = 21 mins for all 13 simulations based on DEM2. The results are reported in Figure 11 above.

Figure 11 shows that the best agreement was found with the parameter combination 1 (or lower values, not tested) at time t = 15 mins, with the combination 3 at time t = 18 mins, and with the combination 4 at time t = 21 mins. This represents Manning's n values of between 0.008 and 0.011 for the roads and of between 0.015 and 0.030 for land, instead of the original values of 0.015 for the roads and 0.050 for land. An alternative method based on the time at which water depth reached 10 cm at all output gauges was also used and it reached similar conclusions.

The main implication of these results is that if roughness coefficients in a flood model are to be set according to published guidelines (where Manning's n values are advised with a precision of 0.001 for many types of surface cover types), the choice of an appropriate value of n may be much less important than the understanding of the artificial roughness introduced by the errors in the DEM/DTM. Also, if attempts are made to calibrate Manning's n values using field measurements during a real flood event, large discrepancies will occur depending on the quality of the DEM/DTM used in the model, and it is unlikely that such calibrated values will be transferable to another site in

Copyright © 2006 Taylor & Francis Group plc, London, UK

another model, even if the nature of the land cover is clearly similar.

5 CONCLUSION

The implications of LiDAR measurement errors in terms of the reliability of flood model results have been investigated using experimental tests based on the modelling of overland flood flow in an urban area using a 2D fully hydrodynamic model, a benchmark error-free DEM and 2 DEMs with errors of various magnitudes. The first conclusion is that the distribution of the flow between the different flow routes was significantly affected by the choice of DEM. The magnitude of the observed differences is such that cases where this would result in large differences in terms of final or maximum inundation extent and water levels are possible. Significant effects were also observed in terms of modelled water levels and flow velocities. Also, the artificial roughness of the DEMs with errors significantly slowed down the flow in the simulation, in a manner similar to what is achieved by greatly reducing values of Manning's *n*. This results in an incorrect representation of the flow dynamics, and has implications in terms of the choice or the calibration of roughness coefficients in river and floodplain models.

ACKNOWLEDGEMENTS

The research reported in this paper was conducted as part of the Flood Risk Management Research Consortium. The FRMRC is supported by grant GR/S76304 from the Engineering and Physical Sciences Research Council, in partnership with the Natural Environment Research Council, the DEFRA/EA Joint Research Programme on Flood and Coastal Defence, UKWIR, the Scottish Executive and the Rivers Agency (Northern Ireland). This financial support is gratefully acknowledged. The authors are also grateful to Glasgow City Council and Infoterra for providing LiDAR data for Glasgow, to WBM for the use of their TUFLOW software, and Ordnance Survey for providing Mastermap® data.

REFERENCES

Ahokas E., Kaartinen H. & Hyyppä J. 2003. A quality assessment of airborne laser scanner data. *International Archives of Photogrammetry and Remote Sensing* Vol. XXXIV, 3/W13.

Aronica G., Hankin B. and Beven K.J. 1998. Uncertainty and equifinaly in calibrating distributed roughness coefficients in a flood propagation model with limited data. *Advances in Water Resources* 22: 349–365.

Bates P.D. and De Roo, A.P.J. 2000. A simple raster-based model for flood inundation simulation. *Journal of Hydrology* 236: 54–77.

Chow, V.T. 1998. *Open Channel Hydraulics*. McGraw-Hill Education.

Cobby, D.M., Mason D.C., Horritt M.S. & Bates P.D. 2003. Two-dimensional hydraulic flood modelling using a finite-element mesh decomposed according to vegetation and topographic features derived from airborne scanning laser altimetry. *Hydrological Processes* 17(10): 1979–2000.

Gomes Pereira L.M. & Wicherson R.J. 1999. Suitability of laser data for deriving geographical information. A case study in the context of management of fluvial zones. ISPRS Journal of Photogrammetry and Remote Sensing 54: 105–114.

Hodgson M.E. & Bresnahan P. 2004. Accuracy of airborne LiDAR-derived elevation: empirical assessment and error budget. *Photogrammetric Engineering and Remote Sensing* 70(3): 331–339.

Marks K. & Bates P.D. 2000. Integration of high-resolution topographic data with floodplain flow models. *Hydrological Processes* 14(11): 2109–2122.

Mason D.C., Cobby D.M., Horritt M.S. & Bates P.D. 2003. Floodplain friction parameterization in two-dimensional river flood models using vegetation heights derived from airborne scanning laser altimetry. *Hydrological Processes* 17(9): 1711–1732.

North Carolina Floodplain Mapping Program 2006. *Internet address: http://www.ncfloodmaps.com*. Last accessed February 2006.

Sithole G. & Vosselman G. 2004. Experimental comparison of filter algorithms for bare-Earth extraction from airborne laser scanning point clouds. *ISPRS Journal of Photogrammetry and Remote Sensing* 59: 85–101.

Stelling G.S. 1984. On the Construction of Computational Methods for Shallow Water Flow Problems. *Rijkswaterstaat Communications, No 35/1984. The Hague, Netherlands.*

Copyright © 2006 Taylor & Francis Group plc, London, UK

One-dimensional flow modelling and a case study of the River Rhine

Tobias Bleninger & John D. Fenton
Institute for Hydromechanics, University of Karlsruhe, Kaiserstrasse, Karlsruhe, Germany

Rolf Zentgraf
Federal Waterways Engineering and Research Institute, Postfach, Karlsruhe, Germany

ABSTRACT: The simulation of rivers by one-dimensional models is examined. The German Federal Waterways Engineering and Research Institute's model CasCade was applied to a comprehensive case study for a long non-uniform section of the Rhine river with extensive floodplains. Results obtained show that the one-dimensional long-wave equations are more accurate than often believed. Large real-time data sets allow model calibration and optimisation beyond the matching of field data, and reproducing unsteady wave characteristics over the whole flow regime. It is then shown theoretically that, possibly surprisingly, river junctions require no special treatment in one-dimensional modelling. However some improvements are suggested – for curved rivers, over flood-plains, and in the treatment of friction. It is concluded that one-dimensional models, including the results of this paper, preserve a balance between requirements of accuracy and simplicity, and have much to offer in the understanding of river systems.

1 INTRODUCTION

1.1 *Rhine River engineering – the CasCade model*

The Rhine river (1320 km, 2000 $m^3 s^{-1}$ average discharge) is one of the longest and most important rivers in Europe (www.iksr.de). Its watershed is highly populated (about 50 million people) and connects the world's largest sea harbour (Rotterdam) with the inland European markets and its large and important industrial complexes. Ships up to 3000 t can navigate one of the most frequented waterways of the world from Rotterdam to Basel (800 km). The Rhine is also an important ecological habitat, source of major drinking water supplies and is of recreational and cultural importance. River engineering therefore has to guarantee optimised navigation conditions and flood protection combined and balanced with natural preservation (Figure 1). The German Federal Waterways Engineering and Research Institute (BAW, www.baw.de) is the central technical and scientific governmental agency of the German Federal Ministry of Transport, Building and Urban Development and the Federal Waterways and Shipping Administration. Its responsibilities are the operation and maintenance of federal waterways such as defining dimensions of fairways, regulating waterways structures or measures for stabilising the river bed. The assessment concerning the short-term and long-term hydraulic-morphological effects as well as the water management and environmental aspects is realised using physical as well as one-dimensional and multi-dimensional hydro-numerical models complementing one another.



Figure 1. Rhine River at Ketsch near Heidelberg, showing large flood plains, branches and lakes, being flow effective during high flows, but ineffective during low flows (Source: Landesmedienzentrum Baden-Württemberg).

Copyright © 2006 Taylor & Francis Group plc, London, UK

A computer model for a 500 km long section of the river Rhine has been developed and operated by the BAW using the in-house software CasCade, a one-dimensional, hydro-numeric modelling system for unsteady, unconfined flow conditions in branched or meshed networks of rivers, canals and flood fields. CasCade covers a major part of the river Rhine and therefore allows a unique system-wide river analysis. Its applications regard the following objectives:

- *Real time flow dynamics – online computation of water level elevation and depth*: CasCade models can easily be connected to the Rhine water gauge online-database, which is continuously updated with real-time data. Unsteady model runs include the previous flow history and use the actual water level time-series as boundary conditions at open boundaries. Additional water gauge data furthermore allows for a real-time model accuracy check. Waterway authorities already operate these models to improve fairway definitions, thus improving navigation conditions.
- *Navigation dynamics – computation of ship travel times*: CasCade post-processors allow for detailed data analysis. For example mean flow velocities can be computed for the navigation channel and used for further analysis of the navigation dynamics, thus transformed into ship travel times. Knowledge of unsteady hydrodynamic features therefore allows for improved logistical handling and better traffic control.
- *River bed dynamics – computation of mean shear stress in main channel*: CasCade post-processors may also compute section-wise shear stress. A system-wide analysis covering the whole flow regime allows for defining critical sections regarding erosion or sedimentation, especially after large floods, thus providing important data reducing the amount of costly field measurements and improving maintenance programs.
- *River engineering dynamics – simulation of impacts of regulating waterways structures*: The continuously updated and operated model allows for more accurate impact prediction beyond the calibrated flow regimes (Figure 2). The model is setup with all geometrical features regarding the whole flow regime. Although changes of regulating waterways structures are included only in an aggregated sense and not as higher-dimensional features, reasonable predictions are possible due to the additional unsteady calibration of the model.
- *Modelling dynamics – nesting/coupling optimisation*: A good knowledge of the system wide river flow behaviour, covering local characteristics over large discharge regimes allows optimising the complementary or coupled usage of additional models (i.e. more dimensional models). More detailed but costly 3-D hydrodynamic or morphology models are therefore applied especially to these sections and flow-regimes, where the 1-D model is passing its limits of applicability, exceeding desired accuracies.

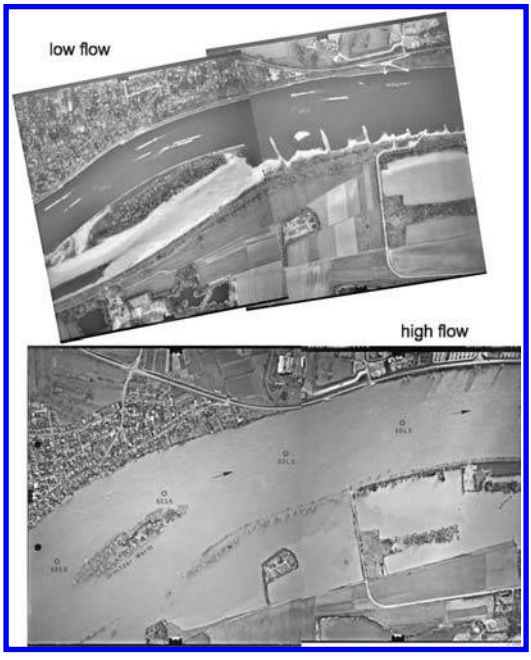


Figure 2. Short section of Rhine River showing waterway structures (groynes) and natural characteristics (islands), resulting in a strong change of the already complex flow characteristics during increasing flows.

1.2 *Case-study – section from Speyer to Worms*

A brief illustration of CasCade capabilities and limitations is shown for the application on the Rhine section from Speyer to Worms (Rhine-km 400.6–443.4). Along this streamwise 42.8 km there is an approximate bed height difference of 6 m resulting in an average bed slope of 0.015%. The width of the main channel ranges from 200 to 350 m and the depth from 2 m (during low flow conditions at 400–900 $m^3 s^{-1}$) to 5 m (during medium flow conditions at 900–1600 $m^3 s^{-1}$). This river section is characterised by its strong heterogeneity with partly very large flood plains (a few kilometres wide), including side branches, lakes and other retention areas (Figure 1). Another part is almost canal-like, where the river passes the cities of Mannheim and Ludwigshafen including the junction with a major tributary river, the Neckar (Figure 3).

The BAW maintains an extensive database, where topography and bathymetry data are available from recent laser and sonar scans respectively, with high spatial resolution. Cross-sections are extracted at each 100 m distance in the streamwise direction and used for the 1-D model setup. River sections separated by

Copyright © 2006 Taylor & Francis Group plc, London, UK

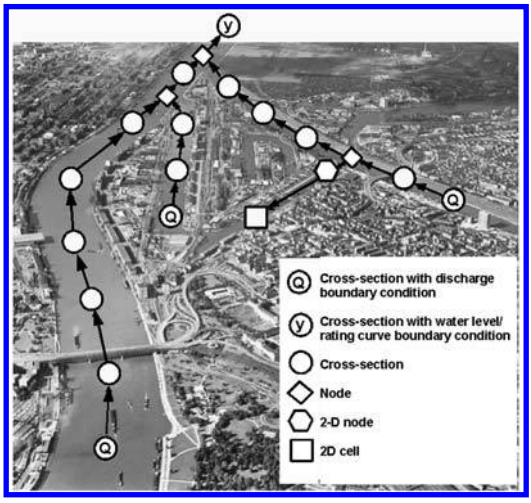


Figure 3. Rhine-Neckar junction and model schematisation as branched network.

islands or old river arms are modelled as separate branches, leading to a looped network model (Figure 3). Aerial photographs, geographical and geological maps, as well as navigational charts, allow locating and including important hydraulic structures and features in the model. The model Pre-Processor allows for subdividing cross-sections according to main roughness characteristics: the main channel, the floodplains, groyne fields or flow ineffective areas (encroachment approach). Model calibration is usually done using longitudinal water level measurements from recent field campaigns where ships travelled with the flow velocity and recorded position and elevation with high accuracy for low and medium flow conditions. Further unsteady calibration is done using the continuous water gauge recordings, with stored data of the last 10 years. Results show, that standard deviation of measured and calculated water level elevations in the main channel are around 2–4 cm for low flow conditions, 4–10 cm for medium flow conditions compared with the field campaign data and even less difference for the unsteady data compared with the water gauge time-series, also for high flow events. Nevertheless higher discrepancies can be observed at sections with strong curvature, at junctions and large floodplains not necessarily only due to limitations of 1-D modelling, but also to restrictions in the actual governing equations as seen by running sensitivity analyses.

Improvements to the 1-D numerical models are proposed, focusing on calibrating the model to adequately represent the observed flow characteristics and not only matching field data. Besides the attempt to improve the 1-D model itself the presented modifications should also clearly be seen as extensions beyond the 1-D approach as an interface to either more dimensional models or coupling to other models (hydrology, water quality, sediment transport, *etc.*).

1.3 *Research needs and achievements*

The simulation of flows and waves in rivers for a long time has been undergoing a development in terms of the sophistication of models which are actually applied, which has been related to computational facilities available. Once only steady gradually-varied problems were studied. Then unsteady one-dimensional problems were able to be simulated, followed by two-dimensional problems. Methods such as the development of the $k - \varepsilon$ model and then Large Eddy Simulation have meant that three-dimensional turbulent problems can now be simulated over limited domains. In general however, for practical problems the data requirements are inordinate, and the actual boundary conditions, the manner in which the fluid encounters resistance, are little better modelled than in the one-dimensional case.

Often field data is limited, and it is superfluous to try to model in a more sophisticated manner than the data warrants. This leads to the desirability of using a relatively simple model, but by performing inverse modelling (calibration) to extract the gross features of physical parameters. The use of one-dimensional modelling enables rather more physical understanding. With more sophisticated models the plethora of results often mean that physical intuition and understanding, perhaps the main benefit of computation, are not forthcoming. Also, in many rivers such as the Rhine, the physical extent is such that only a one-dimensional model is feasible.

In the case of the one-dimensional formulation, however, there remain areas where theoretical developments have not developed as they might. This paper examines several aspects of the one-dimensional modelling used by CasCade and by other one-dimensional computational models and tries to show that there is still much that one-dimensional modelling has to offer, especially if some of the suggested improvements are made:

- The one-dimensional long wave equations are examined, and it is shown that they have fewer essential approximations than has generally been believed.
- Generalised long wave equations are presented for curved rivers. The effects of curvature are examined.
- The problem of a junction of two rivers is considered, and it is shown that no special treatment is necessary; the only modification of the model necessary is that dynamic momentum flux of incoming streams should be included, and that this will be small in many cases.
- Friction in rivers is considered and it is observed that one-dimensional modelling is commensurate

Copyright © 2006 Taylor & Francis Group plc, London, UK

with the information usually to hand. However there has long been room for improvement in the modelling of friction. It is shown that the Weisbach friction formulation has advantages over the traditional Gauckler-Manning-Strickler version, and it is shown how compound friction can easily and rationally be included in 1-D models.

2 THE LONG WAVE EQUATIONS

2.1 *Equations for straight channels*

The one-dimensional equations usually used to model flows and waves in rivers are the long wave or Saint-Venant equations. They are a pair of partial differential equations for mass and momentum conservation, shown here in terms of the surface elevation η and the discharge Q, depending on distance along the channel x and time t, where the stream is assumed to be straight. The equations are

$$\frac{\partial \eta}{\partial t} + \frac{1}{B}\frac{\partial Q}{\partial x} = \frac{q}{B} \tag{1a}$$

$$\frac{\partial Q}{\partial t} + 2\beta\frac{Q}{A}\frac{\partial Q}{\partial x} + \left(gA - \beta\frac{Q^2 B}{A^2}\right)\frac{\partial \eta}{\partial x} = \beta\frac{Q^2 B}{A^2}\bar{S} - gA\frac{Q|Q|}{K^2} + \beta_q q u_q - \frac{Q^2}{A}\frac{\partial \beta}{\partial x}, \tag{1b}$$

where

q	is inflow volume per unit length,
B	is width of surface,
A	is cross-sectional area,
β	is the Boussinesq momentum coefficient,
$\bar{S}$	is mean bed slope at a section,
K	is conveyance, giving the effect of friction,
β_q	is the Boussinesq coefficient of inflow, and
u_q	is the inflow x-component of velocity.

Fenton (2006) suggested that the derivation of the equations can be made with few essential assumptions. The only non-trivial ones are not particularly limiting. They are:

- Variation in the streamwise direction is slow, such that pressure at a point is given by the equivalent hydrostatic pressure due to the water above that point, which is almost everywhere the case, except in the vicinity of local structures;
- The friction forces are given by an empirical formulae such as the Weisbach or Gauckler-Manning-Strickler formulae for the section as a whole, which in the absence of very detailed knowledge of the roughness, nature, and drag force of the bed, is a reasonable one; and
- The integral of the square of the horizontal velocity over a section is approximated by $\beta Q^2/A$, where β is a coefficient of magnitude about 1.1; this is a rough approximation, but the factor β only occurs in terms which are of a relative magnitude of the square of the Froude number $\mathbf{F}^2 = Q^2 B/gA^3$, which is small for many streams.

Generally the one-dimensional long wave equations are a good compromise between requirements of accuracy, and the scarcity of data, especially the nature of shear forces. Equation (1b) contains features worthy of note:

- The quantity $\bar{S}$ actually contains all the details of the underwater topography, and with it the equations are valid for non-prismatic sections (Fenton (2006). It is

$$\bar{S} = -\frac{1}{B}\int_B \frac{\partial Z}{\partial x}\,dy + \text{term from vertical diverging walls,} \tag{2}$$

  where Z is the bed elevation, such that $\bar{S}$ is obviously the mean bed slope at a section. Some formulations include a term like $\partial A/\partial h$, usually known as the non-prismatic contribution, but it seems simpler to represent it in terms of the mean slope. The form of equation (2) shows that to evaluate it accurately, one needs to have a detailed knowledge of the underwater topography. In the case of the Rhine River, such a detailed knowledge is available. But often this is not the case, however, and the term is written only as a representative slope of the river as a whole. As this term is largely counterbalanced by the friction term, which is also usually poorly known, this is quite justifiable.
- The friction term $gAQ|Q|/K^2$ is shown in terms of the conveyance K, which is obtained from friction laws:

$$K = \frac{1}{n}\frac{A^{5/3}}{P^{2/3}} = k_{St}\frac{A^{5/3}}{P^{2/3}} = \sqrt{\frac{8g}{\lambda}}\frac{A^{3/2}}{P^{1/2}} = C\frac{A^{3/2}}{P^{1/2}} \tag{3}$$

  in which P is the wetted perimeter, and n, k_{St}, λ, and C are respectively the roughness coefficients of Manning, Strickler, Weisbach, and Chézy. The friction term is based on boundary stress, which is clear from the derivation of the Chézy and Weisbach forms – what is most notable about this formulation is that it is *not* based on energy, and the dimensionless term $Q|Q|/K^2$ is *not* an "energy slope", as described by many sources.
- The term $\beta_q q u_q$ is the contribution to momentum flux from lateral inflow. In many cases it is poorly known, when it is not zero, but in the case of a

Copyright © 2006 Taylor & Francis Group plc, London, UK

tributary, the β_q is technically necessary to express correctly the momentum transport. Some texts write the whole term as $q(u_q - Q/A)$, which is not correct (and is based on a double counting of the momentum of the inflow as it enters and leaves the control volume).

2.2 *Channels curved in plan*

Fenton and Nalder (1995) derived the one-dimensional equations for the case where the river is curved. A long-stream co-ordinate s was used, generally expected to pass down the perceived centre of the stream. The equations were obtained in terms of the discharge Q, as for the straight-channel case, but in terms of the cross-sectional area A rather than the surface elevation η, which in this case can vary across the channel due to centripetal acceleration. The difference between the equations obtained and the straight channel equations are linear terms in two quantities, $\kappa n_m = n_m/r$ and $\kappa\bar{n} = \bar{n}/r$, where $\kappa = 1/r$ is curvature of the longitudinal s axis along the river and r is the radius of curvature, n_m is the transverse distance between the s co-ordinate axis chosen and the centre of the free surface, and $\bar{n}$ is the distance between the s axis and the centroid of the cross-section. In addition to the approximations for the straight-channel case, also terms proportional to $(n_m/r)^2$ and $(\bar{n}/r)^2$ are ignored. That is, the extra approximation is that the radius of curvature be rather larger than the channel width. This level of approximation is similar to the usual one for the conventional formulation of the Saint-Venant equations for channels presumed to be straight, where the approximation is that (depth / disturbance length)$^2 \ll 1$. The equations are

$$(1-\kappa n_m)\frac{\partial A}{\partial t} + \frac{\partial Q}{\partial s} = q, \tag{4a}$$

$$(1-\kappa\bar{n})\frac{\partial Q}{\partial t} + \beta\frac{Q}{A}(2+3(\kappa n_m - \kappa\bar{n}))\frac{\partial Q}{\partial s} + \left(\frac{gA}{B} - \beta\frac{Q^2}{A^2}(1+2(\kappa n_m - \kappa\bar{n}))\right)\frac{\partial A}{\partial s}$$

$$= gA\bar{S} - gA\frac{Q|Q|}{K^2}(1-\kappa\bar{n}) + \beta_q q u_q \tag{4b}$$

where terms involving $d\kappa/ds$ have been ignored, and the inflow term has been simplified. The latter equation is slightly different from that in Fenton and Nalder (1995). It includes the momentum coefficient β and the friction term has been written more correctly in terms of conveyance rather than "energy slope". The coefficient β may be important particularly in a curve where the longitudinal velocity is greater on the inside of a curve than on the outside so that β is rather larger than 1. In the original paper no attempt was made to solve the field equations to obtain the longitudinal or lateral velocity distributions – the momentum formulation does not require that knowledge in detail.

Equations (4) are of a very similar nature to those for straight channels, equations (1). The only differences are the presence of the dimensionless coefficients κn_m and $\kappa\bar{n}$ in terms of curvature and cross-channel dimensions. The behaviour of waves and flows, the development of numerical methods, the behaviour and properties of those methods, and the re-writing of software, all should be able to be relatively simply done.

3 RIVER JUNCTIONS

3.1 *The canonical problem – rectangular channels*

Almost all research on river junctions has been for the case of steady flow in two rectangular channels with co-planar bottoms, where one enters the other, whose width remains unchanged thereafter. The belief that the problem is difficult, even for this relatively simple geometry, has stultified extension to more complicated geometries and to the general unsteady case. Here we examine a momentum approach to the problem, to guide our extension to more general problems. The energy principle does not contribute much – all that it yields is the energy loss, which is not as important as the relation between upstream and downstream depths that is obtained from momentum considerations.

Consider a rectangular stream entering another at an angle δ as shown in Figure 4. The main stream has the same width upstream and downstream of the junction. The plan of a vertical-sided control volume is shown by a heavy dashed line and the flow force contributions are shown by double-headed arrows. The downstream face of the control surface has not been taken across the region of separation, but it is supposed sufficiently far downstream that the velocity defect due to the separation has been substantially dissipated.

The flow force **M**, consisting of a static component, the hydrostatic force and a dynamic component,

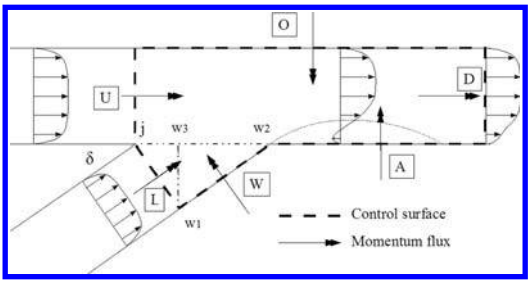


Figure 4. Definition diagram for momentum analysis of a junction of two uniform rectangular streams.

Copyright © 2006 Taylor & Francis Group plc, London, UK

the momentum flux, across a planar part of a control surface, where the velocity crosses the section perpendicularly is $\mathbf{M} = \rho(gAh_c + \beta Q^2/A)\ \hat{\mathbf{n}}$, where symbols are the same as above, with the addition of h_c, the depth of the centroid of the section below the surface, such that Ah_c is the first moment of area of the section about a transverse axis at the water level, and $\hat{\mathbf{n}}$ is a unit vector, normal to the section, directed outwards from the control volume.

The vertical boundaries across which momentum flows, with the corresponding reference letters on Figure 4, are a transverse **U**pstream face across the stream, a similar **D**ownstream face, a **L**ateral stream entering at an angle of δ to the main stream, the side of the main stream **O**pposite to the inflowing stream, and the side **A**djacent to it. The analysis we are about to perform assumes that the square of the Froude number of the incoming flow at L is not large so that the disturbances to the free surface are also not large.

It is the *dynamic* contribution from L that is the most important factor in the analysis. If we consider a momentum balance *transverse* to the main stream, then by a simple theorem from hydrostatics, the component of a static force on any surface is equal to the component of the static force on a projection of that surface perpendicular to the component direction (*e.g.* §2.6 of White (2003)). This means that the static component from L in the transverse direction is approximately equal to that on the rectangular section from the junction point j to w_3, and the component from the wall W is approximately equal to that on the projection w_2w_3. Hence the static component of the whole lateral entry region is approximately that of a hypothetical wall from j to w_2, just as if the tributary were not there. This leaves the only transverse contribution that of the dynamic contribution from the tributary, which can only be balanced by the force contribution from O being slightly larger than that from A and jw_2, so that the water level along O opposite the tributary will be slightly higher and the water level along the junction and A will be slightly lower – the transverse dynamic contribution causes the river locally to tilt slightly transversely. While this seems to violate the initial assumption that the water level does not vary much because of the tributary, the overall deduction that the effect is small for small Froude number is true.

Similarly, if we consider longitudinal flow force, along the main stream, it can be seen that the longitudinal static contribution on L will be approximately equal to the contribution due to its projection, the vertical rectangle marked on the surface by w_1w_3, while the contribution on the wall W is only static, and has the same projection area but its contribution is the reverse of that due to L, and so the static contributions almost completely cancel each other out, and the only flow force contribution to the inflowing stream is its dynamic component in the longitudinal direction, which will be usually relatively small.

To quantify this, we write the longitudinal momentum balance, assuming that on each contributing face the water level is constant, but not for the moment assuming that $h_w = h_L$, to give, after re-arrangement:

$$\tfrac{1}{2}Bh_D^2 + \frac{\beta_D Q_D^2}{gBh_D} - \left(\tfrac{1}{2}Bh_U^2 + \frac{\beta_U Q_U^2}{gBh_U}\right) - \cos\delta\,\frac{\beta_L Q_L^2}{gbh_L} + \tfrac{1}{2}b\cos\delta\left(h_w^2 - h_L^2\right) = 0, \qquad (5)$$

in which b is the width of the tributary. A good approximation is that the water level in both confluent streams is the same, such that $h_L = h_U$, which is supported by evidence (Hager 1987, citing Favre and Vischer). The last term in (5) shows mathematically the approximate balance between the contribution of the wall and that due to the lateral stream. However the actual depth along the wall is not known *a priori*, although in many cases, the water surface drops very little as the tributary enters the main stream, and so $h_w \approx h_L$. As a first approximation a factor $\gamma = h_w/h_L$ could be introduced in the spirit of Hager (1989), and a numerical value slightly less than 1 assigned. The result is an equation connecting h_U and h_D in terms of all the β and Q of the three component streams. If we were to make the further approximation that all the dynamic terms, of magnitude proportional to the square of the Froude number, then the solution of the momentum equation is simply $h_D \approx h_U$.

3.2 *Unsteady flow through junctions of arbitrary section*

Consider a natural river junction as shown in Figure 5. The treatment here is of some generality, so we abandon the nomenclature of Upstream and Downstream, and prefer to identify the channels as 1, 2 and 3. Shown is a possible control volume with vertical planar flow boundaries C_1, C_2, and C_3.

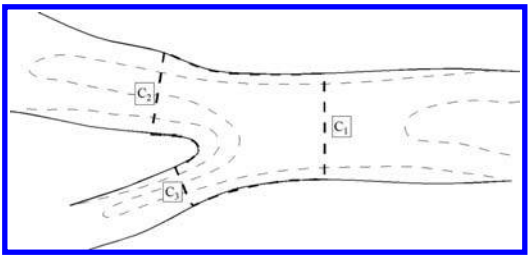


Figure 5. Definition diagram for momentum analysis of a junction of two irregular natural streams.

Copyright © 2006 Taylor & Francis Group plc, London, UK

In this case the solid boundaries that give contributions to the momentum from hydrostatic forces, are irregular, complicated, and very difficult to evaluate, if indeed the bottom topography is known at all well. However for rectangular channels in both transverse and longitudinal directions it was seen above that significant cancellations and simplifications occurred. That suggests further exploration for the case of irregular geometry. The reason is to be found in Gauss' Divergence Theorem in one of its lesser-known forms, (#2.61, equation 3 of Milne-Thomson (1968)) to replace the integral of the pressure contributions over *all* parts of the control volume by an integral of the pressure gradient through the volume, as used by Fenton (2006) in a derivation of equations (1). Gauss' relation is

$$\int_{CS} p\hat{\mathbf{n}}\,dS = \int_{CV} \nabla p\,dV. \tag{6}$$

The basic approximation throughout river hydraulics is that the pressure distribution is equal to the equivalent static head of water above, such that at any point with elevation z, and where η is the water surface elevation above, $p = \rho g(\eta - z)$, and ∇p is the vector with components $\rho g(\partial\eta/\partial x, \partial\eta/\partial y, -1)$. As we will not consider vertical momentum here, we can take just the x and y components of the right side of (6), such that $\nabla_2 = (\partial/\partial x, \partial/\partial y)$ and use these results to give the pressure force $\mathbf{P}_2$ in the two-dimensional horizontal plane on the fluid in the control volume:

$$\mathbf{P}_2 = \int_{CS} \nabla_2 p\,dV = \rho g \int_{A_s} h\nabla_2\eta\,dA_s \tag{7}$$

where the last term is the integral over the surface area A_s of the junction, of the depth h times the surface gradient. In this form the contribution can be approximated readily without gross error, in the spirit of much river hydraulics. If we take the component of the net pressure force along part of the control volume, and just consider the x-component along the volume, in a slice of length Δx and elementary volume ΔV, the term becomes, as $\partial h/\partial x$ is closely constant across the width,

$$\rho g \int_{A_s} h\frac{\partial\eta}{\partial x}\,dA_s = \rho g\frac{\partial\eta}{\partial x}\Delta V = \rho g\frac{\partial\eta}{\partial x}A\Delta x, \tag{8}$$

and this results in the term $gA\,\partial\eta/\partial x$ in the momentum equation for the channel, (1b). This underlying simplicity leads us to suggest that for all the physical processes governing motion in the junction, there is nothing which requires special modelling if momentum is considered. Energy is quite different, because the mixing of two streams at an angle to each other causes extra losses. For momentum, however, all processes are similar to those which occur in the body of the river itself. The process of friction drag is similar, although extra currents will cause some minor differences.

In the case of a junction of two rectangular channels, the water surface slope does vary around the junction, and for higher speed flow, it does dip as it passes the sharp corner w_2 in Figure 4. However, for natural junctions as in Figure 5 we assert that the river surface shows little unusual variation, and that it becomes possible to do away with the concept of a special control volume at the junction. It seems easier and in keeping with the usual one-dimensional approach to rivers if instead, the river junction is considered as a junction between different one-dimensional streams, as shown in Figure 6. This might have been the simplest and most obvious approach from the beginning, but the junction problem has been traditionally believed to be too complicated for such a simple representation.

The CasCade model already incorporates this representation in its looped network formulations. A major problem for the actual case study, as presented previously, has been the lack of data regarding the lateral inflow volume flux. There is no rating curve existing for the Neckar tributary nearby the junction, because of the influence by the Rhine river superimposed on the unknown discharge control by upstream hydropower plants. Furthermore it is not possible to develop a rating curve for a long section upstream of the junction, due to the influence of the Rhine discharge on Neckar water levels and even more important, the influence of the Neckar discharge on Rhine water levels. A calibrated CasCade model was therefore used to artificially develop a rating surface at the junction point. Given downstream water level and discharge, together with given upstream discharge allows computing the Neckar flow and upstream water levels for both. An *a priori* calculation of the rating surface using Equation (5) would improve the modeling of junctions considerably, which still has to be proven.

In view of this apparent simplicity, it seems that the only consideration at a junction is to include the dynamic momentum contribution from the tributaries. Equation (5) for rectangular channels clearly contains

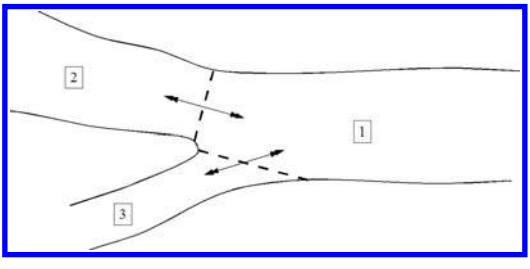


Figure 6. The schematisation which can be used in practice at a junction of two irregular natural streams.

Copyright © 2006 Taylor & Francis Group plc, London, UK

a dynamic contribution from the inflow that becomes, after multiplying through by g:

$$\cos\delta \frac{\beta_L Q_L^2}{b h_L} \quad (9)$$

that does affect the main stream. Here we examine the adequacy of the inflow term $\beta_q\, q\, u_q$ in the general momentum equation (1b) to represent this. We multiply by the length of the finite computational length Δx in the downstream river. It is clear that $\beta_q = \beta_L$, $q\Delta x = Q_L$, and $u_q = \cos\delta\, Q_L/bh_L$, and the expressions are equivalent. Hence we suggest that the only effort or modification necessary to allow for a river junction is to add the dynamic momentum contribution as an inflow contribution, such that over the first computational length the term $\beta_q\, q\, u_q$ be incorporated as a total contribution of $\cos\delta\, \beta_L Q_L^2/A_L$ where the subscripts L pertain to the lateral stream and δ is the angle it makes with the downstream channel.

4 THE CALCULATION OF FRICTION

4.1 *Friction formulations*

The Gauckler-Manning-Strickler equation is empirical – it has no theoretical justification. It is simple and describes friction for a river cross-section as a whole. Rouse (1937) wrote

> "… hydraulicians have been forced to rely to a great extent upon empirical relationships for the expression of energy loss due to turbulence; and as empiricism is at best a rather haphazard means to an end, such relationships in themselves are seldom likely to suggest the correct nature of underlying physical principles. Thus it is that the subject of hydraulics now finds itself somewhat hobbled in its thought by those very methods which contributed greatly to its prestige in past generations.

However, an alternative was already at hand, Keulegan (1938) noted that the theoretical investigations of Prandtl and von Kármán, and the experimental work of Nikuradse, led to rational formulas for velocity distribution and hydraulic resistance for turbulent flow in circular pipes in terms of the dimensionless Weisbach friction coefficient λ. He went on to show how similar rational formulas could be deduced for open channels, although rather than allowing for a general treatment by allowing for the local depth to vary over a section, he adopted the overall section hydraulic radius as the characteristic length.

The optimism of the 1930s was misplaced – the Gauckler-Manning-Strickler law continues to appear as some sort of universal standard, such that experimental and field results are related to it, arbitrary formulae are used to apply it to compound sections and more general problems, and books and tables are published suggesting that friction can be calculated from visual similarity with other rivers. There are a number of arbitrary formulae for calculating the effective friction coefficient for a section, not based on rational criteria. Indeed the ASCE Task Force on Friction Factors in Open Channels (1963) wrote:

> "Many engineers have become accustomed to using Manning's n for evaluating frictional effects in open channels. At the present stage of knowledge, if applied with judgement, both n and λ are probably equally effective in the solution of practical problems. The design engineer who prefers to use n in his (*sic*) computations should continue to do so, but he should recognize the limitations on his method … It is believed that experimental measurements of friction in open channels over a wide range of conditions are better correlated and understood by the use of λ. Furthermore, λ is commonly used by engineers in many other branches of engineering and probably provides the only basis for pooling all experience on frictional resistance in both open and closed conduits. It is recommended, therefore, that engineering teachers and research workers emphasize the use of the friction factor λ …

Clearly the Task Force believed that Manning's n was sufficiently entrenched in practice that it could continue to be used but that it was desirable for researchers and teachers to move the profession in the direction of λ.

4.2 *A drag-force approach to channel friction*

The resistance to flow in open channels has often been thought of, incorrectly, in energy terms, giving rise to the concept of energy gradient. Energy dissipation processes are internal to the flow and are complicated and difficult to describe and quantify. However the concepts of the Chezy resistance coefficient C and the closely allied Weisbach coefficient λ are derived from considerations of wall stress, hence momentum. Also, research into the effects of vegetation on flow has used a momentum approach, in terms of drag forces on individual elements, which has usually then been converted to an equivalent overall Gauckler-Manning-Strickler roughness by processes whose validity is doubtful.

Using momentum/drag it is possible to unify effects due to boundary roughness, bed-forms, vegetation, and structures – using the empirical Gauckler-Manning-Strickler law that is not possible. Consider the combined drag force ΔT on a number of discrete

Copyright © 2006 Taylor & Francis Group plc, London, UK

roughness elements and/or vegetation elements in an elemental slice of channel of length Δx:

$$\Delta T = \frac{\rho}{2} \sum C_D v^2 a, \tag{10}$$

where the summation is over all the drag-producing elements, each of projected area a normal to the flow of local velocity v and with drag coefficient C_D. Theoretically the sum contains a huge number of terms of small quantities (every sand grain, for example). It is not intended that the sum ever be actually evaluated, it is here only as a representation. If the local velocity v is assumed given by a factor γ related to the mean horizontal velocity in the channel Q/A, then $v^2 = \gamma Q^2/A^2$, and

$$\Delta T = \frac{\rho}{2} \frac{Q^2}{A^2} \sum C_D \gamma a. \tag{11}$$

The *mean* shear stress on the channel wall is given by (p 63, Montes (1998)):

$$\tau_0 = \rho \frac{\lambda}{4} \frac{(Q/A)^2}{2}, \tag{12}$$

where λ is the Weisbach friction coefficient, so that, using $\tau_0 = \Delta T / P \Delta x$ gives λ expressed in terms of the drag components:

$$\lambda = \frac{4 \sum C_D \gamma a}{P \Delta x}. \tag{13}$$

This gives a fluid-dynamical explanation for the behaviour of λ, and shows how it is actually made up of *local* components, and how a rational theory of channel friction becomes possible:

- In general, the elements of the sum $\sum C_D \gamma a$ will vary around the boundary, as the bed material changes, as vegetable matter of a different kind grows at the edges, as the local value of γ depends on the local depth, and so on.
- Clearly the drag coefficient terms can be added linearly so that we could write it as a *finite* sum of various contributions

  $$\lambda = \lambda_1 + \lambda_2 + \ldots, \tag{14}$$

  where 1, 2, *etc* might denote gravel on bed, reeds at the side, and so on, each of which can be determined separately by research.
- In the case of the Gauckler-Manning-Strickler equation it is not at all clear how individual components should be combined, and there are several alternatives.
- With some research and experience it would be possible to calculate the sum, and hence the friction coefficient λ, from a knowledge of bed materials of the same form.
- In general, the sum and hence the friction factor λ, will be a function of depth and flow. It, unlike Manning's n (Strickler's k_{St}), is not expected to be constant. Its variability is an expression that we are modelling the actual physics. We do not expect a magic constancy for such a complicated problem.

In the case of a channel with particles of sand or gravel, we can use previous research which has obtained expressions for λ. Colebrook and White proposed an implicit equation for λ in a pipe in terms of relative roughness k/D, the equivalent sand grain roughness divided by the pipe diameter D, and the Reynolds number $\mathbf{R} = UD/\nu$. For channels this can be used with $D = 4A/P$ (Henderson (1966, p 93)). As λ appears implicitly in the equation, it has been thought of as being more difficult than it really is. To try to overcome this Moody (1944) produced a well-known chart for λ as a function of $\mathbf{R}$, with k/D as a parameter; it is not always known that most of the results are simply those corresponding to the Colebrook and White equation. The best solution of all is to use the explicit approximation produced by Haaland (1983):

$$\lambda = \frac{1}{1.8^2} \log_{10}^{-2} \left(\left(\frac{k/D}{3.7} \right)^{10/9} + \frac{6.9}{\mathbf{R}} \right), \tag{15}$$

where again, $D = 4A/P$ for a channel.

4.3 *Use in practice*

In equation (3) the conveyance K in terms of λ is given by

$$K = \sqrt{\frac{8g}{\lambda}} \frac{A^{3/2}}{P^{1/2}} \tag{16}$$

so that in the 1-D momentum equations (1b) and (4b) the friction term appears as

$$-\frac{gAQ|Q|}{K^2} = -\lambda P \frac{Q|Q|}{8A^2}, \tag{17}$$

with an extra curvature factor in the latter case. The friction coefficient λ appears linearly, as does perimeter P, as they are directly related to the force on the boundary, to which the whole term corresponds. If the boundary were a compound boundary, for example, or with different roughness elements, one could write the friction term in terms of a sum

$$-\left(\sum_i \lambda_i P_i \right) \frac{Q|Q|}{8A^2}. \tag{18}$$

If this approach were adopted, it may be less necessary to resort to 2-D or 3-D modelling, as the characteristics of the whole cross-section are incorporated in this 1-D model.

Copyright © 2006 Taylor & Francis Group plc, London, UK

5 CONCLUSIONS

The simulation of rivers has been examined, by one-dimensional models in general, and by the program CasCade in particular. Extensive data management allows for analysis of real-time flow dynamics coupled with navigation dynamics, river bed dynamics and impact analysis of regulating waterway structures. The governing equations have been shown to require few limiting assumptions. Furthermore the problem of the confluence of two or more natural streams has been considered, and the problem has been shown to be able to be approximated by conventional one-dimensional approaches, with the incorporation of the momentum from and to any tributaries or effluent streams. The problem of simulating flood-plain flows was considered, and it was concluded that even though the one-dimensional approach does not solve the problem as well as might be desired, irregularities of roughness, channel and geometry are such that no great sophistication is warranted and further developments of a simple nature are warranted. Methods for calculating friction have been considered, and it has been suggested that the Weisbach formulation is characterised by its universal applicability beyond the main channel hydraulics. It is concluded that the knowledge of frictional characteristics in the bed and the floodplains of a river, and the detailed geometry of both, are usually so limited that the one-dimensional model represents a good compromise between requirements of fidelity of simulation and the greatly increased effort and intrinsic limitations of highly accurate simulation by two- and three-dimensional models.

ACKNOWLEDGMENTS

The authors thank Inga Müller, Master's degree student, for her assistance with the model setup and visualisation.

REFERENCES

ASCE Task Force on Friction Factors in Open Channels 1963. Friction factors in open channels. *J. Hydraulics Div, ASCE* 89: 97–143.

Fenton, J. D. 2006. On the long wave equations, manuscript in preparation.

Fenton, J. D. and G. V. Nalder 1995. Long wave equations for waterways curved in plan. In *Proc. 26th Congress IAHR, London*, Volume 1, pp. 573–578.

Haaland, S. E. 1983. Simple and explicit formulas for the friction factor in turbulent pipe flow. *J. Fluids Engng* 105: 89–90.

Hager, W. H. 1987. Discussion of "Separation zone at open-channel junctions" by Best and Reid (1984). *J. Hydraulic Engng* 113(4): 539–543.

Hager, W. H. 1989. Transition flow in channel junctions. *J. Hydraulic Engng* 115(2): 243–259.

Henderson, F. M. 1966. *Open Channel Flow*. New York: Macmillan.

Keulegan, G. H. 1938. Laws of turbulent flow in open channels. *J. Res. Nat. Bureau Standards* 21: 707–741.

Milne-Thomson, L. M. 1968. *Theoretical Hydrodynamics* (Fifth ed.). London: Macmillan.

Montes, S. 1998. *Hydraulics of Open Channel Flow*. New York: ASCE.

Moody, L. F. 1944. Friction factors for pipe flow. *Trans. ASME* 66: 671–684 (including discussion).

Rouse, H. 1937. Modern conceptions of the mechanics of fluid turbulence. *Transactions, ASCE, Vol. 102, Paper 1965* (also published in facsimile form in *Classic Papers in Hydraulics*, by J. S. McNown and others, ASCE,1982.

White, F. M. 2003. *Fluid Mechanics* (Fifth ed.). New York: McGraw-Hill.

Copyright © 2006 Taylor & Francis Group plc, London, UK

River Po low water training: The importance of mathematical modeling to support designing activities

L. Schippa, S. Pavan & S. Colonna
Engineering Department, University of Ferrara, Italy

ABSTRACT: An extended reach of the major Italian river, the river Po, is suitable for navigation. Regulation works are however needed to ensure good navigation conditions also during low water periods. Designing has been supported by hydraulic mathematical modeling in order to evaluate long term and middle term effects. Mobile bed simulations have been performed using a mathematical model based on one-dimensional shallow water equations and on Exner equation. The model has been numerically implemented with an implicit finite difference algorithm based on the four points Preissman scheme. Both actual and designed river configurations have been modeled in order to evaluate effects on design navigation channel, on sediment balance and bottom evolution, on hydraulic risk and on solid mass fluxes to the river delta.

1 INTRODUCTION

Progresses and improvements in the field of hydraulic research led to significant achievements and developments for what concerns hydraulic modeling. The possibility of creating a mathematical or numerical model based on the deep knowledge of physical phenomena, is of utmost importance in river engineering, and it is going to become one of its fundamental tools.

The value of hydraulic models during the project phase of considerable river regulation works is easy to understand, since they give the opportunity to know in advance the effects of human actions on the natural system and on the surrounding environment. Moreover, they permit to better evaluate project decisions, and to accurately choose the operative procedures which will lead to job's successful outcome.

In this paper, an example of the role of hydraulic modeling in river management is proposed, with the description of the various phases of work and of the interactions with the designing party.

The project's issue is the low water training of river Po, the major river in Italy. Thanks to its depth and to its noticeable width, the Po river results suitable for navigation for a long reach of about 400 kilometers, starting upstream from the city of Cremona, where an important harbor has been built, and closing downstream near the town of Porto Viro, in correspondence of the navigation lock of Volta Grimana, which links the Po river with another navigable channel. However, the lack of river regulation structures dramatically reduces the navigation possibilities during low water periods along the middle reach, between the tributary Mincio's mouth and the city of Ferrara.

To ensure navigability features for an extended period of time, a river regulation work has been planned. It involves a 60 Km long river reach, and includes several submergible groynes and riverbank stabilization structures. The aim of the modeling work here presented is to investigate morphological changes expected in river bed configuration, the overall sediment balance along the river, the consequent flood risk assessment and the variation of solid mass fluxes to the Po delta. Beside these environmental aspects, the model will also give useful indications about low water river course regarding navigation purposes, and about effects induced on the existent structures along the river.

Simulations have been performed with a mobile bed one-dimensional mathematical model based on shallow water equations and on sediment continuity equation, numerically implemented with an implicit computational scheme. Though natural rivers flow patterns are predominantly 2-D, a one-dimensional model has been chosen in order to have the possibility of long term and middle term simulation performance. Since the aim of this analysis is to capture the river evolution trend and the regulation works global effects, the choice of a 1-D model, seems to be the most convenient from the computational point of view. The use of a 2-D model, in fact, would have not result in a more accurate representation of macro-phenomena, in front of a larger computational effort. An appropriate method has however been applied to take in

Copyright © 2006 Taylor & Francis Group plc, London, UK

account bends curvature for morphological changes evaluation. The examined river reach has been properly extended downstream and upstream in order to correctly evaluate its evolution trend. Boundary conditions have been derived from hydrologic historical data and rating curves.

The modeling work has been applied considering two different geometrical configuration: the actual river condition, and the river setting after regulation operations. Simulations results have been analyzed in comparative and absolute terms.

2 THE MATHEMATICAL MODEL

2.1 *Governing equations*

Since physical celerities associated to liquid phase are much greater than the one characteristic of sediment transport phenomena, an uncoupled treatment is allowed. Indicating with h, water depth, and with Q, liquid discharge, the state variables, the one-dimensional shallow water equations written in non-conservative form are:

$$\frac{\partial Q}{\partial t}+\frac{\partial}{\partial x}\left(\frac{Q^2}{\Omega}\right)+g\Omega\frac{\partial h}{\partial x}+g\Omega s_f=0 \quad (1)$$

$$\frac{\partial \Omega}{\partial t}+\frac{\partial Q}{\partial x}-q=0 \quad (2)$$

where g is the gravitational acceleration, Ω the wetted cross-section, x the distance along the river, t the time variable, s_f the friction slope and q the lateral incoming discharge for unit length.

Equations 1–2 constitute a non linear mathematical system, which may be numerically solved once proper initial and boundary conditions are imposed.

From the hydraulic point of view, river cross-sections are clearly divided in two different zones: main channel and over banks. This distinction reflects also on the sediment transport evaluation: the channel, where low flow and moderate flow discharges are contained, is generally covered by granular material and takes part to sediment exchanges; on the contrary over banks are only interested by flood events and can be considered as not erodible zones. Equations 1–2 are applied only within main channel, while over banks hydraulics is treated using a quasi-uniform flow scheme, assuming the same water surface slope as main channel.

Slope friction has been calculated under the hypothesis of uniform flow by means of the Gauckler-Strickler formula:

$$s_f=\frac{Q|Q|}{\Omega^2 gRC^2}\ ;\ C=\frac{K_S R^{1/6}}{\sqrt{g}} \quad (3)$$

where R indicates the hydraulic radius. The Gauckler-Strickler coefficient K_S has been calibrated and it resulted homogeneously equal to $38\,m^{1/3}/s$ for the main channel, while for over banks it varies within the range $3\,m^{1/3}/s$–$30\,m^{1/3}/s$ with a mean value of $15\,m^{1/3}/s$ (Agriculture Ministry, 1990).

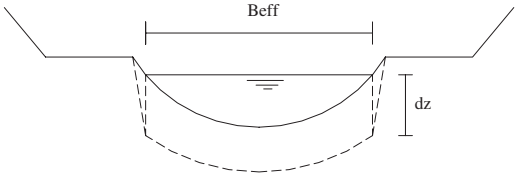


Figure 1. Cross-section uniform evolution model.

Equations 1–2 have been numerically solved applying the Preissman semi-implicit scheme, with implicity parameter equal to 0.7 and spatial weight of 0.5, commonly used values which guarantee computational stability and results accuracy (Chaudry, 1993).

Cross-sections evolution process is influenced by longitudinal and transversal solid transport gradients, mainly associated to the concentration gradient and to lateral gravitational bottom transport. (Lamberti & Schippa, 1996) The present approach assumes the sediment redistribution effect across the cross-section to be complete and homogeneous. As represented in Figure 1, this leads to a uniform vertical translation of channel bed, which corresponds to the eroded sediment volume per channel length.

Solid phase balance equation is written as:

$$\gamma_S B_{eff}\frac{\partial z}{\partial t}+\frac{\partial Q_S}{\partial x}-q_S=0 \quad (4)$$

where Q_S is the apparent volumetric solid discharge (the bed porosity is assumed equal to 0.4), γ_S is the apparent specific weight, B_{eff} is the effective cross-section width which takes part to sediment exchange processes, z is the elevation of channel bottom, q_S is the sediment discharge per unit length deriving from external mass exchanges (e.g. mining activities).

The unknown in Equation 4 is the uniform bed level variation ∂z. Here the Preissman scheme has been applied assuming the spatial weight equal to 0 in the upstream cross section of every single reach, and equal to 1 in its downstream cross-section. This is allowed considering the limited daily evolution of bed level, and ensures high computational stability. The implicity parameter is kept equal to 0.7 as for the liquid phase.

Through comparison with measured values of sediment transport (Agriculture Ministry, 1990), the relation which gives the best solid discharge estimate is the Engelund-Hansen formula:

$$Q_S=0.05B\gamma_S U^2\sqrt{\frac{d_s}{g(s-1)}}\theta^{3/2} \quad (5)$$

Copyright © 2006 Taylor & Francis Group plc, London, UK

where s is the relative sediment density 2.65, B is the water surface width, d_s is the representative sediment diameter, U is the mean flow velocity, θ is the Shield's parameter.

2.2 *Boundary conditions*

For liquid phase, the upstream boundary condition is the temporal sequence of daily mean discharge values, both for the Po reach upstream end and for each of the 14 tributary comprised in the analyzed reach.

For what concerns solid phase, the incoming sediment discharge and the transport mass at tributaries mouths are evaluated assuming a local uniform flow condition and the correspondent transport capacity, as it results from the Engelund-Hansen monomia formula:

$$Q_S = 15.54 \frac{1}{d_s \cdot B^7} k_S s_f^{1.65} Q^{1.7} \tag{6}$$

At a distance of about 90 Km from the upstream cross section, a transversal regulation structure (operating since 1969) is located, in correspondence of a river island named Isola Serafini, immediately upstream of the tributary Adda's mouth. From the modeling point of view, it represents an internal boundary condition, which requires the definition of a relationship between flowing discharge and upstream and downstream water levels. This relation has been derived considering the structure management rule, that is the maintenance of a water surface elevation equal to 41.00 m, except in case of huge flood events, when the barrier is set as wide open and its presence may be neglected.

To represent this internal boundary condition, a fictitious cross-section has been added 100 m downstream the blockage location, in order to isolate this anomalous reach, for which particular balance equations have been used instead of Equations 1–2:

$$Q_{IS} = Q_{IS+1} \tag{7}$$

$$h_{IS} = 41.00\ m\ ;\ h_{IS} = h_{IS+1} \tag{8}$$

in which the under script IS indicates the Isola Serafini cross-section, while $IS + 1$ stands for the downstream fictitious cross-section. Equation 7 expresses the continuity of the flowing discharge, while Equation 8 regulates the structure water elevation respectively in case of ordinary operation and flood event.

The downstream boundary condition consists of a rating curve in correspondence of Polesella station. It has been provided by the hydro-meteorological service, and it is based on measures carried out between 1988 and 1993. It is considered as representative of the last decade with a ±10% variation, and it is actually

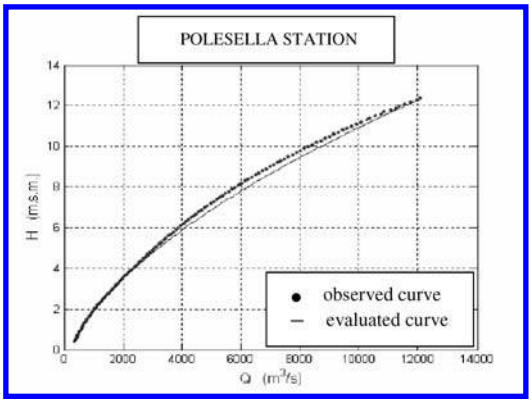


Figure 2. Rating curve at Polesella station.

under validation process. In the model, the discharge scaling is expressed as follows:

$$Q = a\left(h - h_0\right)^b \tag{9}$$

where h is the water level corresponding to the discharge Q, h_0 is the virtual water surface elevation corresponding to null discharge at Polesella, a and b are characteristic parameters dependent on cross-section shape, extrapolated by the minimum square method ($a = 118.89$, $b = 1.76$, $h_0 = 1.50$ m).

Beside, an evolution analysis of the rating curve in correspondence of Pontelagoscuro (about 20 Km upstream from Polesella), has been carried out. On the basis of several measures effectuated between 1988 and 1993, considering a rating curve elaborated in 2000 (G. Benatti, 2000), and the most recent study dated 2003 a stability trend of the bed level configuration is clearly noticeable. This deduction may be extended to the overall low course of the river Po, in particular downstream of the Pontelagoscuro station. This means that the Polesella rating curve may be assumed as invariant for the simulation period and substantially independent from the weak evolution processes of the reach.

3 RIVER DESCRIPTION

The mobile bed model has been applied to a Po reach which starts upstream at La Becca and extends till Polesella with an overall length of 307 Km.

This extension has the function to include the river reach subject to regulation works, to mitigate any discrepancy effect which may derive from boundary conditions, to have reliable data at upstream and downstream ends, and to evaluate works effect over the whole river.

Copyright © 2006 Taylor & Francis Group plc, London, UK

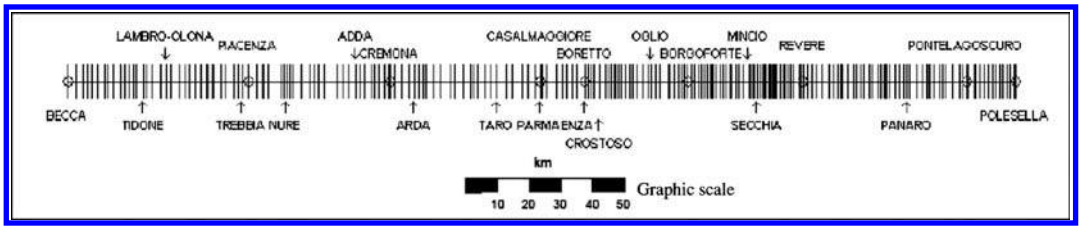


Figure 3. River reach scheme.

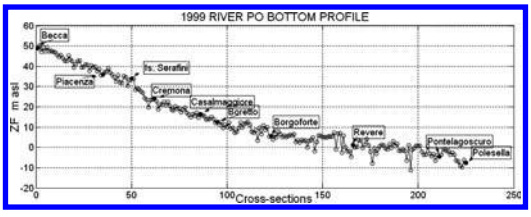


Figure 4. AIPO 1999 surveys: longitudinal profile.

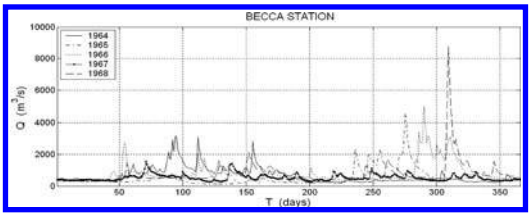


Figure 5. Example of daily discharge hydrogram at Becca station in representative years.

Along the considered reach, river Po receives water from 15 tributaries, that have been schematized with 14 localized incoming discharge.

The cross-section geometry has been described by means of recent field surveys (AdPo, 2001), however proper fictitious cross-sections have been added in order to represent more completely the design configuration in the surroundings of the low water channel settlement work. The resulting river scheme is therefore composed by 225 computational sections meanly spaced by 1.5 Km, each one described by 100 points of known coordinates. In particular, over banks are each described with 30 points, while 40 points are reserved to channel representation.

3.1 *Hydrologic data*

For what concerns hydrologic data, the daily mean incoming discharge at the upstream station, is known in the period 1954–1971, while from 1972 to 1983 only data starting at Piacenza station are available. After statistical considerations, a quantitative relationship has been found between the discharge passing by Piacenza and the upstream water flow at La Becca, assuming a traveling time of a day.

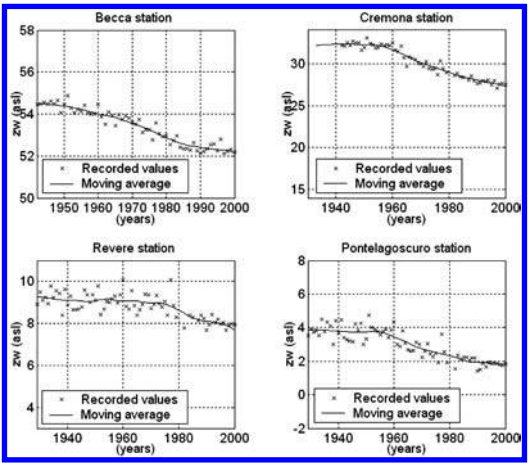


Figure 6. Minimum water elevation trend.

In this way, the discharge data sequence at disposal covers a period of 30 years, and may be considered as a long period representative sequence. It can therefore be used to represent the hydrologic succession of the fifty year simulation time.

3.2 *Hydrometric data*

Water surface elevation data are known in 8 hydrometric stations: Becca, Piacenza, Cremona, Casalmaggiore, Boretto, Borgoforte, Revere and Pontelagoscuro. Among them, minimum annuals elevations have been isolated and examined. In fact, the hydrometric level is a reliable indicator of bed elevation lowering trend, since it is not affected by local anomalies as bottom elevation, usually assumed as the cross-section lowest point elevation, can be (e.g. localized rocks or pits) (Schippa & Pavan, 2004). Referring to Figure 6, one can see a progressive reduction of the noticeable lowering trend initiated in the fifties. In particular at Cremona station erosion is particularly evident because of the presence of Isola Serafini structure, while at Pontelagoscuro station the lowering trend is no longer perceptible, also because of the sea proximity, which level strongly influences low water flow.

Copyright © 2006 Taylor & Francis Group plc, London, UK

3.3 *Sedimentological data*

The sedimentological channel characterization has been derived from field measurements carried out in the nineties (Agriculture Ministry, 1990). Two main aspects are to be highlighted: the granulometric distribution is substantially one-modal, except for the upstream reach where the torrential stream effects lead to a bi-modal distribution; secondly, the sediment diameter progressively reduces as a consequence of sorting.

In the model, the channel has been longitudinally divided in distinct portion, each one characterized by a d_S constant in time and not affected by the bed altimetric evolution, with a lognormal distribution:

$$d_S = 2^{-\left[0.029+(1.89-0.029)(x/L)\right]} \tag{10}$$

where x is the distance from the Becca station (m) and L is the reach extent.

3.4 *Mining activities*

Generally speaking, the causes which affect bed evolution are: the main channel narrowing for navigation purposes, the Isola Serafini transversal structure presence, and the mining activities, which had a predominant role from fifties until nowadays. (Lamberti & Schippa 1994).

Recently, specific laws have been created for river sediment exploiting regulation. It seems therefore reasonable to take in account a progressive reduction of the extractive action, which leads to an hypothetical realistic residual amount of 3 Mm^3/year within the overall reach. This value will be taken as the representative one across the fifty year simulation period. However, to compensate the uncertainty towards mining activities data, a sensitivity analysis has been performed.

The spatial distribution of the extracted volumes along the reach is worked out from the mining installations layout. Consequently, 10% of the extractions has been attributed between Becca and Piacenza, the 40% between Piacenza and Boretto, the 30% between Boretto and Borgoforte, and the remaining 20% between Borgoforte and Polesella.

4 REGULATION DESIGN

Concerning fundamental designing criteria, there are some significant aspects which rule the navigation path project and the preliminary works sizing.

Straight connection reaches between two consequent curves must be avoided, since they may favor shallow water zones and erratic changes in flow direction. To this purpose, the low water channel design tends to go along with the existent roughed out curves, keeping unchanged the natural navigation path length.

Analyzing forces acting on curved flows (centrifugal force and gravitational force), a proportionality between flexure and arch length ($1/R \propto L$) is noticeable, and leads to the choice of a path made of a clotohoids sequence, osculating at inflection points with different expansion parameters and vertexes.

The height of regulation works crest has been set equal to the low flow water elevation (discharge equal to 450 m^3/s), augmented by one meter next to curves vertexes in order to take in account the water surface rise caused by the centrifugal force. Then the height gradually decreases to the lower profile level from the vertex to the work extremes.

From the operative point of view river regulation structures can be longitudinal or transversal regarding flow direction. The position and the conformation of a bend can be fixed and protected by longitudinal over bank defenses, which can be made of loosen rocks (rip-rap) or have wooden retaining walls filled with granular material. Beside, low stage main channel narrowing is obtained by means of low-dipping cross dikes extended from the river banks and pointing to the river axis so as to direct the water flow into the central channel.

The evaluation of the designed configuration leads to the transversal profile reshaping of the involved cross sections. As far as a one-dimensional model is used, simulations are referred to the final morphological setting, neglecting the transient period during which regulation works will not be fully operative. On the other hand, even if the assessment time of a water stream could have relevant effects, its actual influence is hard to evaluate, (Lamberti & Schippa, 1995), and can reasonably be ignored in long term analysis.

The design transversal profile of the examined reach has been drawn accounting for centrifugal force in curved streams, which produces motion field deformations and typical 3-D effects. A transversal secondary recirculation stream adds to the main longitudinal one, resulting in an overall helicoidal motion. At the concave bend side, sediment particles move downward, depositing, while at the convex side they move upward causing bed erosion.

To represent these morphological phenomena, the simple Engelund-Bridge model has been chosen:

$$\frac{D}{D_C} = \left(\frac{r}{r_C}\right)^{\alpha} \quad ; \quad \alpha = 11\tan\varphi \tag{11}$$

Referring to Equation 10 and to Figure 7, φ is the soil slope friction, r is the flexure radius, D the local depth, r_i and D_i are respectively the bend internal radius and depth, r_e and D_e refer to the external bend side, r_C and D_C to the middle channel.

Copyright © 2006 Taylor & Francis Group plc, London, UK

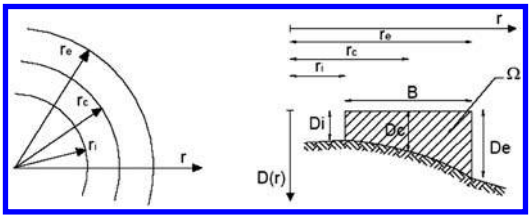


Figure 7. Engelund-Bridge model.

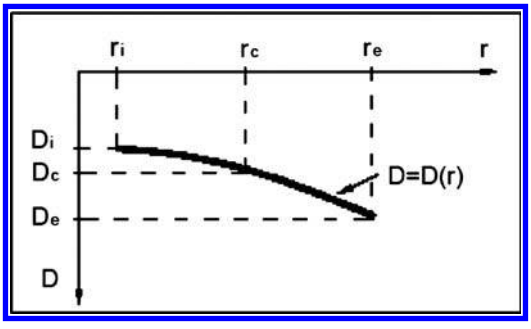


Figure 8. River bend design profile.

In this case the flexure radiuses are known, and correspond to those of the designed low flow channel, defined by a the discharge $Q_P = 450\ m^3/s$.

Assuming quasi-uniform flow conditions for the low flow event, one obtains:

$$\begin{cases} \Omega = \dfrac{Q_P}{C\sqrt{g}\sqrt{s_0}D_c^{1/2}} \\ \Omega = \int_{r_i}^{r_e} D\,dr \end{cases} \tag{12}$$

where s_0 is the longitudinal bottom slope.

Substituting the D expression obtained from Equation 10 inside Equation 11, and balancing the two expressions of Ω, leads to the value of D_C:

$$\frac{Q_P}{C\sqrt{g}}\frac{1}{D_C^{1/2}} = \frac{D_C}{r_C}\frac{1}{(\alpha+1)}r^{\alpha+1}\Big|_{r_i}^{r_e} \Rightarrow D_C \tag{13}$$

The application of Engelund-Bridge formula gives then the bend transversal configuration:

$$D(r) = \frac{D_C}{r_C^{\alpha}}r^{\alpha} \quad , \quad r \in [r_i, r_e] \tag{14}$$

It is very important to consider the definitive river configuration, since the regulation works presence strongly affects the channel geometry, consequently conditioning sediment balance through modifying the effective cross-section width. As an example, Figure 9 depicts the effect of a cross dike, highlighting the noticeable main channel narrowing produced in the final design configuration.

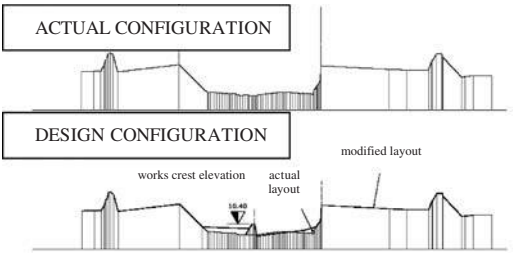


Figure 9. Example of definitive design morphology.

5 SENSITIVITY ANALYSIS

The sensitivity analysis is a useful tool for results comprehension, since it puts in evidence data sets influence on model behavior and simulation outcomes.

In particular, among the parameters affected by an uncertainty grade, the most interesting seem to be those regarding mining activities, on which sediment balance directly depends, and flow resistance, because of its influence on flow regime and transport capacity. They have therefore an important role in defining the river morphologic evolution.

Anyway, it is important to keep in mind the comparative purpose of this work, which mainly aims to analyze the differences in the evolution process of the actual and of designed river configuration (*ante and post operam*) instead of giving an overall evaluation of the phenomena.

The reference values for the sensitivity analysis are the minimum annual water surface elevation zw_{min} and the bed elevation z. As pointed before, zw_{min} can be considered as the more reliable one, since it is not affected by isolated irregularities and localized flow pattern effects.

In view of the fact that the model sensitivity cannot depend from the geometry configuration assumed, the analysis has been performed considering the actual state, correspondent to the surveys of 1999 (AdPo, 2000).

To determine model sensitivity to mining activities, different scenarios have been hypothesized:

1) no mining activities
2) extracted volume equal to 1.5 Mm^3/year (50% less than the reference volume)
3) extracted volume equal to 3.0 Mm^3/year (reference volume)
4) extracted volume equal to 4.5 Mm^3/year (50% more than the reference volume).

Copyright © 2006 Taylor & Francis Group plc, London, UK

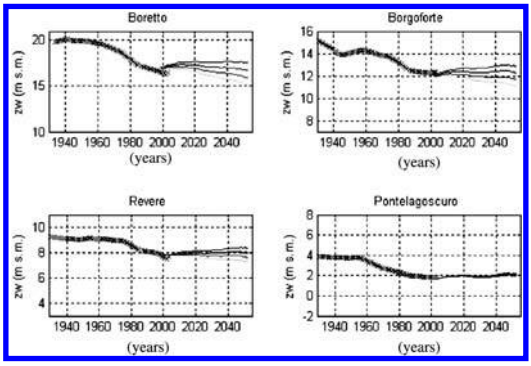


Figure 10. Sensitivity analysis to mining activities in terms of minimum water level evolution trend.

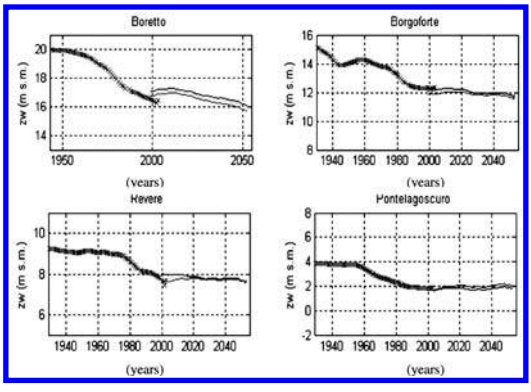


Figure 11. Sensitivity analysis to flow resistance in terms of minimum water level evolution trend.

The graphical results for the main stations located in the river reach mostly involved by regulation works are shown in Figure 10.

Referring to the trend evolution analysis of the last decades (see Fig. 6), the prudential approach which suggests a mining activity of 3 Mm^3/year seems to be the more consistent one, since it continues the observed stabilization tendency. This is particularly evident at Pontelagoscuro station.

As expected, the model sensitivity to sediment extraction is predominant in correspondence of the reaches to which a greater excavation activity is assigned, that is Boretto and Borgoforte.

For what concerns the influence of the flow resistance coefficient, the three chosen possibilities are:

1) $k_S = 34\ m^{1/3}/s$ (10% less than the reference value)
2) $k_S = 38\ m^{1/3}/s$ (reference value)
3) $k_S = 42\ m^{1/3}/s$ (10% more than the reference value)

Figure 11 shows the modest model sensitivity to the flow friction parameter, especially in the downstream zone.

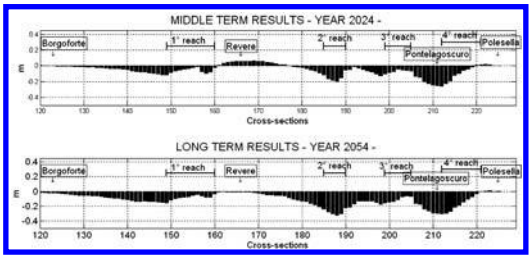


Figure 12. Minimum water elevation variation during simulation: middle term and long term results.

6 RESULTS

6.1 *Bed elevation evolution trend*

As already explained in the previous sections, the most reliable trend indicator is the minimum water level, since it is independent from local effects. However, within long and middle term analysis, it should be properly filtered to eliminate inconsistent values deriving from particular hydrologic events, as for example the 2003 exceptional low flow.

Another possible indicator of bed lowering or overloading is the low flow wetted cross section, estimated assuming quasi-steady conditions. Its value is however influenced by energy slope, which is in turn a channel bed evolution result.

Moreover, the uncertainty grade of data sets and the difficulty of correctly quantifying all linked and involved phenomena, suggest to focus on a comparative evaluation of results, instead of referring to absolute estimates.

Figure 12 shows the difference between the annual minimum water level of actual and designed configuration. Graphics have been obtained from the moving average of minimum water level elevations simulated in each cross-section $\overline{zw}$. The ordinate axis represents the difference for the N-th year of the i-th cross-section: $diff^N(i) = zw_D^N(i) - zw_A^N(i)$, where the term $zw_D^N(i)$ refers to the design configuration, and $zw_A^N(i)$ to the actual state.

The overall bar chart representation puts in evidence a substantially unchanged sediment balance over the reach, showing a sub-reaches succession with stable evolution trends over the time.

Figure 13 represents the annual minimum water level differences between the beginning and the closing of simulations, for both design and actual river geometry:

$$diff_D(i) = \overline{zw_D}^{2054}(i) - \overline{zw_D}^{1999}(i) \quad (15)$$

$$diff_A(i) = \overline{zw_A}^{2054}(i) - \overline{zw_A}^{1999}(i) \quad (16)$$

Copyright © 2006 Taylor & Francis Group plc, London, UK

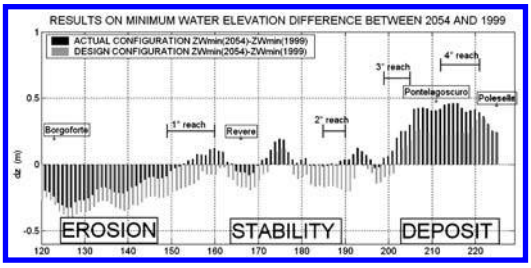


Figure 13. Annual minimum water level differences at the end of simulation.

The notation $\overline{zw}$ indicates the moving average over 5 annual values.

For what concerns the actual configuration, from the analysis of Figure 13, one can see that the first zone, localized between Borgoforte station and the tributary Secchia, presents a slight lowering tendency; from Secchia's mouth until Panaro's mouth the bottom configuration seems to be stable; then, from Panaro's outlet to Polesella station, a channel overloading tendency is noticeable.

Referring to the results of the design configuration simulations, the same reach splitting can be drawn, and the same considerations can be derived for the three sub-reaches, even if from the quantitative point of view the evolution effects seems to be smoother. This result can be interpreted as an assessment of the future bed evolution trend along the considered reach. Beside, it seems that the presence of regulation works would not affect the natural river morphologic development (i.e. lowering or overloading), though a smoothing effect should be taken in account.

The same conclusions may be evinced from the analysis of bottom elevation, always referring to the moving average values over five points. The results analysis also permits to border the regulation works influence zone, which extends to about 5 km upstream and terminates about 20 km upstream of the first modified cross-section.

6.2 *Effects on navigation channel*

To establish the efficiency and the stability of the navigation channel, the analysis has been based on channel bottom morphologic evolution and on annual minimum water depth trend along the reach, at simulation beginning and closing.

The assumption of the definitive channel geometry as design configuration simulation input data, leads to a progressive canalization of modified cross-sections. It is worth keeping in mind that navigability benefits are strictly connected to the river low flow channel canalization grade.

This phenomenon could be evaluated considering middle-long term minimum water depth. To this

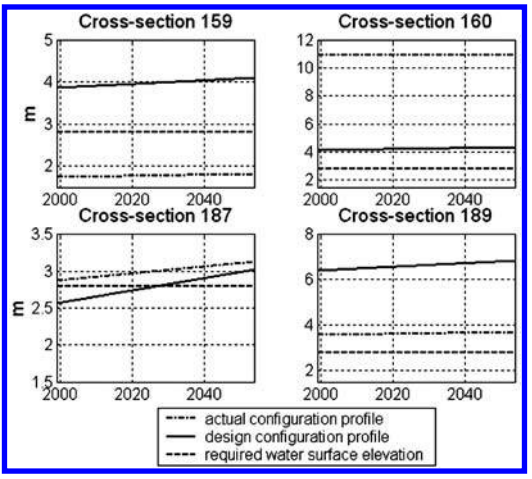


Figure 14. Example of the effects on navigation pattern.

purpose, design low flow ($Q_P = 450\,\mathrm{m^3/s}$) foreseen water depth could be used, in addition to the lowering action expected over fifty years. For the *i*-th cross-section, the estimated water depth at the end of simulation for the actual configuration is:

$$y_A^{2054}(i) = y_A^{1999}(i) + \left|dzw_A(i)\right| \tag{17}$$

$$dzw_A(i) = zw_A^{2054}(i) - zw_A^{1999}(i) \tag{18}$$

where y_A^{1999} is the water depth correspondent to the design discharge ($Q_P = 450\,\mathrm{m^3/s}$) at the simulation beginning (year 1999), zw_A^{1999} and zw_A^{2054} are respectively the minimum water surface elevations at the beginning and at the end of simulation. The same procedure applies to the design configuration.

Figure 14 reports some exemplificative situations, occurring at four different cross-sections representative of the middle river course (between Revere and Panaro's mouth). At a preliminary view one can see that in the long term scene the designed configuration ensures greater water depths than the minimum required for class V boats navigation (dashed line). At section 159 this condition is not fulfilled considering the actual geometry. In some reaches, for example at section 160, the water level consequent to river regulation results lower than the undisturbed one, even remaining over the designed depth. This condition depends on the severe channel modifications due to localized works, and does not affect the deepening tendency of the reach. In certain cross sections, works effects take a longer time to get the definitive navigation setting, like section 167, where an initial unfavorable situation is recuperated within the middle term scene.

Copyright © 2006 Taylor & Francis Group plc, London, UK

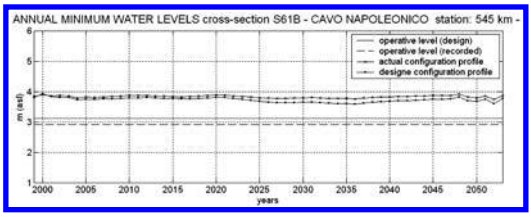


Figure 15. Cavo Napoleonico pump station operation analysis.

6.3 *Effects on existent water supply plants and pump stations*

Within the considered reach, six water supply plants are located. The effects of the designed works are evaluated by controlling if the minimum simulated water levels are in accordance with pumps operation conditions.

The operative water level of every structure has been evaluated considering both the design operation conditions and the minimum recorded water level at which pumps guaranteed their functionality.

Long and middle term simulation results does not show any relevant effect on existing structures, always keeping minimum water levels suitable for their activity.

Results are clearly influenced by hydrologic events, however long term differences between design and actual configuration are unimportant (about 10 cm in 50 years), and regulation works effects may substantially be neglected.

Figure 15 reports as an example the situation at the main pump station present in the analyzed reach.

6.4 *Effects on the Delta sediment feeding and on channel efficiency*

In order to evaluate the effect of regulation works on the sediment feeding to the Po Delta, there are two main aspects to account for: the possible changes in the stable setting of the downstream reach, and the variation of sedimentary fluxes directed to the delta.

For what concerns setting stability, let us consider the model structure: it applies sediment balance to single river reaches delimited by adjacent cross-sections. Referring to Figure 16 for the ending part of the computational scheme one can write:

$$V = \int_T Q_u\,dt - \int_T Q_i\,dt + E \qquad (19)$$

where V is the apparent volume which concludes the sediment balance over the time T, Q_i is the instant incoming discharge, Q_u is the instant outgoing discharge, E is the volume mass associated to external sediment exchanges over the time T, and T is the integration period.

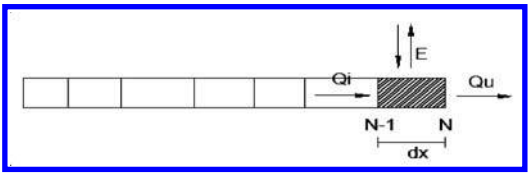


Figure 16. Sediment balance on downstream reach.

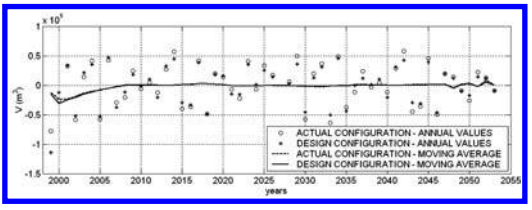


Figure 17. Annual volume balance referred to downstream reach.

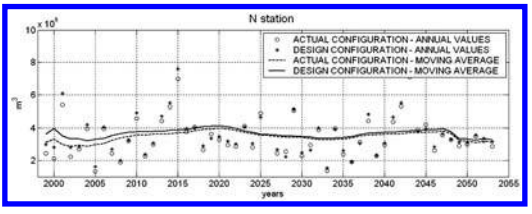


Figure 18. Outgoing apparent solid volume.

Assuming T equal to a year, the closing volume V can be calculated and represented year by year for the design and actual configuration.

Figure 17 does not show any appreciable variation in the long term sediment balance evolution trend of the Po downstream reach. The results can be easily interpreted referring to the moving average representation.

For what concerns the second aspect, let us consider the apparent solid volume coming out from the last model section (towards the delta):

$$V_u^i = \int_T Q_u^i\,dt \qquad i = 1,\ldots,55\,years \qquad (20)$$

The computed values are represented in Figure 18. The sediment flux increase rapidly decreases during simulation, passing from an initial value of about 28% to approximately 13% after five years, 5% after 10 years and 3% after 20 years.

The fundamental equilibrium condition featuring the downstream Po reach suggests a gradual spatial redistribution along the delta 70 km extension of the expected little disturbance effects.

6.5 *Effects on hydraulic risk*

The effects of designed works on flood stage, and therefore on hydraulic risk, have been evaluated by

Copyright © 2006 Taylor & Francis Group plc, London, UK

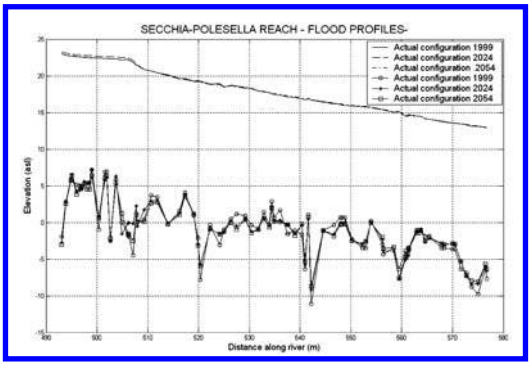


Figure 19. "94 + 51" scene applied to the actual river configuration: simulation of years 1999, 2024, 2054.

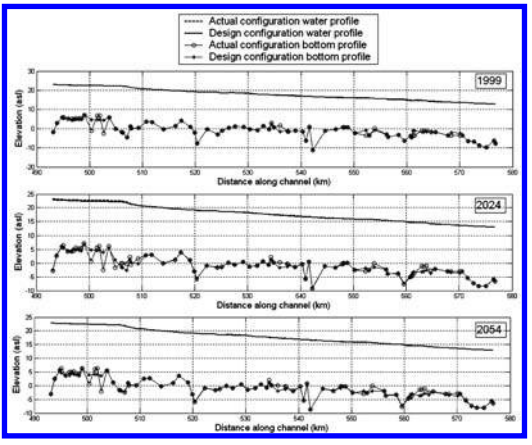


Figure 20. Comparison between design and actual configuration simulation results.

means of a quasi-stationary simulations set. The simulated reach starts from Secchia's mouth and ends at Polesella, including all the designed regulation works locations. It is long about 84 km and it is described by 80 cross-sections.

Simulations have been performed assuming the gradually varied flow, accounting for the reference flood discharge.

Three different phases of river evolution process have been analyzed, considering both design and actual configurations: the initial setting, referred to 1999, the middle (year 2024) and long term (year 2054) settings. Summarizing, the following configurations have been assumed:

- Actual configuration 1999, 2024, 2054
- Design Configuration 1999, 2024, 2054.

Model calibration has been based on the flood reference profile named "94 + 51" (AdPo, 2001), built on Po drainage basin behavior, including the observation of the two main flood vents of the last fifty years. The reference predicted discharge is 13000 m^3/s, the downstream boundary condition has been set as a constant level of 12.89 m above sea level at Polesella station, which corresponds to 13000 m^3/s.

After the calibration phase, a first simulations set has been carried out to see the flood profile evolution trend linked to the actual geometry configuration. Resulting profiles are shown in Figure 19, showing little variations with time.

Subsequently simulation have been performed using the design geometry. The three phases results are represented in Figure 20. By comparing computed profiles, the difference between the design and the actual setting is comprised within the range +10 cm\−25 cm (∼1\2% of local water depth).

The regulation works presence, therefore, does not produce any flood risk increase all over the considered simulation time.

7 CONCLUSIONS

The effect of designed regulation works on the river Po, planned to increase its navigability, have been investigated in order to determine effects on design navigation channel, on sediment balance and bottom evolution, on hydraulic risk and on solid mass fluxes to the river delta.

A mobile bed mathematical model has been used, based on a non-conservative form of shallow water equations and on Exner equation. For numerical implementation the four point Preissman implicit scheme has been used.

An accurate river system description, covering several important aspects, has been carried out. It includes a geometrical description, based on recent field surveys, hydrological and hydrometric data, sedimentological data and information about mining activities.

Simulation have been performed both for the actual and for the designed river setting, in order to have the possibility of comparing results. The geometrical configuration of the design river setting has been drawn following the usual indications about river regulation, and considering the designed works as already fully operative.

A sensitivity analysis has been conducted, in order to evaluate model response to two fundamental parameters variation, that is the amount of mining activities and the value of flow resistance. The analysis confirmed the reliability of the chosen parameters.

Simulation results have then been evaluated from various points of view. First of all, the works influence on the bed elevation evolution trend has been considered, resulting not to be relevant for what concerns the morphological trend.

Positive effects have been find out for what concerns navigation channel efficiency, while supply

Copyright © 2006 Taylor & Francis Group plc, London, UK

plants operating functionality is not affected along the whole examined reach.

The evaluation of the sediment balance in the downstream reach permits to affirm that also the morphological configuration of Po delta will be marginally influenced by regulation works.

Finally, the possible hydraulic risk variation has been investigated, checking that there will be no flood risk increase.

In conclusion, mathematical modeling is not only necessary to confirm individual design work geometrical effects (for which a 2-D model is required), but mainly to evaluate middle and long term effects produced on the overall river system.

ACKNOWLEDGEMENTS

Grateful thanks are due to Ing. Galvani and ARNI for their kindness and for the fruitful discussions.

REFERENCES

AdPo, 2001. Piano stralcio per l'assetto idrogeologico (PAI), Parma. (in Italian)

Benatti G., "Modello di evoluzione altimetrica del fiume Po. Analisi e previsioni di abbassamenti futuri" Graduating thesis, University of Ferrara, Engineering Department, A.A. 1999–2000. (in Italian)

Chaudry M.H., 1993. Open Channel Flow. Prentice Hall inc.

Lamberti A. & Schippa L., 1994. Studio dell'abbassamento dell'alveo del fiume Po: previsioni trentennali di abbassamento a Cremona; supplemento al n.3/4 Luglio-Dicembre 1994 di Navigazione Interna. (in Italian)

Lamberti A. & Shippa L., 1995, Experimental study on adaptation time of a regime alluvial channel. Proceedings VI International Symposium on River Sedimentation – New Delhi (India); November 1995. (in Italian)

Lamberti A. & Schippa L., 1996; Alluvial channel cross-section evolution. A physically based numerical model and experiments. EXCERPTA n. 10, anno 1996, pp. 115–156. (in Italian)

Lamberti A. & Schippa L., 2001. Studio dell'abbassamento dell'alveo del fiume Po: previsioni trentennali di abbassamento a Cremona, Aggiornamento 1993–2000. (in Italian)

Ministero dell'Agricoltura, 1990. Consorzio per il Canale Emiliano Romagnolo, Po AcquaAgricolturaAmbiente; vol.2, L'alveo ed il delta; Ed. il Mulino; Bologna. (in Italian)

Schippa L. & Pavan S., 2004. Modelling river bed evolution in natural alluvial streams. Environmental Hydraulics and Sustainable Water Management, Vol. II, pp 2107–2112.

Copyright © 2006 Taylor & Francis Group plc, London, UK

Sustainable navigation Rhine Delta branches, a reconnaissance of strategies

G.J. Akkerman & M.A. van Heereveld
Royal Haskoning Consultants, Architects and Engineers, Nijmegen, Netherlands

H.J. Barneveld
HKV Consultants, Lelystad, Netherlands

R.J. Smedes
Ministry of Transport, Public Works and Water Management, East Regional Directorate, Arnhem, Netherlands

ABSTRACT: To facilitate sustainable navigation for the Rhine Delta branches, extensive research is being carried out in the Netherlands. A first step of this research is a reconnaissance of potentially feasible fairway improvement strategies. This reconnaissance comprises a wide range of measures and their indicative hydraulic and morphological effects, against the background of ongoing degradation of the main channels and the adverse effects of climate change. Future intensification of fairway traffic calls for enlargement of the fairway channel. With the current maintenance strategy, dredging frequency and volumes will also strongly increase. Hence, apart from other dredging strategies, structural measures are considered so as to reduce the increasing maintenance dredging effort. The reconnaissance of potential measures includes efficacy, practical feasibility, maintenance efforts and economy. Attention is also paid on sustainability. The present paper presents a review of problems, general results and illustrates some potentially feasible measures.

1 BACKGROUND

Navigation at the largest rivers in The Netherlands, the Rhine/Waal system as a part of the Rhine Delta, see Figure 1, has been important for inland transport for some centuries. In the last decades, this importance is even strongly increasing due to further intensification of fairway traffic between the main ports of Rotterdam and Duisburg (Germany) in the years to come. A further growth of navigation commodities in the near future is to be expected. One of the short-term objectives of the project 'Sustainable Fairway Rhine Delta' is the enlargement of the present navigation channel dimensions from 150 m (width) and 2,50 m (depth) to 170 m (width) and 2,70 m (depth) at Agreed Low Discharge and the accompanying Lowest Available Depth (exceeded in 95% of time).

At the same time, ongoing degradation of the main channels and effects of climate change poses upcoming threats to navigability.

The degradation rate in the upper part of the Waal River amounted to 1 to 1.5 m in the last 50 years, although degradation seems to slow down more recently. Due to this bed degradation, problems may arise such as the access to locks, to mooring facilities and to river harbour entrances. In addition, the groynes near the banks are becoming over-exposed during high flows and under-exposed during low flows and groundwater levels drop. On the longer term, even the filled up stabilization of sharp outer bends (fixed layers), in order to maintain sufficient width, may form a barrier on the river bed, limiting the water depth during low flow conditions.



Figure 1. Impression of navigation on the Waal river at low flow.

Ongoing bed degradation in the Rhine/Waal system is, amongst others, a long term consequence of river

Copyright © 2006 Taylor & Francis Group plc, London, UK

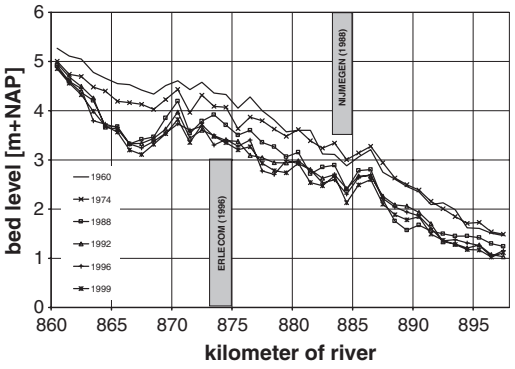


Figure 2. Degradation of part of the main channel of the Waal (longitudinal profile).

training works and flood plain occupation over the last century and a shortage of sediment influx from across the German border. The latter is due to normalisation works and subsidence of the riverbed in the upstream mining areas. This is not a problem that is exclusive to the Rhine Delta rivers: at present, many European rivers suffer severe bed degradation due to the same causes.

The bed degradation on the Waal is illustrated in Figure 2. It is clearly visible how the fixed layer Nijmegen has become more pronounced in time.

Present dredging estimates amount to 300,000 to 500,000 m^3 (measured in profile) on a yearly basis. The exact amount varies strongly over the years, mainly due to the variation in annual (peak) discharges. Recent figures are not known accurately, due to the recently negotiated performance contract with the dredging company. The planned enlargement of the navigation channel dimensions may increase the yearly maintenance dredging to about 1,000,000 m^3 as an order of magnitude, if other measures would not be implemented.

The last decade, the dredging strategy has been changed so as to mitigate the ongoing degradation: nowadays the dredged material is not removed from the river system anymore, but is dumped upstream at deeper locations at a minimum distance from the dredging site (1.5 km). In this way the dredged material is 'circulated'. Although less effective from a dredging point-of-view, it is a more sustainable methodology since it contributes significantly to mitigating the degradation.

2 RESEARCH OBJECTIVES

The present research focuses on an inventory of potential measures that may contribute to improvement of navigation and, at the same time, add to the sustainable development of the river system. An important item for sustainability is reduction of the degradation trend.

The inventory of measures has been based on the outcome of workshops with experts from different disciplines.

In order to elaborate the potential measures to a practical level, the measures have been detailed to a level of functional design. This allowed also providing a rough estimate of the costs involved. Different measures may have a total different distribution of costs during their life cycle: hence, the net present value (NPV) over a 50 years period has been assessed, including maintenance and intermediate reconstruction (if required). The research is to provide directions for further elaboration of sustainable fairway improvement measures and combinations thereof in a subsequent step.

3 RESEARCH METHOD

The working methodology for this research was as follows. At first, a brief analysis was made of the present and future major navigation bottlenecks and the present main measure to maintain sufficient depth and width: maintenance dredging. Figures 3 and 4 illustrate some major bottlenecks on the Waal River.

Navigation bottlenecks can be grouped into two types:

1) Structural bottlenecks which mainly occur in sharp bends and which sustain after high flows recede. The position of these bottlenecks is rather stable. Because of the vast extent of the dredging activities required to maintain sufficient width and depth, this dredging is denoted 'profile dredging', see Figure 3.
2) Bottlenecks which occur during floods, as well as during low and medium flows on a more erratic basis, due to e.g. retarded scour and large bed forms (sand waves). Dredging these local shoals is dispersed and is denoted 'occasional dredging'. While the first type can be checked quite well after the floods recede, the second type has to be monitored on a (nearly) day-to-day basis, see Figure 4.

Next a framework for analysis of potential improvement measures was drawn up (see also [2] and [3]).

The *potential efficacy* was assessed on the basis of engineering judgement, within a team of nautical and morphological experts.

As regards the *impacts* a distinction was made between: impacts on flood levels, change of the discharge distribution at the bifurcation points and interaction with other planned river measures.

Sustainable issues related to the effect on bed degradation, adaptability (=preservation of functionality)

Copyright © 2006 Taylor & Francis Group plc, London, UK

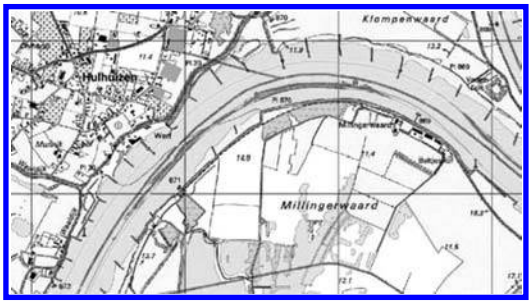


Figure 3. Profile dredging locations near sharp bend in the Waal River (coloured bands).



Figure 4. Occasional dredging locations on the Waal river (red dots).

in case of further climate change, maintenance and navigation hindrance.

The *practical feasibility* addresses the practical workability to realize the measure.

Risk and uncertainties, other than stemming from the realization, relate to e.g. the probability of failure during the lifetime, uncertainties on efficacy, adverse impacts and sustainability.

A *rough cost assessment* was carried out to explore the economical feasibility.

It should be remarked that the measures were judged separately: combinations of measures were not explored yet in this phase of the research.

4 TYPES OF MEASURES

Two groups of measures have been considered:

1) *Sediment management measures*, e.g. dredging of shoals, levelling of scour holes and sediment nourishment;
2) *River training measures*, e.g. application of bed groynes or fixed layers, adaptation of groynes and roughness elements in inner bends.

Some twenty preliminary concepts of individual measures have been identified and explored in the present reconnaissance study. These measures have been analyzed against the background of the aforementioned framework for analysis.



Figure 5. Example of nourishment of external bed material.

Some typical measures are indicated hereafter:

Sediment management measures

- Alternative dredging strategy with dumping a part of the dredged material farther upstream to compensate for the sediment transport deficit upstream;
- Filling of sharp outer bends and reduction of transport capacity by applying 'Smart Soils' technology;
- Dredging of inner bends and nourishment of external coarse material in outer bends, see Figure 5;
- Intensification of the stirring action of ships sailing close to shallows;
- Suppletion of a thin semi-stable upper layer to control the bed degradation;

Structural measures

- Continuation of the proven methodology of applying fixed layers in sharp outer bends;
- Filling up of scour holes near groynes ('flames') and scour holes downstream of present fixed layers, see Figure 6;
- Continuous stable layer along the whole Rhine/Waal river system;
- Bank alignment measures: a 'flow guidance dam' to close-off groyne sections in inner bends at low flows; a flow guidance structure for groyne heads; a 'turbulence dam' to promote erosion in the inner bends.

Some of these measures are proven technology, others however are highly innovative.

5 GENERAL FINDINGS

The current dredging strategy would lead to high efforts and costs for maintaining the enlarged

Copyright © 2006 Taylor & Francis Group plc, London, UK

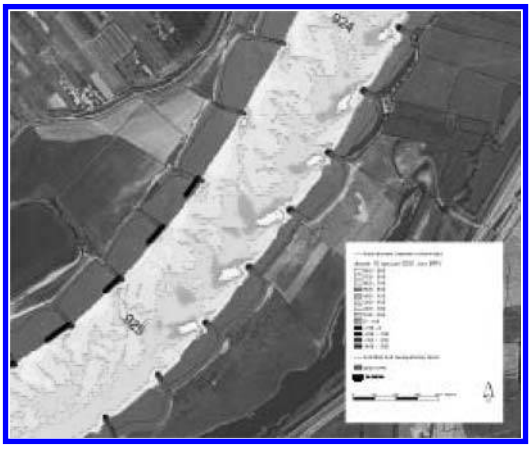


Figure 6. Typical erosion pattern near groynes.

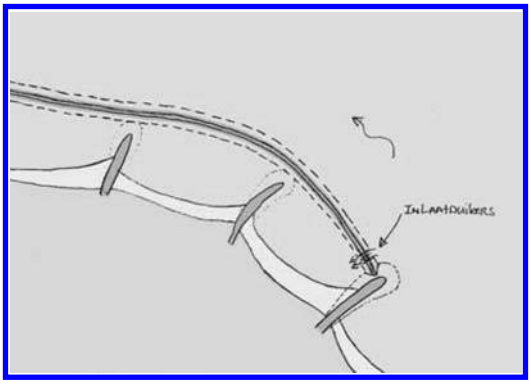


Figure 7. Top view of the flow guidance dam (upstream section).

navigation channel in the new situation. The net present value of these activities could be well over € 200 M. Moreover, hindrance to navigation will be significant. The additional costs for the alternative dredging strategy with dumping of dredged material farther upstream will hardly increase this cost figure but appears to be much more sustainable.

The efficacy of other large-scale sediment management measures, such the as suppletion of a thin semi-stable upper layer, seems to be highly uncertain. At the same time, the savings on the anticipated dredging is not known as well. Other measures, e.g. the deployment of vessels to increase the stirring up action are far beyond practical application. Local measures, i.e. nourishment of coarse (semi-stable) materials in outer bends may be feasible and economical: the net present value for two major bends at the Waal indicate a cost figure of around € 20 M.

The most efficient measures may still be of the structural type, especially when applied locally in bends. These measures may contribute significantly to the reduction of maintenance dredging. Other promising measures are various bank alignment measures. Hereafter, some of these will be highlighted. The efficacy of filling up present scour holes is uncertain, although this measure may contribute well to reducing 'occasional dredging' in an economical way: the net present cost is nearly € 20 at the major occasional dredging sites of the Waal.

Sustainability of the structural measures is especially positive in terms of durability and low cost of maintenance. However, they do not actively mitigate bed degradation. Therefore, structural measures should be combined with sediment management measures, e.g. the alternative dredging option, supported by nourishment with external coarse bed material.

6 ILLUSTRATION OF TWO PROMISING BANK ALIGNMENT MEASURES

The study indicates a number of potentially feasible measures. For illustration purposes, two concepts deemed feasible are described hereafter in more detail.

6.1 *Flow guidance dam*

The flow guidance dam is a dam that is installed in front of the present groynes, see Figures 7 and 8, and serves different purposes:

- Additional resistance at low flows, so as to increase low water levels;
- Reduction of the irregular riverbed patterns in the vicinity of groynes;
- Shelter to the groyne beach section so as to promote environmental conditions.

To avoid adverse effects on flood water levels, the adjoining groynes may need to be removed partly, e.g. by lowering of the crest level.

It is anticipated that this type of flow guidance will give significant savings on the quantity of profile dredging.

The anticipated costs (NPV) of this guidance dam are relatively modest: € 2.5 M per inner bend of 2 km length.

6.2 *Flow guidance structure near groyne heads*

This structure, as shown in Figure 9, is meant to guide the flow more smoothly during low flows in inner bends and, at the same time, provide additional resistance to increase low water levels (these functions do compare with the flow guidance dam).

To promote a more regular flow pattern near the groyne head, the structure consists of separate poles.

Copyright © 2006 Taylor & Francis Group plc, London, UK

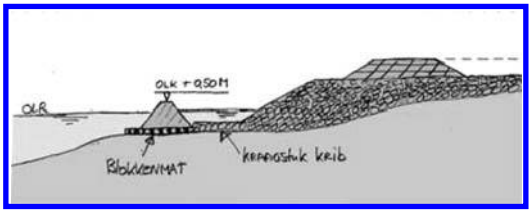


Figure 8. Sketch of the flow guidance dam near a groyne.

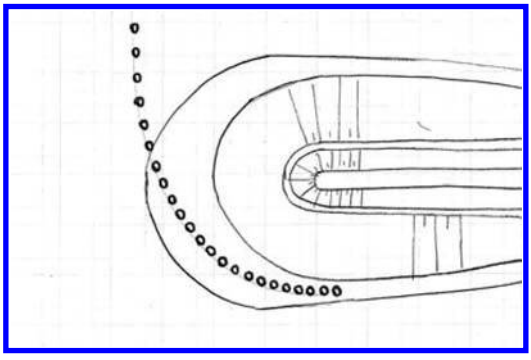


Figure 9. Top view of the 'spoiler' near a groyne head © Royal Haskoning.

The poles introduce small-scale turbulence that disturbs the irregular flow separation around the groyne head and thus impose a 'spoiler' action. The height of the poles will be modest: the top level of the poles may go down from groyne level to around Least Available Depth + 0.5 m at the downstream end. It is likely that adverse impacts on flood water levels can be avoided.

The anticipated costs of this concept (NPV) are around € 5 M for two major sharp bends in the Waal River.

7 CONCLUSIONS

The present study points out that adaptation of current practices on maintaining and extension of the nautical profile may be needed for safeguarding sustainable and economical solutions in the future. New dredging strategies, nourishment of external (coarse) bed material and innovative bank alignment measures can contribute to reduce future maintenance dredging.

Predicting maintenance dredging for future scenario's was proven to be complex and uncertain. Further study is needed.

The potential measures need further detailing and in-depth morphological and hydraulic research of their adequacy in reducing maintenance dredging. Such research may comprise field pilots, scale model investigations, desk studies and mathematical model studies. In addition, lessons learned from field pilots carried out in the German part of the Rhine River should be incorporated.

REFERENCES

Akkerman, G.J., M.A. van Heereveld, et al (2004): Groyne optimisation and river hydrodynamics, 2nd International Conference on Fluvial Hydraulics, Riverflow 2004, June 2004, Napoli, Italy.

Havinga H.H. (2005): Sustainable waterways within the context of navigation and flood management, 3rd International Symposium on Flood Defence, 25–27 May 2005, Nijmegen, the Netherlands.

Havinga H.H. (2006): Sustainable waterways within the context of navigation and flood management, 31st PIANC Congress, May 14–18, 2006, Estoril, Portugal.

Van der Wal M., G.J. Akkerman, J.M.T. Stam (2005): Multifunctional river groynes: Providing nautical depth and mitigation of flood levels, 3rd International Symposium on Flood Defence, May 2005, Nijmegen, the Netherlands.

Copyright © 2006 Taylor & Francis Group plc, London, UK

C.3. River habitat management and restoration

Copyright © 2006 Taylor & Francis Group plc, London, UK

Mathematical modeling of the biogeochemistry of dissolved and sediment associated trace metal contaminants in riverine systems

Arash Massoudieh, Fabian A. Bombardelli, Timothy R. Ginn & Peter G. Green
Dept. of Civil and Environmental Engineering, University of California, Davis, CA, USA

ABSTRACT: A quasi two-dimensional model is presented which is able to simulate biogeochemical processes of metal contaminants in river sediments. The model takes into account horizontal transport of dissolved and particle associated species and the effects of erosion and resuspension on the sedimentary chemistry, using coupled advection-dispersion-reaction equations for both suspended sediments and dissolved species. Transport of species in the sediments is modeled using a set of vertical one-dimensional sub-models which take into account the reactive transport of chemicals, burial, sorption/desorption to/from the solid phase, and diffusive transport of species. A kinetic reversible assumption is used to simulate the mass exchange between suspended sediments and bulk water, as well as the mass exchange between bed-sediments and pore-water. The model is applied to simulate the methylation of mercury in a hypothetical river reach.

1 INTRODUCTION

Biogeochemical processes in sediments have an important role on the mobility and bioavailability of toxic trace metals in aquatic ecosystems, as well as on the cycling of other elements, including carbon, nitrogen and sulfur. The latter elements have in turn important implications for plant productivity and human health (Gadd, 2004). The state of metals in terms of mobility depends highly on the organisms involved and the oxidation state of the environment. The role of microorganisms in the metal speciation and mobility has received more attention recently. As examples of the effects microbial activities on the mobility of metals, it is possible to mention reduction of Fe(III) to Fe(II), Mn(IV) to Mn(II), Cr(VI) to Cr(III), U(VI) to U(IV) and biomethylation of Hg, As, Se, Sn, Te and Pb.

There have been several recent modeling efforts to predict biogeochemical cycles in sediments in lakes and coastal zones (Berg et al., 2003; Boudreau, 1996; Van Cappellen and Gaillard, 1996; Van Cappellen et al., 1993; Van Cappellen and Wang, 1996). In all of these efforts, a one-dimensional column of sediments with fixed or varying boundary conditions at the surface has been adopted in order to model the diverse processes; in other words, the effects of horizontal heterogeneity and hydrodynamic transport of dissolved compounds, sediments, and sediment associated species have been disregarded. This approach may be suitable for water bodies such as lakes and coastal zones, with small lateral heterogeneity; however it does not work well in rivers where the horizontal transport of species in the water body is of critical importance in the cycling of elements. In a riverine system, transport in the water body is responsible for supplying many compounds such as oxygen and sediments containing organic carbon to the bed surface. Also, hydrodynamic transport processes in the water body can influence the redox biogeochemistry of the sediments by resuspending the top sediments and exposing the lower levels to the water column with different chemical composition. For example tidal cycles usually have a very crucial influence on the redox state in tidal marshlands (Neubauer et al., 2005; Twilley and Rivera-Monroy, 2005).

In this paper, a multi-scale model is presented in order to couple the hydrodynamic transport of species in the river with the diffusive transport in the sediments. This model considers transport of dissolved and particle associated species in rivers as well as transport within the sediments due to molecular diffusion, bioturbation (due to activities of benthic organisms), burial and resuspension. The model can be used for any reaction network with a high degree of complexity in reaction kinetics. An application of the model is presented by performing a demonstration simulation on the methylation of mercury in a hypothetical river reach.

Copyright © 2006 Taylor & Francis Group plc, London, UK

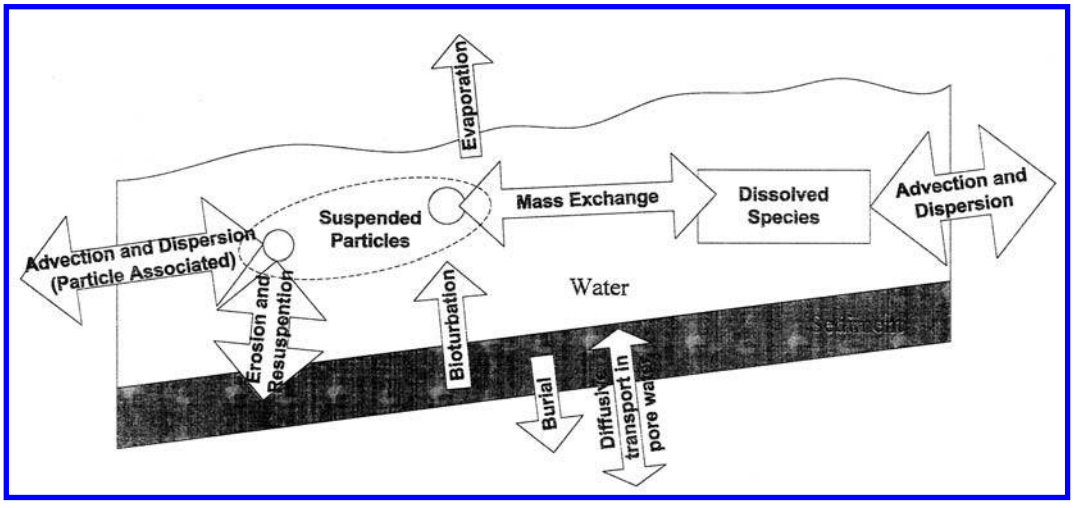


Figure 1. Physical processes considered in the model.

2 MODEL DESCRIPTION

2.1 *Physical transport component*

The multicomponent and multiphase model includes one-dimensional advective-dispersive transport of both dissolved and particle-associated species, as well as suspended particles in the river. The river module is fully coupled with a series of one-dimensional diffusive transport columns representing active bed sediments (See Fig. 1). Bioturbation and burial of species are modeled in the bed sediments using a two-domain diffusive transport process.

Bed sediments exchange species with the water column via both deposition and resuspension of chemical species attached to the grains, and through a diffusive boundary layer between sediments and water column. First order kinetic reversible sorption is assumed for the exchange between solid phase and bulk or pore water in the water column or bed sediments respectively.

A one-dimensional model is used for the transport of species in the river. For each species being modeled a set of two coupled 1-D advection-dispersion equations, one for dissolved species and one for particle associated species are used, respectively:

$$\frac{\partial(C_i)}{\partial t}+\frac{\partial(vC_i)}{\partial x}=\frac{1}{A}\frac{\partial}{\partial x}\left(D_h A\frac{\partial C_i}{\partial t}\right)+k_b\frac{P}{A}\left(c_i(0)-C_i\right)-C_s k_r\left(K_D C_i-S_i\right)+R_i+\frac{q_{in}}{A}\left(C_{i,in}-C_i\right)+k_{at}\left(C_{i,at}-C_i\right) \quad (1)$$

$$\frac{\partial C_s S_i}{\partial t}+v\frac{\partial C_s S_i}{\partial x}=\frac{1}{A}\frac{\partial}{\partial x}\left(D_s A\frac{\partial C_s S_i}{\partial x}\right)+Er.w_p.\frac{P}{A}s_i(0)-w_p r_0.\frac{P}{A}.C_s S_i+\frac{q_{in}}{A}\left(C_{s,in}S_{in}-C_s S_i\right)+k_r C_s\left(K_D C_i-S_i\right) \quad (2)$$

in which, t(s) is time, x(m) is the longitudinal river axis, $C_i(\mu g/mL)$ is the dissolved concentration of chemical i in bulk water, v(m/s) is the velocity along the river, $D_h(m^2/s)$ is the mechanical dispersion coefficient along the river axis, $k_b(s^{-1})$ is the sediment-water exchange coefficient for the dissolved species, $c_i(0)(\mu g/ml)$ is the pore-water concentration at the topmost layer of sediments, P(m) is the wetted perimeter of the stream, $k_r(s^{-1})$ is the mass exchange coefficient between suspended particles and water, $C_s(g.mL^{-1})$ is the concentration of suspended particles, K_D(L/g) is the water-solid distribution coefficient, $S_i(\mu g/g)$ is the sorbed phase concentration, $R_i(\mu g/mL.s)$ is the sum of reaction terms for species i, $q_{in}(m^3s^{-1})$ is the amount of lateral water flux, $C_{i,in}(\mu g/mL)$ is the concentration of species i in the lateral flux, $k_{at}(s^{-1})$ is the atmospheric exchange rate coefficient, $D_s(m^2/s)$ is the dispersion coefficient for suspended particles, $Er(g.m^{-3})$ is the entrainment coefficient, w_p(m/s) is particles fall velocity in the water column, r_0 is the ratio between the concentration of suspended particles at the bed and the average concentration of suspended particles, and $C_{s,in}(\mu g/mL)$ is the concentration of suspended particles in the lateral inflow. In Eq. (1) the second term in the left hand side represents the advective transport of dissolved species; the first term of

Copyright © 2006 Taylor & Francis Group plc, London, UK

the right hand side is the mechanical dispersion; the second term is the exchange of species with benthic sediments; the third term is the exchange of species with suspended sediments; the fifth term is lateral flux of chemicals; and the last term represents exchange of species with atmosphere. In Eq. (2) the second term from the left hand side represents advection of chemicals sorbed to particles due to movement of particles, the first term from the right hand side represents the effect of mechanical dispersion of particles, the second and third terms simulate effects of resuspension and erosion respectively, and forth and fifth terms are respectively lateral inflow of chemical species associated with suspended solids and mass exchange with bulk water.

The one-dimensional transport model described above is coupled with the transport of chemical species in bed sediments. The horizontal diffusive transport of chemicals in bed sediments is ignored due to the larger horizontal scale with respect to the vertical scale. In addition, it is assumed that the effects of bioturbation can be simulated using a diffusive model with a modified diffusion coefficient. Therefore the equations governing the diffusive transport of chemicals in the bed sediments can be written as:

$$\frac{\partial c_i}{\partial t} + w\frac{\partial c_i}{\partial z} = \frac{1}{\theta}\frac{\partial}{\partial z}\left((D_m + D_B)\theta\frac{\partial c_i}{\partial z}\right) + \frac{B_d k_r}{\theta}\left(K_D c_i - s_i\right) + R_i \quad (3)$$

$$\frac{\partial s_i}{\partial t} + w\frac{\partial s_i}{\partial z} = \frac{1}{B_d}\frac{\partial}{\partial z}\left(D_B B_d \frac{\partial c_i}{\partial z}\right) - \frac{B_d k_r}{\theta}\left(K_D c_i - s_i\right) + R_{s,i} \quad (4)$$

where $c_i = c_i(x,z,t)$ is the dissolved concentration in pore water in the bed sediments, $s_i(\mu g/g)$ is the mass concentration of sorbed species, B_d(g/ml) is the bulk density of the sediment materials, D_b(cm^{2}s^{-1}) is the biodiffusion coefficient, D_m(cm^{2}s^{-1}) is the molecular diffusion coefficient of the species in the pore water, θ is the porosity of the bed material, w(cm.s^{-1}) is the burial velocity which depends on the rate of accumulation of newly deposited sediments at the bed surface, and $R_{s,i}$ is the production or elimination of species i due to total intra-phase reaction rate. If we assume that porosity (compaction) is solely a function of depth, the burial velocity (which is the shift occurred in the position of a grain particle in a coordinate system with its origin fixed on the bed surface due to deposition or erosion) can be approximated using the following equation:

$$w(z) = \frac{C_s w_f - Er.C_s}{B_d(z)} \quad (5)$$

in which $C_s w_f$ is the deposition rate and B_d is assumed to be only dependent on depth or the weight of materials above it.

Boundary conditions for equation (3) can be written as:

$$(D_m + D_B)\theta\frac{\partial c_i}{\partial z} = k_b(c_i - C_i) \quad \text{at z=0} \quad (6)$$

$$\frac{\partial c_i}{\partial z} = 0 \quad \text{at z=L} \quad (7)$$

and for equation (4):

$$s_i\big|_{z=L} = 0 \ \text{for w<0} \quad \text{erosion} \quad (8)$$

$$s_i\big|_{z=0} = S_i \ \text{for w>0} \quad \text{deposition} \quad (9)$$

2.2 *Numerical techniques*

A first order in space with an implicit Crank-Nicholson time weighing finite difference method is used to solve coupled equations (1) and (2) for each species. A similar approach is also used to model the vertical transport of chemicals in each column associated with one grid cell of water column (Eqs. 3 and 4). The coupling between the water column and sediment components is performed explicitly using the boundary conditions defined in equations (6)–(9). The reaction terms are computed explicitly as source and sink terms. Fractional time steps are used to simulate fast reaction rates. In this way, a different time step is chosen automatically by the model based on the variation of each reaction term.

3 MODEL APPLICATION (BIOMETHYLATION OF MERCURY IN RIVER)

In order to test the model, it was applied to simulate methylation of mercury in a vertical sediment column and also a hypothetical river reach. For this purpose, the reaction network for the cycling of oxygen, nitrogen, sulfur, iron and manganese was adopted from a previous work (VanCappellen and Wang, 1996) with some simplifications; also a simplified reaction network was built for methylation of mercury. Methylation of mercury is thought to be mainly caused by Sulfate Reducing Bacteria (SRB) (Compeau and Bartha, 1985; Gilmour and Henry, 1991; Winfrey and Rudd, 1990) and thus a relationship is for methylation rate that takes into account the SRB activity was proposed.

3.1 *Microbially-mediated transformations model*

In order to compute the rate of methylation of mercury the activities of SRBs and concentration of H_2S are required. For this purpose, the fate and transport of some major species affecting the activities of

Copyright © 2006 Taylor & Francis Group plc, London, UK

SRB such as O_2, NO_3, Fe and Mn needs to be modeled as well. Since mercury concentration is usually small compared to other major components such as organic matter, oxygen, nitrate, sulfate, iron, etc., the effect of mercury reactions on the concentration of major components was ignored. The reaction network was adopted from recent models (Hunter et al., 1998; VanCappellen and Wang, 1996) with some slight modifications and simplifications. Monod type kinetics with inhibition was used for the oxidant inhibitor multipliers as suggested by Boudreau, 1996; Van Cappellen et al., 1993, (Eq 10a–f). The complete reaction network used in the model can be seen in figure 2.

$$R_1 = -k_1[OM]\frac{[O_2]}{K_{O2}+[O_2]} \quad (10\text{-a})$$

$$R_2 = -k_2[OM]\frac{[NO_3]}{K_{NO3}+[NO_3]}\frac{K'_{O2}}{K'_{O2}+[O_2]} \quad (10\text{-b})$$

$$R_3 = -k_3[OM]\frac{[MnO_2]}{K_{MnO2}+[MnO_2]}\frac{K'_{NO3}}{K'_{NO3}+[NO_3]}\frac{K'_{O2}}{K'_{O2}+[O_2]} \quad (10\text{-c})$$

$$R_4 = -k_4[OM]\frac{[FeOOH]}{K_{FeOOH}+[FeOOH]}\frac{K'_{MnO2}}{K'_{MnO2}+[MnO_2]}\frac{K'_{NO3}}{K'_{NO3}+[NO_3]}\frac{K'_{O2}}{K'_{O2}+[O_2]} \quad (10\text{-d})$$

$$R_5 = -k_5[OM]\frac{[SO_4]}{[SO_4]+K_{SO4}}\frac{K'_{FeOOH}}{K'_{FeOOH}+[FeOOH]}\frac{K'_{MnO2}}{K'_{MnO2}+[MnO_2]}\frac{K'_{NO3}}{K'_{NO3}+[NO_3]}\frac{K'_{O2}}{K'_{O2}+[O_2]} \quad (10\text{-e})$$

$$R_6 = -k_6[OM]\frac{[CH_4]}{[CH_4]+K'_{CH4}}\frac{K'_{SO4}}{[SO_4]+K'_{SO4}}\frac{K'_{FeOOH}}{K'_{FeOOH}+[FeOOH]}\frac{K'_{MnO2}}{K'_{MnO2}+[MnO_2]}\frac{K'_{NO3}}{K'_{NO3}+[NO_3]}\frac{K'_{O2}}{K'_{O2}+[O_2]} \quad (10\text{-f})$$

Secondary reoxidation reactions are assumed to obey simple rate laws as K[reactant1][reactant2] as done by VanCappellen and Wang, (1996).

3.2 *Mercury partitioning and speciation reactions*

As mentioned above, Sulfate-Reducing Bacteria (SRB) have been identified as a primary agent for methylation of mercury. Also recent studies have illustrated that, production of methylmercury is inhibited by accumulation of sulfide, the by-product of activities of SRBs (Gilmour and Henry, 1991). This can be explained by the fact that high concentrations of sulfide will convert a large portion of mercury into HgS and reduce the amount of reactive mercury available for methylation. Therefore the following simplified geochemical reaction network was utilized to simulate mercury cycling:

$$HgS \xleftarrow{k_{Hg,1},k_{Hg,2}} Hg^{2+} + S^{2-} \quad (11\text{-a})$$

$$Hg^{2+} + DOC \xrightarrow{SRB} MMHg \quad (11\text{-b})$$

$$MMHg \xrightarrow{k_d} Hg^{2+} \quad (11\text{-c})$$

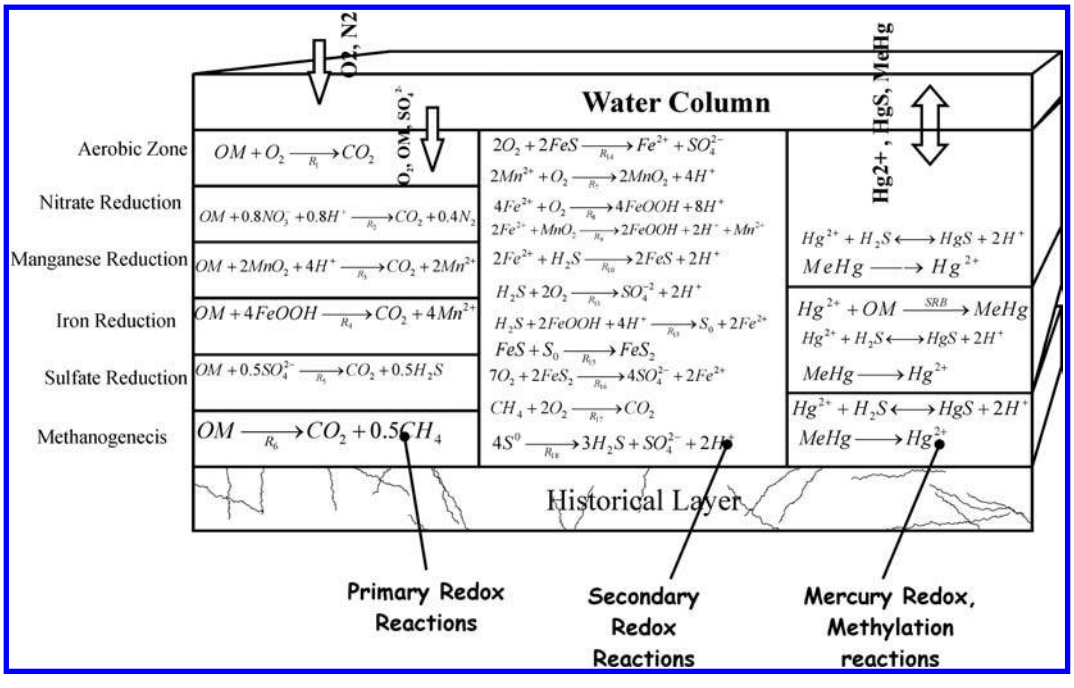


Figure 2. Reaction network used for bacteria mediated biogeochemical transformations of mercury.

Copyright © 2006 Taylor & Francis Group plc, London, UK

$$Hg^{2+} \xrightarrow{k_r} Hg^0 \qquad (11\text{-d})$$

$$Hg^0 \xrightarrow{k_o} Hg^{2+} \qquad (11\text{-f})$$

Because oxidation, reduction and demethylation of mercury are known to be both biotically and abiotically mediated in this work a mass action kinetic rate was used to simulate these collective processes. Methylation rate on the other hand is assumed to be a function of the activity of SRBs and so single Monod kinetics are used. Therefore the system of differential equations describing the mercury reaction network can be written as:

$$\frac{\partial[HgS]}{\partial t} + \ell([HgS]) = \frac{\theta}{B_d} k_{Hg,r}[Hg^{2+}][H_2S] - k_{Hg,f} \qquad (12\text{-a})$$

$$\frac{\partial[Hg^{2+}]}{\partial t} + \ell([Hg^{2+}]) = -k_{Hg,r}[Hg^{2+}][H_2S] + \frac{B_d}{\theta} k_{Hg,f} - k_m[SRB]\frac{OM}{K_{OM}+OM}[Hg^{2+}] + k_d[MMHG] - k_r[Hg^{2+}] + k_o[Hg^0] \qquad (12\text{-b})$$

Table 1. Reaction rate parameter values.

k_1 (yr^{-1})	9.26×10^{-2}(a)	k_2 (yr^{-1})	9.26×10^{-2}(a)
k_3 (yr^{-1})	9.26×10^{-2}(a)	k_4 (yr^{-1})	9.26×10^{-2}(a)
k_5 (yr^{-1})	9.26×10^{-2}(a)	k_6 (yr^{-1})	9.26×10^{-2}(a)
k_7 (yr^{-1})	19.86(a)	k_8 (yr^{-1})	3.47×10^{-1}(a)
k_9 (yr^{-1})	$3.47 \times 10^{+1}$(a)	k_{10} (yr^{-1})	2.37×10^{-3}(a)
k_{11} (yr^{-1})	$1.48 \times 10^{+1}$(a)	k_{12} (yr^{-1})	1.61×10^{-1}(a)
k_{13} (yr^{-1})	6.31×10^{-2}(a)	k_{14} (yr^{-1})	4.42×10^{-2}(a)
k_{15} (yr^{-1})	1.89×10^{-1}(a)	k_{16} (yr^{-1})	7.25×10^{-3}(a)
k_{17} (yr^{-1})	9.46×10^{-3}(a)	k_{18} (yr^{-1})	Not used
k_{19} (yr^{-1})	1.70(a)	k_{20} (yr^{-1})	5.68×10^{-1}(a)
k_{21} (yr^{-1})	3.15(a)	$k_{Hg,f}$(yr^{-1})	1.2×10^{-5} (estimated)
$k_{Hg,f}$ (yr^{-1})	1.2×10^{-5} (estimated)	$k_{Hg,r}$ (yr^{-1})	1.58×10^{-4}
k_m (yr^{-1})	20.1(b)	k_d (yr^{-1})	1.65(b)
k_r (yr^{-1})	11(b)	k_r (yr^{-1})	11(b)
k_0 (yr^{-1})	8.76×10^2(b)		

a. (Berg et al., 2003), b. (Kim et al., 2004)

$$\frac{\partial[MMHg]}{\partial t} + \ell([MMHg]) = k_m[SRB]\frac{OM}{K_{OM}+OM}[Hg^{2+}] - k_d[MMHg] \qquad (12\text{-c})$$

$$\frac{\partial[Hg^0]}{\partial t} + \ell([Hg^0]) = k_r[Hg^{2+}] - k_o[Hg^0] \qquad (12\text{-d})$$

In the above equations, ℓ is the transport operator representing all processes described in the previous section, $k_{Hg,r}$, $k_{Hg,f}$ are rates of dissociation and production of cinnabar (HgS), [SRB] is the activity of sulfate reducing bacteria which will be discussed later, k_m, and k_d are methylation and demethylation rate coefficients respectively, and k_r and k_o are respectively reduction and oxidation rate coefficients for elemental mercury.

For testing the model a demonstration simulation was performed using parameters obtained from literature on a hypothetical river reach. A 30 cm-deep bed-sediment layer was considered. The parameters used for the simulation are listed in tables 1 to 3. Biodispersion was simulated as exponentially decreasing with depth and the compaction effect was taken into account in calculating the diffusion coefficient, dry density and porosity of sediment vs. depth. The profiles were obtained by running the model for a 25 day time frame starting with uniform concentrations of species with depth. Figure 3 shows the concentration of primary components and mercury species in the river. It is noticed that oxygen and nitrate diminish quickly with depth. Also MnO_2 and FeOOH disappear within the top 10 cm of the column. On the other hand the sulfate concentration does not vanish in the top 30 cm due to its high concentration at the surface and the sulfate reduction condition can be seen at depth higher than 10 cm in the sediments (figures are not included). Concentrations of Mn^{2+}, Fe^{2+}, H_2S, FeS, S^0, Hg^{2+}, Hg^0, and MeHg were assumed to be zero in the upstream boundary. The initial concentration of total mercury was assumed to be uniform and equal to 1 nmol/g of sediments which is close to typical values found in San Fransisco Bay (Choe et al., 2004). It is noticed that methyl mercury is mainly produced in the depths greater than 7 cm in the anoxic layers. The magnitude of MeHg produced in the model also

Table 2. Parameters used for the demonstration calculation on a one-dimensional sediment column.

Parameter	Value
Porosity	$0.631 + 0.207e^{-1.02z}$
Density (g/cm^3)	2.41 g cm^{-1}
Burial velocity at the surface or sedimentation rate (cm/yr)	0.12 cm $year^{-1}$
Maximum Biodiffusion coefficient at the surface (cm^2/yr)	$4.6 \times 10^{-6} cm^2 s^{-1}$

Reference : (Berg et al., 2003)

Copyright © 2006 Taylor & Francis Group plc, London, UK

Table 3. Chemical and physical parameters for species used in the model.

	D(cm^2s^{-1})	K′(limiting concentration)	Bulk water concentration	Initial Concentration	Partitioning coefficient (K_D)	Source
$[O_2]_{ini}$	11.7×10^{-6}	20(μmol/mL)	389(μmol/mL)	389(μmol/mL)	N/A	a
$[OM]_{ini}$	N/A	N/A	250000(μmol/gr)	250000(μmol/gr)	N/A	a
$[NO_3^{-1}]_{ini}$ (μmol/ml)	9.8×10^{-6}	N/A	6.2(μmol/mL)	6.2(μmol/mL)	N/A	a
[N2]	9.5×10^{-6}	N/A	669(μmol/mL)	669(μmol/mL)	N/A	a
[H2S]	8.7×10^{-6}	N/A	0(μmol/mL)	0(μmol/mL)	N/A	a
$[SO_4^{-2}]$	5.0×10^{-6}	1600(μmol mL^{-1})	7300(μmol/mL)	7300(μmol/mL)	N/A	b,a
$[MnO_2]$	N/A	10 (μmol g^{-1})	333(μmol/gr)	333(μmol/gr)	N/A	a
$[Mn^{2+}]$	3.1×10^{-6}	N/A	1(μmol/mL)	1(μmol/mL)	28 cm^3g^{-1}	a
[FeOOH]	N/A	20 (μmol g^{-1})	625(μmol/gr)	625(μmol/gr)	N/A	a
$[Fe^{2+}]$	3.4×10^{-6}	N/A	0	0	268 cm^3g^{-1}	a
[HgS]	N/A	N/A	0	1(nmol/gr)	6218 cm^3g^{-1}	c
$[Hg^{2+}]$	5×10^{-6}	N/A	0	0	N/A	c
[MeHg]	5×10^{-6}	N/A	0	0	N/A	c
$[Hg^0]$	5×10^{-6}	N/A	0	0	N/A	c

a. (Berg et al., 2003) b. (VanCappellen and Wang, 1996), c. (Choe et al., 2004)

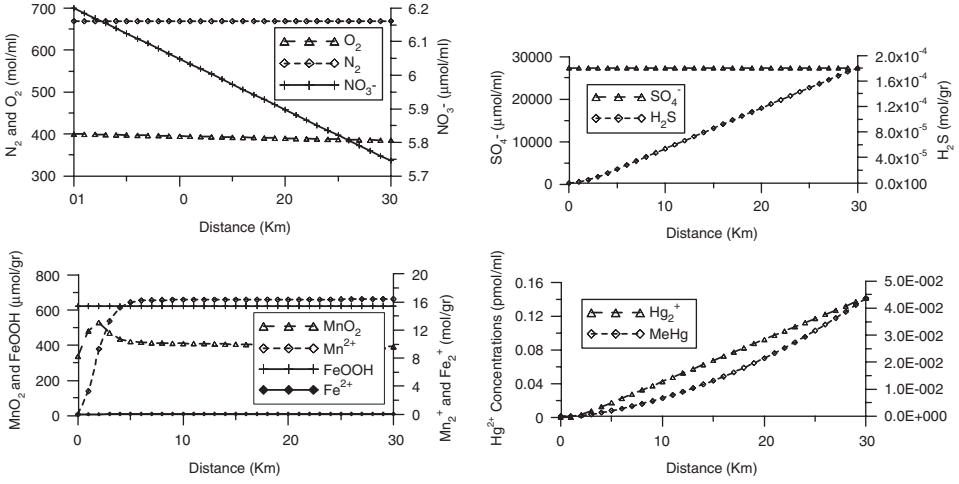


Figure 3. Profiles of species in the river after 25 days of simulation.

conforms with the values found by (Choe et al., 2004) in San Fransisco Bay.

The reach was assumed to have 30 km river length with 5 m depth. The erosion rate was assumed to be constant and equal to 2.16 g/cm^2/day and the deposition rate (fall velocity) was considered to be 0.5 cm/s. The inflow concentration of mercury was assumed to be zero so the only source of mercury was the contaminated sediments. Also in this case oxygen and nitrogen was assumed to be supplied to the water column through kinetic first order Henry's law. Figure 3 shows the variation of concentration of major species in the model. As it can be seen, the concentrations of dissolved oxygen and nitrogen are almost constant in the river reach due to high rate of exchange with the atmosphere, whereas nitrate is consumed by the diagenetic processes in the sediments due to its small concentration at the upstream boundary. Also concentrations of Manganese and Iron species reach to equilibrium relatively quickly. The concentration of Fe^{2+} in the water body is small due to its high oxidation rate in the aerobic water body. The sulfate concentration at the upstream boundary is relatively high and so its concentration remains

Copyright © 2006 Taylor & Francis Group plc, London, UK

almost constant in the reach with a small drop and H_2S concentration is low as expected. In addition Hg^{2+} and MeHg are supplied through the sediments and so their concentration increases monotonically as expected.

4 CONCLUSIONS

A multi-component and multi-species model for the prediction of transport and transformations of metals in riverine systems has been presented. The model couples the advection-dispersion governing equation for dissolved and particle associated species in the water column and diffusive transport of species in the bed sediments through a diffusive boundary layer and also deposition and resuspension mechanisms. The model was applied to simulate transport, transformation and particularly biomethylation of mercury in a hypothetical riverine system. For this purpose a multi-component, biotic/abiotic redox reaction network representing the cycling of major components involved was linked to a simplified reaction network governing mercury transformations. Also the activity of sulfate reducing bacteria (SRB) in the sediments was assumed to control the production of methyl-mercury. Two demonstration calculations for a hypothetical river reach were performed using literature values. Using the total mercury concentration observed in natural systems, resulted in reasonable methylmercury concentrations based on measured data in contaminated water bodies (Choe et al., 2004). Model validation and calibration using field and lab study results is currently underway. Further details and results on the distribution of species in the sediments can be found in a recently submitted paper (Massoudieh A., Bombardelli F. A, and Ginn, T. R., 2006).

REFERENCES

Berg, P., Rysgaard, S. and Thamdrup, B., 2003. Dynamic modeling of early diagenesis and nutrient cycling. A case study in an Arctic marine sediment. American Journal Of Science, 303(10): 905–955.

Boudreau, B.P., 1996. A method-of-lines code for carbon and nutrient diagenesis in aquatic sediments. Computers & Geosciences, 22(5): 479–496.

Choe, K.Y. et al., 2004. Sediment-water exchange of total mercury and monomethyl mercury in the San Francisco Bay-Delta. Limnology And Oceanography, 49(5): 1512–1527.

Compeau, G.C. and Bartha, R., 1985. Sulfate-reducing bacteria: principal methylators of mercury in anoxic estuarine sediment. Appl. Environ. Microbiol., 50(2): 498–502.

Gadd, G.M., 2004. Microbial influence on metal mobility and application for bioremediation. Geoderma, 122(2-4): 109–119.

Gilmour, C.C. and Henry, E.A., 1991. Mercury methylation in aquatic systems affected by acid deposition. Environ. Pollut., 71(2-4): 131–169.

Hunter, K.S., Wang, Y.F. and Van Cappellen, P., 1998. Kinetic modeling of microbially-driven redox chemistry of subsurface environments: coupling transport, microbial metabolism and geochemistry. Journal Of Hydrology, 209(1-4): 53–80.

Kim, D., Wang, Q.R., Sorial, G.A., Dionysiou, D.D. and Timberlake, D., 2004. A model approach for evaluating effects of remedial actions on mercury speciation and transport in a lake system. Science Of The Total Environment, 327(1-3): 1–15.

Massoudieh, A., Bombardelli, F.A. and Ginn, T.R., 2006. Mathematical Modeling of fate and transport of dissolved and particulate mercury in riverine systems, submitted to EWRI world environmental and water resources congress, Omaha, NE, USA.

Neubauer, S.C., Givler, K., Valentine, S.K. and Megonigal, J.P., 2005. Seasonal patterns and plant-mediated controls of subsurface wetland biogeochemistry. Ecology, 86(12): 3334–3344.

Twilley, R.R. and Rivera-Monroy, V.H., 2005. Developing performance measures of mangrove wetlands using simulation models of hydrology, nutrient biogeochemistry, and community dynamics. Journal Of Coastal Research: 79–93.

Van Cappellen, P. and Gaillard, J.-F. (Editors), 1996. Biogeochemical dynamics in aquatic sediments. Reactive Transport in Porous Media, Reviews in Mineralogy, 34.

Van Cappellen, P., Gaillard, J.-F. and Rabouille, C. (Editors), 1993. Biogeochemical transformation in sediments: kinetic models of early diagenesis. Interactions of C, N, P, and S biogeochemical cycles and global change, NATO ASI Series, 14.

VanCappellen, P. and Wang, Y.F., 1996. Cycling of iron and manganese in surface sediments: A general theory for the coupled transport and reaction of carbon, oxygen, nitrogen, sulfur, iron, and manganese. American Journal Of Science, 296(3): 197–243.

Winfrey, M.R. and Rudd, J.W.M., 1990. Environmental-Factors Affecting The Formation Of Methylmercury In Low Ph Lakes. Environmental Toxicology And Chemistry, 9(7): 853–869.

Copyright © 2006 Taylor & Francis Group plc, London, UK

The application of hydrodynamic models as integrative tool between flood protection and ecological demands using a morphologically based evaluation method

C. Hauer, M. Liedermann & H. Habersack

University of Natural Resources and Applied Life Sciences Vienna, Department of Water – Atmosphere and Environment, Institute of Water Management, Hydrology, and Hydraulic Engineering

ABSTRACT: On the basis of a case study at the Kamp River/Lower Austria the possibilities of an integrative evaluation of an ecologically oriented flood protection measure are discussed. Beside the hydrodynamic modelling of predefined flood events, low and mean discharge situations were simulated to evaluate the abiotic conditions for main fish species. The morphological developments of the flood protection measure were documented by terrestrical survey in 2003 and 2004. Furthermore it was possible to create a digital terrain model (DTM) of the former, natural river bed (1890) which was used as the "Leitbild" situation. With a geomorphologically based evaluation method the success of ecologically orientated flood protection measures was discussed according to the "Leitbild" situation using ecological and economical parameters.

1 INTRODUCTION

In August 2002 a catastrophic flood event occurred in Austria and in several countries of Central Europe (Habersack & Moser, 2003). Beside deaths the huge economic damage reflected in some cases the suboptimal management of our river systems. As a reaction to these catstrophic events some governments decided to build so called initial measures for flood protection. In Lower Austria river widenings have been chosen as the first step for an improved flood management. Additionally it was tried to reconstruct typical natural river patterns in these areas of cross section enlargement. A main project is performed at the Kamp River. Such an integrative river restoration aiming for improved better flood protection consisting the European Water Framework Directive (WFD) is only found in pilot protects so far. River widening for flood protection including river restoration was documented in the Netherlands (Baptist et al., 2004). More studies are dealing with river restoration. In Denmark two major projects on River restoration were performed. At the River Brede and the River Skjern the straight, regulated river bed was reconstructed with the former natural meandering character, better hydraulic interaction between the river and its meadows was introduced and former lakes, bogs, ponds and marshes were established (Neilsen, 2002). An example for a restoration protect from France is presented by Poudevigne et al., 2002, where at the River Seine the method of simplification of river processes on certain units was tested. In this study the work was focused on two attributes of the ecosystem at different scales: community organisation and landscape organisation. Reach scale hydraulic assessment of instream restoration is presented by Lacey & Millar (2004). Other river restoration projects and their benefits to aquatic ecology are discussed in Rohde et al., 2004 and Kamp et al., 2004. A target setting for river restoration is presented in Pedroli et al. (2001). Their work concentrates on the concept of setting targets for river restoration as exemplified by the Meuse River. A modelling exercise shows the restraints of current habitat configuration and the potential for habiat restoration along the river. State of the art in relationships between form and processes in a river according to river restoration were discussed in Niezgoda & Johnson (2005) and standards for ecologically successful river restoration were defined by Palmer et al. (2005). The development of an ecohydraulic model for stream and river restoration was tested in a British River by Bockelmann et al. (2004). Further numerical modelling for river restoration processes was also included by Larsen & Greco (2002).

The aim of this paper is to discuss the effectiveness of an integrative method for analysing flood protection and the possibility of achieving a good ecological status (WFD) using a one dimensional cross sectional based model.

Copyright © 2006 Taylor & Francis Group plc, London, UK

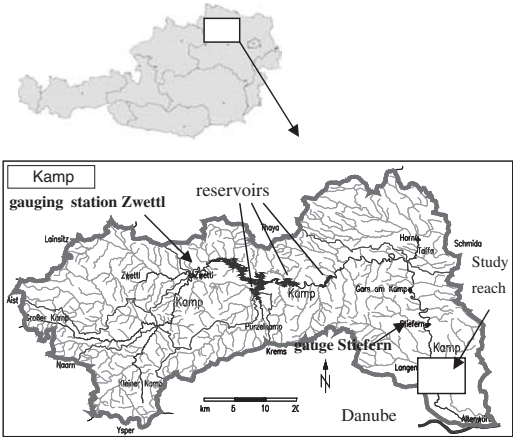


Figure 1. Catchment area of the Kamp River.

Table 1. Hydrological characteristics (Hydrologisches Jahrbuch, 1999).

Gauging station	NQ* [m^3s^{-1}]	MQ** [m^3s^{-1}]	HQ*** [m^3s^{-1}]	NQ:HQ
Neustift	0.04	0.87	18.5	1:462
Zwettl	0.21	5.88	140	1:677
Rosenburg	1.36	7.93	153	1:113
Stiefern	1.84	7.48	162	1:88

* NQ = low flow, ** MQ = mean flow, *** HQ = high flow.

2 STUDY REACH

The study reach of this paper is situated in the northern part of Lower Austria. The origin of the Kamp River is near the village Karlstift (920 m.a.sl.). Its 160 km course discharges into the Danube River (182 m.a.sl.) at Altenwörth. The total catchment area is defined with 1.753 km^2 (Fig. 1).

In the recent past (1954–1957) three large hydropower plants were build. The reservoirs of Ottenstein, Dobra and Thurnberg influenced the sediment transport and the hydrological regime significantly. The whole part of the Kamp River from river station km 73 + 500 to the Danube river can be described as a residual flow zone with no bedload input from upstream and reduced input from tributaries since that time. The hydrologic characteristics of the catchment area are described in Table 1.

The area of riverbed widening for flood protection and for detailed analysis is found between the river station 20.650 km and 21.700 km with a length of 1.050 m. The average bed slope in this part of the Kamp River is defined with 0.0007 m m^{-1}.

3 METHODS

Based on terrestrical surveys, which were taken in the years 1890, 1900, 2002 and 2003, different Digital Terrain Models (DTM) could be constructed of the investigation area at the Kamp River. The historical geometry of 1890 was derived from a data set of 290 points which showed the main characteristics of the river section (riffles, pools, bankfull, etc.). Based on that information breaklines were constructed and based on the interpolation method of Kriging a DTM model with 450 points could be made. The geometry of the year 1900 was taken from a river regulation project. The data set provided cross sectional information every 50 m. The measurement of the river topography in 2002 was done before the riverbed widening (350 points), the geometry data of 2003 (320 points) is representing the situation immediately after the cross sectional enlargement. The data of the cross sectionally based surveys were transferred to a one dimensional hydrodynamic numerical model (HEC – RAS) for analysing different discharge scenarios. These scenarios were split into below bankfull analysis (1.4 m^3s^{-1}; 3 m^3s^{-1}; 5 m^3s^{-1}; 8 m^3s^{-1}; 12 m^3s^{-1}; 16 m^3s^{-1}; and 87 m^3s^{-1}) and into calculations of specific flood events (40 m^3s^{-1}, 50 m^3s^{-1}, 60 m^3s^{-1}, 70 m^3s^{-1}, HQ_1, HQ_5, HQ_{10}, HQ_{30}, HQ_{50}, HQ_{100},HQ_{200}). Only the results of below bankfull analysis were taken for studies on ecological benefits. To link the hydraulic simulation results with suitability indices the method of Bovee (1986) was used. This method of multiplying suitability indices was first utilized in the PHABSIM model (Milhouse, 1989) and is shown in equation 1.

$$SI_{ges} = SI_d \cdot SI_v \cdot SI_{CI} \quad \text{or.} \quad SI_{ges} = \prod_{i=1}^{I} SI_i \qquad (1)$$

where SI_d = Suitability Index depth, SI_v = Suitability Index velocity, SI_{CI} = Suitability Index channel index, SI_{ges} = Suitability Index total, SI_i = Suitability index variable

For generating suitability curves of nase (*Chondrostoma nasus*) the results of the observations by snorkelling at the Pielach River were taken. From the surveyed fish (by snorkelling) Melcher (1999) developed the following suitability classes (Table 2).

For analysing the effects of riverbed widenings to flood protection, the calculated water surface levels of the year 2002 (before widening) and 2003 (after widening) were compared.

4 RESULTS

4.1 *Riverbed widening and flood protection*

The effects of the cross sectional enlargement of 2003 to the water surface levels are presented in Figure 2.

Copyright © 2006 Taylor & Francis Group plc, London, UK

Table 2. SI of nase (Melcher, 1999).

Suitability index [SI]	very high	high	low	no SI
Spa. depth [cm]	15–30	30–45	45–90	<15, >90
Spa. velocity [cm s^{-1}]	100–110	80–120	70–80 130–140	<70, >140
Spa. substrate	Microlithal	Mesolithal		
Juv. depth [cm]	0–30	30–60	60–120	>120
Juv. velocity [cm s^{-1}]	0–5	10–15	20–35	>35
Juv. substrate	Pelal Microlithal	Mesolithal Macrolithal	Psammal Megalithal	

Ad. Table1: Pelal (<0,063 cm), Psammal (0,063–0.2 cm), Akal (0,2–2 cm), Microlithal (2–6.3 cm), Mesolithal (6,3–20 cm), Macrolithal (20–40 cm), Megalithal >40 cm
Spa. – Spawning/Juv. – Juvenile

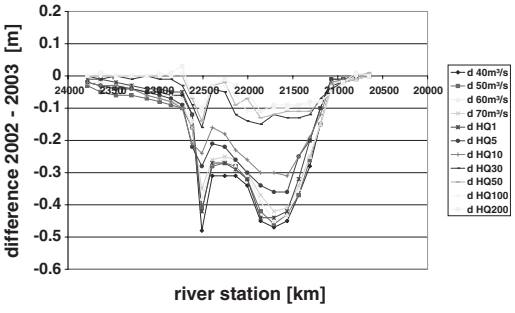


Figure 2. Effects of cross section enlargement on flood protection (d = discharge).

It is obvious, that the lowering of the water levels is clearly found at discharges beneath bankfull (<190 m^3s^{-1}). At discharges with recurrence intervals >10 years the positive effect for flood protection can be neglected (reduction <0.1 m).

Beside the local effects of riverbed widenings, the influence of theses artificial measures is found additionally in upstream direction. The increase of the conveyance through the cross sectional enlargement is documented up to 300 m upstream for discharges around 50 m^3s^{-1}.

4.2 *Effects of restoration measures*

To evaluate the benefits of the restoration measures to aquatic ecology the method of habitat modelling was used. The abiotic data were combined with the preference function of nase, one of the main fish species (Table 2). The analysis was performed for below bankfull discharges. In Figure 3 (a), (c) the percentage of Weighted Useable Areas (WUAs) is documented for the historical natural "Leitbild situation" (1890), the regulated river bed of 1900, the geometry data of 2002 (before widening) and 2003 (after widening).

It was found as an interesting result, that the modelling of the historical "Leitbild" situation showed a

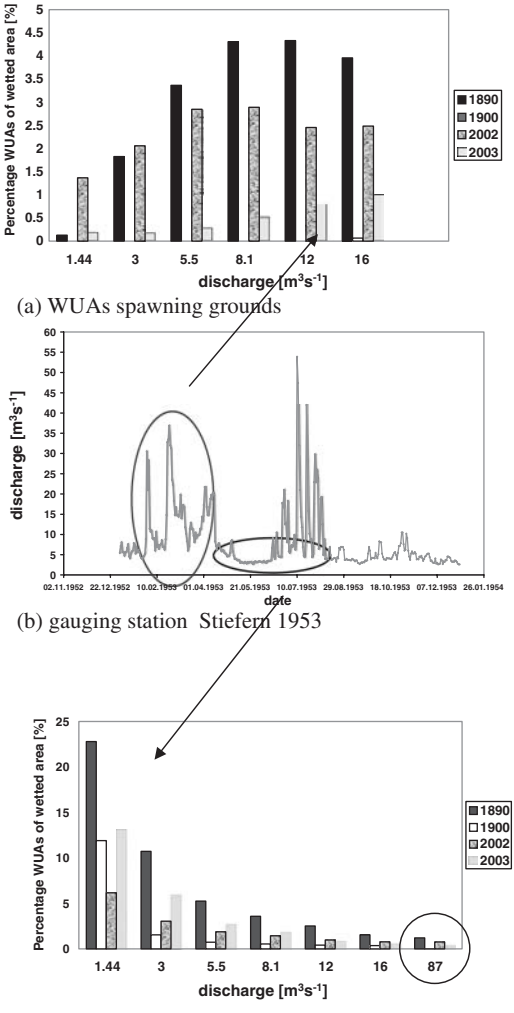


Figure 3. Development of fish habitat quality 1890–2003.

Copyright © 2006 Taylor & Francis Group plc, London, UK

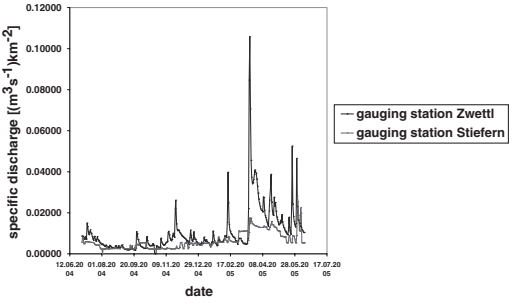


Figure 4. Specific discharge Zwettl/Stiefern (06.2004–06.2005).

good correlation between the maximum percentage of useable areas and the hydrological regime (Fig. 3). Spawning of nase is highly correlated to a certain water temperature and is found in spring-time (Lelek & Penaz, 1963; Maier, 1993). In this period the average flow of the Kamp River is increased caused by the natural regime (Mader et al., 1996). Frequently discharges around 15 m^3s^{-1} (Figure 3b) were documented. During the low flow season in summer with discharges $<3\ m^3s^{-1}$ the channel geometry of the historical river morphology provided also the best habitats for the juvenile nases which are described in Table 2. In cases of small to mid-size flood events ($87\ m^3s^{-1}$), which may happen in summer (Fig. 3b), the historical geometry provided additionally the best refugial habitats (Fig. 3c). The regulation project of 1900 with its straight course caused a total reduction of riffles (Fig. 3a) which are well known as spawning habitats of nase (Stein, 1992; Keckeis, 1991; Maier et al., 1992). Also the juvenile habitats, defined as shallow water areas (Table 2), were reduced compared to the historical "Leitbild" situation. Following on, the construction of the three large power plants caused a massive change in the hydrologic characteristics. In Figure 4 the gauging stations of Zwettl (non influenced, Fig. 1) and Stiefern (influenced by power plants since 1954, Fig. 1) are compared.

Figure 4 shows the reduction of small and mid-size flood events by the hydrological management of the power plants. Therefore a cross sectional decrease of the originally regulated cross section of 1900 arose, from the loss of stream power, for almost 30%. As a result of this loss in dynamics, the bankfull discharge was reduced from $170\ m^3s^{-1}$ to $145\ m^3s^{-1}$. During this 100-years of morphological development (50 years with an influenced regime) the habitats (spawning, juvenile) became a similar characteristic like in the historical "Leitbild" situation (Fig. 3a and Fig. 3c). Only the quantified usable areas were reduced.

The effects of the flood protection measures and the effects of the restoration features are presented in the modelling results of the year 2003 (Fig. 3a and Fig. 3c).

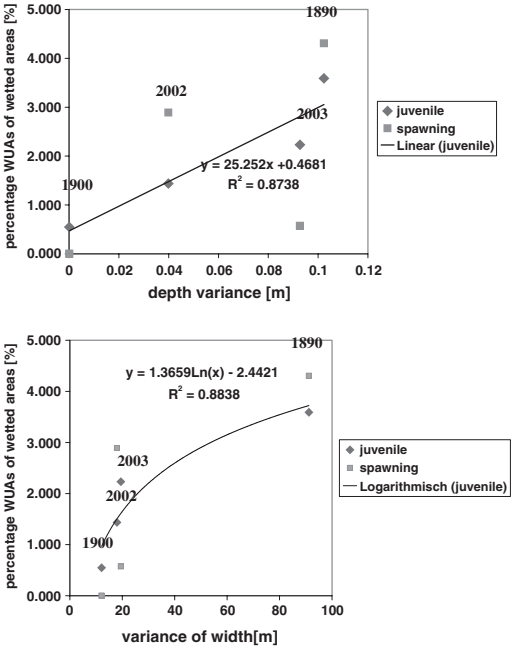


Figure 5. Depth and width variance/useable juvenile habitats.

It is obvious that the habitat characteristics changed totally by the cross section enlargement. The spawning areas were drastically reduced and the shallow water areas, preferred by juveniles, increased.

4.3 *Evaluation method*

For evaluating the benefits of these measures to flood protection and aquatic ecology, according to the Water Frame Work Directive, a morphologically based evaluation method was tested. At the beginning it was necessary to define parameters for channel characterization. Depth- and width variance are often used for describing channel – habitat characteristics (Jungwirth et al., 1984). In Figure 5 the depth and width variance are presented for mean flow ($8.1\ m^3s^{-1}$).

It is obvious that the variance of depth and width is correlating with the percentage of weighted useable areas (WUAs) of juveniles nases (Fig. 5). The modelled spawning grounds, based on the surveyed preferences, showed no response to these parameters. Therefore a new parameter derived from the 1-D modelling results had to be taken to characterize a linear relation between the increase of the 1-D variable and the percentage of the useable spawning areas. Various analysis were performed and finally the variance of bottom shear stress showed the best response to the occurrence of spawning grounds. These results are presented in Figure 6.

Copyright © 2006 Taylor & Francis Group plc, London, UK

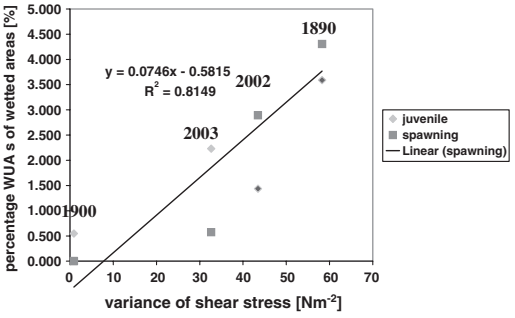


Figure 6. Bottom shear stress/useable spawning habitats.

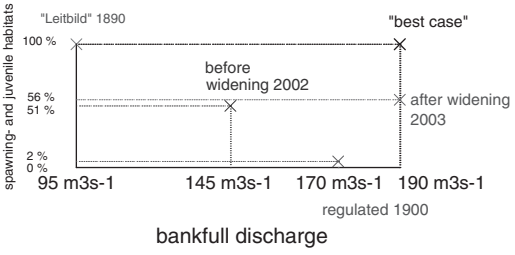


Figure 7. Integrated evaluation of geometric datas.

In Figure 7 the integrated evaluation of the measures at the Kamp River are shown. In x-direction the improvement to flood protection is shown. The increase of the bankfull discharge was taken as parameter to evaluate the success according to flood protection because, as it was proven in Figure 2, the events with a high recurrence interval (>10 years) were only less influenced by the artificial riverbed widening.

In y-direction the percentage of natural habitat characteristics is presented. The values are describing the morphological conditions for spawning- and juvenile habitats based on the variance analysis of the 1-D model (Figs 5–7). Juvenile and spawning habitats were equally weighted. A splitting was further done for depth and width variance.

For interpretating the evaluation method, two totally different points of Figure 7 can be mentioned. The "Leitbild" situation of 1890 is representing the non influenced morphological conditions with its natural characteristics (100%). The opposite situation can be seen in the river regulation of 1900. The natural morphological characteristics was reduced to 2% of the former river bed structure. During the 100 years development (50 years influenced by the hydropower plants) the river restructured itself by erosion and deposition of material (influenced since 1954 by power plants, Fig. 3). Therefore the 51% of natural characteristics calculated for 2002 can be seen as the maximum possible heterogeneity under the consisting boundary conditions (reduced coarse sediment input and discharge regime). The artificial widening, with its restoration measures in 2003, caused an increase of the bankfull discharge up to 190 $m^3 s^{-1}$. Furthermore the morphological situation changed. The analysis of variances of depth, width and shear stress (according to the correlation to certain habitat types) showed that 56% of the natural geomorphologic habitats were found in these areas of artificial widening. But it can be mentioned, based on the knowledge of the River System (literature and modelling), the situation 2003 (190 $m^3 s^{-1}$/56%) is not sustainable. Caused by the reduced sediment transport capacity, effected by the Riverbed widening, aggradation of material is expected. This will lead to a shift of 2003 (190 $m^3 s^{-1}$/56%) towards the situation of 2002 (145 $m^3 s^{-1}$/51%). 2002 can be seen, as it was mentioned, as the best possible morphologic characteristics under the existing boundary conditions. A monitoring of the morphologic development has started to proof the assumption.

5 DISCUSSION

For some cases the problems of mid- to long term development of riverbed widening were documented (Habersack & Nachtnebel, 1995). Hauer et. al. (sub.) investigated the effects of riverbed aggradation to the habitat quality of the rheophilic cyprinid nase over a three year time period at the Sulm River. The results showed that fish react immediately to changes in morphological characteristics. Similar effects can be expected for the initial measures at the Kamp River. The problem of such artificial measures is that in these areas of artificial river bed widening the rivers are not "in regime" anymore. Therefore a regime analysis was done based on the work of Simond & Albertson, 1960. Their studies were taken because their regime equations were found comparable to rivers with less sediment transport like the Kamp River is. The results showed for the historic bankfull discharge (95 $m^3 s^{-1}$) that a bankfull width of 41 m and a bankfull depth of 2.8 m are characterizing a river in regime. Compared to that, the results of the hydrodynamic modelling with the historical geometric data (1890) showed an average width of 48 m and a depth of 2.2 m. That means, there are differences in the singular parameters (width, depth) but the wetted areas [m^2] are quite similar. Therefore it can be mentioned, that the study reach was in regime before river regulation (1900). The regime calculations also emphasis the thesis that the riverbed widening of 2003 is not sustainable. Based on the geomorphologic characteristic and the aggradations of suspended sediments, which increased by the change of wood- to farmland in the catchment area beneath the reservoirs, the bankfull capacity will be reduced and will lead to a development of the measures towards the situation of 2002 (145 $m^3 s^{-1}$/51%).

Copyright © 2006 Taylor & Francis Group plc, London, UK

6 CONCLUSIONS

The results of this study demonstrate that it is possible to use a one dimensional model for an integrative analysis according to the demands of the European Water Framework Directive (WFD). It was shown that variables of the 1-D models (depth-, width- and shear stress variance) are well correlating with the occurrence of spawning- and juvenile fish habitats which were defined by preference analysis. Furthermore an evaluation method was tested, based on the one dimensional parameters, and showed a good response to river characteristics comparing flood analysis and fish habitat characteristics.

ACKNOWLEDGEMENTS

The authors want to thank DI Ines Fordinal for supportive work an the government of Lower Austria for financing the project.

REFERENCES

Babtist, M.J., Penning, W.E., Duel, H., Smits, A.J.M., Geerling, G.W., van der Lee, G.E.M., Van Alphen, J.S.L. 2004. Assessment of the effects of cyclic floodplain rejuvenation on flood levels and biodiversity along the Rhine river. *River Research and Application 20 (3)*: 285–297. May 2004.

Bockelmann, B.N., Fenrich, E.K., Lin, B., Falconer, R.A. 2004. Development of an ecohydraulics model for stream and river restoration. *Ecological Engineering 22 (4-5)*: 227–235 July 1 2004.

Bovee, K.D. 1986. Development and evaluation of habitat suitability criteria for use in the instream flow incremental methodology. *Biological report 86 (7)*, 235 pp, US Fish and Wildlife Service.

Habersack, H., Nachtnebel, H.P. 1995. Short term effects of local river restoration on morphology, flow field, substrate and biota. *Regulated Rivers: Research and management 10*: 291–301.

Hauer, C., Unfer, G., Schmutz, S., Habersack, H. sub. Morphodynamic effects on the Habitat of Juvenile Cyprinids (*Chodrostoma nasus*) in a restored Austrian Lowland river. *submitted in River Research and Application.*

Jungwirth, M., 1984. Auswirkungen des naturnahen Wasserbaus auf die Fischerei II. *Wasserwirtschaft und Wasservorsorge*, BmfLuF, 188 pp.

Kamp, U., Bock, R., Holzl, K. 2004. Assessment of river habitat in Brandenburg, Germany. *Limnologica 34 (3)*: 176–186

Keckeis, H. 1991. Fortpflanzungsbiologie und ökologische Kennzeichnung von Laichgebieten der Nase (*Chondrostoma nasus*) in der Donau. *Workshop Biologie und Gefährdung heimischer Kleinfischarten, Innsbruck.*

Lacey, R.W.J. & Millar, R.G. 2004. Reach scale hydraulic assessment of instream salmonid habitat restoration. *Journal of the American Water Resources Association 40 (6)*: 1631–1644 Dec 2004.

Larsen, E.W., Greco, S.E. 2002. Modelling channel management impacts on river migration: A case study of Woodson Bridge State Recreation Area, Sacramento River, California, USA. *Environmental Management 30 (2)*: 209–224. Aug 2002

Lelek, A. & Penaz, M. 1963. Spawning of *Chondrostoma nasus* in the Brumovka River. *Folia Zoologica. 12*; 121–134.

Maier, K., Turcsany, M., Krieg, M., Tinguely C. 1992. Untersuchungen an einem Laichplatz der Nase (*Chondrostroma nasus*) im Unterlauf der Sense (Schweiz, Kt. Bern). *DGL, erweiterte Zusammenfassung der Jahrestagung 1992*, Band 1, 258–263.

Maier, K.J. 1993. Erfassung und Katalogisierung der wichtigsten Laichgebiete der Nase (*Chondostroma nasus*) in den schweizerischen Rheinflüssen. *BUWAL, Sektion Fischerei*. Bern.

Melcher, A. 1999. Biotische Habitatmodellierung im Zuge eines Gewässerbetreuungskonzeptes anhand der Lebensraumansprüche der Nase (*Chondrostoma nasus*), *Abteilung für Hydrobiologie*, BOKU Wien.

Milhouse, R.T. 1989. Physical Habitat Simulation System Reference Manual – Vers 2. Instream Flow Information Paper No.26. *U.S.Department of the Interior, Fish and Wildlife Service.*

Neilsen, M. 2002. Lowland stream restoration in Denmark: Background and examples. *Journal of the charactered Institution of Water and Environmental Management 16 (3)*: 189–193. Aug 2002.

Niezgoda, S.L. & Johnson, P.A. 2005. Improving the urban stream restoration efford: Identifying critical form and processes relationships. *Environmental Management 35 (5)*: 579–592. May 2005.

Palmer, M.A., Bernhardt, E.S., Allan, J.D., Lake, P.S., Alexander, G., Brooks, S., Carr, J., Dahm, C.N., Shah, J.F., Galant, D.L., Loss, S.G., Goodwin, P., Hart, D.D, Hasset, B., Jenkinson, R., Kondolf, G.M., Lave, R., Meyer, J.L., O'Donnel, T.K., Pagano, L., Sudduth, E. 2005. Standards for ecological successful river restoration. *Journal of Applied Ecology 42 (2)*: 208–217. Apr 2005.

Pedroli, B., de Blust, G., van Looy, K., van Rooij, S. 2001. Setting targets in strategies for river restoration. *Landscape Ecology 17*: 5–18 Suppl. 1

Poudevigne, I., Alard, D., Leuven, R.S.E.W., Nienhuis, P.H. 2002. A system approach to river restoration : A case study in the Lower Seine Valley, France. *River Research and Application 18 (3)*: 239–247. May–Jun 2002.

Rohde, S., Kienast, F., Burgi, M. 2004. Assessing the restoration success of river widenings: A landscape approach. E*nvironmental Management 34 (4*): 574–589 Oct 2004.

Stein, H. 1992. Fischlaichplätze an Fließgewässern, *Kriterien zur Untersuchung, Identifizierung und Bewertung im Rahmen von Beweissicherungen*. Seminar f. Sachverständige der Binnenfischerei. Bonn

Copyright © 2006 Taylor & Francis Group plc, London, UK

River habitat model using energy budget characteristics and experiment on improvement of river physical environment

H. Yabe
Civil Engineering Research Institute for Cold Region, Sapporo, Japan

ABSTRACT: The Cherry salmon (*Oncorhynchus masou formosanum*) spend much of their life in rivers. As is true for any organism, the population of Cherry salmon is influenced by the habitat. The purpose of this study is to make clear the relationship between the population of Cherry salmon parr and the river habitat, toward gaining knowledge necessary for conservation and improvement of the river environment.

This study evaluated the living environment for Cherry salmon parr by their feeding activities. Knowledge on physiology and ecology of Cherry salmon was used for calculation of acquired energy after feeding, and consumed energy for maintaining their position and resting against current. The budget between the two kinds of energy was also calculated. And it verifies the validity of the evaluation by analyzing the relationship between the energy budget and fish population in the sections of river, pools and riffles, and created experimental pools. As a result the optimal environmental conditions for Cherry salmon were clarified. Additionally we conducted the experiment that river channel structure and the amount of organic matter were artificially altered. It was verified that it is possible to increase food for cherry salmon by creating physical structures that improve the retention and accumulation of organic matter, which in turn improves the food environment.

1 INTRODUCTION

River conservation and restoration have become increasingly pressing issues. Cherry salmon (*Oncorhynchus masou formosanum*) are anadromous salmonids that inhabit cold parts of the North Pacific Ocean of Asia and spend much of their life in rivers. Because the fish are susceptible to changes in the riverine environment, they are considered to be an indicator of a river's ecological soundness. However, an efficient method for evaluating a river's ecological soundness has not been established because it is dependent on various factors whose complex interactions greatly influence aquatic life including cherry salmon. Also, the populations of cherry salmon have recently been declining, which has prompted the fishery and tourism industries to call for clarification on the relationship between the changes in a river's physical environment and the fish population. The purpose of this study is to establish a method that quantitatively evaluates a river in terms of its ability to support cherry salmon. Established methods for clarifying the physical environmental factors preferred by the salmon give us knowledge necessary for selecting riparian conservation areas and for improving and restoring the river environment.

The life of cherry salmon is divided into the fry and parr stages (from spring to autumn), the wintering stage, the seaward migration stage, and the upstream spawning stage. The habitat a fish chooses depends on the fish's stage of life. Conservation and improvement of the habitat for fry and parr, which spend one or two years in a river after hatching, are considered particularly important for the preservation and growth of the population. That is why this study addresses the parr stage. The Physical Habitat Simulation Model is a common method for evaluating the habitats of fish. However, existing habitat models including it are not applicable to cases in which the habitat of the target species is difficult to identify; therefore, data on the direct relationship between the population (density/suitability) and the physical environment cannot sufficiently be collected by field surveys or other means. We propose a new habitat evaluation method that incorporates the fish's physiology and behavior, including feeding and resting behavior. The validity of the model is examined by comparing its results with field data.

Next, we attempt to understand the influence of physical structures on fish population. The knowledge from this attempt can be used in habitat improvement and restoration efforts. It has been assumed that a decrease in the number of pools can affect the population of cherry salmon. To test this assumption, we artificially created pools to improve the physical habitat structure of a river reach. The findings in the

Copyright © 2006 Taylor & Francis Group plc, London, UK

examination were applied in our habitat evaluation model described above. Also, it has been pointed out that the straightening of rivers influences the habitat of the benthic animals on which cherry salmon feed. To clarify this, we demonstrated that the habitat for benthic animals could be improved by installing groin works and iron piles that change how organic matter accumulates in a river.

2 FISH HABITAT MODEL

Application of the Physical Habitat Simulation Model (PHABSIM) requires the calculation of a preference curve for each physical-environment factor of a river (Stalnker *et al.*, 1994). Each factor is then converted to weighted usable area (WUA) and evaluated as a total value. Preference curves obtained from field studies conducted in a target river, or from laboratory experiments that reproduce the preferences of fish in a target river, accurately describe the distribution of fish. However, the evaluation of fish distribution is difficult when the data on the direct relationship between population (i.e., density as an indicator of suitability) and the physical environment cannot sufficiently be collected by field surveys or other means, and the preference curve thus lacks accuracy. During a single life stage, a fish does not stay in one microhabitat. Depending on its behaviors such as feeding, resting, and taking refuge during flooding, a fish often changes its microhabitat. Because of this, it is desirable that a preference curve be calculated separately for each behavior, including feeding and resting, with equal consideration given to the interrelation between the relevant factors. Previous studies that addressed this problem – targeting pale chubs, sweet fish or dace – include one that that used equations to calculate preferences separately for feeding, resting, refuge, and spawning, and evaluated the habitat by weighting these behaviors. One study analyzed, based on the disturbance frequency that relates to flow velocity and the amount of food, the energy budget during feeding. Another study improved the fish habitat preference criteria to accommodate the structural features of pools and riffles and their seasonal variations. As described above, it is important to improve on PHABSIM, which quantifies a river's suitability as a fish habitat based solely on a one-to-one relationship between a target species and the physical habitat component of a river, and to evaluate fish habitat based on growth of a target fish and the seasons and by giving consideration to the physiology, and behaviors of the fish.

For cherry salmon, there have been studies in which the fish's distribution points and the corresponding physical structures of a river were collected and analyzed in the wintering period, when the fish tend to be resting. In these cases, application of PHABSIM seems feasible. However, identification of the fish's habitat is difficult in the parr stage, between summer and autumn, when the fish are actively feeding. This is because salmonids, such as cherry salmon, are cautious by nature and exhibit avoidance behavior even when only seeing the shadow a researcher casts, so study through visual observation is difficult, except at certain locations such as pools, due to the fish's extremely rapid movement. Therefore, few studies have directly collected habitat data on the fish, and no clear preference curves have been calculated for the species. Instead, many studies identified the limiting factors and clarified the importance of habitat factors such as flow velocity, water depth, and the availability of pools and cover by analyzing the population density and environmental variables in terms of stream reach and channel unit.

Toward evaluating the habitat of cherry salmon in the parr stage, this study focused on parr feeding activities, attempting to calculate the energy taken in from feeding, the energy expended to maintain optimal position or take rest in the current, and the budget between those, based on physiological and ecological information of the fish. In this study, the validity of the proposed habitat evaluation method was examined for summer and autumn through an analysis of the relationship between energy budget and population density according to river sections (reaches), riffles, pools, and artificial pools in the target river. It is likely that these calculated values can be used to determine fish quantitative populations in various rivers as well as to evaluate the relative distribution of species.

3 HABITAT MODEL BY ENERGY BUDGET

3.1 *Survey procedures*

One-kilometer reaches were studied on the Hidarimata River and the Migimata River, a tributary of Shiribeshi-toshibetsu River in Japan. The rivers are designated as protected rivers, where all aquatic animals and plants are prohibited from being collected. The population density of cherry salmon in these rivers is very high, making the rivers ideal for ecological studies. Eight river sections (Hidarimata River 1 to 4, Migimata River 1 to 4; each section is approximately 50 m long) were chosen for study sites. Investigations of the river conditions and field surveys on fish, drifting insects, the river physical environment and the like were conducted once in late July and once in early October 2004.

To make the fish surveys as accurate as possible, sampling by net casting was combined with sampling by electric shock. Each 15-minute net casting survey was followed by electric shock sampling from the downstream limit to the upstream limit of each survey section. Three sets of net casting plus electric shock

Copyright © 2006 Taylor & Francis Group plc, London, UK

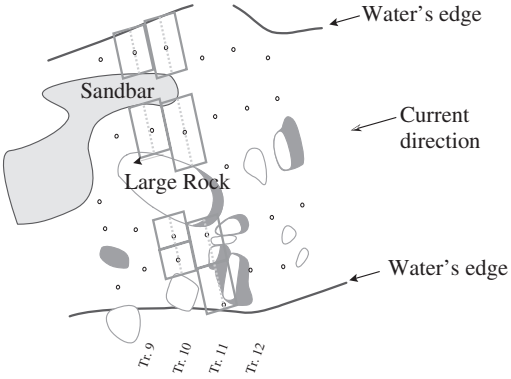


Figure 1. Measurement of river physical structure.

sampling were done, with a between-set interval of 10 minutes. Captured fish were measured for body length and weight.

In the physical habitat structure surveys (Figure 1), each river section was subdivided into cells where channel configuration, flow regime (water depth and flow velocity), riverbed material (loose rock, sunk rock, and grading (roughness)) were measured. In each river section, 30 transects were drawn perpendicular to the center of stream at equidistant intervals, and four survey spots per transect were set at equidistant intervals (total of 120 survey spots). At each survey spot, physical environment, such as the distance from the riverbank, water depth, flow velocity at 60% depth (i.e., 60% of the distance from the surface to the bottom) and flow velocity at the bottom, were measured, and visual observations were made on bottom sediment type, type of microhabitat such as riffle and pool, and canopy opening (closed (0) or open (1)).

Drifting insects were collected with a drift net (50 × 50 cm or 25 × 25 cm) that was set on a flat (i.e., medium water depth and flow velocity) for 30 minutes in the early morning (around 6 a.m.). The flow velocity and the flow rate (water filtered) at the front of the net were measured. To collect falling insects, water pan traps were placed for a whole day on a warm, fine day on both sides of each river section. The mass per area of benthic animals, amount of attached algae, and the sunshine duration were calculated. Discharge observation was made six times each for the Hidarimata River and the Migimata River to record the flow rate and water-surface gradient. The maximum daily rainfall during the study period (July to October) at the Imagane Observatory was 48 mm per day, on August 20, and 50 mm per day, on September 13. There were rainfalls of about 30 mm/2 days and 10 mm/2 days in late August and early September. In both rivers, the peak water level followed two hours after each peak rainfall, and the maximum water level increase was about 60 cm.

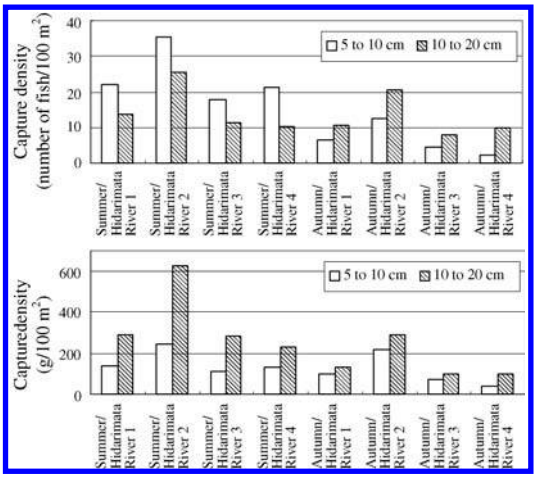


Figure 2. Population density in the Hidarimata River (upper: number of fish, lower: weight).

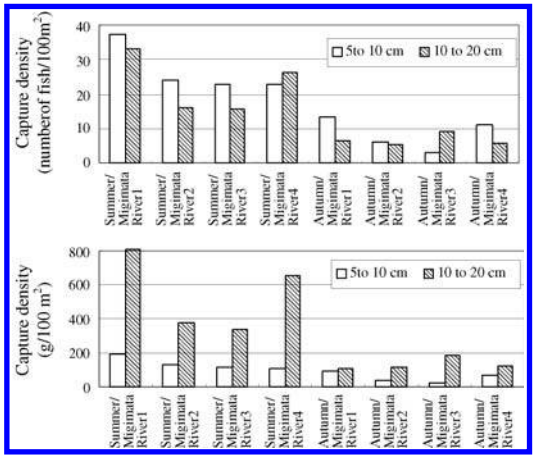


Figure 3. Population density in the Migimata River (upper: number of fish, lower: weight).

3.2 *Results of fish surveys*

3.2.1 *Distribution of cherry salmon*

Summer surveys were conducted in late July, the high-growth period for (under-yearling) parr, and autumn surveys were conducted in early October after the spawning period of adult fish. Figures 2 and 3 show the survey results for each survey section. In autumn, the number and weight of captured fish per area, which was calculated by dividing the number and weight of fish by the water-surface area of each survey section, decreased. In summer on the Hidarimata River, both the number and weight per area were greatest in Section 2, and on the Migimata River the number and weight per area were greatest in Section 1. In autumn on the Hidarimata

Copyright © 2006 Taylor & Francis Group plc, London, UK

Table 1. Results of survey on the physical structure of rivers (for each river).

Item	Section							
	Hidarimata River				Migimata River (left: summer, right: autumn)			
	Section 1	Section 2	Section 3	Section 4	Section 1	Section 2	Section 3	Section 4
Riverbed gradient	1/33	1/35	1/52	1/48	1/47	1/55	1/40	1/57
Water-surface area	274∼247 m^2	229∼233 m^2	183∼177 m^2	207∼205 m^2	133 m^2	163 m^2	165 m^2	205 m^2
Average water-depth	35∼32 cm	36∼32 cm	26∼23 cm	30∼25 cm	28∼32 cm	29∼28 cm	26∼25 cm	22∼24 cm
Average flow velocity	56∼39 cm/s	47∼34 cm/s	73∼48 cm/s	67∼46 cm/s	48∼45 cm/s	58∼47 cm/s	63∼48 cm/s	57∼43 cm/s
Average flow velocity	30∼18 cm/s	28∼16 cm/s	45∼20 cm/s	43∼18 cm/s	28∼19 cm/s	34∼20 cm/s	35∼25 cm/s	33∼22 cm/s
Rate of loose rock	71∼61%	73∼49%	83∼39%	74∼55%	47∼65%	82∼72%	71∼81%	65∼77%
Drifting insects	0.0038∼ 0.048 g/10000	0.0034∼ 0.243 g/10000	0.0032∼ 0.035 g/10000	0.0032∼ 0.035 g/10000	0.0027∼ 0.16 g/10000 L	0.0018∼ 0.04 g/10000 L	0.0018∼ 0.04 g/10000 L	0.0018∼ 0.04 g/10000 L
Benthic animals (wet weight)	2.09∼0.94 g	2.81∼3.55 g	3.29∼1.69 g	2.12∼2.01 g	0.41∼0.29 g	0.49∼1.18 g	2.79∼0.72 g	1.23∼1.78 g
Canopy opening (area)	83∼170 m^2	63∼207 m^2	90∼109 m^2	191∼38 m^2	101∼88 m^2	156∼129 m^2	50∼166 m^2	158∼153 m^2
Canopy opening (%)	20%	34%	20%	18%	15%	12%	25%	21%
Sunshine duration	237∼167 min	329∼241 min	208∼45 min	277∼145 min	175∼48 min	148∼93 min	206∼96 min	193∼96 min

River, both the number and weight per area were greatest in Section 2, and on the Migimata River the number of small-sized fish was great in Section 1 and that of large-sized fish was great in Section 3.

3.2.2 *Physical environment of the rivers*

Table 1 shows the average physical environment values for each section. The weight of falling insects recorded between August 10 and 12 is extremely small; it is possible that terrestrial insects had already become less active by then. Sections 1, 2, 3 and 4 of the Hidarimata River are respectively characterized as a reach with rapid flow and many large rocks; a reach with large rocks, pools, and sandbars; and straight reaches with series of riffles and flats. Sections 1, 2, 3 and 4 of the Hidarimata River are respectively characterized as a straight reach with dispersed large rocks; a right-curving reach with large rocks, pools, and sandbars; and straight reaches with series of riffles and flats. The number of tree species of the riparian woods is similar for the eight sections on the two rivers (from 149 to 160 species), and the species compositions do not differ significantly between the two.

3.3 *Analysis methods*

3.3.1 *Classification of riffle and pool clusters based on the river physical environment*

Habitats were evaluated on the scale of channel unit (i.e., riffle/flat/shallow edge or pool) as well as stream reach (i.e., river survey section). Surveyed sections were quantitatively categorized into riffle, flat, shallow edge or pool clusters according to their physical structures, since distribution of such structures in a river habitat is important for the growth of cherry salmon parr. Principal component analysis did not extract composite variables (principal components) that could explain the overall variation in surveyed sections as a whole; therefore, principal component points were not used. Instead, cluster analysis was conducted using physical measurements (water depth, flow velocity at 60% depth, bottom flow velocity, bottom sediment type, and the rate of loose rock). The degree of dissimilarity among clusters was calculated using Ward's method, which is based on the squared Euclidean distance. Four cases were analyzed: the Hidarimata River in summer and autumn, and the Migimata River in summer and in autumn. As a result of the analysis, all surveyed river channel units were categorized into four clusters. Similarity in water depth, flow velocities, and bottom sediment was fairly strong within each cluster. The four clusters were a pool cluster with great water depth and low flow velocity, a riffle cluster with shallow water depth and high flow velocity, a flat cluster with medium water depth and flow velocity, and a channel-edge shallow cluster with small water depth, low flow velocity and small amount of bottom sediment. Comparison with the river bottom morphology maps, which were produced by field investigation conducted for the sections classified into the cluster types, confirmed the reproducibility of the clusters. The classification reflected the variation in the physical conditions, which is hard to visually identify, such as transverse variation in flow velocity and water depth, and enabled us to describe the channel-edge shallow conditions.

3.3.2 *Application of the energy budget model*

To evaluate habitats in terms of suitability for cherry salmon parr, an energy budget model that incorporates the salmon's feeding characteristics was applied. Salmons have the habit of maintaining their position while facing the current in wait for drifting insects. Flow velocity strongly influences the behavior of

Copyright © 2006 Taylor & Francis Group plc, London, UK

cherry salmon engaged in feeding, and flow rate (and drifting insect supply rate) positively correlates with flow velocity (i.e., the greater the flow velocity, the more insects drift down, making it easier for the fish to feed). However, greater flow velocity means that more energy is required for a fish to maintain position. It was predicted that cherry salmon would choose locations (i.e., optimal position) where they could feed most efficiently.

In this study the energy budget of cherry salmon was evaluated based on the physiology and life of the species as described above. The relationship between energy budget and population density was analyzed. Assuming that the survey spots for physical structure survey set within the surveyed sections are optimal positions of the fish, the net energy intake (NEI) at each optimal position was calculated by subtracting the swimming cost (SC, the energy expended in swimming) from the gross energy intake (GEI, the energy obtained by feeding) (Equation (1)).

$$NEI = GEI - SC \quad (1)$$

The following hypothetical conditions are assumed in models used for estimating GEI and SC:

- The fish rests at whichever depth has the lower flow velocity: the bottom (3 cm above the riverbed), or the 60% depth. (The bottom tends to have lower flow velocity.)
- SC is determined by the flow velocity at the fish's optimal position.
- The fish feeds at whichever depth has the higher flow velocity: the bottom, or the 60% depth. The fish's capture area is defined by maximum capture distance (MCD), which is determined by the flow velocity at the feeding depth.
- The fish eats all the food that drifts into its capture area.

GEI, an index of collectability of food by fish, is calculated by Equation (2) (Hughers *et al.*, 1990):

$$GEI\ (cal/h) = CA \cdot V_{fg} \cdot D \cdot I \quad (2)$$

Where,
CA (m^2): Capture area
V_{fg} (m/s): Flow velocity at a feeding depth
D (cal/g): Drifting insects, converted into energy (4,823 cal/g (dry weight))
I ($g/m^3 \cdot h$): Drifting insect supply rate

MCD was calculated to obtain CA. As shown in Figure 4, MCD can be calculated using Equation (3) (Hughers *et al.*, 1990). In this study, the following values were adopted: RD = 45 cm, V_{max} = 69 cm/s for fish shorter than 10 cm and V_{max} = 93 cm/s for fish 10 cm or longer.

$$MCD = (RD^2 - (V_{fg} \cdot RD/V_{max})^2)^{1/2} \quad (3)$$

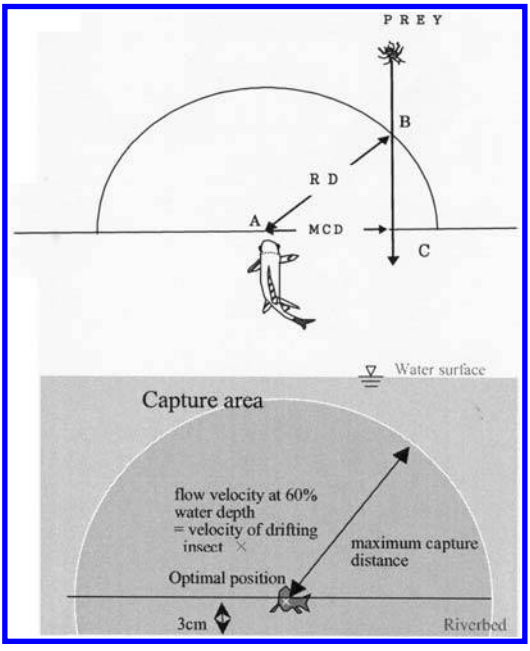


Figure 4. Maximum capture distance (MCD) and capture area (CA).

Where,
RD (m): Distance from food at which fish reacts to it
V_{max} (m/s): Maximum sustainable swimming velocity

CA was calculated using Equation (4) when a hypothetical fish's position was the bottom point (see Figure 4), and using Equation (5) when the position was the 60% depth. When MCD + 3 cm is greater than water depth (d_{fc}), Equation (6) in which calculated CA was the area above the riverbed is used. In that case, areas outside the MCD are included in CA for the simplification of calculation; however, such areas were expected to be relatively small.

$$CA = \pi \cdot MCD^2/2 + 0.03 \cdot 2MCD \quad \text{(Bottom position)} \quad (4)$$

$$CA = \pi \cdot MCD^2 \quad \text{(60\%-depth position)} \quad (5)$$

$$CA = d_{fc} \cdot 2MCD \ (MCD > d_{fc}) \quad (6)$$

SC was obtained using Equation (7) (Fausch, 1984), which allowed the calculation of energy required for the fish to maintain its position in the current. The equation can be adjusted by body weight and thus fish species and growth stage. In this study, the average body weight and the average body weight for fish between 5 and 10 cm long and between 10 and 20 cm long, which were determined by our fish surveys, are

Copyright © 2006 Taylor & Francis Group plc, London, UK

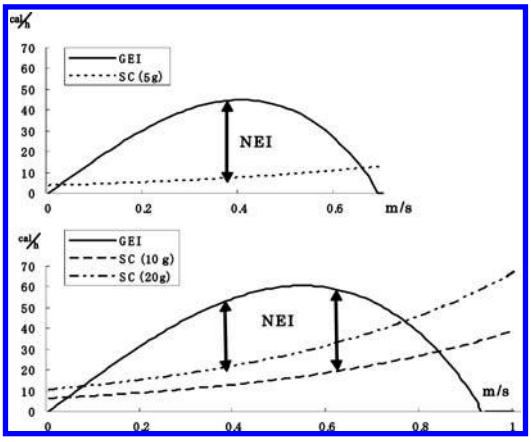


Figure 5. NEI, GEI, SC, and flow velocity.

set for each river and study period. In this way, NEI is calculated.

$$SC\ (cal/h) = 0.9906 \cdot BW^{0.784} \cdot e^{(0.0186 \cdot Vfc)} \quad (7)$$

Where,
BW (g): Body weight
V_{fc} (m/s): Flow velocity at position for rest

3.4 *Results*

3.4.1 *Evaluation based on energy budget and surveyed population density*

Figure 5 shows how values obtained from the energy budget model change according to the flow velocity at position for rest and feeding points. In this case, it was assumed that the flow velocity at optimal position and feeding points were the same and the drifting insect supply rate was constant. The values differed depending on body weight of fish: the lower the body weight and the shorter the capture distance, the narrower is the suitable flow velocity range, and the smaller are the GEI and SC; whereas, the greater the body weight and capture distance, the greater are the GEI and SC. The flow velocity at a feeding point that maximizes GEI was calculated for different body weights. SC becomes smaller as the flow velocity at the optimal position decreases. In using this model to calculate energy budget, it is necessary to use various flow velocities and consider various drifting insect supply rates. By using this model, the mutual relationships between habitat factors during the feeding period of cherry salmon can be expressed, and suitable physical environment based on NEI can be identified for a target river. SC starts rapidly increasing after the flow velocity exceeds 1 m/s, indicating the need for refuge areas in the event of flooding.

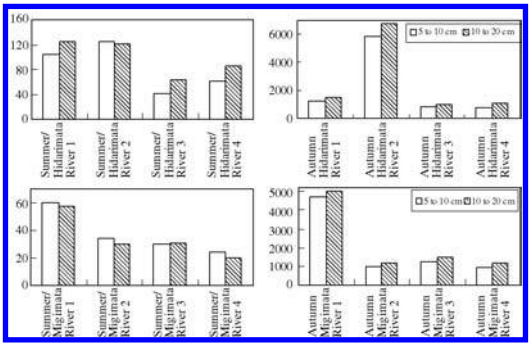


Figure 6. Net energy intake (NEI) (left: summer, right: autumn).

Next, the validity of the values calculated using the energy budget model is examined. The calculated values and surveyed results were compared for the river section cells (120 cells per section) Equation (8) was used to obtain the average NEI per unit water-surface area for each river section and for summer and autumn. Comparisons based on the two body-weight categories were also made.

$$NEI = 1/A \left\{ \sum_i \left[(GEI\ i - SC\ i) A\ i \right] \right\} \quad (8)$$

Where,
Ai: Water-surface area of Cell i

In the Hidarimata River, NEI is the highest in Section 2 in summer and in autumn (Figure 6), which is consistent with the surveyed population density. In the Migimata River, NEI is highest in Section 1 in summer, which agrees well with the surveyed population density. Evaluation of NEI and population density in the Migimata River in autumn was difficult because the population density did not show any variation. NEI was calculated for the four categories classified by cluster analysis. In Section 2 of the Hidarimata River and Section 1 of the Migimata River, where the population densities were high, pool cluster as a share of the total area of the section was high in both seasons (around 30% in summer and 20% in autumn), and the average water depth was high (0.4 to 0.6 m). The values for flow velocity in these two sections resulted in large NEI values (Figure 6). The average flow velocities at 60% depth in the two sections in summer were 0.37 m/s and 0.57 m/s when the average bottom flow velocities were 0.22 m/s and 0.24 m/s. Flow velocity tended to decrease in autumn in both sections. Cells classified as pool clusters in summer that retained that status in autumn accounted for 23% of cells for Section 2 and 29% for Section 1. These percentages were higher than those for the other sections, indicating that there were more stable pools in these sections. Figure 7 shows NEI for the pool cluster (shallow stream-edge

Copyright © 2006 Taylor & Francis Group plc, London, UK

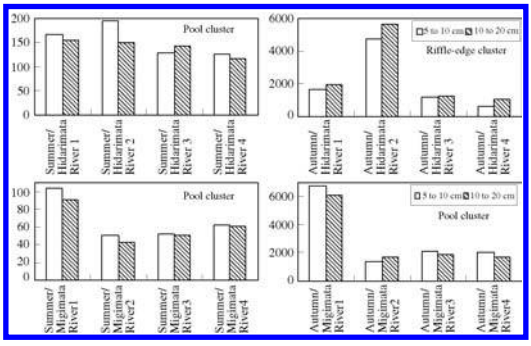


Figure 7. NEI for the pool clusters (left: summer, right: autumn).

cluster for the Hidarimata River in autumn), which clearly shows the relationship between NEI and population density. The results for the Hidarimata River are similar to results for all the clusters regardless of season (Figure 6). However, NEI in autumn for Sections 1, 2, and 4 is greater for smaller fish (5 to 10 cm) than for larger fish (10 to 20 cm), which shows that there is agreement between the population density from captured fish and the density calculated based on NEI. For the Migimata River, NEI for Section 4 is high in summer, which accurately reflects the surveyed population density. But NEI for the same section in autumn is about the same as NEI for other sections, from which it is not possible to identify the relationship between NEI and the surveyed population density.

3.4.2 *Habitat evaluation during flooding*

Whether flooding influences the population density of cherry salmon was evaluated by using the SC, i.e., energy required to maintain optimal position or to rest in the current. In the evaluation we assumed that it is easy for the fish to take refuge during flooding if the SC is small. SC analysis focused on the August 20 flooding, when there was the greatest water level increase recorded during the study period. The flow volume during the flooding was set at 3.8 m^3/s, based on HQ curves (Hidarimata River: $Q = 20.6 \cdot (H + 0.137)^2$; Migimata River: $Q = 13.17 \cdot (H + 0.183)^2$), and the roughness coefficient was set at 0.065 to 0.075, based on observed values. To obtain SC, five or six cross sections for each river section (summer survey results), and the water level and the flow-velocity increase estimated for each survey point (cell) were used in a non uniform flow calculation (Figure 8). In the Hidarimata River, the survey showed that the population density decreased almost uniformly in all four sections from summer to autumn, although SC was high for Section 4 and relatively high for Section 3. In the Migimata River, SC was high for Sections 3 and 4 ,the surveyed population density significantly decreased in Section 4.

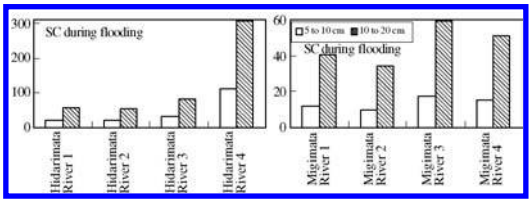


Figure 8. Swimming cost (SC) during flooding.

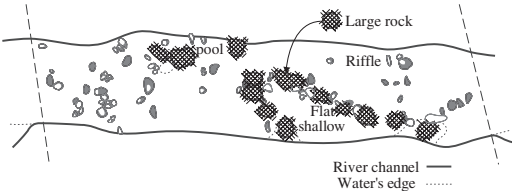


Figure 9. Pool creation experiment (Migimata River 4).

During the flooding it was clarified that flow velocity and water depth increased uniformly in Sections 3 and 4 of the Hidarimata River and Sections 3 and 4 of the Migimata River, where channel physical structures are relatively simple. Increase in water depth and flow velocity were not uniform in Sections 1 and 2 of the Hidarimata River and Sections 1 and 2 of the Migimata River, where channel physical structures are complex, with many sandbars and large rocks. Increase in SC based on the autumn flow regime from SC based on the summer flow regime in the Hidarimata River was great in Section 4, and increase in SC for Section 3 was greater than those for Sections 1 and 2. In the Migimata River the increases in SC for Sections 3 and 4 were 5 to 20 cal/h greater those for Sections 1 and 2.

3.5 *Experiment on improvement of river physical environment*

3.5.1 *Pool-creation experiment*

It was predicted that there would be sections where SC would be high during flooding, and that this would predict to the decrease in population density of cherry salmon there. It is also pointed out that a decrease in the number of pools caused by river improvement works and changes in land use in the river basin can contribute to the decrease in cherry salmon population. To address decrease in the cherry salmon population, we conducted an experiment where pools were artificially created to minimize the energy expenditure required for the fish to maintain position. SC and fish distribution were compared using the evaluation model described above.

In April 2005 in the Migimata River, pools were created in Sections 3 and 4 by repositioning riverbed rocks (Figure 9). Section 2 was used as the reference section. To calculate SC, physical environment surveys

Copyright © 2006 Taylor & Francis Group plc, London, UK

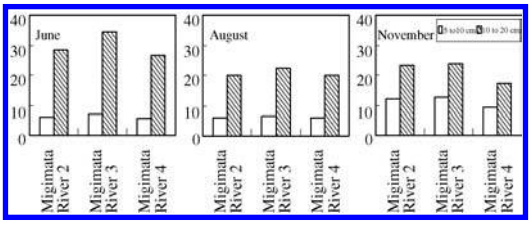


Figure 10. SC of pool creation and reference section.

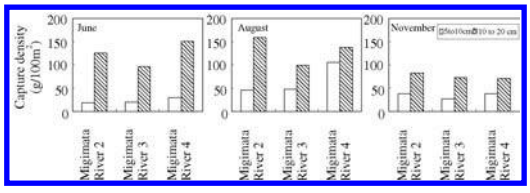


Figure 11. Population density in pool creation and reference section.

were conducted in June, August, and November 2005, using the method described in 3.1 *Survey procedures*. SC was similar in all sections, although it was slightly high in Section 3 in June and August and low in Section 4 in November (Figure 10). Figure 11 shows the survey results of population density for each survey section. The number of small-sized fish was great in Section 4 in June, August. And the population density was almost the same in each section, even though flooding with water-level increase of 50 cm or more occurred three times during the study period. Therefore, it is suggested that the creation of pools did not adversely affect the cherry salmon population. In the November survey the pools we had created in Sections 3 and 4 in April became smaller as the result of natural changes in channel configurations. I will continue monitoring and conducting hydrological investigations, such as by calculating SC during flooding and studying the disappearance process of pools.

3.5.2 *Improvement of the food environment*

GEI changes with the drifting insect supply rate. So the experiment were attempted to improve the food environment of cherry salmon by improving the habitat for benthic animals. The fish feed on both terrestrial and aquatic insects. They mainly eat benthic animals, most of which are aquatic insects, except in summer when there are fewer aquatic insects and cherry salmon become increasingly reliant on terrestrial insects that originate in riparian woods. It is becoming more evident from studies that water quality, flow velocity, riverbed material, organic matter, and other factors influence the benthic habitat. It has been pointed out that the straightening of rivers has reduced the supply of organic matter into rivers and the retention of organic matter, particularly at the upper reaches.

In this study, we artificially altered a channel structure and the amount of organic matter and then monitored changes in the distribution of benthic animals to increase food for cherry salmon. This examination used existing knowledge with which it is possible to characterize the habitat in the most parts (riffles) of the river, except in pools, based on the relationship between the channel's physical structural factors (e.g., water depth, flow velocity) and food factors (e.g., organic matter). This is one of the first empirical studies of its kind, and it is expected to be useful in establishing a method of using benthic habitat factors to evaluate the fish habitat.

We conducted an experiment to increase the accumulation of coarse particulate organic matter (CPOM) by reducing water depth and flow velocity at a section with several riffles on the Atsubetsu river of the Ishikari River System. Through this experiment we examined the changes in benthic animal populations (Negishi *et al.*, 2003).

It was predicted that sedimentation on the riverbed would increase following the creation of experimental river sections where flow velocity was reduced by groin (spur dike in sandbag) installation. Also, iron piles were installed to promote accumulation of CPOM and other matter (i.e., food environment factors). The effect of changes in the physical and food environments on benthic animal populations was examined in mid October 2003. The river section for the experiment is shown in Figure 12. Three riverbed/flow regime modified sections were established downstream of a reference section. Iron piles were installed in the first and second sections, and a groin was made between the second and third sections. The first section had rapid flow because it was upstream of the groin (fast-flow pile works section) and the second section, immediately upstream of the groin, had slow flow (slow-flow pile works section). The third section was downstream from the groin, and the physical environment of the section was affected only by the groin (energy-dissipated section).

The posteriori study was conducted in late November, one month after the preliminary study. Sampling was conducted at 12 locations (i.e., three sampling sites for each section) for benthic animals, organic matter and attached algae. Physical conditions were also measured at each sampling site. The flow velocity decreased most in the slow flow pile works section followed by the energy-dissipated section. The flow velocity decrease was smallest in the fast-flow pile works section. The water depth decreased most in the energy-dissipated section followed by the slow-flow pile works section and the fast-flow pile works section. The flow velocity and water depth also decreased in the reference section. Both the flow velocity and

Copyright © 2006 Taylor & Francis Group plc, London, UK

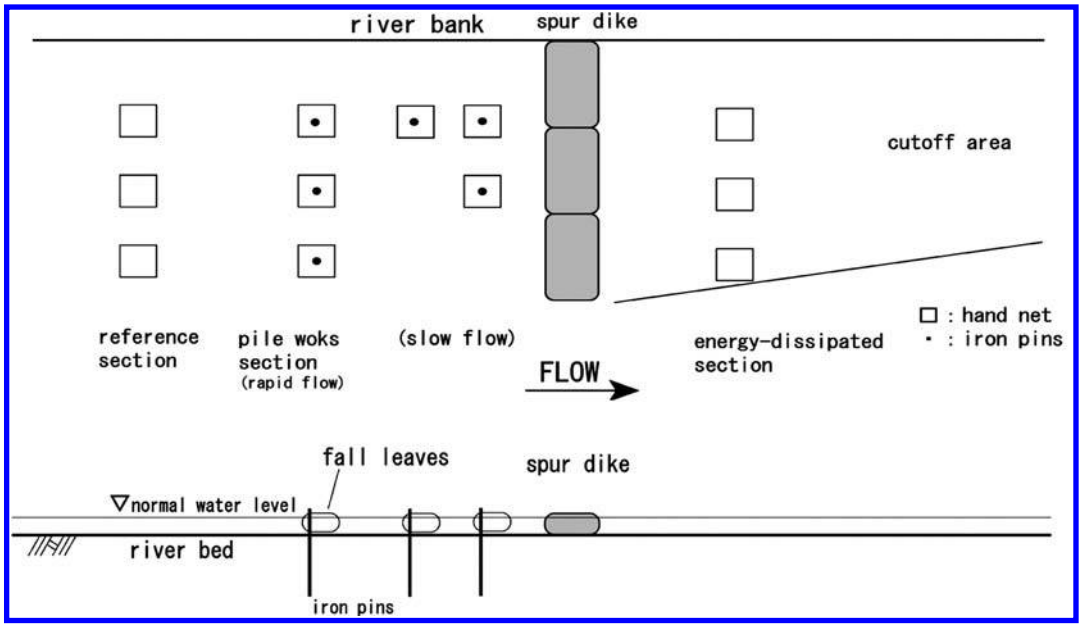


Figure 12. Physical structure improvement experiment on the artificially modified river section (riffle) (upper: plan, lower: cross section).

the water depth increased in the slow-flow pile works section, both slightly decreased in the fast-flow pile works section, and the water depth decreased and the flow velocity increased in the energy-dissipated section. The size of riverbed material decreased in the energy-dissipated section and the slow-flow pile works section, and slightly decreased in the fast-flow pile works section and the reference section. Loose rock as a share of riverbed surface rock decreased by half in the energy-dissipated section, and decreased in the fast-flow pile works section and slow-flow pile works section. As for the food environment, CPOM and fine particulate organic matter (FPOM) greatly increased in the pile works sections, increased in the reference section, but decreased in the energy-dissipated section. Amount of attached algae increased in all sections. Based on these results, the physical conditions and food environment of the pile works sections, particularly the section with slow flow, improved to become close to those of the natural streams. In the energy-dissipated section the physical environment improved but the food environment did not.

Figures 13 and 14 show the result on benthic animal populations. The number of benthic animals decreased in the reference and energy-dissipated sections, but increased in the pile works sections. The taxonomic diversity (number of taxa) did not change in the reference section and decreased in the energy-dissipated section, but nearly doubled in the pile works sections. Changes in population of benthic animals categorized

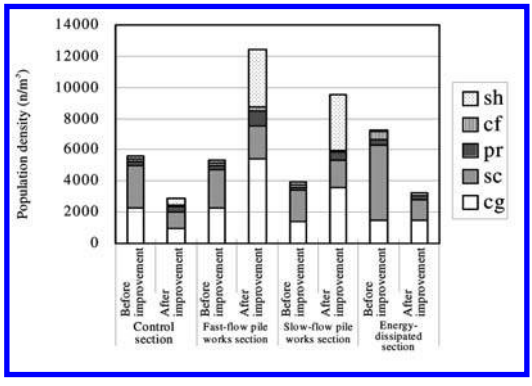


Figure 13. Changes in the number of benthic animals in each section.

by feeding pattern are as follows. In the reference section the number of scrapers and collectors decreased. Shredders slightly increased both in population and taxonomic diversity.

In the pile works sections, shredders sharply increased in population and taxonomic diversity, and collectors and predators increased in population and taxonomic diversity. As a result, scrapers as a share of the total population decreased. In the energy-dissipated section, the number of scrapers sharply decreased, collectors as a share of the total population increased, and shredders were not found. The diversity

Copyright © 2006 Taylor & Francis Group plc, London, UK

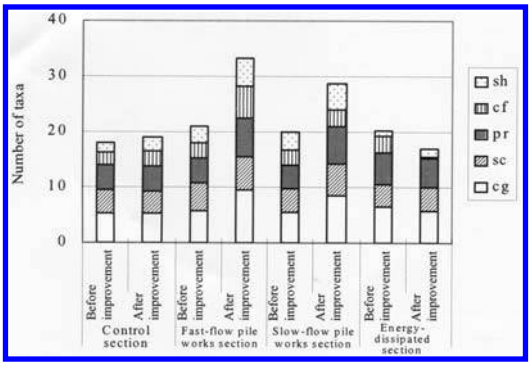


Figure 14. Changes in taxonomic diversity in each section.

index increased in all sections, although the increase was not marked in the energy-dissipated section. In the energy-dissipated section the physical conditions were improved, but the supply of organic matter such as fallen leaves was reduced by groin works, preventing CPOM from accumulating. Therefore, the energy dissipation from groin work installation did not positively influence the population of benthic animals. It was predicted that the physical and food environments in the slow-flow pile works section would improve and the population of benthic animals would increase more than that in the fast-flow pile works section; however, no clear differences were observed between the two sections. Contrary to our prediction, the population of benthic animals slightly increased in the fast-flow pile works section.

For riffles in autumn in the river sections studied, the food environment, not the physical environment, was a limiting factor for the population of benthic animals. It was verified that it is possible to improve the habitat for cherry salmon by creating physical structures that improve the retention and accumulation of organic matter, which in turn improves the food environment.

4 CONCLUSIONS AND FUTURE WORK

Habitat for cherry salmon parr in the feeding stage was evaluated by the energy budget method. The values obtained by this method agree fairly well with the salmon population density obtained by field survey. To hone this method of describing the relationship between the physical structures of habitat and the population distribution of cherry salmon, it is necessary to improve models for the fish's feeding and positioning in the current. The possible parameters that will be considered in developing such models include a physical unit of a series of a riffle and pool, and the distribution of such series in the river channel, detailed three-dimensional data on flow velocities and water depths, and the volumes of each habitat. It will also be necessary to obtain detailed knowledge on the relationship between the insect drift rate and the river channel environment. Further more, we have plan to examine river channel designs and maintenance technologies, including creation of riffles and pools, suitable as cherry salmon habitat. This can be achieved by applying the method developed in this study to fish habitats of rivers with various physical structures and discharge characteristics.

ACKNOWLEDGMENTS

This study was conducted under a grant for sponsored research from the Hokkaido Development Bureau. And it was supported by Hokkaido fish hatchery. Nakajima (Director of salmon resource) and Urabe (Researcher in Donan branch) cooperated and advised in examining. Additionally Sasage, Nakahara, Nunokawa (Engineer of consultants CO) conducted field surveys. We express their gratitude.

REFERENCES

Stalnker, C., Lamb, B.L., Henriken, J., Bovee, K., & Bartholow, J., 1994. The Instream Incremental Methodology – A primer for IFIM – National Ecology Research Center, National Biological Survey.

Hughers, N.F., & Dill, L.M., 1990. Position choice by drift-feeding salmonids-Model and test for Arctic grayling (Thymallus arcticus) in subarctic mountain streams, interior Alaska, Canadian Journal of Fisheries and Aquatic Science 47:2039–2048.

Fausch, K.D., 1984. Profitable stream positions for salmonids-relating specific growth rate to net energy gain, Canadian Journal of Zoology 62:441–451.

Negishi, J.N., & Richardson, J.S., 2003. Responses of organic matter and macroinvertebrates to placements of boulder clusters in a small stream of southwestern British Columbia, Canada, Canadian Journal of Fisheries and Aquatic Science 60:247–258.

Leclerc, M., 2002. Ecohydraulics, last frontier for fluvial hydraulics: research challenges and multidisciplinary perspectives, River Flow 2002:13–25.

Copyright © 2006 Taylor & Francis Group plc, London, UK

Flow-vegetation-sediment interaction: Research challenges

J. Järvelä, J. Aberle & A. Dittrich
Leichtweiss-Institute for Hydraulic Engineering, Technical University of Braunschweig, Germany

H.P. Rauch
Institute for Soil Bioengineering and Landscape Construction, University of Natural Resources and Applied Life Sciences, Vienna, Austria

I. Schnauder
Hydroenvironmental Research Centre, Cardiff School of Engineering, Cardiff University, UK

ABSTRACT: A good understanding of the interaction between flow, vegetation, and sediment is a key issue for successful river restoration and sustainable flood management. However, many of the relevant hydraulic and sedimentological processes are not fully understood. Flow in rivers and floodplains is complex as it is affected by several interconnected factors such as topography, relative submergence, and vegetation characteristics. These factors directly influence the turbulent flow field and thus sediment dynamics. On the basis of recent field and experimental studies with natural vegetation this paper highlights problems associated with existing computational approaches. Key parameters and characterisation concepts for vegetation are discussed with respect to requirements for reliable modelling of sediment dynamics and river morphology. To tackle the problems, integrated research strategies based on the combination of field studies, laboratory experiments, and numerical modelling are proposed.

1 INTRODUCTION

Traditional river engineering in Europe in the last centuries focused mainly on increasing the agricultural production and protecting people and property from flooding. Particularly in densely populated areas, the function of the rivers was minimized to a system to convey effectively water. This development resulted in straightened river courses along with significant reduction of wetland and natural flood retention areas and an ecological degradation of sensitive riverine habitats. It is nowadays often assumed that river engineering works and intensified catchment landuse have increased the magnitude and propagation of flood waves, though the knowledge of the relative importance of the associated mechanisms remains incomplete (e.g. Pinter et al. 2006). There is ample evidence, however, that river scientists are attempting to integrate principles of hydrology, geomorphology and ecology into synthetic frameworks to better understand and predict how river systems function and respond to manipulation (Wohl et al. 2005). New design approaches and decision support systems for river engineering and management can be developed only on the basis of an improved understanding of fluvial processes and more advanced modelling in combination with improved field monitoring and data elaboration (Klaassen 2002). Recent interest in river restoration, environmental flood management, and the application of bioengineering techniques has brought new perspective to the analysis of environmental hydraulics with special regard to vegetated channels (see e.g. Oplatka 1998, Copeland et al. 2001, Shields et al. 2003, Järvelä 2004b, Rauch 2005, Boelscher et al. 2005).

Flow conditions in open-channels depend on many factors such as discharge, cross-sectional shape, bed forms, sinuosity, sediment and substrate, ice cover and vegetation. In this paper we highlight the effect of vegetation on flow phenomena in open channels. Riparian vegetation is a ubiquitous feature of riverine landscapes providing habitat and food sources, aesthetic appeal as well as erosion control (Andrews 1984, Hey & Thorne 1986). The proper understanding of associated physical processes is the basis for the development of reliable modelling tools for hydraulics, sediment transport, river morphology, and pollutant transport. Such models are needed for the development of sustainable river management strategies as well as ecological and biological considerations. The purpose

Copyright © 2006 Taylor & Francis Group plc, London, UK



Figure 1. Flow-vegetation interaction is a complex process as it is influenced by several interconnected factors, including topography, relative submergence, and vegetation characteristics (photo J. Järvelä).

of this paper is to provide a state-of-the-art review of current approaches to address flow-vegetation-sediment interaction and to propose potential solutions to close the gaps in our knowledge.

2 STATE-OF-THE-ART

Vegetation increases flow resistance, changes backwater profiles, and modifies sediment transport and deposition (Yen 2002). The quantification of the net impact of vegetation is, however, difficult and depends on many complex interacting factors, including the geomorphic setting of a channel, physical properties, extent, species, age, and health of vegetation (Darby 1999) and temporal variations such as water stage and growth of vegetation (Bakry et al. 1992, Fisher 1995, Sellin & van Beesten 2002) (Fig. 1). For example, dense vegetation within a channel can alter the effective area of a cross section that conveys the flow and significantly influence local flow properties (Hicks et al. 2006). In vegetated compound channels, floodplain flow interacts with the main channel flow or vegetated zones resulting in additional energy losses (Sellin 1964, Pasche & Rouvé 1985, Knight & Shiono 1996, Thornton et al. 2000, Helmiö 2004).

Besides the influence of vegetation on hydraulics, vegetation is a key player also in erosion, transport, and deposition processes of solids, nutrients, and pollutants. The range of associated problems is widespread including the influence of aquatic vegetation on fine sediment dynamics (e.g. Paterson & Black 1999, Aberle et al. 2004), the proper design of wetlands (Hayes et al. 2000), and the influence of terrestrial vegetation on overland flow that carries sediment to the river system (e.g. Rey 2004). The last issue is of particular interest for hydraulic engineering applications since sediment deposits on the floodplain may significantly reduce the conveyance capacity for future flood events (Dittrich & Järvelä 2006). On the other hand, deposited polluted sediments can be washed away during floods, which may be harmful to the riverine ecosystem.

An important issue to be considered when investigating vegetated river systems is the scale of analysis. Investigations of how vegetation influences the turbulent flow field are generally conducted either at point, cross-sectional or reach scales. The knowledge gained from such investigations is often implicitly upscaled to model flow in long river reaches and catchments. Such models require detailed data on bathymetry and ground cover (e.g. bed roughness, vegetation). Techniques to gather the required data are already available and include airborne laser scanning (ALS), vertical aerial photography, and multi-spectral (MS) scanning (e.g. Hicks et al. 2006). Using GIS systems it is possible to generate Digital Elevation Models (DEM) and to determine ground cover (Hicks et al. 2006), type, structure and density of vegetation (Hug et al. 2004) and bed roughness parameters such as characteristic grain-sizes (Carbonneau et al. 2005). However, the reliability of these models depends on the accurate modelling of the critical physical processes. Therefore, we focus in the following section first on the current knowledge concerning the relationship between vegetation characteristics and flow. This knowledge is a prerequisite for the second part of the literature review, flow-vegetation-sediment interaction.

2.1 *Flow-vegetation interaction*

In this section, advances in the knowledge of flow-vegetation are reviewed beginning with the development of methods to determine bulk resistance coefficients. Thereafter the review is directed towards a more detailed description of the flow processes including velocity distributions and turbulence. In the analysis of vegetal flow, non-submerged and submerged conditions are typically separated, since the flow field considerably changes when flow depth exceeds the height of vegetation. In addition, usually two types of vegetation are defined: rigid and flexible plants. On the basis of this classification, a considerable amount of research has been carried out in developing resistance laws for channels with rigid vegetation (e.g. Li & Shen 1973, Petryk & Bosmajian 1975, Lindner 1982, Pasche & Rouvé 1985, Musleh & Cruise 2006), flexible vegetation (e.g. SCS 1954, Kouwen & Unny 1973, Temple et al. 1987, Kouwen & Fathi-Moghadam 2000, Carollo et al. 2005), and various combinations (e.g. Flippin-Dudley et al. 1998, Freeman et al. 2000, Järvelä 2004a). In these conceptual models, numerous different variables have been used to describe the relationship between the flow and vegetation properties. The variation is for the most part due to the differences in vegetation type and relative submergence.

Copyright © 2006 Taylor & Francis Group plc, London, UK

2.1.1 *Bulk approaches*

In traditional approaches, vegetation is typically reduced to boundary roughness by adjusting the channel and/or floodplain roughness coefficient which combines all sources of flow resistance, including vegetation, into Manning's n. Such cross-section or reach-averaged bulk coefficients have been used widely in the analysis of practical engineering problems and are typically selected with the help of reference publications, such as Chow (1959), Barnes (1967), Arcement & Schneider (1989), Coon (1998) and Hicks & Mason (1999). Simple approaches, such as the Cowan (1956) summation method, have given some guidance to combine the effect of various sources contributing to the total resistance. Another often-used methodology to determine the total flow resistance is the Einstein and Banks (1950) linear superposition principle, which can be applied to point as well as reach scales.

To design vegetated (grass-lined) waterways, Palmer (1945) introduced the *n-VR* method relating Manning's n to the product of average velocity V and hydraulic radius R for various channel slopes and plant-stands. For fully submerged vegetation, Kouwen et al. (1969) criticised the *n-VR* method and introduced a stiffness parameter MEI, flexural rigidity per unit area, which reflects the overall resistance to deformation of a plant stand as a result of a flow passing over it. Three decades later, Temple (1999) argued that the *n-VR* method has remained the primary tool for practical application to grass-lined channel conditions, although alternate approaches for predicting vegetal flow resistance have been proposed.

2.1.2 *Vegetative drag*

For non-submerged flow with cylindrical roughness, Li & Shen (1973) and Petryk & Bosmajian (1975) used plant diameter, longitudinal and lateral distances between the plants, and drag coefficient as independent variables. Li & Shen (1973) identified four factors that need to be taken into account in determining the drag coefficient: 1) the effects of open-channel turbulence; 2) the effect of non-uniform velocity profile; 3) the free surface effects; and 4) the effect of blockage. Lindner (1982) concluded that, in densely vegetated channels, the first two of these are of minor importance and can be neglected. Vogel (1994) reported that the major contributor to the drag of most trees is the drag of the leaves. He found that reshaping of the leaves is a critical process in generating drag. Therefore, branched and leafy plants cannot be treated as simple cylinders. Freeman et al. (2000), Kouwen & Fathi-Moghadam (2000), and Järvelä (2002) reported for natural woody vegetation great variations in the flow resistance with the mean flow velocity, because of plant bending and changing flow depth. Fathi-Moghadam & Kouwen (1997) stated that the vegetation density is always a dominant parameter regardless of tree species or foliage shape and distribution. Kouwen & Fathi-Moghadam (2000) related flow resistance to velocity and a species-specific vegetation index ξE, which accounts for the effects of shape, flexibility, and biomass. Järvelä (2004a) concluded that the essential factors in formulating a resistance equation for woody vegetation are density of vegetation and deformation of plants in a flow. He suggested characterization of leafy woody vegetation based on three variables: 1) leaf area index (LAI); 2) a species-specific drag coefficient $C_{d\chi}$; and 3) a vegetation parameter χ, which accounts for the effects of plant deformation in a flow (velocity effect) and is unique for a particular species.

2.1.3 *Turbulent flow field*

Recently, several studies (e.g. Shimizu & Tsujimoto 1994, Tsujimoto et al. 1996, Naot et al. 1996, Nepf 1999, López & García 2001, Stephan & Gutknecht 2002, Järvelä 2005) have focused on velocity distribution and turbulent characteristics of vegetated channels and floodplains. This field of research was founded in the 1970's to investigate the effect of wind on tree stands and canopies; a review of this topic is given by Finnigan (2000). In the 1990's with an increasing interest in river restoration, this research approach was extended to aquatic vegetation with the aim to characterise the vertical velocity profile above submerged plants. With the development of measurement techniques such as Acoustic Doppler Velocimetry (ADV), the spatial and temporal resolution of flow measurements was improved, revealing the turbulence structure for some simplified cases, such as flow around cylindrical obstacles. Most of these studies have been directed towards an adaptation of the logarithmic law of the wall for flow above submerged aquatic vegetation (López & García 2001, Stephan & Gutknecht 2002, Baptist 2005). The differences in the approaches are due to the modifications of the zero-velocity displacement and roughness height (e.g. deflected plant height; see Stephan & Gutknecht 2002 for a review). Another conceptual modelling approach for velocity distribution is based on the assumption that the vertical velocity profiles have a form of a hyperbolic tangent function. Such profiles are characterised by an inflection point (Ghisalberti & Nepf 2002) and can be derived with the help of the mixing layer analogy (Raupach et al. 1996). Using this approach, the location of the inflection point was found to coincide with the top of the bent vegetation in the physical model by Carollo et al. (2002).

Freeman et al. (2000) reported significant influence of the vegetation canopy on the velocity distribution in the wake. The authors observed that shrubs with open areas beneath the primary leaf mass diverted significant amounts of flow beneath the canopy, leading to an accelerated sub-canopy flow and an increase of the bed shear stresses around the plants. Similar velocity profiles have been measured by Boelscher

Copyright © 2006 Taylor & Francis Group plc, London, UK

et al. (2005) in a field study with natural willows. Their study revealed the dependence of velocity profiles on a seasonal and hydrograph time-scale, which had not been taken into account before. Nepf (1999) investigated flow through groups of emergent cylinders and found a direct relation between the turbulent kinetic energy and the vegetative drag. The fraction of mean energy, which was transferred into turbulence, was dependent on the ratio between form and surface drag of the stems. Turbulence intensities increased with sparser element density due to larger wake zones, but decreased with increasing density due to a reduced mean velocity and eddy scale. For submerged conditions, the turbulent length scales can be classified vertically according to the phenomenological concept of Poggi et al. (2004): 1) the lower regions which are dominated by von Karman vortices associated with the flow around the elements; 2) a mixing layer between the topmost region of the vegetation and the outer flow above; and 3) a boundary layer flow considering the whole vegetation as a rough wall with a zero-velocity displacement towards the vegetation. Further studies revealed the importance of coherent vortex structures similar to near-bed sweeps and ejections for the vertical momentum transfer above the plant canopies (Ghisalberti & Nepf 2002, Stephan & Gutknecht 2002). These flow structures are associated with waving motions of flexible plants, the so-called "honami" phenomenon. Honami enhances the vertical momentum transfer and reduces the stresses on the plants (Ikeda & Kanazawa 1996, Ghisalberti & Nepf 2002, Stephan & Gutknecht 2002).

2.1.4 *Spatial variability*

The spatial variability of the velocity and turbulence characteristics in a group array of cylinders was investigated by Lopez & Garcia (1998) and Choi & Kang (2004) on the basis of the Reynolds Averaged Navier Stokes (RANS) equations. However, the flow field within a canopy is highly three-dimensional, and therefore, it is not clear how to address adequately the spatial heterogeneity of the flow. In fact, most applications deal with spatially averaged roughness parameters that cannot be linked explicitly with local flow properties provided by the RANS equations. These conceptual contradictions have been ignored in most studies. Nevertheless, all the above studies have significantly contributed to the understanding of how vegetation influences flow resistance, and they provide the basis for the current standard in modelling flow-vegetation interaction using 1D (e.g. Yoshida & Dittrich 2002), 2D (e.g. Beffa & Connel 2001), and 3D numerical models (e.g. Stoesser et al. 2003). The shortcoming of how to describe the turbulent flow field in complex flow situations has only recently been specifically tackled in environmental hydraulics by using the Double Averaging Methodology (DAM). The majority of DAM related studies have focused on rough-bed flows (e.g. Nikora et al. 2001, 2005b, Aberle & Koll 2004, Campbell et al. 2005). DAM studies related to flow resistance of vegetation have been reported by Lopez & Garcia (1998, 2001), Nepf & Vivoni (2000), and Righetti & Armanini (2002).

2.2 *Flow-vegetation-sediment interaction*

Numerical models for the assessment of morphological development of river reaches have been developed by Tsujimoto (1999) and Baptist (2005). In these models, state of the art approaches for numerical flow simulations, turbulence modelling as well as sediment transport have been combined to simulate morphological development. Dittrich et al. (2005) used a 3D hydrodynamic model to evaluate flow patterns on floodplains and in vegetated areas to identify areas prone to erosion and sedimentation. The results of their numerical studies were used to assess morphological development and to refine flood management strategies at the River Rhine. Successful numerical simulations of the transportation of fine sediments through emergent vegetation have been carried out by Lopez & Garcia (1998) and Choi & Kang (2004) on the basis of experimental data of Tollner et al. (1982). The challenge within such investigations is the adequate modelling of the turbulent flow field, which is needed to estimate reliably suspended sediment transport. The altered turbulent flow field around plants and the reduced bulk flow velocity may result in enhanced deposition of suspended sediments (Fig. 2). However, vegetation may have also a destabilising effect on the sediments due to high local turbulent intensities and vertical velocity components in their wake. In this context, Choi & Kang (2004) concluded that the use of an isotropic turbulence model results in a significant underestimation of suspended sediment load for open-channel flow with emergent vegetation. Furthermore, Elliot (2000) showed that settling of suspended



Figure 2. Sediment deposits after a flood event on a vegetated riverbank and floodplain (photo H.H. Bernhart).

Copyright © 2006 Taylor & Francis Group plc, London, UK

sediment onto vegetation has the potential to additionally increase the rate of removal of sediment from the flow, indicating the complexity of the relevant processes.

Detailed experimental studies of how bed load is transported through vegetation have only recently been carried out by Specht (2002) and Jordanova & James (2003). Specht (2002) investigated in a series of laboratory experiments how vegetation influences bed load transport rates in compact river channels. Based on these experiments he derived a coefficient which can be used with various bed load transport formulae to account for the effect of both symmetrical and asymmetrical bank vegetation. Besides the altered transport rates, Specht (2002) found that vegetation significantly influences the geometry of sand dunes, which became steeper and more regular in length. Jordanova & James (2003) found that bed load rate through emergent stems is closely correlated with excess bed shear stress. In the study, shear stress exerted on the bed was calculated by subtracting the total stem drag from the total force applied by the flow in the flow direction. However, the results of Jordanova & James (2003) cannot be generalized, since they were obtained for only one sediment size, stem diameter, and stem spacing.

The influence of bank vegetation on gravel bed channel pattern has been investigated, e.g. by Ikeda & Izumi (1990) and Millar (2000). Both studies revealed that bank vegetation does represent an important and quantifiable control on alluvial river patterns. Similar results have been obtained by Gran & Paola (2001) and Coulthard (2005), focusing on the influence of riparian vegetation on braided stream patterns and dynamics. These laboratory studies revealed that vegetation can substantially alter channel geometry and flow characteristics in braided rivers by stabilizing the banks, constraining channel migration, and allowing deeper and narrower channels to develop (Gran & Paola 2001). Furthermore, Coulthard (2005) found that relatively sparse levels of vegetation can alter flow dynamics and cause the deposition of islands in the lee. When vegetation starts to grow on such islands, they can then develop not only downstream but also in upstream and transverse directions (Tsujimoto et al. 1998).

Huang & Nanson (1997) performed a field study in small streams and showed that it is necessary to distinguish between bank vegetation and vegetation growing on the channel bed. They found that dense bank vegetation results in narrower channels whereas channel vegetation increases flow resistance, causes channel widening and hence reduces flow velocity but not necessarily flow depth. Jeffries et al. (2003) investigated in a field study the influence of large woody debris on patterns of sediment deposition within a small forest floodplain and found that patterns of sediment deposition were both greater and more variable than for non-forested floodplains. Boelscher et al. (2005) found in their field study strong local scouring around tree stems, often enhanced by clogging of floating debris and increased sub-canopy flow velocities. Toda et al. (2005) used field observations and numerical modelling studies to determine the effects of the flood flow on the riparian vegetation and the soil environments of floodplains in a gravel-bed river. They found that the amount of particulate nutrients on the floodplain increased during small floods, whereas it decreased during large floods. The latter effect was explained by the removal of fine sands and hence nutrients from floodplains during large flood events.

3 DISCUSSION AND CONCLUSION

The literature review revealed that the effect of the natural characteristics of vegetation on flow resistance and sediment dynamics have not been adequately addressed in hydraulic design and modelling. This is due to the complexity of the flow as it is affected by several interconnected factors such as topography, relative submergence (flow through and over vegetation), vegetation characteristics (e.g. coverage, patchiness), and plant characteristics (e.g. deformation of plants with increasing velocity). Yet, it is not fully clear at which spatial and temporal scales the key flow processes should be investigated. On the other hand, it appears that the available knowledge of the key processes is not fully exploited in current modelling and management approaches because of a lack of appropriate feedback mechanisms between model developers, river scientists, and managers.

It is obvious that solving a local flow problem requires a different approach compared to the hydraulic analysis of a large catchment. In addition, the scale of the analysis is dependent on the nature of the problem. For example, estimation of water stage can be based often on cross-section and reach averaged variables. However, for predicting erosion and sediment transport such averaging may result in significant errors, and a more suitable solution would probably require a 2/3D analysis. To quantify flow-vegetation interaction, a formula or model that will relate measurable characteristics of vegetation to flow properties is desirable. Theoretical (or semi-empirical) approaches should provide a better general understanding of the variation in flow processes. From a practical point of view, a suitable approach should be transparent and straightforward enough to be applied by a practising engineer. However, no approach can deliver reliable results if the physical reality is excessively simplified or if the source data are of low quality. Gathering field data for natural vegetation is far more complicated and time-consuming than describing the properties of simulated vegetation in laboratory conditions. Therefore, a preferable approach uses clearly

Copyright © 2006 Taylor & Francis Group plc, London, UK



Figure 3. Bending and streamlining of vegetation is a critical process, which must be taken into account in developing flow resistance models and in designing scale model experiments; natural willows (a) in comparison to rigid cylinders (b) (photos J. Järvelä).

defined variables, which can be easily and objectively determined. In contrast, many of the hydraulic design methods used currently rely on the professional judgment of an experienced engineer, e.g. in selecting a roughness coefficient.

Although simulation of vegetation under laboratory conditions seems to be preferable, there is still a lack of appropriate methods to incorporate the effect of natural vegetation in hydraulic models. Several methods or formulas have been developed to determine bulk (averaged) flow properties, but most are based on the simulation of vegetation by artificial rigid cylinders. However, in reality natural vegetation exhibits a wide variety of forms and flexibility (Fig. 3). Furthermore, if such cylinders would be upscaled to the nature, they typically would be unrealistically large in diameter. The effect of scale on experimental design and data interpretation needs to be elaborated. Recent experimental investigations with natural plants have provided new insight into the identification of important mechanisms with which vegetation react to flow stresses. These mechanisms comprise 1) the bending of the main stem and branch structure in flow direction; 2) the width and height compression of the leaf mass; and 3) the dynamic, waving motions of the plant induced by the vortex shedding in the wake (Schnauder 2004). This knowledge is important in order to quantify drag exerted by plants (e.g. Armanini et al. 2005, Wilson et al. 2005) and hence for the quantification of flow resistance. As a next step, the research should focus on detailed investigation of the bulk dependencies and the turbulent flow field.

The interaction between the turbulent flow field and vegetation has been investigated mainly with respect to the time averaged velocity profile within and above vegetated areas. However, the flow field within the canopy is highly three-dimensional, and therefore, it is not clear how to adequately address spatial flow heterogeneity. Herein, a promising direction is the DAM approach. Nikora et al. (2005a) showed that this approach is a useful tool for developing numerical models, designing laboratory, field, and numerical experiments, and for data analysis and interpretation. E.g., by adopting the DAM approach, similarity hypotheses and two-dimensional assumptions can be developed and applied even for the flow region in the canopy, which is impossible using the conventional time-averaged variables. Thus, this methodology may significantly improve research tools for studying a wide range of flow-vegetation-biota interaction phenomena (Nikora et al. 2005b).

Although the spatial pattern of the vegetation and plant characteristics significantly influence sediment dynamics, numerical and experimental studies have been based on idealized conditions and are thus far from being generalized for practical purposes. For example, most of the numerical approaches are based on k-ε models, which assume isotropic turbulence, though it is not clear if such turbulence models allow for adequate modelling of turbulence in vegetated zones (Choi & Kang 2004, Baptist 2005). Furthermore, turbulent and form induced stresses significantly influence the flow forces acting on the bed and hence bed shear stress (Nikora et al. 2005a). Bed shear stress, on the other hand, is the key parameter for modelling incipient motion and bed load transport. However, in complex geometries it is not straightforward to determine bed shear stress unambiguously (Rowinski et al. 2005, Nikora et al. 2005a). This is only one of the problems in modelling geomorphologic development. The amount of transported sediment depends not only on flow but as well on sediment characteristics. There is a wide range of empirically derived sediment transport formulae available which yield, for the same hydraulic conditions, differences of up to several hundred percent when estimating bed load transport (Specht 2002). The reason for these differences is associated with experimental boundary conditions, flow forces, grain size distribution, sediment shape, density, etc. So far it is not possible to adequately model movement of natural shaped particles to simulate morphological development. There

Copyright © 2006 Taylor & Francis Group plc, London, UK

remains an abundance of challenges regarding the interaction flow-vegetation-sediment. One challenging question is to what extent turbulence is modulated by moving bed material such as gravel particles (see e.g. Campbell et al. 2005) and dunes (e.g. Maddux et al. 2003). Such knowledge is the prerequisite to relate sediment dynamics to both vegetation patterns and turbulence characteristics, and hence to establish reliable models for morphological development.

Of concern is the fact that the use of some of the hydraulic design methods that were originally derived based on idealised or site-specific conditions, has been extended far beyond the limits of their applicability in current models. For example, approaches suitable for only large relative submergence have been applied to shallow flows because of a lack of information and even ignorance. The shortcomings follow from the very complexity of vegetated flow. The deficiencies in our knowledge should be tackled with novel, scientifically based approaches – not with repetition of conventional ones. Simplification is indeed needed and justified, but first we should get a good understanding what we are simplifying. Otherwise, we face the risk that we focus on modelling and calibrating something irrelevant. Unfortunately, such cases are not rare in the literature. More specifically, the domination of laboratory studies that use simple artificial roughness has not allowed for the identification and assessment of all the important processes and mechanisms that control flow-vegetation-sediment interaction. Such experiments were very important at the beginning of the new field of research, but today there is not much idea to repeat these experiments without questioning the original approaches. The use of new, sophisticated gadgets such as ADVs, LDVs and PIVs does not straightforwardly give reason for the repetition, if real advances in our understanding of the flow processes are to be made.

To conclude, the key to the development of sustainable river management strategies is the proper identification and assessment of physical processes, which dominate the complex interaction between water flow, vegetation, and sediment fluxes. These challenging tasks can only be tackled successfully by a combination of experimental and numerical studies together with theoretical advances in hydrodynamics. Specifically designed laboratory experiments are needed to provide high-quality data for the analytical investigation of flow and sediment transport dynamics. Results of these studies can be used then to further develop numerical models. These models will, once successfully validated with the help of laboratory experiments, reveal the issues, which need to be investigated in more detail in the field and laboratory. Comparative field studies are necessary for the quality control and evaluation of the numerical simulations and laboratory data. Such an integrated research strategy will systematically advance our knowledge in environmental hydraulics and stimulate the exchange between science and practitioners.

ACKNOWLEDGEMENT

The first author gratefully acknowledges the Technical University of Braunschweig for hosting a research visit with the financial support from the Alexander von Humboldt Foundation, Germany. The second author gratefully acknowledges the support of the Deutsche Forschungsgemeinschaft (DFG) under contract DI-651/4-3.

REFERENCES

Aberle, J. & Koll, K. 2004. Double-averaged flow field over static armor layers. In *River Flow 2004, Int. Conf. on Fluvial Hydraulics, Naples, 23–25 June 2004*: 225–233. London: Taylor & Francis.

Aberle, J., Nikora, V. & Walters, R. 2004. Effects of bed material properties on cohesive sediment erosion. *Marine Geology* 207: 83–93.

Andrews, E.D. 1984. Bed-material entrainment and hydraulic geometry of gravel-bed rivers. *Geol. Soc. Amer. Bull.* 95: 371–378.

Arcement, G.J. & Schneider, V.R. 1989. *Guide for selecting Manning's roughness coefficients for natural channels and floodplains.* U.S. Geological Survey Water Supply Paper 2339.

Armanini, A., Righetti, M. & Grisenti, P. 2005. Direct measurement of vegetation resistance in prototype scale. *J. Hydr. Res.* 43(5): 481–487.

Bakry, M.F., Gates, T.K. & Khattab, A.F. 1992. Field-measured hydraulic resistance characteristics in vegetation-infested canals. *Journal of Irrigation and Drainage Engineering* 118(2): 256–274.

Baptist, M. 2005. *Modelling floodplain biogeomorphology.* PhD thesis. Delft: Technical University of Delft.

Barnes, H.H. 1967. *Roughness characteristics of natural channels: color photographs and descriptive data for 50 stream channels for which roughness coefficients have been determined.* US Geological Survey Water-Supply Paper 1849.

Beffa, C. & Connell, R.J. 2001. Two-dimensional flood plain flow I: Model description. *Journal of Hydrologic Engineering* 6(5): 397–405.

Boelscher, J., Ergenzinger, P. & Obenauf, P.-J. 2005. *Hydraulic, Sedimentological and Ecological Problems of Multifunctional Riparian Forest Management -RIPFOR- The Scientific Report.* Heft 65, Berliner Geographische Abhandlungen.

Campbell, L., McEwan, I., Nikora, V., Pokrajac, D., Gallagher, M. & Manes, C. 2005. Bed-load effects on hydrodynamics of rough-bed open-channel flows. *J. Hydr. Engrg.* 131(7): 576–585.

Carbonneau, P.E., Bergeron, N. & Lane, S.N. 2005. Automated grain size measurements from airborne remote sensing for long profile measurements of fluvial grain sizes. *Water Resources Research* 41: W11426.

Copyright © 2006 Taylor & Francis Group plc, London, UK

Carollo, F.G., Ferro, V. & Termini, D. 2002. Flow velocity measurements in vegetated channels. *J. Hydr. Engrg.* 128(7): 664–673.
Carollo, F.G., Ferro, V. & Termini, D. 2005. Flow resistance law in channels with flexible submerged vegetation. *J. Hydr. Engrg.* 131(7): 554–564.
Choi, S.-U. & Kang, H. 2004. Reynolds stress modeling of vegetated open-channel flows. *J. Hydr. Res.* 42(1): 3–11.
Chow, V.T. 1959. *Open-channel hydraulics.* New York: McGraw-Hill.
Coon, W.F. 1998. *Estimation of roughness coefficients for natural stream channels with vegetated banks.* US Geological Survey Water-Supply Paper 2441.
Copeland, R.R., McComas, D.N., Thorne, C.R., Soar, P.J., Jonas, M.M. & Fripp, J.B. 2001. *Hydraulic design of stream restoration projects.* Technical Report, ERDC/CHL TR-01-28. U.S. Army Corps of Engineers, Engineer Research and Development Center, Vicksburg, MS.
Coulthard, T.J. 2005. Effects of vegetation on braided stream pattern and dynamics. *Water Resour. Res.* 41: W04003.
Cowan, W.L. 1956. Estimating hydraulic roughness coefficients. *Agric. Eng.* 37: 473–475.
Darby, S.E. 1999. Effect of riparian vegetation on flow resistance and flood potential. *J. Hydr. Engrg.* 125: 443–454.
Dittrich, A. & Järvelä, J. 2006. Flow-vegetation-sediment interaction. *Water Engineering Research* 6(3): 123–130.
Dittrich, A., Marek, M. & Huppmann, O. 2005. Konzept zur Abschätzung der morphodynamischen Entwicklungen in Fließgewässern und auf ihren Vorländern. *NNA-Berichte* 18(1): 153–161.
Einstein, H.A. & Banks, R.B. 1950. Fluid resistance of composite roughness. *Trans. AGU* 31: 603–610.
Elliott, A.H. 2000. Settling of fine sediment in a channel with emergent vegetation. *J. Hydr. Engrg.* 126(8): 570–577.
Fathi-Moghadam, M. & Kouwen, N. 1997. Nonrigid, nonsubmerged, vegetative roughness on floodplains. *J. Hydr. Engrg.* 123(1): 51–57.
Finnigan, J.J. 2000. Turbulence in plant canopies. *Annual Review of Fluid Mechanics* 32: 519–571.
Fisher, K. 1995. *The impact of temporal and spatial variations in vegetation in rivers.* Report SR 393. Wallingford: HR Wallingford Ltd.
Flippin-Dudley, S.J., Abt, S.R., Bonham, C.D., Watson, C.C. & Fischenich, J.C. 1998. *Evaluation of flow-resistance equations for vegetated channels and floodplains.* Technical Report EL-98-2. U.S. Army Corps of Engineers, Engineer Research and Development Center, Vicksburg, MS.
Freeman, G.E., Rahmeyer, W. & Copeland, R.R. 2000. *Determination of resistance due to shrubs and woody vegetation.* Technical Report, ERDC/CHL TR-00-25. U.S. Army Corps of Engineers, Engineer Research and Development Center, Vicksburg, MS.
Ghisalberti, M. & Nepf, H.M. 2002. Mixing layers and coherent structures in vegetated aquatic flows. *Journal of Geophysical Research* 107(C2): 10.1029/2001JC000871.
Gran, K. & Paola, C. 2001. Riparian vegetation controls on braided stream dynamics. *Water Resour. Res.* 37(12): 3275–3283.
Hayes, D.F., Olin, T.J., Fischenich, J.C. & Palermo, M.R. 2000. *Wetlands Engineering Handbook.* Technical Report, ERDC/EL TR-WRP-RE-21. U.S. Army Corps of Engineers, Engineer Research and Development Center, Vicksburg, MS.
Helmiö, T. 2004. Flow resistance due to lateral momentum transfer in partially vegetated rivers. *Water Resour. Res.* 40(5): W05206.
Hey, R.D. & Thorne, C.R. 1986. Stable channels with mobile gravel beds. *J. Hydr. Engrg.* 112(8): 671–689.
Hicks, D.M. & Mason, P.D. 1999. *Roughness Characteristics of New Zealand Rivers.* Christchurch: NIWA.
Hicks, D.M., Shankar, U., Duncan, M.J., Rebuffe, M. & Aberle, J. 2006. Use of remote-sensing technology to assess impacts of hydro-operations on a large, braided, gravel-bed river: Waitaki River, New Zealand. *IAHS Special Publication, Gravel Bed Rivers.* IAHR. (in press)
Huang, H.Q. & Nanson, G.C. 1997. Vegetation and channel variation; a case study of four small streams in southeastern Australia. *Geomorphology* 18: 237–249.
Hug, C., Ullrich, A. & Grimm, A. 2004. Litemapper-5600-A waveform-digitizing lidar terrain and vegetation mapping system. *International Archives of Photogrammetry, Remote Sensing and Spatial Information Sciences* XXXVI-8/W2: 24–29.
Ikeda, S. & Izumi, N. 1990. Width and depth of self-formed straight gravel rivers with bank vegetation. *Water Resour. Res.* 26(10): 2353–2364.
Ikeda, S. & Kanazawa, M. 1996. Three-dimensional organized vortices above flexible plants. *J. Hydr. Engrg.* 122(11): 634–640.
Järvelä, J. 2002. Flow resistance of flexible and stiff vegetation: a flume study with natural plants. *Journal of Hydrology* 269(1–2): 44–54.
Järvelä, J. 2004a. Determination of flow resistance caused by non-submerged woody vegetation. *International Journal of River Basin Management.* 2(1): 61–70.
Järvelä, J. 2004b. *Flow resistance in environmental channels: Focus on vegetation.* Helsinki University of Technology Water Resources Publications, TKK-VTR-10. http://lib.tkk.fi/Diss/2004/isbn9512270749/.
Järvelä, J. 2005. Effect of submerged flexible vegetation on flow structure and resistance. *Journal of Hydrology* 307(1–4): 233–241.
Jeffries, R., Darby, S.E. & Sear, D.A. 2003. The influence of vegetation and organic debris on flood-plain sediment dynamics: case study of a low-order stream in the New Forest, England. *Geomorphology* 51: 61–80.
Jordanova, A.A. & James, C.S. 2003. Experimental study of bed load transport through emergent vegetation. *J. Hydr. Engrg.* 129(6): 474–478.
Klaassen, G.J. 2002. *Novel approaches in river engineering.* In *D. Bousmar & Y. Zech (eds), River Flow 2002*: 27–43. Lisse: Swets & Zeitlinger.
Knight, D.W. & Shiono, K. 1996. River channel and floodplain hydraulics. In M. Anderson, D.Walling & P. Bates (eds), *Floodplain processes*: 139–182. Chichester: John Wiley.
Kouwen, N. & Fathi-Moghadam, M. 2000. Friction factors for coniferous trees along rivers. *J. Hydr. Engrg.* 126(10): 732–740.
Kouwen, N. & Unny, T.E. 1973. Flexible roughness in open channels. *J. Hydr. Div. ASCE* 99(5): 713–728.

Copyright © 2006 Taylor & Francis Group plc, London, UK

Kouwen, N., Unny, T.E. & Hill, H.M. 1969. Flow retardance in vegetated channels. *Journal of Irrigation and Drainage Division* 95(2): 329–340.
Li, R.-M. & Shen, H.W. 1973. Effect of tall vegetations on flow and sediment. *J. Hydr. Div. ASCE* 99(5): 793–814.
Lindner, K. 1982. *Der Strömungswiderstand von Pflanzenbeständen.* Mitteilungen 75. Leichtweiss-Institut für Wasserbau, Technische Universität Braunschweig.
López, F. & García, M.H. 1998. Open-channel flow through simulated vegetation: Suspended sediment transport modeling. *Water Resour. Res.* 34(9): 2341–2352.
López, F. & García, M.H. 2001. Mean flow and turbulence structure of open-channel flow through non-emergent vegetation. *J. Hydr. Engrg.* 127(5): 392–402.
Maddux, T.B., McLean, S.R. & Nelson, J.M. 2003. Turbulent flow over three-dimensional dunes: 2. Fluid and bed stresses. *J. Geophys. Res.* 108(F1): 6010.
Millar, R.G. 2000. Influence of bank vegetation on alluvial channel patterns. *Water Resour. Res.* 36(4): 1109–1118.
Musleh, F.A. & Cruise, J.F. 2006. Functional relationships of resistance in wide flood plains with rigid unsubmerged vegetation. *J. Hydr. Engrg.* 132(2): 163–171.
Naot, D., Nezu, I. & Nakagawa, H. 1996. Unstable patterns in partly vegetated channels. *J. Hydr. Engrg.* 122(11): 671–673.
Nepf, H.H. 1999. Drag, turbulence and diffusion in flow through emergent vegetation. *Water Resour. Res.* 35(2): 479–489.
Nepf, H.M. & Vivoni, E.R. 2000. Flow structure in depth-limited, vegetated flow. *J. Geophys. Res.* 105(C12): 28547–28557.
Nikora, V., Goring, D.G., McEwan, I. & Griffiths, G.A. 2001. Spatially averaged open channel-flow over rough bed. *J. Hydr. Engrg.* 127(2): 123–133.
Nikora, V., McEwan, I., McLean, S., Coleman, S., Pokrajac, D. & Walters, R. 2005a. Double averaging concept for rough-bed open-channel and overland flows: Theoretical background. *J. Hydr. Engrg.* (submitted)
Nikora, V., McLean, S., Coleman, S., Pokrajac, D., McEwan, I., Campbell, L., Aberle, J., Clunie, D. & Koll, K. 2005b. Double averaging concept for rough-bed open-channel and overland flows: Applications. *J. Hydr. Engrg.* (submitted)
Oplatka, M. 1998. *Stabilität von Weidenverbauungen an Flussufern.* Mitteilungen 156. Zürich: ETH Versuchsanstalt für Wasserbau, Hydrologie und Glaziologie.
Palmer, V.J. 1945. A method for designing vegetated waterways. *Agric. Eng.* 26(12): 516–520.
Pasche, E. & Rouvé, G. 1985. Overbank flow with vegetatively roughened flood plains. *J. Hydr. Engrg.* 111(9): 1262–1278.
Paterson, D.M. & Black, K.S. 1999. Water flow, sediment dynamics and benthic biology. In D.B. Nedwell & D.G. Raffaelli (eds), *Advances in Ecological Research*: 155–193. San Diego: Academic Press.
Petryk, S. & Bosmajian, G.B. 1975. Analysis of flow through vegetation. *J. Hydr. Div. ASCE* 101(7): 871–884.
Pinter, N., van der Ploeg, R.R., Schweigert, P. & Hoefer, G. 2006. Flood magnification on the River Rhine. *Hydrological Processes* 20: 147–164.
Poggi, D., Porporato, A., Ridolfi, L., Albertson, J.D. & Katul, G.G. 2004. The effect of vegetation density on canopy sub-layer turbulence. *Bound.-Layer Meteorol.* 111: 565–587.
Rauch, H.P. 2005. *Hydraulischer Einfluss von Gehölzstrukturen am Beispiel der ingenieurbiologischen Versuchsstrecke am Wienfluss* [Hydraulic impact of a vegetated river bank exemplified by the soil bioengineering test flume of the river Wien]. Ph.D. Thesis. Wien: Universität für Bodenkultur.
Raupach, M.R., Finnigan, J.J. & Brunet, Y. 1996. Coherent eddies and turbulence in vegetation canopies: The mixing-layer analogy. *Bound.-Layer Meteorol.* 78: 351–382.
Rey, F. 2004. Effectiveness of vegetation barriers for marly sediment trapping. *Earth Surface Processes and Landforms* 29: 1161–1169.
Righetti, M. & Armanini, A. 2002. Flow resistance in open channel flows with sparsely distributed bushes. *Journal of Hydrology* 269(1–2): 55–64.
Rowinski, P.M., Aberle, J. & Mazurczyk, A. 2005. Shear velocity estimation in hydraulic research. *Acta Geophysica Polonica* 53(4): 567–583.
Schnauder, I. 2004. *Strömungsstruktur und Impulsaustausch in gegliederten Gerinnen mit Vorlandvegetation.* Univ. Karlsruhe, Inst. f. Wasserwirtschaft u. Kulturtechnik. Mitteilungen 224. Univ. Karlsruhe, Inst. f. Wasserwirtschaft u. Kulturtechnik. http://www.ubka.uni-karlsruhe.de/eva/index.html
SCS 1954. *Handbook of channel design for soil and water conservation.* Soil Conservation Service SCS-TP-61. Washington, D.C.: U.S. Department of Agriculture.
Sellin, R.H.J. 1964. A laboratory investigation into the interaction between the flow in the channel of a river and that over its flood plain. *La Houille Blanche* 19(7): 793–802.
Sellin, R.H.J. & van Beesten, D. 2002. Berm vegetation and its effects on flow resistance in a two-stage river channel: an analysis of field data. In *D. Bousmar & Y. Zech (eds), River Flow 2002*: 319–327. Lisse: Swets & Zeitlinger.
Shields, F.D., Copeland, R.R., Klingeman, P.C., Doyle, M.W. & Simon, A. 2003. Design for stream restoration. *J. Hydr. Engrg.* 129(8): 575–584.
Shimizu, Y. & Tsujimoto, T. 1994. Numerical analysis of turbulent open-channel flow over a vegetation layer using a k-e turbulence model. *Journal of Hydroscience and Hydraulic Engineering* 11(2): 57–67.
Specht, F.-J. 2002. *Einfluß von Gerinnebreite und Uferbewuchs auf die hydraulisch-sedimentologischen Verhältnisse naturnaher Fließgewässer.* Mitt. des Leichtweiß-Instituts für Wasserbau, Heft 153. TU Braunschweig.
Stephan, U. & Gutknecht, D. 2002. Hydraulic resistance of submerged flexible vegetation. *Journal of Hydrology* 269(1–2): 27–43.
Stoesser, T., Wilson, C.A.M.E., Bates, P.D. & Dittrich, A. 2003. Application of a 3D numerical model to a river with vegetated floodplains. *Journal of Hydroinformatics* 5(2): 99–112.
Temple, D.M. 1999. Flow resistance of grass-lined channel banks. *Applied Engineering in Agriculture* 15(2): 129–133.
Temple, D.M., Robinson, K.M., Ahring, R.M. & Davis, A.G. 1987. *Stability Design of Grass-Lined Open Channels.* USDA Agriculture Handbook 667. Washington, D.C.: U.S. Department of Agriculture.

Copyright © 2006 Taylor & Francis Group plc, London, UK

Thornton, C.I., Abt, S.R., Morris, C.E. & Fischenich, J.C. 2000. Calculating shear stress at channel-overbank interfaces in straight channels with vegetated floodplains. *J. Hydr. Engrg.* 126(12): 929–936.

Toda, Y., Ikeda, S., Kumagai, K. & Asano, T. 2005. Effects of flood flow on flood plain soil and riparian vegetation in a gravel river. *J. Hydr. Engrg.* 131(11): 950–960.

Tollner, E.W., Barfield, B.J. & Hayes, J.C. 1982. Sedimentology of erect vegetal filters. *J. Hydr. Div. ASCE* 108(12): 1518–1531.

Tsujimoto, T. 1999. Fluvial processes in streams with vegetation. *J. Hydr. Res.* 37(6): 789–803.

Tsujimoto, T., Kitamura, T. & Tsujikura, H. 1998. Development of sand island with vegetation by repetition of flood and low-stage water. In *Proceedings, 3rd International Conference on Hydroscience and Engineering, Cottbus*.

Tsujimoto, T., Kitamura, T., Fujii, Y. & Nakagawa, H. 1996. Hydraulic resistance of flow with flexible vegetation in open channel. *Journal of Hydroscience and Hydraulic Engineering* 14(1): 47–56.

Vogel, S. 1994. *Life in moving fluids: the physical biology of flow.* 2nd edition. Princeton: Princeton University Press.

Wilson, C.A.M.E., Schnauder, I., Mas, J. & Hoyt, J. 2005. Measuring the drag force of vegetation. In B.-H. Jun, S.-I. Lee, I.W. Seo & G.-W. Choi (eds), *Water engineering for the future – choices and challenges, XXXI IAHR Congress, Seoul, 11–16 September 2005*: 2142–2151. Seoul: IAHR.

Wohl, E., Angermeier, P.L., Bledsoe, B., Kondolf, G.M., MacDonnell, L., Merritt, D.M., Palmer, M.A., Poff, N.L. & Tarboton, D. 2005. River restoration. *Water Resour. Res.* 41: W10301.

Yen, B.C. 2002. Open Channel Flow Resistance. *J. Hydr. Engrg.* 128(1): 20–39.

Yoshida, H. & Dittrich, A. 2002. 1D unsteady-state flow simulation of a section of the upper Rhine. *Journal of Hydrology* 269(1–2): 79–88.

Copyright © 2006 Taylor & Francis Group plc, London, UK

Multi-purpose shallow reservoir: Synergies between ecology and energy production

P. Heller, E. Bollaert & A.J. Schleiss
Laboratory of Hydraulic Constructions, Ecole Polytechnique Fédérale de Lausanne, Lausanne, Switzerland

M. Pellaud & R. Schlaepfer
Laboratory of ecology management, Ecole Polytechnique Fédérale de Lausanne, Lausanne, Switzerland

ABSTRACT: During the last century, most European river networks have been trained, mostly for energy production, flood prevention, and land use. Today, these rivers cope with severe deficiencies. Partially due to climate changes, flood safety becomes an increasing issue. Artificial morphologies and regulated hydraulic regimes disconnected rivers from their floodplain and often strongly disturb river ecology. Also, due to training works, the river's potential for leisure activities is often reduced. Nevertheless, these rivers still offer an important potential for recovery of their initial characteristics. They remain essential for irrigation, drinking water or navigation, as well as energy production. It is possible to reduce such deficiencies and to develop river potential with a multipurpose project. Such a project may become very complex and defining the most feasible solution (for both design and management) requires a new and original approach. A qualitative study of the system highlighting the project's key variables was linked to a quantitative study providing specific answers regarding the project's dimension and management variables. Trough the optimization of the design and management of a shallow reservoir, it was found that returning to a near-natural hydraulic regime for the downstream part of the river was possible without losing over 10% of potential energy production. Ecological aspects of the reservoir have been optimized directly with a specific simulation module. Besides, the reservoir's stable water levels during the summer season allowed development of social activities. This paper provides an integrative approach to optimize energy production while protecting ecological components of a river network.

1 INTRODUCTION

1.1 *Complex problem*

The demographic pressures of last centuries (i.e. population growth, land use) dramatically reduced the space allocated to rivers in industrialized countries. Rivers have been canalized and their flow regulated in order to promote navigation, energy production and flood protection. The ecological processes once associated to the rivers are strongly disturbed and various negative effects on the environment are observed. A particularly brutal impact on the system is caused by hydropeaking. Hydropeaking is defined by the sudden water discharges of power plants during peak energy production and affect the hydraulic, sediment and thermal regimes of rivers (Meile et al. 2005 and Meier 2002).

Nevertheless, rivers still offer great opportunities for development. The growth of electricity demand in addition to the willingness of reducing CO2 emissions and the social rejection of nuclear power stimulates use of hydropower. In parallel, restoration of aquatic biotopes has a strong legal leverage and cannot be overlooked in a river development project.

To guarantee acceptability, new projects have to consider these different aspects in an integrated manner. Hence, satisfying solutions become much more complicated. To agree on a reasonable compromise, many participative methods have been developed (Leach et al. 2001). Stakeholders are included in the projects from its very beginning and in order to satisfy all parties, projects have to become multi-purposed. Models are good candidate to deal with the numerous interactive effects of these complex systems. According to Coyle (2000), a complex system has to be analyzed with a qualitative model followed by a quantitative study. System dynamic is defined as "a complex system analysis method done by a causal analysis, followed by a dynamic transcription, completed by a model and processed with a computer simulation" (EuroDicauTom 1982). A qualitative study is performed with the help of a generic network method (Gomez et al. 1995).

Copyright © 2006 Taylor & Francis Group plc, London, UK

1.2 *Results of qualitative study*

According to the nature of the problem, a preliminary qualitative study has been performed to understand the complexity of the problem (Heller et al. 2005). The study was divided into hydraulic, energetic, financial, socio-economic, underground water and ecological topics. The qualitative results highlight three groups of variables. The first one regroups the size variables which define the construction and the general aspect of the project (i.e. reservoir surface, dam elevation, project configuration). The second group contains the reservoir's operation management (focusing mainly on the downstream flow characteristics) and the third group the project's indicators. The most important indicators are the ecological improvement, the financial viability and the leisure development. This qualitative study also permits to compare the different purposes. The global model is then built on these results.

1.3 *Quantitative expectation and Pareto results*

Based on measured values on the upper Swiss Rhône River, the global model provides quantitative results for costs, energy production and its repartition during the year, flow mitigation and its consequences on the ecological aspects. The model considers the reservoir itself as well as the downstream river.

Results are expressed with the Pareto dominance concept. This concept allows generating many solutions of interest without determining any set of weights (Goldberg 1989).

This project focuses on run-of-river power plants with a shallow reservoir for hydropeaking mitigation and energy production. Such a project is proposed on the strongly canalized upper Rhône River in Switzerland (Bollaert et al. 2000). Due to several retention reservoirs upstream, the river flow regime is considerably influenced by daily and seasonally hydropeaking. As the catchments area contains many glaciers, the water is highly laden with fine sediments (glacial floor). Figure 1 represents such a reservoir in a conceptual manner and Figure 2 a candidate site.

This paper focuses on the relations between energy production and ecological integrity for both the downstream river and the reservoir.

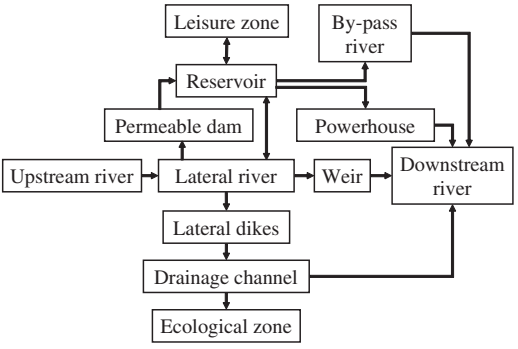


Figure 1. Concept of multi-purpose reservoir.

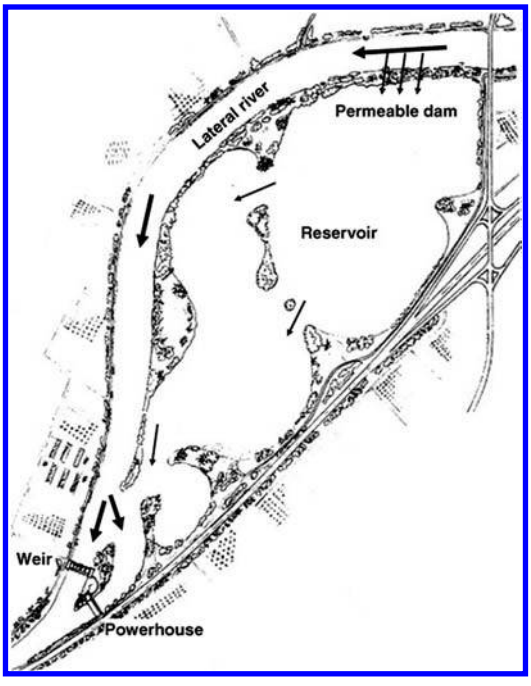


Figure 2. Multi-purpose reservoir potential site (Bollaert et al. 2000).

2 GLOBAL MODEL

2.1 *Global flow-chart*

Results of the qualitative study highlight the necessity of a quantitative analysis. This analysis has to consider the various aspects of the problem (multi-purpose) as well as to permit a sound interpretation of the results (multi-criteria). This quantitative study is performed with a global flow-chart based on the Queuing Multi-Objective Optimizer (QMOO). This optimization tool is presented at §2.2.

Based on the results of the qualitative study, the size variables of the project have to be independent from the management variables. According to an hourly simulation step, a whole year simulation produces 8760 management variables (the downstream flow for each hour during a year). Added to the 20 size variables, this number of variables would excess the capacity of any optimizer. This clearly points out the need for separation of management and size optimizations in

Copyright © 2006 Taylor & Francis Group plc, London, UK

two successive steps. The management optimization is presented further on (§3).

The global flow-chart starts with an arbitrary vector for the internal variables (project size and global management constraints). The external variables represent uncontrollable data (upstream flow, external temperature, upstream water temperature, substrate,…). This vector is dependant from the site characteristics.

According to the data (internal and external) the second step performs the ordinary management optimization. Since this reservoir is also configured to reduce a flood peak, an extraordinary flood optimization tool is provided for extreme flows.

The third step is composed by the different simulation tools. The first one simulates the hydraulic behavior of the project. Based on the hydraulic results, the other tools are run to predict the water temperature in and downstream of the reservoir as well as energy production. In a third round, the ecological, socio-economical and financial simulations are performed. These different tools constitute the multi-objective approach of the problem.

The fourth step aggregates the simulation results into objective functions. Since the QMOO optimizers as well as the usual three-dimensional representation are able to deal with three different objectives, the aggregation must reduce the result into three indicators. Energy and economic aspects of the multi-purpose reservoir can be reduced to a financial assessment. Social and ecological aspects are quantified with different units and therefore constitute the two other axes.

The fifth step contains the global optimizer and produces Pareto solutions. To generate them, the optimizer changes the internal variables vector. Figure 3 illustrates the global flow-chart with its five steps.

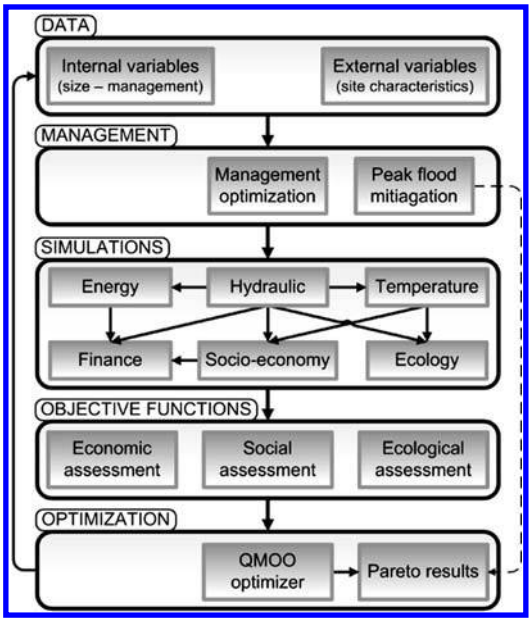


Figure 3. Global flow-chart with its 5 steps.

2.2 *Optimization tool QMOO*

The optimization tool QMOO, namely 'Queuing Multi-Objective Optimizer', has been developed at the EPFL in the Laboratory for Industrial Energy Systems (Leyland 2002). It is based on an evolutionary algorithm. Such algorithms are particularly suited to conflicting multi-objective optimizations (Prasad et al. 2004). Since they are also able to deal with non-linear, discontinuous, disjoint and multi-modal problem (Sharif et al. 2000), they are well adapted for the resolution of complex problems.

The optimizer first generates a random population of solutions. Each member of that population represents an internal variables vector. Performance is then computed for each vector (i.e. its related objective functions vector). The optimizer uses then the performance of the current population to generate, by mixture, the next population. The optimizer stops after a defined number of populations or when the performance seems to be optimal. To reduce the computation time and to produce separate local optima simultaneously, QMOO generates clusters and then focuses its search of solutions. It nevertheless conserves the 'tail regions' of population to explore the full extent of the problem's optimal regions.

Conserving the best solutions produces the optimum Pareto solutions. A Pareto solution is defined as a solution which improves at least one performance dimension without deteriorating any others. This kind of solutions allows generating the best physical solutions independently from any weighted method. It clearly distinguishes a political choice for one solution from the scientific generation of the best solutions.

3 MANAGEMENT OPTIMIZATION MODULE

3.1 *Objective function*

The management of the reservoir is based on an hourly step for a whole year of simulation. It is transformed into a system of equations. This system is written in AMPL code (Fourrer et al. 2002) and solved with the Cplex solver. It is solved with a seven days prediction for a validity of only two days. It is composed of an objective function, variables, data and constraints.

The objective function maximizes, for every hour, the reservoir filling rate, as written in Equation 1.

$$Max\left(\sum_{t} Accumulation(t)\right), t \in [1;168], t \in \mathrm{N} \qquad (1)$$

Copyright © 2006 Taylor & Francis Group plc, London, UK

According to an increasing derivative of the function "height-volume", this objective function minimizes, for a required volume, the variations of the reservoir level. For an accepted downstream water level variation (hydropeaking tolerance), it minimizes the reservoir hydropeaking. This function also implicitly maximizes the energy production (useful head).

The variables are composed by one vector of 8760 positions, i.e. the downstream flow for each hour. This vector constitutes the solution for the management.

The data contain the initial reservoir level and the upstream flow. According to the accepted forecast, the upstream vector is composed by 168 values.

The system constraints are the common physical constraints for such a system, i.e. a maximal reservoir volume (Eq. 2), a minimal reservoir volumes (Eq. 3) and positive downstream flows (Eq. 4).

$$Accumulation(t) \leq \text{Volume_max}, \forall t \quad (2)$$

$$Accumulation(t) \geq 0, \forall t \quad (3)$$

$$Q_{downstream}(t) \geq 0, \forall t \quad (4)$$

They also contain two parameters for the management. The first parameter constraints the rate of downstream water level variation (mathematically the derivative of the level) and the second constraints the maximum variation around the average level. Typical values for these two constraints are 8 cm/h of variation limited by deviations from the mean of ± 15 cm. These constraints are defined for both winter and summer seasons with different values. The seasons are defined according to the average week of forecasted flows. For the transition season (spring and autumn), transition values are computed linearly to the averaged week flow. These four constraints (two for the winter season and two for the summer season) clearly define the major objective of the reservoir, which is to limit the artificial hydropeaking towards downstream. Two additional constraints (one winter and one summer value) limit also the reservoir maximum variation. They are comprised between 0.5 m and 4.5 m, respectively for the summer and winter value. In case of inconsistent mathematical system, the downstream limitations are slightly relaxed by steps of 5%.

The system is solved consecutively 180 times in order to generate 8760 downstream flows, which compose the global year management of the reservoir. This management is called "ordinary management" and does not take care of peak flood events. The splitting of the management optimization from the size optimization corresponds to a reasonable process of optimization and allows reducing, for QMOO, the number of management variables from 8760 to 6 positions.

4 ECOLOGICAL MODEL

4.1 *System overview*

The hydrosystem of interest is comprised of (1) the water detention basin and (2) the downstream portion of the river (Figure 2). The design and management of the basin (point element, scale in the order of a square kilometer) is to influence the whole downstream hydrosystem (scale in the order of hundreds of square kilometers). The scale differences (grain) require different methods to develop an adequate protocol for the assessment of the ecological integrity of each of the two elements. One of the reasons that models were developed was to simplify complex systems and to identify key variables affecting the behavior of such a system. A tradeoff was loss of information on the operating processes with hidden influences (i.e. long term consequences, 'cocktail' effects …). At the resolution of the water detention basin, and based on available knowledge of the ecological processes and parameters at stake, a theoretical ecological model of the basin has been developed with an expert knowledge-based approach to reach ecological integrity. It has been assumed that the current knowledge of artificial ponds/lake engineering would yield better results and convey less risk than following design and management environmental guidelines issued by a model. For the downstream section (i.e. downstream Rhône River), the scale, length of processes and complexity require a model-based approach in order to asses its ecological integrity.

4.2 *Ecological considerations – multi-purpose basin*

The purpose of the water detention basin is to buffer sudden water level variations of the river. The discharge variations will be absorbed by the basin, meaning that the basin's water level is to vary considerably. Within this multi-objective basin, a surface is to be allocated for an 'ecological zone'. These zones are to be protected from anthropologic disturbances and the ecotonal zone (aquatic – terrestrial interface) is to be enlarged and preserved from the harsh disturbances caused by sudden and frequent water variations. To do so, a protective submersible dike is to be engineered (Figure 4). The periodic filling of the ecotonal shallow

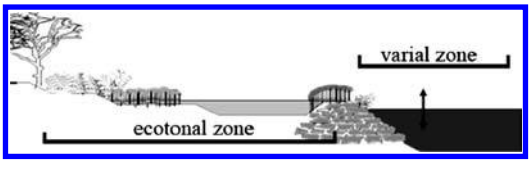


Figure 4. Ecotonal stabilization of the banks for the multi-purpose basin.

Copyright © 2006 Taylor & Francis Group plc, London, UK

zone (<0.5 m) takes place when the basin water level is high, and the water remains trapped when the water basin level falls, ensuring permanent submersion.

Development of vegetation (e.g. reeds, various helophytes) is expected and is necessary to provide shelter and trophic resources for associated fauna.

4.3 *Connection to the downstream channel*

Longitudinal connectivity has to be maintained to perturb as little as possible the migrating patterns of fish and macro-invertebrate populations. Various kinds of artificial-river like bypasses are indicated (Figure 5). Fish-ladder structures alone should be avoided since they are often species-specific and do not work well for aquatic invertebrates.

Particularities of the shown river are (1) the 'natural' segment, and (2) the basin ladder. The natural segment mimics a 'natural' sequence of riffles and pools with vegetated banks of a rather smooth gradient. The basin ladder offers a second chance for migrating fish who 'missed' the river entrance and are blocked by the turbines. The basin ladder plays an important role reducing delays which may derogate fish reproduction (Amoros et al. 1993).

4.4 *Ecological considerations – downstream river*

The downstream part of the river plays a role in the basin management. Literature and expert-knowledge jointly recommend that, under normal conditions, daily fluctuations caused by water restitution should not exceed +/−15 cm with a variation rate inferior to 10 cm·h^{-1} (Valentin 1995; Poff et al. 1997). Moreover, river bed maintenance is to be assured by the periodic transit of morphogenic floods through the basin (Richter et al. 2000; Murle et al. 2003). The ecological integrity of the downstream river is assessed by the aggregation of three modules, (1) a zoobenthos module (2) a fish module and (3) a vegetation module.

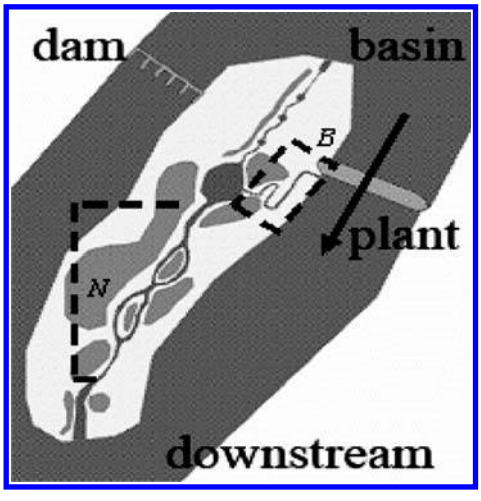


Figure 5. Representation of an artificial river ensuring longitudinal connectivity. (N) represents a 'nature – like' suite of riffles and pools (B) a basin ladder.

4.4.1 *Zoobenthos module*

This module predicts zoobenthos richness on homogenous reaches and is based on (1) river-specific taxonomic richness surveys, (2) associated point physical variables, and (3) hydropeaking effect. Radial Basis Functions (RBF) (Dowla et al. 1995; Lek et al. 1999; Obach et al. 2001; Zhang et al. 2005) are used to model a Preliminary Standardized Richness Index (PSRI). PSRI predicts reach richness reflecting actual hydropeaking conditions (variation rates and variation length). A hydropeaking coefficient zeroed on actual hydropeaking conditions is determined using fuzzy logic (Zadeh 1995; Silvert 2000; Adriaenssens et al. 2004). The hybridization of the PSRI with the fuzzy hydropeaking coefficient yields the predicted zoobenthos richness by reach (Figure 6).

4.4.2 *Fish module*

The fish module predicts the results of an instream habitat model such as PHABSIM (Bovee 1982) or EVHA (Ginot 1998) for four fish habitat guilds following the methodology by Lamouroux (Lamouroux et al. 2002). The habitat indices for each fish habitat guild are subsequently adjusted by independent fuzzy coefficients simulating (1) hydropeaking effects and (2) thermal alteration effects (Valentin 1995). The outputs are guild-specific habitat convenience indices that can be multiplied by reach surface to yield weighted usable surfaces per guild.

4.4.3 *Vegetation module*

The vegetation module is currently under development and will consist in a system of differential equations

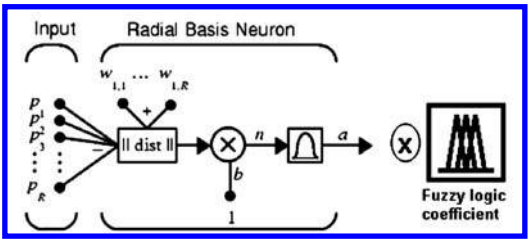


Figure 6. Schematic model representation of the zoobenthos module (modified from The MathWorks Neural Network Toolbox (2004)). Inputs are river-specific taxonomic richness surveys associated with point physical variables; the radial basis neuron yields the PSRI; the fuzzy logic coefficient simulates the hydropeaking effect; the output is a predicted taxonomic richness per reach.

Copyright © 2006 Taylor & Francis Group plc, London, UK

aiming at predicting (1) submerged aquatic vegetation biomass (2) habitat convenience index for helophytes (Wade et al. 2001).

4.4.4 *Aggregation process*

By assessing a weight to each module (i.e. zoobenthos, fish and aquatic vegetation) based on case-specific ecological objectives, actors contribute directly to the aggregation process. A single grade will represent the ecological integrity of the downstream part of the river. Stakeholders are provided with a simulation tool set on sound scientific bases linking a design or management action to an ecological consequence predicted for the downstream section of the river.

5 UPPER SWISS RHONE RIVER STUDY CASE

5.1 *Current state*

Sub-alpine hydrosystems' ecological integrity suffers from various anthropologic actions such as canalization, hydrologic alteration, landscape fragmentation and others. These actions were meant to facilitate man's life around fluvial hydrosystems (i.e. flood protection, navigation, agriculture) and to benefit from the considerable energetic potential of sub-alpine rivers. The resulting pattern is a straight, monotonous and embanked river apparently totally disconnected from its floodplain.

After three decades of large dams' construction, it also suffers from an acute artificial hydropeaking. This hydropeaking transfers significant water flows from summer season to winter season. Reducing the summer morphogenic flood, it generates daily peak flows. Historically the Rhône winter flow was very stabile with an average value of about 50 m^3/s. Nowadays the winter flow varies from 35 m^3/s during the week-end to more than 160 m^3/s during the working days. This represents a water level variation of more than 1 m, which is produced on a very short time (less than one hour).

The dam hydropeaking also generates a thermal transfer from summer to winter season. Consequently, winter water is about one degree warmer than historically and summer season one degree colder (Meier 2002).

These three modifications (geographical uniform flow, hydropeaking and thermal disturbances) have strong effects on the river ecology. It is currently in a very poor state.

5.2 *Smooth hydropeaking flows*

The major reason of such a multi-purpose reservoir is the mitigation of the downstream river hydropeaking. Management optimization based on the year 2003 with following maximal values (Table 1), produces a strong improvement of the downstream flow (Figure 7).

Table 1. Key values of the management optimization.

Variables	Unit	Value
Reservoir surface	km^2	1
Dam elevation	m	8.68
Winter downstream water level speed variation	cm/h	8
Winter downstream water level variation	cm	30
Winter reservoir level variation	m	4.5
Summer downstream water level speed variation	cm/h	15
Summer downstream water level variation	cm	50
Summer reservoir level variation	m	0.8

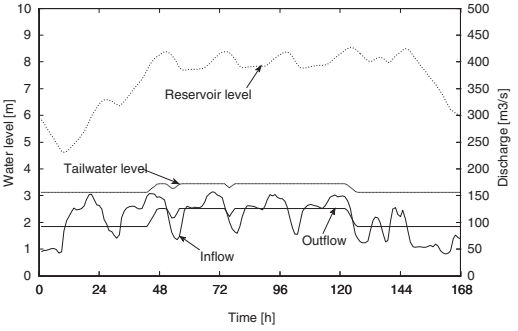


Figure 7. Typical winter week with an improved downstream flow.

The downstream flow improvement is well highlighted with the hydropeaking indicator. This indicator is based on a yearly cumulative flow variation curve. The flow variation, on the horizontal axis, is expressed in $m^3/s/min$. The vertical axis expresses the probability of non-exceeded variation. Since the flow variations are accepted as a major stress on the aquatic ecosystem, this indicator represents the human influences on the hydraulic regime and its effects. The current state can then be compared to a historical state. The same indicator also integrates hydraulic regime improvements of the reservoir. The area between the curves aggregates this improvement into one unique value. Figure 8 illustrates the result.

According to this indicator and to a reduction of 85% of the hydraulic variation stress, it can be accepted that such a reservoir reproduces a near-natural flow.

5.3 *Energy production*

For this multi-purpose reservoir, energy production is seen as an opportunity and not a major objective. Real energy production is always compared to the maximum (physically) possible energy production with a run-of river dam, i.e. the management with a constant reservoir water level. Summarized for the whole year, optimized management produces about 90% of

Copyright © 2006 Taylor & Francis Group plc, London, UK

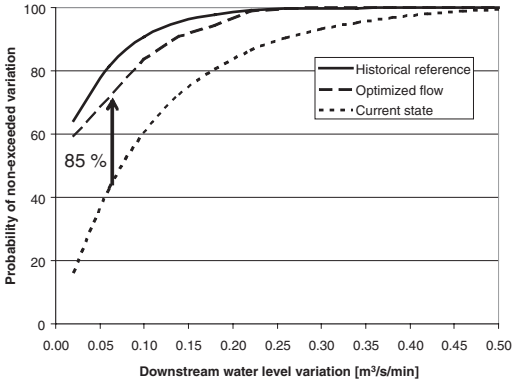


Figure 8. Hydropeaking indicator and reservoir improvement.

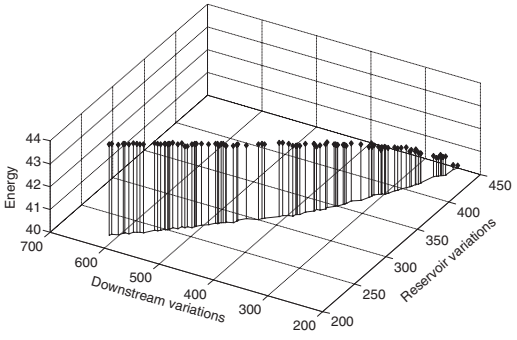


Figure 9. Pareto optimization with energy production (GWh/year), downstream variations (m^3/s/min/year) and reservoir variations (m/an). Z axis starts at 40 GWh/year.

the maximum possible energy. This loss of 10% is principally the consequence of a current deep flow during the winter week-end (Figure 7). To respect the maximum flow variation constraints, the reservoir greatly supports the minimum flow. Therefore it requires over one day to be filled again. During the much more unstable summer flows (historically observed), the reservoir conserves its maximum level nearly permanently (variations less than 30 cm).

5.4 *Pareto results*

The two previous results (hydropeaking and energy) can be summarized with a Pareto illustration. The well-shaped form of the curve obtained from the computations strengthens the *a priori* choice of a Pareto representation.

Figure 9 illustrates the three relations between the reservoir level variations (expressed in m/year), the downstream water level variation (in m^3/s/min/year) and the energy production (in GWh/year).

	Actual	R3	R3 + Basin
Discharge	Branson 2002	Branson 2002	from hydraulic model
Bed width	Actual (50 m)	x 1.5 (75 m)	x 1.5 (75 m)
Bank slopes	Actual (1:2.2 / 1:2.5)	Smooth (1:6)	Smooth (1:6)
Granulometry	d50*=0.1 m	d50=0.07 m	d50=0.07 m
Water temperatures	Branson 2002	Branson 2002	from thermal model

Figure 10. General characteristics used for the three scenarios – Branson stands for discharge values at the gauging station.

Figure 9 underlines a constantly decreasing relation between energy production and reservoir fluctuations. This corresponds, with the equation of the hydropower (Eq. 5), to the relation between the head and the power

$$P = \rho * g * h * Q \tag{5}$$

where ρ = water density, g = normal acceleration, h = water head and Q = water flow. The same figure (Figure 9), on the horizontal plan, highlights another constantly decreasing relation between the downstream and the reservoir water level fluctuations. Following the continuity equation, this result clearly illustrates the antagonistic purposes between reservoir ecological preservation and downstream restoration.

Based on two continuous equations, this optimization presents relative continuous results. The links between the hydraulic aspects and the ecological consequences is the purpose of the next paragraph. Directly related to the final impacts, the hydraulic improvements can generate less continuous results.

5.5 *Aquatic ecological improvements*

In the scope of the current and projected states of the Rhône River, three scenarios were retained for a numerical application of the zoobenthos and fish modules: (1) The Swiss Upper Rhône in its actual configuration, (2) A hypothetic Swiss Upper Rhône River after a third correction (R3) (Canton du Valais, 2006) and (3) a hypothetic Swiss Upper Rhône River after its third correction and with a multi-purpose basin as previously described (Figure 10).

The zoobenthos richness (Figure 11) was predicted as the lowest in the actual configuration of the river and showed to increase subsequently in the R3 configuration and even more in the R3 + Basin configuration. The predicted increase of taxonomic richness is probably due to the river widening (causing a decrease in flow velocity and depth). The subsequent richness increase observed when shifting from the R3 to

Copyright © 2006 Taylor & Francis Group plc, London, UK

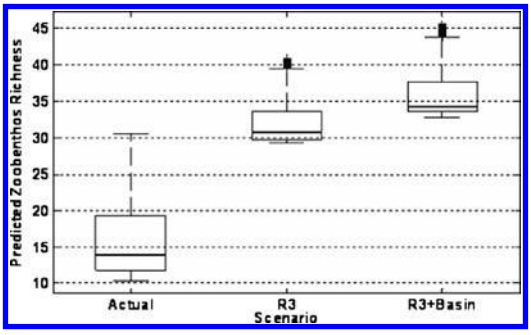


Figure 11. Zoobenthos predictions for the three scenarios.

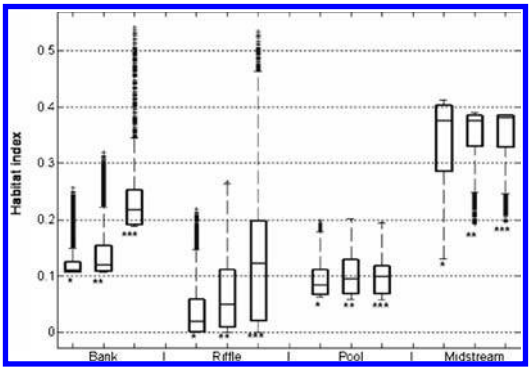


Figure 12. Predicted habitat index for each fish habitat guild (Bank – Riffle – Pool – Midstream) in actual (*), R3(**) and R3 + Basin (***) scenarios.

the R3 + Basin scenario reflects the buffering of the hydropeaking effect in this type of configuration.

Bank habitat guild as well as *Riffle* habitat guild seemed to benefit the most when shifting from the actual scenario to R3 and R3 + Basin (Figure 12). The *Pool* and *Midstream* habitat guilds seemed less affected by a decrease in hydropeaking. Shallow zones as well as riffle zones are most exposed when water fluctuates and should benefit the most when hydropeaking is buffered.

6 CONCLUSION AND PERSPECTIVES

'All models are wrong but some are useful' (Box)

A qualitative approach is required to understand the complexity of a multipurpose project. Qualitative results allow defining rules of design and management for a quantitative model. The purpose of the here presented model is to provide sound scientific bases for an optimized multipurpose management and design of a run-of-river retention basin by integrating social, economic and ecologic aspects. This paper focuses on hydraulics, energy production and ecology.

Establishment of the model's general flow-chart (Figure 3) clearly distinguishes design optimization from management optimization. The formal is based on an evolutionary algorithm. The latter is based on a linear optimization method. The results (Figure 9) permit to separate the scientific aspects (generation of Pareto optimal solutions) from the political aspects (evaluation of weighted criteria to choose of a unique solution). The presented simulation results quantify the predicted improvements of the Rhône River.

The hydraulic model highlights the general improvement of the downstream hydraulic regime. Hence, a near-natural regime may be expected. The energetic model underlines an acceptable loss of energy (about 10% of the theoretical maximal energy production) required for the hydraulic regime restoration. The zoobenthos and fish modules ecologically illustrate the hydraulic regime improvements (Figures 11 and 12). These two modules are the first steps towards a final ecological tool already showing promising results. Consequent tuning and training of the ecological model is still needed before its application is undertaken. However the integration of three different models into a global structure has set the framework for a truly transdisciplinary and innovative approach.

REFERENCES

Adriaenssens, V., DeBaets, B. et al. 2004. Fuzzy rule-based models for decision support in ecosystem management. *The Science of the Total Environment* 319: 1–12.

Amoros, C. & Petts, G.E. 1993. *Hydrosystèmes fluviaux*. Paris.

Bollaert, E., Irniger, P. & Schleiss, A.J. 2000. Management of sedimentation in a multipurpose reservoir in a run-of-river powerplant project on an alpine river. *Proc. of conf. Hydro 2000*: 183–192. Bern, Switzerland.

Bovee, K.D. 1982. A Guide to Stream Habitat Analysis Using the Instream Flow Incremental Methodology. USFWS/OBS, Fort Collins, CO.

Canton du Valais. 2006: http://www.vs.ch/Navig/navig.asp?MenuID=806

Coyle, G. 2000. Qualitative and quantitative modelling in system dynamics: some research questions. *System Dynamics Review*, 16: 225–244.

Devi Prasad, T. & Park, N.S. 2004. Multiobjective Genetic Algorithms for Design of Water Distribution Networks. *J. Water Resour. Plng. Mgmt.* 130(1): 73–82.

Dowla, F.U. & Rogers, L.L. 1995. Solving Problems in Environmental Engineering and Geosciences with Artificial Neural Networks, The MIT press.

EuroDicauTom, A Glossary of Space Terms, ESA 1982, http://europa.eu.int/eurodicautom/Controller.

Fourer, R., Gay, D.M. & Kernighan, B.W. 2003. *AMPL: A Modeling Language for Mathematical Programming*. Duxbury Press, Brooks/Cole Publishing Company.

Ginot, V. 1998. Logiciel EVHA. EValuation de l'HAbitat physique des poissons en rivière ver. 2. Cemagref BEA/LHQ

Copyright © 2006 Taylor & Francis Group plc, London, UK

Goldberg, D.E. 1989. Genetic algorithms in search, optimization and machine learning. Addison-Wesley, Reading Mass.

Gomez, P. & Probst, G. 1995. *Die Praxis des ganzheitlichen Problemlösens*. Bern, Switzerland: Paul Haupt Verlag.

Heller, P., Bollaert, E. & Schleiss, A. 2005. Potential Synergies of Multipurpose Run-of-River Hydroelectric Powerplants. *Proc. of conf. 31 IAHR Congress*: 2121–2130. Seoul, Korea.

Lamouroux, N. & Souchon, Y. 2002. Simple predictions of instream habitat model outputs for fish habitat guilds in large streams. *Freshwater Biology* **47**: 1531–1542.

Leach, W.D. & Pelkey, N.W. 2001. Making Watershed Partnerships Work: A Review of the Empirical Literature. *J. Water Resour. Plng. Mgmt.*, 127: 378–385.

Lek, S. & Guégan, J.F. 1999. Artificial Neural Networks as a tool in ecological modeling, an introduction. *Ecol. Model*. 90, 39–52.

Leyland, G. 2002. Multi-objective optimisation applied to industrial energy problems. PhD Thesis, EPFL Nr. 2572, Lausanne, Switzerland.

Meier, W. 2002. Modellierung der Auswirkungen von Wasserkraftanlagen auf physikalische und chemische Eigenschaften von Bergbächen. PhD Thesis, ETHZ Nr. 14526, Ökostrom Publikation Band 11, Zurich, Switzerland.

Meile, T., Schleiss A.J. & Boillat, J.-L. 2005. Entwicklung des Abflussregimes der Rhone seit dem Beginn des 20. Jahrhunderts. *Wasser, Energie, Luft – eau, énergie, air*, 97(5/6): 133–142.

Murle, U., Ortlepp, J. et al. 2003. Effects of experimental flooding on riverine morphology, structure and riparian vegetation: The River Spöl, Swiss National Park. *Aquatic Sciences* 65(3): 191–198.

Obach, M., Wagner, R. et al. 2001. Modelling population dynamics of aquatic insects with artificial neural networks. *Ecological Modelling* 146: 207–217.

Poff, N.L., Allan, J.D. et al. 1997. The Natural Flow Regime: A paradigm for river conservation and restoration. *Bioscience* 47(11): 769–784.

Richter, B.D. & Richter, H.E. 2000. Prescribing Flood Regimes to Sustain Riparian Ecosystems along Meandering Rivers. *Conservation Biology* 14(5).

Silvert, W. 2000. Fuzzy indices of environmental conditions. *Ecological Modelling* 130: 111–119.

The MathWorks, I. 2004. Neural Network Toolbox User's Guide for use with MatLab. The MathWorks, Inc.

Valentin, S. 1995. Variabilité artificielle des conditions d'habitat et conséquences sur les peuplements aquatiques: effets écologiques des éclusées hydroélectriques en rivière. Laboratoire Hydroécologie Quantitative – Division Biologie des Ecosystèmes Aquatiques – CEMAGREF. Lyon, Université Claude Bernard – Lyon I: 263 pages.

Wade, A., Hornberger, G.M. et al. 2001. On modeling the mechanisms that control in-stream phosphorous, macrophyte, and epiphyte dynamics: an assessment of a new model using general sensitivity analysis. *Water Resources Research* 37(11): 2777–2792.

Zadeh, L.A. 1995. Foreword. Fuzzy Logic Toolbox User's Guide ver.2. I. The MathWorks. Natick, MA.

Zhang, L., Gove, J.H. et al. 2005. Spatial residual analysis of six modeling techniques. *Ecological Modelling* 186: 154–177.

Copyright © 2006 Taylor & Francis Group plc, London, UK

Optimizing the flow pattern in culverts for small upstream migrating fish using a numerical 3D Code

R. Feurich
Institute of Hydraulic Research, University of Innsbruck, Austria

J. Boubée
National Institute of Water & Atmospheric Research Ltd., Hamilton, New Zealand

ABSTRACT: After improving passage for upstream migrating fish in a culvert on Cardinia Creek, Australia, field trials were conducted to test the effectiveness of the modifications. These included velocity measurements, catch and release experiments with fish, electrofishing, and numerical simulations of flow patterns through the culvert. Results indicated that the use of spoiler baffles facilitated the upstream passage of fish, and that numerical simulation was an appropriate tool to predict flow patterns in modified culverts, and could potentially be used to advance the design of spoiler baffle arrays.

1 INTRODUCTION

To complete their life cycle, diadromous freshwater fish need to have free access to and from the sea. These migratory fish are often blocked by natural and anthropogenic instream structures such waterfalls, weirs and overhanging road culverts, with large numbers found congregating below such barriers (Thorncraft & Harris 1996). High mortality from predation, competition, and disease can occur as a result, and some populations may become locally extinct.

In 1980, the Dandenong Valley Authority, Melbourne, Australia, constructed a drop structure on Cardinia Creek at the end of Thompson Road to stabilise a 6.2 m high erosion head. A flood retention basin was formed behind the structure, with low flows diverted into a 42 m long, 1.35 m diameter ARMCO culvert at a slope of 1.19%. From there, flows passed down a rock-lined galvanised chute at 6.7% slope before rejoining the original creek channel. Flood flows were directed over a concrete spillway into the original creek channel.

A total of 15 indigenous fish species are recorded in the Cardinia Creek catchment. Nine of these fish are diadromous, with many returning to freshwater as juveniles. Fish distribution studies by Close et al. (2001), and McGuckin (2001) concluded that the combination of the steep, rock-lined chute and the ARMCO culvert limited fish passage at the Thompson Road drop structure. As the swimming ability of fish is related to their length (Boubée et al. 1999), ensuring upstream passage at potential barriers requires the installation of facilities that cater for the smallest fish species that migrate at that site.

Fish distribution records for Cardinia Creek indicate that the common galaxias (*Galaxias maculatus*) is the dominant species in the lower reaches, particularly during summer. Juveniles return to freshwater in spring when between 45 and 70 mm in length, and slowly make their way upstream during spring and summer. Because of its abundance, this species would benefit from improved access to the upstream catchment. More importantly, Boubée et al. (2003) considered that providing passage for common galaxias would also ensure passage of other indigenous species, including the Australian grayling (*Prototroctes maraena*) that is listed as a vulnerable species by the International Union for Conservation of Nature and Natural Resources (Allen et al. 2002).

In 2002, a rock ramp fishway with a slope of 4.8% was installed to replace the rock-lined galvanised chute at the Thompson Road drop structure. At the same time, the culvert was shortened to about 32 m (Fig. 1). Mark-recapture trials with common galaxias showed that the remaining 32 m of the ARMCO culvert was still a significant barrier to migration (Boubée & McGuckin 2004). In addition, the rock ramp fishway progressively reduced fish migration as flows increased above 0.5 m^3/s.

Due to the poor structural condition of the remaining 32 m of ARMCO culvert, Melbourne Water Corporation, which now manages the structure, judged that it had to be replaced, and this provided an opportunity to improve fish passage. The replacement structure had to

Copyright © 2006 Taylor & Francis Group plc, London, UK

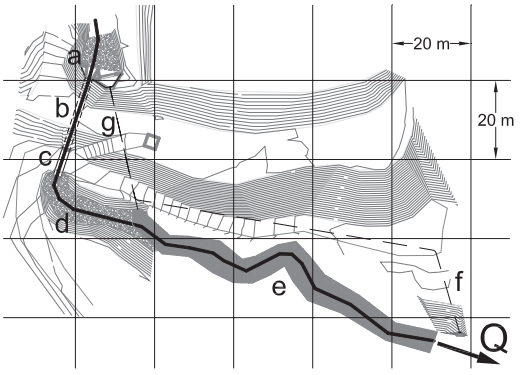


Figure 1. Plan of Cardinia Creek at the Thompson Road drop structure and fishway; a: culvert intakes; b: culvert built 2005; c: open square section built 2005; d: rock lined fishway extended 2005; e: rock lined fishway built 2002; f: Bypass pipe built 2005; g: old culvert modified as bypass 2005. (From Connel Wagner Drawing SES1017/001 dated 16/09/2005.)

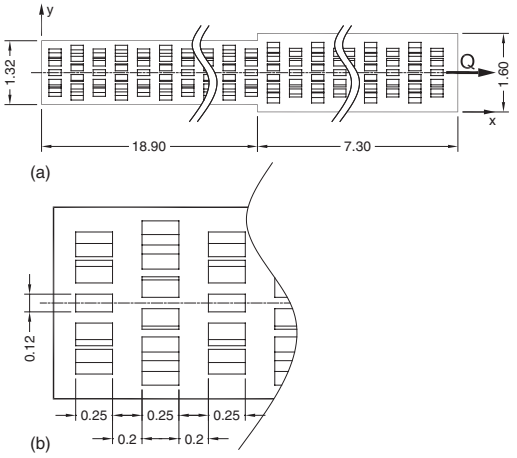


Figure 2. Plan view of the culvert and spoiler baffle array used.



Figure 3. View of the installed culvert outlet and rock ramp fishway. The buried flow bypass pipe exists just to the right of the picture.

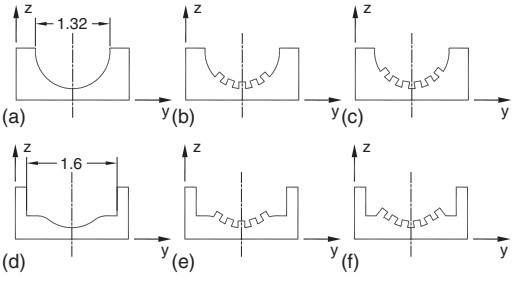


Figure 4. Culvert cross-sections with five and six spoiler baffles; a–c: round culvert section; d–f: square culvert section.

retain the ability to control floods. Of the options considered, the most effective was to replace the ARMCO culvert with concrete reinforced pipes that had spoiler baffles and resting areas for fish installed on the base. Although spoiler baffles are more complex than the weir system of baffles (Ead et al. 2002), observations of common galaxias swimming through different fish baffle systems indicated that these fish are reluctant to pass over weir baffles, but easily negotiate spoiler baffles where they can remain close to the bottom at all times (Authors, pers. obs.). As long as spoiler baffles create a zone 50–100 mm wide with velocities below 0.3 m/s, Boubée et al. (1999) found that small fish could progress upstream in the sustained swimming mode.

Flow records at the Thompson Road drop structure indicated that during the October to January upstream migration period, mean monthly flows were usually below 0.5 m^3/s, but flows up to about 1 m^3/s were occasionally recorded. Passage of fish was therefore required for flows of up to 1 m^3/s.

Field trials (Boubée & McGuckin 2004) and simulation studies (Kopeinig 2004) showed that fish passage was possible in the fishway and existing pipe fitted with spoilers at flows of up to 0.7 m/s, but passage became increasingly restricted at higher flows. Therefore, the chosen design had a pipe connected to the rock-lined channel for fish, with a weir and bypass pipe to progressively take flows above c. 0.2 m^3/s away from the fishway (Fig. 1). Steel flow restriction plates were installed on the headwall to ensure floods could still be controlled. To maximise fish passage, the rock-lined fishway was extended by c. 20 m, and the pipe section for fish reduced to 26.2 m, of which c. 7.3 m was formed out of a box section with a grill over the top to maximise light entry (Figs 2, 3). The slope of the pipe section was also reduced to 0.76%, and rows of five and six rectangular wooden blocks 120 × 120 × 250 mm at 450 mm spacing were attached to the invert (Figs 2, 4).

This paper presents the results of the monitoring and simulation undertaken following installation, and discusses the potential use of numerical simulation for resolving fish passage issues at culverts.

Copyright © 2006 Taylor & Francis Group plc, London, UK

2 METHODS

Field trials were conducted between 15 and 18 November 2005 at the peak of the common galaxias migration. Trials were made following a rain event, and three sets of flow and velocity measurements within the culvert were obtained for calibration of the numerical model.

2.1 *Flow and velocity*

Longitudinal and cross sectional water velocities within the culvert were measured with a Marsh MCBirney meter. Flows both within and outside the culvert was estimated from cross sectional water velocities with RHYHABSIM (Jowett 1989).

2.2 *Numerical simulation*

The complex geometry of a spoiler baffle array in a culvert, together with the need to calculate the free water surface, requires the use of a 3D numerical Code. Consequently, Flow-3D produced by Flow Science Inc. was used in this study.

Flow-3D uses a very simple structural mesh consisting of a hexahedral block subdivided into hexahedrons. In order to account for complex geometries, a multiblock mesh consisting of several adjacent blocks can be built. Into this simple mesh the geometry is inserted as obstacles, which can either be:

– Simple elements termed "Flow-3D primitives"
– XYZ-data, or
– 3D file formats like IDEAS or STL originating from CAD software.

To track the free surface, the VOF (volume of fluid) method is implemented. The principle of the VOF method is very similar to the FAVOR (fractional area volume representation) approach used to represent complex geometries in Flow-3D (Premstaller et al. 2004). Both the free surface and a geometric boundary cutting through an element are represented by additional scalar information indicating the percentage of water and obstacles, respectively, being present in a particular cell. The exact position where the free surface and/or the obstacle cuts through the cell is determined by the scalar information of that and adjoining cells (Fig. 5). Similarly, the normal vector on the plan can be determined. The scalar information is used to fulfill continuity, and in the case of the VOF method, is also used to ensure conservation of momentum.

In addition, so called fixed lines can be set. These force the grid generator to insert a volume boundary at the specified location.

Three numerical simulations were conducted using the three measured culvert discharges and a grid of

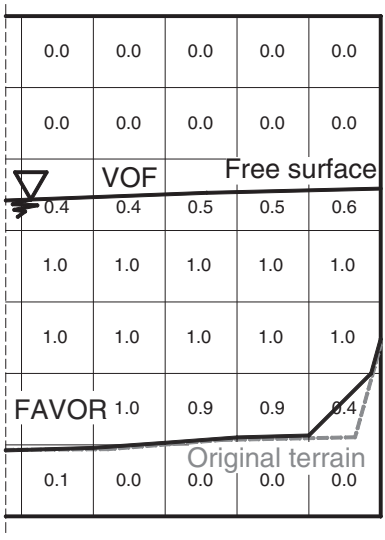


Figure 5. VOF and FAVOR method (from Premstaller et al. 2004).

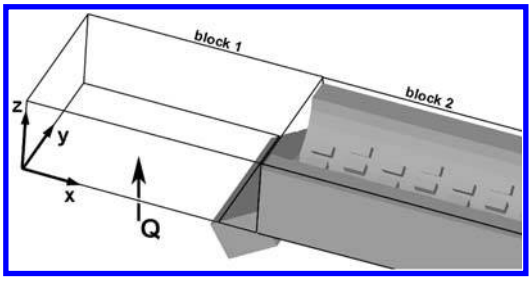


Figure 6. Inflow design used in the model.

700,000 cells with an x, y and z width of 80, 40 and 30 mm respectively. Two blocks were used for the entire grid: one for the inflow area and a finer one for the culvert.

The inflow block used in the model had a 2.5 × 2 m opening on the bottom as this provided slow inflow velocities, and an undisturbed flow field downstream (Fig. 6).

As the outlet flow observed in the field did not affect conditions within the culvert, a free water outflow was used in the model (Fig. 7b) and a 1 m long section free of baffles was added at the end of the culvert (Fig. 7a).

2.3 *Fish passage*

To determine the ability of fish to negotiate the structure, a 3 mm mesh trap that blocked the entire channel was set upstream of culvert inlet. Stained fish (Boubée & McGuckin 2004) were released at the

Copyright © 2006 Taylor & Francis Group plc, London, UK

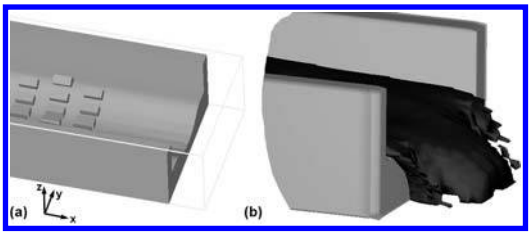


Figure 7. Extension at the end of culvert (a) and free outflow condition (b), used in the model.

Table 1. Flow measured in the stream above the structure and through the fishway.

	Flow (m^3/s)	
Date	Stream	Fishway
15/11/2005	1.45	0.74
17/11/2005	0.34	0.21
18/11/2005	0.26	0.15

culvert outlet, and the proportion recaptured in the trap determined. In addition, the entire rock-lined fishway was electrofished to determine if fish were accumulating in or below the structure. Results were compared with those obtained in 2002 (Boubée et al. 2003).

3 RESULTS

3.1 *Flows and effectiveness of bypass*

Three flows were measured and showed that the bypass pipe was effective at reducing flows in the fishway (Table 1).

3.2 *Numerical simulation*

At the two lowest experimental flows, predicted and measured velocities in the zone important for the fish migration (100 mm above the culvert floor) were very similar (Figs 8–9, 10–11). At the highest flow, for safety reasons no measurements could be made within the culvert, but the simulation indicates that fish migration would have been possible (Fig. 12).

3.3 *Fish passage*

Close to 53% of the 172 stained common galaxias released at the culvert outlet on 17 November 2005 was recaptured at the culvert inlet within 22 hours of release. Flows at this time were 0.21 m^3/s. This compares with only 8.5% making it through the structure over a similar period in 2002 when flow through the culvert was 0.1 m^3/s (Boubée et al. 2003).

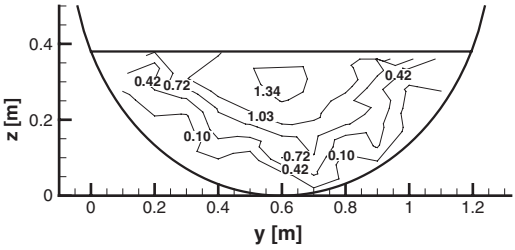


Figure 8. Measured water velocities (m/s) at cross-section x = 17.65 m with Q = 0.211 m^3/s.

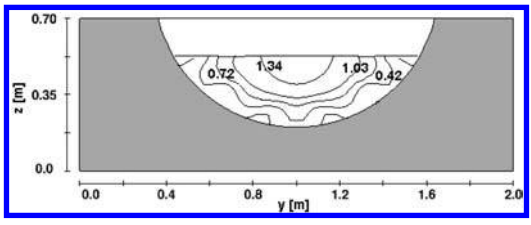


Figure 9. Simulated water velocities (m/s) at cross-section x = 17.65 m with Q = 0.211 m^3/s.

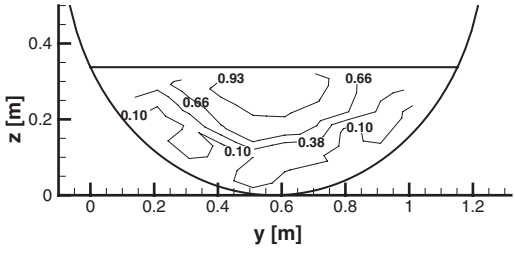


Figure 10. Measured water velocities (m/s) at cross-section x = 17.65 m with Q = 0.1559 m^3/s.

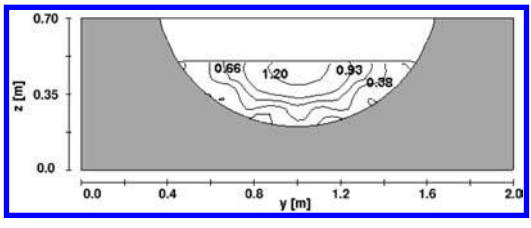


Figure 11. Simulated water velocities (m/s) at cross-section x = 17.65 m with Q = 0.1559 m^3/s.

In addition to the stained fish, 159 unmarked (wild) common galaxias, 24 lamprey (*Mordacia mordax*), 23 juvenile eels (*Anguilla australis*) and 2 tupong (*Pseudaphritis urvillii*) were captured at the culvert inlet. Electrofishing results did not indicate a concentration of fish below the culvert as was seen in 2002 (Boubée et al. 2003). This indicates a considerable improvement in fish passage since modifications were completed.

Copyright © 2006 Taylor & Francis Group plc, London, UK

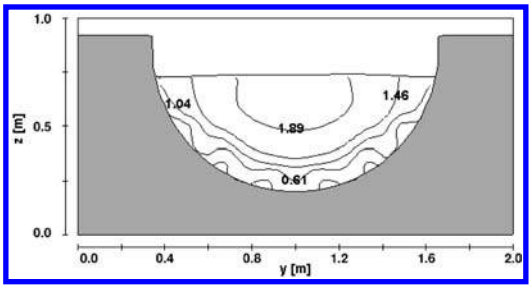


Figure 12. Simulated water velocities (m/s) at cross-section x = 17.65 m with Q = 0.7437 m^3/s.

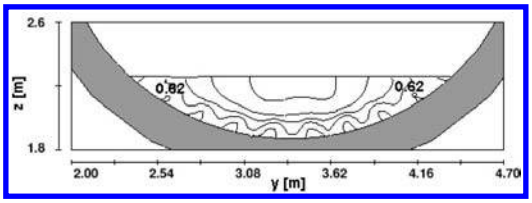


Figure 13. Simulated cross sectional water velocities (m/s) in a 3 m diameter culvert with Q = 0.6 m^3/s.

4 DISCUSSION

Modifications made to the Thompson Road drop structure, including the use of spoiler baffles within the culvert, allowed fish to successfully negotiate what was previously a migration barrier.

The numerical model correctly predicted flow patterns within the modified culvert, and could therefore be used to predict the effects of baffle configuration (e.g. spacing and size) on fish passage in culverts of varying size. For example, our numerical model shows that spoiler baffles of the same size as used in the 1.3 m culvert on Cardinia Creek would produce a low velocity fish passage zone in a 3 m diameter culvert of similar slope and flow (Fig. 13). This may mean that for small fish, baffle height does not need to be increased with culvert size as indicated by Engel (1974 in Rajaratnam et al. 1991). If further modeling and field verification prove this assertion correct, it would considerably simplify the installation and retrofitting of fish passage facilities in culverts of varying size as it would mean that spoiler baffles of the same size and orientation could be installed in a range of culvert.

ACKNOWLEDGEMENTS

We would like to thank David Fisher of Melbourne Water Corporation for the opportunity to undertake this study. Thanks are also due to John McGuckin for field assistance and Tanja Kopeinig for providing the results of her initial modeling studies.

REFERENCES

Allen, G.R.; Midgley, S. M. & Allen, M. 2002. *Field guides to the freshwater fishes of Australia.* Collingwood: CSIRO Publishing.

Boubée, J.; Jowett, I.; Nichols, S. & Williams, E. 1999. *Fish passage at culverts. A review with possible solutions for New Zealand indigenous species*. Wellington: Dept. of Conservation.

Boubée, J.; Williams, E. & McGuckin, J. 2003. Cardinia Creek-Fish Passage at the Thompson Road Drop Structure, Spring 2002. *NIWA Client Report* AUS2002-008.

Boubée, J. & McGuckin, J. 2004. Cardinia Creek – Fish passage at the Thompson Road drop structure – Stage 2. *NIWA Client Report* AUS2004-006.

Close, P.; Koster, W. & Lyon, J. 2001. *An assessment of the aquatic fauna in four Western Port sub-catchments (Victoria) Cardinia, Gum Scrub, Toomuc and Deep Creeks*. Report to Melbourne Water by Freshwater Ecology, Parks Flora and Fauna.

Ead, S.A.; Rajaratnam, N. & Katopodis, C. 2002. Generalised study of hydraulics of culvert fishways. *Journal of Hydraulic Engineering 128*: 1018–1022.

Jowett, I.G. 1989. River hydraulic and habitat simulation, RHYHABSIM computer manual. *New Zealand Fisheries Miscellaneous Report* 49. Christchurch: Ministry of Agriculture and Fisheries.

Kopeinig, T. 2004. *Numerical study of flow through a culvert – Investigation on various modifications using a 3D turbulent Navier-Stokes code*. Diploma Thesis, University of Innsbruck: Institute of Hydraulic Research.

McGuckin, J. 2001. *Riparian and instream habitat, instream barriers and fish survey along Cardina Creek*. Report to Melbourne Water by Streamline Research Pty Ltd.

Premstaller, G.; Rutschmann, P. & Oberhuber, M. 2004. Numerical simulation of flow instabilities in steep, stepped channels. *Riverflow 2004. Proceeding of the International Association of Hydraulic Engineering and Research Symposium.* Napoli: Balkema.

Rajaratnam, N.; Katopodis, C. & Lodewyk, S. 1991. Hydraulics of culvert fishways IV: spoiler baffle culvert fishways. *Canadian Journal of Civil Engineering 18*: 76–82.

Thorncraft, G.A. & Harris, J.H. 1996. *Assessment of rock-ramp fishways*. Report by the NSW Fisheries Research Institute and the Cooperative Research Centre for Freshwater Ecology.

Copyright © 2006 Taylor & Francis Group plc, London, UK

Fuzzy modelling of habitat suitability using 2D and 3D hydrodynamic models: Biological challenges

S.N. Lane, D.C. Mould, P.E. Carbonneau & R.J. Hardy
Department of Geography, University of Durham, UK

N. Bergeron
INRS-Eau, Terre et Environnment, Quebec, Canada

ABSTRACT: The last 10 years has seen a considerable improvement in our ability to measure and to model the complex flow fields in a range of river environments, even to the point that we have numerical schemes and data acquisition strategies that allow us to model the interaction between the detailed geometry of individual clasts and clast clusters and the associated three-dimensional flow and sediment transfer fields. At the same time, habitat modeling has developed significantly, as we have developed methods for coupling hydrodynamic models to measured habitat preferences. Here, we show how we have developed this linkage through coupling of a depth-averaged hydrodynamic model to habitat preferences, using a fuzzy rule-based approach. We demonstrate how this approach can be used to determine habitat suitability for two fish species (Atlantic salmon and Brown trout), in relation to spawning, nursery and rearing habitat, and related to proposed changes in compensation flow releases downstream from a dam, and possible future climate changes to the 2050s. The results demonstrate the crucial need to explore flow-biology interactions at the *within*- reach scale, especially in relation to low flows. In reflecting on these findings, we show that whilst three-dimensional modeling may reduce some of the uncertainties that follow from a depth-averaged approach, its applicability is limited by both the small scale of predictions generated and the lack of ecological knowledge of how to interpret those scales of prediction. The scales of habitat that matter in ecological terms are larger and more continuous, questioning approaches based on modeling 'representative reaches' and necessitating exploration of new ways of coupling biological and hydrodynamic knowledge.

1 INTRODUCTION

In this paper we develop a model for predicting available habitat for two species of fish (*Salmo salar* and *Salmo trutta*) using a combination of two-dimensional hydrodynamic modelling with fuzzy modelling of the consequent habitat, for three different life stages (spawning, nursery and rearing). The model is used: (1) to evaluate the compensation flows required to improve instream habitat for fish; and (2) to understand how future climate changes might impact upon instream habitat. Our examples lead to critical reflection of this kind of habitat modelling as a means of informing river management activities in relation to ecological enhancement.

1.1 *The move from one-dimensional to two-dimensional approaches*

The ecologically-available habitat in a river depends on several key physical parameters, notably flow velocity and depth, wetted perimeter, substrate, temperature and pH (e.g. Elso & Giller, 2001, Maddock et al., 2001, Leclerc, 2005). These are often combined into some form of habitat score such as a Weighted Usable Area (WUA) (see Leclerc, 2005, for review). The best-known example of this is PHABSIM (e.g. Milhous et al., 1984) which is widely used to assess habitat suitability. PHABSIM is based upon a simplified form of the one-dimensional St. Venant equations for width- and depth-averaged flow. It uses a combination of the mass continuity equation and the Manning equation, the latter supported by the Bernoulli equation in order to determine the slope of the energy line. If we make a diffusion wave approximation of the St. Venant equations (i.e. we ignore temporal and spatial accelerations), and specify a Manning type friction law, then this gives the mass continuity and Manning equation used by PHABSIM. This approximation limits PHABSIM to situations where flow is uniform, or approximately uniform (Milhous et al., 1989). Leclerc et al. (1995) note that this will not produce reliable results for areas of river less than $10\,m^2$, so limiting its suitability for smaller streams or where spatial variation in habitat is high. This was confirmed by Ghanem et al. (1996) who obtained a

Copyright © 2006 Taylor & Francis Group plc, London, UK

more accurate representation of spatial patterns of flow velocity with a two-dimensional (2D) model than with a one-dimensional (1D) model. Indeed, application of PHABSIM at smaller spatial scales appears to lead to over-estimation of the amount of available habitat (Crowder & Diplas, 2002).

The main motivation for moving away from a modelling approach like PHABSIM and towards 2D habitat models is that they can deal with the fact that fish are relatively mobile organisms and hence may move over a range of spatial scales. This may include the within-reach scale over a range of time scales, as organisms move between resting and feeding, or as external forces (e.g. river flow) change. Adopting a 2D approach is important as 1D approaches do not represent the substantial within-reach variability in hydraulic variables and this has been commonplace since the 1990s. For instance, Leclerc et al. (1995, 1996) used a finite element solution of the depth-averaged flow equations, including a wetting and drying treatment, with a Habitat Suitability Index (HSI), to explore habitat changes on the Moisie River, Quebec (Leclerc et al., 1995) and the Ashuapmushuan River, Quebec (Leclerc et al., 1996). The HSI was derived from observed vertically-averaged velocity, depth and substrate characteristics for Atlantic salmon fry and parr, using multivariate statistical techniques. The HSIs were driven by the hydraulic model predictions and were used to determine how the percentage usable area varied as a function of discharge. The advantage of using a 2D approach is that it recognises that as some habitat becomes less suitable as flow depth and/or velocity locally rises, so other habitats become more suitable (e.g. if they were originally dry but become wet). This showed that there was a rapid increase in the percentage usable area for both parr and fry habitat up to 50 $m^3 s^{-1}$. Above this threshold, it remained relatively constant for fry, but rose more slowly for parr. Most importantly, they noted that the spatial scale of model predictions was more similar to that of known ecological function: salmonids defend territories that rarely exceed 4 m^2. In a similar study Tiffan et al. (2002) used a depth-averaged model to simulate flow depths and velocities at 36 steady state discharges. The biological model was based upon multivariate logistic regression in which the probability of subyearling fall Chinook salmon presence was predicted from physical habitat parameters predicted by the model. The results showed that estimates of rearing habitat decreased as flows increased and that estimates of the area that fish could become stranded in initially rose, but then fell. However, they noted that even the 16 m^2 resolution adopted was too coarse to characterise adequately the habitat needs of the subyearling fish. The Tiffan et al. biological model was based upon a habitat probabilistic model and Guay et al. (2000) used a similar approach, but compared it with Habitat Suitability Index approaches. They found that the HPI produced better results than the HSI, and they noted that this may be because of the multivariate nature of the HPI approach in which predictions from the hydraulic models are considered simultaneously rather than independently, so dealing with a common criticism of approaches like PHABSIM.

Crowder & Diplas (2000) extend these approaches to determination of energy gradients and 'velocity shelters'/refugia in gravel-bed streams. They recognise that point predictions of hydraulic variables may not always provide a sufficient representation of habitat as spatial variation in those variables is also a crucial fish (e.g. Hayes & Jowett, 1994) and macroinvertebrate (e.g. Lancaster & Hildrew, 1993) requirement. Crowder & Diplas undertook a higher resolution modelling study, which included mesoscale topographic features (e.g. boulders), to generate predictions for input into spatial habitat metrics. These seek to capture the physical habitat difference between two locations with the same velocity but different surrounding velocities in terms of velocity and kinetic energy gradients. For instance, by scaling the spatial change in kinetic energy between two points by the kinetic energy at the point with the smaller velocity, they were able to derive a metric that represents the kinetic energy that must be spent by an organism to move from an area of lower velocity to an area of higher velocity. As these are gradient-based, they will depend upon the spatial scale over which calculations are made, and this will need to be evaluated in relation to the spatial resolution of the mesh used in the model in relation to the behavioural aspects of the organism being considered. The research showed that boulders resulted in a substantially more complex spatial metric and so a greater habitat range for fish. Linking this to observed fish behaviour (Crowder & Diplas, 2002) confirmed that boulders enhanced the potential availability of the right habitat.

1.2 *Why habitat modelling needs to be fuzzy*

The above review emphasises that there has been significant development of habitat modelling approaches using hydrodynamic models over the last 10 years. This progress aside, a number of difficult issues remain. Central to these difficulties is the fact that hydrodynamic models need to be informed by ecological knowledge. Much of this is traditionally based upon field measurements (e.g. of depth and velocity) of where individual organisms have been observed at particular life stages (e.g. Rimmer et al., 1983, Heggenes, 1990, Heggenes, 1991, Heggenes, 1996, Bardonnet & Baglinière, 2000, de Crespin de Billy & Usseglio-Polatera, 2002, Armstrong et al., 2003). Typically, these measurements record a preferred organism preference (where they are living) and not a possible organism preference (where they could live). The latter

Copyright © 2006 Taylor & Francis Group plc, London, UK

is more difficult to estimate, not least because exposure to certain extreme conditions (where an organism could temporarily live) means that certain conditions may only be suitable for a specific period of time, but also because designing experiments to evaluate possible organism habitat is almost impossible. It is quite possible that a number of possible different *combinations* of habitat parameter values are similarly suited to an organism (Jorde et al., 2001). Habitat will only limit organism growth and survival if the densities of fish are sufficiently high relative to the size of the fish (Armstrong et al., 2003). If ecological measurements are made when this is not the case, the organism-habitat relationships will partly reflect other processes and hence will be noisy/uncertain with respect to what could be possible habitat.

Fuzzy models are designed for applicability to situations where only imprecise information is available (Ross, 1995) and they were introduced into habitat modelling by Jorde (e.g. Jorde et al., 2001, Schneider & Jorde, 2003). Given the above observation about the noise that will be implicit in ecological preference data, fuzzy modelling has real appeal for habitat modelling. Fuzzy models are particularly valuable for situations where the noise in our knowledge is non-random and not necessarily quantifiable: the situation is ambiguous (Ross, 1995) rather than uncertain (in the classical statistical sense). Thus, fuzzy analysis commonly maps onto linguistic definitions (good, bad) rather than numerical definitions. The ecological uncertainty surrounding habitat preference, both methodological and substantive, means that developing fuzzy habitat models it is possible to explicitly retain the ambiguity that is implicit in habitat preferences knowledge.

2 METHODOLOGY AND APPROACH

Our methodology and approach has two key dimensions: (1) the development of two-dimensional predictions of flow depth and velocity for shallow gravel bed rivers, using hydrodynamic models; and (2) application of these predictions to a fuzzy habitat model in relation to the species requirements for Atlantic Salmon (*Salmo salar*) and Brown Trout (*Salmo trutta*). Here, we consider two case-studies: (1) possible impacts of changing the release rate of water from a dam to improve instream ecology; and (2) possible impacts of climate change, to the 2050s, upon habitat suitability for instream ecology.

2.1 *Two-dimensional hydrodynamic modelling*

The two-dimensional hydrodynamic modeling was based upon the Finite Element Surface Water Modelling System (FESWMS, Froehlich, 1989). This solves the finite element form of the depth-integrated conservation equations for mass and momentum. This is not a widely adopted numerical scheme, although it has been used in a similar habitat modeling application by Pasternack et al. (2004). Importantly, it allows representation of complex geometries through use of a finite element mesh, that can include individual habitat relevant features such as cobbles and boulders. The model does not make a hydrostatic pressure assumption and has a wetting and drying treatment that allows for the representation of changing discharge. The model can include both wind-driven and Coriolis stresses, but these are assumed to be negligible in the scales of application used here. The model treats the turbulent stresses introduced during depth-averaging using a zero order Boussinesq type turbulence model, with an empirically specifiable eddy viscosity (see Lane, 1998) for review. The model uses a Manning-type parameterization of a quadratic friction law (see also Lane, 1998). Taken together, the eddy viscosity and Manning's n represent the two key calibration parameters available during model simulation. In terms of data requirements, and for application to a reach with a single outflow and inflow, the model requires: (1) a stage-discharge relationship as input to one of the boundaries; (2) stage hydrographs at both boundaries; and (3) channel geometry. At each model node, the model predicts the depth-averaged velocity and water depth, and these are used as input to the habitat model. We do not report on the validation of the hydrodynamic modeling in this paper. We have done this using distributed measurements of water surface elevation and depth-averaged flow velocity with very good levels of agreement. Pasternack et al. (2004) also report on model validation.

2.2 *Fuzzy modeling of habitat suitability*

Our approach focuses on depth and velocity alone. As it is two-dimensional, it implicitly includes consideration of the wetted usable area, as nodes are predicted as wet (depth > 0) and/or dry as a function of model solution.

After verbal consultations with habitat researchers in relation to depth and velocity requirements of Atlantic Salmon and Brown Trout, we classified each into: poor, medium and good; and habitat into six classes: unsuitable, very poor, poor, good, very good and excellent. We then define fuzzy subsets for depth (*Di*) and velocity (*Vi*) that define the grade of membership of each predicted depth (d) or velocity (v) of each of the i (poor, medium or good) subsets:

$$\begin{aligned}
D_p &= \{[d, \mu_{Dp}(d)]; d \in D, \mu_{Dp}(d) \in [0,1]\} \\
D_m &= \{[d, \mu_{Dm}(d)]; d \in D, \mu_{Dm}(d) \in [0,1]\} \\
D_g &= \{[d, \mu_{Dg}(d)]; d \in D, \mu_{Dg}(d) \in [0,1]\} \\
V_p &= \{[v, \mu_{Vp}(v)]; v \in V, \mu_{Vp}(v) \in [0,1]\} \\
V_m &= \{[v, \mu_{Vm}(v)]; v \in V, \mu_{Vm}(v) \in [0,1]\} \\
V_g &= \{[v, \mu_{Vg}(v)]; v \in V, \mu_{Vg}(v) \in [0,1]\}
\end{aligned} \quad (1)$$

Copyright © 2006 Taylor & Francis Group plc, London, UK

where: p is poor, m is medium and g is good; and $\mu Li(l)$ is the grade of membership of the predicted value l(d or v) in Li(Di *or* Vi), which equals one for at least one value of L for each i. In this scheme, when $0 < \mu Li(l) < 1$, l has a partial membership of Li, and this is the sense in which the analysis is fuzzy, with l potentially being a partial member of more than one Li. We then specify a fuzzy rule for Habitat (Hk) based on two premises (for D and V):

$$\text{If } Di \otimes Vj \text{ then } Hk, \text{ for } K \text{ values of } k \tag{2}$$

where K is the number of habitat classes, i is the subset of Depth and j is the subset of velocity. In this case, $i = j = 3$, there are 9 rules, and potentially nine values of k. In order to capture the fuzziness of the analysis, membership of Di and Vj is expressed as a grade that varies between 0 and 1. Thus, we use a product operation rule (Wang, 1994) to define the degree of fulfilment of a particular habitat class:

$$\mu_{Hk} = \mu_{Hk,Di(d)}\mu_{Hk,Vj(v)} \tag{3}$$

where, μHk is the degree of fulfilment of Habitat class k, as defined by each possible combination of Di and Vj (from (2)), given the predicted values of d and v. The nine rules that come from (2) could be used to provide nine habitat classes. However, we use a symmetrical habitat classification, weighting D and V equally in the determination of habitat suitability (Table 1). This can be made more sophisticated by changing the weightings to reflect the known importance of velocity and depth in contributing to a particular habitat class, possibly informed by field data or traditional habitat suitability analyses, or calibrated onto measured relationships between habitat and productivity for a specific reach or set of reaches. We do not explore this here.

The analysis so far provides nine outcomes which indicate the degree of fulfillment of each rule. If there was no fuzziness in the system, then there would only be a single outcome. As the level of fuzziness increases, so the number of outcomes increases to the maximum of nine. In order to provide a single habitat suitability index we defuzzify the analysis to produce a single 'crisp' number. This can be done in a number of ways. Here we scale the total degree of membership of all classes to one, and then introduce the weightings shown in Table 1.

2.3 *Salmo salar and Salmo trutta habitat preferences*

The main additional data source necessary to run the habitat model relates to habitat preferences. On the basis of available data (e.g. Rimmer et al., 1983, Heggenes, 1990, Heggenes, 1991, Heggenes, 1996, Bardonnet & Baglinière, 2000, de Crespin de Billy & Usseglio-Polatera, 2002; Armstrong et al., 2003), we have mapped habitat preferences onto the following set memberships. We have also set a precision as per the table, this defines the fuzziness.

Table 1. The (symmetrical) definition of habitat classes in relation to the rule set defined in (2).

	Velocity		
Symmetrical	Poor (presence rarely found)	Medium (presence sometimes found)	Good (presence often found)
Depth Poor (presence rarely found)	Unsuitable Habitat 0	Very Poor Habitat 1	Poor Habitat 2
Depth Medium (presence sometimes found)	Very Poor Habitat 1	Good Habitat 3	Very Good Habitat 4
Depth Good (presence often found)	Poor Habitat 2	Very Good Habitat 4	Excellent Habitat 5

Table 2. Habitat preferences. All velocities have units ms^{-1} and all depths have units m.

	Poor (rarely found)	Medium (sometimes found)	Good (often found)
Salmo salar (Atlantic Salmon)			
Spawning, Velocity	<0.20	0.20–0.40	0.40–0.54
	>0.80	0.54–0.80	
Spawning, Depth	<0.17	0.17–0.25	0.25–0.38
	>0.76	0.38–0.76	
Nursery, Velocity	<0.15	0.10–0.30	0.20–0.40
	>1.00	0.40–0.10	
Nursery, Depth	<0.10	0.10–0.20	0.20–0.40
	>0.50	0.40–0.50	
Rearing, Velocity	<0.20	0.20–0.50	0.25–0.60
	>1.20	0.60–1.20	
Rearing, Depth	<0.20	0.15–0.30	0.25–0.60
	>0.70	0.60–0.70	
Salmo trutta (Brown Trout)			
Spawning, Velocity	<0.11	0.11–0.35	0.35–0.50
	>0.80	0.50–0.80	
Spawning, Depth	<0.06	0.06–0.25	0.25–0.40
	>0.82	0.40–0.82	
Nursery, Velocity	<0.05	0.05–0.15	0.15–0.20
	>0.20		
Nursery, Depth	<0.05	0.05–0.20	0.20–0.30
	>0.35	0.30–0.35	
Rearing, Velocity	<0.05	0.05–0.10	0.20–0.40
	>0.70	0.40–0.70	
Rearing, Depth	<0.05	0.05–0.50	0.50–0.75
	>1.22	0.75–1.22	

Copyright © 2006 Taylor & Francis Group plc, London, UK



Figure 1. Case study 1: compensation flow redesign.



Figure 2. Case study 2: climate change impacts on low flows.

2.4 *Case-study applications*

We use two case studies. They share the common characteristic of being upland gravel/cobble streams in the Pennines region of northern England, with established populations of Brown Trout. We also include Atlantic Salmon in the analysis as these were thought to be found in these systems before the onset of major regulation and industrialization downstream (and hence both barriers and water quality), which would have most likely precluded salmonid migration to spawning, nursery and rearing grounds. The inclusion of Atlantic salmon is valuable as this is a potential target species in relation to what an undisturbed river catchment might look like. The prime difference between the two systems is in terms of the content for the modeling.

2.4.1 *Designing optimal compensation flow releases*

The first case study is concerned with the optimal way of setting compensation flow releases downstream from a dam, in order to deliver ecological improvements. Traditionally, in the U.K., compensation flow releases were set according to downstream industrial needs. With the decline of industry, opportunities have arisen to redefine releases to deliver ecological enhancement. In the case study here (Fig. 1), the aim was to increase the compensation flow from the current level of 0.03 $m^3 s^{-1}$, to the target level of 0.10 $m^3 s^{-1}$, and then subsequently to much higher levels than feasible: 0.50 $m^3 s^{-1}$ and 1.0 $m^3 s^{-1}$. We modeled a single riffle-pool unit (Fig. 1).

2.4.2 *Assessing future climate change impacts*

In the second example, we explore the impacts of estimated changes in low flow due to climate change. This uses output from a continuous simulation of climate from the start of a baseline period (1960) to 2069. We apply it to a distributed continuous simulation model of runoff. The model was calibrated on measured flows for the 1990s and early 2000s. Model output allowed determination of annual flow duration curves over the full 109 year period. We used this to determine characteristic drought period Q95 flow percentiles for the baseline period and for the 2050s

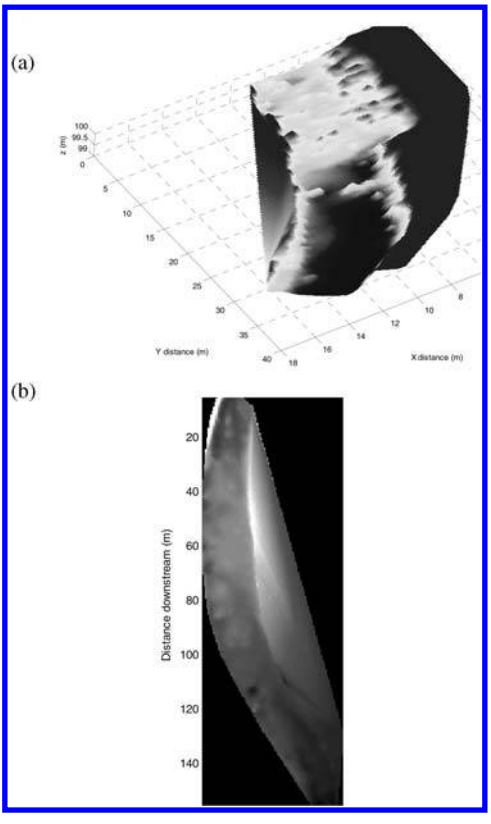


Figure 3. Shaded relief model of the topography at Case Study 1 (3a) and shaded contour model of the topography at Case Study 2 (3b).

(0.106 $m^3 s^{-1}$ and 0.078 $m^3 s^{-1}$ respectively). The modeled site comprised a weakly curved reach with a riffle at the downstream end (Fig. 2).

2.5 *Model geometry and mesh*

For both studies, we determined model geometry (Fig. 3) using high density field survey with Total

Copyright © 2006 Taylor & Francis Group plc, London, UK

Stations. These yielded data files with point spacings of better than 1 point per m^2. The density was varied to reflect the topographic variability of the river bed, including mapping of individual boulders and cobbles where it was clear that these were having (or would have) a substantial impact upon the associated flow characteristics. Topographic data were mapped directly onto the finite element mesh, locally interpolating nodes where the local rate of topographic change necessitated a higher node spacing. Achieving mesh independence in a study like this is not straightforward: as mesh resolution is progressively fined, so the model starts to resolve aspects of topography that are a consequence of data point spacing and data interpolation rather than the real topography (Lane et al., 2004) and this necessitates exploration of different approaches to topographic data representation in models of this kind. This is beyond the scope of this paper, but methods for doing this are reported elsewhere (Lane et al., 2004; Lane, 2005; Hardy et al., 2005).

3 RESULTS

Here, we begin by showing the importance of a two-dimensional analysis as the underlying context for the subsequent quantified changes in habitat suitability index. We then present results for: (1) compensation flow design; and (2) climate change impacts.

3.1 *Spatial patterns of habitat suitability*

Figure 4 shows the spatial patterns of HSI for Atlantic salmon (spawning) in response to the reduction of the characteristic drought period Q95 from 0.106 $m^3 s^{-1}$ (Fig. 4a) to 0.078 $m^3 s^{-1}$ (Fig. 4b). The results demonstrate the crucial role that is played by the bed geometry at these low flows: as the flow is reduced to the 2050s, so the bed topography becomes more strong topographically forced, as indicated by the greater steering shown in the superimposed flow vectors. There is a clear change in the amount of suitable habitat between the two simulations: there is a change in scale between the two Figures, showing that the general suitability is reduced under the 2050s scenario. Further, there are subtle spatial patterns to the associated changes. For instance, by the 2050s, the zone of most suitable habitat has switched towards the true right, 80 to 100 m downstream, reflecting the changing partitioning of flow around the upstream mid channel bar. Particularly at these low flows, small changes in flow magnitude can lead to very different flow routing, and this will have a major impact upon habitat suitability.

Figure 5 shows the spawning habitat changes but for Brown trout. As compared with Figure 4, the changes are much less dramatic. There is a smaller reduction in habitat suitability. However, there are some subtle

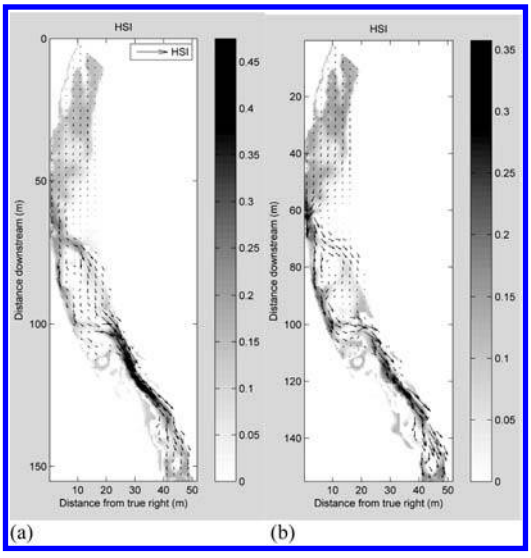


Figure 4. Habitat suitability index estimates for Atlantic salmon spawning habitat in response to climate change. 4a shows the baseline scenario and 4b shows the 2050s scenario.

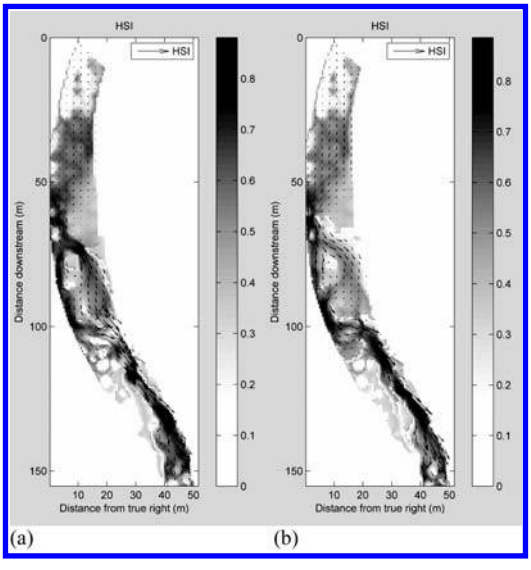


Figure 5. Habitat suitability index estimates for Brown Trout spawning habitat in response to climate change. 5a shows the baseline scenario and 5b shows the 2050s scenario.

changes in the spatial distribution of habitat suitability, notably the emergence of suitable habitat on the true right, between 130 and 150 m downstream. Much of this reflects the upstream steering of flow onto the true right which, as a result, wets part of a previously bar, creating new habitat. As with the case of

Copyright © 2006 Taylor & Francis Group plc, London, UK

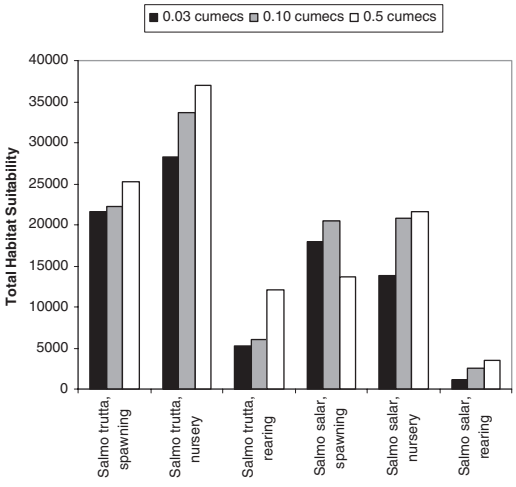


Figure 6. The total habitat suitability for case study site 1, for the three lowest compensation flows simulated.

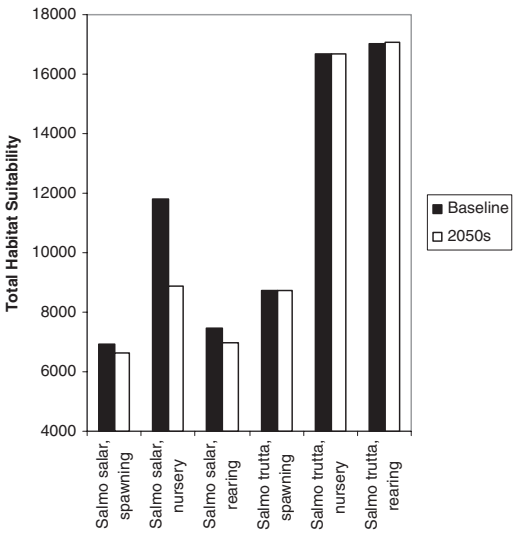


Figure 7. The total habitat suitability for case study site 2, for the drought period Q95, for the baseline and the 2050s.

Atlantic salmon, the spatial changes in flow distribution at these low flows are crucial for determining the spatial patterns of available habitat.

3.2 *Quantitative results: compensation flow redesign*

Figure 6 shows the effects of the three lowest compensation flows tested on the model of Case Study 1.

Figure 6 suggests that the current level of compensation ($0.03\,m^3s^{-1}$) is sub-optimal in terms of habitat suitability for Brown trout as compared with both the $0.10\,m^3s^{-1}$ and $0.50\,m^3s^{-1}$ simulations. However, for Atlantic salmon, this is only true for nursery and rearing life stages: increasing the compensation flow to $0.50\,m^3s^{-1}$ actually leads to a reduction in suitable spawning habitat. There is also variability between life stages and organisms in response to sensitivity to change. However, the key conclusion from this analysis is that the suitability of this reach for both Atlantic salmon and Brown trout habitat, for all life stages, might be improved by an increase in the magnitude of the compensation release.

3.3 *Quantitative results: climate change impacts*

Figure 7 compares simulated total habitat suitability for Case Study site 2, where the drought period Q95 is perturbed from baseline to the 2050s. The most striking aspect of Figure 7 is the difference between the species response in terms of habitat suitability. For *Salmo salar*, the simulations to the 2050s suggest a reduction in suitability for all three life cycles, with a dramatic reduction for nursery habitat, and smaller reductions for spawning and rearing habitat. However, for *Salmo trutta*, there are almost no changes. The reason for this difference in response could be two fold. First, it could reflect differences in organism traits in relation to the distinguishability of different habitat classes: if *Salmo trutta* had less clear preferences, it would be less sensitive to discharge changes. However, inspection of Table 2 suggests that this is not the case. Second, and more likely, it reflects the facts that, in habitat terms, *Salmo trutta* is more tolerant of the reduced Q95 under the 2050 scenario, in relation to the interaction between that flow and the bed topography. The reduced flow produces a velocity and depth field that is still within the range of habitat suitabilities found under the baseline scenario. Again, this emphasizes the important contextual influence of particular local river geometries and individual organism habitat preferences in mediating climate change impacts, as was shown in Figures 4 and 5. In terms of climate change, for in rivers in this region with similar gravel-beds, there is likely to be a net loss of *Salmo salar* suitable habitat due to the impacts of discharge changes upon velocity and depth, and the associate habitat suitability. However, there are important caveats to this observation, and these are discussed below.

4 DISCUSSION

In the discussion, we seek to set this work into broader context by looking at the above research from two perspectives: (1) hydrodynamic; and (2) biological; and then linking these together to think of future ways forward.

Copyright © 2006 Taylor & Francis Group plc, London, UK

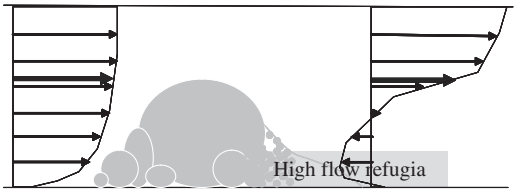


Figure 8. A simple cartoon illustrating the problem of depth-averaged velocity predictions (the thicker arrow) in the presence of a classic gravel-bed river feature (a pebble cluster): as stage rises and the flow depth to obstacle height ratio rises, so the depth-averaged velocity contains progressively less ecologically relevant information, not least because at these higher stages the separation zone in the lee of the cluster may become ecologically critical.

4.1 *Habitat modeling and hydrodynamics*

The starting point for many in terms of depth-averaged modeling of velocity and depth were the perceived inadequacies of representing spatial variability in velocity and depth in one-dimensional schemes. Even if the observed inadequacies of 1D modeling of habitat using diffusion wave approximations are accepted, there remains a logical limit to the extent to which such models can represent the real variability in depth and velocity that matters for organisms. Most life stages of fish, for instance, can readily move upstream or downstream in order to find suitable habitat, refuge or food, and 1D approaches tend to emphasize variability in section rather than downstream (Leclerc, 2005). The question then arises as to whether or not a 2D approach is any better. The process of depth-averaging yields a velocity prediction that (if the profile is semi-logarithmic) is found at approximately 40% of the flow depth above the bed. This will vary substantially where there are deviations from this profile form, notably if there is some form of flow separation such as above or around cobbles or boulders (e.g. Fig. 8), features that are known to be crucial components of good salmon and trout habitat. In theory, organisms can occupy any part of 3D space where there is flow and will do, according to whether they are feeding (where food sources in faster flowing water may be more available), resting (where slower velocities are critical) or seeking refuge (such as behind boulders or in deeper pools). Further, the kind of habitat that is produced by a given bed geometry will change as a function of discharge and stage and, from a hydrodynamic perspective, the information content of the depth-averaged velocity will partly reflect relative submergence effects rather than describing purely changes in velocity at the elevation associated with depth-averaging.

The initial response to this might suggest 3D approaches are needed, supported by the observation that we can now measure three-dimensional river bed topography in both laboratory and field environments

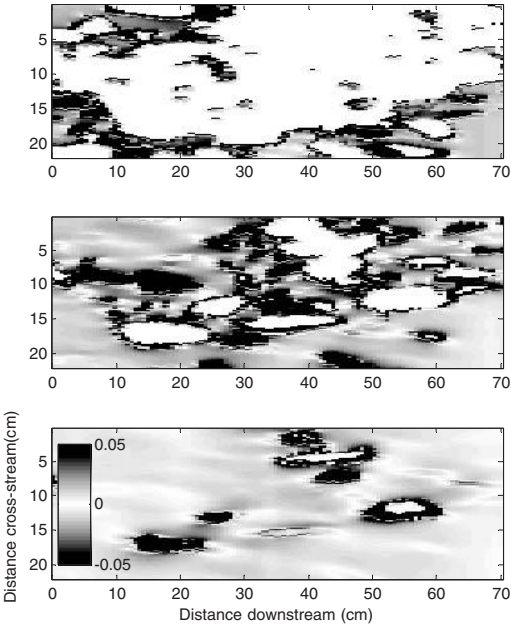


Figure 9. Predictions of planform vorticity at 10, 15 and 20 cm above a gravel/cobble surface from a 3D numerical model. White areas are blocked out by individual stones.

to mm precision and resolution (Butler et al., 2002). There are also novel methods available for representing this topographic information without recourse to boundary-fitted co-ordinates, such as by using blockage or porosity methods (Lane et al., 2004, Hardy et al., 2005). These methods can be used to derive ecologically-relevant information such as vorticity (Fig. 9), which has been linked to habitat usage (Crowder & Diplas, 2002).

The sophistication of these tools is appealing. However, these kinds of predictions immediately represent a problem in terms of ecological interpretation, as the scale of model predictions is commonly significantly smaller than the size of the organisms that the predictions are to be linked to. Figure 10 shows a three-dimensional visualization of the 5 cms^{-1} velocity surface for the same predictions shown in Figure 9. The length of the domain is 0.70 m and the width 0.30 m. The spatial structure of this field is less than the cm scale and will be largely irrelevant to the scale of a fish. We have almost no biological guidance on how to scale up these data to those biologically relevant scales. Thus, the move to 3D may satisfy the reductionist desire of removing progressively more of the uncertainty associated with modeling flows for habitat studies but, even if issues such as data availability and numerical representation, can be dealt with, this does not necessarily yield information that is biologically relevant.

Copyright © 2006 Taylor & Francis Group plc, London, UK

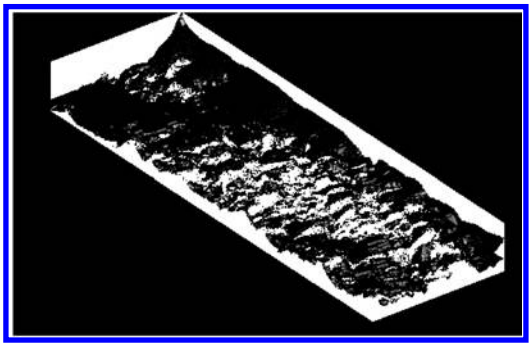


Figure 10. Three-dimensional visualization of the 5 cms^{-1} velocity surface for the same predictions shown in Figure 9, with a 70 cm length and 26 cm width gravel surface.

4.2 *Biological perspectives*

The previous section considered the hydrodynamic modeling presented in this paper in terms of process representation. Here, we look at the issue from a different angle: biological perspectives. The first point to emphasize is that the methodology that described in Section 3 and demonstrated in Section 4 is only relevant for predicting changes in *habitat*.

These can only be ecologically relevant if habitat is the limiting variable (Armstrong et al., 2003). Second, the analysis we present focuses only on depth and velocity and, because this analysis is 2D, wetted area. Velocity, depth and wetted area should map reasonably well onto system productivity if habitat is limiting. For the spatial scale and case-studies that we present, spatial variations in substrate are not significant. However, both compensation flow and climate change will cause adjustment in other variables (e.g. temperature, fine sediment delivery) and these may be as or more important than depth and velocity. In some cases, velocity and depth may be a surrogate for some parameters: for instance, high velocities and deeper flows will have cooler temperatures; faster velocities will have lower fine sediment contents. This is implicit in the habitat preference data used to populate these models (Table 2), because the data are based on observations, where temperature, substrates etc. are themselves difficult to control. This contamination probably can't be avoided. The main issue to be established is the extent to which depth and velocity capture these other variables and, if not, what the other variables are that are required and how they might be incorporated into habitat models.

The third, and final, issue is probably the biologically most relevant. In the same way that hydrodynamic models become most reliably closed at the very smallest of spatial scales, with boundary conditions absolutely and reliably specifiable, this is the scale at which they are likely to be least biologically valuable. Even with the 2D analysis presented in Sections 3 and 4, there are a number of key assumptions made that restrict the biological relevance of the associated results. The key assumption is that the analysis that we present requires us to assume that our reaches are *representative*, which they may not be. Central to this is the question of scale in fisheries biology. In salmonid research, the hierarchical view of scale is well established: larger scale catchment processes (e.g. basin scale sedimentary patterns) are assumed to create the environment within which smaller scale processes (e.g. riffle-pool dynamics) create a template that drives ecology (e.g. Folt et al., 1998, Armstrong et al., 1998). However, it is now recognized that this is a bi-directional process in which small–scale heterogeneity creates the spatial framework within which larger patterns of mobility emerge (Fausch et al., 2002). This represents a crucial challenge to habitat modeling, especially in relation to fish, because different spatial scales of mobility are associated with different stages of the salmonid life cycle (Armstrong et al., 1998). The habitat changes predicted, for instance in response to climate change, may be over-ridden by the ease with which salmonids can migrate to find other locations to spawn. Clearly some life stages are more critical than others: adapting to declining nursery habitat through migration is more difficult as the organisms are less able to migrate.

Both of the case studies we present are biased to the spatial scale at which we can feasibly generate bed geometrical data at ecologically-relevant scales, something that has been observed as common in many habitat studies (Folt et al., 1998). The result is a need to scale upwards (Cunjak, 1996, Lewis et al., 1996, Folt et al., 1998), without sacrificing the local spatial detail that is a crucial part of larger scale salmonid behaviour. This will involve considering the river as a continuously varying (Fausch et al., 2002) patchy environment. Focusing upon single or multiple representative reaches will not capture the ecological footprint available to mobile organisms.

5 CONCLUSION

Herein lies the challenge. On the one hand, the need to generate hydrodynamically meaningful data encourages us to think of progressively smaller spatial scales of enquiry. On the other, biologists are increasingly showing us that biological relevance emerges at much larger scales and over longer time periods than our models can possibly capture (but note, for example, Morin et al., 2000). One way forward may be system scale description of habitat parameters (see Carbonneau et al., 2004, 2005 for a 1 m mapping of an 80 km length of salmonid spawning river). The other is to begin to think about the link between hydrodynamics

Copyright © 2006 Taylor & Francis Group plc, London, UK

and biology in the conventional ways in which we have approached other parameterization difficulties in river research. In hydrodynamic modelling, for instance, because we cannot measure all relevant scales of geometrical variability we parameterise those scales that are not measured into a roughness parameter. This parameter is 'effective' (Lane, 2005): it is designed to represent those sources of friction loss that are not explicitly modeled, and it may not always easily map onto field or laboratory measurements. From a biological perspective, we need a similar research effort that seeks to couple hydrodynamic and biological expertise to develop effective parameters for coupling hydrodynamic and biological models in ways that are practical and feasible for river management.

REFERENCES

Armstrong, J.D., Kemp, P.S., Kennedy, G.J.A., Ladle, M. and Milner, N.J., 2003. Habitat requirements of Atlantic salmon and brown trout in rivers and streams. Fisheries Research, 62, 143–70.

Armstrong, J.D., Grant, J.W.A., Forsgren, H.L., Fausch, K.D., DeGraaf, R.M., Fleming, I.A., Prowse, T.D. and Schlosser, I.J., 1998. The application of science to the management of Atlantic salmon (Salmo salar): integration across scales. Canadian Journal of Fisheries and Aquatic Science, 55(Suppl. 1), 303–11.

Bardonnet, A. and Baglinière, J.-L., 2000. Freshwater habitat of Atlantic salmon (Salmo salar). Canadian Journal of Fisheries and Aquatic Science, 57, 497–506.

Butler, J.B., Lane, S.N., Chandler, J.H. and Porfiri, E., 2002. Through-water close range digital photogrammetry in flume and field environments. Photogrammetric Record, 17, 419–39.

Carbonneau, P.E., Lane, S.N. and Bergeron, N., 2004. Catchment-scale mapping of surface grain size in gravel bed rivers using airborne digital imagery. Water Resources Research, 40, Art. No. W07202 JUL 22 2004.

Carbonneau, P.E., Bergeron, N. and Lane, S.N., 2005. Automated grain size measurements from airborne remote sensing for long profile measurements of fluvial grain sizes. Water Resources Research, 41, Art. No. W11426 NOV 24 2005.

Crowder, D.W. and Diplas, P., 2000. Evaluating spatially explicit metrics of stream energy gradients using hydrodynamic model simulations. Canadian Journal of Fisheries and Aquatic Science, 57, 1497–1507.

Crowder, D.W. and Diplas, P., 2002. Assessing changes in watershed flow models with spatially explicit hydraulic models. Journal of the American Water Resources Association, 38, 397–408.

Cunjak, R.J. 1996. Winter habitat of selected stream fishes and potential impacts from land-use activities. Canadian Journal of Fisheries and Aquatic Science, 53(Suppl. 1), 267–282.

de Crespin de Billy, V. and Usseglio-Polatera, P., 2002. Traits of brown trout prey in relation to habitat characteristics and benthic invertebrate communities. Journal of Fish Biology, 60, 687–714.

Elso, J.I. and Giller, P.S., 2001. Physical characteristics influencing the utilization of pools by brown trout in an afforested catchment in Southern Ireland. Journal of Fish Biology, 58, 201–21.

Fausch, C.D., Torgersen, C.E., Baxter, C.V. and Li, H.W., 2002. Landscapes to riverscapes: bridging the gap between research and conservation of stream fishes. Bioscience, 52, 483–98.

Folt, C.L., Nislow, K.H. and Power, M., 1998. Implications of temporal and spatial scale for Atlantic salmon (Salmo salar) research. Canadian Journal of Fish and Aquatic Science, 55(Supp. 1), 9–21.

Froehlich DC. 1989. Finite Element Surface-Water Modeling System: Two-dimensional Flow in a Horizontal Plane User's Manual. U.S. Department of Transportation, Publication #FHWA-RD-88-177.

Ghanem, A., Steffler, P. and Hicks, F., 1996. Two-dimensional hydraulic simulation of physical habitat conditions in flowing streams. Regulated Rivers: Research and Management, 12, 185–200.

Guay, J.C., Boisclair, D., Rioux, D., Leclerc, M., Lapointe, M. and Legendre, P., 2000. Development and validation of numerical habitat models for juveniles of Atlantic salmon (Salmo salar). Canadian Journal of Fisheries and Aquatic Science, 57, 2065–75.

Hardy, R.J., Lane, S.N., Lawless, M.R., Best, J.L., Elliott, L. and Ingham, D.B., 2005. Development and testing of a numerical code for treatment of complex river channel topography in three-dimensional CFD models with structured grids. Journal of Hydraulic Research, 43, 468–80.

Hayes, J.W. and Jowett, I.G., 1994. Microhabitat models of large drift-feeding brown trout in three New Zealand rivers. North American Journal of Fisheries Management, 14, 710–725.

Heggenes, J. 1990. Habitat utilization and preferences in juvenile Atlantic salmon (Salmo salar) in streams. Regulated Rivers: Research and Management, 5, 341–354.

Heggenes, J. 1991. Comparisons of habitat availability and habitat use by an allopatric cohort of juvenile Atlantic salmon Salmo salar, under conditions of low competition in a Norwegian stream. Holarct. Ecol., 14, 51–62.

Heggenes, J., 1996. Habitat selection by brown trout (salmo trutta) and young atlantic salmon (s. salar) in streams: static and dynamic hydraulic modelling, Regulated Rivers: Research and Management, 12, 155–169.

Jorde, K., Schneider, M., Peter, A. and Zoellner, F., 2001. Fuzzy based models for the evaluation of fish habitat quality and instream flow assessment. Proc 2001 International Symposium on Environmental Hydraulics, Tempe, Arizona.

Lancaster, J. and Hildrew, A.G., 1993. Flow refugia and the microdistribution of lotic macroinvertebrates. Journal of the North American Benthological Society, 12, 385–393.

Lane, S.N. 1998. Hydraulic modelling in hydrology and geomorphology. A review of high resolution approaches. Hydrological Processes, 12, 1131–50.

Lane, S.N., Hardy, R.J., Elliott, L. and Ingham, D.B., 2004. Numerical modelling of flow processes over gravely-surfaces using structured grids and a numerical porosity treatment. Water Resources Research, W01302 JAN 8 2004.

Lane, S.N., 2005. Roughness – time for a re-evaluation? Earth Surface Processes and Landforms 30, 251–3.

Copyright © 2006 Taylor & Francis Group plc, London, UK

Leclerc, M., Boudreault, A., Bechara, J.A. and Corfa, G., 1995. Two-dimensional hydrodynamic modelling: a neglected tool in the Instream Flow Incremental Methodology. Transactions of the American Fisheries Society, 124, 645–662.

Leclerc, M., Boudreault, A., Bechara, J.A. and Belzile, L., 1996. Numerical method for modelling spawning habitat dynamics of landlocked salmon, Salmo salar. Regulated Rivers: Research and Management, 12, 273–285.

Leclerc, M., 2005. Ecohydraulics: a new interdisciplinary frontier for CFD. In Bates, P.D., Lane, S.N. and Ferguson, R.I., Computational Fluid Dynamics: applications in environmental hydraulics, Wiley, Chichester, 429–60.

Lewis, C.A., Lester, N.P., Bradshaw, A.D., Fitzgibbon, J.E., Fueller, K. Hakanson, L., and Richards, C. 1996. Considerations of scale in habitat conservation and restoration. Canadian Journal of Fisheries and Aquatic Science 53(Suppl 1), 440–445.

Maddock, I.P., Bickerton, M.A. and Spence, R., 2001. Reallocation of compensation releases to restore river flows and improve instream habitat availability in the Upper Derwent catchment, Derbyshire, UK. Regulated Rivers, 17, 417–41.

Milhous, R., Updike, M. and Snyder, D. 1989. PHABSIM system reference manual: version 2. U.S. Fish and Wildlife Service FWS/OBS 89/16. (Instream Flow Information Paper 26).

Milhous, R.T., Wegner, D.L. and Waddle, T. 1984. Users guide to the physical habitat simulation system. US Fish and Wildlife Service Biological Services Program. FWS/OBS-81/43.

Morin, J., Boudreau, P., Secretan, Y., Leclerc, M., 2000. Pristine Lake Saint-Francois, St. Lawrence River: Hydrodynamic simulation and cumulative impact. Journal of Great Lakes Research, 26, 384–401.

Pasternack, G. B., Wang, C. L., and Merz, J. 2004. Application of a 2D hydrodynamic model to reach-scale spawning gravel replenishment on the lower Mokelumne River, California. River Research and Applications, 20, 205–225.

Rimmer, D.M., Paim, U. and Saunders, R.L., 1983. Changes in the selection of microhabitat by juvenile atlantic salmon (salmo salar) at the summer-autumn transition in a small river, Canadian Journal of Fisheries and Aquatic Science, 41, 469–475, 1983.

Ross, T.J., 1995. Fuzzy Logic with Engineering Applications, McGraw-Hill, New York, 600 pp.

Tiffan, K.F., Garland, R.D. and Rondorf, D.W., 2002. Quantifying flow-dependent changes in subyearling fall Chinook Salmon rearing habitat using two-dimensional spatially explicit modelling. North American Journal of Fisheries Management, 22, 713–726.

Schneider, M. and Jorde, K., 2003. Fuzzy-rule based models for the evaluation of fish habitat quality and instream flow assessment. Proc IFIM User's Workshop, Fort Collins, CO, June 2003.

Wang, L., 1994. Adaptive fuzzy systems and control. Prentice Hall, New Jersey, 232 pp.

Copyright © 2006 Taylor & Francis Group plc, London, UK

Modeling approach to simulate habitat dynamics

S. Wieprecht, A. Eisner & M. Noack
Universität Stuttgart, Institute of Hydraulic Engineering, Chair of Hydraulic Engineering and Water Resources Management, Stuttgart, Germany

ABSTRACT: Today habitat modeling is a successful and commonly used method for the assessment of river ecology and for the evaluation of mitigation measures. Such models link morphohydraulic parameters with the biological needs of the aquatic fauna and flora. Presently state of the art in habitat modeling is restricted to calculations of habitat availability for different discharge scenarios just under steady state topographical and morphological conditions. However, the consideration of alternating morphological processes plays a key role for many species. In particular the life-cycles of gravel-spawning fish species depend on the temporal and spatial variability of the substrate layer and the accessibility of the interstitial zone. This paper presents the procedure how morphodynamic aspects are implemented in a habitat simulation process with the model CASiMiR. The consideration of these dynamic aspects upgrades the application of habitat modeling as a decision support tool in the framework of River Management issues.

1 INTRODUCTION: HABITAT MODELING

In the field of ecohydraulics habitat modeling is a river management methodology to assess – amongst others – the anthropogenic impacts on aquatic communities. Habitat modeling incorporates key hydro-morphologic parameters that are determined specifically to be used to review the availability of habitats for any particular e.g. target fish species, or life stages of such species. In turn, a number of key indicator species are used to indicate overall ecological integrity.

Habitat models analyze e.g. hydraulic and morphological attributes and perform the linkage to biological preferences or ecological needs respectively. As a result habitat suitability is calculated for different scenarios and visualized by graphs or maps.

1.1 *Applications*

Habitat models are applied in a wide range of river management issues. Among others the assessment of the ecological status of rivers and the identification of habitat deficits are basic applications. The key benefit of habitat simulation models is the possibility to predict – under consideration of certain limitations – biological and ecological developments for given river engineering measures or water management scenarios, which is in particular valuable for decision makers, investors, and stakeholders.

Minimum Flow Requirements, Revitalisation Projects or Environmental Impact Assessments are typical tasks in practice.

The state of the art in river habitat modeling including a wide range of applications is well elaborated by the COST Action 626 “European Aquatic Modeling Network” (2004), funded by the European Union.

1.2 *Parameters for fish habitat modeling*

One main focus in river habitat modeling lies on the simulation of fish habitats, because the integrity of fish habitats is generally accepted as a substantial factor to assess river ecology. Compared to other river organisms a good knowledge about the habitat demands of fish populations is available and the number of species is relatively small. The significant dependency of many fish species on hydraulic and morphological river characteristics is beneficial as well.

To be able to simulate fish habitats three basic parameters are required:

- Water Depth,
- Flow Velocity,
- Substrate Condition.

Further parameters (e.g. temperature or suitable hiding habitat conditions) can be taken into consideration well depending on target fish species and focus of foreseen investigation.

In order to get information about the hydraulic conditions for a certain range of discharges or single flow events, habitat models are usually connected by interfaces to 1D- or 2D hydraulic models that are able to predict water depth, flow velocity, and inundated area for steady and/or unsteady flow.

Copyright © 2006 Taylor & Francis Group plc, London, UK

On the other hand substrate, as a third basic parameter, is generally mapped by visual observation in the field. Thus, this parameter is normally recorded for only one situation. At present the consideration of morphodynamic processes and substrate variability in habitat modeling is missing.

However, morphodynamic processes play a key role for ecological integrity of river habitats. Among other species morphodynamic is of particular importance for gravel-spawning fish species. Their specific habitat demands are described in the following section.

2 BIOLOGICAL RELEVANCE OF HABITAT DYNAMICS: REQUIREMENTS FOR GRAVEL-SPAWNING FISH SPECIES

Many river species require, throughout their life cycle, an array of different habitat types, e.g. spawning habitats, juvenile habitats, or hiding habitats against predators or during extreme events such as floods or high temperature periods. The availability of such habitat diversity in rivers is primarily determined by the flow regime, morphology, and temperature.

Gravel-spawning fish species (e.g. Brown Trout, Grayling, Barbel, and Atlantic Salmon), that are exemplified in this paper, have particular demands on morphodynamic processes.

Beside the essential need for loose gravel of a specific grain size in low flow sections of a river for spawning fish individuals, the deposited eggs are dependent on specific conditions (e.g. oxygen availability) during their growth while hatching fishes must be able to emerge as alevins. Therefore, the significance of substrate characteristics is essential for the ecological assessment of spawning habitats.

In the past human impacts changed the established pattern of natural river dynamics. Today limiting morphological factors to disrupt the reproduction cycle of gravel-spawners are mainly:

– Embeddedness
– and fixed armored layers.

Embeddedness describes the grade of filling of coarse bed material with fine sediments. Thus, especially during the spawning period the interstitial zone is not accessible for fish to deposit their eggs and sufficient oxygen support is missing. Another consideration is the accumulation of fine material after fish eggs are deposited in the spawning habitat. Consequently, the consideration of embeddedness is twofold: one aspect is that fish eggs may be buried; the second aspect is that fry may be blocked from emerging. It is important to note that an increase of fine sediment may result from changed land-use practices in the watershed and must not necessarily be a direct result of alterations of the river course itself, although both usually occur more or less simultaneously and contribute to degradation of habitats.

Secondly, fixed armored layers inhibit the possibility for spawning fish to move the substrate with their tails and bodies in order to clear spaces to deposit their eggs.

To enhance the substrate conditions in potential spawning habitats particular attention should be paid to high-flow events, considering both their frequency and intensity. These flow events are crucial in maintaining a variety of habitats. High-flow events are periodically necessary to remove and transport fine sediment, that would otherwise fill the interstitial spaces in productive gravel habitats, as well as to entrain the armored layer.

According to that, morphydynamic processes and their occurrence must be considered, if spawning habitat suitability is to be modeled.

3 CASIMIR-CONCEPT

The habitat model CASiMiR (Computer Aided Simulation Model for Instream Flow Requirements) was developed in the early 1990s at the Universität Stuttgart, Germany, in order to assess fish and benthic habitats on microscale.

In contrast to most habitat models that use univariate preference curves for the linkage between hydromorphological parameters and biological needs the model CASiMiR is based on a multivariate fuzzy-logic approach (Schneider, 2001). The principle mode of operation of the fish habitat simulation model CASiMiR is described in Figure 1.

This progressive approach allows the implementation of qualitative expert knowledge in a numerical calculation. Furthermore, significant combinations of

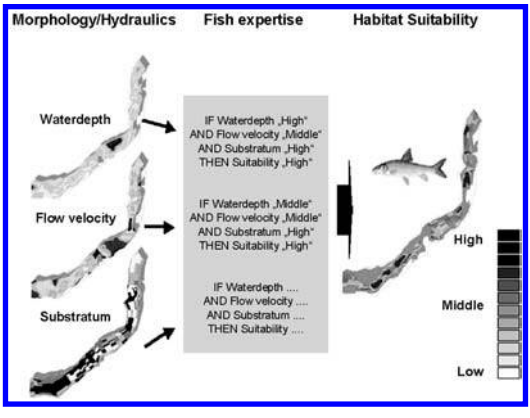


Figure 1. Principle mode of operation of CASiMiR for fish habitat simulations.

Copyright © 2006 Taylor & Francis Group plc, London, UK

abiotic parameters are considered for the examination of habitat suitability, which cannot be performed directly by using univariate preference curves.

In CASiMiR the three basic parameters mentioned above are primarily used for fish habitat modeling: flow velocity, water depth, and substrate condition. While flow velocity and water depth are calculated by conventional hydraulic models, substrate condition is a mapped parameter – usually observed for one situation. Additional parameters, e.g. different cover-types to assess hiding habitats or temperature, can easily be added.

The information that is used to describe the biological preferences in CASiMiR is:

- A set of Fuzzy-rules:
  to define the coherence of selected parameters by imprecise expert knowledge (see Figure 1).
- Related Fuzzy-sets:
  to define the range of each parameter-class, e.g. "high" flow velocity or "middle" water depth.

The implementation of the biological input data into the simulation process in CASiMiR is based on literature review, electro-fishing evaluation, and/or expert knowledge.

As a result the predicted habitat quality can be analyzed for each cell separately and illustrated as habitat maps (right map in Figure 1) or as integrated values over the observed reach. The habitat quality of each cell is expressed by the Habitat Suitability Index (HSI = 1,0 for optimal habitat suitability; HSI = 0 for insufficient habitat suitability).

Depending on the application the habitat simulations are run for unsteady or steady state flow. Near baseflow conditions, steady flow can often be assumed over longer periods of time. Simulation of unsteady flow usually is important for investigations of flood events. For habitat modeling purposes, mostly steady state time steps are used, except for single flood events or surge and sink issues. It is already mentioned, that at present no changes in river bed morphology or topography is considered for hydraulic modeling.

Usually one species and life-stage is modeled at a time. The results can show steady state conditions and discharge dependencies as well as seasonal aspects or single flow events by animation of habitat maps or graphs of integrative values.

Although CASiMiR has already been applied successfully on projects in Europe and the United States, it continues to be improved, becoming more extensive in scope. The improvements include the extension of applicability in habitat modeling from microscale (several hundreds meters) to mesoscale (several kilometers up to river catchment) and the linkage to morphodynamic issues.

4 APPROACH: CONSIDERATION OF MORPHODYNAMIC PROCESSES IN HABITAT MODELING

4.1 *Objectives*

This approach acts as an extension of the conventional habitat modelling with CASiMiR. The consideration of substrate conditions in rivers as a static parameter should be complemented by including morphodynamic processes to converge the overall aim of modeling habitat dynamics.

The following ecological issues are supposed to be answered:

- Improvement of ecological evaluations and predictions of anthropogenic influences. Moreover, it enables the modeling of mitigation scenarios, especially for spawning and rearing habitat conditions of gravel-spawning fish species.
- Identification of spots in river reaches where habitat suitability is reduced due to embeddedness or armored layers.
- Determination of discharges to entrain armored layers.
- Development of biocompatible water management concepts (dynamic flow regulations, reduction or surge and sink impacts that are mainly caused by hydropower operation).

4.2 *Development*

4.2.1 *Influence of embeddedness and armored layers on spawning habitat suitability*

The first part of the approach contributes to identify river reaches of decreased habitat suitability due to the limiting factors embeddedness and armored layer. Based on the fuzzy-logic methodology implemented in CASiMiR the specific morphodynamic attributes will be included by imprecise expert knowledge.

As it takes high efforts to define fuzzy-rules for more than four different parameters simultaneously it is convenient to divide the approach into two subsequent steps. The flow chart in Figure 2 provides its concept.

At first the conventional habitat modeling approach using basic habitat parameters (see Figure 1) is applied, resulting in a Habitat Suitability Index "HSI 1". If "HSI 1" is less than a predefined threshold value (in this example 0.4), habitat suitability is defined as low, based on conventional parameters. In that case the "basic" morphohydraulic conditions do not match the requirements for spawning activities anyway, and therefore no further investigation of embeddedness or armoring processes has to be performed.

For "HSI 1" higher than 0.4 the second step of the concept is applied to consider morphodynamic processes in terms of embeddedness, packing (armored

Copyright © 2006 Taylor & Francis Group plc, London, UK

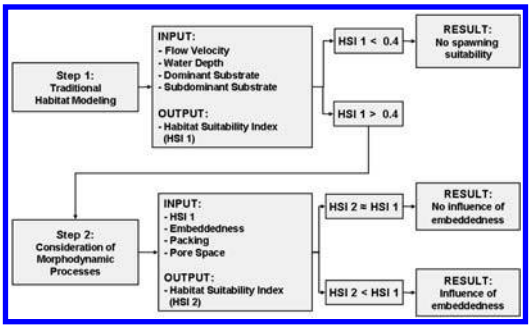


Figure 2. Flow chart to evaluate the influence of embeddedness and armored layers on spawning habitat suitability.

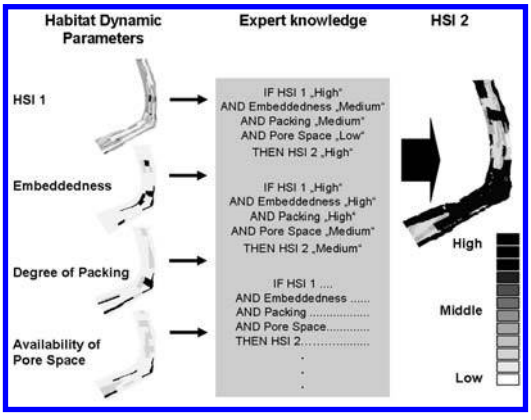


Figure 3. Implementation of "Habitat Dynamic Parameters" into habitat modeling.

layers) and pore space, which constitute the most drastic effect on spawning habitats. Again these so called "Habitat Dynamic Parameters" are linked to biological demands of certain fish species by using fuzzy-rules (see Figure 3) resulting in a "HSI 2"-value. The comparison between "HSI 1" and "HSI 2" describes the influence of additionally considered "Habitat Dynamic Parameters" and therewith their importance.

If "HSI 2" is similar to "HSI 1", embeddedness, packing, and pore space have no influence on habitat suitability. For "HSI 2" less than "HSI 1", the "Habitat Dynamic Parameters" affect the spawning habitat suitability in a negative manner.

In this context the investigation of embeddedness, packing and pore space is done by visual assessment and simple measurements during field observations. Eastman (2004) describes a proposed investigation method of each parameter and its classification.

4.2.2 *Concept for modeling of mitigation measures*

The evaluation of mitigation scenarios to improve spawning habitats for gravel spawners is aimed by the second part of this approach.

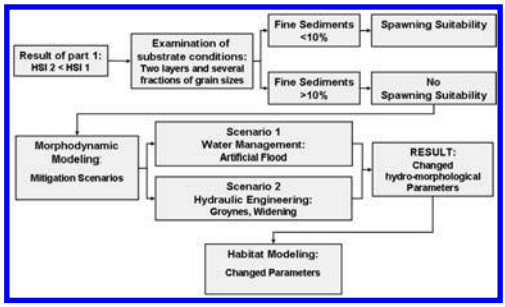


Figure 4. Concept of modeling mitigation measures.

Basically, mitigations are needed if the habitat suitability is affected by embeddedness or armoring processes ("HSI 2" < "HSI 1").

As shown in Figure 4 the major component of this part of the approach is the morphodynamic modeling to simulate the changes of substrate compositions and distributions caused by mitigation measures. For that reason morphodynamic models have to be applied that are able to calculate graded sediment with several particle fractions. Section 5 will explain the procedure in connection with two case studies.

First of all, one or several criteria have to be defined that are useful to evaluate whether a mitigation scenario is beneficial or not. That might be e.g. critical shear stress, thickness of moveable sediment layer or, as mentioned in Figure 4, a certain percentage of fine sediments in the upper layer (<10%).

Mitigation measures in this context can be divided into two main groups:

- Water management scenarios
  (artificial flood, flow regulations, surge and sink effects of e.g. hydropower operation)
- Hydraulic Engineering scenarios
  (Revitalisation projects, widening of river beds, structural measures such as groynes)

Significant changes in morphological and hydraulic characteristics are initialized and can be simulated by morphodynamic modeling.

Afterwards the verification of the fulfilment of the predefined threshold criteria (e.g. percentage of fine sediment <10%) as well as the evaluation of the effects of these modified morphological and hydraulic conditions on habitat supply have to be performed.

This concept enables an optimization process of planned mitigation measures as well as the comparison of different proposed scenarios with regard to habitat quality enhancement.

5 CASE STUDIES: WATER MANAGEMENT AND HYDRAULIC ENGINEERING

The mentioned approach was applied to two mitigation scenarios in Norway and Austria to improve

Copyright © 2006 Taylor & Francis Group plc, London, UK

spawning habitats for gravel-spawning fish species (Noack, 2005).

5.1 *Water management: Artificial flood*

5.1.1 *Situation*

This scenario was applied to the river Surna in Norway in cooperation with SINTEF (Foundation for Scientific and Industrial Research at the Norwegian Institute of Technology).

Due to flow regulations in the catchment area of river Surna in order to optimize hydropower usage, the river is characterized by more or less steady state minimum flow conditions. The natural hydrological characteristic is: MQ $\approx 56\,m^3/s$ with extreme flood discharge up to $400\,m^3/s$. The flow is reduced to about 60% of the annual flow. High flood events are missing. Therefore extensive parts of the river bed of the representative investigated diversion-reach Sandehølen are influenced by embeddedness and armoring processes significantly affecting spawning habitat suitability for Atlantic salmon.

5.1.2 *Objectives*

Based on the CASiMiR approach the influence of embeddedness on spawning habitat suitability had to be quantified.

Additionally it has to be investigated whether an artificial flood before the spawning season of Atlantic salmon would provide suitable substrate conditions for spawning habitats.

Finally an ecological oriented management strategy should be developed on the basis of simulations of different flow regimes.

In this context it must be considered that during spawning and rearing season salmons are endangered by insufficient supply of oxygen due to accumulation of fine sediments in the interstitial zone. Furthermore the mechanical damage to eggs and juvenile fish caused by sediment transport of big grain sizes is also a high potential of danger. Freshly hatched Atlantic salmons react more sensitive to higher discharges than eggs as they depend on shelter in the interstitial and have limited mobility whereas eggs are more resistant due to their stream lined shape.

Consequently, critical discharges have to be determined and strategies developed to avoid sedimentation as well as transport of cobbles and stones during the incubation period.

5.1.3 *Definition of threshold values*

To consider the requirements mentioned above the threshold values listed in Table 1 have been presumed for the study site Sandehølen by consultation of Norwegian fish experts.

Table 1. Threshold values for habitat parameters, Sandehølen, Surna (particularly adapted to specific situation).

Assumptions	Value/threshold
Critical "HSI 1"	>0.4
Grain size of fine particles	<2 mm
Critical percentage of fine sediment	10 %
Critical Shields-Parameter to avoid sedimentation	0.041
Critical grain size to provide shelter for hatched Atlantic Salmon	40 mm

5.1.4 *Input data and modeling base*

The hydraulic input data for the two-stepped fuzzy-logical approach in CASiMiR was processed by using the 2D-hydrodynamic software MIKE 21C provided by DHI (Danish Hydraulic Institute), while the parameters embeddedness, packing, pore space as well as the dominant, subdominant, and present substrate classes were mapped by visual observation. In detail the distribution of graded sediment was mapped for the upper and lower sediment layers separately, whereas the thickness of the upper layer covers approximately 20 cm of substrate. Based on these investigations simplified sieve curves were derived representative for each layer of mapped habitat areas. The dominant grain size of the cover layer is between 12 and 16 cm.

Within the simulation of different artificial flood events the morphodynamic modeling with MIKE 21C incorporates the modules "Graded Sediment Model" and "Morphological Update" allowing the interaction between morphological and topographical changes and the resulting hydraulic conditions. To calculate the sediment transport for each fraction the approach of Meyer-Peter & Müller (1947) has been applied.

As biological input data spawning habitat requirements for Atlantic salmon were provided by Norwegian fish experts based on electro fishing, experience and literature review.

5.1.5 *Results*

Exemplary results are illustrated by habitat suitability maps generated on basis of various simulation runs. For the representative discharge during spawning season of $15\,m^3/s$ Figure 5 illustrates the influence of embeddedness on spawning habitats. In the left map the habitat suitability "HSI 1", determined from basic habitat parameters flow velocity, water depth, and substrate, and in the right map the situation for "HSI 2" after consideration of "Habitat Dynamic Parameters" embeddedness, pore space, and packing.

It is obvious that the consideration of morphodynamic attributes is crucial for the assessment of spawning habitats for Atlantic salmon in that reach. The spawning habitats are widely and significantly reduced by embeddedness.

Exemplarily two areas are marked to demonstrate the influence of cumulative effects of the mapped

Copyright © 2006 Taylor & Francis Group plc, London, UK

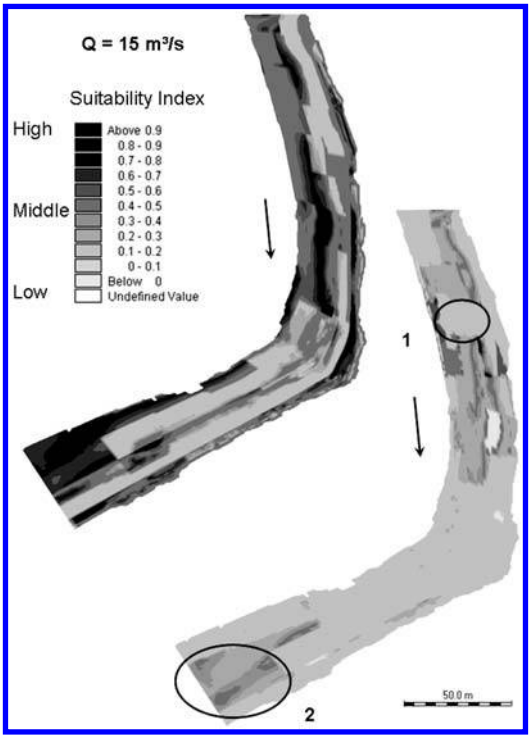


Figure 5. Comparison of habitat modeling without (left map) and with (right map) consideration of embeddedness.

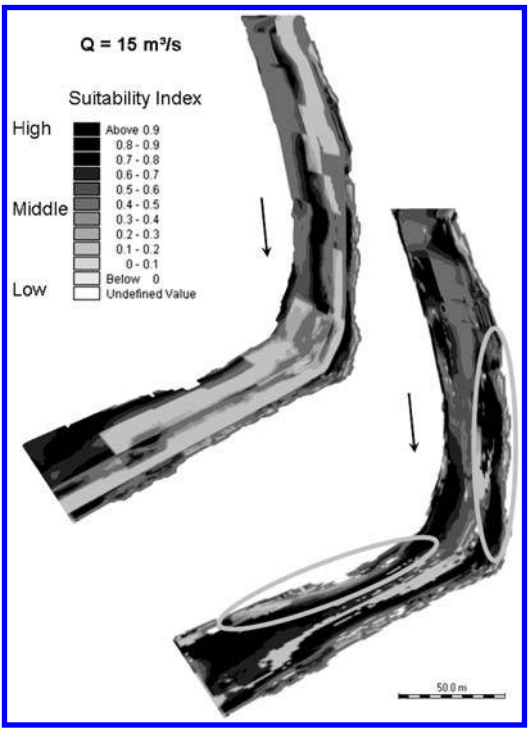


Figure 6. Comparison of habitat modeling before (left map) and after (right map) the proposed artificial flood.

parameters: The impairment of embeddedness (circle 1) results in no suitability and the influence of relatively suitable pore space conditions (circle 2) results in a minor reduction of spawning habitat quality.

To prevent hatched Atlantic salmon from mechanical damage by transported grain sizes larger than 40 mm, it is recommended that the discharge should temporary not exceed a critical limit at which grain sizes larger than 40 mm begin to move. Moreover, a drifting of both, eggs and hatched salmons could be avoided if this critical discharge is not exceeded.

On basis of numerous simulations of different flow events it is recommended that the flow regime during incubation period should not go beyond a discharge of 120 m^3/s. On the other hand the discharge should not drop below 25 m^3/s in order to prevent the deposition of fine sediments into the interstitial zone.

In fact, a smaller flood after the hatching period is recommended to provide nutrients as during this phase the first external feeding is necessary. However, the point in time of such a flood has to be chosen carefully due to the strong relation between hatching and water temperature on the one hand while it might endanger the survival of freshly hatched salmons if they are not strong enough to resist the flow and might be drifted away loosing their protection against predators.

Figure 6 describes the results of the habitat modeling before (left map) and after (right map) the proposed artificial flood under consideration of changed distribution of dominant and subdominant substrate and changed bed topography.

The artificial flood results in an increasing of habitat availability and habitat quality in the investigated reach. Particularly the circled areas in the right map could be improved by redistribution of sediment composition, where before the mitigation measure high percentages of fine sediments reduced the spawning habitat suitability.

5.2 *River engineering: Groynes, widening*

5.2.1 *Situation*

The second application was performed as part of the Interreg III B project ALPRESERV, funded by the European Union. The study site is located at Gestütshof (river Mur) in the Austrian Alps.

The investigation area is situated immediately downstream of the runoff power plant Bodendorf with a concrete weir construction of 17 m height backing up a reservoir of 2.6 km. The natural hydrological characteristic of river Mur at Bodendorf is: MQ $\approx$ 33 m^3/s

Copyright © 2006 Taylor & Francis Group plc, London, UK

Table 2. Threshold values for habitat parameters, Gestütshof, Mur (particularly adapted to specific situation).

Assumptions	Value/threshold
Critical "HSI 1"	>0.4
Grain size of fine particles	<2 mm
Critical percentage of fine sediment	10%
Critical Shields-Parameter to initiate entrainment of armored layer	0.051

and $HQ_1 \approx 130\,m^3/s$. Resulting from the heavily affected sediment regime the reservoir suffers from significant aggradation processes while the downstream section at Gestütshof is predominated by strong armored layers and significant embeddedness.

In addition, the flow velocities as well as the water depths exceed the tolerable values for spawning suitability because of fixed river banks and as a consequence an apparent degradation and narrowing of the river bed.

These conditions cause a significant reduction of spawning habitats for grayling.

5.2.2 *Objectives*

In a first step the influence of the presently existing morphological conditions on spawning habitat suitability has to be analyzed.

Following the basic analysis the effects of a proposed mitigation scenario on the improvement of spawning habitats must be investigated. The mitigation scenario includes the construction of groynes, the implementation of widenings of the river bed, and an adapted sediment flushing concept of the reservoir upstream.

With the aim to reduce armoring and embeddedness processes within the observed river reach the design of groynes and river bed widening has to be optimized.

5.2.3 *Definition of threshold values*

The assumptions mentioned in Table 2 were particularly made for the evaluation and morphodynamic modeling of grayling spawning habitats at the study site Gestütshof:

5.2.4 *Input data and modeling base*

Again, the hydraulic input parameters for the two-stepped fuzzy-logical approach in CASiMiR were provided by the hydrodynamic model MIKE 21C. To analyze the influence of existing morphological conditions on spawning habitat suitability the mentioned sediment attributes were mapped.

For the morphodynamic modeling with MIKE 21C the specification of different substrate layers was investigated by freeze-core sampling up to 60 cm in depth (by 10 cm intervals). Considering the significant interstitial zone for grayling spawning habitats the upper layer for morphodynamic modeling was

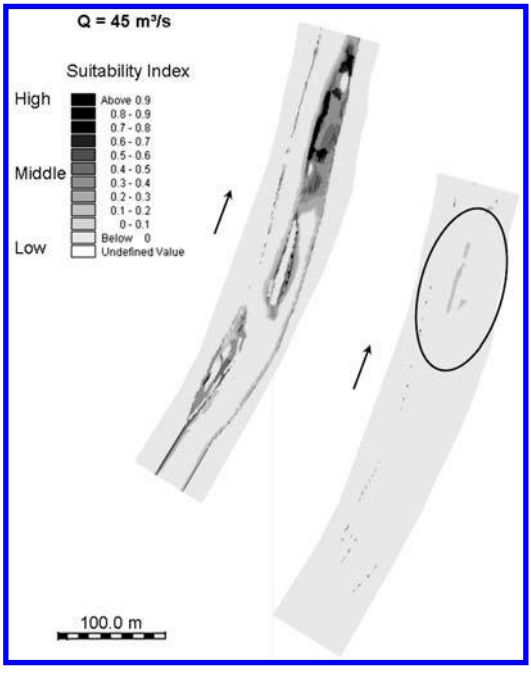


Figure 7. Comparison of habitat modeling without (left) and with (right) consideration of embeddedness.

defined to be 20 cm with a characteristic grain size of 72 mm. Similar to the previous case study the formula of Meyer-Peter and Müller was used to model sediment transport, while the approach of Günter (1971) was applied regarding armoring processes.

The spawning habitat demands for grayling were provided by Austrian fish experts based on electro fishing, experience and literature review.

5.2.5 Results

To be able to analyze the influence of "Habitat Dynamic Parameters" the modeling results are again compared with (left map) and without (right map) consideration of embeddedness, packing and pore space. Figure 7 shows the situation for a discharge of $45\,m^3/s$, as these flow conditions are representative for the grayling spawning season with minor variations between ca. $40\,m^3/s$ (minimum) and ca. $60\,m^3/s$ (maximum).

Consideration of the parameters embeddedness, packing and pore space emphasize that almost no suitable habitats for spawning graylings can de detected anymore. The strong impact of the mapped parameters, particularly packing and pore space, is directly affecting the suitable areas at the end of the study site resulting in a significant reduction of spawning habitat suitability compared to the habitat modeling with just the basic hydraulic parameters water depth, flow velocity and substrate condition. These results correspond

Copyright © 2006 Taylor & Francis Group plc, London, UK

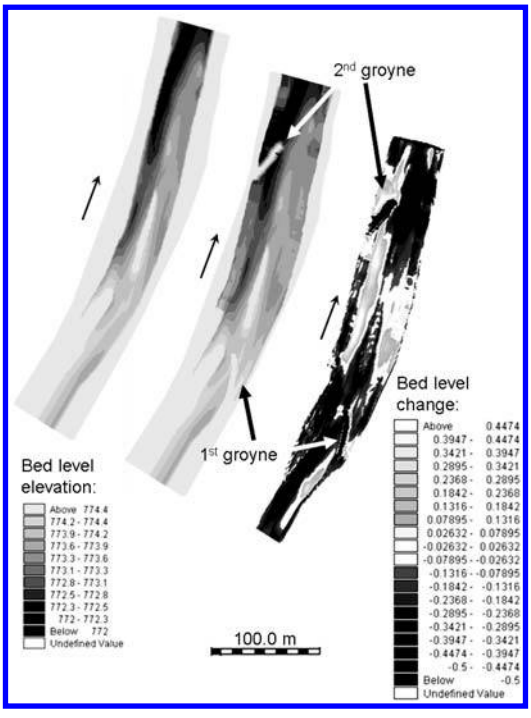


Figure 8. Mitigation measures: Effects of river bed widening and implementation of two groynes on bed elevation (original situation on the left, modified river bed after a 1-year-flood event in the middle).

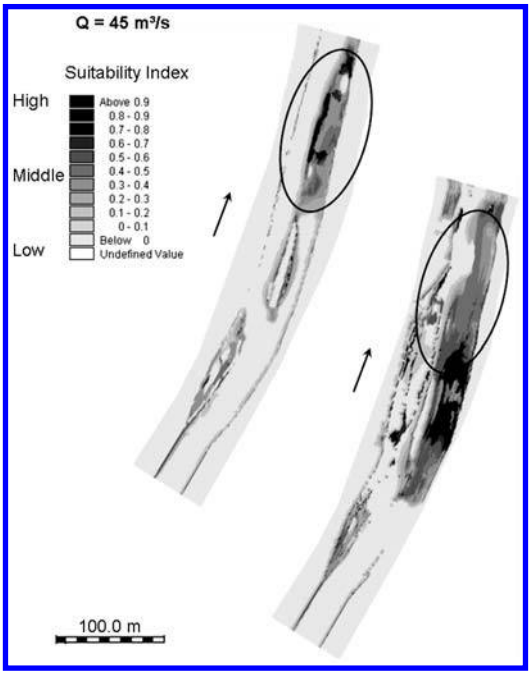


Figure 9. Results of habitat modeling with (right) and without (left) river engineering mitigation measures.

to the biological observations for that specific river section.

Concerning the habitat demands it can be stated that regarding the large areas of no suitability in the basic habitat modeling approach (Figure 7, left map) the flow velocities and water depths are too high for spawning activities.

Consequently, the main purpose of the proposed mitigation scenario includes the implementation of two groynes plus a widening of the river bed combined with a modified flushing concept to change the distribution of flow velocities and water depths as well as the substrate conditions to increase habitat suitability for spawning graylings.

In Figure 8 the bed elevation of the unmodified reach is shown on the left map, while the map in the middle represents the modified reach considering the changed bed topography due to the mitigation measures. The right map illustrates the bed level changes (erosion and accumulation) after a one year flood event. Particularly on the left hand side of the river, the sedimentation results in minor water depths and, combined with river bed widening, a reduction of local flow velocities. Erosion at the end of the study site results in significant substrate changes, however, water depths in this section are still in a tolerable range for spawning activities.

Figure 9 compares modeling results with and without the proposed mitigation measures.

Comparing the resulting suitability of both situations it is obvious that the formerly good habitats (circled in the left illustration) would be reduced by the proposed measures due to coarser substrate conditions and erosion processes caused by the second groyne. However, significant improvements in spawning habitat suitability can de detected in large areas on the right side of the river reach. As an integrated result the habitat availability could be almost doubled by the proposed mitigation measures.

These results could be incorporated in the development of a modified ecological oriented sediment flushing concept at the reservoir upstream.

6 CONCLUSION

Exemplified by two case studies of river reaches with different characteristics in Norway and Austria it is evident that morphodynamic processes, in particular embeddedness and armored layers, have to be considered, if spawning habitat suitability for gravel-spawning fish species has to be assessed.

Copyright © 2006 Taylor & Francis Group plc, London, UK

The significant influence of these "Habitat Dynamic Parameters" on the achieved habitat simulation results corresponds to the attended electro-fishing investigations and fish expert expectations.

The linkage between morphodynamic and habitat models offers a valuable and reliable basis to optimize mitigation measures in river management issues efficiently. The need to integrate habitat modeling in general and a morphodynamic approach particularly into the planning process of mitigation measures has been illustrated by the case studies. It is obvious that the linkage is an important progress for both, habitat modeling as well as morphodynamic modeling, in order to be established as a decision support tool for river managers and stakeholders.

However, further studies are necessary: To be able to improve the efficiency and applicability an operational interface between the morphodynamic and habitat simulation models has to be developed. Intensive research is required to increase the biological knowledge about dependencies between "Habitat Dynamic Parameters" and their limitations on specific river organisms. The habitat demands regarding morphodynamic requirements and threshold values are mentioned in this paper depending on specific conditions at the investigated river sites and which are subsequently not transferable to other sites without an in-depth analysis.

Finally, the consideration of suspended load processes is of high importance to be able to incorporate the parameter embeddedness into the simulations of mitigation scenarios as well. In the approach presented in this paper embeddednessis considered as a mapped parameter to quantify the influence of "Habitat Dynamic Parameters". The simulation of embeddedness processes itself is not included yet.

REFERENCES

COST 626 European Aquatic Modeling Network. 2004. *State-of-the-art in data sampling, modeling analysis and applications of river habitat modeling*. Download: http://folk.ntnu.no/borsanyi/eamn-web/.

Eastman, K. 2004. *Effects of Embeddedness on Fish Habitats: An Approach for Implementation in the Habitat Simualation Model CASiMiR.* Master Thesis. Institute of Hydraulic Engineering, Universität Stuttgart.

Günter, A. 1971. *Die kritische mittlere Sohlschubspannung bei Geschiebemischungen unter Berücksichtigung der Deckschichtbildung und der turbulenzbedingten Sohlschubspannungsschwankungen*. Mitteilungen der Versuchsanstalt für Wasserbau, Hydrologie und Glaziologie, Zürich.

Meyer-Peter, E. and Müller, R. 1948. *Formulas for bed load transport*. Proceedings of 2nd Congress IAHR, Stokholm, Vol. 2.

Noack, M. 2005. *Application, Validation and Optimization of modelling approaches for the implementation of morphodynamic processes in habitat modelling.* Master Thesis. Institute of Hydraulic Engineering, Universität Stuttgart.

Schneider, M. 2001. *Habitat- und Abflussmodellierung für Fließgewässer mit unscharfen Berechnungsansätzen.* Dissertation. Mitteilungen des Instituts für Wasserbau der Universität Stuttgart, Heft 108.

Copyright © 2006 Taylor & Francis Group plc, London, UK

Comparison of suitability for living of ayu, *Plecoglossus Altivelis*, between pools and rapids

T. Nagaya & Y. Shiraishi
CTI Engineering Co., Ltd., Daimyo, Fukuoka, Japan

K.Onitsuka
Dept. of Civil Eng., Kyushu Institute of Tech., Kitakyushu, Japan

M. Higashino & T. Takami
Dept. of Civil Eng., Oita Nat. College of Tech., Oita, Japan

N. Otsuka
Nobeoka Work Office, Ministry of Land, Infrastructure and Transport, Nobeoka, Japan

J. Akiyama
Dept. of Civil Eng., Kyushu Institute of Tech., Kitakyushu, Japan

H. Ozeki
Graduate School, Kyushu Institute of Tech., Kitakyushu, Japan

Y. Nakagawa
Waseda Seminar, Chuo-ku, Fukuoka, Japan

H. Hatanaka
ACTIS Corporation, Higashi-Nippori, Tokyo, Japan

ABSTRACT: It is necessary for inhabitation of aquatic lives such as fish, crab and so on, to preserve the structure consisting of both pool and rapid. Because some fish prefer pools and the other some fish prefer rapids. In particular, the ayu, *Plecoglossus Altivelis*, prefers rapids. The ayu is one of the most expensive fish in fishery in Japan. However, the reason why the ayu prefers rapids has not been investigated. In this study, the field survey, i.e., velocity measurements, flow depth and bed level measurements, recording the behavior of the swimming ayu and also gathering attached algae on the rocks, was conducted both in the pools and rapids under the condition that the ayu cannot feed attached algae in some area (non-ayu area) and also can feed in the other area (normal area). It was found that the growth of attached algae in the rapid is higher than that in the pool. The growth of attached algae in non-ayu area is higher than that in the normal area, due to the ayu feed attached algae on the rocks in the normal area. A logistic model was used for the evaluation of the growth of attached algae. As a result, the difference in the growth of attached algae between in the pool and rapid and also between in non-ayu and normal area can be investigated quantitatively.

1 INTRODUCTION

Ayu, *Plecoglossus altivelis*, inhabits in Japan, Korean peninsula and the east of the continent of China (see Picture 1.). They spawn at the lower reach of the river in autumn and drift downstream to the sea as soon as hatching (see Tsukamoto & Uchida, 1992). After about half year, they migrate to the upper and middle reach of the river and feed on algae adhering on rocks. In autumn, mature ayu spawn and then die. Ayu is one of the most important fish for fishery in Japan so that it is important to conduct the environmental assessment before construction of the hydraulic structures in the river.

It is known that sometimes strong ayu makes a territory almost in the rapids and rarely in the pools.

Copyright © 2006 Taylor & Francis Group plc, London, UK



Picture 1. Ayu, *Plecoglossus altivelis*.

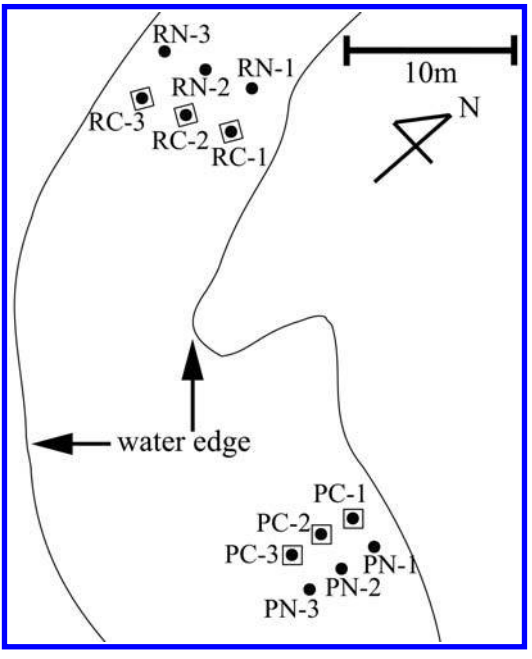


Figure 1. Survey points in pool and rapid (Kitagawa river).

It is supposed empirically that the good attached algae grows up in the rapids in comparison with that in the pools. However, this supposition has not been verified as yet. Further, the difference of behavior of ayu between pools and rapids is not known.

In this study, the field survey, i.e., velocity measurements, flow depth and bed level measurements, recording the behavior of the swimming ayu and also gathering attached algae on the rocks, was conducted both in the pools and rapids under the condition that the ayu cannot feed attached algae in some area (non-ayu area) and also can feed in the other area (normal area).

2 TARGET RIVER AND FIELD SURVEY

Nobeoka city where is located at the middle part of Kyushu Island in Japan. The Gokasegawa river, Hourigawa river and Kitagawa river are running through the Nobeoka city. Those rivers belong to Class A river. The administrator of the Class A river is Ministry of Land, Infrastructure and Transport (MLIT). The Gokasegawa river has a branch. The length and watershed catchment area of the Gokasegawa river are 106 Km and 1820 Km^2, respectively.

The field survey was conducted at 15 K 700 m upstream from the river mouth of the Kitagawa river. The reason of choosing this site, Kitagawa fisherman's cooperative association pointed out that a lot of ayu inhabits in the rapid. Figure 1 shows the sketch of field survey site. The field survey was carried out through 9th to 12th August in 2005.

In contrast, it is well known that the attached algae on the rocks is seceded by the flood. Figure 2 shows the variation of the discharge in the Kitagawa river in 2004, together with another year. Although, a small flood can be seen just before the survey period, the

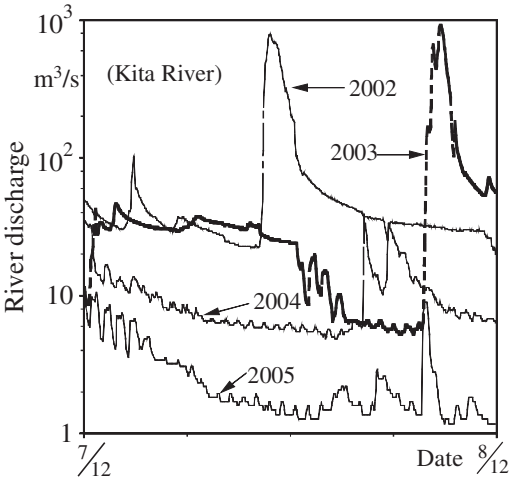


Figure 2. Variation of river discharge in Kitagawa river.

discharge is relatively small. As a result, attached algae was not seceded by this flood.

The number of survey points was 12 as shown in Figure 1. Table 1 shows the survey points and condition. 6 points are located in the rapid and pool, respectively. At the points of RC-1, RC-2 and RC-3 in rapid and also of PC-1, PC-2 and PC-3 in pool, the rock is surrounded by the cage as shown in Figure 3. Therefore, ayu cannot feed the attached algae at such

Copyright © 2006 Taylor & Francis Group plc, London, UK

Table 1. Survey points and measurements items.

Case name	Averaged case name	Rapid or pool	Cage	Measurements items
RC-1, RC-2, RC-3	RC	Rapid	Cage	Velocity and attached algae
RN-1, RN-2, RN-3	RN		No cage	
RC-1(NC)	–			Velocity
PC-1, PC-2, PC-3	PC	Pool	Cage	Velocity and attached algae
PN-1, PN-2, PN-3	PN		No cage	
PC-1(NC)	–			Velocity

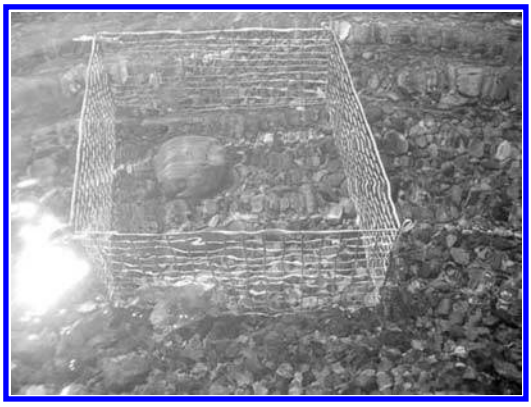


Figure 3. Picture of wire netting (PC-1).

points. On the other hand, ayu can feed on the attached algae at the points of RN-1, RN-2, RN-3, PN-1, PN-2 and PN-3. The flow depth at the pool and rapid was 0.4 m and 1.0 m, respectively.

All the attached algae and also fine sediments adhering on the rocks at all points were scratched by a hard brush and taken off on the first survey day (9th August in 2005). After that, all rocks put back on the river bed for each point. Attached algae and also fine sediments adhering on rocks were collected every 24 hours during the survey period (9th to 12th August). After field survey, TR (total residue) was measured.

The velocity profiles in the vertical direction were measured by an electromagnetic current meter at all the 12 the points. The measuring frequency and measuring time were set to 20 Hz and 51.2 s, respectively. Further, the velocity measurements were also conducted at the RC-1 and PC-1 in the condition that the cage was eliminated (RC-1(NC) and PC-1(NC)) to confirm whether the cage affects on the hydraulic structure or not (non-ayu area).

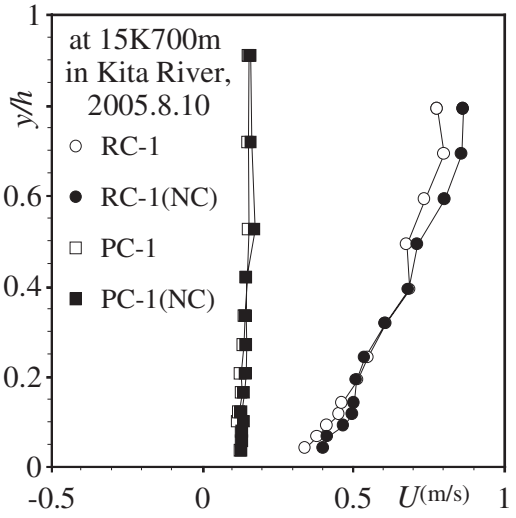


Figure 4. Velocity profiles in pool and rapid with cage and without cage.

The trajectories of swimming ayu both in pool and rapid were recorded by an underwater digital video camera. After recording, the swimming position from the bed, population, the number of feeding were analyzed.

3 RESULTS AND DISCUSSIONS

3.1 *Effect of cage on hydraulic structure*

Figure 4 shows the velocity profiles at the points of RC-1 and PC-1, together with those at the points of RC-1(NC) and PC-1(NC). In which h is the flow depth, y is the vertical coordinate, U is the time averaged flow velocity in the streamwise direction x, U_* is the friction velocity. The calculation method of the friction velocity U_* will be described later. A considerably difference of velocity between with cage and without cage cannot be found.

Figure 5 shows the distribution of the turbulence intensity u' normalized by the friction velocity U_* in pool and rapid, respectively, together with the empirical formula proposed by Nezu (1977) (see Nezu & Nakagawa, 1993).

$$\frac{u'}{U_*} = D_u \exp\left(-\lambda_u \cdot \frac{y}{h}\right) \quad (D_u = 2.26, \quad \lambda_u = 0.88) \qquad (1)$$

The empirical coefficients D_u and λ_u were obtained by Nezu & Rodi (1986).

The distribution of the turbulence intensity in almost cases near the free surface deviate upward from the Nezu's universal formula (1), due to the fluctuation

Copyright © 2006 Taylor & Francis Group plc, London, UK

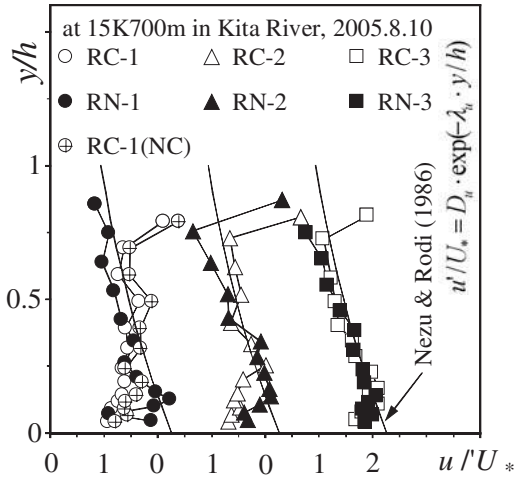


Figure 5(a). Distributions of turbulence intensity in rapid.

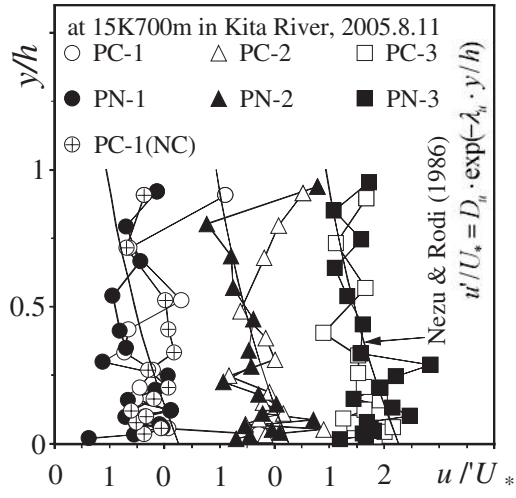


Figure 5(b). Distributions of turbulence intensity in pool.

of the free surface. Further, the distribution of the turbulence intensity at PC-1(NC) is almost the same as that at PC-1. Therefore, it can be said that the cage does not affect on the hydraulic structure and also the Nezu's universal formula is also valid in the natural river. The difference of the volume of attached algae depends on the feeding volume of ayu.

3.2 *The modeling of growth of attached algae considering ayu's feeding*

(a) Time variation of attached algae

Takami et al. (2005) measured both of TR (total residue) and chlorophyll-a in the Gokasegawa river and

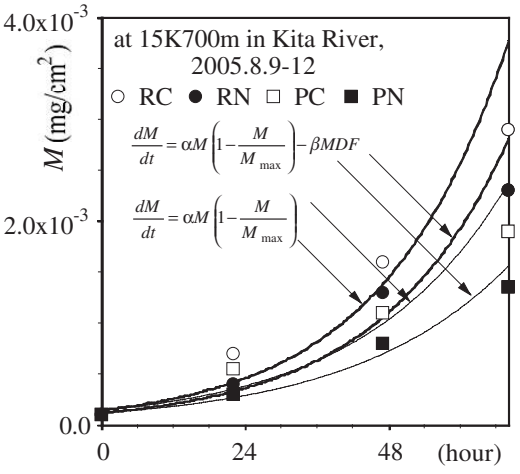


Figure 6. Time variation of TR in pool and rapid.

pointed out that weight of chlorophyll-a is almost equal to 0.1% of TR during April to October. Therefore, it is possible to evaluate the weight of attached algae on the basis of TR data. Figure 6 shows the time variation of the TR.

In which M is the weight of TR. It was found that the variation rate of TR in the rapid is higher than that in the pool and also the variation rate with cage is higher than that without cage. Toda et al. (2005) pointed out that the variation rate of attached algae depends on a balance of growth rate, importation rate, metabolic rate and separation rate per unit area. However, this model is complicated so that a lot of known coefficients are included. In this study, the following simple logistic equation is used for the cases with cage.

$$\frac{dM}{dt} = \alpha M\left(1 - \frac{M}{M_{\max}}\right) \tag{2}$$

In which t is the time, α is specific growth rate and $M_{\max}$ is the environmental capacity of TR which was calculated from chlorophyll-a (see Takami et al., 2005). Eq. (2) can be used under the condition that the importation and separation rate is negligible small. It is known that such a condition is keeping a few days after new attached algae start to grow.

On the other hand, Eq. (2) is valid for the cases with cage, but not valid for the cases without cage. Because ayu feeds the attached algae on the rocks which are not surrounded by the cage. It is necessary for proposing a new logistic model considering ayu's feeding to investigate on the feeding behavior of ayu.

(b) Behavior of feeding ayu

After ayu feeds attached algae on rocks, ayu goes away from the rocks. After that, ayu feeds again soon.

Copyright © 2006 Taylor & Francis Group plc, London, UK

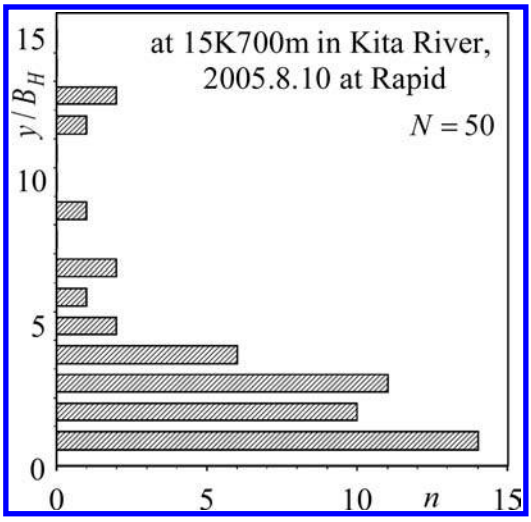


Figure 7(a). Swimming positions of ayu in rapid.

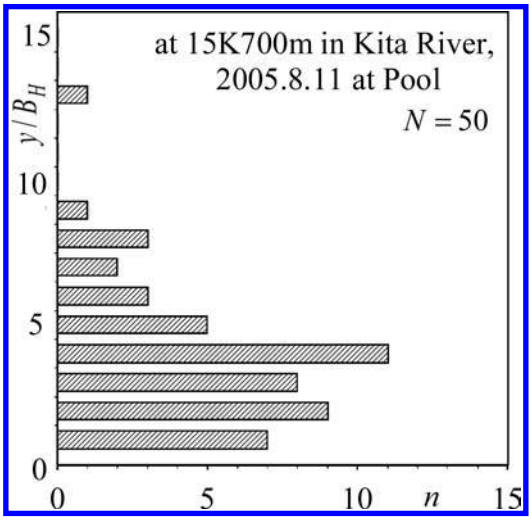


Figure 7(b). Swimming positions of ayu in pool.

Therefore, ayu swims near the rocks. Figure 7 shows the histogram of the swimming position of the ayu from the bottom y normalized by the body height of ayu B_H. In which N is the amount number of observed fish, n is the number of the fish in each layer. It was found that the swimming position of ayu both in the rapid and pool is lower than 10 times of body height of ayu. This implies that the reason why ayu likes the rapid does not depend on the flow depth.

The food intake of the ayu per unit time of unit area is proportion to the population of the ayu per unit area D (number/m^2) and the number of feeding per unit time F (number/s). Table 2 shows the results of D and F. The relative growth rate α is calculated from Eq.(2) by using of data with cage.

Table 2. Coefficients in modified logistic model.

Case name	D number/m^2	F number/s	α	β
RC	0	0	0.021	0
RN	5	0.714		3.63
PC	0	0	0.018	0
PN	25	0.909		1.08

(c) Proposal of a new logistic model considering ayu's feeding

A new logistic model which is considering the feeding of ayu is proposed as the following formula.

$$\frac{dM}{dt} = \alpha M\left(1 - \frac{M}{M_{\max}}\right) - \beta MDF \qquad (3)$$

In which β is the coefficient. When the second term on the right hand side in Eq.(3) is eliminated, Eq.(3) is equal to Eq.(2), because the second term on the right hand side has a significance of the effects of feeding. The coefficient β can be calculated on the basis of data without cage, adopting the relative growth rate α which is obtained from the data with cage. The calculated TR from Eq.(3) is also described in Figure 6 as fine lines. It can be recognized that Eq.(3) can describe the variation of TR without cage cases. Therefore, Eq.(3) can predict the time variation of weight of attached algae in the river.

3.3 *Physical meaning of proposed logistic model*

It is already pointed out that the relatively growth rate α in the rapid is higher than that in the pool, due to the deference of DO (dissolved oxygen), nutrients, velocity and so on between pools and rapids may difference. Kono et al. (2004) measured DO and nutrients both in rapid and pool in the Osegawa river and pointed out that the value of DO and nutrients are the same. Therefore, the difference of α between pool and rapid may depend on the difference of shear near the rocks.

The friction velocity can be calculated from the log-law.

$$\frac{U}{U_*} = \frac{1}{\kappa}\ln\frac{y + \Delta y}{k_s} + A_r \quad (y/h \le 0.2) \qquad (4)$$

In which κ (=0.412) is von Karman constant, A_r (=8.5) is the integration constant, k_s is the equivalent sand roughness and Δy (=0.25k_s) is the reference

Copyright © 2006 Taylor & Francis Group plc, London, UK

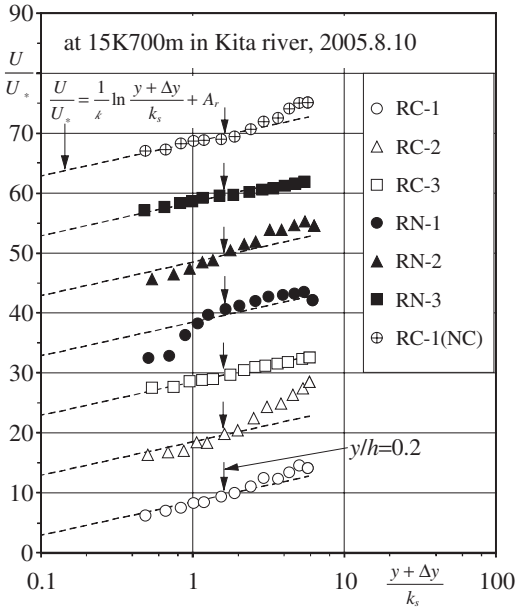


Figure 8(a). Velocity profiles in the rapid.

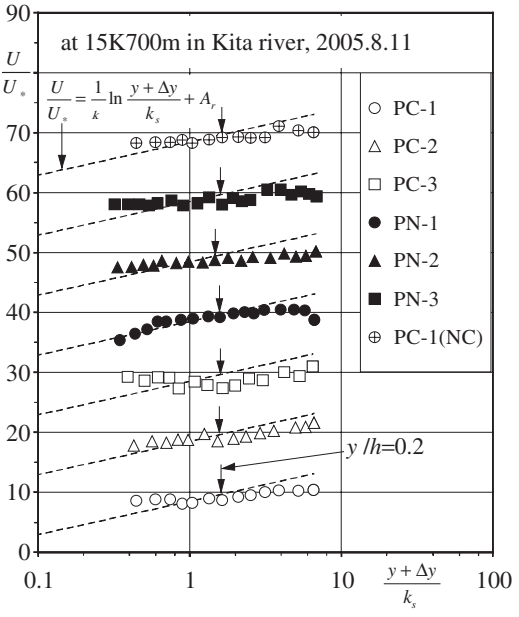


Figure 8(b). Velocity profiles in the pool.

bed level. The equivalent sand roughness k_s can be calculated by the Einstein method as follows:

$$k_s = d_{65} \tag{5}$$

Figure 8 shows the velocity distribution in the pool and rapid, together with the log-law as dashed lines. Although, the velocity profiles slightly deviate from the log-law in the outer region ($y/h > 0.2$), the velocity profiles in the inner region ($y/h \leq 0.2$) can be described by the log-law both in the pool and rapid. Therefore, the evaluation of the friction velocity from the log-law is valid.

Figure 9 shows the relationship between the relative growth rate α, coefficient β and the friction velocity U_*. Although, there is a few data, it is seen that the relative growth rate α increases with an increase of the friction velocity.

Figure 10 shows the relationship between the population of the ayu per unit area D (number/m^2), the number feeding per unit time F (number/s) and the friction velocity U_*. The population of ayu D decrease with an increase of the friction velocity U_*. This is because strong ayu makes the territory in the pool and turn off the other ayu from the territory. The feeding rate F also decrease with an increase of the friction velocity U_*. In the pool, feeding attached algae on the rocks is easy for ayu. On the other hand, in the rapid, feeding is difficult due to ayu must stay near the bed in the high velocity flow.

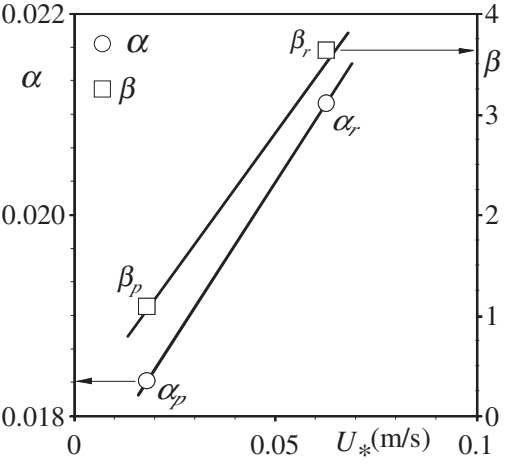


Figure 9. Relationship between the relative growth rate α, coefficient β and the friction velocity U_*.

4 CONCLUSIONS

In this study, the field survey, i.e., velocity measurements, flow depth and bed level measurements, recording the behavior of the swimming ayu and also gathering attached algae on the rocks, was conducted both in the pools and rapids under the condition that

Copyright © 2006 Taylor & Francis Group plc, London, UK

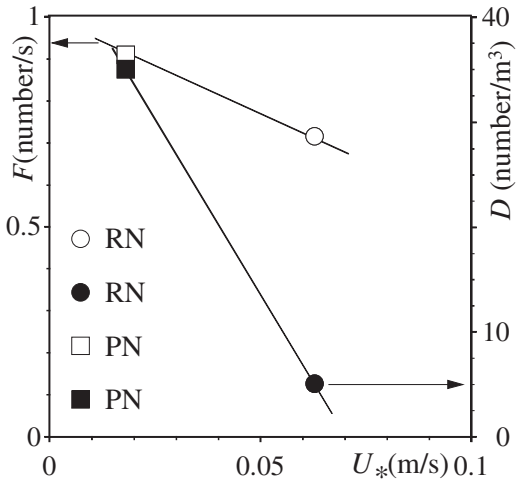


Figure 10. Relationship between the population of the ayu per unit area D, the number feeding per unit time F and the friction velocity U_*.

the ayu cannot feed attached algae in some area (non-ayu area) and also can feed in the other area (normal area).

It was found that the growth of attached algae in the rapid is higher than that in the pool. The growth of attached algae in non-ayu area is higher than that in the normal area, due to the ayu feed attached algae on the rocks in the normal area. A modified logistic model considering feeding of ayu is proposed to evaluate the growth of attached algae. As a result, the difference in the growth of attached algae between in the pool and rapid and also between in non-ayu and normal area can be investigated quantitatively.

ACKNOWLEDGEMENTS

The authors are thankful to K. Nagase who is a manager of Kitagawa fisherman's cooperative association. He taught us not only characteristics of ayu, but also river dynamics. The authors also to M. Suda, H. Kudoh, M. Kai and S. Tsuchida who belong to Nobeoka Gokasegawa fisherman's cooperative association. The authors are also thankful to H. Takao, H. Tsurusaki, K. Kawagoe, T. Takahashi, K. Nishie who belong to Nobeoka Work Office, Ministry of Land, Infrastructure and Transport.

REFERENCES

Hara, N. 1990. Artificial spawning channel for Ayu fish at Lake Biwa, *Proc. Int. Symp. on Fishways, '90 in Gifu*, Japan, 75–80.

Ishida, R. and Ichijo, E. 1990. Artificial river for spawning of ayu, *Proc. Int. Symposium on Fishways, '90 in Gifu*, Japan, 81–84.

Kono, Y., Sato, Y., Higasino, M., Takami, T., Akiyama, J., Onitsuka, K., Nagaya, T. and Otsuka, N. 2004. Field survey on the aquatic environment and ayu habitat in the urban river, *Proc. Ann. Meeting of JSCE in Seibu Brunch*: in CD-ROM (in Japanese).

Nagaya, T. and Matsuo, K. 2002. Evaluation of fish habitat using two-dimensional numerical analysis, *Advances in River Engineering*, 8, 73–78 (in Japanese).

Nagaya, T., Onitsuka, K., Higashino, M., Takami, T., Otsuka, N., Akiyama, J. and Matsumoto, K. 2004. Evaluation of weight of parameter for spawning of ayu, *Plecoglossus altivelis*, and prediction of spawn density per unit area, *Environmental Hydraulics and Sustainable Water Management*, 2 (Eds. J.H.W. Lee & K.M. Lam), A.A. Balkema Publishers, UK, 947–954.

Nagaya, T., Onitsuka, K., Higashino, M., Takami, T., Otsuka, N., Shiraishi, Y. and Akiyama, J. 2005. Prediction of spawning suitability for Ayu, *Plecoglossus altivelis*, with horizontal 2-D numerical simulation, *31th Congress of IAHR*, Korea, 1920–1928.

Nezu, I. and Nakagawa, H. 1993. *Turbulence in Open-Channel Flows*, IAHR Monograph, Balkema, Rotterdam.

Nezu, I. and Rodi, W. 1986. Open-channel flow measurements with a laser Doppler anemometer, *J. Hydraulic Eng.*, ASCE, 112, 335–355.

Onitsuka, K., Nagaya, T., Higashino, M., Takami, T., Otsuka, N., Akiyama, J., Ozeki, H., Matsumoto, K. and Shiraishi, Y. 2005. Suitable flow depth and velocity for spawning of Ayu, *Plecoglossus altivelis*, *31th Congress of IAHR*, Korea, 1850–1858.

Shiraishi, Y., Onitsuka, K., Nagaya, T., Higashino, M., Takami, T., Otsuka, N., Akiyama, J. and Ozeki, H. 2005. Field survey on suitable condition of habitat for ayu, *Plecoglossus altivelis*, *31th Congress of IAHR*, Korea, 1927–1938.

Suzuki, K. 1958. Ecology of ayu of spawning season and spawning bed, *Fishery proliferation*, 5(3): 21–26 (in Japanese).

Takami, T., Higasino, M., Onitsuka, K., Akiyama, J., Nagaya, T. and Otsuka, N. 2005. *Proc. Ann. Meeting of JSCE in Seibu Brunch*: in CD-ROM (in Japanese).

Toda, Y., Nishimura, A. and Ikeda, S. 2005. Numerical simulation on primary production and interspecific competition of stream periphyton, *Anu. J. Hydraulic Eng.*, JSCE, 1447–1452.

Tsukamoto, K. and Uchida, K. 1992. Migration mechanism of the ayu, *Oceanic and Anthropogenic Controls of Life in the Pacific Ocean*, (Eds. V.I. Ilyichev and V.V., Anikiev) Kluwer Academic Publishers, 145–172.

Copyright © 2006 Taylor & Francis Group plc, London, UK

Interaction between flow and growth of Periphyton in sand river

Y. Toda, T. Tsujimoto, T. Ikeda & Y. Tadakuma
Department of Civil Engineering, Nagoya University, Furo-cho, Chikusa, Nagoya, Japan

ABSTRACT: Priphyton is known to be one of major primary producers in river ecosystem. While the growth of periphyton is usually seen on the relatively stable substrata in flowing water such as stone surface of gravel bed streams, large growth of periphyton is sometimes observed in sand river where the flow discharge and water depth are small enough for providing stable habitats for periphyton. In the present study, the field observation was performed to know the growth of periphtyon in a sand river, in which the growth of periphyton on sand bed and the spatial distribution of periphyton were measured at the Yahagi River in Japan. A numerical simulation model was presented to describe the spatial distribution of periphyton biomass at the observed reach. The present numerical simulation model can predict the spatial distribution of periphyton well.

1 INTRODUCTION

Periphyton is known to be one of major primary producers for river ecosystem, and it develops bio-film type communities on solid surface in water (MacIntire (1973), Minshall (1978), Saravia et al. (1998)). In natural streams, the periphyton communities are usually seen on the surface of gravel stones of shallow river bed and/or on the surface of submerged structures. The growth of periphtyon is expected to be rarely observed in sand river reach because of high mobility of bed materials and shortage of solar illumination at the vicinity of river bed due to relatively large water depth compared with gravel reach. Nevertheless, the large growth of periphyton is sometimes seen even in sand rivers where river discharge and water depth are small enough to provide the stable habitats for periphyton.

As for rivers running through agricultural area, river water is often diverted to the agricultural fields for irrigation use, which reduces river discharge during ordinary water stage. This decrease of river discharge may induce the stabilization of bed materials and the resulting large growth of periphyton even on sand bed. In order to understand the base of river ecosystems in sand rivers, it is important to know the growth characteristics of periphtyon on sand bed.

In the present study, the field measurement was performed in a sand river to understand the time growth and the spatial distribution of periphyton biomass on sand bed. Numerical simulation was conducted to know the effect of flow characteristics on the growth of periphyton in the sand river.

2 FIELD OBSERVATION

2.1 *Observation area*

The field observation was performed at the Yahagi River in Japan (figure 1). The length of the river is 117 km, and the catchment area of the river is about 1,830 km^2. The large part of the middle and lower basin of the river is used for agriculture field, and about 30 m^3/s of the river discharge is continuously distributed to the agricultural field during irrigation season at a diversion weir locating at 34.6 km upstream from the river mouth. This water intake reduces the river discharge at the lower reach of the river from 50∼60 m^3/s down to about 20∼30 m^3/s,

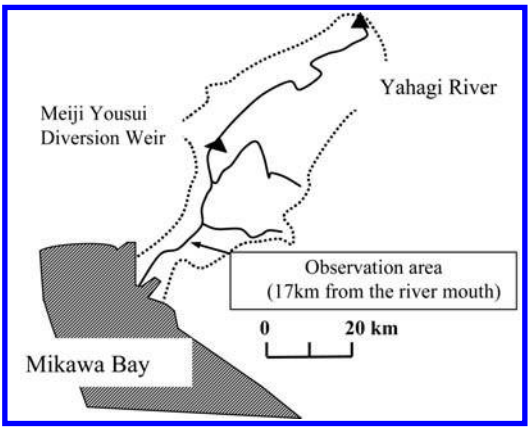


Figure 1. Map of the Yahagi River.

Copyright © 2006 Taylor & Francis Group plc, London, UK

which depresses mobility of river bed materials. Consequently, the river bed at the lower reach of the Yahagi River has been strongly stabilized during ordinary water stage, and the growth of periphyton is sometimes seen on the sand bed surface.

The observation area locates at 17 km upstream from the river mouth. The cross-sectional bed elevation of the observation site is depicted in figure 2. The cross-sectional averaged water depth of the observation site is less than 1 m during ordinary water stage, indicating that the large part of solar illumination can reach to the bed surface.

2.2 *Methods of the observation*

The field observation was conducted to know the growth of periphyton on the surface of the sand bed from July to December in 2005. The discharge during the observation period at the observation area is shown in figure 3. High water stages due to typhoon were observed around September 7 and October 19, and the discharge during November and December had been relatively small and stable. The sand sampled at the observed area was pasted on the square-shaped acrylic plates, each of whose has a dimension of 8 cm × 8 cm. The acrylic plates were settled on a frame, and the frame was installed onto the river bed (figure 4). 3 acrylic plates were picked up weekly, and the periphyton growing on them was removed by a tooth brush. The amount of periphyton was quantified in terms of the amount of chlorophyll a which is known to be a major photosynthetic pigment of plant. The amount of chlorophyll a was measured by using a spectrophotometer in accordance with the method proposed by SCOR/UNESCO (1975).

At October 31, November 16 and December 12 2005, the growth area of periphyton at the observed reach was recorded by D-GPS, in which the boundary between growth and non-growth area was detected by eye observation. The bed material sand was sampled at growth and non-growth area, and the grain size distribution of the sand was measured by using sieves.

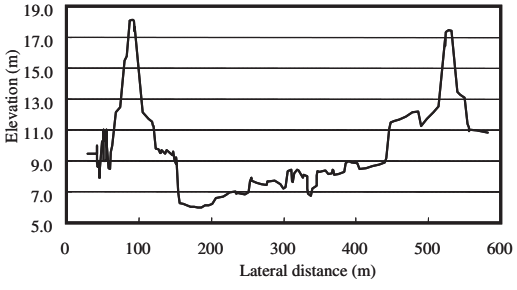


Figure 2. Cross-section of the observed area.



Figure 4. Fixed sand plates settled on the river bed of the observed area.

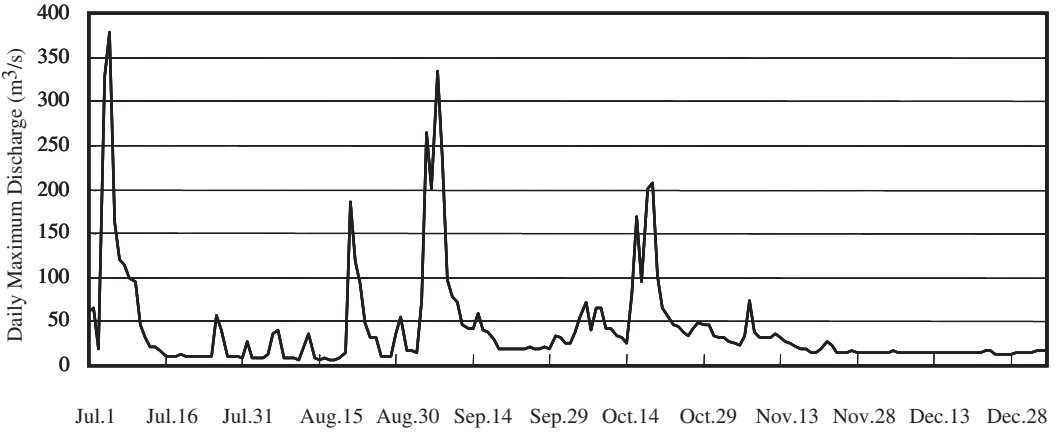


Figure 3. Daily maximum river discharges during observation period.

Copyright © 2006 Taylor & Francis Group plc, London, UK

At December 12, the periphyton growing on the bed surface was sampled, and the amount of periphyton biomass sampled was measured in terms of ignition loss.

3 NUMERICAL SIMULATION

3.1 *Outline of the numerical simulation model*

Flow chart of the present numerical simulation is illustrated in figure 5, which consists of the analysis of frequency of bed material movements and the simulation of growth of periphyton during the period that the bed material sands had been at rest. In the computation of frequency of bed material movements, Shields stress on river bed τ_* was estimated by calculating shallow water equations on the observed river discharge and bed geometry. The critical Sheilds stress τ_{*c} was calculated by using following Iwagaki formula (Iwagaki (1956)):

$$\begin{aligned} d \geq 0.303: \quad & U_{*c}^{\,2} = \tau_c/\rho = 80.9d \\ 0.118 \leq d \leq 0.303: \quad & = 134.6d^{31/22} \\ 0.0565 \leq d \leq 0.118: \quad & = 55.0d \\ 0.0065 \leq d \leq 0.0565: \quad & = 8.41d^{11/32} \\ d \leq 0.0065: \quad & = 226d \end{aligned} \tag{1}$$

in which d is grain size in cm, and U_{*c} is critical friction velocity in cm/sec. Comparing between τ_* and τ_{*c}, the amount of periphyton M was estimated to 0 during the period of $\tau_* > \tau_{*c}$, and it was calculated by the numerical integration of the logistic equation during the period of $\tau_* < \tau_{*c}$.

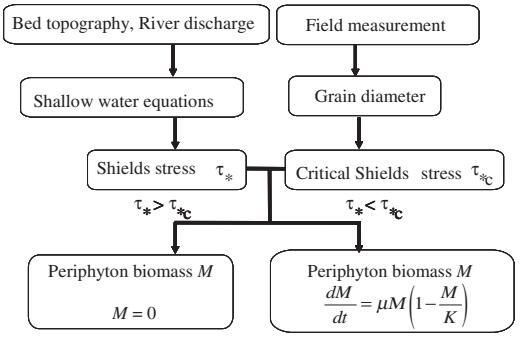


Figure 5. Flowchart of the present numerical simulation.

3.2 *Flow modeling*

The depth-averaged continuity equation and the depth-averaged Reynolds equations in curvilinear coordinates were used for calculating horizontal flow field. Eddy viscosity was estimated by using 0-equation type turbulence closure.

The governing equations for flow field were solved by finite volume method on a staggered grids system. Crank-Nicholson scheme was used for time integration. The 3rd order upwind scheme was employed for advection terms, and the 2nd order central difference was used for the other spatial derivatives.

3.3 *Modeling of growth of periphyton*

The logistic equation, Eq. (2), was used for the governing equation for periphyton growth:

$$\frac{dM}{dt} = \mu M\left(1 - \frac{M}{K}\right) \tag{2}$$

in which M is periphyton biomass per unit area, μ is specific growth rate of periphyton and K is environmental capacity. It is expected that the parameters μ and K are the functions of the environmental conditions relating the periphyton growth. In the present simulation model, the specific growth rate μ was assumed to be a function of solar radiation, water temperature and nutrient concentration. The environmental capacity K was represented by a function of solar radiation at bed surface;

$$\mu = \mu_{\max} f_I(I_b) f_T(T) f_N(N) \tag{3}$$

$$K = K_{\max} g_I(I_{b0}) \tag{4}$$

in which $\mu_{\max}$ is maximum specific growth rate, I_b is daily-averaged solar radiation at river bed, T is water temperature, N is nutrient concentration, $K_{\max}$ is maximum environmental capacity and I_{b0} is daily-averaged solar radiation under fair weather at river bed, respectively. The influence functions of solar radiation f_I, g_I, water temperature f_T and nutrient concentration f_N represent the effects of each environmental factor on specific growth and environmental capacity, and they are expected to take the value between 0 to 1.

The influence functions of solar radiation $f_I(I_b)$ and $g_I(I_{b0})$ were assumed to obey Monod type function;

$$f_I(I_b) = \frac{I_b}{I_{bc} + I_b}, \quad g_I(I_{b0}) = \frac{I_{b0}}{I_{b0c} + I_{b0}} \tag{5a, b}$$

in which I_{bc} and I_{b0c} are the half-saturated values of solar radiation. The influence function of water temperature was given by the following equation;

$$f_T(T) = \exp\left[\alpha_T \frac{(T - T_{opt})^2}{(T_c - T_{opt})^2}\right] \tag{6}$$

Copyright © 2006 Taylor & Francis Group plc, London, UK

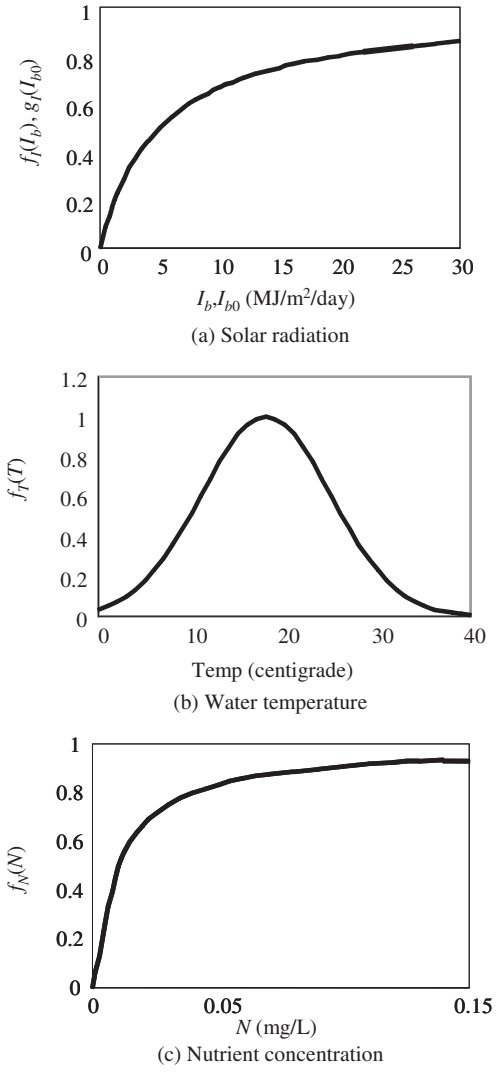


Figure 6. Influence functions used in the present numerical simulation.

in which T_{opt} is the optimal water temperature for the growth of periphyton, α_T and T_c is the numerical parameters. The function for nutrient concentration f_N was modeled by Monod type function;

$$f_N(N) = \frac{N}{N_c + N} \tag{7}$$

in which N_c is the half-saturated value of nutrient concentration. The profiles of the influence functions are depicted in figure 6.

Table 1. Physiological parameters for periphyton growth used in the present numerical simulation.

Item	Value	Reference
$\mu_{\max}$	1.1(day^{-1})	estimated from field data
$K_{\max}$	38.4(mg.chl.a/m^2)	estimated from field data
T_{opt}	18(°C)	Nozaki et al. (2003)
α_T	−2.3	Ikeda et al. (1998)
T_c	3(°C)	Ikeda et al. (1998)
δ	0.05	assumed
λ	0.18(m^{-1})	assumed
I_c	5(MJm^{-2}day^{-1})	Tashiro (2004)
N_c	0.01(mg.N/l)	Nozaki et al. (2003)

3.4 *Computational conditions*

The computational domain was taken at a reach between 16.8 km and 17.6 km from the river mouth. The domain was divided into 20 grids in longitudinal direction and 22 grids in transverse direction. The bed elevation data measured at the observation area was used for the topographical condition for the computation.

The numerical computation was performed under the hydrological and metrological conditions during September 1 and December 31, 2005. The downstream boundary condition for water level was given to the interpolated value of the daily maximum water levels measured at 4 km downstream and 7.5 km upstream from the observation site. The inlet water discharge at the upstream end of the domain was given to the discharge observed at 4 km downstream from the study site, because there is no confluence between the interval. The water temperature and the nutrient concentration during the computational period were given to the values measured at 7 km downstream from the study site.

In the present computation, grain size of the bed material was set to be 1.0 mm, since the mean sand size at the periphyton growth area is about 1.0 mm (figure 9, broken lines). The Manning's roughness coefficient was given to 0.032 by calibrating the result of computation of flowing water area to that observed in the field. The physiological parameters used in the growth simulation for periphyton are summarized in table 1.

4 RESULTS

4.1 *Results of the field observations*

The growth of periphyton on the fixed sand plate was illustrated in figure 7. It is clearly shown that the periphyton biomass rapidly increased during 2 to 3 weeks after the installation. This result suggests that

Copyright © 2006 Taylor & Francis Group plc, London, UK

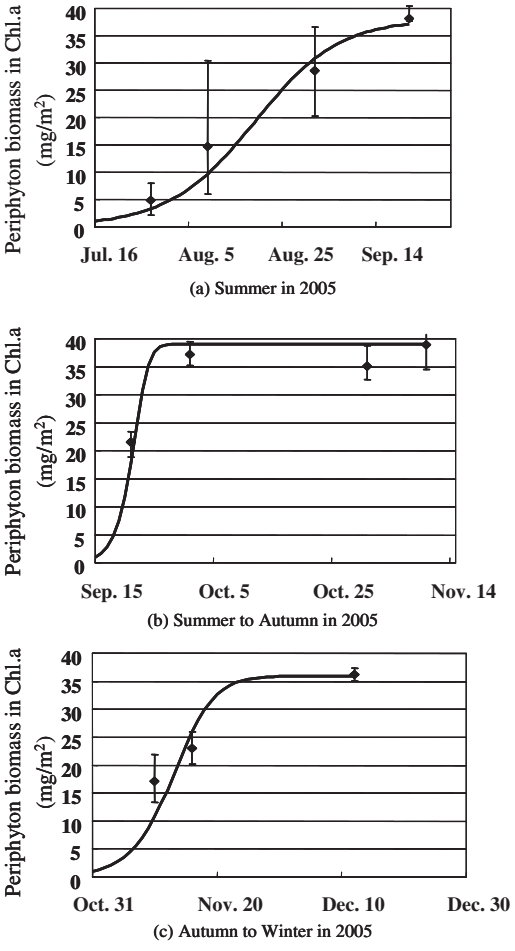


Figure 7. Growth of periphyton on fixed sand plates.

the periphyton can grow on sand surface if the sand has not moved. The fitting results of logistic curves, Eq. 2, were illustrated in solid line in the figure. In fitting the logistic equation, the environmental capacity, K, was given to the maximum value of the periphyton biomass observed during each growth period, and the specific growth rate, μ, was estimated by least square of residuals from the biomass measured in the field. The fitting results of the specific growth rate and the environmental capacity are summarized in table 2. While the variation of environmental capacity is found to be small among the season, a large specific growth rate was observed during September and October at the present study site. The specific growth rate is know to represent the activity of photosynthesis of periphyton, and the result indicates the growth activity becomes large at autumn while solar radiation becomes maximum in summer in Japan.

Table 2. Specific growth rate and environmental capacity estimated from the growth curves measured in the field.

	μ (day^{-1})	K (mg/m^2)
Jul. to Aug.	0.11	38
Sep. to Nov.	0.70	39
Nov. to Dec.	0.33	36

The spatial distribution of periphyton growth area is illustrated in figure 8, in which the solid line indicates the boundary between land and water. At October 31, small periphyton communities were seen at the vicinity of the right side bank. At the October 19, river discharge increased over 200 m^3/s, which might remove the periphyton communities from the river bed. Therefore the small periphyton communities were seen at October 31. During December to November, the river discharge and the fluctuation of it were relatively small compared with September, which might provide stable habitat for periphyton. Therefore the periphyton expanded their communities from the right side bank (figures 8 (b) and (c)).

Since the periphyton growth on sand bed depends on the stability of substrata, the grain size of bed materials might be important for the periphyton growth. The figure 9 shows the grain size distribution of bed materials sampled at the growth and non-growth area of periphyton. The grain size distribution has a considerable scatter for each location, and there is no significant difference between growth and non-growth area.

The spatial distribution of periphyton biomass in terms of ignition loss at December 12, 2005 is illustrated in figure 10. The periphyton biomass becomes large where the water depth is shallow. The difference in grain size was not large between growth and non-growth area, and therefore the growth of periphyton is expected to be affected by the flow characteristics such as water depth and bottom shear stress.

4.2 *Results of the numerical simulations*

The computational results of the spatial distribution of periphyton biomass are represented in figure 11. The computational results of the growth area of periphyton are more diffused than the area measured in the field (figure 8). In the field measurement, the growth area was detected by eye, and the boundary between growth and non-growth area was very clear. However, the periphyton biomass computed varies continuously with the continuous variation of hydraulic properties, which induces more diffused estimation of the growth area of periphyton.

The periphyton biomass computed tends to becomes large near the right side bank, and the growth

Copyright © 2006 Taylor & Francis Group plc, London, UK

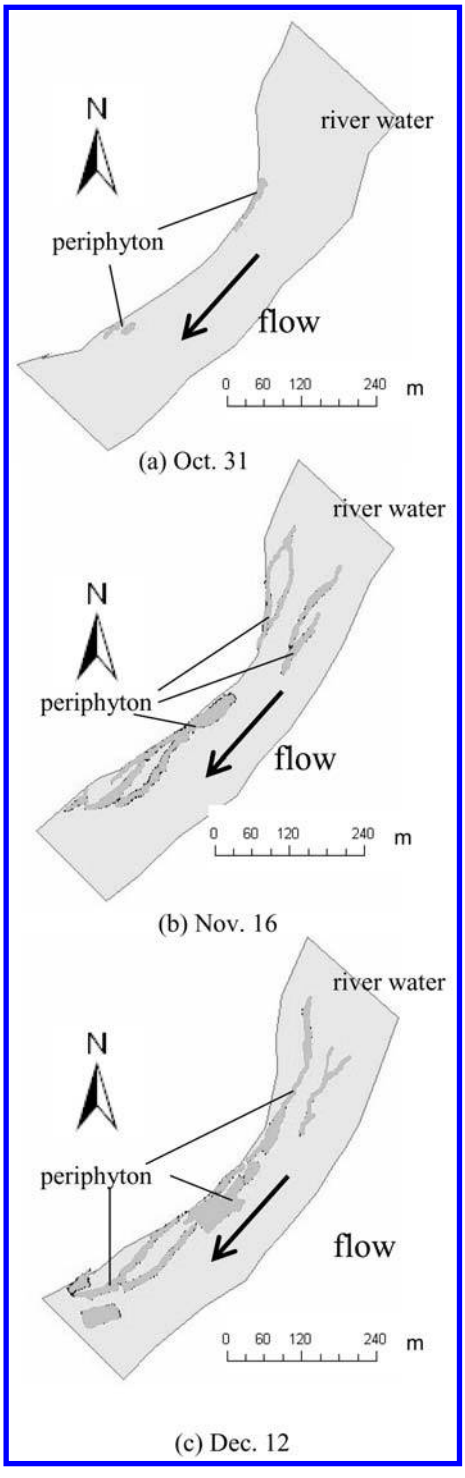


Figure 8. Growth area of periphyton on the observed river bed.

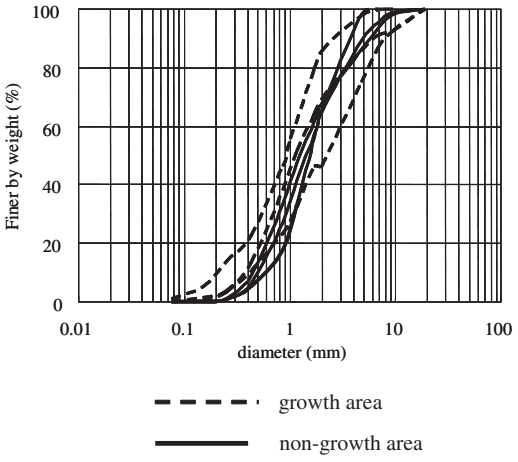


Figure 9. Grain size distribution of bed material sands sampled at growth and non-growth area.

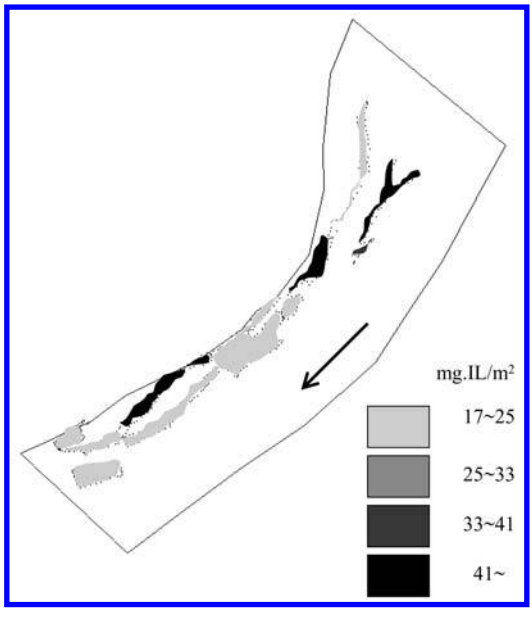


Figure 10. Spatial distribution of periphyton biomass measured at Dec. 12 in 2005.

area expanded in order of October 31, November 16 to December 12. These results agree with the results of field observation, and therefore the present computation can qualitatively estimate the growth of periphyton in the sand river. These results suggest that the growth and the spatial distribution of periphyton are closely correlated with stability of bed material sand, and the flow characteristics strongly influence primary production of periphyton in sand river.

Copyright © 2006 Taylor & Francis Group plc, London, UK

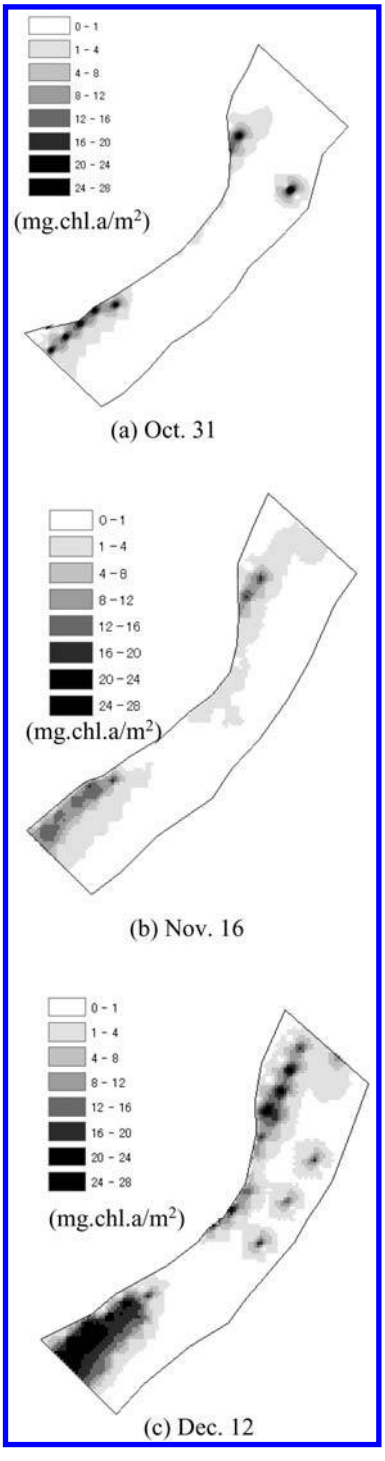


Figure 11. Spatial distribution of periphyton biomass computed.

5 CONCLUSIONS

In the present study, the field observations and the numerical simulations were performed to know the growth characteristics of periphyton in a sand river. The results of the observation and the numerical simulation have revealed the followings;

1) Periphyton can grow on the sand bed river if the bed material sand has not moved.
2) A numerical simulation model is proposed to describe the growth and the spatial distribution of periphyton in sand river. The model can estimate the growth area of periphyton, and the flow characteristics strongly influence primary production of periphyton in sand river.

APPENDIX

The following symbols are used in this paper:

d = grain size of sediment
I_b = daily-averaged solar radiation at river bed
I_{b0} = I_b under fair weather at river bed
I_{bc}, I_{b0c} = half-saturated values of solar radiation
K = environmental capacity for periphyton growth
$K_{\max}$ = maximum environmental capacity
M = periphyton biomass per unit area
N = nutrient concentration
N_c = half-saturated value of nutrient concentration
T = water temperature
T_{opt} = optimal water temperature for periphyton growth
T_c, α_T = numerical parameters representing temperature effect
U_{*c} = critical friction velocity
μ = specific growth rate of periphyton
$\mu_{\max}$ = maximum specific growth rate
τ_* = Shields stress
τ_{*c} = critical tractive force

ACKNOWLEDGEMENT

This study was performed under the financial supports of Grant-in-Aid for Young Scientists (b) (No. 17760405) and Grant-in-Aid for Exploratory Research (No.16656148), JSPS.

REFERENCES

Ikeda, S., Toda, Y. and Sano, T. 1998. Study on hydraulic characteristics and production rate of chlorophyll-a at riffles by field observation, *Journal of Hydraulic, Coastal*

Copyright © 2006 Taylor & Francis Group plc, London, UK

and Environmental Engineering, JSCE, 593, 93–104. (in Japanese)

Iwagaki, Y. 1956. Hydrodynamic study on critical bed shear stress, *Transactions of the Japan Society of Civil Engineers*, JSCE, 41, 1–21. (in Japanese)

MacIntire, C.D. 1973. Periphyton dynamics in laboratory streams: a simulation model and its implications, *Ecological Monograph*, 43, 399–420.

Minshall, G.W. 1978. Autrotrophy in streams, *Bioscience*, 28, 767–771.

Nozaki, K., Kohmatsu, Y., Yamamoto, T., Goto, N. and Mitamura, O. 2003. Photosynthetic activity of a filamentous green alga *Cladophora glomerata* in the middle region of the Yahagi River, *Report of Yahagi River Institute*, 7, 169–173. (in Japanese)

Saravia, L. A., Momo, F. and Lissin, L. D. B. 1998. Modeling periphyton dynamics in running water, *Ecological Modeling.*, 114, 35–47.

SCOR/UNESCO 1975. Determination of photosynthetic pigments in sea water, *Monograph of Oceanographic Methodology*, 1, 1–65.

Tashiro, T. 2004. *Study on Evaluation of Aquatic Ecosystem in a Stream with Less Disturbance after Dam Construction*, Doctoral Thesis, Nagoya University. (in Japanese)

Copyright © 2006 Taylor & Francis Group plc, London, UK

Evaluation of environmental impacts resulting from river regulation works: A case study from Portugal

A.E. Barbosa & E. Alves
Portuguese National Laboratory for Civil Engineering (LNEC), Department of Hydraulics and Environment

R.M.V. Cortes
University of Trás-os-Montes and Alto Douro (UTAD), Forestry Department

P. M. Silva-Santos
University of Trás-os-Montes and Alto Douro (UTAD), Laboratory of Applied Ecology

F. Aguiar & T. Ferreira
Technical University of Lisbon, Higher Institute of Agronomy (ISA)

ABSTRACT: Modifications observed on the hydraulic regime of river systems caused by engineering works led to growing awareness of the impacts caused by these engineering constructions. The need to harmonize and integrate both the hydraulic and the ecological/environmental components has been growing, namely in Portugal. This paper presents the work of a multidisciplinary team that carried out, from 1998 to 2003, an evaluation of the ecological impacts of realignment and construction works implemented at the lower part of Mondego river, in central Portugal, in the 80's. The hydraulic and hydrologic alterations in Mondego river, caused by regularization works, have been analyzed and quantified. The main conclusions of the study are that the changes in the Mondego river geometry induced more homogeneous physical and hydraulic conditions and reduced life diversity. However, the construction of a set of transversal groynes, and discontinuities of the bottom elevation, had an opposite effect. Similar conclusions are reported in the literature.

1 INTRODUCTION

1.1 *River corridors and anthropogenic modifications*

It is very important that rivers are approached to as components of a system that include its bordering and connected environment as well. The understanding of the ecological value of river corridors has been gradually assimilated in the last decades, after observations of the serious damages caused in the past by straight engineering interventions, namely, channelization and changes in rivers cross-section geometry. Modifications on the hydraulic regime of river systems cannot be isolated from the total system that comprehends the river basin, groundwater and the supported ecosystems (e.g.: Brooks, 1988).

Presently it is well known that river biological diversity and productivity are a result of habitat diversity and ecological connections. They are kept and balanced by the dynamic river processes of erosion and deposition which, in turn, depend on the water course hydrologic and sedimentation regimes (Brooks, 1988). Therefore, alterations on any of these physical processes, or a loss of connectivity between any of the three spatial borders of a river, may lead to serious changes on the aquatic communities.

In addition to the spatial variables, a forth temporal variable needs to be taken into account, and it is within these four dimensions that any river system must be comprehensively evaluated and managed (Ward, 1989).

The ecological impacts of dam and diversion channels construction, channelization and changes in the river cross-section geometry, may be synthesized as follows:

i. Significant reduction of habitats diversity, since hydraulic works interfere with the natural continuity of the river physical borders, and make more homogeneous both the river bed and the flooded areas.
ii. Reduction in the native species diversity, caused by the disappearance of the species that depend on seasonal flow differences, and spatial habitat variations to survive. Simultaneously, the exotic species

Copyright © 2006 Taylor & Francis Group plc, London, UK

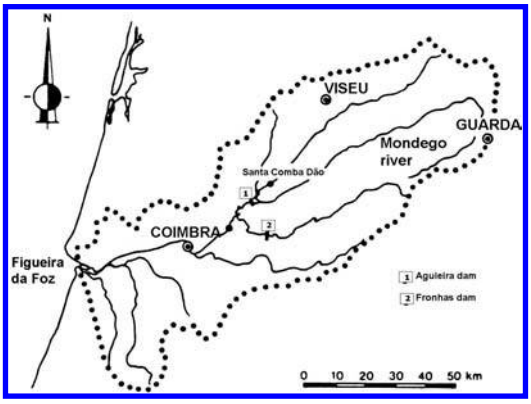


Figure 1. Mondego river basin.

gain a competitive advantage due to the before mentioned alterations.

1.2 *Project framework*

The need to harmonize and integrate both the hydraulic and the ecological/environmental components has been growing since the last four decades. In the past, in Portugal there was a weak connection between such fields of knowledge that today are known to be interdependent.

This paper presents the work of a multidisciplinary team, from two universities (UTAD and ISA) and a state laboratory (LNEC) that carried out, from 1998 to 2003, a study financed by the Portuguese Foundation for Science and Technology. The objectives of the project were to evaluate and quantify ecological impacts of realignment and construction works implemented in rivers. The selected case study was the lower part of Mondego river, in central Portugal (Figure 1), that has been channelized as part of a large river regulation scheme implemented in the 80's.

The study permitted an understanding of the modifications provoked by the river channelization on the local ecosystem. The report by Barbosa *et al.* (2005) presents the study in detail.

1.3 *Study methodology*

The study has been split in different components, being each of the three institutions involved responsible for a sector, as follows:

i) LNEC, in charge of the Project coordination, was responsible for the description of the case study history, including the engineering interventions implement in the Mondego river. The hydraulic and hydrologic alterations caused by the referred to regularization works, have been analysed and quantified by the LNEC team.

ii) LNEC made a literature review in order to synthesize the impacts of river training works, and the concepts of river channelization, restoration and rehabilitation. The aim was to emphasize the need to understand rivers as elements of complex catchment's system that combines surface, subsurface and underground water, quantitative and qualitative variables, all in dynamic interaction, and that are a support to the local ecosystem. The UTAD team put into perspective the importance of biomonitoring results as indicators of the impacts of river regularization works.

iii) The ISA research team was responsible for studying the responses of river plants to channelization, and the effects of habitat disturbance in the ecosystem's invasibility. A comparative study of floral features was conducted among sites in the channelized segment of the Mondego river, and in the near-natural river reaches upstream Coimbra. General differences in plant species composition, distribution and relationship with environment were investigated, with particular attention paid to shifts in richness and cover of native species assemblages, and in the dominance of exotic species (as defined per Richardson *et al*., 2000).

iv) The study of macroinvertebrate and ichthyic communities of the regulated fluvial ecosystem of Mondego river has been the responsibility of the UTAD team.

In order to find out how the hydraulic works in the lower Mondego river affected the aquatic communities (fish and invertebrates) field work campaigns were implemented during June and September of 2000 and 2001. Fauna was sampled and registered and water quality parameters were measured both in the field and in the laboratory.

2 CASE STUDY – MONDEGO RIVER TRAINING AND CHANNEL IMPROVEMENT

2.1 *General description*

The Mondego river is the largest entirely Portuguese river with a catchment area of approximately 6644 km^2. It originates at an elevation of 1547 m in "Estrela" Mountains and flows through a very narrow valley till Coimbra town, where the valley spreads to form a vast alluvial plain, the Lower Mondego region, which consists of 15000 hectares of land with high agricultural aptitude. The river reaches the Atlantic Ocean near the town of Figueira da Foz (Figure 1).

The hydrological regime of the Mondego river is very irregular, with discharges that can be less than 1 m^3/s during several days in a year, and flood discharges up to 3000 m^3/s (natural situation, before river basin interventions). The average annual rainfall is 1124 mm. The river presents torrential

Copyright © 2006 Taylor & Francis Group plc, London, UK



Figure 2. Flooding in the lower Mondego river.



Figure 3. Mondego river: trained main channel.

characteristics due to the precipitation regime and the strong slopes of the river basin.

Along several centuries, the lower part of Mondego river basin was subject to periodic flooding and many attempts to regulate and channelize the river were performed. The construction of a new river bed downstream Coimbra, at late XVIII century, was kept functional along the years but was judged to be insufficient by mid-XX century due to the erosion of the upper part the river basin and the resulting silting and sanding up of the river and the marginal fields, which caused more frequent flooding of the agricultural lands (Figure 2).

2.2 *River training and flood protection works*

In order to attenuate the annual flood effects (inundation of river banks) thus increasing the agricultural potential of the downstream flood plains, and protect the population, a large river regulation project was implemented in the 80's. This project implied the construction of three large dams: Aguieira, Raiva and Fronhas to control the flood discharges, and a significant training of the river in the lower, flat area of its basin, with the opening of adequately designed channel flanked by unsubmergible embankments, in a distance of about 36 km.

In the design of alluvial bed river training the main objective was to define a dinamically stable channel, i. e., a channel with movable bed where the sediment transport capacity is equal to the equilibrium value.

The main channel (Figure 3) was designed for the modified 100-year flood of 1200 m^3/s (at Coimbra) associated with the 25-year flood of the Lower Mondego tributaries. The bankfull cross sectional geometry is of trapezoidal type. The bottom width varies between 88.0 m and 142.2 m and the maximum depth is 6.5 m. To maintain the desired cross section, the channel banks are protected by riprap with mean diameter of 0.15 mm.

The levees along the main channel have lateral fuse-plug weirs, to permit controlled flooding for discharges higher than the design ones.

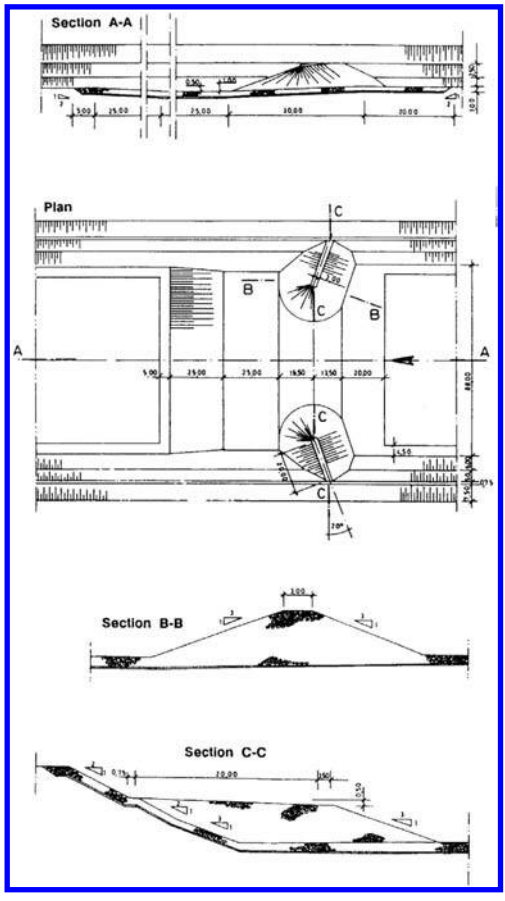


Figure 4. Mondego river groynes. Plan and sections (Lemos *et al*., 1991).

The Lower Mondego river training project included, within an extension of 11873 m downstream Coimbra town, the construction of a set of groyne-type structures, placed in pairs, and combined with discontinuities of the bottom elevation (Figure 4). Groynes

Copyright © 2006 Taylor & Francis Group plc, London, UK

have 20.0 m length and an angle to the flow direction of 70°. Upstream and downstream from each groyne, the channel bed is protected by riprap to prevent streambank erosion.

3 HYDROLOGIC AND HYDRAULIC CONSIDERATIONS

The flow regime of the lower Mondego channelized river reflects the variability of the climate and the physiographic conditions in the river basin and the type of operation of Aguieira, Raiva, Fronhas and Coimbra reservoirs. These reservoirs are part of the Mondego river regulation scheme and are associated with a diversity of water uses (e.g. urban supply, agriculture, industry, energy production). In general, the operation of reservoirs causes changes in either total flow volume or annual distribution of the flow, or both, and in the frequency and magnitude of floods.

To characterize the hydrologic modifications occurred in Mondego river due to the interventions in the river basin two measuring stations were considered: Ponte Santa Clara and Coimbra dam, near Coimbra town. These stations represent the integrated runoff of 74% of the entire Mondego basin and are located immediately upstream the channelized reach of the river.

Historical data from Ponte Santa Clara station between 1939/1940 and 1979/1980 (41 years) was used to analyse the river flow regime before the interventions. This station was discontinued after the construction of Coimbra dam. On the other hand, the period of 1986/1987 to 2003/2004 (18 years) was considered as representative of the present situation (Barbosa *et al*., 2005), after an analysis of the number and size of reservoirs and the date of their construction.

Based on the analysis of the mean daily flows and flood hydrographs some modifications on Mondego flow regime have been identified:

- The average total runoff is 2424 hm^3. This value reflects a slight reduction (14%) in the total runoff due to water diversion for agricultural, urban and industrial supply.
- Although river flows maintain a marked seasonal pattern, there has been a reduction of the monthly mean discharges, between February and June, and an increase of the low flows between July and September. The mean monthly discharges may vary between 16 m^3/s and 205 m^3/s. The flow duration curve presents a more gentle decline, without long periods of zero streamflow, as occurred in natural conditions.
- Aguieira and Fronhas reservoirs ensure the regulation of 80% of the river basin upstream Coimbra town. For approximately 20 consecutive years these reservoirs managed to control the river flood discharges and no inundation of the agriculture fields was registered. However recent flood events (January 27, 2001) have demonstrated that high peak discharges can occur due to the contribution of the many Mondego tributaries. In this event, the maximum flood discharge reached 2000 m^3/s exceeding the design value of the river Mondego main channel, leading to levee failure and extensive flooding of the marginal fields. The flood water remained on the plain for several days destroying many farms and causing severe damages to agriculture.

Concerning the hydraulic conditions on the Mondego river, no information on the trained river bed evolution was available during the present study. However, due to human activities upstream Coimbra dam, namely sand mining, and the construction and operation of Aguieira and Fronhas dams, it is sup-posed that a reduction on the sediment transport had lead to a degradation of the trained mobile river bed.

Accordingly with the work of Belo and Cardoso (1993) significant bed degradation was observed since 1977, in a 33.2 km reach of river Mondego up-stream Coimbra town due to the aforementioned activities.

4 RESPONSES OF RIVER PLANTS TO CHANNELIZATION EFFECTS OF HABITAT DISTURBANCE IN THE ECOSYSTEM'S INVASIBILITY

4.1 *Sampling procedures*

Fito-ecological surveys were carried out in May–June 1999 at six sites placed at regular intervals along the channelized segment and at three sites in the "natural" river. Three longitudinal transects of five 5×25 m plots were laid out at each studied site. The first transect was positioned instream and in the waterlogged margin, while the others were placed on each of the two-stage terraces, whilst the "natural" transects were located in the corresponding areas of the fluvial corridor – i.e. the in-stream and waterlogged margins, inner-bank and outer-banks. The richness and percentage of foliar cover in each plot were visually estimated for each exotic and native species by averaging the results from 2.5×2.5 m sub-plots ($n = 10$ in each plot). Environmental variables that potentially influence the vegetation establishment were estimated for each plot (e.g. substrate, distance from the water) or measured (e.g. conductivity). Site-specific variables were also achieved (e.g. river corridor width).

4.2 *Data treatment*

A correspondence analysis was carried out, so as to evaluate channelization effects by comparing plant

Copyright © 2006 Taylor & Francis Group plc, London, UK

species composition and distribution in 'natural' and channelized plots. The number and foliar cover of native and exotic species were also compared, using non-parametric Mann-Whitney U tests. Data from plots of the channelized river segment were subjected to a canonical correspondence analysis and to a classification using the unweighted pair-group arithmetic average clustering.

4.3 *Results and discussion*

Exotic plant species in fluvial ecosystems are known to be associated with human-disturbance and its establishment and invasive spread frequently conduct to an over-turning of native species assemblages (Hood & Naiman, 2000).

In this study, significant differences in the distribution and vegetation features (richness and cover) were observed, however the number of plant species recorded was very similar, with 150 species present in the 'natural' corridor, 160 species on the channelized part, and 98 were common to both. A small number of exotic species was recorded (around 10% of the total flora), which was coupled with low exotic species richness found per plot (maximum 8 species, average 2.8). However, exotic species were dominant in some plots, especially in the channelized river. *Eryngium pandanifolium*, a swamp-dwelling plant from the South-American subtropical zone, dominated the instream plots and the first terrace at downstream sites, but was substituted by another exotic species, the knotgrass (*Paspalum distichum*) at the upstream ones. The exotic hydrophytes *Azolla filiculoides* and the parrot feather (*Myriophyllum aquaticum)* were also largely disseminated in instream plots. Below the riparian woody vegetation, in shady and wet habitats, dense stands of the South-American species *Tradescantia fluminensis* were established. On the second terrace the increase in exotic cover was due mainly to the presence of the silver wattle (*Acacia dealbata*), a woody Australian species. Knotgrass, silver wattle and *T. fluminensis* were also found at the 'natural' sites, but with the exception of the latter on the inner bank, consistently had a lower degree of cover. Figure 5 presents the comparison of native and exotic species cover between the "natural" and channelized river segments, at the three transects.

Aguiar *et al*. (2001) pointed out two potential reasons for the channelized river's higher susceptibility to exotic invasion. Firstly, the strong disturbance of the physical environment caused by the channelization, regulation and expansion of the irrigation area led to new and favorable environmental conditions to invasion, including a reduction in the intensity and frequency of scouring floods and an increase in the fine sediment and nutrient load. Secondly, the synergistic effect of higher propagule pressure and the successful dispersal capability of the exotic species that were already present.

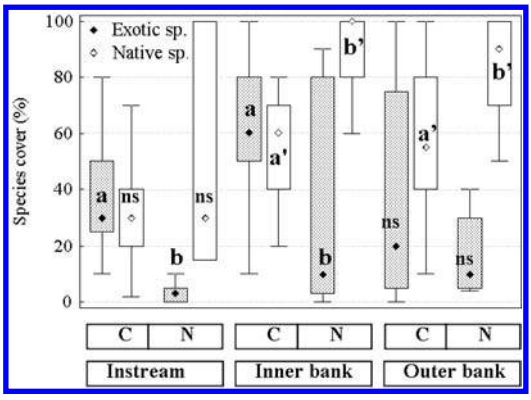


Figure 5. Comparison of species cover for exotic and native species between the channelized (C) and the "natural" (N) river at the three transects. Median (black or white lozenge), non-outlier range, and 25%, 75% percentiles are represented. Columns with different letters indicate significant differences at $p < 0.05$, using Mann-Whitney U tests for comparison tests, within each group of species (a′, b′ for native species, and a, b for exotic species; ns = non-significant test). Note that inner bank and outer bank corresponds to 1st terrace and 2nd terrace for the channelized segments, respectively.

The riparian woody species have rapidly recovered after the channelization project, and the structure and composition of the riparian woody layer of the first terrace, is rather similar with the riparian gallery of the "natural" river, however overstorey herbaceous species had a varying composition, whilst the vegetation of the 2nd terrace clearly diverges in species composition from the "natural" area. This experimental evidence can be related with the loss of interactive pathways, which are maintained in non-impacted floodplain rivers, namely the vertical and lateral connectivity with the river channel (Ward & Stanford, 1995). In the channelized segment of Mondego river, the first terrace is located 2 m above the water, and the original river connections were preserved, but the second terrace, which is positioned 4 m above the water, led to the likely disruption of vertical and lateral interactions with the river channel.

Figure 6 presents the canonical correspondence analysis biplot of the channelized segment data (sites from 1 to 6, with 1 being the site closer to the estuary and 6 the most upstream site), with the selected variables obtained by a forward selection procedure. The first axis clearly represented a transverse gradient of moisture (water→terraces), whereas the second axis displayed the longitudinal gradient of the river (upstream→downstream). Conductivity and channel depth were also aligned with the distance

Copyright © 2006 Taylor & Francis Group plc, London, UK

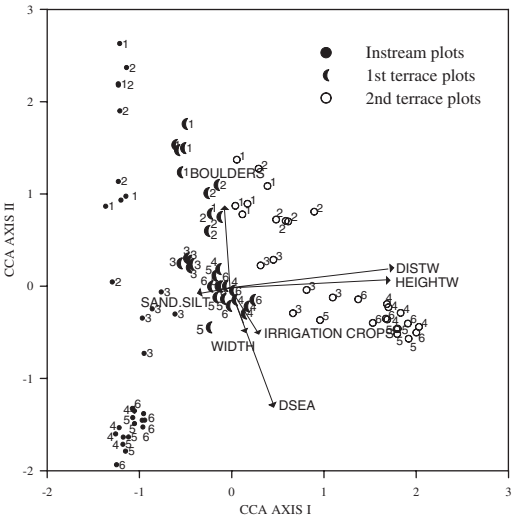


Figure 6. Axis one and two of the canonical correspondence analysis biplot using the floral composition of the channelized Mondego segment. Numbers indicate sites (each site with five plots per transect). Substrate: BOULDERS – boulders (%); SAND.SILT – sand and silt (%); WIDTH – channel width (m); DSEA – distance to the sea (km); DISTW – distance of the plot to the water (m); HEIGTHW – height of the plot above water (m); IRRIGATION CROPS – land use on the site surroundings: irrigation crops and rice fields (adapted from Aguiar *et al*., 2001).

from the sea, channel width and irrigated cropland. Site 3, approximately in the middle of the channelized river is a transitional zone in terms of species composition.

Differences in species composition within and along the channelized segment can be observed, regardless of the same engineering procedures and materials used in the channelization process. This suggests the development of microtopographic variations and habitat patches that influenced vegetation establishment, associated with differences in adjacent land-use along the impacted river, and the diverse existing species pool.

5 STUDY OF MACROINVERTEBRATE AND ICHTHYIC COMMUNITIES OF THE REGULATED MONDEGO RIVER FLUVIAL ECOSYSTEM

5.1 *Sampling sites*

Three sampling sites were set in the regularized central bed of the Mondego river (M2, M3, M4), between Coimbra and the river mouth (Figueira da Foz), and

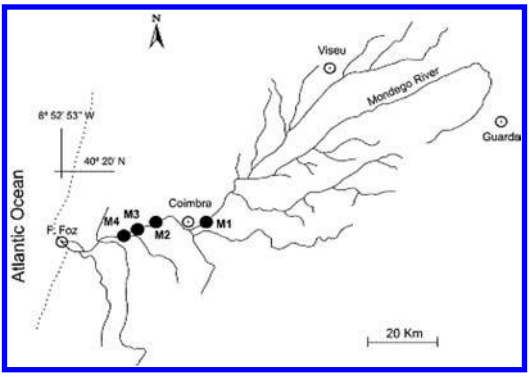


Figure 7. Location of the sampling sites within the Mondego basin. M1 – Reference site; M2, M3 and M4 – Sites on channelized sector.

one located approximately 14 km upstream of Coimbra (M1) – (Figure 7). This last one, was a control site since it was not affected by channelization, although it is located approximately 20 km downstream of the Aguieira Dam. This site has well developed riparian vegetation on the left bank. In contrast, the right bank presents scarce vegetation due to its clear cutting and to the high deposition of materials (small stones, gravel and sand).

The sites in the artificial segment exhibit extensive riprap along the banks, with constant slope of 45°, partially colonized by shrubs and trees (mainly *Populus* spp.). Medium fraction materials (stones and gravel) dominated the riverbed, but were replaced by a lower grain size fraction in the second part of the study after the flood events of 2001. M2 showed a semi-disaggregated groyne with resulting shear stress in the wet channel. A more detailed description of the different characteristics of each meso-habitat is in Table 1. Macroinvertebrate (M) and fish (F) sampling was carried out simultaneously in June (the 6th) and September (the 9th), of 2000 and 2001. Physical and chemical parameters (dissolved oxygen, pH, temperature, conductivity, alkalinity and total suspended solids) were also analysed at the sampling sites during the same periods (Table 2).

5.2 *Benthic macroinvertebrates communities*

Benthic invertebrates were collected from reaches of approximately 100 m in length during a fixed time of 5 minutes (CPUE) by disturbing the substratum upstream of the net using a vigorous kicking and/or feet action. The sampling was performed using a 350 μm mesh net with 600 cm^2 aperture and embraced all the existent biotopes, with an effort proportional to the relative importance of each habitat

Copyright © 2006 Taylor & Francis Group plc, London, UK

Table 1. Characterization of habitats in each sampled site and aquatic communities that were inventoried in each sector: F – fishes; M – macroinvertebrates. Example: M1006 means reference site (M1) sampled in 2000 (second and third code's cypher) in June (fourth code's cypher). The last code refers to habitat type: D- right bank; E- left bank; T- groynes; R- nets; N- riprap; I- sand bank.

Habitat	Mean depth (m)	Dominant substrate	Current ($m\ s^{1}$)	Bank structure	Communities
M1006D	1.20	Stones	0,28	Natural, smooth profile with tree clumps.	F; M
M1009D	1.20		0.28	Natural, smooth profile with tree clumps.	F; M
M1009E	2.50		0.28	Natural with a vertical profile. Riparian vegetation without interruptions.	F
M1016D	1.20		0.28	Natural, smooth profile with tree clumps.	F; M
M1016E	2.50		0.28	Natural with a vertical profile. Riparian vegetation without interruptions.	F
M1019D	1.20		0.28	Natural, smooth profile with tree clumps.	F; M
M1019E	2.50		0.28	Natural with a vertical profile. Riparian vegetation without interruptions.	F
M2006E	0.50	Gravel	0.20	Artificial embankment. 45° slope. Dense riparian vegetation.	F; M
M2006T	0.40	Stones	0.84	Semi-disaggregated submersed weir with stone blocks.	F
M2006R	2.5	Gravel	1.05		F
M2009T	0.40	Stones	0.84	Semi-disaggregated submersed weir with stone blocks.	F
M2009E	0.50	Gravel	0.20	Artificial embankment. 45° slope. Dense riparian vegetation.	F; M
M2016E	0.50	Gravel	0.20	Artificial embankment. 45° slope. Dense riparian vegetation.	F; M
M2016T	0.40	Stones	0.84	Semi-disaggregated submersed weir with stone blocks.	F
M2016R	2.5	Gravel	0.95		F
M2019E	0.50	Gravel	0.20	Artificial embankment. 45° slope. Dense riparian vegetation.	F; M
M2019T	0.40	Stones	0.84	Semi-disaggregated submersed weir with stone blocks.	F
M2019R	2.5	Gravel	1.02		F
M3006D	1.20	Stones	0.15	Artificial embankment. 45° slope. Riparian vegetation with interruptions.	F
M3006N	0.60	Stones	0.25	Rip rap with stone blocks.	F
M3006R	2.0	Gravel	0.55		F
M3009D	1.20	Stones	0.15	Artificial embankment. 45° slope. Riparian vegetation with interruptions.	F; M
M3009N	0.60	Stones	0.25	Rip rap with stone blocks.	F
M3016D	1.20	Stones	0.15	Artificial embankment. 45° slope. Riparian vegetation with interruptions.	F; M
M3016N	0.60	Stones	0.25	Rip rap with stone blocks.	F
M3016R	2.0	Gravel	0.49		F
M3019D	1.20	Stones	0.15	Artificial embankment. 45° slope. Riparian vegetation with interruptions.	F; M
M3019N	0.60	Stones	0.25	Rip rap with stone blocks.	F
M3019R	2.0	Gravel	0.54		F
M4006E	0.70	Sand	0.06	Sand bank with herbaceous vegetation.	F; M
M4006I	1.00	Sand	0.10	Stabilized sand bank with herbaceous and shrubby vegetation.	F
M4006D	1.50	Stones	0.06	Artificial embankment. Riparian vegetation with interruptions.	F
M4006R	2.5	Sand	0.10		F
M4009D	1.50	Stones	0.06	Artificial embankment. Riparian vegetation with interruptions.	F
M4009E	0.70	Sand	0.06	Sand bank with herbaceous vegetation.	F; M
M4009I	1.00	Sand	0.10	Banco de areia estabilizado com vegetaçõo herbácea	F
M4016D	1.50	Stones	0.06	Artificial embankment. Riparian vegetation with interruptions.	F
M4016E	0.70	Sand	0.06	Sand bank with herbaceous vegetation.	F; M
M4016R	2.5	Sand	0.15		F
M4019D	1.50	Stones	0.06	Artificial embankment. Riparian vegetation with interruptions.	F
M4019I	1.00	Sand	0.10	Sand bank with herbaceous vegetation.	F
M4019E	0.70	Sand	0.06	Sand bank with herbaceous vegetation.	F; M
M4019R	2.5	Sand	0.16		F

(Table 1). The nets were washed carefully between collections. The contents of the hand-net were placed in labeled containers, transported to the laboratory, and the specimens sorted alive. 70% ethanol was used for preservation before subsequent identification. Wherever possible, identification was done to species level using the available keys (except Diptera and Oligochaeta).

Copyright © 2006 Taylor & Francis Group plc, London, UK

Table 2. Physical and chemical values at the 4 sampling sites in June/September 2000 and 2001.

Sampling site	D.O. ($mg.L^{-1}$)	pH	Temp (°C)	Cond ($\mu S.cm^{-1}$)	Alkalinity ($mg.L^{-1}$ $CaCO_3$)	TSS ($mg.L^{-1}$)
M1006	9.5	6.5	18.6	76.1	11.8	3
M1009	8.4	7.0	20.6	78.2	14.4	1
M1016	10.2	6.3	22.8	76.3	13.8	3
M1019	9.0	6.5	22.4	79.8	9.3	0
M2006	8.9	6.7	21.1	120.1	22.9	5
M2009	9.1	7.6	23.4	103.0	20.5	1
M2016	6.7	6.4	22.1	128.9	26.4	8
M2019	7.0	7.0	22.3	113.0	18.3	8
M3006	8.6	7.4	25.5	123.5	24.8	8
M3009	10.2	7.7	24.3	149.0	27.7	2
M3016	10.4	8.1	29.0	136.7	31.9	8
M3019	9.6	7.3	25.0	120.9	19.8	5
M4006	9.2	6.9	23.9	149.0	31.8	7
M4009	6.6	6.6	22.4	137.0	35.4	2
M4016	10.4	8.1	24.9	161.0	40.1	20
M4019	7.9	7.2	23.8	129.0	20.9	20

5.3 *Ichthyic communities*

In contrast with benthic collections, fish sampling allowed the discrimination between habitat types in order to detect the influence of hydraulic structures and erosion sedimentation processes (Table 1). Fish were captured using na Electrocatch apparatus, model WFC7-HV, powered by a generator (Honda GX160) of 4.0 KW. Electrofishing used DC current and the voltage was set between 150 to 200 V in order to produce a current from 2.5 to 4 A. This fact, together with a constant capture effort of 7 minutes in each meso-habitat (CPUE), allowed comparable results among the different inventoried habitat types. Electrofishing captures were complemented by 30×2.5 m static multimesh gill net (mesh types: 32 mm, 43 mm, 50 mm, 65 mm and 85 mm), which was placed in the deeper pools for 3–4 hours.

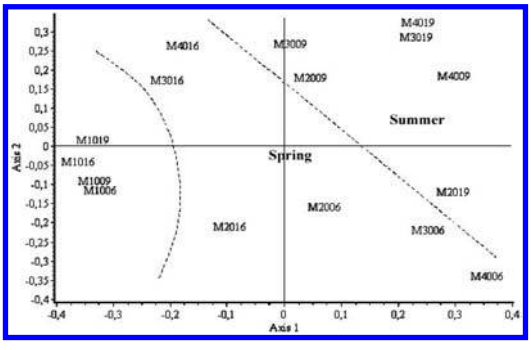


Figure 8. MDS ordination of sampling sites based on benthic invertebrates. Example: M1006 means reference site (M1) sampled in 2000 (second and third code's cypher) in June (last code's cypher).

5.4 *Data treatment*

To compare sites and periods for both sampled communities, the total number of individuals and Shannon diversity index were computed through PRIMER 5.2.2 (Clarke & Gorley, 2001). Multivariate methods were used to detect the spatial and temporal patterns underlying the biotic and abiotic data. Metric Dimensional Analysis (MDS) was used through the package SYN-TAX 2000 (Podani, 2001) and non-Metric Dimensional Analysis (n-MDS) through PRIMER 5.2.2 (Clarke & Gorley, 2001). N-MDS operated on a sample similarity matrix of the Bray-Curtis coefficient instead of the original data matrix, converting the similarity values to rank order (in order to preserve the original relationships between samples). MDS is a related technique, in the sense that it also uses a distance or dissimilarity matrix but, on the contrary, it assumes the existence of linear relationships between variables. The data files were not transformed to enhance the effect of the density variation of organisms among sites.

5.5 *Results*

5.5.1 *Macroinvertebrates communities*

The differences between the reference site and the channelized sector, and the potential effects of the floods in the macroinvertebrate communities were assessed through MDS ordinations of sampling sites. Figure 8 shows a clear separation of the reference

Copyright © 2006 Taylor & Francis Group plc, London, UK



Figure 9. n-MDS ordination of sampling sites based on benthic fauna. In each site was overlapped one circle with proportional radius at relative importance of the sand on the substrate. Abbreviations of the sampling sites are given in Figure 7.

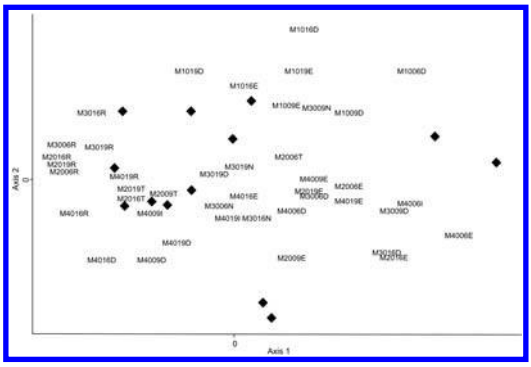


Figure 10. MDS ordination of sampling sites and habitats based on ichthyic communities. Symbols represent fish species. Abbreviations of the sampling sites are given in Figure 7. The last code refers to habitat type (D – right bank, E – left bank, T – groynes, N – riprap, R – nets and I – sand bank).

site (M1) relative to the channelized ones. This site presents, a specific benthic assemblage, characterized by different caddisflies (*Polycentropus* sp., *Plectrocnemia* sp., *Tinodes waeneri*) and stoneflies (*Leuctra fusca*) taxa. On the contrary, some Heteroptera (*e.g. Gerris lateralis* and *Micronecta* sp.) show a preference for the modified sector.

A clear seasonal separation of the sampling sites is another important aspect displayed in Figure 8.

This fact demonstrates the high capacity of recovery of the system since inter-annual differences are obscured by seasonal ones. The importance of riverbed materials in explaining the dynamics of benthic assemblages is illustrated by Figure 9. Here, we can link these changes to the winter peak flows, which cause an extensive deposition of fine sediments, especially clear in site M2. The reduced *stress* value obtained by the n-MDS ordination (0.08) demonstrates a good representation of the global variance.

In the reference site the diversity of benthic organisms was, in general, superior when compared to the channelized sites before the flood events. After this phenomenon, diversity decreased in the reference site, while the total number of individuals did not suffer strong variations. However, in the channelized sites (M2, M3 and M4), the extreme flows were probably responsible for the drastic reduction in invertebrate abundances. Nevertheless, the diversity was not substantially changed in these sites.

5.5.2 *Ichthyic communities*

A total of thirteen *taxa*, six of which were Cyprinidae, were recorded. This family, besides barbel (*Barbus bocagei*), includes three Iberian endemisms (Iberian nase – *Chondrostoma polylepis*, Portuguese roach – *Ch. macrolepidotus*, chub – . *Squalius carolitertii*), and two introduced species (goldfish – *Carassius auratus* and gudgeon – *Gobio gobio*). *Cobitis paludica* was also recorded. Aside from these, two other exotic species were recorded: eastern mosquitofish (*Gambusia holbrooki*), and the centrarchid pumpkinseed (*Lepomis gibbosus*). The migratory diadromous fish species identified were the anadromous sea lamprey (*Petromyzon marinus*), the twaite shad (*Alosa fallax*), the catadromous European eel (*Anguilla anguilla*), and the thinlip mullet (*Liza ramada*).

The influence of floods and channelization on the abundance and diversity of ichthyic communities was not conclusive. However, Figure 10 suggests that the two types of sites (channelized *versus* non-channelized) support different communities. In fact, *Ch. macrolepidotus*, *Gobio gobio* and *Squalius carolitertii* are more represented in the reference site, whereas *B. bocagei* and *Ch. polylepis* are common in both sectors (channelized/non-channelized). The other species (including the exotic ones) are restricted to the artificial segment of the Mondego. The fish populations were discriminated by the meso-habitat in each station, which is also represented in Figure 10. A lack of inter-annual differences may be concluded from this observations, demonstrating a high resilience of fish populations to extreme hydrological events.

It is also possible to see from Figure 10 that a higher number of species exhibit preferences for the meso-habitats T and N (groyne and riprap, respectively). Similarly, a higher density of the majority of species is observed precisely in these habitats.

5.6 *Discussion*

The entire new channel created in the Lower Mondego, after dredging and re-sectioning the old one, and transforming the natural banks in extensive dykes covered by riprap, affected the heterogeneity of habitats with repercussions on different fish and benthic

Copyright © 2006 Taylor & Francis Group plc, London, UK

composition, and had a detrimental effect on species diversity (Ward & Stanford, 1983; Cortes *et al*., 2002). The lack of intolerant species (with high oxygen and low levels of nutrient requirements) in artificialized sectors was replaced by benthic communities with short life cycles which can be explained by the reduction of available or suitable habitat, especially when the channel reflects hydro-geomorphic changes as pointed out by Maitland (1990) and Erskine *et al*. (1999).

Infrequent events, which are regarded as being catastrophic because of their immediate effects on ecosystems or on human activity, are capable of leaving long-lasting traces. In this respect they can affect the organization and composition of the patchwork. In spite of resulting from strong disturbances, flood "scars" generally heal quickly; major floods do not disturb the structure and functioning of the patchwork (Bravard & Gilvear, 1996). The most impressive aspect of the effects of floods on aquatic insects is not the devastation of the fauna that occurs, but rather the remarkable ability of species to recover from such severe perturbations (Ward, 1992). The floods that occurred in the winter of 2000/2001 caused substantial alterations in the fluvial dynamics. The increased transport of solid material originated a strong sedimentation of unstable fine materials, leading to a biological impoverishment and alterations in the functioning of the system. Macroinvertebrate communities underwent a substantial reduction of abundance, with larger incidence in channelized sectors, where sedimentation was higher. Nevertheless, despite the floods, macroinvertebrate communities displayed a high resilience, as obtained by Ortega *et al*. (1991) after a flood in the basin of River Segura (Spain). Macroinvertebrates respond to spatial and temporal variability by changes in the structure of their communities. They show tremendous diversity in their life history patterns, including variation in life cycle length, developmental strategies, and seasonality of the various life history stages (Greenwood & Richardot-Coulet, 1996). Such traits explain also the seasonal variations, which were very clear in the Lower Mondego, probably because in changing environments there is a dominance of short-lived species (Hershey & Lamberti, 1998). Ichthyic communities did not show clear inter-annual or seasonal differences. Moreover, the natural hydrological disturbances seemed to produce a low impact. Roux & Copp (1996) argue that the importance of hydrological variation is necessary to complete the biological cycles and that only frequent flow peaks disrupt these communities.

6 CONCLUSIONS

It is generally known that channelization of river courses leads to a decrease in microhabitats. Therefore mitigation structures providing habitat heterogeneity must be installed immediately after channelization (Brookes, 1988; Armitage, 1995).

This study evaluated the environmental impacts resulting from regularization of the Lower Mondego river, in central Portugal. It has demonstrated the impacts of human-disturbance in the vegetation establishment at the channelized segment, with the generalized increase of exotic species richness and cover, and a native displacement of herbaceous vegetation, diverging from the riparian woody species, which has shown a high resilience to intense, but discontinuous habitat alterations.

Concerning the macroinvertebrates it was observed a clear separation between the reference site and the channelized sectors. For instance, some Heteroptera showed a preference for the modified sector. The role of channelization on the abundance and diversity of the ichthyic communities was not conclusive.

The main conclusions concerning the case study are that most of the changes in the Mondego river geometry induced more homogeneous physical and hydraulic conditions and reduced life diversity. However, the construction of a set of transversal groynes and discontinuities of the bottom elevation had an opposite effect. These results are similar to findings reported in the literature, for instance Brookes (1988) and Torre (2001).

For this particular case Vieira & Ferreira (1997) and Silva-Santos *et al*. (2004) argue that the use of groynes and riprap in the Lower Mondego was environmentally positive. All these mitigation structures in channelized reaches increase the heterogeneity of available habitats for the aquatic communities and have been applied to restore streams all over Europe (Nijland & Cals, 2000).

The study also confirmed that biomonitoring over time is a precious tool for integrated river management.

ACKNOWLEDGEMENTS

This research was partly funded by the Portuguese Foundation of Science and Technology, in the study referred as PRAXIS/3/3.1/CEG/2702/95 and POCTI/CTA/2702/95.

REFERENCES

Aguiar, F.C., Ferreira, M.T. & Moreira, I. 2001. Exotic and native vegetation establishment following channelization of a western Iberian river. *Regulated Rivers: Research & Management*, 17: 509–526.

Armitage, P. D. 1995. Faunal community change in response to flow manipulation. In: *The Ecological Basis for River Management*. D. M. Harper & A. J. D. Ferguson (eds): 59–80. John Wiley & Sons, London.

Barbosa, A. E., Alves, E., Cortes, R. M. V., Santos, P. M. S., Ferreira, T. e Aguiar, F. 2005. *Valorização Ambiental de Obras Fluviais*, Relatório 297/05 – NRE, LNEC, Lisboa, Agosto de 2005, 193 pp.

Copyright © 2006 Taylor & Francis Group plc, London, UK

Belo, J. M., Cardoso, A. H. 1993. Modelling non-equilibrium transport by unsteady flow. Proceedings of XXV Congress of International Association for Hydraulic Research, Volume II, pp. 608–615, Tokyo, Japan.

Brookes, A. 1988. *Channelized Rivers: Perspectives for Environmental Management*. John Wiley & Sons Ltd: Chichester.

Bravard, J.P. & D.J. Gilvear. 1996. Hydrological and geomorphological structure of hydrosystems. In: *Fluvial Hydrosystems*. G. E. Petts & C. Amoros (eds): 98–116. Chapman & Hall, London.

Clarke, K. R. & Gorley, R. N. 2001. *PRIMER v5, User Manual/Tutorial*. [Computer program manual]. PRIMER-E Ltd.

Cortes, R. M. V., Ferreira, M. T, Oliveira, S. V. & Oliveira, D. 2002. Macroinvertebrate community structure in a regulated river segment with different flow conditions. *River Research and Applications*, 18: 367–382.

Erskine, W. D., Terrazolo, N. & Warner, R. F. 1999. River rehabilitation from the hydrogeomorphic impacts of a large hydro-electric power project: Snowy river, Australia. *Regulated Rivers: Research and Management*, 15: 3–24.

Greenwood, M. T. & Richardot-Coulet, M. 1996. Aquatic invertebrates. In: *Fluvial Hydrosystems*. G. E. Petts & C. Amoros (eds): 137–166. Chapman & Hall, London.

Hershey, A. E. & Lamberti, G. A. 1998. Stream macroinvertebrate communities. In: *River ecology and management: lessons from the Pacific coastal ecoregion*. R. J. Naiman & R. E. Bilby (eds): 169–199. Springer-Verlag, New York.

Hood, W.G. & Naiman, R.J. 2000. Vulnerability of riparian zones to invasion by exotic vascular plants. *Plant Ecology*, 148: 105–114.

Lemos, F.O. Ramos, M.C. Rodrigues 1991. Theoretical and practical aspects in river regulation works. *Advances in Water Resources Technology*, G. Tsakiris (ed.), pp. 149–156.

Maitland, P. S. 1990. *Biology of Fresh Waters: Terciary level biology*. 2ond ed. UK: Blackie Academic & Professional.

Nijland, H.J. & Cals, M.J.R. 2000. River restoration in Europe: Pratical Approaches. *Conference on River Restoration. Institute for Inland Water Management and Waste Water Treatment/RIZA*. Lelystad, The Netherlands.

Ortega. M., Suárez, M.L. Vidal-Abarca, M.R. & Ramírez-Díaz, L. 1991. *Aspectos dinámicos de la composición y estructura de la comunidad de invertebrados acuáticos de la Rambla del Móro después de una riada (Cuenca del Rio Segura. SE España)*. Limnética, 7: 11–24.

Podani, J. 2001. *SYN-TAX 2000. Computer Programs for Data Analysis in Ecology and Systematics*. [User's Manual]. Budapest: Scientia Publishing.

Richardson, D.M., Pysek P., Rejmanek, M., Barbour, M.G., Panetta, F.D. & West CJ. 2000. Naturalization and invasion of alien plants: concepts and definitions. *Diversity and Distributions* 6: 93–107.

Roux, A. L. & Copp, G. H. 1996. Fish populations in rivers. In: *Fluvial Hydrosystems*. G. E. Petts & C. Amoros (eds): 167–183. Chapman & Hall, London.

Silva-Santos, P.M., Oliveira, S.V., Cortes, R.M.V. & Albuquerque, A.C. 2004. Natural and anthropogenic variations in a channelized water course in Centre of Portugal. *Limnetica* 23(3–4):257–270.

Torre, A. 2001. *Stream Stabilisation*. Water and Rivers Comission. Report RR 10.

Vieira, P. A. & Ferreira, M. T. 1997. "Impacte Ambiental das Obras de Regularização Fluvial do Baixo Mondego: Contributo para o seu Estudo". *Anais do Instituto Superior de Agronomia*.

Ward, J.V. & Stanford, J.A. 1983. The serial discontinuity concept of lotic ecosystems. In: *Dynamics of Lotic Ecosystems*. T. D. Fontaine & S. M. Bartell (eds): 29–42. Ann Arbor Sciences, Ann Arbor, Michigan.

Ward, J.V. 1989. *The four-dimensional nature of lotic ecosystems,* Journal of the North American Benthological Society, 8, 2–8.

Ward, J. V. 1992. *Aquatic Insect Ecology. Biology and habitat (v.1)*. John Wiley & Sons, Inc.

Ward, J. & Stanford, J.A. 1995. The serial discountinuity concept: expanding the model to flood plain rivers. *Regulated Rivers: Research & Managemen*t, 10(2–4): 159–168.

Copyright © 2006 Taylor & Francis Group plc, London, UK

Methodology and techniques for urban river rehabilitation

J.S. Rocha
Portuguese National Laboratory for Civil Engineering (LNEC), Lisbon, Portugal

ABSTRACT: The rehabilitation of urban rivers is a complex process that requires the knowledge of the adequate hydraulic techniques, and its relations with other type of interventions and constraints in the urban area and in the drainage basin. The paper describes the fundamental steps in rehabilitation of urban rivers.

For the definition of the site the three basic hydromorphological elements described in the Water Framework Directive (WFD) should be considered: the hydrological regime, the river continuity and the morphological conditions.

An extension of the strategy to recover "natural" conditions is presented: the aim is not to obtain the original conditions but rather to establish hydrological and morphological conditions that support all river functions. If this process is not scientifically sounded, the probability of achieving long-term self-sustaining river system will be compromised, as new problems will appear in the future and additional interventions will be maintained in the "new" river.

1 INTRODUCTION

The rehabilitation of urban rivers is based on the application of adequate river techniques. At same time, the use of river techniques must be in accordance with other type of interventions on urban areas.

When the river channel has not suffered significant modifications on urban areas only measures for river basin are to be used. Rarer is the case where there are no modifications in the river basin; this may happen when an urban area is situated near a large river, where only the interventions on river channel are done, and the urban area is a small percentage of the entire river basin area. In this case only measures on river channel and banks are needed. The general situation is to apply both types of measures.

This paper briefly describes the fundamental steps in rehabilitating urban rivers, according to the URBEM project activity chart: site definition, formulation, strategies and the development of technical options for urban river rehabilitation, description of consequences of urban river rehabilitation and the monitoring of rehabilitated urban river. This is a subset of the more general river rehabilitation, well documented in several works in last decade, such as FISRWG (2001) and Doll (2002). The specific case of urban river rehabilitation may be found in Tourbier *et al.* (2005).

The objective of the URBEM research project was "*to develop innovative urban watercourse rehabilitation techniques for use in future schemes*". The rehabilitation of urban rivers includes the knowledge of adequate techniques and its relations with all needed type of interventions, both before and after the implementation of techniques. The technical interventions are divided in two main groups: interventions to be practised in the drainage basin, controlling the hydrological processes, and interventions to protect, maintain and improve the hydromorphological conditions in stream channels (controlling the hydraulic processes in bed and banks).

2 SITE DEFINITION IN URBAN RIVER REHABILITATION

The site definition within the URBEM case studies has displayed both subjective and methodological approaches. In most case studies, about 70%, the sites were defined with existing knowledge, no selection method being applied, Schanze *et al*. (2005).

In the remaining case studies, the site definition is based on a selection method. But these definitions have been determined by three different specific and complementary reasons: city wide, river network based or basin wide assessments.

The site definition will be made by two different main processes, related with the main scope of the intervention, being therefore associated with the technical aspects of river rehabilitation.

One of the main processes is focussed in the river itself, although some urban aspects are necessarily included. In this process the driving forces are on the River Basin Administration or equivalent institutions.

Copyright © 2006 Taylor & Francis Group plc, London, UK

The main object is to rehabilitate the river, situated in an urban area, taking into consideration the target, i.e. a better river, and by consequence also a better urban in the adjacent area, as well as better banks and flood valleys. In this case, it is natural to find an emphasis on the river techniques. A joint work with city administration is needed.

The other main process is focused on the urban rehabilitation near an existing bad river. The main object is to rehabilitate the city, situated near a river, taking into consideration the target a better city, and by consequence also a better river passing there, with its banks and flood valleys being seen as urban zones. In this case, it is natural to find an emphasis on the urban techniques. A joint work with River Basin administration is needed.

The site definition for these two main processes is not the same, although some aspects are necessarily present in both.

When the rehabilitation of an urban river is initiated, it is necessary to define the river reach. There are not strict rules to define the site where the rehabilitation is to be implemented.

However, using the Water Framework Directive (WFD) terminology, it is possible to establish simple criteria to define the site where the rehabilitation is to be done. Considering the type and intensity of efforts to be used in the rehabilitation it is possible to differentiate the type of intervention, and consequently the site definition.

The first basic distinction is the

1 Instream river rehabilitation;
2 River basin rehabilitation (either including or not the instream).

The instream river rehabilitation is concentrated on the main channel, and on its lateral adjacent zones where the flood pass. The site definition comprises, at least, the definition of the downstream and upstream cross sections. This is relatively straightforward but only an expert in flow regimes can find the appropriate cross sections to tackle the hydraulic aspects.

The definition of the adjacent areas, equivalent to the flood prone area, is relatively more difficult, being advisable to use a step by step approach, unless previous data gives directly the right definition. An accurate definition is costly and time consuming. At a first guess a rough definition may be done with the analysis of geomorphology and geology maps, or with the help of the inhabitants, by knowing the history of past river floods, or by analysing existing flood marks.

The other more accurate definitions for the flood prone area will be done based on hydraulic modelling of present, past or future situations. The hydraulic modelling needs good river data to guarantee reliable results. The calibration and validation of hydraulic modelling will be vital because it is the only way to succeed in the proposed river rehabilitation.

For hydraulic modelling, it is necessary to define the contributing river basin. That definition is only required to determine the river discharge to be used in the computation. In some cases the river basin is entirely outside the urban area, whereas in other cases, it is precisely the opposite, i.e., all the area is in the urban area. These two limiting cases are quite different, as far as the implications to the study are concerned. The latter case may generate a chain of scenarios for the reciprocal influence of river basin and instream.

The river basin definition is relatively simple, from a conceptual point of view, it consists of determining the river basin boundaries, where the river processes are generated and transported to the river channel. Indeed, the river basin, a spatial area where complex physical, chemical and biologic processes are generated and transmitted downstream, may also be viewed as a network of small streams going from the river basin boundaries downstream to the lower cross section where the river basin is defined.

In URBEM, it was proposed that the definition of the site should include the three basic hydromorphological elements described in WFD: the hydrological regime (quantity and dynamics of water flow and connection to groundwater bodies), the river continuity and the morphological conditions (river depth and width variation, structure and substrate of the river bed and structure of the riparian zone). Therefore for the site definition it will be necessary to gather all pertinent data related with the above mentioned elements. As each element may impose different types of control and influence on the river system the site limits may not be unique. Consequently, it is not easy to obtain general and simple criteria to help find the border cross sections for the site.

The river basin definition in an urban area may be complex, the sub basins being difficult to find, and the relations between surface processes and under ground networks generating and transporting to the river channel both water and different pollutants, which are not entirely identified for all areas.

In most cases, the river basin is entirely within the urban area. The development of the urban areas creates pressures on river. The WFD also imposes "*the collection and maintenance of information on the type of the significant anthropogenic pressures to which the surface water bodies in each river basin district are liable to be subject*" (Annex II, 1.4).

3 FORMULATION OF RIVER REHABILITATION

The following three steps are recommended to formulate the urban river rehabilitation: 1) to assess the

Copyright © 2006 Taylor & Francis Group plc, London, UK

present situation, including the river basin and the river channel and bank elements; 2) to assess the previous situation, by two alternative ways – (i) the real previous river regime is obtained by gathering a data base and historical facts and documents or (ii) a previous reference situation is obtained by comparison of neighbouring unchanged river basins or by theoretical reasoning and 3) to compare both situations in order to obtain the synthesis of the modifications imposed, during all history, by the presence of urban areas in the river basin.

The identification of the modifications occurred on the river is the basis to define the interventions to be applied to the river rehabilitation.

From the knowledge of hydrological regime and the discharges for different time and space situations, it is possible to characterise the flow conditions in the river channels.

The characterisation of channel flow processes is to include the characterisation of bed and banks and the hydraulic structures. The only way to collect the required data is to survey the site. For important structures the design documents should be referred to, in which hydraulic computations may be included.

To characterise flow regimes and modification of flow regimes in urban areas, the main definitions of physical processes in rivers may help to define spatial and time-scale boundaries. The characterisation of flood plains in rivers is related to the definition of lateral boundaries. The urban drainage systems on rivers provide information on the urban systems that, to some extent, are boundaries for the river system.

The definition of spatial extension of the assessment is to take into account the relative spatial scale of the river and urban areas. In the URBEM project it is recognized that "*river width is a geometric parameter that has a strong influence on the interrelationships between the river and the city. It influences the scale of the river corridor and the waterfront and its uses, the accessibility network, the transponibility, traffic and many other factors in the urban/watercourse environment*".

Indeed, the scale and size of an urban watercourse within the urban morphology is a very important relationship. The river width has been chosen in the methodology of classification of the aesthetic values as one of the starting items for selecting the case study, due to its relevance in the urban context.

The width of a river is a good measure of the importance of a river, and is strongly correlated with many aspects of river system and river basin upstream feeding water, sediments, and other water constituents. It is possible to present an available quantification of the river characteristics based on the order of the rivers. It was observed that the order of the major part of the rehabilitated rivers is between fourth (IV) and ninth (IX) orders. That means with river basin areas and river lengths ranging from 2 km^2 to 300 km^2 and from 2 km to 50 km, Rzhanitsyn (1960).

The modifications in the river net are highly dependent on the space scale of the two areas, the river basin area and the urban area. In urban river rehabilitation, different cases can occur, and for each case different spatial extents of assessment are necessary, Rocha & Alves (2004).

Case 1 – Urban area much smaller than the river basin

The consequences for river modification, during past times, are minor except on the part of the catchment area where the urban area is settled. In this case, only a part of the river may be changed during the past.

Case 2 – Urban area covering the major part of the river basin

The urban influence on the river may be more or less important depending on the location of the urban area is located in the catchment. If the urban area is in the upstream part of the catchment, it might significantly alter the river network in the whole catchment, not only in the urban area, but also in the downstream part. If the urban area is in the downstream part of the river network the consequences to downstream will not be felt, and the urban area will receive a natural river network in the upstream border.

Case 3 – Urban area covering the entire river basin

In this case, usually the river net becomes completely artificial. Indeed, the large towns may occupy more than one river basin. The spatial extension of the river basin is practically coincident with the urban area.

The river network may be extremely disturbed in orders I and II of the stream, because the urbanisation might have destroyed the natural river network. Artificial channels for mixed sewage system and storm water system are built and they quickly drain water from non-permeable urban areas. Many streams have a very limited water flow. Since artificial piping systems and culverted streams have a lower permeability, during some flood events the roads may change into temporary streams. Consequently, the definition of boundaries, either in river network or in river basin areas, is not straightforward in heavily occupied urban areas. The careful analysis of detailed maps and field surveys are needed for a good definition of boundaries for river rehabilitation in urban areas.

In the river environment, the time scale is associated to the river size. The hydrologic processes in a river have times dependent on river basin size. For very small river basins, the significant times range from a few minutes to a few hours. It means that the rain events and associated flow discharges are running in times of order of rain event time and its multiples. For small river basins, the hydraulic events have generally times less than one day. The peaks of river discharges are sharp in a time-discharge graphic and the water level variations along time are fast.

Copyright © 2006 Taylor & Francis Group plc, London, UK

Same processes in larger river basins have a similar variation type but now considering time values increasing from hours to days as the river basin size increases.

However, the presence of two extreme seasonal conditions, the wet period with a large amount of rain, and the dry period with absence or small amount of rain, leads to consider a second time scale for analysing the hydrologic and hydraulic processes, the seasonal variation, and also the monthly variation of hydrologic and hydraulic parameters.

The hydrologic and hydraulic processes vary also year from year. That variation will be analysed in long term time series, with a monthly or daily discrimination.

The river alluvial beds are moved by the successive river regimes along the years. For that particular analysis, it may be necessary to consider even larger time scales, being possible to arrive to centuries as a basis for the definition of river bed trends in the past, and also for the future.

The conclusion is the need to include multiple times scales to set the time boundaries of river rehabilitation. The time scales in river processes are accompanied by equivalent time scales in urban activities: from short time activities, such as emergency actions during dangerous flood events, to daily actions in the everyday life of a city, like garbage collection, cleaning of streets and of river banks; seasonal actions like flora activities; yearly actions like planning, building activities; and finally, to average and long term activities like urban plans or trends in society.

Consequently, the definition of time scales of plans and of detailed projects for river rehabilitation may be different. All time scales will be included in comprehensive river rehabilitation projects, to avoid overlooking any important subject. In small river rehabilitation projects, with some few details in river and urban parts, only one time scale can be used, as for instance in a small intervention in a cross section of a river, where there is only enough instantaneous flood discharge for the project. But, for the same example, if an alluvial river bed is present, it will be advisable to consider the time scale for long period analyses, such as a few decades trend.

If besides a physical intervention, on the hydromorphological features of an urban river, other interventions are performed on the water quality and on the ecological elements of the urban river, it will be necessary to include year time scales. The latter are to cover the daily river discharge variations along the year, or years, because both river processes are very sensitive to river discharge variations and also to the variation of climate parameters (temperature, radiation) along the year.

After the definition of spatial and time boundaries, it is possible to determine the resources for assessing and formulating river rehabilitation. For smaller space scales and longer time scales, the needed resources will be more significant. Of note is the fact that since, in general, different expertise fields are associated to different time scales, multi disciplinary teams will be used in the analysis of river problems.

In the proposed methodology the definition of success indicators and acceptability criteria will be included in the formulation of river rehabilitation.

4 STRATEGIES FOR RIVER REHABILITATION

The main technical strategies for the urban river rehabilitation, or for urban rehabilitation including a river, are the interventions at one or more levels, considering the rationale of the WFD:

- Hydromorphological;
- Water quality;
- Biological.

Also the intervention may be done in one or more of the following situations:

1. Instream river rehabilitation;
2. River basin rehabilitation;
3. Urban area rehabilitation with some or all components of passing rivers.

The strategies for urban river rehabilitation must include the appropriate isolated or combined types of interventions to rehabilitate river and urban areas together, Rocha (2005).

The fundamental question concerns the strategy for the river rehabilitation. Is the aim to renaturalise the river just as it was before the urbanisation? In Europe, this means that there is the intention to recover centuries of history. Only in rare cases this is an attainable strategy.

The most common strategy is to restore some aspects of the previous river environment. The main scope of river rehabilitation must be to obtain good combinations of interventions to restore as much as possible the "natural" conditions of the river.

The "natural" river conditions are very difficult to define. A relative broad set of conditions is possible, which turns it into a fuzzy concept. Consequently, even in a team of river experts, different strategies will be raised, and therefore, it will easy to find different parallel strategies. The combination of strategies for the river itself with other strategies of urban rehabilitation, when applicable, leads to numerous options for the rehabilitation.

Mention must be made of the fact that it is possible to consider an extension of the strategy to recover "natural" conditions: not to obtain the original conditions but rather to obtain completely new conditions where

Copyright © 2006 Taylor & Francis Group plc, London, UK

the natural forces and processes are used to "create" a river environment like the natural one. We may rather designate this river rehabilitation more as "river creation". When this process is not scientifically sound there will be problems to solve in the future, because additional interventions will be needed to maintain the "created" river. The problems may arise easily in the morphological interventions and in the ecological interventions. The corrections for the first one tend to be costly, when compared to the second one. Moreover, the interventions in the water quality are easily done and with lesser doubts in the results, although they can have higher costs when compared with the other two.

The physical constraints are yet to be identified. There are different types of physical constraints: some are associated to the river channel (like minimum or maximum admissible hydraulic parameters, singularities on the river bed, compliance with water quality standards, ecological maintenance, etc.) or to the river basin (permission on or not to carry out water transfers, maintenance or not of some land covers, etc.). Other constraints are associated with urban features (historical buildings or infrastructures, administrative subjects, social status, etc.). Some of the constraints are self explanatory, but others are only known by expertise studies. This sets the ground for debate, because these do not seem to be constraints for some in opposition to others. Again, the identification of constraints is a multidisciplinary work, and the final list of constraints is not a straightforward task, but rather an iterative task, implying some consultation outside the teams, Rocha (2004a).

In URBEM project, a minimum of 29 parameters was proposed to deal with techniques for river rehabilitation. They are divided in 23 related with WFD, 3 with social aspects and 3 with economic aspects. The 23 ecological parameters are divided into 11 for hydromorphological aspects, 8 for chemical aspects and 4 for biological aspects, Tourbier & Gerdorf (2005).

The proposed parameters generally agree with the parameters and indicators proposed in other aspects of rehabilitation interventions, such as success indicators and monitoring.

5 DEVELOPMENT OF TECHNICAL OPTIONS FOR URBAN RIVER REHABILITATION

5.1 *Identification of technical options*

The identification of technical options is mainly an expertise task to be done by a multidisciplinary team covering a large spectrum of skills. Even in the case of a small in stream intervention, a broad overview of different aspects shall be taken into consideration, namely the imposed constrains by the presence of the city, and the public participation, saw as input of data and assistance to decision-making.

The maximum of technical intervention is associated to the description of the consequences. The modelling of consequences is essentially a technical aspect.

To obtain a good set of potential options professional advice must be seek when drawing up a list, Rocha (2004).

Within an urban context there are often constraints that limit the potential for river rehabilitation. The situations that can potentially arise are so diverse that it is not possible to list all the potential constraints that have to be considered.

The following two steps are recommended to identify options for urban river rehabilitation:

1 To choose the measures to be designed for the river basin or/and river channels and banks. The measures have the effect of recovering the previous situation. The more common attitude is to mix measures in an appropriate balance, in order to minimise disturbances to the consolidated urban areas and costs.
2 To design the measures chosen to quantify the interventions, the amount and type of work, costs, duration of the intervention, and so on. The quantification of costs and the detailing of the intervention may raise important questions leading to new choices of measures or to new design for measures. Iterations are expected until a consensual design is obtained.

The assessment of deviations from an ideal state is the basis for the conceptualisation of the rehabilitation of the current urban rivers. Known the actual urban rivers and defined the goals for the interventions, a general procedure will be defined for the interventions in the stream channels, considering that other types of interventions may be simultaneously present at same time.

Measures for a drainage basin and a river site need to be combined in turn, forming "treatment trains" of measures that supplement each other to meet planning targets. The conceptualisation is followed by a pre-design and a final design for construction, in which the measures are designed to meet the particular conditions of a site.

The classical solutions are described in many Manuals and may be quantified. The quantification of the elements of the solutions is essential to determine the likely costs.

To achieve the "good ecological potential" of urban streams a new approach is required. A more natural approach needs to be taken to manage and design channel form and function. In the past, many rivers were stabilised and hardened with concrete and steel

Copyright © 2006 Taylor & Francis Group plc, London, UK

in order to accommodate navigation and to protect urban uses from flooding and erosion. River shorelines were typically designed for a single purpose. Today, there is a growing support for ecology and multiple uses as well as an interest in using "soft engineering" of shorelines at appropriate locations. Such an approach incorporates flood conveyance concerns, aquatic habitat, riparian habitat, water quality, recreation and aesthetics.

Stream bank protection designs that include vegetation satisfy these multiple objectives. Natural channel design can be well accomplished with soil-bioengineering measures that use a combination of living plant material and mechanical means to achieve specific engineering functions.

However the "soft engineering" has limitations and the classical river engineering must always be present in most cases, because some types of measures do not have alternative.

The specifications of the river engineering interventions are divided in five groups considering different aspects of the rivers.

The first group is dedicated to an important characteristic of the urban rivers: these were in the past confined by revetment of the natural riverbed and riverbanks, being in extreme cases covered by panels, which completely hid their presence.

The three following groups are based on the three main views of the rivers: cross sections (bed and banks), longitudinal profile and plan form.

Finally, in the last group some singularities are considered, most of them related with infrastructures like bridges and hydraulic works.

The identification of options will run the different aspects of the actual river status to design the future and desirable status, according to the previously defined objectives.

5.2 *Bank and bed protection*

In hard paved river beds, a layer of natural substrate can be placed on the existing lining or might completely replace the artificial material. Sand, gravel and cobble are placed into the wetted perimeter of streams that are lacking this bed load. The goal is to protect the channel bed from further degradation, to increase habitats for aquatic life forms and to provide spawning areas for some fish species. Sediments, corresponding to the natural size and shape composition are the preferred bed material.

The main interventions on river profiles are done to decrease the bed slope or to decrease only the water surface slope, maintaining the bed slope. The alternative of increasing the bed slope is much rarer, unless in very short lengths, associated to the general decrease of river bed.

The more common option is rock slope protection. This kind of protection, called riprap, consists of rock pieces placed upon the embankment. Rock, as a slope protection material, has a number of desirable features which have led to its widespread application.

Another common flexible type of armour protection is the gabion. Gabion revetments consist of rectangular wire mesh baskets filled with stone. There are two types of gabions: wall type and mattress type. In the wall type, the empty cells are positioned and filled in place for walls in a stepped fashion. Wall type revetment is not fully self adjusting but has some flexibility. When the gabion has a small height (thickness) it is designated by Reno mattress. This confers a relatively high flexibility, very important to suit to bank movements.

Point protection is performed at pockets along stream banks that pose problems. Point protection is an efficient method that can harvest fluvial processes, leading to the deposition of gravel that modifies flow to improve the hydromorphology of streams.

Their influence often extends to untreated portions downstream. Vegetated nodes have a habitat improvement function that can be combined with architectural features in urban areas.

5.3 *Training structures*

One alternative technique is a training structure (groin) or equivalent structure. Training structures, inserted in the river channel, control the direction, velocity, or depth of water flow. They control scour on banks by deflecting the currents. Some of the training structures are linked to the banks and act as protection to the bank. A groin is an elongated artificial obstruction projecting into the stream from bank to control scour by deflection of currents. There are two main types of groins: permeable and impermeable.

5.4 *Transversal barriers*

Timber logs and/or rocks creating a transversal barrier. Like other transverse structures it collects and retain gravel for spawning habitat, deepens existing resting/jumping pools, creates new pools above and/or below the structure and promote deposition of organic debris. Sills also hinder scouring of the channel bed and stabilises it. They are appropriate for degrading rivers, preventing the evolution of degradation. The result is a decrease in the river bed slope.

There is another type of transversal barriers acting mainly on the water depth, not trying to influence the river bed slope. However, they may also have some influence on river bed deposition, for the cases where these conditions occur. A set of these transverse structures creates a cascade of pools, producing, for instance, a permanent water table for all river discharges, even for the minima, in dry period. They are appropriate for mild rivers, where the river bed

Copyright © 2006 Taylor & Francis Group plc, London, UK

evolution is not a problem. The result is a decrease in the water slope for low discharges. For flood discharges they may have a minor influence, because they are submerged without inconvenience.

5.5 *Dredging*

Another type of intervention is dredging of river bed. This action may recover the flow capacity of cross section. The dredging is associated in general with an increase in river bed slope, because the dredging removes the excess of deposition, associated with a trend in decreasing slope.

The useful life of dredging depends on the sediment transport dynamics. The isolated dredging does not modify the sediment yield, and some time forward the river will return to the same bed level. However, for certain local conditions this may be an economic and justified intervention. Some care shall be put on the maintenance of plantonic habitats, and on the stability of river banks.

5.6 *Interventions in the river plan form*

It is very difficult to define the type of interventions in the river plan form, because there is a large spectrum of possibilities. The natural plan forms are controlled by complex relationships between river discharge regimes, sediment supply and geological formations. The presence of urban settlements strongly changed those interrelationships. The interventions to modify the plan forms, from the present situation to a more natural situation, are subject to reduced technical options because the rehabilitation based on geomorphologic criteria continues to be restricted by urban reality.

The rivers have natural bends, the presence of natural long righteous reaches being rare. The definition of the plan form is dependent on the form of the river valleys, and is conditioned by geologic, urban (like buildings and bridges) and hydraulic factors.

Of note is the fact there is a trend to create sinuosity only to provide a good landscape. However this approach needs to be based on valid technical criteria, unless strongly fixed banks are built and sediment supply is not intense.

5.7 *Soft interventions*

Methods of soil-bioengineering play a central role in nature like in slope stabilisation and in river rehabilitation and revitalisation. Soil bioengineering structures are based on synergies of living plants and dead materials as stones, timber or geotextiles and auxiliary objects. These structures are intended to create stable native riparian vegetation, which sufficiently protects riverbanks and improves the landscape, aesthetics and ecology, Faber (2004).

Working with living native plants in river regulation schemes has a long tradition. The utilisation of tree spurs was documented in the Roman Empire. Although none of the current technical machinery and constructions existed in the Middle Ages, durable protection of waterways was achieved with natural and living materials.

Aquatic habitats are highly dependent on the quantity and dynamics of water flow. Aquatic habitat provides cover, food, nesting and spawning sites; shelter and escape cover for fish, amphibians and other wildlife. Habitat protection and improvement refers to in-stream conditions and to riparian habitat. Both are interrelated. Vegetation on the water edges provides shade and an input of leaves that directly affects the quality of the aquatic habitats. The riparian habitat, as a transition area between terrestrial and aquatic environment, is particularly rich in life forms. In-stream habitats such as gravel riffles, deep pools, driftwood piles, sandbars, and boulder clusters are points of interest to any sport-fisherman's association, which often willingly organizes to support improvements. These measures include fish ladders, fish passage improvement and removal of migration barriers.

6 DESCRIPTION OF THE CONSEQUENCES OF URBAN RIVER REHABILITATION

To guarantee the success of the rehabilitated urban river it is necessary to characterise the hydraulics of the urban river, before and after rehabilitation, and to know the sediment transport entering in the reach. The geometric characteristics of the cross sections, the longitudinal slope and the discharges running in the reach are the basic parameters to collect and to analyse. The comparison of the flow behaviour before and after rehabilitation is the basis for describing the consequences of urban river rehabilitation.

The adequate values to be considered in the description of the consequences of technical options will be minimum discharge, possibly zero; a set of three discharges between minimum and bankfull discharge; the bankfull discharge and a few flood discharges (for instance T = 5, 10, 20, 50 and 100 return period years).

The flow depth may be computed by simple hydraulic equations, such as Manning or Strickler equation, or other empirically derived equations for computing the average flow velocity, assuming uniform and turbulent flow conditions, for simpler cases.

For estimating the shear stress, simplified equations are with the channel slope S, as an approximation of the actual energy grade J, to be used when available. It is possible to use h (flow depth) instead of R in wide flows, when the channel width exceeds the 30 fold of the perimeter.

Copyright © 2006 Taylor & Francis Group plc, London, UK

From all data available, it will be possible to compute the sediment transport capacity. It is very important to note the differences between capacity and actual sediment transport. The actual sediment transport is the lesser of two situations: the capacity if the incoming sediment load is higher or the incoming sediment load if the capacity is higher.

The sediment transport capacity may be computed by a large number of equations. This is a very specific technical work to be done by experts.

In sediment river bed there will be complex flow dynamics and erosion/deposition sequences, both being a vital part of the flow regime. On urban rehabilitated rivers, these natural processes are to be maintained to a certain extent, even in the cases of a completely artificial mobile river bed.

The computation of water levels is much more difficult on natural river beds because there are strong variations in roughness coefficients during a passage of flood wave. This will also be a job for experts on river hydraulics to guarantee successful interventions.

For lower velocities, when there is no sediment transport in the river bed, the roughness is only controlled by the grain size of the bed material. For larger discharges there is sediment transport in river bed originating bed configurations, like dunes and ripples, and the adoption of a representative of roughness is much more difficult.

The meanders are the most common plan form in rivers. The plan form of meanders can be approximate by cosine functions. The definition of the axis of a theoretical meander may be obtained by knowing the minimum curvature radius and the meander length along the axis.

The time scale has also some importance. There is the river time scale, where the seasons are a mark of the rivers. The important transport phenomena in rivers are associated with large discharges, in rainy season. On the other hand, the intervention on the river will be done during the low water period.

All computations will be done in accordance with the data available, the stage of the project and the complexity and size of intervention. The heavy computer computations are only to be used in complex and large river rehabilitation cases, simplified computing approaches being enough for most cases. Additionally, the heavy computations will be accompanied by good observation data to calibrate and validate computations. It is non sense to use heavy computations without enough data to calibrate the models.

The computations of present and future status of the urban river are the basis to describe the consequences of options. In computations the use of past experience in river behaviour and in river processes are determinant to obtain good results.

The theoretical analysis of the consequences of urban river rehabilitations will be compared with the behaviour of the river after implementing the rehabilitation. This comparison should always be done to detect deviations from the initial objective, and to define possible corrections and also to confirm the appropriateness of the theoretical analysis used.



Figure 1. The urban River Fervença (Bragança, Portugal) before rehabilitation (view from right bank).



Figure 2. The urban River Fervença (Bragança, Portugal) after rehabilitation (view from centre of river).

LNEC was involved in the analysis of the consequences of successful urban river rehabilitation in river Fervença, in Bragança, Portugal, Figures 1 and 2.

In this case it was obvious the need to verify the behaviour of the river after the rehabilitation to introduce a small additional intervention.

7 MONITORING OF REHABILITATED RIVER

The effectiveness of a project is determined by comparisons between pre- and post-development conditions, and by applying evaluation criteria through indicators of success. The monitoring costs involved are money well spent when findings are disclosed and used in order to convince the public and its representatives

Copyright © 2006 Taylor & Francis Group plc, London, UK

that the projects financed with the taxpayer's money have been a success.

In an optimal case, the lessons learned during the monitoring process are utilized in revising the intervention and the operation of controllable systems.

There are technical reasons to reinforce the need to monitor in the stream channels. Indeed, the rivers are subject to large flood events that involve strong forces in all river bed and river bank founded structures and put in motion the alluvial beds. The large mobility of the rivers imposes a careful monitoring plan.

In the urban river projects the monitoring programme will provide data to follow up the performance of the intervention measures. The appropriate parameter will be identified for each measure. The natural choice of parameters is the set of controlling parameters referred to in 4, but additional parameters may be considered necessary. The sites to monitor are related with the intervention places, some cases inside the boundaries the intervention, other cases outside the boundaries. In general, all parameters will be monitored before and after implementation. In more dynamic or sensible phenomena it is also justified to monitor during implementation.

The methods and patterns of monitoring are associated with the existing know how of each parameter observation. For some of them there are international accepted standards.

The decisions inherent to the non-compliance of pre defined objectives will also be incorporated in the monitoring programme. The decisions may be divided in regular or every day simple decisions, occasional and complex decisions, to be studied carefully when occurring, and urgent or alert decisions when critical or dangerous occurrences happen. All types of decisions may be anticipated, mainly the most dangerous one or most irreversible situations.

In WFD the monitoring has the following objectives: surveillance, operational and investigation.

The monitoring in urban river rehabilitation interventions is more related with the operational monitoring defined in WFD.

Operational monitoring shall be undertaken in order to:

- establish the status of those bodies identified as being at risk of failing to meet their environmental objectives, and
- assess any changes in the status of such bodies resulting from the programmes of measures.

In operational monitoring, enough points will be chosen in order to assess the magnitude and impact of the hydromorphological pressures.

In URBEM project the following hydromorphological controlling factors, or parameters, were proposed for the techniques of urban river rehabilitation, Table 1.

Table 1. Hydromorphological controlling factors in urban river rehabilitation techniques and monitoring frequency.

Parameter name	Descriptor	Monitoring frequency
River discharge	Q	Continuous
River slope	S	6 years
Subterranean discharge	Q_{sub}	3 months
Head loss	ΔH	6 years
River depth	H	Continuous
River width	B	6 years
Median grain size of aluvionar bed	D_{50}	6 years
Median grain size of aluvionar bank	D_{b50}	6 years
Cross sections	Z(x,y)	6 years
Sediment transport capacity of river	Q_s	6 years

Other controlling factors are: physico-chemical, biological, social and economic. The first group include the thermal conditions (T), oxygenation conditions (O), salinity (Sa), acidification status (pH), nutrient conditions (N), turbidity (T_u) and pollution by other substances (P_{ss}) all with a monitoring frequency of 3 months, plus pollution by priority substances (P_{ps}) with 1 month for monitoring frequency.

The biological controlling factors are the compositions and abundance of aquatic flora (CA_{af}) and benthic invertebrate fauna (CA_{bif}) plus composition, abundance and age structure of fish fauna (CA_{ff}) and also riparian vegetation (RV) all factors with 3 years as monitoring frequency.

The social factors are the flooded area (F_a) and the flood risk (H_fV_f), both having a 6-year monitoring frequency.

Lastly, the economic factors are the flood damage cost (FC) and the annualized maintenance cost (MC) respectively, with 6 and 3 year monitoring frequency. The maintenance of interventions will be done based on monitoring results.

For operational monitoring, the frequency of monitoring required for any parameter will be determined by Member States so as to provide sufficient data for a reliable assessment of the status of the relevant quality element. As a guideline, monitoring should take place at intervals not exceeding those shown in the Table 1 unless greater intervals would be justified on the basis of technical knowledge and expert judgement.

Frequencies will be chosen so as to achieve a level of confidence and precision. Estimates of the confidence and precision attained by the monitoring system used will be stated in the river basin management plan.

Monitoring frequencies will be selected taking into account the variability in parameters resulting from both natural and anthropogenic conditions. The times

Copyright © 2006 Taylor & Francis Group plc, London, UK

at which monitoring is undertaken will be selected so as to minimise the impact of seasonal variation on the results, and thus ensure that the results reflect changes in the water body as a result of changes due to anthropogenic pressure. Additional monitoring during different seasons of the same year will be carried out, where necessary, to achieve this objective.

The implementation of the option for urban river rehabilitation will be linked with the implementation of monitoring. Indeed, some of the monitored parameters will be obtained in advance; consequently the monitoring implementation will precede the river rehabilitation, in order to compare the present and future situation.

The time interval between first data, obtained before the river rehabilitation, and the data obtained after the completed river rehabilitation, depends on the decision process, being difficult to reach a consensus among a great number of entities involved in the decision-making process. In general, there is enough time in the decision-making process to be possible to implement in advance the monitoring program.

Monitoring reports will provide opportunity to disseminate any lessons learnt from the behaviour of rivers responding to the rehabilitation.

Besides the correct technical presentation of the results, according to the previous frequency of reporting, the presentation of monitoring results will include a classification of ecological status and ecological potential, as well as chemical status. The latter presentations are defined in WFD.

For urban river rehabilitation the same procedure may be applied, extending the classification to all significant elements of intervention, including also the hydromorphological elements and other structural and non-structural aspects of the intervention.

Indeed, most cases of urban river interventions are to be done in heavily modified and artificial water bodies, where the ecological potential classification will be represented by the lowest of the values for the biological and physico-chemical monitoring results for the relevant quality elements classified in four classes.

The same type of presentation for the compliance of WFD may be adapted and added to cover the case of urban river rehabilitation. The colour codes may be inserted in parts of the river intervention, considering not only the elements included in the WFD, but also all relevant elements specific of each intervention.

ACKNOWLEDGEMENTS

This research was partly funded by the European Commission, in the project URBEM (Urban River Basin Enhancement Methods), EVK-CT-2002-00082.

REFERENCES

Doll, B, Grabow, G., Hall, K., Harman, W., Jennings & Wise, D. (2002) Stream restoration. A natural channel design handbook, North Stream Restoration Institute, U.S.A.

Faber, R. (2004). New techniques for urban river rehabilitation. Specifications for new materials and techniques. Improve instream morphology. Soil bio-engineering. Specifications. Deliverable 8.2 URBEM. Vienna, BOKU.

Federal Interagency Stream Restoration Working Group (2001). Stream corridor restoration. Principles, processes, and practices. USDA – Natural Resources Conservation Service, U.S.A.

Rocha, J. (2005). New techniques for urban river rehabilitation. Methodology. Deliverable 8.1, URBEM. Lisbon, LNEC.

Rocha, J. & Alves, E. (editors) (2004). New techniques for urban river rehabilitation. How to re-naturalise flow regimes. Recommendations Deliverable 8.1. URBEM, Lisbon, LNEC.

Rocha, J. (2004a). New techniques for urban river rehabilitation. Incorporation of wetlands, floodplains and sustainable urban drainage methods into urban schemes. Recommendations Deliverable 8.2, URBEM, Lisbon, LNEC.

Rocha, J. (2004). New techniques for urban river rehabilitation. Specifications for new materials and techniques. Improve instream morphology. River engineering. Specifications Deliverable 8.1, URBEM Lisbon, LNEC.

Rzhanitsyn, N.A. (1960). Morphological and hydrological regularities of the structure of the river net. Translated by Krimgold, D.B., U.S. Department of Agriculture, Original Gidrometeoizdat.

Schanze, J., Olfert. A., Tourbier, J.T., Gersdorf, I. & Schwager, T. (2005). Existing urban river rehabilitation schemes. Deliverable 2.1, URBEM, Dresden, Germany.

Tourbier, J.T. & Schanze, J. (Eds) (2005). Indicators of success in Urban River basin Enhancement metohods, Deliverable 10, URBEM, Dresden, Germany.

Tourbier, J.T. & Schanze, J. (Eds) (2005). Urban River Rehabiliation, Proceedings International Conference on Urban River Rehabiltation, URRC 2005, September 2005, Dresden, Germany.

Copyright © 2006 Taylor & Francis Group plc, London, UK

C.4. Management of risk associated to floods and man-induced river hazards

Copyright © 2006 Taylor & Francis Group plc, London, UK

Flood management system – A newly developed instrument based on WebGIS and CMS and the improvement of basis data

A. Koch, M. Tzschirner & R. Jüpner
Institute for Water Management and Ecotechnology (IWO), Department of Water and Waste Management, University of Applied Sciences Magdeburg, Germany

ABSTRACT: The recent flood events in Germany on the River Rhine, Oder and Elbe, the responsible public authorities were forced to find new strategic ways to handle flood events more efficiently. Results of the floods showed that in spite of increasing technical flood measures, the damages are also rising. Instruments that therefore combine solutions for flood prevention and operative flood protection measures are helpful. Regarding this aim, a "Flood Management System" (FloMS) has been developed, which satisfies the duties and expectations of the responsible regional actors in case of emergency and flood prevention. FloMS consists of two main parts: the GIS and WebGIS for spatial information like flooded and flood-prone areas including flood scenarios and the Content Management System (CMS) for non spatial information. A major output of the project is the creation of different kinds of maps showing the hazards, the potential damage, special risks etc. for defined flood events. Those maps are applied for flood prevention measures and during flood events especially on a local scale. The available basis data, particularly the digital elevation model, had to be improved by additional data. Important line objects as dykes, streets and railways were acquired and implemented in order to run dyke breach simulations, which are e.g. basis for hazard maps.

1 INTRODUCTION

In the recent years, a change of paradigm in flood protection has become obvious. Thereby the "safety society" is being displaced by a risk society with the focus on flood risk management including also flood prevention.

This resulted into a rethinking within the different countries. In Germany, a law for the improvement of flood prevention was enacted in Mai 2005 to strengthen the legal framework for precaution measures of flood protection. In Europe, too, a modern flood management initiative started and even a European Flood guideline is in preparation.

The European Commission is furthermore supporting a variety of (research) projects as FLOODsite, FLOWS, IRMA, ODERREGIO and ELLA, that focus either on transnational flood prevention, integrated flood management or the development of practical instruments and tools as decision support systems. One practical instrument has been developed within ELLA for Stendal County in Saxony-Anhalt, Germany.

Stendal County with approximately 250,000 ha and 148,000 inhabitants is the biggest county in federal state of Saxony-Anhalt. It is situated in the middle part of the River Elbe watershed. In addition to the River Elbe, the Rivers Havel and Aland are important tributaries in this region (see Figure 1).

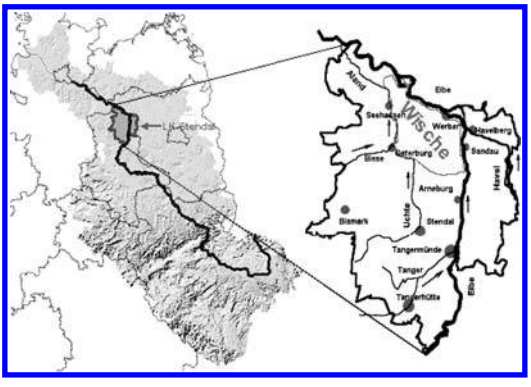


Figure 1. Overview, main towns and rivers of Stendal County in the Elbe watershed.

The terrain of Stendal County is very flat and nearly 30% of the area is former floodplain (e.g. the Wische area).

Concerning flood protection, the responsibilities are in different hands. While the state of Saxony-Anhalt is responsible for building and maintaining flood protection structures, the counties take over the emergency management in case of a flood catastrophe. Due to that the counties are responsible for planning and preparation of the emergency management. But

Copyright © 2006 Taylor & Francis Group plc, London, UK

they have also been given instruments for flood prevention by steering the flood plain management by spatial planning instruments, water management instruments as well as preparing and informing the population properly. By realizing those prevention measures the counties can contribute to reduce the potential damage caused by extreme flood events. The overall damage of the Elbe flood disaster in August 2002 was quite high in Germany. 38 people were killed and the economical damage was estimated to 11.3 billion Euros (IKSE 2004). Saxony-Anhalt had an overall damage of about two billon Euros (HWSK LSA, 2003). In Stendal County, there were luckily no victims and no dyke breaches occurred. But altogether, nearly 30,000 people had to be evacuated and thousands of emergency management forces were in action.

To improve the present flood control system and to decrease future flood damages, an integrated management instrument dealing with all aspects of flood prevention and flood defense has been developed for Stendal County. This Flood Management System (FloMS) is a pilot project for Saxony-Anhalt and has been realized by the Institute for Water Management and Ecotechnology of the University of Applied Sciences in Magdeburg since April 2003.

2 PILOT PROJECT "FLOOD MANAGEMENT SYSTEM – FLOMS"

The aim of developing the flood management system for Stendal County was the provision of all relevant data and information to the responsible authorities before and during a flood event. By the integration and presentation of existing and potential flood scenarios, the county gets an appropriate instrument to support their duties as a catastrophic authority. The system also serves as an information platform for the open public. Furthermore all flood relevant subjects such as water management, spatial planning, nature conservation, agriculture and forestry are considered in the project. Five professors representing different disciplines of the University of Applied Sciences in Magdeburg as well as two local firms are involved in this project (Jüpner, R., Tzschirner M. 2005).

2.1 *Structure/contents*

On the basis of flood scenarios, the application of FloMS is divided into two main parts, the flood prevention and the emergency management.

The flood prevention part is used during flood-free times and consists of:

– Flood plain management (Land-use planning, Natural water retention)
– Technical flood protection (dykes, retention basins etc.)

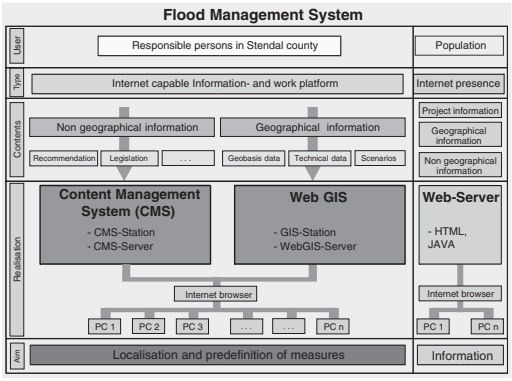


Figure 2. Technical realization of FloMS.

– Further flood prevention (risk-, building- and behavior provision).

In case of a flood event, the emergency management part is applied during:

– Routine measures for flood events up to the emergency alert and
– Disaster measures in case of the declaration of the emergency alert

The most important output data are hazard maps, hazard indication maps and dyke failure scenarios, which are the basis for preventive measures as well as for the hazard defense. Hazard maps mainly contain – according to different flood scenarios- information for emergency means as location of fire brigades, police, hospitals, collapse load of bridges, social facilities (as schools, nursing homes etc.) and special risks as location of water treatment plants, water supply and petrol stations. Hazard indication maps give an overview and depict conflict locations. They consist of information about flood-prone areas (simulated without flood protection structures for extreme flood events) and damage potential (values for different landuses).

2.2 *Technical realization*

FloMS technically consists of two major components (see Figure 2). One is a Geographical Information System (GIS), where geographical data is stored, and a WebGIS, where the data and their generated information are presented to the user via intranet/internet. The other part of FloMS stores all non spatial related data and information. This is accomplished by means of a content management system (CMS) which is based upon the open source software "MediaWiki".

The CMS (Figure 3) offers collected and structured information in different portals and gives helpful links concerning flood prevention and hazard defense. In case of an emergency alert, the web portal provides not

Copyright © 2006 Taylor & Francis Group plc, London, UK

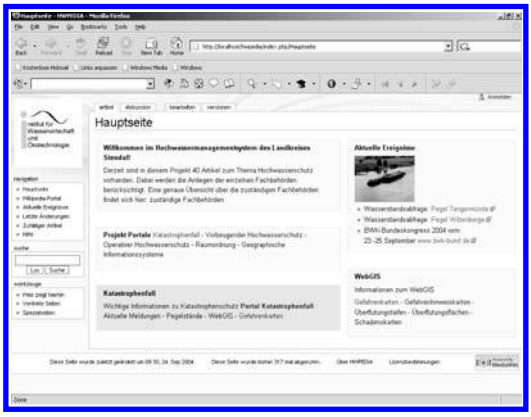


Figure 3. Homepage of the existing FloMS.

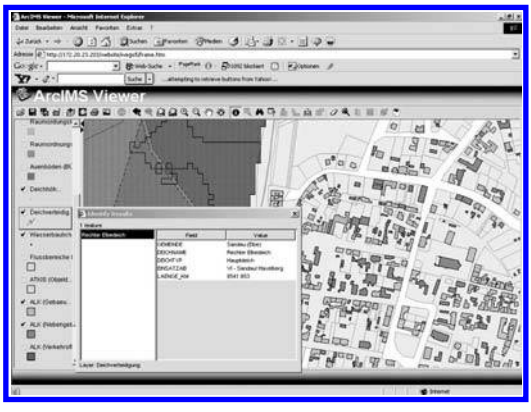


Figure 4. Representation of a scenario via WebGIS.

only emergency action plans, list of phone numbers of contact persons and action forces. It also links to the WebGIS containing maps and geographical data.

The WebGIS (Figure 4) provides different kinds of maps. These are e.g. the hazard indication maps (see section 2.1), the "dyke maps" (issued by the State Authority for Flood Protection and Water Management of Saxony-Anhalt (LHW)) and other maps with additional data containing geographical information. These maps were created with the desktop GIS and are provided to the user via WebGIS. Besides using the geographical data, the user can add its own data according to his/her special requirements of his/her work.

The current work is to improve the data basis of FloMS and to compute dyke breach scenarios as basic for hazard maps (see section 4).

At the moment, all FloMS users mainly of Stendal County but also responsible persons e.g. of the LHW are trained for using FloMS effectively.

2.3 *European project "ELLA"*

With its main focus on improving flood protection, the described interdisciplinary project FloMS became part in the European INTERREG IIIB ELLA-project "ELBE-LABE: spatial planning flood management strategies (ELLA)". ELLA which aims for the improvement of the transnational flood prevention runs from June 2003 to December 2006. Involved are 23 project partners, mostly state and regional authorities of spatial planning, water management or environmental planning, within the Elbe River Basin. Stendal County and the Ministry of Building and Traffic of Saxony-Anhalt (MBV), that is responsible authority for spatial planning, are both project partners within ELLA. The objectives of the transnational project are:

- Implementation of an integrated water management into the regional planning by agreeing upon a common transnational strategy
- Evaluation and improvements of the regional planning instruments and
- Improvement of regional and local land use plans in flood-prone areas

Finding solutions for the upstream-downstream burden that accelerates the process of improving flood prevention is another aim.

The methods being used in the project are risk analysis and their mapping, analysis and evaluation of retention measures in regional planning, agriculture and forestry.

Within ELLA, the main objectives of the pilot project "Stendal" are focused on:

- Improving the regional and local flood prevention by providing information
- Adjusting FloMS (data, information, maps) to the needs of regional and local planning authorities
- Strengthening the cooperation between water management and spatial planning and involving other actors

By realizing those and other tasks, the original project had been enlarged and extended to the end of 2006.

3 INUNDATION MAPS IN SAXONY-ANHALT

Different methods of creating inundation maps exist. Two of them (a static and a dynamic method) are being introduced in the following sections.

3.1 *Static method*

Some of the existing inundation maps had been produced by using a simple static method by intersecting the water level with the terrain. For this method the basis data is the water level and the Digital Elevation Model (DEM).

Copyright © 2006 Taylor & Francis Group plc, London, UK

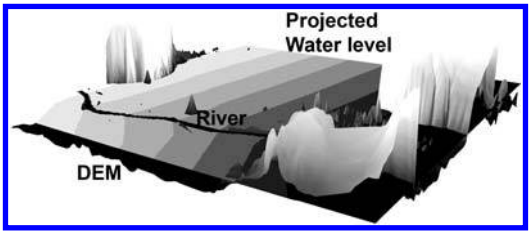


Figure 5. Intersection of the water surface and the DEM.

In GIS the water level is projected from the River into the area up to a certain buffer distance (see Figure 5). The difference between water level and terrain is calculated resulting into the water depth and the water dispersion.

This method does not consider the hydraulic fact of the subsidence of the water level and areas are being filled with water, that are naturally not reached by the water because of orographic related barriers. In general, the result obtained with this simple method is, that the inundation areas are too extended and that the water is too deep. Practical experiences during the Elbe flood in 2002 have confirmed this result.

3.2 *Dynamic method*

For the determination of the flood-prone areas different dynamic methods can be applied. In this project the ArcGIS® (company ESRI) extension FloodArea® (company Geomer) has been used. The basic data is again the water level and the DEM. In the simulation, all eight neighboring raster of one cell are considered. The discharge volume of all raster cells is calculated by using the Manning-Strickler equation, at which the flow depth during an iteration interval is taken from the difference between water level and maximum terrain elevation along the flow path [Assmann, 2003].

Because of the better consideration of the hydraulic situation, this method gives a more realistic picture for certain scenarios. In the example of Figure 6, the water depth and the inundation area are shown. With the static method (6a), a higher water level is calculated (partly more than four meter: black color) whereas the general water depth is not higher than two meter using the dynamic method (6b). Also the inundation area is lower with the dynamic method.

The aim of creating this information is to depict the worst case scenario as overtopping of dykes or failure of flood protection structures during extreme flood events. Structures as dykes were omitted in the simulation on purpose.

But the spreading of the water obtained with this dynamic method is still too wide compared to the reality. The reason is the available DEM including the natural relief and no streets, railways or dams. Those elements would naturally hinder the water flowing.

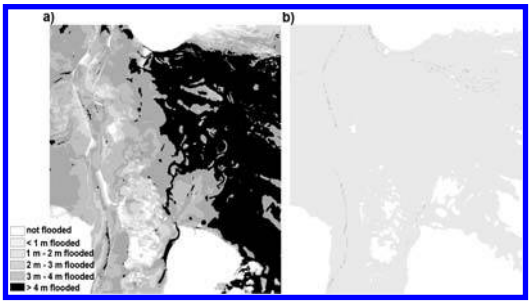


Figure 6. a) Flooded areas with static method, b) Flooded areas with dynamic method.

For local planning the data basis therefore has to be improved (see section 4.2).

3.3 *Practical application of methods*

In Saxony-Anhalt inundation maps created with the static method and followed by adjusting them to historical events exists. The maps are designed for depicting the inundation situation of the whole state of Saxony-Anhalt in a scale of 1:100,000. They give a general overview of the inundation, but they do not include water depth and water extension.

Within the ELLA project, hazard indication maps for the area of Saxony and Saxony-Anhalt have been produced using the dynamic method. They show the water depth and extension but are also on the state scale (1:100,000).

These existing maps are being applied for flood prevention on country scale. For regional and local tasks, especially for the preparation or in case of a flood event, feedbacks from the praxis showed, that the existing maps are not detailed enough for the use on the regional (1:20,000–1:50,000) or local (1:10,000–1:20,000) scale.

For this reason, maps with more detailed and differentiated information have to be created. Of a special interest are such maps that e.g. show the flooded area as a result of dyke breaches.

Out of this demand, the generation of high detailed dyke breach scenarios with a wide practical benefit was the new task. Therefore, the DEM had to be added with line objects as dykes, streets and railways on dams.

4 DYKE BREACH SCENARIOS

In comparison to the determination of the flood-prone areas on state scale, dyke breach scenarios have the advantage that they are more detailed and are on a local scale. In case of a dyke breach, usually only a small part of the water amount flows into the flood-prone

Copyright © 2006 Taylor & Francis Group plc, London, UK

areas behind the dykes, but the main discharge still remains in the river bed.

4.1 *Data basis*

4.1.1 *Water level*

The water level required for the simulation of the dyke breach scenarios is the longitudinal section of the water surface of the River Elbe with point data of 100 m. The 100 year and extreme flood event (100 years event plus 0.50 m), provided by the LHW, have been chosen for the simulation. To use the data in the ArcGIS® extension FloodArea®, the data points have to be raster with at least two pixels width. Therefore the points have been converted into a line first and second into raster.

4.1.2 *DEM*

The DEM is provided by the State Department for Surveying and Geoinformation of Saxony-Anhalt (LVermGeo). It is generated from orthophotos that are usually not older than 4 years, because one quarter of Saxony-Anhalt is renewed every year. The points extracted from the orthophotos are a raster with a clearance of 10×10 m and an elevation accuracy of ± 0.50 m. A more detailed DEM with a raster of 1×1 m and an elevation accuracy of ± 0.20 m is unfortunately only available for the River Elbe within the dyke limits. This more accurate DEM can not be used for the dyke breach scenarios, because the areas behind the dykes are of interest.

Because the available DEM does not include the required line structures, the main focus for creating the dyke breach scenarios has been the acquisition of those data and its implementation into the DEM.

4.2 *Improvement of DEM*

4.2.1 *Data sources*

For the first improvement of the DEM, the dyke structures including their elevation data for the extension of the project area has been provided by the LHW. The data is delivered in different formats, as GIS-shape- or CAD-dxf-files.

More difficult is the acquisition of the other line objects such as streets, roads and railways, because they are not compiled and stored in one hand. For the predominant part of the project area there is no surveying and mapping data of these objects. Only partly, planning data is available, but mostly not in a digital format.

Other important information for the dyke breach scenarios is the elevation of culverts or canalization. Unfortunately these data is also not available for the whole county area and therefore has to be collected by each responsible organization (organization for the maintenance of rivers of second order).

In the consequence the DEM can not be improved optimally by all required line structures.

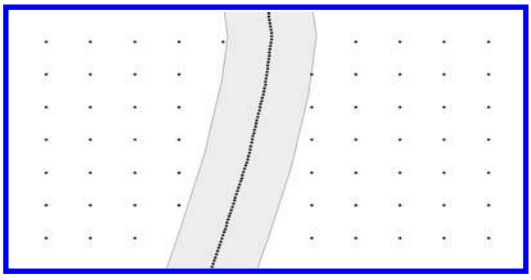


Figure 7. Grabing the elevation points from the TIN surface to the raster.

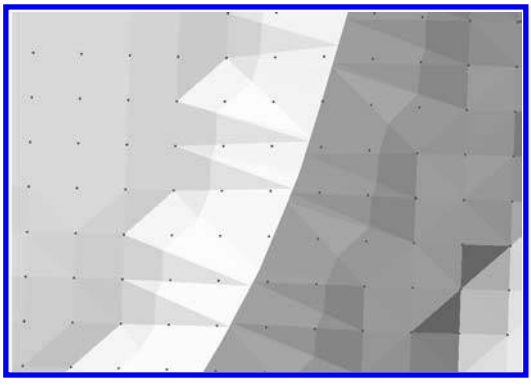


Figure 8. The dyke is integrated into the DEM, buffered with 10 m, and DEM points inside the buffer are erased.

4.2.2 *Data integration*

In order to integrate the data into the DEM, the challenge was the handling of the different structure of data within the GIS. On the one hand, the simulation software requires raster data (as the DEM), but the dyke data exists only as single points in a line without fitting in the raster of the DEM.

The conventional way is to merge the DEM raster with the single data points, buffer the dyke with 10 m (Figure 8) according to the raster width of the DEM and erase the points of the DEM inside the buffer. Then a Triangular Irregular Network (TIN) is created. The buffer is necessary to create a dyke body for the TIN.

Afterwards, the TIN has to be transformed into a raster again (Figure 7).

While relocating the elevation points of the TIN to the raster, elevation point of the dyke crest can be missed according to the raster width of 10 m (Figure 9 a) and b)). For the dyke breach simulation, the real height of the dyke crest is important. As shown in Figure 9 c) and d) the elevation of the dyke crest has to be set on a width which is wider than the clearances of the raster (in this case 10 m). In this wavy it is ensured, that at least one of the raster points is placed on top of the dyke (see Figure 10).

Copyright © 2006 Taylor & Francis Group plc, London, UK

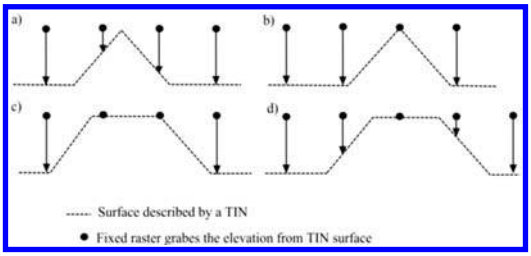


Figure 9. a) and b) not every point of the raster is located on top of the dyke, c) and d) at at least one point is on top of the dyke.

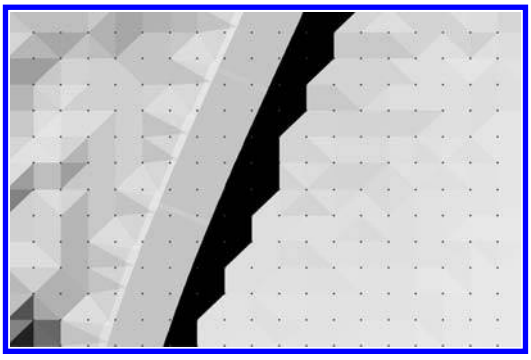


Figure 10. AT least one point is on top of the dyke by the converting from TIN to raster by the developed tool.

Because ArcGIS does not provide a tool for transforming a line into a stripe by keeping the elevation data, a new tool has been developed within this project. The tool works similar to a buffer but it additionally copies additionally the elevation to the edges of the buffer in a right angle to the axis. This process has to be done also for the other line objects.

An easy implementation of line objects into a raster model is enabled by using this helpful tool.

4.3 *Simulation*

After integrating the necessary and available surface data, the locations of simulated dyke breaches had to be defined. The localization was coordinated with the responsible persons of the LHW and Stendal County. Also the boundary conditions for the simulation were agreed on. The results were the following:

- Water level input: 100 year flood event and an extreme flood event
- Width of dyke breach: 90 m (experience values, often applied)
- Simulation time: 48 hours (most of the water is spread by then)

For the simulation the dyke was erased on a length of 90 m at the predefined locations within the DEM.

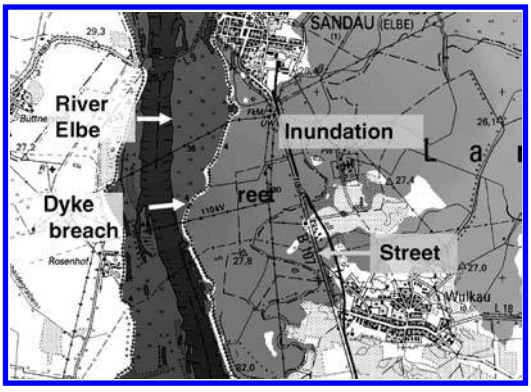


Figure 11. Simplified snap of dyke breach scenario.

Each dyke breach is simulated separately. After 6, 12, 24 and 48 hours the result of the simulation is represented in a map.

With these settings, the simulation runs about 10 days using a new desktop computer (Intel© P4 3.2 MHz, 2 GB RAM).

4.4 *Interim results of the simulation*

The result of a dyke breach scenario is a map of flood-prone areas as a consequence of a certain dyke breach that shows the water depth and extension. The result is strongly depending on the precision of the input data, especially of the DEM. In Figure 11, a snap of a dyke breach scenario can be seen as an overview. In this case, the street could not have been integrated into the DEM yet. For final calculation of dyke breach scenarios, all street elevation data have to be considered. This is elementary because the street can hinder the water spreading, depending on its elevation in relation to the water level. For this reason, proper information about the input data is also required and has to be made transparent e.g. by displaying it on the map.

In spite of the difficulties in obtaining all the required and wishful elevation data, the results are a big step forward for flood management. The maps are a very helpful tool for the authorities in the LHW and Stendal County. The dyke breach scenarios are also the basics for the hazard maps. For critical points in flood-prone areas, e.g. petrol stations, the effect due to dyke breaches can be seen and result into prevention measures.

5 SUMMARY AND OUTLOOK

The Flood Management System was developed as a instrument for optimizing the flood protection in Stendal County. It is based on the experience during the Elbe flood in 2002 and the subsequent detailed

Copyright © 2006 Taylor & Francis Group plc, London, UK

evaluation of the different emergency management activities. In January 2005 the principal establishment of the main contents and the technical solution of using a GIS, WebGIS and CMS were finished and presented. Since then FloMS has been further optimized by

- Improving the data basis by adding important data and developing practical tools for the implementation
- Simulating additional scenarios for depicting in maps with a more detailed scale for a better practical local application
- Intensifying the cooperation between persons and authorities (especially water management and spatial planning) involved in the in flood protection

During the whole project, a close communication and agreements with the responsible actors of Stendal County and state authorities e.g. LHW was maintained. Until the end of the project in the end of 2006, following further outputs are focused:

- Further acquisition of basis data as line objects, especially railway dams and new simulation of the scenarios
- Finishing the hazard maps
- Developing concepts for minimizing the damage potential in flood-prone areas

The integration of the pilot project into ELLA has been a good opportunity for further developing, expanding and adjusting the flood management system to different demands. Also, the transnational experiences in flood prevention and risk management from other riparian countries and counties could have been considered and implemented.

ACKNOWLEDGEMENTS

Stendal County, the Ministry for Building and Traffic of Saxony-Anhalt and the European Union have funded this pilot project. The authors would like to thank them as well as our colleagues Stefan Müller, Agnes Richmann and our former colleague Thilo Weichel for supporting the research within this project.

REFERENCES

Assmann, A. 2005. FloodArea – ArcView-Erweiterung zur Berechnung von Überschwemmungsgebieten, Fa. Ruiz Rodriguez + Zeisler Ingenieurgesellschaft für Wasserbau und Wasserwirtschaft, Anwenderhandbuch, Juni 2003

IKSE 2004. Dokumentation des Hochwassers vom August 2002 im Einzugsgebiet der Elbe, IKSE, Magdeburg 2004

HWSK LSA 2003. "Hochwasserschutzkonzeption des Landes Sachsen-Anhalt bis 2010"; Ministerium für Landwirtschaft und Umwelt, Stand 25. März 2003

Jüpner, R. & Tzschirner, M. 2005: Development of an Integrated Flood Management System for Stendal County in Saxony-Anhalt, Germany – a Pilot Project. in Floods, from defence to management. Proceedings of the Third International Symposium on Flood Defence, Nijmegen, May 2005

Copyright © 2006 Taylor & Francis Group plc, London, UK

Palaeoflood records applied to assess dam safety in SE Spain

G. Benito, M. Rico & V.R. Thorndycraft
Consejo Superior de Investigaciones Científicas, Centro de Ciencias Medioambientales, Madrid, Spain

Y. Sánchez-Moya & A. Sopeña
Instituto de Geología Económica. CSIC-UCM. Facultad de Ciencias Geológicas, Universidad Complutense de Madrid, Madrid, Spain

A. Díez Herrero
IGME, Dep. of Geological Hazards, Madrid, Spain

A. Jiménez
Centro de Estudios Hidrográficos del CEDEX, Madrid, Spain

ABSTRACT: Spanish dam safety regulations recommend the estimation of a return period of 1000 years for the Design Flood and of 10,000 for the Safety Check Flood, which are obtained from Flood Frequency Analysis (FFA) or on the Probable Maximum Flood (PMF). Short gauge records afford little support for the FFA or the hypothetical PMF, which in addition to the absence of an associated probability, limits the utility of these indices for risk-based dam safety decisions. Palaeoflood hydrology was applied to the Guadalentín River, upstream of the Valdeinfierno reservoir (372 km^2), which has a spillway capacity of 550 $m^3 s^{-1}$ (design flood). Palaeoflood data and gauge station records, were combined for the FFA, using the maximum likelihood estimates of the parameters for a Gumbel distribution, providing a discharge of 2350 $m^3 s^{-1}$ for the design flood (1000-yr flood) and 3450 $m^3 s^{-1}$ for the safety check flood (10,000-yr flood). The PMF discharge is 5786 $m^3 s^{-1}$, showing an overestimation of this empirical method.

1 INTRODUCTION

Understanding the magnitude and frequency of extreme floods is critical for the design of hydraulic structures such as dams. Dams are designed, constructed and modified, when necessary, such that a catastrophic failure is prevented during a large flood. Civil engineers when designing a dam must establish the capacity of the dam and the rate at which water can be passed through the dam by means of flood gates and spillways. Dam safety components are established by two concepts: (1) the design flood and (2) the safety check flood. The design flood refers to the flood magnitude for which hydraulic design of spillways and energy dissipating structures have been designed, with a safety margin provided by the freeboard. The safety check flood represents the most extreme flood conditions that the dam structure could support without failure, including a low safety margin (worst flood scenario). Past experience indicate that overtopping represents more than 40% of dam failures, showing that extreme floods constitute an important risk for dam safety (ICOLD 1995).

According to Spanish regulations on dam safety (MOPTMA 1996), dam category depends upon the potential economic losses and human threats on downstream settlements. The Civil Protection Basic Framework on Flood Risk (MJI 1995), therefore, classifies dams into three categories: (A) High Hazard, (B) Significant Hazard, and (C) Low Hazard. A failure in a "high hazard" class of dam may cause loss of life, serious damage to residential, industrial, or commercial buildings; or damage to, or disruption of, important public utilities or transportation facilities such as major highways or railroads. The class "significant hazard" includes dam in which failure poses no threat to life but may cause significant damage to main roads, minor railroads, or cause interruption in the service of public utilities. A failure of a "low hazard" class of dam would at the most result in damage to agricultural land, farm buildings (excluding residences), or minor roads. In this flood risk Directive, the estimation of the design flood is based on probabilistic methods (statistical analysis and hydrometeorologic estimations) in which the use of historical data is highly recommended. The Spanish Committee on Large Dams (Comité Español

Copyright © 2006 Taylor & Francis Group plc, London, UK

Table 1. Number of significant loss of life (N) according to national regulations and selection of design flood (modified from Berga 1998).

Dam hazard category	Loss of life	Impacts*	Design flood	Safety check flood
High	>N	Excessive	% PMF or 1000–5000	% PMF or 5000–10,000
Significant	0–N	Significant	% PMF or 500–1000	% PMF or 1000–5000
Low	0	Minimal	100	100–500

* Economic, social, environmental & political impacts.

de Grandes Presas 1997, Penas et al. 1997) recommends the estimation of a return period of 1000 years for the design flood and of 10,000 years for the safety check flood (Table 1). The estimation of such low frequency floods are based on either probabilistic or deterministic approaches.

The deterministic method relies on the concept of the Probable Maximum Flood (PMF) or the greatest amount of precipitation theoretically possible within a region (Maximum Probable Precipitation, PMP) subsequently maximized through "moisture maximization" and other numerical methods, finally turned into runoff or flood discharge, this depending on the characteristics of the drainage basin (Berga 1998). This methodology is complex especially in large basins due to the timing of different flood hydrographs and different land use scenarios. In addition, this deterministic approach is limited due to the lack of probability value associated to the PMF, which impedes its use on the decision support for flood risk analysis.

In most European countries, the dam design determines the probability that a storm will cause the dam to overflow and consequently destroy the structure. In Spain, most of the existing dams were designed with flood gates to handle flows upto the 500-yr flood i.e. a flood that occurs on average once in five hundred years (recurrence probability of 0.002). This statistical analysis is based either on streamflow gauge records or on hydrometeorological analysis from precipitation associated with different return periods. If the reliability of flood design and safety check flood estimation is to be improved, there is a critical need to specifically extend the record of the instrumental period (systematic period) of extreme floods. This record is usually limited to only a few dozens of years and the largest floods are therefore under-rated in the data. Information on hydrological variability and extreme floods can be completed using either or both palaeoflood hydrology and/or written chronicles of historical floods. Long records of extreme floods are then applied successfully in the design of dams and flood gates, combining palaeofloods, historical and instrumental records within the statistical analysis or testing the analysis performed in the calculation of the PMF. The statistical analysis can also contribute/benefit from regionalisation to generate statistics of extremes from combining records from several sites.

Recently, a new Dam Safety Program was launched by the Spanish Government, in which different methodological approaches to dam-safety design criteria are being revised at pilot areas. In this study, a combination of methods for the estimation of the design and safety check floods have been used in the upper Guadalentín basin, SE Spain. The specific objectives of the study are to: (1) extend the instrumental flood record to past using palaeoflood and historical data; (2) combine systematic and non-systematic information on the flood frequency analysis (FFA); (3) compare the results of the FFA using palaeoflood and historical data with those obtained from hydrometeorological methods and from the PMF; (4) estimate the design flood and the safety check flood; (5) discuss the contribution of palaeoflood hydrology to dam safety issues in Spain.

2 STUDY AREA

The Guadalentín River is located in SE Spain and is a major tributary of the Segura River which flows into the Mediterranean. The study reach is located at the upper reach of the Guadalentín, at the junction of the Rambla Mayor and Caramel River (Fig. 1), and upstream of the tail of the Valdeinfierno reservoir. The Guadalentín River has a Mediterranean regime and it is known as one of the most torrential rivers in Spain. The mean monthly discharges show two maxima: (1) in spring with a twinfold peak in February–March and May–June, a (2) in fall (September to November) during which the most catastrophic floods have been produced. The gauge station is located at the Valdeinfierno dam with a drainage area of 540 km^2. This record covers the periods 1933–1949 and 1968 onwards, the largest peak discharge recorded being 178 m^3s^{-1} in 1946. It is important to note that most of the gauge record corresponds to mean daily discharges.

Palaeoflood studies were conducted at the Caramel River (El Posadero site), upstream of Valdeinfierno Reservoir. At this point the drainage basin is 311 km^2, with a mean discharge of 0.6 m^3s^{-1} and peak discharge of 178 m^3s^{-1}, as recorded at the gauge station. At the El Posadero site, the Caramel River and Rambla Mayor join at the entrance of a narrow bedrock canyon carved in Cretaceous limestones. The gorge is 15–30 m wide with bedrock walls 40 m high and a gravel bed channel. During flooding, flow is hydraulically controlled by the narrow canyon entrance, producing a hydraulic damming of the flow upstream of the constriction, which favoured the accumulation of flood deposits at the entrance sides. Palaeoflood sedimentation also occurred high along the canyon

Copyright © 2006 Taylor & Francis Group plc, London, UK

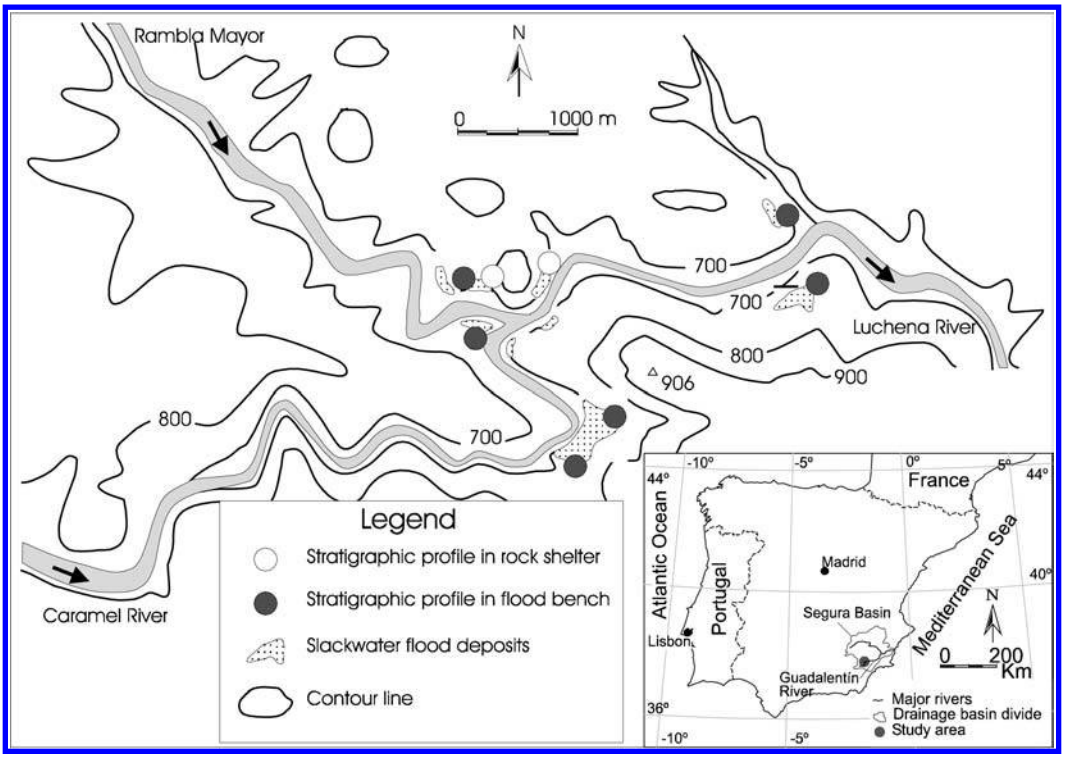


Figure 1. Location of the study area and stratigraphic profiles at the Rambla Mayor and Caramel River.

sides, bedrock caves and upstream of the canyon tributary gullies. Additional, documentary flood information of the Guadalentín at Lorca was obtained from bibliographic sources.

At the upper part of the basin, two dams where built mainly for irrigation purposes, and secondarily as flood control reservoirs. The most upstream one, Valdeinfierno, is located 5.2 km downstream of the study site, draining a catchment area of 540 km^2. The Valdeinfierno dam was built in 1806 for irrigation use and rebuilt in 1897 with a gravity structure of 51 m in height. It is 165 m in length and can hold a reservoir volume of 14 hm^3, with a spillway capacity of 673 $m^3 s^{-1}$ and a safety check flood of 850 $m^3 s^{-1}$.

The Puentes dam drains a catchment area of 1388 km^2 and has a long history of catastrophic failures that affected the city of Lorca (13 km downstream). The Puente's dam construction started in 1647, but a year later, during the construction works, a flood caused the collapse of the structure. The dam was rebuilt in 1790 but a few years later, on April 30th 1802, the failure of the dam produced a catastrophic flood that caused 608 deaths in Lorca as well as large economic losses. In 1884 the Puentes dam was rebuilt with a spillway capacity of 945 $m^3 s^{-1}$, although few years later was infilled by sediments. A new dam was built in 2000 close to the site of the former one, with a design flood of 2026 $m^3 s^{-1}$ and a safety check flood of 3626 $m^3 s^{-1}$.

3 METHODOLOGY

Palaeoflood hydrology is the reconstruction of the magnitude and frequency of recent, past, or ancient floods using geological evidence (Baker et al. 2002). The term "palaeo" has contributed to the general misconception that palaeoflood techniques are only used for estimating very old floods over geological timescales. However, most palaeoflood studies involve the study of the last 5000 years, and in this study there is a great emphasis on the last millennium. Palaeoflood hydrology is indeed defined by the fact that flood evidence is derived from lasting physical effects of floods on natural indicators, such as slackwater flood deposits, silt lines or scour lines.

During high flood stages in river canyons eddies, back-flooding and water stagnation occur at the gorge sides, producing low velocities and/or flow stagnation (slack water) that favours deposition from suspension of clay, silt and sand. These fine-grained deposits, known as slackwater flood deposits, are stage

Copyright © 2006 Taylor & Francis Group plc, London, UK

indicators of floods and can be preserved in stratigraphic sequences (Benito et al. 2003a) providing detailed and complete records of flood events that extend back several thousand of years (Baker & Kochel 1988). Slackwater flood deposits were found at three sedimentary settings: (1) forming flood benches at the sides upstream of narrow bedrock constrictions, (2) upstream of tributary valleys and (3) in rock alcoves (small caves or rock shelters formed in exposed bedrock on the valley sides) (Fig. 1). Stratigraphic and sedimentological analyses of the deposits were carried out both in the field and the laboratory, with sediment peels of the stratigraphic profiles, measuring approximately 80 cm × 50 cm in size, made in the field. Individual flood units were identified through a variety of sedimentological indicators (Baker & Kochel 1988, Benito et al. 2003b): the identification of clay layers at the top of a unit; erosion surfaces; bioturbation indicating the exposure of a sedimentary surface; angular clast layers, where local alcove or slope materials were deposited between flood events; and changes in sediment colour. As well as identifying individual flood units, sedimentary flow structures were also described in order to elucidate any changing dynamics during a particular flood event and/or infer flow velocities that can improve discharge estimation (Benito et al. 2003b).

Slackwater flood deposit chronology was determined using radiocarbon dating of charcoal collected from individual flood units. Necessary preparation and pre-treatment of the sample material for radiocarbon dating was carried out by the ^{14}C laboratory of the Department of Geography at the University of Zurich (GIUZ). The dating itself was done by AMS (accelerator mass spectrometry) with the tandem accelerator of the Institute of Particle Physics at the Swiss Federal Institute of Technology, Zurich (ETH). Calibration of the radiocarbon dates was carried out using the CalibeETH 1.5b (1991) programme of the Institute for Intermediate Energy Physics ETH Zürich, Switzerland, using the calibration curves of Kromer & Becker (1993), Linnick et al. (1986) and Stuiver & Pearson (1993).

The discharge estimations associated with the slackwater flood deposits at the Luchena River were calculated using the US Army Corps of Engineers River Analysis System computer program-HECRAS (Hydrologic Engineering Center 1995). The computation procedure is based on the solution of the one-dimensional energy equation, derived from the Bernoulli equation, for steady gradually varied flow. Palaeoflood discharge reconstruction was based on the calculation of the step-backwater profile which best matches geological evidence of the flood stage.

Twenty cross-sections about 25 to 100 metres apart were obtained from field survey along a 1800 m reach where the stratigraphical sections are located. Cross-sections and flood deposit elevations, the input data for the hydraulic models, were surveyed along both study reaches using a Trimble 4700 kinematic differential GPS, with additional data using a Sokkia total station where satellite visibility was poor. The GPS comprised two GPS receivers (a fixed base station with known co-ordinates and a rover to measure the cross-sections) with a radio link between them both to allow real time data processing.

The accuracy of the discharge estimations depends on stability of the cross-section geometry through time. In stable, bedrock-confined channels, channel geometry at maximum stage is known. In this study, the gravel bed channel is susceptible for scour and fill of the channel which reduces the accuracy of the palaeodischarge modelling. Assuming recent channel bed aggradation due to the downstream reservoir construction, the resulting values would underestimate the peak flood discharges. In the modelling, it was assumed for the calculations that flow was subcritical along the modelled reach. Manning's n values of 0.03 and 0.04 over the valley floor and margins, respectively, were assigned. A sensitivity test performed on the model shows that for a 25% variation in roughness values, an error of 4% was introduced into the discharge results. Critical flow was selected as boundary conditions at the most downstream cross-section where the channel narrows into a bedrock section where a deep pool was created.

Discharge values associated with each slackwater bench were estimated upon calculated water surface profiles matching flood unit elevations at different sites along the longitudinal profile. Rating curves relating individual flood unit elevations with flood discharges were established at each site. High water marks from the largest instrumental flood that occurred in 1973 were also fitted in the model to estimate flood discharges.

Traditional methods of flood frequency analysis (FFA) assume that the distribution of the unknown magnitudes of the largest floods is well-represented by the gauged record or can be obtained by statistical extrapolation from recorded floods (usually modest floods). The value of palaeoflood data is the potential to include physical evidence of large floods, or limits on flood magnitude, over long time periods. The basic hypothesis in the statistical modelling of palaeoflood information is that a certain threshold of water level exists and that over a specified time interval (from one year to thousands of years), all exceedances of this level have been recorded through geological palaeoflood evidence left along the river channels such as sediment deposits. It is also assumed a stationary of the long term incidence of floods. Palaeoflood data were organised in different threshold levels exceeded by flood waters over a given time period. In each threshold, individual floods are introduced as

Copyright © 2006 Taylor & Francis Group plc, London, UK

minimum, maximum, exact or range values of discharge, as well as the age dating. Data organisation on exceeded levels or thresholds reduces the potential palaeoflood discharge underestimation.

4 RESULTS

4.1 *Palaeoflood stratigraphy*

Nine stratigraphic profiles were described in a reach of 2.5 km in length. The slackwater flood deposit units varies between a few centimetres and 40 cm of fine to very fine sands and silts, with occasional clay, with gradual fining upward sequences. Massive, parallel lamination and cross-bedding are the dominant sedimentary structures.

A flood unit sequence usually culminates with climbing ripple structures overlaid by silt lamina which represents the end of the flood deposition. The oldest flood deposits were dated as 1985 ± 50 ^{14}C yrs BP (radiocarbon years before present), although the stratigraphic record contains major gaps between 2000 and 1000 BP (years before present).

The most complete section forms a flood bench on the right side of the Caramel River at the entrance of the gorge. The stratigraphic profile is ca. 7 m in thickness and provided evidence of at least 24 floods over the last 1000 years. The lower ten flood units have been dated between 1020 ± 50 and 945 ± 45 ^{14}C yrs BP, suggesting a period of frequent relatively small floods on the basis of the very fine and fine sand grain size and the thin layers. The top of this flood sequence is overlain by slope deposits which indicate a break in flood sedimentation of ca. 300 years (2-sigma age range overlaps). Overlying this are five flood layers, the lower one dated to 340 ± 45 ^{14}C yrs BP, which also have fine and very fine sand grain-size but they are generally thicker. These flood layers are capped by a 42 cm-thick colluvial layer, indicating a second break in flood sedimentation. The upper part of the section is represented by nine modern flood deposits, with a basal date of 205 ± 45 ^{14}C yrs BP, a middle date of 120 ± 45 ^{14}C yrs BP, and the upper flood layer likely left by the 1973 flood. Field evidences suggest that the 1973 flood was the largest event over the last 1000 years.

On the right side of the Rambla Mayor, also near the entrance of the gorge, a 2 m thick flood bench shows evidence of at least nine flood units with an oldest date of 190 ± 45 ^{14}C yrs BP, a middle date of 105 ± 45 ^{14}C yrs BP, and the upper deposits dated as modern. This stratigraphy is equivalent in flood unit number and chronology to the upper part of the previous stratigraphic profile.

The palaeoflood and historical flood information point out to an increase in the flood frequency and magnitude in modern times which can be attributed to climate variability accentuated by intensive deforestation and land use practices during the last 400 years.

4.2 *Discharge estimation*

Discharge values associated with each slackwater bench were estimated upon calculated water surface profiles matching the upper unit elevations at different sites along the longitudinal profile. The accuracy of the palaeodischarge estimates is reduced by the potential for scour and fill of the gravel channel bed. In the most complete stratigraphic profile, the lower 10 flood units (dated as 1020 ± 50 and 945 ± 45 ^{14}C yrs BP) are associated with minimum estimated discharges of 15 $m^3 s^{-1}$ and 580 $m^3 s^{-1}$. The second set of flood units comprising five flood units (with a basal date of 340 ± 45 ^{14}C yrs BP) is associated with minimum discharges between 580 $m^3 s^{-1}$ and 680 $m^3 s^{-1}$ (Fig. 2). In this section the third fill set (at least nine flood units) containing a dating at the lower portion of this set of 205 ± 45 ^{14}C yrs BP matched with discharge estimates between 730 $m^3 s^{-1}$ and 1033 $m^3 s^{-1}$ (Fig. 2). These discharges are minimum estimates since the water depth above the flood units are unknown, and therefore, discharge values may be considered as conservative. However, high water marks of the 1973 flood found along the study reach provided an associated discharge of 1616 $m^3 s^{-1}$, which shows that "exact" discharges may be 35% higher than the minimum estimates.

4.3 *Flood frequency analysis*

In the Valdeinfierno gauge station, the quality of the instrumental data is discontinuous, with most data corresponding to mean daily discharges. These mean daily discharges were transformed into peak discharges using nearby gauge data, but the degree of uncertainty was very high. Therefore, only peak discharges were used together with the palaeoflood data in the flood frequency analysis. The FFA was carried out with the MAX program (Stedinger et al. 1988), which computes the maximum likelihood estimates of the parameters of selected probability distributions. A critical assumption is that all the floods above specified discharge thresholds are recorded in the stratigraphy. In this study, only the floods postdating AD 1000 were used, since it was inferred that the stratigraphic record is complete for this time period. The exact date of each flood is not known, but the documentary flood record obtained in Lorca shows a great degree of agreement between the catastrophic historical floods and the number of floods recorded in the stratigraphy for specific time periods. Therefore, for practical purposes, each

Copyright © 2006 Taylor & Francis Group plc, London, UK

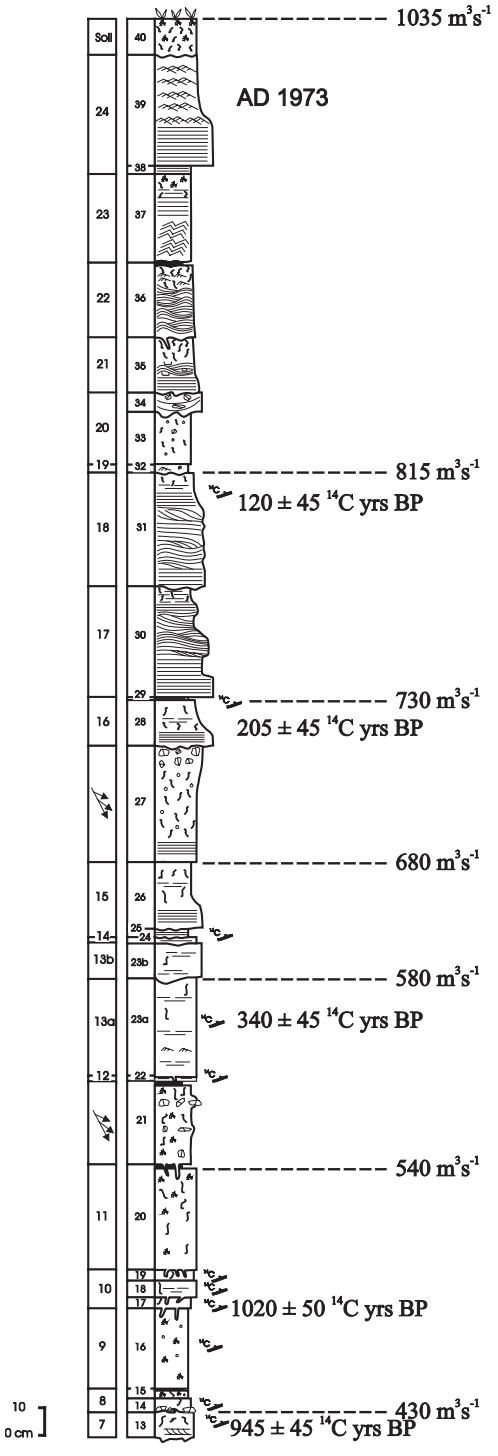


Figure 2. Stratigraphic profile, radiocarbon dates (years before present, yrs BP) and associated discharges ($m^3 s^{-1}$).

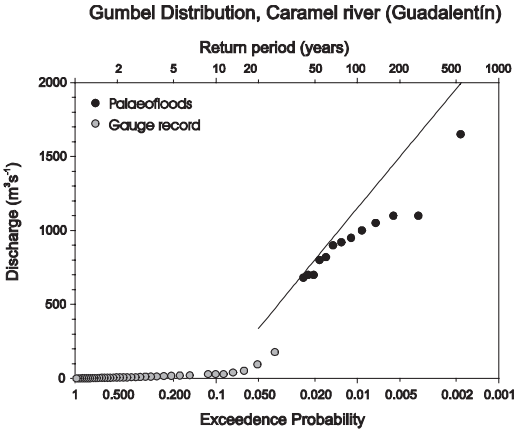


Figure 3. Gumbel distribution using gauge data (Valdeinfierno station) and palaeoflood records.

palaeoflood unit was assigned to a particular year of the historical flood record.

In this analysis, the best optimisation of the parameters was obtained using the Gumbel distribution. Plotting positions were assigned on the basis of the Weibull equation (Fig. 3). The analysis were conducted using only the last 1000 years palaeoflood record since it was noted major gaps in the previous stratigraphic record. According to this analysis the floods with return periods (T) of 100, 500, 1000, 5000 and 10,000 years correspond to discharges of 1150, 1950, 2300, 3100 and 3450 $m^3 s^{-1}$ respectively. These data are within the same order of magnitude of the rainfall-runoff analysis using a semidistributed model performed by CEDEX (Spanish Ministry of Development), in which discharges of 935, 1722, 2121, 3204 and 3727 $m^3 s^{-1}$ were calculated for the same return periods.

5 DISCUSSION

The palaeoflood data shows physical evidence of flood discharges with magnitudes almost 10 times higher than the ones recorded by the gauge station. In the studied stratigraphic profiles there is a good agreement on the number of flood units over specific time periods. A good agreement between the stratigraphic record and the documented catastrophic floods in Lorca was also found. This agreement among different data sources support the value of the palaeoflood evidence found in the study area. The potential for scour and fill of the gravely channel bed of the study reach reduces the accuracy of the palaeodischarge modelling, however, the deposits have fairly good chronological control and there is no indication of major cut and fill alluvial facies.

Copyright © 2006 Taylor & Francis Group plc, London, UK

The FFA using palaeoflood and gauge data shows that the current design flood ($673\,m^3s^{-1}$) and the safety check flood ($850\,m^3s^{-1}$) for the Valdeinfierno dam are underestimated. The analysis using the palaeoflood data provided discharges of $2300\,m^3s^{-1}$, for the 1000-yr flood (design flood), and $3450\,m^3s^{-1}$ for the 10,000-yr flood (safety check flood). Similar conclusions can be extracted from the hydrological study performed by CEDEX in which the 1000 and 10,000-yr floods were estimated in 2121 and $3727\,m^3s^{-1}$.

Palaeoflood data can also be used for testing the analysis performed in the calculation of the PMF. The PMF has been used as a standard for hydrological analyses in dam safety for several decades (National Research Council 1985). By definition, the PMF has no return period but arbitrarily it was assigned a return period of 10,000 to 1,000,000 years at the upper and lower confidence limits for flood frequency analysis (National Research Council 1985). The PMF has been estimated for the Guadalentín River at the Valdeinfierno dam using an empirical equation based on the Meteorological World Organisation recommendations (OMM 1990), with a modification for the Spanish catchments introduced by CEDEX. According to this equation, the PMF estimated for the study reach is $5786\,m^3s^{-1}$. This value shows that the extrapolated discharges of the 10,000 year palaeoflood return period is about 60% of the calculated PMF, indicating that the calculated PMF discharges are very large overestimates. Similarly, palaeoflood studies performed for dam safety purposes by the U.S. Bureau of Reclamation, show that the upper limit for palaeoflood magnitude is up to an order of magnitude smaller than the one implied by PMF calculations (Enzel et al. 1993; Levish et al. 1996). In the USA the extrapolated discharges of the 10,000 year palaeoflood return period are between 5 to 20% of the calculated PMF (Levish et al. 1996). The value of the PMF for dam safety studies is uncertain due to the lack of physical potential of these basins to generate the calculated peak discharges. Estimated discharges from the physical evidence left by floods over periods of thousands of years provide more realistic results, which can be combined with gauge station data using appropriate statistical tools and subsequently be of great value for the planning of large scale hydrological projects (e.g. Ostenaa et al. 1994; Ostenaa & Levish 1996).

6 CONCLUSIONS

This paper illustrates that palaeodischarge estimations can be obtained from sedimentological evidence of floodwater elevations reached by past floods. These palaeoflood data are based on "real" evidence of flood stages providing advantages over the uncertainties of other methods such as the hydrometeorological models or the deterministic (PMF) estimations. In the Guadalentín River, the 2000-yr flood record from palaeofloods indicates that floods of a larger magnitude (upto $1616\,m^3s^{-1}$) than any recorded in the instrumental record ($<180\,m^3s^{-1}$) have occurred in the past. The palaeoflood discharges can be combined with the gauge record to estimate high flood quantiles (500, 1000, 5000, 10,000 year return periods with discharges of 1150, 1950, 2300, 3100 and $3450\,m^3s^{-1}$ respectively), without relying on statistical extrapolations from short instrumental records. The current design flood ($673\,m^3s^{-1}$) and the safety check flood ($850\,m^3s^{-1}$) for the Valdeinfierno dam are underestimated, and they should be modified to $2300\,m^3s^{-1}$ for the design flood and $3450\,m^3s^{-1}$ for the safety check flood. Discharges obtained from the PMF ($5786\,m^3s^{-1}$) overestimated the discharge results, and they do not provide a realistic estimation of dam safety features (dam and spillway designs).

ACKNOWLEDGEMENTS

Our palaeoflood research has been funded by the Spanish Commission of Science and Technology through the projects "Incorporation of palaeoflood and historical flood data in the calculation of dam safety – PALEOCAP" (CICYT project no. REN2001-1633-RIES), and "Infiltration on channel beds and recharge of aquifers related to floods and palaeofloods in ephemeral rivers- PALEOREC" (CICYT project no. CGL2005-01977/HID). Further funding support was provided by the Centro de Estudios Hidrográficos of the CEDEX and the European Commission projects "Systematic, Palaeoflood and Historical data for the improvement of flood Risk Estimation – SPHERE" (contract no. EVG1-CT-1999-00010) and "FloodWater recharge of alluvial Aquifers in Dryland Environments – WADE (contract no. GOCE-CT-2003-506680). The manuscript benefited from comments from an anonymous reviewer.

REFERENCES

Baker, V.R. & Kochel, R.C. 1988. Flood sedimentation in bedrock fluvial systems. In V.R Baker, R.C. Kochel. & P.C. Patton (eds.), *Flood Geomorphology*, 123–137. USA: John Wiley & Sons Ltd.

Baker, V.R., Webb, R.H. & House, P.K. 2002. The Scientific and societal value of paleoflood hydrology. In P.K., House, R.H., Webb, V.R., Baker, D.R. Levish (eds.), *Ancient Floods, Modern Hazards: Principles and Applications of Paleoflood Hydrology*. Water Science and Application Series, vol. 5, 127–146. Washington, DC: American Geophysical Union.

Benito, G., Sánchez-Moya, Y. & Sopeña, A. 2003a. Sedimentology of high-stage flood deposits of the Tagus River, Central Spain. *Sedimentary Geology* 157: 107–132.

Benito, G., Sopeña, A., Sánchez, Y., Machado, M.J. & Pérez González, A. 2003b. Palaeoflood Record of the Tagus

Copyright © 2006 Taylor & Francis Group plc, London, UK

River (Central Spain) during the Late Pleistocene and Holocene. *Quaternary Science Reviews* 22: 1737–1756.
Berga, L. 1998. New trends in hydrological safety. In L. Berga (ed.), *Dam Safety*: 1099–1106. Rotterdam: Balkema.
Comité Español de Grandes Presas 1997. *Guías Técnicas de seguridad de Presas y Embalses*. Guía No. 4. Avenida de Proyecto, 107 pp.
Enzel, Y., Ely, L.L., House, P.K. & Baker, V.R. 1993. Paleoflood evidence for a natural upper bound to flood magnitudes in the Colorado river basin. *Water Resources Research* 29: 2287–2297.
Hydrologic Engineering Center 1995. *HEC-RAS, River Analysis System, Hydraulics Reference Manual*, (CPD-69). pag. var.
ICOLD 1995 *Dam failures. Statistical Analysis*. Bulletin 99. Paris: Icold.
Kromer, B. & Becker, B. 1993. German oak and pine C-14 calibration, 7200–9439 BC. *Radiocarbon* 35: 125–135.
Levish, D.R., Ostenaa, D.A. & O'Connell, R.H. 1996. Paleohydrologic bounds and the frequency of extreme floods on the Santa Ynez river, California. *1996 California Weather Symposium, A Prehistoric look at California Rainfall and Floods*: 1–19.
Linnick, T.W., Long, A., Damon, P.E. & Ferguson, C.W. 1986. High-precision radiocarbon dating of bristlecone-pine from 6554 to 5350 BC. *Radiocarbon* 28: 943–953.
Ostenaa, D. & Levish, D. 1996. *Reconnaissance paleoflood study for Ochoco Dam, Crooked River Project, Oregon: Seismotectonic.* Report 96-2, Denver: U.S. Bureau of Reclamation, Seismotectonic and Geophysics Group.
Ostenaa, D., Levish, D. & O'Connell, D. 1994. *Paleoflood study for Bradbury Dam. Reclamation Review Draft, Seismotectonic*. Report 94-3. Denver: U.S. Bureau of Reclamation, Technical Service Center. (Unpublished report).
MJI 1995. *Directriz Básica de Planificación de Protección Civil ante el Riesgo de Inundaciones*. Madrid: Resol. 31 enero, BOE, 38.
MOPTMA 1996. *Reglamento Técnico sobre Seguridad de Presas y Embalses*. Madrid: Orden de 12 de marzo, B.O.E., 78pp.
National Research Council 1985. *Safety of dams, flood and earthquake criteria*. Washington: National Academy Press, 321pp.
Organización Meteorológica Mundial (OMM) 1990. *Manual para la estimación de la precipitación máxima probable. Instituto Nacional de Meteorología de España*.
Penas, J., Berga, L. & de Andrés, M. 1997. *Clasificación de presas en función del riesgo potencial*. Guía Técnica. Serie Monografías. Madrid: Ministerio de Medio Ambiente, 55 pp.
Stedinger, J., Therivel, R. & Baker, V.R. 1988. Flood frequency analysis with historical and paleoflood information, Salt and Verde Rivers, Arizona. In *Proceedings of the Eighth Annual Meeting of the U.S. Committee on Large Dams, Salt River Project, Phoenix, Arizona*: 3.1–3.35.
Stuiver, M. & Pearson, G.W. 1993. High-precision bidecadal calibration of the radiocarbon timescale, AD 1950–500 BC and 2500–6000 BC. *Radiocarbon* 35: 1–23.

Copyright © 2006 Taylor & Francis Group plc, London, UK

Development of a flood inundation model for extreme flood analysis

Kun-Yeun Han & Gwangseob Kim
Department of Civil Engineering, Kyungpook National University, Daegu, Korea

Kyu-Hyun Choi
River Information Center, Seoul, Korea

Jong-Tae Lee
Department of Civil Engineering, Kyonggi University, Seoul, Korea

ABSTRACT: Two-dimensional flood inundation model and quantitative precipitation estimation(QPE) model were developed to evaluate the impact of levee failure for flood analysis. For improved areal rainfall estimation, cokriging technique was adopted to optimally merge radar reflectivity data into rain-gauges data by getting the better information of spatial variability of rainfall fields from weather radar and getting the better quantitative information from rain gauges. For the improved inundation model development, the mathematical formulation of the suggested model incorporates two-dimensional shallow water equations for flood inundation analysis.

The developed model was applied to analyze the inundation flow from the levee break of Gamcheon river during the typhoon Rusa on October 31 through September 1, 2002. To verify the simulated results, wide range field surveys have been performed including the collection of GIS database, land use condition, flooded area, and flow depths. Velocity distributions and inundation depths were presented to demonstrate the robustness of the model. Simulation results have good agreements with the observed data in terms of flood level and flooded area. Methodologies considering radar-rainfall estimation, rainfall-runoff analysis and inundation analysis in this study will contribute to the establishment of the nationwide flood disaster prevention system

1 INTRODUCTION

The climatic change of summer rainfall pattern in Korean peninsula can be summarized as the total number of rain day decreases, nevertheless, the total amount of rainfall increases, and the total number of days, whose daily rainfall amount is greater than 80 mm, increases. Floods are the most frequent natural hazards in Korea: typhoon Rusa took 213 lives and caused $5 billion worth of damage in 2002, and typhoon Memi took 117 lives and caused $4.5 billion worth of damage in 2003 (http://www.kma.go.kr). To evaluate the probable flooding damages, we need an accurate numerical model for flood and inundation analysis as well as accurate spatial rainfall estimation technique. Therefore a comprehensive approach is essential to analyze the flood and inundation effectively.

The analysis of flood wave resulting by the sudden collapse of a dam or river levee is studied continuously after development of a set of hyperbolic partial differential equations, well known as Saint-Venant equations. Katopodes and Strelkoff (1978) developed two-dimensional numerical model using characteristic curves but it is relatively complex to use. Kawata and Nakagawa (1984) and Tachi et al.(2001) represented the relationships between flood waves and obstacles in protected lowlands such as buildings, trees etc. Han et al.(1998, 2003, 2004) analyzed the characteristics of flood waves in protected low lands caused by levee breaks. In this study, a 2-D flood inundation model was developed to evaluate the impact of levee failure in a natural basin for flood analysis.

The variability of rainfall has the most critical influence on the performance of hydrologic models. Traditionally, hydrologic models have depended on rain gauge networks to provide the areal-averaged rainfall information. It will provide incorrect representation of the spatial characteristics of rainfall fields, especially in convective weather systems where rainfall amounts vary significantly over small regions. The spatial variability of rainfall in mountainous regions is very large because of orographic influences (Li et al., 1995). Korea is mountainous and marked by deep, narrow valleys. A complex system of mountain ranges and spurs extends across the country. Therefore accurate spatial rainfall information is essential to analyze the rainfall runoff process appropriately. Therefore

Copyright © 2006 Taylor & Francis Group plc, London, UK

accurate spatial rainfall information is essential to analyze the rainfall runoff process appropriately. In this study, we introduced an ordinary cokriging technique which optimally merges radar reflectivity data into rain-gauges data (Krajewski, 1987).

The purpose of this study is to develop an integrated model of the advanced spatial rainfall estimation technique and flood inundation analysis to simulate two-dimensional surface flow during floods.

2 MODEL DESCRIPTION

In this study, two-dimensional flood inundation analysis model was developed to evaluate the impact of levee failure in a natural basin for flood analysis. The mathematical formulation of the suggested model incorporates 2-dimensional shallow water equations for flood inundation analysis. The two-dimensional unsteady shallow water equations consist as follows:

$$\frac{\partial h}{\partial t}+\frac{\partial q_x}{\partial x}+\frac{\partial q_y}{\partial y}=0 \tag{1}$$

$$\frac{\partial Q_x}{\partial t}+\frac{\partial}{\partial x}\left(\frac{Q_x^2}{A_x}\right)+\frac{\partial}{\partial y}\left(\frac{Q_xQ_y}{A_y}\right)+gA_x\left[S_{fx}+\frac{\partial H}{\partial x}\right]=0 \tag{2}$$

$$\frac{\partial Q_y}{\partial t}+\frac{\partial}{\partial y}\left(\frac{Q_y^2}{A_y}\right)+\frac{\partial}{\partial x}\left(\frac{Q_yQ_x}{A_x}\right)+gA_y\left[S_{fy}+\frac{\partial H}{\partial y}\right]=0 \tag{3}$$

where Q_x, Q_y are the flow rates in the x- and y-directions, respectively; q_x, q_y are flow rates per unit width in the x- and y-directions; A_x, A_y are the cross sectional areas; s_{fx}, s_{fy} are the friction slopes in the x- and y-directions; g is gravitational acceleration, h is water depth; and H is water surface elevation.

The developed model consisted of unstructured mesh basis to analyze complex flow problems associated with complicated topography and boundary of protected lowlands. Figure 1 shows a sample element of unstructured mesh. Where c denotes the center element in computation; 1, 2, 3, 4 are adjacent elements number; G_i is coordinate of centroid of mass for each element; a_i is area of each element; n_i is coordinate of corner points of center element; L_{ij} is distance between centroid of element i and boundary with element j; and SL_i is length of i-side.

The two-dimensional unsteady shallow water equations for unstructured meshes are can be written as

$$\frac{\partial q_i}{\partial i}+\frac{\partial h}{\partial t}=0 \tag{4}$$

$$\frac{\partial Q_i}{\partial t}+\frac{\partial}{\partial i}\left(\frac{Q_i^2}{A_i}\right)+gA_i\left[S_{fi}+\frac{\partial H}{\partial i}\right]=0 \tag{5}$$

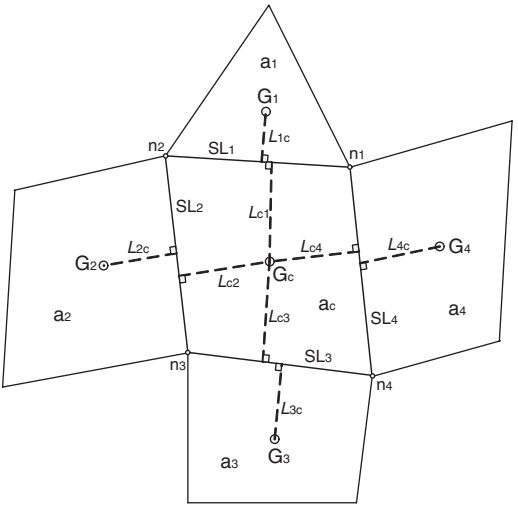


Figure 1. Sample element for two-dimensional flood analysis.

where Q_i is the flow rates in the i-direction; q_i is flow rates per unit width in the i-direction; A_i is the cross sectional area; s_{fi} is the friction slope in the i-direction; g is gravitational acceleration; h is water depth; and H is water surface elevation.

The friction slope, S_{fi}, can be written as follows using Manning's formula

$$S_{fi}=\frac{n_i^2|Q_i|Q_i}{\varphi^2A_i^2R_i^{4/3}} \tag{6}$$

where n_i is Manning's roughness coefficient; ψ is 1 for SI units and 1.49 for US Customary units; $R_i=(A_i/P_i)$ is hydraulic radii, P_i denotes the perimeter for i-direction. Equation 5 can be written as

$$M_i+\left\{S_{fi}+\frac{\partial H}{\partial i}\right\}=0 \qquad \text{where} \quad Mi=\left(\frac{\partial Q_i}{\partial t}+\frac{\partial}{\partial i}\left(\frac{Q_i^2}{A_i}\right)\right)/gA_i \tag{7}$$

Arial and directional components of unstructured element are computed by Equations (8) and (9).

$$\theta_k=\tan^{-1}\left(\frac{y_k}{x_k}\right) \tag{8}$$

$$\frac{1}{2}\sum_{k=1}^{n}\det\begin{vmatrix}x_k & x_{k+1}\\ y_k & y_{k+1}\end{vmatrix}=0 \tag{9}$$

Copyright © 2006 Taylor & Francis Group plc, London, UK

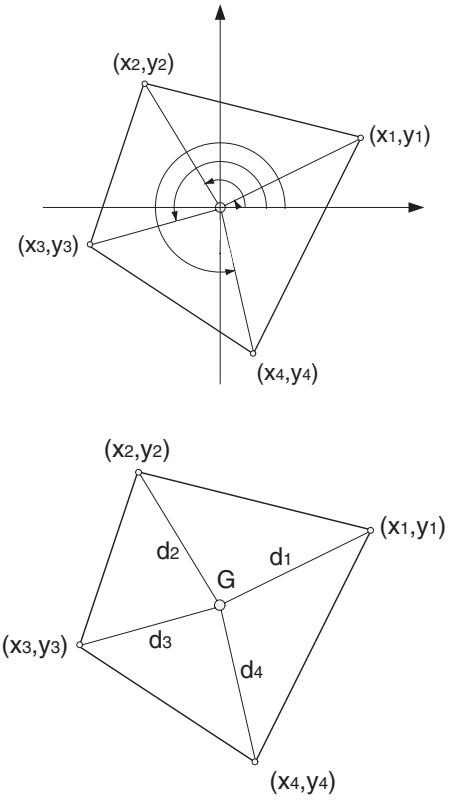


Figure 2. Schematic of arial and directional components of unstructured element.

The elevation of centroid was estimated using inverse distance method.

$$z_G = \frac{\sum_{r=1}^{n} d_r z_r}{\sum_{r=1}^{n} z_r} \tag{10}$$

where z_r is elevation of corner points; $d_r = \{(x_r - x_G)^2 + (y_r - y_G)^2\}^{1/2}$

Optimal time step, Δt is estimated using Courant-Friedrichs-Lewy (CFL) stability condition. The differences in flow rates Q and water depth h were estimated respectively as

$$\Delta Q_c^j = -\left\{ \sum_{i=1}^{3 \text{ or } 4} q \,|\, \Gamma_i \cdot \delta_i \right\} \tag{11}$$

$$\Delta h_c^j = \frac{\Delta Q_c^j \cdot \Delta t}{a_c} \tag{12}$$

where δ_i is length of i-side.

At time step $j+1$, the water surface elevation H of element c can be estimated as

$$H_c^{j+1} = H_c^j + \Delta h_c^j \tag{13}$$

The model is able to compute maximum stage and peak discharge efficiently in channel and protected lowland.

3 RAINFALL ESTIMATION USING GEOSTATISTICAL APPROACH

Based on the assumption that rain gauge networks give us the accurate rainfall quantity at a point and weather radar gives us accurate spatial distribution of rainfall fields, a geostatistical approach is employed to describe the spatial structure of rainfall fields. Geostatistical estimation techniques such as kriging give us unbiased linear estimations with minimum error variance. A linear estimator for rainfall estimation can be written as

$$\hat{P}_0 = \sum_{i=1}^{N_G} \alpha_i P_i + \sum_{j=1}^{N_R} \beta_j M_j \tag{14}$$

where M is radar reflectivity data, P is rain gauge data. N_G is the number of rainfall gauges, and N_R is the number of radar bins. Now we have two sets of coefficients: those that multiply the rainfall measurements and those that multiply the radar reflectivity measurements. The two sets of coefficients have different units.

The estimation problem is reduced to estimating the coefficients of α's and β's. The estimation error, defined as the difference between the estimate and the actual value of P_0 is

$$\hat{P}_0 - P_0 = \sum_{i=1}^{N_G} \alpha_i P_i + \sum_{j=1}^{N_R} \beta_j M_j - P_0. \tag{15}$$

The coefficients must be such that the variance of the estimation error is as small as possible. The coefficients can be determined by minimizing the Equation (16)

$$E[(\hat{P}_0 - P_0)^2] = E\left(\sum_{i=1}^{N_G} \alpha_i (P_i - G) + \sum_{j=1}^{N_R} \beta_j (M_j - S_j) - (P_0 - G) \right)^2 \tag{16}$$

Figure 3 represents the schematic diagram of the computation processes of the spatial rainfall data including quality control process of rain gauge and radar reflectivity data, computation of multi resolution constant altitude plan position indicator (CAPPI), and merging filtered radar reflectivity data into rain gauge data ordinary cokriging.

Figure 4 shows the schematic diagram describing the procedures of spatial rainfall estimation and flood analysis by developed model.

Copyright © 2006 Taylor & Francis Group plc, London, UK

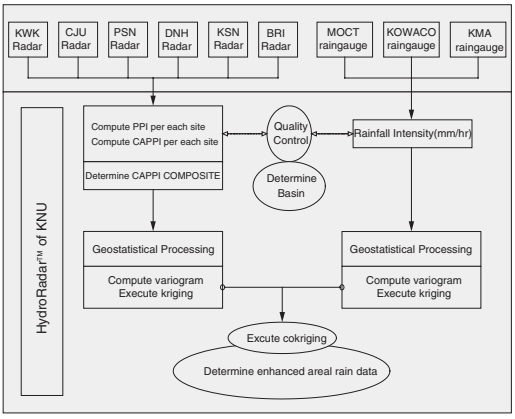


Figure 3. Schematic diagram of the computation processes of the spatial rainfall data.

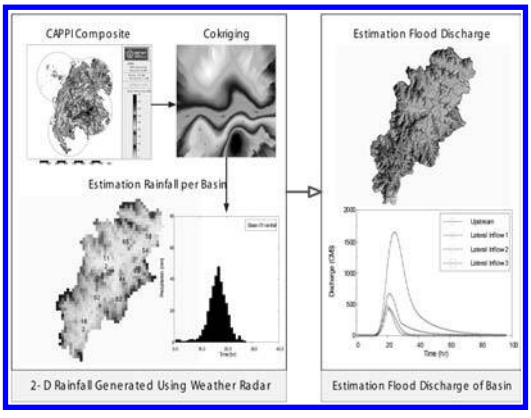


Figure 4. Schematic diagram describing the procedures of spatial rainfall estimation and flood analysis by the developed model.

4 RESULTS AND DISCUSSION

The model was applied to analyze the inundation flow from the levee break of the Gamcheon river during the typhoon Rusa on October 31 through September 1, 2002. Rusa was the most violent typhoon to hit South Korea since 1959. During the typhoon Rusa, 213 people were dead and 33 people were missing. The total damage estimates were more than 5 billion US$. The rainfall field estimated using rain gage data and radar reflectivity data by cokriging was able to describe the spatial structure of rainfall fields more accurately than that using only rain gage data. Results show that rainfall fields estimated by ordinary cokriging give the improved results than that of traditional approach. Figure 5 represents topography and watershed characteristics of the Gamcheon basin. The watershed

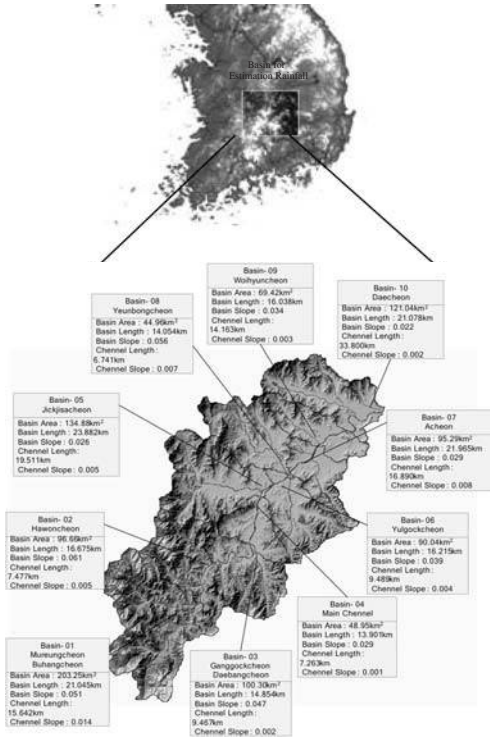


Figure 5. Topography and watershed characteristics of the Gamcheon basin.

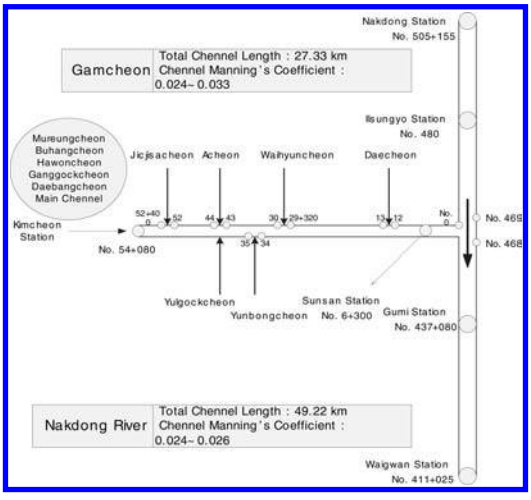


Figure 6. Schematic diagram describing characteristics of channel networks in Gamcheon river system.

was subdivided to ten small watersheds as shown in the Figure 5. Figure 6 shows the schematic diagram describing characteristics of channel networks in the Gamcheon river system. The Muskingum and

Copyright © 2006 Taylor & Francis Group plc, London, UK

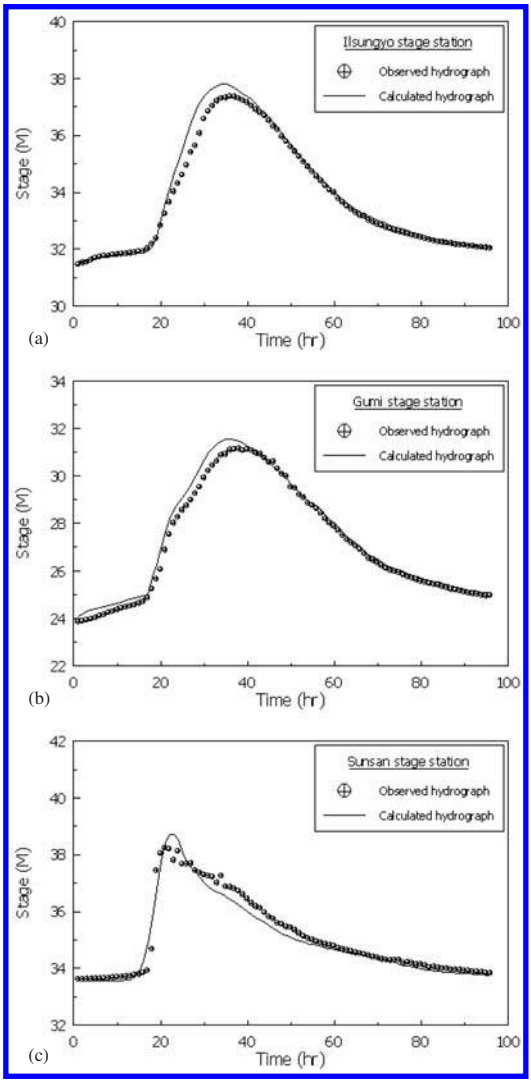


Figure 7. Observed and calculated stages at (a) Ilsungyo, (b) Gumi, and (c) Sunsan.

Clark methods were used for the flood routing. To verify the simulated results, wide range field surveys have been performed including the collection of NGIS(National Geographic Information System) database, land use condition, flooded area, and flow depths. Figure 7 shows the observed and calculated stages at Ilsungyo, Gumi, and Sunsan stations respectively. Sunsan station is located at the downstream of the Gamcheon river, Ilsungyo and Gumi stations are located up- and down-stream of the Gamcheon river inflow along the Nakdong river respectively. Results show good agreement between the simulated and observed data. Velocity distributions and inundation

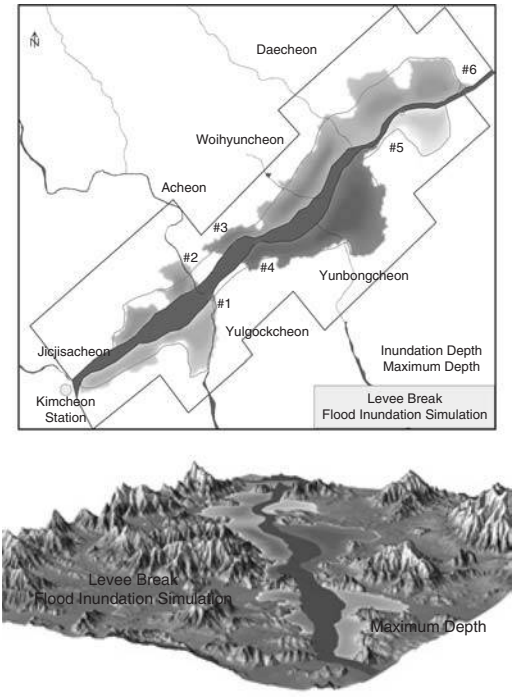


Figure 8. Observed flooded area (solid line) and the simulated flooded area (shaded area).

depths for different time were presented. Model results have good agreements with the observed data in terms of flood level and flooded area. Figure 8 represents the observed flooded area (solid line) and the simulated flooded area (shaded area). Overall results show good agreements with observed data and demonstrate the robustness of the model. The developed model will contribute to the establishment of the national integrated flood disaster prevention system and the river or protect lowland management system.

ACKNOWLEDGEMENTS

This study was supported by the 2003 Core Construction Technology Development Project(03-SANHAKYOUN-C03-01) through the Urban Flood Disaster Management Research Center in KICTTEP of MOCT, KOREA.

REFERENCES

Fread, D.L. (1988). *The NWS DAMBRK Model: Theoretical Background/User Documentation*, Office of Hydrology, National Weather Service(NWS), Maryland, USA.

Copyright © 2006 Taylor & Francis Group plc, London, UK

Han, K.Y., Kim, G., and Choi, K.H. (2004). "Inundation analysis for basinwide flood management." *The 3rd Seminar on the Technology of Disaster Management on Urban Flood*, Seoul, Korea.

Han, K.Y., Lee, J.T., and Choi, K.H. (2003). "Levee breach and flood inundation modeling in urban areas." *30th IAHR Congress*, Greece.

Han, K.Y., Lee, J.T., and Park, J.H. (1998). "Flood inundation analysis resulting from levee-break." *Journal of Hydraulic Research*, Vol. 36, No. 5, pp. 747–760.

Li, L., Schmid, W., and Joss, J. (1995). "Nowcasting of motion and growth of precipitation with radar over complex orography." *Journal of Applied Meteorology*, Vol. 34, pp. 1286–1300.

Krajewski, W.F. (1987). "Cokriging radar-rainfall and rain-gauge data." *Journal of Geophysical Research*, Vol. 92, pp. 9571–9580.

Katopodes, N. and Strelkoff, T. (1978). "Computing two-dimensional dam-flood waves." *Journal of Hydraulic Engineering*, ASCE, Vol. 104, No. 9, pp. 1269–1288.

Kawata, Y., and Nakagawa, H. (1984). "Flood disasters in the Misumi river-Flooding and damages of houses." *Annuals of the Disaster Prevention Research Institute*, Kyoto University, Vol. 27B-2, pp. 1–18.

Tachi, K., Suetugi, T., Kobayashi, H., and Tomaru, M. (2001). "Flood damage mitigation effect of groves in the flood plain, study on the Yosasa river basin." *Annual Journal of Hydraulic Engineering*, Vol. 45, pp. 913–918.

Copyright © 2006 Taylor & Francis Group plc, London, UK

A management system to optimize reservoir control in the case of floods

R. Pohl & A. Bornschein
Dresden University of Technology, Germany

ABSTRACT: Many multipurpose reservoirs are situated in the low mountain range of Germany. Most of them are necessary for drinking water supply and flood protection as well. Other utilizations are recreation, water power and the downstream low water regulation during dry seasons. The operation rules of the reservoirs have to be optimized to meet the different requirements of use. One tool within this framework is a management system for river basins including all reservoirs and their specific operation rules affecting the downstream reaches. As an optimization objective for instance the minimization of inundation risks can be defined. In this case the risk can be defined as hydraulic and hydrologic safety of the reservoir itself and the risk due to inundation and damaging in the downstream regions. Considering the European Water Framework Directive the ecological aspect of reservoir management is one more point in the optimization process. To establish a pilot project the software TALSIM will be applied to river catchments in the ore mountains (Saxony).

1 INTRODUCTION

In the last few years some big flood events occurred in the catchments of the rivers Elbe, Danube and Odra in Germany (Figure 1). Heavy damages occurred. Thus 21 people were killed and substantial parts of the infrastructure were destroyed during the 2002 flood.

The total loss in Germany was estimated to be 11.9 billion €. These floods have dramatically called attention to limits and deficits of flood risk management in the affected areas. It became obviously that there was a need to develop and implement improved instruments of flood risk management by the integration of different professional disciplines and experts in different fields.

The German Federal Ministry of Education and Research (BMBF) funded the national research program RIMAX (risk management of extreme flood events). The program has duration of 3 years (www.rimax-hochwasser.de). It focuses on flood events with a return period greater than 100 years and with high damage potential.

The program consists of three major subjects:

– Integrated concepts of flood risk management
– Technical flood protection



Figure 1. River Elbe with flooded open air cinema in Dresden during the 2002 flood event (photograph: Bornschein).

Copyright © 2006 Taylor & Francis Group plc, London, UK

– General issues (e.g. Education, Networking, Flood awareness and Risk communication)

The general issues should warrant the knowledge transfer into practice and education as well as the national and Europe-wide network of research activities. The research program stresses on implementation, which means, that the funded projects have to collaborate with responsible organizations at different political levels.

The research program includes more than 30 research projects with partners from universities, engineering consultants, governmental organizations and dam authorities. The first projects started in summer 2005. There is a wide range of research themes such as ground water management in urban areas in the case of extreme floods, reservoir and polder management, geo-textiles, stability of dikes and levees, flood retention in river networks, flood prediction and management, flood impacts on water supply, risk management and risk prediction using historical flood data information.

2 OBJECTIVES OF THE PROJECT

The presented project is a joint project between the Institute of Hydraulic Engineering and Applied Hydromechanics of the University of Technology Dresden and the Institute of Hydraulic Engineering and Water Management of the University of Technology Darmstadt, both are situated in Germany.

The research work of the project is focused on the improving of tools to analyze, evaluate and to manage flood risks. The future aim is to integrate the flood risk management including the reservoir operation strategies into the river catchments management.

In the end the flood risk of a certain flood event should be reduced in terms of both the failure probability of the dams and the consequences (damages, costs, impacts etc.) in the downstream areas. This means that an optimization has to be carried out to find the reservoir operation rules with the lowest environmental impact and the highest structure safety (dams, weirs, levees). Two strategies are possible: On the one hand a risk management system can be established due to pre-calculations of possible flood events including the consideration of retention in reservoirs and polders. On the other hand a just in time calculation can help to achieve better operation rules during a flood event.

In a catchments area the reservoirs and dams, the structures in the downstream regions like weirs, dikes and levees, the urban areas, industries and agricultural might be at risk. Furthermore the preservation and the improvement of the ecological system in the river basin, in the reservoirs and the river network are very important requirements of the risk management system.

3 INPUT DATA

The system which comes out of the research project has to include the calculation of the discharge in the whole catchments area (precipitation-runoff-calculation), retention calculation of the reservoirs and the computation of wave propagation downstream the dams with the determination of inundation areas. Furthermore the damages occur due to the flooding have to be calculated.

This needs a wide range of input data which are described in the following paragraphs.

3.1 *Digitalized morphological data*

A digitalized morphological data set is the basis for the whole system. It determines the river morphology, the geographical data set for precipitation run off calculation and provides the information of land use and soil properties as well as the location of buildings and bridges (Figure 2).

The profiles of river cross section are often determined by terrestrial surveying. Additionally laser scan data or digital topographical maps are used for the whole watershed and the floodplains.

3.2 *Precipitation and discharge*

To model the areal precipitation for the whole watershed, the polygon method will be used.

This method is used because of the non uniform measurement station spacing. To determine the areas belonging to each station, lines are drawn between adjacent stations on the map. The perpendicular bisectors of these lines form a pattern of polygons with one station inside each polygon (see Figure 3). These are the areas in which the measured precipitation of each station will be used to calculate a certain event for the whole watershed.



Figure 2. Morphological data set with vegetation and buildings from laser scan (confluence of the rivers Wilde Weißeritz and Rote Weißeritz at the town of Freital; data: LTV 2005).

Copyright © 2006 Taylor & Francis Group plc, London, UK

Furthermore data are needed to estimate the maximum possible precipitation (DVWK 1997 and DWD 1997), the discharge of a flood event with a certain reoccurrence (LfUG 1993) and the soil-moisture at a certain event.

To validate the calculated discharge from precipitation-runoff-analysis gauge data will be needed. Considering bigger flood events where the discharge measurement didn't work it is also possible to validate the discharge by use of hydraulic water level calculation and comparison with measured water levels along the river banks or at bridges and buildings.

3.3 *Operation strategies and rules for dams, reservoirs and polders*

The operation rules of a controlled reservoir determine the future reservoir water level and the outflow hydrograph depending on the inflow hydrograph, the initial reservoir water level, the actual season and the precipitation forecast. These operation rules depend on reservoir purposes like flood protection, water supply, low water regulation, fishing and recreation benefits.

There are different common operation strategies for reservoir storages and release decisions like the following:

- Determination of a minimal and maximal outflow discharge; the minimal outflow discharge often depends on ecological reasons; the maximal outflow discharge could be determined by the inbank capacity in a downstream river reach.
- For flood control purposes free reservoir storage has to provide enough volume to keep a flood of a certain reoccurrence within the reservoir. This could mean to discharge more water downstream in anticipation of a flood event.
- Water supply for drinking water or industrial water demands a defined release discharge to meet the needs.
- Controlled outflow to balance the downstream flow (reservoir storage management plan).
- Low water regulation (to ensure a critical water level for commercial navigation, thinning of wastewater inflow, fulfilment of a water supply demand downstream).
- The reservoir outflow depends on the reservoir inflow.
- Release decisions depending on other states of the system (actual water level in other reservoirs in the same or in other catchments areas, actual discharge in a special river reach, the snow height in the catchments area, actual precipitation, actual soil moisture and others).

All release decisions may vary with respect to the time. The outflow discharge is limited by the gate opening and or the spillway capacity (Figure 4).

In the case of a multipurpose reservoir there are often competing purposes. One example could be flood protection and water supply. Flood protection needs an initially large empty flood control storage resulting in a low water level. Water supply needs a high water level because of required supply safety and the need of water extraction in different water levels to guarantee the water quality.

But in the case of an extreme flood event it is difficult to control the outflow. In Figure 5 the inflow, outflow and storage hydrographs of the Malter reservoir in Saxony are shown during the flood event in August 2002. The volume of the whole flood wave was 11 times bigger than the flood detention storage of the reservoir and almost triple of the total storage

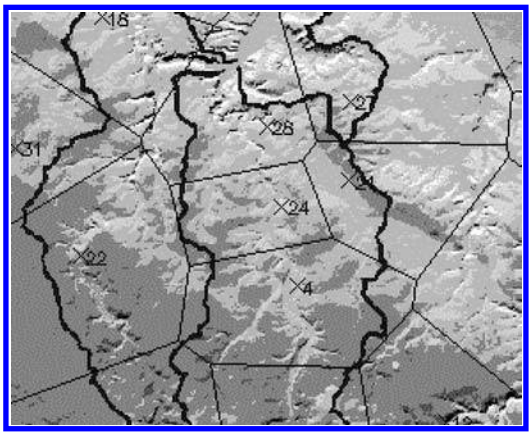


Figure 3. Polygon method to calculate the areal precipitation distribution in the catchments area of the Weißeritz river (x = the location of a precipitation station; – = border of the related areas).



Figure 4. The intake of the spillway of the Malter dam on 13th August 2002.

Copyright © 2006 Taylor & Francis Group plc, London, UK

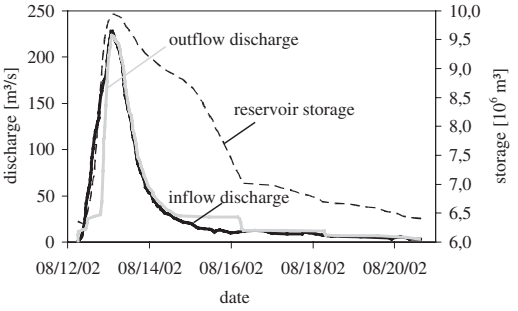


Figure 5. Inflow and outflow hydrographs as well as reservoir capacity of the Malter reservoir during the flood in August 2002 (LfUG 2002).

volume of the reservoir. The inflow and outflow peak are almost the same.

Polders often have more simple operation rules. In the case of an uncontrolled polder the inflow begins when the water level in the river exceeds a certain level. If there is a gated inflow structure the filling of the polder can be delayed until the flood peak arrives.

4 OPTIMIZATION CRITERIA

The optimization process is mainly based on a multi-criterion matrix which includes different types of optimization criteria.

4.1 *Freeboard and overtopping of dam*

The new German standard (DIN 19700) gives two design cases for dams. Furthermore the hydraulic safety of the dams has to be considered (Pohl & Horlacher 1996 and Pohl 1999). In the risk management the failure frequency of gates and valves at dams has to take into consideration (Pohl 2000 and Martin & Pohl 2002).

If the water level in a reservoir or in the river reaches a certain level the dam or levee could be overtopped. Because of the possibly unstoppable erosion process due to overtopping and the following completely destruction this must be avoided at all costs (Aigner et. al. 2002 and Bornschein & Pohl 2003). So the level of the dam crest or the top of a levee or dike is a very strong criterion for maximum water level.

4.2 *Stability of dams and levees*

There are different stability criteria for each type of hydraulic structure like dams, dikes, levees, weirs. They are e.g. described in dam or levee standards and guidelines. Typical failure modes are sliding, overturning, erosion due to piping or overtopping.

The difference in water level outside and inside a levee has an influence on seepage and can reduce levee stability.

Just before overtopping extraordinary water surface elevation can reduce the stability of a dam. In general safety coefficients below 1 indicate insufficient stability and therefore a severe failure risk.

4.3 *Inundation damages*

The inundation of industrial and urban areas or forests and farmland results in different types of damages which are:

- Asset damages (economic, public and private)
- Production downtimes (during and after the flood event)
- Casualties
- Damage to cultural buildings or sites with considerable ideal losses
- Ecological impacts

Some of these damages were recorded or can be expressed monetarily. An advanced description of possible damage due to high water levels is a stage-damage-function. This is a summary statement of direct economic cost of flood water inundation for a specific river reach (US Army 1996). This function depends on the land use and the kind of structures within the considered area (residential structures, non-residential structures).

There is a wide range of different stage-damage-functions. Therefore the above mentioned RIMAX program includes also research groups dealing with damage functions.

But some damages can be described only qualitatively. Therefore an evaluation system with qualitative description has to be used. A very simple example is the classification of damages into groups as high, mean, low and none.

4.4 *Ecological impacts*

The operation of dams, the installation of weirs as well as the set up of dikes and levees change the landscape and have ecological impacts.

A qualitative calculation of this impact is very difficult or often impossible. One has to distinguish between the ecological impacts in mean level and low level times and in the case of a flood event.

In times of a low water level the water temperature and oxygen content have often negative impacts on protozoa, fishes and plants. The reservoir operation rules could help to avoid critical states in the stream.

But also a flood itself has negative ecological impacts although a flood is a natural phenomenon. Too frequent and too long inundation of floodplains or polders can hurt the flora and fauna. Since the velocity is high fishes may floating away during a flood event.

Copyright © 2006 Taylor & Francis Group plc, London, UK

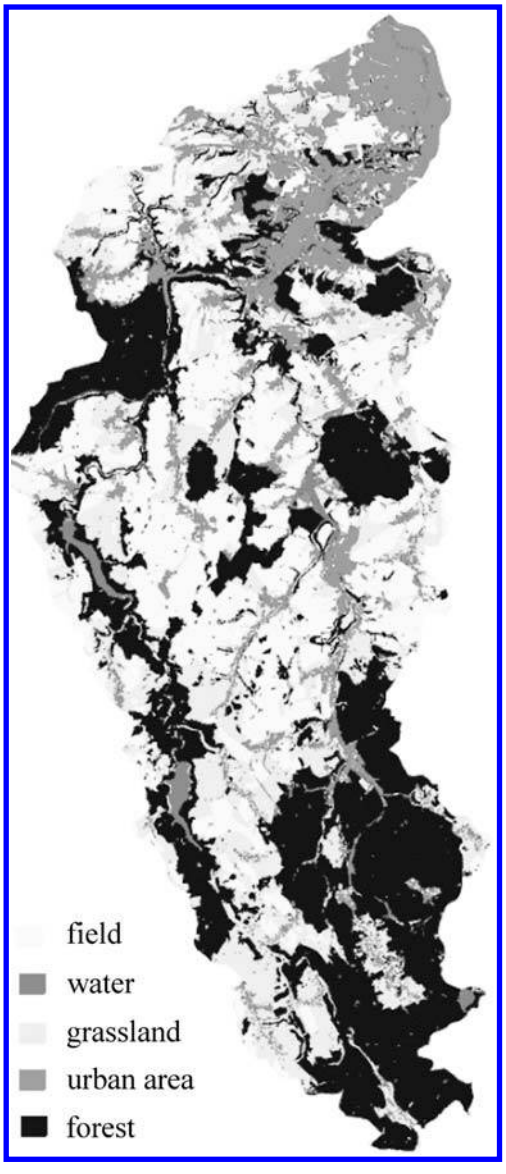


Figure 6. Land use in the Weißeritz watershed (LTV 2005).

5 CALCULATION PROCEDURE

To find out the optimum operation strategy several calculation steps have to be included in a calculation procedure. The separate computation steps that have to be repeated many times can be described as follow:

1 Precipitation-runoff-calculation in the whole watershed using TALSIM. The result is the discharge hydrograph in each river reach (Q(t)).
2 Determination of stage-discharge-relation at each cross section using a water level calculation for different flood scenarios.
3 Determination of a relation between a certain water level and the possible damage at a certain river reach
   – allocation of a flooded area to a certain water level at each cross section
   – selection of the appropriate stage-damage-function depending on the major land use in the flooded area
   – addition of all damages related to a water level at each cross section
4 determination of the relation between the amount of damage and the river discharge using the results from step 2 and 3
5 determination of a multi-criteria objective function for optimization purposes including monetary and non-monetary criteria
6 search of this operation strategy with the lowest damage for all possible flood events or the most of them.

To check the different operation strategies it is necessary to use artificial flood events with a reoccurrence period of about 20 to 100 years and beyond and the series of historical flood events if recorded.

5.1 *Precipitation-runoff analysis using TALSIM*

The TALSIM software has been developed to solve water management problems including reservoirs at Darmstadt University, chair of hydrology and SYDRO-Consultants. Water management systems like a multi reservoir system or a river basin can be modelled.

The description of the water management system needs different artificial system elements. A system element yields a certain output under certain defined input conditions. Different system elements have been connected to create the whole water management system.

The following elements are available: single discharger, reservoir, customer, transport element (= river reach), branch and single catchments area. An element is described by characteristics and parameters. Characteristics can be determinate clearly like a cross section shape of a river reach. Parameters need a calibration and validation process like the roughness parameter of the river bed. A special element uses different methods to transform the input data into the output data.

The level of discretization of the water management system depends on possible cost and effort as well as how detailed the output is needed.

To calculate the precipitation-runoff process three models are implemented. The most simple is to define

Copyright © 2006 Taylor & Francis Group plc, London, UK

a fixed discharge coefficient for each single catchment area depending on land use, altitude and subsoil properties.

More advanced is the widely used soil-conservation service method (SCS-method) or curve number method considering soil texture, land use and soil moisture. The Curve number and the total precipitation of the last 21 days are necessary for input.

The highest effort needs a complex soil moisture and ground water calculation. This model needs a wide range of detailed measured data and is only recommended for smaller catchments areas.

TALSIM is not a hydrodynamic model. The flood routing and water retention in a river network are approximated using the conceptual model of *Kalinin-Miljukov.*

5.2 *Water level calculation and determination of inundation area*

To connect the damages due to the inundation with the precipitation-runoff-model a one-dimensional hydrodynamic model has been introduced into the calculation.

A possible hydrodynamic model is HEC-RAS developed by the Hydrologic Engineering Center of the US Army Corps of Engineers (USA). It solves the one-dimensional shallow water equation and can be used for both steady state and dynamic water level calculation. Backwater effects of bridges and weirs as well as more complex cross sections can be considered.

The water level from the hydrodynamic model together with the digital morphological data set let to the inundated area due to a certain river discharge.

5.3 *Polder*

There is no special element or tool to describe a controlled polder within TALSIM. Therefore a combination of different elements has to be established.

The polder itself is represented by the element "Reservoir". A water-level-storage-relation must be known as input. The distribution of the flow at the inflow cross section of the polder can be modelled using the element "branching" with a threshold model (Figure 7). If the discharge reaches a critical value the inflow into the polder begins.

To determine the actual characteristics of inflow structure it is possible to set "selectivity" for it. Another possibility is to set a variable threshold $Q_{crit.}$

The outflow from the polder can be included in an element "river reach". The definition of a weir or an operation rule is necessary at this cross section.

5.4 *Model calibration*

Previous flood events among them the 2002 event in Saxony are used to calibrate the model. First the

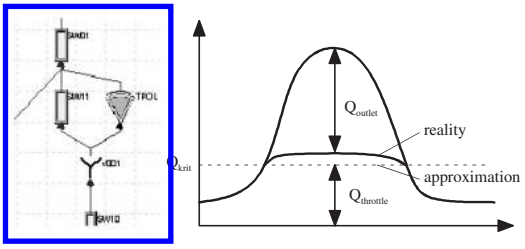


Figure 7. System elements of TALSIM describing a polder with rectangles = river reaches and triangle = reservoir (left) and the principle of the threshold model for the polder inflow (right).

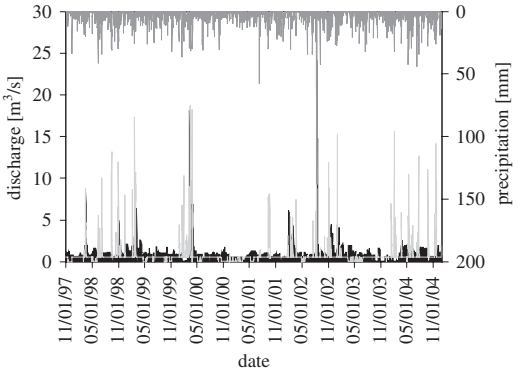


Figure 8. Measured (–) and simulated (–) water level at the gauge Lehnmühle UP together with precipitation data (–) of the station Fichtelberg.

modelling of the precipitation-runoff-relation has to be verified. Figure 8 shows the precipitation measured at the rain gauge Fichtelberg versus the measured and calculated discharge at the gauge Lehnmühle in the period from November 1997 to November 2004.

At the moment the agreement is not sufficient due to the assumption that the measured precipitation at one rain gauge is equal to the areal precipitation of the whole catchments area of the discharge gauge, which is about 60 km^2. Therefore further data and calibration are needed.

Another calibration is necessary for the hydrodynamic model and calculation of the water level. Water level and discharge measurements are required. The water level of the extreme 2002 flood event is available. More data of this quality would be desirable. This event represents a reoccurrence interval of about 500 years for the Weißeritz watershed (LfUG 2004).

6 CASE STUDY

To evaluate the effectiveness and usability of the calculation model two case studies will be carried out. The Weißeritz case study will be presented shortly.

Copyright © 2006 Taylor & Francis Group plc, London, UK

Table 1. Catchments area, river length and altitude of the Weißeritz River (LfUG 2004).

Catchments area	Area [km^2]	River length [km]	Altitude max. [m a.s.l.]	Altitude min. [m a.s.l.]
Wilde Weißeritz	163	52.9	735	185
Rote Weißeritz	154	35.4	765	185
Weißeritz	67	14.2	185	110
Total	384	102.5		

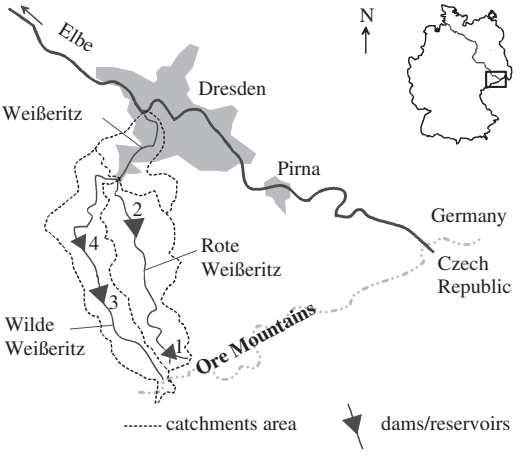


Figure 9. Catchment areas of the three Weißeritz rivers with existing dams (the numbers of the dams refers to table 2).

Table 2. Dams in the Weißeritz catchments.

Catchments area	No. of the dam	Name of the dam or Storage system	Storage [10^6 m^3]
Rote Weißeritz	1	Altenberg	1.036
	2	Malter	9.2
Wilde Weißeritz	3	Lehnmühle	23.53
	4	Klingenberg	17.49

Three rivers belong to the Weißeritz watershed. The Rote (red) Weißeritz River and the Wilde (wild) Weißeritz River have their sources in the Ore Mountains (Figure 9). The Weißeritz River (also named Vereinigte (united) Weißeritz River) originates due to the confluence of these two rivers at the town of Freital (figure 2). The Weißeritz River runs into the Elbe River at Dresden.

There are four reservoirs situated in the Weißeritz watershed all directly connected with the natural river system (Figure 9 and Table 2). The Rote Weißeritz River begins at the Altenberg reservoir. Furthermore



Figure 10. The Klingenberg gravity dam in the Weißeritz catchment area (photograph: LTV).

the Malter dam is situated at the Rote Weißeritz River. This is a multipurpose reservoir for flood retention, water supply and recreation.

There are the Klingenberg dam (Figure 10) and the Lehnmühle dam in the catchment area of the Wilden Weißeritz River. The main purpose of these two reservoirs is the drinking water supply for the town of Freital and the city of Dresden. Another purpose is flood control.

There are 21 precipitation stations within and near the Weißeritz watershed.

7 FIRST RESULTS

First calculations were made to check the reliability and the results of a reservoir or polder retention model. In the case of reservoirs and polders it was very important to find the right point in time to open the outlets (dams) or inlets (polder). As already expected the results were sensitive to the reliability of the forecast of the discharge hydrograph.

As an example a polder with a reservoir surface of $A_p = 2\,km^2$ was taken into consideration. The mean discharge in the river (in the frame of this example the Elbe river, also a federal navigation waterway) was set to the mean discharge $MQ = 400\,m^3/s$ whereas the peak flow was $Q = 4500\,m^3/s$. The time to peak was set to 48 h. It was assumed that the river was 250 m wide and the longitudinal bottom slope was $I = 0.0003$. The elevation of the river bed was 102.0 m a.s.l. The *Strickler* coefficient of the river bed was $k_{st} = 36\,m^{1/3}/s$ ($n = 0.0277\,s/m^{1/3}$).

The polder bottom was set to 105 m a.s.l. and the inflow of the polder had a fixed overflow crest at a level of 105.2 m a.s.l. There were two dike gates each 20 m wide. If the water level reached 108.0 m a.s.l. the 1st of two dike gates was opened. When opening the 2nd dike gate the water level had to be at 109.5 m a.s.l. The dike crest is set to 110.5 m a.s.l and for the crest width 1414 m was chosen.

The calculation uses a time step of $dh = 0.08\,h$. If the dike gates are opened in perfect matter just before the discharge reaches its maximum the peak reduction is more than $300\,m^3/s$, it is about 7% (Figure 11).

Copyright © 2006 Taylor & Francis Group plc, London, UK

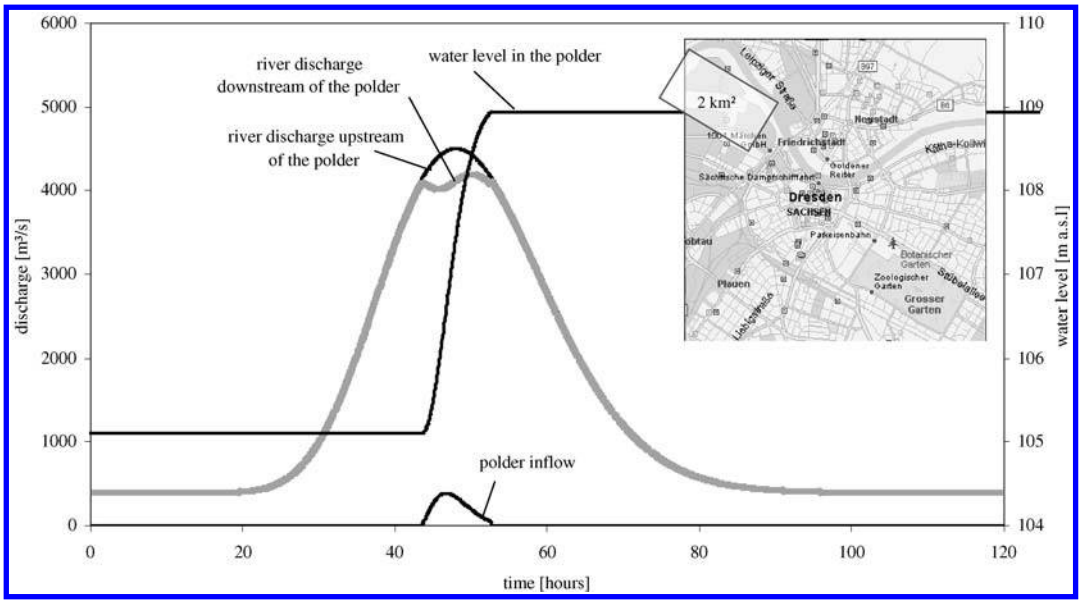


Figure 11. Example for controlled polder flooding with sufficient reduction of peak discharge.

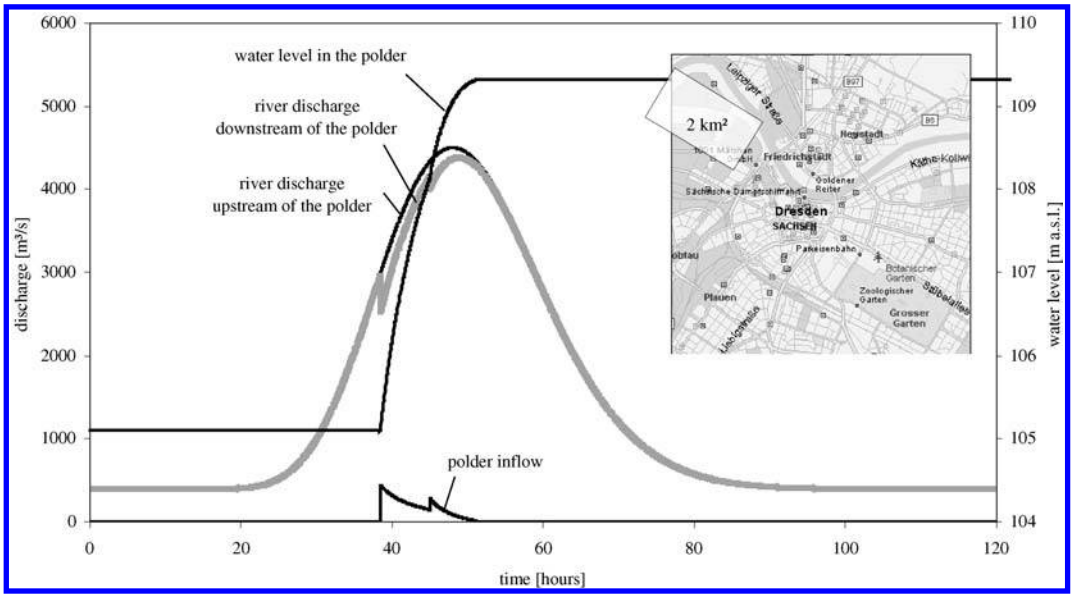


Figure 12. Insufficient peak discharge reduction due to inexact prediction of river flow discharge.

Copyright © 2006 Taylor & Francis Group plc, London, UK

Due to inexact forecast and an early opening of the inlets the retention effect could be completely lost. In Figure 12 the discharge hydrograph is shown. The polder was flooded to early and the peak discharge reduction is less than 3%.

It is obvious that the peak discharge reduction ability of a reservoir or a polder is very sensitive on opening time of the inflow gates and this decision needs a very good runoff forecast.

Flood damage reduction studies often recommended polders or the rebuilding of dikes more far away from the river to reduce the risk of inundation. But only controlled polders with controlled inflow gates have significant peak discharge reduction ability.

8 CONCLUSIONS AND FURTHER INVESTIGATIONS

A calculation procedure for the optimization of reservoir operation rules considering inundation damages as well as ecological impacts is presented.

The optimization of reservoir operation strategies needs a computation model and a multi criteria function.

A computation model can be established using available software and data describing the catchment areas and the reservoirs. The further issue is to connect these different models in an efficient way.

The description of optimization criteria is more complicated. It needs the combined consideration of monetary and non-monetary damages due to flood events. We have to remark a lack of data about the most of the non-monetary damages so that additional research has to be done.

REFERENCES

Aigner, D., Bornschein, A. & Pohl, R. 2002. Der Dammbruch von Glashütte. In *Wasserwirtschaft, Wassertechnik*; Heft 7: 6–10.

Bornschein, A. & Pohl, R. 2003. The Dam Break during the Flood in Saxon/Germany in August 2002. In *Proc. XXX IAHR-Congress*, Thessalonica, Greece, August 2003.

Bornschein, A. & Pohl, R. 2005. Lessons learned from the 2002 flood in Saxony, Germany. In *Proc. 40th Defra Flood and Coastal management Conference*, York, England: 05B.3.1 – 05B.3.12.

DVWK 1997. Maximierte Gebietsniederschlagshöhen für Deutschland. DVWK-Mitteilungen 29, Bonn, Germany.

DWD 1997. Starkniederschlagshöhen für Deutschland. KOSTRA-DWD-2000, Deutscher Wetterdienst, Offenbach, Germany.

LfUG 1993. Gewässerkundliche Hauptzahlen – Hydrologisches Handbuch Teil 1, Landesamt für Umwelt und Geologie des Freistaates Sachsen, Dresden, Germany.

LfUG 2004. Ereignisanalyse – Hochwasser August 2002 in den Osterzgebirgsflüssen. Sächsisches Landesamt für Umwelt und Geologie, Dresden, Germany.

LTV 2005. Daten zu den Einzugsgebieten der Weißeritz und der Müglitz sowie der Talsperren, Landestalsperrenverwaltung des Freistaates Sachsen, Pirna, Germany.

Martin, H. & Pohl, R. 2002. Hydraulic dam safety from the viewpoint of gate and valve operation. In *Flood Defence 2002*, Vol. 2, Science Press, Beijing, New York: 1438–1445.

Pohl, R. 1988. Aspekte zur Freibordbemessung an Talspeichern. In *Wasserwirtschaft-Wassertechnik* 38(1): 15–17.

Pohl, R. 1999. Estimation of the probability of hydraulic-hydrological failure of dams. In *Proc. Int. Workshop on risk analysis in dam safety assessment* Taipei, Taiwan, R.o.C.: 143–157.

Pohl, R. 2000. Failure frequency of gates and valves at dams and weirs. In *Int. Journal on Hydropower & Dams* issue No. 6: 77–82.

Pohl, R. & Horlacher, H.-B. 1996. Safety aspects in reservoir operation: power utilization, water supply, freeboard allowance. In *International conference on aspects of conflicts in reservoir development & management* London 3–5 Sept.: 443–451.

US Army 1996. Risk-based analysis for flood damage reduction studies. Manual No. 1110-2-1619. Department of the Army, US Army Corps of Engineers, Washington, DC, USA.

Copyright © 2006 Taylor & Francis Group plc, London, UK

Using results of mathematical modeling of debris flows for optimization of a river channel form to convey debris flows and floods

R. Fazarinc
Water Engineering Ltd., Ljubljana, Slovenia

B. Majes & M. Mikoš
Faculty of Civil and Geodetic Engineering, University of Ljubljana, Ljubljana, Slovenia

ABSTRACT: This paper is about how the final channel form of the Predelica Torrent and the Koritnica River was designed and optimized in order to convey future torrential floods and possible future debris flows of different magnitudes and densities, generated from the Stože slope in W Slovenia. For this purpose two mathematical non-commercial models have been used, a 1-D model DEBRIS1D in the narrow canyon of the Predelica Torrent, and a 2-D model PCFLOW2D in the Koritnica valley. A sensitivity analysis on rheologic parameters (dynamic viscosity, yield shear stress, pseudo Manning roughness coefficient) was performed with the PCFLOW2D model. Furthermore, the influence of the size of the computational numerical grid (2×2 m, 4×4 m) and the selected boundary conditions (dry vs. wet debris flow) on the numerical results was determined. The calibrated 2-D model was used for the final design of the river channel geometry, and to optimize the proposed widening of the local narrow in the Predelica Torrent.

1 INTRODUCTION

On November 17, 2000, the Stože debris flow devastated the Koritnica River valley, a typical narrow alpine valley in W Slovenia. It was the largest event of this kind in the last century in Slovenia. More than 1 million m^3 of debris material flowed as a wet debris flow from the Stože landslide area through a narrow channel of the Predelica Torrent for 4 km to the village of Log pod Mangartom and further downstream along the Koritnica River (Fig. 1).

The debris flow reached the village in a few minutes, killed 7 people in their homes, destroyed or damaged 29 residential or farm buildings and devastated nearly 15 ha of agricultural land. As the main triggering factor, prolonged rainfall of 1638.4 mm in 46 days prior to the event with the return period well above 100 years (Table 1) was recognized by a hydrologic analysis (Mikoš et al. 2004b).

If the Stože debris flow magnitude is compared to other case studies documented in the Alps (van Steijn 1996), it can be put into the group of "very high-magnitude" events. Even though its return period cannot be estimated from historical data, one can roughly estimate it to be well above 100 years.

The maximum flow velocity of the debris flow was estimated to be well over 10 m/s in the steep and narrow channel of the Predelica Torrent, and between 3 and 5 m/s in the more open valley of the Koritnica River.



Figure 1. Debris flow deposits in Log pod Mangartom on November 22, 2000. The Predelica Torrent flows from above into the Koritnica River, coming with clear emerald green water from the right (photo: authors, November 2000).

These estimated values were confirmed using one 1-D (non-commercial DEBRIS1D) and two 2-D mathematical models for debris flows (commercially available FLO-2D, non-commercial PCFLOW2D) (Četina et al. 2006). The hazard zones in the valley were determined using the before mentioned 2-D mathematical models for debris flows and different scenarios for further land sliding in the Stože area. For debris-flow hazard assessment a combination of a 1-D model (routing from source areas along steep and/or narrow

Copyright © 2006 Taylor & Francis Group plc, London, UK

Table 1. Measured rainfall depths (mm) at the rainfall gauging station in Log pod Mangartom compared with the statistical values given for different recurrence intervals for this gauging station.

Measured values (Autumn 2000)	
Rainfall depth [mm]	Period
174.0	12.10.2000 (1 Day)
481.6	11.11. – 17.11.2000 (7 Days)
1042.7	18.10. – 17.11.2000 (1 Month)
1638.4	03.10. – 17.11.2000 (46 Days)
1666.4	18.09. – 17.11.2000 (2 Months)

Statistical values (reference period 1961–1990)				
Reccurence interval	Duration			
	1 Day	7 Days	1 Month	2 Months
2 years	170	359	496	756
5 years	226	453	684	1018
10 years	263	515	808	1192
25 years	309	594	966	1411
50 years	344	652	1082	1574
100 years	378	710	1198	1735

channels) and a 2-D model (deposition areas: fans or valley floors) is frequently used (Lenzi et al. 2003; Bertolo & Wieczorek 2005; Mikoš et al. 2006).

During the debris-flow event, around 400,000 m^3 of debris material were deposited along the debris flow pathway upstream the valley, and nearly 700,000 m^3 were deposited in the valley itself, locally with a thickness up to 10 m. Early in 2001, an outline scheme for temporary river engineering measures was designed in order to stimulate natural river erosion processes.

This scheme has proved to be highly effective, because in 5 years more than half of the debris-flow deposit was eroded from the valley by natural river erosion processes (Fig. 2; Mikoš & Fazarinc 2005). As a basis for this scheme, the results of the hydrologic analysis (Mikoš et al. 2004b), analysis of grain-size distribution of debris-flow deposits (Fig. 3), preliminary evaluation of cross-sectional sediment transport capacities (Mikoš et al. 2004a), and 2-D mathematical modelling of debris flows were used (Četina et al. 2006).

This paper discusses the sensitivity analysis of the PCFLOW2D mathematical model, which was validated using the data from the 2000 Stože debris flow, and the way it was applied for optimization of the river channel geometry. Furthermore, the results of the PCFLOW2D model were used to map debris-flow hazard zones according to the 3 classes of debris-flow intensity (Petraschek & Kienholz 2003) in order to plan future land use in the area (Četina et al. 2006).

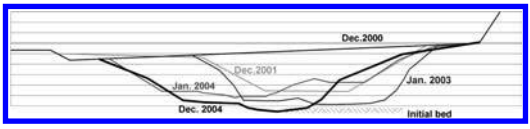


Figure 2. The time evolution of a typical cross section of the Koritnica River after the debris flow event in November 2000. The vertical step is 1 m.

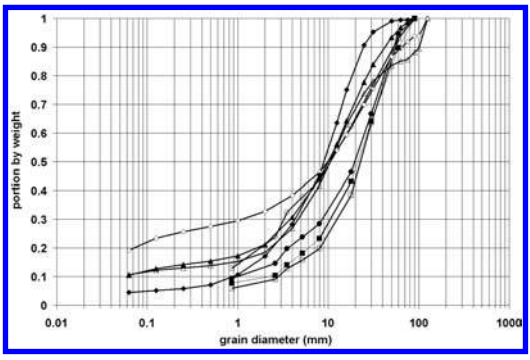


Figure 3. Grain size distribution of debris flow deposits in Log pod Mangartom.

2 DESCRIPTION AND CALIBRATION OF THE 2-D MODEL

2.1 *Description of the PCFLOW2D model*

In the DEBRIF1D and the PCFLOW2D models the same formulation is used for the resistance slope S_f, adapted from O'Brien & Julien (1993):

$$S_f = \frac{\tau_y}{\gamma_m h} + \frac{K\eta V}{8\gamma_m h^2} + \frac{n^2 V^2}{h^{4/3}} + S_e + S_b \quad (1)$$

in which τ_y = the yield shear stress of a sediment-water mixture; γ_m = the specific weight of a sediment-water mixture; h = the flow depth; K = the non-dimensional friction parameter of the laminar flow ($K = 24$ for smooth wide rectangular channels but increases with roughness and irregular cross-section geometry; Julien & O'Brien 1997; FLO-2D 2006); η = dynamic viscosity of the mixture; V = flow velocity; n = "pseudo Manning" roughness coefficient; S_e = resistance slope due to eddy losses at sharp channel expansions, equal to the difference of the values of kinetic terms in two subsequent cross-sections (Rajar 1978); S_b = resistance slope due to bends, which was calculated by a simple equation, known from steady state river hydraulics (Rajar 1978):

$$S_b = 2\frac{B_b}{r_b}\frac{V^2}{2g} \quad (2)$$

Copyright © 2006 Taylor & Francis Group plc, London, UK

in which B_b = water surface width in the bend; r_b = radius of curvature; V = flow velocity; g = acceleration due to gravity.

Using the Cartesian coordinate system, the continuity (Equation 3) and momentum equations (Equations 4 and 5), which describe the two-dimensional, incompressible unsteady depth-averaged debris flow, are written in the following form (Četina 2000):

$$\frac{\partial h}{\partial t}+\frac{\partial (hu)}{\partial x}+\frac{\partial (hv)}{\partial y}=0 \tag{3}$$

$$\frac{\partial (hu)}{\partial t}+\frac{\partial (hu^2)}{\partial x}+\frac{\partial (huv)}{\partial y}= -gh\frac{\partial h}{\partial x}-gh\frac{\partial z_b}{\partial x}-ghS_{fx}+\frac{\partial}{\partial x}(hv_{ef}\frac{\partial u}{\partial x})+\frac{\partial}{\partial y}(hv_{ef}\frac{\partial u}{\partial y}) \tag{4}$$

$$\frac{\partial (hv)}{\partial t}+\frac{\partial (huv)}{\partial x}+\frac{\partial (hv^2)}{\partial y}= -gh\frac{\partial h}{\partial y}-gh\frac{\partial z_b}{\partial y}-ghS_{fy}+\frac{\partial}{\partial x}(hv_{ef}\frac{\partial v}{\partial x})+\frac{\partial}{\partial y}(hv_{ef}\frac{\partial v}{\partial y}) \tag{5}$$

where t = time, h = water depth, u and v = depth-averaged velocity components in the x and y directions, z_b = bottom level, g = gravity constant and v_{ef} = effective viscosity. The terms S_{fx} and S_{fy} express energy line slopes, analogous to Equation 1.

The set of coupled partial differential equations (Equations 3 to 5) is solved by the Finite Volume Method proposed by Patankar (1980). This robust numerical algorithm is also used in the 2D-UFM model (Pianese & Barbiero 2003), but not in the FLO-2D model that uses the Finite Difference Method (FLO-2D 2006). A fully implicit scheme is used in the PCFLOW2D for time integration, providing a stable and accurate solution even at relatively high Courant numbers (up to about 10). It is possible to simulate both subcritical and supercritical flow (Četina & Rajar 1994, Četina et al. 1996).

2.2 *Calibration of the PCFLOW2D model*

The value of non-dimensional friction parameter K was always taken as 2285, a value that has been used effectively for most urban studies (FLO-2D 2006) and that lies in the range for sparse vegetation (K = 1000–4000; Woolhiser 1975; see Table 8 in FLO-2D Users' Manual; FLO-2D 2006). Similar value of $K = 2480$ was used when modelling the 1998 Sarno debris flows using the FLO-2D (Aleotti & Polloni 2003).

The boundary conditions at the upstream boundary were hydrographs $Q(t)$ determined from the DEBRIS1D simulations. An assumption of uniform velocity distribution at the inflow cross section was also applied, as more detailed information from upstream 1D computations was not available.

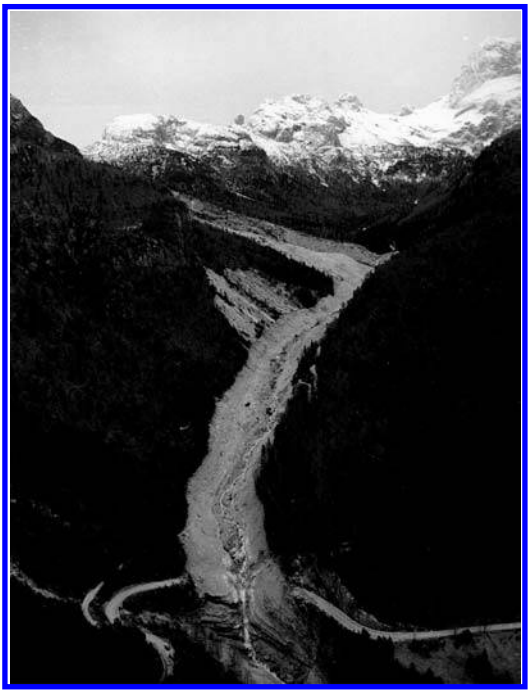


Figure 4. The flowpath of the Stože debris-flow from the source area along the channel of the Mangart torrent across the main road Bovec (Slovenia) – Tarvisio (Italy). The clearly visible erosional scar was used for the calibration of the DEBRIS1D model (photo: authors, November 2000).

At the downstream end two types of boundary conditions were used: (a) Critical flow: at all downstream control volumes where there was an outflow from the computational domain, critical velocities depending on the instantaneous water depth were prescribed in the direction perpendicular to the outflow boundary; (b) Uniform conditions at the downstream end, where zero gradients of water depths and velocities perpendicular to the outflow boundary were prescribed.

The boundary condition (b) gave more realistic results but it caused some stability problems. Condition (a) was more robust without causing stability problems but the results just upstream of the outflow boundary were a little less accurate, although the results were not essentially different.

For the calibration of the DEBRIS1D and PCFLOW-2D models the measured maximum levels (Fig. 4) and inundation limits along the whole computational domain were taken into account (Fazarinc 2002), because no other direct debris-flow measurements were available. In cases with more frequent events, a large range of different debris-flow monitoring devices and methods are available (Itakura et al. 2005).

Copyright © 2006 Taylor & Francis Group plc, London, UK

Table 2. Selected combinations of dynamic viscosity and yield shear stress for fixed pseudo Manning roughness coefficient $n = 0.05\ \mathrm{s.m^{-1/3}}$ with case numbers.

	μ[Pa.s]					
τ_y [N/m^2]	0	10	20	50	100	1000
0	2 & 3	14	8		9	
20	7	1	11	18	6	17
50		19				
100	10	15	12		5	
10,000		16				4

Calibration was made by determining the proper values of the three rheological parameters in Equation 1, expressing flow resistance: (1) yield shear stress τ_y; (2) viscosity η; (3) pseudo Manning roughness coefficient n. In the literature the values of these parameters may be found to vary over a very wide range, differing by several orders of magnitude, especially the first two. In the calibration process three methods for determination of these values were used: (a) values available in the literature; (b) results of geo-mechanical laboratory experiments: $\gamma_m = 18.75\ \mathrm{kN/m^3}$, $\gamma_s = 22\ \mathrm{kN/m^3}$ (Majes et al. 2002), and (c) values obtained by a trial-and-error procedure starting with values suggested in the literature. Method (c) was taken as the most relevant, even in the case of non-agreement with the other 2 methods.

Two rheological parameters were used with values obtained from back-calculations when applying DEBRIS1D, and geo-mechanical laboratory measurements (yield stress $\tau_y = 20\ \mathrm{Pa}$, and viscosity $\eta = 10\ \mathrm{Pa.s}$). The value of the pseudo Manning coefficient n was calibrated, and a uniform value $n = 0.05\ \mathrm{s.m^{-1/3}}$ was used overall. A numerical grid of $2 \times 2\ \mathrm{m}$ was used, and buildings were taken into account in the numerical grid as "dry" grid cells. Usually no field data are available on debris-flow front velocities, thus calibration of the pseudo Manning coefficient is done using the inundation boundaries.

A comparison of maximum inundation levels, computed by the calibrated PCFLOW2D model and those observed in the field, shows a good correlation.

3 SENSITIVITY ANALYSIS

3.1 *Sensitivity analysis on rheological parameters*

Sensitivity analysis of the PCFLOW2D model was performed using the original geometry prior to the debris-flow event in November 2000 by changing all three rheologic parameters: dynamic viscosity μ, yield shear strength τ_y and pseudo Manning roughness coefficient n (19 sensitivity cases in Table 2).

For all sensitivity cases the boundary condition at the upstream boundary was taken into account as determined by the DEBRIS1D model: volume $V = 740{,}000\ \mathrm{m^3}$ and the hydrograph $Q(t)$ with the maximum discharge $Q = 5684\ \mathrm{m^3/s}$. The computed maximum discharge fits between the semi-theoretical equation satisfying the Froude similarity (Rickenmann 1997): $Q = 0.1\ V^{0.833} = 7746\ \mathrm{m^3/s}$ and the empirical equation for the relationship between the peak discharge Q_p and the debris-flow volume V for granular debris flows in Japan (Mizuyama et al. 1992): $Q_p = 0.135\ V^{0.780} = 5109\ \mathrm{m^3/s}$.

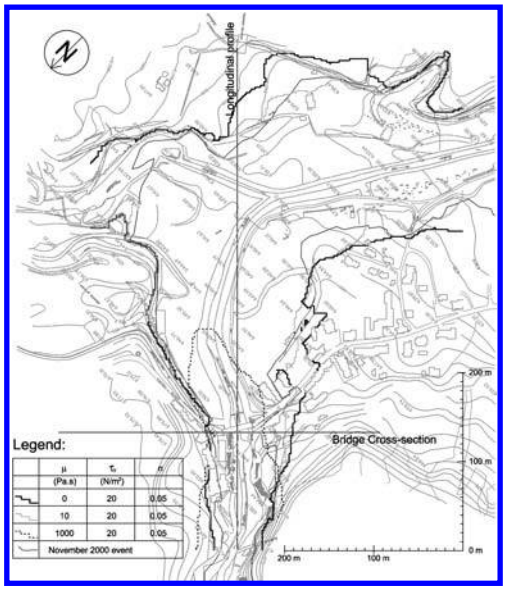


Figure 5. The sensitivity of the PCFLOW2D model on rheological parameters as computed for 3 sensitivity cases #1, #7 and #17 (see Table 2) to show the influence of dynamic viscosity μ to the envelope of debris flows.

3.1.1 *The influence of dynamic viscosity μ*

The sensitivity analysis has shown moderate to high influence of dynamic sensitivity on hydraulic parameters of debris flows. The influence of dynamic viscosity was determined at a constant (validated) value of yield shear stress. The results are given in Figures 5–7.

The differences between cases are moderate: with increasing viscosity, flow-depths rise in the upper part and decrease in the lower part of the domain. The differences in the flow-depths at the upper boundary are for realistic values of viscosity $\mu \leq 100\ \mathrm{Pa.s}$ between 1 m and 3 m on average. The largest differences can be observed along the Predelica Torrent (narrow section, followed by a sudden widening of the domain). In the other part of the domain, along the Koritnica River, these differences zeroed out, or, as in the lower part, flow depths at higher viscosities were even smaller than those computed with relatively small values of viscosity. These increased flow depths

Copyright © 2006 Taylor & Francis Group plc, London, UK

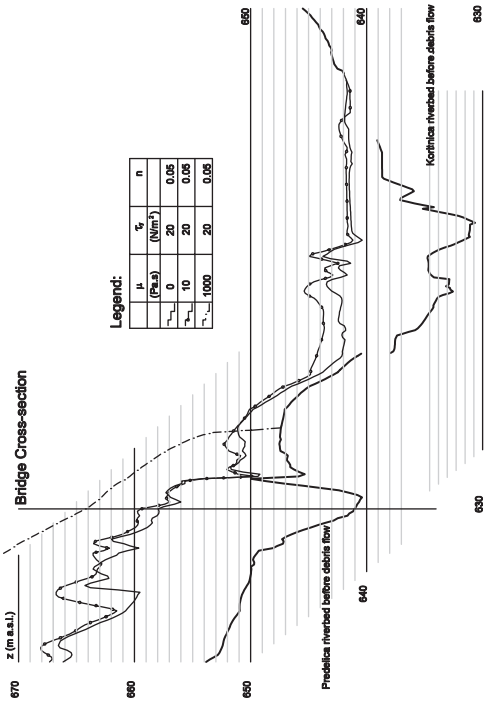


Figure 6. The sensitivity of the PCFLOW2D model on rheological parameters as computed for 3 sensitivity cases #1, #7 and #17 (see Table 2) to show the influence of dynamic viscosity μ to the envelope of debris flows – shown in the longitudinal profile along the Predelica Torrent. The distortion of the vertical to horizontal scale is 10 : 1.

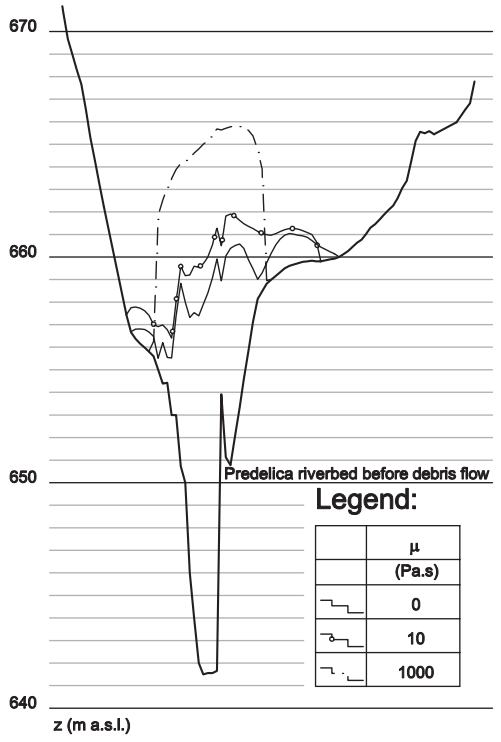


Figure 7. The sensitivity of the PCFLOW2D model on rheological parameters as computed for three sensitivity cases #1, #7 and #17 (see Table 2 for details) to show the influence of dynamic viscosity μ to the envelope of debris flows – shown in the cross section of the temporary bridge (see Figure 6 for the location of this cross section). The distortion of the vertical to horizontal scale is 10:1.

Table 3. The influence of dynamic viscosity on travel time through domain t and the maximum discharge at outflow Q_{out} for fixed calibrated yield shear stress $\tau_y = 20$ Pa and for fixed calibrated Manning roughness coefficient $n = 0.05$ s.m$^{-1/3}$.

μ[Pa.s]	0	10	20	50	100	1000
t(s)	96	103	112	120	170	∞
Q_{out} (m^3/s)	3374	2973	2436	1433	686	0

can be explained by the more pronounced flow afflux at sudden geometrical changes at large viscosity values. Large viscosity increases the energy gradient (due to larger energy losses) and so the flow depths in the lower part of the domain are smaller than those for low viscosity values.

With very high viscosity (case #17, $\mu = 1000$ Pa.s) the debris-flow stops around the bridge at Gorenji Log (the upper part of Log pod Mangartom village). However, this situation is unrealistic, because such a dry debris flow triggered at the Stože slope would not be able to reach Gorenji Log. At low viscosity (case #7, $\mu = 0$ Pa.s) the results are identical to those for water flow without any rheologic characteristics (case #2, $\tau_y = 0$ Pa). Increasing viscosity decreases the debris-flow front velocity and thus also the travel time of the debris-flow front through the domain and the maximum discharge at the outflow (Table 3).

The hazard situation in Gorenji Log (the computational domain), where debris-flow velocities and impacts forces are highest, is favorable when the debris flow is as wet as possible or with low clay content (smaller viscosity). On the other hand, less viscous debris flows travel much faster, and the attenuation of the front is less pronounced thus raising the hazard in Spodnji Log (the lower part of Log pod Mangartom village).

3.1.2 *The influence of yield shear stress* τ_y

Similarly to viscosity analysis, the influence of yield shear stress was determined at a constant but validated value of dynamic viscosity. At very high yield shear stress $\tau_y = 10{,}000$ N/m^2 flow depths are higher in the upper part of the domain (Gorenji Log) and lower

Copyright © 2006 Taylor & Francis Group plc, London, UK

Table 4. Selected combinations of dynamic viscosity and yield shear stress for two pseudo Manning roughness coefficients with case numbers.

n [s.m$^{-1/3}$]	0.03			0.07		
μ [Pa.s]	0	10	100	0	10	100
τ_y[N/m^2]						
0	20	21	22	29	30	31
20	23	24	25	32	33	34
100	26	27	28	35	36	37

in the lower part of the domain (Spodnji Log) when compared to low (ordinary) yield shear stress values between 0 and 100 N/m^2. For such low values, identical results are obtained, and yield shear stress has no important influence on debris flow. Much larger influence may be given to dynamic viscosity than to yield shear stress. When both rheological parameters are set to zero ($\tau_y = 0$ Pa, $\mu =$ Pa.s), the average flow depths decrease between 0 and 2 m.

For values of yield shear stress between 0 and 100 N/m^2, the maximum discharge of the outflow hydrograph stays nearly the same (decreases from 2981 to 2954 m^3/s). A noticeable decrease in maximum discharge to 1055 m^3/s is caused by high yield shear stress $\tau_y = 10{,}000$ N/m^2.

The travel time of the debris-flow front through the domain was in all sensitivity cases practically constant (103 s), and so yield shear stress had no influence on debris-flow front velocity.

The influence of yield shear stress on hydraulic parameters of debris flows is low during the travel phase. This is not true during the triggering and especially the deposition phase of a debris flow, when the influence of yield shear stress is of high importance. This was confirmed during the calibration using the DEBRIS1D model (Četina et al. 2006).

3.1.3 *The influence of pseudo Manning roughness coefficient n*

The pseudo Manning roughness coefficient covers two influences, namely that of dispersivity caused by collisions of particles in the debris flow front, and that of roughness and channel form. Three values of pseudo Manning roughness coefficient were analyzed: $n = 0.05$ s.m$^{-1/3}$ (case #60), $n = 0.03$ s.m$^{-1/3}$ (low dispersivity and favorable channel form, as with hydraulics of Newtonian fluids), and $n = 0.07$ s.m$^{-1/3}$ (high dispersivity and natural torrential channels). Additional sensitivity cases for changed pseudo Manning values are given in Table 4.

The influence of the pseudo Manning coefficient is largest in the upper part of the domain (narrow channel, sudden confinement, high flow velocities), where the kinematic-inertial flow regime is clearly predominating. The differences in flow depths are between 2 and 4 m in the reaches with very irregular channel geometry, and much smaller (practically negligible) in the reaches with regular channel geometry. Another flow regime type is the macroviscous regime where viscosity starts to be the dominating parameter.

The influence of the pseudo Manning coefficient on debris-flow front velocity is determined by the time it travels through the domain: by increasing n from 0.03 s.m$^{-1/3}$ to 0.05 s.m$^{-1/3}$ or 0.07 s.m$^{-1/3}$, the time of travel increases from 86 s to 103 s or 104 s. The debris flow travels slightly faster at smaller roughness or at lower dispersivity. The maximum discharge at the outflow slightly decreases from 3037 m^3/s to 2973 m^3/s when n changes from 0.03 s.m$^{-1/3}$ to 0.05 s.m$^{-1/3}$.

When analyzing the influence of the pseudo Manning coefficient, one may conclude that the optimized channel form for conveying debris flows would have rather smooth and uniform cross sections, thus reducing the danger of flow impoundments. On the other hand such a solution increases the flow velocities and impact forces on structures. Lowering of n values can also be achieved by extracting large particles from a debris-flow mass by flow breakers or separating grills.

For this specific case study, the effect of the pseudo Manning coefficient on hydraulic parameters of debris flows is moderate. It might well have been much larger at higher channel slopes and less regular channel geometries.

3.2 *The influence of the numeric grid size*

The influence of the numeric grid size was studied by comparing the results of simulations using two sizes: 2 × 2 m and 4 × 4 m. The rheological parameters were the same as in the basic case ($\tau_y = 20$ N/m^2, $\mu = 10$ Pa.s, $n = 0.03$ s.m$^{-1/3}$) and the geometry was selected to be the same as it was prior to the November 2000 event.

The differences between both simulations were within 1 m, with more pronounced details with the 2 × 2 m grid. The main cause for this was the more detailed geometry than that with the 4 × 4 m grid and the size of the phenomenon in nature, being better described by the 2 × 2 m grid. A less dense grid also attenuated the local extreme flow depths. Also in the case of a muddy debris-flow in the Wartschenbach (Austria), a 2 × 2 m grid was found to be clearly the better choice over a 5 × 5 m grid (Laigle et al. 2003). In some cases (Lenzi et al. 2003) also a 1 × 1 m grid was applied. Though, many study cases applied much larger grids: 20 × 20 m grid (Aleotti & Polloni, 2003), 25 × 25 m grid (García et al. 2003), or 30 m DTM (Bertolo & Wieczorek, 2005).

The maximum discharges at inflow $Q_{in} = 5684$ m^3/s decreased at outflow to $Q_{out} = 2973$ m^3/s with the

Copyright © 2006 Taylor & Francis Group plc, London, UK

2×2 m grid, and to $Q_{out} = 2860$ m^3/s with the 4×4 m grid, respectively. This difference is mainly restricted to the maximum discharge. Other values of the hydrograph were quite similar. Also, the travel time of the debris-flow front through the domain was practically the same for both grid sizes.

For this case study the influence of the numerical grid size on hydraulic parameters of debris flows was low.

3.3 *The influence of the outflow boundary condition*

In some cases, due to instabilities, the domain was prolonged for less than 100 m and then the critical flow conditions were selected. Normally, uniform conditions at the downstream end were considered as the better solution when compared to the critical flow conditions.

4 OPTIMIZATION OF THE CHANNEL GEOMETRY

One of the key issues of debris-flow modeling was the optimization of the proposed river engineering measures. The basic starting point for the new channel design was to find a combination that would be ecologically acceptable, financially feasible and would yield the selected level of safety for the village and infrastructure in the case of new debris flows triggered on the Stože slope. The main question when optimizing the geometry of new channels was how to ensure flood safety to a 100-year flood (77 m^3/s for the Predelica Torrent, 211 m^3/s for the Koritnica River) and how to form new channels in 5 to 12 m thick debris-flow deposits to effectively convey possible future debris flows.

Early in 2001, a preliminary design of final river engineering measures in the Predelica Torrent and the Koritnica River was prepared. The channels were designed in cross sections and in the longitudinal profile in such a way that the optimal hydraulic conductivity was secured without the need to excavate all the debris flow deposits. The fastest solution would be if all the debris deposits would be mechanically removed and transported to dumping sites. However, there is not enough room for dumping such a volume of material.

The computed debris-flow levels without the widening of the narrow section of the Predelica Torrent are similar to those obtained for the geometry prior to the event and for the boundary conditions when calibrating the model and performing the sensitivity analysis (volume $V = 740{,}000$ m^3 and the hydrograph $Q(t)$ with the maximum discharge $Q = 5684$ m^3/s).

In 2001 proposed mitigation measures between the Stože slope and the village of Log pod Mangartom (two earthen dams, two reinforced concrete debris-flow breakers) were later reduced to only one debris-flow breaker (erected early in 2005), thus a new boundary condition was selected for the optimization of the channel geometry. Therefore, for all optimization cases the new boundary condition at the upstream boundary was taken into account as determined by the DEBRIS1D model, namely the debris-flow volume $V = 910{,}000$ m^3 and the hydrograph $Q(t)$ with the maximum discharge $Q = 7090$ m^3/s. Also this maximum discharge fits between the semi-theoretical equation satisfying the Froude similarity: $Q_p = 0.1\ V^{0.833} = 0.1\ 910{,}000^{0.833} = 9202$ m^3/s and the empirical equation for granular debris flows in Japan: $Q_p = 0.135\ V^{0.780} = 0.135\ 910{,}000^{0.780} = 6003$ m^3/s.



Figure 8. Downstream view on the debris-flow breaker, made of reinforced concrete, 11.5 m high, erected early in 2005 some 150 m upstream of the temporary bridge in Gorenji Log at the upstream end of the narrow in the Predelica Torrent.

The 2-D modeling proved that Gorenji Log is not safe by lowering the riverbed to the initial level (excavating debris-flow deposits) only. Therefore, additional modeling was done, taking into account the following proposed measures around the bottle neck in the Predelica Torrent (cross section of the temporary bridge across the Predelica Torrent in Gorenji Log):

a) Deflecting wall on its right hand side to prevent riverbank overtopping.
b) Widening of the narrow section from the existing 24–28 m to uniform 33 m, 40 m, and 48 m, respectively, to lower debris-flow levels.

The widening and smoothing of the natural rock walls of the narrow reach upstream of the temporary bridge would lower the pseudo Manning coefficient. This measure would support the influence of the debris-flow breaker (see Fig. 8), erected 150 m upstream of the bridge at the upstream end of the narrow. A breaker would separate the coarse and fine fractions within a debris flow, decrease kinetic energy of the flow front and thus change its rheologic parameters.

Copyright © 2006 Taylor & Francis Group plc, London, UK

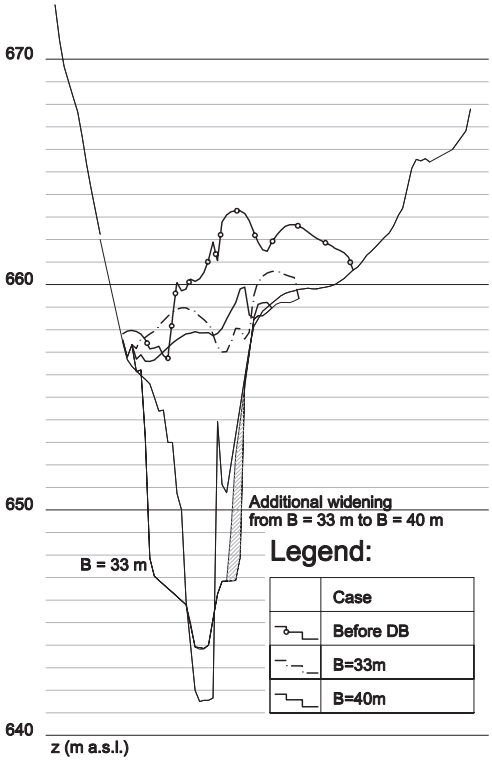


Figure 9. The optimization of the channel geometry using the results of the PCFLOW2D model as computed for three optimization cases #1, #3 (B = 33 m), and #3 (B = 40 m) to show the influence of the widening of the narrow to the envelope of debris flows – shown in the cross section of the temporary bridge (see Figure 6 for the location of this cross section). The distortion of the vertical to horizontal scale is 10:1.

Several channel geometries were taken into consideration when modeling their influence. The three most important optimization cases were:

1 Situation prior to the November 2000 event.
2 Situation immediately after the November 2000 event.
3 The proposed final situation according to the preliminary design of the river channels with the proposed widenings of the narrow (uniform width 33 m, 40 m, and 48 m) in the Predelica Torrent.

As the optimal solution for widening of the critical cross section of the Predelica Torrent through the temporary bridge in Gorenji Log, its widening to 40 m was selected. Due to the mass momentum there was an obvious rise of the maximum debris-flow table along the right bank. This rise was maximal at the maximum selected width of the narrow, i.e. at 48 m. Hence, the maximal possible widening of the cross section to the uniform 48 m did not prove to be optimal.

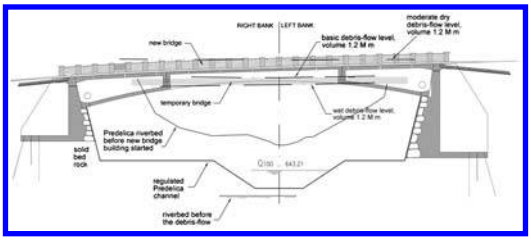


Figure 10. Cross-sectional upstream view of the new concrete bridge in Gorenji Log (see Figure 11 for the location of the bridge). The debris-flow levels computed for different debris-flow wetness are also indicated. The actual construction of the bridge is shown on Fig. 13.

In the reach upstream of the bridge the computed debris-flow levels decreased with increasing width of the narrow (Fig. 9). With all three selected widenings of the narrow, no overtopping of debris flows across the right-hand bank could be expected. Additionally, the proposed widenings eliminated the need to erect a deflecting wall along the right bank to prevent overtopping; such a wall was proposed by some experts immediately after the disaster.

Our goal was to design the new concrete bridge (Fig. 10) higher than the computed maximum debris-flow table to avoid its destruction. However, due to restrictions in space (especially the existing buildings to be preserved) this was not achieved for all cases. The moderately dry debris flow having relatively low flow velocities and thus higher levels would overtop the bridge construction.

The results of the channel geometry optimization were taken into account when preparing the final river engineering plan (Fig. 11).

Immediately downstream of the bridge, the envelopes for all three proposed widenings are quite similar. The reason lies in the similarly regulated channel geometry. A smaller debris-flow level rise can be observed downstream of the bridge. A sudden widening downstream of the bridge leading to an afflux can be nominated as a possible cause. Therefore, the maximal possible widening of the narrow is not to be considered as the optimal solution, even though it might optically seem as if it was.

The widening of the narrow upstream of the bridge should be in accordance with the width of the cross section next to the bridge. A local narrow to make the new concrete bridge shorter would cause the local rise of the debris-flow level and could cause overtopping. As a consequence of this, the optimal widening of the narrow in the reach of the bridge in Gorenji Log was determined to be around 40 m. This width should be kept also for some 40 to 50 m downstream of the bridge in order to avoid the local afflux of debris flows.

Early in 2006, we proceeded with the implementation of the optimized final river engineering plan

Copyright © 2006 Taylor & Francis Group plc, London, UK

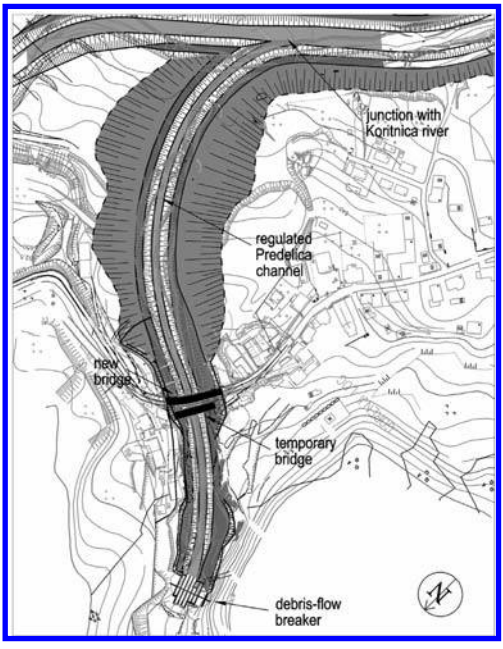


Figure 11. The ground plan of the lower reach of the Predelica Torrent and the junction with the Koritnica River with proposed final channel geometry; showing also the position of the erected debris-flow breaker, the existing steel temporary bridge, and the new concrete bridge under construction.



Figure 12. The temporary bridge, erected in January 2001 (photo: authors, January 2001).

by erecting the new concrete bridge in Gorenji Log (Figs 12–13).

5 CONCLUSIONS

The PCFLOW2D model, a 2-D mathematical model, was successfully calibrated using field data from the November 2000 debris flow from the Stože slope in W



Figure 13. Ongoing construction works of a new concrete bridge in Gorenji Log (photo: authors, May 2006). The cross section of this bridge is given in Fig. 10.

Slovenia. The rheological parameters in the calibrated model were as follows: dynamic viscosity $\eta = 10$ Pa.s, yield shear stress $\tau_y = 20$ Pa, and the pseudo Manning roughness coefficient $n = 0.05$ s.m$^{-1/3}$. A computational grid 2×2 m was applied.

A sensitivity analysis of the PCFLOW2D model on rheological parameter has shown moderate to high influence of dynamic sensitivity on hydraulic parameters of debris flows. The influence of yield shear stress on hydraulic parameters of debris flows remained low during the travel phase of debris flows – this is not true during the triggering and especially during the deposition phase of a debris flow, when the influence of yield shear stress is of high importance. In this case study the influence of the pseudo Manning roughness coefficient and the computational grid on hydraulic parameters of debris flow was low and moderate. It might well have been much larger at higher channel slopes and less regular channel geometries. The most important parameter was definitely the geometry itself.

The mathematical modeling of debris flows using the DEBRIS1D and the PCFLOW2D models has proved that the proposed river engineering scheme with the longitudinal profile 2 to 3 m above the original river bed and with the widened cross sections will give even better flow conditions when compared with the situation prior to the November 2000 debris-flow event.

A step-wise mitigation of the Stože debris-flow devastation in the Koritnica river valley is under way after the initial immediate relief actions performed in winter 2000/2001. Combining field observations and laboratory experimental results with the results of mathematical modeling of possible future debris flows enabled the preparation of a sound river engineering plan. This plan has so far respected natural river erosion processes by stimulating sediment transport (washing away of debris-flow deposits instead of their mechanical removal to dumping sites) in the first

Copyright © 2006 Taylor & Francis Group plc, London, UK

years after the debris flow. When completed, the plan will assure relatively natural outlook of this alpine river flowing in the Triglav national park.

REFERENCES

Aleotti, P. & Polloni, G. 2003. Two-dimensional model of the 1998 Sarno debris flows (Italy): preliminary results. In Dieter Rickenmann (ed.), Cheng-lung Chen (ed.), *Debris-Flow Hazards Mitigation: Mechanics, Prediction, and Assessment; Proc. of the third int. conf DFHM., Davos, 10–12 September, 2003:* 553–563. Rotterdam: Millpress.

Bertolo, P. & Wieczorek, G.F. 2005. Calibration of numerical models for small debris flows in Yosemite Valley, California, USA. *Natural Hazards and Earth System Sciences* 5(6): 993–1001.

Četina, M. 2000. Two-dimensional modelling of free surface flow. *Acta hydrotechnica* 18(29): 3–37.

Četina, M. & Rajar, R. 1994. Two-Dimensional Dam-Break Flow Simulation in a Sudden Enlargement. In P. Molinaro (ed.), L. Natale (ed.), *Modelling of Flood Propagation over Initially Dry Areas; Proc. of the Int. Conf., Milan,* Italy.

Četina, M., Rajar, R. & Zakrajšek, M. 1996. Recent developments in dam-break flow computations in Slovenia. In Fritz Zollinger (ed.), Gernot Fiebiger (ed.), *Proc. intern. symp., Garmisch-Partenkirchen, 24–28 June 1996*. Klagenfurt: Interpraevent.

Četina, M., Rajar, R., Hojnik, T., Zakrajšek, M., Krzyk, M. & Mikoš, M. 2006. Case study: Numerical simulations of debris flow below Stože, Slovenia. *Journal of Hydraulic Engineering* 132(2): 121–130.

Fazarinc, R. 2002. *Mathematical modeling of the debris flow in Log pod Mangartom*. Unpublished M.Sc. Thesis. University of Ljubljana, Ljubljana, Slovenia.

FLO-2D 2006. *FLO-2D, Users Manual, Version 2006.01*. Civil and Water Resources Engineering, Beckenridge, USA.

García, R., López, J.L., Noya, M., Bello, M.E., González, N., Paredes, G., Vivas, M.I. & O'Brien, J.S. 2003. Hazard mapping for debris-flow events in the alluvial fans of northern Venezuela. In Dieter Rickenmann (ed.), Cheng-lung Chen (ed.), *Debris-Flow Hazards Mitigation: Mechanics, Prediction, and Assessment; Proc. of the third int. conf DFHM., Davos, 10–12 September, 2003:* 589–599. Rotterdam: Millpress.

Itakura, Y., Inaba, H. & Sawada, T. 2005. A debris-flow monitoring devices and methods bibliography. *Natural Hazards and Earth System Sciences* 5(6): 971–977.

Julien, P.Y. & O'Brien, J.S. 1997. Selected notes on debris flow dynamics. In Aronne Armanini (ed.), Masanori Michiue (ed.), *Recent Developments on Debris Flows.* Berlin: Springer.

Laigle, D., Hector, A.-F., Hübl, J. & Rickenmann, D. 2003. Comparison of numerical simulation of muddy debris-flow spreading to records of real events. In Dieter Rickenmann (ed.), Cheng-lung Chen (ed.), *Debris-Flow Hazards Mitigation: Mechanics, Prediction, and Assessment; Proc. of the third int. conf DFHM., Davos, 10–12 September, 2003:* 635–646. Rotterdam: Millpress.

Lenzi, M.A., D'Agostino, V., Gregoretti, C. & Sonda, D. 2003. A simplified numerical model for debris-flow hazard assessment: DEFLIMO. In Dieter Rickenmann (ed.), Cheng-lung Chen (ed.), *Debris-Flow Hazards Mitigation: Mechanics, Prediction, and Assessment; Proc. of the third int. conf DFHM., Davos, 10–12 September, 2003:* 611–622. Rotterdam: Millpress.

Majes, B., Petkovšek, A. & Logar, J. 2002. The comparison of material properties of debris flows from Stože, Slano blato and Strug landslides. *Geologija* 45(2): 457–463.

Mikoš, M., Rojnik, F. & Fazarinc, R. 2004a. River engineering measures in an alpine river after a major debris flow event. In Matjaž Mikoš (ed.), Dieter Gutknecht (ed.), *Schutz des Lebensraumes vor Hochwasser, Muren, Lawinen und Hangbewegungen, Proc. intern. symp., Riva del Garda, 24–27 May 2004*. Klagenfurt: Interpraevent.

Mikoš, M., Četina, M. & Brilly, M. 2004b. Hydrologic conditions responsible for triggering the Stože landslide, Slovenia. *Engineering Geology* 73(3–4): 193–213.

Mikoš, M. & Fazarinc, R. 2005. Natural erosion processes in the Koritnica river, W Slovenia, after the Stože debris flow. In Byong-Ho Jun (ed.), *Water Engineering for the Future, Choices and Challenges, Proc. XXXI IAHR congress, Seoul, 11–16 September 2005*: 3757–3769. Madrid: IAHR.

Mikoš, M., Fazarinc, R., Majes, B., Rajar, R., Žagar, D., Krzyk, M., Hojnik, T. & Četina, M. 2006. Numerical simulation of debris flows triggered from the Strug rock fall source area, W Slovenia. *Natural Hazards and Earth System Sciences* 6(2): 261–270.

Mizuyama, T. Kobashi, S. & Ou, G. 1992. Prediction of debris flow peak discharge. In Fritz Zollinger (ed.), Gernot Fiebiger (ed.), *Proc. intern. symp., Bern, 29 June – 3 July 1992*. Klagenfurt: Interpraevent.

O'Brien, J.S. & Julien, P.Y. 1988. Laboratory analysis of mudflow properties. *Journal of Hydraulic Engineering* 114(8): 877–887.

Patankar, S.V. 1980. *Numerical Heat Transfer and Fluid Flow*. New York: McGraw-Hill.

Petrascheck, A. & Kienholz, H. 2003. Hazard assessment and mapping of mountain risks in Switzerland. In Dieter Rickenmann (ed.), Cheng-lung Chen (ed.), *Debris-Flow Hazards Mitigation: Mechanics, Prediction, and Assessment; Proc. of the third int. conf DFHM., Davos, 10–12 September, 2003:* 25–38. Rotterdam: Millpress.

Pianese, D. & Barbiero, L. 2003. Formulation of a two-dimensional unsteady debris-flow model for analysis of debris-flow hazards and countermeasures thereof. In Dieter Rickenmann (ed.), Cheng-lung Chen (ed.), *Debris-Flow Hazards Mitigation: Mechanics, Prediction, and Assessment; Proc. of the third int. conf DFHM., Davos, 10–12 September, 2003:* 705–716. Rotterdam: Millpress.

Rajar, R. 1978. Mathematical Simulation of Dam-Break Flow. *Journal of Hydraulic Engineering* 104(7): 1011–1026.

Rickenmann, D. 1997. Empirical relationships for debris flows. *Natural Hazards* 19: 47–77.

van Steijn, H. 1996. Debris-flow magnitude-frequency relationships for mountainous regions of Central and Northwest Europe. Geomorphology 15: 259–273.

Woolhiser, D.A. 1975. Simulation of unsteady overland flow. In K. Mahmood (ed.), V. Yevjevich (ed.), *Unsteady Flow in Open Channels.* Fort Collins: Water Resources Publications.

Copyright © 2006 Taylor & Francis Group plc, London, UK

Climate change, sediment delivery and flood risk explored using two-dimensional inundation modelling

S.N. Lane, R.J. Hardy & D. Yu
Department of Geography, University of Durham, Science Laboratories, Durham, UK

V. Tayefi & S.C. Reid
Formerly, School of Geography, University of Leeds, Leeds

ABSTRACT: Much concern has been expressed about the potential impacts of changing climate upon future flood risk. However, there has been much less attention given to the ways in which changes in catchment function in general, and sediment delivery in particular, might themselves impact upon flood risk. This includes the effects of climate change upon sediment delivery and hence upon changes in river channel conveyance and hence flood risk. In this paper, we present the results of two types of modeling. The first presents predictions of future sediment delivery rates under future climate changes (estimated for the 2050s and 2080s) in order to provide first order estimates of rates of channel aggradation in an upland river with a gravelly bed. The second couples measured channel geometry changes, over short timescales, to flood events with 1 in 0.5 year and 1 in 2 year return periods, for both the present, and for future climates (the 2050s and 2080s). This coupling is achieved through a coupled 1D-2D model, with a full solution of the 1D St.Venant equations for the channel and a 2D diffusion wave treatment on the floodplain. Our results show that, for the system and flood return periods studied, sedimentation rates are the primary control upon the frequency of overbank flows and the magnitude of flood inundation extent. However, these interact non-linearly with future climate changes to increase future flood risk dramatically. This leads us to make three important observations: (1) we must consider what happens when historical flood events are modelled contemporary geometrical surveys in aggrading systems, as this is likely to yield unrealistically low friction parameters during the parameterization process; (2) we must factor the indirect impacts of future climate change upon sediment delivery into estimates of future flood risk; and (3) we must think about how river management activities impact upon the sedimentation process and make sure that the mechanisms by which a channel maintains conveyance when subject to sediment delivery are not undermined by river management activities.

1 INTRODUCTION

1.1 *Climate change and flood risk*

The magnitude, frequency and extent of floodplain inundation will be a direct function of the hydrological response of a catchment. As future climates may be responsible for increases in the magnitude of peak flows (e.g. Middelkoop et al., 2001, Milley et al., 2002) and given recent major flooding events across Europe, future climate change is likely to be a contributing factor to more frequent flood events (Hunt, 2002).

1.2 *The impacts of changing conveyance*

The magnitude of a peak flow is not the only control on flood risk: a flood begins when main channel water levels are sufficient to exceed local bank height, which is a function of channel conveyance. Conveyance is a function of three primary properties: (1) the elevation and shape of river channel cross-sections; (2) the slope of the energy line; and (3) surface roughness properties. Thus, channel conveyance acts as a crucial connection between climate change impacts upon river flows and the onset and magnitude of flood inundation. Traditionally, changing conveyance due to aggradation or degradation has not been factored into flood risk assessment. This may reflect a traditional view of sediment delivery as some kind of local (in time and space) disturbance to an equilibrium channel morphology, where cross-sectional areas adjust to some characteristic bankfull flow. When sediment is delivered, it is thought to be just a matter of time before channel capacity re-establishes itself through transport of that sediment downstream through the river system. However, this overlooks extensive geomorphological evidence of alluviation, potentially rapidly over short

Copyright © 2006 Taylor & Francis Group plc, London, UK

time periods (e.g. Macklin & Lewin, 2003), including aggradation. For example, Harvey (2002) reports that the long-term response of a major input of sediment to Bowderdale and Langdale Becks in the Howgill Fells was partial stabilisation of associated sedimentation zones and not downstream progradation.

Concurrently, there is a growing recognition that reductions in channel conveyance due to sedimentation could be contributing to flood risk (e.g. James, 1999, Stover & Montgomery, 2001, Korup et al., 2004, Pinter & Heine, 2005). We have no knowledge as to how such changes might compare with future climate changes in relation to future flood risk.

1.3 *Climate change and sediment delivery*

There is a second reason to be concerned about the potential impacts of changing conveyance upon flood risk. This is due to the possibility that climate change may impact on sediment delivery in a way that exacerbates in-channel sedimentation. Increased sediment delivery from hillslopes and channel banks to river systems may follow from climate related changes in precipitation. If this delivery leads to in-channel sedimentation it could further exacerbate flood risk (e.g. Stover & Montgomery, 2001). Given that climate change is likely to have a major impact upon the distribution, frequency and magnitude of rainfall patterns (Brooks et al., 1993, 2004), these changes could have major impacts upon coarse sediment generation in upland environments (Buma & Dehn, 1998).

1.4 *Aims*

Given the potential importance of conveyance changes due to sedimentation for future flood risk, and the potential climate changes upon sedimentation, this paper aims to understand, for a gravel-bed river in an upland temperate environment, the possible relative contributions of climate change, sedimentation and sediment delivery upon future flood risk. The approach we adopt is based upon simulation modeling, using a hillslope failure model to estimate coarse sediment delivery rates (Reid et al., in press, a) and a coupled 1D-2D hydraulic model to assess the effects of in-channel sedimentation (Tayefi et al., in press).

2 METHODOLOGY

2.1 *Study site*

Our study site is in a temperate upland environment in the north of England (Fig. 1). In terms of catchment characteristics, this is a good study site as it has shown to be representative of the upper reaches of a number of rivers in the region in terms of probable geomorphological changes during the Holocene



Figure 1. The location of the study site, including the catchment (top diagram) and reach of river studied (bottom diagram). Diagram from Lane et al. (in press, a).

period (Coulthard et al., 2005). These are largely characterised by the reduction of valley gradient and the widening of valley floodplain width, both of which lead to aggradation and rapid downstream fining of surface sediment. In choosing this site, we are therefore focusing upon those rivers associated with coarse sediment (in the gravel fraction and coarser) and a climatic regime that is strongly influenced by the North Atlantic Oscillation, with weather that is strongly influenced by North Atlantic pressure systems when the index is positive and partly influenced by continental originating air masses when the index is negative. Generally, this results in a humid climate, with (relatively) warm winters and (relatively) cool summers.

The study site has been the subject of intensive investigation since July 2000, as a result of a problem of gravel sedimentation, in terms of both catchment hydrology and sediment delivery and river channel response and flood risk. The catchment comprises a mixture of limestone and gritstone, some of which is

Copyright © 2006 Taylor & Francis Group plc, London, UK

covered by thick post-glacial drift material. Almost all of the hillslopes and moorland surfaces are covered with a thin layer of peaty soils. Tributaries (locally known as Gills) extend steeply up the hillslopes and onto the moorland, are commonly dissected into drift material, and this has been observed to be a major source of delivered sediment (Reid et al., in press, a). Some of the moorland has been drained by shallow open drains, although these are now not routinely maintained, and some have been subject to attempts to block them.

The river flows out of a confined, bedrock reach at Hubberholme (Fig. 1), where the valley gradient reduces, the valley widens, and the river becomes alluvial, with well developed floodplain systems. The study reach for the flood risk analysis extends from Hubberholme to Starbotton (Fig. 1) and is predominantly sinuous, although straighter reaches are interspersed between intensely meandering reaches. At Starbotton, a major landslide blocks the valley and measurements suggest that not much sediment passes downstream beyond Starbotton (Reid et al, in press, b). The floodplain land use is a mixture of managed hey meadow (of conservation value). The river was subject to extensive management in the 1980s (Hey & Winterbottom, 1990) as a result of flooding between 20 and 30 times per year on average. Some of this engineering activity was reversed in the late 1990s and 2000s as a result of a perceived failure of the 1980s scheme.

2.2 *Coarse sediment delivery modeling: SEDMAP*

The approach to modelling is explained in full in Reid et al. (in press) and only a summary is provided here. SEDMAP is based on a modified form of SHALSTAB (Montgomery & Dietrich, 1994, Montgomery et al., 1998), leading to determination of failure likelihood (slope stability) without and with a soil and root cohesion treatment. In SHALSTAB, slopes and channel banks can fail at full or partial saturation. In practice, failed material may then be transferred to the drainage network whether or not there is hydrological connection between the failure site and the network. However, in SEDMAP, we follow the theoretical analysis of Legros (2002). Legros shows that water at the bed of a failed material may significantly increase the associated transfer distance, so increasing its connectivity with the drainage network. Thus, we modify SHALSTAB to require hydrological connection into the location for failed sediment to be delivered to the drainage network. Our method provides discrete predictions of failed sediment areas and, with assumptions regarding soil depth, failed sediment volumes. Reid et al. (in press, b) assessed the model by comparing measured failure locations to modeled failure locations and obtained a good level of agreement. They also used coarse sediment sensors to compare when the model predicted sediment delivery to when it was observed and, again, the agreement was good. Provisional estimates suggest that the ratio of coarse sediment to fine sediment in the mix of failed sediment is about 11% and we use this to compare delivered sediment rates to surveyed river bed level changes.

We drive the model using a modified form of TOPMODEL, which is a continuous simulation hydrological model. This is modified from the Beven and Kirkby (1979) formulation to include a treatment that allows for saturated parts of the landscape to be disconnected from the drainage network (Lane et al., 2004). In the study site, we observed negligible sediment storage within the tributaries and the main stem of the river above Hubberholme (Fig. 1) and, with the coarse:fine sediment ratio, this allows us to convert estimates of sediment delivery from the catchment to estimates of coarse sediment delivery to the river channel between Hubberholme and Starbotton.

The model was applied using measured rainfall data from a nearby gauge to provide a baseline set of data (representative of the 1960–1990 period). These rainfall data were then scaled using UKCIP (2002) climate predictions for the region to provide rainfall estimates for the 2050s and 2080s. These provide monthly rainfall estimates which were downscaled using a range of downscaling approaches (see Reid et al., in review). The topographic data required by the model were supplied at 2.0 m resolution from a specially flow Lidar survey.

2.3 *Channel response to coarse sediment delivery*

The sediment delivery method gave us a first approximation of mean coarse sediment delivery rates. In order to assess these rates, and also to provide us with an understanding of the spatial structure of sediment deposition along the 6 km reach and cross-section data for the coupled 1D-2D hydraulic model, we have been surveying a series of 60 cross-sections (average spacing 100 m) in March and December of each year, since 2001. These surveys were based upon instrumented cross-sections, located and recovered using Real-time Kinematic GPS.

2.4 *Modelling floodplain inundation*

Tayefi et al. (in press) reviewed three options for modelling upland floodplain inundation with complex topographic and topological structure: (1) lateral extension of cross-sections across the floodplain; (2) representation of the floodplain as a series of connected storage cells; and (3) a coupled one-dimensional model of the main channel and two-dimensional diffusion wave model of the floodplain. The latter was based on methods reported in Yu and Lane (2006a, 2006b) and Lane (2005) in which we

Copyright © 2006 Taylor & Francis Group plc, London, UK

explicitly represent floodplain topography and topology rather than representing its effects implicitly through upscaling of a roughness parameter. On the basis of comparisons of measured and modeled inundation extent for an event on the 4th February 2004, Tayefi et al. found a significantly better level of agreement with the coupled 1D-2D model than with either the extended section or storage cell approaches. Thus, we use the coupled 1D-2D approach in this paper (see Lane et al., in press, for a full review). The main channel flow was modelled using HEC-RAS, which allows description of the river channel as a series of discrete cross sections perpendicular to the flow direction. Water surface elevation and other hydraulic characteristics of flow were calculated at each cross section and all hydraulic structures defined in the domain (e.g. lateral weirs). These were coupled with a weir equation and used as the boundary conditions for the floodplain inundation model, which uses the depth-averaged mass conservation equations and a simplification of the shallow water momentum equations, based upon ignoring the spatial and temporal acceleration terms and adopting a Manning friction equation (Bradbrook et al., 2004, Yu & Lane, 2006a, 2006b). The floodplain was discretised to an 8 m resolution, following Yu and Lane (2006a, 2006b). Fluxes between cells were set to zero where cells fell adjacent to impervious boundaries. Flow exchanges between the main river and floodplain were calculated based on water levels in the adjacent cells and some form of boundary condition, in this case a weir equation.

The model required a number of boundary conditions. First, the channel cross-section surveys provided the geometrical boundary conditions. In this paper, we compare the geometrical boundary conditions for two dates: December 2002; and March 2004. Second, the model required floodplain topography and this was based upon remotely-sensed Lidar data, filtered for trees and hedgerows (assumed to be pervious to flow at the scale of model application, but compare with Cobby et al., 2003) using automated image processing techniques. These data were supported by Ordnance Survey Landline data on field and other boundaries, held in the same co-ordinate system as that used for both the cross-section and LiDAR data surveys. These data needed additional field based classification into whether or not the boundaries were pervious, and over what spatial extent. Third, we needed flow and stage conditions. We specified measured water levels at the upstream end of the reach, which were converted to flows by using the Flood Estimation handbook Rainfall-Runoff model. This allowed us to model two events: one with a 1: 0.5 year event and one with a 2 year event. We were also able to use the rainfall-runoff model with the UKCIP (2002) predictions to generate estimates of future flows for the 2050s and 2080s. At the downstream end of the reach, we specified a reach slope and a normal depth condition, but extended the sections downstream so that this boundary condition had no impact upon results in the area of interest.

3 RESULTS

The results are structured into two sections. First, we describe how coarse sediment delivery is estimated to change in response to different downscaled climate changes for the 2050s and 2080s. Second, we present results from the coupled 1D-2D floodplain flow model and assess how predictions of inundation duration and areal extent change in response to both measured geometrical changes and future climate change impacts upon flow magnitude.

3.1 *Coarse sediment delivery under climate scenarios*

Under the baseline scenarios we estimate an average of 70.4 sediment generating events per year, although only 0.8 events per year affect more than 0.1% of the catchment area. Most events are highly localized to the channel margins. These events delivered an annual average of 24,300 cubic meters of sediment, which is equivalent to an average annual bed level rise for the 6 km study reach of about 10 cm.

Figure 2 shows predicted changes with respect to baseline under the three types of climate downscaling: (1) magnitude refers to proportionate application of the predicted precipitation changes, applied to each rain day in the data; (2) frequency refers to delivering forecast increases in rainfall through an increase in the number of days on which rainfall events occur; and (3) variability refers to keeping the number of rain days constant and adding the predicted increase in rainfall to only those days on which rainfall occurs, in proportion to the magnitude of the rainfall that occurs. For the 2050s, the average number of events increases by around 10%, regardless of downscaling scenario used. However, there is a marked difference in the predicted failure volume, with much more sediment produced under the magnitude and variability scenarios. This is because of the different nature of the downscalings. Under the frequency scenario, the additional days of rainfall result in an increase in the number of very small failures, largely channel marginal ones. Under the magnitude and variability scenarios, the increase in rainfall predicted for the 2050s occurs primarily as an increase in the size of existing events, more so for the variability scenario. This emphasizes the need to distinguish between different types of climate change impacts. If climate change impacts primarily increase the level of catchment wetness (i.e. the frequency scenario) this is likely to result in a smaller increase in

Copyright © 2006 Taylor & Francis Group plc, London, UK

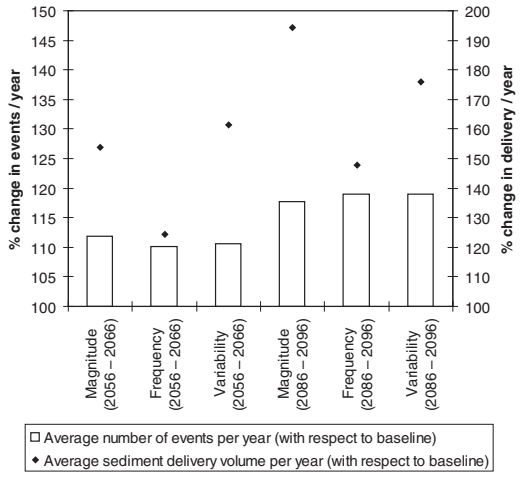


Figure 2. Predictions of coarse sediment delivery rates expressed as a percentage of the baseline estimates.

coarse sediment delivery than if the impacts result in an increase in the intensity of storm events, as in the variability (and to a lesser extent, the magnitude) scenarios. Indeed, the coarse sediment sensor results (Reid et al., in press, a) show that coarse sediment delivery in this environment is particularly sensitive to short-lived intense storm events, and not antecedent wetness.

These patterns are amplified for the 2080s. Again, the number of failure events does not vary significantly between downscaling methods, at just below a 20% increase. However, the sediment volume delivery per year increases by between 50 and 100%, according to the downscaling scenario used. These are quite dramatic increases and emphasise that the impacts of climate change upon coarse sediment delivery could be very significant for this kind of upland environment. Annual average aggradation rates are forecast to rise between 12 and 15 cm per year for the 2050s and 16 and 20 cm per year for the 2080s which, when compared with average annual aggradation rates of 10 cm per year at present are quite dramatic rises.

3.2 *Flood inundation model results*

Figure 3 shows the results from the flood inundation model, run with the December 2002 geometry and a 1 in 0.5 year flood event. The river flow is from right to left and predictions are superimposed on a digital elevation model of the reach. The upper part of the reach also illustrates the floodplain structure in terms of walls etc. Each image has a computational time step of 10 units and the 20 time-steps shown correspond to about 2 hours of simulation

It is clear from Figure 3 that the nature of flood inundation in this system is complex. Inundation begins early at a number of locations down the river, notably associated with floodplain low points. The total inundated area expands quite rapidly between 40 and 70 time steps and then slows quite significantly. The images show that the structure of the floodplain has a major effect upon the time-space patterns of inundation, with the walls, largely impervious to flows except where there are gates, having a major impact on inundation.

The prime reason for using this model was to compare the effects of short term changes in aggradation with longer term changes in climate. If we focus on the short term changes in aggradation, and compare the flood characteristics of the 1 in 0.5 year and 1 in 2 year events for the December 2002 and March 2004 measured cross-sections, the results are quite striking. This 16 month period has a reduction in bankfull discharge of 6.2% during which there was a measured average aggradation along the reach of 0.12 m. For the 1 in 0.5 year event, the average duration during which flows exceeded bankfull increased by 9.5%. The result was a 5.7% increase in inundated area. For the 1 in 2 year event, the increase in inundated area was 7.1%.

We then ran the 2002 geometry with flows estimated for the climate change scenarios for the 2050s and the 2080s. The inundation area increased by 12.2% by the 2050s and 21.6% by the 2080s for the 1 in 0.5 year event.

Finally, we ran the 2004 geometry with the 2050s and 2080s. This increased in inundated area over the baseline flows and 2002 geometry of 38.2% for the 2050s and 52.1% for the 2080s. This emphasizes the non-linear nature of the interaction between geometrical changes and changes in flow due to climate.

4 DISCUSSION

The main finding that emerges from the above results is that relatively short duration channel configuration changes, in this case over a 16 month period, can lead to substantial changes in inundated areas for 1 in 0.5 and 1 in 2 year floods, in an upland environment associated with coarse sediment transfer. For the 1 in 0.5 year event, the increase in inundated area was almost one half of the increase in inundated area estimated as resulting from simulated climate change to the 2050s. The non-linear nature of the onset of floodplain inundation (i.e. associated with the onset of overbank flow) meant that when these geometrical changes were combined with forecast climate changes, the increases in inundated area were amplified over the increases associated with each change in isolation. In other words, in this case study, in-channel sedimentation increases the sensitivity of flood inundation to future climate changes.

Following from these findings, a number of important research questions and river management issues

Copyright © 2006 Taylor & Francis Group plc, London, UK

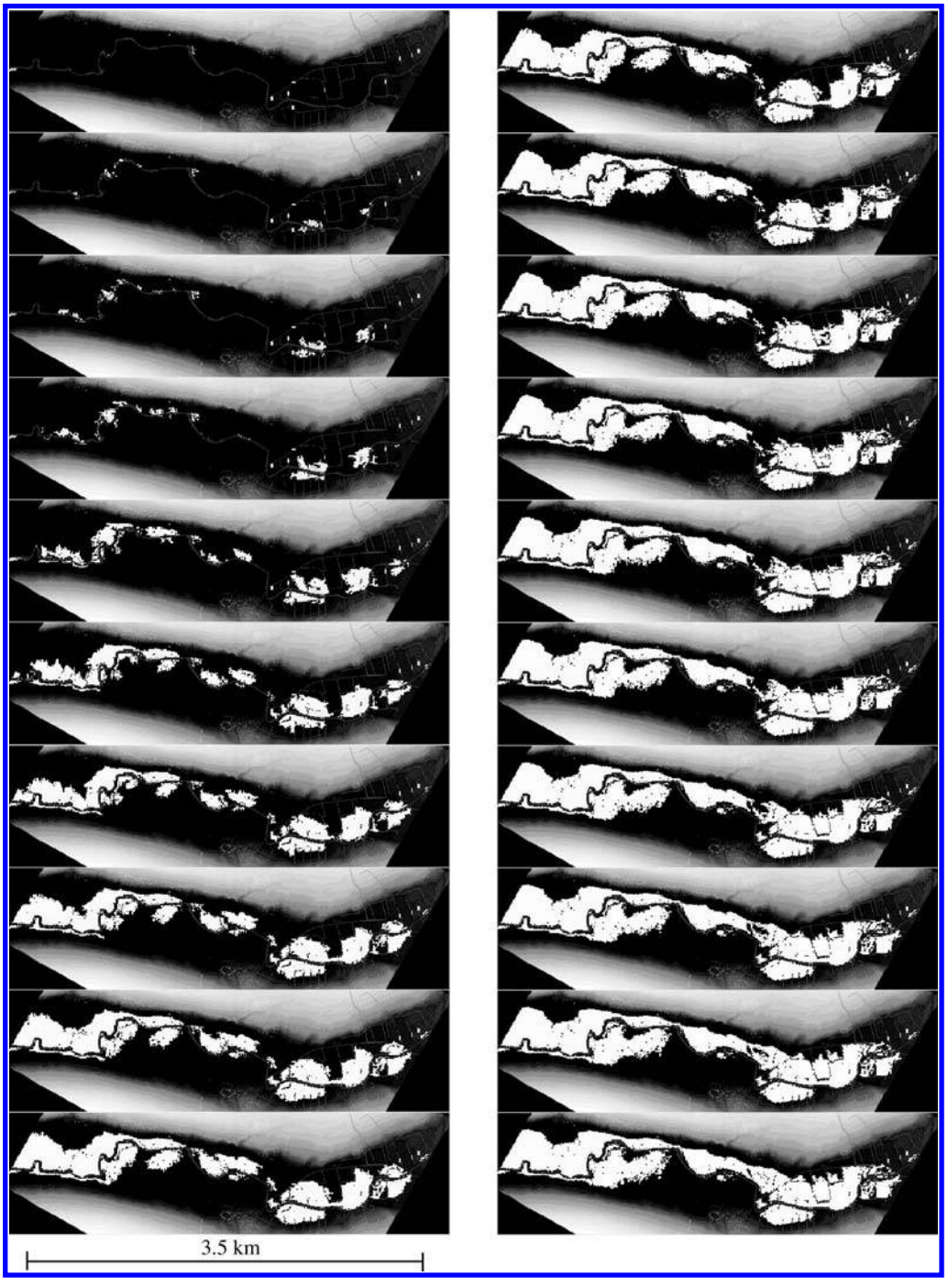


Figure 3. Model predictions of inundation for the 1 in 0.5 year event with the 2002 geometry. Each image is shown every 10 computational time steps and a total of 2 hours is simulated. The flow is from right to left.

Copyright © 2006 Taylor & Francis Group plc, London, UK

emerge. First, much attention is currently being given to detecting climate change signals in time-series of river flows. The evidence is not conclusive (e.g. Robson, 2002). However, this emphasis on flow is misleading as it does not necessarily provide any indication of the impacts of climate change upon flood risk. The kinds of geomorphological changes described here do not impact on flows, but they do impact upon the return periods and magnitudes of floodplain inundation, such that there could be a major increase in the magnitude and frequency of inundation events in any river, or river reach, that is aggradational, with no change in the magnitude and frequency of imposed flows.

Second, the sediment delivery model shows that the effects of climate change upon coarse sediment delivery may, in some situations, lead to a very significant increase in future flood risk. This is an indirect impact, independent of changes in river flow, although the latter may be important in controlling the spatial patterns of sediment transfer and hence the nature of any future river bed aggradation. Current cross-section surveys suggest annual average aggradation rates of about 10 cm per year, which are similar to the baseline simulations from the coarse sediment delivery model. We know that UK upland rivers can go through distinct cycles of alluviation in response to both short and long-term climatic fluctuations (e.g. Macklin et al., 1992). At present, upland landscapes are thought to be more sensitive to climatic fluctuations as a result of historical land use change (Macklin & Lewin, 2003). For instance, Coulthard and Macklin (2001) used modelling to show a severely non-linear interaction between climate change and deforestation in a similar upland river catchment.

The sediment delivery model results suggest increases in annual average aggradation rates of between 50 and 100%, which would be sufficient to make the annual aggradation rate equivalent to climate change impacts on flows to the 2050s. It appears that the indirect impacts of the climate change signal upon sediment delivery will act so as to reinforce the importance of short-term aggradation upon the magnitude and frequency of floodplain inundation, and that short-term variability in aggradation rates may be superimposed on top of a longer-term, aggradational trend. Hence, the changing flood risk identified here will be strongly impacted upon by climate change, not only because of the direct impacts of climate upon the magnitude and frequency of high flow events, but also because of the indirect effects of changing climate upon coarse sediment delivery which in turn will impact upon coarse sediment delivery and hence aggradation rates. There has been much debate over the extent to which land management impacts on catchment hydrology might be contributing to changing flood magnitude and frequency (see review in O'Connell et al., 2005). There has been much less acknowledgement of the extent to which land management practices have sensitised river basins to climate change (Coulthard et al., 2002, Macklin & Lewin, 2003) and in so doing are indirectly exacerbating flood magnitude and frequency. This case study emphasises the need to broaden the current focus of debate on the impacts of climate change upon river flows to include a much stronger engagement with catchment sediment delivery processes and how these interact with climate change.

There are three important practical issues that arise from these findings. The first is concerned with practical aspects of flood risk mapping. Commonly, flood risk mapping is based upon specially-commissioned geometrical surveys, application to one-dimensional hydraulic models, and model calibration based upon adjustment of model parameters, notably channel friction (commonly Manning's n), to predict the water level recorded in historical events. If there has been bed aggradation since that historical event, then a lower value of n will be required to reproduce that event than if the historical flood had been combined with historical geometrical survey. Thus, when modelling future events, this type of calibrated model will under-estimate water levels, and hence inundated area, inundation depth and flood risk, as a result of having a calibrated value of n that is too low. The converse would occur in systems that are degradational. Where this approach is being used in aggradational systems, it is highly likely that we are under-estimating future flood risk.

The second issue relates to river management in response to sediment aggradation problems. On the basis of observations, including the cross-section surveys, that began in July 2000, as well as the historical analyses of other data available for the area, it is possible to identify a distinct style of in-channel sedimentation and lateral channel adjustment, in response to the deposition of coarse sediment (Lane et al., in press). Most of the sedimentation occurs in distinct zones, commonly where the channel is weakly or strongly sinuous. This deposition is asymmetrical, commonly localized on point bars, attached to either meander bends or the inside edge of weakly sinuous reaches. Concurrent with this deposition is the erosion of mixed fine and coarse material from channel banks on the channel margin opposite the zone of deposition, and this is central to maintaining bankfull capacity. We can hypothesise that this transfer of coarse sediment to storage, through channel migration, should be an integral contribution to the observed rapid downstream fining, as well as a mechanism that leads to long-term valley fill. Given this response to in-channel sedimentation, it is important to consider the range of river management options available. The 1980s river management scheme chose to manage sedimentation through a combination of a gravel trap (to allow more

Copyright © 2006 Taylor & Francis Group plc, London, UK

manageable removal of sediment) and river channel realignment to increase sediment throughput, coupled to bank protection measures. Aside from the problem that enhancing sediment throughput will simply deliver sediment more readily to downstream locations, river bank stabilization is a particular problem in relation to flood risk. It prevents the *erosion* that is necessary to maintain channel bankfull capacity in response to river bed aggradation. There is still a general view in some river management communities that bank erosion (as opposed to artificially enhanced bank erosion, such as due to stock poaching) is a problem that has to be prevented, rather than a natural geomorphological response to high rates of sediment delivery. Consultant reports from the late 1990s for the reach of river considered in this paper advocated focusing management on stretches where eroding banks should be stabilised (e.g. RKL Arup, 1999a, 1999b). This assumes that a channel can be engineered to be robust, to transfer sediment through it and so to absorb changes in sediment supply with only minor adjustment in its form. However, channel morphology and stability in fact reflect the net sediment budget (e.g. Hooke, 2003), which in turn reflects: (i) the net erosion and deposition observed; and (ii) the supply and connectivity of sediment from the hillslopes and upstream reaches. Where river management restricts: (a) lateral movement of the river; and (b) transfer of sediment into floodplain storage; the channel bed becomes responsive (e.g. Schumm, 1979, Harvey, 2001, Hooke, 2003); and one response is aggradation. This will reduce channel conveyance and lead to the kinds of impacts described above in relation to flood risk. Thus, in addition to naturally high rates of sediment delivery, this kind of river management exacerbates flood risk. The Holocene record (e.g. Macklin & Lewin, 2003) tells us that these systems can experience large increases in sediment delivery over relatively short time periods and it is this historical record that emphasises the need to incorporate changes in conveyance due to sediment aggradation more explicitly into flood risk assessment and river management.

The third management question then becomes what should be done to manage river systems undergoing high rates of sediment delivery and consequent bank erosion and increased flood risk, if bank erosion is not an acceptable situation? The only option that recognizes the natural function of such river systems, aside from active dredging of sediment which may be unacceptable for ecological reasons, is to reduce the rate of sediment delivery to the system. The simulations from the coarse sediment delivery show that just four out of twelve tributaries were responsible for over 80% of delivered coarse sediment and that less than 1% of the area of each sub-catchment was delivering sediment. We simulated the effects of localized tree planting using native woodland through changing the root cohesion term in the sediment delivery model and found that this resulted in almost an 85% reduction in coarse sediment delivery rates. This is substantial, and provides a very different approach to managing the problems caused by coarse sediment aggradation in upland river systems.

5 CONCLUSION

This paper has shown the importance of considering the effects of coarse sediment delivery and the associated bed aggradation in the case study of a temperate upland environment. Whilst based on a case-study, it has some very important implications for climate change studies, flood risk assessment and river management more generally. In this study, for a flood with a 1 in 0.5 year event, short-term bed aggradation (over a 16 month period) was shown to result in about half the inundated area increase that results from applying climate changes estimated for the 2050s to the same event. Consideration of the joint impacts of climate change and bed aggradation emphasised the non-linear nature of system response, and the possibly severe and synergistic effects that come from combined direct effects of climate change and sediment delivery. Such effects are likely to be exacerbated further as a result of the impacts of climate change upon coarse sediment deliver and our modeling results suggested serious increases in aggradation rates to the 2050s and the 2080s.

When couched in conventional flood frequency terms, these changes do not result in a change in the return period of extreme flow events, but rather a reduction in the return period of the flow events that lead to floodplain inundation. Thus, analyses that focus upon the changing magnitude and frequency of flow events will overlook a key influence upon the return period and magnitude of flood inundation events.

Our analysis suggests that if more attention to to be placed on coarse sediment aggradation and its impact upon flood risk, then this needs to adopt a different approach to river management. Rather than managing the sediment once it is in the river system, more attention needs to be given to managing the sediment delivery process through reducing sediment source impacts. Our coarse sediment delivery modeling provides a framework for reducing delivery rates in a way that is, ultimately, much more sustainable.

Finally, whilst this research is based upon an upland case study, the observations will apply to flood risk issues in any upland or piedmont system, where there is coarse sediment delivery and accumulation, but also where active river management precludes the possibility of coarse sediment transfer into floodplain storage. Research by Pinter and Heine (2005) shows that river engineering on a river with a sand and silt-bed may also

Copyright © 2006 Taylor & Francis Group plc, London, UK

lead to systematic increases in stage for a given flow, and this may make these kinds of issues of relevance in other river systems.

ACKNOWLEDGEMENTS

This research was funded by a Ph.D. scholarship awarded to VT by the Iranian Science, Research and Technology Ministry and by NERC Connect Grant NER/D/S/2000/01269 awarded to SNL, Professor A. McDonald (AMcD) and Professor M.J. Kirkby and by Environment Agency R&D award E1-108 awarded to AMcD and SNL. Downscaled climate data were provided by the UK Climate Impacts Programme funded by the U.K.'s Department of the Environment, Farming and Rural Affairs. The Design and Imaging Unit, Durham, assisted with Figure production.

REFERENCES

Beven, K.J. and Kirkby, M.J., 1979. A physically based variable contributing area model of basin hydrology. Hydrological Sciences Bulletin, 24, 43–69.

Bradbrook, K.F., Lane, S.N., Waller, S.G. and Bates, P.D., 2004. Two dimensional diffusion wave modelling of flood inundation using a simplified channel representation. International Journal of River Basin Management, 3, 1–13.

Brooks, S.M., Crozier, M.J., Glade, T.W. and Anderson, M.G., 2004. Towards establishing climatic thresholds for slope instability: Use of a physically-based combined soil hydrology-slope stability model. Pure and Applied Geophysics, 161, 881–905.

Brooks, S.M., Richards, K.S. and Anderson, M.G., 1993. Approaches to the study of hillslope development due to mass movement, Progress in Physical Geography, 17, 32–49.

Buma, J. and Dehn, M., 1998. A method for predicting the impact of climate change on slope stability, Environmental Geology, 35, 190–196.

Cobby, D,M., Mason, D.C., Horritt, M.S. and Bates, P.D., 2003. Two-dimensional hydraulic flood modelling using a finite-element mesh decomposed according to vegetation and topographic features derived from airborne scanning laser altimetry. Hydrological Processes, 17, 1979–2000.

Coulthard, T.J. and Macklin, M.G., 2001. How sensitive are river systems to climate and land-use changes? A model based evaluation. Journal of Quaternary Science, 16, 347–351.

Coulthard, T.J., Lewin, J. and Macklin, M.G., 2005. Modelling differential catchment response to environmental change. Geomorphology, 69, 222–41.

Coulthard, T.J., Macklin, M.G. and Kirkby, M.J., 2002. A cellular model of Holocene upland river basin and alluvial fan evolution. Earth Surface Processes and Landforms, 27, 269–288.

Harvey, A.M., 2001. Coupling between hillslopes and channels in upland fluvial systems: implications for landscape sensitivity, illustrated from the Howgill Fells, northwest England. Catena, 42, 225–250.

Harvey, A.M., 2002. Effective timescales of coupling within fluvial systems. Geomorphology, 44, 175–201.

Hey, R.D. and Winterbottom, A.N., 1990. River engineering in National parks: the case of the River Wharfe, U.K. Regulated Rivers: Research and Management, 5, 35–44.

Hunt, J.C.R., 2002. Floods in a changing climate: a review. Philosophical Transactions of the Royal Society of London A 360, 1531–1543.

James, A., 1999. Time and the persistence of alluvium: River engineering, fluvial geomorphology, and mining sediment in California. Geomorphology, 31, 265–90.

Korup, O., McSaveney, M.J. and Davies, T.R.H., 2004. Sediment generation and delivery from large historic landslides in the Southern Alps, New Zealand. Geomorphology, 61, 189–207.

Lane, S.N., 2005. Roughness – time for a re-evaluation? Earth Surface Processes and Landforms, 30, 251–3.

Lane, S.N., Brookes, C.J., Kirkby, M.J. and Holden, J., 2004. A network index based version of TOPMODEL for use with high resolution digital topographic data. Hydrological Processes, 18, 191–201.

Lane, S.N., Tayefi, V., Reid, S.C., Yu, D. and Hardy, R.J., in press. Interactions between sediment delivery, channel change, climate change and flood risk in a temperate upland environment. Forthcoming in Earth Surface Processes and Landforms.

Legros, F., 2002. The mobility of long-runout landslides. Engineering Geology, 63, 301–331.

Macklin, M.G. and Lewin, J., 2003. River sediments, great floods and centennial-scale Holocene climate change. Journal of Quaternary Science, 18, 101–5.

Macklin, M.G., Rumsby, B.T. and Heap, T., 1992. Flood alluviation and entrenchment: Holocene valley floor development and transformation in the British uplands. Geological Society of America Bulletin, 104, 631–643.

Middelkoop, H., Daamen, K., Gellens, D., Grabs,W., Kwadijk, J.C.J., Lang, H., Parmet, B.W.A.H., Schädler, B., Schulla, J. and Wilke, K., 2001. Impact of climate change on hydrological regimes and water resources management in the Rhine basin. Climatic Change, 49, 105–128.

Milley, P.C.D., Wetherald, R.T., Dunne, K.A. and Delworth, T.L., 2002. Increasing risk of great floods in a changing climate. Nature, 415, 514–517.

Montgomery, D.R. and Dietrich, W.E., 1994. A physically based model for the topographic control on shallow landsliding, Water Resources Research, 30, 1153-1171.

Montgomery, D.R., Sullivan, K. and Greenberg, H., 1998. Regional test of a model for shallow landsliding, Hydrological Processes, 12, 943–955.

Pinter, N. and Heine, R.A., 2005. Hydrodynamic and morphodynamic response to river engineering documented by fixed-discharge analysis, Lower Missouri River, USA. Journal of Hydrology, 302, 70–91.

Reid, S.C., Lane, S.N., Berney, J.M. and Holden, J., in press, a. The timing and magnitude of coarse sediment transport events within an upland gravel-bed river. Paper forthcoming in Geomorphology.

Reid, S.C., Lane, S.N., Montgomery, D.R. and Brookes, C.J., in press, b. Does hydrological connectivity improve identification of coarse sediment delivery in upland environments? Paper forthcoming in Geomorphology.

Copyright © 2006 Taylor & Francis Group plc, London, UK

RKL Arup, 1999a. Dynamic Assessment of Unstable Reaches of the Upper Wharfe, Environment Agency Final Report.
RKL Arup, 1999b. Upper Wharfedale "Best Practice" Project – Erosion Risk Assessment, Environment Agency Report.
Robson, A.J., 2002. Evidence for trends in UK flooding. Philosophical Transactions of the Royal Society of London A 360, 1327–1343.
Schumm, S.A., 1979. Geomorphic thresholds: the concept and its applications. Transactions of the Institute of British Geographers, 4, 485–515.
Stover, S.C. and Montgomery, D.R., 2001. Channel change and flooding, Skokomish River, Washington. Journal of Hydrology, 243, 272–86.
Tayefi, V., Lane, S.N., Hardy, R.J. and Yu, D., in press. A comparison of 1D and 2D approaches to modelling flood inundation over complex upland floodplains. Paper forthcoming in Hydrological Processes.
Yu, D. and Lane, S. N., 2006a. Urban fluvial flood modelling using a two-dimensional diffusion wave treatment: 1. Mesh resolution effects. Forthcoming in Hydrological Processes.
Yu, D. and Lane, S.N., 2006b. Urban fluvial flood modelling using a two-dimensional diffusion wave treatment: 2. Development of a sub grid-scale treatment. Forthcoming in Hydrological Processes.

Copyright © 2006 Taylor & Francis Group plc, London, UK

Consideration of protection works in hazard assessment – A case study

W. Gostner
Patscheider & Partner Engineers, Mals, Italy

B. Mazzorana
Public Water Authority, Province of South Tyrol, Italy

ABSTRACT: The paper describes an approach that makes it possible to consider protection works in hazard assessment properly. With the help of event trees the probability of flood events is combined with the failure probability of protection works. Probability of flood events is studied with classical methods of hydrology. Failure probability of protection works is examined by means of a semi-probabilistic approach respectively by expert judgement. Hydraulic modelling of different flood scenarios allows to compare hazard zones with and without consideration of protection works.

1 INTRODUCTION

Hazard assessment plays a key role in management of natural dangers such as floods, debris flows, snow avalanches, rock fall, etc. In order to plan and realize sustainable measures, communities and authorities recognize that, first of all, a thorough investigation of natural dangers is required. Exact knowledge of the hazard potential forms the base for efficient land use planning, reliable design of protection works and useful emergency concepts.

Therefore in recent years hazard mapping has become an important tool in hazard assessment. Different methodologies reflecting the needs of the area where they have been developed exist.

On the other hand, usually where financial and administrative conditions allowed it, structural protection works of different kinds have been realized in the past in order to reduce the hazard potential of natural dangers.

However, in hazard mapping most of the adopted procedures don't consider the impact of protection measures yet. In the present paper an approach is described which makes it possible to quantitatively judge the effectiveness of protection works in hazard zone mapping.

The approach has been developed by means of a case study that deals with an alpine torrent where clear water floods and debris flow event occurred in the past and that has been trained by different structural measures.

First of all there is a brief description of the studied torrent in order to point out clearly its main characteristics and the potential hazards related to it. Then an introduction into the method of hazard mapping is made. Further on stays the explanation of the developed method and at the end of the paper the application to the present case is described.

2 THE UPPER EISACK TORRENT

2.1 *General characteristics of the watershed*

The upper Eisack lies in the north of Italy closed to the border to Austria. Shortly after its origin it reaches the village of Brenner which is situated to the relatively small debris fan. It therefore represents the potentially endangered area. At this point the watershed of the torrent covers an area of 3,24 km^2 (Fig. 1).

The highest elevation of the watershed is at an altitude of 2.166 m a.s.l., whereas the mean elevation of the village of Brenner is at 1.370 m a.s.l. The main reach of the torrent has a length of 2,6 km. The main reach has a longitudinal slope of 23,5% in the upper



Figure 1. Watershed of the upper Eisack torrent.

Copyright © 2006 Taylor & Francis Group plc, London, UK



Figure 2. The flooded village of Brenner in 1956.



Figure 3. Check dam series with damaged check dams.

part, of 14% in the central part and of 38% in the lower part. The mean slope of the debris fan is around 8%.

The lower part of the watershed is covered by conifers, whereas the upper and central part are mainly characterized by pastureland.

In terms of geology the principal rock formation of the watershed are metamorphic stones such as lime schist and lime phylitte. The main debris sources are to be found, rather untypical for an alpine torrent, along the central part of the main reach. In the upper part of the watershed, where in alpine torrents sediment delivery usually takes place, no significant debris sources exist.

2.2 *History of events and protection works*

Besides of smaller flood events in recent history one catastrophic event is known. In 1956 on August 20th after heavy rains in the central part of the torrent large erosion processes took place. A debris flow developed and the village of Brenner was flooded. Registered precipitation states that the rainfalls in the period between August 16th and August 20th were the heaviest within the last 80 years.

After this event several protection works took place. In the central part of the torrent a series of 45 masonry check dams was built, immediately upstream of the village a debris retention basin with a volume of around 1400 m^3 was realized and through the village the torrent got an artificial trapezoidal flow profile.

However, site surveys have revealed that at present around one third of the check dams is damaged and no longer in a perfect state (Fig. 3). Among other things, this circumstance has been one of the main motivations to carry out the present study: the consideration of protection works in hazard assessment is of utmost importance to understand their effectiveness.

2.3 *Available debris volume*

The available debris volume that can by mobilized in an event is one of the key factors when dealing with debris flows in alpine torrents. Assuming that the erosion depth in an event can amount up to 20% of the river bed width, as observed in the past (Lehmann 1993), and that in the same event the side banks can be eroded in a triangular shaped manner, the available debris volume within the erodible part can be estimated at 28,800 m^3.

This estimation is confirmed through empirical relationships, as f.i. proposed by D'Agostino (1996), Takei (1984) or Rickenmann & Zimmermann (1993). This formulae give volumes of 25,000–35,000 m^3.

2.4 *Hazard features of the torrent*

The investigation of the watershed allows the following conclusions:

- The upper Eisack is a torrent where debris flow events and clear water floods with bed load transport can take place. The debris sources are to be found in the central reach of the torrent, having a potential volume of around 30,000 m^3.
- Due to the realization of the check dam series debris flow activity has been reduced to a minimum, i.e. debris flow events only can take place in the case of failure of several check dams.
- As the watershed has a rather small extension, in case of floods the mobilized sediment is likely delimited by the transport capacity of the clear water discharge.
- The maximum sediment concentration in a debris flow is probably low, due to the moderate slope of 14% in the erosion reach.

3 PROCEDURE OF HAZARD ZONE MAPPING

Usually, in hazard assessment different hazard degrees are defined, distinguished by different colors. The differentiation of the hazard zones is obtained by combining the probability of catastrophic events with their intensity.

Copyright © 2006 Taylor & Francis Group plc, London, UK

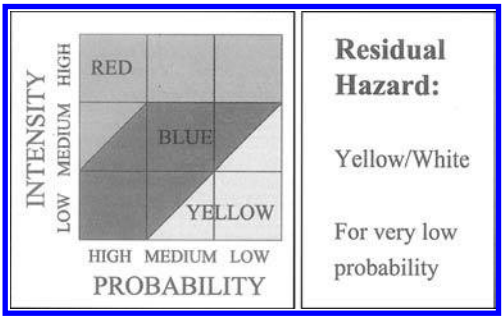


Figure 4. Matrix for determination of hazard degree.

Table 1. Criteria for intensity of mountain hazards.

Process	Low intensity	Medium intensity	High intensity
Rockfall	$E < 30$ kJ	30 kJ $< E < 300$ kJ	$E > 300$ kJ
Landslide	$Vs < 2$ cm/year	Vs: dm/year	$Vs >$ dm/year
Debris flow	—	$D < 1$ m or $v < 1$ m/s	$D > 1$ m and $v > 1$ m/s
Static flooding	$h < 0.5$ m	$0.5 < h < 2$ m	$h > 2$ m
Dynamic flooding	$q < 0.5$ m^2/s	$0.5 < q < 2$ m^2/s	$q > 2$ m^2/s
Bank erosion	$t < 0.5$ m	$0.5 < t < 2$ m	$t > 2$ m
Avalanche	$P < 3$ kN/m^2	$3 < P < 30$ kN/m^2	$P > 30$ kN/m^2

E = kinetic energy, Vs = mean annual velocity of landslide, D = thickness of debris front, v = flow velocity, h = flow depth, q = specific discharge, t = extent of lateral erosion, P = avalanche pressure exerted on an obstacle.

Figure 4 shows the matrix that has been applied in the present study. It was presented by FOWM (1997) and it distinguishes four degrees of hazard zones: high danger where life is endangered in- and outside of buildings and heavy damages can be expected (red zone), medium danger where human life is at risk only outside of buildings (blue zone), and low danger without danger of life (yellow zone). Finally, a residual hazard zone where probability of occurrence is very low is determined.

The intensity of an event may be characterized by different parameters depending on the type of the event. When dealing with mountain hazards, the criteria shown in Table 1 are used (after Petraschek & Kienholz 2003).

The probability of an event is directly related to its return period. The method of FOWM (1997) defines return periods of 30, 100 and 300 years as events with low, medium and high probability respectively.

Knowing the events with the defined return periods, their probability of occurrence can be calculated. Table 2 illustrates the probability of occurrence of the events, related to the period of one year.

Table 2. Relation between probability and return period.

Probability	Return period (Years)	Probability
High	30	0.033
Medium	100	0.01
Low	300	0.0033

4 THE ROLE OF PROTECTION WORKS

4.1 *General considerations*

Structural protection works are active measures with the aim to reduce the intensity respectively probability of an event. Thus, hazard mapping becomes substantially more reliable if the role of protection works is considered in a proper manner. The elaboration of scenarios should be integrated directly within the frame of the analysis (Romang et al. 2000).

Methods used in classical risk analysis f.i. concerning the safety of nuclear power plants or of large dams have been used for the development of the approach described in the present paper.

4.2 *Event trees*

A risk analysis is sustained by a logical tree whose function is to decompose the problem into its parts in a logical structure such as (Salmon & Hartford 1995):

1 Identification of initiating events;
2 Lay out of all possible combinations and sequences of following events;
3 Consideration of the outcome of each sequence along the branches.

Among the different types of logical trees the most appropriate to apply in natural hazard assessment are event trees. Their principal concepts are described in the following.

The probability of the occurrence of an event is given by the product of the probability of the primary process w_0 and the relative probabilities of the consecutive processes

$$w = w_0 w_1 w_2 \ldots\ldots w_n \quad (1)$$

where n is the number of consecutive processes. For the relative probabilities one has to consider that the probability that a process does not occur is

$$w_{ni} = 1 - w_{ij} \quad (2)$$

where w_i is the relative probability of the process i. Accordingly, the sum of the probabilities from all the events that share the same primary process is equal to the probability of the primary process (Beffa 2000). Figure 5 shows an abstraction of an event tree for extreme precipitation induced failure.

Copyright © 2006 Taylor & Francis Group plc, London, UK

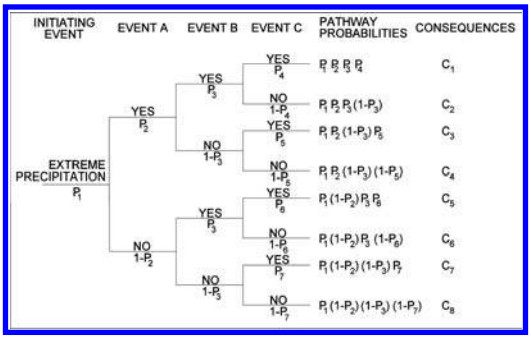


Figure 5. Exemplification of an event tree (after Darbre, 2000).

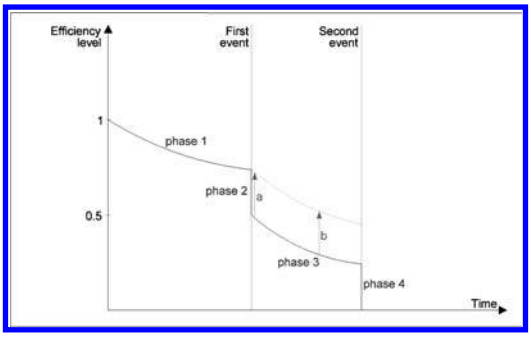


Figure 6. Component reliability during its working period.

In the present case the primary process is given by a flood event with a certain probability respectively return period, whereas the consecutive processes are defined by the reaction of the system, especially of the protection works.

4.3 *Probability determination of structural collapse*

4.3.1 *General considerations*

Figure 5 demonstrates that a given event causes several reactions with different probabilities. The response of protection works on a flood event might be either the perfect functioning without any damage at the structure, the partially functioning with some damages or the collapse of the structure.

Moreover, the efficiency of the same protection structure can vary in course of time as follows (Fig. 6):

- Phase 1: efficiency decrease of endogenous type, due to progressive deterioration of the materials and the permanent loadings on the structure;
- phase 2: during an extreme event the efficiency may decrease abruptly in time;
- phase 3: after the extreme event the decreasing of the efficiency is analogous to that in phase 1, but faster.

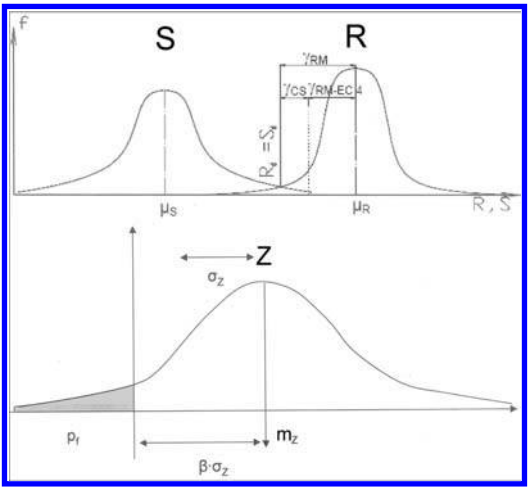


Figure 7. Distribution of S and R.

- phase 4: this represents the final collapse of the structure.

However, in the present study only two cases are considered: the perfect functioning of the structure respectively the collapse of the structure.

Thus, the key task in the next step is to quantify the collapse probability of the protection works. Once the collapse probability is known, the probability of non collapse can be determined using Equation 2.

Two different approaches have been utilized. The first is based on the semi-probabilistic concept established in the Eurocodes for the correct dimensioning of supporting structures. The second takes advantage of the precious experience of technicians involved over many years in the planning, realization and maintenance of river protection works.

4.3.2 *Semi-probabilistic approach*

The Eurocodes consider the fact that structures aren't either safe or non safe. Indeed, a structure has a certain failure probability depending on different variables, i.e. external or internal actions and material resistance.

The semi-probabilistic approach starts from the assumption that actions S and resistance R are aleatory variables with a normal distribution around their mean value m_S and m_R respectively. Consequently, the difference $Z = R - S$ that determines the failure probability has again a normal distribution (Fig. 7).

The failure probability can also be described by the so-called index of reliability

$$\beta = \frac{m_z}{\sigma_z} \tag{3}$$

where β is the index of reliability, m_z the mean value and σ_z the standard deviation of Z. In order to increase the factor β respectively to decrease the failure

Copyright © 2006 Taylor & Francis Group plc, London, UK

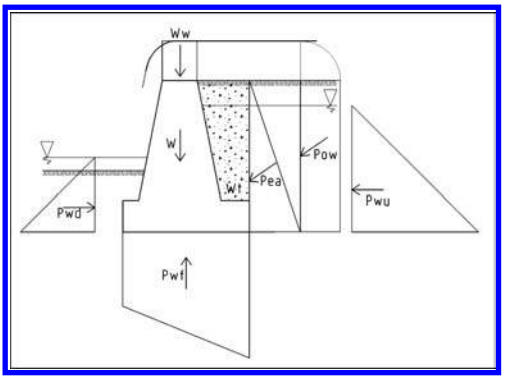


Figure 8. Forces acting on a check dam.

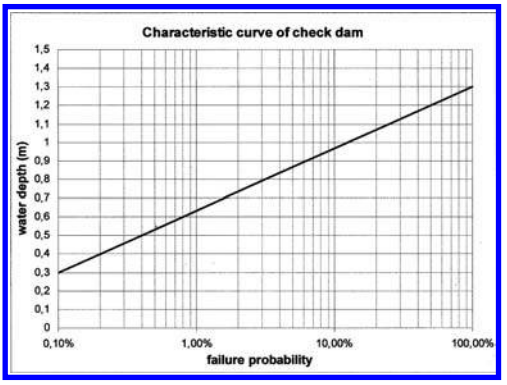


Figure 9. Correlation between water depth over check dam and failure probability for the check dams on the Eisack torrent.

probability partial safety factors are introduced which allow to increase the action respectively to decrease the resistance of the material.

In civil engineering the partial safety factors are defined with the background that a failure probability of $1 \cdot 10^{-6}$ for a single structure is acceptable. However, in Geotechnics a failure probability of $1 \cdot 10^{-3}$ for sustaining structures is accepted (Meyerhof 1995). Therefore, if the partial safety factors proposed in Eurocode 7 – Geotechnical design (1997) for the USL (ultimate state limit) are applied in the dimensioning procedure, a sustaining structure will have a failure probability of $1 \cdot 10^{-3}$. On the other hand, if the partial safety factors are set to an overall value of 1, the failure probability of the structure will be equal to 1.

Coming back to the present case, the failure probability of check dams has to be analyzed. The actions on a check dam can be subdivided into active earth pressure P_{ea}, hydrostatic pressure upstream P_{wu}, pressure due to the water or sediment-water-mixture overflowing the check dam P_{ow}, hydrostatic pressure downstream P_{wd}, water pressure beneath the foundation P_{wf}, own weight W, weight of the upstream earth fill W_e and weight of the overflowing water respectively water-sediment-mixture W_w (Fig. 8). The passive earth pressure downstream is not taken into account, as there are substantial uncertainties concerning its entity.

The structure has to be verified regarding its safety for translation and rotation, the bearing capacity of the soil and the safety for siphoning. To actions and resistance usually an unequivocal, clearly defined value can be assigned. Only the depth of the overflowing water depends on the discharge, in other words on the return period. For a given structure two water depths can be searched: utilizing the partial safety factors as proposed by the Eurocode and searching the water depth at which all the verifications are fulfilled, is the case which corresponds to a failure probability of $1 \cdot 10^{-3}$.

On the other hand, if the partial safety factors are set to an overall value of 1, at the corresponding water depth the failure probability is equal to 1.

Furthermore, assuming a logarithmic behaviour, a function can be defined that correlates the water depth and the failure probability of the structure.

As the check dams on the Eisack torrent are similar in terms of geometry and construction, a single function, valid for the whole check dam series, has been worked out (Fig. 9).

The semi-probabilistic approach offers the advantage that it is certainly based on a scientific and well recognized background, as the Eurocodes have adopted it in different subjects. The major disadvantage consists in the fact that the methodology presumes a perfect structure, i.e. a structure immediately after completion with an efficiency level of 1 (Fig. 6). For a slightly or heavily damaged structure assumptions based on subjective judgement have to be made. From that point of view the empirical approach proposed in the next chapter seems to be more consistent.

4.3.3 *Empirical approach – Expert judgement*

Key personnel in public water authorities has many years of experience in planning, realizing and maintaining of protection structures. The idea of the proposed approach is to gather this experience in order to judge the failure probability of a structure in a best possible manner.

Thus, an expert questioning finalized to the deeper understanding has been organized and structured as follows:

In the first step, the estimation step, the experts get a detailed photographical documentation of the check dams as well as the available project documents (basin characteristics, assumed peak flow for the dimensioning of the structure, available information about past sediment transport or debris flow events). Then the experts fill out a prepared evaluation form.

After having evaluated the single damage or defect types, the experts estimate the failure probability of the considered structure, assuming an impact event of

Copyright © 2006 Taylor & Francis Group plc, London, UK

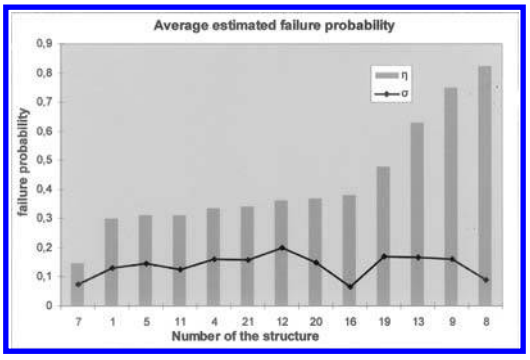


Figure 10. Average values and standard deviations of the estimations.

a reference return period of 100 years (a horizontal line in the cross section indicates the flow height related to this return period).

In addition the experts evaluate the relative importance of each detected defect type by assigning a specific percentage that reflects the relative weight of the severity of the detected damage type in the estimation process.

In the second step, the data analysis step, the damage or defect types are grouped into two larger damage categories:

1 External damage categories: defined as any action due to groundwater flow, weir overfall, water and earth pressure that change the external configuration of the considered structure.
2 Structure related damage categories: defined either as equilibrium changes or any sort of deformations and degradations of the structure.

Through a multiple correlation between the average value of the sums of the assigned ratings to the external damage factors and the average value of the sums of the assigned ratings to the structure related damage factors with the average failure probability estimated by the experts a failure probability indicator can be proposed:

$$Z = 0.03 \cdot \Sigma X_i + 0.02 \cdot \Sigma Y_i \quad (4)$$

where Z is the estimated failure probability, ΣX_i is the sum of the assigned ratings for the detected external damage factors, ΣY_i is the sum of the assigned ratings for the detected structure related damage factors.

Figure 10 shows the failure probability estimations of the experts. The standard deviations of the failure probability estimations do not seem to depend on the average failure probability estimations. Furthermore, the figures indicate that the expert's relative weight assignments to the two categories are surprisingly homogeneous.

As already mentioned above the failure probability indications are related to a well defined input event intensity. In order to derive useful failure probability indications also for higher intensity input events and therefore for events of lower occurrence probability or higher return period in this work an extrapolation procedure based on the two parameter Weibull distribution has been adopted.

The assumption is that the shape parameter γ depends on the structure material, so for a given value of the parameter γ and for a given failure probability estimation for a 100 years return period input event, the location parameter of the Weibull distribution is found by a secant iteration method.

The so fixed parameters of the Weibull distribution permit the determination of other return periods.

Concluding, both of the proposed approaches can be utilized for the development of event trees. However, in the present paper the semi-probabilistic approach is presented.

5 APPLICATION TO THE PRESENT CASE

5.1 *Adopted methodology*

The adopted methodology consists in a modular and gradual structure. The procedure can be interpreted as the modelling of a process chain where the different processes have to be considered as a cause-effect-relation. Parameters that can not be defined exactly must be assumed for the modelling of each process. Therefore it was necessary to conduct a sensitivity analysis in each step of the study in order to test the reaction of the system on the variation of the different assumptions. Herewith possible events can be constrained and plausible scenarios defined. The following steps have been worked out:

– Generation of clear water hydrographs. Analysis begins with a rainfall-runoff-model. Precipitation data based on the local meteorological conditions are combined with the hydrological characteristics of the watershed to define clear water hydrographs at different points of interest.
– Elaboration of flood scenarios. Event trees are developed that permit to consider existing protection works properly in order to define flood scenarios which take into account the wholeness of the real conditions. In this step different transport formulae for bed load transport and debris flow are used.
– Numerical modelling of the urbanized area. A two-dimensional numerical model is used. Clear water floods and debris flows are analyzed in order to define the hazard zones.

5.2 *Generation of clear water hydrographs*

In the watershed of the upper Eisack torrent no rainfall gauges are installed, thus no direct measurements of

Copyright © 2006 Taylor & Francis Group plc, London, UK

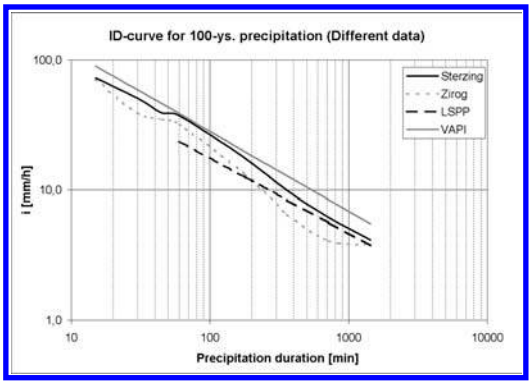


Figure 11. Comparison of intensities for precipitations with a return period of 100 years.

precipitations are available. Therefore, statistical evaluation of precipitation data recorded at gauges near the watershed as well as regionalized analytical functions proposed by Villi (1994) in the context of the project VAPI (Valutazione delle Piene in Italia) were used (Figure 11).

Extensive sensitivity analysis led to the following basic observations for the assumption of rainfall scenarios:

1 Data from the rain gauge in Sterzing, distant from the upper Eisack torrent around 20 km, can be used as precipitation data.
2 Floods in the upper Eisack torrent are caused by precipitation with short duration and high intensity, i.e. storms triggered by convective air circulation. Therefore, rainfall events with a duration of 60 minutes are considered.
3 In order to simulate the variation in rainfall intensity throughout the storm, hyetographs according to the alternating block method are used. This method, described in Chow et al. (1988) is a simple way of developing a design hyetograph from an IDF-curve. In this way, it is possible to incorporate the observation that generally 90% of the precipitation falls within a third of the duration of the whole storm.

In order to compute clear water hydrographs at different points of interest, the watershed is subdivided in several subbasins. The formation of the clear water hydrographs, based on the chosen rainfall scenarios, is modelled with the software HEC-HMS. The software includes several components which, based on different optional methods provide the possibility to model runoff volumes, runoff hydrographs and the routing of the hydrograph through the channel.

In Figure 12 hydrographs obtained with the rainfall-runoff model for different return periods are shown at the entrance into the village of Brenner.

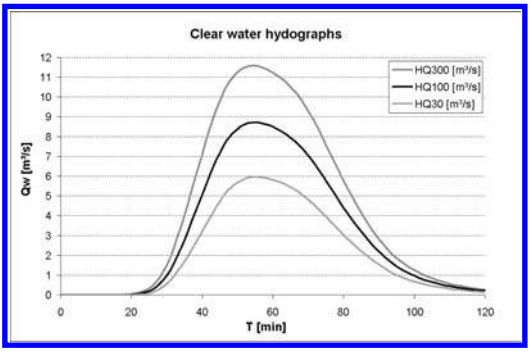


Figure 12. Clear water hydrographs at the entrance into the village.

Table 3. Basic assumption for the development of event trees.

Return period (Years)	Q_{max} (m^3/s)	H_w (m)	P_f	V (m^3)
30	3.05	0.60	$8 \cdot 10^{-3}$	7.800
100	4.44	0.78	$2{,}8 \cdot 10^{-2}$	9.800
300	5.89	0.94	$8{,}3 \cdot 10^{-2}$	11.800

5.3 *Elaboration of flood scenarios*

Development of event trees is based on the basic assumptions summarized in Table 3 and described explicitly in the following.

– Maximum discharges Q_{max} in the part of the check dam series are 3.05, 4.44 and 5.89 m^3/s for the flood events with return periods of 30, 100 and 300 years.
– The water depth over the check dam H_w can be calculated with the Poleni formula

$$Q = \frac{2}{3}\mu b\sqrt{2g}\,h^{3/2} \quad (5)$$

where Q is the discharge, μ the weir coefficient that can be set equal to 0.489, b is the width of the check dam and h is the flow depth. For the considered return periods the water depths are 0.60, 0.78 and 0.94 m.
– The failure probability P_f which is directly related to the water depth (Figure 9) amounts at $8 \cdot 10^{-3}$ for a 30-ys flood, $2{,}8 \cdot 10^{-2}$ for a 100-ys flood and $8{,}3 \cdot 10^{-2}$ for a 300-ys event.
– Concerning the maximum sediment load, the assumption is made that it is distributed equally on the check dam series. Consequently, having estimated a total sediment potential of 30,000 m^3 behind each check dam a volume of 670 m^3 can be mobilized.
– Moreover, a debris flow can only develop if a certain amount of sediment is mobilized. In other

Copyright © 2006 Taylor & Francis Group plc, London, UK

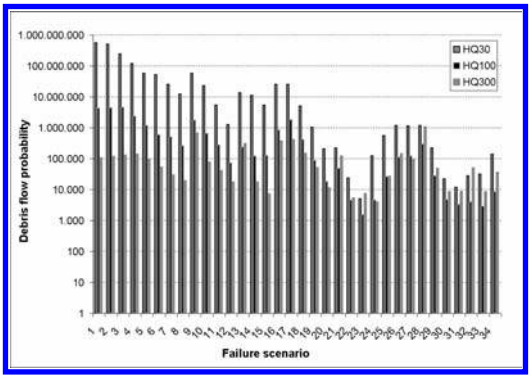


Figure 13. Return periods of debris flow events for the different scenarios.

Table 4. Debris flow probability P_{DF} for the considered flood events.

Return period (Years)	P_{DF} (%)
30	1.4
100	25.6
300	48.4

words, if the mobilized volume is not enough for a debris flow, the flood has the characteristics of a clear water flood with bed load transport or of a hyperconcentrated flow. The modelling of different scenarios, as described in chapter 5.4.2, allows to set the threshold V for a debris flow at 7800 m^3 for a 30-ys flood, at 9800 m^3 for a 100-ys. flood and 11,800 m^3 for a 300-ys. flood. Therefore, at least 11 check dams have to collapse in order to mobilize enough sediment for the development of a debris flow.

Based on this assumptions event trees are elaborated. The probability of the failure of 11 check dams is calculated by defining the scenarios that might physically occur. Considering that the check dam series is composed of 45 dams and supposing that the structures are failing from upstream to downstream, one after each other, 34 (45–11) scenarios can be defined. Scenario no. 12 f.i. stands for the rupture of check dam no. 12 and its 10 following check dams.

At each check dam the event tree is divided in two branches, where one represents the failure probability of the check dam and the other the probability of withstanding the load. According to Equation 2 the sum of the two branches gives the value of 1.

Further on, the probability for the development of a debris flow corresponds, as shown in Equation 1, to the product of the failure probabilities of 11 single check dams.

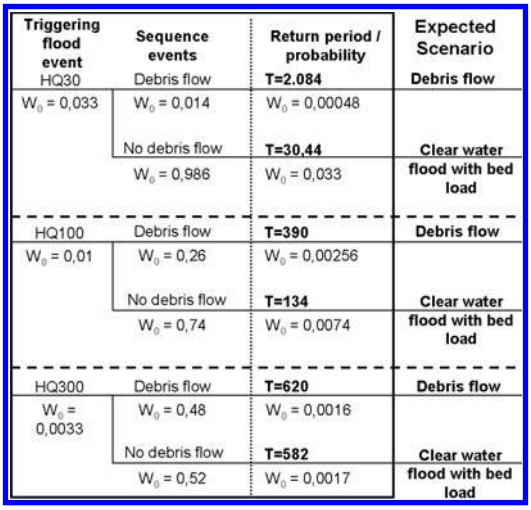


Figure 14. Event tree for flood events in the upper Eisack.

Finally, the overall probability that a debris flow occurs is represented by the sum of the 34 scenarios for a debris flow event.

Worth mentioning are the assumptions concerning damaged check dams. In the present case it is presumed that the failure probability of a moderate damaged check dam is five times higher than that of a check dam in perfect state, whereas for a heavily damaged check dam a 10 times higher probability is assumed.

Furthermore, in the failure case of a check dam the water depth on the downstream check dam is increased due to the mobilized sediment. Consequently, the failure probability is increasing successively along the check dams.

Figure 13 shows the return periods for the occurrence of debris flows for each of the considered scenarios. The figure points out the weak points of the system. Scenario no. 23 and no. 25 have the lowest return periods. This can be explained by the fact that downstream of check dam no. 23 several structures are heavily damaged. Hence, refurbishment measures have to start first in that zone.

The sum of the single scenarios gives the overall probability for a debris flow (Table 4).

Based on this calculations the event tree for the global system behaviour can be built (Figure 14). This event tree summarizes the event trees developed for the single scenarios described above. The figure states that a debris flow event in the upper Eisack torrent at the moment has a return period of at least 390 years, precisely for a 100-ys flood. Thus, a debris flow event at the upper Eisack torrent has still a very low return period.

On the other hand, a comparative analysis shows that for a check dam series without any damage the return period for a debris flow event is around

Copyright © 2006 Taylor & Francis Group plc, London, UK

5100 years. This proves that proper maintenance of protection works is of primary importance for their efficiency.

Due to the above considerations hazard mapping in the village of Brenner requires the following scenarios:

- modelling of 30-ys, 100-ys and 300-ys flood with bed load,
- modelling of a debris flow event in order to delimitate the residual hazard zone.

5.4 *Numerical modelling in the urbanized area*

5.4.1 *Clear water floods with bed load*

When modelling clear water floods, consideration of bed load is crucial as the debris retention basin situated immediately upstream of the village doesn't have a large volume.

The sediment transport capacity can be calculated by the formula proposed by Smart & Jäggi (1983). Assuming that enough sediment is available and thus the flood hydrograph can fully exploit its transport capacity, a total bed load of 1240 m^3 for a 30-ys flood, 1860 m^3 for a 100-ys flood and 2510 m^3 for a 300-ys. flood has been calculated.

5.4.2 *Debris flows hydrographs*

A debris flow hydrograph is developed based on a 100-ys flood event. It is assumed that maximum solid concentration at the front of the debris flow is not larger than 50%, due to the relatively moderate slope in the debris flow initiation zone.

The debris flow hydrograph is elaborated based on an approach proposed by Gostner et al. (2003) that utilizes for the debris flow front a criterion after Takahashi (1991) and for the debris flow body a transport formula presented by Tognacca et al. (2000).

Figure 15 shows the debris flow hydrograph at the entrance into the village. It can be noticed that lateral tributaries, joining the main reach after the debris flow initiation zone, reduce the maximum solid concentration to a value of 40%. Therefore the behaviour of the debris flow after the front has passed might also be of Newtonian type.

5.4.3 *Modelling of the urbanized area*

For the investigation of the flood and deposition processes in the village, the numerical model FLO-2D (O'Brien 2001) is used. FLO-2D is a two-dimensional flood routing model and allows the use of both clear water hydrographs and debris flows.

The input data of the model are a DEM, eventually the geometry of the channel, the incoming hydrograph and the rugosity of the grid elements.

In order to have both satisfactory accuracy and a reasonable calculation time for the model a grid size of 4 m for the floodplain is used and the trapezoidal

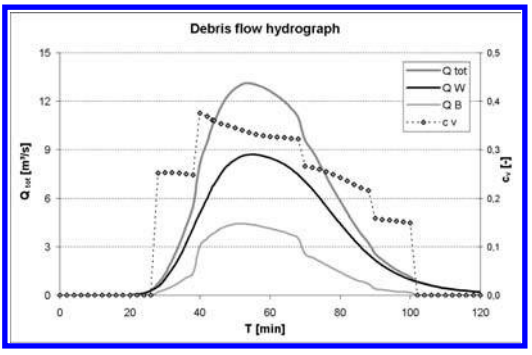


Figure 15. Debris flow hydrograph at the entrance in the village.

channel downstream of the debris retention basin is modelled one-dimensionally.

As the solid concentration of the debris flow after the front is relatively low as well as assumptions regarding the rheological parameters of the debris flow are quite speculatory, it seems justified that the debris flow is modelled as a Newtonian fluid. However, an increased rugosity, compared with the clear water floods, has to be adopted.

The model FLO-2D doesn't allow changes in topography throughout an event, therefore the debris retention basin situated upstream of the village has to be considered in a qualitative manner:

- Concerning clear water floods, due to the reduced transport capacity of the flood, the bed load is depositing in the debris retention basin. When the maximum discharge is reached, around 50% of the bed load has settled down and the topography has changed accordingly.
- For the debris flow a simplified way is adopted: it is assumed that as long as the retention basin is not completely filled up, the debris flow solids are retained and only clear water flows out of the basin. Once the basin is full the characteristics of the surge are no longer affected by the basin. The modified geometry of the filled retention basin is taken into account properly.

5.5 *Hazard mapping*

If protection works are taken into account, almost the whole flooded zone lies within a yellow zone due to inundations provoked by a 300-ys. flood with bed load.

On the contrary, if protection works were not considered properly, big part of the village would be in a blue hazard zone, as the 100-ys. flood would provoke a debris flow with the same return period.

However, the elaboration of event trees has clearly proven that at present a debris flow event has a return period >300 years.

Copyright © 2006 Taylor & Francis Group plc, London, UK

5.6 *Recommendations for measures*

The study allows to propose the following measures:

- At present the return period of a debris flow is >300 years. Nevertheless, the event trees have shown some weak points in the system. If the deterioration of the check dams continues, hazard potential in the village of Brenner can increase significantly. First of all, the check dams downstream of check dam no. 23 should be replaced.
- Enlarging the debris retention basin it is possible to prevent inundations of the village even for a 300-ys. event.

Both the refurbishment of the check dams and the enlargement of the debris retention basin contribute to reduce significantly the hazard potential in the village of Brenner. A zone with residual risk will always remain, when ever with a very low probability of occurring.

6 CONCLUSIONS

An approach that permits to consider in a proper manner protection works in hazard mapping has been described in this study.

The approach has been developed by means of a case study where a check dam series and a debris retention basin have been taken into account in hazard mapping for the village of Brenner.

With the help of event trees the return period of different flood scenarios can be properly investigated. The key step therein consists in relating the probability of flood events with the failure probability of the protection structures.

Failure probability can be either estimated by a semi-probabilistic approach or by an expert hearing. In the present study the semi-probabilistic approach has been presented in detail. However, in the semi-probabilistic approach a structure in a perfect state is implicitly presumed and damaged structures have to be considered by engineering judgement. Therefore an expert hearing might be the more consistent way for further developments.

REFERENCES

Beffa, C. 2000. A Statistical Approach for Spatial Analysis of Flood Prone Areas. *International Symposium on Flood Defence, September 20–23, Kassel*

Chow, V.T., Maidment, D.R. & Mays, L.W. 1988. *Applied Hydrology*. McGraw-Hill International Editions

D'Agostino, V. 1996. Analisi quantitativa e qualitativa del trasporto solido torrentizio nei bacini montani del Trentino Orientale. *Scritti dedicati a Giovanni Tournon.* Associazione Italiana di Ingegneria Agraria – Associazione Idrotecnica Italiana. (in Italian)

Darbre, G.R. 2000. Evaluation du Risque. *Cycle Postgrade en aménagements hydraulics 1999–2001*

Egli, T. 1996. Hochwasserschutz und Raumplanung. *ORL Bericht 100/1996*. vdf Hochschulverlag ETH Zürich

Eurocode 7. 1997. *Geotechnical Design*.

Federal Office for Water Management (FOWM). 1997. *Consideration of Flood Hazards in Land-use Practice*. EDMZ. Bern. (in German)

Gostner, W., Bezzola, G.R., Schatzmann, M. & Minor, H.E. 2003. Integral analysis of debris flow in an Alpine torrent – the case study of Tschengls. In Rickenmann & Chen (eds), *Debris-Flow Hazard Mitigation: Mechanics, Prediction and Assessment.* Millpress, Rotterdam.

Lehmann, Ch. 1993. Zur Abschätzung der Feststofffracht in Wildbächen. Grundlagen und Anleitung. *Geographisches Institut der Universität Bern, Verlag Geographica Bernensia.* (in German)

Meyerhof, G.G. 1995. Development of geotechnical limit state design. *Canadian Geotechnical Journal* 32: 128–136

O'Brien, J. 2001. *FLO-2D. Users Manual.* Version 2001.06

Petraschek, A & Kienholz, H. 2003 Hazard assessment and mapping of mountain risks in Switzerland. In Rickenmann & Chen (eds), *Debris-Flow Hazard Mitigation: Mechanics, Prediction and Assessment.* Millpress, Rotterdam

Rickenmann, D. & Zimmermann, M. 1993. The 19878 debris flows in Switzerland: documentation and analysis. *Geomorphology*. 8: 175–189

Romang, H., Kienholz, H. & Böll, A. 2000. Wirksamkeit und Kosten von Wildbachschutzmaßnahmen. *Internationales Symposium Interpraevent 2000.* Villach/Austria, Volume 3: 271–282. (in German)

Salmon, G.M. & Hartford, D.N.D. Risk analysis for dam safety: Part II of II. *Int. Water Power & Dam Construction*. April, 38–39

Smart, G.M. & Jäggi, M.N.R. 1983. Sediment transport on steep slopes. *Mitteilungen der Versuchsanstalt für Wasserbau, Hydrologie und Glaziologie*, 64, Eidgenössische Technische Hochschule (ETH), Zürich, Switzerland, 191 pp.

Takahashi, T. (1991). *Debris flow*. IAHR Monograph Series. Rotterdam: Balkema.

Takei, A. 1984. Interdependence of sediment budget between individual torrents and a river system. *International Symposium Interpraevent*. Villach. Austria., Volume 2: 35–48

Tognacca, Ch., Bezzola, G.R. & Minor, H.E. Threshold criterion for debris-flow initiation fue to channel-bed failure. In G.F. Wieczorek & N.D. Naeser (eds), *Debris-Flow Hazard Mitigation: Mechanics, Prediction and Assessment; Proceedings 2nd International DFHM Conference, Taipei, Taiwan, August 16–18, 2000*: 89–97, Rotterdam: Balkema.

Villi, V. 1994. Valutazione delle piogge estreme nell'Italia Nord-Orientale. *La valutazione delle piene in Italia.* CNR, Roma. (in Italian)

Copyright © 2006 Taylor & Francis Group plc, London, UK

Innovative aspects of design concept for comprehensive flood scheme for Water of Leith, Dunedin, South Island, New Zealand

M.G. Webby & T.G. Parsons
Opus International Consultants, Wellington, New Zealand

S.E. Coleman & B.W. Melville
Department of Civil and Environmental Engineering, The University of Auckland, Auckland, New Zealand

G. Palmer & G. Collings
Otago Regional Council, Dunedin, New Zealand

ABSTRACT: The Water of Leith is a steep mountain stream which has been heavily modified in the past to facilitate intensive urban development of an alluvial floodplain at the lower end. An extreme flood in 1929 resulted in major channel breakout of floodwaters and extensive floodplain inundation. A 1999 review of the flood hazard for the stream identified serious channel capacity and other deficiencies at several locations across the floodplain. Following this review, a comprehensive scheme was developed to address these deficiencies. This paper provides a brief overview of the catchment and the flood hazard issues associated with the stream, and describes three innovative aspects of the scheme developed to improve flood security.

1 DESCRIPTION OF WATER OF LEITH CATCHMENT

The Water of Leith is a steep mountain stream which falls about 600 m over a distance of 10.6 km before discharging into the Otago Harbour (see Figure 1). The Leith and its major tributary, Lindsay Creek, drain a catchment of approximately 42 km2. The catchment extends up to a maximum elevation of 740 m and is mostly covered in a mix of native forest, regenerating scrub, plantation forest and pasture with tussock grasslands above 600 m. However the lower part of the catchment consists of an intensely developed urban floodplain at the north end of Dunedin City.

The middle part of the catchment features a very narrow gorge with steep vee-shaped and actively eroding ravines branching laterally off it. The gorge widens out at the lower end and urban development has extended upstream from the floodplain onto flat areas adjacent to the stream. In the lower part of the catchment, the stream flows across the floodplain for a distance of approximately 3 km before reaching the harbour. Lindsay Creek joins the Water of Leith approximately 2.1 km upstream of the harbour outlet.

Although it is predominantly a boulder and cobble bed stream in the lower gorge and lower part of the catchment, the Water of Leith has been heavily modified to facilitate urban development of both areas.



Figure 1. April 2006 flood event in the Water of Leith immediately downstream of a sharp ninety degree bend through the University of Otago Campus (view looking downstream).

Channel modifications in the lower gorge include concrete-lined banks and concrete walls in places, several grade control weirs and two coarse sediment traps. In the upper part of the urban floodplain, a concrete supercritical flow channel has been constructed which was originally intended to extend to the outlet although it has never been completed. Over the lower part of the urban floodplain through the University

Copyright © 2006 Taylor & Francis Group plc, London, UK

of Otago Campus, the stream features concrete-lined banks and a coble bed with regularly spaced grade control weirs. There is also a gauging station weir on the stream and a number of road and pedestrian bridges which cross it, including an historic one. The original stream outlet has also been extended seawards by about 0.7 km with an artificial concrete-lined double channel system through an old harbour reclamation.

2 FLOOD HISTORY

The Leith Catchment experienced a devastating flood in 1929 which inundated an extensive part of Dunedin City. This flood was estimated at the time to have had a peak discharge of as much as 400 m3/s but recent re-evaluation of the rainfall and slope / area gauging data measured during the event has put the magnitude of the peak discharge in the order of 220 m^3/s.

The 1929 flood followed one only six years earlier in 1923 which also resulted in extensive inundation of the urban floodplain. However anecdotal evidence from this event indicates that it was smaller than the 1929 one. Another flood in 1877 is considered to have been of a similar magnitude to the 1929 one although there are no data for it. At that time the extent of floodplain development was very limited.

The stream flow below the Lindsay Creek confluence has been gauged since 1963. The largest flood since the historic 1929 one has been the February 1991 event with a peak discharge of 114 m^3/s. Figure 1 shows a photograph of a slightly smaller flood event in April 2006 in the heavily modified natural channel through the University of Otago Campus.

3 KEY FLOOD HAZARD FACTORS

Although only limited damage and disruption occurred during the 1991 flood event, there was a concern that another flood of similar magnitude to the 1929 one could occur with major breakouts occurring through the University of Otago Campus. Such breakouts would potentially cause severe damage across the floodplain as far south as the city's central business district (the floodplain is much more intensively developed than in 1929 and the likely inundation zone includes significant facilities such as part of the main hospital). The February 1991 flood event was only just contained at a very sharp ninety degree bend through the University Campus which induced a standing wave pattern with waves estimated to be up to 1.3 m high (Figure 2). The expansion of flood flows from the modified stream channel to the artificial concrete-lined double channel system 200 m downstream of this sharp bend was also observed to be very inefficient, producing an uneven distribution of flow between the two channels (Figure 3).



Figure 2. Flow round a sharp ninety degree bend through the University of Otago Campus during the February 1991 flood event (view looking upstream).



Figure 3. Flow entering the artificial double channel system from the modified natural channel upstream of the Forth Street Bridge during the February 1991 flood event (view looking upstream).

Other significant issues include the limited flow capacity of many bridges, the lack of any energy dissipation facility at the end of the supercritical flow channel in the upper part of the urban floodplain reach, the potential for large amounts of sediment and woody debris to be flushed out of the actively eroding ravines off the main stem of the Water of Leith in the middle part of the catchment, the performance of the existing boulder traps and scouring of the stream bed through the heavily modified urban floodplain reach.

4 PRELIMINARY INVESTIGATION OF FLOOD HAZARDS AND CHANNEL CAPACITY ENHANCEMENT MEASURES

Following the transfer of responsibility for catchment management from the Dunedin City Council

Copyright © 2006 Taylor & Francis Group plc, London, UK

to the Otago Regional Council in 1995, the Otago Regional Council commenced a study of flood hazards in the Water of Leith catchment. This culminated in the publication of the Water of Leith Flood Hazard Report (Otago Regional Council, 1999) in 1999 and the Lindsay Creek Flood Hazard Report (Otago Regional Council, 2001) in 2001. In the case of the Water of Leith, serious channel capacity deficiencies were identified in parts of the partially urbanized lower section of the gorge in the middle catchment and in the lower part of the urban floodplain reach downstream of the exit from the supercritical flow channel.

In mid 2003, the Otago Regional Council commissioned Opus International Consultants to embark on a major programme of investigations to develop a comprehensive flood scheme for the water of Leith and Lindsay Creek to enable the 1% annual exceedance probability (AEP) flood to be satisfactorily passed with freeboard. These investigations initially involved a thorough review of the flood hydrology taking account of the estimated magnitude of the historic 1929 flood. Subsequently several MIKE11 one-dimensional computational hydraulic models of separate parts of the Water of Leith and Lindsay Creek were constructed and calibrated against observed flood data. These models were used to evaluate reaches of both stream channels with restricted flood capacity and then to investigate possible in-channel or out-of-channel works to achieve the required flood capacity. The possible modification of two water supply dams to provide flood detention and the feasibility of other in-channel detention pond options were also investigated. The potential for erosion of the stream bed and banks at the downstream end of the supercritical flow channel where no stilling basin structure exits was examined. Debris traps to capture large woody debris flushed out of the upper and middle parts of the Water of Leith catchment and the Lindsay Creek catchment were also designed (these have since been constructed).

This paper focuses on three innovative aspects of the overall flood scheme concept developed for the Water of Leith:

- the design of a woody debris trap for the lower urbanized part of the gorge in the middle catchment
- the design of channel enhancements for the sharp ninety degree bend through the University of Otago Campus
- the design of a more efficient channel expansion from the modified natural channel to the artificial concrete-lined double channel system.

5 FLOOD HYDROLOGY REVIEW

The flood hydrology review involved careful re-examination of all flow gauging data, application of corrections to some of the gauging data to account for both the angle of skew of the gauging transect to the channel centreline and the location of the transect on a stream bend, revision of the stage / discharge rating curves for the gauging station, revision of the streamflow record from 1962 to 2002 on the basis of the revised rating curves and a flood frequency analysis of the annual flood maxima series. The latter analysis incorporated the estimated magnitude of the historic 1929 flood. The results of the flood frequency analysis are summarised in Table 1 with the magnitude of the 1% AEP flood estimated to be 171 m^3/s.

Table 1. Estimated flood magnitudes for the Water of Leith based on a Log Pearson 3 distribution.

Return period (years)	AEP (%)	Flood discharge (m^3/s)
Mean annual		34
10	10	84
50	2	142
100	1	171
200	0.5	202
500	0.2	247

6 DESIGN OF WOODY DEBRIS TRAP FOR LOWER GORGE

As part of the flood scheme, a debris trap was proposed to be constructed on the Water of Leith in the lower urbanized gorge section of the middle catchment. It was intended that this debris trap would capture large woody debris transported under extreme flood conditions from the heavily forested parts of the upper and middle catchments. This would prevent such debris from getting snagged on any of the bridges in the lower catchment and which could otherwise result in breakout of floodwaters onto the floodplain.

A coarse sediment trap already existed in an old abandoned quarry about 0.8 km downstream. However, this boulder trap (which consists of a steel grille across the stream) rapidly gets clogged with smaller scale vegetative debris and then overtops, behaving effectively as a sharp crested weir.

The proposed site for the woody debris trap was located where the channel followed a gradual right hand turn, widening out to form a boulder beach area on the left with the main (low flow) channel then experiencing a gradual left hand turn down to the confluence with a small tributary stream. This is shown in Figure 4 with the direction of flow being from top to bottom. The boulder beach area is a natural deposition area for both boulders and woody debris due to centrifugal force effects.

Based on a literature search, a concept was developed for the woody debris trap of a line of vertical

Copyright © 2006 Taylor & Francis Group plc, London, UK

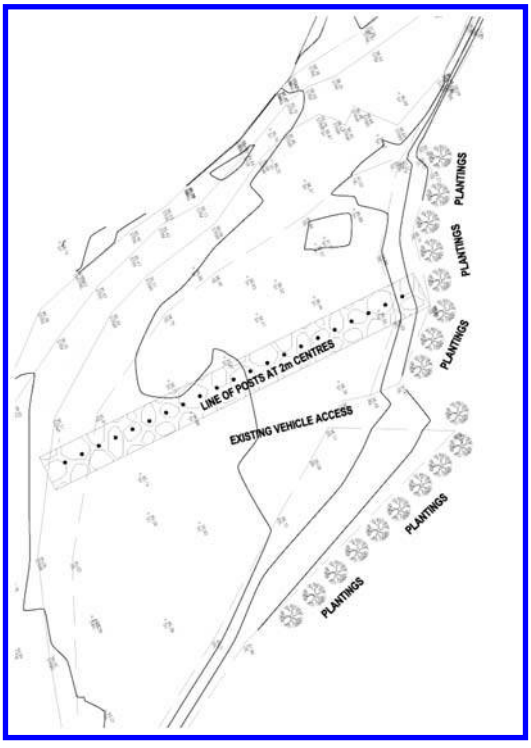


Figure 4. Layout of the woody debris trap designed and constructed in the lower gorge section of the Water of Leith (flow from top to bottom).

poles angled at forty-five degrees to the direction of flow across the boulder beach area (Figure 4). This was based on some examples of similar traps constructed in the German Bavarian Alps with a downstream pointing vee-shaped row of poles across the flanks and a row of poles perpendicular to the direction of flow across the main channel (Wallerstein and Thorne, 1995). These examples had been extensively tested in physical hydraulic models and had also been shown to work effectively in practice. In the case of the proposed water of Leith debris trap, the chosen configuration consisted of only one half of the vee-shaped row of poles with the row stopping short of the low flow channel to leave this unrestricted for recreational purposes (Figure 4).

The design process for the debris trap included both MIKE11 one-dimensional model simulations of the backwater effect of a partially blocked trap and detailed MIKE21 two-dimensional model simulations of the flow pattern across the boulder beach area to assist with orientation of the row of poles forming the trap.

The debris trap was constructed in late 2005. It was first exposed to a large flood event in April 2006. Figure 5 shows of a photograph of the trap near the



Figure 5. Woody debris trap in operation during the April 2006 flood event (view looking upstream).



Figure 6. Woody debris trap after the April 2006 flood event (view looking downstream).

peak of the flood with evidence of a significant amount of woody debris captured. Figure 6 shows another photograph of the trap after the flood event. In addition to the woody debris captured, a significant quantity of boulders was deposited in front of the row of poles forming the trap with some boulders estimated to be as large as 800 mm in diameter. The volume of boulder material deposited was significantly less than the volume of sediment material captured by the boulder trap 0.8 km further downstream. The woody debris trap was considered to have performed very effectively in its first major test.

7 DESIGN OF CHANNEL CAPACITY ENHANCEMENTS FOR SHARP NINETY DEGREE BEND

The heavily modified stream channel for the Water of Leith through the University of Otago Campus

Copyright © 2006 Taylor & Francis Group plc, London, UK



Figure 7. Geometry of the sharp ninety degree bend through the University of Otago Campus.

with near vertical concrete banks and closely spaced grade control weirs incorporates a sharp ninety degree bend with a radius to width ratio in the order of 6. The University's Information Technology Services (ITS) Building spans the stream channel near the downstream end of the bend with a line of columns supporting the building along the edge of the existing inside bank.

Figure 7 shows the geometry of the bend. The existing channel is about 11.5 m wide and has a bed slope of 1.2%. The grade control weirs have a shallow trapezoidal shape although they are partially covered by a gravel beach on the inside of the bend. The cobbles on the pools between the weirs have a median diameter of 200–300 mm.

MIKE11 model simulations of flood flows through the University Campus reach identified the outside of the sharp bend as the most critical location for channel breakout of floodwaters in the event of an extreme flood. Although the MIKE11 model of the Water of Leith below the exit from the supercritical flow channel was used to help determine a general concept for enhancing channel capacity round the bend (principally channel widening with lowering of grade control weirs and raising outside wall), it was considered prudent to establish a more detailed design concept for the recommended measures using a physical hydraulic model. Such an approach would elucidate the complex flow behaviour round the bend including the interaction between flood flows, the grade control weirs and the cobble-lined bed.

A 1:50 scale physical model of the bend was constructed in the Fluid Mechanics Laboratory of the University of Auckland's Department of Civil and Environmental Engineering. The model covered a 340 m long reach of the stream channel through the University of Otago Campus which extended approximately 100 m upstream of the start and 100 m downstream of the end of the sharp bend. The model was initially constructed as a fixed bed model with projecting grade control weirs above the bed surface. Following testing of various channel capacity enhancement measures in the fixed bed model, the model was converted to a mobile bed to test the final modified channel configuration with an erodible bed. The prototype bed material was represented by 3.35–6.7 mm size fine gravel in the model.

The fixed bed model was initially calibrated for the existing channel geometry against estimated flood levels for the February 1991 flood event (Figures 2 and 3). Measured surface wave heights of 1 m in prototype terms measured at the location of the University's ITS Building were comparable with wave heights from photographs of the actual flood event as indicated by Figure 8. The model was then tested for the 1% and 0.5% AEP floods of magnitude 171 and 202 m^3/s respectively.

Subsequently the fixed bed model was modified to represent the following bend configurations:

(a) the existing channel geometry with the grade control weirs lowered
(b) the existing channel widened from 11.5 m to 16 m with the grade control weirs lowered
(c) the widened fixed bed between the grade control weirs converted to a mobile bed with the grade control weirs lowered.

The effect of incorporating a mobile bed in the model was very dramatic. Even with the maximum amount of channel widening applied (within the constraints of the University's ITS Building spanning the stream), the mobile bed was highly erodible with scour holes more than 3 m deep forming upstream of each grade control weir on the outside of the bend for the 1% AEP flood (site investigations have since revealed the existence of a hard cemented boulder layer about 2 m below the surface of stream bed which would limit the depth of prototype scour in practice).

The erodible bed also induced a significant increase in super-elevated flood levels (up to 1 m) round the outside of the bend compared to those for the corresponding fixed bed case as seen in Figure 9 for the 1% AEP flood case. The magnitude of the surface wave

Copyright © 2006 Taylor & Francis Group plc, London, UK

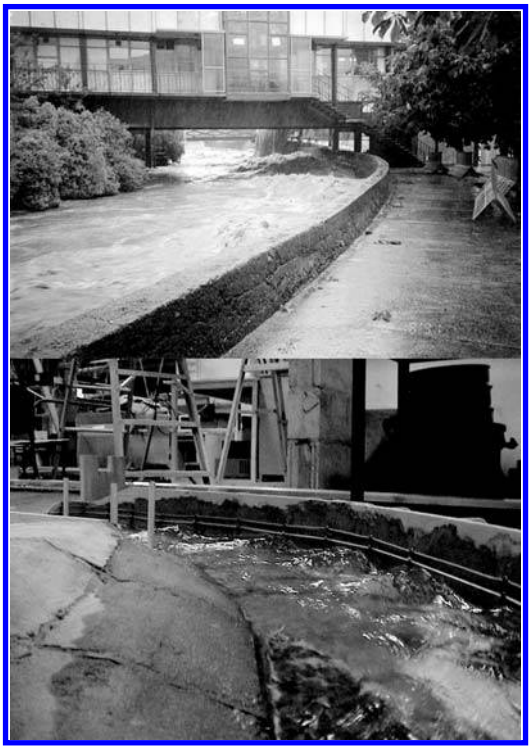


Figure 8. Comparison of prototype and model surface waves round the outside of the sharp ninety degree bend through the University of Otago Campus (top view – prototype, bottom view – model).

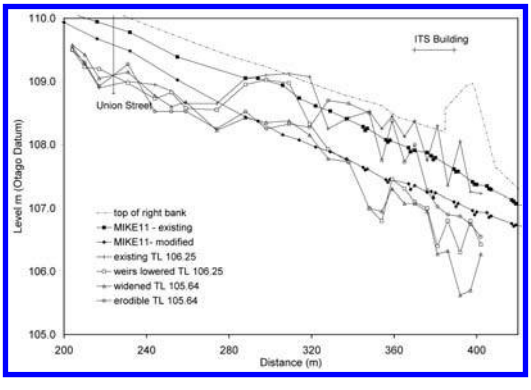


Figure 9. Comparison of flood levels measured in the model round the outside of the sharp ninety degree bend for the 1% AEP flood.

heights round the outside of the bend also increased with the erodible bed case. The magnitude of flow velocities round the outside of the bend were typically of the order of 3.5–4 m/s in prototype terms for the erodible bed case which was considerably lower than for the fixed bed situation (flow velocities were as high as 6–6.5 m/s for the latter case).

The magnitude of both surface wave heights and flow velocities round the outside of the bend increased with increasing flood discharge for both the fixed bed and erodible bed cases.

The results of the model tests were used to refine the general concept for the channel capacity enhancement round the bend. Broadly this consists of:

- widening the channel from 11.5 m to 16 m to provide the maximum possible waterway width
- incorporating a low level footpath on the inside of the bend to improve public access to the stream and assist with meeting the University's objectives for pedestrian routes through the Campus
- modifying the grade control weirs by cutting down the shallow trapezoidal shape on the outside of the bend
- raising the height of the wall on the outside of the bend to provide the required amount of freeboard

It was originally proposed to modify the structural support system for the University's ITS Building to allow channel widening, However recent site investigations have indicated that the existing columns are founded deeper than originally thought and it might be possible to retain the columns in their present position with some additional foundation support.

The treatment of the prototype erodible bed round the bend has yet to be finalised. Two options exist: either partially armour the bed with rock riprap material during construction of the proposed channel modifications, or increase the outside wall height, allow bed scouring to occur in the interim and place rock riprap material in the future when required.

8 DESIGN OF EFFICIENT EXPANSION FROM MODIFIED NATURAL CHANNEL TO ARTIFICIAL CHANNEL SYSTEM

The geometry of the transition from the heavily modified natural channel to the artificial double channel system downstream of the sharp ninety degree bend through the University Campus is quite complex (Figure 10). The transition lies between the Clyde Street and Forth Street Bridges. The channel slope reduces from 1.2% to 0.46% at a point just upstream of the Clyde Street Bridge and from 0.46% to 0.13% below the Forth Street Bridge (which marks the start of the double channel system). The modified natural channel down to the Forth Street Bridge has near-vertical concrete banks and a cobble-lined bed with closely spaced grade control weirs. There is a side-spill weir just upstream of the Forth Street Bridge to allow floodwaters to spill from the main channel into the left overflow channel. The weir is aligned with the

Copyright © 2006 Taylor & Francis Group plc, London, UK

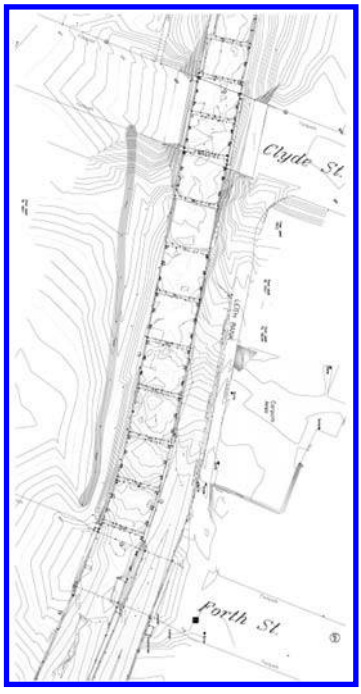


Figure 10. Geometry of the expansion from the modified natural channel and the artificial double channel system between the Clyde Street and Forth Street Bridges (flow from top to bottom).

central pier of the Forth Street Bridge. A high dividing wall between the main and overflow channels continues downstream of the Forth Street Bridge as an extension of the central pier.

Figure 3 demonstrates that the geometry of the Clyde Street to Forth Street channel expansion does not allow for an efficient distribution of flow between each component of the double channel system under flood conditions.

It is not possible to satisfactorily simulate the complex flow behaviour in the Clyde Street to Forth Street channel expansion of the Water of Leith with either a one-dimensional or two-dimensional computational hydraulic model. For this reason it was recommended that a physical hydraulic model of the Clyde Street to Forth Street channel expansion be constructed and tested to establish a detailed design concept.

A 1:65.78 scale model of the channel expansion based on an initial concept of widening the modified natural channel upstream of the Clyde Street Bridge on the left bank, incorporating a new gradual left bank expansion wall downstream of this bridge and extending laterally the existing grade control weirs was constructed in the Hydraulics Laboratory of Opus International Consultants' Central Laboratories. This particular length scale was chosen so that the combined width of the main channel and overflow channel at the downstream boundary of the model just matched the width of the laboratory flume in which the model was set up. Figure 10 shows that there is a slight change in alignment of the prototype expansion between the two bridges. In order to fit the model into the laboratory flume it was necessary to ignore this change in alignment (the effects of this were considered to be very minor). The model covered a reach extending upstream of the Clyde Street Bridge (so that it overlapped with the bend model) and 100 m downstream of the Forth Street Bridge where the main and overflow channels of the double channel system attain their full width.

The model was originally configured as a fixed bed model to represent the initial modification concept for the channel expansion. However it was found that the backwater profile predicted by the model for the 1% AEP flood was markedly different from that predicted by an approximate MIKE11 model of the modified channel expansion. Consequently the model was set up as a mobile bed model (with 4.2 mm gravel chip used to represent the 200–400 mm size prototype bed material) and temporarily reconfigured to simulate the existing channel geometry.

The model was run in this temporary configuration for the February 1991 flood event. It was found for this flood event that the mobile bed was highly erodible with scour holes forming on the bed in front of each grade control weir and corresponding standing waves forming on the water surface. Any eroded bed material that reached the fixed bed of the double channel system was rapidly flushed downstream. Although it is normal practice to run a mobile bed setup in a model over a long period of time to establish an equilibrium bed profile, a slightly different approach was adopted to try and expedite the test programme. The pool levels were progressively lowered over a series of runs to achieve an approximate match between the simulated water surface profile in the model and the flood level data for the February 1991 event estimated from photographs taken just prior to the peak. The amount of pool "scour" required to achieve a good match between the model water surface profile and the observed flood level data was found to very large. This was consistent with the results of the mobile bed tests on the bend model with the widened channel configuration where extremely large scour depths on the outside of the bend were observed, albeit for a widened channel geometry rather the existing channel geometry.

Having achieved an adequate understanding of bed behaviour under flood conditions in the existing channel situation, the initial modification concept for the channel expansion was restored in the model and tested with a mobile bed. In contrast to the existing channel situation, it was found that the mobile bed was

Copyright © 2006 Taylor & Francis Group plc, London, UK



Figure 11. Surface wave action in the model of the modified channel expansion between the Clyde Street and Forth Street Bridges for the 1% AEP flood (view looking upstream).

no longer erodible under 1% AEP flood conditions. However it has to be acknowledged that the model setup in the flume ignored the scouring effect of the highly asymmetric flow distribution round the upstream sharp bend which the bend physical model had identified.

Figure 11 shows a view of the wave action in the model configured to represent the initial modification concept for the channel expansion. The occurrence of a standing wave on the surface in front of each grade control weir is still evident even though the degree of projection of the weir crest above bed level is much less that for the scoured bed condition of the existing channel geometry.

The model was further modified to represent an alternative channel modification concept which retained the essential channel widening component of the initial concept but which incorporated a low level path along the left bank downstream of the sharp bend to enhance the public amenity value of the stream and to provide an alternative pedestrian route through the University Campus. The low level path terminated immediately downstream of the Clyde Street Bridge at the start of the channel expansion. It was accepted that this path would be inundated on average 1–2 times per year and more frequently under the Clyde Street Bridge but these occasions would provide only temporary disruption. One advantage of this alternative concept over the initial concept was that it would not be necessary to laterally extend the grade control weirs over the reach between the sharp bend and the Forth Street Bridge.

Testing of the alternative channel modification concept in the model generally confirmed the suitability of the concept although it also helped identify useful

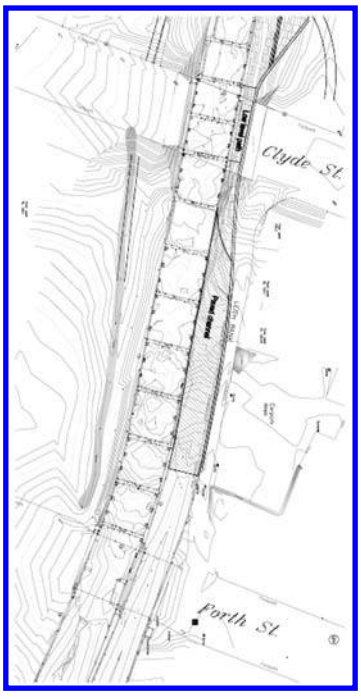


Figure 12. Final recommended layout for the modified channel expansion between the Clyde Street and Forth Street Bridges.

refinements. The cobble-lined bed with this alternative channel geometry showed slight evidence of movement in the case of the 0.5% and 0.2% AEP floods.

Figure 12 shows the final geometry recommended for the Clyde Street to Forth Street channel expansion. Key components of this geometry include:

- widening of the channel on the left bank upstream of the Clyde Street Bridge
- a shaped contraction past the left abutment of the Clyde Street Bridge
- a shaped left bank expansion wall downstream of the Clyde Street Bridge
- lowering the crest of the side-spill weir to just above the top of the transverse grade control weirs
- a continuous left bank low level path just above the top of the grade control weirs with an alternating sequence of steep and flat sections to promote energy dissipation of flood flows through the formation of weak hydraulic jumps
- extension of the paved left overflow channel upstream to the Clyde Street Bridge
- filling in with suitable cobble and boulder material the deeper scour holes in the pools between the grade control weirs upstream of the Forth Street Bridge.

Copyright © 2006 Taylor & Francis Group plc, London, UK

9 CONCLUSIONS

The combination of a steep mountain stream and a heavily modified channel across an intensively developed floodplain provide a challenging environment in which to design and construct improved flood security measures. This paper has described three innovative aspects of a comprehensive flood scheme in such a setting for the Water of Leith at the north end of Dunedin City, New Zealand. A woody debris trap was designed and constructed and, in its first major test, performed exceptionally well. Channel capacity enhancement measures round a sharp ninety degree bend (which is presently the most critical location for flood breakout) in the heavily modified natural channel were designed with the aid of a mobile bed physical hydraulic model. A more efficient channel expansion from the modified natural channel to an artificial double channel system was also designed with the aid of another mobile bed physical hydraulic model. Both the bend and channel expansion enhancements incorporate features to improve the public amenity value of the stream.

REFERENCES

Otago Regional Council 1999. *Water of Leith Flood Hazard Report.* Dunedin: Otago Regional Council.

Otago Regional Council 2001. *Lindsay Creek Flood Hazard Report.* Dunedin: Otago Regional Council.

Wallerstein, N & Thorne, C.R. 1995. Debris Control at Hydraulic Structures in Selected Areas of Europe. First Interim Report prepared for US Army Research Development and Standardisation Group – UK. Contract No. N68171-95-9133. Project No. WK2Q5C-7793-EN01.

Copyright © 2006 Taylor & Francis Group plc, London, UK

YTSS. Yangtze Special Session

Copyright © 2006 Taylor & Francis Group plc, London, UK

Changes of sediment deposition and erosion at Chongqing reach in backwater area of Three Gorges Project

A.Y.J. Lu, C.W. Xu & L.Q. Zuo
Nanjing Hydraulic Research Institute State's Key Laboratory of Hydrology, Water Resources and Hydraulic Engineering Science, Nanjing, China

B.Z.Y. Wang
State Key Laboratory of Hydroscience and Engineering, Tsinghua University, Beijing, China

ABSTRACT: The plane distribution of water flows and sediment deposition and erosion at Chongqing reach are studied with a 2-D numerical model, especially the backflows at the confluence of the Jialingjiang River flowing into the Yangtze River, and the backflows owing to irregular local banks. According to the water flows and sediment conditions the amount of sediment deposition and distribution for the period of 2003～2032 are calculated. Deposition mainly occurs on the meandering reaches with uneven bank lines, backwater areas, and wide and shallow reaches as well. The bank lines will become more straight and smoother due to sediment deposition near the banks.

1 INTRODUCTION

Three Gorges Project constructed on the Yangtze River, which is called "Gold Watercourse" is of multiple benefits of flood control, power generation and navigation. Experience gained from the existing hydro projects in China shows that in the backwater area of reservoirs the problems related sediment will gradually aggravate with time (Dou et al, 1988). The sediment problems of the Three Gorges Project affects the development and prosperity of Chongqing Harbor, which has a great importance on the development of national economy in the southwest areas of China. During the construction of Three Gorges Project, Chongqing City became the municipality directly under the Central Government of China, and its municipal construction has been rapidly performing. In recent years, the municipal construction has changed the bank line of Chongqing reach: Chaotiamen bank line has extended 50～100 m toward the river channel, the bank line of left bank upstream the Chongqing Yangtze River Bridge has extended 100～200 m toward the river, and those of other reaches have changed to some extent. The influence of the modification of the bank lines on flood prevention and navigation has attracted concern of people and researchers.

Yangtze River is the largest river in China, with abundant water and large drainage areas, and there are many tributaries flowing into the river. Discharges of tributaries have a great influence on water flow and sediment motion in the Yangtze River, especially those with large drainage areas, abundant water and sediment. The river and tributaries are of different flood periods, their water levels affect with each other, the flow velocity and sediment carrying capacity decrease as a result of the reservoir operation, so as to make large quantity of sediment deposit and to result in shoals near the mouths of the tributaries, directly affecting navigation of the stream and tributaries.

Applications of 1D mathematical models to sediment transport simulation were reported as early as in the 1960s (Dou, 1963; Lin et al., 1981; Chang, 1982; Han, 1987; Holly and Rahuel, 1990). These models have been used to calculate long term sediment deposition and erosion for fluvial river channels. In the past few decades, 2D and 3D mathematical models for sediment transport have been developed to predict river regime and riverbed deformation due to engineering projects (Dou et al., 1987; van Rijn, 1987; Li, 1989; Shimizu et al., 1990; Spasojevic and Holly, 1990; Olsen, 1999; Zhou, 1997; Lu, 1998; Lu et al., 2002, 2004; Wu et al., 2000). The numerical models assume either an equilibrium or a non-equilibrium state of sediment transport. The models for suspended load transport mostly assume non-equilibrium sediment transport. The state of bed load transport (equilibrium or non-equilibrium) is essentially a key issue in the modeling of local sediment deposition and riverbed erosion. The existing 2D sediment mathematical models mostly highlight simulation of water

Copyright © 2006 Taylor & Francis Group plc, London, UK

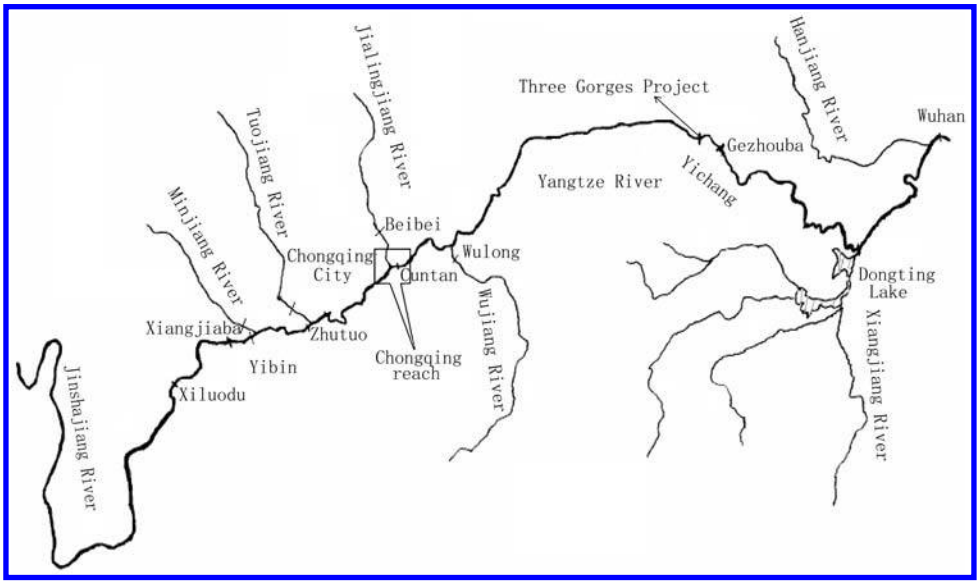


Figure 1. Sketch of middle and upstream Yangtze River.

flows and sediment in a single river. The 2D sediment mathematical model in the boundary fitting orthogonal curvilinear coordinate system developed by the authors overcomes the difficulty of complex boundary between the river and its tributaries (Lu, 1998). It is employed to simulate water flow motion and riverbed deformation of the 44 km-long Chongqing reach (Qiezixi—Tongluoxia) located about 25 km upstream of a tributary of Yangtze River, Jialingjiang River (Fig. 1).

2 CHONGQING REACH AND ITS WATER FLOWS AND SEDIMENT CHARACTERISTICS

Chongqing reach is located in the wide river reaches with hills in the upstream of Yangtze River. From the plane configuration, the present reach is meandering, especially the channel of the Yangtze River is continuously meandering, and the ratio of lengths between the meandering reach and straight transition reach is 1:1. The Jialingjiang River, from north to south, flows into the Yangtze River on the left bank at Chaotianmen, as shown in Figure 2. The channel is narrow, usually only 1000 m in flood season and 600 m in low-water periods, some reaches are 2000 m in flood season and 250 m in low flow season. The banks are steep and usually made up of bedrock, with huge rocks protruding towards the river. The bank line is not smooth, but it is stable. The riverbed consists of gravel and sand, with the median diameter being about 60 mm. There are some bedrocks surfacing out at part of the



Figure 2. Chongqing reach and its computational domain.

reach, resulting in stone reefs. From the longitudinal section, the riverbed is uneven with deep pools and shallow ridges, showing a shape of indention. The afflux of Jianglingjiang River makes Chongqing reach be of estuarine characteristics. The above-mentioned results in the complexity of water flows and sediment motion of Chongqing reach. Cuntan station, a hydrological station on Chongqing reach, has a catchment area of 866559 km^2, and Beibei station on Jialingjiang River has a catchment area of 157900 km^2, occupying 18.2% of the catchment area of Cuntan station. About 75% of the total annual runoff for the stations Cuntan and Beibie mainly occurs during the flood period. 18.6% of the amount of runoffs of Cuntan station is

Copyright © 2006 Taylor & Francis Group plc, London, UK

Table 1. Size distribution of gravel bed load at Cuntan station.

Grain size (mm)	1∼10	10∼20	20∼50	50∼75	75∼100	100∼150	150∼200
Percentage (%)	0.83	9.47	38.00	24.40	13.30	10.90	2.80

Table 2. Size distribution of sand bed load at Cuntan station.

Grain size (mm)	0.025∼0.05	0.05∼0.10	0.10∼0.15	0.15∼0.20	0.20∼0.25	0.25∼0.50	0.50∼1.00
Percentage (%)	10.50	13.00	31.50	26.00	11.00	6.00	2.00

from Jialingjiang River, and it is nearly of the same percentage during the flood and low-water periods. Perennial mean sediment load by suspended load of Jialingjiang River is 148000000 t, about 1/3 of sediment load of Cuntan station (Dou et al, 1988). During the low-water period, the percentage of sediment load from Jialingjiang River is larger, reaching 41.7%. The median diameter of suspended load at Cuntan station is 0.0275 mm, and that of the Beibei station is close to that of Cuntan station.

Perennial mean transport of gravel bed load at Cuntan station is 277000 t/y, and the median diameter is 51 mm (Table 1), with the maximum being 202 mm. the size distribution of sand bed load is given in Table 2. Generally, the narrow and deep reaches are of coarse riverbed material, and the wide and shallow ones has fine material; the main stream carries coarse material, and the beach area is of fine material.

3 MODEL VERIFICATION

In this paper, verification and calculation of water flows and sediment deposition and erosion are performed to Chongqing reach in the upstream of Yangtze River. It is about 43.6 km in length, the upper boundary is Qiezixi (687.6 km away from Yichang), and the lower boundary is Tongluoxia (644 km away from Yichang) and Jialingjiang.

3.1 *Generation of computational domain and orthogonal curvilinear grid mesh*

The computational domain includes the reach from Qiezixie (inlet) to Tongluoxia on Yangtze River and the reach from Jinkou (about 25 km away from the afflux) to the afflux on Jialingjiang River. Its river regime is shown in Fig. 2. A grid system of 407×63 is arranged, among which, 248×31 nodes are arranged for the reach from Qiezixi to the afflux, 248×31 nodes for Jialingjiang River, and 159×63 nodes for the reach from the afflux to Tongluoxia. The resulting orthogonal curvilinear grid mesh is shown in Fig. 2. The nodes have intersection angles of 88°∼92° except for some nodes close to the banks. The spacing between each two nodes is 80∼120 m along the longitudinal direction and 10∼40 m along the lateral direction.

3.2 *Verification of water levels*

On March 8, September 22 and November 22, 1986, the discharges at Cuntan station are 3170 m^3/s, 22600 m^3/s and 6400 m^3/s, respectively, as for at Beibei station, they are 447 m^3/s, 1710 m^3/s and 716 m^3/s, respectively. Differences between the calculated and measured instantaneous water levels are all smaller than 0.1 m except individual water levels (Lu, 2001).

3.3 *Verification of velocity distribution and simulation of flow fields*

When the discharge of Jialingjiang River is 716 m^3/s or 1710 m^3/s, the calculated and measured values of velocities for Section Wen-O III are in good agreement (Lu, 2001). When the discharge at Cuntan station is 6400 m^3/s or 22600 m^3/s, the calculated distribution of velocities along the river width for Cuntan section are also in good agreement with the measured ones (Lu, 2001). Distribution of velocities of Cuntan section fully shows the controlling action of river topography, that is, large velocity in deep channels and small one in beach areas.

It is simulated that with the increase of discharges, water flows gradually submerge beach areas and backflows are caused by local topography. Especially when the discharge of Jialingjiang River is small (1710 m^3/s), the confluence ratio is small ($R = 0.076$) and the discharge of Cuntan station is 22600 m^3/s, it is simulated that the river of Yangtze River has an effect on its tributary, Jialingjiang River, resulting in that the estuarial water flows of the latter become tranquil flows, with the velocity being only 0.2∼0.4 m/s; while when the confluence ratio is 0.45, $Q_{Jia} = 4860\ m^3/s$, $Q_{Cun} = 11350\ m^3/s$, water flows from Jialingjiang River directly flow towards the right bank on Yangtze River and large area of backflow at the left bank is thus formed, about 400 m in length and about 300 m in width (Fig. 3); when the confluence ratio is much larger ($R = 0.72$), $Q_{Jia} = 10500\ m^3/s$, $Q_{Cun} = 14500\ m^3/s$, the

Copyright © 2006 Taylor & Francis Group plc, London, UK

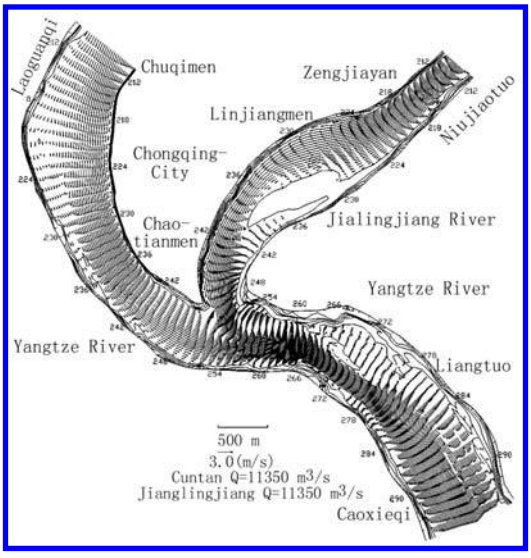


Figure 3. Flow fields at the afflux when $Q_{Cun} = 11350\ m^3/s$, $Q_{Jia} = 4860\ m^3/s$ and $R = 0.45$.

velocity of water flows from Jialingjiang River directly flowing toward the right bank is up to 5 m/s, and the backflow area is 600 m in length and 400 m in width (Lu, 2001).

3.4 *Verification of sediment concentration and its gradation distribution*

Based on the measured sediment concentration and gradation in Jialingjiang River and Jiulongtan on Yangtze River on September 22 and November 22, 1986, sediment concentration fields for various grain sizes are calculated. The calculated values of mean sediment concentration along the river width for Section Wen-O III on Jialingjiang River and Cuntan station on Yangtze River are in good agreement with the measured ones, and their gradation is close to the measured one (Lu, 1998; Lu, 2001).

3.5 *Verification of riverbed deposition and erosion*

A period from the middle of January to the middle of November 1986 is selected for verification of riverbed deposition and erosion, and there are 88 time intervals, with the time step of 3∼4 days on average, that is, 5∼6 days during non-flood season and 1∼2 days during flood season. Calculation of sediment concentration of suspended load is conducted for 6 groups of grain sizes, and percentage of various grain sizes employs the annual mean value. Table 3 gives the percentage and settling velocities of various grain sizes on the inlets of Yangtze River and Jialingjiang River. Calculation of sediment transport of bed load is conducted

Table 3. Sediment concentration and settling velocities of suspended load.

Grain size (mm)	0.005	0.0169	0.0368	0.0736	0.169	0.368
Ps (%)						
Yangtze River	23.6	20.9	25.9	17.6	8.0	4.0
Jialingjiang River	17.7	19.9	28.9	24.1	7.0	2.4
Settling velocity (mm/s)	0.016	0.180	0.855	3.39	16.40	51.10

for 7 groups of grain sizes (Table 1), with the grain size being 1∼200 mm, among which, as for the pebble bed load with grain size of 10∼200 mm, the empirical equation by Nanjing Hydraulic Research Institute based on the measured data is employed (Dou, 1988), that is,

$$g_b = 8.0\times10^{-12} mQ^{2.60} \quad (1)$$

where m is the efficiency coefficient of instruments; $m = 11.6$. Because there is no measured data of pebble bed load on Jialingjiang, during calculation sediment transport rate by use of discharge ratio of the river is estimated for Jialingjiang River. As for the gravelly bed load of 1∼10 mm, it is calculated by the percentage of 3% of pebble bed load, and the sandy bed load smaller than 1 mm is taken into account during calculation of deposition and erosion of suspended load. The initial gradation of riverbed material is based on Table 1, and change of components of riverbed material is also considered, that is, the narrow and deep reaches are of coarse riverbed material, and the wide and shallow ones are of fine material; the riveris of coarse material, and the beach area is of fine material.

3.5.1 *Jinshaqi reach in the estuary of Jialingjiang River*

During January∼June of 1986, though there is large discharge from the upper boundary from April to June and the confluence ratio is larger than 0.2, with the maximum being 0.7, water flows in Yangtze River have no effect on Jialingjiang River, however, water flows in Jialingjiang River have certain effect on Yangtze River. As for Jinshaqi reach, there is little deposition; during July∼September, that is, the flood period for Yangtze River, the confluence ratio gradually decreases, and it is usually about 0.10 and the maximum sediment concentration of Jialingjiang River is 2.6 kg/m^3, with the mean value being smaller than that during April∼June, affected by water flows of Yangtze River, velocity and sediment carrying capacity decrease, resulting in large amount of deposition on Jinshaqi reach, up to 370000 m^3 and mainly on

Copyright © 2006 Taylor & Francis Group plc, London, UK

Table 4. Verification of deposition and erosion for various reaches (10^4 m^3).

Rivers and reaches		Distance (km)	Amount of deposition from Mar. to Sept. 1986		Amount of erosion from Sept. to Nov. 1986		Scour rate (%)	
			Calculated	Measured	Calculated	Measured	Calculated	Measured
Yangtze River	Jiulongtan	669∼674	187.4	181.7	−97.0	−115.2	51.8	63.4
Jialingjiang River	Jinshaqi	0∼3	37.7	37.8	−20.9	−25.3	55.4	66.9
	Shimen	10∼12	20.0	23.1	−11.5	−11.6	57.5	50.2

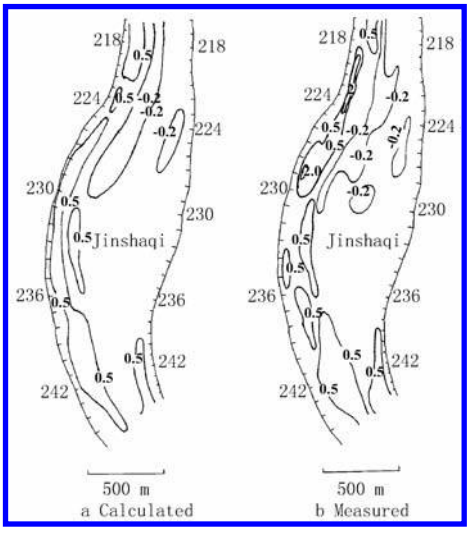


Figure 4. Deposition and erosion at Jinshaqi reach on Jialingjiang River from Mar. to Sept. 1986

its right channel; after October, that is, the ebbing period for Yangtze River, effect of Yangtze River on Jialingjiang River gradually decreases, the confluence ratio increases and the discharge from Jialingjiang River is nearly clear water with the sediment concentration being only 0.01 kg/m^3, the deposited sediment on Jinshaqi reach during the flood period are started to erode, till the middle of November, about 200000 m^3 is washed away by water flows. Table 4 gives a comparison between the calculated and measured amount of deposition and erosion. Figure 4 shows a comparison between the calculated and measured locations during March∼September. It is seen that the calculated amount of deposition and erosion and corresponding locations are close to the measured ones.

3.5.2 *Shimen reach on Jialingjiang River*

Shimen reach is located 10∼12 km upstream Jialingjiang River. The width of the widest and shallowest reach is about 2 times that of the deep channel in the upstream, and the velocity and sediment carrying capacity of the wide reach is fairly smaller than those of the deep channel reach, resulting in that during the flood period large quantity of sediment carried by water flows deposit in the wide reach, and during the ebb period, water flows return and the velocity increases, the deposited sediment during the flood period is eroded, and the riverbed basically recover the topography during the low-water period. The calculated distribution of locations during March∼September 1986 (Lu, 2001) and the calculated amount of deposition and erosion during March∼September and September∼November 1986 are close to the measured ones (Table 4).

3.5.3 *Jiulongtan reach on Yangtze River*

Jiulongtan reach is located 669∼674 km upstream Yichang. During the flood period sediment deposition is mainly resulted from rapid widening of the reach, decrease of velocity and sediment carrying capacity. The calculated distribution of locations during March∼September 1986 (Lu, 2001) and the calculated amount of deposition and erosion during March∼September and September∼November 1986 for Jiulongtan are also close to the measured ones (Table 4).

4 CALCULATION OF DEPOSITION AT CHONGQING REACH AFTER THE IMPOUNDMENT OF THREE GORGES PROJECT (2003∼2032)

4.1 *Calculation conditions*

According to the data of 1D mathematical models by Yangtze River Scientific Research Institute, that is, discharge, sediment concentration as well as its gradation of Qiezixi section (inlet) on Yangtze River during 2003∼2032 and water level hydrograph of Tongtianba (Shengjitang) (outlet), the deposition process of the present reach is calculated. Among which, discharge of Jialingjiang River is obtained by subtraction of discharge of Qiezixi section from that of Cuntan; sediment concentration process of Jialingjiang River is obtained by relationship (Lu, 2001) between sediment transport rate and discharge at Beibei station

Copyright © 2006 Taylor & Francis Group plc, London, UK

Table 5. Amount of deposition at Chongqing reach calculated by mathematical models and its comparison with the test results of physical model by Nanjing Hydraulic Research Institute (10^4 m^3).

Reach	Lijiatuo∼ Jiulongtan	Jiulongtan∼ Huangsha	Huangsha∼ Chuqimen	Chuqimen∼ Chaotianmen	Chaotianmen∼ Cuntan
No. of starting and ending sections	96∼119	119∼140	140∼217	217∼245	245∼317
Location of starting and ending (km)	675∼673	673∼670	670∼662.2	662.2∼659.5	659.5∼653
Distance (km)	2.0	3.0	7.8	3.2	6.5
Calculated values by mathematical models after impoundment of 18 years (175 m) (2026)	99.9	922.0	1244.4	146.2	1446.0
Calculated values by physical models of Nanjing Hydraulic Research Institute after impoundment of 18 years (175 m)	116.3	819.9	1270.0	170.1	998.7
Mathematical model – physical model	−16.1	102.1	37.4	−23.9	447.3

Reach	Cuntan∼ Tongtianba	Lijiatuo∼ Tongtianba	Ciqikou∼ Niujiaotuo	Niujiaotuo∼ Mouth
No. of starting and ending sections	317∼345	96∼345	85∼192	192∼248
Location of starting and ending (km)	653∼649	675∼649	16∼5	5∼0
Distance (km)	4.0	26.0	11.0	5.0
Calculated values by mathematical models after impoundment of 18 years (175 m) (2026)	800.2	4658.7	2019.4	1131.9
Calculated values by physical models of Nanjing Hydraulic Research Institute after impoundment of 18 years (175 m)	780.9	4155.9	2917.9	1187.1
Mathematical model – physical model	19.3	502.8	−898.5	−55.2

on Jialingjiang River during 1961∼1970; gradation of sediment concentration employs the perennial mean gradation at Beibei station.

During June 2003∼June 2007, Three Gorges Project employs the impoundment scheme of 135 m; During July 2007∼July 2009 the impoundment scheme of 156 m is employed; After August 2009 the impoundment scheme of 175 m is employed. During 2003∼July 2009, the study reach is basically in a natural state, and its riverbed will show evolution characteristics of natural riverbed. After August 2009, owing to the effect of backwater, the study reach will be located in the fluctuating backwater area, water levels will increase, and velocity and sediment carrying capacity will decrease, resulting in sediment deposition.

4.2 *Amount of deposition at Chongqing reach before change of bank line and its comparison with the test results of long model of Nanjing Hydraulic Research Institute*

In order to check the precision of the present model to simulate sediment deposition after the construction of Three Gorges Reservoir, amount of deposition at Chongqing reach before change of bank line should be compared with the test results of long models. As for the long model of Nanjing Hydraulic Research Institute for fluctuating backwater areas of Three Gorges Project, tests on sediment deposition for 80 years were once performed to the impoundment scheme of 175 m (Dou, 1988), they were demonstration tests for water levels of Three Gorges Project. For the impoundment scheme of 175 m, the level of 156 m is employed for the first 10 years and after that, the level of 175 m is employed. During model tests, considering that at the level of 156 m the study reach is basically not affected by backwater, thus its corresponding discharge hydrograph was not simulated, therefore, the test results of the 28th year in the research report are equivalent to the amount of deposition of 18th year after the impoundment of 175 m. Table 5 gives the Amount of deposition at Chongqing reach of 18th year after the impoundment of 175 m calculated with the topography of 1986 being the initial one and its comparison with the test results of long model of Nanjing Hydraulic Research Institute. It is seen from the table that as for the 26 km-reach from Lijiatuo to Tongtianba, the amount of deposition calculated by mathematical models is 46587000 m^3, that by physical model tests is 41559000 m^3, with the difference being only 5028000 m^3. Except individual reaches, differences of the amount of deposition for various reaches and Jialingjiang River between mathematical and physical model tests are small.

4.3 *Amount of deposition at Chongqing reach after change of bank line*

4.3.1 *Amount of deposition*

Table 6 gives the amount of deposition at Chuanjiang reach after the impoundment till 2022

Copyright © 2006 Taylor & Francis Group plc, London, UK

Table 6. Amount of deposition at Yangtze River reach at different years of impoundment (10^4 m^3).

Reach		Qiezixi~ Lijiatuo	Lijiatuo~ Jiulongtan	Jiulongtan~ Huangsha	Huangsha~ Chuqimen	Chuqimen~ Chaotianmen
No. of starting and ending sections		2~96	96~119	119~140	140~217	217~245
Location of starting and ending (km)		687.6~675	675~673	673~670	670~662.2	662.2~659.5
Distance (km)		12.6	2.0	3.0	7.8	3.2
2022	Amount of deposition	1243.8	84.3	785.5	1170.0	153.1
	Accumulative amount of deposition	1243.8	1328.1	2113.6	3283.6	3436.7
2032	Amount of deposition	1665.4	117.6	961.4	1412.9	194.8
	Accumulative amount of deposition	1665.4	1783.0	2744.4	4157.3	4352.1

Reach		Chaotianmen~ Cuntan	Cuntan~ Tongtianba	Lijiatuo~ Tongtianba	Qiezixi~ Tongtianba
No. of starting and ending sections		245~317	317~345	96~345	2~345
Location of starting and ending (km)		659.5~653	653~649	675~649	687.6~649
Distance (km)		6.5	4.0	26.0	38.6
2022	Amount of deposition	1402.5	801.5	4396.8	5640.7
	Accumulative amount of deposition	4839.2	5640.7		
2032	Amount of deposition	1655.4	903.7	5245.8	6911.2
	Accumulative amount of deposition	6007.5	6911.2		

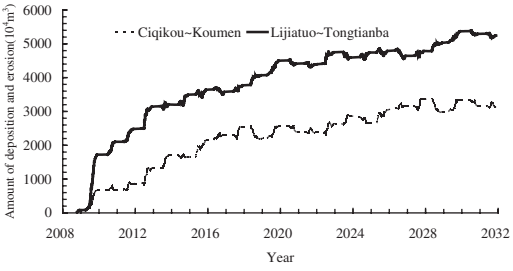


Figure 5. Change of amount of deposition and erosion at Chongqing reach with time.

and 2032, respectively. Figure 5 shows the change of the amount of deposition at Lijiatuo-Tongtianba reach with time. It is seen that untill the completion of the impoundment in 2032, there will be a deposition of 69112000 m^3 at Qiezixi-Tongtianba reach. The spatial distribution of this deposition is as follows: 16654000 m^3 for Qiezixi-Lijiatuo reach, 1176000 m^3 for Lijiatuo-Jiulongtan reach, 9614000 m^3 for Jiulongtan-Huangsha reach, 14129000 m^3 for Huangsha-Chuqimen reach, 1948000 m^3 for Chuqimen-Chaotianmen reach, 16554000 m^3 for Chaotiamen-Cuntan reach, and 9037000 m^3 for Cuntan-Tongtianba. The law of change of amount of deposition with time is as follows: during October~November after the flood period Three Gorges Reservoir begins to impound, when the water level gradually rises to 175 m from 145 m, the water level of the study reach increases, velocity and sediment carrying capacity decrease, resulting in sediment deposition. Before the flood period, the water level decreases to 145 m, the water level of the study reach is of little rise, thus the riverbed of the main channel of the study reach is slightly eroded. Therefore, the process of amount of deposition has an alternative deposition and erosion within a year, showing an increasing tendency in general. Deposition mainly occurs during the period from October to May of the next year, and erosion occurs during June~September, and it fully shows the function of Three Gorges Reservoir, that is, to store clear water and release eddy water, so as to ensure the effective capacity of Three Gorges Project.

Table 7 gives the amount of deposition at Jinkou-mouth reach on Jialingjiang River after the impoundment till 2022 and 2032, respectively. Fig. 5 shows the change of the amount of deposition at Ciqikou-mouth reach with time. It is seen that the deposition law of tributaries is basically the same as that of the trunk stream, that is, there is an increasing tendency in general and it is slightly eroded during the flood period. Till the impoundment in 2032, there is amount of deposition of 56115000 m^3 at Jinkou-mouth reach, among which, 24728000 m^3 for Jinkou-Ciqikou reach, 20210000 m^3 for Ciqikou-Niujiaotuo reach and 11197000 m^3 for Niujiaotuo-mouth reach.

4.3.2 *Location of deposition*

The calculated riverbed topographies are shown in Figs. 6a, 6b, 6c and 6d for Lijiatuo-Chuqimen reach, Chuqimen-Yuduchuanchang reach, Duchuanchang-Tongtianba reach and Ciqikou-Zengjiayan reach in 2032. It is seen that the deposition mainly occurs on the

Copyright © 2006 Taylor & Francis Group plc, London, UK

Table 7. Amount of deposition at Jialingjiang River reach at different years of impoundment ($10^4 m^3$).

Reach		Jinkou∼ Ciqikou	Ciqikou∼ Niujiaotuo	Niujiaotuo∼ Mouth	Ciqikou∼ Mouth	Jinkou∼ Mouth
No. of starting and ending sections		2∼85	85∼192	192∼248	85∼248	2∼248
Location of starting and ending (km)		25∼16	16∼5	5∼0	16∼0	25∼0
Distance (km)		9	11	5	16	25
2022	Amount of deposition	1882.9	1522.0	856.4	2378.3	4261.3
	Accumulative amount of deposition	1882.9	3404.9	4261.3		
2032	Amount of deposition	2472.8	2021.0	1119.7	3140.8	5613.5
	Accumulative amount of deposition	2472.8	4493.8	5613.5		

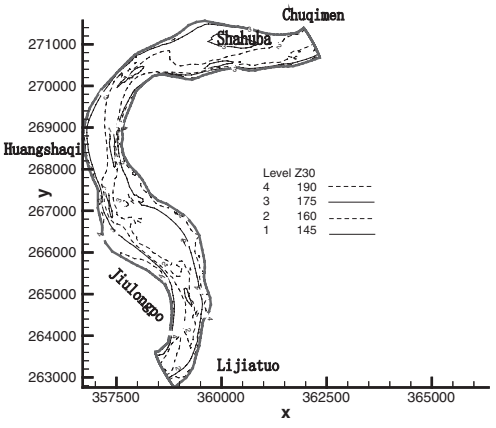


Figure 6a. Topography of Lijiatuo-Chuqimen reach on Yangtze River in 2032.

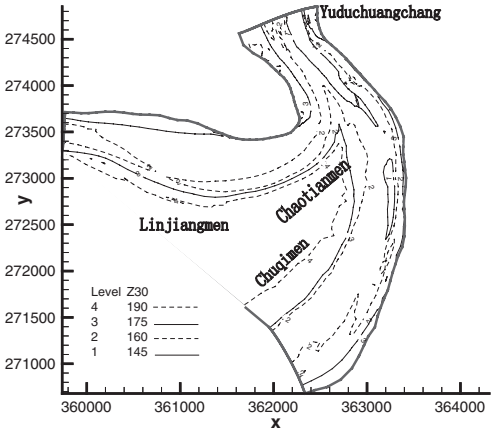


Figure 6b. Topography of Chuqimen-Yuduchuanch ang reach on Yangtze River in 2032.

protruding banks of the meandering channels, meandering locations with uneven bank lines, backwater areas as well as wide and shallow reaches, and the bank lines of deposited riverbed becomes more straight and smooth.

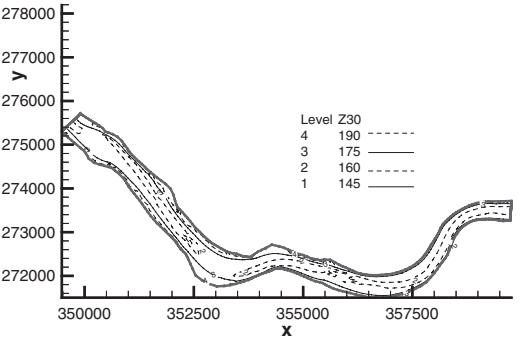


Figure 6c. Topography of Ciqikou-Zengjiayan reach on Jialingjiang River in 2032.

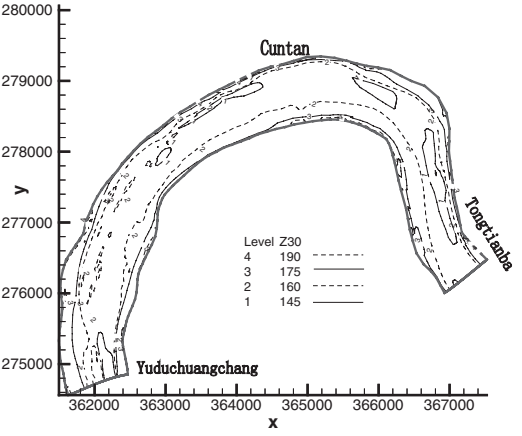


Figure 6d. Topography of Yuduchuanchang-Tongtianba reach on Yangtze River in 2032.

5 CONCLUSIONS

This paper studies the plane distribution of water flows and sediment deposition and erosion at Chongqing reach, especially the backflows at the confluence of the two rivers, that is, Yangtze River and Jialingjiang River,

Copyright © 2006 Taylor & Francis Group plc, London, UK

and those owing to irregular local banks. The calculated water levels, distribution of velocities, sediment concentration and its gradation, amount of deposition and erosion as well as its locations of Jiulongtan on Yangtze River and Shimen and Jinshaqi on the Jialingjiang River are in good agreement with the measured data.

According to the water flows and sediment conditions, the amount of sediment deposition and locations during 2003 ~ 2032 are calculated. At the end of the 30th year of impoundment of the reservoir the amount of deposition in the 38.6 km-long Qiezixi-Tongtianba reach will be 69.112 million m^3 whereas in the 25 km-long Jinkou-mouth reach will be 56.135 million m^3. Deposition mainly occurs on the meandering reaches with uneven bank lines, backwater areas as well as wide and shallow reaches. The bank lines will become more straight and smoother.

ACKNOWLEDGEMENTS

This work was supported by China's National Key Basic Research and Development Program (or 973 Program, No. 2003CB415206) and the National Natural Science Foundation of China (No. 50379027).

REFERENCES

Chang, H. H., 1982, Mathematical model for erodible channels. *J. Hydraul. Div., Am. Soc. Civ. Eng*., Vol. 108, No. 5, pp. 678–689.

Dou Guoren, 1963, Suspended load transport and calculation of erosion and deposition in tidal currents. *Journal of Hydraulic Engineering, (2)*: 13–25 (in Chinese).

Dou Guoren, Wan Shengan, Lu Changshi, et al., 1988, Study on sediment physical model on 175 m scheme for long reach of fluctuating backwater zone of Three Gorges Project. *Report of Nanjing Hydraulic Research Institute* (in Chinese)

Dou Guoren, Zhao Shiqing, & Huang Yifen, 1987, Study on two-dimensional total sediment transport mathematical model. *Journal of Hydro-Science and Engineering, (2)*: 1–12 (in Chinese).

Han Qiwei & He Mingmin. 1987, Mathematical model (1D) of reservoir deposition and riverbed evolution. *Journal of Sediment Research, (3)*:14–29 (in Chinese).

Holly, F. M. Jr, & Rahuel, J. L., 1990, Numerical Physical Framework for Mobil-bed Modelling. *J. of Hydraulic Research, 28(4)*: 401–416.

Li Yitian, 1989, 2D sediment mathematical model for channels. *Journal of Hydraulic Engineering,20(2)*:26–35, (in Chinese).

Lin Bingnan, Huang Juqing, & Li Xinchun, 1981, Tide sediment transport mathematical model for Qiantang River Estuary. *Journal of Sediment Research (Nisha Yanjiu) (2)*:16–29 (in Chinese).

Lu Yongjun, 1998, Study on 2D mathematical model of water and sediment movement at the branch river estuary. *Journal of Hydraulic Engineering, 29 (10)*: 60–68 (in Chinese).

Lu Yongjun, 2001, 2D mathematic model for deposition and erosion and influence of navigation in Chongqing reach after impoundment of Three Gorges Project for 30 years. *Report of Nanjing Hydraulic Research Institute* (in Chinese)

Lu Yongjun, Dou Guoren, Han Longxi, & Shao Xuejun. 2004, 3D Mathematical Model for Suspended Load Transport by Turbulent Flows and its Applications. *Science in China Ser. E*, 47(2) 237–256.

Lu Yongjun, Li Haolin, Dong Zhuang, Lu Jianyu, & Hao Jialing. 2002, Two-Dimensional Tidal Current and Sediment Mathematical Model for Oujiang Estuary and Wenzhou Bay. *China Ocean Engineering*, 16(1): 107–122.

Olsen, N. R. B. 1999, Two-dimensional numerical modeling of flushing processes in water reservoirs. *J. Hydraul. Res*., Vol. 37, No. 1, pp. 3–16.

Shimizu, Y., Yamaguchi, H., & Itakura, T., 1990, Three-dimensional computation of flow and bed deformation. *J. Hydr. Engrg*., ASCE, Vol. 116, No. 9, pp. 1090–1108.

Spasojevic, M., & Holly, F. M., Jr., 1990, 2-D bed evolution in natural watercourses—New simulation approach. *J. Waterw., Port, Coastal, Ocean Eng.*, Vol. 116, No. 4, pp. 425–443.

Van Rijn, L. C. , 1987. Mathematical modeling of morphological processes in the case of suspended load transport,Delft Hydra. Communication No.382, Delft, the Netherlands.

Wu, W. M., Rodi, W., & Wenka, T., 2000, 3D numerical model for suspended load transport in open channels. *J. Hydr. Engrg*., ASCE, Vol. 126, No. 1, pp. 4–15.

Zhou Jianjun, 1997, Research report of calculation of 2D sediment mathematical model of the dam area of Three Gorges Project. *Collection of sediment research reports for the dam area of Three Gorges Project on Yangtze River (Vol. 1)*, pp. 575–624, Patent Literature Press,Beijing (in Chinese).

Copyright © 2006 Taylor & Francis Group plc, London, UK

A preliminary study on the local abrupt descent of downstream water level near the Three Georges Dam

Zhaohua Sun, Yitian Li & Ming Li
State key laboratory of water resource and hydropower engineering science, Whuhan University, Wuhan, China

Ying Huang
Changjiang Waterway Engineering Bureau, Wuhan, China

ABSTRACT: The Yangtze River transforms from gravel bed channel into sand bed channel in the reach of Yichang to Shashi, which is close to the Three Georges Dam and undergone the immediate clear water erosion after impoundment. Prediction of how water level and long profile will response to the dam in dry season has draw wide concerns, for their likely influence on navigation condition. Based on historical data collection and analysis, it is found that the water level drop in this reach is controlled not only by channel erosion but also by pivotal reach segment with special geological and morphological features. Because of its control function, an abrupt descent of water level is formed, that will become even higher gradient slope in future.

1 INTRODUCTION

The Yangtze River, with a total length of more than 6300 km, is divided into upper and middle reaches at Yichang, where the river exits from the upper rock-confined valley into the Jingjiang fluvial plain. In the downstream reach near Yichang, the river transform from confined gravel bed channel into alluvial sand bed channel. After the construction of the Three Georges Project (TGP) at Yichang, dam effects would take places in this section more immediate than other reaches. As channel incision and water level drop is common on other regulated rivers, how fast would the post-dam channel adjustment occur in this reach and to what extent the water level would drop have draw much concerns. Numerical models have indicated that water level decrement would amount to about 0.5 m (5000 m^3/s) in dry season at Yichang after 5 years clear water erosion (Changjiang River Scientific Research Institute, 2002), but the actual process is even unnoticeable in the past three years. With channel degradation shifts to downstream sand bed reaches, will the upstream water level be affected and get into obvious periods of decreasing? Whether the streamwise uneven scour depth would result in abrupt descent of water level at some locations? At present, these are questions very cared by engineers, especially in waterway management near the dam.

In numerous catchments throughout the world human intervention has strongly altered natural river dynamics. The response of flow processes and channel morphology to engineering and regulation of alluvial streams have been studied widely both on gravel channels and sand bed channels, for hazard mitigation, infrastructure stability and environmental conservation, but few on navigation (Kondolf, 1997; Surian & Rinaldi, 2003). The middle and upper reaches of the Yangtze River differing in geology, channel geomorphology and bed composition, as the transitional section between them, dam effect issues surrounding the immediate downstream of the TGP will inevitably be complex. Documented historical data of changes that have occurred in response to human impacts is helpful for prediction of the future evolution of the river. This paper examines the gauged information in this reach in the past few decades and investigates the relationships between low flow hydraulic features and channel adjustment, based on which, some predictive description about the future evolution is given.

2 STUDY AREA

2.1 *Regional setting*

The upper Yangtze is deeply incised into rocky canyons with high slope. At the exit of the Three Gorges, the TGP (dam impoundment in 2003) and Gezhouba Project (dam impoundment in 1981) were constructed. In the middle Yangtze, the slope decreases dramatically. Downstream from Shashi, a typical meandering river pattern is formed (Fig. 1). In the 1960s and the 1970s, a set of cutoff projects were used to manage

Copyright © 2006 Taylor & Francis Group plc, London, UK

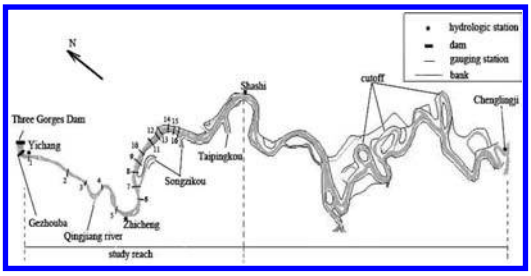


Figure 1. Location of the study reach.

the fluvial environment and the course of the river was shortened by approximately 78 km. The study reach from Yichang to Shashi is about 140 km long with confined channel boundary and low sinuosity in planform. A little tributary named Qingjiang joins the main stream about 39 km downstream Yichang, but its runoff only amounts to less than 5% of the Yangtze's at Zhicheng. At Songzikou (74 km from Yichang) and Taipingkou (138 km from Yichang), there are diversions linking the Yangtze River with Dongting Lake, but they are usually dry in low flow season.

In this reach, the low flow water level is of navigational interests for two reasons. One is related to the threshold water depth in the downstream ship-lock entrance of the Gezhouba Project. If the water level of Yichang dropped too much to make the water depth less than the designed 4.0 m depth at lock entrance, ships would not be able to get through. Another reason is about the slope gradient at some location. After the TGP enclosure, more ships are reported to have difficulty in upstream navigate in certain location in dry season, so engineers wondered if water level has descended abruptly in that reach, which is causing a high gradient.

2.2 *Historical events*

Both human disturbance and extreme hydrologic event have impacts on the channel adjustment history in this reach, including dam construction, river cutoff projects, gravel mining, sediment excavate and major floods:

(1) Two cutoff projects were implemented at Zhongzhouzi and Shangchewan in the 1960s and another natural-cutoff occurred in 1972 at Shatanzi. Although these changes were not taken place in the study reach, but they aroused backward erosion and water level had been changed in upstream reaches.
(2) From 1971, for the purpose of the Gezhouba Dam construction intense gravel mining and sediment excavate had taken place in neighborhood of Yichang. Records show that $14.55 \times 10^6 m^3$ sediment had been mined from 1972 to 1981. Affected by this, average channel degradation between Yichang and Qingjiang River confluence was amount to 0.91 m.
(3) The Gezhouba Dam is a run-of-river project and it locked the Yangtze River in 1981. After impoundment, the dam released water had taken $22.40 \times 10^6 m^3$ sediment away from 1981 to 1986. Integrating with gravel mining, average bed degradation upstream of the Qingjiang River confluence is about 0.4 m to 0.5 m in this period.
(4) In the extreme flood of 1998, about $53.42 \times 10^6 m^3$ sediment was flushed out of the Gezhouba reservoir. The downstream reach undergone obvious deposition. Top elevation of some bars in Yichang reach was increased by 5 m and the deposition depth averaged to 1.85 m in the reach of more than 30 km long.
(5) After the TGP closure in Jun 2003, water level behind the dam was increased from about 60 m to 135 m above mean sea level. Down stream channel degradation is still ongoing.

Those events affect different segments of the whole reach and their impacts often compound with one another. In order to roughly separate the effects of those impacts, the past few decades is divided into several consecutive periods: 1961–1970, 1971–1980, 1981–1987, 1987–1998, 1998–2003 and 2003–2005.

3 DATA COLLECTION AND METHODS

The Yangtze River Water Resource Committee (YRWRC) has set gauging stations along the Yangtze River from the 1950s. Three major gauging stations were chosen for this study at Yichang, Zhicheng and Shashi, representing the upper, middle and lower part of this reach. Among them, water level gauging data is available from the 1950s and daily mean discharge can be obtained at Yichang(1950–2005) and Shishi (data before 1990 not available). The focus of this paper in on low flow, so that only data in January to March is collected. In this period, the discharge of Zhicheng and Shashi can be calculated by adding the discharge of Qingjiang into Yichang. In addition to the hydrologic data gauging by YRWRC, the Changjiang Waterway Engineering Bureau (CWEB) has set 16 water gauges in this reach to survey the water level change after 2003. Their distance from Yichang are 0 km, 20 km, 27 km, 43 km, 57 km, 71 km, 76 km, 80 km, 83 km, 87 km, 92 km, 98 km, 103 km, 106 km, 109 km and 112 km (Fig. 1). From those gauging sites, simultaneous water level along the reach can be obtained. It will give convenience to the present study for detailed understand of the slope in each segment. The water level from different sources or in different periods may have the different base level; these factors are all considered and taken into account.

Copyright © 2006 Taylor & Francis Group plc, London, UK

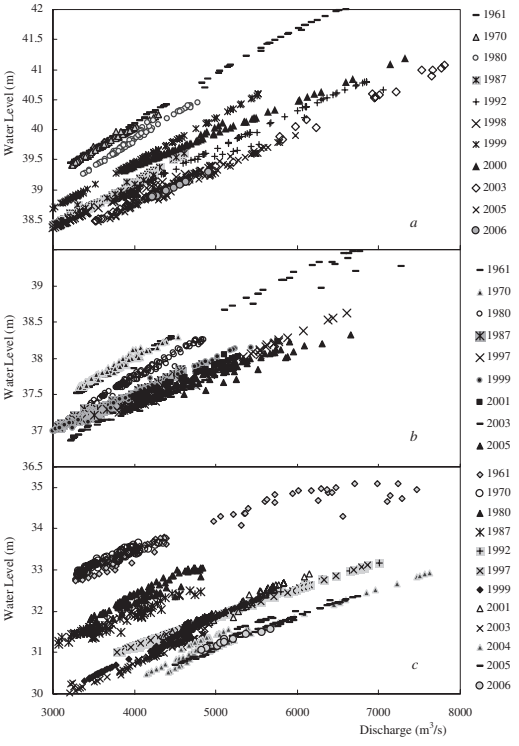


Figure 2. Stage-discharge relation of different station; *a*.Yichang, *b*.Zhicheng *c*.Shashi.

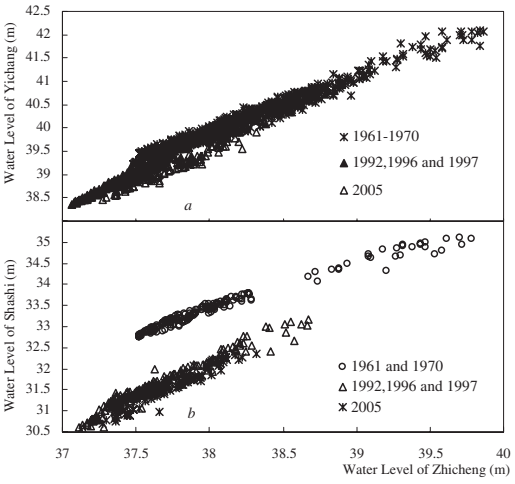


Figure 3. Correlation of water level between stations; *a*. Yichang-Zhicheng, *b*. Shashi-Zhicheng.

In the study reported here, records of discharge and water level in this reach were collected to examine the spatial and temporal changes of water level. The exploration is performed by three means:①For each gauging station, the stage-discharge relations of different periods are plotted (Fig. 2). Because only the first three months of every year is investigated, the discharge variation is limited in a certain scope. By this way, the changing process of low flow water level of different parts of the reach can be indicated.②On the basis of one site study, the relationships between different sites were depicted for different periods. As Zhicheng located in the middle of the other two stations, the value of daily water level is plotted in manners of Shashi-Zhicheng and Yichang-Zhicheng (Fig. 3). Because interval between those stations is not a very long distance and the flow isclose to a quasi-steady state in dry season, the inter-station discharge difference can be ignored. The daily water level has the foundation to be compared, so the result will be credible.③From the data of the 16 water gauges, some characteristics of water surface profile can be plotted. In order to eliminate the influence of unsteady flow, only data series of those times is chosen when the discharge and water level at Yichang keep steady for several days. The above hydrological analysis work will figured out the water level changing in history, which is helpful for present state assessment.

From the 1980s, the YRWRC has implemented long distance channel morphology survey for several times. Morphology information available for this study is from survey of 1980 and 2002. From the channel morphology map of 1980 and 2002, 103 and 294 cross sections were taken from Yichang to Shashi respectively from the two maps. Because the two sets of morphology data spanned a long period of 22 years, it will provide evidence of channel adjustment if there were any those changes. Besides the direct morphological comparison, the data can also serve as boundary condition for 1D numerical hydrodynamic model, with which a quantitative analysis can be given about the flow character in different periods. The CWEB also has carried out some geology and geomorphology survey in recent years, but their work only covered some segment in this reach. Anyhow, those data will provide supplementary information for this study.

4 RESULT AND DISCUSSION

4.1 *Hydrological data analysis*

From the stage-discharge relation plotted in Figure 2, the corresponding consequence of the major historical events can be clearly figured out.

(1) Yichang: Before 1970, the water level at Yichang was quite stable. This can be referred as undisturbed state. From 1970 to 1987, the water level had dropped by 0.2 m, which might caused by the intense gravel mining in this period. The largest extent of water level decrement happened between

Copyright © 2006 Taylor & Francis Group plc, London, UK

1980 and 1987, with the value of 0.8 m (4500 m^3/s). It is the period when the Gezhouba Dam finished construction. After 1987, the water level changing is not obvious until 1998. It seems that the water level adjustment was getting into another stable state. After the flood in 1998, the water level at Yichang elevated for the deposition caused by sediment from the reservoir. Although the flood interrupted the descending process, the water level quickly changed to the state before the flood. By 2003, the water level dropped to the position little lower than 1998. Even after the TGP construction, it showed no more decline trend.

(2) Zhicheng: Before 1970, the water level is under a natural stable state. In the period of 1971–1980 and 1981–1987, it experienced continued decreasing. But from 1987 until 2001, the water level remained another quasi-equilibrium. This state is kept even after 2003. The post-dam water level is unnoticeable. In general, the total changing of water level at this station is about 0.6 m (4500 m^3/s), which is less than that of Yichang.

(3) Shashi: This station is adjacent to the river cut-off project accomplished in the 1960s and early 1970. In the 1970s, the water level dropped about 0.8 m (4500 m^3/s) for the impact of downstream river cutoffs. Between 1980 and 1987, the water level continued to decrease but with lower speed, unlike that at Yichang. After 1987, the decreasing speed got increase. To 1992, the water level finished a descent of 0.6 m (4500 m^3/s). It seems that the Gezhouba's influence on this station had taken effects. After then, the water level became stable, which can be indicated by the points of 1992–2001. Unlike the trend of Yichang and Zhichen, obvious water level decline taken place at Shashi right after 2003, the TGP dam closure. But it appeared that the drop main occurred in 2003, the subsequent two year showing no clear change. Because this station is in sand bed reach, the total water level drop is much larger than the other two.

The water level change at the three stations shows both similarity and difference. From the historical data, we can find that the distribution of stage-discharge points show stable appearance before and after rapid changes in the 1970s and 1980s. Those periods can be picked out to set up the inter-station relation. The period of 1961–1970 is chosen to represent the undisturbed natural condition; 1992–1998 can be chosen to indicate the equilibrium after early human disturbance; 2005 represents the post-dam condition. The relations show that the water level has both dropped at Yichang and Shashi corresponding to the same Zhicheng level from the 1960s (Fig. 3). The Yichang-Zhicheng relation changed little from the 1960s while Shashi-Zhicheng changed obviously. The good relation between Yichang and Zhicheng indicated that the middle and upper part of this reach must dominate by some same factors. Those relations can also be revealed in the changing corresponding to historical events in Figure 2.

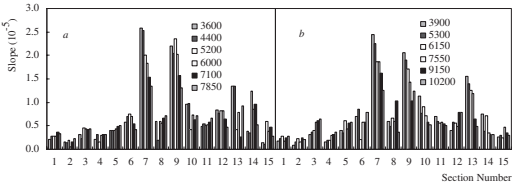


Figure 4. Local slop of water surface at different discharges, the number on x-axis indicates the section between every two gauging sites; *a*. in year 2003, *b*. in year 2005.

Gauging data of long profile is absent before 2003. The data from the water gauges set by CWEB gives information of recent years' low flow profile. Some selected data is depicted in Figure 4. The slop along this reach is quite uneven, with high gradient in the middle reach. In sections 7–9, the reach length occupies 1/11 of the whole, but the energy loss almost accounts for one third of the whole energy dissipation. An interesting phenomenon is: in the high gradient section the slope becomes steeper with discharge decreasing, but this is not the case in low-gradient sections. In fluvial rivers, low flows profile is to some degree control by channel morphology. The characters indicated by Figure 4 implied that channel morphology of certain sections may play an important role in upstream water level maintaining. This may also be the reason for the modes of water level changing at different stations, as Figure 2 and Figure 3 demonstrate.

4.2 *Morphological change and its impact*

Some geological survey discovered that there is underlying gravel layers buried beneath uneven depth of alluvial deposition in most part of the study reach. The sketch of top elevation of the gravel layer is depicted in Figure 5 with channel profile of 1980 and 2002. It shows that the alluvial layer depth is deeper in the upper and lower reach than the middle reach. According to this, some early research predicated that water lowering would take place in upper reach during the TGP post-dam erosion process (Changjiang River Scientific Research Institute, 2002). Comparing with the channel profile of 1980, bed elevation only obviously lowered in few locations until 2002, although the top of underlying gravel layer is not reached. In the middle part (70 km to 100 km), channel profile is almost not changed. Survey data of CWEB from 1999 to 2005 coincide with this trend.

By 1D numerical hydrodynamic model, low flow process is simulated under the 1980 and 2002 condition. The model is calibrated with the gauged discharge and water level series at Yichang, Zhicheng and Shashi

Copyright © 2006 Taylor & Francis Group plc, London, UK

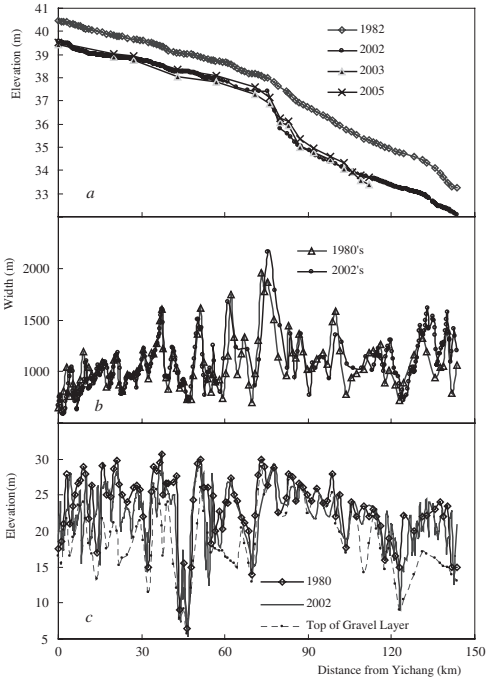


Figure 5. Channel width and profile in different periods; *a*. low flow profile of 5000 m^3/s, *b*. water surface width of 5000 m^3/s, *c*. channel profiles.

in 1982, 2002 respectively. Given the same discharge of 5000 m^3/s, the water profile and surface width is calculated (Fig. 5). It is obvious that water level had drop notably between 1982 and 2002 but the width only increased a little in the lower part. The magnitude of water level drop is much higher in the lower part reach and a tuning point is formed at the location about 75 km from Yichang. Around this location, an abrupt water level descent appeared. It is also the place where the top elevation of the underlying gravel layer is high. Below this reach segment, channel changes from wide to narrow and channel profile begins to decline. This reach segment can be named as pivotal segment. It should be pointed out that the roughness coefficient in 2002 is much larger than that in 1982. This may result from the channel erosion process from the 1980s.

The water gauges of CWEB provide low flow profiles from 2003. The gauged data in 2003 and 2005 (5000 m^3/s) is plotted with the calculation results. Though the TGP began to trap sediment after 2003, low flow profile changed little till 2005.

4.3 *Discussion*

In this reach, water level change is affect by channel erosion, downstream influence and channel geomorphology. From historical data analysis, their roles and correlations can be revealed. Water level lowering in the upper reach before 1987 and in the lower reach before 1992 is absolutely consequence of channel erosion. But water level lowering of Shashi to some extent attributes to downstream erosion, which can be seen as downstream influence. Water level of Zhicheng is affected both by Yichang and Shashi. Although the Yichang-Zhicheng relation is quite good, but water level of Zhicheng lowered much in 1970–1980 when Yichang's dropped little. This must be affected by water level drop of Shashi in the same period. After 1987, this trend was not continued, which implied that when water level had dropped to some degree the control function of channel morphology began to take effect. This means the water level descent at Shashi would no longer have impact on the upstream reach of the pivotal segment, including Yichang and Shashi.

After 1987, water level of Yichang kept a relative stable state disregard the flood of 1998. One the one hand it maybe the function of the pivotal segment, on the other hand it may indicate that bed armoring was gradually formed in Yichang reach, because channel profile of 2002 shows the underlying gravel layer is still not reached. Whatever the reason, the water level at Yichang is unlikely to drop large extent after the TGP construction, so is Zhicheng.

After the TGP dam closure, channel erosion has certain taken place in the reach near Shashi and its downstream. The obvious water level drop from 2003 to 2004 at Shashi provides evidence for this process. Considering the deep alluvium of the Jingjiang reach, the relative stable state of water level after 2004 can not be taken for equilibrium. With erosion going on, the downstream water level drop will cause the high gradient section even higher.

5 CONCLUSION

Channel adjustments on human disturbed rivers have straightforward impacts on low flow water level, which will possibly affect waterway condition. On the basis of more than 40 years long database, the following main conclusions can be drawn from the analyses that have been presented.

(1) Because of the particular geologic surroundings of the study reach, magnitude and rate of water level lowering is not only controlled by channel erosion but also by pivotal reach segment, where a high gradient local slop is formed.
(2) After the water level dropped to a certain extent, upstream reach from the pivotal segment is no longer obviously affected by the downstream reach erosion and water level drop. Whether this relation will be remained after the TGP dam closure is still need more research.

Copyright © 2006 Taylor & Francis Group plc, London, UK

(3) Water levels at Yichang and Zhicheng has good correlation and they are unlikely to decrease with dam effects of the TGP, while the abrupt descent around the pivotal segment will drive the local slop gradient even higher.

ACKNOWLEDGEMENT

The study is supported by National Key Basic Research and Development Program (No. 2003 CB415200).

REFERENCES

Changjiang River Scientific Research Institute. 2002. Analysis and computation about riverbed erosion process downstream Three Gorges Reservoir by 1-D numerical model. In Sediment research of Tree Gorges Project (Vol. 7): 258–311, Beijing: Intellectual Property Press.

Kondolf, G.M. 1997. Hungry water: effects of dams and gravel mining on river channels. Environmental Management 21(4): 533–551.

Surian, N. & Rinaldi, M. 2003. Morphological response to river engineering and management in alluvial channels in Italy. Geomorphology 50: 307–326.

Copyright © 2006 Taylor & Francis Group plc, London, UK

Habitat suitability index model of four major Chinese carp species in the Yangtze River

A.Y.J. Yi & Z.Y. Wang
State Key Laboratory of Hydroscience and Engineering, Tsinghua University, Beijing, China

B.Y.J. Lu
Nanjing Hydraulic Research Institute, Nanjing, China

ABSTRACT: Human activities, especially dam construction and river training projects are changing the river environment and stream habitat in the Yangtze River in China. As a consequence, aquatic organisms, especially, rare species and fishes with economic value are affected. Therefore, it is necessary to study the changing characteristics of the river that affect the aquatic community habitat, such as substrate, water depth, water temperature, velocity, water quality, etc. There are four species of carps in the Yangtze River that have the most importance to the fresh water fishery in China. They are the black carp (Mylopharyngodon piceus), the grass carp (Ctenop haryngodon idellus), the silver carp (Hypoph thal michthys molitrix) and the big-head carp (Aristichyths nobilis), which are the four major Chinese carp Species. A model is developed in this paper of the habitat Suitability Indices for the four major Chinese carp Species. Based on research on the main eco-factors influencing growth and reproduction, 10 main aquatic eco-factors are analyzed, including water temperature; velocity; water depth; dissolved oxygen; un-iomized ammonia; vegetative cover; and amount of pools, backwaters, and marshes. The Suitability Index (*SI*) curves of the ten eco-factors for these species are obtained. The stream habitat for the carp species is assessed with the model, which integrates these eco-factors. The model is validated by application to 15 groups of data.

1 INTRODUCTION

In recent years, human activities and exploitation of rivers have altered flow patterns and aquatic habitat. Large dams alter flow regimes, retain sediment and nutrients, interrupt fish migration, cause changes in water quality and temperature, and destroy riparian habitats (Ligon et al. 1995, McCully 1996). As a consequence, the quality of riverine ecosystems across the globe is declining and at the same time the pressure on water resources is further increasing. There is a general need for tools to analyze, assess and quantify the impacts of human activities on physical processes and ecological functions in such systems to help finding better solutions for adaptive management of watersheds (Schneider & Jorde 2006).

Habitat evaluations of rivers and streams have become important tools for estimation of the amount of habitat that is available for a given species within a study reach as a function of flow. One of the most common one-dimensional techniques is the Physical Habitat Simulation System (PHABSIM). PHABSIM uses the methodology known as the Instream Flow Incremental Methodology (IFIM) and is one of the most widely used tools for assessing flow management practices (Bovee et al. 1986). New applications of PHABSIM are also including 2D hydrodynamics (Katopodis 2003). Recently, two-dimensional models (RIVER 2D and SMS) have been developed for detailed hydraulic analysis of spatially explicit habitat units at the microhabitat scale (Steffler & Waddle 2002). Scientists chose RIVER 2D because of the ease with which the model reaches a steady-state solution without compromising accuracy. The aquatic habitat simulation models (AHSMs) generally have physical and biological modeling components and compare measured or simulated physical parameters at a location with habitat suitability criteria. (Schneider & Jorde 2006) A more general critique is that AHSMs have widely been used to determine instream flow regulations simply based on instream physical habitat and neglecting the need to address wider ecosystem related aspects such as channel maintenance flows, overbank flows, the lateral connectivity with the floodplain or with smaller tributaries, etc. (Hudson et al. 2003). The computer model CASiMiR (Computer

Copyright © 2006 Taylor & Francis Group plc, London, UK

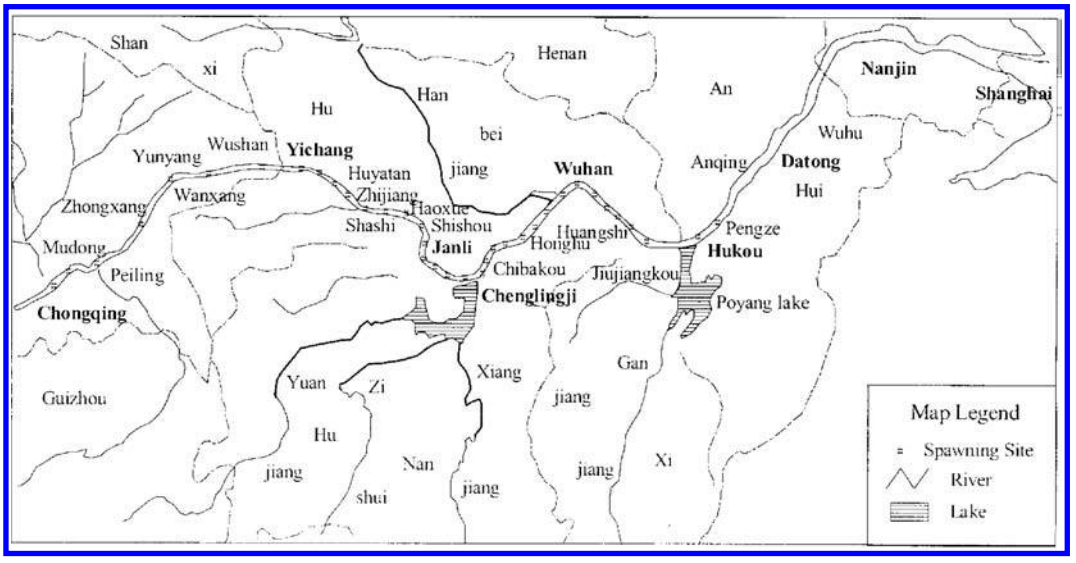


Figure 1. The spawning site of the four major Chinese carp species in the Yangtze River.

Aided Simulation Model for Instream Flow Requirements) was developed at the University of Stuttgart's Institute for Hydraulic Engineering. It is a surface water habitat model, in which – among other things – fish habitat can be investigated (Schneider 2001, Jorde 1996). The model uses additional information for the regulation of hydraulic parameters. This enables the assessment of, for example, water depth, flow velocity, or sediment transport as conditions are modified.

There is still a lack of understanding of the habitat process and none of the models are mature enough for assessment of habitat of all different species. The basic principle guiding habitat-modeling is that the majority of water organisms have specific demands for the suitability of their environment. Selection of the indicator fish species in the studied stream habitat is important. There are four Chinese carp species, i.e. the black carp (Mylopharyngodon piceus), the grass carp (Ctenop haryngodon idellus), the silver carp (Hypoph thal michthys molitrix), and the big-head carp (Aristichyths nobilis) in the Yangtze River, which are the main species of economic value to the fresh water fishery in the river. The four carps reproduce in the Yangtze River and grow in the riparian lakes, such as the Tongting and Poyang Lakes. These carps live in lakes with different environment but their spawning sites of the carps in the river have the similar environmental conditions. A model is developed in this paper of the habitat suitability indices for the four major Chinese carp. Based on the research of the main eco-factors influencing the growth and reproduction in the Yangtze River, 10 main aquatic eco-factors are analyzed, including water temperature; velocity; water depth; dissolved oxygen; un-iomized ammonia; vegetative cover; and amount of pools, backwaters, and marshes. The stream habitat for the carp species is assessed with the model, which integrates these eco-factors.

2 HABITAT OF CARP SPECIES IN THE YANGTZE RIVER

The 6300-km long Yangtze River is the largest and longest river in China and the third in the world in length. It flows from west to east and pours into the East China Sea at Shanghai. The Yangtze River has a watershed area of 1.80 million km^2. In China, the river is called the Changjiang, with special names for different stretches. From the source to Yichang (the Three-Gorges Dam) is the upper reach, from Yichang to Hukou (Poyang Lake mouth) is the middle reach, from Hukou to Datong is the lower reach and below Datong is the estuary (Wang & Lee, 2004).

The middle reach of the Yangtze River is 898 km long, has a drainage area of about 680,000 km^2, and is the main reproduction area of the carp. A 393 km long reach from Yichang to Chenglingji is one of the most important habitats of the four carp species. There are 12 spawning sites for the carp species in this reach (Fig. 1), with 43% of the total egg production in the Yangtze River. From 1970s, increasing human activities in the river basin has affected the reproduction of fish in the river and the amount of the four major Chinese carp species decreased sharply. Especially during 1997–2003 when the construction of Three Gorges Dam, resulted in the clearing of 8 spawning areas in the reservoir. Thus the flux of fries through Jianli during the spawning season reduced quickly.

Copyright © 2006 Taylor & Francis Group plc, London, UK

The impoundment of the reservoir delays the spawning season of the carp of the some of the spawning sites downstream of the reservoir, and decreases the amount of fry at each site. Some sites can not provide the carp with adequate spawning conditions.

3 HABITAT SUITABILITY INDEX MODEL

Carp habitat quality analysis is based on basic components consisting of food, water quality, and reproduction requirements. Variables which have been shown to affect growth, survival, abundance, or other measures of well-being of carp are placed in the appropriate component.

Ten aquatic eco-factors, which mainly influence the habitat of the four major Chinese carp species, are selected for the modeling as follows: (1) Percentage of vegetative cover in shallow areas during spring and summer (V_1); (2) Percentage of pools, backwaters, and marsh areas during average summer flow (V_2); (3) Average water temperatures for adults (V_3, °C); (4) *DO* concentrations for juvenile and adult carp (V_4, mg/L); (5) Water-level fluctuation during spawning season (V_5, m); (6) Average water temperature during spawning within specified areas (V_6, °C); (7) Average water temperature during hatching within specified areas (V_7, °C); (8) Flow velocity during hatching within specified areas (V_8, m/s); (9) Minimum *DO* concentrations within specified areas during hatching (V_9, mg/l); and (10) NH_3-N concentrations (V_{10}, mg/l).

The suitable ranges of the 10 main eco-factors for carp are determined using the research results of biological scientists. The Suitability Index (*SI*) curves of each eco-factor for these species are developed based on those results. By analyzing these eco-factors, a habitat assessment model is developed, which combines these factors and can be used for assessing habitat changes due to human activities or hydraulic processes.

3.1 *Suitability index curve*

The suitability index (*SI*) curve is a curve that quantifies the physical habitat such as water temperature, flow velocity, and *DO* concentration. The habitat suitability ranges from unsuitable (0) to optimal habitat suitability (1). The intermediate values represent the suitability range based on a specified hydraulic variable.

The habitat suitability model is divided into three parts: food component, water-quality component and reproduction component.

Food component: Percentage of vegetative cover (V_1) is included because areas with abundant vegetation provide habitat for various food organisms. In addition, the amount of vegetation reflects the general productivity of the habitat, and carp are opportunistic feeders on vegetation and detritus, as well as animal matter. Percent pools, backwaters, and marsh areas (V_2) is included because this variable quantifies the amount of area available for production of food for the species.

Water quality component: Water temperature (V_3) and *DO* (V_4) affect growth, survival, and feeding. NH_3-N (V_{10}) is included because too much NH_3-N may be harmful for survival and reproduction.

Reproduction component: Percentage of vegetative cover (V_1) is important because the preferred spawning substrate is vegetation. Percentage pools, backwaters, and marsh areas (V_2) are included because these variables quantify the amount of spawning habitat. The water depth is not a key factor affecting the reproduction, but the water level range (V_5) is important, because higher levels of depth change may cause a higher rate of spawning. Flow velocity during hatching (V_8) is included because carp fry should have a certain velocity to prevent them from depositing. Temperature (V_6, V_7) and dissolved oxygen (V_9) are important water-quality variables which can affect embryo survival and development.

By summarizing the research of the fisheries biologists, the factors *SI* for the four major Chinese carp species in the Yangtze River were developed. The data sources are listed in Table 1, and the *SI* curves are shown in Figure 2.

3.2 *Habitat suitability function*

Edwards (1982) developed an *HSI* model for carp in the USA. The authors modified the model by considering the features of the Chinese carp and the Yangtze River.

Habitat Suitability Index:

$$HSI = (C_F C_{WQ} C_R)^{1/3} \tag{1}$$

In which C_F represents the food component given by

$$C_F = (V_1 V_2)^{1/2} \tag{2}$$

C_{WQ} represents the water quality component given by

$$C_{WQ} = \frac{V_3 + V_4 + V_{10}}{2} \tag{3}$$

C_R represents the reproduction component given by

$$C_R = (V_5 V_6 V_7 V_8 V_9)^{1/5} \tag{4}$$

The values of V_1–V_{10} are determined from Figure 2.

Copyright © 2006 Taylor & Francis Group plc, London, UK

Table 1. Eco-factors for the four major Chinese carp species.

Variables	Eco-factors	Research results of biologists
V_1	Percentage of vegetative cover in shallow areas during spring and summer	In both riverine and lacustrine habitats, carp prefer enriched, well-vegetated waters with a mud or silt substrate (McCrimmon 1968). Adults spend summer and early autumn in shallow areas of dense vegetation (May & Gloss 1979).
V_2	Percentage of pools, backwaters, and marsh areas	The carp prefer areas of slow current. In the Missouri River, common carp occurred in pools and chutes ($\leq$60 cm/s) and in the main channel borders (60–120 cm/s) (Schmulbach et al. 1975), but were most abundant in marshes and backwaters ($\leq$20 cm/s) (Kallemeyn & Novotny 1977). Deep pools with abundant cover, including logs, brush, and other objects, provide feeding and resting areas in swift rivers (Pflieger 1975). Although occasionally found in high gradient streams, carp is more common in low to moderate gradient streams. In high gradient streams, carp occur in warm backwaters and in organically polluted sections (Sigler 1958, Pflieger 1975).
V_3	Temperature (Adult)	A range of 20–32°C is suitable for growth under laboratory conditions and optimum in 25–32°C. The carp will die when temperatures are $<$0.5°C and $>$40°C (Zhang & Fan 2004). The growth rate decreases when the temperature is $<$15°C (Yang 1996). The carp begins feeding when temperature is over 5°C, increasing with temperature, and is greatest for temperatures between 25–30°C (Xiong 2003). Under laboratory conditions, feeding and growth increase for temperatures between 22–30°C, are optimum at 30°C (Cui. et al. 1995).
V_4	*DO* (Juvenile and adult)	The four major Chinese carp species feed more and grow faster along with higher *DO* concentrations, they will die when *DO* is $<$0.5 mg/l (Zhang & Fan 2004). Adults are very tolerant of low *DO* concentrations, a condition common in warm, fertile waters (Sigler 1955, McCrimmon 1968). Adults will also feed in the oxygen-depleted hypolimnion ($<$2 mg/l *DO*) (Hover 1976). Adults can gulp surface air when the *DO* is $\leq$0.5 mg/l (Yashouv 1956). Respiration is elevated at 3–5 mg/l *DO* (T $\sim$ 13–23°C) (Itazawa 1971, Davis 1975). The *DO* should remain at least 6–7 mg/l for good growth (Huet 1970).
V_5	Water level fluctuation	Rising of water level makes the carp spawn, and spawning ceases when water level falls (Yih & Liang 1964). Most carp spawn when water level rises, the wider the rise rang, the bigger the flux of fry. On 9–21 May, 1997, the water level at Jianli rose 3.17 m, and flow increased 6550 m^3/s caused the first fry flux; and 6–15 June, 1997, water level rose 3.47 m, and flow increased 10,300 m^3/s, caused the second fry flux (The Technology Report of Fish Resources and Environment Monitoring, 2004).
V_6	Temperature (Spawning)	Spawning begins when temperature $>$18°C (Yang 1996). The four major Chinese carp species in the Yangtze River stop spawning when temperature $<$18°C, the optimum is 21–24°C, the top temperature in Yichang reach during laying season is 27°C, the carps still spawning (Li 2001). The species generally will not spawn in waters with an average temperature $<$18°C, and optimum in the range of 21–24°C (The Technology Report of Fish Resources and Environment Monitoring, 2004). The spawning temperature for black carp is 22–30°C and the optimum temperature is 25 $\sim$ 28°C (Large fresh water fish species in China- black carp, 2006).
V_7	Temperature (Hatching)	Embryos are tolerant water temperatures between 18 and 30°C, the optimum is 22–28°C, fetation ceases or abnormality results when temperature is $<$17°C or $>$30°C (Wang 2003).
V_8	Flow velocity (Spawning and hatching)	Preferred spawning areas have a flow velocity of 0.2–0.9 m/s. A velocity increase of 0.25–0.50 m/s is better for spawning (Yih & Liang 1964). The eggs and fries will not sink when velocity $>$0.2 m/s (Cao et al. 1987). The eggs begin sinking as water velocity is $<$0.27 m/s, and most of the eggs sink if the velocity is $<$0.18–0.25 m/s, and all eggs deposit if the velocity is $\leq$0.1 m/s (H. Y. Tang, & Z. T. Yu, et al. 1996).
V_9	DO (Hatching)	Fetation needs a *DO* concentration in the range of 5–8 mg/l, and should not be $<$4 mg/l, if $<$2 mg/l, the eggs will die by suffocation (Wang 2003). Eggs are tolerant of fluctuating *DO* concentrations, and some may survive short exposures to *DO* concentrations as low as 1.2 mg/l (at T = 25°C). The percentage of hatching increases with increasing *DO* concentrations. At 3 mg/l *DO*, 40% of the embryos hatched; at 6 mg/l, 65% hatched; and at 9 mg/l, 92% hatched (Kaur & Toot 1978).
V_{10}	NH_3-N(Adult and juvenile)	Experiments show that grass carp enjoy an uniform growth rate in a NH_3-N range between 0.042 and 0.240 mg/l, and also an uniform growth rate for a concentrations between 0.306 and 0.414 mg/l, but there are notable growth differences when concentration is below or above 0.240 mg/l. thus, ammonia toxicity affects are present for concentrations $>$0.240 mg/l (Zhu et al. 1995). The 24 h LC_{50} (50% lethal concentration) of silver carp and big-head carp is 0.46 mg/l and 0.91 mg/l, respectively (Lei & Jin 1979). Experiments show that the 96 h LC_{50} of 1.73 cm, 2.62 cm, and 7.07 cm grass carp is 0.469 mg/l, 1.325 mg/l, 1.386 mg/l, respectively (Zhou 1986).

Copyright © 2006 Taylor & Francis Group plc, London, UK

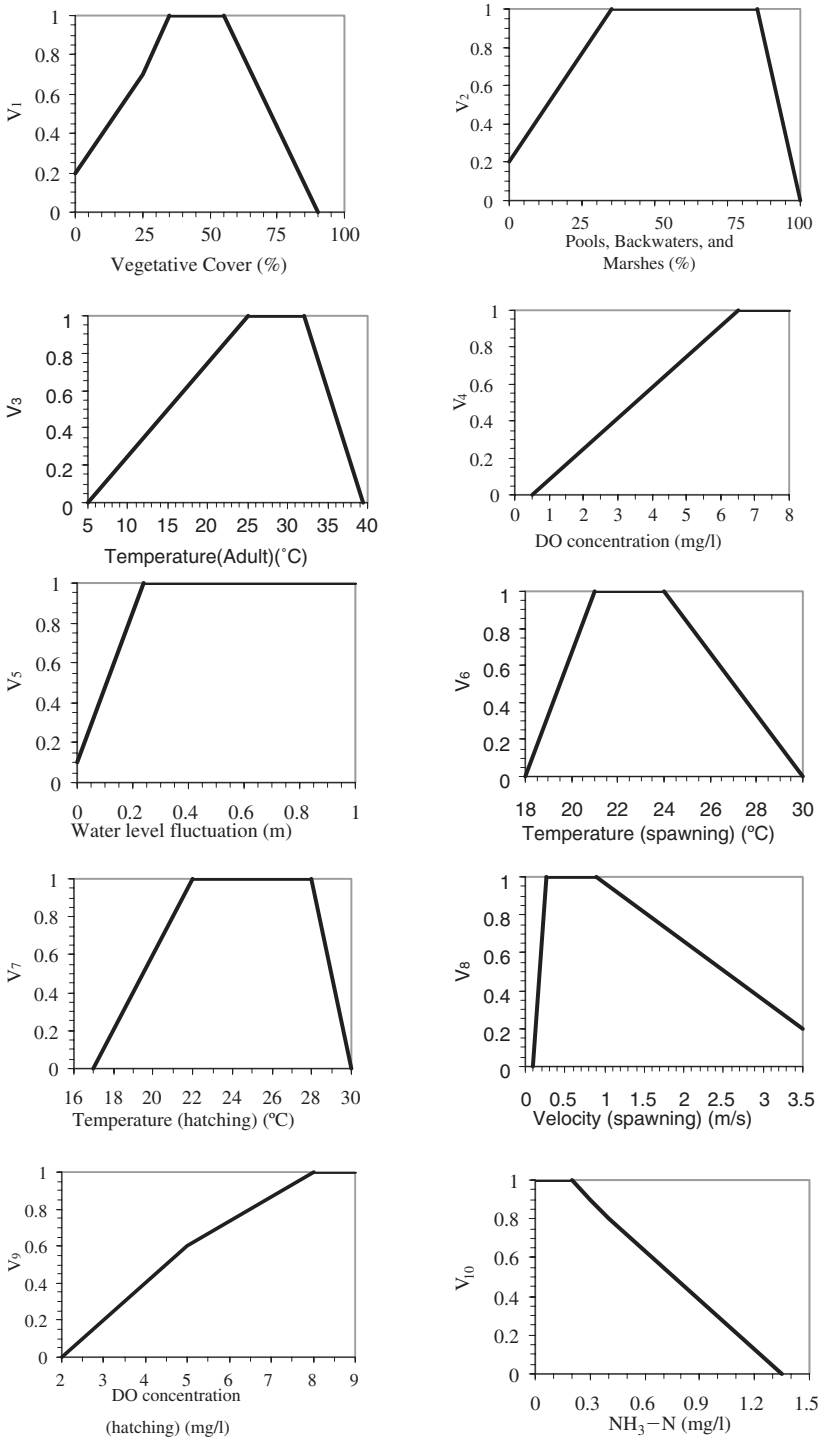


Figure 2. Suitability index curves for habitat of the four major Chinese carp species.

Copyright © 2006 Taylor & Francis Group plc, London, UK

Table 2. Reproduction suitability index.

Daily stage fluctuation (m)	V_5	Spawning temperature (°C)	V_6	Hatching temperature (°C)	V_7	Hatching flow velocity (m/s)	V_8	Hatching *DO* (mg/L)	V_9	C_R	Flux of fry (10^7 offal)
0.24	1.00	21.2	1	21.1	0.82	1.59	0.79	7.99	1	0.92	156.67
0.17	0.77	22.4	1	22.4	1	1.96	0.67	7.35	0.91	0.86	11.82
0.35	1.00	20.5	0.87	20.6	0.72	1.4	0.85	7.57	0.94	0.87	72.18
0.28	1.00	21.3	1	21.3	0.86	1.4	0.85	7.57	0.94	0.93	191.53
0.28	1.00	20.4	0.84	20.5	0.7	1.54	0.8	7.64	0.95	0.85	73.13
0.12	0.55	21.2	1	21.6	0.92	1.68	0.76	7.64	0.95	0.82	34.80
0.16	0.73	23.1	1	22.4	1	1.8	0.72	7.64	0.95	0.87	85.08
0.12	0.55	21.6	1	21.6	0.92	1.35	0.86	7.57	0.94	0.84	31.08
0.36	1.00	21.4	1	21.6	0.92	1.5	0.82	7.57	0.94	0.93	206.61
0.30	1.00	19.5	0.6	21.2	0.84	1.36	0.86	7.45	0.93	0.83	58.43
0.15	0.70	21.3	1	22.7	1	1.74	0.74	7.43	0.92	0.86	68.36
0.27	1.00	20.5	0.87	20.6	0.72	1.34	0.87	7.38	0.92	0.87	53.98
0.29	1.00	20.8	0.95	21.1	0.82	1.77	0.73	7.38	0.92	0.88	68.68
1.05	1.00	21.1	1	21.1	0.82	1.24	0.89	7.57	0.94	0.93	8.90
1.06	1.00	23.5	1	22.5	1	1.84	0.71	7.57	0.94	0.92	3.84

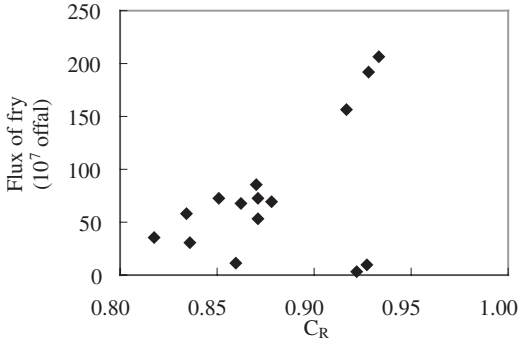


Figure 3. Relation between flux of carp fry and the calculated habitat suitability index for reproduction (C_R) at Jianli.

4 VALIDATION

The reproduction component is validated using 15 groups of sample data during 1997–2003 at Jianli station. The reproduction suitability index is validated by the flux of fry. The results are listed in Table 2.

Figure 3 shows the relation between the calculated *HSI* and flux of carp fry. The flux of carp fry increases with the index *HSI*. It seems that the flux of fry increases linearly with *HSI* as *HSI* is larger than 0.8.

5 CONCLUSIONS

Human activities change the river and ecological environment, reduce aquatic biodiversity, and influence aquatic organisms. Habitat evaluations of rivers and streams have become important tools for estimation of the amount of habitat that is available for a given species within a study reach as a function of flow.

In this paper, the main species of economic value for fresh water fishery in the Yangtze River-four Chinese carp are studied. Ten aquatic eco-factors, which mainly influence the habitat of four major Chinese carp, are selected for the modeling. The suitable ranges of 10 main eco-factors for carp are determined and the Suitability Index (SI) curves of each eco-factor for these species are developed. By analyzing these eco-factors, a habitat assessment model is developed, which combines these factors and can be used for assessing habitat changes due to human activities or hydraulic processes. The validation result shows that the relation between calculate HSI for reproduction and adult carp fry flux is evident.

ACKNOWLEDGEMENT

The study is supported by the 973 program of the Ministry of Science and Technology of China (2003CB415206).

REFERENCES

Bovee, K. D. 1986. Development and evaluation of habitat suitability criteria for use in the instream flow incremental methodology. *US Fish and Wildlife Service, Instream Flow Information Paper No. 21, Biologic Report*. 86(7).

Cao, W. X., Yu, Z. T. & Xu, Y. X. 1987. The influence of Three Gorges project on fish resources in Yangtze River and multiplication approach. *The transaction of the influence of Three Gorges project on ecology and environment and countermeasures*. Beijin. Science Pro.: 2–20(in Chinese).

Copyright © 2006 Taylor & Francis Group plc, London, UK

Cui, Y. B., Chen, S. L. & Wang S. M. 1995. Effect of Temperature on the Energy Budget of the Grass Carp, Ctenopharyngodon Idellus Val, *Oceanologia et Limnologia Sinica.* 26(2): 169–174. (in Chinese)

Davis, J. C. 1975. Minimal dissolved oxygen requirements of aquatic life with emphasis on Canadian species: A review. *J. Fish. Res. Board Can*. 32(12):2295–2332.

Edwards, E. A. & Twomey, K. 1982. Habitat Suitability Index Models: Common Carp. *Biological Services Program and Division of Ecological Services*.:3–4, 13–16.

Hover, R. J. 1976. *Vertical distribution of fishes in the central pool of Eufaula Reservoir, Oklahoma*. M.S. thesis, Oklahoma State Univ. Stillwater. 72.

Hudson, H. R., Byrom, A. E. & Chadderton, W. L. 2003. A critique of IFIM – instream habitat simulation in the New Zealand context. *Science for Conservation*: 231. Department of Conservation, Wellington, New Zealand.

Huet, M. 1970. *Textbook of fish culture: breeding and cultivation of fish. Fishing News* (Books) Ltd., London.: 436.

H. Y. Tang, Z. T. Yu, et al. Sinking speed and loss rate of drifting spawn in Dangjiangkou Reservoir. *Reservoir Fisheries* , 1996, (4):25–27, 43.

Itazawa, Y. 1971. An estimation of the minimum level of dissolved oxygen in water required for normal life of fish. *Bull. Jap. Soc. Sci. Fish*. 37(4): 273–276.

Jorde, K. 1996. Ecological Evaluation of Instream Flow Regulations Based on Temporal and Spatial Variability of Bottom Shear Stress and Hydraulic Habitat Quality. *Proceedings, 2nd International Symposium on Habitat Hydraulics, Ecohydraulics 2000.* Quebec City, Canada. B: 163–174.

June, F. C. 1977. Reproductive patterns in seventeen species of warmwater fishes in a Missouri River reservoir. *Env. Biol. Fish*. 2(3): 285–296.

Kallemeyn, L. W. & Novotny, J. F. 1977. Fish and fish food organisms in various habitats of the Missouri River in South Dakota, Nebraska, and Iowa. *USDI Fish and Wildl. Serv., FWS/OBS-77/25*: 100.

Katopodis, C. 2003. Case Studies of Instream Flow Modelling for Fish Habitat in Canadian Prairie Rivers. *Canadian Water Resources Journal.* 28(2): 199–216.

Large fresh water fish species in China- black carp, *China Fishing*, 2006, 2:36–39.

Laur, K. & H. S. Toor. 1978. Effect of dissolved oxygen on the suivival and hatching of eggs of scale carp. *Prof. Fish-Cult*. 40(1):35–37.

Lei, Y. Z. & Jin, S. D. 1979. Primary Test of Ammonia Toxicity to fry. *Fresh-water fishery of Liaoning*. (3): 11. (in Chinese)

Ligon, F. K., Dietrich, W. E., and Trush, W. J. 1995. Downstream Ecological Effects of Dams. *Bioscience*, 45(3): 183–192.

Li, S. F. 2001. *A Study on Biodiversity and its Conservation of Major Fishes in the Yangtze River*. Shanghai Sci. & Tec. Publ. (in Chinese)

May, B. E. & Gloss, S. P. 1979. Depth distribution of Lake Powell fishes. *Utah Div. Wildl. Res. Publ.* 78–1: 19.

McCrimmon, H. R. 1968. Carp in Canada. *Fish Res. Board Can. Bull.* 165: 93.

McCully, P. 1996. *Silenced Rivers – the Ecology and Politics of Large Dam.* Zed Books, London.

Pflieger, W. L. 1975. *The fishes of Missouri.* Missouri Dept. Conserv. Jefferson City. 343.

Schmulbach, J. C., Gould, G. & Groen, C. L. 1975. Relative abundance and distribution of fishes in the Missouri River. Gavins Point Dam to Rulo, Nebraska. *Proc. S. Dak. Acad. Sci*. 54:194–222.

Schneider, M. 2001. Habitat-und Abflussmodellierung für Fließgewässer mit unscharfen Berechnungsansätzen – Weiterentwicklung des Simulations models CASIMIR.

Schneider, M. & Jorde, K. 2006. Use of Fuzzy Logic in Fish Habitat Modeling: A New Approach Incorporation Imprecise Expert Knowledge. *River Research and Applications.* (under review)

Sigler, W. F. 1955. An ecological approach to understanding Utah's carp populations. *Utah Acad. Sci. Arts Letters Proc*. 32:95–104.

Sigler, W. F. 1958. The ecology and use of carp in Utah. *Utah State Univ. Agric. Exp. Sta. Bull*. 405: 63.

Steffler, P. & Waddle, T. 2002. Mesh generation program for River2D two-dimensional depth averaged finite element: introduction to mesh generation and user's manual. *University of Albert, Edmomton, Canada.*: 31.

The technology report of fish resources and environment monitoring. 2004. The Three Gorges Project ecology and environment monitoring system: 5(in Chinese).

Wang, Q. 2003. Main factors influence the embryo of the four major Chinese carps. *Cultivation and Feedstuff*. (5): 29–30. (in Chinese).

Wang, Z. Y. & Lee, H. W. 2004. *Integrated River Management*. Textbook for PhD. students: 321.

Xiong, Y. C. 2003. Knowledge cathedra of fish nutrition, ninth class, fish habits type and food choice. *Fishery Guide to be Rich*. (9): 53–54. (in Chinese)

Yang, W. L. 1996. The relationship between water temperature and fish culture. *Henan Agriculture*. (11):17. (in Chinese)

Yashouv, A. 1956. Problems of carp nutrition. *Bamidgeh* 8(5):79–87.

Yih, P. L. & Liang, T. S. 1964. Natural conditions of the spawning grounds of the "domestic fishes" in Yangtze River and essential external factor for spawning. *Acta Hydrobiologica Sinca*. 5(1): 1–15. (in Chinese)

Zhang, J. J. & Fan C. H. 2004. Aquiculture should pay attention to water temperature and water quality. *Fishery Guide to be Rich.*: 27. (in Chinese)

Zhou, Y. X. 1986. The Acute Toxicity and Subacute Toxicity of Ammonia to Grass Carp. *Acta Hydrobiologica Sinca*. 10(1): 32–38. (in Chinese)

Zhu, Y., Wu, S. J., & Hua, D. 1995. The Harmful Effect of the Ammonia on the Growth of Grass Carp (Ctenopharyngodon Idellus). *Journal of Fisheries of China*. 10(2): 177–179. (in Chinese)

Copyright © 2006 Taylor & Francis Group plc, London, UK

Influence of flow and sediment inputs on channel sediment delivery ratio: An example of the Yichang – Hankou Reach, Yangtze River, China

J.X. Xu
Institute of Geographical Sciences and Natural Resources Research, Chinese Academy of Sciences, Beijing, China

ABSTRACT: The channel sediment delivery ratio (*SDR*) of the Yichang – Wuhan reach in the middle Yangtze River has been determined using the concept of sediment budget at channel-reach scale, based on which the variation in *SDR* from 1956–1997 has been studied in response to the variation in sediment load and flow inputs. The *SDR* showed a increasing overall trend, but its variation can be divided into 4 stages: (1) increased rapidly from 1955 to 1962; (2) still increased from 1963 to 1975, but the rate of increase became slower; (3) rapidly decreased from 1976 to 1979; and (4) increased rapidly from 1980 to 1997. Some indices describing flow and sediment load characteristics have been related to the *SDR*, and then a multiple regression equation has been established between *SDR* and these influencing factors. The multiple regression equation indicates that channel sediment delivery ratio of the Yichang-Hankou# river reach increases with the increases in river flow and the ratio of the sediment diverted from the three outfalls, and decreases with the increases in the suspended load at Yichang station, the ratio of the flow diverted from the three outfalls and the flood discharge at Yichang station.

1 INTRODUCTION

Erosion, transport and deposition are basic processes in a fluvial system (Schumm, 1977). The relation of the three processes or three components can be generalized by the concept of sediment budget (Dietrich & Dunne, 1978; Trimble, 1981), namely, for a given fluvial system, the sediment yield equals the sum of erosion amount from all sources minus the sum of sediment deposition or storage within the system. Because a fluvial system may be divided into two sub-systems, hillslope system and river channel system, sediment delivery can also be differentiated into two coupled components. Thus, sediment budget can be established for these two sub-systems separately, and so can be the sediment delivery ratio. Under this consideration, Xu has established the channel sediment budget for the channel of lower Yellow River (Xu, 2002) and studied the channel sediment delivery ratio (Xu, 2003). Much study has been made for the sediment transport and deposition in the middle reaches of theYangtze River (Li & Ni, 1998; Li et al., 2000a; Li et al., 2000b; Xu, 2005), but channel sediment delivery ratio has not yet been involved. The present study will deal with channel sediment delivery ratio in response to the variations in flow and sediment load imposed by the upper drainage basin.

2 OUTLINES OF THE STUDIED RIVER REACH, DATA SOURCE AND METHOD

Yichang, above which the drainage area of the Yangtze River is 100.5 million km^2, is the dividing point between the upper and middle reaches of the Yangtze River (Fig. 1) and controls the river flow and sediment load from the upper to the middle Yangtze River. The mean annual water discharge is 13883 m^3/s at Yichang station, and suspended sediment load is 500.94 million tons, respectively. Below Yichang, the river leaves mountainous areas and enters a vast alluvial plain known as the Middle and Lower Yangtze River Plain. The Yichang-Wuhan reach may be divided into four sub-reaches according to channel morphology: (1) The sub-reach from Yichang to Zhicheng is a single channel, locally confined by terraces and bedrock hills. In this sub-reach, the transition from a gravel bed to a sand bed occurs. (2) The sub-reach from Zhicheng to Ouchikou, known as upper Jingjiang, 168 km in length, is a meandering channel, with some alluvial islands appearing occasionally. (3) The sub-reach from Ouchikou to Chenglingji, known as lower Jingjing, 170 km in length, is a typical meandering channel. Natural bend neck-cutoffs occurred frequently. (4) The sub-reach from Chenglingji to Wuhan has an "island" channel pattern, namely, some stable mid-channel

Copyright © 2006 Taylor & Francis Group plc, London, UK

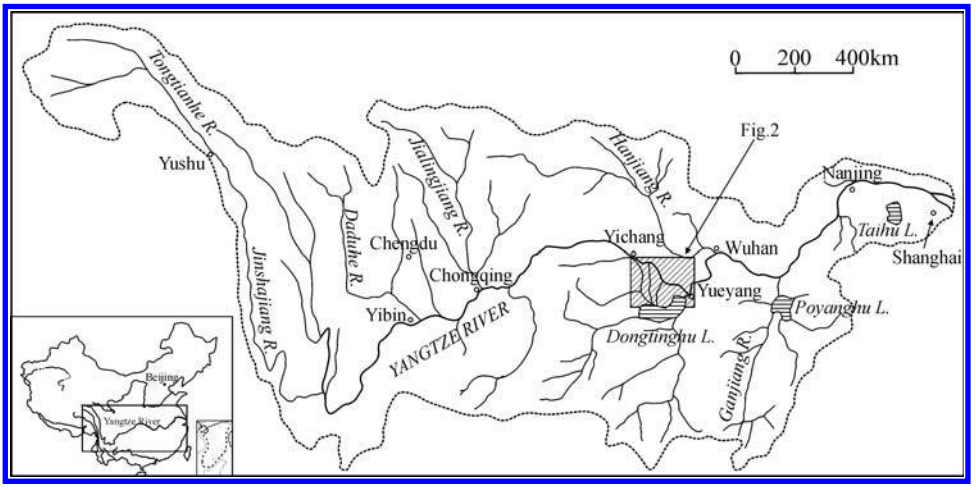


Figure 1. A diagram of the studied river reach.

alluvial islands are well developed, the surface height of which is roughly the same as floodplain, separating the channel to a multi-thread one.

The Lower Jingjiang is characterized by frequent occurrence of natural bend neck-cutoffs in history. In 1967 and 1969, two bend neck-cutoffs were induced by man, at Zhongzhouzi and Shangchewan, to improve the navigation channel. In 1972, a natural cutoff occurred at Shatanzi. Due to these three cutoffs, the length of the river was reduced by 78 km, and the channel sinuosity of the lower Jingjiang decreased from 3.0 to 2.0. These cutoffs significantly increased the local channel slope, and therefore enhanced the river's sediment carrying ability, resulting in degradation below the point at which the cutoff occurred. The lowering of bed due to scour may cause backward erosion upstream from the cutoff point, also resulting in bed degradation. The increased sediment load due to upstream degradation may cause sediment deposition downstream the scoured reach. Thus, the occurrence of cutoffs induced strong channel adjustment, which may have some influence on channel sediment budget in the Yichang-Wuhan reach.

Due to the coupling between the Yangtze River and the Dongtinghu Lake (Fig. 2), the channel sediment budget of the Yichang-Wuhan reach is complicated. Between the mainstem of the upper and lower Jingjiang reaches and the Dongtinghu Lake, a channel network of distributaries developed in history, and thus the mainstem of Jingjiang, the distributary channels and the Dongtinghu Lake constitute a coupled system, known as "river-lake coupled system". This system has a great influence on channel sediment budget. Part of the sediment load from the upper Yangtze River is diverted through the distributaries to the Dongtinghu Lake and deposited there, significantly reducing the sediment load of the main stem downstream. High artificial levees were built along both banks of the Jingjiang River in history, for flood protection. To release the flood of the main stem to the distributaries in case an abnormal flood occurs, some "gaps" were left on the levee. In history, there were many such "gaps", but by 1954, only four remained, known as "Four outfalls" in Chinese, known as Songzhi, Taiping, Ouchi and Tiaoxian. In 1959, a sluice gate was built at Tiaoxian, and in 1970, the sluice gate was closed, and since then only 3 outfalls were left. There is a waterway linking the Dongtinghu Lake and the Yangtze River. The water of the Lake, including the water from the rivers emptying to the lake and from the three outfalls, may flow to the Yangtze River main stem though this waterway which is gauged at Chenglingji hydro-metric station. The Hanjiang River, a major tributary of the Yangtze River, joins the main stem near Hankou. The flow and sediment load of the Hanjiang to the Yangtze main stem is measured at Xiantao station. As long-term data are not available at Xiantao station, the flow and sediment loads measured at Huangzhuang station are used to represent the loads to the Yangtze main stem. Hankou station just in Wuhan on the Yangtze is the end of the Yichang-Wuhan reach, and the flow and sediment loads measured at this station are the outputs of flow and sediment load of the studied reach. Additionally, another tributary, the Qingjiang River joins the main stem near Yidu. The flow and sediment load from the Qingjiang River to the Yangtze River account for only 1.7% and 0.4% of the loads of the Yangtze measured at Yichang station (Li and Ni, 1998), and thus,

Copyright © 2006 Taylor & Francis Group plc, London, UK

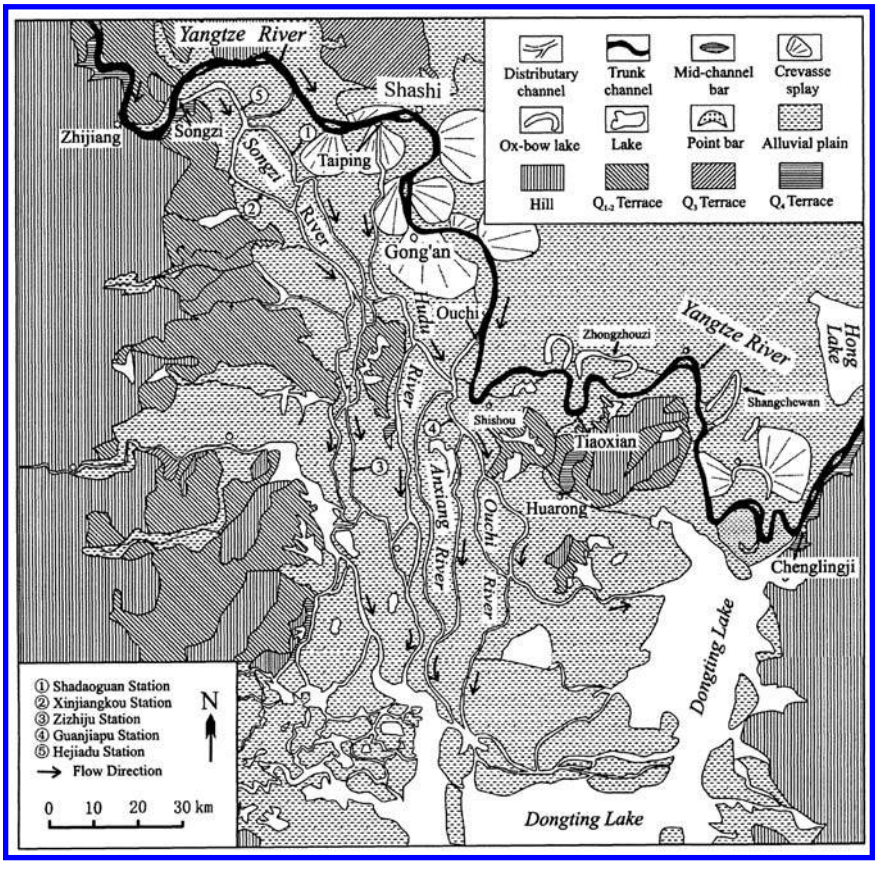


Figure 2. The relationship between the Yangtze River and the Dongtinghu Lake.

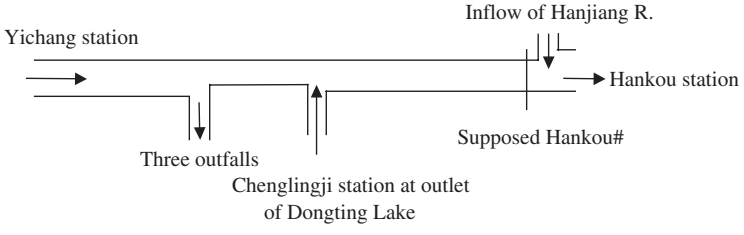


Figure 3.

they are not taken into account. The sediment input and output for the Yichang-Wuhan reach are generalized as Fig. 3.

In terms of sediment budget concept, the following can be written for the Yichang-Hankou# reach:

The sediment storage of the Yichang-Wuhan reach = Σsediment input – Σ sediment output, or

$$S_{Y\text{-}H}=(Q_{s,Yichang}+Q_{s,Chenglingji}+Q_{s,Huangzhuang})-(Q_{s,3outfalls}+Q_{s,Hankou}) \quad (1)$$

where S_{Y-H} is the sediment storage in the Yichang-Wuhan reach, $Q_{s,Yichang}$ is annual suspended sediment load at Yichang station, representing the sediment input to the studied river reach from the upstream drainage basin of the upper Yangtze River. $Q_{s,Hankou}$ is annual suspended sediment load at Hankou station, representing the sediment load output from the studied river reach. $Q_{s,Chenglingji}$ is annual suspended sediment load at Chenglingji station, representing sediment load from the Dongtinghu Lake to the Yangtze

Copyright © 2006 Taylor & Francis Group plc, London, UK

River. $Q_{s,Huangzhuang}$ is mean annual suspended load at Huangzhuang station, representing the sediment inflow from the Hanjiang River to the river reach. $Q_{s,3outfalls}$ is the sum of annual suspended loads measured at the three outfalls, i.e., Songzhikou, Taipingkou, and Ouchikou, representing the sediment load outflow from the Yangtze main stem to the Dongtinghu Lake. The unit for all the variables is 10^4 t/yr.

As the confluence between the Hanjiang and Yangtze Rivers is just above Hankou station, the sediment load inflow from the Hanjiang River immediately flows out of the studied river reach and therefore basically has no influence on sediment deposition in the studied river reach. Thus, for simplicity, we introduce a supposed control point just above the Hanjiang-Yangtze confluence, which is called Hankou#, as the end of the Yichang-Wuhan reach. After doing so, the sediment load from the Hanjiang River may be excluded when considering the channel sediment storage in the Yichang-Hankou# reach. The sediment load ($Q^{s,Hankou\#}$) at Hankou# can be calculated as the sediment load at Hankou station on the Yangtze River minus that at Huangzhuang station on the Hanjiang River. Thus, the sediment storage of the Yichang-Hankou# reach can be written as follows:

$$S_{Y\text{-}H\#} = \Sigma \text{ sediment input} - \Sigma \text{ sediment output} = (Q_{s,Yichang} + Q_{s,Chenglingji} - Q_{s,3outfalls}) - (Q_{s,Hankou} - Qs,Huangzhuang) \quad (2)$$

And therefore, the channel sediment delivery ratio ($SDR_{Y-H\#}$) of the Yichang-Hankou# reach can be expressed as

$$SDR_{Y\text{-}H\#} = (\Sigma \text{ sediment output})/ \Sigma \text{ sediment input} = Q_{s,Hankou} - Q_{s,Huangzhuang})/(Q_{s,Yichang} + Q_{s,Chenglingji} - Q_{s,3outfalls}) \quad (3)$$

The annual sediment delivery ratio of the Yichang-Hankou# river reach has been calculated using Equation (3). All the data involved are from the relevant hydro-metric stations, as mentioned above. It should be pointed out that the sediment budget established in this study is only for suspended sediment load, with bed-load ignored, because no bed-load data are available, as is the case for most rivers in the world. The studied river reach has sand-bed, and thus bed-load transport rate is rather low, compared with suspended load. According to some incomplete measurements made at Yichang station, the ratio of bed-load to suspended load is only 1%–2% (Institute of Geography, Chinese Academy of Sciences and Yangtze River Institute of Water Conservancy and Hydro-power Research, 1985). Thus, ignoring bed load does not make much difference.

After annual sediment deposition is determined, it is further related to the variables of river flow and sediment load of the studied river reach using empirical statistical approaches, to elucidate the response of sediment deposition to the changing river flow and sediment load input.

The indices of flow and sediment load that are used in the present study are as follows: (1) Annual river flow ($Q_{w,Yichang}$) and suspended load ($Q_{s,Yichang}$) and mean suspended sediment concentration ($C_{mean,\ Yichang}$) at Yichang station; (2) Annual flow ($Q_{w,3outfalls}$) and suspended load ($Q_{s,3outfalls}$) flowing to the Dongtinghu Lake through the three distributaries, represented by the sum of river flow or suspended load at the stations on Eastern Songzhihe, Western Songzhihe, Huduhe, Anxianghe and Ouchihe Rivers; the mean suspended sediment concentration ($C_{mean,3outfalls}$) of the distributed river flow is also used, calculated as $C_{mean,3outfalls} = Q_{s,3outfalls}/Q_{w,3outfalls}$. (4) Annual river flow ($Q_{w,Chenglingji}$) and suspended load ($Q_{s,Chenglingji}$) and mean suspended sediment concentration ($C_{mean,Chenglingji}$) at Chenglingji station, representing the features of the water and sediment flowing from the Dongtinghu Lake to the Yangtze main stem.

3 RESULTS

3.1 *Temporal variations in the components of channel sediment budget and sediment delivery ratio*

As pointed out earlier, the components of channel sediment budget for the Yichang-Hankou# reach include sediment input at Yichang station ($Q_{s,Yichang}$), the sediment load outflow from the Yangtze main stem to the Dongtinghu Lake ($Q_{s,3outfalls}$), the sediment input from the Dongting Lake at Chenglingji station ($Q_{s,Chenglingji}$), and sediment output at the end of the reach, Hankou# ($Q_{s,Hankou\#}$). The temporal variations of the 4 variables have been shown in Fig. 4.

Fig. 4a shows that the temporal variation in annual suspended load at Yichang station may be divided into two stages. From 1951 to 1979, although there were some fluctuations, no overall trend can be seen. However, from 1980 to 1997, a clear decreasing trend appeared. This decreasing trend may be related to two factors. The implementation of soil and water conservation measures and the building of large numbers of reservoirs and checkdams since the 1980s reduced the sediment supply to the Yangtze River. The Gezhouba Reservoir, located above Yichang and used for water storage since 1983, also reduced the sediment input of the studied river reach.

The sediment diversion through distributaries expressed by $Q_{s,3outfalls}$ showed a clear decreasing trend. The sediment outflow at Hangkou# ($Q_{s,Hankou\#}$) showed an increase with time and reached a peak around 1980, followed by a decline. The increase in

Copyright © 2006 Taylor & Francis Group plc, London, UK

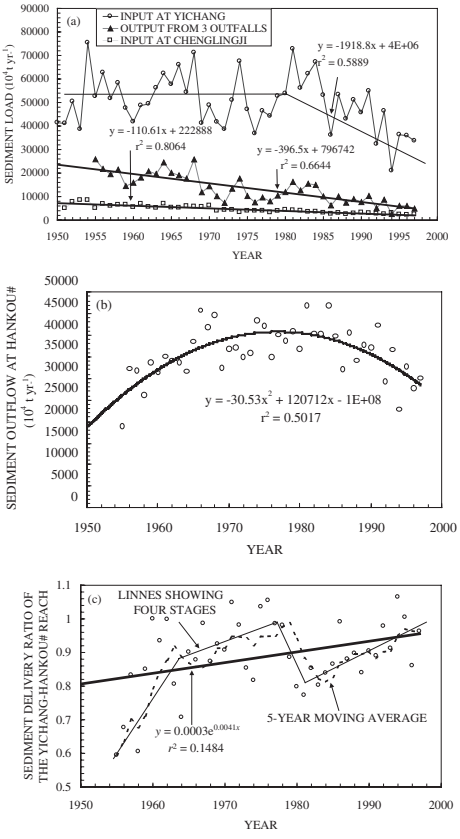


Figure 4. Temporal variations in four components of the channel sediment budget of the Yichang- Hankou# reach.

(a) Inflow sediment at Yichang station ($Q_{s,Yichang}$), outflow sediment through "three outfalls" ($Q_{s,3outfalls}$) and inflow sediment from the Dongting lake ($Q_{s,Chenglingji}$)
(b) Sediment outflow at Hankou#
(c) Sediment delivery ratio of the Yichang-Hankou# reach.

sediment outflow during the period 1955–1979 may be related with the increase in $Q_{s,3outfalls}$, which led to a relative increase in the "net" input of sediment, and also with the man-made bend neck-cutoffs, which enhanced the sediment carrying ability of the river and thus, more sediment could be transported to the end of the river reach. The increase in $Q_{s,Hankou\#}$ after 1980 result from the decrease in the sediment input at Yichang station.

The temporal variation in channel sediment delivery ratio ($SDR_{Y-H\#}$) of the Yichang-hankou# reach has been plotted in Fig. 4c. As an overall tendency, $SDR_{Y-H\#}$ increased with time T, and the correlation coefficient between $SDR_{Y-H\#}$ and T is 0.385, significant at a level of $p < 0.01$. However, the 5-year moving average indicates that the variation in $SDR_{Y-H\#}$ can be divided into 4 stages. From 1955–1962, it increased

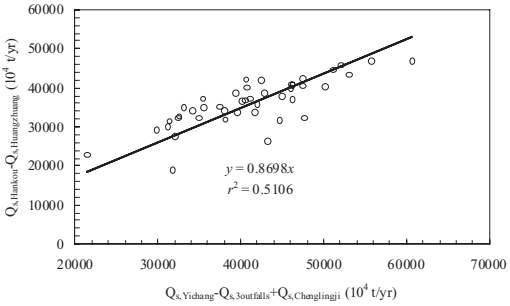


Figure 5. The relationship between the annual input ($Q_{s,Yichang} + Q_{s,3outfalls} + Q_{s,Chenglingji}$) and output ($Q_{s,Hankou} - Q_{s,Huangzhuang}$) sediment of the the Yichang-Hankou# river reach.

rapidly. From 1963–1975, it also increased, but the rate of increase decreased. From 1976–1979, it declined rapidly, but from 1980–1997, it increased rapidly. The relationship between sediment input and output of the Yichang-Hankou# reach is shown in Fig. 5, where the regression equation is given as: Annual sediment output $= 0.8698 \times$ Annual sediment input.

3.2 *Sediment delivery ratio of the Yichang-Hankou# reach as influenced by sediment load and river flow conditions*

As the sediment input and output of the studied river reach were different in the periods before and after 1980, and so was the sediment delivery ratio. Thus, the period 1955–1997 was divided into two stages, 1955–1979 and 1980–1997, in the following study.

3.2.1 *Influence of flow conditions*

The flow conditions include the annual flow at Yichang station ($Q_{w,Yichang}$), the annual outflow through "three outfalls" ($Q_{w,3outfalls}$) and its ratio ($R_{w,div}$) to the total flow at Yichang, and the annual flood discharge ($Q_{max,Yichang}$) at Yichang. The $SDR_{Y-H\#}$ has been plotted against $Q_{w,Yichang}$, $Q_{w,3outfalls}$ and $Q_{max,Yichang}$ in Fig. 6, where the periods 1955–1979 and 1980–1997 are distinguished by different symbols. The figure shows that in all the four plots the correlation for the period 1980–1997 is much closer than that for the period 1955–1979. This can be related to the human impacts, especially to the man-made bend neck-cutoffs in the lower Jingjiang River in 1967 and 1969. Afterwards, the river length was reduced by 78 km, and the channel sinuosity decreased from 3.0 to 2.0 (Lu, 1996). The resultant strong scour lowered the elevation of river bed of the Yangtze main stem near the "three outfalls", which means a relative rise of the river bed of the distributaries. As a result, less floodwater could flow out of the main stem to the Dongtinghu

Copyright © 2006 Taylor & Francis Group plc, London, UK

Lake. The yearly lowest water stage at Shashi station was used as an index to reflect the elevation of river bed (Xu, 2005). From 1950 to 1967, although there were some fluctuations, no trend of declining in the yearly lowest water stage at Shashi station can be seen. Afterwards, it declined rapidly. It became stable again around 1980. Obviously, it is the man-made bend neck-cutoffs in 1967 and 1969 that resulted in strong scour, and therefore the lowering of water stage (Xu, 2005).

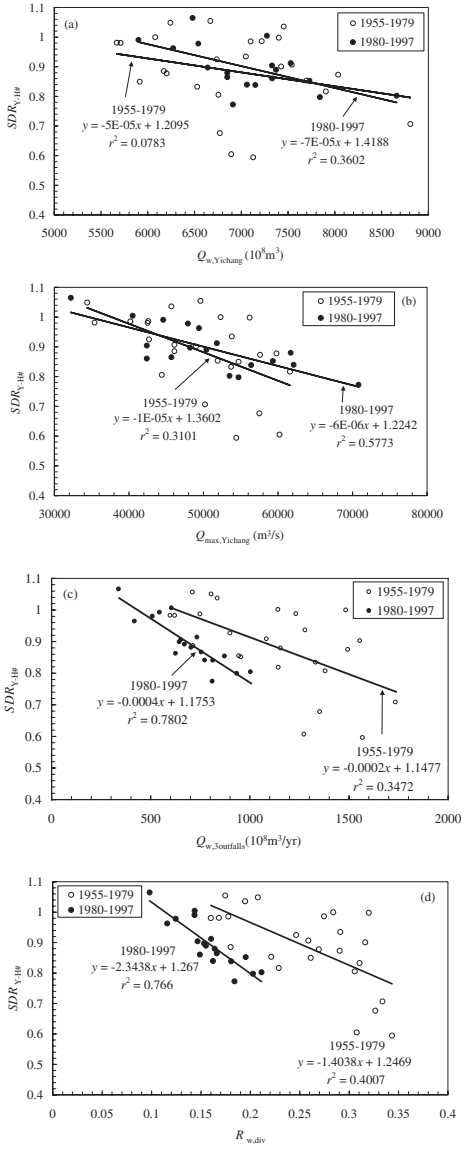


Figure 6. The relationships of sediment delivery ratio ($SDR_{Y-H\#}$) of the Yichang-Hankou# river reach with annual river flow ($Q_{w,Yichang}$) (a) and flood discharge ($Q_{max,Yichang}$) (b) at Yichang station and the water diversion ($Q_{w,3outfalls}$) (c) from the 3 outfalls and its ration ($R_{w,div}$) (d) to the river flow at Yichang station.

Fig. 6a shows that the correlation coefficient between $SDR_{Y-H\#}$ and $Q_{w,Yichang}$ is much higher than that between $SDR_{Y-H\#}$ and $Q_{max,Yichang}$. For the period 1980–1997, the $SDR_{Y-H\#} - Q_{max,Yichang}$ squared correlation coefficient (r^2) is 0.5773, much larger than the critical r^2 at $p < 0.01$, 0.1546. The r^2 of $SDR_{Y-H\#}$ with $Q_{w,3outfalls}$ and $R_{w,div}$ are even higher, which are 0.7802 and 0.7660 for the period 1980–1997. Thus, the influence of outflow from the three outfalls on channel sediment deliver ratio is larger than those of flood and annual water discharges. This is because the $R_{w,div}$ has a marked decreasing trend (Fig. 7). A decrease in outflow from the three outfalls means a equal increase in the flow in the main stem below the three outfalls, a factor that would result in an increase in sediment carrying ability. In general, sediment carrying ability of the river is proportional with the square of water discharge (Q) (Qian et al., 1987). If the increase in Q is ΔQ, then the sediment transport rate related with Q and ΔQ are aQ^2 and $a(\Delta Q)^2$, respectively, given the state of equilibrium in sediment transport. Here a is a constant. After the increase of ΔQ in water discharge, the discharge becomes $(Q + \Delta Q)$, and the sediment that the river can carry becomes $a(Q + \Delta Q)^2 = aQ^2 + a(\Delta Q)^2 + 2a(Q\,\Delta\,{}^*Q)$, which is larger than the sum of sediment transport related with Q and ΔQ, $aQ^2 + a(\Delta Q)^2$. This implies that if the sediment transport equilibrium exists previously, the sediment carrying ability after the increase in water discharge would exceed the supplied sediment load. Thus, scour may occur. Obviously, this factor may increase the river's sediment delivery ratio, and therefore results in the negative correlation of $SDR_{Y-H\#}$ with $Q_{w,3outfalls}$ and $R_{w,div}$ (Fig. 6c and 6d). In this study, $R_{w,div}$ and $R_{s,div}$ are defined as the ratio of water and sediment outflow from the 3 outfalls to those at Yichang station, respectively.

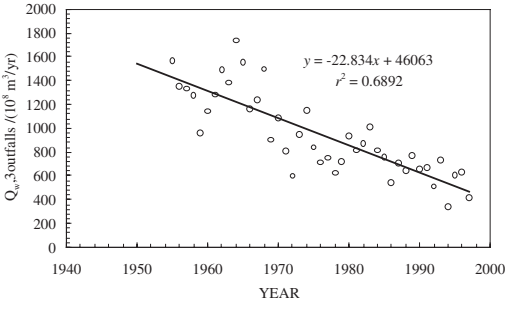


Figure 7. Water diversion ($Q_{w,3outfalls}$) from the 3 outfalls varying with time.

Copyright © 2006 Taylor & Francis Group plc, London, UK

The negative correlation between $SDR_{Y-H\#}$ and $Q_{w,Yichang}$ (Fig. 6b) can be explained by strong sediment deposition induced by overbank flows when large floods occur. As considerable amount of sediment is deposited in floodplain, the sediment transported downstream decreases, leading to a decrease in $SDR_{Y-H\#}$.

3.2.2 *Influence of sediment load*

The annual channel sediment delivery ratio of the Yichang-hankou# reach is positively correlated with annual suspended load at Yichang station (Fig. 8), and the r^2 for the period 1980–1997 is as high as 0.7730.

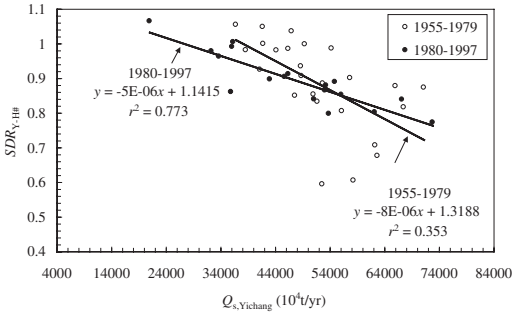


Figure 8. Relationship between sediment delivery ratio ($SDR_{Y-H\#}$) of the Yichang-Hankou# reach and annual sediment load ($Q_{rms,Yichang}$) at Yichang station.

3.3 *Multiple regression analysis*

To establish the relationship between the variation in annual channel sediment delivery ratio ($SDR_{Y-H\#}$) in the Yichang-Hankou# reach and the river's flow and sediment conditions, a multiple regression analysis has been performed. The influencing variables include annual river flow ($Q_{w,Yichang}$ in $10^8 m^3$/yr), annual suspended load ($Q_{s,Yichang}$ in $10^4 t^3$/yr) and annual maximum water discharge ($Q_{max,Yichang}$ in m^3/s) and the ratio ($R_{w,div}$) of annual river flow diverted through the three outfalls to the annual river flow at Yichang station, and the ratio ($R_{s,div}$) of annual suspended load diverted through the three outfalls to the annual suspended load at Yichang station. The multiple regression equations are established for the period 1955–1997 in general, and for the period 1980–1997 in particular. As pointed out earlier, the channel conditions for the periods 1955–1979 and 1980–1997 are different. In the former period, the strong adjustment following the three bend neck-cutoffs that occurred in 1967, 1968 and 1972 was underway, but before the beginning of the latter period, it may be thought that the quasi-equilibrium had been re-established. Thus, the relationship for the period 1980–1997 can be used to represent the situation of the channel at quasi-equilibrium.

The correlation matrix among $SDR_{Y-H\#}$ and all the influencing variables has been calculated for the periods 1955–1979 (Table 1) and 1980–1997 (Table 2). The multiple regression equations have been established for the periods 1955–1979 and 1980–1997,

Table 1. The correlation matrix among $SDR_{Y-H\#}$ and $Q_{w,Yichang}$, $Q_{s,Yichang}$, $Q_{max,Yichang}$, $R_{w,div}$ and $R_{s,div}$ (1955–1997).

	$Q_{w,Yichang}$	$Q_{s,Yichang}$	$R_{w,div}$	$R_{s,div}$	$Q_{max,Yichang}$	$SDR_{Y-H\#}$
$Q_{w,Yichang}$	1.00	0.70	0.40	0.38	0.49	−0.43
$Q_{s,Yichang}$	0.70	1.00	0.53	0.46	0.71	−0.64
$R_{w,div}$	0.40	0.53	1.00	0.97	0.33	−0.50
$R_{s,div}$	0.38	0.46	0.97	1.00	0.33	−0.48
$Q_{max,Yichang}$	0.49	0.71	0.33	0.33	1.00	−0.56
$SDR_{Y-H\#}$	−0.43	−0.64	−0.50	−0.48	−0.59	1.00

Table 2. The correlation matrix among $SDRY - H\#$ and $Q_{w,Yichang}$, $Q_{s,Yichang}$, $Q_{max,Yichang}$, $R_{w,div}$ and $R_{s,div}$ (1980–1997).

	$Q_{w,Yichang}$	$Q_{s,Yichang}$	$R_{w,div}$	$R_{s,div}$	$Q_{max,Yichang}$	$SDR_{Y-H\#}$
$Q_{w,Yichang}$	1.00	0.76	0.82	0.75	0.57	−0.80
$Q_{s,Yichang}$	0.76	1.00	0.86	0.89	0.81	−0.88
$R_{w,div}$	0.82	0.86	1.00	0.97	0.66	−0.88
$R_{s,div}$	0.75	0.89	0.97	1.00	0.68	−0.84
$Q_{max,Yichang}$	0.57	0.81	0.66	0.68	1.00	−0.76
$SDR_{Y-H\#}$	−0.80	−0.88	−0.88	−0.84	−0.76	1.00

Copyright © 2006 Taylor & Francis Group plc, London, UK

respectively. The regression equation based on data from the period 1980–1997 is as follows:

$$SDR_{\text{Y-H\#}} = 1.1863 + 2.5521\times10^{-6}Q_{\text{w,Yicahng}} - 3.5568\times10^{-6}Q_{\text{s,Yichang}} - 3.4159R_{w,\text{div}} + 2.5050R_{\text{s,div}} - 1.1049\times10^{-6}Q_{\text{max,Yichnag}} \quad (4)$$

For the above equation, number of samples $N = 18$, multiple correlation coefficient $R = 0.9394$, the result of F-test is $F = 18.034$, with the probability of significance $p = 0.00003$, and the standard error of estimate is $SE = 0.0321$. The multiple regression equation indicates that channel sediment delivery ratio of the Yichang-Hankou# river reach increases with the increases in river flow and the ratio of the sediment diverted from the three outfalls, and decreases with the increases in the suspended load at Yichang station, the ratio of the flow diverted from the three outfalls and the flood discharge at Yichang station.

Based on data from 1955–1997, the multiple regression equation has been established as follows:

$$SDR_{\text{Y-H\#}} = 1.2824 + 1.2364\times10^{-5}Q_{\text{w,Yichang}} - 3.3434\times10^{-6}Q_{\text{s,Yichang}} - 0.3910R_{w,\text{div}} - 3.8817\times10^{-6}Q_{\text{max,Yichang}} \quad (5)$$

The units for the variables are shown in Table 2. For the above equation, number of samples $N = 43$, multiple correlation coefficient $R = 0.7010$, the result of F-test is $F = 9.18$, with the probability of significance $p = 0.00003$, and the standard error of estimate is $SE = 0.0825$.

It should be pointed out that in the above equation, $R_{\text{w,div}}$ was not selected, because the two variables expressing water and sediment diversion through the three outfalls, $R_{\text{w,div}}$ and $R_{\text{s,div}}$, are closely correlated, the effect of one can be represented by an other. Thus, only $R_{\text{w,div}}$ was selected. Table 1 shows that all the correlation coefficients between $SDR_{\text{Y-H\#}}$ and influencing variables are not high, but the correlation coefficients between $R_{\text{w,div}}$ and $R_{\text{s,div}}$ is very high. If both $R_{\text{w,div}}$ and $R_{\text{s,div}}$ are selected to enter the equation, the quality of the equation would be much lower.

4 CONCLUSIONS

The channel sediment delivery ratio (*SDR*) of the Yichang – Wuhan reach in the middle Yangtze River has been determined using the concept of sediment budget at channel-reach scale, based on which the variation in *SDR* from 1956–1997 has been studied in response to the variation in sediment load and flow inputs. The *SDR* showed a increasing overall trend, but its variation can be divided into 4 stages: (1) increased rapidly from 1955 to 1962; (2) still increased from 1963 to 1975, but the rate of increase became slower; (3) rapidly decreased from 1976 to 1979; and (4) increased rapidly from 1980 to 1997. Some indices describing flow and sediment load characteristics have been related to the *SDR*, and then a multiple regression equation has been established between *SDR* and these influencing factors. The multiple regression equation indicates that channel sediment delivery ratio of the Yichang-Hankou# river reach increases with the increases in river flow and the ratio of the sediment diverted from the three outfalls, and decreases with the increases in the suspended load at Yichang station, the ratio of the flow diverted from the three outfalls and the flood discharge at Yichang station.

ACKNOWLEDGEMENT

The financial support from the National Major Basic Research Program of China (grant number 2003CB415202) is gratefully acknowledged.

REFERENCES

Dietrich, W.E. Dunne, T. 1978. Sediment budget for a small catchment in mountainous terrain., Zeitschrift fur Geomorphologie 29: 191–205.

Institute of Geography, Chinese Academy of Sciences and Yangtze River Institute of Water Conservancy and Hydropower Research, 1985. River Channel Processes of the Middle and Lower Yangtze River. Beijing: Science Press. (in Chinese)

Li, Y.T. Deng J.Y. Sun Z.H. Li R. 2000a. Sediment deposition and variation of flood storage in The Dongtinghu Lake. Journal of Hydraulic Engineering, (12): 48–52. (in Chinese)

Li, Y.T. Li, R. Deng, J.Y. 2000b. A study of sediment transport and flood control in the middle reach of Yangtze River. Journal of Sediment Research, (3):12–20. (in Chinese)

Li, Y.T. Ni, J.R. 1998. Influence of sediment transport on water level elevation in the middle reach of Yangtze River. Journal of Applied Basic Sciences and Engineering, 6(3): 5–11. (in Chinese)

Lu, J.Y. 1996. Study on laws of runoff and sediment diverted from three outfalls on the Jingjiang reach of the Yangtze River. Journal of Sediment Research, (4):54–61. (in Chinese)

Qian, N. Zhang, R. Zhou, Z.D. 1987. River Channel Processes. Beijing: Science Press (in Chinese).

Schumm, S.A. 1977. The Fluvial System. New York: John Wiley & Sons, 1–338.

Trimble, S.W. 1981. Changes in sediment storage in Coon Creek Basin, Driftless Area, Wisconsin, 1853–1975, Science, 214:181–183.

Xu, J.G. 2005. Response of channel sediment budget to flow and sediment inputs: an example of the Yichang – Wuhan reach, Yangtze River, China. Acta Geographica Sinica, 60 (2): 337–348. (in Chinese)

Xu, J.X. 2002. Relation between the erosion and sedimentation zones in the Yellow River, China. Geomorphology, 48(4): 365–382.

Xu, J.X. 2003. A study of sediment delivery by floods in the lower Yellow River, China, Hydrological Sciences Journal, 48(4): 553–566.

Copyright © 2006 Taylor & Francis Group plc, London, UK

Restore water levels in the river channel downstream of the Three Gorges Reservoir: A numerical simulation

G. Zhou, H. Wang, D.D. Jia & X.J. Shao
Dept. of Hydraulic Engineering, Tsinghua University, Beijing, China

ABSTRACT: Among the many physical processes triggered by the impoundment of the Three Gorges Reservoir, the degradation of river channel downstream of the project will develop very quickly in the next few decades. This paper presents results of a numerical study on the effectiveness of proposed measures to reduce bed scour and to maintain water stage during dry seasons, by placing a layer of articulated concrete mattresses on the river bed at several selected locations in a reach 63 km long of the Yangtze River.

1 INTRODUCTION

The Three Gorges Reservoir (TGR) has substantially reduced sediment supply to the downstream river channels since its impoundment in June 2003. Comparison of observed sediment transport rates before and after the impoundment of the Reservoir indicates a significant drop in sediment transport after the impoundment (Figure 1). Numerical simulation results (IWHR & YSRI, 1990, as cited in Lu et al 1997) predicted that, in the first 30 years after its impoundment, the siltation of TGR would cause a 70% reduction in both the average concentration and the total amount of sediment transport downstream of the project, as shown in Table 1. The sediment concentration at the outlet of the reservoir would not recover and restore to its original level until 100 years later, when the reservoir siltation process achieves an equilibrium.

The river bed scour downstream of the Gezhouba Shiplock, located 2 km upstream of the Yichang Station, would be most severe in the next few decades due to the impoundment and siltation of TGR. Lowered water stages at Yichang Station caused by channel degradation could pose a great problem for the navigation traffic trying to get through the Gezhouba shiplocks. The present water level at Gezhouba is already 1 meter lower than the designed operational level, because of the bed scour after the completion of the Gezhouba Dam in 1983 (Lu Yongjun et al 2002). When the operation of TGR introducing another round of bed scour and water stage reduction, the navigation condition at the shiplocks would be worsened and normal traffic could be interrupted more frequently during the dry seasons. Water level drop will also affect the aquatic environments and ecosystem processes in the alluvial channels. In such a case, river training works are usually applied to prevent or stop scour and restore water stages.

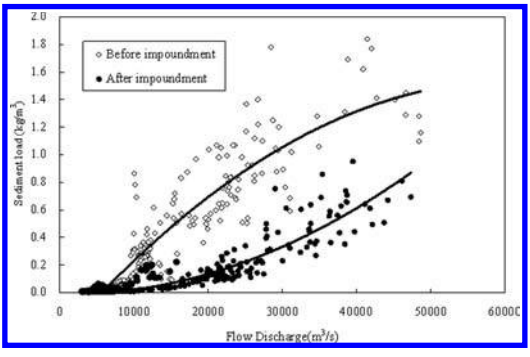


Figure 1. Measured sediment load ~ flow discharge relation at Yichang Station before and after Three Gorges Reservoir impoundment.

The purpose of this study is to evaluate the effectiveness of the proposed engineering measures to maintain water level on this section of the Yangtze River channel. A 2-D numerical simulation model for flow and sediment tansport is used for the calculation.

2 STUDY AREA

This numerical simulation applies a 2-D model to calculate water flow and sediment transport in a channel

Copyright © 2006 Taylor & Francis Group plc, London, UK

Table 1. Predicted water and sediment discharge after impoundment of the Three Gorges Reservoir and comparison with observations before construction of the reservoir.

Years after impoundment (1)	Annually averaged Discharge ($\times 10^3$ m^3/s) Before (2)	After (3)	(3)/(2) (%) (4)	Total sediment transport per year (million tons) Before (5)	After (6)	Sediment concentration kg/m^3 Before (7)	After (8)	(8)/(7) (%) (9)
1–10	14.4	14.0	97.2	556	165	1.22	0.37	30.3
11–20	14.4	13.9	96.5	556	156	1.22	0.36	29.5
21–30	14.4	13.9	96.5	556	178	1.22	0.4	32.8
31–40	14.4	13.9	96.5	556	207	1.22	0.47	38.5
41–50	14.4	13.9	96.5	556	256	1.22	0.58	47.5
51–60	14.4	13.9	96.5	556	323	1.22	0.74	60.7
61–70	14.4	13.9	96.5	556	372	1.22	0.85	69.7
71–80	14.4	13.9	96.5	556	408	1.22	0.93	76.2
81–90	14.4	13.9	96.5	556	420	1.22	0.96	78.7
91–100	14.4	13.9	96.5	556	427	1.22	0.97	79.5

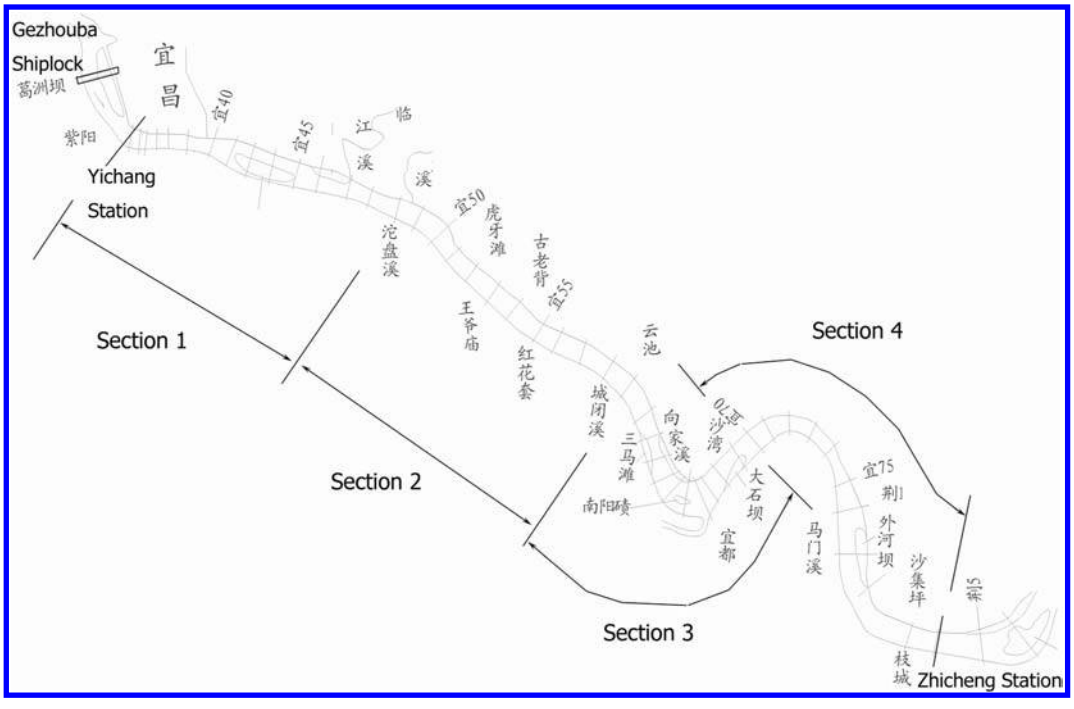


Figure 2. The study area.

section from Yichang Station to Zhicheng Station, with a total length of 63 km (Fig. 2).

In this hilly area, planform of the channel section is mostly straight with a few river bends and major sand bars, as the Yangtze River runs out of the mountainous area into the Great Jiang-han Plain. Within the next few decades, the operation of the Three Gorges Reservoir will dominate the seasonal variation of water stages of the river reach between the City of Yichang and the downstream Zhicheng Station, and will impose a long-term impact on the navigation conditions at Gezhouba Shiplock. Detailed processes of bed degradation caused by such an impact can be predicted using numerical simulations that take into

Copyright © 2006 Taylor & Francis Group plc, London, UK

account the reduction of sediment supply due to the siltation of the TGR. Effectiveness of proposed measures, e.g., increase of bed roughness through bottom pavement methods, can also be estimated and optimized for maintaining water stages during dry seasons ($Q_{min} = 3000\ m^3/s$). Such measures should not create problems for flood control during flood seasons ($Q_{max} = 76000\ m^3/s$).

3 MATHEMATIC MODELS

3.1 *Governing equations for water flow*

Wind-induced surface stresses are ignored in the mathematical model for water flow, and the depth integrated conservation equations can be written as follows:

$$\frac{\partial Z}{\partial t}+\frac{1}{J}\left[\frac{\partial(h_2 q)}{\partial \xi}+\frac{\partial(h_1 p)}{\partial \eta}\right]=0 \tag{1}$$

$$\frac{\partial q}{\partial t}+\beta\left(\frac{1}{J}\frac{\partial(h_2 qU)}{\partial \xi}+\frac{1}{J}\frac{\partial(h_1 pU)}{\partial \eta}-\frac{pV}{J}\frac{\partial h_2}{\partial \xi}+\frac{qV}{J}\frac{\partial h_1}{\partial \eta}\right)$$
$$-fp+\frac{gH}{h_1}\frac{\partial Z}{\partial \xi}+\frac{qg|\vec{q}|}{(CH)^2}=\frac{\nu_e H}{h_1}\frac{\partial E}{\partial \xi}-\frac{\nu_e H}{h_2}\frac{\partial F}{\partial \eta} \tag{2}$$

$$\frac{\partial p}{\partial t}+\beta\left(\frac{1}{J}\frac{\partial(h_2 qV)}{\partial \xi}+\frac{1}{J}\frac{\partial(h_1 pV)}{\partial \eta}+\frac{pU}{J}\frac{\partial h_2}{\partial \xi}-\frac{qU}{J}\frac{\partial h_1}{\partial \eta}\right)$$
$$+fq+\frac{gH}{h_2}\frac{\partial Z}{\partial \eta}+\frac{pg|\vec{q}|}{(CH)^2}=\frac{\nu_e H}{h_2}\frac{\partial E}{\partial \eta}+\frac{\nu_e H}{h_1}\frac{\partial F}{\partial \xi} \tag{3}$$

$$E=\frac{1}{J}\left[\frac{\partial(h_2 U)}{\partial \xi}+\frac{\partial(h_1 V)}{\partial \eta}\right],\quad F=\frac{1}{J}\left[\frac{\partial(h_2 V)}{\partial \xi}-\frac{\partial(h_1 U)}{\partial \eta}\right] \tag{4}$$

$$h_1=\sqrt{\left(\frac{\partial x}{\partial \xi}\right)^2+\left(\frac{\partial y}{\partial \xi}\right)^2},\quad h_2=\sqrt{\left(\frac{\partial x}{\partial \eta}\right)^2+\left(\frac{\partial y}{\partial \eta}\right)^2} \tag{5}$$

where ξ, η are orthogonal curvilinear horizontal coordinates, respectively; h_1, h_2 are Lame coefficients in the ξ, η directions, respectively; U, V are depth-averaged velocity components in the ξ, η directions, respectively; the unit discharge vector is $\rightharpoonup_q = (q, p) = (UH, VH)$, where $q = UH$, $p = VH$; Z is water level relative to the reference plane; H is total depth; β is the correction factor for non-uniformity of the vertical velocity profile, $\beta = 1.016$; f is Coriolis parameter; g is gravitational acceleration; C is Chezy coefficient; ν_e is depth mean effective vortex viscosity; $J = h_1 h_2$ is the Jacobian of ordinates transformation.

A staggered grid system is applied in the model, with Z, C and ν_e located at the center of each grid cell, q, p, U and V at the center of the grid boundary, respectively (Fig. 3). The numerical model uses a finite difference method in the orthogonal curvilinear coordinate system. The finite difference equations corresponding to the differential equations are expressed in an alternating direction implicit form. All the discretization procedures use a second-order central difference

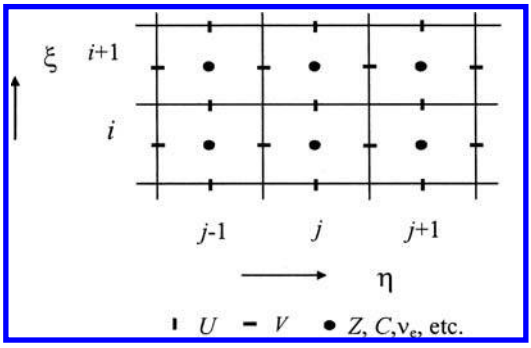


Figure 3. The staggered grid system.

scheme, except the time differentials of water level in the continuity equation which use a forward difference scheme. For the advective accelerations in the momentum equations, a combination of the first-order upwind scheme and second-order central difference is applied.

The computational domain has a total of 385 × 29 grids in an orthogonal curvilinear coordinate system (Fig. 4).

In the longitudinal direction, the grid steps vary within a range of 100 m∼200 m, with an average value of 150 m. In the lateral direction the grid size varies from 24 m to 40 m, with a mean value of 32 m.

Measured contour of the channel section dated October 1998 was used in this study as the initial bed topography, as shown in Figure 5. Observed daily discharges and water stages in the year 1999 at Yichang Station and Zhicheng Station were applied as the boundary condition.

From the above we note that sin $\theta = (x + y)z$ or:

$$K_t=\left(1-\frac{R^2\tau}{c_a+\nu\tan\delta}\right)^4 k_1 \tag{6}$$

where c_a = interface adhesion; δ = friction angle at interface; and k_1 = shear stiffness number.

3.2 *Governing equations for sediment transport*

The governing equations for sediment transport included the 2-D unsaturated suspended load transport equation and the transport equation for bed load. A total of 16 size groups of the non-uniform bed material were considered. The transport equations for suspended load are:

$$\frac{\partial(HS_k)}{\partial t}+\frac{1}{J}\left[\frac{\partial(HS_k Uh_2)}{\partial \xi}+\frac{\partial(HS_k Vh_1)}{\partial \eta}\right]-\frac{1}{J}\left[\frac{\partial}{\partial \xi}\left(H\varepsilon_\xi\frac{h_2}{h_1}\frac{\partial S_k}{\partial \xi}\right)\right.$$
$$\left.+\frac{\partial}{\partial \eta}\left(H\varepsilon_\eta\frac{h_1}{h_2}\frac{\partial S_k}{\partial \eta}\right)\right]+\alpha_k\omega_k(S_k-S_{*k})=0 \tag{7}$$

Copyright © 2006 Taylor & Francis Group plc, London, UK

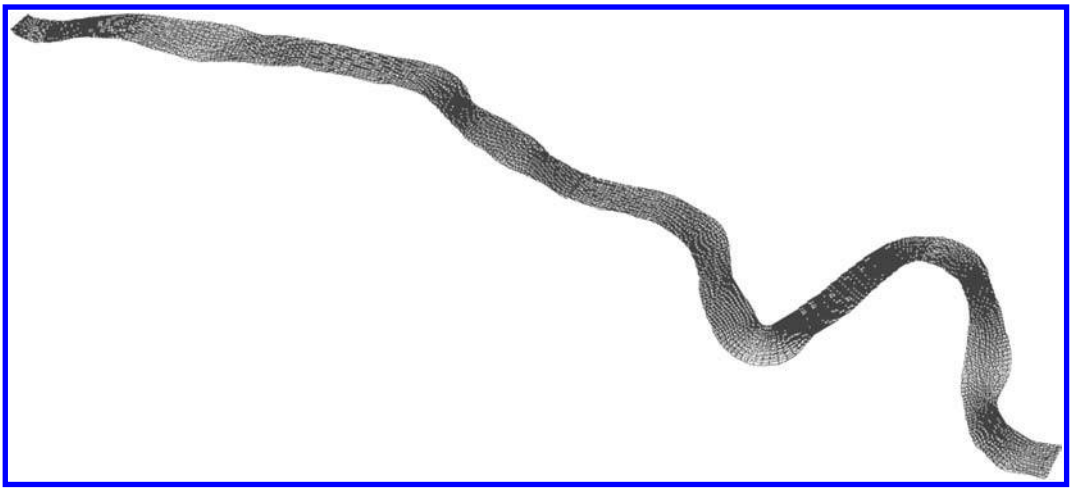


Figure 4. Grid system in an orthogonal curvilinear coordinate.

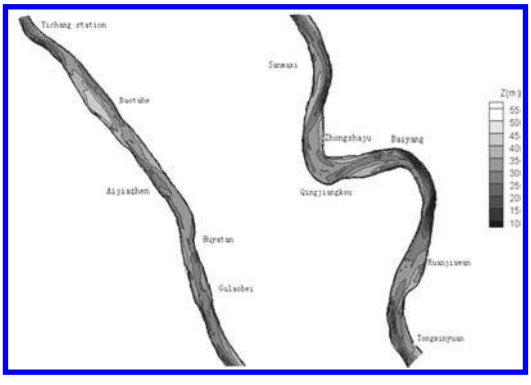


Figure 5. Measured topography of the river reach.

$$\varepsilon_\xi = \frac{\left(k_t U^2 + k_t V^2\right) H\sqrt{g}}{\sqrt{U^2 + V^2}\,C} \tag{8}$$

$$\varepsilon_\eta = \frac{\left(k_t U^2 + k_t V^2\right) H\sqrt{g}}{\sqrt{U^2 + V^2}\,C} \tag{9}$$

Bed degradation due to suspended load transport is evaluated using the following

$$\rho_s \frac{\partial Z_{bsk}}{\partial t} = \alpha_k \omega_k \left(S_k - S_{*k}\right) \tag{10}$$

Bed degradation due to bed load transport is calculated using the following

$$\rho_b \frac{\partial Z_{bgk}}{\partial t} = \frac{1}{J}\left[\frac{\partial}{\partial \xi}\left(g_{b\xi k} h_2\right) + \frac{\partial}{\partial \eta}\left(g_{b\eta k} h_1\right)\right] \tag{11}$$

where subscript k indicates the size group; S_k, S_{*k} are depth-averaged sediment concentration and carrying capacity of size group k (in kg/m^3), respectively; ε_x, ε_y are longitudinal and transverse diffusion coefficients, respectively; k_t, k_l are longitudinal and transverse components of the depth-averaged diffusion coefficient, respectively; ω_k is fall velocity of size group k (m/s); α_k is the saturation-restoration coefficient for size group k, assumed as constants in this study, i.e., $\alpha_k = 1.0$ for sour process ($S_k < S_{*k}$) and $\alpha_k = 0.25$ for siltation process ($S_k > S_{*k}$); ρ_s, ρ_b are dried bulk density of suspended-load and bed-load, respectively; Z_{bsk}, Z_{bgk} are deposition depth resulted from suspended-load and bed-load transports, respectively; $g_{b\xi k}$, $g_{b\eta k}$ are unit-width bedload transport rates of size group k in the ξ and η directions, respectively. The bedload transport rates were evaluated using an empirical formula that uses the depth averaged velocity as the driving variable.

The fall velocity of sediment particles is calculated using the following formula developed by Zhang Ruijin (1961), which is similar to the Rubey formula for settling velocity, except that the coefficients were calibrated differently:

$$\omega = \left[\left(13.95\frac{\nu}{D}\right)^2 + 1.09\frac{\gamma_s - \gamma}{\gamma} gD\right]^{1/2} - 13.95\frac{\nu}{D} \tag{12}$$

The river channel in the study area has a cobble-and-sand bed, and the following method (*Li* 1987) is applied to evaluate the carrying capacity S_*, which calculate the transport rate of a particular size group k out of the non-uniform bed materials:

$$S_{*k} = P_k S_*(\omega) \tag{13}$$

Copyright © 2006 Taylor & Francis Group plc, London, UK

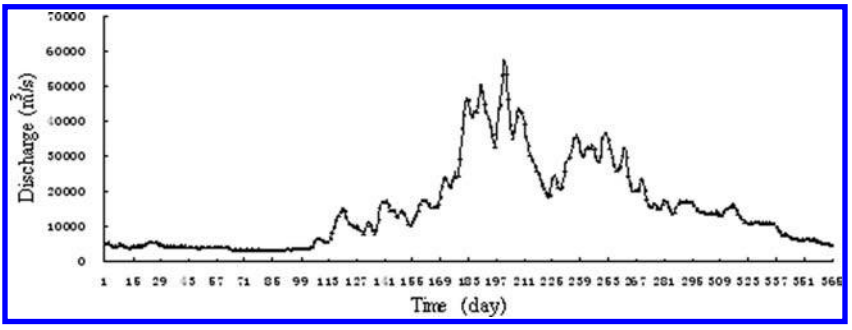


Figure 6. Measured daily-averaged discharges at Yichang Station (1999 data).

in which

$$S_*(\omega) = K\left(\frac{U^3}{gh\varpi}\right)^m$$

$$\varpi = \left(\sum_{l=1}^{n} p_{sl}\omega_l^m\right)^{1/m}$$

$$P_k = a_k P_{bk} \Big/ \sum_{k=1}^{N} a_k P_{bk}$$

$$a_k = (1-\Lambda_k)\left(1-e^{-R_k}\right)\Big/\omega_k$$

$$\Lambda_k = \omega_k \Big/ \left[u_* e^{-\omega_k^2/2u_*^2} + \omega_k \psi\left(\omega_k/u_*\right)\right]$$

$$\psi(\xi) = \int_{-\infty}^{\xi} e^{-t^2/2}dt \Big/ \sqrt{2\pi}\,, \quad R_k = \frac{6\omega_l}{\chi u_*}$$

where $S_*(\omega)$ is the total carrying capacity (expressed as suspended load concentration) for the non-uniform bed-material; K, m are constants to be calibrated; P_k is the share of carrying capacity for size group k in total carrying capacity; p_{sl} , ω_l are the fraction of size group l in the incoming suspended load and its corresponding fall velocity, respectively;P_{bk} is the fraction of size group k in the bed material.

4 MODEL CALIBRATION

In the present paper, the numerical model for flow of water was calibrated first. The sediment transport model was calibrated after all the parameters in the flow simulation model were determined.

4.1 *Calibration of the Flow Simulation Model*

Daily-averaged discharges observed in 1999 at Yichang Station were applied as the upper boundary conditions of the study area, as shown in Figure 6. Daily water stages at Zhicheng Station observed in 1999 were applied as the lower boundary conditions, as shown in Figure 7. In this study, river bed roughness were evaluated from observed

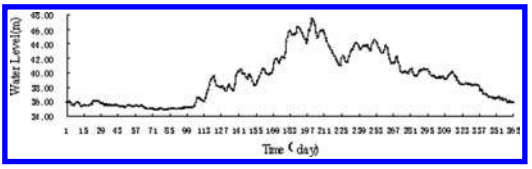


Figure 7. Measured daily-averaged water stages at Zhicheng Station (1999 data).

stage-discharge relations. The time interval in the numerical calculation was 6 seconds.

Flow patterns for various discharges in different seasons ($Q = 3140\ m^3/s$, $21000\ m^3/s$, $50000\ m^3/s$) at a 90 degree river bend are shown in Figure 8.

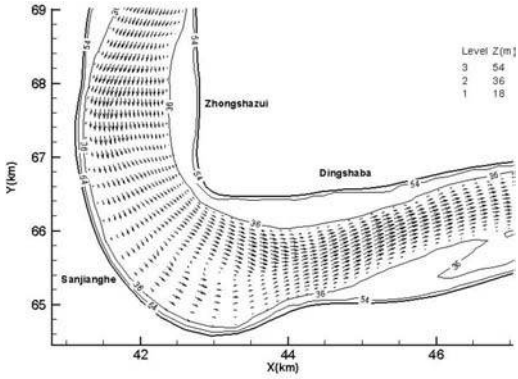
It can be seen from the simulated patterns that flow patterns during dry seasons are quite different from that in flood seasons. Both the inundated areas and the direction of velocity vectors will change significantly when discharge varies. Figure 9 shows calculated water surface profile. Comparison of observed and calculated water stages at Yichang Station is shown in Figure 10, which suggests results from simulations agree with measurements.

4.2 *Calibration of the Sediment Transport Model*

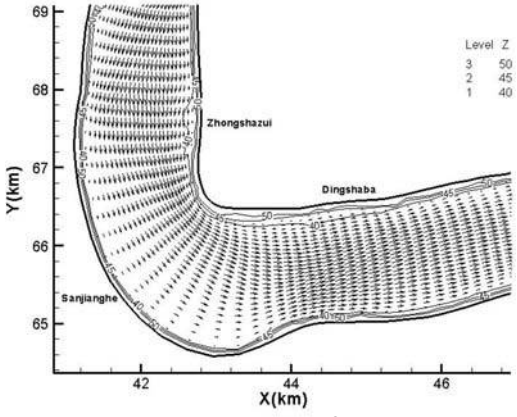
The sediment transport model was calibrated using observed data of bed contours, river cross-sections, sediment concentrations and water stages. Topographical measurements for this reach taken in October 1998 and November 1999 were used to obtain the observed volume of scour or deposition. The daily averaged hydrological data collected in the year 1999 were used as initial and boundary conditions for the simulation model to reproduce the observe scour or deposition in this river reach.

The 63 km long channel is divided into 4 sections (Fig. 2). Volume of scour and deposition for each section during 1999 were calculated and compared with observations. Table 2 lists the observed and calculated amounts of deposition and scour, which suggest

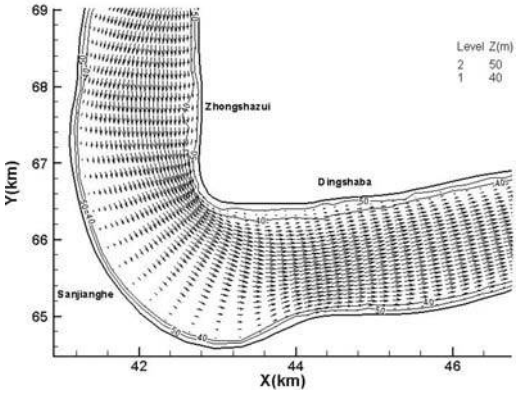
Copyright © 2006 Taylor & Francis Group plc, London, UK



a) Q= 3140m^3/s



b) Q= 21000m^3/s



c) Q= 50000m^3/s

Figure 8. Calculated flow pattern at the first bend (Q = 3140, 21000, and 50000 m^3/s).

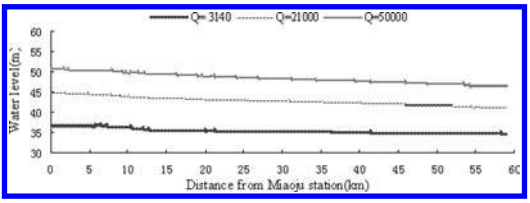


Figure 9. Calculated water surface profiles (Q in m^3/s).

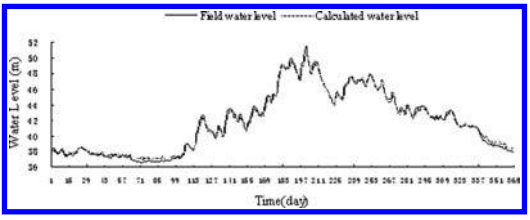


Figure 10. Comparison between field measurements and calculated water stages at Yichang Station.

Table 2. Observed and calculated volume of scour and deposition.

Section	1	2	3	4
Distance from Yichang (km)	0∼15	16∼31	32∼47	47∼63
Observed (10^4 m^3)	−3536.9	−23.9	+696.3	+1450.6
Calculated (10^4 m^3)	−3025.34	−356.434	+647.3009	+1462.45

Note: The "−" signs indicate bed scour; "+" signs indicate deposition.

that: 1) in the upstream part of the study area bed scour occurred and in the downstream part deposition occurred; 2) the model calculation is capable of simulating the sediment transport pattern in this type of river channel with complicated sour and deposition processes. Scour volume of section 2 was overestimated due to the lack of measured size distribution for bed materials, which should be used as initial conditions. Obviously the local armoring process was more complex than what was predicted.

5 SIMULATION OF LONG-TERM CHANNEL DEGRADATION

The simulation model was applied to predict degradation processes of a 20-year period beginning at the impoundment of the TGR in June 2003. The upper boundary conditions of water discharge and sediment supply from the Reservoir were provided by the same numerical simulation model that produced the results listed in Table 1. The observed long-term average

Copyright © 2006 Taylor & Francis Group plc, London, UK

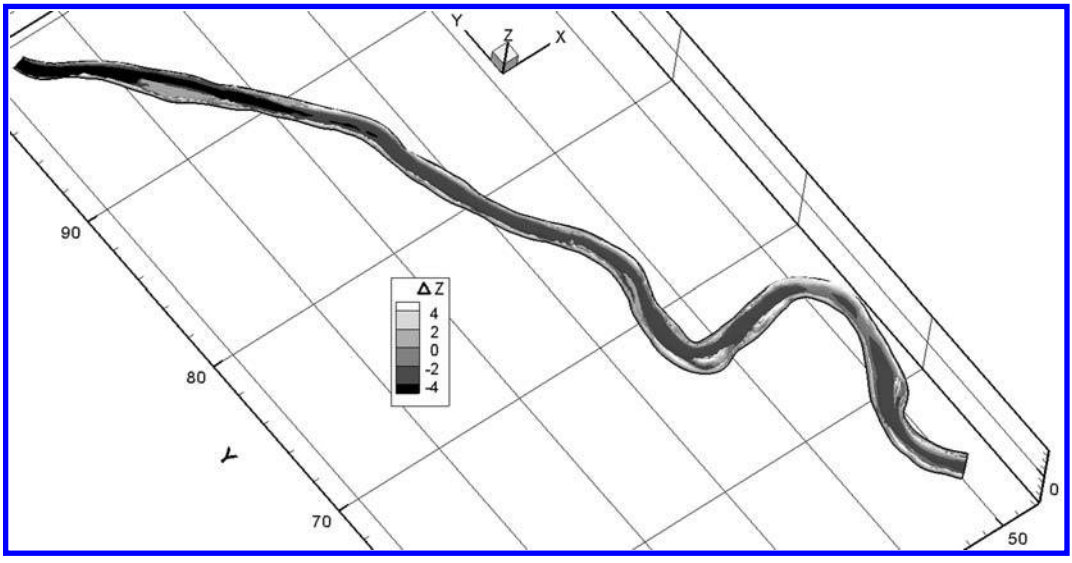


Figure 11. Predicted accumulated depth of scour and deposition in 20 years' time (units in meters)

Table 3. Predicted scour and deposition in the study area after reservoir impoundment.

	Accumulated volume of scour and deposition below the water surface at Q = 10000 m^3/s ($\times 10^4$ m^3)						
	Distance from Yichang Station (km)						
Year	0 ~ 10	10 ~ 20	20 ~ 30	30 ~ 40	40 ~ 50	50 ~ 59	Total
1	−1186.49	−843.66	−64.82	443.92	918.30	254.69	−478.07
5	−1780.90	−1577.44	−1203.30	−1185.98	−257.39	−765.90	−6770.91
10	−1929.21	−1841.87	−1441.17	−1768.27	−673.23	−1139.08	−8792.82
15	−1929.11	−1852.39	−1407.70	−1722.39	−760.09	−1122.64	−8794.33
20	−1943.72	−1880.55	−1409.87	−1802.30	−836.97	−1105.49	−8978.90

water stage ~ discharge relations at Zhicheng Station were used for the lower boundary conditions in this simulation.

Figure 11 shows the distribution of predictions of accumulated depth of scour and deposition in the study reach 20 years after the TGR impoundment. Calculation results expressed as the total volume of scour and deposition in each river sections are listed in Table 3, which indicates that the entire area will be subject to a net scour of about 90 million m^3 in the next two decades.

During the first 10 years, channel degradation will develop very rapidly and the total volume of net scour will reach 88 million m^3 at the end of the first decade. In the next 10 years, the scour would virtually stop and the river channel would be stabilized, due to the armoring process.

There is little possibility that the river channel in this hilly area would migrate laterally, because of the geological conditions that impose restraints on the channel planform. The scour will mainly occur in the main channel while deposition will occur on the floodplain along the river.

Model predictions of the armoring process are shown in Figure 12, from which it can be seen that the armoring process will be more obvious in the upstream part of the study reach, e.g., the first section in Fig. 2, where the median size will increase from $D_{50} = 0.34$ mm to $D_{50} = 3.4$ mm and becomes stabilized in 5 years' time after impoundment.

In contrast, smaller increases median sizes were predicted for the downstream sections. Close to the lower boundary, the size of bed materials became finer than before.

The long-term scour would result in water level drops from the 2003 water level along the entire study reach, with a maximum of 1.26 m at the Yichang Station, as shown in Figure 13. Such a systematic and

Copyright © 2006 Taylor & Francis Group plc, London, UK

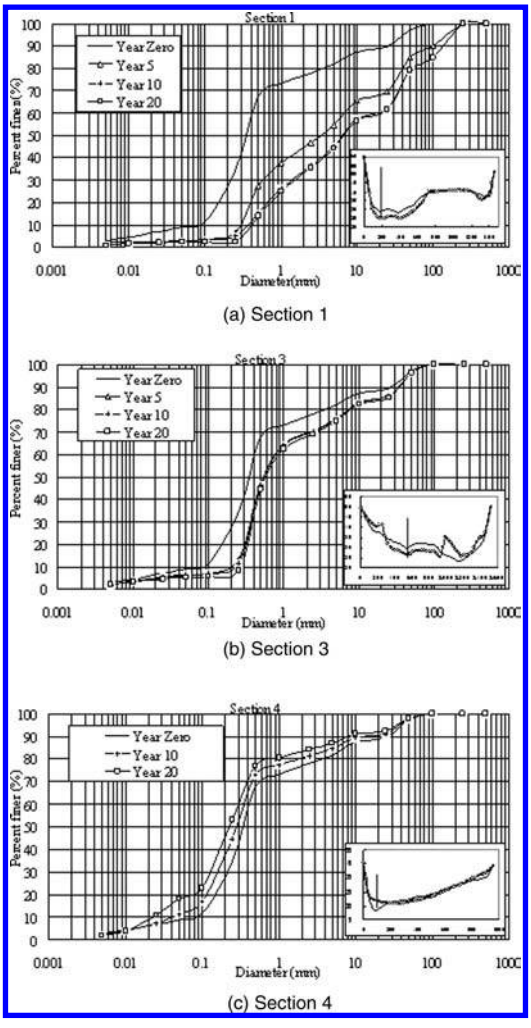


Figure 12. Predicted armoring process at various locations along the channel.

long-term water level drop will not only create difficulties for the operation of the Gezhouba Shiplock but also will have negative impacts on the environment and ecology in this area.

6 RESTORE THE WATER LEVEL BY BED PAVEMENT

The proposed measures to prevent bed scour and to restore water level include laying a layer of articulated concrete mattresses or stone ripraps on the river bed, at several selected sections between Yichang Station and Zhizheng Station. In this numerical simulation, the water level rises due to such measures were estimated for the selected five locations between Yichang and Zhicheng, as locations A to D shown in Figure 14.

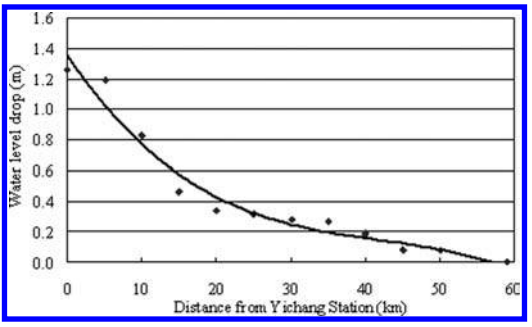


Figure 13. Predicted water level drop at Yichang Station due to channel degradation.

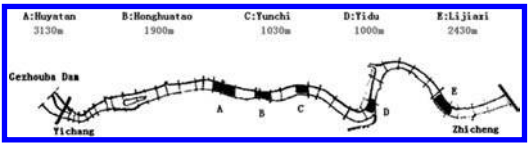


Figure 14. The length and location of selected sections for bed pavements.

Table 4. Predicted water level recovery (ΔWL) after bed pavements (for $Q = 5000\ m^3/s$).

Series Number	Controlled reaches	Thickness (m)	ΔWL of Yichang(m)		
			1.00*n*	1.35*n*	1.48*n*
s8-1	A+B+C	0.5	0.05	0.13	0.16
s8-2	A+B+C	1.0	0.08	0.17	0.21
s9-1	A+B+C+D	0.5	0.06	0.15	0.02
s9-2	A+B+C+D	1.0	0.11	0.20	0.26
s10-1	A+B+C+D+E	0.5	0.07	0.26	0.32
s10-2	A+B+C+D+E	1.0	0.15	0.3	0.38

The pavements will be constructed for a portion of the river bed which could be submerged when the discharge is $5010\ m^3/s$. Such pavements can raise the river bed elevation by 0.5 m to 1.0 m, and the local roughness of the channel will also increase by a certain magnitude. The predicted effects of various pavement schemes, listed in Table 4, are obtained by assuming various magnitudes of roughness increase, expressed as increases in the Chezy coefficient, *n*.

Let roughness height K_s be equal to D_{50}, and assume that the K_s will be increased from 5.7 mm to 78 mm after pavements are completed, the Chezy coefficient *n* are found to have increased by 35%. If stone ripraps of larger sizes are used for pavements, e.g., K_s becomes 150 mm, the Chezy coefficient *n* will be increased by a magnitude of 48%. For various *n* values, the water level rise was calculated accordingly. The simulation results are based on the assumption that the paved areas of the river bed will no long be subject to further scour.

Copyright © 2006 Taylor & Francis Group plc, London, UK

7 CONCLUSIONS

This study presents results from a 2-D water flow and sediment transport model, which is developed to calculate the transport of graded sediments downstream of the Three Gorges Reservoir. The model is validated using field observations from the study area on the Yangtze River.

Long-term river channel degradation processes were calculated for the study area, which is a 63 km long reach downstream of Yichang. Simulation results suggest that during the first 20 years after the impoundment of TGR, the accumulated total amount of bed scour will be 89 million m^3 (which only includes those areas of the bed that could be inundated by a discharge of $Q = 10000\ m^3/s$). River bed scour at such a scale will cause a water level drop of 1.26 m at Yichang Station, from the present stage for the discharge of 5000 m^3/s. This would create difficulties for the operation of the Gezhouba Shiplock and would have negative impacts on the environment and ecology in this area.

The effectiveness of bed pavement measures has been evaluated by numerical calculations. It was found out that such measures could prevent the development of bed scour and restore water stages to a certain extent. Calculation results indicate that the water stage at Yichang can be raised by up to 0.38 m for the discharge of 5000 m^3/s, if pavement measures are applied at all the 5 selected locations. However, the numerical simulations were based on assumed increases of roughness coefficient, *n*, due to bed pavements. Such assumptions require confirmation or modification through experiments or field observations in the future.

ACKNOWLEDGEMENTS

Partial financial support from China's National Key Basic Research and Development Program (Grant No. 2003CB415206) and the National Natural Science Foundation of China (Project No. 50479004, 50221903) is gratefully acknowledged.

REFERENCES

Dong, Yaohua. 2000. 2-D Mathematical Model for Training of the Reaches below TGP. CSRTGP6: 344–359.

Fan, Beilin et al. 2000. Computation of Sediment Transport in the Reach from Jiangkou to Guanyinsi below TGP. CSRTGP7: 382–412.

Fang, Chunming. 2000b. 2-D Computation of Sediment Transport in the Douhudi Reach of the Yangtze. CSRTGP7: 413–421.

Gao, Kaichun et al. 2000. Coupling 1-D and 2-D Mathematical Model for Gravel Shoal Reaches below TGP. CSRTGP6: 486–529.

Han, Q. W. 1980. A study on the non-equilibrium transportation of suspended load Proc. 1st Int. Symp. on River Sedimentation, IRTCES, Beijing.

Holly, F. M., Jr., and Rahuel, J. L. 1990. New numerical/physical framework for mobile-bed modeling, Part I: Numerical and physical principles. *J. Hydraul. Res.* 28(4): 401–416.

Huang, Yue. 2000a. 1-D Mathematical Modeling of Fluvial Processes in the Reach from Yichang to Datong below TGP. CSRTGP7: 258–311.

Huang, Yue. 2000b. Computation of Channel Evolution in the Reach from Yichang to Datong after construction of the Xiluodu Project. CSRTGP7: 339–359.

IWHR(China Institute of Water Resources and Hydropower Research) & YSRI (Yangtze River Scientific Research Institute), 1990. *Preliminary Report on the Bed Erosion Processes downstream of the Three Gorges Reservoir*. Technical Report.

Li, Yitian. 1987. Size distribution of bed materials under the condition of equilibrium transport state. *Nisha Yanjiu*(*Sediment Research*), (1): 82–87. (In Chinese)

Lu, Yong-jun, Yuan, Mei-qi, Jia, Rui-min, et al. 1997. Impact of the Three Gorges Project on the downstream river channels and possible countermeasures. *Shuidao Gangkou* (*Waterway&Port*), (2): 11–29. (In Chinese)

Lu Yongjun, Chen Zhicong, Zhao Lianbai, Shao Xuejun, Yang Meiqing, Li Yunzhong. 2002. Impact of the Three Gorges Project on the Water Level and Navigation Channel in the Near-dam Reach Downstream The Gezhouba Project. *Engineering Sciences.* 4(10): 67–72..(in Chinese)

Lu, Yongjun et al. 2000a. 2-D Mathematical Modeling of Water Depth in the Navigation Channel with Movable Bed below the Gezhouba Dam. CSRTGP6: 330–343.

Lu, Yongjun. 2000b. Coupling 1-D and 2-D Mathematical Model for Training of Shoal Reaches below TGP. CSRTGP6: 530–549.

Mao, Jixin et al. 1998. Computation of Degradation in the Reach from Yichang to Datong below the TGP. CSRTGP7: 115–148.

Mao, Jixin et al. 2000. Computation of Channel Evolution in the Reach from Yichang to Datong after construction of the Xiangjiaba Project. CSRTGP7: 360–381.

Olsen, N. R. B. 1999. Two-dimensional numerical modeling of flushing processes in water reservoirs. *J. Hydraul. Res.*, 37(1): 3–16.

Peng Yang , Zhang Hongwu , Zhang Yu. 2005. 2-D numerical modeling for unsteady flow and sediment transport in Chongqing reach. *Journal of Hydrologic Engineering*. 24(1): 47–52. (in Chinese)

Wu, Weiming. 2004. Depth-averaged 2-D numerical modeling of unsteady flow and nonuniform sediment transport in open channels. *Journal of Hydraulic Engineering,* ASCE.: 1013–1024.

Xie Zuotao, Zhang Xiaofeng, Yuan Jing, Xu Quanxi, Yang Fangli. 2005. Study and application of 2-D horizontal mathematical model for flow and sediment in generalized curvilinear coordinate. *Journal of Sediment Research.* 6: 58–64. (in Chinese)

Zhang, Ruijin. 1961. *River Dynamics*. Beijing: China Industrial Press: 13–21.

Zhu, J. 1992. FAST2D: A computer program for numerical simulation of two-dimensional incompressible flows with complex boundaries. Rep. No. 690, Institute of Hydromechanics, Karlsruhe Univ., Karlsruhe, Germany.

Copyright © 2006 Taylor & Francis Group plc, London, UK

The evolution analysis of Fengcheng reach under the changing conditions

L. Chen, J. He, Z.G. Wang & W.S. Xu
Key Laboratory of Water Resources and Hydropower Engineering, Key Lab. of the Water and Sediment Sciences of Ministry of Education, Wuhan University, Wuhan, China

ABSTRACT: Impoundment of upstream reservoir, construction of Ganjiang highway bridge and actualization of navigation regulation project changed the incoming water & sediment condition and boundary condition of Fengcheng reach and consequently brought to the reformation process which caused adjustment of local river regime. Based on flied data and model experiment, river evolution and reformation process tendency in Fengcheng reach under changing conditions was analyzed. Furthermore interaction between reformation process and changing conditions was interpreted as well as the influence to navigation and near-shore project. It is concluded that after change of the condition general scour occurs. Left branch downstream highway bridge has gradually declined while mid branch has developed to be the main channel. Evolution tendency presents as shoal line recession in Sha-shoal and thalweg swing rightwards in mid bending part and thalweg deepen and widen in mid branch. The reformation will influence navigation condition and near-shore project in a long run.

1 INTRODUCTION

River evolution is affected by three essential factors, incoming water & sediment condition, channel boundary condition and downstream erosion base level. When these mutual interacting factors reach to a homeostasis, channel keeps stable, yet when factors changed, a new reformation process occurs.

Fengcheng Reach (shown in Figure 1) locates downstream of Ganjiang River in Jiangxi province. Fengcheng highway bridge and the controlling node Leigongnao divide this reach into three parts: upper straight part, mid bending part and lower branching part. Western mountain (peak height-60 m) alternates with mesa in the left bank, and west levee connects discontinuously. Gandong Levee lies on the right side of the reach with flood control standard of 50-year frequency.

The channel is relatively narrow in upper straight part and mid bending part, while in lower branching part channel broadens gradually at 2000 m downstream Shishang. Side bar Peng-shoal and Dong-shoal locates at the left side of upper straight part, and side bar Sha-shoal locates at the right side of the mid bending part of the reach. There are two central sand-bars lying in the middle of the lower branching part. Left Xin-bar has lower height with narrow surface and divides flow into left and mid branch in low water period. Right Zhong-bar has higher height with nearly 1000 m broad surface and divides flow into middle and right branch which join together 3500 m downstream in middle and high water period.

The riverbed of this reach is composed by gravel and coarse sand while 7∼8 m height below is anti-scouring grit stone. Riverbed particle median diameter is 5∼19 mm, in which diameter lager than 1 mm occupies 70%∼90%, maximum particle diameter is from 40∼20 mm and minimum is over 0.2 mm. Side bars is consisted mainly by sand with median diameter of 0.43∼2.7 mm, and particle with diameter lager than 1 mm occupies 8%∼20%.

The mean annual discharge in Fengcheng reach is 1890 m^3/s and the mean annual runoff is $596.4 \times 108\ m^3$ (as much as the Yellow River). The mean annual sediment runoff (refers to suspended load) is only 912×104 t.

Either river bed or banks of this reach has fine stability. And with less incoming sediment, the river regime in Fengcheng reach presented to be stable in natural condition and annual variation of scouring and silting was small before 1990.

In the early 1990s, the construction of Gangjiang highway bridge, water intake & drainage project of Fengcheng thermal power plant and navigation channel dredging project in Xin-bar middle branch have changed the boundary condition of Fengcheng Reach. On the other hand, the impoundment of Wanan reservoir upstream has changed the incoming water & sediment conditions. Annual runoff distribution tended to be even. Trimestral runoff of April, May and June occupies 40.87% of the annual runoff while it had occupied 51.18% before. Changes in sediment transportation also occurred: the annual average sediment runoff was 464.36×104 t from 1993 to 2003, only half

Copyright © 2006 Taylor & Francis Group plc, London, UK

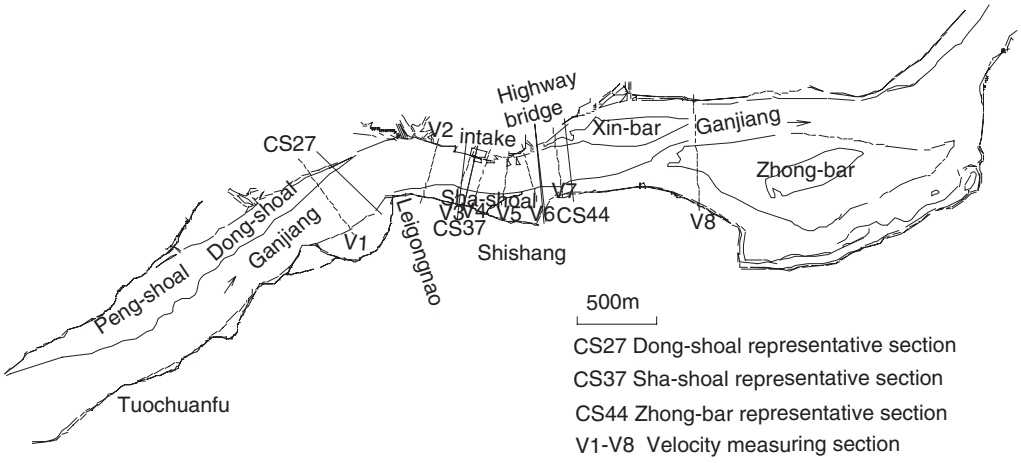


Figure 1. Planform in Fengcheng reach.

of the amount before 1990, trimestral sediment runoff of April, May and June decreased from 66.59% to 57.63% of annual sediment runoff. All these variations have induced the reformation process in Fengcheng reach and probably brought to the adjustment of local river regime. Based on the field data and physical model, the prediction of evolution tendency under the changing conditions in Fengcheng reach is analyzed.

2 RECENT EVOLUTION

2.1 *In upper straight part*

Thalweg varied in a relatively small range in upper straight part before and after the change of boundary conditions. The thalweg kept in the left side upstream, and transferred to the right in the vicinity of Tuochuanfu. In upper straight part below Tuochuanfu, the thalweg cling to the right bank. Side bar Peng-shoal and Dong-shoal is basically stable, and the range of sliting and scouring there was rather small.

2.2 *In mid bending part*

Flow was deflected to the opposite side by controlling node Leigongnao, thalweg correspondingly transferred to the left bank. In mid bending part, the thalweg kept to the concave side of the bend and swung in a small range. Hereinto, the thalweg moved leftwards for about 30 m from 1985 to 1992, and kept on moving leftwards for about 30 m from 1992 to 1997. From 1997 to 2003, the thalweg swung back to the right. Till 2003, the thalweg had almost moved back to the location where it lay in 1985.

The Sha-shoal head was in a state of erosion from 1985 to 2003. And the bed level variation at intake section in the middle Sha-shoal is shown in Figure 2.

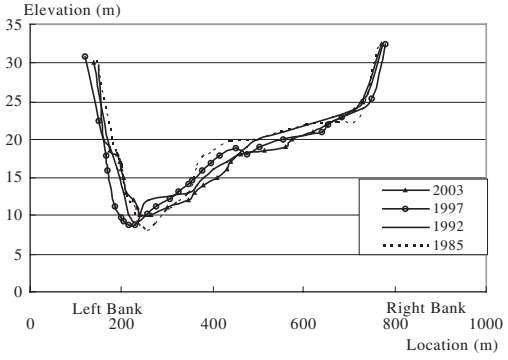


Figure 2. Bed level variation at intake section.

As Figure 2 shows, section morphology was stable in intake section from 1985 to 2003, the thalweg height only changed in a small range. The height of the deepest point in section thalweg ranged from 7.94 m∼10.0 m. Meanwhile the height variation in Sha-shoal was about 3.5 m, which exceeded the variation range (=2.06 m) in thalweg. From 1985 to 2003, the thalweg swung rightwards together with the downcut of Sha-shoal and the deposition in the thalweg.

2.3 *In lower branching part*

Before 1992, the thalweg entered into the left branch smoothly along the left bank of Xin-bar, and stretching in the left branch afterward. After 1992, the Xin-bar head extended forwards for about 5∼7 m, it invaded into the left branch and blocked the flow movement in left branch. Sediments deposited at left side of Xin-bar, and Xin-bar tended to spread leftwards. Meanwhile, the Xin-bar tail also had a leftward deflection and blocked the flow movement in left branch furthermore.

Copyright © 2006 Taylor & Francis Group plc, London, UK

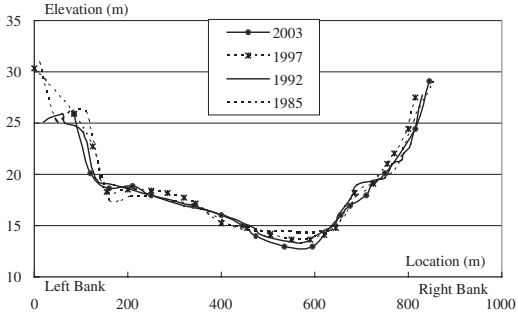


Figure 3. Bed level variation at Xin-bar head section.

The bed level variation of the typical section at Xin-bar head is shown in Figure 3. It is found that, the gradual deposition occurs at 160 m from initial point, and height of which rises beyond 18.0 m. The left branch declined gradually while the middle branch developed rapidly.

The thalweg kept to the left bank from Xin-bar tail to Zhong-bar tail and transited to the right bank at Zhong-bar tail, the thalweg changed little in this part and swung rightwards for about 90 m from 1985 to 2003. The regulation works on Zhong-bar including three spur dikes was advantageous for river regime in Zhong-bar.

2.4 *Variation of downstream erosion base level*

Figure 4 shows the variation of the relation between discharge in Zhangshu (23 km upstream Fengcheng reach) and water level in Fengcheng from 1993.

It is figured out in Figure 4 that the gauge-discharge curve varies in a certain extent: when discharge is 2000 m^3/s, variation amplitude of water level is 0.59 m; when discharge is 4000 m^3/s, variation amplitude is 0.42 m; when discharge is 8000 m^3/s, variation amplitude is 0.65 m; when discharge is 10000 m^3/s, variation amplitude is 0.39 m. From 1993 to 2003, the variation of water level is relatively large. Although it does not present as holistic descend, the water level in 2000~2003 is lower than it is in the early 1990s'. Erosion caused by artificial sand excavation and reduce of incoming sediment have lowered the bed level downstream, consequently decreased the downstream erosion base level.

3 PREDICTION OF EVOLUTION TENDENCY BY MODEL EXPERIMENT

3.1 *Model design*

In order to make clear about river evolution in different hydraulic condition as well as do an evolution tendency prediction of this reach, a moveable-bed physical model has been established.

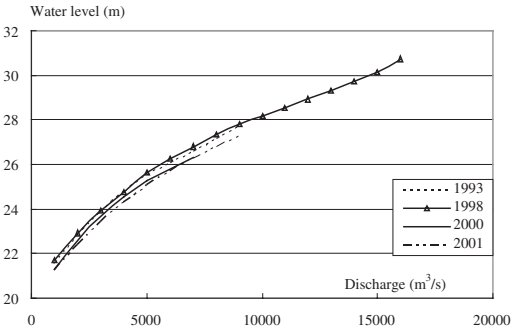


Figure 4. Relation curve between discharge in Zhangshu and water level in Fengcheng.

The reach which the model simulated is from Tuochuanfu to Fengcheng stage gauging station with a length of 13.5 km. Considering about the length, width and depth of the simulating reach, physical model has been defined to be distorted with horizontal scale of 250, vertical scale of 100 and distortion ratio of 2.5. The model has simulated bed load and suspended load. The main similarity scales have been chosen as follows:

(1) Settling velocity scale and model sand size scale

In distorted physical model, flow convection & gravity deposition ratio similarity and turbulent diffusion & gravity deposition ratio similarity cannot be satisfied at one time. The turbulent diffusion & gravity deposition ratio similarity has been chosen to ascertain the settling velocity scale

$$\lambda_\omega = \lambda_u \left(\frac{\lambda_H}{\lambda_L} \right)^{\frac{1}{2}} \quad (1)$$

where λ_u refers to settling velocity scale; λ_H refers to horizontal scale; λ_L refers to vertical scale.

Meanwhile model sand size scale formula that satisfied the suspended load sediment movement similarity can be induced as

$$\lambda_d = \frac{\lambda_\omega^{\ 2}}{\lambda_{\frac{\gamma_s - \gamma}{\gamma}} \lambda_\xi} \quad (2)$$

Thereinto:

$$\xi = \sqrt{\left(\frac{13.95 \frac{\nu}{d}}{\sqrt{\frac{\rho_s - \rho}{\rho} gd}} \right)^2 + 1.09} - \frac{13.95 \frac{\nu}{d}}{\sqrt{\frac{\rho_s - \rho}{\rho} gd}}$$

(2) Incipient velocity scale

Model and prototype incipient velocity have been calculated respectively according to the incipient velocity

Copyright © 2006 Taylor & Francis Group plc, London, UK

formula

$$u_c = 1.14\sqrt{\frac{\gamma_s - \gamma}{\gamma} gd}\left(\frac{h}{d}\right)^{\frac{1}{6}} \quad (3)$$

where γ_s and γ refer to the unit weight of sediment and h, d refer to water depth and grain diameter.

The suspended load incipient velocity scale has been calculated as

$$\lambda_{uc} = u_{cp} / u_{cm} \quad (4)$$

where u_{cp}, u_{cm} refer to incipient velocity of prototype and model.

(3) Sediment concentration scale

Based on the imbalanced sediment transportation formula

$$\frac{d_s}{d_x} = -\frac{\alpha\omega}{q}(s - s_*) \quad (5)$$

and Zhang Rui-jin's sediment transport capacity formula

$$S_* = \frac{\rho_s}{8c_1\frac{\rho_s - \rho}{\rho}}(f - f_s)\frac{u^3}{gR\omega} \quad (6)$$

sediment concentration scale formula can be induced as

$$\lambda_s = \lambda_{s_*}$$
$$\lambda_s = \frac{\lambda_{\rho_s}}{\lambda_{\frac{\rho_s - \rho}{\rho}}\eta^{1/2}} \quad (7)$$

where η refers to variability.

(4) Riverbed reformation time scale

Based on sediment balance equation

$$\frac{\partial q_s}{\partial x} + \rho'\frac{\partial Z_0}{\partial t} = 0 \quad (8)$$

and concentration scale which has been mentioned above, riverbed reformation time scale can be derived as follows

$$\lambda_{t_s} = \frac{\lambda_l \lambda_{\rho'}}{\lambda_u \lambda_s} \quad (9)$$

where λ_L, $\lambda_{\rho'}$, λ_u, λ_s respectively refer to vertical scale, sediment dry density scale, velocity scale and sediment concentration scale.

More detailed similarity is shown in Table 1.

Table 1. Scale of similitude statement.

Similarity	Scale		Remark
Geometric similarity	Horizontal scale Vertical scale	250 100	
Current movement similarity	Velocity scale Roughness scale Discharge scale	10 1.36 250000	
Suspended load sediment movement similarity	Settling scale Incipient scale Size scale Sediment concentration scale	6.3 10 0.437~0.548 0.048	Plastic sand density 1.05 t/m^3
Sandiness bed load sediment movement similarity	Incipient scale Size scale Riverbed Reformation Time scale	10 11 160	Coal density 1.39 t/m^3

Table 2. Flow profile verification results.

Discharge	Measuring section	Z_p(m)	Z_m(m)	Difference (m)
665 m^3/s	V1	19.05	19.03	−0.02
	V2	19	18.99	−0.01
	V3	18.95	18.94	−0.01
	V4	18.92	18.93	0.01
555 m^3/s	V5	18.7	18.7	0
	V6	18.69	18.68	−0.01
	V7	18.6	18.62	0.02
	V8	18.5	18.52	0.02
2020 m^3/s	V3	21.33	21.3	−0.03

Z_p – water level in prototype, Z_m – water level in model.

3.2 *Model verification*

Verification test including flow profile verification, velocity distribution verification and riverbed scouring/erosion verification has been conducted to verify resistance similarity, current movement similarity and riverbed reformation similarity respectively.

In flow profile verification, water level has been measured in 8 measuring sections (V1–V8 have been figured out in Figure 1) under different discharges (665 m^3/s, 555 m^3/s and 2020 m^3/s). The result is shown in Table 2 that model flow profile was accord with observed prototype data, the max difference between prototype and model water level was less than ±0.03 m.

In velocity distribution verification, the section mean velocity in vertical has been measured and verified in 8 measuring sections (V1–V8 have been figured out in Figure 1) under different discharges. The result shows that the velocity distribution was consistent with observed prototype data, the max difference

Copyright © 2006 Taylor & Francis Group plc, London, UK

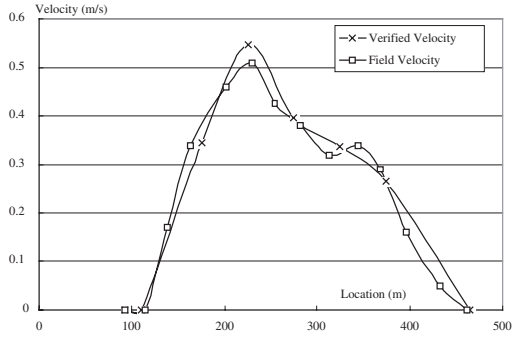


Figure 5. Velocity distribution in V5 ($Q = 665\ m^3/s$).

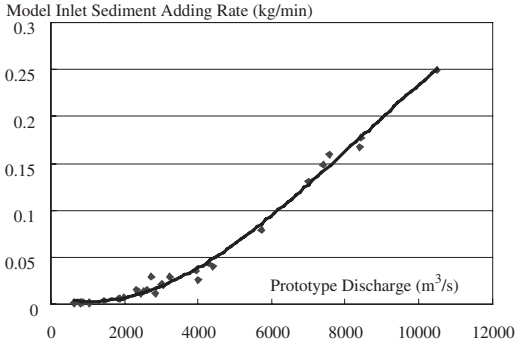


Figure 6. Relationship between sediment adding rate at model inlet and prototype discharge.

between prototype and model section mean velocity in vertical was less than 0.1 m/s. Figure 5 shows the velocity verification in V5 ($Q = 665\ m^3/s$).

In riverbed scouring/erosion verification, Dec 1997 1:5000 terrain field data has been chosen as initial terrain while Dec 2003 1:5000 terrain field data as terminate terrain. The discharge process of Zhangshu gauging station (23 km upstream Fengcheng reach) has been adopted as intake discharge. The generalized discharge hydrograph from Jan 1998 to Dec 2003 and intake sediment adding rate shown as Figure 6 have been adopted as controlling condition.

The verification test result shows that the thalweg tendency, scouring/erosion position as well as scouring/erosion amounts were basically consistent with terrain field data. Comparison between verification terrain and prototype terrain in CS44 is shown in Figure 7. It is indicated that the chosen of distortion ratio, sediment discharge scale and riverbed reformation time scale were suited and reasonable.

The verification test indicates that the model has satisfied resistance similarity, current movement similarity, suspended load sediment movement similarity, bed load sediment movement similarity and riverbed deformation similarity etc.

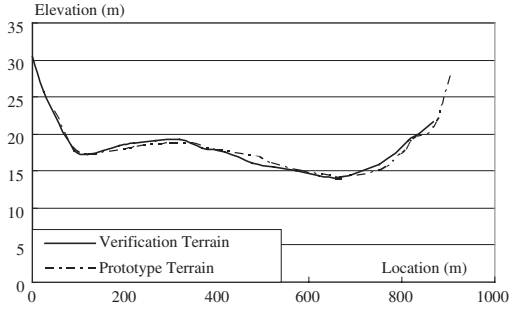


Figure 7. Comparison between verification terrain and prototype terrain in CS44.

Table 3. Eigen values of representative years.

Year	W ($10^8\ m^3$)	W_S (10^4 t)	Q (m^3/s)	S (kg/m^3)	Remark
1994	786.7	994	2494	0.126	High-flow year
1998	827	588	2622	0.071	High-flow year
1996	534	555	1693	0.104	Moderate-flow year
1999	587	292	1861	0.05	Moderate-flow year
2003	446.5	189	1416	0.042	Low-flow year

W – Annual Runoff, W_S – Annual sediment runoff, Q – Annual mean discharge, S – Annual Average Sediment concentration.

3.3 *Evolution tendency prediction*

Based on the data of Zhangshu gauging station, 5 representative years have been selected as typical water & sediment condition of the model test. The eigen values of these representative years are shown in Table 3.

The model experiment has indicated that under the representative water & sediment conditions, different part of Fengcheng Reach has different evolution trend.

In upper straight part, both silting and scouring were comparatively small in different representative years. But there was still slight deposition in Peng-shoal and Dong-shoal in flood season. The deposition was more obvious after moderate-flow year than after high-flow year. As Figure 8 shows that the max deposition thickness in Dong-shoal in flood season of 1998 is 10 cm while in flood season of 1999 the max deposition thickness reaches to 97 cm.

In mid bending part, the influence in Sha-shoal and Zhong-bar left side were rather small after low-flow year and moderate-flow year, while they presented to be scouring after high-flow year. As Figure 9 shows that comparing to the moderate-flow year, the 17 m

Copyright © 2006 Taylor & Francis Group plc, London, UK

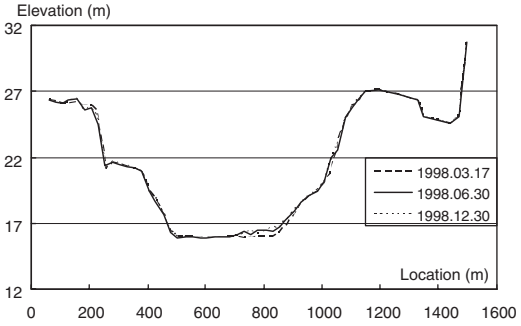


Figure 8(a). The silting/scouring variation of CS27 (Dong-shoal) in 1998 (high-flow year).

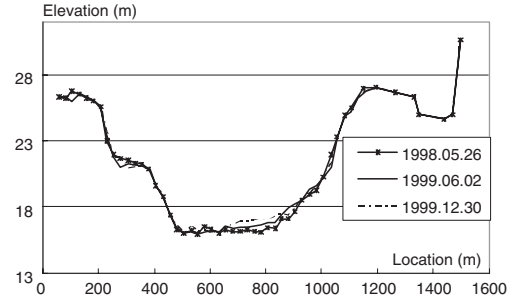


Figure 8(b). The Silting/Scouring Variation of CS27 (Dong-shoal) in 1999 (moderate-flow year).

contour line recedes back for 11.2 m after high-flow year, at the same time the section deepest point swings right for about 10 m. Scouring still occurred in Sha-shoal and Zhong-bar left side during the flood season in moderate-flow year, but the scouring extent was not that obvious than in high-flow year. The 17 m contour line at Sha-shoal receded back for 7.85 m in flood season of 1999 (moderate-flow year) while it is 11.5 m in 1998 (high-flow year).

In lower branching part, as the left branch was mostly blocked, the change of the hydraulic condition had little influence at left branch. While in the middle branch, the main channel was scoured down cutting and leftwards. It is figured out in Figure 10 that the deepest point downcut for 30 cm and moves rightwards for 25 m after high-flow year.

In upper straight part, the thalweg and main stream cling to the left bank upstream Leigongnao, the velocity near Peng-shoal and Dong-shoal at the left bank is not that small, so the deposition could not stay long there. Peng-shoal and Dong-shoal would keep stable and have little chance to extend sideward and lengthways.

In mid bending part, as the thalweg and main stream downstream had switched from left branch to mid branch, flow straightened especially in flood season.

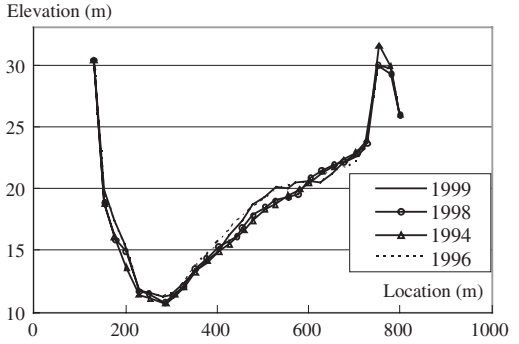


Figure 9. The silting/scouring variation of CS37 (Sha-shoal) between years.

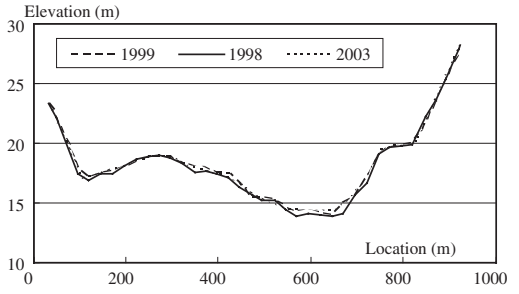


Figure 10. The silting/scouring variation of CS44 (Zhong-bar) between years.

On the other hand, the bed composition is thick with the particle median diameter of 5～19 mm while composition of side bar is relatively thin with the particle median diameter of 0.43～2.7 mm which is easy to be scoured. So Sha-shoal and Zhong-bar left side have a trend of scouring in flood season and the thalweg tends to swing rightward.

In lower branching part, the left branch tends to decline. The thalweg and the mainstream will settle in the mid branch whether in low-water or in flood condition. The downcut and swinging rightwards will continue in mid branch, and the mid branch has a trend of deepen and widen.

4 REFORMATION PROCESS IN CHANGING CONDITIONS

4.1 *Change of the influencing condition*

(1) The impoundment of Wan-an reservoir upstream in 1992 has changed the incoming water & sediment conditions. After the impoundment, the incoming sediment reduces as half as it was before impoundment, and the incoming flow and sediment distribution tend to be even.

Copyright © 2006 Taylor & Francis Group plc, London, UK

(2) The Gangjiang highway bridge which lies upstream of the branching part was built in 1992. The piers' vertical axes directed to the middle branch and had a relatively large deflection angle with the left branch. The navigation channel dredging project in the late 1990s lowers the thalweg elevation of mid branch.
(3) As the erosion and the sand excavation downstream of the Fengcheng reach, the downstream erosion base level has decreased.

4.2 *Analysis of the reformation process in changing conditions*

With the relatively thick bed composition, fine bank control and less sediment runoff, the river regime of Fengcheng reach keeps stable in natural condition. Along with the impoundment of Wan-an reservoir, Fengcheng reach was scoured by the unsaturated runoff. By diversion effect of the highway bridge, the unsaturated runoff was led to the mid branch, and brought to the erosion in mid branch and the deposition at the inlet of the left branch. The main stream and the thalweg successively transferred to the mid branch from the left branch. The subsequent navigation channel dredging lowers the thalweg elevation of the mid branch and further promoted the development of the mid branch and the decline of the left branch. The mid branch had totally replaced left branch to be the main channel. The deflection of the main stream may cause the local scouring in riverbed and bank on the right side of the transitional reach to the branching part. As the particle composition of the side bar is thinner than that of the riverbed, the local scouring will present to be the shoreline recession of Sha-shoal and the left side of Zhong-bar. The thalweg in mid bending part tends to swing right rather than downcut. In addition, as it is too narrow as a main channel, the mid branch has the requirement of deepen and widen rightward.

4.3 *Influence on navigation condition and near-shore project*

(1) After the construction of the highway bridge, the navigation condition became worse because the piers axes had a large inclination with the left branch which was the former navigation channel. As the mid channel developed to be the main channel, the navigation channel shifted to the mid branch, the inclination between piers axes and navigation channel greatly decreased, navigation condition had improved a lot. On one hand, the trends that the shoal line of Sha-shoal scouring backwards and the thalweg swinging rightwards may make the navigation channel more smooth and straight. On the other hand, the decrease of downstream erosion base level may possibly bring to the flow depth inadequate in navigation channel.
(2) The water intake of Fengcheng thermal power plant lies in the mid bending part where the thalweg clings to the left bank at present, so the intake can operate normally now. But with the adjustment of the local river regime, the thalweg here has a trend of swinging rightwards and the left side near water intake has a trend of deposition. It is disadvantageous to the operation of the water intake.

Although the adjustment of local river regime is rather slow at present, countermeasures should be studied.

5 CONCLUSION AND SUGGESTION

(1) The river regime of Fengcheng reach keeps stable in natural condition. After the change of the incoming water & sediment condition and boundary condition, the local river regime adjustment has occurred. The left branch gradually declined while the mid branch developed to be the main channel. At present, the main stream and the thalweg settle in the mid branch at all discharge range.
(2) The reformation process gradually turns peace. There will not be large scale evolution variation in Fengcheng reach while adjustment in local river regime still exists. The evolution tendency presents as shoal line recession in Sha-shoal and thalweg swinging rightwards in mid bending part and thalweg deepen and widen rightwards in mid branch.
(3) The adjustment of local river regime may have influence on navigation condition and near-shore project. Although these adjustments evolve rather slowly at present, countermeasures should be studied.

ACKNOWLEDGEMENTS

The work is Supported by National Key Basic Research and Development Program (973 Program) (2003CB415205), the National Natural Science Foundation of China (50479036).

REFERENCES

J.H. Xie, River Evolution and Regulation, Water Conservancy & Electric Power Press, 1997
J.X. Xu, Influence of Boundary Conditions to Riverbed Evolution Downstream Reservoir, Geographical Research, 1983(4):60–69

Copyright © 2006 Taylor & Francis Group plc, London, UK

J.Y. Zhang, L. Chen & M.W. Wu, Influence of inflow angle on development of meander, Hydro-Science and Engineering, 2003(1):63–66

L.Y. You, D.S. Jin, Problems of Transformation Process Downstream Reservoir, Geographical Research, 1990(4):38–47

L. Chen, B.L. Xie & C.Z. Cui, Analysis on Fluvial Process of Lujiahe Shallow Reach of the Yangtze River, Advances in Water Science, 2000(10):241–246

L. Chen, C.Z. Cui & B.L. Xie, Selection of Model Sand of Total Sediment movable-bed model in Lujiahe reach, Sediment Research Towards the 21th Century, Sichuan University Press, 2000, 10:341–345

L. Chen & J.Y. Zhang, Experimental Study on Development of River Pattern in the Process of River Reformation, Journal of Hydraulic Engineering, 2003(7):42–45

L. Chen, C.Z. Cui & B.L. Xie, Distortion Movable2bed Model of River on Piedmont Alluvial Fan and Slope Distortion, Sediment Research, 2003(4):36–40

M.R. Jia, Influence of Riverbed Evolution of the Lower Reach of the Three Gorges Project on the Channel Analyzed from Downstream Bed Erosion of Danjiangkou and Gezhouba Reservoir, Journal of Waterway and Harbor, 1996(3): 1–13

N. Qian, R. Zhang & Z.D. Zhou, River Evolution, Science Press, 1987

Q.W. Han & Z.J. Tong, Influence of Changing Water & Sediment Process on Riverbed Evolution Downstream Reservoir, Proceedings of 2nd International Symposium on River Sedimentation [C], Guanghua Press, 1983:673–679

Copyright © 2006 Taylor & Francis Group plc, London, UK

Impacts of the Three Gorges Project on flood in the middle reach of Yangtze River

Yitian Li, Yun Liu, Zhaohua Sun & Jinyun Deng
State Key Laboratory of Water Resource and Hydropower Engineering Science, Wuhan University, Wuhan, China

ABSTRACT: In the Yangtze River basin, the most severe flood disaster mainly occurred in the middle reach, especially in the Jingjiang reach and Dongting Lake Area, which just locate downstream the Three Georges Project (TGP). In these areas, the bed erosion due to the construction of the TGP will make the flood control issues more complicated. This paper provides a short background on the present flood situation and details in methodology and analysis in order to provide a reasonable prediction of flood evolution in future. Conclusions are drawn regarding the effective use of gauged historical data and mathematical model. After the dam operation, although channel degradation takes place immediately in the near-dam reach, water level changed little around Chenglingji station, which locates at the outlet of the Dongting Lake. Based on these conclusions, some measures are presented to alleviate the probably flood deterioration.

1 INTRODUCTION

The area of the middle reach of Yangtze River, in immediately downstream of the Three Georges Project (TGP) is 6.8×10^5 km^2. The main stream, tributaries and lakes connect with each other to form a complex river network (Fig. 1). The middle Yangtze River is the region with the most severe flood disasters in the whole basin, especially in the Jingjiang reach and Dongting Lake area. The flood level in the Jingjiang reach is higher than the ground elevation because of the deposition of sediment, and the discharge often exceed the maximal flood discharge that the channel can pass. In recent years, the phenomenon of 'low discharge with high water level' has occurred frequently (Fig. 2), which show the flood disaster situation of the Jingjiang reach and Dongting Lake Area is worse and worse.

At Songzikou, Taipingkou, and Ouchikou, there are diversions linking the Yangtze River with Dongting Lake, but they are usually dry in low flow season. Besides the three diversions, four tributaries join Dongting Lake in the south. The outlet of the lake joins the main stream of the Yangtze River at Chenglingji station. The area and the volume of the Dongting Lake are rapidly reduced because of the deposition of sediment in the lake, and the water delivered into the Dongting Lake is reduced because of the shrinking of the three diversions. Although the reduction of sediment transportation from the main stream to the lake area may reduce the deposition in the Dongting Lake, the high flood stage in recent years show that the flood situation hasn't been alleviated. After dam impoundment, although the TGP has large storage capacity to regulate flood, its volume for flood prevention is still relatively insufficient. Thus, flood detention area is still needed in addition to the reservoir operation.

Because the sediment trap of the TGP Dam reduce the downstream sediment discharge, channel degradation is inevitable. It will induce the change of the relationship between the Yangtze River and the Dongting Lake, which will bring a new problem of flood prevention. Present researches mainly focus on single aspect, the main stream or the Dongting Lake. Few consider two as a whole, which make it difficult to have a comprehensive understanding of impacts of the TGP on flood in the middle reach of Yangtze River.

In this paper, According to the characteristics of flood disaster in the middle reach of Yangtze River, causes of flood disaster are analyzed. A flood regulation model and a 1-D numerical model of flow and sediment transport are set up to predict the change of flood in the middle of Yangtze River in the early period after the TGP's operation. Finally, flood control measures are put forward.

2 CAUSES OF FLOOD DISASTER IN THE MIDDLE REACH OF YANGTZE

2.1 *The flood characteristics*

The flood of Yangtze River is caused by rainstorm. The great spatial-temporal differences of floods and rainstorms result from the geographical and climatic difference in different regions. Normally, the rainstorms

Copyright © 2006 Taylor & Francis Group plc, London, UK

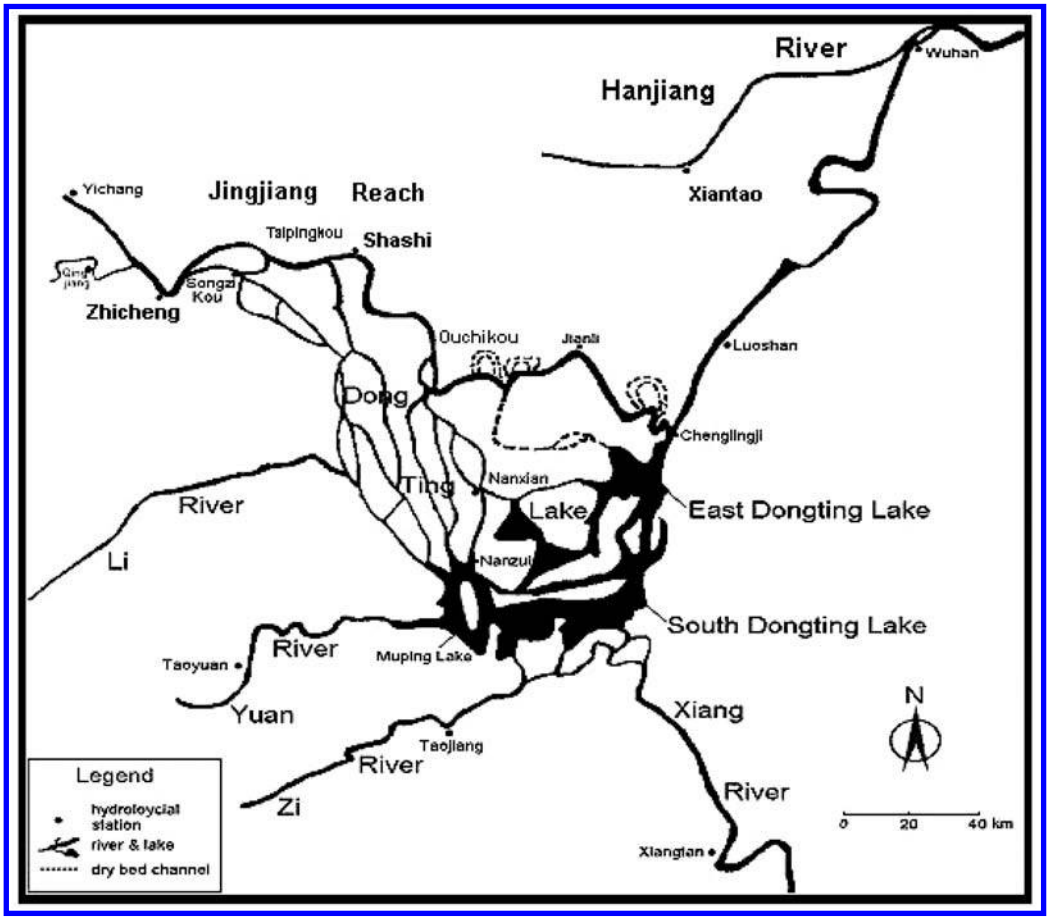


Figure 1. The study area in the middle Yangtze River.

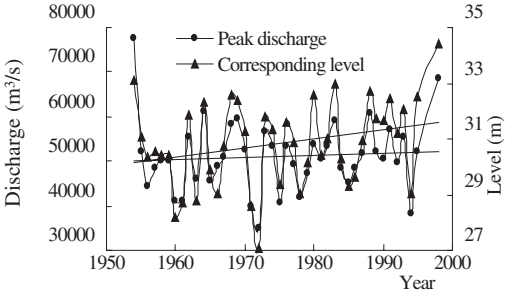


Figure 2. Annual peak discharge and corresponding water level at Luoshan station.

move from the south to the north and from the lower reach to the upper reach.

In normal condition, the floods of different region are not encountered. So the large flood disaster is not caused. If the weather, rainfall and its movement are abnormal, the probabilities of flood encounter of different regions increase and regional or basin level flood will occur.

The river network and regime of water level and discharge are all extremely complicated in the middle reach of Yangtze River, and the source and composition of the floods have great changes as the regional difference of rainstorm every year. The composition of annual volume of floods upstream from Luoshan station is displayed in Table 1. The drainage area upstream from Yichang station is 77.7% of that of Luoshan station, so that flood from Yichang is the main source of the floods. The reach from Yichang to Luoshan, including the Qingjiang River and the tributaries of the Dongting Lake have the regions of rainstorm, so the flood volume during flood season is large. The control area of the four tributaries of the Dongting Lake is 16.1% of the control area of Hankou station, which is the important compositive part of the flood.

Copyright © 2006 Taylor & Francis Group plc, London, UK

Table 1. Composition of average annual flood volume near Chenglingji station (1951–1983).

Period	15d		30d	
Item	Flood volume (10^8m^3)	Percent	Flood volume (10^8m^3)	Percent
Zhicheng	489.1	72.8	860.8	73.2
Xiangtan	48.04	7.15	85.9	7.3
Taojiang	19.05	2.84	32.5	2.8
Taoyuan	73.32	10.92	126.3	10.8
Sanjiangkou	22.37	3.33	36.8	3.1
Four tributaries	162.79	24.23	281.5	24
Region	13.45	2.0	33.1	2.8
Luoshan	611.75	100	1175.5	100

(Xiangtan (Xiang River), Taojiang (Zi River), Taoyuan (Yuan River), Sanjiangkou (Li River), four tributaries (Xiang, Zi, Yuan, Li River), Zhicheng (Yangtze River), Luoshan (YangtzeRiver)).

Table 2. Flood passing capacity of the reach in the middle reach of Yangtze (m^3/s).

Reach	Flood passing capacity
Shashi	5000
Jianli	46000
Chenglingji	60000
Hankou	71600
Hukou	83400

The characteristics of the floods are that they have high peaks and large volume of water and keep in a long time. But large volume of water conflict with the flood passing capacity of the channel (Table 2), which is the main reason of the flood disaster in the middle reach of Yangtze River.

2.2 *Variation of sediment transport*

The sediments of Yangtze River, especially bedloads, mainly come from the upstream from Yichang station. When sediment transportation amount of Yichang, the four tributaries of the Dongting lake and Hankou (the outlet in this region) have only a few changes (the effect of Hanjiang River is not treated), the average annual deposition quantity is about 1.8×10^8t. Although the change of the deposition quantity is little, the places of the deposition are transferring. With the reduction of the deposition of the Dongting Lake, the quantity of the deposition of the reach from Luoshan to Hankou is increasing, and the speed of the reduction and the increase is approximate same (Fig. 3).

Because of the deposition, the three outlet tributaries shrink gradually and the diversions ratio of

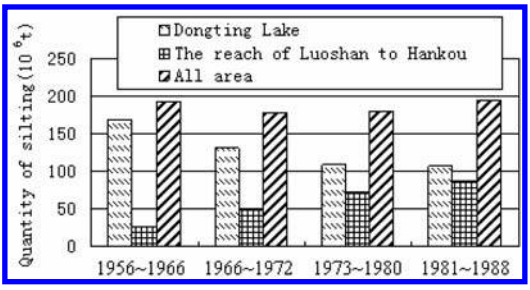


Figure 3. Proportions of sedimentation.

Table 3. The change of average discharge under conditions of the different water levels at Qilishan station.

Level Period	32 m	30 m	25 m	20 m
1963∼1966	36833	19184	10439	4212
1981∼1985	26462	16168	9488	3663
1960s–1980s	10371	3016	951	549
1980s/1960s	72%	84%	91%	87%

Wusong elevation system, unit of discharge: m^3/s.

sediment is reduced so that the function of the trap sediment of the Dongting Lake is weakened (Li et al, 2004). The reduction of deposition in the Dongting Lake loses the long-range balance of sediment transportation in the middle reach of Yangtze River so that new places of deposition are formed, or the slope of the riverbed downstream from Chenglingji station is adjusted to enhance the ability of sediment transportation.

The main stream of the Yangtze River and the Dongting Lake are interactional, and the sediment transportation rapidly drives up the water level near Chenglingji station, which blocks the water outflow of the Dongting Lake. Generally, slope during flood season of the Dongting Lake is relatively smooth, and the water level of the Dongting Lake is close to that near Chenglingji station, however, the raising of the water level near Chenglingji station makes more water volume kept in the Dongting Lake, which causes the raising of the water level of the whole lake (Li et al, 2000; Li et al, 2001a,b). Table 3 shows that the discharge through Chenglingj station is reduced at the same stage.

3 TENDENCY OF FLOOD DISASTER IN THE MIDDLE REACH OF YANGTZE

3.1 *The methodology of studies*

3.1.1 *The flood regulation model*

In the Jingjiang reach and Dongting Lake Area of the middle reach of Yangtze, with many river systems and

Copyright © 2006 Taylor & Francis Group plc, London, UK

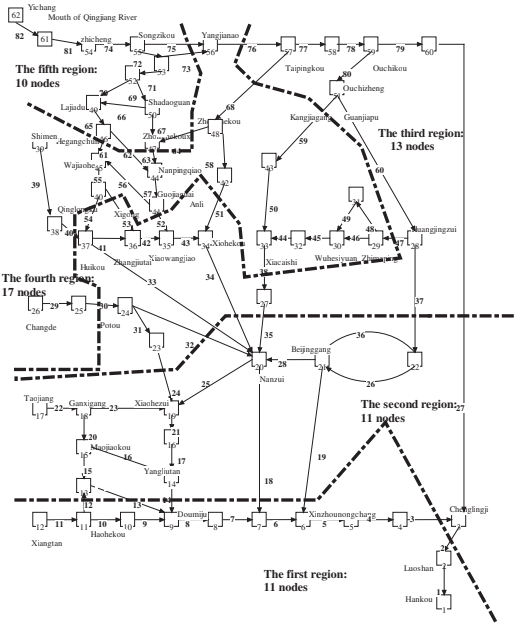


Figure 4. The outline picture of river networks in the middle reach of Yangtze and flood division areas.

complex river networks and many separate flood division areas, it's difficult to simulate stream movement by hydraulic model of single channel. So, hydraulic model of river networks is most suitable to simulate flood propagation. However, under conditions of special relation between the Yangtze River and the Dongting Lake, with complex river networks, big matrixes are formed so that it's difficult to compute. Moreover, stage-discharge relationships are complex so that it's difficult to ascertain the condition of the lower boundary. At present, Some models of flood regulation with the Yangtze River and the Dongting lake in the middle reach of Yangtze are set up, which is mostly made up of river networks. However, these models divide the whole areas into many little areas, which loses the integrity of the relationship of the Yangtze River and the Dongting lake in the middle reach of Yangtze, and loses the conservation of the water volume and the momentum, and depresses the computational speed and precision.

Hydrological model has a good precision to forecast the water level. It may provide the condition of the lower boundary. By using the junctions group method for unsteady flow in multiply connected networks (Li, 1997). A model that combines hydrological model with hydraulic model is set up (Fig. 4), which can be properly applied for the flood regulation in the middle reach of Yangtze. Its calculation speed and accuracy are improved.

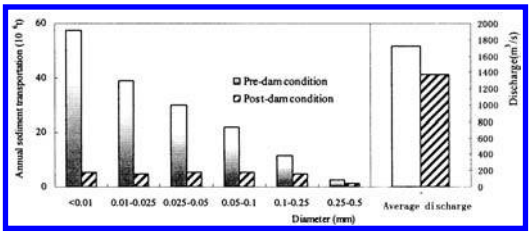


Figure 5. Annual sediment transportation capacity of each grain group size of different periods downstream from the Danjiangkou reservoir.

3.1.2 *Erosion and deposition model downstream from the reservoir*

The TGP has been put to use. In a long time, the long reach downstream from the TGP will be eroded because of the trapping sediment function of the reservoir. Current researches are very much on the erosion change downstream from the TGP. Some literatures (Han & He, 1995; Han & Yang, 2000; Wang & Han, 1997) analyzed the evolvement of the reach from Yichang to Chenglingji by the 1D steady suspended load model with a slight erosion or deposition, including the erosion and the descent of the water level on the main stream of the Yangtze River. However, many reservoirs throughout the world show the phenomenon that the upper reach is eroded and the lower reach is deposited in the early period after the reservoir's operation. It is disadvantageous to the flood prevention. For example, after the reservoir in the Spey River in Scotland operated 50 years, some of lower reaches are deposited to drive up the riverbed. Although the reservoir may adjust flood process, flood disasters are more than ones before building the reservoir (David. 2004). Thus erosion simulation downstream from the TGP need study, and it is necessary to build an erosion model downstream from the reservoir in order to estimate the erosion impacting on flood prevention in the early period after the TGP's operation.

The change process of erosion and sediment transportation capacity from the Danjiangkou Reservoirs (Fig. 5) indicate that through the riverbed erosion and sediment concentration recovery process, sediment transportation capacity of each grain group size after the reservoir's operation can't exceed it s original level before the reservoir's operation (Li et al, 2003), which is common erosion law downstream from the reservoir.

In order to forecast the erosion process downstream from the TGP in the early period after the TGP's operation, The 1D unsteady mathematical model for total sediment transport (suspended load and bed load), including the main stream of Yangtze and the Dongting lake downstream from the TGP is established, which is suitable to simulate sediment concentration recovery process downstream from the reservoirs.

Copyright © 2006 Taylor & Francis Group plc, London, UK

Table 4. The regulating result of the TGP for the 1% exceedance floods.

Typical flood	Maximal flood volume near Chenglingji station ($10^8 m^3$)		Reduction of the water level without the TGP and with the TGP (m)	
	Without the TGP	With the TGP	Shashi	Chenglingji
1954	313.7	279.8	0.89	1.77
1995	268.6	263.4	0.19	1.84
1998	338.1	273.4	1.01	1.87

3.2 *Regulating capacity of the TGP for floods of the middle Yangtze*

3.2.1 *The regulation mode of the TGP*

The flood prevention emphases of the TGP are the Jingjiang reach. According to the design operation scheme, the highest limit of the regulation is to control the water level at Shashi station on 45.00 m. There are two regulation modes of the TGP: the compensation regulation mode aimed at the Jingjiang area to control the water level at Shashi station and the compensation regulation mode aimed at the Chenglingji area to keep Jingjiang reach safe as well as to reduce the flood diversion near the Chenglingji station.

For the floods in the upper Yangtze River, the first mode can adjust the discharge at Zhicheng station in order to ensure the water level at Shashi station under 45.00 m; for the floods in the whole Yangtze River and in the middle reach of Yangtze, the second mode can adjust the discharge at Chenglingji station by using the TGP effectively.

3.2.2 *The regulating capacity of the TGP*

The flood regulation model is put into use to simulate different criteria floods, with and without the TGP. The upper boundary conditions are 1% design floods including the basin-wide flood in 1954 , the tributary flood in the middle Yangtze in 1995 and the flood in the upper Yangtze River in 1998. The computational results are analyzed.

As shown in Table 4, for the 1% floods in 1954 and in 1998, the function of flood regulation is obvious because of operating the TGP, and Jingjiang spreading area is not used; for the 1% flood in 1995, the function of the TGP is less, and the flood spreading areas of the Dongting Lake and the Honghu are used.

The TGP has a function of reducing the water level of the Dongting Lake and the main stream. The bigger the flood proportion of the main stream is, the more obvious the function of the reservoir is. It reflects that the probability that the flood encounters in the middle reach of Yangtze is reduced and the beginning time of the peak water level of main stations is earlier than before the TGP. For the main stream, the effect on the upper water level reduction is more obvious; but the influence period is very short. The closer it is to the lower reach, the less reduction of water level is, and the influence period is longer. The range of water level reduction relates with the compositive proportion of the flood. For the Dongting Lake, the water level reduction of the three outlet diversions in the Yangtze River is obvious. And there are no influences on the upper reaches of four tributaries of the Dongting Lake.

3.3 *The erosion process of the lower reach in the early period after the TGP's operation*

The input data of the model is supported by the computational result (1960–1970) of Yangtze River Scientific Research Institute (YRSRI). The flow & sediment process downstream the TGP is the upstream boundary condition of the simulation reach from Yichang to Hankou. The flow & sediment process of the tributaries, Qingjiang River and Hanjiang River, corresponds to the typical year. The stage-discharge relationships at Hankou station are the lower control condition of the water level. According to the gauged data, the long-term stage-discharge relationships at Hankou station keep steady. Moreover, in the early period after the TGP's operation, the stage-discharge relationships changes little too, so it is feasible to take the relationships as the downstream boundary. As a result the stage-discharge relationships between 1981 and 1993 at Hankou station are adopted. The computational erosion result is analyzed.

3.3.1 *The erosion process*

In the first twentieth year, the riverbed erosion from Yichang to Shashi will have finished, and the riverbed erosion from Shashi to Jianli will not come to the end. Furthermore, the upper erosion near the TGP will cause a slight deposition in the reach from Jianli to Chenglingji at the beginning, and the riverbed erosion of that reach will start in the fifth year (Fig. 6). Table 5 lists average depth of the reach erosion from Yichang to Chenglingji. From the tenth year, the deposition tendency from Chenglingji to Hankou starts to decrease, and the riverbed starts erosion. By the end of the 20 years, the succeeded erosion volume will been close to the deposition in the first ten years.

Table 6 compares the erosion and deposition computational results of our model, the YRSRI model (2002) and the model of China Institute of Water Resources and Hydro-Power Research (CIWRHPR) in the first twentieth year after operating the TGP. The table shows that our computational erosion quantity in the whole reach is relatively smaller than previous study. The sediment budget from Chenglingji to Hankou keeps balance.

The terrain of the model in this paper is that of 1981, but the terrains of the YRSRI model and the

Copyright © 2006 Taylor & Francis Group plc, London, UK

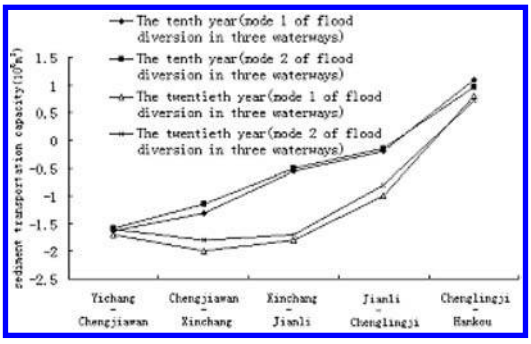


Figure 6. The comparison of erosion and deposition of riverbeds in different mode of flood diversion in three waterways in the tenth, twentieth year after the TGP's operation. (Mode 1 of flood diversion in three waterways is that the diversions ratio of flow and sediment in three waterways changes with reduction of the water level of the main stream because of erosion, and Mode 2 is that it keeps invariable when three waterways and the main stream are synchronously eroded.)

Table 5. Average depth of the erosion between the Yichang reach and the Chenglingji reach in the twentieth year after the TGP's operation (m).

Item	Yichang-Shashi	Shashi-Jianli	Jianli-Chenglingji
The width of rivers	1300	1525	1500
Average depth of the erosion	1.09	1.6	0.75

Table 6. The comparison of the quantity of erosion and deposition in the twentieth year after the TGP's operation (10^8 m^3).

Reach Model	Yichang-Chenglingji	Chenglingji-Hankou	Yichang-Hankou
YRSRI	−14.68	−2.87	−17.55
CIWRHPR	−14.22	−3.2	−17.42
This article	−6.57	0.83	−5.74

CIWRHPR model are that of 1993. If the quantity of erosion and deposition from 1981 to 1993 is deductible, the erosion result computing by this model is less 8.11×10^8 m^3 than that of YRSRI, and is less 7.65×10^8 m^3 than that of CIWRHPR.

3.3.2 *The reduction of the water level*

The erosion and deposition of the long reach downstream from the TGP and its influence on flood

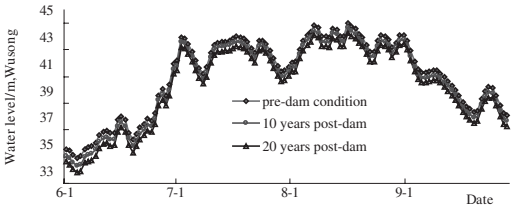


Figure 7. Computational water level process at Shashi station in 1998 under conditions of different terrains.

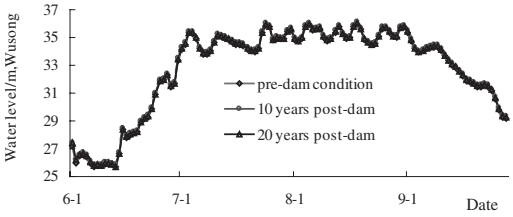


Figure 8. Computational water level process at Chenglingji station in 1998 under conditions of different terrains.

prevention have cause more attention (Han & He, 1995). According to the analysis of this paper, the channel erosion process after dam closure is not as rapid as previous prediction. So the change of flood prevention in the middle reach of the Yangtze River needs more examination (Han & He, 1995,1997; Wang & Han, 1997).

In order to estimate the influence of the erosion and deposition in the main stream on flood prevention, according to the riverbed terrain from Yichang to Hankou, computing by this model, in the tenth and twentieth year after the TGP, there is no erosion and deposition on the three outlet diversions of the Yangtze River. The flood water level processes in different period are computed. The gauged discharge processes of the tributaries and the main stream from June to September in 1998 is adopted. The flood water level processes at present, the tenth year after the TGP's operation and the twentieth year after the TGP's operation are computed.

Figures 7 and 8 show the flow process at Shashi and Chenglingji. As the figure indicates, because the lower Jingjiang reach is eroded, the water level at Shashi station reduces obviously. The low water level reduces more than the flood water level. Because of some indistinct change happening in the reach from Chenglingji to Hankou, the water level at Chenglingji station does not change obviously unlike people thought to reduce generally. Table 7 lists the water level change in the upper Jingjiang reach, the lower Jingjiang reach, the outlet of the Dongting Lake and inner stations of the west Dongting Lake. According to the table, although

Copyright © 2006 Taylor & Francis Group plc, London, UK

Table 7. The highest water level in 1996 and in 1998 (Wusong elevation system, m).

	Terrain without the TGP		The tenth terrain with the TGP		The twentieth terrain with the TGP	
The station	1996	1998	1996	1998	1996	1998
Chenglingji	35.44	35.98	35.56	36.1	35.48	36.02
Jianli	36.80	38.16	36.78	38.08	36.71	38.03
Shashi	42.85	45.02	42.48	44.65	42.14	44.31
Nanzui	37.08	37.44	37.11	37.45	37.03	37.35
Xiaohezui		36.97		37.04		36.95

the lower Jingjiang reach is eroded heavily, the reduction of the water level at Jianli station is little because of the backwater near Chenglingji station, and the reduction of the low water level at Shashi station is more; because of big influence of the water discharge of the three outlet diversions and the influence of the water level at Chenglingji station, the water level change of the west Dongting Lake is not obvious. Table 5 shows that the flood water level in 1996 has the same law, which is irrespective to the compositive proportion of incoming water.

The integrated function of the TGP is that the stress on flood prevention of the upper Jingjiang reach is alleviated, but the situation of flood prevention near Chenglingji has little change. Of course, those are the qualitative analysis, the quantity relating to the combination of the flood and the computational precision of the erosion of the lower reach.

3.3.3 *The analysis of the rationality of the computational result*

Sediment concentration recovery process in the lower reach after the TGP operation should has the same law with downstream from other reservoirs, which is that sediment transportation capacity of each grain group size downstream dams can't exceed its original level before the reservoir's operation.

Figure 9 presents the sediment content recovery process at Luoshan and Hankou station after the TGP's operation. The figure shows that the sediment transportation capacity of all the stations of the model of this article, the gauged data in 2003 and the gauged data in 2004 don't exceed their average levels before the reservoir's operation. However, according to the computational result of YRSRI and CIWRHPR, the computational reach has erosion of large volume at the beginning. The reason is that the sediment transportation capacity of grain group size more than 0.1 mm is greatly increased. In the early 30 years after the TGP's operation, the annual sediment transportation capacity of grain group size bigger than 0.1 mm increases 3.6 times than before the reservoir's operation.

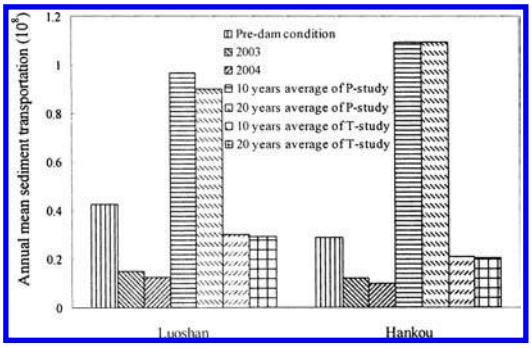


Figure 9. Sediment transportation capacity of grain size more than 0.1 mm. (P-study represents the result of previous study and T-study represent the result of study in this paper.)

4 MITIGATION MEASURES OF FLOOD DISASTER IN THE MIDDLE REACH OF YANGTZE

Flood disasters are caused by many factors including nature and human activity. Natural factors, such as rainfall and geography, belong to objective fact. The factors of human activity are such as keeping the water and soil, building the bank, repairing the channel and so on.

In the Yangtze River basin, flood & sediment problem influences the whole basin. So flood disasters should be cured through thinking about strategy and measures from the point of whole basin. After running the TGP, riverbed erosion downstream from the reservoir will impact on flood prevention. According to the character of flood & sediment disaster, corresponding disaster mitigation measures are put forward.

(1) Improving the regulation mode of the TGP and constructing reservoirs in the upper Yangtze River.

During the course of preliminary designing the regulation mode of the TGP, the compensation regulation mode of the TGP aimed at the Jingjiang area is studied emphatically. In addition, the compensation regulation mode of the TGP aimed at the Chenglingji area is also studied. Under the condition of keeping the Jingjiang reach safe, we may adjust the regulation mode to properly reduce the compensation discharge to the Chenglingji area, and to reduce the flood diversion near Chenglingji station, and to improve the flood control effect of the TGP on ordinary flood.

The floods in the Yangtze River characterize high peak, large discharge. Constructing reservoirs in the upper Yangtze River can make the flood detention capacity in the upper Yangtze River increase. And it is a long-term measure to cut the peak discharge that those reservoirs cooperate with the TGP

Copyright © 2006 Taylor & Francis Group plc, London, UK

to controls the floods in the Yangtze River. As a result, the loss of flood diversion will decrease. The joint regulation of reservoirs in the upper Yangtze River and the TGP will improve the flood control ability in the middle and lower reaches of the Yangtze River.

(2) Increasing clear water with less sediment diversion from the Yangtze River to the Dongting Lake and improving the relation between the Yangtze River and the Dongting Lake.

The result of this paper and current results indicate that the Jingjiang reach will have plenty of erosion in the early period after the TGP's operation, and the Lower Jingjiang River will also erode continuously at the end of 20 years after the operation of the TGP. Quantity of water from the Yangtze River into the Lake through the three outlet divisions will reduce largely, and the outlet pathways will shrink so that erosion of the lower Jingjiang reach will be more drastic.

Enlarging the division of the three outlets by dredging pathways and building gate can increase clean water with less sediment diverted from the Yangtze River to the Dongting Lake. On the one hand, the discharge in the Jingjiang reach will reduce largely so that the danger of caving bank causing by large erosion reduces; river bed shape is prevented from changing and the sediment entering the reach from Chenglingji to Hankou decreases. On the other hand, the three outlet divisions will be scoured and the end reach of Li River and Yuan River, the branches of the Dongting Lake, will be scoured too. Then, when the Dongting Lake joins the Jingjiang River, Chenglingji which is the outlet of the Dongting Lake will be scoured. And the benchmark level of the outlet of the Dongting Lake will depress so the whole level of the Dongting Lake will depress and the flood carrying capacity of the Yangtze River and the Dongting Lake will increase.

(3) Assistant structural and nonstructural measures.

In the middle reach of the Yangtze River, all kinds of flood control measures are supplemented each other. Although they have remarkable effect on dealing with big floods in the past, they have many shortages need to be improved.

After running the TGP, the conditions of flow & sediment downstream from the TGP change, and the river shape of local reach will adjust. Former danger projection section may come to change and the stability of the bank slope and retaining wall projects may be influenced. So project measures, such as revetment dikes, bank protection, should be adopted.

Nonstructural measures are also adopted, such as monitoring channels change in future, predicting floods, flood alarm, and so on. At present, it is the most important task to monitor and analyze change of the channel in the middle reach of the Yangtze River in order to bring forward the corresponding measure.

5 CONCLUSION

In this paper, causes of flood disaster are analyzed based on the change of sediment transportation in the middle reach of the Yangtze River; the tendency of flood disaster is estimated, and disaster mitigation measures are put forward from the point of whole basin.

(1) Main reasons of flood disaster in the middle reach of the Yangtze River are that encounters of local flood are complicated; high peak and large amount of water conflict with the flood passing carrying capacity of the channel; and sediment transfer causes the change of the water level.

(2) The flood regulation model is put into use to simulate different criteria floods with and without the TGP. For the basin-wide floods in the whole Yangtze River, the flood regulation of the TGP has obvious function. For the floods in the middle reach of the Yangtze River, the function of the TGP will decrease.

In the early 20 years after the TGP's operation, the reach from Yichang to Chenglingji will be eroded. But little changes take place in the reach from Chenglingji to Hankou.

The influence of the erosion of the main stream downstream from the TGP in the first decade and in the second decade after the TGP's operation on the flood process is compared. The influence to the upper Jingjiang reach is more than that of the lower Jingjiang reach and the water level at Chenglingji station does not change. But the total change isn't obvious. So after the TGP's operation, the situation of flood prevention in the upper Jingjiang reach is alleviated, and the situation near Chenglingji reach changes little.

(3) After the impounding of the TGP, riverbed erosion downstream from the reservoir will impact on flood prevention. Disaster mitigation measures are put forward, such as improving the regulation mode of the TGP, constructing reservoirs in the upper Yangtze River, increasing clean water with less sediment diversion from the Yangtze River to the Dongting Lake, strengthening flood control project, strengthening dike protection and monitoring channel change in future.

ACKNOWLEDGEMENTS

The study is supported by National Key Basic Research and Development Program (No. 2003CB4-15200).

Copyright © 2006 Taylor & Francis Group plc, London, UK

REFERENCES

David J. Gilvear., 2004, Patterns of the Channel Adjustment to Impoundment of the Upper River Spey, Scotland (1942–2000). River Research and Applications 20: 151–165

Han Q.W., He M.M., 1995, Erosion of River Reach Downstream Three Gorges Reservoir and Its Influence on Flood Prevention. Journal of Hydroelectric Engineering 3: 34–46

Han Q.W., He M.M., 1997, Tendency of River Channel Evolution in Yangtze River's Middle and Lower Reaches after Three Gorges Project being Completed. Journal of Yangtze River Scientific Research Institute 3: 12–20

Han Q.W., Yang K.C., 2000, The Tendency of River Pattern Variation in the Lower Jingjiang River after Completion of the Three Gorges Project. Sediment Research. Vol. 3: pp. 1–11

Li Y.T., 1997, A junctions group method for unsteady flow in multiply connected networks. Journal of Hydraulic Engineering 3: 49–57

Li Y.T., Deng J.Y., Sun Z.H. & Li R. 2000, Sediment deposition and variation of flood storage capacity in Dongting Lake. Journal of Hydraulic Engineering 12: 48–52

Li Y.T., Deng J.Y., Sun Z.H. & He Y. 2001a, A Study on Flood Storage Capacity in Dongting Lake. Sediment Research 6: 1–7

Li Y.T., He Y., Deng J.Y. & Sun Z.H. 2001b, An analysis of flood storage capacity change in Dongting Lake. Journal of Safety and Environment 1(6): 26–30

Li Y.T., Sun Z.H. & Deng J.Y., 2003, A Study on Riverbed Erosion Downstream from the Three Gorges Reservoir. Journal of Basic Science and Engineering 11(3): 283–295

Li Y.T., Sun Z.H., Deng J.Y. & Zhang W., 2004, Variation of sediment transport and flood disaster in the middle reach of Yangtze River. Sediment Research 12: 33–39

Wang C.H., Han Q.W., 1997, Research of Tendency of the Jingjiang reach Evolution after Three Gorges Project being Completed. Report of China Institute of Water Resources and Hydro-Power Research. BeiJing

Yangtze River Scientific Research Institute, 2002, computational analysis of the reach from Yichang to Datong Downstream the Three Gorges Reservoir, Research of sediment problem of the Three Gorges Reservoir Vol. 7: 258–311

Copyright © 2006 Taylor & Francis Group plc, London, UK